Russian Journal of Applied Chemistry, Vol. 76, No. 1, 2003, pp. 1–6. Translated from Zhurnal Prikladnoi Khimii, Vol. 76, No. 1, 2003, pp. 3–8.

INORGANIC SYNTHESIS AND INDUSTRIAL INORGANIC CHEMISTRY

Precipitation of Bismuth(III) Tartrates from Nitrate Solutions

O. A. Logutenko, V. I. Evseenko, Yu. M. Yukhin, and L. I. Afonina

Institute of Chemistry of Solids and Mechanochemistry, Siberian Division, Russian Academy of Sciences, Novosibirsk, Russia

Received September 16, 2003

Abstract—The precipitation of bismuth(III) from nitrate solutions on addition of aqueous solutions of tartaric acid and sodium tartrate was studied by X-ray phase analysis, thermogravimetry, IR spectroscopy, and chemical analysis. Conditions for the formation of $[Bi(NO_3)(H_2O)_3]C_4H_4O_6$ and $[Bi(C_4H_4O_6)(C_4H_5O_6)]\cdot 3H_2O$ were determined.

Bismuth(III) compounds with tartaric acid and its salts are widely used in medicine for treatment of various diseases and also in the synthesis of bismuth-containing oxide materials [1, 2]. Usually they are prepared by precipitation of bismuth(III) from nitrate solutions with tartaric acid or its alkali metal salts [3]. As the composition ot the precipitated products is sensitive to the synthesis conditions [pH of the medium, ratio of tartrate ions and bismuth(III) in the aqueous phase, temperature, etc.], and tartaric acid itself has several donor centers and four labile protons, compounds of various compositions can be formed in these systems. It was shown that bismuth(III) can form the following compounds with tartrate ions: $BiC_4H_5O_7\cdot nH_2O$ [3, 4], $Bi(OH)_2Bi(OH)(C_4H_3O_6)$ [5], and $Bi(C_4H_4O_6)(C_4H_5O_6)\cdot 3H_2O$ [4, 6]. Reactions of these compounds with solutions of ammonia and of alkali metal hydroxides and acetates yield three-component complex compounds, both insoluble, e.g., $C_4H_3O_6BiM$ ($M = K^+$, Na^+, Li^+, NH_4^+) [3], $[Bi(C_4H_4O_6)_2]NH_4\cdot nH_2O$ [7], and soluble in water, e.g., $C_4H_4O_7BiNa$ [3], $Na(BiO)_2C_4H_3O_6$ and $Na(BiO)_3C_4H_2O_6$ [8], $Bi(HC_4H_4O_6)_4^-$, and $[Bi(OH)_3\cdot C_4H_4O_6]^{2-}$ [9].

Bismuth(III) compounds are usually synthesized by hydrolytic processing of nitrate solutions obtained by dissolution of metallic bismuth in HNO_3. Therefore, it is of practical interest to study the precipitation of Bi(III) tartrate from nitrate solutions of the composition similar to that of the process solutions.

In this work, we studied how the concentration of tartrate ions, temperature, and pH affect the degree of Bi(III) precipitation from nitrate solutions, and also the composition and purity of the precipitated products.

Precipitation of Bi(III) was carried out by adding aqueous solutions of sodium tartrate $C_4H_4O_6Na_2$ or tartaric acid $C_4H_6O_6$ to a solution of $Bi(NO_3)_3$ containing (g l^{-1}): Bi(III) 440 and free nitric acid 74. The solution of $Bi(NO_3)_3$ was prepared by dissolving Vi 00 grade metallic bismuth (no less than 99.98% Bi) in 9 M HNO_3; its composition corresponded to solutions usually used in the technology of bismuth(III) compounds. The volume ratio of the initial and final bismuth-containing solutions was 1 : 10; it was adjusted by adding distilled water. The experiments were carried out in fluoroplastic vessels equipped with stirrers. The mixture was stirred for 2 h. After sedimentation for 1 h, the precipitate was filtered off, washed on the filter with distilled water, and dried in air. The X-ray phase analysis of the precipitated products was carried out on a DRON-3 diffractometer using CuK_α radiation (rotation rate of the counter 0.5 deg min^{-1}, I = 1000). The DTA and TG curves for the samples under study were taken on an MOM derivatograph (Hungary) at a heating rate of 10 deg min^{-1}. The IR absorption spectra in the range 400–4000 cm^{-1} were recorded on a Specord IR-75 spectrophotometer. Samples were prepared in the form of pellets with calcined KBr. The electron micrographs of products were taken on a JSMT-20 scanning microscope with a 200 Å resolution. The specific surface area of the samples was measured by thermal desorption of argon, monitored chromatographically. Macroamounts of Bi(III) in the liquid and solid phases were determined by EDTA titration using xylenol orange as indicator, and its microamounts were determined photocolorimerically in the presence of KI. The concentrations of metal ions (Bi, Pb, Ag, Cu, Fe, Zn) were determined by the atomic absorption method on a Saturn 2M spectrophotometer. The precipitated products were

1070-4272/03/7601-0001$25.00

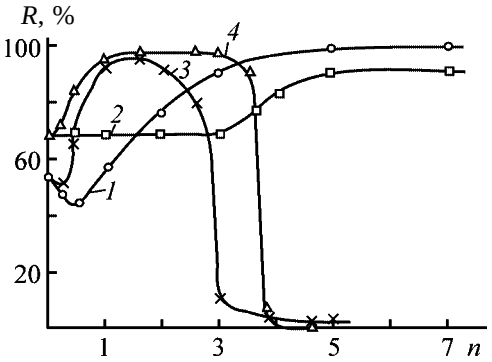

Fig. 1. Degree of Bi(III) precipitation *R* as a function of the molar ratio *n* of tartrate ions to Bi(III) in solution. Agents added to a bismuth-containing solution: (*1, 2*) tartaric acid and (*3, 4*) sodium tartrate. Temperature, °C: (*1, 3*) 23 and (*2, 4*) 60.

preliminarily dissolved in HNO_3 (1 : 1). The concentration of nitrate ions was determined photometrically with sodium salicylate after dissolution of the precipitates by treatment with a sodium hydroxide solution (2 M) at 70–90°C.

The study of the influence of the tartaric acid concentration on the degree of bismuth precipitation *R* (Fig. 1, curves *1* and *2*) shows that, as the concentration of tartrate ions in solution increases, the degree of bismuth(III) precipitation at 23±1°C first slightly decreases, passes through a minimum at the molar ratio of tartrate ions and Bi in solution *n* equal to 0.5, and then increases, reaching 98.8% at *n* = 5. Increased process temperature results in decreased degree of Bi(III) precipitation. The degree of Bi(III) precipitation at 60±1°C remains constant and independent of tartaric acid concentration up to *n* = 3, and at higher *n* the degree of precipitation grows, reaching 91.1% at *n* = 5.

According to the X-ray analysis (Fig. 2), the basic nitrates $[Bi_6O_4(OH)_4](NO_3)_6 \cdot 4H_2O$ (23°C) and $[Bi_6O_4(OH)_4](NO_3)_6 \cdot H_2O$ (60°C) are formed in the system in the absence of tartrate ions. The X-ray patterns of these compounds (Fig. 2, curves *1*, *2*) contain the characteristic diffraction peaks: *d*/*n* 1.68, 2.11, 2.39, 2.77, 2.82, 3.30, 3.81, and 8.42 Å for the tetrahydrate and 1.51, 1.73, 2.17, 2.50, 2.84, 3.75, 4.31, and 7.37 Å for the monohydrate [10, 11]. The precipitates obtained at the initial molar ratio of tartrate ions and bismuth in solution less than 1 are X-ray amorphous; in this case, Bi(III) seems to be precipitated as a mixture of oxohydroxonitrate and nitratotartrate. At *n* equal to 1, diffraction peaks with *d*/*n* 2.24, 3.72, 5.57, and 10.92 Å are clearly seen in the X-ray patterns of the precipitates (Fig. 2, curve *3*). This pattern does not correspond to any of the known bismuth compounds. However, according to the chemical analysis, the samples contain (%) Bi 49.00, C 9.74, H 1.42, and N 2.46; the molar ratio of Bi(III) and tartrate and nitrate ions in the precipitate is 1 : 1.1 : 1.2, which suggests that, under these conditions, a compound of the composition $[Bi(NO_3)(H_2O)_3]C_4H_4O_6$ mainly precipitates. The possibility for its formation was reported in [12].

The precipitates obtained at 23°C and *n* no less than 2 and also at 60°C and *n* no less than 3 consist of a compound with the composition $[Bi(C_4H_4O_6) \cdot (C_4H_5O_6)] \cdot 3H_2O$, which contains two different tartrate ligands, (+)-tartrate$^-$ and (+)-tartrate^{2-}. This is confirmed by the X-ray phase and chemical analyses. The diffraction peaks characteristic of this compound (*d*/*n* 1.84, 2.15, 2.46, 3.31, 4.36, 6.74, and 9.08 Å) [6] are present in the X-ray pattern (Fig. 2, curve *4*), and the molar ratio of Bi(III) and tartrate ions in the precipitate is 1 : 2 (the product contains 37.00% Bi, 17.61% C, and 2.64% H). The orthorhombic crystal structure of this compound (space group $P2_12_12_1$) includes a three-dimensional network with bridging and chelating bonds of polydentate hydroxocarboxylate ligands, and the coordination number of Bi(III) is 4 [6].

The thermal (DTA, TG, DTG) analysis of Bi(III) oxohydroxonitrates and tartrates in air reveals a number of endo- and exothermic stages, demonstrating the possibility of obtaining α-Bi_2O_3 by thermal decomposition of Bi(III) tartrates. Comparison of the thermograms of the samples obtained by Bi(III) precipitation from nitrate solutions in the absence of tartaric acid (Fig. 3a) and at *n* equal to 1 (Fig. 3b) and 5 (Fig. 3c) shows that the total weight loss increases with increasing *n*. This is due to an increase in the content of tartrate ions in the precipitated products. The thermal analysis of bismuth(III) oxohydroxonitrate reveals stepwise dehydration, dehydroxylation, and decomposition of nitrate with the formation of Bi_2O_3 [13]. The thermal decomposition of Bi(III) nitratotartrate starts from water removal (endothermic effect at 100°C) and decomposition of nitrate and tartrate ions (exothermic effects at 130, 240, and 320°C). Bismuth(III) tartrate trihydrate obtained at *n* = 5 loses weight in two stages: first water is removed (endothermic effect at 140°C), and then tartrate ions decompose with endothermic effects at 270 and 340°C. It is seen from the thermograms that heating of all the samples gives Bi_2O_3 as the final product. The endothermic effect at 730°C is due to the polymorphous transition of α-Bi_2O_3 into the high-temperature modi-

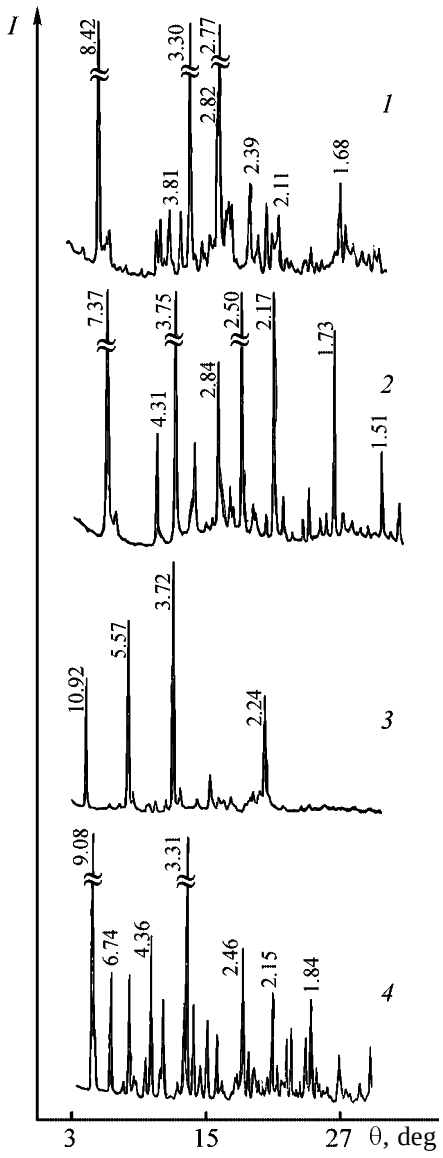

Fig. 2. Diffraction patterns of Bi(III) precipitates obtained from nitrate solutions by adding (*1, 2*) water and (*3, 4*) tartaric acid. (*I*) Signal intensity and (θ) Bragg angle. *n*: (*1, 2*) 0, (*3*) 1, and (*4*) 5. Temperature, °C: (*1*) 23 and (*2–4*) 60.

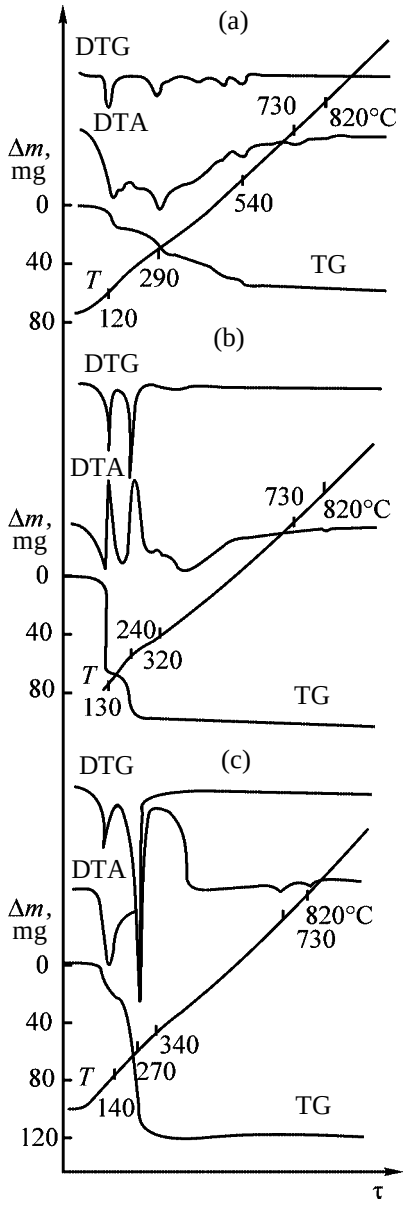

Fig. 3. Thermograms of Bi(III) precipitates obtained from nitrate solutions by adding (a) water and (b, c) tartaric acid. 23°C; sample weight 200 mg. (Δ*m*) Weight loss and (τ) time. *n*: (a) 0, (b) 1, and (c) 5.

fication β-Bi_2O_3, and the endothermic effect at 820°C is due to melting of Bi_2O_3 [14]. To transform Bi(III) oxohydroxonitrate into the oxide, it is necessary to calcine it at a temperature of no less than 540 ± 20°C, whereas Bi(III) tartrates can be transformed into the oxide by their thermal decomposition at 320 ± 20°C.

The study of the effect exerted by pH of the medium on the degree of Bi(III) precipitation has shown that, at the molar ratio of tartrate ions and Bi(III) equal to 2.1, 23°C, and the concentration of H^+ ions of 0.073, 0.34, 0.41, 0.61, 1.03, and 1.33 M the concentration of Bi(III) in solution is 20.9, 2.6, 1.0, 2.1, 11.5, and 12.8 g l^{-1}, respectively, i.e., the maximal degree of Bi(III) precipitation (97.5%) is reached at the 0.4–0.5 M concentration of hydrogen ions. The concentration of free nitric acid in precipitation of bismuth ditartrate by adding tartaric acid to a solution of $Bi(NO_3)_3$ is 0.75 M. To achieve the maximal precipitation, it is necessary to neutralize the solution by adding NaOH or $NH_3 \cdot H_2O$. However, the degree of Bi(III) precipitation sharply decreases at the concen-

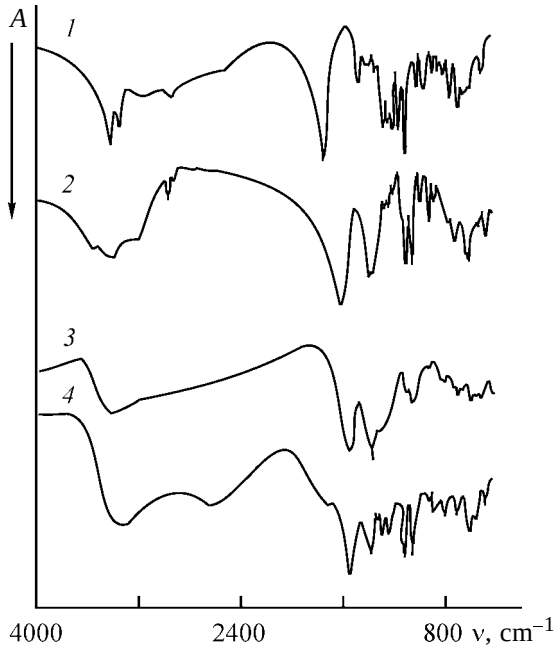

Fig. 4. IR absorption spectra of (*1*) tartaric acid, (*2*) sodium tartrate, (*3*) $[Bi(NO_3)(H_2O)_3]C_4H_4O_6$, and (*4*) $[Bi(C_4H_4O_6)\cdot(C_4H_5O_6)]\cdot 3H_2O$. (*A*) Absorption and (ν) wave number.

tration of free HNO_3 in solution less than 0.3 M, which may be due to formation of soluble tartrate-containing complexes. As the concentration of free HNO_3 in solution increases over 0.6 M, the degree of Bi(III) precipitation as a dihydrate also decreases, and at 1.33 M H^+ it is as low as 70.9%.

The degree of Bi(III) precipitation as a function of the concentration of sodium tartrate is plotted in Fig. 1 (curves *3*, *4*), which shows that this degree first increases, passes through a maximum at the molar ratio of tartrate ions and Bi(III) of 1.6 (R = 98%), and then sharply decreases, i.e., the precipitate dissolves. Such a pattern is due to the capability of Bi(III) to form water-soluble complexes with tartrate ions. The increase in the sodium tartrate concentration initially results in the precipitation of basic Bi(III) nitrates and tartrates of various compositions. The chemical analysis has shown that the products precipitated at n 1 and 2 contain, respectively (%): Bi 49.7, Na 1.43, NO_3^- 11.32 and Bi 35.0, Na 6.1 and NO_3^- 17.13. The sodium–bismuth(III) molar ratio in the precipitate is 0.25 and 1.5, respectively. At $n > 2$ (23°C) and $n > 3$ (60°C), the degree of Bi(III) precipitation sharply decreases, which is due to formation of water-soluble $Bi(HC_4H_4O_6)_4^-$ complex ions [9].

The IR absorption spectra of bismuth(III) tartrates were compared to those of tartaric acid and its sodium salt. The carboxy groups in the IR spectrum of tartaric acid (Fig. 4, curve *1*) give a broad band in the range 3300–2500 cm^{-1} corresponding to O–H stretching vibrations of carboxy groups bound in dimers. A band with a maximum at 1720 cm^{-1} corresponds to stretching vibrations of the C=O bonds of free carboxy groups. A band with well-defined maxima at 3320 and 3400 cm^{-1} corresponds to stretching vibrations of hydroxy groups involved to various extents in the hydrogen bonding.

The IR spectrum of sodium tartrate $C_4H_4O_6Na_2$ (Fig. 4, curve *2*) contains bands of the COO^- group with C–O bonds of the order 1.5 at 1610 (asymmetric stretching vibrations) and 1410 cm^{-1} (symmetric stretching vibrations), indicating the transformation of the carboxy groups to the anionic form. A broad band with several maxima in the range 3560–3200 cm^{-1} corresponds to hydroxy groups involved in various hydrogen bonds and to molecular water present in a certain amount in the associated form.

A similar IR pattern is observed with the compound $[Bi(NO_3)(H_2O)_3]C_4H_4O_6$ obtained at the 1 : 1 molar ratio of tartrate ions and Bi(III) (Fig. 4, curve *3*). However, along with the absorption bands of the deprotonated carboxy group (1590 and 1390 cm^{-1}), broadened bands in the range 1400–1280 cm^{-1} and a pronounced shoulder at 1310 cm^{-1} are observed in the spectrum, which most likely originate from the absorption of nitrate ions. A broad band with a pronounced maximum at 3400 cm^{-1} is due to the O–H stretching vibrations of water molecules and hydroxy groups of tartrate ions involved in hydrogen bonding.

Similar to the spectrum of tartaric acid, the IR spectrum of bismuth ditartrate (Fig. 4, curve *4*) contains, along with the absorption bands of carboxylate groups (1590 and 1390 cm^{-1}), also the bands of carboxy groups: a broad band in the range 3200–2400 cm^{-1}, which corresponds to the stretching vibrations of OH groups of carboxylic acids involved in hydrogen bonding, and a band at 1720 cm^{-1} of the stretching vibrations of the C=O bond in the carboxy group. This spectral pattern is quite consistent with the composition $[Bi(C_4H_4O_6)(C_4H_5O_6)]\cdot 3H_2O$.

The electron micrographs (Fig. 5a) show that Bi(III) nitratotartrates obtained at 23 and 60°C consist of relatively large aggregates of the size from 3 to 40 μm, with signs of a block structure. The aggregates consist of smaller crystals. Bismuth(III) ditartrate trihydrate obtained at 23°C consists of oriented intergrown pieces of elongated prismatic (almost needle-like) crystals of the size of about 3–10 μm, whereas

crystals of the product obtained at an elevated temperature (60°C) have a size of 20–60 μm (Fig. 5*c*).

When Bi(III) is precipitated from nitrate solutions by adding a sodium tartrate solution, an X-ray amorphous product is obtained; its aggregates, having a size of 1–5 μm, consist of submicrometer X-ray amorphous particles (Fig. 5d). The specific surface areas of sodium tartrates obtained at 23 and 60°C are, respectively, for the nitratotartrate 0.8 and 0.7, for the ditartrate 0.6 and 0.4, and for the sodium-containing tartrate 1.5 and 1.1 $m^2\ g^{-1}$, i.e., the specific surface area of Bi(III) tartrates decreases with increasing temperature.

Bismuth(III) compounds are usually synthesized from nitrate solutions starting from Vi-1 grade bismuth which contains Ag and Pb as the main impurities. The Bi(III) tartrate $[Bi(C_4H_4O_6)(C_4H_5O_6)]\cdot 3H_2O$ was precipitated by adding tartaric acid to a solution of $Bi(NO_3)_3$ at 23 ± 1°C and the 5 : 1 ratio of tartrate ions to Bi(III) in solution. Enlarged tests were carried out with a Bi(III)-containing solution, which was obtained by dissolving Vi-1 grade bismuth containing 0.06 wt % Ag and 1.2 wt % Pb. The mixture was stirred for 2 h and settled. The mother solution containing 0.69 $g\ l^{-1}$ of Bi(III) was separated by decanting. The precipitate of Bi(III) tartrate was washed with one portion of a nitrate solution with pH 1.0 and two portions of distilled water. The resulting Bi(III) tartrate contained (wt %) Pb 0.55, Ag 1.5×10^{-4}, Cu 2.5×10^{-4}, Fe 1.0×10^{-3}, and Zn 2.5×10^{-4}, i.e., the removal of Pb(II) from Bi(III) was inefficient. Therefore, to synthesize high-purity Bi(III) tartrate, it is necessary to use the Vi 00 grade metal (≥99.98% Bi) or to preliminarily remove impurity metal ions by precipitating Bi(III) from nitrate solutions as its oxohydroxonitrate [15]. To remove impurity metal ions from Bi(III), we diluted the initial nitrate solution by a factor of 2 with distilled water and added a 2.5 M solution of $(NH_4)_2CO_3$ with stirring to the solution containing 220 $g\ l^{-1}$ of Bi(III) and 37 $g\ l^{-1}$ of free HNO_3, until pH of the pulp became 0.9. The precipitate was washed with two portions of distilled water, and the resulting oxohydroxonitrate $[Bi_6O_5(OH)_3](NO_3)_5\cdot 3H_2O$ was dissolved in 6.0 M HNO_3. The precipitation of Bi(III) ditartrate trihydrate by adding tartaric acid to the resulting solution under the above-mentioned conditions gave a product containing (wt %) Pb 5.0×10^{-4}; Ag 3×10^{-6}; Cu 2×10^{-6}; Fe 1.0×10^{-4}; Zn 8×10^{-5}; and Ca, Mg, and Na $< 1.0 \times 10^{-4}$.

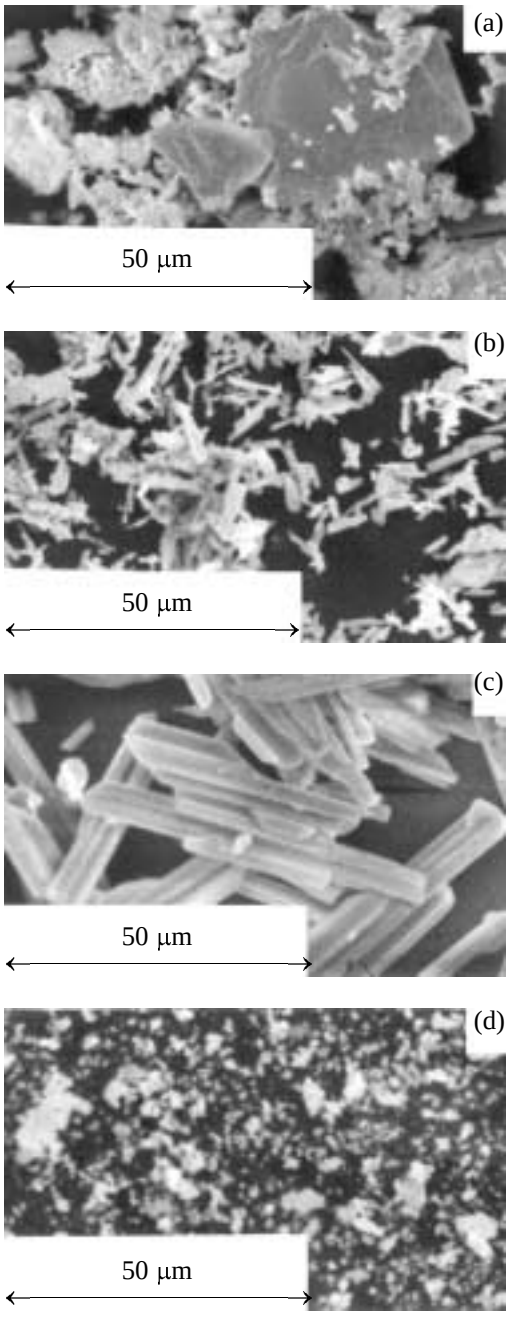

Fig. 5. Electron micrographs of (a) nitratotartrate, (b) ditartrate, and (c) sodium-containing tartrate of Bi(III) obtained on adding (a–c) tartaric acid and (d) sodium tartrate to a solution of $Bi(NO_3)_3$. Temperature (°C): (a, b, d) 23 and (c) 60.

CONCLUSIONS

(1) It is appropriate to synthesize the Bi(III) ditartrate $[Bi(C_4H_4O_6)(C_4H_5O_6)]\cdot 3H_2O$ by its precipitation from bismuth-containing nitrate solutions by adding tartaric acid at the molar ratio of tartrate ions and

Bi(III) in solution no less than 2, H^+ concentration of 0.4–0.5 M, and temperature of 22 ± 3°C.

(2) When synthesizing high-purity Bi(III) ditartrate, it is necessary to use high-purity Bi(III), or, if using technical-grade Bi(III), to preliminarily perform hydrolytic purification of bismuth by its precipitation as oxohydroxonitrate.

(3) Bi(III) is precipitated as the nitrotriaquatartrate $[Bi(NO_3)(H_2O)_3]C_4H_4O_6$ from a solution with the 1 : 1 molar ratio of tartrate ions and Bi(III), whereas the precititation with sodium tartrate gives sodium-containing tartrates.

REFERENCES

1. Briand G.G. and Burford N., *Chem. Rev*., 1999, vol. 99, no. 9, pp. 2601–2657.
2. Yukhin, Yu.M. and Mikhailov, Yu.I., *Khimiya vismutovykh soedinenii i materialov* (Chemistry of Bismuth Compounds and Materials), Novosibirsk: Sib. Otdel. Ross. Akad. Nauk, 2001.
3. Girard, M., *Bull. Soc. Chim. Fr*., 1957, no. 2, pp. 240–245.
4. Turkevich, N.M., *Ukr. Khim. Zh*., 1953, vol. 19, pp. 276–281.
5. Kirchhoff, G.A., Spektr, M.O., and Akon'yants, E.A., *Khim.-Farm. Prom–st*., 1933, no. 3, pp. 122–123.
6. Herrmann, W.A., Herdtweck, E., Scherer, W., *et al*., *Chem. Ber*., 1993, vol. 126, pp. 51–56.
7. Sagatys, D.S., O'Reily, E.J., Patel, S., *et al*., *Aust. J. Chem*., 1992, vol. 45, pp. 1027–1034.
8. Tsimbler, M.E., *Ukr. Khim. Zh*., 1952, vol. 18, pp. 376–380.
9. Tikhonov, A.S., *Zh. Obshch. Khim*., 1954, vol. 24, no. 1, pp. 37–41.
10. Lazarini, F., *Cryst. Struct. Commun*., 1979, vol. 8, pp. 69–74.
11. Afonina, L.I., Yukhin, Yu.M., and Vorsina, I.A., *Sib. Khim. Zh*., 1993, no. 3, pp. 13–19.
12. *Gmelins Handbuch der anorganischen Chemie. Wismut*, Weinheim: Chemie, 1964, 8th ed.
13. Mikhailov, Yu.I., Yukhin, Yu.M., Shcherbinina, V.I., and Logvinenko, V.A., *Zh. Neorg. Khim*., 1991, vol. 36, no. 8, pp. 1913–1918.
14. Gattow, G. and Schutze, D., *Z. Anorg. Allg. Chem*., 1964, vol. 328, nos. 1–2, pp. 44–68.
15. Yukhin, Yu.M., Mikhailov, Yu.I., Afonina, L.I., and Podkopaev, O.P., *Vysokochist. Veshch*., 1996, no. 4, pp. 62–67.

Russian Journal of Applied Chemistry, Vol. 76, No. 1, 2003, pp. 7–11. Translated from Zhurnal Prikladnoi Khimii, Vol. 76, No. 1, 2003, pp. 9–13.

INORGANIC SYNTHESIS AND INDUSTRIAL INORGANIC CHEMISTRY

Interaction of Titanium Tetrachloride with Products of Thermal Decomposition of Basic Magnesium Carbonate

S. A. Morozov, A. A. Malkov, and A. A. Malygin

St. Petersburg State Technological Institute, St. Petersburg, Russia

Received June 4, 2002

Abstract—The interaction of titanium tetrachloride vapor with products formed in thermal decomposition of basic magnesium carbonate in the temperature range 200–800°C was studied.

Published data on modification of magnesium-containing solid matrices with titanium tetrachloride show that application of the gas-phase technique is mainly limited to pure magnesium oxide [1–6]. Other magnesium compounds are mostly modified in the liquid phase. In synthesizing magnesium oxide, various hydroxocarbonate compounds with different phase compositions and structural characteristics have been obtained and characterized [7]. In view of the wide use of compounds of this kind in catalysis, as fillers, and as binder components [2, 3, 8, 9], it is of current interest to consider the possibility of gas-phase modification of these compounds with titanium(IV) chloride.

EXPERIMENTAL

The samples used in the study were obtained by thermal decomposition of basic magnesium carbonate [ultrapure grade, TU (Technical Specifications) 6-09-2118–77] in a flow of dried air (flow rate 50 ml min^{-1}) for 4 h at a temperature chosen from the range 200–800°C. X-ray phase analysis of products formed in thermal treatment was made with a DRON-2 diffractometer (Ni-filtered CuK_α radiation, range of angles θ 2°–40°) using the ASTM file. The specific surface area of the initial samples was determined by the method involving low-temperature adsorption of air [10]. The reaction of titanium tetrachloride with products formed by thermally induced transformations of basic magnesium carbonate was studied at 200°C on a thermogravimetric setup with a quartz spring balance with the spring stretching factor of 3.33 mg g^{-1}. With 0.10–0.12-g samples, this allows monitoring to within ±0.5 mg g^{-1} of mass changes under conditions of a continuous supply of reagent vapor and removal of gaseous reaction products. The products synthesized were analyzed for the content of titanium [11] and chlorine [12].

The phase compositions of products formed in successive transformations of basic magnesium carbonate is listed in Table 1. It can be seen that, at calcination temperatures below 400°C, the solid matrix contains both magnesium oxide and magnesium carbonate. At 400°C and above, the product is entirely composed of magnesium oxide, and the size of coherent domains increases from 4.3 (400°C) to 15.6 nm (800°C).

Analysis of thermogravimetric curves of $TiCl_4$ chemisorption (Fig. 1a) shows that all the samples are characterized by a gradual decrease in the reaction rate in the course of treatment with reagent vapor, which is manifested in decreasing mass gain at equal intervals of time. The overall change in the mass and in the titanium content of reaction products at equal duration of chemisorption as a function of the temperature of sample preparation passes through a maximum at 400°C (Fig. 2). A similar dependence on the temperature of calcination of basic magnesium carbonate has been observed previously for the specific surface area of the samples obtained [7]. Therefore, to characterize the reactivity of the surface of the products, the gains in the mass and titanium content were related to unit surface area (Fig. 2b, Table 2). The dependences obtained indicate that the highest activity in reaction with $TiCl_4$, as regards the change in mass in the initial stage and the maximum gain in mass, both related to unit surface area, is observed with samples obtained at 200 and 300°C.

The Cl/Ti ratio in the composition of all the products (Table 2) is close to the stoichiometric ratio in titanium tetrachloride; moreover, no decrease in mass, common in processes carried out on SiO_2 and Al_2O_3, is observed in the stage of removal of the physically

1070-4272/03/7601-0007$25.00

Table 1. Phase composition of products formed in calcination of basic magnesium carbonate*

T_c, °C	*d*/*n*, nm	I/I_0, %	Phase according to ASTM		Size of coherence domain, nm
			d/*n*, nm	I/I_0, %	
		$MgO \cdot 2MgCO_3$			
Initial sample	0.598	100	0.605	100	
	0.300	10	0.301	25	
	0.226	15	0.226	35	
	0.212	35	0.212	70	
	0.200	10	0.200	20	
		$MgO \cdot 2MgCO_3$			
200–300	0.606	33	0.605	100	
	0.348	18	0.350	85	
	0.227	5	0.226	35	
		MgO			
400	0.210	100	0.210	100	
	0.150	45	0.149	52	4.3
500	0.243	5	0.243	10	
	0.211	100	0.210	100	6.6
	0.150	43	0.149	52	
600	0.243	6	0.243	10	
	0.210	100	0.210	100	9.1
	0.149	43	0.149	52	
800	0.243	6	0.243	10	
	0.211	100	0.210	100	15.6
	0.150	48	0.149	52	

* T_c, calcination temperature; *d*/*n*, interplanar spacing; I/I_0, relative intensity.

adsorbed reagent and gaseous reaction products (Fig. 1a). This suggests complete binding of the gaseous reagent with the magnesium-containing compounds of the given series.

As noted in [1, 2, 5], in samples containing solely the magnesium oxide phase, along with the exchange reaction between the gaseous reagent and surface functional groups,

$$–Mg–O–H + TiCl_4 \rightarrow –Mg–O–TiCl_3 + HCl, \quad (1)$$

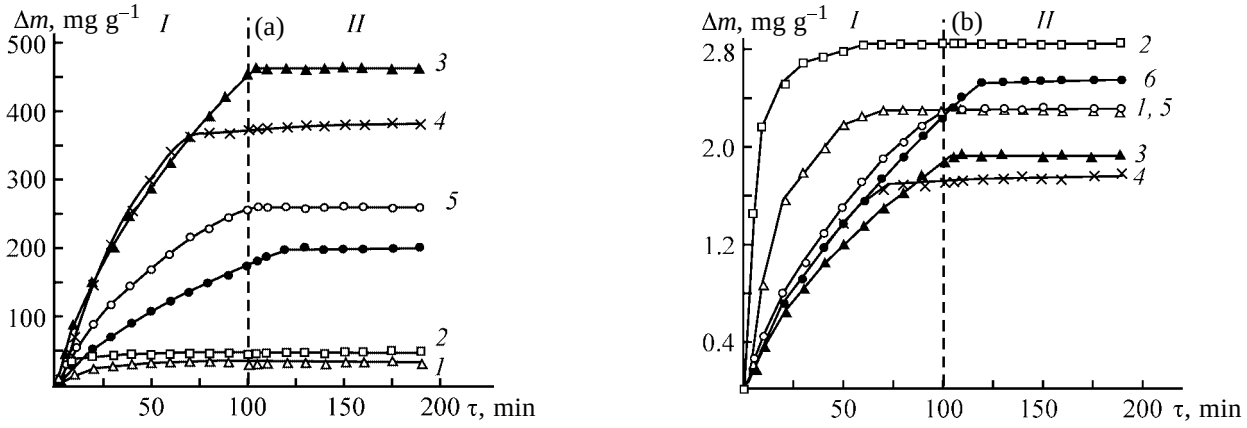

Fig. 1. (a) Change in sample mass, Δm, in reaction with $TiCl_4$ vapor at 200°C and (b) that related to unit area of the initial surface. (*I*) Stage of $TiCl_4$ chemisorption and (*II*) stage of removal of physically adsorbed reagent. Sample preparation temperature (°C): (*1*) 200, (*2*) 300, (*3*) 400, (*4*) 500, (*5*) 600, and (*6*) 800.

Table 2. Chemical composition of products formed in reaction of $TiCl_4$ with products of thermal transformations of basic magnesium carbonate

T_c, °C	S_{sp}, $m^2\ g^{-1}$	Content, mmol g^{-1}		Cl/Ti	Ti_S, atoms nm^{-2}	Ti_S/N_{Ti}
		Ti	Cl			
200	15	0.24	1.21	5.04	9.99	3.5
300	17	0.34	1.42	4.18	12.58	4.4
400	240	2.18	9.11	4.18	8.01	2.8
500	215	1.80	7.35	4.08	6.98	2.4
600	110	1.44	5.70	3.96	9.93	3.5
800	80	1.00	4.05	4.05	9.03	3.2

the reaction with the forming HCl and with $TiCl_4$ yielding magnesium chloride are also possible:

$$MgO + 2HCl \rightarrow MgCl_2 + H_2O, \quad (2)$$

$$–Mg–O–H + HCl \rightarrow –Mg–Cl + H_2O, \quad (3)$$

$$–Mg–O–H + TiCl_4 \rightarrow –Mg–Cl + Ti(OH)Cl_3, \quad (4)$$

$$MgO + TiCl_4 \rightarrow MgCl_2 + TiOCl_2 \begin{matrix} \nearrow 0.5TiO_2, \\ \searrow 0.5TiCl_4. \end{matrix} \quad (5)$$

Formation of E–Cl groups was observed in reactions of vapors of volatile chlorides and hydrogen chloride with Al_2O_3 and ZnO matrices, which are characterized by mainly ionic type of E–O bonds and contain basic centers, in addition to acid centers, on the surface [13–17].

On the assumption that the reagent molecules are fully bound to the matrix, chemical analysis data were used to estimate the possible gain in mass of samples in their interaction with $TiCl_4$:

$$\Delta m = M_{Ti}Ti + M_{Cl}Cl, \quad (6)$$

where Δm is the gain in mass (mg g^{-1}); Ti, the content of titanium in a sample (mmol g^{-1}); M_{Ti}, the molar mass of titanium (g mol^{-1}); M_{Cl}, the molar mass of chlorine (g mol^{-1}); Cl, the content of chlorine in a sample (mmol g^{-1}).

The calculated gain in mass was compared with that determined experimentally during the reaction and and upon its completion by measuring the sample mass (Table 3). For samples obtained at 400–800°C, the calculated and experimental changes in mass are in good agreement, suggesting that, for the given samples containing solely the magnesium oxide phase, the interaction with $TiCl_4$ also proceeds via exchange reactions [1–5].

For samples obtained at 200 and 300°C, which contain a residual phase of magnesium carbonate, the discrepancies between the calculated and experimental gains in mass are significant. In view of the data in Table 1, this may be due to removal of carbon dioxide from the matrix, occurring in parallel with addition of titanium(IV) and chlorine-containing groups under the action of $TiCl_4$ vapor.

Thus, in the case of hydroxocarbonate samples, reactions (1)–(5) listed above presumably occur in parallel with exchange of carbonate ions for chloride ions with the formation of magnesium chloride and titanium oxide as solid products:

$$2MgCO_3 + TiCl_4 = 2MgCl_2 + TiO_2 + CO_2. \quad (7)$$

It is this factor that may lead to additional mass loss and to a decrease in the gravimetrically recorded gain in the sample mass.

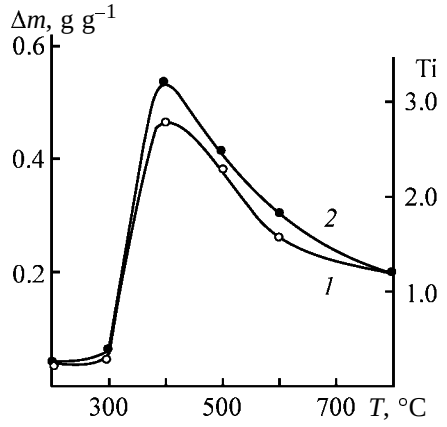

Fig. 2. (*1*) Gain in mass, Δm, and (*2*) content of titanium(IV), Ti, in the product formed upon interaction with $TiCl_4$ vapor vs. sample preparation temperature, *T*.

Table 3. Gain in sample mass upon interaction of $TiCl_4$ with basic magnesium carbonate calcined at 200–800°C

T_c, °C	Gain in mass, mg g^{-1}		$\Delta m_c/\Delta m_{exp}$
	calculated, Δm_c	experimental, Δm_{exp}	
200	46.95	37.04	1.27
300	66.63	47.82	1.39
400	427.37	463.37	0.92
500	346.78	384.97	0.90
600	271.04	261.36	1.04
800	191.47	201.29	0.95

Table 4. Assessment of the probability that $TiCl_4$ and hydrogen chloride may react with magnesium-containing compounds

Reaction	Gibbs energy ΔG, kJ mol^{-1}, at 200°C
$Mg(OH)_2 + TiCl_4 \rightarrow MgCl_2 + TiO_2 + 2HCl$	–129.9
$2MgCO_3 + TiCl_4 \rightarrow 2MgCl_2 + TiO_2 + 2CO_2$	–136.8
$2MgO + TiCl_4 \rightarrow 2MgCl_2 + TiO_2$(anatase)	–172.6
$MgO + 2HCl \rightarrow MgCl_2 + H_2O$	–71.6

To verify this assumption, we calculated the amount of CO_2 that can be removed by topochemical reaction (7). According to differential-thermal analysis of the starting compound, the content of CO_2 in the products formed upon thermal treatment at 200 and 300°C is, respectively, 15.7 and 19.3 mg g^{-1} [7], which is close to the difference between the calculated and experimental gain in mass in interaction of the matrices with $TiCl_4$ vapor, equal to, respectively, 17.4 and 18.8 mg g^{-1}. At temperatures higher than 400°C, when decomposition of magneisum carbonate in the initial matrix is virtually complete, satisfactory agreement is observed between the gains in mass calculated from chemical analysis data and found experimentally.

Taking into account the aforesaid and proceeding from the interaction schemes considered, we may assume that the amount of titanium(IV) in the products synthesized must exceed its possible content for the case when only surface reactions involving functional groups of the initial matrix occur to give a titanium-containing monolayer. In other words, topochemical reactions presumably occur at the given temperature in parallel with surface reactions of substitution and addition. Thermodynamic assessment of the feasibility of the reactions at 200°C, based on the standard Gibbs energies calculated using the thermodynamic constants of the reaction participants [18], is done in Table 4. The Gibbs energy is negative for all the reactions, which means that they may, in principle, occur at the given temperature.

To confirm quantitatively the above assumption, we calculated the limiting concentration of titanium(IV) on the surface of magnesium oxide for the case of dense monolayer packing of $TiCl_4$ molecules.

The effective landing area w for $TiCl_4$ molecules was calculated using the Brunauer–Emmett formula [19]

$$w = 1.091(M/N_A\rho)^{2/3}, \quad (8)$$

where w is the landing area for a molecule (nm^2); M, the molar mass of the chloride (g mol^{-1}); N_A, Avogadro's constant (at. mol^{-1}); and ρ, the density of liquid $TiCl_4$ (g cm^{-3}).

For titanium tetrachloride, the landing area

$$w = 1.091(190/6.02 \times 10^{23} \times 1.728)^{2/3} = 0.35 \text{ nm}^2. \quad (9)$$

The limiting content of titanium(IV) in the monolayer is, correspondingly, given by

$$N_{Ti} = 1/w = 2.86 \text{ at nm}^{-2}. \quad (10)$$

For all the samples, the experimentally found content of titanium, Ti_S, exceeds the calculated monolayer concentration on the surface (Table 2). Thus, the interaction of TiCl both with intermediates formed in thermal transformation of basic magnesium carbonate and with magnesium oxide under the temperature conditions of the process, considered here, involves, in addition to exchange reactions at the surface, topochemical transformations accompanied by formation of a product layer, presumably composed of bulk magnesium chloride and titanium dioxide.

CONCLUSIONS

(1) The nature of interaction with $TiCl_4$ vapor is determined by the chemical and phase composition of products formed in thermal transformation of basic magnesium carbonate. Exposure to $TiCl_4$ vapor of magnesium-containing products of thermal treatment at 200 and 300°C, which contain a large amount of magnesium carbonate compounds, leads to their replacement magnesium chloride compounds, accompanied by evolution of carbon dioxide into the gas phase.

(2) The general pattern involves, together with surface reactions, topochemical conversions accompanied by formation of a product layer presumably composed of bulk magnesium chloride and titanium dioxide.

ACKNOWLEDGMENTS

The study was in part supported financially by the Russian Foundation for Basic Research (project no. 01-03-32 345) and Ministry of Education of the Russian Federation.

REFERENCES

1. Eley, D.D., Keir, D.A., and Rudham, R., *Trans. Faraday Soc.*, 1976, vol. 72, no. 7, pp. 1685–1692.
2. Ermakov, Yu.I., Zakharov, V.A., and Kuznetsov, B.N., *Zakreplennye kompleksy na okisnykh nositelyakh v katalize* (Immobilized Complexes on Oxide Supports in Catalysis), Novosibirsk: Nauka, 1980.
3. Stiles, A.B., *Catalyst Supports and Supported Catalysts. Theoretical and Applied Concepts*, Boston: Butterworths, 1987.
4. Simon, A. and Grobler, A., *J. Polym. Sci., Polym. Chem. Ed.*, 1980, vol. 18, no. 10, pp. 3111–3118.
5. Baulin, A.A., Semenova, A.S., Stefanovich, L.G., *et al.*, *Vysomol. Soedin.*, 1974, vol. 16, no. 12, pp. 2688–2693.
6. Zakharov, V.A., Perkovets, D.V., Bukatov, G.D., *et al.*, *Kinet. Katal.*, 1988, vol. 29, no. 4, pp. 903–908.
7. Morozov, S.A., Malkov, A.A., and Malygin, A.A., *Sintez i khimicheskoe modifitsirovanie oksida magniya parami* (Synthesis and Chemical Modification of Magnesium Oxide with $TiCl_4$ and H_2O Vapor), Available from VINITI, April 15, 1998, no. 1135-V98.
8. *Handbook of Fillers and Reinforcements for Plastics*, Katz, H.S. and Milewski, J.V., Eds., New York: Van Nostrand Reinhold, 1978.
9. Vaivad, A.Ya., *Magnezial'nye vyazhushchie veshchestva* (Magnesia-Based Binders), Riga: Zinatne, 1971.
10. Samoilov, V.M. and Ryabov, A.N., *Kinet. Katal.*, 1978, vol. 19, no. 1, pp. 250–252.
11. Bulatov, M.I. and Kalinkin, I.P., *Prakticheskoe rukovodstvo po fotokolorimetricheskim metodam analiza* (Manual of Photocolorimetric Analysis), Leningrad: Khimiya, 1986.
12. Charlot, G., *Les methods de la chimie analytique. Analyse quantitative Minerale*, Paris: Masson, 1961, 4th ed.
13. Avrutina, E.A., Gusev, A.V., Kol'tsov, S.I., *et al.*, *Zh. Prikl. Khim.*, 1981, vol. 54, no. 9, pp. 2125–2127.
14. Damyanov, D. and Vlaev, L., *Bull. Chem. Soc. Jpn.*, 1983, vol. 56, pp. 1841–1846.
15. Kytökivi, A., Lakomaa, E.-L., and Root, A., *Langmuir*, 1996, vol. 12, no. 18, pp. 4395–4403.
16. Filimonov, V.N., *IK-spektroskopiya adsorbirovannykh molekul i stroenie poverkhnostnykh soedinenii na okislakh metallov: Spektroskopiya fotoprevrashchenii v molekulakh* (IR Spectroscopy of Adsorbed Molecules and Structure of Surface Compounds on Metal Oxides: Spectroscopy of Phototransformations in Molecules), Leningrad: Nauka, 1977.
17. Paukshtis, E.A., *Infrakrasnaya spektroskopiya v geterogennom kislotno-osnovnom katalize* (IR Spectroscopy in Heterogeneous Acid–Base Catalysis), Novosibirsk: Nauka, 1992.
18. Barin, I. and Knacke, O., *Thermochemical Properties of Inorganic Substances*, Berlin: Springer, 1973.
19. Kel'tsev, N.V., *Osnovy adsorbtsionnoi tekhniki* (Fundamentals of Adsorption Technology), Moscow: Nauka, 1984.

Russian Journal of Applied Chemistry, Vol. 76, No. 1, 2003, pp. 12–16. Translated from Zhurnal Prikladnoi Khimii, Vol. 76, No. 1, 2003, pp. 14–17.

INORGANIC SYNTHESIS AND INDUSTRIAL INORGANIC CHEMISTRY

Synthesis and Thermal Expansion of Complex Niobium(V) Phosphates with Bivalent Elements

A. I. Orlova, V. I. Pet'kov, M. V. Zharinova, A. K. Koryttseva, M. V. Sukhanov, G. N. Kazantsev, S. G. Samoilov, and V. S. Kurazhkovskaya

Lobachevsky State Univesity, Nizhni Novgorod, Russia
Institute of Energy Physics, State Scientific Center of the Russian Federation, Obninsk, Kaluga oblast, Russia
Lomonosov State University, Moscow, Russia

Received February 11, 2002

Abstract—Thermal expansion of niobium phosphates, new representatives of the family of structural analogs of $[NaZr_2(PO_4)_3]$, was studied. These compounds possess high thermomechanical stability because of the unique ability of their structure to expand–contract along different crystallographic directions under thermal treatment.

Thermal expansion of a material is an important characteristic determining its behavior under conditions of multiple abrupt changes in temperature ("thermal shock"). Crystalline substances, including ceramics with low and ultralow expansion, and particularly those with low anisotropy of thermal expansion, are characterized by high thermomechanical stability.

The family of phosphates, structural analogs of $NaZr_2(PO_4)_3$ (NZP, Nasicon), known from the 1980s, is unique in behavior of its representatives under heating. Their structure is characterized by expansion–contraction along different crystallographic directions, which leads to low average thermal expansion for most of them. Moreover, the ability of their structure to incorporate strongly diverse cations (with oxidation state in the range from +1 to +5) because of the broad isomorphism ensures formation of a large number of compounds and solid solutions with controllable properties, including thermal properties. Therefore, phosphates of the NZP family are of indubitable interest for materials science specialists.

The structure of $NaZr_2(PO_4)_3$ and its analogs [1], which can be regarded as a derivative of the structure of iron sulfate $Fe_2(SO_4)_3$ [2, 3], is formed by a tetrahedral-octahedral framework of the $[T_2(PO_4)_3]^{n-}$ type, composed of PO_4 and TO_6 groups sharing common oxygen vertices, where T stands for elements in various oxidation states, and n is the framework charge. Cations are connected in the framework by strong covalent bonds, and it is this factor that ultimately determines its small deformations under heating.

Various cations, compensating the negative charge n of the framework, may occupy positions of two types, M1 and M2, in framework voids. The general crystal-chemical formula of the compounds, which takes into account the number of positions M, is described as $(M1)(M2)_3[T_2(PO_4)_3]$.

A separate group among framework phosphates of this kind is constituted by compounds with electrically neutral frameworks ($n = 0$), with unoccupied positions M1 and M2. They can be represented as the series

$$T^{IV}T^{V}(P^{V}O_4)_3 \rightarrow T^{III}_{1/2}T^{V}_{3/2}(P^{V}O_4)_3$$

$$\rightarrow T^{II}_{1/3}T^{V}_{5/3}(P^{V}O_4)_3 \rightarrow T^{I}_{1/4}T^{V}_{7/4}(P^{V}O_4)_3.$$

Apparently, cations in the oxidation state +5 (T^V) are involved in formation of any framework of this kind.

Representatives of phosphates with $T^{IV}T^{V}$ and $T^{III}_{1/2}T^{V}_{3/2}$ are known. These are phosphates containing T^{IV} = Zr, Nb, Ti, Ge, V; T^V = Nb, Sb, Ta [4–10], and T^{III} = Sb, Nd, Eu, Bi; T^V = Sb, Nb, Ta [11–13]. Most of these are related to the structural type NZP, space group $R\bar{3}c$ or $R\bar{3}$. One of conditions for formation of such a structure is that the relative difference between the radii of the cations T^{IV}–T^V and T^{III}–T^V, $\Delta r/r_{min}$, should not exceed 0.3.

A study of thermal decomposition of phosphates with the above composition established that all the compounds studied are characterized by nearly zero

1070-4272/03/7601-0012$25.00

thermal expansion with nearly zero expansion anisotropy along different crystallographic directions [6–8, 14].

The set of the already synthesized and studied phosphates described by the above formula series is rather limited. At the same time, it should be kept in mind that the compositions proposed cannot be always obtained. The possible limiting factors are chemical and crystal-chemical features of framework-forming cations.

This study was aimed to synthesize phosphates of the general formula $T^{II}_{1/3}T^{V}_{5/3}(PO_4)_3$ with T^{II} = Mg, Co, Ni and T^{V} = Nb and analyze their thermal expansion. There are no published data on phosphates of such composition. With account of the nature of cations (their radii, charges, electronegativities) and the formation of an electrically neutral framework (n = 0), anticipated in view of the stoichiometry chosen, it would be expected that the new compounds have structure with trigonal crystal system (rhombohedral unit cell) and nearly zero thermal expansion.

EXPERIMENTAL

Phosphates of niobium(V) and bivalent metals of the type $B_{1/3}Nb_{5/3}(PO_4)_3$, where B = Mg, Co, Ni, were synthesized by the solid-phase method. As starting reactants served MgO, $CaCO_3$, $Sr(NO_3)_2$, $CoCl_2 \cdot 6H_2O$, $Ni(NO_3)_2 \cdot 6H_2O$, $(NH_4)_2HPO_4$, and Nb_2O_5. The synthesis included several stages. A mechanical mixture of reactants taken in stoichiometric amounts was ground in an agate mortar and kept at 450°C for 4 h. Then the mixture was subjected to isothermal treatment at 600, 800, 900, 1000, and 1100°C for 24–60 h with intermediate dispersion in each stage.

The phosphates obtained were studied by IR spectroscopy, X-ray phase analysis, electron-microprobe analysis, and high-temperature X-ray diffraction analysis.

The microprobe analysis was made on a Camebax instrument with a Link AN-10 000 energy-dispersive detector, with the ZAF-correction technique used to calculate compositions. The accuracy with which the composition of samples was determined was 2.5 mol %.

IR spectra were recorded on a Specord 75-IR spectrophotometer in the wave number range 1800–400 cm^{-1}. Samples in the form of a finely dispersed suspension in isopropyl alcohol were deposited onto a KBr substrate.

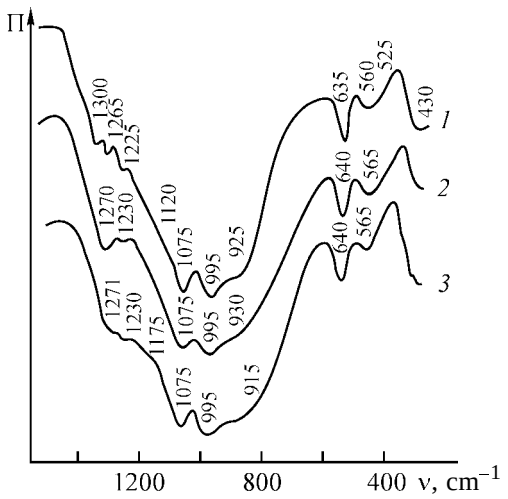

Fig. 1. IR spectra of phosphates of the type $B_{1/3}Nb_{5/3}(PO_4)_3$ with B = (*1*) Mg, (*2*) Co, and (*3*) Ni. (П) Transmission and (ν) wave number.

X-ray diffraction patterns of powder samples were recorded on a DRON-3.0 diffractometer with filtered CuK_α radiation (λ = 1.54078 Å) in the range of angles 2θ 10°–80°. The angle measurement error did not exceed 0.015°. This led to an error in lattice parameters equal to 0.005 and 0.01 Å along the a and c axes, respectively.

The behavior of the phosphates under heating was studied by powder high-temperature X-ray diffraction analysis on a DRON-3M diffractometer with a GPVT-1500 high-temperature attachment in filtered CoK_α radiation (λ = 1.78892 Å) [15]. The samples were heated at an average rate of 10 deg min^{-1}. Reflections were recorded in the temperature range 20–800°C with a temperature step of 200°C. The temperature was measured with a Pt–Pt/Rh thermocouple, whose readings were verified by simultaneous measurement of lattice parameters of a reference substance (Al_2O_3). The axial coefficients α_a and α_c were calculated by a procedure based on the least-squares method [16].

It follows from the results of X-ray diffraction analysis that individual phases are obtained for all the niobium(V) phosphates studied. According to the results of electron-microprobe analysis, these samples are homogeneous and have compositions close to the theoretical composition corresponding to the formula $B_{1/3}Nb_{5/3}(PO_4)_3$. Their X-ray diffraction patterns are similar in positions and relative intensities of diffraction peaks. As regards the distribution of vibration frequencies, the IR spectra (Fig. 1) are also closely similar and indicate that the compounds under study are orthophosphates.

Table 1. X-ray diffraction data for phosphates of the type $B_{1/3}Nb_{5/3}(PO_4)_3$ (B = Mg, Co, Ni)

hkl	$NbTi(PO_4)_3$ [17]		Mg		Co		Ni	
	d, Å	I/I_0, %	*d*, Å	I/I_0, %	*d*, Å	I/I_0, %	*d*, Å	I/I_0, %
102	6.144	60	6.174	42	6.143	37	6.255	43
104	4.414	100	4.471	100	4.416	100	4.437	100
110	4.279	59	4.316	80	4.293	72	4.309	77
113	3.695	58	3.718	82	3.707	78	3.719	82
204	3.072	77	3.089	73	3.085	68	3.083	70
116	2.783	29	2.796	53	2.792	52	2.799	55
124	2.496	12	2.511	27	2.509	25	2.513	27
300	2.470	23	2.491	28	2.486	27	2.490	24
218	1.961	12	1.970	13	1.971	12	1.974	14
314	1.925	10	1.942	19	1.938	15	1.940	15
226	1.847	11	1.860	12	1.859	9	1.861	11
2.1.10	1.729	13	1.741	14	1.737	16	1.739	14
410	1.617	13	1.635	20	1.631	18	1.631	16

The diffraction patterns were indexed with the use of an analog, $NbTi(PO_4)_3$, which is characterized by rhombohedral symmetry [17] and belongs to the structural type of $NaZr_2(PO_4)_3$ (NZP) (Table 1).

The results of X-ray diffraction analysis are in good agreement with IR data. The spectral pattern characteristic of NZP phases is similar to that of the substances containing tetra- and pentavalent elements, e.g., $TaV(PO_4)_3$ [10].

Table 2. Crystallographic parameters of phosphates of the type $B_{1/3}Nb_{5/3}(PO_4)_3$ (B = Mg, Co, Ni)

B	*r*, Å	$\Delta r/r_{min}$	*a*	*c*	*V*, Å
			Å		
Mg	0.72	0.125	8.642	22.11	1430
Co	0.75	0.172	8.642	22.09	1429
Ni	0.69	0.078	8.637	22.08	1429

Table 3. Data of high-temperature X-ray diffraction analysis for phosphates of the type $B_{1/3}Nb_{5/3}(PO_4)_3$ (B = Mg, Co, Ni)

B	$\alpha \times 10^6$, deg^{-1}		
	α_a	α_c	α_{av}
Mg	–2.3	3.4	–0.39
Co	–1.5	4.4	0.45
Ni	–2.2	3.0	–1.92

The unit cell parameters calculated for the phosphates $B_{1/3}Nb_{5/3}(PO_4)_3$ (B = Mg, Co, Ni) (Table 2) are close and vary only slightly within the range from 8.657 to 8.642 Å for *a* and 22.08 to 22.11 Å for *c*.

The double phosphates of niobium(V) and bivalent metals Mg, Co, and Ni, characterized by the above techniques, were studied under heating. First, the thermal limits of existence of the compounds obtained were found. It was established that, having formed at 600°C as crystalline phases, they retained their composition and structure up to 900°C. Raising the temperature led to decomposition of the NZP phosphates, with the high-temperature modification α-$NbOPO_4$ (space group *P*4/*n*) [18] becoming the predominant phase.

Changes in the structure of the phosphates under thermal treatment in the range from room temperature to 800°C were judged from the linear thermal expansion coefficients $\alpha_a = \Delta_a/(a\Delta T)$ and $\alpha_c = \Delta_c/(c\Delta T)$. The coefficients α_a and α_c, calculated from X-ray diffraction data, are listed in Table 3.

As expected, the phosphates under study, having an electrically neutral framework, little expand upon heating. The experimentally determined crystallographic parameters *a* and *c* vary only slightly within the temperature range studied. The structure exhibits anisotropy of thermal expansion: contraction along the *a*-axis ($\alpha_a < 0$) and expansion along the *c*-axis ($\alpha_c > 0$), which is characteristic, as already mentioned, of the family of NZP phosphates. The differences in α_a and α_c values in the series of Mg–Co–Ni phosphates are insignificant, although a certain decrease in

contraction along the *a*-axis and increase in expansion along the *c*-axis are observed for the $Co_{1/3}Nb_{5/3}(PO_4)_3$ phosphate, compared with its Mg and Ni analogs.

Also, the unit cell parameters *a* and *c* at different temperatures were calculated from data furnished by high-temperature X-ray diffraction analysis (Fig. 2). A tendency is observed for the parameter *a* of the hexagonal unit cell in the phosphates $B_{1/3}Nb_{5/3}(PO_4)_3$, (B = Mg, Co, Ni) to decrease and the parameter *c* to increase with increasing temperature. Such a behavior is commonly characteristic of phosphates with NZP structure. Apparently, the crystallographic parameters *a* and *c* change only slightly upon heating.

The average thermal expansion was calculated for the phosphates studied (Table 3). These compounds show either insignificant average thermal expansion, or contraction ($\alpha_{av} < 0$). Apparently, the results of the study supplement published data on phosphates exhibiting low thermal expansion, which are represented now by a small number of compounds. The list includes $NbM(PO_4)_3$, where M = Ti, Zr, Sn, Hf [6, 7, 14].

The unique ability of materials based on phosphates with NZP structure to exhibit virtually zero expansion upon heating may be luckily combined with such properties as high hydrothermal stability and radiation hardness, capacity for forming, high strength and hardness of ceramics prepared on their base, environmental stability, etc. The properties listed above are of value for materials for space and laser technologies, petrochemistry and other fields of chemistry, development of catalysts and catalyst supports, neutron-absorbing ceramics, hard tool ceramics, refractory composites, and other functional materials.

CONCLUSION

Thermal expansion of new compounds, belonging to the class of orthophosphates with framework structure, was studied. Phosphates of niobium(V) and bivalent metals Mg, Co, and Ni, of the type $B_{1/3}Nb_{5/3}(PO_4)_3$, supplemented the family of structural analogs of $NaZr_2(PO_4)_3$ (NZP or Nasicon), which are characterized by low or ultralow thermal expansion and the resulting stability to thermal shocks. It was shown that the low value of the average thermal expansion coefficient, $\alpha_{av} \approx 10^{-6}$–$10^{-7}$ deg^{-1}, is due, as in the case of all phosphates of similar structure, to expansion–contraction along different crystallographic axes.

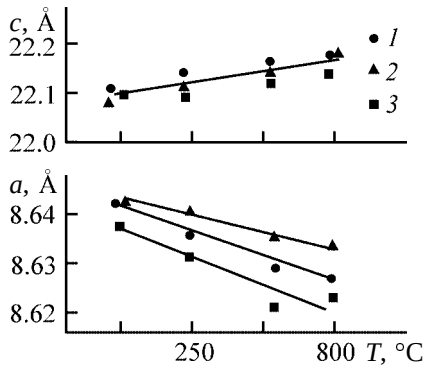

Fig. 2. Unit cell parameters *a* and *c* of phosphates of the type $B_{1/3}Nb_{5/3}(PO_4)_3$ with B = (*1*) Mg, (*2*) Co, and (*3*) Ni vs. temperature *T*.

ACKNOWLEDGMENTS

The study was supported financially by the Russian Foundation for Basic Research (project nos. 01-03-33013 and 02-03-32181).

REFERENCES

1. Hong, H.Y.-P., *Mater. Res. Bull.*, 1976, vol. 11, no. 2, pp. 173–182.
2. Sizova, R.G., Blinov, V.A., Voronkov, A.A., *et al.*, *Kristallografiya*, 1981, vol. 26, no. 2, pp. 293–300.
3. Nanjundaswamy, K.S., Padhi, A.K., Goodenough, J.B., *et al.*, *Solid State Ionics*, 1996, vol. 92, pp. 1–10.
4. Leclaire, A., Borel, M.-M., Grandin, A., and Raveau, B., *Acta Crystallogr., Sect. C*, 1989, vol. 45, no. 5, pp. 699–701.
5. Masse, R., Durif, A., Guitel, J.C., and Tordjman, I., *Bull. Soc. Fr. Miner. Cristallogr.*, 1972, vol. 95, no. 1, pp. 47–55.
6. Taylor, D., *Brit. Ceram. Trans. J.*, 1991, vol. 90, no. 2, pp. 64–69.
7. Govindan Kutty K.V., Asuvathraman, R., Mathews, S.K., and Varadaraju, U.V., *Mater. Res. Bull.*, 1994, vol. 29, no. 10, pp. 1009–1016.
8. Dhas, N.A. and Patil, K.C., *J. Mater. Chem.*, 1995, vol. 5, no. 9, pp. 1463–1468.
9. Agaskar, P.A., Grasselli, R.K., Buttrey, D.J., and White, B., *Stud. Surf. Sci. Catal. 110* (3rd Congr. on Oxidation Catalysis), 1997, pp. 219–226.
10. Rangan, K.K. and Gopalakrishnan, J., *Inorg. Chem.*, 1995, vol. 34, no. 7, pp. 1969–1972.
11. Jouanneaux, A., Verbaere, A., Guyomard, D., *et al.*, *Eur. J. Solid State Inorg. Chem.*, 1991, vol. 28, pp. 755–765.

12. Jouanneaux, A., Fitch, A.N., Oyetola, S., *et al*., *Eur. J. Solid State Inorg. Chem*., 1993, vol. 30, nos. 1–2, pp. 125–137.
13. Oyetola, S., Verbaere, A., Guyomard, D., and Piffard, Y., *J. Solid State Chem*., 1988, vol. 77, pp. 102–111.
14. Oota, T. and Yamai, I., *J. Am. Ceram. Soc*., 1989, vol. 69, no. 1, pp. 1–6.
15. Filatov, S.K., *Vysokotemperaturnaya kristallokhimiya* (High-Temperature Crystal Chemistry), Leningrad: Nedra, 1990.
16. Finkel', V.A., *Vysokotemperaturnaya rentgenografiya metallov* (High-Temperature X-ray Diffraction Analysis of Metals), Moscow: Metallurgiya, 1968.
17. Berry, F.J., Greaves, C., and Marco, J.F., *J. Solid State Chem*., 1992, vol. 96, pp. 408–413.
18. Chahboun, H., Groult, D., and Raveau, B., *C. R. Acad. Sci. Paris, Ser. II*, 1987, vols. 3–4, no. 14, pp. 807–810.

Russian Journal of Applied Chemistry, Vol. 76, No. 1, 2003, pp. 17–19. Translated from Zhurnal Prikladnoi Khimii, Vol. 76, No. 1, 2003, pp. 18–20.

INORGANIC SYNTHESIS AND INDUSTRIAL INORGANIC CHEMISTRY

Complex Formation of Calcium Ions and Monosubstituted Succinic Acid Derivatives in Aqueous Solutions

G. V. Mitrofanova

Mining Institute, Kola Scientific Center, Russian Academy of Sciences, Apatity, Murmansk oblast, Russia

Received September 25, 2002

Abstract—Complex formation of calcium ions with succinic acid monoamide and methyl hydrogen succinate at 25°C and ionic strength $I = 0.3$ (KCl) was studied by pH-potentiometric titration. The stability constants of the complexes were determined.

Fatty acid collecting agents used for dressing of phosphorus-containing ores are obtained from vegetable raw materials. They are insufficiently effective for flotation of ores with complicated mineralogical composition, especially under conditions of water recycling. One of promising ways for the development of effective collecting agents that are less sensitive to the salt composition of the pulp liquid phase is the use of compounds containing two different functional groups.

Nitrogen- or oxygen-containing monosubstituted succinic acid derivatives are of interest in this respect [1–3]. They are readily available owing to high reactivity of the anhydride ring in reactions of the anhydride with methanol or ammonia.

The pulp liquid phase formed during dressing of apatite (a calcium-containing mineral) contains a significant amount of calcium ions, which strongly affect the flotation process. Therefore, it was important to estimate stability of calcium compounds in aqueous solutions of succinic acid monoamide and monoester. The complex formation of unsubstituted succinic acid with calcium ions was studied in [4], and the stability constants of the resulting compounds were determined.

The aims of this work were to estimate the effect of amidation or esterification of one of carboxy groups in succinic acid on the stability of calcium salts and to determine the constants of Ca(II) complex formation with succinic acid monoamide and monomethyl ester.

EXPERIMENTAL

Methyl hydrogen succinate [5] and succinic acid monoamide were prepared by the reactions of succinic anhydride with methanol and ammonia, respectively. Succinic acid monoamide was recrystallized three times from ethanol and dried under reduced pressure. Methyl hydrogen succinate was used without additional purification. The compounds synthesized were identified by melting points and neutralization equivalents (see table).

The Ca(II) complex formation with monosubstituted derivatives of succinic acid was studied by pH-potentiometric titration. The experimental conditions were the same as in the earlier study of Ca(II) complex formation with unsubstituted succinic acid [4]: 25°C and ionic strength $I = 0.3$ supported by KCl. The ionization constants B of the compounds HL under consideration, which are required to calculate the complex formation constants, were determined previously under the same conditions [6].

The pH was measured with glass and silver chloride electrodes on an I-120.1 pH meter with an accuracy of ± 0.01 pH unit.

The concentration of monosubstituted succinic acid derivatives was 0.10–0.15 M, and the concentration of the added $Ca(NO_3)_2$ solution, 0.1 M. The concentration ratios Ca(II) : HL were 1 : 5 and 1 : 3.

Characteristics of monosubstituted succinic acid derivatives

Compound	mp, °C		Neutralization, mol-equiv	
	found	[5]	found	calculated
Methyl hydrogen succinate	57	58	131.3	132.1
Succinic acid monoamide	156	157	116.2	117.0

1070-4272/03/7601-0017$25.00

The concentrations of succinic acid monosubstituted derivatives HL in solution were calculated from the precise weights of their portions and refined by pH-potentiometric titration. Chemically pure grade calcium nitrate and potassium chloride were used. The content of Ca(II) in solutions were determined by complexometric titration. The concentration of KOH solution prepared by dilution of its saturated solution [6] was refined by potentiometric titration. All the solutions were prepared in freshly boiled distilled water.

Solutions of a succinic acid monosubstituted derivative, $Ca(NO_3)_2$, and KCl were placed in a temperature-controlled cell. After adding each portion (0.1 ml) of the titrant (0.3 M KOH), the pH values were measured. The equilibrium was considered as attained if pH remained constant for 2–3 min. The glass electrode was calibrated by buffer solutions before each measurement. The calibration straight line was determined by the least-squares procedure and then used to refine the pH values obtained during titration. The pH meter readings were checked by a buffer solution with pH 4.01 after each titration. If the measured pH differed from this value by more than 0.02, the results were discarded. Points of the titration curve in the range pH 3.0–6.0 were used in the calculations.

The protonation constants of succinic acid monoamide and methyl succinate anions,

$$B = \frac{[HL]}{[L^-][H^+]},$$

were determined by the potentiometric titration at 25°C and ionic strength I = 0.3 (KCl). Three to five replicate determinations were performed for each acid. In each determination, the protonation constant was calculated as the average of the calculated values for each point of the titration curve. The error in $\log B$ was taken as the probable deviation of the arithmetic mean at a confidence level of 0.95. The calculated $\log B$ values for succinic acid monoamide and methyl hydrogen succinate were 4.51 ± 0.01 and 4.42 ± 0.01, respectively (I = 0.3, T = 25°C).

The following equilibria were taken into account when calculating the stability constants of calcium complexes with succinic acid derivatives:

$$H^+ + L^- \rightleftarrows HL, \quad (1)$$

$$Ca^{2+} + L^- \rightleftarrows CaL^+, \quad (2)$$

$$Ca^{2+} + 2L^- \rightleftarrows CaL_2. \quad (3)$$

Hydrolysis of Ca^{2+} ions was not taken into account, as being negligible at pH < 6 [7].

The equilibrium concentrations of species in solution were calculated from the following equations of material balance and mass action law:

$$c_L = [HL] + [L^-] + [CaL^+] + [CaL_2],$$

$$c_H = [HL] + [H^+],$$

$$c_M = [Ca^{2+}] + [CaL^+] + [CaL_2],$$

$$B = \frac{[HL]}{[L^-][H^+]}, \qquad \beta_{CaL^+} = \frac{[CaL^+]}{[Ca^{2+}][L^-]},$$

$$\beta_{CaL_2} = \frac{[CaL_2]}{[Ca^{2+}][L^-]^2},$$

where c_L, c_H, and c_M are total concentrations of the ligand, hydrogen ions, and metal ions, respectively; B, protonation constant of a monosubstituted succinic acid derivative; and β_{CaL_2} and β_{CaL^+}, stability constants of the corresponding calcium compounds.

The formation function $\bar{n}$ for the system under study has the following form:

$$\bar{n} = \frac{\beta_{CaL^+}[L^-] + 2\beta_{CaL_2}[L^-]^2}{1 + \beta_{CaL^+}[L^-] + 2\beta_{CaL_2}[L^-]^2}.$$

This equation can be transformed to

$$\bar{n} + (\bar{n} - 1)[L^-]\beta_{CaL^+} + (\bar{n} - 1)[L^-]^2\beta_{CaL_2} = 0.$$

The experimental data were treated by the least-squares procedure. The number of independent determinations of complex formation constants for each compound was 8–10. The obtained β_{CaL^+} and β_{CaL_2} values for Ca(II) complexes with succinic acid monoamide and methyl hydrogen succinate at I = 0.3 (KCl) and T = 25°C were recalculated to zero ionic strength by the Davies equation. The experimental data were approximated by $y = a + bx$ functions with at confidence level of 0.95 and with the confidence interval no greater than 2. The logarithms of the complex formation constants are presented below together with the previous data [4] on the stability of calcium succinates, given for comparison.

Compound	$\log \beta^0_{CaL^+}$	$\log \beta^0_{CaL_2}$
Succinic acid	2.08 ± 0.02	3.41 ± 0.06
Methyl hydrogen succinate	1.91 ± 0.02	3.56 ± 0.03
Succinic acid monoamide	1.86 ± 0.05	3.58 ± 0.06

These data show that the stability of calcium complexes with succinic acid monoamide and methyl hydrogen succinate is virtually independent of the nature of substituted carboxy group. Comparison of the $\log\beta^0$ values for the compounds under study and calcium succinates shows that replacement of one carboxy group by an amide or ester group decreases the stability of the 1 : 1 Ca(II) complexes. Since succinic acid has two carboxy groups, it was suggested [8] that the probable structure of its Ca(II) chelate contains a seven-membered ring. In contrast to the acid, the monosubstituted derivatives under consideration contain one anion and one nonionic (amide or ester) group showing no tendency to form a coordination bond. The composition of the monosubstituted derivatives under study and the stability constants found in this work suggest that succinic acid monoamide and methyl hydrogen succinate behave as monodentate ligands. In the case of 1 : 2 calcium complexes with the monosubstituted derivatives, the $\log\beta^0_{CaL_2}$ values are greater than in the case of the Ca(II) complex with succinic acid.

CONCLUSIONS

(1) The complex formation of Ca(II) with methyl hydrogen succinate and succinic acid monoamide was studied. The stability constants of the 1 : 1 and 1 : 2 Ca(II) complexes were determined by potentiometric titration.

(2) The stability of the 1 : 1 Ca(II) complexes decreases on replacement of one of carboxy groups in the succinic acid molecule by a nonionic ester or amide group.

ACKNOWLEDGMENTS

The author is grateful to S.I. Pechenyuk (Institute of Chemistry and Technology of Rare Elements and Mineral Raw Materials, Kola Scientific Center, Russian Academy of Sciences) for advises and helpful discussion.

REFERENCES

1. Ivanova, V.A., Mitrofanova, G.V., and Shlykova, G.A., in *Optimizatsiya protsessov obogachsheniya mineral'nogo syr'ya* (Optimization of Ore Dressing Processes), Apatity: Kol'sk. Nauchn. Tsentr, Ross. Akad. Nauk, 2001, pp. 69–83.
2. RF Patent 2 150 330.
3. USSR Inventor's Certificate no. 1 084 076.
4. Mitrofanova, G.V., *Zh. Prikl. Khim.*, 2002, vol. 75, no. 5, pp. 730–733.
5. *Organic Synthesis. An Annual Publication of Satisfactory Methods for the Preparation of Organic Chemicals*, Allen, C.F.H., Drake, N.L., and Smith, L.I., Eds., New York: Chapman and Hall, 1940–1945, vols. 20–25.
6. Kumok, V.N. and Skorik, N.A., *Laboratornye raboty po khimii kompleksnykh soedinenii* (Laboratory Works on the Chemistry of Complex Compounds), Tomsk: Tomskii Univ., 1983.
7. Inczedy, J., *Analytical Application of Complex Equilibria*, Budapest: Akad. Kiado, 1976.
8. Bukolov, I.E., Astakhov, K.V., Zimin, V.I., and Tairov, V.S., *Zh. Neorg. Khim.*, 1962, vol. 7, no. 7, pp. 1577–1582.

Russian Journal of Applied Chemistry, Vol. 76, No. 1, 2003, pp. 20–22. Translated from Zhurnal Prikladnoi Khimii, Vol. 76, No. 1, 2003, pp. 21–23.

INORGANIC SYNTHESIS AND INDUSTRIAL INORGANIC CHEMISTRY

Preparation of Iron Oxide Pigments for Mineral Paints from Solid Iron-Containing Waste

A. N. Epikhin and A. V. Krylova

Mendeleev Russian University of Chemical Engineering, Moscow, Russia

Received June 13, 2002

Abstract—The possibility was examined for preparing various iron oxide pigments for mineral paints from solid industrial waste of metallurgical, chemical, and mechanical engineering plants by synthesizing yellow pigment, goethite, and preparing other pigments on its basis. The influence exerted by the kind of waste and conditions of goethite synthesis on the main properties of the pigments was elucidated.

It is known that hundreds thousands of tons of practically unusable solid waste containing from less than 15 to more than 90 wt % iron are formed annually at metallurgical, chemical, mechanical engineering, and other industrial plants. There are indications in the literature that various iron oxide pigments can be prepared from, e.g., solid waste of sewage treatment at electroplating plants [1, 2] and from ash of sulfuric acid manufacture [3].

Recently, synthesis of goethite (α-FeOOH yellow pigment) from iron sulfate followed by reprocessing into pigments of other colors is the most promising method for production of high-quality finely dispersed iron oxide pigments.

It was shown previously [4, 5] that waste of Severonikel' nonferrous metallurgical plant, spent iron catalyst from Nevinnomyssk chemical plant, and waste of Cheboksary mechanical engineering plant can be used for preparing, via synthesis of goethite, magnetic iron oxide powder γ-Fe_2O_3 for tape recorder carriers; its properties are controlled by the waste composition and conditions of goethite synthesis.

In this work, we examined the possibility of preparing various iron oxide pigments for mineral paints from these types of waste via synthesis of goethite.

The average elemental compositions of the wastes studied, as determined by X-ray spectral analysis, are compared in Table 1.

To prepare iron sulfate solutions, the waste was leached by alternating treatments with sulfuric acid solutions and water. The optimal conditions for leaching and washing, solution compositions, procedures for removing impurities, and features of processes on an enlarged installation have been described previously [4–6].

Goethite was synthesized and converted to other pigments by the following scheme:

$$\text{Solid waste} \xrightarrow{H_2SO_4} FeSO_4 \xrightarrow{OH^-, O_2} \underset{\text{Yellow}}{\alpha\text{-FeOOH}} \xrightarrow{N_2,\ \Delta} \underset{\text{Red}}{\alpha\text{-}Fe_2O_3} \xrightarrow{H_2,\ \Delta} \underset{\text{Black}}{Fe_3O_4} \xrightarrow{O_2,\ \Delta} \underset{\text{Reddish brown}}{\gamma\text{-}Fe_2O_3}.$$

The products of successive transformations yellow goethite → red hematite (α-Fe_2O_3) → black magnetite (Fe_3O_4) → reddish brown maghemite (γ-Fe_2O_3) are commercial pigments. The goethite crystals have acicular shape, which is preserved in all the subsequent stages of goethite conversion.

Table 1. Elemental composition of the waste

Waste	Elemental composition, wt %
Nonferrous metallurgy sluge (NMS)	Fe 28.1; Si 18.1; Ca 2.7; Mg 1.8; Al 1.0; Ti 0.3; S 1.0; Na 0.9; K 0.8; Co 0.44; Cr 0.3; Cu 0.3; Ni 0.22; Mn 0.18; Zn 0.1; Cl 0.1; V 0.06; P 0.06; Ru, Rb, and Pt <0.01; the remainder O
Spent catalyst (SC)	Fe 85.5, Ca 2.5, Al 1.2, K 0.6, the remainder O
Mechanical engineering calcination sludge (MECS)	Fe 16.1, Si 14.0, Mn 3.5, S 3.1, Al 1.5, Cu 1.0, Cl 0.4, Zn 0.3, Ti 0.2, K 0.16, Mg 0.12, Cr 0.1, Na <0.1, Ni <0.1, the remainder O

1070-4272/03/7601-0020$25.00

Table 2. Properties of the pigments synthesized

Sample	Property	Pigment				Waste	Conditions of goethite synthesis		
		yellow	red	black	reddish brown		precipitant	T, °C	W, l h^{-1} l^{-1} solution
P1	CP, g m^{-2}	17.7	15.1	11.5	16.3	NMS	KOH	20	206
	OA, g/100 g	68	51	39	41				
P2	CP, g m^{-2}	14.3	10.9	9.0	10.1	SC	KOH	20	100
	OA, g/100 g	44	39	39	46				
P3	CP, g m^{-2}	16.9	8.3	10.0	12.6	SC	KOH	20	206
	OA, g/100 g	53	33	42	39				
P4	CP, g m^{-2}	15.0	7.9	12.5	14.1	SC	KOH	20	750
	OA, g/100 g	50	34	37	42				
P5	CP, g m^{-2}	16.4	7.8	9.8	12.3	SC	KOH	45	206
	OA, g/100 g	49	39	29	39				
P6	CP, g m^{-2}	17.4	14.2	–		SC	Na_2CO_3	20	206
	OA, g/100 g	56	49	–	–				
P7	CP, g m^{-2}	19.7	18.7	–	–	MECS	KOH	20	206
	OA, g/100 g	61	48	–	–				

In the course of synthesis of the goethite pigment, we used a new method of nucleus-free precipitation with alkali (KOH) at pH > 13 and, for comparison, the traditional sodium carbonate precipitation. The temperature and the rate of the air feed into the suspension were varied in the course of the synthesis, with the precipitant/$FeSO_4$ volume ratio being constant in most experiments (n = 2). The suspension was stirred with a stirrer at a rate of 200 rpm.

α-FeOOH was dehydrated in a nitrogen flow at 300°C to obtain α-Fe_2O_3, which was reduced with hydrogen at 380°C to Fe_3O_4. The latter was oxidized to γ-Fe_2O_3 in air at 200°C. The space velocities of the gases in various stages of the synthesis were (ml min^{-1} g^{-1}) nitrogen 30, hydrogen 25, and air 60. The quality of the pigments synthesized was characterized by the covering power CP (g m^{-2}) and oil absorption OA (g/100 g), which were measured by standard procedures [7]. The pigment color was evaluated visually.

Table 2 shows how the properties of the pigments synthesized vary depending on the kind of waste and synthesis conditions.

The yellow and red pigments synthesized from different wastes under the similar conditions have high characteristics for all samples (P1, P3, and P7), with the P3 sample (from spent catalyst) having the best covering power and oil absorption. Compared to P1 pigment (from metallurgical sludge), the black and reddish brown pigments P3 are better in covering power and nearly similar in oil absorption.

The characteristics of the samples of all colors depend on the rate of the air feed into the suspension in the W range studied (samples P2–P4). The minimal value of W was optimal for the yellow pigment, and its maximal value, for the red pigment. For the black and reddish brown pigments, the optimal covering power was attained at the minimal value of W, and the optimal oil absorption, at the middle or maximal value.

The yellow pigments from the spent catalyst, obtained by alkali precipitation and precipitation with sodium carbonate (samples P3 and P6, respectively), have similar characteristics, and the red pigment from the spent catalyst obtained by alkali precipitation has better characteristics. The pigments of all the colors synthesized at elevated and standard temperatures (samples P5 and P3, respectively) have similar characteristics, except for the black pigment P5 having lower oil absorption. Thus, by varying various parameters of the goethite synthesis, it is possible to vary within a certain interval the properties of the pigments synthesized.

Among yellow pigments, sample P4 from the spent catalyst has the highest color characteristic. Sample P6 obtained by sodium carbonate precipitation has the middle color characteristic. The color characteristic of the sample P7 from mechanical engineering sludge is

Table 3. Properties of commercial iron oxide pigments [7]

Brand or composition	Color	CP, g m^{-2}	OA, g/100 g
Zh-0	Yellow	12–15	35–50
Zh-1	″	15–20	35–60
Zh-2	″	15–20	35–70
K, grade 1	Red	6–7	26–35
K, grade 2	″	7–8	25–35
English Red	″	10–15	35–50
Indian Red	″	10–15	30–40
Fe_3O_4	Black	6–10	20–30
α-Fe_2O_3	Reddish brown	7–15	30–50

the worst, which may be due to a high content of the manganese oxide impurity. Sample P5 obtained at higher temperature of the goethite synthesis and sample P2 obtained at a low velocity of the air feed have a dark color. The peak of their absorption was shifted toward longer wavelengths, which may be due to increased particle size [7].

The properties of the commercial iron oxide pigments are characterized in Table 3 [7].

Yellow pigments of the indicated brands are used in industry as stencil and special-purpose paints, as additives to color cements, as thermosensitive pigments (up to 280°C), etc. Red pigments are used in construction and for painting ships and plastics. Black pigments are used in paints instead of carbon black, for coloring fiber glass, and as an intermediate in production of artist paints. The Fe_3O_4 powder is used for xerocopying. In pigment properties, γ-Fe_2O_3 is similar to α-Fe_2O_3.

In covering power and oil absorption, the P2 and P4 yellow pigments obtained correspond to Zh-0 commercial standard; samples P3, P5, and P6, to Zh-1 standard; and samples P1 and P7, to Zh-2 standard. Red sample P4 corresponds to K standard, grade 2; sample P3 corresponds to this standard in oil absorption, and sample P5, in covering power. Samples P1, P2, P6, and P7 in their characteristics are similar to English Red pigment. Sample P5 corresponds to the black standard, and samples P2–P5, to the reddish brown standard.

CONCLUSIONS

(1) In the main characteristics, iron oxide pigments (yellow, red, black, and reddish brown) synthesized from solid waste correspond to commercial pigments.

(2) Along with the use of Na_2CO_3, a nucleus-free method of alkaline precipitation is suitable for synthesizing goethite as intermediate in production of pigments.

(3) Choice of the conditions of the goethite synthesis allows control of the main characteristics of pigments.

REFERENCES

1. Prasad, T.P., *Res. Ind.*, 1993, vol. 38, no. 3, pp. 168–169.
2. USSR Inventor's Certificate no. 1 507 830.
3. USSR Inventor's Certificate no. 1 623 963.
4. Epikhin, A.N., Krylov, I.O., Kiselev, M.R., *et al.*, *Zh. Prikl. Khim.*, 1995, vol. 68, no. 2, pp. 1427–1432.
5. Epikhin, A.N., Kuznetsov, L.D., Kiselev, M.R., *et al.*, *Zh. Prikl. Khim.*, 1996, vol. 69, no. 9, pp. 1518–1524.
6. Epikhin, A.N., *Cand. Sci. Dissertation*, Moscow, 1998.
7. Korsunskii, L.F., Kalinskaya, T.V., and Stepin, S.N., *Neorganicheskie pigmenty: Spravochnik* (Inorganic Pigments: Handbook), Leningrad: Khimiya, 1992.

Russian Journal of Applied Chemistry, Vol. 76, No. 1, 2003, pp. 23–28. Translated from Zhurnal Prikladnoi Khimii, Vol. 76, No. 1, 2003, pp. 24–30.

INORGANIC SYNTHESIS AND INDUSTRIAL INORGANIC CHEMISTRY

Complex Formation in Electrolyte Solutions in the Course of Plating Protective Coatings on Titanium

S. V. Gnedenkov, O. A. Khrisanfova, A. G. Zavidnaya, S. L. Sinebryukhov, V. V. Kon'shin, S. B. Bulanova, and P. S. Gordienko

Institute of Chemistry, Far Eastern Division, Russian Academy of Sciences, Vladivostok, Russia

Received August 16, 2002

Abstract—Conditions for complex formation in aqueous electrolyte solutions containing salts of aluminum and hydroxy carboxylic acids were studied by ^{27}Al and ^{19}F NMR spectroscopy. The formation of complex anions in the electrolytes at various pH and their discharge on the anode under conditions of a microplasma process allowed preparation of surface layers containing α-Al_2O_3 on VT1-0 titanium. The interrelation between the composition and properties of the coatings was studied.

It is known that the physicochemical and service properties of coatings formed on metals and alloys under microplasma anodizing conditions essentially differ from the properties of common anodic films [1]. We have shown in [2] that certain factors should be taken into account when selecting the electrolyte composition and oxidation conditions for directed synthesis of surface layers of required composition on metals and alloys under the microarc oxidation conditions. Among such factors are possible changes in the forms of anionic complexes in solution depending on pH, both in the bulk of the electrolyte and in a local area of the near-electrode space.

Electrolytes containing various anionic complexes were used previously in the microarc oxidation of aluminum [3], titanium [4], and some other metals [5]. The resulting coatings had various physicochemical properties determined by their phase and chemical compositions. At the same time, the composition of the complex anions at various pH of the electrolyte, the interactions between various anions in solutions before and during oxidation, and also the mechanism of the complex formation are poorly understood.

To obtain on aluminum protective coatings exhibiting high resistance to wear and heat owing to the presence of α-Al_2O_3, an electrolyte containing aluminum tartrate complexes and also fluorides [6, 7] was developed. In [6], aluminum alloys were selected as model materials ensuring high concentration of aluminum ions in the near-anode space during oxidation. Depending on pH, the complex formation can involve various functional groups of tartaric acid: carboxy (–COOH), hydroxo (–OH), or both [8]. The presence of such complexes in an electrolyte solution strongly affects the composition and properties of the forming surface structures [9].

Proceeding from model concepts developed for aluminum and its alloys [6, 9], we believe that development of a process for obtaining solid layers on the titanium surface by its oxidation in electrolytes containing anions of hydroxy carboxylic acids should be based on the following principles.

(1) Fluorine compounds do not form insoluble compounds with titanium (in contrast to aluminum); therefore, their presence in the electrolyte will result in active etching of the substrate, thus hindering the formation of a continuous uniform coating.

(2) To ensure formation of anionic complexes with hydroxy acid ligands, aluminum(III)-containing components should be added to the electrolyte.

(3) It is necessary to minimize formation of titanium(IV) complexes with hydroxy acid salts by selecting appropriate electrolyte composition and varying its pH, as the existence of such complexes in solution will result in the formation of coatings based on titanium oxides and in decreased concentration of aluminum oxide in the film.

With the aim to obtain heat-resistant solid coatings on titanium, we studied in this work the complex formation in electrolytes containing aluminum salts and certain hydroxy carboxylic acids, both aliphatic (lactic, tartaric, and citric) and aromatic (salicylic). For this purpose, we created conditions favoring

1070-4272/03/7601-0023$25.00

the formation of aluminum(III) complexes with the above-listed hydroxy acids in solution. Then, using electrolytes containing complex anions, we formed coatings on titanium under the microplasma conditions and studied their composition and properties.

EXPERIMENTAL

Samples of VT1-0 grade titanium (99.4% Ti) in the form of 5×30-mm plates were oxidized. Aluminum sulfate $Al_2(SO_4)_3 \cdot 18H_2O$ and oxalate $Al_2(C_2O_4)_3 \cdot nH_2O$, and also hydroxy carboxylic acids and their salts (potassium tartrate $K_2C_4H_4O_6 \cdot 0.5H_2O$, lactic acid $C_3H_6O_3$, potassium citrate $K_3C_6H_5O_7$, and salicylic acid $C_7H_6O_3$) were added to the electrolyte used in the oxidation. The electrolyte pH was adjusted with KOH and H_2SO_4. Sodium fluoride NaF was added when studying the electrolytes by ^{19}F NMR. All the chemicals used in the work were of chemically pure grade. The formation voltage was selected individually for each electrolyte solution within the limits 170–300 V. The current density did not exceed 1 A cm^{-2}, the oxidation time, 5–10 min, and the electrolyte temperature, +25°C. The electrolyte was cooled using a refrigerating unit whose heat exchanger was placed directly in the electrolytic cell.

The phase composition of coatings on a metallic substrate was determined with a DRON 3.0 X-ray diffractometer (CuK_α radiation). The relative contents of phases in films were estimated from the ratios of intensities of their strongest lines. The NMR experiments were carried out on a Bruker WP-80 SY radiospectrometer at room temperature with external stabilization by deuterium. The chemical shifts δ_i of ^{27}Al and ^{19}F are given relative to $[Al(H_2O)_6]^{3+}$ and $CFCl_3$ references, respectively, using the relationship $\delta_i = (\nu_i - \nu_0)/\nu_0$ (ν_0 and ν_i are the frequencies of the signals of the reference and sample under study). The microhardness of coatings was measured on a Neofot-2 device using cross-sectional microsections prepared with the use of epoxy resin. The differential thermal (DTA) and thermogravimetric (TG, DTG) analysis was performed with a Q-1500D derivatograph (MOM, Hungary) in the course of heating coated samples in open platinum crucibles in air or under helium at a rate of 5 deg min^{-1} to 1000°C, with the aim to evaluate the probability of afteroxidation of the titanium substrate during annealing in air. The helium flow rate through the chamber was 10 l h^{-1}.

The mechanism of the complex formation of certain metals in solutions of tartaric acid and its salts was studied in [10, 11]. It was found that, depending on solution pH, aluminum(III) can form cationic, neutral, and anionic tartrate complexes. The formation of complexes involving oxotitanium(IV) ions TiO^{2+} is the most typical for titanium in a strongly acidic medium, where the most stable complexes with tartaric acid ligands are formed. At pH < 1, titanium(IV) forms $[Ti(OH)_2(C_4H_5O_6)(C_4H_6O_6)]^+$ cationic complexes. In the range pH 1–7, the migration of titanium-containing complexes to anode increases, suggesting the conversion of cationic and neutral species into the anionic species $[Ti(OH)_2(C_4H_4O_6)_2]^{2-}$, $[Ti(OH)_2(C_4H_2O_6)]^{2-}$, and $[Ti(OH)_2(C_4H_4O_6) \cdot (C_4H_3O_6)]^{3-}$ with the charge increasing with pH [12]. The migration of complexes to the anode is reduced in an alkaline medium owing to hydrolysis of titanium-containing components with the formation of single-charged ions.

Aluminum(III) anionic complexes, in contrast to titanium(IV) complexes, are more stable in an alkaline medium (pH 9–10); therefore, when aluminum and titanium compounds are present simultaneously in solution, it is appropriate to select high pH values to decrease the probability of the titanium(IV) complex formation with tartrate ions and hence to reduce the effect of titanium-containing compounds on the composition of a film formed on the anode.

Figure 1 shows the ^{27}Al NMR spectra of solutions (pH 2.5–12) containing aluminum salts (sulfate or oxalate), their mixtures with hydroxy acids (salicylic or lactic), and salts of hydroxy acids (potassium tartrate or citrate).

Aluminum(III) cations in solution have either octahedral or tetrahedral environment depending on the solvent properties and the ligand type [13]. The ^{27}Al NMR chemical shifts of octahedral complexes are in the region of 0 ppm, and those of tetrahedral complexes are shited downfield (–70 to –100 ppm). Thus, the ^{27}Al chemical shifts furnish information on the structure of aluminum complexes. A signal with the ^{27}Al NMR chemical shift of 0 ppm corresponding to the $[Al(H_2O)_6]^{3+}$ complex was recorded in an aqueous solution of aluminum sulfate at pH 2.5 (Fig. 1, spectrum *1*). When tartrate anions $[C_4H_4O_6]^{2-}$ are added to the electrolyte at pH 10, a broad signal with δ = –34 ppm corresponding to the aluminum tartrate complex $[Al(OH)(C_4H_2O_6)]^{2-}$ [6] appears (Fig. 1, spectrum *2*). An increase in pH to 11 owing to hydrolysis results in hydrolysis and breakdown of the aluminum(III) tartrate complex, as demonstrated by the appearance of the ^{27}Al NMR signal with δ = –80 ppm corresponding to the tetrahedral aluminum

complex $[Al(OH)_4]^-$ (Fig. 1, spectrum *2*). In a solution of aluminum oxalate at pH 2.5, aluminum exists as the complex $[Al(C_2O_4)_3]^{3-}$ (δ = –10 ppm) (Fig. 1, spectrum *4*). When aluminum oxalate is added to solutions containing potassium tartrate, the complex $[Al(OH)(C_4H_2O_6)]^{2-}$ is formed at pH < 12, giving a broad ^{27}Al NMR signal at δ = –26 ppm (Fig. 1, spectrum *5*). The hydrolysis of oxalate-containing solutions results in the formation of the tetrahedral complex $[Al(OH)_4]^-$ at higher pH (pH 12) than in sulfate-containing solutions (pH 11), which is due to the existence in such systems of the complex $[Al(C_2O_4)_3]^{3-}$ along with $[Al(OH)(C_4H_2O_6)]^{2-}$ (Fig. 1, spectrum *3*).

The ^{27}Al NMR spectra of solutions containing aluminum oxalate and lactic acid are shown in Fig. 1, spectra *6* and *7*. A signal with δ = –13.9 ppm is observed in the spectra at pH 9. This is the signal of an aluminum anionic complex with lactic acid, which exists without changes within a broad pH range, pH 3–10 (Fig. 1, spectrum *7*). The tetrahedral complex $[Al(OH)_4]^-$, which gives a signal with δ = –79.9 ppm (Fig. 1, spectrum *6*), is formed at pH 11.4 as a result of the hydrolysis of the lactate complex. The obtained data agree with the results of studying the structure of aluminum complexes with lactic and citric acids by ^{27}Al NMR [14]. For solutions containing aluminum salts and lactic acid, several signals were observed, originating from the replacement of water molecules in the complex $[Al(H_2O)_6]^{3+}$ by lactate ions (pH 3–5) [14]. An increase in pH to 7–8 resulted in the hydrolysis of this compound up to formation of the anionic complex $[Al(OH)_4]^-$ (pH 10–11).

Aluminum(III) complexes with citrate and salicylate ions have certain specific features. According to [14], the presence of three carboxy groups and one hydroxy group in the citrate ligand complicate the determination of structural characteristics of the complexes (as is also the case with the lactate ligand), because of numerous possible coordination modes of the ligand. In particular, formation of a structure suggested in [15], in which aluminum is linked to two carboxy groups and one hydroxy group, forming two five-membered rings, is quite possible.

Salicylic acid, which belongs to the class of aromatic hydroxy acids, also forms complexes with aluminum(III) ions. Signals with δ = –15.3 and δ = –10.6 ppm are observed in the range of pH 3–10 in the systems aluminum oxalate–potassium citrate and aluminum oxalate–cirtic acid, respectively. These signals suggest formation of aluminum anionic complexes with citrate and salicylate ions in solution (Fig. 1, spectra *8*, *9*).

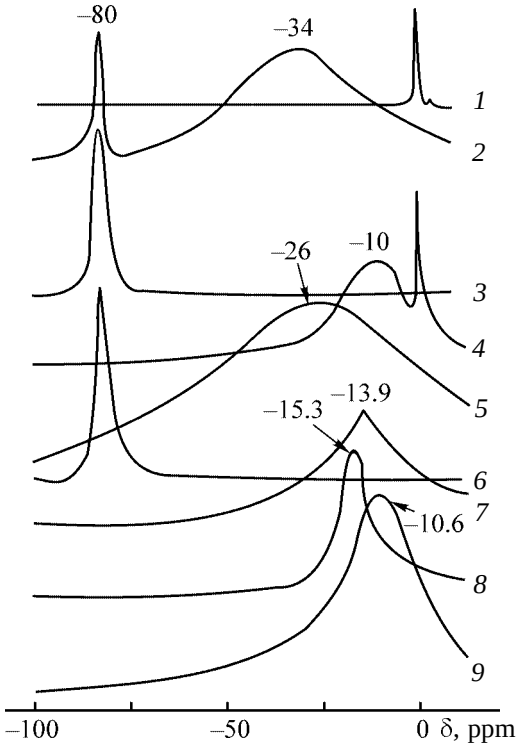

Fig. 1. ^{27}Al NMR spectra of solutions of aluminum salts and hydroxy acids. (δ) Chemical shift; the same for Fig. 2. (*1*) Aluminum sulfate, pH 2.5; (*2*) aluminum sulfate + potassium tartrate, pH 10–11; (*3*) aluminum oxalate + potassium tartrate, pH 12; (*4*) aluminum oxalate, pH 2.5; (*5*) aluminum oxalate + potassium tartrate, pH 10.8; (*6*) aluminum oxalate + lactic acid, pH 11.4; (*7*) aluminum oxalate + lactic acid, pH 9.0; (*8*) aluminum oxalate + potassium citrate, pH 9.85; and (*9*) aluminum oxalate + salicylic acid, pH 9.0.

In contrast to data in [14], the positions of the ^{27}Al NMR signals corresponding to aluminum(III) complexes with anions of the above-listed hydroxy acids or their salts did not change in the range of pH 3–10, i.e., the complexes formed in the solution are stable under these conditions. Based on our experimental data and on the approach developed in [8, 9], we can presume the composition of the aluminum complexes with the hydroxy acids in solutions. The following anionic complexes can be formed in the range of pH 9–10: $[Al(OH)_2(C_3H_4O_3)]^-$, M = 149, with lactic acid; $[Al(C_4H_2O_6)]^-$, M_r = 173 and $[Al(OH)(C_4H_2O_6)]^{2-}$, M = 190, with tartaric acid; $[Al(C_6H_4O_7)]^-$, M_r = 215, $[Al(OH)(C_6H_4O_7)]^{2-}$, M = 232, and $[Al(OH)_2 \cdot (C_6H_4O_7)]^{3-}$, M = 249, with citric acid; and $[Al(OH)_2 \cdot (C_7H_4O_3)]^-$, M 197, $[Al(C_7H_4O_3)_2]^-$, M = 275, and

Table 1. Formation conditions, composition, and microhardness μ of coatings on titanium

Electrolyte	Concentration, g l^{-1}	pH	μ, MPa	Phase composition of coating*
$K_2C_4H_4O_6 \cdot 0.5H_2O$, $Al_2(SO_4)_3 \cdot 18H_2O$	10 2	3.2	3200	TiO_2-rutile
$K_2C_4H_4O_6 \cdot 0.5H_2O$, $Al_2(SO_4)_3 \cdot 18H_2O$	10 2	9.8	5000	Al_2TiO_5, α-Al_2O_3, TiO_2-rutile
$K_2C_4H_4O_6 \cdot 0.5H_2O$, $Al_2C_6O_{12} \cdot nH_2O$	10 10	10.8	5500	Al_2TiO_5, α-Al_2O_3,
$C_3H_6O_3$, $Al_2C_6O_{12} \cdot nH_2O$	10 31.8	9.8	4300	Al_2TiO_5
$K_3C_6H_5O_7$, $Al_2C_6O_{12} \cdot nH_2O$	8.1 15.8	9.8	4250	TiO_2-rutile, Al_2TiO_5
$C_7H_6O_3$, $Al_2C_6O_{12} \cdot nH_2O$	6.9 31.8	9.8	4800	Al_2TiO_5, α-Al_2O_3

* Components are given in the order of decreasing content in the coating.

$[Al(OH)(C_7H_4O_3)_2]^{2-}$, M = 292, with salicylic acid (M is the molecular weight of the complex anion).

Without using other physical methods, the available data do not allow an unambiguous conclusion on the composition and structure of the complexes formed in the electrolytes. The difference in the position of signals in the NMR spectra of these compounds is no more than an evidence for their different compositions and structures.

Since information furnished by the ^{27}Al NMR spectra is relatively poor compared to the ^{19}F NMR spectra, we added fluoride ions to the solutions containing aluminum salts and tartrate ions. Then we studied the aqueous solutions of aluminum fluoride–tartrate complexes by ^{19}F and ^{27}Al NMR spectroscopy. The ^{19}F NMR spectra show that aluminum fluoride–tartrate complexes $[AlF_n(C_4H_4O_6)_{6-n}]^{3-}$ (n = 1–6) are present in aqueous solutions along with aluminum aquafluoride complexes (Fig. 2). In such systems, in contrast to bidentate oxalate ions, tartrate ions behave as monodentate ligands [16].

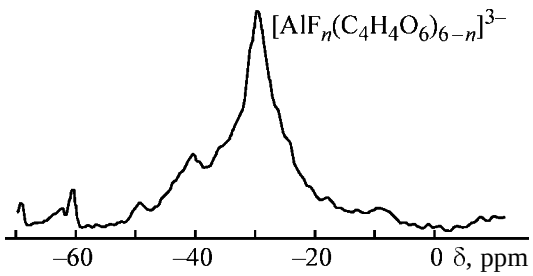

Fig. 2. ^{19}F NMR spectrum of aluminum(III) fluoride–tartrate solution.

A question arises: To what extent are the composition and properties of electrolytic oxide layers affected by the structure of complexes present in the electrolyte? To answer this question, we obtained coatings on titanium from solutions containing aluminum sulfate and oxalate and anions of lactic, tartaric, citric, and salicylic acids, using the microplasma anodizing method. We found that such layers consist of titanium and aluminum oxides (rutile TiO_2, α-Al_2O_3, and Al_2TiO_5) in various combinations depending on pH and composition of the electrolyte (Table 1). According to the X-ray phase analysis, in view of the estimated microhardness of the resulting surface layers, we found that the coatings obtained from the electrolyte at pH from 3 to 5 contain titanium dioxide (rutile) responsible for their moderate microhardness (up to 3200 MPa). Surface layers with a higher hardness (5500 MPa), consisting of the double oxide Al_2TiO_5 and aluminum oxide α-Al_2O_3, were formed in alkaline solutions of the electrolytes at pH 10.0–10.8. At such pH, more favorable conditions are created for the formation of anionic complexes involving aluminum(III) ions and hydroxy acids.

At the same time, with the examined electrolytes, we failed to eliminate the oxidation of the titanium substrate by selecting anodic oxidation modes. It resulted in the formation of titanium dioxide and the double oxide Al_2TiO_5, which reduce the hardness of the coatings compared to the coatings on aluminum consisting of α-Al_2O_3 and having the microhardness of up to 7000 MPa [6].

We estimated the heat resistance of coatings obtained in the microplasma mode at various electrolyte

Table 2. Thermal stability of coatings on titanium

Composition no.	Electrolyte	Concentration, g l^{-1}	Annealing conditions	Temperature, °C		Phase composition of coatings	
				onset of oxidation	onset of intense oxidation	before annealing	after annealing
1	Sample without coating		Helium Air	680 650	780 760	X-ray amorphous phase	TiO_2-rutile
2	$C_3H_6O_3$, $Al_2C_6O_{12}\cdot nH_2O$	10 31.8	Helium Air	780 750	910 900	Al_2TiO_5	Al_2TiO_5 TiO_2-rutile
3	$K_2C_4H_4O_6\cdot 0.5H_2O$, $Al_2C_6O_{12}\cdot nH_2O$	10 10	Helium Air	790 760	920 910	Al_2TiO_5, α-Al_2O_3	Al_2TiO_5, α-Al_2O_3, TiO_2-rutile
4	$K_3C_6H_5O_7$, $Al_2C_6O_{12}\cdot nH_2O$	8.1 15.8	Helium Air	700 680	900 890	TiO_2-rutile, Al_2TiO_5	
5	$C_7H_6O_3$, $Al_2C_6O_{12}\cdot nH_2O$,	6.9 31.8	Helium Air	800 780	915 910	Al_2TiO_5, α-Al_2O_3	Al_2TiO_5, α-Al_2O_3, TiO_2-rutile

pH (within the range 10.0–10.8). It was shown above that this pH range ensures the formation of anionic aluminum complexes with hydroxy acids in solution. The discharge of the complexes on the anode allows preparation of coatings containing aluminum oxide α-Al_2O_3, ensuring their high hardness and heat resistance.

We estimated the temperatures of the initial and accelerated titanium oxidation by the points in which the experimental TG curve deviates from the extrapolated straight lines, and also by the inflection points in the DTG curve. Also, we determined the phase composition of the coatings before and after annealing. The corresponding experimental data are given in Table 2.

Figure 3 shows the DTA, TG, and DTG curves recorded in the course of annealing the samples coated in an electrolyte containing salicylic acid (similar curves are characteristic for all the samples studied). According to Table 2, such coatings have the best protective properties. No thermal effects and weight changes were detected in the DTA curves of all the coated titanium samples (Table 2) up to the temperature of the initial oxidation (680–800°C). The thermal effect originating from the transition of α-Ti (hexagonal modification) to β-Ti (cubic modification) is observed at 880°C. The temperature of this transition should not depend on the annealing atmosphere, which is indeed the case (Fig. 3). Above 890–920°C, the sample weight quickly grows, as seen from the TG curve (the stage of accelerated oxidation). At these temperatures, the coating continuity is broken, which is due to a certain extent to the difference in the thermal expansion coefficients of the coating material and titanium substrate; as a result, oxygen penetrates to the metallic matrix and causes its active oxidation. At the same time, according to the data of [6], aluminum-based coatings exhibited a higher heat resistance. Up to 870°C, the composition, properties, and weight of samples did not change; the coating did not melt, was not destroyed, and acted as a heat-resistant crucible. Weaker protective properties of coatings on titanium, as compared to coatings on aluminum obtained in a similar electrolyte, are attributable not only to the difference in the phase composition of the

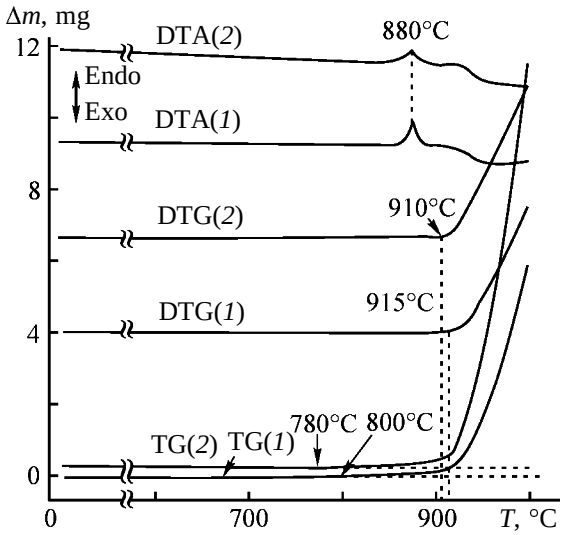

Fig. 3. DTA, TG, and DTG curves for samples coated from the electrolyte containing salicylic acid. Heating rate 5 deg min^{-1}. (Δm) Change in the sample weight and (T) temperature. Annealing (*1*) in a helium atmosphere and (*2*) in air.

layers under study (smaller content of α-Al_2O_3), but also to the effect of the substrate (aluminum or titanium), which is manifested at temperatures higher than 620°C. As the aluminum substrate is completely molten above this temperature [6], the difference in the thermal expansion coefficients of the substrate and coating is of no importance above 620°C and, therefore, it cannot affect the continuity of surface layers responsible for the intensity of oxygen penetration to the matrix. In the case of titanium samples (mp 1668°C) with surface layers obtained by microarc oxidation, the difference in the thermal expansion coefficients of the substrate and coating will be of importance within the temperature range under study.

According to Table 2, all coatings under study exhibit protective properties both in air and in a helium atmosphere, decelerating oxidation of the titanium substrate. The coatings obtained from electrolyte nos. 3 and 5 exibit a higher degree of protection (Table 2), which is due to the presence of α-Al_2O_3 in them. The temperatures of the initial and accelerated substrate oxidation are higher for these samples than for the samples obtained from the other electrolytes. This may be due not only to the coating structure, but also to its morphology, porosity, homogeneity, and presence of cracks. It follows from Table 2 that the phase composition of coatings on titanium before and after annealing, both in air and in helium, changes insignificantly, indicating the high heat resistance and low oxygen permeability of the coatings. The protective properties strengthen as the concentration of aluminum oxide in the surface layers increases. Presumably, the complexes with higher molecular weights, burning down in a plasma channel on the anode, liberate considerable energy, which, in turn, promotes the formation of the high-temperature modification of aluminum oxide in the surface layer. Furthermore, the benzene ring of salicylic acid can affect the nature, temperature, and time of plasma chemical reactions occurring at the anode and, correspondingly, the composition and properties of the forming surface layers.

CONCLUSION

The formation of complexes in electrolyte solutions containing aluminum salts and hydroxy carboxylic acids was proved by the ^{27}Al and ^{19}F NMR spectroscopy. These complexes, being fairly stable in a wide pH range, determine the composition and properties of oxide layers formed in these electrolytes on titanium under the action of microplasma oxidation. The presence of α-Al_2O_3 in the coatings is responsible for their elevated microhardness and thermal stability compared to the substrate. At the same time, differences in the composition and structure of the complexes detected in the electrolyte by NMR do not give rise to considerable differences in the composition and protective properties of the forming layers.

REFERENCES

1. Gordienko, P.S. and Gnedenkov, S.V., *Mikrodugovoe oksidirovanie titana i ego splavov* (Microarc Oxidation of Titanium and Its Alloys), Vladivostok: Dal'-nauka, 1997.
2. Khrisanfova, O.A., Volkova, L.M., Gnedenkov, S.V., *et al.*, *Zh. Neorg. Khim.*, 1995, vol. 40, no. 4, pp. 558–562.
3. Timoshenko, A.V., Magurova, Yu.V., and Artemova, S.Yu., *Fiz. Khim. Obrab. Mater.*, 1996, no. 2, pp. 57–64.
4. Yarovaya, T.P., Gordienko, P.S., Rudnev, V.S., *et al.*, *Elektrokhimiya*, 1994, vol. 30, no. 11, pp. 1395–1396.
5. Gruss, L. and McNeil, W., *Electrochem. Technol.*, 1963, vol. 1, nos. 9–10, pp. 283–287.
6. Gnedenkov, S.V., Khrisanfova, O.A., Zavidnaya, A.G., *et al.*, *Zh. Prikl. Khim.*, 2000, vol. 73, no. 11, pp. 541–547.
7. Gnedenkov, S.V., Khrisanfova, O.A., Zavidnaya, A.G., *et al.*, *Surf. Coat. Technol.*, 2000, no. 23, pp. 24–28.
8. Pyatnitskii, I.V., *Usp. Khim.*, 1963, vol. 32, no. 1, pp. 93–117.
9. Gnedenkov, S.V., Khrisanfova, O.A., Zavidnaya, A.G., *et al.*, *Surf. Coat. Technol.*, 2001, no. 145, pp. 146–151.
10. Motekaitis, R.J. and Martell, A.E., *Inorg. Chem.*, 1984, vol. 23, pp. 18–23.
11. Grigalashvili, K.N. and Pyatnitskii, I.V., *Analiticheskaya khimiya i ekstraktsionnye protsessy* (Analytical Chemistry and Extraction Processes), Kiev: Naukova Dumka, 1970.
12. Zholnin, A.V. and Dolmatov, Yu.D., *Zh. Neorg. Khim.*, 1969, vol. 14, no. 5, pp. 1222–1218.
13. Petrosyants, S.P. and Buslaev, Yu.A., *Zh. Neorg. Khim.*, 1990, vol. 44, no. 11, pp. 1766–1776.
14. Karlik, S.J., Tarien, E., Elgavish, G.A., and Eichorn, G.L. *Inorg. Chem.*, 1983, vol. 22, no. 3, pp. 525–529.
15. Tsimbler, E.N., Derenovskii, V.I., and Prosyanik, N.S., *Tr. Inst. Inzh. Vodn. Khoz.*, 1959, no. 8, pp. 159–167.
16. Kon'shin, V.V., Solvation and Complex Formation of Aluminum and Magnesium in Aqueous-Organic and Peroxide Solutions, *Cand. Sci. Dissertation*, Vladivostok, 1990.

Russian Journal of Applied Chemistry, Vol. 76, No. 1, 2003, pp. 29–32. Translated from Zhurnal Prikladnoi Khimii, Vol. 76, No. 1, 2003, pp. 31–34.

PHYSICOCHEMICAL STUDIES OF SYSTEMS AND PROCESSES

Thermodynamic Properties of Anabasine Hydrochloride and Its Analogs

B. K. Kaskenov, Zh. K. Tukhmetova, S. M. Adekenov, Sh. B. Kasenova, E. S. Mustafin, A. D. Kagarlitskii, and A. Zh. Turmukhambetov

Institute of Phytochemistry, Ministry of Education and Science of Kazakhstan Republic, Karaganda, Kazakhstan

Received March 13, 2002

Abstract—The heats of solution of anabasine hydrochloride $C_{10}H_{14}N_2HCl$ and of the reaction of its aqueous solution with crystalline $AgNO_3$ at various dilutions were determined. The standard enthalpies of formation of anabasine hydrochloride and its 36 analogs were calculated. The temperature dependence of the anabasine hydrochloride heat capacity was studied within the 173–448 K range.

A study of thermochemical and thermodynamic properties of alkaloids is of practical and theoretical interest for purposeful synthesis of new derivatives with preset properties. Up to now, data on thermochemical and thermodynamic constants (both experimental and calculated) of anabasine and its derivatives were lacking. The goal of this work is the experimental study of thermochemical and thermodynamic properties of anabasine hydrochloride and calculation of the standard enthalpy of formation of anabasine hydrochloride and its derivatives.

Calorimetric determination of the enthalpy of $C_{10}H_{14}N_2HCl$ solution in water and of the reaction of its aqueous solution with crystalline $AgNO_3$ was performed at dilutions (salt : water molar ratios) of 1 : 6000, 1 : 9000, and 1 : 18 000 under isothermal conditions. The experimental error and variance homogeneity in determination of thermal effects were calculated using Student and Bartlett tests [1].

We calculated the heat of combustion of anabasine hydrochloride by Karash and Frost methods [2] and the heat of melting, by the empirical equation recommended in [3]. The enthalpies of formation $\Delta_f H^0$ (298.15) of $C_{10}H_{14}N_2HCl$ analogs were calculated using the enthalpy increments of anions [4, 5].

EXPERIMENTAL

Chemically pure grade anabasine hydrochloride was used. The enthalpy of solution of anabasine hydrochloride in water was measured in a DAK-1-1A isothermal differential automatic calorimeter. The thermal effects were recorded with a KSP-4 potentiometer and, in parallel, with an IP-4 precision integrator. The time of prethermostating of the compound to be measured was 2 h. The calorimeter was calibrated by applying a calibrated voltage to a built-in electric motor and was checked by measuring the heat of solution of triple-recrystallized KCl at 1 : 1600, 1 : 2400, and 1 : 3200 (salt : water molar ratios) dilutions. The averaged measured heat of KCl solution, $17\,860 \pm 283$ J mol^{-1}, is in good agreement with the value of $17\,577 \pm 34$ J mol^{-1} obtained in [6].

The heat of solution of anabasine hydrochloride in water ΔH_s^m

$$C_{10}H_{14}N_2HCl(cr) + nH_2O(l) = C_{10}H_{14}N_2HCl(soln, nH_2O) + \Delta H_s^m, \quad (1)$$

was found at n = 6000, 9000, and 18 000 (Table 1).

The experimental values of ΔH_s^m at various dilutions (Table 1) were used for calculating the enthalpy of solution of anabasine hydrochloride at infinite (standard) dilution ΔH_s^0. The molal concentrations m_1, m_2, and m_3 and the corresponding $\Delta H_{s(1)}^m$, $\Delta H_{s(2)}^m$, and $\Delta H_{s(3)}^m$ were calculated. The dependence of the enthalpy of solution (kJ mol^{-1}) on the molal concentration $m^{1/2}$ is described by the equation

$$\Delta H_s^m(C_{10}H_{14}N_2HCl) = 5.29 - 469.59m^{1/2}, \quad (2)$$

similarly to data of [7].

Using Eq. (2), we calculated the standard enthalpy

1070-4272/03/7601-0029$25.00

Table 1. Enthalpy of $C_{10}H_{14}N_2HCl$ solution in water. Dilution (salt : water molar ratios): (1) 1 : 6000, (2) 1 : 9000, and (3) 1 : 18 000

Sample of $C_{10}H_{14}N_2HCl$, g	ΔH_s, J	ΔH_s^m, kJ mol^{-1}
Dilution 1		
0.0092	0.111	2.397
0.0091	0.095	2.074
0.0091	0.099	2.162
0.0091	0.100	2.183
0.0092	0.112	2.419
Average		$\Delta H_{s(1)}^m = 2.25 \pm 0.19$
Dilution 2		
0.0062	0.076	2.436
0.0062	0.072	2.307
0.0063	0.080	2.523
0.0062	0.071	2.275
0.0062	0.075	2.404
Average		$\Delta H_{s(2)}^m = 2.39 \pm 0.12$
Dilution 3		
0.0032	0.057	3.539
0.0031	0.055	3.525
0.0031	0.057	3.653
0.0031	0.052	3.333
0.0031	0.058	3.718
Average		$\Delta H_{s(3)}^m = 3.55 \pm 0.18$

Table 2. Enthalpy of reaction of aqueous solution of $C_{10}H_{14}N_2HCl$ with $AgNO_3$. Dilution (salt : water molar ratios): (1) 1 : 6000, (2) 1 : 9000, and (3) 1 : 18 000

Sample of $AgNO_3$, g	ΔH_r, J	ΔH_r^m, kJ mol^{-1}
Dilution 1		
0.0079	1.035	22.25
0.0078	1.015	22.10
0.0078	1.021	22.23
0.0078	1.025	22.32
0.0079	1.043	22.42
Average		$\Delta H_{s(1)}^m = 22.26 \pm 0.15$
Dilution 2		
0.0053	0.761	24.39
0.0053	0.751	24.07
0.0053	0.763	24.44
0.0053	0.769	24.64
0.0053	0.765	24.51
Average		$\Delta H_{s(2)}^m = 24.41 \pm 0.26$
Dilution 3		
0.0027	0.400	25.16
0.0026	0.383	25.02
0.0026	0.381	24.89
0.0026	0.387	25.28
0.0026	0.382	24.96
Average		$\Delta H_{s(3)}^m = 25.06 \pm 0.20$

of solution of anabasine hydrochloride in water, $\Delta H_s^0 = 5.29 \pm 0.33$ kJ mol^{-1}. This value is essential for calculating the standard heats of formation of anabasine derivatives.

The enthalpy of solution was used for determining the heat of the reaction of aqueous anabasine hydrochloride with crystalline $AgNO_3$ (Table 2):

$$C_{10}H_{14}N_2HCl(soln, nH_2O) + AgNO_3(cr) = C_{10}H_{14}N_2HNO_3(soln, nH_2O) + AgCl\downarrow(cr.) - \Delta H_r^m \quad (3)$$

The progress of reaction (3) was monitored by X-ray phase analysis (formation of crystalline AgCl) and NMR spectroscopy (formation of anabasine nitrate). Crystalline $C_{10}H_{14}N_2HNO_3$ was separated from the filtrate.

The isobaric heat capacity of anabasine hydrochloride was measured on an IT-C-400 device with the error not exeeding ±10.0% [8]. The time of measurements over the 173–448 K range, including the treatment of the experimental data, did not exceed 2.5 h. The device was calibrated by measuring the calorimeter heat conductance K_c. Five experiments were performed at each temperature, the results were averaged, and the root-mean-square deviation $\bar{\delta}$ for the heat capacity and the random error $^0\Delta$ for the molar heat capacity were estimated. The calorimeter operation was controlled by measuring the heat capacity of α-Al_2O_3. The $C_p^0(298.15)$ value obtained, 76.0 J mol^{-1} K^{-1}, is in good agreement with the reference value of 79.0 J mol^{-1} K^{-1} [9]. The results are listed in Table 3.

From the data obtained, the equation describing the $C_p^0 = f(T)$ dependence for anabasine hydrochloride over the temperature range 298.15–448 K is as follows (J mol^{-1} K^{-1}):

$$C_p^0 = (145 \pm 8) + (284 \pm 16) \times 10^{-3}T - (24.7 \pm 1.3) \times 10^5 T^{-2}. \quad (4)$$

To calculate $\Delta H^0(298.15)$ of $C_{10}H_{14}N_2HCl$, we estimated its standard heat of combustion by the methods of Karash and Frost [2]. In the Karash's

method, the presence of oxygen, nitrogen, and chlorine in the compound is estimated. In the Frost's method, the effects of cyclenes and double bonds in their rings are additionally taken into consideration. The averaged heat of combustion of $C_{10}H_{14}N_2HCl$ is –5860 kJ mol^{-1}.

Taking into account the heat of combustion of $C_{10}H_{14}N_2HCl$

$$2C_{10}H_{14}N_2HCl(l) + 27.5O_2(g) = 20CO_2(g) + 15H_2O(l) + 2N_2(g) + Cl_2(g) - \Delta H^0_{comb}, \quad (5)$$

we calculated the standard enthalpy of formation of liquid $C_{10}H_{14}N_2HCl$, which is equal to –229.9 kJ mol^{-1}. It should be noted that methods of Karash and Frost are suitable only for calculating ΔH^0 of combustion of liquid hydrocarbons. The data required for calculating $\Delta_f H^0$ (298.15) of $C_{10}H_{14}N_2HCl(l)$ by scheme (5) (excluding ΔH^0_{comb}) are taken from the handbook [10]. Since at 298.15 K anabasine hydrochloride is crystalline, its $\Delta_f H^0$ (298.15) should be calculated for the solid state. We estimated ΔH^0_m(298.15) of $C_{10}H_{14}N_2HCl$ by the empirical equation [3],

$$\Delta H^0_m = 44.4T_m - 4400, \quad (6)$$

valid for highly polar halides, and obtained the value of 17.0 kJ mol^{-1}. The standard enthalpy of formation of crystalline anabasine hydrochloride was calculated by the equation

$$\Delta_f H^0(298.15)C_{10}H_{14}N_2HCl(cr) = \Delta_f H^0(298.15)C_{10}H_{14}N_2HCl(l) - \Delta H^0_m \quad (7)$$

and amounts to –239.9 ± 12.0 kJ mol^{-1}.

Then, using ΔH^0 of solution of $C_{10}H_{14}N_2HCl$ in standard aqueous solution (5.29 kJ mol^{-1}),

$$\Delta_f H^0(298.15)C_{10}H_{14}N_2HCl(soln, H_2O, standard state) = \Delta_f H^0(298.15)C_{10}H_{14}N_2HCl(cr) + \Delta H^0_s, \quad (8)$$

we calculated the standard enthalpy of formation of $C_{10}H_{14}N_2HCl$ in aqueous solution: –234.6 kJ mol^{-1}.

Using the equation

$$[\Delta_f H^0(298.15)C_{10}H_{14}N_2H^+(soln, H_2O, standard state)] = [\Delta_f H^0(298.15)C_{10}H_{14}N_2HCl(soln, H_2O, standard state)] - [\Delta_f H^0(298.15)Cl^-(soln, H_2O, standard state)], \quad (9)$$

Table 3. Experimental heat capacities of $C_{10}H_{14}N_2HCl$

T, K	$C_p \pm \bar{\delta}$, J K^{-1} g^{-1}	$C^0_p \pm {}^0\Delta$, J mol^{-1} K^{-1}
173	0.6027 ± 0.0094	120 ± 5
198	0.6936 ± 0.0096	138 ± 5
223	0.8573 ± 0.0195	170 ± 11
248	0.9248 ± 0.0138	184 ± 16
273	0.9656 ± 0.0311	192 ± 17
298.15	1.0159 ± 0.0315	202 ± 17
323	1.0997 ± 0.0101	219 ± 6
348	1.1273 ± 0.0235	224 ± 13
373	1.1751 ± 0.0358	233 ± 20
398	1.2309 ± 0.0155	245 ± 9
423	1.2776 ± 0.0156	254 ± 9
448	1.3093 ± 0.0333	260 ± 18

we calculated the standard enthalpy of formation of $[C_{10}H_{14}N_2H]^+$ in aqueous solution: – 67.4 kJ mol^{-1}.

This value was used for calculating $\Delta_f H^0$ (298.15) of 36 anabasine derivatives. In [4, 5], the system of thermochemical enthalpy increments was developed, allowing calculation of the standard heats of formation of crystalline compounds by the scheme

$$\Delta_f H^0(298.15)M_m(X_\alpha O_\beta)_n = [m\Delta_f H^0(298.15)M^{n+}(soln, H_2O, standard state)]K + n\Delta_f H^i(298.15)X_\alpha O_\beta^{m-}, \quad (10)$$

where $\Delta_f H^i$(298.15) is the enthalpy increment of the anion, and K is proportionality coefficient.

To calculate $\Delta_f H^0$(298.15) of derivatives by scheme (1), it is sufficient to know $\Delta_f H^0$(298.15, soln, H_2O, standard state) of the cation, since K and $\Delta_f H^i$(298.15) of anions are tabulated in [4, 5]. The error of calculation is ±5.0%. As applied to anabasine derivatives, scheme (10) can be presented as follows (by an example of $C_{10}H_{14}N_2HNO_3$):

$$\Delta_f H^0(298.15)C_{10}H_{14}N_2HNO_3(cr) = [\Delta_f H^0(298.15)C_{10}H_{14}N_2H^+(soln, H_2O, standard state)]K + \Delta_f H^i(298.15)NO_3^-. \quad (11)$$

The $\Delta_f H^0$ values for 36 anabasine derivatives, calculated by scheme (11), are listed in Table 4.

CONCLUSIONS

(1) The enthalpy of solution of anabasine hydrochloride in water at various dilutions was experimentally determined for the first time, and the stan-

Table 4. Standard heats of formation of anabasine derivatives

Compound	$-\Delta_f H^0(298.15)$, kJ mol^{-1}	Compound	$-\Delta_f H^0(298.15)$, kJ mol^{-1}
$C_{10}H_{14}N_2HF$	391	$[C_{10}H_{14}N_2H]_4P_2O_7$	2299
$C_{10}H_{14}N_2HBr$	187	$[C_{10}H_{14}N_2H]H_2PO_2$	674
$C_{10}H_{14}N_2HI$	120	$[C_{10}H_{14}N_2H]_3AsO_4$	1072
$C_{10}H_{14}N_2HClO_4$	197	$[C_{10}H_{14}N_2H]H_2AsO_4$	1013
$C_{10}H_{14}N_2HClO_3$	174	$[C_{10}H_{14}N_2H]_5As_3O_{10}$	2430
$C_{10}H_{14}N_2HBrO_3$	161	$[C_{10}H_{14}N_2H]_2CO_3$	797
$C_{10}H_{14}N_2HIO_3$	317	$[C_{10}H_{14}N_2H]_2C_2O_4$	957
$[C_{10}H_{14}N_2H]_2S$	140	$C_{10}H_{14}N_2HAlO_2$	976
$[C_{10}H_{14}N_2H]_2SO_4$	1037	$C_{10}H_{14}N_2HBO_2$	805
$[C_{10}H_{14}N_2H]_2S_2O_3$	803	$C_{10}H_{14}N_2HReO_4$	904
$[C_{10}H_{14}N_2H]SeO_4$	720	$C_{10}H_{14}N_2HMnO_4$	639
$[C_{10}H_{14}N_2H]_2TeO_4$	890	$[C_{10}H_{14}N_2H]_2Cr_2O_7$	1669
$[C_{10}H_{14}N_2H]_2SO_3$	788	$[C_{10}H_{14}N_2H]_2CrO_4$	1015
$[C_{10}H_{14}N_2H]_2SeO_3$	621	$[C_{10}H_{14}N_2H]_2WO_4$	1217
$[C_{10}H_{14}N_2H]_2TeO_3$	650	$[C_{10}H_{14}N_2H]MoO_4$	1045
$C_{10}H_{14}N_2HNO_3$	279	$C_{10}H_{14}N_2HVO_3$	973
$C_{10}H_{14}N_2HNO_2$	174	$C_{10}H_{14}N_2HNbO_3$	1153
$[C_{10}H_{14}N_2H]_3PO_4$	1444	$[C_{10}H_{14}N_2H]_2Se$	177

dard enthalpy of anabasine hydrochloride solution, standard enthalpies of formation of liquid and crystalline $C_{10}H_{14}N_2HCl$, and its heats of combustion and melting were calculated by indirect methods from these data.

(2) The enthalpy of reaction of aqueous $C_{10}H_{14}N_2 \cdot HCl$ with $AgNO_3$ at various dilutions was determined.

(3) The heat capacity of $C_{10}H_{14}N_2HCl$ was determined over the range 173–448 K, and the equation $C_p^0 = f(T)$ was derived for the 298.15–448 K range.

(4) The standard heats of formation for 36 anabasine derivatives were calculated.

REFERENCES

1. Spiridonov, V.P. and Lopatkin, A.A., *Matematicheskaya obrabotka fiziko-khimicheskikh dannykh* (Mathematical Treatment of Physicochemical Data) Moscow: Mosk. Gos. Univ., 1970.
2. Kazanskaya, A.S. and Skoblo, V.A., *Raschety khimicheskikh ravnovesii* (Calculation of Chemical Equilibria) Moscow: Vysshaya Shkola, 1974.
3. Morachevskii, A.G. and Sladkov, I.B., *Termodinamicheskie raschety v metallurgii* (Thermodynamic Calculations in Metallurgy), Moscow: Metallurgiya, 1985.
4. Kasenov, B.K., Abishev, D.N., and Bukharitsyn, V.O., *Termokhimiya arsenatov shchelochnykh metallov* (Thermochemistry of Alkali Metal Arsenates), Alma-Ata: Nauka, 1988.
5. Kasenov, B.K., Aldabergenov, M.K., and Pashinkin, A.S., *Termodinamicheskie metody v khimii i metallurgii* (Thermodynamic Methods in Chemistry and Metallurgy), Almaty: Rauan, 1994.
6. Mishchenko, K.P, and Poltoratskii, G.M., *Thermodynamika and stroenie vodnykh i nevodnykh rastvorov elektrolitov* (Thermodynamics and Structure of Aqueous and Nonaqueous Solutions of Electrolytes), Leningrad: Khimiya, 1976.
7. Krestov, G.A., *Termodinamika ionnykh protsessov v rastvorakh* (Thermodynamics of Ionic Processes in Solutions), Leningrad: Khimiya, 1984.
8. Platunov, E.S., *Teplofizicheskie izmereniya v rezhime* (Thermal Physical Measurements in Regime), Moscow: Energiya, 1973.
9. Robie, R.A, Hewingway, B.C., and Fisher, I.K., *Thermodynamic Properties of Minerals at 10^5 Pa Pressure and at High Temperatures*, Washington: US Government, 1978.
10. Ryabin, V.A., Ostroumov, M.A., and Svit, T.F., *Termodinamicheskie svoistva veshchestv: Spravochnik* (Thermodynamic Properties of Substances: Handbook), Leningrad: Khimiya, 1977.

Russian Journal of Applied Chemistry, Vol. 76, No. 1, 2003, pp. 33–36. Translated from Zhurnal Prikladnoi Khimii, Vol. 76, No. 1, 2003, pp. 35–38.

PHYSICOCHEMICAL STUDIES OF SYSTEMS AND PROCESSES

Solubility in the Fullerene C_{60}–Fullerene C_{70}–*o*-$C_6H_{14}(CH_3)_2$ System

O. V. Arapov, B. M. Aksel'rod, A. A. Pronkin, N. A. Charykov, and O. Yu. Ryazanova

St. Petersburg State Technological Institute, St. Petersburg, Russia

Received May 23, 2002

Abstract—The solubility diagram of the ternary fullerene-containing system C_{60}–C_{70}–*o*-xylene at 25 and –20°C was studied.

Up to now, there have been virtually no systematic studies on solubility in fullerene-containing multicomponent systems. At the same time, there are published experimental data on the solubility of fullerenes in a number of binary systems like fullerene C_{60}–solvent or fullerene C_{70}–solvent [including aromatic solvents (e.g., benzene, toluene, dichlorobenzenes, xylenes, etc.), CCl_4, CS_2, alkanols, diols, etc.]. Compared to C_{60}, the solubility of C_{70} is studied less comprehensively, apparently, because of its more difficult accessibility. As to polythermal data on the solubility of C_{60} and C_{70}, there are published data for several solvents only (carbon tetrachloride, toluene, hexane, *o*-xylene, *o*-dichlorobenzene, and a few other solvents). These studies covered the temperature range from –20 to 110°C. The experimental data on the solubility of fullerenes C_{60} and C_{70} in the most common solvents were published, in particular, in [1–5].

According to these works, individual fullerenes C_{60} and C_{70} do not form solid solutions with solvents. However, formation of crystal solvates of a fixed composition, e.g., $C_{60}\cdot 2CCl_4$, $C_{60}\cdot 2C_6H_5CH_3$, $C_{60}\cdot 0.5C_6H_5CH_3$, $C_{60}\cdot 2C_6H_4(CH_3)_2$, etc., was reported in [6, 7]. In some cases (e.g., $C_{60}\cdot 2CCl_4$), polythermal phase equilibria in fullerene–solvent system are complicated by polymorphic (α–β) transitions occurring typically at comparatively low temperatures (<0°C). The same holds for crystal solvates of fullerene C_{70} for which formation of crystal solvates is less typical.

We could not find any published data on mutual solubility of two different fullerenes in one solvent or of an individual fullerene in solvent mixtures, except for the work [8] devoted to solubility diagrams in the C_{60}–C_{70}–toluene system at 25°C and in the C_{60}–C_{70}–*o*-xylene system at 80°C. It should be noted that, along with purely scientific interest, studies of the solubility diagrams of such ternary and more complex systems are of undoubted practical interest, associated with the prospects for a more or less complete prechromatographic separation of fullerene mixture components (above all, the main mixture components, C_{60} and C_{70}) based on the difference in their solubilities.

EXPERIMENTAL

In this work, we used fullerenes C_{60} and C_{70} (99.9 and 99 wt % pure, respectively; content of the main determinable impurities ca. 0.1 wt % C_{70} in C_{60} and ca. 1 wt % C_{60} in C_{70}), available from Klaster, St. Petersburg, as well as analytically puregrade *o*-xylene.

In solubility studies for the C_{60}–C_{70}–*o*-xylene system at 25°C, the solution prepared by isothermal saturation for 24 h was evaporated, which yielded *a fortiori* equilibrium (freshly precipitated) solid phase, which was used for repeated isothermal saturation for 4–6 h at 25.00 ± 0.05°C. Thus, we obtained reproducible solubilities of C_{60} and C_{70}, namely, of 9.25 ± 0.1 and 15.17 ± 0.2 g l^{-1}, respectively.

We studied experimentally the solubility in the C_{60}–C_{70}–*o*-xylene system at –20°C by the freezing-out technique. To this end, the prepared solid solution $C_{60}+C_{70}$ ($m \approx 2$ g) and the solvent, *o*-xylene (≅10 ml), were stirred with a magnetic stirrer at 25°C; the saturation time was 48–72 h. The resulting solution was separated from the solid phase by filtration and then placed into a Peltier cooler and frozen out for

1070-4272/03/7601-0033$25.00

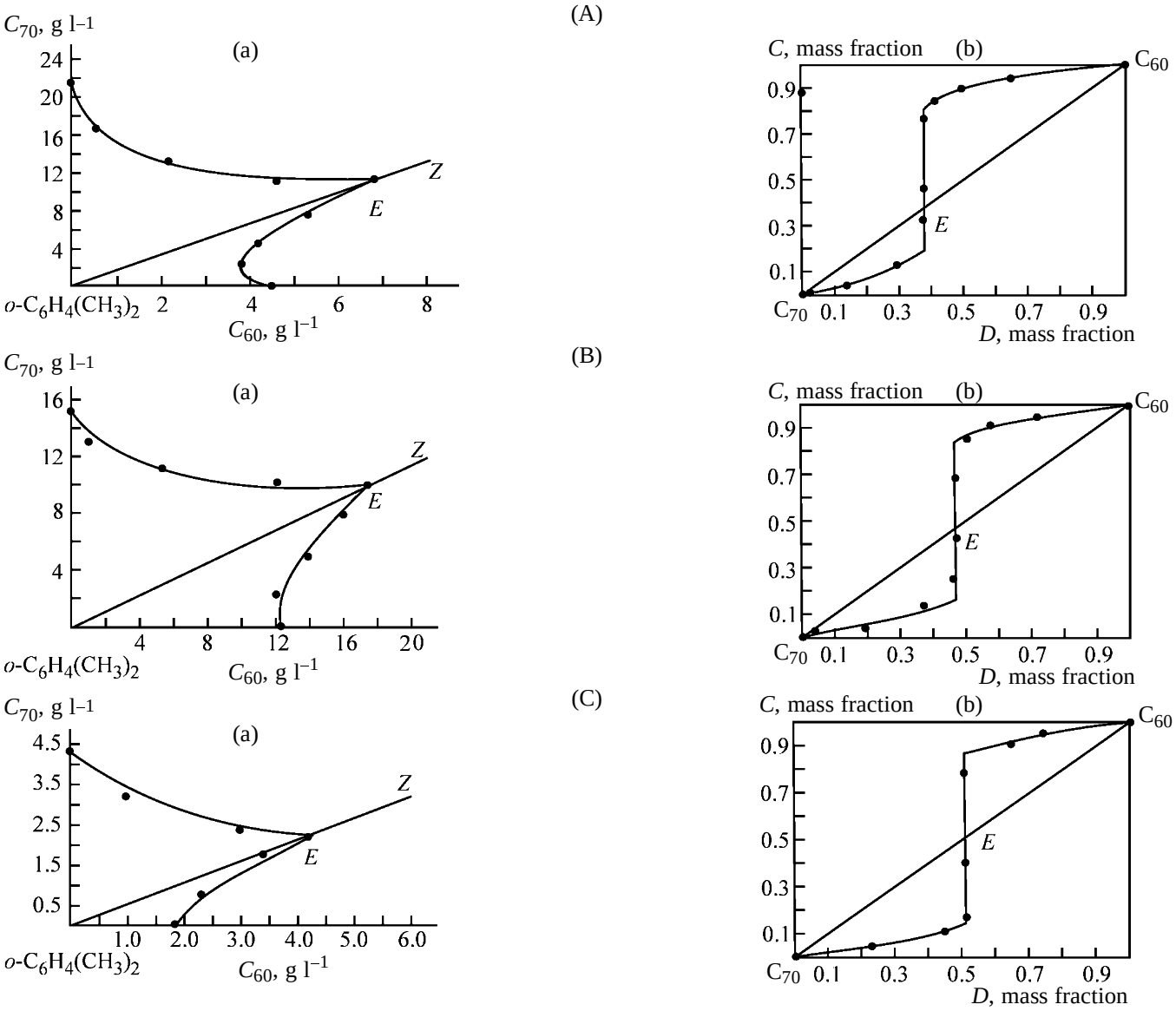

Fig. 1. (a) Solubility diagrams and (b) diagrams of distribution of the fullerene components between the liquid and solid phases in the C_{60}–C_{70}–*o*-xylene system at (A) 80 [8], (B) 25, and (C) –20°C. (C_{70}, C_{60}) Solubility of C_{70} and C_{60}, respectively; (*C*) C_{60} content in solid solution; and (*D*) C_{60} content in liquid solution.

8–10 h at 20 ± 0.2°C with determination of the solution composition at regular intervals. Next, the equilibrium solution of the liquid phase was separated from the solid phase, and the liquid and solid phases were analyzed spectrophotometrically [9]. The solubilities of $C_{60} \cdot 2o\text{-}C_6H_4(CH_3)_2$ and $C_{70} \cdot 2o\text{-}C_6H_4(CH_3)_2$ at –20°C were estimated by this method at 1.81 ± 0.2 and 3.74 ± 0.2 g l^{-1}, respectively.

The content (*x* values) of the fullerene components C_{60} and C_{70} in the solid solutions $(C_{60})_x(C_{70})_{1-x} \cdot n\,o\text{-}C_6H_4(CH_3)_2$ was determined by the Schreinemakers method of wet residues. To determine the content of the solvent in the solid solutions, the solid phase was separated from the mother liquor, washed with diethyl alcohol, dried, weighed, and heated under isothermal conditions at 120°C for 2 h. Next, the solid phase was weighed once again, and the content of the solvent in the solid phase *n* was determined from the mass difference. The experiments yielded for all the solid solutions at –20°C the compositions $(C_{60})_x(C_{70})_{1-x} \cdot n\,o\text{-}C_6H_4(CH_3)_2$ with $n = 2 \pm 0.3$. This is a bisolvate; the deviation from 2 is due to the residual amount of *o*-xylene in the solid phase. At 25°C we observed a mixed pattern: The crystallization branch of C_{60}-rich solid solutions exhibited crystallization of bisolvate solid solutions $(C_{60})_x(C_{70})_{1-x} \cdot$

$2o$-$C_6H_4(CH_3)_2$ with $n = 2 \pm 0.2$, and the crystallization branch of C_{70}-rich solid solutions, crystallization of nonsolvated solid solutions $(C_{60})_x(C_{70})_{1-x}$.

C_{60}–C_{70}–o-$C_6H_4(CH_3)_2$ system (at 80°C). The solubility in this system was studied earlier [8]. For clarity and comparison, we presented in Fig. 1A the solubility diagram and the diagram of distribution of the fullerene components between the liquid and solid phases (the mass fraction of C_{60} in the $C_{60} + C_{70}$ mixture in the liquid and solid phases is the Jaenicke index of the fullerene components).

As seen from Fig. 1A, at 80°C [8] the salting-in effect is observed in the crystallization branch of the C_{60}-rich solid solutions, i.e., the C_{60} solubility tended to increase with increasing C_{70} concentration. By contrast, the crystallization branches of the C_{70}-rich solid solutions exhibited a salting-out effect, i.e., the C_{70} solubility tended to decrease with increasing C_{60} concentration.

At 80°C, substitution solid solution of the composition $(C_{60})_x(C_{70})_{1-x}$ free of o-$C_6H_4(CH_3)_2$ crystallize in the system; a discontinuity is observed in crystallization of solid solutions (the immiscibility region corresponds to $0.21 < x < 0.82$). In addition, there is one nonvariant eutonic point (point *E*) corresponding to mutual saturation with two solid solutions of the same qualitative composition. Also, Ponomarev *et al.* [8] mentioned a peculiar run of the crystallization branch of solid solutions rich in C_{60} [monovariant liquidus curve is almost tangent to the secant *0Z* drawn from the figurative point of the solvent o-$C_6H_4(CH_3)_2$] and showed that this tangency contradicts the criteria of the solution resistance to infinitesimal state changes [10].

Solubility in the C_{60}–C_{70}–o-$C_6H_4(CH_3)_2$ system at 25°C. The experimental data on the composition of the equilibrium liquid phase for this system are presented in Fig. 1B. In this system, the crystallization branch of C_{60}-rich solid solutions also exhibits a salting-in effect (the solubility of C_{60} tends to increase with increasing C_{70} concentration). By contrast, the crystallization branch of C_{70}-rich solid solutions exhibits a salting-out effect (the C_{70} solubility tends to decrease with increasing C_{60} concentration). Figure 1B also shows the distribution diagram (mass fraction of C_{60} in the $C_{60} + C_{70}$ mixture in the liquid and solid phases). The system exhibits a discontinuity in crystallization of solid solutions (it is slightly wider compared to that at 80°C); the immiscibility region corresponds to $0.17 < x < 0.84$; there is one eutonic nonvariant point (point *E*) corresponding to the mutual saturation with two solid solutions of different

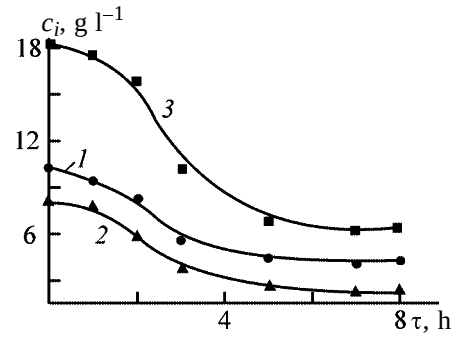

Fig. 2. Variation with the cooling time τ of the concentration of the fullerene components c_i in the solution saturated at 25°C and subsequently cooled in a temperature-controlled cooler at –20°C. (*1*) C_{60}, (*2*) C_{70}, and (*3*) $C_{60} + C_{70}$ (typical data for solution *E* in Fig. 2); the same for Figs. 3 and 4.

qualitative compositions. Figure 1B also shows a peculiar run of the crystallization branch of C_{60}-rich solid solutions: Similar to the case at 80°C, in the close-to-eutonic region, the monovariant liquidus curve is tangent to the secant 0*Z* drawn from the figurative point of the solvent, o-$C_6H_4CH_3$.

Solubility in the C_{60}–C_{70}–o-$C_6H_4(CH_3)_2$ system at –20°C. The solubility diagram at this temperature is of interest in view of the fact that polythermal crystallization in prechromatographic separation of fullerenes always proceeds via low-temperature recrystallization of solid solutions. The melting point of o-xylene is -25.1 ± 0.1, which makes the temperature region much below –20°C inaccessible.

According to our data, the fullerene C_{60}–fullerene C_{70}–o-xylene system at –20°C is characterized by substitution solid solutions of the composition $(C_{60})_x \cdot (C_{70})_{1-x} \cdot 2o$-$C_6H_4(CH_3)_2$ with a discontinuity. The DTA curves of the solid solution $(C_{60})_x(C_{70})_{1-x} \cdot n\,o$-$C_6H_4(CH_3)_2$ obtained for the 25–100°C range suggest the presence of two solvent molecules of crystallization in both kinds of solid solution. The TGA data suggest, for example, that the solid solution $(C_{60})_{0.88}(C_{70})_{0.12} \cdot 2o$-$C_6H_4(CH_3)_2$ loses the crystallization o-xylene in two stages within 43–72°C. The temperature corresponding to the loss of the crystallization solvent is strongly dependent on the composition of the primary bisolvate and decreases by tens of degrees with increasing mass fraction of C_{70} (decrease of *x*).

Figure 1C shows the experimentally determined composition of the equilibrium liquid phase. At –20°C, this system exhibits a salting-in effect in the crystallization branch of C_{60}-rich solid solutions and a salting-out effect in that of C_{70}-rich solid solutions. Figure 1C also shows the distribution diagram indicat-

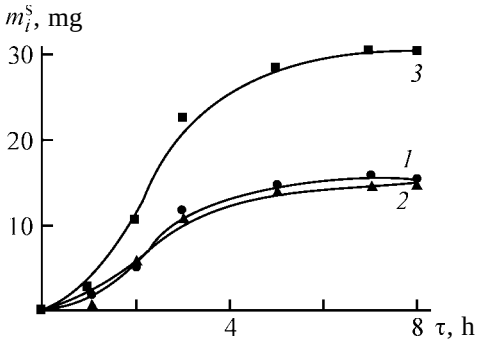

Fig. 3. Variation with time τ of the mass of the fullerene components m_i^s in the solid solutions obtained upon cooling in a temperature-controlled cooler (–20°C) 2.5 ml of the solution saturated at 25°C.

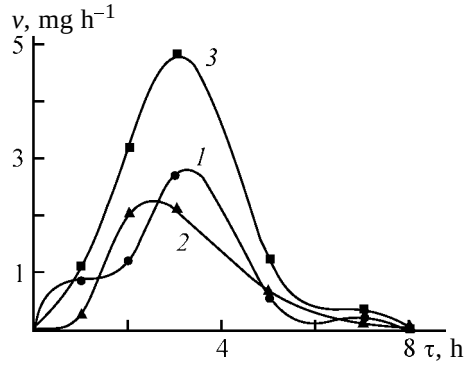

Fig. 4. Variation with the cooling time τ of the freezing-out rate for the solid solution $(C_{60})_x(C_{70})_{1-x} \cdot 2o\text{-}C_6H_4(CH_3)_2$ obtained upon cooling in a temperature-controlled cooler (–20°C) 2.5 ml of the solution saturated at 25°C. $v = dm/dt$ is the solid phase separation rate.

ing that the system exhibits a discontinuity in crystallization of solid solutions; the immiscibility region gets even wider and now corresponds to $0.14 < x < 0.86$. Also, the system has one eutonic nonvariant point (point *E*) corresponding to mutual saturation with two solid solutions of the same qualitative composition. In this case, similar to the cases of 80 and 25°C, the monovariant liquidus curve is nearly tangent to the secant 0*Z* drawn from the figurative point of the solvent *o*-$C_6H_4CH_3$.

Studies of freezing-out of fullerenes at –20°C revealed a peculiar fact. Thermodynamically, the presence of a solid phase in a crystalline form implies "a perturbation of the solution corresponding to finite changes in the state" [10]; hence, in our case, further separation of the solid phase to attain steady-state solution concentrations proceeded at a very low rate, namely, within several hours (Figs. 2–4). This involved changes in the composition of the "supersaturated solution" (Fig. 2) and the mass of the fullerenes separated into the solid phase (Fig. 3). Figure 4 shows that the rate of separation of the fullerene components varies nonmonotonically; this process is characterized by a certain "pseudoinduction" period (0.5–1 h); the separation rate attains a maximum (after 2–4 h), and only then it tends to decrease to zero (after 8–10 h). This period is unusually long, and this very fact by no means fits the classic phase formation theory.

CONCLUSIONS

(1) An experimental study of the phase diagram of the C_{60}–C_{70}–*o*-xylene system at –20°C revealed formation of extremely slowly degrading metastable states corresponding to supersaturated liquid solutions.

(2) Comparison of the solubility diagrams of the ternary system C_{60}–C_{70}–*o*-xylene at 80, 25, and –20°C showed the identity of the phase diagrams at all the three temperatures: Each diagram exhibits two crystallization branches of solid solutions (solvated and nonsolvated) of the fullerenes in each other, exhibiting a discontinuity and a eutonic nonvariant.

(3) The topology of the phase diagrams of the C_{60}–C_{70}–*o*-xylene system in polythermal conditions suggests the principal possibility of separation of C_{60} and C_{70} (and probably of other fullerenes) by polythermal recrystallization.

REFERENCES

1. Xihuang, Z., Zhemnan, G., Wu, J., *et al*., *Carbon*, 1994, vol. 32, pp. 935–948.
2. Sivaraman, N., Dhamodaran, R., Kalliapan, I., *et al*., *J. Electrochem. Soc*., 1994, vol. 141, pp. 156–189.
3. Ceolin, N., Agafonov, V., Andre, D., *et al*., *Chem. Phys. Lett*., 1993, vol. 208, no. 34, pp. 259–267.
4. Kushch, N.D., Majchrzak, I., Ciesielski, W., *et al*., *Chem. Phys. Lett*., 1993, vol. 215, pp. 317–321.
5. Bezmel'nitsyn, X.X., Eletskii, A.V., and Okun', M.V., *Physics—Uspekhi*, 1998, vol. 41, no. 14, pp. 1091–1114.
6. Korobov, M.V., Mirakyan, A.L., Avramenko, N.V., *et al*., *J. Phys. Chem. B*, 1999, vol. 103, pp. 1339–1349.
7. Avramenko, N.V., Mirakyan, A.L., Korobov, M.V., *et al*., *J. Thermal Anal. Calorim*., 1998, vol. 52, no. 3, pp. 831–849.
8. Ponomarev, A.N., Aksel'rod, B.M., Barchenko, V.T., *et al*., *Zh. Fiz. Khim*., 2000, vol. 74, no. 11, pp. 2031–2034.
9. Ponomarev, A.N., Yudovich, M.E., Charykov, N.A., *et al*., *Opt. Spectrosk*., 2002, vol. 88, pp. 195–198.
10. Storonkin, A.V., *Termodinamika geterogennykh sistem* (Thermodynamics of Heterogeneous Systems), Leningrad: Leningr. Gos. Univ., 1967, parts 1, 2; 1969, part 3.

Russian Journal of Applied Chemistry, Vol. 76, No. 1, 2003, pp. 37–43. Translated from Zhurnal Prikladnoi Khimii, Vol. 76, No. 1, 2003, pp. 39–45.

PHYSICOCHEMICAL STUDIES OF SYSTEMS AND PROCESSES

Extraction Equilibria in the Fullerene C_{60}–Fullerene C_{70}–Solvent Systems

O. V. Arapov, A. A. Pronkin, N. A. Charykov, V. I. Seregin, and K. B. Strel'nikov

St. Petersburg State Technological Institute, St. Petersburg, Russia

Received May 23, 2002

Abstract—A new method was proposed for separation of light fullerenes C_{60} and C_{70} based on realization of two-phase extraction equilibria in multicomponent fullerene-containing systems C_{60}–C_{70}–solvent I–solvent II and C_{60}–C_{70}–solvent I–solvent II–"inert component." The principal possibility and high efficiency of the extraction separation of light fullerenes were demonstrated.

The presently known regularly structured carbon forms are subdivided into molecular and covalent crystals. Molecular crystals are formed from individual cluster molecules. Covalent crystals are characterized by polymeric structures. It is convenient to describe the structure of covalent clusters in terms of infinite graphs. Diamond is characterized by a fourth-order uniform graph. By realizing this graph in a three-dimensional space, it is possible to depict the diamond structure corresponding to the closest packing of carbon atoms. Graphite is described by a disconnected graph consisting of an infinite number of two-dimensional lattices. Each lattice can be realized on a plane as a hexagonal network. The third allotropic modification of carbon, carbyne, is described in terms of infinite number of simple paths which all can be arranged on a straight line. In 1973, Soviet chemists Bochvar and Gal'perin [1] performed theoretical calculations and concluded that carbo-*s*-icosahedron should be a stable molecule with a singlet ground state.

In the middle 1980s, astrophysicists, using new optical spectrophotometers, revealed in the spectra of "carbon stars" (red giants) and comet tails an absorption band at 216 nm. Researchers assumed that such objects and interstellar dust can contain small clusters of carbon atoms, C_n. American physicists Rolling, Cox, and Calder tested an assumption that C_n can exist under laboratory conditions. They performed high-vacuum evaporation of graphite when exposed to a powerful laser beam. Using a mass spectrometer, these researchers detected in a graphite vapor a set of C_n clusters containing 1–150 carbon atoms. It should be noted that small clusters ($n < 40$) contained both even and odd numbers of carbon atoms, and larger ones, even numbers only. In 1985, Kroto *et al*. [2] reproduced this experiment, though under somewhat different conditions, and obtained mass spectra with peaks corresponding to m/z of 720 and 840. Kroto *et al*. assumed that these peaks correspond to individual molecules, C_{60} and C_{70}, and advanced a hypothesis that the C_{60} molecule has a form of a truncated icosahedron with the I_h symmetry, and the C_{70} molecule, a more extended ellipsoid-like structure with the D_{5h} symmetry. These assumptions were subsequently confirmed. Polyhedral carbon clusters were termed fullerenes.

A detailed mechanism of formation of fullerenes still remains to be elucidated. By now, only general ideas have been advanced concerning the carbon skeleton growth via successive addition of C_2 particles, which, evidently, dominate in graphite vapor [3].

The structural difference between fullerenes and graphite consists, above all, in that the former comprise pentagons. The very first pentagon surrounded by hexagons gives corannulene with a nonplanar structure. The same result can be obtained with formation of a heptagon [4]. The peculiar structural features of fullerenes, namely, all bonds unsaturated and no substituents, allow only two types of primary reactions: detachment of electrons and addition of electrons or groups. Fullerenes exhibit electrophlicity and are good electron acceptors. They are prone to addition of nucleophiles, as well as of free radical and carbenoid moieties. Virtually all the reactions known for fullerenes were realized for C_{60} and C_{70}. As to the chemical properties of higher fullerenes, the information is scarce.

Certain physical properties and structure of ful-

1070-4272/03/7601-0037$25.00

lerene C_{60} were reported by Prassides *et al*. [5]: cubic crystal structure, space group *Fm*3*m* (T > 260 K) and *Pa*3 (T < 260 K); carbon cage diameter 7.1 Å; bond length C=C 1.391, C–C 1.455 Å; nonvalent distance between the C_{60} molecules in a crystal 3.1 Å; volume modulus 18 GPa; density 1.65 g cm^{-3}. Spectral characteristics: electron affinity 2.6–2.8 eV; ionization potential 7.6 eV; band gap 1.9 eV; ^{13}C NMR chemical shift 142.68 ppm; IR frequencies 528, 577, 1183, 1429 cm^{-1}; Raman frequencies 1250, 1422, 1467, 1573 cm^{-1}; and refractive index 2.2 (630 nm). The structure of the C_{70} cluster was determined by electron diffraction [6]. It was found that it has a fullerene-type structure of the ellipsoidal form, point group D_{5h}. The C–C bond length varies from 1.37 to 1.47 Å. The shortest bonds are those linking the vertices of two different pentagons, and the longest are those located in five-membered rings. The "height" of the molecule is equal to 7.8 Å. The equatorial section of C_{70} has a diameter of 6.94 Å. Formally, the D_{5h}-C_{70} cluster can be obtained from two halves of the C_{60} cluster with five pairs of carbon atoms inserted in the equatorial plane.

The D_{5h}-C_{70} cluster, similar to I_h-C_{60}, contains only isolated five-membered rings. The C_{70} molecule contains atoms of five types, and its spectra exhibit the corresponding number of signals. The carbon atoms in C_{70} molecule are nonequivalent, which is responsible for different chemical shifts observed in the ^{13}C NMR spectra. Fowler [7] and Iijima [8] discussed the structures of higher fullerenes with the number of carbon atoms $n \geq 84$, as well as of those with a greater n (giant fullerenes), including extended fullerene-type carbon structures. It was suggested to simulate the structure of giant fullerenes by spherical models. It can be assumed that giant fullerenes have a complex "matreshka" or bulb-like structure. Certain giant fullerenes can have a cylindrical form or give more complex network structures (capsulenes, barrelenes, tubulenes, torenes) [8].

By now, crystalline C_{60} samples and doped systems like M_nC_{60} have been synthesized. Such salts with alkali metals at n = 3 exhibit superconducting properties: compounds with K ions have T_c = 18 K and those with Rb ions, T_c = 28 K [9]. The reliably reproducible critical temperature T_c achieved for the cesium–rubidium salt Cs_2RbC_{60} is equal to 33 K [5]. It was found that superconducting transition temperatures for some halogen-doped fullerenes exceed 60 K [10]. Fullerenes were used for preparing films having nonlinear optical properties suitable for application in optical limiters (shutters) and light diodes, as well as for generation of third harmonics in optical laser radiation. Also described are optical elements consisting of fullerene C_{60}, which exhibits high nonlinear third-order susceptibility, and a polymer or a glass as the binder [11]. Thin fullerene films are used in wave guides. Materials having magnetic properties were prepared by dispersing globular C_n (n = 60, 70, 84) bound to La, Na, K, Cs, or Rb ions in a polymeric material [12]. Magnetic materials containing C_n exhibit stable ferromagnetic properties at room temperature and can be easily prepared. Materials containing C_{60} and its derivatives are suitable for tunnel diodes, electroluminescent devices, organic solar elements, optical memory devices, field-effect transistors, etc. [13].

Fullerenes exhibit photoelectric properties such as photoconductivity and photovoltaic effect. This makes them suitable for manufacturing various devices underlain by induced processes such as current generation by illuminating fullerene interfaces. Semiconductor materials containing C_{60} or C_{70} are responsible for rectifying and photosensitive properties of devices utilizing these materials. It was shown [14] that heterostructures based on semiconducting conjugated polymers and acceptors chosen from amongst fullerenes are suitable as photodiodes and photovoltaics; also described is their use as optical memory cells. The experiments reported in [15, 16] showed that crystalline C_{60} powder can be converted to diamond by nonhydrostatic compression. This allows preparation of diamond-like (possibly, optically transparent in the visible range) films with physical and chemical properties close to those of single-crystalline diamond. This application field of fullerenes and/or their mixtures seems the most promising today.

Intercalation compounds of fullerenes with transition metals exhibit a catalytic effect in hydrogenation; they can be prepared by reaction of transition metal compounds with fullerene or fullerene-containing soot, involving activation in solution [17]. Hydrogenated or fluorinated fullerenes are suitable as solid lubricants or additives to lubricating oils [18]. Fullerene-containing fuel compositions were developed for internal-combustion engines; they include gasoline, allotropic forms of carbon soluble in hydrocarbons, and a dispersing agent [19]. Engines utilizing such fuel compositions are characterized by reduced emissions of undesired exhaust gases. Compounds containing fullerenes and hydrogenated catalysts are suitable for application in adsorption, concentration, and purification processes, as well as for storage, transfer, hydrogen reduction, and regeneration of acid

storage batteries [20]. Electric batteries also utilize fullerene-containing anodes and/or cathodes. Solar cells employ C_{60}-doped semiconductors for creating *n*, *i*, and *p* conductivities in formation of homo- and heterojunctions. Such solar cells have long service lives, and their manufacture requires no toxic materials [21].

In 1990, Kratchmer *et al*. [22] described for the first time a method for preparing several grams of carbon clusters by graphite electrode burning in an electric arc under He. The mass ratio of the main components obtained by this procedure, C_{60}/C_{70}, is typically 4/1. The content of higher clusters is ca. 1% of the fullerene mass. Also, fullerenes can be prepared by heating carbon-containing compounds in a hot plasma in front of a refractory shielding plate for collecting fullerene-containing solid products. Another method for preparation of fullerenes is burning carbon-containing substances (e.g., C_6H_6) at 1400–3000 K followed by collection of fullerene-containing condensates with the C_{70}/C_{60} ratio within 0.26–5.7 [24]. The yield and composition of fullerenes are governed by selectively controlled burning conditions and other parameters such as the C/O ratio, pressure, temperature, keeping time, diluent concentration, and gas supply rate. Also, graphite can be heated by directly passing electric current or using ultra-high-frequency radiation under an inert gas atmosphere [25, 26].

The resulting mixture of fullerene-containing products should be separated. This is usually done by fullerene extraction from fullerene soot [27, 28]. Light fullerenes C_{60} and C_{70} can be separated by different methods: chromatography [28, 29], low-pressure sublimation [30], or a method based on the difference in the polythermal solubilities of light fullerenes [29, 31, 32]. The latter method is of interest, above all, for prechromatographic separation of fullerenes; it allows isolation of individual 90–95% pure fullerenes in a yield of up to 80% of the total fullerene content.

EXPERIMENTAL

In this work, fullerenes were synthesized by the standard method of graphite rod erosion in a high-temperature plasma under helium [22]. This yielded fullerene-containing soot with a total fullerene content of ca. 8.4 wt %. The fractional composition, %, of fullerenes was as follows: C_{60} 81.3, C_{70} 17.9; sum of higher fullerenes C_{76}, C_{84}, etc. 0.8. Next, the fullerene mixture was extracted with *o*-xylene in a Soxhlet-type counterflow extractor. The residual amount of the fullerene sum in the fullerene soot was under 0.1%. The fullerene mixture in the form of *o*-xylene solutions with a total fullerene concentration of ca. 7.8 g l^{-1} was separated chromatographically on two series-connected columns packed with graphite-like filler. This gave C_{60} and C_{70} of 99.9 and 99.0 wt % purity, respectively (the only significant impurity is C_{70} in C_{60} and C_{60} in C_{70}) in the yields of 85 and 60%, respectively. The concentrations of fullerenes C_{60} and C_{70} in the liquid phase were determined spectrophotometrically from the optical densities of solutions in *o*-xylene at the wavelengths λ_1 = 335.7 and λ_2 = 472.0 nm [33]; solid mixtures of fullerenes were first dissolved without residue in *o*-xylene and then analyzed similarly. The concentrations of organic solvents (*o*-xylene, isobutylamine, monoethanolamine, etc.) in the coexisting phases were determined chromatographically on 3700 (Khromatograph plant, Moscow) and LKhM-8MD (N_2 carrier gas, Chromaton N AW DMCS, mobile phase PEG-6000) gas chromatographs. In analysis of liquid phases for H_2O content we used helium as the carrier gas and Porapak Q as the sorbent. The content of the solvents in the solid phases was determined gravimetrically, by evaporation to a constant weight at a temperature of up to 150°C and residual pressure of about 15 mm Hg.

The aim of this work is to test the suitability, in principle, of the extraction methods based on realizing two-phase liquid I–liquid II equilibria for separation and purification of the fullerene components. As far as we know, such equilibria in fullerene-containing systems have not been studied previously.

Suitable for this purpose are systems whose main components (solvents) have a fairly large concentration range of immiscibility. The physicochemical properties of the coexisting phases should differ significantly; in this case, the distribution coefficients of the fullerene components between the phases can be expected to differ significantly from unity. The distribution coefficients should also be significantly different for fullerenes C_{60} and C_{70}. The most rigorous requirement related to the process feasibility is that the solubility of fullerenes C_{60} and C_{70} in both equilibrium phases should be significant, namely, no less than 50–100 mg of fullerenes in 1 l of solution.

Fullerene C_{60}–fullerene C_{70}–*o*-xylene–isobutylamine–H_2O system at 25°C. Analysis of the coexisting phases showed that the content, wt %, of the main components of the solvent (*o*-xylene, isobutylamine, and H_2O) is as follows: *o*-xylene 3, isobutylamine 81, H_2O 16 for the lower (amine) phase and *o*-xylene 65, isobutylamine 35, and H_2O 0.1 for the upper

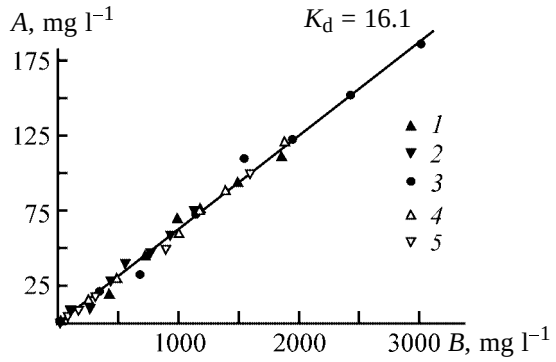

Fig. 1. Distribution of fullerenes C_{60} and C_{70} between the amine and *o*-xylene phases at 25°C. Fullerene content in (*A*) isobutylamine and (*B*) *o*-xylene phase. System: (*1–3*) C_{60}–C_{70}–*o*-xylene–isobutylamine–H_2O, (*4*) C_{60}–*o*-xylene–isobutylamine–H_2O, and (*5*) C_{70}–*o*-xylene–isobutylamine–H_2O. Fullerene: (*1, 4*) C_{60}, (*2, 5*) C_{70}, and (*3*) $C_{60} + C_{70}$.

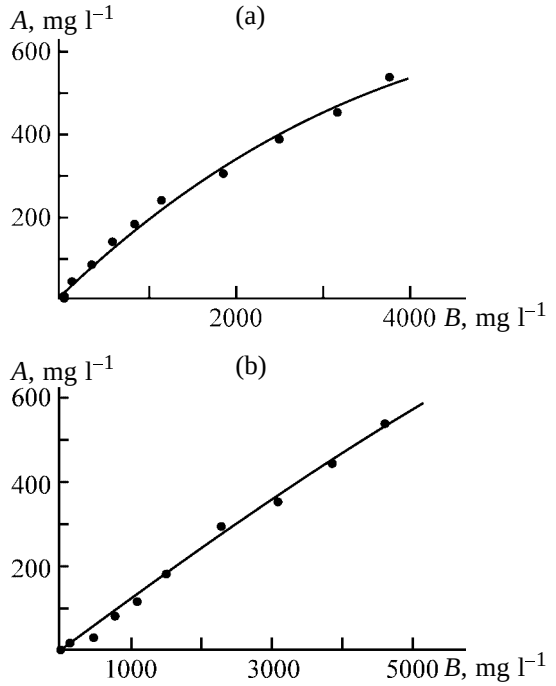

Fig. 2. Distribution of fullerenes (a) C_{60} and (b) C_{70} between the monoethanolamine and *o*-xylene phases in the fullerene C_{60}–fullerene C_{70}–*o*-xylene–monoethanolamine system at 25°C. Content of fullerenes C_{60} and C_{70} in (*A*) *o*-xylene and (*B*) monoethanolamine phase.

(xylene) phase. The content of these components in the phases is virtually independent of the fullerene content, as the coexisting phases are extremely dilute with respect to fullerene components. The total mole fraction of these components was estimated at $X_f \cong 10^{-4}$–10^{-6} and $X_f \cong 10^{-3}$–10^{-5} for the amine and xylene phases, respectively.

Figure 1 shows the distribution of the fullerene components C_{60} and C_{70} between the amine and xylene phases for the quaternary systems C_{60}–*o*-xylene–isobutylamine–H_2O and C_{70}–*o*-xylene–isobutylamine–H_2O and the quinary system C_{60}–C_{70}–*o*-xylene–isobutylamins–H_2O at 25°C. In these diagrams, the content of the macrocomponents (*o*-xylene, isobutylamine, and H_2O) is fixed, as well as the ratio of fullerenes C_{60} and C_{70} in the quinary system. The obtained distribution diagrams proved to have an unexpectedly simple form of straight lines (this allowed their uniform geometric representation in Fig. 1). The distribution coefficients of C_{60} and C_{70} in all the three studied systems proved to be invariant, irrespective of whether both or one of the fullerenes were present in solution (the fullerenes did not compete during extraction and were extracted independently). Moreover, the distribution coefficients of both fullerenes C_{60} and C_{70} proved to be equal, namely, $K_d = 16.1$.

This fact is fairly difficult to interpret. Straight-line distribution diagrams are typical, above all, for systems with ideal (with respect to the components being extracted) phases. It is unlikely that fullerenes are extracted in the form of monomers solvated by solvent molecules (in any case, this contradicts the data reported by Golubkov *et al*. for *o*-xylene solutions [34, 35]). It remains to be suggested that fullerenes form a mixture of individual associates like $(C_{60})_p(Solv)_{rl}$ and $(C_{70})_q(Solv)_{r2}$ and are extracted in these forms, and the coexisting phases are ideal specifically with respect to the extracted species rather than to unassociated monomers.

The fact that the distribution coefficients in extraction of C_{60} and C_{70} are identical means that extraction separation in the fullerene C_{60}–fullerene C_{70}–*o*-xylene–isobutylamine–H_2O system is impossible.

Fullerene C_{60}–fullerene C_{70}–*o*-xylene–monoethanolamine system at 25°C. Figures 2a and 2b show the distribution of the fullerene components C_{60} and C_{70} between the monoethanolamine and *o*-xylene phases in the quaternary system C_{60}–C_{70}–*o*-xylene–monoethanolamine at 25°C.

The content of the macrocomponents, *o*-xylene and monoethanolamine, is fixed in the diagram (because of the extremely low mutual solubility of *o*-xylene and monoethanolamine of ca. 1 wt %). Also fixed is the overall ratio of C_{60} and C_{70} (46.5 wt % C_{60}). Figure 3 presents the relative mass content of C_{60} (in the $C_{60} + C_{70}$ mixture) in the coexisting phases as a function of the C_{70} concentration in the monoethanolamine phase of the C_{60}–C_{70}–*o*-xylene–monoethanol-

amine system at 25°C. For clarity, the overall composition of the fullerene mixture being distributed (Y_{ov} = 46.5 wt % C_{60}) is shown with a dotted line.

The distribution diagrams for the C_{60}–C_{70}–*o*-xylene–monoethanolamine system are more complex than those for the fullerene C_{60}–fullerene C_{70}–*o*-xylene–isobutylamine–H_2O system. The distribution diagrams for C_{60} and C_{70} are curved (concave toward the concentration simplex axes) throughout the concentration range studied. It should be noted that, in the case of fullerene C_{60} (Fig. 2a), the curvature is much stronger compared to C_{70} (Fig. 2b). At all the concentrations, the monoethanolamine phase is richer in both fullerenes than the *o*-xylene phase, since the coefficients of fullerene distribution between these phases are always significantly over unity. Figures 2a and 2b suggest that, with increasing concentration, the distribution coefficients for C_{60} tend to monotonically increase from ca. 2 (for dilute solutions with the total fullerene concentration in the monoethanolamine phase c_f < 100 mg l^{-1}) to 7 (for concentrated solutions with the maximal total concentration $c_f \cong$ 8400 mg l^{-1}). By contrast, the distribution coefficients for C_{70} tend to monotonically decrease with increasing concentration from 12 (for dilute solutions) to 8.5 (for concentrated solutions). Figure 3 shows that, with increasing total fullerene concentration, the relative mass concentration of C_{60} (in the C_{60} + C_{70} mixture) in the coexisting phases gradually approaches the overall composition of the mixture being distributed (Y_{ov} = 46.5 wt % C_{60}), shown in Fig. 3 with a dotted line. In solutions dilute with respect to the fullerene components, fullerene C_{70} passes predominantly (relative to C_{60}) to the monoethanolamine phase, and fullerene C_{60}, to the *o*-xylene phase. In concentrated solutions, this effect is leveled. The relative contents of fullerene C_{60} (in C_{60} + C_{70} mixture) in the coexisting phases approach each other and the overall composition of the fullerene mixture, i.e., the selectivity of the phase distribution for C_{60} and C_{70} is lost.

Thermodynamically, it is fairly clear that the coexisting phases (or even one of them) are nonideal with respect to extractable species (Figs. 2, 3). The fact that both phases are nonideal with respect to nonassociated fullerene components C_{60} and C_{70} was mentioned earlier [34, 35]. However, the appearance of the distribution diagrams suggests that at least one of the liquid phases in the system under study is not even ideally associated, i.e., it is not ideal with respect to the associated and solvated extractable fullerene species. We observed such ideal association in the case of the fullerene C_{60}–fullerene C_{70}–*o*-xylene–isobutylamine–H_2O system. In view of the facts that the system with isobutylamine also contains the *o*-xylene-based phase and that the distribution diagrams for the fullerene components are straight lines, it can be assumed that specifically the monoethanolamine phase is nonideally associated.

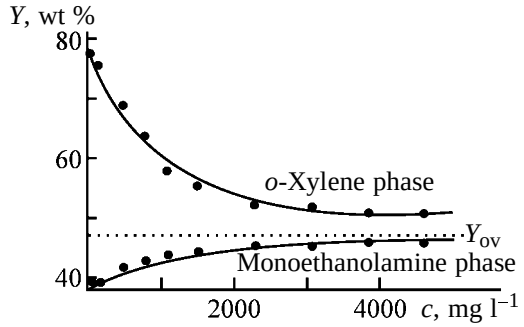

Fig. 3. Relative content of C_{60} (in the C_{60} + C_{70} mixture) *Y* in the coexisting phases as a function of the C_{70} concentration *c* in the monoethanolamine phase of the fullerene C_{60}–fullerene C_{70}–*o*-xylene–monoethanolamine system. Dotted line: overall composition of the fullerene mixture being distributed, Y_{ov} = 46.5 wt % C_{60}.

It should be noted that fullerenes C_{60} and C_{70} can be separated by extraction in the fullerene C_{60}–fullerene C_{70}–*o*-xylene–monoethanolamine quaternary system at 25°C. Figures 2 and 3 suggest that the fullerene components can be efficiently separated only in the case of comparatively dilute solution with the total fullerene concentration c_f < 2000 mg l^{-1}. The best results are obtained at still lower concentrations: c_f < 500 and even $c_f \ll$ 100 mg l^{-1}. It should be mentioned, however, that very dilute solutions (c_f < 100 mg l^{-1}) are unfavorable, because large amounts of the solvents involved, which should be subsequently evaporated, make the process power- and labor-consuming. At high concentrations (c_f > 2000 mg l^{-1}), the separation is also inefficient because of fairly low separation factors. Hence, the optimal concentration for separation of C_{60} + C_{70} mixtures of an averaged composition (from 20 to 80 wt % of C_{60} in the C_{60} + C_{70} mixture) is 500 ± 200 mg l^{-1}.

Fullerene C_{60}–fullerene C_{70}–*o*-xylene–dimethylformamide (DMF)–H_2O system at 25°C. Analysis of the system showed that the content, wt %, of the main solvent components (*o*-xylene, DMF, and H_2O) in the coexisting phases is as follows: *o*-xylene 14, DMF 67, and H_2O 19 in the lower (DMF) phase, and *o*-xylene 48, DMF 44, and H_2O 8 in the upper (*o*-xylene) phase.

Figures 4a and 4b show the distribution of the fullerene components C_{60} and C_{70} between the DMF and *o*-xylene phases in the C_{60}–C_{70}–*o*-xylene–DMF–

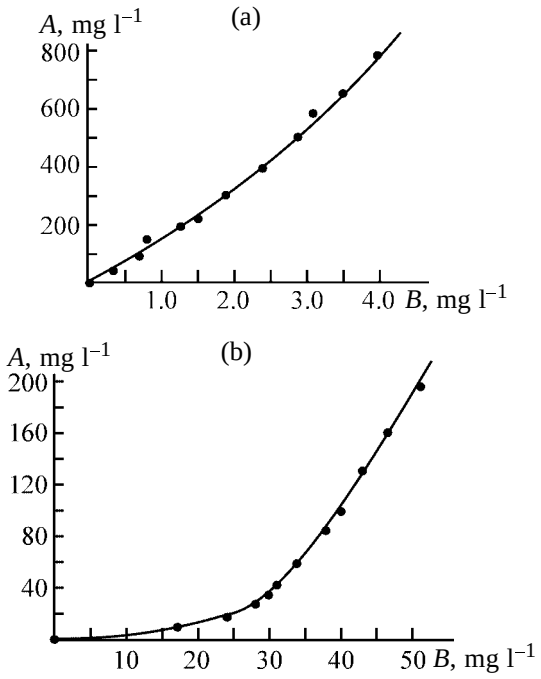

Fig. 4. Distribution of (a) C_{60} and (b) C_{70} between the DMF and *o*-xylene phases in the fullerene C_{60}–fullerene C_{70}–*o*-xylene–DMF–H_2O system at 25°C. C_{60}, C_{70} fullerene content in (*A*) *o*-xylene phase and (*B*) DMF phase.

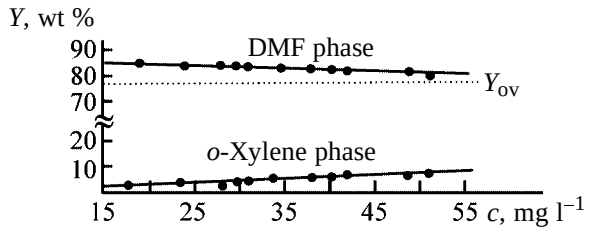

Fig. 5. Relative content of C_{60} in the $C_{60} + C_{70}$ mixture in the coexisting phases *Y* as a function of the C_{70} concentration *c* in the DMF phase of the fullerene C_{60}–fullerene C_{70}–*o*-xylene–DMF–H_2O system at 25°C. Dotted line: overall composition of the fullerene mixture being distributed, Y_{ov} = 77.7 wt % C_{60}.

H_2O quinary system at 25°C. The overall composition of the C_{60}–C_{70} mixture used was fixed at 77.7 wt % C_{60}.

The distribution diagrams for C_{60} and C_{70} also proved to be curved throughout the concentrated range studied. It should be noted that, in the distribution diagram for fullerene C_{70}, the curvature is much stronger compared to C_{60}, and the *o*-xylene phase is always richer in both fullerenes than the DMF phase. The distribution coefficients (the concentration ratio of the *o*-xylene to DMF phase) vary for C_{60} insignificantly with increasing concentration and are estimated at ca. 200 (Fig. 4a). The distribution coefficients for C_{70} vary more strongly with increasing concentration; they monotonically increase from 1 (for dilute solutions with the C_{70} concentration in the *o*-xylene phase of under 20 mg l^{-1}) to 4 (for concentrated solutions with the C_{70} concentration in the *o*-xylene phase of over 200 mg l^{-1}) (Fig. 4b).

Of principal importance is the fact that the separation factor equal to the ratio of the C_{60} and C_{70} distribution coefficients is large, namely, $50 < K_s < 200$, which offers promise for phase separation. Indeed, the *o*-xylene phase predominantly accumulates C_{60} (80–84 wt %), and the DMF phase, C_{70} (92–97 wt %). Figures 4 and 5 suggest that the separation is the most efficient in dilute solutions, though in comparatively concentrated solutions the separation is very efficient as well. Evidently, the optimal concentrations for separation of C_{60} and C_{70} are 800–1000 mg l^{-1}. It is impossible to markedly increase the total fullerene concentration in solution relative to the indicated range, as a solid phase is immediately formed in the DMF phase, which disturbs the extraction equilibrium.

Thermodynamically, Figs. 4 and 5 also suggest that both coexisting phases are nonideal with respect to the extractable species.

CONCLUSIONS

(1) The extraction equilibria liquid I–liquid II were studied in the C_{60}–C_{70}–*o*-xylene–monoethanolamine quaternary system and C_{60}–C_{70}–*o*-xylene–dimethylformamide–H_2O and C_{60}–C_{70}–*o*-xylene–isobutylamine–H_2O quinary systems at 25°C.

(2) The diagrams of distribution of the fullerene components between the coexisting liquid phases were obtained. It is possible to achieve noticeable extractive separation of C_{60} and C_{70} in the monoethanolamine system at the total fullerene concentration in the *o*-xylene phase of 500 ± 200 mg l^{-1}. The optimal concentration for separation in the dimethylformamide system is $c_f = 900 \pm 100$ mg l^{-1}. No extractive separation was achieved in the isobutylamine-containing system.

ACKNOWLEDGMENTS

This work was financially supported by the Council for Grants at the RF President's Office (project code 00-15-99334).

REFERENCES

1. Bochvar, D.A. and Gal'perin, E.G., *Dokl. Akad. Nauk SSSR*, 1973, vol. 209, pp. 610–612.

2. Kroto, H.W., Heath, J.R., O'Brien, S.C., *et al*., *Nature*, 1985, vol. 318, pp. 162–163.
3. Smalley, R.E., *Acc. Chem. Res*., 1992, vol. 25, pp. 98–107.
4. Sokolov, V.I., Troitskaya, L.L., and Bulygina, L.A., *Izv. Ross. Akad. Nauk, Ser. Khim*., 1993, no. 10, pp. 1799–1802.
5. Prassides, K., Kroto, H.W., Taylor, R., *et al*., *Carbon*, 1992, vol. 30, no. 8, pp. 1799–1802.
6. McKenzie, D.R., Davis, C.A., Cockayne, D.J.H., *et al*., *Nature*, 1992, vol. 355, pp. 622–624.
7. Fowler, P.W., *J. Chem. Soc., Faraday Trans*., 1990, vol. 86, no. 12, pp. 2073–2077.
8. Iijima, S., *Nature*, 1991, vol. 354, pp. 56–59.
9. Haddon, R.C., *Acc. Chem. Res*., 1992, vol. 25, pp. 127–133.
10. US Patent 5380703.
11. JPN Patent 06102547.
12. JPN Patent 05109121.
13. JPN Patent 06273811.
14. US Patent 5331183.
15. Sandre, E. and Cyrot-Lackmann, F., *Solid State Commun*., 1994, vol. 90, pp. 431–437.
16. Canadian Patent 02059185.
17. EUR Patent 635515.
18. JPN Patent 60-24720.
19. US Patent 5234474.
20. JPN Patent 05270801.
21. Ajil, H., Alvarez, M.M., Anz, S.J., *et al*., *J. Phys. Chem*., 1990, vol. 94, pp. 8630–8633.
22. Kratchmer, W., Lamb, L.D., Fostiropoulos, K., *et al*., *Nature*, 1990, vol. 347, pp. 354–359.
23. JPN Patent 06032606.
24. US Patent 5273729.
25. French Patent 2710049.
26. EUR Patent 568918.
27. US Patent 5904852.
28. Chatterjee, K., Parker, D.H., Wurz, P. *et al*., *J. Org. Chem*., 1992, vol. 57, pp. 3253–3254.
29. Coustel, N., Bernier, P., Aznar, R., *et al*., *J. Chem. Soc., Chem. Commun*., 1992, no. 19, pp. 1402–1403.
30. US Patent 5304366.
31. Ponomarev, A.N., Axel'rod, B.M., Klepikov, V.V., *et al*., Abstracts of Papers, *5th Biennial Int. Workshop "Fullerenes and Atomic Clusters,"* St. Petersburg, 2001, p. 330.
32. Ponomarev, A.N., Aksel'rod, B.M., Barchenko, V.T., *et al*., *Zh. Fiz. Khim*., 2000, vol. 74, no. 11, pp. 2031–2034.
33. Ponomarev, A.N., Yudovich, M.E., Nikitin, V.A., *et al*., *Opt. Spectrosk*., 2000, vol. 88, no. 2, pp. 195–197.
34. Golubkov, V.V., Shakhmatkin, B.A., Charykov, N.A., and Aksel'rod, B.M., *Zh. Fiz. Khim*., 2002, vol. 76, no. 3, pp. 561–563.
35. Golubkov, V.V., Shakhmatkin, B.A., Charykov, N.A., and Aksel'rod, B.M., *Zh. Fiz. Khim*., 2001, vol. 75, no. 10, pp. 1819–1822.

Russian Journal of Applied Chemistry, Vol. 76, No. 1, 2003, pp. 44–47. Translated from Zhurnal Prikladnoi Khimii, Vol. 76, No. 1, 2003, pp. 46–49.

SORPTION AND ION-EXCHANGE PROCESSES

Modification of Carbon Materials To Impart to Them Fungicidal and Antimicrobial Properties

S. S. Stavitskaya, A. N. Tomashevskaya, V. E. Goba, and N. T. Kartel'

Institute of Sorption and Endoecology Problems, National Academy of Sciences of Ukraine, Kiev, Ukraine

Received April 22, 2002

Abstract—New copper-containing fungicides based on peat and granulated and powder-like anthracite were prepared and studied; the optimal conditions of their preparation were determined.

Although numerous chemical agents for plant protection (in particular, fungicides) are available, search for new more effective and convenient-to-use preparations is still an urgent problem due to increasing requirements to safety for humans and preservation of the activity at prolonged storage.

Though copper-containing fungicides are well known [1–5], in this work we tried to prepare new copper-containing fungicides with carbon materials as supports.

It was found [6–11] that, in sorption of copper(II) compounds on activated carbons, various forms of sorbed copper(II) are formed, depending on the process conditions, chemical nature of the sorbent surface, and structure of the carbon material. The carbon surface is active, it can bear an electrical charge and contain various functional groups. Hence, contact with salt solutions can be accompanied by the exchange of anions (with the release of OH^- ions into solutions) and cations (with acidic functional groups in the oxidized samples). At anion exchange in the presence of copper(II) salts, hydroxides and basic salts are formed in the carbon pores. Also [8–11], at contact with concentrated solutions, the multilayer coverage of the pore surface with copper(II) compounds is possible. Such preparations (impregnated carbons), in which granules (particles) of activated carbon support are filled with a certain compound, are widely used as chemosorbents, catalysts, etc. [8–11].

As for carbon materials modified with copper(II) compounds, it is known [8–10] that they can contain a water-soluble (WS) fraction sorbed in the interlayer or intrapore space and an acid-soluble fraction in the form of basic salts or copper(II) bound by cation exchange. Such a variety of the forms of bound copper(II) allows synthesis of preparations with the controlled amount and rate of release of fungicidal and antimicrobial copper(II) species into the environment. As a result, we can obtain highly active fungicides (bactericides) with a lower content of copper(II) and lower toxicity compared to known copper-containing agents.

The aim of this work was to prepare modified carbon materials with fungicidal and antimicrobial properties, to determine the optimal synthesis conditions, and to obtain a series of experimental samples for full-scale tests. For this purpose we prepared about 30 samples, mainly based on granulated and powdered anthracite.[1] In some cases, natural peat was used as copper support. Modification was performed in the static sorption mode: a weighed portion (5–1000 g) of the carbon material was shaken for 4 h with the required volume (15–5000 ml) of a copper(II) chloride solution of appropriate concentration. To determine the optimal synthesis conditions, we varied the type of the initial material, its granulation, copper(II) salt concentration, pH value, etc. In special tests we recorded the copper(II) sorption isotherms (Fig. 1) and performed washing out of weakly bound (WS) copper(II) (Fig. 2) and desorption of copper(II) (sorbed or bound by ion exchange) from the sorbent surface.

As seen from Table 1, the samples studied contained different amounts of sorbed copper(II). Using sorption isotherms and the ratio of the sample weight to solution volume, we can calculate the required amount of copper(II) in the preparation. Copper(II) is strongly sorbed on both anthracite and peat (Fig. 1).

[1] Due to the short supply of special-purpose activated carbons for rapidly expanding areas of their application, utilization of cheap carbon materials, e.g., activated anthracite, is an urgent problem. Search for new processes to obtain valuable products from the waste of powdered anthracite production is also important.

1070-4272/03/7601-0044$25.00

Table 1. Conditions of modification of carbon materials to impart to them fungicidal and antimicrobial activity

Sample no.	Carbon sorbent, treatment procedure	Treatment with $CuCl_2$, mg-equiv l^{-1}	c_{Cu}, wt %
1	Peat	5	540
2	″	3	16
3	″	2	14
4	″	1	24
5	″	0.1	0.45
6	″	0.01	0.05
7	APA*	5	37.6
8	″	3	3.8
9	″	2	4.2
10	″	1	4.3
11	APA treated with 1% NaOH solution and washed with water	0.1	1.1
12	APA treated with NH_3 vapor and washed with water	0.1	1.1
13	APA	0.015	0.08
	AGA,** particle size, mm:		
14	1–0.5	5	60.8
15	0.5–0.2	5	60.8
16	0.2–0.1	5	60.8
17	0.2–0.1	2	3.2
18	AGA treated with 1% NaOH solution and washed with water	0.1	1.2
19	AGA treated with NH_3 vapor and washed with water	0.1	1.2
20	Anthracite washed with water and 0.1 M KOH solution (0.01–0.0005 mm particle size)	4	64.0
21	Anthracite (0.01–0.0005 mm particle size)	0.1	12.8

* (APA) Activated powdered anthracite.
** (AGA) Activated granulated anthracite.

As seen from Table 1, at high copper(II) concentrations the content of sorbed copper(II) is almost independent of the anthracite granulation. With decreasing concentration of the initial $CuCl_2$ solution, the content of sorbed copper(II) on the finer anthracite particles became smaller than that on the coarser particles.

Along with the fractional composition of the carbon material, pH of the initial solution also affects sorption of copper(II) and forms of its binding with

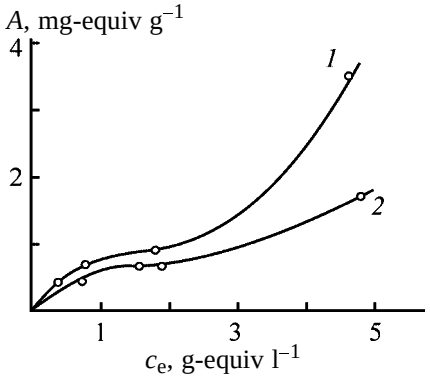

Fig. 1. Isotherms of copper(II) sorption A from industrial copper-containing solution on (*1*) granulated activated anthracite and (*2*) peat. (c_e) Equilibrium concentration of copper(II). (*1*) Sample no. 15, m = 5 g, V = 25 ml, contact time 5 h; (2) sample no. 5, m = 20 g, V = 100 ml, contact time 4 h.

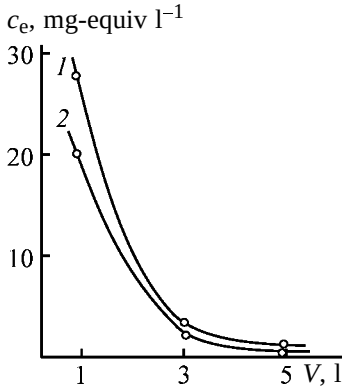

Fig. 2. Desorption of copper(II) ions from copper-modified anthracite samples by triple treatment with distilled water (3 × 5 l). (c_e) Equilibrium concentration of copper(II) and (V) water volume. Copper(II) content in anthracite, %: (*1*) 1.5 and (*2*) 3.

Table 2. Fungicidal and antimicrobial activity of copper-containing carbon materials in laboratory tests

Sample no. (Table 1)	Carbon material	Fraction composition, mm	Inhibition of spore growth, %, in indicated time, h			Antimicrobial activity* with respect to indicated cultures				
			3	24	80	1_3	5_a	8982	8163	549
	Untreated peat	Natural	14.3	40.0	–	+	+	++	+	+
	Untreated anthracite	0.5–0.2	2.5	47.0	61.8	+	+	+	+	+
1	Peat	Natural	100.0	92.3	100.0	+	+	+	+	++
2	″	″	97.9	90.0	100.0	+++	+++	+++	+	+++
3	″	″	97.6	90.0	100.0	+++	+++	+++	++	+++
4	″	″	96.6	94.0	100.0	+++	+++	+++	++	+++
5	″	″	55.2	93.5	–	Not determined				
6	″	″	8.0	51.6	–	Not determined				
7	Anthracite	Powdered	97.7	97.0	100.0	+	+	++	++	+
8	″	″	100.0	90.0	100.0	+++	+++	+++	++	+++
9	″	″	100.0	94.0	100.0	+++	+++	+++	++	+++
10	″	″	100.0	94.0	99.1	+	+++	+++	++	++
12	″	″	99.0	95.0	–	Not determined				
13	″	″	–	–	–	Not determined				
14	″	1–0.5	100.0	98.0	100.0	+	+	+	+	+
15	″	0.5–0.2	97.7	94.0	100.0	+	+	+	+	+
16	″	0.2–0.1	96.6	92.0	100.0	+	++	+	+	+
17	″	Commercial	93.9	89.4	–	Not determined				
Reference	$3Cu(OH)_2 \cdot CuCl_2 \cdot xH_2O$	–	40.4	51.0	79.8	++	++	+++	++	++
Water (blank test)			–	–	–	+	+	+	+	+

* Antibacterial activity was determined using the phytopathogenic cultures *Predomanas lachrymans* (1_3 and 5_a strains) and *Ervinia* (8982, 8163, and 549 strains); (+) weak sensitivity, sterile area diameter 15 mm; (++) moderate sensitivity (15–25 mm); and (+++) high sensitivity (more than 25 mm).

the sorbent. However, this effect is appreciable only in dilute solutions and at rather low pH values, whereas in concentrated solutions sorption is almost independent of pH.

The conditions of copper(II) desorption are important, because the amount and forms of desorbed copper(II) strongly affect the fungicidal and phytotoxic properties of carbon materials.

Experiments on the kinetics of copper(II) washing out with water from samples with a fairly high metal content showed that copper(II) is actively washed out in the first 5 min. This fact suggests that the diffusion factors do not noticeable affect the copper desorption, and at longer contact with water the copper desorption increases only slightly. The residual copper(II) content after treatment with water for 1 h was 6.4 mg g^{-1}. We failed to remove all the sorbed copper from the samples with water, which suggests that it occurs in activated carbon in different chemical forms.

Based on our experimental results and preliminary data on the fungicidal activity, obtained at the Ukrainian Research Institute of Plant Protection (Kiev, Ukraine), we prepared a pilot series of the samples for the field plant protection tests. We determined the sorption capacity and desorption of copper(II) in single and multiple treatments with water (Fig. 2). As seen, in successive treatments copper(II) is gradually washed out.

Our preparations (Table 1) were tested under the laboratory conditions. We determined the growth inhibition factors for the fungus spores of *Alternaria tenrus, Phytophthora infestans*, etc., which are pathogens of crops, causing potato and tomato phytophthora infection, potato alternariosis, and root rot of many plants (Table 2). For some samples we also determined the antimicrobial activity.

Analysis of our experimental data showed that unmodified carbon materials exhibit no fungicidal and antimicrobial properties (Table 2). With addition of copper(II), almost all the samples acquire the fungicidal activity. It should be noted that the strong inhibition of the spore growth was observed with both the

anthracite samples impregnated with concentrated (1–5 N) copper(II) chloride solutions, which probably contain all the above forms of bound copper and significant amounts of weakly bound water-soluble species, and with the samples treated with dilute solutions, which contain smaller amounts of readily removable copper(II). Therefore, there are good grounds to expect that such preparations can provide the required fungicidal effect at lower copper(II) consumption.

Sample nos. 17 and 18, treated after sorption with alkali, showed high activity; the fungicidal activity of modified peat may be of practical interest. After such a treatment, copper(II) in the sorbent can occur as oxychloride, i.e., in the form similar to the reference compound $3Cu(OH)_2 \cdot CuCl_2 \cdot xH_2O$, $x = 0–3$ or hydroxide; certain its fraction also can be bound by the cation-exchange mechanism.

Comparison of the fungicidal activity of the samples (Table 2) showed that some samples, e.g., modified copper-containing samples of anthracite (sample nos. 8–10) and peat (sample nos. 2–4) are more effective in the spore growth inhibition and in suppression of a series of phytopathogenic bacteria as compared to the reference. Since the above preparations were obtained using concentrated solutions and they contained significant amounts of water-soluble copper(II), we assume that their antimicrobial properties are predominantly determined by the released copper(II).

The results of the laboratory tests on the fungicidal and antimicrobial activity of copper-containing carbon materials suggest that they are promising for agricultural use.

In the field tests, we used the samples with various forms of bound copper(II), prepared by impregnation of carbon material with both concentrated and dilute solutions of copper(II) chloride. After sorption, the samples were washed to remove excess copper(II) with distilled water (sample no. 16) and with water and alkaline solution (sample no. 20). In the latter case, we assume that the major fraction of copper in the sample occurs in the form close to $3Cu(OH)_2 \cdot CuCl_2 \cdot xH_2O$.

The vegetation tests showed phytotoxicity of sample nos. 16 and 20, whereas sample no. 21 with a small content of copper(II) exhibited no such activity; no phytotoxicity was observed in the field tests. Sample no. 21 with the copper content by an order of magnitude smaller than in the reference exhibited a fungicidal activity in the field tests.

CONCLUSION

Copper-modified anthracites show promise as fungicidal and antibacterial preparations for vegetable growing and storage.

REFERENCES

1. Kul'skii, L.A., Savluk, O.S., and Kayumova, G.Kh., in *Intensifikatsiya protsessov obezzarazhivaniya vody* (Intensification of Water Disinfection), Kiev: Naukova Dumka, 1978, pp. 5–9.
2. Romanian Patent 89 310.
3. Khovrychev, M.P., Korolev, P.N., and Bulgakova, V.G., *Mikrobiologiya*, 1978, vol. 47, no. 2, pp. 442–445.
4. Khovrychev, M.P. and Rabotnova, I.L., *Mikrobiologiya*, 1972, vol. 41, no. 4, pp. 672–674.
5. Savluk, O.S., Tomashevskaya, I.P., and Bukharskaya, L.P., *Khim. Tekhnol. Vody*, 1986, vol. 8, no. 6, pp. 65–67.
6. Tarkovskaya, I.A., *Okislennyi ugol'* (Oxidized Carbon), Kiev: Naukova Dumka, 1981.
7. Emel'yanov, V.B., Tarkovs'ka, I.A., and Rubanik, S.K., *Dopov. Akad. Nauk Ukr. RSR, Ser. B*, 1965, no. 2, pp. 214–217.
8. Tarkovskaya, I.A., Stavitskaya, S.S., Larina, A.A., and Farberova, E.M., *Khim. Tekhnol.*, 1990, vol. 69, no. 4, pp. 47–51.
9. Tarkovskaya, I.A., Stavitskaya, S.S., and Tikhonova, L.P., *Zh. Prikl. Khim.*, 1996, vol. 69, no. 4, pp. 602–607.
10. Tarkovskaya, I.A., Stavitskaya, S.S., and Tikhonova, L.P., *Khim. Tekhnol. Vody*, 1997, vol. 19, no. 2, pp. 143–149.
11. Tarkovskaya, I.A., Stavitskaya, S.S., and Strelko, V.V., in *Yubileinyi sbornik k 100-letiyu so dnya rozhdeniya M.M. Dubinina* (Jubilee Collection to M.M. Dubinin's Centenary), Moscow: Inst. Fiz. Khim., Ross. Akad. Nauk, 2001, pp. 130–135.

Russian Journal of Applied Chemistry, Vol. 76, No. 1, 2003, pp. 48–54. Translated from Zhurnal Prikladnoi Khimii, Vol. 76, No. 1, 2003, pp. 50–56.

SORPTION AND ION-EXCHANGE PROCESSES

Effect of Deposition and Stabilization Conditions on the Texture Properties of Aluminum Hydroxides

A. A. Lamberov, O. V. Levin, S. R. Egorova, D. A. Evstyagin, and A. G. Aptikasheva

Kazan State Technological University, Kazan, Tatarstan, Russia
Novokuibyshevsk Catalyst Plant, Limited Liability Company, Novokuibyshevsk, Samara oblast, Russia

Received February 27, 2002

Abstract—Methods of low-temperature adsorption of nitrogen and X-ray phase analysis were applied to study structural characteristics of aluminum hydroxides synthesized under industrial conditions. A mechanism of formation of the porous structure of aluminum hydroxides was suggested.

Aluminum oxide is widely used in manufacture of adsorbents and catalysts, being, therefore, a large-tonnage product of industrial chemistry. Recent studies have shown that synthesis of a support is one of the most important procedures in catalyst manufacture technology. As a support frequently serves active aluminum oxide (AAO), determining the dispersity and distribution of the active component and diffusion limitations on mass-transfer processes in a catalyst [1, 2].

It is commonly believed that there exists the optimal pore size of a catalyst for any particular type of raw materials. However, despite that the literature contains a voluminous material concerning the synthesis techniques and the structure of aluminum hydroxides and oxides of varied morphology, data on the influence of particular industrial procedures on the texture of aluminum oxide obtained by reprecipitation are rather scarce [3–7].

The aim of this study was to establish the mechanism of texture formation in AAO in the course of its industrial synthesis and to analyze the influence exerted by the conventional procedures on its texture characteristics.

EXPERIMENTAL

Aluminum hydroxides (AH) were synthesized under industrial conditions by batch precipitation using the sulfate process. The hydroxide samples were analyzed for the content of impurities: Na^+ ions (in terms of Na_2O), by flame photometry on a Flapho-4 instrument; SO_3^{2-} ions, by a procedure described in [8]. The texture characteristics were determined on an ASAP 2010 Micromeritics universal analyzer of surface area and porosity. Adsorption isotherms were measured at 77 K, degassing was done at 773 K to a residual pressure of 10^{-4} mm Hg. The specific surface area S_{sp} was determined by thermal desorption of nitrogen. S_{sp} was calculated with account of the adopted surface area of the nitrogen molecule (0.162 nm^2). The density of nitrogen in the normal liquid state was 0.808 g cm^{-3}. The relative error in S_{sp} measurements was ±3%. The pore volume

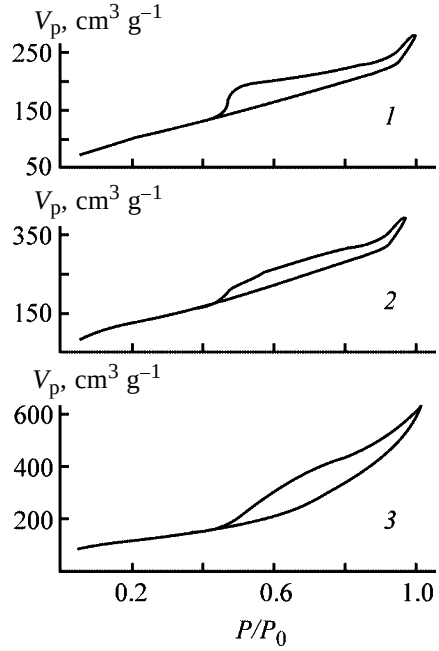

Fig. 1. Isotherms of adsorption–desorption of nitrogen (77 K) from AH samples. (V_p) Measured pore volume and (P/P_0) relative pressure of nitrogen. Precipitation temperature, °C: (*1*) 40, (*2*) 50, and (*3*) 80.

1070-4272/03/7601-0048$25.00

Table 1. Effect of precipitation temperature T_p on the texture characteristics of aluminum hydroxides

T_p, °C	S_{BET}, $m^2\ g^{-1}$	V_p, $cm^3\ g^{-1}$		Distribution of pores, $cm^3\ g^{-1}$/%, with respect to diameter, Å			$I^* \cdot 10^4$, $cm^3\ g^{-1}\ Å^{-1}$, at indicated diameter, Å			SO_3^{2-}	Na_2O
		V_Σ	V	13–50	50–100	>100	16–22	36–37	42–46	%	
40	370	0.44	0.46	0.31/68	0.04/9.4	0.11/24	–	520	–	2.24	0.016
50**	460	0.61	0.63	0.37/59	0.11/17	0.15/21	70	280	–	1.82	0.012
60	404	0.71	0.72	0.31/43	0.30/42	0.11/15	30	175	175	1.79	0.013
70	405	0.84	0.85	0.28/32	0.27/32	0.30/36	35	160	130	2.27	0.016
80	423	0.97	0.98	0.36/37	0.29/30	0.33/34	30	180	20	1.78	0.011

* I is the intensity of pore size distribution peaks.
** The porogram has a peak at 82 Å (intensity 0.002 $cm^3\ g^{-1}\ Å^{-1}$).

V_p and pore size distribution were calculated from the desorption portion of the isotherm, using the standard Barrett–Joyner–Highland procedure [9]. The measurement error was ±13%. X-ray studies were carried out with a DRON-2 diffractometer (FeK_α radiation with β-filter). The range of 2θ angles in which measurements were made was 0°–100°.

It is reasonable to start the discussion of the results obtained with analysis of adsorption isotherms (Fig. 1), since the shape of the hysteresis loop is related to a certain type of the pore structure.

AH precipitated at 40°C shows a type II adsorption isotherm with a hybrid hysteresis loop H2–H3 by the IUPAC classification. The cumulative specific surface area S_Σ exceeds the specific surface area found by BET ($S_\Sigma : S_{BET}$ = 1.27 for the given sample). This indicates that the deposit has tubular pores with constrictions [9, 10].

Raising the precipitation temperature to 50°C changes the type of the hysteresis loop from H2–H3 to H3. The steep slope of the adsorption branch points to the absence of mesopores with medium diameters, and the narrow hysteresis loop, to uniformity of the pores. A hysteresis loop of this type is characteristic of slitlike pores between two parallel plates, open on all sides.

Raising the AH precipitation temperature further does not change the type of isotherms and hysteresis loops; a certain broadening of the hysteresis loop indicates an increasing diversity of pores, and the steeper adsorption branch of the isotherm at medium and high relative pressures confirms the formation of mesopores of large diameter.

The texture characteristics of the AH synthesized are listed in Table 1. In view of the fact that larger part of AH samples had finely porous structure and the peaks in pore size distributions in porograms (Fig. 2) lie fairly close to one another, we used the intensities of these peaks assuming that they are proportional to the contribution of pores of a given diameter to the total pore volume.

The pore structure of AH precipitated at 40°C (S_{sp} = 370 $m^2\ g^{-1}$; V_p = 0.44 $cm^3\ g^{-1}$) is characterized by high-intensity peak of the pore size distribution (0.052 $cm^3\ g^{-1}\ Å^{-1}$) at 37 Å, and, in accordance with the descending run of the porogram in the initial portion of the curve, there is a peak with undeterminable intensity in the range of narrow (<14 Å) pores. The pore volume is 0.31 $cm^3\ g^{-1}$ (68% of V_p) in the range 13–50 Å and 0.043 $cm^3\ g^{-1}$ (9.4% of V_p) in the range 50–100 Å (Table 1, Fig. 2).

With account taken of the type of the hysteresis loop and data of [11], it may be assumed that the hy-

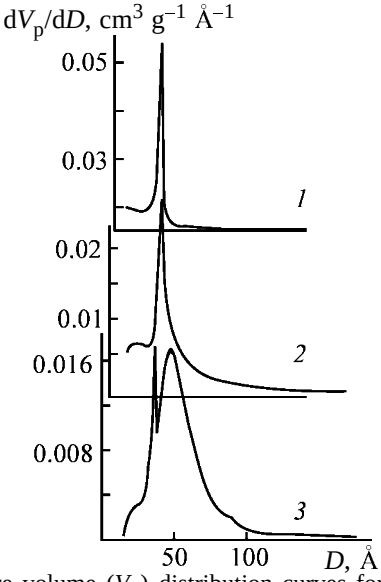

Fig. 2. Pore volume (V_p) distribution curves for AH samples. (D) Pore diameter; the same for Fig. 3. Precipitation temperature, °C: (*1*) 40, (*2*) 50, and (*3*) 60.

Table 2. Variation of texture characteristics with time for AH samples precipitated at low temperature*

τ, days	S_{BET}, $m^2\ g^{-1}$	V_p	V_{des}	$I \times 10^4$, $cm^3\ g^{-1}\ Å^{-1}$, at indicated diameter, Å					Distribution of pores, $cm^3\ g^{-1}$/%, with respect to diameter, Å		
		$cm^3\ g^{-1}$		23	36	46	51	66	50	50–80	>80
1**	224	0.50	0.50	8sh	30sh***	40sh	45sh	66sh	0.05/10	0.21/43	0.24/47
25	259	0.45	0.46	15sh	97	65sh	68sh	80	0.11/23	0.26/56	0.10/21
75	286	0.52	0.52	18sh	92	–	105sh	130	0.10/20	0.35/68	0.06/12

* (τ) Aging time.
** The porogram contains a broad peak of pore volume distribution at 80 Å (I = 0.0070 $cm^3\ g^{-1}\ Å^{-1}$).
*** Peak in the pore volume distribution at 33 Å; (sh) in the form of a shoulder.

droxide precipitate is formed by fibrillar fragments of "gel-like" boehmite [10].

Raising the precipitation temperature to 50°C leads to the appearance of peak in the pore size distribution at 16 Å with intensity of 0.007 $cm^3\ g^{-1}\ Å^{-1}$, and the intensity of the peak at 37 Å decreases from 0.052 to 0.028 $cm^3\ g^{-1}\ Å^{-1}$. The specific surface area of this AH is 459 $m^2\ g^{-1}$, and the pore volume, 0.63 $cm^3\ g^{-1}$. Such a strong increase in the specific surface area is probably due to dispersion of fibrillar particles of gel-like boehmite to give plates of "microcrystalline boehmite" [10], which form, via undirected mutual coordination, slit-like pores of the diameter exceeding 50 Å. The volume of pores with the diameter less than 50 Å is 0.372 $cm^3\ g^{-1}$, which is close to the corresponding value for AH obtained at 40°C (0.31 $cm^3\ g^{-1}$); however, it constitutes only 59% of V_p. It may be stated that the increase in the pore volume is due to the formation of secondary porosity in the range 50–100 Å,

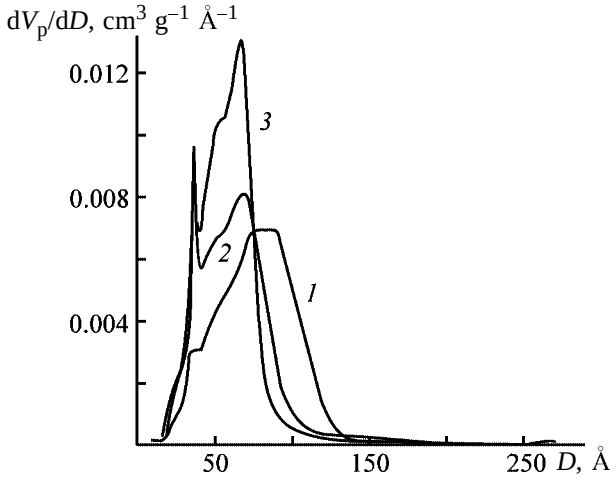

Fig. 3. Pore volume (V_p) distribution curves for AH samples precipitated at low temperature, (*1*) 1, (*2*) 25, and (*3*) 75 days after the synthesis.

without appearance of any peak in the pore size distribution.

Raising the precipitation temperature further leads to a gradual shift of the peak in the pore size distribution at 42 Å to larger diameters (to 50–60 Å), whereas the position of the peaks at 25 and 36 Å remains virtually unchanged. The measured pore volume first grows (T_p = 50–60°C) in the range 50–100 Å (to 0.30–0.36 $cm^3\ g^{-1}$) and then ($T_p \geq 70$°C) at diameters exceeding 100 Å (also to 0.30–0.33 $cm^3\ g^{-1}$), and the specific surface area decreases. In the diameter range 13–50 Å, all the hydroxides synthesized have approximately the same pore volume of 0.30–0.36 $cm^3\ g^{-1}$.

The hydroxides obtained at $T \leq 50$°C are the most labile systems in which crystallization and structuring of a precipitate occur spontaneously in the course of time (Table 2, Fig. 3). For example, a broad peak in the pore size distribution at the pore diameter of 80 Å, observed for AH obtained at 20°C, is probably shifted upon storage to about 66 Å as a result of partial dispersion of pore-forming particles, which is indicated by a considerable increase in the specific surface area of the hydroxide.

To bring crystallization processes in low-temperature AH ($T_p \leq 50$°C) to completion, the hydroxide is stabilized in industrial practice by keeping its dispersion in mother liquor at 102°C for 1 h. Variation of the texture of cold-precipitated AH with the temperature of its stabilization is illustrated in Table 3 and Fig. 4.

The initial cold-precipitated hydroxide has a bidisperse structure with peaks of about the same intensity at 20 and 36 Å in the pore size distribution, low pore volume (0.37 $cm^3\ g^{-1}$), and large specific surface area (357 $m^2\ g^{-1}$) (Table 3, Fig. 4).

Table 3. Effect of stabilization temperature T_{st} on texture characteristics of AH precipitated at 20°C

T_{st}, °C	Na_2O, %	SO_3^{2-}, %	S_{BET}, $m^2\ g^{-1}$	V_{des}, $cm^3\ g^{-1}$	Diameter D, Å, and intensity $I \times 10^4$, $cm^3\ g^{-1}\ Å^{-1}$					
					D_1	I_1	D_2	I_2	D_3	I_3
30	0.080	1.62	357	0.35	20.2	175	35.9	173	–	–
50	0.040	1.83	291	0.34	25.4	58	36.0	641	–	–
60	0.025	2.64	274	0.31	25.0	58	35.6	560	–	–
70	0.020	1.81	297	0.37	25.4	78	–	–	40.4	326
80	0.020	1.27	334	0.42	25.1	100	–	–	40.4	476
90	0.086	1.73	318	0.41	25.4	96	36.6	202	46.0	271
102	0.070	1.46	306	0.42	25.4	80	36.6	176	50.0	270

Raising the stabilization temperature to 60°C increases the intensity of the peak in the pore size distribution at 36 Å from 0.173 to 0.560 $cm^3\ g^{-1}\ Å^{-1}$, and the peak at 20 Å is shifted to 25 Å, with its intensity decreasing from 0.175 to 0.058 $cm^3\ g^{-1}\ Å^{-1}$. In the process, the type of the hysteresis loop remains virtually unchanged. It may be assumed that fibrils of gel-like pseudoboehmite with the pore size distribution peak at 36 Å are formed under these conditions. Further increase in the stabilization temperature leads to a decrease in the intensity of the peak at 36 Å from 0.560 to 0.202 $cm^3\ g^{-1}\ Å^{-1}$ (90°C) and appearance of a peak at 40 Å, gradually shifted to around 50 Å with increasing stabilization temperature. No significant change in the specific surface area or pore volume occurs in the process. Consequently, it may be assumed that pores 40 Å in diameter are formed within a structure constituted by fibrillar fragments as a result of hydrothermal transformations of the hydroxide. This is indicated by a change of the type of the hysteresis loop from H3 to H2, which points to formation of bottle-shaped pores. It may be assumed that no microcrystalline boehmite is formed in stabilization of low-temperature hydroxide, which is indicated by the absence of pores more than 100 Å in diameter. The total pore volume remains rather small.

To elucidate the mechanism of texture formation in AH, we studied its morphology by X-ray phase analysis. The results obtained are listed in Table 4, whence follows that, depending on AH precipitation and stabilization temperatures, the precipitate contains pseudoboehmite, gibbsite, and bayerite in various ratios.

Raising the temperature of AH precipitation and stabilization makes the content of bayerite in the precipitate lower and the size of bayerite microcrystals larger. If account is taken of the fact that bayerite microcrystals are characterized by presence of slitlike micropores 15–20 Å in diameter [10, 12], then the high-intensity peaks in the pore size distribution, observed at 18–20 Å for low-temperature AH samples (Table 4, sample nos. 1 and 8) are due to the presence in the precipitate of a hydroxide of just bayerite morphology. Raising the temperature of stabilization or precipitation leads to disappearance of these peaks, with another peak appearing, instead, in the pore size distribution at 22–25 Å. The intensity of this peak does not correlate with the content of gibbsite or bayerite in AH.

The content of trihydroxides decreases when the precipitation is performed at lower pH. For example, the content of gibbsite in AH obtained at 20°C and stabilized at 50°C decreases from 11% to zero with the precipitation pH decreasing from 9.6 to 8.8. As follows from Table 4, the precipitation pH affects the rate of hydrolysis to a much greater extent than the process temperature does. For example, stabilization at 100°C of AH precipitated at 20°C decreases the

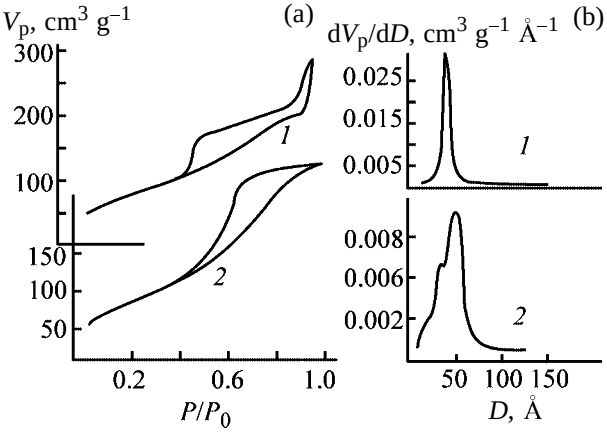

Fig. 4. (a) Isotherms of adsorption–desorption of nitrogen and (b) pore volume (V_p) distribution curves for AH precipitated at 20°C. (D) Pore diameter and (P/P_0) relative pressure of nitrogen. AH stabilization temperature, °C: (*1*) 60 and (*2*) 102.

Table 4. Effect of synthesis conditions on the phase composition of AH

Sample no.	Temperature of AH preparation, °C		Pseudoboehmite									Phase composition,* wt %		
			crystallite size along indicated crystallographic axis, Å			defectiveness along indicated crystallographic axis, %			unit cell size, Å					
	T_p	T_{st}**	*b*	*a*	*c*	*b*	*a*	*c*	*b*	*a*	*c*	Pbm	Byr	Gbs
1	20	30	9.70	26.80	21.70	5.2	26.6	10.0	12.9	3.7	2.7	34.5	41.7	20.8
2	20	70	16.03	55.42	36.94	11.5	24.0	3.0	13.0	3.7	2.7	81.5	–	–
3	20	102	18.25	65.16	24.89	10.0	24.7	5.8	12.7	3.7	2.8	91.1	–	8.8
4	20	50	9.70	44.00	22.12	13.9	24.7	5.2	12.9	3.7	2.7	97.7	–	–
5	60	50	19.99	68.67	30.85	8.5	20.4	8.0	12.5	3.7	2.8	58.0	30.2	11.7
6	50	100	19.67	63.67	41.44	5.6	2.0	5.9	12.5	3.7	2.8	96.6	–	–
7	50	70	20.33	52.06	14.36	11.6	21.4	6.9	12.6	3.7	2.8	97.0	–	–
8	40	50	10.68	43.1	55.07	10.7	2.8	6.8	12.8	3.7	2.7	32.7	46.1	21.2
9	40	102	21.25	81.54	79.02	9.3	1.8	3.0	12.6	3.7	2.8	80.0	16.6	3.3
10	20	50***	14.50	60.70	33.86	10.4	22.8	7.8	12.7	3.7	2.8	91.8	–	7.7
11	20	50****	16.60	54.98	25.49	9.81	23.1	6.3	12.8	3.7	2.7	88.9	–	10.9

* Pbm, pseudoboehmite; Byr, bayerite; Gbs, gibbsite.
** pH 9.2.
*** pH 9.4.
**** pH 9.6.

content of gibbsite from 21 to 9% (pH 9.4), and lowering the precipitation pH to 8.8 leads to disappearance of gibbsite in the precipitate already at 50°C.

According to the results of X-ray phase analysis, gibbsite and bayerite crystallize in the form of coarse microcrystals 130 to 1000 Å in size, and pores of about the same diameter are not manifested in the porograms. Raising the precipitation and stabilization temperatures leads to higher amount of a hydroxide with the pseudoboehmite morphology in the precipitate, and it is this hydroxide that determines the texture characteristics of the precipitate.

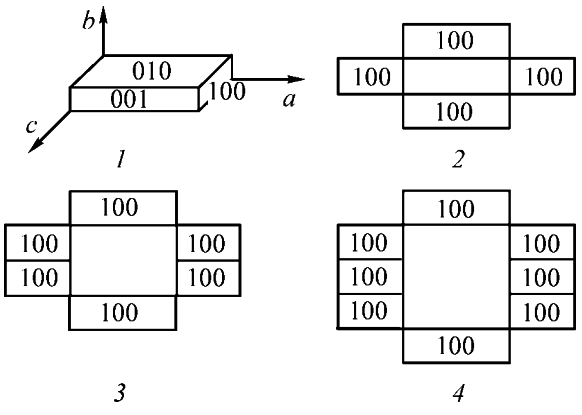

Fig. 5. (*1*) Microcrystalline structure of pseudoboehmite and (*2–4*) ways of its coordination. Fragment: (*2*) I ($D \approx$ 22–25 Å), (*3*) II (D = 37 Å), and (*4*) III ($D \approx 40-60$ Å).

A microcrystallite of pseudoboehmite is shown schematically in Fig. 5. With account of the structure of the double polymeric molecule of pseudoboehmite [10], the (010) plane of the microcrystallite, containing vectors *a* and *c*, is saturated with terminal hydroxy groups, and the (100) plane, containing vectors *b* and *c*, is the most defective (Table 4). This points to a noncoherent coordination of boehmite microcrystalites in this plane [10].

At the same time, coordination between primary microcrystallites of pseudoboehmite is the most probable in the (010) plane via formation of bridging OH groups or hydrogen bonds. The cleavage planes of unit cells of pseudoboehmite contain excess water (up to 1.7 mol per mole of Al_2O_3) firmly bound by H bonds in the interplanar space, which is indicated by strong broadening of diffraction peaks corresponding to the (010) plane. It is this water that ensures lability of contacts between pseudoboehmite microcrystallites.

Comparison of data on the phase composition of AH and their texture characteristics allows the following interpretation of the data obtained. Pores 20–25 Å in diameter, appearing in the course of AH structuring, may be due to mutual coordination of like faces,

Table 5. Peaks in the pore size distribution in AH samples

Temperature of AH preparation, °C		Peaks in pore diameter distribution at indicated D, Å					
		calculation			experiment		
T_p	T_{st}	D_1	D_2	D_3	D_1	D_2	D_3
20	70	23	33	–	25	36	–
20	102	27	38	55	25	37	50
20	50*	17	23	33	17	25	36
60	50	28	40	48	25	40	45
50	70	27	38	61	25	36	60
20	50**	25	36	–	26	36	–
20	50***	23	33	–	25	36	–

* pH 9.2. ** pH 9.4. *** pH 9.6.

formed by the (010) and (001) planes, of pseudoboehmite microcrystallites along the *a*-axis, to give fragment I in Fig. 5.

Pores 32–36 Å in diameter are probably formed via coordination of the (010) planes of microcrystallites to give fragment III (Fig. 5), with translation of the image in the direction perpendicular to the plot plane. Pores with larger diameters are formed via noncoherent dimerization of microcrystallites along the *b*-axis. The calculated and actual values of the pore size distribution peaks are listed in Table 5.

The main criterion characterizing the strength of intercrystallite binding in pseudoboehmite is its unit cell size along the *b*-axis, determined by the amount of interplanar water. For example, at the unit cell size exceeding 12.5 Å (H_2O content higher than 1.4 mol per mole of Al_2O_3), the hydroxide is described as gel-like pseudoboehmite, which is characterized by bottle-shaped pores formed via directed mutual coordination of primary particles of pseudoboehmite, small pore volume, and labile intercrystallite contacts of "coagulation" nature (van der Waals or hydrogen bonds) [10, 11]. The contacts are easily destroyed under peptization or other external actions. Virtually all AH samples precipitated at low temperature can be related to gel-like pseudoboehmites even after stabilization. Further structuring of the precipitate occurs via noncoherent coordination of the (100) planes of pseudoboehmite microcrystallites (which is indicated by high defectiveness along the crystallographic axis *a*) to give fibrillar fragments in the direction perpendicular to the plane of the figure.

If the size of the unit cell of pseudoboehmite along the *b*-axis is less than 12.5 Å, then the hydroxide is a microcrystalline pseudoboehmite with large pore volume formed via undirected mutual coordination of microcrystallites to give slitlike pores without any clearly pronounced peak in the pore size distribution and firm contacts between primary particles. These contacts are of "crystallization" nature [11] (content of interplanar water less than 1.4 mol per mole of Al_2O_3) and do not disintegrate under the action of peptizing agent. Hydroxides obtained at 50°C are formed of microcrystalline pseudoboehmite to a greater extent.

It follows from Table 4 that, for most of the hydroxides synthesized, the crystallite size along the *b*-axis exceeds the size of the unit cell of pseudoboehmite along the same axis. Therefore, it was assumed that the probable dominant "crystallization center" [13] is fragment II (Fig. 5) formed via mutual coordination of dimeric microcrystallites to give pores 33–37 Å in diameter. For example, hydroxides synthesized at 20°C (pH 8.8–9.6) and stabilized at 50°C contain 90% pseudoboehmite and have a virtually unimodal pore structure ($V_p \approx 0.40$ cm^3 g^{-1}) with the pore size distribution peak at 37 Å (60–70% of V_p) having intensity of 0.05–0.07 cm^3 g^{-1} Å^{-1}.

The formation of pores of large diameters in stabilization of AH prepared at low temperature is probably due to occurrence of hydrothermal conversion within fibrillar structures [10], which are accompanied by a discrete local increase in pore diameter (Fig. 5, fragment III). This is indicated by a change in the type of the hysteresis loop from H2–H3 to H2 (bottle-shaped pores). No destruction of fibrillar fragments occurs in stabilization, which is confirmed by insignificant changes in the specific surface area and pore volume.

The diameters of the forming pores were calculated in terms of the suggested mechanism of AH structur-

ing, and the calculated and true values are listed in Table 5.

Synthesis of the hydroxides at temperatures above 50°C leads to destruction of fibrillar particles along the longest axis [in the (100) plane] to give short fragments with pores 37 and 42 Å in diameter (which is indicated by the 30% greater specific surface area of these samples), forming secondary pores of diameter more than 100 Å via undirected mutual coordination [probably, in the (010) plane]. The forming pores of the secondary pore system constitute up to 60% of the pore volume in high-temperature hydroxides.

CONCLUSIONS

(1) Industrial cold-precipitated hydroxides ($T_p \approx$ 50°C) are gel-like pseudoboehmites with small pore volume (up to 0.4 $cm^3 g^{-1}$) associated with pores 25 and 36 Å in diameter. Their pore structure is due to fibrillar pseudoboehmite fragments containing pores with diameters mainly in the range 36–37 Å. Stabilization of cold-precipitated hydroxides leads to formation of bottle-shaped pores as a result of hydrothermal synthesis within fibrillar structures, with distribution peaks appearing in the range 40–60 Å. The specific surface area and pore volume remain virtually unchanged upon stabilization.

(2) Hot-precipitated hydroxides (T_p > 50°C) are formed of finely crystalline pseudoboehmite with slitlike pores open on all sides. The pore structure is due to undirected mutual coordination of platelike particles, with crystalline contacts formed between them. The hydroxides are characterized by large pore volume (>0.6 $cm^3 g^{-1}$) without any clearly pronounced peak in the pore size distribution.

(3) It is proposed that conventional discrimination of hydroxides into microcrystalline and gel-like should be based on the size of the unit cell of pseudoboehmite along the *b*-axis. The unit cell is equal to, or greater in size than 12.5 Å for gel-like pseudoboehmite, and less than, or equal to 12.5 Å for microcrystalline pseudoboehmite.

(4) The morphology of the hydroxides is determined by the conditions of their synthesis and stabilization temperature. Raising the precipitation and stabilization temperature and lowering the pH value favors formation of an aluminum hydroxide with pseudoboehmite morphology. Trihydroxides (bayerite and gibbsite) take no part in the formation of the texture of the precipitate.

(5) Based on the results obtained, a model of texture formation in aluminum hydroxide precipitate is proposed and peaks in pore size distribution are calculated. The calculated and actual positions of peaks in the distribution are close.

REFERENCES

1. Radchenko, E.D., Nefedov, B.K., and Aliev, R.R., *Promyshlennye katalizatory gidrogenizatsionnykh protsessov neftepererabotki* (Industrial Hydrogenation Catalysts in Oil Refining), Moscow: Khimiya, 1987.
2. Irisova, K.N., Kostromina, T.S., and Nefedov, B.K., *Nositeli katalizatorov gidroochistki na osnove aktivnoi okisi alyuminiya* (Supports for Hydrorefining Catalysts Based on Active Aluminum Oxide), Moscow: TsNIITEneftekhim, 1983.
3. Fedorov, B.M., Balashov, V.L., and Berenblyum, A.S., *Kinet. Katal.*, 1990, vol. 31, no. 3, pp. 673–680.
4. Leshchev, N.P., Kamenskii, A.A., Silin, N.G., *et al.*, *Neftepererab. Neftekhim.*, 1985, no. 1, pp. 5–6.
5. Nasirov, R.K., Talisman, E.L., Makeeva, G.N., *et al.*, *Neftepererab. Neftekhim.*, 1994, no. 9, pp. 13–16.
6. Korontsevich, A.Yu., Moroz, E.M., Vorob'ev, V.N., *et al.*, *Zh. Prikl. Khim.*, 1985, vol. 58, no. 1, pp. 29–33.
7. Poezd, I.P., Radchenko, E.D., and Poezd, D.F., *Proizvodstvo aktivnoi okisi alyuminiya – nositelya katalizatorov dlya gidrogenizatsionnykh protsessov: Tematicheskii obzor* (Manufacture of Active Aluminum Oxide, a Support for Hydrogenation Catalysts: Topical Review), Moscow: TsNIITEneftekhim, 1979.
8. *TU* (Technical Specification) *38.601-13-062–90: Aluminum Oxide as Drying Agent*.
9. Gregg, S.J. and Sing, K.S.W., *Adsorption, Surface Area and Porosity*, London: Academic, 1982.
10. *Physical and Chemical Aspects of Adsorbents and Catalysts*, Linsen, B.G., Ed., London: Academic, 1970.
11. Shepeleva, M.N., Shkrabina, R.A., Okkel', L.G., *et al.*, *Kinet. Katal.*, 1988, vol. 29, no. 1, pp. 195–200.
12. Chukin, G.D. and Seleznev, Yu.L., *Kinet. Katal.*, 1989, vol. 30, no. 1, pp. 69–74.
13. Buyanov, R.A. and Krivoruchko, O.P., *Izv. Sib. Otd. Akad. Nauk SSSR, Ser. Khim.*, 1982, no. 14, pp. 28–35.

Russian Journal of Applied Chemistry, Vol. 76, No. 1, 2003, pp. 55–59. Translated from Zhurnal Prikladnoi Khimii, Vol. 76, No. 1, 2003, pp. 57–61.

SORPTION AND ION-EXCHANGE PROCESSES

Extraction of Lanthanide(III) and Yttrium(III) Nitrates with a Toluene Solution of Trialkylbenzylammonium Naphthenate

A. K. Pyartman, A. A. Kopyrin, and D. A. Zhikharev

St. Petersburg State Technological Institute (Technical University), St. Petersburg, Russia

Received June 12, 2002

Abstract—Extraction of lanthanides(III) [La(III)–Lu(III)] and yttrium(III) with toluene solution of trialkylbenzylammonium naphthenate mixture was studied. The equations of extraction isotherms taking into account formation of the extractable complexes $(R_4N)_2[Ln(NO_3)_3A_2]$ (A is naphthenate anion) were obtained. The extraction constants of lanthanides [La(III)–Lu(III] and yttrium(III) were calculated.

Organic solutions of quaternary ammonium base (QAB) salts with organic anions are widely used for extractive recovery and separation of nonferrous and platinum metals [1, 2]. We found no information on extraction isotherms of rare-earth metals(III) (Ln) with such binary extractants. In order to fill this gap in the extraction chemistry of lanthanide(III) and yttrium(III), we studied extraction of theses metals (as nitrates) with a toluene solution of trialkylbenzylammonium naphthenate.

The concentration of trialkylbenzylammonium naphthenate (TABANP) in toluene was 0.42 M. The general formula of TABANP is $C_6H_5(C_7H_{15}–C_9H_{19})_3N^+A^–$, where $A^–$ is the naphthenate anion. In our experiments we used a mixture of naphthenic acids (natural carboxylic acids containing carboxy groups bound to five-membered rings, M_{av} = 220).

Trialkylbenzylammonium naphthenate was prepared as follows: (1) an organic solution of trialkylbenzylammonium chloride was converted to the hydroxide by triple contact with aqueous 5–7 M NaOH; (2) the excess alkali was removed by repeated scrubbing of the organic phase with distilled water until pH of the wash water decreased to 8–9; (3) trialkylbenzylammonium hydroxide was mixed with stoichiometric amount of naphthenic acids and this mixture was dissolved in toluene (chemically pure grade). The resulting binary extractant was washed with distilled water to pH 7.

The concentration of naphthenic acids in the organic phase was determined by two methods: two-phase potentiometric titration [2] and titration with aqueous alkali of the organic phase diluted with ethyl alcohol, with phenolphthalein as indicator. The amount of the QAB salt was determined by the method reported in [3]. Ln(III) nitrates were prepared by dissolving the corresponding Ln(III) oxides (ultrapure grade) in nitric acid (analytically pure grade). Extraction was carried out in graduated tubes at the 1 : 1 ratio of the organic and aqueous phases. Changes in the volumes of the organic and aqueous phases did not exceed 2 rel. %. The Ln(III) concentration in both the initial and equilibrium aqueous phases was determined by titration with a standard aqueous solution of disodium ethylenediaminetetraacetate in the presence of xylenol orange as indicator [4]. The Ln(III) concentration in the organic phase was determined as the difference between its content in the initial and equilibrium aqueous phases taking into account the changes in the volumes of the aqueous and organic phases after extraction.

The relative errors in preparing solutions were within ±0.5%; in determining Ln(III) concentration, ±(0.5–2)%; and in determining the distribution coefficients, ±(1–3)%. The IR spectra of the organic phase (thin liquid layer between KBr plates) were recorded on UR-20 IR spectrometer (Germany) within the 700–1900 cm^{-1} range against the pure solvent (toluene).

Figure 1 shows the extraction isotherms of Ln nitrates with 0.420 M TABANP in toluene at 298 ± 0.5 K. It is seen that all the extraction isotherms show saturation with respect to Ln(III) at $C_S : [Ln^{3+}](o) \rightarrow 2 : 1$ {C_S is the total TABANP concentration in the organic phase and $[Ln^{3+}](o)$ is the equilibrium Ln(III) concentration in the organic phase; the indices (a) and (o) refer to the aqueous and organic phases, respectively}. This fact shows that lanthanides(III) are extracted in the form of mixed-ligand complexes $(R_4N)_2[Ln(NO_3)_3A_2]$ [5].

1070-4272/03/7601-0055$25.00

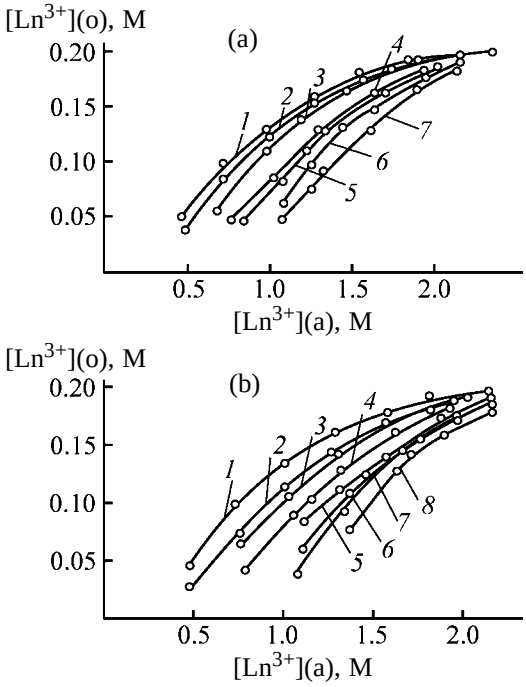

Fig. 1. Extraction isotherms of Ln(III) nitrates with 0.420 M TABANP in toluene at T = 298 K and pH 3. $[Ln^{3+}](o)$ and $[Ln^{3+}](a)$ are the equilibrium Ln(III) concentrations in the organic and aqueous phases, respectively. (a) Ln(III): (*1*) La, (*2*) Pr, (*3*) Sm, (*4*) Gd, (*5*) Dy, (*6*) Er, and (*7*) Yb; (b) Ln(III): (*1*) Ce, (*2*) Nd, (*3*) Eu, (*4*) Tb, (*5*) Ho, (*6*) Tm, (*7*) Lu, and (*8*) Y.

Extraction of Ln(III) with TABANP can be described by the equation of a heterogeneous chemical reaction

$$Ln^{3+}(a) + 3NO_3^-(a) + 2R_4NA(o) = (R_4N)_2[Ln(NO_3)_3A_2](o). \quad (1)$$

The concentration extraction constant is expressed by

$$K_{ex}^2 = \frac{[(R_4N)_2Ln(NO_3)_3A_2](o)}{[Ln^{3+}](a)[NO_3^-]^3(a)[R_4NA]^2(o)} = \frac{D_{ex}}{[NO_3^-]^3(a)[R_4NA]^2(o)}, \quad (2)$$

where D_{ex} is the LnIII) distribution coefficient.

The correlation between the concentration (K_{ex}^2) and thermodynamic ($K_{ex}^{0.2}$) extraction constants is described by

$$K_{ex}^{0.2} = K_{ex}^2 \frac{Y[(R_4N)_2Ln(NO_3)_3A_2](o)}{Y_\pm^4 Y^2(R_4NA)(o)}, \quad (3)$$

where Y_j(o) are the molar activity coefficients of the extractable complex and free TABANP in the organic phase, and $Y_\pm$ is the mean ionic molar activity coefficient of Ln(III) nitrates in the aqueous phase.

Assuming that

$$\frac{Y[(R_4N)_2Ln(NO_3)_3A_2](o)}{Y^2(R_4NA)(o)} = \text{const} = 1,$$

Eq. (3) can be transformed to the form

$$K_{ex}^{0.2} = K_{ex}^2/Y_\pm^4. \quad (4)$$

Analysis of published data on the mean ionic molar activity coefficients of Ln(III) nitrates [6–9] showed that their dependence on the Ln(III) molar concentration is fairly well described by Eq. (5) given in [10]:

$$\ln Y_\pm = C^{1/3}(a) + BC(o), \quad (5)$$

where C(a) is the molar concentration of Ln(III) nitrate in the aqueous solution, and A and B are empirical parameters. The dependence described by Eq. (5) is divided in two separate portions, corresponding to the 0.5–0.6 M and 0.6–3.0 M concentration ranges. The parameters A and B were reported in [5, 11].

The mathematical treatment of the extraction isotherms was performed assuming that two extractable complexes (i = 2 and 3) are formed in the organic phase. The following set of material balance equations was used:

$$C_S = [R_4NA](o) + 2K_{ex}^{0.2}[Ln^{3+}](a)[NO_3^-]^3(a)[R_4NA]^2(o)Y_\pm^4, \quad (6)$$

$$[Ln^{3+}](o) = K_{ex}^{0.2}[Ln^{3+}](a)[NO_3^-]^3(a)[R_4NA]^2(o)Y_\pm^4, \quad (7)$$

where C_S is the total TABANP concentration in the organic phase, $[Ln^{3+}](o)$ and $[Ln^{3+}](a)$ are the Ln(III) equilibrium concentrations in the organic and aqueous phases, respectively, and $[R_4NA](o)$ is the concentration of free TABANP in the organic phase. Equations (6) and (7) were solved for $K_{ex}^{0.2}$ by the nonlinear least-squares technique [12].

Some results of the mathematical treatment of the extraction isotherms performed assuming formation of only one extractable complex, $(R_4N)_2[Ln(NO_3)_3]A_2$, are listed in Table 1. These data show that the calculated values of $\log K_{ex}^{0.2}$ are virtually independent of the composition of the aqueous and organic phases. The calculated Ln(III) concentrations in the organic

Table 1. Calculated parameters of the extraction isotherms of Ln(III) nitrates with 0.420 M TABANP in toluene at T = 298.15 K

$[Ln^{3+}](a)$	$[Ln^{3+}](o)$	$[Ln^{3+}]_{calc}(a)$	Difference, %	$Y_{\pm}$	$\log D_{ex}$	$\log K_{ex}^{0.2}$
			Lanthanum(III)			
0.465	0.050	0.9494	1.27	0.217	–0.97	2.24
0.722	0.100	0.0971	2.91	0.198	–0.86	2.27
0.985	0.129	0.1340	–3.91	0.192	–0.88	2.16
1.820	0.159	0.1617	–1.67	0.194	–0.91	2.18
1.545	0.180	0.1777	1.28	0.201	–0.93	2.30
1.839	0.192	0.1892	1.43	0.214	–0.98	2.36
2.162	0.197	0.1972	–0.08	0.234	–1.04	2.22
			Cerium(III)			
0.473	0.046	0.0521	–13.33	0.214	–1.01	2.18
0.723	0.101	0.1024	–1.40	0.200	–0.85	2.25
1.011	0.135	0.1417	–4.96	0.195	–0.87	2.17
1.294	0.162	0.1664	–2.73	0.199	–0.90	2.17
1.584	0.179	0.1824	–1.87	0.208	–0.95	2.16
1.805	0.191	0.1904	0.33	0.219	–0.98	2.30
2.147	0.197	0.1984	–0.70	0.242	–1.04	2.17
			Neodymium(III)			
0.484	0.026	0.0248	4.72	0.210	–2.27	1.83
0.756	0.074	0.0761	–2.89	0.209	–1.01	1.77
1.005	0.116	0.1157	0.23	0.208	–0.94	1.80
1.270	0.144	0.1475	–2.45	0.215	–0.95	1.74
1.572	0.170	0.1716	–0.95	0.230	–0.97	1.76
1.818	0.182	0.1843	–1.27	0.248	–1.00	1.72
2.032	0.192	0.1919	0.06	0.266	–1.20	1.81
			Dysprosium(III)			
0.840	0.046	0.0459	0.18	0.232	–1.26	1.04
1.075	0.083	0.0842	–1.49	0.241	–1.11	1.02
1.235	0.109	0.1099	–0.83	0.251	–1.05	1.03
1.340	0.129	0.1251	3.03	0.260	–1.02	1.09
1.703	0.164	0.1644	–0.26	0.299	–1.02	1.03
2.027	0.186	0.1847	0.67	0.347	–1.04	1.09
			Yttrium(III)			
1.364	0.077	0.0771	–0.17	0.358	–1.25	–1.15
1.629	0.128	0.1243	–2.88	0.421	–1.10	–1.10
1.714	0.142	0.1372	–3.36	0.445	–1.08	–0.08
1.890	0.160	0.1593	0.45	0.502	–1.07	–0.14
2.171	0.181	0.1826	–0.88	0.615	–1.08	–0.20

Note: $[Ln^{3+}](a)$ and $[Ln^{3+}](o)$ are the equilibrium Ln(III) concentrations in the aqueous and organic phases, respectively. The difference between the calculated and experimental values of the Ln(III) concentrations in the organic phase is given.

phase agree with the experiment to within 1–4 rel. %. Thus, our model adequately describes the extraction isotherms of Ln(III) nitrates with TABANP in toluene.

The average values of the extraction constants with rms deviations are given in Table 2. These results show that $\log K_{ex}^{0.2}$ decreases from lanthanum(III) to lutetium(III), and Y is the least extractable. Thus, trialkylbenzylammonium naphthenates can be used for separating cerium-group lanthanides(III) from other lanthanides(III) and yttrium(III) from lanthanides(III).

Figure 2 shows the IR spectra of $(R_4N)(RCOO)$ and $(R_4N)[M(NO_3)_3(RCOO)_2]$, where M = Er(III),

Table 2. Average values of the extraction constants ($\log K_{ex}^{0.2}$) of Ln(III) nitrates with 0.420 M trialkylbenzylammonium naphthenate in toluene at 298.15 K

Ln(III)	$\log K_{ex}^{0.2}$
La	2.24 ± 0.05
Ce	2.20 ± 0.05
Pr	1.95 ± 0.06
Nd	1.78 ± 0.04
Sm	1.70 ± 0.04
Eu	1.54 ± 0.03
Gd	1.27 ± 0.03
Tb	1.22 ± 0.04
Dy	1.05 ± 0.03
Ho	0.81 ± 0.10
Er	0.59 ± 0.06
Tm	0.40 ± 0.03
Yb	0.15 ± 0.06
Lu	0.08 ± 0.06
Y	–0.13 ± 0.05

Note: The errors are given as rms deviations (σ).

Pr(III), and Y(III). The bands of antisymmetric (ν^{as}) and symmetric (ν^{s}) stretching vibrations of carboxy groups are the most sensitive to complexation with metal ions [13, 14]. For free TABANP, these bands are observed at approximately 1480 and 1400 cm^{-1}, respectively. The difference between the frequencies of the symmetric and antisymmetric stretching vibrations $\Delta = \nu^{as} - \nu^{s}$ is ~80 cm^{-1}, which indicates that in TABANP the quaternary ammonium cations are bound to naphthenate anions by predominantly electrostatic forces. Formation of the extractable complex $(R_4N)\cdot[Er(NO_3)_3(RCOO)_2]$ results in a high-frequency shift of the antisymmetric absorption band (ν^{as} ~1600 cm^{-1}), and a low-frequency shift of the symmetric absorption band (ν^{s} ~ 1370 cm^{-}) (Fig. 2). As a result, the difference $\Delta = \nu^{as} - \nu^{s}$ increases to approximately 230 cm^{-1}. This means that Ln(III) cations are bound to carboxy groups [13, 14] by coordination bonds.

The spectra of the complexes $(R_4N)[Ln(NO_3)_3\cdot(RCOO)_2]$ also contain the absorption bands of the nitrate anions (ν^{as} ~1320, ν^{s} ~1500, ν_2^{s} ~1040 cm^{-1}, ν_5^{as}/ν_3^{s} ~835, and ν_6 ~730–750 cm^{-1}). The difference $\Delta = \nu_1^{s} - \nu_4^{as}$ is about 200 cm^{-1}, which shows that nitrate anions are coordinated with Ln(III) cations [13, 14]. These IR data confirm our above conclusion about formation of mixed-ligand $(R_4N)[Ln(NO_3)_3\cdot(RCOO)_2]$ complexes in the organic phase.

CONCLUSIONS

(1) Extraction of lanthanide and yttrium nitrates from aqueous solutions with trialkylbenzylammonium naphthenate in toluene was studied within a wide concentration range of these metals at 298.15 K. The extraction isotherms show saturation with respect to Ln(III) at $C_S : [Ln^{3+}](o) \rightarrow 2 : 1$.

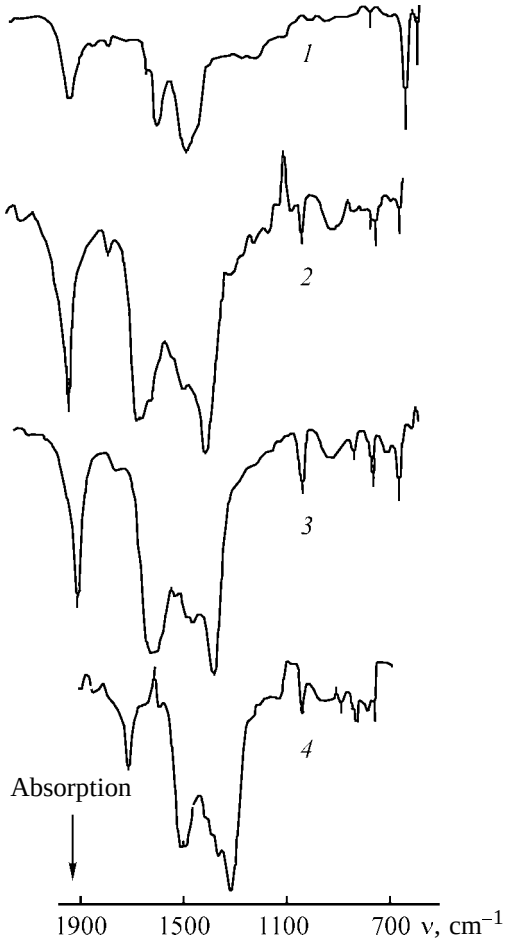

Fig. 2. IR spectra of compounds: (*1*) TABANP, (*2*) $(R_4N)\cdot[Er(NO_3)_3(RCOO)_2]$, (*3*) $(R_4N)[Pr(NO_3)_3(RCOO)_2]$, and (*4*) $(R_4N)[Y(NO_3)_3(RCOO)_2]$. (ν) Wave number.

(2) The complexes $(R_4N)[Ln(NO_3)_3(RCOO)_2]$ are formed in the organic phase. The extraction constants of Ln(III) were calculated. IR spectrosopic studies showed that carboxy and nitrate anions are mainly coordinated with Ln(III) cations.

(3) Extraction of lanthanides (III) with trialkylbenzylammonium naphthenates in toluene decreases in going from lanthanum(III) to lutetium(III). The extractability of yttrium(III) is considerably lower than that of lanthanides (III). Trialkylbenzylammonium naphthenates can be used for separating cerium-group lanthanides(III) from other lanthanides(III) and yttrium(III) from lanthanides(III).

REFERENCES

1. Khol'kin, A.I. and Kuz'min, V.I., in *Khimiya ekstraktsii* (Extraction Chemistry), Novosibirsk, Nauka, 1984, pp. 53–67.
2. Gran, G., Determination of the Equivalence Point in Potentiometric Titration, *Analyst*, 1962, vol. 77, no. 920, pp. 661–671.
3. Fedyanin, L.B., Stepanov, S.I., Sergievskii, V.V., and Frolov, Yu.G., *Khim. Tekhnol. Org. Vysokomol. Soedin., Tr. Mosk. Khim-Tekhnol. Inst. im. D.I. Mendeleeva*, 1987, no. 80, pp. 20–25.
4. *OST* (Branch Standard) *48-209–81, revision no. 2, 1991: Rare-Earth Metal Oxides. Rules of Acceptance and Methods of Analysis.*
5. Pyartman, A.K., Kovalev, S.V., Keskinov, V.A., and Kopyrin, A.A., *Radiokhimiya*, 1997, vol. 39, no. 2, pp. 145–148.
6. Rard, J.A., Miller, D.G., and Spedding, F.H., *J. Chem. Eng. Data*, 1977, vol. 24, no. 4, pp. 348–354.
7. Rard, J.A. and Spedding, F.H., *J. Chem. Eng. Data*, 1982, vol. 27, no. 4, pp. 451–461.
8. Rard, J.A. and Spedding, F.H., *J. Chem. Eng. Data*, 1981, vol. 26, no. 4, pp. 391–395.
9. Pitzer, K.S., Peterson, T.R., and Silvester, L.-F., *J. Solution Chem.*, 1978, vol. 7, no. 1, pp. 45–46.
10. *Chemical Thermodynamics in Industry: Models and Computation*, Barry, T.I., Ed., Oxford: Blackwell Scientific, 1985.
11. Pyartman, A.K., Kovalev, S.V., and Keskinov, V.A., *Radiokhimiya*, 1997, vol. 39, no. 4, pp. 349–352.
12. Dennis, J.E. and Schnabel, R.B., *Numerical Methods for Unconstrained Optimization and Nonlinear Equations*, New Jersey: Prentice-Hall, 1983.
13. Bellamy, L.J., *The Infra-Red Spectra of Complex Molecules*, New York: Wiley, 1957.
14. Bellamy, L.J., *Advances in Infrared Group Frequencies*, London: Methuen, 1968.

Russian Journal of Applied Chemistry, Vol. 76, No. 1, 2003, pp. 60–64. Translated from Zhurnal Prikladnoi Khimii, Vol. 76, No. 1, 2003, pp. 62–66.

SORPTION AND ION-EXCHANGE PROCESSES

Composite Ion Exchangers Based on KU-23 and KM-2P Cation Exchangers and Nickel(III) Hydroxide and Their Use for Purification of Nickel Sulfate Solutions To Remove Cobalt(II) Impurity

A. A. Blokhin, D. Yu. Maiorov, A. A. Kopyrin, and V. P. Taushkanov

St. Petersburg State Technological Institute, St. Petersburg, Russia

Received May 23, 2002

Abstract—A method of preparing composite ion exchangers based on macroporous cation exchangers and nickel(III) hydroxide was developed, and their suitability for deep purification of nickel(II) sulfate solutions to remove small amounts of cobalt(II) was demonstrated.

Cobalt(II) is the most difficultly removable impurity in nickel(II) salts. On the other hand, the cobalt content in nickel(II) compounds is rigidly limited. The most efficient method of cobalt(II) separation from nickel(II) salts is based on different stability of Co(III) and Ni(III) hydroxides (HO) and involves treatment of nickel(II) salts with freshly deposited $Ni(OH)_3$ [1–4]. Cobalt(II) is oxidized and precipitated as Co(III) HO, while nickel(III) is reduced to Ni(II) and passes into the solution. This method is fairly labor-consuming and does not always provide the required degree of cobalt recovery. As follows from [5], more efficient purification of Ni(II) to remove Co(II) can be attained by passing a solution of Ni(II) salt through a column packed with a granulated ion exchanger containing Ni(III) HO, e.g., with a macroporous cation exchanger with Ni(III) HO introduced into its granules.

The goal of this work is to develop a method of preparing composite ion exchangers based on KU-23 sulfonic cation exchanger or KM-2p carboxylic cation exchanger and nickel(III) HO and assess the suitability of the ion exchangers obtained for purification of Ni(II) salts to remove Co(II).

EXPERIMENTAL

Nickel(III) and cobalt(III) hydroxides were prepared by successive treatment of 0.2 M metal(II) sulfate solutions with 0.5 M solutions of NaOH and $Na_2S_2O_8$. The precipitates formed were kept to mature for 24 h, separated from the mother liquor, washed with water, dried in air at 70°C, crushed, and sieved. Experiments were performed with 0.2–0.5-mm grains of Ni(III) HO.

Preliminarily, the cation exchangers were conditioned by the standard method: successive treatment with NaOH and HCl solutions including intermediate and final washing with water [6]. Experiments were performed under static and dynamic conditions. The ratio of the ion exchanger weight (g) to the solution volume (ml) in the experiments under static conditions was 1 : 100, and time of phase contact, 5–7 days. In experiments under dynamic conditions, we used the preliminarily fractionated composite ion exchangers with 0.5–1.0-mm grains in the air-dry state. Ion exchangers were placed into 10-ml glass columns (the bed height to inner diameter ratio $H : D$ was 15 : 1). The rate of the solution flow through the column was close to 1 specific volume (sp. vol.) per hour. The sorption kinetics was studied by the limited volume method [6, 7]. The effective diffusion coefficients of Co(II) ions were calculated by Dryden–Kay equation [7], and the activation energies were found from the temperature dependence of the diffusion coefficients. The Ni(II) concentration in the solutions was determined complexometrically and (at low concentrations) photocolorimetrically [8]. pH of solutions was measured with glass (ESL-47-07) and AgCl (EVP-AM-3) electrodes and an I-120 ion meter. The nickel(II) content in samples of composite ion exchangers was determined by dissolution of the mineral constituent in 1 M H_2SO_4 with the subsequent determination of Ni(II) in the solution. The Co(II) behavior was

1070-4272/03/7601-0060$25.00

monitored using ^{60}Co tracer. The specific β-radioactivity (counts per unit time) of samples was measured on a KRK-1-01A device with a BDIB-01-1 counter equipped with a PSO2-4 scaler.

To determine the Ni(III) and Co(III) HO redox potentials, the voltage of the cell

$$\begin{array}{c|c|c} \text{Ni, } \underset{[Co(OH)_3]}{Ni(OH)_3} & 1\ \text{M}\ NiSO_4 & \text{Ag,} \\ & & \text{AgCl, } KCl_{sat} \end{array}$$

was measured with an ShCh-1413 digital voltmeter. Preliminarily, electrodes were prepared by pressing one of the compounds studied [composite ion exchanger, Ni(III) or Co(III) HO] ground to the powdered state onto an etched nickel plate with the developed surface. This plate was placed into a fluoroplastic casing equipped with a lead connected to the plate. The mounted electrode was placed in a small bath filled with a 1 M $NiSO_4$ solution. An AgCl electrode was used as a reference electrode.

The first stage of preparing composite ion exchangers based on cation exchangers and Ni(III) HO involved saturation of cation exchangers with Ni(II) ions. The maximal capacity of both cation exchangers with respect to Ni(II) ion was attained at pH close to the onset of the $Ni(OH)_2$ precipitation (pH 6.2–6.3). Therefore, saturation of cation exchangers with Ni(II) ions was performed at pH 6.0–6.2. To find the optimal Ni(II) concentration for saturation of cation exchangers, we measured the isotherms of Ni(II) sorption. It follows from Fig. 1 that the sorption isotherms flatten out at the Ni(II) equilibrium concentration of 0.03–0.04 M.

However, to reduce the volume of the solution passed through the column, a 0.1 M Ni(II) solution was taken. In this case, the total dynamic capacity of the cation exchanger with respect to Ni(II) was 2.2 mmol g^{-1} for KU-23 and 2.8 mmol g^{-1} for KM-2p, which practically coincided with the maximal capacity observed in the sorption isotherms at equilibrium (Fig. 1). After saturation with Ni(II) ions, the cation exchangers were washed with 2–3 sp. vols. of distilled water and were then treated with 5 sp. vols. of 0.5 M NaOH to convert the sorbed Ni(II) into the HO form. Then, the cation exchangers were treated with an $Na_2S_2O_8$ solution to convert $Ni(OH)_2$ into Ni(III) HO. In the process, the cation exchanger color changed from green to black. Observation of microscopic sections of the cation exchanger granules (magnification 100) showed that oxidation of Ni(II) HO to Ni(III) HO was uniform throughout the section. It was noted that the $Na_2S_2O_8$ solution washed out a part of nickel from the column packed with the cation

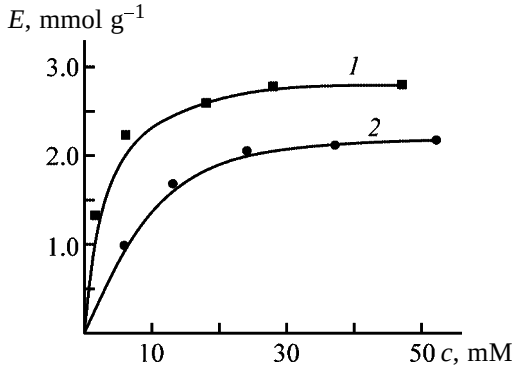

Fig. 1. Isotherms of nickel(II) sorption from solution with pH 6.1 ± 0.05 on cation exchangers (*1*) KM-2p and (*2*) KU-23. (*E*) Capacity of ion exchanger with respect to nickel(II) ion and (*c*) concentration of Ni(II) in the equilibrium solution.

exchanger, especially from the column with KU-23. At the optimal concentration of $Na_2S_2O_8$ (~0.2 M), the washout did not exceed 4–10% (depending on the support), and the cation exchanger grains rapidly turned black. Finally, the ion exchangers were washed to remove excess oxidant. The nickel content was 2.7 and 1.9 mmol g^{-1} in the obtained samples of the composite ion exchangers based on KM-2p and KU-23 cation exchangers, respectively.

The chemical stability of the combined ion exchangers was evaluated by washout of Ni(II) ions with 2 M $NaNO_3$ solutions of various acidities. It was found that the mineral constituent of the composite cation exchangers did not dissolve in solutions with pH 6–8. However, even small acidification caused noticeable dissolution. In solutions with pH 5, 2–3% of the total amount of nickel contained in the composite ion exchangers and in granulated Ni(III) HO dissolved. In solutions with pH < 1, dissolution of the mineral constituent was virtually complete.

Sorption of cobalt(II) ions on Ni(III) HO should proceed due to its oxidation and formation of poorly soluble Co(III) HO in the cation exchanger phase by the reaction

$$Ni(OH)_3 + Co^{2+} \rightleftarrows Co(OH)_3 + Ni^{2+}.$$

In general, the properties of Ni(III) HO in cation exchanger granules may differ from those of Ni(III) HO in the pure form. To predict the use of composite ion exchangers for removing Co(II) from solutions of Ni(II) salts, we compared the redox potentials of both forms of Ni(III) HO and of Co(III) HO. As seen from Table 1, the $Ni((OH)_3/Ni(OH)_2$ redox potential for Ni(III) HO in the composite ion exchanger based on KM-2p resin and pure Ni(III) HO are virtually the

Table 1. Redox potentials of materials containing Ni(III) and Co(III) HO

Material	$\varphi_{M(OH)_i/AgCl,Ag}$	$\varphi_{M(OH)_i/H^+,H_2}$	$\varphi^0_{M(OH)_i/H^+,H_2}$ [9]
	V		
Ni(III) HO	0.18 ± 0.02*	0.40 ± 0.02**	0.48
KM-2p–Ni(III) HO	0.16 ± 0.02*	0.38 ± 0.02**	–
Co(III) HO	–0.10 ± 0.02*	0.12 ± 0.02**	0.17

* ($\varphi_{M(OH)_i/AgCl,Ag}$) Potential vs. AgCl electrode.
** ($\varphi_{M(OH)_i/H^+,H_2}$) Potential vs. hydrogen electrode.

same and close to the reference data [9]. At the same time, they are noticeably higher than the potential of $Co((OH)_3/Co(OH)_2$ couple. Therefore, at the contact of an ion exchanger containing Ni(III) HO with a solution containing Co(II), Co(II) should undergo oxidation and precipitate in the form of Co(III) HO.

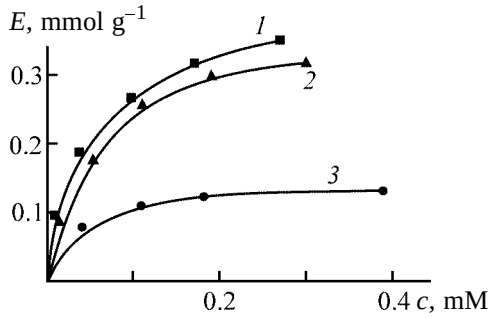

Fig. 2. Isotherms of cobalt(II) sorption from 1 M $NiSO_4$ solution at pH 6.1 ± 0.05 on ion exchangers (*1*) KM-2p–Ni(III) HO, (*2*) Ni(III) HO, and (*3*) KU-23–Ni(III) HO.

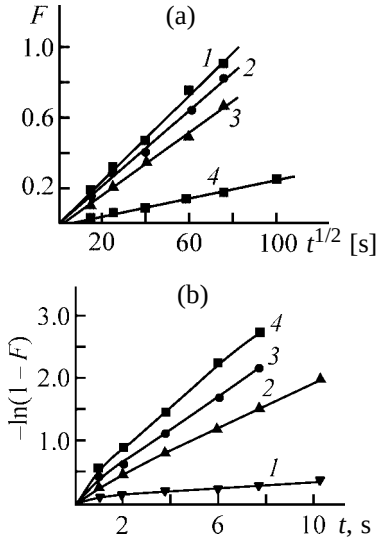

Fig. 3. Plots (a) F–$t^{1/2}$ and (b) $-\ln(1-F)$–t for Co(II) sorption from 1 M $NiSO_4$ on KM-2p–Ni(III) HO ion exchanger. Initial concentration of Co(II) 1 mM, pH 6.10 ± 0.05. Temperature, K: (*1*) 293, (*2*) 308, (*3*) 324, and (*4*) 338.

To find optimal conditions of sorption of Co(II) ions from 1 M solution of $NiSO_4$, we studied the influence of the solution acidity and measured the sorption isotherms. The capacity of the ion exchangers with respect to Co(III) increases with increasing pH and reaches a maximum at pH 6.0–6.3 [at higher pH, Ni(II) HO starts to precipitate]. Within the entire range of Co(II) concentrations in the solution, the capacity of the composite ion exchanger based on KM-2p resin with respect to cobalt(II) is practically equal to the capacity of pure Ni(III) HO (Fig. 2). The capacity of the composite ion exchanger based on KU-23 resin is substantially lower, which is caused by the lower content of Ni(III) HO in it.

The study of the kinetics of Co(II) sorption from 1 M $NiSO_4$ on the composite ion exchanger based on KM-2p resin and on pure Ni(III) HO showed that the rate of Co(II) sorption on both ion exchangers depends on the ion exchanger grain size and is virtually independent of the intensity of solution agitation. This shows that the internal diffusion is the rate-determining stage of the sorption. This is confirmed by the noticeable increase in the sorption rate after interrupting the process for 30 min, the linear dependence of the degree of equilibrium attainment F on $t^{1/2}$ (time), deviation from the straight line of the $-\ln(1-F)$ vs. t plot in the region of low F values (Fig. 3), and the value of Biot B' test (Table 2). It follows from Table 2 that the composite ion exchanger KM-2p–Ni(III) HO has better kinetic characteristics than pure Ni(III) HO. The effective diffusion coefficient D of Co(II) in sorption on the composite ion exchanger is approximately three orders of magnitude higher than that on pure Ni(III) HO. The activation energy E_a (59–62 kJ mol^{-1}) is close to the limiting value of E_a characteristic for processes controlled by internal diffusion [7]. Presumably, the rate of the chemical reaction also affects the process kinetics.

Removal of the Co(II) impurity from Ni(II) salt solutions under dynamic conditions was studied as

Table 2. Kinetics of cobalt(II) sorption from 1 M $NiSO_4$ solution with pH 6.1

Ion exchanger	T, K	$t_{0.5}$,* min	D, $cm^2\ s^{-1}$	B'	E_a, kJ mol^{-1}
Nickel(III) HO	293	3380	3.9×10^{-12}	111	
	308	273	1.5×10^{-11}	343	62 ± 3
	323	94	7.8×10^{-11}	521	
	338	54	1.2×10^{-10}	455	
KM-2p–Ni(III) HO	293	327	2.0×10^{-9}	76	
	308	64	7.6×10^{-9}	80	59 ± 3
	323	36	3.1×10^{-8}	110	
	338	25	4.8×10^{-8}	113	

* ($t_{0.5}$) Half-time of exchange (sorption).

applied to purification of 1 M $NiSO_4$ solution to remove cobalt (1 mM) at pH 6.0. When the solution was passed through a column with pure granulated Ni(III) HO, the flow rate rapidly decreased and, after passing 10 sp. vols., did not exceed 0.1% of the initial value at fully opened clips at the input and output of the column and excess hydraulic pressure of about 0.1 MPa. This is caused by mechanical breakdown of the ion exchanger, which makes it useless in columns, although that, presumably, under other conditions a stronger ion exchanger can be obtained, as demonstrated in [5]. With composite ion exchangers, there are no such problems. When KM-2p cation exchanger containing Ni(III) HO was used, the Co(II) content in the solution of Ni(II) sulfate was decreased by a factor of more than 100 (to the background level) after passing 80 sp. vols. of the solution (Fig. 4a). The composite ion exchanger based on KU-23 resin gives somewhat worse results.

Since the mineral constituent of the composite ion exchangers readily dissolves in acids, the regeneration was performed as follows. After saturation with Co(II), the ion exchanger was washed with water to remove the initial solution, and then 1 M H_2SO_4 was passed through the column. Virtually complete Co(II) desorption is attained after passing 10 sp. vols. of the acid (Fig. 4b). The average concentration of the macrocomponent, Ni(II) in the desorbate, was 0.1–0.12 M. After desorption, the cation exchanger was washed with water, and then it was again saturated with Ni ions and treated with solutions of alkali and oxidant as described above. After three cycles of preparation–sorption–regeneration, the total dynamic capacity of the composite ion exchanger based on KM-2p resin with respect to cobalt(II) did not change noticeably as compared to the first cycle.

CONCLUSIONS

(1) A method was proposed for preparing composite ion exchangers based on macroporous cation exchangers and Ni(III) hydroxide by ion-exchange saturation of cation exchangers with Ni(II) ions and successive treatment with alkali and oxidant with intermediate and final washing with water.

(2) The composite ion exchanger based on KM-2p carboxylic cation exchanger is not inferior to pure granulated nickel(III) hydroxide in selectivity to cobalt ions and noticeably exceeds it in kinetic characteristics.

(3) The suitability of the composite ion exchanger based on KM-2p cation exchanger and Ni(III) hydroxide for exhaustive purification of nickel sulfate solutions to remove cobalt(II) impurities was confirmed. The composite ion exchanger based on KU-23 cation exchanger is less efficient.

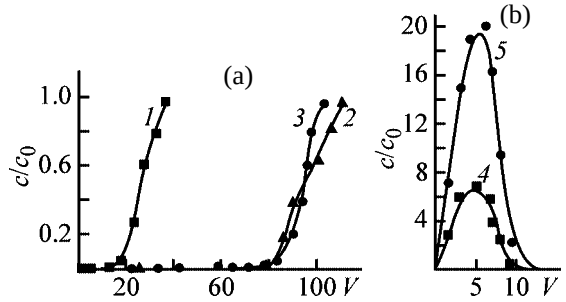

Fig. 4. Output curves of (a) Co(II) sorption from 1 M $NiSO_4$ solution with pH 6.1 on ion exchangers (*1*) KU-23–Ni(III) HO and (*2, 3*) KM-2p–Ni(III) HO in the (*2*) first and (*3*) third sorption cycles and (b) Co(II) desorption from (*4*) KU-23–Ni(III) HO and (*5*) KM-2p–Ni(III) HO with 1 M H_2SO_4. Initial concentration of Co(II) 1 mM. (c/c_0) Ratio of Co(II) concentration in the initial solution to its concentration in the eluate and (V) volume of the passed solution [number of specific (column) volumes].

REFERENCES

1. Gudima, N.V. and Shein, Ya.P., *Kratkii spravochnik po metallurgii tsvetnykh metallov* (Concise Handbook on Non-Ferrous Metallurgy), Moscow: Metallurgiya, 1975.
2. Karyakin, Yu.V. and Angelov, I.I., *Chistye khimicheskie veshchestva* (Pure Chemical Substances), Moscow: Khimiya, 1974.
3. Reznik, I.D., Sobol', S.I., and Khudyakov, V.M., *Kobal't* (Cobalt), Moscow: Mashinostroenie, 1995, vol. 2.
4. JPN Patent 57-55 659.
5. Vol'khin, V.V., in *Khimiya i tekhnologiya neorganicheskikh sorbentov* (Chemistry and Technology of Inorganic Sorbents), Perm: Perm. Politekh. Inst., 1980, pp. 3–19.
6. Marhol, M., *Ion Exchangers in Analytical Chemistry. Their Properties and Use in Inorganic Chemistry*, Prague: Academia, 1982.
7. Kokotov, Yu.A. and Pasechnik, V.A., *Ravnovesie i kinetika ionnogo obmena* (Equilibrium and Kinetics of Ion Exchange), Leningrad: Khimiya, 1970.
8. Charlot, G., *Les methods de la chimie analytique. Analyse quantitative minerale*, Paris: Masson, 1961, 4th ed.
9. Tur'yan, Ya.V., *Okislitel'no-vosstanovitel'nye reaktsii i potentsialy v analiticheskoi khimii* (Redox Reactions and Potentials in Analytical Chemistry), Moscow: Khimiya, 1989.

Russian Journal of Applied Chemistry, Vol. 76, No. 1, 2003, pp. 65–70. Translated from Zhurnal Prikladnoi Khimii, Vol. 76, No. 1, 2003, pp. 67–72.

APPLIED ELECTROCHEMISTRY AND CORROSION PROTECTION OF METALS

Electrodeposition of Chromium–Cobalt Alloy Coatings from Sulfate Electrolytes

B. A. Spiridonov

Voronezh State Technical University, Voronezh, Russia

Received March 11, 2002

Abstract—The influence of electrolysis conditions on the kinetics of formation of the chromium–cobalt alloy in acid sulfate electrolytes containing monoethanolamine was studied along with the composition, current efficiency, and physicochemical characteristics of the coatings.

Electrodeposition of chromium and chromium alloys from nontoxic solutions containing chromium(III) compounds remains an urgent problem. Because of strong tendency of chromium(III) ions to complexation, chromium plating sulfate electrolytes are unstable, which is one of their major drawbacks. The composition of chromium(III) complexes depends on many factors including chromium sulfate concentration, pH, temperature, nature of ligands, etc. [1]. Two chromium(III) sulfate modifications, violet and green, exist, depending on the composition of complexes. Violet chromium(III) sulfate in aqueous solutions forms hexaaqua cations $[Cr(H_2O)_6]^{3+}$ [2], which are slowly hydrolyzed at 20–25°C [3]. At higher temperatures (40–45°C), the hydrolysis is markedly accelerated, and green chromium(III) sulfate (GCS) is formed. The conversion of violet chromium(III) sulfate to GCS is accompanied by a shift of the peaks in their absorption spectra to longer wavelengths [4]. In moderately dilute and concentrated solutions, GCS forms polynuclear anionic complexes consisting of several coordination spheres. In these complexes, Cr^{3+} ions are bound by hydroxo or oxo bridges and by SO_4^{2-} ions [1, 3]. The modification of chromium(III) sulfate solutions essentially affects chromium plating [5–7]. Chromium virtually is not deposited from violet solutions and is deposited with a very low current efficiency (CE_{Cr} = 5–7%) from GCS solutions. The higher current efficiency (up to 35–40%) was attained in chromium plating from "modified" solutions obtained by aging of GCS (keeping at 20–25°C for 20–25 days) [7]. The modified GCS is more stable; it retains its composition for a long time (6 months), as indicated by spectral measurements. The absorption peaks for the modified GCS (λ_1 = 415–416, λ_2 = 582–583 nm; $\varepsilon_1 \approx \varepsilon_2$ = 37) occupy an intermediate position between the peaks for the violet solution and GCS [4].

The addition into the solutions of modified GCS of monoethanolamine (MEA) or urotropin [7] allows deposition of mirror-lustrous protective and decorative chromium coatings 10–15 μm thick. The sulfate electrolytes containing urea [8], glycine [5], formic acid [9], or other complexing additives are more stable. However, chromium coatings deposited from them are also thin. The use of pulsed current makes it possible to increase the thickness of chromium coatings to 40 μm [10]. Recently, new electrolytes containing oxalic acid have been developed, allowing the thickness of chromium coatings to be increased to 100 μm [11, 12].

The thickness of coatings can be increased by increasing electrolysis time τ_{el} at a given current density. At the same time, pH_s and T_s in the near-cathode region vary with increasing τ_{el}. This results in formation of basic chromium compounds and initiates complex transformations in solutions of modified GCS. It was found by thermography [13] that, at the cathodic current density D_c = 30 A dm^{-2}, the temperature T_s of chromium plating electrolyte based on modified GCS increases to 35°C after 10 min and to 45°C after 20 min of electrolysis. As a result, modified GCS in the near-cathode layer is converted into GCS, and the current efficiency by chromium decreases drastically. Therefore, it is appropriate to examine the influence exerted by electrolysis conditions (D_c, pH, etc.) on the current efficiency by chromium and chromium alloys and on their composition and physicochemical properties at τ_{el} not exceeding 10–15 min. At the same time, it should be noted that study of the electrodeposition kinetics of chromium

1070-4272/03/7601-0065$25.00

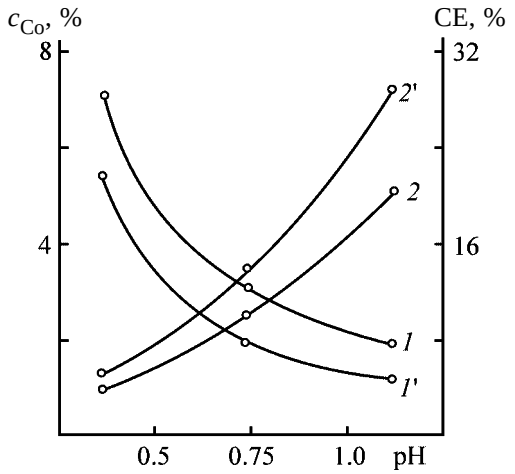

Fig. 1. Influence of electrolyte pH on (*1*, *1*') cobalt content c_{Co} in the chromium–cobalt alloy and (*2*, *2*') current efficiency by the alloy CE. τ_{el} = 5 min, T = 25°C. D_c, A dm^{-2}: (*1*, *2*) 25 and (*1*', *2*') 35.

and chromium alloys at a longer electrolysis time is also of certain interest.

It was established previously [14] that protective properties of chromium coatings deposited from MEA-containing solutions of modified GCS can be improved by electrochemical modification with cobalt. The introduction of $CoSO_4$ into the Cr–Co plating electrolyte based on modified GCS makes it possible to extend the range of D_c values at which lustrous coatings are deposited and increases the throwing power of the electrolyte [15]. The use of pulsed current has been recommended in [16, 17] to stabilize the composition of the plated Cr–Co alloy. In this work, we continued a study of the electrodeposition of Cr–Co alloy from MEA-containing solution of modified GCS along with a study of some physicomechanical properties of the alloy.

EXPERIMENTAL

The study was performed in an electrolyte containing (M) 0.5 modified GCS, 0.5 Na_2SO_4, and 0.032 MEA. To the electrolyte, from 1 to 5 g l^{-1} $CoSO_4$ was added. The current efficiency by the alloy CE_{al} was determined gravimetrically using a copper coulometer and with account taken of the alloy composition. The content of cobalt in the alloy was determined spectrophotometrically with nitroso-R salt, and the chromium content, by oxidation to chromium(VI). The cathodic polarization was studied galvanodynamically (6 mA min) on a P-5827 M potentiostat using a KSP self-recording potentiometer. All potentials are given relative to silver chloride electrode which served as a reference. Platinum was used as auxiliary electrode. The character of the total and partial polarization curves was shown in [17]. Here we report the partial current densities of formation of hydrogen, chromium(II) ions, and metallic cobalt and chromium. The partial currents were determined by decomposition of the total current on the basis of data on the current efficiencies by hydrogen, cobalt, and chromium. The current spent for chromium(II) ion formation by the reaction $Cr^{3+} + e \rightarrow Cr^{2+}$ was determined from the difference between the total current and partial currents of formation of hydrogen, cobalt, and chromium. The polarization curves were taken galvanostatically in a hermetically sealed two-chamber cell for 15 min. The amount of evolved hydrogen was determined volumetrically. The quality of the cathodic deposits was judged from the outward appearance. The reflectivity of the coatings was studied on an FM-58 M photometer, and their morphology, on an MIN-7 microscope. The hardness of the cathodic deposits H_V was determined on a PMT-3 device. The indicator load was 100 g. The internal stresses (ISs) were determined by the method of flexible cathode [18, 19].

The composition of the Cr–Co alloy and the current efficiency by the alloy CE_{al} as functions of the electrolyte pH and D_c are shown in Fig. 1. As seen, with the pH increasing from 0.5 to 1.0, the cobalt content in the alloy decreases from 4 to 2.2% at D_c = 25 A dm^{-2} (curve *1*), and CE_{al} increases from 5.8 to 16.2% (curve *2*). This trend keeps for D_c within 15–30 A dm^{-2}, i.e., in the range corresponding to deposition of lustrous coatings. At D_c = 35 A dm^{-2} the maximal current efficiency by the alloy is attained, 40%.

At pH varied within the indicated range (Table 1), the partial current spent for alloy deposition (at D_c = 20 A dm^{-2}) increases by a factor of about 8.2, that of chromium deposition, by a factor of 7.8, and that of hydrogen formation decreases by a factor of 1.7. The partial rate of cobalt deposition decreases simultaneously. These data explain why the current efficiency by the alloy increases and the alloy becomes enriched with chromium. Apparently, a decrease in the rate of the discharge of Cr^{2+} ions is due to the formation of a cathodic film from basic chromium(III) compounds (the solubility product $SP_{Cr(OH)_3} = 6.31 \times 10^{-31} < SP_{Cr(OH)_2} = 2 \times 10^{-15}$), which exerts a stronger effect at higher pH.

It should be noted that the formation of colloidal $Cr(OH)_3$, which forms a passivation film owing to the

Table 1. Partial current densities of formation of hydrogen, chromium(II), cobalt, and chromium at various pH of the electrolyte (T = 25°C)

pH	D_c, A dm^{-2}	$-E$, V	i_{H_2}	$i_{Cr^{2+}}$	i_{Co^0}	i_{Cr^0}
			A dm^{-2}			
0.5	20	1.22	15.19	4.40	0.19	0.22
	30	1.41	19.02	10.10	0.16	0.38
	40	1.63	22.76	16.42	0.12	0.70
0.75	20	1.05	14.00	5.24	0.15	0.61
	30	1.25	18.46	10.43	0.10	1.01
	40	1.44	21.83	16.62	0.09	1.46
1.0	20	0.82	9.10	9.08	0.11	1.71
	30	1.13	10.70	14.23	0.08	4.99

absorption on active sites of the cathode, is fairly efficiently suppressed in the electrolyte containing MEA as a luster-producing and buffer additive [7]. Without MEA, the coatings are deposited in a very narrow D_c range and are dull. In the presence of MEA, the alloy coatings deposited in the indicated pH range are mirror-lustrous. Increasing pH to 1.0 makes narrower the D_c range, and at D_c = 35 A dm^{-2} dull coatings are deposited. At pH > 1.0 and D_c > 35 A dm^{-2}, the quality of the coatings is appreciably impaired, which is evidently due to incorporation of basic chromium(III) compounds. The coatings become coarsely disperse and brittle, with a developed crack pattern.

The development of crack pattern in the cathodic deposits under certain electrolysis conditions is typical not only for chromium alloys but also, and to a greater extent, for chromium coatings deposited from commercial electrolytes [20] (based on CrO_3) and from sulfate electrolytes. One of the reasons why the crack pattern is formed is the appearance of internal stresses owing to incorporation of hydrogen. The forming chromium hydrides are instable and can crystallize in the form of hexagonal crystals Cr_2H–CrH or face-centered cubic crystals CrH–CrH_2 [21]. Spontaneous transformation of the metastable hexagonal modification of chromium into the stable body-centered cubic modification is accompanied by a decrease in the deposit volume and by appearance of large internal stresses. As the cobalt content in the alloy increases, for example, from 1 to 5% (Fig. 2, curve *1*), ISs decrease by a factor of approximately 1.3, which is evidently due to decreased hydrogenation [17].

The cathodic current density markedly affects ISs. For example, with D_c increasing from 30 to 60 A dm^{-2}, ISs increase by a factor of approximately 1.5 (at the cobalt content in the alloy of 5%). This may be due to incorporation of basic chromium compounds and to increased hydrogen absorption. The dependence of ISs on D_c for chromium coatings deposited from sulfate electrolytes is similar [22].

As seen from Fig. 3, increasing the cobalt content in the alloy increases the hardness of the cathodic deposits. The H_V for the 1% cobalt alloy obtained at

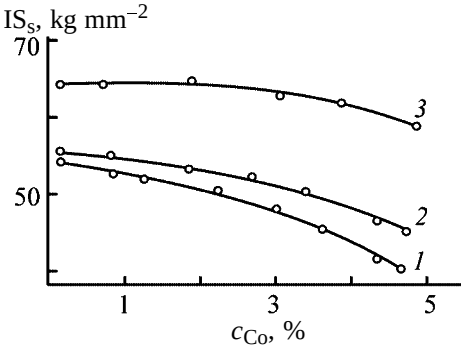

Fig. 2. Internal stresses ISs in the cathodic deposits of the alloy vs. the cobalt content in the alloy c_{Co}. pH 0.75; the same for Figs. 3 and 5. D_c, A dm^{-2}: (*1*) 30, (*2*) 40, and (*3*) 60.

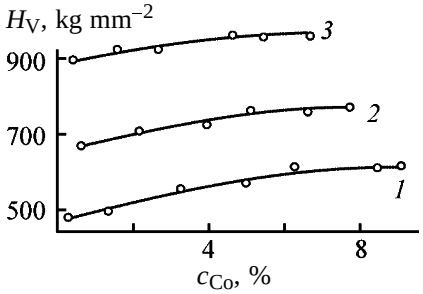

Fig. 3. Microhardness H_V of the chromium–cobalt alloy vs. the cobalt content in the alloy c_{Co}. D_c, A dm^{-2}: (*1*) 40, (*2*) 50, and (*3*) 60.

Table 2. Partial current densities of formation of hydrogen, chromium(II), cobalt, and chromium at various electrolysis times

τ_{el}, min	D_c, A dm^{-2}	i_{H_2}	$i_{Cr^{2+}}$	i_{Co^0}	i_{Cr^0}
		A dm^{-2}			
5	20	13.64	4.67	0.37	1.32
	30	18.05	9.52	0.26	2.17
	40	21.24	15.42	0.22	3.12
10	20	13.80	4.85	0.28	1.07
	30	18.26	9.76	0.19	1.79
	40	21.56	15.61	0.17	2.66
20	20	14.00	5.24	0.15	0.61
	30	18.46	10.43	0.10	1.01
	40	21.83	16.62	0.09	1.46

D_c = 40 A dm^{-2} (curve *1*) is 490 kg mm^{-2}, and for the 9% cobalt alloy obtained under similar conditions it increases to 620 kg mm^{-2}. The increase in H_V may be due to the formation of a solid solution in the alloy containing up to 10% cobalt [17]. As known [23], the hardness H_V of solid solutions is always higher than that of the components. The hardness is strongly affected by the cathodic current density. For example, with D_c increased from 40 to 60 A dm^{-2}, the hardness of the Cr–Co alloy containing 5% Co increases from 580 (Fig. 3, curve *1*) to 960 kg mm^{-2} (curve *3*). The similar effect of D_c on the hardness of cobalt coatings has been demonstrated in [24–26]. Electrolytic chromium is characterized by high hardness, which is ascribed to incorporation of hydrogen and oxygen, internal stresses, and grain size [20]. The dependence of H_V of chromium on its hydrogen content was not confirmed by the available experimental data. On heating, hydrogen is comparatively easily evolved from electrolytic chromium, and at 500°C virtually no hydrogen remains, with the hardness remaining the same. The direct correlation of H_V with CE has not been revealed either. The major factors determining H_V of electrolytic chromium are the presence of oxygen in it and the grain size. The effect exerted by oxygen on the chromium hardness is due to the distribution of dispersed chromium oxide in its bulk. The dependence of H_V of the chromium–cobalt alloy on the electrolyte pH is presented in Fig. 4. With pH increasing, e.g., from 0.5 to 0.75 (D_c = 60 A dm^{-2}), H_V increases from 720 (curve 1) to 925 kg mm^{-2} (curve *2*), which can be explained by incorporation of basic chromium(III) compounds into the cathodic deposit, increasing the oxygen content.

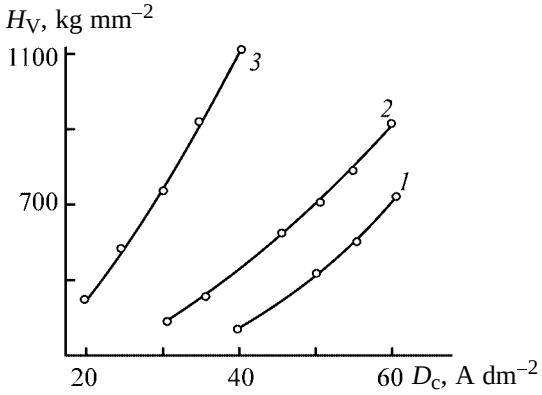

Fig. 4. Influence of the cathodic current density D_c on the microhardness H_V of the Cr–Co alloy. Electrolyte pH: (*1*) 0.5, (*2*) 0.75, and (*3*) 1.0.

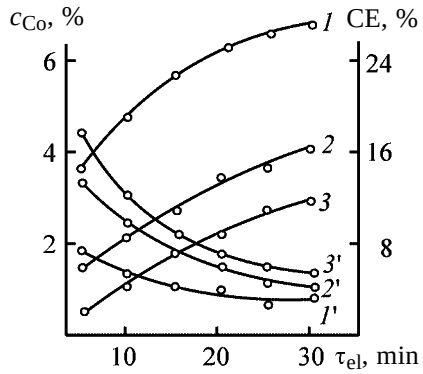

Fig. 5. Influence of the electrolysis time τ_{el} on (*1–3*) cobalt content in the alloy c_{Co} and (*1'–3'*) current efficiency by the alloy CE. D_c A dm^{-2}: (*1, 1'*) 30, (*2, 2'*) 40, and (*3, 3'*) 60.

Table 2 shows that, as τ_{el} increases from 5 to 20 min, the partial current of hydrogen evolution increases and that of Cr–Co alloy formation decreases. As a result, CE_{al} decreases, e.g., from 14 to 6.5% at D_c = 40 A dm^{-2} (Fig. 5, curve *2'*). It should be noted that the partial current of hydrogen evolution decreases at D_c = 20–40 A dm^{-2}, with the decrease being more pronounced at longer τ_{el}, and the alloy is enriched with cobalt. For example, the alloy deposited at D_c = 40 A dm^{-2} contains 1.5% cobalt after τ_{el} = 5 min and 3.5% cobalt after 20 min of electrolysis (Fig. 5, curve *2*). With the electrolysis time increased to 30 min, the cobalt content increases by about 4%. One of the reasons why the alloy becomes chromium-depleted at longer τ_{el} is the pH_s growth favoring formation of chromium(III) hydroxide impeding chromium deposition. Another reason is the increase in T_s after 20 min of electrolysis, which is accompanied by GCS formation and by even sharper decrease in the chromium current efficiency. Evidently, this tendency is retained when chromium is deposited jointly with cobalt.

It should be noted that, with increasing τ_{el}, the chromium(II) ion formation accelerates (Table 2). For example, at D_c = 40 A dm^{-2} the partial current of chromium(II) formation increases from 15.42 to 16.62 A dm^{-2}. Accumulation of Cr^{2+} ions should increase the rate of the formation of metallic chromium, in accordance with the reaction $Cr^{2+} + 2e \rightarrow Cr^0$. At the same time, Table 2 shows that actually the rate of chromium formation decreases by a factor of 2.2 with increasing τ_{el} (Table 2). This suggests occurrence of the more probable three-electron reaction $Cr^{3+} + 3e \rightarrow Cr^0$. Such a scheme of electrolytic reduction of chromium from sulfate electrolytes has been considered previously [27, 28].

With increasing τ_{el}, the ISs in the cathodic deposits grow, which is due to increase in pH_s and hydrogen absorption of the coatings promoted by incorporation of chromium(III) hydroxide. As a result, the quality of the coatings is impaired. Lustrous coatings are deposited at τ_{el} shorter than 30–35 min; semilustrous coatings, at longer electrolysis times; and dull coatings, at τ_{el} > 60 min.

CONCLUSIONS

(1) The method of partial curves showed that, as pH of the electrolyte is increased from 0.5 to 1.0, the partial current of hydrogen and cobalt formation decreases and that of chromium formation grows. Under these conditions, the alloy is enriched with chromium, and the current efficiency by the alloy increases.

(2) With increasing t_{el}, the partial currents of chromium and cobalt formation decrease and that of hydrogen formation grows, the relative content of cobalt in the alloy increases, and the current efficiency by the alloy decreases substantially, especially after 30 min of electrolysis. The fact that the partial current of chromium(III) ion formation increases with electrolysis time and the current efficiency by the alloy does not grow suggests occurrence of the three-electron reaction of the formation of metallic chromium at its joint deposition with cobalt.

(3) The internal stresses decrease with increasing cobalt content in the alloy and grow with increasing cathodic current density. The cathodic current density markedly affects the alloy hardness. For example, with D_c increased from 20 to 40 A dm^{-2}, the hardness grows from 480 to 1100 kg mm^{-2}.

(4) To obtain protective and decorative Cr–Co alloy coatings up to 20 μm thick, we recommend an electrolyte containing modified green chromium(III) sulfate and monoethanolamine.

REFERENCES

1. Remy, H., *Lehrbuch der anorganischen Chemie*, Leipzig: Geest und Portig, 1961, vol. 2.
2. Grinberg, A.A., *Vvedenie v khimiyu kompleksnykh soedinenii* (Introduction to Coordination Chemistry), Leningrad: Goskhimizdat, 1951.
3. Lavrukhina, A.K. and Yukina, L.V., *Analiticheskaya khimya khroma* (Analytical Chemistry of Chromium), Moscow: Nauka, 1979.
4. Falicheva, A.I., *Elektrokhimiya*, 1968, vol. 4, no. 7, pp. 856–858.
5. Kudryavtsev, N.T., Pshilusski, Ya.B., and Potapov, I.I., *Izv. Vyssh. Uchebn. Zaved., Khim. Khim. Tekhnol*., 1962, vol. 5, no. 2, pp. 617–621.
6. Falicheva, A.I., *Zh. Vses. Khim. O–va im. D.I. Mendeleeva*, 1964, vol. 9, no. 8, pp. 555–557.
7. Falicheva, A.I., Chromium Plating from Electrolytes Containing Chromium(III) and Chromium(VI) Compounds, *Doctoral Dissertation*, Sverdlovsk, 1971.
8. Iosida, T., *J. Chem. Soc. Jpn. Ind*., vol. 56, no. 9, pp. 649.
9. Danilov, F.I., and Ben-Ali, M.N., *Elektrokhimiya*, 1989, vol. 25, no. 3, pp. 409–412.
10. Shalimov, Yu.N., Falicheva, A.I., and Spiridonov, B.A., *Zashch. Met*., 1977, vol. 13, no. 15, pp. 623–625.
11. Edigaryan, A.A. and Polukarov, Yu.N., *Zashch. Met*., 1996, vol. 32, no. 5, pp. 504–508.
12. Edigaryan, A.A. and Polukarov, Yu.N., *Zashch. Met*., 1998, vol. 34, no. 2, pp. 117–120.
13. Falicheva, A.I., Shalimov, Yu.N., and Ionova, I.G., *Zashch. Met*., 1972, vol. 8, no. 4, pp. 499–503.
14. Falicheva, A.I., Spiridonov, B.A., Shalimov, Yu.N., and Zhernokleeva, S.V., *Zashch. Met*., 1975, vol. 11, no. 5, pp. 622–623.
15. Falicheva, A.I., Spiridonov, B.A., and Shalimov, Yu.N., *Zashch. Met*., 1976, vol. 12, no. 3, pp. 342–344.
16. RF Patent 2 130 091.
17. Spiridonov, B.A., and Falicheva, A.I., *Zh. Prikl. Khim*., 2001, vol. 74, no. 11, pp. 1784–1787.
18. Shluger, M.A., in *Teoriya i praktika elektroliticheskogo khromirovaniya* (Theory and Practice of Chromium Electroplating), Moscow: Akad. Nauk SSSR, 1957, p. 147.
19. Lur'e, Yu.Yu., *Spravochnik po analiticheskoi khimii* (Handbook on Analytical Chemistry), Moscow: Khimiya, 1979.

20. Vagramyan, A.T. and Solov'eva, Z.A., *Dokl. Akad. Nauk SSSR*, 1949, vol. 68, no. 2, pp. 321–324.
21. Saali, A., *Khrom* (Chromium), Moscow: Metallurgiya, 1971.
22. Gulyaev, A.A., Hydrogen Absorption by Chromium Deposits Obtained from Electrolytes Containing Chromium(III) Compounds, *Cand. Sci. Dissertation*, Voronezh, 1973.
23. Fedot'ev, N.P., Bibikov, N.N., Vyacheslavov, P.M., and Grilikhes, S.Ya., *Elektroliticheskie splavy* (Electrolytic Alloys), Moscow: Mashgiz, 1962.
24. Lainer, V.I. and Kudryavtsev, N.T., *Osnovy gal'vanostegii* (Principles of Electroplating), Moscow: Metallurgizdat, 1957, part 2.
25. Shreider, A.V., in *Teoriya i praktika elektroliticheskogo khromirovaniya* (Theory and Practice of Chromium Electroplating), Moscow: Akad. Nauk SSSR, 1957, pp. 77–95.
26. *Prikladnaya elektrokhimiya* (Applied Electrochemistry), Kudryavtsev, N.T., Ed., Moscow: Khimiya, 1975.
27. Zabotin, P.I., and Kozlovskii, M.T., *Izv. Akad. Nauk Kaz. SSR, Ser. Khim.*, 1956, issue 6, no. 10, pp. 64–68.
28. Falicheva, A.I., *Izv. Vyssh. Uchebn. Zaved., Khim. Khim. Tekhnol.*, 1976, vol. 19, no. 11, pp. 1734–1737.

Russian Journal of Applied Chemistry, Vol. 76, No. 1, 2003, pp. 71–75. Translated from Zhurnal Prikladnoi Khimii, Vol. 76, No. 1, 2003, pp. 73–77.

APPLIED ELECTROCHEMISTRY AND CORROSION PROTECTION OF METALS

Composition of the Cobalt Sulfide Coating after Its Electrochemical Reduction

G. Valiuliene, A. Žeriene, V. Jasulaitiene, and I. Možginskiene

Institute of Chemistry, Vilnius, Lithuania

Received July 19, 2002

Abstract—X-ray photoelectrom spectroscopy was used to study the composition of the initial and electrochemically reduced cobalt coating formed by the adsorption procedure involving treatment of a carbon glass electrode in a solution of Co(II) ammine complexes, hydrolytic washing in water, and conversion to sulfide in Na_2S solution.

Sulfides of many metals have low electrical resistivity [1] and can be used as electroconducting sublayers for decorative metal plating of plastics and in manufacture of printed-circuit boards. Nonstoichiometric copper sulfide ($Cu_{2-x}S$), whose formation, composition, and electrochemical properties are studied in detail [2–8], is widely used for this purpose. Electrochemical deposition of metals can occur only after reduction of $Cu_{2-x}S$ to metal [7, 8]. To obtain a reliable metal coating, it is, however, necessary to perform plating in two or three cycles.

Cobalt sulfide coatings [9] formed in one cycle are also used today as electroconducting layers. Nickel can be deposited on it in two or three cycles, as on $Cu_{2-x}S$. Formation, electrochemical activity, and modification of the cobalt sulfide layer have been described in [9–12]. At the same time, the composition of such coatings after reduction was not studied.

In this work, we used X-ray photoelectron spectroscopy (XPS) to determine the composition of the cobalt sulfide coatings before and after electrochemical reduction.

EXPERIMENTAL

The cobalt sulfide coating was formed by the adsorption procedure involving treatment of the working electrode in a solution containing 0.18 M $CoSO_4 \cdot 7H_2O$ and 0.12 M $(NH_2OH)_2 \cdot H_2SO_4$, to which NH_4OH (25% solution) was added to pH 11.0. This was followed by hydrolytic washing with distilled water, conversion to sulfide in 0.13 M Na_2S aqueous solution, and washing with distilled water. This comprised one cycle of formation of the cobalt sulfide coating. The coatings studied by XPS were formed in three cycles, each 30 s, at $25 \pm 1°C$.

The sulfide coatings were electrochemically reduced in a 0.1 M $KClO_4$ solution at $T = 20 \pm 1°C$ in a YaSE-2 standard cell. An SU-1200 carbon glass with a working surface area of 1 cm^2 was the working electrode. Saturated silver chloride electrode was the reference electrode, and platinum gauze, the auxiliary electrode. The potentials E were recalculated relative to standard hydrogen electrode. The voltammograms (VA) were measured with a PI-50-1 potentiostat and a PR-8 programmer and were recorded with an XY RECORDER A3 self-recording potentiometer. The scanning rate of the potential was 6×10^{-2} V s^{-1}.

The composition of the sulfide coatings was studied by X-ray photoelectron spectroscopy (XPS) on an ESCALAB-MK II Vacuum Generator Scientific spectrometer (the United Kingdom). As a source of soft X-ray radiation served a magnesium anode (1253.6 eV, 300 W). The pressure in the analytical chamber of the spectrometer was 1.33×10^{-8} Pa. An AG-2 argon gun (beam energy 20 eV, current 20 μA) in a preparative chamber was used to study the depth distribution of elements. The rate of the surface etching was 2 nm min^{-1}, and etching time, 30, 60, and 120 s. The accuracy of the method was ±0.1 at. %. In study of the Co sulfide coatings by XPS, we recorded the Co2$p_{3/2}$ photoelectron spectra. The empirical factors of sensitivity of these elements were taken from the literature [13], and the recorded spectra were compared with the reference spectra [14].

In [10], the electrochemical behavior of a cobalt sulfide coating in 0.1 M $KClO_4$ was studied by cyclic voltammetry. It was found that the Co(III) compounds

1070-4272/03/7601-0071$25.00

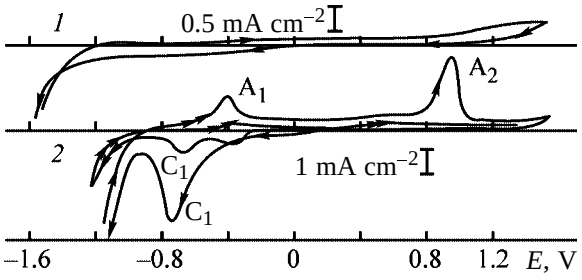

Fig. 1. Cyclic potentiodynamic curves taken in 0.1 M $KClO_4$ solution. Two deposition cycles; T = 20°C; V_{sc} = 5×10^{-2} V s^{-1}. Electrode: (*1*) carbon glass and (*2*) carbon glass coated with cobalt sulfide.

are reduced to Co(II) in the potential range from –0.4 to –0.9 V (Fig. 1). Namely, reduction of CoOHS to CoS and $Co(OH)_2$ (cathodic current peak C_1) was suggested.

In the XPS study of the sulfide coating, we paid attention to the distribution of Co, O, and S elements over the surface and throughout the depth of the coating (Fig. 2). Our results show that the surface of the initial and reduced coatings contains up to 65 at. % oxygen. About 20 at. % oxygen was found in deeper layers of the coating. The measured binding energies E_b of Co2$p_{3/2}$ (780.6±0.1 eV) and O1*s* (531.0±0.3, 529.7±0.1 eV) electrons (Table 1; Figs. 3a, 3b) sug-

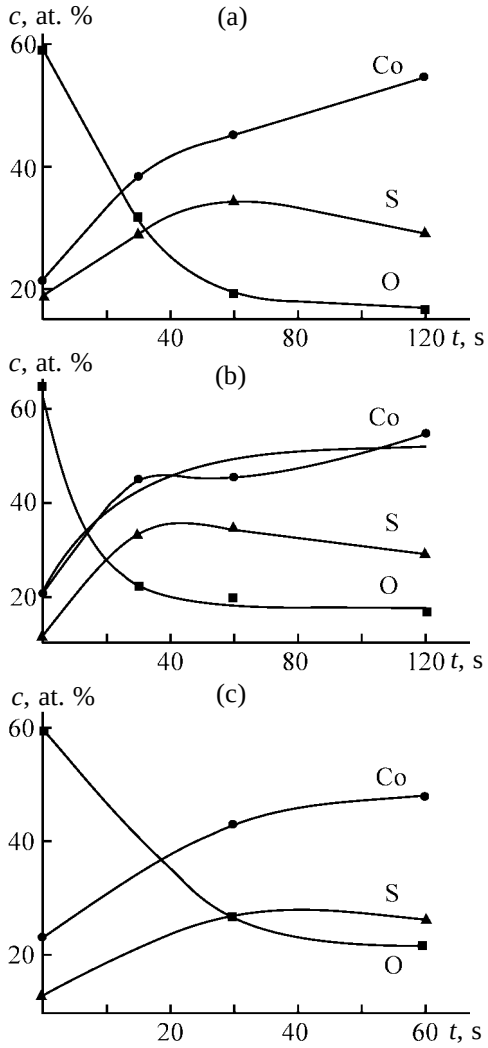

Fig. 2. Content of the elements c in the cobalt sulfide coating formed in three cycles vs. the time t of etching with Ar^+ ions. Coating: (a) initial and (b, c) reduced in 0.1 M $KClO_4$ solution at the potential scanned from E_{st} to –0.85 and –1.3 V, respectively.

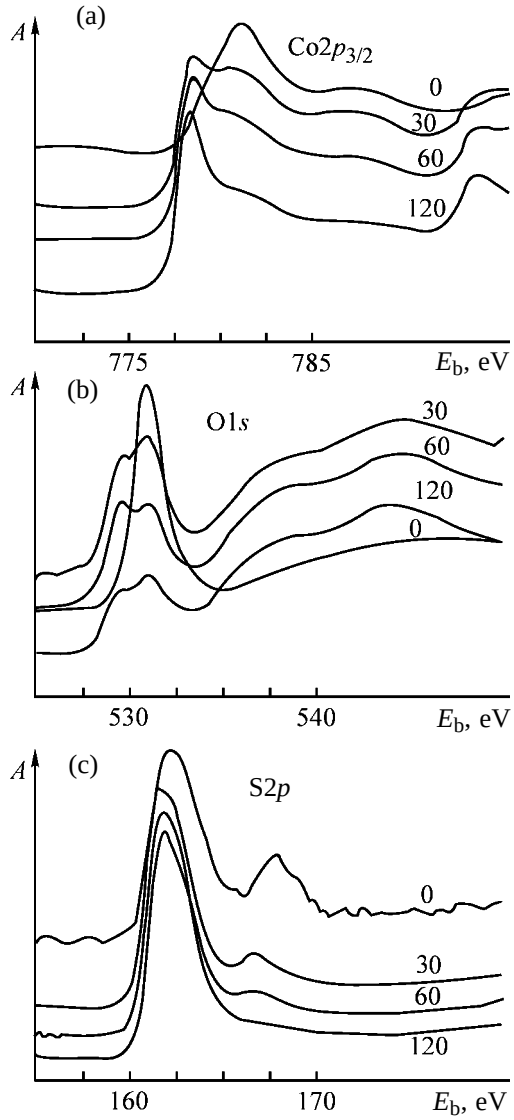

Fig. 3. XPS of the cobalt sulfide coatings. (*A*) Intensity and (E_b) binding energy; the same for Figs. 4, 5. (a) Co2$p_{3/2}$, (b) O1*s*, and (c) S2*p*; the same for Figs. 4, 5. The etching time (s) is denoted at curves; the same for Figs. 4 and 5.

Results of XPS analysis of the cobalt sulfide coating*

Coating no.**	t, s	E_b, eV			I_O/I_{Co}		I_s/I_{Co}		Coating composition
		Co2$p_{3/2}$	O1s	S2p	OH^-	SO_3^{2-}	CoS	$CoSO_3$	
1	0	778.1, 780.9	529.7, 531.1	162.6, 167.8	1.88	1.9	7	2.7	$Co(OH)_3$
	30	778.1, 780.9	529.7, 531.1	162.3, 166.7	1.39	0.98	1.53	0.27	CoS
	60	778.1, 780.9	529.7, 531.1	162.3, 166.7	1.02	0.71	1.44	0.19	$CoSO_3$, CoOHS
2	0	778.0, 780.9	529.7, 531.1	162.7, 166.9	2.02	5	10.4	5.2	$Co(OH)_2$
	30	778.0, 780.9	529.7, 531.1	162.8	1.0	0.38	1.35	0.13	CoS
	60	778.0, 780.9	529.7, 531.1	162.8	0.92	0.29	1.25	0.12	$CoSO_3$
3	0	778.1, 780.5	529.7, 531.0	162.3, 167.5	1.84	1.93	5.16	1.25	Co, CoS
	30	778.1, 780.5	529.7, 531.0	162.3	1.1	0.47	1.55	0.17	$Co(OH)_2$
	60	778.0, 780.6	529.7, 531.1	162.3	0.77	0.36	1.33	0.09	$CoSO_3$

* (I_O/I_{Co}, I_s/I_{Co}) Intensity ratio of oxygen to cobalt and of sulfur to cobalt, as calculated from Figs. 3–5; (t) time of Ar^+ etching.
** Coating no.: (1) initial and (2, 3) reduced at the potential scanned from the steady-state potential to –0.85 and –1.3 V, respectively.

gest that oxygen occurs in the forms of $Co(OH)_2$, $Co^{III}OHS$, and $CoSO_3$. These compounds were detected not only on the surface, but also in deeper layers of the coating. At the same time, a large amount of oxygen on the surface may be due to adsorption and chemisorption of the oxygen compounds of cobalt and also of water and oxygen molecules.

Apart from oxygen compounds of cobalt, the cobalt sulfide coatings formed in three cycles contain CoS (E_bS2p = 166.7 ± 0.1 eV) (Table 1, coating no. 1). This compound was detected after the upper layer 1 or 2 nm thick was etched with Ar^+ ions. The amount of $CoSO_3$ abruptly decreases with depth. The intensity ratios calculated from the S2p and Co2$p_{3/2}$ spectra for cobalt(II) sulfide and sulfate are different on the surface of the sulfide coating and at a depth of 2 nm (Table 1). Compared to $CoSO_3$, the amount of CoS amount is larger by a factor of approximately 2.6 on the surface and by a factor of 5.6 and 7.5 at a depth of 1 and 2 nm, respectively. This fact suggests that $CoSO_3$ is formed solely on the coating surface, whereas in deeper layers CoS dominates. $CoSO_3$ may be formed owing to oxidation of S^{2-} with Co(III) [15]:

$$6CoOOH + 6S^{2-} + 3H_2O = CoSO_3 + 5CoS + 12OH^-. \quad (1)$$

Accprding to reaction (1), the amount of forming $CoSO_3$ should be smaller by a factor of 5 than that of CoS. The S2p spectra (Fig. 3c) shows that the amount of sulfite ($E_b \approx$ 166.7 eV) is smaller than that of sulfide ($E_b \approx$ 162.1–162.7 eV). The coating contains about 19 at. % S on the surface and from 29 to 34 at. % S in deeper layers (Fig. 2a). The binding energies in the S2p spectrum do not correspond to elemental sulfur (E_b = 164.1 ± 0.1 eV), i.e., it is absent in the coating. This result is in agreement with the voltammetric data. The current peak of sulfur reduction was not revealed in the voltammograms of reduction of the cobalt sulfide coatings (Fig. 1).

In the sulfide coating reduced at the potential E scanned from the steady-state potential E_{st} to –0.85 V, the $CoSO_3$ amount on the surface (I_S/I_{Co} = 5.2) is two times that in the initial coating (I_S/I_{Co} = 2.7). The $CoSO_3$ amount in deeper layers abruptly decreases (I_S/I_{Co} = 0.12).

In the coating partially reduced to E = –0.85 V, cobalt sulfide CoS (E_b = 778.0 ± 0.1 eV) is present both on the surface and in deeper layers, because the reduction occurs at E < –1.0 V [10], i.e., in the range of hydrogen evolution [16]. The CoS content on the surface is 1.5 times higher than in initial coating. The I_S/I_{Co} ratio for CoS, as calculated from the Co2$p_{3/2}$ and S2p spectra (Figs. 4a, 4c), is 10.4 and 7.0 for the initial and reduced coatings, respectively (Table 1, coating nos. 1, 2). Apparently, the increased amount of CoS on the surface of the reduced coating is due to the reduction of the Co(III) compound, i.e., CoOHS (Fig. 1, curve *2*, cathodic current peak C_1), which occurs in the range of E from –0.4 to –0.9 V with formation of CoS and $Co(OH)_2$. The results obtained confirm the assumption [10] that the current peak C_1 at E = –0.75 V in the cyclic voltammogram taken in a 0.1 M $KClO_4$ solution is due to the reduction of the Co(III) compound containing not only oxygen but also sulfur, i.e., of CoOHS.

CoS obtained by deposition from aqueous solutions of salts is sparingly soluble (SP 10^{-22}) [17]. The solubility of the CoS precipitate decreases further with time. This is explained by appearance of new bonds

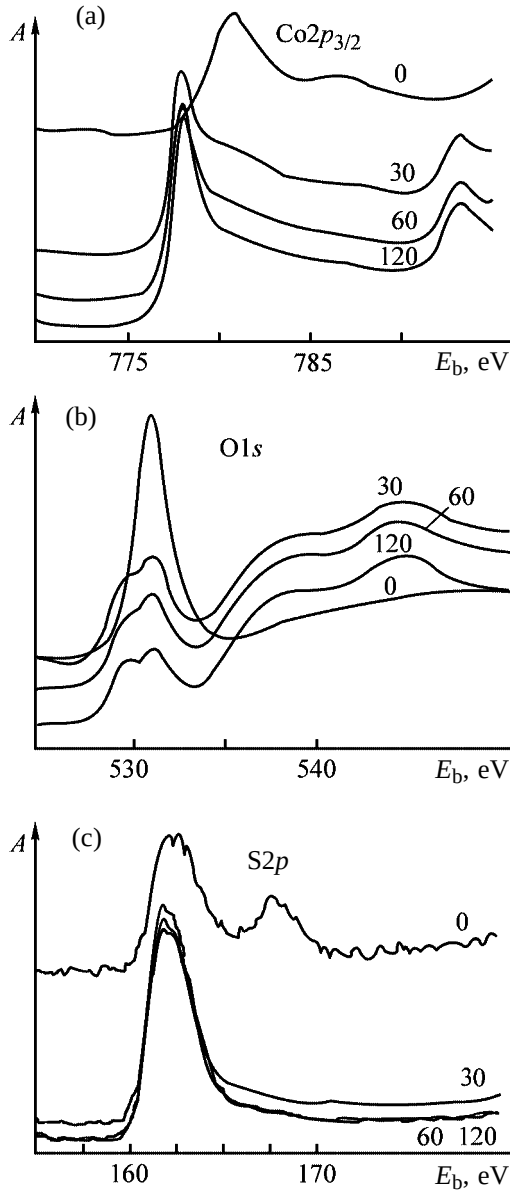

Fig. 4. XPS of the cobalt sulfide coatings reduced in 0.1 M $KClO_4$ solution at the potential E scanned from E_{st} to –0.85 V.

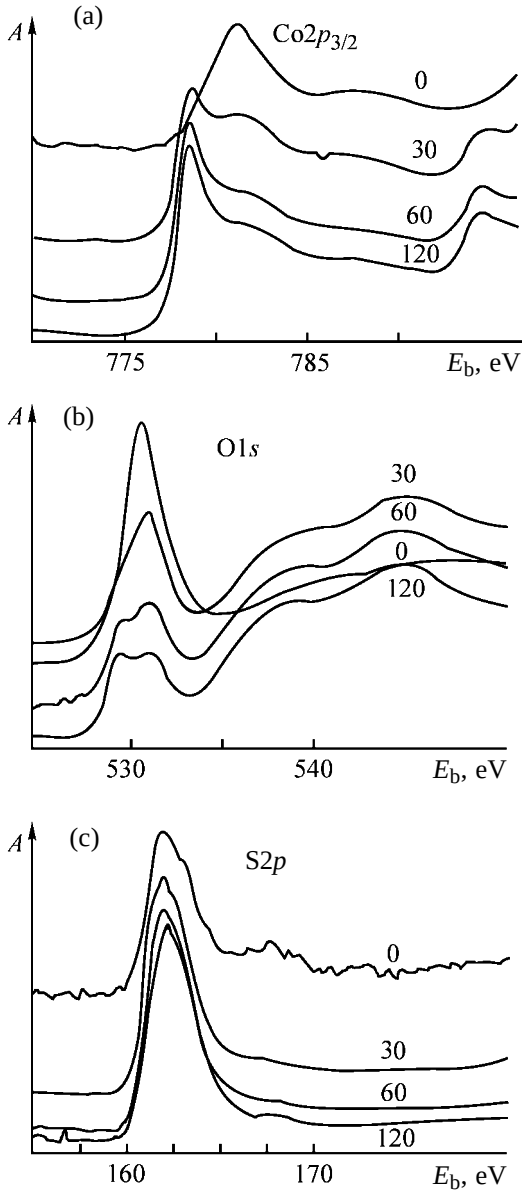

Fig. 5. XPS of the cobalt sulfide coatings reduced in 0.1 M $KClO_4$ solution at the potential E scanned from E_{st} to –1.3 V.

due to oxidation of Co(II) to Co(III) and hydrolysis to $Co^{III}OHS$. We found no published XPS data for CoOHS.

After the reduced coating was etched with Ar^+ ions for 30 and 60 s, the I_S/I_{Co} intensity ratio decreased to 1.35 and 1.25, respectively (Table 1, coating no. 2). Probably, the decrease in the CoS decrease at depths of 1 and 2 nm is due to the formation of $Co(OH)_2$, which is a product of CoOHS reduction. Cobalt(II) hydroxide, $Co(OH)_2$, can block the electrode surface, change its electrical properties, and impede further reduction of CoOHS.

We studied the composition of the sulfide coatings reduced at the potential E scanned from E_{st} to –1.3 V, i.e., after the potential of CoS reduction was attained. The results (Table 1, Figs. 5a–5c) show that the surface layer of the coating consists of $Co(OH)_2$, CoS, and $CoSO_3$. Cobalt sulfite was present solely on the surface and was absent at a depth of 1 nm. The oxygen to cobalt intensity ratio I_O/I_{Co} (Table 1, coating no. 3) for $Co(OH)_2$ and CoS decreases. Cobalt(II) sulfide was detected both on the surface and at a depth of 1–2 nm.

The I_S/I_{Co} ratio for CoS, calculated from the

spectral data (Figs. 5a, 5c) is 5.16. This value is lower than that for initial sulfide coating (Table 1, coating no. 1). This result may be due to the reduction of CoS to metallic Co at the potential *E* scanned down to –1.3 V, which is supported by the Co L_3VV Auger spectra (kinetic energy E_k 772.5, 774.3 eV). Metallic cobalt was found both on the surface and at a depth of 1–2 nm. It should be noted, however, that the CoS reduction after electrochemical treatment to –1.3 V is incomplete. This conclusion was confirmed not only by X-ray photoelectron spectroscopy but also by cyclic voltammetry.

CONCLUSIONS

(1) The composition of the cobalt sulfide coating was studied by X-ray photoelectron spectroscopy. The coating reduced in 0.1 M $KClO_4$ solution and the initial coating contain about 60 at. % oxygen on the surface and ~20 at. % oxygen in deeper layers. This result may be due to adsorpton and chemisorption of oxygen compounds of cobalt and also of water and oxygen molecules.

(2) The initial cobalt sulfide coating is a mixture of the compounds CoS, $CoSO_3$, $Co(OH)_2$, and CoOHS, whereas the reduced coating is a mixture of Co^0, CoS, $CoSO_3$, and $Co(OH)_2$. The presence of Co(II) compounds shows that the reduction is incomplete, even after attaining the potential of extensive hydrogen evolution.

(3) The large amount of CoS in the partially reduced (to –0.85 V) cobalt sulfide coating shows that the cathodic peak in the cyclic voltammograms at *E* = –0.75 V is due to the reduction of CoOHS.

REFERENCES

1. Koch, D.F.A., *Modern Aspects of Electrochemistry*, Bockris, J.O'M., and Conwey, B.E., Eds., New York: Plenum, 1975, vol. 10, pp. 211–237.
2. Golovchanskaya, R.G. and Kruglikov, S.S., *Itogi Nauki Tekh., Ser.: Elektrokhim.*, 1987, vol. 25, pp. 79–143.
3. Žebrauskas, A., *Chem. Technol.* (Lithuania), 1996, no. 1(3), pp. 39–44.
4. Vinkevičius, J., Možginskiene, I., and Jasulaitiene, V., *J. Electroanal. Chem.*, 1998, vol. 442, pp. 73–82.
5. Pilite, S., Valiuliene, G., Želiene, A., and Vinkevičius, J., *Chemija*, 1996, no. 2, pp. 96–103.
6. Naruškevičius, L.L. and Rosovskis, G.I., *J. Adhesion Sci. Technol.*, 1994, vol. 8, no. 9, pp. 1007–1015.
7. Chumakov, A.A., Golovchanskaya, R.G., and Kuznetsov, V.N., *Izv. Vyssh. Uchebn. Zaved., Khim. Khim. Tekhnol.*, 1985, vol. 28, no. 2, pp. 125–126.
8. Vinkevičius, I., Možginskiene, I., Želiene, A., and Pilite, S., *Zh. Prikl. Khim.*, 1997, vol. 70, no. 12, pp. 1987–1992.
9. Naruškevičius, L.L., Rosovskis, G.I., Simkunaite, B., *et al.*, *Chem. Technol.* (Lithuania), 2001, no. 4 (21), pp. 31–35.
10. Želiene, A. and Valiuliene, G., *Chem. Technol.* (Lithuania), 1999, no. 1(10), pp. 24–31.
11. Vinkevičius, J., Švickus, N., and Jasulaitiene, V., *Trans. IMF*, 2001, vol. 79, pp. 33–37.
12. Vinkevičius, J., Švickus, N., Jasulaitiene, V., and Gudaviciute, I., *J. Solid State Electrochem.*, 2002, vol. 6, pp. 209–214.
13. *Practical Surface Analysis by Auger and X-Ray Photoelectron Spectroscopy*, Briggs, D. and Seah, M.P., Eds., New York: Wiley, 1983.
14. Wagner, C.D., Riggs, W.M., Davis, L.E., *et al.*, *Handbook of X-Ray Photoelectron Spectroscopy*, Minnesota: Perkin–Elmer, 1978.
15. *Comprehensive Inorganic Chemistry*, Bailar, J.C., Emeleus, H.J., Nikolm, R., and Trotman-Dickenson, A.F., Eds., Oxford: Pergamon, 1975, vol. 3.
16. Dobos, D., *Electrochemical Data, Handbook for Electrochemists and Universities*, Budapest: Akad. Kiado, 1975.
17. Spitsyn, V.I., and Martynenko, L.I., *Neorganicheskaya khimiya* (Inorganic Chemistry), Moscow: Mosk. Gos. Univ., 1994.

Russian Journal of Applied Chemistry, Vol. 76, No. 1, 2003, pp. 76–79. Translated from Zhurnal Prikladnoi Khimii, Vol. 76, No. 1, 2003, pp. 78–81.

APPLIED ELECTROCHEMISTRY AND CORROSION PROTECTION OF METALS

Separation of Platinum(IV) and Iron(III) with Liquid Membranes under Electrodialysis Conditions

T. Zh. Sadyrbaeva

Institute of Inorganic Chemistry, Riga Technical University, Salaspils, Latvia

Received September 3, 2002

Abstract—The recovery of platinum(IV) from hydrochloric acid solutions containing an excess amount of iron(III) with liquid tri-*n*-octylamine–1,2-dichloroethane membranes under conditions of galvanostatic dialysis was studied. The influence exerted by the current density and by the composition of aqueous solutions and liquid membranes on the rate of platinum(IV) transport and efficiency of separation of the metals was analyzed and the optimal process conditions were determined.

Recovery of platinum metals from hydrochloric acid solutions in the presence of macroscopic impurities of non-noble metals is of primary practical interest. The ability of platinum metals to form stable anionic chloro complexes under the conditions under which the nonferrous metals and iron are present as impurities allows use of anion-exchange extraction with amine salts [1, 2] and high-voltage dialysis [3] for their separation. However, in systems with amines, the high stability of the forming compounds makes back extraction of platinum metals difficult, which hinders application of the extraction techniques [4]. It has been shown previously that application of an electric field facilitates back extraction of platinum, palladium, and ruthenium from tri-*n*-octyalime (TOA) solutions [5]. Electrodialysis of liquid TOA-containing membranes has been used to recover palladium from dilute acid solutions [6] and separate the metal from excess amounts of iron, nickel [7], and copper [8].

The aim of this study was to analyze electrodialytic transport of platinum from binary hydrochloric acid mixtures with iron(III) across TOA-based liquid membranes bounded by cellophane films.

EXPERIMENTAL

Electrodialysis was carried out in an assembled five-chamber fluoroplastic cell comprising electrode chambers, feeding and receiver solution chambers, and a liquid membrane in the system

(–)Pt, H_2SO_4	H_2PtCl_2 $FeCl_3$ HCl	TOA Dichloroethane	HCl	Pt,(+) H_2SO_4
	MK		MK	

The volume of the liquid membrane was 2 cm^3; its thickness, 0.2 cm; phase contact area, 7.1 cm^2. Cellophane films bounding a liquid membrane were preliminarily soaked in water. The electrode chambers filled with 0.15 M H_2SO_4 solution (volume 17 cm^3) were separated from the chambers containing the feeding and receiving solutions (volume 13 cm^3) with MK-40 solid cation-exchange membranes. Direct current was fed through platinum electrodes.

The liquid-membrane solution was prepared by dissolving a weighed portion of TOA (pure grade, main substance content 95%) in 1,2-dichloroethane. In view of the possible reaction of TOA with the solvent to give a salt of quaternary ammonium base [9], freshly prepared solutions were used. The feeding solution was prepared by dissolving H_2PtCl_6 (pure grade) and $FeCl_3 \cdot 6H_2O$ (analytically pure grade) in hydrochloric acid of appropriate concentration (0.1 M HCl, as a rule). Commonly, 0.1 M HCl was used as receiving solution.

The concentration of metals in aqueous solution was determined spectrophotometrically: platinum, with tin(II) chloride [10]; iron, with sulfosalicylic acid [11]. In determining the content of iron(III) in the presence of a large excess of platinum, the optical density was measured relative to the solution being analyzed. The measurements were done on an SF-46 spectrophotometer.

Platinum(IV) forms highly stable complexes with chloride ions and exists in hydrochloric acid solutions mainly as the hexachloride complex $[PtCl_6]^{2-}$ [10]. Tri-*n*-octylamine recovers platinum(IV) in a wide range of HCl concentrations by, predominantly, the

1070-4272/03/7601-0076$25.00

interphase anion exchange mechanism [4]:

$$H^+(a) + Cl^-(a) + R_3N(o) \rightleftarrows R_3NHCl(o), \quad (1)$$

$$2R_3NHCl(o) + [PtCl_6]^{2-}(a) \rightleftarrows (R_3NH)_2[PtCl_6] + 2Cl^-(a), \quad (2)$$

where (a) stands for the aqueous phase, and (o), for the organic phase; R_3N is TOA.

On applying an electric field, the platinum complex being extracted is transported across the liquid membrane and disintegrates at the interface with the receiving solution by a reaction reverse to (2). The membrane recovery of platinum occurs by co-directed transport of $[PtCl_6]^{2-}$ anions and chloride ions, and, therefore, high HCl concentration in the receiving solution is not required, in contrast to dialysis processes. The electric field intensifies the transport of $[PtCl_6]^{2-}$ across each of the liquid membranes and ensures back extraction into a weakly acidic receiving solution. In the zero-current mode, there is virtually no transmembrane transport of platinum in the system studied.

The rate of platinum recovery from a binary mixture containing 2.14×10^{-2} M $H_2[PtCl_6]$ and 3.64×10^{-2} M $FeCl_3$ is proportional to the current density in the range 0–8.5 mA cm^{-2} (Fig. 1). Platinum is recovered into the receiving 0.1 M HCl solution selectively; the degree of iron(III) recovery in 1 h is about 0.1%. The metals are separated because amine salts more actively extract iron than platinum at higher HCl concentrations. In dilute HCl solutions, iron(III) forms cationic and neutral complexes [12]. In the course of electrodialysis, loss of Fe^{3+} from the feeding solution is as high as 25–35% because of its adsorption by a solid cation-exchange membrane.

The variation of voltage in the galvanostatic mode is characterized by a steep fall at the beginning of the process, with an "electric breakdown" of the liquid membrane possible at high current densities after several tens of minutes of electrodialysis (Fig. 2). The initial rise in the electrical conductivity of the organic phase is due to an increase in the total concentration of ions in the liquid membrane as a result of extraction of hydrochloric acid and $[PtCl_6]^{2-}$ by amine [reactions (1) and (2)]. The electric breakdown, associated with accumulation of water in the organic phase and formation of through aqueous channels [13], leads to the loss of transporting and selective properties by the membrane. The time when the breakdown occurs depends on the current density and on the nature of organic solvent and ion being recovered. Liquid membranes based on TOA in dichloroethane work without breakdown in recovery of platinum for about 2.5 h at current density of 6.4 mA cm^{-2} and equal acidities of the feeding and receiving solutions, with more than 50% of platinum and about 0.3% of iron transferred across the liquid membrane (Fig. 3). The

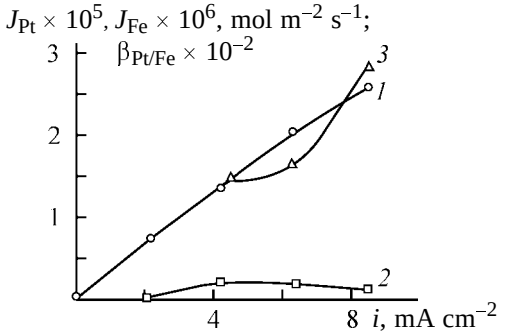

Fig. 1. Rates of transport of (*1*) platinum(IV), J_{Pt}, and (*2*) iron(III), J_{Fe}, and (*3*) metal separation factor $\beta_{Pt/Fe}$ vs. current density i. C_{TOA} = 0.1 M, τ = 60 min.

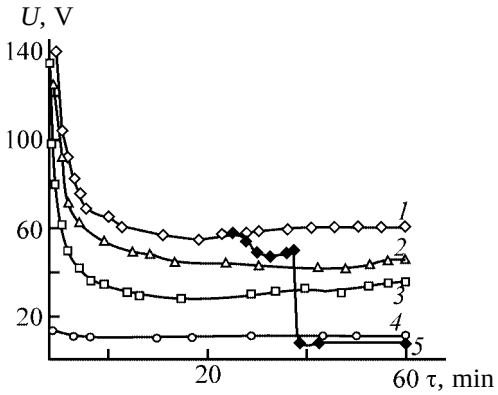

Fig. 2. Effect of current density on the variation of voltage U. (τ) Process duration. i, mA cm^{-2}: (*1*, *5*) 8.5, (*2*) 6.4, (*3*) 4.2, and (*4*) 2.1.

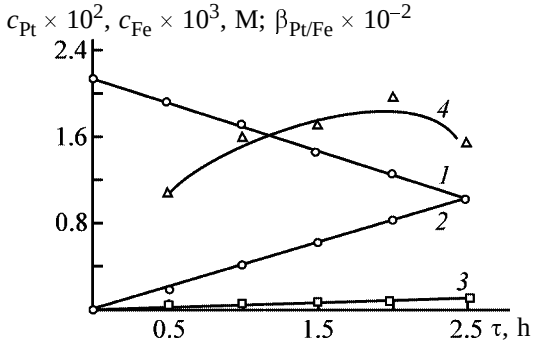

Fig. 3. Kinetic curves describing (*1*) platinum(IV) recovery from the feeding solution, accumulation of (*2*) platinum(IV) and (*3*) iron(III) in the receiving solution, and (*4*) variation of the metal separation factor $\beta_{Pt/Fe}$. $c_{Pt} = 2.1 \times 10^{-2}$ M, $c_{Fe} = 3.6 \times 10^{-2}$ M in 0.1 M HCl; i = 6.4 mA cm^{-2}. (c_{Pt}, c_{Fe}) Pt(IV) and Fe(III) concentrations and (τ) process duration.

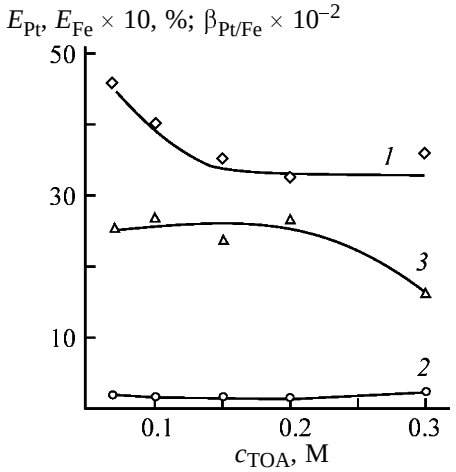

Fig. 4. Degrees of recovery of (*1*) platinum(IV), E_{Pt}, and (*2*) iron(III), E_{Fe}, and (*3*) metal separation coefficient $\beta_{Pt/Fe}$ vs. carrier concentration c_{TOA}. I = 6.4 mA cm^{-2}, τ = 120 min.

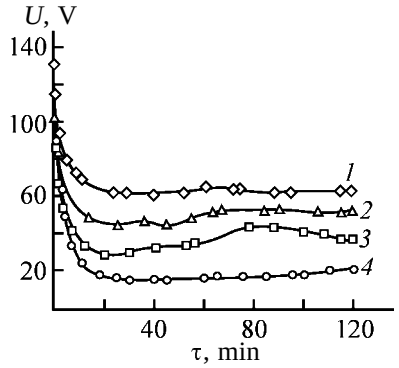

Fig. 5. Effect of carrier concentration on variation of voltage U. I = 6.4 mA cm^{-2}. (τ) Process duration. c_{TOA}, M: (*1*) 0.07, (*2*) 0.1, (*3*) 0.15, and (*4*) 0.3.

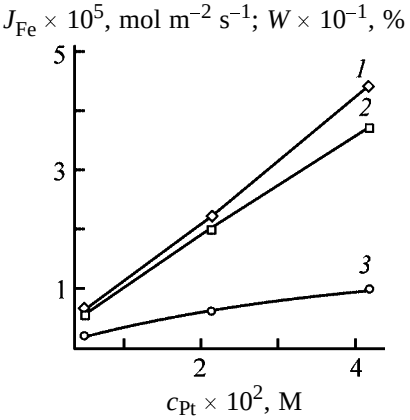

Fig. 6. Rates of transfer, J_{Pt}, into (*1*) liquid membrane and (*2*) receiving solution and (*3*) current efficiency W by platinum(IV) vs. its concentration c_{Pt} in the feeding solution. c_{TOA} 0.1 M, i = 6.4 mA cm^{-2}, τ = 60 min.

best separation of the metals is achieved under the experimental conditions in 2 h of electrodialysis. The efficiency and stability of liquid membranes with TOA in recovery of platinum exceeds that in the previously studied process of palladium transport [6].

The effect of the carrier concentration in the organic phase on the rate and selectivity of platinum recovery is shown in Fig. 4. In contrast to dialysis membrane extraction, raising the concentration of TOA to 0.15 M impairs the rate of platinum transport since chloride ions compete with $[PtCl_6]^{2-}$ in current transport across the interface between the membrane and the receiving solution. The excess of carrier acts in electrodialysis as supporting electrolyte. It should be noted that raising the TOA concentration leads to a pronounced increase in the electrical conductivity of the liquid membrane (Fig. 5).

Raising the concentration of platinum in the feeding solution to 4.2×10^{-2} M at constant concentration of iron leads to a proportional increase in the rate of $[PtCl_6]^{2-}$ transfer across both phase boundaries and in the current efficiency (Fig. 6). However, under excess of hydrochloric acid in the feeding solution, current is mainly carried across the liquid membrane by chloride ions and the current efficiency by $[PtCl_6]^{2-}$ anions does not exceed 10%.

Lowering the concentration of HCl in the feeding solution to 1×10^{-3} M makes higher the degree of platinum recovery, current efficiency, and metal separation factor (Table 1). The increase in the rate of platinum transport is due to a decrease in the content of chloride ions competing with $[PtCl_6]^{2-}$ anions for the trioctylammonium cation.

The type and concentration of acid in the receiving solution is not an important factor under electrodialysis conditions (Table 2).

The rate of platinum recovery into the liquid membrane is independent of the composition of the receiving solution, and the transmembrane transfer decreases somewhat in those cases when an electric breakdown occurs in the course of an experiment. Liquid membranes are the most stable if recovery is done into hydrochloric acid solutions, whereas systems with nitric acid are characterized by their shortest service life.

CONCLUSIONS

(1) Under electrodialysis conditions, liquid membranes containing tri-*n*-octylamine in dichloroethane ensure transport of $[PtCl_6]^{2-}$ into dilute acid solutions

Table 1. Effect of the acidity of the feeding solution on the rate of platinum transfer and the separation of the metals. c_{TOA} 0.1 M, i = 6.4 mA cm^{-2}, τ = 60 min

Concentration in feeding solution, M			E_{Pt}	W_{Pt}	E_{Fe}	$\beta_{Pt/Fe}$	$J^*_{Pt} \times 10^5$, mol m^{-2} s^{-1}
Pt(IV)	Fe(III)	HCl	%				
2.5×10^{-2}	3.1×10^{-2}	10^{-3}	22.8	8.7	0.13	189	2.86
2.2×10^{-2}	3.5×10^{-2}	10^{-2}	20.3	6.8	0.11	184	2.25
2.1×10^{-2}	3.6×10^{-2}	10^{-1}	18.5	6.1	0.12	161	2.01

* J is the transmembrane flux.

Table 2. Effect of the composition of the receiving solution on transport of metals. $c_{Pt} = 2.1 \times 10^{-2}$ M, $c_{Fe} = 3.6 \times 10^{-2}$ M; i = 6.4 mA cm^{-2}; τ = 60 min

Receiving solution, M	E_{Pt}	E_{Fe}	$\beta_{Pt/Fe}$	$J^*_1 \times 10^5$	$J^*_2 \times 10^5$
	%			mol m^{-2} s^{-1}	
HCl:					
0.01	18.5	0.15	123	2.35	2.02
0.1	18.5	0.12	161	2.21	2.01
H_2SO_4:					
0.01	19.9	0.19	108	2.37	2.17
0.1	14.7	0.13	113	2.17	1.6
HNO_3:					
0.01	15.3	0.16	96	2.29	1.67
0.1	15.4	0.15	103	2.29	1.68

* J_1 and J_2 are the flux of platinum into the membrane and the transmembrane flux, respectively.

and efficient separation of platinum(IV) from iron(III) in recovery from hydrochloric acid media.

(2) The rate of electrodialytic transport of $[PtCl_6]^{2-}$ is determined by the current density, composition of the feeding solution, and carrier concentration in the liquid membrane.

(3) The longer service life of liquid membranes without electric breakdown is achieved in recovery of platinum from hydrochloric acid solutions at moderate current densities.

REFERENCES

1. Ivanova, S.N., Druzhinina, I.A., Plotnikova, G.I., *et al.*, *Izv. Sib. Otd. Akad. Nauk SSSR, Ser. Khim. Nauk*, 1984, issue 15, no. 15, pp. 86–93.
2. Warshawsky, A., *Sep. Purif. Meth.*, 1983, vol. 12, no. 1, pp. 1–9.
3. Ezerskaya, N.A. and Solovykh, T.P., *Izv. Akad. Nauk SSSR, Ser. Khim.*, 1969, no. 5, pp. 993–999.
4. Gindin, L.M., *Ekstraktsionnye protsessy i ikh primenenie* (Extraction Processes and Their Use), Moscow: Nauka, 1984.
5. Kulikova, L.D., Petrichenko, O.I., Sadyrbaeva, T.Zh., and Yansone, A.K., *Izv. Akad. Nauk Latv. SSR, Ser. Khim.*, 1989, no. 3, pp. 316–322.
6. Sadyrbaeva, T.Zh. and Purin, B.A., *Izv. Akad. Nauk Latv. SSR, Ser. Khim.*, 1990, no. 3, pp. 311–316.
7. Sadyrbaeva, T.Zh. and Purin, B.A., *Latv. Kim. Z.*, 1993, no. 3, pp. 301–308.
8. Sadyrbaeva, T.Zh. and Purin, B.A., *Khim. Tekhnol.*, 2001, no. 10, pp. 17–22.
9. Popov, A.N. and Timofeeva, S.K., *Izv. Akad. Nauk Latv. SSR, Ser. Khim.*, 1990, no. 6, pp. 707–714.
10. Ginzburg, S.I., Ezerskaya, N.A., Prokof'eva, I.V., *et al.*, *Analiticheskaya khimiya platinovykh metallov* (Analytical Chemistry of Platinum Metals), Moscow: Nauka, 1972.
11. Charlot, G., *Les methods de la chimie analytique. Analyse quantitative minerale*, Paris: Masson, 1961, 4th ed.
12. Zolotov, Yu.A., Iofa, B.Z., and Chuchalin, L.K., *Ekstraktsiya galogenidnykh kompleksov metallov* (Extraction of Metal Halide Complexes), Moscow: Nauka, 1973.
13. Golubev, V.N. and Purin, B.A., *Dokl. Akad. Nauk SSSR*, 1977, vol. 232, no. 6, pp. 1340–1342.

Russian Journal of Applied Chemistry, Vol. 76, No. 1, 2003, pp. 80–84. Translated from Zhurnal Prikladnoi Khimii, Vol. 76, No. 1, 2003, pp. 82–86.

APPLIED ELECTROCHEMISTRY AND CORROSION PROTECTION OF METALS

Interaction of Electrolyte for Alkaline Zinc Plating with Calcium Compounds in the Course of Chemical Washing

A. Pigaga, A. Selskis, M.-G. Klimantavičiute, and A. Sveikauskaite

Institute of Chemistry, Vilnius, Lithuania

Received June 18, 2002

Abstract—The interaction between diluted electrolyte for alkaline zinc plating and calcium compounds ($CaCl_2$ solutions, phosphogypsum and cement dust suspensions) was studied to determine the promise of their use for chemical washing.

Zinc coatings occupy a distinctive position among corrosion-protection coatings since about 50% of surfaces coated with metals are zinc plated. Originally, cyanide electrolytes were used, then, weakly acidic electrolytes, and now alkaline electrolytes are in use because of their high throwing power and high current efficiency at fast plating rates and owing to the fact that the coatings obtained are nicely lustrous. These electrolytes conform to modern nature preservation requirements because the concentrations of zinc are low and luster-producing agents are environmentally safe.

One of ways to save metals and water and to diminish pollution is to use the so-called chemical washing, first proposed by Lanzi for rendering harmless discharged chromium-plating electrolytes and cyanide-containing solutions directly in the catching bath [1].

In washing of articles after alkaline zinc plating, sludge formation was observed in washing water because of partial decomposition of zincate ions and formation of poorly soluble zinc compounds. In washing in deionized water, formation of a bulky, slowly settling precipitate was observed. In washing in tap water containing 57 mg l^{-1} Ca^{2+} and 13 mg l^{-1} Mg^{2+}, a minor volume of a compact precipitate settled fast, with the residual concentration of zinc in solution being lower. Presumably, cations in tap water favor precipitation of zinc. Additional experiments demonstrated that precipitation of zinc is promoted by solutions of calcium salts, with magnesium salts exerting virtually zero influence on zinc precipitation.

Zincate ions form with calcium(II) hydroxide a poorly soluble finely crystalline precipitate of calcium zincate, $CaZn_2(OH)_6 \cdot 2H_2O$ [2]. Its structure and the conditions and rates of its formation and decomposition have been much studied, and calcium zincate has found application in Zn/NiOOH and Zn/AgO batteries [3–9] and as a component of wood binders [10], luminophores, insulators and glasses, and polymerization catalysts [8].

Calcium zincate $CaZn_2(OH)_6 \cdot 2H_2O$ crystallizes in the monoclinic system [2], with two its forms, tetragonal and hexagonal, known. According to X-ray diffraction analysis, the unit cells of both forms are identical [8]. Hexagonal crystals are formed by slow crystallization (during several days), and tetragonal crystals, by fast precipitation from supersaturated solutions.

The aim of this study was to analyze the interaction of a diluted electrolyte for alkaline zinc plating with calcium compounds ($CaCl_2$ solutions, suspensions of phosphogypsum and cement dust) to determine the promise of their use for chemical washing.

About 4 ton of phosphogypsum is formed in manufacture of 1 ton of orthophosphoric acid [11]. By the content of the main substance, gypsum ($CaSO_4 \cdot 2H_2O$) (up to 98%), it corresponds to natural gypsum of the highest quality (91–95%). The chemical composition of phosphogypsum manufactured by Lifosy Joint-Stock Company (in terms of dry substance) is as follows (%): CaO 31–37, SO_3 44–54, SiO_2 0.3–0.6, R_2O_3 0.5–1.5, Na_2O 0.24–0.32, K_2O 0.04–0.08, P_2O_5 total 0.91–2.86, P_2O_5 water-soluble 0.52–2.65, F total 0.14–0.48, and F water-soluble 0.015–0.33 [12]. Moisture content of phosphogypsum 20–25%, calcination loss (400°C) 37–42%, density 750–800 kg m^{-3}, specific surface area 260–290 m^2 kg^{-1}. Phosphogypsum particles are $CaSO_4 \cdot 2H_2O$ crystals

1070-4272/03/7601-0080$25.00

5–500 μm long, 1–50 μm wide, and 0.05–0.5 μm thick.

Data on the sorption properties of phosphogypsum are scarce. It is known that phosphogypsum can be used to remove Sr^{2+} and Pb^{2+} [13], and also phosphates and borates from industrial wastewater [14], and to perform preliminary purification of concentrated phenol-containing discharges [15]. A method for purification of phosphoric acid to remove fluorine has been developed [16].

Cement dust, exhibiting properties of both an alkaline agent and a sorbent, can be used to remove heavy metals {17–19] and a number of hazardous organic substances [19, 20] from industrial wastewater. In Lithuania, Akmenes Cementas Joint-Stock Company produces annually 20–30 thousand tons of cement dust of the following chemical composition (%): Al_2O_3 3–8, Fe_2O_3 2–5, SiO_2 11–15, CaO 38–48, CaO free 3–7, MgO 2–4, $(Na,K)_2O$ 2–8, and SO_3 3–8. According to X-ray phase analysis, the dust is mainly constituted by calcite $CaCO_3$ (~80%), quartz α-SiO_2 (10–15%), and basic calcium silicate $Ca_5 \cdot (SiO_4)_2(OH)_2$ the rest [16].

EXPERIMENTAL

A Limeda NBTs electrolyte for alkaline zinc plating was used in the study. It was prepared in accordance with GOST (State Standard) 9.305–84 and had the following composition (g l^{-1}): ZnO 15, NaOH 110; luster-producing additives NBTs-0 and Limeda NBTs-K 5 ml l^{-1} each. Immediately before an experiment, the electrolytes were diluted with deionized water.

The concentrations of Zn^{2+} and Ca^{2+} in the solutions under study were determined by plasma atomic-emission spectrometry on a Beckman SpectraSpan VI instrument at wavelengths of 206, 200 and 317, 933 nm, respectively.

X-ray diffraction patterns of precipitates were obtained on a DRON-2 X-ray diffractometer in CuK_α radiation. Micrographs of the precipitates were obtained on a JXA-50A scanning electron microscope–microanalyzer. Reagents of chemically pure and analytically pure grades were used.

Phosphogypsum, a waste formed in industrial processing of Kola apatite, was delivered by Lifosa Joint-Stock Company [TU (Technical Specification) 6 111 045-03–92], and cement dust, by Akmenes Cementas [TU 5 290 342-04–92, GOST (State Standard) 310.2, content of free CaO 4.7%].

Table 1. Residual concentrations of zinc(II) and calcium(II) in solution upon introduction of Limeda NBTs electrolyte into deionized water or $CaCl_2$ solution

Amount of zinc(II) introduced, mg l^{-1}	Residual concentration of Zn^{2+} (Ca^{2+}), mg l^{-1}		
	deionized water	$CaCl_2$ solution, g l^{-1}	
		2	10
48	9.2/2.1*	–/1.5	1.5 (3300)/1.9
240	76/26	–/2.0	2.6 (3200)/2.0
790	510/210	–/9.5	3.2 (810)/3.2
1090	880/260	–/17	4.1 (260)6.1
1570	1260/310	–/69	17 (56)/26
2000	2000/1620	–/410	37 (50)/41
2770	2770/2380		45 (24)/94
3430	3400/3400		115 (19)/150

* After settling for 1 h/24 h.

To determine the efficiency of Zn^{2+} precipitation, 0.2–25 ml of Limeda NBTs electrolyte was mixed with 50 ml of a $CaCl_2$ solution (2 or 10 g l^{-1}), the mixture was filtered after 1 or 24 h of settling, and the residual concentrations of Zn(II) and Ca(II) were found.

Table 1 shows that, upon introduction of the electrolyte into the $CaCl_2$ solutions, the concentration of zinc decreases by up to a factor of 200, compared with the case of the corresponding dilution with deionized water. Precipitate formation was also observed upon 5–250-fold dilution of the electrolyte with deionized water, which is due to decomposition of zincate ions to give ZnO (as established by an X-ray diffraction study):

$$Zn(OH)_4^{2-} \rightleftarrows ZnO + 2OH^- + H_2O. \quad (1)$$

In solutions containing $CaCl_2$, zinc(II) precipitates much faster and to a greater extent, with calcium(II) coprecipitated, which confirms the formation of a mixed compound containing calcium and zinc:

$$2Zn(OH)_4^{2-} + Ca^{2+} + 2H_2O \rightleftarrows CaZn_2(OH)_6 \cdot 2H_2O + 2OH^-. \quad (2)$$

An X-ray diffraction study demonstrated that precipitates obtained upon introduction of the Limeda NBTs electrolyte into solutions with 2 or 10 g l^{-1} $CaCl_2$ to Ca : Zn molar ratios equal to 1 or 2 are composed of $CaZn_2(OH)_6 \cdot 2H_2O$ with a minor impurity of ZnO. The interplanar spacings and the reflection intensities for the compound $CaZn_2(OH)_6 \cdot 2H_2O$

Table 2. Residual concentrations of zinc(II) at varied duration of agitation, τ

τ, min	Residual concentration of Zn^{2+}, mg l^{-1}						
	deionized water	$CaCl_2$ solution, 10 g l^{-1}	phosphogypsum suspension, 40 g l^{-1}				cement dust suspension, 40 g l^{-1}
0	400	400	100	200	400	1000	400
5	370	14	4.1	19	27	51	8.2
10	360	3.5	3.9	9.1	11	16	8.9
15	160	3.5	2.7	4.9	5.5	6.0	8.7
30	91	3.5	2.7	4.6	5.1	5.4	11
60	69	3.3	2.8	4.3	5.0	5.1	12
120	63	3.1	2.6	4.6	4.7	4.9	11
180	59	3.6	1.8	4.1	4.4	4.6	14

Table 3. Residual concentrations of zinc(II) and calcium(II) upon introduction of Limeda NBTs electrolyte into deionized water, $CaCl_2$ solutions, and suspensions of phosphogypsum or cement dust. Duration of agitation 10 min, and that of settling, 5 min, after each introduction

Introduced amount of zinc(II), mg l^{-1}	Residual concentration of Zn^{2+} (Ca^{2+}), mg l^{-1}						
	deionized water	$CaCl_2$ solution, g l^{-1}				phosphogypsum suspension, g l^{-1}		cement dust suspension, g l^{-1}
		1	5	10	25	20	40	40
570	490	5.2(110)	2.4(560)	4.1(1700)	7.9(6500)	5.0	5.2(180)	9.9(800)
1140	980	82(58)	7.0(280)	7.3(800)	6.3(3900)	5.4	5.7(170)	10(560)
1710	1270	210(22)	43(175)	17(125)	7.1(980)	10	9.5(160)	24(560)
2290	2000	300(6.9)	94(81)	26(34)	14(520)	22	18(150)	47(400)
2860	2500	410(0.7)	210(56)	75(29)	26(210)	25	20(140)	84(160)
3430	2800	610(0.5)	300(30)	130(13)	50(130)	26	22(120)	180(140)
4000	3300	1020(0.2)	430(0.6)	230(10)	88(87)	35	27(73)	420(110)
4570	3600	3580(0.2)	630(0.6)	400(11)	120(71)	180	32(67)	710(82)
5140	4000	3830(0.2)	850(0.5)	530(8.9)	140(39)	190	170(65)	870(54)
5700	4200	4260(0.2)	1080(0.3)	670(7.1)	210(25)	260	190(32)	1190(52)

are in good agreement with the data of [2]. The precipitate is mainly formed by rhombic plates 50–250 μm long or aggregates of these, 100–200 μm in diameter.

Another set of experiments was concerned with the kinetics of calcium zincate precipitation upon introduction of a zinc-plating electrolyte into a $CaCl_2$ solution or phosphogypsum (cement dust) suspension under continuous agitation of the reaction mixture with a magnetic stirrer. The results listed in Table 2 indicate that the rates of formation of a poorly soluble calcium zincate are fairly high and are acceptable for chemical washing purposes.

Further, the process of chemical washing was simulated. A 300-ml portion of deionized water or of an aqueous solution of 1.0, 5.0, 10, or 25 g l^{-1} $CaCl_2$ was placed in a volumetric vessel, 15 ml of electrolyte was introduced, the mixture was agitated with a magnetic stirrer for 10 min and settled for 5 min, the precipitate volume was determined, a 15-ml sample of the solution was taken and filtered, and the residual concentrations of zinc and calcium were determined by atomic-emission spectrometry. This procedure of introduction–sampling–analysis of the solutions was repeated nine times. The results of the experiment, which are listed in Table 3, and X-ray diffraction data indicate that the major part of zinc(II) (~90%) is precipitated from solution in the form of calcium zincate.

The efficiency of washing grows with $CaCl_2$ concentration; however, with this concentration raised

from 10 to 25 g l^{-1}, the volume of the precipitated phase increased from 8 to 37% because of the formation of voluminous $Ca(OH)_2$. Therefore, the optimal $CaCl_2$ concentration is 5–10 g l^{-1}, since at lower concentrations the solutions are exhausted fast.

The phosphogypsum suspension acts no less effectively, and the volume of the precipitated phase does not exceed 20%. The precipitate is mainly composed of calcium zincate with impurity of zinc oxide and unreacted gypsum.

The cement dust suspension is much inferior in efficiency to $CaCl_2$ solutions and phosphogypsum suspension, with this fact not being associated with exhaustion of reactive Ca(II) ions in solution (Table 3). The reason is that the cement dust additionally alkalizes the reaction mixture.

The gradual increase in the concentration of zinc(II) in solution is due to a decrease in the concentration of reactive calcium(II) ions and rise in the degree of calcium zincate dissociation with increasing solution alkalinity.

The solubility of calcium zincate was studied as a function of concentration as follows. To 20 ml of zinc-plating electrolyte was added 10 ml of $CaCl_2$ solution (50 g l^{-1}) and 0–20 ml of NaOH solution (400 g l^{-1}), the mixture was diluted with distilled water to 50 ml, agitated for 4 h, and filtered, and the Zn(II) concentration was determined. The figure shows that the solubility of calcium zincate grows with increasing solution alkalinity.

In the course of chemical washing, the precipitate should be separated from the solution by filtration or centrifugation after a Zn(II) concentration of 300–400 mg l^{-1} is reached, and the filtrate is to be added to acidic and alkaline wastes for neutralization. To separate the precipitate, it is desirable to lower the pH of the reaction mixture. For this purpose, a dilute H_2SO_4 solution is introduced or CO_2 bubbled through to make the pH 11.5–11.7. The Zn(II) concentration in solution decreases to 15–40 mg l^{-1}. It is necessary to avoid pH < 11.5, since in this case voluminous $Zn(OH)_2$ is formed. In manufacture, it is much more convenient to use inexpensive CO_2, which makes it possible to set easily the required pH value. The filtrate can be recycled.

The precipitate obtained from $CaCl_2$ solutions can be used in electroplating, manufacture of trace-element fertilizers and pigments, and ceramic fillers, and also for preparing zinc-phosphating solutions.

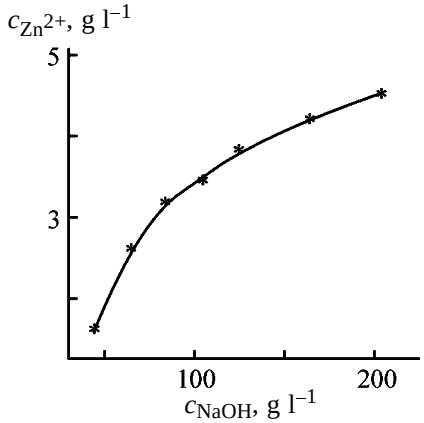

Residual concentration of Zn(II), $c_{Zn^{2+}}$, vs. NaOH concentration c_{NaOH}. Initial concentrations of Zn(II) and $CaCl_2$ are, respectively, 4.8 and 10 g l^{-1}.

CONCLUSIONS

(1) A procedure is proposed for washing with calcium chloride solutions or phosphogypsum suspensions of articles after alkaline zinc plating. The optimal process conditions are established. Compared to washing in water, the concentration of zinc in the catching bath is 100–200 times lower because of the formation of poorly soluble finely crystalline calcium zincate $CaZn_2(OH)_6 \cdot 2H_2O$.

(2) The precipitate, mainly composed of calcium zincate with impurity of zinc oxide, can be used in zinc phosphating for preparing phosphating solutions, as trace element fertilizer in agriculture, and in some other industries.

REFERENCES

1. Weiner, R., *Die Abwässer der Galvanotechnik und Metallindustrie*, Saulgau: Leuze, 1973.
2. Liebau, F. and Amel-Zadeh, A., *Krist. Techn.*, 1972, vol. 7, pp. 221–227.
3. Romanov, V.V., *Zh. Prikl. Khim.*, 1961, vol. 34, no. 6, pp. 1317–1321.
4. Romanov, V.V., *Zh. Prikl. Khim.*, 1962, vol. 35, no. 6, pp. 1293–1302.
5. Sharma, R.A., *J. Electrochem. Soc.*, 1986, vol. 133, no. 11, pp. 2215–2219.
6. Sharma, R.A., *J. Electrochem. Soc.*, 1988, vol. 135, no. 8, pp. 1875–1882.
7. Wang, Y.-M., *J. Electrochem. Soc.*, 1990, vol. 137, no. 9, pp. 2800–2803.
8. Jain, R., Adler, T.C., McLarnon, F.R., and Cairns, E.J., *J. Appl. Electrochem.*, 1992, vol. 22, no. 11, pp. 1039–1048.

9. Zhang, C., Wang, J.M., Zhang, L., *et al*., *J. Appl. Electrochem*., 2001, vol. 31, no. 9, pp. 1049–1054.
10. JPN Patent Appl. 50–109 229.
11. *Tekhnologiya fosfatnykh i kompleksnykh udobrenii* (Technology of Phosphate and Complex Fertilizers), Evenchik, S.D. and Brodskii, A.A., Eds., Moscow: Khimiya, 1987.
12. Kazilionas, A., Leškevičienė, V., Vektaris, B., and Valančius, Z., *Chem. Technol*. (Kaunas), 1998, no. 3(9), pp. 38–46.
13. Belinskaya, F.A. and Mel'do, T.A., *Zh. Prikl. Khim*., 1997, vol. 70, no. 5, pp. 738–742.
14. Kazymbetova, M.S., Tanasheva, M.R., and Nurakhmetov, N.N., Abstracts of Papers, *7-e Vsesoyuznoe soveshchanie po fiziko-khimicheskomu analizu* (7th All-Union Meet. on Physicochemical Analysis), Frunze, October 4–6, 1988, pp. 600–601.
15. Panov, V.P., Zykova, I.V., and Lysenko, I.V., *Zh. Prikl. Khim*., 1999, vol. 72, no. 8, pp. 1396–1398.
16. USSR Inventor's Certificate no. 674 977.
17. Burnham, J.C., Hatfield, N., Bennett, G.F., and Logan, T.J., *Innovations and Uses for Lime, ASTM STP 1135*, Walker Jr., D.D., Hardy, T.B., Hofman, D.C., and Stanley, D.D., Eds., Philadelphia: Am. Soc. for Testing Materials, 1992, pp. 128–141.
18. Klimantavičiūtė, M.G., Virbalytė, D., Šalkauskas, M., and Juškėnas, R., *Chem. Technol*. (Kaunas), 2000, no. 1(14), pp. 21–25.
19. El-Awady, M.H. and Sami, T.M., *Bull. Environ. Contam. Toxicol*., 1997, vol. 59, no. 4, pp. 603–610.
20. El-Awady, M.H. and Hamdy, M., *Egypt. J. Appl. Sci*., 1996, no. 11(7), pp. 191–201.

Russian Journal of Applied Chemistry, Vol. 76, No. 1, 2003, pp. 85–87. Translated from Zhurnal Prikladnoi Khimii, Vol. 76, No. 1, 2003, pp. 87–89.

APPLIED ELECTROCHEMISTRY AND CORROSION PROTECTION OF METALS

Variation of Electrolyte Density in Electrode Pores during Discharge of Sealed Lead Batteries

V. V. Bayunov, M. M. Barsukova, Yu. A. Podalinskii, and G. A. Kolikova

Istochnik Research Institute of Batteries, Joint-Stock Company, St. Petersburg, Russia

Received May 17, 2002

Abstract—The difference of the electrolyte densities in the container and within pores of the active electrode paste was determined in discharge of sealed lead batteries with absorbed electrolyte. The data obtained can be used in designing sealed batteries.

To calculate and plot discharge curves when designing lead batteries, it is necessary to take into account the variation of the electrolyte concentration in the container and within electrode pores. It is known that, during discharge of a lead battery, the densities of electrolyte in the container and within pores of the active electrode paste are different. In [1], the density of electrolyte within pores of the positive and negative electrodes of a starter battery was determined after 5 min and 10 and 20 h of discharge. In the 5-min and 10-h modes of discharge, the difference ΔP of the electrolyte densities in the container and within pores of the positive and negative electrodes was, respectively, 0.18–0.065 and 0.13–0.035 g cm^{-3}. However, data on how the electrolyte density within the electrode pores varies with battery discharge in different discharge modes were not reported in [1].

In order to determine the electrolyte density within electrode pores, we performed an experimental study of nonportable lead batteries with discharge capacity of 600 A h and rated electrolyte density of 1.240 g cm^{-3} at 20°C. During discharge of the batteries in the course of 10, 5, 3, 1, 0.5, and 0.25 h, the circuit was broken after exhausting 25, 50, 75, and 100% of the discharge capacity, and the open-circuit voltage (OCV) and electrode potentials were measured, after which the discharge of the batteries was continued. The discharge was terminated in accordance with the technical specification requirements at final voltage U_f of 1.8 V in the 3–10-h modes and 1.75 V in the 0.25–1-h modes.

During dc discharge of lead batteries, there is a voltage drop across the internal resistance R of the batteries, which is constituted by the active resistance and the polarization resistance R_p. The latter comprises the following resistances: transition resistance R_t, reaction resistance R_r, diffusion resistance R_d, and crystallization resistance R_c. These polarization resistances are determined by the respective overvoltages. When the circuit is broken to determine the OCV, the digital voltmeter only measures the overvoltages of diffusion, η_d, and reaction, η_r (or that of crystallization, η_c). It is difficult to record the transition overvoltage η_t because of the high rate of the process (occurring within micro- or milliseconds), which should be taken into account in calculations [2]. However, the current densities in a nonportable lead battery in 0.25–10-h discharge modes are low and the transition overvoltage η_t is close to zero. Therefore, the experimental data, even if obtained with a digital voltmeter, require no correction.

The results of calculation of the differences of electrolyte densities in the container and within pores of the active paste of the electrodes, ΔP, with account of the experimental OCV values for batteries with different degrees of discharge are shown in Fig. 1. The

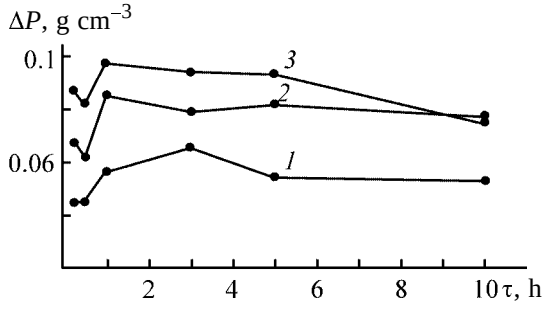

Fig. 1. Variation with the discharge duration τ of the difference ΔP of electrolyte densities in the container and within electrode pores of a battery with liquid electrolyte. Degree of discharge, %: (*1*) 25, (*2*) 50, and (*3*) 100.

1070-4272/03/7601-0085$25.00

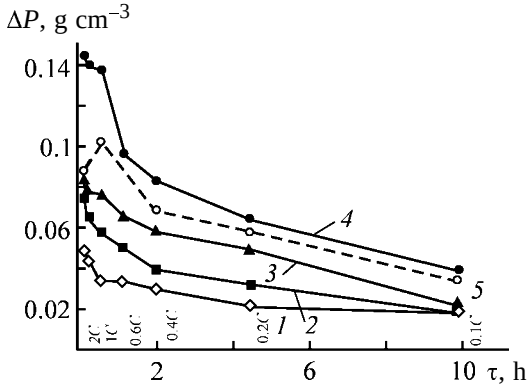

Fig. 2. Variation with the discharge duration τ of the difference Δ*P* of electrolyte densities in the separator and within electrode pores of sealed batteries with absorbed electrolyte. Degree of discharge, %: (*1*) 25, (*2*) 50, (*3*) 75, (*4*) 100, and (*5*) 100 at U_f = 1.75–1.80 V.

data obtained indicate that the difference Δ*P* of electrolyte densities at the same degree of discharge varies in the 1–10-h discharge modes only slightly. With increasing degree of discharge, Δ*P* grows.

Theoretical calculations and experimental determination of the emf (OCV) of lead batteries, carried out by many authors, have been reported with the difference of acid concentration within the pores of positive and negative electrodes disregarded [3]. Here, the Δ*P* value is calculated using experimental data and those reported in [3]. The experimental OCV value corresponds to the real concentration of electrolytes within pores of the positive and negative electrodes at a particular instant of measurement and determines the calculated averaged Δ*P* value. Comparison of the differences of electrolyte densities in the container and in the electrode pores of 100% discharged nonportable batteries with similar data obtained in [1] shows that their values are rather close. For example, for the 0.25–10-h discharge modes considered, Δ*P* is 0.097–0.075 g cm^{-3}. The calculated Δ*P* values obtained for 1–10-h discharge modes are also close to the average Δ*P* values for positive and negative electrodes, reported in [1].

A characteristic tendency in the development of lead batteries is the desire to simplify and make less expensive, to the maximum possible extent, their service maintenance. This is achieved by partly or totally sealing the lead battery. One of specific features of sealed lead batteries is that an immobilized electrolyte, gel-like or absorbed, is used in these batteries. Replacement of a liquid electrolyte with a gel-like electrolyte decreases its electrical conductivity and the diffusion coefficient. According to published data, this also leads to an increase in the discharge capacity of the negative electrode and decrease in that of the positive electrode. In view of the lowering of the freezing point of the electrolyte by 13–15°C, the frost resistance of the battery increases, which affects positively its service characteristics at low temperature [4, 5].

At present, electrolytes are mostly immobilized using a glass-fiber separator with high bulk porosity and good wettability with a sulfuric acid solution. The fine structure of the fibers in such a separator allows it not only to separate electrodes, but also to retain an electrolyte within its pores. Both kinds of immobilization, with gel-like electrolyte or that absorbed by the glass fiber, ensure a high rate of oxygen transport to the negative electrode, where it recombines [5, 6].

In view of the significant difference between the electrode operation conditions in lead batteries with liquid and immobilized electrolytes, a necessity arises for determining, in design of sealed lead batteries, the difference of electrolyte densities in the separator and within pores of the active paste in electrodes.

In the present study, experiments were performed with SG-6 sealed batteries with absorbed electrolyte of the density of 1.280 g cm^{-3}. The OCV and voltage *U* were measured during battery discharge with currents of 0.1*C*, 0.2*C*, 0.4*C*, 0.6*C*, 1*C*, 2*C*, and 3*C* A (where *C* is numerically equal to the rated 20-h discharge capacity) after exhausting 25, 50, 75, and 100% of the discharge capacity. The discharges were terminated in accordance with the requirements of the corresponding technical specifications at final voltages U_f of, respectively, 1.75, 1.70, 1.65, 1.60, 1.55, 1.45, and 1.25 V. In SG-6 batteries, the current density at discharges of 0.05–3*C* is 0.0017–0.1 A cm^{-2}, i.e., the overvoltage η_t is close to zero and can be disregarded in calculations. The results of experimental studies and calculations are shown in Fig. 2 in the form of dependences of Δ*P* on the discharge duration τ.

For all the discharge modes, the difference of electrolyte densities in the container and within pores, Δ*P*, grows with the degree of discharge increasing from 25 to 100%; in particular, in discharge with currents of 0.1*C* and 3*C*, by factors of 2.2 and 3.0, respectively. At equal degrees of discharge, the difference of electrolyte densities, Δ*P*, grows with the discharge current increasing from 0.1*C* to 3*C* by a factor of 2.6 at 25% discharge and by a factor of 3.6 at 100% discharge.

Comparison of the differences Δ*P* of electrolyte densities in batteries with liquid and absorbed electrolytes (Figs. 1, 2) shows that this quantity is 2.9–

3.9 times lower, compared to batteries with liquid electrolyte, in batteries with absorbed electrolyte at 25–50% discharge in the 10-h discharge mode, and 1.3–1.1 times lower in the 0.5-h discharge mode. At 100% discharge, the difference of electrolyte densities, ΔP, in batteries with absorbed electrolyte is 1.9 times smaller than that in batteries with liquid electrolyte in the 10-h discharge mode, and 1.8 times greater in the 0.5-h discharge mode.

It should be noted that these figures will be somewhat different if batteries with absorbed electrolyte are discharged to a lesser extent. The results obtained in calculating the difference of electrolyte densities, ΔP, for 100% discharged SG-6 batteries at the same final voltages as those for the liquid-electrolyte batteries under study are shown in Fig. 2, curve *5*. Comparison of curves *4* and *5* shows a decrease in ΔP with increasing final discharge voltage. ΔP is 2.2 times smaller than that in batteries with liquid electrolyte in the 10-h discharge mode, and 1.1 times greater in the 0.5-h discharge mode.

Despite the fact that the rated electrolyte density in SG-6 batteries exceeds that in the liquid-electrolyte batteries under study (1.28 and 1.24 g cm^{-3}), the ΔP value is smaller in 1–10-h discharge modes for batteries with absorbed electrolyte, which, presumably, can be accounted for by the increasing rate of electrolyte diffusion as a result of the greater difference of electrolyte concentrations in the separator and within electrode pores. In short-discharge modes, the discharge is ensured by acid accumulated within the electrode pores and the adjacent separator layer, and, therefore, the ΔP value for sealed batteries exceeds that for batteries with liquid electrolyte.

The run of curve *5* in Fig. 2 and the curves in Fig. 1 also points to the presence of a certain reserve of electrolyte in batteries with liquid electrolyte in short discharge modes and to the possibility of obtaining higher discharge capacity on lowering the final discharge voltage.

The experimental data on the difference of electrolyte densities in the container and within pores of the active paste in electrodes of sealed batteries, obtained in this study, make it possible to determine how the voltage varies with exhausted discharge capacity for all discharge modes of sealed batteries being designed, prior to fabrication and tests of their prototypes.

CONCLUSIONS

(1) Calculated differences of the electrolyte densities in the container and within pores of the active electrode paste were found for a sealed lead battery with absorbed electrolyte on the basis of experimental data. The dissimilarity between the values obtained and the analogous parameters of a lead battery with liquid electrolyte was demonstrated.

(2) The data obtained make it possible to determine the basic characteristic, variation of voltage during discharge, for sealed lead batteries being designed.

REFERENCES

1. Bessonova, T.M., Zhivotinskii, P.B., and Marasanova, A.N., *Sbornik rabot po khimicheskim istochnikam toka* (Coll. of Works on Chemical Power Sources), Leningrad: Energiya, 1975, issue 10, pp. 140–144.
2. Vetter, K.J., *Elektrochemische Kinetik*, Berlin: Springer, 1961.
3. Dasoyan, M.A., *Khimicheskie istochniki toka: Spravochnoe posobie* (Chemical Power Sources: Reference Book), Leningrad: Energiya, 1969.
4. Aguf, I.A., Dasoyan, M.A., Lyzlov, N.Yu., and Grigalyuk, N.K., *Elektrotekhnicheskaya promyshlennost'* (Electrotechnical Industry), Ser. 22: *Khimicheskie i fizicheskie istochniki toka: Obzor informatsii* (Chemical and Physical Power Sources: Review), Moscow: Informelektro, 1984, pp. 1–67.
5. Aguf, I.A., Tsenter, B.I., Mrga, I., and Mitski, K., *Elektrotekhnicheskaya promyshlennost'* (Electrotechnical Industry), Ser. 22: *Istochniki toka: Obzor informatsii* (Power Sources: Review), Moscow: Informelektro, 1989, pp. 1–28.
6. Taganova, A.A. and Bubnov, Yu.I., *Germetichnye khimicheskie istochniki toka: Elementy i akkumulyatory: Sposoby i ustroistva zaryada* (Sealed Chemical Power Sources: Cells and Batteries, Charging Methods and Devices), St. Petersburg: Khimizdat, 2002.

Russian Journal of Applied Chemistry, Vol. 76, No. 1, 2003, pp. 88–94. Translated from Zhurnal Prikladnoi Khimii, Vol. 76, No. 1, 2003, pp. 90–96.

CATALYSIS

Complexes of Copper(I) with Dimercapto Compounds as Catalysts for Oxidation of Mercaptans and Hydrogen Sulfide with Molecular Oxygen in Aqueous Solutions

G. A. Bagiyan, I. K. Koroleva, N. V. Soroka, and A. V. Ufimtsev

Konstantinov Institute of Nuclear Physics, Russian Academy of Sciences, Gatchina, Leningrad oblast, Russia

Received September 2, 2002

Abstract—The conditions for formation of complexes of copper(I) with mercapto compounds in aqueous-alkaline solutions and the catalytic activity of these complexes in oxidation of mercaptans and hydrogen sulfide was studied. The kinetic characteristics of these catalysts were compared with those of catalysts based on cobalt phthalocyanines. A method was proposed for suppressing formation of the thiosulfate ion in oxidation of H_2S to elemental sulfur.

Catalytic oxidation of mercaptans plays a key part in industrial processes for purification of hydrocarbon raw materials to remove sulfur compounds [1] impairing the quality of motor fuels and poisoning catalysts in various stages of manufacture of synthetic rubber. The content of mercaptan sulfur in the raw materials is within the range from hundredths to tenths of a percent. Extraction of hydrogen sulfide from natural gas containing 1 (Orenburg gas field) to 25% (Astrakhan gas field) H_2S and its subsequent oxidation to elemental sulfur involves numerous catalytic stages aimed to convert the maximum possible amount of the initial H_2S into sulfur [2]. Cobalt phthalocyanines (CoPC), proposed in the 1960s, proved to be the most effective catalysts for oxidation of mercaptans into disulfides. In the years that passed, a great number of CoPC derivatives have been tested: from water-soluble mononuclear complexes intended for oxidation of mercaptans in the bulk of an aqueous-alkaline solution formed in Merox extraction process to polynuclear (M > 5000 Da) complexes acting as catalysts at the interface between the aqueous and organic phases in Merox demercaptanization of naphthas [3]:

$$2RSH + O_2 \rightarrow RSSR + H_2O_2, \quad (1)$$

$$4RSH + O_2 \rightarrow 2RSSR + 2H_2O. \quad (2)$$

It is known that, in aqueous-alkaline solutions in an excess of thiol compounds, Cu^{2+} ions are reduced to Cu^+, and further, thiolate anions form either soluble complexes with Cu^+ (if additional hydrophilic functional groups are present in a thiol compound) or poorly soluble Cu^+ mercaptides in the case when Cu^+ has monofunctional mercaptans as ligands [4]. The formation constants of Cu^+ complexes with thiol compounds are so high that the concentration of free Cu^+ ions in aqueous solutions does not exceed 10^{-10}–10^{-17} M, depending on the pH of the medium at total concentration of copper compounds in solution in the range 10^{-4}–10^{-6} M [5]:

$$RSH \rightleftarrows RS^- + H, \quad (3)$$

$$2RS^- + Cu^{2+} \rightleftarrows RSSR + Cu^+, \quad (4)$$

$$2RS^- + Cu^+ \rightleftarrows [Cu(SR)_2]^-, \quad (5)$$

$$RS^- + Cu^+ \rightleftarrows CuSR\downarrow. \quad (6)$$

Hence follows that the catalytic properties of copper(I) in oxidation of thiol compounds are due to complex species rather than to Cu^+ aqua ions.

A study of the catalytic oxidation of thiol compounds in relation to their structure in aqueous solutions revealed that the rate of oxidation of difficultly oxidized aliphatic mercaptans in aqueous-alkaline solutions increases dramatically [6] if into their solutions, along with Cu^+, minor amounts of readily oxidizable dimercapto compounds (DMCs) (I) are introduced, such as dimercaptopropionic, dimercaptosuccinic, and dimercaptopropanesulfonic acids and dimercaptopropylamine (Fig. 1):

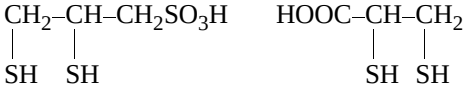

1070-4272/03/7601-0088$25.00

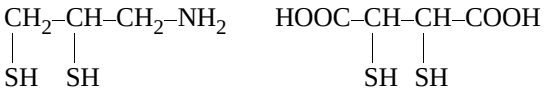

In this case, Cu^+ mercaptides are dissolved and the previously inert mercaptans start to oxidize with kinetic characteristics typical of DMC oxidation. This effect can be used to develop novel catalysts for mercaptan oxidation, which have not been used previously in purification of petroleum products to remove mercaptans. Here, the main components of the catalyst are DMCs and their complexes with copper (DMC + Cu^+), introduced into an alkaline solution. In this case, the catalyst complex DMC + Cu^+ does not require development of any special flowsheet in purification of hydrocarbon raw materials to remove mercaptans, being totally compatible with the flowsheets employing CoPC.

The scheme of this process is as follows: hydrocarbon raw materials are brought in contact in an extractor, in a counterflow, with an alkaline (15–20% NaOH) solution of the catalyst, and mercaptans, which are weak acids (pK_a 10–10.5) pass in the form of anions, mercaptides, into the aqueous-alkaline solution. In this solution, when it comes in contact with atmospheric oxygen in the regeneration apparatus, mercaptides are oxidized to disulfides. The disulfides, which are insoluble in aqueous solutions, are extracted from the aqueous phase in the settling apparatus, being accumulated in a small volume of the upper organic layer and then removed from the system [7].

The DMCs mentioned differ only slightly in their catalytic properties in oxidation of mercaptans in the presence of Cu^+ ions, but only dimercaptopropanesulfonic acid (unithiol) is manufactured in Russia on the industrial scale for use in medicine to cure poisoning

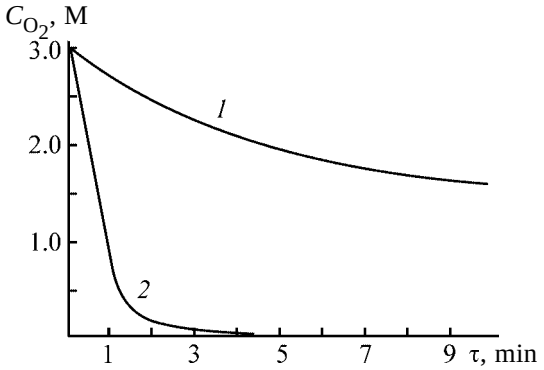

Fig. 1. Catalytic oxidation of butyl mercaptan BuSH. (c_{O_2}) Oxygen concentration and (τ) reaction time. Solution composition (M): (*1*) $CuSO_4$, 1.25×10^{-6}; $BuSH_0$, 1×10^{-2}, pH 11; (*2*) 1 + unithiol, 1×10^{-4}.

with heavy metals. Therefore, a catalyst on its base is, in principle, of interest for demercaptanization of hydrocarbons. The mechanism of the catalytic action of DMC + Cu^+ catalysts is based on two conjugated reactions: DMC oxidation by molecular oxygen in the coordination sphere of Cu^+ ions and thiol–disulfide exchange, which occurs outside the coordination sphere of the Cu^+ ion and results in that mercaptans dissolved in the alkaline medium are converted into disulfides and DMCs oxidized in the first reaction pass into their original reduced form. At relatively low Cu^+ concentrations the occurring reactions can be represented by Scheme 1.

Effective homogeneous catalysts for mercaptan oxidation must be characterized by high catalytic activity and long-term stability in 15–20% alkali solutions. The kinetics of butyl mercaptan oxidation in the presence of a complex of unithiol with copper(I) was studied in most detail: the dependence of the rate of mercaptan oxidation on the unithiol concentration,

Scheme 1

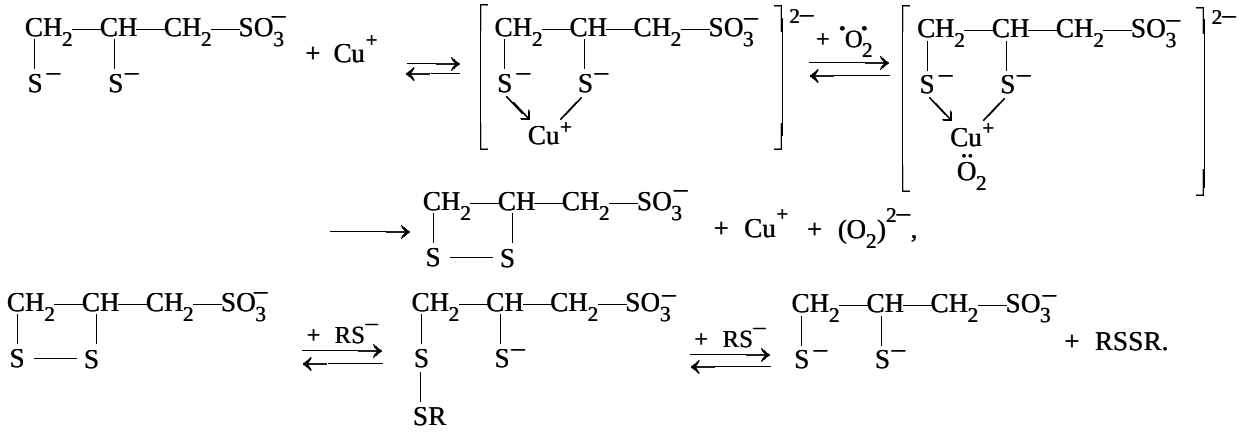

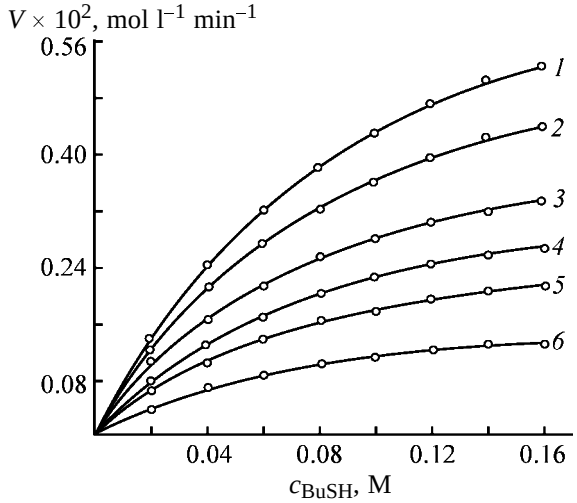

Fig. 2. BuSH oxidation rate V at relatively low Cu(I) concentrations in the catalyst solution. Concentration: $BuSH_0$ 1.75×10^{-1} and unithiol 4×10^{-3}. (c_{BuSH}) BuH concentration; the same for Fig. 4. Cu(I) concentration, g-ion l^{-1}: (*1*) 2.5×10^6, (*2*) 2.0×10^6, (*3*) 1.60×10^6, (*4*) 1.25×10^6, (*5*) 1.0×10^6, and (*6*) 6.25×10^7.

content of copper(I) ions in solution, and concentration of butyl mercaptan was analyzed.

EXPERIMENTAL

A procedure for determining the catalytic activity was chosen with account taken of the conditions in which the oxidation is kinetically controlled. The most adequate in this regard is the technique described in [8]. The oxidation was done with technical-grade oxygen under atmospheric pressure in an alkaline solution of the catalyst in a batch installation. The reactor was a 0.5-l glass vessel equipped with a three-blade impeller stirrer, bubbler for oxygen supply, reflecting partitions, reflux condenser, and contact thermometer connected to an electric relay. To maintain the temperature at the required level, a cooling finger was inserted into the vessel, and the reactor itself was heated with a Nichrome coil. The temperature was controlled to within ± 0.5°C, the stirrer rotation rate was 2700 rpm. Kinetic curves of butyl mercaptan oxidation were recorded at 20°C. The concentration of copper(I) ions was varied between 1.0×10^{-6} and 1.0×10^{-5} M, and that of unithiol, between 1.0×10^{-3} and 1.0×10^{-2} M. The initial concentration of mercaptides in the alkaline solution was varied between 0.690 and 0.082 M. The solution of mercaptides was prepared by mixing appropriate amounts of freshly distilled butyl mercaptan with a 10% solution of NaOH. The catalyst complex was prepared separately by dissolving weighed portions of unithiol and $CuSO_4 \cdot 5H_2O$ in distilled water. The mercaptide and catalyst solutions were mixed and the reaction mixture was thermostated directly in the reaction vessel in an atmosphere of argon. Oxygen was fed into the vessel at 20°C; the reaction time was counted from the beginning of oxygen supply into the reactor. The oxidation course was monitored by the content of mercaptides in the alkaline solution, by sampling the reaction mixture at certain intervals of time. The content of mercaptides in the reaction mixture was determined by potentiometric titration with 0.01 N $[Ag(NH_3)_2]NO_3$ in conformity with GOSTs (State Standards) 22 985–78 and 17 323–71.

The graphical dependence of the oxidation rate on the mercaptan concentration at different reagent concentrations in solution is shown in Figs. 2–4. It can

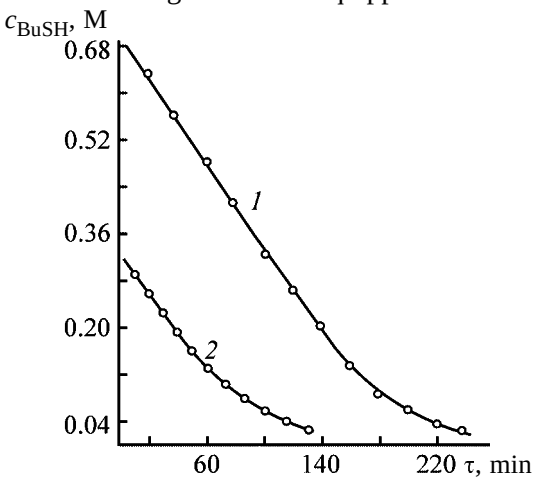

Fig. 3. BuSH oxidation kinetics at varied initial concentrations of mercaptan. Concentration: Cu(I) 1.25×10^{-6} g-ion l^{-1} and unithiol 4×10^{-3} M. (c_{BuSH}) BuSH concentration and (τ) reaction time. Initial BuSH concentration, M: (*1*) 6.5×10^{-1} and (*2*) 3.2×10^{-1}.

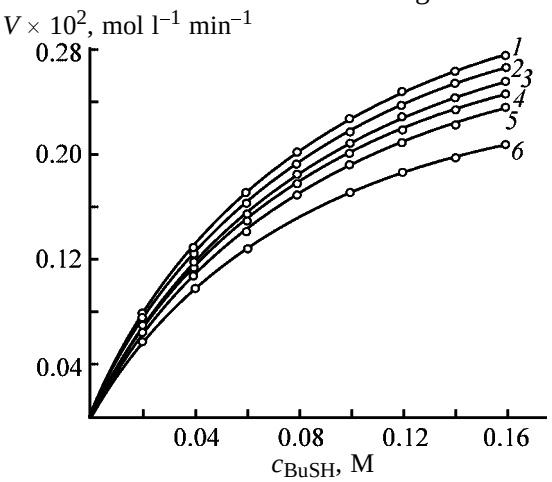

Fig. 4. BuSH oxidation rate V at varied unithiol concentration in the catalyst solution. Concentration, M: $BuSH_0$ 1.75×10^{-1} and $CuSO_4$ 1.25×10^{-6}. Unithiol concentration, M: (*1*) 1×10^2, (*2*) 5×10^3, (*3*) 3.5×10^3, (*4*) 2.2×10^3, (*5*) 1.5×10^3, and (*6*) 8×10^4.

be seen that the reaction kinetics is described by the Michaelis equation [9, 10]

$$V = -\mathrm{d[RSH]}/\mathrm{d}t = V_{max}[\mathrm{RSH}]/([\mathrm{RSH}] + K_m), \quad (7)$$

where V is the reaction rate, [RSH] is the mercaptan concentration, and V_{max} and K_m are constants.

With increasing mercaptan concentration, the reaction rate does not grow unlimitedly, but tends to a value V_{max} reached at the highest concentrations of the catalytically active complex species. The physical meaning of the Michaelis constant K_m is as follows: If the mercaptan concentration is chosen to be [RSH] = K_m, then the reaction rate is equal to half the maximum possible value, i.e., $V = -\mathrm{d[RSH]}/\mathrm{d}t = V_{max}/2$. Such a dependence means that the reaction rate is limited by the concentration of the catalytically active complex species. Their concentration becomes the highest at mercaptan concentrations of about K_m, and then it no longer depends on the mercaptan concentration because of the saturation. Thus, this reaction is first-order at very low mercaptan concentrations and zero-order at a sufficiently high concentration. It is the latter case that occurs in catalytic oxidation of mercaptans in high-sulfur raw materials. Therefore, the quantity τ_1^{-1}, reciprocal of the time of conversion (e.g., 95% oxidation), can serve as a measure of the catalyst performance. Let us consider how the reaction rate depends on the concentrations of the catalyst components. The rate is virtually independent of the unithiol concentration in a wide range (Fig. 4). As for the dependence of the reaction rate on the copper(I) concentration, the situation is complicated by the following circumstance. As shown previously [6], the complex of copper(I) with unithiol exists in two forms, monomeric and dimeric, characterized by different catalytic activities. In the dimeric complex, the O_2 molecule is a bridging ligand, in which connection the steady-state concentration of the catalytically active oxygen-containing complex is higher for the dimeric form of the complex, compared to its monomeric form:

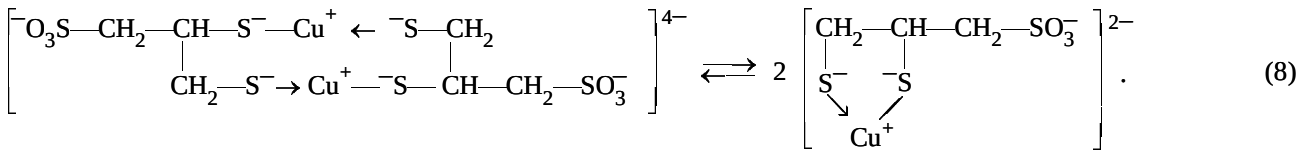

(8)

Therefore, the mechanism of oxidation of coordinated dimercapto compounds in such a dimeric complex differs from the scheme presented for the monomeric form of the complex: electrons pass from four thiolate anions to the bridging O_2 molecule, and water molecule, rather than the O_2^{2-} anion, is the reduction product in this case (Scheme 2). At low copper(I) concentrations, the reaction is first-order with respect to copper(I), since the dimeric complex is mainly dissociated; whereas at sufficiently high copper(I) concentrations the reaction order must be 0.5, i.e., the reaction rate is to be proportional to a square root of the copper concentration. It is this behavior that is observed experimentally (Fig. 5).

As shown by experiments, the oxidation rates of butyl and ethyl mercaptans are the same under comparable conditions, and that of the sulfide ion is half the oxidation rate of mercaptans, which would be expected since the sulfide ion loses two times greater number of electrons in oxidation, compared to the mercaptide ion. By contrast, in the presence of CoPC catalysts, high-molecular-weight mercaptans are oxidized more readily than low-molecular-weight mercaptans. For example, Co disulfophthalocyanine oxidizes butyl mercaptan 4.5 times faster than ethyl mercaptan, which, in turn, is oxidized several times faster than the sulfide ion. Moreover, in contrast to the kinetic characteristics of the DMC + Cu^+ systems, the reaction is first-order with respect to the catalyst and mercaptan concentrations [11].

In view of the fundamentally different kinetic characteristics of the catalysts compared, the time necessary for 95% oxidation of butyl mercaptan with the initial concentration of 0.2 M was chosen as a catalytic activity criterion.

Experiments demonstrated that butyl mercaptan is 95% oxidized in an alkaline solution at copper(I) and unithiol concentrations of, respectively, 5×10^{-6} and 5×10^{-4}–5×10^{-3} M in 35–40 min, whereas the industrial Co disulfophthalocyanine ensures the same conversion in 100 min at a concentration in solution of 5×10^{-6} M. With Co polyphthalocyanine, 95% conversion of butyl mercaptan into disulfide is reached in 20 min. It is noteworthy that the activity of the catalyst based on Cu^+ and dimercaptopropionic acid ensures the same conversion in 20 min. Thus, compar-

Scheme 2

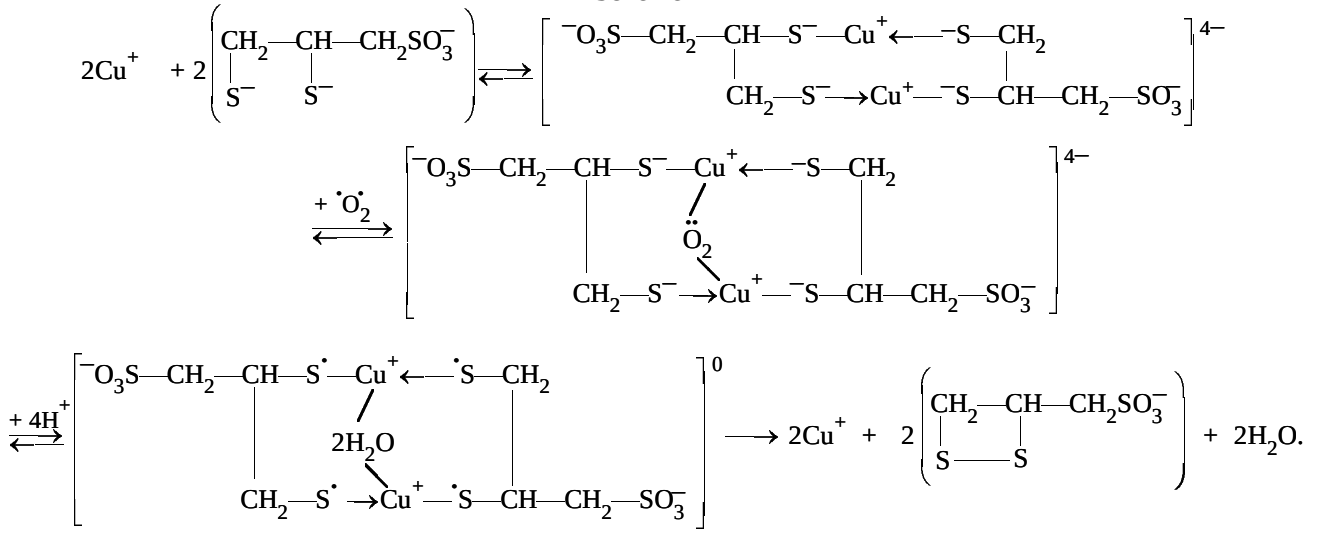

ison of the activity of DMC + Cu^+ catalysts with that of the industrially used CoPC catalysts shows that the unithiol-based system is 2.5 times more active than Co diphthalocyanine and 1.5 times less active than Co polyphthalocyanine, and the system based on Cu^+ and dimercaptopropionic acid exhibits higher activity than Co polyphthalocyanine.

The above data on the catalytic activity are an important, but insufficient characteristic of the catalysts, since, at their close catalytic activities, of key importance for the effective industrial use of the catalysts must be their stability in alkaline solutions. That is why experiments were performed on prolonged keeping of the catalysts in a 10% NaOH solution, with periodic sampling to measure the dependence of the catalytic activity on the time of keeping of the catalyst solutions. The initial concentrations (M) of the catalysts compared were the same as those in industrial processes, i.e., 3×10^{-4} disulfophthalocyanine, 1.5×10^{-4} polyphthalocyanine, and 5×10^{-3} unithiol + 1×10^{-3} $CuSO_4$. The variation of the activity of the catalyst solutions with time is shown in Fig. 6. It can be seen that after 7 days the activity of the DMC + Cu^+, disulfophthalocyanine, and polyphthalocyanine catalysts decreased by, respectively, factors of 1.4, 17, and 60. After 2 weeks the respective figures were 2.5, 120, and 120. In subsequent sampling, the activity was only measured for the DMC + Cu^+ catalyst, to decrease 5-fold in 6 weeks, compared with that of a freshly prepared solution. Thus, it was established that the DMC + Cu^+ catalysts much better retain their

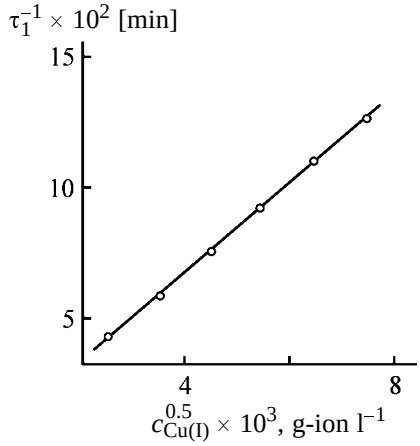

Fig. 5. BuSH oxidation rate vs. concentration $c_{Cu(I)}$ of Cu(I) ions in the catalyst solution at high Cu(I) concentrations. (τ) Time of 95% conversion. Concentrations: $BuSH_0$ 1.75×10^{-1} M, unithiol 4×10^{-3} M, Cu(I) 4×10^{-6}–6×10^{-5} g-ion l^{-1}.

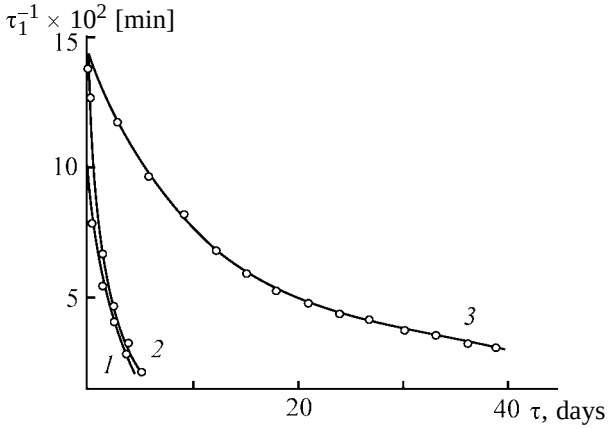

Fig. 6. Variation of the catalytic activity of the complexes in prolonged keeping in a 10% NaOH solution. (τ_1) Time of 95% conversion and (τ) time of keeping in an alkali solution. Catalyst (g l^{-1}): (*1*) disulfophthalocyanine, 2.0; (*2*) polyphthalocyanine, 1.0; (*3*) complex of copper (0.17 g l^{-1} $CuSO_4$) with unithiol, 1 g $^{-1}$.

activity in prolonged storage in alkaline solutions than the CoPC catalysts do [12, 13].

It is known that CoPC catalysts cannot sustain elevated temperatures in alkaline solutions: their activity falls dramatically at 70–80°C. The DMC + Cu^+ catalysts show no changes in catalytic activity on being kept for 1 h in a 10% NaOH solution at 95°C and subsequent cooling of the solution to 20°C. The same result was obtained on heating a DMC + Cu^+ catalyst solution in a 20% diethanolamine solution at 107°C for 1.5 h.

It was of interest to test the capabilities of DMC + Cu^+ catalysts in a more intensive process involving purification of natural gas to remove hydrogen sulfide, with elemental sulfur obtained simultaneously. Most frequently, natural gas with high H_2S content (≥1.5%) is purified in the industry by intensive processes associated with preliminary H_2S absorption by ethanolamine solutions, subsequent desorption of H_2S from ethanolamine solutions at 120°C, and its oxidation in a flow of O_2 to elemental sulfur (Claus process). This technique has an important disadvantage, high sorbent loss of up to 100 g of ethanolamine per ton of natural gas. All other "wet" methods for H_2S oxidation do not compare in intensity with this process and can only be used at low H_2S content in natural gas (<0.5%), because Na_2CO_3 solutions should not be strongly saturated with hydrogen sulfide. Such a saturation could lead to predominant formation of thiosulfate and sulfate ions in the solutions, with the H_2S absorption capacity of the solutions decreasing in proportion to this accumulation [14]. Preliminarily, the oxidation of H_2S to polysulfides and elemental sulfur in sodium carbonate solutions in the presence of DMC + Cu^+ catalysts was studied and it was established that, in H_2S oxidation, elemental sulfur is not the only and even not the major reaction product. Indeed, experiments aimed to determine the stoichiometry of H_2S (1.5 M) oxidation in Na_2CO_3 solutions containing 2×10^{-3} M unithiol and 4×10^{-4} M Cu^+ demonstrated that elemental sulfur and thiosulfate ions are formed in a 1 : 4 molar ratio. The short-chain polysulfides formed in the catalytic stage react outside the coordination sphere of the complex with excess O_2 by the radical-chain mechanisms, finally yielding thiosulfate ions [15]:

$$HS^- + RSSR \rightleftarrows RSSH + RS^-, \quad (9)$$

$$RSSH \rightleftarrows RSS^- + H^+, \quad (10)$$

$$RSS^- + RSSR \rightleftarrows RSSSR + RS^-, \quad (11)$$

$$RSS^- + RSSSR \rightleftarrows RSSSSR + RS^-, \quad (12)$$

$$RSS^- + R(S)_7R \rightleftarrows R(S)_8R + RS^-, \quad (13)$$

$$R(S)_8R \rightarrow S_6\downarrow + RSSR. \quad (14)$$

The undesirable appearance of radicals can be prevented by introducing effective radical scavengers into the system. For example, 0.2–1 M ammonium thiosulfate and 0.03–3 M elemental sulfur are introduced, together with CoPC, into the absorbing solution. However, these measures ensure quantitative conversion of H_2S into sulfur at H_2S concentration in solution not exceeding 2×10^{-2} M in 3–20 min [16] and, therefore, cannot be used in processing of gases with high H_2S content. In the present study, an aminodisulfide, $(H_2NCH_2CH_2S–)_2$, cystamine, manufactured in Russia industrially, was used to effectively suppress radical-chain reactions in H_2S oxidation. Aminodisulfides are known to be, together with aminothiols, active scavengers of many kinds of radicals. Here, it should be emphasized once more that the oxidation of both mercaptans and hydrogen sulfide occurs in the thiol–disulfide reaction, including that with active short-chain polysulfides, rather than in the coordination sphere of the complex. Thus, it would be expected that, as a result of consecutive reactions, these active polysulfide species will be transformed into $R(S)_nR$ species, which are inert toward O_2. With the chain of sulfur atoms growing, as a result of these reactions, to $R(S)_8R$ or $R(S)_{10}R$, 6- and 8-membered sulfur rings are formed from them. Indeed, the presence in the absorbing solution of cystamine with concentration of 1–1.5 M, in addition to DMC + Cu^+, totally suppresses formation of oxygen-containing sulfur compounds in oxidation of 1.5 M S^{2-} with half-oxidation time of 6 min in the presence of 2×10^{-3} M unithiol and 4×10^{-4} g-ion l^{-1} Cu^+.

Thus, the system proposed ensures a two orders of magnitude more intensive process than that in the above-considered conventional technique with CoPC. Analysis for the content of thiosulfate ions in solutions shows that their concentration does not exceed 1%. The difficulty of analysis of thiosulfate ions in the presence of a large excess of cystamine gives no way of determining with sufficient accuracy in laboratory conditions how much less than 1% is the amount of thiosulfate ions formed in the system. This could be done reliably in experiments on a continuous pilot installation from the extent of preservation of the buffer capacity of the absorbing solution in the stage of H_2S absorption.

Calculations show that, if by-product thiosulfate ions are formed in amount less than 0.1%, the catalytic system developed is more attractive economically than separate ethanolamine treatment of natural gas to

remove H_2S with elemental sulfur subsequently obtained by the Claus method. An additional advantage of cystamine introduction into the catalytic system is that cystamine as a base can also be employed as an effective absorbent binding the H_2S acid from the gas flow, instead of using the conventional ethanolamine, and can perform, in the stage of catalytic interaction between H_2S and O_2, a second important function by suppressing the undesirable radical-chain reactions.

CONCLUSIONS

(1) New effective catalysts for oxidation of mercaptans and hydrogen sulfide are proposed, based on complexes of copper(I) with dimercapto compounds, which can be used in purification of the wide fraction of light hydrocarbons to remove mercaptans and in purification of natural gas to remove hydrogen sulfide, with elemental sulfur obtained simultaneously.

(2) A study of the kinetic characteristics of the new catalysts demonstrated that the catalytically active species in the practically important range of concentrations is the dimeric form, which binds more effectively an oxygen molecule in the coordination sphere of copper(I).

(3) In oxidation of H_2S to elemental sulfur, the undesirable formation of a by-product, thiosulfate ions, was suppressed by introducing cystamine into the catalyst solution, with the high intensity of catalytic oxidation of H_2S into elemental sulfur preserved.

ACKNOWLEDGMENTS

The authors are grateful to A.V. Ilatovskii for assistance in preparing the manuscript.

REFERENCES

1. Borisenkova, S.A., *Neftekhimiya*, 1991, vol. 31, no. 3, pp. 391–408.
2. Agaev, G.A. and Chernomyrdin, V.S., *Tekhnicheskii progress v ochistke prirodnogo gaza ot serovodoroda okislitel'nymi metodami* (Technical Progress in Purification of Natural Gas To Remove Hydrogen Sulfide by Oxidative Techniques), Moscow: Mingazprom, 1980.
3. Sharipov, A.Kh. and Kovtunenko, S.V., *Neftekhimiya*, 1997, vol. 37, no. 6, pp. 563–567.
4. Hemmerich, P. and Sigwart, C., *Experientia*, 1963, vol. 19, no. 2, pp. 488–492.
5. Bagiyan, G.A., Valeev, A.K., Koroleva, I.K., and Soroka, N.V., *Zh. Neorg. Khim.*, 1983, vol. 28, no. 8, pp. 2016–2025.
6. Bagiyan, G.A., Koroleva, I.K., Soroka, N.V., and Ufimtsev, A.V., in *Breslerovskie chteniya* (Bresler Readings), St. Petersburg: Peterb. Inst. Yadernoi Fiziki, Ross. Akad. Nauk, 2002, pp. 270–290.
7. Ivanova, N.N., Pavlova, V.V., Glebova, N.A., *et al.*, *Seroochistka legkogo uglevodorodnogo syr'ya* (Purification of Light-Hydrocarbon Raw Materials To Remove Sulfur), Moscow: TsNIITEneftekhim, 1975.
8. Fomin, V.A. and Mazgarov, A.M., *Neftekhimiya*, 1978, vol. 18, no. 3, pp. 298–303.
9. Panchenkov, G.M. and Lebedev, V.P., *Khimicheskaya kinetika i kataliz* (Chemical Kinetics and Catalysis), Moscow: Khimiya, 1974.
10. Bresler, S.E., *Vvedenie v molekulyarnuyu biologiyu* (Introduction to Molecular Biology), Moscow: Nauka, 1966.
11. Fomin, V.A., Liquid-Phase Catalytic Oxidation of Mercaptans with Molecular Oxygen, *Cand. Sci. Dissertation*, Kazan, 1980.
12. USSR Inventor's Certificate no. 869300.
13. USSR Inventor's Certificate no. 908069.
14. USSR Inventor's Certificate no. 1401665.
15. Simonov, A.D., Keier, N.P., and Kundo, N.N., *Kinet. Katal.*, 1973, vol. 14, pp. 989–999.
16. USSR Inventor's Certificate no. 1510898.

Russian Journal of Applied Chemistry, Vol. 76, No. 1, 2003, pp. 95–98. Translated from Zhurnal Prikladnoi Khimii, Vol. 76, No. 1, 2003, pp. 97–100.

CATALYSIS

Effect of High-Temperature Steam Treatment of High-Silica Zeolites of the ZSM-5 Type on Their Acidity and Selectivity of Formation of Lower Olefins from Straight-Run Naphthas

V. I. Erofeev, L. V. Adyaeva, and N. V. Ryabova

Department of Scientific and Technical Development, Tomsk Petrochemical Concern, Joint-Stock Company, Tomsk, Russia
Institute of Petroleum Chemistry, Siberian Division, Russian Academy of Sciences, Tomsk, Russia

Received May 16, 2002

Abstract—The effect of high-temperature steam treatment of high-silica zeolites of the ZSM-5 type on their acidity and selectivity of formation of lower olefins from straight-run naphthas was studied.

High-silica zeolites (HSZs) of the ZSM-5 type exhibit high activity in many transformations of hydrocarbons [1–4]; however, they are rapidly deactivated owing to active coking. The coking on the catalyst surface can be supressed by addition of special modifying components or appropriate pretreatment [5–13]. In this connection, it is advisable to study how the high-temperature steam treatment affects the acid and catalytic characteristics of HSZs of the ZSM-5 type in conversion of straight-run naphtha (SRN) to lower olefins and aromatic hydrocarbons.

EXPERIMENTAL

High-silica zeolites of the ZSM-5 type with silica modulus of 30 were produced by hydrothermal synthesis from alkaline aluminosilica gels by the procedure described previously [14]. The resulting samples of zeolites were decationized by treatment with 25% aqueous NH_4Cl at 90°C for 2 h, dried at 110°C, and calcined at 550°C for 8 h (Na_2O content less than 0.1%). As shown by IR spectroscopy and X-ray analysis (Mo anode, Ni filter), the synthesized zeolites correspond to HSZs of the ZSM-5 type with 90–95% degree of crystallinity. The coke amount in the samples was determined by thermal gravimetric analysis on an MOM derivatograph (Hungary). After completion of the catalytic experiments, the reaction products adsorbed on the catalyst surface were removed with a flow of gaseous nitrogen. The carbon-containing residue remaining on the catalyst surface under these conditions was considered as coke. After removal of adsorbed hydrocarbons with gaseous nitrogen, the reactor was cooled and the coked catalyst was discharged into a hermetically sealed vessel. A weighed portion of the catalyst sample was placed into a platinum crucible and heated in air at a rate of 10 deg min^{-1} with the simulatneous recording of the thermal and weight loss effects. The sensitivity of the derivatograph in the weight measurements was 5×10^{-4} g.

To study the influence of high-temperature steam treatment (HTST) on the acid and catalytic characteristics, the HSZ samples were subjected to high-temperature steam pretreatment at 550 and 700°C. The acid characteristics of HSZs were studied by thermal desorption of ammonia by the procedure described previously [15]. The catalytic characteristics of HSZs in conversion of SRN were studied on a flow-type installation [13]. As the initial hydrocarbon raw material we used SRN produced by the Surgut Gas-Processing Plant with the following composition: paraffins 56.89, naphthenes 32.76, and aromatic hydrocarbons 8.54% (here and hereinafter, wt %).

The results of studying the effect of HTST on the activity and selectivity of HSZs in conversion of SRN are listed in Table 1. With increasing reaction temperature from 500°C to 650°C at the space velocity of SRN of 3 h^{-1}, the degree of SRN conversion increases from 85 to 90%. With heating, the yield of lower olefins C_2–C_4 increases from 6.7 to 26.0%, and the yield of aromatic hydrocarbons, from 33.5 to 37.8%. The content of aromatic hydrocarbons C_6–C_9 in the liquid catalyzate at the pyrolysis temperature of 600°C is 88.3%. With increasing duration of HTST of HSZ at 550°C from 7 to 15 h, the yield of lower olefins in the products of SRN pyrolysis at 700°C abruptly increases to 40.9%. An increase in the temperature of

1070-4272/03/7601-0095$25.00

Table 1. Effect of HTST on the yield of products of SRN conversion on HSZ

Treatment conditions		T_{react}, °C	Yield based on SRN, %							Content, %	
T, °C	τ, h		gas	methane	ethane	C_2–C_4 alkenes	ethylene	propylene	arenes	C_2–C_4 alkenes in gas	arenes in the catalyst
Initial HSZ		500	59.2	6.4	7.8	6.7	1.2	3.4	33.5	11.3	82.1
		550	57.2	9.6	9.0	11.6	3.5	5.3	36.4	20.3	85.0
		600	57.2	13.1	9.8	16.4	6.4	6.7	37.8	20.7	88.3
		650	58.5	11.5	7.7	26.0	11.3	9.9	35.8	44.4	86.3
550	7	500	25.5	1.0	1.5	12.7	3.6	5.7	12.9	49.8	17.3
		550	35.7	1.9	2.4	21.3	6.3	8.6	19.9	59.7	30.9
		600	44.2	3.6	3.2	28.5	8.6	11.5	26.5	54.5	47.5
550	15	550	34.3	1.6	1.7	23.9	6.6	10.8	13.5	69.8	20.5
		600	44.9	3.3	2.7	33.2	9.7	14.1	13.9	73.9	25.2
		650	52.0	5.8	3.5	37.3	13.5	16.4	15.6	71.7	32.5
		700	58.3	8.7	4.5	40.9	15.15	16.9	17.8	70.2	42.7
700	1	550	23.2	1.4	1.4	15.5	4.4	7.3	9.2	66.8	11.9
		600	35.6	2.9	2.2	24.7	7.6	11.2	10.5	69.4	16.3
		650	49.7	4.9	2.7	31.1	9.8	13.4	12.9	62.6	25.6
		700	51.9	8.1	4.0	35.7	12.0	14.7	16.4	68.8	34.1
700	2	550	22.3	0.9	1.1	14.8	3.6	6.2	7.9	66.4	10.2
		600	34.9	2.2	1.8	25.3	6.9	10.6	8.7	72.5	13.4
		650	43.6	4.1	2.5	32.3	9.9	12.4	12.9	74.1	22.9
		700	53.2	7.1	3.5	38.8	13.6	14.5	15.3	72.9	32.7
700	6	550	8.3	0.4	0.3	6.4	1.2	3.1	6.3	77.1	6.9
		600	14.2	0.9	0.6	10.2	2.7	5.7	6.5	71.8	7.5
		650	26.3	2.3	1.4	19.3	5.9	9.4	7.2	73.4	9.8
		700	46.8	5.9	3.2	33.7	11.2	14.2	11.9	72.0	22.4

1-h HTST of HSZ from 550°C to 700°C results in decreased SRN conversion; however, the yield of lower olefins is 35.7% at the pyrolysis temperature of 700°C. An increase in the duration of HTST of the catalyst at 700°C to 6 h abruptly decreases the catalyst activity and the yield of lower olefins C_2–C_4. Apparently, prolonged action of steam on the catalyst sample partially destroys the crystal structure of zeolite.

Thus, the optimal condition of HTST of the catalyst is treatment of HSZ at 550°C for 15 h. Under these conditions, at the SRN pyrolysis temperature of 700°C and the space velocity of 3 h^{-1}, we obtained on HSZ 40.9% yield of lower olefins C_2–C_4, among them ethylene 15.2% and propylene 16.9%; the conversion of HSZ was 71% (Table 1). This behavior of HSZ subjected to HTST at various high temperatures and for a long time is caused by variation of the acid characteristics of the zeolite-containing catalysts. In this connection, we studied how HTST affects the acid characteristics of HSZs. The acid characteristics were evaluated by thermal desorption of ammonia.

Two forms of ammonia desorption are observed in the thermal desorption curve of the initial HSZ: low-temperature form I of ammonia desorption with the peak temperature T_{max} 194°C and high-temperature form II with T_{max} 406°C. The concentrations of acid centers are 623 and 526 μmol per gram of the catalyst, respectively (Fig. 1a, Table 2). High-temperature steam pretreatment of HSZ at 550°C for 7 h shifts the two peaks of ammonia desorption to lower temperatures and significantly decreases the concentration of acid centers: the low-temperature form I of ammonia desorption is characterized by the peak at T_{max} 179°C (289 μmol per gram), and high-temperature form II, by T_{max} 298°C (171 μmol per gram). The total concentration of acid centers in comparison with the initial HSZ decreases by a factor of 2.5. As the time of HTST of HSZ at 550°C is further increased to

Table 2. Effect of HTST on the acid characteristics of HSZ

Treatment conditions		T_{max}, °C		Amount of acid centers, μmol g^{-1}		
T, °C	τ, h	form I	form II	form I	form II	total
Initial HSZ		194	406	623	526	1149
550	7	179	298	289	171	460
550	15	165	295	170	62	232
700	1	174	290	138	93	231
700	2	155	290	155	69	224
700	6	179	260	87	55	142

15 h, both forms of ammonia desorption are shifted to lower temperatures, and the concentration of acid centers of both types decreases (Fig. 1a, Table 2).

The study of effect exerted by HTST of HSZ at 700°C on its acid characteristics showed that, as a result of treatment of the catalyst for 1 h, the concentration of acid centers, especially that of strong (Brønsted) acid centers [6, 8–9, 11], considerably decreases. On the contrary, weak (Lewis) acid centers are more resistant to HTST and are not destroyed even at prolonged HTST for 15 h and more (Fig. 1b, Table 2) [7, 12].

Thus, when the HTST temperature is increased to 700°C and HTST time, to 15 h and more, the strong Brønsted centers are destroyed, the strength and concentration of weak Lewis acid centers decrease, and, as a result, the selectivity of formation of lower olefins from SRN increases. It is advisable to perform HTST of zeolite-containing catalysts at a temperature not exceeding 550°C, since under these conditions strong acid centers transform to moderately strong Brønsted acid centers and the rates of aromatization and coke formation, proceeding actively on strong Brønsted acid centers, decrease. HTST of zeolite-containing catalysts at elevated temperatures results in hydrolysis of the Si–O–Al bonds and removal of aluminum from the zeolite skeleton (conversion into Al_2O_3) owing to dehydroxylation [16]. Variation of the selectivity of SRN conversion on zeolite-containing catalysts under the effect of HTST is caused primarily by removal of aluminum from cationic sites during HTST. This increases the selectivity of formation of C_2–C_4 olefins from SRN and decreases the rates of aromatization and coke formation.

The DTA of the samples after their operation in pyrolysis of SRN revealed an exothermic effect in the range 450–650°C with a clearly pronounced peak at 580°C and a high-temperature shoulder; this suggests a wide spectrum of coke deposits. The total weight of the coke deposit in the spent HSZ sample is 7.2%. As a result of HTST of HSZ, the weight of the coke deposit in the spent catalyst sample after pyrolysis of SRN decreases to 5.6%. The peak (T_{max}) in the DTA curve is shifted to lower temperatures (560°C), and an additional exothermic peak with a maximum at 330°C appears, i.e., a more "friable" low-temperature coke is formed in the course of SRN pyrolysis.

CONCLUSIONS

(1) Upon high-temperature steam treatment of high-silica zeoilites of the Pentasil type (ZSM-5), the acid centers in the zeolite are redistributed, which

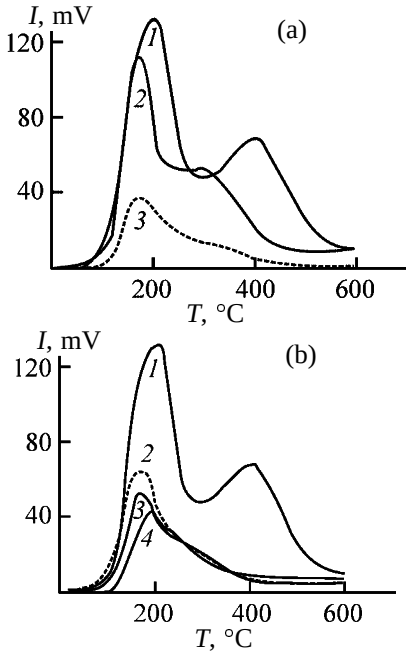

Fig. 1. Spectra of thermal desorption of ammonia. (*I*) Signal intensity and (*T*) temperature. (*1*) Initial HSZ; HTST time, h: (a) (*2*) 7 and (*3*) 17; (b) (*2*) 1, (*3*) 2, and (*4*) 6. Temperature of HTST, °C: (a) 550 and (b) 700.

results in predomination of weak Lewis acid centers over strong Brønsted acid centers.

(2) In pyrolysis of straight-run naphthas, high-temperature steam treatment of high-silica zeolites results in increased yield of lower olefins C_2–C_4 and decreased yield of aromatic hydrocarbons and coke deposits, formed more actively on strong Brønsted centers of the zeolite-containing catalyst.

REFERENCES

1. Minachev, Kh.M. and Kondrat'ev, D.A., *Usp. Khim.*, 1983, vol. 52, no. 12, pp. 1921–1273.
2. Isakov, Ya.I. and Minachev, Kh.M., *Neftekhimiya*, 1990, vol. 30, no. 3, pp. 291–325.
3. Minachev, Kh.M. and Dergachev, A.A., *Usp. Khim.*, 1990, vol. 59, no. 4, pp. 1522–1544.
4. Minachev, Kh.M. and Dergachev, A.A., *Izv. Akad. Nauk SSSR, Ser. Khim.*, 1993, no. 6, pp. 1018–1027.
5. Mamedov, S.E., Aminbekov, A.F., and Mamedov, A.B., *Neftekhimiya*, 1998, vol. 38, no. 2, pp. 107–110.
6. Erofeev, V.I., Ryabov, Yu.V., Korobitsyna, L.L., and Bol'shakov, G.F., *Dokl. Akad. Nauk SSSR*, 1985, vol. 283, no. 1, pp. 148–151.
7. Sinitsyna, O.A., Chumakova, V.I., Moskovskaya, N.F., *et al.*, *Vestn. Mosk. Gos. Univ., Ser. 2*, 1986, vol. 27, no. 6, pp. 550–553.
8. Ryabov, Yu.V. and Erofeev, V.I., *Izv. Akad. Nauk SSSR, Ser. Khim.*, 1986, no. 9, pp. 1966–1970.
9. Lomako, V.I. and Erofeev, V.I., *Zh. Fiz. Khim.*, 1986, vol. 60, no. 12, pp. 3004–3007.
10. Spiridonov, S.E., Khadzhiev, S.N., Yaralov, N.G., and Limonova, T.V., *Kinet. Katal.*, 1986, vol. 27, no. 1, pp. 201–209.
11. Erofeev, V.I., Ryabov, Yu.V., and Bol'shakov, G.F., *Dokl. Akad. Nauk SSSR*, 1987, vol. 293, no. 6, pp. 1400–1403.
12. Ryabov, Yu.V., Korobitsyna, L.L., and Erofeev, V.I., *Zh. Fiz. Khim.*, 1987, vol. 61, no. 7, pp. 1817–1820.
13. Erofeev, V.I., Adyaeva, L.V., and Ryabov, Yu.V., *Zh. Prikl. Khim.*, 2001, vol. 74, no. 2, pp. 231–234.
14. RF Patent 1527154.
15. Vosmerikov, A.V. and Erofeev, V.I., *Zh. Fiz. Khim.*, 1995, vol. 69, no. 5, pp. 787–790.
16. Echevskii, G.V., Nosyreva, G.N., and Ione, K.G., *Izv. Akad. Nauk SSSR, Ser. Khim.*, 1986, no. 5, pp. 996–1004.

Russian Journal of Applied Chemistry, Vol. 76, No. 1, 2003, pp. 99–104. Translated from Zhurnal Prikladnoi Khimii, Vol. 76, No. 1, 2003, pp. 101–106.

PROCESSES AND EQUIPMENT OF CHEMICAL INDUSTRY

Mass Exchange in Absorption in Fluid–Gas Jet Apparatus with Elongated Mixing Chamber

A. N. Blaznov, V. A. Kunichan, D. V. Chashchilov, and Yu. N. Denisov

Biisk Technological Institute, Polzunov State Technical University of Altai, Biisk, Altai krai, Russia

Received February 8, 2002

Abstract—Mass exchange in absorbers having the form of fluid–gas jet apparatus with elongated mixing chamber is considered. An approach to calculation of the mass-exchange coefficients and gas absorption rate in a flow of a gas–fluid emulsion in the mixing chamber is proposed. Results obtained in industrial operation of the absorber are presented.

Use of jet apparatus with elongated mixing chamber as small-size absorbers seems to be promising for the modern industry [1, 2]. Absorbers of this kind can be used both for physical absorption and (most effectively) for chemisorption. In this case, engineering calculation of jet absorbers requires that, in addition to hydrodynamic parameters, mass-exchange characteristics (phase boundary area and mass-exchange coefficient) should also be calculated.

The phase contact surface is produced in a jet absorber as a result of mixing of flows of the working fluid (absorbent) and gas being sucked in and has the form of a gas–fluid emulsion or foam, depending on the volume content of the dispersed phase. In [1, 2], studies of dispersion and coalescence in fluid–gas jet apparatus with elongated mixing chamber for the water–air system were reported. On the basis of the results obtained, expressions were proposed for determining the area of the phase boundary formed via disintegration of gas bubbles by the fluid jet and for finding how this area changes upon coalescence in motion of a two-phase flow in the mixing chamber of the jet apparatus.

At the same time, there are no published data on mass transfer in jet apparatus with elongated mixing chamber, which could be used to calculate the mass-transfer coefficient. In view of this fact, the aim of this study is to propose expressions for determining the mass-transfer coefficient in absorption in a jet apparatus with elongated mixing chamber.

As is known, the mass-transfer coefficient is determined by the coefficients of mass transfer from the gas phase to the phase boundary and from the phase boundary to the fluid phase [3]. In absorption at small size of gas bubbles and developed turbulent flow of the fluid–gas emulsion, the main resistance to mass transfer is exhibited by the fluid phase since, for poorly soluble gases, the rate of molecule diffusion in a gas much exceeds that of molecules in the fluid. In this connection, the resistance in the gas phase is commonly neglected in calculating the mass-transfer coefficient under conditions of both physical adsorption and chemisorption, with the mass-transfer coefficient being approximately equal to the coefficient of mass transfer from the phase boundary to the liquid phase [3–5]. This coefficient, β_f, is commonly determined under turbulent flow conditions in terms of the Higby model accounting for the nonstationarity of the mass transfer [4, 5]:

$$\beta_f = 2(D_f/\pi t)^{1/2}, \quad (1)$$

where D_f is the molecular diffusion coefficient of the component being absorbed in the fluid phase ($m^2\ s^{-1}$), and t is the period of surface renewal (s).

As the surface renewal period t can be taken the time in which a bubble moves relative to the flow to a distance equal to its diameter. If the velocity of relative motion of a bubble in the flow is denoted by w, then the time of surface renewal can be found from the expression

$$t = d_b/w, \quad (2)$$

where d_b is the bubble diameter (m), and w is the relative velocity of bubble motion in the flow ($m\ s^{-1}$).

Substitution of (2) into Eq. (1) brings this equation to the form

$$\beta = 2(D_f w/\pi d_b)^{1/2}. \quad (3)$$

1070-4272/03/7601-0099$25.00

In the criterial form, expression (3) takes the form [5]

$$\mathrm{Sh} = 1.13\,\mathrm{Pe}^{1/2}, \quad (4)$$

where $\mathrm{Sh} = \beta_f d_b/D_f$ is the Sherwood number, and $\mathrm{Pe} = w d_b/D_f$ is the diffusion Peclet number.

The main difficulty in applying Eq. (4) to calculation of the mass-transfer coefficient consists in determining the velocity w of the relative motion of a bubble. This velocity in a turbulent flow can be found in terms of Kolmogorov's theory of isotropic turbulence. In this case, as relative motion velocity of particles of the dispersed phase in a flow is employed the difference of velocities of turbulent pulsations on the particle scale, $(w^2)^{1/2}$, found using the Kolmogorov–Obukhov "two-thirds rule" [6, 7] from the expression

$$w^2 = (\varepsilon_{fr} d_b/\rho)^{2/3}, \quad (5)$$

where ε_{fr} is the rate of energy dissipation in the mixing chamber of the jet apparatus (W m^{-3}), and ρ is the continuous phase density (kg m^{-3}).

For a cylindrical mixing chamber, the ε_{fr} value is defined as the rate of hydraulic loss of the flow energy for friction against pipe walls [1, 8]:

$$\varepsilon_{fr} = \lambda \frac{\rho v_m}{2D}, \quad (6)$$

where λ is the hydraulic friction coefficient; v_m, velocity of the two-phase flow in the mixing chamber (m s^{-1}); D, the mixing chamber diameter (m).

The hydraulic friction coefficient can be found for a two-phase flow from the known expressions [5, 9].

Mass transfer across the phase boundary from the gas phase to the fluid is described by the material balance equation [3]

$$G_g = -\beta_f F(c_f^* - c_f), \quad (7)$$

where G_g is the flow rate of the gas-phase component being absorbed (kg s^{-1}); F, the phase boundary area (m^2); c_f^*, the equilibrium concentration of the gas phase component in the fluid at the phase boundary (kg m^{-3}); c_f, the concentration of the gas-phase component in the fluid core (kg m^{-3}).

It has been noted [3, 4] that gas absorption is the most effective in the case accompanied by an irreversible instantaneous chemical reaction between the gas-phase component and absorbent, dissolved in a fluid. In this case, the concentration of the gas-phase component in the core of the fluid flow, c_f, is zero, and the driving force of the mass-transfer process is the highest. In this connection, calculation of jet absorbers for fast isothermal chemisorption is considered additionally in what follows.

In general form, the rate of mass transfer is defined by the differential equation

$$G_g = \frac{d V_g \bar{c}_g}{d\tau} = V_g \frac{d\bar{c}_g}{d\tau} + \bar{c}_g \frac{dV_g}{d\tau}, \quad (8)$$

where V_g is the volume of the gas being absorbed (m^3) and c_g is the concentration of the component being absorbed in the gas phase (kg m^{-3}).

Of interest for experimental verification of the appropriateness of the approach proposed are two extreme cases of the mass-transfer process: (1) gas mixture is 100% composed of gases that can be absorbed by the absorbent and (2) the absorbable gases constitute a lesser fraction of the mixture.

As shown in [1], absorption in a jet apparatus is a complex phenomenon involving simultaneously occurring processes of dispersion, coalescence, and mass transfer in a dispersed system. Coalescence leads to an increase in bubble size in the course of their residence in the mixing chamber of the jet apparatus, whereas mass transfer acts in the opposite direction. If the gas phase contains only absorbable gas, the rate of chemisorption is high. In this case, the change in the phase boundary area as a result of coalescence can be neglected and calculation can be done for the case of dissolution of a single gas bubble by the absorbent. In another case, when the gas phase contains a large amount of gases unabsorbable by the absorbent, the absorption rate should be calculated with account of the volume content of the gas phase in the emulsion.

In the first case, the concentration of the gas being absorbed within a bubble remains constant during the entire time of bubble dissolution in the fluid. The first term in Eq. (8) is zero, and the mass transfer from the gas phase into the fluid is accompanied by a change in the gas bubble volume:

$$G_g = \bar{c}_g \frac{dV_g}{d\tau}. \quad (9)$$

With the bubble assumed to be spherical, the decrease in the bubble volume by dV_g can be expressed via a decrease in its diameter by dd_b:

$$dV_g = V_{in} - V_{fin} = \frac{\pi d_b^3}{6} - \frac{\pi(d_b - dd_b)^3}{6}. \quad (10)$$

On the assumption that $d d_b$ is negligible as compared to d_b, expression (10) can be simplified to

$$dV_g = \frac{\pi d_b^2 d d_b}{2}. \quad (11)$$

Expressing the phase boundary area in (7) in terms of bubble diameter and using Eqs. (11) and (9), we obtain an equation relating the bubble diameter and the time of its residence in the absorbent:

$$\frac{d d_b}{d\tau} = -2\beta_f \frac{c_f^*}{\bar{c}_g}. \quad (12)$$

Substitution of the expression (3) for the mass-transfer coefficient brings Eq. (12) to the form

$$\frac{d d_b}{d\tau} = -2.26 (D w/d_b)^{1/2} \frac{c_f^*}{\bar{c}_g}. \quad (13)$$

Integration of Eq. (13) within the limits from d_b^0 to d_b and from 0 to τ yields

$$d_b = \left[(d_b^0)^{3/2} - \frac{3.39 (D w)^{1/2} \tau c_f^*}{\bar{c}_g} \right]^{2/3}, \quad (14)$$

where d_b^0 is the bubble diameter at the initial instant of time (m), and τ is the time of bubble residence in the absorbent (s).

Expression (14) defines the running diameter of a single bubble composed of an entirely absorbable gas as a function of the time of its contact with the absorbent. The time of total dissolution of a gas bubble is given by

$$\tau = \frac{(d_b^0)^{3/2} \bar{c}_g}{3.39 (D w)^{1/2} c_f^*}. \quad (15)$$

The study demonstrated that the sizes of gas bubbles in gas–fluid emulsions are not the same, being described by the corresponding particle size distributions. In determining the time necessary for gas to be absorbed in polydisperse emulsions, the maximum bubble size d_{max}, which is stable against the action of turbulent pulsations in emulsion, should be used in (15) as d_b^0. In accordance with experimental data, the maximum bubble diameter is proportional to the volume surface mean diameter and can be found using the formula [10]

$$d_{max} = C d_{32}^0, \quad (16)$$

where C is the proportionality coefficient.

According to [10], the coefficient C was found to vary within the range 1.47–2.63 in a study of fluid emulsions in stirred vessels. In a study of dispersion and coalescence in a jet apparatus, the average value of C was 1.5 [1, 2].

The volume surface mean diameter d_{32}^0 of bubbles formed at the initial instant of time in disintegration in the mixing chamber of the jet apparatus can be found from the expression [1, 2]

$$d_{32}^0 = 1.05 \frac{\sigma^{3/5}}{\rho^{1/5} \varepsilon^{2/5}} (1 + 9\varphi), \quad (17)$$

where σ is the surface tension (N m^{-1}); ε, the rate of energy dissipation in the initial part of the mixing chamber (W m^{-3}); φ, the volume gas content of the emulsion.

The rate of energy dissipation can be found from the expression [1, 2]

$$\varepsilon = \frac{\rho v^3 d^2}{10 D^3} (1 - d^4/D^4), \quad (18)$$

where v is the fluid jet velocity at the nozzle exit (m s^{-1}), and d is the nozzle diameter (m).

In the case when the concentration of the component being absorbed from the gas phase is low, the volume of the gas phase in a unit volume of the emulsion is virtually constant and the second term in Eq. (8) can be neglected. The mass transfer, which is accompanied by a change in the concentration of the component being absorbed in the gas phase, is given by

$$G_g = V_g \frac{d \bar{c}_g}{d\tau}. \quad (19)$$

Substitution of (19) into (8) gives the material balance equation

$$\frac{d \bar{c}_g}{d\tau} = -\beta_f \frac{F c_f^*}{V_g}. \quad (20)$$

The quantity F/V_g, which determines the ratio of the phase boundary area to the gas phase volume, is the specific phase boundary area for the gas phase and is related to the volume surface mean diameter d_{32} by

$$F/V_g = 6/d_{32}. \quad (21)$$

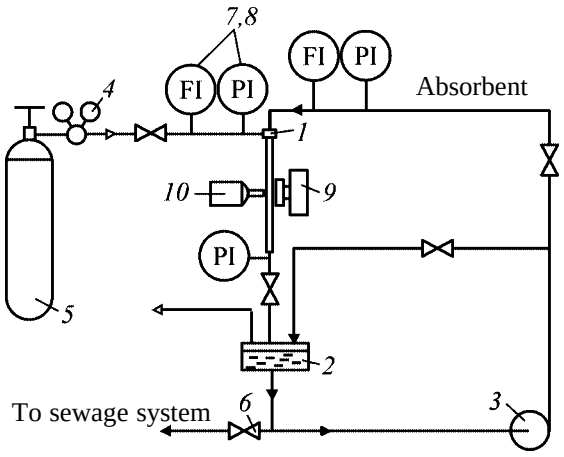

Fig. 1. Schematic of the experimental setup. For explanations, see text.

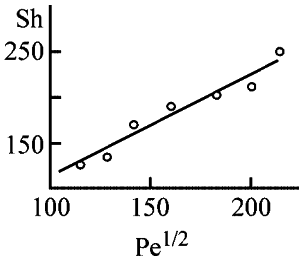

Fig. 2. Mass transfer in a system constituted by CO_2 and 3% aqueous solution of NaOH in the form of a criterial dependence $Sh = f(Pe^{1/2})$.

At a considerable volume content of gas in the emulsion, the phase boundary area decreases with time as a result of coalescence. In this case, the quantity d_{32} in expression (21) varies with the time of bubble residence in the apparatus in accordance with the dependence suggested in [1]:

$$d_{32} = d_{32}^0\left[1 + K_{\text{eff}}\frac{\varphi^{1/2}(\varepsilon_{\text{fr}}/\rho)^{1/3}\tau}{(d_{32}^0)^{2/3}}\right]^{3/2}, \qquad (22)$$

where K_{eff} is the coefficient of collision efficiency (for the water–air system, $K_{\text{eff}} = 0.014$ [1]).

Thus, in calculating the residence time of bubbles in the mixing chamber that would be sufficient to reduce the concentration of the gas being absorbed to a prescribed level, Eq. (20) is to be solved for τ together with expressions (3), (5), and (22).

To verify the validity of our approach to calculation of mass exchange in jet absorbers, we performed experiments on chemisorption of a totally absorbable gas.

EXPERIMENTAL

Experiments were performed on a setup shown schematically in Fig. 1. The setup comprises a vertical jet apparatus *1* with changeable nozzles and changeable elongated cylindrical glass mixing chamber, tank *2* for the working fluid (absorbent) with a cooling jacket, and a centrifugal pump *3*. The pipe for gas supply into the apparatus is connected through a pressure reducer *4* to a cylinder *5* with compressed CO_2. The flow rates of fluid and gas are controlled with valves *6* in the fluid and gas pipelines. The flow rate and pressure of the flows of the working fluid and gas being ejected are monitored with rotameters *7* and pressure gages *8*. To record bubble sizes, the setup is equipped with a photographic camera *9* and a synchronized flash-lamp *10*.

The setup described was used in a study of absorption in a jet apparatus with elongated mixing chamber. A vertical jet apparatus had a nozzle 6 mm in diameter and a glass mixing chamber with the diameter of 10 mm and length exceeding 35 chamber diameters. A 3% aqueous solution of NaOH served as working fluid (absorbent), and pure CO_2, as the phase being absorbed. The gas content of the emulsion in the experiments did not exceed 0.1. The bubble size was determined by taking photographs at the main part of the mixing chamber at a distance of 50 to 800 mm from the nozzle exit.

The photographs taken were used to determine the volume surface mean diameter of bubbles. With the flow velocity in the mixing chamber known, the residence time of bubbles in the absorbent and experimental values of the mass-transfer coefficient were calculated from the variation of bubble sizes with time, using expression (12). The diffusion coefficient was calculated by the Arnold formula [3, 4].

The results of experiments on mass exchange in a jet absorber are represented by points in Fig. 2 in the form of a criterial dependence $Sh = f(Pe^{1/2})$. The solid line shows the data obtained by calculation with expressions (4)–(6). The results of the experiments are described by expression (4) with the maximum deviation of ±10%. The rather good agreement between the experimental and calculated data demonstrates the applicability of our approach to calculation of the mass-transfer coefficient in jet apparatus with elongated mixing chamber under chemisorption conditions in terms of the Higby model, with averaged difference of the velocities of turbulent pulsations on the bubble scale used as the relative velocity of bubble motion.

The results of the experiments demonstrated that, for the largest CO_2 bubbles to dissolve, it suffices that the mixing chamber length should be 1 m at a velocity of the two-phase flow in the mixing chamber equal to 1.5 m s^{-1}.

Our results allow calculation of the geometric dimensions of absorbers based on jet apparatus with elongated mixing chamber. A hydrodynamic calculation can be done to determine the optimal size (diameter) of the nozzle and the mixing chamber and to choose the optimal flow rates of the fluid and gas phases and the injection coefficient with the use of expressions proposed for calculation of hydrojet pumps [11, 12]. The parameters obtained are used as input data for a mass-exchange calculation, which, carried out using expressions proposed in [1, 2], yields the phase boundary area and, with expressions (15) and (20), the residence time sufficient for total absorption of a noxious gas or for lowering its concentration in the discharge to below the maximum permissible concentration. The residence and the flow velocity in the chamber can be used to determine the length of the mixing chamber, which may have smooth cylindrical or stepped shape.

The results obtained were employed to design a jet absorber used in an industrial installation for purification of gas discharges formed in synthesis of ethyl α-bromoisovalerate. The installation comprises a jet apparatus, a tank for absorbent, and a centrifugal pump. The jet apparatus, which is made of fluoroplastic, has a nozzle *1* of diameter 16 mm and an elongated cylindrical mixing chamber *2* of diameter 38 mm and length 800 mm (Fig. 3). The exit from the mixing chamber is turned by 90° with respect to the axis of the mixing chamber to create a counterpressure.

The chemical reactions occurring in synthesis of ethyl α-bromoisovalerate yield hydrogen chloride, hydrogen bromide, and sulfur dioxide. In addition, the heating in the course of the reaction leads to evaporation of minor amounts of the reactants and liquid reaction products, which are also noxious. The purification of gas discharges is carried out continuously during the entire synthesis process. The degree of purification of gas discharge at the apparatus outlet is about 99.9%, which conforms to the sanitary regulations.[1]

[1] The absorption installation based on a jet apparatus with elongated mixing chamber, described in this communication, has been working at Altaivitaminy Private Company (Biisk) since 1997.

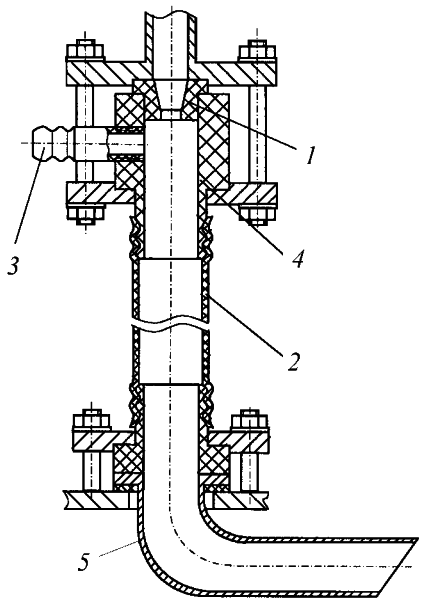

Fig. 3. Diagram of jet apparatus with elongated mixing chamber: (*1*) nozzle, (*2*) mixing chamber, (*3*) gas feed pipe, (*4*) receiving chamber, and (*5*) drain tube.

CONCLUSIONS

(1) An approach to calculating mass exchange in absorption in jet apparatus with elongated mixing chamber is suggested.

(2) Expressions for calculating the absorption rate are suggested.

(3) The expressions have been verified experimentally under conditions of chemisorption of a totally absorbable gas.

(4) An absorption installation based on a jet apparatus with elongated mixing chamber has been designed and put into industrial service.

REFERENCES

1. Blaznov, A.N., Kunichan, V.A., and Chashchilov, D.V., *Zh. Prikl. Khim.*, 2001, vol. 74, no. 4, pp. 621–625.
2. Blaznov, A.N., A Study and Design of Absorbers Based on Fluid–Gas Jet Apparatus with Elongated Mixing Chamber, *Cand. Sci. Dissertation*, Biisk, 2001.
3. Ramm, V.M., *Absorbtsiya gazov* (Absorption of Gases), Moscow: Khimiya, 1976, 2nd ed.
4. Danckwerts, P.V., *Gas–Liquid Reactions*, New York: McGraw-Hill, 1970.
5. Sokolov, V.N. and Domanskii, I.V., *Gazozhidkostnye*

reaktory (Gas–Fluid Reactors), Leningrad: Mashinostroenie, 1976.

6. Kolmogorov, A.N., *Dokl. Akad. Nauk SSSR*, 1941, vol. 30, no. 4, p. 299.
7. Obukhov, A.M., *Izv. Akad. Nauk SSSR, Ser. Geogr. Geofiz.*, 1941, vol. 5, nos. 4–5, p. 452.
8. Piterskikh, G.P. and Valashek, E.R., *Khim. Prom–st.*, 1956, no. 1, pp. 35–41.
9. Brounshtein, B.I. and Fishbein, G.A., *Gidrodinamika, masso- i teploobmen v dispersnykh sistemakh* (Hydrodynamics and Mass and Heat Exchange in Disperse Systems), Moscow: Mashinostroenie, 1977.
10. Sprow, F.B., *Am. Inst. Chem. Eng. J.*, 1967, vol. 13, no. 5, pp. 995–998.
11. Lyamaev, B.F., *Gidrostruinye nasosy i ustanovki* (Hydrojet Pumps and Installations), Leningrad: Mashinostroenie, 1988.
12. Korennov, B.E., Water–Air Ejectors with Elongated Cylindrical Mixing Chamber, *Cand. Sci. Dissertation*, Moscow, 1980.

Russian Journal of Applied Chemistry, Vol. 76, No. 1, 2003, pp. 105–107. Translated from Zhurnal Prikladnoi Khimii, Vol. 76, No. 1, 2003, pp. 107–110.

ORGANIC SYNTHESIS AND INDUSTRIAL ORGANIC CHEMISTRY

Preparative Synthesis of Functionally Substituted Esters of 1-Adamantanecarboxylic Acid

N. G. Kozlov, E. A. Dikusar, and V. I. Potkin

Institute of Physical Organic Chemistry, National Academy of Sciences of Belarus, Minsk, Belarus

Received July 2, 2002

Abstract—A procedure was developed for preparing 1-adamantanecarboxylic acid esters functionally substituted in the alcoholic moiety.

Compounds of the adamantane series exhibit high and diverse biological activity. Effective drugs based on adamantane have been developed, such as Midantane, Memantine, Gludantan, Remantadine, and Adapromine [1]. Some of adamantane derivatives exhibit antiviral, curare-like, myorelaxing, anti-choline esterase, psychostimulating, neurotropic, and local anesthetic activity [2]; compounds with a high surface activity were also found [3]. The main synthetic route to adamantane derivatives involves chemical modificatiomn of substituents in the hydrocarbon framework. Nitrogen-containing adamantane derivatives have been studied most comprehensively [4, 5].

One of promising routes to new adamantane-containing biologically active compounds is preparation of esters. In this case, it is possible to combine in one molecule an adamantane moiety with other functional groups, e.g., aromatic, acetylenic, or bicyclic [6].

Here we report on a new convenient route to functionally substituted esters of 1-adamantanecarboxylic acid, involving the reactions of 1-adamantylcarbonyl chloride **I** with alcohols **II**–**XII** in diethyl ether in the presence of pyridine [7]. Esters **XIII**–**XXIII** are formed under mild conditions (room temperature). No prolonged stirring, heating, or precipitation is required; the reactants can be mixed in any order. The reaction, performed in sealed vessels, is complete in 24–36 h; the yield of esters is 65–83%.

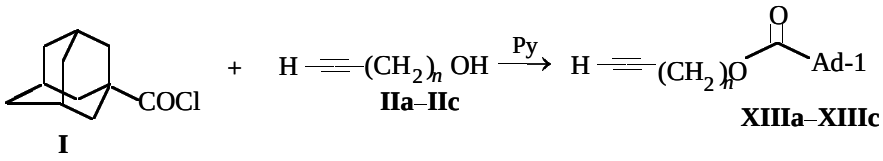

I **IIa**–**IIc** **XIIIa**–**XIIIc**

II, **XIII**, n = 1 (**a**), 2 (**b**), 3 (**c**)

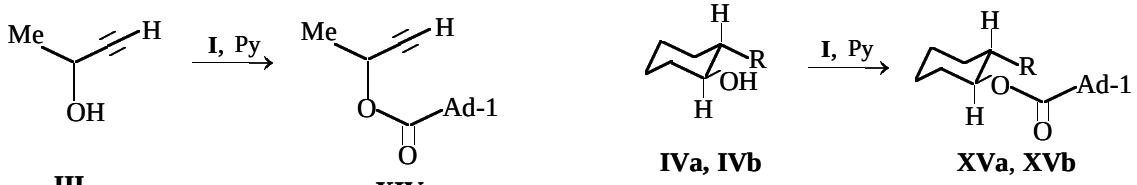

III **XIV** **IVa**, **IVb** **XVa**, **XVb**

IV, **XV**, R = H (**a**), Me (**b**)

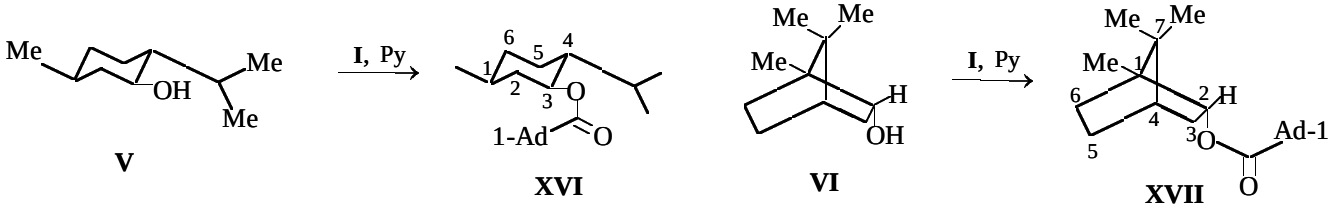

V **XVI** **VI** **XVII**

1070-4272/03/7601-0105$25.00 © 2003 MAIK "Nauka/Interperiodica"

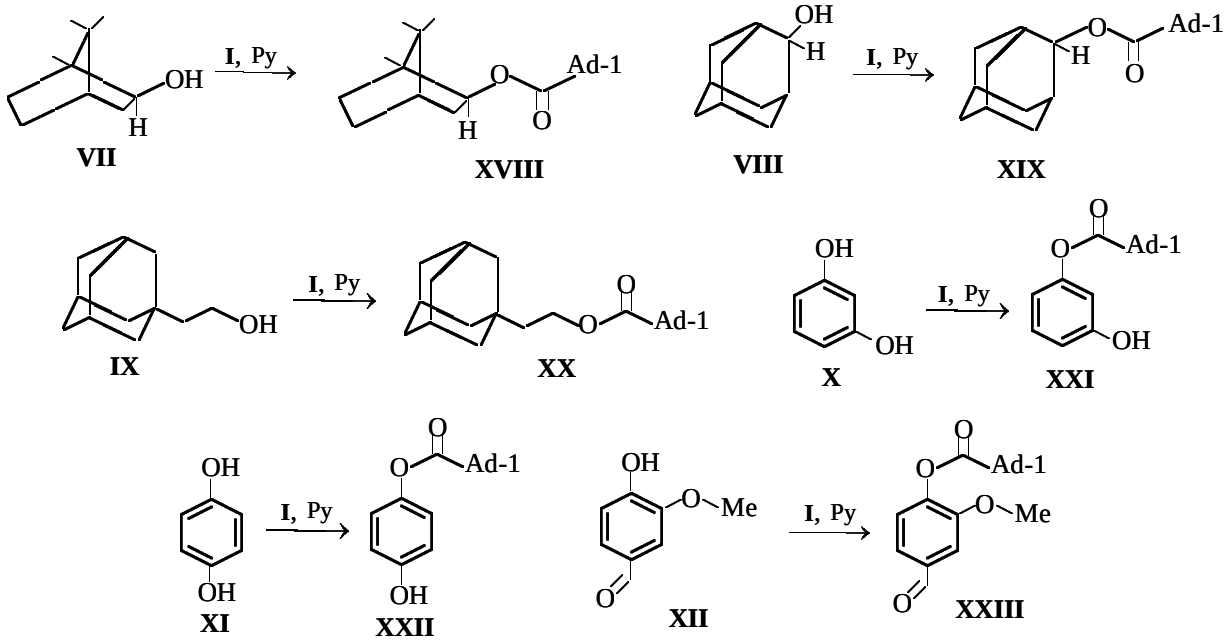

Primary alcohols (**IIa**–**IIc**, **IX**), secondary alcohols (**III**–**VIII**), and phenols (**X**–**XII**) are readily esterified with chloride **I**. Dihydric phenols **X** and **XI** form momoesters only, even at the reactant ratio **I** : (**X** or **XI**) = 3 : 1. Tertiary alcohols (e.g., 2-methyl-2-propanol or 2-methyl-3-butyn-2-ol) do not form the corresponding esters even under severe conditions (prolonged refluxing in dioxane at 100–102°C in the presence of pyridine).

1-Adamantanecarboxylic acid esters are colorless viscous liquids (**XIIIa**, **XVb**, **XVI**) or crystalline substances (**XIIIb**, **XIIIc**, **XIV**, **XVa**, **XVII**–**XXII**); their characteristics are listed in the table.

The IR and NMR spectra of the synthesized esters are consistent with their structure. The IR spectra contain stretching vibration bands of the C=O (1727 ± 5; for **XXIII**, 1742 cm^{-1}) and C–O (1225 ± 15 and 1070 ± 15; for **XXIII**, 1290 and 1155 cm^{-1}) groups. The spectra of acetylenic derivatives **XIIIa**–**XIIIc** and **XIV** also contain absorption bands at 3280 ± 25 (≡C–H) and 2150 ± 15 cm^{-1} (C≡C). Aromatic esters **XXI**–**XXIII** exhibit C–H absorption bands at 3090, 3070, 3030 ± 5; 858, 777, 767, and 680 (**XXI**); 830 and 800 (**XXII**); 865 and 785 cm^{-1} (**XXIII**), and also the bands belonging to the aromatic ring at 1604 and 1487 (**XXI**); 1600 and 1511 (**XXII**); 1601, 1593, and 1509 cm^{-1} (**XXIII**). The spectra of phenols **XXI** and **XXII** contain O–H absorption bands at 3375 (**XXI**) and 3445 cm^{-1} (**XXII**), and also C–OH bands at 1065 ± 5 cm^{-1}. The IR spectrum of aromatic methoxy aldehyde **XXIII** contains the bands of the HC=O (1697 cm^{-1}) and C–O–C (1110 cm^{-1}) groups.

The ^1H NMR spectra of all the esters **XIII**–**XXIII** contain multiplets at 1.6 (6H), 1.9 (6H), and 2.1 ppm (3H), typical of 1-substituted adamantane derivatives. Compounds **XIIIa**–**XIIIc** and **XIV** containing terminal acetylenic groups also give a proton signal at 2.0–2.4 ppm. The CH_2O proton signals in the spectra of **XIIIa**–**XIIIc** and **XX** are observed at 4.1 ppm, and in esters **XV**–**XIX** derived from alicyclic alcohols the α-CH proton in the alcoholic residue gives a signal at 4.7–4.9 ppm. The spectra of these esters also contain signals characteristic of cyclohexane (**XV**), menthane [**XVI**; a doublet of the C^1–CH_3 protons at 0.74 ppm (^3J 1.6 Hz) and a doublet of two methyl groups in the isopropyl substituent at 0.94 ppm (^3J 6.7 Hz)], and camphane [**XVII, XVIII**; singlets of three methyl groups at C^1 (0.8 ppm) and C^7 (1.0 ppm) atoms]. The aryl protons in **XXI**–**XXIII** are manifested at 6.4–7.5 ppm. Also, the spectrum of **XXIII** exhibits a CHO singlet at 9.9 ppm and an OCH_3 singlet at 3.9 ppm.

EXPERIMENTAL

The IR spectra were recorded on a Protege-460 IR Fourier spetrophotometer (Nicolet) from thin films (**XIIIa**, **XVb**, **XVI**) or KBr pellets. The ^1H NMR spectra were recorded on a Tesla BS-567A spectrometer (100 MHz) from 5% solutions in $CDCl_3$, with TMS as internal reference.

The molecular weight was determined by cryoscopy in benzene.

Properties of esters **XIII**–**XXIII**

Ester	Yield, %	mp, °C	Found, %		Formula	Calculated, %		*M*	
			C	H		C	H	found	calculated
XIIIa	79	1.0791* 1.5060	77.28	8.56	$C_{14}H_{18}O_2$	77.03	8.31	214.1	218.3
XIIIb	77	48–49	77.84	8.95	$C_{15}H_{20}O_2$	77.55	8.68	225.8	232.3
XIIIc	83	56–57	78.44	9.19	$C_{16}H_{22}O_2$	78.01	9.00	239.0	246.3
XIV	81	46–47	77.93	8.90	$C_{15}H_{20}O_2$	77.55	8.68	227.4	232.3
XVa	70	29–30	78.13	10.18	$C_{17}H_{26}O_2$	77.82	9.99	249.3	262.4
XVb	80	1.0409* 1.5025	78.45	10.41	$C_{18}H_{28}O_2$	78.21	10.21	262.9	276.4
XVI	78	1.0237* 1.4990	79.50	10.93	$C_{21}H_{34}O_2$	79.19	10.76	306.7	318.5
XVII	82	176–177	80.03	10.25	$C_{21}H_{32}O_2$	79.70	10.19	303.2	316.5
XVIII	84	145–146	80.01	10.32	$C_{21}H_{32}O_2$	79.70	10.19	308.6	316.5
XIX	72	172–173	80.34	9.85	$C_{21}H_{30}O_2$	80.21	9.62	307.0	314.5
XX	82	82–83	80.88	10.12	$C_{23}H_{34}O_2$	80.65	10.00	330.1	342.5
XXI	65	107–108	75.22	7.65	$C_{17}H_{20}O_3$	74.97	7.40	260.4	272.3
XXII	68	179–180	75.21	7.60	$C_{17}H_{20}O_3$	74.97	7.40	262.3	272.3
XXIII	79	118–119	72.71	7.11	$C_{19}H_{22}O_4$	72.59	7.05	303.1	314.4

* Numerator, d_{20}^{20}; denominator, n_D^{20}.

Column chromatography was performed with neutral alumina, Brockmann grade II.

1-Adamantanecarboxylic acid chloride **I** was prepared by refluxing 1-adamantanecarboxylic acid with a 1.5-fold excess of $SOCl_2$ in benzene [5].

1-Adamantanecarboxylic acid esters XIII–**XXIII**. Anhydrous pyridine (3.5 mmol) was added to a solution of 3 mmol of chloride **I** and 3 mmol of alcohols or phenols **II**–**XII** in 70 ml of absolute diethyl ether. The mixture was slightly shaken and allowed to stand at 18–23°C for 24–36 h. The precipitate of pyridine hydrochloride was filtered off and washed with 30 ml of diethyl ether; the combined filtrates were washed with water and saturated aqueous solution of sodium hydrogen carbonate. The ether solution was dried over $CaCl_2$, the solvent was distilled off, and the residue was dried in a vacuum. Ethers **XIIIa**, **XVb**, and **XVI** were purified by column chromatography on Al_2O_3, eluent hexane. Compounds **XIIIb**, **XIIIc**, **XIV**, **XVa**, and **XVII**–**XXIII** were purified by low-temperature crystallization from hexane.

CONCLUSIONS

(1) Functionally substituted primary and secondary alcohols and phenols are readily esterified under mild conditions with 1-adamantanecarboxylic acid chloride in the presence of pyridine.

(2) Dihydric phenols form monoesters only; tertiary alcohols do not undergo esterification.

ACKNOWLEDGMENTS

The study was financially supported by the Belarussian Republican Foundation for Basic Research (project no. Kh 03-079) and INTAS (grant 99-00 806).

REFERENCES

1. Mashkovskii, M.D., *Lekarstvennye sredstva* (Drugs), Moscow: Novaya Volna, 2001, vols. 1, 2.
2. Morozov, I.S., Petrov, V.I., and Sergeeva, S.A., *Farmakologiya adamantanov* (Pharmacology of Adamantanes), Volgograd: Volgograd. Med. Akad., 2001.
3. Vashkevich, E.V., Yurashevich, N.Ya., Kozlov, N.G., *et al.*, *Zh. Prikl. Khim.*, 2001, vol. 74, no. 11, pp. 1833–1839.
4. Bagrii, E.I., *Adamantany: poluchenie, svoistva, primenenie* (Adamantanes: Preparation, Properties, Applications), Moscow: Nauka, 1989.
5. Ford, R.C., *Adamantane: The Chemistry of Diamond Molecules*, New York: Dekker, 1976.
6. Schulte, K. and Rucker, G., *Prog. Drug Res.*, 1970, vol. 14, pp. 387–563.
7. Dikusar, E.A., Yuvchenko, A.P., Zvereva, T.D., *et al.*, *Zh. Obshch. Khim.*, 1996, vol. 66, no. 11, pp. 1813–1817.

Russian Journal of Applied Chemistry, Vol. 76, No. 1, 2003, pp. 108–113. Translated from Zhurnal Prikladnoi Khimii, Vol. 76, No. 1, 2003, pp. 111–116.

ORGANIC SYNTHESIS AND INDUSTRIAL ORGANIC CHEMISTRY

Oxidation of Sulfides with Hydrogen Peroxide to Sulfoxides and Sulfones

A. Kh. Sharipov

Institute of Petrochemistry and Catalysis, Academy of Sciences of Bashkortostan Republic and Ufa Scientific Center, Russian Academy of Sciences, Ufa, Bashkortostan, Russia

Received July 2, 2002

Abstract—Oxidation of sulfides with hydrogen peroxide to sulfoxides and then sulfones was studied. The conditions optimal for the formation of sulfoxides and sulfones were found.

Oxidation of sulfides with hydrogen peroxide is a widely used synthetic route to sulfoxides and sulfones [1]. Although sulfoxides are readily oxidized further to sulfones, under definite conditions the reaction can be stopped at the stage of sulfoxide formation. Oxidation of sulfides to sulfoxides occurs at relatively low temperatures and in short time. The second stage, oxidation of sulfoxides to sulfones, requires higher temperatures and longer time. Sulfones can be prepared both by direct oxidation of sulfides and by oxidation of sulfoxides. In some cases, the latter route is preferable, since each oxidation stage can be performed under optimal conditions; as a result, higher yield and purity of the target product can be attained [2].

In this work we studied oxidation of dimethyl sulfide (DMS), tetramethylene sulfide (TMS), and petroleum sulfide concentrate (PSC) with hydrogen peroxide to the corresponding sulfoxides and oxidation of these sulfoxides to sulfones.

EXPERIMENTAL

The reaction mixtures were analyzed by GLC with a Tsvet 4-67 chromatograph [flame ionization detector; 2100 × 4-mm column; stationary phase 10% polyethylene glycol succinate on Chromaton N-AW-HMDS, 0.2–0.25 mm fraction, washed with water and treated with hexamethyldisilazane; carrier gas nitrogen, GOST (State Standard) 9293–74]. The stationary phase used retains water and allows determination of the nonaqueous oxidation products [3]. Analysis conditions: column temperature 140–180°C, vaporizer temperature 200–240°C, carrier gas flow rate 40–60 ml min^{-1}, sample volume 0.1–0.2 μl. The component contents were determined by internal normalization of the peak areas using benzene as reference. The absolute determination error was 0.4% at a confidence level of 98%.

The oxidation products of petroleum sulfides cannot be analyzed chromatographically because of the low thermal stability of petroleum sulfoxides and high boiling temperature of the sulfone concentrate obtained from them. Therefore, the content of sulfoxide sulfur in the oxidation products was determined by nonaqueous titration of the product with a solution of $HClO_4$ in dioxane [4], and the content of sulfones, by IR spectroscopy, from the intensity of the absorption band of the sulfone stretching vibrations at about 1320 cm^{-1} [5]. The concomitant compounds, mainly sulfoxides, do not absorb in this range. Also, the content of sulfonic and carboxylic acids was determined by potentiometric titration [6].

Oxidation was performed as follows. A flask was charged with a required amount of the starting compound and heated to a required temperature, after which H_2O_2 was added. The mixture was heated at the prescribed temperature with vigorous stirring. The instant of H_2O_2 addition was considered as the reaction start. After the reaction completion, the flask was cooled, and samples of the product were taken. The content of H_2O_2 in the oxidation products was determined by titration with a $KMnO_4$ solution [7]. To each sample we added MnO_2 to decompose the unchanged H_2O_2 and terminate oxidation. After that, the sample was filtered and analyzed.

Hydrogen peroxide was used as 27.5% (here and hereinafter, wt %) aqueous solution [GOST (State Standard) 177–88]. TMS and DMS were 98 and 99.5% pure, respectively. The sulfide concentrate was recovered from the 260–360°C fraction of Arlan crude oil

1070-4272/03/7601-0108$25.00 © 2003 MAIK "Nauka/Interperiodica"

Table 1. Oxidation of DMS to DMSO (τ = 10 min)

T, °C	H_2O_2 : DMS molar ratio	Composition of dehydrated oxidation product, %				H_2O content in oxidation product, wt %
		DMS	DMSO	DMSF	H_2O_2	
0	0.75	4.5	92.6	0.4	0.8	44.5
	1.1	1.2	94.2	1.2	1.0	45.4
	1.2	0.8	91.5	2.4	2.2	46.2
5	0.8	4.0	93.7	0.9	1.1	43.8
	1.0	1.0	94.8	3.0	1.5	45.0
	1.2	0.6	92.1	3.5	1.8	46.7
10	0.7	3.1	92.2	0.8	0.9	44.3
	1.1	0.9	94.2	3.1	1.2	46.1
	1.3	0.8	92.0	3.8	1.8	47.2

Table 2. Oxidation of DMSO to DMSF

T, °C	H_2O_2 : DMSO molar ratio	τ, h	Composition of dehydrated oxidation product, %		Acidity, g KOH l^{-1}	Yield of DMSF, %
			DMSO	H_2O_2		
40	1.1	20	12	2.3	6.0	48
	1.2	25	10	1.6	6.4	55
	1.3	30	8	1.6	7.4	62
60	1.1	15	6	1.5	6.8	61
	1.2	20	2	1.5	8.0	68
	1.3	25	2	1.4	8.4	72
80	1.1	10	1	0.8	7.5	68
	1.2	15	–	0.8	8.4	70
	1.3	20	–	0.4	9.2	66

[8]; it contained 8.8% sulfide sulfur and 12.8% total sulfur and had the average composition $C_{14.5}H_{27.0}S$.

In experiments on oxidation of DMS to dimethyl sulfoxide (DMSO), we examined the influence of temperature and H_2O_2 : DMS ratio on the yield of reaction products (Table 1). Oxidation was performed at 0.5 and 10°C. The very low boiling point of DMS (37.2%) caused certain problems. Since the reaction is exothermic, even at 10°C it is necessary to take special measures to prevent evaporation of DMS in the initial oxidation stage. In the range 0–10°C, the temperature affects the product composition insignificantly; the yield of DMSO is fairly high. The major influence on the product composition is exerted by the H_2O_2 : DMS molar ratio. When this ratio is as low as 0.7–0.8, the products contain a large amount of unchanged DMS, and dimethyl sulfone (DMSF) is absent. At the H_2O_2 : DMS molar ratio increased to 1.1–1.2, DMS is fully consumed and DMSF appears. This fact suggests the consecutive mechanism of DMSF formation via DMSO. The product obtained by oxidation of DMS is a transparent aqueous solution. To isolate DMSO, the oxidation product was heated at reduced pressure (30–40 mm Hg) on a water bath (40–50°C) to remove water, after which DMSO was distilled in a vacuum (bath temperature 72–82°C, 10–15 mm Hg). The purity of the distilled DMSO was 99.6%, bp 189°C, n_D^{20} 1.4785, d_4^{20} 1.1000.

Found, %: C 30.82; H 7.62; S 41.01.

C_2H_6OS. Calculated, %: C 30.76; H 7.69; S 41.02.

Oxidation of DMSO to DMSF was studied at 40, 60, and 80°C (Table 2). The H_2O_2 : DMSO molar ratio was varied from 1.1 to 1.3, and the oxidation time, from 10 to 30 min. The oxidation product obtained under the above conditions was evaporated at 700 mm Hg to remove about 30–40% of water. Then the oxidation product was cooled to 5°C to crystallize dimethyl sulfone. The crystals were separated, re-

crystallized from water, and dried in a water-jet-pump vacuum. The resulting DMSF is a colorless crystalline substance readily soluble in organic solvents; purity 99.8%, mp 109°C, bp 238°C.

Found, %: C 25.59; H 6.36; S 34.02.

$C_2H_6O_2S$. Calculated, %: C 25.53; H 6.38; S 34.04.

Oxidation of TMS to tetramethylene sulfoxide (TMSO) was studied at 20, 40, and 60°C (Table 3). These data show that, after oxidation for 1 h at 20°C, the content of DMSO in the dehydrated oxidation products was 94%, and after oxidation for 3 h it reached 97%. The content of TMSO after oxidation for 1 h at 60°C was 98%. Thus, oxidation of TMS to TMSO occurs with a high rate. At all the examined temperatures, the formation of TMSO is virtually complete in 1–3 h. Oxidation occurs in a two-phase system and is accompanied by a large heat release in a short time. The reaction mixture undergoes autocatalytic self-heating, which results in intense decomposition of excess H_2O_2. Therefore, H_2O_2 was added gradually to maintain its optimal concentration in the mixture in the course of the process.

The oxidation product obtained by oxidation of TMS under the above conditions is a single-phase transparent colorless aqueous solution. To isolate TMSO, the oxidation product was treated with MnO_2 to remove residual H_2O_2, heated at reduced pressure (30–40 mm Hg) to remove water (bath temperature 40–50°C), and vacuum-distilled (bath temperature 140–160°C, vapor temperature 85–100°C, residual pressure 3–5 mm Hg).

Tetramethylene sulfoxide is thermally unstable. Its loss in the course of distillation was evaluated from the decrease in the content of sulfoxide sulfur. The average loss of sulfoxide sulfur is 3%, which corresponds to 10% loss of TMSO. Under the optimal conditions, the yield of TMSO is 89–91%. The purity of the distilled product is 99.6%, bp 45°C (3 mm Hg), n_D^{20} 1.5203, d_4^{20} 1.1816.

Found, %: C 45.72; H 7.83; S 30.5.

C_4H_8OS. Calculated, %: C 46.1; H 7.7; S 30.8.

Oxidation of TMSO to tetramethylene sulfone (TMSF) was performed at 60, 70, 80, 90, and 100°C (Table 4). The reaction occurs in the homogeneous system with a lower heat effect and at a lower rate than oxidation of TMS to TMSO. After oxidation for 8 h at 60°C, the content of TMSF in the dehydrated oxidation product was 60%, and after oxidation for 10 h, 88%. After oxidation for 5 h at 80°C, the content of TMSF was as high as 99%. The optimal oxidation temperature is 80–90°C. To attain a high yield of TMSF, H_2O_2 should be taken in a 35% excess. The product obtained by oxidation of TMSO under these conditions is an aqueous solution containing 35–40% TMSF, 60–50% water, and 4–7% impurities. Tetramethylene sulfone is infinitely miscible with water, forms no binary azeotrope with water, and strongly differs from water in the boiling point. However, TMSF cannot be isolated from the oxidation products by common distillation, since it is thermally unstable and starts to decompose at temperatures above 170°C, forming in the presence of oxygen acidic compounds and condensation products. According to analyses, the oxidation product always contaions residual H_2O_2, which promotes decomposition of TMSF in the course of distillation to acetic and sulfuric acids. Therefore, prior to distillation, the oxidation product was treated with 6% aqueous alkali to decompose H_2O_2, after which it was fractionated on a 2–3-TP batch distillation column; the temperature in the still was 100°C, and the residual pressure, 20 mm Hg. TMSF was isolated from the oxidation product in 96% yield and was 99.7% pure.

We also examined the possibility of recovering TMSF from the oxidation product by extraction with organic solvents. The extractant should selectively recover TMSF with minimal extraction of impurities; it should be sparingly soluble in water and should also meet such general requirements as availability, stability under regeneration conditions, and low cost [9]. The best suited are aromatic hydrocarbons, in particular, benzene. Study of the phase equilibria showed that, in extraction of TMSF from the oxidation product with benzene, the separation of TMSF from impurities is fairly efficient; the impurities mostly remain in the aqueous phase. Under the optimal extraction conditions (benzene : oxidation product weight ratio 2.4 : 1, 25°C, six extraction steps), the recovery of TMSF from the oxidation product is 94–96%. Distillation of benzene from the extract was performed at 200 mm Hg. The energy consumption for distillation of benzene from the extract is much less than that for distillation of water from the oxidation product (because of considerably higher heat capacity and heat of vaporization of water).

Tetramethylene sulfone obtained by this procedure is a colorless hygroscopic solid (at room temperature) with pleasant odor, soluble in water, ethanol, benzene, acetone, and other organic solvents; the product purity

Table 3. Oxidation of TMS to TMSO (H_2O_2 consumption 1.05 mol per mole of TMS)

T, °C	τ, h	Composition of dehydrated oxidation product, %				Acidity, mg KOH per gram oxidation product
		TMS	TMSO	TMSF	unidentified component	
20	1	3.49	94.69	–	1.82	0.24
	3	0.86	97.64	–	1.50	0.36
	6	0.20	97.97	–	1.83	0.44
40	1	1.31	06.84	–	1.85	0.33
	3	–	98.48	–	1.52	0.42
	6	–	97.82	–	2.18	0.51
60	1	0.11	98.09	0.15	1.65	0.41
	3	–	98.66	0.39	0.95	0.48
	4	–	98.69	0.41	0.90	0.61
65	3	–	97.80	1.35	0.75	0.58

Table 4. Oxidation of TMSO to TMSF (H_2O_2 consumption 1.35 mol per mole of TMSO)

T, °C	τ, h	Composition of dehydrated oxidation product, %				Acidity, mg KOH per gram oxidation product
		TMSO	TMSF	unidentified components		
				light*	heavy**	
60	8	39.30	60.42	0.11	0.17	2.1
	10	11.41	88.23	0.15	0.21	3.7
70	6	2.30	98.10	0.37	0.91	5.2
	8	1.21	99.11	0.30	0.39	4.58
80	5	0.49	97.38	0.19	0.21	5.2
	6	0.107	99.22	0.38	0.29	5.94
90	5	0.04	97.38	1.02	1.56	9.8
	6	0.08	99.22	0.55	0.15	10.2
100	4	0.07	97.74	0.18	1.21	10.3
	5	0.03	98.20	0.65	1.12	12.4

* Retention time in chromatographic column shorter than that of TMSF.
** Retention time in chromatographic column longer than that of TMSF.

is 99.8%, bp 283°C, n_D^{30} 1.4812, d_4^{30} 1.2644.

Found, %: C 39.92; H 6.64; S 27.21.

$C_4H_8O_2S$. Calculated, %: C 39.98; H 6.70; S 27.16.

Oxidation of PSC to sulfoxides was performed at 80, 90, and 100°C (Table 5). With increasing temperature, products with SO_3H and COOH groups are actively formed, and the PSC oxidation rate grows. For example, as the temperature is increased from 80 to 100°C, the acidity of the aqueous phase obtained after oxidation for 15 min grows from 0.9 to 2.6 g KOH l^{-1} and the content of sulfoxide sulfur in the oxidation product increases by a factor of 2. The sulfonic and carboxylic acids that are formed effectively catalyze oxidation of sulfides to sulfoxides, as demonstrated by the example of PSC oxidation in the presence of butane-, hexane, and *p*-toluenesulfonic acids and CH_3COOH. Oxidation of PSC in the presence of sulfonic and acetic acids occurs with a higher yield of sulfoxides than oxidation on the presence of only one of these acids [10]. Sulfones appear in the oxidation product only after conversion of the major fraction of sulfides to sulfoxides, whereas acids are formed already in the very first minutes of oxidation simultaneously with sulfoxides. After oxidation, the aqueous and hydrocarbon layers were separated. The hydrocarbon layer (sulfoxide concentrate) was neutralized with an Na_2CO_3 solution, washed with an Na_2SO_4 solution, and kept under reduced pressure (80–100 mm Hg) to remove emulsified and dissolved water.

Table 5. Oxidaiton of PSC into sulfoxides (H_2O_2 consumption 1.2 mol per mole of sulfide sulfur)

T, °C	τ, min	Sulfoxide sulfur in oxidation product, %	Acidity, g KOH l^{-1}				Oxidation of sulfides to sulfoxides, %
			hydrocarbon phase		aqueous phase		
			SO_3H	CO_2H	SO_3H	CO_2H	
80	5	0.9	0.11	0.30	0.45	0.25	10.2
80	15	3.4	0.15	0.35	0.62	0.30	38.6
90	5	4.7	0.23	0.50	0.45	0.35	53.4
90	15	6.3	0.25	0.62	0.81	0.40	71.5
100	15*	6.6	0.20	0.61	2.02	0.63	75.0
100	30**	7.4	0.25	0.80	3.95	0.75	84.0

* 0.8% sulfones.
** 11% sulfones.

Table 6. Oxidation of sulfoxide concentrate to sulfones (H_2O_2 consumption 1.4 mol per mole of total sulfur, 100°C)

τ, h	Catalyst, mol mol^{-1} total sulfur		Content of sulfones, %	Acidity, g KOH l^{-1}	Viscosity at 20°C, $mm^2\ s^{-1}$
	H_2SO_4	CH_3CO_2H			
6.0	–	–	36.0	6.2	957.6
9.0	–	–	44.2	8.2	964.5
5.0	–	0.15	82.7	12.0	1424.5
6.5	–	0.15	83.8	12.2	1490.0
5.5	0.1	–	86.3	14.6	1502.28
6.5	0.15	–	88.2	16.4	1610.0
5.0	0.08	0.1	94.0	11.2	1354.3
5.5	0.08	0.1	95.4	11.0	1360.1
6.5	0.08	0.1	97.0	11.0	1414.0
10.0	0.08	0.1	97.6	11.2	1489.2

The composition of the dehydrated sulfoxide concentrate was determined with a Finnigan Type 4021 gas chromatograph–mass spectrometer (the United States). Because of the low thermal stability of sulfoxides, it was impossible to analyze the sulfoxide concentrate directly. Therefore, the sulfoxides were preliminarily reduced to sulfides with HI [11]. The chromatograms and total mass spectra of the initial sulfides used to prepare sulfoxides and of sulfides obtained by back reduction of sulfoxides proved to be identical. Hence, oxidation of sulfides is not accompanied by structural changes. The sulfoxide concentrate from the 260–360°C fraction of Arlan crude oil mainly consists of heterocyclic sulfoxides, in particular, 15–18% monothiacycloalkanes, 38–40% dithiacycloalkanes, 23–25% trithiacycloalkanes, and 18–20% tetrathiacycloalkanes.

The sulfoxide concentrate also contains unoxidized sulfides, substituted thiophenes, and hydrocarbons.

The sulfoxide concentrate is a viscous oily liquid of light yellow color with a weak characteristic odor; it is soluble in the majority of organic solvents, and the solubility in water is 7.8 g l^{-1}. The glass transition point is –67°C. The product starts to decompose at 120–140°C. The sulfoxide sulfur content is 7.4%, and the total sulfur content, 11%; n_D^{20} 1.5092, d_4^{20} 1.0195, *M* 267; $C_{12.8}H_{24.7}SO_{1.3}$.

The dependence of the content of sulfones in the oxidation product as influenced by the amount of acid catalysts and time of oxidation of sulfoxides to sulfones was studied at 100°C (Table 6). It was found that, in the absence of catalysts, the oxidation is slow. The presence of acids in the reaction medium also leads to increased yield of sulfones. As in oxidation of PSC, in the presence of a mixture of acids the reaction rate and the yield of the target product increase. For example, when oxidation of the sulfoxide concentrate to sulfones is performed for 5–7 h in the pres-

ence of CH_3COOH and H_2SO_4, the yield of sulfones increases to 95–97%. After oxidation in this mode, the aqueous acid layer was separated after settling for 30 min. The oxidation product was washed with water to remove traces of acids, dried in a water-jet-pump vacuum, and vacuum-distilled (1 mm Hg, bath temperature 110–165°C).

The composition of the resulting sulfone concentrate was studied by mass spectrometry. The sulfone concentrate is a mixture of various thiacycloalkane 1,1-dioxides, aromatic sulfides, and alkylthiophenes; it is a brown viscous liquid with a specific petroleum odor, readily soluble in organic solvents and virtually insoluble in water; n_D^{20} 1.4814, d_4^{20} 1.0312, total sulfur content 12.4%, sulfoxide sulfur absent, *M* 298, average composition $C_{12.0}H_{22.6}SO_{2.4}$.

CONCLUSION

The yield of sulfoxides and sulfones in oxidation of sulfides and sulfoxides, respectively, with hydrogen peroxide was studied in relation to the reaction temperature, time, and substrate : H_2O_2 ratio. Formation of sulfoxides occurs under milder conditions and at considerably higher rates than formation of sulfones.

REFERENCES

1. Patai, S., Rappoport, L., and Stirling, C.J.M., *The Chemistry of Sulfoxides and Sulfones*, New York: Wiley, 1988, pp. 1202–1206.
2. Kirk, R.E. and Othmer, D.F., *Encyclopedia of Chemical Technology*, New York: Wiley, 1982, vol. 21.
3. Sharipova, I.A., Nasyrov, Kh.M., Sharipov, A.Kh., and Mazitov, M.F., *Zh. Org. Khim.*, 1997, vol. 33, no. 9, pp. 1374–1376.
4. Wimer, D.C., *Anal. Chem.*, 1958, vol. 30, no. 12, pp. 2060–2062.
5. Sharipov, A.Kh., Suleimanova, Z.A., and Faizrakhmanov, I.S., *Neftekhimiya*, 1994, vol. 34, no. 5, pp. 459–466.
6. Dudina, R.I., Vlasova, L.V., Avdeeva, L.B., and Rezanova, L.N., in *Kataliticheskii sintez organicheskikh soedinenii sery*, Novosibirsk: Sib. Otdel. Akad. Nauk SSSR, 1979, pp. 62–64.
7. *GOST* (State Standard) *177-88: Hydrogen Peroxide. Technical Specification*, Moscow: Izd. Standartov, 1988.
8. Chertkov, Ya.B., Spirkin, V.G., and Demishev, V.N., *Neftekhimiya*, 1965, vol. 5, no. 4, pp. 551–556.
9. Sharipov, A.Kh., *Khim. Prom–st.*, 2000, no. 7, pp. 3–11.
10. Sharipov, A.Kh., Suleimanova, Z.A., Faizrakhmanov, I.S., and Masagutov, R.M., *Neftekhimiya*, 1991, vol. 31, no. 1, pp. 86–92.
11. Masagutov, R.M., Kruglov, E.A., Popov, J.N., and Sharipov, A.Kh., Abstracts of Papers, *Tenth Int. Symp. on the Organic Chemistry of Sulphur*, Bangor: Univ. College of North Wales, 1982, pp. 129–131.

Russian Journal of Applied Chemistry, Vol. 76, No. 1, 2003, pp. 114–116. Translated from Zhurnal Prikladnoi Khimii, Vol. 76, No. 1, 2003, pp. 117–120.

ORGANIC SYNTHESIS AND INDUSTRIAL ORGANIC CHEMISTRY

Lightfastness of Polymeric Color Filters with Metal-Containing Dyes and Heterocyclic Azo Dyes as Absorbing Agents

N. B. Sokolova, L. P. Kovzhina, N. M. Dmitrieva, and T. A. Karsakova

St. Petersburg State Technological Institute, St. Petersburg, Russia

Received June 20, 2002

Abstract—Color filters containing in the cellulose acetobutyrate matrix a combination of a metal-containing organic dye and an azo dye derived from thiophene or furan were prepared, and their lightfastness was studied.

Polymeric film color filters are widely used in modern optical devices and well compete with glass filters, being light, elastic, convenient in service, and cheap. However, in the lightfastness they are inferior to glass filters prepared, as a rule, using inorganic salts and metal oxides. Therefore, one of major problems in development of film color filters is the choice of the most lightfast dye formulations. In this case, either available dyes with a high lightfastness are used, which is not always possible, or dyes enhancing the lightfastness of each other are combined.

Yellow-orange dyes are used in color filters most widely, both as absorbing agents in cutting filters and as additives to blue, green, and red dyes for suppressing "parasitic" transmission in the blue range. Such dyes include monoazo dyes derived from five-membered heterorings: pyrazole, thiophene, furan, etc. The lightfastness of these dyes, taken separately, in various polymeric matrices and their photodecomposition in binary mixtures with triphenylmethane, anthraquinone, and azo (derived from benzene) dyes were studied previously [1–4]. In this work, we studied mixtures of monoazo dyes of the thiophene and furan series with metal-containing green and green-blue dyes.

Among numerous azo dyes of the thiophene and furan series, we chose anthranilic acid and *m*-xylidine derivatives **I**–**IV** as the most and the least lightfast dyes, respectively [1, 2], and among hydrophobic metal-containing dyes, Alcohol-Soluble Blue Z (C.I. 74350) (**V**) and iron complexes of 1-nitroso-2-naphthol (**VI**), 1,2-naphthylenediamine (**VII**), and 1,2-anthracenediamine (**VIII**):

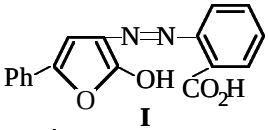

I

λ_{max} = 440 nm

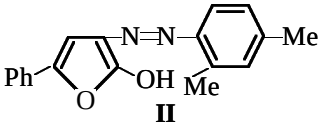

II

λ_{max} = 440 nm

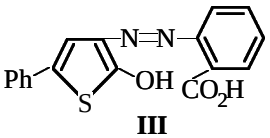

III

λ_{max} = 470 nm

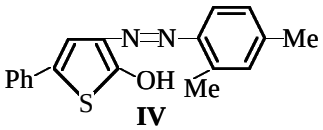

IV

λ_{max} = 480 nm

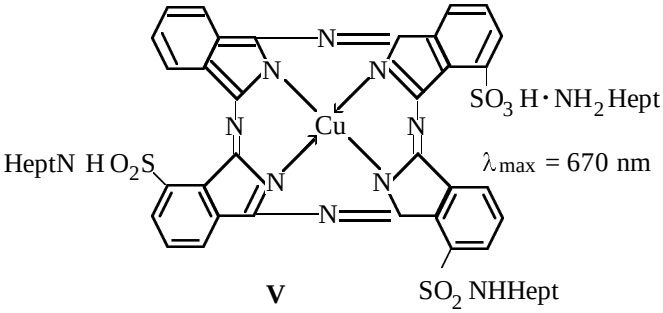

V

λ_{max} = 670 nm

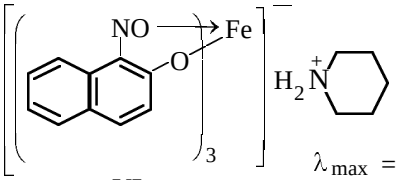

VI

λ_{max} = 730 nm

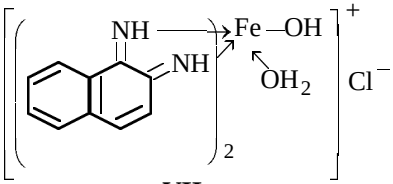

VII

λ_{max} = 700 nm

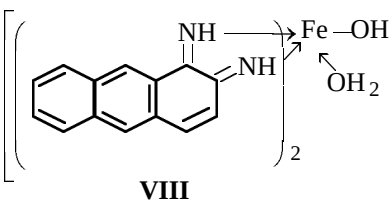

VIII

λ_{max} = 740 nm

1070-4272/03/7601-0114$25.00 © 2003 MAIK "Nauka/Interperiodica"

Color filters were prepared on the cellulose acetobutyrate base (film thickness 0.15 mm). To obtain the required spectral characteristic, we studied the spectra of the dyes in the solvent (chloroform : acetone, 85 : 15 by volume) and calculated the required concentrations of the dyes in the film, taking into account the thicknesses of the cell and film. We prepared 8 films with individual dyes **I**–**VIII** and 16 films with combinations of one of dyes **I**–**IV** with one of dyes **V**–**VIII**.

The lightfastness of dyes in films containing individual dyes and their combinations was studied in an installation for accelerated photochemical aging. Samples were irradiated with a xenon lamp whose spectrum is the most similar to the spectrum of solar light. The total irradiation time was 10 h; during this period, we monitored photochemical degradation of dyes by recording at regular intervals (15 and 30 min; 1, 2, 3, ..., 10 h) the electronic absorption spectra of the film against the colorless cellulose acetobutyrate film sample irradiated under the same conditions.

As analytical wavelength we chose λ_{max} of the dye absorption. In films with binary dye formulations, we first measured the optical density at the analytical wavelength of the metal-containing dye and then calculated the optical density originating from the heterocyclic azo dyes as the difference between the measured optical density at the analytical wavelength of the yellow component and the optical density at the same wavelength, generated by the metal-containing dye. Then we calculated separately the degrees of photodegradation (PD, %) of the yellow (azo dyes derived from thiophene and furan) and blue-green (metal-containing dyes) components:

$$\mathrm{PD} = \frac{D_0 - D_t}{D_0} \times 100\%,$$

where D_0 is the optical density of the nonirradiated sample at the analytical wavelength and D_t is the optical density at the same wavelength after irradiation for time t.

Data on photodegradation of films containing individual dyes and their binary mixtures were analyzed to reveal the effect of the dyes on the lightfastness of each other. For this purpose, we determined the difference ΔPD in photodegradation of the dye in the individual (PD_i) film and binary formulation (PD_f):

$$\Delta\mathrm{PD} = \mathrm{PD_i} - \mathrm{PD_f}.$$

Photodegradation of individual yellow monoazo dyes derived from thiophene and furan was studied previously [4]. Data on the photodegradation of dyes after irradiation for 1 h are compared in Tables 1 and 2. This irradiation time allows comparison of our data on the metal-containing dyes with available data for other dyes [2–4].

Table 1. Photodegradation of azo dyes **I**–**IV** in cellulose acetobutyrate films using mixtures of dyes **I**–**IV** with metal-containing dyes **V**–**VIII** (irradiation for 1 h)

Dye	PD	ΔPD
	%	
I + **V**	21.1	+2.9
I + **VI**	17.3	+6.7
I + **VII**	16.0	+8.0
I + **VIII**	20.2	+3.8
II + **V**	92.0	–3.0
II + **VI**	16.2	+72.8
II + **VII**	29.9	+59.1
II + **VIII**	42.1	+46.9
III + **V**	12.8	+2.2
III + **VI**	16.0	–1.0
III + **VII**	3.0	+12.0
III + **VIII**	8.1	+6.9
IV + **V**	62.0	+8.0
IV + **VI**	7.8	+62.2
IV + **VII**	52.1	+17.9
IV + **VIII**	60.3	+9.7

These data allow the following conclusions.

(1) The lightfastness of azo dyes derived from thiophene and furan, as a rule, increases when these dyes are used in combination with metal-containing organic dyes. The effect of metal-containing dyes is more pronounced with less lightfast dyes derived from *m*-xylidine. The lightfastness of dyes derived from anthranilic acid, which are more resistant to photochemical degradation, increases also but to a lesser extent. It is advisable to use dyes based on *m*-xylidine in combination with **VI**, and dyes based on anthranilic acid, in combination with **VII**.

(2) Metal-containing organic dyes **V**–**VIII**, when taken separately, exhibit considerably higher lightfastness than heterocyclic dyes; when used in combination with azo dyes, dyes **V**–**VIII** exhibit either the same (dye **V**) or still higher lightfastness. It is interesting that this variation of the lightfastness is independent of the structure of the azo dye added (Table 2). Most probably, this is due to the fact that all the metal-containing dyes studied degrade photochemically

Table 2. Photochemical degradation of metal-containing dyes **V**–**VIII** in acetobutyrate films containing individual dyes **V**–**VIII** and their binary mixtures with azo dyes **I**–**IV** (irradiation for 1 h)

Dye	PD	ΔPD
	%	
V	1.3	
VI	2.0	
VII	4.0	
VIII	7.5	
V + **I**	2.8	–1.5
V + **II**	1.9	–0.6
V + **III**	1.5	–0.2
V + **IV**	0.9	+ 0.4
VI + **I**	1.4	+ 0.6
VI + **II**	0.2	+ 1.8
VI + **III**	0.2	+ 1.8
VI + **IV**	0.3	+ 1.7
VII + **I**	5.5	–1.5
VII + **II**	2.5	+ 1.5
VII + **III**	2.5	+ 1.5
VII + **IV**	2.5	+ 1.5
VIII + **I**	0.5	+ 7.0
VIII + **II**	0.9	+ 6.6
VIII + **III**	0.7	+ 6.8
VIII + **IV**	0.6	+ 6.9

by the reductive mechanism and, being oxidants, stabilize azo dyes [2]. Also, in the case of iron quinonimine complexes **VII** and **VIII**, heterocyclic azo dyes, probably, additionally coordinate with the iron atom, which stabilizes both dyes.

Thus, binary mixtures of heterocyclic azo dyes and metal-containing organic dyes are good absorbing agents for polymeric film color filters, since they enhance the lightfastness of each other. In preparing a filter with required spectral characteristics, it is always possible to choose a pair of dyes ensuring the maximal lightfastness of the filter.

EXPERIMENTAL

Heterocyclic monoazo dyes were prepared by procedures described in [1], and dyes **VI**–**VIII**, according to [5–7]. Commercially produced Alcohol-Soluble Blue Z dye (Blue for Nitrolacquer) was purified by column chromatography on silica gel, eluent ethanol.

Polymeric film color filters on cellulose acetobutyrate base were prepared by casting the polymeric formulations containing appropriate dyes onto polished glass with a restricting frame determining the filter size [4].

The lightfastness of color filters in the polymeric matrix was studied in a Standard Xenon Long-Life Fade Meter XFL-1 installation for accelerated photochemical aging [2]. The progress of photodegradation was monotored spectrophotometrically at the analytical wavelength with an SF-16 spectrophotometer. The spectra were recorded against a colorless acetobutyrate film irradiated under the same conditions.

CONCLUSION

To obtain lightfast band color filters on polymeric film base, it is advisable to attain the required spectral characteristic by using metal-containing hydrophobic green-blue dyes in combination with monoazo dyes derived from thiophene and furan.

ACKNOWLEDGMENTS

The study was performed within the framework of the project supported by the program “Scintific Research of Higher Schools in Priority Fields of Science and Engineering,” section 203.02 (P-06.015).

REFERENCES

1. Kovzhina, L.P., Sokolova, N.B., Dmitrieva, N.M., and Pesenko, E.V., *Zh. Prikl. Khim.*, 1996, vol. 69, no. 3, pp. 477–482.
2. Kovzhina, L.P., Sokolova, N.B., Dmitrieva, N.M., and Popova, T.N., *Zh. Prikl. Khim.*, 1998, vol. 71, no. 12, pp. 2024–2028.
3. Kovzhina, L.P., Sokolova, N.B., Dmitrieva, N.M., and Vins, T.Yu., *Zh. Prikl. Khim.*, 1999, vol. 72, no. 9, pp. 1507–1509.
4. Sokolova, N.B., Kovzhina, L.P., Dmitrieva, N.M., and Blinova, N.V., *Zh. Prikl. Khim.*, 2002, vol. 75, no. 2, pp. 263–265.
5. Veller, E.A., El’tsov, A.V., Ivanova, L.A., and Sokolova, N.B., Abstracts of Papers, *Vsesoyuznaya nauchno-tekhnicheskaya konferentsiya “Sintez i promyshlennoe primenenie krasitelei i promezhutochnykh produktov”* (All-Union Scientific and Technical Conf. “Synthesis and Industrial Application of Dyes and Intermediates”), Rubezhnoe, 1981, p. 8.
6. El’tsov, A.V., Sokolova, N.B., Shul’gina, E.S., and Dmitrieva, N.M., *Zh. Prikl. Khim.*, 1993, vol. 66, no. 7, pp. 1561–1574.
7. El’tsov, A.V., Sokolova, N.B., Shul’gina, E.S., and Dmitrieva, N.M., *Zh. Prikl. Khim.*, 1994, vol. 67, no. 9, pp. 1537–1542.

Russian Journal of Applied Chemistry, Vol. 76, No. 1, 2003, pp. 117–123. Translated from Zhurnal Prikladnoi Khimii, Vol. 76, No. 1, 2003, pp. 121–127.

MACROMOLECULAR CHEMISTRY AND POLYMERIC MATERIALS

Comparative Study of Intercalation of Zero-Valent Silver into the Cellulose Matrix by Raster and Transmission Microscopy

N. E. Kotelnikova, G. Wegener, M. Stoll, and V. N. Demidov

Institute of Macromolecular Compounds, Russian Academy of Sciences, St. Petersburg, Russia
Institute for Wood Research, University of Munich, Munich, Germany
St. Petersburg State Technological Institute, St. Petersburg, Russia

Received August 7, 2001; in final form, November 2002

Abstract—Diffusion–reduction interaction between microcrystalline cellulose and aqueous solution of $AgNO_3$ was studied in the absence (taking into account the reducing properties of cellulose) and in the presence of specific reductants. The resulting intercalates of cellulose and zero-valent silver were examined by raster and transmission electron microscopy. The morphological changes in cellulose after intercalation of silver nanoclusters as well as the nanocluster size distribution in the cellulose matrix were characterized.

Electron microscopy is widely used to study the structure of natural materials such as wood and cellulose [1]. Cellulose interaction with various agents starts under heterogeneous conditions on its surface and causes changes in the chemical structure of cellulose and/or in the supramolecular structure of cellular membranes. This leads subsequently to structural modification of the entire fiber [2].

Our recent studies concerned preparation and properties of new metal-containing derivatives of microcrystalline cellulose (MCC) [3–7]. Examination by raster electron microscopy (REM) showed that the cellulose morphology substantially changed when its sodium, potassium, and lithium derivatives were obtained [3, 4]. REM examination also clearly demonstrated that intercalation of clusters of zero-valent metals (silver, platinum, palladium) into the cellulose matrix also led to changes in the cellulose morphology. The intercalation procedure affects the cluster distribution on the fiber surface. The use of transmission electron microscopy (TEM), a direct method making it possible to observe the inner fiber structure, allowed evaluation of the size and distribution of nanosize clusters not only on the sample surface but also in the bulk [5, 6].

It has been shown [7] that, in cellulose samples containing silver clusters obtained by various methods, the silver content on the surface [data of X-ray photoelectron spectroscopy (XPS)] appreciably exceeds that in the bulk [data of elemental and X-ray fluorescence analysis (XFA)]. After intercalation, the chemical composition of samples changes, with the decrease in the carbon content corresponding to increase in the silver content.

In this work, using REM and TEM, we made a comparative study of the initial MCC and the MCC samples containing silver nanoclusters (cellulose–Ag), with the aim to elucidate in detail the changes in the cellulose fiber morphology upon intercalation of silver clusters and to characterizate the cluster size and size distribution in the fiber bulk.

EXPERIMENTAL

Raster electron microscopy. Micrographs were obtained with a Leitz/AMR 1200B raster electron microscope at 15 kV. The samples were placed in a special chamber on aluminum supports coated with carbon and were subjected to spraying in an argon atmosphere using a gold–palladium target. Raster microscopy was carried out in combination with energy dispersive X-ray spectral analysis, which was performed with the same microscope equipped with a Kevex 7000 X-ray spectrometer. For this analysis, the samples placed on carbon-coated aluminum supports were used without spraying. The electron beam was focused on the chosen object or point, and measurements were carried out at different magnifications at 25 kV for 300 s.

Transmission electron microscopy. Samples of

1070-4272/03/7601-0117$25.00

Table 1. Some characteristics of cellulose–Ag samples containing silver nanoclusters

Sample no.*	Reductant	Reduction conditions	Sample color	Silver cluster size	Silver content, wt %	
					in bulk (XFA)	on the surface (XPS)
1	–	–	White	–	–	–
2	Cellulose	90–100°C	Yellow	Small; Ag_3–Ag_{11}	0.6	<1.0
3	″	$NH_3 \cdot H_2O$, 70°C	Reddish-brown	Small, Ag_3–Ag_{11}; Ag_{1000}	0.6	1.5
4	″	Cellulose heating at 250°C	Yellow	Small; Ag_3–Ag_{11}	1.3	1.2
5	″	Glycerol, $NH_3 \cdot H_2O$	Reddish-brown	Small, big; Ag_3–Ag_{11}; Ag_{1000}	6.1	12.6
6	″	1,10-Phenanthroline, glycerol, $NaHCO_3$, 90°C	Grey-green	Giant; Ag > 5000	3.0	4.1
7	$NaBH_4$	90°C	Yellow	Small; Ag_3–Ag_{11}	5.3	2.2
8	″	(repeated treatment)	Grey-brown	Giant; Ag > 1000	6.2	2.6
9	KH_2PO_2, H_3PO_4	90°C	Grey	Giant; Ag > 10 000	7.6	16.5
10	Hydroquinone		″	″	3.4	1.3
11	$NaBH_4$		″	Giant		

* no. 1, initial MCC; nos. 2-10, cellulose-Ag samples; no. 11, Ag^0 sample.

MCC and cellulose–Ag intercalates were dried with water–ethanol mixtures with increasing content of ethanol. Then they were placed in a standard spurr epoxy resin and heated at 70°C. Ultrathin sections were placed on carbon-coated nets and examined with a Zeiss EM 10C transmission electron microscope equipped with an amplifier at 80 kV.

Some characteristics of cellulose–Ag samples are listed in Table 1. The morphological structure of MCC obtained from cotton cellulose (CC) somewhat differs from that of the initial CC. Thus, the main structural element of CC is a fiber having the shape of a strongly twisted ribbon [8]. The main structural element in its inner part is the primary wall. Cellulose of this wall forms thin fibrils visible under the polarizing microscope or after dyeing with certain dyes.

Fig. 1. REM micrographs of MCC sample (sample no. 1): (a) general fiber view, magnification 5000; (b) butt part, magnification 3000.

Fibers located in the primary wall form a typical surface relief with a helical fibrillar structure. This relief is retained in MCC (Figs. 1a, 1b, sample no. 1) and can be clearly seen at high magnification. Fibers 10–20 mm in diameter form long flexible bands. At low magnification, MCC bands have the shape of short rodlike particles tending to aggregate.

When MCC is obtained by mild acid hydrolysis of natural cellulose, its main part (over 90 wt %) does not dissolve in the hydrolyzing mixture, and the unit cell of crystalline cellulose is neither destroyed nor changed [9]. The surface relief of cellulose probably changes after its hydrolysis and subsequent drying, leading sometimes to fibril aggregation. However, the fibers themselves look swollen and porous, which is especially pronounced in their inner craters (Fig. 1b).

Silver intercalation into the cellulose matrix proceeds in two stages [5]: diffusion of the aqua complex $[Ag(H_2O)_2]^+$ into the cellulose matrix and reduction of silver ions to zero oxidation state. These stages mostly occur simultaneously. Cellulose itself exhibits reducing properties because of the presence of terminal aldehyde groups. Therefore, ionic silver can be reduced to zero-valence state without adding specific reductants. Sample no. 2 obtained in this way contains a very small amount of Ag^0. Nevertheless, it is sufficient to change markedly its morphological structure

as compared to that of the initial cellulose. Large cracks appear on the fiber surface and on butt ends. Inner voids swell and become deeper, and large pores with the diameter ranging from 0.1 to 1.0 μm can be observed inside the fiber (Fig. 2a).

The reaction medium strongly influences the reducing power of cellulose. Sample no. 3 obtained in aqueous ammonia contains more Ag^0 on the fiber surface than sample no. 2. However, the amount of Ag^0 is still small and cannot be visualized by electron-microscopic examination.

Temperature also exerts a pronounced effect on the redox reaction of cellulose with Ag(I). The reducing power of cellulose increases after its preliminary heating at high temperatures. Cellulose heating at 250°C (sample no. 4) (Fig. 2b) increases the amount of Ag^0 but considerably alters the morphological structure, which is due to degradation of inner layers of MCC fibers. Fibers degrade in the transverse direction. Many small fibers appear and their shape changes: the length-to-width ratio is close to unity (Fig. 2b).

At combined effect of elevated temperatures and complexing medium, the effect of Ag^+ reduction with the cellulose matrix becomes still more pronounced. For example, the Ag^0 content on the surface of a sample obtained in aqueous glycerol medium at heating to high temperatures is 12.5 wt %, and that in the bulk is 6.1 wt % (sample no. 5). Aggregations of light-colored particles located on the MCC fiber surface (Figs. 3a–3c) are agglomerates of giant silver clusters. The cluster distribution on the surface where their concentration is high is irregular (Fig. 3a). The presence of voids and a large number of thin pores in butt fiber parts (with the diameter ranging from 0.02 to 0.2 μm) suggests that specifically these voids and pores facilitate penetration of reagents inside the fibers (Fig. 3b). The energy-dispersive X-ray analysis of the sample confirms the presence of silver in fibers (Fig. 3c) [7]. Silver clusters are strongly bound to the fiber surface. Their amount does not decrease after repeated washing with hot water. Silver agglomerates formed on the surface of MCC fibers during reduction were compared with the surface of a model sample of metallic silver powder obtained by reduction of $AgNO_3$ with sodium borohydride $NaBH_4$ (in the absence of cellulose) (sample no. 11, Fig. 3d). This comparison shows that they belong to different morphological types and the morphological elements on the surface of silver powder in the model sample are much larger than those in sample no. 5.

If the reaction takes place in aqueous glycerol medium in the presence of 1,10-phenanthroline (a competing ligand), giant silver clusters are obtained in sample no. 6 (Figs. 4a and 4b). Their concentration on the surface of MCC fibers is 4.1 wt %, and that in the bulk is 3.0 wt %. Globular silver particles and large silver agglomerates can be seen (Fig. 4a). They are strongly bound to the fiber and are not removed from the surface even after washing with hot water. Considerable additional fiber splitting is observed (Fig. 4b), and a system of pores 0.2–0.6 μm in diameter appears inside the fibers (Fig. 4b, lower right corner).

Fig. 2. REM micrographs of cellulose–Ag samples: (a) sample no. 2, magnification 2800; (b) sample no. 4, magnification 3000.

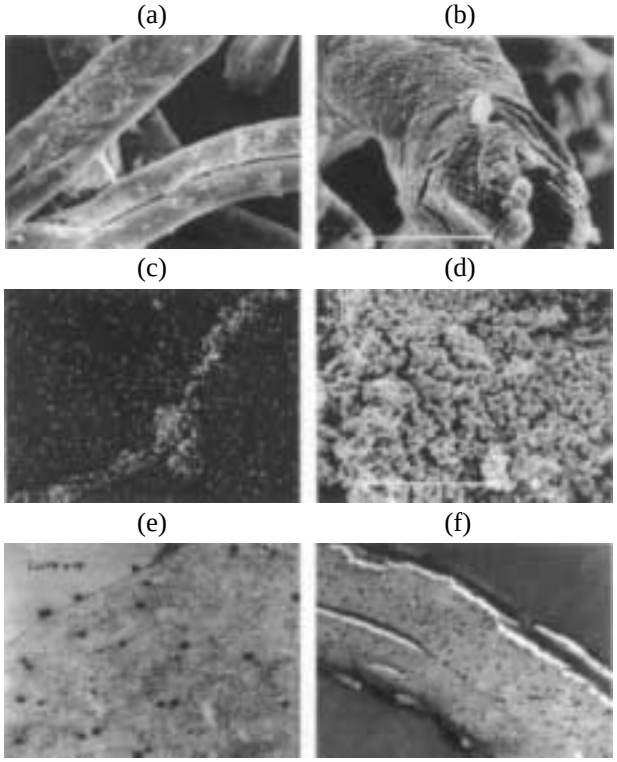

Fig. 3. (a–c) REM and (e, f) TEM micrographs of cellulose–Ag sample no. 5 and (d) sample no. 11 (metallic silver powder): (a) general fiber view, magnification 2000; (b) butt part, magnification 5000; (c) energy-dispersive X-ray analysis of silver particle distribution on the fiber surface; (d) magnification 5000; (e) fiber cross section, magnification 60000; and (f) longitudinal fiber cross section, magnification 14400.

Table 2. Characteristics of silver clusters [10–12]

Sample color	Plasmon line in the diffuse reflection spectrum, λ, nm	Number x of silver atoms in clusters Ag_x	Cluster size
Yellow	440–480	3–11	Small
Reddish-brown	480–490	11–22; 1000	Small; giant
Red	490–500	3000	Giant
Purple-red	500–580	5000	″
Green	590–605	5000–10 000	″
Grey	–	> 10 000	Giant; colloidal particles

The amount of reduced silver and the size of the resulting silver clusters in the cellulose matrix strongly depend not only on the reductant type, reaction temperature, and reaction medium but also on the procedures of sample washing and subsequent drying. Some published data on the relationship between the number x of silver atoms in Ag_x clusters, on the one hand, and sample color and wavelength λ in the diffuse reflection spectrum of silver clusters [10–12], on the other hand, are given in Table 2. These data, in combination with the results listed in Table 1, suggest that intercalation results in formation of giant silver clusters as major silver species in the cellulose matrix. Moreover, the color of many samples after reduction corresponds to that of small silver clusters, but after drying the samples become darker. Cluster growth is evidently initiated by the temperature effect during sample drying. For example, sample no. 2 having a low silver content is yellow immediately after reduction but becomes grayish-green after drying. In other words, the resulting sample contains a mixture of silver clusters of different size ranging from very small to giant.

(a) (b)

(c)

Fig. 4. (a, b) REM and (c) TEM micrographs of cellulose–Ag sample no. 6: (a) general fiber view, magnification 5000; (b) view of degraded fiber part, magnification 5000; in the lower right corner, sample part with a system of pores 0.2–0.6 μm in diameter, magnification 6000; (c) transverse cross section, magnification 30 000.

(a) (b)

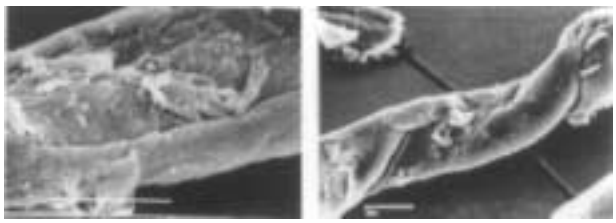

Fig. 5. REM micrographs of cellulose–Ag sample no. 8. Magnification: (a) 2900 and (b) 1600.

The use of specific reductants gives MCC samples with a high Ag^0 content both on the fiber surface and in the bulk. The largest amount of reduced silver in cellulose samples was obtained with $NaBH_4$ or KH_2PO_2 used as reductants.

With $NaBH_4$, only small silver clusters were obtained in the cellulose matrix (Table 1, sample no. 7). The amount of intercalated silver attains 4.9 (elemental analysis) or 5.3 wt % (XFA). Repeated reduction with $NaBH_4$ leads to additional growth of silver clusters and to the appearance of large cluster agglomerates on the surface (Fig. 5a, sample no. 8). The sample surface and fiber ends swell, and fibers additionally degrade. The cracks and breaks formed are parallel to fibril direction (Fig. 5b).

When KH_2PO_2 was used as a reductant, a sample with a high silver content on the surface (16.5 wt %) was obtained (Fig. 6a, sample no. 9). Giant silver clusters were formed. A strong destructive effect was detected on butt ends of greatly swollen fibers (Fig. 6b). The inner surfaces of voids also markedly swell and stick together. This probably prevents penetration of reagents inside the fibers. Helical fibers also appear. A similar effect has already been observed in cotton fluff nitration [2].

With hydroquinone as reductant, 3.4 wt % of Ag^0 with the average silver content of 300 atoms per cluster is intercalated into the cellulose matrix in the first stage (sample no. 10) [7]. As the reduction proceeds further, cluster continues to grow, with its size reaching 1000 and more atoms. When the reaction is complete, subsequent cooling and drying lead to the closure of butt end passages (Fig. 7a). Silver clusters are weakly bound to the fiber surface. Thorough washing causes their complete removal. The surface relief (Fig. 7b) resembles that of the cellulose sample subjected to thermal treatment. Regular crack distribution after silver removal probably indicates that clusters (before their removal) were regularly distributed in fibers. The distance between cracks is a multiple of 10, being mainly 10 or 20 μm. These data confirm previous results, which indicate that cellulose fibers contain periodical structural elements formed by a fibrillar ribbon twisted in a helix [13]. A similar pattern, as indicated by REM, is observed in cellulose nitration [2].

When viewed under a transmission electron microscope, fibers of the initial MCC have a shape of cross sections. The presence of Ag^0 clusters in fibers of cellulose–Ag intercalates was first visualized by us using TEM (Figs. 3e, 3f, 4c, 6c).

The micrographs of sample no. 5 (Figs. 3e, 3f) show spherical silver particles distributed relatively regularly in the sample bulk. This distribution is retained regardless of the method of fiber preparation for microscopic examination (Fig. 3e, fiber section transverse to its axis; Fig. 3f, fiber section along the axis). Large agglomerates of silver clusters are also located on the fiber surface. These conclusions agree with data obtained by REM and XPS. The histogram of numerical size distribution of silver clusters obtained by statistical processing of micrographs has a single maximum, i.e., the distribution is unimodal (Fig. 8). The calculation based on the histogram of the root-mean-square diameter distribution of silver clusters d_s shows that most of the clusters have the diameter less than 30 nm. The area occupied by silver clusters in the fiber section is about 4% of the total section area. It was established that the cluster distribution in these fibers exhibits certain regularity. The greatest number of clusters is on the surface. With increasing distance from the surface, it gradually decreases, with this decrease being described by a hyperbolic function.

Figure 4c shows the transverse section of fiber of sample no. 6. In contrast to sample no. 5, the distribution of silver clusters is irregular and bimodal

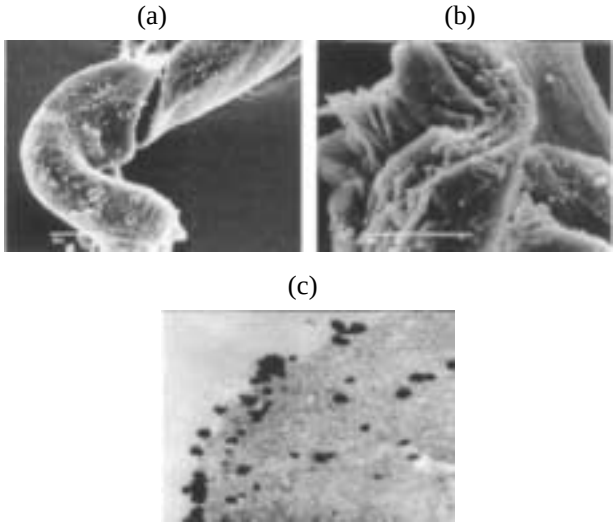

Fig. 6. (a, b) REM and (c) TEM micrographs of cellulose–Ag sample no. 9. Magnification: (a) 3000, (b) 2000, and (c) 60000.

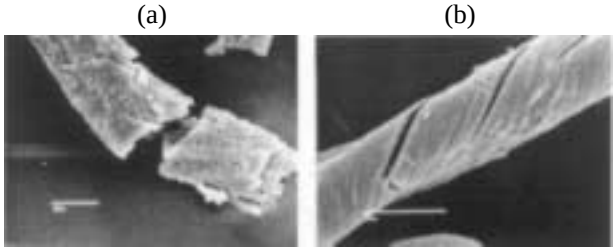

Fig. 7. REM micrographs of cellulose–Ag sample no. 10. Magnification: (a) 1600 and (b) 2600.

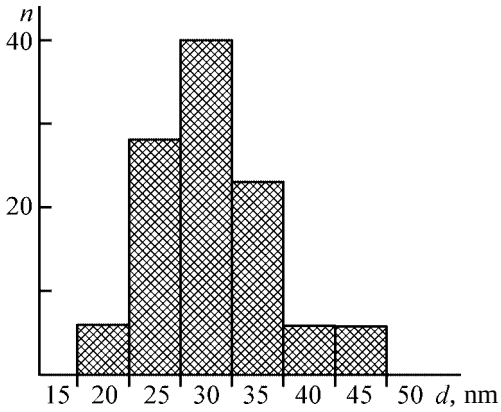

Fig. 8. Histogram of numerical silver cluster size distribution in a cellulose–Ag sample (no. 5) according to TEM data: (*n*) number of nanoclusters and (*d*) their diameter; the same for Fig. 9.

with the maxima corresponding to d_s 10 and 60 nm (Fig. 9). The silver content in the fiber bulk is smaller than in sample no. 5, which agrees with analytical data. The area occupied by silver clusters is 1.5% of the total cross-sectional area.

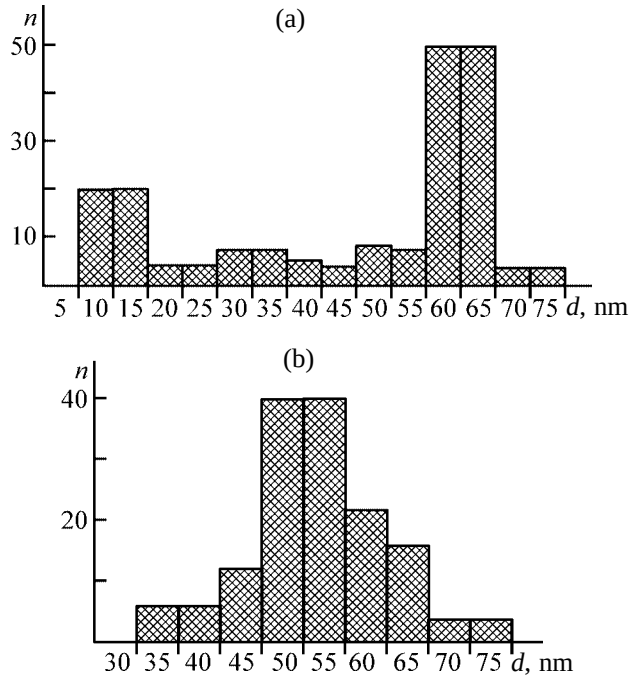

Fig. 9. Histograms of numerical silver cluster size distribution in cellulose–Ag samples according to TEM data. Sample no.: (a) 6 and (b) 9. For designations, see Fig. 8.

Silver clusters in sample N 9 (Fig. 6c) are large and are also concentrated both on the surface (16.5 wt %) and in the fiber bulk (7.6 wt %). In some places on the surface they form giant agglomerates. The cluster distribution is unimodal. However, it is not so regular as that in sample no. 5 (Fig. 8), and the average cluster size is 1.5–2.0 times greater (Fig. 9b). The d_s value for the maximum number of clusters is 48–58 nm. The area occupied by them in the fiber cross section is 5.1% of the total cross-sectional area.

Thus, the observed silver clusters in the samples have different sizes but can be characterized as nanoclusters. Note that the resolution of the transmission microscope used in this study does not allow observation of clusters smaller than 1 nm. Smaller clusters probably also exist in the samples. However, it may be assumed that the histograms reflect the real distribution patterns.

It should be emphasized that the use of high-resolution TEM allowed the first observation of intercalated silver nanoclusters directly in the cellulose matrix bulk and the characterization of their size and size distribution. The use of mutually complementing REM and TEM methods also furnished detailed information about changes in the MCC morphology accompanying intercalation of silver clusters. The main changes are observed on the surface of MCC fibers, because diffusion of reagents and reduction of silver ions occur under heterogeneous conditions. Thus, on the surface the texture changes: fibrils become disordered, reconstructed, and in some cases the surface becomes completely smooth. In many cases fibers become curved and twisted. Moreover, REM examination furnished additional information about inner fiber layers. Intercalation leads to the degradation of these layers, making the inner surface open. The butt ends of fibers are often open for observation, and thin pores appearing as a result of chemical processes can be seen.

CONCLUSIONS

(1) The diffusion–reduction interaction of microcrystalline cellulose with aqueous $AgNO_3$ solutions directly in the cellulose matrix and in the presence of $NaBH_4$ and KH_2PO_2 reductants was studied by REM and TEM, which allowed visualization of intercalation of zero-valent silver nanoclusters into the cellulose matrix.

(2) Morphological changes in cellulose both on the fiber surface (fibril disordering and crack formation) and in the inner layers (distribution of inner voids and appearance of a pore system) were compared and characterized.

(3) Nanocluster sizes and their distribution in the matrix were characterized; it was shown that these parameters depend on the reduction conditions and on particular reductant.

ACKNOWLEDGMENTS

The authors are grateful to the German Research Society (DFG) for financial support, to M. Wenzkowski for assistance in carrying out the electron-microscopic study, to E. Windeisen for the discussion of the results, and to E.F. Panarin for valuable remarks.

REFERENCES

1. Fengel, D. and Wegener, G., *Wood. Chemistry, Ultrastructure, Reactions*, Berlin: Walter de Gruyter, 1989.
2. Ludwig, M. and Fengel, D., *Wood. Sci. Technol.*, 1992, vol. 26, pp. 393–401.
3. Kotelnikova, N.E., Fengel, D., Kotelnikov, V.P., and Stoll, M., *J. Inorg. Organomet. Polym.*, 1994, vol. 4, no. 3, pp. 315–323.
4. Kotelnikova, N.E., Fengel, D., Kotelnikov, V.P., *et al.*, *Cellulose Chem. Technol.*, 2002, vol. 36, no. 1, pp. 280–287.

5. Kotelnikova, N.E., Paakkari, T., Serimaa, R., *et al*., *Macromol. Symp*., 1997, vol. 114, pp. 165–171.
6. Kotelnikova, N.E., Paakkari, T., Serimaa, R., *et al*., *Macromol. Symp*., 1999, vol. 138, pp. 175–180.
7. Kotelnikova, N.E., Adsorption-Chemical Modification of Cellulose by Biologically Active Substances, *Doctoral (Chem.) Dissertation*, St. Petersburg, 2002.
8. Petropavlovsky, G.A. and Kotelnikova, N.E., *Acta Polym*., 1985, vol. 36, no. 2, pp. 118–123.
9. Kotelnikova, N.E., Petropavlovsky, G.A., Shevelev, V.A., *et al*., *Cellulose Chem. Technol*., 1976, vol. 4, no. 10, pp. 391–399.
10. Gratzel, M., *Energy Resources through Photochemistry and Catalysis*, Gratzel, M., Ed., New York: Academic, 1983.
11. Gubin, S.P., *Khimiya klasterov. Printsipy klassifikatsii i struktura* (Cluster Chemistry. Principles of Classification and Structure), Moscow: Nauka, 1987.
12. *Clusters and Colloids. From Theory to Applications*, Schmid, G., Ed., Weinheim, VCH, 1994.
13. Kotelnikova, N.E., Fengel, D., and Kotelnikov, V.P., *Metal-Containing Polymeric Materials*, Pittman, C.U., Jr., *et al*., Eds., New York: Plenum, 1994, pp. 403–407.

Russian Journal of Applied Chemistry, Vol. 76, No. 1, 2003, pp. 124–127. Translated from Zhurnal Prikladnoi Khimii, Vol. 76, No. 1, 2003, pp. 128–132.

MACROMOLECULAR CHEMISTRY AND POLYMERIC MATERIALS

Devoted to the Memory of Yurii Pavlovich Kudryavtsev

IR Spectra of Carbynoid Films Prepared by Dehydrofluorination of Polyvinylidene Fluoride

I. G. Margamov, S. E. Evsyukov, L. A. Pesin, E. M. Baitinger, P. S. Semochkin, I. V. Gribov, N. A. Moskvina, and V. L. Kuznetsov

Chelyabinsk State Educational University, Chelyabinsk, Russia
Nesmeyanov Institute of Organoelement Compounds, Russian Academy of Sciences, Moscow, Russia
Institute of Physics of Metals, Ural Division, Russian Academy of Sciences, Yekaterinburg, Russia

Received May 22, 2002

Abstract—IR and X-ray photoelectron spectra of the products of chemical carbonization of polyvinylidene fluoride were recorded and discussed.

Synthesis of high-quality carbyne which is a unidimensional modification of carbon is an urgent problem. These are several chemical methods for preparing carbynoid materials[1] in the form of powders, fibers, or films [1]. One of the simplest procedures for preparing carbynoid materials is chemical dehydrohalogenation of some halogen-containing polymers [1]. To determine the prospects for practical application of carbynoids, their structural stability and properties should be studied.

In this work the dehydrofluorination products of polyvinylidene fluoride (PVDF) films were studied by IR and X-ray photoelectron (XPE) spectroscopy. We studied two sample series chemically treated under different conditions. The first series was obtained by treatment of the initial PVDF films at room temperature for a time from 2 min to 2 h with a mixture of a saturated ethanolic solution of potassium hydroxide (20%) and acetone in a 1 : 9 volume ratio. The samples of the second series were treated for a time from 10 min to 16 h with a mixture of saturated ethanolic solution of potassium hydroxide and tetrahydrofuran (THF) in a 2 : 3 ratio. Then the samples were successively washed with ethanol, acetone, and water. No additional treatment was performed.

The IR absorption spectra were recorded in the range 400–4000 cm^{-1} at room temperature on a double-beam Specord 75-IR spectrometer. The standard spectrometer error in the ranges 400–2000 and 2000–4000 cm^{-1} is ±1 and ±2 cm^{-1}, respectively. The shapes of the spectra are well reproduced. In the far IR region (400–1200 cm^{-1}), we failed to record the IR spectra owing to strong absorption of C–F bond at the film thickness of about 0.1 mm.

The X-ray photoelectron spectra were recorded on an ES IFM-4 spectrometer [2]. Two coaxial cylindrical coils producing magnetic filed with required configuration along the photoelectron beam were used as the energy analyzer. The transmission energy was 320 eV. The residual pressure in the vacuum chamber was no higher than 10^{-9} mm Hg. Photoelectrons (E 1486.6 eV) were excited with Al$K_{\alpha_{1,2}}$ radiation.

The IR spectra of the partially dehydrofluorinated PVDF films of the first series are shown in Fig. 1, and those of the initial PVDF film and the films of the second series, in Fig. 2. The shape of the spectra in the 1500–4000 cm^{-1} range strongly depends on the treatment time, with the spectral transformations being more pronounced after prolonged dehydrofluorination. This may be due to a change in the concentration of the double carbon–carbon bonds (1500–1800 cm^{-1}) [1, 3], water molecules (1700, 3400 cm^{-1}) [4], CH bonds (2900–3100 cm^{-1}) [3], hydroxy groups (3000–3700 cm^{-1}) [5, 6], and HF molecules (3000–4000 cm^{-1}) [5]. In addition, the absorption in the range 2200–3700 cm^{-1} increases after the treatment.

The fact that the band in the range 1500–1800 cm^{-1} grows with the treatment time is likely due to an in-

[1] Carbynoids are carbon macromolecular compounds having mainly chain structure and containing carbyne [polyyne or(and) cumulene] fragments along with defective liner carbon chains [interchain cross-linking, heteroatom substituents (atoms and groups), etc.].

1070-4272/03/7601-0124$25.00

crease in the number of conjugated double carbon–carbon bonds [1]. A weak band at 1720 cm^{-1} in the spectra of all the films indicates the presence of carbonyl groups in small amounts [3, 4]. This band appears as a shoulder on the main band in the range 1500–1800 cm^{-1} and does not contribute to the intensity of this band. Probably, the carbonyl groups were formed in the course of film preparation by heating of a PVDF solution in DMF on a support [7]. These groups can behave as local initiators of dehydrofluorination [7].

It should be noted that water molecules can contribute to the absorption in this range. At first glance, this is indicated by a strong increase in the absorption in the 3200–3700 cm^{-1} range with the treatment time. However, the increase in the intensity of the band in the range 1500–1800 cm^{-1} does not correlate with that of the band in the range 3200–3700 cm^{-1}: the maximal growth of the first band is observed in the first dehydrofluorination steps when the intensity of the second band remains virtually the same. Thus, the absorption of water molecules in the first examined range is negligible.

The absence of the band at 2175 cm^{-1} indicates the absence of triple carbon–carbon bonds in the films [3]. The presence of double bonds and the absence of triple bonds in the films would indicate formation of $–(–CH=CF–)_n–$ intermediate in the first dehydrofluorination step. Finally, in this step the hydrogen and fluorine concentrations decrease approximately by half as compared to those in the initial film. Hence, the fluorine content in these films should not be lower than a half of the carbon content. To confirm this assumption, we studied the XPE spectra in a wide range of binding energies for the samples of the first and the second series treated for 2 and 16 h, respectively. The spectra were recorded 2 months after dehydrofluorination. In both cases, fluorine and oxygen were detected, along with carbon, on the sample surface. The fluorine and oxygen concentrations were determined relative to the carbon concentration by the conventional procedure [8] taking into account the photoionization cross sections, sample thickness, and transmission function of the spectrometer. The oxygen content in the samples was about 20 and 16 at. %, respectively. The fluorine content (23 and 28 at. %, respectively) was appreciably lower than the expected values. Probably, this fact does not prove formation of exclusively the cumulene structure after the treatment and may be a result of a lower fluorine concentration in the surface layer as compared to the deeper layers inaccessible for XPE analysis. At the same time, the absence of triple carbon–carbon bonds may be due to

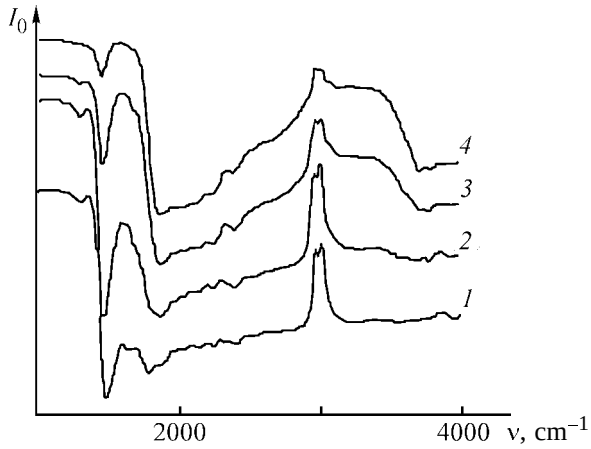

Fig. 1. IR spectra of PVDF films dehydrofluorinated for (*1*) 2, (*2*) 8, (*3*) 25, and (*4*) 45 min (first series). (I_0) Absorption and (ν) wave number; the same for Fig. 2.

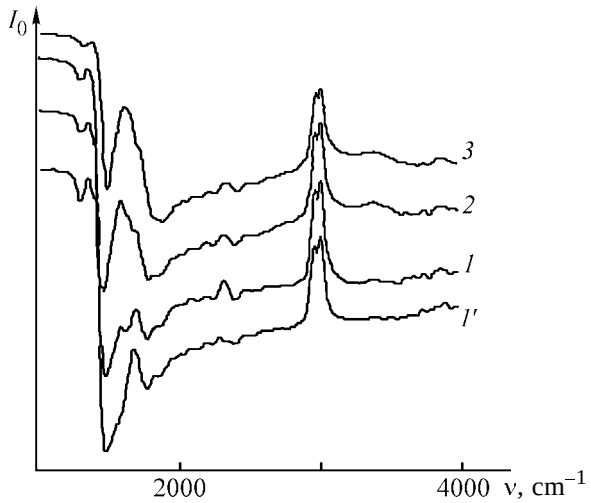

Fig. 2. IR spectra of (*1'*) the initial PVDF film and the products of its dehydrofluorination for (*1*) 10, (*2*) 60, and (*3*) 100 min (second series).

strong interchain cross-linking and oxidative degradation of carbynoid fragments (both polyyne and cumulene) on storage:

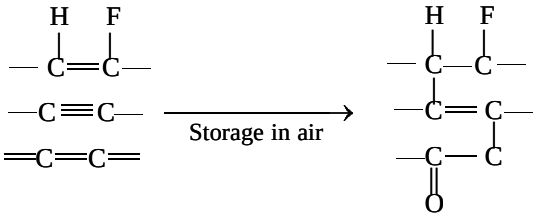

This assumption is confirmed by the fact that the films lose flexibility and are destroyed on prolonged storage.

The XPE spectra of the films were repeatedly recorded 7.5 years after their treatment. We failed to

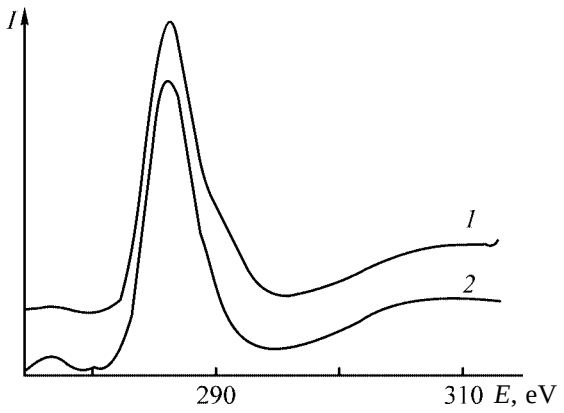

Fig. 3. XPE spectra (range of carbon inner electron shell) of a carbynoid film of the second series dehydrofluorinated for 16 h, recorded in (*1*) 1994 and (*2*) 2001. (*I*) Intensity and (*E*) binding energy.

record the spectra of the first film since it completely degraded to a fine powder. The second film was broken down into large fragments which were glued without gaps on an adhesive tape. When the spectra were recorded (~335 min), the relative oxygen and fluorine concentrations monotonically decreased from 22 to 14 and from 9.4 to 6.4%, respectively. Thus, during storage of the samples, the oxygen content increased and the fluorine content appreciably decreased. Furthermore, the film was defluorinated when the XPE spectra were recorded. Defluorination of the samples stored for 7.5 years is also confirmed by a change in the shape of the C1*s* band (Fig. 3): the intensity of the shoulder assigned to the inner electron shell of the carbon atom of the CF_2 groups appreciably decreased.

Defluorination of the initial [9] and dehydrofluorinated PVDF films [10] exposed to X-ray radiation was observed previously. We also found that the fluorine content in the surface layer of dehydrofluorinated PVDF films increased during prolonged storage of the samples, which was due to spontaneous elimination of hydrogen fluoride from labile groups and its diffusion from the bulk of the sample to its surface. We failed to quantitatively characterize this process by the elemental composition of the surface layer due to desorption of HF from the sample. We suggest that the surface fluorine concentration in the samples dehydrofluorinated to a small extent, i.e., with a high initial fluorine content in the surface layer, will decrease on prolonged storage. On the contrary, since chemical carbonization develops in the direction from the surface to the bulk of the sample, prolonged fluorine diffusion form the bulk to the surface of strongly dehydrofluorinated samples can increase (as compared to the fluorine concentration measured immediately after the synthesis) the fluorine concentration in the surface layer accessible for XPE analysis.

Two bands in the 2900–3100 cm^{-1} range of the spectra shown in Figs. 1 and 2 and three closely located bands in this range in the spectra of strongly carbonized samples are assigned to stretching vibrations of the CH bonds. The intensity of the CH bands of the samples of both series, dehydrofluorinated for a short time, is slightly higher than that of the initial film. As the decarbonization time increases, the intensity of this band changes nonmonotonically. In the first series, the overall trend toward a decrease is more pronounced than in the second series. The nonmonotonic decrease is due to the fact that the contribution of side reactions of nucleophilic substitution of halide anions with ethoxy anions to the total dehydrofluorination changes in the course of the process. When dehydrofluorination of PVDF film is activated with acetone, the contribution of these reactions is lower than in the case when THF is used for this purpose.

The absorption in the range 2200–3700 cm^{-1} also depends on the dehydrohalogenation time and procedure. We divided this range into regions S_1 (2200–2800 cm^{-1}) and S_2 (3200–3700 cm^{-1}). Bellamy [6] assigned the absorption in the first range to vibrations of hydroxy groups bonded by strong hydrogen bonds. The bands in the second region were assigned to the stretching vibrations of OH groups [4]. The formation of H-bonded hydroxy groups can be semiquantitatively estimated from the ratio of the peak areas in the first and the second regions (S_1/S_2). The most reliable measurements of these areas can be performed for the highly dehydrofluorinated samples (first series, dehydrofluorination time 15–60 min). In this case, S_1/S_2 is almost constant and close to 0.6. This probably indicates that the content of OH groups bonded by strong hydrogen bonds is appreciable and constant. This assumption is correct at least for the samples dehydrofluorinated for a long time.

Formation, accumulation, and transformation of hydroxy groups is one of the main features of PVDF dehydrofluorination and aging of the reaction products. Nucleophilic substitution of fluorine atoms with hydroxy groups occurs most readily in allyl fragments owing to the effect of allyl activation [11]. This reaction yields reactive hydroxyallyl groups II. On storage of the samples, these groups degrade to form HF and carbonyl groups:

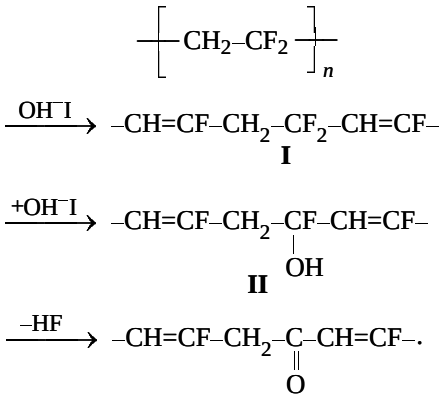

Since atmospheric oxygen has virtually no effect of PVDF dehydrofluorination [3], in the course of the alkali treatment, oxygen-containing groups are formed mainly by the nucleophilic substitution pathway. Secondary transformation of hydroxy groups contribute mainly to the accumulation of carbonyl groups in the course of sample storage. Thus, transformation of the broad band in the range 2200–3700 cm^{-1} on storage of the dehydrofluorinated samples may be due to multistage process involving oxidation, hydrolysis, isomerization, and(or) tautomerization. In addition, as the carbynoid structure is formed, the absorption due to free and localized electrons can appear. To confirm this assumption, special studies in a wide spectral range are required.

CONCLUSIONS

(1) Dehydrofluorination of PVDF in the presence of acetone is more effective than that in the presence of THF.

(2) The IR spectra of modified polyvinylidene fluorides contain the bands of C=C, CH, and OH groups.

(3) The structural differences in the samples dehydrofluorinated for different times in the presence of various activators are preserved after prolonged storage of these samples in air.

(4) Films of polyvinylidene fluoride and products of its partial dehydrofluorination eliminate HF in the course of recording the XPE spectra.

ACKNOWLEDGMENTS

This work was financially supported in part by the Russian Foundation for Basic Research (regional grant 01-02-96475 p2001ural).

REFERENCES

1. *Carbyne and Carbynoid Structures*, Heimann, R.B., Evsyukov, S.E., and Kavan, L., Eds., Dordrecht (Netherlands): Kluwer Academic, 1999.
2. Sokolov, O.B. and Kuznetsov, V.L., *Razvitie eksperimental'nykh vozmozhnostei metoda elektronnoi spektroskopii s ispol'zovaniem magnitnogo energoanalizatora* (Expansion of the Experimental Potential of Electron Spectroscopy with the Use of Magnetic Energy Analyzer), Chelyabinsk: Chelyab. Politekh. Inst., 1990.
3. Korshak, V.V., Kudryavtsev, Yu.P., Korshak, Yu.V., *et al*., *Dokl. Akad. Nauk SSSR*, 1987, vol. 294, no. 1, pp. 127–130.
4. Goncharov, G.N., Zorina, M.L., and Sukharzhevskii, S.M., *Spektroskopicheksie metody v geokhimii* (Spectroscopy in Geochemistry), Leningrad: Leningr. Gos. Univ., 1982, pp. 204–205.
5. Nakamoto, K. *Infrared and Raman Spectra of Inorganic and Coordination Compounds*, London: Wiley, 1986.
6. Bellamy, L.J., *The Infra-Red Spectra of Complex Molecules*, London: Methuen, 1954.
7. Evsyukov, S.E., Kudryavtsev, Yu.P., and Korshak, Yu.V., *Usp. Khim.*, 1991, vol. 60, no. 4, pp. 764–798.
8. Pesin, L.A., Baitinger, E.M., Kovalev, I.N., *et al*., *Zh. Strukt. Khim*., 1999, vol. 40, no. 3, pp. 493–499.
9. Duca, M.D., Plosceanu, C.L. and Pop, T., *J. Appl. Polym. Sci*., 1998, vol. 67, pp. 2125–2129.
10. Margamov, I.G., Pesin, L.A., Kudravtsev, Yu.P., and Evsyukov, S.E., *Appl. Surf. Sci*., 1999, vol. 148, nos. 3–4, pp. 183–188.
11. *Khimicheskaya entsiklopediya* (Chemical Encyclopedia), Knunyants, I.L., Ed., Moscow: Sov. Entsiklopediya, 1988, vol. 1.

Russian Journal of Applied Chemistry, Vol. 76, No. 1, 2003, pp. 128–131. Translated from Zhurnal Prikladnoi Khimii, Vol. 76, No. 1, 2003, pp. 133–137.

MACROMOLECULAR CHEMISTRY AND POLYMERIC MATERIALS

Dissolution of Silk Fibroin in *N*-methylmorpholine-*N*-oxide and Its Mixtures with Organic Solvents

E. S. Sashina, N. P. Novoselov, and K. Heinemann

St. Petersburg State University of Technology and Design, St. Petersburg, Russia
Thuringian Institute of Textile and Plastics, Germany

Received June 2, 2002

Abstract—Preparation of concentrated solutions of natural silk fibroin in *N*-methylmorpholine-*N*-oxide and its mixtures with protonic and aprotic solvents was experimentally studied. Solutions with the fibroin concentration of 6 wt % and more were prepared.

Active efforts are made today to develop processes for producing various materials from wastes of natural fibers [1]. These processes involve preparation of working solutions of natural polymers and their conversion into, in particular, fibers and films. Natural fibers, e.g., cellulose, can be dissolved without derivatization in tertiary amine oxides [2].

Fibers of polymer blends can be produced from solutions of proteins such as fibroin of natural silk. These fibers are characterized by improved hydrophilicity, dyeability, folding resistance, etc. Dissolution of a protein depends on its structure, molecular weight and structure of its macromolecules, and polarity and steric arrangement of the side groups. Mutual interaction of side groups of fibroin (Fig. 1) restricts free rotation around single bonds of the peptide chain, thus making it relatively rigid. A fibroin macromolecule contains nonpolar amino acid residues (aliphatic residues of alanine, leucine, isoleucine, valine, and proline and aromatic residues of phenylalanine and tryptophan), polar amino acid residues (serine, threonine, and tyrosine residues containing hydroxy groups, cysteine residues with SH groups, carboxy and amide groups of aspartic and glutamic acids, and amino groups of lysine) [3, 4]. The fibroin macromolecules are closely packed owing to higher content of hydrophobic residues as compared to that of hydrophilic polar groups. The content of oriented chains reaches 40–60%. Fibroin sparingly swells in water and is soluble in concentrated solutions of LiCNS, LiBr, $CuCl_2$, $Ca(CNS)_2$, and $ZnCl_2$, copper ammonia solution ($CuSO_4$ + NH_4OH), phosphoric acid, and some other inorganic solvents [3–8].

The mechanism of dissolution of fibroin in concentrated aqueous solutions of salts and acids is not understood. Probably, ions of the solvent interact with charged groups of the side chains of the fibroin, thus cleaving hydrogen bonds between the macromolecules. These ions indirectly affect the macromolecular conformation via a change in the solvent structure. The internal regions of the ordered polymer do not contact with the solvent. Hydration of side polar groups results in loosening of the water structure and its diffusion inside polymeric fibrils. Structuring of water by interaction with the nonpolar groups

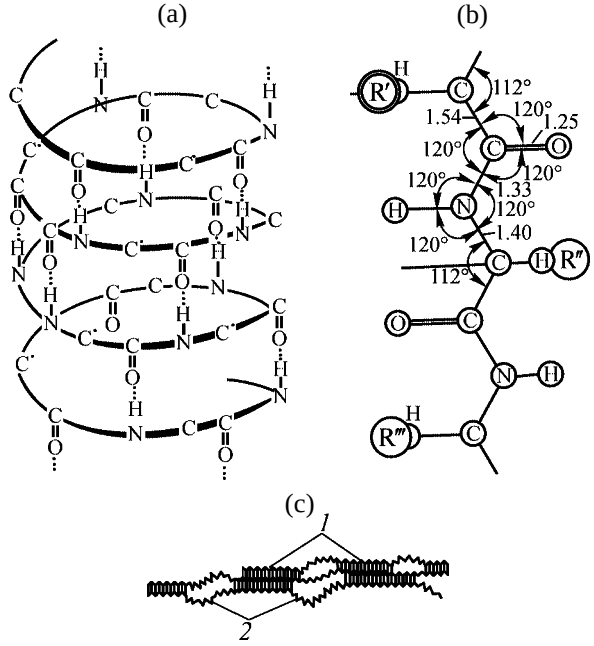

Fig. 1. Scheme of a polypeptide chain [4]: (a) helical structure, (b) unfolded chain, and (c) arrangement of polypeptide chains in the fiber. Region: (*1*) crystalline and (*2*) amorphous.

1070-4272/03/7601-0128$25.00

prevents its diffusion into the protein. Degradation of the water structure in the presence of salts results in conformational transformations of the macromolecule and penetration of water into the crystalline regions of the polymer.

Structural transformations of macromolecules are observed not only in the presence of ions breaking the water structure but also under the action of structure-making ions which become surrounded by a shell of water molecules ordered owing to interaction with nonpolar side groups of the protein. Disordering of water around hydrophobic fragments results in conformational transformations of the polymer, followed by its dissolution [9]. We suggest that fibroin of natural silk is dissolved in concentrated aqueous solutions of salts owing to interaction of the solvent ions with the side groups and a change in the conformation of the macromolecules, which favors their unwrapping and penetration of water inside the protein. Disadvantages of salt solutions of fibroin are their structure-breaking effect on the polymer and the necessity of subsequent dialysis of the solution to remove the salt.

Dissolution of silk fibroin in nonaqueous solvents is of special scientific and technological interest. As shown previously [2], up to 1.96 and 3.84% of silk is dissolved in *N*-methylmorpholine-*N*-oxide monohydrate (NMMO) at 120°C and in *N*-methylazacycloheptane-*N*-oxide at 140°C, respectively.

EXPERIMENTAL

To prepare silk solutions suitable for industrial processing, we studied dissolution of silk fibroin in NMMO. We used silk fibroin of silkworm, treated to remove sericin, fats, waxes, and mineral compounds and stapled in samples 34.6 μm in diameter and 3.6 mm long. The solubility was studied by polarizing microscopy at 160× magnification. The fiber did not dissolve after keeping in the solvent at 95–130°C for 4 h. The fiber diameter increased by a factor of 1.5 (105°C) and 2–3 (120, 130°C). Thus, silk fibroin only swells in NMMO monohydrate (13.3 wt % water, mp 71–74°C) at temperature of 105°C and higher. As determined by X-ray diffraction, the crystallite size does not noticeably change after swelling (Fig. 2, curves *1*, *2*), i.e., NMMO monohydrate interacts only with amorphous fibroin. Clearly, critical (threshold) energy of interaction of fibroin macromolecules with the solvent, which is required for the rupture of intermolecular hydrogen bonds in crystalline parts of the polymer and dissolution of the polymer, is higher than that of cellulose macromolecules.

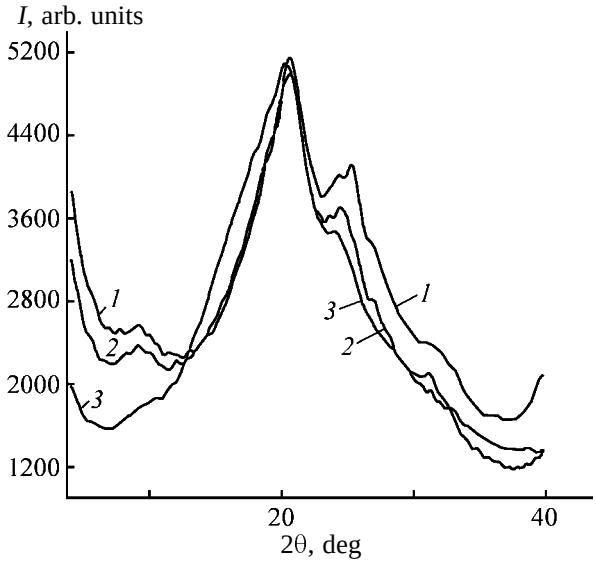

Fig. 2. X-ray patterns of (*1*) the initial washed silk, (*2*) swollen and dried sample, and (*3*) sample precipitated from a solution in $NMMO \cdot 0.8H_2O$. (*I*) Intensity and (θ) Bragg's angle.

Previously [10, 11] we analyzed the influence of the water content in the solvent on the energy of interaction of the solvent with cellulose macromolecules. Thermochemical studies and theoretical calculations show that the energy of interaction of NMMO with hydroxy groups of cellulose is inversely proportional to the water content in the solvent. In this work we studied the fibroin solubility in NMMO with different water content, which was adjusted by removing water at 95–110°C and a pressure of 30–60 mbar. The residual water content was determined gravimetrically and by the melting point of NMMO. As seen from Table 1, the fibroin is dissolved at the water content in NMMO no more than 10 wt %, which corresponds to the composition $NMMO \cdot 0.8H_2O$. Transparent light yellow fibroin solutions with the polymer concentration of 5 wt % and higher are formed. The X-ray

Table 1. Fibroin solubility in NMMO with different water content

H_2O content in NMMO, wt %	Molar composition of the solvent	T_d,* °C	Fibroin concentration in the solvent, wt %
13.3	$NMMO \cdot 1.0H_2O$		Insoluble
11.5	$NMMO \cdot 0.85H_2O$		Insoluble
10.6	$NMMO \cdot 0.77H_2O$	120	≥6
8.4	$NMMO \cdot 0.6H_2O$	>120	≥6
4.4	$NMMO \cdot 0.3H_2O$	>120	≥6

* (T_d) Dissolution temperature

Table 2. Fibroin solubility in NMMO–water–alcohol systems

Alcohol	NMMO : water : alcohol molar ratio	T_m,* °C	Fibroin solubility
Methanol	1 : 0.45 : 0.78	60–70	–
	1 : 0.3 : 0.6	90–100	Soluble at 120°C
	1 : 0.3 : 0.7	90	″
Ethanol	1 : 0.45 : 0.78	70	–
	1 : 0.3 : 0.6	65	–
1-Propanol	1 : 0.45 : 0.78	105	–
	1 : 0.3 : 0.6	100–105	–
2-Propanol	1 : 0.45 : 0.78	> 110	Soluble
	1 : 0.3 : 0.6	105	–
1-Butanol	1 : 0.45 : 0.78	>140	Soluble
	1 : 0.3 : 0.6	90–100	–
2-Butanol	1 : 0.45 : 0.78	>140	Soluble
	1 : 0.3 : 0.6	90–95	–
1-Pentanol	1 : 0.45 : 0.25	>120	Soluble
	1 : 0.3 : 0.46	120	–
	1 : 0.3 : 0.9	50–55	–
2-Pentanol	1 : 0.45 : 0.25	>140	Soluble
	1 : 0.3 : 0.46	120–125	″
	1 : 0.3 : 0.6	80–85	–
	1 : 0.3 : 0.9	60–65	–
3-Pentanol	1 : 0.45 : 0.25	>120	Soluble
	1 : 0.3 : 0.46	120–125	″
	1 : 0.3 : 0.6	80–85	–
	1 : 0.3 : 0.9	60–65	–

* (T_m) Melting point; the same for Tables 3 and 4.

Table 3. Fibroin solubility in NMMO–water–aprotic solvent systems

Aprotic solvent	NMMO : water : cosolvent molar ratio	T_m, °C	Fibroin solubility
DMSO	1 : 0.45 : 0.25	>140	–
	1 : 0.45 : 0.5	130–135	Soluble
	1 : 0.35 : 0.5	90–100	″
	1 : 0.35 : 0.79	80–90	″
	1 : 0.35 : 1.58	65–75	<3%
	1 : 0.35 : 3.15	Liquid	<1%
	1 : 0.3 : 0.5	>140	–
	1 : 0.3 : 0.9	120–125	Soluble
	1 : 0.3 : 1.2	120	″
	1 : 0.3 : 1.5	90	″
	1 : 0.3 : 1.8	75	″
	1 : 0.3 : 2.4	65	<3%
DMFA	1 : 0.45 : 0.25	>140	–
	1 : 0.45 : 0.5	140	Soluble
	1 : 0.35 : 0.84	80–90	″
	1 : 0.35 : 1.69	75–80	<1%
	1 : 0.3 : 0.8	>140	–
	1 : 0.3 : 1.2	140	Soluble
	1 : 0.3 : 1.6	90–100	<5%
	1 : 0.3 : 2.4	80	<3%
DMAA	1 : 0.45 : 0.25	>140	–
	1 : 0.45 : 0.5	140	Soluble
	1 : 0.35 : 0.7	130	″
	1 : 0.35 : 1.4	105–115	<1%
	1 : 0.3 : 1	130	Soluble
	1 : 0.3 : 1.5	125	″

pattern of fibroin precipitated from the solutions (Fig. 2, curve *3*) differs from those of the initial (curve *1*) and swollen and dried polymer (curve *2*). As compared to the initial sample, the reflections in the range 8°–10° and 25°–27° of the X-ray pattern of precipitated fibroin are absent.

To decrease the melting point of the solvent and hence the dissolution temperature, we introduced low-molecular-weight organic diluents. It is important that the diluent should not decrease the solubility. Our previous comparative studies of aprotic and protic diluents show [12] that aprotic compounds effectively breakdown the NMMO structure, thus accelerating the dissolution and decreasing the viscosity and T_m of the solvent. On the contrary, protic diluents are structure-making additives which compete with hydroxy groups of cellulose for formation of hydrogen bonds with the N–O group of the amine oxide. In [13] we studied the influence of aprotic diluents on the enthalpy of interaction of binary solvent with cellulose. It was found that the heat effect of the interaction of cellulose with the DMSO complex of NMMO monohydrate is higher than that of pure NMMO monohydrate. We suggest that DMSO additionally polarizes the N–O groups. Here we tested as diluents aprotic [DMSO, dimethylformamide (DMF), dimethylacetamide (DMAA)] and protic solvents (lower alcohols $C_nH_{2n+1}OH$, where n = 1–5, 2-pyrrolidone, [14] ε-caprolactam, and δ-valerolactam).

As seen from Tables 2–4, only limited amounts of protic solvents can be added to NMMO. The fibroin is soluble in a $NMMO \cdot nH_2O \cdot m$ diluent mixture when $(n + m)$ is no higher than 0.8. At higher $(n + m)$ values the solubility sharply decreases. In the case of aprotic solvents, especially DMSO, the fibroin solubility is retained in a wider concentration range (Table 3), which allows control of the melting point of the solvent and hence of the dissolution temperature. The most efficient additive is DMSO. Introduction of up to 2–3 mol of DMSO per mole of NMMO

Table 4. Fibroin solubility in NMMO–water–lactam systems

Lactam	NMMO : water : lactam molar ratio	T_m, °C	Fibroin solubility
2-Pyrrolidone	1 : 0.3 : 0.4	80–90	Soluble
	1 : 0.3 : 0.5	80–90	"
	1 : 0.3 : 0.7	50–60	–
	1 : 0.3 : 1	Liquid	–
ε-Caprolactam	1 : 0.3 : 0.4	80–90	Soluble
	1 : 0.3 : 0.5	80–85	"
	1 : 0.3 : 0.7	60	–
	1 : 0.3 : 1	Liquid	–
δ-Valerolactam	1 : 0.3 : 0.4	80–100	Soluble
	1 : 0.3 : 0.5	80–95	"
	1 : 0.3 : 0.7	50–60	–
	1 : 0.3 : 1	Liquid	–

Table 5. Thermolysis temperature T_{therm} of fibroin solutions

Molar composition of the solvent	Fibroin concentration in the solution, wt %	T_{therm}, °C
NMMO · $0.3H_2O$	–	174
NMMO · $0.3H_2O$	5	160
NMMO · $0.3H_2O$ · 0.9DMSO	5	152
NMMO · $0.3H_2O$ · 1.8DMSO	5	162
NMMO · $0.3H_2O$ · 0.4pyrrolidone	5	174
NMMO · $0.3H_2O$ · 0.4valerolactam	5	158

does not decrease the fibroin solubility and effectively lowers the melting point and viscosity of the solution.

The onset temperature of thermolysis of amine oxide in 5% fibroin solutions ranges from 150 to 170°C depending on the solvent composition (Table 5).

CONCLUSIONS

(1) Dissolution of silk fibroin in *N*-methylmorpholine-*N*-oxide was studied. The threshold energy of interaction between the solvent and the polymer, required for polymer dissolution, is reached at a 10 wt % water content in *N*-methylmorpholine-*N*-oxide, which corresponds to the composition *N*-methylmorpholine-*N*-oxide · $0.8H_2O$.

(2) The melting point of the solvent decreases when water is partially replaced by an equimolar amount of alcohol. Branched alcohols are more efficient for this purpose.

(3) Partial replacement of water in the solvent by 2-pyrrolidone, ε-caprolactam, and δ-valerolactam decreases the melting point of the solvent with no loss of its solvency.

(4) Additives of aprotic compounds, especially DMSO, effectively decrease the melting point and viscosity of fibroin solutions in *N*-methylmorpholine-*N*-oxide, with the solvency of *N*-methylmorpholine-*N*-oxide being preserved in a wide range of components ratios in the solvent.

REFERENCES

1. *Werkstoffe aus nachwachsenden Rohstoffen: 3 Int. Symp.*, Erfurt, September 5–6, 2001.
2. US Patent 3 447 939.
3. Yunusov, L., *Fiziko-khimicheskie sviostva natural'nogo shelka v protsesse pererabotki kokonov* (Physicochemical Properties on Natural Silk in the Course of Cocoon Processing), Tashkent: Fan, 1978.
4. Rubinov, E.B., Mukhamedov, M.M., Osipova, L.Kh., and Burnakshev, I.Z., *Shelkosyr'e i kokonomotanie* (Raw Silk and Silk Reeling), Moscow: Legpromizdat, 1986.
5. McCormick, C.L., Callais, P.A., and Hutchinson, H., *Macromolecules*, 1985, vol. 18, pp. 2394–2401.
6. Petrus, L., Gray, D. G., and BeMiller, J.N., *Carbohydr. Res.*, 1995, vol. 268, pp. 319–323.
7. Kettenbach, G., Klufers, P., and Mayer, P., *Macromol. Symp.*, 1997, vol. 120, pp. 291–301.
8. Yakubova, N.Ya., Zakirov, I.Z., and Geller, B.E., *Khim. Volokna*, 1972, no. 3, pp. 17–18.
9. Worley, J.D. and Klots, I., *J. Chem. Phys.*, 1966, vol. 45, pp. 2868–2871.
10. Novoselov, N.P., Sashina, E.S., and Tret'yak, V.M., *Zh. Fiz. Khim.*, 1999, vol. 73, no. 1, pp. 78–82.
11. Novosjolow, N.P. and Sachina, Y.S., *Cellulose Chem. Technol.*, 1999, vol. 33, nos. 5–6, pp. 361–380.
12. Novoselov, N.P. and Sashina, E.S., *Izv. Vyssh. Uchebn. Zaved., Khim. Khim. Tekhnol.*, 1999, vol. 42, no. 4, pp. 91–97.
13. Novoselov, N.P., Sashina, E.S., and Kozlov, I.L., *Zh. Fiz. Khim.*, 2001, vol. 75, pp. 1254–1257.
14. FRG Patent 10 005 163.

Russian Journal of Applied Chemistry, Vol. 76, No. 1, 2003, pp. 132–136. Translated from Zhurnal Prikladnoi Khimii, Vol. 76, No. 1, 2003, pp. 138–142.

CHEMISTRY OF FOSSIL FUEL

Fuel Oil Pyrolysis Initiated by Propane–Butane–Oxygen Flame

V. V. Makarov, G. I. Ksandopulo, and V. M. Potekhin

St. Petersburg State Technological Institute, St. Petersburg, Russia

Received July 16, 2002

Abstract—The parameters of fuel oil pyrolysis initiated by propane–butane–oxygen flame were studied as influenced by the temperature in the pyrolysis zone, time of the fuel oil contact with the initiating flame, and fuel oil feed rate. The experimental data on thermal and flame-initiated fuel oil pyrolysis were compared.

One of the major lines in development of petrochemical industry is increase in the production of lower olefins, e.g., ethylene and propylene. Ethylene is produced in industry by pyrolysis of hydrocarbons with steam in tubular furnaces; the best raw material for ethylene production is ethane, and its treatment under fairly severe conditions yields up to 76–78 wt % of ethylene [1].

Naphtha fractions with various boiling ranges are widely used as raw materials for pyrolysis. In contrast to the pyrolysis of gaseous hydrocarbons, pyrolysis of naphtha fractions yields, along with pyrolysis gas rich in C_2–C_4 unsaturated hydrocarbons, also significant amount of liquid products containing aliphatic and cyclic C_5 and higher olefins, C_6–C_8 aromatic hydrocarbons, and other valuable materials [2].

However, the composition of materials for pyrolysis gradually changes. At present, heavy oil distillates are widely used for pyrolysis along with gaseous materials and light oil fractions. Further improvement of common pyrolysis furnaces is performed and new alternative pyrolysis processes are developed [1]. Such alternative processes involve pyrolysis in the presence of heterogeneous catalysts, high-temperature pyrolysis using gaseous heat carriers, pyrolysis in the presence of initiating additives, hydropyrolysis, pyrolysis in molten metals and metal salts, thermal contact processes, and pyrolysis in the initiating flame [3–7]. An example of the latter process is the flame-initiated pyrolysis (FIP) of fuel oil.

EXPERIMENTAL

In the experiments we used M-40 fuel oil with the following main parameters: density (at 293 K) 1 kg m^{-3}, ash residue 0.15 wt %; content (wt %): solid impurities 1, water 2, and sulfur 0.5–3.5; the heat of combustion recalculated on the dry fuel oil 39770 J g^{-1}.

The scheme of a flow-type unit for FIP of the fuel oil, operating under atmospheric pressure, is shown in the figure. The reactor is made of Cr1849TiCu stainless steel and consists of three zones, mm: zone of preheating (573 K) 160 mm long, pyrolysis zone (773–923 K) 140 mm, and initiation zone (combus-

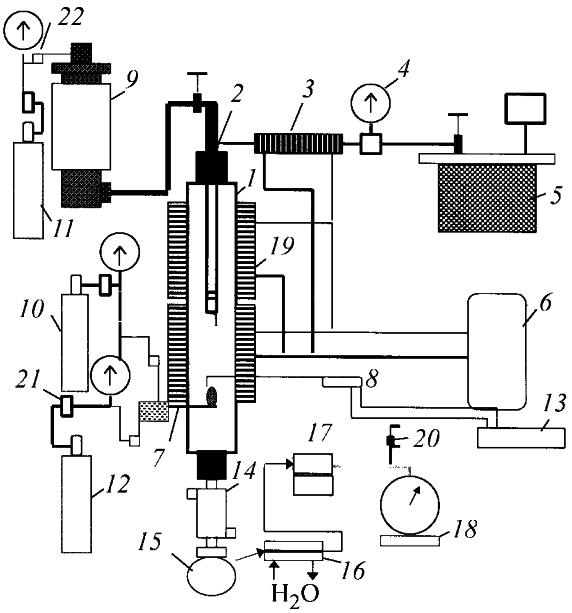

Scheme of experimental unit for flame-initiated pyrolysis of fuel oil: (*1*) metallic pyrolysis reactor, (*2*) pulverizer, (*3*) electrical heater, (*4*) gage, (*5*) steam generator, (*6*) automated system for heating and maintaining the required temperature, (*7*) diffusion burner, (*8*) thermocouple, (*9*) reservoir for feeding the starting hydrocarbons, (*10–12*) gas cylinders, (*13*) potentiometer, (*14*) cooling system, (*15*) sediment collector, (*16*) reflux condenser, (*17*) system for liquid separation, (*18*) wet-gas meter, (*19*) electrical heaters, (*20*) sampler, (*21*) throttles, and (*22*) needle valves.

1070-4272/03/7601-0132$25.00

Table 1. Initiated and noninitiated fuel oil pyrolysis. Feeding rates of water in the steam generator and of fuel oil 6 and 3.45 $cm^3\ min^{-1}$, respectively; residence time of fuel oil in the flame and pyrolysis zones 0.1 and 0.5 s, respectively

Composition	Pyrolysis at indicated temperature,* K						
	I, 773	I, 803	I, 823	T, 873	I, 873	T, 923	I, 923
Pyrolysis gas, vol %:							
Σ_{hyd}	29.3	28.3	27.9	90.8	27.1	90.1	24.7
CO	33.4	33.8	33.8	–	33.2	–	34.1
CO_2	4.2	4.2	4.2	–	4.3	–	4.2
H_2	33.1	330.7	34.7	9.2	35.4	9.9	37.0
Hydrocarbon fraction of pyrolysis gas, vol %							
CH_4	39.1	39.3	40.2	22.1	40.2	22.1	41.8
C_2H_6	3.1	3.2	3.1	5.2	2.3	5.3	3.0
C_2H_4	39.7	40.1	40.8	28.8	41.3	28.9	42.8
C_3H_8	3.2	3.2	2.0	14.0	0.8	13.8	0.8
C_3H_6	7.5	7.6	7.6	14.3	9.0	14.4	6.5
C_2H_2	0.2	0.2	0.2	–	0.3	–	0.3
ΣC_4H_8	3.7	3.1	3.5	8.3	3.7	8.2	3.9
ΣC_4**	3.5	3.3	2.6	4.3	2.4	4.2	1.4
ΣC_5	Traces	Traces	Traces	1.1	Traces	1.1	Traces
ΣC_6	″	″	″	1.9	″	2.0	″
Gasification, %	11.5	12.1	12.3	3.6	12.9	5.9	13.2

* Pyrolysis: (I) initiated and (T) thermal; the same for Table 3.
** ΣC_4, except ΣC_4H_8

tion and pyrolysis) 30 mm. The initiating burner was placed in the reactor at the boundary of the pyrolysis and initiation zones. The composition of the propane–butane gas mixture was as follows, vol %: propane 76.2, butane 17.6, isobutane 5.9, and ethane 0.3; oxygen was supplied to the burner in stoichiometric amounts.

The type of the initiating flame is selected is accordance with its physicochemical parameters such as the temperature of the stoichiometric flame (1900°C), shape and size of the flame (elongated flare, 30–40 mm height), length of the area in which the H atoms are detected (30–45 mm along the axis of the flow of reaction products), and maximal concentration of H atoms in the flame (4×10^{15} cm^{-3}) [3].

In the course of pyrolysis initiation with propane–butane–oxygen flame at 1800–1900°C flame temperature, significant amounts of hydrogen atoms (up to 4×10^{15} cm^{-3}) and other reactive radicals (HO_2, $OH^{\bullet}$, $CH_3^{\bullet}$, $C_2H_5^{\bullet}$, $CHO^{\bullet}$, $O^{\bullet\bullet}$, etc. [3]) diffuse into the fuel oil, which strongly accelerates pyrolysis of the feed. The flame capacity in the experiments was characterized by the content of oxygen relative to the feed (wt %). In all the cases the (propane–butane) : oxidant ratio was 1 : 5; the flow rates of the oxidant and propane–butane mixture at the burner inlet were 710 and 140 $cm^3\ min^{-1}$, respectively.

The gaseous products (vol %) of the fuel oil pyrolysis were analyzed by gas chromatography; for quantitative analysis of the chromatographic patterns, we used the method of internal normalization taking into account the sensitivity coefficients and also the absolute calibration procedure.

The aim of this work was to increase the yield of lower olefins (ethylene, propylene, and butenes). In our experiments we varied the pyrolysis temperature, contact time, and the fuel oil feed rate. The contact time was changed by varying the steam flow rate at the pulverizer inlet or the fuel oil feed rate at a constant steam flow rate. The temperature of the steam and fuel oil in the experiments was 423 and 383 K, respectively. The results of fuel oil pyrolysis are listed in Tables 1–3.

As seen from published data [1], pyrolysis of fuel oil is characterized by extensive coking. Taking into account this fact, we varied the temperature in the pyrolysis zone within 773–923 K, whereas the temperature in the preheating zone was constant (573 K).

Along with studying the effect of temperature on the fuel oil pyrolysis initiated by propane–butane

Table 2. Initiated fuel oil pyrolysis. Temperature in the pyrolysis zone 773 K, fuel oil feed rate 3.45 $cm^3\ min^{-1}$, and flame capacity 29 wt %

Composition	Residence time of fuel oil in the flame zone, s				
	0.1	0.07	0.05	0.04	0.03
Pyrolysis gas, vol %:					
Σ_{hyd}	29.3	30.3	31.0	32.9	34.7
CO	33.4	33.1	32.7	32.8	32.1
CO_2	4.2	4.3	4.4	4.3	4.5
H_2	33.1	32.3	31.9	30.0	28.7
Hydrocarbon fraction of pyrolysis gas, vol %					
CH_4	39.1	37.8	34.0	33.9	33.1
C_2H_6	3.1	3.3	3.4	3.4	3.4
C_2H_4	39.7	38.6	37.1	36.8	37.0
C_3H_8	3.2	3.5	3.7	3.9	4.4
C_3H_6	7.5	7.6	8.8	9.3	10.2
C_2H_2	0.2	0.2	Traces	Traces	Traces
ΣC_4H_8	3.5	6.1	8.2	8.4	8.4
ΣC_4*	1.7	2.9	3.1	3.3	3.5
ΣC_5	Traces	Traces	0.7	Traces	Traces
ΣC_6	″	″	1	1	″
Gasification, %	11.5	11.3	11.0	8.9	6.2

* ΣC_4, except ΣC_4H_8.

Table 3. Initiated and noninitiated fuel oil pyrolysis. Temperature in the pyrolysis zone 798 K, rate of water feeding in the steam generator 8 $cm^3\ min^{-1}$, residence time of fuel oil in the flame and pyrolysis zones 0.08 and 0.4 s, respectively, and flame capacity 29 wt %

Composition	Pyrolysis at indicated fuel oil feed rate, $cm^3\ min^{-1}$					
	I, 0.65	I, 1.25	T, 5.4	I, 5.4	T, 12.0	I, 12.0
Pyrolysis gas, vol %:						
Σ_{hyd}	27.9	26.9	92.8	29.8	92.1	35.2
CO	33.7	34.6	–	30.9	–	28.1
CO_2	4.4	4.4	–	5.9	–	6.6
H_2	34.0	34.1	8.6	33.4	7.9	30.1
Hydrocarbon fraction of pyrolysis gas, vol %						
CH_4	43.9	31.6	21.3	32.0	20.1	28.1
C_2H_6	Traces	Traces	5.2	2.4	5.3	4.5
C_2H_4	42.1	46.3	28.6	41.8	27.7	35.8
C_3H_8	2.1	6.6	21.8	7.5	21.4	9.1
C_3H_6	6.5	7.8	10.0	8.0	11.0	9.6
C_2H_2	0.2	0.1	–	0.1	–	0.1
ΣC_4H_8	3.5	4.7	6.7	4.8	6.7	4.5
ΣC_4*	1.7	2.9	3.5	3.4	3.7	3.5
ΣC_5	Traces	Traces	1.0	Traces	2.0	2.0
ΣC_6	″	″	1.0	″	2.1	2.8
Gasification, %	11.3	11.4	3.2	12.4	3.4	14.1

* ΣC_4, except ΣC_4H_8.

flame, we performed the experiments on the pyrolysis without initiator. The operation parameters and experimental conditions were determined in the course of thermal pyrolysis, and then the initiating flame was added.

As seen from Table 1, as the temperature is increased from 773 to 923 K, the content of ethylene in the hydrocarbon fraction of the pyrolysis gas gradually increases, and at 923 K it comprises 42.8 vol %; the content of propylene and butenes in the pyrolysis gas varies within 6.5–9.0 and 3.1–8.4 vol %, respectively. As compared to thermal pyrolysis at the residence time in the flame of 0.5 s and 923 K, initiation with propane–butane flame increases the content of ethylene in the hydrocarbon fraction of pyrolysis gas by 13.3 vol %, whereas the content of propylene and butenes decreases by 7.9 and 4.3 vol %, respectively. It should be noted that the variation of the pyrolysis temperature by 150°C only slightly affects the volume content of the target products. However, in the entire temperature range studied the content of ethylene in the pyrolysis gas at initiated pyrolysis is higher than that in the noninitiated process.

The gasification degree varies within 11.5–13.2 and 3.6–5.9% for initiated and thermal processes, respectively. The gasification degree is defined as the amount of fuel oil (wt %) that passed into the gas phase.

The effect of the residence time of fuel oil in the initiating flare zone is illustrated in Table 2. The residence time was varied by changing the flow rate of the supplied steam. As seen, as the residence time of fuel oil in the initiating flare zone is decreased from 0.1 to 0.03 s, the volume content of ethylene and methane in the pyrolysis gas decreases, whereas the volume content of ΣC_4H_8, C_3H_6, and C_3H_8 increases; the ethane concentration remains almost constant.

When the contact time in the pyrolysis zone was decreased to 0.2 s and the residence time in the initiating flare zone, to 0.03 s, the gasification degree in flame-initiated fuel oil pyrolysis became close to that in thermal pyrolysis. As seen from the comparison of experimental results obtained in initiated (Table 2) and noninitiated (Table 1) pyrolysis at similar gasification degrees, the volume content of unsaturated hydrocarbons in the pyrolysis gas increases relative to saturated hydrocarbons. Initiation of the fuel oil pyrolysis at gasification degree of 6.2 wt % as compared to thermal pyrolysis (gasification degree 5.9 wt %) increases the content of ethylene and butenes in the hydrocarbon fraction of the pyrolysis gas by 8.1 and 0.2%, respectively, whereas the content of propylene decreases by 4.2%. In this case, the temperature difference in the thermolysis zone was 150 K.

The residence time in the reaction zone is predominantly determined by the rate of steam supply to the fuel oil pulverizer, whereas the increase in the feed rate of the fuel oil, which falls into the reactor as fine drops (with size less than 100 μm), does not noticeably affect the residence time of the fuel oil in the reaction zone. At the same time, the composition of the pyrolysis gas changes with changing the fuel oil feed rate (Table 3). With increasing fuel oil feed rate, the content of hydrocarbons in the pyrolysis gas increases from 27.9 to 35.2 vol %. Simultaneously, despite the increase in the gasification degree, the content of ethylene in the pyrolysis gas decreases from 42.1 to 35.8 vol %.

As seen from the comparison of experimental data obtained in the course of thermal and flame-initiated pyrolysis (Table 3) at similar feed rates of the fuel oil, the yield of unsaturated hydrocarbons in the course of pyrolysis strongly increases with respect to saturated hydrocarbons. At low feed flow (1 : 1.4 fuel oil : steam ratio), the content of lower olefins in the pyrolysis gas strongly increases , whereas the content of saturated C_3–C_4 hydrocarbons decreases. Thus, in initiation of pyrolysis with propane–butane flame, with increasing fuel oil feed rate the volume content of ethylene and methane in the pyrolysis gas decreases and the content of heavier hydrocarbons C_3–C_4 increases.

Our experimental data showed that, despite variation of the process conditions in a fairly wide range, the flame-initiated fuel oil pyrolysis mainly follows the "olefin" pathway. We identified only C_1–C_4 components in the gaseous mixture. The absence of heavier hydrocarbons in the pyrolysis products suggests that the process involves profound breakdown of the fuel oil molecules with formation of lower unsaturated and saturated C_1–C_4 hydrocarbons, which determine the final composition of the hydrocarbon fraction of the pyrolysis gas.

Among the pyrolysis products we also detected carbon oxides and hydrogen, probably arising from combustion of the initiating propane–butane mixture and fuel oil pyrolysis.

CONCLUSIONS

(1) In the course of pyrolysis of fuel oil initiated by propane–butane–oxygen flame (29 wt % capacity) and performed at 773–923 K and gasification degree of about 6 wt %, the content of ethylene and butenes

in the hydrocarbon fraction of the pyrolysis gas increases by 7.9–8.1 and 0.2 vol %, respectively, whereas the content of propylene decreases by 4.0–4.2 vol %.

(2) At pyrolysis temperature from 773 to 923 K, residence time of the fuel oil in the initiating flame zone of 0.1 s, flame capacity of 29 wt %, and fuel oil : steam ratio of 1 : 1.7, the gasification degree is 13–14%, and the content of ethylene in the hydrocarbon fraction of the pyrolysis gas reaches 40–42 vol %.

REFERENCES

1. Mukhina, T.N., Barabanov, M.L., Babash, S.E., *et al.*, *Piroliz uglevodorodnogo syr'ya* (Pyrolysis of Hydrocarbon Materials), Moscow: Khimiya, 1987.
2. Yampol'skii, Yu.P., *Elementarnye reaktsii i mekhanizm piroliza uglevodorodov* (Elementary Reactions and Mechanism of Hydrocarbon Pyrolysis), Moscow: Khimiya, 1990.
3. Ksandopulo, G.I. and Dubinin, V.V., *Khimiya gazofaznogo goreniya* (Chemistry of the Gas-Phase Combustion), Moscow: Khimiya, 1987.
4. Antipov, Yu.V. and Korul'kin, M.Yu., *Neftepererab. Neftekhim.*, 1994, no. 8, pp. 22–24.
5. Ksandopulo, G.I., Kolesnikov, B.Ya., and Odnorog, D.S., *Fiz. Goren. Vzryva*, 1975, vol. 11, no. 1, pp. 131–134.
6. USSR Inventor's Certificate no. 1 268 558.
7. Ksandopulo, G.I., Kolesnikov, B.Ya., and Odnorog, D.S., *Fiz. Goren. Vzryva*, 1975, vol. 11, pp. 412–418.

Russian Journal of Applied Chemistry, Vol. 76, No. 1, 2003, pp. 137–139. Translated from Zhurnal Prikladnoi Khimii, Vol. 76, No. 1, 2003, pp. 143–145.

CHEMISTRY OF FOSSIL FUEL

Oxidation of Diesel Oil in the Presence of Metallic Copper

E. M. Kuramshin, O. B. Zvorygina, V. K. Gumerova, R. F. Khalimov, and U. B. Imashev

Ufa State Petroleum Technical University, Ufa, Bashkortostan, Russia

Received May 27, 2002

Abstract—The kinetic parameters of autooxidation of DL-0.2 diesel oil in the presence of copper were determined in the range 120–140°C. The possibility of using Ionol for stabilization of diesel oil under these conditions was studied.

High efficiency of diesel engines in comparison with carburetor engines causes great interest in stabilization of diesel oils (DOs) [1–3]. At a temperature of 100–140°C, providing proper operation of fuel system units of diesel engines, DO contacting structural materials is rather actively oxidized with dissolved oxygen, whose content reaches 4–5 vol % [4]. Oxidation of DO is accompanied by formation of tarry compounds which are deposited on filters and units of fuel-controlling and fuel-supplying apparatus and fuel injectors. This disturbs the normal operation of engines and, as a result, increases the toxicity and smoke content of exhaust gases. It is known that copper is a highly active catalyst of oxidation of hydrocarbon fuels [5]. In this work we examined the effect of copper on the kinetics of DO oxidation and the possibility of DO stabilization with classic oxidation inhibitor, Ionol.

EXPERIMENTAL

Uptake of O_2 in oxidation of DL-0.2 commercial diesel oil was studied on a gasometric installation of the static type [6]. Into a 15-ml temperature-controlled conical glass reactor equipped with a stirrer, 5 ml of the fuel was placed, and oxygen was bubbled for 10 min. The amount of oxygen taken up, $\Delta[O_2]$ (mol l^{-1}), was evaluated by the formula

$$\Delta[O_2] = V_{O_2}/V_f \times 22.4,$$

where V_{O_2} is the oxygen uptake (ml) and V_f is the fuel volume (ml).

Autooxidation of DO proceeds with acceleration, and the kinetics of O_2 uptake is described by the relationship $\Delta[O_2]^{1/2} = bt$ characteristic of hydrocarbon fuels [6]. In the coordinates $\Delta[O_2]^{1/2}$–t, the experimental points fall on a straight line. The parameter b characterizing the susceptibility of DO to autooxidation is determined as the slope of the experimental straight line.

Metallic copper was used as a powder, plate, or ring. The particle size of the powder was determined with a BIOLAM microscope and a micrometric network of the OS type with the scale factor of 1×10^{-2} mm. Based on numerous measurements, the average radius of copper particles was taken equal to 2×10^{-2} mm.

These results allowed estimation of the copper particle volume, assuming that particles are spherical ($V = 4/3\pi r^3 = 3.2 \times 10^{-5}$ mm^3), the average weight of one particle ($m = \rho V = 2.7 \times 10^{-7}$ g at $\rho_{Cu} = 8.4 \times 10^{-3}$ g mm^{-3}), the total number of particles in the weighed portion of 5.4×10^{-3} g Cu per 5 ml of fuel (2×10^4 particles), and also the surface area of one particle ($S = 4\pi r^2 = 50 \times 10^{-4}$ mm^2) in the weighed portion of copper powder (1 cm^2 per 5 ml of fuel or 200 cm^2 per 1 l of fuel).

The size of the copper plate was $10 \times 15 \times 0.2$ mm. The copper ring was made from a copper tube 10 mm in diameter (the element of the fuel system of a diesel engine), the wall thickness of the ring was 1 mm, and the ring width was 2 mm.

Experiments on autooxidation of crude DO with oxygen in the presence of metallic copper at 120°C for 7 h with parallel measurement of the oxygen uptake, $\Delta[O_2]$, and the optical density of fuel, A, characterizing tarring in the system, showed that these parameters reach the limiting values by the end of the run and are 0.22 and 1.6 mol l^{-1}, respectively (Fig. 1). Cessation of DO autooxidation is apparently due to

1070-4272/03/7601-0137$25.00

Table 1. Influence of the surface area of metallic copper S_{Cu} and temperature on the kinetic parameter of DO autooxidation b

Copper	S_{Cu}, $cm^2\ l^{-1}$	T, °C	$b \times 10^5$, $mol^{1/2}\ l^{-1/2}\ s^{-1}$	b/b_0	$[(b - b_0)/(b_0S)] \times 10^3$, $l\ cm^{-2}$
Absent	–	120	1.1	–	–
Powder	50	120	2.1	1.9	18.2
	120	120	2.3	2.1	9.1
	210	120	3.2	2.9	9.0
	126	120	3.0	2.7	13.7
	126	130	5.3	4.8	30.8
	126	140	7.5	6.8	46.2
Plate	60	120	3.2	2.9	11.5
Ring	166	120	3.2	2.9	11.5

deactivation of the catalytically active metal surface.

Adsorption purification of DO on silica gel significantly enhances the thermal oxidation resistance of fuel: the limiting values of $\Delta[O_2]$ and A decrease by factors of 5 and 2, respectively. The kinetic curves of O_2 uptake in the initial stage of DO oxidation ($\Delta[O_2] \le 1 \times 10^{-2}$ mol l^{-1}) in the presence of copper powder are typical of autoaccelerating processes (Fig. 1); the curves are made linear in the coordinates $\Delta[O_2]^{1/2}$–time, which allows characterization of the process using the parameter b ($\Delta[O_2]^{1/2} = bt$). The temperature dependence of b in the range 120–140°C is reasonably adequately described by the Arrhenius equation

$$\ln b = 9.32 - 64 \times 10^3/(RT),$$

where $R = 8.31$ J $mol^{-1}\ K^{-1}$.

As known, in heterogeneous catalytic oxidation, the specific activity of a material having a catalytic effect is characterized by the b/b_0 value and by the ratio $(b - b_0)/(b_0S)$, where b_0 and b are the quantitative measures of the susceptibility of the fuel to autooxidation in the absence and in the presence of this material, respectively; S is the metal surface area, cm^2 per liter of fuel [4]. The results of the study (Table 1) showed that the specific activity of copper powder with respect to DO at 120°C is $(13.6 \pm 4.6) \times 10^{-3}$ $l\ cm^{-2}$ and the ratio $b/b_0 = 2.4 \pm 0.5$. It should be noted that similar values are characteristic of copper in T-6 jet engine fuel: $(b - b_0)/(b_0S) = 5 \times 10^{-3}$ $l\ cm^{-2}$ and $b/b_0 = 2.51$ [4].

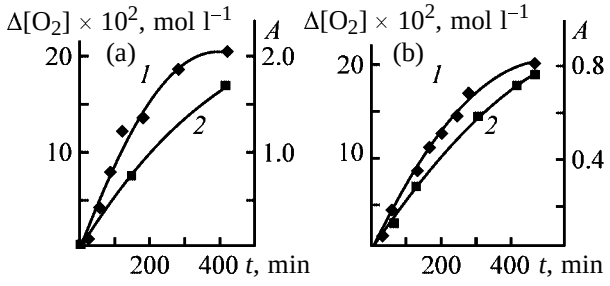

Fig. 1. (*1*) Kinetics of oxidation of diesel oil $\Delta[O_2]$ and (*2*) variation of optical density A in the presence of copper at 120°C. (*t*) Time. Diesel oil: (a) crude and (b) purified on silica gel.

It is evident that the increased oxidizability of DO is caused by accelerated decay of hydroperoxides ROOH to radicals under the action of metallic copper. This is suggested by the parabolic dependence of O_2 uptake on time (Fig. 1) and the fact that the dependence of the autooxidation parameter b on S_{Cu} tends to a certain limit (Table 1). According to the data obtained, with increasing surface area of copper from 0 to 50 cm^2 per liter of fuel, b is doubled, whereas further increase in S_{Cu} does not result in significant growth of the autooxidation rate. It is apparent that, at $S_{Cu} \ge 126$ $cm^2\ l^{-1}$, hydroperoxide molecules formed in the bulk are adsorbed at the copper surface and a constant initiation rate ($b = 0.5ak_i^{12}$) is maintained in the system owing to heterogeneous decay of ROOH. Replacement of the copper powder by copper plate or copper ring (fragment of copper tube, the element of fuel apparatus of diesel engine) does not disturb the shape of the dependence of b on S_{Cu} (Table 1).

A conventional inhibitor of radical-chain oxidation, Ionol PhOH, added to the fuel containing copper powder ($S_{Cu} = 126$ $cm^2\ l^{-1}$), efficiently inhibits oxidation, causing appearance of induction periods (t_i = 37–90 min at 120°C); their duration is in direct proportion to PhOH concentrations in the range $(1.3–2.7) \times 10^{-4}$ M. These results allow estimation of the initiation rate W_i:

$$W_i = 2[PhOH]/t_i = (1.1 \pm 0.1) \times 10^{-7}\ mol\ l^{-1}\ s^{-1}.$$

Table 2. Influence of inhibitor concentration [PhOH] and temperature on the parameter of DO autooxidation b and inhibition coefficient n in the presence of copper powder, S_{Cu} = 126 $cm^2\ g\ l^{-1}$

T, °C	[PhOH] × 10^2, wt %	[PhOH] × 10^3, M	$b \times 10^5$, $mol^{1/2}\ l^{-1/2}\ s^{-1}$	$n = b_0/b$
120	0	0	3.0	–
	0.3	0.12	2.50	1.2
	0.6	0.23	1.25	2.4
	1.0	0.38	1.45	2.1
	1.6	0.60	0.70	4.3
	4.0	1.50	0.78	3.8
	6.0	2.25	0.43	7.0
	12.0	4.50	0.44	6.8
130	0	0	5.5	–
	1.0	0.38	3.7	1.5
	2.0	0.76	1.9	2.6
	2.5	0.95	0.9	6.1
	3.0	1.14	0.6	9.2
140	0	0	7.8	–
	1.0	0.38	7.7	1.0
	2.0	0.76	6.2	1.3
	3.3	1.26	3.7	2.1

The study of the dependence of the autooxidation parameter b and inhibition coefficient n ($n = b_0/b_{PhOH}$) on the Ionol concentration showed that, at 120°C and [PhOH] > 0.06 wt %, b decreases by a factor of 7 and then does not vary noticeably (Table 2). However, with increasing temperature, the inhibition activity of Ionol noticeably decreases: the inhibition coefficient n is 4.3, 2.6, and 1.3 at 120, 130, and 140°C, respectively. At 140°C and concentration of 0.02 wt % ([PhOH] = 7.6×10^{-4} M), virtually no inhibition of autooxidation is observed; therefore, other inhibitors are required for stabilization of DO at elevated temperatures.

CONCLUSIONS

(1) Diesel oil contacting metallic copper at 120–140°C is subject to active oxidation and tarring in the initial stage of the process. The factor of the copper catalytic effect at 120°C is 2.4 ± 0.5.

(2) Adsorption purification of diesel oil on silica gel appreciably suppresses its susceptibility to autooxidation. Ionol added to the fuel decreases its oxidizability at 120°C by a factor of 7 but is ineffective at higher temperatures.

REFERENCES

1. Danilov, A.M., *Neftekhimiya*, 1992, vol. 32, no. 4, pp. 374–382.
2. Popova, T.V., Vishnyakov, T.P., Yurechno, V.V., and Frolov, V.N., *Khim. Tekhnol. Topl. Masel*, 1995, no. 3, pp. 18–20.
3. Koshelev, V.N., Golubeva, N.A., Klinaev, E.V., and Kelarev, V.N., *Khim. Tekhnol. Topl. Masel*, 1996, no. 4, pp. 29–31.
4. Kuramshin, E.M. and Imashev, U.B., *Okislenie i stabilizatsiya dizel'nykh topliv* (Oxidation and Stabilization of Diesel Oils), Moscow: TsNIITEneftekhim, 1995.
5. Denisov, E.T. and Kovalev, G.I., *Okislenie i stabilizatsiya reaktivnykh topliv* (Oxidation and Stabilization of Jet Engine Fuels), Moscow: Khimiya, 1983.
6. Kuramshin, E.M., Gumerova, V.K., Zlotskii, S.S., *et al.*, *Zh. Prikl. Khim.*, 2001, vol. 74, no. 4, pp. 608–612.

Russian Journal of Applied Chemistry, Vol. 76, No. 1, 2003, pp. 140–143. Translated from Zhurnal Prikladnoi Khimii, Vol. 76, No. 1, 2003, pp. 146–149.

CHEMISTRY OF FOSSIL FUEL

Preparation of Transformer Oil Body by Extraction Refining of 300–500°C Fraction of Low-Paraffinicity Oil

A. A. Gaile, N. M. Dyurik, L. V. Semenov, A. N. Chagovets, A. V. Ustalov, L. L. Koldobskaya, and G. F. Stepanova

St. Petersburg State Technological Institute, St. Petersburg, Russia
Slavneft Oil and Gas Company, Joint-Stock Company, Moscow, Russia
Slavneft–Mendeleev Yaroslavl Oil Refining Plant, Open Joint-Stock Company, Yaroslavl, Russia

Received May 30, 2002

Abstract—A raffinate meeting the requirements for the transformer oil body was obtained from the 300–350°C fraction of low-paraffinicity oil by five-step countercurrent extraction of aromatic hydrocarbons and organoelement compounds with aqueous methyl Cellosolve in the presence of pentane.

Hydraulic oils and transformer oil body are produced from the 200–300 and 300–350 or 300–400°C fractions of low-paraffinicity oil, respectively. Low-paraffinicity oils, among them Troitsk-Anastasievsk oil, contain virtually no *n*-alkanes, which allows production of low-freezing oils without dewaxing as the most expensive stage. However, the aromatic hydrocarbon content in the fraction 200–430°C of the Troitsk-Anastasievsk oil amounts to 40% (hereinafter, wt %, unless otherwise stated) [1]. According to the existing technical specifications, the optimal content of arenes in it should be within 18–22%, the major part of arenes being represented by monocycloarenes [2, 3].

Transformer oils can be produced from the 300–400°C fraction by solvent extraction followed by hydrogenation. For example, this combined method is used in production of T-1500U transformer oil [TU (Technical Specification) 38.401-58-107]. The advantage of solvent-extracted oils is in high gas resistance coefficient, which is caused by the optimal content of aromatic hydrocarbons (18–22%). As their drawbacks, we can indicate high dielectric loss tangent tan α, which is due to excessive resin content, resulting in deteriorated insulating characteristics and oxidation resistance of the oil. The resin content can be reduced from 3.2 to 1.2–1.3% by additional adsorption refining of a solvent-extracted oil. In this case, tan α decreases from 2.2 to 0.24–0.29%, meeting the requirements of the technical specifications to T-750 transformer oil [3].

Solvent extraction of oil fractions is performed with phenol, furfural, or *N*-methylpyrrolidone [4, 5]. However, all these solvents are relatively high-boiling, which complicates their regeneration. *N*-Methylpyrrolidone, the most selective and high-boiling of them, forms azeotropic mixtures with a series of saturated hydrocarbons of the 200–400°C fraction, which causes oiling of the solvent and complicates its regeneration, thus deteriorating the solvent extraction efficiency [6]. Regeneration of a solvent by aqueous backwashing or back extraction of arenes from the extract phase with saturated hydrocarbons is insufficiently efficient, causing complication of the process flowsheet and increase in the power consumption. Furthermore, all the indicated solvents have certain inherent drawbacks: phenol, low selectivity with respect to arenes and high toxicity; furfural, low thermal oxidation resistance; and *N*-methylpyrrolidone, high cost and corrosion activity [7–9].

To obtain the transformer oil body from low-paraffinicity oil fractions, sulfuric acid refining is used. However, this method does not longer meet the modern environmental criteria, because of formation of large amounts of acid tar to be utilized or disposed of.

The goal of this work is to examine the possibility of production of the transformer oil body from the 300–350°C fraction of low-paraffinicity oil by solvent extraction using a low-boiling extraction system readily regenerable by distillation.

Since the oil in hand contains no *n*-alkanes, one may draw an analogy between the composition of its kerosene–gas-oil fractions and that of 200–320°C fraction dewaxed by adsorption on zeolites (denormalization product of the Parex plant). Previously we

1070-4272/03/7601-0140$25.00

Table 1. Parameters of countercurrent extraction refining of the 300–350°C fraction of Troitsk–Anastasievsk oil

Characteristic	Pilot experiment (no. 1)	Optimal conditions (experiment no. 2)
Number of theoretical steps of extraction	5	5
Temperature, °C	30	30
Water content in methyl Cellosolve, wt %	5	5
Weight ratio:		
aqueous methyl Cellosolve : raw material	3 : 1	4 : 1
pentane : raw material	0.7 : 1	1 : 1

reported on extraction of aromatic hydrocarbons from such denormalization product to obtain a component for a pollution-free diesel fuel with an arene content of no more than 10–15% [10–13].

Oils from the West Siberian oil-and-gas province (raw material for most of the Russian refineries) are classified with A^1 type [1]. This is essentially paraffin-base crude, in which naphthenes are represented primarily by monocycloalkanes. It is known that the solubility of saturated hydrocarbons, having the same amount of carbon atoms, in polar solvents increases in the order *n*-alkanes < isoalkanes < monocycloalkanes < polycycloalkanes.

The solubility of alkanes in polar solvents increases with increasing degree of branching. For example, the solubility of 2-methylheptane and 2,5-dimethylhexane in 2-methoxyethanol (methyl Cellosolve) at 50°C is 26.0 and 31.1%, respectively [14].

In contrast to West-Siberian oils, in the kerosene–gas-oil fractions of low-paraffinicity oils polycycloalkanes and isoalkanes predominate. Therefore, extraction of organoelement compounds and aromatic hydrocarbons from low-paraffinicity oils is a more difficult problem as compared to separation of denormalization products, more so of straight runs of West Siberian oils with high *n*-alkane content. The success in solving this problem depends primarily on the solvent selectivity. Among the known relatively low-boiling solvents, methyl Cellosolve is one of the most selective solvents with respect to arenes. For example, at 25°C, its selectivity with respect to toluene in the octane–toluene system, expressed as the limiting activity coefficient ratio of these hydrocarbons in a diluent, was found to be 7.92, whereas that of methanol, acetone, and pyridine is 4.57, 5.45, and 6.46, respectively [15].

More selective solvents are known (compared to methyl Cellosolve) such as sulfur dioxide, 2,2,2-trifluoroethanol, hexafluoro-2-propanol, acetonitrile, and nitromethane [16]. However, each of these solvents has drawbacks complicating its practical use as a solvent. Sulfur dioxide demonstrates high corrosion activity and high reactivity towards unsaturated hydrocarbons. Also, a refrigerating medium is required in extraction with this solvent. Polyfluoro alcohols are highly expensive, and nitromethane is dangerously explosive. Acetonitrile has a density close to that of the raw material, making it difficult to separate the extract and raffinate phases; also, at high temperature of regeneration, hydrolysis of aqueous acetonitrile can occur with formation of acetic acid, thus initiating corrosion of the equipment.

Among the advantages of methyl Cellosolve are high thermal and hydrolytic stability, sufficiently high density (ρ_4^{20} = 0.996), relatively low toxicity (MPC = 80 mg m^{-3} [17]), and low cost. Also, an important advantage of this solvent is in higher selectivity with respect to polycycloarenes [18, 19] and sulfur-containing components of oil fractions [20].

As in solvent extraction refining of the denormalization product of the Parex plant [11], in this work, to improve the selectivity of methyl Cellosolve, we used the heterogeneous solvent system containing 5% water and pentane as a nonpolar diluent.

As a raw material we used a fraction of Troitsk–Anastasievsk oil, whose characteristics were as follows: boil-off range (standard distillation) 302–354°C, refractive index n_D^{20} 1.5026, density ρ_4^{20} 0.901, sulfur content 0.16%, sulfury content 30 vol % (31.9 wt %), kinematic viscosity at 50°C 7.4 $mm^2\ s^{-1}$, and flash point (open vessel) 168°C.

Extraction experiments were performed in two modes, namely, pilot and optimal (Table 1). Five-step countercurrent extraction was carried out according to the classical flowsheet using a system of separating funnels [21]. Results obtained in the pilot experiments are given in Table 2.

Table 2 shows that the resulting raffinate contains the desired amount of arenes, but rather large amount of saturated hydrocarbons still remains in the extract

Table 2. Characteristics of the raffinate and extract obtained in experiment nos. 1 and 2

Characteristic	Raffinate		Extract	
	no. 1	no. 2	no. 1	no. 2
Yield, %	79.5	81.9	20.5	12.1
ρ_4^{20}	0.896	0.893	0.920	0.937
n_D^{25}	1.4925	1.4912	1.5545	1.5585
Kinematic viscosity at 50°C, $mm^2\ s^{-1}$	7.17	7.15	–	–
Sulfury content:				
vol %	18.6	18.2	75.8	86.3
wt %	20.3	19.66	76.9	87.3
Degree of arene recovery, %	–	–	49.4	49.5

Table 3. Results of testing of transformer oil

Characteristic	Standard value	Actual value
Kinematic viscosity at 50°C, $mm^2\ s^{-1}$:		
at 50°C, no more than	9	7.88
at –30°C, no more than	1500	977
Acid number, mg KOH g^{-1} oil, no more than	0.02	Not detected
Flash point, °C, no less than	135	163
Water-soluble acids and bases	Not detected	Not detected
Mechanical admixtures	〃	〃
Solidification temperature, °C, no higher than	–45	–53
Copper corrosion test	Passed	Passed
n_D^{20}, no more than	1.4950	1.4890
Color units, no more than	1.0	0.5
Oxidation resistance:		
volatile low-molecular-weight acids, mg KOH g^{-1} oil, no more than	0.005	0.002
weight fraction of oil foot, %, no more than	0.01	0.004
acid number of oxidized oil, mg KOH g^{-1} oil, no more than	0.1	0.01
Dielectric loss tangent, %, no more than	2.2	0.24
Density at 20°C, $g\ cm^{-3}$, no more than	0.895	0.890

(their loss with the extract is about 7% of the estimated total in the raw material).

To increase the solvent extraction selectivity and the arene content in the extract, we increased the pentane : raw material weight ratio to 1 : 1. Simultaneously, the aqueous methyl Cellosolve : raw material weight ratio was increased from 3 : 1 to 4 : 1, to maintain the attained degree of recovery of arenes and also their content in the raffinate. The other conditions of countercurrent extraction remained unchanged. The results of experiment no. 2 are given in Table 2.

The results show that the arene content in the extract increased by more than 10%, and the raffinate yield, by 2.4% (Table 2). The loss of saturated hydrocarbons with the extract decreased from 7 to 3.4% of the theoretical total amount in the raw material, i.e., by more than half. The higher aromaticity of the extract in experiment no. 2 is demonstrated also by the physicochemical characteristics (increased density and refractive index). In this case, the raffinate quality was somewhat improved also, i.e., in experiment no. 2, we reached more selective separation of the raw material into aromatic and paraffin fractions.

Pentane and the major part of methyl Cellosolve were removed from the extract and raffinate phases by distillation on a 20 TP column. Small amount of residual methyl Cellosolve (1.5–3.0% against the total in the raffinate and extract) was stripped with water. The methyl Cellosolve can be also removed from the raffinate and extract by purging with an inert gas as in the industrial process for selective refining of Texaco oils [7].

The raffinate obtained under the optimized condi-

tions was additionally refined by adsorption on bleaching clay, which was taken in amount of 3% against the raffinate. Then Agidol oil additive was added (3%). Test results for the resulting transformer oil revealed that the product meets the requirement of TU (Technical Specifications) 38.401-58-49–92 for TKp transformer oil in all respects (Table 3).

CONCLUSIONS

(1) Five-step countercurrent extraction of arenes and organoelement compounds from the 300–350°C fraction of low-paraffinicity oil at 4 : 1 aqueous (5% water) methyl Cellosolve to raw material and 1 : 1 pentane to raw material weight ratios allowed a decrease in the sulfury content from 30 vol % in the initial raw material to 18 vol % in the extract. In this case, the yield of the raffinate was about 82%, and the arene content in the extract, 87%, demonstrating sufficiently high selectivity of the process.

(2) Transformer oil obtained on the basis of the above raffinate meets the requirements of TU 38.401-58-49–92 in all respects leaving a wide margin. For example, the dielectric loss tangent was 0.24% against 2.2% by standards.

REFERENCES

1. Petrov, Al.A., *Uglevodorody nefti* (Petroleum Hydrocarbons), Moscow: Nauka, 1984.
2. Lipshtein, R.A. and Shakhnovich, M.I., *Transformatornoe maslo* (Transformer Oil), Moscow: Energoatomizdat, 1983.
3. Shabalina, T.N., Surovskaya, G.V., Grigor'ev, V.V., and Suzdal'tsev, N.I., *Khim. Tekhnol. Topl. Masel*, 2001, no. 4, pp. 30–32.
4. Kazakova, L.P. and Krein, S.E., *Fiziko-khimicheskie osnovy proizvodstva neftyanykh masel* (Physicochemical Principles of Petroleum Oil Production), Moscow: Khimiya, 1978.
5. Shkol'nikov, V.M. and Kolesnik, I.O., *Sovershenstvovanie protsessov selektivnoi ochistki i deasfal'tizatsii maslyanogo syr'ya na osnove primeneniya novykh rastvoritelei* (Improvement of Selective Refining and Deasphalting of Lube Stock Using Novel Solvents), Moscow: TsNIITEneftekhim, 1986.
6. Berkovich, S.R., Martynenko, A.G., Potashnikov, G.L., and Vishnevskii, A.V., *Neftepererab. Neftekhim.*, 1987, no. 10, pp. 9–11.
7. Bittrich, H.J., Gaile, A.A., Lempe, D., *et al.*, *Razdelenie uglevodorodov s ispol'zovaniem selektivnykh rastvoritelei* (Separation of Hydrocarbons with Selective Solvents), Leningrad: Khimiya, 1987.
8. Gaile, A.A., Somov, V.E., and Varshavskii, O.M., *Aromaticheskie uglevodorody: vydelenie, primenenie, rynok: Spravochnik* (Aromatic Hydrocarbons: Separation, Applications, and Market: A Handbook), St. Petersburg: Khimizdat, 2000.
9. Gantsev, V.A., Sukhorukov, A.M., Nigmatullin, R.G., *et al.*, in *3-ii Kongress neftegazopromyshlennikov Rossii* (3rd Congr. of Oil-and-Gas Manufacturers of Russia), Section E: *Neftepereraborka i neftekhimiya – problemy i perspektivy* (Petroleum Refining and Chemistry—Problems and Prospects), Ufa: Inst. Neftekhimpererab., Akad. Nauk Resp. Bashkortostan, May 23, 2001, pp. 125–128.
10. Kaifadzhyan, E.A., Gaile, A.A., Somov, V.E., and Semenov, L.V., *Zh. Prikl. Khim.*, 1998, vol. 71, no. 2, pp. 237–240.
11. Kaifadzhyan, E.A., Gaile, A.A., Somov, V.E., and Semenov, L.V., *Zh. Prikl. Khim.*, 1998, vol. 71, no. 3, pp. 386–389.
12. Kaifadzhyan, E.A., Gaile, A.A., Somov, V.E., and Semenov, L.V., *Zh. Prikl. Khim.*, 1998, vol. 71, no. 4, pp. 601–603.
13. Gaile, A.A., Kaifadzhyan, E.A., Semenov, L.V., *et al.*, *Zh. Prikl. Khim.*, 1998, vol. 71, no. 12, pp. 2003–2008.
14. Landauer, A., Lichtenthaler, R.N., and Prausnitz, J.M., *J. Chem. Eng. Data*, 1980, vol. 25, no. 2, pp. 152–153.
15. Park, J.H., Hussan, A., Couasnon, P., *et al.*, *Anal. Chem.*, 1987, vol. 59, no. 15, pp. 1970–1976.
16. Gaile, A.A., Semenov, L.V., Zalishchevskii, G.D., and Varshavskii, O.M., in *Ekstraktsionnaya dearomatizatsiya neftyanykh fraktsii: Sbornik trudov OOO PO "KINEF"* (Extraction Dearomatization of Oil Fractions: Collection of Works of KINEF Production Association, Limited Liability Company), Gaile, A.A. and Somov, V.E., Eds., St. Petersburg: Sankt-Peterburg. Gos. Univ., 2002, pp. 5–34, 164–285.
17. *Khimicheskii entsiklopedicheskii slovar'* (Chemical Encyclopedia), Knunyats, I.L., Ed., Moscow: Sov. Entsiklopediya, 1983.
18. Leshchev, S.M. and Onishchuk, V.I., *Neftekhimiya*, 1992, vol. 32, no. 4, pp. 367–373.
19. Leshchev, S.M. and Sinitsyna, A.V., *Neftekhimiya*, 1997, vol. 37, no. 6, pp. 552–556.
20. Kozin, V.G., Physicochemical Principles of Extraction of Organosulfur Compounds from Diesel Fractions, *Doctoral Dissertation*, Ufa, 1989.
21. Alders, L., *Liquid–Liquid Extraction; Theory and Laboratory Practice*, Amsterdam: Elsevier, 1959.

Russian Journal of Applied Chemistry, Vol. 76, No. 1, 2003, pp. 144–147. Translated from Zhurnal Prikladnoi Khimii, Vol. 76, No. 1, 2003, pp. 150–153.

CHEMISTRY OF FOSSIL FUEL

Manufacture of Hydraulic Oil by Solvent Extraction Refining of 225–290°C Fraction of Low-Paraffinicity Oil

A. A. Gaile, N. M. Dyurik, L. V. Semenov, A. N. Chagovets, A. V. Ustalov, E. A. Kaifadzhyan, and G. F. Stepanova

St. Petersburg State Technological Institute, St. Petersburg, Russia
Slavneft Oil and Gas Company, Joint-Stock Company, Moscow, Russia
Slavneft–Mendeleev Yaroslavl Oil Refining Plant, Open Joint-Stock Company, Yaroslavl, Russia

Received May 30, 2002

Abstract—A raffinate meeting the requirements for the hydraulic oil body was obtained from the 225–290°C fraction of low-paraffinicity oil by extraction refining with aqueous methyl Cellosolve in the presence of pentane.

At the Slavneft–Mendeleev Yaroslavl Oil Refining Plant, Open Joint Stock Company, hydraulic oils are produced from the 200–300°C fraction of Troitsk-Anastasievsk oil. The aromatic hydrocarbon content in this fraction is about 25% (hereinafter wt %, unless otherwise stated). However, according to existing technical specifications, the optimal content of aromatic hydrocarbons in environmentally friendly low-viscous hydraulic oils and fluids should be no more than 5.5% [1–3].

Low-aromaticity neutrals are obtained by hydrogenation of the kerosene–gas-oil fraction of aromatic-base crude oil; however, to prevent cracking, hydrogenation of arenes into cycloalkanes should be performed at high pressure (~28 MPa), which requires high capital investments and power inputs [2]. White oils (medicinal, perfume, compressor, and cable oils) with an arene content of 0.5–2% are produced by sulfonation with oleum or sulfuric anhydride [4].

Sulfonation of arenes is also used for manufacture of AMG-10 hydraulic oil. However, this method does not meet the modern environmental requirements, because of formation of large amounts of acid tar to be neutralized or disposed of.

Therefore, white oils are now produced beyond Russia mostly using a two-stage process involving hydrofining (to remove organoelement compounds) followed by hydrocracking at a pressure of 25–35 MPa on Pt, Pd, and Ni catalysts [4]. Realization of such a high-pressure two-stage process also requires high capital investments and power inputs. The goal of this work is to check the possibility of manufacturing hydraulic oil body by extraction refining of the 225–290°C fraction of low-paraffinicity oil using a relatively low-boiling extraction system readily regenerable by distillation. Previously, a procedure was proposed for manufacturing the component of pollution-free diesel oil from the dewaxed 200–320°C fraction using the methyl Cellosolve–water–pentane extraction system [5]. The same extraction system was successfully employed for manufacture of the transformer oil body from the 300–350°C fraction of low-paraffinicity oil [6]. However, hydraulic oil production requires deeper dearomatization of the raw material as compared to both transformer oil and diesel fuel production.

EXPERIMENTAL

As a raw material we used a fraction of Troitsk–Anastasievsk oil, whose characteristics were as follows: fraction composition (°C): 225 (initial boiling temperature), 233 (10%), 248 (50%), 273 (90%), 283 (95%), and 290 (dry point); density ρ_4^{20} 0.861, refractive index n_D^{25} 1.4750, arene content 22.8%, sulfur content 0.07%, kinematic viscosity at 50°C 2.2 $mm^2\ s^{-1}$, and flash point (open vessel) 96°C.

For extraction refining of the 225–290°C fraction, we selected the methyl Cellosolve–water–pentane extraction system (process temperature 30°C, five steps of countercurrent extraction). These basic parameters of the process were taken the same as in extraction refining of the 300–350°C fraction, in order to use the same installation for manufacturing both the hydraulic and transformer oil bodies from different raw materials.

1070-4272/03/7601-0144$25.00

Table 1. Parameters of countercurrent extraction refining of the 225–290°C oil fraction (1 : 1 pentane to raw material weight ratio)

Experiment no.	Water content in methyl Cellosolve, wt %	Solvent : raw material weight ratio
1	2	4 : 1
2	2	7 : 1
3	4	8 : 1

To adapt the processes to the 225–290°C fraction, we only changed the water content in the solvent and the solvent to raw material weight ratio (Table 1).

Extraction experiments were carried out using a system of five thermostatically controlled separating funnels [7]. In light of the need in deeper refining of the 225–290°C fraction as compared to the transformer oil fraction, to enhance the solvency of methyl Cellosolve, in pilot experiment nos. 1 and 2 we reduced the water content in the solvent from 5 to 2%. Note that the use of anhydrous methyl Cellosolve is impracticable because of the low critical temperature of dissolution in pentane (32°C).

Table 2 shows that, in experiment no. 1, we failed in attaining the desired arene content in the raffinate. To increase the degree of arene recovery, in experiment no. 2 we increased the solvent to raw material volume ratio from 4 : 1 to 7 : 1, all other conditions being equal. In this case we obtained the raffinate of the desired quality. However, in this case, the extraction selectivity was insufficient: the arene content in the extract was below 60%, and the loss of saturated hydrocarbons with the extract, 13.16% (counting on the raw material) or 17% of their potential content in the raw material.

Therefore, to increase the process selectivity, in experiment no. 3 we increased the water content in methyl Cellosolve to 4%. At the same time, we increased the solvent to raw material volume ratio to 8 : 1, to maintain the desired quality of the raffinate. The results of experiment no. 3 are better in all respects as compared to experiment no. 2: lower arene content in the raffinate and higher raffinate yield, arene content in the extract, and degree of arene recovery. The loss of saturated hydrocarbons with the extract in experiment no. 3 decreased to 11.58% (counting on the raw material) or to 15% of their potential content in the raw material.

It is possible to further improve the process selectivity, i.e., to increase the raffinate yield and arene content in the extract and to decrease the loss of saturated hydrocarbons with the extract. However, for this purpose, we should further increase the solvent to raw material and pentane to raw material ratios, which will inevitably increase the power consumption for regeneration of the solvents and also in the capital cost due to the need in increasing diameter of the extractor and distillation columns.

The results show that extraction refining of the 225–290°C fraction of Troitsk–Anastasievsk oil requires more stringent process conditions, including higher solvent to raw material ratio, as compared to those used in extraction of arenes from the denormalization products from the Parex plant (Kirishinefteorgsintez Production Association) [8]. This is caused by predominance in Troitsk–Anastasievsk oil of polycycloalkanes and highly branched alkanes, which are more readily soluble in polar solvents, particularly, in methyl Cellosolve, as compared to monocycloalkanes and monomethylalkanes of the diesel fraction of West Siberian oils.

In this work, methyl Cellosolve and pentane were recovered from the extract and raffinate phases by distillation on a 20 TP column. Small residual amounts of methyl Cellosolve (~2%) were removed from the

Table 2. Characteristics of the raffinate and extract obtained in experiment nos. 1–3

Characteristic	Experiment no. 1		Experiment no. 2		Experiment no. 3	
	raffinate	extract	raffinate	extract	raffinate	extract
Yield, %	78.1	21.9	67.5	32.5	68.7	31.3
n_D^{20}	1.4651	–	1.4612	–	1.4609	1.5112
ρ_4^{20}	–	–	–	–	0.836	0.910
Sulfury content, vol %	8.0	–	4.5	–	4.0	63.1
Arene content, %	8.3	75.6	5.1	59.5	4.5	86.5
Degree of arene recovery, %	–	72.6	–	84.8	–	

Table 3. Results of testing the raffinate as the AMG-10 hydraulic oil body

Characteristic	Standard value (TU 38.301-29-21)	Raffinate from run no. 3
Density at 20°C, g cm^{-3}, no more than	0.850	0.837
Initial boiling temperature, °C, no higher than	210	225
Kinematic viscosity at 50°C, mm^2 s^{-1}:		
at 50°C, no less than	2.2	2.2
at –30°C, no less than	200	142
Flash point in closed vessel, °C, no less than	93	105
Solidification temperature, °C, no higher than	–72	–72
Mechanical admixtures, %	–	–
Moisture content, %	–	–
Sulfury content, vol %, no more than	4.5	4.2
n_D^{20}	–	1.4595
Aniline point, °C, no lower than*	76.5	70.4
Acid number, mg KOH g^{-1} oil, no more than	0.03	0.02
Rubber swelling in AMG-10 oil, %, no more than	4–7	6

* This characteristic of AMG-10 is not critical for rejection.

extract and raffinate by aqueous stripping. In the large-scale process, methyl Cellosolve residuals can be removed from the extract and raffinate not by aqueous washing, but by live steam distillation or purging with an inert gas.

In extraction refining of relatively light fractions with methyl Cellosolve, the possibility of formation of azeotropic mixtures with hydrocarbons boiling below 200°C should be taken into account.

It is known that azeotropic mixtures characterized by positive deviation from the Raoult's law are formed if the following condition is realized [9]:

$$\gamma_1^0 > P_2^0/P_1^0$$

where γ_1^0 is the activity coefficient of the hydrocarbon at infinite dilution in the azeotropizer component and P_1^0 and P_2^0 are the saturated vapor pressures of the hydrocarbon and azeotropizer component at the boiling point of the azeotropic mixture.

With arenes, methyl Cellosolve forms systems characterized by small deviations from ideality (activity coefficient of arenes in methyl Cellosolve at infinite dilution γ^0 ~3–5). Therefore, methyl Cellosolve having bp 124.4°C can form azeotropic mixtures only with arenes whose boiling point differs from that of methyl Cellosolve by no more than 30°C, i.e., with such solvents as toluene, xylenes, and cumene, but not with mesitylene (bp 164.7°C) and arenes C_{10}.

The limiting activity coefficients of saturated hydrocarbons in methyl Cellosolve are considerably higher. Therefore, methyl Cellosolve can form azeotropic mixtures even with decane (bp 174.6°C) [10]. Also methyl Cellosolve can form tangential azeotropic mixtures with undecane (bp 195.6°C) and branched alkanes C_{11}.

The initial boiling temperature of the fraction in hand is 225°C (standard distillation), which corresponds to an initial boiling temperature of about 200°C on the actual boiling point curve. Therefore, the 225–290°C fraction should contain no C_{11} alkanes, and we observed no formation of azeotropic mixtures of methyl Cellosolve with hydrocarbons in solvent regeneration.

However, if the initial boiling temperature of a fraction were lower by 10–15°C, it is not improbable that C_{11} alkanes capable of forming azeotropic mixtures with methyl Cellosolve would enter this fraction. In this case, the process flowsheet should include separators for these azeotropic mixtures. However, no oiling of methyl Cellosolve with hardly removable trace arenes will occur even if the initial boiling temperature under standard distillation conditions is lowered to 190–200°C.

The raffinate obtained after extraction refining of the 225–290°C fraction of low-paraffinicity oil meets the basic requirements of TU (Technical Specifications) 38.301-29-21 for AMG-10 hydraulic oil body (Table 3).

Thus, AMG-10 hydraulic oil body can be manufactured by extraction refining of the 225–290°C fraction of low-paraffinicity oil. This method should be con-

sidered as an alternative to sulfuric acid refining as an environmentally unfavorable process, as well as hydrogenation as requiring the use of pure hydrogen and high-pressure equipment.

CONCLUSION

Five-step countercurrent extraction refining of the 225–290°C fraction of low-paraffinicity oil containing 23% arenes, at 8 :1 solvent (methyl Cellosolve–4% H_2O) to raw material and 1 : 1 pentane to raw material weight ratios, allowed decrease in the sulfury content in the raffinate to 4.5 vol % (raffinate yield about 69%). The raffinate thus obtained meets the requirements to the AMG-10 hydraulic oil body.

REFERENCES

1. Shabalina, T.N., Filippova, G.I., Kalyapina, Yu.T., *et al*., *Khim. Tekhnol. Topl. Masel*, 1993, no. 7, pp. 5–7.
2. Shabalina, T.N., Development of a Method for Production of Neutrals Using Hydrocatalytic Processes, *Doctoral Dissertation*, Moscow, 1999.
3. *Topliva, smazochnye materially, tekhnicheskie zhidkosti. Assortiment i primenenie: Spravochnik* (Fuels, Oils, and Technical Fluids. Range and Applications: A Handbook), Shkol'nikov, V.M., Ed., Moscow: Tekhinform, 1999.
4. Potanina, V.A., Marcheva, E.N., and Bogdanov, Sh.K., *Kachestvo i tekhnologiya proizvodstva belykh masel* (Quality and Production Process of White Oils), Moscow: TsNIITEneftekhim, 1981.
5. RF Patent no. 2 139 910.
6. Gaile, A.A., Dyurik, N.M., Semenov, L.V., *et al*., *Zh. Prikl. Khim*., 2003, vol. 76, no. 1, pp. 146–149.
7. Alders, L., *Liquid–Liquid Extraction; Theory and Laboratory Practice*, Amsterdam: Elsevier, 1959.
8. Kaifadzhyan, E.A., Gaile, A.A., Somov, V.E., and Semenov, L.V., *Zh. Prikl. Khim*., 1998, vol. 71, no. 3, pp. 386–389.
9. Kogan, V.B., *Azeotropnaya i ekstraktivnaya rektifikatsiya* (Azeotropic and Extractive Distillation), Leningrad: Khimiya, 1971.
10. Ogorodnikov, S.K., Lesteva, T.M., and Kogan, V.B., *Azeotropnye smesi: Spravochnik* (Azeotropic Mixtures: A Handbook), Leningrad: Khimiya, 1971.

Russian Journal of Applied Chemistry, Vol. 76, No. 1, 2003, pp. 148–152. Translated from Zhurnal Prikladnoi Khimii, Vol. 76, No. 1, 2003, pp. 154–158.

CHEMISTRY OF FOSSIL FUEL

Ozonolysis of Asphaltenes from Semicoking Tar of G17 Coal

V. V. Platonov, A. N. Kudrya, and S. V. Proskuryakov

Leo Tolstoy Tula State Pedagogical University, Tula, Russia
St. Petersburg State Technological Institute, St. Petersburg, Russia

Received July 3, 2002

Abstract—Liquid-phase ozonolysis of asphaltenes from the semicoking tar of G17 coal was studied.

In structural studies of asphaltenes, ozone is of particular interest as a specific agent cleaving double bonds [1–9]. Identification of low-molecular-weight (water-soluble) and high-molecular-weight (water-insoluble) products of asphaltene ozonolysis by ^{1}H and ^{13}C NMR spectroscopy, gas chromatography–mass spectrometry (GC–MS), gas–liquid (GC) and thin-layer (TLC) chromatography, UV/Vis spectroscopy, and ESR allows detailed characterization of the molecular structure of asphaltenes of various origins, which, in turn, is necessary for their efficient application.

In this work we studied liquid-phase ozonolysis of asphaltenes from the semicoking tar of G17 coal.

EXPERIMENTAL

Coal characteristics: moisture content W^{d} 2.9, ash residue A^{c} 8.7, yield of volatiles V^{daf} 36.6% (based on air-dry coal); elemental composition, % daf: C 80.8, H 5.7, N 1.0, O 11.7, S_{tot} 0.8. Yield of semicoking tar, % of organic matter of coal (OMC): 15.1; chemical group composition of semicoking tar, % of anhydrous tar: organic bases 1.15, carboxylic acids 0.85, phenols 18.96, hydrocarbons 32.90, neutral oxygen-, nitrogen-, and sulfur-containing compounds 25.11, asphaltenes 86, and resinous substances + loss 12.43 [10].

Characteristics of asphaltenes: molecular weight M = 277.5; elemental composition, % daf: C 77.8, H 8.2, N 2.6, O 11.4; functional composition, g-equiv mol^{-1}: phenolic groups (PG) 0.42, quinoid groups (QG) 0.40, keto groups (KG) 0.27, alcoholic groups (AG) 0.38, alkoxy groups (AOG) 0.22, and heterocyclic oxygen (O_c) 0.76.

In the mineral fraction of asphaltenes, we identified by emission spectrum, X-ray fluorescence, and X-ray phase analyses the following elements: Fe, Mg, Al, Si, Ti, Ni, Sn, Sb, V, Mn, Cr, Zn, Zr, Pt, Rh, Hg, Ge, Ga, Pb, Ca, Na, K, Ce, Co, and Nd. The IR spectra of asphaltenes contained absorption bands (ν, cm^{-1}) of the following structural fragments: aromatic rings (3030–3080, 1600, 1500, 1440–1465), with the increased intensity of the bands at 1600 and 1500 suggesting formation of fused structures; CH_2 groups exhibiting stretching (2840, 2940, 2925, 2850) and bending (720–740, 970, 1470) vibration bands, whose high intensity suggests high content of hydrogenated rings; phenolic hydroxyls (3570–3670, 1140–1230, 1310–1410); methoxy groups (2850); quinoid groups (1645, 1665, 1675, 1745); cyclic and naphthenic alcohols (1030–1120, 1260–1350, 3630–3700); oxygen- and nitrogen-containing heterocycles (1565, 1500, 1015–1030, 845–870, 740–800).

Asphaltenes have relatively high molecular weight (154–589); they contain alicyclic, aromatic, and heterocyclic rings fused in the linear or angular fashion.

From the practical viewpoint, one of promising ways of asphaltene processing is homogeneous pyrolysis, as it can yield additional amounts of hydrocarbons and other valuable products. However, the yield of pyrocarbon is relatively high, which calls for development of alternative procedures for processing asphaltenes. One of such procedures is ozonolysis.

Homogeneous ozonolysis of asphaltenes was performed in an installation consisting of an ac generator, an ozonizer equipped with a water-cooled jacked and tungsten electrodes, a bubbling reactor, a temperature control system, a control valve for feeding air, and a bottle packed with silica gel ASKM for drying the air fed to the ozonizer. The volume fraction of ozone in the ozone–air mixture was 2.5%. The reaction was performed in chloroform at $20 \pm 1°C$ for 30 h. The optimal reaction time was chosen in a series of pre-

1070-4272/03/7601-0148$25.00

liminary experiments in the course of which samples of the reaction mixture were taken and analyzed by TLC and IR and UV/Vis spectroscopy. The reaction performed for a time longer than 25–30 h caused no further significant changes in the composition of the ozonolysis products.

Active transformations of asphaltenes under the action of ozone start after an induction period (2–3 h) and are the most significant in the first 12–15 h. The ozonolysis mechanism is not unambiguous and constant throughout the process, as judged from the trends in variation of the content of various functional groups with time.

In the first stage of the process, the content of aromatic rings drastically decreases, and ozonides are formed. The content of phenolic groups and heterocyclic oxygen drastically decreases also, but the relative content of quinones somewhat increases.

This is followed by decomposition of ozonides and formation of carboxy and keto groups with dramatic decrease in the content of quinoid groups. Finally, the amount of aliphatic substituents decreases and naphthenic rings are cleaved, which is indicative of the occurrence of radical oxidation with atomic and molecular oxygen formed by partial decomposition of ozone.

Thus, the revealed trends in transformations of asphaltenes in the course of ozonolysis allow an important conclusion that there are two reaction pathways: classical ozonolysis involving cleavage of peripheral aromatic rings and heterocycles via ozonides and radical oxidation with atomic and molecular oxygen, apparently occurring after saturation with ozone of the multiple bonds in aromatic rings.

The mechanism of cleavage of "internal" aromatic rings in fused asphaltene structures is different and apparently involves intermediate formation of quinones, which accounts for a certain increase in their content in the initial stage of ozonolysis.

The induction period is most probably due to the slowest stage of the process, addition of ozone to multiple bonds with the formation of ozonides. Then, as the ozonides decompose, the rate of asphaltene oxidation by various pathways sharply grows.

Thus, the kinetic features of ozonolysis revealed by prompt analytical procedures form a theoretical basis for controlling the process so as to stop it at the required stage, in particular, at the stage of ozonide formation.

After ozonolysis completion, the reaction mixture was refluxed with distilled water for 2 h to fully decompose ozonides, and the organic and aqueous phases were separated in a separatory funnel. The weight gain of the organic phase after removal of the solvent was 66.15 wt %.

To identify acidic components of the aqueous layer, the aqueous phase was chromatographed on an activated Silufol plate in the system ethanol–25% ammonia–water (volume ratio 50 : 15 : 2.5). A reference mixture of acids was chromatographed simultaneously. The plates were developed under UV light (254 and 366 nm) and then sprayed with a 0.25% solution of Bromocresol Purple (reagent for carboxylic acids) and a 0.2% solution of diazotized *p*-nitroaniline (reagent for phenols).

We identified oxalic (the major component of water-soluble products), salicylic, succinic, benzoic, and phthalic acids.

An aliquot of the aqueous layer was titrated potentiometrically with 1 N aqueous-alcoholic KOH. From the first potential jump corresponding to titration of oxalic acid, we evaluated its yield: 22.5% based on the initial asphaltenes.

The composition of organic products of asphaltene ozonolysis was found by combination of the data of IR and UV/Vis spectroscopy, cryoscopy, elemental and quantitative functional analysis, and TLC.

Under the optimal TLC conditions (petroleum ether–acetone–benzene, volume ratio 25 : 40 : 15), we obtained 26 close-cut fractions (see table).

It is seen that the isolated components are characterized by broad ranges of the molecular weight (150–295) and composition (% daf: C 53.2–86.8, H 3.7–13.3, and O 7.7–35.6). Among functional groups, the carboxy and keto groups are present in the largest amounts: 0.74–1.92 and 0.60–1.62 g-equiv mol^{-1}, respectively. The content of hydroxy groups is also significant: 0.49–0.81 g-equiv mol^{-1}. Quinoid groups were identified in four compounds, with the content of 1.70–1.99 g-equiv mol^{-1}. Alkoxy, ester, and lactone groups and heterocyclic oxygen are untypical of the isolated components: only two or three structures were detected.

The presumed structural formulas of the isolated compounds are listed below.

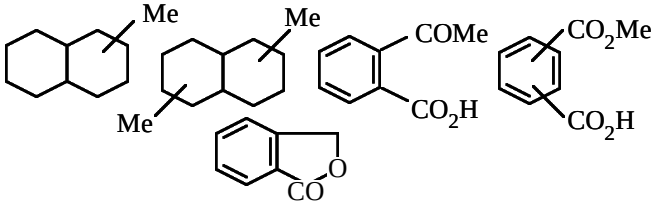

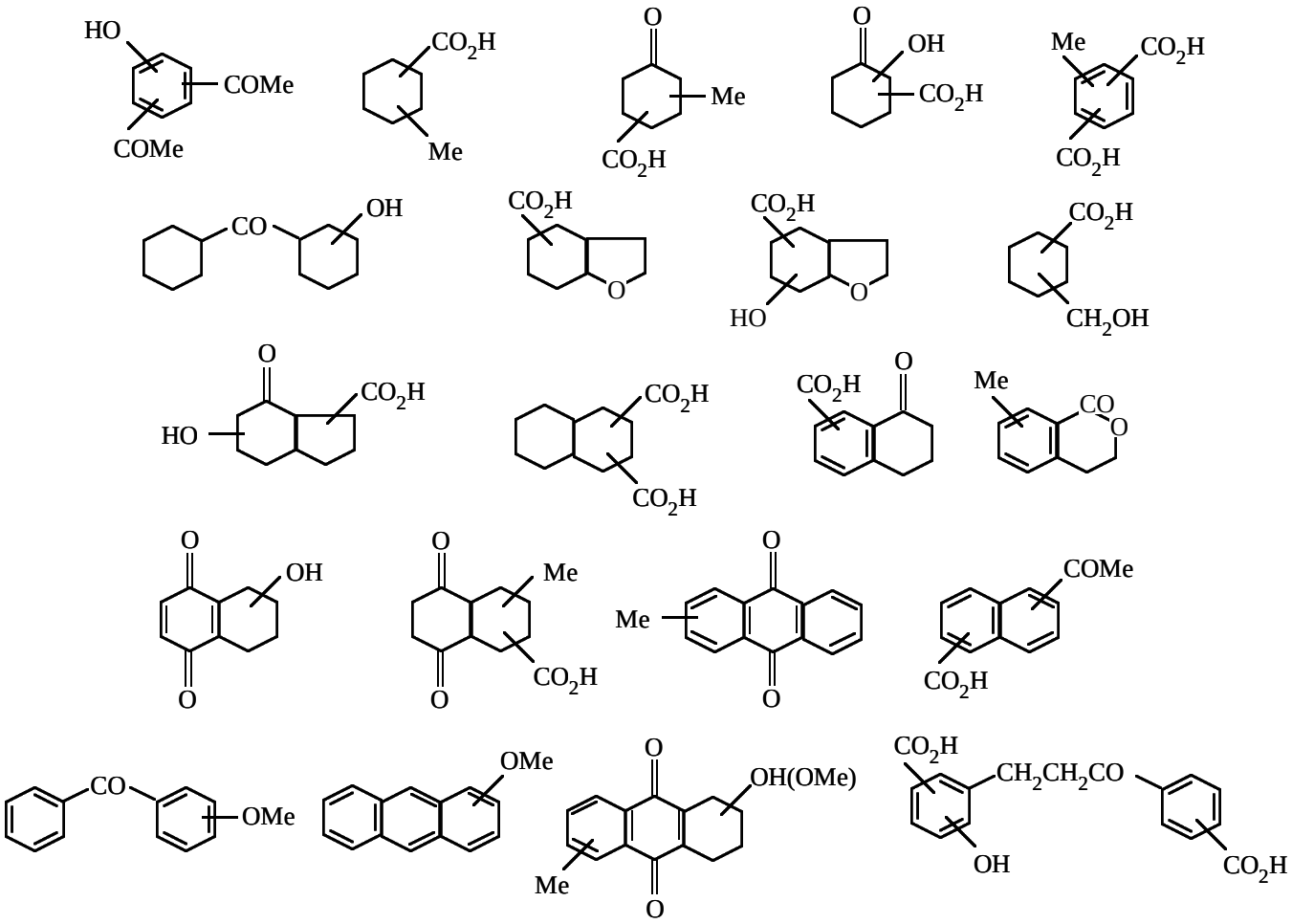

Except methyl- and dimethyldecalins, which are the only detected hydrocarbons, the organic phase mainly consists of functional (mostly bifunctional) mono-, bi-, and tricyclic compounds containing carboxy, keto, and hydroxy groups. The high content of aromatic rings along with naphthenic rings may be due to secondary formation of aromatic rings in the course of ozonolysis by oxidative dehydrogenation of naphthenes. Quinoid structures are all the more secondary; they are formed by intermediate oxidation of "internal" aromatic rings of the initial asphaltenes. The carboxy and keto groups are formed by oxidative degradation of alkyl substituents and naphthenic rings.

The whole set of our results allows certain practical conclusions.

Firstly, mild ozonation can be successfully used as an additional procedure for confirming the structure of high-molecular-weight asphaltenes by converting them into low-molecular-weight compounds, and also for revealing the structural correlations between the initial and oxidized asphaltenes and for elucidating possible transformation pathways of various components of oxidized asphaltenes.

For example, for several pathways of possible transformations of one of the initial asphaltenes, we calculated the activation energy E_a by the procedure [11] based on the assumption that the bond energies in the activated complex are additive:

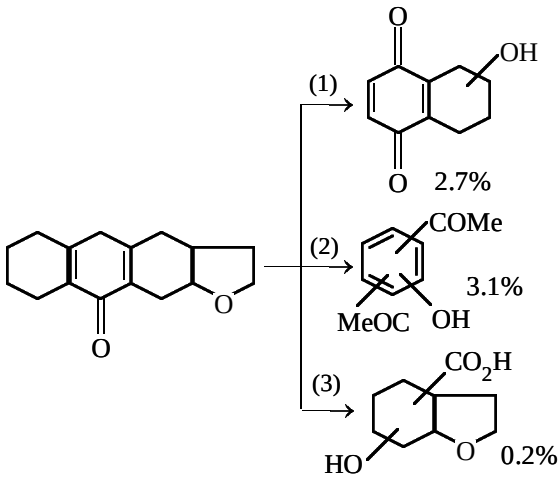

The calculated activation energies are as follows:

Characteristics of asphaltene ozonolysis products*

Fraction no.	*M*, formula, elemental and functional composition
1	*M* 158; $C_{11.4}H_{20.9}$; C 86.8, H 13.2
2	*M* 170; $C_{12.3}H_{22.6}$; C 86.7, H 13.3
3	*M* 164; $C_{9.0}H_{7.9}O_{3.0}$; C 65.9, H 4.8, O 29.3, CG 0.98, KG 0.91
4	*M* 185; $C_{9.3}H_{8.2}O_{4.1}$; C 60.0; H 4.4; O 35.6; CG 0.97; EG, LR 0.83
5	*M* 149; $C_{9.1}H_{8.1}O_{2.0}$; C 73.0; H 5.4; O 21.6; EG, LR 0.85
6	*M* 160; $C_{8.3}H_{10.4}O_{3.1}$; C 62.3, H 6.5,O 31.2, KG 1.62, PG 0.81
7	*M* 150; $C_{8.5}H_{14.9}O_{2.1}$; C 67.6, H 9.9, O 22.5, CG 0.74
8	*M* 161; $C_{8.3}H_{12.4}O_{3.1}$; C 61.5, H 7.7, O 30.8, CG 0.76, KG 0.70
9	*M* 165; $C_{7.3}H_{10.4}O_{4.2}$; C 53.2, H 6.3, O 40.5, CG 0.75, KG 0.63, AG 0.72
10	*M* 187; $C_{9.4}H_{8.2}O_{4.2}$; C 60.0, H 4.4, O 35.6, CG 1.82
11	*M* 211; $C_{13.1}H_{22.2}O_{2.0}$; C 74.3, H 10.5, O 15.2, KG 0.60, AG 0.70
12	*M* 180; $C_{9.5}H_{14.8}O_{3.2}$; C 63.5, H 8.2, O 28.3, CG 0.88, O_c 0.74
13	*M* 190; $C_{9.2}H_{14.3}O_{4.1}$; C 58.1, H 7.5, O 34.4, CG 0.80, AG 0.68, O_c 0.70
14	*M* 169; $C_{8.6}H_{15.0}O_{3.0}$; C 60.8, H 8.9, O 30.3, CG 0.82, AG 0.74
15	*M* 203; $C_{10.2}H_{16.3}O_{4.1}$; C 60.0, H 8.0, O 32.0, CG 0.75, KG 0.68, AG 0.62
16	*M* 204; $C_{11.3}H_{18.6}O_{3.1}$; C 66.7, H 9.1, O 24.2, CG 0.77, AG 0.60
17	*M* 198; $C_{11.5}H_{10.5}O_{3.1}$; C 69.5, H 5.3, O 25.2, CG 0.97, KG 0.87
18	*M* 170; $C_{10.5}H_{10.5}O_{2.1}$; C 74.1; H 6.2; O 19.7; EG, LR 0.91
19	*M* 185; $C_{10.4}H_{10.4}O_{3.1}$; C 67.4, H 5.6, O 27.0, AG 0.65, QG 1.85
20	*M* 220; $C_{12.2}H_{8.4}O_{4.1}$; C 66.7, H 3.7, O 29.6, CG 0.94, QG 1.92
21	*M* 229; $C_{15.5}H_{10.3}O_{2.1}$; C 81.1, H 4.5, O 14.4, QG 1.99
22	*M* 214; $C_{14.1}H_{12.2}O_{2.0}$; C 79.2, H 5.7 O 15.1, KG 0.90, AOG 0.71
23	*M* 216; $C_{15.6}H_{12.5}O_{1.0}$; C 86.5, H 5.8, O 7.7, AOG 0.74
24	*M* 215; $C_{13.1}H_{10.1}O_{3.0}$; C 72.9, H 4.7, O 22.4, CG 0.83, KG 0.92
25	*M* 250; $C_{14.8}H_{9.8}O_{3.9}$; C 70.9, H 3.9, O 25.2, AOG 0.34, PG 0.49, QG 1.70
26	*M* 295; $C_{16.8}H_{13.9}O_{5.0}$; C 68.4, H 4.7, O 26.9, CG 1.92, KG 0.65, PG 0.68

* (CG) Cresol groups, (EG) ester groups, and (LR) lactone rings.

E_a^1 = 148.75, E_a^2 = 168.02, and E_a^3 = 338.55 kJ mol^{-1}.

It is seen that pathway (3) with the highest activation energy is characterized by the yield as low as 0.2%, whereas the two other pathways whose activation energies are approximately two times lower give ~15 times higher product yields: 2.7 and 3.1%.

The contribution of pathway (1) is somewhat lower than that of pathway (2), despite lower E_a. This may be due to further degradation of the product of reaction (1), involving the quinone ring and occurring before the product concentration is measured.

Secondly, we have found a way of efficient processing of asphaltene raw materials which are accumulated in large amounts at petrochemical and coal-tar chemical plants and have no applications yet.

High-molecular-weight asphaltene compounds can be converted by ozonolysis into valuable products and raw materials for organic synthesis. In particular, high yield of oxalic acid (22.5% based on the initial asphaltenes) makes economically feasible its recovery from water-soluble ozonolysis products. Succinic and salicylic acids can be obtained as by-products.

Among the components of the organic phase, of considerable interest are polycarboxylic acids as additional significant source of raw materials for heat-resistant fibers, plastics, and lubricants, and also quinones as starting compounds for preparing dyes.

CONCLUSIONS

(1) Homogeneous ozonolysis of asphaltenes from the semicoking tar of G17 coal was studied, and variation of the structure of products was monitored.

(2) The ozonolysis products contain aromatic and alicyclic structures substituted with phenolic, quinoid, carboxy, keto, and ester groups, oxygen-containing heterocycles, and six-membered lactones.

(3) The major pathways of asphaltene ozonolysis were suggested.

REFERENCES

1. Eliseev, V.S., Comprehensive Study of the Structure of Petroleum Asphaltenes Using Ozonolysis, *Cand. Sci. Dissertation*, Moscow, 1979.
2. Yatsenko, E.A., Gutsalyuk, V.G., and Sdobnov, E.I., *Tr. Inst. Khim. Nauk Akad. Nauk Kaz. SSR*, 1964, vol. 11, no. 1, pp. 130–132.
3. Filimonova, T.A., *Neftekhimiya*, 1976, vol. 16, no. 5, pp. 769–771.
4. Bernatek, E. and Thoresen, F., *Acta Chem. Scand.*, 1955, vol. 9, no. 4, pp. 521–525.
5. Sister, M., Carol, B., and Nagy, B., *Anal. Chem.*, 1967, vol. 39, no. 11, pp. 1310–1313.
6. Strocci, A., *Riv. Ital. Sost. Grasse*, 1973, vol. 50, no. 11, pp. 413–418.
7. Platonov, V.V., Klyavina, O.A., and Vol'-Epshtein, A.B., *Khim. Tverd. Topl.*, 1987, no. 1, pp. 88–92.
8. Kamneva, A.T. and Korolev, Yu.G., *Laboratornyi praktikum po khimii topliva* (Practical Laboratory Course of Fuel Chemistry), Moscow: Mosk. Khimiko-Tekhnol. Inst. im. D.I. Mendeleeva, 1976.
9. Moin, F.B., *Usp. Khim.*, 1967, vol. 36, no. 7, pp. 1223–1243.

Russian Journal of Applied Chemistry, Vol. 76, No. 1, 2003, pp. 153–155. Translated from Zhurnal Prikladnoi Khimii, Vol. 76, No. 1, 2003, pp. 159–161.

BRIEF COMMUNICATIONS

Conversion of Tantalum(V), Niobium(V), and Titanuim(IV) Sulfates and Chlorides to Their Fluorides

V. G. Maiorov and A. I. Nikolaev

Tananaev Institute of Chemistry and Technology of Rare Elements and Mineral Raw Materials, Kola Scientific Center, Russian Academy of Sciences, Apatity, Murmansk oblast, Russia

Received September 3, 20002

Abstract—A process was developed for converting tantalum(V), niobium(V), and titanium(IV) sulfate and chloride to their fluorides in order to improve separation of these elements.

Large deposits of rare-earth titanoniobates, loparite and perovskite, are located on the Kola Peninsula. Some procedures of their breakdown yield acidic sulfate and chloride solutions containing tantalum(V), niobium(V), and titanium(IV) [1–5]. Numerous studies on separation of rare metals from these solutions were summarized in [6]. Especially numerous papers deal with extractive recovery of Ta(V), Nb(V), and Ti(IV) from chloride solutions. For example, more than twenty papers on extraction of these metals with tributyl phosphate were published. Increased interest in this problem was caused by researchers' attempts to develop an extraction procedure for treatment of loparite chlorination products formed in industrial processing of loparite ore in Russia [7]. However, these attempts failed. Serious problems originated from the dependence of the extractability of Nb(V) and especially Ta(V) on the history (preparation procedures) of the solutions of these metals, from deterioration of extractive recovery and separation of Nb(V) from Ta(V) due to copolymerization of Nb(V) with Ta(V), and of Nb(V) and Ta(V) with Ti(IV) and Zr(IV) and other metals, and a sharp decrease in the extractability of Ta(V) on standing or heating of solutions [6]. These facts, along with such negative factors as relatively low solubility of Nb(V) and Ta(V) in hydrogen chloride solutions, active joint extraction of foreign metals, and their difficult removal from the target metals make extractive separation of Ta(V), Nb(V), and Ti(IV) from chloride solutions unfeasible. Still greater problems arise in extractive separation of Ta(V), Nb(V), and Ti(IV) from sulfate solutions [6].

The most efficient separation and purification of the metals under consideration is attained with fluoride system, which is successfully used in industry [8]. In this system, Ta(V), Nb(V), and Ti(IV) are jointly extracted with organic acids from solutions prepared by breakdown of rare-metal titanoniobates with sulfuric or hydrochloric acids [1–5] and then are backwashed with hydrofluoric acid. Ta(V) and Nb(V) are recovered from the resulting fluoride solutions by extraction with tributyl phosphate (TBP) [9] or octanol [10]. Owing to conversion of sulfate and chloride complexes into fluoride derivatives and the fact that organic acids recover metals by the ion-exchange mechanism virtually without mineral acids, the liberated H_2SO_4 and HCl can be reused for breakdown of the initial titanoniobate [6]. After extractive recovery of Ta(V) and Nb(V), the spent aqueous fluoride solutions can be subjected to dialysis or pyrolysis [1, 2] to obtain commercial titanium dioxide and regenerate HF for its reuse for backwashing metals from the organic extracts. The above-noted procedures are promising for developing a low-waste procedure for processing of rare metal raw materials.

Among effective organic acid extractants, the cheapest and the most commercially available is di(2-ethylhexyl) hydrogen phosphate (HDEHP). Our experimental results on extractive recovery of Ta(V), Nb(V), and Ti(IV) with HDEHP from sulfuric acid process solutions obtained by different procedures of breakdown of loparite, perovskite, and sphene with sulfuric acid are listed in Table 1. The data on backwashing of the metals are given in Table 2. In our experiments we used technical-grade HDEHP containing about 7 vol % of main component, about 7 vol % of mono(2-ethylhexyl) dihydrogen phosphate (H_2MEHP), and isooctyl alcohol. Kerosene and RED-1 (C_{12}–C_{16} paraffins hydrocarbons) were used as diluents.

The extraction was performed at 18–20°C. After one or two contacts of the organic phase with the

1070-4272/03/7601-0153$25.00

Table 1. Extractive recovery of Ta(V), Nb(V), and Ti(IV) from sulfuric acid solutions with 40 vol % HDEHP solution in organic diluent

Run no.	Content in the initial solution, M				Diluent	$V_o : V_a$	Degree of recovery, %		
	Ta(V)	Nb(V)	Ti(IV)	H_2SO_4			Ta(V)	Nb(V)	Ti(IV)
1	0.0018	0.030	0.022	2.6	Kerosene	1 : 1	~100	~100	~100
2	0.0018	0.030	0.022	6.5	″	1.6 : 1	~100	~100	~100
3	0.0003	0.015	0.075	5.0	″	0.4 : 1	–	99.4	97.4
4	0.0003	0.015	0.075	10.0	″	0.2 : 1	85.7	90.9	98.2
5	0.0003	0.015	0.075	10.0	″	0.3 : 1	96.7	95.4	99.1
6	–	0.006	0.072	10.0	RED-1	0.5 : 1	–	90.2	94.0
7	0.0025	0.015	0.22	7.9	″	1 : 1	57	43	43
8*	0.0025	0.015	0.22	7.9	″	1 : 1	73	63	92

* Extraction at 40°C.

Table 2. Backwashing of Ta(V), Nb(V), and Ti(IV) from 40 vol % HDEHP solution in organic diluent with 7.5 M aqueous HF

Content in HDEHP, M			Diluent	$V_o : V_a$	Degree of recovery, %		
Ta(V)	Nb(V)	Ti(IV)			Ta(V)	Nb(V)	Ti(IV)
0.0020	0.050	0.063	Kerosene	10 : 1	~100	~100	72.6
–	0.012	0.14	RED-1	2 : 1	–	99.7	97.3
–	0.012	0.14	″	5 : 1	–	98.2	96.4
0.0003	0.015	0.41	″	4.5 : 1	>66	97.8	97.5

aqueous hydrogen fluoride solution, Ta(V), Nb(V), and Ti(IV) are virtually exhaustively backwashed from the organic phase. Because V_o is substantially larger than V_a, the target metals are concentrated in the aqueous fluoride backwashes by a factor of about 10. Table 1 (run nos. 7 and 8) shows that heating considerably improves the extraction of the rare elements with HDEHP. We found also that addition of neutral oxygen-containing solvents (e.g., TBP) improves the extractive recovery of Ta(V) and Nb(V). The amount of this additive, however, should not be large (e.g., for TBP, no more than 3–5 vol %), because higher concentrations of additives prevent backwashing of the metals with aqueous HF. The similar technique was successfully used by us for converting Ta(V), Nb(V), and Ti(IV) chlorides to their fluorides [4]. In this process, both the degree of extracive recovery of the rare metals with HDEHP and the degree of their backwashing were close to 100%.

In conclusion it should be noted that the contact of HDEHP with concentrated mineral acids should be avoided. For example, contact of HDEHP with aqueous HF and H_2SO_4 with concentration exceeding 8 and 10 M, respectively, results in fast decomposition of this extractant [11].

CONCLUSIONS

(1) Ta(V), Nb(V), and Ti(IV) are virtually completely recovered from aqueous sulfuric acid with di(2-ethylhexyl) hydrogen phosphate and are backwashed from the organic phase with aqueous HF.

(2) Conversion of Ta(V), Nb(V), and Ti(IV) to their fluorides by backwashing from the organic phase with aqueous hydrogen fluoride is promising for development of low-waste procedures for processing rare-earth titanoniobates.

REFERENCES

1. Sklokin, L.I., Zots, N.V., Shestakov, S.V., *et al.*, *Tsvetn. Met.*, 2000, no. 10, pp. 48–53.
2. Kalinnikov, V.T., Nikolaev, A.I., and Sklokin, L.I., *Tsvetn. Met.*, 2001, no. 12, pp. 96–98.
3. RF Patent no. 2149908.

4. Zots, N.V., Kasikova, N.I., Kasikov, A.G., *et al*., in *Metallurgiya tsvetnykh i redkikh metallov: Sbornik nauchnykh trudov Rossiisko-indiiskogo simpoziuma* (Metallurgy of Nonferrous and Rare Metals: Proc. of the Russian-Indian Symp.), Moscow, 2002, pp. 10–16.
5. Kalinnikov, V.T., Zots, N.V., Nikolaev, A,I,, *et al*., in *Metallurgiya tsvetnykh i redkikh metallov: Sbornik nauchnykh trudov Rossiisko-indiiskogo simpoziuma* (Metallurgy of Nonferrous and Rare Metals: Proc. of the Russian-Indian Symp.), Moscow, 2002, pp. 199–203.
6. Nikolaev, A.I. and Maiorov, V.G., *Ekstraktsiya niobiya i tantala* (Extraction of Niobium and Tantalum), Apatity: Kol'sk. Nauchn. Tsentr, Ross. Akad. Nauk, 1995.
7. Elyutin, A.V. and Dozorova, R.B., in *Razvitie redkometal'noi promyshlennosti v Rossii na osnove loparita: Sbornik trudov IV nauchnoi konferentsii* (Development of Russian Rare-Metal Industry Based on Loparite: Proc. IV Scientific Conf.), St. Petersburg, May 22–24, 2001, pp. 102–103.
8. Babkin, A.G., Maiorov, V.G., and Nikolaev, A.I., *Ekstraktsiya niobiya, tantala i drugikh elementov iz ftoridnykh rastvorov* (Extraction of Niobium, Tantalum, and Other Elements from Fluoride Solutions), Leningrad: Nauka, 1988.
9. Maiorov, V.G. and Nikolaev, A.I., *Hydrometallurgy*, 1996, vol. 41, pp. 71–78.
10. Maiorov, V.G., Nikolaev, A.I., Sklokin, L.I., *et al*., *Zh. Prikl. Khim*., 2001, vol. 74, no. 6, pp. 920–923.
11. Nikolaev, A.I., Maiorov, V.G., Zozulin, A.N., *et al*., *Zh. Obshch. Khim*., 1994, vol. 64, no. 6, pp. 941–944.

Russian Journal of Applied Chemistry, Vol. 76, No. 1, 2003, pp. 156–157. Translated from Zhurnal Prikladnoi Khimii, Vol. 76, No. 1, 2003, pp. 162–163.

BRIEF COMMUNICATIONS

Solubility of Calcium Sulfate Dihydrate in Nitric Acid at 20°C

Yu. A. Vershkova, O. A. Tareeva, K. G. Ivlev, and E. P. Lokshin

Tananaev Institute of Chemistry and Technology of Rare Elements and Mineral Raw Materials, Kola Scientific Center, Russian Academy of Sciences, Apatity, Murmansk oblast, Russia

Received June 18, 2002

Abstract—The solubility of gypsum in 0–30 wt % nitric acid solutions at 20°C was studied. The data were compared with the results obtained at 60°C.

Methods involving preliminary leaching of calcium ions with nitric acid show promise for recovery of calcium-containing rare-metal raw materials (perovskite, sphene) [1–3]. The forming solutions contain free nitric acid, nitrates of calcium and rare-earth elements, and, to a small extent, nitrates of other impurity elements. Most of calcium ions can be precipitated from the leaching solution by addition of sulfuric acid, and the nitric acid solution after concentrating can be reused to break down the concentrates. Reuse of nitric acid solutions is also of interest due to the fact that under certain conditions rare-earth elements do not precipitate jointly with calcium sulfate [4] and can be accumulated in the solution and subsequently recovered by extraction.

Methods are being developed for extracting lanthanides by nitric acid leaching of phosphogypsum, $CaSO_4 \cdot 2H_2O$, and phosphohemihydrate, $2CaSO_4 \cdot H_2O$, which are by-products in production of wet-process phosphoric acid from Khibiny apatite concentrate [5–7]. In the course of leaching, phosphohemihydrate recrystallizes into phosphogypsum, and calcium sulfate dissolves in the nitric acid solutions.

To estimate the efficiency of the calcium ion precipitation from nitric acid leaching solutions and the amount of calcium sulfate dissolving in nitric acid during leaching of phosphogypsum, we determined experimentally the dependence of the solubility of calcium sulfate dihydrate on the nitric acid concentration at 20°C.

The solubility of calcium sulfate dihydrate in nitric acid was studied by the isothermal method. Analytically pure grade chemicals were used. The initial solutions with a prescribed HNO_3 concentration and excess $CaSO_4 \cdot 2H_2O$ were kept in hermetically sealed temperature-controlled flasks at 20 ± 0.5°C with stirring until the equilibrium was attained. The process was monitored by analysis of the liquid phase at regular intervals for the content of Ca^{2+} and SO_4^{2-} ions by standard photometric and gravimetric procedures. The presence of two endothermic peaks in the ranges 124–150 and 178–192°C in the thermograms and the X-ray phase analysis data for the samples of the bottom phase confirm the existence of $CaSO_4 \cdot 2H_2O$ under the examined conditions.

As seen from the results obtained (see figure), the dependence of the gypsum solubility on the nitric acid concentration at 20°C passes through a maximum in the range 22–25 wt % HNO_3. Data on the $CaSO_4 \cdot 2H_2O$ solubility at 60°C [8] are presented for comparison. The observed direct temperature dependence of the $CaSO_4 \cdot 2H_2O$ solubility in nitric acid confirms the previous results [4].

The results obtained are useful for engineering calculations and physicochemical substantiation of flowsheets for reprocessing of calcium-containing rare-metal raw materials. In particular, we can state that

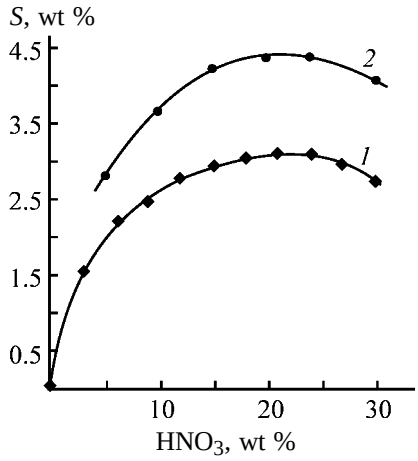

Solubility S of $CaSO_4 \cdot 2H_2O$ in nitric acid at (*1*) 20 and (*2*) 60°C [8].

1070-4272/03/7601-0156$25.00 © 2003 MAIK "Nauka/Interperiodica"

the low residual concentration of calcium ions in recycled nitric acid solutions must not impede their reuse for breaking down sphene concentrate.

ACKNOWLEDGMENTS

The work was financially supported by the program "Leading Scientific Schools" (project no. 00-15-97364).

REFERENCES

1. Kostrikin, V.M., Melent'ev, B.N., and Reznichenko, V.A., in *Mineral'noe syr'e* (Mineral Raw Materials), Moscow: Nedra, 1966, issue 3, pp. 63–69.
2. Motov, D.L. and Petrov, V.B., in *Khimiya i tekhnologiya redkikh elementov* (Chemistry and Technology of Rare Elements), Apatity: Kol'sk. Filial Akad. Nauk SSSR, 1976, pp. 95–99.
3. Motov, D.L. and Petrov, V.B., *Zh. Prikl. Khim.*, 1977, vol. 50, no. 9, pp. 1926–1930.
4. Vershkova, Yu.A., Masloboev, V.A., and Lokshin, E.P., Abstracts of Papers, *Konferentsiya "Metallurgicheskie tekhnologii i ekologiya"* (Conf. "Metallurgical Technologies and Ecology"), St. Petersburg, November 9–12, 1999, pp. 25–26.
5. Kijkowska, R. and Pawlowska-Kozinska, D., *Prage Nauk. Inst. Techn. Niorg. Nawoz. Miner. P. Wroch.*, 1986, no. 30, pp. 17–26.
6. Lebedev, V.N., Smirnova, I.P., Masloboev, V.A., and Mikhlin, E.B., in *Fiziko-khimicheskie i tekhnologicheskie problemy pererabotki syr'ya Kol'skogo poluostrova* (Physicochemical and Technological Problems of Reprocessing Raw Materials from Kola Peninsula) St. Petersburg: Nauka, 1993, pp. 56–60.
7. Kosynkin, V.D., Shatalov, V.V., Selivanovskii, A.K., *et al.*, *Khim. Tekhnol.*, 2001, no. 1, pp. 27–36.
8. Karmyshov, V.F., Popova, V.A., and Zakharova, M.I., *Zh. Prikl. Khim.*, 1982, vol. 55, no. 4, pp. 904–905.

Russian Journal of Applied Chemistry, Vol. 76, No. 1, 2003, pp. 158–159. Translated from Zhurnal Prikladnoi Khimii, Vol. 76, No. 1, 2003, pp. 164–165.

BRIEF COMMUNICATIONS

Electrotreatment of Wastewaters from High-Octane Fuel Production To Remove Methyl *tert*-Butyl Ether and Methanol

S. V. Vorob'eva and O. V. Smirnov

Tyumen Center, International Academy of Ecology and Life Protection Sciences, Tyumen, Russia

Received October 2, 2001; in final form, January 2002

Abstract—The possibility is examined of removing methyl *tert*-butyl ether from wastewaters by electrotreatment.

Industrial wastes from gas-condensate stabilization plants contain methanol, sodium carbonate and hydrocarbonate, *tert*-butanol, isobutene dimers, and methyl *tert*-butyl ether $CH_3OC(CH_3)_3$ (MTBE). The standard flowsheet of wastewater treatment in such plants includes hydrocyclones, oil removers, floatation machines, and tanks for treated wastewater. A line of wastewater treatment to remove MTBE and associated acetone, dimeric isobutene, methanol, and hydrocarbons is connected in parallel. MTBE cannot be oxidized biochemically. At the input of the line, the MTBE concentration amounts to 20–40 mg g^{-1}. At the output, it should be no more than 0.001 mg g^{-1}. The facilities and pipelines should be leakproof.

At the Surgut gas-condensate stabilization plant, the output of the treatment plant for removal of MTBE is 4.0 m^3 day^{-1}. The chemical oxygen demand (COD) of the wastewater to be treated is 7 g l^{-1}, the oil product content, 100–200 mg l^{-1}, and pH 6.5–8.5. The MTBE concentration at the output is 10 mg l^{-1} and that of the suspended material, up to 100 mg l^{-1}.

The use of electrotreatment for such wastes was reported in [1–5]. In this work we studied the efficiency of electrotreatment to remove MTBE from wastewaters containing 14.5 mg l^{-1} MTBE in the presence of 68 g l^{-1} methanol. The concentrations of MTBE, methanol, *tert*-butanol, and hydrocarbons were determined chromatographically, using a thermal conductivity detector. Electrotreatment was performed with an Akvalon electrode array [3, 4] (voltage on the flat electrodes 24 V, interelectrode distance 3–4 mm, and power consumption 40 W).

The electrode array consisted of four plates 14.5 cm high (two of them 6.4 cm wide, and two, 3.9 cm). Such an electrode arrangement allowed both uniform or nonuniform electrical field conditions. As filters we used foamed propylene fiber cartridges (horizontal filtration to the center; countercurrent washing with water). In one series of experiments we used aluminum electrodes (treatment time 120 min using 6-min pulses and 1-min breaks) and in the other series, large-width aluminum internal electrodes and small-width iron external electrodes (treatment time 60 min with the same pulses). The dispersion formed in the course of electrotreatment was agitated in breaks between pulses.

After electrotreatment with the aluminum electrode array, the MTBE concentration decreased from 14.5 to 6.8 mg l^{-1}. More considerable effect was observed with the combined electrode array. We failed to recover MTBE exhaustively. The methanol concentration decreased to 60.7 g l^{-1} after electrotreatment with combined electrode array for 30 min and to 42 g l^{-1} after treatment with Al electrode array for 60 min.

One more series of experiments was performed, to determine the efficiency of electrotreatment of wastewaters formed after regeneration of reforming columns, containing Na_2CO_3, Na_2SO_3, and 1.01 mg l^{-1} of iron ions (pH 7.5, dry residue 9500 mg l^{-1}). After electrotreatment with Al electrode array for 60 min, the dry residue was 9540 mg l^{-1} and iron concentration, 0.41 mg l^{-1}; and with the combined electrode array, 9340 and 0.7 mg l^{-1}, respectively.

Increased efficiency of wastewater treatment in the electrical field is due to the fact that, in this case, coagulation with participation of organic molecules [5] and associates is followed by their chemisorption on some coarser aggregates formed from the regenerated coagulant [$Fe(OH)_2$ + $Fe(OH)_3$ + $Al(OH)_3$] and multiple-charged Al and Fe cations. Because of the weak polarity, the common electrokinetic effects can

1070-4272/03/7601-0158$25.00

be only partly manifested in the course of coagulation. At the same time, certain contributions to this process are provided by dielectrophoresis, including dipolophoresis [1].

CONCLUSION

The use of external uniform or nonuniform electrical fields at a strength of up to 100 V cm^{-1} for treating industrial wastewaters from gas condensate stabilization plants allows reduction of the contents of such oxygen-containing organic fuel additives as methyl *tert*-butyl ether and methanol.

REFERENCES

1. Lavrov, I.S. and Smirnov, O.V., *Zh. Prikl. Khim.*, 1969, vol. 42, no. 7, pp. 1547–1553.
2. Granovskii, M.G., Lavrov, I.S., and Smirnov, O.V., *Elektroobrabotka zhidkostei* (Electrotreatment of Liquids), Leningrad: Khimiya, 1976.
3. Smirnov, O.V., Smirnova, L.F., and Lyutikov, V.A., *Zh. Prikl. Khim.*, 1998, vol. 71, no. 9, pp. 1486–1492.
4. Batrakov, V.E., *Khim. Zhizn'*, 2001, nos. 7–8, pp. 32–39.
5. Proskuryakov, V.A. and Smirnov, O.V., *Ochistka nefteproduktov i neftesoderzhashchikh vod elektroobrabotkoi* (Electrotreatment of Oil Products and Oil-Containing Waters), St. Petersburg: Khimiya, 1992.

Russian Journal of Applied Chemistry, Vol. 76, No. 1, 2003, pp. 160–161. Translated from Zhurnal Prikladnoi Khimii, Vol. 76, No. 1, 2003, pp. 166–167.

BRIEF COMMUNICATIONS

Synthesis of 1,3-Bis(trialkylammonio)-2-propanol Dihalides Exhibiting Retardant Activity toward Rape

A. I. Merkis, L. L. Novickiene, V. K. Daukšas, Z. A. Šaltite, L. I. Miliuviene, and V. A. Gaveliene

Institute of Botanics, Vilnius, Lithuania
Vilnius University, Vilnius, Lithuania

Received July 9, 2002

Abstract—1,3-Bis(trialkylammonio)-2-propanol dihalides were prepared, and their retardant activity was studied in relation to the chemical structure.

No retardants (compounds inhibiting the growth of plant pedicels and increasing their productivity) effective toward rape are known [1]. Relatively low retardant activity is exhibited by *N,N*-dimethylmorpholinium [2, 3] and *N,N*-dimethylpiperidinium [4] chlorides.

With the aim of revealing a correlation between the retardant activity and chemical structure and of searching for new retardants effective toward rape, we have converted 1,3-bis(dialkylamino)-2-propanols **Ia**–**Ic** [5–7] into 1,3-bis(trialkylammonio)-2-propanol dihalides **IIa**–**IIc**, **IIIa**–**IIIc**, and **IVa**–**IVc** and studied their biological activity. Quaternization was performed with iodomethane, 1-chloro-2-propene, or benzyl chloride:

$$\underset{\textbf{Ia–Ic}}{R_2NCH_2CHOHCH_2NR_2} \xrightarrow{R'X} \underset{\textbf{IIa–IIc, IIIa–IIIc, IVa–IVc}}{[R'R_2N^+CH_2CHOHCH_2N^+R_2R']2X^-},$$

where NR_2 = $N(C_2H_5)_2$ (**Ia**), piperidino (**Ib**), morpholino (**Ic**); NR_2 = $N(C_2H_5)_2$; R' = CH_3, X = I (**IIa**); R' = $CH_2CH{=}CH_2$, X = Cl (**IIb**); R' = $CH_2C_6H_5$, X = Cl (**IIc**); NR_2 = piperidino; R' = CH_3, X = I (**IIIa**); R' = $CH_2CH{=}CH_2$, X = Cl (**IIIb**); R' = $CH_2C_6H_5$, X = Cl (**IIIc**); NR_2 = morpholino; R' = CH_3, X = I (**IVa**); R' = $CH_2CH{=}CH_2$, X = Cl (**IVb**); R' = $CH_2 \cdot C_6H_5$, X = Cl (**IVc**).

The yield was 85–99%. The composition and structure of the compounds were proved by UV and ^{1}H NMR spectroscopy and by elemental analysis (see table). The absorption band of the aromatic ring in the UV spectra of **IIc**–**IVc** is located at about 264 nm ($\log\varepsilon$ = 2.8–3.0), and the chemical shift of the hydroxyl proton in the ^{1}H NMR spectra of **IIa**–**IVa**, in the region of δ = 4.9 ppm.

The retardant activity was studied with respect to rape plantules and roots under laboratory conditions [8] and in field experiments.[1]

The height, diameter, anatomic structure, and resistance to lodging of pedicels, and the plant productivity were estimated [9].

We found that salt **IVb** inhibits the growth of rape plantules and pedicels, appreciably increases the green and dry weight of roots, and stimulates formation of components of rape harvest as compared to the control. Compounds **IIa**, **IIc**, **IIIa**–**IIIc**, **IVa**, and **IVc** are considerably less active or inactive at all. Thus, replacement of the morpholine fragment in the molecule of **IVb** by the piperidine or diethylamine fragments, as well as replacement of the 2-propenyl substituent by methyl or benzyl substituents, sharply decreases the retardant activity toward rape.

EXPERIMENTAL

The UV spectra were taken on a Specord UV-VIS spectrophotometer in 95% ethanol, and the ^{1}H NMR spectra, on a Tesla BS-487C spectrometer (80 MHz, solvent CF_3CO_2H, internal reference TMS).

1,3-Bis(*N*, *N*-dialkyl-*N*-methylammonio)-2-propanol diiodides IIa–IVa. Iodomethane (42.6 g, 0.3 mol) was added dropwise with stirring to 0.1 mol of **Ia**–**Ic**. The mixture was kept at 50–60°C for 0.5 h

[1] Field experiments were performed in the pilot area of the Lithuanian Institute of Agriculture (Dotnuva Academy).

1070-4272/03/7601-0160$25.00

Yields, melting points, and elemental analyses of **IIa**–**IIc**, **IIIa**–**IIIc**, and **IVa**–**IVc**

Compound	Yield, %	mp, °C	Found, %/Calculated, %				Formula
			C	H	Cl	N	
IIa	90	156–157	31.96/32.11	6.70/6.63	–/–	5.88/5.76	$C_{13}H_{32}I_2N_2O$
IIIa	91	194–196	35.60/35.31	5.99/6.32	–/–	5.52/5.49	$C_{15}H_{32}I_2N_2O$
IVa	85	235–237	30.52/30.37	5.37/5.49	–/–	5.21/5.45	$C_{13}H_{28}I_2N_2O_3$
IIb	98	204–205	57.52/57.45	10.28/10.21	20.03/19.95	7.81/7.88	$C_{17}H_{36}Cl_2N_2O$
IIIb	98	201–203	60.31/60.15	9.62/9.56	18.77/18.69	7.54/7.38	$C_{19}H_{36}Cl_2N_2O$
IVb	86	168–170	52.90/53.26	8.83/8.41	18.11/18.50	7.07/7.31	$C_{17}H_{32}Cl_2N_2O_3$
IIc	99	205–206	66.06/65.92	8.81/8.85	15.42/15.57	6.24/6.15	$C_{25}H_{40}Cl_2N_2O$
IIIc	85	234–235	67.70/67.63	8.44/8.41	14.88/14.79	5.83/5.84	$C_{27}H_{40}Cl_2N_2O$
IVc	92	180–183	62.23/62.11	7.76/7.51	14.89/14.67	5.62/5.79	$C_{25}H_{36}Cl_2N_2O_3$

and cooled to 20°C; the precipitate was filtered off, washed with anhydrous diethyl ether, dried in a vacuum, and recrystallized from acetone–ethyl acetate (1 : 3 by volume).

1,3-Bis(*N*, *N*-dialkyl-*N*-2-propenylammonio)-2-propanol dichlorides IIb–IVb. A mixture of 0.1 mol of **Ia**–**Ic** and 30.6 g (0.4 mol) of 1-chloro-2-propene was refluxed for 60 days and cooled; the precipitate was worked up as described for **IIa**–**IVa** and recrystallized from acetone–ethyl acetate (1 : 5 by volume).

1,3-Bis(*N*, *N*-dialkyl-*N*-benzylammonio)-2-propanol dichlorides IIc–IVc. A mixture of 0.1 mol of **Ia**–**Ic** and 50.6 g (0.4 mol) of benzyl chloride was heated at 100°C for 50 h and cooled; the precipitate was worked up as described above for **IIa**–**IVa.**

CONCLUSIONS

(1) A procedure was developed for preparing 1,3-bis(trialkylammonio)-2-propanol dihalides by N-alkylation of 1,3-bis(dialkylamino)-2-propanols.

(2) Among the compounds prepared, 1,3-bis(*N*-2-propenylmorpholinio)-2-propanol dichloride exhibits retardant activity toward rape.

REFERENCES

1. Zhou, W. and Leul, M., *Plant Growth Regulation*, 1999, vol. 27, no. 2, pp. 99–104.
2. Mel'nikov, N.N., *Usp. Khim.*, 1976, vol. 35, no. 8, pp. 1473–1503.
3. Knypl, J.C. and Junas, K.M., *Acta Soc. Bot. Polon.*, 1977, vol. 46, no. 1, pp. 129–133.
4. Rademacher, W. and Evans, J.R., *Proc. Plant Growth Regulation Soc. of America: 23th Annual Meet.*, Calgary, Alberta (Canada): Univ. of Calgary, July 14–18, 1996, pp. 236–241.
5. Urbanska, A. and Tkaczynski, T., *Acta Pol. Pharm.*, 1976, vol. 33, no. 4, pp. 447–455.
6. Vassiliades, M.C., *Bull. Soc. Chim. Fr.*, 1937, vol. 4, no. 6, pp. 1131–1136.
7. Kochetkov, N.K. and Vorotnikova, T.A., *Zh. Obshch. Khim.*, 1959, vol. 29, no. 2, pp. 532–535.
8. Miliuviene, L.I., *Fiziol. Biokhim. Kul't. Rast.* (Kiev), 2000, vol. 32, no. 4, pp. 288–296.
9. Novickiene, L., Gaveliene, V., Miliuviene, L., *et al.*, *Biologija* (Vilnius), 1998, no. 3, pp. 45–49.

Russian Journal of Applied Chemistry, Vol. 76, No. 1, 2003, p. 162. Translated from Zhurnal Prikladnoi Khimii, Vol. 76, No. 1, 2003, p. 168.

BOOK REVIEWS

Gaile, A.A., Proskuryakov, V.A., Semenov, L.V., Pul'tsin, N.M., Parizheva, N.V., Zakharov, A.P., Apter, Yu.M., and Solodova, N.I., *Predel'nye koeffitsienty aktivnosti uglevodorodov: Spravochnik* (Limiting Activity Coefficients of Hydrocarbons in Specific Solvents: A Handbook), Gaile, A.A., Ed.

St. Petersburg: Sankt-Peterburg. Gos. Univ., 2002

The handbook covers experimental activity coefficients of hydrocarbons C_5–C_9, including alkanes, cycloalkanes, alkenes, alkadienes, alkynes, and arenes at infinite dilution in more than 500 polar solvents, obtained by GLC at the St. Petersburg State Technological Institute. Note that a significant part of these data was previously published only in dissertations.

It follows from comparison with the fundamental handbook (Gmehling, J., Menke, J., and Schiller, M., *Activity Coefficients at Infinite Dilution*, Frankfurt on Main, 1994) that the reviewed handbook covers more than a half of all the known selective solvents. Data given in this handbook are of importance for choosing optimal separating agents in extraction, extractive and azeotropic distillations, and absorption, i.e., in the processes widely used in oil-refining and petrochemical industries. Data on the limiting activity coefficients of hydrocarbons can be used for predicting their solubility, and the selectivity of a solvent can be judged from the activity coefficient ratios of components to be separated. Also these data are widely used in modeling phase equilibria liquid–liquid and liquid–vapor using semiempirical Wilson, NRTL, UNIQUAC, and other equations.

The handbook is of interest for specialists working in the fields of physical chemistry, oil processing, and petrochemistry.

I. V. Tselinskii

1070-4272/03/7601-0162$25.00

Russian Journal of Applied Chemistry, Vol. 76, No. 1, 2003, p. 163. Translated from Zhurnal Prikladnoi Khimii, Vol. 76, No. 1, 2003, p. 169.

BOOK REVIEWS

Blinov, L.N., *Khimiko-ekologicheskii slovar'-spravochnik* (Chemical-Ecological Dictionary—Reference Book)

St. Petersburg: Lan', 2002, 272 pp.

In recent decades, such disciplines as ecology, safe mode of life, ecological chemistry, and chemistry of the environment have appeared in the curricula of secondary- and higher-school institutions. The increasing attention is given to preservation in quite a number of other general and special courses. In this connection, numerous special terms have appeared, not used widely previously. The chemical-ecological dictionary—reference book under discussion is the first publication of this kind, which is intended to serve to a wide audience of readers, and schoolchildren and junior students in the first place. The book, written in well-understandable manner, presents interpretation of about 1400 various terms of generally chemical and ecological nature.

The first edition of the reference book, considered here, proves to be much more "chemical" than "ecological," despite the apparent conventionality of such a distinction. No more than 8–10% of the total number of entries are devoted, according to our estimate, to ecological terms proper. Sufficiently detailed evidence is given about all elements of the periodic table, much attention is given to the terminology used to describe the chemical bond (atomic and molecular orbitals, bonding molecular orbital, metal–metal bond, chemical bond), to issues concerning the nomenclature of chemical compounds (systematic nomenclature of anions, cations, acids, acid and basic salts, bases, oxides, organic compounds).

The book written by L.N. Blinov, a known specialist, professor of St. Petersburg State Polytechnic University, can well be used as additional textbook of chemistry in a wide variety of educational institutions. It seems advisable to enhance, in subsequent editions of the book, its ecological component by including entries concerning the pollution of the environment with heavy metals, and mercury in the first place, evidence about radiation accidents that have occurred in Russia and their consequences. Such compounds as tetraethyllead, fluorochloromethanes, and dioxins deserve separate consideration. It would be well to characterize potassium superoxide, the most important component of formulations serving to evolve oxygen and absorb carbon dioxide in self-contained objects. When considering metals, it would be appropriate to specify the amount of their production in Russia and, in some cases, place emphasis on the environmental problems associated with their manufacture. This, in particular, refers to aluminum, whose manufacture inflicts severe damage on the environment, is accompanied by discharge of fluoride compounds, and possibly leads to formation of benzopyrene in anode mass baking.

Blinov has demonstrated a rather valuable initiative, which deserves any kind of support.

A. G. Morachevskii

1070-4272/03/7601-0163$25.00

Russian Journal of Applied Chemistry, Vol. 76, No. 1, 2003, p. 164. Translated from Zhurnal Prikladnoi Khimii, Vol. 76, No. 1, 2003, p. 170.

ANNIVERSARIES

Nataliya Aleksandrovna Smirnova (to 70th Anniversary of Her Birthday)

On January 4, 2003, Nataliya Aleksandrovna Smirnova, a corresponding member of the Russian Academy of Sciences, professor, and head of the Chair of Physical Chemistry at St. Petersburg State University, was 70.

N.A. Smirnova is a prominent physical chemist and honorable representative of the physicochemical school of St. Petersburg University. Her basic research made a significant contribution to several parts of modern physical chemistry: molecular theory of solutions, theory of phase equilibria, and molecular-statistical theory of complex fluid systems of various kinds.

Smirnova is the author of about 300 scientific publications, including monographs and textbooks. Wide acceptance has been gained by the monograph *Metody statisticheskoi termodinamiki v fizicheskoi khimiii* (Methods of Statistical Thermodynamics in Physical Chemistry), the first and very successful manual of statistical thermodynamics for chemists (1st edition, 1973; 2nd edition, 1983; translated abroad). Numerous Smirnova's original investigations were summarized in her monograph *Molekulyarnye teorii rastvorov* (Molecular Theories of Solutions, 1988), she was the author of the most important chapters in collective monographs *Termodinamika razbavlennykh rastvorov* (Thermodynamics of Dilute Solutions) and *Termodinamika ravnovesiya zhidkost'–par* (Thermodynamics of the Liquid–Vapor Equilibrium), and in IUPAC publication *Uravneniya sostoaniya* (Equations of State).

The investigations carried out by Smirnova and her disciples have the fundamental nature and are characterized by high scientific level, being, at the same time, aimed at solution of important applied problems. These include development of effective methods for calculation of phase equilibria in order to optimize separation processes, methods for calculation of thermodynamic properties and phase equilibria in systems composed of oil and natural gas in a very wide range of conditions, analysis of factors influencing precipitation of asphaltenes from crude oil, establishment of regular trends in physicochemical behavior of mixed surfactant solutions, etc.

Also fruitful are Smirnova's pedagogic activities:

She has been delivering general courses of lectures on physical chemistry and statistical thermodynamics and special courses at the chemical faculty and working with graduates, postgraduates, and doctoral candidates. Among Nataliya Aleksandrovna's disciples are doctors and candidates of science and known scientists. Smirnova has been delivering lectures at leading universities in many countries all over the world and participating in the work of international scientific conferences, both as speaker and as conference organizer. Smirnova's works have been twice honored with awards of St. Petersburg University and a State Prize of the USSR. She conducts important scientific-organizational work, being a member of a number of Scientific Councils and a member of Editorial Boards of *Zhurnal Prikladnoi Khimii* (Russian Journal of Applied Chemistry) and *Zhurnal Fizicheskoi Khimii* (Russian Journal of Physical Chemistry).

Editorial Board of *Zhurnal Prikladnoi Khimii*, Russian Academy of Sciences

1070-4272/03/7601-0164$25.00

Russian Journal of Applied Chemistry, Vol. 76, No. 1, 2003, p. 165. Translated from Zhurnal Prikladnoi Khimii, Vol. 76, No. 1, 2003, p. 171.

OBITUARIES

Sergei Sergeevich Markov (October 23, 1906–November 20, 2002)

Prikladnaya Khimiya Russian Scientific Center and the entire domestic chemical science have suffered an irreplaceable loss.

On November 20, 2002, Sergei Sergeevich Markov, research worker at the Center, doctor of chemistry, professor, laureate of Lenin and State Prizes, passed away at the age of 96. Having graduated from the Leningrad Pharmaceutical, and then from the Leningrad Technological, institutes, Sergei Sergeevich started his scientific activities at the State Institute of Applied Chemistry (GIPKh) and devoted to this institute 73 years of his working life, having worked his long way up from laboratory assistant to deputy director of the Institute for scientific work.

Death deprived us of an outstanding scientist, prominent specialist and organizer in the field of technical chemistry and space technology. All Prof. Markov's activities have been associated with the development of domestic chemical industries and creation of the Russian school of chemical engineers with a broad spectrum of capabilities.

Technology for nepheline processing, production of aluminum oxide from bauxites, synthesis of compounds of magnesium, iodine, and bromine and inorganic fluoro compounds—all these issues have been the subject of his interests and have been powered by his ideas.

Special mention should be made of Sergei Sergeevich's works on organization of industry for manufacture of manganese compounds, on whose synthesis he has been working till the last days of his life.

The originality and national importance of these investigations and industrial implementation of research developments are characterized by the fact that, in 1937, the scientific degree of the candidate of science was conferred to Markov without backing a dissertation, and in 1943, he was awarded the State Prize of the USSR for the development of GAP (GIPKh active pyrolusite).

During the World War II, Sergei Sergeevich remained in besieged Leningrad and supervised, together with the staff members of GIPKh, manufacture of defense-related products for the Leningrad front.

In postwar years, continuing his work on problems concerning the technology of manufacture of fluoride and manganese compounds, compounds of magnesium, iodine, and bromine, and various nitro compounds, Prof. Markov devoted his efforts to the developing space technology.

His works on creation of rocket propellant components and their use in special technologies culminated in that, in 1967, Markov was awarded, together with other members of a group, his second State Prize, and in 1976, a Lenin Prize for works on technology for synthesis of a new class of nitro compounds.

Sergei Sergeevich has trained a sizable pleiad of specialists working in various fields of the national economy. His disciples include candidates and doctors of science and directors of companies, and with all of them he unselfishly shared his ideas, professional and everyday experience, and knowledge.

Production shops to which Sergei Sergeevich made a prominent creative contribution are still working at plants in Slavgorod, Perm, Nevinnomyssk, Dneprodzerzhinsk, Samara, Moscow, St. Petersburg, Saki, Krasnoperekopsk, Baku, Novotroitsk, Nebit Dag, Neftechala, Salavat, and Biisk; his studies in chemistry of manganese have gained worldwide acceptance.

Markov's merits have been honored with high State awards.

The rich legacy bequeathed to us by Sergei Sergeevich is constituted by his disciples, his numerous papers and inventions, and fruitful scientific ideas he had no time to implement himself.

An attentive and sensitive person and manager, he has been always deeply respected by staff members of the Institute and plants where he has ever been and worked.

The unexceptionable honesty, culture, devotion to work and colleagues, and enormous working capacity and energy of Sergei Sergeevich have always caused sincere delight of those around him.

Together with his relatives and friends, we deeply grieve over the irreplaceable loss and will preserve Sergei Sergeevich Markov's respectful memory in our hearts.

Staff members of the Prikladnaya Khimiya Russian Scientific Center

1070-4272/03/7601-0165$25.00 © 2003 MAIK "Nauka/Interperiodica"

Russian Journal of Applied Chemistry, Vol. 76, No. 2, 2003, pp. 167–170. Translated from Zhurnal Prikladnoi Khimii, Vol. 76, No. 2, 2003, pp. 177–180.

INORGANIC SYNTHESIS AND INDUSTRIAL INORGANIC CHEMISTRY

A Study of Calcium Chloride Purification

A. A. Fakeev, L. V. Vasil'eva, and A. I. Sukhanovskaya

State Research Institute of Chemical Reagents and Ultrapure Chemical Substances, Moscow, Russia

Received February 27, 2002

Abstract—Two methods of calcium chloride purification were studied: crystallization from aqueous solutions and joint precipitation of impurities from aqueous solutions onto inorganic collectors (hydrated aluminum or zirconium oxides). The purification factors were calculated and a high efficiency of purification of calcium chloride solutions with hydrated zirconium dioxide as collector was established.

Calcium chloride is widely used in metallurgical, chemical, chemical-pharmaceutical, aircraft, and coal industries, in glass manufacture, agriculture, everyday chemistry, etc. [1].

In chemical industry, calcium chloride is, along with calcium nitrate, a key compound for preparing the most practically important calcium products (calcium carbonate, phosphate, chromate, etc.) [2].

In recent years, ultrapure calcium compounds (calcium carbonate, fluoride, and phosphate) have found application in fabrication of optical fibers, single crystals, and luminophores, [3, 4]. This required the development of novel methods for thorough purification of the accessible raw material, calcium chloride.

In the system $CaCl_2$–H_2O, compounds of the following compositions crystallize: $CaCl_2 \cdot 6H_2O$, $CaCl_2 \cdot 4H_2O$, $CaCl_2 \cdot 2H_2O$, $CaCl_2 \cdot H_2O$, and $CaCl_2$, whose solubilities are 42.9, 53.60, 67.20, and 77.32, and >80 wt %, respectively [1, 5].

The efficiency of crystallization purification of calcium chloride could be estimated from data on phase equilibria in water–salt systems containing this salt. However, the relevant data are scarce. The systems $CaCl_2$–M^nCl_n–H_2O, where M^n is Co(II) [6, 7], Cu(II) [8], NH_4^+ [9], K [10], or Mg(11) are of simple eutonic type at 25°C; those in which M^n is Cu(I) [8], Mn(II) [12], Zn [13], or Cd [14] are binary compounds. Analysis of the data presented suggests that crystallization from aqueous solutions is an effective method for separation of calcium chloride from Co(II), Cu(I), Cu(II), Mn(II), Zn, Cd, NH_4^+, K, and Mg chlorides.

Crystallization of $CaCl_2$ from HCl solutions is promising, since in this case, the yield of the target product increases substantially ($CaCl_2$ solubility in a 26–28% HCl solution is 4 times lower at 0°C and twice lower at 15°C than that in H_2O [1]); however, this process has not been studied. It has been proposed to purify $CaCl_2$ solutions to remove iron ions by treatment with carbonate-containing compounds (ammonium carbonate solution) at 71–100°C and pH 4–7. A product containing 8×10^{-5} wt % iron has been obtained [15].

A way to prepare $CaCl_2$ phosphors by precipitation of sparingly soluble sulfide and phosphate impurities, separation of precipitate, and boiling of the solution with activated carbon has been described. The quality of the product obtained has not been reported [16].

Joint precipitation of impurities with calcium carbonate at 60–80°C and pH 5–7 has been proposed as a method for purification of $CaCl_2$ solutions, and the possibility of using purified solution for preparing luminophore has been demonstrated [17, 18].

Treatment of $CaCl_2$ solutions with complexing reagents (sodium diethyldithiocarbamate [17–19], 8-oxyquinoline [20]) is highly efficient in removal of iron, heavy metals, and other impurities.

Analysis of the above data on $CaCl_2$ purification shows that published data are rather scarce. Promising among the known purification methods are crystallization of $CaCl_2$ from aqueous solutions and joint precipitation of impurities onto inorganic collectors.

The aim of the present study was to analyze the process of calcium chloride purification.

EXPERIMENTAL

Two methods of calcium chloride purification were studied: crystallization from aqueous solutions and

1070-4272/03/7602-0167 $25.00 © 2003 MAIK "Nauka/Interperiodica"

Table 1. Impurity fractionation in crystallization of $CaCl_2$ from aqueous solutions at 25°C

Impurity, wt %	α	K_{pur} for $CaCl_2 \cdot 6H_2O$ crystals	
		with washing	without washing
^{59}Fe:			
1×10^{-4}	0.60	10.0 ± 0.3	78.0 ± 2.3
1×10^{-5}	0.50	6.2 ± 0.2	70.0 ± 2.1
1×10^{-5}	0.60	5.0 ± 0.1	56.0 ± 1.2
^{54}Mn:			
5×10^{-6}	0.50	9.0 ± 0.3	96.6 ± 2.9
5×10^{-6}	0.60	8.5 ± 0.2	89.5 ± 2.8
^{51}Cr:			
5×10^{-6}	0.50	8.1 ± 0.2	96.2 ± 2.5
5×10^{-6}	0.60	7.2 ± 0.2	86.5 ± 2.5
^{63}Ni:			
5×10^{-6}	0.50	8.0 ± 0.2	78.6 ± 2.2
5×10^{-6}	0.60	7.1 ± 0.2	72.3 ± 2.2
^{57}Co:			
5×10^{-6}	0.50	8.0 ± 0.2	90.7 ± 2.7
5×10^{-6}	0.60	6.0 ± 0.2	75.3 ± 2.2

joint precipitation of impurities from aqueous solutions onto inorganic collectors.

The study was performed using radioactive tracers ^{59}Fe, ^{60}Co, ^{54}Mn, ^{51}Cr, ^{64}Cu, and ^{63}Ni. The radiation was recorded simultaneously from several isotopes using an IN-96B automated multichannel gamma spectrometer (France) and a semiconductor detector (single-crystal germanium). The relative measurement error was ±2–3%. Beta radiation (^{63}Ni) was measured with a BDIS 3-05 transducer with detector (thallium-activated NaI), PS-2 counter unit, and scintillating granules. The relative accuracy of the measurement was ±10%. The results of radiometric analysis were used to calculate the crystal purification factors K_{pur} as the ratio of the specific activities of crystals (solution) before and after crystallization (purification), related to unit mass of $CaCl_2 \cdot 6H_2O$), and the degree α of precipitation of the main substance ($CaCl_2 \cdot 6H_2O$) into the solid phase during crystallization [21].

The purification of $CaCl_2$ by crystallization was studied as follows: radioactive isotopes of the corresponding metals were introduced into 100 ml of a 78% solution of $CaCl_2 \cdot 6H_2O$ [14–1 ultrapure grade, TU (Technical Specification) 6-09-3834–80], and the mixture was stirred and kept for 1 day for isotopic exchange to occur. Then, the solution was evaporated on a water bath to obtain solid phase in varied yield and cooled to room temperature under continuous agitation. The crystals precipitated were separated on a Büchner funnel ("blue tape" filtering paper) and firmly squeezed between two sheets of filtering paper to remove mother liquor. The squeezed crystals were twice washed with a saturated solution of initial $CaCl_2$, whose volume was equal to the crystal mass, and then squeezed again. The specific activities of the initial solution, mother liquor, squeezed crystals before washing, and doubly washed crystals (after dissolution in water) were determined, and K_{pur} were calculated.

Analysis of the results obtained (Table 1) shows that the degree of $CaCl_2$ purification by crystallization from aqueous solution to remove iron, manganese, chromium, nickel, and cobalt ion impurities is not too high. The low degree of purification of the $CaCl_2 \cdot 6H_2O$ crystals (Table 1) is due to occlusion of the mother liquor, since additional washing of the crystals makes K_{pur} higher for all of the impurities studied. According to published data, calcium and cobalt (copper and manganese) chlorides do not form solid solutions in joint crystallization from aqueous solutions [6–8, 12].

The results obtained are accounted for by the characteristic high solubility of $CaCl_2$ and stability of metastable supersaturated solutions. This leads to changes in the crystal growth mechanism, facilitates formation of aggregates, closed cavities, and capillaries, and causes surface deterioration and the resulting pronounced entrapment of mother liquor by the crystals, which is responsible for the low degree of purification of unwashed crystals (Table 1).

Additional washing of the isolated $CaCl_2 \cdot 6H_2O$ crystals with a saturated aqueous solution of this compound markedly increases the degree of purification (Table 1). Despite the necessity for processing of large volumes of mother liquors, the crystallization method shows industrial promise. Compared with calcium nitrate crystallization [21], the method in question is more efficient for preparing small amounts of ultrapure calcium salts in laboratory.

Also, purification of $CaCl_2$ solutions with inorganic collectors was studied. It has been established previously [21] that purification of calcium nitrate solutions to remove 3*d*-metal impurities with the use of hydrated aluminum and zirconium oxides is highly effective. It has been proposed to purify calcium chloride solutions by coprecipitation of impurities onto a $CaCO_3$ collector [15, 17, 18]. However, this collector is, as a rule, effective only for iron impurity [15, 21]. Therefore, hydrated aluminum, $Al_2O_3 \cdot nH_2O$, or zirconium oxides, $ZrO_2 \cdot nH_2O$, precipitated in a solution being purified were used in this study for purification of $CaCl_2$ aqueous solutions.

Table 2. Distribution of iron(III), chromium(III), manganese(II), and copper(II) impurities upon purification of a 20% $CaCl_2$ solution on inorganic collectors*

c, wt %	K_{pur} for indicated impurity					c, wt %	K_{pur} for indicated impurity				
	Fe(III)	Cr(III)	Mn(II)	Co(II)	Cu(II)		Fe(III)	Cr(III)	Mn(II)	Co(II)	Cu(II)
Collector–$Al_2O_3 \cdot nH_{20}$						Collector–$ZrO_2 \cdot nH_{20}$					
5×10^{-4}	100 ± 3					5×10^{-4}	300 ± 9				
5×10^{-5}	120 ± 3					5×10^{-5}	1200 ± 35				
1×10^{-5}		100 ± 3	10 ± 0.3	25.0 ± 0.7		1×10^{-5}		250 ± 7	100 ± 3		
5×10^{-6}					20.0 ± 0.6	5×10^{-6}				70 ± 2	150 ± 4

* (c) Impurity concentration.

Table 3. Quality of initial and purified $CaCl_2$ and $CaCl_2 \cdot 6H_2O$ samples and the best foreign products (according to catalogues)

Sample	Impurity content, $c \times 10^6$, wt %					
	Fe(III)	Mn(II)	Cu(II)	Cr(III)	Ni(II)	Co(II)
Laboratory:						
Initial	500	20	50	50	8	<5
Purified	20	<2	<2	<2	<2	<0.5
Analytical-purity grade, TU 6-09-4578–78, Russia	200					
14-1 special-purity grade, TU 6-09-3834–80, Russia	50		1		Ni(II)–Co(II), 30	
Extra pure, Riedel-de-Häen, Germany	500		500			
Suprapur,* E.Merck, Germany	5	1	0.5		0.5	0.5

* $CaCl_2 \cdot 4H_2O$.

Solutions of radioactive isotopes were introduced into a 20 wt % solution of $CaCl_2$ (25 ml), the solution was stirred for 3 h for the isotope exchange to occur, and a sample was taken for radiometric measurements. Then, calculated amounts of a 20% solution of $Al(NO_3)_3$ (17-3 ultrapure grade, TU 6-09-3657–74) or $ZrOCl_2$ (chemically pure grade, TU 6-09-3677–74, 2.0 wt % relative to the $CaCl_2 \cdot 6H_2O$ mass by analogy with the data of [21]) were introduced into the solution, and a 10% solution of NaOH [18-3 special-purity grade, OST (All-Union Standard) 6-01-302–74] was gradually added under agitation to pH 8.0. The mixture was stirred for 1 h, the precipitated hydrated aluminum or zirconium oxides were separated on a TsLN-2 centrifuge, and the purified solution was sampled for radiometric analysis. The method of analysis and the procedure for calculating K_{pur} are described above.

Analysis of the results obtained (Table 2) shows that the purification of $CaCl_2$ solution with $ZrO_2 \cdot nH_2O$ collector is a highly effective process. For $Al_2O_3 \cdot nH_2O$, the degree of $CaCl_2$ purification is somewhat lower and differs significantly from the results obtained previously for $Ca(NO_3)_2$ solutions [22]. This can be accounted for by higher stability of chloride complexes in aqueous solutions [23].

The data on coprecipitation of metal ions onto $ZrO_2 \cdot nH_2O$ (Table 2) correlate well with the values of the first constants of their hydrolysis [24] and supplement the previously established selectivity series [25].

Large-scale laboratory experiments on $CaCl_2$ purification by crystallization from aqueous solutions were performed. An aqueous solution of $CaCl_2$ was prepared by dissolving an analytically pure reagent at 70°C, filtering the solution on a "blue tape" filtering paper, evaporating it on a water bath to about 60% yield, and cooling the mixture to room temperature under continuous agitation. The crystals precipitated were carefully separated and washed with a saturated solution of $CaCl_2$ (14-1 special-purity grade), whose volume was equal to the mass of the separated $CaCl_2 \cdot 6H_2O$ crystals. Then the crystals were dried at 25–28°C and subjected to spectrochemical analysis [26].

A comparison of the quality of the initial $CaCl_2$ samples and those purified by crystallization from aqueous solution (Table 3) showed that this method is

promising for preparing a special-purity-grade product. For preparing ultrapure calcium salts, the $CaCl_2$ crystallization is a more effective method than the previously described technique using calcium nitrate [21].

CONCLUSIONS

(1) Purification of $CaCl_2$ by crystallization from aqueous solutions was studied using radioactive tracers. The purification factors were calculated. It was found that the low values of K_{pur} for $CaCl_2 \cdot 6H_2O$ crystals are due to occlusion of the mother liquor. It was shown that $CaCl_2$ crystallization is promising method for preparing an ultrapure product.

(2) Purification of aqueous $CaCl_2$ solutions by coprecipitation of impurities onto inorganic collectors ($Al_2O_3 \cdot nH_2O$ or $ZrO_2 \cdot nH_2O$) was studied using radioactive tracers. A high efficiency of the $ZrO_2 \cdot nH_2O$ collector for purification of $CaCl_2$ solutions was demonstrated.

REFERENCES

1. Pozin, M.E., *Tekhnologiya mineral'nykh solei* (Technology of Mineral Salts), Leningrad: Khimiya, 1974.
2. Karyakin, Yu.V., and Angelov, I.I., *Chistye chimicheskie veshchestva* (Pyre Chemical Substances), Moscow: Khimiya, 1974.
3. *Fiziko-khimicheskie osnovy proizvodstva opticheskogo stekla* (Physicochemical Foundations of Optical Glass Manufacture), Demkina, L.I., Ed., Leningrad: Khimiya, 1976.
4. Kosintsev, F.I., *Zh. Vsesoyuz. Khim. O–va im. D.I. Mendeleeva*, 1984, vol. 29, no. 6, pp. 72–74.
5. *Spravochnik khimika* (Chemist's Reference Book), Nikol'skii, B.P., Ed., Leningrad: Khimiya, 1965, vol. 3.
6. Bernath, A., *Z. anorg. allgem. Chem.*, 1927, vol. 163, nos. 3/4, pp. 396–404.
7. Bassett, H., Gordon, H.F., and Henshall, J.H., *J. Chem. Soc.*, 1937, pp. 971–973.
8. Shirokova, G.N., Shokin, I.N., and Kuznetsova, A.G., *Trudy Mosk. Khimiko-Tekhnol. Inst. im. D.I. Mendeleeva* (Proceedings of the Mendeleev Institute of Chemical Engineering, 1965, no. 49, pp. 73–77.
9. Ivanov, S.A., *Sbornik nauchnykh trudov Yaroslavl. Pedag. Inst.* (Coll. of Sci. Works of Yaroslavl Pedag. Inst.), 1977, no. 164, pp. 67–69.
10. Assarson, G.O., *J. Am. Chem. Soc.*, 1950, vol. 72, no. 4, pp. 1433–1436.
11. Perova, A.P., *Soobshchenie o nauchn. rabotakh Vsesoyuzn. Khim. O–va im. D.I. Mendeleeva*, 1955, no. 2, pp. 46–48.
12. Zhelnin, B.I., and Gorshtein, G.I., *Zh. Prikl. Khim.*, 1972, vol. 45, no. 6, pp. 1347–1348.
13. Hudgins, C.M., *J. Chem. Eng. Data*, 1964, vol. 9, pp. 434–437.
14. Bassett, H., and Strain, R., *J. Chem. Soc.*, 1952, pp. 1795–1797.
15. USSR Inventor's Certificate, no. 998353
16. Romanian Patent 75724.
17. Angelov, I.I., *Materialy V soveshchaniya po lyuminestsentsii* (Proc. V Meeting on Luminescence), Tartu: Akad Nauk ESSR, 1956, pp. 338–346.
18. Mezentseva, I.A., Samarskaya, E.I., Shindakova, N.V., *et al.*, *Nauchnye trudy Vsesoyz. Naucho-Issled. Inst. Lyuminoforov* (Sci. Works of the All-Russia Research Institute of Luminophores), 1986, no. 31, pp. 27–31.
19. Angelov, I.I., Shwarts, M.M., Buris, E.V., and Khainson, S.I., *Trudy Vsesoyzn. Nauchno-Issled. Inst. Khim. Reaktivov* (Proc. of the All-Russia Research Institute of Chemical Reagents), 1958, no. 22, pp. 159–162.
20. Golota, A.F., Valetto, D.I., and Golota, A.A., *Nauchnye trudy Vsesoyz. Naucho-Issled. Inst. Lyuminoforov* (Sci. Works of the All-Russia Research Institute of Luminophores), 1970, no. 4, pp. 145–149.
21. Fakeev, A.A., and Sukhanovskaya, A.I., *Zh. Prikl. Khim.*, 2001, vol. 74, no. 12, pp. 1921–1924.
22. Fakeev, A.A., Kurmanguzhina, L.K., and Sukhanovskaya, A.I., *Zh. Prikl. Khim.*, 2002, vol. 75, no. 5, pp. 724–729.
23. Davydov, Yu.P., *Sostoyanie radionuklidov v rastvorakh* (State of Radionuclides in Solutions), Minsk: Nauka i Tekhnika, 1978.
24. Baes, C.F., and Mesmer, R.E., *The Hydrolysis of Cations*, New York: Wiley–Interscience, 1976.
25. Bekrenev, A.V., and Pyartman, A.K., *Zh. Neorg. Khim.*, 1995, vol. 40, no. 6, pp. 938–942.
26. Chupakhin, M.S., Sukhanovskaya, A.I., Krasil'shchik, V.Z., *et al.*, *Metody analiza chistykh khimicheskikh reaktivov* (Methods for Analysis of Pure Chemical Reagents), Khimiya, 1984.

Russian Journal of Applied Chemistry, Vol. 76, No. 2, 2003, pp. 171–174. Translated from Zhurnal Prikladnoi Khimii, Vol. 76, No. 2, 2003, pp. 181–184.

INORGANIC SYNTHESIS AND INDUSTRIAL INORGANIC CHEMISTRY

Optimization of Olivine Processing To Obtain Magnesium Meliorant

V. N. Makarov, N. K. Manakova, T. N. Vasil'eva, and A. T. Belyaevskii

Tananaev Institute of Chemistry and Technology of Rare Elements and Mineral Raw Materials, Kola Scientific Center, Russian Academy of Sciences, Apatity, Russia

Received September 16, 2002

Abstract—Problems associated with the optimization of processing of olivine from mining wastes and, in particular, from dressing tailings of vermiculite ores with sulfuric acid in order to obtain a magnesium meliorant characterized by alkaline reaction were considered. The influence of a seed on the course of silica gel coagulation and on the filtration of the forming solutions was studied.

Atmospheric precipitation near mining and smelting plants is characterized by increased acidity. Although the strongest impact of acid rains on the environment is observed on territories closely adjacent to nonferrous metallurgy plants, the influence of these rains is also pronounced at a considerable distance from the plants. In particular, acid rains in Kola peninsula also fall in regions virtually lacking any industrial plants, including nature reserves. This atmospheric precipitation, which is characterized by pH ranging from 3.6 to 4.7, contains 2.1 to 52.7 mg l^{-1} of sulfate ions [1].

Under the action of acid rains, a number of necessary nutritious elements, Mg^{2+}, Ca^{2+}, and Mn^{2+} cations in the first place, are selectively leached from plants and soil of forest ecosystems [1].

To compensate for the deficiency of cations, it is necessary to use meliorants that would replenish the nutritious substances. In view of the increased acidity of soil in zones affected by acid rains, the meliorants must possess a neutralizing capacity and also improve the soil structure. With account of the large areas of deteriorated forests, the meliorants must be comparatively low-cost and readily accessible.

An important factor in making lower the cost of a meliorant is cheapness of raw materials. The most promising in this regard are mining wastes. Annually, industrial countries produce hundreds of millions of tons of ferrous and various nonferrous metals. Most part of ores is separated, in the course of ore dressing, in the form of nonmetalliferous minerals from the valuable minerals and discarded as waste into tailing dumps. The maintenance of tailing dumps is rather expensive. Finely dispersed tailings react with atmospheric agents. Flotoreagents, which are sorbed on the surface on nonmetalliferous minerals, and products of oxidation of sulfides are leached into surface and ground waters. In the course of oxidation of ore dressing tailings, readily soluble sulfates of heavy metals pass into the environment [2]. The large volume of the mining waste accumulated gives no reason to believe that they could be processed in near future. Therefore, the primary objects of study and targets for utilization technologies are mining wastes that can be reprocessed into ecological-purpose materials [3].

Meliorants can be manufactured from mining wastes mainly composed of silicates (olivinites, dunites, etc.) or magnesium hydrosilicates (serpentinites).

In particular, meliorants can be obtained from serpentine-containing materials, which are wastes formed in processing of copper-nickel, vermiculite, and some other ores. However, serpentine materials are to be activated in order to obtain the final product. This involves certain energy expenditure, which is not always justified.

Use of mining wastes mainly composed of anhydrous magnesium silicates, olivines, which are frequently richer in magnesium oxide than serpentines, offers more promise for manufacture of meliorants. In this case, strip-pit olivinites of the Kovdor phlogopite deposit, dressing tailings of vermiculite ores, strip-pit

1070-4272/03/7602-0171 $25.00 © 2003 MAIK "Nauka/Interperiodica"

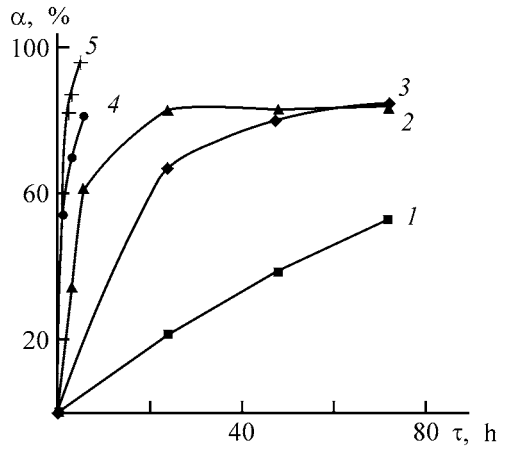

Fig. 1. Degree of olivine processing, α, vs. processing time τ. Processing temperature (°C): (*1*) 20; (*2*) 40; (*3*) 60; (*4*) 80; (*5*) 80, with addition of a seed.

dunites from chromite deposits of the Monchegorsk region, and other products of this kind can serve as raw materials. Although vermiculite tailings are characterized by lower content of magnesium oxide, they contain minerals including other nutritious substances: calcium and phosphorus in apatite, potassium in hydrophlogopite, and manganese in olivine and vermiculite, which can also be converted into assimilable form. At the same time, the dressing tailings are rather cheap and readily accessible.

In acid treatment of olivine, nutritious substances contained in it are converted into a form assimilable by plants [4]. However, the technique proposed in [4] has two important disadvantages; olivine processing takes a long time (72 h) and the product obtained is characterized by a stable acid reaction. Formation of a silica gel poses considerable difficulties, since, in producing a magnesium fertilizer, silica passes into the final product because of the impossibility of filtration. At the same time, there is no way of neutralizing acid salts and acid residues formed in olivine processing, since magnesium hydrosilicates are formed in the neutral or alkaline medium in the presence of silicic acid.

To manufacture a neutral meliorant, it is necessary to optimize the olivine processing so as to enable separation of silica and to prevent reverse reactions in neutralization of acid salts and acid residues.

EXPERIMENTAL

In studying the reaction of olivine with H_2SO_4, dressing tailings of vermiculite ores were used. In view of the fact that fine fractions of this product contained a large amount of sungulite, and coarse fractions contained pieces of dike rocks, which are poor in magnesium minerals, the vermiculite tailings were subjected to preliminary sizing. The +0.125–3.0-mm fraction was used in the experiments.

Mineral composition of the raw material (%): olivine 45.3, vermiculite 12.65, apatite 10.04, magnetite 8.66, diopside 21.17, and sungulite 0.8.

Chemical composition of the raw material (wt %): MgO 25.0, K_2O 0.12, CaO 14.0, Na_2O 0.26, Al_2O_3 0.92, FeO 4.25, Fe_2O_3 5.81, H_2O 1.12, SiO_2 33.46, and P_2O_5 4.46.

A 15-g portion of the material was poured over with 50 ml of a 40% H_2SO_4 solution. The temperature was varied between 20 and 80°C, and the processing time, between 3 h and 3 days.

After the experiment was complete, the solid residue was washed with distilled water and dried. A white powder containing new formations was separated from the product obtained. Then the granulometric composition of the residue was studied and residual contents of the starting minerals—olivine, pyroxenes, vermiculite, and apatite, were determined mineralogically. A finely dispersed product was additionally subjected to X-ray diffraction analysis on a DRON-2 diffractometer (Cu_{K_α} radiation), and also studied on a FLOUSORB II 2300 laboratory electronic device for measuring the specific surface area and porosity and on a Hitachi scanning electron microscope.

The washing solutions were analyzed chemically for the content of calcium, magnesium, and iron ions.

The degree of olivine processing, measured in the course of time at different temperatures, is shown in Fig. 1. At room temperature, the process is slow, and, therefore, the subsequent experiments were done at 40, 60, and 80°C. On raising the temperature, the olivine conversion is much accelerated: at 80°C olivine is virtually entirely (80%) processed in 6 h.

Equation (1) describes the reaction of olivine with acid

$$Mg_2SiO_4 + 4H^+ + (n - 2)H_2O = 2Mg^{2+} + SiO_2 \cdot nH_2O. \quad (1)$$

The study performed demonstrated that, together with acid processing of olivine, formation of magnesium hydrosilicates with serpentine-like structure is observed:

$$6Mg^{2+} + 4SiO_2 \cdot nH_2O = Mg_6(OH)_8[Si_4O_{10}] + 4(n - 1)H_2O. \quad (2)$$

In this case, a considerable amount of magnesium ions recovered into solution are bound. Raising the temperature promotes the olivine processing, but, even to a greater extent, accelerates the formation of hydrosilicates. As a result, the recovery of magnesium ions into solution decreases. It seems reasonable that, for reverse reactions to occur, the solution pH should be made higher. Therefore, it is impossible to obtain a neutral meliorant directly by acid processing of olivine. Presumably, a technology for obtaining such a product must include several stages, with neutralization only carried out after separating the active silica.

It is known that the longest characteristic time in silica coagulation is the induction period of nucleation of primary colloid particles, which then combine into coarse aggregate. Silica coagulation is much accelerated in the presence of specially introduced particles of amorphous SiO_2, acting as nuclei [5]. To prevent formation of magnesium hydrosilicates and to accelerate silica coagulation, a seed, having the form of amorphous SiO_2 obtained from nepheline, vermiculite, or sungulite, was introduced into the reaction vessel together with raw materials and acid. The experiments were done with vigorous stirring. The solutions were filtered in hot state to prevent $MgSO_4$ crystallization. After an experiment was complete, the solid residue was washed with hot distilled water (70°C).

The experiments demonstrated that addition of amorphous SiO_2 as a seed makes it possible to obtain coagulated silica and well filterable solutions, to prevent a reverse reaction of binding of magnesium ions from solution, and to decrease the H_2SO_4 concentration to 25%, with total recovery of magnesium ions into solution ensured.

Figure 2 shows kinetic curves describing the completeness of recovery of magnesium ions in relation to the amount of seed. With the amount of a seed additive prepared from nepheline increasing to 15% relative to the amount of the starting material, the recovery of magnesium ions reaches 100%. A sungulite seed is less effective, with the recovery equal to only 76%. It is not improbable that the closeness of the inherited structure of the seed to magnesium hydrosilicates gives no way of ruling out the reverse reactions. However, a vermiculite-based seed is nearly as effective as that based on nepheline. With increasing amount of the seed added (Fig. 3), the humidity of the final product decreases.

Electron-microscopic studies demonstrated that newly formed silica has a lamellar structure (Fig. 4), whereas amorphous SiO_2 obtained by sulfuric acid treatment of nepheline [5] is represented by densely packed rounded particles.

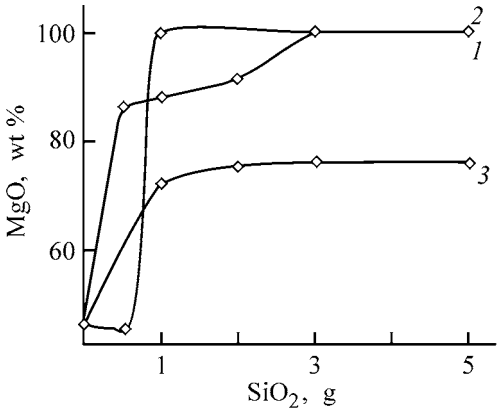

Fig. 2. Amount of recovered MgO vs. amount of SiO_2 seed introduced. Seed: (*1*) nepheline, (*2*) vermiculite, and (*3*) sungulite; the same for Fig. 3.

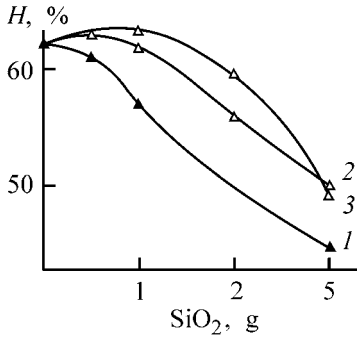

Fig. 3. Sample humidity *H* vs. amount of SiO_2 seed introduced.

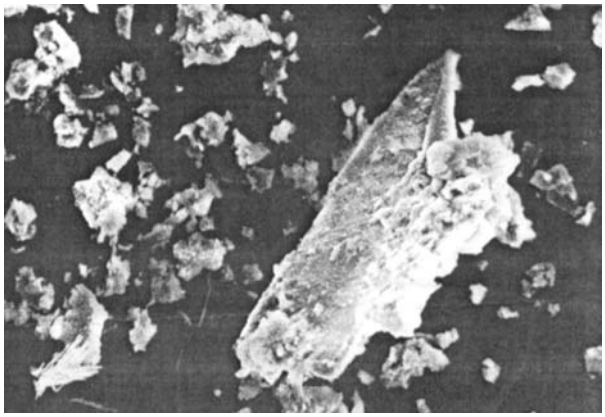

Fig. 4. Electron micrograph of a finely dispersed sample obtained with addition of a vermiculite seed.

CONCLUSIONS

(1) Complete processing of olivine and vermiculite contained in vermiculite tailings takes 6 h in 25% sulfuric acid at 80°C.

(2) Addition of amorphous SiO_2 as a seed precludes the reverse reaction of magnesium ion binding from solution and ensures complete leaching-out of magnesium.

(3) The optimal amount of the silica seed in terms of dry substance is 15 wt % relative to the amount of the starting raw material.

(4) Separation of a silica precipitate from the magnesium-containing solution enables manufacture of a neutral meliorant by a known method.

ACKNOWLEDGMENTS

The study was supported by the Program "Leading Scientific Schools" (project no. 00-15-97364).

REFERENCES

1. Lukina, N.V. and Nikonov, V.V., *Biogeokhimicheskie tsikly v lesakh Severa v usloviyakh aerotekhnicheskogo zagryazneniya* (Biogeochemical Cycles in Northern Forests under Conditions of Aerospace Contamination), Apatity: Kola Nauchn. Tsentr, Ross. Akad. Nauk, 1996, part 1, p. 213.
2. Makarov, V.N., *Ekologicheskie problemy khraneniya i utilizatsii gornopromyshlennykh otkhodov* (Ecological Problems Associated with Storage and Utilization of Mining Wastes), Apatity: Kola Nauchn. Tsentr, Ross. Akad. Nauk, 1998, part 1.
3. Makarov, V.N., *Mineralogicheskie kriterii kompleksnoi pererabotki rudovmeshchayushchikh giperbasitov* (Mineralogical Criteria for Comprehensive Processing of Ore-Containing Hyperbasites), Apatity, 1989.
4. USSR Inventor's Certificate, no. 1 392 066.
5. Zakharov, V.I., Kalinnikov, V.T., Matveeev, V.A., and Maiorov, D.V., *Khimiko-tekhnologicheskie osnovy i razrabotka novykh napravleniii kompleksnoi pererabotki i ispol'zovaniya shchelochnykh alyumosilikatov* (Chemical-Technological Foundations and Development of New Directions of Comprehensive Processing and Use of Alkaline Aluminosilicates), Apatity, 1995.

Russian Journal of Applied Chemistry, Vol. 76, No. 2, 2003, pp. 175–179. Translated from Zhurnal Prikladnoi Khimii, Vol. 76, No. 2, 2003, pp. 185–189.

INORGANIC SYNTHESIS AND INDUSTRIAL INORGANIC CHEMISTRY

Distribution of Copper, Nickel, Cobalt and Iron between Products of Smelting of Copper Concentrate Obtained by Flotation of Converter Matte

N. A. Fedorova, L. B. Tsymbulov, and L. Sh. Tsemekhman

Institut Gipronikel' Joint-Stock Company, St. Petersburg, Russia

Received November 21, 2002

Abstract—An experimental study of the equilibrium between the bottom phase (sulfide melt or copper) and slag in neutral and oxidizing atmospheres yielded dependences of the content of dissolved copper, nickel, and cobalt in the slag on that of sulfur in the sulfide melt and also the dependence of the content of dissolved copper and nickel on that of nickel in the metallic melt. The distribution coefficients of the metals between copper and slag were determined and compared with the results of other investigations.

Nickel-containing copper concentrate obtained by flotation of the converter matte (composition, wt %: Cu 67–70, Ni 2–5, Fe 2–5, Co 0.1–0.3, S 20–21) is processed in various ways [1–7].

The distribution of the metal between a target product (sulfide melt or metallic melt based on copper) and the slag is one of the most important characteristics of any smelting technology. Commonly, this factor is evaluated by the metal distribution coefficient L_M defined as the ratio of metal weight fractions in the sulfide (metallic), $X_{[M]}$, and slag phases, $X_{(M)}$:

$$L_M = X_{[M]}/X_{(M)}.^1 \quad (1)$$

It is a common practice to subdivide copper-based metallic melts, depending on their copper and sulfur content, into blister copper containing 0.5–1 wt % Ni and 0.03–0.05 wt % S and "sulfurous" copper containing 5–6 wt % Ni and 1.5–2.0 wt % S.

The wide variety of technologies used in smelting of the copper concentrate assumes significant differences in the L_M values. The reason is that the compositions of the sulfide (metallic) melts and slag are different, as also are the compositions of the gas phase over the melt, which is characterized by partial oxygen pressure P_{O_2}.

The available published data obtained in studying the distribution of nickel and copper in processing of the copper concentrate produced by flotation of the converter matte are considered in this study.

Yazawa [8, 9] studied the distribution of metals between a sulfur-free copper-based metallic melt and the slag under partial oxygen pressure of 10^{-11}–10^{-8} atm in the gas phase at a temperature of 1200°C. The equilibrium between iron-silicate slag saturated with silicon dioxide, on the one hand, and copper, on the other, in the temperature range 1217–1307°C at partial oxygen pressure varied from 10^{-11} to 10^{-7} atm was studied in [10]. The solubility of copper in the iron-silicate slag saturated with silicon dioxide was determined in [11] under the conditions of equilibrium with a liquid Cu–Au melt at $P_{O_2} = 10^{-10}$–10^{-7} atm and 1250–1350°C. The coefficients of copper, nickel, and iron distribution at 1500°C between the liquid Cu–Ni–Fe alloy and the slag (which is a mixture of FeO_x–SiO_2–CaO oxides saturated with MgO) were calculated from the activity coefficients of the alloy components at partial pressures of oxygen in the range 10^{-10}–10^{-6} atm [12]. These activity coefficients were determined by the quasi-equilibrium gas-flow method using Knudsen's double mass-spectrometric cell. In [13], the results obtained in an experimental study of the distribution of metals in equilibrium in the systems constituted by (i) sulfurous copper, sulfide melt, and slag and (ii) blister copper and slag in an atmosphere of argon and in an oxidizing atmosphere with $P_{O_2} = 1.6 \times 10^{-5}$–$2.9 \times 10^{-5}$ atm at 1300°C were considered. Abramov *et al.* [14] studied the influence exerted by the content of silicon dioxide in a slag at $P_{O_2} = 1.4 \times 10^{-5}$ atm and 1300°C on the distribution of metals in

[1] A reverse ratio between the metal weight fractions can also be found in the literature. In the present study, the L_M values are represented as the $x_{[M]}/x_{(M)}$ ratio.

1070-4272/03/7602-0175 $25.00 © 2003 MAIK "Nauka/Interperiodica"

Table 1. Comparison of the distribution coefficients of copper L_{Cu} and nickel L_{Ni} according to published data

L_{Cu}	L_{Ni}	P_{O_2}, atm	T, K	Reference
300–55	600–25	10^{-11}–10^{-8}	1473	[9]
325–25	–	10^{-11}–10^{-7}	1490–1580	[10]
110–21	–	10^{-10}–10^{-7}	1523–1623	[11]
160–23	200–8.3	10^{-10}–10^{-6}	1773	[12]
–	24–6.5	2.9×10^{-5}–1.6×10^{-5}	1573	[13]
–	27–30	Ar	1573	
20–12	5.9–2.1	1.4×10^{-5}	1573	[14]
11.1–5.9	2.3–0.9	6.1×10^{-5}–2.1×10^{-4}	1553	[15]

Table 2. Composition of starting materials

Material	Content, wt %					Material	Content, wt %				
	Cu	Ni	Fe	Co	S		Cu	Ni	Fe	Co	S
Copper sulfide	75.3	4.1	0.8	0.08	16.9	Blister copper	97.8	0.48	0.2	0.08	–
Copper concentrate	67.0	4.0	4.4	0.21	21.6	Sulfurous copper	92.2	5.8	0.1	0.02	1.9

the equilibrium system constituted by sulfurous copper, sulfide melt, and slag. The dependence of the distribution coefficients on the SO_2 concentration in the gas phase (P_{O_2} = 6.1×10^{-5}–2.1×10^{-4} atm) at 1280°C was studied under equilibrium conditions in the system formed by sulfurous copper, sulfide melt, and slag [15]. The distribution coefficients found in these studies are listed in Table 1.

Analysis of the data obtained indicates that the majority of the investigations [8–13, 15] are concerned with the effect of P_{O_2} on the solubility of copper in slag.

The copper content in slag grows (L_{Cu} value decreases) with increasing P_{O_2}. The effect of slag composition on the distribution of nonferrous metals has been studied to a lesser extent [13–15]. The least studied is the influence exerted by the activities of components in a copper-rich melt (sulfide melt, sulfurous copper, or blister copper) on the distribution of copper and impurities concomitant in cooper–nickel production (nickel, cobalt, and iron). The only study [11] was concerned with the influence of the activity of copper on its distribution between metallic melt and slag. It was found that copper solubility in the slag linearly grows with its increasing activity in the Cu–Au melt, with this dependence becoming more pronounced with increasing partial pressure of oxygen.

It follows from Table 1 that the most topical issue to be studied is the effect of the composition of sulfide and metallic melts on the distribution of copper and metal impurities between the smelting products. Such a study would cover all versions of technologies for processing of the nickel-containing copper flotation concentrate, from smelting to give copper sulfide to that producing blister copper.

Three sets of experiments were performed in this study. The first of these was concerned with the effect of the sulfide melt composition on the distribution of metals between products of smelting in an argon atmosphere. The second and the third sets were devoted to the effect of copper composition (sulfurous and blister copper, respectively) in an oxidizing atmosphere. In the first and second sets, a neutral atmosphere was created using high-purity argon which contained (wt %): O_2 0.0002, N_2 0.001, H_2 0.0002, CH_4 0.0001, and CO_2 0.00002. The partial pressure of oxygen in this gas mixture was 4×10^{-8} atm at 1300°C.

In the first set of experiments, a synthetic iron-silicate slag (7 g) containing 20–23 wt % SiO_2 and copper (45 g) with varied sulfur content (17–22 wt %) were used. Mattes of varied composition were obtained by taking an industrial sulfide melt from a reverberatory furnace and the starting concentrate in various proportions.

In the second and third set of experiments, a synthetic iron-silicate slag (7 and 20 g, respectively) containing 22–30% SiO_2 was mixed with copper (45 g in the second set and 20 g in the third) containing various amounts of nickel and sulfur. Copper of varied composition was obtained by taking sulfurous and blister copper in various proportions. The composition of the starting materials is listed in Table 2.

A weighed sample of a stock consisting of slag and a sulfide component (or metal) in an alundum crucible was placed in a high-temperature furnace with $LaCrO_3$ heater. The stock was heated to 1300°C with an inert gas flowing over its surface. To attain the equilibrium faster, the melt was agitated by bubbling of argon[2] ($P_{O_2} = 4 \times 10^{-8}$ atm) in the first and second sets, and with a SO_2–CO_2 gas mixture[3] ($P_{O_2} = 6 \times 10^{-5}$ atm) in the third, for 20 min and allowed to stay for the same time. In the first and second sets, the melt was cooled after settling in the reactor to 700°C in an atmosphere of argon and then in air. In the third set, a slag sample was taken after settling of the melt, and the melt remaining in the crucible was gradually cooled within the furnace to 1000°C under a flow of the working gas mixture and then in air.

The sulfide component and copper formed in smeltings were subjected to chemical analysis.

The content of metals in the slag was determined by scanning electron microscopy (SEM) and X-ray fluorescence microanalysis (XFMA). In the authors' opinion, it is this approach that makes it possible to obtain reliable data on the concentrations of metals dissolved in the slag. As is known [16], slag also includes mechanical aggregates (beads of the sulfide or metallic phase), which strongly distort the equilibrium distribution pattern obtained, e.g., by chemical analysis.

The experimental data on the equilibria between sulfide melts and slag are given in Fig. 1.

Figure 1 shows that the content of Cu, Ni, and Co is virtually independent of the sulfur content in a sulfide melt within the range of compositions under study and the observed scatter of data has random nature and is determined by the experimental error.

The coefficients of metal distribution between the sulfide melt and slag are listed in Table 3. They are also virtually independent of the composition of the sulfide melt. Together with the data obtained in the present study, Table 3 also lists the results of [14, 15].

The difference in the distribution coefficients of copper, found in this study and in [14, 15], is attributable not only to a difference in partial oxygen pressures, but also to the fact that, in the former case, copper dissolved in the slag was determined by the XFMA method, and in [14, 15], chemical methods taking into account not only dissolved copper, but also mechanical losses were used. The distribution coefficients of nickel obtained in the present study are also higher than those reported in [14, 15], which is due to higher nickel content in the sulfide melt. The distribution coefficients of iron and cobalt are in good agreement with the data of [15].

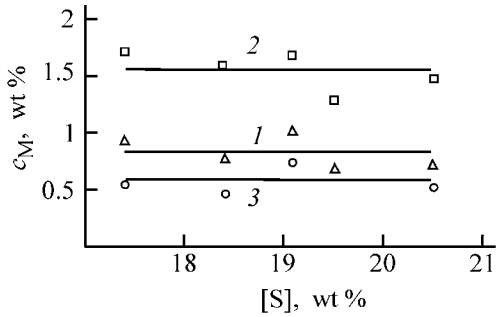

Fig. 1. Metal content c_M in the slag vs. sulfur content in the sulfide melt. M: (*1*) Cu, (*2*) Ni, (*3*) Co.

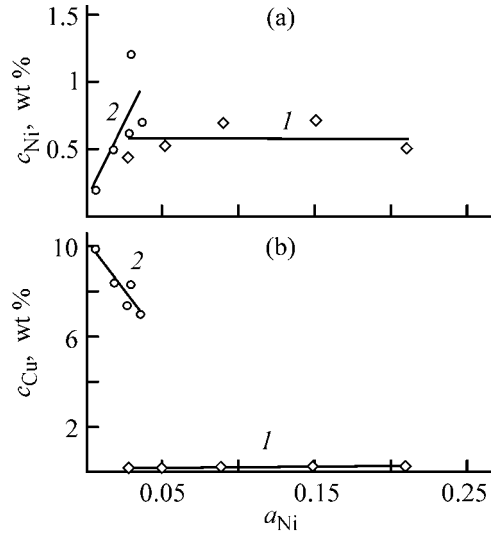

Fig. 2. Dependence of the content of (a) nickel and (b) copper in the slag on nickel activity a_{Ni} in copper in the equilibrium system copper–slag in (*1*) neutral and (*2*) oxidizing atmosphere. (*1*) Ar, (*2*) SO_2.

The results obtained in studying of the copper–slag system in an argon atmosphere are presented in Figs. 2a and 2b, curves *1*. The activities of nickel in copper containing up to 1.2 wt % nickel and about 3 wt % oxygen were taken from [17], where activities of copper and nickel in melts saturated with oxygen were determined. The activities of nickel at its content in copper higher than 1.2 wt % were taken from [18],

[2] The necessity for using argon in the first set of experiments was due to the fact that it is impossible to obtain a sulfide melt with varied sulfur content in an oxidizing atmosphere with rather high P_{O_2}.

[3] The composition of the oxidizing gas mixture was chosen in accordance with the composition of the gas phase formed in smelting of the copper concentrate to obtain blister copper.

Table 3. Coefficients of metal distribution, L_M (M: Cu, Ni, Fe, Co), between sulfide melt and slag

Content, wt %			P_{O_2}, atm	L_{Cu}	L_{Ni}	L_{Fe}	L_{Co}	Reference
Ni	Cu	S						
1.0–1.3	79–81	14.4–19.0	1.4×10^{-5}	11.4	1.0	0.03–0.07	–	[14]
0.3–1.1	72–79	16.0–19.2	6.1×10^{-5}–2.1×10^{-4}	7.1–5.3	0.9–0.2	0.01–0.02	0.07–0.05	[15]
3–5	61–78	17.4–20.5	4×10^{-8}	75–104	2–3	0.04–0.15	0.04–0.25	Present study

Table 4. Coefficients of copper, L_{Cu}, and nickel, L_{Ni}, distribution between copper and slag at varied nickel content in the bottom phase in neutral and oxidizing atmospheres

Neutral atmosphere			Oxidizing atmosphere			Neutral atmosphere			Oxidizing atmosphere		
c_{Ni}, wt %	L_{Cu}	L_{Ni}	c_{Ni}, wt %	L_{Cu}	L_{Ni}	c_{Ni}, wt %	L_{Cu}	L_{Ni}	c_{Ni}, wt %	L_{Cu}	L_{Ni}
0.6	584	1.35	0.22	9.98	1.10	4.4	267	6.34	1.15	11.77	0.95
1.3	391	2.57	0.68	13.92	1.36	6.4	302	12.54	1.41	11.68	2.01
2.4	311	3.31	1.05	13.23	1.75						

where oxygen-free copper–nickel melts were studied, since in this case, the concentration of sulfur in copper grows, and even its minor content results in a dramatic decrease in the concentration of oxygen in copper, which, therefore, can be neglected.

It is seen from the data obtained that the copper content in slag remains almost unchanged (c_{Cu} = 0.2–0.3 wt %) with the nickel activity varying within a rather narrow interval. The content of nickel in the slag also remains virtually unchanged (c_{Ni} = 0.5–0.7 wt %) when its activity in copper is varied.

The coefficients of copper and nickel distribution in the copper–slag system in an argon atmosphere ($P_{O_2} = 4 \times 10^{-8}$ atm) are listed in Table 4. The variation of the nickel distribution coefficients is completely dependent on the variation of the nickel content. It is well seen that the copper distribution coefficient is only slightly affected by the variation of the bottom phase composition.

The results obtained in studying the copper and nickel distribution between copper and slag in an oxidizing atmosphere are shown in Figs. 2a and 2b, curves *2*, and in Table 4. It is seen from Fig. 2 that the content of nickel in the slag markedly grows with its increasing activity in the metallic melt. The copper content in the slag decreases rather sharply even upon a minor increase in the nickel activity in an alloy.

The data obtained are in good agreement with the data of [11], which show that the copper solubility in a slag grows with increasing partial pressure of oxygen (distribution coefficients decrease). However, the content of copper in the slag is almost independent of the copper activity in the alloy at high copper content (95–100 wt %) and low partial pressures of oxygen.

As seen from Table 4, the distribution coefficient of copper decreases substantially on passing from argon to an oxidizing atmosphere, which is due to the increasing content of dissolved copper in the slag. Raising the partial pressure of oxygen has virtually no effect on the nickel distribution coefficient, which lies in the range 1–2 in both cases at nickel content in copper of up to 1.5%. However, a certain tendency toward an increase in the content of nickel dissolved in the slag is observed in the oxidizing atmosphere (Fig. 2a).

Now, it is appropriate to compare the coefficients of copper and nickel distribution between copper and slag, obtained in this study, with the results of other studies, listed in Table 1.

The distribution coefficients of copper in an argon atmosphere are in good agreement with the coefficients obtained at low partial pressures of oxygen (10^{-11} atm) [9, 10]. The distribution coefficients of nickel in an argon atmosphere are much lower than the values obtained in [13] for compositions of copper and slag close to those in the present study. The difference in L_{Ni} is mainly related to the higher nickel

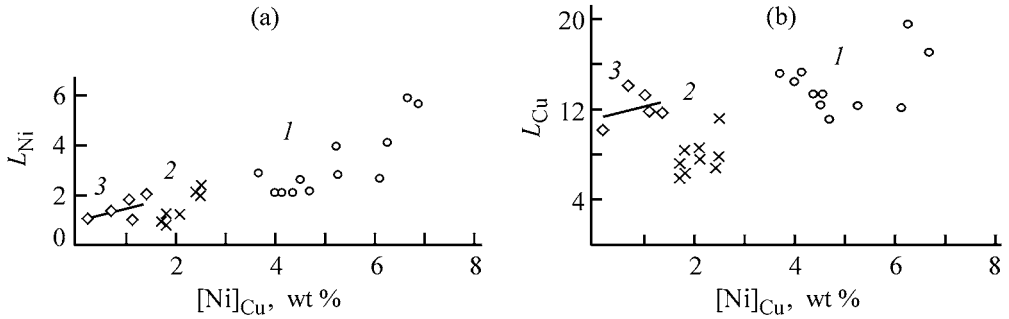

Fig. 3. Distribution coefficients of (a) nickel, L_{Ni}, and (b) copper, L_{Cu}, vs. $[Ni]_{Cu}$ in copper in the equilibrium system copper–slag according to different references. (*1*) [14], (*2*) [15], (*3*) present study. Experimental conditions: P_{O_2} (atm), c_{SiO_2} (wt %): (*1*) 1.4×10^{-5}, 13.4–29.2; (*2*) 6.1×10^{-5}–2.05×10^{-4}, 16–23; (*3*) 6×10^{-5}, 25–30.

content in the slag in the present study. A similar pattern is observed when the L_{Ni} values obtained here are compared with the data of [13] for an oxidizing atmosphere. The copper distribution coefficients in the oxidizing atmosphere with $P_{O_2} = 6 \times 10^{-5}$ atm (present study) are in good agreement with the data of [14, 15] obtained at close P_{O_2} values. For convenience of comparison, these data are presented graphically in Figs. 3a and 3b. In the authors' opinion, the distribution coefficients of copper are somewhat underestimated in [14, 15], since the content of copper in the slag was determined by chemical methods.

CONCLUSIONS

(1) The solubility of copper, nickel, and cobalt in a slag in an argon atmosphere is independent of the content of sulfur in a sulfide melt (17–21 wt %), being, on the average, 0.7–1.0 wt % Cu, 1.3–1.7 wt % Ni, and 0.5–0.7 wt % Co.

(2) The content of dissolved copper and nickel in an argon atmosphere is also independent of the composition of the metallic bottom phase, being, on the average, 0.2–0.3 wt % Cu and 0.5–0.7 wt % Ni, at nickel activity a_{Ni} 0.027–0.211.

(3) The solubility of copper and nickel in the slag in an oxidizing atmosphere increases from 7 to 10 wt % for Cu and from 0.2 to 1.2 wt % for Ni with increasing activity of nickel in the bottom phase (a_{Ni} 0.006–0.036).

REFERENCES

1. Kostyukovich, V.F., Abramov, N.P., Sukharev, S.V., *et al., Tsvetn. Met.*, 1998, no. 2, pp. 33–35.
2. Astaf'ev, A.F., Lukashev, L.P., Tsemekhman, L.Sh., *et al., Tsvetn. Met.*, 1987, no. 4, pp. 28–32.
3. Landoln, C., Dutton, A., Fritz, A., and Segsworth, S., *Proc. Paul E. Queneau Int. Symp. Extractive Metallurgy of Copper, Nickel and Cobalt*, 1993, vol. 2, pp. 1497–1527.
4. Tsemekhman, L.Sh., Lukashev, L.P., Ermakov, G.P., *et al., Tsvetn. Met.*, 1986, no. 5, pp. 25–27.
5. Onishchin, B.P., Khe Khuankhua, Tsemekhman, L.Sh., *et al., Tsvetn. Met.*, 1998, no. 1, pp. 26–29.
6. Miroevskii, G.P., Golov, A.N., and Koklyanov, E.B., *Tsvetn. Met.*, 2001, no. 2, pp. 41–47.
7. Golov, A.N., Study and Development of Ecologically Pure Autogenous Technology of Processing Low-Iron Copper-Rich Concentrates To Give Copper of Prescribed Composition, *Cand. Sci. (Chem.) Dissertation*, Moscow, 2001.
8. Yazawa, A., *Can. Met. Quart.*, 1974, vol. 13, no. 3., pp. 443–453.
9. Yazawa, A., *Sbornik nauchnykh trudov NII "Gipronikel'"* (Collection of Scientific Works of Research Institute "Gipronikel'"), 1991., pp. 32–46.
10. Oishi, T., Kamuo, M., Ono, K., and Moriyama, J., *Met. Trans., B.*, 1983, vol. 8, pp. 101–104.
11. Toguri, J.M., Santander, N.H., *Met. Trans.*, 1972, vol. 3., pp. 586–588.
12. Itagaki, K., Hino, M., Pagador, R., and Surapunt, S., *Ber. Bunstngesell. Phys. Chem.*, 1998, vol. 102, no. 9., pp. 1304–1308.
13. Serebryakov, V.F., Ezrokhina, A.M., and Tsemekhman, L.Sh., *Tsvetn. Met.*, 1994, no. 11, pp. 22–25.
14. Abramov, N.P., Pavlinova, L.A., and Bochkova, L.V., *Trudy AO "Institut Gipronikel'"* (Proc. Joint-Stock Company "Institut Gipronikel'"), 2000, pp. 107–112.
15. Abramov, N.P., Voikhanskaya, N.L., D'yachenko, V.T., *et al., Vestnik Ural. Gos. Tekhn. Univ.—Ural. Politekhn. Inst.* (Yekaterinburg), 2000, no. 1(19), pp. 33–34.
16. Vanyukov, A.V. and Zaitsev, V.Ya., *Shlaki i sheiny tsvetnoi metallurgii* (Slags and Mattes in Nonferrous Metallurgy), Moscow: Metallurgiya, 1969.
17. Kulkarni, A.D. and Johnson, R.E., *Met. Trans.*, 1973, vol. 4., pp. 1723–1727.
18. Berezutskii, V.V. and Lukashenko, G.M., *Ukr. Khim. Zh.*, 1987, vol. 53, no. 10, pp. 1029–1032.

Russian Journal of Applied Chemistry, Vol. 76, No. 2, 2003, pp. 180–186. Translated from Zhurnal Prikladnoi Khimii, Vol. 76, No. 2, 2003, pp. 190–195.

INORGANIC SYNTHESIS AND INDUSTRIAL INORGANIC CHEMISTRY

Distribution of Rare and Radioactive Elements in Processing of Baddeleyite Concentrate from Kovdor Deposit

V. N. Lebedev, E. P. Lokshin, and N. A. Mel'nik

Tananaev Institute of Chemistry of Rare Elements and Mineral Raw Materials, Kola Scientific Center, Russian Academy of Sciences, Apatity, Russia

Received September 19, 2002

Abstract—Specific features of the distribution of rare elements and radionuclides in processing of the baddeleyite concentrate by various methods to obtain pure zirconium compounds and in its chemical purification were studied. The products in which they are concentrated can be regarded as concentrates of niobium(V), tantalum(V), scandium(III), and radionuclides.

The main Russia's source of zirconium is the baddeleyite concentrate (BC) manufactured by Kovdorskii GOK Joint-Stock Company. The commercial BC, containing no less than 97.5–98.5% ZrO_2 + HfO_2, is commonly used without chemical processing in manufacture of refractory materials, ceramics, and abrasives. Zirconium dioxide in BC is twice as expensive as that in zircon. Therefore, use of BC for production of zirconium compounds is inexpedient. However, account should be taken of the fact that the Kovdor BC contains, in addition to hafnium, which is present in zirconium minerals and is of limited use, also the deficient niobium, tantalum, and scandium. According to chemical and X-ray fluorescence analyses, commercial BC contains (wt %): Nb_2O_5 0.6–0.8, Ta_2O_5 0.18–0.23, and Sc_2O_3 0.045–0.055. The total cost of these components at world prices is close to the cost of BC, and the ratio of their costs is 1 : 4 : 6. Consequently, if the problem of recovery of accessory rare elements in chemical processing is solved, BC may become quite competitive with zircon as regards the manufacture of various zirconium-containing chemical products. In addition, the high content of ZrO_2 in BC (low content of impurities) leads to lower reagent expenditure and simpler technology of its processing, compared with that for zircon, which may also improve the economical attractiveness of BC as raw material for manufacture of zirconium compounds.

In studying the methods for BC processing [1–6], the behavior of compounds of niobium, tantalum, and scandium (further, rare elements) and radioactive elements has not been analyzed. Incomplete data on their distribution in chemical processing of BC were reported in [7].

Approximately 80% of niobium(V) and tantalum(V) is present in the commercial concentrate in the form of isomorphic impurities, and 20%, as constituents of accessory minerals—uranopyrochlore, pyrochlore, zirkelite, etc. Radioactive elements are represented by uranium and thorium (specific activity of up to 70 kBq kg^{-1}). The radionuclides are mainly associated with the minerals mentioned above. In minor amounts, they are present as isomorphic impurity. Scandium(III) is virtually completely present in baddeleyite as an isomorphic impurity.

Various methods for BC decomposition are known: (1) high-temperature sintering with compounds of alkali and alkaline-earth metals [1–3], (2) sulfuric acid processing [1, 4], (3) sintering with ammonium sulfate [1, 5], (4) decomposition with the use of fluorinating reagents [1, 6], and (5) chlorination [1].

The present study is concerned with the behavior of rare and radioactive elements in chemical purification of BC by the method described in [8], and also in production of pure zirconium compounds with methods 1–3 used to process BC.

EXPERIMENTAL

BC conforming to the requirements of TU (Technical Specifications) 48-0572-17-252–91 and 1762-

1070-4272/03/7602-0180 $25.00 © 2003 MAIK "Nauka/Interperiodica"

Table 1. Distribution of rare and radioactive elements impurities in sulfuric acid purification of BC

Product	Yield, %	Content, wt %					Specific activity *A*, kBq kg^{-1}
		Sc	Nb_2O_5	Ta_2O_5	U	Th	
BC:							
initial	100	0.03–0.038	0.6–0.8	0.2–0.23	0.02–0.05	0.01–0.015	80–130
purified	98–99	0.03–0.038	0.5–0.65	0.18–0.2	0.011–0.02	0.003–0.007	17–25
purified, –0.044-mm fraction	97–98	0.03–0.038	0.5–0.65	0.18–0.2	0.08–0.015	0.002–0.005	15.8
Hydrate cake	1–2	0.003–0.006	4–8	1.5–3.0	0.5–1.5	0.15–0.3	1000–3000

003-00186759–2000 was commonly used in the study. Occasionally, the content of impurities, especially those radioactive, in the BC was higher.

Rare and impurity elements in precipitates were analyzed by X-ray fluorescence and spectral methods, and those in solutions, by chemical-analytical and atomic-adsorption techniques. The specific radioactivity of ^{232}Th and ^{226}Ra and the content of U and Th were determined by radiometry and gamma-spectrometry on certified instruments.

In chemical purification of BC with hydrochloric [1] or sulfuric [7, 8] acid, the content of main components can be brought to 99–99.5 wt %; however, hydrochloric acid does not react with accessory minerals containing radionuclides, niobium(V), and tantalum(V). Under the optimal conditions, sulfuric acid decomposes these minerals, but virtually does not react with baddeleyite. The most complete purification achieved in sulfuric acid processing is that to remove compounds of phosphorus, calcium, magnesium, iron, and radioactive impurities. Silicon present in the form of olivine and some other silicates is separated in the course of purification, but silicon contained in zircon, pyroxenes, and garnets is not removed from BC. In the course of purification, rare and radioactive elements are converted, together with most of other impurities removed from the concentrate, into an insoluble form, specifically hydrate cake. Table 1 lists the distribution of admixtures of rare and radioactive elements in sulfuric acid purification of BC.

Rare elements isomorphically incorporated in the ZrO_2 lattice remain in the purified product. This is confirmed by the fact that their concentration in the product purified remains the same upon additional grinding of the initial BC. Although the concentrations of tantalum, niobium, and uranium compounds in the hydrate cake are rather high, their recovery from this product is hardly justified economically because of the relatively low amount of rare elements finding their way into this product (recovery into the cake less than 0.5% for Sc, 17–18% for Nb_2O_5, and 12–15% for Ta_2O_5). However, deep processing of the hydrate cake may be advisable for ecological reasons.

In BC processing by sintering, the concentrate was ground and simultaneously mixed with CaO and $CaCl_3$ at mass ratio of 1 : 0.55 : 0.12. The stock was sintered at 1150°C for 4 h. The degree of BC decomposition in sintering was 80–85%. The cake was decomposed with hydrochloric or nitric acid. In cake dissolution, most of impurities passed into solution simultaneously with zirconium(IV), with the insoluble residue enriched with niobium(V) and tantalum(V) and depleted of radionuclides.

The niobium(V) to tantalum(V) ratio varied from 3.4 for BC to 2.5 in the insoluble residue and 5.9–6.2 in solutions. The recovery of zirconium(V) into solution in decomposition of the cake with nitric acid was somewhat lower than that in the case of hydrochloric acid and occurred at higher acidity. The enrichment of the insoluble residue with niobium(V) and, to a greater extent, tantalum(V) occurred as a result of hydrolysis. Chloride solutions were purified by crystallization of zirconium(IV) oxochloride, and nitric acid solutions, by extraction.

Recrystallization of zirconium(IV) oxochloride is a standard procedure for obtaining pure zirconium(IV) compounds [9, 10]. After dissolution and separation of the insoluble residue, the solution was evaporated and the resulting precipitate of zirconium(IV) oxochloride was repulped in 20% hydrochloric acid at s : l ratio of 1 : 4.5. The amount of acid necessary for repulpation corresponded to its expenditure for cake decomposition. After three counterflow washings-repulpations with one intermediate dissolution of the oxochloride under heating, ZrO_2 obtained from the oxochloride by calcination was close to special-

Table 2. Content of rare and radioactive elements in products obtained in hydrochloric acid decomposition of cake

Product	Mass, g	Content wt %					Specific activity *A*, kBq kg^{-1}
		Sc	Nb_2O_5	Ta_2O_5	U	Th	
Initial BC	100	0.036	0.68	0.2	0.025	0.019	52
Insoluble residue	17.5	0.036	0.72	0.29–0.33	0.005	0.008	11.9
$ZrOCl_2$ residue after two repulpations	250	N.f.*	N.f.	N.f.	$<1 \times 10^{-4}$	$<4 \times 10^{-4}$	<0.34
ZrO_2 from $ZrOCl_2$ obtained after three repulpations	73.5	N.f.	N.f.	N.f.	$<1 \times 10^{-4}$	$<2 \times 10^{-4}$	<0.25
Precipitate separated from mother liquor with $NH_3 \cdot H_2O$ solution	7.2	0.36	7.6	1.3	0.27	0.23	700

* Not found; the same for Table 4.

Table 3. Distribution coefficients of components in extraction of zirconium(IV) from solution formed upon BC decomposition

Acidity of equilibrium aqueous phase, M	Distribution coefficient								
	Zr	Hf	Sc	Nb	Ni	Ca	Fe	Si	U + Th
2	0.36	0.02	0.06	0.2	0.5	0.05	0.01	1.7	3.6
4	0.82	0.05	0.29	0.12	0.1	0.04	0.02	0.5	6.9
6	3.1	0.26	0.19	0.05	0.06	0.02	0.01	0.2	17
6*	3.2	0.22	0.19	0.06	0.08	0.04	0.03	0.2	16
2**	0.12	0.06	0.04	N.f.	0.06	0.04	0.03	1.3	42

* Including 2 N HCl.

** In reextraction.

purity 9-2 brand (TU 6-09-4709–79), with calcium compounds removed to residual level of 0.01 wt %. Average composition of the mother liquor obtained after precipitation of zirconium(IV) oxochloride (g l^{-1}): ZrO_2 + HfO_2 4–7, CaO 150–170, Fe_2O_3 8–13, Sc 0.13–0.16, Nb_2O_5 1.8–2.4, Ta_2O_5 0.28–0.35, U 0.1–0.13, Th 0.07–0.09; A = 1.25–1.5 kBq kg^{-1}. The yield of the mother liquor was 100 ml per 100 g of cake. After its neutralization with an $NH_3 \cdot H_2O$ solution, a precipitate was isolated into which the rare and radioactive elements contained in the mother liquor passed.

The content of rare impurities and radionuclides in the products obtained is given in Table 2.

Judging from the composition of the precipitate, the main part of scandium(III), niobium(V) and radionuclides (Sc 72, Nb 80.5, U 77.8, and Th 87.2% relative to their respective amounts in BC) and nearly half of Th(V) find their way into it.

The extraction technique for processing of nitric acid solutions of zirconium(IV) is, as a rule, analyzed for the case of hafnium(V) isolation [9–11]. The extraction process was studied in order to obtain pure compounds of zirconium(IV). The nitric acid solution contained 103.1 g l^{-1} ZrO_2 at acidity of 7.4 M HNO_3. Zirconium(IV) was extracted with solution of 80% tributyl phosphate (TBP) in dodecane. The experimentally found distribution coefficients of the components are listed in Table 3.

The distribution coefficients of the impurities decreased with increasing acidity because of their salting-out by the better extractable zirconium(IV). Introduction of hydrochloric acid raised somewhat the separation coefficient of zirconium(IV) and hafnium(IV), but favored passing of admixtures of iron- and calcium-containing compounds into the organic phase. On the whole, the distribution data are close to the known values [12] and indicate that purification is possible. Radioactive elements can be isolated in the reextraction stage. Difficulties may be only encountered when dealing with compounds of silicon.

The extraction was carried out on a cascade comprising 40 stages of the mixer–settler type, with stage

volume of 450 ml (see scheme). In accordance with the values of the separation coefficients, 3 to 4 stages are necessary for purification; however, it has been found previously in a similar system [12, 13] that 12 stages are insufficient for obtaining pure zirconium(IV) at phase ratio org : aq = 2.5 : 1 in the washing stage because of the gradual accumulation of admixtures of silicon and titanium compounds, mainly as gels in the organic phase.

Scheme of extraction purification of zirconium.

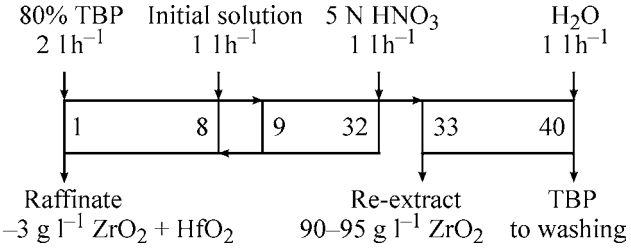

To separate radionuclides, the organic phase obtained after reextraction was periodically removed from the process and treated with a Na_2CO_3 solution or a fluorine-containing reagent. It was found that there exist unextractable forms of zirconium(IV), bound to silicon and calcium. The precipitate isolated from the fluoride or carbonate reextract contained (wt %): ZrO_2 20–50; CaO 5–20; SiO_2 3–20; Al_2O_3 1–5; Nb_2O_5, Fe_2O_3, and TiO_2 <0.01 each.

Zirconium(IV) was isolated from the reextract in the form of basic sulfate or oxalate. In the content of controllable impurities, ZrO_2 obtained by calcination of oxalate was also close to special-purity 9-2 brand (TU 6-09-4709–79) and contained no (<0.01 wt %) hafnium. The activity of samples was 0.9–1.4 kBq kg^{-1}, including $(2–4) \times 10^{-4}$ wt % U and $(0.5–2) \times 10^{-3}$ wt % TH. The content of radionuclides was lowered to 0.4–0.6 kBq kg^{-1} by single preliminary extraction with 10% TBP from the initial solution and from the reextract.

The operation of the extracting apparatus was complicated by the formation and motion along the cascade of interphase gel-like precipitates, which had to be removed periodically. Their composition approximately corresponded to that of the precipitate formed in the carbonate reextract and differed only in lower activity and presence of admixtures of titanium, niobium, and tantalum compounds. The precipitate formed in the raffinate with an $NH_3 \cdot H_2O$ solution contained (wt %): Sc 0.2–0.4, Nb_2O_5 7–9, and Ta_2O_5 1.1–1.3. This indicated that the impurities nearly completely passed into this product, with the exception of the amount lost with interphase precipitates. The content of hafnium(IV) in the sum of zirconium(IV) and hafnium(IV) was 45–65%.

The distribution of less-common and radioactive elements in BC processing by sintering with $(NH_4)_2SO_4$ was evaluated [3]. Sintering of BC with $(NH_4)_2SO_4$ at 500°C and a 10-fold excess of the decomposing agent yields 99% decomposition [1]. Zirconium is present in the cake as ammonium sulfate-zirconate (ASZ).

The baddeleyite concentrate was decomposed in a 6-fold excess of $(NH_4)_2SO_4$ at 400–450°C, the cake was dissolved in water, and the insoluble residue was filtered off. The degree of decomposition was 95–96.5%. Niobium(V) and tantalum(V) were distributed approximately evenly between the solution and insoluble residue because of their poor solubility in sulfuric acid solutions, whereas scandium, uranium, and thorium mainly passed into solution in amount proportional to the degree of BC decomposition. ASZ with $NH_4 : Zr : SO_4$ ratio of 1 : 1 : (1.3–1.75), to which the formula $(NH_4)_4[Zr_4O_2(OH)_4(HSO_4)_2(SO_4)_5 \cdot 8H_2O$ has been ascribed [14], was isolated from the resulting supersaturated solution after keeping for 8–24 h with periodic agitation. The isolation process was accelerated upon introduction of an ASZ seed. The yield of zirconium(IV) into the precipitate was 68–72%, rare elements could be concentrated in the mother liquor after its evaporation and recrystallization, or by using the mother liquor to dissolve the cake.

The slow crystallization favored a high degree of purification to remove virtually any of the impurities. Washing of ASZ with a saturated $(NH_4)_2SO_4$ solution and calcination gave ZrO_2 containing admixtures of Sc, Mg, Ca, Fe, Al, Ti, Nb, Ta, and Cr in amount of less than 0.01 wt % each. The highest degree of purification, compared with other techniques, was achieved in removing silicon: its content decreased from 0.69 wt % in the concentrate to 0.001 wt % in ZrO_2. Sufficiently successful was purification to remove uranium, to 2.0×10^{-3} wt %, but the whole amount of thorium remained in ASZ and could not be removed by recrystallization. To achieve deeper purification, ASZ was converted into a hydroxide, the hydroxide was dissolved in hydrochloric acid and basic zirconium sulfate (BZS) was precipitated. After calcination of ASZ, ZrO_2 contained (wt %): Mg, Ca, Sc < 0.01; Fe, Al, Mn, Si, and Cr < 0.001; Cu < 0.0001; Ti < 0.005; U < 0.002; Th < 0.003; Nb_2O_5 < 0.005; Ta_2O_5 < 0.005.

Table 4. Impurity content of zirconium sulfates

Extraction technique	Yield, %	Content, wt % relative to ZrO_2						Specific activity *A*, kBq kg^{-1}
		Sc	Nb	Fe	Si	Ca	Ti	
Evaporation	50	0.069	N.f.	0.03	0.02	0.1	0.01	3.9
	80	0.042	0.01	0.03	0.02	0.1	0.01	3.9
	70	0.09	N.f.	0.01	0.003	0.03	0.01	3.1
Salting-out	50	0.09	N.f.	<0.01	0.003	0.1	0.01	2.8
	80	0.046	N.f.	<0.01	0.003	0.1	<0.01	2.6
Recrystallization	70	0.11	N.f.	<0.01	0.001	0.03	<0.01	2.2

Thus, niobium(V) and tantalum(V) are approximately evenly distributed among the insoluble residue and the mother liquor formed upon ASZ precipitation, and major amount of scandium(III) is accumulated in the mother liquor. An acceptable level of separation of radionuclides can only be achieved by multistage processing.

The baddeleyite concentrate is decomposed by sulfuric acid at 300°C in the course of 4–5 h [1, 4]. Because of the high rate of H_2SO_4 evaporation, the process is carried out either in a large excess of the acid, or with the use of an autoclave or reflux condenser. At H_2SO_4 expenditure of 150% with respect to the stoichiometry (2.5 kg of $H_2SO_4 \cdot H_2O$ per 1 kg of BC), the degree of decomposition was 86–91% for the –0.074-mm fraction. The decomposition became somewhat more pronounced in a 3–5-fold excess of the acid (not used in the experiments). Presumably, the decomposition was not complete because of the blocking of baddeleyite particles by a precipitate of the forming zirconium sulfate. According to the results of X-ray phase analysis, zirconium(IV) was present in the reaction mass as $Zr(SO_4)_2 \cdot 4H_2O$; in thermal treatment of the sulfate mass, $Zr(SO_4)_2 \cdot H_2O$ and $Zr(SO_4)_2$ were formed successively.

Zirconium sulfate readily dissolved to a concentration of 120–170 g l^{-1}, depending on the concentration of sulfuric acid in solution. Although the undecomposed residue (0.12–0.15 kg per 1 kg of BC) is enriched with niobium(V) and tantalum(V) (1.5–2.0 and 0.8–0.9 wt %, respectively) because of their hydrolysis, a major part of niobium (~65%) and tantalum (~40–45%) passes into solution. The specific activity of the residue increases by 15–20% because of the precipitation of radium sulfate. Scandium and other impurities pass into solution in proportion to the degree of BC decomposition. The solution obtained was used to recover various zirconium(IV) compounds.

Since the undecomposed residue is recycled into the sulfatization process, the extent to which niobium(V) and tantalum(V) pass into solution increases significantly.

Crystallization of $Zr(SO_4)_2$ has been used to obtain pure zirconium dioxide [9]. Zirconium sulfate crystallized when the acidity increased to 6–8 M, which was effected by introduction of H_2SO_4 or by evaporation. Table 4 lists data on the composition of $Zr(SO_4)_2$ obtained by various techniques (the content of impurities is given in terms of ZrO_2). The content of tantalum(V) was not determined, but it may be assumed that its behavior in sufficiently concentrated sulfuric acid solutions is similar to that of niobium.

As follows from Table 4, extraction and recrystallization of $Zr(SO_4)_2$ leads to its purification to remove all impurities except scandium(III), which is concentrated in the first fractions of the precipitates formed. Presumably, the bridging bonds of zirconium sulfate can accommodate anionic complexes of scandium, which are predominant in the sulfuric acid medium [15]. The insufficient degree of purification to remove radioactive impurities is presumably due to coprecipitation of radium sulfate. The content of niobium(V) and tantalum(V) in the precipitate formed in the mother liquor with ammonium was 3.5–7.5 and 0.65–1.3 wt %, respectively.

Ammonium sulfate-zirconate was isolated from solutions formed in sulfuric acid decomposition of BC by neutralization with $NH_3 \cdot H_2O$ to an $NH_3 : Zr$ molar ratio of no less than 2 and acidity of 0.75–1.0 M. The amount of precipitated zirconium(IV) was 85–90%. Judging from the relative concentrations of the components, the composition corresponded to the $(NH_4)_2SO_4 \cdot ZrOSO_4$ salt. The content of controllable impurities in ASZ approximately corresponded to that in zirconium sulfate, but the whole amount of scandium remained in solution, and niobium(V) and tantalum(V) were distributed among the solution and

precipitate, depending on the precipitation conditions. Purification to remove radioactive impurities proceeded to a fuller extent, to 1.4 kBq kg^{-1}, with uranium removed better than thorium.

Potassium fluorozirconate was extracted from the sulfuric acid solution upon introduction KF and NH_4F into a hot solution in amount of 110% with respect to the stoichiometry. A single phase, K_2ZrF_6, was revealed by X-ray phase analysis in the precipitate formed upon cooling. Niobium(V) and tantalum(V) remained in solution, although formation of potassium fluorometallates is also characteristic of these metals. Scandium(III) partly precipitated in the form of scandium trifluoride or potassium fluoroscandate with distribution coefficient of 0.3, and remained in the concentrate of hafnium(IV) upon recrystallization of the preciopitate. The precipitate formed in the mother liquor with $NH_3 \cdot H_2O$ contained (wt %): Nb_2O_5 3.7, Ta_2O_5 0.49, and Sc 0.19. Niobium(V) and tantalum(V) can be selectively recovered from fluorine-containing sulfate solutions by extraction.

Thus, in various methods for BC processing by decomposition with H_2SO_4, niobium(V) and tantalum(V) are distributed among the insoluble residue and the mother liquor, and the major part of scandium(III) is accumulated in the mother liquor. Nonradioactive zirconium(IV) compounds can be obtained in all variants; however, techniques for final concentration of radionuclides require further development.

CONCLUSIONS

(1) A study of specific features of the distribution of rare elements and radionuclides in various methods for processing of the baddeleyite concentrate to obtain pure zirconium compounds and in its chemical purification revealed the products and wastes in which the rare and radioactive elements are concentrated.

(2) Comparison of the behavior of rare elements and radionuclides in chemical purification of the baddeleyite concentrate with that in processing of the concentrate to obtain zirconium compounds confirms that uranium and thorium are mainly contained in accessory minerals, whereas scandium(III) and major part of niobium(V) and tantalum(V) crystallize isomorphically to baddeleyite.

(3) The possibility of concentrating radionuclides and part of niobium(V) and tantalum(V) in sulfuric acid purification of the baddeleyite concentrate was demonstrated.

(4) Simultaneous production of pure zirconium compounds and recovery of rare and radioactive elements into separate concentrates is achieved the most effectively by processing the baddeleyite concentrate by the sintering method, with the formation and subsequent recrystallization of zirconium oxychloride or extraction processing of nitric acid solutions.

REFERENCES

1. Kolenkova, M.A., Shumenko, V.N., Dorokhina, M.N., and Safuanova, N.A., *Novoe otechestvennoe syr'e i sposoby ego pererabotki* (New Domestic Raw Material and Methods for Its Processing), issue 2, Moscow: TsNII Ekonom. Informats. Tsvetn. Met., 1980.
2. Voskoboinikov, N.B., Skiba, G.S., Smirnova, L.A., and Nosova, L.A., *Tekhnologiya mineral'nogo syr'ya i svoistva soedinenii redkikh elementov* (Technology of Mineral Raw Materials and Properties of Compounds of Rare Elements), Apatity: Kola Nauchn. Tsentr Ross. Akad. Nauk, 1996, pp. 5–9.
3. Kalinnikov, V.T., Lebedev, V.N., Lokshin, E.P., *et al.*, *Fiziko-khimicheskie problemy sozdaniya novykh konstruktsionnykh keramicheskikh materialov: Syr'e, sintez, svoistva: Doklady 1V Vserossiskoi konferentsii* (Physicochemical Problems Associated with Development of New Ceramic Construction Materials: Raw Materials, Synthesis, Properties: Proc. IV All-Russia Conf.), Syktyvkar: Ural'sk. Otd. Ross. Akad. Nauk, 2001, pp. 187–188.
4. Motov, D.L. and Godneva, M.M., *Fiziko-khimicheskie problemy sozdaniya novykh konstruktsionnykh keramicheskikh materialov: Syr'e, sintez, svoistva: Doklady IV Vserossiiskoi konferentsii* (Physicochemical Problems Associated with Development of New Ceramic Construction Materials: Raw Materials, Synthesis, Properties: Proc. IV All-Russia Conf.), Syktyvkar: Ural'sk. Otd. Ross. Akad. Nauk, 2001, p. 212.
5. Lebedev, V.N., Abstracts of Papers, *2-oi Mezhdunarodnyi simpozium "Problemy kompleksnogo ispol'zovaniya rud"* (2nd Int. Symp. "Problems Associated with Integrated Use of Ores"), St. Petersburg: SPb Gorn. Inst., 1996, p. 207.
6. RF Patent 2 103 400.
7. Lokshin, E.P., Lebedev, V.N., Lyakhov, V.P., *et al.*, *Fiziko-khimicheskie problemy sozdaniya novykh konstruktsionnykh keramicheskikh materialov: Syr'e, sintez, svoistva: Doklady IV Vserossiskoi konferentsii* (Physicochemical Problems Associated with Development of New Ceramic Construction Materials: Raw Materials, Synthesis, Properties: Proc. IV All-Russia Conf.), Syktyvkar: Ural'sk. Otd. Ross. Akad. Nauk, 2001, p. 196.
8. RF Patent 2 139 250.

9. Bol'shakov, K.A., *Tekhnologiya redkikh i rasseyannykh elementov* (Technology of Rare and Scattered Elements), Moscow: Vysshaya Shkola, 1969, vol. 2.
10. Miller, G.L., *Zirconium*, London: Butterworth Scientific, 1954.
11. Solovkin, A.S. and Yagodin, G.A., *Ekstraktsionnaya khimiya tsirkoniya i gafniya* (Extraction Chemistry of Zirconium and Hafnium), Moscow: VINITI, 1969.
12. Kolenkova, M.A., Sazhina, V.A., Koshkarova, N.A., *et al., Nauchnye trudy MISiS* (Sci. Works of Moscow Institute of Steel and Alloys), no. 117, Moscow: Metallurgiya, 1979, pp. 40–43.
13. Lebedev, V.N., Masloboev, V.A., and Sergeeva, S.D., *Tekhnologiya mineral'nogo syr'ya i svoistva soedinenii redkikh elementov* (Technology of Mineral Resources and Properties of Compounds of Rare Elements), Apatity: Kola Nauchn. Tsentr Ross. Akad. Nauk, 1966, pp. 39–45.
14. Nekhamkin, L.G., Kozlova, V.K., Laube, L.G., and Zaitsev, L.M., *Zh. Neorg. Khim.*, 1971, vol. 16, no. 5, pp. 1291–1296.
15. Kolosov, V.I., Ivanov-Emin, B.N., Korotaeva, L.G., *et al.*, *Radiokhimiya*, 1967, vol. 24, issue 4, pp. 473–478.

Russian Journal of Applied Chemistry, Vol. 76, No. 2, 2003, pp. 187–190. Translated from Zhurnal Prikladnoi Khimii, Vol. 76, No. 2, 2003, pp. 196–200.

INORGANIC SYNTHESIS AND INDUSTRIAL INORGANIC CHEMISTRY

Sulfidization of Acid-Soluble Barium Compounds with Sulfurous Petroleum Coke

L. A. Malysh, L. G. Gaisin, A. G. Prokhorov, K. V. Tkachev, and M. F. Volkova

Ural'skii nauchno-issledovatel'skii khimicheskii institut s Opytnym zavodom Federal State Unitary Company, Yekaterinburg, Russia

Khimicheskii zavod im. L.Ya. Karpova Open Joint-Stock Company, Mendeleevsk, Tatarstan, Russia

Received September 19, 2002

Abstract—The influence exerted by sulfur contained in petroleum coke on sulfidization of acid-soluble barium compounds formed in reductive calcination of recycled barium sulfate in sodium sulfide production was studied.

A low-waste technique for manufacture of sodium sulfide [1–3] is based on the interaction of barium sulfide with sodium sulfate by the reaction

$$BaS + Na_2SO_4 = BaSO_4 + Na_2S. \quad (1)$$

Barium sulfide is regenerated by reductive calcination of the forming barium sulfate

$$BaSO_4 + 2C = BaS + 2CO_2, \quad (2)$$

and, consequently, the barium raw material is not spent, and only its replenishment is necessary. However, in reduction of $BaSO_4$ with carbon, the main reaction (2) is accompanied by side reactions [4] associated with loss of sulfur and formation of acid-soluble (as) barium compounds:

$$BaS + CO_2 + 1.5O_2 = BaCO_3 + SO_2, \quad (3)$$

$$BaS + 4CO_2 = BaCO_3 + SO_2 + 3CO, \quad (4)$$

$$BaS + H_2O + CO_2 = BaCO_3 + H_2S, \quad (5)$$

$$2BaSO_4 + C = 2BaSO_3 + CO_2, \quad (6)$$

$$BaSO_4 + CO = BaSO_3 + CO_2. \quad (7)$$

Admixtures of a barite concentrate, added to compensate for the loss of barium, also form silicates, ferrites, and other acid-soluble barium compounds.

The industrial BaS melt contains 65–75% water-soluble (ws) barium compounds in terms of BaS_{ws} and 15–20% acid-soluble barium compounds in terms of BaS_{as}. In manufacture of $BaCl_2$ by the hydrogen chloride technique [4], acid-soluble barium salts react with HCl to give the target product. In the technique for Na_2S production in aqueous leaching of the melt, acid-soluble barium compounds are not involved in the formation of the target product and, being accumulated in $BaSO_4$ being recycled, affect adversely the technical and economic characteristics of the process.

The aim of this study was to minimize the yield of acid-soluble barium compounds in reductive calcination of the stock by converting them into BaS, e.g., by the reaction

$$2BaCO_3 + 2S + C = 2BaS + 3CO_2, \quad (8)$$

with the use of sulfurous petroleum coke as sulfidizing agent.

Petroleum coke manufactured from domestic oils with 1–2% sulfur content contains sulfur in the form of cyclic structures possessing high thermal stability. The extent of desulfurization of sulfurous petroleum cokes at 900–1000°C does not exceed 10–17% [5, 6], which points to the possibility of using the sulfur contained in petroleum coke in reduction-sulfidization processes. Sulfur-containing components of volatiles can also be used as active sulfidizing agents.

1070-4272/03/7602-0187 $25.00 © 2003 MAIK "Nauka/Interperiodica"

Table 1. Chemical composition of stock components

Parameter	Barite concentrate	Recycled barium sulfate	WIR*	Petroleum coke		
				no. 1	no. 2	no. 3
Content, wt %:						
$BaSO_4$	91.51	99.53	37.83			
BaS_{ws}	0.11		3.00			
BaS_{as}	3.10	0.41	49.04			
H_2O	0.63	0.08	0.17	0.36	0.50	0.58
Acid-insoluble impurities, without $BaSO_4$	4.25		5.52			
C			0.58	91.95	89.90	92.53
S				2.45	1.78	0.68
Yield of volatiles				7.52	9.93	6.79
Ash content				0.53	0.17	0.68

* Water-insoluble residue upon leaching of BaS melt.

EXPERIMENTAL

To carry out the study, samples of a water-insoluble residue containing a complex of acid-soluble barium compounds, together with $BaSO_4$ being recycled, were prepared. The samples were obtained by leaching in water a BaS melt from Soda Joint-Stock Company, Sterlitamak, separating the water-insoluble residue, reacting a BaS solution with powdered Na_2SO_4 of pure grade [GOST (State Standard) 4166–76], and filtering the suspension to obtain recyclable $BaSO_4$. The resulting substances were thoroughly washed with hot water to remove S^{2-} ions (with the process monitored with indicator paper impregnated with lead acetate) and dried.

The chemical composition of the samples obtained and of those used to study the barite concentrate and petroleum coke is listed in Table 1. The grain size of all the stock components is 0.25 mm.

The study was carried out as follows. The stock was prepared, with the petroleum coke taken in amount (in terms of 100% C) of 125% with respect to the stoichiometry of reaction (2); reductive calcination of the stock was done in static mode in a muffle furnace at 1000°C for 15 and 30 min in alundum crucibles with caps; then the resulting BaS melt was subjected to chemical analysis. The melt was analyzed, after being cooled in desiccator, for BaS_{I_2} and BaS_2O_3 by iodometry, for BaS_{ws} and BaS_{as} by complexonometry, and for water-insoluble residue and carbon by gravimetry.

The results of chemical analysis were used to calculate the degree of $BaSO_4$ reduction (η_1), and degrees of $BaSO_4$ conversion into BaS_{I_2} (η_2), BaS_{ws} (η_3), and BaS_{as} (η_4) and of BaS_{as} conversion into BaS_{ws} (η_5) and BaS_{I_2} (η_6) by the formulas

$$\eta_1 = \frac{(m_{st}BaSO_{4st} - m_mBaSO_{4m}) \times 100}{m_{st}BaSO_{4st}},$$

$$\eta_2, \eta_3, \eta_4 = \frac{1.3778 m_{st}BaS_m \times 100}{m_{st}BaSO_{4st}},$$

$$\eta_5, \eta_6 = \frac{m_mBaS_m \times 100}{m_{st}BaSO_{4as.st}},$$

where m is the stock mass (g); m_m, the melt mass (g); $BaSO_{4st}$, $BaSO_{4m}$, and BaS_m, the contents of $BaSO_4$ in, respectively, the stock and the melt and the content of water- or acid-soluble barium compounds in terms of BaS in the melt (wt %); $BaS_{as.st}$, the content of acid-soluble barium compounds in terms of BaS in the stock (wt %); 1.3778, the coefficient of BaS recalculation to $BaSO_4$.

The results obtained in the experiment are listed in Table 2. In the first stage of the study, experiments on calcination of reactive $BaCO_3$ of pure grade (GOST 4158–80) (run nos. 1–6) and WIR (run nos. 7–12), in a mixture with petroleum coke, were conducted.

In the second stage (run nos. 13–27), petroleum coke was used to reduce mixtures of reactive $BaSO_4$ of pure grade (GOST 3158–75) with $BaCO_3$ (run nos. 13–18), of recycled $BaSO_4$ with WIR (run nos. 25–27), and of the barite concentrate of class A, KB-2 brand (GOST 4682–84) (run nos. 19–24).

The effect of sulfur contained in petroleum coke on the sulfidization of acid-soluble barium compounds was assessed in run nos. (1–12) on the basis of η_5 and

Table 2. Results obtained in a study of the influence exerted by sulfur contained in petroleum coke on the sulfidization of acid-soluble barium compounds (reduction temperature 1000°C, amount of petroleum coke in terms of 100% C 125%)

Run no.	Petroleum coke no.	τ, min	Melt composition, wt %				BaS_{as}*, wt %	η_1	η_2	η_3	η_4	η_5	η_6
			BaS_{I_2}	BaS_{ws}	BaS_{as}	$BaSO_4$ + ash		%					
1	1	15	1.59	5.31	4.29	4.93	–/65.6					42.5	12.7
2	2	15	2.01	4.66	4.05	4.76	–/67.5					37.4	16.1
3	3	15	0.03	4.45	5.66	4.30	–/54.7					35.6	0.2
4	1	30	0.99	3.35	3.64	9.04	–/71.3					26.4	7.8
5	2	30	1.86	3.29	5.29	5.41	–/58.5					25.8	14.6
6	3	30	0.01	2.77	5.91	6.29	–/53.6					21.8	0.1
7	1	15	4.22	8.35**	9.73	2.62	–/25.7					67.8	34.3
8	2	15	4.56	7.64**	10.00	2.63	–/17.4					63.1	37.7
9	3	15	4.12	7.77**	10.34	2.90	–/15.4					62.8	33.7
10	1	30	4.31	7.31**	11.29	2.45	–/8.8					59.1	34.8
11	2	30	4.29	6.90**	11.18	3.03	–/8.5					56.5	35.1
12	3	30	4.29	6.96**	11.48	3.21	–/7.1					56.3	34.7
13	1	15	62.29	63.02	3.44	26.47	1.38/–	77.6	72.9	73.7	1.6		
14	2	15	70.67	71.38	4.75	20.68	2.54/–	83.7	77.1	77.9	2.8		
15	3	15	61.24	62.18	5.06	27.93	2.98/–	76.6	71.0	72.0	3.5		
16	1	30	80.45	82.32	4.06	13.03	1.74/–	90.2	83.7	85.6	1.8		
17	2	30	80.70	87.74	5.21	6.11	2.90/–	95.4	84.4	91.8	3.0		
18	3	30	74.99	79.13	8.89	8.58	6.66/–	93.4	81.0	85.4	7.2		
19	1	15	43.02	45.35	6.46**	39.43	2.94/–	66.9	56.9	60.0	3.9		
20	2	15	50.78	52.56	7.64**	33.14	3.98/–	74.0	64.8	67.1	5.1		
21	3	15	33.15	37.37	7.96**	45.31	4.55/–	59.7	45.4	51.2	6.2		
22	1	30	76.90	80.94	6.62**	8.43	2.52/–	97.8	87.5	92.1	2.9		
23	2	30	79.53	83.17	7.17**	6.01	3.03/–	99.8	89.6	93.7	3.4		
24	3	30	79.13	81.14	8.88**	6.55	4.75/–	99.4	89.4	91.7	5.4		
25	1	30	90.08	93.70**	4.01	2.02	–/12.79	98.9	95.5	99.3	0.00		
26	2	30	87.59	91.39**	4.65	2.54	0.05/–	98.4	92.8	96.8	0.05		
27	3	30	81.98	86.24**	4.78	8.28	0.17/–	94.1	87.3	91.9	0.18		

* Numerator, formed; denominator, spent.

** Less the content of BaS in the raw material.

η_6 values and the amount of spent BaS_{as}, related to that introduced into the stock in the form of $BaCO_3$ and WIR; in run nos. 13–27, this was done on the basis of the η_4 value. In addition, the completeness of the process was assessed on the basis of η_1–η_3.

As seen from Table 2, run nos. 1–6, in which $BaCO_3$ was calcined, clearly reveal an increase in the conversion of BaS_{as} into BaS_{wr} (η_5) in relation to the sulfur content of the petroleum coke. However, the degree of BaS_{as} conversion into BaS_{I_2} (η_6) shows another behavior: it reaches a higher value with petroleum coke no. 2 as reducing agent. This coke is characterized by higher content of volatiles containing methane, hydrogen and organosulfur compounds, which intensify the reduction process [5]. The low content of sulfur in petroleum coke no. 3 accounts for the virtually zero extent of sulfidization of acid-soluble barium compounds in run nos. 3 and 6 (η_6 of 0.2 and 0.1%, respectively), although η_5 has rather high values. Apparently, in these runs, as also in some others (run nos. 1, 2, 4, and 5), $BaCO_3$ is reduced in the presence of carbon [14] in accordance with the equation

$$BaCO_3 + C = BaO + 2CO \quad (9)$$

with the subsequent conversion of BaO into $Ba(OH)_2$ upon melt dissolution, with the latter barium compound determined as BaS_{ws}.

Raising the time of stock reduction to 30 min leads to oxidation of the BaS formed to BaS_2O_3 and $BaSO_4$,

with the corresponding decrease in η_5 and η_6. The same behavior is observed in experiment nos. 7–12, devoted to WIR calcination. In this case, too, keeping the melt in the reaction zone for 30 min resulted in a decrease in η_5, with a dramatic fall of the amount of spent BaS_{as} relative to that introduced into the stock: from 25.7 to 8.8% (petroleum coke no. 1), from 17.4 to 8.5% (petroleum coke no. 2), and from 15.4 to 7.1% (petroleum coke no. 3). The apparent increase in the η_5 and η_6 values in these runs, compared with the results obtained in run nos. 1–6, occurred because of the reduction of $BaSO_4$ contained in WIR.

In the following set of experiments (run nos. 13–27), the same tendency toward a decrease in the degree of $BaSO_4$ conversion into BaS_{as} (η_4) with increasing content of sulfur in a petroleum coke was revealed, and higher degree of $BaSO_4$ reduction (η_1) was obtained in run nos. 14 and 17 with petroleum coke no. 2 containing the largest amount of volatiles. In this case, raising the duration of calcination from 15 to 30 min exerts positive influence on the process characteristics, and, therefore, reduction of a mixture of $BaSO_4$ being recycled and WIR was done at a single experiment duration of 30 min.

Noteworthy is the fact that the reduction in a mixture with WIR of the barite concentrate and $BaSO_4$ being recycled occurs to a fuller extent (η_1 of 99.8 and 98.4%, respectively), compared with the case of a mixture of reactive reagents $BaSO_4$ and $BaCO_3$ (η_1 = 95.4%). Apparently, in the first case, the high intensity of the process is achieved because of the presence of catalyzing components (Fe_2O_3 etc.) in the stock [5, 7], with additional increase in the case of $BaSO_4$ being recycled resulting from the more developed phase boundary in the freshly precipitated product.

However, of practical interest for the method of Na_2S production is the degree of $BaSO_4$ conversion into BaS_{I_2} (η_2), since it is BaS that is the supplier of S^{2-} ions to the finished product, Na_2S. The reduction of a mixture of $BaSO_4$ being recycled and WIR with a petroleum coke containing 2.45% sulfur yielded a η_5 value of 95.5%. In this case, the loss of acid-soluble barium compounds, caused by their sulfidization, was 12.79% relative to their content in the initial stock (η_4 = 0).

Calculations performed on the basis of the experimental data obtained demonstrated that, in processing the barite concentrate of the KB-2 brand, the content of sulfur in the petroleum coke should not exceed 3.0%, since an excess of sulfur complicates neutralization of furnace gases. The requirements to the content of sulfur in a petroleum coke should be determined in relation to the amount of SiO_2, Fe_2O_3, and Al_2O_3 impurities in the barite concentrate and that of acid-soluble barium compounds in $BaSO_4$ being recycled.

CONCLUSIONS

(1) The sulfidizing action of sulfurous petroleum coke on the reductive calcination of barite raw materials is established. This favors minimization of the yield of acid-soluble barium compounds, which is important for the technology of sodium sulfide manufacture.

(2) It is shown that, with a petroleum coke containing 2.45% sulfur used, a 95.5% conversion of $BaSO_4$ into BaS_{I_2} is achieved in reduction of $BaSO_4$ being recycled, and the conversion of $BaSO_4$ to BaS_{as} is zero, compared with 87.3 and 0.18%, respectively, for the petroleum coke containing only 0.68% of sulfur.

(3) Noteworthy is the positive influence exerted by catalyzing components of the stock, e.g., Fe_2O_3, and by developed phase boundary in freshly precipitated $BaSO_4$ on the process of reduction with sulfurous petroleum coke of the barite concentrate and $BaSO_4$ being recycled, with 98.9–99.8% $BaSO_4$ reduction achieved.

REFERENCES

1. RF Patent 2142907.
2. Busygin, V.M., Gaisin, L.G., Tkachev, K.V., and Prokhorov, A.G., *XIV Mendeleevskii s''ezd po obshchei i prikladnoi khimii* (XIV Mendeleev Congress on General and Applied Chemistry), Moscow, 1998, vol. 2, pp. 253–254.
3. Tkachev, K.V., Gaisin, L.G., Prokhorov, A.G., *et al.*, *Khim Prom–st.*, 2001, no. 9, pp. 44–49.
4. Akhmetov, T.G., Busygin, V.M., Gaisin, L.G., and Porfir'eva, R.T., *Khimicheskaya tekhnologiys neorganicheskikh veshchestv* (Chemical Technology of Inorganic Substances), Moscow: Khimiya, 1998.
5. Trutnev, G.A., A Study of Application of High-Sulfur Petroleum Coke in Some Chemical Technology Processes, *Cand. Sci. Dissertation*, Ufa, 1978.
6. Koshkarova, M.E., Use of Sulfurous Petroleum Coke as Reducing Agent in Non-Ferrous Metallurgy and Chemical Industry, *Cand. Sci. Dissertation*, Moscow, 1984.
7. Alekseev, V.I., A Study of Reductive Calcination of Barite Concentrates, *Cand. Sci. Dissertation*, Kharkov, 1977.

Russian Journal of Applied Chemistry, Vol. 76, No. 2, 2003, pp. 191–194. Translated from Zhurnal Prikladnoi Khimii, Vol. 76, No. 2, 2003, pp. 201–204.

INORGANIC SYNTHESIS AND INDUSTRIAL INORGANIC CHEMISTRY

Refining of Lead To Give Bismuth-Enriched Drosses

O. G. Zarubitskii

Vernadskii Institute of General and Inorganic Chemistry, National Academy of Sciences of Ukraine, Kiev, Ukraine

Received June 3, 2002

Abstract—The results obtained in testing an improved technique for reagent refining of crude lead, which yields bismuth-enriched drosses in the form of a powder, are presented. The advantages of the method put into industrial practice are described.

The pyrometallurgical method proposed by Kroll and Betterton [1, 2] is mainly used at lead works to remove bismuth admixtures from refined crude lead (lead bullion). This, the most complicated procedure is carried out after silver removal. It involves dissolution of blocks of circulating bismuth drosses at 400°C and subsequent introduction of magnesium and calcium into melted crude lead at 360–370°C. These metals react with bismuth to form intermetallic compounds: Ca_3Bi_2, Mg_3Bi_2, Mg_2CaBi_2, which are poorly soluble in lead and are deposited on the bath surface. They are extracted as the so-called "enriched" bismuth drosses with bismuth content of 3–5%. Then the bath is cooled to 340–350°C and "lean" circulating drosses containing 0.5–2% Bi are extracted. Repeated circulation of drosses can increase the bismuth content up to 5–11%, to give a lead–bismuth alloy containing 8–15% Bi [1]. The increase in the bismuth content from 5–11 to 8–15% results from removal of magnesium and calcium from the drosses with molten NaOH. A 5–6% fraction of Bi passes into the resulting alkaline melts.

The existing technology for Pb–Bi alloy production does not ensure isolation of bismuth-enriched (to more than 8–15%) products and is characterized by repeated dross circulation, which leads to loss of the target metal and involves additional consumption of reagents (magnesium, calcium, and sodium hydroxide).

Various methods for dross enrichment with bismuth have been proposed. For example, centrifugal refining can enrich drosses to Bi content of 18–21% at its initial concentration of 5.7% [3]. Air bubbling through liquid metal (cupellation) at 900–950°C can raise the bismuth content of a Pb–Bi alloy being treated from 14 to 40–60%, with simultaneous removal of antimony, tin, arsenic, and tellurium [4]. This method has been implemented in industry.

Of special interest are the publications [5–7] describing the possibility of using organic compounds in pyrometallurgical processing of lead–bismuth alloys. For example, in purifying bismuth to remove lead and copper by adding sulfur to a metallic melt, friable yields can be obtained if carbon or masut is introduced into the metal being refined [5]. It is recommended [6] that coal-tar pitch should be added to a melt to enrich dross with bismuth, which yields an alloy containing 40% Bi and 60% Pb. Dry drosses are obtained by adding sawdust to crude lead (modified Kroll and Betterton method [6, 7]). However, the authors of [5, 7] did not consider the mechanism by which the above-mentioned organic compounds affect the metallurgical processes under consideration.

EXPERIMENTAL

Our experiments and pilot tests made it possible to develop and put into industrial practice an improved method for lead refining, which provides lead alloys with high bismuth content. The technological process consists in the following. First, magnesium and calcium are introduced into crude lead at 375–400°C (rather than the commonly used circulating dross), and then the temperature of the refining bath is raised to 475–490°C and circulating drosses are loaded. After settling for 25–35 min, dead oil (0.13–0.18 kg per 1 ton of lead to be refined) is introduced in portions with continuos agitation at 400–470°C. After liquation, solid powdered drosses (30–40% Bi, 50–60 Pb, 5–10 Zn, 0.015–0.02 Ag) are extracted, cooled to room temperature, and classified by sieving with 0.10–0.15 mm mesh. Drosses remaining on the sieve

1070-4272/03/7602-0191 $25.00 © 2003 MAIK "Nauka/Interperiodica"

are loaded in the lead bath for recirculation, whereas sifted drosses (–0.10–0.15-mm class) are remelted to obtain a lead–bismuth alloy. After the removal of dry drosses, the temperature is lowered to 330°C, and circulating bismuth drosses are taken off. The refining process is finished according to the standard scheme.

Powder drosses of the +0.10–0.15-mm class, containing (%) 12–17 Bi, 50–55 Pb, 25–40 Zn, and 0.06–0.07 Ag, are purified to remove silver, which diminishes the expenditure of metallic zinc by approximately 50%, and loss of silver and bismuth, by approximately 30%. Thus, in contrast to the common technologies, this method does not involve a labor-consuming procedure of lead bullion purification to remove zinc introduced into lead to recover silver.

Powder drosses of the –0.10–0.15-mm class are remelted under a layer of slam (spent $PbCl_2$–$ZnCl_2$–KCl–NaCl electrolyte used at the plant in electrochemical reactors for separating lead–bismuth alloys in ionic melts [8]). In this case, the following reactions occur

$$Mg_3Bi_2 + 3PbCl_2 = 3MgCl_2 + 3Pb + 2Bi,$$

$$Ca_3Bi_2 + 3PbCl_2 = 3CaCl_2 + 3Pb + 2Bi.$$

Such a procedure is expedient because lead, which was previously dumped as a salt in a chloride mixture, is returned into the production cycle. The resulting lead–bismuth alloy contains 55–65% Bi and the balance lead.

In pilot tests, we used dead oils of BN-IV and BN-V brands, which have softening points of 70 and 90°C, respectively. Special bitumens of A and G brands, and also pitches and other products of straight-run masut distillation, can be used for this purpose.

The tests have shown that the initial introduction of calcium and magnesium into crude lead at 375–400°C and subsequent addition of circulating drosses at higher temperature (475–490°C) diminish the loss of active metals (magnesium and calcium) and thus make lower the process costs. According to this technique, the purification to remove bismuth is carried out at bath saturation with bismuth higher than 2%. The introduction of calcium and magnesium at 375–400°C ensures high dissolution rate at minimum loss of the active metals, which can be oxidized by atmospheric oxygen or moisture. At 475–490°C the dissolution of circulating drosses proceeds faster, the solubility of all the components added is higher at elevated temperature, and, simultaneously, lead is deoxidated and cooled. Thus, complete use of the reagents is achieved, and drosses very rich in bismuth are obtained in small amounts. This is also important for the subsequent introduction of a solid product of heavy oil residuals, e.g., dead oil, to be carried out successfully. Under these conditions, fine particles of bismuth intermetallics do not aggregate, which makes it possible to obtain bismuth-rich drosses.

In carrying out this operation, dry powder drosses with high bismuth content (33–37%) are formed as a phase on the lead surface. The results of X-ray diffraction, mass-spectrometric, microscopic, and chemical analyses suggest that the forming particles of intermetallic compounds, and especially bismuth intermetallide Mg_3Bi_2, are wetted with bituminous hydrocarbons (asphaltenes etc.). This phenomenon eliminates wetting of intermetallic particles by liquid lead, because the adsorption energy of hydrocarbons on the surface of solid intermetallic particles is higher than the energy of lead adsorption. Consequently, bismuth drosses are formed as powders containing no coarse conglomerates with adsorbed or adhering lead. This results in that the bismuth drosses are obtained in powdered (dry) form and contain much lesser amounts of lead and greater amounts of bismuth. According to a mass-spectrometric analysis of the gas content of samples, the fine powder contains 2.5 and 3 times greater amount of, respectively, hydrogen and carbon dioxide than the coarse fraction does. This may indicate that bitumen is mostly adsorbed on fine-fraction particles of bismuth drosses.

Our physicochemical study has shown that powder drosses with particle size less than 0.10–0.15 mm are largely composed of bismuth intermetallides (mainly Mg_3Bi_2 in amount of 30–35%, according to X-ray analysis). Drosses with particles larger than 0.10–0.15 mm additionally contain intermetallic compounds of zinc and lead. It was established that the fine fraction of dry powder drosses with particle size less than 0.15 mm contains (%) 43–50 Bi, 35–45 Pb, 0.1–0.5 Zn, 0.002–0.003 Ag, and Ca and Mg the rest. Drosses of the +0.10–0.15-mm class are complex intermetallic compounds of zinc, bismuth, lead, silver, calcium, and magnesium.

The expenditure for production of bismuth from an alloy containing 55–65% Bi is considerably less than that for production of the same amount of Bi from an alloy with bismuth content of 15% (this is the maximum Bi content ensured by the currently existing procedures). In this case, the expenditure of electric power and electrolyte, number of electrolyzers, floor

area, and maintenance staff are diminished. This is confirmed by the following simple calculation of, e.g., the electric power expenditure.

Let us assume that a plant accomplishes electrochemical separation of a lead–bismuth alloy containing, on average, 12% Bi and 88% Pb by the formerly used technology, i.e., it is necessary to transfer electrochemically 88 tons of Pb from anode to cathode in order to produce 12 tons of Bi. If, however, a lead–bismuth alloy enriched with bismuth to 60% by the new technology is subjected to electrolysis, it is necessary to dissolve at the anode and precipitate at the cathode only 8 tons of Pb in order to obtain the same amount of Bi (12 tons). Consequently, the amount of lead to be electrolyzed in the second variant is 11 times less than that in the case of the standard technology. The expenditure of electric power, number of electrolyzers, etc. will be equally diminished.

The results obtained in industrial tests of the lead refining technique under consideration, which yields a bismuth-enriched Pb–Bi alloy, are presented below.

The experiments were carried out in cauldrons with capacity of 125–130 tons of crude lead (lead bullion). The sequence of operations was described above. The size classification of powder drosses yielded 5.3–6.0 tons of a fine fraction containing 43.7–50.6% Bi and 2.8–3.8 tons of grit with Bi content of 12.6–17.2%. After remelting of the fine fraction under a fluxing agent ($PbCl_2$–$ZnCl_2$–KCl–NaCl), 4.2–4.5 tons of alloy with Bi content of 55.1–59.9% were obtained. The process was implemented industrially and ensured a significant technological and economic effect. The environmental safety was improved, because we used a lesser number of electrochemical reactors producing lead by high-temperature electrolysis of a lead chloride melt.

A somewhat different technique for lead–bismuth alloy enrichment was also developed and applied in industry. At one of lead-manufacturing plants, a Bi–Pb alloy is separated by electrolysis in hexafluorosilicon electrolyte, following the Betts procedure [1, 9]. A semi-finished product with Bi content of 8–15% is used as the starting alloy. It is desirable to raise the content of this metal, but to no more than 30%. If the bismuth content in Pb–Bi anode plates is greater, the anodic process is significantly complicated. As lead is dissolved, the solid alloy lattice is disrupted and narrow channels are formed, in which lead hexafluorosilicate is crystallized. At the same time, a large amount of bismuth is dissolved and deposited at the cathode. Small pieces of the anode are crumbled and entrained by slam. The surface layer of the pieces consists of virtually pure bismuth, and the inner layer, of electrochemically unreacted lead. Industrial tests have shown that the Betts method for processing of Pb–Bi alloys containing more than 30% Bi is inexpedient.

Taking into account the aforesaid, we proposed, developed, and implemented industrially a somewhat different method for enrichment of bismuth drosses. The method, which is simpler and less expensive, consists in the following. To refine lead containing 0.5 ± 0.1% Bi, a mixture of bitumen (45–75 wt %) and sawdust (25–55 wt %) is added, and the process is performed at lower temperature (370–390°C). As a result, powder drosses containing 23–27% Bi are obtained and delivered to hydroelectrolytic processing by the Betts method. This procedure involves separation of drosses and thus eliminates the additional stage of bath heating to a temperature of 400–470°C, at which drosses are separated in the method described above. The addition of sawdust (which is less expensive than bitumen) prevents the possible inflammation of bitumen particles floating-up to the surface of a lead bath. Sawdust contains moisture, which evaporates to cool the upper layers of molten lead. It should be noted that sawdust is introduced into the liquid metal being refined not simultaneously with dead oil, but later, when obtaining "dry" powder drosses. In addition, sawdust plays the same part in the separation of intermetallic compounds of bismuth as dead oil.

This method makes lower the cost of bismuth removal from lead because of the use, in addition to bitumen, of such a less expensive material as sawdust. Labor conditions are improved owing to the elimination of the possibility of bitumen inflammation. The energy expenditure, labor intensity, and reagent consumption are much lowered owing to a significant decrease in the amount of lead–bismuth alloy to be processed by an electrolyzer in a hexafluorosilicon acid solution.

CONCLUSIONS

(1) A modified Kroll and Betterton method for lead purification to remove bismuth has been proposed and subjected to pilot tests. The improvement consists in that dead oil or its mixture with sawdust is introduced into metal melt in a certain stage of refining to yield rich bismuth drosses in the form of a powder. The separation of the product is also a specific feature of the process.

(2) The method for lead and bismuth separation, which was developed and implemented industrially, makes it possible to produce a bismuth–lead alloy containing up to 55–65% Bi.

ACKNOWLEDGMENTS

The author is grateful to I.P. Brovin and V.A. Shleenkov (DVGMK, Far-Eastern Mining and Swelting Combine) for help in the study.

REFERENCES

1. Smirnov, M.P., *Rafinirovanie svintsa i pererabotka poluproduktov* (Lead Refining and Semiproduct Processing), Moscow: Metallurgiya, 1977.
2. Betterton, J.O. and Lebedeff, Y., *Trans. Metallurg. Soc. Am. Inst. Met. Eng.*, 1936, vol. 121, pp. 205–209.
3. Khodov, N.V., Suturin, S.N., Meshkov, E.I., *et al.*, *Byull. Tsvet. Metallurgiya*, 1982, no. 6. pp. 22–24.
4. USSR Inventor Certificate, no. 653916.
5. Polyvyannyi, I.R., Ablanov, A.D., Batyrbekova, S.A., and Sysoev, L.N., *Metallurgiya vismuta* (Metallurgy of Bismuth), Alma-Ata: Nauka, 1973.
6. Zelenova, E.I., *Byull. Tsvet. Metallurgiya*, 1971, no. 15, pp. 33–37.
7. German Patent 1132731.
8. Zarubitskii, O.G., *Tsvetn. Met.*, 1990, no. 6, pp. 41–42.
9. Shivrin, G.N., *Metallurgiya svintsa i tsinka* (Metallurgy of Lead and Zinc), Moscow: Metallurgiya, 1982.

Russian Journal of Applied Chemistry, Vol. 76, No. 2, 2003, pp. 195–197. Translated from Zhurnal Prikladnoi Khimii, Vol. 76, No. 2, 2003, pp. 205–207.

PHYSICOCHEMICAL STUDIES OF SYSTEMS AND PROCESSES

A Study of Rectification and Liquid–Vapor Phase Equilibrium in Systems Phenol–Water–Hydroxyacetone and Phenol–Water–α-Methylstyrene

V. Yu. Aristovich, Yu. V. Aristovich, A. Yu. Sokolov, and J. V. Fulmer

Novye Technologii Limited Liability Company, St. Petersburg, Russia
General Electric Plastics, Mount-Vernon, IN, USA

Received July 30, 2002

Abstract—Distillation processes and the liquid–vapor phase equilibrium in the systems phenol–water–hydroxyacetone and phenol–water–α-methylstyrene at atmospheric pressure were studied. The direction of the distillation lines was established and the possibility of preparing pure phenol and concentrating other components, i.e., impurities, in various regions of distillation of the systems was determined.

Owing to the increasing stringency of requirements to the quality of phenol used for production of various polymers, including those exhibiting heat resistance, it is necessary to study in more detail processes of distillation of a mixture of phenol with concomitant impurities in the stage of phenol isolation as a commercial product. Among the main impurities determining the quality of commercial phenol are water, α-methylstyrene, and 2-methylbenzofuran, with the last compound being a product of reaction between hydroxyacetone and phenol in the final stages of phenol isolation.

Data on liquid–vapor phase equilibrium in mixtures of phenol with water, α-methylstyrene, and hydroxyacetone form a physicochemical basis for determining the optimal conditions of phenol rectification to remove concomitants. Published data are only available for the system phenol–water–α-methylstyrene at 66.65 hPa [1]. At the same time, commercial phenol is commonly isolated from aqueous solutions under nearly atmospheric conditions.

Experiments on determining the liquid–vapor equilibria were performed on a Bushmakin device modified by Smirnova and Morachevskii in order to study stratification liquids [2]. The presence of an azeotrope in the hydroxyacetone–water system was judged from data of gas-liquid chromatography (Hewlett–Packard 5890 chromatograph). The mixtures were distilled on a film rectification column with efficiency of 25 theoretical plates. Prior to all experiments, nonvolatile antioxidants were added to the solutions to prevent oxidation of the active components of the mixtures studied. The rectification of aqueous hydroxyacetone mixtures did not reveal presence of an azeotrope with the lowest boiling point, since the hydroxyacetone concentration in the first fractions (T_b =100.0°C, P = 1013 hPa) was less than 0.01 wt %.

Data on the liquid–vapor equilibrium are listed in Table 1 for the binary system water–hydroxyacetone

Table 1. Data on liquid (X)–vapor (Y) equilibrium in the system hydroxyacetone (1)–water (2)

P, hPa	T, °C	X_1	Y_1
		mol %	
433	104.0	69.13	55.18
433	80.5	9.67	4.87
433	77.8	4.49	2.18
433	77.6	1.91	1.08
433	77.5	0.68	0.31
433	77.5	0.43	0.20
993	129.4	48.54	39.79
1000	106.8	26.90	9.60
981	101.0	9.67	5.13
997	100.1	3.93	2.04
993	99.5	1.91	1.21
978	99.5	0.85	0.45
992	99.5	0.44	0.17

1070-4272/03/7602-0195 $25.00 © 2003 MAIK "Nauka/Interperiodica"

Table 2. Data on liquid (X_i)–vapor (Y_i) equilibrium in the system phenol (1)–water (2)–hydroxyacetone (3)

P, hPa	T, °C	X_1	X_3	Y_1	Y_3	$\alpha = \frac{Y_3 X_1}{X_3 Y_1}$	$K = \frac{Y_3}{X_3}$
		mol %					
987	130.4	81.53	5.96	28.62	2.52	1.20	0.42
987	140.2	84.55	4.21	35.48	1.94	1.10	0.46
985	147.4	89.03	3.19	39.51	1.44	1.02	0.45
988	153.2	91.55	2.05	47.69	1.12	1.05	0.55
1002	160.1	92.65	1.21	55.31	0.87	1.20	0.72
1006	165.6	93.48	0.80	63.63	0.64	1.18	0.80
1005	168.9	95.14	0.48	68.81	0.41	1.18	0.85
1002	174.7	97.05	0.14	77.5	0.15	1.34	1.07
986	179.7	99.06	0.063	96.91	0.079	1.28	1.25
988	114.9	69.15	0.043	22.55	0.004	0.29	0.09
982	117.6	68.37	0.88	21.87	0.17	0.60	0.19
1000	135.5	57.12	29.11	9.45	17.12	3.55	0.59
988	147.8	78.94	14.22	25.41	10.07	2.20	0.71
990	161.2	89.02	5.84	50.40	5.57	1.68	0.95
982	169.8	94.40	2.61	69.13	2.67	1.40	1.02
973	177.0	96.84	0.35	92.27	0.37	1.11	1.06
974	178.6	98.98	0.09	94.48	0.12	1.40	1.33
986	124.6	77.9	0.051	14.96	0.018	1.84	0.35

and in Table 2 for the ternary phenol–water–hydroxyacetone system.

The experiments performed made it possible to construct diagrams of distillation lines and regions (Fig. 1a). The family of the distillation lines is divided into two distillation regions *1* and *2*. The strong dependence of the concentrations and the relative volatility of hydroxyacetone on the phenol : water ratio is characteristic of the distillation lines in region *1* adjacent to phenol and occupying the major part of the concentration triangle. In some cases, the relative volatility is lower than unity.

Analysis of the curve of the extremal concentrations of hydroxyacetone (Fig. 1a, *dashed line*) shows that, at a given hydroxyacetone concentration in the initial mixture, pure commercial phenol can be isolated

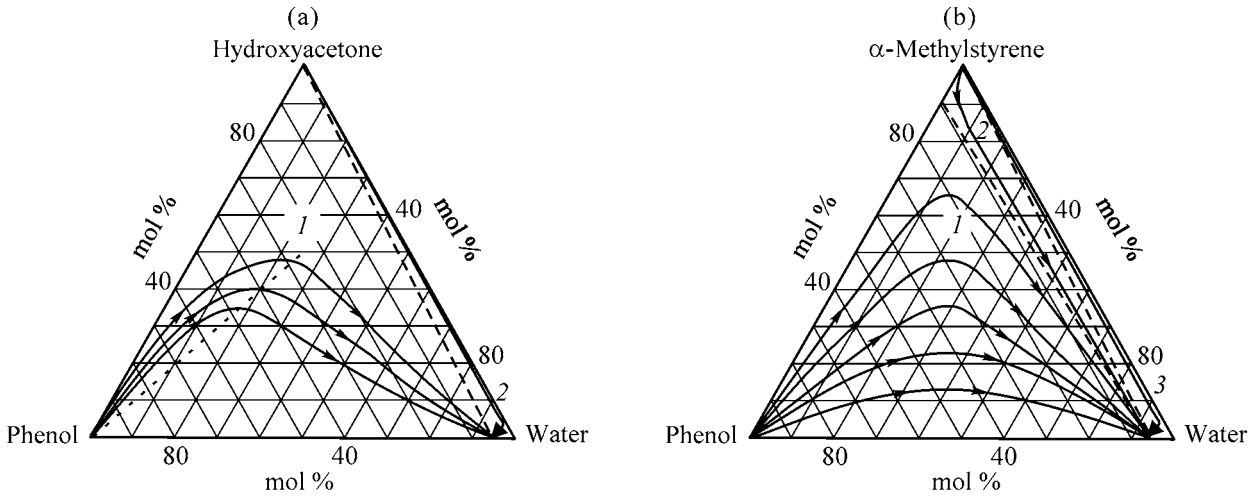

Fig. 1. Diagram of distillation regions and lines in the systems (a) phenol–water–hydroxyacetone and (b) phenol–water–α-methylstyrene at atmospheric pressure.

Table 3. Data on liquid (X_i)–vapor (Y_i) equilibrium in the system phenol (1)–water (2)–α-methystyrene (3)

Experiment no.	P, hPa	T, °C	X_1	X_3	Y_1	Y_3	Experiment no.	P, hPa	T, °C	X_1	X_3	Y_1	Y_3
			mol %							mol %			
1	1015	118.13	64.00	20.72	3.07	7.47	6	1008	133.16	33.05	59.32	5.18	22.83
2	1012	142.38	79.59	12.89	4.85	2.91	7	1009	155.74	67.37	29.56	31.03	33.51
3	1012	160.45	88.82	5.75	43.00	7.33	8	1013	167.80	86.29	12.80	54.20	21.16
4	1013	168.94	95.87	2.37	67.45	6.40	9	1016	174.52	94.34	5.08	70.98	11.96
5	1014	175.64	98.35	0.92	81.83	2.58	10	1014	177.90	97.56	2.12	87.02	6.16

Table 4. Data on liquid (X_i')–liquid (X_i'') equilibrium in the system phenol (1)–water (2)–α-methystyrene (3) at 20°C

Run no.; the same as in Table 3	X_1'	X_3'	X_1''	X_3''	Run no.; the same as in Table 3	X_1'	X_3'	X_1''	X_3''
	mol %					mol %			
1	0.68	0.01	22.92	69.39	6	0.52	0.00	13.95	66.18
2	1.21	0.01	40.12	30.93	7	1.27	0.02	35.17	38.14

in region *1* only up to a certain phenol/water ratio. The most complete concentrating of hydroxyacetone is possible in region *2*, which is adjacent to water. The distillation line separating regions *1* and *2* is shown in Fig. 1a by dashed line.

Table 3 lists data on the liquid–vapor equilibrium in the phenol–water–α-methystyrene system at atmospheric pressure. In run nos. 1, 2, 6, and 7, the condensate of sampled vapor stratified. The compositions of its lower and upper layers are given in Table 4. The diagram of the distillation lines and regions for the system is shown in Fig. 1b. There exist three distillation regions. Pure phenol can be isolated in region *1*, which is adjacent to phenol. Isolation of pure α-methystyrene is possible in region *3*, which is adjacent to water.

CONCLUSIONS

(1) The experimentally obtained data on the liquid–vapor equilibrium in the systems water–hydroxyacetone and in the ternary system phenol–water–hydroxyacetone made it possible to assess conditions of phenol rectification in its mixtures with water and hydroxyacetone.

(2) The experimental data on the liquid–vapor equilibrium in the phenol–water–hydroxyacetone ternary system at atmospheric pressure were used to determine the conditions of phenol rectification in mixtures with water and α-methylstyrene.

ACKNOWLEDGMENTS

The authors thank Dr. A.G. Morachevskii from St. Petersburg State University for his attention in the course of preparation of this article to publication.

REFERENCES

1. Byk, S.Sh., Serebrennaya, I.I., and Shcherbakova, P.R., Khim. Prom–st., 1963, no. 7, pp. 507–509.
2. Smirnova, N.A., and. Morachevskii, A.G., *Vestnik Len. Gos. Univ.*, 1959, vol. 2, no. 10, pp. 106–109.

Russian Journal of Applied Chemistry, Vol. 76, No. 2, 2003, pp. 198–202. Translated from Zhurnal Prikladnoi Khimii, Vol. 76, No. 2, 2003, pp. 208–211.

SORPTION AND ION-EXCHANGE PROCESSES

Sorption Properties of α-Aluminum Oxide Modified with Decationized Silica Sol

T. F. Kuznetsova, A. I. Rat'ko, and S. I. Eremenko

Institute of General and Inorganic Chemistry, National Academy of Sciences of Belarus, Minsk, Belarus

Received December 4, 2001; in final form, June 2002

Abstract—The method of sorption of tetrachloromethane vapor at the solid/gas interface was applied to study the sorption and structural properties of a mesoporous aluminum oxide material obtained by deposition of amorphous hydrated silicon(IV) oxide onto α-aluminum oxide particles submerged in decationized silica sol.

Varieties of colloid silica, from silicic acids to sols, are commonly deposited on surfaces in order to diminish or raise their adhesion to other substances. The resulting thin SiO_2 films enable modification of the surface properties of the substrate and expand the application fields of its valuable volume properties. For example, a dense coating on a titanium oxide pigment can protect it from photocatalytic degradation [1], and a porous coating deposited on a selective catalyst and exhibiting a sieving effect precludes undesirable side reactions in the catalytic process [2]. However, despite the interest in properties and deposition of various silica coatings [1–5], there are virtually no published data on how the sorption characteristics of substances change upon SiO_2 deposition. In contrast to the structure of the conventional bulk silica gel, whose formation is much contributed by stages of gel formation, syneresis, and drying [6], the structure of thin SiO_2 films is the most sensitive to the last stage, which is more important than the others, and the time of structure formation is much shorter than that in xerogel SiO_2 [5].

The aim of the present study was to apply the method of sorption of tetrachloromethane vapor at the gas/solid interface to analysis of the structural properties of aluminum oxide materials obtained by deposition of amorphous hydrated SiO_2 onto α-Al_2O_3 particles submerged in decationized silica sol. Upon drying, such substances, which are densified when necessary to a desirable extent, are potential sensors, membranes, or catalysts, and mixtures of a colloid silica with highly dispersed Al_2O_3 may serve as thin-layer coatings in cellular supports with developed surface [7].

As substrate for a silica coating was used α-Al_2O_3 with specific surface area $S_{sp} = 27 \times 10^3$ m^2 kg^{-1} and density of 3700 kg m^{-3}. A decationized silica sol with pH 3.5 and SiO_2 content of 2.0 wt % was obtained by passing diluted aqueous solution of Na_2SiO_3 through a column packed with KU-2 sulfo cation-exchange resin in hydrogen form [8]. Then, a certain amount of silica sol, corresponding to Si : Al molar ratios of 0.1 : 0.9, 0.3 : 0.7, 0.5 : 0.5, 0.6 : 0.4, and 0.7 : 0.3 was delivered by a dosing pump to a vessel with aqueous suspension of aluminum oxide powder, which contained 2.5×10^{-3} kg α-Al_2O_3 per 1 kg of H_2O. Simultaneously, $NH_3 \cdot H_2O$ was added to pH 7.5, and then hydrochloric acid to pH 5.6. After keeping the gel in liquid state for 0.5 h the solid phase was separated by decantation, washed with distilled water to complete absence of a reaction for Cl^- ions in washing water, and dried in air, first at room temperature and then at 393 K for 4 h. The corresponding bulk silica gel was prepared from acidic decationized silica sol in the absence of α-Al_2O_3.

Adsorption–desorption isotherms of CCl_4 vapor were measured gravimetrically at 293 K after preliminary vacuum treatment of samples at 413 K for 16 h. The specific surface area was calculated from the monolayer capacity by the BET equation in linear form at relative pressures $p/p_0 = 0.05–0.25$ with surface area occupied by a CCl_4 molecule taken to be 0.322 nm^2. The amount of adsorbed vapor was expressed in volumes V of the liquid adsorbate per 1 kg of adsorbent. The limiting sorption volume of pores, V_p, was found by the Gurvich method [9] from the amount of vapor sorbed at saturation. The shape of mesopores was assessed in accordance with IUPAC

1070-4272/03/7602-0198 $25.00

recommendations from the shape of the adsorption–desorption hysteresis loop [10]. The average pore radius r_p was found using the relation

$$r_p = 2V_p/S_{sp}, \quad (1)$$

and the radius of globules of aluminum oxide materials, r, by the formula

$$r = 3/\rho S_{sp}, \quad (2)$$

where ρ is the density of the solid.

To analyze the isotherms of adsorption of CCl_4 vapor, comparison curves were also plotted, in which the adsorption on a sample under study (ordinate) was represented as a dependence on the adsorption on a standard sample at the same relative vapor pressure (abscissa). The latter adsorption was expressed as reduced adsorption $V/V_{0.4}$, where $V_{0.4}$ is the amount of vapor adsorbed at $p/p_0 = 0.4$. As standard served Fransil EL nonporous SiO_2 with hydroxylated surface [11].

The thickness of the SiO_2 monolayer was calculated on the assumption that silicon dioxide tetrahedra form a densely packed hexagonal structure. With this kind of packing, the SiO_2 mass per 1 m^2 of the aluminum oxide surface $m = 103.75 \times 10^{-6}$ kg, in accordance with the expression

$$m = \frac{Mu}{a}, \quad (3)$$

where M is the relative molecular weight of SiO_2; u, the atomic mass unit equal to 1.66×10^{-27} kg; a, the area occupied by a silicon dioxide tetrahedron, equal to 0.096×10^{-18} m^2.

Then the SiO_2 volume per 1 m^2 $V = 0.47 \times 10^{-9}$ m^3 in accordance with the expression

$$V = \frac{Mu}{a}\frac{1}{\rho}, \quad (4)$$

where ρ is the silica density, equal to 2200 kg m^{-3}.

Since the calculation was done for 1 m^2 of the aluminum oxide surface, the SiO_2 monolayer thickness was taken to be 0.47 nm.

IR spectra of samples compacted in pellets with KBr were measured on MIDEC M 2000 IR Fourier spectrometer (USA) in the spectral range 4000–400 cm^{-1} at resolution of 4 cm^{-1} and number of scans equal to 4. The spectra obtained were processed using Galactic GRAMS/32 software (USA).

The data presented in Fig. 1 show that sample nos. 1 and 8, i.e., α-Al_2O_3 and SiO_2 obtained from decationized sol at pH 5.6, have mesoporous and microporous structure and are described, according to the IUPAC classification [10], by isotherms of, respectively, type IV and I. The shape and reversibility of isotherm *8* (SiO_2) indicate that the calculated specific surface area and average sizes of pores and globules are effective, apparent, and the effective pore radius of the sample is less than 1 nm [10]. To summarize, to dense α-Al_2O_3 globules (r = 30 nm) corresponds a specific surface area of 27×10^3 m^2 kg^{-1}, and to SiO_2 ($r \approx 1$ nm), an apparent specific surface area of 1120×10^3 m^2 kg^{-1} (see table).

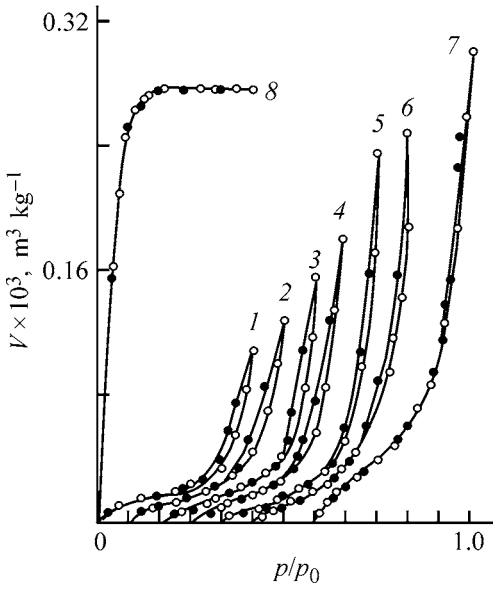

Fig. 1. Isotherms of adsorption–desorption of CCl_4 vapor on α-Al_2O_3 samples (*1*) without treatment with decationized silica gel and (*2–7*) after such treatment and (*8*) silica gel obtained from acidic decationized silica sol. (V) Amount of CCl_4 vapor adsorbed in volume of liquid adsorbate per 1 kg of adsorbent, (p/p_0) relative vapor pressure of the adsorbate, and (p_0) saturated vapor pressure of the adsorbate. *Digits at curves* correspond to sample numbers in the table.

The starting decationized SiO_2 sol is composed of minute globules ($r \approx 1.5$–2.0 nm), which corresponds, at SiO_2 density of 2200 kg m^{-3}, to a mass of a separate particle of about $(3.9–9.2) \times 10^{-24}$ kg, or, if it were a separate molecule, to relative molecular mass of 2300–5500 [8]. The increase in capillary contraction forces in the course of dehydration of the silica gel obtained leads to an isotherm of type I, characteristic of microporous gels (Fig. 1).

The isotherms of CCl_4 vapor sorption by sample nos. 2–7 obtained at various Si : Al ratios are revers-

Sorption and structural parameters of samples obtained

Sample no.	Si : Al, mol : mol	Type of isotherm	$S_{sp} \times 10^{-3}$, $m^2\ kg^{-1}$	$V_p \times 10^3$, $m^3\ kg^{-1}$	r_p, nm	ρ, $kg\ m^{-3}$	r	t^*
							nm	
1	0 : 1.0	IV	27	0.11	8.1	3700	30.0	–
2	0.1 : 0.9	IV	25	0.13	10.4	3609	30.8	0.8
3	0.3 : 0.7	IV	24	0.16	13.3	3398	32.7	2.7
4	0.5 : 0.5	IV	24	0.18	15.0	3145	35.3	5.3
5	0.7 : 0.3	IV	27	0.24	17.7	2832	42.4	12.4
6	0.8 : 0.2	IV	27	0.25	18.5	2647	45.3	15.3
7	0.9 : 0.1	IV	42	0.30	14.3	2439	29.3	–
8	1.0 : 0	I	1120**	0.28	0.5**	2200	1.2**	–

* t is the thickness of the silica coating.

** Apparent values.

ible at low relative vapor pressures, and show hysteresis loops at higher p/p_0, which corresponds to type IV of isotherms of physical sorption [10]. The shape of the irreversible part of isotherms in Fig. 1 varies between the samples, which points to the presence of mesopores with different shapes and sizes, formed by various ensembles of particles. The hysteresis loop in isotherms *2–7* narrows and shifts somewhat to the right with increasing isotherm number. The very narrow hysteresis loops of isotherms *2–7* are a combination of hysteresis H1 at the beginning of the loop and H3 at its end at high p/p_0. The first kind of hysteresis is characteristic of open cylindrical pores formed by agglomerates of contacting globules and connected with neighboring pores by several throats, and the second kind is tipical of particle aggregates with other types of packing.

The initial portions of comparison curves *2–6* for samples obtained at Si : Al molar ratios in the range from 0.1 : 0.9 to 0.8 : 0.2 are, in contrast to isotherm *7*, straight lines passing through the origin of the coordinates, which points to the absence of micropores (Fig. 2). The rise observed in curves *5–7* begins at $V/V_{0.4}$ values corresponding to p/p_0 of 0.59, 0.52, and 0.40 and precedes the beginning of hysteresis loops in the isotherms shown in Fig. 1 ($p/p_0 \approx 0.70$). Such upward deviations of the comparison curves of the samples in the region preceding the beginning of the hysteresis loop point to the occurrence of capillary condensation not accompanied by hysteresis [12]. For sample nos. 2–4, the points of rise in adsorption in the comparison curves coincide with the onset of hysteresis in the sorption isotherms.

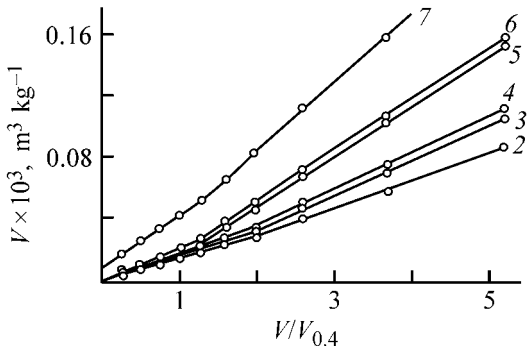

Fig. 2. Comparison curves for the samples obtained. (V) Volume of CCl_4 vapor adsorbed on a sample under study, ($V/V_{0.4}$) reduced adsorption of CCl_4 vapor on a standard Fransil EL sample at the same p/p_0 values as those for the sample under study, and ($V_{0.4}$) amount of CCl_4 vapor adsorbed at equilibrium p/p_0 equal to 0.4.

It can be seen from the table that, with the Si : Al molar ratio changing from 0.1 : 0.9 to 0.8 : 0.2, the average particle radius in sample nos. 2–6 increases from 30.8 to 45.3 nm, the thickness of the silica coating, from 0.8 to 15.3 nm, and the number of silica layers on the surface at monolayer thickness of 0.47 nm, from 1.7 to 32.6. The limiting sorption volumes of pores in sample nos. 1–8 increase from 0.11×10^{-3} $m^3\ kg^{-1}$ for the starting α-Al_2O_3 to 0.30×10^{-3} $m^3\ kg^{-1}$ for a sample obtained at Si : Al molar ratio of 0.9 : 0.1. The steep rise in the thickness of the silica coating occurs at Si : Al molar ratios exceeding 0.5 : 0.5. The adsorption of a CCl_4 monolayer is virtually the same for all porous sample nos. 1–6 (Fig. 1), and, consequently, the set of mesopores formed as a result of SiO_2 deposition on the surface of aluminum oxide at Si : Al molar ratios in the range from 0.1 : 0.9 to 0.8 : 0.2 affects the adsorption in the monolayer region only slightly. The average pore radius increases from 8.1 nm in sample no. 1 to 18.5 nm in sample no. 6 and 14.3 nm in sample no. 7.

Figure 3 shows an IR spectrum of α-Al_2O_3 treated with decationized silica sol at a ratio of 0.5 : 0.5. The sample is characterized by a narrow band of stretching vibrations (SiO) at 1093 cm^{-1} and retains most of its hydroxy groups. The configuration of the formula unit of silica in modified α-Al_2O_3 is not distorted. Presumably, deposition of hydrated SiO_2 on the aluminum oxide surface, which acts in acid medium as anion adsorbent, begins with the interaction of SiOH groups with surface AlOH groups and continues as growth of silica layers. It is difficult to determine what polymeric variety of SiO_2: discrete particles of silica sol, particles formed directly on the surface of α-Al_2O_3, or silica gel floccules, are responsible for this growth.

As a rule, narrowing of the hysteresis loops and their rightwards shift are observed with increasing size of contacting globules and decreasing coordination number of their packing [13]. In the presence of firmly bound agglomerates of aluminum oxide globules, the former assumes filling of contacts with SiO_2 being deposited, with loss of a part of the surface area, and the latter is meaningless. The loop width also decreases when the capillary condensation with hysteresis is overlapped by a condensation not accompanied by hysteresis, as in the case of cylindrical mesopores closed at one end [12]. Such a capillary condensation without hysteresis is revealed by comparison curves of sample nos. 5–7 (Fig. 2). To summarize, cylindrical mesopores constituted by spaces between α-Al_2O_3 globules, in which noticeable capillary condensation may occur, change their shape upon treatment with decationized silica sol, with one of their ends closing.

The formation of a silica coating, which is very fast process, strongly differs from gelation, aging, and drying the corresponding SiO_2 bulk gel, which leads to fundamental difference between their physical properties [5]. Even at high SiO_2 content in sample no. 7, its porous structure strongly differs from that of sample no. 8: volume filling of pores is replaced by polymolecular filling, and the isotherm changes from type I to type IV. The comparison curve for this sample in Fig. 2 makes an intercept on the ordinate axis and has steeper slope than the curves for other samples, which points to an increase in the surface area, accompanied by a decrease in the average pore radius in the sample from 18.5 to 14.3 nm. This circumstance and the fact that CCl_4 vapor adsorption on sample no. 7 occurs as adsorption on a mesoporous material whose globule radius of 29.3 nm is close to a similar value for α-Al_2O_3, but the limiting sorption volume exceeds nearly 2.7-fold the same parameter for α-Al_2O_3, are both due to the appearance of a phase of aggregated SiO_2 particles, which introduces a certain volume of shallow mesopores into the structure.

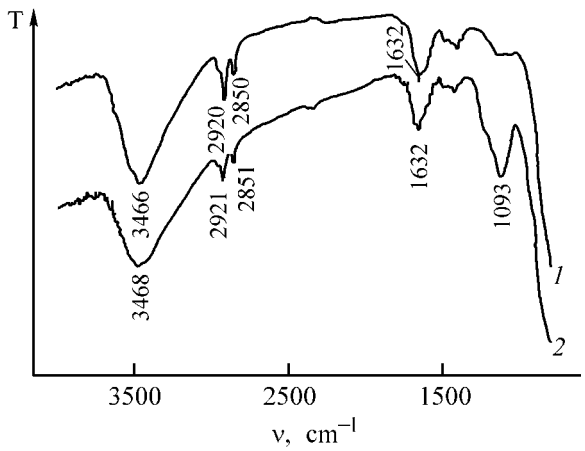

Fig. 3. IR spectra of α-Al_2O_3 samples (*1*) without treatment with decationized silica sol and (*2*) after such treatment. (T) Transmission, and (ν) wave number. Si : Al molar ratio: (*1*) 0 : 1 and (*2*) 0.5 : 0.5.

CONCLUSIONS

(1) Deposition of amorphous hydrated SiO_2 on α-Al_2O_3 particles submerged in decationized silica sol allows control over the size and shape of pores in the aluminum oxide and their limiting sorption volume. Raising the Si : Al molar ratio leads to an increase in the limiting sorption volume and average radii of pores and α-Al_2O_3 globules. The type IV of the isotherm of adsorption–desorption of tetrachloromethane vapor, the shape of the hysteresis loop, and the occurrence of adsorption in the monolayer region, which are all characteristic of α-Al_2O_3, do not change significantly.

(2) The hysteresis loop in the isotherm becomes narrower and is shifted to higher p/p_0 values.

REFERENCES

1. Bergna, H.E., Firment, L.E., and Swartzfager, D.S., *The Colloid Chemistry of Silica*, Bergna, H.E., Ed., *Advances in Chemistry Series*, vol. 234, Washington, DC, 1994, pp. 561–578.
2. Yokoyama, N., Nakazato, T., and Tarutani, T., *Bull. Chem. Soc. Japan*, 1980, vol. 53, no. 4, pp. 850–863.
3. Davis, J.A. and Leckie, J.O., *J. Colloid Interface Sci.*, 1980, vol. 74, no. 1, pp. 32–43.
4. Barrow, N.J. and Bowden, J.W., *J. Colloid Interface Sci.*, 1987, vol. 119, no. 1, pp. 236–250.

5. Brinker, C.J., Hurd, A.J., Frye, G.C., *et al.*, *J. Non-Cryst. Solids*, 1990, vol. 121, nos. 1–3, pp. 294–302.
6. Fenelonov, V.B., Tarasova, D.V., and Gavrilov, V.Yu., *Kinet. Kataliz*, 1977, vol. 18, no. 2, pp. 480–487.
7. Stiles, A.B., *Catalyst Supports and Supported Catalysts. Theoretical and applied concepts*, Boston: Butterworths, 1987.
8. Kuznetsova, T.F., Lemeshonok, G.S., and Eremenko, S.I., *Kolloid. Zh.*, 2000, vol. 62, no. 5, pp. 623–627.
9. Gurvich, L.M., *Zh. Ross. Fiz.-Khim. O–va, Chast' Khim.*, 1915, vol. 47, no. 4, pp. 805–827.
10. *IUPAC Pure Appl. Chem.*, 1985, vol. 57, no. 4, pp. 603–619.
11. Cutting, P.A. and Sing, K.S.W., *Chem. Ind.*, 1969, no. 268, pp. 268–269.
12. Gregg, S.J. and Sing, K.S.W., *Adsorption, Surface Area and Porosity*, London: Academic, 1982.
13. Iler, R.K., *The Chemistry of Silica*, New York: Wiley–Interscience, 1979.

Russian Journal of Applied Chemistry, Vol. 76, No. 2, 2003, pp. 203–206. Translated from Zhurnal Prikladnoi Khimii, Vol. 76, No. 2, 2003, pp. 212–215.

SORPTION AND ION-EXCHANGE PROCESSES

Method for Determining the Concentration of Isolated Silanol Groups on Silica Surface with Dimethylchlorosilane

A. M. Varvarin and L. A. Belyakova

Institute of Surface Chemistry, National Academy of Sciences of Ukraine, Kiev, Ukraine

Received July 15, 2002

Abstract—The chemical interaction between dimethylchlorosilane and silica of varied degree of hydroxylation was subjected to a systematic study. The optimal conditions for complete substitution of isolated silanol groups with dimethyl hydride silyl groups were found. It is suggested that the reaction of dimethylchlorosilane with the surface of silicon dioxide can be used to determine the concentration of free silanol groups in the surface layer of silica.

It is known that main active centers on the surface of silica are isolated ≡Si–OH groups [1, 2]. Most of chemical reactions occurring on the silica surface involve the silanol groups of silicon dioxide [3–5]. The silanol groups on the silica surface play an important part in adsorption and ion exchange [1, 2, 5]. Residual silanol groups on the surface of chemically modified silicas strongly affect the adsorption, chromatographic, and catalytic properties of silica-containing materials.

There exist various methods for determining the concentration of silanol groups on the silica surface [4]. These methods are mostly based on a chemical reaction between the silanol groups and an appropriate reagent, with subsequent quantitative analysis of the reaction products formed.

In this study, it is suggested that the concentration of isolated silanol groups on the silica surface should be determined by means of chemical reaction between dispersed silicon dioxide and dimethylchlorosilane (DMCS).

Silica was studied in the form of aerosil subjected to vacuum treatment at 200, 400, or 600°C. These pretreatment temperatures are frequently used in studying the adsorption and chemisorption properties of silicon dioxide [3].

As established previously [6], the chemical reaction of silica with DMCS proceeds quantitatively with only free silanol groups involved:

$$\equiv Si–OH + (CH_3)_2Si(Cl)H \rightarrow \equiv Si–O–Si(CH_3)_2H + HCl\uparrow. \quad (1)$$

To determine the optimal conditions for complete substitution of isolated silanol groups with dimethyl hydride silyl groups, the interaction between DMCS vapor and surface of silica vacuum-treated at 200, 400, or 600°C was studied in relation to temperature (Fig. 1) and time (Fig. 2) of reaction. The conditions

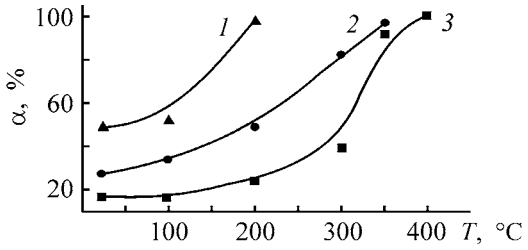

Fig. 1. Degree of substitution of free OH groups, α, vs. temperature *T* of reaction between DMCS and surface of aerosil vacuum-treated for 2 h. Reaction duration 1 h. Vacuum-treatment temperature (°C): (*1*) 200, (*2*) 400, and (*3*) 600.

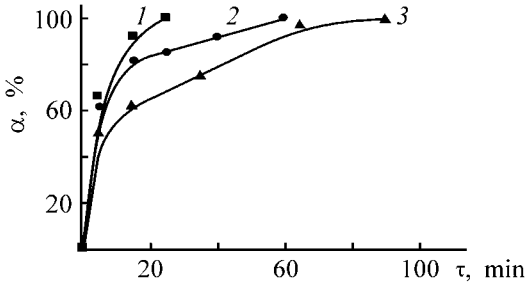

Fig. 2. Degree of substitution of free OH groups, α, vs. duration τ of reaction between DMCS and surface of aerosil. Vacuum pretreatment of silica for 2 h at (*1*) 600, (*2*) 400, and (*3*) 200°C. Reaction temperature (°C): (*1*) 400, (*2*) 350, and (*3*) 200.

1070-4272/03/7602-0203 $25.00 © 2003 MAIK "Nauka/Interperiodica"

Conditions for quantitative substitution of free OH groups on the aerosil surface as a result of DMCS chemisorption and concentration *c* of these groups in the surface layer of silica with varied degree of hydroxylation

Temperature, °C		Reaction duration, min	*c*,* mmol g^{-1}	
of vacuum treatment	of reaction		I	II
200	200	90	1.11 ± 0.05**	1.12 ± 0.05**
400	350	60	1.08 ± 0.05	0.98 ± 0.05
600	400	30	0.74 ± 0.04	0.72 ± 0.04

* I, by alkaline hydrolysis of dimethyl hydride silyl groups; II, by grafting of trimethyl silyl groups (for the conditions of quantitative substitution of free OH groups with trimethyl silyl groups in chemisorption of hexamethyldisilazane, see text.).

** The absolute error was found using Student's method [7]. The calculation was done at confidence probability of 0.95 and number of degrees of freedom equal to 10 in determining the amount of OH groups with DMCS and 5 when hexamethyldisilazane was used.

for complete substitution of isolated silanol groups with dimethyl hydride silyl groups are summarized in the table. As seen from the data presented (see table and Figs. 1 and 2), in the case of silica vacuum-pretreated at 200°C, complete substitution of silanol groups with dimethyl hydride silyl groups occurs at 200°C already in 1.5 h. In the case of silica vacuum-treated at 400°C, the reaction of electrophilic substitution of the proton from the silanol group occurs at 350°C in 1 h; the optimal reaction temperature and duration for silica vacuum-treated at 600°C are 400°C and 0.5 h. IR spectra of silicas (Fig. 3) modified with DMCS under the conditions of complete substitution of silanol groups contain no absorption band at 3750 cm^{-1}, which is associated with stretching vibrations of the O–H bonds in free OH groups, whereas the absorption bands associated with asymmetric (2970 cm^{-1}) and symmetric (2910 cm^{-1}) stretching and deformation (1420 cm^{-1}) vibrations of the C–H bond, and also the absorption band (2160 cm^{-1}) of stretching vibrations of Si–H bonds in grafted dimethyl hydride silyl groups [8] are present.

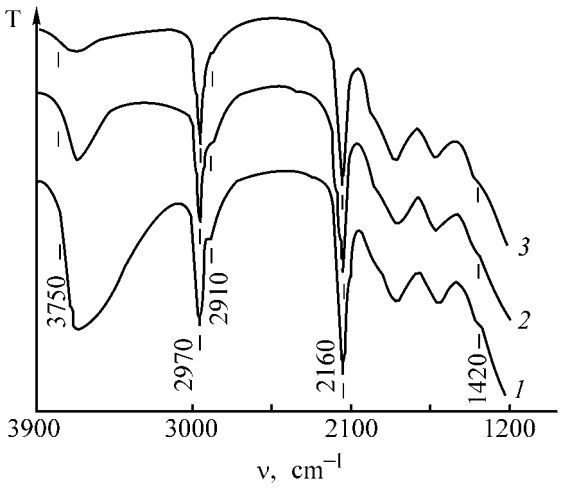

Fig. 3. IR spectra of aerosil modified with DMCS. Vacuum-pretreatment of silica for 2 h at (*1*) 200, (*2*) 400, and (*3*) 600°C. (T) Transmission and (ν) wave number. Reaction temperature (°C): (*1*) 200, (*2*) 350, and (*3*) 400°C. Reaction duration (h): (*1*) 1.5, (*2*) 1.0, and (*3*) 0.5.

It should be noted that the efficiency of DMCS chemisorption on the silica surface depends not only on the temperature and duration of a chemical reaction, but also on the temperature of preliminary vacuum treatment of SiO_2: the higher the temperature of vacuum treatment of silica, the lower the degree of substitution of isolated silanol groups with dimethyl hydride silyl groups at the same reaction temperature (Fig. 1). This is due, as established previously [6, 9], to a decrease in the electron density on oxygen atoms of the silanol groups attacked in the course of dehydroxylation of the silica surface.

Thus, the investigation of the chemical interaction of dispersed silicas with various degrees of surface hydroxylation with DMCS makes it possible to select the optimal conditions for quantitative occurrence of this chemical reaction for any particular case. As follows from scheme (1), in the case of a quantitative course of the reaction, the concentration of dimethyl hydride silyl groups formed on silica surface is equal to that of isolated silanol groups and can be found from the volume of hydrogen evolved in alkaline hydrolysis of dimethyl hydride silanol groups [10]:

$$\equiv Si{-}O{-}Si(CH_3)_2H + H_2O \rightarrow \equiv Si{-}O{-}Si(CH_3)_2OH + H_2\uparrow. \quad (2)$$

This method for determining the concentration of free OH groups on the surface of silicon dioxide does not require any sophisticated equipment or expensive reagents. The table lists the data obtained in determining the concentration of isolated silanol groups by means of alkaline hydrolysis of dimethyl hydride silyl groups (from the volume of hydrogen evolved). Also presented are data obtained gravimetrically (in quantitative chemisorption of hexamethyl disilazane on silica) in a vacuum setup with quartz spring balance [3]. Both the techniques yield virtually the same results.

It should be noted that the indubitable advantage of the method for determining the content of isolated

silanol groups by means of alkaline hydrolysis of preliminarily chemisorbed dimethyl hydride silyl groups consists in that adsorbed water does not hinder determination of the concentration of silanol groups in silica: tetramethyldisiloxane $H(CH_3)_2Si–O–Si(CH_3)_2H$, which is formed when DMCS is brought in contact with water, is a volatile compound and is easily removed from the silica surface in vacuum-treatment of products formed in electrophilic substitution of the proton in silanol groups and an excess amount of DMCS [11].

Thus, the method proposed can be used to determine the concentration of isolated silanol groups on the surface of silicas hydroxylated to varied extent and to find the content of residual (or secondary) silanol groups in chemically modified silicas.

EXPERIMENTAL

The concentration of free silanol groups was determined for highly dispersed amorphous silica, A-300 aerosil with specific surface area of 300 $m^2 g^{-1}$, pretreated in a vacuum at 200, 400, and 600°C.

The modification of silicon dioxide with DMCS was performed as follows. Silica was placed in a quartz reactor, the reactor was evacuated, and silica was kept, first, in a vacuum at 200°C for 2 h and then in saturated DMCS vapor at 200°C for 1.5 h. The excess amount of the reagent and the hydrogen chloride evolved were pumped out of the reactor at 200°C for 1 h. In the case of a pretreatment of silica at 400 and 600°C, the reaction with DMCS was carried out at 350°C for 1 h and at 400°C for 0.5 h, respectively, with subsequent vacuum treatment at the reaction temperature for 1 h.

The extent of the reaction between the silanol groups of the silica surface and DMCS was monitored by IR spectroscopy on an IKS-29 spectrophotometer (LOMO, Russia) in the frequency range 4200–1200 cm^{-1}.

To determine the concentration of isolated OH groups on the silica surface (from DMCS chemisorption), a 0.2–0.4-g portion of silica quantitatively modified with dimethyl hydride silyl groups was taken. The volume of hydrogen evolved in the course of alkaline hydrolysis of chemically attached dimethyl hydride silyl groups was measured on a setup similar to the Tserevitinov device [10]. As locking fluid served water saturated with hydrogen. For this purpose, gaseous hydrogen was passed through water under vigorous stirring for several minutes.

The amount of free OH groups on the silica surface, c_{OH} (mmol g^{-1}), was calculated using the formula

$$c_{OH} = \frac{V_0}{m \times 22.4},$$

where m is the weighed portion of silica (g), and V_0 is the volume of evolved hydrogen, recalculated to the standard conditions (ml).

The hydrogen volume was reduced to the standard conditions by the equation

$$V_0 = \frac{V_T \times 273.2(B - p)}{760(273.2 + T)},$$

where V_T is the hydrogen volume (ml) measured at temperature T and barometric pressure B; B, the barometric pressure (mm Hg); p, the water vapor pressure (mm Hg) at temperature T; T, the temperature at which the gas volume is measured (°C) [12].

The amount of isolated OH groups on the silica surface was determined gravimetrically (on the basis of hexamethyldisilazane chemisorption) in an evacuated installation with McBain–Bakr quartz spring balance [13]. The spring extension (sensitivity 0.53 mm mg^{-1}) was measured with a V-630 cathetometer. The chemical reaction of hexamethyldisilazane with the surface of silicon dioxide was carried out at 200°C in the course of 1 h, with subsequent vacuum-treatment of the excess amount of the reagent and the reaction products at 200°C for 1 h [3].

The content of grafted trimethyl silyl groups, c_{TMS} (mmol g^{-1}), which is equal to the initial amount of free OH groups, c_{OH}, on the silica surface, was calculated by the formula

$$c_{TMS} = \frac{\Delta l \varphi}{mM},$$

where Δl is the difference between the cathetometer readings before and after chemisorption of hexamethyl disilazane (mm); φ, the calibration coefficient of the spring (mg mm^{-1}); M, the molar mass of the grafted fragment (g); m, the true mass of silica (g).

The true mass of silicon dioxide (mass after dehydroxylation) was found using the formula

$$m = m_0 - \frac{\Delta l \varphi}{1000},$$

where m_0 is a weighed portion of air-dried silica (g) and Δl is the difference between the cathetometer readings (mm) before and after vacuum treatment of silica at 200, 400, or 600°C.

CONCLUSIONS

(1) The optimal conditions for complete substitution of free silanol groups with dimethyl hydride silyl

groups were established on the basis of a study of the interaction between dimethylchlorosilane vapor and the surface of silica vacuum-treated at 200, 400, or 600°C in relation to reaction temperature and duration.

(2) A method was suggested for determining the concentration of isolated silanol groups on the surface of silica with varied degree of hydroxylation by means of alkaline hydrolysis of grafted dimethyl hydride silyl groups.

REFERENCES

1. Kiselev, A.V. and Lygin, V.I., *Infrakrasnye spektry poverkhnostnykh soedinenii i adsorbirovannykh veshchestv* (IR Spectra of Surface Compounds and Adsorbed Substances), Moscow: Nauka, 1972.
2. Iler, R.K., *The Chemistry of Silica*, New York: Wiley–Interscience, 1979.
3. Tertykh, V.A. and Belyakova, L.A., *Khimicheskie reaktsii s uchastiem poverkhnosti kremnezema* (Chemical Reactions Involving Surface Silica), Kiev: Naukova Dumka, 1991.
4. Vansant, E.F., Van der Voort, P., and Vrancken, K.C., *Characterization and Chemical Modification of the Silica Surface*, Amsterdam: Elsevier, 1995.
5. *Khimiya poverkhnosti kremnezema* (Chemistry of Silica Surface), vol. 2, Chuiko, A.A., Ed., Kiev: UkrINTEI, 2001.
6. Varvarin, A.M. and Belyakova, L.A., *Collection of Abstracts of V Polish-Ukrainian Symp. "Theoretical and Experimental Studies of Interfacial Phenomena and Their Technological Application,"* September, 4–9, 2000, Odessa, 2000, pp. 221–222.
7. Charykov, A.K., *Matematicheskaya obrabotka rezul'tatov khimicheskogo analiza* (Mathematical Processing of Chemical Analysis Data), Leningrad: Khimiya, 1984.
8. Bellamy, L.J., *Advances in Infrared Group Frequencies*, London: Methuen, 1968.
9. Varvarin, A.M. and Belyakova, L.A., *Kolloid. Zh.*, 1994, vol. 56, no. 2, pp. 164–170.
10. *Prakticheskoe rukovodstvo po analizu monomernykh i polimernykh kremniiorganicheskikh soedinenii* (Manual of Analysis of Monomeric and Polymeric Organosilicon Compounds), Kreshkov, A.P., Ed., Moscow: Goskhimizdat, 1962.
11. Yoshinaga, K., Yoshida, H., Yamamoto, Y., *et al.*, *J. Colloid Interface Sci.*, 1992, vol. 153, no. 1, pp. 207–211.
12. Perel'man, V.I., *Kratkii spravochnik khimika* (Concise Chemist's Handbook), Moscow: Khimiya, 1964.
13. *Eksperimental'nye metody v adsorbtsii i molekulyarnoi khromatografii* (Experimental Methods in Adsorption and Molecular Chromatography), Nikitin, Yu.S. and Petrova, R.S., Eds., Moscow: Mos. Gos. Univ., 1990.

Russian Journal of Applied Chemistry, Vol. 76, No. 2, 2003, pp. 207–210. Translated from Zhurnal Prikladnoi Khimii, Vol. 76, No. 2, 2003, pp. 216–219.

SORPTION AND ION-EXCHANGE PROCESSES

Influence of the Structure of Anion-Exchange Resin on Complexation with Transition Metal Ions

E. E. Ergozhin, A. K. Chalov, R. A. Iskakova, and A. I. Nikitina

Besturov Institute of Chemical Sciences, Ministry of Education of the Republic of Kazakhstan, Almaty, Kazakhstan

Received November 23, 2001; in final form, November 2002

Abstract—Polarography and potentiometry was applied to study the influence exerted by the degree of cross-linking of an ion-exchange resin based on allyl bromide, diglycidil ether of resorcinol, and polyethylenepolyamine on its complexing ability. The shift of the potential of half-wave of reduction of the complex ion and data of potentiometric titration with and without complexing metal were used to calculate the coordination numbers and stability constants of complexes with cations of various metals.

A study of specific features of the complexation between ion-exchange resins and metals and determination of the stability constants and composition of complex compounds are of theoretical and practical interest. The complexing ability of polymers is widely used in hydrometallurgy for recovery and concentration of ions of transition, rare, and noble metals [1].

Complex compounds are commonly studied by spectrophotometry, polarography, high-frequency titration, and potentiometry. However, polarographic studies of complex compounds are scarce [2–4].

The aim of the present study was to analyze the influence exerted by the structure of an ion-exchange resin based on allyl bromide (AB), diglycidil ether of resorcinol (DGER), and polyethylenepolyamine (PEPA) on its complexing ability, by polarography in the stage of prepolymerization and by potentiometry after additional curing.

EXPERIMENTAL

The ion-exchange resin under study was synthesized by a procedure described in [5]. Part of the polymer was precipitated in diethyl ether and dried, and solutions of various concentrations were prepared. The rest of the reaction mass was subjected to additional curing at 80°C.

Polarograms of reduction of metal cations in their complexes with the polymer were measured with solution 0.01 N H_2SO_4 in 25% dimethylformamide (DMF) as supporting electrolyte. The choice of 0.01 N H_2SO_4 and DMF as supporting electrolyte for polarography is due to the fact that it is in this medium that complex compounds of an anion-exchange resin based on AB, DGER, and PEPA with transition metals, including Cu^{2+}, possess sufficient solubility in the necessary range of anion-exchange resin concentrations. In polarographic measurements, the content of the ion-exchange resin was varied from 0.1 to 20 g l^{-1}. The concentration of metal salts, $CoSO_4$, $NiSO_4$, and $CuSO_4$, was 2×10^{-3} M. As reference served saturated calomel electrode. Characteristic of the mercury drop electrode: $m^{2/3}t^{1/6} = 4.28$ mg$^{2/3}$ s$^{-1/2}$. The electrolytic cell was thermostated at 25 ± 0.1°C. Oxygen was removed from the solutions by bubbling argon through them for 10 min.

The apparent dissociation constant pK_α, the Bjerrum complex-formation function n, and the stability constant log K_n were calculated from the data of [1].

The main factor governing the formation of coordination compounds is that metal ions tend to compensate for the electron deficiency at the expense of the electron pairs of the donor contained in the functional groups of the polymer.

Anion-exchange resins absorb metal cations from solutions of their salts by the scheme

$$n\mathrm{R_3N}\ldots\mathrm{HOH} + \mathrm{M^{2+}} \rightarrow [(\mathrm{R_3N})_n\mathrm{M}]^{2+} + n\mathrm{H_2O}.$$

The sorption equilibrium is affected by the following factors: nature of the anion-exchange resin and complexing metal, and also the state of the metal in

1070-4272/03/7602-0207 $25.00 © 2003 MAIK "Nauka/Interperiodica"

Table 1. Potentials of half-wave of reduction of complexes formed by ion-exchange resin based on AB, DGER, and PEPA with various metals (concentration of ion-exchange resin 1 g l^{-1}, that of a salt 2×10^{-3} M)

Cation	$E_{1/2}$, V	$\Delta E_{1/2}$, V	pH value
Co^{2+}	–0.11	0.05	3.0–6.5
Ni^{2+}	–0.12	0.09	3.0
Cu^{2+}	–0.15	0.13	3.0
Cu^{2+*}	–0.20	0.18	5.0

* Concentration of ion-exchange resin 10 g l^{-1}.

solution; concentration of coordination-active amino groups and the complexing metal; solution composition (pH value, ionic strength of the solution).

It is known [6] that reduction of a complex ion on a mercury drop electrode occurs at rather strong electrode polarization, and complexation is associated with a shift of the potential of half-wave of reduction to more negative values. The $E_{1/2}$ potential of the complex must be more negative than the half-wave potential of the free ion, since the cation must become free of ligands in the course of reduction, and this involves energy expenditure. With a knowledge of how $E_{1/2}$ depends on the concentration of the complexing agent (and this dependence is, as a rule, linear), one can calculate the equilibrium stability constant of the complex, log K, and its composition, The higher the log K value, the stronger the complex and the more negative the half-wave potential of its discharge in solution.

It was established in studying the complexing ability of the ion-exchange resin based on AB, DGER, and PEPA in solution in the presence of various metal

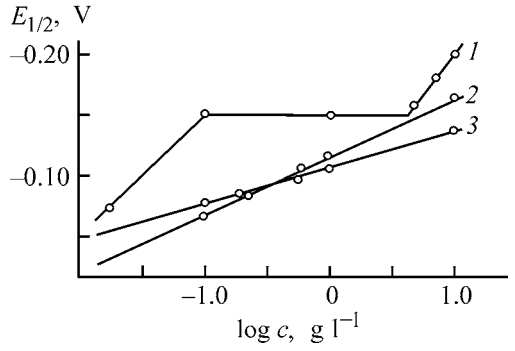

Fig. 1. Potential of half-wave of reduction $E_{1/2}$ of complex ions with various metals on the concentration c of the ion-exchange resin. (*1*) Cu^{2+}, (*2*) Ni^{2+}, and (*3*) Co^{2+}.

ions that the potential of half-wave of reduction of the forming complex and its shift $\Delta E_{1/2}$ relative to $E_{1/2}$ of reduction of a free metal cation depend on the nature of the metal (Table 1).

Analysis of the data in Table 1 shows that the anion-exchange resin forms the strongest complex with copper cations, since the maximum shift $\Delta E_{1/2}$ is observed in this case.

To obtain quantitative characteristics of the composition and stability of complex compounds formed by various metal ions with the ion-exchange resin based on AB, DGER, and PEPA, the change in $E_{1/2}$ of reduction of the complexes on raising the content of the ion-exchange resin was studied in the range 0.1–20 g l^{-1}.

It can be seen from Fig. 1 that the dependence of $E_{1/2}$ on the logarithm of the polymer concentration is linear for the Co^{2+} and Ni^{2+} cations, which points to the existence of a single strong complex in solution [6]. If the stability constants of successive complexes differ strongly, this dependence has the form of a number of linear portions with sharp bends, with the number of the portions corresponding to the number of complexes present in solution. It is the dependence of this kind that is observed for the Cu^{2+} cation. It follows from this dependence that the ion-exchange resin mentioned above gives with copper ions two complexes with different strengths, one of which, as also complexes with Co^{2+} and Ni^{2+}, is formed at pH 3.0 and the other exists in the pH range 5.0–5.5.

The slope tan α of the dependence of $E_{1/2}$ on the logarithm of the sorbent concentration was used to determine the coordination number p by the equation [7]

$$p = \frac{n}{0.059} \tan \alpha,$$

where n is the number of electrons involved in the reaction, i.e., the valence of the metal cation.

The slope can be calculated from two $E_{1/2}$ values and the corresponding logarithms of the concentration of the ion-exchange resin:

$$\tan \alpha = \frac{(E_{1/2})_2 - (E_{1/2})_1}{\log c_2 - \log c_1}.$$

The coordination numbers calculated for complexes of the ion-exchange resin with various metal cations are listed in Table 2. It can be seen that Co^{3+}, Ni^{2+}, and Cu^{2+} coordinate, respectively, one, two, and three or four (depending on the sorbent concentration) amino groups of the anion-exchange resin.

The stability constants of the complexes formed by the ion-exchange resin based on AB, DGER, and PEPA with various metal ions (Table 2) were calculated by the equation [7]:

$$\log K = \frac{n(\Delta E_{1/2} + p\frac{0.059}{n}\log c)}{0.059}.$$

The highest $\log K$ value (Table 2) and the maximum shift $\Delta E_{1/2}$ (Table 1) are observed for complexes of the ion-exchange resin with copper. Metal cations can be arranged in order of decreasing complexing ability as follows: $Cu^{2+} > Ni^{2+} > Co^{2+}$.

The different strengths of the complexes formed by the sorbent with the given cations result in their different sorption capacities for metal ions (Table 2), which decrease in the same order as the strength of the respective complexes.

The composition and strength of the complexes formed with the insoluble sorbent after additional curing of the prepolymer were determined by potentiometric titration of the anion-exchange resins, with ions of the complexing metal absent or present and the pH value and concentration of uncomplexed metal ions monitored simultaneously.

The functional groups of the ion-exchange resins were neutralized to a greater extent using sodium nitrate, which is indifferent toward these groups, creates the ionic strength of a solution, and forms no complexes with anion exchange resins. With increasing ionic strength of a solution, the electron-donor properties of the ionogenic groups of the anion exchange resin become more pronounced, and the density of hydration sheaths of unprotonated amino groups decreases, which favors the higher complexing ability of the anion exchange resin. That is why the sorption properties of ion-exchange resins were studied at an ionic strength of the contacting solution equal to unity.

In potentiometric titration of polyfunctional polyelectrolytes in the presence of transition metal ions, the run of the curves changes because of the complexation (Fig. 2). It can be seen from the dependences obtained that protonation of a part of amino groups or their complexation with metal makes pH lower in all cases, with this decrease the stronger, the greater the amount of metal ions sorbed by the polymer.

The coordination properties of the ion-exchange resin were studied at metal ion concentration of 0.025 M, since at ion concentrations lower than 0.05 M the Bjerrum complex-formation function and the coordinated number of ligand groups have closer values [8].

Table 2. Coordination numbers and stability constants of complexes formed by ion-exchange resin based on AB, DGER, and PEPA with ions of various metals, found by polarography (concentration of the ion-exchange resin 1 g l^{-1}, that of a salt 2×10^{-3} M)

Salt	p	$\log K$	Sorption capacity, mg g^{-1}
$CoSO_4$	1	1.7	114.7
$NiSO_4$	2	3.0	133.4
$CuSO_4$	3	4.4	314.2
$CuSO_4^*$	4	10.1	–

* Concentration of ion-exchange resin 10 g l^{-1}.

For a cellular ion-exchange resin with less rigid 3D lattice, polarography gives the coordination numbers of 3 and 4 for copper ions, 2 for nickel ions, and 1 for cobalt ions; in the case of a densely cross-linked ion-exchange resin $n = 1$ for all the above ions, which points to the formation of a complex of 1 : 1 composition. The stability constants of the complexes, calculated from potentiometric titration data, are as follows: 6.2 for complexes with copper ions, 5.5 for nickel, and 5.3 for cobalt.

These data demonstrate the advantage of cellular sorbents with higher degree of cross-linking over soluble sorbents. This can be presumably accounted for by the following: in the former case, each amino group bounds one ion, and in the latter, 0.25–0.30 metal ions [9].

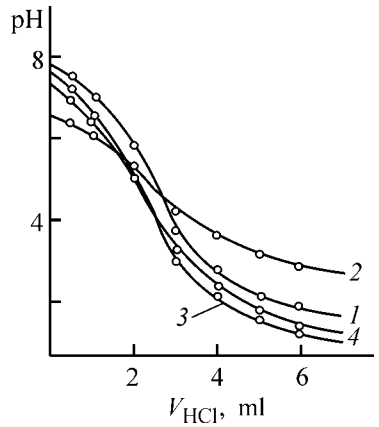

Fig. 2. Potentiometric titration curves for anion-exchange resin (*1*) without metal ions and in the presence of (*2*) Cu^{2+}, (*3*) Ni^{2+}, and (*4*) Co^{2+}. HCl concentration 0.1 M. (V_{HCl}) Volume of acid.

Table 3. Comparative characteristics of the complexing ability of various PEPA-based ion-exchange resins with respect to cobalt, nickel, and copper ions (concentration of ion-exchange resin 1 g l^{-1}, that of a salt 2×10^{-3} M)

Salt	log *K*				
	AB–DGER	DGER	PECH	ECH–styrene	ECH–styrene*
$CoSO_4$	1.7/5.3**	3.20	3.62	4.78	3.15
$NiSO_4$	3.0/5.5	3.90	4.70	4.52	2.82
$CuSO_4$	4.4/6.2	4.10	4.53	4.46	2.97
$CuSO_4$***	10/10	–	–	–	–

* Chloromethylated copolymer.

** Polarographic/potentiometric determination method.

*** Concentration of ion-exchange resin 10 g l^{-1}.

Comparison of the stability constants obtained (Table 3) with characteristics of the complexing ability of polyelectrolytes based on PEPA and various copolymers of epichlorohydrin (ECH), polyepichlorohydrin (PECH), and DGER [1] suggests that the strongest complex with copper ions is formed by the polymer based on AB, DGER, and PEPA (polymer concentration in solution 10 g l^{-1}). Practical use of the given ion-exchange resin will allow selective recovery of copper ions.

CONCLUSION

It is demonstrated that the structure of the anion exchange resin strongly affects the complexing ability of ion-exchange resins synthesized from allyl bromide, diglycidil ether of resorcinol, and polyethylenepolyamine. The most stable are complexes with copper ions.

REFERENCES

1. Ergozhin, E.E. and Menligaziev, E.Zh., *Polifunktsional'nye ionoobmenniki* (Polyfunctional Ion-Exchange Resins), Alma-Ata: Nauka, 1986.
2. Korshunov, I.A. and Malyutina, N.I., *Zh. Obshch. Khim.*, 1950, vol. 20, no. 3, pp. 403–406.
3. Iaih Vivek Kumar, Teneja Ajay, and Seth, D.S., *Proc. Nat. Acad. Sci., India A*, 1997, no. 3, pp. 243–247.
4. Cukrowski Ignacy, *Analyst*, 1997, no. 8, pp. 827–833.
5. Chalov, A.K., Ergozhin, E.E., Iskakova, R.A., and Sarsenov, S.K., *Izv. Min. Obraz. Nauk. Resp. Kazakhst., Nats. Akad. Nauk Resp. Kazakhst., Ser. Khim.*, 2001, no. 1, pp. 22–25.
6. Heyrovsky, J. and Kuta, J., *Zaklady polarografie*, Praha: Nakladatelstvi ceskoslovenske academie ved., 1962.
7. Vinogradova, E.N., Gallai, Z.A., and Finogenova, Z.M., *Metody polyarograficheskogo i amperometricheskogo analiza* (Methods for Polarographic and Ammetric Analysis), Moscow: Mos. Gos. Univ., 1960.
8. Bjerrum, J., *Metal Ammine Formation in Aqueous Solution, Theory of Reversible Step Reactions*, Copenhagen: P. Haase, 1957.
9. Ergozhin, E.E. and Utkelov, B.A., *Khelatnye polimernye reagenty* (Chelate Polymeric Reagents), Almaty: Gylym, 1998.

Russian Journal of Applied Chemistry, Vol. 76, No. 2, 2003, pp. 211–216. Translated from Zhurnal Prikladnoi Khimii, Vol. 76, No. 2, 2003, pp. 220–224.

SORPTION AND ION-EXCHANGE PROCESSES

Mutual Influence of Rare-Earth Metals(III) in Their Joint Extraction from Aqueous Solutions with a Toluene Solution of Trialkylbenzylammonium Naphthenate

A. K. Pyartman, A. A. Kopyrin, D. A. Zhiharev, and V. A. Keskinov

St. Petersburg State Technological Institute, St. Petersburg, Russia

Received September 30, 2002

Abstract—Extraction of nitrates of lanthanides(III) [La(III)–Lu(III) and also yttrium(III)] from their aqueous multicomponent systems with a toluene solution of trialkylbenzylammonium naphthenate was studied at 298 K and pH 3. Physicochemical and mathematical models describing the distribution and mutual influence of lanthanides(III) [Ln(III)] in their joint extraction from multicomponent aqueous solutions as influenced by the total Ln(III) concentration in the aqueous phase and composition of their mixture was developed.

Organic binary solutions of salt of quaternary ammonium bases (QAB) with organic anions are widely used for extractive recovery and separation of nonferrous and platinum metals [1]. We found no published information on extraction of lanthanides(III) [Ln(III)] with binary trialkylbenzylammonium naphthenate (TABANP) solutions in organic diluents.

In this study, we developed physicochemical and mathematical models describing the distribution and mutual influence of lanthanides(III) in their joint extraction from multicomponent solutions as a function of the total concentration and composition of Ln(III) mixture in the aqueous phase, taking into account that extractable complexes $(R_4N)_2[Ln(NO_3)_3A_2]$ (A, naphthenate anions) are formed in the organic phase.

The extraction of lanthanide(III) nitrates from aqueous solution with TABANP organic solution is described by the following equations:

$$2R_4NA_{(o)} + Ln^{3+}_{(a)} + 3NO^-_{3\,(a)} \rightleftarrows (R_4N)_2[Ln(NO_3)_3A_2]_{(o)}. \quad (1)$$

The extraction systems under consideration contain N kinds of Ln(III) metals. The main parameters characterizing the composition of these systems are as follows: $c_{Ln\,(a)}$ is the total (analytical) concentration of the sum of Ln(III) in the aqueous phase; $c_{Ln\,(o)}$, the total (analytical) concentration of the sum of Ln(III) in the organic phase; c_s, the total (analytical) extractant concentration in the organic phase; $\{R_4NA\}_{(o)}$, the equilibrium concentration of free TABANP in the organic phase; $\alpha^k_{(a)}$, the fraction of kth Ln(III) in the aqueous phase; $\alpha^k_{(o)}$, the fraction of kth Ln(III) in the organic phase

$$\alpha^k_{(a)} = c^k_{Ln\,(a)}/c_{Ln\,(a)}, \quad (2)$$

$$\alpha^k_{(o)} = c^k_{Ln\,(o)}/c_{Ln\,(o)}. \quad (3)$$

Here $c^k_{(a)}$ and $c^k_{(o)}$ are the total (analytical) concentrations of kth Ln(III) in the aqueous and organic phases, respectively.

For the organic phase, the following material balance equation is valid:

$$c_s = \{R_4NA\}_{(o)} + 2\sum_{k=1}^{N}(R_4N)_2[Ln^k(NO_3)_3A_2]_{(o)}. \quad (4)$$

A correlation between the equilibrium concentrations of the reacting species in both aqueous and organic phases and the concentration constant of the heterogeneous reaction of extraction of Ln(III) with TABANP is described by the equation

$$K^2_{ex,\,k} = \frac{\{(R_4N)_2[Ln^k(NO_3)_3A_2]\}_{(o)}}{\{R_4NA\}^2_{(o)}\{NO^-_3\}^3_{(a)}\{Ln^{3+(k)}\}_{(a)}}, \quad (5)$$

where $\{NO^-_3\}_{(a)} = 3\sum_{k=1}^{N}\{Ln^{3+(k)}\}_{(a)} = 3c_{Ln\,(a)}$.

1070-4272/03/7602-0211 $25.00 © 2003 MAIK "Nauka/Interperiodica"

The main parameters characterizing the extraction systems under consideration and the correlation between them can be determined from the following expressions.

Concentration of *k*th Ln(III) in the organic phase

$$c^{k}_{\mathrm{Ln\,(o)}} = 27\left(c_{\mathrm{Ln\,(a)}}\right)^4 \alpha_{\mathrm{Ln\,(a)}} K^2_{\mathrm{ex},k} \{\mathrm{R_4NA}\}^2_{\mathrm{(o)}}. \quad (6)$$

Total Ln(III) concentration in the organic phase

$$c_{\mathrm{Ln\,(o)}} = 27\left(\sum c_{\mathrm{Ln\,(a)}}\right)^4 \sum_{k=1}^{N} \alpha^{k}_{\mathrm{(a)}} K^2_{\mathrm{ex},k} \{\mathrm{R_4NA}\}^2_{\mathrm{(o)}}. \quad (7)$$

Fraction of *k*th Ln(III) in the organic phase

$$\alpha^{k}_{\mathrm{(o)}} = \frac{\alpha^{k}_{\mathrm{(a)}} K^2_{\mathrm{ex},k}}{\sum_{k=1}^{N} \alpha^{k}_{\mathrm{(a)}} K^2_{\mathrm{ex},k}}. \quad (8)$$

Overall distribution coefficient of the sum of Ln(III)

$$D^{\Sigma}_{\mathrm{ex}} = 27\left(c_{\mathrm{Ln\,(a)}}\right)^3 \sum_{k=1}^{N} \alpha^{k}_{\mathrm{(a)}} K^2_{\mathrm{ex},k} \{\mathrm{R_4NA}\}^2_{\mathrm{(o)}}. \quad (9)$$

Distribution coefficient of *k*th Ln(III)

$$D^{k}_{\mathrm{ex}} = 27\left(c_{\mathrm{Ln\,(a)}}\right)^3 K^2_{\mathrm{ex},k} \{\mathrm{R_4NA}\}^2_{\mathrm{(o)}}. \quad (10)$$

Correlation between D^{Σ}_{ex} and $D^{\mathrm{k}}_{\mathrm{ex}}$

$$D^{k}_{\mathrm{ex}} = D^{\Sigma}_{\mathrm{ex}} \frac{K^2_{\mathrm{ex},k}}{\sum_{k=1}^{N} \alpha^{k}_{\mathrm{(a)}} K^2_{\mathrm{ex},k}}. \quad (11)$$

Separation factors of Ln(III) pairs

$$\beta_{k/(k+1)} = \frac{K^2_{\mathrm{ex},k}}{K^2_{\mathrm{ex},k+1}}. \quad (12)$$

For the organic phase, the material balance equation can be transformed to the following form:

$$c_{\mathrm{s}} = \{\mathrm{R_4NA}\}_{\mathrm{(o)}} + 54\left(c_{\mathrm{Ln\,(a)}}\right)^4 \sum_{k=1}^{N} \alpha^{k}_{\mathrm{(a)}} K^2_{\mathrm{ex},k} \{\mathrm{R_4NA}\}^2_{\mathrm{(o)}}. \quad (13)$$

The total material balance in the extraction system containig (1…, *k*…, *N*) Ln(III) in both aqueous and organic phases can be evaluated by solving the following set of nonlinear equations:

$$c^{0,1}_{\mathrm{Ln\,(a)}} V^0_{\mathrm{a}} = \{\mathrm{Ln}^{3+(1)}\}_{\mathrm{(a)}} V_{\mathrm{a}} + V_{\mathrm{o}} 27\left(c_{\mathrm{Ln\,(a)}}\right)^4 \alpha^{1}_{\mathrm{(a)}} K^2_{\mathrm{ex},1} \{\mathrm{R_4NA}\}^2_{\mathrm{(o)}}, \quad (14)$$

$$c^{0,k}_{\mathrm{Ln\,(a)}} V^0_{\mathrm{a}} = \{\mathrm{Ln}^{3+(k)}\}_{\mathrm{(a)}} V_{\mathrm{a}} + V_{\mathrm{o}} 27\left(c_{\mathrm{Ln\,(a)}}\right)^4 \alpha^{k}_{\mathrm{(a)}} K^2_{\mathrm{ex},k} \{\mathrm{R_4NA}\}^2_{\mathrm{(o)}}, \quad (15)$$

$$c^{0,N}_{\mathrm{Ln\,(a)}} V^0_{\mathrm{a}} = \{\mathrm{Ln}^{3+(N)}\}_{\mathrm{(a)}} V_{\mathrm{a}} + V_{\mathrm{o}} 27\left(c_{\mathrm{Ln\,(a)}}\right)^4 \alpha^{N}_{\mathrm{(a)}} K^2_{\mathrm{ex},N} \{\mathrm{R_4NA}\}^2_{\mathrm{(o)}}. \quad (16)$$

where $c^{0,k}_{\mathrm{Ln\,(a)}}$ is the concentration of *k*th Ln(III) in the initial aqueous solution; V^0_{a}, V_{a}, and V_{o} are the volumes of the initial aqueous, equilibrium aqueous, and equilibrium organic phases, respectively.

The material balance with respect to nitrate anions is described by the equation

$$3\sum_{k=1}^{N} c^{0,k}_{\mathrm{Ln\,(a)}} V^0_{\mathrm{a}} = \{\mathrm{NO_3^-}\}_{\mathrm{(a)}} V_{\mathrm{a}} + V_{\mathrm{o}} 81\left(c_{\mathrm{Ln\,(a)}}\right)^4 \sum_{k=1}^{N} \alpha^{k}_{\mathrm{(a)}} K^2_{\mathrm{ex},k} \{\mathrm{R_4NA}\}^2_{\mathrm{(o)}}. \quad (17)$$

The system of Eqs. (13)–(17) consists of (*N* + 2) nonlinear equations with (*N* + 2) independent variables. This system of equations can be solved numerically, taking into account the following constraints:

$$0 < \{\mathrm{R_4NA}\}_{\mathrm{(0)}} < c_{\mathrm{s}}, \quad (18)$$

$$0 < \{\mathrm{Ln}^{3+(k)}\}_{\mathrm{(a)}} V_{\mathrm{a}} < c^{0,k}_{\mathrm{Ln(a)}} V^0_{\mathrm{a}}. \quad (19)$$

The system of nonlinear equations (13)–(17) was solved for (*N* + 2) unknown quantities [$c_{\mathrm{Ln\,(o)}}$, $\{\mathrm{R_4NA}\}_{\mathrm{(o)}}$, $\alpha^{k}_{\mathrm{(a)}}$ (*k* = 1, …, *N*) by the Newton–Raphson method with replacement of the partial derivatives with the corresponding finite differences [2].

The revealed general pattern of the mutual influence of Ln(III) cations in their joint extraction from *N*-component aqueous solution with trialkylbenzylammonium naphthenate in toluene can be reduced to the following.

(1) In all the systems, the Ln(III) distribution coefficients are functions of the following parameters: concentration extraction constants K^2_{ex}, free extractant concentration in the organic phase $\{\mathrm{R_4NA}\}_{\mathrm{(o)}}$, fractions of *k*th Ln(III) in the aqueous phase, and equilibrium concentration of nitrate anions in the aqueous phase.

With increasing concentration of nitrate anions in the aqueous phase, the Ln(III) distribution coefficients grow, and, therefore, the Ln(III) concentration in the organic phase grows too. As a result, the concentration of the free extractant $\{\mathrm{R_4NA}\}_{\mathrm{(o)}}$

decreases, which, in turn, makes smaller the distribution coefficients D_{ex}^{Σ} and D_{ex}^{k}. Therefore, with increasing Ln(III) nitrate concentration in the aqueous phase, D_{ex}^{Σ} and D_{ex}^{k} pass through a maximum whose position depends on the nature of a particular Ln(III) and on the extractant concentration.

(2) The fraction of *k*th Ln(III) in the organic phase depends on K_{ex}^{2}; equilibrium concentration of free extractant, $\{R_4NA\}_{(o)}$; and fraction of *k*th Ln(III) in the aqueous phase, $\alpha_{(a)}^{k}$. With increasing $\alpha_{(a)}^{k}$, the $\alpha_{(o)}^{k}$ increases too.

(3) If only one extractable species is formed in the organic phase, the separation factor of the neighboring lanthanides(III) $\beta_{k/(k+1)}$ is determined by the ratio of the concentration extraction constants of these Ln(III), being dependent of the free extractant concentration.

For extraction of the individual Ln(III) nitrates, the dependences of the concentration extraction constants on the ionic strength of the aqueous phase *I* are fitted by the empirical equation [3–5]

$$\log K_{ex}^{2} = \log K_{ex}^{0,2} + \tilde{a}\Delta Z^{2}\sqrt[3]{I} + b_k I, \quad (20)$$

where $\tilde{a} = -0.1942$, $\Delta Z^2 = -12$. is the linear combination of the charge numbers of the species involved in the extraction equilibrium, and b_k is the empirical parameter specific for particular Ln(III).

The results reported in [6, 7] show that the extraction constant of lanthanide(III) nitrate A from binary mixture of lanthanide(III) nitrates A + B at I = const ($I = I_A + I_B$) and variable A/B ratio linearly varies with contribution of lanthanide B to the total ionic strength

$$\log K_{ex}^{2,A}(I = I_A + I_B) = \log K_{ex}^{2,A}(I = I_A) - \lambda_A I_B \quad (21)$$

and similarly for B

$$\log K_{ex}^{2,B}(I = I_A + I_B) = \log K_{ex}^{2,B}(I = I_B) - \lambda_B I_A. \quad (22)$$

In the limiting case

$$\lambda_A \simeq \lambda_B \simeq \lambda,$$

$$\log K_{ex}^{2,A}(I = I_B) \simeq \log K_{ex}^{2,B}(I = I_A).$$

Then

$$\lambda = [\log K_{ex}^{2,A}(I = I_B) - \log K_{ex}^{2,B}(I = I_A)]/2I. \quad (23)$$

Taking into account Eq. (21), Eq. (23) can be transformed to the form

$$\lambda = \left(\log K_{ex}^{i,0,A} - \log K_{ex}^{i,0,B}\right)/2I + (b_A - b_B)/2. \quad (24)$$

For solution containing only two different Ln(III) ($I^{\Sigma} = I_A + I_B$), Eq. (21) can be transformed to the form

$$\log K_{ex}^{2,A} = \log K_{ex}^{2,0,A} + \tilde{a}\Delta Z^{2}\sqrt[3]{I^{\Sigma}} + b_k I^{\Sigma} + \lambda I_B. \quad (25)$$

This equation can be reformulated for *N*-component solution:

$$\log K_{ex}^{2,k} = \log K_{ex}^{2,0,k} + \tilde{a}\Delta Z^{2}\sqrt[3]{I^{\Sigma}} + b_k I^{\Sigma} + \sum_{j=1}^{N}\lambda_{k,j} I_j. \quad (26)$$

where I_j is the contribution of *j*th component to the total ionic strength I^{Σ}; $\lambda_{k,j}$ are the empirical parameters which, to a first approximation, can be evaluated by the equation

$$\lambda_{k,j} = \left(\log K_{ex}^{0,k} - \log K_{ex}^{0,j}\right)/2I^{\Sigma} + (b_k - b_j)/2. \quad (27)$$

Taking into account Eq. (27) describing the concentration extraction constants as functions of the ionic strength of the aqueous phase for multicomponent mixtures, the system of nonlinear equations (13)–(17) can be transformed to the following

$$c_s = \{R_4NA\}_{(o)} + 54\left(c_{Ln(a)}\right)^4 \sum_{k=1}^{N}\alpha_{(a)}^{k} K_{ex,k}^{0,2} F(I)\{R_4NA\}_{(o)}^{2}, \quad (28)$$

$$c_{Ln(a)}^{0,1} V_a^0 = \{Ln^{3+(1)}\}_{(a)} V_a + V_o 27\left(c_{Ln(a)}\right)^4 \alpha_{(a)}^{1} K_{ex,1}^{0,2} F(I)\{R_4NA\}_{(o)}^{2}. \quad (29)$$

$$c_{Ln(a)}^{0,k} V_a^0 = \{Ln^{3+(k)}\}_{(a)} V_a + V_o 27\left(c_{Ln(a)}\right)^4 \alpha_{(a)}^{k} K_{ex,k}^{0,2} F(I)\{R_4NA\}_{(o)}^{2}, \quad (30)$$

$$c_{Ln(a)}^{0,N} V_a^0 = \{Ln^{3+(N)}\}_{(a)} V_a + V_o 27\left(c_{Ln(a)}\right)^4 \alpha_{(a)}^{N} K_{ex,N}^{0,2} F(I)\{R_4NA\}_{(o)}^{2}, \quad (31)$$

$$3\sum_{k=1}^{N} c_{Ln(a)}^{0,k} V_a^0 = \{NO_3^-\}_{(a)} V_a + V_o 81\left(c_{Ln(a)}\right)^4 \sum_{k=1}^{N}\alpha_{(a)}^{k} K_{ex,k}^{0,2} F(I)\{R_4NA\})_{(o)}^{2}, \quad (32)$$

$$F(I) = 10^{\tilde{a}\Delta Z^{2}\sqrt[3]{I^{\Sigma}} + b_k I^{\Sigma} + \sum_{j=1}^{N}\lambda_{k,j} I_j},$$

$$I^{\Sigma} = 6\sum_{k=1}^{N}\{Ln^{3+(k)}\}_{(a)} = 6c_{Ln(a)}, \quad I^{j} = 6\{Ln^{3+(j)}\}_{(a)}.$$

Logarithms of thermodynamic constants of reaction (1) and empirical parameters b_{Ln} in Eq. (20) for extraction Ln(III) nitrates with 0.60 M toluene solution of TABANP at T = 298.15 K

Ln(III)	$\log K_{ex}^{0,2}$	b_{Ln}
La	2.24 ± 0.05	0.228 ± 0.005
Ce	2.20 ± 0.05	0.233 ± 0.004
Pr	1.95 ± 0.06	0.250 ± 0.005
Nd	1.78 ± 0.04	0.252 ± 0.004
Sm	1.70 ± 0.04	0.266 ± 0.003
Eu	1.54 ± 0.03	0.271 ± 0.004
Gd	1.27 ± 0.03	0.277 ± 0.005
Tb	1.22 ± 0.04	0.278 ± 0.004
Dy	1.05 ± 0.03	0.290 ± 0.003
Ho	0.81 ± 0.10	0.303 ± 0.004
Er	0.59 ± 0.06	0.323 ± 0.005
Tm	0.40 ± 0.03	0.331 ± 0.004
Yb	0.15 ± 0.06	0.345 ± 0.005
Lu	0.08 ± 0.06	0.357 ± 0.004
Y	–0.13 ± 0.05	0.375 ± 0.004

Note. The errors are given as rms deviations σ.

The logarithms of the thermodynamic constants of Ln(III) extraction by reaction (1), $\log K_{ex}^{0,2}$, and the empirical parameters b_k are listed in the table.

In our experiments TABANP was taken as 0.6 M toluene solution. The general formula of TABANP is $C_6H_5(C_7H_{15}-C_9H_{19})_3N^+A^-$, where A^- is the naphthenate anion. We used a mixture of naphthenic acid isomers recovered from crude oil (natural carboxylic acids containing carboxy groups bound to five-membered rings, M_{av} = 220).

Trialkylbenzylammonum naphthenate was prepared from trialkylbenzylammonum chloride as follows. An organic solution of trialkylbenzylammonium chloride was converted to the hydroxide by triple contact with 5–7 M aqueous NaOH. Excess alkali was removed by repeated scrubbing of the organic phase with distilled water until pH of the wash water decreased to 8–9. The resulting solution of trialkylbenzylammonium hydroxide was mixed with a stoichiometric amount of naphthenic acids and this mixture was dissolved in toluene (chemically pure grade). The resulting binary extractant was washed with distilled water to pH 7.

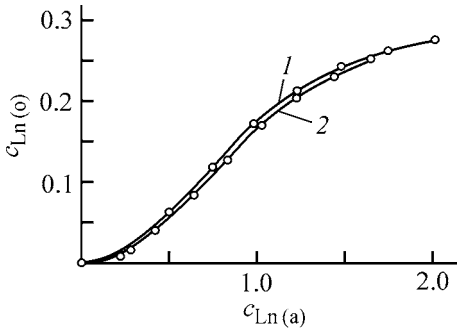

Fig. 1. Isotherms of joint extraction of Ln(III) nitrates from aqueous Ln(III) concentrates of varied composition with 0.60 M TABANP in toluene. ($c_{Ln(o)}$) and ($c_{Ln(a)}$) Ln(III) concentrations in the organic and aqueous phases, respectively. Concentrate: (*1*) no. 1 and (*2*) no. 2

The concentration of naphthenic acids in the organic phase was determined by two methods: two-phase potentiometric titration [8] and titration with aqueous alkali of the organic phase diluted with ethyl alcohol, with phenolphthalein as indicator. The amount of the QAB salt was determined by the method reported in [9].

Solutions of Ln(III) nitrates were prepared by dissolving the corresponding Ln(III) oxides in nitric acid (analytically pure grade). We used two different commercial concentrates containing Ln(III) oxide mixture of the following compositions (wt % recalculated to oxide): (concentrate no. 1) La 8.8, Ce 17.5, Pr 12.5, Nd 6.0, Sm 5.5, Eu 7.3, Gd 9.3, Tb 16.8, Dy 10.6, and Ho 5.7; (concentrate no. 2) La 6.6, Ce 8.2, Pr 7.9, Nd 6.4, Sm 5.2, Eu 1.8, Gd 7.3, Tb 1.2, Dy 6.3, Ho 1.3, Er 3.1, Tm 0.5, Yb 2.1, Lu 0.6, and Y 41.5. Extraction was carried out in graduated tubes at a 1 : 1 ratio of the organic and aqueous phases. Changes in the volumes of the organic and aqueous phases did not exceed 2 rel. %. The ΣLn(III) concentration in both the initial and equilibrium aqueous phases was determined by titration with a standard aqueous solution of disodium ethylenediaminetetraacetate in the presence of xylenol orange as indicator [10]. The ΣLn(III) concentration in the organic phase was determined as the difference between the ΣLn(III) contents in the initial and equilibrium aqueous phases. To determine the concentrations of particular Ln(III) in their mixture, lanthanides were precipitated as oxalates, calcined to oxides, and then subjected to atomic emission analysis on a Labtest device (USA) with ionization in inductively coupled argon plasma [10].

The relative errors were within ±0.5%, in preparing solutions; ±(0.5–2)%, in determining Ln(III) concentration; and ±(1–3)%, in determining the distribution coefficients.

The isotherms of joint extraction of lanthanide(III) nitrates from their concentrates with 0.60 M TABANP in toluene (Fig. 1) show saturation with respect to Ln(III) at $c_S : c_{Ln(o)} \Rightarrow 2 : 1$.

The logarithms of the distribution coefficients of particular La(III)–Ln(III) and Y(III) are plotted against the total equilibrium concentration of Ln(III) in the aqueous concentrate (M) in Fig. 2. In these plots, the solid lines represent the results of our model calculations performed using parameters listed in the table, and the points are our experimental results. Figures 2a and 2b show that the calculated distribution coefficients agree with the experimental values to within 3–5 rel.%. Thus, our model describes adequately the extraction of lanthanides(III) from their multicomponent mixtures with the use of TABANP in toluene.

Figures 2a and 2b show that, with the Ln(III) concentration in the aqueous phase increasing above 250 g/l, the distribution coefficients of particular Ln(III) and the difference between the distribution coefficients of the neighboring elements decrease. The best extraction separation of Ln(III) concentrates into groups and into individual elements using TABANP as extractant was achieved at an equilibrium Σ Ln(III) concentration of 120–200 g/l. Under these conditions, the distribution coefficients and the difference between the distribution coefficients of neighboring Ln(III) are maximal. The difference between the distribution coefficient is the largest for the pairs Ce(III)/Pr(III), Pr(III)/Nd(III), and Eu(III)/Gd(III) for concentrate no. 1, and for pairs Ce(III)/Pr(III), Pr(III)/Nd(III), Eu(III)/Gd(III), Dy(III)/Ho(III), and Er(III)/Tm(III) for concentrate no. 2. It should be noted that Y(III) is the least extractable with TABANP, compared with La(III)–Lu(III).

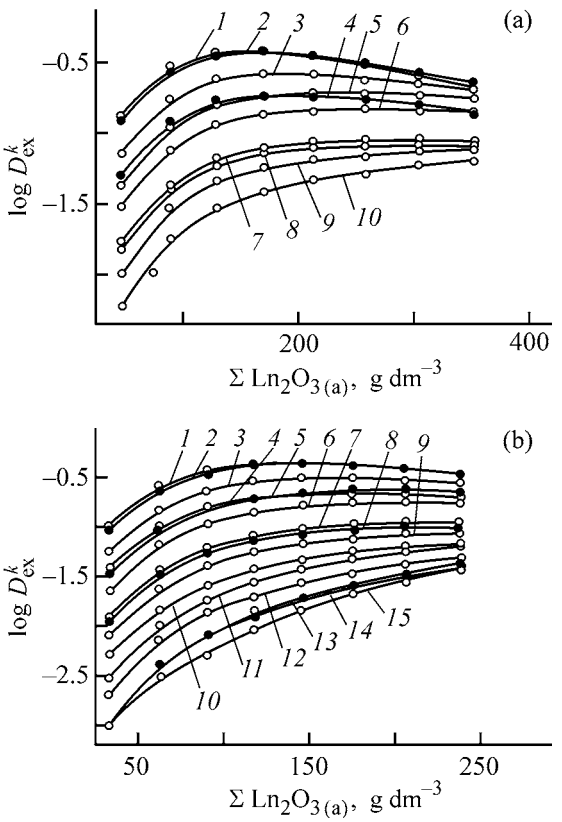

Fig. 2. Logarithm of distribution coefficients of particular Ln(III), $\log D_{ex}^k$, between 0.6 M TABANP in toluene and aqueous concentrate containing sum of Ln(III) as influenced by the total concentration of lanthanides(III) mixture in the aqueous concentrate, $\Sigma\,Ln_2O_{3\,(a)}$. Concentrate: (a) no. 1 and (b) no. 2. Ln(III): (a) (*1*) La, (*2*) Ce, (*3*) Pr, (*4*) Nd, (*5*) Sm , (*6*) Eu , (*7*) Gd , (*8*) Tb, (*9*) Dy, and (*10*) Ho ; (b) (*1*) La, (*2*) Ce, (*3*) Pr, (*4*) Nd, (*5*) Sm, (*6*) Eu, (*7*) Gd , (*8*) Tb, (*9*) Dy, (*10*) Ho, (*11*) Er, (*12*) Tm, (*13*) Yb, (*14*) Lu, and (*15*) Y .

CONCLUSIONS

(1) The physicochemical and mathematical models of extraction of La(III)–Lu(III) and Y(III) nitrates from their multicomponent aqueous solutions with the use of trialkylbenzylammonium naphthenate in toluene was developed taking into account the mutual influence of lanthanides at different concentrations and compositions of Ln(III) mixtures.

(2) Extraction of particular Ln(III) nitrates from their multicomponent aqueous solutions with trialkylbenzylammonium naphthenate in toluene was studied within a wide range of Ln(III) nitrate concentrations in the aqueous phase at 298.15 K. The extraction isotherms were obtained. The extraction isotherms show saturation with respect to Ln(III) at $c_S : c_{Ln\,(o)} \Rightarrow 2 : 1$.

(3) Extraction of lanthanide(III) nitrates with trialkylbenzylammonium naphthenates in toluene decreases in going from lanthanum(III) to lutetium(III). The extractability of yttrium(III) is considerably lower than that of La(III)–Lu(III). Trialkylbenzylammonium naphthenates can be used for separating cerium-group lanthanides(III) from other lanthanides(III) and yttrium(III) from lanthanides(III). The best separation of the sum of lanthanides(III) into groups and individual metals by extraction with TABANP is attained at the equilibrium ΣLn(III) concentration in the aqueous phase 120–200 g/l.

REFERENCES

1. Khol'kin, A.I. and Kuz'min, V.I., in *Khimiya ekstraktsii* (Extraction Chemistry), Novosibirsk, Nauka, 1984.
2. Dennis, J.E. and and Schnabel, R.B., *Numerical Methods for Unconstrained Optimization and Solution of Nonlinear Equations*, New York: Prentice-Hall, 1983.

3. Bjerrum, N., *Z. Anorg. Chem.*, 1919, vol. 109, pp. 275–292.
4. Pyartman, A.K., Kopyrin, A.A., Kovalev, S.V., and Keskinov, V.A., *Radiokhimiya*, 1997, vol. 39, no. 2, pp. 141–144.
5. Pyartman, A.K., Kopyrin, A.A., Puzikov, E.A., and Bogatov, K.B., *Zh. Prikl. Khim.*, 1993, vol. 66, no. 12, pp. 2728–2732.
6. Pyartman, A.K., Puzikov, E.A. Kopyrin, A.A., and Bogatov, K.B., *Radiokhimiya*, 1995, vol. 37, no. 1, pp. 52–59.
7. Pyartman, A.K., Kopyrin, A.A., Puzikov, E.A., and Bogatov, K.B., *Zh. Prikl. Khim.*, 1994, vol. 67, no. 4, pp. 762–766.
8. Gran, G., *Analyst*, 1962, vol. 77, no. 920, pp. 661–671.
9. Fedyanin, L.B., Stepanov, S.I., Sergievskii, V.V., and Frolov, Yu.G., Khim. Tekhnol. Org. Vysokomol. Soedin., *Tr. Mosk. Khim.-Tekhnol. Inst. im. D.I. Mendeleeva*, 1987, no. 80, pp. 15–16.
10. *OST* (Branch Standard) *48-209-81*, revision no. 2, 1991: *Rare-Earth Metal Oxides. Rules of Acceptance and Methods of Analysis*, Moscow: Gos. Kom. SSSR po Standartam, 1991.

Russian Journal of Applied Chemistry, Vol. 76, No. 2, 2003, pp. 217–222. Translated from Zhurnal Prikladnoi Khimii, Vol. 76, No. 2, 2003, pp. 225–230.

APPLIED ELECTROCHEMISTRY AND CORROSION PROTECTION OF METALS

Electrically Conducting and Photosensitive Polymers Derived from CuSalbn-1,4

T. V. Semenistaya, A. V. Shchukarev, and G. A. Shagisultanova

Herzen State Educational University, St. Petersburg, Russia

Mekhanobr-Analit Regional Analytical Center, Private Company, St. Petersburg, Russia

Received October 21, 2002

Abstract—A new electrically conducting photosensitive polymer was prepared by electrochemical polymerization of [CuSalbn-1,4]. Poly-[CuSalbn-1,4] was studied by X-ray photoelectron spectroscopy, voltammetry, and the photoelectrochemical methods.

Previously [1], we have prepared and isolated crystalline platinum, palladium, nickel, and copper complexes with tridentate bis(salicylidene)-1,4-butylenediamine ligand (Salbn-1,4^{2-}). These complexes contain four methylene groups in the aliphatic diamine moiety, unlike complexes with Salen and Salpn-1,3 [2–6] ligands containing two and three methylene groups, respectively.

Electrochemical synthesis of electrically conducting photosensitive poly-[PdSalbn-1,4] and parameters of reversible electro- and photoredox processes occurring in the bulk of the polymer were reported in our previous paper [1]. In this study, we prepared poly-[CuSalbn-1,4] by an electrochemical procedure and studied its physicochmeical and electrochemical properties.

Copper(II) bis(salicylidene)-1,4-butylenediamine complex [CuSalbn-1,4] was prepared by the modified procedure from [7]. To a methanolic solution of $Cu(CH_3COO)_2 \cdot H_2O$ (2.2 mM, 30 ml CH_3OH) was added a methanolic solution of [Salbn-1,4]$^{2-}$ in 5 wt % excess. To prevent hydrolysis of copper(II) acetate, the solution was acidified with acetic acid. The resulting dark green solution was heated at 100°C, evaporated by half, cooled, and kept at 0°C for 12 h. Dark green crystals were filtered off, washed with CH_3OH and C_2H_5O, and dried in air. Yield 60–65%.

Found (%): C 60.34, H 5.25, N 7.83.

$CuC_{18}H_{18}N_2O_2$.

Calculated (%): C 60.47, H 5.07, N 7.84.

Gruber *et al.* [8] studied the paramagnetic properties of [CuSalbn-1,4] and determined its magnetic moments at room temperature.

The C1*s*, O1*s*, N1*s*, and Cu2*p* binding energies and the atomic concentrations of the elements in different chemical states in the initial ligand H_2Salbn-1,4 and complex [CuSalbn-1,4] are listed in Table 1.

The electronic absorption spectra of H_2Salbn-1,4 in acetonitrile and [CuSalbn-1,4] in various solvents are shown in Fig. 1. The spectrum of the free ligand contains strong π–π^* intraligand charge-transfer band at λ_{max} = 315 nm (ε = 8400 l mol^{-1} cm^{-1}). In the spectrum of [CuSalbn-1,4], a shoulder with λ_{max} = 300 nm (ε = 7500 l mol^{-1} cm^{-1} is observed in the range of absorption of the uncoordinated ligand. The spectrum of an acetonitrile solution of the complex contains an additional band with λ_{max} = 375 nm and high molar extinction coefficient of 9000 l mol^{-1} cm^{-1}. The shape of this band is similar to that of allowed π–π^* elec-electronic transitions. The peak position of this band

Table 1. C1*s*, O1*s*, N1*s*, and Cu2*p* binding energies and atomic concentrations of C, O, N, and Cu in [H_2Salbn-1,4] and [CuSalbn-1,4] (XPS data)

Band	H_2Salbn-1,4		CuSalbn-1,4	
	BE, eV	*c*, %	BE, eV	*c*, %
C1*s*	285.0	57.74	285.0	55.70
	286.3	26.41	286.4	24.71
N1*s*	398.9	5.64	399.4	6.33
	399.7	1.58		
			401.7	0.50
	402.9	0.68	403.5	0.87
O1*s*			531.4	6.90
	532.9	7.93	532.4	0.53
Cu2*p*3/2			934.7	4.45

1070-4272/03/7602-0217 $25.00 © 2003 MAIK "Nauka/Interperiodica"

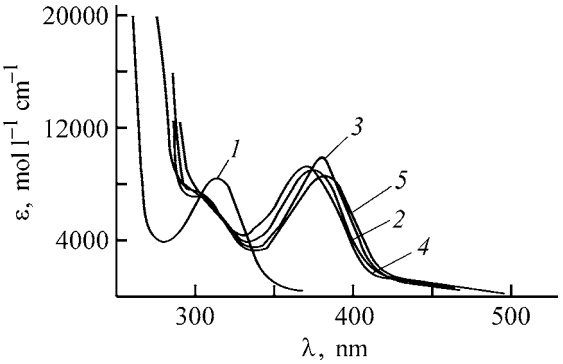

Fig. 1. Electronic absorption spectra of (*1*) H_2Salbn-1,4 in acetonitrile and of [CuSalbn-1,4] in (*2*) CH_3CN, (*3*) CH_2Cl_2, (*4*) C_2H_5OH, and (*5*) $CHCl_3$. (ε) Extinction and (λ) wavelength.

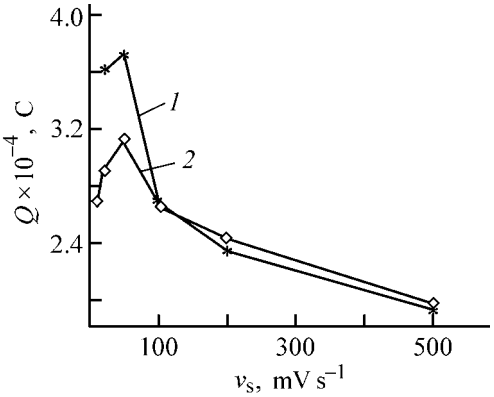

Fig. 2. Quantity of electricity Q vs. the potential sweeping rate v_s in 1×10^{-3} M solution of [CuSalbn-1,4] in (*1*) CH_3CN and (*2*) CH_2Cl_2.

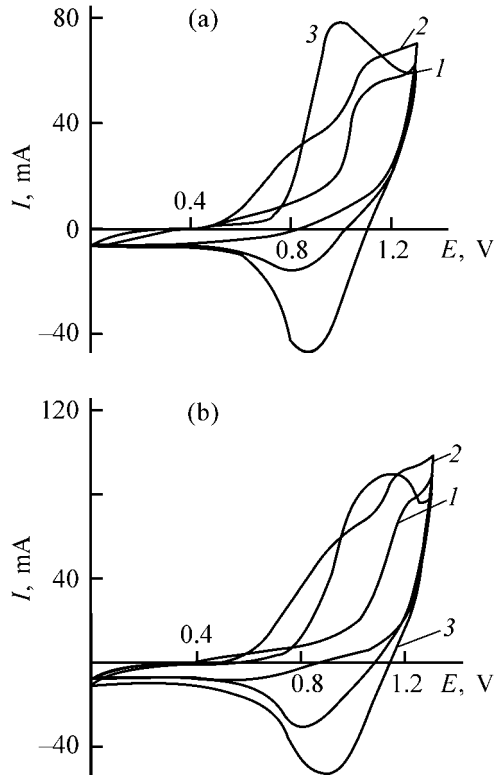

Fig. 3. Cyclovoltammograms of 1×10^{-3} M solution of [CuSalbn-1,4] in (a) CH_3CN and (b) CH_2Cl_2. $v_s = 0.5$ V s^{-1}; the same for Figs. 7 and 8. (*I*) Current and (*E*) potential; the same for Fig. 4. (b) Scale of *I* axis is doubled. Cycle: (*1*) first, (*2*) fifth, and (*3*) twenty-fifth.

depends on the solvent polarity, i.e., the solvatochromic effect is observed. When the solvent polarity increases [z (kcal mol^{-1}) 63.2 ($CHCl_3$), 64.2 (CH_2Cl_2), 71.3 (CH_3CN), 79.6 (C_2H_5OH)], a hypsochromic shift of the band is observed [λ_{max} (nm) 383 ($CHCl_3$), 380 (CH_2Cl_2), 375 (CH_3CN), and 370 (C_2H_5OH)], which is typical of charge-transfer transitions [9].

Polymeric [CuSalbn-1,4] was prepared by the electrochemical procedure previously used to synthesize poly-[PdSalbn-1,4] [1]. Electropolymerization of [CuSalbn-1,4] was performed in CH_3CN and CH_2Cl_2 under potentiostatic and potentiodynamic conditions of accumulation of the electroactive substance on the electrode positively polarized from 0.0 to +1.3 V. The concentration of the complex ranged from 0.5 to 3.0 mM.

(a) Electrochemical polymerization under potentiodynamic conditions was performed in a 1×10^{-3} M solution of [CuSalbn-1,4] in CH_3CN or CH_2Cl_2, containing 0.1 M tetrabutylammonium perchlorate (TBAP) as the supporting electrolyte.

We have recorded the cyclovoltammograms at different potential sweeping rates v to find an optimum (Fig. 2) The fact that the current peak is directly proportional to the sweeping rate at $v_s < 0.05$ V s^{-1} indicates that the electroreduction is controlled by adsorption [10]. At $v_s < 0.05$ V s^{-1}, the complex is completely reduced during the first cycle. Thus, the thickness of a polymeric film h can be calculated by the procedure described in [11] from the quantity of electricity determined from the chronovolatmograms. At potential sweeping rates higher than 0.05 V s^{-1}, the polymeric complex is incompletely reduced and oxidized during a single cycle. In this case, the redox processes occur under conditions of semi-infinite diffusion of the electroactive compound toward the electrode surface. Probably, the rate-determining step of the reduction and oxidation of the polymeric complex is electron transfer across the polymeric film. By analogy with liquid-phase processes, the rate of electron transfer can be characterized by the diffusion coefficient D_{ct}. At these potential sweeping rates, the charge transfer rate was calculated by the Randles–Shevchik equation [12].

Cyclovoltammograms of [CuSalbn-1,4] are shown in Fig. 3. In successive sweeping cycles, the complex

polymerizes. For comparison, we chose the potentiodynamic curves recorded during the first, fifth, and twenty-fifth cycles. As seen from Fig. 3, the anodic current peak at E = 1.1 V is shifted to 1.0 V after continuous potential sweeping in an acetonitrile solution for 23 min (25 cycles). A broad peak at 0.85 V is present in the cathodic region of the voltammogram recorded at the reverse sweeping. The cyclovoltammograms of [CuSalbn-1,4], recorded in CH_2Cl_2, contains an anodic peak at 1.1 V and a cathodic peak at 0.85 V. Poly-[CuSalbn-1,4] films with the maximal thickness (0.06 μm) were grown in a CH_3CN solution in the course of 23–25 min with electrochemical polarization under potentiodynamic conditions. In CH_2Cl_2, 0.04-μm films were prepared in 17–20 min. The film thickness does not change on longer sweeping. The maximal peak current of anodic oxidation in CH_3CN and CH_2Cl_2 is 71 and 50 mA, respectively.

The electrode coated with poly-[CuSalbn-1,4] was placed in a solution of a pure supporting electrolyte. Cyclovoltammograms of poly-[CuSalbn-1,4] were recorded with potential sweeping from 0.0 to +1.3 V (Fig. 4). As seen from Fig. 4, the charge transfer in the polymer is reversible, i.e., the redox transformations of the polymer on the electrode surface are also reversible.

The stability of poly-[CuSalbn-1,4] depends on the solvent in which it has been prepared. The polymer prepared in CH_3CN is less stable on storage in a pure supporting electrolyte exposed to open air than the polymer prepared in CH_2Cl_2. The polymer synthesized in CH_2Cl_2 degrades irreversibly in the course of prolonged potential sweeping.

To obtain thicker polymeric films, we studied the dependence of the thickness of the film grown for τ_{acc} = 500 s on the [CuSalbn-1,4] concentration (Fig. 5). As seen from Fig. 5, the thickness of the poly-[CuSalbn-1,4] film increases with the complex concentration increasing up to 2×10^{-3} M. At higher concentrations, the film thickness decreases owing to partial degradation of the polymer. In CH_2Cl_2, the thickness of the polymeric films linearly increases with the complex concentration. The maximal thickness of the poly-[CuSalbn-1,4] film grown in CH_3CN (0.08 μm) is reached within 500 s at complex concentration of 2.0×10^{-3} M. In CH_2Cl_2, films with the maximal thickness (0.067 μm) were grown by potential sweeping for 1500 s at complex concentration of $(2.5–3.0) \times 10^{-3}$ M.

(b) Complex [CuSalbn-1,4] was electrochemically polymerized on a platinum electrode under the potentiostat conditions in CH_3CN and CH_2Cl_2 solutions at the optimal potentials. The potentiostatic curves were recorded in solutions of pure supporting electrolyte.

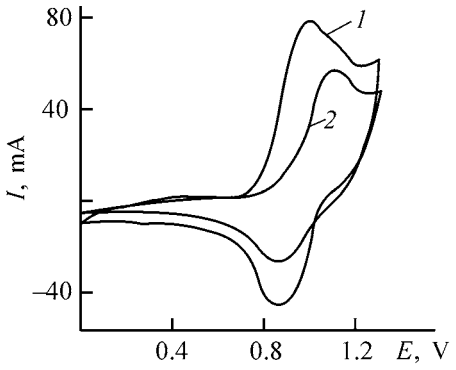

Fig. 4. Cyclovoltammograms of poly-[CuSalbn-1,4] in 0.1 M TBAP solution in (*1*) CH_3CN and (*2*) CH_2Cl_2. v_s = 0.5 V s^{-1}; the same for Fig. 5

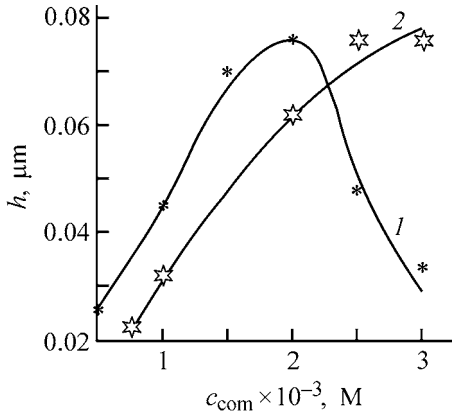

Fig. 5. Thickness h of poly-[CuSalbn-1,4] film prepared under potentiodynamic conditions in (*1*) CH_3CN and (*2*) CH_2Cl_2 vs. the [CuSalbn-1,4] concentration c_{com}.

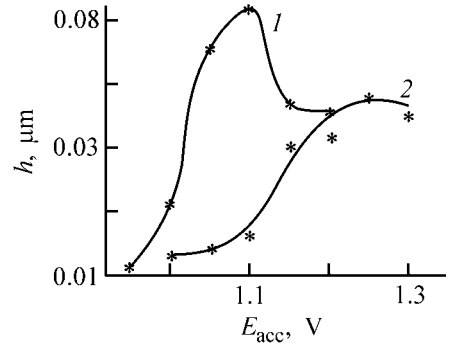

Fig. 6. Thickness h of poly-[CuSalbn-1,4] film prepared in (*1*) CH_3CN and (*2*) CH_2Cl_2 vs. the accumulation potential E_{acc}. $c_{com} = 10^{-3}$ M, τ_{acc} = 10 min, v_s = 0.5 V s^{-1}.

For example, the accumulation potential in CH_3CN and CH_2Cl_2 is 1.1 and 1.25 V, respectively (Fig. 6). The accumulation time is 10 min. It should be noted

Table 2. Electron binding energies and atomic concentrations of elements in the reduced and oxidized forms of poly-[CuSalbn-1,4] (XPS data)

Band	Forms of poly-[CuSalbn-1,4]			
	oxidized		reduced	
	BE, eV	*c*, %	BE, eV	*c*, %
C1*s*	285.0	48.28	285.0	53.62
	286.3	23.58	286.4	22.48
	287.3	4.18	287.8	2.59
	288.8	3.09	289.4	2.28
N1*s*	399.2	3.68	399.2	2.79
	400.4	1.37	400.4	1.44
	402.5	0.50	402.9	0.43
O1*s*	531.2	3.51	531.1	2.37
	532.4	6.18	532.3	7.17
	533.6	3.64	533.8	2.92
Cu2*p*3/2	932.6	0.09	932.8	0.26
	934.5	0.38	934.5	0.53
Cl2*p*3/2	198.2	0.16	198.5	0.17
	200.6	1.34	200.7	0.52

that the color of the polymers prepared in these solvents under the same conditions (complex concentration 1×10^{-3} M, accumulation time 10 min, optimal potentials) differs. Poly-[CuSalbn-1,4] prepared in CH_3CN is emerald green, whereas the polymer grown in CH_2Cl_2 is red-brown. Probably, the mechanisms of polymer formation in these solvents differ.

The dependence of the thickness of a poly-[CuSalbn-1,4] film on the accumulation time, characterizing the kinetics of polymer growth at the optimal potential, is shown in Fig. 7. The film with the maximal thickness (0.074 μm) was grown in the course of 21 min from an acetonitrile solution of [CuSalbn-1,4] (E_{acc} = 1.1 V). The limiting thickness of the film prepared in CH_2Cl_2 solution (E_{acc} = 1.25 V) in 7 min is 0.093 μm. The film thickness does not grow with increasing accumulation time.

The dependence of the charge diffusion coefficient along the polymeric chain on the thickness of a poly-[CuSalbn-1,4] film is shown in Fig. 8. The maximal diffusion coefficient D_{ct} (1.05×10^{-12} cm^2 s^{-1}) was observed in the film grow in CH_3CN in the course of 21 min. In CH_2Cl_2, the maximum (D_{ct} = 0.57×10^{-12} cm^2 s^{-1}) is attained at accumulation time of 10 min.

Thus, films of poly-[CuSalbn-1,4] with the maximum thickness of 0.093 μm can be grown within 7 min from 1×10^{-3} M solution of the complex in CH_2Cl_2 under potentiostatic conditions at E_{acc} = 1.25 V.

Poly-[CuSalbn-1,4] was analyzed by X-ray photoelectron spectroscopy (XPS). The binding energies and atomic concentrations of the components of XPS spectra of the oxidized and reduced forms of poly-[CuSalbn-1,4] are presented in Table 2. The copper XPS spectrum indicates the presence of Cu(I) (BE = 932.6 eV) and Cu(II) (BE = 934.5 eV) in the polymer. The Cu(I)/Cu(II) ratio in the oxidized and reduced forms differs. The Cu(I) content in the reduced form (33% of the total copper content) is higher than that in the oxidized form (20%). It should be noted that the band with BE of about 937.2 eV, which is typical of Cu(Mesal)$_2$ polymers [13] and is assigned to Cu(II) atoms forming strong Cu–O–Cu bonds, is absent in the spectra. Probably, additional methylene groups of the H_2Salbn-1,4 ligand prevent formation of these dimers.

The electrochemical behavior of poly-[CuSalbn-1,4] is characterized by an electrochromic effect owing to the formation of oxidized and reduced forms of the polymer. The oxidized form was prepared by polymerization under potentiostatic conditions in CH_3CN

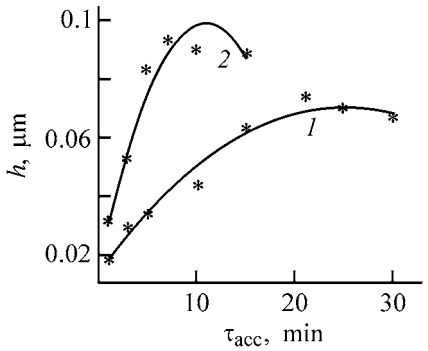

Fig. 7. Thickness *h* of poly-[CuSalbn-1,4] film vs. the accumulation time τ_{acc} (*1*) at E_{acc} = 1.1 V in CH_3CN and (*2*) E_{acc} = 1.25 V in CH_2Cl_2.

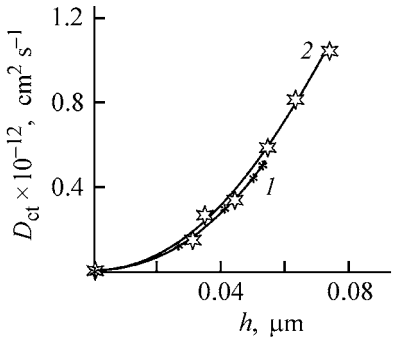

Fig. 8. Charge transfer rate vs. the thickness *h* of poly-[CuSalbn-1,4] film grown (*1*) in CH_2Cl_2 at E_{acc} = 1.15 V and (*2*) in CH_3CN at E_{acc} = 1.1 V. (D_{ct}) diffusion coefficient.

and CH_2Cl_2 at E = 1.1 and 1.25 V, respectively. The color of the oxidized form of poly-[CuSalbn-1,4] prepared in CH_3CN and CH_2Cl_2 is emerald green and red-brown, respectively. The reduced form accumulated at low potential (E = 0.1 V) in 5 min has light green color, irrespective of the color of the oxidized form. When the applied voltage is switched off, an equilibrium potential E_{eq} = 0.51 and 0.56 V is spontaneously attained in several hours in CH_3CN and CH_2Cl_2, respectively. These potentials determine the redox state of the polymer.

The electronic absorption spectrum of oxidized poly-[CuSalbn-1,4] prepared in CH_3CN under potentiostatic conditions (E_{acc} = 1.1 V) is shown in Fig. 9. To record the electronic spectra, the polymeric film was supported on a quartz plate coated with platinum by a vacuum procedure. The spectrum contains two bands with λ_{max} = 395 and 615 nm. We failed to record the electronic absorption spectrum of the reduced form.

The dependence of the photopotential of the reduced form of the polymer on the exposure time is shown in Fig. 10. The polymer was prepared in CH_3CN and was reduced to E = 0.1 V (light green color) in acetonitrile solution of TBAP. The photoelectric experiment was performed by the procedure described in our previous paper [2]. As seen from Fig. 10, reduced poly-[CuSalbn-1,4] (E_{red} = 0.1 V) is photooxidized to the stationary state in 40 s. The maximum photopotential corresponding to the maximum accumulation of oxidized fragments of the complex in the polymer exposed to light is 177 mV. The fact that the photopotential does not change after repeated excitation cycles indicates the stability of the polymeric films to light. The photopotential of the film, measured on a cylindrical electrode, is 100 mV.

CONCLUSIONS

(1) Electrochemical synthesis of poly-[CuSalbn-1,4] was performed for the first time. In spite of the fact that the methylene chain of the [H_2Salbn-1,4] is longer than that of [H_2Salen] and [H_2Salpn-1,3], [MSalbn-1,4] complexes form stable electrically conducting and photoactive polymers characterized by fast charge transfer. The thickness of these polymeric films is typical of compounds of this class.

(2) Poly-[CuSalbn-1,4] with the maximal thickness of 0.24 μm was prepared in CH_2Cl_2 under potentiostatic conditions at E_{acc} = 1.2 V for 7 min. The charge diffusion coefficient in poly-[CuSalbn-1,4] is $D_{ct} = 2.95 \times 10^{-12}$ cm^2 s^{-1}. The maximum photopotential of poly-[PdSalbn-1,4] and poly-[CuSalbn-1,4] is 133 and 177 mV, respectively.

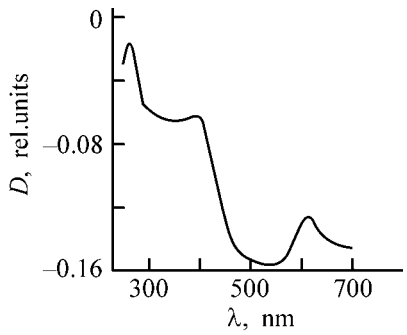

Fig. 9. Electronic absorption spectrum of oxidied poly-[CuSalbn-1,4] (E_{ox} = 1.1 V, CH_3CN, Bu_4NClO_4, τ_{acc} = 20 min, emerald green polymer). (D) Optical density and (λ) wavelength.

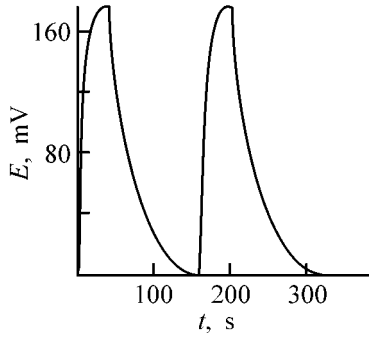

Fig. 10. Photopotential E of poly-[CuSalbn-1,4] in 0.1 M solution of TBAP in CH_3CN vs. the time t of exposure to polychromatic light. Film thickness h = 0.04 μm, E = 0.1 V.

ACKNOWLEDGMENTS

This work was supported financially by the Russian Foundation for Basic Research (project no. 01-03-33155) and by the Ministry of Education, Russian Federation (project no. E00-5.0.-210).

REFERENCES

1. Shagisultanova, G.A., Ardasheva, L.P., Gubasova, T.N., *et al.*, Abstracts of Papers, *XX Int. Conf. of Photochemistry*, Moscow, July 30–August 4, 2001, pp. 483–484.
2. Popova, E.O., Orlova, I.A., and Shagisultanova, G.A., *Koord. Khim.*, 2000, vol. 26, no. 10, pp. 733–737.
3. Shagisultanova, G.A., Orlova, I.A., Ardasheva, L.P., and Popova, E.O., *Macromol. Symp.*, 1998, vol. 136, pp. 91–97.
4. Shagisultanova, G.A. and Ardasheva, L.P., *Koord. Khim.*, 1999, vol. 25, no. 11, pp. 843–849.

5. Orlova, I.A., Synthesis and Properties of Electroactive Polymers Derived from Transition Metal Complexes with Schiff Bases, *Cand. Sci. Dissertation*, Moscow, 1997.
6. Shagisultanova, G.A. and Ardasheva, L.P., *Koord. Khim.*, 1999, vol. 25, no. 5, pp. 411–415.
7. Gruber, S.J., Harris, C.M., and Sinn, E., *Inorg. Chem.*, 1968, vol. 7, pp. 268–273.
8. Gruber, S.J., Harris, C.M., and Sinn, E., *J. Inorg. Nucl. Chem.*, 1968, vol. 30, pp. 1805–1830.
9. Lever, A.B.P., *Inorganic Electronic Spectroscopy*, Amsterdam: Elsevier, 1984.
10. Galus, Zb., *Teoretycznue Podstawy Elektroanalisy Chemicznej*, Warszawa: Naukowe, 1971.
11. Khannanov, N.K., Yatsun, T.F., Shafirovich., V.Ya., and Strelets, V.V., *Izv. Akad. Nauk SSSR, Ser. Khim.*, 1983, no. 20, pp. 1282–1287.
12. Plambeck, J.A., *Electroanalytical Chemistry. Basic Principles and Applications*, New York: Wiley, 1982.
13. Gubasova, T.N., Synthesis and Study of Polymeric Complexes of Nickel(II), Palladium(II), and Copper(II) with Schiff's Bases, *Cand. Sci. Dissertation*, St. Petersburg, 2002.

Russian Journal of Applied Chemistry, Vol. 76, No. 2, 2003, pp. 223–225. Translated from Zhurnal Prikladnoi Khimii, Vol. 76, No. 2, 2003, pp. 231–233.

APPLIED ELECTROCHEMISTRY AND CORROSION PROTECTION OF METALS

On Passivating Action of Silicate-Alkaline Solutions on Metals

V. N. Ovchiyan

Institute of General and Inorganic Chemistry, National Academy of Sciences of the Republic of Armenia, Yerevan, Armenia

Received October 10, 2002

Abstract—A mechanism for enhancing the stability of the passive state of metals in silicate solutions is described on the basis of a study of the corrosion-electrochemical behavior of the metals in concentrated alkaline and silicate-alkaline solutions.

Concentrated silicate-alkaline solutions find use in many branches of industry. These solutions serve as technological medium in integrated processing of silicate and aluminosilicate rocks and are used to manufacture silicon dioxide, detergents, etc.

Corrosion of metals, caused by the media mentioned above, is characterized by a number of specific features [1, 2]. Of interest in this context is a study of the electrochemical behavior of steel in solutions of this kind. However, only few investigations have been carried out in this direction [3].

It is known that metallic construction materials used in technology are mostly thermodynamically unstable. They react with the ambient and are frequently passivated through formation on their surface of insoluble (or difficultly soluble) films of oxide, hydroxide, or salt nature.

The stability of the passive state of metals depends on the nature of a protective film and its heterogeneity. Structural defects in the film are either due to imperfection of the surface structure of a metal or arise in the course of film formation. One of ways to improve the corrosion stability of a metal is to form on its surface a less defective protective.

EXPERIMENTAL

In the present study, the electrochemical behavior of 08kp steel in concentrated alkaline (AS) and silicate-alkaline (SAS) solutions was analyzed. Polarization curves were measured by changing the potential stepwise, from the range of active dissolution to repassivation, at 0.1-V intervals and keeping the steel at each potential for 15 min. The measurements were done at elevated temperature in an autoclave whose design was described in [4].

The solutions employed were fabricated using sodium hydroxide of analytically pure grade and high-purity amorphous silicon dioxide with impurity content of less than 10^{-3}%.

Corrosion cracking was studied under continuous stretching stress on wire samples passed through a vessel with a solution.

A study of the corrosion-electrochemical behavior of iron and steel in AS and SAS at 80°C has shown [5, 6] that, under the given conditions, the metals tend to undergo passivation. The region of the passive state is rather wide and lies within –0.8…–0.4 V (relative to silver chloride electrode). The stationary potential of iron and steel in both the solutions is within the range –0.3…–0.4 V, which points to the possibility of a spontaneous transition of metals to the passive state. Therefore, under standard conditions, they spontaneously undergo passivation in an alkaline medium at low temperature and dissolve at a slow rate.

It has been shown [5, 7, 8] that, although the passivating layer formed on iron in AS has complex composition and structure, the passivation of iron is due to formation of an exceedingly thin surface layer of iron oxide γ-Fe_2O_3.

The equilibrium potential of the reaction of γ-Fe_2O_3 formation in an AS containing 300 g l^{-1} NaOH is –0.896 V at 20°C. If account is taken of a minor overvoltage, this value is in good agreement with the experimental passivation potential of iron, equal to –0.85 V [5].

IR spectral and thermogravimetric studies of products formed in reaction of iron with alkaline solutions

1070-4272/03/7602-0223 $25.00 © 2003 MAIK "Nauka/Interperiodica"

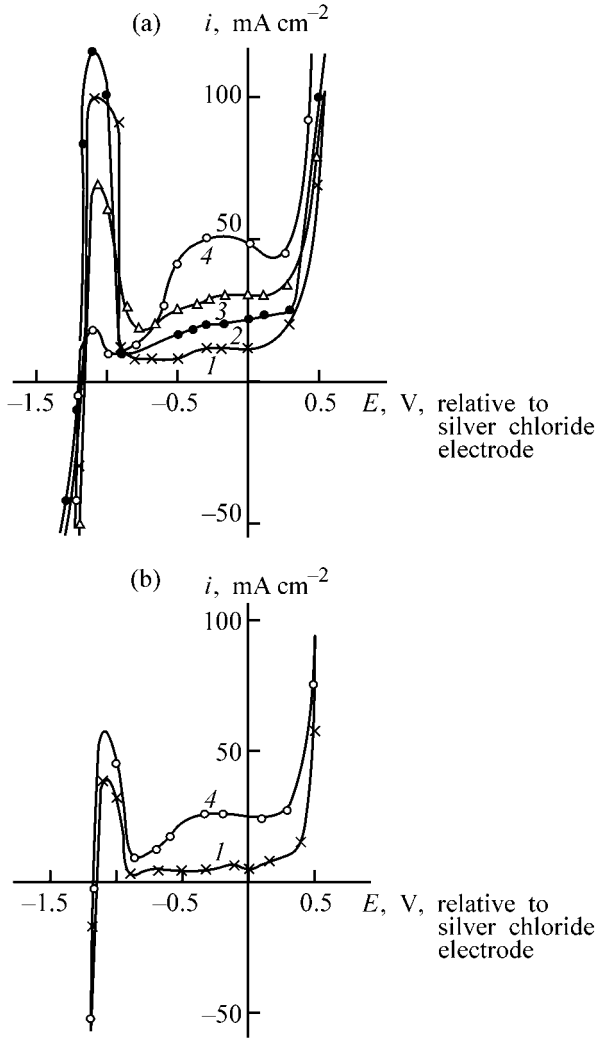

Fig. 1. Potentiostatic polarization curves for carbon steel in (a) AS and (b) SAS at different temeratures. (*i*) Current density, and (*E*) potential. Temperature (°C): (*1*) 160, (*2*) 180, (*3*) 200, and (*4*) 230.

have shown that these products are mostly composed of amorphous hydrated iron oxides, which crystallize in the course of time [9].

The fact that the dissolution rates at the corrosion potential for iron in AS and SAS are equal indicates that the nature of the compound responsible for the metal passivation is the same. However, the corrosion rate in the passive state is much lower in SAS, compared with AS, and, in the state of active dissolution (at potentials more negative than –0.85 V), this difference is also preserved [6].

The thin passivating film formed on iron in an AS is not homogeneous in structure and electrochemical properties. Some of its parts with defective structure, which show the lowest degree of saturation of free valences, become active centers of preferable adsorption of hydroxy ions [10]. Under the conditions of SAS, there further occurs an adsorption-chemical interaction between iron oxide and silicate ions possessing electron-donor properties. Monomeric SiO_4^{4-} ions, which are the most mobile, are adsorbed first. This is also favored by the fact that distances between metal ions in iron oxide and oxygen atoms in the monomeric silicate ion are close (0.27 nm). As a result, first the structurally imperfect regions of the passivating film are healed, which leads to higher stability of the passivated state [6, 11], and then monomeric and more complex ions condense on the silicate compound formed.

The part played by silicate ions in the enhancement of the passive state consists in the formation of ferrosilicates of complex composition [9, 12] on certain, energetically most favorable parts of the surface film of the passivated metal. As a result, the passivated state of the metal in SAS is determined by higher-quality protective film with smaller number of defects.

The experimental data obtained are in good agreement with the results of a study of the surface of passivated iron electrode at its interface with an alkaline medium by impedance measurements. The passivating film formed in SAS has lower capacitance and somewhat higher resistance than the film formed in AS, with the above characteristics only slightly dependent on the ac voltage frequency.

SAS exert similar influence on the corrosion-electrochemical behavior of other metals—chromium, nickel, and molybdenum, and steels alloyed with these elements [1, 13].

At 160–230°C (see Fig. 1a) the stationary potentials of steel in an AS containing 300 g l^{-1} NaOH are shifted with respect to those at low temperatures toward negative values and fall within the active dissolution range. Their values are very close, and, therefore, as a characteristic of the corrosion resistance of steel at various temperatures may serve anodic current peaks in the polarization curves (see Fig. 1a), which are due to the formation of a passivated film. With increasing temperature, the rate of the anodic process passes through a maximum, being the highest at 180°C. These data are in agreement with the results obtained in studying steel corrosion in an AS (300 g l^{-1} NaOH) at various temperatures [14].

The rate of the anodic process in an SAS containing 300 g l^{-1} NaOH + 50 g l^{-1} SiO_2 (see Fig. 1b) at 160°C at a potential of the onset of passivation under

conditions of a stable passive state is lower than that in AS. At 230°C, silicate ions stimulate dissolution of steel in the active state. The onset of passivation is observed at high current densities *i*. In the given case, the abovementioned specific feature of the influence exerted by silicon dioxide is confirmed. This feature consists in that the inhibiting action would only be expected in those cases when the surface layers on the metal possess, to lesser or greater extent, protective properties [6].

Much later, a similar effect of healing action on defects in an oxide film was also observed for molybdate ions in aerated aqueous media [15].

Previously [16], an assumption has been made that the inhibiting action of minor additions of water-soluble silicates on the steel corrosion in boiler water is related to formation of solid ferrosilicate films.

As is known, an alkaline medium may cause corrosion cracking of metals. This frequently occurs with steels in passivated state, whose surface is covered with a protective film. Under the influence of mechanic stresses, the film is weakened in places, and then the construction steel, which, on the whole, retains high stability against uniform corrosion, is subjected to rather intensive intercrystallite or transcrystallite disintegration in separate zones. It can be readily imagined how dangerous is this for apparatus working under pressure.

A study of the kinetics of corrosion cracking demonstrated that, owing to the higher passivating capacity of SAS, compared with AS, higher-quality and stronger protective films are formed on the metal in SAS. As a result, steel becomes more stable against corrosion cracking. Also established was the effect of silicon dioxide in SAS on the duration of tests under stretching stress until appearance of corrosion cracks and disintegration of a wire sample. For example, at a SiO_2 concentration of 100 g l^{-1} in SAS containing 300 g l^{-1} NaOH at 100°C, a wire sample of steel 10 disintegrates after approximately 3 months of tests, whereas in AS with the same concentration of NaOH, disintegration occurs already on the ninth day.

The presence of silicon ions largely eliminates electrochemically heterogeneous regions on the surface of the oxide film on the metal and prevents localization of the corrosion process, with, correspondingly, the stability of steels against corrosion cracking enhanced.

CONCLUSIONS

(1) A significant improvement of the corrosion resistance of metals in concentrated alkaline solutions in the presence of silicate ions is established.

(2) Silicate ions stimulate the corrosion process in the region of active dissolution of metals.

REFERENCES

1. Ovchiyan, V.N., Avanesova, L.M., Sedrakyan, S.M., *et al.*, *Arm. Khim. Zh.*, 1986, vol. 39, no. 2, pp. 88–93.
2. Ovchiyan, V.N., Oganesyan, A.R., and Avanesova, L.M., *Arm. Khim. Zh.*, 1991, vol. 44, no. 6, pp. 344–350.
3. Saakyan, K.G., *Zashch. Met.*, 1975, vol. 11, no. 1, pp. 41–42.
4. Gerasimov, V.V., *Korroziya reaktornykh materialov* (Corrosion of Reactor Materials), Gerasimov, V.V., Ed., Moscow: Atomizdat, 1960, pp. 16–20.
5. Ovchiyan, V.N. and Voskanyan, S.S., *Arm. Khim. Zh.*, 1977, vol. 30, no. 2, pp. 380–382.
6. Ovchiyan, V.N., Voskanyan, S.S., and Danil'yants, E.S., *Arm. Khim. Zh.*, 1978, vol. 31, no. 6, pp. 393–398.
7. Nagayama, M. and Cohen, M., *J. Electrochem. Soc.*, 1962, vol. 109, no. 9, pp. 781–785.
8. Rozenfel'd, I.L., *Ingibitory korrozii metallov* (Inhibitors of Metal Corrosion), Moscow: Khimiya, 1977.
9. Stepanyan, Ts.R., Zulumyan, N.O., and Ovchiyan, V.N., *Arm. Khim. Zh.*, 1988, vol. 41, no. 5, pp. 255–260.
10. Leont'ev, I.P. and Khidikel', M.A., *Usp. Khim.*, 1983, vol. 52, no. 4, pp. 596–600.
11. Oganesyan, A.R. and Ovchiyan, V.N., *Arm. Khim. Zh.*, 1987, vol. 40, no. 12, pp. 737–742.
12. Lyakhov, O.G. and Varfolomeev, Yu.M., *Vodosnabzh. Santekhn.*, 1974, no. 7, pp. 15–17.
13. Ovchiyan, V.N., Danil'yants, L.S., Sedrakyan, S.M., *et al.*, *Arm. Khim. Zh.*, 1986, vol. 39, no. 2, pp. 93–98.
14. Ovchiyan, V.N. and Barsegyan, M.D., *Izv. Akad. Nauk ArmSSR, Ser. Tekhn. Nauk.*, 1976, vol. 29, no. 6, pp. 58–61.
15. Eldin, A.M.S. and Wang, L.E., *Desalination*, 1996, vol. 107, no. 1, pp. 29–43.
16. Akol'zin, P.A., *Protivokorrozionnaya zashchita stali plenkoobrazovatelyami* (Corrosion Protection of Steel with Film-Forming Agents), Moscow: Metallurgiya, 1989.

Russian Journal of Applied Chemistry, Vol. 76, No. 2, 2003, pp. 226–228. Translated from Zhurnal Prikladnoi Khimii, Vol. 76, No. 2, 2003, pp. 234–236.

CATALYSIS

Nature of Catalytic Activity of Defective Calcium Hydroxyapatites

A. S. Dykman

Vserossiiskii Nauchno-issledovatel'skii Institut Neftekhimicheskikh Protsessov Joint-Stock Company, St. Petersburg, Russia

Received August 1, 2002

Abstract—The nature of the catalytic activity of defective calcium hydroxyapatites was studied. The activity of synthesized defective hydroxyapatites in vapor-phase dehydration of trimethylcarbinol, methylphenylcarbinol, α-hydroxyisobutyric acid, and in decomposition of 4,4-dimethyl-1,3-dioxane into isoprene was analyzed.

Calcium phosphates, which have been described as catalysts and supports for catalysts for hydration and dehydration, vapor-phase hydrolysis, isomerization, and alkylation [1, 2], were applied to industrial synthesis of isoprene (in the second stage of decomposition of 4,4-dimethyl-1,3-dioxane, DMD) [2–4]. We used in this process basic calcium phosphates whose X-ray pattern is typical of stoichiometric calcium hydroxyapatite $Ca_{10}(PO_4)_6(OH)_2$ (molar ratio $CaO/P_2O_5 = 3.34$), but differ from it in their composition: the CaO/P_2O_5 ratio in these compounds varies from 2.66 to 3.34. It has been shown in numerous studies [2–7] that such calcium phosphates belong to the series of defective calcium hydroxyapatites (DCHA) with composition $Ca_{10-x}H_x(PO_4)_6(OH)_{2-x}$ or $Ca_{10-x}(HPO_4)_x(PO_4)_{6-x}(OH)_{2-x}$ (where $0 \le x \le 2$).

These compounds, which are derivatives of the stoichiometric $Ca_{10}(PO_4)_6(OH)_2$ hydroxyapatite, have been given their name because of the presence of a calcium defect (calcium vacancy) in the structure. To maintain the charge balance, one proton is "incorporated" into the lattice instead of each absent calcium ion and one hydroxyde ion "is removed" [3, 6, 7].

Commercial DCHA-based catalysts developed with the author's participation (conventionally designated as KF-70, KBF, and KBF-76) were successively introduced into industrial practice and have been used at Russian synthetic-caoutchouc plants in the second stage of isoprene synthesis from isobutylene and formaldehyde.

The KF-70, KBF, and KBF-76 catalysts have aroused considerable interest of researchers. Results obtained in studying their catalytic activity in dehydration of aliphatic alcohols [8], isoamyl alcohol [9], 2-methyl butanol [10], and esters [11], and in other thermocatalytic reactions [12] have been published. Bett *et al.* [7], having generalized data on the composition and catalytic properties of DCHA, concluded that their acidity and catalytic activity result from the presence of protons in their structure. Protons in DCHA are in the form of the hydrophosphate ions, HPO_4^{2-} [2, 3, 5, 6]. As a proof of the hypothesis, data on dehydration of butanol-2 in the presence of a number of DCHA with varied degree of defectiveness have been reported [10]. According to these data, the activity of the catalysts grows with decreasing CaO/P_2O_5 ratio in a sample, i.e., with increasing amount of hydrophosphate ions in the structure of hydroxyapatites [7, 13].

However, it has been shown by means of IR spectroscopy [4] that, within the operation temperature range of DCHA-based catalysts (250–500°C), hydrophosphate ions react with one another rather rapidly (within several hours) to be converted into condensed phosphate ions $P_nO_{3n+1}^{-(n+2)}$, with the catalyst retaining its initial activity. Consequently, the acidity and catalytic activity of DCHA cannot be directly determined by the presence of HPO_4^{2-} groups [4].

It seems more correct to suggest that the acidity and catalytic activity of DCHA are determined by the presence of a film of phosphoric acid formed on the catalyst surface in the reaction of condensed phosphates with water at elevated temperature. The hydrolytic decomposition of condensed phosphates can be schematically represented by the reaction

$$(n + 1)P_nO_{3n+1(\text{solid})}^{-(n+2)} + H_2O_{(\text{vapor})} \rightarrow (n + 2)P_{n-1}O_{3n-2(\text{solid})}^{-(n+1)} + 2H_3PO_{4(\text{vapor})}.$$

1070-4272/03/7602-0226 $25.00 © 2003 MAIK "Nauka/Interperiodica"

It seems that the greater the amount of phosphoric acid in the film, the greater the amount of acid removed on treating the catalyst with water vapor.

The aim of this study was to reveal the relationship between the composition of defective calcium hydroxyapatites, the amount of phosphoric acid they evolve, and their catalytic activity in dehydration of alcohols and acids and in decomposition of DMD.

EXPERIMENTAL

As objects of study served DCHA samples with varied defectiveness. The physicochemical parameters of these compounds are listed in Table 1. According to X-ray diffraction analysis, the samples have phase composition of hydroxyapatite.

To determine the amount of phosphoric acid released by a catalyst, we put the samples in a quartz reactor, which was placed, in turn, in an electric furnace. Distilled water was delivered to the reactor through an evaporator, using a controlled-volume pump. The water vapor released from the reactor was condensed in a condenser. We determined the content of phosphoric acid in the condensate by the procedure described in [14]. The method used allows phosphorus(V) to be determined only as orthophosphate ions, and, therefore, to convert condensed phosphates into orthophosphates, we boiled the samples before measurements.

We studied the activity of DCHA as catalysts in dehydration of trimethylcarbinol, methylphenylcarbinol, and α-hydroxyisobutyric acid and in decomposition of DMD. We tested the catalysts on the installation described above. The raw material was delivered into the reactor in a mixture with water, the duration of an experiment was 2 h. The catalyzates were analyzed by gas-liquid chromatography.

The dependence of the amount of H_3PO_4 released by 1 m^2 of the DCHA surface on the CaO/P_2O_5 ratio is given in the figure. As the CaO/P_2O_5 ratio decreases, i.e., as the content of condensed phosphates increases, the amount of released phosphoric acid grows. The greatest amount of H_3PO_4 was observed for the sample with the maximum defectiveness (sample no. 1). Stoichiometric hydroxyapatite (sample no. 4) hardly releases any phosphoric acid.

Data on the catalytic activity of DCHA samples in dehydration of trimethylcarbinol, methylphenylcarbinol, and α-hydroxyisobutyric acid (conversion of α-hydroxyisobutyric acid into methacrylic acid), and in decomposition of DMD are listed in Table 2.

Table 1. Physicochemical properties of synthesized DCHA samples with varied degree of defectiveness

Sample no.	CaO/P_2O_5, mol/mol	S_{sp}, $m^2\ g^{-1}$	Bulk density, $g\ cm^{-3}$
1	2.72	86	0.62
2	3.04	85	0.64
3	3.26	71	0.68
4	3.34	79	0.69

Table 2. Conversion of trimethylcarbinol, methylphenylcarbinol, α-hydroxy isobutyric acid, and 4,4-dimethyl-1,3-dioxane at various CaO/P_2O_5 ratios in DCHA (weight ratios: H_2O : trimethylcarbinol = 1 : 1, H_2O : methylphenylcarbinol = 1 : 1, H_2O : α-hydroxyisobutyric acid = 4 : 1, H_2O : DMD = 2 : 1)

T, °C	CaO/P_2O_5, mol/mol	Conversion (%) at indicated volumetric rate of raw material supply, h^{-1}				
		1	2	4	6	8
Trimethylcarbinol						
300	2.72	–	99.7	97.0	91.2	63.0
	3.04	–	93.0	74.0	68.5	44.6
	3.26	–	30.9	19.8	16.4	9.7
	3.34	–	7.6	9.8	4.4	1.1
Methylphenylcarbinol						
250	2.72	99.5	–	–	–	–
	3.04	60.3	–	–	–	–
	3.26	21.6	–	–	–	–
	3.34	6.3	–	–	–	–
α-Hydroxyisobutyric acid						
280	2.72	–	97.7	–	–	–
	3.04	–	54.9	–	–	–
	3.26	–	15.3	–	–	–
4,4-Dimethyl-1,3-dioxane						
320	2.72	98.1	78.9	52.2	–	32.0
	3.04	53.3	32.1	15.2	–	10.4
	3.26	30.9	23.2	8.7	–	3.9
	3.34	28.3	22.5	8.5	–	3.3

It was found that defective calcium hydroxyapatite with the highest content of condensed phosphates (sample no. 1) is the most active in the reactions under study and a sample of stoichiometric calcium hydroxyapatite has the lowest activity. Thus, the activity of DCHA in dehydration of alcohols and acids and in

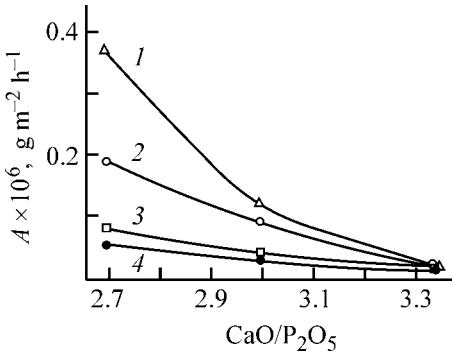

Amount of phosphoric acid released by the DCHA surface, A vs. CaO/P_2O_5 molar ratio. Temperature 300°C. Water supply (vol/vol of catalyst per 1 h): (*1*) 16, (*2*) 8, (*3*) 4, and (*4*) 2.

decomposition of DMD grows with increasing amount of released phosphoric acid, which seems to be present in the form of a film on the catalyst surface and is removed when the catalyst is treated with water vapor.

To elucidate the part played by DCHA in the catalytic reactions under study, we carried out experiments on dehydration of trimethylcarbinol and decomposition of DMD on quartz, to which phosphoric acid was delivered during the experiment. In this case, we hardly observed any dehydration of trimethylcarbinol or decomposition of DMD. This suggests that phosphoric acid released by DCHA is present on its surface as a relatively firmly adhering film, which determines the catalytic activity of calcium phosphates belonging to the hydroxyapatite structure.

CONCLUSIONS

(1) A set of calcium phosphate catalysts with various molar ratios CaO/P_2O_5 has been synthesized. These catalysts are defective calcium hydroxyapatites with composition $Ca_{10-x}(HPO_4)_x(PO_4)_{6-x}(OH)_{2-x}$ ($0 \le x \le 2$).

(2) Hydrophosphate ions HPO_4^{2-} cannot be directly responsible for the catalytic activity of defective calcium hydroxyapatites, since they are converted to condensed phosphate ions $P_nO_{3n+1}^{-(n+2)}$ at the working temperatures of the catalyst (250–500°C).

(3) The catalytic activity of defective calcium hydroxyapatites is determined by the release of phosphoric acid formed in the reaction of condensed phosphates with water. The acid is presumably present on the catalyst surface in the form of a film.

(4) The catalytic activity of calcium hydroxyapatites in dehydration of trimethylcarbinol, methylphenylcarbinol, and α-hydroxyisobutyric acid and decomposition of 4,4-dimethyl-1,3-dioxane grows with increasing amount of phosphoric acid released by the catalysts.

REFERENCES

1. Freidlin, L.Kh. and Sharf, V.Z., *Kinet. Kataliz*, 1960, vol. 1, no. 2, pp. 247–256.
2. Dykman, A.S., Batalin, O.E., Bitepazh, Yu.A., and Osmolovskii, G. M., Abstracts of Papers, *III Vsesoyuznoye soveshchanie po fosfatam* (III All-Union Conf. on Phosphates), Riga, 1971, pp. 182–183.
3. Dykman, A.S., Batalin, O.E., Vasil'eva, T.M., *et al.*, Abstracts of Papers, *IV Vsesoyuznaya konferentsiya "Fiziko-khimicheskoe issledovanie fosfatov"* (IV All-Union Conf. "Physicochemical Study of Phosphates"), Minsk, 1976, pp. 105–106.
4. Dykman, A.S., Batalin, O.E., Baklanova, G.F., *et al.*, Abstracts of Papers, *IV Vsesoyuznaya konferentiya "Fiziko-khimicheskoe issledovanie fosfatov"* (IV All-Union Conf. "Physicochemical Study of Phosphates"), Minsk, 1976, pp. 104–105.
5. Posner, A.S. and Petroff, A., *J. Res. Nat. Bureau Stand.*, 1957, vol. 58, pp. 2761–2771.
6. Berry, E.E., *J. Inorg. Nucl. Chem.*, 1967, vol. 29, pp. 317–326.
7. Bett, J.A.S., Christner, L.G., and Hall, W.K., *J. Am. Chem. Soc.*, 1967, vol. 89, pp. 5535–5541.
8. Ogorodnikov, S.K., Katsnelson, M.G., Levin, Yu.M., *et al., Osn. Org. Sintez Neftekhimiya* (Yaroslavl'), 1989, no. 25, pp. 32–34.
9. Liakumovich, A.K., Guliyants, S.T., and Balandina, N.A., *Prom–st'. Sint. kauchuka, shin i rezinotekhnicheskikh izdelii*, NTRS, Moscow, 1989, no. 2, pp. 3–5.
10. Mazaeva, V.A., Slivinskii, E.V., Bol'shakov, D.A., and Loktev, S.M., *Neftekhimiya*, 1990, vol. 30, no. 3, pp. 384–388.
11. Smagin, V.M., Popov, S.V., Kamneva, S.A., and Strel'chik, B.S., *Kinetika-4: Vsesoyuznaya konferentsiya po kinetike geterogenno-kataliticheskikh reaktsii: Materialy konf.* (Proc. Kinetika-4: All-Union Conf. on Kinetics of Heterogeneous Catalytic Reactions), Yaroslavl, 1988, Moscow, 1988, pp. 169–170.
12. Golovko, L.V. and Kashina, S.V., *Proizv. Ispol'z. Elastomerov*, 1990, no. 4, pp. 9–11.
13. Bett, J.A.S. and Hall, W.K., *J. Catal.*, 1968, vol. 10, pp. 105–112.
14. Shafran, I.G., Pavlova, M.V., and Titova, S.A., *Khimicheskie reaktivy i preparaty: Trudy IREA* (Chemical Reagents and Preparations: Proc. IREA), Issue 28, Moscow, 1966.

Russian Journal of Applied Chemistry, Vol. 76, No. 2, 2003, pp. 229–233. Translated from Zhurnal Prikladnoi Khimii, Vol. 76, No. 2, 2003, pp. 237–241.

CATALYSIS

Changes in the Composition, Structure, and Activity of Catalysts in Hydrogenation of Diene Hydrocarbons of the C_5–C_9 Fraction of Pyrolysis Naphtha

A. A. Lamberov, R. G. Romanova, E. Yu. Sitnikova, Kh. Kh. Gil'manov, and S. V. Trifonov

Kazan State Technological University, Kazan, Tatarstan, Russia

Nizhnekamskneftekhim Open Joint-Stock Company, Nizhnekamsk, Tatarstan, Russia

Received June, 13, 2002

Abstract—A comparative study was performed of changes in the composition, structure, and catalytic activity of catalysts in selective hydrogenation of C_5–C_9 fraction of pyrolysis naphtha. The main reasons for catalyst deactivation in the course of industrial exploitation were considered.

At present, the stringent requirements are imposed on the quality and purity of pyrolysis naphtha fraction, in particular, on the content of diene hydrocarbon impurities. One of the most widespread methods for removing such impurities is catalytic hydrogenation [1]. Catalysts containing palladium supported by aluminum oxide are the most efficient in hydrogenation of diene hydrocarbons [2–7]. In spite of successful exploitation of these catalysts in hydrogenation of diene, the decrease in the catalyst activity is a serious problem. Unfortunately, the reasons for catalyst deactivation have not been analyzed previously, and here we try to fill this gap.

It is known [8] that deactivation can occur because of catalyst poisoning with toxic inorganic substances. Another reason is blocking of the active centers of the catalyst surface through deposition of coke.

In this work, we studied deactivation of catalysts for selective hydrogenation of dienes of the C_5–C_9 fraction.

EXPERIMENTAL

Samples of a deactivated catalyst were taken from various levels of a reactor, as shown in the scheme (Fig. 1).

Low-temperature nitrogen adsorption, IR spectroscopy, thermogravimetry, photocolorimetry, X-ray fluorescence analysis, emission spectroscopy, and chemical analysis were used to study the composition, structure, and surface characteristics of the catalyst.

The specific surface area, porosimetric volume, and pore volume distribution were measured by low-temperature nitrogen adsorption on an ASAP-2400 Micromeritics device. To obtain adsorption-desorption isotherms at 77 K, 0.8–1.0 g of the finely crushed catalyst was placed in the analyzer ampule, which was heated to 523 K, evacuated to 0.1 mm Hg for 4 h, and then filled with nitrogen and weighed. Degassing was performed to 0.03 mm Hg. In calculations, $\rho(N_2)$ was taken to be 0.808 g cm^{-3}, and the crosssection area of the nitrogen molecule S, 0.1620 nm^2. The pore volume and size distribution of pores were measured with relative error of ±13%, and the specific surface area, with error of ±3%. The curves of pore volume distribution with respect to pore diameter were calculated in terms of the cylindrical pore model [9].

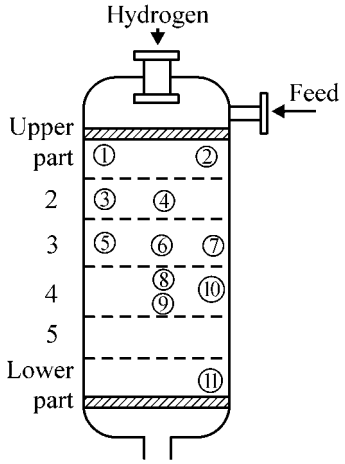

Fig. 1. Scheme of the reactor and points of catalyst sampling (samples nos. 1–11).

1070-4272/03/7602-0229 $25.00 © 2003 MAIK "Nauka/Interperiodica"

Table 1. Activity of fresh and spent catalyst for hydrogenation of pyrolysis naphtha (PN) (characteristics of the initial PN: DN = 27.5 g of I_2 per 100 g, BN = 83.8 g Br_2 per 100 g)

Testing conditions			Fresh sample		Sample no. 1		Sample no. 11	
V, h^{-1}	H_2/CG	T_{rawmat},* K	DN	BN	DN	BN	DN	BN
2	300	303	0	12.0	0	27.8	0.3	54.3
2	300	316	0	12.2	0	31.0	0.1	46.1
2	300	323	0	12.2	0	30.1	0	43.7
2	300	333	0	18.3	0	29.5	0	42.6
8	100	310–311	0	24.0	0	49.0	0.9	55.4

* Temperature of the feed at the reactor inlet.

The IR spectra were measured at the temperature of adsorption on a Shimadzu 8300 Fourier spectrometer with resolution of 4 cm^{-1} and the number of scans equal to 50. Carbon monoxide was used as a probe for monitoring the state of the palladium surface [10, 11].

The content of Pd and Fe was monitored by X-ray fluorescence and photocolorimetric analyses. The X-ray fluorescence analysis was performed on a VRA-20 analyzer by the method of additives. The catalyst was crushed to 0.2-mm powder, and 0.1-g sample was added to 3 g of H_3BO_3, the mixture was thoroughly mixed, and pellets 39 mm in diameter were compacted. An analytical signal from the pellet was measured and compared with signals of two analogous pellets in which the known portions of the analyzed element were additionally introduced.

The content of palladium in the catalyst was monitored photocolorimetrically by absorption of a green palladium complex with Sn(II) chloride after recovery of the metal from the calcined and finely divided catalyst sample with a boiling mixture of hydrochloric, nitric, and hydrofluoric acids.

The Fe content in the catalyst was monitored photocolorimetrically by absorption of the Fe(III) complex with sulfosalicylic acid in aqueous ammonia.

The macro- and microelemental composition of catalysts was monitored by emission spectrum analysis on a DFS-458 spectrometer and an MF-2 microphotometer, using an external reference (active Al_2O_3 with the known content of elements).

Calorimetric studies were performed on a DSK-111 Setaram calorimeter.

The catalytic activity was tested in a reactor with working volume of the catalyst of 6–10 cm^3 at a working pressure of 46 atm and temperature of 303–353 K, feed space velocity of 2–4 h^{-1}, and hydrogen to feed ratio from 100 : 1 to 300 : 1. Preliminarily, samples were reduced in the reactor. A 0.25–1.00-mm fraction of the catalyst was taken.

The diene number (DN) was determined by the reaction of unsaturated compounds, containing conjugated double bonds, with maleic anhydride in boiling toluene in the presence of iodine. The bromine number (BN) was found as the amount of bromine reacting with an aliquot portion of the feed. BN characterizes the content of components reacting with bromine only and determines the olefinic unsaturation of the compounds.

To monitor the changes in the catalyst activity in the course of exploitation, we studied the activity of the fresh catalyst and catalyst samples after a year of their operation in hydrogenation of the C_5–C_9 fraction (nos. 1 and 11; Table 1).

As seen from Table 1, under the same conditions, the BN of the catalyzate obtained with catalyst samples nos. 1 and 11 is higher than that with the fresh catalyst, which indicates a substantial decrease in the catalyst activity in the course of exploitation. In addition, the catalyst is deactivated to a greater extent in the lower part of the reactor than in the upper part, as indicated by an increase in BN and appearance of diene compounds in the catalyzate for sample no. 11 at a temperature lower than 316 K.

To reveal the reasons for deactivation, we studied evolution of the composition and surface and structural characteristics of the catalyst. The pore structure of the catalyst was monitored in the course of its deactivation by low-temperature nitrogen adsorption. The specific surface area, pore volume, pore diameter distribution, and peaks in the distribution and their intensities are listed in Table 2. The absolute values of the pore volume within various intervals of pore diameters and contribution of these fractions to the total pore volume were also calculated. As seen from Table 2, the content of fine pores (about 35 Å) de-

Table 2. Changes in characteristics of the catalyst pore structure in the course of its exploitation

Sample	S_{sp}, $m^2\ g^{-1}$	V_{pore}, $cm^3\ g^{-1}$	Average pore diameter, Å	Specific volume V ($cm^3\ g^{-1}$) of pores with indicated diameter d (Å) and its fraction relative to the total pore volume ω, %						Maxima of pore distribution d_{max} (Å) and their intensity $I \times 10^5$, cm^3 (Å g)$^{-1}$							
				<50		50–100		>100		1		2		3		4*	
				V	ω	V	ω	V	ω	d_{max}	I	d_{max}	I	d_{max}	I	d_{max}	I
Fresh	66.0	0.3823	231.0	0.0122	3.2	0.0228	6.0	0.3474	90.9	35	130	125	123	165	120	250	50
no. 1	64.1	0.3893	242.0	0.0105	2.7	0.0205	5.3	0.3583	92.0	35	115	125	125	165	123	240	55
no. 2	64.1	0.3974	247.0	0.0088	2.2	0.0188	4.7	0.3698	93.1	34	95	135	134	164	135	250	58
no. 5	64.0	0.3972	246.0	0.0101	2.5	0.0204	5.1	0.3667	92.3	35	109	125	126	162	126	250	55
no. 6	63.1	0.3844	244.0	0.0096	2.5	0.0194	5.0	0.3554	92.5	34	103	130	126	168	126	250	55
no. 11	62.0	0.3637	234.0	0.0088	2.4	0.0168	4.6	0.3380	92.9	34	92	–		165	126	250	55

* Maximum as shoulder.

creases in the course of catalyst exploitation by approximately 10–20% throughout the reactor volume, which insignificantly decreases the specific surface area of the catalyst.

The distribution of pore volumes with respect to diameter for the fresh catalyst and that after 1-year operation, taken from different levels of the reactor (samples nos. 1 and 11), is shown in Fig. 2. Two maxima peaks are seen: narrow at 35 Å and broad at 125–165 Å. The major fraction of the total pore volume belongs to pores with diameter greater than 100 Å (90.0–92.9%).

The greatest changes in the catalyst pore structure occur in the lower part of the reactor (sample no. 11): the fraction of small pores decreases, the peak of large pores shifts from 125–145 to 160 Å (Fig. 2), which corresponds to a decrease in the total pore volume (Table 2). Thus, in the course of the catalyst operation, the pore structure changes, with these changes being the most pronounced for the catalyst in the lower part of the reactor.

To reveal the probable deactivating effect of inorganic substances sorbed on the catalyst surface, we determined the elemental composition of the catalyst samples. It should be noted that the catalyst samples taken from the upper (no. 1) and lower (no. 11) parts of the reactor substantially differ in color. Samples taken from the upper level had reddish color due to substantial amounts of dusty particles, probably, iron(III) oxide. These particles were readily removed by expulsion or by washing with 0.1 M HCl. At the lower levels of the reactor, a part of the catalyst had a dark color. In deactivated samples, the content of the active component, Pd, was determined photocolorimetrically (after chemical dissolution of the catalyst) and by X-ray fluorescence analysis (without preliminary preparation in the form of granules). It was found that the Pd content in the spent catalyst varies insignificantly

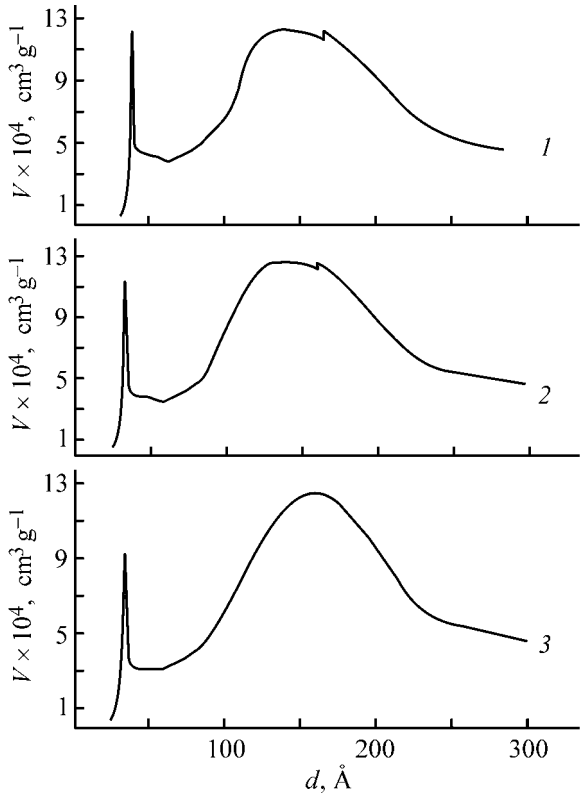

Fig. 2. Distribution of specific pore volume V with respect to diameter d for samples: (*1*) fresh, (*2*) spent no. 1, and (*3*) spent no. 11.

Table 3. Elemental composition of hydrogenation catalyst

Element	Content (wt %) in a sample			
	standard	fresh	no. 1	no. 11
Al	>30	>30	>30	>30
Be	0.00110	0.00018	0.00021	0.00016
Ca	1.40000	0.00550	0.02700	0.02700
Cr	0.00380	0.00030	0.00310	0.00016
Cu	0.02900	0.00010	0.00090	0.00050
Mg	1.10000	0.01500	0.08400	0.01700
Mn	0.01400	0.00080	0.00870	0.00120
Na	0.03000	0.18000	0.23000	0.18000
Ni	0.00370	0.00080	0.00170	0.00120
Pb	0.00140	0.00060	0.00160	0.00070
Si	0.16000	0.04600	0.07300	0.07300

(within the limits of the experimental error) as compared to samples of the fresh catalyst. Thus, the decrease in the catalyst activity is not associated with Pd loss.

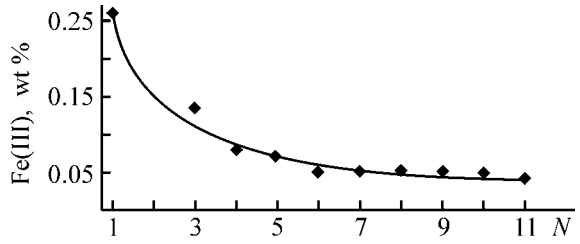

Fig. 3. Distribution of the iron(III) content in the catalyst throughout the reactor. (*N*) number of a sampling point.

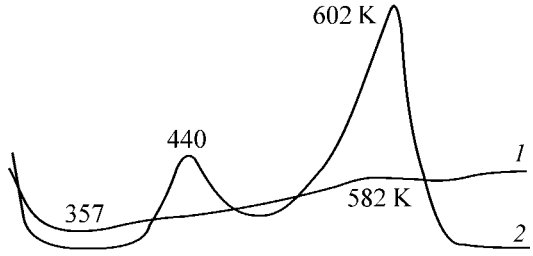

Fig. 4. Calorimetric analysis of spent catalyst samples (*1*) no. 1 and (*2*) no. 11.

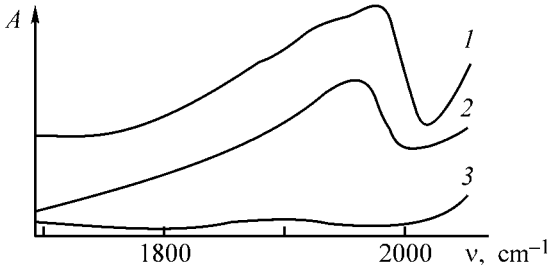

Fig. 5. IR spectra of CO adsorbed on metal Pd particles of (*1*) fresh catalyst, (*2*) spent sample no. 1, and (*3*) spent sample no. 11. (*A*) Adsorption and (ν) wave number.

The Fe(III) content in the catalyst was found by X-ray fluorescence and photocolorimetric analyses. The data obtained show that in the spent catalyst the Fe(III) content increases as compared to the fresh sample (0.023 wt % Fe). The distribution of Fe(III) in the catalyst throughout the reactor is shown in Fig. 3. As seen, a higher Fe(III) content is observed in the upper layers of the catalyst, with the content of Fe(III) in sample no. 1 exceeding by a factor of 6–10 that in sample no. 11). Thus, in the course of exploitation, Fe(III) oxide accumulates in the upper layers of the catalyst, where it forms a dust sediment on the granule surface.

The microelement composition of the catalyst samples determined by emission spectral analysis is shown in Table 3. Preliminarily, samples were cleaned to remove the dust. Granules of reddish (sample no. 1) and dark (sample no. 11) color were taken.

As seen, chromium, copper, magnesium, manganese, and lead compounds are accumulated in the upper part of the reactor. The content of chromium, copper, and manganese in the upper part of the reactor increases as compared to the fresh catalyst sample by approximately a factor of 10, and the content of magnesium and lead, by factors of 6 and 3, respectively. In the lower catalyst layers, the content of the above elements is less than that in the upper catalyst layers. Thus, in the course of the catalyst exploitation, catalytic poisons delivered with the feed are accumulated on the catalyst surface. However, the absolute amount of the above metals is small, and we cannot suggest that their accumulation is the main reason for the catalyst deactivation.

To reveal the nature of agents deactivating the catalyst surface, we performed a DSC study of the fresh catalyst and spent sample nos. 1 and 11 (Fig. 4). All the samples show an endothermic effect at 357 K, which is accompanied by weight loss within the 313–393 K range. This effect is caused by water desorption from the catalyst surface. In addition, two exothermic effects are observed at 423–540 and 582–602 K for samples of spent catalyst. Since Al_2O_3 undergoes no phase transitions within these temperature intervals [12], we can suggest that these effects correspond to combustion of the organic compounds (various polymers, coke) formed on the catalyst surface. The intensities of the effects for sample nos. 1 and 11 relate as about 1 : 4, which indicates that sample no. 11 contains a greater amount of coke, which obviously blocks the catalyst activity.

The IR data also indicate blocking of the catalyst active centers in deactivation. The IR spectrum of CO adsorbed on Pd metal particles (Fig. 5) shows that

the catalyst surface changes in deactivation. The spectrum of the fresh sample is characterized by intense bands at 1927 and 1978–2000 cm^{-1}, assigned to ν(CO) of Pd–CO and Pd–C(O)–Pd groups [13]. The absorption of sample no.1 in this spectral region is similar. By contrast, sample no. 11 shows virtually no absorption in the 1978–2000 cm^{-1} range, and the intensity of the band at 1927 cm^{-1} is substantially lower. These results show that the number of Pd atoms accessible to chemisorption of CO in the catalyst that has operated in the lower part of the reactor decreases. The decrease in the catalyst activity in the course of hydrogenation of pyrolysis naphtha is probably due to a decrease in the number of the reactive Pd particles on the catalyst surface, resulting from their blocking by the organic deposits.

CONCLUSION

Deactivation of the catalyst in the upper and lower parts of the reactor is caused by different factors: in the upper parts, it is due to accumulation of catalytic poisons, namely, chromium, copper, manganese, magnesium, and lead compounds delivered to the reactor with the feed; in the lower parts, it is due to blocking of the active centers by organic deposits. Deactivation substantially affects the catalyst pore structure: the fine pore constituent and the number of Pd particles accessible to molecules of the feed decrease.

REFERENCES

1. Khrenov, E.G., Perminova, E.A., Fal'kov, I.G., *et al.*, *Katalizatory i protsessy selektivnogo gidrirovaniya v neftekhimicheskoi i khimicheskoi promyshlennosti* (Catalysts and Processes of Selective Hydrogenation in Petrochemical and Chemical Industry), Moscow: TsNIITEneftekhim, 1993.
2. Navalikhina, M.D. and Krylov O.G., *Usp. Khim.*, 1998, vol. 67, no. 7, pp. 656–688.
3. Berenblyum, A.S., Mund, S.L., Karel'skii, V.V., *et al.*, *Kinet. Katal.*, 1986, vol. 27, no. 1, pp. 205–209.
4. Turkova, T.V., Kipnis, M.A., Motova, O.N., and Shashkov, A.Yu., *Neftepererab. Neftekhim.*, 1994, no. 5, pp. 15–17.
5. Lakhman, L.I., Tumanova, V.A., Karel'skii, V.V., *et al.*, *Neftepererab. Neftekhim.*, 1978, no. 10, pp. 56–57.
6. Cherkashin, G.M., Shuikina, L.P., Parenago, O.P., and Frolov, V.M., *Kinet. Katal.*, 1985, vol. 26, no. 5, pp. 1110–1113.
7. Tomas, Ch.L., *Catalytic Processes and Proven Catalysts*, New York: Academic, 1970.
8. Hughes, R., *Deactivation of Catalysts*, London: Academic, 1984.
9. Gregg, S.J. and Sing, K.S.W., *Adsorption, Surface Area and Porosity*, London: Academic, 1982.
10. Paukshtis, E.A., *IK-spektroskopiya v geterogennom kislotno-osnovnom katalize* (IR Spectroscopy in Heterogeneous Acid–Base Catalysis), Novosibirsk: Nauka, 1992.
11. Lamberov, A.A., Romanova, R.G., and Liakumovich, A.G., *Kinet. Katal.*, 1999, vol. 40, no. 3, pp. 472–479.
12. Fedorov, B.M., Danyushevskii, V.Ya., Balashov, V.L., and Berenblyum, A.S., *Kinet. Katal.*, 1991, vol. 32, no. 2, pp. 447–454.
13. Davydov, A.A., *IK-spektroskopiya v khimii poverkhnosti okislov* (IR Spectroscopy in Chemistry of Surface Oxides), Novosibirsk: Nauka, 1984.

Russian Journal of Applied Chemistry, Vol. 76, No. 2, 2003, pp. 234–237. Translated from Zhurnal Prikladnoi Khimii, Vol. 76, No. 2, 2003, pp. 242–245.

CATALYSIS

Hydrogenation and Skeleton Rearrangements of α-Pinene on Heterogeneous Catalysts

Yu. P. Bazhenov, L. Z. Kas'yanova, A. I. Bokin, B. I. Kutepov, A. N. Khazipova, E. A. Travkin, N. A. Shchadneva, R. I. Khusnutdinov, and U. M. Dzhemilev

Kauchuk Private Company, Sterlitamak, Bashkortostan, Russia

Institute of Petrochemistry and Catalysis of the Republic of Bashkortostan, Ufa Scientific Center, Russian Academy of Sciences, Ufa, Bashkortostan, Russia

Received May 14, 2002

Abstract—Hydrogenation and isomerization of α-pinene on heterogeneous catalysts were studied, and conditions were found for hydrogenation of pinene to *cis*-pinane on nickel catalysts and for its dehydrogenation to *p*-cymene on decationized zeolite Y.

α-Pinene, which is a bicyclic monoterpenoid, is an important product of wood chemical industry. α-Pinene widely occurs in nature; it is present in oils obtained from most of coniferous tree species and is the major component of turpentine. Due to the presence of a double bond and a strained four-membered ring, α-pinene readily undergoes various transformations, primarily hydrogenation and skeleton isomerization [1–3].

α-Pinene is widely used in industry, in particular, in production of synthetic camphor, camphene, myrcene, fragrances (linalool, citronellol, geraniol, pinocarveol, myrtenol, etc.), and paint-and-varnish materials [1–3].

The α-pinene hydrogenation product, pinane, is also an important chemical: its autooxidation yields a stable hydroperoxide used as initiator of low-temperature copolymerization of butadiene with styrene [4].

Pinane required for preparing the hydroperoxide is usually synthesized by hydrogenation of α-pinene with molecular hydrogen on metal-containing catalysts [5–10]. In particular, it has been suggested [5, 6] to use supported Ru- and Pd-containing catalysts for α-pinene hydrogenation. Hydrogenation of α-pinene can also be performed on Ni-containing catalysts, but under more severe conditions: $p_{H_2} \geq 1.0$ MPa and reaction time no less than 14–20 h [7–10].

Our goal was to find catalysts effecting hydrogenation of α-pinene to pinane under mild conditions ($p_{H_2} \leq 0.6$ MPa, $T \leq 150$°C). The major attention was given to hydrogenation of α-pinene on Pd- and Ni-containing catalysts for hydrogenation of other organic substances, commercially produced in Russia.

EXPERIMENTAL

Experiments on α-pinene transformations were performed in a 100-ml isothermal pressure reactor containing a finely dispersed (0.04–0.1 mm) catalyst; the ideal mixing mode was ensured by vigorous shaking. The amount of loaded α-pinene was 50 ml, and the amount of the catalytic system relative to substrate, c_c = 1–10 wt %. The temperature in the reactor, T_r, was varied from 20 to 150°C, and the hydrogen pressure, p_{H_2}, from 0.2 to 1.0 MPa. Also, hydrogenation of α-pinene was studied in a tubular bubbling reactor charged with a pelletized catalyst (V_c = 100 ml); the process was performed in a flow of hydrogen, in the batch mode with respect to α-pinene.

The IR spectra were recorded on a UR-20 spectrometer; samples were prepared as KBr pellets, mulls in mineral oil, or neat liquids. The ^{1}H and ^{13}C NMR spectra were recorded on a Jeol FXQ spectrometer (90 and 22.5 MHz, respectively) in $CDCl_3$ solutions; the chemical shifts (δ, ppm) are given relative to TMS. The mass spectra (70 eV) were taken on a Finnigan MAT-112S gas chromatograph–mass spectrometer. A chromatographic analysis was performed with a Chrom-5 chromatograph, column length 1.2 m, stationary phase 5% SE-30 on Chromaton N-AW-HMDS, carrier gas helium.

The reaction was performed with sulfate α-pinene purified by distillation (99.0 wt % purity). The reac-

1070-4272/03/7602-0234 $25.00 © 2003 MAIK "Nauka/Interperiodica"

tion products (pinane, dipentene, terpinolene, camphene, *p*-cymene) were isolated by fractional distillation in a vacuum (purity no less than 98.0 wt %, according to GLC) and identified by IR, ^{1}H NMR, and ^{13}C NMR spectroscopy and by refractive indices, using reference samples and published data [1–11]. The *cis* configuration of pinane prepared on the nickel catalyst follows from the signal pattern given by the gem-dimethyl (C^9, C^{10}; δ 1.02–1.04 ppm) and C^8 methyl groups (δ 1.18 ppm) [1–11].

***cis*-Pinane (2,6,6-tetramethylbicyclo[3.1.1]heptane)**. Yield about 100%; bp 166–167°C, n_D^{20} 1.4624. IR spectrum (thin liquid film), ν, cm^{-1}: 750, 790, 850, 950, 995, 1005, 1025, 1045, 1100, 1120, 1150, 1220, 1250, 1275, 1320, 1340, 1360, 1370, 1380, 1452, 1458, 1465, 2895. ^{1}H NMR spectrum ($CDCl_3$), δ, ppm: 1.02 d (3H, $C^{10}H_3$), 1.04 s (3H, C^9H_3), 1.18 s (3H, C^8H_3), 1.26–1.36 m (3H, C^1H, C^2H, C^5H), 1.66–2.44 m (6H, C^3H_2, C^4H_2, C^6H_2). ^{13}C NMR spectrum ($CDCl_3$), δ_C, ppm: 23.06 (C^9), 23.39 (C^{10}), 24.17 (C^8), 26.83 (C^4), 28.52 (C^3), 34.25 (C^6), 36.25 (C^2), 39.06 (C^7), 41.72 (C^5), 48.49 (C^1). Mass spectrum, *m*/*z* (I_{rel}, %): 41 (100), 35 (86.2), 95 (74.4), 39 (59.2), 27 (58.7), 82 (57.2), 83 (53.9), 67 (49.3), 69 (49.3), 81 (45).

Found, %: C 86.86; H 13.11.
$C_{10}H_{18}$.
Calculated, %: C 86.88; H 13.12.

***p*-Cymene (1-methyl-4-isopropylbenzene)**. Yield about 80%, bp 177–177.57°C, n_D^{20} 1.4624. IR spectrum (thin liquid film), ν, cm^{-1}: 690, 767, 860, 1040, 1095, 1170, 1192, 1520, 1618, 1690, 1820, 2860, 2915, 3010. ^{1}H NMR spectrum ($CDCl_3$), δ, ppm: 1.02 d (3H, $C^{10}H_3$), 1.17 s (3H, C^8H_3), 1.25 s (3H, C^9H_3), 2.26 s (3H, C^{10}, CH_3), 2.66–2.98 m (1H, C^7H, CH), 7.06 s (4H, C^2H, C^3H, C^5H, C^6H, arom.). ^{13}C NMR spectrum ($CDCl_3$), δ, ppm: 20.98 (C^{10}), 24.17 (C^8, C^9), 33.79 (C^7), 126.26 (C^3, C^5), 135.04 (C^1), 145.84 (C^4). Mass spectrum, *m*/*z* (I_{rel}, %): 119 (100), 134 (23.7), 91 (16.1), 39 (10.1), 120 (9.7), 41 (7.6), 27 (6.6), 77 (6.6), 17 (6.6), 65 (6.2).

Found, %: C 89.45; H 10.52.
$C_{10}H_{14}$.
Calculated, %: C 89.49; H 10.51.

Preliminary experiments showed that α-pinene undergoes no thermal transformations under the conditions examined ($T \le 160$°C, nitrogen pressure $p \le 0.8$ MPa). In the presence of γ-Al_2O_3, SiO_2 (kieselguhr or KSM synthetic silica gel), or Sibunit [12], used as supports for the tested catalysts, the maximal conversion of α-pinene under the above conditions did not exceed 3–5 wt %, with the major transformation product being the isomer of α-pinene, dipentene. Similar results were obtained with hydrogen taken instead of nitrogen. Thus, the concentration of catalytically active centers on the surface of these supports is low.

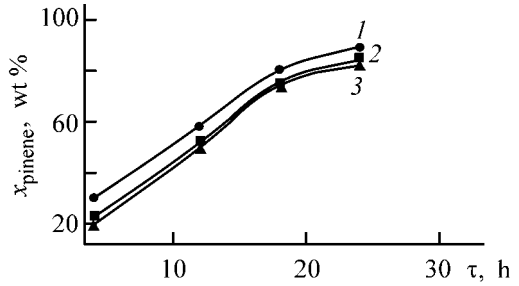

Fig. 1. Variation with time τ of the conversion of α-pinene, x_{pinene}, in its hydrogenation on palladium catalysts (150°C, 2 h, p_{H_2} = 0.6 MPa, c_c = 10 wt %): (*1*) 2 wt % Pd/Sibunit, (*2*) 2 wt % Pd/γ-Al_2O_3, and (*3*) 0.5 wt % Pd/γ-Al_2O_3.

However, α-pinene showed an unusual behavior on decationized zeolites of various structural types (mordenite, Y) whose surface contains Brønsted (B^-) acid centers with different strengths [13].

If the reaction is performed on mordenite in the H form under N_2, the conversion x_{pinene} (wt %) of α-pinene at 150°C, pressure of 0.3 MPa, and c_c = 10 wt % reaches 75% in 2 h. The reaction products contain dipentene, terpinolene, and camphene (1 : 1 : 0.1):

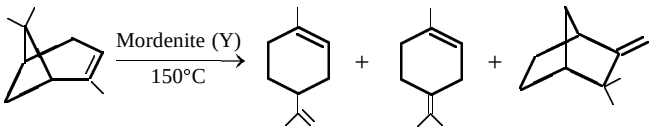

α-Pinene Dipentene Terpinolene Camphene

On ~50% decationized zeolite Y, whose surface contains stronger B^- centers, α-pinene undergoes not only isomerization, but also dehydrogenation yielding *p*-cymene:

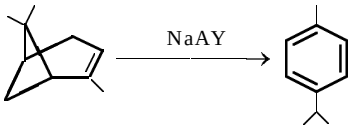

α-Pinene *p*-Cymene

This reaction may be of considerable practical interest owing to a high (~80% based on the initial α-pinene) yield of *p*-cymene.

When α-pinene is heated in an H_2 atmosphere in the presence of Pd- and Ni-containing catalysts supported by α-Al_2O_3, SiO_2, or Sibunit, the major reaction pathway is hydrogenation to pinane:

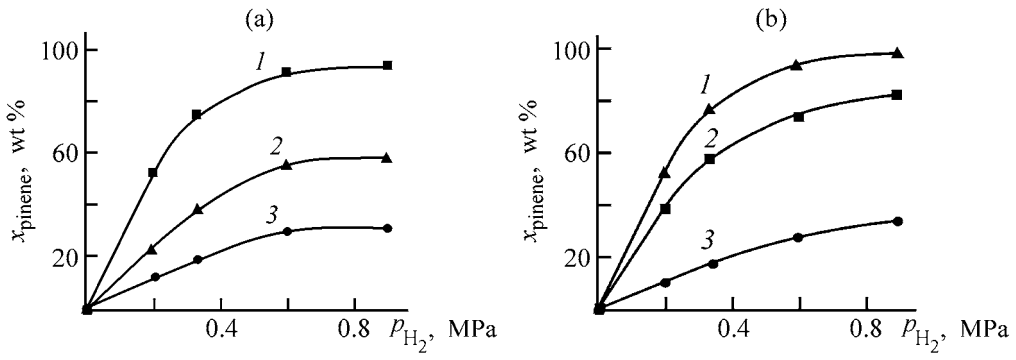

Fig. 2. Conversion of α-pinene, x_{pinene}, on GM-3 catalyst vs. hydrogen pressure p_{H_2}. Reaction time 6 h. c_c, %: (a) 1.5 and (b) 3. *T*, °C: (a) (*1*) 150, (*2*) 100, and (*3*) 75; (b) (*1*) 130, (*2*) 100, and (*3*) 50.

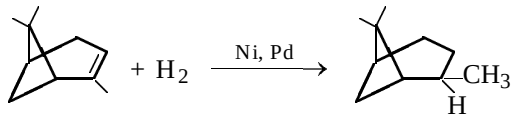

α-Pinene Pinane

Figure 1 shows variation of the α-pinene conversion, x_{pinene}, with time on various Pd-containing catalysts. The highest conversion is observed on 2 wt % Pd/Sibunit (IK-53 brand). The highest activity of this catalyst is probably due to the largest surface area of the metal. At the same time, all the catalysts exhibit similar selectivities: The yield of pinane based on the converted α-pinene is 92–95% with all the catalysts.

Usually, hydrogenation catalysts are subjected before use to reductive hydrogen treatment. It is known [14] that too high treatment temperatures may affect the ratio of the hydride and atomic hydrogen species in the catalyst and hence the catalytic activity. However, when the hydrogen treatment temperature was raised from 100 to 300°C, the Pd-containing catalysts we studied did not show such an effect.

Table 1. Hydrogenation of α-pinene on the commercial Ni/kieselguhr catalyst at p_{H_2} = 0.6 MPa

c_c, wt %	T_r, °C	τ, h	x_{pinene},* wt %
2.5	130	4	78.0
2.5	150	4	100.0
5.0	100	4	45.0
5.0	130	4	100.0
5.0	150	2	100.0

* (x_{pinene}) Conversion of α-pinene (selectivity with respect to pinane is close to 100%).

In production of isoprene, admixtures of acetylenic hydrocarbons are hydrogenated on nickel silicate catalysts which are prepared by precipitation of basic nickel(II) carbonate on kieselguhr, followed by filtration, washing, drying, pelletizing, and reductive decomposition [15]. The catalysts contain 25 to 50 wt % nickel.

Experiments on hydrogenation of α-pinene on the catalyst produced using this procedure by the Kauchuk Private Company showed that the complete conversion of α-pinene with quantitative yield of pinane is attained in 2 h at 150°C and p_{H_2} = 0.6 MPa with the 0.04–0.1-mm fraction of the catalyst obtained by crushing the pellets and activated at 400°C in a hydrogen flow for 2 h (Table 1).

A still more active powdered nickel-containing catalyst GM-3 was obtained [15] when the drying of the catalyst mass and its activation in a hydrogen flow (~400°C, 2–4 h) were combined in a single stage. The results of hydrogenation on the catalyst prepared by this procedure are shown in Fig. 2.

As seen from Fig. 2, GM-3 catalyst is more active than all the catalysts studied previously.

Gan [15] has shown that the pore volume, overall specific surface area, and specific surface area of metallic nickel in GM-3 catalyst are 2–3 times higher compared to the catalyst prepared by the conventional procedure and amount to 0.5–0.56 $cm^3\,g^{-1}$, 250–280 $m^2\,g^{-1}$, and 100–130 $m^2\,g^{-1}$ Ni, respectively. It is known that, after decomposition of basic nickel carbonate, Ni/kieselguhr catalysts contain a readily reducible phase of nickel oxide and also nickel hydrosilicates, which are reduced at temperatures above 300°C. We found that GM-3 catalyst samples prepared by reduction in an H_2 flow at 400–450°C for

Table 2. Influence of temperature T and time τ of reduction of GM-3 catalyst on the conversion of α-pinene, x_{pinene} (100°C, p_{H_2} = 0.3 MPa, hydrogenation time 2 h, c_c = 3.0 wt %)

T, °C	τ, h	x_{pinene}, wt %
350	4	60.2
350	8	60.8
400	2	90.6
400	3	100.0
450	2	95.3
450	3	100.0
500	2	85.0
500	3	79.0

2–3 h are the most active in α-pinene hydrogenation (Table 2).

The lower activity of the catalyst samples reduced at $T \le 350$°C is probably due to incomplete reduction of nickel hydrosilicates; treatment at temperatures exceeding the optimum (at 500°C) also results in lower catalyst activity, probably due to partial sintering of the forming nickel crystallites.

The stability of the catalytic properties of nickel silicate systems in hydrogenation of α-pinene was studied in a tubular bubbling reactor with a commercial sample of pelletized Ni/kieselguhr catalyst reduced in a hydrogen flow at 350°C for 6 h. We found that, at 150°C, outlet hydrogen pressure of 0.4 MPa, and molar ratio α-pinene : H_2 = 1 : 2, complete conversion of α-pinene into pinane was observed within 5–6 h, and the catalytic properties of the sample did not change after ten operation cycles. An important feature of the Ni-containing catalyst is that it allows hydrogenation of α-pinene to pinane with 96% selectivity.

CONCLUSIONS

(1) Hydrogenation of α-pinene on Pd- and Ni-containing heterogeneous catalysts was studied, and conditions were found for selective preparation of pinane: 150°C, 2 h, p_{H_2} = 0.6 MPa, commercial Ni/kieselguhr catalyst activated in an H_2 flow at 400–450°C for 2–3 h.

(2) *p*-Cymene was prepared in high yield (80%) by isomerization and dehydrogenation of α-pinene on 50% decationized zeolite Y at 150°C for 2 h in the presence of N_2 (p = 0.3 MPa).

REFERENCES

1. Erman, W.F., *Chemistry of the Monoterpenes: An Encyclopedic Handbook*. New York: Marcel Dekker, 1982.
2. Bratus, I.N., *Khimiya dushistykh veshchestv* (Chemistry of Fragrances), Moscow: Pishchevaya Prom–st., 1979.
3. Sinel'nikova, A.V., Tikhonova, T.S., and Polyakova, I.P., *Teoriya i praktika proizvodstva i pererabotki kanifoli i skipidara* (Theory and Practice of Production and Processing of Rosin and Turpentine), Gor'kii: TsNIILKhI, 1982.
4. Antonovskii, V.L., *Organicheskie perekisnye initsiatory* (Organic Peroxide Initiators), Moscow: Khimiya, 1972.
5. US Patent 4310714.
6. Allandrien, C., Descotes, G., Praly, J.P., and Sobadie, J., *Bull. Soc. Chim. Fr.*, 1977, no. 4, pp. 519–523.
7. Krasuska, A. and Guberska, *J., Przem. Chem.*, 1981, vol. 60, no. 5, pp. 259–261.
8. Polish Patent 127559.
9. Fisher, G.S., Stinson, J.S., and Goldblatt, L.A., *J. Am. Chem. Soc.*, 1953, vol. 75, no. 8, pp. 3675–3678.
10. Ko, S.H. and Chou, T.C., *Can. J. Chem. Eng.*, 1994, vol. 72, no. 10, pp. 862–873.
11. Zweifel, G. and Brown, H.C., *J. Am. Chem. Soc.*, 1964, vol. 86, no. 2, pp. 393–397.
12. Plaksin, G.V., *Khim. Inter. Ustoich. Razv.*, 2001, vol. 9, no. 5, pp. 609–620.
13. Kazanskii, V.B., *Usp. Khim.*, 1988, vol. 57, no. 12, pp. 1937–1962.
14. Krylov, O.V. and Navalikhin, M.D., *Coll. of Plenary Lectures, III Konferentsiya po nauchnym osnovam prigotovleniya i tekhnologii katalizatorov RF i SNG* (III Conf. of the Russian Federation and CIS on the Scientific Principles of Catalyst Production and Processing), Novosibirsk, May 27–31, 1996, pp. 147–178.
15. Gan, T.O., *Zh. Prikl. Khim.*, 1992, vol. 64, no. 8, pp. 1804–1805.

Russian Journal of Applied Chemistry, Vol. 76, No. 2, 2003, pp. 238–243. Translated from Zhurnal Prikladnoi Khimii, Vol. 76, No. 2, 2003, pp. 246–251.

ENVIRONMENTAL PROBLEMS OF CHEMISTRY AND TECHNOLOGY

Determination of Herbicides of the Chlorophenoxycarboxylic Acid Type in Natural and Drinking Water by Capillary Zone Electrophoresis

N. V. Komarova and L. A. Kartsova

Lyumeks Research and Production Company for Analytical Instrument Making, St. Petersburg, Russia
St. Petersburg State University, St. Petersburg, Russia

Received June 13, 2002

Abstract—The method of capillary electrophoresis was applied to separate and quantitatively determine herbicides belonging to the class of chlorophenoxycarboxylic acids: 2,4-dichlorophenoxyoleic, 2,4-dichlorophenoxypropionic, 2,4,5-trichlorophenoxyacetic, 2,4-dichlorophenoxyacetic, and phenoxyacetic, and the final product of their decomposition in an aqueous medium of 2,4-dichlorophenol. The influence exerted by α- and β-cyclodextrin on the selectivity of the separation system under study was analyzed. The hindering effect of humic acids on the separation and determination of phenoxycarboxylic acids by capillary electrophoresis was assessed.

Gas chromatography [1, 2] and high-efficiency liquid chromatography [3, 4], most widely used to analyze pesticides of the type of chlorophenoxycarboxylic acids, require prolonged sample preparation, which includes derivation, and sophisticated and expensive equipment. A fast, simple, and sufficiently reliable method for analysis of herbicides is capillary electrophoresis [5–10]. This technique for electromigration separation of ions is based on their different velocities of motion in an electric field, depending on charge and ionic radius. Being an intraphase separation technique, the capillary electrophoresis is inferior to gas chromatography and high-efficiency liquid chromatography in selectivity, but much exceeds them in efficiency.

The most widely used as herbicides are chlorophenoxycarboxylic acids (PCA) and their derivatives: 2,4-dichlorophenoxyoleic (2,4-DO), 2,4-dichlorophenoxypropionic (2,4-DP), 2,4,5-trichlorophenoxyacetic (2,4,5-T), 2,4-dichlorophenoxyacetic (2,4-D), 2-methyl-4-chlorophenoxyacetic (2M-4C), and phenoxyacetic (PAA) acids.

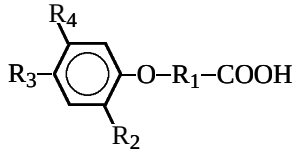

The presence of halogen atoms in PCA molecules ensures higher herbicide activity, which is at a maximum with two chlorine atoms in the benzene ring, i.e., in the case of 2,4-D and its homologues.

The properties of some frequently used (and, consequently, controlled for residual content) herbicides are illustrated in Table 1. A relatively low persistence

Table 1. Selected properties of the most frequently used herbicides of the PCA class

Compound	M, g mol^{-1}	T_m, °C	pK_a	Substituent				Solubility in water at 20°C, g l^{-1}	MPC in water, mg l^{-1}
				R_1	R_2	R_3	R_4		
PAA	152.2	99	Not found	CH_2	H	H	H	12	1.0* [11]
2,4-D	221.04	141–142	2.64	CH_2	Cl	Cl	H	0.540	0.03* [11], 1.0** [12]
2M-4C	200.5	118–120	3.07	CH_2	CH_3	Cl	H	1.5	0.02** [12]
2,4,5-T	255.5	153–156	2.85	CH_2	Cl	Cl	Cl	0.278	U.f.***
2,4-DP	235.1	117–119	3.0	$(CH_2)_2$	Cl	Cl	H	0.35	0.50* [11], 0.62** [12]
2,4-DM	249	117–119	4.8	$(CH_2)_3$	Cl	Cl	H	0.053	0.01* [11]
2,4-DCP	163.01	43–45	7.9	$C_6H_3(Cl)_2OH$				4.5	0.002** [12]

* Maximum permissible concentration (MPC) in drinking water. ** MPC in natural water. *** Use forbidden.

1070-4272/03/7602-0238 $25.00 © 2003 MAIK "Nauka/Interperiodica"

has been observed for this class of ecotoxicants; their highest stability (300–500 days) is typical of soils, and the lowest (120 days), of water bodies [13]. The stability of herbicides in various media depends both on their physicochemical characteristics and on the nature of a biological medium, temperature, humidity, UV radiation, etc. The class of PCA belongs to medium-toxicity compounds. Nevertheless some PCA representatives exhibit postponed toxic effects. For example, 2,4,5-T is characterized by embryotropic effect, and use of this preparation in Russia is prohibited. Mention should be made of the importance of determining, together with residual amounts of herbicides, also the content of their decomposition products, many of which also exert toxic influence on the environment. For PCA, such an accesory component is 2,4-dichlorophenol (2,4-DCP).

As already noted, capillary electrophoresis, being highly efficient, is, however, characterized by insufficient selectivity. Use of macrocyclic agents (crown ethers, cryptands, cyclodextrins) as additives to the leading electrolyte allows control over the selectivity of separation of complex mixtures of organic and inorganic compounds, owing to, in the first place, the unique ability of microcycles to form inclusion complexes of the host–guest type with the substances being analyzed [14].

Natural cyclodextrins (CD) are nonionic macrocyclic chiral carbohydrates composed of D–(+) residues of glucopyranose (each in chair conformation) interconnected by α-1,4-bonds. The CD molecules have the shape of a truncated cone with hydrophobic inner cavity and hydrophilic outer part (with primary hydroxy groups at the narrower end, and secondary, at the wider one). The identification is based on inclusion of bulky hydrophobic fragments of substances being analyzed into the CD cavity and interaction of secondary hydroxy groups of the macrocycle with polar groups of a component. The possibility of formation of inclusion complexes is determined by steric factors (matching between the size of the CD cavity and that of a molecule being analyzed), hydrophobic interactions, solvation effects, and hydrogen bonding [15]. The most widely used and commercially available are α-, β-, and γ-CD having, respectively, 6, 7, and 8 glucopyranose residues (β-CD occupying an intermediate position as regards the cavity size is in the highest demand). Figure 1 shows structural formulas and schematic images of α- and β-CD molecules. In capillary electrophoresis, CD is included in the main electrolyte, with the selectivity of the separation system depending on the type and concentration of a macrocycle used, presence of organic modifiers in the buffer solution, and temperature.

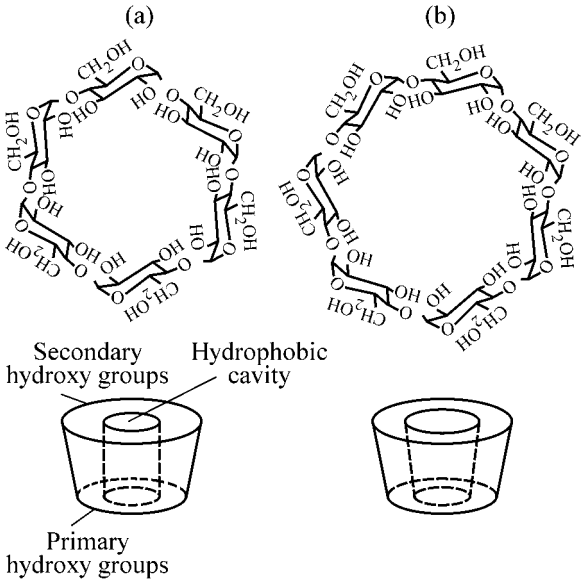

Fig. 1. Structural formulas and schematic images of molecules of (a) α- and (b) β-CD.

The aim of this study was to develop a procedure for determining PCA concentrations in natural, drinking, and waste water that would include their separation and final determination by capillary zone electrophoresis, with preliminary concentration by solid-phase extraction.

EXPERIMENTAL

As standards were used the following acids: PAA, 2,4-D, 2M-4C, 2,4,5-T, 2,4-DP, 2,4-DM (Supelco, USA); 2,4-DCP (Ekros, St. Petersburg). As macrocyclic additives served α- and β-CD (Supelco, USA). The leading electrolyte was prepared from sodium tetraborate (standard buffer solution). The preparation of humic acids was extracted from soil by the standard method [16]. Acetone, acetonitrile, and hydrochloric acid were of chemically pure grade. The cartridges for concentration were of the Diapak S16 type (Bio-KhimMak Joint-Stock Society, Moscow).

A Kapel'-105 unit for capillary electrophoresis with alternating polarity and SF detector (Lyumeks Research and Production Company for Analytical Instrument Making, St. Petersburg) was used.

As auxiliary devices served rotary evaporator, water-jet pump, and centrifuge. The data acquisition and processing were done using an IBM PC with Multikhrom software (Ampersend Joint-Stock Company, Moscow).

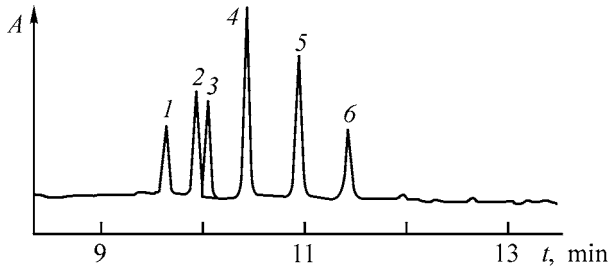

Fig. 2. Separation of PCA and 2,4-DCP by capillary zone electrophoresis. Capillary: quartz, effective length 60 cm, inner diameter 75 μm; leading electrolyte: borate buffer solution, 10 mM, pH 9.2; sample introduction at 30 mbar · 15 s; working voltage +20 kV; detection: UV, 205 nm; temperature +20°C; the same for Fig. 4. Concentrations of components to be determined (mg l^{-1}): (2,4-DM, 2,4-DP, 2,4,5-T) 2 and (2,4-D, 2,4-DCP, PAA) 1; the same for Figs. 3 and 4. (*A*) Optical density and (*t*) time; the same for Figs. 3 and 4. Component: (*1*) 2,4-DM, (*2*) 2,4-DP, (*3*) 2,4,5-T, (*4*) 2,4-D, (*5*) 2,4-dichlorophenol, and (*6*) PAA; the same for Figs. 4 and 5.

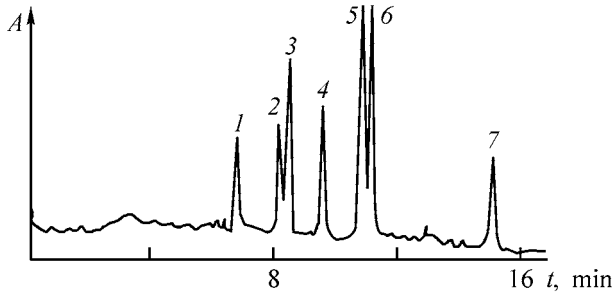

Fig. 3. Separation of PCA by capillary zone electrophoresis in the presence of β-CD. Leading electrolyte: borate buffer solution, 10 mM with addition of 2 mM of β-CD. 2M-4C concentration 2.5 mg l^{-1}. Component: (*1*) 2,4-DM, (*2*) 2,4,5-T, (*3*) 2,4-dichlorophenol, (*4*) 2,4-DP, (*5*) 2M-4C, (*6*) 2,4-D, and (*7*) PAA.

An unused Diapak S16 concentrating cartridge was washed successively with 5 ml of acetonitrile and 5 ml of distilled water acidified to pH 2.0.

A 250-ml water sample was acidified with hydrochloric acid to pH 2.0 and passed through the Diapak S16 cartridge at a rate of 15 ml min^{-1}. Then the cartridge was dried with air for 20 min and the substances to be determined were eluted with 4 ml of acetone. The eluate was evaporated to dryness under a water-jet-pump vacuum at room temperature, and the residue was dissolved in 1 ml of distilled water. The solution obtained was centrifuged (6000 rpm, 2 min) and analyzed by means of capillary electrophoresis.

An unmodified polyimide-coated quartz capillary with total (effective) length of 70 (60) cm and inner diameter of 75 μm was used. As leading electrolyte served sodium tetraborate solution with concentration of 10 mM, pH 9.18. The sample was introduced hydrodynamically at 450 mbar s. The working voltage was +20 kV. Peaks were recorded in the UV spectral range at a wavelength of 205 nm. All the measurements were done at +20°C.

Before analysis, the capillary was successively washed with 0.5 M NaOH solution for 10 min, distilled water for 5 min, and leading electrolyte for 15 min. Between analyses, the capillary was washed with the working buffer solution for 2 min.

Among various kinds of capillary electrophoresis, preference is commonly given to zone electrophoresis [17, 18], in which components of a sample introduced as a separate zone at the capillary inlet are separated in the electric field because of their different electrophoretic mobilities and detected as discrete zones. The electrophoretic motion of ions in the capillary is overlapped by an electrooscmotic flow (EOF), i.e., fluid flow under the action of an applied electric field, which accomplishes passive transfer of the sample zone in the capillary. Chlorophenoxycarboxylic acids dissociate in neutral and alkaline solutions to form organic anions, which favors their determination in the capillary–zone–electrophoresis mode. In optimizing the conditions for separation of a six-component mixture containing five herbicides to be determined and products of their degradation, the geometric dimensions of the capillary, methods and characteristics of sample introduction, composition and concentration of the leading electrolyte, working voltage, and temperature were varied. Figure 2 shows an electrophoregram obtained under the optimal conditions.

Being characterized by high separation efficiency, capillary electrophoresis has insufficient selectivity. For example, it is important to determine, in some analyses for herbicides of the PCA class, 2M-4C acid, whose mobility is close to that of 2,4-D, which hinders their separation in the zone–electrophoresis mode. It is impossible to separate 2M-4C and 2,4-D under the conditions of Fig. 2, since these two compounds form a single peak. Addition of natural unmodified α- and β-CD make it possible to improve the resolution of the system through formation of inclusion complexes, with the selectivity determined, in the first place, by the type and concentration of a CD used [19]. A seven-component PCA mixture containing six herbicides (including 2M-4C) and products of their decomposition was separated using borate buffer so-

lutions with addition of individual α- or β-CD, with the CD concentration varied from 1 to 10 mM at constant sodium tetraborate concentration (10 mM). It was shown that addition of α-CD does not affect mixture separation in the whole range of concentrations studied, with 2,4-D and 2M-4C still yielding a single peak. At the same time, introduction of β-CD improves the efficiency (twice) and selectivity of separation. The optimal amount of the macrocycle added is 2 mM (Fig. 3). In this case, peak inversion is observed: the time of migration decreases for 2,4,5-T and 2,4-DCP to a greater extent than for other components of the mixture, which can be attributed to formation of host–guest complexes with varying stability (apparently, 2,4-DCP forms the strongest complex with β-CD). The increase in efficiency is an independent indication of complexation: moving in the EOF direction, neutral β-CD molecules with anions in cavities favor more effective mass transfer of the anions

It was intended to use natural water as a real medium to be analyzed, and it is for this reason that the hindering effect of humic acids on the separation and determination of PCA by zone electrophoresis was studied. The dominant natural organic components of water bodies are humic (HA) and fulvic acids (FA), which account for 50 to 98% of organic carbon in natural water [20]. The molecular masses of these acids vary between hundreds and tens of thousands of atomic mass units, depending on conditions of HA extraction, sample from which HA are extracted, and degree of their purification and fractionation. The method of zone electrophoresis was applied to perform a set of experiments on model systems for assessing the influence exerted by HA on PCA separation. The HA concentration was varied within the range 0–250 mg l^{-1} at constant PCA concentrations. The electrophoregrams obtained are shown in Fig. 4. These data were used to construct plots reflecting the dependence of the efficiency of PCA separation on the HA concentration in solution (Fig. 5). It was established that HA do not affect the separation of PCA mixtures at concentrations lower than 50 mg l^{-1}. With the HA concentration in the solution being analyzed increasing from 50 to 250 mg l^{-1}, the efficiency of separation of neighboring peaks decreases markedly because of the broadening of zones of individual components, caused by mass overloading of the separation system.

PCA are commonly extracted from water bodies by the classical liquid–liquid [21] or solid-phase extraction with the use of cartridges filled with reversed-phase sorbents [22]. Solid-phase extraction of a mixture of PCA and, separately, HA from model solutions on Diapak S16 concentrating cartridges, with subsequent separation and determination by capillary electrophoresis, was studied. It was shown that PCA and HA are sorbed completely, and desorption of PCA is characterized by degrees of extraction close to 100%, whereas HA are not desorbed from a cartridge under the given conditions. In addition, experiments on solid-phase extraction of a mixture con-

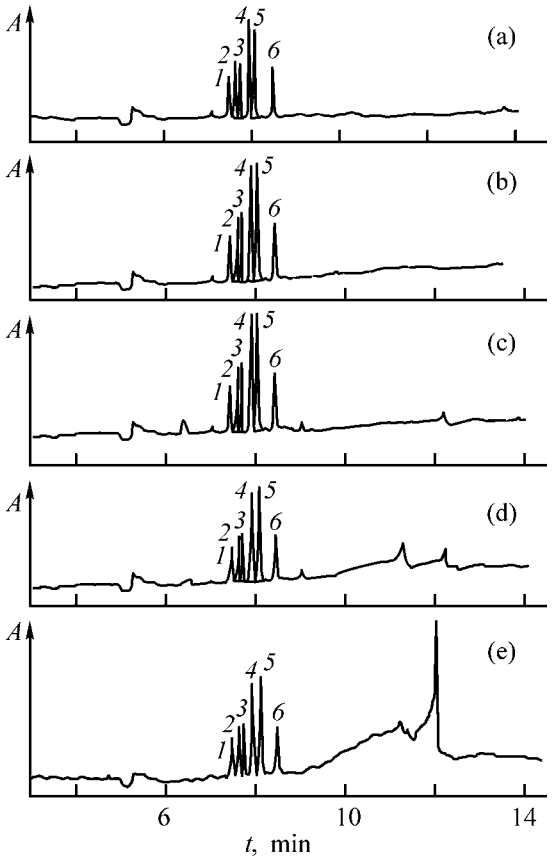

Fig. 4. Effect of HA on the PCA separation by capillary zone electrophoresis. HA concentration in the initial mixture (mg l^{-1}): (a) 0, (b) 10, (c) 50, (d) 100, and (e) 250.

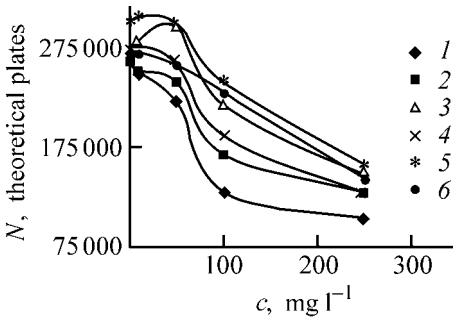

Fig. 5. PCA separation efficiency N vs. concentration c of HA in a solution being analyzed.

Table 2. Degree R of PCA recovery from model mixtures in solid-phase extraction (n = 15, P = 0.95)

Compound	Area under peak		R, %	S_r^*
	calibration solution	solution after solid-phase extraction		
2,4-DM	8.02	6.52 ± 0.59	81.3 ± 7.4	0.16
2,4-DP	11.99	9.89 ± 1.03	84.3 ± 8.6	0.18
2,4,5-T	11.84	9.82 ± 0.92	84.7 ± 7.8	0.17
2,4-D	24.27	18.81 ± 2.16	81.5 ± 8.9	0.21
2,4-DCP	23.17	2.94 ± 0.99	12.6 ± 4.3	0.60
PAA	11.59	8.04 ± 0.87	71.3 ± 7.5	0.19

* Relative standard deviation.

taining PCA and HA simultaneously revealed total desorption of PCA and partial desorption of HA, which indicates that the substances being determined react with humic acids. The degrees of extraction, calculated for the components under study, are listed in Table 2. The low degrees of extraction of the accessory component 2,4-DCP are due to its ability to be co-distilled with highly volatile substances in evaporation. For each of the acids, linear ranges of the concentrations being determined were established and the detection limit was calculated. For example, the minimum detectable concentrations in water bodies are 0.0005 mg l^{-1} for 2,4-DM, 2,4-DP, 2,4,5-T, and 2,4-D and 0.001 mg l^{-1} for PAA.

Real samples (drinking and tap water, water from artesian wells, and natural water from the Volkhov and Terek Rivers) were analyzed for the PCA content; the determinations were verified by the method of additives.

CONCLUSIONS

(1) The possibility of using capillary electrophoresis for separation and quantitative determination in the form of anions of herbicides belonging to the class of chlorophenoxycarboxylic acids was demonstrated.

(2) It is proposed to improve the selectivity of separation of analytes by adding β-cyclodextrin to the leading electrolyte, with the optimal concentration of the macrocycle equal to 2 mM.

(3) It was shown that humic acids do not hinder analysis of natural water when present in concentration not exceeding 50 mg l^{-1}.

(4) Solid-phase extraction on Diapak S16 concentrating cartridges was used in the stage of sample prepparation; the minimum detectable concentrations of herbicides were 0.0005 mg l^{-1} for for 2,4-DM, 2,4-DP, 2,4,5-T, and 2,4-D and 0.001 mg l^{-1} for PAA at sample volume of 250 ml.

REFERENCES

1. Ding, W.H., Liu, C.H., and Yeh, S.P., *J. Chromatogr.*, 2000, vol. 896, pp. 111–116.
2. Butz, S. and Snan, H.J., *J. Chromatogr.*, 1993, vol. 643, pp. 227–232.
3. Balinova, A., *J. Chromatogr.*, 1993, vol. 643, pp. 203–209.
4. Vandecasteele, K., Gaus, J., Debreuck, W., and Welraevens, K., *Anal. Chem.*, 2000, vol. 72, pp. 3093–3101.
5. Craston, D.H. and Saeed, M., *J. Chromatogr.*, 1998, vol. 827, pp. 1–12.
6. Penmetsa, K.V., Leidy, R.B., and Shea, D., *J. Chromatogr.*, 1996, vol. 745, pp. 201–208.
7. Mechref, Y. and Rassi, Z.E., *Anal. Chem.*, 1996, vol. 68, pp. 1771–1777.
8. Eash, D.T. and Bushway, R.J., *J. Chromatogr.*, 2000, vol. 880, pp. 281–294.
9. Garrison, A.W., Schmitt, P., and Kettrup, A., *J. Chromatogr.*, 1994, vol. 688, pp. 317–327.
10. Brumley, W.C. and Brownrigg, C.M., *J. Chromatogr.*, 1994, vol. 646, pp. 377–383.
11. *Pit'evaya voda: Gigienicheskie trebovaniya k kachestvu vody tsentralizovannykh sistem pit'evogo vodosnabzheniya. Kontrol' kachestva: Sanitarnye pravila i normy* (Drinking Water: Hygienic Requirements to Quality of Water in Centralized Water Supply Systems, Quality Monitoring: Sanitarty Regulations), Moscow: Inf. Tsentr, Goskomsanepidnadzor Rossii, 1996.
12. *Normativnye dannye po predel'no dopustimym urovnyam zagryazneniya vrednymi veshchestvami ob''ektov okruzhayushchei sredy: Spravocnyi material* (Standardized Data on Maximum Permissible Levels of Contamination with Harmful Substances of Environmental Objects) St. Petersburg: Petropolis, 1994.

13. Lunev, M.M., *Pestitsidy i okhrana agrofitotsenozov* (Pesticides and Protection of Agrophytocenoses), Moscow: Kolos, 1992.
14. *Host Guest Complex Chemistry Macrocycles. Synthesis, Structures, Applications*, Vogtle, F. and Weber, E., Eds., Berlin: Springer, 1985.
15. Zolotov, Yu.A., Formanovskii, A.A., Pletnev, I.V., *et al.*, *Makrotsiklicheskie soedineniya v analiticheskoi khimii* (Macrocyclic Compounds in Analytic Chemistry), Moscow: Nauka, 1993.
16. Orlov, D.S., *Guminovye kisloty pochv i obshchaya teoriya gumifikatsii* (Humic Acids and General Theory of Humification), Moscow: Mos. Gos. Univ., 1990.
17. Engelhardt, H., Beck, W., and Schmitt, T., *Capillarelektroforese: Metoden und Moglichkeiten*, Wiesbaden: Vieveg, 1994.
18. *Handbook of Cappillary Electroforesis*, Landers, J.P., Ed., Boca Raton: CRC, 1994.
19. Zerbinati, O., Trotta, F., and Giovannoli, C., *J. Chromatogr.*, 2000, vol. 875, pp. 423–430.
20. Orlov, D.S., *Gumusovye kisloty pochv* (Himic Acids in Soil), Moscow: MGU, 1974.
21. *Metody opredeleniya mikrokolichestv pestitsidov v produktakh pitaniya, kormakh i vneshnei srede* (Methods for Determining Microscopic Amounts of Pesticides in Foodstuffs, Fodder, and Environment), Moscow: Kolos, 1983.
22. Maistrenko, V.N., Khamitov, R.Z., and Budnikov, G.K., *Ekologo-analiticheskii monitoring superekotoksikantov* (Ecological-Analytical Monitoring of Superecotoxicants), Moscow: Khimiya, 1996.

Russian Journal of Applied Chemistry, Vol. 76, No. 2, 2003, pp. 244–247. Translated from Zhurnal Prikladnoi Khimii, Vol. 76, No. 2, 2003, pp. 252–255.

ENVIRONMENTAL PROBLEMS OF CHEMISTRY AND TECHNOLOGY

Effect of Impurities on Results of Redoxometric Determination of Molecular Oxygen in Natural and Waste Water by Winkler Method

S. B. Sapogova, A. V. Kaverin, A. M. Pisarevskii, and I. P. Polozova

Research Institute of Chemistry, St. Petersburg State University, St. Petersburg, Russia

Received September 18, 2002

Abstract—The possibility of determining dissolved oxygen in natural and waste water by the potentiometric variant of the Winkler method, with samples prepared using the Ross procedure and blank sample technique employed, was studied.

For many decades the Winkler method [1–3] has been the standard technique for chemical analysis for dissolved oxygen in pure and conditionally pure water. Oxygen is determined by the Winkler method in two stages. In the first stage, molecular oxygen is fixed in an alkaline medium via its reduction with Mn(II) ions. In the second stage, the sample is acidified to pH ~ 2 and KI is added. Under these conditions, iodide ions are stoichiometrically oxidized to I_2 by Mn(IV) ions formed in the first stage. Then, I_2 is titrated with a sodium thiosulfate solution, with starch as indicator. The Winkler method allows dissolved oxygen to be determined within a wide concentration range, O_2 0.1–12 mg l^{-1}, with an absolute error of about 0.04–0.06 mg l^{-1} [4].

Shortcomings of the method, associated with the low stability of starch and of dilute solutions of sodium thiosulfate, have been noticed. These shortcomings are especially pronounced at concentrations of dissolved oxygen lower than 2 mg l^{-1}. At these concentrations the relative error of oxygen determination increases to 20 rel.% [5]. At the same time, it is this range of low oxygen concentrations that acquires the highest importance in connection with the deterioration of ecological situation in water reservoirs. The accuracy of O_2 determination by the Winkler method in natural and waste water decreases dramatically because of the systematic errors caused by the presence of contaminants. In particular, presence of reducing impurities (Fe^{2+}, S^{2-}, SO_3^{2-}, etc.) in water being analyzed leads to underestimated concentrations of dissolved oxygen, and, by contrast, presence of oxidizing impurities (nitrites, peroxides, Fe^{3+}, etc.) manifests itself in overestimated results. For this reason, variations of the Winkler method [4, 6–8] are used to neutralize the effect of impurities. These modifications consists in addition of various reagents (complexing substances, oxidants, and reducing agents) to water being analyzed and in choice of conditions under which the interfering effect of one or another impurity can be neglected. Whenever possible, the effect of impurities is taken into account by means of the blank sample method.

Among the existing variants of the classical method, the widest acceptance has been gained by the technique proposed by an American scientist Ross [9]. According to this variant, the Winkler method is supplemented with a procedure for sample preparation: prior to oxygen fixation, a solution of sodium hypochlorite is added to water to be analyzed, with oxidation of the reducing agents contained in water:

$$SO_3^{2-} + ClO^- \rightarrow SO_4^{2-} + Cl^-,$$

$$NO_2^- + ClO^- \rightarrow NO_3^- + Cl^-.$$

Then, the excess amount of hypochlorite ions and some oxidants are decomposed by addition of a potassium thiocyanate solution:

$$4ClO^- + NCS^- + 2OH^- \rightarrow NCO^- + 4Cl^- + H_2O + SO_4^{2-}.$$

In this case, the components of the NCO^-/NCS^- redox system do not impede the second stage of the Winkler analysis [10].

1070-4272/03/7602-0244 $25.00 © 2003 MAIK "Nauka/Interperiodica"

Previously [11], the possibility of determining the dissolved oxygen in the iodine–iodide system (I_3^-/I^- by the Winkler method, with potentiometric measurements used instead of iodometric titration, has been demonstrated. The redoxometry is based on the high selectivity of the platinum indicator electrode toward the I_3^-/I^- system, which is achieved owing to irreversible modification of the electrode surface by the components of this system. It was established that modified indicator electrodes are frequently insensitive to side electrochemical reactions. This allows redoxometric measurements under conditions close to equilibrium in solutions of the iodine–iodide system at concentrations of up to 10^{-6} M (in terms of iodine). The concentration of iodine (dissolved oxygen) was determined from a change in the emf of galvanic cell (I) as a result of coulometric generation of a standard addition of iodine.

$$\text{Ag} \mid \text{AgCl, KCl}_{\text{sat}} \mid \text{Solution of } I_3^-/I^- \text{ system} \mid \text{Pt} \quad (1)$$

The potentiometric measurements and electrochemical generation of iodine were performed in a four-electrode cell with generating unit having unseparated cathode and anode spaces. The determination technique and calculation procedure were described in detail in [11, 12].

It is necessary to note that use of the Ross procedure in potentiometric determination within the framework of the Winkler method yields correct results only when the selectivity of the indicator electrode in the I_3^-/I^- system toward the redox system NCO^-/NCS^- ensures attainment of a partial equilibrium at the electrode–solution interface and provides a 100% current efficiency by iodine in electrochemical generation. Otherwise, it could hardly be expected that the potentiometric determination would yield correct results.

Therefore, the aim of this study was to analyze the possibility of potentiometric determination of dissolved oxygen in contaminated reservoirs with the use of the Ross method. Potentiometric analysis was also used for determining the impurity concentration in a blank test.

EXPERIMENTAL

The problem of reversibility, in principle, of redox measurements in solutions of the coexisting systems I_3^-/I^- and NCO^-/NCS^- was studied in two stages.

In the first stage was studied the current efficiency by iodine in no-diaphragm generation of a standard addition of iodine in mixed solutions of the following composition typical of the Ross procedure: 5×10^{-4} equiv. l^{-1} NCO^-, 1.5×10^{-3} equiv. l^{-1} NCS^-, and 2×10^{-1} M KI, to which H_2SO_4 was added to pH 2.5. The results obtained demonstrated that, under the conditions of the Ross method at generation current density of 20 mA cm^{-1}, the current efficiency by iodine is $99.4 \pm 1.6\%$ ($n = 7$, $p = 0.95$), i.e., the NCO^-/NCS^- system is electrochemically inactive under the experimental conditions.

In the second stage, the reversibility of platinum electrode toward the iodine–iodide system in the solutions containing components of the NCO^-/NCS^- redox system was verified. For this purpose, the dependence E–$\log[I_3^-]$ was studied in pure solutions of the iodine–iodide system (3×10^{-5}–1×10^{-3} M I_2 l^{-1}, 2×10^{-1} M KI, pH 2.5) and in solutions containing Ross reagents (composition indicated above). The iodine concentration in the solutions studied was set by successive electrochemical generation. The E–$\log[I_3^-]$ dependences in pure solutions of the I_3^-/I^- system and in solutions containing the NCO^-/NCS^- system are linear; the slopes of the calibration lines are the same for both solutions and coincide, within the measurement error, with the theoretical value [29.6 mV $\times$ $(pI_3^-)^{-1}$].

The experiments performed demonstrated that equilibrium redoxometric measurements can be performed in the system I_3^-/I^-, despite the presence of components of the NCO^-/NCS^- redox system. This makes potentiometry with sample preparation by the Ross procedure suitable for O_2 determination.

The analytical characteristics of the potentiometric variant of the Ross method were studied in model solutions of reducing agents. $NaNO_2$ and Na_2SO_3, typical "contaminants" of natural water, were chosen for this purpose. Their concentration was taken to be 10^{-4} eqiv. l^{-1}, which corresponds to 0.8 mg l^{-1} O_2 (in terms of oxygen). Table 1 compares the results of potentiometric and titrimetric determinations of O_2. It can be seen that the application of the Ross method of sample preparation was successful for the reducing agents used: the results for pure water and model aqueous solutions containing contaminants differ by no more than 0.5%. A large positive error associated with the presence of additional dissolved oxygen introduced by KNCS and NaClO Ross reagents was only observed at lower oxygen concentrations. Comparison of the reproducibility characteristics of titrimetric and redoxometric determinations shows that they are about the same (~1%) at high O_2 concentrations, and only on lowering the O_2 concentration to

Table 1. Results of determination of dissolved O_2 by the Ross method in model solutions of reducing agents (reducing agent concentration 0.8 mg O_2 l^{-1})

Reducing agent	O_2, mg l^{-1}					
	potentiometry			titrimetry		
	By Winkler	by Ross	Δ, %	By Winkler	by Ross	Δ, %
$NaNO_2$	9.41	9.41	0	9.42	9.37	–0.5
	8.43	8.44	+0.1	8.47	8.44	–0.3
	1.95	2.03	+4.1	1.99	2.03	+2.0
	1.41	1.53	+8.5	1.41	1.53	+8.5
Na_2SO_3	9.41	9.42	+0.1	9.42	9.40	–0.2
	8.43	8.39	–0.5	8.47	8.40	–0.8
	1.95	1.92	–1.5	1.99	1.92	–3.5
	1.41	1.52	+7.8	1.41	1.52	+7.8

Note. Results of O_2 determination by Winkler method refer to pure water and are accepted as reference data in comparisons with the Ross method; n = 3–5.

2 mg l^{-1}, the potentiometric method becomes advantageous: the error in determining oxygen by the potentiometric method is 0.04–0.06 mg l^{-1}, i.e., approximately twice lower than that in the case of titrimetry.

In studying the model solutions of other reducing agents (sodium thiosulfate, ascorbic, citric, tartaric, and oxalic acids), underestimated values were obtained, despite the use of the Ross method. The concentration of dissolved O_2, found in this case, was lower than the expected value by 0.5–0.9 mg O_2 l^{-1}. These results indicate that the efficiency of the Ross procedure of sample preparation is insufficient. In other words, the degree of impurity oxidation did not reach 100% in any of the solutions. Since $Na_2S_2O_3$ and ascorbic acid react with molecular I_2 in quantitative yield, it becomes possible to take their contribution into account, in determining oxygen, by means of the blank sample method. In this case, the sequence of analytical operations is as follows:

Table 2. Iodometric determination of reducing agents (O_2^{red})

Reducing agent	O_2^{red}, mg l^{-1}				
	preset	O_2^{pot}	S^{pot}	O_2^{tit}	S^{tit}
Ascorbic acid	0.86	0.86	0.01	0.86	0.02
	3.89	3.89	0.01	3.89	0.03
$Na_2S_2O_3$	0.79	0.78	0.01	0.77	0.04
	3.88	3.88	0.01	3.88	0.02

Note. 1 mg O_2 l^{-1} = 1.25×10^{-4} equiv. l^{-1}, n = 7.

(1) Iodometric determination of active redox impurities. In an electrochemical cell containing a sample of water being analyzed and a supporting electrolyte (0.2 M KI, pH 2.5), an iodine addition $[I_3^-]_1$ was generated. After the stationary emf E_1, indicating the completion of the reaction of I_2 with a reducing agent, was attained, the second addition of iodine $[I_3^-]_2$ was generated. The second emf value, E_2, was recorded. The concentration of the reducing agent in oxygen units (mg l^{-1}) was calculated by the formula common for the standard addition method:

$$O_2^{red} = \left([I_3^-]_1 - \frac{[I_3^-]_2}{(10^{2\Delta E/\theta} - 1)}\right) \times 16\,000.$$

where $\Delta E = E_2 - E_1$; $\theta = 2.3RTF^{-1}$, R is the gas constant (J K^{-1} mol^{-1}), T is temperature (K), and F = 96 500 C.

Table 2 lists the results of an iodometric determination of $Na_2S_2O_3$ and ascorbic acid by potentiometry, in comparison with the data furnished by the commonly accepted titrimetric procedure. As expected, the titrimetic determination is accompanied in this concentration range by large random errors exceeding by a factor of 2–3 the error of the potentiometric method (O_2 concentration 0.01 mg l^{-1}). The same behavior was already observed in the case of the Ross method.

Since the reactions of oxidation of oxalic, tartaric, and citric acids by I_2 are kinetically hindered, it was impossible to determine them in the blank sample.

Table 3. Determination of dissolved O_2 with preliminary analysis for the reducing agent

Reducing agent	O_2^{red}, mg l^{-1}	O_2, mg l^{-1}				Reducing agent	O_2^{red}, mg l^{-1}	O_2, mg l^{-1}			
		without impurity, by Winkler	with impurity					without impurity, by Winkler	with impurity		
			by Winkler	ΣO_2^*	Δ, %				by Winkler	ΣO_2^*	Δ, %
Ascorbic acid	1.66	9.40	7.82	9.48	+0.9	$Na_2S_2O_3$	0.80	9.40	8.57	9.37	–0.3
	1.61	8.46	6.82	8.43	–0.2		0.81	8.45	7.63	8.44	–0.1
	1.60	8.46	6.86	8.46	0		0.77	8.45	7.67	8.44	–0.1

* The concentration of dissolved O_2 in a solution of the reducing agent, ΣO_2, is the sum of the concentration of dissolved O_2, determined in the presence of the reducing agent, and that of the reducing agent, O_2^{red}.

(2) Determination of dissolved O_2 by the classical Winkler method, with correction made for the expenditure of I_2 (O_2) for oxidation of the reducing impurity (Table 3). As in the case of the Ross method, the results obtained using the classical Winkler method for pure water served as reference data. As seen from Table 3, their accuracy is about the same as that for the Ross method. It should be noted that in those cases when O_2 can be determined with preliminary iodometry of a sample, this variant has an advantage over the Ross method, because it yields two parameters of a sample: concentrations of O_2 and impurity.

CONCLUSIONS

(1) The high selectivity of the platinum indicator electrode in the redox system I_3^-/I^-, making it possible to perform reversible measurements despite the presence of components of the NCO^-/NCS^- system and other systems, was confirmed. This circumstance justified the application of the Winkler method with potentiometric determination of I_2 to analysis of contaminated water both in the Ross variant and in combination with the blank sample method.

(2) Potentiometric determination of dissolved O_2 by the Ross method is simple technically and attractive for serial determinations. At the same time, analysis for dissolved oxygen by the Winkler method, with correction made for active redox impurities (blank sample), is more informative. It was shown for several examples that neither the Ross variant nor the blank sample method can serve as a universal technique for analysis of contaminated natural and waste water for dissolved oxygen. The choice of a variant is governed by the nature of a particular impurity.

ACKNOWLEDGMENTS

The study was supported by the Federal Program "Universities of Russia" (grant no. UR.05.01.031).

REFERENCES

1. *ISO 5813–83, Quality of Water: Determination of Dissolved Oxygen: Iodometric Method*.
2. Carritt, D.E., and Carpenter, J.H., *J. Mar. Res.*, 1966, vol. 24, no. 3, pp. 286–318.
3. Carpenter, J.H., *Lymnol. Oceanogr.*, 1965, vol. 10, no. 1, pp. 135–140.
4. *D-888, Standard Test Methods for Dissolved Oxygen in Water*, Annual Book of ASTM Standards, 1977, part 31, pp. 531–540.
5. Chernyakova, A.M., Sallivan, D.P., Stunzhas, P.A., *et al.*, *Okeanologiya*, 1983, vol. 23, no. 4, pp. 681–687.
6. *D-1589, Standard Test Methods for Dissolved Oxygen in Waste Water*, Annual Book of ASTM Standards, 1974, part 31, pp. 524–530.
7. Hitchman, M.L., *Measurement of Dissolved Oxygen*, New York: John Wiley, 1987.
8. Standard Methods for the Examination of Water and Wastewater, Washington: APHA, 1985, 16th edn. 635 p.
9. Ross, F.F., Water Waste Treat. J., 1964, vol. 9, pp. 528–530.
10. Lur'e, Yu.Yu., and Rybnikova, A.I., *Khimicheskii analiz proizvodstvennykh stochnykh vod* (Chemical Analysis of Industrial Sewage), Moscow: Khimiya, 1966.
11. Pisarevsky, A.M., and Kaverin, A.V., *Zh. Prikl. Khim.*, 1999, vol. 72, no. 10, pp. 1658–1662.
12. Kaverin, A.V., Pisarevsky, A.M., and Polozova, I.P., *Proc. 8th Intern. Conf. on Electroanalysis (ESEAC-2000)*, Bonn (Germany), June 11–15, 2000, part A., Bonn, 2000, p. 16.

Russian Journal of Applied Chemistry, Vol. 76, No. 2, 2003, pp. 248–252. Translated from Zhurnal Prikladnoi Khimii, Vol. 76, No. 2, 2003, pp. 256–260.

ORGANIC SYNTHESIS AND INDUSTRIAL ORGANIC CHEMISTRY

Synthesis and Antioxidant Properties of Bis[ω-(3,5-dialkyl-4-hydroxyphenyl)alkyl] Sulfides

A. E. Prosenko, E. I. Terakh, E. A. Gorokh, V. V. Nikulina, and I. A. Grigor'ev

Novosibirsk State Pedagogical University, Novosibirsk, Russia

Vorozhtsov Institute of Organic Chemistry, Siberian Division, Russian Academy of Sciences, Novosibirsk, Russia

Received October 10, 2002

Abstract—The reaction of ω-(3,5-dialkyl-4-hydroxyphenyl)-1-chloroalkanes with sodium sulfide yielded the corresponding sulfides, which were tested as antioxidants in two model reactions: oxidation of lard and Vaseline oil.

Sulfur-containing derivatives of sterically hindered phenols are effective inhibitors of free-radical oxidation of various polymeric materials and lipid substrates [1–4]. A distinctive feature of sulfur-containing phenolic antioxidants (SPAOs) is the presence of two reaction centers: phenolic moiety and bivalent sulfur atom. As a result, these compounds can inhibit oxidation in two ways: by reactions with peroxy radicals and with hydroperoxides. Furthermore, the antioxidant activity of SPAOs is enhanced by intramolecular synergism [3].

Among SPAOs is known bis[3-(3,5-di-*tert*-butyl-4-hydroxyphenyl)propyl] sulfide (SO-3 stabilizer, Tiofan), having high inhibiting activity in oxidation of polyethylene, polypropylene [5, 6], and animal fats [1]. Biological studies have shown that SO-3 exhibits hepatoprotective, immunostimulating, and antiischemic effects [7–9]. In this study, we prepared and tested for antioxidant activity a series of structural analogs of SO-3, bis[ω-(3,5-dialkyl-4-hydroxyphenyl)alkyl] sulfides, differing in the extent of steric shielding of the phenolic OH group and in the length of the *p*-alkyl chain linking the phenolic and sulfide moieties.

The sulfides were prepared by the reaction of the corresponding ω-(3,5-dialkyl-4-hydroxyphenyl)-1-chloroalkanes **I** with sodium sulfide nonahydrate:

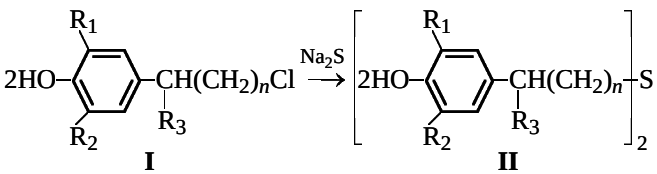

where $R_1 = R_2 =$ Me, $R_3 = H$, $n = 2$ (**Ia**, **IIa**); $R_1 =$ Me, $R_2 = t$-Bu, $R_3 = H$, $n = 2$ (**Ib**, **IIb**); $R_1 = R_2 = t$-Bu, $R_3 = H$, $n = 1$ (**Ic**, **IIc**), $n = 2$ (**Id**, **IId**), $n = 3$ (**Ie**, **IIe**), $n = 4$ (**Ig**, **IIg**); $R_1 = R_2 = t$-Bu, $R_3 =$ Me, $n = 2$ (**If**, **IIf**).

Syntheses were performed in refluxing 2-propanol for 4–8 h at a molar ratio of the initial chloroalkane **I** to sodium sulfide of 1 : 0.62. Yields of sulfides **II** 57–90%. The compositions and structures of sulfides **II** were confirmed by elemental analysis and NMR spectra.

The antioxidant activity of sulfides **II** was tested in autooxidation of lard (Novosibirsk Meat-Canning Plant) and Vaseline oil (Tatkhimfarmpreparaty Chemical Pharmaceutical Production Association, Kazan). As references we used Ionol (2,6-di-*tert*-butyl-4-methylphenol), TB-3 stabilizer [bis(3,5-di-*tert*-butyl-4-hydroxybenzyl) sulfide], and also a synergistic mixture of Ionol with didodecyl sulfide (DDS) in 1 : 0.5 molar ratio.

The kinetic studies showed that all the sulfides **II** synthesized exhibit high antioxidant activity and efficiently inhibit oxidation of lard and Vaseline oil (see table). They surpass in the antioxidant power the monofunctional antioxidant Ionol and a mixture of Ionol with DDS. This fact suggests that the high inhibiting power of sulfides **II** is due to the bifunctional mechanism of the antioxidant effect and to intramolecular synergism.

In oxidation of Vaseline oil, the mixture of Ionol with DDS exhibits a pronounced synergistic effect due to a combination of the antiradical activity of Ionol and antiperoxide activity of DDS [10]. However, no synergistic effect of these compounds was observed

1070-4272/03/7602-0248 $25.00 © 2003 MAIK "Nauka/Interperiodica"

Antioxidant properties of bis[ω-(3,5-dialkyl-4-hydroxyphenyl)alkyl] sulfides

Antioxidant*	Induction period τ, min		
	lard, [PhOH] = 1 μmol g^{-1}, 130°C	Vaseline oil, [PhOH] = 2.5 μmol g^{-1}	
		175°C	180°C
$R(CH_2)_3S(CH_2)_3R$ (**IIa**)	115	–	238
$R^1(CH_2)_3S(CH_2)_3R^1$ (**IIb**)	190	–	300
$R^2(CH_2)_2S(CH_2)_2R^2$ (**IIc**)	225	221	–
$R^2(CH_2)_3S(CH_2)_3R^2$ (**IId**)	290	171	113
$R^2(CH_2)_4S(CH_2)_4R^2$ (**IIe**)	322	179	–
$R^2CH(CH_2)_2S(CH_2)_2CHR^2$ (**IIf**) CH_3 CH_3	281	169	–
$R^2(CH_2)_5S(CH_2)_5R^2$ (**IIg**)	305	202	–
$R^2CH_2SCH_2R^2$ (TB-3)	209	49	–
R^2CH_3 (Ionol)	169	64	33
DDS	34	–	5
Synergistic mixture Ionol + DDS	169	–	79
Control	34	10	5

* R = 2,5-dimethyl-4-hydroxyphenyl, R^1 = 3-methyl-5-*tert*-butyl-4-hydroxyphenyl, and R^2 = 3,5-di-*tert*-butyl-4-hydroxyphenyl.

in oxidation of lard. This result is probably due to different rates of oxidation of lard and Vaseline oil, and also to different thermal stabilities of hydroperoxides formed by oxidation of these substrates.

The susceptibility of hydrocarbons to oxidation is determined by the ratio of the rate constants of chain propagation, k_2, and quadratic chain termination, k_6:

$$RO_2^{\cdot} + RH \xrightarrow{k_2} ROOH + R^{\cdot}, \quad (1)$$

$$RO_2^{\cdot} + RO_2^{\cdot} \xrightarrow{k_6} \text{Products}. \quad (2)$$

Unsaturated compounds are characterized by higher $k_2/k_6^{1/2}$ ratio; correspondingly, under equal other conditions, they are oxidized faster [11]. Lard containing residues of unsaturated fatty acids is oxidized faster than Vaseline oil, which results in accumulation of larger amount of hydroperoxides exhibiting lower thermal stability [12]. Therefore, in oxidation of lard, hydroperoxides are accumulated rapidly, and DDS present in the system has no time to fully deactivate them. In oxidation of Vaseline oil, hydroperoxides are formed at a lower rate and are more stable, and in this case, the mixture of Ionol with DDS exhibits a synergistic effect.

The synthesized sulfides **II** differing in the extent of steric shielding of the phenolic OH group can be ranked in the following order with respect to the capability to inhibit oxidation of Vaseline oil: **IIb** > **IIa** > **IId**. The decrease in the effect of the antioxidants in this order corresponds to a decrease in the rate of their reaction with peroxy radicals [12]

$$PhOH + RO_2^{\cdot} \rightarrow PhO^{\cdot} + ROOH. \quad (3)$$

In oxidation of lard, the antioxidant activity of the sulfides increased as the phenolic OH group became more shielded in the order **IIa** < **IIb** < **IId**, which corresponds to the decreasing reactivity of the phenoxy radicals in the reaction

$$PhO_2^{\cdot} + RH \rightarrow PhOH + R^{\cdot}. \quad (4)$$

It is known that the role of reaction (4) in inhibited oxidation of aliphatic and alkylaromatic hydrocarbons is insignificant. However, in the case of lipid substrates containing relatively weak C–H bond, the contribution of reaction (4) becomes significant, and the inhibiting power of phenolic compounds with respect to oxidation of lipids depends on the stability of the generated phenoxy radicals to a greater extent.

The structure of the *p*-alkyl substituent linking the phenolic and sulfide fragments affected the antioxidant power of sulfides **II** to a lesser extent than did the structure of the *o*-substituents. Among sulfides **IIc**–**IIg**, sulfide **IIe** was the most effective inhibitor with respect to lard, and **IIc**, with respect to Vaseline oil.

TB-3 showed poor antioxidant activity as compared to sulfides **II**, which may be due to the low thermal stability of TB-3 as a benzyl derivative. It is notable that at a lower temperature of 130°C (autooxidation of lard) TB-3 somewhat surpassed Ionol in the antioxidant properties but was inferior to Ionol at 180°C (autooxidation of Vaseline oil).

Thus, sulfides **II** show considerable promise as effective inhibitors of oxidation of various organic substrates and surpass the available analogs in the antioxidative activity.

EXPERIMENTAL

The ^{1}H NMR spectra were recorded on a Bruker spectrometer (500 MHz) in $CDCl_3$ relative to external TMS. The melting points were determined with a PTP device. The initial ω-(3,5-dialkyl-4-hydroxyphenyl)-1-chloroalkanes **I** were prepared according to [13] from the corresponding ω-(3,5-dialkyl-4-hydroxyphenyl)alkanols.[1] TB-3 stabilizer was prepared according to [14].

Bis[3-(3,5-dimethyl-4-hydroxyphenyl)propyl] sulfide IIa. Chloropropane **Ia** (5 g, 25.2 mmol) and sodium sulfide nonahydrate (3.78 g, 15.7 mmol) were dissolved in 30 ml of 2-propanol. The mixture was refluxed for 4 h, cooled, neutralized with HCl, and treated with petroleum ether. The extract was washed with water and dried over Na_2SO_4; the solvent was distilled off. The product was purified chromatographically (silica gel, petroleum ether–diethyl ether, 3 : 1). Yield of **IIa** 2.6 g (57%), mp 63–64°C. ^{1}H NMR spectrum, δ, ppm: 1.86 m (4H, $CH_2C\underline{H}_2CH_2$), 2.23 s (12H, Me), 2.52 t (4H, CH_2S), 2.60 t (4H, $ArC\underline{H}_2$), 4.55 s (2H, OH), 6.79 s (4H, H_{arom}).

Found, %: C 73.99; H 8.38; S 8.77.
$C_{22}H_{30}O_2S$.
Calculated, %: C 73.70; H 8.43; S 8.94.

Bis[3-(3-methyl-5-tert-butyl-4-hydroxyphenyl)-propyl] sulfide IIb was prepared similarly from 5.0 g (20.8 mmol) of **Ib**. The product was purified chromatographically (silica gel, petroleum ether–diethyl ether, 6 : 1). Yield 2.8 g (61%); a resinous substance. ^{1}H NMR spectrum, δ, ppm: 1.42 s (18H, *t*-Bu), 1.88 m (4H, $CH_2C\underline{H}_2CH_2$), 2.22 s (6H, Me), 2.25 t (4H, CH_2S), 2.62 t (4H, $ArC\underline{H}_2$), 4.64 s (2H, OH), 6.83 s (2H, H_{arom}), 6.96 s (2H, H_{arom}).

Found, %: C 75.64; H 9.44; S 6.89.
$C_{28}H_{42}O_2S$.
Calculated, %: C 75.97; H 9.56; S 7.24.

Bis[2-(3,5-di-tert-butyl-4-hydroxyphenyl)ethyl] sulfide IIc was prepared similarly from 5.0 g (18.6 mmol) of **Ic** (synthesis time 8 h). The reaction product was recrystallized from 2-propanol. Yield 3.2 g (70%), mp 104°C. ^{1}H NMR spectrum, δ, ppm: 1.43 s (36H, *t*-Bu), 2.80 m (8H, $C\underline{H}_2C\underline{H}_2$), 5.08 s (2H, OH), 7.01 s (4H, H_{arom}).

Found, %: C 77.12; H 10.23; S 6.81.
$C_{32}H_{50}O_2S$.
Calculated, %: C 77.05; H 10.10; S 6.43.

Bis[3-(3,5-di-*tert*-butyl-4-hydroxyphenyl)propyl] sulfide IId was prepared similarly from 5.0 g (17.7 mmol) of **Id** and recrystallized from 2-propanol. YIeld 4.3 g (90%), mp 71–73°C. ^{1}H NMR spectrum, δ, ppm: 1.43 s (36H, *t*-Bu), 1.89 m (4H, $CH_2C\underline{H}_2CH_2$), 2.55–2.58 t (4H, CH_2S), 2.61–2.64 t (4H, $ArC\underline{H}_2$), 5.03 s (2H, OH), 6.97 s (4H, H_{arom}).

Found, %: C 77.35; H 10.23; S 6.03.
$C_{34}H_{54}O_2S$.
Calculated, %: C 77.51; H 10.33; S 6.08.

Bis[4-(3,5-di-*tert*-butyl-4-hydroxyphenyl)butyl] sulfide IIe was prepared similarly from 5.0 g (16.8 mmol) of **Ie** and recrystallized from 2-propanol. Yield 3.1 g (70%), mp 89–90°C. ^{1}H NMR spectrum, δ, ppm: 1.43 s (36H, *t*-Bu), 1.66 m (8H, $ArCH_2C\underline{H}_2C\underline{H}_2$), 2.52–2.55 m (8H, $ArC\underline{H}_2$, CH_2S), 5.02 s (2H, OH), 6.96 s (4H, H_{arom}).

Found, %: C 77.65; H 10.59; S 6.12.
$C_{36}H_{58}O_2S$.
Calculated, %: C 77.92; H 10.53; S 5.78.

Bis[3-(3,5-di-*tert*-butyl-4-hydroxyphenyl)butyl] sulfide IIf was prepared similarly from 5.0 g (16.8 mmol) of **If** and recrystallized from 2-propanol. Yield 3.4 g (76%), mp 84–85°C. ^{1}H NMR spectrum, δ, ppm: 1.21–1.24 d (6H, $CH\underline{Me}$), 1.43–1.44 s (36H, *t*-Bu), 1.76–1.79 m (4H, $CHC\underline{H}_2CH_2$), 2.38–2.41 t (4H, CH_2S), 2.72 m (2H, $ArC\underline{H}$), 5.02 s (2H, OH), 6.95 s (4H, H_{arom}).

Found, %: C 77.51; H 10.30; S 6.00.
$C_{36}H_{58}O_2S$.
Calculated, %: C 77.92; H 10.53; S 5.78.

[1] The compounds were kindly submitted by A.P. Krysin (Novosibirsk Institute of Organic Chemistry, Siberian Division, Russian Academy of Sciences).

Bis[5-(3,5-di-*tert*-butyl-4-hydroxyphenyl)pentyl] sulfide IIg was prepared similarly from 5.0 g (16.1 mmol) of **Ig** and recrystallized from methanol. Yield 3.2 g (69%), mp 76–78°C. ^{1}H NMR spectrum, δ, ppm: 1.43 s (36H, *t*-Bu), 1.46–1.47 m (4H, $ArCH_2CH_2C\underline{H}_2$), 1.60–1.63 m (8H, $ArCH_2C\underline{H}_2C\underline{H}_2$), 2.50–2.53 t (8H, $ArC\underline{H}_2$, CH_2S), 5.00 s (2H, OH), 6.96 s (4H, H_{arom}).

Found, %: C 78.38; H 10.50; S 5.33.
$C_{36}H_{62}O_2S$.
Calculated, %: C 78.29; H 10.72; S 5.50.

Oxidation of lard was performed at 130°C under conditions of oxygen bubbling; the reaction cell was similar to that described in [15]. The lard sample weight was 50 g, and the concentration of antioxidants, 1 μmol per gram of lard. In the course of oxidation, 1-g portions of lard were withdrawn to determine the concentration of peroxides by iodometric titration [16]. The initial peroxide number of the lard was 0.002% iodine. The kinetic curves of the oxidation were plotted (Fig. 1a), and the induction period (time in which the peroxide number of 0.1 was attained) was determined graphically.

Oxidation of Vaseline oil was performed in a gasometric unit similar to that described in [17] at oxygen pressure of 1 atm. The total volume of the oil sample was 5 ml; the concentration of antioxidants was 2.5 μmol per gram of oil. Oxidation was performed at 175 or 180°C. The kinetic curves were plotted (Fig. 1b), and the induction period was determined as the intersection point of the tangents to the initial and final portions of the kinetic curves.

Three or four replicate runs were performed, and the average induction periods (deviations ≤3%) were determined.

CONCLUSIONS

(1) A series of bis[ω-(3,5-dialkyl-4-hydroxyphenyl)alkyl] sulfides differing in the extent of steric shielding of the phenolic OH group and in the length of the *p*-alkyl chain linking the phenolic and sulfide moieties were prepared.

(2) The sulfides synthesized are bifunctional antioxidants and are characterized by intramolecular synergism; the relative activities of these compounds are different, depending on the substrate.

(3) The sulfides show high performance as inhibitors of lard and Vaseline oil oxidation; they show promise as antioxidants of various fuels, lubricants, polymeric materials, and lipid substrates.

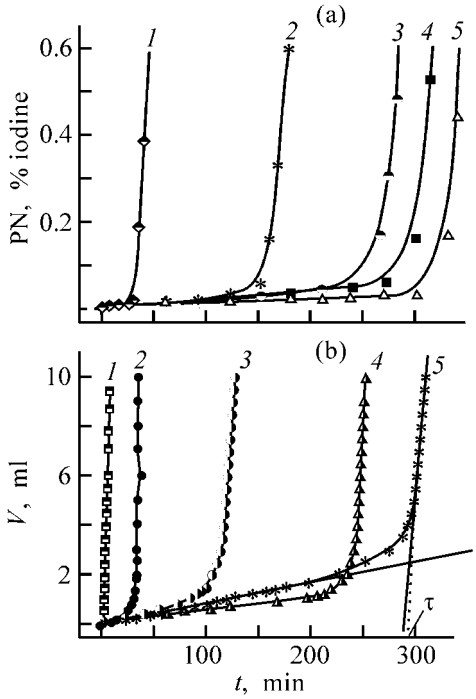

Fig. 1. Kinetic curves of oxidation of (a) lard and (b) Vaseline oil: (*1*) no inhibitor; inhibitor added: (*2*) Ionol, (*3*) (a) **IIc** and (b) **IId**, (*4*) (a) **IId** and (b) **IIa**, and (*5*) (a) **IIe** and (b) **IIb**. (PN) Peroxide number, (*V*) volume of oxygen taken up, and (*t*) time.

REFERENCES

1. Prosenko, A.E., Terakh, E.I., Kandalintseva, N.V., *et al., Zh. Prikl. Khim.*, 2001, vol. 74, no. 11, pp. 1839–1843.
2. Pinko, P.I., Terakh, E.I., Prosenko, A.E., and Grigor'ev, I.A., *Zh. Prikl. Khim.*, 2001, vol. 74, no. 11, pp. 1843–1847.
3. Pinko, P.I., Terakh, E.I., Gorokh, E.A., *et al., Zh. Prikl. Khim.*, 2002, vol. 75, no. 10, pp. 1694–1698.
4. USSR Inventor's Certificate, no. 1 131 869.
5. RF Patent 1 072 420.
6. RF Patent 1 007 405.
7. Bakhtina, I.A., Antip'eva, E.V., Prosenko, A.E., *et al., Byull. Sib. Otd. Ross. Akad. Med. Nauk*, 2000, vols. 97–98, nos. 3–4, pp. 24–29.
8. Fridlyand, I.F., Prosenko, A.E., Klepikova, S.Yu., *et al., Med. Immunol.*, 2001, vol. 3, no. 2, p. 243.
9. Dushkin, M.I., Kandalintseva, N.V., Prosenko, A.E., and Lyakhovich, V.V., Abstracts of Papers, *VI Mezhdunarodnaya konferentsiya "Bioantioksidant"* (VI Int.

Conf. "Bioantioxidant"), Moscow, April 16–19, 2002, pp. 175–176.

10. *Ingibirovanie protsessov okisleniya polimerov smesyami stabilizatorov* (Inhibition of Polymer Antioxidation Using Mixtures of Stabilizers), Levin, P.I., Ed., Moscow: NII Khimpolimer, 1970.
11. Yurchenko, N.I. and Gol'denberg, V.I., *Kinet. Katal.*, 1980, vol. 21, no. 3, pp. 606–611.
12. Roginskii, V.A., *Fenol'nye antioksidanty: Reaktsionnaya sposobnost' i effektivnost'* (Phenolic Antioxidants: Reactivity and Performance), Moscow: Nauka, 1988.
13. Gorbunov, V.N., Maslov, N.N., and Gurvich, Ya.A., *Khimiya i tekhnologiya stabilizatorov polimernykh materialov* (Chemistry and Technology of Stabilizers for Polymeric Materials), Moscow: Khimiya, 1981.
14. USSR Inventor's Certificate, no. 1376511.
15. Emanuel', N.M. and Lyaskovskaya, Yu.N., *Tormozhenie protsessov okisleniya zhirov* (Inhibition of Fat Oxidation), Moscow: Pishchepromizdat, 1961.
16. Zinov'ev, A.A., *Khimiya zhirov* (Chemistry of Fats), Moscow: Pishchepromizdat, 1952.
17. Tsepalov, V.F., in *Issledovanie sinteticheskikh i prirodnykh antioksidantov in vivo i in vitro: Sbornik uchenykh statei* (In vivo and in vitro Studies of Synthetic and Natural Antioxidants: Coll. of Scientific Papers), Moscow: Nauka, 1992, pp. 16–26.

Russian Journal of Applied Chemistry, Vol. 76, No. 2, 2003, pp. 253–257. Translated from Zhurnal Prikladnoi Khimii, Vol. 76, No. 2, 2003, pp. 261–265.

ORGANIC SYNTHESIS AND INDUSTRIAL ORGANIC CHEMISTRY

Synergistic Effects in SO-3 Antioxidant and Its Structural Analogs, as Compared to Trialkylphenol–Dialkyl Sulfide Mixtures

E. I. Terakh, A. E. Prosenko, V. V. Nikulina, and O. V. Zaitseva

Novosibirsk State Pedagogical University, Novosibirsk, Russia

Received October 10, 2002

Abstract—The inhibiting activity of SO-3 antioxidant and its structural analogs in the model reaction of autooxidation of Vaseline oil was compared to that of synergistic mixtures of 2,4,6-trialkylphenols and didodecyl sulfide.

Sulfur-containing derivatives of sterically hindered phenols are highly effective inhibitors of free-radical oxidation of hydrocarbon substrates and occupy a prominent place among antioxidants. The high inhibiting activity of sulfur-containing phenolic antioxidants (SPAOs) is accounted for by a combination of the bifunctional mechanism of the antioxidant effect with the intramolecular synergistic effect, owing to which these compounds surpass in antioxidant activity the synergistic mixture of Ionol with didodecyl sulfide (DDS) [1–4]. Elucidation of the mechanism of intramolecular synergism is of scientific and applied importance, since it would allow development of new SPAOs surpassing the available analogs in activity. To solve this problem, it is necessary to study the interrelation between the SPAO structure and the effect of intramolecular synergism.

In this study, we analyzed the intermolecular synergistic effects in mixtures of 2,4,6-trialkylphenols (TAPs) with DDS and compared the extents of intramolecular synergism in bis[3-(3,5-di-*tert*-butyl-4-hydroxyphenyl)-propyl] sulfide (SO-3 antioxidant) and its structural analogs, as applied to the model reaction of autooxidation of Vaseline oil (Tatkhimfarmpreparaty Chemical Pharmaceutical Production Association, Kazan). The structures of the compounds under consideration are given in Tables 1 and 2.

In the experiments, we determined the induction periods of oxidation of Vaseline oil in the presence of DDS, trialkylphenols, and SPAO taken separately (τ_{DDS}, τ_{PhOH}, and τ_{SPAO}, respectively) and of the synergistic mixtures trialkylphenol + DDS ($\tau_{PhOH+DDS}$). The effects of intermolecular synergism in TAP + DDS mixtures were characterized by the quantities $\Delta\tau_{inter}$ and $\Delta\tau'_{inter}$:

$$\Delta\tau_{inter} = \tau_{PhOH+DDS} - (\tau_{DDS} + \tau_{PhOH}),$$

$$\Delta\tau'_{inter} = \tau_{PhOH+DDS}/(\tau_{DDS} + \tau_{PhOH}).$$

Studies of the antioxidant activity of TAP + DDS mixtures showed that their effect is nonadditive: In all the cases, the induction periods were longer than the sum of the induction periods in the presence of the components taken separately (Table 1). The extent of the synergistic effect in TAP + DDS mixtures largely depended on the qualitative and quantitative composition of the synergistic mixtures.

According to the classification accepted in [5], the synergism observed in this case is of the kinetic type and is due to the effect of mixture components (TAP, DDS) on different oxidation stages. For example, sterically hindered phenol terminates oxidation chains by reacting with peroxy radicals:

$$PhOH + RO_2^{\cdot} \rightarrow PhO^{\cdot} + ROOH, \qquad (1)$$

and DDS decomposes hydroperoxides:

$$R–S–R \xrightarrow{ROOH} R–SO–R \xrightarrow{ROOH} R–SO_2–R,$$

suppressing degenerate chain branching:

$$ROOH \rightarrow RO^{\cdot} + HO^{\cdot}.$$

1070-4272/03/7602-0253 $25.00 © 2003 MAIK "Nauka/Interperiodica"

Table 1. Synergism in TAP + DDS mixtures (180°C, [PhOH] = 2.5 μmol g^{-1})

PhOH*	[DDS], μmol g^{-1}	[PhOH] : [DDS] molar ratio	τ	$\tau_{DDS} + \tau_{PhOH}$	$\Delta\tau_{inter}$	$\Delta\tau'_{inter}$
			min			
Ionol	0.00	1 : 0	33	–	–	–
	1.25	1 : 0.5	79	38	41	2.08
	2.50	1 : 1	172	38	134	4.53
TMP	0.00	1 : 0	32	–	–	–
	1.25	1 : 0.5	168	37	131	4.54
	2.50	1 : 1	378	37	341	10.22
α-TP	0.00	1 : 0	52	–	–	–
	1.25	1 : 0.5	131	57	74	2.30
	2.50	1 : 1	165	57	108	2.89
I	0.00	1 : 0	30	–	–	–
	1.25	1 : 0.5	77	35	42	2.20
	2.50	1 : 1	187	35	152	5.34
II	0.00	1 : 0	27	–	–	–
	1.25	1 : 0.5	129	32	97	4.03
	2.50	1 : 1	241	32	209	7.53
III	0.00	1 : 0	40	–	–	–
	1.25	1 : 0.5	236	45	191	5.24
IV	0.00	1 : 0	31	–	–	–
	1.25	1 : 0.5	71	36	35	1.97
	2.50	1 : 1	126	36	90	3.50

* 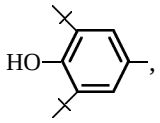
Ionol

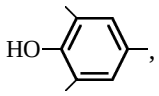
2,4,6-Trimethylphenol (TMP)

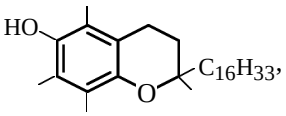
α-Tocopherol (α-TP)

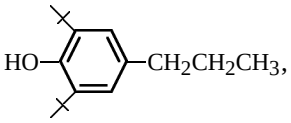
I

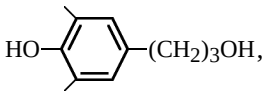
II

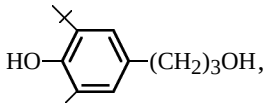
III

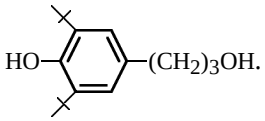
IV

Table 2. Synergistic effects of sulfur-containing phenolic antioxidants (180°C, [PhOH] = 2.5 μmol g^{-1})

Sulfide*	τ_{SPAO}, min	PhOH + DDS synergistic mixtures		Δτ, min	Δτ'	$\Delta\tau_{intra}$, min	$\Delta\tau'_{intra}$
		PhOH	[PhOH] : [DDS] molar ratio				
SO-3	113	Ionol	1 : 0.5	75	2.97	34	1.43
		I	1 : 0.5	78	3.23	36	1.47
		IV	1 : 0.5	77	3.14	42	1.59
V	300	**III**	1 : 0.5	255	6.67	64	1.27
VI	238	TMP	1 : 0.5	201	6.43	70	1.42
		α-TP	1 : 0.5	181	4.18	107	1.82
		II	1 : 0.5	206	7.44	109	1.84
VII	198	Ionol	1 : 1	160	5.21	26	1.15
		I	1 : 1	163	5.66	11	1.06
		IV	1 : 1	162	5.50	72	1.57

* 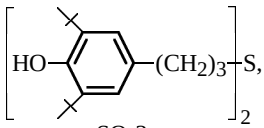
SO-3

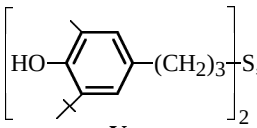
V

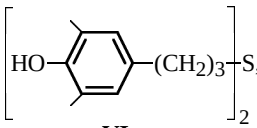
VI

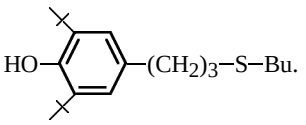
VII

Thus, both antioxidants protect each other from rapid consumption [6, 7].

Along with the kinetic synergism, TAP–DDS mixtures may also exhibit chemical synergism based on chemical reactions between the antioxidants and their transformation products [5]. For example, as demonstrated by the example of 2,6-di-*tert*-butyl-4-methylphenol (Ionol), DDS can react with oxidation products of phenolic antioxidants, regenerating the initial form of the inhibitor [7–9]. The sophisticated mechanism of synergistic interactions in TAP–DDS mixtures is indicated by the fact that, when the component ratio is varied (DDS concentration increased by a factor of 2), the induction periods grow nonlinearly.

The inhibiting activity of TAP used in combination with DDS varies depending on *o*- and *p*-substituents. The dimethyl substitution is apparently more effective than di-*tert*-butyl substitution. For example, at the molar ratios of TAP and DDS of 1 : 0.5 and 1 : 1, the mean values of $\Delta\tau'_{inter}$ for Ionol and phenols **I** and **IV** are 2.08 and 4.46, respectively, whereas for TMP, α-TP, and phenol **II** they are 3.62 and 6.88, respectively. Among the TAPs examined in combination with DDS, TMP is the most effective.

As for synergistic compositions based on 3-(3,5-dialkyl-4-hydroxyphenyl)-1-propanols **II**–**IV** in which the *p*-substituent is constant and the *o*-substituents are varied, the strongest inhibiting effect was observed with the **III** + DDS mixture, and the weakest, with the **IV** + DDS mixture; compound **III** taken separately is also more effective than **II** and **IV**.

The antioxidant activity of SPAOs was studied with SO-3 and its structural analogs **V**–**VII** as examples. These compounds differ in the extent of the steric shielding of the phenolic OH group and in the molar ratio of the phenolic and sulfide groups.

All the sulfides examined efficiently inhibit oxidation of Vaseline oil; in their inhibiting power they surpass both the structurally related TAPs and their synergistic mixtures with DDS (Table 2). This fact suggests that the SPAOs exhibit bifunctional mechanism of the antioxidant effect. The synergistic effect, which can be quantitatively characterized by the parameters $\Delta\tau$ and $\Delta\tau'$

$$\Delta\tau = \tau_{SPAO} - (\tau_{DDS} + \tau_{PhOH}),$$

$$\Delta\tau' = \tau_{SPAO}/(\tau_{DDS} + \tau_{PhOH}).$$

is strongly pronounced.

The strong synergistic effect in SPAO is apparently due to its intramolecular nature and to the favorable steric arrangement of the phenolic and sulfide fragments, so that the hydroperoxide molecule formed from the corresponding radical with the participation of the phenolic group of the inhibitor can be inactivated by the sulfide moiety without escaping into the bulk of the substrate:

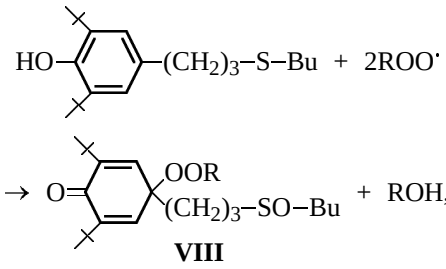

VIII (2)

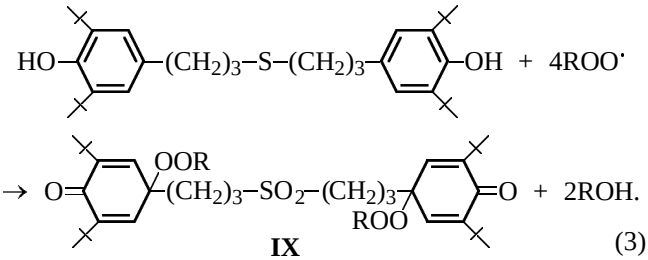

IX (3)

Thus, the reaction of the antioxidant with an active radical yields a thermally stable alkanol and not the hydroperoxide.

The extent of intramolecular synergism in SO-3 and sulfides **V**–**VII** can be characterized by the quantities $\Delta\tau_{intra}$ and $\Delta\tau'_{intra}$:

$$\Delta\tau_{intra} = \tau_{SPAO} - \tau_{PhOH+DDS},$$

$$\Delta\tau'_{intra} = \tau_{SPAO}/\tau_{PhOH+DDS}.$$

Among the sulfides examined, differing in the structure of *o*-alkyl substituents, the inhibiting activity increased in the order SO-3 > **VI** > **V**. A similar trend was observed with the structural analogs of these SPAOs, phenols **II**–**IV**.

It is known that the antioxidant activity of phenolic compounds is governed by two factors: extent of steric shielding of the phenolic OH group and energy of the PhO–H bond. Making larger the volume of the *o*-alkyl substituents, on the one hand, diminishes the energy of the PhO–H bond, which facilitates reaction (1), but, on the other hand, results in that this reaction becomes more hindered sterically. As a consequence, the most active in radical substitutions are phenolic antioxi-

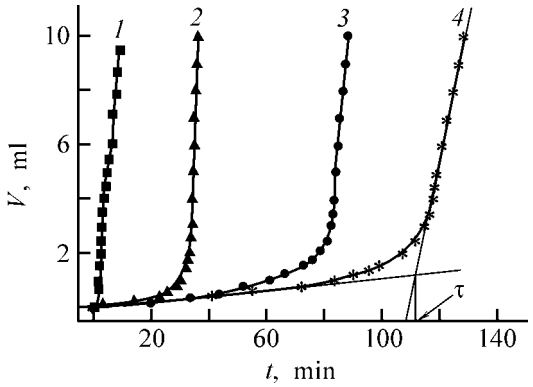

Kinetic curves of Vaseline oil oxidation. Inhibitor: (*1*) none, (*2*) Ionol, (*3*) Ionol + DDS, and (*4*) SO-3. (*V*) Volume of oxygen taken up and (*t*) time. For comments, see text.

dants with one *o*-methyl group and one *o-tert*-butyl group [10], compounds **III** and **V** in our case.

The extent of intramolecular synergism in SO-3 and sulfides **V** and **VI** was evaluated by comparison of the induction periods in the presence of these sulfides and the mixtures based on structurally related phenols **II**–**IV** containing the same *p*-substituent. No correlation was observed between the antioxidant activity of the sulfides and the extent of intramolecular synergism. The quantity $\Delta\tau'_{intra}$ was maximal for sulfide **VI**, whereas the longest induction period in oxidation of Vaseline oil was observed with sulfide **V**.

The influence of the sulfur content on the antioxidant properties of SPAOs was examined with SO-3 and sulfide **VII** as examples. The extent of intramolecular synergism in SO-3 appeared to be somewhat higher than in **VII**: The mean $\Delta\tau'_{intra}$ values were 1.50 and 1.26, respectively. At the same time, the absolute inhibiting activity of **VII** was higher than that of SO-3 by a factor of 1.75. Apparently, the antioxidant activities of these compounds do not correlate with the extent of intramolecular synergism. The higher antioxidant activity of **VII** is due to the fact that sulfoxide **VIII** formed by reaction (2) can reduce an additional hydroperoxide molecule formed in the substrate without participation of the phenolic groups of the antioxidant. Oxidative transformations of SO-3 [reaction (3)] yield sulfone **IX**, incapable of inactivating additional hydroperoxide molecule; therefore, SO-3 is less effective as inhibitor.

EXPERIMENTAL

Oxidation of Vaseline oil was performed in a gasometric unit similar to that described in [11], at oxygen pressure of 1 atm. The total oil volume was 5 ml; the concentrations of antioxidants were 1.25 and 2.5 μmol per gram of oil. The oxidation was performed at 180°C. The kinetic curves were plotted (see figure), and the induction period τ was determined graphically as the intersection point of the tangents to the initial and final portions of the kinetic curves. Three or four replicate runs were performed; the average induction periods (deviations ≤3%) are listed in Tables 1 and 2.

Ionol and α-TP were purchased from Acros Organics; TMP, from Lancaster; 3-(3,5-dialkyl-4-hydroxyphenyl)-1-propanols **II**–**IV** were prepared at the Novosibirsk Institute of Organic Chemistry, Siberian Division, Russian Academy of Sciences); and the other antioxidants were synthesized as described in [12]. The main substance content in the antioxidants was no less than 97–99%.

CONCLUSIONS

(1) Mixtures of 2,4,6-trialkylphenols with dodecyl sulfide show a pronounced synergistic effect in inhibition of Vaseline oil oxidation; the extent of this effect depends on the molar ratio of the components and the structure of the phenolic component.

(2) The sulfur-containing phenolic antioxidants surpass in the inhibiting activity the mixtures of structurally related 2,4,6-trialkylphenols with dodecyl sulfide, suggesting the occurrence of intramolecular synergism. The extent of intramolecular synergism depends on the structure of the *o*-alkyl substituents and relative content of sulfur in the inhibitor molecule.

(3) The results of the experiments performed can be used for development of new high-performance sulfur-containing phenolic antioxidants with pronounced intramolecular synergism.

REFERENCES

1. RF Patent 1 072 420.
2. Prosenko, A.E., Terakh, E.I., Kandalintseva, N.V., *et al., Zh. Prikl. Khim.*, 2001, vol. 74, no. 11, pp. 1839–1843.
3. Prosenko, A.E. and Terakh, E.I., Abstracts of Papers, *VI Mezhdunarodnaya konferentsiya "Bioantioksidant"* (VI Int. Cond. "Bioantioxidant"), Moscow, April 16–19, 2002, pp. 480–481.
4. Pinko, P.I., Terakh, E.I., Gorokh, E.A., *et al., Zh. Prikl. Khim.*, 2002, vol. 75, no. 10, pp. 1694–1698.
5. Karpukhina, G.V. and Emanuel', N.M., *Dokl. Akad. Nauk SSSR*, 1984, vol. 276, no. 5, pp. 1163–1167.

6. *Ingibirovanie protsessov okisleniya polimerov smesyami stabilizatorov* (Inhibiton of Polymer Oxidation Using Mixtures of Stabilizers), Levin, P.I., Ed., Moscow: NII Khimpolimer, 1970.
7. Emanuel', N.M. and Lyaskovskaya, Yu.N., *Tormozhenie protsessov okisleniya zhirov* (Inhibition of Fat Oxidation), Moscow: Pishchepromizdat, 1961.
8. Voigt, J., *Die Stabilisierung der Kunststoffe gegen Licht und Wärme*, Berlin: Springer, 1966.
9. Kharitonova, A.A., Shilenko, E.I., Tsepalov, V.F., *et al.*, *Kinet. Katal.*, 1982, vol. 23, no. 3, pp. 745–747.
10. Roginskii, V.A., *Fenol'nye antioksidanty: Reaktsionnaya sposobnost' i effektivnost'* (Phenolic Antioxidants: Reactivity and Performance), Moscow: Nauka, 1988.
11. Tsepalov, V.F., in *Issledovanie sinteticheskikh i prirodnykh antioksidantov in vivo i in vitro: Sbornik uchenykh statei* (In vivo and in vitro Studies of Synthetic and Natural Antioxidants: Coll. of Scientific Papers), Moscow: Nauka, 1992, pp. 16–26.
12. USSR Inventor's Certificate, no. 1370952.

Russian Journal of Applied Chemistry, Vol. 76, No. 2, 2003, pp. 258–260. Translated from Zhurnal Prikladnoi Khimii, Vol. 76, No. 2, 2003, pp. 266–268.

ORGANIC SYNTHESIS AND INDUSTRIAL ORGANIC CHEMISTRY

Synthesis of New Surface-Active β-Amino Amides, Agents for Fixation of Dyes on Cotton Fibers, from *N*-[Tri(hydroxymethyl)methyl]acrylamide

G. S. Simonyan, R. S. Arutyunyan, N. M. Beileryan, and E. A. Grigoryan

Yerevan State University, Yerevan, Armenia

Geratsi State Medical University, Yerevan, Armenia

Received July 16, 2002

Abstract—Amines containing amido and hydroxy groups were prepared. Their surface activity was studied, and the possibility of their use as cotton fiber modifiers was examined.

Surface-active amines (SAAs) containing various functional groups are used in various branches of industry [1], in particular, in production and dyeing of fibers [2, 3].

Usually, cotton and cellulose fibers cannot be dyed with acid dyes suitable for wool. For dyeing viscose fibers, small amounts of agents containing basic functional groups, e.g., synthetic resins or amino compounds modifying the fiber surface, are added to viscose spinning solution. Therefore, molecules containing amino, amido, hydroxy, and other functional groups exhibiting affinity for various types of dyes (direct, acid, active) may also be effective as modifiers improving the dyeability of cotton and cellulose fibers.

In this study, we prepared, following the procedure described in [4, 5], new nonionic SAAs **I**–**V** containing amino, amido, and hydroxy groups:

$$CH_2{=}CHC(=O)NHC(CH_2OH)_3 + R^1R^2NH \longrightarrow R^1R^2NCH_2CH_2C(=O)NHC(CH_2OH)_3,$$

where (R^1 + R^2) = $(CH_2)_5$ (**I**), $(CH_2)_2O(CH_2)_2$ (**II**); R^1 = R^2 = C_2H_5 (**III**), C_3H_7 (**IV**); R^1 = H, R^2 = C_6H_{13} (**V**).

We studied the colloidal-chemical properties of these compounds and their modifying effect on cotton fibers in the course of dyeing.

The SAAs were identified by ^{1}H NMR spectroscopy (Bruker ACG 250 spectrometer, D_2O, internal reference TMS) and mass spectrometry (TUEL 1MS-DX 300 device).

The SAAs were prepared as follows. A mixture of equimolar amounts of the amine and *N*-[tri(hydroxymethyl)methyl]acrylamide in water was kept at 293 K until the reaction was complete. The surface-active amines were separated from water by lyophilic drying and dried at room temperature.

3-Piperidinopropanoic acid *N*-[tri(hydroxymethyl)-methyl]amide I. *M* = 260; *m*/*z* = 261; $[M + H]^+$. ^{1}H NMR spectrum, δ, ppm: 3.5 s (6H, CH_2OH), 2.25 t (2H, $CH_2C{=}O$), 2.55 t (2H, NCH_2), 2.45 t [4H, $(CH_2)_2N$], 1.5 m [6H, $(CH_2)_3$], 8.05 s (NH), 4.05 s (3H, OH).

3-Morpholinopropanoic acid *N*-[tri(hydroxymethyl)methyl]amide II. *M* = 262; *m/z* = 263, $[M + H]^+$. ^{1}H NMR spectrum, δ, ppm: 3.5 s (6H, CH_2OH), 2.25 t (2H, $CH_2C{=}O$), 2.5 t (2H, NCH_2), 2.4 t [4H, $(CH_2)_2N$], 3.55 t [4H, $O(CH_2)_2$], 7.9 s (NH), 4.05 s (3H, OH).

3-(Diethylamino)propanoic acid *N*-[tri(hydroxymethyl)methyl]amide III. *M* = 248; *m/z* = 249, $[M + H]^+$. ^{1}H NMR spectrum, δ, ppm: 3.5 s (6H, CH_2OH), 2.2 t (2H, $CH_2C{=}O$), 2.6 t (2H, NCH_2), 2.5 t [4H, $(CH_2)_2N$], 0.95 t (6H, CH_3), 7.85 s (NH), 3.85 s (3H, OH).

3-(Dipropylamino)propanoic acid *N*-[tri(hydroxymethyl)methyl]amide IV. *M* = 276; *m/z* = 277,

1070-4272/03/7602-0258 $25.00 © 2003 MAIK "Nauka/Interperiodica"

Properties of surface-active amines **I**–**V**

SAA	Yield, %	Found, %			Formula	Calculated, %			σ_{CMC},* dyne cm^{-1}	CMC × 10^2, M
		C	H	N		C	H	N		
I	98	55.45	9.35	10.91	$C_{12}H_{24}N_2O_4$	55.38	9.23	10.77	57	15.40
II	100	50.52	8.45	10.80	$C_{11}H_{22}N_2O_5$	50.38	8.37	10.69	52	11.40
III	97	53.10	9.58	11.20	$C_{11}H_{24}N_2O_4$	53.27	9.68	11.29	68	0.95
IV	96	56.40	10.2	10.0	$C_{13}H_{28}N_2O_4$	56.52	10.14	10.14	55	0.36
V	98	56.35	10.0	10.0	$C_{13}H_{28}N_2O_4$	56.52	10.14	10.14	36	0.16

* (σ_{CMC}) Surface tension at CMC.

$[M + H]^+$. ^1H NMR spectrum, δ, ppm: 3.5 s (6H, CH_2OH), 2.2 t (2H, $CH_2C{=}O$), 2.6 t (2H, NCH_2), 2.4 m [4H, $(CH_2)_2N$], 1.4 m (4H, CH_2CH_3), 0.85 t (6H, CH_3), 7.65 s (NH), 4.05 s (3H, OH).

3-(Hexylamino)propanoic acid *N*-[tri(hydroxymethyl)methyl]amide V. *M* = 276; *m/z* = 276, $[M + H]^+$. ^1H NMR spectrum, δ, ppm: 3.5 s (6H, CH_2OH), 2.2 t (2H, $CH_2C{=}O$), 2.6 t (2H, NCH_2), 2.5 t (2H, CH_2N), 0.9 t (3H, CH_3), 1.3 m [8H, $CH_3(CH_2)_4$], 7.6 s (2H, NH), 4.05 s (3H, OH).

The critical micelle concentration, CMC (M), of SAAs was determined from the isotherms of electrical conductivity (S m^{-1}) and surface tension σ (dyne cm^{-1}). The surface tension of aqueous SAA solutions was measured by the method of the maximum bubble pressure on a Rebinder device [6], and the electrical conductivity, as described in [7]. The measurement temperature was 303 ± 0.1 K.

The foaming power was evaluated by determining the foam stability of 1% aqueous SAA solutions from the ratio of the foam column height measured 5 min after foaming to its initial height [1].

Colloidal-chemical studies showed that the amines synthesized are micelle-forming surfactants (see table). As expected (see table, figure), the CMC and σ decrease with increasing length of the alkyl groups in SAA molecules (σ of water at 303 K is 71.18 dyne cm^{-1}).

The SAAs examined show no foam stability, which is significant for modifiers of cotton and cellulose fibers. Taking into account the structures of SAAs and their σ values, we chose compounds **II** and **V** as modifiers of cotton tricot fabrics.

Two modification procedures were used. In the first procedure, tricot fabrics (bath ratio 50) were treated for 20–30 min at 353–363 K with 5–10% aqueous solutions of **II** and **V**. After treatment, the fabric was gently squeezed, washed with two portions of water, and dried in air. In the second procedure, to enhance the effect of SAAs, dimethylolurea was added at the end of treatment performed according to the first procedure. After that, the fabric was squeezed without washing and dried in air. For cross-linking and fixation of the modifier on the fibers, the fabrics were heat-treated for 5 min. Then the modified fabrics were dyed with a 3 g l^{-1} aqueous solution of Acid Blue anthraquinone dye for 30–40 min at 358–363 K (bath ratio 30). The fabrics dyed were washed with water and dried.

The tests showed that the tricot fabrics modified by the first procedure are dyed to moderate tints; with **V**, the tints are lighter than with **II**. It should be noted that the second procedure makes it possible to obtain darker tints fairly resistant to wet treatment.

Thus, amine-containing acid amides improve the dyeability of cotton fibers with acid dyes.

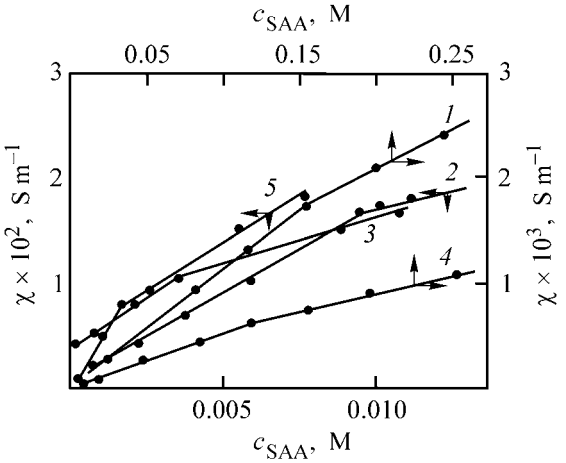

Isotherms of specific electrical conductivity χ of SAAs in water at 303 K. (c_{SAA}) SAA concentration. SAA: (*1*) **I**, (*2*) **III**, (*3*) **IV**, (*4*) **II**, and (*5*) **V**.

CONCLUSIONS

(1) Amines containing amido and hydroxy groups were prepared; they exhibit micelle-forming power and are poor foaming agents.

(2) The surface-active amines synthesized are active modifiers of cotton fibers in their dyeing with acid dyes.

REFERENCES

1. *Poverkhnostno-aktivnye veshchestva* (Surfactants), Abramzon, A.A. and Gaevoi, G.M., Eds., Leningrad: Khimiya, 1979.
2. Serebryakova, Z.G., *Poverkhnostno-aktivnye veshchestva v proizvodstve iskusstvennykh volokon* (Surfactants in Production of Manmade Fibers), Moscow: Khimiya, 1986.
3. *Kratkaya khimicheskaya entsiklopediya* (Concise Chemical Encyclopedia), Knunyants, I.L., Ed., Moscow: Sovetskaya Entsiklopediya, 1963, vol. 2, p. 77.
4. *Khimiya alkenov* (Chemistry of Alkenes), Patay, S., Ed., Leningrag: Khimiya, 1969.
5. Simonyan, G.S., Beileryan, N.M., Pirumyan, E.G., *et al.*, *Kinet. Katal.*, 2001, vol. 42, no. 4, pp. 526–530.
6. *Praktikum po kolloidnoi khimii* (Practical Course of Colloid Chemistry), Neiman, E.R., Ed., Moscow: Vysshaya Shkola, 1972.
7. Astvatsatryan, S.A., Arutyunyan, R.S., Beileryan, N.M., and Gevorkyan, A.V., *Uchen. Zap. Erevan. Gos. Univ.*, 1984, no. 2, pp. 84–87.

Russian Journal of Applied Chemistry, Vol. 76, No. 2, 2003, pp. 261–263. Translated from Zhurnal Prikladnoi Khimii, Vol. 76, No. 2, 2003, pp. 269–271.

ORGANIC SYNTHESIS AND INDUSTRIAL ORGANIC CHEMISTRY

Modification of Coal Humic Acids with Formaldehyde

I. N. Ryabova and G. A. Mustafina

Institute of Organic Synthesis and Coal Fuel Chemistry of the Republic of Kazakhstan, Karaganda, Kazakhstan

Received May 31, 2002

Abstract—Optimal conditions for condensation of coal humic acids with formaldehyde in alkaline medium were determined. The conversion of formaldehyde as influenced by temperature, reaction time, component ratio, and catalyst content was studied.

Humic acids (HAs) and products based on them are extensively studied today, because they contain various functional groups and can be used as environmentally safe and available raw materials for production of ion-exchange materials, soil structuring agents, etc.

However, low mechanical strength, strong swellability in water and aqueous acidic solutions, and complete dissolution in alkaline solutions hinder wide use of humic acids. Modification of HAs can enhance their reactivity, thermal and chemical resistance, and sorption properties and can affect their solubility [1, 2]. It was found that the modified products surpass HAs in some respects and show promise for industrial use.

In particular, HAs can be modified with formaldehyde (FA) and urea. However, if it is assumed that, in the case of FA, the reaction mechanism is similar to that by which phenol-formaldehyde oligomer is formed {schemes (1) and (2) [3]}, then, for the subsequent condensation with urea, the intermediate hydroxymethyl derivatives should be preserved to the maximum possible extent [scheme (1)]:

$$ArH + CH_2O = ArCH_2OH, \quad (1)$$

$$ArCH_2OH + ArH = ArCH_2Ar + H_2O. \quad (2)$$

If curing by the resol type is intended, then the highest content of FA is possible and desirable.

The aim of this study was to find the optimal conditions of polycondensation of HAs and FA in alkaline medium and to determine the effect of modification on the ion-exchange properties of the reaction products.

EXPERIMENTAL

We studied condensation as influenced by temperature (x_1), reaction time (x_2), molar component ratio (x_3), and catalyst content (x_4). Alkali was taken in a minimal amount required for complete conversion of the acid into salt, and only in this case, the reaction proceeds in aqueous solution under the homogeneous conditions; in neutral and acidic solutions, HAs are insoluble.

The process was optimized using the mathematical experimental design [4] based on a 4×5 matrix. The experimental results were obtained, and partial dependences $y_i = f(x_i)$ for the above process parameters (Fig. 1) plotted, in accordance with the spec-

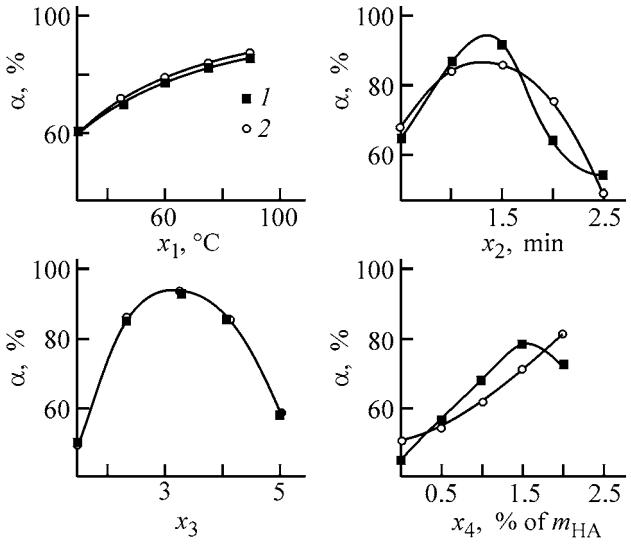

Fig. 1. Conversion α of FA in reaction with HAs vs. temperature x_1, reaction time x_2, HA : FA molar ratio x_3, and weight fraction of catalyst x_4. (*1*) Experimental and (*2*) calculated data.

1070-4272/03/7602-0261 $25.00 © 2003 MAIK "Nauka/Interperiodica"

Table 1. Levels of the parameters studied

Parameter	Level				
	1	2	3	4	5
x_1, K	303	318	333	348	363
x_2, h	0.5	1.0	1.5	2.0	2.5
x_3, HA : FA	1 : 1	1 : 2	1 : 3	1 : 4	1 : 5
x_4, % relative to m_{HA}	0	0.5	1.0	1.5	2.0

Table 2. Properties of the initial and modified compounds

Compound	SEC(Ca^{2+}), mg-equiv g^{-1}	Content of acid groups, mg-equiv g^{-1}	pK_i	pH of aqueous suspension
Initial coal	0.27	2.93	–	5.4
HA	0.88	4.35	4.50	3.8
HFP-1	1.40	5.48	4.54	3.3
HFP-2	1.39	5.87	4.51	2.9

ified conditions (Table 1). The reaction course was monitored by FA conversion.

The partial dependences of FA conversion y_i on parameters x_i were approximated with the following functions:

$$y_1 = 0.049\exp(-16.73/x_1), \quad (3)$$

$$y_2 = 0.38 + 0.74x_2 - 0.28x_2^2, \quad (4)$$

$$y_3 = 0.224 + 2.54x_3 - 2.19x_3^2, \quad (5)$$

$$y_4 = 0.74\exp(0.266x_4). \quad (6)$$

The generalized equation in terms of optimization parameters [4] is as follows:

$$y = y_1y_2y_3y_4 \times 0.69^{-4}. \quad (7)$$

The maximal FA conversion is observed under the following conditions: HA : FA molar ratio 1 : 3, 75°C, reaction time 1 h, and concentration of base catalyst 2% relative to the HA weight.

The kinetic curves of formation of hydroxymethyl derivatives are shown in Fig. 2; the highest yield is observed in the first 10–30 min, depending on the ini-

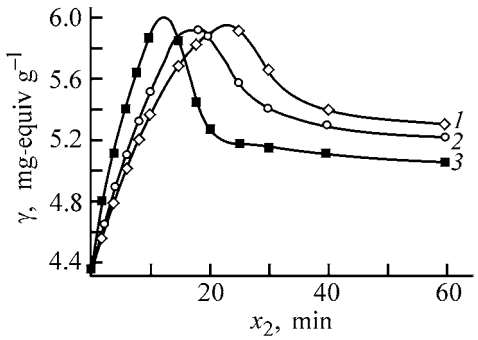

Fig. 2. Variation with time of the content of the acid groups γ at 333 K and HA : FA molar ratio of (*1*) 1 : 1, (*2*) 1 : 2, and (*3*) 1 : 3. (x_2) Reaction time.

tial component ratio. In all the cases, the maximal content of the hydroxymethyl groups is constant and equal to 5.9 mg-equiv g^{-1}, or about 25% of the initial content of the acid groups. The increase in the FA content only makes earlier the onset of condensation. Hence, to obtain the highest content of the hydroxymethyl derivatives at HA : FA molar ratio 1 : 3, catalyst weight fraction 2%, and 60°C, the reaction time can be decreased to 10 min.

Since an increase in the complexity of the polymeric chain can affect the sorption capacity of the ion exchanger, it was necessary to compare the polyelectrolytic and sorption properties of the modified products with those of the initial HAs. For this purpose, we determined the ionization constants (pK_i) and static exchange capacities (SEC) for calcium cations of the initial compound and two modified humic-formaldehyde polymers (HFPs) differing in the preparation conditions, namely, in the component molar ratio and reaction time [1 : 1 and 60 min for HFP-1; 1 : 2 and 15 min for HFP-2).

Addition of FA may cause redistribution of the electron density in the condensed HA system, enhancing the acid properties of weak acid groups and thus increasing the SEC. However, nearly similar pK_i values for the compounds in question suggest that this is hardly the case, and SEC is more probably determined by the content of the acid groups.

As seen from Table 2, the sorption capacity of the modified products increases by nearly a factor of 2, and the decrease in the reaction time does not affect noticeably the sorption capacity. This is probably due to the fact that the steric environment of the hydroxymethyl groups sorbing calcium cations hinders their participation in condensation. Thus, hydroxymethyl derivatives, as well as the condensation products, can be used as sorbents or soil-structuring agents. However, preparation of HFP-2 type products is preferable for the subsequent curing, because formation of meth-

ylene bridges from hydroxymethyl groups allows preparation of partially cross-linked polymers with higher molecular weight. As a result, the mechanical strength of these compounds increases, whereas their solubility in alkaline medium decreases, which expands the range of application of the modified polymers.

Humic acids were prepared from oxidized coal of the Oikaragaiskoe field; first the coal was treated with alkali and then humic acids were precipitated from aqueous solution with hydrochloric acid. Formaldehyde was used as 33% aqueous solution; the content of FA was monitored potentiometrically by oximation [5].

The resulting products were precipitated with 2 M hydrochloric acid; the precipitates were filtered off and washed to negative reaction of the filtrate with silver nitrate. The content of the acid groups in the products was determined by conductometry [6]. The experimental results were processed using the QUATTRO PRO 4.0 software.

The exchange capacity was determined under static conditions, using the ion exchangers in the H^+ form. Weighed portions of the samples (~0.4 g) were equilibrated with 50 ml of a 0.02 M calcium chloride solution. The concentration of metal cations in the equilibrium solutions was determined by complexomeric titration [7].

The averaged apparent ionization constants were evaluated graphically from potentiometric titration curves, for which purpose weighed portions of the samples (~0.4 g) were placed in 30 ml 1 M NaCl solution and titrated with 0.1 M NaOH solution.

CONCLUSIONS

(1) The optimal conditions for polycondensation of humic acids with formaldehyde are as follows: molar ratio of reagents molar ratio 1 : 3, 60°C, reaction time 60 min, catalyst weight 2% relative to that of humic acids.

(2) The maximal amount of the intermediate products is formed in the first 10–30 min, depending on the reagent ratio, but the magnitude of the maximum is independent of this ratio.

(3) Modification of humic acids with formaldehyde increases the sorption capacity for calcium cations, with the average ionization constant remaining unchanged.

REFERENCES

1. Lyubchenko, V.I., Dumbai, I.N., Gubanova, E.N., *et al., Khim. Tverd. Topl.*, 1999, no. 2, pp. 38–46.
2. Kasatochkin, V.I., Nefedova, L.N., and Larina, N.K., *Khim Tverd. Topl.*, 1971, no. 7, pp. 19–28.
3. Gutsalyuk, V.G., Nevskii, V.M., and Safronova, A.S., *Areno-formal'degidnye oligomery* (Arene-Formaldehyde Oligomers), Alma-Ata: Nauka, 1986.
4. Malyshev, V.P., in *Veroyatnostno-determinirovannoe planirovanie eksperimenta* (Probabilistic-Deterministic Experimental Design), Alma-Ata: Nauka, 1981, pp. 11–52.
5. Siggia S., and Hanna, J.G., **Quantitative Organic Analysis via Functional Groups**, New York: Wiley–Interscience, 1979.
6. Dzhalyabova, L.V., Aleksandrov, I.V., and Kameneva, A.I., *Khim. Tverd. Topl.*, 1981, no. 5, pp. 28–33.
7. Schwarzenbach, G. and Flaschka, H., *Die Komplexometrische Titration*, Stuttgart: Ferdinand Enke, 1965.
8. Libinson, G.S., *Fiziko-khimicheskie svoistva karboksil'hykh kationitov* (Physicochemical Properties of Carboxylic Cation Exchangers), Moscow: Nauka, 1969.

Russian Journal of Applied Chemistry, Vol. 76, No. 2, 2003, pp. 264–270. Translated from Zhurnal Prikladnoi Khimii, Vol. 76, No. 2, 2003, pp. 272–278.

MACROMOLECULAR CHEMISTRY AND POLYMERIC MATERIALS

Fast Reactions in Polymer Syntheses

K. S. Minsker, A. A. Berlin, V. P. Zakharov, G. S. D'yakonov, A. G. Mukhametzyanova, and G. E. Zaikov

Bashkir State University, Ufa, Bashkortostan, Russia

Semenov Institute of Chemical Physics, Russian Academy of Sciences, Moscow, Russia

Kazan State Technological University, Kazan, Tatarstan, Russia

Emanuel Institute of Biochemical Physics, Russian Academy of Sciences, Moscow, Russia

Received June 13, 2002

Abstract—Specific features of fast polymerization processes necessitate use of new highly productive compact plug-flow tubular turbulent reactors. Theoretical examination of turbulent mixing in the reaction zone is made, allowing control of fast polymerization in polymer synthesis.

It has been demonstrated in studying liquid-phase synthesis of macromolecular compounds that many of such reactions are very fast (characteristic reaction time $\tau_{ch} < 0.1–0.01$ s). In this case, even very slow delivery of a polymerization initiator, use of dilute reagent solutions, and vigorous stirring cannot ensure isothermal polymerization. Chemical reactions of this type start long before the reagents delivered to the reaction zone are mixed. These reactions are diffusion controlled, being limited by reagent mixing kinetics, primarily, by the turbulence level in the reaction space, since the reagent mixing time is mostly longer than the characteristic reaction time ($\tau_{mix} > \tau_{ch}$).

This essentially new class of chemical reactions including syntheses of many polymeric products appears to be virtually not understood [1]. Among them are electrophilic polymerization of isobutylene, styrene, *p*-chlorostyrene, and cyclopentadiene; ionic polymerization of formaldehyde; irreversible polycondensation; copolymerization of isobutylene with isoprene and styrene; synthesis of chlorobutyl rubber; cationic polymerization of piperylene; formation of growth centers with Ziegler–Natta catalytic systems; initiation, particularly, in syntheses of stereoregular isoprene and butadiene rubbers and ethylenepropylene elastomers.

It has been demonstrated in a simple experiment modeling fast electrophilic polymerization of isobutylene in the presence of $AlCl_3$ (243 K) that the reaction proceeds essentially (to 80–95 wt %) locally, i.e., directly in the catalyst delivery zone [2]. In this case, the reaction mass temperature is not the same in different zones of the apparatus, depending on the local monomer and catalyst concentrations. Topochemically, fast polymerization is brush flame-like, with typical gradients of temperature, reagent concentrations (Figs. 1c, 1d), and product along the reaction zone. In this case, the reaction zone resembles a combustion front. In performing fast polymerization in bulk mixer apparatus, it is virtually impossible to achieve isothermal conditions in the reaction zone, so that, in actual processes, the temperature in the bulk of the reactor may rise by tens of degrees and no adequate modeling of the kinetic parameters can be made by the classical methods. As a result, among the specific features of fast polymerization are nonuniform molecular structure of the resulting polymeric products and, therefore, their performance characteristics, scatter of molecular characteristics of the polymer (molecular weight MW and molecular-weight distribution MWD), and, finally, irreproducibility of experiments.

An important result obtained analyzing experimental data and solving the inverse problem for the case of cationic polymerization of isobutylene, as an example of fast polymerization, was the establishment of the possibility of attaining a macroscopic

1070-4272/03/7602-0264 $25.00

quasiideal plug-flow mode in turbulent flows confined by an impermeable cylindrical wall, having no match in the present-day technology. This mode provides quasi-isothermal reaction conditions by virtue of formation of a plane front of reagent concentrations and temperature over the interval confined by strictly fixed radii R_{max} and R_{min} of the jet reaction zone (Figs. 1a and 1b). Also, this mode ensures highly efficient mixing of the reagents and, as a result, leads to uniform radial distribution of the reagent concentrations and temperature throughout the reaction zone. Taking into account the longitudinal turbulent mixing of reagents distinguishes this mode from the known ideal plug-flow mode in laminar flows.

The quasi-ideal plug-flow mode is achieved at reagent flow velocity V in the reaction zone sufficiently high to provide high turbulence level. In this case, important factors influencing the reagent mixing time τ_{mix} and molecular-weight characteristics of the resulting polymeric products (MW and MWD) are the geometry and design of the reaction volume. Conditions of establishment of the quasi-ideal plug-flow turbulent mode (planar reaction front) in fast polymerization are determined by the relationship $\tau_{mix} = R^2/D_{turb} < \tau_{ch} = 1/k_t$ (Figs. 1a and 1b), where D_{turb} is the turbulent diffusion coefficient ($m^2\ s^{-1}$) and k_t, chain termination rate constant (s^{-1}). Therefore, there exists a critical radius R_{cr} corresponding to transition from the quasi-ideal plug-flow mode to the brush flame mode:

$$R_{cr} = \sqrt{D_{turb}/k_t}. \quad (1)$$

With decreasing reaction mixture velocity V within the turbulent mode limits, the "erosion" of the temperature front in the reaction zone through longitudinal turbulent diffusion and heat transfer in the direction opposite to that of flow motion results in that the temperature is virtually constant throughout the reaction volume (quasi-isothermal mode). This is the basic distinction from the ideal plug-flow mode. Making D_{turb} higher by raising V or changing design of the reaction zone leads to the corresponding increase in the reagent conversion. In this case, the residence time of the reagents in the reaction zone, τ_r, decreases, and the reaction zone itself becomes more compact (Fig. 2). Furthermore the temperature fluctuations in the reaction zone are smoothed, regardless of the fact that the total product yield and heat liberation increase [2].

The establishment of the possibility of attaining the quasi-ideal plug-flow mode described by Eq. (1) in the reaction zone allowed development of a new class of chemical apparatus, based on tubular turbulent reactors (Fig. 3) [3, 4]. The use of such compact highly productive power- and resource-saving reactors operating in the quasi-ideal plug-flow mode

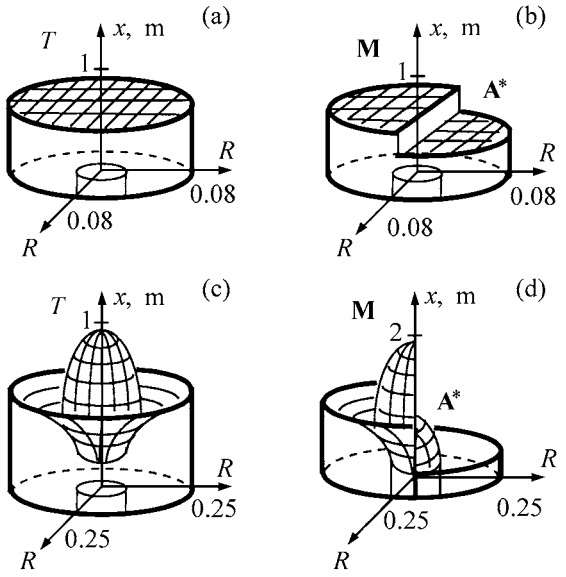

Fig. 1. (a, c) Temperature fields and (b, d) concentration fields of growth centers $\mathbf{A}^*$ and monomer **M** formed in fast polymerization of isobutylene in a flow with R = 0.08 (a, b) and 0.25 m (c, d). Conversion of monomer (wt %): (a, b) 99.3 and (c, d) 65.0. ΔT (K): (a, b) 28 and (c, d) 22. $c_{\mathbf{M}}$ = 1 M, c_{Al} = 4.5 mM, D_{turb} = 0.025 $m^2\ s^{-1}$, $k_p = 10^5$ l $mol^{-1}\ s^{-1}$, k_t = 20 s^{-1}, and T_0 = 300 K. (x) Coordinate. (a, b) Planar front of the reaction controlling the quasi-isothermal regime in the reaction zone and (c, d) brush flame-like process.

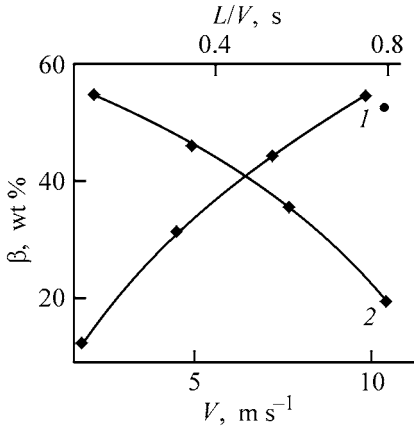

Fig. 2. Poly(isobutylene) yield β vs. (*1*) reaction mixture velocity V and (*2*) characteristic reaction time L/V. L = 2 m, $c_{\mathbf{M}}$ = 2 M, c_{Al} = 4.5 mM, R = 0.25 m, and T_0 = 300 K.

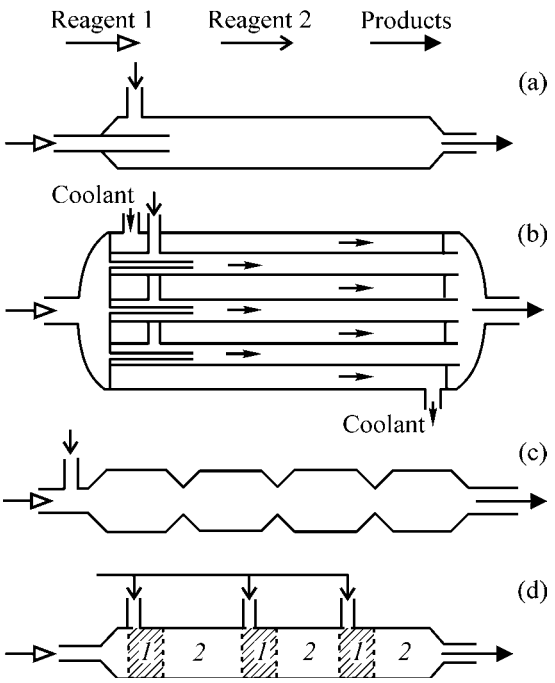

Fig. 3. Schematics of tubular turbulent reactors: (a) constant diameter of the reaction zone, (b) shell-and-tube design (c) divergent-convergent design, and (d) zonal reactor: (*1*) reaction zone and (*2*) cooling zone.

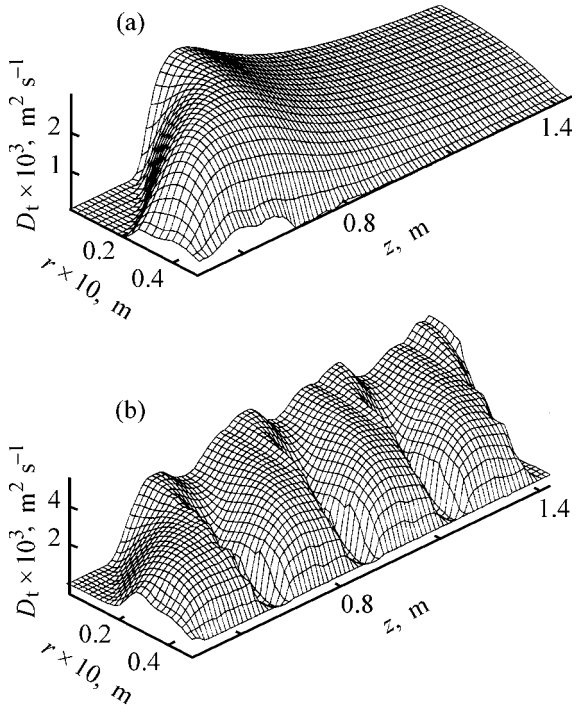

Fig. 4. Distribution of the turbulent diffusion coefficient D_{turb} in the reaction zone of (a) cylindrical and (b) divergent-convergent reactors. Re = 2×10^5, R_{cr} = 0.025 m, V = 4 m s^{-1}, and ρ = 1000 kg m^{-3}. (r, z) Radial and longitudinal coordinates.

(Fig. 3) is the optimal solution of the problem of fast polymerization.

This new type of apparatus combines the advantages of plug-flow tubular reactors and stirred continuous reactors, also demonstrating its own distinctive features and technological advantages such as (a) possibility of achieving high turbulence level along the anture length of a divergent-convergent apparatus (Fig. 4) [5]; (b) effect of the kinetic and hydrodynamic parameters of the process on the optimal size of the reaction zone [2]; (c) influence of the reaction zone geometry on the yield and composition of the product (Fig. 2); (d) possibility of attaining the ideal plug-flow turbulent mode at $\tau_{ch} \geq \tau_{mix}$, which is of great importance, allowing the process to be performed under quasi-isothermal conditions; (e) possibility of obtaining self-similar flows at Reynolds number Re $\geq 800/f$, where $f = 0.117 + 0.0488\gamma - 0.0012\gamma^2 + 1.374 \times 10^{-5}\gamma^3 - 5.9 \times 10^{-8}\gamma^4$ and γ is the diffuser divergence angle, specifically, at $\gamma = 30-80°$ and Re $\geq 950 \pm 50$ [6]; (f) possibility of controlling fast polymerization by, e.g., varying the reaction zone geometry (d, L) and hydrodynamic parameters in the reactor (V, D_{turb}) [7].

Previously we obtained for divergent-convergent tubular turbulent reactors operating in the self-similar flow mode relationships for the mean turbulent diffusion coefficient D_{turb}, specific kinetic energy K of turbulence and its dissipation ε, and also for the characteristic times of turbulent (τ_{turb}), micro- (τ_{micro}), and mesomixing (τ_{meso}), which allow optimization of the reactor design and operation mode [7]:

$$D_{turb} = 0.012 f V_c d_c,\ K = 0.048 f^2 V_c^2,\ \varepsilon = 0.021 f^3 V_c^3/d_c,$$

$$\tau_{turb} = 80.65 l^2/f V_c d_c,\ \tau_{micro} = 119.4[\nu d_c/(f^3 V_c^3)]^{0.5},$$

$$\tau_{meso} = 3.62(l^2/d_c)^{1/3}/(f V_c). \quad (2)$$

Here V_c is the reagent flow velocity in the confuser (m s^{-1}), d_c, the diameter of the narrow section of the reaction zone (m); ν, the kinematic viscosity (m^2 s^{-1}); l, the reaction zone length (m).

Comparison of the characteristic times can reveal the mechanism controlling the smoothing of the reagent concentration fields in the reaction zone, which, in its turn, allows control of the mass transfer and optimization of the reactor design.

Performing fast polymerization in plug-flow turbulent tubular reactors (planar reaction front) allowed development of a new method for estimating some kinetic parameters, particularly, the chain propagation

and termination rate constants k_p and k_t for cationic polymerization of isobutylene [2]. It is typical of the plug-flow mode that the effective time of reagent residence in the reaction zone, $\tau_r = (L/V)_{ef}$, controlling the reaction zone length L at which the polymer yield amounts to 90%, is related to with kinetic parameters of the process by

$$\left(\frac{L}{V}\right) = -\frac{1}{k_t}\ln\left\{1 + \frac{k_t}{k_p[\mathbf{A}^*]_0}\ln\left[0.1 + 0.9\exp\left(\frac{k_p[\mathbf{A}^*]_0}{k_t}\right)\right]\right\}, \quad (3)$$

where $[\mathbf{A}^*]_0$ is the initial catalyst concentration.

A study of the polymer yield as a function of L or V at various catalyst concentrations and $R_{cr} > R$ allowed experimental determination of the rate constants for certain elementary reactions occurring in fast polymerization of isobutylene. For example, at 243 K, k_p and k_t were estimated to be 10^6 l mol^{-1} s^{-1} and 17.5 ± 5 s^{-1}. Note that the experimental k_p is, in general, consistent with published data, and k_t was estimated for the first time.

From the experimental characteristic residence time τ_r we estimated the rate constant of chlorination of butyl rubber with chlorine ($k \sim 150 \pm 50$ l mol^{-1} s^{-1} [8, 9]). This polymer-analogous reaction was carried out in a divergent-convergent tubular turbulent reactor (diffuser radius R_d = 0.025 m, confuser radius $R_c = R_d/2$, L = 2 m, reactor volume ~0.004 m^3) filled with special Teflon packing. Based on the results obtained, the indicated reaction was related to a new class of fast chemical reactions [1], and it was concluded that it is advisable to perform this reaction in tubular turbulent reactors.

In many cases, polymer synthesis among them, the major stages of the process are slow themselves, but are preceded by some primary fast reactions. For example, this is the case in polymer synthesis with Ziegler–Natta catalytic systems.

With the use of such systems as V–Al, Ti–Al, Nd–Al, etc. for synthesis of, e.g., ethylene–propylene, *cis*-1,4-isoprene, *trans*-1,4-isoprene, and *cis*-1,4-butadiene rubbers, the characteristic time of chain propagation is about 10^2 s or more. At the same time, the rate of initiation to give growth centers is faster by many orders of magnitude, i.e., it is a fast reaction controlled by reagent mixing. As a result, when a catalyst and a co-catalyst are delivered directly to a mixing vessel, the resulting distribution of the forming growth centers is nonuniform at both micro- and macrolevels. This leads also to a nonuniform monomer distribution throughout the reactor, which deteriorates molecular characteristics of the resulting polymers and, therefore, their quality.

Characteristics of ethylene–propylene–ethylidenenorbornene terpolymer rubbers obtained without and with divergent-convergent pre-reactor

Characteristic	Flow chart	
	without stage separation	with stage separation
Content of monomeric units, %:		
ethylidenenorbornene	28	29
terminal vinylidene	0.29	0.19
Content of blocks of ethylene units, %		
long	0.17	0.06
short	1.1	0.9
Fraction of propylene units in long blocks, %	1.9	2.6
Degree of branching, %	0.29	0.17

It appeared expedient to separate the fast stage of growth center formation from the slow stage of copolymerization of olefins and dienes on Ziegler–Natta catalysts. It was demonstrated that, for each of these stages, it is possible to provide ideal or practically ideal conditions. For the first, fast stage, this can be done using a divergent-convergent tubular turbulent pre-reactor [4], and for the second, slow stage, with a stirred continuous reactor. With the use of a divergent-convergent tubular turbulent pre-reactor, the reagent mixing time τ_{mix} is always shorter than the reaction mixture residence time τ_r. This guarantees that all the potential growth centers of polymerization enter the continuous polymerizer in the already formed state, and the ideal mixing model appears to be valid in this case.

Such measures as optimization of the V–Al catalytic system composition and homogenization of flows going to the polymerizer (including separation of the fast stage of formation of growth centers and slow stage of copolymerization of ethylene and propylene using a divergent-convergent tubular turbulent pre-reactor) remarkably improved the quality of ethylene-propylene rubbers (see table) and reduced the amount of off-grade products and wastes [10].

In manufacturing ethylene-propylene rubbers, the presence of a gas–liquid interface result in that the diffusion limitations and reaction mixture separation into components (diluent, monomers, hydrogen, etc.) occur upon delivery of the initial flows directly in

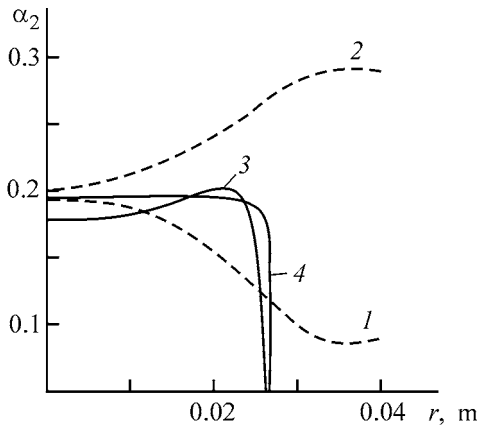

Fig. 5. Distribution of the volume fraction of the dispersed phase, α_2, across the radius of the tubular reactor, *r*, in (*1, 2*) diffuser and (*3, 4*) confuser parts. d_d = 0.08 m, d_c = 0.05 m, L_{dc} = 0.27 m, and V = 16 m s^{-1}. Continuous phase density ρ_1 (kg m^{-3}): (*1, 3*) 6.93, (*2*) 1111, and (*4*) 998.2. Dispersed phase density ρ_2 (kg m^{-3}): (*1, 3*) 640, (*2*) 0.689, and (*4*) 1111.

stirred continuous reactor are responsible for formation of the compositionally inhomogeneous copolymer both in a single polymerizer and in reactors connected in parallel. The use of divergent-convergent tubular turbulent pre-reactor allows efficient saturation of a hydrocarbon diluent with gaseous monomers and hydrogen and continuous supply of a homogeneous gas–liquid mixture to continuous polymerizers connected in parallel. In this case, the multiphase flow in the tubular channels of the divergent-convergent reactor is characterized by the occurrence of some circulation zones. Near an impermeable wall, the particles start to move in the direction opposite to the main flow under the action of a pressure gradient. In this region, the liquid flow is in rotatory motion, which results in an unexpected phenomenon: under the action of the centrifugal force, phase separation starts, depending primarily on the density of components involved in dispersion [11]. With remarkable difference between the densities of the continuous (ρ_1) and dispersed phases (ρ_2) and at $\rho_1 < \rho_2$, in the peripheral parts of the reactor, the volume fraction of the dispersed phase α_2 decreases by virtue of rejection of particles toward the impermeable wall or reactor periphery under the action of the centrifugal force (Fig. 5). In the case of $\rho_1 > \rho_2$, α_2 in the circulation zone increases. However, a uniform two-phase flow characterized by a homogeneous distribution of α_2 throughout the reactor section is formed in the narrow section of the reactor, i.e., in the confuser (Fig. 5).

Based on a numerical solution of the equations of two-phase flow motion with the corresponding boundary condition with respect to the geometrical parameters of the mixing zone and physical and dynamic parameters of the disperse system, Takhavutdinov *et al.* [12] derived a relation for the specific interfacial area, i.e., for the size of dispersed inclusions [12]:

$$\varepsilon = 0.625\left(\frac{f_E f^3 V^3}{d_c}\right)\left[1 + \left(\frac{U_2}{U_1 + U_2}\right)^2\left(\frac{\rho_1}{\rho_2}\right)^{-0.3}\right], \quad (4)$$

$$d_2 = 0.099(\sigma/\rho_1)^{0.6}\varepsilon^{0.4}, \quad (5)$$

$$f_E = -0.221 + 0.362(d_d/d_c) - 0.186(d_d/d_c)^2 - 0.031(d_d/d_c)^3 - 0.048(L_{dc}/d_d) - 7.92 \times 10^{-3}(d_d/d_c)(L_{dc}/d_d) - 3.08 \times 10^{-3}(L_{dc}/d_d)(d_d/d_c)^2 - 0.015(L_{dc}/d_d)^2 + 5.15 \times 10^{-3}(d_d/d_c)(L_{dc}/d_d)^2,$$

where U_1 and U_2 are the flow rates of, respectively, continuous and dispersed phases (m^3 s^{-1}); L_{dc}, the length of the diffuser-confuser unit (m); σ, the surface tension (mPa s).

The results obtained allow optimization of the operational parameters of a divergent-convergent tubular turbulent pre-reactor with account taken of the effects of phase separation and inhomogeneous distribution of components in the disperse system. For example, such an optimization has been done for the case of full-scale copolymerization of ethylene with propylene on Ziegler–Natta catalysts [10].

In synthesis of stereoregular *cis*-1,4-isoprene rubbers on Ti–Al (SKI-3) and Nd–Al catalytic systems (SKI-5), the above-described separation of the stages of formation of growth centers and polymerization with the use of a tubular turbulent pre-reactor also allows improvement of molecular characteristics of the resulting products [13, 14]. In the standard process, a catalyst and a monomer are introduced in the first reactor of the cascade of stirred continuous polymerizers. In this case, mixing of the reagents and formation of a catalytic system are inefficient.

Installing a divergent-convergent pre-reactor before the cascade of stirred continuous polymerizers provided an increase in the *cis*-1,4-units in the macromolecules of stereoregular polyisoprene and also improvement in the product homogeneity [15]. This ensured for the first time a correlation between the plasticity of the industrial product and its Mooney viscosity. As a result, it became possible to improve the product quality to the theoretical level and to obtain SKI-5 stereoregular 1,4-isoprene rubber of various grades in

the same apparatus, which could not be done with the existing stirred continuous reactors. Furthermore, in synthesis of SKI-5, the process output increased from 34 ± 1 to 40 ± 1 t h^{-1}, the amount of the Nd–Al catalyst was reduced by a factor of 2–4, and the rate of skin formation on the inner walls of process equipment decreased by about an order of magnitude. Also, the efficiency of the chain-transfer agent, diisobutyl aluminum hydride, increased. It was demonstrated in laboratory experiments that, in performing the stages of formation of growth centers and initiation of isoprene polymerization with the Ti–Al catalytic system, use of divergent-convergent tubular turbulent reactors ensures an increase in the molecular weight of the resulting polymers (Fig. 6).

Polymeric products synthesized on Ziegler–Natta catalysts mostly demonstrate wide MW distribution. One of the reasons is the occurrence of several types of growth centers with different kinetic activities.

Solution of the inverse MWD problem allows derivation of growth center activity distribution functions (Fig. 7). Each maximum in the distribution curve corresponds to at least one type of growth centers characterized by certain chain termination probability. The curves $\Psi(\ln \beta)\beta = \beta^2\varphi(\beta) - \ln M$, where β is the reciprocal of the mean degree of polymerization M_p characterizing the chain termination probability and equal to $(1/m)(r_0/r_p)$ (r_p is the chain propagation rate, r_0, integral termination rate, and m, molecular weight of the monomer), allow estimation of the number and relative contribution of each type of growth centers separately, using normal distribution functions [16].

A study of the growth center activity distribution for the case of isoprene polymerization on Ti–Al catalytic systems revealed that, with reactive turbulent mixing instead of standard mixing used in synthesis of isoprene rubber in the growth center formation and initiation stages, the active centers responsibe for formation of the low-molecular-weight fraction disappear (Fig. 7), allowing production of polymers with higher MW and narrow MWD [17].

Finally, performing the fast stage (growth center formation and initiation) in tubular turbulent jet reactors and the slow stage (copolymerization olefins and dienes), in stirred continuous reactors, with the resulting considerable increase in the turbulence level in the first stage, allows a significant improvement of the molecular-weight characteristics of the polymeric products obtained, control over the number of growth centers, and decrease in catalyst consumption in industrial processes.

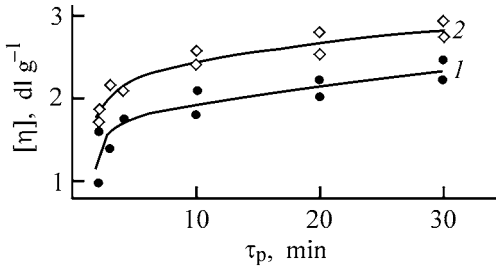

Fig. 6. Intrinsic viscosity [η] vs. the polymerization time τ_p in polymerization of isoprene on the $TiCl_4$–$Al(i\text{-}C_4H_9)_3$–piperylene catalytic system. c_{Ti} = 3.2 mM, $c_{\mathbf{M}}$ = 1.5 M, Ti : Al : piperylene = 1 : 0.83 : 4. (*1*) Without stage separation and (*2*) with stage separation using a tubular turbulent pre-reactor; the same for Fig. 7.

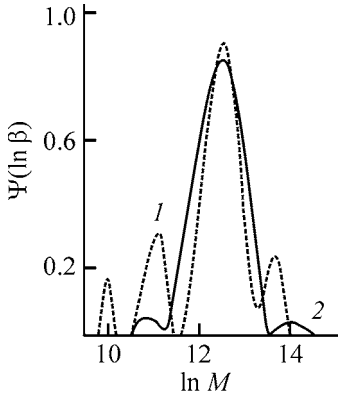

Fig. 7. Growth center activity distribution for the $TiCl_4$–$Al(i\text{-}C_4H_9)_3$–piperylene catalytic system in polymerization of isoprene in toluene. $c_{\mathbf{M}}$ = 1.5 M, c_{Ti} = 7 mM, Ti : Al : piperylene = 1 : 1.02 : 4. (*M*) Degree of polymerization.

CONCLUSIONS

(1) The specific features of fast polymerization processes make it expedient to use compact tubular turbulent reactors in industrial synthesis of polymers.

(2) Slackening of the diffusion limitations in polymer synthesis by virtue of intensification of turbulent mixing in the reaction zone allows estimation of kinetic parameters of polymerization and polymer-analogous reactions, optimization of the molecular-weight characteristics of the resulting polymeric products, and, finally, control of the process as a whole.

REFERENCES

1. Minsker, K.S. and Berlin, A.A., *Fast Polymerization Processes*, Amsterdam: Gordon and Breach, 1996.
2. Sandalov, Yu.A., Minsker, K.S., and Zaikov, G.E., *Polymers Derived from Isobutylene: Synthesis, Properties, Application*, Ser.: *New Concepts in Polymer Science*, Utrecht: VSP BV, 2001.

3. Berlin, A.A., Minsker, K.S., and Zakharov, V.P., *Dokl. Ross. Akad. Nauk*, 1999, vol. 365, no. 3, pp. 360–363.
4. Minsker, K.S., Zakharov, V.P., and Berlin, A.A., *Teor. Osn. Khim. Tekhnol.*, 2001, vol. 35, no. 2, pp. 172–177.
5. Takhavutdinov, R.G., D'yakonov, G.S., Deberdeev, R.Ya., and Minsker, K.S., *Khim. Prom–st.*, 2001, no. 5, pp. 41–49.
6. Minsker, K.S., Berlin, A.A., Takhavutdinov, R.G., *et al., Dokl. Ross. Akad. Nauk*, 2000, vol. 372, no. 3, pp. 347–350.
7. Minsker, K.S., Berlin, A.A., Zakharov, V.P., Takhavutdinov, R.G., *et al., Dokl. Ross. Akad. Nauk*, 2001, vol. 381, no. 1, pp. 78–81.
8. Berlin, A.A., Minsker, K.S., and Deberdeev, R.Ya., *Dokl. Ross. Akad. Nauk*, 2000, vol. 375, no. 2, pp. 218–221.
9. Minsker, K.S., Berlin, A.A., Deberdeev, R.Ya., and Ivanova, S.R., *Khim. Prom–st.*, 2000, no. 11, pp. 26–28.
10. Busygin, V.M., D'yakonov, G.S., Minsker, K.S., and Berlin, A.A., *Summa Tekhnol.*, 2000, vol. 3, no. 4, pp. 48–49.
11. Minsker, K.S., D'yakonov, G.S., Takhavutdinov, R.G., *et al., Dokl. Ross. Akad. Nauk*, 2002, vol. 382, no. 4, pp. 509–512.
12. Takhavutdinov, R.G., D'yakonov, G.S., Mukhametzyanova, A.G., *et al., Khim. Prom–st.*, 2002, no. 1, pp. 22–27.
13. Minsker, K.S., Berlin, A.A., Rakhimov, R.Kh., *et al., Zh. Prikl. Khim.*, 1999, vol. 72, no. 6, pp. 996–1001.
14. Rakhimov, R.Kh., Minsker, K.S., Kutuzov, P.I., *et al., Kauchuk Rezina*, 1999, no. 4, pp. 2–3.
15. Minsker, K.S., Berlin, A.A., Rakhimov, R.Kh., *et al., Russ. Polym. News*, 1999, vol. 4, no. 3, pp. 1–3.
16. Sigaeva, N.N., Usmanov, T.S., Shirokova, E.A., *et al., Dokl. Ross. Akad. Nauk*, 1999, vol. 365, no. 2, pp. 221–224.
17. Minsker, K.S., Zakharov, V.P., Berlin, A.A., and Monakov, Yu.B., *Dokl. Ross. Akad. Nauk*, 2001, vol. 381, no. 3, pp. 373–376.

Russian Journal of Applied Chemistry, Vol. 76, No. 2, 2003, pp. 271–274. Translated from Zhurnal Prikladnoi Khimii, Vol. 76, No. 2, 2003, pp. 279–283.

MACROMOLECULAR CHEMISTRY AND POLYMERIC MATERIALS

Synthesis of Copolymers of Unsaturated β-Diketones with Styrene and Methyl Methacrylate

I. S. Voloshanovskii, O. V. Shevchenko, T. D. Butova, and T. I. Manaeva

Mechnikov National University, Odessa, Ukraine

Received June 3, 2002

Abstract—Copolymerization of styrene and methyl methacrylate with various unsaturated β-diketones was studied. The influence exerted by the reaction temperature, structure of β-diketone, and its content in the comonomer mixture on the kinetic parameters of copolymerization and molecular weights of the products was examined.

In the past decades, there has been a great deal of interest in synthesis and application of polymers containing various functional groups in the pendant chains [1, 2]. Functional polymers are prepared by polymer-analogous transformations, polycondensation, or homo- and copolymerization of appropriate monomers. The last procedure seems to be more efficient; however, it has been studied relatively poorly because the initial monomers are difficultly accessible.

β-Diketones are well-known chelating agents. However, there have been only few reports of polymers prepared from unsaturated β-diketones. Homo- and copolymerization of methacryloylacetone (MAC) [3, 4] and its derivatives [5] have been studied fairly well. Polymeric ligands and metal complexes derived from *p*-vinylbenzoylacetophenone have been prepared [6]. β-Diketone monomers suitable for preparing functional polymers have been reported [7, 8].

Our goal was to carry out a kinetic study of copolymerization of various unsaturated β-diketones with styrene or methyl methacrylate (MMA).

EXPERIMENTAL

In the experiments, we used linear

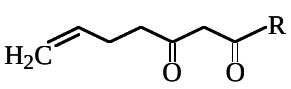

{R = CH_3 [7-octene-2,4-dione (lin.CH_3)], CF_3 [1,1,1-trifluoro-7-octene-2,4-dione (lin.CF_3)], C_6H_5 [1-phenyl-6-heptene-1,3-dione (lin.C_6H_5)]} and branched β-diketones:

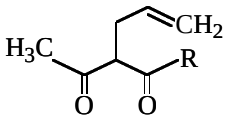

{R = CH_3 [3-allylpentane-2,4-dione (br.CH_3)], CF_3 [3-allyl-1,1,1-trifluoropentane-2,4-dione (br.CF_3)], C_6H_5 [2-allyl-1-phenylbutane-1,3-dione (br.C_6H_5)].

For comparison, we also tested MAC. The monomers were prepared, purified, and identified according to [3, 9, 10].

All the unsaturated β-diketonates synthesized, except MAC, undergo no radical homopolymerization in the presence of initiators [benzoyl peroxide, BP; azobis(isobutyronitrile), AIBN] at temperatures of up to 90°C. This may be due to steric hindrance and also to appreciable resonance stabilization of the monomers. These factors apparently govern the reactivity in polymerization for all the unsaturated β-diketonates synthesized. However, such monomers as MAC and the β-diketones synthesized, according to the existing concepts, must readily enter copolymerization. Furthermore, the C–C bond linking two different units in the backbone will be stronger if the substituents in the units have different electronegativities [11]. The electronegativity of monomers can be evaluated using the Alfrey–Price *Q*–*e* scheme which quantitatively relates the reactivity (*Q* factor) and polarity (*e* factor) of the monomers. The *e* factor is +0.57 for MAC and –0.80 for styrene [4], which suggests a high stability of MAC–styrene copolymers.

We have studied bulk copolymerization of all the unsaturated β-diketones synthesized with styrene and

1070-4272/03/7602-0271 $25.00 © 2003 MAIK "Nauka/Interperiodica"

Table 1. Molecular weights of copolymers and kinetic parameters of copolymerization of unsaturated β-diketones with styrene at various comonomer ratios* (BP initiator, c_{in} = 0.01 M, 80°C; the same for Tables 2–4)

β-Diketone	β-Diketone : styrene volume ratio	v_{pol}^{in}, % min^{-1}	Molecular weight $M \cdot 10^{-5}$				
			M_n	M_w	M_s	M_w/M_n	M_s/M_w
Lin.CH_3	1 : 2	0.09	0.254	0.544	0.47	2.14	1.74
	1 : 10	0.13	0.420	0.953	1.61	2.27	1.69
Lin.CF_3	1 : 2	0.12	0.299	0.647	1.12	2.16	1.73
	1 : 10	0.13	0.584	1.270	2.11	2.17	1.66
Lin.C_6H_5	1 : 2	0.11	0.377	0.852	1.45	2.26	1.70
	1 : 10	0.18	0.541	1.300	2.14	2.40	1.65
Br.CH_3	1 : 1	0.08	0.599	1.670	3.26	2.79	1.95
	1 : 10	0.18	0.676	1.440	2.39	2.15	1.66
Br.CF_3	1 : 1	0.08	0.222	0.544	1.02	2.45	1.88
	1 : 10	0.18	0.582	1.290	2.16	2.22	1.67
Br.C_6H_5	1 : 2	0.10	0.364	0.765	1.33	2.10	1.74
	1 : 10	0.17	0.632	1.350	2.25	2.14	1.67
MAC	1 : 1	0.09	0.401	1.244	3.23	3.10	2.60
	1 : 10	0.14	0.675	1.650	3.15	2.44	1.91

* (v_{pol}^{in}) Initial polymerization rate; molecular weight: (M_n) number-average, (M_w) weight-average, and (M_s) sedimentation-average; (M_w/M_n) degree of polydispersity of the polymer; (M_s/M_w) width of molecular-weight distribution.

of some of them with MMA. Experiments were performed in ampules and dilatometers at 80 and 70°C and various volume ratios of the comonomers. The reaction kinetics was monitored dilatometrically. Prior to all the experiments, the ampules and dilatometers were purged with argon to remove oxygen. The molecular weights of the copolymers were determined by gel-permeation chromatography on a Waters-200 device calibrated using monodisperse polystyrene references (Waters).

The kinetic parameters of copolymerization of β-diketones with styrene, intiated by BP, and molecular weights of the copolymers are listed in Table 1. In all the cases, the polymerization rate and the molecular weight of the polymer decrease with increasing concentration of monomeric β-diketone. With both linear and branched monomers (in the latter case, to a greater extent), the copolymerization rate tends to decrease in the order $C_6H_5 > CF_3 > CH_3$.

It is interesting that both the polymerization rate and the molecular weights of copolymers decrease with increasing content of β-diketones. For example, in the case of br.CF_3 and br.C_6H_5, the polymerization rate decreases by approximately a factor of 2.5 and 1.7, respectively, and the molecular weights of the resulting polymers decrease to approximately the same extent. With lin.CH_3, the reaction rate decreases by a factor of 1.5, and the molecular weight of the copolymer, by a factor of 1.7; with lin.C_6H_5, these factors are 1.7 and 1.5, respectively. With increasing content of the unsaturated β-diketone in the initial mixture (for branched β-diketones and MAC), the degree of polydispersity of the copolymers, M_w/M_n, grows (Table 1), this ratio being the highest for MAC copolymers.

These trends might be due to decreased activity of the radicals generated from the β-diketones, which could result in slower chain propagation and hence in slower polymerization and lower molecular weight of the product. Indeed, in polymerization of MAC, the propagating radical is conjugated with the quasiaromatic ring, being therefore less reactive. However, in the other monomers, there is no such conjugation. Nevertheless, the general pattern is similar with all the monomers.

For example, the parameters characterizing copolymerization of MAC, except the molecular weights of the products, are very similar to those obtained with lin.CH_3 (Figs. 1a, 1b). Thus, specifically the quasiaromatic chelating ring in the β-diketone molecules, rather than the decreased activity of the radicals and position of the double bond (in MAC and in the linear and branched monomers it is different) is the major factor responsible for the features observed.

Burnett *et al.* [12] have shown that diethyl malonate forms very stable complexes with nitroxyl radicals

owing to strong interaction of the unpaired electron with two carbonyl groups. In homo- and copolymerization of unsaturated β-diketones, the propagating radicals apparently form similar complexes. Complexation of the radicals makes them incapable of being involved in chain propagation, and polymerization occurs with only the "free" radicals. The system behaves as if the monomer had lower reactivity, but actually decreased is the steady-state concentration of the propagating radicals [13]. A similar effect will apparently be observed with all the monomers containing the β-diketone ring; therefore, such monomers polymerize slowly, yielding polymers with lowered molecular weight. A similar effect has been observed with the metal complexes; in this case, the radicals were scavenged by metal ions [14]. We showed in this study that such an effect is also characteristic of metal-free β-diketones. Complexes with radicals are also formed by simpler electron-rich compounds (alkenes, aldehydes, ketones), but these complexes have considerably lower stability constants [15]. The compounds containing developed π systems (β-diketones, porphyrins) form very stable complexes with radicals. It is interesting that the complexation of monomers containing a heteroatom with radicals involves the lone electron pairs of heteroatoms [13], rather than π electrons of the double bond.

Shapiro *et al.* [16] have studied by ^{1}H NMR spectroscopy the complexation of radicals with metal porphyrins and with their metal-free analogs. In the latter case, π–*p*–(π) complexes involving the porphyrin π system and the *p* electrons of the monomer are formed. Gridnev and Nechvolodova [17] obtained, when studying polymerization of vinylpyrrolidone, direct evidence of termination of propagating radicals on the porphyrin macroring. Depending on the structure of the porphyrin (presence of meso substituents), the propagating radicals add either at the *meso*-position or at the α- or β-position of the pyrrole rings; one porphyrin molecule can terminate two radicals. A similar effect was observed in polymerization of other monomers: acrylic acid, vinyltriazole, 4-vinylpyridine, etc. Formation of peroxy radicals in these experiments was fully excluded, since these radicals decompose porphyrins so that the Soret band disappears. If polymerization is performed in the presence of a metal porphyrin, the polymeric radicals are scavenged by metal atoms [18], similarly to polymerization in the presence of metal β-diketonates. In the process, an adduct containing the Co–C bond is formed, and the nature of the monomer from which the radical has been generated plays a decisive role in the complexation. For example, in polymerization of styrene, a secondary radical is generated, which readily forms a complex with Co(II), whereas tertiary radicals generated from MMA form no adducts because of steric hindrance.

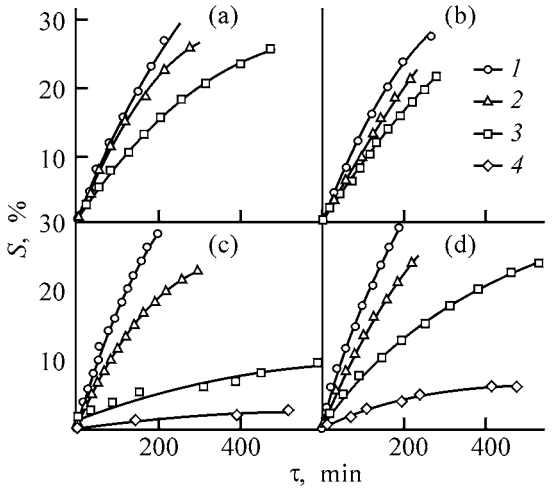

Fig. 1. Extent of polymerization *S* vs. time τ. BP initiator, c_{in} = 0.01 M, 80°C. (a) MAC, (b) lin.CH_3, (c) br.CH_3, and (d) br.CF_3. β-Diketone : styrene volume ratio: (*1*) 1 : 10, (*2*) 1 : 5, (*3*) 1 : 1, and (*4*) 5 : 1.

The kinetic parameters of copolymerization of branched β-diketones with styrene in a wide range of comonomer concentrations are given in Table 2 and in Figs. 1c and 1d. At low concentrations of β-diketones, the polymerization rates are close for all the monomers. At the comonomer ratios of 1 : 1 and especially 5 : 1, the polymerization rates drastically decrease, and the rates become different for different

Table 2. Kinetic parameters of copolymerization of unsaturated β-diketones with styrene at various ratios of comonomers (BP initiator, c_{in} = 0.01 M, 80°C)

β-Diketone	β-Diketone : styrene volume ratio	τ, min	Copolymer yield, %	v_{pol}^{m*}	v_{pol}^{in}
				% min^{-1}	
Br.CH_3	1 : 10	235	32.6	0.14	0.18
	1 : 5	295	23.4	0.08	0.12
	1 : 1	600	9.5	0.02	0.08
	5 : 1	690	2.7	0.004	0.008
Br.CF_3	1 : 10	201	29.7	0.15	0.18
	1 : 5	246	25.5	0.10	0.12
	1 : 1	540	24.5	0.05	0.08
	5 : 1	490	6.5	0.01	0.02
Br.C_6H_5	1 : 10	230	34.2	0.15	0.17
	1 : 5	232	31.5	0.14	0.16
	1 : 2	340	30.0	0.09	0.10
	1 : 1	360	22.2	0.06	0.08

* (v_{pol}^{m}) Mean polymerization rate.

Table 3. Kinetic parameters of copolymerization of lin.C_6H_5 with styrene at various temperatures (BP initiator, c_{in} = 0.01 M)

Lin.C_6H_5 : styrene volume ratio	T, °C	τ, min	Copolymer yield, %	v_{pol}^{m}	v_{pol}^{in}	E_a, kJ mol^{-1}
				% min^{-1}		
1 : 10	70	460	38.4	0.08	0.09	69
	80	260	38.8	0.15	0.18	
1 : 5	70	490	34.1	0.07	0.08	69
	80	260	33.7	0.13	0.16	
1 : 2	70	510	26.7	0.05	0.06	58
	80	280	25.8	0.09	0.11	

Table 4. Kinetic parameters of copolymerization of unsaturated β-diketones with MMA at various ratios of comonomers (BP initiator, c_{in} = 0.05 M, 80°C)

β-Diketone	β-Diketone : MMA volume ratio	τ, min	Copolymer yield, %	v_{pol}^{m}, % min
Lin.CH_3	1 : 2	360	54.2	0.15
	1 : 5	360	60.1	0.17
Lin.C_6H_5	1 : 1	420	54.1	0.13
	1 : 2	420	66.6	0.16
	1 : 5	420	78.0	0.19
Lin.CF_3	1 : 2	360	66.6	0.18
	1 : 5	360	87.0	0.24

monomers. The kinetic curves virtually level off, indicating that the polymerization ceases.

The temperature dependence of the copolymerization rate was studied with lin.C_6H_5 as example (Table 3). The calculated effective activation energy E_a is 69 kJ mol^{-1} at low β-diketone concentrations; at higher concentrations, it decreases to 58 kJ mol^{-1}. Comparison of this value with the activation energy of homopolymerization of MAC (0.12 M in ethanol), E_a = 58 kJ mol^{-1} [19], shows that they closely coincide. The results of copolymerization of some β-diketonate monomers with MMA are listed in Table 4. With MMA, compared to styrene, an increase in the β-diketone concentration has a weaker effect on the mean copolymerization rate.

CONCLUSIONS

(1) Copolymerization of unsaturated β-diketones of various structures with styrene or methyl methacrylate yields copolymers containing β-diketone units.

(2) The copolymerization rate and molecular weight of the copolymers decrease, and the polydispersity grows as the content of unsaturated β-diketone in the polymerizing mixture is increased. This may be due to complexation of the propagationg radicals with the quasiaromatic β-diketonate ring.

REFERENCES

1. Pomogailo, A.D., *Kataliz immobilizovannymi kompleksami* (Catalysis with Immobilized Complexes), Moscow: Nauka, 1991.
2. Sherington, D., *Usp. Khim.*, 1991, vol. 60, no. 7, pp. 1494–1512.
3. Despic, A. and Kasanovic, D.I., *Makromol. Chem.*, 1959, vol. 29, no. 3, pp. 151–155.
4. Kopeikin, V.V., Pakarin, E.F., Milevskaya, I.S., and Redi, I.S., *Vysokomol. Soedin., Ser. A*, 1977, vol. 19, no. 4, pp. 861–866.
5. Thamizharasi, S., Peddy, A., and Venkata Rami, *Polymer*, 1992, vol. 33, no. 11, pp. 2421–2423.
6. Chapin, E.C. Twohig, E.F., Keys, L.D., and Gorski, K.U., *J. Appl. Polym. Sci.*, 1982, vol. 27, no. 3, pp. 811–820.
7. Gloris, M.E. and Galves, N., *Tetrahedron*, 1991, vol. 47, no. 37, pp. 8031–8042.
8. Bi Siwei, *Synth. React. Inorg. Met.-Org. Chem.*, 1999, vol. 29, no. 7, pp. 1283–1297.
9. Voloshanovskii, I.S., Butova, T.D., and Shevchenko, O.V., *Zh. Obshch. Khim.*, 1999, vol. 69, no. 9, pp. 1504–1507.
10. Voloshanovskii, I.S., Manaeva, T.I., Shevchenko, O.V., and Mamontov, V.P., *Zh. Prikl. Khim.*, 2000, vol. 73, no. 2, pp. 283–287.
11. *Vinyl Polymerization*, Ham, G.E., Ed., New York: Marcel Dekker, 1969.
12. Burnett, G.M., Cameron, G.G., and Cameron, J., *J. Chem. Soc., Faraday Trans. 1*, 1973, vol. 69, no. 5, pp. 864–870.
13. Kabanov, V.A., Zubov, V.P., and Semchikov, Yu.D., *Kompleksno-radikal'naya polimerizatsiya* (Radical Complex Polymerization), Moscow: Khimiya, 1987.
14. Goluev, V.B., Zubov, V.P., Valuev, L.I., *et al.*, *Vysokomol. Soedin.*, 1969, vol. 11, no. 12, pp. 2689–2694.
15. Golikov, I.V., Svitych, R.B., and Yablonskii, O.P., *Zh. Strukt. Khim.*, 1976, vol. 17, no. 3, pp. 474–478.
16. Shapiro, Yu.E., Dozorova, N.P., Golikov, I.V., and Smirnov, B.P., Abstracts of Papers, *VII Vsesoyuznoe soveshchanie "Fizicheskie i matematicheskie metody v koordinatsionnoi khimii"* (VII All-Union Meet. "Physical and Mathematical Methods in Coordination Chemistry"), Chisinau: Shtiintsa, 1980, p. 198.
17. Gridnev, A.A. and Nechvolodova, E.I., *Teor. Eksp. Khim.*, 1989, vol. 25, no. 6, pp. 727–732.
18. Nokel', A.Yu., Gridnev, A.A., and Semeikin, A.S., *Izv. Vyssh. Uchebn. Zaved., Khim. Khim. Tekhnol.*, 1988, vol. 31, no. 10, pp. 52–55.
19. Movchan, T.I., Voloshanovskii, I.S., and Pomogailo, A.D., *Izv. Ross. Akad. Nauk, Ser. Khim.*, 1993, no. 12, pp. 2060–2064.

Russian Journal of Applied Chemistry, Vol. 76, No. 2, 2003, pp. 275–279. Translated from Zhurnal Prikladnoi Khimii, Vol. 76, No. 2, 2003, pp. 284–288.

MACROMOLECULAR CHEMISTRY AND POLYMERIC MATERIALS

Synthesis of Water-Soluble Chemodegradable *N*-Vinylpyrrolidone–Crotonic Acid–2-Hydroxyethyl Methacrylate Terpolymers Containing Interchain Urethane Cross-Links, as Carriers of Substances with Antimicrobial Activity

M. V. Solovskii, N. V. Nikol'skaya, V. M. Denisov, A. V. Adamov, E. B. Tarabukina, and S. I. Klenin

Institute of Macromolecular Compounds, Russian Academy of Sciences, St. Petersburg, Russia

Received September 25, 2002

Abstract—Water-soluble branched *N*-vinylpyrrolidone–crotonic acid–2-hydroxyethyl methacrylate terpolymers containing labile interchain urethane cross-links were prepared. Their molecular-weight characteristics were determined, and the hydrolytic stability under conditions close to those in a living body was evaluated. Polymeric salts of gentamicin were prepared from linear and branched chemodegradable *N*-vinylpyrrolidone terpolymers.

Chemodegradable polymers based on *N*-vinylpyrrolidone (VP) and containing labile interchain cross-links readily hydrolyzable in a living body show much promise as carriers for biologically active substances (BASs). Owing to degradability, the molecular weight of such (co)polymers can exceed the limit of 40 000 determined by the possibility of elimination through kidneys. In a living body, such polymers will undergo gradual hydrolysis (biodegradation) to low-molecular-weight fragments that can be removed by kidney filtration. Previously, we prepared branched chemodegradable copolymers of VP with allylamine, containing –CH=N– cross-links which are readily hydrolyzed under conditions close to those in a living body [1]. Another chemically labile fragment is the urethane fragment –O–C(=O)–NH– [2, 3].

The goal of this study was to prepare branched chemodegradable polymers containing interchain urethane cross-links, to analyze their molecular-weight characteristics, to evaluate the rate of their hydrolysis in saline at 37°C, and to test them as carriers for gentamicin antibiotic.

As the initial linear copolymers, we chose previously prepared [4] VP–crotonic acid (CA)–2-hydroxyethyl methacrylate (HEMA) terpolymers **I**:

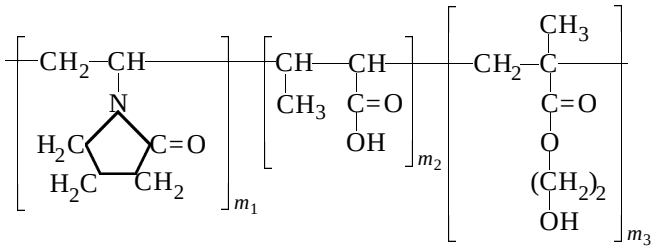

I

$$m_1 + m_2 + m_3 = 100 \text{ mol \%}.$$

These water-soluble terpolymers, biocompatible with a living body, have been successfully used as carriers for two BASs with different mechanisms of the biological effect [5]. The presence of primary hydroxy groups in terpolymers **I** enabled their cross-linking with hexamethylene diisocyanate (HMDIC), which yielded chemodegradable branched terpolymers **II** with urethane cross-links:

1070-4272/03/7602-0275 $25.00 © 2003 MAIK "Nauka/Interperiodica"

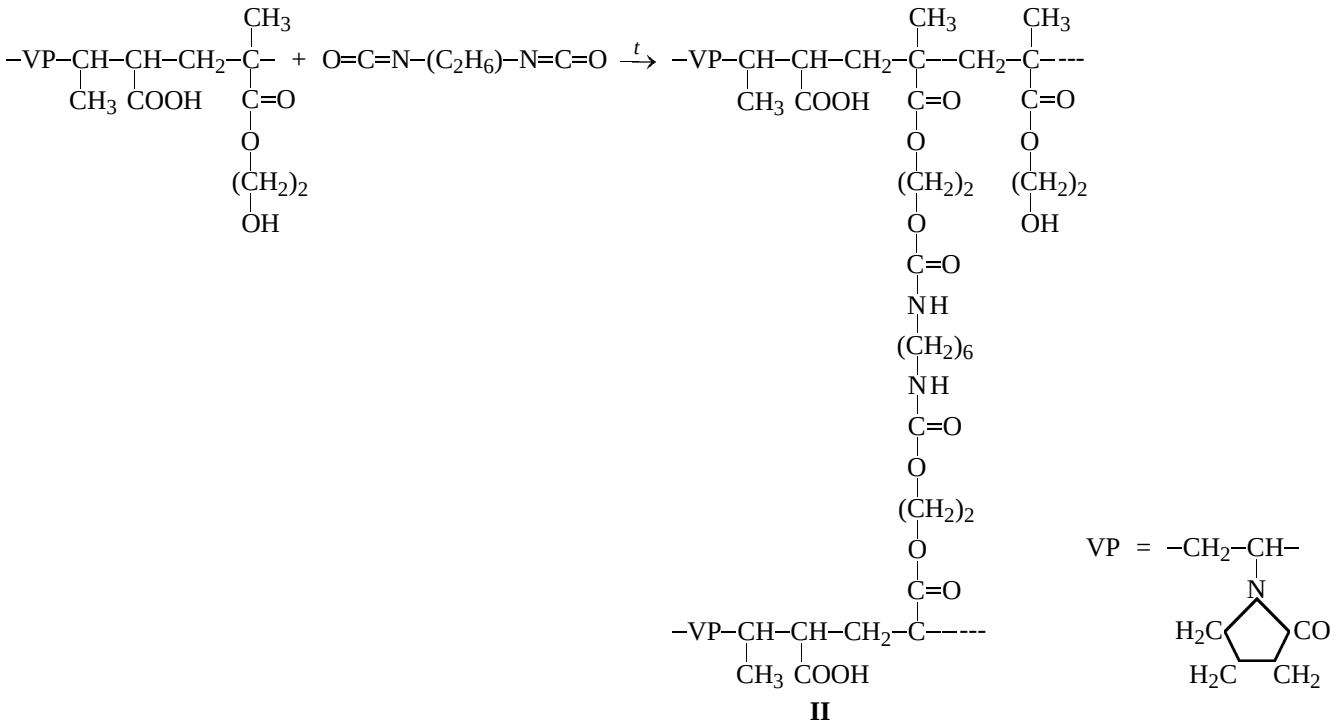

II

The presence of carboxy groups allowed incorporation into **II** of an aminoglycoside antibiotic, gentamicin, via an ionic bond. The properties of the initial terpolymers **I** and conditions of their reaction with HMDIC are listed in Table 1. It is seen that terpolymers **I** have low molecular weights (22000–28000) and relatively low content of functional hydroxy and carboxy groups (11.8–20.7 mol %).

The reaction of terpolymers **I** with HMDIC was performed in DMF at 130°C in an inert atmosphere, i.e., under the conditions of synthesis of linear polyurethanes [6–8]. We varied the copolymer concentration, [HMDIC] : [OH] molar ratio, and reaction time τ. With the other conditions being the same, increased [HMDIC] : [OH] molar ratio resulted in higher intrinsic viscosity of the product (Table 1, terpolymers **IIc** and **IId**). Upon the reaction with the diisocyanate, the intrinsic viscosity of **I** and its molecular weight (Table 2) increased by a factor of approximately 2, suggesting the formation of interchain urethane crosslinks. We determined the conditions under which the

Table 1. Reaction of VP–CA–HEMA terpolymers with HMDIC in DMF at 130°C in an argon atmosphere

Terpolymer	m_1	m_2	m_3	$[\eta]_{in}$, dl g^{-1},	c_{cop}, wt %	[HMDIC] : [OH] molar ratio	τ, h	Reaction product	Yield, %	$[\eta]$, dl g^{-1}
	mol %									
Ia	62.7	20.7	16.6	0.08*	9.9	1 : 1	8	**IIa**	92.9	0.13
	62.7	20.7	16.6	0.08*	12.3	2 : 1	6	**IIb**	74.1	0.16
Ib	72.4	15.8	11.8	0.10**	14.0	1 : 1	0.5	**IIc**	61.1	0.15
	72.4	15.8	11.8	0.10**	14.0	2 : 1	0.5	**IId**	93.7	0.19
	72.4	15.8	11.8	0.10**	14.0	1.5 : 1	3	**IIe**	81.8	0.20

* M_{SD} = 22000. ** M_{SD} = 28000.

Table 2. Hydrodynamic characteristics of linear and branched VP–CA–HEMA terpolymers

Terpolymer	$S \times 10^{13}$, Sv	$D \times 10^7$, cm^2 s^{-1}	M_{SD}	Terpolymer	$S \times 10^{13}$, Sv	$D \times 10^7$, cm^2 s^{-1}	M_{SD}	Terpolymer	$S \times 10^{13}$, Sv	$D \times 10^7$, cm^2 s^{-1}	M_{SD}
Ib	2.0	7.5	28000	**IIb**	2.3	6.7	36000	**IIe**	2.7	4.3	67000

reaction of **I** with HMDIC was not accompanied by gelation. The sedimentation and diffusion coefficients of the initial terpolymer **Ib** and branched terpolymers **IIb** and **IIe** and their molecular weights M_{SD} obtained by a combination of the sedimentation and diffusion methods are listed in Table 2. The molecular weight M_{SD} of **IIb** is 36000, and that of **IIe**, 67000.

The structure of product **IIb** obtained by the reaction of linear terpolymer **Ia** with HMDIC was confirmed by its ^{1}H NMR spectrum (Fig. 1a). Upfield signals at 0.5–1.2 ppm (solvent dimethylacetamide-d_9) belong to the protons of the HEMA and CA units, and the signals at 1.2–1.5 ppm, to backbone methylene protons of the HEMA units, backbone CH proton of the CA units, and four methylene groups of the cross-linking units. The signal at about 3.3 ppm belongs to the NCH_2 protons in the vinylpyrrolidone units and cross-links. The signal at about 3.7 ppm is due to the proton of the vinylpyrrolidone NCH group involved in the backbone (–CH– fragment).

Taking into account the composition of the initial terpolymer, contribution of the CA and HEMA methylene groups to the total integral signal intensity of 3.00 units (Fig. 1b), and contributions of two methylene protons of the HEMA units, one proton of the CA unit, and four methylene protons of the cross-linking unit to the total integral signal intensity of 2.16 units we calculated the composition of branched terpolymer **IIb**. The calculation showed that about 40% of HEMA units (about 6.6 mol %) are cross-linked by

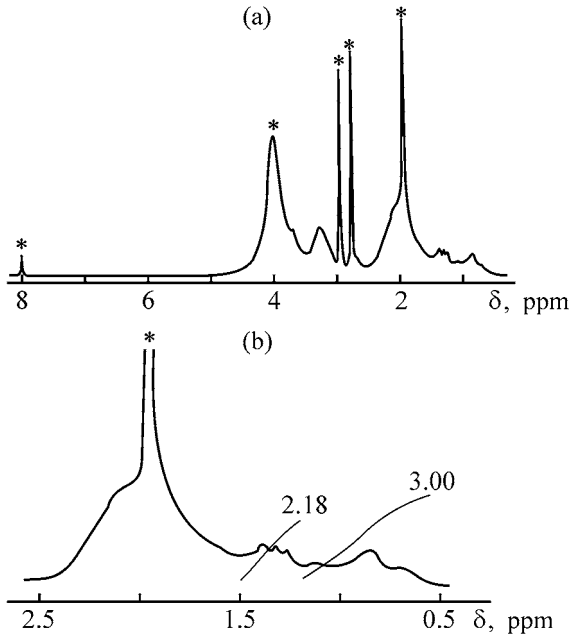

Fig. 1. ^{1}H NMR spectrum of copolymer **IIb** in dimethylacetamide-d_9: (a) total spectrum and (b) upfield region. (δ) Chemical shift. The residual proton signals of the solvent are denoted by *asteriscs*.

HMDIC; hence, the content of unchanged HEMA units is about 10 mol %.

Actually the content of interchain cross-links is lower than 6.6 mol %, since a part of the cross-linking agent is consumed for formation of intrachain (intramolecular) urethane cross-links:

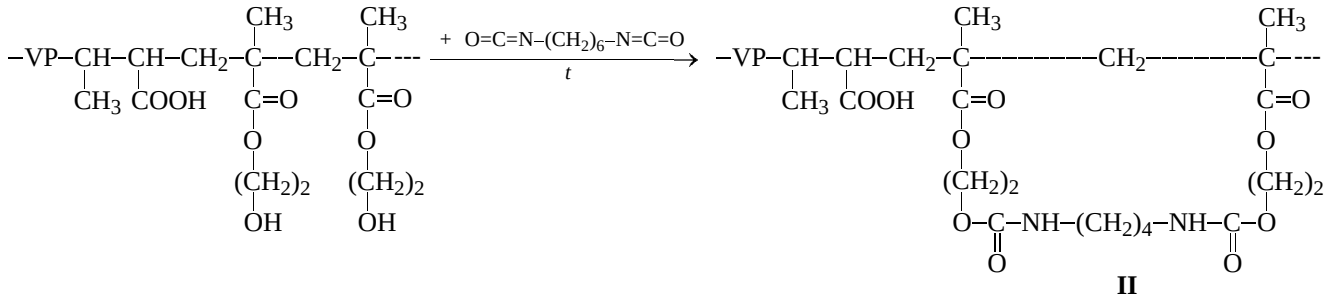

As for the selectivity of hydrolysis of bonds in interchain cross-links in terpolymers **II**, it may be assumed that the urethane groups are hydrolyzed first. According to [9], CO_2 evolution is observed on keeping polyurethane samples in model solutions (pH 7.0, 37°C). THe degradation of polyurethane in model solutions involves cleavage of C–O bonds in the urethane group and formation of carbamic acid and alcohol. Carbamic acid decomposes with the release of CO_2 and formation of the primary amine:

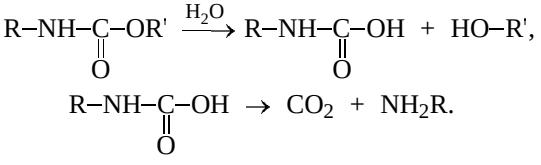

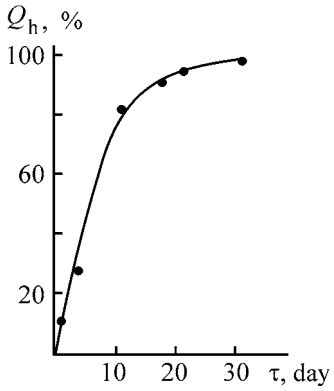

Fig. 2. Kinetics of **IIe** hydrolysis in physiological saline at 37°C. c_{cop} = 10 mg ml^{-1}. (Q_h) Degree of hydrolysis and (τ) time.

Hydrolysis of ester bonds in HEMA units is hindered because of the steric effect of the backbone.

Hydrolysis of branched terpolymer **IIe** (M_{SD} = 67000) in physiological saline (pH 7.0) at 37°C was studied viscometrically. We found (Fig. 2) that terpolymer **IIe** is hydrolyzed under these mild conditions to 96% in 31 days. The high hydrolysis rate is due to the lability of the interchain urethane cross-links and relatively low molecular weight of the terpolymer.

Table 3. Polymeric salts of gentamicin

Polymeric carrier	Salt	Yield, %	Content of gentamicin base, %		MSC,* μg ml^{-1}
			calculated	found	
Ib	**IIIa**	72.9	10	9.5	0.50
	IIIb	72.8	20	20.2	0.25
IId	**IIIc**	93.7	10	9.6	0.50
	IIId	93.8	20	20.8	0.25
Gentamicin base			100		0.25

* (MSC) Minimal suppressing concentration with respect to *Staphylococcus aureus*, strain 38, in terms of the antibiotic content in the preparation.

Table 4. Hydrolysis of polymeric gentamicin salts in physiological saline at 25°C

Salt	Elimination of antibiotic from polymeric carrier, %, in indicated time, h						
	1	2	3	4	5	6	24
IIIa	2.8	5.6	8.9	10.0	11.2	12.3	28.0
IIIb	1.6	3.6	5.3	6.7	8.1	9.2	20.1
IIIc	2.9	4.5	5.6	6.7	7.5	8.1	19.2

From terpolymers **Ib** and **IId**, we prepared gentamicin salts by the reaction of gentamicin base with the carboxy groups of the terpolymers, following the procedure described in [10]. Polymeric gentamicin salts **III** (Table 3) were obtained in 73–94% yield; they contained 10–20 wt % bound antibiotic and showed high acitvity against staphylococcus.

We have studied the rate of elimination of gentamicin base from the polymeric carrier (salts **IIIa**–**IIIc**) in physiological saline at 25°C by dialysis through a semipermeable cellophane membrane. We found that 19–28% of the antibiotic is eliminated in 1 day (Table 4). These data show that the antimicrobial activity of gentamicin incorporated in polymeric salts can be prolonged. It is remarkable that the antibiotic is eliminated from branched terpolymer **IId** more slowly than from linear terpolymer **Ib**.

EXPERIMENTAL

Terpolymers **I** were prepared and analyzed according to [4].

The reaction of **Ib** with HMDIC was performed as follows. A 0.5-g portion of **Ib** was dissolved in 3.23 ml of DMF, and 18.72 μl of distilled HMDIC was added. The mixture was transferred into a 50-ml ampule which was purged with argon and placed in an oil bath heated to 130±5°C. After 3 h, the ampule was cooled and opened; the viscous solution in the ampule was diluted with 0.5 ml of ethanol. The reaction product was precipitated into diethyl ether, collected on a glass frit, and vacuum-dried. Yield of branched terpolymer **IIe** 408.8 mg (81.8%), intrinsic viscosity 0.20 dl g^{-1}.

The intrinsic viscosity of terpolymers **I** and **II** was measured in an Ubbelohde viscometer (0.1 N aqueous sodium acetate, 25°C).

The hydrodynamic studies of terpolymers **I** and **II** (solutions in DMF) were performed by diffusion–sedimentation analysis. High-speed sedimentation experiments were performed with an MOM 3180 analytical ultracentrifuge with a Philpott–Svensson refractometric optical system at a rotor rotation rate of 45000 rpm in a cell with artificial formation of the sedimentation boundary at 21.0°C. The forward diffusion was studied in a polarization diffusometer [11]; the concentration gradient was recorded with a Lebedev polarization–interferometric system.

The molecular weights M_{SD} were determined by the Svedberg formula [11] allowing calculation of the molecular weight of a macromolecule without considering its structure and conformation:

$$M_{SD} = \frac{S_0}{D}\frac{RT}{1 - v\rho_0},$$

where S_0 is the sedimentation constant; D, the forward diffusion coefficient; R, the universal gas constant; and T, temperature. The floatability factor $(1 - v\rho_0)$ was taken from [12].

The resulting M_{SD} values are nicely consistent with the molecular weights $M_{S\eta}$ determined by sedimentation-viscometric analysis with the formula [13]

$$M_{S\eta} = \left(\frac{N_A}{\beta}\right)^{3/2}\left(\frac{S_0\eta_0}{1 - v\rho_0}\right)^{3/2}[\eta]^{1/2},$$

where β is the hydrodynamic invariant taken equal to the mean experimental value for flexible-chain polymers, $\beta = 2.3 \times 10^6$ [13]; N_A is the Avogadro number.

Hydrolysis of branched chemodegradable terpolymer **IIe** in physiological saline at 37°C was monitored by a decrease in time of the reduced viscosity of the terpolymer solution (initial concentration of **IIe** 10 mg ml^{-1}). The degree of hydrolysis of **IIe** was calculated by the formula given in [1].

Polymeric gentamicin salts **IIIa** and **IIIb** were prepared from **Ib**, and salts **IIIc** and **IIId**, from **IId**, following the procedure described in [10]. The content of gentamicin base in the polymeric salts was determined by complexation with trinitrobenzenesulfonic acid [14]. The rate of gentamicin release from salts **III** was evaluated according to [10].

The antimicrobial activity of polymeric gentamicin salts **III** against *Staphylococcus aureus*, strain 38, was studied by the method of twofold serial dilutions in a liquid culture medium [15].

CONCLUSIONS

(1) Water-soluble branched terpolymers containing interchain urethane cross-links were prepared by reaction of *N*-vinylpyrrolidone–crotonic acid–2-hydroxyethyl methacrylate terpolymers with hexamethylene diisocyanate.

(2) The hydrodynamic characteristics of the resulting branched terpolymers were studied, and the rate of their hydrolysis in physiological saline at 37°C was evaluated.

(3) Polymeric gentamicin salts exhibiting high antimicrobial activity were prepared from the linear and branched terpolymers. The kinetics of gentamicin elimination from the polymeric carrier was studied.

ACKNOWLEDGMENTS

The study was supported financially by the grants of the Institute of Macromolecular Compounds, Russian Academy of Sciences, within the framework of the Scientific Program of the St. Petersburg Scientific Center (section 2.2).

REFERENCES

1. Solovskii, M.V., Nikol'skaya, N.V., Korneeva, E.V., *et al.*, *Zh. Prikl. Khim.*, 2001, vol. 74, no. 4, pp. 643–648.
2. Lipatova, T.E., Alekseeva, T.T., Bakalo, L.A., *et al.*, *Polim. Med.* (Poland), 1980, vol. 10, no. 1, pp. 20–27.
3. *Biodestruktiruyushchie polimernye materialy: Sbornik nauchnykh trudov* (Biodegradable Polymeric Materials: Coll. of Scientific Papers), Lipatova, T.E., Ed., Kiev: Naukova Dumka, 1982, pp. 39–43.
4. Solovskii, M.V., Pavlov, G.M., Korneeva, E.V., *et al.*, *Zh. Prikl. Khim.*, 2002, vol. 75, no. 2, pp. 286–290.
5. Solovskii, M.V. and Panarin, E.F., *Dokl. Ross. Akad. Nauk*, 1998, vol. 359, no. 4, pp. 503–506.
6. Braun, D., Cherdron, H., and Kern, W., *Praktikum der makromolekularen organischen Chemie*, Heidelberg: Alfred Huthig, 1971.
7. Toroptseva, A.M., Belogorodskaya, K.V., and Bondarenko, V.M., *Laboratornyi praktikum po khimii i tekhnologii vysokomolekulyarnykh soedinenii* (Practical Laboratory Course of Chemistry and Technology of Macromolecular Compounds), Leningrad: Khimiya, 1972.
8. Omel'chenko, S.I., in *Sintez i fizikokhimiya polimerov: Poliuretany* (Synthesis and Physical Chemistry of Polymers: Polyurethanes), Kiev: Naukova Dumka, 1977, issue 21, pp. 35–44.
9. Lipatova, T.E. and Veselovskii, R.A., *Vysokomol. Soedin., Ser. A*, 1969, vol. 11, no. 7, pp. 1459–1464.
10. Solovskii, M.V., Nikol'skaya, N.V., and Denisov, V.M., *Khim.-Farm. Zh.*, 2000, vol. 34, no. 11, pp. 21–24.
11. Tsvetkov, V.N., Eskin, V.E., and Frenkel, S.Ya., *Struktura makromolekul v rastvorakh* (Structure of Macromolecules in Solutions), Moscow: Nauka, 1964.
12. Solovskij, M.V., Panarin, E.F., Gorbunova, O.P., *et al.*, Eur. Polym. J., 2000, vol. 36, pp. 1127–1135.
13. Tsvetkov, V.N., *Zhestkotsepnye polimernye molekuly* (Rigid-Chain Polymeric Molecules), Leningrad: Nauka, 1986.
14. Snyder, S.L. and Sobocinski, P.Z., *Anal. Biochem.*, 1975, vol. 64, no. 2, pp. 284–288.
15. Navashin, S.M. and Fomina, I.P., in *Ratsional'naya antibiotikoterapiya* (Efficient Therapy with Antibiotics), Moscow: Meditsina, 1982, pp. 40–41.

Russian Journal of Applied Chemistry, Vol. 76, No. 2, 2003, pp. 280–283. Translated from Zhurnal Prikladnoi Khimii, Vol. 76, No. 2, 2003, pp. 289–292.

MACROMOLECULAR CHEMISTRY AND POLYMERIC MATERIALS

Radical Polymerization of Acrylamide in Aqueous–Dimethyl Sulfoxide Solutions in the Presence of Sodium Acetate

V. F. Kurenkov and O. A. Antonovich

Kazan State Technological University, Kazan, Tatarstan, Russia

Received April 9, 2002

Abstract—The kinetic features of nonisothermal polymerization of acrylamide in aqueous, mixed aqueous–dimethyl sulfoxide, and DMSO solutions in the presence of potassium persulfate as initiator and sodium acetate as complexing agent were studied by differential thermal analysis.

Radical polymerization of acrylamide (AA) in concentrated solutions under nonisothermal conditions is a promising procedure for production of water-soluble high-molecular-weight polyacrylamide (PAA) [1]. In this case, polymerization can proceed at a high rate and to a high degree of conversion [2–6]. In addition, as the reaction temperature grows owing to the heat released in polymerization, the viscosity of the reaction mixture decreases and the flexibility of macroradicals increases, so that they more efficiently suppress intermolecular imidization yielding the water-insoluble polymer. Synthesis of PAA under nonisothermal conditions has not been studied adequately, and data on the influence of the complexing power of CH_3COONa (SA) on polymerization of AA are scarce [7–10]. Here, we report on the main features of nonisothermal radical polymerization of AA in concentrated solutions in water, mixtures of water with dimethyl sulfoxide (DMSO), and straight DMSO in the presence of SA.

EXPERIMENTAL

The substances and experimental procedure are similar to those described previously [9, 10]. The polymerization kinetics were studied by differential thermal analysis. Polymerization was carried out in 15-cm^3 cylindrical glass ampules. A solution of AA and SA was charged into an ampule and the ampule blown with helium for 30 min and hermetically sealed with a rubber stopper. A solution of the initiator, $K_2S_2O_8$ (PPS), was introduced into the ampule by a syringe through the rubber stopper, and the ampule was placed in a heating furnace. All the experiments were carried out at the initial temperature of 25°C, and then the temperature in the furnace was raised at a constant rate of 1.8 deg min^{-1} with a heater used in differential thermal analysis. In the course of polymerization, we recorded the variation of the temperature difference between the reaction mixture and ethanol (reference) with time.

After the polymerization was complete, the solution was diluted with water and the polymer was precipitated into acetone. Then, the polymer was filtered, washed with acetone, and dried under reduced pressure at room temperature to constant weight.

The intrinsic viscosity of PAA [η] was measured with an Ubbelohde viscometer (d = 0.56 mm) in 0.5 M NaCl at 25°C. The viscosity-average molecular weight of PAA $\overline{M}_\eta$ was evaluated by the formula [11]

$$[\eta] = 7.19 \times 10^{-3} \overline{M}_\eta^{0.77}.$$

The experimental data on nonisothermal polymerization were processed under the following assumptions: the total polymerization heat is expended for heating of the reaction mixture, the heat capacities of the monomer and polymer are the same, and evaporation of the solvent is neglected. In this case, the relation between the rate of variation of the reaction mixture temperature, dT/dt, in the course of polymerization and the rate of monomer consumption, –d[AA]/dt, is described by the simplified equation [3, 12]

$$dT/dt = (-\Delta H/C)(-d[AA]/dt),$$

where ΔH is the polymerization heat and C is the heat capacity of the reaction mixture.

1070-4272/03/7602-0280 $25.00 © 2003 MAIK "Nauka/Interperiodica"

Parameters of AA polymerization in various media

Water : DMSO, vol % : vol %	Molar ratio ([SA]/[AA]) × 10^2	v, deg s^{-1}	$k_p/k_t^{1/2}$	Reaction order		$\overline{M}_\eta \times 10^{-6}$
				with respect to AA	with respect to PPS	
100 : 0	0	0.42*	3.30	1.25	0.50	–
100 : 0	0.40	3.50*	4.52	1.38	0.78	–
80 : 20	0	0.62	–	–	–	–
80 : 20	1.34	1.51	–	–	–	2.65
60 : 40	0	0.46	–	–	–	–
60 : 40	1.34	1.25	–	–	–	1.90
50 : 50	0	0.40	1.25	1.25	–	–
50 : 50	1.34	1.20	1.35	1.35	–	–
40 : 60	1.34	1.14	–	–	–	1.25
20 : 80	1.34	1.04	–	–	–	0.70
0 : 100	0	–	0.79	0.94	0.47	–
0 : 100	1.34	1.00	1.36	1.02	–	0.25
0 : 100	2.01	–	–	1.37	0.60	–

* Values for $v \times 10^4$, mol l^{-1} s^{-1}.

The initial polymerization rate $v = dT/dt$ was determined from variation of the temperature of the reaction mixture with time. The results are listed in the table. Based on the experimental linear dependences $\log v = f(\log [AA])$ and $\log v = f(\log [PPS])$, we determined the reaction orders with respect to the monomer and initiator in the absence and in the presence of SA (see table). The positive values of the reaction orders in polymerization in aqueous solutions, in a 1 : 1 water–DMSO mixture, and in DMSO show that v grows with increasing initial concentrations of the monomer and initiator. In all the systems studied, with increasing concentration of AA in the initial mixture, the $\overline{M}_\eta$ values for PAA vary in parallel with v (Fig. 1), in good agreement with the general pattern of radical polymerization. The increased reaction orders with respect to AA and PPS, found in polymerization in the presence of SA, suggest a complicated mechanism of polymerization of AA in the presence of the complexing agent. The increase in the reaction order with respect to the monomer, observed on adding SA, is caused by participation of AA in the complexation with SA. The increase in the reaction order with respect to the initiator suggests an increase in the contribution of monomolecular termination to the total balance of chain termination reactions.

Deviation of the reaction orders with respect to the monomer and initiator from 1.0 and 0.5, respectively, did not allow determination of the individual rate constants of chain propagation, k_p, and termination, k_t. Therefore, we found the $k_p/k_t^{1/2}$ values determined from the dependence of $1/\overline{P}$ on $v/[AA]^2$, where $\overline{P}$ is the average degree of polymerization. The resulting $k_p/k_t^{1/2}$ values are listed in the table. It is seen that v grows upon addition of SA as a result of an increase in the $k_p/k_t^{1/2}$ ratio, which can be assigned to increased k_p.

According to IR, ^{1}H NMR [13], and NMR [14] data, the effect of SA on polymerization of AA is caused by complexation of SA with amide groups of the propagating radical. As a result of the com-

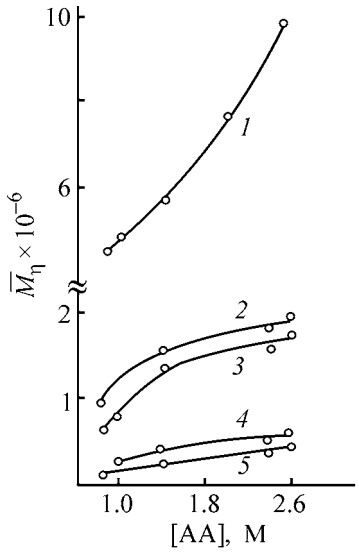

Fig. 1. $\overline{M}_\eta$ of PAA vs. AA concentration in polymerization in (*1*) aqueous solutions, (*2*, *3*) mixture water : DMSO = 1 : 1, and (*4*, *5*) DMSO (*1*, *2*, *4*) in the absence and (*3*, *5*) in the presence of 0.034 M SA. [PPS] = 0.82×10^{-3} M.

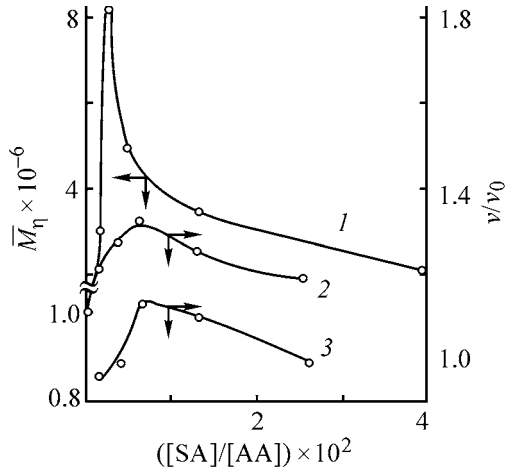

Fig. 2. Relative rate of AA polymerization, v/v_0, in (*1*) aqueous solution, (*2*) 1 : 1 water–DMSO mixture, and (*3*) DMSO solution vs. the molar ratio [SA]/[AA]. [AA] = 1.41 and [PPS] = 0.82×10^{-3} M. v_0: (*1*) 0.42×10^{-4} mol l^{-1} s^{-1}; (*2*) 0.4 and (*3*) 1.17 deg s^{-1}.

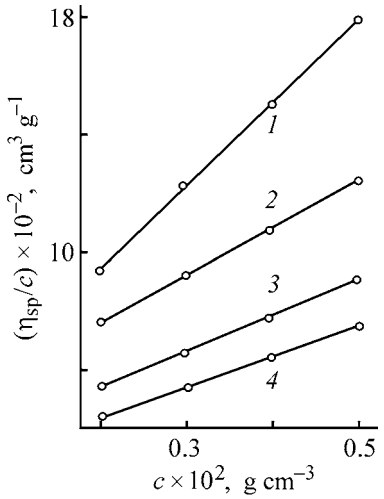

Fig. 3. Reduced viscosity of the solutions, η_{sp}/c, vs. concentration c of PAA ($\overline{M}_\eta = 2.1 \times 10^6$) in (*1*) aqueous solution and in the water–DMSO mixtures: (*2*) 4 : 1, (*3*) 3 : 2, and (*4*) 1 : 1.

plexation, changes in the conjugation energy and polarity of the macroradical enhanced its reactivity in the events of chain propagation and promoted the increase in the $k_p/k_t^{1/2}$ ratio observed in the experiments.

The influence of SA concentration on the relative rate of AA polymerization, v/v_0 in aqueous solutions, in the 1 : 1 water–DMSO mixture, and in DMSO solutions is shown in Fig. 2. It is evident that, in all the media, the v/v_0 values grow with increasing concentration of SA and, after passing through a maximum, decrease. The observed $v/v_0 = f$[SA] dependence with a maximum is due to the dual function of SA as a complexing agent and a salt additive affecting the conformation of macroradicals in solution. Addition of small amounts of SA leads to higher v and, evidently, when the concentration of macroradicals that form complexes reaches a maximum, the highest v values are observed. The subsequent decrease of the v values in the presence of SA can be assigned to a decrease of root-mean-square sizes of molecular globules $(\bar{r}^2)^{1/2}$ as a result of deterioration of the solvent quality owing to addition of large amounts of SA. A similar decrease of $(\bar{r}^2)^{1/2}$ in solutions of lithium bromate was accompanied by a decrease in the rate of AA polymerization [15].

Data presented in the table and Fig. 1 suggest that, in polymerization of AA in the presence of SA, v and $\overline{M}_\eta$ grow in parallel with increasing water content in the mixed water–DMSO solvent. The v values in aqueous–DMSO media in the absence of SA vary in a similar manner (see table), in good agreement with the results of isothermal polymerization of AA [16, 17]. The observed decrease in v in the series water > water : DMSO = 1 : 1 > DMSO is caused by the increase in the $k_p/k_t^{1/2}$ ratio and in the reaction order with respect to the monomer. According to published data for isothermal polymerization of AA in aqueous–DMSO media [17], the variation of $k_p/k_t^{1/2}$ is caused by rise in k_p owing to an increase in the activation energy of reaction.

The above kinetic effects are mainly due to variation of the reactivity of the reacting species as a result of complexation (H-bonding) of propagating radicals and monomer with the solvent [18]. According to NMR data [19], an increase in the polarity of the medium on adding water (ε = 80) to less polar DMSO (ε = 46.6) enhances the capability of the solvent to form intermolecular H-bonds. Formation of H-complexes between the C=O group of AA and water decreases the electron density at the CH_2= group and increases v. In addition, complexation between the C=O group of AA and S=O group of DMSO may also exert a certain effect on v [20]. This effect becomes more pronounced with increasing content of DMSO in the solvent; it affects the activity of AA during polymerization. One more reason for the above rise in v is an increase in $(\bar{r}^2)^{1/2}$ values with growing content of water in the mixed solvent water–DMSO. In this study, the rise in $(\bar{r}^2)^{1/2}$ was judged from the increased reduced viscosity of PAA solutions η_{sp}/c at c = const (Fig. 3, passing from curve *4* to curve *1*), since, as a first approximation, we can assume that $(\eta_{sp}/c) \sim (\bar{r}^2)^{1/2}$ [21]. It is evident that a rise in $(\bar{r}^2)^{1/2}$ with increasing water content in the solvent leads to higher local concentration of the monomer

in the area of active centers and to higher rate of AA polymerization.

The increase in $\overline{M}_\eta$ on adding water to DMSO can be caused by decreased contribution of chain transfer involving mobile hydrogen atoms of the methyl groups of DMSO.

CONCLUSIONS

(1) With increasing concentration of the monomer and initiator, v grows and the dependence of v on the concentration of CH_3COONa passes through an extremum. The v values, the $k_p/k_t^{1/2}$ ratio, and the reaction order with respect to the monomer increase on adding CH_3COONa and in the order DMSO < water : DMSO = 1 : 1 < water.

(2) The $\overline{M}_\eta$ grows with increasing concentration of acrylamide and water content in the binary solvent water–DMSO.

(3) The influence of CH_3COONa on v is due to complexation of CH_3COONa with the propagating radical, and the influence of the composition of the water–DMSO mixture on v is due to complexation of the propagating radicals with the solvent owing to formation of H-bonds and also to variation of the conformational state of macroradicals.

REFERENCES

1. Kurenkov, V.F. and Abramova, L.I., *Polym.-Plast. Technol. Eng.*, 1992, vol. 31, nos. 7–8, pp. 659–704.
2. Thomson, R.A.M., Ong, Ch.K., Rosser, C.M., and Holt, J.M., *Makromol. Chem.*, 1983, vol. 184, no. 9, pp. 1885–1892.
3. Kay, T.A. and Rodriguez, F.J., *J. Appl. Polym. Sci.*, 1983, vol. 28, no. 2, pp. 663–666.
4. Kurenkov, V.F., Baiburdov, T.A., and Stupen'kova, L.L., *Vysokomol. Soedin., Ser. A*, 1987, vol. 29, no. 2, pp. 348–351.
5. Kurenkov, V.F., Baiburdov, T.A., and Stupen'kova, L.L., *Zh. Prikl. Khim.*, 1987, vol. 60, no. 10, pp. 2311–2316.
6. Kurenkov, V.F., Baiburdov, T.A., and Stupenkova, L.L., *Eur. Polym. J.*, 1990, vol. 26, no. 8, pp. 915–918.
7. Boghina, C.M., Marinescu, N.N., Marinescu, M.M., *et al.*, Abstracts of Papers, *Int. Symp. on Macromolecular Chemistry*, Bucharest, 1983, Sect. 1, pp. 113–117.
8. Kurenkov, V.F., Verizhnikova, A.S., and Myagchenkov, V.A., *Fiziko-khimicheskie osnovy sinteza i pererabotki polimerov* (Physicochemical Foundations of Synthesis and Recovery of Polymers), Gorky: Gork. Gos. Univ., 1988, pp. 35–40.
9. Kurenkov, V.F., Aleeva, Yu.V., Verizhnikova, A.S., and Myagchenkov, V.A., *Izv. Vyssh. Uchebn. Zaved., Khim. Khim. Tekhnol.*, 1989, vol. 32, no. 2, pp. 69–73.
10. Kurenkov, V.F., Aleeva, Yu.V., Kuleshov, V.P., and Myagchenkov, V.A., *Zh. Prikl. Khim.*, 1991, vol. 64, no. 1, pp. 150–154.
11. Klein, J. and Conrad, K.-D., *Makromol. Chem.*, 1980, vol. 181, no. 6, pp. 227–240.
12. Tonoyan, O.A., Leikin, A.D., Davtyan, S.P., *et al.*, *Vysokomol. Soedin., Ser. A*, 1973, vol. 15, no. 8, pp. 1847–1851.
13. Osmanov, T.O., Gromov, V.F., Khomikovskii, P.M., and Abkin, A.D., *Vysokomol. Soedin., Ser. A*, 1979, vol. 21, no. 8, pp. 1766–1772.
14. Kurenkov, V.F., Nurullina, E.V., Minkin, V.S., and Myagchenkov, V.A., *Vysokomol. Soedin., Ser. A*, 1994, vol. 36, no. 7, pp. 1076–1080.
15. Osmanov, T.O., Gromov, V.F., Khomikovskii, P.M., and Abkin, A.D., *Dokl. Akad. Nauk SSSR*, 1978, vol. 240, no. 4, pp. 910–913.
16. Kurenkov, V.F., Akhmed'yanova, R.A., Severinov, A.V., and Myagchenkov, V.A., *Khim. Tekhnol. Elementoorg. Soedin. Polim.* (Kazan), 1977, vol. 16, no. 6, pp. 20–23.
17. Gromov, V.E., Galperina, N.J., Osmanov, T.O., *et al.*, *Eur. Polym. J.*, 1980, vol. 16, no. 6, pp. 529–535.
18. Kabanov, V.A., Zubov, V.P., and Semchikov, Yu.D., *Kompleksno-radikal'naya polimerizatsiya* (Radical Complex Polymerization), Moscow: Khimiya, 1987.
19. Zhuravleva, I.L., Zav'yalova, E.N., Bogachev, Yu.S., and Gromov, V.F., *Vysokomol. Soedin., Ser. A*, 1986, vol. 28, no. 4, pp. 873–877.
20. Bondarenko, S.G., Nikolaev, A.F., lavrov, N.A., and Stepanov, E.M., *Zh. Prikl. Khim.*, 1982, vol. 55, no. 12, pp. 2728–2732.
21. Tanford, Ch., *Physical Chemistry of Macromolecules*, New York: Wiley, 1963.

Russian Journal of Applied Chemistry, Vol. 76, No. 2, 2003, pp. 284–288. Translated from Zhurnal Prikladnoi Khimii, Vol. 76, No. 2, 2003, pp. 293–297.

MACROMOLECULAR CHEMISTRY AND POLYMERIC MATERIALS

Structure and Properties of Zinc-containing Copolymers Based on (Meth)Acrylate Monomers

N. V. Kuznetsova, L. V. Kabanova, M. A. Lazarev, and D. F. Grishin

Research Institute of Chemistry, Lobachevsky State University, Nizhni Novgorod, Russia

Received June 13, 2002

Abstract—The kinetic parameters of radical emulsion copolymerization of zinc-containing copolymers with esters of acrylic and methacrylic acids were studied. The effective relative activities of the monomers were calculated from experimental data and the properties of the metal-containing copolymers were assessed as influenced by the structure of the organic monomers.

Thanks to their biocidal, thermal, and physicomechanical properties, zinc-containing polymers are of much interest for preparing special-purpose materials [1]; such polymers can find application as polymer materials with wide biocidal spectrum. Zinc-containing copolymers based on acrylates and methacrylates exhibit enhanced heat resistance and high adhesion to various materials (metal, wood, concrete, etc.), which allows their use for preparing heat-resistant coatings.

It has been found [2–4] that physicomechanical, thermal, and biological properties of zinc-containing polymers and colloidal-chemical characteristics of their latexes are determined by the ligand environment of the zinc atom and by its concentration in the initial monomeric mixture and in the resulting copolymer.

Moreover, synthesis of polymers from zinc-containing monomers is of particular interest because they involve metal atoms able to interact both with the monomer and with the growing macroradical. Similarly to metal halides (Lewis acids) [5, 6], organometallic monomers can directly affect the elementary stages of macromolecule synthesis, including polymeric chain growth.

In this study, we analyzed the reactivity of zinc methacrylate acetate (ZMA) in reactions of emulsion polymerization with esters of acrylic and methacrylic acids.

EXPERIMENTAL

Zinc methacrylate acetate was prepared by the known procedure [1]. Latexes of ZMA copolymers with methyl methacrylate (MMA), ethyl methacrylate (EMA), butyl methacrylate (BMA), and butyl acrylate (BA) were prepared by emulsion polymerization [2].

The size of the latex particles was determined by turbidimetry [7]. To prepare latex films, a required amount of latex was cast on a Teflon plate and dried in air for 5 days at $20 \pm 2°C$.

The content of zinc-containing polymers in the sol–gel fraction were determined by extraction (in the course of 1 month) in a Soxhlet apparatus, using organic solvents with different dielectric constants [8].

The molecular weight of the internodal chain sections (M_c), characterizing the degree of polymer cross-linking, was determined by the Flory–Rener method [9].

The effective relative activities of monomers (r_1 and r_2) were evaluated by the Fineman–Ross procedure [10].

We studied the features of emulsion polymerization of ZMA with monomers of the methacrylate (MMA, EMA, BMA) and acrylate (BA) series. It was found that a stable latex is formed in a wide concentration range only in copolymerization of ZMA with BMA (Table 1). No zinc-containing copolymer is formed in the reactions of ZMA with MMA and EMA. It was demonstrated that, under the conditions studied, homopolymerization of MMA and EMA occurs in relatively low yields (38.3 and 61.3%, respectively); the reaction mixture separates into two phases and no stable latex is formed. Our experimental results are in good agreement with data on emulsion homopolymerization of

1070-4272/03/7602-0284 $25.00 © 2003 MAIK "Nauka/Interperiodica"

Table 1. Properties of ZMA copolymers with (meth)acrylate monomers*

Monomer	c_{Zn}, wt %	M_c, g mol^{-1}	g, wt %	$\eta/\eta_0 - 1$	R, nm	γ, wt % h^{-1}
BMA	0	0	0	0.4	112	–
	2.19	41000	63.0	5.3	132	–
	2.64	31000	60.0	6.5	138	–
	4.53	18000	70.2	4.5	150	–
	5.76	17000	76.7	3.7	155	–
	7.03	15000	82.2	2.1	162	–
BA	0	–	–	0.63	95	–
	1.9	–	–	0.71	106	–
	2.5	–	24.3	0.73	110	–
	3.6	13500	25.0	1.23	122	–
	5.4	–	28.0	2.81	>170	–
	7.1	1457	30.2	–	–	–
	10.7	731	40.0	–	–	–
	14.3	667	55.4	–	–	–
MMA	0	–	–	–	–	38.3
	0.7	–	51.4	–	–	–
	1.0	400	55.65	–	–	–
	3.19	400	99.0	–	–	81.4
	6.05	400	–	–	–	–
	11.0	400	–	–	–	–
	18.6	400	100	–	–	–
EMA	0	–	–	–	–	61.5
	3.1	12500	62.0	–	–	98.0
	6.2	8200	82.2	–	–	–
	8.3	–	98.0	–	–	–
	15.5	2035	97.9	–	–	–
	24.8	–	100	–	–	–

* (g) Content of insoluble gel fraction and (γ) conversion of organic monomer.

lower methacrylates in the presence of oxyethylated alkylphenols as emulsifiers [11].

It was found that, with the concentration of ZMA in the reaction mixture increasing to 3.2 wt %, the conversion of the organic comonomer grows appreciably from 38.3 and 61.5 to 81.4 and 98.0 wt % for MMA and EMA, respectively. This is probably due to complexation of zinc atoms with the growing macroradical, which accelerates polymerization and, thus, increases the polymer yield.

The ZMA–BMA copolymer has a cross-linked structure [2, 3], which can be quantitatively characterized by the internodal molecular weight M_c and content of insoluble gel fraction, g.

Using extraction with butyl acetate, we separated the ZMA–BMA copolymers into gel and sol fractions; their washed and dried samples were analyzed. It was found that, in ZMA–MMA copolymers containing from 0.7 to 18.6 wt % zinc, zinc occurs almost exclusively (up to 98%) in the gel fraction.

The gel fraction of ZMA–MMA copolymers was used to determine the internodal molecular weight, which characterizes the network density. For copolymers containing 0.7 to 18.6 wt % zinc, M_c constitutes ~400, which is the lowest value attainable for both acrylate and methacrylate monomers. It should be noted that a slightly lower value was only obtained for rigidly cross-linked polyurethanes [12]. It was found that this value is independent of the conversion of the organic monomer. For example, for ZMA–MMA copolymer containing 3.19 wt % zinc, M_c is constant beginning from 30% conversion of the organic monomer up to its complete exhaustion.

The internodal molecular weight M_c (Fig. 1) in the concentration range studied can be described by the following equations:

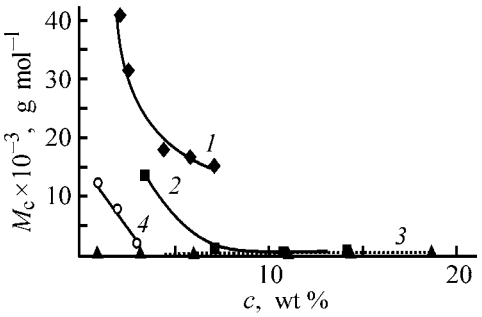

Fig. 1. Internodal molecular weight M_c vs. zinc content c in the monomer mixture for copolymers (*1*) ZMA–BMA, (*2*) ZMA–BA, (*3*) ZMA–MMA, and (*4*) ZMA–EMA.

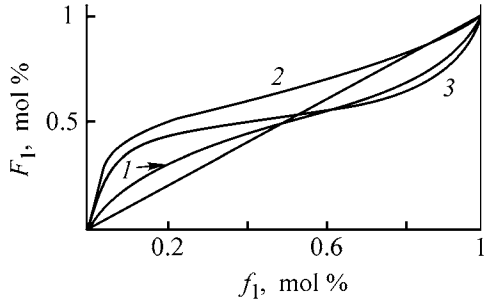

Fig. 2. Composition of copolymers F_1 vs. the composition of the initial monomer mixture f_1 for copolymers (*1*) ZMA–BMA, (*2*) ZMA–BA, and (*3*) ZMA–MMA.

$$M_c(\text{MMA}) = 400 \pm 50,$$

$$M_c(\text{EMA}) = 39\,134[\text{Zn}]^{-1} + 425,$$

$$M_c(\text{BMA}) = 81\,033[\text{Zn}]^{-1} + 2164,$$

$$M_c(\text{BA}) = 6573[\text{Zn}]^{-1} - 5394.$$

A rather abrupt decrease in the internodal molecular weight M_c, characterizing strengthening of the polymer cross-linking on passing from BMA to BA [e.g., at 7-wt % content of zinc in copolymer it constitutes 15 000 and 1500 g mol^{-1}, respectively (Table 1)], is probably due to steric hindrance in copolymerization of ZMA with methacrylate monomers (BMA) as compared with acrylates (BA).

The content of the gel fraction at zinc content in copolymer of up to 10 wt % can be described by the following expressions:

$$g(\text{MMA}) = 19.1[\text{Zn}] + 38,$$

$$g(\text{EMA}) = 7.0[\text{Zn}] + 40,$$

$$g(\text{BMA}) = 5.9[\text{Zn}] + 65,$$

$$g(\text{BA}) = 2.45[\text{Zn}] + 16.8.$$

It should be noted that, in copolymerization of ZMA with methacrylates (MMA, EMA, and BMA) the content of the gel fraction grows with increasing degree of cross-linking (Table 1). The internodal molecular weight M_c and the content of gel fraction g in the copolymer increase in the order BMA < EMA < MMA.

By analogy with the emulsion polymerization of styrene involving metal-containing monomers [13], we suggest that copolymerization of ZMA with MMA and EMA involves formation of a rigidly cross-linked core in the initial stage. Free MMA and EMA are probably linked as blocks to give an unstable coarse dispersion.

As shown previously, a similar polymerization mechanism has been observed by Wojnarowski and coworkers in emulsion polymerization of styrene with disubstituted acrylates and methacrylates of Group I and II metals. In this case, it is assumed that the copolymer blocks grow in different phases [13, 14].

Using the data on the emulsion copolymerization of ZMA with MMA, BMA, and BA, we plotted the dependences of the copolymer compositions on the composition of the initial monomer mixture (Fig. 2) and calculated the effective relative activities of monomers r_1 and r_2 for the above monomer pairs. The alternation of the monomer units in the copolymers was determined (Table 2). As seen from a comparison of

Table 2. Effective relative activities and parameters Q and e for (meth)acrylate monomers in copolymerization with ZMA (M_2)

M_1	r_1	r_2	Q_1	e_1	r_1r_2	Δe
MMA	0.10 ± 0.01	0.20 ± 0.05	0.74	0.40	0.020	2.10
EMA	–	–	0.56	0.17	–	1.87
BMA	0.36 ± 0.05	0.31 ± 0.05	0.72	–0.23	0.112	1.47
BA	0.06 ± 0.01	0.90 ± 0.10	0.50	1.06	0.054	2.76

different methacrylate monomers (MMA and MBA), the strongest tendency toward alternation is observed for the ZMA–MMA monomer pair, for which the copolymer composition is constant in a wide concentration range (Fig. 2, curve *1*, plateau). Moreover, the product of the effective relative activities of monomers $r_1 r_2$ is minimal and close to zero (Table 2). A similar trend is found for the ZMA-BMA monomer pair (Fig. 2, curve *2*). However, in this case, the alternation of the monomer units is less pronounced than in ZMA–MMA copolymer. It should be noted that, on passing from ZMA–MMA to ZMA–BMA pairs, the effective cross-linking density increases to a lesser extent.

We found that (Table 1), at equal content of zinc, the ZMA–BA copolymers have lower internodal molecular weight as compared with ZMA–BMA copolymers. For example, at a zinc content in the copolymer of 7 wt %, M_c of ZMA–BMA copolymer is close to 15000, whereas for ZMA–BA copolymer it is an order of magnitude lower (~1500). At the same time, the product of the relative activities of the monomers ($r_1 r_2$ = 0.054) in ZMA–BA copolymer is smaller than in the case of ZMA–BMA copolymer ($r_1 r_2$ = 0.11) (Table 2).

It is known [15] that the electron-acceptor properties of a monomer in the *Q*–*e* Alfrey–Price scheme are characterized by the electronegativity parameter *e*. For the monomers studied (Table 2) this value increases in the order BMA < EMA < MMA and BMA < BA. The alternation of the monomer units in the copolymer and the degree of polymer cross-linking increase in the same order.

According to the Alfrey–Price scheme [14], the alternation of the monomer units in the copolymer becomes more pronounced with increasing difference in the *e* parameter between the copolymerizing monomers. In particular, the most regular alternation is observed for typical donors and acceptors.

Previous studies of the copolymerization of ZMA with MMA and BMA have revealed the electron-donor nature of MMA ($Q = 3.0 \pm 0.3$, $e = -1.7 \pm 0.2$) [3].

We found that the particle size of latexes of ZMA–BMA and ZMA–BA copolymers grows with increasing effective density of cross-linking in accordance with the following equations (Fig. 3):

$$R(\text{BMA}) = 6.95[\text{Zn}] + 116,$$

$$R(\text{BA}) = 7.27[\text{Zn}] + 94.$$

The specific viscosity of latexes of ZMA–BA copolymers is lower as compared with ZMA–BMA (Fig. 4).

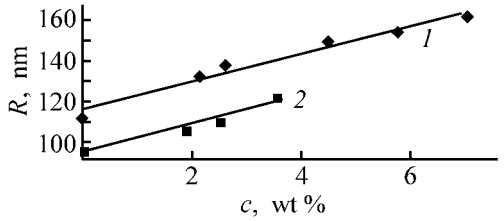

Fig. 3. Size *R* of copolymer latex particles vs. the zinc content *c* in copolymers (*1*) ZMA–BMA and (*2*) ZMA–BA.

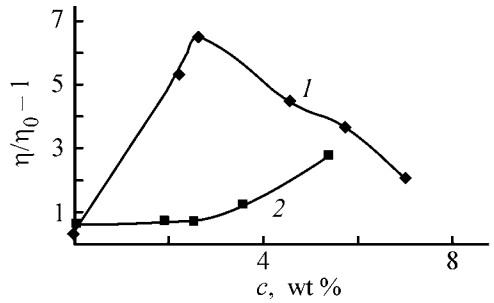

Fig. 4. Specific viscosity $\eta/\eta_0 - 1$ of latexes of copolymers (*1*) ZMA–BMA and (*2*) ZMA–BA vs. the zinc content in the mixture *c*.

As is known [16], the latex viscosity is determined by the interaction of functional groups present on the particle surface. With increasing effective degree of cross-linking, the amount of these groups must decrease. As a result, the viscosity of the latexes of more cross-linked polymers is smaller than that of latexes of ZMA–BMA copolymers at equal zinc content in the copolymer.

CONCLUSIONS

(1) In copolymerization of zinc methacrylate acetate with (meth)acrylate monomers, stable latexes are formed only with butyl methacrylate and butyl acrylate. The initial stage of polymerization involves formation of a rigidly cross-linked core. In the case of methyl methacrylate and ethyl methacrylate, the free (meth)acrylate monomer is linked as a block with the formation of a coarse dispersion.

(2) The effective relative activities of monomers in polymerization of zinc methacrylate acetate with methyl methacrylate, ethyl methacrylate, and butyl methacrylate show that the alternation of the monomeric units in the copolymers becomes more pronounced in the order ethyl methacrylate < butyl methacrylate < methyl methacrylate, i.e., with increasing electron-acceptor properties of the organic monomer. With increasing degree of cross-linking of zinc methacrylate acetate copolymers with methacrylate and

acrylate monomers, the tendency toward alternation of the monomer units is enhanced.

(3) The colloidal-chemical properties of latexes of zinc methacrylate acetate copolymers with (meth)-acrylate monomers depend on the parameters of cross-linking of these copolymers, which are determined by the nature of the organic monomer.

REFERENCES

1. Pomogailo, A.D. and Savost'yanov, V.S., *Metallsoderzhashchie monomery i polimery na ikh osnove* (Metal-Containing Monomers and Polymers Based on Them), Moscow: Khimiya, 1988.
2. Kabanova, L.V., Kuznetsova, N.V., Aleksandrov, Yu.A., *et al.*, *Kolloidn. Zh.*, 1999, vol. 61, no. 2, pp. 211–214.
3. Kabanova, K.V., Kuznetsova, N.V., and Aleksandrov, Yu.A., *Zh. Prikl. Khim.*, 2000, vol. 73, no. 3, pp. 480–484.
4. Kuznetsova, N.V., Kabanova, K.V., Aleksandrov, Yu.A., and Smirnov, V.F., in *Ekologicheskie problemy biodegradatsii promyshlennykh, stroitel'nykh materialov i otkhodov proizvodstv* (Environmental Problems of Biodegradation of Commercial and Building Materials and Industrial Wastes), Penza: PDZ, 2000, pp. 168–170.
5. Grishin, D.F. and Semenycheva, L.L., *Usp. Khim.*, 2001, vol. 70, no. 5, pp. 486–510.
6. Kabanov, V.A., Zubov, V.P., and Semchikov, Yu.D., *Kompleksno-radikal'naya polimerizatsiya* (Radical Complex Polymerization), Moscow: Khimiya, 1987.
7. *Laboratornye raboty i zadachi po kolloidnoi khimii* (Practical Works and Problems on Colloidal Chemistry), Frolov, Yu.G., Ed., Moscow: Khimiya, 1986.
8. Rafikov, S.R., Budtov, V.P., and Monakov, D.B., *Vvedenie v fizikokhimiyu rastvorov polimerov* (Introduction to Physical Chemistry of Polymer Solutions), Moscow: Nauka, 1978.
9. Rogers, C.E., Stannett, V., and Szwarc M., *J. Phys. Chem.*, 1959, vol. 63, no. 2, pp. 406–410.
10. Odian, G., *Principles of Polymerization*, New York: McGraw–Hill, 1970.
11. Zabotin, K.P. and Shmeleva, A.N., *Fiziko-khimicheskie osnovy sinteza i pererabotki polimerov* (Physicochemical Principles of Synthesis and Treatment of Polymers), Gor'kii: Gor'k. Gos. Univ., 1986, pp. 33–35.
12. Lipatov, Yu.S., Kercha, Yu.Yu., and Sergeev, L.M., *Sruktura i svoistva poliuretanov* (Structure and Properties of Polyurethanes), Kiev: Naukova Dumka, 1970.
13. Wojtczak, K. and Sucharcka-Galas, K., *Polimery*, 1982, vol. 27, no. 11, pp. 425–427.
14. Wojnarowski, T.J. and Silin, L., *Polimery*, 1973, vol. 18, no. 3, pp. 128–130.
15. *Copolymerization*, Ham, G.E., Ed., New York: Interscience, 1964.
16. Baran, A.A., *Polimersoderzhashchie dispersnye sistemy* (Polymer-Containing Disperse Systems), Kiev: Naukova Dumka, 1986.

Russian Journal of Applied Chemistry, Vol. 76, No. 2, 2003, pp. 289–293. Translated from Zhurnal Prikladnoi Khimii, Vol. 76, No. 2, 2003, pp. 298–303.

MACROMOLECULAR CHEMISTRY AND POLYMERIC MATERIALS

Synergistic Phenomena in Modification of Polyolefins with Mixtures of Isocyanates and Epoxides

R. R. Spiridonova, S. S. Galibeev, A. M. Kochnev, and V. P. Arkhireev

Kazan State Technological University, Kazan, Tatarstan, Russia

Received October 16, 2001; in final form, July 2002

Abstract—Modification of commercial polyolefins with binary mixtures of isocyanates and epoxides was studied; the influence of the order of adding components on the performance of the modifying system was examined.

Under the impact of severe external factors, polymeric materials undergo irreversible transformations causing changes in the degree of crystallinity, molecular mobility, strength, and other parameters. This results in partial or complete loss of the main properties determining the wide use of polymeric materials in modern engineering. Stabilization of polymers is aimed at suppressing undesirable changes, improving the quality, and prolonging the service life of finished polymeric products. Antioxidative stabilization of polymers [1] can be provided by introducing individual reactive compounds containing functional groups (e.g., epoxy, isocyanato) or synergistic mixtures in which combination of different types of antioxidants ensures considerable enhancement of the stabilizing effect. The second alternative shows much promise.

In this study, we assessed the performance of synergistic mixtures based in isocyanates (ISs) and epoxides (EPs) in chemical modification of polyolefins (POs) and examined regular trends in the effect of these antioxidants. Our goal was to improve the processing and service characteristics of the polymeric products, in particular, to make them less expensive and prolong their service life by retarding aging and reducing the loss of stabilizers due to exudation.

The approach to choosing and formulating effective synergistic mixtures is based on studying the effect of the components taken separately and in combination. The choice of ISs and EPs was governed by the fact that the effect of these compounds, taken separately, on the PO properties has been studied in sufficient detail. The thermostabilizing effect of ISs and EPs, taken separately or in combination, is due to the reaction of their functional groups with terminal unsaturated bonds of POs [2–4], which, being potentially active centers of macromolecule degradation, negatively affect the whole set of properties of commercial POs (Table 1). Deactivation of such centers by reactions with isocyanato and epoxy groups ensures strong stabilizing effect, and the use of ISs and EPs in combination may result in nonadditive enhancement of various properties. The use of binary modifying systems instead of mechanical blending allows incorpora-

Table 1. Effect of the modification of polypropylene (PP) with toluene-2,4-diisocyanate (TDI) and ED-20 epoxy–4,4'-isopropylidenediphenol resin on the content of terminal vinylene units and heat resistance of the polymer*

Modifier, wt %	$\log I_{888} / \log I_{1380}$	$T_{on.ox}$	T_{ox}^0	$T_{\Delta m=5\%}$	$T_{\Delta m=50\%}$
		°C			
–	1.277	291	353	262	370
TDI:					
0.67	1.069	308	369	268	384
1.3	0.919	318	373	274	400
ED-20:					
0.67	1.115	326	373	274	398
1.33	–	316	351	279	388

* (I_{888}, I_{1380}) Intensities I of the absorption bands at 888 (out-of-plane bending vibrations of terminal vinylidene groups) and 1380 cm^{-1} (symmetric bending vibrations of the methyl groups), respectively; ($T_{on.ox}$) temperature of oxidation onset; (T_{ox}^0) equilibrium oxidation temperature; ($T_{\Delta m=5\%}$, $T_{\Delta m=50\%}$) temperatures of 5 and 50% weight loss, respectively.

1070-4272/03/7602-0289 $25.00 © 2003 MAIK "Nauka/Interperiodica"

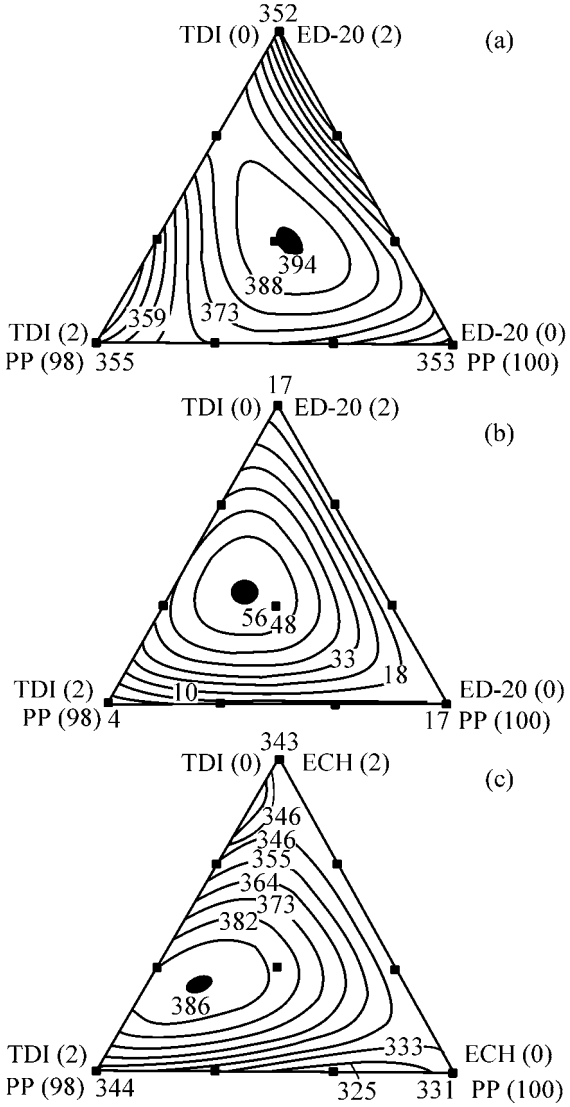

Fig. 1. Isolines of (a, c) oxidation temperature and (b) induction period of oxidation. System: (a, b) PP + TDI + ED-20 and (c) PP + TDI + ECH. *Figures in parentheses* denote the content of the corresponding compounds (wt %); the same for Fig. 4.

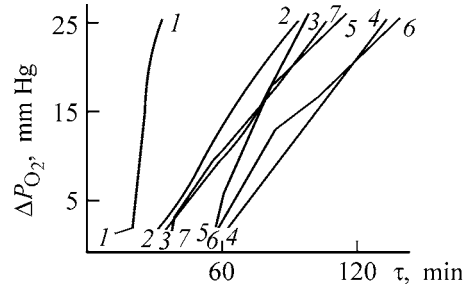

Fig. 2. Autooxidation kinetic curves for the system LDPE–TDI–ECH. (ΔP_{O_2}) Oxygen uptake measured as pressure change and (τ) time. (*1*) Initial LDPE, (*2*) LDPE + ECH (2 wt %), (*3*) LDPE + ECH (1.33 wt %), (*4*) LDPE + ECH (1.33 wt %) + TDI (0.67 wt %), (*5*) LDPE + TDI (0.67 wt %), (*6*) LDPE + ECH (0.67 wt %) + TDI (0.67 wt %), and (*7*) LDPE + TDI (1.33 wt %).

tion of active molecular groups directly into the polymer chain; in this way, the process for introducing a stabilizer is simplified and the ideal molecular distribution is attained; furthermore, exudation and evaporation of the stabilizers are excluded.

A study of the heat resistance of PP modified with IS–EP mixtures revealed synergistic effects at certain component ratios. For example, the equilibrium temperature of PP oxidation considerably increases (by 41°C, Fig. 1a), and the induction period becomes 40 min longer (Fig. 1b), on adding a mixture of 0.67 wt % TDI and 0.67 wt % ED-20. Still stronger effects are observed with epichlorohydrin (ECH) used instead of ED-20: T_{ox}^{0} increases by 55°C (Fig. 1c), and $T_{on.ox}$, by 79°C, compared with the unmodified PP. This stabilizing system also retards oxidation of low-density polyethylene (LDPE, Fig. 2).

We also examined how the order of adding the components of the stabilizing mixture affects the stability of POs. Four addition modes were tested: (I) IS was added to PO melt first, and, after rolling for 5 min, EP was added; (II) EP was added first, and IS, 5 min later; (III) IS and EP were added simultaneously; (IV) IS and EP were preliminarily copolymerized for 2 h and then added to the PO melt. As seen from Table 2, the highest $T_{on.ox}$ and the longest induction period of autooxidation τ_{ind} are observed when the components are preliminarily copolymerized.

It should be noted that the copolymerization time τ (h) of the components of the modifying mixture PP + 0.67 wt % ED-20 + 0.67 wt % additive (MDI or SKU-PFL) appreciably affects the induction period τ_{ind} of PP autooxidation (Table 3); the strongest effects were attained in the case when the preliminary copolymerization was performed for 1–2 h. As the copolymerization time is increased further, the stabilizing effect monotonically decreases and, finally, fully disappears. This effect is due to initial formation of a more active species in which the centers capable of reacting with PO unsaturated bonds are preserved; at higher conversions, the content of these centers decreases, and the thermostabilizing effect becomes weaker.

Our assumption is confirmed by an increase, following the hyperbolic law, in the viscosity of the TDI–ECH system in the course of polymerization at 50°C and by changes in the thermal stability of the products formed in model reactions of copolymerization of 1-hexene, TDI, and ECH added in different modes (Table 4). Mode I: An equimolar amount of ECH was added to 1-hexene, then a catalyst (tertiary amine) was

Table 2. Influence of the mode of component addition on the efficiency of PP stabilization (modifier: 0.67 wt % ED-20 + 0.67 wt % additive)

Additive*	Mode of component addition							
	I		II		III		IV	
	τ_{ind}, min	$T_{on.ox}$, °C	τ_{ind}, min	$T_{on.ox}$, °C	τ_{ind}, min	$T_{on.ox}$, °C	τ_{ind}, min	$T_{on.ox}$, °C
MDI	58	283	56	311	47	274	57	245
SKU–PFL	36	275	52	309	–	290	77	354
TDI	53	305	25	394	31	372	62	396

* (MDI) Diphenylmethane-4,4'-diisocyanate and (SKU–PFL) product of reaction of polyoxymethylene glycol with TDI.

introduced, the mixture was heated at 60°C for 1 h, after which an equimolar amount (with respect to the other components) of TDI was added, and the reaction was continued for an additional 1 h. Mode II: The same except that TDI was added to 1-hexene first. Mode III: all the three components taken in equimolar ratio were mixed, and the mixture was heated at 60°C for 1 h.

The reaction products were transparent solids differing in color (from white to yellow) and insoluble in organic solvents; in view of the functionality of the chosen IS, this fact suggests formation of cross-linked three-dimensional (3D) structures.

The sample prepared using mode II showed the highest thermal degradation temperature. In this case, first the copolymerization of EP with 1-hexene occurred, after which IS was added. This fact confirms that ether fragments grafted to the PO macromolecule are more stable than amide fragments.

Analysis of the temperatures corresponding to the first step of the weight loss (apparently, due to evaporation of unchanged 1-hexene) also gives interesting results. In all the three samples, the weight loss starts at about 50–55°C, which corresponds to the boiling point of 1-hexene, and is complete at different temperatures, with the highest temperature being observed in the case of mode II. This may be due to formation in this case of a more densely cross-linked 3D structure hindering evaporation of the unchanged monomer. Evaporation of 1-hexene is complete only with the onset of degradation.

As shown above, the chemical reactions of ISs and EPs with PP yield grafted amide and ether structures. Also, as known from the literature [5] and shown by analysis of model reactions of ISs and EPs, reactions of bi- and polyfunctional compounds yield 3D cross-linked products insoluble in organic solvents. After performing the reaction in the TDI–ED-20–1-hexene system for 4 h with the temperature gradually raised from 50 to 100°C, the IS and EP taken in equimolar ratio are fully exhausted, and approximately 30% of the olefin remains unchanged.

Table 3. Thermostabilizing effect of the modifying mixture at varied time τ of copolymerization of the components

Additive	τ_{ind} (min) at indicated τ, h				
	0	1	2	3	4
MDI	46	72	58	47	–
SKU–PFL	37	59	78	40	18

Table 4. Heat resistance of copolymerization products of 1-hexene, ECH, and TDI as influenced by the mode of the component addition (DTA data)*

Addition mode	T_t	$T_{\Delta m=5\%}$	T_1
	°C		
I	426	98	53–95
II	512	116	54–239
III	440	68	52–147

* (T_t) Temperature of thermal degradation and (T_1) temperature range of the first step of the weight loss.

Table 5. Rate constants of the reaction at equimolar IS : EP ratio

T, °C	Initial IS concentration, M	$k \times 10^2$, l mol^{-1} min^{-1}
20	0.27	8.85
30	0.29	10.0
40	0.30	14.21

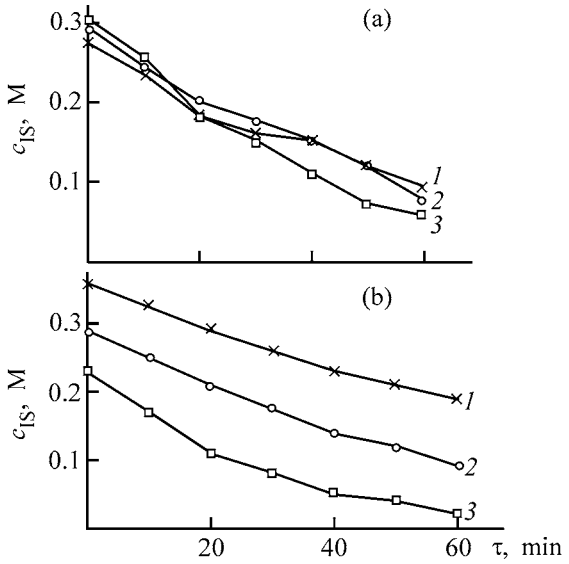

Fig. 3. Concentration of isocyanate groups, c_{IS}, vs. copolymerization time τ. (a) TDI : ECH molar ratio 1 : 1; copolymerization temperature, °C: (*1*) 20, (*2*) 30, and (*3*) 40. (b) Copolymerization temperature 30°C; TDI : ECH molar ratio: (*1*) 2 : 1, (*2*) 1 : 1, and (*3*) 1 : 2.

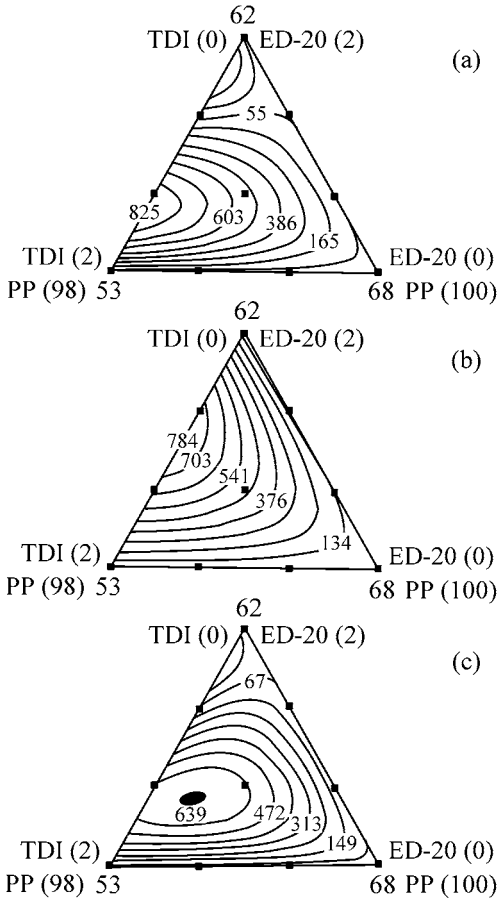

Fig. 4. Isolines of relative elongation for the system PP + TDI + ED-20: (a) modifiers added simultaneously, (b) TDI added first, and (c) ED-20 added first.

Thus, the synergistic effect of IS–EP mixtures (with ECH as example) may be due to formation of a more active stabilizer in the reaction between the initial monomers and can be enhanced by concurrent grafting of the IS–EP reaction product to residual unsaturated bonds of a PO:

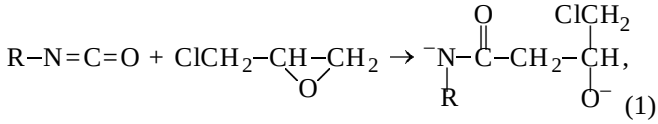

(1)

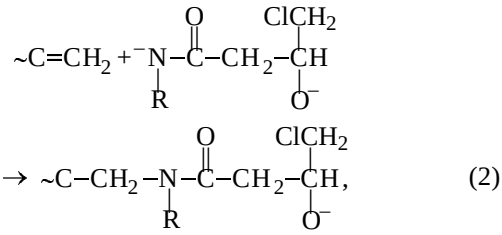

(2)

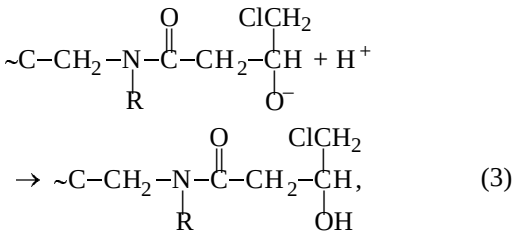

(3)

where (1) is the stage of dianion formation; (2), reaction of the dianion with the α-olefin; (3), chain termination.

A kinetic study of the reaction (Figs. 3a, 3b; Table 5) showed that it obeys a second-order equation

$$-\frac{dc_{IS}}{dt} = k c_{IS} c_{EP},$$

where k is the second-order rate constant; c_{IS} and c_{EP} are the IS and EP concentrations, respectively.

Presumably, such reactions occur in POs, yielding fairly large fragments grafted to the polymer macromolecule; these fragments may form a separate phase in the polymeric matrix, thus affecting the heat resistance, processability, and service characteristics of the polymer. For example, only on adding the modifiers in combination, the relative elongation increases by an order of magnitude (Figs. 4a–4c), with the breaking stress growing too.

The considerable rise in the relative elongation on adding TDI and ED-20 to polypropylene may be due to modification of the amorphous phase by lengthy fragments grafted to the PO macromolecule; these fragments must impart rubber-like properties to PO. The contribution of the elastic component to the total

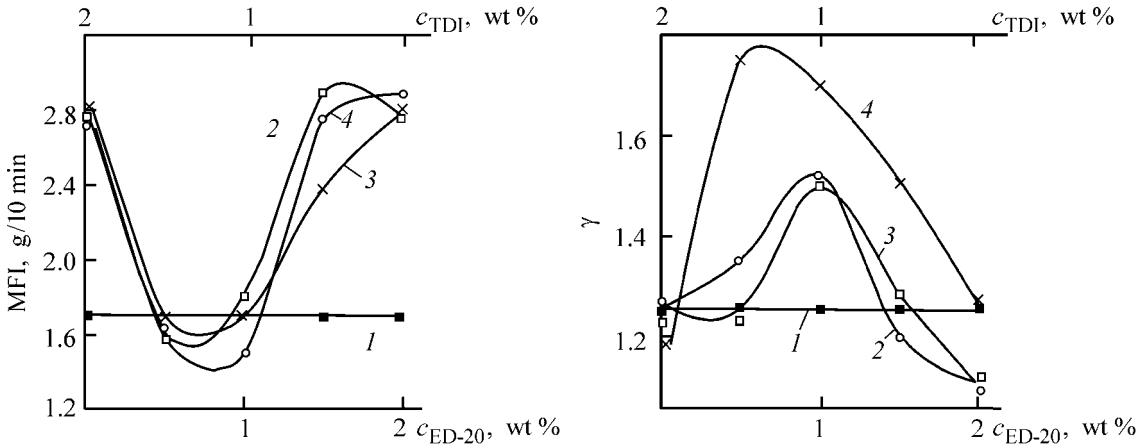

Fig. 5. Melt flow index MFI and intrinsic viscosity γ of PP modified with TDI and ED-20 vs. the content of TDI (c_{TDI}) and ED-20 (c_{ED-20}): (*1*) initial PP, (*2*) ED-20 added first, (*3*) TDI added first, and (*4*) both modifiers added simultaneously.

deformation increases by a factor of 2–4 on adding mixtures of modifiers to PP, compared with the unmodified polymer (Table 6). The elastic deformation grows at the expense of the viscous component.

The stress–strain curves also show that modification of PP with IS–EP mixtures enhances its hyperelastic properties. Whereas the stress–strain curve for the unmodified samples is typical of crystalline POs, addition of binary mixtures makes this curve similar to that obtained for rubbers. In modified samples, no decrease in the stress is observed at the instant of necking; similarly to rubbers, the stress grows with the strain; and the plateau characteristic of crystalline POs is less pronounced.

Formation of grafted 3D structures in the course of PO modification with IS–EP mixtures affects the rheological parameters: The viscosity of solutions and melts grows, the resistance of PO to fivefold extrusion is enhanced, and the melt flow index (MFI) decreases (Fig. 5). Its decrease to the level characteristic of the control sample does not impair the processability of the modified formulations.

Table 6. Contributions of the elastic, viscoelastic, and viscous deformations in the system PP + TDI + ED-20 (modifier: 1.33 wt % TDI + 0.67 wt % ED-20)

Mode of modifier addition*	Deformation, %		
	elastic	viscoelastic	viscous
Initial PP	2.8	2.4	94.8
I	10.5	1.1	88.4
II	4.6	2.1	93.3
III	9.2	1.8	89.0

* (I) TDI added first, (II) ED-20 added first, and (III) both components added simultaneously.

Thus, modification of POs with mixtures of epoxy compounds and isocyanates leads, at certain ratios of the components, to manifestation of the synergistic effect not only in the heat resistance, but also in service properties.

CONCLUSIONS

(1) Copolymerization of isocyanates with epoxy compounds and olefins was studied. Introduction of binary mixtures based on isocyanates and epoxides into crystalline polyolefins enhances their heat resistance and certain physicomechanical properties, with the synergistic effects observed. The modification efficiency was studied in relation to the order of adding components.

(2) The synergistic effect is accounted for by the formation of a more active species upon introduction of the components of the binary mixture into polyolefins.

REFERENCES

1. Shlyapnikov, Yu.A., Kiryushkin, S.G., and Mar'in, A.P., *Antiokislitel'naya stabilizatsiya polimerov* (Antioxidative Stabilization of Polymers), Moscow: Khimiya, 1986.
2. Kotschnev, A., Archireev, V., Shageeva, F., and Kondratyeva, T., *Eur. Polym. J.*, 1988, vol. 24, no. 12, pp. 1177–1180.
3. Arkhireev, V.P. and Abdulkhakova, Z.Z., *Plast. Massy*, 1980, vol. 3, pp. 13–15.
4. Galibeev, S.S., Influence of Small Additions of Reactive Compounds on the Efficiency of Polyolefin Modification, *Cand. Sci. Dissertation*, Kazan, 2000.
5. Saunders, J.H. and Frish, K.C., *Polyurethanes. Chemistry and Technology*, part 1: *Chemistry*, New York: Interscience, 1962.

Russian Journal of Applied Chemistry, Vol. 76, No. 2, 2003, pp. 294–302. Translated from Zhurnal Prikladnoi Khimii, Vol. 76, No. 2, 2003, pp. 304–312.

MACROMOLECULAR CHEMISTRY AND POLYMERIC MATERIALS

Hydrodynamic Behavior of Epoxy and Phenol-Formaldehyde Oligomers in Solution during Thermal Precondensation

A. N. Krasovskii, D. V. Novikov, V. N. Filippov, V. D. Zaporozhets, and L. Sh. Nigmanova

Pigment Open Joint-Stock Research and Production Company St. Petersburg, Russia

Institute of Macromolecular Compounds, Russian Academy of Sciences, St. Petersburg, Russia

St. Petersburg State University of Motion Pictures and Television, St. Petersburg, Russia

Received July 8, 2002

Abstract—The concentration dependences of the relative viscosity of epoxy-4,4'-isopropylidenediphenol (Epikot 1009, E-05) and phenol-formaldehyde (DFFr) resins in Cellosolve solutions in the concentration range c = 5–60%, as well as the kinetics of thermal precondensation of a mixture of E-05 and DPFr resins in solution at molar ratios N_1/N_2 = 0.6–1.5, were studied by the method of capillary viscometry. The cluster structure of the surface of coatings on the metal sheet formed by cross-linked epoxy-phenol polymer in various kinetic stages of precondensation of the mixture of E-05 and DFFr resins in solution was studied by electron microscopy with gold decoration. The optimal concentrations of resins in solution and the precondensation kinetics of oligomer mixtures essential for formulating the compounds were calculated.

In preparing coatings of epoxy-phenol polymers, account should be taken [1] of the fact that the compatibility of epoxy-4,4'-isopropylidenediphenol and phenol-formaldehyde resins in solution is determined by the nature of intermolecular interactions of the oligomers in various kinetic stages of thermal precondensation. Markevich *et al*. [1] showed that molecules of epoxy-4,4'-isopropylidenediphenol and phenol-formaldehyde oligomers (EOs and POs, respectively) are associated in solution. It was found later [2–6] that the size and structure of the EO and PO associates are determined by the molecular weight (MW) of the oligomers, composition of the mixture, and thermal history of the solution. The viscosity of the EO–PO mixture in solutions is determined by the time of thermal precondensation of resins and passes through an extremum, which is due to changes in the size and structure of mixed associates [5, 6].

As shown previously [2–4], the degree of polymerization (DP) of EP and the solvent polarity determine the shape of the concentration dependences of the relative viscosity η_{rel} on c of EO in solutions. These dependences are described by the expression

$$\ln \eta_{rel} = ([\eta]_0 c)^a, \quad (1)$$

Here, $[\eta]$ is the intrinsic viscosity, and c is the concentration [7].

In EO solutions (DP = 2–4) in chloroform, the η_{rel}–c curves for oligomer molecules whose size does not exceed that of the Kuhn statistic segment (27 Å, DP ≅ 5 [8]) satisfy the condition $[\eta]_c > [\eta]$, where $[\eta]_c = d\ln \eta_{rel}/dc$ ($c > 0$) is the running intrinsic viscosity [9]. In this case, the power index a in expression (1) is over unity. For EO with DP > 5, the η_{rel}–c curves are characterized by the conditions $[\eta]_c < [\eta]$ and $a < 1$ [9]. According to [1, 3, 8], stable heterocomplexes are formed in solutions of the EO–PO mixture in Cellosolve (C) via of intermolecular hydrogen bonding between these oligomers.

Studies of the structure of cross-linked epoxy-phenol polymers [10, 11] have shown that a uniform chemical network is formed on the polymer coating surface at EO-to-PO molecular weight ratios close to 4 : 1, the optimal M_n(EO) being close to 3500. Markevich *et al*. [1, 8] believe that thermal precondensation of a resin mixture in solution is required for increasing the compatibility between EO and PO and for the subsequent formation of a uniform chemical network upon thermal curing of EO and PO. This conclusion has been confirmed in studies of the mechan-

1070-4272/03/7602-0294 $25.00 © 2003 MAIK "Nauka/Interperiodica"

ical properties of epoxy-phenol polymer films and the protective characteristics of a coating in various kinetic stages of precondensation of the EO–PO mixture in solution at 393 K [8, 12].

Nizhnik *et al*. [12] studied the precondensates (precondensation time 2 h at 393 K [12]) based on a mixture of epoxy-4,4'-isopropylidenediphenol (E-05) and phenol-formaldehyde (FPF-1) resins in a C solution for a set of 15 E-05 samples differing in molecular weight. A uniform correlation was established between the relative elongation ε/δ of the films of cross-linked epoxy-phenol polymer and the ultimate rupture stress δ (Fig. 1). For films prepared by cold mixing of EO and PO in solution, there is no correlation between ε/δ and δ. It can be suggested that association of oligomers in solution is governed by a uniform mechanism predetermining the precondensation kinetics of the mixture and the structure of the cross-linking sites in the chemical network of the cross-linked polymer in the coating.

The structural changes in various kinetic stages of precondensation of resin mixture in solution must affect the densities of the aggregates (or associates) of oligomers, as well as the degree of association of the molecules, *s*. It is highly probable that, during precondensation of the resin mixture, the EO and PO aggregates break down to give mixed aggregates of oligomers and an infinite cluster. Specifically in this case, the viscosity of the oligomer mixture in solution and the protective properties of coatings based on cross-linked epoxy-phenol polymers must be determined by the kinetic modes of precondensation.

It is known [13] that the correlations between the parameters of the oligomer aggregates in solutions, as well as those between the characteristics of clusters of macromolecules constituting the network of the cross-linked epoxy-phenol polymer, can be studied using the fractal cluster model [13, 14]. This model predicts how the density of aggregates in solution and clusters of macromolecules on the surface of the cross-linked epoxy-phenol polymer varies in different stages of precondensation of resin mixtures. We have shown previously [11] that the distribution and the topology of the cross-linking sites of the chemical network of the cross-linked polymer vary with the molecular weight of EO. At M_n(EO) = 2100, the coating surface contains discrete clusters of macromolecules ("lattice animals") constituting the nonuniform chemical network of a cross-linked polymer, and a single uniform network of the cross-linked polymer corresponds to M_n(EO) ≅ 3400 [11]. At the same time, the fundamental aspects of aggregation of oligomers in various

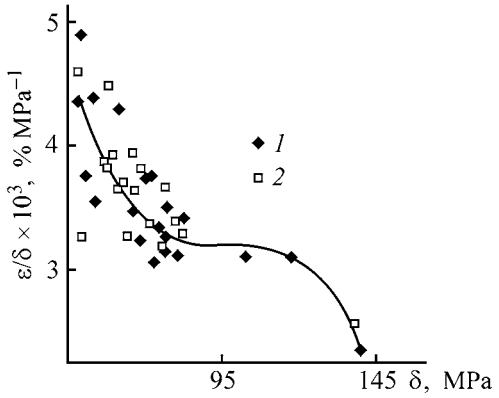

Fig. 1. Relative elongation ε/δ of the films of cross-linked epoxy-phenol polymer vs. the ultimate rupture stress δ for precondensates of (*1*) epoxy-4,4'-isopropylidenediphenol E-05 and phenol-formaldehyde FPF-1 resins prepared at 393 K within 2 h for a set of 15 samples of the E-05 resin and (*2*) cold mixtures of these resins [12].

stages of precondensation of EO and PO in solution and in formation of the chemical network of the cross-linked epoxy-phenol polymer still remain to be understood [1].

The aim of this study was to optimize EO–PO formulations and the kinetic modes of precondensation of a mixture of resins in solution to ensure formation of a uniform chemical network of the cross-linked epoxy-phenol polymer. We studied the hydrodynamic behavior and aggregation of EO and PO molecules and their mixtures in solutions in various kinetic stages of thermal precondensation. Also, we analyzed the cluster structure of the network of the cross-linked polymer based on EO and PO.

EXPERIMENTAL

We studied the concentration dependences of the relative viscosity of epoxy-4,4'-isopropylidenediphenol resins Epikot 1009 (Shell Corporation) and E-05 (Pigment Research and Production Company) and phenol-formaldehyde resin DFFr based on diphenylolpropane and formaldehyde (Pigment Research and Production Company) in C solutions in the concentration range c = 5–60 wt %, as well as that of a mixture of E-05 and DFFr resins in solution with mass ratio varied from 1.5 : 1 to 4 : 1 [15].

The molecular-weight distribution in sample nos. 1–3 (Table 1) was determined by gel-permeation chromatography (Shodex KF-803 columns, solvent tetrahydrofuran, sample volume 5–10 μl, eluent flow rate 1 ml min^{-1}, spectrophotometric detector, λ =

Table 1. Characterization of oligomer samples at 298 K

Sample no.	Oligomer	EN,* %	$[\eta]$, $cm^3\ g^{-1}$	PD	$M_n \pm 10\%$	M_w/M_n	$n_D^{20} \pm 0.0005$
1	Epikote 1009	1.2	0.140	13–35	3600	2.65	– (1.438)**
2	E-05	1.8	0.134	10–17	2850	2.70	1.555 (1.485)
3	DFF	–	0.061	2–5	1030	3.85	1.484 (1.512)

* EN is the epoxide number.

** Figures in parentheses are the refractive indices n_D^{20} for solutions of sample nos. 1–3 in C at *c* 42 (no. 1), 38 (no. 2), and 60.2% (no. 3), respectively; n_D^{20}(C) = 1.4062.

250 nm) [16]. The relative viscosity $\eta_{rel} = \eta/\eta_0$ (η is the solution viscosity and η_0 is the C viscosity) was measured on a Ubbelohde viscometer (capillary thickness 0.6 mm, shear rate 300 s^{-1}, C flow time 89 s, 298 K) (Figs. 2, 3, 4a). The refractive indices of the solutions were measured on a URL-1 refractometer (Fig. 4b). The intrinsic viscosity $[\eta]$ was determined by the procedure described in [7], and the running intrinsic viscosity $[\eta]_c$ at $c > 0$ and the power index *a* in Eq. (1), by the expression

$$[\eta]_c = d\ln\eta_{rel}/dc = a[\eta]([\eta]c)^{a-1} = a\ln\eta_{rel}/c, \quad (2)$$

$$[\eta]c/\ln\eta_{rel} = ([\eta]c)^{1-a}. \quad (3)$$

The parameters *a* and $[\eta]_c$ were calculated to within 7% (Tables 2, 3).

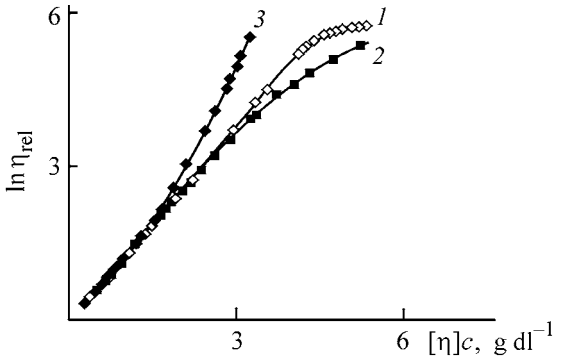

Fig. 2. Relative viscosity η_{rel} of sample nos. 1–3 vs. the concentration *c* in the C solution in the $\ln\eta_{rel}-[\eta]c$ coordinates at 298 K. *Figures at curves* correspond to sample nos.; the same for Fig. 6.

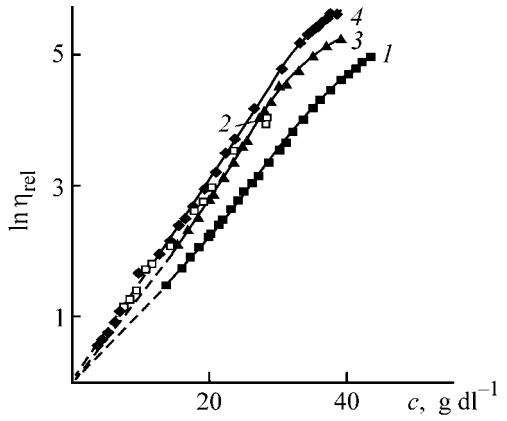

Fig. 3. Relative viscosity η_{rel} of the precondensates of epoxy-4,4'-isopropylidenediphenol and phenol-formaldehyde resins in C solution vs. the concentration *c* of the resin mixture in the $\ln\eta_{rel}-c$ coordinates at 298 K. N_1(EO)/N_2(PO) molar ratio: (*1*) 0.7, (*2*) 0.8, (*3*) 0.9, and (*4*) 1.5.

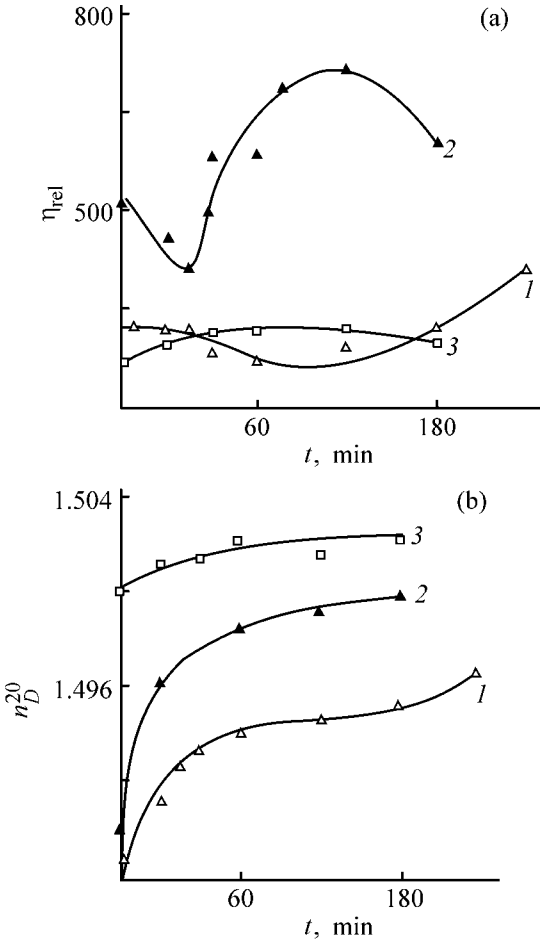

Fig. 4. Kinetic curves of (a) the relative viscosity η_{rel} and (b) refractive index n_D^{20} of a mixture of E-05 and DPFr resins in a EC solution vs. the precondensation time *t* at 298 K. N_1/N_2 molar ratio: (*1*) 0.6, (*2*) 0.8, and (*3*) 1.5.

Table 2. Parameters of aggregates of oligomer molecules* (sample nos. 1–3) in C solutions at 298 K [oligomer radius R 3.2 (sample no. 1), 3.0 (sample no. 2), and 1.5 nm (sample no. 3)]

Sample no.	c, g dl^{-1}	$[\eta]c \pm 0.1$	$a \pm 0.03$	$D \pm 0.05$	$s \pm 0.2$	c_s, g dl^{-1}	$\rho \pm 0.02$	$\langle R\rangle/R \pm 7\%$
1**	4.25	0.59	1.04	1.47	14.9	0.29	0.95	6.3
	12.0	1.68	1.04	1.47	43.5	0.28	0.36	13.0
	29.6	4.14	0.64	1.83	554	0.05	0.63	73.5
	31.4	4.39	0.25	2.4	–	–	0.64	–
2	2.8	0.37	1.05	1.46	26.8	0.10	0.98	12.9
	6.5	1.00	1.05	1.46	60.8	0.11	0.64	22.7
	12.3	1.65	0.92	1.56	91.8	0.13	0.42	24.2
	26.7	3.58	0.64	1.83	341	0.08	0.53	31.0
	33.4	4.48	0.64	1.83	–	–	–	–
3	6.6	0.40	1.14	1.40	1.12	5.9	0.53	1.49
	17.3	1.00	1.14	1.34	2.02	8.56	0.24	1.34
	26.4	1.61	1.24	1.34	3.05	8.65	0.20	3.21
	34.6	2.11	1.40	1.25	3.45	10.2	0.146	3.62
	45.0	2.75	1.40	1.25	4.56	9.86	0.105	3.65

* D is the fractal dimension; c_s, is the concentration of clusters; $\langle R\rangle$, the radius of the aggregates.

** For sample no. 1 in solution, the transition to a continuous fluctuation network of intermolecular contacts corresponds to $c > 29.6$ g dl^{-1}.

Table 3. Parameters of mixed aggregates in C solutions of EO and PO [precondensation time t = 1.5 h, N_1/N_2 0.7 (sample no. 1) and 1.5 (sample no. 2), 298 K. [η] 0.115 (sample no. 1) and 0.154 dl g^{-1} (sample no. 2), radius of a "unit" mixed aggregate of EO and PO 3.1 nm]

Sample no.	c, g dl^{-1}	$[\eta]c \pm 0.1$	$a \pm 0.03$	$D \pm 0.05$	$s \pm 7\%$	$\rho \pm 0.02$	$\langle R\rangle/R \pm 7\%$	$\langle R\rangle \pm$ nm
1	21.4	2.46	1.08	1.44	1.7	0.57	1.43	4.1
	35.6	4.06	0.90	1.58	2.3	0.36	1.67	5.2
	37.1	4.26	0.90	1.58	2.4	0.64	1.72	5.3
	40.0*	4.60	0.52	2.0	193	0.76	13.9	43
	50.0	5.75	0.52	2.0	303	0.77	17.4	54
2	5.2	0.80	1.04	1.47	2.8	0.80	2.0	6.2
	10.7	1.65	1.04	1.47	5.8	0.42	3.3	10.2
	17.7	2.72	0.90	1.58	27.8	0.41	8.2	25.4
	29.1	4.48	0.90	1.58	34.1	0.58	9.9	30.7
	35.5*	5.47	0.48	2.1	116	0.64	11.9	36.9
	37.5	5.78	0.48	2.1	180	0.69	12.6	39.1
	43.4	6.68	0.48	2.1	330	0.73	17.0	52.0

* In the vicinity of the threshold concentration c^*, the aggregate radius $\langle R\rangle$ is close to the correlation radius ξ [11, 17].

The formulations corresponded to EP-547 varnish [15] based on E-05 and DFFr resin containing 5.6% butoxy groups. Precondensation of the resin mixture was carried out in a C solution at 393 K; the N_1(EO)/N_2(PO) molar ratio was varied from 0.6 to 1.5. Precondensation time t = 0.4–4 h. The first sample for measuring the viscosity and refractive index n_D^{20} for the resin mixture in solution was taken 30 min after mixing the resins; further samples were taken during precondensation of the resins at 30-min intervals after the temperature of 393 K was attained (Figs. 4, 5). A catalyst in the form of 25% H_3PO_4 solution in C in amount of 0.24–0.26% of the oligomer mixture content was introduced after thermal precondensation was complete [15].

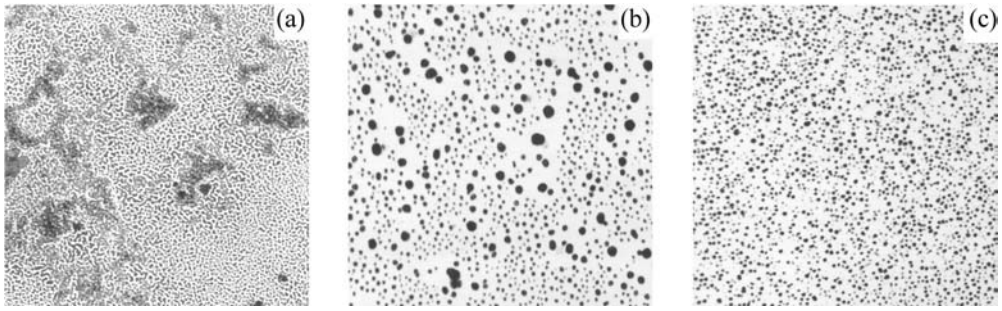

Fig. 5. Electron micrographs of the decorating gold particles on the surface of cross-linked epoxy-phenol polymer based on sample nos. 2 and 3 at N_1/N_2 = 0.7. Magnification: (a) 30 000 and (b, c) 60 000. Time, h, of precondensation of the coating on canning sheet metal: (a) 0.25, (b) 0.5, and (c) 2.0.

Coatings with thickness of 4–6 μm were prepared by casting 20% solution of the precondensate in C, also containing 0.79% organosilicon oligomer KO-815 [15], on tin-plated sheet metal (surface concentration of tin 8.4 g m^{-2}) and cured in air at 452–483 K for 15 min [18, 19]. The chemical stability of the cured coatings was tested in model media; these included 3% aqueous solutions of NaCl and acetic acid, 2% aqueous solution of tartaric acid, and distilled water at 120 atm (393 K) for 1 h [18, 19]. Cured coatings corresponding to the precondensation time t = 2.5 h exhibit satisfactory chemical stability in the model systems studied.

The cluster structure of the samples of cross-linked epoxy-phenol polymer coatings was studied by electron microscopy with gold decoration. The coating surface was preactivated with an aqueous solution of silver nitrate, which was followed by thermal sputtering of gold at 1.33×10^{-3} Pa to effective layer thickness of 0.4 nm. The coating surface activation consisted in partial reduction of $AgNO_3$ by quinonemethide groups of the polymer, yielded by thermal reduction of the secondary hydroxy groups of phenol-formaldehyde resin [20], and subsequent nucleation of silver nanoparticles, which act as nucleation centers for the decorating gold particles. Carbon replicas with decorating gold particles were prepared by the procedure from [21] and examined with an EVM 100 L electron microscope. The electron micrographs of the surface of cross-linked epoxy-phenol coatings (Fig. 5) obtained for precondensates of a mixture of E-05 and DFFr resins at a molar ratio N_1/N_2 = 0.6 were processed on a PC using the cluster lattice model [11, 17].

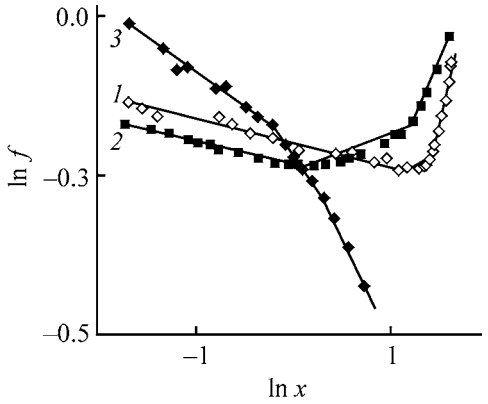

Fig. 6. $f([\eta]c)$ curves for sample nos. 1–3 in C solution, plotted in the $\ln f - \ln x$ coordinates.

When plotted in the $\ln \eta_{rel} - [\eta]c$ coordinates, the concentration dependences of the relative viscosity, $\eta_{rel} - c$, of the EO samples in C solution lie under the bisector of the angle at $[\eta]c = VN$ = 1–6, where $V = [\eta]M$ is the hydrodynamic volume of the oligomer molecules (M is molecular weight), $N = c/MN_A$ is the number of moles, and N_A is the Avogadro number [7]. The $\eta_{rel} - c$ curve plotted in these coordinates for sample no. 3 in C solution in the $[\eta]c < 3$ region lies above the bisector of the angle, since $[\eta]c/[\eta] > 1$ (Fig. 2). For the precondensates studied [N_1(EO)/N_2(PO) = 0.6–1.5], the $\eta_{rel} - c$ curves lie under the angle bisector (Fig. 3).

The $\eta_{rel} - t$ kinetic curves of the resin mixture viscosity exhibit extrema in the course of thermal precondensation of oligomers for all the N_1/N_2 parameters studied (Fig. 4a). With increasing precondensation time t, the refractive index n_D^{20} of the resin mixtures in solution tends to grow, with the dependence leveling off at $t \geq 3$ h (Fig. 4b), which suggests changes in the density of the EO and PO aggregates [9].

To estimate the threshold concentration c^* corresponding to sharp changes in both the $[\eta]c$ parameter and the effective hydrodynamic volume $\langle V \rangle$ of the EO and PO aggregates in solution [11], we calculated the dependences of the $f(x) = [\eta]c/\ln \eta_{rel}$ ratio on the parameter $x = [\eta]c$ (Figs. 6, 7). The $f(x)$ curve plotted in the $\ln f - \ln x$ coordinates for EO solution

in C (Table 1, sample no. 2) consists of three linear portions (Fig. 6, Table 2). A similar curve was obtained for sample no. 1. In the case of the C solution of sample no. 3, the $f(x)$ dependence exhibits a decrease in $f(x)$ in the $[\eta]c$ = 0.1–2 range and, when plotted in the logarithmic coordinates, it consists of three linear portions.

According to the cluster model [14], the density π of the fractal aggregate tends to decrease with increasing hydrodynamic volume $\langle V\rangle$

$$\pi = sV/\langle V\rangle = w^{(D-3)/D}(\langle R\rangle/R)^{(D-3)/D}. \quad (4)$$

Here, $s = w(\langle R\rangle/R)^D$ is the degree of aggregation; D is the fractal dimension; R and $\langle R\rangle$ are the radii of the oligomer and oligomer aggregate, respectively; w = 0.637 is the coefficient of random packing of rigid spheres [13].

To a first approximation, we have for relative viscosity η_{rel} of macromolecules in solution

$$\ln \eta_{rel} = VN_s(\langle V\rangle/V_s) = VN_s/\rho = [\eta]c/\rho s = ([\eta]c)^a. \quad (5)$$

Here, $N_s = c/MsN_A$ is the number of moles of the aggregates of particles, and $a = (3 - D)/D$ [11, 22].

Equations (2)–(5) give

$$\rho s = x/\ln \eta_{rel} = x^{1-a}, \quad (6)$$

$$\rho = (a[\eta]/[\eta]c)^{a/(a-1)} = w^a(x/\ln \eta_{rel})^{a/(a-1)}. \quad (7)$$

Figure 6 shows that the three portions in the $f(x)$ curve for EO solutions in C are due to a successive transitions from isolated oligomer molecules with D_1 = 1.46 (c < 7.2 g dl^{-1}) to aggregates of particles with D_2 = 1.56 (c = 7.2–13.9 g dl^{-1}) and D_3 = 1.83 (c = 14–26.7 g dl^{-1}). For sample no. 2, a transition to a continuous network of intermolecular contacts of macromolecules in the vicinity of $c^* \cong$ 27 g dl^{-1} is characterized by $D_4 \cong$ 1.8 (Table 2). For sample no. 1, the $f(x)$ curve also consists of three portions, namely, those with D_1 = 1.47 (c < 29 g dl^{-1}), D_2 = 1.83 (c = 29–31 g dl^{-1}), and D_3 = 2.4 (c > 31 g dl^{-1}). In the case of PO solutions in C, the three portions of the $f(x)$ curve are due to fractal transitions from D_1 = 1.4 (c < 17.3 g dl^{-1}) to D_2 = 1.34 (c = 17.3–26.4 g dl^{-1}) and D_3 = 1.25 (c > 26 g dl^{-1}, Table 2). Our data show that the degree of aggregation of EO in C solution at $c \cong c^*$ (s > 500 sample no. 1) significantly exceeds that of PO at $c \cong$ 26 g dl^{-1} ($s \cong$ 3, sample no. 3).

The $f(x)$ curves for EO–PO precondensates, plotted in the ln f–ln x coordinates, exhibit three linear portions with D_1 = 1.47 (c < 12 g dl^{-1}), D_2 = 1.54 (c = 12–36 g dl^{-1}), and D_3 = 2.2 (c > 36 g dl^{-1}) (Fig. 7). In the first two portions, the degree of aggregation s of the EO and PO molecules is lower than that of solutions of EO in C, though beeng significantly higher than that of solutions of PO (Tables 2, 3).

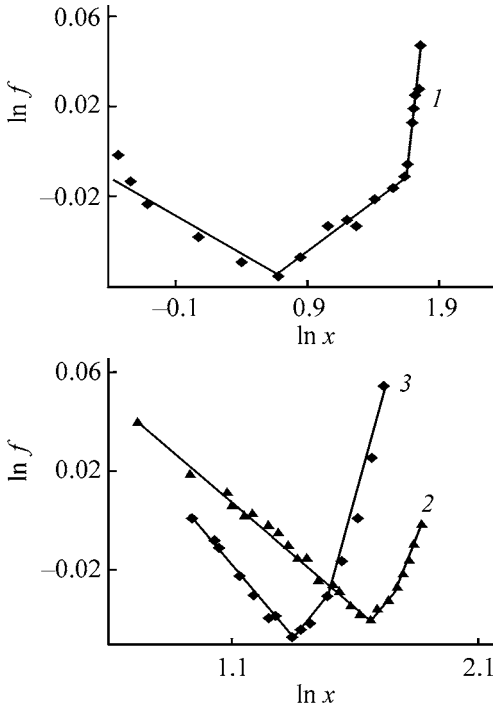

Fig. 7. $f([\eta]c)$ curves for EO–PO precondensates in the C solution plotted in the ln f–ln x coordinates. N_1(EO)/N_2(PO) molar ratio: (*1*) 1.5, (*2*) 0.7, and (*3*) 0.9.

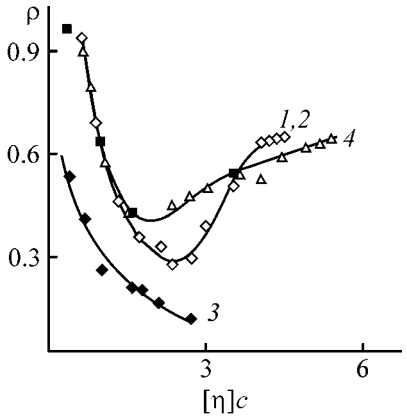

Fig. 8. Density of oligomer aggregates in solution ρ vs. $[\eta]c$ at 298 K. (*1–3*) Sample nos.; (*4*) precondensate of a resin mixture obtained at the molar ratio N_1/N_2 = 1.5 in sample nos. 2 and 3.

The density of the aggregates of EO molecules and mixed EO–PO aggregates varies nonmonotonically with increasing concentration c of the oligomers in solution (Fig. 8). The minimum of the density ρ of the aggregates in solution for sample no. 1 corresponds

Table 4. Parameters of the cluster structure of cross-linking sites of the chemical network of cross-linked epoxy-phenol polymer in various stages of precondensation of the EO–PO mixture in C solution at $N_1/N_2 = 0.6$

t, h	$\rho_{latt} \pm 0.01$	$D \pm 0.03$	ξ, nm	$m^* \pm 0.03$
0.25	0.86	1.92	250	3.4
0.5	0.64	1.73	80 (235)**	2.8
0.8	0.50	1.7	40 (42)	3.2
2.0	0.84	1.94	50 (38)	3.1

* m is the coordination number.

** Figures in parentheses are the parameters of the clusters corresponding to the fraction of large gold particles formed on the silver metal nuclei through reduction with quinonemethide groups of PO.

to $[\eta]c = 2.4$, and that for the EO – PO precondensate, to $[\eta]c \cong 2$. Near the threshold concentration c^*, corresponding to the formation of a physical network of intermolecular contacts, ρ asymptotically approaches $\rho \cong 0.69$ characteristic of percolation of self-similar particles (or clusters of oligomer molecules) in a simple cubic lattice [13] (Table 3).

The radius of the aggregates $\langle R \rangle$ was calculated by the expression

$$\langle R \rangle / R = w^{-1/D}(x/\ln \eta_{rel})^{1/(2D-3)}. \quad (8)$$

Near the threshold concentration c^*, the radius of the EO aggregates sharply grows with increasing molecular weight of the oligomer. For sample no. 1 at $c^* = 29.6$ g dl^{-1}, $\langle R \rangle = 235$ nm, and for sample no. 2 at $c^* = 26.7$ g dl^{-1}, $\langle R \rangle = 93$ nm (Table 2), which is consistent with the Rayleigh scattering data for the EO solutions in C [6]. For example, according to [6], the ratio of the rms radii of the aggregates of oligomers is 2.8 for two EO samples (M_n 5310 and 4954) and 2.5 for sample nos. 1 and 2 (M_n 3600 and 2850).

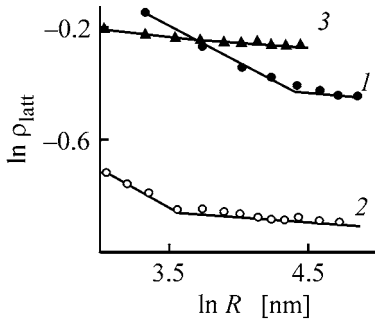

Fig. 9. Lattice density ρ_{latt} of clusters vs. the radius R of the circle circumscribed about the cluster. Coatings on the sheet metal of cross-linked epoxy-phenol polymer, $N_1/N_2 = 0.6$. Precondensation time, h: (*1*) 0.5, (*2*) 0.8, and (*3*) 2.0.

Figure 6 presents the electron micrographs of carbon replicas with gold decorating particles, corresponding to samples of cross-linked epoxy-phenol polymer coatings for various precondensation times t of the resin mixture. In analyzing the micrographs, the space-correlated groups of the gold particles were represented clusters of macromolecules on a two-dimensional lattice [13]. In the coatings corresponding to precondensation times of 0.25, 0.5, and 0.8 h, we revealed two regions where two fractions of particles of different size were localized, as well as two cluster types of different densities and topologies. The fraction of large particles corresponds to the most active centers of gold crystallization on the nuclei of silver metal reduced by quinonemethide groups of the PO units of the cross-linked epoxy-phenol polymer. Large gold particles occur as isolated inclusions in voids of an infinite cluster [11, 13] built from small gold particles corresponding to the EO aggregates.

With increasing precondensation time t, the density of two types of clusters is redistributed. For the coating sample corresponding to $t = 0.8$ h, we revealed a minimum of the lattice density ρ_l of the infinite cluster (Table 4). The fraction of the surface occupied by the PO molecule clusters decreases, which suggests formation of mixed aggregates containing EO and PO. A completely uniform continuous chemical network of a cross-linked polymer whose cross-linking sites contain EO and PO units is formed at $t = 2$ h. Within $t = 0.8$–2.0 h, the lattice density ρ_{latt} and the fractal dimension D of the clusters tend to increase (Fig. 9), and the correlation radius ξ asymptotically approaches $\xi = 50$ nm. These data evidence the formation of an infinite cluster of EO and PO.

The concentration dependences of the relative viscosity η_{rel}–c of EO in C solutions evidence a transition to the continuous fluctuation network of intermolecular contacts at $c^*(EO) \cong 27$ g dl^{-1} (Table 2, sample no. 2). The degree of aggregation for EO significantly exceeds that for EO (~340 against ~3 at $c \cong 26$ g dl^{-1}). In the case of the EO–PO precondensate [molar ratio $N_1(EO)/N_2(PO) = 1.5$, precondensation time 2.5 h], the transition from discrete mixed-type EO–PO aggregates ($D = 1.58$) to infinite cluster ($D \cong 2.1$) occurs at $c^* \cong 35\%$, Table 3).

The extrema in the kinetic curves of the relative viscosity η_{rel}–t for EO–PO mixtures in C solutions (Fig. 4a) suggest, above all, breakdown of the EO

aggregates. The rate of breakdown of the EO aggregates into "simple" particles depends on the degree of aggregation, *s*, of oligomers. The run of the $\eta_{rel}-t$ curves is determined by the N_1/N_2 ratio. A minimum in these curves is due to excess PO molecules in the mixture, and a maximum, to excess EO molecules. For example, breakdown of the EO aggregates in the EO–PO mixture in solution at $N_1/N_2 = 1.5$ is complete in the kinetic stage of precondensation corresponding to the viscosity maximum at $t \cong 1.5$ h. Formation of mixed EO–PO aggregates corresponds to the kinetic stage of the decline in viscosity, $\eta_{rel}-t$ at $t \cong 3$ h (Fig. 4a, curve *1*). Similarly, a viscosity minimum for the EO–PO mixture in solution ($N_1/N_2 = 0.6$) at $t = 0.25$ h is due to breakdown of the EO and PO aggregates. Formation of mixed aggregates is complete at $t > 4$ h (Fig. 4a, curve *3*).

Electron-microscopic data suggest that the uniform chemical network of the cross-linked epoxy-phenol polymer corresponds to the precondensation time $t = 1.5$–2 h ($N_1/N_2 = 0.6$). In this case, the correlation radius ξ of the clusters of macromolecules is 50 nm, $D = 1.94$ (Table 4). In the initial ($t = 0.25$ h) and intermediate ($t = 0.8$ h) stages of precondensation of the resin mixture, EO and PO do not form a single network. With precondensation time increasing from 0.4 to 2.5 h, the correlation radius ξ passes through a minimum: It first decreases from ca. 250 to 50 nm and then increases to 500 nm at $t > 2$ h, which is consistent with the run of the $\eta_{rel}-t$ curves (Fig. 4a) and with the Rayleigh scattering data for EO – PO solutions [6].

Thus, in various kinetic stages of precondensation of the mixture of EO and PO resins in solution, and on the surface of the cross-linked epoxy-phenol polymer, we revealed a cluster structure of the oligomer aggregates and of the cross-linking sites of the chemical network. Thermal precondensation of the resin mixture in solution involves structural evolution of the aggregates, namely, breakdown of the EO and PO aggregates and formation of mixed EO–PO aggregates and of an infinite cluster.

CONCLUSIONS

(1) The cluster mechanism of aggregation of the particles in solution determines the kinetics of thermal precondensation of resin mixtures and the structure of the chemical network of the cross-linked epoxyphenol polymer. This mechanism accounts for the formation of self-similar mixed-type aggregates of epoxy-4,4'-isopropylidenediphenol and phenol-formaldehyde oligomers from aggregates of the corresponding oligomers in solution, which differ in density and degree of particle aggregation. A uniform network of cross-linked epoxy-phenol polymer is formed when the density of the aggregates of epoxy-4,4'-isopropylidenediphenol and phenol-formaldehyde oligomers approaches that of an infinite cluster in the vicinity of the threshold concentration of particles in solution.

(2) The cluster model of aggregation and distribution of the cross-linking sites of the chemical network on the surface of the cross-linked epoxy-phenol polymer obtained by thermal precondensation of epoxy-4,4'-isopropylidenediphenol and formaldehyde oligomers in solution accounts for the dependence of the relative elongation of polymer films (for a set of samples of epoxy-4,4'-isopropylidenediphenol oligomers with different molecular weights) on the ultimate rupture stress. In this case, the film strength depends on the density of the cross-linking sites, which, in turn, depends on the parameter N_1/N_2. Films prepared by cold mixing of oligomers in solution do not show a uniform chemical network of cross-linked polymer, since mixed-type aggregates and an infinite cluster are not formed.

REFERENCES

1. Markevich, M.A., Kuzaev, A. I., Vladimirov, L.V., *et al.*, *Vysokomol. Soedin., Ser. A*, 1985, vol. 27, no. 5, pp. 1000–1008.
2. Kurmakova, I.N., Amfiteatrova, T.A., Kabanov, N.M., *et al.*, *Vysokomol. Soedin., Ser. B*, 1985, vol. 27, no. 12, pp. 906–909.
3. Krasovskii, A.N., Polyakov, D.N., Baranov, V.G., and Mnatsakanov, S.S., *Vysokomol. Soedin., Ser. A*, 1991, vol. 33, no. 6, pp. 1221–1227.
4. Kurmakova, I.N., Trifonova, Yu.F., Ivanov, A.I., *et al.*, *Vysokomol. Soedin., Ser. B*, 1988, vol. 30, no. 1, pp. 5–7.
5. Sukhareva, L.A., Sorokin, M.F., Kochnova, Z.A., *et al.*, *Lakokras. Mater. Ikh Primen.*, 1982, no. 4, pp. 30–31.
6. Sukhareva, L.A., Sorokin, M.F., Kochnova, Z.A., and Svetlakova, T.N., *Lakokras. Mater. Ikh Primen.*, 1982, no. 1, pp. 10–11.
7. Tsvetkov, B.N., Eskin, V.E., and Frenkel, S.Ya., *Struktura makromolekul v rastvorakh* (Structure of Macromolecules in Solutions), Moscow: Nauka, 1964.
8. Markevich, M.A., Structural and Kinetic Aspects of the Processes of Formation of Epoxy-4,4'-Isopropylidenediphenol Oligomers and 3D Polymers Thereof, *Doctoral Dissertation*, Chernogolovka, 1986.
9. Krasovskii, A.N., Krasheninnikov, V.A., and Kharlampiev, A.A., *Vysokomol. Soedin., Ser. A*, 1997, vol. 39, no. 2, pp. 250–258.

10. Markevich, M.A., Vladimirov, L.V., Prut, E.V., and Enikolopyan, N.S., *Mekh. Kompoz. Mater.*, 1985, no. 1, pp. 25–28.
11. Krasovskii, A.N., Novikov, D.V., Krasheninnikov, V.A., *et al.*, *Zh. Prikl. Khim.*, 2001, vol. 74, no. 1, pp. 124–134.
12. Nizhnik, I.N., Aleksandrov, V.N., Fartunin, V.I., and Rozenberg, B.A., *Lakokras. Mater. Ikh Primen.*, 1989, no. 2, pp. 16–18.
13. Feder, J., *Fractals*, New York: Plenum, 1988.
14. Gennes, P.-G. de, *Scaling Concepts in Polymer Physics*, Ithaca: Cornell Univ., 1979.
15. *Lakokrasochnye materialy dlya zashchity konservnoi tary* (Paint and Varnish Materials for Can Protection), Lyalyushko, S.M., Ed., Moscow: NIITEKhim, 1981.
16. Gorshkov, A.V., Verenish, S.S., Evreinov, V.V., and Entelis, S.G., *Chromatographia*, 1988, vol. 26, pp. 338–342.
17. Krasovskii, A.N. and Novikov, D.V., *Zh. Prikl. Khim.*, 1999, vol. 72, no. 9, pp. 1518–1527.
18. Aleksandrov, V.N., Tarasov, A.N., and Rozenberg, B.A., *Lakokras. Mater. Ikh Primen.*, 1985, no. 6, pp. 35–38.
19. Tarasov, A.I., Shuvarin, N.A., Aleksashina, M.V., and Eselev, A.D., *Lakokras. Mater. Ikh Primen.*, 1979, no. 6, pp. 30–32.
20. Kochnova, Z.A., Khrisanova, T.A., and Sorokin, M.F., *Lakokras. Mater. Ikh Primen.*, 1989, no. 2, pp. 82–89.
21. Novikov, D.V. and Varlamov, A.V., *Kolloidn. Zh.*, 1997, vol. 5?59, no. 3, pp. 355–359.
22. Baranov, V.G., Brestkin, Yu.V., and Frenkel, S.Ya., *Dokl. Akad. Nauk SSSR*, 1986, vol. 290, no. 2, pp. 369–372.

Russian Journal of Applied Chemistry, Vol. 76, No. 2, 2003, pp. 303–306. Translated from Zhurnal Prikladnoi Khimii, Vol. 76, No. 2, 2003, pp. 313–316.

MACROMOLECULAR CHEMISTRY AND POLYMERIC MATERIALS

Modification of Synthetic Latexes with Colloidal Silver

E. V. Sanatin, N. F. Levecheva, Yu. A. Savina, T. B. Boitsova, E. I. Volkova, and V. V. Gorbunova

St. Petersburg State Technological Institute, St. Petersburg, Russia
Herzen State Educational University, St. Petersburg, Russia

Recived June 9, 2001; in final form, November, 2002

Abstract—Butadiene-styrene and acrylate latexes were studied as matrices for preparing colloidal silver. Colloidal-chemical and strength properties of the modified latexes and Primal E1950 latex films were studied. The heat resistance of these materials was determined.

Development of processes for producing new materials for electronics and medicine (e.g., antiseptic applicators containing finely divided particles) is of great scientific and practical importance [1–3]. The published data on formation of colloidal metals in a latex matrix are scarce [4, 5].

Since metal-containing elastomeric nanocomposites cannot be prepared by direct mixing of a macromolecular binder with finely divided metals, preparation of these materials by a procedure involving generation of colloidal metal in aqueous solution and coagulation of latex rubber is a topical problem.

In this work we studied colloidal-chemical and physicomechanical properties of latexes and latex films modified with colloidal silver. This study was organized as follows: first we chose a procedure for preparing finely divided metal in an aqueous solution, then we performed this reaction in rubber latex, and finally we determined colloidal-chemical, physicochemical, and thermal parameters of the composites.

Colloidal silver in a latex matrix was prepared by a photochemical procedure that allows control of the metal reduction in a matrix of any rigidity by varying the irradiation time [6, 7].

The photolytes were prepared using $AgNO_3$ as the electrolyte.

To choose the latex matrix, we analyzed the properties, first of all the colloidal-chemical behavior, of various polymer dispersions. Special attention was paid to the distribution of polymer particles in the dispersion medium.

We studied latexes of acrylate [Primal E1950 (Room & Haas), Acronal 271 (BASF), DMMA (Voronezhsintezkauchuk)], butadiene-styrene [SB-278, SB-139G, SB-852 (RHODIA), BS-75 (Voronezhsintezkauchuk)], and styrene-acrylate [GB-016, DL-430, DS-910 (RHODIA)] polymers. All latexes were prepared using anionic emulsifiers, presumably RSO_3Na or $ROSO_3Na$, where R = C_{10}–C_{16}.

Since the system can be destabilized at high $AgNO_3$ concentrations [8], the amount of $AgNO_3$ introduced into the latexes ranged from 0.17 to 1.7 wt %.

To prepare colloids in an aqueous medium, latex (8 wt %) was mixed with an electrolyte (2 wt %) with a definite $AgNO_3$ concentration. A latex film was obtained from the resulting solution by the surface renewal method [9]. All the components of the system were concentrated during drying and formation of the film.

The surface tension of the latex modified with the electrolyte was determined with a Du-Nouy tensiometer; the acidity of the dispersions, with a pH-154 pH meter; their viscosity, on a V3-4 orifice [10]; the tensile strength of the films, on an RMI-5 tensile-testing machine [11].

Dry modified films were irradiated with 254- and 365-nm light of UFO-254 and DRT-375 mercury lamps. Formation of colloidal silver was determined spectrophotometrically (SF-46) from the rise in the characteristic plasmon absorption in the range 300 – 800 nm.

Parameters of thermal oxidative degradation of the polymers (temperature range of thermolysis, ac-

1070-4272/03/7602-0303 $25.00 © 2003 MAIK "Nauka/Interperiodica"

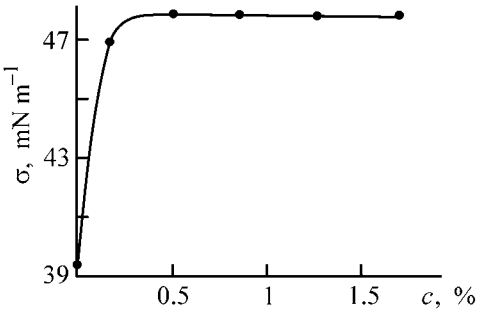

Fig. 1. Surface tension σ of Primal E1950 latex vs. the electrolyte content *c*.

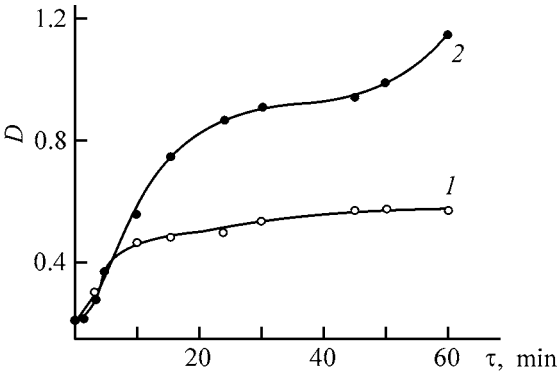

Fig. 2. Kinetic curve of photochemical formation of silver colloid in the latex. (*D*) Optical density of modified latex and (τ) irradiation time. Wavelength λ_{exc} (nm): (*1*) 254 and (*2*) 365.

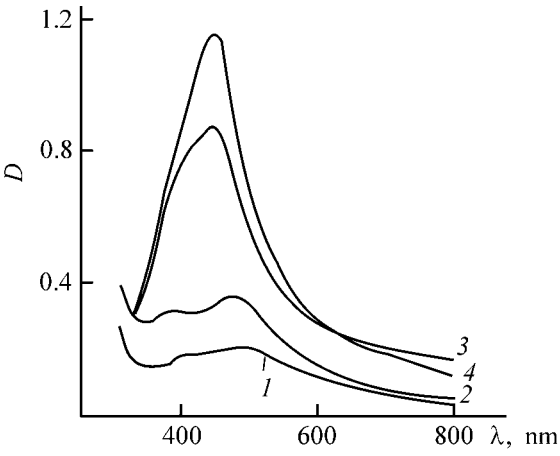

Fig. 3. Absorption spectra of colloidal silver in the matrix of modified latex (0.17 wt % $AgNO_3$) irradiated with 365-nm light for (*1*) 5, (*2*) 10, (*3*) 20, and (*4*) 60 min. (*D*) Optical density and (λ) wavelength.

tivation energy of thermolysis) were determined on a Thermophlex differential scanning calorimeter (Perkin–Elmer).

We observed coagulation of the latex dispersions after introduction of $AgNO_3$ solutions in concentration higher than 0.85 wt % [12]. This is presumably due to reaction of the electrolyte with the surfactant introduced into the latex during its polymerization. This assumption was confirmed by a model experiment in which an anion-active surfactant, $C_9H_{19}SO_3N$, was reacted with $AgNO_3$.

$$AgNO_3 + C_9H_{19}SO_3Na \rightarrow C_9H_{19}SO_3Ag\downarrow + NaNO_3.$$

This reaction decreases the surfactant concentration [8], thus decreasing the thickness of the electrical double layer. As a result, the dispersion coagulates.

We found that only Primal E1950 latex was stable at electrolyte concentrations higher than 0.85 wt %, since it probably contained nonionic surfactants. Latexes stabilized with nonionic surfactants do not obey the Deryagin–Landau–Verwey–Overbeek (DLVO) law [8] since they are coated with relatively thick hydration shell preventing formation of the electrical double layer at the interface. We used this latex as the optimal matrix for preparing colloidal silver.

An increase in the surface tension after introducing an $AgNO_3$ solution of a prescribed concentration into the latex (Fig. 1) is due to partial binding of the anionic surfactant [13]. The pH (5) and the relative viscosity of the dispersion (17 s) remained the same.

In some experiments, silver alkylsulfonate was irradiated for 1 h. The white precipitate turned cherry-red, which points to the presence of silver nanoparticles. Similar processes were observed in a latex film. Probably, the structure of polymeric particles is transformed into hexagonal packing under the action of capillary forces, and silver alkylsulfonate present between these particles initiates formation of silver clusters.

A kinetic study of silver reduction showed (Fig. 2) that the rate-determining step of the photosynthesis is that preceding cluster formation and initiated by silver alkylsulfonate. Subsequent growth of silver particles occurs mainly by the photocatalytic mechanism. As determined by UV spectroscopy (Fig. 3, curve *1*), an ill-resolved band of metastable clusters and particles of subcritical size is formed in the first steps of UV irradiation of a latex film containing silver cations. Upon longer exposure to UV radiation (Fig. 3, curves *3*, *4*) a strong plasmon band appears at 480 nm. The location of this band remains the same on further irradiation. This indicates the formation of silver nanoparticles of the same size governed by the structure of the latex matrix [14].

Since we failed to determine the final silver concentration in the film by common procedures, we give

Kinetic parameters of thermolysis of Primal E1950 latex modified with $AgNO_3$

$AgNO_3$ concentration, wt %	ΔT, °C	E_a, kJ mol^{-1}	ln K_0^*	$AgNO_3$ concentration, wt %	ΔT, °C	E_a, kJ mol^{-1}	ln K_0^*	$AgNO_3$ concentration, wt %	ΔT, °C	E_a, kJ mol^{-1}	ln K_0^*
0 (initial latex)	366–424	263	42	0.17	369–424** / 367–417	257 / 262	40 / 42	0.85	370–419 / 374–419	334 / 457	54 / 77

* K_0 is the rate constant of polymer thermolysis.

** Data for unirradiated and irradiated films are given in the numerator and denominator, respectively.

in all the dependences the silver concentration in the initial solution.

The strength of the irradiated film of the initial latex (0.270 MPa) is higher than that of the unirradiated film (0.164 MPa). The onset temperature ΔT and the activation energy E_a of thermal degradation of the polymer increases after irradiation (see table). This is probably due to additional intermolecular cross-linking under exposure to UV light [15]. The strength of the irradiated films decreases up to electrolyte concentration of 0.17 wt % (Fig. 4) and then increases up to a concentration of 0.5 wt %. The decrease in the film strength at low concentrations of $AgNO_3$ is possibly due to the structural nonuniformity at the molecular and supramolecular levels and microcracking of the modified latex film upon exposure to UV light [13]. With the electrolyte concentration increasing from 0.17 to 0.5 wt %, the film becomes more rigid. Further increase in the electrolyte concentration to 1.7 wt % has no effect on the rigidity. This complex dependence may be due to the fact that silver nanoparticles are formed only in the definite concentration range of the electrolyte.

The heat resistance of the modified film also grows with the electrolyte concentration increasing from 0.17 to 0.85 wt %.

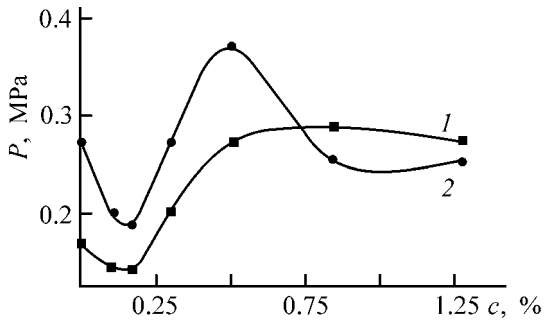

Fig. 4. Tensile strength P of (*1*) unirradiated and (*2*) irradiated Primal E1950 latex films vs. the electrolyte content in the latex, c.

CONCLUSIONS

(1) Silver nanoparticles were prepared by photochemical reduction of Ag^+ in a latex film. The best matrix for preparing silver nanoparticles is Primal E1950 latex.

(2) The formation of colloidal silver in the latex–$AgNO_3$ system is initiated by silver alkylsulfonate.

(3) Modification of Primal E1950 latex film with colloidal silver enhances its strength and heat resistance.

ACKNOWLEDGMENTS

This fork was supported financially by the Russian Foundation for Basic Research (project no. 02-03-32 829).

REFERENCES

1. Natanson, E.M. and Ul'berg, Z.R., *Kolloidnye metally metallopolimery* (Colloidal Metals and Metal-Polymers), Kiev: Naukova Dumka, 1971.
2. Thomas, J.M., *Pure Appl. Chem.*, 1983, vol. 92, no. 10, pp. 1517–1528.
3. Schmid, G., *Chem. Rev.*, 1992, vol. 91, no. 8, pp. 1709–1727.
4. Naohis Ynagihara, *Chem. Lett.*, 1998, no. 4, pp. 304–306.
5. Mayer, A.B.R., Grebner, W., and Wannermacher, R., *J. Phys. Chem.*, 2000, vol. 104, no. 6, pp. 1176–1182.
6. Boitsova, T.B., Loginov, A.V., and Gorbunova, V.V., *Macromol. Symp.*, 1998, vol. 136, pp. 103–107.
7. Loginov, A.V., Gorbunova, V.V., and Boitsova, T.B., *Zh. Obshch. Khim.*, 1997, vol. 67, no. 2, pp. 189–201.
8. Lebedev, A.V., *Kolloidnaya khimiya sinteticheskikh lateksov* (Colloidal Chemistry of Synthetic Latexes), Leningrad: Khimiya, 1976.

9. Afanas'eva, L.N., Kaluzhskaya, M.O., Kosareva, V.V., and Fedorova, V.Kh., New Procedure for Preparing Latex Film, *Information Sheet of the Leningrad Inter-branch Terrirory Center of Scientific and Technical Inf.*, no. 1281–79.
10. Eliseeva, V.I., *Polimernye dispersii* (Dispersion of Polymers) Moscow: Khimiya, 1980.
11. Lazarev, S.Ya, Reikhsfel'd, V.O., and Erkova, L.N., *Laboratornyi parktikum po sinteticheskim kauchukam: Uchebnoe posobie dlya vuzov* (Laboratory Course on Synthetic Rubbers: Handbook for Institutes of Higher Education) Leningrad: Khimiya, 1986.
12. Neiman, R.E., *Koagulyatsiya sinteticheskikh lateksov* (Coagulation of Synthetic Latexes), Voronezh: Voronezh. Gos. Univ., 1984.
13. Erkova, L.N. and Chechik, O.S., *Lateksy* (Latexes), Leningrad: Khimiya, 1983.
14. Boitsova, T.B., Gorbunova, V.V., and Loginov, A.V., *Zh. Obshch. Khim.*, 1999, vol. 69, no. 12, pp. 1937–1943.
15. Guillet, G.E., *New Y. Chem*. 1974, vol. 42, p. 509.

Russian Journal of Applied Chemistry, Vol. 76, No. 2, 2003, pp. 307–309. Translated from Zhurnal Prikladnoi Khimii, Vol. 76, No. 2, 2003, pp. 317–319.

MACROMOLECULAR CHEMISTRY AND POLYMERIC MATERIALS

Thermal Oxidative Degradation of Caprolactam in Melting and Storage in Molten State in the Presence of Some Trace Impurities

N. P. Gankov

Ekomedbio EAD Business Innovation Center, Sofia, Bulgaria

Received January 22, 2002

Abstract—The influence of trace amounts of cyclohexanol, cyclohexanone, and cyclohexanone oxime on the quality and stability of caprolactam melt was considered.

Caprolactam is the main raw material for production of polycaproamide fibers. It is well known that caprolactam is stable to heat treatment in an inert medium; however, even trace amounts of impurities make it unstable [1]. The presence of concomitant impurities, such as cyclohexanol, cyclohexanone, and cyclohexanone oxime, is inevitable and is caused by the process conditions.

Under conditions of caprolactam melting, these impurities are oxidized under the action of minor amounts of oxygen present in the inert gas or adsorbed on crystalline caprolactam, which can affect its characteristics.

The influence of impurities on the particular characteristics of caprolactam was considered previously [2–5]; however, more specific information on the maximum permissible concentrations of each impurity was not given.

Previously [6], we found that trace amounts of cyclohexanol, cyclohexanone, and cyclohexanone oxime inhibit polymerization and cause formation of a polymer with cross-linked structure and high polydispersity. Up to now, these processes have not been studied adequately.

We found no published data on thermal oxidation processes in melting of impure caprolactam and its storage in the liquid state.

To study the effect of trace impurities, cyclohexanol, cyclohexanone, and cyclohexanone oxime in the amount of 10^{-3}–10^{-1} wt % (the amounts of these impurities in commercial caprolactam are usually smaller) were added to crystalline caprolactam containing 99.9553% main substance. Caprolactam samples with impurities were preliminarily homogenized. The samples were melted at 85°C in hermetically sealed glass ampules. Before sealing, the ampules filled with caprolactam and additives were blown with nitrogen for a long time. The main characteristics of caprolactam were determined by the procedures described previously [7].

The dependences of the main quality characteristics of caprolactam and the degree of oxidation on the type and amount of impurities (wt % relative to caprolactam) are shown in Fig. 1.

Determination of permanganate extinction number (PEN) involves determination of the optical density of a caprolactam solution in sulfuric acid 10 min after addition of a definite amount of a $KMnO_4$ solution.

Figure 1a shows that the presence of cyclohexanone oxime in caprolactam affects PEN insignificantly. Cyclohexanol and cyclohexanone appeared to be more active in this case, with their effect strongly depending on their concentrations. The PEN value noticeably decreases at the content of cyclohexanol and cyclohexanone exceeding 10^{-1} wt % and becomes lower than that prescribed by the standard. Previously [4] it has been established that aniline has the strongest effect on PEN.

The optical density A_{290} of a 50% aqueous solution of caprolactam was determined on a spectrophotometer at a wavelength λ = 390 nm. The color expressed in Hasen degrees X_{390} was determined from the optical density of 50% aqueous solution of caprolactam at wavelength λ = 390 nm.

1070-4272/03/7602-0307 $25.00 © 2003 MAIK "Nauka/Interperiodica"

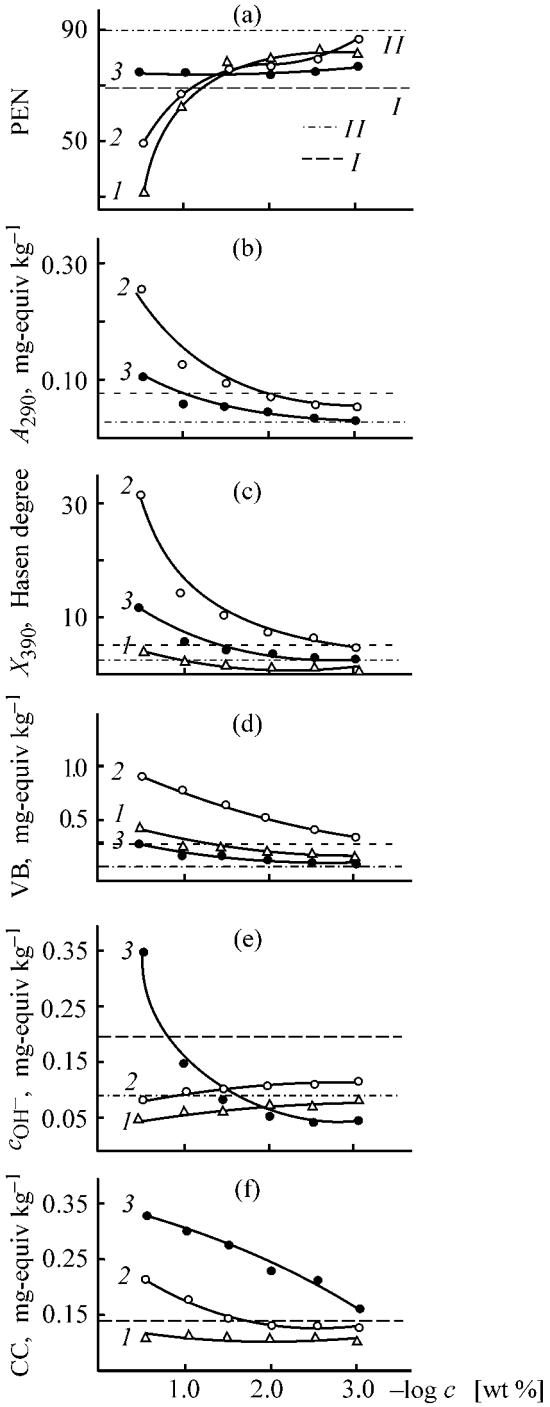

Fig. 1. Dependences of (a) permanganate extinction number (PEN), (b) optical density of 50% aqueous solution of caprolactam at λ = 290 nm A_{290}, (c) coloration of 50% aqueous solution of caprolactam at λ = 390 nm X_{390}, (d) content of volatile bases VBs, (e) alkalinity of caprolactam c_{OH^-}, and (f) content of carbonyl compounds CCs on the impurity content c. Impurity: (*1*) cyclohexanol, (*2*) cyclohexanone, and (*3*) cyclohexanone oxime. (*I*) Level prescibed by BDS (Bulgarian State Standard) 10780–88 and (*II*) value for the initial caprolactam sample.

In studying the variation of the optical density A_{290} and coloration X_{390} of caprolactam, it was found that the concentration dependences of these characteristics are similar (Figs. 1b, 1c). As expected, in comparison with the other impurities, a significant influence is exerted by cyclohexanone, whose carbonyl group gives a peak in the UV range at a wavelength of 290 nm. In parallel, the cyclohexanone impurity increases the integral absorption in a wide UV range. Thus, at the cyclohexanone concentration higher than 10^{-2} wt %, the optical density exceeds the value prescribed by the standard. A similar concentration dependence is observed in the presence of cyclohexanone oxime; however, the optical density reaches the value prescribed by the standard at its concentration exceeding 10^{-1} wt %. The concentration dependence in the presence of cyclohexanol is not shown in Fig. 1, since aliphatic alcohols do not absorb in the near-UV range.

It is well known that, in storage of caprolactam melt, the coloration of caprolactam increases, which is caused by oxidation processes, mainly oxidation of trace impurities. This assumption is based on the fact that the coloration of caprolactam thoroughly purified by sublimation in a vacuum remains constant for a long time, while the coloration of caprolactam contaminated with impurities increases steadily, especially in storage in the liquid state in the light or under UV irradiation.

The coloration of caprolactam is governed by the amount of cyclohexanone. It was established that in the presence of 10^{-3} wt % cyclohexanone, the coloration of caprolactam exceeds the value prescribed by the standard. The amount of cyclohexanone oxime exerts a weaker effect on the coloration of caprolactam: only at concentrations higher than 10^{-1} wt % the degree of its coloration exceeds the prescribed level. At concentrations less than 10^{-1} wt % cyclohexanol decreases the coloration as compared to the initial sample of caprolactam, i.e., it inhibits oxidation processes (Fig. 1c).

It has been established that the coloration is strongly affected by the presence of nitrobenzene and Fe(III) ions [4].

Determination of volatile bases (VBs) involves alkali decomposition of ammonium salts and other VB derivatives contained in caprolactam. The studies showed that cyclohexanone contributes most significantly to the content of VBs. As seen from Fig. 1d, even at 10^{-3} wt % content of this impurity the amount of VBs exceeds the prescribed level. Cyclohexanol affects the content of VBs only slightly, and cyclohexanone oxime, still more weakly. It was found that only at large amounts of cyclohexanone oxime, exceeding

10^{-1} wt %, the content of VBs is higher than the value prescribed by the standard. Aniline is the most critical impurity with respect to the content of VBs [4].

Alkalinity or acidity was determined by titration of aqueous solution of caprolactam with a 0.01 N solution of H_2SO_4 or NaOH in the presence of a mixed indicator (1.0 g of Methyl Red and 0.5 g of Methylene Blue in 1000 cm^3 of ethanol or methanol). The impurities in question excert appreciably different effect on the alkalinity of caprolactam. In this regard, the most active impurity is cyclohexanone oxime, its effect strongly depends on its concentration. Figure 1e shows that, at small content of cyclohexanone oxime, the alkalinity of caprolactam decreases and becomes lower than that of the initial caprolactam. At the cyclohexanone oxime concentration exceeding 10^{-1} wt %, the alkalinity becomes higher than that prescribed by the standard and increases steeply. This influence of cyclohexanone oxime can be accounted for by the fact that, under the conditions of melting and in prolonged storage in the liquid state, caprolactam undergoes hydrolysis to give cyclohexanone and hydroxylamine. The high reactivity of these compounds promotes various side reactions. Hence, the total effect will depend on the relative concentrations of its initial form and products of chemical transformations [4].

In the case of cyclohexanone and cyclohexanol, the pattern is the opposite. With increasing content of the above impurities, the alkalinity of caprolactam decreases. In the presence of 10^{-3} wt % cyclohexanol, the alkalinity of the samples is lower than that of the initial caprolactam. With increasing content of this impurity in the examined range, the tendency for decrease in the alkalinity is retained. Cyclohexanone exerts a similar effect.

Previously [8–10] it has been established that, for production of high-quality polycaproamide fibers, the concentration of carbonyl compounds should not exceed 0.15 mg-equiv g^{-1}.

Figure 1f shows that cyclohexanol hinders thermal oxidation processes and, to some extent, is an inhibitor. This is apparently caused by the ability of cyclohexanol to form complexes with free radicals arising in thermal oxidative degradation [11]. In the presence of cyclohexanol, caprolactam melt is characterized by the lowest content of carbonyl compounds, virtually independent of the amount of impurities. It is also seen that, in the presence of cyclohexanone and cyclohexanone oxime, carbonyl compounds are accumulated in caprolactam melt. With increasing content of these impurities, especially in the case of cyclohexanone oxime, the amount of carbonyl compounds increases.

The increasing content of carbonyl compounds in the presence of impurities may be due to formation and decomposition of hydroperoxides, which are a source of aldehyde groups [12]. In the presence of cyclohexanone, the amount of carbonyl compounds accumulated in caprolactam melt is smaller compared to cyclohexanone oxime.

CONCLUSIONS

(1) A noticeable decrease in the permanganate extinction number and alkalinity of caprolactam in the presence of 10^{-1} wt % cyclohexanol and cyclohexanone was established. The cyclohexanone oxime impurity affects the permanganate extinction number only slightly and has a complex effect on the alkalinity.

(2) Cyclohexanone affects most strongly the optical density and coloration of caprolactam and also the content of volatile bases.

(3) Cyclohexanone oxime and, to a lesser extent, cyclohexanone promote noticeable accumulation of carbonyl compounds in caprolactam. Cyclohexanol inhibits thermal oxidative processes in caprolactam during melting and prolonged storage in the molten state.

REFERENCES

1. Riech, A. and Schon, W., *Kunststoffe*, 1967, vol. 587, no. 1, pp. 49–52.
2. Pishev, D., Stanev, E., Gankov, N., *et al.*, *Godishn. VKhTI* (Sofia), 1988, vol. 30, no. 1, pp. 237–246.
3. Fisyuk, L.T., Lezhnina, L.A., and Butkin, V.T., *Khim. Volokna*, 1978, no. 1, pp. 5–7.
4. Nikulina, L.E., Koroleva, V.R., and Mizerovskii, L.N., *Izv. Vyssh. Uchebn. Zaved., Khim. Khim. Tekhnol.*, 1974, vol. 17, no. 5, pp. 778–780.
5. Nikulina, L.E. and Koroleva, V.R., *Khim. Volokna*, 1968, no. 6, pp. 16–18.
6. Gankov, N.P., *Zh. Prikl. Khim.*, 1998, vol. 71, no. 10, pp. 1712–1715.
7. Ignat'ev, Yu.S., Al'tshuler, S.S., and Gyul'handan'yan, E.M., *Khim. Volokna*, 1980, no. 3, pp. 51–52.
8. Pakshver, A.B. and Konkin, A.A., in *Kontrol' proizvodstva khimicheskikh volokon* (Monitoring of Production of Chemical Fibers), Moscow: Khimiya, 1967, pp. 275–293.
9. Gankov, N.P., *Zh. Prikl. Khim.*, 1996, vol. 69, no. 11, pp. 1908–1912.
10. Gankov, N.P., *Zh. Prikl. Khim.*, 1997, vol. 70, no. 10, pp. 1755–1756.
11. Nikulina, L.E., Koroleva, V.R., and Chuchko, V.A., *Khim. Volokn.*, 1972, no. 1, pp. 21–22.
12. Gordon, G.Ya., *Stabilizatsiya sinteticheskikh polimerov* (Stabilization of Synthetic Polymers), Moscow: Goskhimizdat, 1963.

Russian Journal of Applied Chemistry, Vol. 76, No. 2, 2003, pp. 310–313. Translated from Zhurnal Prikladnoi Khimii, Vol. 76, No. 2, 2003, pp. 320–323.

MACROMOLECULAR CHEMISTRY AND POLYMERIC MATERIALS

Flame Retardants for Wood, Based on Urea-Formaldehyde Resin with Mineral Fillers

G. V. Plotnikova, A. N. Egorov, and A. K. Khaliullin

East-Siberian Institute, Ministry of Internal Affairs, Irkutsk, Russia

Irkutsk Institute of Chemistry, Siberian Division, Russian Academy of Sciences, Irkutsk, Russia

Received March 29, 2001; in final form, November 2002

Abstract—The efficiency of flame retardants for wood, based on urea-formaldehyde resin with mineral fillers is studied.

Wood is among the most widely used materials. Its advantages are well known, as well as the major drawback, namely, high inflammability.

Wood and related materials are virtually equal in fire points and specific heats of combustion [1]. Ignition of wood can occur both from open flame and from hot objects and gases. Heat flow from the flame initiates pyrolysis of wood materials.

Thermal decomposition of wood proceeds in two stages. In the first stage (up to 280°C), endothermic decomposition takes place, and the second stage is divided into two substages, namely, combustion of gases formed in thermal decomposition (flame burning) and combustion of charcoal formed (smoldering).

Raising the charcoal yield at the expense of combustible gaseous decomposition products can considerably reduce the inflammability of wood. This can be achieved by decreasing the heating rate of the material in order to form a layer of charcoal having low thermal conductivity, directing pyrolysis toward formation of incombustible gases, and providing conditions for prevention of charcoal smoldering.

In practice, the methods to decrease the combustibility of wood are as follows: applying flame-retardant coating ensuring formation of a coke layer and impregnation of wood and related materials or introduction of dehydrating agents into their structure.

The most advanced method for flame retardation in timber-based materials under conditions of a building yard is to apply flame-retardant coatings. When affected by a local short-term fire hazard source, flame-retardant coatings hamper burning of wooden structures, facilitate fire extinguishing, and, in some cases, prevent fire events.

Polymers demonstrating a tendency toward carbonization are capable of retarding burning of wood. In recent years, extensive studies of their application for flame retardation has been carried out. For example, it has been demonstrated that wood impregnated with urea oligomers passes into the category of difficultly inflammable materials [1]. However, despite the advances in science and engineering in the field of wood preservation, no efficient method reducing the inflammability of wood, suitable for mass construction application, has been developed. The drawbacks of the existing methods are either the complexity of fireproofing treatment, or in short supply of materials, or the resulting deterioration of mechanical and decorative characteristics.

In this work, we studied the effect of the composition of urea-formaldehyde resin (UFR) filled with natural minerals on the flame-retardant efficiency of coatings on wooden structures.

EXPERIMENTAL

As a binder for the coatings we used KF-Zh urea-formaldehyde resin [GOST (State Standard) 14231–88] ensuring the desired mechanical and adhesion characteristics. The formulations were filled with finely crushed mica (phlogopite), mineral wool, basalt fiber, and graphite. To reduce the combustibility, a fire retardant (diammonium hydrogen phosphate) was added.

The formulations were prepared as follows. First, the fire retardant was dissolved in the resin. Then

1070-4272/03/7602-0310 $25.00 © 2003 MAIK "Nauka/Interperiodica"

Table 1. Flame retardation efficiency of composites studied*

Formulation no.	Composition, %	P_m, %	τ_{max}, s	T_{max}, °C	ΔT_{max}, °C
1	UFR 38, mineral wool 6, phlogopite 44, and diammonium hydrogen phosphate 12	3.2	300	227	27
2	UFR 45, graphite 10, phlogopite 12, and diammonium hydrogen phosphate 13	4.9	300	250	50
3	UFR 46, graphite 16, phlogopite 16, and diammonium hydrogen phosphate 12	3.2	300	260	60
4	UFR 45, graphite 16, phlogopite 16, basalt fiber 3, and diammonium hydrogen phosphate 12	1.4	300	210	10
5	UFR 45 and graphite 16	5.3	300	250	50
6	UFR 45, graphite 16, and diammonium hydrogen phosphate 12	4.8	300	280	80
7	UFR 100	45	240	290	90

* (τ_{max}) Time of attainment of the maximal temperature, (T_{max}) maximal temperature in the reaction cell, and (ΔT_{max}) maximal temperature rise.

the fillers were added, and the resulting mixture was thoroughly stirred, to obtain a homogeneous mass. To optimize the composition, the contents of all the components were varied.

Sample preparation, finishing, and testing were carried out in conformity with the current regulations [2, 3]. The formulations were applied on the samples of straight-grained pinewood. The side surfaces of the samples were planed, and the ends were filed and rubbed with emery. The samples were 30 × 60 × 150 mm in size. Before applying the flame-retardant formulation, the samples were kept in a disiccator over saturated $Zn(NO_3)_2 \cdot 6H_2O$ solution at 23 ± 5°C to constant weight (to within 0.2 g).

The samples were coated from all sides. Each formulation was applied on ten samples. After finishing, the samples were dried to constant weight at 22°C (relative air humidity 50%).

The flame-retardant efficiency of the formulations was determined with a "Ceramic tube" apparatus. Each sample was held in torch flame for 5 min (initial temperature of flue gases 200°C). In the course of testing, the maximal temperature of the reaction cell and the time at which the maximal temperature was attained were recorded. Cooled samples were weighed, and the weight loss P (%) was estimated as

$$P = \frac{m_1 - m_2}{m_1} \times 100,$$

where m_1 and m_2 are the sample weights (g) before and after testing, respectively.

For each formulation, we determined the arithmetic mean weight loss P_m estimated for 10 parallel runs. This parameter was used as a criterion for evaluating the group of the flame-retardant efficiency. The formulations for which the weight loss was within 9% belong to the top group (group I).

According to COMECON Standard 2437–80, wooden construction materials flame retarded with group I formulations should be tested in a torch flame for 10 min to be classed with nonflammable materials [4].

In this study, the test samples were exposed to torch flame with venting switched on. The flue gas temperature was measured at 30-s intervals. Also the self-maintained burning time was measured for each sample. After testing, we measured the length of undamaged pieces of the samples and their residual weight. From these data, we estimated the extents of damage α_m (by mass) and α_l (by length). These parameters, along with the time τ of self-maintained burning and flue gas temperature T, were accepted as criteria in evaluating the combustibility of the test materials. Flameretarded wood is classified with nonflammable materials if the criteria given below are met.

	T, °C	τ, s	α_l, %	α_m, %
I*	Not higher than 235	30	85	80
II	Not higher than 250	60	90	85

* Estimated from data on three replicate tests: (I) arithmetic mean and (II) maximal value.

From the total amount of samples studied (50), we selected six most efficient flameretardant formulations. The results are given in Table 1.

The smallest weight loss of mass and minimal rise in temperature were observed in samples flame-retarded with formulations nos. 4 and 1. Evidently,

Table 2. Flame-retardation test results*

Characteristic	Composite no.					
	1	2	3	4	5	6
Flue gas temperature, °C	219/222	265/275	260/267	190/217	253/257	290/300
Self-maintained burning time, s	15/22	48/54	39/44	0/0	20/29	69/75
Extent of damage, % (by length)	44/50	82/90	77/84	30/41	68/74	90/98
Extent of damage, % (by weight)	10/13	50/59	55/67	8/10	62/73	70/81

* The numerator represents the arithmetic mean for three replicate runs, and denominator, the maximal value among them.

the flame-retardant properties of the coatings are controlled essentially by the nature of filler rather than by its content. The best protective characteristics were demonstrated by formulation no. 4 containing lower amount of the filler as compared to formulation no. 1.

External examination of the samples after testing revealed no sag or cracking of protecting coating, or wood carbonization. The samples coated with formulation nos. 2 and 3 showed only slightly pronounced evidence of peeling. The formulations obtained provide good protection of wood against thermal decomposition; evolution of combustible gaseous products is insignificant, and, therefore, the time of self-maintained burning is short. In samples treated with formulation nos. 5–7, the coatings partly peeled, and wood exhibited traces of carbonization and indications of burning spread under the coating.

For these samples, the flue gas temperature approached 265°C and higher, which corresponds to the onset of degradation of the macromolecules [5]: anhydrocellulose is subject to deeper degradation (thermally unstable C–C and C–O bonds within the ring are ruptured), which is accompanied by liberation of CO_2, CO, H_2O, CH_4, and H_2. Ignition of the gases leads to initiation of combustion. Burning involves the following reactions:

$$2H_2 + O_2 \rightarrow 2H_2O + Q,$$

$$CH_4 + 2O_2 \rightarrow CO_2 + 2H_2O + Q,$$

$$2CO + O_2 \rightarrow 2CO_2 + Q.$$

The liberated heat partly goes to heating of next sections of a sample, resulting in their pyrolysis and inflammation. Therefore, both the time of self-maintained burning and flue gas temperature increase, i.e., the formulations under consideration do not protect wood against thermal degradation and subsequent burning.

Presumably, the maximal rise in temperature, observed for formulation no. 6 consisting of UFR, graphite, and diammonium hydrogen phosphate, can be attributed to insufficient adhesion of the coating to wood. Apparently, formulation no. 6 (UFR + graphite) has the least adhesion. Introduction of crushed mica (phlogopite) considerably improves the adhesion.

The results obtained allow classification of the formulations given in Table 1 with group I in their flame-retardant efficiency. Therefore, we conducted additional tests, to characterize the combustibility of wainscots finished with the flame-retardant formulations. The results are summarized in Table 2.

Among the formulations studied, formulation nos. 1 and 4 meet the requirements to nonflammable materials; samples finished with formulation no. 4 did not exhibit self-maintained burning and showed lower flue gas temperature and extents of damage by mass and length. Visual inspection of these samples revealed that the flame-retardant coatings have good adhesion to wood. They demonstrated no cracking or evidence of carbonization of wood under the coating.

Finally, the best flame-retardant characteristics were shown by the UFR-based coatings containing diammonium hydrogen phosphate (10%) as a fire retardant, and phlogopite with additions of basalt fiber or mineral wool as a filler. The higher flame-retardant characteristics of the coating containing basalt fiber as compared to similar formulation but containing

mineral wool can be attributed to lower thermal conductivity of the former (thermal conductivity coefficients of basalt fiber and mineral wool are 0.033–0.040 and 0.15–0.19 $W\,m^{-2}\,K^{-1}$, respectively). As a result, considerably lower thermal conductivity of basalt fiber ensures better protective characteristics of the coating even at its content lower by half as compared to mineral wool.

CONCLUSIONS

(1) The composition of flame-retardant coatings for wood, based on urea-formaldehyde resin with mineral fillers, is optimized.

(2) The flame-retardant characteristics of the formulations are controlled essentially by the nature of filler, rather than by its percentage.

REFERENCES

1. *Pozharnaya opasnost' stroitel'nykh materialov: Spravochnik* (Fire Risk for Construction Materials: A Handbook), Baratov, A.N., *et al.*, Eds., Moscow: Khimiya, 1988.
2. *NPB* (Fire Safety Standards) *251–98: Flame-Retardant Composites and Agents for Wood and Related Materials: General Requirements. Testing Procedures.*
3. *GOST* (State Standard) *16363–76, Standards of Accident Prevention, Wood: Determination of Flame-Retardant Characteristics of Coatings and Impregnating Products by the Ceramic Tube Method.*
4. *Sposoby i sredstva ognezashchity drevesiny: Rukovodstvo* (Methods and Means for Fire Protection of Wood: A Manual), Moscow: VNIIPO, 1994.
5. Orlova, A.M. and Petrova, E.A., *Pozharovzryvobezopasnost'*, 2000, no. 2, pp. 8–17.

Russian Journal of Applied Chemistry, Vol. 76, No. 2, 2003, pp. 314–316. Translated from Zhurnal Prikladnoi Khimii, Vol. 76, No. 2, 2003, pp. 324–326.

MACROMOLECULAR CHEMISTRY AND POLYMERIC MATERIALS

Rheological Characteristics of Moist Microcrystalline Cellulose Pastes

I. N. Pavlov, V. A. Kunichan, and Yu. N. Denisov

Biisk Technological Institute, Altai State Technical University, Biisk, Altai krai, Russia

Received June 4, 2002

Abstract—The suitability of the contact method for drying moist finely ground product classed, according to its properties, with pastes was considered. The rheological characteristics of microcrystalline cellulose pastes were studied experimentally in relation their moisture content. The study was based on the Metzner procedure with the moist product with mechanical stirrers in a mixer.

Microcrystalline cellulose (MCC), which is a finely ground powder in the ready-for-use form, finds wide application in various industries [1–3]. The MCC production is expanding, and the corresponding technology is being improved. Among the most important characteristics of ready-for-use MCC is its particle-size distribution [4–6]. For preparing MCC with the desired particle-size distribution, it was suggested to combine the MCC drying and grinding in the framework of the contact method involving mechanical stirring in a horizontal twin-shaft blade mixer [7, 8].

In the contact method of drying in the MCC production technology, the initial moisture content is 48–52%. Such a product yielded by filtration or centrifugation is classed with pastes [9], despite its being comparatively friable. Designing equipment for processing of moist MCC paste and appropriate control system requires a knowledge of the rheological characteristics of these pastes at varied moisture content. However, there are no published data on these properties of MCC pastes with moisture content within 5–52%.

This work was aimed at determining the rheological characteristics of MCC pastes differing in moisture content.

The rheological characteristics of pastes are largely determined by the solid phase concentration, shape of solid particles, size of the particles, and the nature of interparticle binding [10, 11]. With growing concentration, the paste viscosity tends to vary nonlinearly with the deformation rate or shear stress. This is due to the appearance of a 3D structure in the network, which is responsible for strongly pronounced viscosity anomaly and formation of a strong, elastic structure. Further thickening of the suspension results in the formation of a structured system.

The flow of highly concentrated suspensions and, in particular, pastes is typically described by the Ostwald–de Ville power law [12–14]

$$\tau = K(\mathrm{d}w/\mathrm{d}x)^m, \quad (1)$$

where $\mathrm{d}w/\mathrm{d}x$ is the shear rate, s^{-1}; K, consistency coefficient; m, non-Newtonian behavior coefficient.

Theoretical description of the rheological characteristics of moist MCC pastes is a complex task, which necessitates their experimental study. Since only the apparent viscosity of the product can be considered in the case of MCC, we used the Metzner–Otto procedure for studying its rheological properties [15, 16]. In this case, the apparent viscosity of the medium in mixing of the mass with mechanical stirrers is determined by the equation

$$\mu_{app} = K(\mathrm{d}w/\mathrm{d}x)^{m-1}. \quad (2)$$

EXPERIMENTAL

In our studies, we employed a laboratory setup based on a horizontal twin-shaft blade mixer (see its schematic in Fig. 1). The working elements of the mixer are two Z-shaped blades. To widely vary the blade rotation rate, the drive was equipped with a dc motor, and the rotation rate was controlled with an autotransformer. The rotation rate of the driven shaft of the mixer was monitored with an electronic digital tachometer. The desired temperature was maintained with a ther-

1070-4272/03/7602-0314 $25.00 © 2003 MAIK "Nauka/Interperiodica"

mostat and facilities for monitoring the temperature and varying the flow rate of the heat carrier. For convenience of measuring the useful power expenditure for stirring, the measurement system was preliminarily calibrated by creating the desired torque at the shaft of mixer stirrers with a friction mechanism. We determined the dependences of the electric power on the mechanical power for various rotation rates of the driving shaft of the mixer.

In [17], we studied the stirring of a non-Newtonian medium in a mixer over a wide viscosity range, established the criterial dependence, and determined its constituent empirical coefficients

$$K_N = A\mathrm{Fr}_c^{\alpha}\mathrm{Re}_c^{\psi}, \quad (3)$$

where K_N is the power criterion; Re_c and Fr_c are the Reynolds and Froude centrifugal criteria, respectively; A, α, and ψ are empirical coefficients.

A study of the rheological characteristics of MCC pastes involved the following assumptions: The apparent viscosity of moist MCC under study is equivalent to the viscosity of the Newtonian fluid employed as the model fluid whose stirring under the same conditions (at the same rotation rate of the stirrer) consumes the same power; the viscosity of the Newtonian fluid during stirring is equal to that measured with a capillary viscometer at the same shear rate; the average shear rate in the apparatus is proportional to the rotation rate of the stirrer.

The rheological characteristics of the MCC pastes were studied at mixer filling coefficient of 0.8, at various rotation rates of the blades and in the following operation modes: (1) mixer blades rotate toward each other ("pull" operation mode) and (2) mixer blades rotate in the opposite directions ("push" operation mode).

Based on the data on stirring power, we determined the corresponding Reynolds centrifugal criterion and calculated the apparent viscosity

$$\mu_{app} = \frac{n_{av} d^2 \rho_b}{\mathrm{Re}_c}, \quad (4)$$

where n_{av} is the average stirrer rotation frequency, s^{-1}; D is the stirrer diameter, m; ρ_b is the bulk density of moist MCC, kg m^{-3}.

The shear rate in the apparatus is proportional to the rotation rate

$$\gamma = Bn_{av}, \quad (5)$$

where B is a coefficient depending on the mixer type.

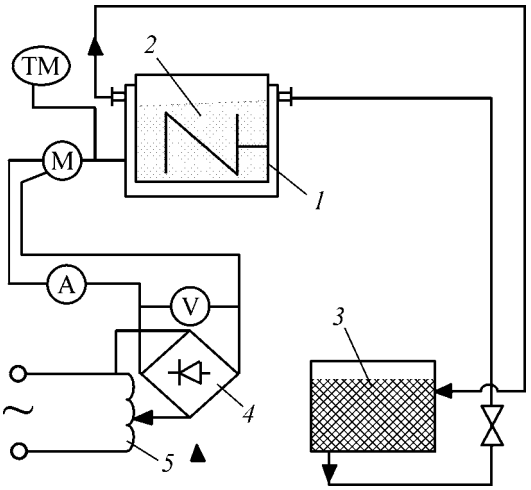

Fig. 1. Schematic of the experimental setup: (*1*) mixer, (*2*) product, (*3*) thermostat, (*4*) rectifier; (*5*) autotransformer, (TM) tachometer, (M) motor, (A) ammeter, and (V) voltmeter.

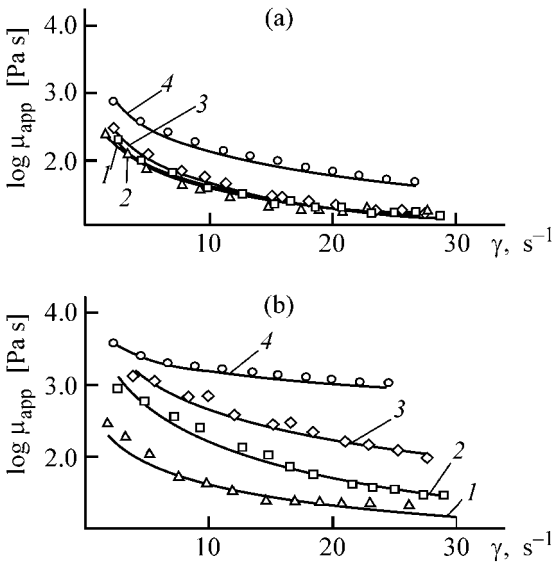

Fig. 2. Apparent viscosity μ_{app} of the MCC pastes vs. the shear rate γ in the (a) "push" and (b) "pull" modes of mixer blade operation modes. Moisture content W, %: (*1*) 10, (*2*) 30, (*3*) 40, and (*4*) 50.

According to [13], for this mixer type

$$B = 4\pi. \quad (6)$$

Our experimental data, namely, the dependence of the apparent viscosity on the shear rate and moisture content of MCC, were subjected to least-squares fitting, and the coefficients for Eq. (2) were obtained [17].

The results are shown in Figs. 2a and 2b. Solid lines represent the least-squares fits, and points, the experimental values.

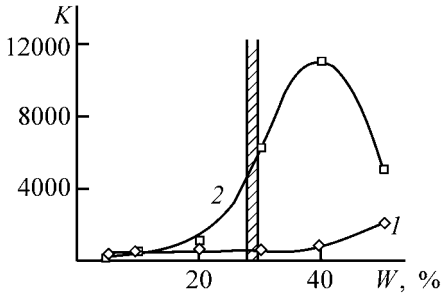

Fig. 3. Consistency coefficient *K* vs. the moisture content *W* of the paste. Mixer blade rotation mode: (*1*) "push" and (*2*) "pull"; the same for Fig. 4.

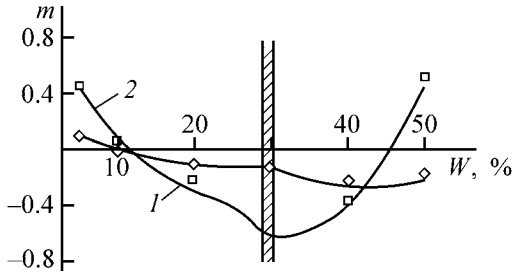

Fig. 4. Non-Newtonian behavior coefficient *m* vs. the moisture content of the paste, *W*.

Figures 3 and 4 show how the consistency coefficient *K* and the non-Newtonian behavior coefficient *m* vary with the operation mode of the mixer. The cross-hatched region denotes the range within which the physical structure of the MCC pastes changes [17].

Also, we studied how the effective viscosity varies with the shear rate for MCCs differing in the moisture content (Figs. 2a, 2b). We found that, unlike the "push" mode, stirring of MCC in the "pull" mode of blade operation is accompanied by its pressing between the mixer blades. This was responsible for a significantly larger power consumed in the latter case for stirring of MCC with moisture content of 30–50%. However, for MCC with moisture content of 5–20%, the results for the "pull" and "push" modes proved to be comparable.

Our results show that, with increasing shear rate, the apparent viscosity of the pastes tends to decrease. Such an abnormal variation of the viscosity of moist MCC pastes allows the media studied to be classed with non-Newtonian pseudoplastic fluids. Figures 2a and 2b show that, with increasing moisture content of MCC, the apparent viscosity of the pastes grows, with the shear rate remaining unchanged.

CONCLUSIONS

(1) Rheological properties of moist pastes of microcrystalline cellulose under mechanical stirring were studied. The nature of the non-Newtonian behavior of the pastes with varying shear rate was elucidated. The pastes studied were classed with pseudoplastic fluids.

(2) The patterns of variation of the apparent viscosity of the pastes with the shear rate and moisture content were elucidated.

REFERENCES

1. Sarybaeva, R.I., *Dlya nashego zdorov'ya: Tsellyuloza v forme poroshka ili gelya i vozmozhnosti ee ispol'zovaniya otraslyami, proizvodyushchimi produkty pitaniya: Obzor* (For Our Health Sake: Cellulose in the Form of a Powder or a Gel and Its Suitability for Food-Producing Industries: Review), Frunze: Ilim, 1988.
2. Petropavlovskii, G.A. and Kotel'nikova, N.E., *Khim. Drev.*, 1979, no. 6, pp. 3–21.
3. Sarybaeva, R.I., Vasil'kova, T.V., Sultankulova, A.S., and Trushkina, N.I., *Tsellyuloza v forme poroshka: Poluchenie. Svoistva. Primenenie: Annotirovannyi ukazatel' literatury 1951–1984 gg*. (Powdered Cellulose: Preparation. Properties. Application: Annotated Index of Literature for 1951–1984), Frunze: Ilim, 1986.
4. USSR Inventor's Certificate, no. 1 432 062.
5. Mukhiddinov, D.N., Yunusov, Yu.Kh., Yufa, A.I., *et al.*, *Khim. Prom–st.*, 1984, no. 5, pp. 307–308.
6. USSR Inventor's Certificate, no. 1 630 271.
7. Pavlov, N.I. and Kunichan, V.A., *Materialy Vserossiiskoi nauchno-prakticheskoi konferentsii "Prikladnye aspekty sovershenstvovaniya khimicheskikh tekhnologii i materialov* (Proc. Russian Scientific and Practical Conf. "Applied Aspects of Improving Chemical Technologies and Materials"), Biisk: Altaisk. Gos. Tekh. Univ., 1998, pp. 80–83.
8. Pavlov, I.N. and Kunichan, V.A., *Khim. Rast. Syr'ya* (Barnaul), 1999, no. 2, pp. 90–92.
9. Romankov, P.G. and Rashkovskaya, N.B., in *Sushka v khimicheskoi i legkoi promyshlennosti* (Drying in Chemical and Light Industries), Moscow: Profizdat, 1958, pp. 23–43.
10. *Rheology. Theory and Applications*, Eirich, F.R., Ed., New York: Academic, 1956, vol. 1.
11. Frolov, V.F., *Teor. Osn. Khim. Tekhnol.*, 1993, vol. 27, no. 1, pp. 56–63.
12. Zhurba, A.M. and Kurilov, S.V., *Teor. Osn. Khim. Tekhnol.*, 1995, vol. 29, no. 4, pp. 351–356,
13. Zhurba, A.M. and Kurilov, S.V., *Khim. Neft. Mashinostr.*, 1985, no. 3, pp. 12–14.
14. Aiba, Sh., Humphrey, A.E., and Millis, N.F., *Biochemical Engineering*, New York: Academic, 1973.
15. Metzner, A.B., Feehs, R.H., Ramos, H.P., *et al.*, *Am. Inst. Chem. Eng. J.*, 1961, vol. 7, p. 3.
16. Metzner, A.B. and Taylor, J.S., *Am. Inst. Chem. Eng. J.*, 1960, vol. 6, pp. 109–114.
17. Pavlov, I.N., Study and Development of a Technology and Implementation of the Process of Contact Drying of Microcrystalline Cellulose, *Cand. Sci. Dissertation*, Biisk, 2001.

Russian Journal of Applied Chemistry, Vol. 76, No. 2, 2003, pp. 317–319. Translated from Zhurnal Prikladnoi Khimii, Vol. 76, No. 2, 2003, pp. 327–329.

MACROMOLECULAR CHEMISTRY AND POLYMERIC MATERIALS

Rheological and Magneto-Rheological Properties of Formulations Based on Magnetite and Aqueous Emulsions of Water-Soluble Polymers in Transformer Oil

T. G. Lazareva and E. V. Shinkareva

Institute of General and Inorganic Chemistry, National Academy of Sciences of Belarus, Minsk, Belarus

Received May 13, 2002

Abstract—Rheological and magneto-rheological properties of magnetite dispersions in transformer oil were studied as influenced by the concentration of a modifying solution of water-soluble polymers (polyvinyl alcohol and carboxymethyl cellulose) and by the magnetic field strength.

Fluid systems structurizing in an electric or magnetic field are dispersions of electro- and magneto-sensitive materials in nonconducting or weakly conducting media. When an electric or magnetic field is applied to these liquids, their rheological properties change significantly due to formation of anisotropic structures via orientation of the filler particles in the field [1–3].

Such materials can be used in robotics, mechanical engineering, optical, instrument-making, automobile, aircraft, and other industries in various devices such as antivibrators (shock absorbers and buffers), compressors, temperature-controlled cooling fans, valves, clutches, polishing units, etc. The design of such devices is determined by the function of structurizing fluid system and by systems of application of external fields [4–7].

To prepare materials sensitive to mechanical and magnetic fields, we studied the rheological and magneto-rheological properties of magnetite dispersions in emulsions of water-soluble polymers [polyvinyl alcohol (PVA) and carboxymethyl cellulose (Na-CMC)] in transformer oil.

EXPERIMENTAL

In our study, we used commercial magnetite (particle size <5 μm) and dehydrated transformer oil as dispersion medium. The oil was mixed with a 0.5% solution of NaCMC (7HOF and M31F brands) and 1% solution of PVA (16/1 brand); the modifying agent to transformer oil weight ratio was varied from 1 : 99 to 10 : 90. The resulting mixtures were dispersed with a UZDM-2 ultrasonic unit (44 KHz). Then, magnetite (5 wt %) was added to the oil–water emulsion. The rheological measurements were performed on a Rheotest-2 device at 30–70°C.

The magnetite dispersion in dehydrated transformer oil is a non-Newtonian liquid, whose viscosity strongly depends on the shear stress or shear rate (Fig. 1a, curve *1*) [8]. The mode of the fluid flow in a mechanical field, namely, the decrease in the viscosity with increasing shear stress (section *I*) with the subsequent attainment of a uniform flow at which the viscosity is independent of the shear stress (section *II*), indicates that the dispersion can be easily structured and possesses a property of plasticity, i.e., filler particles can be oriented at certain shear stresses (section *I*) with the subsequent attainment of the uniform flow mode (section *II*).

Upon modification of the transformer oil with Na-CMC and PVA solutions, the shape of the flow curves of magnetite dispersion changes, with the appearance of sections in which the fluid viscosity decreases (plasticity) or increases (dilatancy). The nature of the flow curves depends on the viscosity of Na-CMC solutions. With addition of 1 or 5 wt % highly viscous Na-CMC solution (e.g., 7HOF brand), the oil viscosity at 30°C increases to 30–45 MPa s, with peaks at small shear stresses of 0.5–1.0 Pa (Fig. 1a, curves *2*, *3*). With the content of modifying agent increasing to 10 wt %, the oil viscosity increases to

1070-4272/03/7602-0317 $25.00 © 2003 MAIK "Nauka/Interperiodica"

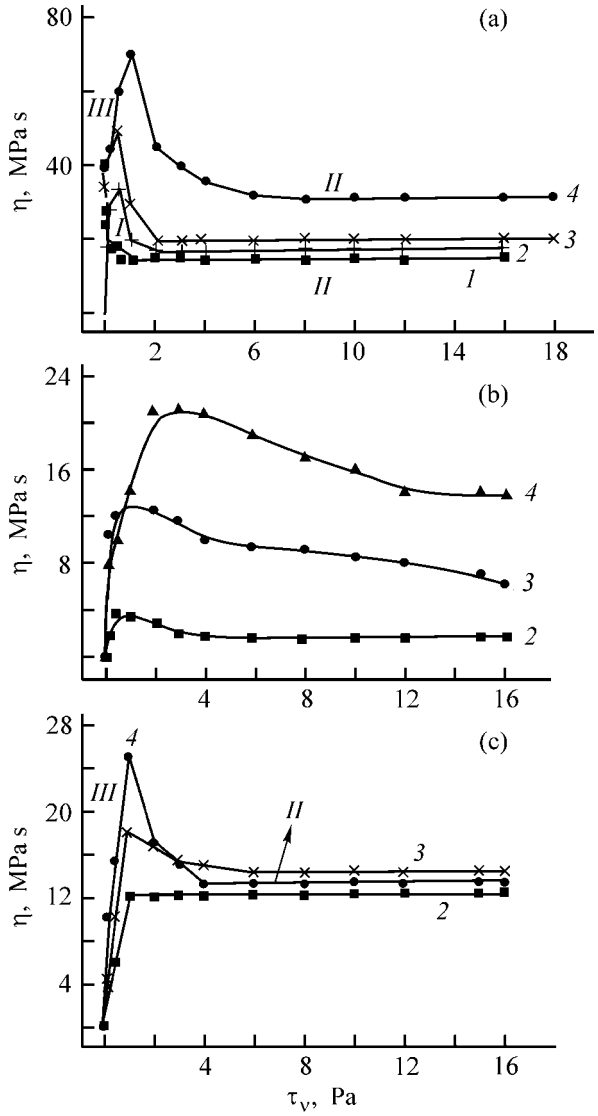

Fig. 1. Viscosity η vs. the shear stress τ_v at 30°C for 5 wt % magnetite dispersion in (*1*) dehydrated transformer oil and (*2*–*4*) transformer oil containing Na-CMC and PVA solutions. Additive: (a) 7HOF, (b) 9M31F, and (c) PVA. Additive content, wt %: (*2*) 1, (*3*) 5, and (*4*) 10.

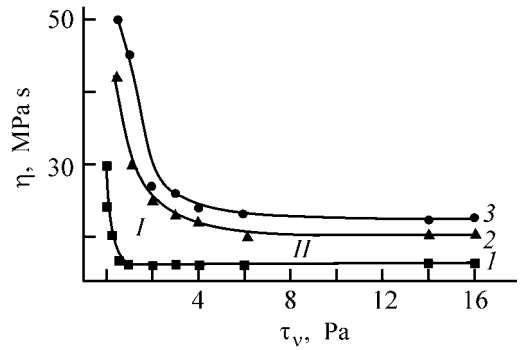

Fig. 2. Viscosity η vs. the shear stress τ_v for magnetite dispersion in dehydrated transformer oil. Magnetic field strength, mT: (*1*) 0, (*2*) 34, and (*3*) 44.

65 MPa s, with the viscosity peak shifting toward higher shear stresses (Fig. 1, curve *4*). On raising the temperature to 70°C, the maxima in the oil viscosity strongly shift toward higher shear stresses. The effect of anisotropic structuring, at which the viscosity is independent of the shear stress (section *II*), is observed at shear stresses of 1.5–2.0 Pa and 5 Pa at concentration of Na-CMC polymer in the transformer oil of 1–5 and 10 wt %, respectively. Similar dependences were observed upon addition of less viscous Na-CMC and PVA solutions.

The effects observed are probably due to changes in the nature of intermolecular interactions of magnetite particles, with molecules of water-soluble polymers sorbed on their surface. In this case, first the system of intermolecular interactions occurring in the system changes under the effect of the mechanical field, with the viscosity increasing and dilatancy appearing (Fig. 1, section *III*); in the next step, the filler particles are structured in the mechanical field, giving rise to plastic properties (section *I*), and then an anisotropic solution is formed (Fig. 1, section *II*).

As seen from Fig. 2, the viscosity of magnetite dispersions in dehydrated transformer oil increases on applying magnetic field, without changes in the flow curves. At the same time, the shape of the flow curves of magnetite dispersions in the transformer oil modified with water-soluble polymers gradually changes in a magnetic field (Fig. 3). With addition of Na-CMC solution (7HOF brand, up to 5 wt %) at the magnetic field strength of 20–34 mT, the peaks in the flow curves become less pronounced (Fig. 3a, curves *1*–*4*), and at H = 44 mT the flow curve changes, i.e., the viscosity of the system decreases with increasing shear strength (Fig. 3a, curve *5*).

Such variations in the rheological properties observed in a magnetic field are probably due to changes in the intermolecular interactions of magnetite particles in the transformer oil modified with water-soluble polymers and orientation (additional to mechanical ordering) of magnetite particles in the magnetic field. As seen from experimental data, the system exhibits either plasticity or dilatancy, depending on the composition of the initial medium and magnetic field strength.

CONCLUSIONS

(1) Magnetite dispersions based on emulsions of transformer oil modified with water-soluble polymer solutions (polyvinyl alcohol and carboxymethyl cel-

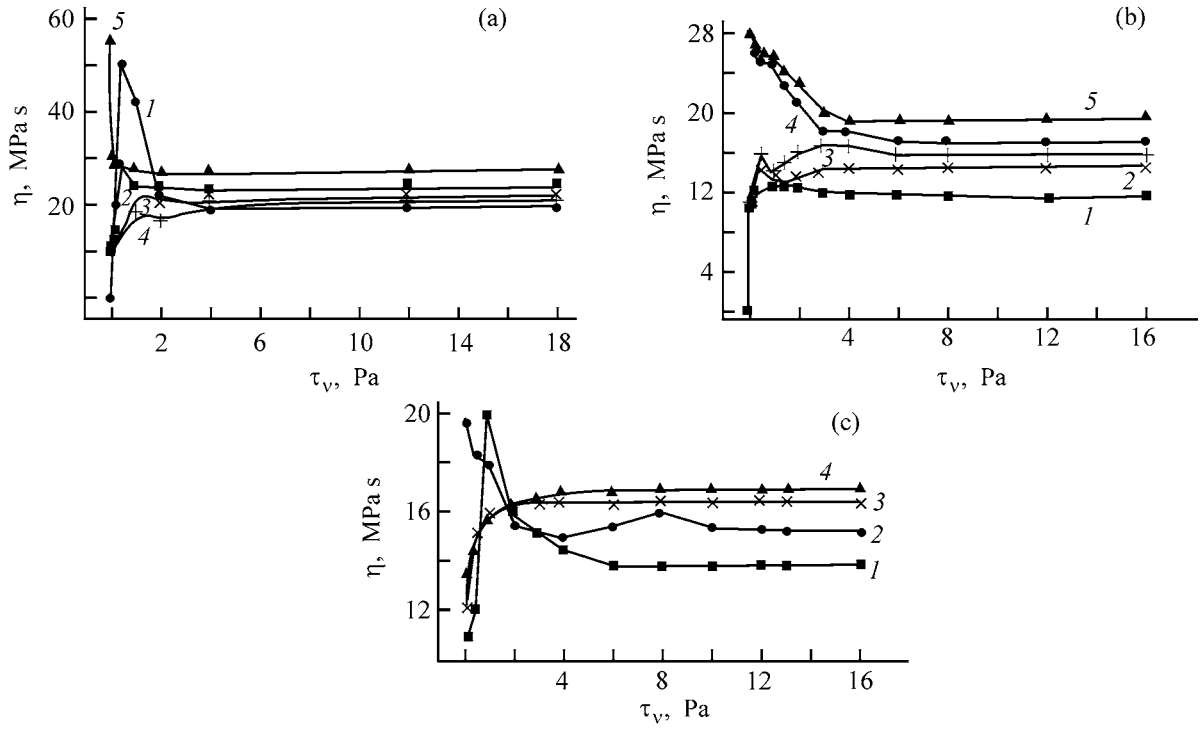

Fig. 3. Viscosity η vs. the shear stress τ_v for magnetite dispersion in transformer oil containing 5 wt % (a) Na-CMC : (7HOF), (b) Na-CMC : (9M31F), and (c) PVA. Magnetic field strength, mT: (*1*) 0, (*2*) 16, (*3*) 20, (*4*) 34, and (*5*) 44.

lulose) exhibit flow curves differing in both plasticity and dilatancy.

(2) Magnetic field strongly affects the flow curves of the system and its rheological properties, with the structuring of the system depending on the composition of the oil–water emulsion and magnetic field strength.

REFERENCES

1. Lazareva, T.G. and Korobko, E.V., *Proc. II Int. Conf. of Intelligent Materials*, Williamsburg, June 5–8, 1994, pp. 783–792.
2. Lazareva, T.G., Shitik, I.G., and Gaiduk, Yu.S., *Vestsi Nats. Akad. Navuk Bel., Ser. Khim. Navuk*, 1998, vol. 3, pp. 34–38.
3. Bibik, E.E., *Reologiya dispersnykh sistem* (Rheology of Disperse Systems), Leningrad: Khimiya, 1981.
4. Clair, J.D., *Proc. 5 Int. Conf. on Electro-Rheological Fluids, Magneto-Rheological Suspensions and Associated Technology*, Sheffield (the United Kingdom), July 10–14, 1995, pp. 20–28.
5. Jiang, F.O., Wang, Z.W., Wu, J.Y., and Zhow, L.W., Abstracts of Papers, *Int. Conf. on Electro-Rheological Fluids, Magneto-Rheological Suspensions and Their Applications*, Yonezawa (Japan), July 22–25, 1997, p. 163.
6. Bullogh, W.A., *Proc. of 4 Eur. and 2 MIMR Conf. on Smart Materials and Structures*, the United Kingdom, July 6–8, 1998, pp. 767–769.
7. Kordonsky, W. and Goliny, Don, *Proc. of 4 Eur. and 2 MIMR Conf. on Smart Materials and Structures*, the United Kingdom, July 6–8, 1998, pp. 275–281.
8. Schranm, G., *A Practical Approach to Rheology and Rheometry*, Karlsruhe, 1994.

Russian Journal of Applied Chemistry, Vol. 76, No. 2, 2003, pp. 320–322. Translated from Zhurnal Prikladnoi Khimii, Vol. 76, No. 2, 2003, pp. 330–332.

BRIEF COMMUNICATIONS

Estimation of Efficiency of Removal of Heavy Metal Ions as Hydroxides from Sewage

V. P. Svyatokhina, O. Yu. Isaeva, S. V. Pestrikov, and N. N. Krasnogorskaya

Ufa State Aeronautical Technical University, Ufa, Bashkortostan, Russia

Received April 16, 2001; in final form, May 2002

Abstract—The minimum solubilities of heavy metal hydroxides were calculated and compared with the maximum permissible concentrations of metal ions in various water reservoirs. The efficiency of the reagent method for sewage purification, based on precipitation of heavy metal hydroxides, was estimated.

Among various (chemical, physicochemical, etc.) methods for purification of sewage from galvanic industries to remove toxic heavy metal ions, the reagent methods based on precipitation of poorly soluble hydroxides have received the widest acceptance [1]. Taking into account only the low solubility products of the hydroxides [2], we can hardly explain the fact that the maximum permissible concentrations (MPC) of heavy metal ions in sewage subjected to reagent purification are exceeded manyfold.

The evidence concerning the mechanism by which precipitates of metal hydroxides are formed [3, 4] indicates that hydrolysis of heavy metal ions is accompanied by formation of both mono- and polynuclear hydroxide complexes. Therefore, it is impossible to calculate the solubilities of the hydroxides solely on the basis of their solubility products.

The sewage formed in galvanic industries is characterized by low content of metal ions, and, therefore, we can assume that the contribution of polynuclear interactions is insignificant [5]. Thus, the formation of hydroxide complexes in dilute solutions over hydroxide precipitates is described by Eq. (1).

$$M^{z+} + nOH^- \rightleftarrows M(OH)_n^{z-n}. \quad (1)$$

Here z is the charge of an ion; $n = 1, 2, 3,\ldots$

The aim of this study was to calculate the solubilities of heavy metal hydroxides and compare the values obtained with the MPC for metal ions in various water reservoirs.

As the precipitation of metal hydroxides is accompanied by other physicochemical phenomena (adsorption, coprecipitation, formation of basic salts, aging of precipitates, etc.), the approach proposed in the study can be considered the first stage in mathematical simulation of this complicated process.

The solubility of a metal hydroxide, S, is equal to the total concentration of all chemical forms of metal ions in solution, which result from partial dissolution of a precipitate (taking a hydroxide of a double-charged metal as an example):

$$S = [M^{2+}] + [MOH^+] + [M(OH)_2] + [M(OH)_3^-] + [M(OH)_4^{2-}] + \ldots \quad (2)$$

The concentration of the metal ion M^{2+} can be calculated from the solubility product $SP = [M^{2+}][OH^-]^2$, and the concentrations of hydroxo complexes, by using published data on the stepwise [5] or total [6] formation constants, hydrolysis constants [7, 8], or equilibrium constants for cases involving a solid phase. The calculations were carried out as applied to analysis of sewage purification processes, and, therefore, the solubility products were taken for freshly prepared hydroxides having the greatest solubility [9], and the equilibrium constants, for room temperature and nearly zero ionic strength of solution.

We used the hydrolysis constants described by the following equations [8]

$$M^{2+} + H_2O \overset{k_{10}}{\rightleftarrows} MOH^+ + H_3O^+,$$
$$M^{2+} + 2H_2O \overset{k_{20}}{\rightleftarrows} M(OH)_2 + 2H_3O^+,$$
$$M^{2+} + 3H_2O \overset{k_{30}}{\rightleftarrows} M(OH)_3^- + 3H_3O^+,$$
$$M^{2+} + 4H_2O \overset{k_{40}}{\rightleftarrows} M(OH)_4^{2-} + 4H_3O^+.$$

1070-4272/03/7602-0320 $25.00 © 2003 MAIK "Nauka/Interperiodica"

Taking into account the ionic product of water $K_w = [H_3O^+][OH^-]$, we can bring Eq. (2) by simple transformations to the form

$$S = \frac{SP}{K_w^2}\left([H^+]^2 + K_{10}[H^+] + K_{20} + \frac{K_{30}}{[H^+]} + \frac{K_{40}}{[H^+]^2} + \ldots\right). \quad (3)$$

Similarly, Eq. (2) for hydroxides of triple-charged metals can be represented as

$$S = \frac{SP}{K_w^3}\left([H^+]^3 + K_{10}[H^+]^2 + K_{20}[H^+] + K_{30} + \frac{K_{40}}{[H^+]} + \ldots\right). \quad (4)$$

Substituting various $[H^+]$ values in Eqs. (3) and (4), we can determine the pH range in which the solubility S is the lowest.

In this study, we calculated the minimum solubilities for copper(II), zinc(II), cadmium(II), cobalt(II), nickel(II), lead(II), manganese(II), iron(III), and chromium(III) hydroxides and compared the values obtained with MPCs for various water reservoirs. It is ions of these metals that are contained in the sewage of plants having electroplating shops and purifying their wastewater by the reagent method.

As an example, we calculated the solubility of nickel(II) hydroxide as a function of pH with $SP = 10^{-11.89}$ for freshly precipitated nickel hydroxide [10] (2 h after precipitation) and hydrolysis constants [8] $\log K_{10} = -9.86$, $\log K_{20} = -19.0$, $\log K_{30} = -30.0$, and $\log K_{40} = -44.0$. The solubility of nickel hydroxide (mg l^{-1}) as a function of pH is shown in the figure. The calculation demonstrated that the minimum solubility (~110 mg l^{-1}) is observed in the pH range 9.7–10.7.

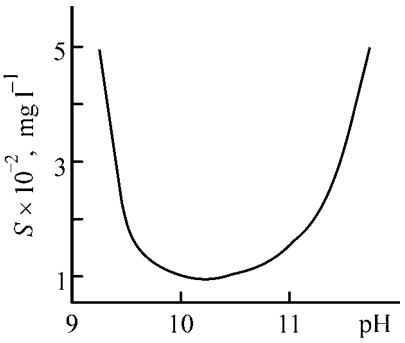

Calculated content of nickel(II) in solution, S, vs. pH value for the case of nickel precipitation as hydroxide.

The maximum permissible concentration of nickel(II) ions in sanitary-hygienic water reservoirs is 0.1 mg l^{-1}, and that in fish farming pools, 0.01 mg l^{-1}. It follows from the data obtained that, when nickel(II) is precipitated as the hydroxide, its solubility at the optimal pH exceeds the MPC by a factor of 1000–10 000 (depending on a water reservoir). Thus, nickel(II) is among metals easily penetrating into the environment when the reagent method is used for sewage purification.

The calculated values of pH ensuring the minimal solubility of hydroxides of other heavy metals are listed in the table. The data obtained are represented as S_{min}/MPC ratios.

It follows from the table that the reagent method fails to satisfy MPC requirements for fish-farming reservoirs for any of the metal ions except chromium(III). In the case of household-drinking water-supply reservoirs, the MPC level can only be attained for chromium(III), copper(II), and manganese(II).

pH value, minimum solubility of heavy metal hydroxides, and MPC for various water reservoirs*

Cation	pH value	S_{min}, mg l^{-1}	MPC, mg l^{-1}		S_{min}/MPC	
			I	II	I	II
Fe(III)	4–11	2.6	0.3	0.1	9	26
Cr(III)	8.5–10	0.02	0.5	0.07	0.04	0.3
Zn(II)	9–11	3	1.0	0.01	3	300
Cd(II)	11–13	10	0.001	0.005	10 000	2000
Co(II)	10–12	0.15	0.1	0.01	1.5	15
Ni(II)	9.7–10.7	110	0.1	0.01	1100	11 000
Cu(II)	8–12	0.17	1	0.001	0.17	170
Mn(II)	11.2–12.5	0.1	0.1	0.01	1	10
Pb(II)	10.5–11.5	5	0.03	0.1	167	50

* Water reservoir: (I) for household and drinking water supply, (II) for fish-farming.

Sewage is purified to remove heavy metal ions by neutralization with alkaline reagents to pH ≤ 8.5, i.e., at pH values different from the optimal pH listed in the table. Under these purification conditions, the solubility of heavy metal hydroxides [except iron(III) hydroxide] is much higher.

Thus, the reagent method for sewage purification by precipitation of heavy metal hydroxides should be regarded as ineffective.

REFERENCES

1. Bek, R.Yu., *Vozdeistvie gal'vanotekhnicheskikh proizvodstv na okruzhayushchuyu sredu i sposoby snizheniya nanosimogo ushcherba* (Effect of Electroplating Industry on the Environment and Methods for Reducing the Damage), Novosibirsk: Gos. Publ. Nauchn. Tekhn. Bibl., Sib. Otd. Akad. Nauk SSSR, 1991.
2. *Spravochnik khimika* (Chemist's Handbook), Nikol'skii, B.P., Ed., Moscow: Khimiya, 1964, vol. 3.
3. Khaiduk, I., *Usp. Khim.*, 1961, vol. 30, no. 10, pp. 1124–1174.
4. Cherkinskii, Yu.S., *Khimiya polimernykh neorganicheskikh vyazhushchikh veshchestv* (Chemistry of Polymeric Inorganic Binders), Moscow: Khimiya, 1967.
5. Butler, J.N., *Ionic Equilibrium* (A Mathematical Approach), Reading, Massachusetts: Addison–Wesley, 1964.
6. Lidin, R.A., Andreeva, L.L., and Molochko, V.A., *Spravochnik po neorganicheskoi khimii: Konstanty neorganicheskikh veshchestv* (Handbook of Inorganic Chemistry: Constants of Inorganic Substances), Moscow: Khimiya, 1987.
7. Nazarenko, V.A., Antonovich, V.P., and Nevskaya, E.M., *Gidroliz ionov metallov v razbavlennykh rastvorakh* (Hydrolysis of Metal Ions in Dilute Solutions), Moscow: Atomizdat, 1979.
8. Povar, I.G., *Zh. Analit. Khim.*, 1998, vol. 53, no. 12, pp. 1289–1292.
9. Vasserman, I.M., *Khimicheskoe osazhdenie iz rastvorov* (Chemical Precipitation from Solutions), Leningrad: Khimiya, 1980.
10. Kumok, V.N., Kuleshova, O.M., and Karabin, L.A., *Proizvedenie rastvorimosti* (Solubility Product), Novosibirsk: Nauka, 1983.

Russian Journal of Applied Chemistry, Vol. 76, No. 2, 2003, pp. 323–324. Translated from Zhurnal Prikladnoi Khimii, Vol. 76, No. 2, 2003, pp. 333–334.

BRIEF COMMUNICATIONS

On the Possibility of Replacing Standard Chromium-Plating Electrolytes with Sulfate-Oxalate Solutions of Cr(III)

A. A. Edigaryan and Yu. M. Polukarov

Institute of Physical Chemistry, Russian Academy of Sciences, Moscow, Russia

Received February 20, 2002

Abstract—A method for preparing sulfate-oxalate chromium-plating solutions by reducing Cr(VI) from industrial chromium-plating electrolytes to Cr(III) with a Na_2SO_3 solution is proposed.

Replacing environmentally unsafe standard chromium-plating solutions with unharmful electrolytes based on chromium(III) is a priority task of modern electroplating technology. It was shown in [1–3] that the oxalate-sulfate chromium-plating electrolyte makes it possible to obtain with high current efficiency coatings of any thickness, which compare well in mechanical properties and corrosion resistance with coatings formed using standard chromium-plating solutions.

The simplest and technologically most acceptable technique for preparing sulfuric acid chromium-plating solutions in a galvanic shop would be direct reduction of Cr(VI) from standard plating electrolytes to Cr(III). In [4–6], methods were proposed for reducing Cr(VI) to Cr(III). In [4], Cr(III) compounds were obtained by saturating a $CrO_3 + H_2SO_4$ solution with gaseous SO_2 to complete the reduction of Cr(VI) to Cr(III). The excess of SO_2 was removed from the solution by boiling. In [5, 6], CrO_3 or $Na_2Cr_2O_7$ was reduced in a sulfuric acid medium with formaldehyde. However, this failed to ensure complete reduction of Cr(VI). As is known, Cr(VI) inhibits reduction of Cr(III) from sulfuric acid solutions to metal. Therefore, this method cannot be recommended for use to obtain sulfuric acid chromium-plating solutions. Below, a procedure is proposed for reducing Cr(VI) to Cr(III) with a Na_2SO_3 solution directly in standard chromium-plating solutions. The reduction by the reaction

$$2CrO_3 + 3Na_2SO_3 + 3H_2SO_4 \rightarrow Cr_2(SO_4)_3 + 3Na_2SO_4 + 3H_2O \quad (1)$$

yields in solution the necessary components, chromium and sodium sulfates. The reaction proceeds till complete reduction of Cr(VI) ions to Cr(III).

EXPERIMENTAL

A Na_2SO_3 solution was introduced in small portions into a standard $CrO_3 + H_2SO_4$ solution in a certain excess with respect to the amount that was calculated in accordance with Eq. (1) and took into account the hydrolysis of sodium sulfate upon heating the solution. The exothermic reaction of Cr(VI) reduction in an acid medium proceeds vigorously, with strong heating of the solution and evolution of SO_2 as a result of H_2SO_3 decomposition at elevated temperatures. In milder reduction mode, without solution heating, no SO_2 is evolved. The completeness of reduction of Cr(VI) ions was tested by staining the solution with 1,5-diphenylcarbazide. When necessary, the solution was boiled for 1.5–2 h after the reaction was complete, to total removal of SO_2 from the solution. The resulting solution of Cr(III) and sodium was adjusted to $Cr_2(SO_4)_3$ and Na_2SO_4 concentration of 130–140 g l^{-1}. $Na_2C_2O_4$, $Al_2(SO_4)_3 \cdot 18H_2O$, and NaF were introduced into the solution. The recommended composition of the chromium-plating solution is as follows [2] (g l^{-1}): $Cr_2(SO_4)_3$ 130–140, $Na_2C_2O_4$ 25–30, $Al_2(SO_4)_3 \cdot 18H_2O$ 110, Na_2SO_4 130–140, and NaF 15. To stabilize the solution prepared, it was allowed to stay at 90–95°C for 30 min. The working mode was the following: pH 1.0–2.0, temperature 40–45°C, current density 20–50 A dm^{-2}, depending on the solution acidity. The volume current density was up to 10 A l^{-1}. At the above current densities and solution pH values, the electrolyte shows prolonged stable work. The optimal mode for obtaining lustrous chro-

1070-4272/03/7602-0323 $25.00 © 2003 MAIK "Nauka/Interperiodica"

mium deposits is as follows: pH 1.4, current density 30 ± 15 A dm^{-2}, current efficiency 30–35%, rate of coating deposition 1.5–1.8 μm min^{-1}, irrespective of the coating thickness. The electrolyte prepared by reduction of Cr(VI) from standard chromium-plating solutions has the same characteristics as the electrolyte prepared on the basis of Cr(III) sulfate and can be used to deposit protective and decorative coatings and obtain thick chromium layers.

The current efficiency by chromium grows with increasing $Cr_2(SO_4)_3$ concentration and reaches the limiting value at 130 g l^{-1}. Raising the $Cr_2(SO_4)_3$ concentration further does not affect the current efficiency by chromium and, therefore, is inexpedient because of the increasing loss of chromium with finished articles.

Electrodeposition of chromium from an oxalate-sulfate solution allows wide variation of the $Na_2C_2O_4$ concentration in solution. Decreasing this concentration to 40% of that recommended for the composition given above makes somewhat lower the throwing power of the electrolyte, without impairing the coating quality, and raising the concentration by 100% leads to only slight decrease in the throwing power.

Raising the concentration of $Al_2(SO_4)_3 \cdot 18H_2O$ in solution to 100 g l^{-1} leads to an increase in the admissible current densities and improves the throwing power of the electrolyte; however, making this concentration higher than 110 g l^{-1} gives no additional positive effect, being, therefore, inexpedient.

Introduction of NaF into the solution leads to much higher current efficiency without impairing the deposit quality; the optimal salt concentration is 20 g l^{-1}.

The electrolyte proposed contains two expended components, $Cr_2(SO_4)_3$ and $Na_2C_2O_4$, with the concentration of the latter falling as a result of oxidation at the anode and reduction at the cathode. The decrease in the concentration of $Cr_2(SO_4)_3$ in the solution on passing through it about 60 A h l^{-1} of electricity (which corresponds to a decrease in the salt concentration in solution by 50 g l^{-1} relative to the initial value) results in that the current efficiency falls from 30–35% to 25%. To prevent the decrease in the current efficiency, a chromium(III) salt should be added to the electrolyte with account of the amount of electricity passed.

The expenditure of $Na_2C_2O_4$ is compensated for by its introduction into the solution when necessary.

One of factors hindering the industrial use of chromium-plating electrolytes based on Cr(III) ions is oxidation of Cr(III) ions to Cr(IV) at the anode and the resulting necessity for separation of the anode and cathode spaces, which complicates the technology of the galvanic process. Use of sulfate-oxalate solutions and anodes made of platinum-plated titanium makes it possible to carry out the process without separating membranes, since Cr(VI) forming at the anode is 100% reduced to Cr(III) by products of partial cathodic reduction, i.e., by Cr(II) ions. As a result of current expenditure for additional formation of Cr(II) ions, the current efficiency by chromium decreases from 30–35 to 25% without any degradation of the deposit quality [7].

Coatings of thickness 20 μm have (depending on current density) a strength within the range $(8.8–15) \times 10^3$ MPa and internal stretching stresses of $(1.2–7.0) \times 10^2$ MPa. According to X-ray diffraction data, the deposits are X-ray-amorphous; in chemical composition, determined by X-ray photoelectron spectroscopy (XPS), and in the corrosion-protective and electrochemical behavior the deposits are close to chromium carbide $Cr_{23}C_6$ [3, 8].

CONCLUSIONS

(1) A simple method is proposed for obtaining sulfate-oxalate solutions for chromium plating by reducing Cr(VI) from standard electrolytes with sodium sulfite.

(2) Sulfate-oxalate solutions obtained by reduction from standard electrolytes make it possible to deposit chromium coatings of arbitrary thickness with high current efficiency.

(3) The deposits obtained are X-ray-amorphous and close in chemical composition and corrosion-electrochemical properties to chromium carbide $Cr_{23}C_6$.

REFERENCES

1. Edigaryan, A.A. and Polukarov, Yu.M., *Zashch. Met.*, 1998, vol. 34, no. 2, pp. 117–122.
2. Edigaryan, A.A. and Polukarov, Yu.M., *Zashch. Met.*, 1999, vol. 35, no. 1, pp. 5–7.
3. Safonov, V.A., Vykhodtseva, L.N., Edigaryan, A.A., *et al.*, *Elektrokhimiya*, 2001, vol. 37, no. 2, pp. 148–156.
4. UK Patent 1583105.
5. USSR Inventor's Certificate, no. 199619.
6. USSR Inventor's Certificate, no. 241882.
7. Edigaryan, A.A. and Polukarov, Yu.M., *Zashch. Met.*, 1998, vol. 34, no. 6, pp. 609–612.
8. Lubnin, E.N., Edigaryan, A.A., and Polukarov, Yu.M., *Zashch. Met.*, 2000, vol. 36, no. 4, pp. 339–343.

Russian Journal of Applied Chemistry, Vol. 76, No. 2, 2003, pp. 325–327. Translated from Zhurnal Prikladnoi Khimii, Vol. 76, No. 2, 2003, pp. 335–337.

BRIEF COMMUNICATIONS

A Mass-Spectrometric Study of Gaseous Products of Thermal Desorption from Diamond and Graphite

B. Ya. Zorin, S. Yu. Plastinin, and E. P. Smirnov

St. Petersburg State Technological Institute, St. Petersburg, Russia

Received January 10, 2002

Abstract—The method of thermal desorption in a vacuum, with gaseous products recorded by mass-spectrometry, was applied to study the state of the surface of diamond and graphite.

Diamond and graphite are carbon materials widely used in various fields of science and technology. Studying the state of the surface of these materials is of scientific and practical importance.

It has been established by numerous studies using chemical and physicochemical analytical techniques that, when interacting with the surface of diamond and graphite, oxygen forms various functional oxy groups: hydroxy, carboxy, carbonyl, ester and ether, etc. [1, 2].

The aim of the present study was to determine the thermal stability of the functional oxy groups of diamond and graphite by analyzing the gaseous products evolved in linear heating of diamond and graphite, with these products recorded simultaneously by mass-spectrometry.

Thermal desorption spectra (Figs. 1 and 2) were obtained by plotting envelopes in the coordinates molecular ion peak intensity–temperature.

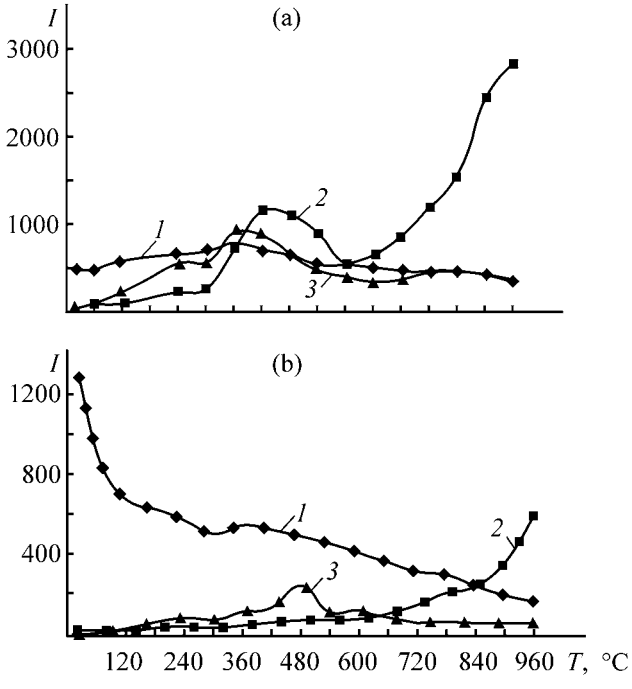

Fig. 1. Thermal desorption spectra of (a) AM-3 diamond and (b) GSM-5 graphite. (*I*) Intensity of molecular ion peaks (H_2O, CO, CO_2) and (*T*) temperature; the same for Fig. 2. (*1*) H_2O, (*2*) CO, and (*3*) CO_2; the same for Fig. 2.

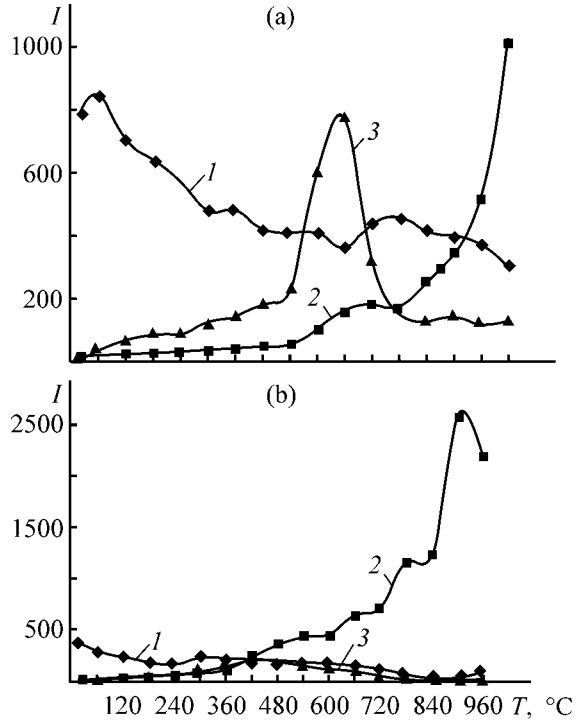

Fig. 2. Thermal desorption spectrum of (a) GSM-5 graphite modified with sodium ions and (b) AM-3 diamond modified with titanium oxide.

1070-4272/03/7602-0325 $25.00 © 2003 MAIK "Nauka/Interperiodica"

EXPERIMENTAL

As objects of study served initial and modified powders of natural diamond of the AM-3 brand and graphite of the GSM-0.5 brand. The specific surface area of the samples under study was found using the method of low-temperature adsorption of nitrogen before and after modification to be 12 and 1.7 $m^2 g^{-1}$ for, respectively, diamond and graphite. The concentration of modifying elements was 1.0 μmol m^{-2} for sodium ions on the graphite surface and 7.0 μmol m^{-2} for titanium ions in the titanium oxide layer. Before measuring the mass spectra, the samples were heated to 100°C in an inert medium for 30 min to remove physically sorbed water.

A 10–30-mg portion of a sample under study was placed in a quartz reactor connected, with the use of a special seal, to the vacuum system of an MI-1201 mass-spectrometer. To monitor the temperature, a Chromel–Alumel thermocouple was inserted into the bottom part of the reactor. The thermo-emf was measured with a KSP-4 potentiometer. The sensitivity of the MI-1201 mass-spectrometer was improved by using a VEU-1 secondary electron multiplier with an RTO-1 unit (wide-band current recorder). The mass spectra were recorded by an N-117 light-beam oscilloscope. Mass spectra of gaseous products of thermal desorption were recorded 5 or 6 times at any given temperature and then processed mathematically. The results of this processing were used to evaluate the experimental error. The desorption was carried out in a vacuum at residual pressures of 10^{-3}–10^{-5} Pa, with the temperature raised linearly from 20 to 1000°C at a rate of 10–12 deg min^{-1}. Spectra of thermal desorption from the initial diamond and graphite are presented in Figs. 1a and 1b.

The thermal desorption spectrum of diamond shows a peak at about 400°C for CO_2, and a peak at about 450°C and steep rise in the tempeature range 850–1000°C for CO. No peaks are observed in the range 20–960°C in the spectrum of water.

The thermal desorption spectrum of graphite (Fig. 1b) differs significantly from that of diamond. For example, the temperature at which a peak is observed for CO_2 is about 480°C, and the spectrum for CO shows a steady gradual rise, becoming steep only at about 900°C. The spectrum for water exhibits a steep decrease in the range from 20 to 120°C and then decreases steadily and gradually, with a minor peak at 360°C.

The common feature of all the thermal desorption spectra of diamond and graphite samples is desorption of CO_2 at lower temperatures, compared with that of CO. Carbon monoxide makes a greater contribution than carbon dioxide to the total number of carbon atoms removed from the surface.

For diamond, the peaks of CO, CO_2, and H_2O desorption at about 400°C are due to decomposition of oxy groups containing carbonyl, carboxy, and quinone groups. The desorption of water is due to dehydration of oxy groups containing hydrogen atoms, i.e., hydroxy groups.

A similar pattern of distribution among groups is also characteristic of graphite, with a quantitative difference consisting in that the yield of water is, in this case, 2–3 times that for diamond.

The results obtained are in good agreement with the data of Japanese researchers, who heated diamond in a vacuum and recorded the forming gaseous products by mass spectrometry. They established that the onset of intense gas evolution corresponds to a temperature of 360°C, and at 900°C the evolution of carbon dioxides ceases [3].

Modification of oxidized graphite samples with alkali metal ions, and, in particular, sodium ions, leads to proton substitution in the functional oxy groups to give alcoholates or phenolates [4]. A thermal desorption spectrum of the sample obtained is shown in Fig. 2a. It can be seen that a CO_2 peak is observed at about 600°C, with its intensity exceeding approximately 4-fold the corresponding peak for an unmodified sample.

It may be assumed that the substitution of hydrogen ions in the hydroxy groups on the graphite surface with sodium ions catalyzes the surface diffusion of oxygen from oxy groups to the active centers of carboxy groups decomposing at 600°C.

As second type of modification of functional oxy groups on the surface of diamond and graphite was growth of a titanium oxide layer (about 100 Å thick) by the chemical assembly technique [5]. The spectra obtained for diamond are shown in Fig. 2b. Modification of the surface of oxidized diamond with a titanium oxide layer leads to a dramatic increase in the CO yield at temperatures higher than 600°C. In contrast to the preceding set of experiments, this effect can be attributed to occurrence of a solid-phase reaction at the interface between the diamond surface and the titanium oxide layer. In the process, the role of diamond oxidizer is played by oxygen ions diffusing upon heating to these temperatures from the lattice of titani-

um oxide TiO_2, with, presumably, partial reduction of titanium(IV) ions to Ti(III).

CONCLUSIONS

(1) Thermal desorption of CO_2 occurs at lower temperatures than that of CO. Carbon monoxide makes a greater contribution than carbon dioxide to the total amount of carbon atoms removed from the surface in thermal desorption.

(2) Modification of the diamond and graphite surfaces allows control over the shift of temperature ranges in thermal desorption.

REFERENCES

1. Sappok, R. and Boehm, H., *Chemie der Oberfläche des dia manten. Carbon*, 1968, vol. 6, pp. 283–293.
2. Sappok, R. and Boehm, H., *Chemie der Oberfläche des dia manten. Carbon*, 1968, vol. 6, pp. 573–583.
3. Matsumo, S., Sato, Y., Setaka, N., and Goto, M., *Chem. Lett.*, 1973, no. 12, pp. 1247–1250.
4. Smirnov, E.P., Taushkanova, O.G., and Aleskovskii, V.B., *Dokl. Akad. Nauk SSSR*, 1986, vol. 290, no. 4, pp. 901–904.
5. Gordeev, S.K. and Smirnov, E.P., *Neorg. Mater.*, 1984, vol. 20, no. 1, pp. 101–104.

Russian Journal of Applied Chemistry, Vol. 76, No. 2, 2003, pp. 328–329. Translated from Zhurnal Prikladnoi Khimii, Vol. 76, No. 2, 2003, pp. 338–339.

BRIEF COMMUNICATIONS

Polymeric Formulations Based on Iron and Cobalt Molybdophosphates and Polyacrylates

L. A. Egorova, N. I. Radishevskaya, and T. I. Izaak

Tomsk State University, Tomsk, Russia

Department of Structural Macrokinetics, Tomsk Scientific Center, Siberian Division, Russian Academy of Sciences, Tomsk, Russia

Received October 2, 2002

Abstract—The possibility of using synthesized iron(III) and cobalt(II) molybdophosphates as dyes in dyeing of copolymers and polymeric formulations based on methacrylic acid and methyl methacrylate and also as pigments deposited onto natural and inorganic supports for heterogeneous dyeing of polymeric materials was studied.

Dyeing of polymeric materials has always been and still is an important problem of modern materials science The widely used organic pigments frequently fail to ensure the necessary working properties and loose brightness in the course of time under the action of light, which impairs the commercial value of plastic building materials and household articles. Some problems can be solved by introducing light-resistant inorganic pigments. Promising in this regard are heteropoly compounds making it possible to obtain brightly colored and light-resistant formulations for finishing building materials and consumer goods. The increased interest in iso-and heteropoly compounds is due to the wide variety of physicochemical and functional properties of the structural forms obtained.

This study is concerned with the properties of polymeric (polyacrylate) materials dyed with iron(III) and cobalt(II) molybdophosphates. Iron(III) and cobalt(II) molybdophosphates were obtained using two methods: (i) directly from 12-molybdophosphoric acid and (ii) from molybdenum(VI) oxide by its alkaline fusion with sodium hydrophosphate and reaction with iron(III) and cobalt(II) chlorides in acid and weakly acid aqueous media [1, 2].

The salts obtained are brightly colored: iron(III) 12-molybdophosphates are yellow, and cobalt(II) 11-molybdophosphates, lylac. Iron(III) and cobalt(II) molybdophosphates, which are soluble in organic solvents, homogeneously dye copolymers of acrylic acid CH_2=CHCOOH and methyl methacrylate CH_2=C(CH_3)$COOCH_3$, obtained by block polymerization (60°C, benzoyl peroxide as initiator). The intermolecular interactions in the polymeric formulations were studied by IR spectroscopy in the spectral range 4000–400 cm^{-1} (Specord-M80). The dominant wavelength and color purity of the salts obtained were calculated from reflectance spectra measured on a Specord-M40 spectrophotometer in the wavelength range 350–900 nm.

Homogeneous introduction of a heteropoly ion into the structure of acrylic polymers leads to a shift of the absorption band at 1730 cm^{-1}, associated with the functional group COO^- of the copolymer, to lower frequencies (1580 cm^{-1}, C=O bond vibrations), which is presumably due to coordination of the COO^- group upon the introduction of a heteropoly compound. The absorption band of the starting polymer, which is observed at 1730 cm^{-1}, corresponds to stretching vibrations of an un-ionized carboxy group and appears because of the partial coordination of COOH groups [3].

The formation of a coordination bond between a metal atom and the oxygen of the carboxy group causes redistribution of the electron density between COO^- bonds and gives rise to two frequencies of a symmetric and an asymmetric vibrations [4, 5]. Similar changes occur, according to IR spectral data, upon introduction of iron(III) and cobalt(II) molybdophosphates into polyacrylate systems. The spectrum of a polymer dyed, e.g., by iron(III) molybdophosphate (Fig. 1) contains absorption bands at ν_{as} = 1580 cm^{-1} and ν_s = 1385 cm^{-1}. The difference of these frequencies $\Delta\nu = \nu_{as} - \nu_s$ is a measure of the covalence of bonding between the heteropoly compound and oxygen. The calculated value of $\Delta\nu$ is 195 cm^{-1}, which is lower than the known value of 225 cm^{-1} [5], and,

1070-4272/03/7602-0328 $25.00 © 2003 MAIK "Nauka/Interperiodica"

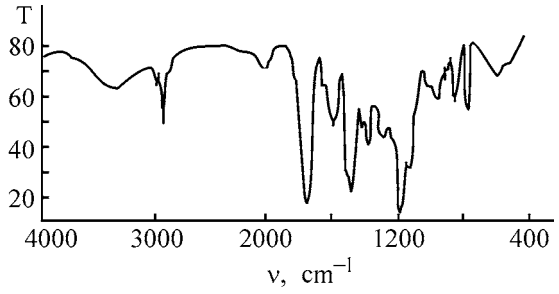

Fig. 1. IR spectrum of acrylic copolymer dyed with iron(III)12-molybdophosphate. (T) Transmission and (ν) wave number.

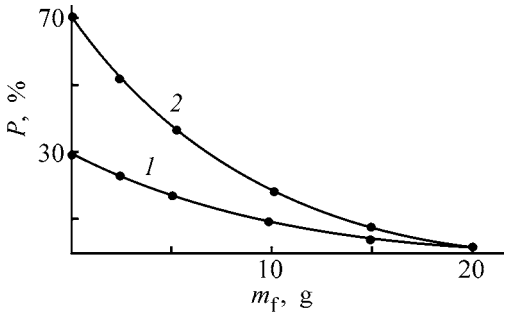

Fig. 2. Color purity P of a pigment vs. mass m_f of filler (silica gel). Pigment mass 1 g. (*1*) Cobalt(II) 11-molybdophosphate and (*2*) iron(III) 12-molybdophosphate.

consequently, the bonding between the heteropoly compound and the carboxy group is mainly ionic. A broad band peaked at 1950 cm^{-1}, characteristic of vibrations of the M–O=C bond, is observed in the range 2000–1900 cm^{-1}. A pronounced peak corresponding to stretching vibrations of the Fe–O bond appears at 520 cm^{-1} [3, 4, 6]. The homogeneous dyeing of the copolymer is apparently due to coordination of the heteropoly compound with oxygen-containing fragments.

Polymers can also be dyed with heteropoly salts deposited onto natural silicate supports. The deposition of heteropoly compounds can be done in the course of their synthesis. The pigments obtained can be further used for heterogeneous dyeing of polymers. The results obtained in a study of how the color purity depends on the mass of silica gel filler are shown in Fig. 2. It can be seen that, with increasing mass fraction of the filler (silica gel), the color purity decreases steadily. For iron(III) molybdophosphate the color purity is higher, and cobalt(II) molybdophosphate has pleasant delicate coloration. The calculations performed demonstrate that the optimal amount of filler is about 5 g per 1 g of pigment.

Dyed fillers, such as silica gel support, diopside, tremolite, and wollastonite, and also ground porcelain, make it possible to decrease dramatically the expenditure of the pure pigment and can be used in heterogeneous dyeing of polymeric materials. As would be expected, the color of the cobalt(II) salt, which has lacunar structure (P : Mo = 1 : 11), is defined by the *d*–*d* transition (455–465 nm). The color of iron(III) molybdophosphate, which has the Keggin structure (P : Mo = 1 : 12), depends to a greater extent on the influence exerted by the environment of the heteropoly ion on the *d*–*d* transition (λ_d = 570 nm).

The polymeric formulations obtained have bright color and are not bleached under sunlight. Dyed methyl methacrylate samples were subjected to the action of a UV light (DRL-400 lamp) for 45 h and to outdoors daylight for half a year. No changes in their optical properties were observed. The formulations obtained on the basis of polymethyl methacrylate and heteropoly compounds show promise as components for modern building materials.

CONCLUSIONS

(1) Iron(III) and cobalt(II) molybdophosphates, which are soluble in organic solvents, homogeneously dye copolymers of acrylic acid and methyl methacrylate, which is due to coordination of the heteropoly ion with oxygen-containing fragments of the acrylic polymer.

(2) Heteropoly salts of iron(III) and cobalt(II), supported by such fillers as silica gel, wollastonite, diopside, tremolite, and ground porcelain can be used in heterogeneous dyeing of polymethyl methacrylate and other acrylic polymers.

REFERENCES

1. Radishevskaya, N.I., Egorova, L.A., and Kozik, V.V., *Zh. Prikl. Khim.*, 2000, vol. 73, no. 7, pp. 1066–1068.
2. Radishevskaya, N.I., Egorova, L.A., and Kozik, V.V., *Izv. Vyssh. Uchebn. Zaved., Fiz.*, 2000, no. 10, pp. 92–93.
3. Silverstein, R.M., Clayton, G.C. and Morril, T.C., *Spectrometric Identification of Organic Compounds*, New York: John Wiley & Sons, 1974.
4. Nakamoto, K., *Infrared and Raman Spectra of Inorganic and Coordination Compounds*, New York: John Wiley & Sons, 1986.
5. Ergozhin, E.E., *Vysokopronitsaemye ionity* (Highly Permeable Ion-Exchange Resins), Alma-Ata: Nauka, 1979.
6. Dechant, J., Danz, R., Kimmer, W., *et al.*, Ultrarotspektroskopieshe Untersuchungen an Polymeren, Berlin: Akademie, 1972.

Russian Journal of Applied Chemistry, Vol. 76, No. 2, 2003, pp. 330–331. Translated from Zhurnal Prikladnoi Khimii, Vol. 76, No. 2, 2003, pp. 340–341.

BRIEF COMMUNICATIONS

Synthesis of Bis(Amido Sulfimides) from 2-Sulfoterephthalic Acid Imide Chloride

T. A. Aslanov

Institute of Polymeric Materials, National Academy of Sciences of Azerbaijan, Sumgait, Azerbaijan

Received May 13, 2002

Abstract—A series of bis(amido sulfimides) were prepared by condensation of 2-sulfoterephthalic acid imide chloride with aliphatic and aromatic diamines.

Trimellitic acid and its derivatives are widely used as monomers in production of polyimide polymers [1, 2]. Synthesis of less studied 2-sulfoterephthalic acid imide, 4-sulfoisophthalic acid imide, and their esters was reported in [3].

This paper describes previously unknown 2-sulfoterephthalic acid imide chloride **I** [4] and its amide derivatives **II**–**VII** containing amide and imide groups, which show promise as monomers for preparing poly(amido imides).

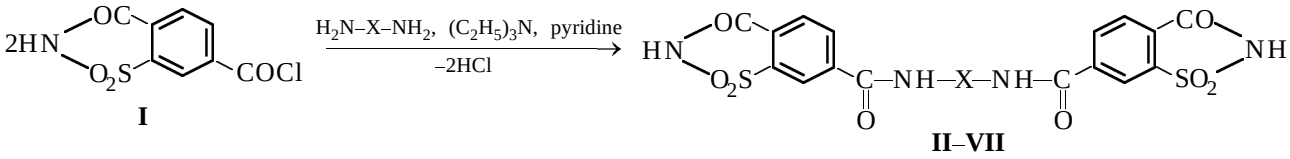

R = $(CH_2)_2$ (**II**), $(CH_2)_4$ (**III**), $(CH_2)_6$ (**IV**), 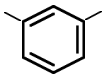 (**V**), 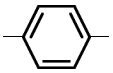 (**VI**), and 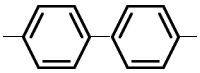 (**VII**).

Condensations of **I** with diamines were performed at 40–45°C; a solution of acid chloride was gradually added with stirring to a solution of an appropriate diamine in dimethylacetamide, and an equimolar amount of triethylamine was added to bind the HCl released.

The reactions give bis(amido sulfimides) **II**–**VII** in high yields. The compositions and structures of **II**–**VII** were confirmed by elemental analysis (see table) and IR spectroscopy. The IR spectra of **II**–**VII** contain C–N absorption bands at 1660–1600 cm^{-1}, bands at 1380–1300 and 1200–1130 cm^{-1} belonging to asymmetric stretching vibrations of the SO_2 group in the saccharin ring, and N–H bands at 3350–3310 cm^{-1} [4, 5].

EXPERIMENTAL

Dimethylacetamide, triethylamine, and pyridine were purified as described in [6, 7]; diamines, by recrystallization and vacuum distillation; and hexamethylenediamine, by distillation in an argon flow at 198–199°C (mp 40°C).

2-Sulfoterephthalic acid imide chloride I. A 250-ml round-bottomed flask with a reflux con-

1070-4272/03/7602-0330 $25.00 © 2003 MAIK "Nauka/Interperiodica"

Bis(amido sulfimides) **II**–**VII**

Compound no.	Yield, %	Found, %				Formula	Calculated, %				*M*	
		C	H	N	S		C	H	N	S	found	calculated
I	85	40.3	1.60	5.66	12.9	$C_8H_4NO_4SCl$	39.10	1.63	5.70	13.08	244	245.5
II	94	46.0	2.88	11.3	13.3	$C_{18}H_{14}N_4O_8S_2$	45.18	2.92	11.71	13.38	473	478
III	91	47.0	3.45	10.85	12.5	$C_{20}H_{18}N_4O_8S_2$	47.43	3.55	11.06	12.64	502	506
IV	90	50.1	4.15	10.3	12.0	$C_{22}H_{22}N_4O_8S_2$	49.44	4.12	10.48	11.98	531	534
V	84	51.1	2.58	10.44	12.22	$C_{22}H_{14}N_4O_8S_2$	50.19	2.66	10.64	12.16	520	526
VI	83	49.9	2.54	10.37	12.40	$C_{22}H_{14}N_4O_8S_2$	50.19	2.66	10.64	12.16	521	526
VII	78	54.5	2.86	8.87	10.31	$C_{28}H_{12}N_4O_8S_2$	49.83	2.99	9.30	10.63	595	602

denser and a calcium chloride tube was charged with 2.1 g (0.01 mol) of PCl_5 and 2.27 g (0.01 mol) of sulfoterephthalic acid imide. The mixture was stirred. In the process, the mixture spontaneously warmed up to 40–45°C. After completion of the exothermic reaction, the temperature was raised to 95–100°C, and the heating was continued for an additional 2 h. After reaction completion, $POCl_3$ was distilled off in a water-jet-pump vacuum. Then 50 ml of benzene was added, and the mixture was stirred for 10–15 min. The solvent and $POCl_3$ were distilled off from the filtrate. The remaining oily product was successively washed on a glass frit with dry carbon tetrachloride, chloroform, and benzene, after which it was recrystallized successively from dry toluene and acetone. The resulting light brown product was dried in a desiccator to constant weight.

Bis(amido sulfimide) VII derived from 2-sulfoterephthalic acid imide chloride and *p,p*'-diaminobiphenyl. A three-necked round-bottomed flask with a power-driven stirrer and a tube for nitrogen outlet was charged with 30 ml of dimethylacetamide and 1.85 g (0.01 mol) of *p,p*'-diaminobiphenyl. Then 5 g (0.02 mol) of chloride **I** was added in an inert atmosphere. Triethylamine or pyridine was added to neutralize the HCl released. The reaction temperature was maintained at 40–45°C. After adding the whole amount of **I**, the mixture was stirred for an additional 30 min. In the course of the reaction, a dark product formed. After reaction completion, 150 ml of distilled water was added, and the mixture was filtered through a glass frit. The product was dried at room temperature and then brought to constant weight in a vacuum oven.

Bis(amido sulfimides) derived from *m*- and *p*-phenylene-, ethylene-, tetramethylene-, and hexamethylenediamines were prepared similarly.

CONCLUSION

Previously unknown 2-sulfoterephthalic acid imide chloride was prepared, and bis(amido sulfimides) showing promise as monomers were prepared by its reactions with diamines.

REFERENCES

1. Suvorov, B.V., Zhubanov, B.A., and Mashkevich, S.A., *Trimellitovaya kislota i polimery na ee osnove* (Trimellitic Acid and Polymers Derived from It), Alma-Ata: Nauka, 1975.
2. Arkhipova, I.A., Zhubanov, B.A., Kim, L.V., and Ivashchenko, N., *Zh. Prikl. Khim.*, 1976, vol. 49, no. 6, pp. 1399–1402.
3. Tagiev, B.A. and Aslanov, T.A., *Azerb. Khim. Zh.*, 1997, nos. 1–4, pp. 62–66.
4. Smiles, S. and Harrison, D.C., *J. Chem. Soc.*, 1922, vol. 121, p. 2022.
5. Kazitsyna, L.A. and Kupletskaya, N.B., *Primenenie UF, IK, YaMR i mass-spektroskopii v organicheskoi khimii* (Applications of UV, IR, NMR, and Mass Spectroscopy in Organic Chemistry), Moscow: Mosk. Gos. Univ., 1979.
6. Gordon, A.J. and Ford, R.A., *The Chemist's Companion. A Handbook of Practical Data, Techniques, and References*, New York: Wiley, 1972.
7. Becker, H., Berger, W., Domschke, G., *et al.*, *Organikum. Organisch-chemisches Grundpraktikum*, Berlin: Wissenschaften, 1976.

Russian Journal of Applied Chemistry, Vol. 76, No. 2, 2003, pp. 332–334. Translated from Zhurnal Prikladnoi Khimii, Vol. 76, No. 2, 2003, pp. 342–344.

Professor Vladimir Yakovlevich Kurbatov (To 125th Anniversary of His Birthday)

Vladimir Yakovlevich Kurbatov made a major contribution to investigations into the nature of the liquid state, thermal properties of liquids, and their structural features, to improvement of teaching of physical and colloid chemistry at St. Petersburg Technological Institute and other higher-school institutions, and to studies of D.I. Mendeleev's creative heritage; he also was a known historian of architecture, art critic, and student of local lore.

He was born on January 24, 1878, in St. Petersburg into the family of an office employee, court councilor Yakov Ivanovich Kurbatov (1845–1881). The early death of the head of the family with three infants led to severe financial difficulties. Already at the age of 14, when being a secondary-schoolboy, V.Ya. Kurbatov had to do coaching and try to earn a living in other ways. Nevertheless, he finished gymnasium with gold medal in 1896 and entered the natural department of the physico-mathematical faculty of St. Petersburg University. In those years, the university had no special laboratory or chair of physical chemistry; however, D.P. Konovalov (1856–1929, academician of the Academy of Sciences of the USSR since 1923), who headed the chair of inorganic chemistry after D.I. Mendeleev (1834–1907) left the university, delivered a separate course of lectures on physical chemistry beginning in 1895. Since 1897, lectures on some sections of physical chemistry (electrochemistry, photochemistry) were also delivered by privatdocent V.A. Kistyakovskii (1865–1952, academician of the Academy of Sciences of the USSR since 1929). By that time, Konovalov was already very well known; the essential results of his classical study "On Pressure of Solution Vapor" (1884) were described in all courses of lectures and textbooks of physical chemistry, beginning in the 1890s. Detailed recollections of Konovalov's scientific and pedagogical activities were left by one of the most prominent representatives of his school, A.A. Baikov (1870–1946, academician of the Academy of Sciences of the USSR since 1923) [1].

In 1897, V.Ya. Kurbatov, when still being a student, commenced scientific research at the laboratory of inorganic chemistry under Konovalov's supervision. In 1900, Vladimir Yakovlevich graduated from the

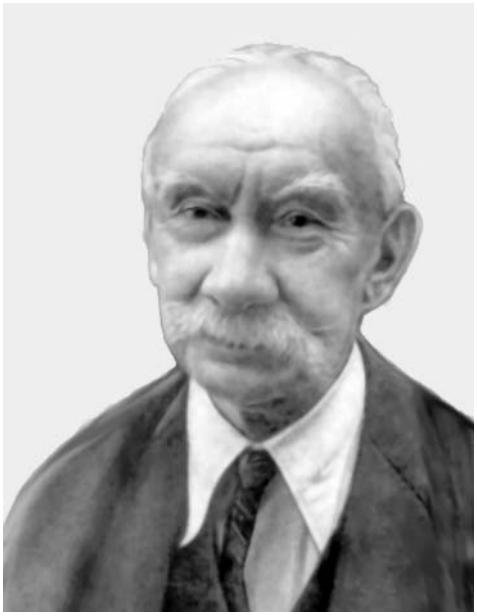

university; his diploma work was honored with minor A.M. Butlerov Prize, awarded by the Russian Physicochemical Society. From 1900 till 1907, V.Ya. Kurbatov was a laboratory assistant at the chemical laboratory of the university. Already beginning in 1902, *Zhurnal Russkogo Fiziko-Khimicheskogo Obshchestva* (Journal of the Russian Physicochemical Society) regularly published interesting results of his experimental studies concerned with the properties and structure of various liquids, temperature dependence of specific heat, and heat of evaporation. Vladimir Yakovlevich took active part in meetings of the Society and made reports of his new investigations.

In 1903–1913, V.Ya. Kurbatov repeatedly went to business trips abroad. In particular, in 1905, he worked at the laboratory of H. Le Chatelier (1850–1936) in Paris. The same laboratory was the place of on-the-job training of other known representatives of Konovalov's school: Baikov, B.G. Karpov (1870–1940), M.S. Vrevskii (1871–1929, academician of the Academy of Sciences of the USSR since 1929), I.I. Zhukov (1880–1949, academician of the Academy of Sciences of the USSR since 1946), and others.

The first summary of the results obtained in experimental studies of more than 30 organic liquids

1070-4272/03/7602-0332 $25.00 © 2003 MAIK "Nauka/Interperiodica"

was given in V.Ya. Kurbatov's monograph *O molekulakh, obrazovannykh soedineniem tozhdestvennykh grupp. Yavlenie assotsiatsii* (On Molecules Formed by Combination of Identical Groups. Association Phenomenon), published as separate edition in St. Petersburg in 1908. The most important concepts of this study have been commented by Yu.I. Solov'ev [2] and V.V. Razumovskii [3]. According to the concepts developed by V.Ya. Kurbatov, various kinds of anomalies in water, alcohols, and other liquids can be accounted for by the existence of complex molecules (associates), which disintegrate when temperature is raised. Based on a study of specific heats and heats of evaporation of liquids, the scientist came to important, by that time, conclusions that, in particular, "crystal-forming forces reflect on the properties of a substance in the liquid state" [3].

In 1907–1909, V.Ya. Kurbatov taught physical chemistry at St. Petersburg Technological Institute; in 1909–1921, he worked at various educational institutions of St. Petersburg (Petrograd). Simultaneously, he continued experimental studies of properties of liquids. By 1916, V.Ya. Kurbatov had studied the properties of more than 150 liquids and generalized the results he obtained in a large paper "On Specific Heat of Liquids," which was published in *Izvestiya Petrogradskogo Tekhnologicheskogo Instituta* (Transactions of Petrograd Technological Institute) (1917, vol. 24, pp. 1–383.

V.Ya. Kurbatov became a professor at the chair of physical chemistry of St. Petersburg Technological Institute in 1921, and head of this chair in 1922; in 1925–1927 he was elected deputy rector for educational work. The main direction of his scientific research remained the same. By 1927, he accumulated a vast body of experimental data on specific heats of various liquids, including some liquid metals (Hg, Na, K, Cd, Pb), heats of evaporation and boiling points of liquids at different pressures, surface tension and capillary properties of liquids. This material was discussed and systematized in his third generalizing paper published in *Izvestiya Teknologicheskogo Instituta im. Lensoveta* (Transactions of Lensovet Technological Institute, 1927, vol. 1, pp. 1–238).

In subsequent years, the total number of organic liquids whose specific heat and other properties were studied by V.Ya. Kurbatov and his pupils became as large as 450 [3]. Such a vast amount of experimental data made it possible to draw certain conclusions about the influence exerted by one or another functional group of a compound on its properties. The results obtained became part of reference books, were regularly published and reported at major scientific conferences and meetings of the All-Union Mendeleev Chemical Society.

Beginning in 1919, V.Ya. Kurbatov carried out a large set of investigations in the field of colloid solutions and jellies. Despite the technological aim of these studies, the author came to a number of important conclusions of general theoretical nature, formulated conditions for formation and preservation of jellies and colloids, and put forward the "crystal-polyamphionic" and then "polyionic-halise" theories of electrolyte solutions. These new approaches to the nature of solutions were described, among other issues, in his monograph *Fiziko-khimicheskie teorii i ikh prilozhenie v tekhnike* (Physicochemical Theories and Their Application in Technology) (Leningrad, 1929, 856 pp.) and other publications [3].

Being Mendeleev's and Konovalov's follower, V.Ya. Kurbatov always closely associated his scientific research with solution of concrete technological problems. Already in the first years of his scientific activities, he carried out a set of investigations concerned with the nature of hardened steels; later, he was invited as consultant in construction of chemical plants and served as a member of Scientific-technological councils at a number of applied institutes. V.Ya. Kurbatov actively cooperated with the Scientific and technological department of VSNKh (Supreme Council of National Economy), created in Petrograd in 1918.

Together with his colleagues from he Technological Institute, V.Ya. Kurbatov was among the authors of the well-known "Memorandum on Importance of Chemistry in Economical Development of the USSR," presented to the Soviet Government in 1928. The Committee for Chemicalization at Council of People's Commissaries of the USSR, created later, played an important part in the restoration and reconstruction of the existing chemical plants and construction of new plants [4]. V.Ya. Kurbatov's idea that a close association between the scientific and applied research is necessary was described in a brochure *Nauka—osnova khimicheskoi promyshlennosti* (Science as Basis of Chemical Industry) (Leningrad, 1929, 69 pp.).

V.Ya. Kurbatov made a major contribution to studies of Mendeleev's scientific legacy and to popularization of his concepts and works. Already at the First Mendeleev Congress, held in the year when the great scientist died (St. Petersburg, December 20–30, 1907), V.Ya. Kurbatov presented a large report "General Survey of D.I. Mendeleev's Scientific Activities" [5]. A detailed analysis of the periodic law discovered by

Mendeelev was made in V.Ya. Kurbatov's monograph *Zakon D.I. Mendeleeva* (D.I. Mendeleev's Law) (Leningrad, 1925, 453 pp.). Vadinir Yakovlevich took part in writing a book of recollections of Mendeleev [6] and wrote a book for schoolchildren about the great Russian scientist [7]. It should also be mentioned that V.Ya. Kurbatov proposed in 1925–1926 a hyperboloid form of Mendeleev's periodic system of chemical elements [3].

During the whole time of his scientific and pedagogical activities, V.Ya. Kurbatov paid much attention to publication of textbooks of widely varying level. In the series *Biblioteka rabochego* (Worker's Library) he wrote in a popular manner *Nachala khimii* (Fundamentals of Chemistry) (Petrograd, 1923, 368 pp.). He wrote *Vvedenie k izucheniyu i prakticheskim zanyatiyam po fizicheskoi khimii* (Introduction to Studies and Laboratory Works in Physical Chemistry) (Leningrad, Leningrad Technological Institute, 1926, 237 pp.) for students of the Technological Institute and *Khimiya kolloidov i studnei* (Chemistry of Colloids and Jellies) for students of the Military Academy (Leningrad, 1925, 232 pp.).

In August 1934, the degree of doctor of chemical science was conferred on V.Ya. Kurbatov. In 1941–1944, Vladimir Yakovlevich taught at Kazan Institute of Chemical Engineering. In 1944, he became Honored Scientist and Technologist of Tatar Autonomous Soviet Socialist Republic.

Having returned from evacuation in 1944, V.Ya. Kurbatov headed the chair of inorganic chemistry at Leningrad Sanitary-Hygienic Institute and became head of the chair of physical chemistry at Lensovet Technological Institute in January 1949.

V.Ya. Kurbatov was not only a prominent scientist in the field of physical and colloid chemistry; he was also well-known as historian of architecture, student of local lore, a connoisseur of Russian art, and that of St. Petersburg and environs in the first place. Vladimir Yakovlevich was very closely associated with members of the *Mir Iskusstva* (World of Art) Society which appeared in the very end of the XIX century, among whose main organizers were such outstanding persons of the Russian culture as A.N. Benua (1870–1960), S.P. Dyagilev (1872–1929), and others. In his reminiscences [8], A.P. Ostroumova-Lebedeva (1871–1955), a known artist and active member of the Society, mentioned more than once this aspect of V.Ya. Kurbatov's activities. St. Petersburg and environs, their gardens and parks, were the favorite subjects in the creative work of Benua, M.S. Dobuzhinskii (1875–1957), and Ostroumova-Lebedeva. The monograph on St. Petersburg [9], written by V.Ya. Kurbatov, was decorated, together with a large number of photographs, with numerous engravings by Ostroumova-Lebedeva. The scientist also wrote books about environs of St. Petersburg: Gatchina, Pavlovsk, Peterhof, and others, a great number of papers about gardens, parks, and museums of St. Petersburg.

Vladimir Yakovlevich Kurbatov passed away on February 12, 1957, at the age of 79. Elder generations of graduates from the Technological Institute remember this comprehensively educated, modest, and well-wishing person, who made a major contribution to the development of the domestic chemical science and training of specialists at the Technological Institute and other higher-school educational institutions. Of high and independent value are his descriptions of the architectural ensembles and museums of St. Petersburg and environs. The whole V.Ya. Kurbatov's life was devoted to science and art.

REFERENCES

1. Baikov, A.A., *Sobranie trudov* (Collection of Works), Moscow: Akad. Nauk SSSR, 1952, vol. 1.
2. Solov'ev, Yu.I., *Istoriya ucheniya o rastvorakh* (History of the Theory of Solutions), Moscow: Akad. Nauk SSSR, 1959.
3. Razumovskii, V.V., *Zh. Obshch. Khim.*, 1953, vol. 23, no. 4, pp. 529–537.
4. *150 let Leningradskogo tekhnologicheskogo instituta im. Lensoveta* (150 Years of Lensovet Technological Institute), Leningrad: Khimiya, 1978.
5. Kurbatov, V.Ya., *Trudy Pervogo Mendeleevskogo s''ezda po obshchei i prikladnoi khimii* (Proc. First Mendeleev Congress on General and Applied Chemistry), St. Petersburg, 1909, pp. 36–45.
6. Kurbatov, V.Ya., *D.I. Mendeleev v vospominaniyakh sovremennikov* (D.I. Mendeleev in Recollections of His Contemporaries), Moscow: Atomizdat, 1969, pp. 106–109.
7. Kurbatov, V.Ya., *Mendeleev*, Leningrad: Detgiz, 1954.
8. Ostroumova-Lebedeva, A.P., *Avtobiograficheskie zapiski: 1900–1916* (Autobiographic Notes: 1900–1916), Moscow: Iskusstvo, 1945.
9. Kurbatov, V.Ya., Peterburg: *Khudozhestvenno-istoricheskii ocherk i obzor khudozhestvennogo bogatstva stolitsy* (Artistic-Historical Treatise and Review of the Artistic Treasures of the Capital), St. Peterburg: Izd. Obshchiny Sv. Evgenii, 1913.

A. G. Morachevskii

Russian Journal of Applied Chemistry, Vol. 76, No. 2, 2003, pp. 335–336. Translated from Zhurnal Prikladnoi Khimii, Vol. 76, No. 2, 2003, pp. 345–346.

BOOK REVIEWS

Kozin, L.F. and Volkov, S.V., *Vodorodnaya energetika i ekologiya* (Hydrogen Power Engineering and Ecology), Kiev: Naukova Dumka, 2002, 336 pp.

The monograph by known Ukrainian scientists, Professor L.F. Kozin and Academician S.V. Volkov (National Academy of Sciences of the Ukraine), considers and discusses the state of modern power engineering and global problems encountered, in the first place, by countries not provided to a full extent with domestic natural energy carriers. The authors emphasize that, at present, electric power is mostly generated at thermal and nuclear power plants and hydroelectric power stations, and only its minor part, by ecologically safe devices employing renewable sources of energy.

Electric power generation at thermal power plants, especially those using coal, entails severe contamination of the environment with oxides of sulfur, nitrogen, and metals, and deteriorates life conditions on the Earth.

Nuclear power plants allow large-scale production of electric and thermal power. At present, Ukrainian nuclear power plants produce 39.6–42.2% of the total electric power consumed in the country. However, their operation requires an exceedingly high culture of maintenance and strict observance of the necessary technological mode. The consequences of the Chernobyl disaster will be felt by many generations of those living in the Ukraine and adjacent provinces of Belarus and Russia. The Ukraine has not solved up to now the problem of processing of the nuclear waste, which is still put into storage.

The main attention is given by the monograph to prospects for development of hydrogen power engineering, discusses the possibility of combining this power source with nuclear power plants, with nuclear-hydrogen power plants to be created in, probably, distant future. The authors also consider such problems as origin of oil in the Earth, formation of ozone holes, and put forward their own hypotheses.

The book comprises a brief foreword (pp. 3 and 4), nine sections, conclusion, and a list of references. Small first (pp. 5–13) and second (pp. 14–16) sections analyze energy-related and ecological problems of most general nature. In particular, the authors note that the so-called "post-Chernobyl syndrome" affected adversely the prospects for development of nuclear power engineering, including scientific research in this field not only in the Ukraine, but also in some other countries.

The third section of the monograph (pp. 17–46) contains evidence concerning the resources and consumption of combustibles (oil, natural gas, coal, and lignite) in various countries and presents a vast body of numeric data, mainly for recent years. According to the available estimates, up to 75% of the proven resources of coal and lignite are found in the territory of Russia, United States, and Ukraine. Russia and the United States are leaders in production of natural gas. The authors call attention to the correlation between the gross national product and the consumption of energy resources per capita. It is noted that the deficiency of energy resources in the Ukraine and their high cost favored the breakdown of industry, degradation of agriculture, deterioration of the living standards of the population, and other negative phenomena of the last decade.

The fourth section (pp. 47–96) is devoted to the development of nuclear power engineering in the Ukraine and to analysis of its scientific, technological, and ecological problems. At present, nuclear power plants of the country have in operation 16 power units, with the problem of utilization of nuclear waste being topical. The authors pay special attention to the Chernobyl disaster, the reasons why it occurred, and elimination of its consequences. After the disaster at the fourth power unit of the Chernobyl nuclear power plant in 1986, three power units had been in operation, with the last of these removed from service in December 2000.

The fifth section (pp. 86–96) presents evidence concerning the scale of energy production in the Ukraine. The thermal power plants produce about 54.5–57.1% of the electric and thermal power generated in the country; however, the industry is in deep crisis. The charges for fuel transportation have increased, and the overwhelming majority of units have exhausted their expected service life. Their being worn out and obsolescence lead to increased fuel expenditure and impair other operation characteristics. The Ukraine's

1070-4272/03/7602-0335 $25.00 © 2003 MAIK "Nauka/Interperiodica"

hydroelectric power stations have nearly totally exhausted the potential resources of hydroelectric energy and can produce no more than 5.0–5.5% of the total output of electric power in the country. Various unconventional power sources can only satisfy 1–2% of the country's demand.

The sixth (pp. 97–200) and seventh (pp. 201–216) sections, which are devoted to hydrogen and hydrogen power engineering, in fact occupy the central position in the monograph and contain the results of numerous investigations carried out by the authors of the book in this field. Hydrogen is the most widely occurring element in the Earth and the ecologically unique type of fuel whose combustion products are water vapor or liquid water. The physicochemical properties of hydrogen and metal hydrides and methods for obtaining hydrogen are considered in detail. Particular attention is given to hydrogen production by reacting water with aluminum alloyed with various components positively influencing the rate of the process. According to the data presented by the authors, world's output of hydrogen was 83 million tons in 2000.

The eighth section of the book (pp. 272–292), devoted to ecology and environment, contains an analysis of reasons for various negative natural phenomena and processes. To these belong the greenhouse effect, ozone holes, acid rains, and "thermal contamination" of the planet. The authors, in particular, believe that freons have nothing to do with the appearance of ozone holes over Antarctic, and put forward their own considerations on the issue. It is also noted that the human technological activities do not exert, as yet, any detrimental effect on the thickness of the ozone layer over the planet. The reasons for the appearance of acid rains and the pollution of the human environment with harmful combustion products of natural gas, oil, coal, lignite, and combustible shale are discussed.

The ninth section (pp. 293–315) prognosticates what power sources will be in use in the third millennium. In the authors' opinion, the main power sources will be solid fuel (coal, shale, peat), hydrogen, nuclear sources of heat and electric power, and various renewable power sources.

In the conclusion (pp. 316–319), the authors note once again the deficiency of energy resources in the Ukraine and formulate concrete proposals aimed at satisfying the country's demand for energy carriers. At present, not only the nuclear fuel cycle, but also the conventional thermal fuel cycle, are not provided with energy carriers. Their deficiency creates real difficulties in manufacture of competitive industrial goods and poses a threat to the stability of the national economy and to the national safety.

The bibliographic list (pp. 320–334) contains 373 references to studies published mostly in recent years.

The monograph written by scientists with rather wide range of interests luckily combines an analysis of the concrete situation with energy in the Ukraine and discussion of quite a number of global problems. The main attention is given to the hydrogen power engineering and methods for production of hydrogen. Also presented are the authors' hypotheses concerning the mechanisms of oil formation and appearance of ozone holes. The book is well written, interesting to read, and contains a vast factual material; the authors do not abuse the reader with excess of special terminology. Despite the disputable nature of some of the problems discussed, the book can be recommended for reading to a wide audience of readers. The reference material summarized by the authors will undoubtedly be of interest for specialists in power engineering and ecology.

A.G. Morachevskii and V.S. Shpak

Russian Journal of Applied Chemistry, Vol. 76, No. 2, 2003, p. 337. Translated from Zhurnal Prikladnoi Khimii, Vol. 76, No. 2, 2003, p. 347.

BOOK REVIEWS

Habashi, F., *Textbook of Pyrometallurgy*, Quebec City: Laval Univ., 2002, 592 pp.

Professor F. Habashi, a Canadian scientist, supplemented the voluminous set of his publications[1] with a new textbook describing pyrometallurgical processes in ferrous and nonferrous metallurgy. The whole material is presented in the form of 38 small chapters grouped into five parts. The first of these, "Introduction" (chapters 1–4, pp. 1–75) contains evidence about the history of high-temperature metallurgical processes. Mention is made of works of leading Western scientists J. Berzelius (1778–1848), H. Bessemer (1813–1898), W. Kroll (1889–1973), and others. The evolution in use of various procedures for isolation and subsequent refining of a great number of nonferrous and rare metals, and also iron, is considered. The first part of the book discusses in the general context theoretical, technological, and equipment-related problems. Temperature dependences of the standard Gibbs energy in a wide range of temperatures are presented for oxides, chlorides, and fluorides of a great number of metals. Special attention is given to environment protection from contamination in performing typical metallurgical processes (steel manufacture, processing of sulfide ores of heavy metals).

The second part of the textbook, "Engineering Aspects" (chapters 5–11, pp. 79–182), considers processes and apparatus of metallurgical shops. Various types of furnaces, refractories used, energy-saving processes, methods for separation of the solid and gaseous phases, oxidation processes, and metallothermic reactions are described.

The third part, "Preliminary Treatment" (chapters 12–19, pp. 183–302), contains evidence about various kinds of preprocessing of raw materials, concentrates, and minerals. The following basic procedures are described: preliminary thermal treatment (smelting, hardening, dehydration, calcination, oxidation); alkaline fusion; sulfatization of oxides by various methods; oxidation of sulfides, disulfides and related materials; formation of mattes; chlorination and fluorination. Each of the procedures discussed is illustrated with concrete examples.

The fourth part, "Metal Separation: Reduction, Conversion and Other Processes" (chapters 20–30, pp. 303–442), groups chapters describing, for the most part, production of metals from their compounds. It considers properties of various reducing agents (coal, coke, carbon(II) oxide and its mixture with hydrogen, hydrogen), discusses in detail reduction of oxides and other compounds of iron, reduction of nonferrous metal oxides with carbon, hydrogen and metals, and also reduction of complex oxides, halides, and sulfides. The same part of the book considers some other processes involving copper, lead, and nickel sulfides.

The fifth part of the book, "Refining" (chapters 31–38, pp. 443–451), is concerned with refining processes. The introductory chapter describes typical processes of purometallurgical refining (refining of iron, copper, and lead) and gives a classification of the main refining procedures: selective oxidation of impurities, removal of dross and mattes from melts, chemical transport reactions involving the gas phase, and physical refining methods (vacuum treatment, zone melting, distillation). The following chapters consider in ample detail the procedures and methods of high-temperature refining, with concrete examples provided.

Appendixes A, B, C, and D describe textbooks and monographs of general nature and those devoted to separate metals or groups of these (A), educational films (B), rather simple worked examples (C), and test questions for the main parts of the textbook (D). The book is provided with an index (pp. 579–592).

In contrast to the conventional practice of the Russian educational literature, F. Habashi's book luckily combines presentation of problems concerning both ferrous and nonferrous metallurgy under the common header "pyrometallurgy." Another important distinction of the book is an excellent set of illustrations, numerous clear photographs, including those in color, and graphic schemes not overburdened with unimportant details. F. Habashi's textbook can serve as an example of concise and clear presentation of a vast and important branch of metallurgy.

A. G. Morachevskii and I. N. Beloglazov

[1] For earlier F. Habashi's books, see *Zh. Prikl. Khim.*, 2000, vol. 73, no. 1, pp. 167–168; 2001, vol. 74, no. 10, p. 1724.

1070-4272/03/7602-0337 $25.00 © 2003 MAIK "Nauka/Interperiodica"

Russian Journal of Applied Chemistry, Vol. 76, No. 3, 2003, pp. 339–341. Translated from Zhurnal Prikladnoi Khimii, Vol. 76, No. 3, 2003, pp. 353–355.

INORGANIC SYNTHESIS AND INDUSTRIAL INORGANIC CHEMISTRY

Transformation of Calcium Sulfate Hemihydrate into Dihydrate upon Granulation in the Presence of Admixtures

L. P. Firsova

Moscow State University, Moscow, Russia

Received November 14, 2002

Abstract—The effect of admixtures on parameters of granules obtained from calcium sulfate hemihydrate in the course of pelletizing and stimulated phase transition into dihydrate was studied.

Large-tonnage production of phosphoric acid leads to accumulation of production waste in the form of phosphogypsum. A part of this waste is used as secondary raw material in manufacture of construction materials (gypsum cardboard, plaster, cement, etc.). At the same time, the amount of spent phosphogypsum materials increases annually by several millions of tons, thus contaminating the environment. Therefore, it is urgent to develop new methods for phosphogypsum utilization. For example, phosphogypsum can be used in melioration and plant growing as an important source of nutrients, microelements, and other biologically active substances [1, 2]. The amount of granulated meliorant based on calcium sulfate hemihydrate is largely determined by the chemical composition, size distribution, and strength of granules, which are affected by physicochemical processes accompanying the transition of calcium sulfate hemihydrate into dihydrate. The topochemical transformation of $CaSO_4 \cdot 0.5H_2O$ into $CaSO_4 \cdot 2H_2O$, including that in the presence of rare-earth elements (REEs), was studied previously [3–5]. In this work, we studied how the bioactive admixtures of metal [manganese(II) and zinc(II) salts and boron (in the form of boric acid) affect granulation and the topochemical transformation of hemihydrate into dihydrate.

EXPERIMENTAL

Calcium sulfate hemihydrate from the Voskresensk Plant of Mineral Fertilizers was preserved prior to granulation to prevent premature phase transition into the dihydrate. Commercial powder was washed with several portions of hot saturated solution of $CaSO_4 \cdot 2H_2O$ and then with acetone to remove residual phosphoric acid and absorbed water, after which it was dried in air to remove acetone. The resulting $CaSO_4 \cdot 0.5H_2O$ powder consisted of 10–250-μm druses formed by hexagonal prisms 1 to 30 μm long. The preserved phosphogypsum contained 6.5–7.0% H_2O (based on anhydrite), which is higher than the theoretical value, i.e., a minor portion of hemihydrate had time to transform into the dihydrate. The $P_2O_{5\,tot}$ content in phosphogypsum was about 3.2–0.5%, and the powder porosity was 65.1%.

Calcium sulfate hemihydrate was granulated after moistening with aqueous solutions, which were unsaturated with respect to this salt and contained various additives. The wet mixtures were prepared by mixing a weighed portion of air-dry hemihydrate powder with a prescribed volume of aqueous solutions containing 1–5% bioactive salts (manganese or zinc sulfate) and acids (sulfuric, orthophosphoric, or boric). The liquid-to-solid (liq : sol) ratio for wetting the powder was optimized experimentally to obtain chiefly 2–8-mm spherical granules. When the liq : sol ratio was smaller than the optimal value determined for the wetting solution of the prescribed composition, the granulated mixture disintegrated on the plate or too small granules were formed. At the liq : sol ratios exceeding the optimal value, the water-logged mixture spreaded over the plate or coarse irregular clumps were formed instead of spherical granules. The powder was mixed with the solution for 30–60 s. After that, a wet mixture of a specified composition was transferred into a plate-like granulator. The granulator plate made of stainless steel was 250 mm in diameter and had a 75-mm-high edge. The rotation velocity of the plate was varied from 50 to 80 rpm; angle of inclination, from 20° to 40°; and granulation time, from 5 to 60 min.

Strengthening of granules was performed by matur-

1070-4272/03/7603-0339$25.00

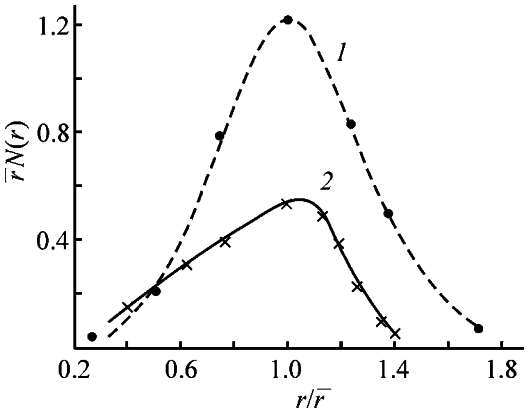

Fig. 1. Distribution $rN(\bar{r})$ of granules with respect to the relative size $r/\bar{r}$, depending on the type of acids added to calcium sulfate hemihydrate. Acid, wt %: (*1*) H_2SO_4, 3; (*2*) H_3BO_3, 2.

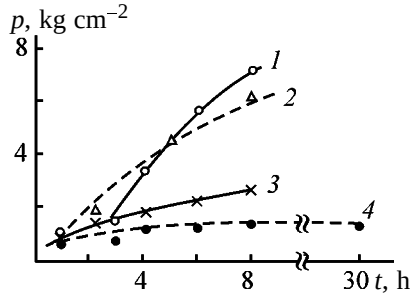

Fig. 2. Mechanical strength p of granules vs. the time t of maturing in the presence of various admixtures. Admixture, wt %: (*1*) H_2SO_4, 2.5; (*2*) $ZnSO_4$, 3.0 (maturing in a desiccator); (*3*) $ZnSO_4$, 2.0 (maturing in a solution); and (*4*) H_3BO_3, 2.0.

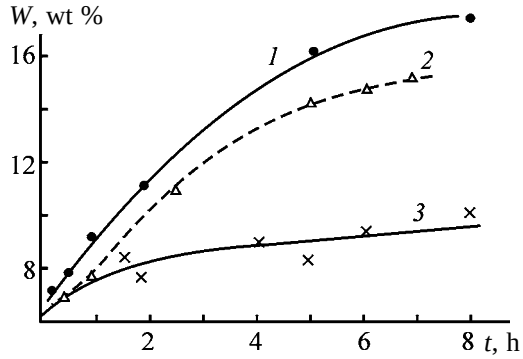

Fig. 3. Content of water of crystallization N in granules vs. the time t of maturing in the presence of various admixtures. Admixture, wt %: (*1*) H_2SO_4, 5.0; (*2*) $MnSO_4$, 3.0 (after 1 h of maturing in a solution); and (*3*) $MnSO_4$, 3.0 (after maturing in a desiccator).

ing. The $CaSO_4 \cdot 0.5H_2O$ granules obtained by pelletizing of a wet powder were carefully transferred from the granulator plate into special vessels, where they were strengthened owing to the topochemical transformation of the hemihydrate into the dihydrate $CaSO_4 \cdot 2H_2O$. Maturing was performed in a wet atmosphere in a dessicator and in the vessels with solutions similar in composition to the wetting solutions.

In the course of the pelletizing and maturing, portions of granules were taken to determine total water and water of crystallization. Absorbed water in the weighed portions of the powdered granules was determined from the mass loss after washing in acetone and drying in air to constant weight. Water of crystallization in air-dry granules and powders was determined thermogravimetrically after calcining the samples to constant weight.

The strength of the granules of a certain size in various stages of maturing and topochemical transition was evaluated from the breaking stress, as the average value obtained in 15–20 replicate measurements on an extensometer. The granules were sampled by sieving through metallic or Nylon sieves. Prior to sieving, wet granules were dried from the surface with a filtering paper.

The results of the study are presented in Figs. 1–3. It was shown that the total moisture content of the charge necessary for maturing, ensuring formation of 1–5-mm granules, was virtually independent of the type of admixture in a wetting solution (27–34%). At the indicated moisture content and under the similar granulation conditions (angle of plate inclination, rotation velocity, and maturing time), the average size of the obtained granules and the character of their size distribution are largely determined by the composition of the wetting solution (Fig. 1). On moistening the charge with solutions containing sulfuric or phosphoric acid, the size distribution density exhibits no marked deviations from the normal distribution. The same is true for manganese and zinc sulfate admixtures. At the same time, in the presence of boric acid, the portion of small granules increases asymmetrically, i.e., deviation from the normal distrubution is observed.

A study of breaking of the 2–3- and 3–5-mm granules obtained and matured under the similar conditions using different wetting solutions showed that the strength and strengthening kinetics also depend on the composition of the wetting solution (Fig. 2).

The granules formed in the presence of boric acid admixture have the minimal strength. Probably, this fact can also be responsible for the particular granulometric distribution of the product obtained in pelletizing of the H_3BO_3-containing charge.

As follows from Figs. 2 and 3, the granule strength-

ening kinetics correlates with the kinetics of the uptake of water of crystallization and reflects the topochemical transformation of the hemihydrate into dihydrate. The kinetics of the uptake of water of crystallization and the corresponding stages of the phase transition (Fig. 3) show that the transformation of calcium sulfate hemihydrate into dihydrate starts virtually simultaneously with the onset of wetting of the phosphogypsum powder, with the phase transition rates during maturing and pelletizing of granules dependent on the composition of wetting solutions and the type and content of admixtures in them.

CONCLUSION

Results obtained in measuring the size and strength of granules obtained in pelletizing of phosphogypsum moistened with solutions containing admixtures of sulfuric, phosphoric, or boric acid and of manganese or zinc sulfate show that the parameters of the granulometric distribution and the breaking stress of granules depend on the type and content of admixtures introduced into the batch being pelletized. These dependences correlate with the corresponding dependences depicting the uptake of water of crystallization and the stages of the topochemical transformation of calcium sulfate hemihydrate into dihydrate.

REFERENCES

1. USSR Inventor's Certificate no. 1 724 655.
2. USSR Inventor's Certificate no. 1 724 654.
3. Berdonosova, D.G., Burlakova, E.V., Ivanov, L.N., and Melikhov, I.V., *Zh. Prikl. Khim.*, 1989, vol. 62, no. 2, pp. 245–250.
4. Melikhov, I.V., Rudin, V.N., and Vorob'eva, L.I., *Izv. Akad. Nauk SSSR, Neorg. Mater.*, 1988, no. 3, pp. 448–452.
5. Melikhov, I.V., Rudin, V.N., and Vorob'eva, L.J., *Mendeleev Commun.*, 1991, no. 1, pp. 33–34.

Russian Journal of Applied Chemistry, Vol. 76, No. 3, 2003, pp. 342–345. Translated from Zhurnal Prikladnoi Khimii, Vol. 76, No. 3, 2003, pp. 356–359.

INORGANIC SYNTHESIS AND INDUSTRIAL INORGANIC CHEMISTRY

Method for Enhancing the Stability of Potassium Fluoride Hydrogen Peroxide Solvates $KF \cdot nH_2O_2$ (n = 1, 1.5, 2)

V. V. Buyanov, V. P. Nikol'skaya, K. V. Titova, and I. P. Suprun

State Research Institute of Biological Instrument Making, State Scientific Center, Moscow, Russia
Institute of Problems of Chemical Physics, Chernogolovka, Russia

Received August 28, 2002

Abstract—The possibility of enhancing the stability of potassium fluoride hydrogen peroxide solvates by adding various chemical compounds was examined. Solid inorganic and organic acids, amines, and related compounds, and also their mixtures were tested.

Potassium fluoride hydrogen peroxide solvates $KF \cdot nH_2O_2$ (n = 1, 2) are among the most stable compounds containing hydrogen peroxide. The high decontaminating activity of this group of hydrogen peroxide solvates and their stability made it possible to develop a series of disinfectants based on $KF \cdot nH_2O_2$ [1] with a wide spectrum of antimicrobial effect.

Samples of $KF \cdot nH_2O_2$ obtained under laboratory conditions by the removal of water and excess H_2O_2 from a solution of KF in aqueous hydrogen peroxide in a vacuum at 40–60°C decompose with the following rates (% day^{-1}): $KF \cdot H_2O_2$, 0.0124 (observation time τ = 10 years); $KF \cdot 1.5H_2O_2$, 0.0374 (τ = 7 years); and $KF \cdot 2H_2O_2$, 0.0282 (τ = 8 years) [1].

As other solid forms of hydrogen peroxide, potassium fluoride hydrogen peroxide solvates undergo catalytic decomposition under the action of trace impurities originating from the starting substances, air, and surface of vessels and tools during the synthesis. As compared to the samples dehydrated in a vacuum, the samples of $KF \cdot nH_2O_2$ dried in a flow of heated air, and also those prepared in a metallic vessel on a model installation with a film rotary evaporator, are less stable [1]. For example, $KF \cdot 1.5H_2O_2$ or samples of similar compositions kept for one year decompose with the following rates (% day^{-1}): 0.0085 (dried in a vacuum), 0.0131 (dried with heated air), and 0.055 (dried in a rotary evaporator). The considerable increase in the decomposition rate in going from drying in vacuum to drying under conditions similar to those used in industry shows that it is necessary to develop measures for stabilizing the hydrogen peroxide solvates, especially in the case of their long-term storage.

In this work we developed procedures for stabilizing potassium fluoride hydrogen peroxide solvates using compounds of various types: acids, acid salts, amines, other compounds with complexing properties, and also their mixtures.

EXPERIMENTAL

Potassium fluoride forms the following solvates with hydrogen peroxide: $KF \cdot H_2O_2$, $KF \cdot 2H_2O_2$, and $KF \cdot 3H_2O_2$ [2]. The trisolvate is unstable. The other two solvates are sufficiently stable to be used as disinfectants. The equimolar mixture of the mono- and disolvates with the overall composition $KF \cdot 1.5H_2O_2$ also appeared to be stable.

We studied the influence of various additives on the stability of hydrogen peroxide solvates using laboratory samples obtained by dehydration in a vacuum. Stabilizing components were introduced into a solution of hydrogen peroxide and added to solid potassium fluoride dihydrate. The amount of the additives did not exceed 1%, because it was found with others hydrogen peroxide solvates that an increase in the amount of the added stabilizers often decreases the stability of samples owing to the deterioration of crystallization conditions and formation of poor-quality crystals with the reduced stability [3].

The kinetic curves of the thermal decomposition were obtained using potassium fluoride hydrogen peroxide monosolvate $KF \cdot H_2O_2$ in the pure state and also with acid additions. The experiments were carried out in a device described earlier [4]. To study the stability in prolonged storage, we chose the solvate $KF \cdot 1.5H_2O_2$ containing more hydrogen peroxide. The samples were stored in polymer reservoirs in the dark at 20 ± 2°C. As the comparative characteristic we used the coefficient of the decomposition rate K

1070-4272/03/7603-0342$25.00

Table 1. Stability of $KF \cdot H_2O_2$ in the presence of additives [4]. Amount of stabilizing agent 1 wt % relative to $KF \cdot H_2O_2$

Stabilizing agent	$k_1 \times 10^3$ at 120°C	$k_{1\,\text{no stab}} : k_{1\text{stab}}$	*K*, wt % H_2O_2/day, at 50°C in indicated time, days			
			9	16	23	35
–	1.40	1	14.4	32.2	38.5	39.7
$KHSO_4$	0.41	3.4	0.7	0.9	1.8	2.6
Acid:						
oxalic	0.25	5.5	0.6	1.1	1.7	2.3
boric	0.38	3.7	0	0	0.2	0.9
citric	0.54	2.6	0.5	1.1	1.6	2.2
KHF_2	0.15	9.3	0	0	0	0.2

(H_2O_2 loss, % day^{-1}) at the exposure time from 2 to 10 years. The decomposition rate of the samples after the first 2–3 months of storage became approximately constant.

Potassium fluoride hydrogen peroxide monosolvate decomposes under isothermal conditions in the temperature range 90–125°C. The rate constants of its decomposition in the pure state and in the presence of additions, calculated by Kolmogorov–Erofeev's equation

$$[-\ln(1 - \eta)]^{1/3} = k(\tau - \tau_0),$$

are listed in Table 1. For pure $KF \cdot H_2O_2$ without additions, the rate constant is $k_1 = 1.40 \times 10^{-3}$ min^{-1} at 120°C. The kinetic curves taken in the presence of additions at the same temperature give considerably smaller (by a factor of 2–9) rate constants. The stability of these samples in storage at elevated temperatures appreciably grows.

To study the stability of $KF \cdot 1.5H_2O_2$ in long-term storage, we used not only acids and acid salts, but also other compounds. The data for the compounds that, according to preliminary kinetic data, showed a stabilizing effect are listed in Table 2.

It is seen that inorganic and organic acids exhibit a noticeable stabilizing effect with respect to potassium fluoride sesquisolvate in its long-term storage, reducing the decomposition coefficient by a factor of no less than 2.5. Benzoic, salicylic, and acetylsalicylic acids show the highest stabilizing activity. Amines also have a high stabilizing activity. Mixed stabilizing agents act in various ways. Citric acid in a mixture with oxalic acid or hexamethylenetetramine provides a double increase in the stability as compared to each of these compounds separately. The highest stabilization is reached when potassium hydrofluoride is added to $KF \cdot 1.5H_2O_2$: the rate of the solvate decomposition in the presence of 0.5% KHF_2 decreases by a factor of 8.

It is difficult to unambiguously propose a mechanism responsible for the stabilizing effect of the compounds under study. The stabilizing agents found for $KF \cdot nH_2O_2$ are not a unique example of successful search for stabilizing additives to solid forms of hydrogen peroxide. Numerous stabilizing agents were suggested for $Na_2CO_3 \cdot 1.5H_2O_2$, which is commercially produced as a bleaching component of detergents. The main principle of their selection is based on the necessity to bind transition metal impurities into slightly soluble and catalytically low-active salts and to protect the solvate from the action of moisture [2]. The moisture adsorbed on crystals of sodium carbonate hydrogen peroxide solvate creates a microfilm of an alkaline solution in which hydrogen peroxide rapidly decomposes. However, along with additives that bind transition metals and prevent moistening of the solvate, there are numerous patents concerning the stabilization of sodium carbonate hydrogen peroxide solvate by compounds and mixtures lacking these two priority properties. The mechanism of their stabilizing effect has not been elucidated, nor has it been described even hypothetically.

The assumption that binding of trace transition metal impurities (Fe, Cr, Mn, Cu) with acids into difficultly soluble salts is the factor responsible for a decrease in their catalytic activity seems improbable in the case of potassium fluoride hydrogen peroxide solvates, as fluorides of these metals are also difficultly soluble. A reasonable explanation could be a shift of pH of the solution microfilm on the surface of $KF \cdot nH_2O_2$ crystals toward lower values as compared to the weakly alkaline medium free from stabilizing acids. However, the stabilizing effect of amines and related compounds remains unclear, as some of them, e.g., tetramethylammonium hydroxide, have proper-

Table 2. Stability of $KF \cdot 1.5H_2O_2$ in long-term storage in the presence of stabilizing additives

Stabilizing agent, wt %	τ, year	*K*, wt % H_2O_2/day	Relative increase in stability
	$KF \cdot 1.5H_2O_2$		
–	8	0.0374	1
Acid:			
acetic, 0.5	4.7	0.0097	3.8
benzoic, 0.5	3.8	0.0067	5.6
citric, 0.5	4.8	0.0149	2.5
oxalic, 1.0	6.6	0.0128	2.9
boric, 1.0	4.2	0.0166	2.2
salicylic, 1.0	3.7	0.0080	4.6
acetylsalicylic, 0.5	5.0	0.0076	4.9
KHF_2, 0.5	4.7	0.0050	7.5
Amines and related compounds:			
Na_2EDTA, 0.5	3.7	0.0103	3.6
urea, 0.5	4.6	0.0066	3.7
urethane, 0.5	6.5	0.0070	5.3
nitroguanidine, 0.5	3.8	0.0065	5.8
$(CH_3)_4NOH$, 0.5	3.8	0.0059	6.3
diphenylguanidine, 0.5	6.4	0.0138	2.7
diphenylamine, 0.5	3.6	0.0070	5.3
hexamethylenetetramine, 0.5	0.3	0.0145	2.6
Other (mixed) stabilizing agents:			
Detergent (Lotos for machine washing), 0.5	4.2	0.0152	2.4
Na_2SiO_3, 0.5	3.6	0.0165	2.3
sodium stearate, 0.5	5.0	0.0099	3.8
Na_2EDTA, 0.5 + urea, 0.5	4.3	0.0132	2.8
citric acid, 0.5 + hexamethylenetetramine, 0.25	3.9	0.0079	4.7
citric acid, 0.5 + oxalic acid, 0.25	3.5	0.0059	6.3
salicylic acid, 0.1 + hexamethylenetetramine, 0.25	3.9	0.0091	4.1
salicylic acid, 0.5 + hexamethylenetetramine, 0.5	3.9	0.0069	5.4
	PKF-2		
–	5.0	0.0402	1
KHF_2, 0.5	5.0	0.0061	6.7

Table 3. Stability of PFK-1 and PFK-3 samples at 20 ± 2°C in the presence of acid additives

Stabilizing agent, wt %	τ, year	*K*, wt % H_2O_2/day	Relative increase in stability
	PFK-1		
–	10.0	0.0124	1
KHF_2:			
0.5	6.7	0.0013	9.5
1.0	10.0	0.0052	2.4
KHF_2, 1.0 + sulfonol, 0.5	8.3	0.0025	5.9
Acetylsalicylic acid, 0.5	1.8	0.0028	4.4
Acetylsalicylic acid, 0.1 + Sulfonol, 0.14	4.7	0.0068	1.8
Sulfanilic acid, 0.1 + Sulfonol, 0.25	3.2	0.0062	2.0
	PFK-3		
–	8.1	0.0282	1
Acid:			
citric, 0.1	6.0	0.0249	1.1
oxalic, 0.1	6.4	0.0232	1.1
KHF_2, 0.1	4.3	0.0042	6.7

ties of strong bases and shift the pH to the opposite direction.

The stabilizing agents effective for $KF \cdot 1.5H_2O_2$ obtained under laboratory conditions were used to prepare disinfecting agents based on potassium fluoride hydrogen peroxide solvates: PFK-1 (based on $KF \cdot H_2O_2$), PFK-2 (based on $KF \cdot 1.5H_2O_2$), and PFK-3 (based on $KF \cdot 2H_2O_2$). The samples were prepared on a model installation using a film rotary evaporator for drying.

The stabilizing effect of the compounds on the PFK-2 sample is similar to their action on the laboratory samples of $KF \cdot 1.5H_2O_2$ (this is shown in Table 2 with the most striking example of the stabilization with KHF_2).

The data on the stabilization of PFK-1 sample with the stabilizing agents that are the most effective for $KF \cdot 1.5H_2O_2$ are shown in Table 3.

Comparison of Tables 2 and 3 shows that the pure PFK-1 sample is approximately three times as stable as PFK-2. In the presence of additives, the degree of the increase in the stability of the PFK-1 sample is the same as in the case of PFK-2.

The data on the effect of additives on the stability of the PFK-3 sample, the richest in hydrogen peroxide, are given in Table 3. It is seen that the pure PFK-3 sample in the case of its long-term storage is somewhat more stable than the PFK-2 sample. This is probably due to the fact that the PFK-3 sample is based on the pure hydrogen peroxide solvate $KF \cdot 2H_2O_2$, whereas the base of the PFK-2 sample is a mixture of two compounds, namely, potassium fluoride mono- and disolvates, which, apparently, prevents formation of the well-shaped crystals of the solvates in their joint crystallization and leads to reduced stability of the sample. In the case of the PFK-3 sample, only potassium hydrofluoride retains a stabilizing effect, increasing the sample stability by a factor of 6.7. The other additives (citric and oxalic acids) only slightly reduce the decomposition coefficients.

We have selected potassium hydrofluoride as the main stabilizing agent for PFK preparations. The disinfectants obtained with this agent have passed tests successfully and have been accepted for the production and application in the Russian Federation [1].

CONCLUSIONS

(1) Various procedures were considered for the stabilization of potassium fluoride hydrogen peroxide solvates and also of disinfectants based on them. Addition of solid organic acids to the solvates in the amount of 0.5–1.0 wt % decreases the rate of their decomposition in long-term storage ($20 \pm 2°C$) by a factor of 3–5; addition of amines, by a factor of 3–6; and addition of potassium hydrofluoride, by a factor of 7–9.

(2) The most effective stabilizing agent KHF_2 was used to obtain the PFK-1, PFK-2 and PFK-3 disinfectants, which were tested under actual operation conditions. The decomposition rate of the samples with KHF_2 added, at the shelf life of no less than 5 years, is as follows: PFK-1 0.0013, PFK-2 0.0050, and PFK-3 0.0042 % day^{-1}.

REFERENCES

1. Buyanov, V.V., Nikol'skaya, V.P., Pudova, O.P., *et al*., *Peroksosol'vaty v dezinfektologii* (Hydrogen Peroxide Solvates in Disinfection Science), Chernogolovka: Inst. Problem Khim. Fiz., Ross. Akad. Nauk., 2000.
2. Titova, K.V., Nikol'skaya, V.P., and Buyanov, V.V., *Koordinatsionnye soedineniya peroksida vodoroda* (Coordination Compounds of Hydrogen Peroxide), Inst. Problem Khim. Fiz., Ross. Akad. Nauk., 2000.
3. Titova, K.V., Kolmakova, E.I., and Rosolovskii, V.Ya., *Zh. Neorg. Khim.*, 1985, vol. 30, no. 9, pp. 2222–2227.
4. Titova, K.V., Kolmakova, E.I., and Rosolovskii, V.Ya., *Fiziko-khimicheskie svoistva i sposob stabilizatsii peroksogidrata karbonata natriya* $Na_2CO_3 \cdot 1.5H_2O_2$ (Physicochemical Properties and Ways of Stabilization of Sodium Carbonate Hydrogen Peroxide Solvate $Na_2CO_3 \cdot 1.5H_2O_2$), Available from VINITI, Moscow, March 2, 1983, no. 1254–84.

Russian Journal of Applied Chemistry, Vol. 76, No. 3, 2003, pp. 346–350. Translated from Zhurnal Prikladnoi Khimii, Vol. 76, No. 3, 2003, pp. 360–364.

INORGANIC SYNTHESIS AND INDUSTRIAL INORGANIC CHEMISTRY

Conditions for the Chemical Precipitation of the Starting Substances from Solutions for the Synthesis of Aluminospinels

A. E. Sokolovskii, N. M. Bobkova, and E. V. Radion

Belarussian State Technological University, Minsk, Belarus

Received October 22, 2002

Abstract—The precipitation of hydroxides from the Mg^{2+}–Al^{3+}–An^{-}–H_2O system (An = NO_3^-, Cl^-, SO_4^{2-}) at the initial spinel molar ratio Mg^{2+} : Al^{3+} = 1 : 2 was studied. The optimal conditions were found for obtaining the precipitates exhibiting the best properties in the manufacturing sense; their subsequent heat treatment yields a single phase of aluminomagnesium spinel.

Aluminomagnesium spinel is a promising structural material combining a number of valuable properties [1–3]. It is difficult to obtain a compact ceramics from spinel, though numerous attempts were undertaken to carry out such a synthesis using mineralizers, pulverizing pyrolysis, and thermal treatment of polycrystalline samples of oxide mixtures [1, 4]. One of possible ways to prepare high-density oxide ceramics may be the coprecipitation of ultrafine powders followed by thermal decomposition of the intermediate product.

According to [5], the use of ultradispersed powders with the particle sizes less than 1 μm, obtained by coprecipitation from concentrated solutions of salts, makes it possible to reduce the temperature of sintering ceramic products based on aluminomagnesium spinel to 1600°C. Moreover, it is possible to obtain the stoichiometric MgO–Al_2O_3 spinel as powders with a prescribed degree of dispersion by adjusting the pH and temperature of solutions [6]. Contrary to the traditional method of synthesizing powders of the $MgAl_2O_4$ spinel by a solid-phase reaction between the oxides at 1600°C, their preparation by coprecipitation from aqueous solutions reduces the temperature of the spinel synthesis (1450°C) and increases the activity of the powders [7]. When magnesium and aluminum nitrates are used as starting materials, the powders contain only the spinel phase with the average particle size of about 14 μm, and when chlorides are used, traces of Al_2O_3 are detected in the powders along with the spinel phase, the average size of the spinel particles being about 12 μm [7].

The aim of this work was to study the precipitation of hydroxides in the Mg^{2+}–Al^{3+}–An^{-}–H_2O system and to substantiate the optimal conditions for obtaining precipitates for the subsequent synthesis of the single-phase aluminomagnesium spinel $MgO \cdot Al_2O_3$ at a temperature as low as possible.

EXPERIMENTAL

We studied the precipitation of hydroxides in the Mg^{2+}–Al^{3+}–An^{-}–H_2O system by pH-metric titration (an I-160 pH meter equipped with a microprocessor and a temperature-controlled cell), turbidimetric titration (an FEK-56M photocolorimeter with a TPR titration outfit), and chemical analysis.

We used 1 M solutions of aluminum and magnesium nitrates, chlorides, and sulfates (analytically pure grade) as the starting solutions for obtaining hydroxides. The concentration of magnesium(II) was determined by complexometric titration with Eriochrome Black T in ammonia buffer [8], and the concentration of aluminum(III), by complexometric back-titration with a zinc salt and Xylenol Orange in an acidic solution [9].

To study the precipitation, we prepared 0.4 M solutions with the exact ratio Mg^{2+} : Al^{3+} = 1 : 2. A 1 M KOH (analytically pure grade) solution was a precipitating agent. The pH was monitored with an I-160 pH meter. The equilibrium pH after adding the KOH solution was attained slowly; therefore, we determined pH in 1 h after adding the whole amount of the alkali.

After separating the precipitate by filtration, we determined the residual amounts of magnesium(II) and aluminum(III) in the filtrate as described above. Under these conditions, Mg^{2+} ions, which were present in

1070-4272/03/7603-0346$25.00

combination with Al^{3+} ions, did not interfere with the determination of Al^{3+}, whereas Al^{3+} ions interfered with the determination of Mg^{2+}, as they bound the indicator. Therefore, we used triethanolamine to mask Al^{3+} ions [10].

The aim of the pH-metric studies was to find regular trends in the precipitation of Mg^{2+} and Al^{3+} hydroxides. In these experiments, we varied the temperature (25 and 40°C) and composition of the solution being titrated (solutions of Mg^{2+}, Al^{3+}, and Mg^{2+}–Al^{3+}). A 0.1 M KOH solution was the titrant (Fig. 1). The titration curves of the solutions for each composition at 25 and 40°C are almost indistinguishable, i.e., the temperature only slightly affects the precipitation.

A single weakly pronounced step is observed in the curves of pH-metric titration of 0.01 M Mg^{2+} solution at the OH/M ratio of about 2 (Fig. 1a). The buffer region of the titration curve is in the range of pH ~10–10.5. As the first drops of alkali are added, pH almost immediately reaches 10, and the hydroxide starts to precipitate.

The buffer region corresponding to the hydrolysis of aluminum(III) in the range pH 3–4 starts in the titration curves of the 0.01 M solution of Al^{3+} immediately after adding the first portions of alkali. At the end of this region, a single step is observed at the OH/M ratio of about 3 (Fig. 1b). The hydroxide starts to precipitate at the onset of the step at pH ~5; the precipitation is complete at the end of the step at pH ~11. On the further addition of alkali, the precipitate of aluminum hydroxide dissolves to give hydroxoaluminate ions. However, this process occurs without any steps in the titration curves.

The buffer region in the titration curves of the Mg^{2+}–Al^{3+} solution with the molar ratio $Mg^{2+}:Al^{3+}$ = 1 : 2 (the same as in spinel) starts just after adding the first portions of alkali. This region corresponds to the aluminum(III) hydrolysis and lies at pH ~4–5 as in the titration curves of pure Al^{3+} (Fig. 1c). It ends with a step at OH/M ≈ 2, which corresponds to the complete transformation of aluminum(III) into aluminum hydroxide. After the end of the step, a short buffer region is observed at pH ~9. This region is completed with the second step at the OH/M ratio of about 2.5–2.75, which corresponds to the end of the magnesium(II) hydrolysis. At the same time, the titration curves of the ion mixture show some distinctive features. When magnesium(II) is titrated (Fig. 1a), the buffer region before the step is in the range of pH ~10–10.5. The titration of aluminum(III) is completed at almost the same pH (Fig. 1b). In the titration curve of the mixture, the buffer region at pH ~9 corresponds to the titration of magnesium(II) after the complete neutralization of Al^{3+}. Correspondingly, the step at the end of the magnesium(II) titration is substantially larger than in the case of the titration of pure Mg^{2+}. This means that the precipitate of aluminum(III) hydroxide exerts certain effect on the precipitation of magnesium(II) hydroxide.

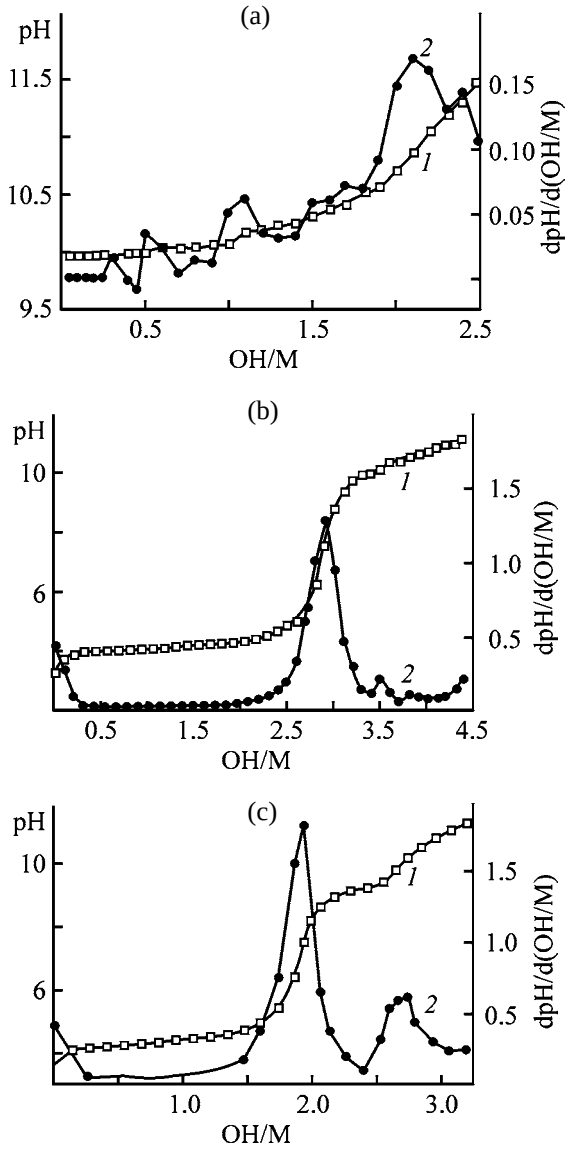

Fig. 1. Titration curves [(*1*) integal and (*2*) differential] of 0.01 M solutions of (a) Mg^{2+}, (b) Al^{3+}, and (c) Mg^{2+}–Al^{3+}.

The precipitation of hydroxides in the Mg^{2+}–Al^{3+}–NO_3^-–H_2O system was studied by the turbidimetric titration with an alkali, and the titration curves for aluminum(III), magnesium(II), and aluminum(III)–

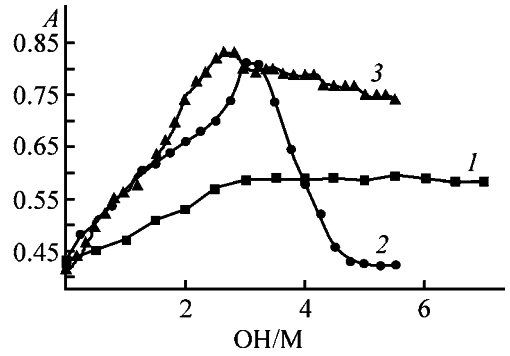

Fig. 2. Curves of turbidimetric titration of solutions of (*1*) Mg^{2+}, (*2*) Al^{3+}, and (*3*) Mg^{2+}–Al^{3+}. (*A*) Light absorption; the same for Fig. 3.

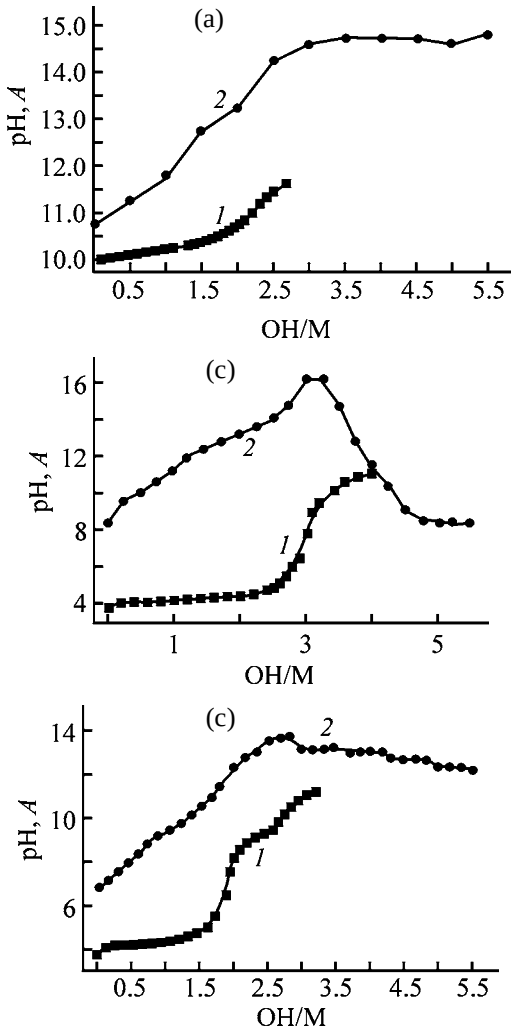

Fig. 3. Curves of (*1*) pH-metric (*2*) and turbidimetric titration of solutions of (a) Mg^{2+}, (b) Al^{3+}, and (c) Mg^{2+}–Al^{3+}.

magnesium(II) solutions were obtained (Fig. 2). The experimental technique and conditions were as follows. The apparent light absorption A_{app} of a colorless suspension was measured with a yellow–green color filter in a cell with the 25-mm-thick absorbing layer, which ensured the measurement of A_{app} under optimal conditions. Before the beginning of the titration, the starting spinel molar ratio $Mg^{2+} : Al^{3+}$ = 1 : 2 was set in the solution. The titrating agent was 0.1 M KOH. To construct the titration curves, we recalculated the added volume of alkali to the OH/M ratio.

As the alkali was added in the course of the turbidimetric titration, precipitates were gradually formed, and, correspondingly, the turbidity of all the solutions in the initial portions of the curves increased (Fig. 2, curves *1–3*). The precipitation of magnesium(II) was complete at OH/M = 2.5, as above this value the turbidity remained unchanged (Fig. 2, curve *1*). The titration curve of aluminum(III) has a more complicated shape (Fig. 2, curve *2*), which is caused by the amphoteric nature of its hydroxide. The precipitate is formed up to OH/M = 3 (A_{app} increases), whereas at OH/M > 3.25 it dissolves, as evidenced by the fact that the solution turbidity decreases as alkali is added. At OH/M ≈ 4.75, A_{app} does not noticeably change since the precipitate has completely dissolved. The titration curve of the aluminum(III)–magnesium(II) solution (Fig. 2, curve *3*) differs from both curves described above. The main difference is associated with the fact that aluminum(III) hydroxide does not dissolve in the presence of magnesium(II). Consequently, during joint precipitation of the hydroxides, a chemical reaction between the ions occurred. The maximal amount of the precipitate determining the maximal A_{app} values is formed in the range of OH/M = 2.5–2.8. At OH/M ≈ 3.0, the precipitate partially dissolves; however, the decrease in the turbidity is insignificant as compared to the titration curve of aluminum(III).

To compare the data obtained by two independent methods, we plotted the curves of turbidimetric and pH-metric titration in Fig. 3. To bring the curves to the same scale along the *y*-axis, the A_{app} values were normalized in the course of the computer processing by multiplying by a correction coefficient. The turbidity of the solutions changes only at the expense of the formation or dissolution of precipitates, and pH is determined by several processes occurring successively and in parallel. Hence, by comparing the curves obtained, we can refine the optimal pH range within which the precipitation becomes complete. To do this, we must draw a perpendicular from the maximum point in the $A_{app} = f(\text{OH/M})$ curve to the *x*-axis. Then, from the point of its intersection with the pH = f(OH/M) curve, we must draw a perpendicular to

Influence of pH and starting salts on the completeness of Mg^{2+} and Al^{3+} precipitation

Compound	*T*, °C	pH	Residual concentration, M	
$Mg(NO_3)_2 + Al(NO_3)_3$	20	10.97	0.0003	0.012
	20	11.38	0.00015	0.0038
	20	10.39	0.0005	0.0009
	65	11.12	0.00015	0.0178
	20	9.78	0.0005	0.00067
	20	12.05	0.000125	0.083
$MgCl_2 + AlCl_3$	20	10.56	0.000375	0.0069
	20	8.86	0.00425	0.0001
	20	9.66	0.00045	0.0001
$MgSO_4 + Al_2(SO_4)_3$	20	10.98	0.00031	0.0135
	20	9.47	0.000525	0.000375
	20	9.26	0.001	0.0025

the *y*-axis and determine the pH value. For magnesium(II) it is 11.5 (Fig. 3a), for aluminum(III), 8.9–9.9 (Fig. 3b), and for the solution containing both ions, 9.5–10.0 (Fig. 3c). It is noteworthy that, in all the cases, the pH value determined by this procedure appears to be higher than the pH in the points of equivalence.

These results are in full agreement with the experimental data on the apparent volume of the precipitates [11]. Specifically in the above-given pH ranges the precipitates have the smallest volume, are deposited quickly, and are easily filtered, i.e., they are the most compact and the easiest to process [11]. Therefore, based on the data obtained by the three independent methods, the range of OH/M = 2.5–2.7 is optimal.

As follows from the results of pH-metric and phototurbidimetric titration, Mg^{2+} and Al^{3+} hydroxides are precipitated in a fairly wide pH range. At the same time, to obtain hydroxide precipitates that will be subsequently used as precursors for obtaining spinels, the stoichiometric ratio $Mg^{2+} : Al^{3+} = 1 : 2$ must be kept. Therefore, to find the optimal pH range and examine the influence of the anion, we studied the precipitation of aluminum(III) and magnesium(II) hydroxides at different pH using different Mg^{2+} and Al^{3+} salts. The results (table, Fig. 4) show that the dependences of the residual ion concentrations on pH of the Mg^{2+} and Al^{3+} solutions differ from each other. At low pH, Mg^{2+} ions are precipitated incompletely, and at high pH so do Al^{3+} ions. Temperature does not exert a substantial effect on the precipitation completeness but affects the rate of the equilibrium attainment. The optimal pH range in which Mg^{2+} and Al^{3+} precipitate almost completely is 9.5–10.5, which corresponds to the second step in the titration curve (Fig. 1c). Such a value of pH can be obtained when using ammonium hydroxide as a precipitant. According to the reference data on the precipitation of Mg^{2+} and Al^{3+} ions from their individual solutions [10], on the one hand, Mg^{2+} ions should not precipitate in the range of pH 9.5–10.5, and on the other hand, Al^{3+} ions should be converted almost completely into hydroxoaluminate ions. Therefore, the chemical analysis of the filtrate suggests a chemical reaction between Mg^{2+} and Al^{3+} ions during the precipitation with alkali.

It was found that heating of the samples synthesized under the above-given optimal conditions to 1000°C results in 41.07–43.57% weight loss [11]. This is almost twice lower than the weight loss reported in [5] for the samples prepared in a similar manner. The weight loss is completed at a lower temperature compared to the other precipitates, especially those obtained from nitrate solutions (865°C instead of 1000–1100°C) [11]. Moreover, the peaks corresponding to the interplanar spacings typical for the $MgO \cdot Al_2O_3$ spinel (0.2014, 0.243, 0.143 nm) were

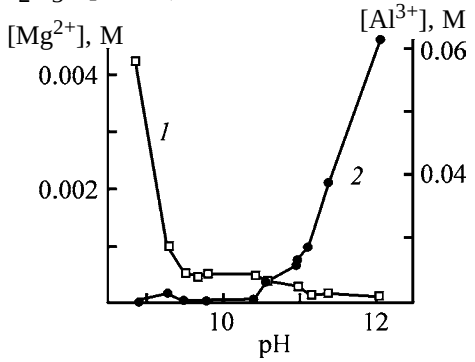

Fig. 4. Influence of pH on residual concentrations of (*1*) Mg^{2+} and (*2*) Al^{3+} ions.

observed even in the samples calcined at 320°C, and this is the only phase detected in the temperature range 320–1250°C.

The results of our studies allow us to develop scientific principles of synthesizing the $MgO \cdot Al_2O_3$ spinel from chemically precipitated mixtures. This will allow preparation of the spinel in a highly dispersed state with a high yield and the subsequent sintering of materials based on it at a considerably lower temperature.

CONCLUSIONS

(1) The optimal pH range for the precipitation of precursors for the synthesis of aluminomagnesium spinel was found by a combination of independent research methods.

(2) The single phase of aluminomagnesium spinel is formed by the heat treatment of the precipitates obtained under the optimal conditions.

REFERENCES

1. Hamano, K., Hakagawa, Z., and Sakaguchi, M., *Rep. Res. Lab. Eng. Mater. Tokyo Inst. Technol.*, 1984, vol. 50, no. 9, pp. 101–111.
2. Evans, A.G. and Langdon, T.G., *Structural Ceramics*, Oxford: Pergamon, 1976.
3. Hori, S., Yoshimura, M., and Somiya, S., *Mater. Sci. Lett.*, 1985, vol. 4, no. 4, pp. 413–417.
4. Toropov, N.A. and Sirazhiddinov, N.A., *Uzb. Khim. Zh.*, 1963, no. 5, pp. 38–42.
5. Chemekova, T.Yu. and Filippova, O.L., *Izv. Akad. Nauk SSSR, Neorg. Mater.*, 1990, vol. 26, no. 3, pp. 656–657.
6. Witkowski, T.S. and Munro, J.B., *Refract. J.*, 1989, vol. 64, pp. 437–442.
7. Louci, M., Arvunescu, I., and Eustafievici, M., *Mater. Constr.*, 1993, vol. 23, no. 1, pp. 54–56.
8. Schwarzenbach, G. und Flaschka, H., *Die komplexometrische Titration*, Stuttgart: Ferdinand Enke, 1965.
9. Petrukhin, O.M., *Analiticheskaya khimiya* (Analytical Chemistry), Moscow: Khimiya, 1992.
10. Lur'e, Yu.Yu., *Spravochnik po analiticheskoi khimii* (Handbook on Analytical Chemistry), Moscow: Khimiya, 1989.
11. Bobkova, H.M., Radion, E.V., and Sokolovskii, A.E., *Steklo Keram.*, 2002, no. 9, pp. 16–18.

Russian Journal of Applied Chemistry, Vol. 76, No. 3, 2003, pp. 351–357. Translated from Zhurnal Prikladnoi Khimii, Vol. 76, No. 3, 2003, pp. 365–372.

INORGANIC SYNTHESIS AND INDUSTRIAL INORGANIC CHEMISTRY

Effect of Peptization on Texture and Physicomechanical Properties of Aluminum Hydroxides

A. A. Lamberov, O. V. Levin, S. R. Egorova, D. A. Evstyagin, and A. G. Aptikasheva

Kazan State Technological University, Kazan, Tatarstan, Russia
Novokuibyshevsk Catalyst Plant, Public Joint-Stock Company, Novokuibyshevsk, Samara oblast, Russia

Received February 27, 2002

Abstract—The method of low-temperature adsorption of nitrogen was applied to study structural characteristics of commercial peptized aluminum hydroxides. An increase or decrease in the porometric volume, depending on the nature and concentration of the peptizing agent, was analyzed. The phenomena observed are explained in terms of the mechanism suggested for formation of the pore system in commercial aluminum hydroxides. The dependence of the physicomechanical properties of active aluminum oxide on synthesis conditions and texture characteristics of commercial aluminum hydroxides was studied.

It is known that texture is formed in active aluminum oxide (AAO) not only during precipitation of aluminum hydroxide (AH), but also in the course of subsequent process operations. One of stages of the process used to obtain γ-Al_2O_3 by reprecipitation of alumina is peptization of washed hydroxide with pseudoboehmite morphology. This procedure is performed to impart to AH masses the necessary thixotropic and strength characteristics [1–4].

As a rule, commercial AHs are blended, i.e., obtained by mixing in a necessary ratio (most frequently, 1 : 1) hydroxides formed by hot and cold (after stabilization) precipitation. The influence exerted by the conditions of industrial precipitation and stabilization on the AH structure was studied previously [5].

The aim of this study was to analyze the influence exerted by the nature and concentration of a peptizing agent on the texture of cold- and hot-precipitated AH, and a mixture of these, and to reveal a correlation between the texture and physicomechanical properties of industrial AH.

EXPERIMENTAL

Aluminum hydroxides were synthesized under industrial conditions by the method of batch precipitation using the sulfate process. Blended AHs were prepared by mixing cold- and hot-precipitated hydroxides in 0.8 : 1.0 ratio. The peptization was done by treating AH with mineral acid solutions in a mixing machine at 160°C. The measurement conditions have been described previously [5].

The mechanical strength was determined on a semiautomatic device with a knife with blade width of 0.8 mm [8]. The bulk density ρ_b was found using a vibrator device [8]. The porometric volume V_p and pore size distribution were calculated from the desorption branch of an isotherm by the standard Barrett–Joyner–Highland procedure [6, 7].

It is known [6, 9] that cold-precipitated AH have the most labile structure because of the weak intercrystallite bonds (coagulation contacts, van der Waals interactions) between primary particles and the considerable content of interlayer water in the unit cell of pseudoboehmite. Therefore, the influence exerted by the nature of peptizing agent on the texture of cold-precipitated AH was studied in the first place. The data obtained are listed in Table 1 and shown in Fig. 1a.

The hysteresis loop of the adsorption isotherm of the initial AH is of the H2 type, which points to the presence of bottle-shaped pores in fibrillar fragments of the gel-like pseudoboehmite.

The initial cold-precipitated AH (Fig. 1a) is characterized by a broad peak of height 0.007 $cm^3\ g^{-1}\ Å^{-1}$ in the pore size distribution at around 78 Å, which accounts for about 72% of the porometric volume. It may be assumed that the observed peak in the pore size distribution is a sum of two peaks at 72 and 90 Å with close heights. Also seen in the porogram are shoulders at 52 (~0.0045 $cm^3\ g^{-1}\ Å^{-1}$), 34 (0.0030 $cm^3\ g^{-1}\ Å^{-1}$), and 24 Å (0.0012 $cm^3\ g^{-1}\ Å^{-1}$). The specific surface area of AH is 225 $m^2\ g^{-1}$, and

1070-4272/03/7603-0351$25.00

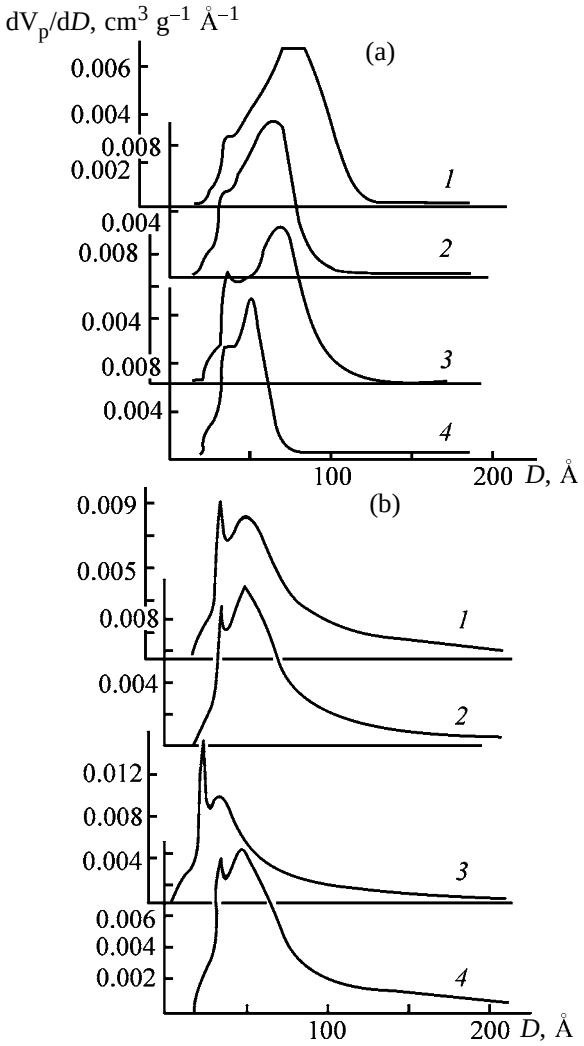

Fig. 1. Pore volume V_p distributions for (a) cold- and (b) hot-precipitated AH. (D) Pore diameter; the same for Fig. 3. (*1*) Initial AH; AH subjected to peptization with 0.04 M acid solution: (*2*) HNO_3, (*3*) H_3PO_4, and (*4*) CH_3COOH.

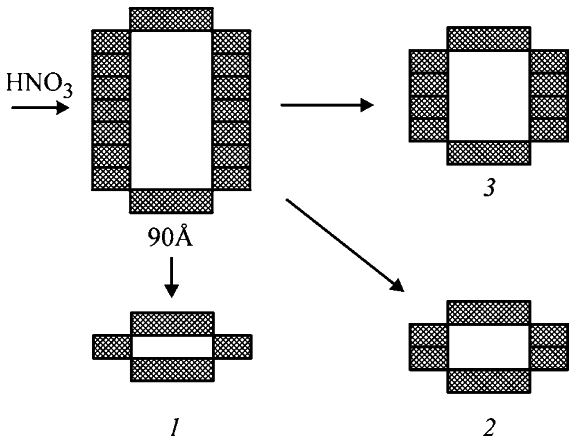

Fig. 2. Scheme of breakdown of pore-forming fragments of gel-like pseudoboehmite. Fragment: (*1*) I (D = 25 Å), (*2*) II (D = 36 Å), and III (D = 42 Å).

the porometric volume, 0.50 cm^3 g^{-1}.

Treatment with 0.4 M nitric acid shifts (Fig. 1a) the main peak (78 Å) with height of 0.0092 cm^3 g^{-1} Å^{-1}, which accounts for 61% of the porometric volume (0.28 cm^3 g^{-1}), to smaller values (72 Å). The heights of peaks in the pore size distribution increase by 60, 66, and 50% for the peaks at, respectively, 52, 34, and 24 Å. The specific surface area of AH increases by approximately 10% (from 225 to 257 cm^3 g^{-1} Å^{-1}), with the porometric volume remaining virtually unchanged. Peptization with 0.04 M acetic acid leads to complete disappearance of peaks at 72 and 90 Å, with only three peaks with much greater height observed in the porogram (Fig. 1a). As seen from Table 1, the heights of almost all peaks in the pore size distribution grow to the same extent, by a factor of 3, whence follows that CH_3COOH much exceeds HNO_3 in the peptizing activity.

Peptization with orthophosphoric acid breaks down the hydroxide to a lesser extent. The height of the peak in the pore size distribution at 90 Å decreases from 0.007 to 0.004 cm^3 g^{-1} Å^{-1}. The height of the peaks in the pore size distribution at 72 and 34 Å grows to a much greater extent than in the case of nitric acid, from 0.007 to 0.010 cm^3 g^{-1} Å^{-1} and from 0.003 to 0.007 cm^3 g^{-1} Å^{-1}, respectively.

The high reproducibility of the diameters of pores in AH and their discrete breakdown in peptization can be understood in terms of the previously suggested mechanism of AH texturing. It is most probable that the peptizing agent attacks places of contact between microcrystallites at (010) planes; breakdown of pore-forming fragments can be represented by the scheme in Fig. 2.

Probably, intermediate structures with another number of microcrystallites in the fragment coordinated along the *b* axis, which are not revealed in porograms of the samples studied, may also exist.

Starting from the fact that the porometric volume of AH remains virtually unchanged upon peptization, as also does the type of the hysteresis loop, it may be assumed that acid peptization leads to rearrangement of the pore system within fibrillar structures, with the liberated microcrystallites involved in formation of more "stable" AH fragments with pore size close to that of the already existing pores, which is indicated by the increase in the specific surface area of the hydroxide (Table 1). The most stable structural units in a fibrillar particle are, probably, fragments I and II, which contain the minimum number of coordinated particles.

Table 1. Effect of the nature of peptizing agent on the texture of cold-precipitated AH. Concentration of peptizing agent 0.04 M

Parameter*	Peptizing agent			
	absent	HNO_3	H_3PO_4	CH_3COOH
Cold precipitation				
$I \times 10^4$, $cm^3\ g^{-1}\ Å^{-1}$, for indicated diameter, Å:				
24	12	18	23	33
34	30	50	72	94
52	45	72	72	136
72–78	70	92	101	0
90	70	25	40	0
S_{sp}, $cm^2\ g^{-1}$	225	257	326	304
V_p, $cm^3\ g^{-1}$	0.50	0.49	0.61	0.46
V_p, $cm^3\ g^{-1}$, for indicated diameters, Å:				
8–50	0.11	0.17	0.33	0.33
50–100	0.361	0.369	0.427	0.284
D_{av}, Å	67	56	56	44
K_{av}, kg mm^{-1}	3.08	4.07	3.44	3.90
Grain diameter,** mm	2.11	2.16	2.41	2.18
ρ_b, g cm^{-3}	0.73	0.72	0.55	0.66
SO_3^{2-}, %	1.17	1.10	0.95	1.05
Na_2O, %	0.034	0.034	0.034	0.034
Hot precipitation				
$I \times 10^4$, $cm^3\ g^{-1}\ Å^{-1}$, for indicated diameter, Å:				
24	21	21	29	22
35	94	84	151	98
48	82	99	104	104
~60	75	81	63	80
S_{sp}, $cm^2\ g^{-1}$	319	319	364	333
V_p, $cm^2\ g^{-1}$	0.78	0.74	0.78	0.75
V_p, $cm^3\ g^{-1}$, for indicated diameters, Å:				
8–50	0.24	0.34	0.36	0.36
50–100	0.47	0.40	0.42	0.40
D_{av}, Å	72	66	65	64
K_{av}, kg mm^{-1}	0.78	1.53	1.51	0.94
Grain diameter,** mm	3.34	3.26	3.32	3.39
ρ_b, g cm^{-3}	0.28	0.34	0.34	0.30
SO_3^{2-}, %	0.62	0.81	0.72	0.82
Na_2O, %	0.032	0.032	0.032	0.032

* I, height of peaks in pore size distribution; $D_{av} = 4V_{des}/S_{des}$; K_{av}, average strength coefficient for Al_2O_3 grains.
** Die diameter 3.5 mm; the same for Table 2.

This is confirmed by the increase in the height of peaks in the pore size distribution at 25 and 36 Å upon peptization. Irrespective of the nature of the acid anion, the peptizing agent attacks the places of contact between pseudoboehmite microcrystallites [probably, at the (010) plane]], which is accompanied by partial deaggregation of the porous system. The peptizing activity of the acids studied, judged from the degree of breakdown of pores with largest diameters, decreases in the order $CH_3COOH > HNO_3 > H_3PO_4$.

Acid peptization leads to partial dissolution of the hydroxide to give basic salts, which, as shown in [10, 11], diffuse into the thinnest pores and fill them, thus reducing the contribution of these pores to the porometric volume. In the case of peptization with HNO_3 and CH_3COOH, the forming basic salts are

Table 2. Effect of the nature of peptizing agent on the texture and physicomechanical properties of blended AHs

Parameter	Peptizing agent, M, for indicated sample							
	no. 1, absent	no. 2, HNO_3, 0.007	no. 3, H_3PO_4, 0.008	no. 4, H_3BO_3, 0.010	no. 5, CH_3COOH, 0.010	no. 6, CH_3COOH, 0.020	no. 7, CH_3COOH, 0.020	no. 8, CH_3COOH, 0.040
$I \times 10^4$, $cm^3\ g^{-1}\ Å^{-1}$, for indicated diameter, Å:								
25	8	5	8	5	14	10	18	21
36	118	97	118	117	113	88	98	108
170	23	34	27	31	33	41	38	46
S_{sp}, $cm^2\ g^{-1}$	224	235	236	229	248	230	270	281
V_{des}, $cm^3\ g^{-1}$	0.587	0.668	0.607	0.617	0.672	0.711	0.712	0.670
V_p, $cm^3\ g^{-1}$, for indicated diameters, Å:								
18–50	0.105	0.082	0.096	0.088	0.122	0.103	0.122	0.136
50–100	0.094	0.152	0.111	0.102	0.162	0.164	0.169	0.197
>100	0.387	0.434	0.399	0.427	0.388	0.443	0.421	0.364
K_{av}, kg mm^{-1}	2.51	2.64	2.57	2.84	2.52	2.70	3.35	3.30
Grain diameter, mm	2.51	2.73	2.53	2.50	2.69	2.76	2.35	2.33
ρ_b, g cm^{-3}	0.54	0.55	0.52	0.54	0.51	0.51	0.50	0.49
SO_3^{2-}, %	1.20	1.10	1.06	1.16	0.94	1.06	0.84	0.97
Na_2O, %	0.039	0.028	0.037	0.031	0.030	0.029	0.037	0.030

water-soluble, which reduces the height of the peak in the pore size distribution at 34 Å. With H_3PO_4, no diffusion of basic phosphates occurs because of their low solubility [12]. It may be assumed that basic salts are accommodated in pores with diameter exceeding 40 Å, which must diminish the corresponding peaks in the pore size distribution. However, account should also be taken of the formation of an additional porometric volume (pores 25 and 34 Å in diameter) by products formed in breakdown of larger pores. The observed changes in the heights of peaks in the pore size distribution at 25 and 34 Å are due to occurrence of both these processes.

The texture of hot-precipitated AH is characterized by a shoulder at around 24 Å (0.0021 $cm^3\ g^{-1}\ Å^{-1}$), a peak at 35 Å (0.0094 $cm^3\ g^{-1}\ Å^{-1}$), and a broad asymmetric peak at 48 Å, which is probably a superposition of peaks at 46 and 60 Å (Table 1, Fig. 1b).

Acid peptization affects the specific surface area most strongly, and the porometric volume, to much lesser extent. Treatment with 0.04 M nitric acid (Fig. 1b) makes larger the height of the peak at 48 Å, with the heights of the other peaks either remaining unchanged (25 Å) or decreasing (35 Å). The last fact may be due to filling of these pores with basic salts of aluminum, which are formed in peptization. The volume of pores less than 68 Å in diameter increases from 0.24 to 0.34 $cm^3\ g^{-1}$, and that of pores with diameter exceeding 68 Å decreases from 0.47 to 0.40 $cm^3\ g^{-1}$, and it is this circumstance that leads to a certain decrease in the total porometric volume from 0.78 to 0.74 $cm^3\ g^{-1}$, with S_{sp} = 319 $m^2\ g^{-1}$ unchanged. Peptization with 0.04 M acetic acid (Fig. 1b) leads to similar changes in texture.

The peptizing action of 0.04 M H_3PO_4 on the AH texture is somewhat different from that considered above (Fig. 1b). It follows from porograms that porometric curves of the samples subjected to peptization with HNO_3 and CH_3COOH run above the porometric curve of the initial AH at 17–78 Å, and below it at pore diameters exceeding 78 Å. It may be assumed that, in AH peptization, the rise in the porometric volume is due to breakdown of pore-forming particles responsible for porosity at diameters larger than 78 Å.

The higher peptizing activity of H_3PO_4 with respect to AH is indicated by the fact that the point of intersection of the porometric curves measured before and after AH peptization lies at 53 Å. The significant increase in the height of the peak at 35 Å, from 0.0094 to 0.0151 $cm^3\ g^{-1}\ Å^{-1}$, is probably due to stronger beakdown of pores with diameters in the range 53–78 Å to give fragments with pores 35 Å in diameter, and also to the absence of water-soluble salts of aluminum and H_3PO_4, which could fill these pores.

In the given case, the increase in the specific surface area from 319 to 364 $m^2 g^{-1}$ is probably due just to the formation of thin pores with the distribution peak at 35 Å, rather than to breakdown of pore-forming fragments, which is indicated by the preservation of the total porometric volume (0.78 $cm^3 g^{-1}$).

Thus, in peptization of hot-precipitated AH, the porometric volume changes to a much lesser extent, which is probably due to higher strength of contacts between microcrystalline pseudoboehmite particles forming the secondary porosity, and the peptizing activity of the acids under study decreases in the order $H_3PO_4 > CH_3COOH \geq HNO_3$.

In mixing of precipitates [9], finely porous cold-precipitated hydroxide is accommodated within pores of high-temperature AH, which leads to a certain decrease in the porometric volume and formation of a precipitate with intermediate type of texture (Table 2, Fig. 3a).

The AH texture is defined by a strong peak at 36 Å (0.011 $cm^3 g^{-1} Å^{-1}$) and a broad peak at 170 Å (0.0023 $cm^3 g^{-1} Å^{-1}$). The porogram also shows a peak in the pore size distribution at 25 Å in the form of a shoulder (0.0008 $cm^3 g^{-1} Å^{-1}$). The porometric volume is distributed as follows ($cm^3 g^{-1}$): <50 Å, 0.105 (18%); 50–100 Å, 0.094 (16%); >100 Å, 0.387 (66%).

Peptization of blended AH with nitric acid does not lead to any significant change in the pore size distribution: no new pores are formed, with only the heights of the peaks in the pore size distribution changing (Table 2). A virtually similar pattern is observed in peptization of the same hydroxide with other acids (H_3PO_4, H_3BO_3) taken in about the same concentrations; however, the change in the total porometric volume and specific surface area of AH is less pronounced in this case.

Use of acetic acid (0.01 and 0.02 mol mol^{-1} Al_2O_3) favors even greater increase, to 0.0041 $cm^3 g^{-1} Å^{-1}$, in the height of the peak in the pore size distribution at 170 Å. However, even at such a high concentration of the peptizing agent, there occurs no breakdown of fragments responsible for pores 170 Å in diameter. And only raising the CH_3COOH concentration to 0.04 M (Table 2) leads to an increase in the height of the peak at 36 Å and to partial breakdown of secondary pores, which is indicated by the increasing height of the peak in the pore size distribution at 170 Å and to its shift to smaller values (140 Å) (Fig. 3b).

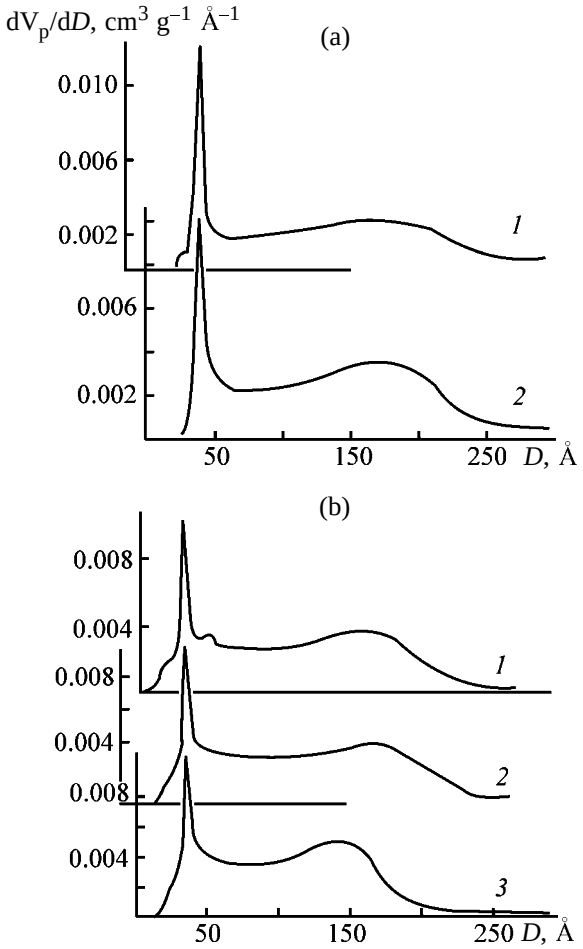

Fig. 3. Pore volume (V_p) distribution curves for blended AH peptized with (a) HNO_3 and (b) CH_3COOH. Acid concentration (M): (a) (*1*) 0.003 and (*2*) 0.007; (b) (*1*) 0.01, (*2*) 0.02, and (*3*) 0.04.

The formation of the peak in the pore size distribution at 170 Å is probably due to the appearance of a secondary porous system via mutual coordination of the fragments shown in Fig. 2. As "binder" serve basic aluminum salts, whose minor amounts are contained in the cold-precipitated hydroxide. In the course of peptization, gel-like pseudoboehmite (cold-precipitated hydroxide) is partly dissolved to give an additional amount of basic aluminum salts, with the resulting further mutual coordination of the fragments mentioned above.

Thus, the texture of the blended AH changes in stages. In the first stage, the partial dissolution of gel-like pseudoboehmite and the formation of basic salts give rise to a secondary porous system. With increasing concentration of the peptizing agent (to approximately 0.02 M for CH_3COOH), the share of secondary pores grows, which leads to a rise in the total porometric volume. The forming basic salts of alumi-

num partly fill the thinnest pores 36 Å in diameter, which is indicated by a decrease in the height of the corresponding peak in the distribution. In the second stage (at concentrations exceeding 0.04 M for CH_3COOH), probably, the pore-forming fragments responsible for the primary porosity partially break down, as shown in Fig. 2. This leads to a decrease in the overall size of these fragments and to a shift of the peak in the size distribution of secondary pores to lower values. The mutual coordination of fragments formed in breakdown gives rise to pores 36 Å in diameter, which is indicated by the increasing height of the corresponding peak in the pore size distribution upon peptization with 0.04 M acid.

The strength characteristics of the cold- and hot-precipitated hydroxides are listed in Table 1.

As shown in [13], the mechanical properties of dispersed materials are commonly related to pore volume and radius, to strength of a unit contact between the particles, and to number of contacts per unit grain cross-section area.

The not-too-large porometric volume and the high bulk density (0.73 g cm^{-3}) of the cold-precipitated hydroxide point to a high packing density and large number of contacts between AH particles. As a result, forming with such an AH gives extrudates with high strength coefficient of 3.08 kg mm^{-1}, which substantially shrink in calcination (Table 1).

The strength of contacts between primary AH particles is determined by the interplanar spacing (along the *b* axis) in the unit cell of pseudoboehmite. The contacts between particles in low-temperature AH are of coagulation nature and can be easily disintegrated under the action of the peptizing agent, which leads to a decrease in the average pore diameter, and the breakdown makes larger the specific surface area. No significant increase in the packing density occurs in peptization, which is indicated by the observed change in the bulk density and pore volume. The intensity of disintegration of contacts between particles in gel-like pseudoboehmite under the action of an acid forms a basis for the practical definition of the "chemical activity" of AH [14], which, in combination with the shrinkage upon drying [9], can be used to determine the formability and strength characteristics.

Another reason for the increase in the strength coefficient in peptization is the formation of basic salts of aluminum with anions of the peptizing acid, which are situated at places of contact between AH particles and form a thin X-ray amorphous film in inner cavities and on the outer surface of grains, which improves the physicomechanical properties of AH. A similar process occurs when Al_2O_3 grains are treated with aluminum nitrate solutions [15]. The diffusing ability of the forming aluminum salts is determined by the solubility of these salts in water, and aluminum phosphates are water-insoluble [6, 12], which, probably, results in that the increase in the strength coefficient upon peptization is the smallest. Owing to the processes listed above, the strength coefficient of cold-precipitated AH increases by 11–32% upon peptization. The absence of correlation between the shrinkage of extrudates in calcination and their strength characteristics [9] is probably due to different diffusing abilities of basic aluminum salts formed in peptization.

Hot-precipitated hydroxide is more aggregated, which is indicated by the large porometric volume (0.78 cm g^{-1}) and low bulk density (0.28 g cm^{-3}). Peptization of hot-precipitated hydroxides also leads to partial dissolution of gel-like pseudoboehmite (but its amount is much smaller than in the preceding case). The insignificant changes in the texture characteristics of AH indicate that intercrystallite contacts are virtually not disintegrated at all because of their higher "crystallinity." For the above reasons, aluminum salts are formed in AH of this kind in much lesser amounts, and, therefore, the absolute value of the strength coefficient of grains is much lower than that in the case of cold-precipitated AH. However, the relative increase in the strength characteristics in peptization of hot-precipitated AH with a solution of H_3PO_4 is 21 to 100%, which much exceeds that in the case of cold-precipitated AH. The porometric volume, bulk density, and texture characteristics indicate an insignificant densification of the hydroxide upon peptization. Therefore, it may be assumed that the rise in the strength coefficient of grains is largely due to the formation of basic aluminum salts.

Commercial blended AHs (Table 2) are characterized by intermediate, between those for cold- and hot-precipitated AH, values of bulk density, strength coefficient, and grain shrinkage.

As follows from the data obtained, peptization leads to a decrease in the bulk density of AH from 0.54 to 0.51 g cm^{-3}, with the porometric volume increasing from 0.59 to 0.71 cm^3 g^{-1}. Despite the rise in the degree of precipitate aggregation, the strength characteristics increased from 2.51 to 2.70 kg mm^{-1}. The phenomenon observed can be attributed to hydroxide strengthening by the forming basic aluminum salts, which is indicated by the substantial decrease

in the height of the pore size distribution peak at 36 Å from 0.0118 to 0.0088 $cm^3 g^{-1} Å^{-1}$.

Raising the concentration of the CH_3COOH peptizing agent to 0.04 M leads to a decrease not only in the porometric volume, but also in the bulk density of AH, which points to an increase in the degree of aggregation of the precipitate, whose effect on the strength characteristics cannot already be compensated for by the action of the basic salts, with the result that the strength parameters of the grains are impaired.

Thus, the increase in the strength characteristics of blended hydroxides in peptization is determined by the amount of cold-precipitated AH and the nature of the peptizing agent. All the factors leading to a decrease in the content of gel-like pseudoboehmite in synthesis of a hydroxide (higher temperature and pH of precipitation) impair the physicomechanical characteristics of the support grains.

In peptization, the gel-like pseudoboehmite is dispersed and interacts with the acid to give basic salts. These salts diffuse into the AH cavities and places of contact between pseudoboehmite particles and form in calcination an X-ray amorphous film improving the physicomechanical properties of AAO. It is for this reason that peptization with an acid yielding water-insoluble aluminum salts leads to a much lesser improvement of the strength characteristics of AH.

CONCLUSIONS

(1) Pore-forming fragments of cold-precipitated aluminum hydroxide are discretely broken down at places of contact between primary particles at (010) planes to give pores of smaller diameter and basic aluminum salts, which are situated at places of contact between primary particles and within the thinnest pores.

(2) Hot-precipitated hydroxides change their texture characteristics upon peptization to a much lesser extent, which is probably due to higher strength of intercrystallite contacts. Peptization probably leads to partial transformation of finely crystalline pseudoboehmite into a gel-like substance through rehydration of the unit cell of pseudoboehmite [incorporation of interlayer water at the (010) plane].

(3) Secondary pores are probably formed in blended hydroxides in the stage of peptization as a result of sticking of the fragments responsible for the primary porosity (<100 Å) by basic salts formed in peptization.

(4) The physicomechanical properties of cold- and hot-precipitated aluminum hydroxides are determined by the packing density and nature of contacts between pseudoboehmite particles. Peptization of the hydroxides with acids leads to an increase in the mechanical strength of grains because of the disintegration of coagulation contacts between particles of gel-like pseudoboehmite and its partial dissolution to give basic aluminum salts, which make stronger the places of contact between the pseudoboehmite particles.

(5) The mechanical strength of grains based on blended aluminum hydroxides is determined by the amount of gel-like pseudoboehmite (cold-precipitated aluminum hydroxide) introduced and by the nature of the peptizing agent.

REFERENCES

1. Poezd, D.F., Radchenko, E.D., Panchenkov, T.M., *et al.*, *Proizvodstvo aktivnoi okisi alyuminiya – nositelya dlya alyumoplatinovykh katalizatorov riforminga: Tematicheskii obzor* (Manufacture of Active Aluminum Oxide, a Support for Aluminoplatinum Reforming Catalysts: Subject Review), Moscow: TsNITE-Neftekhim, 1973.
2. Fedorov, B.M., Fialko, V.M., Rubinchik, E.A., *et al.*, *Kinet. Katal.*, 1992, vol. 33, no. 4, pp. 940–945.
3. Shepeleva, M.N., Ismagilov, Z.R., and Shkrabina, R.A., *Kinet. Katal.*, 1991, vol. 32, no. 2, pp. 455–460.
4. Levin, O.V., Sidel'kovskaya, V.G., Aliev, R.R., *et al.*, *Khim. Tekhnol. Topl. Masel*, 1997, no. 2, pp. 29–31.
5. Lamberov, A.A., Levin, O.V., Egorova, S.R., *et al.*, *Zh. Prikl. Khim.*, 2003, vol. 76, no. 1, pp. 50–56.
6. *Physical and Chemical Aspects of Adsorbents and Catalysts*, Linsen, B.G., Ed., London: Academic, 1970.
7. Gregg, S.J. and Sing, K.S.W., *Adsorption, Surface Area and Porosity*, London: Academic, 1982.
8. *TU* (Technical Specification) *38.601-13-062–90: Aluminum Oxide as Dehydrating Agent 90 M*, Novokuibyshevsk Plant of Catalysts, 1990.
9. Shepeleva, M.N., Shkrabina, R.A., Okkel', L.G., *et al.*, *Kinet. Katal.*, 1988, vol. 29, no. 1, pp. 195–200.
10. Vlaev, L.G., Ivanov, I.D., and Damyanov, D.P., *Kinet. Katal.*, 1993, vol. 34, no. 1, pp. 147–151.
11. Vlasov, E.A., Ryzhak, E.A., and Levitskii, E.A., *Kinet. Katal.*, 1972, vol. 13, no. 5, pp. 1311–1314.
12. Lidin, R.A., Andreeva, L.L., and Molochko, V.A., *Spravochnik po neorganicheskoi khimii* (Handbook of Inorganic Chemistry), Moscow: Khimiya, 1987.
13. Shepeleva, M.N., Ismagilov, Z.R., Ovsyannikova, I.A., *et al.*, *Kinet. Katal.*, 1991, vol. 32, no. 1, pp. 125–131.
14. *TU 2163-007-05766557: Thermally Activated Aluminum Oxide*, Ishimbai Special Plant of Catalysts, 2000.
15. Agievskii, D.A., Kvashonkin, V.I., Zadko, I.I., *et al.*, *Kinet. Katal.*, 1985, vol. 25, no. 4, pp. 928–933.

Russian Journal of Applied Chemistry, Vol. 76, No. 3, 2003, pp. 358–360. Translated from Zhurnal Prikladnoi Khimii, Vol. 76, No. 3, 2003, pp. 373–375.

PHYSICOCHEMICAL STUDIES OF SYSTEMS AND PROCESSES

Gibbs Energy and Entropy of Mixing in the $NaNO_2$–KNO_3 System

V. I. Glazov, G. P. Dukhanin, and M. Kh. Dkhaibe

Volgograd State Technical University, Volgograd, Russia

Received November 14, 2002

Abstract—The activity and activity coefficients of the components of the $NaNO_2$–KNO_3 system, determined from the experimental data on the saturated vapor pressure at 798, 823, and 848 K, are used to calculate the relative and excess partial molar Gibbs energies ($\Delta\bar{G}_i$ and $\Delta\bar{G}_i^{exc}$), entropies ($\Delta\bar{S}_i$ and $\Delta\bar{S}_i^{exc}$), and integral relative and excess thermodynamic functions (ΔG, ΔG^{exc}, ΔS, and ΔS^{exc}) of the system.

Among various physicochemical properties of salt systems, of particular importance are the thermodynamic functions, which reflect rigorous laws associated with the structure of melts and interionic interactions and are common for all chemical systems.

When a melt is formed from pure components, the thermodynamic functions characterizing the given system change. These changes are characterized by the Gibbs energy ΔG, enthalpy ΔH, and entropy ΔS of mixing.

Based on the activities a_i and activity coefficients γ_i of the system components determined from the data on the saturated vapor pressure [1–3], we calculated the relative partial Gibbs energy $\Delta\bar{G}_i$ and the excess partial molar Gibbs energy $\Delta\bar{G}_i^{exc}$ for potassium nitrate and sodium nitrite [4].

$$\Delta\bar{G}_i = 2.3RT\log a_i$$

$$\Delta\bar{G}_i^{exc} = 2.3RT\log\gamma_i$$

The calculation results are presented in Table 1.

The relative and excess partial Gibbs energies were used to calculate the relative integral molar and excess integral molar Gibbs energies and the excess integral molar Gibbs energy.

$$\Delta G = x_1\Delta\bar{G}_1 + x_2\Delta\bar{G}_2,$$

$$\Delta G^{exc} = x_1\Delta\bar{G}_1^{exc} + x_2\Delta\bar{G}_2^{exc},$$

where x_1 and x_2 are mole fractions of potassium nitrate and sodium nitrite in the binary system.

The calculation results are presented in Table 2 and Fig. 1. The integral molar Gibbs energy of the ideal system at 798 K is plotted as a dashed line (Fig. 1, curve *5*).

We calculated the partial molar relative and excess

Table 1. Relative and excess partial molar Gibbs energies of KNO_3 and $NaNO_2$ in melts with $NaNO_2$ and KNO_3, respectively

c, mol %	Extensive property, kJ mol^{-1}, at indicated temperature, K					
	$-\Delta\bar{G}_i$			$-\Delta\bar{G}_i^{exc}$		
	798	823	848	798	823	848
$NaNO_2$ melt						
KNO_3:						
10	22.25	21.38	20.59	6.67	5.62	4.35
20	15.69	15.82	14.73	5.01	4.74	3.38
40	9.44	9.11	8.93	3.39	2.84	2.47
50	7.21	7.09	6.85	2.63	2.35	2.03
60	5.91	5.44	5.36	2.46	1.97	1.76
80	2.84	2.62	2.52	1.36	1.12	0.94
90	1.36	1.28	1.20	0.67	0.57	0.44
KNO_3 melt						
$NaNO_2$:						
90	1.09	1.01	0.97	0.34	0.28	0.21
80	2.37	2.25	2.22	0.92	0.73	0.67
60	5.20	5.16	4.89	1.82	1.59	1.23
50	6.78	6.62	6.46	2.19	1.86	1.57
40	8.69	8.48	8.26	2.66	2.06	1.85
20	14.07	13.96	13.87	3.39	3.06	2.52
10	19.76	19.10	19.02	4.48	3.34	2.82

1070-4272/03/7603-0358$25.00

entropies of mixing of KNO_3 and $NaNO_2$ in their binary system [5]:

$$\Delta\bar{S}_i = -2.3R \log a_i$$

$$\Delta\bar{S}_i^{exc} = -2.3R \log \gamma_i$$

The calculation results are presented in Table 3.

The $\Delta\bar{S}_i$ and $\Delta\bar{S}_i^{exc}$ values were used to calculate the integral molar relative and excess entropies [5] of the system $NaNO_2$–KNO_3:

$$\Delta S = x_1\Delta\bar{S}_1 + x_2\Delta\bar{S}_2,$$

$$\Delta S^{exc} = x_1\Delta\bar{S}_1^{exc} + x_2\Delta\bar{S}_2^{exc},$$

The calculation results are given in Table 4.

The integral molar relative and excess entropies [5] of the system $NaNO_2$–KNO_3 are plotted in Fig. 2. The integral entropy of mixing for the ideal system [5] at 798 K is plotted as a dashed line (Fig. 2, curve *5*).

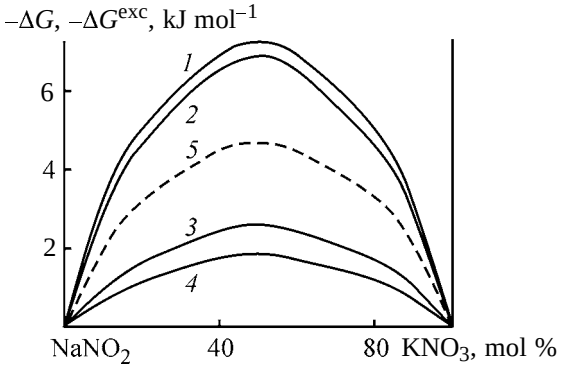

Fig. 1. (*1*, *2*) Relative and (*3*, *4*) excess integral molar Gibbs energies ΔG, ΔG^{exc} for the $NaNO_2$–KNO_3 system; (*5*) integral molar Gibbs energy for the ideal system at 798 K. Temperature (K): (*1*, *3*) 798 and (*2*, *4*) 848; the same for Fig. 2.

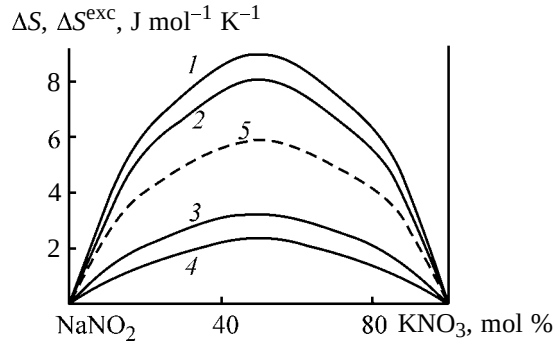

Fig. 2. (*1*, *2*) Integral molar relative and (*3*, *4*) excess entropes ΔS, ΔS^{exc} for the $NaNO_2$–KNO_3 system; (*5*) integral molar entropy of mixing for the ideal system at 798 K.

Table 2. Relative and excess integral molar Gibbs energies of the $NaNO_2$–KNO_3 system

c_{KNO_3}, mol %	Extensive property, kJ mol^{-1}, at indicated temperature, K					
	$-\Delta G$			$-\Delta G^{exc}$		
	798	823	848	798	823	848
10	3.21	3.05	2.93	0.97	0.82	0.63
20	5.03	4.96	4.64	1.74	1.53	1.21
40	6.90	6.74	6.51	2.43	2.09	1.73
50	7.00	6.86	6.66	2.44	2.11	1.81
60	7.02	6.65	6.52	2.52	2.01	1.79
80	5.08	4.89	4.79	1.78	1.51	1.26
90	3.20	3.06	2.98	1.05	0.84	0.67

Table 3. Relative and excess partial molar entropies of KNO_3 and $NaNO_2$ in melts with $NaNO_2$ and KNO_3, respectively

c, mol %	Extensive property, kJ mol^{-1}, at indicated temperature, K					
	$\Delta\bar{S}_i$			$\Delta\bar{S}_i^{exc}$		
	798	823	848	798	823	848
	$NaNO_2$ melt					
KNO_3:						
10	27.88	25.98	24.28	8.73	6.83	5.13
20	19.66	19.22	17.37	6.28	5.76	3.98
40	11.83	11.07	10.53	4.25	3.45	2.91
50	9.04	8.62	8.08	3.34	2.85	2.79
60	7.41	6.62	6.32	3.08	2.39	2.07
80	3.56	3.18	2.97	1.70	1.36	1.11
90	1.70	1.55	1.42	0.84	0.69	0.52
	KNO_3 melt					
$NaNO_2$:						
90	1.36	1.23	1.15	0.42	0.35	0.25
80	2.97	2.74	2.62	1.15	0.88	0.79
60	6.45	6.28	5.76	2.28	1.93	1.45
50	8.50	8.04	7.62	2.84	2.28	1.86
40	10.90	10.30	9.75	3.33	2.51	2.18
20	17.63	16.96	16.35	4.25	3.72	2.97
10	24.76	23.20	22.43	5.61	4.06	3.33

The partial and integral enthalpies, Gibbs energies, and entropies are interrelated as follows [4]:

$$\Delta\bar{H}_i = \Delta\bar{G}_i + T\Delta\bar{S}_i,$$

$$\Delta H = \Delta G + T\Delta S,$$

Table 4. Integral molar relative and excess entropies of the $NaNO_2$–KNO_3 system

c_{KNO_3}, mol %	Extensive property, kJ mol^{-1}, at indicated temperature, K					
	ΔS			ΔS^{exc}		
	798	823	848	798	823	848
10	4.06	3.71	3.46	1.25	1.00	0.75
20	6.31	6.04	5.57	2.18	1.86	1.43
40	8.60	8.20	7.67	3.07	2.54	2.03
50	8.77	8.33	7.85	3.09	2.44	2.33
60	8.80	8.09	7.69	3.18	2.51	2.11
80	6.37	5.94	5.65	2.21	1.83	1.48
90	4.01	3.72	3.52	1.32	1.03	0.80

Substituting the above values of $\Delta\bar{G}_i$, $\Delta\bar{S}_i$, ΔG, and ΔS into these relations, we obtain

$$\Delta\bar{H}_i = 0 \text{ and } \Delta H = 0.$$

The lack of thermal effect in mixing the components is characteristic of ideal systems [4]. At the same time, for certain nonideal systems, referred to as athermal systems, the heats of mixing are also low [6]. In this case,

$$\Delta G^{exc} = -T\Delta S^{exc},$$

and the properties show deviations from ideality mainly owing to the entropy term.

As seen from Fig. 1, the curves of the integral relative and excess molar Gibbs energies exhibit negative deviations from ideal behavior and pass through a minimum at 50 mol %. The integral curves of the relative and excess molar entropies of mixing show positive deviations from ideality and pass through a maximum at the same composition (Fig. 2).

This behavior of the integral thermodynamic functions shows that the component particles in the system studied are to a certain extent ordered, i.e., the interaction Na(I)–K(I) of unlike particles dominates over that of like particles.

In the $NaNO_2$–KNO_3 system, the properties show smaller deviations from ideality than in the previously studied system KNO_3–$NaNO_3$ [6]. This may be due to a decrease in the interaction of unlike cations upon replacement of the NO_3^- anion by NO_2^-.

CONCLUSIONS

(1) The relative and excess partial molar Gibbs energies ($\Delta\bar{G}_i$ and $\Delta\bar{G}_i^{exc}$) and entropies ($\Delta\bar{S}_i$ and $\Delta\bar{S}_i^{exc}$) were calculated from the activities and activity coefficients of the system components.

(2) The relative and excess partial molar Gibbs energies and entropies were used to calculate the integral relative and excess thermodynamic functions ΔG, ΔG^{exc}, ΔS, and ΔS^{exc} in the system $NaNO_2$–KNO_3.

(3) The concentration dependences of the thermodynamic functions are presented. The integral molar Gibbs energy of the system exhibits negative deviations from the ideal behavior and passes through a minimum at 50 mol %. The entropy of mixing shows positive deviations and passes through a maximum at the same composition. This behavior of the thermodynamic functions shows that the component particles in the system studied are ordered to a certain extent.

REFERENCES

1. Glazov, V.I., Golod, V.F., and Golovanov, P.S., *Zh. Prikl. Khim.*, 1984, vol. 57, no. 10, pp. 2351–2352.
2. Glazov, V.I., Dukhanin, G.P., and Losev, V.A., *Zh. Prikl. Khim.*, 2002, vol. 75, no. 6, pp. 908–910.
3. Glazov, V.I., Dukhanin, G.P., and Losev, V.A., *Zh. Prikl. Khim.*, 2002, vol. 75, no. 6, pp. 911–912.
4. Morachevskii, A.G., *Termodinamika zhidkikh splavov* (Thermodynamics of Liquid Alloys), Leningrad: Leningr. Politekh. Inst. im. M.I. Kalinina, 1981.
5. Morachevskii, A.G., and Sladkov, I.B., *Termodinamicheskie raschety v metallurgii* (Thermodynamic Calculations in Metallurgy), Moscow: Metallurgiya, 1985.
6. Glazov, V.I., Dukhanin, G.P., and Shrainer, K.K., *Zh. Prikl. Khim.*, 1994, vol. 67, no. 7, pp. 1062–1064.

Russian Journal of Applied Chemistry, Vol. 76, No. 3, 2003, pp. 361–363. Translated from Zhurnal Prikladnoi Khimii, Vol. 76, No. 3, 2003, pp. 376–378.

SORPTION AND ION-EXCHANGE PROCESSES

Sorption Behavior of Copper(II) on Freshly Precipitated Aluminum Hydroxide

S. A. Evtyukhov and V. G. Berezyuk

Ural State Technical University, Yekaterinburg, Russia

Received August 28, 2002

Abstract—The isotherms of copper(II) sorption from aqueous solutions on freshly precipitated aluminum hydroxide obtained by hydrolysis of pentahydroxomonochlorodialuminum were studied. The sorption efficiency of copper(II) was studied as influenced by pH. Sorption of copper(II) by two different mechanisms is discussed.

Sorption of contaminants on freshly formed precipitates is widely used for decontamination of natural and wastewater. Numerous published data on theoretical and practical aspects of sorption of microelements on metal hydroxides were analyzed and generalized in [1]. This analysis showed that sorption is a complicated phenomenon depending on numerous parameters. Therefore, it is impossible to develop a general model adequately describing diverse sorption systems.

At the same time, simplified models based on a limited set of the main parameters can be developed and successfully used for calculation of sorption equilibrium isotherms characterizing the efficiency of industrial sorption processes.

In this work we studied sorption of copper(II) from aqueous solution on freshly precipitated aluminum hydroxide prepared by hydrolysis of pentahydroxomonochlorodialuminum, the most efficient modern flocculant, which is directly introduced into solution to be decontaminated from copper. This study is of interest because copper(II) is a typical toxic metal contaminating wastewater.

All experiments were carried out under static conditions at 18–20°C. The volume of the working solutions was 100 ml. The Cu^{2+} cations were introduced by dissolution of $CuSO_4$ in a solution containing a prescribed amount of $Al_2(OH)_5Cl$. Aluminum hydroxide was precipitated by adding the stoichiometric amount of NaOH. The required pH was adjusted by adding H_2SO_4 or NaOH. The resulting suspension was stirred and allowed to stand for 2 h to attain the equilibrium. On settling, the liquid phase was separated by filtration and the equilibrium Cu^{2+} concentration was determined by the standard method [2]. The mathematical treatment of the experimental results was performed by the common technique of mathematical statistics [3].

Figure 1 shows the typical isotherms of copper(II) sorption on aluminum hydroxide. The shape of the initial portions of these isotherms is fitted by the equations of Henry isotherm [4, 5]:

$$c_s = Kc_l, \quad (1)$$

where c_s is the sorbate concentration in the solid phase, c_l is the sorbate concentration in the liquid phase, and K is the constant of sorption equilibrium related to the Gibbs free energy of sorption by the equation

$$\Delta G = -RT\ln K, \quad (2)$$

where R is the gas constant and T is temperature (K).

This equation shows that K characterizes the sorbate–sorbent affinity. The degree of the sorption recovery of a sorbate S (%) can be determined by the expression

$$S = K/(K + 1). \quad (3)$$

The type of model isotherm suitable for describing the nonlinear portion of the experimental sorption isotherm should be thermodynamically consistent and sufficiently simple. We believe that the most favorable is so-called exchange sorption isotherm [6] which in the case of equivalent exchange is described by the equation

$$c_s = \frac{K\Gamma c_l}{c_0 + (K-1)c_l}, \quad (4)$$

1070-4272/03/7603-0361$25.00

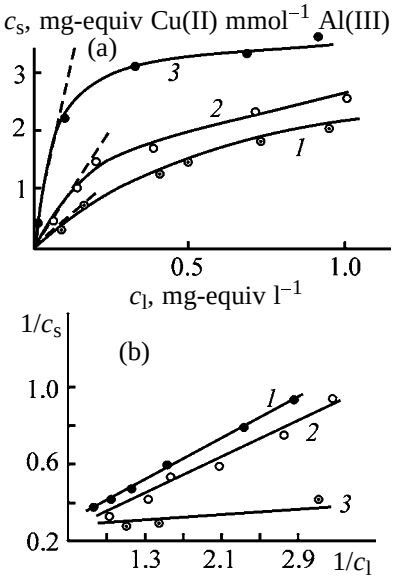

Fig. 1. (a) Isotherms of Cu^{2+} sorption on freshly precipitated aluminum hydroxide and (b) linearized form of Cu^{2+} sorption isotherms. V = 0.2 l, sorbent weight 10.8 mg. (c_s) Cu(II) concentration in the aluminum hydroxide phase; (c_l) Cu(II) concentration in the liquid phase. pH: (*1*) 4.78, (*2*) 5.65, and (*3*) 6.18.

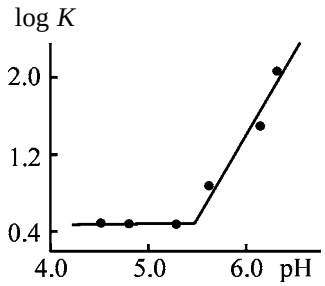

Fig. 2. Plot of log$K$ vs. pH in sorption of Cu^{2+} on freshly precipitated aluminum hydroxide. (K) Sorption constant characterizing thermodynamics of sorption.

where Γ is the limiting sorption capacity of a sorbent, c_0 is the initial sorbate concentration in the liquid phase, and K is the sorption constant.

The K values listed in the table show that sorption of Cu^{2+} on $Al(OH)_3$ is thermodynamically favorable.

Parameters of Eq. (4) describing sorption of Cu^{2+} ions on freshly formed $Al(OH)_3$

pH_{eq}	K	Γ, mg-equiv/mol	c_0, mg-equiv/l
4.52	3.36	6.88	7.02
4.78	3.01	20.1	30.4
5.32	2.92	19.3	22.0
5.65	7.02	9.82	18.8
6.18	28.6	3.68	3.82
6.32	144	3.68	5.84

Equation (4) can be transformed to the form

$$c_s^{-1} = \frac{c_0 c_l^{-1}}{K\Gamma} + \frac{K-1}{K\Gamma}. \quad (5)$$

This equation shows that $1/c_s$ is a linear function of $1/c_l$ (Fig. 1).

The values of the limiting sorption Γ given in the table show that, at the limiting saturation of sorbent sites of aluminum hydroxide with Cu^{2+}, the ratio of Cu^{2+} and Al^{3+} ions in the aluminum hydroxide matrix varies from 2 to 10. Thus, the amount of Cu(II) ions sorbed on aluminum hydroxide exceeds the amount of aluminum atoms in the aluminum hydroxide phase. We believe that this excess sorption of copper(II) is caused by incorporation of Cu^{2+}-containing species into the aluminum hydroxide polymeric matrix by the mechanism of formation of mixed polymeric chains. Thus, the total adsorption Γ of copper(II) is a superposition of the ion-exchange sorption and sorption by the mechanism of copper(II) incorporation into the aluminum hydroxide. This superposition can be expressed by the equation:

$$\Gamma = x_1\Gamma_1 + x_2\Gamma_2, \quad (6)$$

where x_1 and x_2 are the copper(II) fractions sorbed by the incorporation and ion-exchange mechanisms, respectively; Γ_1 and Γ_2 are the values of copper(II) sorption by the first and second mechanisms.

To better understand the contribution of these mechanisms to the total sorption, we studied how the sorption constant K is influenced by pH.

These data show also that, at pH < 5.4, K remains virtually constant, whereas at pH > 5.6 K substantially increases with increasing pH.

It is known that, if a metal is sorbed by the ion-exchange mechanism, the following equation is valid [1]:

$$\log K = A + z\text{pH}, \quad (7)$$

where A is constant and z is the charge of exchangeable ion.

As seen from Fig. 2, the plot of log$K$ vs. pH is divided into two different portions: at pH < 5.5 $z \sim 0$ and at pH > 5.5 log$K$ is expressed by the equation

$$\log K = -9.69 + 1.82\text{pH}, \quad (8)$$

which shows that z is approximately 1.8.

Mechanisms of sorption of ionic species on metal hydroxides were analyzed in detail in [1]. This analysis showed that, from the thermodynamic viewpoint, the sorption by ion-exchange mechanism

$$R\text{–}OH + 0.5M^{2+} \rightleftarrows R\text{–}O(0.5M^{2+}) + H^{+} \quad (8)$$

via replacement of protons of hydroxy groups of the metal hydroxide by hydrated sorbable ions is indistinguishable from the electrochemical mechanism treating sorption as fixation of potential-determining ions.

Taking into account that at pH < 5.5 $z \sim 0$, we can assume that the main mechanism of sorption in this pH range is incorporation of electroneutral species of Cu(II) into the polymeric $Al(OH)_3$ chains ($z \sim 0$).

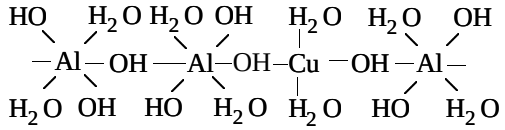

At the same time, at pH > 5.5 z is close to the value corresponding to the sorption by the mechanism of ion exchange. These data show also that sorption by the mechanism of incorporation is increasing with increasing pH.

Because the hydration number of Al^{3+} (as a rule, equal to 6) is higher than that of Cu^{2+}, incorporation of copper(II) into $Al(OH)_3$ polymers can be accompanied by elimination of water molecules from the Cu^{2+} coordination sphere. These effects should occur for all cations of transition metals with the coordination number less than 6 in their coprecipitation with aluminum hydroxide.

CONCLUSIONS

(1) Isotherms of copper(II) sorption on aluminum hydroxide were obtained and treated in terms of the model of equivalent exchange sorption.

(2) Assumption was made that sorption of copper(II) on aluminum hydroxide is a superposition of the ion exchange of Cu^{2+} ions for protons of the hydroxy groups of aluminum hydroxide and incorporation of Cu(II) species into the polymeric matrix of the sorbent.

REFERENCES

1. Egorov, Yu.V., *Statika sorbtsii mikrokomponentov oksigidratami* (Statics of Sorption of Microcomponents on Oxyhydrates), Moscow: Atomizdat, 1975.
2. Lur'e, Yu.Yu., *Analiticheskaya khimiya promyshlennykh stochnykh vod* (Analytical Chemistry of Industrial Wastewater), Moscow: Khimiya, 1984.
3. Tikhonov, A.N. and Ufimtsev, M.V., *Statisticheskaya obrabotka rezul'tatov eksperimentov* (Statistical Treatment of Experimental Results), Moscow: Mosk. Gos. Univ., 1988.
4. Zhukhovitskii, A.A. and Shvartsman, L.A., *Fizicheskaya khimiya* (Physical Chemistry), Moscow: Metallurgiya, 2001.
5. Volovik, L.S., Kovalevs'ka, E.I., Mank,V.V., *et al*., *Kolloidna khimiya* (Colloid Chemistry), Mank,V.V., Ed., Kiev, 1999.

Russian Journal of Applied Chemistry, Vol. 76, No. 3, 2003, pp. 364–367. Translated from Zhurnal Prikladnoi Khimii, Vol. 76, No. 3, 2003, pp. 379–382.

SORPTION AND ION-EXCHANGE PROCESSES

Formation of Hydroxide Complexes in the Fe^{3+}–Cd^{2+}–NO_3^-–H_2O System

A. E. Sokolovskii and E. V. Radion

Belarussian State Technological University, Minsk, Belarus

Received November 6, 2002

Abstract—Hydrolysis in the Fe^{3+}–Cd^{2+}–NO_3^-–H_2O system was studied by spectrophotometry, pH-metric titration, dialysis, and sorption techniques. Mutual influence of cations in their hydrolytic and sorption behavior was discussed from the viewpoint of the heteronuclear complex formation.

Iron(III) salts are widely used as collectors in water treatment to remove toxic metal ions. Particularly, Hg^{2+} ions are precipitated in the course of hydrolysis of Fe^{3+} ions [1]. The formation of an iron(III)–mercury(II) heteronuclear hydroxide complex was established [2]. The hydrolytic interaction of Fe^{3+} and Cd^{2+} ions was not studied previously, and this was the subject of the present work.

EXPERIMENTAL

The initial solutions of iron(III) and cadmium(II) nitrates were prepared by the dissolution of carbonyl iron and cadmium hydroxide in chemically pure grade nitric acid.

The concentrations of Cd^{2+} and Fe^{3+} in solutions were determined by direct complexometric titration with Eriochrome Black T [3] and sulfosalicylic acid in acetate buffer solution [4], respectively. When Fe^{3+} and Cd^{2+} ions were present simultaneously in solutions, their total content was determined by direct complexometric titration in the presence of sulfosalicylic acid and then the concentration of Fe^{3+} was determined by iodometric titration in a separate aliquot. The contents of free HNO_3 in the initial solutions was determined potentiometrically in the presence of EDTA [5].

The initial iron(III) and cadmium(II) solutions were used to prepare Cd^{2+}–NO_3^-–H_2O and Fe^{3+}–Cd^{2+}–NO_3^-–H_2O solutions with various OH/M molar ratios. The concentrations of metal ions and free nitric acid in the initial solutions were determined. The amount of KOH required to neutralize the free acid and to establish a certain OH/M ratio and the amount of $NaNO_3$ required to maintain a constant ionic strength were calculated from these data. Then the calculated amounts of the initial solutions of metal salts, 0.2 M KOH, and 1 M $NaNO_3$ were mixed. In the case of partial neutralization of the free acid, the OH/M molar ratio was designated by the minus sign. The solutions prepared were kept at a required temperature for 7 days to attain the equilibrium.

The experiments were carried out under the following conditions: concentration of metal ions 0.01 M, total concentration of metal ions in the Fe^{3+}–Cd^{2+}–NO_3^-–H_2O system 0.02 M at the $Fe^{3+} : Cd^{2+} = 1 : 1$ molar ratio, temperature 25 ± 0.1°C, and ionic strength 0.3 M ($NaNO_3$).

Hydrolysis was studied by pH-metric titration, spectrophotometry, dialysis, and sorption (KB-4P-2 cation exchanger in the H^+ form). An I-160 ionometer with a temperature-controlled cell was used to measure the pH values. The absorption spectra were recorded on an SF-46 spectrophotometer. The procedures of dialysis and processing of its results are described elsewhere [6]. Solutions were aged in the dialyzer for 7 days.

KB-4P-2 cation exchanger was pretreated and analyzed for the moisture content according to [7, 8]. Sorption was studied at 25 ± 0.1°C under static conditions; the establishment of the equilibrium distribution of ions between the solution and resin was always proved. The solution was in contact with the cation exchanger for 7 days. The data of the chemical analysis of equilibrium solutions were used to calculate the value S of sorption of metal ions by the resin (mmol per gram of the resin dried at 105°C).

The absorption spectra of cadmium(II) solutions with various molar ratios OH^-/Cd^{2+} are shown in

1070-4272/03/7603-0364$25.00

Fig. 1a. In the UV region of all the spectra, there are a weak band (λ = 255 nm, $\varepsilon \approx 35$) caused by the charge transfer [9] in cadmium(II) aqua complex and a still weaker band (λ = 330 nm, $\varepsilon \approx 0.9$) caused by the charge transfer in cadmium(II) mononuclear hydroxo complexes [9]. As the OH^-/Cd^{2+} ratio is increased, the absorption bands grow in intensity, which suggests occurrence of equiliblia involving protons [9]. Within the examined pH range (1.82–1.90), cadmium(II) exists as aqua ions and $Cd(OH)^+$ hydroxo complexes [10]. Therefore, the changes in the spectra with changing pH are attributable to the formation of hydrolyzed cadmium(II) species.

On the whole, the spectra of Fe^{3+}–Cd^{2+}–NO_3^-–H_2O solutions (Fig. 1b) are similar to the spectra of the Fe^{3+}–NO_3^-–H_2O system [11]. The maximum at 250 nm corresponding to the absorption of iron(III) aqua complexes [9, 12] is retained. The dependence of the ratios of the light absorption in Fe^{3+}–Cd^{2+}–NO_3^-–H_2O and Fe^{3+}–NO_3^-–H_2O solutions at λ = 320 nm [11] on the OH/M ratio is shown in Fig. 2. Two almost linear portions are clearly seen. The inflection is observed at OH/M = 0, indicating that, with increasing OH/M ratio, the iron(III) hydrolysis is enhanced in the presence of cadmium(II) to a greater extent than in the straight Fe^{3+}–NO_3^-–H_2O solution.

The pK_a of the $Cd(H_2O)_4^{2+}$ aqua complex is 10.2 [10]; therefore, the first jump in the titration curve of the Cd^{2+} solution corresponds to the neutralization of free nitric acid, and the second, to the formation of a cadmium hydroxide precipitate. The precipitation starts at pH 7.3 and is complete at the OH/M ratio of 1.8.

Three jumps are observed in the titration curve of the Fe^{3+}–Cd^{2+} solution (Fig. 3). The precipitation starts at pH 2.7, which corresponds to the onset of the first jump. The first jump is observed at the ratio OH/ΣM = 1.7, the second, at 1.8, and the third, at 2.5. Judging from the pH values, the first jump is attributable to the neutralization of iron(III) ions [11], and the third, to the neutralization of cadmium(II) ions. The presence of the second jump cannot be explained on the basis of the neutralization curves of the individual ions, suggesting occurrence of a reaction between the hydrolyzed iron(III) and cadmium(II) species.

The values of cation sorption in the systems Cd^{2+}–NO_3^-–H_2O and Fe^{3+}–Cd^{2+}–NO_3^-–H_2O by the weakly acidic cation exchanger KB-4P-2 (H^+) are plotted vs. OH/M ratio in Fig. 4. As the OH/M ratio is increased, the sorption of Cd^{2+} ions considerably increases, probably owing to the formation of mononuclear hydroxo complexes. The KB-4P-2 cation exchanger sorbs both cations from Fe^{3+}–Cd^{2+}–NO_3^-–H_2O solutions in approximately equal amounts (curves *2*, *3*). At the OH/ΣM ratios from –1 to 0, the sorption of iron(III) (curve *2*) is somewhat greater than that of cadmium(II) (curve *3*) and is virtually independent of the OH/ΣM ratio. Sorption of both ions rises sharply as OH/ΣM is increased further. Sorption of cadmium(II) (curve *3*) is significantly lower than that from the individual solution (curve *1*), and

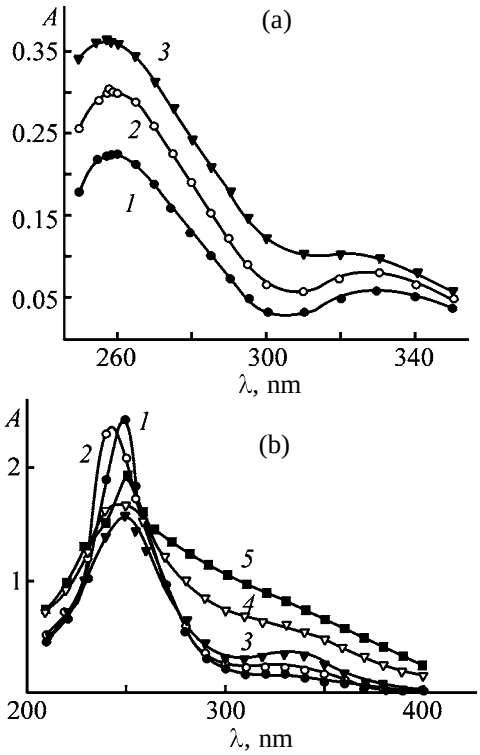

Fig. 1. Absorption spectra of solutions: (a) Cd^{2+}–NO_3^-–H_2O and (b) Fe^{3+}–Cd^{2+}–NO_3^-–H_2O. (*A*) Optical density and (λ) wavelength. Molar ratio OH/M: (a) (*1*) –1, (*2*) –0.5, and (*3*) 0.5; (b) (*1*) –1, (*2*) –0.5, (*3*) 0, (*4*) 0.5, and (*5*) 1.

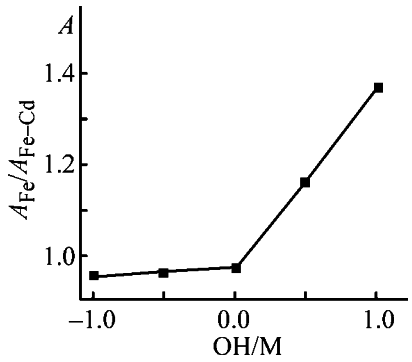

Fig. 2. Ratio A_{Fe}/A_{Fe-Cd} of Fe^{3+}–NO_3^-–H_2O and Fe^{3+}–Cd^{2+}–NO_3^-–H_2O solutions at λ = 320 nm as a function of the OH/M ratio.

Dialysis coefficients K_d of iron(III) and cadmium(II)

OH/M	Fe^{3+}–NO_3^-–H_2O, K_d (Fe)	Fe^{3+}–Cd^{2+}–NO_3^-–H_2O,		Cd^{2+}–NO_3^-–H_2O, K_d (Cd)
		K_d (Fe)	K_d (Cd)	
–1	0.91	0.9	1	1
–0.5	0.89	0.88	1	1
0	0.82	0.80	0.98	1
0.5	0.64	0.59	0.89	1
1	0.34	0.24	0.75	

sorption of iron(III) (curve *2*) is close to that from the Fe^{3+}–NO_3^-–H_2O solution [11]. Thus, in the system Fe^{3+}–Cd^{2+}–NO_3^-–H_2O, cadmium(II) ions lose their individuality, and their sorption changes in parallel with that of iron(III), suggesting formation of heteronuclear hydroxo complexes in the system.

The dialysis coefficients of iron(III) and cadmium(II) in individual and mixed solutions are given in the table. The distribution of various cadmium(II) and iron(III) species in the Fe^{3+}–Cd^{2+}–NO_3^-–H_2O system was calculated from the data obtained according to [13] (Fig. 5). In the Cd^{2+}–NO_3^-–H_2O system, the dialysis coefficient of cadmium(II) is 1 for all OH/M ratios, which agrees with the conclusions of [10] that only aqua complexes and mononuclear hydroxo complexes are present in cadmium(II) solutions. The dialysis coefficients of iron(III) and cadmium(II) in mixed and individual solutions differ. Up to the ratio OH/ΣM = 0, the dialysis coefficients of iron(III) in Fe^{3+}–NO_3^-–H_2O and Fe^{3+}–Cd^{2+}–NO_3^-–H_2O solutions are approximately equal, whereas, as the OH/ΣM ratio is increased further, the dialysis coefficients in the Fe^{3+}–Cd^{2+}–NO_3^-–H_2O system become less than those in the individual solution. This fact suggests enhancement of iron(III) hydrolysis in the presence of cadmium(II), with an increase in the content of Fe(III) in polynuclear hydroxo species.

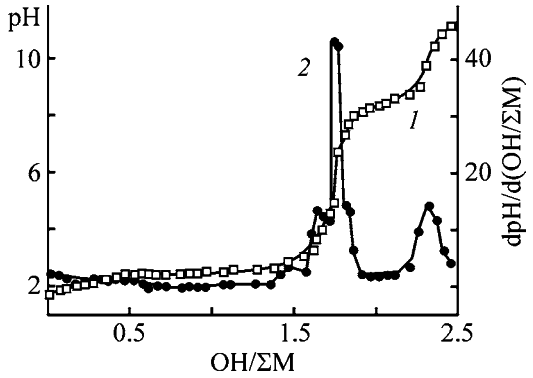

Fig. 3. Curves of pH-metric titration of Fe^{3+}–Cd^{2+}–NO_3^-–H_2O solutions: (*1*) integral and (*2*) differential.

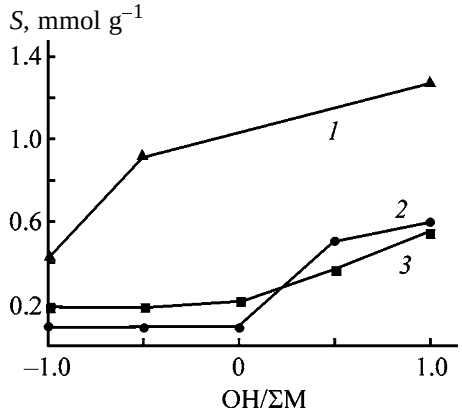

Fig. 4. Sorption *S* of iron(III) and cadmium(II) from Cd^{2+}–NO_3^-–H_2O and Fe^{3+}–Cd^{2+}–NO_3^-–H_2O solutions by KB-4P-2 cation exchanger. Sorption of (*1*) Cd^{2+} in the Cd^{2+}–NO_3^-–H_2O system; (*2*) Fe^{3+} and (*3*) Cd^{2+} in the Fe^{3+}–Cd^{2+}–NO_3^-–H_2O system.

The content of aqua complexes in the iron(III) solution decreases and that of mononuclear species increases in the OH/ΣM range from –1 to 0 (Fig. 5). The content of hydroxo complexes is relatively low. A further increase in the OH/ΣM ratio results in a fast growth of the content of polynuclear species, which agrees well with the spectrophotometric data. In the Fe^{3+}–Cd^{2+}–NO_3^-–H_2O solution, cadmium(II) is in the form of aqua ions in the OH/ΣM range from –1 to 0. The relative content of its mononuclear species, which is not shown in the diagram, is several orders of magnitude lower. As the OH/ΣM ratio increases, the relative content of cadmium(II) aqua complexes decreases, and the content of its polynuclear species grows. As polynuclear complex formation is untypical of cadmium(II), the data obtained suggest the presence of iron(III)–cadmium(II) heteropolynuclear hydroxo complexes in the solution. The dialysis coefficients of cadmium(II) are higher than those of iron(III), suggesting that the relative content of cadmium(II) in polynuclear species is less than that of iron(III) at their equal concentrations.

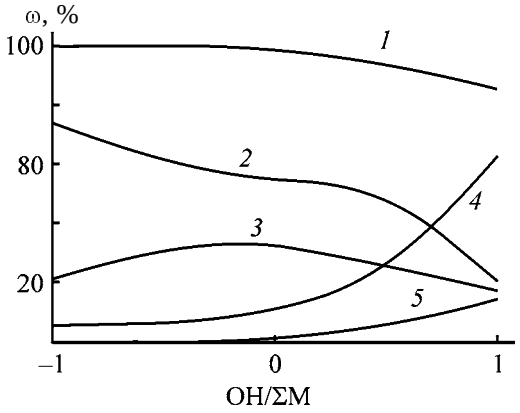

Fig. 5. Relative content of species ω in the Fe^{3+}–Cd^{2+}–NO_3^-–H_2O system as a function of OH/ΣM ratio. Species: (*1*) $Cd(H_2O)_4^{2+}$, (*2*) $Fe(H_2O)_6^{3+}$, (*3*) $FeOH(H_2O)_5^{2+}$, (*4*) Fe(III) in polynuclear species, and (*5*) Cd(II) in polynuclear species.

CONCLUSIONS

(1) It was found by independent methods that, in Fe(III)–Cd(II) solutions, the cations interact with each other, which causes their mutual influence in sorption and hydrolytic processes.

(2) Heteronuclear hydroxo complexes are formed in solutions of the Fe^{3+}–Cd^{2+}–NO_3^-–H_2O system at the ratios OH/ΣM > 0.

REFERENCES

1. Bakeev, T.B., Study of Hydrolytic and Reductive Removal of Mercury from Aqueous Solutions, *Cand. Sci. Dissertation*, Karaganda, 1993.
2. Sheremet, E.N., *Koord. Khim.*, 1998, vol. 24, no. 5, pp. 339–342.
3. Schwarzenbach, G. and Flaschka, H., *Die komplexometrische Titration*, Stuttgart: Ferdinand Enke, 1965.
4. Umland, F., Janssen, A., Thierig, D., und Wünsch, G., *Theorie und praktische Anwendung von Komplexbildnern*, Frankfurt am Main: Akademische, 1971.
5. Bulatov, N.I. and Bulatova, A.A., *Zh. Anal. Khim.*, 1983, vol. 24, no. 5, pp. 339–342.
6. Radion, E.V., Zalevskaya, T.L., and Baev, A.K., *Vestsi Akad. Navuk Bel. SSR, Ser. Khim. Navuk*, 1989, no. 4, pp. 3–5.
7. Aivazov, B.V., *Vvedenie v khromatografiyu* (Introduction to Chromatography), Moscow: Vysshaya Shkola, 1983.
8. Ol'shanova, K.M., Potapova, M.A., and Morozova, N.M., *Praktikum po khromatograficheskomu analizu* (Practical Works on Chromatographic Analysis), Moscow: Vysshaya Shkola, 1970.
9. Lever, A.B.P., *Inorganic Electronic Spectroscopy*, Amsterdam: Elsevier, 1984.
10. Davydov, Yu.P., *Sostoyanie radionuklidov v rastvorakh* (State of Radionuclides in Solutions), Minsk: Nauka i Tekhnika, 1978.
11. Sokolovskii, A.E., Radion, E.V., and Rudakov, D.A. *Zh. Prikl. Khim.*, 2002, vol. 75, no. 11, pp. 1780–1783.
12. Radion, E.V., Zalevskaya, T.L., and Baev A.K., *Vestsi Akad. Navuk Bel., Ser. Khim. Navuk*, 1992, no. 2. pp. 45–48.
13. Kapylovich, M.N., Radion, E.V., and Baev, A.K., *Koord. Khim.*, 1995, vol. 21, no. 1, pp. 66–71.

Russian Journal of Applied Chemistry, Vol. 76, No. 3, 2003, pp. 368–373. Translated from Zhurnal Prikladnoi Khimii, Vol. 76, No. 3, 2003, pp. 383–388.

SORPTION AND ION-EXCHANGE PROCESSES

Synthesis of Calcium and Magnesium Phosphates from Natural Carbonates and Study of Their Activity in Reactions with Lead(II) Ions

N. V. Kitikova, I. L. Shashkova, and A. I. Rat'ko

Institute of General and Inorganic Chemistry, State Scientific Institution, National Academy of Sciences of Belarus, Minsk, Belarus

Received July 20, 2001; in final form, July 2002

Abstract—Chemical and thermal methods for obtaining calcium and magnesium phosphates from natural carbonate raw materials were studied. The activity of these compounds in uptake of lead(II) ions from solution was evaluated.

Phosphates and carbonates of alkaline-earth metals are actively studied as sorbents for ions of heavy and non-ferrous metals [1–14]. The mechanism of their action is peculiar. The recovery of metal ions from a solution is a result of chemical reactions occurring between solid phosphates or carbonates of alkaline-earth metals and multicharged metal cations, yielding compounds with lower solubility products. By this process, metal ions are removed from solutions to a significant extent. It was shown earlier [4–9] that 1 g of calcium phosphate binds up to 25 mg-equiv of ions of heavy and non-ferrous metals in these reactions. This exceeds by almost an order of magnitude the capacity of ion-exchange materials traditionally used to recover metal ions from solutions.

Unlike phosphates, carbonates are cheap natural materials. However, phosphates have significant advantages in using for water treatment.

First, the pH range for the formation of phosphates of heavy and nonferrous metals to be recovered is very wide, namely, from 1 (iron phosphate [4, 9]) to 10–12. Carbonates can be used for the removal of metal ions from solutions only in neutral or alkaline media to yield either carbonates or hydroxides of multicharged metal ions [11, 13].

Second, the solubility of phosphates of heavy and non-ferrous metals is lower than that of the corresponding carbonates and hydroxides by several orders of magnitude [15]. Correspondingly, when phosphates are used, the degree of solution purification is many times higher.

In view of these advantages of using phosphates for the removal of metal ions from solutions and also of the fact that natural carbonates are often chemically inactive and require preliminary activation by chemical, thermal, or mechanical methods [16] for the use in sorption processes, it becomes economically expedient to convert calcium and magnesium carbonates to the phosphates.

A simple way of obtaining calcium and magnesium hydrophosphates by the treatment of natural dolomite with phosphoric acid at room temperature is described in [17]. The resulting phosphates have a cost quite reasonable for the practical use.

Phosphates can be also obtained from natural carbonates by chemical or thermal methods, which would expand the assortment of sorption materials intended for water treatment and water preparation required to meet sanitary regulations concerning noxious metal ions.

Unlike phosphates, hydrated phosphates precipitated from aqueous solutions do not lose chemical activity on dehydration up to 800–900°C [18], which is important for their practical application. They can be obtained in the granular form by the calcination of granules with a clay binder at 600°C.

Here we report on the synthesis of calcium magnesium phosphates from natural chalk $CaCO_3$ and dolomite $CaMg(CO_3)_2$ by chemical and thermal methods and also on their activity in the treatment of aqueous solutions to remove lead(II) ions.

EXPERIMENTAL

Dolomite and chalk industrially produced in the Vitebsk oblast of Belarus Republic were used as raw

1070-4272/03/7603-0368$25.00

materials. According to the DTA data, dolomite contained 84% calcium magnesium carbonate, and, according to X-ray phase analysis (XPA), it contained impurities of quartz, iron oxide, and mica. Natural chalk (Volkovysk) was calcite containing 96% main substance. Our experiments were carried out using sifted fractions of dolomite and chalk with the particle size of 0.09–0.25 mm.

Phosphates were synthesized from natural carbonates by two methods: by chemical precipitation at pH 10 after preliminary dissolution of the carbonate in concentrated HNO_3 and by sintering $CaCO_3$ and $MgCO_3$ with ammonium phosphate in the stoichiometric amounts at 900°C.

The chemical precipitation was performed by two procedures. According to the first procedure [19], a Ca- and Mg-containing solution was alkalized to pH 10 using $NH_3 \cdot H_2O$ and rapidly combined with a solution of ammonium phosphate with pH 10, which was obtained by the addition of $NH_3 \cdot H_2O$ to H_3PO_4. In the second procedure, an acidic solution of dolomite or chalk was mixed with a solution of H_3PO_4, and then calcium and magnesium phosphates were precipitated with concentrated $NH_3 \cdot H_2O$ at pH 10. In both cases, the molar ratio $M_{in} : P$ (M_{in} = Ca or Ca + Mg) in the initial solution was varied from 1.5 to 2.0. The samples synthesized were washed with a dilute ammonia solution, filtered, and dried in air, first at room temperature and then at 70°C.

The phase composition of the synthesized samples was determined by XPA (DRF-2 diffractometer, CuK_α radiation) and IR spectroscopy (UR-20 spectrometer, KBr pellets, weighed sample 2 mg).

The chemical compositions were determined after dissolution of the weighed samples of 50.00 ± 0.01 mg in concentrated nitric acid. The content of calcium(II), and also the total amount of calcium(II) and magnesium(II) were determined by complexometric back-titration with a solution of zinc sulfate [20]; the content of magnesium(II), by titration of the solution after preliminary precipitation of calcium oxalate [21]; and the content of ammonia, by distilling off from an alkaline solution (Kjeldahl's method) [22]. The content of phosphorus(V) was determined by the colorimetric method in the form of a phosphorovanadomolybdate complex [21]. The error in the determination of the elements was ± 0.02 mmol g^{-1}.

The value of the absorption of lead(II) ions under static conditions A_{Pb} (mg-equiv g^{-1}) by the phosphates synthesized was used, as previously [13, 17, 18], as the measure of their chemical activity in recovery of heavy and non-ferrous metal ions from solutions. For this purpose, a weighed sample of the sorbent (0.2 g) was placed in 25 ml of a 0.2 N solution of lead(II) nitrate and kept for a day with intermittent stirring at 18 ± 2°C. The solution was separated from the solid phase, and the residual content of lead(II) in the solution after filtration was determined by complexometric back-titration [20]. The error of the determination of A_{Pb} was ± 0.02 mg-equiv g^{-1}.

The chemical composition of the synthesized phosphates (Tables 1, 2) strongly depends on the nature of the starting natural material. According to the XPA data, the products dried at 70°C are amorphous substances. When natural chalk is used as a raw material (Table 1), the molar ratio Ca : P and the water content allow the resulting compounds to be identified as the phosphate $Ca_3(PO_4)_2 \cdot 2H_2O$ exhibiting slight deviations from the stoichiometry. The samples obtained by the first procedure correspond to the stoichiometry to a greater extent. When phosphates are precipitated from dolomite solutions, cations of calcium, magnesium, and ammonium enter into the resulting materials (Table 2), and the composition of these products corresponds to the empirical formula $Ca_3Mg_2NH_4(PO_4)_{3.67} \cdot 8H_2O$ or $Ca_6Mg_4NH_4(PO_4)_7 \cdot 14H_2O$. Thus, the chemical composition of the triple phosphates corresponds to the neutral salts with the ratio $M_{nat} : P = 1.5$ (M_{nat} = Ca + Mg + NH_4). The composition of the samples was closer to the stoichiometry when they were synthesized by both the first and the second precipitation procedures in the presence of excess calcium and magnesium ions in the starting solutions. Furthermore, at excess of metal cations in solution, the content of ammonium ions in the product was lower (sample nos. 11, 12).

The IR spectra of the phosphates obtained from a solution of chalk (see figure, curves *1, 2*) contain strong absorption bands with maxima at 1060–965 and 620–570 cm^{-1}, corresponding to the stretching, $\nu(PO_4)$, and bending, $\delta(PO_4)$, vibrations of orthophosphate ions PO_4. The spectra of the phosphates obtained from dolomite solutions (curves *3, 4*) contain, along with these bands, also bands with maxima at 1475 and 1410 cm^{-1}, corresponding to the bending vibrations of ammonium ions $\delta(NH_4^+)$, and 1275, 910, and 800 cm^{-1}, corresponding to the bending vibrations δ(POH) and γ(POH) of $H_2PO_4^-$ anions [23, 24].

Along with the above-mentioned methods for determining the phase composition of the synthesized materials, we also used the thermal method. Almost all of the known phosphates crystallize on heating at temperatures of up to 900°C [25]. It is seen from

Table 1. Composition and properties of compounds precipitated from chalk solutions at pH 10

Sample no.	Precipitation technique*	M_{in} : P molar ratio	Product before heat treatment					Heat treatment at 900°C	
			Ca	PO_4	H_2O	Ca : P molar ratio	A_{Pb}, mg-equiv g^{-1}	phase composition	A_{Pb}, mg-equiv g^{-1}
			% (mol)						
1**	I	1.5	33.80 (3.00)	55.39 (2.07)	10.22 (2.02)	1.45	16.19	β-$Ca_3(PO_4)_3$	20.44
2	I	1.5	33.90 (3.00)	54.39 (2.03)	10.11 (1.99)	1.48	18.06	″	23.94
3**	I	2.0	34.41 (3.00)	54.48 (2.01)	10.31 (2.00)	1.50	16.75	″	22.06
4	I	2.0	33.73 (3.00)	54.47 (2.04)	10.10 (1.99)	1.47	17.44	″	21.94
5**	II	1.5	33.16 (3.00)	56.62 (2.16)	9.72 (1.95)	1.39	21.00	″	22.00
6	II	1.5	33.52 (3.00)	56.05 (2.11)	9.96 (1.98)	1.42	20.25	″	23.88
7**	II	2.0	33.21 (3.00)	55.98 (2.13)	9.91 (1.99)	1.41	18.00	″	23.59
8	II	2.0	32.96 (3.00)	55.20 (2.12)	10.05 (2.03)	1.42	19.00	″	22.76

* (I) Quick combining of M_{in}^{2+}- and PO_4^{3-}-containing solutions with pH 10 (M_{in} = Ca, Mg); (II) precipitation with concentrated $NH_3 \cdot H_2O$ from acid solution containing M_{in}^{2+} and PO_4^{3-} ions; the same for Table 2.
** Dissolved carbonate was preliminarily filtered to remove insoluble impurities.

Table 2. Composition and properties of compounds precipitated from dolomite solutions at pH 10

Sample no.	Precipitation technique	M_{in} : P molar ratio	Product before heat treatment							Heat treatment at 900°C	
			Ca	Mg	NH_4	PO_4	H_2O	M_{nat} : P molar ratio	A_{Pb}, mg-equiv g^{-1}	phase composition	A_{Pb}, mg-equiv g^{-1}
			% (mol)								
9*	I	1.5	16.78 (3.00)	6.82 (2.03)	2.63 (1.04)	52.06 (3.90)	19.21 (7.62)	1.42	13.70	$Ca_3Mg_3(PO_4)_4$ + $Ca_7Mg_2(PO_4)_6$ + α-$Mg_2P_2O_7$	12.63
10	I	1.5	16.40 (3.00)	6.62 (2.10)	2.50 (1.02)	50.83 (3.92)	18.16 (7.38)	1.41	13.60	″	12.25
11*	I	2.0	18.73 (6.00)	7.34 (3.92)	1.44 (1.03)	51.49 (6.95)	19.60 (13.96)	1.50	16.00	$Ca_3Mg_3(PO_4)_4$ + $Ca_7Mg_2(PO_4)_6$	16.50
12	I	2.0	18.05 (6.00)	7.06 (3.91)	1.24 (0.92)	48.74 (6.82)	19.11 (14.13)	1.52	14.40	″	16.36
13*	II	1.5	16.73 (3.00)	6.77 (2.02)	2.52 (1.00)	50.95 (3.85)	19.43 (7.74)	1.43	13.10	$Ca_3Mg_3(PO_4)_4$ + $Ca_7Mg_2(PO_4)_6$ + α-$Mg_2P_2O_7$	14.38
14	II	1.5	16.48 (3.00)	6.51 (1.97)	2.42 (0.98)	49.57 (3.80)	19.62 (7.94)	1.44	12.60	″	14.06
15*	II	2.0	17.07 (3.00)	6.99 (2.04)	2.65 (1.03)	50.44 (3.73)	19.95 (7.78)	1.49	13.61	″	12.19
16	II	2.0	16.15 (3.00)	6.72 (2.08)	2.54 (1.05)	49.45 (3.87)	19.44 (8.02)	1.45	13.81	″	12.54

* Dissolved carbonate was preliminarily filtered to remove insoluble impurities.

Tables 1 and 2 that the heat treatment of the phosphates obtained from a chalk solution results in crystallization of β-$Ca_3(PO_4)_2$. We have shown earlier [18] that the crystallization of phosphates free from impurities on heat treatment indicates that the starting compounds are also phosphates. The heat treatment of the phosphates precipitated from the dolomite solution results in the crystallization of compounds identified as double calcium and magnesium orthophosphates $Ca_3Mg_3(PO_4)_4$ and $Ca_7Mg_2(PO_4)_6$, and also of the pyrophosphate $Mg_2P_2O_7$. The formation of magnesium pyrophosphate $Mg_2P_2O_7$ is due to the presence of ammonium ions in the synthesized compounds. The removal of ammonia results in the release of hydrogen ions participating in the polymerization [26]. This salt was not detected in the X-ray pattern of sample nos. 11 and 12, which may be due to the low content of ammonia.

The IR data agree with the XPA results for the heat-treated samples. The bands in the spectra of the samples precipitated from chalk solutions become stronger owing to the formation of a crystalline structure. The bands at 425 and 450 cm^{-1} of the bending vibrations of phosphate ions $\delta(PO_4)$ appear. The spectrum as a whole characterizes only orthophosphate anions. The spectra of samples synthesized from dolomite solutions contain, along with the bands characteristic of orthophosphate, weak bands with the maxima corresponding to stretching antisymmetric, $\nu_{as}(POP)$ (1010 and 980 cm^{-1}), and symmetric, $\nu_s(POP)$ (780 and 740 cm^{-1}), vibrations of the P–O–P bonds in condensed phosphate species [26, 27].

Thus, according to our data, the synthesized compounds are calcium and magnesium phosphates free from impurities of acid phosphates, and the lower $M_{nat} : P$ ratio, as compared to the stoichiometry, is apparently due to the presence of impurities of other metal ions, e.g., iron ions.

Our data on the chemical activity of the materials synthesized under various conditions are also given in Tables 1 and 2, which contain the data for both the starting materials dried at 70°C and the products of their heat treatment at 900°C. As indicated above, calcium and magnesium phosphates preserve the chemical activity after the heat treatment. As these data were obtained for the sample synthesized from reagent-grade salts [25], it seemed appropriate to find whether calcium and magnesium phosphates obtained from natural raw materials containing certain soluble and insoluble impurities have similar properties.

The absorption capacity for lead(II) ions of calcium phosphates obtained from chalk (Table 1) before the heat treatment is 16–20 mg-equiv g^{-1}, and it only slightly depends on the synthesis conditions. The X-ray phase analysis of the products of the reaction of the phosphates synthesized by the first procedure with lead(II) ions shows that the compound $Pb_5(PO_4)_3OH$ is the main product. A similar reaction with phosphates synthesized by the second procedure yields also lead nitrate phosphate $Pb_2PO_4NO_3 \cdot H_2O$, which is responsible for a slight increase in the absorption of lead(II) ions by samples synthesized by the second way. The increase in the chemical activity of the phosphates based on chalk after their heat treatment is due to the removal of water of crystallization.

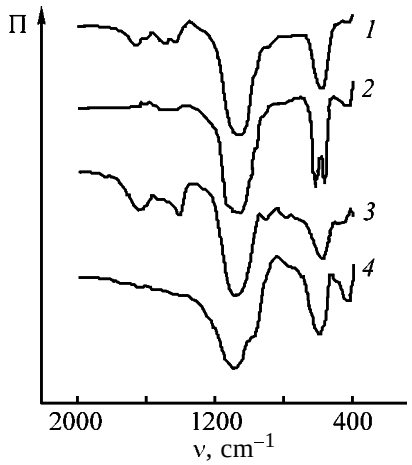

IR spectra of phosphates synthesized from (*1, 2*) chalk and (*3, 4*) dolomite: (*1, 3*) before and (*2, 4*) after heat treatment. (*T*) Transmission and (ν) wave number.

The phosphates precipitated from dolomite solutions (Table 2) absorb less lead(II), and their activity is 12.6–16.0 mg-equiv g^{-1} lead(II). As shown above, the precipitation conditions affect the chemical activity of the forming phases. The heat treatment of ammonium-containing phosphates results in a decrease in their chemical activity owing to the formation of $Mg_2P_2O_7$, which is chemically inert in reactions with metal ions.

No appreciable difference was observed in properties of the compounds obtained by precipitation in the presence or in the absence of insoluble impurities, i.e., with or without filtration of the solutions of the initial carbonates.

Anhydrous calcium and magnesium phosphates were also obtained by sintering with carbonates. The $M_{in} : P$ ratio in the starting mixtures was 1.5. The phase composition and chemical activity of the phosphates obtained by sintering of natural carbonates with ammonium phosphates at 900°C are presented in

Table 3. Phase composition and chemical activity of calcium and magnesium phosphates obtained by sintering of chalk and dolomite with ammonium phosphates at 900°C

System	Phase composition	A_{Pb}, mg-equiv g^{-1}
$CaMg(CO_3)_2$ (natural)–$NH_4H_2PO_4$	$CaMgP_2O_7$ + $(CaMg)_3(PO_4)_2$	6.38
$CaMg(CO_3)_2$ (natural)–$(NH_4)_3PO_4$	$CaMgP_2O_7$ + $(CaMg)_3(PO_4)_2$	2.50
$CaCO_3$ (natural)–$NH_4H_2PO_4$	β-$Ca_2P_2O_7$ + β-$Ca_3(PO_4)_2$	6.25
$CaCO_3$ (natural)–$(NH_4)_3PO_4$	β-$Ca_2P_2O_7$	1.94
$CaCO_3$ (cp grade)–$NH_4H_2PO_4$	β-$Ca_3(PO_4)_2$	1.64
$CaCO_3$ (cp grade)–$(NH_4)_3PO_4$	β-$Ca_2P_2O_7$	0

Table 3. To examine the possible effect of impurities present in natural minerals, we used two samples of calcium carbonate, namely, natural chalk and chemically pure grade calcium carbonate.

The sintering of natural carbonates with ammonium phosphates at 900°C yields orthophosphates containing impurities of calcium diphosphate and amorphous calcium oxide (Table 3). The capacity of this mixture for lead(II) is 1.9–6.4 mg-equiv g^{-1}. Fairly high A_{Pb} values (about 6 mg-equiv g^{-1}) for the products of sintering natural carbonates with ammonium phosphates at 900°C are due to the presence of unchanged amorphous calcium oxide when chalk is used and by the presence of a mixture of calcium and magnesium oxides when dolomite is used. Therefore, the phosphates obtained from chalk and dolomite have almost equal chemical activity. The use of ammonium phosphates considerably affects the chemical activity. When ammonium hydrophosphate is applied, the chemical activity is much higher, which is due to incomplete reaction between the carbonates and ammonium phosphate. According to the published data [25], to obtain pure orthophosphates, the temperature should be raised to 1100°C. At the same time, the sintering of chemically pure reagent chalk with ammonium phosphates results in the formation of the pure orthophosphate β-$Ca_3(PO_4)_2$ at 900°C. Its capacity for lead(II) is 0–1.64 mg-equiv g^{-1}. Impurities present in natural calcite cause the temperature of $Ca_3(PO_4)_2$ crystallization to increase.

The comparison of the chemical activities of the anhydrous phosphates obtained by sintering of carbonates with phosphates and by dehydration of the hydrates precipitated from solutions (Tables 1–3) shows that samples of the first type, in contrast to those of the second type, are inactive in reactions with metal ions. Thus, the genesis of calcium and magnesium phosphates is an important factor determining their chemical activity.

CONCLUSION

Neutral calcium and magnesium phosphates can be obtained from natural carbonates by chemical and thermal methods. The precipitated phosphates are sorption-active up to the temperature of 900°C, whereas anhydrous phosphates obtained by sintering of carbonates with ammonium phosphates at 900°C are chemically inactive in reactions with multicharged metal ions.

REFERENCES

1. Lazic, S. and Vukovic, Z., *J. Radioanal. Nucl. Chem. Articles*, 1991, vol. 149, no. 1, pp. 161–168.
2. Suzuki, S., Nakane, H., Ohshima M., *et al.*, *J. Soc. Mater. Sci. Jpn.*, 1992, vol. 41, no. 465, pp. 939–944.
3. Ganglitz, R., Holterdorf, M., Franke, W., and Marx, G., *Radiochim. Acta*, 1992, vol. 59, no. 2, pp. 253–257.
4. Shashkova, I.L., Rat'ko, A.I., and Kitikova, N.V., *Zh. Prikl. Khim.*, 1997, vol. 70, no. 11, pp. 1787–1793.
5. Shashkova, I.L., Shul'ga, N.V., and Samuskevich, V.V., *Zh. Neorg. Khim.*, 1998, vol. 43, no. 1, pp. 52–57.
6. Shashkova, I.L., Rat'ko, A.I., and Kitikova, N.V., *Zh. Neorg. Khim.*, 1998, vol. 43, no. 9, pp. 1431–1436.
7. Shashkova, I.L., Rat'ko, A.I., and Kitikova, N.V., *Izv. Ross. Akad. Nauk, Neorg. Mater.*, 1999, vol. 35, no. 9, pp. 1–5.
8. Shul'ga, N.V., Shashkova, I.L., and Samuskevich, V.V., *Zh. Prikl. Khim.*, 1999, vol. 72, no. 11, pp. 1852–1858.
9. Shashkova, I.L., Rat'ko, A.I., and Kitikova, N.V., *Colloids Surf. A: Physicochem. Eng. Aspects*, 1999, vol. 160, pp. 207–215.
10. Nagasawa, H., Morita, M., Miyake, M., *et al.*, *Gyps. Lime*, 1990, no. 229, pp. 408–412.
11. Gudz', N.Ya. and Maksin, V.I., *Khim. Tekhnol. Vody*, 1991, vol. 13, no. 5, pp. 428–436.

12. Nikiforov, A.I., Il'ina, L.A., and Sudarushkin, Yu.K., *Izv. Vyssh. Uchebn. Zaved., Khim. Khim. Tekhnol.*, 1999, vol. 42, no. 4, pp. 138–142.
13. Shashkova, I.L., Rat'ko, A.I., Mil'vit, N.V., *et al.*, *Zh. Prikl. Khim.*, 2000, vol. 73, no. 6, pp. 914–919.
14. Shashkova, I.L., Rat'ko, A.I., Panasyugin, A.S., *et al.*, *Zh. Prikl. Khim.*, 2001, vol. 74, no. 2, pp. 249–254.
15. Lur'e, Yu.Yu., *Spravochnik po analiticheskoi khimii* (Handbook on Analytical Chemistry), Moscow: Khimiya, 1989.
16. Komarov, V.S., *Adsorbtsionno-strukturnye, fiziko-khimicheskie i kataliticheskie svoistva glin Belorussii* (Adsorptive-Structural, Physicochemical, and Catalytic Properties of Clays of Belorussia), Minsk: Nauka i Tekhnika, 1970.
17. Shashkova, I.L., Kitikova, N.V., Rat'ko, A.I., and D'yachenko, A.G., *Izv. Ross. Akad. Nauk, Neorg. Mater.*, 2000, vol. 36, no. 8, pp. 990–994.
18. Kitikova, N.V., Shashkova, I.L., and D'yachenko, A.G., *Zh. Prikl. Khim.*, 2002, vol. 75, no. 2, pp. 211–216.
19. Heughebaert, J.C. and Montel, G., *Bull. Soc. Chim. Fr.*, 1970, nos. 8–9, pp. 2923–2924.
20. Schwarzenbach, G. and Flaschka, H., *Die komplexometrische Titration*, Stuttgart: Ferdinand Enke, 1965.
21. Charlot, G., *Les methods de la chimie analytique. Analyse quantitative minerale*, Paris: Masson, 1961, 4th ed.
22. Kuvshinnikov, I.M., Makarevich, V.M., Levshina, A.A., *et al.*, *Metody analiza fosfatnogo syr'ya, fosfornykh udobrenii, kormovykh fosfatov* (Methods of the Analysis of Phosphate Raw Materials, Phosphorous and Complex Fertilizers, Fodder Phosphates), Moscow: Khimiya, 1975.
23. Pechkovskii, V.V., Mel'nikova, R.Ya., Dzuyba, E.A., *et al.*, *Atlas infrakrasnykh spektrov fosfatov: Ortofosfaty* (Atlas of Infrared Spectra of Phosphates: Orthophosphates), Moscow: Nauka, 1981.
24. Corbridge, D.E.C. and Lowe, E.J., *J. Chem. Soc.*, 1954, no. 2, pp. 493–502.
25. Konstant, Z.A. and Dindune, A.P., *Fosfaty dvukhvalentnykh metallov* (Phosphates of Divalent Metals), Riga: Zinatne, 1987.
26. Shchegrov, L.N., *Fosfaty dvukhvalentnykh metallov* (Phosphates of Divalent Metals), Kiev: Naukova Dumka, 1987.
27. Mel'nikova, R.Ya., Pechkovskii, V.V., Dzuyba, E.A., *et al.*, *Atlas infrakrasnykh spektrov fosfatov: Kondensirovannye fosfaty* (Atlas of Infrared Spectra of Phosphates: Condensed Phosphates), Moscow: Nauka, 1985.

Russian Journal of Applied Chemistry, Vol. 76, No. 3, 2003, pp. 374–377. Translated from Zhurnal Prikladnoi Khimii, Vol. 76, No. 3, 2003, pp. 389–392.

SORPTION AND ION-EXCHANGE PROCESSES

Conversion of Respirator Charge into Carbon Sorbents

S. S. Stavitskaya, V. M. Vikarchuk, T. P. Petrenko, and N. T. Kartel'

Institute of Sorption and Endoecology Problems, National Academy of Sciences of Ukraine, Kiev, Ukraine

Received March 13, 2002

Abstract—A simple and efficient liquid-phase procedure was developed for the oxidative-degradation regeneration of the spent respirator charge yielding oxidized carbon with fairly high sorption capacity to heavy metal ions with a minimal loss in the strength and in the amount of the carbon material.

Gas protection is the oldest field of the activated carbon application [1]. To improve the protection efficiency, the respirator carbons are treated with various modifying agents containing metal oxides, hydroxides, carbonates, and other salts. In the case of modified carbons, detrimental and toxic compounds are removed from respirable air by physical sorption, chemisorption, and catalytic conversion into harmless products.

The typical composition of modifying agents is well known. According to [2, 3], 100-kg portion of activated carbon is impregnated using three solutions: (1) copper hydroxycarbonate (6 kg), ammonium carbonate (5 kg), 25% aqueous ammonia (10 l), and water (10 l); (2) potassium dichromate (6 kg) and water (34 l); and (3) silver nitrate (170 g) and water (0.5 l).

As seen from the above data, the resulting activated carbon sorbent-catalyst contains 12–15 wt % of inorganic additives.

Due to accumulation of spent respirators and aging of strategic stocks, their complete utilization (especially for the sake of national economy) becomes an urgent problem. However, high content of modifying agents hinders direct use of the sorbent-catalyst charge as activated carbon because of its environmental impact. Thus, it is necessary to develop procedures for conversion of the respirator charge into activated carbon.

Depending on the nature of the modifying agent to be removed, regeneration and reactivation of activated carbons can be performed by various procedures [4, 5]: displacement desorption, thermal treatment in an inert or oxidizing atmosphere or in a vacuum, desorption with superheated or live steam, extraction with various organic solvents, and external high-energy treatment (ultrahigh frequency fields, radiation-chemical or electrochemical processes, etc.).

In this work we developed a simple and efficient procedure of conversion of the spent respirator charge into a sorbent with a minimal loss of the carbon material. This procedure is based on the liquid-phase oxidative-degradation treatment of the respirator charge with a nitric acid solution, i.e., on demineralization with simultaneous partial oxidation of carbon surface and organic compounds occurring in the pores of the initial material.

Regeneration can be accompanied by partial loss of carbon material (due to burning out, corrosion, and dissolution) and surface oxidation of carbons to form proton-donor functional groups capable of ion exchange. These processes are accelerated (catalyzed) by transition metal ions, whose content in the charge is fairly high. Hence, optimization of the regeneration conditions is required.

EXPERIMENTAL

The respirator charge sample was regenerated in refluxing 25% HNO_3 for 4 h. The sample was separated from the liquid phase, washed with water to pH 7, and then successively treated with 5% ammonia, distilled water, 3% hydrochloric acid (conversion into the H form [1]), and again with distilled water to pH 7. After drying, the structural and sorption properties of the resulting sorbent were determined by common procedures [6]: static sorption capacity for Na^+ cations and Cl^- anions, by titration with NaOH and HCl solutions; sorption capacity for Methylene Blue and iodine in aqueous solutions, spectrophotometrically; pore structure and pore volume distribution, by mercury porosimetry; and specific

1070-4272/03/7603-0374$25.00

Table 1. Carbon properties

Carbon properties	Carbon after regeneration	SKT-3 carbon, TU* 6-16-2727–84
Granulometric composition: residue, wt %, on the sieve with hole size *d*, mm	1 mm, 67.7; 0.5 mm, 33.3	3.6 mm, no more than 20; 2.8, 2.0 mm, no more than 61; 1.0 mm, no more than 0.7
Content, wt %, no more than:		
moisture	15.8	13
ash		15
Granule abrasion resistance, %, no less than	75	71
Bulk density, g dm^{-3}, no more than	560	550
Total pore volume for moisture, $cm^3\ g^{-1}$	0.75	No more than 0.7
Dynamic activity for benzene, min, no less than	130	125
Static capacity for benzene, g l^{-1}, no less than	158	145

* Technical Specifications.

Table 2. Structural and sorption properties of respirator carbon before and after treatment*

Sample	Ash content, %	Moisture content, %	P, g cm^{-3}	W_s, $cm^3\ g^{-1}$	S_{sp}, $m^2\ g^{-1}$	pH	MB, mg g^{-1}
Initial	19.9	15.8	0.56	0.3	505	7.75	53
Oxidized	6.4	13	–	0.4	570	5.8	60
Activated	6.2	5	–	0.4	650	–	71
SKT-3 [7]	–	10	0.58	0.33–0.36	–	–	–

Sample	I_2, %	NaOH, mg-equiv g^{-1}	HCl, mg-equiv g^{-1}	V_Σ, $cm^3\ g^{-1}$	V_{mi}, $cm^3\ g^{-1}$	V_{me}, $cm^3\ g^{-1}$	V_{ma}, $cm^3\ g^{-1}$
Initial	25.4	–	–	0.442	–	–	–
Oxidized	19	1.8	0.0	0.56	–	–	–
Activated	–	0.2	0.4	0.74	0.36	0.28	0.018
SKT-3 [7]	–	–	0.6	0.28	0.27	0.05	0.27

* (P) Bulk density, (pH) pH of aqueous solution, (MB) sorption of Methylene Blue, (I_2) sorption of iodine; (V_{mi}, V_{me}, and V_{ma}) volumes of micro-, meso-, and macropores, respectively.

pore area, chromatographically, by thermal desorption of argon.

Then, the oxidized carbon was additionally annealed at 850°C for 1 h in an argon flow to decompose surface oxides and to convert the oxidized material into common activated carbon [1]. The resulting activated carbon was tested in parallel with the sample of the oxidized carbon by the standard procedures.

Our experimental data (Tables 1, 2; Fig. 1) allowed us to classify the resulting carbon sorbents and to determine their analogs in accordance with [7].

As seen, the samples prepared by regeneration of respirator charge mainly correspond to commercial carbon SKT-3, whose properties are regulated by

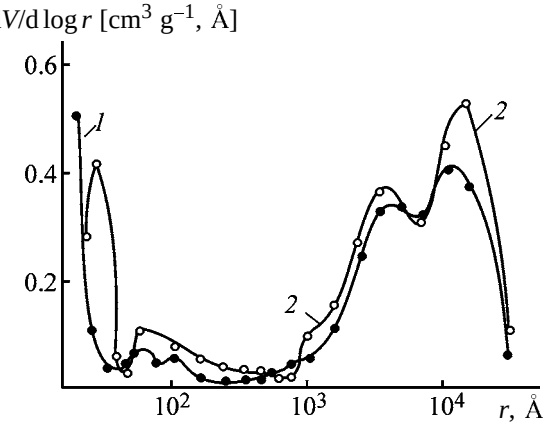

Fig. 1. Differential curve dV/dlog$r$ of pore radius (r) distribution in the (*1*) initial and (*2*) oxidized carbon.

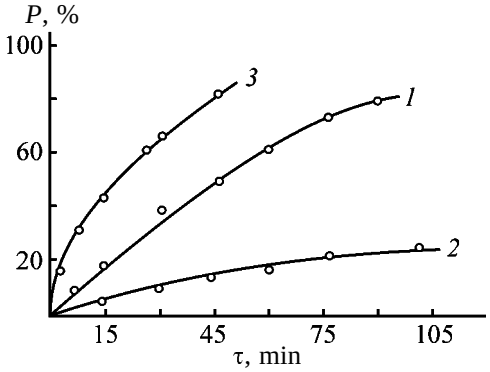

Fig. 2. Kinetics of decomposition of 1% hydrogen peroxide solution in (*1*) initial, (*2*) oxidized, and (*3*) activated respirator carbons. (*P*) Degree of decomposition and (τ) time.

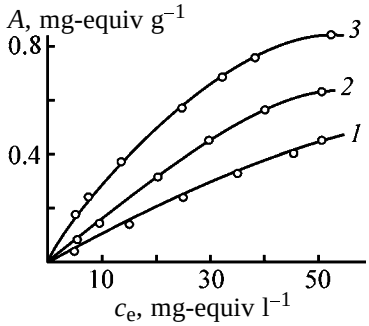

Fig. 3. Isotherms of sorption *A* of (*1*) chromium(III), (*2*) copper(II), and (*3*) iron(III) ions from aqueous nitrate solutions. (c_e) Equilibrium concentration of metal ions.

TU (Technical Specifications) 6-16-2727–84 "SKT-3 Activated Carbon."

It was found that, after prolonged oxidative regeneration, the ash content decreased from 19.9 to 6.4%. Probably, due to the removal of the impregnating salts (13.5% content), the sorption pore volume for benzene W_s (determined by the desiccator procedure [6]) and the total pore volume V_Σ also slightly increased: from 0.30 and 0.44 to 0.40 and 0.56 $cm^3\ g^{-1}$, respectively. The resulting sample exhibited the cation-exchange properties with the exchange capacity of 1.8 mg-equiv g^{-1}. Moreover, after such oxidative treatment carbons preserved their strength, and no loss of the carbon material was observed.

Additionally, we studied the catalytic properties of two samples of the carbon material prepared by regeneration of the respirator charge using a 1% model solution of hydrogen peroxide. The results are shown in Fig. 2 as the kinetic curves of H_2O_2 decomposition in the initial and oxidized carbon material. The concentration of hydrogen peroxide in solution was determined by titration with potassium permanganate [1, 8].

As seen, the highest and lowest decomposition rates are observed with activated and oxidized carbons, respectively, which agrees with published data. The initial respirator charge containing ions of copper and other metals exhibits fairly high catalytic activity, because the transition metal ions, as a rule, accelerate decomposition of hydrogen peroxide.

We also studied the ion-exchange properties of the oxidized sample toward copper(II), chromium(III), and iron(III) ions (Fig. 3). It was found that this carbon cation exchanger strongly retains Fe^{3+} and Cu^{2+} ions, whereas the sorption of Cr^{3+} ions is lower; this phenomenon is typical for the majority of oxidized carbons under the similar conditions [1].

Thus, regeneration of the respirator charge by liquid-phase oxidative degradation yields two types of carbon sorbents: activated carbon with the sorption properties similar to those of commercial SKT-3 carbon and its oxidized modification exhibiting cation-exchange properties.

Similarly to SKT-3 carbon, the activated carbon prepared by regeneration (conversion) of the respirator charge can be used to remove organic compounds of various classes (volatile solvents, dyes, gasoline, diesel oil, etc.) from gas exhausts and also as catalyst support to disinfect gas wastes containing organic contaminants, carbon oxides, etc.

CONCLUSIONS

(1) The liquid-phase procedure of oxidative-degradation regeneration (conversion) of spent respirator charge (without loss in the strength and in the amount of the carbon material) was developed. This procedure causes demineralization and simultaneous partial oxidation of the carbon surface, imparting to it cation-exchange properties.

(2) Additional thermal treatment of the oxidized material in an inert atmosphere yields the activated form of the regenerated carbon sorbent.

(3) Some physicochemical, structural, and sorption properties of the initial respirator carbons and modified carbon materials were determined by the standard procedures. In the set of properties, the resulting regenerated carbon is similar to SKT-3 brand commercial carbon.

REFERENCES

1. Tarkovskaya, I.A., *Okislennyi ugol'* (Oxidized Carbon), Kiev: Naukova Dumka, 1981.

2. Tarkovskaya, I.A., *Sto "professii" uglya* (A Hundred Jobs of Coal), Kiev: Naukova Dumka, 1983.
3. Von Kinle, H. and Bader, E., *Aktivkohle und ihre industrielle Anwendung*, Stuttgart: Enke, 1980.
4. Lukin, N.D. and Antsypovich, I.S., *Regeneratsiya adsorbentov* (Sorbent Regeneration), Leningrad: Khimiya, 1983.
5. Tarkovskaya, I.A., Tomashevskaya, A.N., Shvets, D.I., and Puzii, G.V., *Khimicheskaya, kataliticheskaya i radiatsionnaya regeneratsiya uglerodnykh sorbentov* (Chemical, Catalytic, and Radiation Regeneration of Carbon Sorbents), Chisinau: Shtiintsa, 1986.
6. Kel'tsev, N.V., *Osnovy adsorbtsionnoi tekhniki* (Principles of Adsorption Techniques), Moscow: Khimiya, 1984.
7. *Ugli aktivnye: Katalog* (Activated Carbons: Catalog), Cherkassy: NIITEKhIM, 1990.
8. Babko, A.I. and Pyatnitskii, I.V., *Kolichestvennyi analiz* (Quantitative Analysis), Kiev: Naukova Dumka, 1961.

Russian Journal of Applied Chemistry, Vol. 76, No. 3, 2003, pp. 378–382. Translated from Zhurnal Prikladnoi Khimii, Vol. 76, No. 3, 2003, pp. 393–397.

SORPTION AND ION-EXCHANGE PROCESSES

Effect of the Surface Nonuniformity of Dispersed Diabase on Properties of Composites

E. N. Iordanova, V. G. Korsakov, M. N. Tsvetkova, and D. T. Mitev

St. Petersburg State Technological Institute, St. Petersburg, Russia
Zlatarov University, Burgas, Bulgaria

Received January 23, 2001; in final form, November 2002

Abstract—Adsorption of acid–base (Hammett) indicators and Fe(III) hydroxo complexes on the surface of dispersed diabase containing 45–52% silica, which is a promising polymer filler, was studied. Changes in the energy-related characteristics of the surface in the course of grinding and chemical modification of diabase with carbon from a mixture of CCl_4 and CH_4 were analyzed.

Controlling the energy-related characteristics of the surface of dispersed solids is a promising direction in developing structural and functional polymeric composites with prescribed properties. By varying the dispersity and the composition of functional groups, one can affect the donor–acceptor properties of components, interactions at the interface between the dispersed component and the polymer, and properties of composites. Wide use of inexpensive natural materials instead of synthetic materials as fillers of polymeric composites is hindered by their inhomogeneity. The reproducibility of properties can be improved, and the interaction energy at the interface between the dispersed filler and the polymer and the structure of the interfacial layer can be optimized by polymer grafting [1], local chemical modification of the surface, or synthesis of nanometer coatings by chemical assembly technique [2]. This is only possible for dispersed materials whose particles have a strong 3*D* (mainly covalent) framework and bear reactive functional groups on the surface.

In this work we examined the possibility of chemically modifying with carbon the surface of dispersed diabase produced as waste in manufacture of building materials and also studied the functional composition and energy nonuniformity of the initial and modified samples.

EXPERIMENTAL

Diabase samples [magmatic rock strongly modified by secondary processes, with silica content of 45–52% [3]; Dzhebel deposit, Bulgaria; mineralogical (phase) composition: plagioclase, pyroxene, olivine, hornblende] were ground in a ball mill and fractionated (particle diameter in different fractions 20–125 μm). The diabase surface was modified with carbon on a laboratory setup (Fig. 1) in fixed bed in a quartz reactor from a mixture of CCl_4 and CH_4 at 500°C for 1 h. Methane was purified with active copper and sorbents to remove oxygen and water vapor in units *1* and *2* and was saturated with tetrachloromethane vapor in a bubbler *3* and fed into reactor *4* having the form of a quartz tube 260 mm long and 46 mm in diameter with external Nichrome coil for heating. A quartz grid with 0.5–1-mm openings was welded within the reactor at a height of 60 mm. The grid was covered with glass fiber fabric on which a 50-g portion of diabase was placed. The temperature of the diabase bed was measured with a thermocouple and controlled and recorded with EPP-09 electronic potentiometers *5* and *6*. The reaction proceeds in accordance with the equation

$$CH_4 + CCl_4 \rightarrow 2C + 4HCl.$$

Hydrogen chloride formed in the reaction was absorbed with a 0.1 N NaOH solution in vessel *7*.

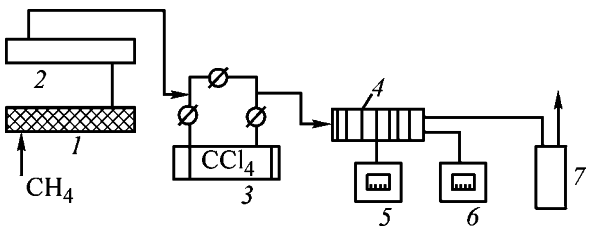

Fig. 1. Schematic of the laboratory setup for modification of dispersed diabase with carbon in fixed bed (for explanations, see text).

1070-4272/03/7603-0378$25.00 © 2003 MAIK "Nauka/Interperiodica"

Changes in donor–acceptor properties of the diabase surface were evaluated by Tanabe's spectrophotometric version [4] of the indicator method, based on adsorption of acid–base (Hammett) indicators with known pK_a in the range from –4 to 12.8 [4, 5]. The optical densities D_0 of the initial indicator solutions were measured with an SF-26 spectrophotometer, after which suspensions of modified diabase in these solutions were prepared and optical densities D_1 of the solutions were measured after the adsorption equilibrium was attained and the solution was separated from the sediment by decanting or centrifuging. To take into account the influence exerted on the optical density by changes in the pH value on contact of a sample with solution and partial dissolution of the sample, a suspension of the initial and modified diabase in distilled water was prepared, the sediment formed was separated after 30 min, an indicator solution was added, and the optical density D_2 was measured. The content of active centers q_{pK_a} (mmol g^{-1}) with a given pK_a value was calculated by the formula

$$q_{pK_a} = \frac{c_{in}V_{in}}{D_0}\left|\left|D_0 - D_1\right|/m_1 \pm \left|D_0 - D_1\right|/m_2\right|,$$

where c_{in} and V_{in} are the concentration and volume of the indicator solution, m_1 and m_2 are weighed portions of diabase, and the ± sign corresponds to oppositely directed changes in D_1 and D_2 with respect to D_0.

The distribution of adsorption centers over the surface of the samples studied was plotted in the coordinates $q_{pK_a} = f(pK_a)$.

The overall energy-related characteristics of the surface of modified diabase were determined using a high-sensitivity method based on potentiometric recording of the potential curves of adsorption of iron hydroxoaqua complexes from solution [6, 7]. A reversible redox system Fe^{3+}/Fe^{2+} and an electrochemical cell with indifferent (platinum) electrode and calomel reference electrode were used in measurements. The concentration of Fe(III) and Fe(II) ions in the starting solution was 10^{-4} and 10^{-5} M, respectively. The potentials of the indifferent electrode in the starting solution and in a suspension of diabase in this solution were measured. The potential curves were calculated using the equation

$$\Delta\mu_Q = \Delta\varphi_m F + RT\ln Q,$$

where $\Delta\mu_Q$ is the adsorption potential for hydroxo complexes of iron ions; $\Delta\varphi_m$, the difference of potentials of the indifferent electrode in the starting solution and in the suspension; F, the Faraday number. The surface fraction Q (filling of the surface with adsorbed iron hydroxoaqua complexes at constant solution concentration) is determined by the amount m of the solid in the suspension.

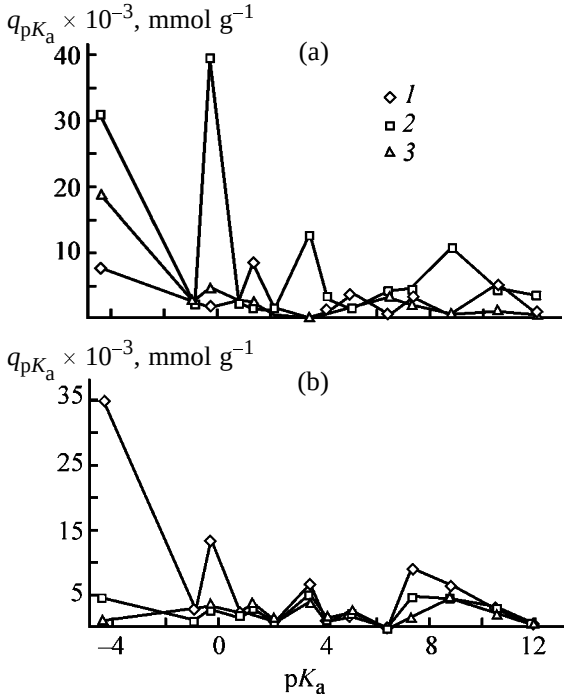

Fig. 2. Distribution with respect to donor–acceptor properties of adsorption centers over the surface of (a) initial diabase of different fractions and (b) that modified with carbon. (q_{pK_a}) Content of centers with the corresponding pK_a value; the same for Fig. 3. Diabase particle size (μm): (*1*) 40, (*2*) 40–80, and (*3*) 80–125.

In the given method, the concentration measurements commonly made in studying adsorption isotherms are replaced by the potential measurements in dilute solutions, which allows a study at low surface filling of dispersed materials with the adsorbate (down to Q = 0.01–0.001). Therefore, this method is used to prognosticate the properties of fillers for polymers, catalysts, and other active materials [8, 9].

Figure 2 [for clarity, the points in 1D distributions (histograms) are connected] shows that the surface of the initial diabase samples is characterized by high nonuniformity depending on dispersity, which is probably due to the complex mineralogical (phase) composition of diabase. Lewis (electron-donor and -acceptor) adsorption centers characterized by pK_a values of –4.4 and –0.29 and Brønsted (proton-donor and -acceptor) centers with pK_a 1.3, 3.4, 5.0, 6.4, 8.8, 10.5 are present on the surface of diabase of different fractions. Figure 3a shows the content Lewis base and Brønsted acid and base centers as functions of the fraction size. The total content of adsorption centers

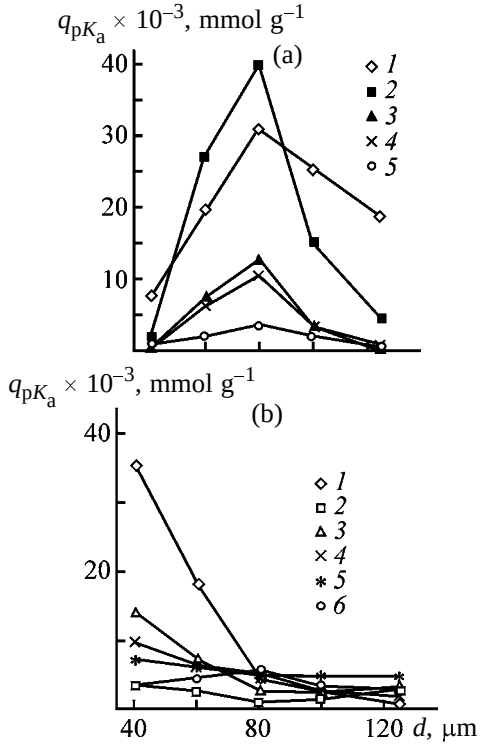

Fig. 3. Content of acid–base centers on the surface of (a) initial and (b) modified diabase as a function of dispersity. (*d*) Particle size of diabase. pK_a value: (a) (*1*) –4.4, (*2*) –0.29, (*3*) 3.46, (*4*) 8.8 and (*5*) 12.8; (b) (*1*) –4.4, (*2*) –0.91, (*3*) –0.29, (*4*) 7.3, (*5*) 8.8, and (*6*) 12.8.

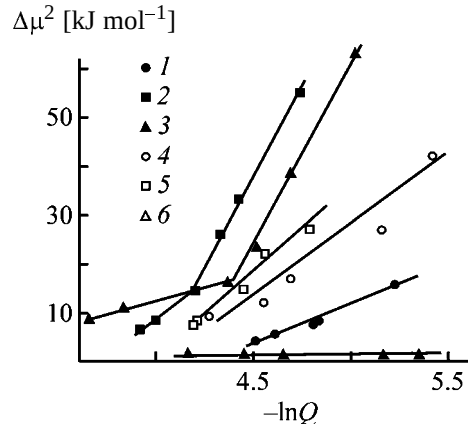

Fig. 4. Potential curves of adsorption of iron(III) ions on (*1–3*) initial and (*4–6*) modified diabase, plotted in the coordinates of the Dubinin equation. (Δμ) Adsorption potential of Fe(III) ions and (*Q*) surface filling. Fraction size (μm): (*1, 4*) 40, (*2, 5*) 40–80, and (*3, 6*) 80–125.

and centers with pK_a –0.29 is the highest for the 40–80-μm fraction. The increase in the content of the centers upon grinding of the initial diabase (80–125 μm) to 40–80 μm is due to a rise in the specific surface area, surface activation (formation of macroradicals), and changes in the phase composition as a result of mechanochemical processes. However, subsequent grinding to less than 40 μm leads to a decrease in the content of the centers, which is probably due to interaction of particles at the most active centers. The most sensitive to grinding are Lewis centers with pK_a –0.29 and –4.4 (radicals formed in dehydration and dehydroxylation of the diabase surface in the course of grinding), Brønsted acid centers with pK_a 3.46 (OH groups), and Brønsted base centers with pK_a 8.8, which may be formed in dissociation of substituted functional groups of the –O–Me type.

In modification of the diabase surface with carbon, the composition of active centers is little dependent on the dispersity, but the number of centers changes (Fig. 2b). A large number of Lewis centers (possibly carbon macroradicals) with pK_a –4.4 and –0.29 appear on the surface of dispersed diabase (<40-μm fraction). Their content increases to a much greater extent than does the surface area upon grinding (Fig. 3b). This points to weaker influence of the phase (mineralogical composition) heterogeneity of particles on the surface properties. For the <40-μm fraction, the number of Brønsted base centers with pK_a 7.3 and 8.8 also grows. However, the content of these centers for all fractions of modified diabase is much lower than that for the 80-μm fraction of the initial sample.

Changes in the qualitative and quantitative composition of active centers upon grinding and modification of diabase lead to changes in the overall energy-related characteristics found potentiometrically. Figure 4 shows the potential curves of adsorption of Fe(III) hydroxoaqua complexes on the diabase surface in the coordinates of the Dubinin equation [10] $\Delta\mu^2 = f(\ln Q)$. The equation was derived in this form by Dubinin [10] for porous adsorbents. However, it is also successfully used for describing monolayer adsorption onto solid surfaces from solutions [11], since only the assumption of a Gaussian distribution of the volume of the adsorption space with respect to potentials was made in deriving this equation.

Figure 4 shows that the potential curves plotted in these coordinates include one or several linear (homotatic) portions corresponding to filling of centers of varied nature. (The term "homotatic" is used in the adsorption theory, e.g., in the Ross–Olivier method [12], for designation of areas of the same type on an energetically nonuniform surface.)

In accordance with the physical meaning of the Dubinin equation, the slopes of the $\Delta\mu^2$ regression with respect to $\ln Q$ characterize the surface nonuniformity and its changes in the course of chemical modification. The surface of the initial diabase is non-

uniform because of the diversity of the mineralogical composition; mechanochemical processes and chemical modification lead to changes in the surface composition. The results are summarized in the table.

Samples of the initial diabase of the 80–125- and 40–80-μm fractions are characterized by high surface nonuniformity. As seen from the table, the slopes of the $\Delta\mu$–$\ln Q$ dependences are only slightly different (82 and 86) for these fractions in the $\ln Q$ range from –4.3 to –5.0. However, the potential curve for the 80–125-μm fraction contains a portion with smaller slope at fillings $Q \geq 0.02$, which may be due to phase heterogeneity of the initial sample before grinding. The potential curve for the <40-μm fraction has only a single portion, i.e., the surface becomes more uniform after grinding.

Much stronger influence is exerted on the surface uniformity by modification of coarsely dispersed diabase with carbon. The slope of the linear dependence $\Delta\mu^2$–$\ln Q$ decreases by two orders of magnitude for the 80–125-μm fraction. The slopes of the linear portions for 40–80- and <40-μm fractions of modified diabase are close (which points to filling of adsorption centers of the same type) and much exceed that for the 80–125-μm fraction. The increase in the adsorption potential and in the slope of the $\Delta\mu^2$–$\ln Q$ regression after modification of the <40-μm fraction of diabase (see table) indicates that the surface activity becomes higher.

The linear regressions of the potential curves intersect the abscissa at $\ln Q$ from –4.0 to –4.2 (Q from 0.01 to 0.15), i.e., the adsorption potential is zero at the surface filling exceeding 0.02.

The low adsorption potentials of modified diabase of the 80–125-μm fraction can be accounted for by the fact that carbon deposited onto the diabase surface blocks oxygen-containing donor–acceptor centers on the surface of the initial coarsely dispersed sample (containing a comparatively small amount of functional groups). This leads to hydrophobization of the surface and precludes adsorption of hydroxo complexes (which are adsorbed by the outer-sphere mechanism into a film of adsorbed water [6]). Naturally, the coefficient of the $\Delta\mu^2$–$\ln Q$ correlation decreases at the exceedingly narrow range of variation of the chemical potential.

The results of potentiometric measurements are in full agreement with the data obtained in studying the distribution of adsorption centers with respect to donor–acceptor properties (Figs. 2 and 3b), according to which the highest content of these centers on the initial diabase is observed for the 40–80-μm fraction, and after modification the content of all the centers decreases. An increase in the adsorption energy after modification is only observed for the <40-μm fraction, i.e., modification must presumably enhance the reactivity of these samples and the interaction energy at the filler–polymer interface.

Regression equation for $\Delta\mu^2$–$\ln Q$ correlation

Diabase fraction size, μm	Regression equation	Correlation coefficient
Initial samples		
80–125	$82\Delta\mu^2 - 310$	0.994
40–80	$86\Delta\mu^2 - 240$	0.996
<40	$16\Delta\mu^2 - 70$	0.982
Samples modified with carbon		
80–125	$0.63\Delta\mu^2 - 1.30$	0.810
40–80	$34\Delta\mu^2 - 130$	0.976
<40	$28\Delta\mu^2 - 110$	0.942

In other words, the initial and modified samples with different dispersities differ both in the composition of adsorption centers and in overall energy-related characteristics of the surface, which must reflect on their properties as fillers for composites and, in particular, for rubbers.

To evaluate the influence exerted by the surface properties of initial and modified diabase samples on the physicomechanical characteristics of rubbers, vulcanizates were prepared from SKMS-30ARKP (nonpolar) and SKN-40AM (polar) rubbers with 50 wt parts of filler per 100 wt parts of rubber. The vulcanization was effected with a sulfur vulcanizing group. For comparison, vulcanizates containing the same volume amount of chalk and PGM-33 carbon black were prepared.

Physicomechanical tests demonstrated that vulcanizates based on SKMS-30ARKP rubber are characterized by weak enhancing effect: nominal rupture strength σ_r ~2 MPa (σ_r = 1.3, 2.7, and 16.7 MPa for, respectively, rubber without filler and that with chalk and carbon black). This is in agreement with the increasing elasticity of the rubbers: relative elongation ε = 430% (ε = 320, 420, and 300%, respectively). The rise in dispersity upon diabase grinding and the surface modification of diabase with carbon improve somewhat the nominal strength and the modulus of elasticity of the rubbers and do not affect the degree of equilibrium swelling of vulcanizates in benzine, i.e., leave unchanged the density of the 3D network. This confirms the weak interaction between nonpolar SKMS-30ARKP rubber and fillers.

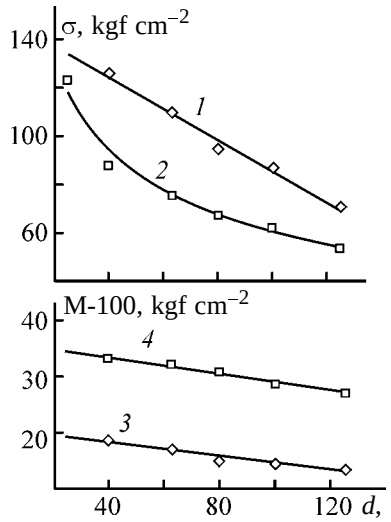

Fig. 5. (*1, 2*) Nominal rupture strength σ and (*3, 4*) stress at 100% relative elongation, M-100, for vulcanizates based on SKN-40AM rubber vs. dispersity *d* of filler: (*1, 3*) initial and (*2, 4*) modified diabase.

Much stronger influence is exerted by the type and dispersity of a filler on the properties of vulcanizates based on SKN-40AM rubber containing nitrile groups. As seen from Fig. 5, the nominal strength, modulus of elasticity, and relative elongation of the rubbers depend on the particle size and on modification of the diabase surface with carbon. The strength of rubbers filled with dispersed diabase of 20-, 40-, 63-, and 80-μm fractions is 10–12 MPa, which is 2 times the value for similar rubbers with chalk (~6 MPa). The strength of rubbers modified with carbon decreases and their modulus grows, which can be accounted for by an increase in their density and decrease in the energy of cross-linking bonds (density and strength of the network). This is also confirmed by the fact that rubbers with carbon-modified diabase of the 20-μm fraction exhibit high oil-and-gas resistance (close to that of rubbers filled with PGM-33 carbon black).

Therefore, the initial dispersed diabase can be used as weakly reinforcing filler for rubbers, together with such widely used mineral fillers as chalk and kaolin. Dispersion and modification of the initial diabase with carbon enhance its adsorption activity. This favors an increase in the number of weak cross-linking bonds and in the density of the 3D network, especially for vulcanizates based on polar rubbers, and leads to substantial improvement of physicomechanical characteristics in comparison with rubbers filled with active chalk.

CONCLUSIONS

(1) The possibility of directed control of energy-related characteristics of the diabase surface by dispersion and chemical modification of diabase with nanometer layers of carbon in fixed bed is demonstrated.

(2) The increase in the content of donor–acceptor centers in dispersion of diabase is due to larger specific surface area, surface activation, and changes in phase composition. Modification of the diabase surface with carbon leads to higher content of Lewis centers and weaker influence of phase heterogeneity on the energy-related characteristics of the surface.

(3) Changes in the composition and content of donor–acceptor centers in dispersion and modification with carbon improve physicomechanical characteristics of vulcanizates based on polar rubbers and diabase, which allows wide use of this inexpensive natural material as filler for composites, instead of deficient mineral fillers.

REFERENCES

1. Ivanchev, S.S. and Dmitrenko, A.V., *Usp. Khim.*, 1982, vol. 51, pp. 1178–1188.
2. Aleskovskii, V.B., *Khimiya nadmolekulyarnykh soedinenii* (Chemistry of Supramolecular Compounds), St. Petersburg: Sankt-Peterb. Gos. Univ., 1996.
3. Petrov, R.R., Demin, A.M., Ezhov, A.I., *et al.*, *Petrograficheskii slovar'* (Petrographic Dictionary), Moscow: Nedra, 1981.
4. Tanabe, K., *Solid Acids and Bases. Their Catalytic Properties*, Tokyo: Kodansha, 1970.
5. Nechiporenko, A.P., Burenina, T.A., and Kol'tsov, S.I., *Zh. Obshch. Khim.*, 1984, vol. 55, no. 9, pp. 1907–1912.
6. Korsakov, V.G., *Prognozirovanie svoistv materialov* (Prognostication of Properties of Materials), St. Petersburg: Leningr. Gos. Tekhnol. Inst., 1988.
7. Aleskovskii, V.B. and Korsakov, V.G., *Fiziko-khimicheskie osnovy ratsional'nogo vybora aktivnykh materialov* (Physicochemical Foundations for Rational Choice of Active Materials), St. Petersburg: Leningr. Gos. Univ., 1980.
8. Korsakov, V.G. Aleskovskii, V.B., Yur'evskaya, I.M., and Myasnikova, A.A., *Dokl. Akad. Nauk SSSR*, 1978, vol. 242, no. 2, pp. 661–664.
9. Rudik, T.V., Myasnikova, A.A., Ershov, V.A., *et al.*, *Zh. Prikl. Khim.*, 1988, vol. 61, no. 2, pp. 410–412.
10. Dubinin, M.M., *Adsorbtsiya i poristost'* (Adsorption and Porosity), Moscow: Akad. Khim. Zashchity, 1972.
11. Pietrzik, S., *Roczn. Chem.*, 1970, vol. 44., no. 4, pp. 817–824.
12. Jaycock, M.J. and Parfitt, G.D., *Chemistry of Interfaces*, New York: Wiley, 1981.

Russian Journal of Applied Chemistry, Vol. 76, No. 3, 2003, pp. 383–386. Translated from Zhurnal Prikladnoi Khimii, Vol. 76, No. 3, 2003, pp. 398–401.

APPLIED ELECTROCHEMISTRY AND CORROSION PROTECTION OF METALS

Separation of Cobalt and Tungsten Carbide by Anodic Dissolution of Hard Alloys in Phosphoric Acid Solutions

V. V. Malyshev and S. A. Butov

Kiev Polytechnic Institute, Ukrainian National Technical University, Kiev, Ukraine

Received June 24, 2002; in final form, January 2003

Abstract—Anodic behavior of the VK–6 alloy in phosphoric acid solutions was studied potentiometrically, voltammetrically, and by X-ray phase and metallographic analyses. The potential range was determined in which the phase of cobalt–tungsten alloy dissolves with formation of soluble compounds of the above metals and the tungsten carbide phase does not dissolve. The results obtained can be used in reprocessing of hard alloy scrap.

Tungsten carbide–cobalt alloys were the first metal–ceramic hard alloys (HAs) applied in industry [1]. Their use is still wide. To return valuable HA components into the production, it is necessary to search for a way for secondary reprocessing of wastes containing these components. Suitable raw materials for the HA production are matrices of spent drilling and cutting instrument and scrap.

Current methods for separating HA components use different treatment conditions and chemical reagents [2]. The drawback of the dissolution of HA components in acids and their mixtures is toxicity of the applied chemicals. In part, this drarwback is avoided in a reprocessing method [3] based on anodic dissolution of spent diamond and HA instrument in a chloride–hydroxide melt. In this method, tungsten and carbon are transferred to the melt in the form of tungstate and carbonate, respectively, whereas materials impregnating HA matrices are accumulated near the cathode in the form of highly disperse metallic powders. The final product in the suggested method is tungsten oxide WO_3, which requires further reprocessing prior to being returned into the manufacture of HA instrument.

In this work, we studied the separation of cobalt and tungsten carbide WC by anodic dissolution in phosphoric acid. A phosphoric acid solution as electrolyte, unlike molten media, allows selective separation of the HA components and ensures separation of WC suitable for return into the production. A strong tendency of tungsten and its carbide to passivation in aqueous solutions determines the specificity of their electrochemical behavior. Mainly, the electrode potentials, cathodic reactions of electrochemical separation of gases, and the oxidation processes involving them have been studied in solutions of hydrochloric and sulfuric acids [4, 5]. The electrochemical separation of hydrogen on WC has been studied in [6], and the recombination of adsorbed hydrogen atoms was believed to be the limiting stage. The shape of the anodic polarization curves for W in H_2SO_4 solutions corresponds to passage of the active dissolution to the passive state of the metal [4, 5].

The anodic dissolution of the electrodes made of WC–Co alloy, metallic cobalt, and tungsten carbide WC was studied in a three-electrode cell. The working electrolyte was 1.25 M H_3PO_4. The solid alloy electrodes were small bars made of VK-6 alloy (WC–6% Co) obtained by traditional technology of powder metallurgy [2]. Tungsten carbide electrodes were prepared by hot pressing of tungsten and carbon powders at 2200°C and 1000 kg mm^{-2}. Cobalt electrodes were plates of ultrapure metallic foil. The surface area of the electrodes was 1–2 cm^2. Prior to measurements, the working electrodes were thoroughly abraded and polished by the procedures proposed for the corresponding materials [7]. Immediately before measurements, the polished surface was washed with alcohol and distilled water. The auxiliary electrode was a platinum plate with a surface area of 1.0–1.5 cm^2. The electrode potentials were measured relative to a saturated calomel electrode located outside the cell and coupled to it with a salt bridge. All measurements were done in nitrogen at 18°C. The steady-state potentiostatic curves were obtained with a PI-50-1 potentiostat by fixing a steady-state current. For measurements of the variations of current with time, the same potentiostat and a PDL-4 recorder were used. The metal-

1070-4272/03/7603-0383$25.00

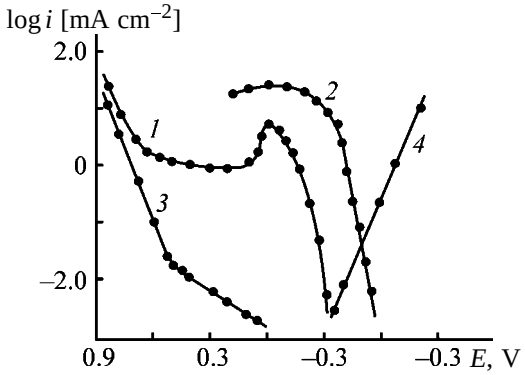

Fig. 1. Steady-state potentiostatic polarization curves log *i*–*E* for anodic dissolution of (*1*) VK-6 hard alloy, (*2*) Co, and (*3*) WC; (*4*) curve of hydrogen evolution on tungsten carbide electrode in 1.25 M H_3PO_4. 18°C; the same for Fig. 2.

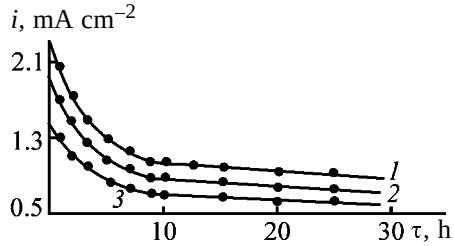

Fig. 2. Variatoin with time τ of the rate *i* of dissolution of Co–W alloy from VK-6 hard alloy. Electrode potential, V: (*1*) –0.15, (*2*) –0.20, and (*3*) –0.25.

lographic analysis was performed on a Neophot-21 electron microscope. The phase composition of the samples was identified on a DRON-4.0 diffractometer, and that of gases, on a Selmichrom-1 chromatograph. The carrier gas was argon or helium. The data obtained were processed on an IBM-486 computer. The concentration curves of the Co and W distribution over the cross sections were obtained on an MS-46 Cameca X-ray microanalyzer. The partial currents for metal dissolution were determined from comparison of the recorded current with the value obtained from analysis of the solutions.

The typical steady-state potentiostatic polarization curves for the anodic dissolution of VK-6, Co, and WC and those of the recovery of hydrogen ions on tungsten carbide electrode are presented in Fig. 1. The polarization curves taken on cycling potential are reproduced with virtually no hysteresis. Moreover, the behavior of the curves is not noticeably affected by mixing. The steady-state potential of the VK-6 electrode is –0.32 to –0.34 V, i.e., it lies between the steady-state potentials of the components (–0.55 to –0.57 V for carbon and –0.09 to –0.11 V for tungsten carbide). In the polarization curves taken on VK-6 electrode (curve *1*), three sections are clearly

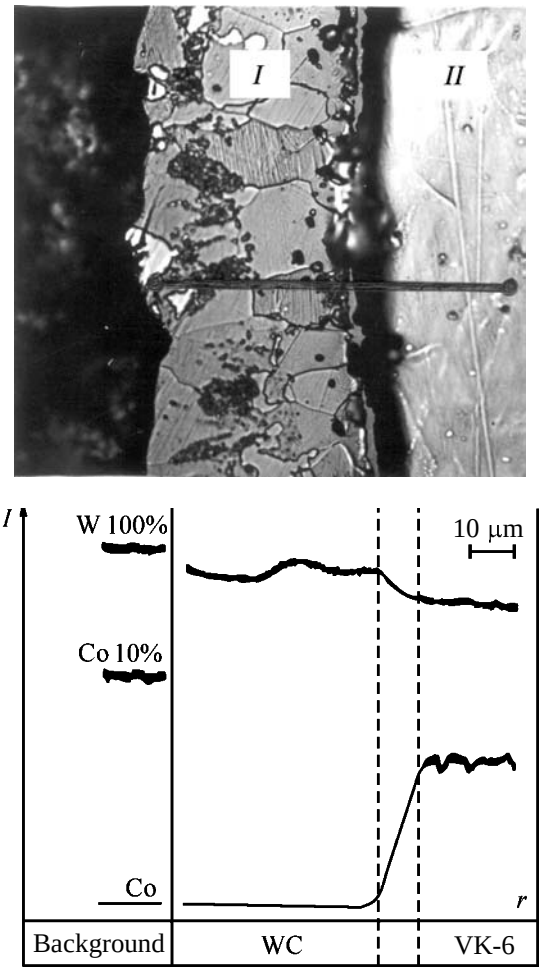

Fig. 3. Photomicrograph of the cross sectional of VK-6 alloy anodically dissolved in 1.25 M H_3PO_4 and the concentration curves *I*–*r* for Co and W distribution between the electrode region subjected to anodic dissolution and the intact region. Electrode potential –0.10 V, dissolution time 10 h, magnification 600. Electrode region: (*I*) subjected to dissolution and (*II*) intact.

observed. The logarithm of the current density increases linearly in the first section (–0.30 to –0.05 V), sharply drops at –0.02 V, remains virtually constant with potential increasing to 0.7 V (section II), and exponentially increases again at higher potentials (section III).

The VK-6 samples were anodically dissolved in the potentiostatic mode at the potentials varied from –0.25 to –0.05 V, i.e., within the first section of the potentiostatic curve. In the process, the current slowly decreases with time (commonly during 10–12 h) and then remains virtually constant (Fig. 2). In the cross-sectional view of the VK-6 alloy subjected to anodic dissolution, two zones are observed (Fig. 3): the base not subjected to dissolution and the partially dissolved

layer. According to the X-ray phase analysis, the layer subjected to dissolution contains WC, whereas metallic cobalt and tungsten are absent. These data are also confirmed by X-ray spectral microanalysis. The W content (93.1–93.8%) in the dissolved layer is lower than that in the tungsten reference, which corresponds to its weight content in the carbide.

To confirm the predicted dissolution mechanism, the VK-6 samples were anodically dissolved at various potentials corresponding to sections I and II of the polarization curve, and at varied dissolution times. The results of analysis of the solutions obtained are presented in the table. With increasing potential, the rate of dissolution of Co and W and the Co/W weight ratio in the dissolved fraction increase. The chromatographic analysis revealed gaseous CO_2 evolving at the anode at the potentials more positive than 0.70 V.

The composition of the solutions after anodic dissolution of the alloys (see table) and the results of the metallographic analysis, X-ray phase analysis, and X-ray spectral microanalysis allow a conclusion that section I of the polarization curve corresponds to separate dissolution of the Co–W phase, with the WC grains remaining in the material. Such dissolution process can be represented by the reactions

$$Co \rightarrow Co^{2+} + 2e, \quad E^0 \approx -0.59 \text{ V}; \qquad (1)$$

$$W + 4H_2O \rightarrow WO_4^{2-} + 8H^+ + 6e, \quad E^0 \approx -0.12 \text{ V}. \qquad (2)$$

The W content in the total mass of the dissolved metals is 11.3–14.2% (Table 1), which corresponds to its solubility in metallic cobalt [8]. It should be also noted that most of the anodic current corresponds to the Co dissolution. Therefore, the polarization curves taken with VK-6 and Co electrodes are similar in appearance and quantitative characteristics (Fig. 1, curves *1*, *3*).

The joint dissolution of Co and W markedly accelerates with increasing potential. As the potential of –0.02 V is attained, the current sharply drops to 15–20% of the maximal value. According to the X-ray phase analysis, tungsten oxide WO_3 and cobalt phosphate are major components of the passivating film. With further increase of the potential, the current starts to grow slowly, and after a potential of 0.7 V is attained, it increases sharply. This is due to the fact that the contribution of the reaction

$$WC + 6H_2O \rightarrow WO_4^{2-} + CO_2 + 12H^+ + 10e,$$

$$E^0 \approx 0.02 \text{ V}, \qquad (3)$$

Rates of dissolution of cobalt and tungten from VK-6 alloy at various electrode potentials. 1.25 M H_3PO_4, 18°C

E, V	τ, h	Dissolution rate, g m^{-2} h^{-1}		W, wt %
		Co	W	
–0.33	30	0.095	b.s.l*	–
–0.25	20	3.419	b.s.l	–
–0.20	20	10.652	1.391	11.3
–0.15	20	18.006	2.876	12.6
–0.10	10	25.556	4.571	14.1
–0.05	10	28.373	5.319	14.2
0.80	5	16.625	48.315	87.9

* (b.s.l.) Below the sensitivity limit of atomic absorption spectroscopy.

to the anodic process considerably increases at the potentials more positive than its reversible potential. In this case, virtually the whole amount of dissolved W, except for a minor amount obtained by reaction (1) and calculated from data on the Co dissolution, is formed by reaction (3). This conclusion is also supported by the data on the contribution of the partial reactions to the total anodic process.

In the absence of oxygen in a solution, the cathodic current is due to hydrogen evolution (Fig. 1, curve *4*). Extrapolation of the polarization curve to the potential axis E_{cor} corresponds to the currents of the same order as for the Co dissolution without polarization. This also suggests that the rate of dissolution of the Co–W phase from the solid alloys depends on the sample thickness, Co content in the alloy, and size of Co and WC grains. Indeed, replacement of the WC–6% Co alloy (1.0–2.0-μm grains) by the WC–5% Co alloy (0.5–1.0-μm grains) increases the dissolution rate by a factor of 1.1–1.3.

Selective dissolution of the Co–W phase can be used for reprocessing of hard alloy scrap. In this case, it is desirable that the separation of Co from WC be performed at low energy consumption. After dissolving the Co–W phase, the residual WC should be ground, and then it can be used again in manufacture of hard alloy instrument.

REFERENCES

1. Kiffer, R. and Benezovskii, F., *Tverdye splavy* (Hard Alloys), Tret'yakov, V.I., Ed., Moscow: Metallurgiya, 1971.
2. *Svoistva, poluchenie i primenenie tugoplavkikh soedinenii: Spravochnik* (Properties, Production, and Ap-

plication of Refractory Compounds: Reference Book), Kosolapova, T.Ya., Ed., Moscow: Metallurgiya, 1986.

3. Shapoval, V.I., Malyshev, V.V., and Sushinskii, N.M., *Ekotekhnol. Resursosberezh.*, 1999, no. 6, pp. 46–50.
4. Vas'ko, A.T., *Elektrokhimiya molibdena i vol'frama* (Electrochemistry of Molybdenum and Tungsten), Kiev: Naukova Dumka, 1977.
5. Vas'ko, A.T., and Kovach, S.K., *Elektrokhimiya tugoplavkikh metallov* (Electrochemistry of Refractory Metals), Kiev: Tekhnika, 1983.
6. Baibatyrov, E.N., Palanker, V.Sh., and Sokol'skii, D.V., *Elektrokhimiya*, 1974, vol. 10, no. 1, pp. 162–164.
7. Dasoyan, M.Ya., Pal'mskaya, I.Ya., and Sakhorova, E.V., *Tekhnologiya elektrokhimicheskikh pokrytii* (Electrochemical Coating Technology), Leningrad: Mashinostroenie, 1989.
8. Hansen, M., and Anderko, K., *Constitution of Binary Alloys*, New York: McGraw-Hill, 1958.

Russian Journal of Applied Chemistry, Vol. 76, No. 3, 2003, pp. 387–390. Translated from Zhurnal Prikladnoi Khimii, Vol. 76, No. 3, 2003, pp. 402–405.

APPLIED ELECTROCHEMISTRY AND CORROSION PROTECTION OF METALS

Tin Electroplating from Sulfate Electrolyte Containing Syntanol, Formalin, and Coumarin

G. I. Medvedev, L. A. Nekrasova, and N. A. Makrushin

Novomoskovsk Institute, Mendeleev Russian University of Chemical Engineering, Novomoskovsk, Tula oblast, Russia

Received April 29, 2002

Abstract—Tin electroplating from sulfate electrolyte containing organic additives was studied. The electrolyte formulation for preparing lustrous smooth tin coatings was developed.

Our previous study [1–4] on tin electroplating from sulfate electrolyte containing organic additives show that introduction of Syntanol, Formalin, butane-, 2-butene-, and 2-butyne-1,4-diols, and benzyl and propargyl alcohols favors formation of lustrous coatings.

In this work we studied tin electroplating from sulfate electrolyte containing Syntanol, Formalin, and coumarin. Coumarin is a luster-producing and smoothing additive to the nickel plating solution [5].

We studied tin electroplating in the electrolyte containing from 5 to 50 g l^{-1} $SnSO_4$ and from 90 to 100 g l^{-1} H_2SO_4. Synthanol DS-10, coumarin, and Formalin (37 % formaldehyde solution) were introduced in amounts of 1–4 g l^{-1}, 0.1–2 g l^{-1}, and 1–10 ml l^{-1}, respectively.

The coumarin solubility in the electrolyte was found to be 2 g l^{-1}. The equilibrium concentration is attained within 20 h. Tin films 6–15 μm thick were deposited on copper supports. The polarization curves were recorded with a P-5828 potentiostat. The luster of the samples was measured on an FB-2 photoelectric luster meter.

The degree of the surface filling with the organic additives θ was estimated from the polarization data by the equation [6]

$$\theta = 1 - \exp(\Delta E/b),$$

where ΔE is the cathodic polarization; b is the constant of the Tafel equation, determined form the polarization curves in the ΔE–$\log i_c$ coordinates.

The smothing power of the electrolytes P was determined by direct profilographic measurements of the sample surface with a sinusoid microprofile. The calculation was performed by the equation [7]

$$P = 2.3a/[2\pi h_{av}\log(H_0/H_i)],$$

where a is the wave amplitude of the sinusoid microprofile (μm), h_{av} is the average thickness of the coating (μm), and H_0 and H_i are the initial and final amplitude of the sinusoid microprofile, respectively (μm).

The capacitance of the electrical double layer in the course of electrolysis was measured by the sequential substitution scheme using a P-5021 ac bridge operating at 30 kHz.

Tin was plated at 18–25°C without stirring or with stirring of the electrolyte with a petal stirrer.

We studied the appearance of the coating as influenced by the organic additives to an electrolyte containing, respectively, 30 and 100 g l^{-1} of $SnSO_4$ and H_2SO_4. Dull coatings were obtained in the presence of 1–4 g l^{-1} Syntanol. Low-quality coatings were plated from the electrolytes containing Formalin (1–10 ml l^{-1}), coumarin (0.1–2 g l^{-1}), or both these additives. Dull coating are formed in the electrolyte containing Syntanol (1–4 g l^{-1}) and coumarin (0.1–2 g l^{-1}), or Syntanol and Formalin (6–8 ml l^{-1}).

The quality of the coatings is substantially improved after addition of coumarin to the electrolyte containing Syntanol (2–3 g l^{-1}) and Formalin (6–8 ml l^{-1}). At the coumarin concentration of 0.5–1 g l^{-1}, lustrous coatings with dark strips along the edges are obtained. At the coumarin concentration from 1.5 to 2 g l^{-1}, the whole cathode surface is lustrous.

When the Formalin concentration is out of the indicated range, silvery coatings are formed. At the Syntanol concentration of 1 g l^{-1}, the range of the current densities providing formation of lustrous coatings strongly narrows down. At the Syntanol concentration of 4 g l^{-1}, the range of the current densities

1070-4272/03/7603-0387$25.00

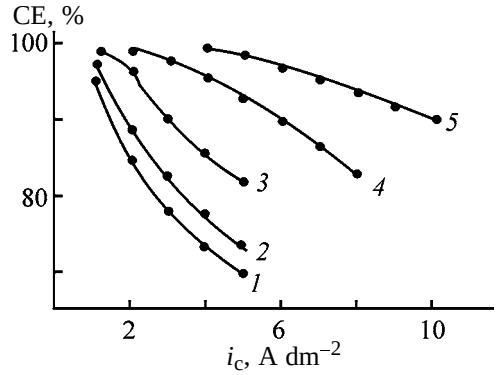

Fig. 1. Current efficiency (CE) of tin electroplating as a function of the current density i_c. Electrolyte contains 100, 2, and 2 g l^{-1} of H_2SO_4, Syntanol, and coumarin, respectively, and 6 ml l^{-1} of Formalin; mechanical stirring. $SnSO_4$ concentration, g l^{-1}: (*1*) 5, (*2*) 10, (*3*) 20, (*4*) 30, and (*5*) 50.

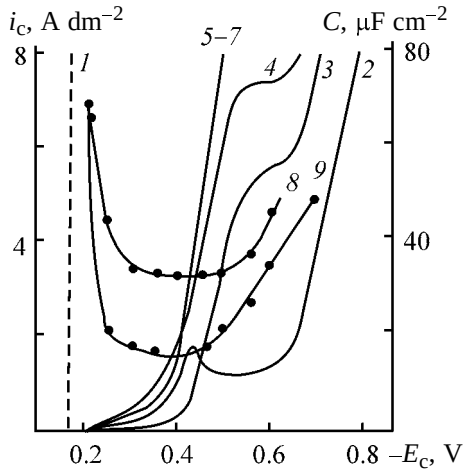

Fig. 2. (*1–7*) Cathodic polarization curves of tin, recorded on a rotating disc electrode, and (*8, 9*) the capacitance of the electrical double layer *C* as a function of cathodic potential E_c (vs. SHE) in the tin plating solutions. Electrolyte contains 30 and 100 g l^{-1} of $SnSO_4$ and H_2SO_4, respectively. (i_c) Cathodic current density. (*1, 8*) Initial electrolyte; (*2–7, 9*) the electrolyte containing Syntanol and coumarin (2 g l^{-1} each) and 6 ml l^{-1} of Formalin. Cathode rotation rate (rpm): (*1, 2*) 0, (*3*) 100, (*4*) 500, (*5*) 900, (*6*) 1500, and (*7*) 2000.

providing formation of lustrous coatings does not change, but the electrolyte foams on stirring, which complicates tin plating.

The range of working current densities providing formation of lustrous coatings was also studied as influenced by the $SnSO_4$ concentration. We found that the current density required to obtain lustrous coating increased as the $SnSO_4$ concentration was increased from 5 to 50 g l^{-1} in the electrolyte containing H_2SO_4 (90–100 g l^{-1}), Syntanol (2–3 g l^{-1}), Formalin (6–8 ml l^{-1}), and coumarin (1.5–2 g l^{-1}). At the $SnSO_4$ concentration of 5, 10, and 20 g l^{-1}, the lustrous coatings are plated at i_c = 1–5 A dm^{-2}; at [$SnSO_4$] = 30 g l^{-1}, at i_c = 2–8 A dm^{-2}; and at [$SnSO_4$] = 50 g l^{-1}, at i_c = 4–10 A dm^{-2}.

The sulfuric acid concentration in the electrolyte should be in the range 90–100 g l^{-1}. At the concentrations below 90 g l^{-1}, the electrolyte is unstable in the course of tin plating and the range of i_c providing formation of lustrous coatings narrows down. At the sulfuric acid concentration higher than 100 g l^{-1}, the range of current densities for obtaining lustrous coatings does not change. It should be noted that high-quality lustrous coatings are plated only in the stirred electrolyte. Without stirring, dull coatings are formed.

The dependence of the current efficiency (CE) on the current density in the electrolyte with the organic additives is shown in Fig. 1. The current efficiency decreases with increasing i_c and grows with increasing the $SnSO_4$ concentration. At the $SnSO_4$ concentration of 5 g l^{-1} and i_c = 1–5 A dm^{-2}, CE ranges from 96 to 71% and at the $SnSO_4$ concentration of 50 g l^{-1} and i_c = 4–10 A dm^{-2}, from 99.9 to 90.1 % (Fig. 1, curves *1, 5*).

To determine the effect of the organic additives on tin plating, we recorded cathodic polarization curves on a rotating disc electrode. As seen from Fig. 2, in the presence of the organic compounds, the cathodic polarization ΔE_c increases and the cathodic polarization curves flatten out at the limiting currents (curves *1, 2*). Curves *1* and *2* were recorded on the stationary disc electrode. At the rotation rate of the disc electrode increased from 200 to 500 rpm, i_{lim} increases, and the cathodic polarization decreases (curves *3, 4*). When the rotation rate increases to 900–2000 rpm, the section of the limiting current disappears and ΔE_c is 320 mV (curves *5–7*).

The plateau of the limiting current in the polarization curves is due to adsorption of the organic compounds on the cathode surface, which is confirmed by variation of the capacitance of the electrical double layer. As seen from Fig. 2 (curves *8, 9*), the capacitance of the electrical double layer decreases after introduction of the organic compounds. In the range of potentials E from –0.3 to –0.4 V, the capacitance decreases from 32 to 18 μF cm^{-2}. At higher cathodic potentials, the organic compounds are desorbed from the electrode surface and the continuity of the adsorption layer gets broken, thus increasing the capacitance of the double layer.

The dependences of the coverage of the cathode surface θ (curve *1*) and of the degree of the coating

luster (curve *2*) on the current density are shown in Fig. 3. The degree of the coating luster increases and the surface coverage decreases with increasing current density i_c. The surface coverage θ ranges from 13.8 to 6.8 % at i_c providing formation of lustrous coatings. It should be noted that the lustrous coatings are plated from the electrolyte with organic additives only in a definite range of i_c and θ. Probably, at the optimal values of these parameters the roughness of the growing films is minimal.

We measured the smoothing power of the sulfate electrolyte as influenced by the cathodic current density and the coumarin and $SnSO_4$ concentrations. The results are shown in Fig. 4. As seen from Fig. 4, the electrolytes containing Syntanol, Formalin, and coumarin smooth the coating surface. When i_c increases from 1 to 5 A dm^{-2} in the electrolyte containing 10 g l^{-1} $SnSO_4$, *S* decreases from 0.5 to 0.4 (Fig. 4, curve *1*). At the same time, at the $SnSO_4$ concentration of 30 g l^{-1} and i_c = 1–8 A dm^{-2}, the smoothing power increases from 0.62 to 0.98 (Fig. 4, curve *2*). The dependences of the smoothing power of the electrolytes containing 10 and 30 g l^{-1} $SnSO_4$ on the coumarin concentration in the range 0.25–2 g l^{-1} differ. As seen from Fig. 4, the *S*–*c* dependence at the $SnSO_4$ concentration of 10 g l^{-1} passes through a minimum (curve *3*), and at the $SnSO_4$ concentration of 30 g l^{-1}, through a maximum (curve *4*). The smoothing power of the electrolyte containing 30 g l^{-1} $SnSO_4$ is higher.

The mechanism of surface smoothing can be explained in the framework of the conventional adsorption–diffusion theory [7] which suggests that the polarization curves recorded on a rotating disc electrode at various rotation rates qualitatively simulate the cathodic process on profile micropeaks (high rotation rate) and microvalleys (low rate). To estimate the influence of various additives, the cathodic potential in the electrolyte with an additive (or additives) was measured at two rates of electrode rotation. If the polarization increases with increasing rotation rate, the additive(s) will have the smoothing effect.

Analysis of the cathodic polarization curves recorded in a tin sulfate electrolyte on a rotating disc electrode (Fig. 2, curves *3*–*7*) shows that these curves do not simulate the distribution of tin plating rates over the microprofile. This is probably due to adsorption of organic compounds on the electrode surface. Intensification of the hydrodynamic conditions affects formation and degradation of the adsorption layer. In this case, tin plating on all microprofile sections ac-

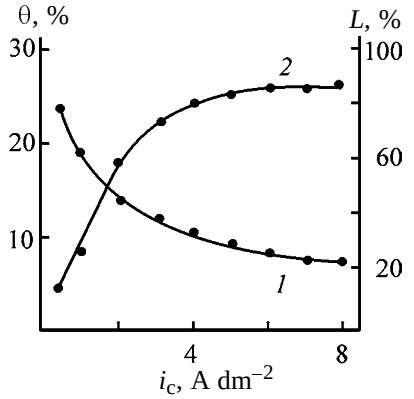

Fig. 3. (*1*) Coverage of the cathode surface θ and (*2*) degree of coating luster *L* as functions of the cathodic current density i_c. Electrolyte contains, respectively, 30, 100, 2, and 2 g l^{-1} of $SnSO_4$, H_2SO_4, Syntanol, and coumarin and 6 ml l^{-1} of Formalin; mechanical stirring.

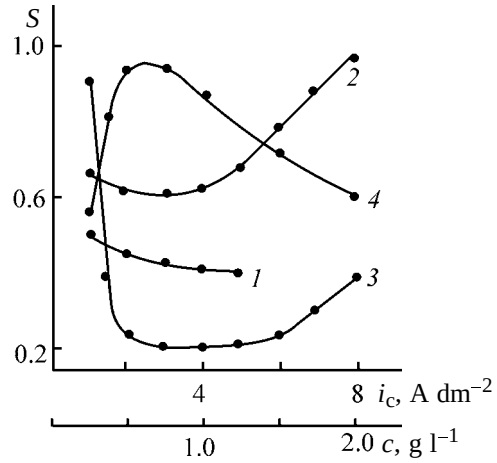

Fig. 4. Smoothing power *S* of tin sulfate electrolytes as a function of the (*1, 2*) cathodic current density i_c and (*3, 4*) coumarin concentration *c*. Electrolyte contains, respectively, 100 and 2 g l^{-1} of H_2SO_4 and Syntanol and 6 ml l^{-1} of Formalin; mechanical stirring. (*1, 2*) Electrolyte + 2 g l^{-1} coumarin + 10 and 30 g l^{-1} $SnSO_4$, respectively; (*3, 4*) electrolyte + 10 and 30 g l^{-1} $SnSO_4$, respectively.

celerates, i.e., the change in the tin plating rate looks like a manifestation of the antismoothing effect. It should be also noted that this phenomenon was observed during tin plating from the sulfate electrolyte with other organic additives [1–4] and during electrodeposition of an Sn–Sb alloy [8].

Based on the above results, we propose the following formulation of the sulfate electrolyte for plating lustrous and smooth tin coatings: $SnSO_4$ (5–50 g l^{-1}), H_2SO_4 (90–100 g l^{-1}), Syntanol DS-10 (2–3 g l^{-1}), coumarin (1.5–2 g l^{-1}), and 37% formaldehyde solu-

tion (6–8 ml l^{-1}); i_c = 1–10 A dm^{-2}. The current efficiency of tin electroplating is 71–99.9%. The electrolyte temperature is 18–25°C. At higher temperature, the electrolyte becomes turbid and low-quality deposits are formed. The electrolyte should be mechanically stirred. To decrease contamination of the electrolyte with the anodic slime, the tin anodes should be placed in woven polypropylene bags.

The electrolyte was highly stable during prolonged lab trials. However, after prolonged operation, a light yellow precipitate deteriorating the film quality was accumulated on the bath bottom. The precipitate should be filtered off at regular intervals.

The IR spectrum of the precipitate (KBr pellet) contains a strong broad band of OH stretching vibrations in the range 3400–3600 cm^{-1} [9]. The band at 895 cm^{-1} can be due to bending vibrations of the Sn–O–H group [10]. In addition, weak coumarin bands are observed at 3040, 1720, 1610, 1260, 1180, 1125, and 760 cm^{-1}. We suggest that the precipitate is a mixture of tin hydroxide and coumarin.

The $SnSO_4$, H_2SO_4, Formalin, and coumarin concentrations in the electrolyte were adjusted on the basis of chemical analysis data [11]. After passage of 100 A l^{-1} of electricity, 1 g l^{-1} of Syntanol should be added to the bath. Coumarin can be added in the amount exceeding its solubility. In this case, the coumarin concentration equal to its solubility is maintained throughout the tin plating. Excess coumarin is introduced in woven polypropylene bags in the amount no less than the weekly consumption. The presence of coumarin in the bags placed between the electrodes is monitored visually. In this case, the analysis of the electrolyte for coumarin is not required, since its concentration is self-adjusted. The coumarin consumption is 0.01 g A^{-1} h^{-1}.

CONCLUSIONS

(1) Lustrous tin coatings are plated from the sulfate electrolyte containing Syntanol, Formalin, and coumarin at i_c = 1–10 A dm^{-2} depending on the $SnSO_4$ concentration.

(2) The organic additives inhibit tin electroplating. The cathodic polarization curves recorded on a rotating disc electrode in the presence of these additives flatten out at limiting current. The length of this plateau increases and the cathodic polarization decreases with increasing rotation rate.

(3) The coverage of the cathode surface decreases and the degree of coating luster grows with increasing i_c. Lustrous coatings are formed at the coverage from 6.8 to 13.8%.

(4) The smoothing power of the sulfate electrolyte containing the organic additives was studied. These electrolytes exhibit the positive smoothing effect which depends on i_c and on the coumarin and $SnSO_4$ concentrations.

(5) The distribution of tin electroplating rate over the microprofile cannot be simulated by the polarization curves recorded at different rates of electrode rotation, since the adsorption layer inhibiting the electrodeposition is sensitive to the hydrodynamic conditions.

(6) A self-adjusted electrolyte for electroplating of smooth and lustrous tin coatings was developed.

REFERENCES

1. Medvedev, G.I. and Gorbunova, I.M., *Zh. Prikl. Khim.*, 1990, vol. 63, no. 4, pp. 807–812.
2. Medvedev, G.I. and Mashutina, G.G., *Zh. Prikl. Khim.*, 1992, vol. 65, no. 4, pp. 789–795.
3. Medvedev, G.I. and Makrushin, N.A., *Zh. Prikl. Khim.*, 2001, vol. 74, no. 11, pp. 1787–1790.
4. Medvedev, G.I., Makrushin, N.A., and Dubenkov, A.N., *Zh. Prikl. Khim.*, 2002, vol. 75, no. 2, pp. 227–230.
5. *Blestyashchie elektroliticheskie pokrytiya* (Lustrous Electroplated Coatings), Matulis, Yu.Yu., Ed., Vilnius: Mitis, 1969.
6. Valentelis, L.Yu., Kamuntavichene, I.Yu., and Matulis, Yu.Yu., *Tr. Akad. Nauk. Lit. SSR, Ser. B*, 1970, vol. 63, no. 4, pp. 129–136.
7. Kruglikov, S.S., *Itogi Nauki Tekh., Ser.: Khim. Elektrokhim.*, 1965, pp. 117–147.
8. Medvedev, G.I., Kruglikov, S.S., and Fursova, N.Yu., *Zh. Prikl. Khim.*, 2001, vol. 74, no. 11, pp. 1763–1764.
9. Bellamy, L.J., *The Infra-Red Spectra of Complex Molecules*, London: Methuen, 1954.
10. Nakamoto, K., *Infrared Spectra of Inorganic and Coordination Compounds*, New York: Wiley, 1963.
11. Vyacheslavov, P.M. and Shmeleva, N.M., *Kontrol' elektrolitov i pokrytii* (Monitoring of Electrolytes and Coatings), Leningrad: Mashinostroenie, 1965.

Russian Journal of Applied Chemistry, Vol. 76, No. 3, 2003, pp. 391–395. Translated from Zhurnal Prikladnoi Khimii, Vol. 76, No. 3, 2003, pp. 406–410.

APPLIED ELECTROCHEMISTRY AND CORROSION PROTECTION OF METALS

Potentiometric and Spectrophotometric Determination of the Ionic Composition of Concentrated Sodium Polysulfides

V. S. Vorobets, S. K. Kovach, and G. Ya. Kolbasov

Vernadsky Institute of General and Inorganic Chemistry, National Academy of Sciences of the Ukraine, Kiev, Ukraine
Uzhgorod National University, Uzhgorod, Ukraine

Received June 17, 2002; in final form, January 2003

Abstract—The concentrations of ionic species in polysulfide electrolytes of photoelectrochemical converters, calculated from the results of potentiometric and spectrophotometric measurements in concentrated polysulfide solutions, are presented. The possible processes that occur at the semiconducting CdSe photoelectrode and involve electrically active species are discussed.

Concentrated polysulfide solutions are used as electrolytes in photoelectrochemical converters of solar radiation [1, 2]. Such solutions contain, in addition to water and alkali metal cations, OH^-, HS^-, S^{2-}, MS^- (M = Na, K), and S_x^{2-} (x = 2–5) ions [3–7]. The equilibria between various polysulfide species are described by the equation [3]

$$(x - 1)S_{x+1}^{2+} + HS^- + OH^- = xS_x^{2-} + H_2O, \quad (1)$$

where x = 2–4.

To describe and control processes occurring in electrochemical converters, it is necessary to perform a quantitative analysis of the electrolyte composition.

The aim of this study was to determine the ionic composition of concentrated polysulfide solutions by spectrophotometry and potentiometry.

EXPERIMENTAL

The concentration of sulfide ions was determined by a direct potentiometric procedure assuming the existence of a calibration plot φ-vs-log$[S^{2-}]$, where φ is the potential of the sulfide-selective electrode (SSE) in solution [8]. It is known that the sulfide ion undergoes hydrolysis in aqueous solutions:

$$S^{2-} + H_2O = HS^- + OH^-. \quad (2)$$

It is assumed in [8] that, already at alkali concentration c = 1 M, the entire amount of alkali metal sulfide introduced into solution is present in the form of sulfide ions, and, therefore, it suffices to prepare solutions with just this alkali concentration for constructing the calibration plot. However, as follows from [9] and data on the second dissociation constant of H_2S [4], equilibrium (2) is not completely shifted to the left even at very high alkali concentrations (~8 M), and a perceptible amount of hydrosulfide ions is present in solution. Therefore, the calibration plot should be constructed using the conversion formulas [10]

$$[S^{2-}] = \frac{S_t}{1 + K_h/[OH^-]}, \quad (3)$$

$$[OH^-] = 0.5\{c_{OH^-} - K_h + [(K_h + c_{OH^-})^2 + 4K_hS_t]^{1/2}\}, \quad (4)$$

where $[S^{2-}]$ and $[OH^-]$ are the concentrations of sulfide and hydroxide ions; c_{OH^-}, the concentration of introduced alkali; S_t, the sum of the concentrations of HS^- and S^{2-} ions (for sulfide solutions, $S_t = [HS^-] + [S^{2-}] = c_{Na_2S}$); and K_h, the hydrolysis constant

$$K_h = [HS^-][OH^-]/[S^{2-}]. \quad (5)$$

The potential of the indicator electrode was measured with an OR-205/1 pH-meter with an accuracy of 0.25 mV. An industrial EA-2 argentite electrode served as the indicator electrode, and an EVL-1M silver chloride electrode, as reference. Polysulfide solutions were obtained by dissolving required amounts of $Na_2S \cdot 9H_2O$ (analytically pure), NaOH, and S (both of ultrapure grade) in deaerated double-distilled water, after which argon (ultrapure grade) was bubbled through for 20 min. The resulting solutions

1070-4272/03/7603-0391$25.00

Table 1. Distribution of ionic species in concentrated polysulfide electrolytes*

Species	Concentration, M, at indicated $c_{NaOH} : c_{Na_2S} : c_S$ molar ratio			
	1 : 1 : 1	1 : 1 : 1.5	1 : 1 : 2	1 : 1 : 0
$[S^{2-}]_c$	5.41×10^{-2}	3.16×10^{-2}	1.47×10^{-2}	8.32×10^{-2}
$[HS^-]_c$				6.82×10^{-2}
$[S^{2-}]_p$	5.51×10^{-2}	3.39×10^{-2}	1.44×10^{-2}	
$[HS^-]_p$	5.51×10^{-1}	3.81×10^{-1}	1.88×10^{-1}	
$[OH^-]$	1.55	1.38	1.19	
$[S_2^{2-}]$	6.28×10^{-3}	7.39×10^{-3}	7.94×10^{-3}	
$[S_3^{2-}]$	1.24×10^{-1}	1.67×10^{-1}	2.19×10^{-1}	
$[S_4^{2-}]$	2.49×10^{-1}	3.85×10^{-1}	5.18×10^{-1}	
$[S_5^{2-}]$	1.83×10^{-3}	3.24×10^{-3}	5.025×10^{-3}	
$[NaS^-]$	1.3×10^{-4}	2.25×10^{-4}	4.84×10^{-4}	
$[S^{2-}]_{sp}$				9.36×10^{-2}
$[HS^-]_{sp}$				7.66×10^{-2}

* $[S^{2-}]_c$, $[HS^-]_c$, $[S^{2-}]_p$, $[HS^-]_p$, $[S^{2-}]_{sp}$, and $[HS^-]_{sp}$ are the ion concentrations found, respectively, from the calibration plots, from the difference of SSE potentials in sulfide and polysulfide solutions with the same content of alkali and sodium sulfide, and from spectrophotometric data. The $K_h = 15.5$ value [9] was used in the calculations.

were stored in hermetically sealed vessels. All measurements were done at the ionic strength of solution $I = 5$ M, adjusted with NaCl.

The concentration of sulfide ions $[S^{2-}]_c$, found from the calibration plot for a set of polysulfide solutions, are listed in Table 1.

However, the given method gives no way of determining the concentration of hydrosulfide ions in a polysulfide solution since the sum S_t is unknown. Previously, a method has been proposed for determining the concentrations of HS^- and S^{2-} ions and the total concentration of polysulfide ions $S_n = \sum_{i=2}^{5} S_i^{2-}$ from the difference of SSE potentials in sulfide and polysulfide solutions. The former has the same composition as the latter with respect to alkali and sodium sulfide, but contains no sulfur. The difference between SSE potentials in sulfide and polysulfide solutions is given by the expression [10]

$$\Delta\varphi = \varphi_s - \varphi_n = b\log[c_{Na_2S}/(c_{Na_2S} - S_n) - A],$$

$$A = b\log\frac{\dfrac{2K_h}{c_{OH^-} - K_h + [4K_h c_{Na_2S} + (K_h + c_{OH^-})^2]^{1/2}} + 1}{\dfrac{2K_h}{c_{OH^-} - K_h + [4K_h(c_{Na_2S} - S_n) + (K_h + c_{OH^-})^2]^{1/2}} + 1}. \quad (6)$$

After calculating the total concentration of polysulfide ions S_n by Eq. (6), S_t can be found from

$$S_t = c_{Na_2S} - S_n,$$

and then the concentrations of OH^-, HS^-, and S^{2-} ions can be determined using Eqs. (3)–(5). The results obtained in calculating the concentration of sulfide ions from the difference of SSE potentials ($[S^{2-}]_p$) are also listed in Table 1. As follows from Table 1, the difference between the concentrations of sulfide ions, found by the above methods, does not exceed 7%.

In this study, we examined the absorption spectra of concentrated polysulfide solutions ($c_{NaOH} = c_{Na_2S} = 1$ M) with varied ratio X_S of sulfur and alkali metal sulfide introduced into the solution. The absorption spectra were measured with a Specord M-40 spectrophotometer in the wave number range 25×10^3–50×10^3 cm^{-1} at small thickness of the optical cell ($d = 4.14 \times 10^{-4}$ cm). Figure 1a shows an absorption spectrum of a solution with the composition (M) 1NaOH : 1Na_2S : 2S. Origin 6.0 software was applied to resolve separate absorption bands and determine their parameters: position x_c of a band, its width, and peak height h. It is known that polysulfide ions absorb at wave numbers of 23×10^3–37×10^3 cm, and sulfide and hydrosulfide ions, and also the ion pair NaS^-, at 40×10^3–47×10^3 cm^{-1}. To improve the accuracy of the parameters being determined, the absorption spectra were processed in two stages. In the first stage, the absorption bands of the HS^-, S^{2-}, and NaS^-

ions were subtracted from the overall spectrum and the parameters of the absorption bands of polysulfide ions were determined (see Fig. 1b). In the second stage, the contributions from the absorption bands of polysulfide ions were subtracted from the overall spectrum and the parameters of the absorption bands of the HS^-, S^{2-}, and NaS^- ions were found. The calculated data are listed in Table 2. It can be seen that mainly S_3^{2-} and S_4^{2-} ions are present in solution nos. 1–3, and their redistribution toward higher content of S_4^{2-} occurs with increasing X_S. At $X_S = 2$ a new band corresponding to the ion pair NaS^- appears in the absorption spectra at $(40 \pm 5) \times 10^3$ cm^{-1} [5].

Approximate concentrations of polysulfide ions can be estimated using published values of the constants of equilibria between different polysulfide ions, $K_{2/3}$, $K_{3/4}$, and $K_{4/5}$, by solving a system of equations describing equilibria in concentrated polysulfide solutions.

In addition to equilibria (1) and (2), account should also be taken, in concentrated polysulfide solutions, of ion association processes [5]

$$Na^+ + S^{2-} = NaS^-. \quad (7)$$

Writing the equilibrium constants corresponding to processes (1), (2), and (7)

$$K_{2/3} = \frac{[S_2^{2-}]^2}{[S_3^{2-}][HS^-][OH^-]}, \quad (8)$$

$$K_{3/4} = \frac{[S_3^{2-}]^3}{[S_4^{2-}]^2[HS^-][OH^-]}, \quad (9)$$

$$K_{4/5} = \frac{[S_4^{2-}]^4}{[S_5^{2-}]^3[HS^-][OH^-]}, \quad (10)$$

$$K_h = \frac{[HS^-][OH^-]}{[S^{2-}]}, \quad (11)$$

$$K_t = \frac{[NaS^-]}{[Na^+][S^{2-}]}. \quad (12)$$

(K_t is the ion association constant), together with material balance conditions for sodium sulfide, sulfur, and hydroxide ion introduced:

$$c_{Na_2S} = [HS^-] + [S^{2-}] + [NaS^-] + S_n, \quad (13)$$

$$c_{S_0} = \sum_{i=2}^{5} (i - 1)[S_i^{2-}], \quad (14)$$

$$[OH^-] = c_{OH^-} + [HS^-], \quad (15)$$

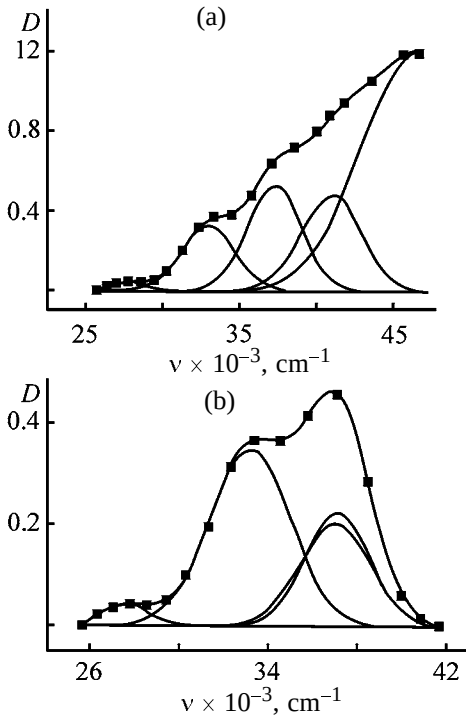

Fig. 1. (a) Absorption spectrum of a solution (M) 1NaOH : 1Na_2S : 2S and results of its processing with Origin 6.0 software and (b) absorption spectrum of the same solution after subtraction of the contributions from absorption bands of the HS^-, S^{2-}, and NaS^- ions. Optical cell thickness $d = 4.14 \times 10^{-4}$ cm. (D) Optical density and (ν) wave number.

yields a system of Eqs. (8)–(15), whose solution enables calculation of the distribution of polysulfide species in concentrated solutions. Since the ionic strength of all the solutions was maintained constant (~5 M) at strongly dominating Na^+ cation, the concentration equilibrium constants in Eqs. (8)–(11) were considered to be invariable.

The results obtained in calculating the concentrations of ion species in solution nos. 1–3 from Table 2 are listed in Table 1. The calculations were done using the constants of equilibrium between different polysulfide ions $K_{2/3}$, $K_{3/4}$, and $K_{4/5}$, and also the constants K_h and K_t [5, 9]. The concentrations of HS^-, S^{2-}, and OH^- ions, and also S_n, were determined from the measured difference of SSE potentials in sulfide and polysulfide solutions, as described above. As follows from Table 1, HS^-, S_3^{2-}, and S_4^{2-} ions predominate in concentrated polysulfide solutions at $c_{NaOH} = c_{Na_2S} = 1$ M and varied X_S (X_S = 1–2). The concentrations of other ion species are much lower, in good agreement with spectrophotometric data (Table 2). A certain discrepancy between the experimental and

Table 2. Parameters of absorption bands of ionic species in polysulfide solutions, obtained with Origin 6.0 software

Solution no.	$c_{NaOH} : c_{Na_2S} : c_S$ molar ratio	$x_c \times 10^{-3}$, cm^{-1}	h	Species
1	1 : 1 : 1	46.3	1.434	HS^-
		37.4	0.181	S_2^{2-}
		37.1	0.104	S_4^{2-}
		33.0	0.138	S_4^{2-}
2	1 : 1 : 1.5	47.0	1.601	HS^-
		36.8	0.088	S_4^{2-}
		36.75	0.112	S_3^{2-}
		32.9	0.262	S_4^{2-}
		27.7	0.041	S_3^{2-}
3	1 : 1 : 2	46.4	1.185	HS^-
		41.0	0.548	NaS^-
		37.1	0.224	S_4^{2-}
		37.0	0.204	S_3^{2-}
		33.1	0.349	S_4^{2-}
		27.6	0.039	S_3^{2-}

calculated data may be due to inadequate extrapolation of the equilibrium constants $K_{2/3}$, $K_{3/4}$, and $K_{4/5}$ to high ionic strengths and also to experimental errors in measuring the absolute values of optical density of strongly absorbing substances in micrometer-size cells. Table 1 lists the concentrations of sulfide and hydrosulfide ions, determined in a solution of composition (M) $1\,NaOH : 1\,Na_2S : 2S$ by potentiometry and spectrophotometry. The error is 12.3%.

It was shown in [11] that singly charged species are potential-determining species on a cadmium selenide semiconductor photoelectrode. The assumption that HS^- ions are electrically active species at the photoelectrode makes it possible to suggest the possible mechanism of the electrochemical process occurring at the CdSe photoelectrode under illumination, which includes discharge of an electrically active HS^- species and desorption of oxidized products from the semiconductor surface

$$HS^- + 2h^+ \rightarrow H^+ + S_{ads}, \quad (16)$$

$$S_{ads} + S_x^{2-} = S_{x+1}^{2-}, \quad (17)$$

where h^+ are holes generated in the valence band of the semiconductor under photoexcitation.

In the range $1.5 < X_S \leq 2$, the HS^- concentration is still sufficiently high (Table 1) to ensure high photocurrents; however, binding of hydroxide ions in solution by H^+ ions formed in accordance with Eq. (16) shifts equilibria (1) toward formation of longer polysulfide ions:

$$3S_3^{2-} + H_2O = 2S_4^{2-} + HS^- + OH^-,$$

$$4S_4^{2-} + H_2O = 3S_5^{2-} + HS^- + OH^-.$$

At high illumination intensity and $X_S \geq 2$, when the concentration of the electrically active species HS^- strongly decreases, diffusion of electrically active species toward the surface of the semiconductor photoelectrode becomes the rate-determining stage of the photoelectrochemical process. A calculation of the limiting diffusion current for typical values of the diffusion coefficient $D = 0.7 \times 10^{-5}$ $cm^2\ s^{-1}$ and diffusion layer thickness $\delta = 1 \times 10^{-2}$ cm in an electrolyte of composition (M) $1NaOH : 1Na_2S : 2S$, with concentration $c_{HS^-} = 0.19$ M of electrically active species, demonstrated that $I_{diff} = 12.8$ mA cm^{-2}. This corresponds to experimental photocurrents on a CdSe photoanode in polysulfide electrolyte [6].

With the concentration of HS^- ions decreasing further at $X_S > 2$, the diffusion current will become smaller, also in agreement with experimental data of [6], according to which I_{SC} (short-circuit current) substantially decreases at $X_S > 2$.

Thus, the electrolyte composition (M) $1NaOH : 1Na_2S : 1.5S$ ensures high stability of CdSe photoelectrodes because of the fast removal of adsorbed sulfur from the surface, with the highest efficiency

achieved in this case owing to the high concentration of the adsorbed electrically active species HS^-. The decrease in efficiency, observed at $X_S > 1.5$, is due to enhancement of ion association (formation of NaS^- species), increasing absorption of visible light in the electrolyte, and more stringent diffusion limitations at $X_S > 2$ (resulting from the significant decrease in the concentration of the electrically active HS^- species).

CONCLUSIONS

(1) Concentrations of the sulfide ion in concentrated sodium polysulfide solutions were determined by direct potentiometry and from the difference of potentials of a sulfide-selective electrode in sulfide and polysulfide solutions, with the discrepancy between the concentrations found by the above methods not exceeding 7%.

(2) It was found that HS^- ions are electrically active species in the system constituted by the CdSe photoelectrode and a polysulfide electrolyte. The possible stage mechanism of transformations occurring in the given system under illumination, which includes discharge of the electrically active HS^- species and desorption of oxidized products from the semiconductor surface, was considered.

(3) A calculation of the limiting diffusion current in an electrolyte of composition (M) 1NaOH : $1Na_2S$: 2S demonstrated that diffusion of electrically active HS^- species toward the photoelectrode surface is the rate-determining stage of the electrochemical process occurring in the system constituted by the CdSe photoelectrode and a polysulfide electrolyte at high illumination intensity and $X_S > 2$.

REFERENCES

1. Hodes, G., *Energy Resource through Photochemistry and Catalysis*, Gratzel, M., Ed., New York: Academic, 1983, pp. 421–465.
2. Kuz'mins'kii, V., Kolbasov, G.Ya., and Tevtul', Ya.Yu., *Netraditsiini elektrokhimichni sistemi peretvorennya energii* (Unconventional Electrochemical Systems for Energy Conversion), Kiev: Akademperiodika, 2002.
3. Giggenbach, W., *Inorg. Chem.*, 1972, vol. 11, no. 6, pp. 1201–1207.
4. Giggenbach, W., *Inorg. Chem.*, 1971, vol. 10, no. 7, pp. 1333–1338.
5. Vorobets, V.S., Kovach, S.K., and Kolbasov, G.Ya., *Ukr. Khim. Zh.*, 2001, vol. 67, no. 9, pp. 12–16.
6. Vorobets, V.S., Kovach, S.K., and Kolbasov, G.Ya., *Zh. Prikl. Khim.*, 2002, vol. 75, no. 2, pp. 237–242.
7. Giggenbach, W., *Inorg. Chem.*, 1974, vol. 13, no. 7, pp. 1724–1730.
8. Papp, J., *Cellulose Chem. Technol.*, 1971, vol. 5, no. 2, pp. 147–159.
9. Kovach, S.K., Vorobets, V.S., and Vas'ko, A.T., *Ukr. Khim. Zh.*, 1988, vol. 54, no. 2, pp. 150–154.
10. Kovach, S.K., Vorobets, V.S., and Vas'ko, A.T., *Ukr. Khim. Zh.*, 1989, vol. 55, no. 1, pp. 51–53.
11. Kolbasov, G.Ya. and Gorodyskii, A.V., *Protsessy fotostimulirovannogo perenosa zaryada v sisteme poluprovodnik–elektrolit* (Photostimulated Charge Transfer in Semiconductor–Electrolyte System), Kiev: Naukova Dumka, 1993.

Russian Journal of Applied Chemistry, Vol. 76, No. 3, 2003, pp. 396–398. Translated from Zhurnal Prikladnoi Khimii, Vol. 76, No. 3, 2003, pp. 411–413.

APPLIED ELECTROCHEMISTRY AND CORROSION PROTECTION OF METALS

Manufacture of Corrosion Inhibitors from Secondary Raw Materials

Z. A. Tadzhikhodzhaev

Institute of Chemical Engineering, Tashkent, Uzbekistan

Received March 28, 2002

Abstract—Metal corrosion inhibitors based on secondary raw materials from chemical and by-product coke plants are developed and their inhibiting properties are studied in acid and hydrogen sulfide-containing solutions.

Wide range of inhibitors are known, as both individual compounds and various formulations. However, inhibitors currently used are based mostly on reagent-grade components, which, naturally, is reflected in their cost.

In view of increasing demand for special inhibitors, it appears advisable to use secondary raw materials (process wastes, by-products, still bottoms, etc.) for their manufacture [1–4].

It is quite reasonable to expect that the use of secondary raw materials for manufacture of acid and hydrogen sulfide corrosion inhibitors not only should exert a significant influence on progress in many branches of the industry, but it will also allow considerable process advancement, eliminating many power- and labor-consuming operations and thus reducing the production cost. Of course, manufacture of corrosion inhibitors from secondary raw materials is advantageous from the environmental standpoint also. In this work we studied new inhibitors for metal protection against acid and hydrogen sulfide corrosion, based on by-products from caprolactam production.

EXPERIMENTAL

As starting materials for preparation of corrosion inhibitors we used toluene and cyclohexane oxidation products, T-product [5, 6] and Pod oil [TU (Technical Specifications) 113-03-476–82] [7], respectively.

Inhibitor I was prepared as follows. A mixture of T-product and still bottoms of isoquinoline (IsSB) was heated to 60°C, and epichlorohydrin (ECH) was added using a dropping funnel. The reaction mixture was heated at 100–110°C for 5–6 h. Then 5% aqueous NaOH was added, and the mixture was allowed to stand at 100°C for 1 h.

Inhibitor II was obtained similarly using Pod oil and still bottoms of higher pyridinium bases (HPBSB) as starting products.

Inhibitor I was tested in the dynamic mode at 20, 40, and 60°C with stratal water [8, 9] of the Krasnoyarsk oil field (Zhigulevskneft' Oil-and-Gas Production Department), containing 333–408 mg l^{-1} hydrogen sulfide. The inhibitor concentration c_{inh} was varied from 100 to 400 mg l^{-1}. In blank experiments, the corrosion of the same material (St. 3 steel) was studied without inhibitor.

The inhibiting characteristics of inhibitor I are given in Table 1 for the optimal component ratio (T-prod-

Table 1. Protective characteristics of inhibitor I with respect to St. 3 steel in hydrogen sulfide-containing solutions

c_{inh}, mg l^{-1}	Protective action, %, at indicated temperature, °C		
	20	40	60
	Composite I*		
100	90.2	86.2	82.4
200	94.4	92.8	91.2
300	96.4	93.2	92.8
400	96.6	93.4	92.8
	T-product		
100	27.2	25.0	Not determined
200	30.0	28.2	〃
300	49.8	48.6	〃
400	56.4	55.4	〃

* For optimal composition.

1070-4272/03/7603-0396$25.00

uct : IsSB : ECH : NaOH = 46.5 : 23.3 : 23.3 : 7.0).

The results show that, at an inhibitor I concentration of 100 mg l^{-1} and a temperature of 20–50°C, the protective action is 82.4–90.2%, depending on the inhibitor formula. With increasing inhibitor concentration from 100 to 400 mg l^{-1}, the protective action increases, approaching 92.8 and 96.6% at 20 and 60°C, respectively. The maintenance of the protective action at elevated temperatures is of no small importance for inhibitors. Table 1 shows that the protective action decreases with increasing temperature from 20 to 60°C, but still remains high.

The results obtained suggest the applicability of I as a metal corrosion inhibitor in hydrogen sulfide-containing solutions.

T-product taken individually is of no interest: it demonstrates the protective action below 56.4%, which is considerably lower as compared to inhibitor I under the same conditions.

The compositions of inhibitors II are given in Table 2.

Inhibitor II was tested with St. 3 steel in acid (HCl, H_2SO_4) solutions (Table 3).

The protective action of inhibitor II in 4 N HCl increases with increasing inhibitor concentration, whereas that in 4 N H_2SO_4 is virtually independent of the inhibitor concentration.

The presence of secondary raw materials from caprolactam production in formulations I and II initiates formation of a film on the sample, thus making a barrier at the metal–solution interface. The presence of pyridinium and quinoline bases provides a synergistic effect in hydrogen sulfide-containing corrosive medium. The use of ECH promotes formation of complex branched radicals, which, along with the inhibiting effect, also demonstrate a blocking action. Generally, it may be suggested that composites I and II demonstrate so-called "intramolecular synergism," as containing oppositely charged groups, each capable of adsorption interaction with the metal surface.

Therefore, the observed high inhibiting performance of formulations I and II is originated primarily from the possibility of formation of a compact adsorption layer on the metal surface. Additionally, some other inhibiting effects can also contribute to the total protective action.

Table 2. Compositions of inhibitors II

Sample index	Component content, wt %			
	Pod oil	HPBSB	ECH	5% NaOH
II*	33.3	23.4	33.3	10.0
II/1	43.5	43.5	–	13.0
II/2	43.5	–	43.5	13.0
II/3	–	43.5	43.5	13.0
II/4	33.3	33.3	33.4	–

* Optimal formula.

Table 3. Protective characteristics of inhibitor II with respect to St. 3 steel in acid solutions

Sample index	c_{inh}, mg l^{-1}	Protective action at 80°C, %	
		4 N HCl	4 N H_2SO_4
II	0.2	96.5	93.5
II	0.25	96.9	93.8
II	0.35	97.7	93.7
II	0.4	98.5	Not determined
II	0.5	99.3	″
II/1	0.3	86.4	83.0
II/2	0.3	58.8	52.5
II/3	0.3	93.3	89.1
II/4	0.3	94.2	91.3

ACKNOWLEDGMENTS

The author is grateful to the staff of the Corrosion Inhibitors Laboratory, Research Institute for Development and Use of Oil Field Pipes (VNIITneft', Samara, Russia) and also to employees of the Corrosion Preventing Laboratory, Research and Design Institute for Oil and Gas Production (UzNIPIneftegas) for their help in conducting corrosion tests.

CONCLUSION

Multicomponent metal corrosion inhibitors based on secondary raw materials from caprolactam production are developed. They demonstrate high protective action at relatively high temperatures in hydrogen sulfide-containing and acid solutions (HCl, H_2SO_4).

REFERENCES

1. Maiko, L.P., Drebenkova, I.V., Falyushina, I.P., and Tsaryuk, T.Ya., Abstracts of Papers, *Vtoraya nauchno-tekhnicheskaya konferentsiya "Resursosberegayushchaya i ekologicheski chistaya tekhnologiya"* (Second Scientific and Technical Conf. "Resource-Saving

and Environmentally Clean Technology"), Grodno (Belarus), 1996, p. 193.
2. RF Patent no. 2064976.
3. Starchak, V.G., Chelyabieva, V.N., Kurmakova, I.N., *et al*., *Ekotekhnol. Resursosberezh*., 1998, no. 3, pp. 25–28.
4. RF Patent no. 2120496.
5. Tadzhikhodzhaev, Z.A., *Zh. Prikl. Khim*., 2000, vol. 73, no. 2, pp. 335–337.
6. USSR Inventor's Certificate no. 1724624.
7. Uzbek Patent no. 2309.
8. Rozenberg, V.F., Zhanko, A.I., Inozemtseva, V.D., and Grigorovskaya, L.A., *Korroz. Zashch. Okruzh. Sredy: Ekspress-Inform*., 1984, no. 5, pp. 19–20.
9. Rozenberg, V.F., Matveev, Yu.M., and Zhanko, A.I., *Tr. VNIITneft'* (Kuibyshev), 1974, issue 4, pp. 165–168.

Russian Journal of Applied Chemistry, Vol. 76, No. 3, 2003, pp. 399–406. Translated from Zhurnal Prikladnoi Khimii, Vol. 76, No. 3, 2003, pp. 414–421.

CATALYSIS

Catalytic Properties of the System Fe_2O_3–Ga_2O_3 in Ammonia Oxidation

N. I. Zakharchenko

Zhukovsky National Aerospace University, Kharkov, Ukraine

Received June 26, 2002

Abstract—The catalytic properties of the system Fe_2O_3–Ga_2O_3 in high-temperature oxidation of ammonia and the influence exerted by the phase composition of the system on the physicochemical and catalytic properties of the catalysts were studied.

Catalytic oxidation of ammonia to nitrogen(II) oxide is the basis for the industrial procedure for manufacture of nitric acid [1]. The high cost, short supply, and irreversible loss of industrial catalysts (Pt, Rh, and Pd alloys) in industrial processes pose a topical problem of a search for effective nonplatinum catalysts (NCs). Iron(III) oxide, which is a promising component of NC, is used in the industry as a component of the second stage of a combined system for ammonia oxidation [1, 2]. The high activity and selectivity with respect to NO is commonly preserved and the thermal and chemical stability of Fe_2O_3 enhanced by using various modifying additives and, in particular, metal oxides [1–9]. Gallium(III) oxide Ga_2O_3 is employed as a modifying additive to catalysts containing iron oxide [1, 10], but the Fe_2O_3–Ga_2O_3 system has not been studied in a wide range of compositions.

This study is concerned with the catalytic and physicochemical properties of the system Fe_2O_3–Ga_2O_3 for NH_3 oxidation at high temperatures in a wide range of compositions.

The catalysts were prepared according to [11] by thermal decomposition in air of hydrated iron and gallium nitrates $Fe(NO_3)_3 \cdot 9H_2O$ and $Ga(NO_3)_3 \cdot 9H_2O$ of chemically pure grade, taken in appropriate proportions. The temperature of the final treatment of catalyst grains was 1143 K. X-ray phase analysis was made on a Siemens D-500 powder diffractometer with CuK_α radiation and graphite monochromator in the path of the diffracted beam. The phases in X-ray diffraction patterns were identified using the JCPDS file included in the software package shipped with the diffractometer. The phase composition of the catalytic system studied is listed in Table 1.

IR absorption spectra were measured on a Perkin–Elmer 577 spectrophotometer in the range 200–2000 cm^{-1} using KBr technique.

The selectivity of the catalysts with respect to NO was determined on a flow-through installation with a quartz reactor 2×10^{-2} m in diameter [12]. The height of the bed of catalyst grains, 2×3 mm in size, was $(4–12) \times 10^{-2}$ m; content of ammonia in the ammonia–air mixture (AAM), about 10 vol %; contact time, 6.89×10^{-2} s (normal conditions), which is the optimal value according to previously obtained data [4]; pressure, 0.101 MPa. The test temperature of 1123 K was close to the optimal value for a single-component iron oxide catalyst; in some sets of experiments it was varied within 913–1273 K.

The composition of products formed in NH_3 oxidation and thermal decomposition of NO on the catalysts was determined chromatographically by the known procedure [13], with the gas mixture analyzed for the content of NH_3, O_2, N_2, NO, NO_2 before and after passing through the catalyst bed. The detection limit of the analytical procedure was (vol %) 3.0×10^{-3} for NH_3, 3.5×10^{-3} for NO, and 5.0×10^{-3} for O_2, N_2, and N_2O.

The limiting NH_3 load on the catalysts was determined using a procedure [3] consisting in that the load on the catalysts is raised to the critical state of "estinguishment," i.e., to disturbance of the heat balance of the catalysts upon transition of the reaction from the diffusion to the kinetic region.

Te specific surface area of the catalysts was measured by low-temperature adsorption of nitrogen and calculated by the BET equation using the standard technique [14].

The particle size of the catalysts was determined on a JEM-7Y electron microscope [15]. Suspensions of

1070-4272/03/7603-0399$25.00

Table 1. Phase composition of the catalytic system Fe_2O_3–Ga_2O_3

Ga_2O_3, wt %	Phase composition*	Crystal structure	Lattice constant, nm
0	α-Fe_2O_3	Trigonal, α-Al_2O_3 type	a = 0.5434
0–14.1	$\alpha_{s.s}$	"	a decreases linearly with Ga_2O_3 content in α-Fe_2O_3 increasing from 0.5434 to 0.5384 wt %
14.2	$\alpha_{s.s}$ saturated	"	a = 0.5384
14.3–33.9	$\alpha_{s.s}$ + $\chi_{s.s}$	–	–
34.0–70.2	$\chi_{s.s}$ ($Ga_{2-x}Fe_xO_{3}{}_{s.s}$, x = 0.7–1.4)	Rhombic, χ-Al_2O_3 type	a decreases linearly with increasing Ga_2O_3 content in solid solution
70.3–82.6	$\chi_{s.s}$ + $\beta_{s.s}$	–	–
82.7	$\beta_{s.s}$ saturated	Monoclinic, θ-Al_2O_3 type	a = 0.5854
82.8–99.9	$\beta_{s.s}$	"	a decreases linearly with α-Fe_2O_3 content in β-Ga_2O_3 increasing from 0.5802 to 0.5854 wt %
100.0	β-Ga_2O_3	"	a = 0.5802, b = 0.3040, c = 1.2230

* $\alpha_{s.s}$ is a solid solution of gallium(III) oxide in rhombohedral α-Fe_2O_3; $\chi_{s.s}$, $Ga_{2-x}Fe_xO_3$ solid solution with x = 0.7–1.4 and structure of χ-Al_2O_3; $\beta_{s.s}$, solid solution of α-Fe_2O_3 in gallium(III) oxide, with β-Ga_2O_3 structure.

catalyst samples were prepared by diluting weighed portions of a substance in distilled water with ultrasonic dispersion on a UZDV-2 device. As substrates served carbon films deposited by thermal sputtering of graphite.

The binding energies of surface oxygen to the catalysts were determined from the temperature dependence of the equilibrium oxygen pressure over the surface of the compounds [16].

The catalytic properties of the system Fe_2O_3–Ga_2O_3 are presented in Fig. 1 and Table 2. In the products formed in NH_3 oxidation on the catalysts under study, only N_2 and NO were found, with no "breakthrough" Y of ammonia observed. Thus, the overall conversion of the starting substance is 100%, with only the ratio of the amounts of NO and N_2, i.e., the selectivity of the catalysts with respect to NO (or to nitrogen), varying. Thermal dissociation of NO leads to a decrease in the apparent selectivity of the

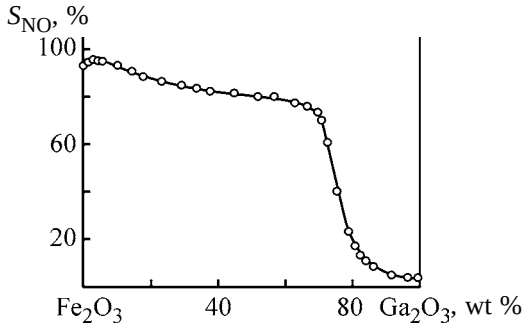

Fig. 1. Catalyst selectivity with respect to nitrogen(II) oxide, S_{NO}, vs. composition of the system Fe_2O_3–Ga_2O_3.

catalysts with respect to nitrogen(II) oxide:

$$2NO = N_2 + O_2. \quad (1)$$

Experimental data on the degree of thermal dissociation of nitrogen(II) oxide on the catalysts of the given system are listed in Table 3.

At the chosen test temperature and the optimal contact time of 6.89×10^{-3} s, from 0.3% (low-active and poorly selective β-Ga_2O_3) to 2.1% (the most active and highly selective composition with Ga_2O_3 content of 3.0 wt %) NO undergoes thermal dissociation. The process leads to a 2.0% decrease in selectivity with respect to nitrogen(II) oxide for the most active catalyst; the selectivity of the low-active β-Ga_2O_3 is virtually not affected (Table 3). Catalysts of other compositions are characterized by intermediate values of these quantities relative to the catalysts considered above (Table 3).

With increasing linear flow velocity of reactants, i.e., with the contact time decreasing to 1.1×10^{-3} s (critical conditions of catalyst extinguishment), no thermal dissociation of NO is observed, in agreement with data on other NCs for NH_3 oxidation [1, 4, 5, 8, 9].

According to the results of X-ray phase analysis, a number of solid solutions based on Fe_2O_3 and Ga_2O_3 are present in the system at the chosen test parameters (temperature, partial pressure of oxygen). A similar conclusion was made in [17, 18], concerned with the phase diagram of the system Fe_2O_3–Ga_2O_3. At a gallium oxide content of up to 14.2 wt %,

Table 2. Properties of the catalytic system Fe_2O_3–Ga_2O_3 at 1123 K*

Ga_2O_3, %	S_{NO}, % ($\tau = 6.89 \times 10^{-2}$ s)	s, $m^2\ g^{-1}$	$X \times 10^{-3}$, $m^3\ h^{-1}\ m^{-2}$	Y, rel. %
0	93.0	5.1	5.62	0.35
1.0	93.6	6.5	7.16	0.16
2.0	94.2	8.0	8.81	0.06
3.0	95.3	9.0	9.92	0.04
4.0	95.0	8.5	9.36	0.05
6.0	94.5	7.7	8.48	0.07
10.0	92.9	6.2	6.83	0.19
14.2	90.2	4.8	5.29	0.39
18.0	88.3	4.7	5.18	0.41
23.0	86.2	4.6	5.07	0.43
29.0	84.0	4.5	4.96	0.45
34.0	82.8	4.4	4.85	0.47
38.0	82.0	4.4	4.85	0.47
45.0	81.1	4.3	4.74	0.50
52.0	80.0	4.2	4.63	0.52
57.0	79.1	4.1	4.52	0.53
64.0	77.0	3.9	4.30	0.58
67.0	75.8	3.8	4.19	0.60
70.2	73.2	3.6	3.97	0.64
71.0	70.0	3.5	3.86	0.66
73.0	60.1	3.4	3.75	0.68
76.0	40.0	3.1	3.42	0.75
79.0	22.3	2.8	3.08	0.83
81.0	16.8	2.6	2.86	0.88
82.7	12.9	2.4	2.64	0.93
84.0	11.3	2.3	2.53	0.97
87.0	8.0	2.1	2.31	1.04
92.0	4.9	1.8	1.98	1.14
97.0	3.9	1.7	1.87	1.19
100.0	3.5	1.6	1.76	1.22

* S_{NO} is the catalyst selectivity with respect to NO; s, the specific surface area of a catalyst; X, the limiting load of ammonia on a catalyst.

iron(III) oxide forms a rhombohedral solid solution $x\alpha$-$Fe_2O_3 \cdot (1 - x)Ga_2O_3$ with the structure of the α-Al_2O_3 type (Table 1). For example, in the X-ray diffraction pattern of the catalyst containing 3.0 wt % Ga_2O_3, the main reflections correspond to interplanar spacings of 0.3682, 0.2693, 0.2511, 0.2214, 0.1846, 0.1695, 0.1484, and 0.1454 nm, which are typical of the rhombohedral structure of α-Fe_2O_3 (hematite) [19], but are shifted to greater reflection angles, which corresponds to a decrease in the lattice constant a from 0.5434 to 0.5423 nm. As the Ga_2O_3 concentration in the solid solution $x\alpha$-$Fe_2O_3 \cdot (1 - x)Ga_2O_3$ is increased further, the lattice constant a decreases to 0.5384 nm (Table 1). No Ga_2O_3 lines were observed in the diffraction patterns of the rhombohedral solid solutions with $c_{Ga_2O_3} \leq 14.2$ wt %. This indicates that, in this composition range, the catalysts are solid solutions of Ga_2O_3 in α-Fe_2O_3.

Table 3. Degree of NO decomposition, R_{NO}, and decrease in selectivity with respect to nitrogen(II) oxide, ΔS_{NO}, for catalysts of the system Fe_2O_3–Ga_2O_3 at 1123 K Gas mixture composition, vol %: NO 9.5, N_2 71.3, O_2 4.6, $H_2O_{(vapor)}$ 14.6; contact time 6.89×10^{-2} s; $R_{NO} = 0$ at $\tau = 1.1 \times 10^{-3}$ s

Ga_2O_3, wt %	Phase composition	R_{NO}, %	ΔS_{NO}, %
0	α-Fe_2O_3	1.2	1.1
3.0	$\alpha_{s.s}$	2.1	2.0
10.0	$\alpha_{s.s}$	1.5	1.4
14.2	$\alpha_{s.s}$ saturated	1.1	1.0
29.0	$\alpha_{s.s} + \gamma_{s.s}$	1.1	0.9
34.0	$\gamma_{s.s}$	1.0	0.8
70.2	$\gamma_{s.s}$	0.8	0.6
76.0	$\gamma_{s.s} + \beta\alpha_{s.s}$	0.7	0.3
82.7	$\beta_{s.s}$ saturated	0.6	0.1
92.0	$\beta_{s.s}$	0.4	$\ll$0.1
100.0	β-Ga_2O_3	0.3	$\ll$0.1

In the Ga_2O_3 content range 0.1–3.0 wt %, the selectivity and specific surface area of the catalytic system grow with increasing Ga_2O_3 content (Fig. 1, Table 2). Raising the content of Ga_2O_3 in the system Fe_2O_3–Ga_2O_3 to more than 3.0 wt % leads to a monotonic decrease in the selectivity and specific surface area of the catalysts (Fig. 1, Table 2).

The composition of a two-component catalytic system with Ga_2O_3 content of 3.0 wt % is the most efficient as regards its selectivity (95.3%) and is characterized by the largest specific surface area (9.0 $m^2\ g^{-1}$); this composition exceeds in catalytic parameters the individual components of the system.

An increase in the specific surface area of a system, compared with that of the starting oxide components (Ga_2O_3 content range 0.1–3.0 wt %), is a common trend in the practice of catalyst fabrication [1, 20–22]. Klyachko-Gurvich and Rubinshtein [20] attributed this phenomenon to a decrease in the lattice energy of a solid solution, compared with the lattice energies of the starting components forming such a solid solution. Milligan [21] accounted for the increase in the surface area of a binary system, compared with the starting oxides, by mutual protective action in the process of catalyst preparation, which consists in adsorption of one component onto the surface of crys-

tallites of the other component, with the result that their growth is hindered and the forming system becomes even more dispersed.

In the Ga_2O_3 content range 82.8–99.9 wt %, there is another solid solution, that of hematite in β-Ga_2O_3, in the Fe_2O_3–Ga_2O_3 system. The main reflections in the X-ray diffraction patterns for, e.g., a composition containing 90 wt % Ga_2O_3 (0.3702, 0.2960, 0.2821, 0.2553, 0.2400, 0.2342, 0.2113, 0.1981, 0.1884, 0.1600, 0.1523, 0.1448, 0.1342, and 0.1037 nm) are characteristic of a solid solution of α-Fe_2O_3 in β-Ga_2O_3, with monoclinic lattice of the θ-Al_2O_3 type [19]. No lines of Fe_2O_3 were observed in the monoclinic solid solution. With increasing Fe_2O_3 content of the solid solution based on Ga_2O_3, the lattice constant grows linearly from 0.5802 to 0.5854 nm (Table 1). Raising the Ga_2O_3 content of the monoclinic solid solution leads to a monotonic decrease in the selectivity and specific surface area of the catalysts in the given range of compositions (Fig. 1, Table 2). The selectivity with respect to NO and the specific surface area of the catalysts, solid solutions of hematite in β-Ga_2O_3, are the lowest, being much exceeded by the similar characteristics of catalysts of the system Fe_2O_3–Ga_2O_3 with other quantitative compositions (Fig. 1, Table 2). The selectivity of β-Ga_2O_3 (3.5%) and its specific surface area (1.6 $m^2\ g^{-1}$) are the lowest among all the compositions from the system Fe_2O_3–Ga_2O_3.

In the Ga_2O_3 content range 34.0–70.2 wt %, solid solutions $Ga_{2-x}Fe_xO_3$ (x = 0.7–1.4) with rhombic structure of the χ-Al_2O_3 type were found in the system Fe_2O_3–Ga_2O_3. With the composition of Ga_{2-x}·Fe_xO_3 changing from $Ga_{0.6}Fe_{1.4}O_3$ to $Ga_{1.3}Fe_{0.7}O_3$, the selectivity (82.9 and 73.1%) and the specific surface area (4.4 and 3.6 $m^2\ g^{-1}$) of the catalysts decrease steadily (Fig. 1, Table 2). Catalysts with χ-Al_2O_3 structure ($Ga_{2-x}Fe_xO_3$) are characterized by relatively high values of selectivity and specific surface area (Fig. 1, Table 2).

In the Ga_2O_3 content ranges 14.3–33.9 and 70.3–82.6 wt %, χ-type solid solutions $Ga_{2-x}Fe_xO_3$ coexist, according to X-ray phase and electron microscopic analyses, with a rhombohedral solid solution of Ga_2O_3 in hematite ($\alpha_{s.s}$) and monoclinic solid solution of α-Fe_2O_3 in β-Ga_2O_3 ($\beta_{s.s}$), respectively, in the form of their mixtures. With the content of the low-active β-type solid solution increasing in the Ga_2O_3 content range 70.3–82.6 wt %, the selectivity and specific surface area of catalysts fall dramatically (Fig. 1, Table 2). The differences between the catalytic properties of χ-type solid solutions $Ga_{2-x}Fe_xO_3$ and rhombohedral solid solutions of Ga_2O_3 in α-Fe_2O_3 ($\alpha_{s.s}$) are less significant (Fig. 1).

Thus, the selectivity of the system depends on the composition and, in particular, on the content of the components (Ga_2O_3, Fe_2O_3) in solid solutions based on iron(III) and gallium(III) oxides and the quantitative relationship between solid solutions of two-phase systems.

High-temperature oxidation of ammonia on catalysts proceeds by two parallel pathways [1, 23]:

$$4NH_3 + 5O_2 = 4NO + 6H_2O, \quad (2)$$

$$4NH_3 + 3O_2 = 2N_2 + 6H_2O. \quad (3)$$

The occurrence of reactions by the redox mechanism [23] predetermines a regular relationship between the selectivity and the strength of binding of chemisorbed oxygen to the catalyst surface [23, 24]. As measure of the strength of oxygen binding to a catalyst may serve the heat of chemisorption [23, 24]. For catalysts of certain nature (metals, metal oxides), there exists the optimal energy of oxygen binding to the surface of compounds at which the selectivity with respect to NO is the highest [23–25]. Deviations from the optimal oxygen binding energy make the selectivity of the catalysts with respect to NO lower, and that with respect to N_2 higher.

The experimental binding energies of surface oxygen to solid solutions, q_s, are listed below (oxidized state of the catalyst surface):

Composition of a system	q_s, kJ mol^{-1} O_2
α-Fe_2O_3	144.6
β-Ga_2O_3	231.5
$\alpha_{s.s}$ (2.0 wt % Ga_2O_3)	135.2
$\alpha_{s.s}$ (3.0 wt % Ga_2O_3)	134.3
$\alpha_{s.s}$ (10.0 wt % Ga_2O_3)	144.8
$\alpha_{s.s}$ saturated (14.2 wt % Ga_2O_3)	146.3
$\alpha_{s.s}$ + $\chi_{s.s}$ (29.0 wt % Ga_2O_3)	151.4
$\chi_{s.s}$ (34.0 wt % Ga_2O_3)	153.2
$\chi_{s.s}$ (70.2 wt % Ga_2O_3)	161.9
$\chi_{s.s}$ + $\beta_{s.s}$ (76.0 wt % Ga_2O_3)	194.3
$\beta_{s.s}$ saturated 82.7 (wt % Ga_2O_3)	223.0
$\beta_{s.s}$ 92.0 (wt % Ga_2O_3)	229.8

The energies of oxygen binding to the β-Ga_2O_3 surface and to catalysts, solid solutions at Ga_2O_3 content higher than 9.9 wt %, exceed the corresponding value for Fe_2O_3.

When a product of deeper NH_3 oxidation, namely, NO, is formed, a greater number of oxygen–catalyst

bonds is ruptured as compared to formation of molecular nitrogen. This means that the catalyst selectivity with respect to NO decreases with increasing binding energy of adsorbed oxygen [23, 25], and such a behavior is, indeed, observed for β-Ga_2O_3 and most of solid solutions in the system Fe_2O_3–Ga_2O_3 with Ga_2O_3 content exceeding 9.9 wt % (Fig. 1, Table 2). The dramatic increase in the binding energy of adsorbed oxygen to the surface of catalysts, solid solutions based on β-Ga_2O_3 and also two-phase systems $\chi_{s.s}$ + $\beta_{s.s}$ (70.2–99.9 wt % gallium oxide; Tables 1 and 2), in comparison with α-Fe_2O_3 leads to a pronounced decrease in the selectivity of these catalysts with respect to NO (Fig. 1). Upon introduction of gallium(III) oxide (up to 9.9 wt %) into α-Fe_2O_3, the binding energy of oxygen to the surface of modified catalysts decreases as compared to that for α-Fe_2O_3. This means that a complex interaction changing the energy state of the surface of the rhombohedral solid solution, compared to α-Fe_2O_3 and Ga_2O_3, occurs between separate components in the catalytic system (in the given range of compositions). The specific surface area of the catalysts increases in comparison with that of separate components (Table 2), which can be attributed to a decrease in the lattice energies of solid solutions, compared to the lattice energies of the constituent substances [20]. There appear areas on the catalyst surface that are characterized by lower oxygen binding energies, compared to that of a single-component iron oxide catalyst. The decrease in the energy of oxygen binding to the surface of modified catalysts, compared to α-Fe_2O_3, leads to higher selectivity of the catalysts with respect to NO (Table 2).

Probably, the composition of a modified catalyst with the Ga_2O_3 content of 3.0 wt % is the optimal as regards the energy-related characteristics of the catalyst surface and, consequently, also the catalyst selectivity with respect to NO. Both raising and lowering the Ga_2O_3 content relative to the optimal value lead to a decrease in the specific surface area of the catalyst (Table 2), increase in the binding energy of adsorbed oxygen to the catalyst surface, and decrease in the catalyst selectivity with respect to NO (Fig. 1).

The limiting NH_3 load on the catalysts grows with an increase in their specific surface area (Table 2) determined at the given technique of catalyst preparation by the composition of the system. The limiting load depends on the rate of the surface chemical reaction, which, in turn, is determined by the number of active centers and the chemical composition of the catalysts [3, 23, 24]. In fact, all active centers of a heterogeneous catalyst come into play under critical conditions, and the number of these centers grows with increasing specific surface area of the system. The limiting load characterizes the activity and the maximum output capacity of the catalysts [1, 26]. The highest limiting load is observed for the catalyst with the largest specific surface area, solid solution of Ga_2O_3 (3.0 wt %) in α-Fe_2O_3 [9.92×10^3 m^3 $NH_3/(h\ m^2)$], and the lowest, for the catalyst with the smallest specific surface area, β-Ga_2O_3 [1.76×10^3 m^3 $NH_3/(h\ m^2)$] (Table 2).

Under the critical conditions of the process ($\tau = 1.1 \times 10^{-3}$ s), no successive decomposition of NO by scheme (1) is observed (Table 3), but a part of unchanged NH_3 is detected after passing through the catalyst bed, i.e., ammonia breakthrough occurs (Table 2). With increasing specific surface area of the catalysts, the breakthrough becomes less pronounced, in agreement with the higher activity of such catalysts under critical conditions of the reaction course, which varies with the composition of the Fe_2O_3–Ga_2O_3 system. The strongest breakthrough is observed for the β-Ga_2O_3 catalyst (1.22 rel. %), i.e., for a catalyst with the smallest specific surface area, and the weakest, for a solid solution of Ga_2O_3 (3.0 wt %) in α-Fe_2O_3 with the highest activity (0.04 rel. %).

The characteristics of the system Fe_2O_3–Ga_2O_3, analyzed in this study, pass through extrema for a solid solution of Ga_2O_3 (3.0 wt %) in α-Fe_2O_3. The catalyst of this composition has the highest selectivity with respect to nitrogen(II) oxide (Fig. 1), largest specific surface area and limiting load, and lowest amount of ammonia breakthrough under critical conditions of the reaction (Table 2). Gallium(III) oxide β-Ga_2O_3 is characterized by the lowest selectivity with respect to NO, smallest specific surface area and limiting load, and highest level of ammonia breakthrough under the critical conditions of the process (Table 2).

The components of the Fe_2O_3–Ga_2O_3 system form a number of solid solutions, including two-phase mixtures of solid solutions (Table 1). As follows from the data obtained, the properties of catalysts in such systems vary continuously from characteristics of one component to those of the corresponding saturated solid solution (within the range of existence of a single phase); from characteristics of one solid solution to those of another (two-phase regions of existence of solid solutions (Fig. 1; Tables 1 and 2). The only exception is the region of solid solutions of Ga_2O_3 (up to 14.2 wt %) in α-Fe_2O_3, in which the physicochemical characteristics pass through extrema at 3.0 wt % Ga_2O_3 (Fig. 1; Tables 2 and 3).

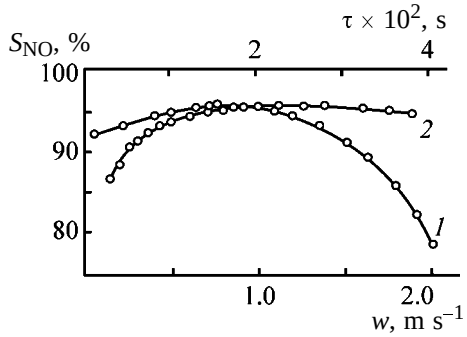

Fig. 2. Selectivity of iron–gallium catalyst, S_{NO}, vs. (*1*) linear flow velocity of AAM, w, at $\tau = 2.25 \times 10^{-2}$ s (operating conditions) and (*2*) contact time τ (operating conditions) at $w = 0.77$ m s^{-1}. Test temperature 1103 K; catalyst composition (wt %): Fe_2O_3 97.0 and Ga_2O_3 3.0; the same for Fig. 3.

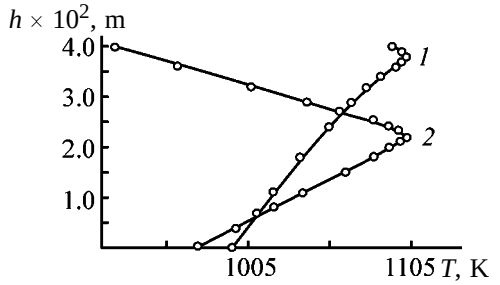

Fig. 3. Distribution of temperature T along the height h of the iron–gallium catalyst bed. Linear flow velocity of AAM (m s^{-1}): (*1*) 0.77 and (*2*) 2.22.

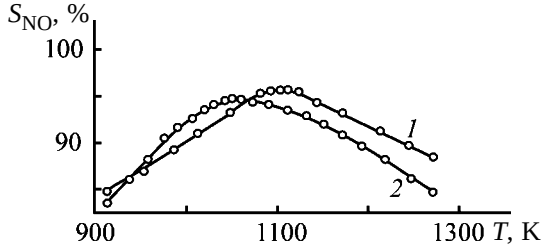

Fig. 4. Catalyst selectivity S_{NO} vs. process temperature T. Linear flow velocity of AAM 19 m s^{-1} (normal conditions). Catalyst: (*1*) σ-Fe_2O_3 97.0, Ga_2O_3 3.0 wt %; (*2*) α-Fe_2O_3.

Of practical interest among catalysts belonging to the system Fe_2O_3–Ga_2O_3 are only compositions with gallium(III) oxide content $c_{Ga_2O_3} \leq 9.9$ wt %, which are the most active and selective and even outperform α-Fe_2O_3. The properties of a two-component catalyst of the optimal composition (Fe_2O_3 97.0 and Ga_2O_3 3.0 wt %), a highly active and selective catalyst in the Fe_2O_3–Ga_2O_3 system, have not been studied [1] and, therefore, are considered below.

The dependence of the selectivity on the contact time (Fig. 2) points to a kinetically complicated mechanism of NH_3 oxidation [1, 3–5, 7–9] on a heterogeneous catalyst.

The abrupt decrease in the catalyst selectivity at a contact time $\tau < 1.0 \times 10^{-2}$ s is due to the occurrence of a side reaction of nitrogen defixation [1, 27] in accordance with the equation

$$4NH_3 + 6NO = 5N_2 + 6H_2O. \quad (4)$$

The slow decrease in the selectivity at a contact time $\tau > 3.2 \times 10^{-2}$ s is mainly due to NO dissociation by scheme (1) [1]. The optimal contact time of the catalyst is 6.89×10^{-2} s under normal conditions, n.c. (2.25×10^{-2} s under operating conditions, o.c.).

The influence exerted by the linear flow velocity of reactants on the catalyst selectivity (Fig. 2) points to the outer-diffusion control of the process [1, 3–5, 7–9], in which the reaction rate is limited by NH_3 diffusion from the flow core to the catalyst surface.

The optimal linear flow velocity of AAM for the catalyst is 0.77 m s^{-1} (o.c.) (0.19 m s^{-1} under n.c.). Raising the linear flow velocity of the reactants shifts the "hot zone" toward the end of the catalyst bed, i.e., lowers the temperature of its "front" layer (Fig. 3). For example, at $w = 2.22$ m s^{-1} the temperature of the front layer of the catalyst falls to 933 K, which favors the occurrence of side reactions. In particular, the rate of nitrogen defixation in accordance with Eq. (4) at this temperature is close to its maximum value [1, 27]. In addition, the low temperature of the front layer, within which oxidation of NH_3 is the most intensive, favors the occurrence of a parallel process (3) [1], which impairs the catalyst selectivity with respect to NO. According to [1, 4, 5, 8, 9], the low linear flow velocities of AAM favor the occurrence of a side reaction of NO dissociation, which leads to a gradual decrease in the catalyst selectivity with respect to nitrogen(II) oxide, since the rate of NO decomposition at 1103 K is slow [1, 28].

Raising the linear flow velocity of reactants to critical values ($\tau = 1.1 \times 10^{-3}$ s) leads to catalyst "extinguishment," i.e., to disturbance of the heat balance because of the dramatic increase in heat losses.

The temperature dependence of the catalyst selectivity is shown in Fig. 4. As compared to iron(III) oxide, the two-component catalyst is characterized by higher selectivity at $T \geq 1073$ K, thus being an effective high-temperature catalyst for NH_3 oxidation [1, 3–5, 8, 9].

The peak selectivity of the catalyst (95.5%) is shifted to higher temperatures, compared to α-Fe_2O_3 (1103 and 1053 K, respectively). The catalyst is characterized by wide interval of temperatures (90 K) with

high selectivity (at the level of 94.0%), compared to Fe_2O_3 for which this interval is only 50–60 K.

The kinetic characteristics of the reaction were determined from the temperatures of "ignition" and "extinguishment" of a catalyst pellet, i.e., the temperatures at the critical points. The reaction rate was calculated using the method for determining the temperature limits of the outer-diffusion region with the use of the effect of catalyst pellet extinguishment on lowering the temperature of AAM [29]. The surface temperature of the catalyst was measured with a Chromel–Alumel thermocouple inserted into the lower side of the pellet relative to the AAM flow direction. To prevent heat loss, a layer of catalyst grains (2.0_3.0) × 10^{-3} m in diameter was placed between the pellet and the reactor walls.

The kinetic parameters of the process were calculated using the equation proposed by Buben [30] and solved for two reaction rates at constant oxygen concentration. The Buben equation has the form

$$(1 + a)^2[1 + (m - 1)a/b] - [a(1 - a/b)]/\varepsilon = 0, \quad (5)$$

$$a = T/T_0 - 1, \quad b = Q\beta c_0/(\alpha T), \quad \varepsilon = RT_0/E,$$

where m is the reaction order with respect to ammonia; T, the temperature of the catalyst surface at the critical point (K); T_0, the AAM temperature; c_0, the NH_3 concentration in the flow; α and β, the mass- and heat-transfer coefficients, respectively, calculated by the known equations [31]; Q, the heat effect of the reaction; E, the activation energy of the reaction.

The kinetic parameters of the reaction of NH_3 oxidation on a two-component catalyst are as follows: catalyst ignition temperature 531 K, content of ammonia in AAM 10.0 vol %, activation energy E of the reaction 9.62 kJ mol^{-1}, and reaction order with respect to ammonia 0.20.

The data on the catalytic properties of the system Fe_2O_3–Ga_2O_3 can be used in developing theoretical and practical foundations for design of high-performance modified catalysts for NH_3 oxidation.

CONCLUSIONS

(1) The catalytic properties of the system Fe_2O_3–Ga_2O_3 in high-temperature NH_3 oxidation were studied at component contents in the range 0–100.0 wt %.

(2) The influence exerted by the phase composition of the system on the physicochemical and catalytic properties of the catalysts and, in particular, on their activity and selectivity with respect to NO was demonstrated. It was established that the activity and selectivity of the system depend on composition, in particular, on the content of solid solution components and quantitative relationship between the solid solutions of the system.

(3) The characteristics of the process occurring on an iron–gallium catalyst with 3.0 wt % Ga_2O_3, which is the most active and selective catalyst in the system Fe_2O_3–Ga_2O_3, were determined.

REFERENCES

1. Karavaev, M.M., Zasorin, A.P., and Kleshchev, N.F., *Kataliticheskoe okislenie ammiaka* (Catalytic Oxidation of Ammonia), Moscow: Khimiya, 1983.
2. Epshtein, D.A., Tkachenko, I.M., Dobrovol'skaya, N.V., *et al*., *Dokl. Akad. Nauk SSSR*, 1958, vol. 122, no. 5, pp. 874–877.
3. Morozov, N.V., Luk'yanova, L.I., and Temkin, M.I., *Kinet. Katal*., 1966, vol. 7, no. 1, pp. 172–175.
4. Zakharchenko, N.I. and Seredenko, V.V., *Zh. Prikl. Khim*., 1999, vol. 72, no. 11, pp. 1921–1923.
5. Zakharchenko, N.I., *Zh. Fiz. Khim*., 2001, vol. 75, no. 6, pp. 985–990.
6. USSR Inventor's Certificate no. 1 182 721.
7. Kurin, N.M. and Zakharov, M.S., *Kataliz v vysshei shkole* (Catalysis in Higher School), Balandin, A.A., Ed., Moscow: Mosk. Gos. Univ., 1962, vol. 2.
8. Zakharchenko, N.I., *Zh. Prikl. Khim*., 2001, vol. 74, no. 2, pp. 226–231.
9. Zakharchenko, N.I., *Kinet. Katal*., 2001, vol. 42, no. 5, pp. 747–753.
10. Podurovskaya, O.N., *Katalizatory dlya okisleniya ammiaka (Bibliografiya patentov, zayavok i avtorskikh svidetel'stv)* (Catalysts for Ammonia Oxidation (Bibliography of Patents, Patent Applications, and Inventor's Certificates)), Moscow: NIITEKhIM, 1972.
11. Zasorin, A.P., Zakharchenko, N.I., and Karavaev, M.M., *Izv. Vyssh. Uchebn. Zaved., Khim. Khim. Tekhnol*., 1980, vol. 23, no. 10, pp. 1274–1276.
12. *Analiticheskii kontrol' proizvodstva v azotnoi promyshlennosti* (Analytical Control of Production in Nitrogen Industry), Demin, L.A., Ed., issue 8: *Kontrol' proizvodstva v tsekhe slaboi azotnoi kisloty* (Production Control in Weak Nitric Acid Shop), Moscow: Goskhimizdat, 1958.
13. Alkhazov, T.G., Gasan-zade, G.Z., Osmanov, M.O., and Sultanov, M.Yu., *Kinet. Katal*., 1975, vol. 16, no. 6, pp. 1230–1234.
14. Panichkina, V.V. and Uvarova, I.V., *Metody kontrolya dispersnosti i udel'noi poverkhnosti metallicheskikh*

poroshkov (Methods for Controlling the Dispersity and Specific Surface Area of Metal Powders), Kiev: Naukova Dumka, 1973.

15. Luk'yanovich, V.M., *Elektronnaya mikroskopiya v fizikokhimicheskikh issledovaniyakh: Metodika i primenenie* (Electron Microscopy in Physicochemical Studies: Methods and Application), Moscow: Akad. Nauk SSSR, 1960.
16. Sazonov, V.A., Popovskii, V.V, and Boreskov, G.K., *Kinet. Katal.*, 1968, vol. 9, no. 2, pp. 307–311.
17. Van Hook, H.J., *J. Am. Ceram. Soc.*, 1965, vol. 48, no. 9, pp. 470–472.
18. Drys, M. and Trzebiatowski, W., *Roczn. Chem.*, 1968, vol. 42, pp. 203–210.
19. *Powder Diffraction Data File*, Philadelphia: ASTM, Joint Committee in Powder Diffraction Standards, 1967.
20. Klyachko-Gurvich, A.L. and Rubinshtein, A.M., *Problemy kinetiki i kataliza: Nauchnye osnovy podbora katalizatorov geterogennykh kataliticheskikh reaktsii* (Problems of Kinetics and Catalysis: Scientific Foundations for Selection of Catalysts for Heterogeneous Catalytic Reactions), Moscow: Nauka, 1966, pp. 41–52.
21. Milligan, W.O. and Adams, C.R., *J. Phys. Chem.*, 1953, vol. 57, no. 9, pp. 885–890.
22. Dzis'ko, V.A., Karnaukhov, A.P., and Tarasova, D.V., *Fizikokhimicheskie osnovy sinteza okisnykh katalizatorov* (Physicochemical Foundations for Synthesis of Oxide Catalysts), Novosibirsk: Nauka, 1978.
23. Golodets, G.I., *Geterogenno-kataliticheskie reaktsii s uchastiem molekulyarnogo kisloroda* (Heterogeneous Catalytic Reactions Involving Molecular Oxygen), Kiev: Naukova Dumka, 1977.
24. Boreskov, G.K., *Geterogennyi kataliz* (Heterogeneous Catalysis), Moscow: Nauka, 1986.
25. Il'chenko, N.I., Pyatnitskii, Yu.I., and Pavlenko, N.V., *Teor. Eksp. Khim.*, 1998, vol. 34, no. 5, pp. 265–281.
26. *Tekhnologiya katalizatorov* (Technology of Catalysts), Mukhlenov, I.P., Ed., Leningrad: Khimiya, 1989.
27. Ganz, S.N. and Vashkevich, A.M., *Zh. Prikl. Khim.*, 1970, vol. 43, no. 1, pp. 13–18.
28. Zhidkov, B.A., Orlova, S.S., Bochenko, G.A., and Plygunov, A.S., *Khim. Tekhnol.*, 1979, no. 1, pp. 5–8.
29. Beskov, V.S., Karavaev, M.M., Garov, D.V., and Arutyunyan, V.A., *React. Kinet. Catal. Lett.*, 1976, vol. 4, no. 3, p. 351–357.
30. Buben, N.Ya., *Zh. Fiz. Khim.*, 1945, vol. 19, nos. 4–5, pp. 250–253.
31. Kasatkin, A.G., *Osnovnye protsessy i apparaty khimicheskoi tekhnologii* (Basic Processes and Apparatus of Chemical Technology), Moscow: Khimiya, 1973.

Russian Journal of Applied Chemistry, Vol. 76, No. 3, 2003, pp. 407–414. Translated from Zhurnal Prikladnoi Khimii, Vol. 76, No. 3, 2003, pp. 422–429.

CATALYSIS

Development of Pyrolysis Catalysts Based on Barium Chloride for Industrial Use

S. V. Kolesov, M. A. Tsadkin, and R. N. Gimaev

Bashkir State University, Ufa, Bashkortostan, Russia

Received July 2, 2002

Abstract—The catalysts of pyrolysis of straight-run naphtha, platforming raffinate, and thermal cracking naphtha, based on barium chloride, were developed. The strength characteristics of preformed catalysts with addition of graphite, alkylamide of synthetic fatty acid (SFA), phenol-furan resin, and clay were studied.

Catalytic pyrolysis of naphtha fractions formed in petroleum refining to ethylene/propylene in the presence of $BaCl_2$ [1, 2] can be feasible only if the form of the salt catalyst will be suitable for the industrial process. Since in a fixed-bed reactor the use of a finely divided catalyst results in significantly increased hydrodynamic resistance to flow of the feed, and in the case of coking the catalyst bed becomes impermeable at all, $BaCl_2$ in the form of crystalline powder cannot be used as a catalyst in the industrial process. Finely dispersed powder is unsuitable for a fluidized-bed reactor (fluid-process) either, because the catalyst particles can be carried away with the flow of the feed and products. The feed flow rate under conditions of catalytic pyrolysis (τ = 5–20 s) is insufficient to produce a fluidized bed [2]. Hence, the catalyst form should provide its efficient operation in a fixed-bed reactor.

Many promising catalysts, in particular potassium metavanadate, were mainly considered in the supported form [3, 4]. With the available and cheap active component, $BaCl_2$, simpler and more efficient procedures of production of commercial catalysts can be considered. For fixed-bed reactors, the optimal shapes are granules, pellets, rings, etc., produced by pressing and extrusion. Along with the possibilities of imparting the required geometric parameters, these procedures allow modification of catalysts owing to introduction of various additives, from auxiliary substances facilitating molding to components serving as cocatalysts.

The pelletized catalysts were produced by molding on a highly productive pelletizing machine Fette-Exacta-21 in the form of 5 × 6-mm pellets, providing minimal hydrodynamic resistance to the flow of the feed [5].

The study of molding process allowed determination of the main conditions for production of suitable catalyst forms.

Variation of the degree of dispersion of the $BaCl_2$ powder showed that the best strength characteristics of pellets are obtained with the 0.25–0.50-mm fraction (Table 1). The strength of pellets is significantly enhanced with thermal pretreatment of the catalyst mass or in subsequent calcination of pellets. Preliminary calcination of the powder fraction at 175–300°C, i.e., at a temperature higher than the temperature of dehydration of $BaCl_2$ crystal hydrates [6], increases the strength of the resulting pellets by a factor of 2–5. Further heating to 500°C produces no positive effect (Table 1).

The structural-mechanical characteristics of pelletized catalysts are largely determined by the features of contacts between the solid particles in molding of the catalysts, namely, by the strength of adhesion between the particles. This strength can be enhanced by decreasing the surface energy in the contact area as a result of formation of adsorption layers of surfactants added to the system. The granule strength can also be enhanced by using lubricating agents which decrease the concentration of internal stresses in the contact areas of particles in the course of compaction. The strengthening effect of some additives can be caused by formation of a three-dimensional skeleton in the form of a chemically cross-linked network, e.g., when using thermosetting resins.

Moistening of the catalyst mass before molding (up to 5% water) enhances the strength of the catalyst pellets. However, in this case, the granule strength varies in a wide range. Addition of surfactants, e.g., alkylamide of SFA of the C_{10}–C_{13} fraction in the amount of 0.25–3 wt %, does not result in strengthen-

1070-4272/03/7603-0407$25.00

Table 1. Strength characteristics* of pelletized catalysts based on $BaCl_2$

Catalyst mass		Thermal treatment conditions		Crushing strength, kgf per pellet	
fraction of $BaCl_2$ powder, mm	addition, wt %	*T*, °C	τ, h	axial direction	radial direction
0.16–1.00 nonfractionated	–	–	–	0.7–1.5	0.6–0.9
0.50–1.00	–	–	–	0.4–0.9	0.2–0.5
0.16–0.25	–	–	–	8.0–1.5	0.2–0.6
0.25–0.50	–	–	–	1.4–2.1	0.8–1.3
0.25–0.50	–	175	10	8.0–12.0	2.0–9.0
0.25–0.50	–	175	20	10.0–15.0	4.0–9.0
0.25–0.50	–	175	25	10.0–16.0	4.0–9.0
0.25–0.50	–	300	10	10.0–16.0	9.0–14.0
0.25–0.50	–	400	10	11.0–16.0	9.0–12.0
0.25–0.50	–	500	10	10.0–16.0	9.0–12.0
		Graphite			
0.16–1.00	3.00	–	–	19.0–23.0	16.0–21.0
0.16–0.25	0.25	–	–	21.0–24.0	7.0–13.0
0.16–0.25	1.00	–	–	34.0–48.0	20.0–27.0
0.16–0.25	3.00	–	–	45.0–65.0	32.0–37.0
0.16–0.25	5.00	–	–	39.0–50.0	31.0–38.0
0.25–0.50	3.00	–	–	38.0–43.0	30.0–37.0
		Diethanolamide of SFA			
0.25–0.50	0.25	–	–	10.0–16.0	0.5–3.0
0.25–0.50	0.50	–	–	4.0–6.0	1.0–3.0
0.25–0.50	3.00	–	–	2.0–3.0	1.0–4.0
		Phenol–furan resin			
0.25–0.50	0.5	–	–	1.0–1.3	0.5–1.3
0.25–0.50	0.25	–	–	0.6–0.9	0.6–0.8
0.25–0.50	5.0	–	–	1.0–1.2	0.5–1.2
0.25–0.50	0.5	300	0.5	6.0–9.0	5.0–9.0
0.25–0.50	2.5	300	0.5	10.0–15.0	4.0–12.0
0.25–0.50	5.0	300	0.5	20.0–24.0	18.0–24.0
0.25–0.50	5.0	400	0.5	50.0–64.0	47.0–60.0
0.25–0.50	5.0	500	0.5	55.0–61.0	55.0–60.0
0.25–0.50	5.0	600	0.5	56.0–66.0	51.0–65.0
		Clay			
0.25–0.50	5.0	–	–	59.0	38.0

* The strength characteristics were determined on an Erweka-TBH28 device.

ing of granules. The use of superfine graphite in the amount of 1–5 wt % (based on the catalyst) as a forming additive is more efficient. At a graphite concentration of 3 wt %, the strength of the resulting catalysts is 8–16 kgf per pellet with a narrow spread in values. At the optimum choice of characteristics of components (dispersion), formulation, and the conditions of pretreatment of the raw materials, we were able to obtain the catalyst with the crushing strength in the axial and radical directions of 55 and 35 kgf per pellet, respectively. Such catalysts are quite acceptable for operation in industrial reactors with a fixed catalyst bed.

As a rule, the strength of pellets in the radical direction is lower than the strength in the axial direction [5], which results in their destruction during random loading and discharge. From this standpoint, the catalyst forms isotropic in strength are desirable, which is reached by using thermosetting resins as an

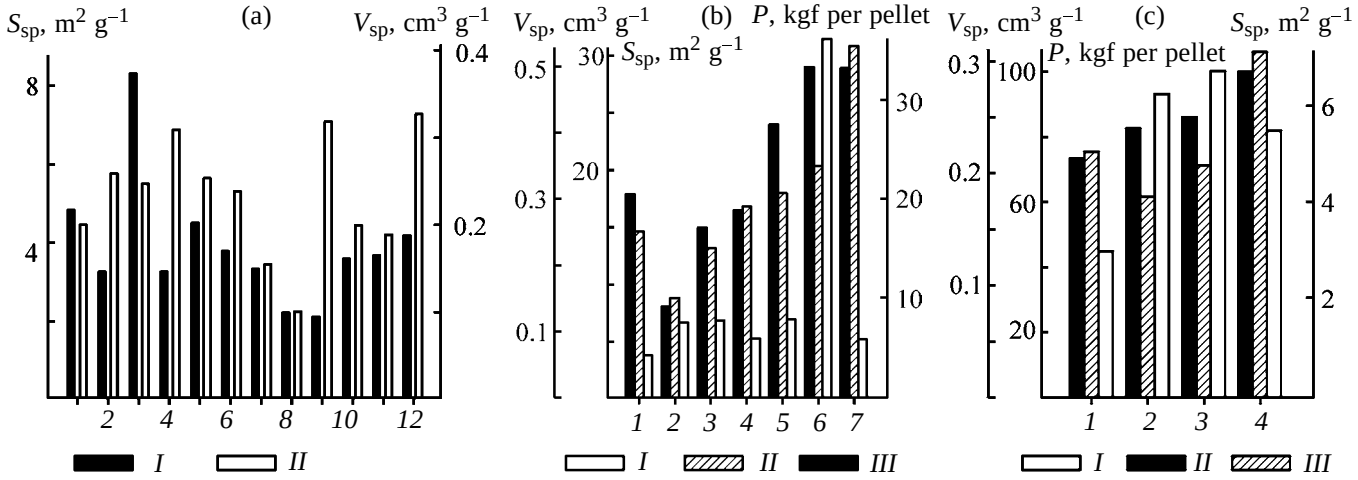

Fig. 1. (*I*) Specific surface area S_{sp}, (*II*) specific pore volume V_{sp}, and (*III*) mechanical strength P of barium-containing catalysts. (a) (*1*) Initial catalyst, (*2*) pellets calcined at 175°C, (*3*) pellets prepared with precalcination of the powder at 175°C, (*4*) pellets calcined at 300°C, and (*5*) pellets prepared with precalcination of the powder at 300°C; addition, wt %: (*6*) graphite 1, (*7*) graphite 3, (*8*) graphite 5, (*9*) diethanolamide of SFA 1, (*10*) water 5, (*11*) graphite 0.25 + water 1, and (*12*) phenol–furan resin 5. (b) (*1*) Catalyst without additive; addition of clay as binding agent (wt %): (*2*) 1.0, (*3*) 5.0, (*4*) 10.0, (*5*) 20.0, (*6*) 30.0, and (*7*) 45.0. (c) (*1*) Pelletized catalyst with 3 wt % graphite; addition of sodium tetrachloroaluminate (wt %): (*2*) 3.0, (*3*) 10.0, and (*4*) 25.0.

auxiliary additive in molding. In particular, we tested Polifuron-321 phenol–furan resin. The strength of the catalyst pellets containing 0.5–5 wt % phenol–furan resin and calcined at 300–400°C for 30–60 min reaches 50–60 kgf per pellet in all directions (Table 1).

The thermal treatment and additive affect not only the strength but also the structural characteristics of the catalysts: the specific surface area and pore volume change. Calcination of the initial $BaCl_2$ and the resulting pellets increases the surface area (Fig. 1a). Addition of water, graphite, and diethanolamide of SFA significantly decreases the specific surface area as compared to the initial catalyst.

The influence of the above factors on the pore structure of the catalyst granules is ambiguous. Whereas thermal treatment of the initial material and the resulting catalyst always increases the pore volume, the influence of additives strongly depends on their nature and content in the mixture. Addition of up to 5 wt % water does not noticeably affect the pore volume, and addition of diethanolamide of SFA (1 wt %) significantly increases the pore volume. Graphite added in the amount of 1 wt % somewhat increases the pore volume as compared to the catalyst molded without thermal treatment and additives. Larger amounts of graphite decrease the porosity of the pellets.

According to published data [7], only the outer surface of a catalyst operates in catalytic pyrolysis, and an increase in the inner surface area plays a negative role, promoting undesirable side processes.

In production of molded catalysts, it is possible to add agents that not only modify the mechanical and structural characteristics but also enhance the catalytic activity. It is of interest to produce catalysts using natural clays as binding agents. Aluminosilicates, zeolites, and zeolite-containing catalysts are widely used in catalytic pyrolysis [8–11]. Despite the presence of Brønsted and Lewis acid centers at the catalyst surface, the trends in the yield and composition of gaseous products of hydrocarbon pyrolysis at 700–800°C are similar to those in the thermal pyrolysis [11]. It is assumed that the active centers arising in dehydroxylation of the aluminosilicate surface participate in high-temperature pyrolysis. Centers containing acid–base pairs Al^+O^- can serve as such centers [12].

We studied the catalysts containing natural clay of the montmorillonite group of the Kuganak deposit, based on aluminosilicates with the structure of $xAl_2O_3 \cdot ySiO_2 \cdot H_2O$. With the clay content of up to 5 wt %, the catalysts are easily molded by pelletizing and give the products with satisfactory strength (Table 1). The catalysts with a higher content of clay (30 and 50 wt %) are best molded by extrusion with preliminary moistening to water content of 25%. After drying and calcination of extruded granules at 350–400°C, the catalysts with the crushing strength of

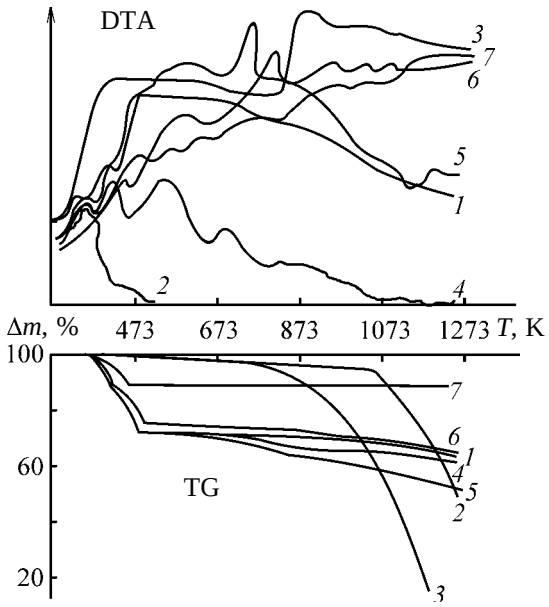

Fig. 2. DTA and TG curves of pelletized catalysts based on $BaCl_2$. (Δm) Weight variation and (T) temperature. Barium chloride: (*1*) without thermal treatment and (*2*) calcined at 300°C; addition, wt %: (*3*) graphite 3, (*4*) phenol–furan resin 3, (*5*) phenol–furan resin 5, (*6*) phenol–furan resin 3 and clay 30, and (*7*) clay 30. OD-102 derivatograph; heating rate 15 deg min^{-1}.

178–240 kgf per granule in the axial direction and 140–205 kgf per granule in the radial direction are obtained. In molding with clay, the structural characteristics of the catalyst are improved with increasing content of additive from 1 to 30 wt % (Fig. 1b).

Extrusion molding from a plastic mixture allows production of catalysts in the form of continuous regular macroscopic lattice or cellular structures. These structures of the catalysts primarily ensure favorable gas-dynamic condition in the reactor. With increasing pressure in the reactor above 0.1 MPa, the yield of the main target products of pyrolysis (ethylene and propylene) decreases and the yield of methane grows. The pressure in the reaction area also depends on the pressure differential in flow of the reaction gas mixture through the catalyst bed, which is governed by the size and shape of the catalyst particles. For example, in a bed of a catalyst in the form of cylindrical granules, the pressure is, on the average, 1.5–1.7 times higher than in the catalyst bed with particles in the form of Raschig rings. In a bed of a catalyst based on potassium vanadate modified with boron compounds and molded as Raschig rings, the yield of ethylene at 790–795°C is, on the average, 0.5–1.0% higher than that in a bed of the catalyst with cylindrical granules. It is evident that the regular cellular or lattice structure ensures the best gas-dynamic regime.

Attempts to produce catalyst blocks by addition of $BaCl_2$ to the initial plastic clayey mixture resulted in production of fragile blocks easily breking after calcination. Applying barium chloride from aqueous solution to a preliminarily formed alumino ceramic block allowed us to increase the $BaCl_2$ content to 45 wt %. However, cellular blocks with such a content of $BaCl_2$ are destroyed upon subsequent calcination at 800°C. The strength of alumino ceramic block is retained if the amount of added $BaCl_2$ does not exceed 18 wt %. In this case, the surface characteristics and pore structure of the alumino ceramic matrix do not change.

In molding of catalysts, additives modifying the catalytic activity can be introduced relatively easily. The catalysts based on a mixture of $BaCl_2$ with sodium tetrachloroaluminate $NaAlCl_4$ are of interest. These catalysts exhibit high activity in cracking and isomerization. The physical state of $NaAlCl_4$ (melt) at the temperature of the catalytic pyrolysis hampers its use. However, on its addition with graphite or clay binder to the catalytic mixture to be molded, suitable catalyst granules can be produced. On addition of the complex in the amount of 3–25 wt % based on the catalyst, the strength appreciably grows: to 98 kgf per pellet (Fig. 1c).

The other, no less important characteristic of heterogeneous pyrolysis catalyst is the thermal stability. The results of thermal gravimetric studies of the pelletized catalyst prepared from noncalcined and preliminarily calcined $BaCl_2$ powder are presented in Fig. 2.

The resulting catalysts were tested in catalytic pyrolysis in the range 500–800°C on a pilot installation equipped with a flow-type reactor with a fixed bed of granulated catalyst, a line for preheating of the feed, and a system of series-connected condensers for condensation of liquid products.

The results of pyrolysis of straight-run naphtha, platforming raffinate, and thermal cracking naphtha on the pelletized catalyst containing 3 wt % graphite are listed in Table 2. The catalyst produced with addition of natural aluminosilicate (clay) as a binder showed satisfactory activity in naphtha pyrolysis (Table 3).

In the range 650–750°C, with the catalyst containing 10 wt % $NaAlCl_4$, the pyrolysis pathway changes considerably. In pyrolysis of straight-run naphtha at 650–700°C, the yield of ethylene is lower than the yields of propylene and butylenes (Table 3), and the

Table 2. Yield *Y* and composition of gaseous products in pyrolysis of naphtha on the catalyst. Binder: 3 wt % graphite

T, °C	τ,* h	*Y*, wt %	Composition of gaseous products, wt %									
			H_2	CH_4	C_2H_4	C_2H_6	C_3H_6	C_3H_8	ΣC_4H_8	ΣC_4H_{10}	ΣC_{5-}	H_2S
Platforming raffinate												
475	30.0	67.4	0.19	20.47	30.95	7.11	27.92	1.54	7.47	1.34	3.01	–
550	5.0	70.6	0.22	18.70	32.19	6.45	28.58	0.90	9.39	2.01	1.56	–
550	10.0	75.9	0.15	20.14	32.03	5.46	27.19	1.67	8.19	1.57	3.60	–
550	20.0	82.0	0.20	21.09	32.19	6.12	28.73	1.21	7.14	0.96	2.36	–
550	30.0	89.4	0.22	22.05	32.27	6.21	29.89	1.16	5.10	1.01	2.09	–
600	0.5	71.3	0.23	22.41	30.47	6.40	28.14	1.19	7.30	1.65	2.21	–
600	1.0	89.5	0.23	23.14	32.60	6.19	28.49	1.25	5.41	1.12	1.57	–
700	0.5	78.4	0.25	23.19	32.96	6.53	27.25	1.20	6.12	1.60	0.90	–
700	1.0	91.3	0.27	24.11	32.90	5.14	28.21	1.06	5.32	1.10	1.89	–
Thermal cracking naphtha												
450	20.0	46.4	0.16	18.30	30.17	4.25	19.00	4.52	11.99	4.67	6.79	0.06
450	30.0	51.3	0.17	20.18	31.66	3.52	21.41	4.31	11.69	4.39	2.55	0.12
475	10.0	55.8	0.17	19.40	30.89	6.53	18.89	3.05	10.95	2.07	7.16	0.08
475	20.0	59.7	0.18	19.80	30.73	4.39	19.29	3.73	10.43	5.37	5.95	0.13
500	5.0	54.0	0.16	22.21	30.33	5.17	18.73	3.14	7.56	5.33	7.26	0.11
500	10.0	72.1	0.18	22.17	31.80	5.23	18.99	2.71	10.67	2.71	5.41	0.13
500	20.0	76.8	0.19	23.83	32.40	3.68	19.74	3.16	7.54	3.39	5.93	0.14
500	30.0	79.5	0.21	24.17	32.70	2.76	21.06	3.05	9.81	3.45	2.67	0.12
550	5.0	71.2	0.21	23.47	31.70	3.42	18.07	2.63	8.16	3.08	9.17	0.09
550	10.0	82.4	0.20	24.62	32.68	2.83	19.76	2.46	7.55	4.19	5.89	0.18
550	20.0	83.9	0.20	25.62	32.35	2.71	18.30	2.46	7.45	2.56	8.26	0.10
550	30.0	88.7	0.24	26.30	32.44	2.94	21.31	3.03	8.89	2.55	2.20	0.10
600	0.5	70.8	0.22	21.93	31.45	3.51	20.44	4.69	10.37	4.64	2.63	0.12
600	10.0	88.0	0.24	22.01	32.53	3.22	21.25	4.27	10.38	2.92	3.05	0.13
700	0.5	77.9	0.25	22.46	31.69	3.00	20.80	4.45	12.07	2.69	2.48	0.11
700	1.0	91.0	0.28	23.12	32.81	2.86	20.89	4.02	10.04	4.27	1.59	0.12

* (τ) Contact time.

content of these latter in pyrolysis gas noticeably exceeds the characteristics of the thermal process. This is in good agreement with published data on the catalytic activity of $NaAlCl_4$ in cracking of hydrocarbons with primary formation of C_4 olefins. However, at 725°C and higher temperatures, the content of ethylene in the products increases, and that of butylenes decreases. In this case, the yield of ethylene exceeding 38% based on the feed was reached, with the degree of gas formation exceeding 80%. On the whole, the product composition becomes typical for a high-temperature radical process.

It is well known [13, 14] that, for activation of electrophilic catalysts based on complex metal chlorides in low-temperature catalytic degradation of hydrocarbons, participation of water or other proton donors is required. The role of water in activation of $MAlCl_4$ is governed by its dissociative adsorption on the catalyst surface. Correspondingly, metal chlorides catalytically active under these conditions play the role of Brønsted acids.

The degree of dilution of the feed with superheated steam affects the yield of ethylene (Table 4). Some increase in the total gas formation and increase in the yield of ethylene take place at steam supply of no more than 75% of the feed. In addition, a noticeable amount of carbon oxides appears in the gas.

The liquid products of pyrolysis are enriched with aromatic hydrocarbons (Table 5).

Testing for the operation life of the catalyst showed that the catalyst formed with 3 wt % graphite retains its activity in the total gas formation and selectivity with respect to the yield of ethylene and propylene for

Table 3. Yield of gaseous* pyrolysis products of naphthas on various forms of barium-containing catalysts

T, °C	*V*,** h^{-1}	Yield of products, wt % based on the feed							
		$CH_4 + H_2$	C_2H_4	C_2H_6	C_3H_6	C_3H_8	ΣC_4H_8	ΣC_4H_{10}	total
Straight-run naphtha/granulated catalyst with 30 wt % clay									
650	0.5	9.1	28.2	10.0	14.9	2.0	6.5	0.8	71.5
700	0.5	12.6	29.1	7.3	15.1	1.1	9.1	0.7	75.0
725	0.5	17.6	32.9	7.2	13.8	0.9	7.0	0.1	79.5
750	0.5	25.2	34.9	7.1	12.0	0.8	5.5	0.1	85.6
Straight-run naphtha/pelletized catalyst with 10 wt % $NaAlCl_4$									
650	0.5	6.8	12.5	6.4	17.5	0.9	13.7	Traces	57.8
650	1.0	6.9	10.9	6.9	18.2	0.2	14.4	–	57.5
700	0.5	12.4	28.4	28.0	7.0	18.3	1.0	14.8	81.5
700	1.0	11.5	21.4	8.1	23.4	0.9	14.9	–	80.2
725	0.5	19.8	32.9	7.0	18.9	0.8	3.0	–	82.4
725	1.0	17.0	30.0	9.1	18.3	1.2	5.5	–	81.1
750	0.5	25.7	38.9	6.2	12.2	0.6	0.4	–	84.0
750	1.0	20.0	33.1	8.0	17.2	0.7	4.8	–	83.8
Straight-run naphtha/cellular catalyst with 18 wt % $BaCl_2$									
650	0.5	3.59	3.9	2.7	26.1	0.1	8.3	4.61	49.3
700	0.5	17.5	22.0	3.9	25.9	0.8	12.5	2.2	84.8
725	0.5	22.4	28.9	4.4	19.0	0.4	12.7	0.1	87.9
725	1.0	19.9	27.1	1.0	22.9	0.3	16.4	0.2	87.8
725	2.0	13.7	23.4	4.0	24.8	0.2	19.3	0.3	85.7
725	2.5	13.6	23.2	4.0	24.9	0.1	19.1	0.3	85.2
750	0.5	26.3	31.0	0.4	12.6	0.1	10.1	0.1	80.6

* Hydrocarbons C_5 are condensed together with liquid products in a condenser.
** *V* is the feed space velocity.

Table 4. Yield and composition of gaseous pyrolysis products of straight-run naphtha on granulated catalysts at dilution of the feed with steam. Temperature 725°C, feed space velocity 0.5 h^{-1}

Dilution, wt % based on feed	Yield of products, wt % based on feed								
	$CH_4 + H_2$	C_2H_4	C_2H_6	C_3H_6	C_3H_8	ΣC_4H_8	ΣC_4H_{10}	carbon oxides	total
Catalyst with 3 wt % graphite									
–	19.1	31.6	7.9	10.9	0.7	5.5	0.2	–	75.9
50	20.8	32.5	4.6	12.9	1.0	6.5	0.1	1.2	79.6
100	25.0	31.9	4.0	12.0	0.6	4.0	0.8	1.9	80.2
Catalyst with 3 wt % clay									
–	17.6	32.9	7.2	13.8	0.9	7.0	0.1	–	79.5
50	18.1	34.8	9.1	16.8	1.0	7.0	0.3	1.4	88.5
100	20.0	34.0	8.0	16.1	0.4	5.1	0.1	2.0	85.7

700 h at 500°C. In this case, the coke yield based on the feed does not exceed 2.5 wt % in 30 h at 700°C for all the catalyst modifications (Fig. 3). It is particularly remarkable that the catalyst containing $NaAlCl_4$ as an additive is characterized by insignificant coking. Depending on the modification, the coke deposit at the catalyst surface can reach 10–20 wt %, which does not affect the process characteristics.

Table 5. Composition of light resin formed in pyrolysis of straight-run naphtha in the presence of various barium-containing catalysts.* Feed space velocity 0.5 h^{-1}

Component of pyrocondensate	Catalyst I				Catalyst II				Catalyst III			
	content, wt %, at indicated pyrolysis temperature, °C											
	650	700	725	750	650	700	725	750	650	700	725	750
Paraffin–naphthene–olefin fraction	43.5	41.6	41.2	39.9	44.7	41.7	41.4	39.4	44.4	43.9	43.7	39.0
Benzene	15.9	16.1	16.9	12.0	12.7	13.6	16.9	15.6	12.1	10.9	9.3	9.9
Toluene	10.9	10.7	10.0	9.3	12.0	10.9	10.3	9.9	16.0	16.3	15.2	15.7
Ethylbenzene	2.1	2.0	1.1	0.9	4.3	3.7	3.4	3.1	3.4	7.3	7.0	4.8
p,m-Xylenes	8.9	7.0	4.3	4.0	7.0	6.4	5.2	4.0	7.1	7.2	8.4	3.0
o-Xylene, cumene	3.4	3.2	3.1	2.8	7.2	34	1.9	0.8	1.1	0.9	0.4	0.6
Mesitylene	0.4	0.3	0.2	0.1	0.3	0.1	–	–	0.1	–	–	–
Styrene, pseudo-cumene	4.5	7.5	8.8	15.2	2.8	5.2	12.4	15.3	6.5	7.6	11.0	14.9
Indene	2.0	3.7	8.2	10.0	2.7	6.6	7.0	7.3	4.3	3.9	4.3	9.9
Unidentified components	8.4	7.9	6.2	5.8	6.3	8.4	1.5	4.6	5.0	2.0	0.7	2.2

* Catalyst molded (I) with 3 wt % graphite, (II) with 30 wt % clay, and (III) with 10 wt % $NaAlCl_4$.

Auto-retardation of coking in the course of the process is characteristic for all modifications of the catalysts.

The study of the coke deposit distribution on pellet sections showed that coke is formed mainly in a thin near-surface layer. In the process, the variation of the pore structure and specific surface area of the catalyst is insignificant. In particular, the specific surface areas of the initial catalyst and catalyst coked at 500°C are 3.62 and 3.43 $m^2 g^{-1}$, and the pore volume is 0.22 and 0.28 $cm^3 g^{-1}$, respectively. In this connection, some decrease in the rate of coke deposition at the catalyst may be due to partial desorption of intermediate condensation products, precursors of coke, into the gas phase. This results in some increase in the yield of heavy resins at the expense of a decrease in the coke yield, and it does not affect the yield of the main gaseous products of pyrolysis.

CONCLUSION

Effective catalysts for production of light olefins by naphtha pyrolysis can be produced on the basis

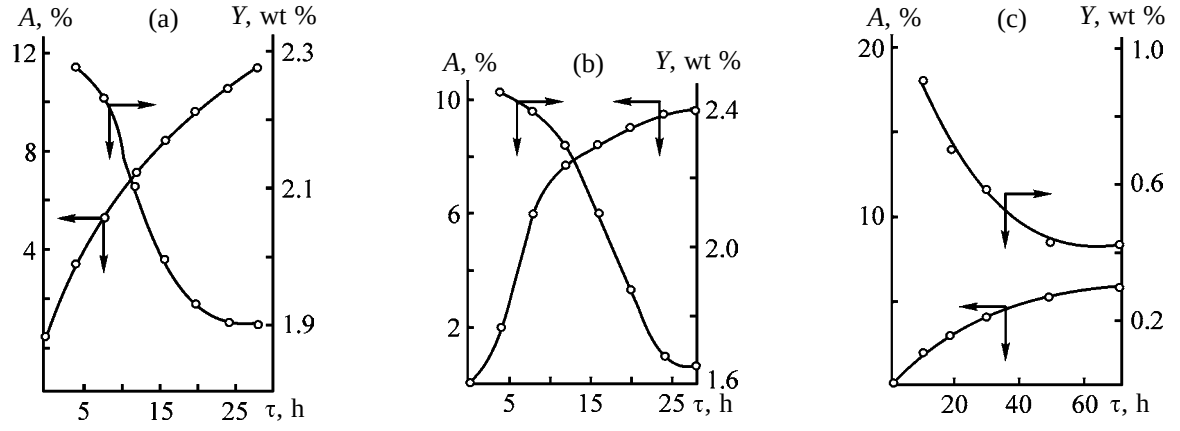

Fig. 3. Coking *A* (% of the catalyst weight) in the course of pyrolysis of straight-run naphtha on barium-containing catalysts molded with various additives. Process temperature 700°C, feed space velocity 0.5 h^{-1}. (*Y*) Coke yield (wt % based on feed) and (τ) process duration. Additive, wt %: (a) 3 graphite, (b) 30 clay, and (c) 10 $NaAlCl_4$.

of barium chloride. These catalysts fully meet the requirements to heterogeneous pyrolysis catalysts.

REFERENCES

1. Tsadkin, M.A., Gimaev, R.N., and Ivanova, S.R., *Neftepererab. Neftekhim*., 1987, no. 2, pp. 47–48.
2. Tsadkin, M.A., Ivanova, S.R., Kabirova, R.Yu., *et al*., *Khim. Tekhnol. Topl. Masel*, 1988, no. 2, pp. 8–9.
3. Adel'son, S.V., Vorontsova, T.A., Mel'nikova, S.A., *et al*., *Neftekhimiya*, 1979, vol. 19, no. 4, pp. 577–582.
4. Chernykh, S.P., Malinovskii, A.S., Adel'son, S.V., *et al*., *Nefteperab. Neftekhim*. (Moscow), 1991, no. 6, pp. 3–5.
5. Satterfield, C., *Heterogeneous Catalysis in Practice*, New York: McGraw-Hill, 1980.
6. Furman, A.A., *Neorganicheskie khloridy (khimiya i tekhnologiya)* [Inorganic Chlorides (Chemistry and Technology)], Moscow: Khimiya, 1980.
7. Vasil'eva, N.A. and Buyanova, R.A., *Neftekhimiya*, 1979, vol. 19, no. 4, pp. 583–586.
8. Tagiev, D.B., Shafirova, E.B., Zeinalova, F.A., *et al*., *Zh. Prikl. Khim*., 1981, vol. 54, no. 2, pp. 356–358.
9. Minachev, Kh.M., Tagiev, D.B., Zul'fugarov, Z.G., *et al*., *Neftekhimiya*, 1980, vol. 20, no. 3, pp. 408–411.
10. Khadzhiev, S.N. and Topchieva, K.V., *Mekhanizm kataliticheskikh reaktsii. Materialy III Vsesoyuznoi konferentsii* (Mechanism of Catalytic Reactions. Proc. III All-Union Conf.), Novosibirsk, 1982, pp. 59–61.
11. Rustamov, M.I., Farkhadova, G.T., Ismailov, E.G., *et al*., *Neftekhimiya*, 1997, vol. 37, no. 4, pp. 347–353.
12. Borovkov, V.Yu., The Nature and Characteristics of Acid–Base Centers of Amorphous Aluminosilicates, High-Silica Zeolites, and Aluminum Oxide from the Evidence of the IR Diffuse Scattering Spectroscopy, *Doctoral Dissertation*, Moscow, 1988.
13. Berlin, A.A., Gumerova, E.F., Ivanova, S.R., *et al*., *Vysokomol. Soedin., Ser. B*, 1987, vol. 29, no. 8, pp. 604–607.
14. Minsker, K.S., Ivanova, S.R., and Babkin, V.A., *Dokl. Ross. Akad. Nauk*, 1995, vol. 343, no. 5, pp. 646–650.

Russian Journal of Applied Chemistry, Vol. 76, No. 3, 2003, pp. 415–421. Translated from Zhurnal Prikladnoi Khimii, Vol. 76, No. 3, 2003, pp. 430–436.

CATALYSIS

Manganese–Aluminum–Calcium Catalysts Prepared by "Chemical Mixing" in Water

V. A. Troshina, I. A. Mamaeva, G. I. Salomatin, M. P. Yaroshenko, G. M. Tesakova, Z. A. Tertichnik, and E. Z. Golosman

Novomoskovsk Institute of Nitrogen Industry, Public Joint-Stock Company, Novomoskovsk, Tula oblast, Russia

Received June 14, 2002

Abstract—X-ray phase and differential thermal analyses, IR spectroscopy, and temperature-programmed reduction method were applied to study the formation of a manganese–aluminum–calcium system prepared by mixing manganese hydroxocarbonate and calcium aluminates in water, which can be used as catalyst in deep oxidation of organic substances. The influence exerted by preparation conditions on the extent of chemical interaction in the system was considered.

Catalysts prepared by mixing metal hydroxocarbonates (MHC) with calcium aluminate in water or aqueous ammonia are successfully used to accelerate various chemical processes [1].

It was found previously that, in formation of formulations of this kind from MHC and calcium aluminates, carbonate ions from the MHC structure are partly or completely replaced by aluminate and(or) hydroxide ions formed in dissolution and hydrolysis of calcium aluminates. In this case, the replacement of CO_3^{2-} with aluminate ions may occur both with structural rearrangement of MHC into metal hydroxoaluminate (e.g., for ZnHC and MgHC in water and aqueous ammonia) and without it (CoHC, MnHC, NiHC in water). In the latter case, solid solutions of aluminum ions in the MHC lattice are formed. The involvement of hydroxide ions in the exchange leads to formation of metal hydroxides, which may further decompose to oxides.

In preparing catalysts from the given systems, it is preferable that products of replacement of carbonate ions with aluminate ions should be formed, since such compounds enhance the properties of the resulting catalysts (activity, thermal stability, service life, etc.) [1]. Thus, a key issue in obtaining catalysts based on calcium aluminates is directed synthesis of compounds incorporating ions of an active metal and aluminum.

There is virtually no published evidence concerning cement-containing systems with manganese hydroxocarbonate. At the same time, it is known that manganese compounds are effective catalysts for redox reactions and, in particular, deep oxidation of organic substances. In this context, it was of interest to study in detail the manganese–aluminum–calcium catalytic system, in which the high activity of manganese ions would combine with such properties of cements as high mechanical strength and thermal stability.

The aim of this study was to analyze specific features of formation of catalysts based on a system comprising MnHC and calcium aluminates by the method of "chemical mixing" widely used in the technology of cement-containing catalysts. The so-called chemical mixing assumes that the interaction of the starting components to give precursors of the active phase occurs in the stage of mixing of the starting substances with a liquid reagent. The stock obtained in mixing is then dried, calcined, and pelletized. In the given case, calcium aluminates are mainly involved in formation of the active phase of the catalysts, and their binding properties are employed to a lesser extent. The properties of the catalysts obtained are strongly affected by the mixing conditions: temperature, time, liquid : solid ratio (l : s), and medium (water or aqueous ammonia). The use of aqueous ammonia as liquid reagent in preparing many of the cement-containing systems developed previously is due to the fact that MHCs dissolve in this solution to form ammine complexes, which facilitates further interaction with the products formed in dissolution and hydrolysis of calcium aluminates to give metal hydroxoaluminates (or hydroxocarbonatoaluminates). In the case of catalyst formation in an aqueous medium, the interaction is localized at the interface between the solid phase of virtually insoluble MHC and solution

1070-4272/03/7603-0415$25.00

of calcium aluminates, and, therefore, the extent of the occurring transformation is lower. Nevertheless, water was used as liquid reagent in the given case, since, in contrast to other MHCs studied, MnHC does not dissolve under the action of aqueous ammonia to give ammine complexes [8], and the degree of hydration of calcium aluminates in the presence of $NH_3 \cdot H_2O$ markedly decreases [1, 4]. Thus, it is inadvisable to use ammonia water in the given case; moreover, adoption of an aqueous medium markedly improves the environmental characteristics of the technology.

The goals of this study were to reveal how preparation parameters affect the formation of the active phase of manganese–aluminum–calcium catalysts and to analyze the structural, strength, and catalytic properties of the catalysts developed with varied content of the active component.

EXPERIMENTAL

As starting components for preparing catalyst samples served manganese hydroxocarbonate $MnCO_3 \cdot m\mathrm{Mn(OH)}_2 \cdot nH_2O$ [GOST (State Standard) 7205–77] and high-alumina cement of the talum[1] type [$CA : CA_2$ = 0.26), TU (Technical Specification) 5737-006-00 284 345–99]. Manganese hydroxocarbonate was mixed with calcium aluminates in water, and the resulting stock was dried at 100°C and calcined at 400°C; dried and calcined catalysts were pelletized (specific compaction pressure P_{sp} = 200 MPa). The temperature and time of mixing were varied in the experiments; the l : s ratio was varied within the range (1.5–3) : 1. Simultaneously, mechanical mixtures of the starting components were studied.

X-ray phase analysis (XPA) was performed on DRON-2 and DRON-3 diffractometers with CuK_α radiation and graphite monochromator. IR spectral study of samples compacted into pellets with KBr was carried out on a Specord 75-IR spectrophotometer. Differential-thermal analysis was made on an OD-102 derivatograph; samples were heated in air to 1000°C at a rate of 5 deg min^{-1}. The temperature-programmed reduction was done on a KL-1 integrated installation in a hydrogen flow, at a heating rate of 5 deg min^{-1}. The specific surface area was measured by the BET technique on the basis of low-temperature adsorption of nitrogen. The total porosity was found from the true and apparent densities of the samples. The pore volume distribution with respect to radii was studied on a Carlo Erba Sorptomatik instrument. The mechanical strength of pelletized catalysts was determined under static conditions by crushing grains with load applied to the sample edge (Shkol'nik and MP-2S instruments). The activity of the samples was tested in deep oxidation of benzene on a laboratory flow-through setup at W = 30 000 h^{-1} and initial concentration of benzene in the air flow of 4–6 g m^{-3}. The activity was evaluated by the temperature at which 50% conversion of benzene was reached ($T_{\alpha=50\%}$).

It was shown previously that mixing of MnHC with talum in water leads to partial replacement of carbonate ions in the structure of MnHC by aluminate and hydroxide ions formed in dissolution and hydrolysis of calcium aluminates. This gives calcium carbonate (in the form of calcite) and aluminum-containing precursors of the active phase of the catalysts: solid solutions based on the crystal lattice of MnHC, with partial replacement of carbonate ions by aluminate ions, and on the gibbsite lattice with introduction of manganese ions. The maximum amount of interaction products is formed at middle compositions: 30–40% manganese compounds in terms of Mn_3O_4. Therefore, a composition with 40% Mn_3O_4 was chosen for a more detailed study of the basic aspects of manganese–aluminum–calcium catalyst formation under various conditions.

An X-ray phase analysis of samples prepared by mixing in water for 5 h demonstrated that, with increasing mixing temperature, the interaction rate grows (Fig. 1a): the intensity of reflections from the initial phases (MnHC, CA, CA_2) decreases and the intensity of lines corresponding to the forming compounds, $CaCO_3$ (in the form of calcite) and gibbsite, increases. The highest rate of the occurring transformations is observed at 75–90°C.

Figure 1b shows for a sample prepared at 90°C how the intensity of diffraction reflections from the starting and forming compounds varies with time. Calcium monoaluminate was completely hydrated within the first 2 h of treatment, and the degree of conversion of calcium dialuminate after 5 h of mixing was about 70%. By the end of the process, the intensity of the lines corresponding to MnHC was 40–45% of the initial value. The amount of forming gibbsite increased during the entire time of mixing; in addition, in contrast to hydrated talum (without MnHC additives), samples contained a minor amount of bayerite. The intensity of the lines corresponding to calcium carbonate increased only during the first 4 h of treatment. After 3 h of mixing, the formation of

[1] Talum is a mixture of calcium monoaluminate $CaO \cdot Al_2O_3$ and calcium dialuminate $CaO \cdot 2Al_2O_3$. Hereinafter the common designations of the chemistry of cements are used: A = Al_2O_3, C = CaO, H = H_2O.

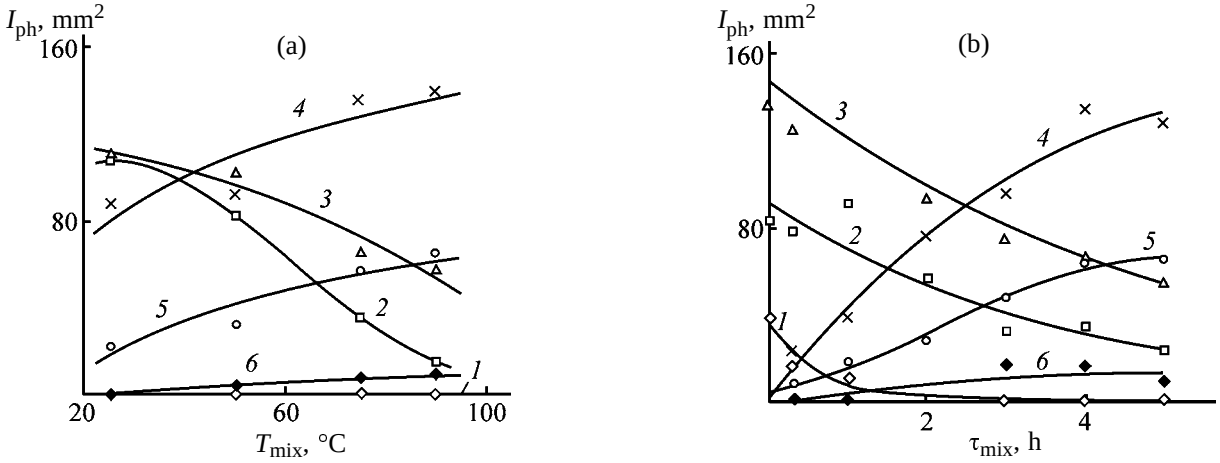

Fig. 1. Intensity I_{ph} of diffraction reflections from the forming and initial phases for samples prepared by mixing in water vs. (a) temperature T_{mix} and (b) time τ_{mix} of mixing (90°C). Phase: (*1*) CA, (*2*) CA_2, (*3*) MnHC, (*4*) $CaCO_3$, (*5*) gibbsite + bayerite, and (*6*) CCA.

calcium hydroxocarbonatoaluminate $C_3A \cdot CaCO_3 \cdot 12H_2O$ (CCA) was observed, with its amount in a sample remaining further unchanged. Thus, the maximum extent of reaction between the starting substances is reached in 3–5 h.

The IR data obtained are in good agreement with the results of XPA. In particular, with increasing time (Fig. 2) and temperature of mixing, the intensity of the absorption bands at 870 and 730 cm^{-1} belonging to MnHC decreases and the bands at 880 and 720 cm^{-1} corresponding to $CaCO_3$ appear. In addition, an increase in intensity and change in profile are observed for absorption bands in the range of stretching (3400–3700 cm^{-1}) and bending (900–1100 cm^{-1}) vibrations of OH^- groups of gibbsite, which results in that its spectrum becomes similar to that of bayerite. On the whole, raising the time of mixing to more than 3 h, and the temperature of mixing to above 75°C does not lead to any significant changes in the spectra of the samples.

The formation of $CaCO_3$ and the decrease in the intensities of diffraction reflections from MnHC in X-ray diffraction patterns and absorption bands associated with MnHC in the IR spectra of the samples result from partial replacement of carbonate ions in the structure of MnHC by hydroxide and aluminate ions formed in dissolution and hydrolysis of calcium aluminates [7].

The exchange of CO_3^{2-} ions for hydroxide ions leads to partial disintegration of the MnHC structure to give, probably, X-ray amorphous compounds $Mn(OH)_2 \cdot nH_2O$ and $MnO_x \cdot yH_2O$, with the possible incorporation of manganese ions into the lattice of the forming gibbsite. In the process, a system of new hydrogen bonds is formed in the structure of $Al(OH)_3$, the characteristics of the existing OH^- groups are changed, and new OH^- groups appear, which leads to partial transformation of its structure into bayerite. As a result, the profile of the absorption bands associated with stretching and bending vibrations of the OH^- groups of gibbsite in the IR spectra and X-ray diffraction characteristics change, and it is this fact that was observed in studying the samples. In particular, a detailed X-ray diffraction study revealed a shift of the diffraction reflections from gibbsite with respect to tabulated values. For example, depending on the mixing temperature, values ranging from d = 4.81 Å (90°C) to d = 4.78 Å (25–50°C) were observed for the reflection with d = 4.82 Å. This means that lowering the mixing temperature leads to stronger

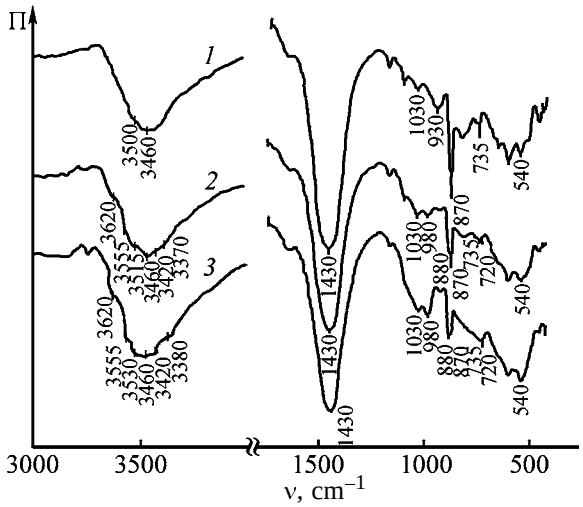

Fig. 2. IR spectra of samples prepared by mixing for varied time. (П) Transmission and (ν) wave number. Mixing time (h): (*1*) 0.5, (*2*) 2, and (*3*) 3.

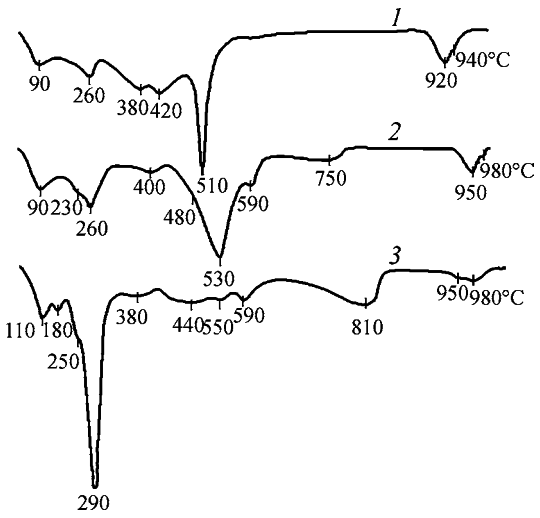

Fig. 3. DTG curves of samples prepared by mixing for varied time. Mixing time (h): (*1*) 0 (mechanical mixture of MnHC with talum), (*2*) 0.5, and (*3*) 3.

disordering of the structure of aluminum hydroxide, probably, owing to an increase in the content of manganese ions in its lattice.

Formation of disordered $MO–Al_2O_3$ solid solutions based on the MO lattice in thermal treatment [1–7] is an evidence of the involvement of aluminate ions in the exchange. Calcination of the samples in a hydrogen flow at 500°C yielded manganese oxide MnO whose diffraction peaks do not superimpose on reflections corresponding to other phases [7]. According to X-ray diffraction data, the forming MnO has a smaller lattice constant, compared to that for MnO obtained from MnHC (4.438 Å). In this case, a_{0MnO} = 4.431–4.437 Å for catalysts obtained under various conditions, and a_{0MnO} = 4.438 Å for the starting mechanical mixture of substances. In addition, depending on the mixing conditions, the intensity of reflections from MnO, I_{MnO}, in the samples under study was 30–50% of the intensity of MnO lines in a reduced mechanical mixture of the reagents. This may be due, first, to binding of manganese compounds into difficultly reducible solid solutions with the result that only a part (30–50%) of manganese compounds is reduced and, second, to formation in the course of reduction of highly dispersed, X-ray amorphous particles of MnO, which leads to broadening of its reflections in X-ray diffraction patterns and to a decrease in their intensity. The dispersity α (Å) of the resulting manganese oxides also depends on the mixing temperature, being equal to 120 Å for a sample prepared at 90°C and 145 Å for catalysts obtained at 25–75°C, in contrast to a mechanical mixture of MnHC with talum, for which α_{MnO} = 180 Å.

These results point to the formation in calcined samples of $MnO_x–Al_2O_3$ solid solutions based on the MnO_x lattice and, consequently, to the presence (as a precursor) in the initial uncalcined samples of a solid solution of aluminate ions in the MnHC lattice.

In view of the partial decomposition of manganese hydroxocarbonate in the course of the reaction [7], an assumption was made that both incorporation of manganese ions into the lattice of $Al(OH)_3$ formed in hydration of calcium aluminates and incorporation of aluminum ions into the structure of $Mn(OH)_2$ are possible under conditions of simultaneous formation of X-ray amorphous manganese and aluminum hydroxides. In addition, modification with Al ions of the forming X-ray amorphous $MnO_x \cdot yH_2O$ is also not improbable, i.e., X-ray-amorphous manganese compounds $Mn(OH)_2$ and $Mn_x \cdot yH_2O$ with incorporation of aluminum ions may serve as another precursor of the $MnO–Al_2O_3$ solid solutions.

Noteworthy is the fact that the minimum values of I_{MnO} and the largest deviations of a_{0MnO} of reduced catalysts from the tabulated values are characteristic of catalysts prepared at medium temperatures (50–75°C). Presumably, the greatest extent of interaction between MnHC and talum to give manganese–aluminum-containing solid solutions based on the MnHC, $Mn(OH)_2 \cdot nH_2O$, and $MnO_x \cdot yH_2O$ lattices is achieved under these conditions.

Figure 3 shows DTG curves of samples obtained at varied mixing time. These curves were interpreted on the basis of the results obtained in [7, 9, 10] and XPA data. It is noteworthy that the intensities of effects associated with $Al(OH)_3$ decomposition (260–290°C) and $CaCO_3$ dissociation grow with increasing mixing time, and also there appear minor thermal effects at 180 and 230–250°C, related to decomposition of calcium hydroxocarbonatoaluminate (CCA). With increasing mixing time, the intensity of the thermal effect associated with the $Mn_3O_3 \rightarrow Mn_3O_4$ transformation at 920–940°C decreases and it is shifted to higher temperatures (950–990°C). Of particular interest is the change in the curve profile in the range 350–600°C. The effects associated with MnHC decomposition (380, 420°C) and $MnO_2 \rightarrow Mn_2O_3$ transformation (510°C), observed for a mechanical mixture of the starting components (Fig. 3, curve *1*), are shifted to higher temperatures and partly overlap after 30 min of mixing (Fig. 3, curve *2*), with the peak at 380°C shifted to 400°C, the effect at 420°C shifted to 480°C and superimposed on the $MnO_2 \rightarrow Mn_2O_3$ effect (530°C), and an effect appearing at 590°C. Further increase in the mixing time makes lower the intensity

of the effect at 530–540°C, with the result that the profile of the DTG curves at 400–600°C is gradually smoothed; after 3 h of mixing the profile virtually does not change any more. The data presented indicate that a chemical reaction occurs in the course of mixing, with the maximum extent of this reaction reached after 3–5 h of treatment. The profiles of the DTG curves of samples prepared at different temperatures are similar; however, the intensities of the effects associated with $Al(OH)_3$ and $CaCO_3$ decomposition grow with increasing mixing temperature, and a minor effect related to decomposition of calcium hydroxocarbonatoaluminate appears at 230°C, with the maximum extent of the occurring transformations reached at 75–90°C.

Thus, according to differential-thermogravimetric analysis, the optimal mixing conditions are the following: temperature 75°C and time 3 h.

In discussing the results obtained by the method of temperature-programmed reduction of samples in a flow of hydrogen, the following is noteworthy. The thermochromatogram of the initial mechanical mixture of the components shows effects of MnHC decomposition (300–470°C). The chromatogram of a "mixed" sample contains peaks associated with dehydration of gibbsite (250–350°C) and dissociation of calcium carbonate (550–670°C): in the interval 400–630°C, a number of minor effects is observed, which can be attributed to decomposition of residual MnHC modified with aluminum ions and to reduction of manganese oxides. Thus, the data furnished by the method of temperature-programmed reduction are in good agreement with the derivatographic data; however, decomposition of $CaCO_3$ in a reductive medium (H_2) occurs at a temperature lower by nearly 150°C than that in the oxidative medium (air). This phenomenon, which has also been observed in studying other cementcontaining systems, is associated with the catalytic action of reduction products on the thermal dissociation of $CaCO_3$.

Noteworthy is the fact that manganese oxide MnO forming in the course of reduction at temperatures of up to 750°C has lattice constant rather close to the tabulated value (4.445 Å): 4.441 for mixed catalyst and 4.444 Å for a mechanical mixture, in contrast to 4.431 and 4.437 Å for the same samples heated to 500°C, which is probably due to ordering of its structure in the course of heating. The intensity of diffraction reflections from MnO for a mixed sample (I_{MnO} = 250 mm^2) is lower than that for a mechanical mixture (I_{MnO} = 570 mm^2), and its dispersity α_{MnO} = 300 Å is 2 times higher. Comparison of these data with the results for catalysts reduced at temperatures of up to 500°C shows that raising the temperature of heating in a flow of hydrogen from 500 to 750°C leads to caking of MnO, and in the case of the initial mixture of MnHC with talum, its dispersity changes from 180 to 600 Å, whereas for a sample obtained by mixing in water, the decrease in MnO dispersity is less pronounced: from 145 to 300 Å. This phenomenon points to higher thermal stability of the mixed catalyst and, consequently, to positive effect of the solid solutions formed in fabrication of catalysts on their stability.

On the basis of the analytical data and the results of XPA and thermogravimetric analysis of samples prepared under different conditions, the degrees of conversion of the starting substances into reaction products were calculated. It was found that, with increasing temperature and time of mixing, the extent of the reaction grows and reaches a maximum at temperatures of 75–90°C and mixing times of 3–5 h. It should be noted that the overall conversion of Al_2O_3 in the composition of calcium aluminates exceeds its conversion into $Al(OH)_3$ and calcium hydroxocarboaluminate (DTG data). At the same time, a good agreement was obtained as regards the conversion of CaO in the system. On the basis of these data and the results of [7], it may be assumed that the discrepancy for Al_2O_3 can be attributed to formation of a solid solution based on the MnHC lattice. For a sample prepared at 75°C in the course of 5 h, approximately 10% of the total amount of Al_2O_3 is presumably introduced into the lattice of manganese compounds.

To refine the optimal composition of manganese–aluminum–calcium catalysts, which must ensure the best structural, strength, and catalytic properties, a set of samples with varied content of the active component was prepared. The catalysts were obtained with account of the optimal preparation parameters (75°C, 3 h).

The dependence of the specific surface area of samples calcined at 400°C on composition shows a maximum at 30–40% Mn_3O_4 (140 $m^2 g^{-1}$). The maximum extent of surface development at medium compositions is presumably due to formation of talum hydration products: highly dispersed $Al(OH)_3$ phases, and to reaction of MnHC with talum to give at these compositions the greatest amount of highly dispersed compounds, manganese–aluminum-containing solid solutions.

The total porosity of calcined samples increases somewhat with increasing manganese content, being at the level of 28–35%. A study of the pore volume distribution with respect to radii demonstrated that, for

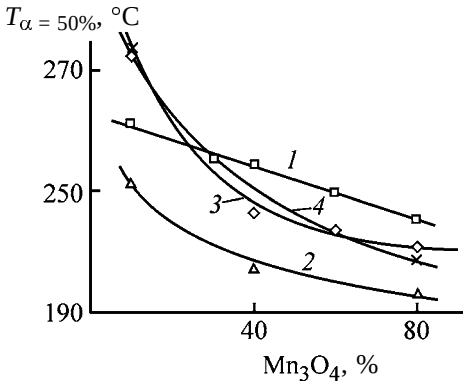

Fig. 4. Activity of samples in test reaction of deep oxidation of benzene vs. manganese content Mn_3O_4. ($T_{\alpha=50\%}$) Temperature of 50% conversion. (*1*, *2*) Uncalcined and calcined (400°C) mechanical mixtures of components, respectively; (*3*, *4*) uncalcined and calcined (400°C) catalysts, respectively.

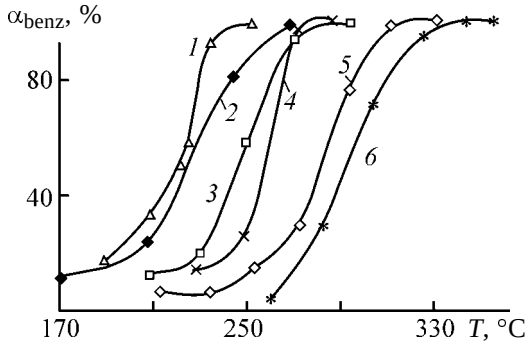

Fig. 5. Conversion of benzene, β_{enz}, vs. temperature *T* of the process, obtained on various catalysts. Catalyst: (*1*) sample with 40% Mn_3O_4, (*2*) GTT, (*3*) NTK-10-7f, (*4*) NTK-4, (*5*) NTK-10-2f, and (*6*) NKO-2-5.

a calcined mechanical mixture containing 40% Mn_3O_4 (S_{sp} = 53 $m^2 g^{-1}$), the main contribution to the surface development comes from pores with radii of 50–100 Å (60%) and 195–405 Å (25%); pore with radii of 100–195 Å account for 12% of the volume, and the volume of very fine pores (0–50 Å) is very small (about 3%). In the case of a finished catalyst (S_{sp} = 140 $m^2 g^{-1}$), the distribution pattern changes significantly: the share of fine pores (0–50 Å) increases dramatically (to 28%); the volume of coarse pores (395 Å) is small (7%); the volume of medium pores constitutes 28% (50–100 Å) and 38% (100–150 Å).

With increasing content of manganese compounds, the mechanical strength of calcined catalysts grows, falling within 20–40 MPa at compositions with 20–80% Mn_3O_4, which corresponds to the strength level of other cement-containing catalysts prepared by similar technology.

Figure 4 shows how the activity of manganese–aluminum–calcium catalysts in the test reaction of deep oxidation of benzene depends on the content of manganese. The activity of uncalcined mechanical mixtures of the starting components (curve *1*) grows with increasing content of manganese; that of calcined (400°C) mixtures of MnHC with talum (curve *2*) also grows with increasing content of manganese compounds, especially at Mn_3O_4 contents of up to 30–40%. In the case of finished catalysts [uncalcined (curve *3*) and catalysts calcined at 400°C (curve *4*)], a considerable rise in activity is also observed at compositions of up to 30–40% Mn_3O_4, and, therefore, raising further the content of the active component in the samples is inadvisable.

The maximum activity is observed for mechanical mixtures of MnHC with talum, calcined at 400°C, which is probably due to the formation (evidenced by XPA data) of a considerable amount of β-MnO_2, which exhibits the highest activity in deep oxidation reactions. However, the activity of mechanical mixtures is unstable and decreases in the course of time. For example, it was found in testing the initial mixture of MnHC with talum (containing 40% Mn_3O_4) that the conversion of benzene decreases from 97 to 58% after 1.5 h of tests at 210°C.

The activity of finished samples remains virtually unchanged after calcination at 400°C; in addition, it is somewhat lower than that of calcined mechanical mixtures, which is in all probability due to formation of solid solutions containing Mn compounds. However, the catalysts are stable in the course of time and, as shown by further experiments, possess high thermal resistance, which is more important as regards the catalyst operation.

To evaluate the thermal stability, a finished sample (75°C, 5 h) and the starting mechanical mixture with 40% Mn_3O_4 were subjected to superheating in the reaction medium at 650°C for 1.5 h, with the activity at the working temperatures determined after that. The tests demonstrated that superheating leads to a certain decrease in the activity of the mixed sample: the temperature of 50% conversion increases by 35°C; in the case of a mechanical mixture of the starting compounds, the decrease in activity is more pronounced; the temperature of 50% conversion increases by nearly 70°C. Thus, the binding of a part of Mn compounds into solid solutions, which occurs in the interaction of MnHC with talum, stabilizes the active component and thus exerts positive effect on the thermal stability of the catalysts. The data presented are in good agreement with changes in the dispersity of manganese

oxides MnO after high-temperature calcination in a reductive medium.

Figure 5 shows the dependence of the conversion of benzene on the process temperature, obtained on different catalysts: copper–zinc–chromium–aluminum NTK-4, copper–nickel–aluminocalcium NKO-2-5 with addition of palladium, copper–nickel–manganese–aluminocalcium GTT, copper–zinc–aluminocalcium NTK-10-2f, copper–zinc–manganese–aluminocalcium NTK-10-7f, and mixed manganese–aluminocalcium sample (40% Mn_3O_4). It can be seen from Fig. 5 that the last catalyst is one of the best in the given set. Its cost price is not too high, compared with that of the other catalysts, and its preparation technology is rather simple and virtually waste-free. Therefore, use of the catalysts developed in this study for purification of waste gases to remove organic impurities may prove effective and economically advantageous, which confirms that further investigations in this direction are promising.

CONCLUSIONS

(1) A combined study of the formation of catalysts obtained on the basis of the system constituted by manganese hydroxocarbonate and calcium aluminates by the method of chemical mixing revealed that the extent of interaction between the starting components to give precursors of the active phase (manganese–aluminum-containing solid solutions) is affected by the conditions of the mixing stage: temperature and time.

(2) A study of the structural, strength, and catalytic properties of samples with varied content of the active component led to a conclusion that raising the content of manganese to more than 30–40% Mn_3O_4 is inadvisable.

(3) It was found that partial binding of manganese compounds into solid solutions stabilizes the active component and has positive effect on the thermal resistance of the catalysts.

REFERENCES

1. Yakerson, V.I. and Golosman, E.Z., *Katalizatory i tsementy* (Catalysts and Cements), Moscow: Khimiya, 1992.
2. Grechenko, A.N., Zaldat, G.I., Bobrov, B.S., and Golosman, E.Z., *Zh. Neorg. Khim.*, 1992, vol. 37, no. 4, pp. 724–728.
3. Artamonov, V.I., Mamaeva, I.A, Boevskaya, E.A., *et al.*, *Zh. Neorg. Khim.*, 1978, vol. 23, no. 4, pp. 903–908.
4. Grechenko, A.N., Physicochemical Foundations for Improving the Activity and Strength of Nickel–Aluminocalcium Catalysts, *Cand. Sci. Dissertation*, Moscow, 1984.
5. Yaroshenko, M.P., Grechenko, A.N., Salomatin, G.I., *et al.*, *Zh. Prikl. Khim.*, 1989, vol. 62, no. 7, pp. 1447–1453.
6. Nechugovskii, A.I., Grechenko, A.N., and Golosman, E.Z., *Zh. Prikl. Khim.*, 1990, vol. 63, no. 8, pp. 1747–1751.
7. Troshina, V.A., Mamaeva, I.A., Salomatin, G.I., *et al.*, *Zh. Prikl. Khim.*, 2001, vol. 74, no. 3, pp. 361–366.
8. Karapet'yants, M.Kh. and Drakin, S.I., *Obshchaya i neorganicheskaya khimiya: Uchebnik dlya vuzov* (General and Inorganic Chemistry: Textbook for Higher Schools), Moscow: Khimiya, 1992, 2nd ed. revised and supplemented.
9. *The Chemistry of Cements*, Taylor, H.F.W., Ed., New York: Academic, 1964, vol. 1.
10. Rode, E.Ya., *Kislorodnye soedineniya margantsa* (Oxygen Compounds of Manganese), Moscow: Akad. Nauk SSSR, 1952.

Russian Journal of Applied Chemistry, Vol. 76, No. 3, 2003, pp. 422–427. Translated from Zhurnal Prikladnoi Khimii, Vol. 76, No. 3, 2003, pp. 437–442.

CATALYSIS

Fabrication of Manganese–Aluminum–Calcium Catalysts by "Hydrothermal Synthesis"

V. A. Troshina, M. P. Yaroshenko, I. A. Mamaeva, G. I. Salomatin, G. M. Tesakova, Z. A. Tertichnik, and E. Z. Golosman

Novomoskovsk Institute of Nitrogen Industry, Public Joint-Stock Company, Novomoskovsk, Tula oblast, Russia

Received July 19, 2002

Abstract—X-ray phase and differential thermal analyses, IR spectroscopy, and temperature-programmed reduction method were applied to study the formation of manganese–aluminum–calcium catalysts prepared by "hydrothermal synthesis."

Cement-containing formulations find increasing use as catalysts for a number of chemical processes. In particular, a great number of catalysts based on the system comprising metal hydroxocarbonates (MHCs, where M = Cu, Zn, Ni, Co, Mg) and calcium aluminates are known [1].

Manganese–aluminium–calcium formulations showed high performance as catalysts of redox reactions and, in particular, afterburning processes. In this context, a necessity arose for developing an efficient method for preparing catalysts of this kind with widely varied properties.

Previously, we studied formation of catalysts prepared on the basis of the system comprising manganese hydroxocarbonate (MnHC) and calcium aluminates by the method of "chemical mixing" [2]. In this method, the interaction of starting components to give precursors of the active phase occurs in the stage of mixing of the starting substances with a liquid reagent, with the role of calcium aluminates mainly consisting in the formation of the active phase and their binding properties used to a lesser extent. Further experiments demonstrated that these catalysts can also be obtained by such an efficient and convenient process as hydrothermal synthesis (HTS), which includes forming of granules and their subsequent keeping in a humid air medium [humid air treatment (HAT)] and then in hot water in the stage of hydrothermal treatment (HTT). In this case, the interaction of the starting components to give precursors of the active state proceeds in a finished catalyst granule and is accompanied by strengthening of the granule through hydration of calcium aluminate components [1, 3]. This method assumes involvement of calcium aluminates both in the formation of the active phase and in the creation of a mechanically strong structure. The HTS technology makes it possible to combine these processes and to replace the labor-consuming stage of pelletizing by the more efficient forming.

The aim of this study was to analyze specific features of formation of catalysts prepared on the basis of the system comprising MnHC and calcium aluminates by the HTS technique and to examine the influence exerted by conditions of preparation of samples on their catalytic properties.

EXPERIMENTAL

As starting components for preparing samples served $MnCO_3 \cdot mMn(OH)_2 \cdot nH_2O$ [GOST (State Standard) 7205–77] and high-alumina cement of the talum[1] type ($CA : CA_2 = 0.26$), TU (Technical Specification) 5737-006-00 284 345–99. A mechanical mixture of MnHC and talum was mixed with water at a low l : s ratio (0.3 : 1); the resulting plastic mass was formed on a laboratory forming device into extrudates (d = 4 mm), which were subjected to humid air treatment and then to HTT: keeping in hot water at 90°C. The granules obtained were dried at 100°C and calcined at 400°C. In the course of experiments, the conditions of HAT and HTT were varied.

A composition with 40% Mn_3O_4 was chosen for the experiment, since the extent of interaction between MnHC and talum to give solid solutions containing manganese and aluminum was the highest at this composition [2].

[1] Talum is a mixture of calcium monoaluminate $CaO \cdot Al_2O_3$ and calcium dialuminate $CaO \cdot 2Al_2O_3$. Hereinafter the common designations of the chemistry of cements are used: A = Al_2O_3, C = CaO, H = H_2O.

1070-4272/03/7603-0422$25.00 © 2003 MAIK "Nauka/Interperiodica"

The procedures used to study the samples were described in [2].

To analyze the transformations occurring in a catalyst grain in relation to the time of its keeping in humid air at room temperature (20–25°C), an additional experiment was carried out in order to observe "in slow motion" the overall pattern of active phase formation in manganese–aluminum–calcium catalysts obtained using the technology in question.

An X-ray phase analysis (XPA) of the samples obtained demonstrated that, during the first 10 h of HAT, the amount of calcium monoaluminate decreases substantially (Fig. 1a, curve *1*) and a calcium carbonate phase appears in the form of calcite (curve *4*). The formation of $Al(OH)_3$ (gibbsite) was observed after 36 h of HAT (curve *5*). A pronounced decrease in the intensity of MnHC lines was observed after approximately 48 h of HAT (curve *3*); in the same time interval, consumption of CA_2 started (curve *2*) and the calcium hydroxocarbonatoaluminate (CCA) phase, $C_3A \cdot CaCO_3 \cdot 12H_2O$ (curve *6*), appeared. With the time of HAT increasing from 2 to 20 days, hydration of CA_2, decomposition of MnHC, and formation of $CaCO_3$ and $Al(OH)_3$ (in the form of gibbsite and bayerite) became more intensive; further keeping in humid air did not result in any significant changes in the content of these phases in the system. The reflections from calcium mono- and dialuminates completely disappeared after 42 days of HAT, with the minimum intensity of lines associated with residual MnHC, about 30% of the initial value, reached in the process.

It has already been noted previously [2, 4] that the decrease in the intensity of X-ray lines associated with MnHC and the appearance of reflections characteristic of $CaCO_3$ is due to partial extraction of carbonate ions from the MnHC lattice and their replacement by aluminate and hydroxide ions.

The involvement of OH^- ions in the exchange assumes that X-ray amorphous manganese compounds of the $MnO_x \cdot yH_2O$ type are formed in the system. In this case, introduction of manganese ions into the lattice of gibbsite formed in hydration of calcium aluminates is possible, with the X-ray diffraction characteristics of gibbsite changed. Indeed, an X-ray diffraction study of the samples revealed that the positions of the diffraction peaks of the forming gibbsite differ from the tabulated values. The maximum shift of the diffraction lines of gibbsite was observed for samples kept in humid air for 15–20 days and more. For example, a shift to d = 4.78 Å was observed for the peak with d = 4.82 Å.

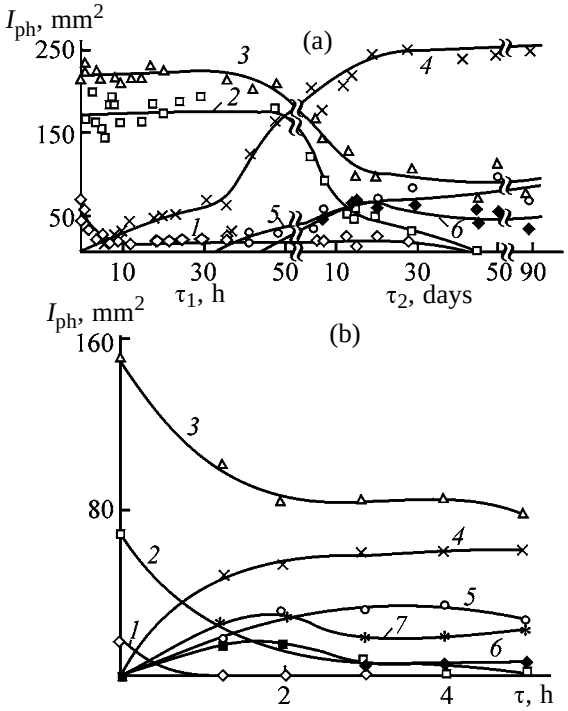

Fig. 1. Intensities of diffraction peaks from the forming and initial phases, I_{ph}, in catalyst granules vs. duration of HAT, τ_1 and τ_2, and (b) HTT, τ, stages. Phase: (*1*) CA, (*2*) CA_2, (*3*) MnHC, (*4*) calcite, (*5*) gibbsite + bayerite, (*6*) CCA, and (*7*) aragonite.

The involvement of aluminate and hydroxide ions in the exchange leads to formation of Mn–Al-containing solid solutions based on the lattices of manganese compounds, from which $MnO–Al_2O_3$ solid solutions based on the crystal lattice of MnO are formed in subsequent heating to 500°C in a hydrogen flow [2, 4]. An X-ray study of samples heated to 500°C in H_2 flow also revealed the presence of a defective MnO phase. In this case, the maximum deviation of the lattice constant of MnO, compared with the tabulated value of 4.445 Å, was observed for the samples kept in humid air for 20 days and more. For these samples, a_{0MnO} = 4.430 Å and the dispersity α_{MnO} = 145 Å, whereas for a mechanical mixture of the starting reagents the respective values are 4.437 and 175 Å. The results obtained indicate that calcined samples contain $MnO–Al_2O_3$ solid solutions based on the crystal lattice of MnO, and, consequently, Mn–Al-containing solid solutions based on MnHC, $MnO_x \cdot yH_2O$, and $Mn(OH)_2$ lattices are formed in uncalcined samples as precursors. The binding of a part of manganese compounds into solid solutions is also evidenced by the fact that the intensity of MnO reflections in reduced samples is about 40% of that in a mechanical mixture of the starting components.

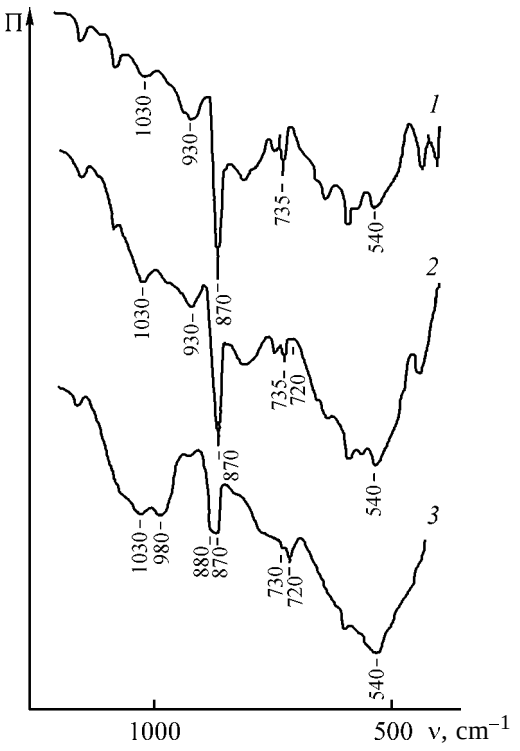

Fig. 2. IR spectra of samples subjected to HAT of varied duration without HTT. (∏) Transmission and (ν) wave number. Sample after forming with HAT for time (days): (*1*) 0, (*2*) 2, and (*3*) 20.

Thus, according to XPA data, chemical transformation occur in catalyst granules in the HAT stage at room temperature. The extent of these transformations grows with increasing time of treatment. However, the rate of the reaction is very slow, and, therefore, more than 20 days are necessary for the maximum content of the forming phases to be reached, which is unacceptable for commercial technology.

To accelerate the chemical reactions occurring in forming of catalysts by the HTS technique, an HTT stage is used. To study the transformations occurring in the catalyst granules in this stage, a formed and dried sample obtained without HAT was subjected to prolonged hydrothermal treatment at 90°C with sampling at certain intervals (Fig. 1b). According to XPA data, the rate of chemical transformations is high in this stage. Calcium monoaluminate was completely consumed in 1 h, and calcium dialuminate, in 4 h of HTT. The intensity of lines associated with residual MnHC after 3–5 h of treatment was 40–45% of the initial value. During the first hour of treatment, the formation of a considerable amount of gibbsite with shifted diffraction peaks (for instance, the peak with d = 4.82 Å was shifted to d = 4.79 Å) and a minor amount of bayerite was recorded. The content of these phases remained virtually unchanged during HTT for more than 3 h. An increase in the intensity of lines related to calcium carbonate was also observed during HTT for up to 3–4 h, with this compound formed as calcite and aragonite. Thus, virtually 100% extent of interaction is reached in the HTT stage in 3–4 h.

To reveal the influence exerted by preliminary HAT on the properties of granules in preparing manganese–aluminum–calcium catalysts, sample reduced in a hydrogen flow after HTT without HAT was compared with that subjected to preliminary HAT and then HTT and characterized by the same conversion of the starting reagents. It was found that for the latter sample the deviations of the lattice constants of the forming MnO are somewhat larger (4.430 Å against 4.434 Å), and the dispersity is higher (145 Å against 180 Å). For the sample with HAT, the intensity of MnO reflections is somewhat lower (190 mm^2 as compared to 240 mm^2 for a catalyst without HAT). The data obtained indicate that, for a sample subjected to preliminary HAT, the extent of interaction between the starting substances to give solid solutions containing manganese and aluminum ions is greater.

An attempt was made to intensify the HAT stage by raising the process temperature. For this purpose, a formed sample was kept in humid air at a temperature varied within 10–90°C for 5 h. Raising the HAT temperature accelerated the transformations occurring in this stage. This is indicated by the fact that, with increasing temperature, the intensity of reflections associated with calcite (the amount of aragonite formed was virtually temperature-independent) and $Al(OH)_3$ (gibbsite and bayerite) grows, and that of reflections associated with the starting compounds, MnHC and calcium aluminates, falls, with the maximum reaction rate reached at 75–90°C. At the same time, a study of samples subjected to HTT demonstrated that raising the temperature of preliminary HAT to above 50°C does not appreciably accelerate the interaction in the subsequent HTT stage. Thus, according to XPA data, it is advisable to perform the stage of HAT of catalyst granules at temperatures not exceeding 50°C.

The results of an IR study of the samples obtained are given in Fig. 2. Only the region in which the spectral changes are the most pronounced is shown. With increasing HAT duration (Fig. 2), the intensity of absorption bands at 870 and 730 cm^{-1}, characterizing the bending vibrations of CO_3^{2-} in MnHC, decreases. New absorption bands, associated with bending vibrations of carbonate groups in the forming calcium carbonate, appear at 880 and 720 cm^{-1}, and their

intensity grows. The intensity of absorption in the range of bending vibrations of hydroxide groups of the forming $Al(OH)_3$, and the profile of the absorption band becomes characteristic of bayerite, with peaks at 1030 and 980 cm^{-1} [5]. Analysis in the range of stretching vibrations of OH^- groups is hindered by pronounced broadening of the corresponding bands. The spectrally detected presence of $Al(OH)_3$ in the form of bayerite, rather than gibbsite, can apparently be accounted for by introduction of manganese ions, which leads to a shift of double layers in packages of the gibbsite structure [6], thus transforming this structure into that of bayerite. The maximum extent of the occurring transformation is achieved in approximately 20 days of HAT (Fig. 2, curve *3*).

The IR spectra of samples subjected after HAT to hydrothermal treatment show that, with increasing time of preliminary HAT, the intensity of the absorption bands at 870 and 730 cm^{-1} decreases and that of the absorption bands at 880 and 720 cm^{-1}, associated with bending vibrations of carbonate groups in, respectively, MnHC and $CaCO_3$, increases. A steady increase in intensity and change in the profile of the OH^- bending vibraiton bands at 1030 and 980 cm^{-1} is observed, which points to the appearance of a bayerite structure. In accordance with spectral data, the greatest extent of interaction in the HTT stage is reached after preliminary HAT for 2 days.

The spectra of samples subjected to only HAT at different temperatures show that, with increasing process temperature, the extent of the occurring transformations grows to reach a maximum at 75°C. For samples subjected to subsequent HTT, the most pronounced spectral changes, similar to those described above, are observed at temperatures of preliminary HAT of up to 30°C, and, therefore, raising the treatment temperature further is inadvisable.

Figure 3 shows the results of a differential thermogravimetric (DTG) analysis of the samples. The thermal effects were identified on the basis of published [2, 4, 7, 8] and XPA data. The DTG curves of catalysts kept for varied time in humid air (Fig. 3) show that, upon treatment of a mixture of MnHC and talum with water, the thermal effects of MnHC decomposition (385°C) and β-MnO_2 conversion into β-Mn_2O_3 (520, 540°C) are shifted to higher temperatures, compared with a mechanical mixture of the starting components, and their superposition is observed. This leads to the appearance of a strong effect peaked at 550°C (curve *2*) [2]. As the time of HAT becomes longer, the intensity of this effect decreases and it is first gradually shifted to the low-temperature region

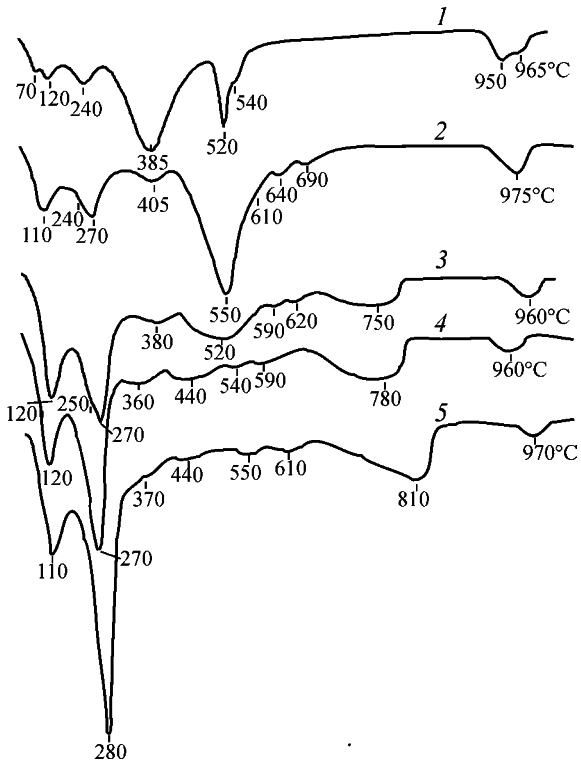

Fig. 3. DTG curves of samples subjected to HAT of varied duration without HTT. (*1*) Starting mechanical mixture of MnHC and talum; sample after forming with HAT for time (days): (*2*) 0, (*3*) 2, (*4*) 5, and (*5*) 20.

(510–520°C) and then, with the HAT duration increasing further (to 5 days), starts to split into two effects, those at 440–460 and 540–550°C. On the basis of a comparison with XPA data, these effects can be attributed to decomposition of MnHC modified with aluminum ions and to MnO_x conversion. In addition, the DTG curves show effects of decomposition of gibbsite (270–290°C) and calcium carbonate (720–810°C), whose intensity grows with increasing HAT duration; however, the profile of the DTG curves remains virtually unchanged after 2–5 days of treatment.

The DTG curves of the same samples subjected to HTT show that, at longer time of preliminary HAT, the effects associated with decomposition of gibbsite (290–300°C) and $CaCO_3$ (800–830°C) grow in intensity, and the profile of the effects in the range 400–650°C is gradually smoothed. These changes are mainly characteristic of catalysts kept in humid air medium for up to 2–5 days; further preliminary HAT does not lead to any significant changes in the DTG curves of the samples.

Raising the temperature of preliminary HAT to above 30°C does not cause any substantial changes,

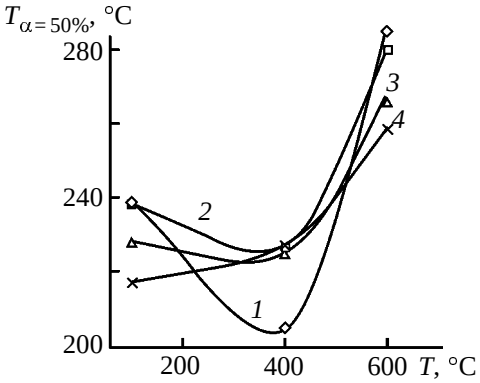

Fig. 4. Activity of samples prepared under various conditions vs. temperature *T* of calcination in air. ($T_{\alpha=50\%}$) Temperature of 50% conversion. Sample: (*1*) starting mixture of MnHC and talum, (*2*) no. 1 (after HTT without preliminary HAT), (*3*) no. 2 (2 days of HAT + HTT), and (*4*) no. 3 (>20 days of HAT after HTT).

either, in the profile of the DTG curves for samples subjected to HTT. Thus, the results of the differential thermogravimetric study confirm that it is advisable to perform preliminary HAT at temperatures not exceeding 30°C.

Comparison of a thermochromatogram of a catalyst after HTT without preliminary HAT and that subjected to prolonged HAT (>20 days) and then to HTT shows that, in the case of a sample without HAT, the intensity of the effect at 200–300°C, which corresponds to liberation of water in the course of gibbsite decomposition, is much lower, and that of effects at 350–450°C, related to liberation of water and CO_2 in decomposition of residual MnHC modified with aluminum ions, is much higher, indicating much higher conversion of the starting substances into the reaction products for the sample subjected to preliminary HAT. MnO formed in the course of catalyst reduction at temperatures of up to 750°C has the lattice constant close to the tabulated value (4.445 Å): 4.444 for a sample after HAT and 4.446 Å for a catalyst without HAT. For these catalysts, the intensities of diffraction peaks related to manganese oxide, I_{MnO}, are 350–370 mm^2, and the MnO dispersity α_{MnO} = 220–225 Å. For a mechanical mixture of MnHC with talum, reduced under similar conditions, I_{MnO} = 570 mm^2 and α_{MnO} = 600 Å. Thus, the dispersity of MnO in the samples obtained is more than 2 times higher than that of the starting mixture of MnHC with talum, and the intensity of diffraction peaks corresponding to MnO is much lower, which points to the formation of X-ray amorphous compounds of manganese. All this indicates a higher thermal stability of the given catalysts and, consequently, a positive influence of the transformations occurring in catalyst fabrication to give solid solutions.

We showed previously that the activity of manganese–aluminum–calcium catalysts in deep oxidation of benzene grows with increasing content of the active component, with the rise being the steepest at Mn_3O_4 concentrations of up to 30–40% [2].

Tests with the catalysts containing 40% Mn_3O_4, prepared by the HTS technique, show that the activity of uncalcined catalysts grows after prolonged preliminary keeping in humid air. The highest activity is observed for the samples kept in humid air for 20 days and more; in particular, for these samples the temperature of 50% conversion, $T_{\alpha=50\%}$, is 215–220°C. The lowest activity is exhibited by the samples after short HAT or without it, and also by a mechanical mixture of the starting components; for instance, for uncalcined samples $T_{\alpha=50\%}$ is 235–240°C.

Thus, the increase in the extent of reaction between MnHC and talum to give Mn–Al-containing solid solutions, favored by preliminary HAT of granules, has a positive effect on the activity of the catalysts obtained.

A distinctive feature of the catalysts under consideration is that their activity changes after calcination in air at various temperatures. Figure 4 shows the dependence of the activity on the calcination temperature for samples prepared under different conditions. In the case of a mechanical mixture of MnHC with talum, the dependence passes through a maximum at 400°C (curve *1*). For a sample without preliminary HAT this dependence also shows an extremum, but the decrease in the temperature of 50% conversion after calcination at 400°C is not so pronounced (curve *2*). A study of a catalyst subjected to preliminary HAT for 2 days and then to HTT demonstrated that its activity remains virtually unchanged after thermal treatment at 400°C (curve *3*). For a sample kept for more than 20 days in humid air and then subjected to HTT, the dependence of $T_{\alpha=50\%}$ on the calcination temperature is somewhat different: the activity decreases steadily with increasing temperature of thermal treatment (curve *4*).

A mechanical mixture of MnHC with talum exhibits the highest activity among the samples studied ($T_{\alpha=50\%}$ = 205°C), which is due to the formation of a large amount (according to XPA) of active β-MnO_2; however, the activity of the mixture decreases substantially in the course of time, probably because of the caking of β-MnO_2. Binding of a part of manganese compounds into solid solutions makes lower the

initial activity of the samples, compared with calcined mechanical mixture, but they are stable with time [2].

Among the uncalcined catalysts, the highest activity is observed for sample no. 3 subjected to prolonged (>20 days) treatment and characterized by the greatest extent of interaction between MnHC and talum: for this catalyst, $T_{\alpha=50\%}$ = 217°C. In addition, its activity decreases after calcination to a lesser extent, compared with other samples and, especially, mechanical mixture. For example, $T_{\alpha=50\%}$ = 285°C for the starting mixture of MnHC with talum, calcined at 600°C, and $T_{\alpha=50\%}$ = 259°C for the catalyst under consideration, i.e., this sample is not only more active, but also more thermally stable. These facts well correlate with data on MnO dispersity in samples reduced at high temperature.

Thus, the extent of interaction between MnHC and talum, which occurs in fabrication of manganese–aluminum–calcium catalysts, affects their activity and thermal stability. The increase in the extent of interaction to give defective structures, Mn–Al-containing solid solutions based on the lattices of MnHC, $Mn(OH)_2$, $MnO_x \cdot yH_2O$, and $Al(OH)_3$, favored by preliminary HAT of granules, leads to an increase in the activity and stability of catalysts.

The catalysts obtained show fairly high activity in deep oxidation, compared with other catalysts [2], which confirms that further investigations in this direction are promising.

CONCLUSIONS

(1) A comprehensive study of the formation of catalysts prepared on the basis of the system constituted by manganese hydroxocarbonate and calcium aluminates by the method of hydrothermal synthesis revealed that the extent of interaction between Mn hydroxocarbonate and talum to give Mn–Al-containing solid solutions based on the lattices of manganese hydroxocarbonate, $Mn(OH)_2$, $MnO_x \cdot yH_2O$, and aluminum hydroxide depends on the temperature and time of humid air and hydrothermal treatment.

(2) An increase in the extent of interaction between the starting components, favored by prolonged humid air treatment of granules, has positive effect on the catalytic properties of the catalysts obtained and, in particular, on their activity and thermal stability.

REFERENCES

1. Yakerson, V.I. and Golosman, E.Z., *Katalizatory i tsementy* (Catalysts and Cements), Moscow: Khimiya, 1992.
2. Troshina, V.A., Mamaeva, I.A., Salomatin, G.I., *et al*., *Zh. Prikl. Khim*., 2003, vol. 76, no. 3, pp. 430–436.
3. Grechenko, A.N., Physicochemical Foundations for Improving the Activity and Strength of Nickel–Aluminum–Calcium Catalysts, *Cand. Sci. Dissertation*, Moscow, 1984.
4. Troshina, V.A., Mamaeva, I.A., Salomatin, G.I., *et al*., *Zh. Prikl. Khim*., 2001, vol. 74, no. 3, pp. 361–366.
5. Vol'ska, E. and Shaida, V., *Zh. Prikl. Spektrosk*., 1983, vol. 38, no. 1, pp. 160–164.
6. *Physical and Chemical Aspects of Adsorbents and Catalysts*, Linsen, B.G., Ed., London: Academic, 1970.
7. *The Chemistry of Cements*, Taylor, H.F.W., Ed., New York: Academic, 1964, vol. 1.
8. Rode, E.Ya., *Kislorodnye soedineniya margantsa* (Oxygen Compounds of Manganese), Moscow: Akad. Nauk SSSR, 1952.

Russian Journal of Applied Chemistry, Vol. 76, No. 3, 2003, pp. 428–430. Translated from Zhurnal Prikladnoi Khimii, Vol. 76, No. 3, 2003, pp. 443–445.

CATALYSIS

Chemical Purification of Ultrafine Cutting Diamonds

I. I. Obraztsova and A. N. Eremenko

Institute of Coal and Coal Fuel Chemistry, Siberian Division, Russian Academy of Sciences, Kemerovo, Russia

Received June 13, 2002

Abstract—A procedure was developed for recovery and purification of ultrafine diamonds.

Superdispersed systems based on clusters or ultrafine diamonds (UFD) are actively studied today, because of theoretical interest and wide possibilities of their practical use.

Ultrafine diamonds are widely used in preparation of abrasive materials, tools, and pastes, in composite and electrochemical plating, in production of mechanical rubber goods, and as additives to diesel oils and lubricants. Diamonds show much promise in systems of magnetic recording, in superfine surface finishing, when the surface quality is a decisive factor, and in preparation of new cutting ceramic materials. At the same time, growth of diamond films and composites based on them is also urgent.

One of the main problems in chemical processing of coal is the low selectivity of catalysts, because coal contains compounds of various structures (C–C, C–N, C–S bonds, etc.), whose selective conversion occurs under different conditions. Therefore, development of versatile catalysts is hardly possible, and it seems necessary to search and study catalysts selective with respect to separate types of compounds. In this connection, it is interesting to study the reactivity of the C–C bonds using cluster diamonds as a model.

Explosion method is the main procedure for UFD synthesis; it is based on the detonation conversion of carbon-containing explosives with a negative oxygen balance [1, 2]. This process yields a carbon blend containing UFD (20–60%) and non-diamond impurities (micrographite, carbon black). The detonation blend has a developed and active surface (~400 $m^2 g^{-1}$) and exhibits specific adsorption and colloidal properties due to elevated reactivity of superdispersed carbon structures characterized by high density of defects. The explosion synthesis procedure is well developed, and several modes of its process are patented. However, relatively low efficiency of purification and recovery of diamonds from the carbon- and metal-containing reaction blend hinders the growth of the cluster diamond production.

The reactivity of diamonds and composition of impurities determine selection of the treatment and purification procedures. The aim of the process is the recovery of the target product with minimal losses, and relatively high chemical stability of the diamond phase allows this process to be performed fairly efficiently.

As seen from published data [3], in the first stage of the diamond recovery the catalyst and carbide phase are dissolved in acids or their mixtures [3]. In the second stage, the non-diamond carbon phases are selectively oxidized with various reagents. In the third stage, the compounds insoluble in water and acid solutions (except hydrofluoric acid) are removed if their content is greater than 1%. Then, the purified diamond crystals are washed with water and dried.

It should be noted that the separation of diamond from graphite, which can be performed by physical and chemical methods [4], is the most difficult stage of the process. In the chemical procedure, graphite is selectively oxidized to carbon oxides. In contrast to physical procedures, chemical treatment provides higher purification and, in some cases, smaller loss of the target product.

However, the main disadvantages of physical and chemical purification procedures are rather complex equipment, large losses of the diamond powder, and use of extremely aggressive compounds with release of environmentally hazardous components.

We developed chemical procedures for recovery and purification of UFDs from the carbon–diamond blend providing a high yield of the diamond phase with a high quality of the target product. These procedures can be performed without additional equipment under milder conditions as compared to the known methods.

1070-4272/03/7603-0428$25.00

EXPERIMENTAL

The diamond blend prepared by the explosion procedure is a specifically smelling viscous black mass.

In the oxidation stage, the diamond blend was washed, dried, and oxidized; then the resulting product was washed and dried.

First the blend sample was washed with distilled water to pH 7 and complete removal of the strange smells; fivefold washing was usually sufficient. The washing water was decanted and, after neutralization, transmitted into a sewage system.

The washed sample was filtered and centrifuged. Then it was dried at 200°C with intermittent stirring to the residual content of water of 5–7%. After drying, the resulting black mass could be readily broken in pieces. The yield of the dry carbon-containing blend was 15–20 wt % based on the initial reaction product.

This pretreatment removes a significant fraction of impurities from the blend and yields a pure friable product appropriate for subsequent treatment.

Then, the blend was treated with an oxidizing mixture consisting of HNO_3 (64–89 wt %) and H_2SO_4; the blend : oxidizing mixture weight ratio was 1 : (20–25). The oxidation was performed in the batch mode by addition of nitric acid in small portions after complete decomposition of the previous portion.

Addition of HNO_3 in small portions provides loosening of the blend and increases its volume and thus improves the UFD recovery.

Sulfuric acid was added only in the initial step to accelerate oxidation. No overheating of the reaction mixture was observed under the above operation conditions, and, thus, the temperature control of the reaction mixture can be eliminated.

As the reaction proceeds, the color of the reaction mixture changed from black to gray. The number of oxidation cycles and the amount of acids required for complete oxidation varied insignificantly. When the blend became gray, the reaction vessel was cooled. The total oxidation time was about 20 h.

The reaction product was washed with distilled water. The gray diamond phase after stirring was settled, and the solution containing acids was decanted and transferred into a sewage system after neutralization. This operation was performed several times up to neutral reaction (pH 7) of the washing solution.

Then, the diamond phase was separated from excess water by centrifuging and treated with acetone. The mixture was stirred and centrifuged; acetone was separated and used in washing of the other portions of the diamond blend. This procedure was repeated 2–3 times.

The resulting mass was dried in air at room temperature, ground in a porcelain mortar, and put into a vessel for storage.

The yield of the gray diamond blend was 40–50 wt % of the dry black mass. According to published data, the UFD yield obtained by the other procedures varies within 20–30%. As seen from XRD data, the average particle size in the UFD blend was 4–5 nm and the content of nonoxidized impurities in the final product was less than 0.1%, whereas in the previously reported procedures [5] the content of impurities reaches 1.1–5.7%.

To accelerate the recovery of the diamond phase, K_2SO_4, $K_2Cr_2O_7$, or MnO_2 was added into the reaction mixture, which loosens the blend, increases its volume, and thus improves the recovery of the UFD particles. These compounds accelerate the oxidation of the carbon blend by a factor of 2–3. The yield of the product increases to 60% based on the dry blend weight.

The experimental data on the oxidation of the diamond blend under various conditions are listed in the table. As seen, the resulting UFDs are characterized by elevated dispersity with a stable particle size.

Our procedure for recovery and purification of UFD phase from the diamond–carbon blend allows wide variation of the experimental conditions (temperature, pressure, medium, etc.) and thus provides control of the UFD properties. The surface of diamonds recovered by this procedure contains various functional groups: nitrate, keto, carbonate, sulfate, etc.

We found that, at thermal treatment of the diamond powder under an inert gas atmosphere at 400–800°C, nearly 1.7 mmol of CO_2 per gram UFD is liberated. The presence of various functional groups on the diamond surface suggests the possibility of its use as sorbent. We studied the UFD sorption power with respect to copper(II), cobalt(II), and nickel(II) sulfates. The sorption power was characterized by the amount of the salt sorbed from solution per gram of the diamond powder.

It was found that the UFD surface sorbed 0.15 mmol g^{-1} $CuSO_4$, liberating in solution 0.09 mmol g^{-1} of H^+ ions. In the case of $CoSO_4$, these parameters were 0.38 and 0.024 mmol g^{-1}. No sorption of $NiSO_4$ was observed.

Oxidation conditions of the carbon–diamond blend. Temperature 200°C, average size of the UFD crystallites 4.3 ± 0.4 nm

Sample weight, g	Catalysts, mmol	H_2SO_4*	HNO_3*	Blend : oxidizing mixture weight ratio	τ, h	Yield, %
		ml				
50	–	150	500	1 : 21.6	18	46
60	–	150	600	1 : 20.7	23	53
2	–	6	24	1 : 24.9	8	50
2	K_2SO_4, 5.75	4	20	1 : 19.9	4	61
60	K_2SO_4, 12.75	300	570	1 : 24.1	14	50
5	$K_2Cr_2O_7$, 5	10	60	1 : 23.2	2.5	56
4	MnO_2, 5	10	50	1 : 24.9	3	45

* Concentrated acid.

It is known [6] that the storage of ultrafine products is a complex problem. Owing to excess Gibbs energy related to the large contribution of the surface component, the system of superdispersed particles tends to aggregate. The UFD powder prepared by our procedure is characterized by elevated dispersity and fairly stable particle size. Moreover, our UFD powder shows no tendency to graphitization in prolonged storage and successive use, and its quality meets the international standards (according to the data of Tajrinu Trading Co., Ltd., Japan). Our procedure for the recovery of ultrafine diamonds from the diamond–carbon blend is patented [7].

CONCLUSIONS

(1) A procedure is developed for purification and recovery of ultrafine diamonds under milder conditions without additional process equipment; the yield of the high-quality diamond phase is higher by a factor of 1.5–1.7 as compared to the known procedures.

(2) Addition into the reaction mixture of small amounts of various metal salts decreases the reaction time by a factor of 2–3 and increases the product yield to 60%.

(3) The resulting ultrafine diamonds exhibit the elevated dispersity and uniformity with a stable particle size; they show no tendency to graphitization in prolonged storage and use.

REFERENCES

1. Lyamkin, A.I., Petrov, E.A., Ershov, A.P., *et al*., *Dokl. Akad. Nauk SSSR*, 1988, vol. 302, no. 3, pp. 611–613.
2. Volkov, K.V., Danilenko, V.V., and Elin, V.I., *Fiz. Goren. Vzryva*, 1990, vol. 26, no. 3, pp. 123–125.
3. Kruk, V.B., Lepikhova, T.G., and Vishnevskii, E.B., *Sint. Almazy*, 1976, issue 5, pp. 26–27.
4. Putyatin, A.A., Nikol'skaya, I.V., and Kalashnikov, Ya.A., *Sverkhtverd. Mater*., 1982, no. 2, pp. 20–28.
5. USSR Inventor's Certificate 1 794 888.
6. Gubin, S.P., *Zh. Vses. Khim. O–va im. D.I. Mendeleeva*, 1987, no. 1, pp. 3–11.
7. RF Patent 2 081 821.

Russian Journal of Applied Chemistry, Vol. 76, No. 3, 2003, pp. 431–433. Translated from Zhurnal Prikladnoi Khimii, Vol. 76, No. 3, 2003, pp. 446–448.

ENVIRONMENTAL PROBLEMS OF CHEMISTRY AND TECHNOLOGY

Flocculation of Kaolin Suspensions with Poly-1-vinyl-1,2,4-triazole, Its Quarternary Ammonium Salt, and Their Mixtures with Anionic Polyelectrolytes

V. A. Izvozchikova, O. G. Zakharova, G. A. Voskoboinik, and Yu. D. Semchikov

Research Institute of Chemistry, Lobachevsky State University, Nizhni Novgorod, Russia
Lobachevsky State University, Nizhni Novgorod, Russia

Received April 19, 2002

Abstract—Homo- and copolymers of 1-vinyl-1,2,4-triazole with acrylamide and quarternary salt of polyvinyltriazole were prepared. The flocculation power of these (co)polymers was studied using model kaolin suspensions.

The majority of natural and artificial suspensions consists of negatively charged particles, and, thus, positively charged polyelectrolytes are preferable for their flocculation. At present, such flocculants are predominantly prepared using polymers and copolymers of two main groups: ammonium and pyridinium.

The most available commercial flocculants are the Praestols (copolymers of acrylamide with sodium acrylate and with *N*,*N*'-trimethylammoniopropylacrylamide chloride, Akromidan (copolymer based on poly(methacroyloxyethyl)trimethylammonium methyl sulfate), and KF copolymer based on quarternary poly-2-methyl-5-vinylpyridine, developed at the Volgograd University.

The comparative data on the flocculation power with respect to model and real systems showed that the Praestol, Akromidan, and KF domestic cationic flocculants are competitive products [1, 2].

Since the assortment of available cationic flocculants is very limited and their flocculation properties are similar, search for new flocculants of this type is urgent. It was found [3] that vinyltetrazole polymers are effective flocculants.

In this work, we studied the flocculation power with respect to model kaolin suspensions of homo- and copolymers of 1-vinyl-1,2,4-triazole (VT), its quarternary ammonium salts, and their mixtures with anionic polyelectrolytes.

EXPERIMENTAL

In our work we used of 1-vinyl-1,2,4-triazole with the following properties: bp 49°C (1 mm Hg); n_D^{20} 1.51, and d^{20} 1.0857.

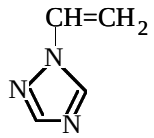

The VT polymers and quarternary salts of poly-VT were prepared by the procedures given elsewhere [4]. Polymerization of VT to high conversions (80%, monitored gravimetrically) was performed in a 40% aqueous solution at 60°C under argon in the presence of the redox system [polyethylenepolyamine : $(NH_4)_2S_2O_8$ = 1 : 3]. The intrinsic viscosity [η] of the resulting polymer was 2.75 dl g^{-1} (distilled water, 25°C). Then, the quarternary salt was prepared.

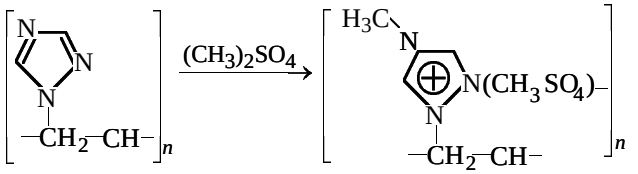

For this purpose, dimethyl sulfate (2.6 g) and poly-VT (0.85 g) were mixed in DMSO (6.65 ml) and heated for 11 h at 60°C under argon. The resulting salt was washed with isopropyl alcohol and dried to constant weight in a vacuum desiccator. The polymer yield was 85%, and the degree of alkylation was 84% (elemental analysis). The copolymerization of VT with acrylamide (AA) was performed up to 95% conversion (VT content in copolymer ~80 wt %).

The flocculation power of the polymers was evaluated from the kinetic dependences of the suspension

1070-4272/03/7603-0431$25.00

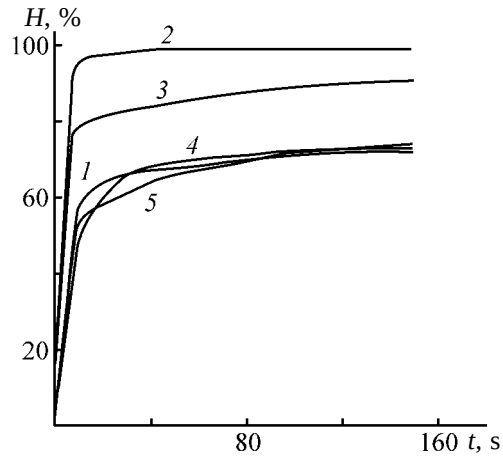

Fig. 1. Optical transmission H of 0.4 wt % aqueous kaolin suspensions as a function of time t; (co)polymer concentration 0.05 wt %. Flocculant: (*1*) none, (*2*) polyacrylamide, (*3*) polyvinyltraizole, (*4*) polyacrylamide–polyvinyltraizole mixture (1 : 1 weight ratio), and (*5*) copolymer of acrylamide with vinyltriazole (0.2 : 0.8 molar ratio).

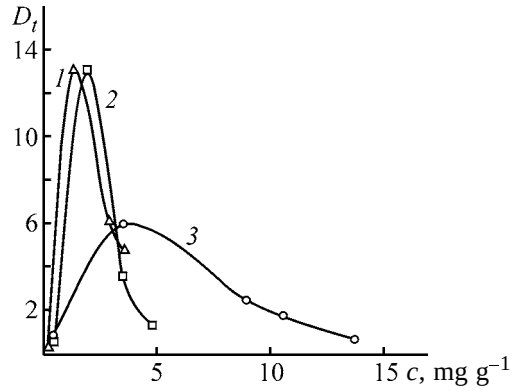

Fig. 2. Suspension clarification efficiency D_t as a function of the concentration of poly-VT c at various contents of kaolin. Kaolin content, wt %: (*1*) 1.0, (*2*) 0.8, and (*3*) 0.4.

clarification efficiency D_t and optical transmission H (%):

$$D_t = \tau_0/\tau - 1, \quad \tau = 2.3A/l,$$

where τ_0 is the supernatant turbidity in the absence of the flocculant; τ, supernatant turbidity after the flocculant addition; l, cell thickness, and A, optical density.

The optimal flocculant concentration (mg flocculant per gram kaolin) corresponding to maximal D_t was determined.

The kaolin concentration was varied in the 0.1–1.0 wt % range. The kaolin weighed portion was placed in water (20 ml), and after 30 min the polymer solution was added; the suspension volume was brought to 100 ml, it was stirred for 2 min and stored for 1 h. Then, the optical density of the supernatant was measured on a KF-77 photocolorimeter (λ 490 nm). When the clarification kinetics was studied, the measurements of the optical transmission were started immediately after the stirring.

The kinetic dependences of the optical transmission of suspensions in the presence of various polymers are shown in Fig. 1. As seen, polyacrylamide exhibits the greatest flocculation power, the flocculation power of poly-VT is significantly lower, and the copolymers of VT and AA and the mixtures of poly-AA and poly-VT exhibit virtually no flocculation power. This is probably due to the fact that, as compared to homopolymers, the VT-AA copolymers have a lower thermodynamic affinity for water, and thus more compact conformations are typical for the copolymer macromolecules. This assumption agrees with the intrinsic viscosities of poly-VT and VT-AA copolymers, which are 2.75 and 0.76 dl g^{-1} (water solvent, 25°C). The lower intrinsic viscosity of the copolymer compared to the homopolymer is probably due to lower molecular weight and compression of macromolecular aggregates with decreasing thermodynamic affinity of copolymers.

In any case, the decrease in the intrinsic viscosity of the copolymer is directly related to the hydrodynamic globule radius and correspondingly to its flocculation power.

Then, the flocculation power of quarternary poly-VT (poly-1-vinyl-4-methyl-1,2,4-traizolium methyl sulfate) was determined. The dependences of the clarification efficiency of various flocculants in suspensions with various kaolin concentrations are shown in Fig. 2. As seen, the best flocculation is observed for suspensions with the kaolin concentration of 0.8–1.0 wt %. The dependences of the clarification efficiency on the polymer concentration pass through a maximum, typical for flocculants.

It is known that, in some cases, the flocculation efficiency can be improved by adding mixtures of cationic and anionic polyelectrolytes [5]. In our tests, we used copolymer of AA with sodium acrylate (0.75 : 0.25 molar ratio); the kinematic viscosity of 0.5% solution was 394 cSt [6]. The required suspensions were prepared by the procedure given above; the concentration of polyelectrolytes in all the cases was 0.001%. As seen from Fig. 3, in the case of fairly concentrated solutions (0.4–1.0 wt % kaolin content) the clarification efficiency decreases with polyelectrolyte addition, but it increases in the case of dilute low-turbid dispersions (<0.4 wt % kaolin content).

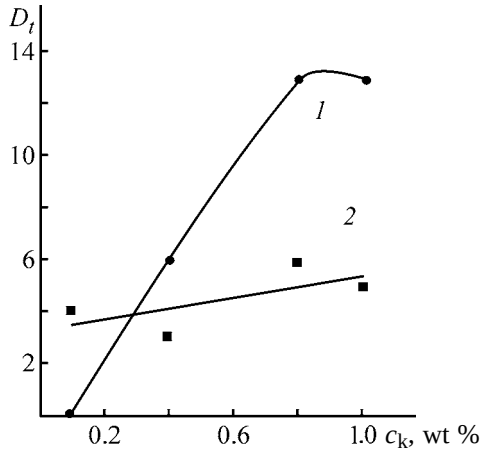

Fig. 3. Suspension clarification efficiency D_t as a function of the kaolin content c_k. Flocculant, mg g^{-1}: (*1*) poly-VT salt, 1–4, and (*2*) mixture of poly-VT with anionic polyelectrolyte, 0.1–1.0.

As known, the dependence of the flocculation efficiency on the polymer molecular weight should be considered to evaluate the feasibility of the flocculants prepared. For example, the intrinsic viscosity of such effective flocculants as KF and Praestol (650 and 655 brands) varies within 4.02–6.89 dl g^{-1} [2], which is greater than that of the polymer studied in this work by a factor of 4–5. The Praestol molecular weight is $(2.62–5.13) \times 10^6$. It was found [7] that the highest performance of the nitrogen-containing flocculants based on poly-1,2-dimethyl-5-vinylpyridinium methyl sulfate is observed for the samples with the molecular weight of 3×10^6. At the same time, the clarification efficiency with respect to kaolin suspensions of the samples with the molecular weight $\bar{M}_\eta \leq 2 \times 10^6$ did not exceed that of the agents studied in this work.

CONCLUSION

The flocculation powers of homo- and copolymers of 1-vinyl-1,2,4-triazole with acrylamide and of quaternary ammonium salt of polyvinyltraizole were compared. The highest flocculation power was found for polyvinyltriazolium dimethyl sulfate, whose performance with respect to dilute suspensions (less than 0.4 wt % kaolin content) can be improved by addition of anionic polyelectrolyte (copolymer of acrylamide with sodium acrylate).

ACKNOWLEDGMENTS

The authors are grateful to T.G. Ermakova with coworkers (Favorskii Institute of Chemistry, Siberian Division, Russian Academy of Sciences, Irkutsk, Russia) for the supply of the required monomers.

This work was financially supported by the grant TOO-9.2-2046.

REFERENCES

1. Balandina, P.V. and Semchikov, Yu.D., *Vestn. Nizhegorod. Gos. Univ.*, 2000, no. 1(2), pp. 36–39.
2. Navrotskii, A.V., Dryabina, S.S., Malysheva, Zh.N., *et al.*, *Zh. Prikl. Khim.*, 2000, vol. 73, no. 12, pp. 1940–1944.
3. Vereshchagin, L.I., Kruglova, V.A., Buzilova, S.R., *et al.*, Abstracts of Papers, *Vsesoyuznaya konferentsiya "Uspekhi khimii azotnykh geterotsiklov"* (All-Union Conf. "Advances in Chemistry of Nitrogen-Containing Heterocycles"), Rostov-on-Don, 1983, pp. 225–226.
4. Ermakova, T.G., Tatarova, L.A., Gritsa, A.I., *et al.*, *Khim. Geterotsikl. Soedin.*, 1984, no. 10, pp. 1412–1414.
5. Kurenkov, V.F., Snegirev, S.V., Dervoedova, S.A., and Churikov, F.I., *Zh. Prikl. Khim.*, 1999, vol. 72, no. 11, pp. 1892–1896.
6. Izvozchikova, V.A., Knyazeva, T.E., Myasnikova, I.B., *et al.*, Abstracts of Papers, *Vserossiiskaya nauchno-prakticheskaya konferentsiya "Ekonomicheskie i tekhnologicheskie aspekty sinteza i primeneniya polimernykh flokulyantov dlya ochiski khozyaistvennykh, bytovykh i stochnykh vod i obezvozhivaniya osadkov" (Flok-2000)*, (Russian Scientific and Practical Conf. "Economical and Practical Aspects of Synthesis and Use of Polymeric Flocculants for Treatment of Municipal and Industrial Wastewaters and for Dehydration of Precipitates" (Floc-2000)), Dzerzhinsk, 2000, pp. 9–10.
7. Navrotskii, A.V., Novakov, I.A., Makeev, S.M., *et al.*, *Khim. Tekhnol. Vody*, 2000, no. 2, pp. 192–196.

Russian Journal of Applied Chemistry, Vol. 76, No. 3, 2003, pp. 434–438. Translated from Zhurnal Prikladnoi Khimii, Vol. 76, No. 3, 2003, pp. 449–453.

PROCESSES AND EQUIPMENT OF CHEMICAL INDUSTRY

Influence of Surfactants on the State of Starch Hydrogels under High Shear Stresses

A. A. Yusova, I. M. Lipatova, and A. P. Moryganov

Institute of Chemistry of Solutions, Russian Academy of Sciences, Ivanovo, Russia

Received November 18, 2002

Abstract—Specific influence of high shear loads on starch hydrogels containing oxyethylene-based surfactants was studied. It was found that a number of oxyethylated fatty alcohols can produce a steady thickening effect on starch hydrogels under high-rate shear strains owing to mechanochemically initiated complexing with starch amylose.

Starch hydrogels (pastes) are widely used in various industries. They are made technologically suitable by heat treatment with chemical cleaving agents aimed at breaking down their primary structure formed by swollen starch grains. One way to significantly reduce the process time and the heat consumed in starch cleavage is mechanical treatment of paste in a rotary pulse flow apparatus (RPA) [1]. For technological purposes, in particular, for improving the film-forming and wetting powers, starch hydrogels are often added with surfactants. In [2], we studied how surfactants affect the efficiency of the mechanical cleavage of starch hygrogels. Studies of the properties of mechanically (using RPA) produced starch hydrogels as influenced by various surfactants revealed an interesting phenomenon which has not been previously described in the literature: Oxyethylated fatty alcohols can cause steady thickening of starch hydrogels when exposed to strong mechanical loads. In view of the fact that this phenomenon can be of not only theoretical but also practical interest, it is reasonable to study in more detail the influence of high shear loads on starch hydrogels containing oxyethylene-based surfactants.

EXPERIMENTAL

Our study was concerned with corn starch [GOST (State Standard) 7697–82]. Starch hydrogels intended for subsequent mechanical treatment were prepared by cooking a starch suspension on a water bath at 90°C for 15 min.

Sonication was performed in a UZDN-2T disintegrator at the frequency F = 22 kHz. The treatment time was 4 min, and treatment temperature, 80°C. The volume density of the acoustic energy was estimated calorimetrically at 1.34 W cm^{-3}.

Mechanical treatment was carried out on a laboratory RPA [3]. The rotor rotation rate was varied from 1000 to 5000 rpm. The treatment time was 4–30 s, and temperature, 80°C.

The relative viscosity of the hydrogels was measured with a VPZh-2 capillary viscometer according to GOST (State Standard) 33–36 at 80°C.

Rheological characteristics of starch hydrogels were measured on a Rheotest-2 rotary viscometer with a coaxial-cylinder working unit at a rate gradient within 1.5–1312 s^{-1} at 30°C.

The surface tension of starch hydrogel at the air interface was measured with a Rebinder's instrument [4] at 80°C.

The surfactants studied in this work were all oxyethylated, primarily fatty, alcohols with the general formula $C_nH_{2n+1}O(C_2H_4O)_mH$ (see table) [5]. Sample nos. 6 and 8 were oxyethylated alkylphenols with the general formula $C_nH_{2n+1}C_6H_4O(C_2H_4O)_mH$. The surfactant concentrations were varied within 0–0.01 M.

Figure 1 shows how the viscosity of starch hydrogels, mechanically treated in an RPA, varies with the concentration of the surfactant added before the treatment (curves *3–5*). It is seen that, with increasing concentration of the surfactant added before the treatment from 0 to 3×10^{-3} M, the viscosity of the starch hydrogels tends to substantially increase. Further increase in the concentration of the added surfactant tends to somewhat decrease the viscosity. Curve *2* in Fig. 1

1070-4272/03/7603-0434$25.00

Characterization of oxyethylated fatty alcohols.* Treatment in RPA: n = 4000 rpm, τ = 4 s; c_{CMC} = 3 wt %; C_{surf} = 3.0×10^{-3} M

Sample no.	Surfactant	n	m	HLB	MW, aver. cond.	DT
1	Oxanol L-2	10–12	2.0	6.3	260	5.35
2	Syntanol DT-2	10–13	2.0	2.8–4.2	273	5.55
3	Oxanol L-3	10–12	3.0	8.0	304	5.00
4	Syntanol ES-3	12–14	3.0–3.5	2.6–3.6	326	4.57
5	OS-2 agent	14–18	2.0	4.9–5.3	359	4.55
6	Neonol AF 9/4	9	4.0	2.5	396	1.25
7	Oxanol KD-6	9	6.0	3.2	484	0.75
8	Neonol AF 9/6	8–10	6.0–8.0	12.8	435	1.05
9	Syntanol DS-10	10–18	8.0–10.0	3.1–6.2	610	0.78
10	OS-20 agent	18	20.0	14.8–17.0	1150	0.79

* n is the number of carbon atoms in the alkyl radical of alcohol; m, degree of oxyethylation; HLB, hydrophilic–lipophilic balance; and DT, degree of thickening.

shows how the viscosity of starch hydrogel varies with the concentration of the surfactant added after the treatment. There is no significant thickening in this case. Thus, starch hydrogels thicken upon introducing the surfactant only when exposed to strong mechanical loads. In an RPA, the liquid material is exposed to a combined effect of high shear stresses and ultrasonic cavitation. To find out which of these factors plays the deciding role in the thickening effect, we exposed the starch hydrogels containing surfactants to sonication not complicated by shear loads. The sonication conditions were such that the integrated ultrasonic energy transferred to the unit mass of the gel was identical to that in the RPA. The acoustic power for calculations was determined by chemical dosimetry. Curve *1* in Fig. 1 shows how

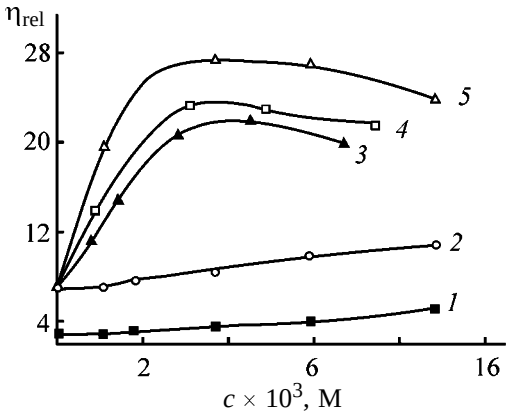

Fig. 1. Relative viscosity η_{rel} of starch gels (3 wt %) as a function of the surfactant concentration c. Mechanical treatment of starch gels: (*1*) in a UZDN-2T disintegrator, (*2–5*) in an RPA (n = 3000 rpm, τ = 4 s); (*1, 3–5*) joint and (*2*) separate treatment. Sample nos.: (*1–3*) 2, (*4*) 5, and (*5*) 4.

the viscosity of starch paste sonicated in the presence of the added surfactant varies with its concentration. The run of this curve is similar to that for the starch hydrogels mechanically treated in an RPA with subsequent introduction of surfactant additives (curve *2*). Sonication in the presence of surfactants did not cause starch hydrogels to thicken. Similar curves were obtained for the other agents studied in this work. This means that the deciding role in thickening of starch hydrogels in the presence of surfactants studied is played by high-rate shear strains rather than by ultrasonic cavitation.

Another issue to be clarified before making any assumptions concerning the thickening mechanism was the possibility/impossibility of such a thickening in aqueous gel-like materials based on other polysaccharides. To clarify this issue, we subjected Na-CMC hydrogels and sodium alginate solution to mechanical treatment in an RPA in the presence of surfactant in various concentrations. Such a treatment did not increase the viscosity of the studied polysaccharides relative to those treated without surfactant. Thus, it seems likely that only starch is able of substantial thickening when mechanically treated in an RPA in the presence of a number of surfactants. This suggests that the viscosity of starch hydrogels increases owing to complexing between starch amylose and surfactant molecules under high shear stresses.

It is known [6] that amylose is capable of forming nonstoichiometric compounds with alcohols and some hydrocarbons. The X-ray diffraction patters obtained by Zavadskii *et al.* [7] proved formation of such complexes with certain surfactants at elevated temperatures under static conditions. The agents utilized in this work do not cause any marked changes in

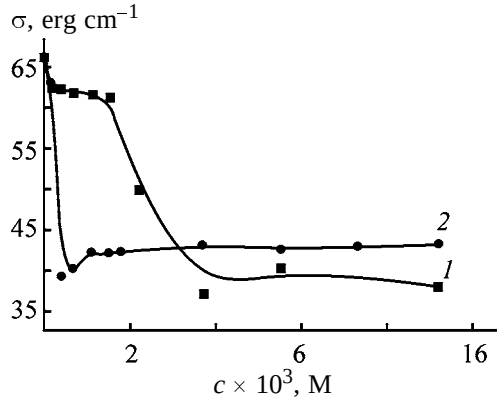

Fig. 2. Surface tension isotherms σ for the starch gel (3 wt %)–surfactant system (sample no. 2) in the case of (*1*) joint and (*2*) separate mechanical treatment in an RPA. n = 3000 rpm, τ = 4 s; the same for Fig. 6. (*c*) Surfactant concentration.

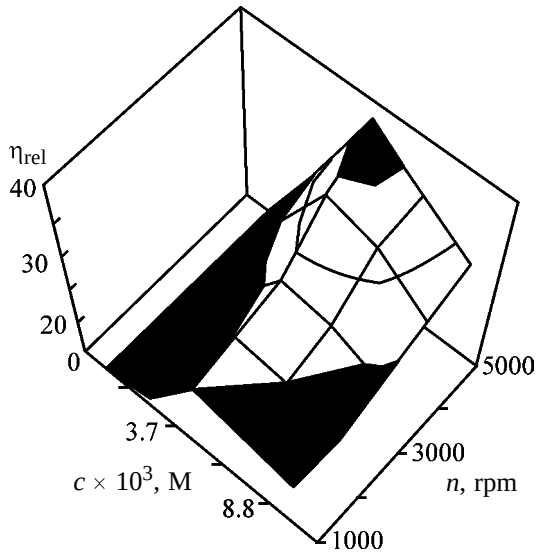

Fig. 3. Relative viscosity η_{rel} of starch hydrogels (3 wt %) vs. the concentration c of the surfactant additive (sample no. 2) and vs. the rate n of treatment in an RPA. Time of treatment in an RPA τ = 4 s.

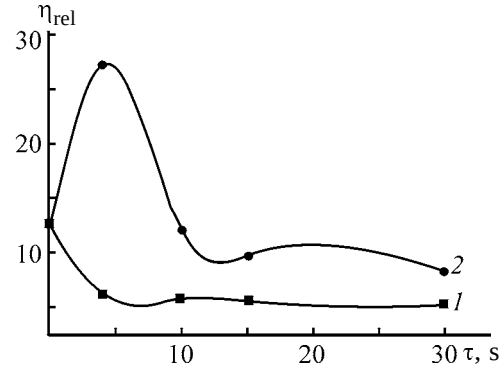

Fig. 4. Relative viscosity η_{rel} of the gel (3 wt %)–surfactant system (sample no. 2) as a function of the time τ of mechanical treatment in an RPA. Surfactant concentration 1.8×10^{-3} M, n = 3000 rpm.

starch hydrogels indicative of formation of amylose–surfactant complexes both under ordinary conditions and at elevated temperatures. Intensive mechanical treatment and, above all, high-rate shear strains seem to be responsible for conformational changes of the helical amylose molecules. At the same time, a combination of high shear loads and ultrasonic cavitation causes breakdown of the micelles and degradation of the surfactant molecules [8]. All this favors formation of complexes between highly mobile surfactant molecule and unfolded amylose macromolecules. This assumption is supported by the surface tension isotherms obtained for the 3% starch hydrogels added with the surfactants either before (Fig. 2, curve *1*) or after (Fig. 2, curve *2*) treatment in an RPA. It is seen that, in the latter case, the isotherm exhibits an ordinary pattern: Even insignificant amounts of the added surfactant tend to substantially decrease the surface tension. In the case of treatment of starch added with a surfactant, the surface tension did not decrease at the surfactant concentration of up to 2.0×10^{-3} M. Similar surface tension isotherms were obtained for the other surfactant samples studied in this work (see table, sample nos. 1–5). The concentrations of the additives at which the isotherms exhibit the ordinary pattern varied within $(1.5–2.5) \times 10^{-3}$ M. Such a "lag" in the onset of decrease in the surface tension with increasing surfactant concentration suggests that the surfactant molecules are bound by the amylose macromolecules. The isotherms for sample nos. 6–10 exhibit an ordinary pattern. Evidently, at the concentration corresponding to the onset of a sharp decline of the surface tension, amylose, occurring in the hydrogel in the free form, exhibits the most pronounced complexing power.

The degree of thickening of starch hydrogels with oxyethylated alcohols is determined both by the concentration of the additive and the intensity of mechanical treatment, i.e., by the shear rate $\dot{\gamma}$. Both dependences have extrema. The 3D diagram in Fig. 3 illustrates the combined effect of these factors. When both c_{add} and $\dot{\gamma}$ take extremal values, the viscosity can increase by several orders of magnitude.

Figure 4 shows how the viscosities of the mechanically treated 3 wt % starch hydrogels vary with the time of treatment in an RPA when the surfactant is added before (curve *2*) and after (curve *1*) treatment. The viscosity of the hydrogels mechanically treated in the presence of surfactants passes through a maximum at the treatment time of 4 s. Further increase of the time of mechanical treatment causes the viscosity to decrease, i.e., the forming complexes seem to break down.

It was of interest to elucidate whether the increase in the viscosity of starch pastes is related to increase in their structurization, which is manifested in enhancement of the viscosity anomaly. The degree of deviation of the rheological behavior of liquid systems from that of Newtonian fluids can be judged from the position of the flow curves, which are, essentially, the logarithmic dependences of the dynamic viscosity on the shear stress. Figure 5 presents the flow curves for the 6% starch pastes mechanically treated in an RPA in the presence of the surfactant in various concentrations. The viscosity tends to grow with increasing additive concentration, but the slope of the curve does not change. This means that the viscosity increases owing to growing asymmetry of the structural elements, rather than to the structural component, i.e., to strengthening of the fluctuation network of the gel. For example, in the ordinary state, the helical amylose macromolecules have a loose coil conformation [9]. Under mechanical treatment, they unfold in the shear field and remain unfolded owing to complexing with oxyethylated alcohols, which is specifically responsible for a steady viscosity increase.

Thus, thickening of starch hydrogels when treated in an RPA in the presence of oxyethylated alcohols under high-rate shear strains is due to complexing with amylose initiated by this treatment and ultrasonic cavitation. It was of interest to correlate the structure of the surfactant with its capability to cause thickening of starch hydrogels when treated in an RPA.

The table presents the degrees of oxyethylation *m* for the studied surfactants, as well as the lengths of the alcohol residues characterized by the number of carbon atoms *n* in the alkyl radical of the alcohol. Also, the table lists the hydrophilic-lipophilic balances (HLBs) of the agents utilized, as well as the degrees of thickening. The latter are, essentially, the ratios of the viscosities of starch hydrogel treated in an RPA in the presence and absence of surfactant, respectively. Clearly, there is no correlation between the above-listed characteristics and the degree of thickening. However, there is a certain relationship between the decrease in the thickening power of the surfactant and increase in its molecular weight (Fig. 6). Sample nos. 6 and 8 virtually do not cause the viscosity to increase, and sample nos. 7, 9, and 10 cause the viscosity to decrease, i.e., behave as conventional noncomplexing surfactants.

Thus, we showed the possibility of widely varying the viscosity of the mechanically cleaved starch hydrogels without affecting the starch concentration. This can be utilized, e.g., in mechanical preparation of

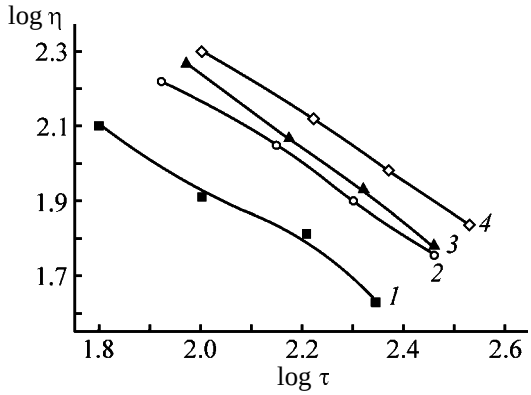

Fig. 5. Flow curves $\log\eta$–$\log\tau$ of the jointly mechanically treated starch (6 wt %)–surfactant system (sample no. 2). Surfactant concentration, M: (*1*) 0, (*2*) 1.1, (*3*) 2.2, and (*4*) 4.4.

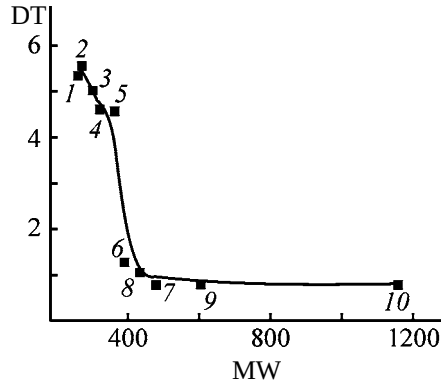

Fig. 6. Degree of thickening DT of starch hydrogel (3 wt %) treated in an RPA in the presence of a number of surfactants based in oxyethylene with different molecular weights MW. Figures at points correspond to sample nos. in the table.

starch size with easily controllable viscosity. By varying the size viscosity without affecting the starch content and the mechanical treatment conditions, in accordance with the thread density, it will be possible to easily optimize the size distribution over the thread cross section.

CONCLUSIONS

(1) Certain surfactants from the series of oxyethylated fatty alcohols can exert a steady thickening effect on starch hydrogels under high-rate shear strains realized in rotary pulse apparatuses. The plots of the degree of thickening vs. the surfactant concentration and the rate gradient have extrema.

(2) The thickening effect of surfactants is due to the high-rate shear-initiated complexing between the starch amylose and surfactant molecules.

(3) The capability of oxyethylated fatty alcohols for mechanochemically initiated complexing with amylose tends to weaken with increasing molecular weight of the surfactant.

REFERENCES

1. Lipatova, I.M., Padokhin, V.A. Moryganov, A.P., *et al*., *Tekst. Prom–st*., 1998, no. 5, pp. 32–33.
2. Yusova, A.A., Lipatova, I.M., Kumeeva, T.Yu., and Moryganov, A.P., *Izv. Vyssh. Uchebn. Zaved., Tekhnol. Tekst. Prom–sti*., 1999, no. 5, pp. 62–67.
3. Lipatova, I.M., Yusova, A.A., and Moryganov, A.P., *Zh. Prikl. Khim*., 2000, vol. 73, no. 8, pp. 1372–1376.
4. Kurilova, V.A. and Volkova, N.V., in *Novye polimenye materialy i materialovedenie v legkoi promyshlennosti* (New Polymer Materials and Materials Science in Light Industry), Moscow: TsNIITEIlegprom, 1978, vol. 1, pp. 14–17.
5. *Poverkhostno-aktivnye veshchestra: Spravochnik* (Surfactants: Reference Book), Abramzon, A.A. and Gaevoi, G.M., Eds., Leningrad: Khimiya, 1979.
6. *Nestekhiometricheskie soedineniya* (Nonstoichiometric Compounds), Mandelkern, L., Ed., Moscow: Khimiya, 1971.
7. Zavadskii, A.E., Kulikova, I.V., and Ledneva, I.A., *Tekst. Khim*., 1998, no. 1(13), pp. 16–20.
8. Schönfeldt, N., *Grenzflachenaktive Äthylenoxid-Addukte*, Stuttgart: Wissenschaftliche, 1976.
9. Richter, M., Augustat, S., and Schierbaum, F., *Ausgewählte Methoden der Stärkechemie*, Leipzig: Fachbuchverlag, 1968.

Russian Journal of Applied Chemistry, Vol. 76, No. 3, 2003, pp. 439–441. Translated from Zhurnal Prikladnoi Khimii, Vol. 76, No. 3, 2003, pp. 454–456.

ORGANIC SYNTHESIS AND INDUSTRIAL ORGANIC CHEMISTRY

Synthesis and Properties of Photosensitive Complex Perchlorates of *d* Metals with 3(5)-Hydrazino-4-amino-1,2,4-triazole as Ligand

I. A. Ugryumov, M. A. Ilyushin, I. V. Tselinskii, and A. S. Kozlov

St. Petersburg State Technological Institute, St. Petersburg, Russia

Received July 13, 2002

Abstract—A number of complex perchlorates based on 3(5)-hydrazino-4-amino-1,2,4-triazole were synthesized. The physicochemical properties and the sensitivity of these complexes to laser monopulse were studied, as well as their photosensitivity as influenced by the metal cation.

Over 70% of the Russia's mineral raw materials is extracted now using explosives. Increasing the efficiency and safety of blast-hole drilling activities is one of the high-priority lines of development of mining and oil and gas industries in the XXI century.

Optical priming charges (OPCs) find ever widening application in various branches of science [1, 2]. In view of the fact that detonation excitation in charges of photosensitive explosives is due to absorption of the laser pulse energy, OPCs are favorably distinguished by safer and more reliable performance from the presently used conventional priming charges.

In the search for new photosensitive energetic compounds suitable for OPC applications among the series of *d*-element complexes and with the aim to elucidate the influence exerted by the central ion on the sensitivity of the metal complex to laser monopulse, we synthesized and studied complex perchlorates of Cu(II), Co(II), Ni(II), and Cd(II) with 3(5)-hydrazino-4-amino-1,2,4-triazole (HATr) as ligand. The choice of the latter was dictated by a high sensitivity to laser monopulse exhibited by di(3(5)-hydrazino-4-amino-1,2,4-triazole)copper(II) perchlorate (**I**) [3, 4].

EXPERIMENTAL

The complexes were synthesized by the general scheme

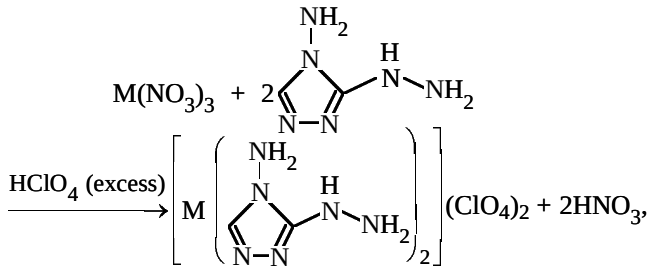

where M = Cu^{2+}, Co^{2+}, Ni^{2+}, Cd^{2+}.

The reactions were run in an excess of perchloric acid at room temperature.

To a 0.002 M solution of HATr in 10 ml of 2-propanol acidified with 5 ml of $HClO_4$ (57%), a 0.01 M solution of appropriate metal nitrate in 10 ml of 2-propanol was added. The resulting mixture was stirred for 1 h at room temperature. The precipitate that formed was filtered off, washed with water and 2-propanol, and dried in a vacuum desiccator at 50°C.

Compound I. IR spectrum, cm^{-1}: 3320 m, 1670 w (NH_2), 1560 m, 1360 m [triazole ring (TrC)], 1100 s (ClO_4).

Found, %: C 9.72, H 2.92, N 34.03.
$C_4H_{12}N_{12}Cl_2O_8Cu$.
Calculated, %: C 9.81, H 2.45, N 34.32.

Compound II. IR spectrum, cm^{-1}: 3320 m, 1660 m (NH_2), 1590 w, 1370 m (TrC), 1110 s (ClO_4).

Found, %: C 9.85, H 2.77, N 34.89.
$C_4H_{12}N_{12}Cl_2O_8Co$.
Calculated, %: C 9.90, H 2.48, N 34.65.

Compound III. IR spectrum, cm^{-1}: 3320 m, 1660 m (NH_2), 1585 m, 1360 m (TrC), 1110 s (ClO_4).

Found, %: C 10.09, H 2.78, N 34.90.
$C_4H_{12}N_{12}Cl_2O_8Ni$.
Calculated, %: C 9.90, H 2.48, N 34.66.

Compound IV. IR spectrum, cm^{-1}: 3320 m, 1650 m (NH_2), 1570 m, 1355 w (TrC), 1100 s (ClO_4).

Found, %: C 8.73, H 2.75, N 30.98.
$C_4H_{12}N_{12}Cl_2O_8Cd$.
Calculated, %: C 8.92, H 2.23, N 31.20.

1070-4272/03/7603-0439$25.00

Table 1. Derivatographic analysis of the synthesized complexes

Thermal decomposition	T, °C	T_{peak}, °C	Residue, %	
			found	calculated
$[Co(HATr)_2](ClO_4)_2$	30–230		–	–
↓	230–285	265	54.8	56.1
$[Co(HATr)]ClO_4$	285–380	300	16.1	15.4
↓				
CoO	380→			
$[Ni(HATr)_2](ClO_4)_2$	30–250		–	–
↓	250–335	300	56.2	56.1
$[Ni(HATr)]ClO_4$	335–385	360	15.6	15.4
↓				
NiO	385→			
$[Cd(HATr)_2](ClO_4)_2$	30–290		–	–
↓	290–350	325	59.2	60.4
$[Cd(HATr)]ClO_4$	350–390	370	24.4	23.8
↓				
CdO	390→			

The IR spectra (films or Nujol mulls) were recorded on a Perkin–Elmer M-457 spectrometer.

The thermograms were obtained with an MOM derivatograph (Hungary) (20–500°C temperature range, heating rate 5 deg min^{-1}).

The sensitivity to laser monopulse was studied on a laser setup with the following parameters: λ = 1.06 μm, τ_{pulse} = 30 ns, and d_{beam} = 0.48 mm. The samples were pressed into copper capsules, 5 mm in diameter and 2 mm high, under the pressure of 400 kg cm^{-2}.

The absorption bands in the IR spectra of the complexes in the region of the stretching vibrations of the triazole ring (1560, 1320 cm^{-1}) are shifted by 15–30 cm^{-1} relative to those of the free ligand. The absorption bands corresponding to the stretching and bending vibrations of the $–NH_2$ groups did not change noticeably on complexing (3320, 1650–1670 cm^{-1}). Also, a strong absorption band of the ClO_4^- ion was recorded at 1100–1110 cm^{-1}. The fact that this band is not split suggests that the ClO_4^- ion occurs in the outer sphere of the complex and takes no part in coordination.

Since elemental analysis confirmed the fact that, in all cases, we obtained complexes containing two inner-sphere ligands, the coordination number M being equal to 4(6), and that the perchlorate ion took no part in coordination, it can be suggested that these compounds contain a bidentate ligand. The invariant position of the absorption bands of the exocyclic $–NH_2$ groups and a blue shift of the bands of the triazole ring relative to the free ligand suggest that the ligand is coordinated via the nitrogen atoms in the heterocyclic. The presence of a substituent at the heterocycle nitrogen atom N^3 and the assumed bidentate nature of this ligand suggest, most probably, coordination via the N^1 and N^2 atoms in the heterocycle, which is common for such complex salts of triazole [5].

A study of thermal decomposition of the resulting salts under nonisothermal conditions at the heating rate of 5 deg min^{-1} revealed a fairly high thermal stability of the products with the onset temperature of intensive decomposition T_{OID} above 230°C (Table 1).

Compounds **II**–**IV** decomposes in three stages. In the first stage, at 230, 250, and 290°C, respectively, they exhibit exothermic peaks with the mass loss corresponding to decomposition of one ligand and one perchlorate ion (45.2, 43.8, and 40.8%, respectively), which is, evidently, due to oxidation of the heterocycle with the outer-sphere cation. The second stage also involves exothermic effects with T_{OID} of 285, 335, and 350°C, respectively, corresponding to decomposition of the second ligand and of the remaining pechlorate ion. At 380–390°C, the residue decomposes into the corresponding metal oxide.

Thermal decomposition of **I** involves one stage, due, evidently, to a higher catalytic activity of copper(II) cation compared to cobalt(II), nickel(II), and cadmium(II) cations, which is responsible for more intensive oxidation in thermal decomposition of this compound.

The complex salts prepared in this work were tested for sensitivity to laser monopulse; the results are presented in Table 2. Here, E_{cr} is the minimal energy required for initiating detonation of a complex.

The results of the tests performed in this work suggest that compounds **I**–**IV** are energetic photosensitive substances. Their sensitivity to laser monopulse is governed by the oxidative power of the metal ion expressed as the sum of the ionization potentials $I_1 + I_2$ (Table 2). The larger this sum, the higher the sensitivity of the compound to laser radiation: Cu > Cd > Ni > Co.

Koroban *et al.* [6] elucidated the role played by the metal cation in decomposition of complex *d*-metal perchlorates based on hydrazine derivatives. That study revealed the predominant inner-sphere oxidation of the ligand by the anion, with the metal cation participating in the initial stages. The data reported in [6]

Table 2. Laser initiation of the detonation of the complexes synthesized

Complex	E_{cr}, J	Sum of the ionization potentials of the metal cation $I_1 + I_2$, eV
$[Cu(HATr)_2](ClO_4)_2$	1.1×10^{-5}	28.02
$[Cd(HATr)_2](ClO_4)_2$	5.03×10^{-4}	25.90
$[Ni(HATr)_2](ClO_4)_2$	5.75×10^{-4}	25.78
$[Co(HATr)_2](ClO_4)_2$	1.36×10^{-3}	24.92

and in the present study suggest the following oxidation mechanism for the studied complexes in the initial stages:

$$2ClO_4^- + M^{2+} \rightarrow ClO_4^\bullet + M^+ + ClO_4^-, \quad (2)$$

$$ClO_4^- + M^+ \rightarrow ClO_4^\bullet + M^0. \quad (3)$$

A two-stage reaction between the metal cation and perchlorate anion yields a highly active perchlorate radical participating in the subsequent oxidation of the ligand.

CONCLUSIONS

(1) New energetic photosensitive compounds were synthesized. The role played by the metal cations in these complex salts under laser initiation was elucidated.

(2) The compounds synthesized are suitable for application in commercial optical priming charges.

ACKNOWLEDGMENTS

This work was financially supported by the Russian Federation Ministry of Education, under the Chemistry and Chemical Products Intercollegiate Program.

REFERENCES

1. Tarzhanov, V.I., Litvinov, B.V., and Zinchenko, A.D., *Gorn. Zh.*, 1999, no. 10, pp. 94–98.
2. Chernai, A.V., Sobolev, V.V., and Sharabura, A.D., *Fiz. Tekh. Vys. Energ.*, 2001, vol. 11, no. 2, pp. 115–120.
3. Ilyushin, M.A., Tselinskii, I.V., and Smirnov, A.B., *Sb. Nauchn. Tr. Nats. Gorn. Akad. Ukr.*, 2001, vol. 3, no. 11, pp. 42–50.
4. Cudzilo, S. and Szmigielsky, R., *Biol. WAT*, 2000, vol. 49, no. 12, pp. 5–17.
5. Sinditskii, V.P. and Fogel'zang, A.E., *Ross. Khim. Zh.*, 1997, vol. 41, no. 4, pp. 74–80.
6. Koroban, V.A., Guk, V.P., and Panina, E.V., *Khim. Fiz.*, 1990, vol. 9, no. 12, pp. 1665–1669.

Russian Journal of Applied Chemistry, Vol. 76, No. 3, 2003, pp. 442–447. Translated from Zhurnal Prikladnoi Khimii, Vol. 76, No. 3, 2003, pp. 457–462.

ORGANIC SYNTHESIS AND INDUSTRIAL ORGANIC CHEMISTRY

Synthesis and Structure of Nanocomposites in the Aromatic Ester Dendrimer–SiO_2 System

N. N. Khimich, L. A. Koptelova, and G. N. Khimich

Grebenshchikov Institute of Silicate Chemistry, Russian Academy of Sciences, St. Petersburg, Russia
Institute of Macromolecular Compounds, Russian Academy of Sciences, St. Petersburg, Russia

Received July 24, 2002

Abstract—The possibility for preparing an organic–inorganic nanohybrid without chemical bonds between its components by the sol–gel procedure was studied.

Nanocomposites are intensively studied in modern materials science [1]. These studies gave rise to fundamentally new materials with peculiar optical, nonlinear optical, ion-conductive, and other properties [2–4].

Among nanocomposites known to date, we chose organic–inorganic hybrids prepared by the sol–gel method, which is one of the simplest, environmentally cleanest, and most convenient procedures [5]. To a first approximation, this method involves (in the case of formation of SiO_2 matrix) hydrolysis of tetraalkoxysilane with subsequent polycondensation of the liberated silanols to form a three-dimensional network incorporating the components added in advance. Nanocomposites are formed owing to various interfacial interactions between the organic (i.e., polymers) and inorganic (the three-dimensional network or its fragments) components. The nanocomposites in which the organic and inorganic components are chemically bound are characterized by the best mechanical properties and highest heat resistance. Preparation of these systems requires modification of the organic component with, e.g., commercially available derivatives of tetraalkoxysilanes: (3-glycidoxypropyl)trimethoxysilane [6], (3-aminopropyl)triethoxysilane [7], and 3-(triethoxysilyl)propyl isocyanate [8].

The trialkoxysilane derivatives are cohydrolyzed with tetraethoxysilane, which provides uniform distribution of the organic component chemically bonded with the inorganic matrix. Nanohybrids can be also formed without special binders. In this case, the active functional groups of the organic component (OH or NH_2) polycondense with silanol liberated in the hydrolysis of tetraalkoxysilanes to form chemical bonds between the components of the system [9, 10].

However, there are nanohybrids with the microstructure formed exclusively by van der Waals and hydrophilic–hydrophobic interactions or hydrogen bonds [11]. To our knowledge, organic–inorganic hybrids with the microstructure determined mainly by physical interactions of the components have not been prepared previously by the sol–gel procedure. This is due to the fact that the organic components of these systems should be sufficiently hydrophobic and should not contain active functional groups, whereas polar solvents such as alcohols and water are necessarily used in modern sol–gel organic synthesis [2]. This confines the range of organic components introduced into the SiO_2 matrix to strongly polar structures soluble in aqueous solutions.

The systematic studies of sol–gel synthesis of monolithic silica gel [12–14] show that this process can be performed in low-polar nonaqueous systems. This prevents uncontrolled phase separation (introduction of a lyophobic organic component into the lyophilic system) and formation of a nonuniform material in the first steps of the sol–gel process. In this work we studied features of formation of organic–inorganic hybrids with the microstructure mainly determined by van der Waals and hydrophobic–hydrophilic interactions of the organic an inorganic components.

EXPERIMENTAL

The organic component of the composite was an ester dendrimer of the second (1) and third (2) generations with benzene groups in external layer:

1070-4272/03/7603-0442$25.00

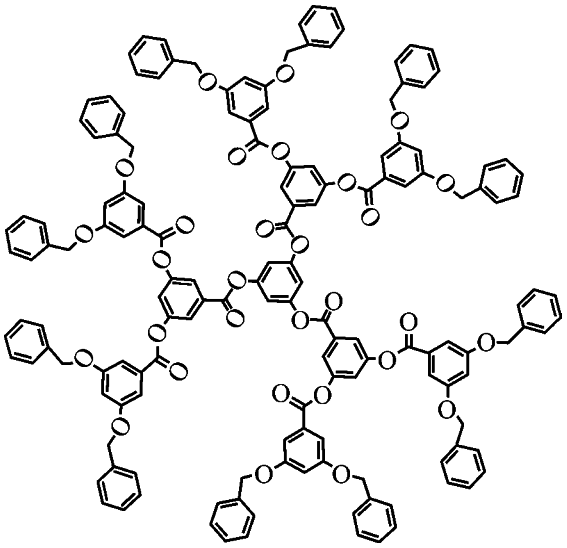

1, $C_{153}H_{114}O_{30}$; MW 2430.74.

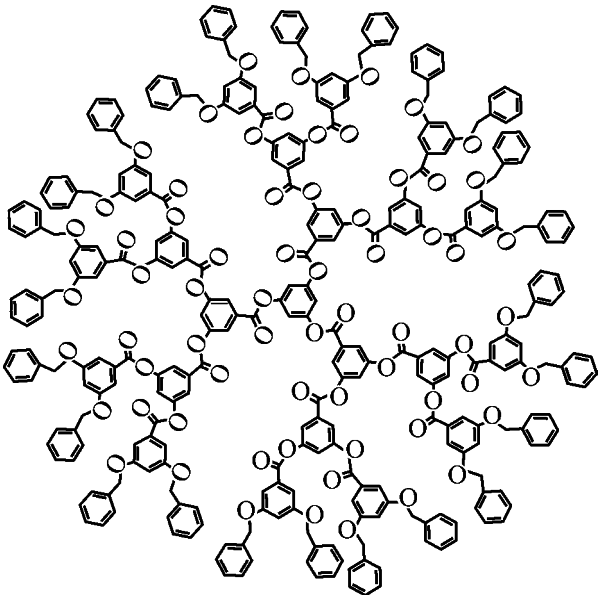

2, $C_{321}H_{234}O_{66}$; MW 5147.25.

Compounds **1** and **2** were prepared by the divergent procedure schematically shown below:

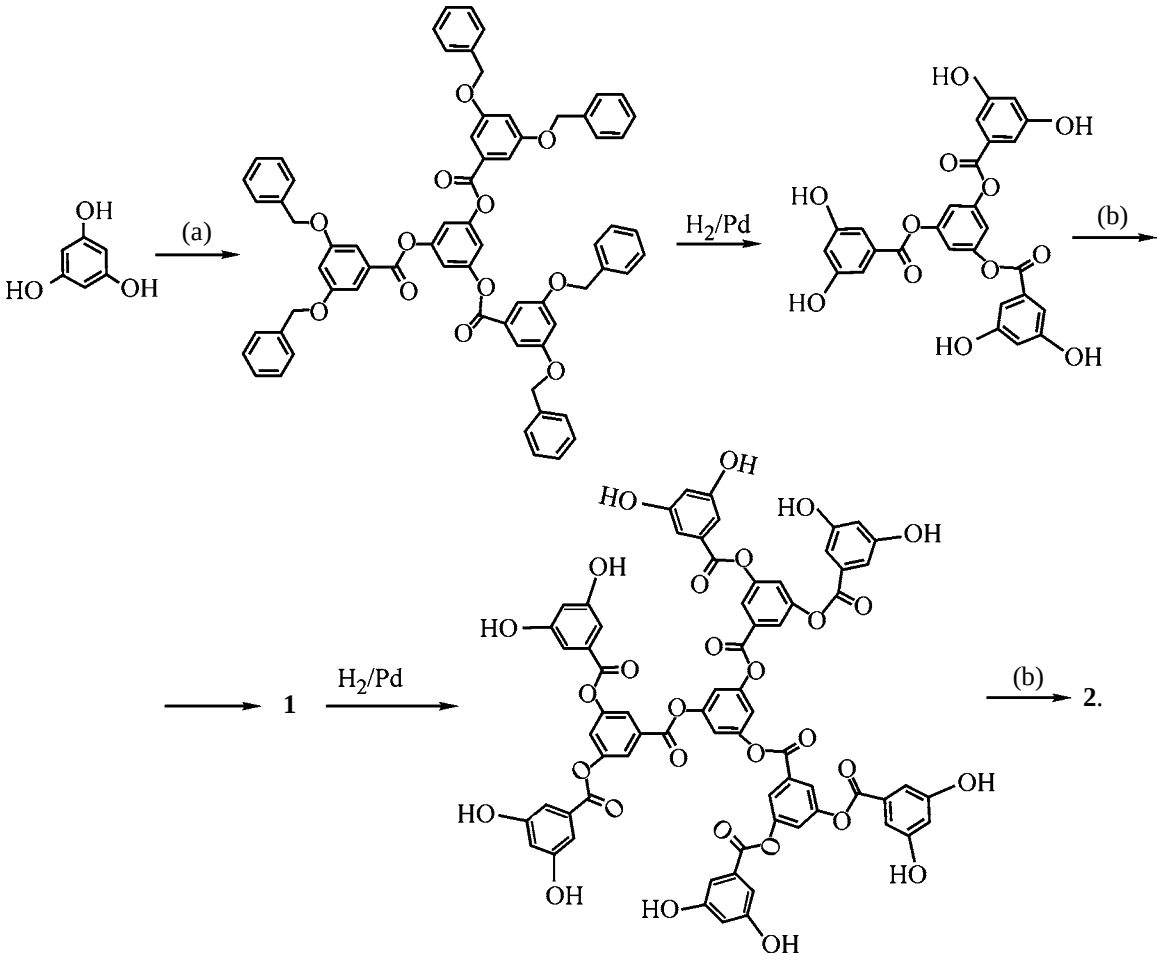

Phloroglucinol and 3,5-dibenzyloxybenzoic acid were used as the central core and the branching agent, respectively. (a) CH_2Cl_2, 3,5-dibenzyloxybenzoyl chloride, *N*,*N*-dimethylaminopyridine, 20°C; (b) dry acetone, 3,5-dibenzyloxybenzoic acid, dicyclohexylcarbodiimide, complex of *N*,*N*-dimethylaminopyridine with *p*-toluenesulfonic acid, 20°C.

The procedure for preparing **1** and **2** [15] was substantially modified. In particular, to increase the purity and yield of 3,5-dibenzyloxybenzoyl chloride [16], it was prepared in a benzene solution of thionyl chloride. We failed to perform hydrogenolysis of benzyl esters on the palladium catalyst by the procedure in [15]. These compounds were hydrogenated using dimethylacetamide as the solvent. Compounds **1** and **2** were purified by preparative column chromatography on a silica gel (40–100 μm) using petroleum ether–dichloromethane (gradient form 10 : 1 to 1 : 1) as the eluent. The purity was determined by ^1H and ^{13}C NMR spectroscopy (Bruker dpx-300, 300 MHz).

$CDCl_3$ and DMSO-d_6 were used as solvents, and tetramethylsilane, as internal reference. Compound **1**:

Found, %: C 75.23, H 4.60.
$C_{153}H_{114}O_{30}$. Calculated, %: C 75.54, H 4.72.

^1H NMR, δ, ppm, $CDCl_3$: 5.12 (24H, s, CH_2), 6.91 (6H, t, *J* 2.0 Hz), 7.24 (3H, s), 7.3–7.55 (75H, m), 8.01 (6H, d, *J* 2.0 Hz). ^{13}C NMR, δ, ppm, $CDCl_3$: 70.2, 108.3, 113.1, 121.0, 124.2, 127.6, 128.0, 128.4, 130.4, 131.1, 136.2, 151.1, 151.3, 159.7, 162.5, 164.1.

Compound **2**:

Found, %: C 74.70, H 4.58, O 20.32.
$C_{321}H_{234}O_{66}$. Calculated, %: C 74.90, H 4.58, O 20.52.

^1H NMR, δ, ppm, DMSO-d_6: 5.15 (48H, s, CH_2), 7.01 (12H, s), 6.2–7.5 (147H, m), 7.76 (6H, s), 7.88 (3H, s), 8.05 (12H, s), 8.12 (6H, s). ^{13}C NMR, δ, ppm, DMSO-d_6: 70.5, 108.9, 114,3, 122.1, 123.1, 128.5, 128.7, 129.3, 129.8, 131.2, 131.8, 137.4, 141.3, 153.0, 153.8, 160.5, 163.7, 165.1.

The nanocomposites containing **1** and **2** were prepared as follows. To a solution of tetramethoxysilane (TMOS) (2.0 g) in acetic acid (5.0 g), a toluene solution of **1** and **2** or pure toluene was added with vigorous stirring at 70°C. Five samples were obtained. The amounts of **1** and **2** m_1 and m_2, used in preparation of nanocomposites **1a**, **1b**, **2a**, and **2b** and gel **3** at the acetic acid : TMOS : toluene ratio of 5 : 2 : 5, are given below:

Sample	**1a**	**1b**	**2a**	**2b**	**3**
m_1, g	0.075	0.15	–	–	–
m_2, g	–	–	0.075	0.15	–

The resulting homogeneous solutions were placed without cooling in hermetically sealed polypropylene test tubes 15 mm in diameter (three test tubes for each sample) and kept at 70°C for 5 days. Then the test tubes were cooled, and their content was transferred into test tubes with 1-mm holes. Wet samples were dried at 60°C for 8 days, 80°C for 1 day, 90°C for 1 day, and 100°C for 3 days at the heating rate of 5 deg h^{-1}.

We measured the open porosity W_{open} and apparent porosity of the samples by the Archimedian procedure. Of course, these measurements were performed with the samples that did not crack during drying or measurements. The sample hardness was determined on a PMT-3 microhardness gage. The thermal analysis curves were recorded on a Q-1500D derivatograph by heating to 1000°C at a rate of 20 deg min^{-1}. The percentage of SiO_2 in composites **1a** and **2a** and gel **3** was determined from the thermal analysis curves. Electron microscopic study of the gels was performed on an EM-125 electron microscope at the accelerating voltage of 75 kV. For this purpose, cellulose–carbon replicas of the surface of fresh chips of the samples were prepared. TMOS, toluene, acetic acid, and organic amides were distilled on a 10 TP column, collecting 0.1–0.3°C fractions.

We used dendrimer molecules of the second and third generation as the organic component of the nanohybrid, since these molecules, owing to their monodispersity and spherical structure of their framework, are convenient models for studying interphase interactions of the components. Unfortunately, complex synthesis of dendrite molecules restricts their use for preparing nanocomposites. Experiments on introduction of dendrimers in the three-dimensional silica framework are mainly performed with polyamidamines, the most available dendrimers to date [6, 9, 17, 18]. The aromatic ester dendirmes studied here as the organic components have the following advantages over polyamidamines: more symmetrical structure and the presence of benzene rings in the internal sphere of the molecules. This structure of aromatic ester dendrimers (contrary to polyamide dendrimers whose internal sphere consists of mobile aliphatic chains) increases their rigidity, makes their molecules more spherical, and provides the absence of nucleophilic groups in the internal sphere of the molecules.

At the same time, compounds **1** and **2** differ only in the generation degree, i.e., in the size of their molecules, spherical to a first approximation. The sizes for the dendrimers of the second **1** and third **2** generation, indirectly estimated from the data of [19], are 2–3 and 3–5 nm, respectively. As shown below, this has a key effect on formation of nanocomposites.

Chemical reactions occurring in the course of transformation of TMOS into the SiO_2 matrix under the action of acetic acid without adding water were described in detail in our previous paper [20]. It should only be noted that no visual deterioration of the homogeneity and monolithic charter of the dispersed phase during syneresis was observed. However, the content of the initial dendrimer in the disperse phase of **1a** and **2a** it is low (<1–2%); in **1b** it reaches 10, and in sample **2b** is high as 25% of the initial content.

Dried composites **1a** and **2a** were obtained in the form of monolithic transparent cylinders; **1b**, in the form of partially cracked cylinders; and sample **2b** was completely cracked. Gel **3** prepared as the reference without the organic component was a monolithic transparent cylinder. The physicochemical properties of the samples are summarized in the table.

These results can be explained as follows. The components of sample **2b** and, to a lesser extent, **1b** are in the form of a mechanical mixture. A sharp decrease in the density and hardness of these samples and an increase in their porosity as compared to gel **3** indicate that the organic component interferes with the sol–gel process. On the contrary, an increase in the density and a decrease in the porosity and hardness of samples **1a** and **2a** suggest formation of the organic–inorganic hybrid.

In addition, a sharp increase in the hardness of composite **1a** and a decrease in the carbon content in the composite (as indicated above, the dendrimer was introduced in the same amounts in the samples) as compared to samples **2a** and **3** indicates more complete formation of the SiO_2 matrix with lower residual content of the $Si–O–CH_3$ bonds. This can be due to definite physical interactions of the organic component with the three-dimensional SiO_2 matrix.

This assumption is confirmed by TG and DTA curves of samples **1a**, **2a**, and **3** (Fig. 1). The characteristic peaks in the DTA curves in the range 100–250°C are due to intense evaporation of volatile products of the sol–gel process (methanol, excess acetic acid, methyl acetate, water, etc.). It should be noted that the maxima of these peaks in the curves for **1a** and **2a** are shifted by 20°C to high temperatures as compared to that of gel **3**. At 300–650°C, the unhydrolyzed methoxy groups and the organic components burn out and thermally decompose. The exothermic peaks in the DTA curves of **1a** and **2a** are strongly shifted to high temperatures as compared to gel **3**. Of special note is the fact that the DTA curve of **1a** contains a sharp peak at 610°C, and an inflection point at 500°C is observed in its TG curve. Clearly, both organic components are structurally similar and consist of the same fragments. Thermolysis of these components (evaporation of these high-molecular-weight compounds is improbable) should occur by the similar mechanism and at close temperatures. Hence, the fact that the hardness and thermolysis temperature of composite **1a** are appreciably higher than those of **2a** suggests the presence of an appreciable amount of the organic component of composite **1a** in the SiO_2

Physicochemical properties of the samples

Sample	SiO_2, %	ρ_{app}, g cm^{-1}	W_{open}, %	Hardness, kg mm^{-2}
1a	70	1.36	29.5	53.5
1b		0.95	52.5	12.0
2a	68	1.26	30.5	25.0
2b		–	–	–
3	77	1.20	34.0	23.0

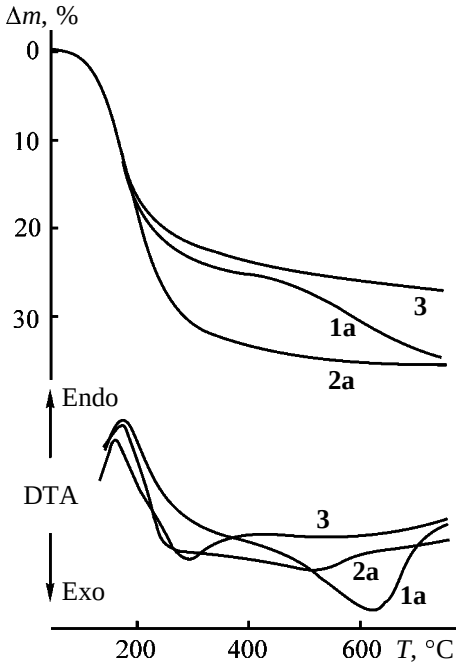

Fig. 1. TG and DTA curves for composites **1a** and **2a** and gel **3**. (Δ*m*) Weight loss and (*T*) temperature.

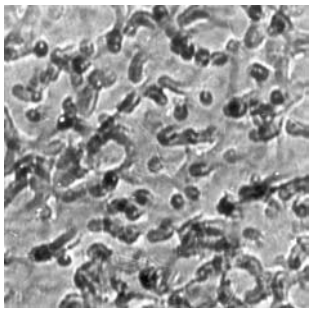

Fig. 2. Electron micrograph of gel **3**. Magnification 90 000.

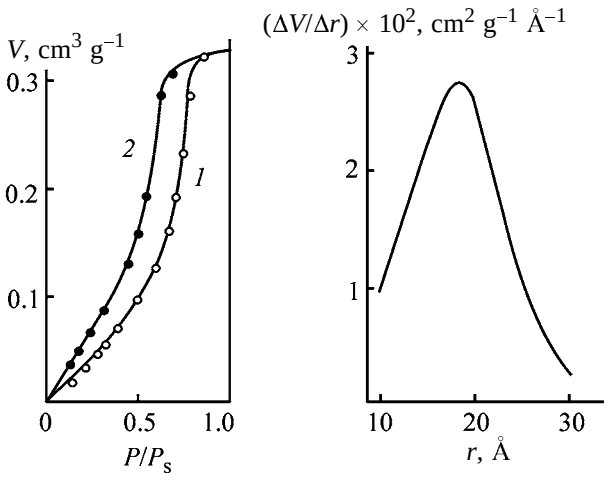

Fig. 3. Isotherm of (*1*) adsorption and (*2*) desoprtion of ethanol on gel **3** at 18°C and (*3*) pore-size distribution derived from the isotherm. (*V*) pore volume in 1 g of the sample, (P/P_s) ratio of ethanol pressure to its saturated vapor pressure, and (*r*) pore radius.

matrix. This is possible only owing to hydrophilic–hydrophobic and van der Waals interactions. To account for substantially higher energy of this interaction in composite **1a** as compared to sample **2a**, let us consider the structure of these samples.

Hybrids **1a** and **2a** are structurally similar to gel **3** (Fig. 2). The diameter of visible nanopores is 22–26 nm. However, the number of channel pores in hybrid **1a** is seemingly higher, and their nanostructure differs. It is known [4] that the pores of the SiO_2 matrix prepared by the sol–gel procedure form TMOS are filled with particles of a fine dispersion. The size of these particles can be estimated from the isotherm of ethanol adsorption on gel **3** and from the pore-size distribution (Fig. 3). Clearly, the molecular size of dendrimer **1** is slightly smaller than the pore diameter. At 9% content of dendrimer **1** in composite **1a** W_{open} = 29.5; however, introduction of the organic component in the amount of 6–7% sharply deteriorates the composite properties. It is also evident that the molecular size of the organic component matches the diameter of pores of the inorganic matrix, which provides strong intermolecular interaction between them. Since the size of dendrimer molecules in hybrid **2a** is substantially larger (3–5 nm), the energy of intermolecular interaction of the component in this system only negligibly compensates the energy loss in formation of the SiO_2 matrix under nonoptimal conditions.

CONCLUSIONS

(1) Organic–inorganic hybrids were prepared by the sol–gel procedure. The properties of these hybrids are exclusively determined by hydrophilic–hydrophobic and van der Waals interactions.

(2) The energy of these interaction at a definite molecular size of the organic component can be so high that it can provide sharp increase in the hardness and heat resistance of the composite.

(3) Unlike chemically bound organic–inorganic hybrids, even a slight change in the concentration of one of the components of a composite formed by hydrophilic–hydrophobic and van der Waals interactions strongly deteriorates its properties.

ACKNOWLEDGMENTS

This work was finacially supported by the St. Petersburg Scientific Center, Russian Academy of Sciences.

REFRENCES

1. Pomogailo, A. D., *Usp. Khim.*, 2000, vol. 69, pp. 60–88.
2. Sung, P.-H., Wu, S.-L., and Lin, C.Y., *J. Mater. Sci*., 1996, vol. 31, pp. 2443–2454.
3. Ruiz-Hitzky, E., Arahda, P., Casal, B., and Galvah, J. C., *Adv. Mater*. 1995, vol. 7, pp. 180–186.
4. Yoshida, M. and Prasad, P.N., *Chem. Mater*., 1996, vol. 8, pp. 235.
5. Brinker, C.I. and Scherer, G.W., *Sol–Gel Science*, New York: Academic, 1990.
6. Gong, A., Chen, Y., Zhang, X.I., *et al*., *J. Appl. Polym. Sci*., 2000, vol. 78, no. 12, pp. 2186–2190.
7. Zhao, Z.D., Ou, Y.C., Gao, Z.M., Qi, Z.N., and Wang, F.S., *Acta Polym*., 1996, pp. 228–235.
8. Marino, I.G., Bersani, D., Lottici, P.P., *et al*., *J. Raman Spectrosc*., 2000, vol. 31, no. 7, pp. 555–558.
9. Saegusa, T., *J. Macromol. Sci. Chem*., 1991, vol. 28, no. 9, pp. 817–829.

10. Tamaki, R. and Yoshiki, C., *Appl. Organomet. Chem.*, 1998, vol. 12, nos. 10–11, pp. 755–762.
11. Brust, M., Bethell, D., Kiely, C.S., and Sehiffrin, D.S., *Langmuir*, 1998, vol. 14, pp. 5425–5429.
12. Khimich, N.N. and Stolyar, S.V., *Zh. Prikl. Khim.*, 1998, vol. 71, no. 10, pp. 1590–1595.
13. Khimich, N.N., Venzel', B.I., Drozdova, I.A., and Suslova, L.Ya., *Dokl. Ross. Akad. Nauk*, 1999, vol. 366, no. 3, pp. 361–363.
14. Khimich, N.N., Venzel', B.I., and Koptelova, L.A., *Dokl. Ross. Akad. Nauk*, 2002, vol. 385, no. 6, pp. 790–792.
15. Yeates, S.G., *J. Chem. Soc., Perkin Trams. 1*, 1996, no. 7, pp. 649–656.
16. De Gennes, P.J. and Hervet, N.J., *Phys. Lett.*, 1983, vol. 44, pp. 351–352.
17. Nunez, C.M., Andrady, A.L., Guo, R.K., *et al.*, *J. Polym. Sci., Part A: Polym. Chem.*, 1998, vol. 36, no. 12, pp. 2111–2117.
18. Wege, V.U. and Grubbs, R.H., *Polym. Prepr.*, 1995, vol. 36, p. 239.
19. Kleppinger, R., Reynaers, H., Desmedt, K., *et al.*, *Macromol. Rapid Commun.*, 1998, vol. 19, pp. 1111–1114.
20. Khimich, N.N., Venzel', B.I., Drozdova, I.A., and Koptelova, L.A., *Zh. Prikl. Khim.*, 2002, vol. 75, no. 7, pp. 1125–1130.

Russian Journal of Applied Chemistry, Vol. 76, No. 3, 2003, pp. 448–451. Translated from Zhurnal Prikladnoi Khimii, Vol. 76, No. 3, 2003, pp. 463–466.

MACROMOLECULAR CHEMISTRY AND POLYMERIC MATERIALS

Degree of Cross-Linking of Epoxy–Acrylate Polymers Prepared by Photopolymerization

G. V. Gatiyatullina, E. M. Battalov, Yu. A. Prochukhan, and R. R. Muslukhov

Institute of Organic Chemistry, Ufa Scientific Center, Russian Academy of Sciences, Ufa, Bashkortostan, Russia

Received May 13, 2002

Abstract—The degree of cross-linking of epoxy–acrylate polymers prepared by photopolymerization of epoxy–acrylate oligomers was evaluated from the swellability in trichloroethylene.

UV-curable epoxy–acrylate oligomers are used as adhesives, sealants, as protective coatings in waveguide systems, and in radioelectronics for protection of printed-circuit boards [1, 2]. The properties of these polymers are largely determined by the degree of their cross-linking. The degrees of cross-linking of epoxy–acrylate polymeric compounds prepared, e.g., by radiation curing were studied previously [3]. At the same time, no data are available on the degree of cross-linking of epoxy–acrylate polymers prepared by photopolymerization.

In this study we evaluated the density of cross-linking of some UV-cured epoxy–acrylate polymers from their swellability in trichloroethane.

EXPERIMENTAL

Epoxy–acrylate oligomers were prepared by esterification of acrylic acid (AA) with equimolar amounts of epoxy oligomers at 120°C in the presence of polymerization inhibitor (hydroquinone) and tertiary amine as a catalyst of epoxy ring opening:

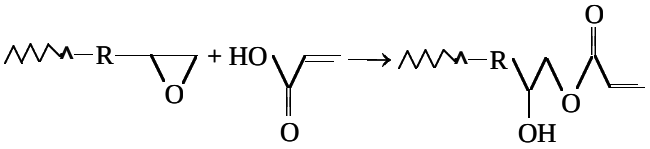

where R is an oligomeric block of an epoxy oligomer.

As epoxy oligomers we used UP-612, Oksilin (product of etherification of glycerol with epichlorohydrin), and ED-16. Acrylic acid was distilled before use. The oligomers mainly contain diacrylates and epoxy acrylates. Their structural formulas are given below.

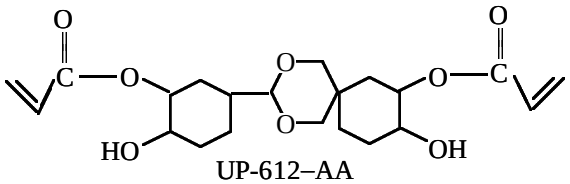

UP-612–AA

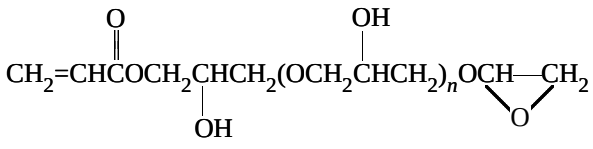

Oksilin–AA

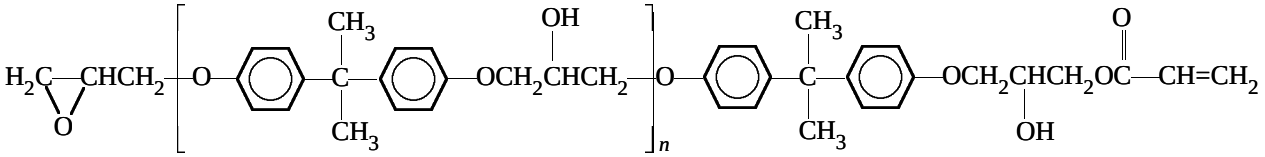

ED-16–AA

The structures of the oligomers were determined by ^{13}C and ^{1}H NMR spectroscopy. The NMR spectra were taken on a Bruker AM-300 spectrometer (^{1}H, 300 MHz; ^{13}C, 76.46 MHz; solvent $CDCl_3$; internal reference TMS). The spectra were interpreted using two-dimensional correlation technique (COSY H–H, C–H). The molar content of epoxy groups in the epoxy–acrylate oligomer decreases from 24 (in the

1070-4272/03/7603-0448$25.00

initial epoxide) to 9 mol % (oligomers studied in this work). The composition of the oligomers does not change in the course of 6-month storage. The molecular weights and molecular-weight distributions of the oligomers were determined by GPC using polystyrene references. The double bonds and epoxy number in the oligomers were determined by elemental analysis.

Samples of UP-612–AA, Oksilin–AA, and ED-16–AA polymers for studying the degree of cross-linking were prepared as films from acetone solutions of the initial oligomers in the presence of a photoinitiator. Benzophenone (BP) was recrystallized from ethanol; benzoin isobutyl ether (IBEB) was purified according to [4–6]. The UV-induced polymerization was performed using a PRK-400 medium-pressure mercury lamp. The distance from the lamp to the irradiation objects was 14 cm in all the runs. The film thickness was about 20 μm. The sol fraction was extracted from the polymers with trichloroethylene in a Soxhlet apparatus. The cross-linking density was calculated from the sol–gel analysis data. First, the number-average molecular weight of chains between the network points $\overline{M}_c$ was determined according to the Charlesby theory [7]:

$$\overline{M}_c = \overline{M}_w(s + s^{1/2})/2(1 + s),$$

where s is the sol fraction content. Then, the degree of cross-linking was evaluated as

$$\overline{M}_w/\overline{M}_c - 1 = \delta,$$

where δ is the cross-linking coefficient.

The volumetric degree of equilibrium swelling of epoxy–acrylate polymers was determined with a Dogadkin device in various solvents at 50°C:

$$q = V_1/m_0,$$

where V_1 is the volume of the solvent absorbed by the polymer and m_0 is the weight of the cross-linked polymer sample.

The deformation and strength properties of films were measured with an IR 5047-50 tensile-testing machine, with automatic data recording.

The degrees of swelling of epoxy–acrylate polymers derived from ED-16–AA and UP-612–AA are plotted in Fig. 1 vs. irradiation time. All the epoxy–acrylate polymers tested swell only slightly in any solvents; the swellabilities of the polymers prepared in an inert medium and in air differ insignificantly (Fig. 1, curves *1*, *3*). It is seen that the degree of

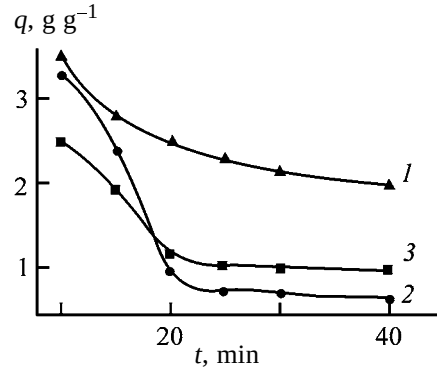

Fig. 1. Degree of swelling of polymers q as a function of UV irradiation time t (5% BP, trichloroethylene, 50°C): (*1*, *2*) ED-16–AA and UD-612–AA, respectively, polymerized in air; (*3*) ED-16–AA polymerized in an inert atmosphere.

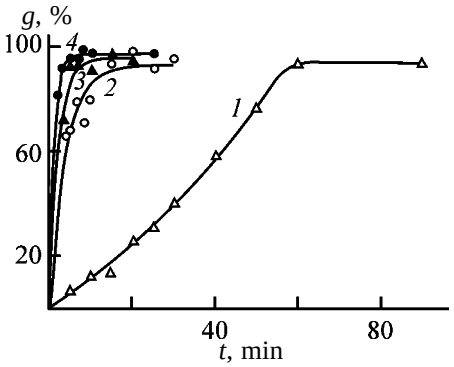

Fig. 2. Gel fraction content g in the polymer derived from ED-16–AA as a function of UV irradiation time t. Initiator, wt %: (*1*) BP, 5; (*2*) BP, 10; (*3*) IBEB, 5; and (*4*) IBEB, 10; the same for Figs. 4 and 5.

cross-linking of the polymer derived from UP-612–AA is higher compared to ED-16–AA at the same time of UV curing. The kinetic curves of gelation of ED-16–AA oligomer during irradiation in the presence of various polymerization initiators (BP, IBEB) are shown in Fig. 2. At IBEB concentrations of 5 and 10 wt % and BP concentration of 10 wt %, the gelation is mainly complete in 3–7 min (curves *2*–*4*), and at a BP content of 5 wt % the gelation of the oligomer follows approximately linear law (curve *1*).

Although, according to the IR spectra, the content of hydroxy and epoxy groups decreases in the course of UV irradiation (Fig. 3), we cannot unambiguously evaluate the contributions of epoxy and secondary hydroxy groups to the mechanism of the polymer cross-linking. Our results agree with those obtained in [8, 9].

The participation of hydrocarbon fragments of the oligomer in cross-linking under conditions of UV curing cannot be ruled out either. For example, Kachan

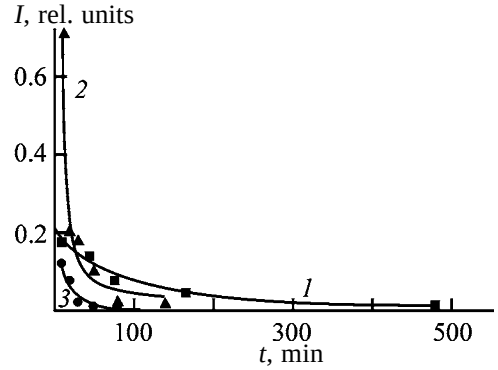

Fig. 3. Variation of the IR spectrum of the compound ED-16–AA + 5% BP with irradiation time *t*. (*I*) Absorption. Bands: (*1*) OH bending, (*2*) CH_2=CH stretching, and (*3*) carbonyl in BP.

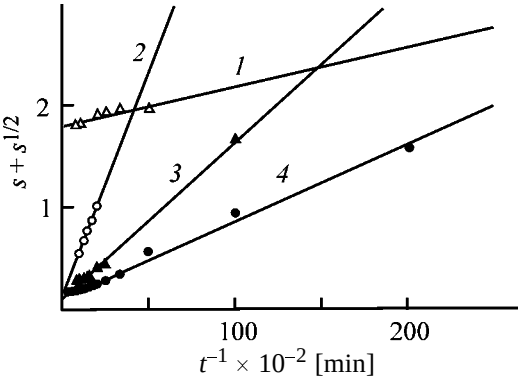

Fig. 4. Variation of the parameter $s + s^{1/2}$ of the polymer derived from ED-16–AA with UV irradiation time *t*.

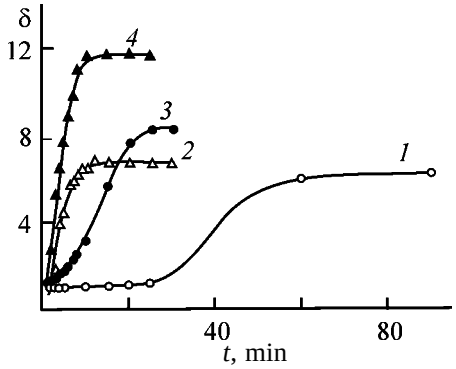

Fig. 5. Kinetic curves of cross-linking of the polymer derived from ED-16–AA. $\delta = M_w/M_c - 1$; (*t*) irradiation time.

and Shrubovich [10] reported on structural changes in benzophenone upon its UV irradiation in saturated hydrocarbons and polyethylene. The structures of both BP and saturated hydrocarbon undergo changes. The possibility of reaction of hydroxy groups with singlet oxygen in polymers is assumed in [11]; singlet oxygen can be generated by quenching of singlet and triplet excited states of BP. It should be particularly emphasized that the photoinitiator consumption during the polymerization is large, suggesting that BP is directly involved both in the cross-linking of epoxy acrylates (Fig. 3) and in formation of by-products of BP photolysis.

Figure 4 illustrates the dependence

$$s + s^{1/2} = p_0/q_0 + 1/q_0 nU,$$

where *s* is the content of the soluble fraction corresponding to definite irradiation dose *U*; *n* is the degree of polymerization calculated from the weight-average molecular weight of the oligomer; and q_0 and p_0 are the probabilities of cross-linking and degradation.

We assumed that the UV energy is absorbed linearly throughout the polymerization period. The ratio of the probabilities of degradation and cross-linking of the epoxy–acrylate polymer derived from ED-16–AA, p_0/q_0, calculated from data in Fig. 3, is 0.10–0.14, i.e., cross-linking is much more probable than degradation. For comparison, the ratio p_0/q_0 for polyethylene subjected to ionizing radiation is close to 0.3 [10].

The parameter M_c was calculated from the strain–stress dependences for the same samples of polymers derived from ED-16–AA, UP-612–AA, and Oksilin–AA as those taken for swellability measurements, using the formula [12]

$$\sigma = \frac{RT\rho_2}{M_c}(\alpha_c - \alpha_c^{-2}),$$

where $\alpha_c = l/l_0$, *l* and l_0 are the lengths of the strained and initial samples, ρ_2 is the polymer density, and *T* is temperature.

We obtained M_c ranging from 190.0 to 1000. The parameters M_c evaluated for the same polymers from the swellability range from 100 to 1000. The physical and chemical methods can give different values of M_c; however, in any case, the epoxy–acrylate polymers can be classed with densely cross-linked materials.

The kinetic curves of cross-linking of ED-16–AA (Fig. 5) upon UV irradiation show that the cross-linking rate depends both on particular photoinitiator and on the irradiation time. The flattening out of the kinetic curves of cross-linking indicates that the polymerization under these conditions is complete. The induction period (Fig. 5, curve *1*) is probably due to BP consumption for formation of benzpinacones [10, 11]. With benzoin isobutyl ether as photoinitiator, the gelation occurs at a higher rate than with benzophenone.

CONCLUSIONS

(1) Polymers with a high degree of cross-linking are prepared by photopolymerization of epoxy–acrylate oligomers in the presence of various initiators.

(2) The degree of cross-linking of the final product can be controlled by varying the UV irradiation time.

(3) With respect to the degree of cross-linking, epoxy–acrylate polymers can be ranked in the following order: UP-612–acrylic acid > ED-16–acrylic acid > Oksilin–acrylic acid.

REFERENCES

1. *Epoksiakrilovye smoly. Obzornaya informatsiya. Khimicheskaya promyshlennost'. Ser.: "Epoksidnye smoly i materialy na ikh osnove"* (Epoxy–Acrylate Resins. Review. Chemical Industry. Ser.: Epoxy Resins and Materials Based on Them), Moscow: NIITEKhIM, 1981.
2. Irzhak, V.I., Rozenberg, B.A., and Enikolopyan, N.S., *Setchatye polimery (sintez, struktura, svoistva)* (Network Polymers (Synthesis, Structure, Properties)), Moscow: Nauka, 1979.
3. Smirnova, V.K., Kalinina, N.A., Efremov, G.A., *et al.*, *Plast. Massy*, 1989, no. 4, pp. 45–48.
4. Battalov, E.M., Sugrobov, V.I., and Leplyanin, G.V., *Plast. Massy*, 1990, no. 5, p. 75.
5. Lipscomb, N.T. and Tarshiani, Y., *J. Polym. Sci., Polym. Chem. Ed.*, 1988, vol. 26, pp. 529–540.
6. Ledwith, A., *J. Oil Colour Chem. Assoc.*, 1976, no. 59, pp. 157–165.
7. Charlesby, A. and Pinner, S.H., *Proc. Roy. Soc., Ser. A*, 1959, vol. 249, p. 367.
8. Zhorina, L.A., Knunyants, M.I., Nechvolodova, E.M., *et al.*, *Vysokomol. Soedin.*, 1979, vol. 21, no. 11, pp. 811–813.
9. Rogovina, S.Z., Stakhovskaya, M.A., Markevich, M.A., *et al.*, *Dokl. Akad. Nauk SSSR*, 1977, vol. 235, no. 1, pp. 140–143.
10. Kachan, A.A. and Shrubovich, V.A., *Fotokhimicheskoe modifitsirovanie sinteticheskikh polimerov* (Photochemical Modification of Synthetic Polymers), Kiev: Naukova Dumka, 1973.
11. Guillet, J.E., *Polymer Photophysics and Photochemistry: An Introduction to the Study of Photoprocesses in Macromolecules*, Cambridge: Cambridge Univ. Press, 1985.
12. Rafikov, S.R., Budtov, V.P., and Monakov, Yu.B., *Vvedenie v fizikokhimiyu rastvorov polimerov* (Introduction to Physical Chemistry of Polymer Solutions), Moscow: Nauka, 1978.

Russian Journal of Applied Chemistry, Vol. 76, No. 3, 2003, pp. 452–456. Translated from Zhurnal Prikladnoi Khimii, Vol. 76, No. 3, 2003, pp. 467–471.

MACROMOLECULAR CHEMISTRY AND POLYMERIC MATERIALS

Thermochemical Reactions of Polyacrylonitrile with Fullerene C_{60}

Yu. N. Sazanov, M. V. Mokeev, A. V. Novoselova, V. L. Ugolkov, G. N. Fedorova, A. V. Gribanov, and V. N. Zgonnik

Institute of Macromolecular Compounds, Russian Academy of Sciences, St. Petersburg, Russia
Institute of Machine Science, Russian Academy of Sciences, St. Petersburg, Russia

Received June 2, 2002

Abstract—Reactions occuring in mixtures of polyacrylonitrile with fullerene C_{60} at 20–1000°C were studied by thermal analysis. The greatest thermal effects were observed in diffusion-controlled reactions of anionic polyacrylonitrile with fullerene. Carbonizate is formed with the yield of about 60%, which is of practical interest.

Polyacrylonitrile (PAN) is one of the most interesting polymers, and features of its formation and transformation are still the matter of discussion [1–4]. In this work, we studied structural features of PAN caused by the presence of reactive groups. These groups govern the reactivity of PAN toward fullerene, whose influence on formation and properties of other polymers was described earlier [5–8].

Generally, three types of PAN reactions with fullerene can be distinguished. Firstly, fullerene can affect PAN formation in the course of acrylonitrile polymerization. Secondly, fullerene can react with PAN prepared in advance by one or another procedure; depending on polymerization conditions, PAN can contain various reactive groups. Thirdly, fullerene can add to numerous products of PAN thermal transformation at various temperatures. In this case, both the direct reactions of fullerene with PAN at elevated temperatures and reactions with low-molecular-weight products of PAN thermal transformation are of the most interest.

Since PAN, similarly to its low-molecular-weight analogs (nitriles), is an electrophilic agent and fullerene is also an electrophilic molecule and, in addition, a strong radical inhibitor, it will suppress radical polymerization of acrylonitrile. It was shown previously [9] that, under the specific conditions of anionic polymerization, only small amounts of fullerene can add to PAN molecules, exerting no substantial influence upon the properties of modified PAN.

Therefore, of the most interest are thermochemical transformations of PAN in a broad temperature range in the presence of fullerene. In this work, we considered reactions of PAN synthesized by both radical and anionic mechanisms with fullerene C_{60} at heating in an inert atmosphere and in a vacuum within the 20–1000°C range.

EXPERIMENTAL

PAN was prepared by both radical [10] and anionic [11] methods, The PAN–C_{60} mixtures of known composition were homogenized by grinding in air. Covalently bound PAN·C_{60} was synthesized by anionic polymerization of the monomer in the presence of fullerene [9].

The thermal analysis of the reaction mixtures (50-mg samples) in the self-generated atmosphere was performed on a MOM derivatograph in crucibles with lids and Al_2O_3 covering layer at 10 deg min^{-1} heating rate. The thermal analysis in an inert atmosphere was performed on a NOETSCH device in special crucibles with 5-mg samples at 10 deg min^{-1} heating rate. The thermolysis in a vacuum was performed on a TVA device by the method described in [12] at variable heating rate (from 3 to 10 deg min^{-1}) and sample weight (from 50 to 200 mg).

It was shown in [3, 4, 13] that thermal transformations of PAN (homolytic and heterolytic) synthesized mainly by radical polymerization are accompanied by liberation of a number of low-molecular-weight volatile products such as hydrogen, hydrogen cyanide, ammonia, dicyan, acrylonitrile, vinylacetonitrile, pyrrole, pyridine, naphthyridine, etc. Their content

1070-4272/03/7603-0452$25.00

depends on the surrounding atmosphere, temperature and time of heating, PAN structure, etc. Intermediates are formed in the initial stage of elimination of volatile nitrogen derivatives as a result of secondary transformations of partially cyclized PAN. It is known that cyclic structures appear in PAN at 170–210°C in the form of naphthyridine rings [14, 15]. At further temperature rise, along with increase in the content of cyclic successions in the PAN chains, volatile products (HCN, acrylonitrile, sometimes NH_3) appear, i.e., PAN starts to lose weight, which is detected by TGA.

It is seen from Fig. 1a that noticeable weight loss due to secondary degradation of partially cyclized PAN starts at 261°C for PAN prepared by the radical mechanism (R-PAN). Below this temperature, R-PAN loses about 9 wt % at the expense of elimination of the sorbed solvent. In the first stage of R-PAN degradation, which proceeds at a high rate within the 261–298°C range, the sample loses 13.5 wt %. This process is accompanied by a strong exothermic effect with a maximum at 268°C, which is assigned to a combination of spontaneous cyclization of PAN and liberation of volatile products of thermal rearrangement of nitrogen-containing rings formed at this temperature. At further temperature rise, the second stage of R-PAN degradation and cyclization (300–420°C) starts with decreasing rate of the weight loss. At 420°C, R-PAN loses another 18.5 wt %, and this is followed by carbonization, which gives the carbonized residue of about 27 wt %. In this stage, no substantial thermal effects are observed except certain change in the heat capacity caused by carbonization.

Curves in Fig. 1a characterize the kinetics of the weight loss of PAN containing various amounts of fullerene. As seen, both the initial weight loss below 261°C and the loss in the first stage of thermal degradation of the R-PAN structure are virtually the same as for R-PAN without fullerene. Thus, the mechanisms of initiation of the polymer thermal degradation related to the R-PAN structure are not radical for which fullerene could be an inhibitor. As for the subsequent stage of the R-PAN carbonization, fullerene starts to gradually escape from the R-PAN carbonizate within the 400–600°C range; the process becomes especially noticeable at 600–750°C. However, the amount of carbonized residue obtained at 1000°C indicates that the part of fullerene remains in the carbonizate; this amount does not correspond to its content in the initial mixture.

Fig. 1b shows that the samples containing 20–30% fullerene exhibit the exothermic effects in the 266–268°C range, almost equal in the temperature and

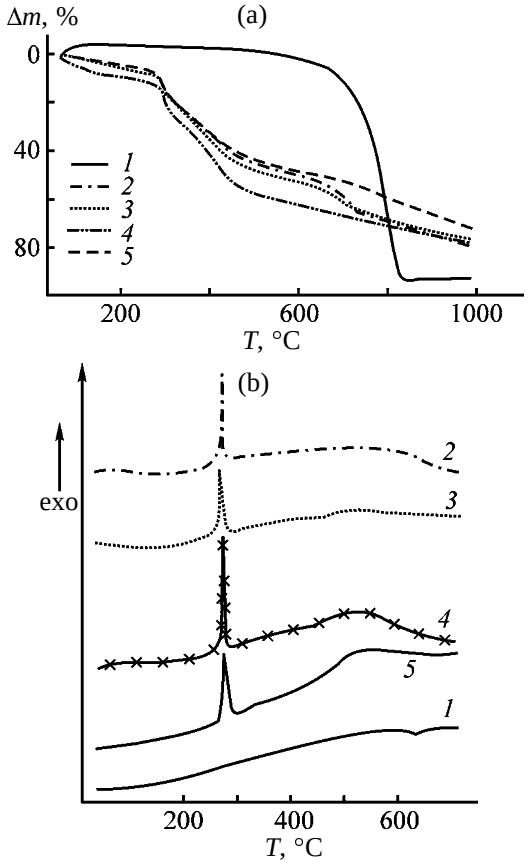

Fig. 1. (a) TG and (b) DSC curves of R-PAN mixtures with fullerene. (Δ*m*) Weight loss and (*T*) temperature; the same for Figs. 2 and 3. Fullerene content (%): (*1*) 100, (*2*) 30, (*3*) 20, (*4*) 0.7, and (*5*) 0.

enthalpy, and their heat capacities become similar in the carbonization region.

It follows from Fig. 2 that, under similar conditions, anionic PAN (A-PAN) is more sensitive to the presence of fullerene.

(1) In the stage of removal of the adsorbed solvent before the onset of cyclization, almost twofold decrease in the weight loss is observed.

(2) Although in the first stage of cyclization the thermal degradation of A-PAN is kinetically similar to that for R-PAN, the quantitative parameters for samples with various fullerene contents differ. For instance, the temperatures of the onset of the first stage of intense cyclization–degradation vary in the 30°C range, and the weight loss recalculated to pure A-PAN (14 wt %) varies from 9 to 20 wt %. Approximately the same difference is observed in the second stage of the thermal degradation at 300–450°C.

(3) Similarly to R-PAN in the carbonization stage, a part of fullerene remains in the carbonizate structure,

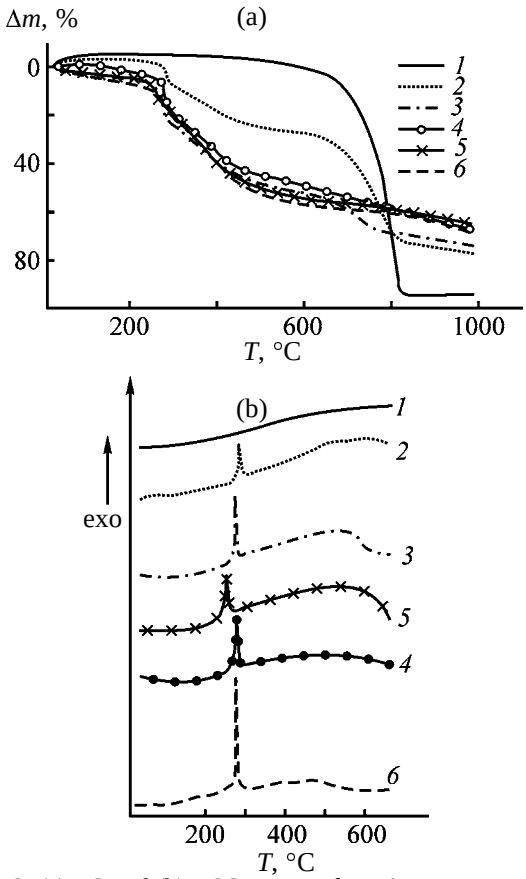

Fig. 2. (a) TG and (b) DSC curves of R-PAN mixtures with fullerene. Fullerene content (%): (*1*) 100, (*2*) 50, (*3*) 30, (*4*) 10, (*5*) 0.7, covalently bound, and (*6*) 0.

but the quantitative ratios of the carbonized residues depend on the amount of the introduced fullerene in a more complicated manner, which is especially clear at the A-PAN : fullerene ratio of 50 : 50. Such a sample is characterized by the lowest content of adsorbed solvent and the highest temperature of the initial stage of weight loss. In addition, in spite of noticeable acceleration of the weight loss at the temperatures higher than 700°C caused by fullerene sublimation, the carbonized residue (about of 25%) at 1000°C contains approximately half of fullerene.

(4) The DSC data show differences in the heat release accompanying the first stage of cyclization. For pure A-PAN, this stage is characterized by a very narrow and large in amplitude exothermic effect. Small amounts of fullerene draw apart the temperature boundaries of this peak and shift its maximum to lower temperatures. Increase in the fullerene content to 30–50% again narrows the exothermic peak and somewhat elevates the temperature of its maximum.

In view of the above differences in the kinetics of A-PAN thermochemical transformations in an inert atmosphere in the presence of fullerene as compared to R-PAN, the behavior of A-PAN containing covalently bound fullerene under the same conditions is of interest [9]. In accordance with TG and DSC data, the release of volatile products in the first stage of the thermal degradation starts at a lower temperature, 239°C with a maximum at 249°C. In this stage, the release of thermal degradation products decreases to 6.5 wt %. In the subsequent stages of carbonization, the content of the carbonized residue exceeds by 5–10% this value for samples with unbound fullerene. These differences show that fullerene covalently bound with A-PAN definitely affects the kinetics of PAN carbonization.

The features of A-PAN carbonization in the presence of substantial amounts of fullerene and their comparison with the behavior of A-PAN, in which even small amounts of fullerene are covalently bound with the macromolecule, allows the conclusion that there is a definite critical concentration of C_{60} below which the reagents do not react thermochemically. Probably, in an inert atmosphere and at small masses of the reactants, the reaction is kinetically controlled, which is confirmed by small difference in the heat effects in the majority of the experiments. The similar trend was found earlier, when the thermal effects of PAN fiber transformation were studied in relation to various kinetic and diffusion factors [10, 16].

Taking this into account, we performed a series of experiments with tenfold larger portions of PAN at heating in the self-generated atmosphere. The TG and DTA curves for certain A-PAN samples with various fullerene contents are shown in Fig. 3. In spite of general similarity of the thermochemical degradation pattern in an inert atmosphere, sample weights, and heat treatment conditions, which were similar to those of the industrial process, additions of fullerene noticeably affected the quantitative characteristics (temperatures of thermal effects and weight loss). The weight losses in the stage of PAN cyclization in the 270–350°C range differ substantially. On the one hand, the relative amount of volatile products in the initial stage of the A-PAN thermal degradation increases; on the other hand, fullerene strongly affects the kinetics of the release of these products. This is confirmed by an increase in the exothermic effects of the initial stage and shift of their maxima to higher temperatures. As above, the thermal effect of decomposition of A-PAN with covalently bound fullerene is particularly intense, which confirms noticeable role of the chemical bond of fullerene with PAN in its thermo-

chemical transformations. The main difference suggesting active participation of fullerene in A-PAN carbonization is noticeable increase in the amount of the carbonized residue at 1000°C: to almost 60%. Apparently, an increase in the sample weight favors carbonization at temperatures higher than 500°C under conditions of diffusion control. This facilitates cross-linking owing to suppressed elimination of volatile products of thermal degradation by the scheme of the framework microreactor.

The composition and state of the surrounding atmosphere is a substantial parameter in cross-linking of the samples studied. Under conditions of thermal transformations of PAN with fullerene in the self-generated atmosphere, a number of aggressive products exist in the reaction mixture, whose reactions with fullerene lead to formation of numerous bonds, similarly to coke synthesis, and formation of carbonizates in high yield.

To confirm this assumption, we performed a series of experiments on vacuum thermolysis of the samples on a TVA device, which allows differential recording of the pressure variation and of the amount of the carbonized product. Figure 4 shows the TVA curves for mixtures of A-PAN with fullerene, similar to those in Fig. 3. As seen, release of volatile thermal degradation products in the stage of PAN cyclization starts at 130–190°C. The reaction, as under the other conditions of heating, is avalanche-like with a sharp maximum at 160–210°C. The samples lose up to 50–60% of their weight at 230°C. Then, above 350°C, further release of volatile products is observed, which is complete at 530°C (the curve with a maximum), and from 750 to 900°C the next carbonization stage proceeds. The effect of fullerene on A-PAN vacuum thermolysis is appreciable: fullerene shifts the onset of the first stage of gas liberation by 30–50°C to lower temperatures. However, the total amount of the carbonized residue at 900°C does not exceed 30% and does not differ from the same value for A-PAN without fullerene. Thus, the use of the heat treatment method ensuring fast removal of reactive products of the stepwise degradation of PAN sharply shifts carbonization to the kinetic region. The prevalence of degradation over cross-linking leads to complete decomposition of the product in accordance with the previously noted features of this process [17].

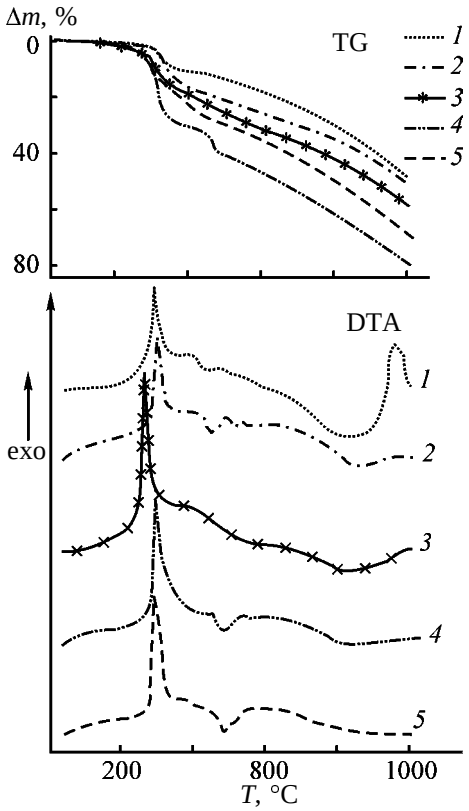

Fig. 3. TG and DSC curves of A-PAN mixtures with fullerene. Fullerene content (%): (*1*) 50, (*2*) 30, (*3*) 0.7 (covalently bound), (*4*) 0.5, and (*5*) 0.

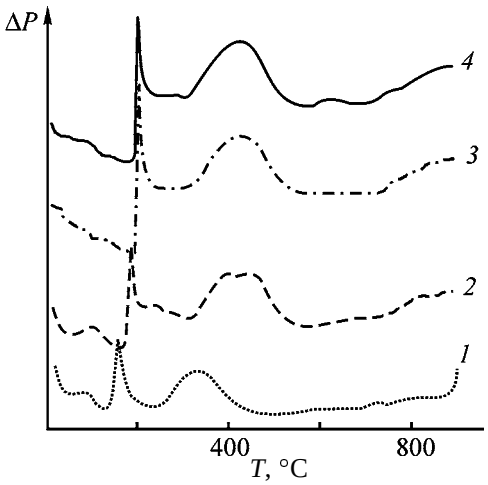

Fig. 4. TVA curves of A-PAN mixtures with fullerene. (Δ*P*) Pressure change and (*T*) temperature. Fullerene content (%): (*1*) 50, (*2*) 0.7 (covalently bound), (*3*) 0.5, and (*4*) 0.

CONCLUSIONS

(1) It was shown by thermal analysis that, in the course of thermal treatment of mixtures of polyacrylonitrile prepared by anionic mechanism with fullerene, they react with formation of carbonizate in a yield to 60%.

(2) The carbonization parameters depend on conditions of thermal treatment and the amount of the reac-

tion mixture. The yield of the carbonization product is appreciable when the reaction is diffusion-controlled.

ACKNOWLEDGMENTS

The authors are indebted to E.M. Kulikov for assistance in the experimental part of work.

REFERENCES

1. Henrici-Olive, G. and Olive, S., *Adv. Polym. Sci*., 1979, vol. 32, pp. 125–152.
2. Varshavskii, V.Ya., *Vysokomol. Soedin., Ser. A*, 1983, vol. 25, pp. 823–830.
3. Kanovich, M.M. and Rudenko, A.P., *Khim. Volokna*, 1982, no. 3, pp. 19–21.
4. Konkin, A.A., *Uglerodnye i drugie zharostoikie voloknistye materialy* (Carbon and Other Heat-Resistant Fibrous Materials), Moscow: Khimiya, 1974.
5. Pozdnjakov, A.O., Pozdnjakov, O.F., Redkov, B.P., *et al*., *Tech. Phys. Lett.*, 1996, vol. 22, no. 9, pp. 86–87.
6. Shibaev, L.A., Antonova, T.A., Vinogradova, L.V., *et al*., *Pis'ma Zh. Tehn. Fiz*., 1997, vol. 23, no. 18, pp. 19–21.
7. Mokeev, M.V., Vinogradova, L.V., Zgonnik,V.N., and Gribanov, A.V., Abstracts of Papers, *Int. Symp. "New Approaches in Polymer Synthesis and Macromolecular Formation,"* St. Petersburg, June 16–20, 1997, abstract P0-002.
8. Shibaev, L.A., Egorov, E.M., Zgonnik, V.N., *et al*., *Vysokomol. Soedin., Ser. A*, 2001, vol. 43, no. 2, pp. 211–216.
9. Novoselova, A.V., Vinogradova, L.V., and Zgonnik, V.N., *Vysokomol. Soedin., Ser. A*, 2001, vol. 43, no. 1, pp. 1–6.
10. Sazanov, Yu.N., Shirokov, N.A., and Goltsin, B.E., *Thermochim. Acta*, 1978, vol. 24, pp. 81–88.
11. Erusalimskii, B.L. and Novoselova, A.V., *Faserforsch. Textiltechn.*, 1975, vol. 26, pp. 293–297.
12. Sazanov, Yu.N. and Sysoev, V.A., *Eur. Polym. J*., 1974, vol. 10, pp. 867–869.
13. Gribanov, A.V. and Sazanov, Yu.N., *Zh. Prikl. Khim*., 2000, vol. 73, no. 3, pp. 465–469.
14. Takata, T., Ishii, H., Nishiyama, Y., and Tamiyama, M., *Kobunshi Kogaku*, 1961, vol. 18, no. 192, pp. 236–239.
15. Takata, T., Hizoi, I., and Tamiyama, M., *J. Polym. Sci., Part A*, 1964, vol. 2, pp. 1567–1585.
16. Sazanov, Yu.N., Shirokov, N.A., and Goltsin, B.E., *Thermochim. Acta*, 1979, vol. 32, pp. 73–79.
17. Zil'berman, E.N., *Usp. Khim*., 1986, vol. 55, no. 1, pp. 62–78.

Russian Journal of Applied Chemistry, Vol. 76, No. 3, 2003, pp. 457–459. Translated from Zhurnal Prikladnoi Khimii, Vol. 76, No. 3, 2003, pp. 472–474.

MACROMOLECULAR CHEMISTRY AND POLYMERIC MATERIALS

Fullerene C_{60} Aggregates in Polymethyl Methacrylate Films

B. M. Ginzburg, A. S. Smirnov, S. K. Filatov, L. A. Shibaev, E. Yu. Melenevskaya, A. V. Novoselova, and A. A. Shepelevskii

Institute of Machine Science, Russian Academy of Sciences, St. Petersburg, Russia
St. Petersburg State University, St. Petersburg, Russia
Institute of Macromolecular Compounds, Russian Academy of Sciences, St. Petersburg, Russia

Received July 31, 2002

Abstract—The structure of aggregates of fullerene C_{60} introduced into films of radical polymethyl methacrylate in the stage of solution preparation was studied by wide-angle X-ray diffraction.

Previously, we have studied the effect of small additions of fullerene C_{60} on thermal degradation of polymers [1–3]. Preparation of fullerene–polymer compositions can be accompanied by microphase segregation with formation of fullerene aggregates in the polymer matrix. In turn, the structure of such aggregates can affect the composition properties [3]. In this work, we studied the structure of fullerene C_{60} aggregates in a film of atactic polymethyl methacrylate (PMMA) prepared by radical polymerization.

EXPERIMENTAL

Atactic PMMA with the molecular weight M = 85000 was dissolved in *o*-dichlorobenzene to obtain 10 wt % concentration. The same solution of fullerene C_{60} was also prepared. Then, these solutions were mixed in proportions required to obtain the fullerene concentration in the PMMA film of 1 and 10%. Films were prepared by casting on a cover glass. The solvent was evaporated from the PMMA and PMMA + fullerene solutions at room temperature in air. The film thickness was about 70 μm.

A study with a MIN-8 polarization optical microscope showed that the films were transparent, i.e., they were homogeneous on the optical level (<0.5 μm). Wide-angle X-ray diffraction patterns of films was measured on a DRON-2.0 diffractometer with graphite crystal monochromator in CuK_α irradiation.

The powder pattern of fullerene C_{60} powder on a glass support is shown in Fig. 1. The reflections are indexed in the face-centered cubic crystal lattice of fullerene C_{60} [4]. The fullerene reflections are narrow and intense, so that the scattering from the support can be neglected. The relative reflection intensities and the corresponding interplanar spacings (with the error of 0.01–0.02 Å) are in good agreement with the reference data [4].

The average crystallite dimensions L_{hkl} in [*hkl*] direction were calculated by the Scherrer formula [5] using measured widths of the reflection profiles. The minimal crystallite size (neglecting the effects of the lattice distortion and primary beam width) calculated from the width of a series of the most intense reflections is 300–400 Å.

Fullerene aggregates in the PMMA matrix show no similar ordering. The diffraction patterns of PMMA films with fullerene on a glass support are shown in Fig. 2. To take into account the scattering from the support, the scattering pattern was subtracted from the difraction patterns. The difference patterns allowed refinement of the position and shape of diffuse maxima.

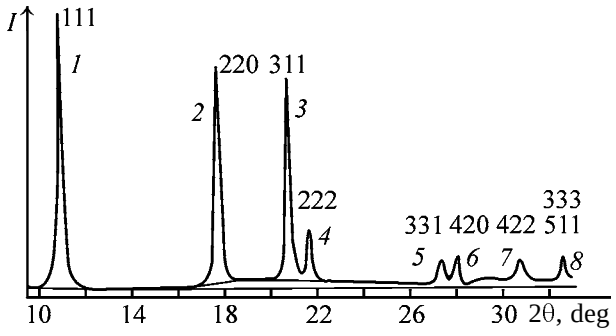

Fig. 1. Wide-angle powder pattern of C_{60} fullerene powder: (*I*) intensity and (2θ) Bragg angle; the same for Fig. 2. Indices of the face-centered crystal lattice are indicated. Bragg angle corresponding to peak maximum, deg: (*1*) 10.83, (*2*) 17.77, (*3*) 20.91, (*4*) 21.82, (*5*) 27.63, (*6*) 28.30, (*7*) 31.01, and (*8*) 32.94.

1070-4272/03/7603-0457$25.00

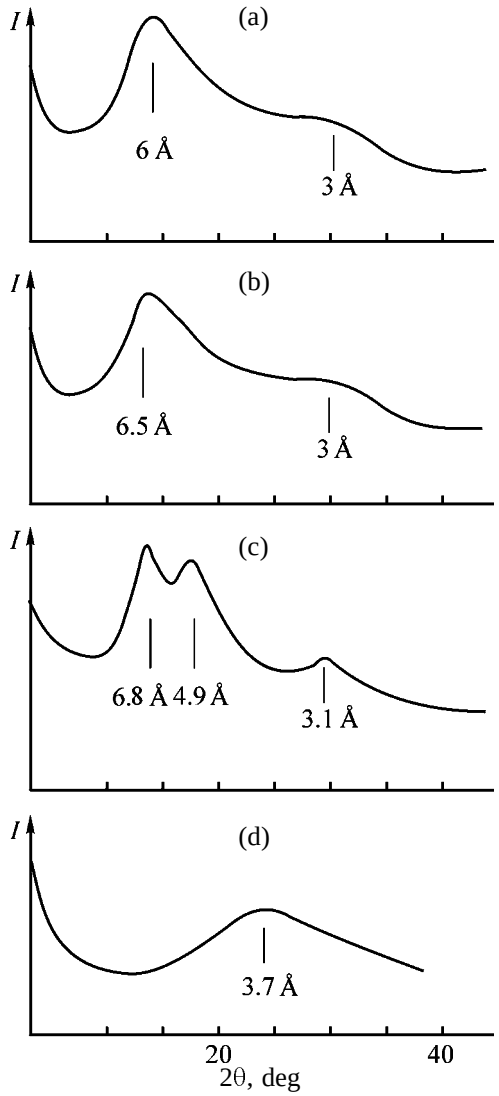

Fig. 2. Wide-angle diffraction patterns of films on a glass support: (a) pure PMMA, (b) PMMA + 1% C_{60}, (c) PMMA + 10% C_{60}, and (d) glass support.

Comparison of the experimental data for C_{60} aggregates in the PMMA matrix and crystallites of pure C_{60} fullerene

Sample	Position of reflection* $2\theta_m$, deg	Interplanar spacing d, Å
C_{60} aggregates in PMMA	13	6.8
	18	4.9
Face-centered cubic lattice of C_{60}, reflection:		
200	12.47	7.09
220	17.77	5.01

* CuK_α radiation.

In diffraction patterns of pure PMMA, two orders of the amorphous halo correspond to intermolecular distance $d \sim 6$ Å. The C_{60} introduced into the PMMA matrix does not form a strictly ordered crystal lattice. However, microphase segregation occurs in the system, i.e., weakly ordered C_{60} aggregates are formed. In films with 1% fullerene, its weak aggregation is due either to the small amount of fullerene aggregates or to weak C_{60} aggregation, when the most part of the fullerene is dispersed to separate molecules.

The data for samples containing 10% fullerene allow more definite conclusions. The interplanar spacings corresponding to two diffuse maxima were estimated as 6.8 and 4.9 Å. The shortest interplanar spacings calculated for the C_{60} crystal lattice are listed in the table, and only the second one (4.9 Å) is manifested in the experimental powder pattern as a strong 220 reflection, while the interplanar spacing of 6.8 Å is not manifested in the C_{60} powder pattern (Fig. 1), in spite of the conformity with the calculations for the C_{60} crystal lattice. It should be noted that the calculated reflections 200 and 220 for the C_{60} crystal lattice are the most intense [4]. The corresponding crystallographic planes determine the structure and are the main in the nucleation of the C_{60} crystal lattice. However, the PMMA matrix prevents further ordering, "freezing" the nucleus structure.

The dimensions of the coherent scattering regions for C_{60} aggregates in the PMMA matrix, estimated by the Scherrer formula at 15–25 Å, are evidently underestimated. They were obtained without taking into account distortions, which are obviously very strong. In addition, to reveal the reflection, the repetition of at least three or four motives (4–5 planes) is required. The interplanar spacing in the C_{60} crystal lattice in the [110] direction is 10 Å. Taking into account that

$$L_{hkl} = \bar{N} d_{hkl}, \quad (1)$$

where $\bar{N}$ is the average number of planes in the L_{hkl} distance and d_{hkl} is the interplanar spacing, we can suggest that the lower limit of the real size of the C_{60} nucleus is 40–50 Å. In each plane (110) of the unit cell, six C_{60} molecules are arranged (Fig. 3). Hence, only in the [110] direction the nucleus contains 24–30 C_{60} molecules. Since for C_{60} aggregates the second reflection (close to reflection 100) is observed, in the [100] direction the nucleus contains also at least 4–5 planes. Hence, the nucleus volume corresponds to 100 C_{60} molecules.

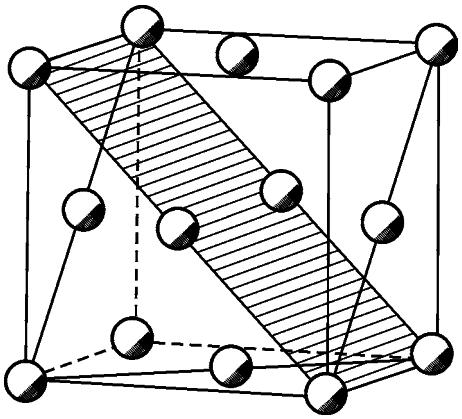

Fig. 3. Scheme of the unit cell of face-centered crystal lattice of C_{60} fullerene. The (100) plane is cross-hatched.

Thus, when the method for preparing PMMA films from common solutions with fullerene C_{60} is used, the microphase segregation occurs, and 40–50-Å C_{60} aggregates with imperfect mesomorphous ordering, containing about 100 fullerene molecules, are formed.

ACKNOWLEDGMENTS

The work was done in the framework of the program "Fullerenes and Atomic Clusters" (project "Controlled Synthesis of Fullerenes and Other Atomic Clusters").

REFERENCES

1. Ginzburg, B.M., Pozdnyakov, A.O., Zgonnik, V.N., *et al*., *Pis'ma Zh. Tekh. Fiz*., 1996, vol. 22, no. 4, pp. 73–77.
2. Shibaev, L.A., Antonova, T.A., Vinogradova, L.V., *et al*., *Zh. Prikl. Khim*., 1998, vol. 71, no. 5, pp. 835–841.
3. Ginzburg, B.M., Shibaev, L.A., and Ugolkov, V.L., *Zh. Prikl. Khim*., 2001, vol. 74, no. 8, pp. 1293–1302.
4. Korolev, Yu.M., Kozlov, V.V., Polikarpov, V.M., and Antipov, E.M., *Vysokomol. Soedin., Ser. A*, 2001, vol. 43, no. 11, pp. 1933–1940.
5. Kitaigorodskii, A.I., *Rentgenostrukturnyi analiz melkokristallicheskikh i amorfnykh tel* (X-ray Diffraction Analysis of Finely Crystalline and Amorphous Substances), Moscow: GITTL, 1952.

Russian Journal of Applied Chemistry, Vol. 76, No. 3, 2003, pp. 460–463. Translated from Zhurnal Prikladnoi Khimii, Vol. 76, No. 3, 2003, pp. 475–478.

MACROMOLECULAR CHEMISTRY AND POLYMERIC MATERIALS

Kinetics of Radical Polymerization of a Monomer Derived from Monoethanolamine Vinyl Ether and 1,4-Benzoquinone: A Polarographic Study

E. E. Ergozhin, B. A. Mukhitdinova, S. A. Shoinbekova, A. I. Nikitina, and B. M. Nuranbaeva

Bekturov Institute of Chemical Sciences, Ministry of Education and Science of the Kazakhstan Republic, Almaty, Kazakhstan

Received February 27, 2002

Abstract—Radical polymerization of a disubstituted monomer derived from monoethanolamine vinyl ether and 1,4-benzoquinone was studied by classical polarography. The optimal conditions for the synthesis of the redox polymer were found. The polymerization rate constants, preexponential term in the Arrhenius equation, and activation energy were calculated.

The versatility of redox and ion-exchange polymers, on the one hand, and the limited range of monomers suitable for their synthesis, on the other hand, require more intense studies in this field, with the aim to develop novel sorption processes [1, 2]. The problem of preparing new redox monomers from cheap and readily available precursors remains very urgent, since the available redox resins do not always meet the existing requirements. Among promising precursors are quinones, which widely occur in the nature and are fairly comprehensively studied. Previously [1–5] we described redox polymers based on various quinones and prepared by chemical modification of polystyrene and styrene–diene copolymers with quinones, di- and trihydroxybenzenes, and their halo derivatives.

With the aim to extend the assortment of redox resins and simplify their preparation, we developed a procedure for single-stage synthesis of new unsaturated monomers [6] from readily available and cheap monoethanolamine vinyl ether (MEAVE) and various quinones. This reduced the cost of redox ion exchangers and made their production profitable; the capability for reversible oxidation–reduction allows repeated use of these resins, which is important for commercial applications.

One of reliable, highly sensitive, and quick methods for analysis of macromolecular compounds is polarography. It is widely used in kinetic studies of polymerization of vinyl monomers [7–12]. It is known that the principal characteristic of the reactivity of unsaturated monomers is the polymerization rate constant. However, only in a few papers [12–14] this quantity was determined polarographically. The relationship between the rate constants of radical polymerization of monomers and the potentials of the half-waves of their reduction on a mercury dropping electrode were established in [13].

In this work we studied by classical polarography the kinetics of radical polymerization of a disubstituted monomer derived from MEAVE and 1,4-benzoquinone (MEAVE–1,4-BQ), calculated the polymerization rate constants at various temperatures, the activation energy, and the preexponential term in the Arrhenius equation.

EXPERIMENTAL

Monoethanolamine vinyl ether was dried over freshly distilled K_2CO_3 and distilled from calcium hydride; bp 114°C, n_D^{20} 1.4382.

1,4-Benzoquinone (pure grade) was recrystallized from methanol; mp 116°C after purification.

Azobis(isobutyronitrile) (AIBN) was recrystallized from absolute methanol; mp 102–103°C.

The monomer, 2,5-bis[*N*-(2-vinyloxy)ethyl]amino-1,4-benzoquinone $C_{14}H_{18}N_2O_4$, was prepared as follows. MEAVE was added in 6 : 1 ratio to a solution of 1,4-BQ in 1,4-dioxane (28.2 g l^{-1}, or 0.26 M) at 25°C with continuous stirring. After 15 min, distilled

1070-4272/03/7603-0460$25.00

Table 1. Elemental composition and some physicochemical properties of the monomer derived from MEAVE and 1,4-BQ and of its polymer

Compound	Calculated, %/Found, %				Yield, %	T_m, °C	[η],* dl g^{-1}	ρ,** g cm^{-3}	SEC**	ROC***
	C	H	N	O					mg-equiv g^{-1}	
Monomer	60.43/60.47	6.47/6.58	10.07/11.08	23.03/12.87	62.36	172–175	–	0.4442	–	–
Polymer	60.43/60.49	6.47/6.49	10.07/11.00	23.03/22.02	67.80	216–218	0.43	1.0714	8.7	4.2

* The intrinsic viscosity was determined at 25°C in DMF.
** The density and static exchange capacity were determined according to [15].
*** The redox capacity was determined according to [1].

water was added, the precipitate was filtered off, reprecipitated, and dried first in air and then in a vacuum oven at 40–50°C to constant weight. The chemical composition and some physicochemical properties of the MEAVE–1,4-BQ are listed in Table 1.

Polymerization of MEAVE–1,4-BQ was performed as follows. AIBN, 1–7 wt % relative to the monomer, was added into an ampule containing a solution of the monomer in dimethylformamide (DMF; 0–44 g l^{-1}). The ampule was purged with argon, sealed, thoroughly shaken, and placed in a thermostat heated to 55–75°C. After reaction completion, the ampule was quickly transferred in a beaker filled with ice, cooled, and opened. The precipitate was filtered off and dried first in air at 20–25°C and then in a vacuum oven at 40–50°C. The polymer yield was 50.0–67.8%. The optimal conditions are as follows: monomer concentration in DMF 25 g l^{-1} (0.0899 M); AIBN amount 5 wt % relative to the monomer (1.25 g l^{-1}, or 0.762 × 10^{-2} M); 68°C; 120 min. The main physicochemical characteristics of the polymer are given in Table 1.

The IR spectra of the new quinoid derivative of MEAVE contains the following absorption bands, cm^{-1}: NH stretching 3256; NH bending 1552; C=O stretching 1660; C=C stretching 1568, 1440; =C–N stretching 1328; and C–O–C stretching 1200. The absorption band of quinoid rings in the spectrum of the polymer becomes broader, which is typical of polymeric quinones, and these bands are shifted toward higher frequencies to 1680 cm^{-1}. The bands at about 3040 cm^{-1} characteristic of the vinyl group disappear, whereas the bands at 2936 and 1496 cm^{-1} belonging to the –CH_2– groups grow in intensity.

The polarograms were taken in a temperature-controlled cell at 25±0.5°C with a PU-1 polarograph equipped with a mercury dropping electrode having the open-curcuit capillary characteristic $m^{2/3}t^{1/6}$ = 4.38 mg$^{2/3}$ s$^{1/2}$. As reference electrode was used saturated calomel electrode. Prior to polarographic measurements, the solutions were purged with argon to remove oxygen. The half-wave potentials were determined by graphic solution of the wave equation in the coordinates $\log i/(I - i)$ vs. E, where i is the current at voltage E and I is the diffusion current [16, 17].

Experiments on studying the kinetics of radical polymerization of the new disubstituted redox monomer based on MEAVE and 1,4-BQ, 2,5-bis[*N*-(2-vinyloxy)ethyl]amino-1,4-benzoquinone (MEAVE–1,4-BQ), were performed as described above; after a certain time, the ampules were successively opened, and samples were taken for polarographic analysis. The samples were diluted with DMF to stop the reaction. Polarographic measurements were performed in 25% DMF, with phosphate buffer solution (pH 7.4) as supporting electrolyte. The conversion was judged from the amount of the unchanged monomer. Experiments revealed a linear relationship between the heights of the polarographic waves and the monomer concentration in the solution. The monomer content was determined from the calibration plot.

Analysis of the reaction mixture furnished information on the degree of conversion and allowed construction of the polymerization curves (Fig. 1).

To calculate the overall polymerization rate constants, we determined the reaction order. The logarithmic dependence of the polymerization rate on the initiator concentration (Fig. 2) and the linear depen-

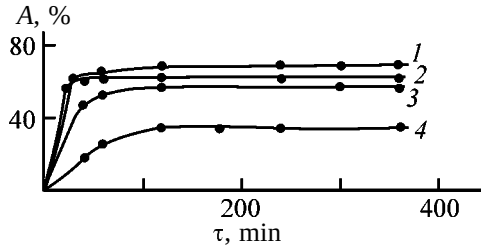

Fig. 1. Kinetic curves of MEAVE–1,4-BQ polymerization: (*A*) polymer yield and (τ) time. Temperature, °C: (*1*) 68, (*2*) 75, (*3*) 62, and (*4*) 55.

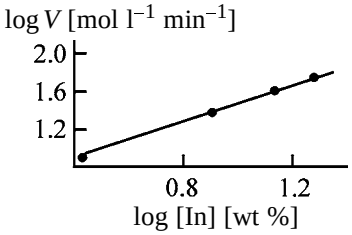

Fig. 2. Logarithmic plot of the polymerization rate, $\log V$, vs. initiator concentration $\log[\mathrm{In}]$.

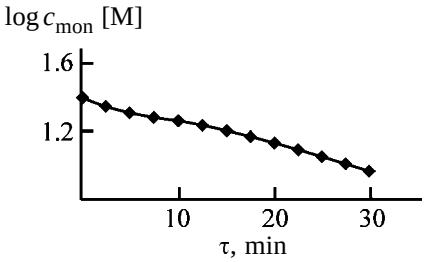

Fig. 3. Plot of $\log c_{mon}$ vs. time τ of MEAVE–1,4-BQ polymerization.

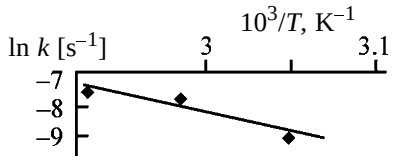

Fig. 4. Logarithm of the rate constant $\ln k$ of MEAVE–1,4-BQ polymerization as a function of temperature T.

dence of $\log c$ of the monomer on the reaction time (Fig. 3) show that the reaction is first-order with respect to the initiator (n = 0.80) and monomer (m = 0.86) and is described by relationships characteristic of first-order reactions.

The rate constants of MEAVE–1,4-BQ polymerization calculated by the first-order kinetic equation [18, 19] and the preexponential terms k_0 in the Arrhenius equation $k = k_0 e^{-E/RT}$ are listed in Table 2.

The plot of $\ln k$ vs. $1/T$ is a straight line; from its slope, we determined the activation energy of the process, $E = 4.57 \left|\tan\alpha\right| \xi$, where α is the slope of the straight line and ξ is the scale ratio of the abscissa and ordinate (Fig. 4).

Table 2. Kinetic characteristics of polymerization of the monomer based on MEAVE–1,4-BQ

T, K	$10^3/T$, K^{-1}	$k \times 10^4$, s^{-1}	$\ln k$	$k_0 \times 10^{15}$, s^{-1}
328	3.05	1.22	–9.015	1.379
335	2.99	3.72	–7.898	1.681
341	2.93	5.38	–7.530	1.141
348	2.87	5.48	–7.508	0.498

In the chosen scale, $\tan\alpha = \tan 32° = 0.6249$, $\xi = 10^3$, and activation energy $E = 4.571 \times 0.6249 = 2.86$ kcal mol^{-1} (11.95 kJ mol^{-1}).

The synthesized disubstituted monomer derived from MEAVE and 1,4-BQ readily polymerizes, in contrast to the starting MEAVE, which, as reported in [20, 21], does not form homopolymers in the presence of radical initiators. Apparently, this is due to the reactivity of the radical, which is the decisive factor in homopolymerization. The higher the electron density localized on the double bond, the more reactive is the monomer [7, 10]. The polarographic parameters are also determined by the electron density localized on the double bond: the higher the electron density, the more negative is the half-wave potential of the reduction of the double bond, i.e., the more negative the potential, the readier is the polymerization, which is indeed the case with MEAVE–1,4-BQ.

CONCLUSIONS

(1) Radical polymerization of the new disubstituted derivative based on monoethanolamine vinyl ether and 1,4-benzoquinone was studied, and optimal conditions were found for formation of the polymeric redox resin.

(2) The kinetics of radical homopolymerization was studied, and the rate constants, activation energy, and preexponential term in the Arrhenius equation were calculated.

REFERENCES

1. Ergozhin, E.E. and Mukhitdinova, B.A., *Redoksionity* (Redox Ion Exchangers), Alma-Ata: Nauka, 1983.
2. Ergozhin, E.E. and Mukhitdinova, B.A., *Okislitel'no-vosstanovitel'nye ionoobmenniki* (Redox Ion Exchangers), Almaty: Redaktsionno-Izd. Otd., Vyssh. Attest. Komissiya Resp. Kazakhstan, 2000.
3. Ergozhin, E.E., Mukhitdinova, B.A., Bakirova, R.Kh., *et al.*, *React. Polym.*, 1991/1992, vol. 16, pp. 321–334.
4. Ergozhin, E.E., Mukhitdinova, B.A., and Dusenbenova, Z.K., *React. Polym.*, 1992, vol. 18, pp. 15–23.
5. Ergozhin, E.E., Mukhitdinova, B.A., Dusenbenova, Z.K., *et al.*, *Polymer*, 1993, vol. 34, no. 14, pp. 3096–3106.
6. Shoinbekova, S.A., New Nitrogen-Containing Redox Monomers and Polymers Based on Them, *Cand. Sci. Dissertation*, Almaty, 1999.
7. Bezuglyi, V.D., *Polyarografiya v khimii i tekhnologii polimerov* (Polarography in the Polymer Chemistry and Technology), Moscow: Khimiya, 1968.

8. Shur, A.M., Filimonov, B.F., and Filimonova, M.M., *Vysokomol. Soedin.*, 1961, vol. 3, no. 11, pp. 1661–1663.
9. Bobrova, M.N. and Matveeva, A.N., *Zh. Obshch. Khim.*, 1956, vol. 26, no. 7, pp. 1857–1860.
10. Bezuglyi, V.D. and Dmitrieva, V.N., *Zh. Prikl. Khim.*, 1957, vol. 30, no. 5, pp. 744–750.
11. Bezuglyi, V.D., Alekseeva, T.A., and Dmitrievskaya, L.I., *Vysokomol. Soedin., Ser. A*, 1967, vol. 7, no. 5, pp. 1185–1189.
12. Ergozhin, E.E., Mukhitdinova, B.A., Shoinbekova, S.A., *et al.*, *Zh. Prikl. Khim.*, 2001, vol. 74, no. 11, pp. 1847–1849.
13. Alekseeva, T.A., Bezuglyi, V.D., Dmitrieva, V.N., *et al.*, *Vysokomol. Soedin.*, 1963, vol. 5, no. 9, pp. 1382–1387.
14. Bezuglyi, V.D., Alekseeva, T.A., Dmitrievskaya, L.I., *et al.*, *Vysokomol. Soedin.*, 1964, vol. 6, no. 1, pp. 125–129.
15. Toroptseva, A.M., Belogorodskaya, K.V., and Bondarenko, V.M., *Praktikum po khimii i tekhnologii vysokomolekulyarnykh soedinenii* (Practical Course of Chemistry and Technology of Macromolecular Compounds), Leningrad: Khimiya, 1972.
16. Mairanovskii, S.G., Stradyn', Ya.P., and Bezuglyi, V.D., *Polyarografiya v organicheskoi khimii* (Polarography in Organic Chemistry), Leningrad: Khimiya, 1975.
17. Heyrovsky, J. and Kuta, J., *Zaklady polarografie*, Prague: Ceskoslov. Acad. Ved, 1962.
18. Panchenkov, G.M. and Lebedev, V.P., *Khimicheskaya kinetika i kataliz* (Chemical Kinetics and Catalysis), Moscow: Mosk. Gos. Univ., 1961.
19. Emanuel', N.M. and Knorre, D.G., *Kurs khimicheskoi kinetiki* (Course of Chemical Kinetics), Moscow: Vysshaya Shkola, 1974.
20. Shostakovskii, M.F. and Chekulaeva, I.A., *Izv. Akad. Nauk SSSR, Otd. Khim. Nauk*, 1953, no. 2, pp. 368–373.
21. Nurkeeva, Z.S. and Seitov, A.Z., in *Radiatsionnye effekty v geterogennykh sistemakh* (Radiation Effects in Heterogeneous Systems), Alma-Ata: Gylym, 1983, pp. 63–68.

Russian Journal of Applied Chemistry, Vol. 76, No. 3, 2003, pp. 464–467. Translated from Zhurnal Prikladnoi Khimii, Vol. 76, No. 3, 2003, pp. 479–482.

MACROMOLECULAR CHEMISTRY AND POLYMERIC MATERIALS

Influence of Filler on the Pore Structure of Films of Ultra-High-Molecular-Weight Polyethylene Xerogels

P. M. Pakhomov, E. V. Nazarova, T. A. Anan'eva, Yu. N. Mikhailova, and S. D. Khizhnyak

Tver State University, Tver, Russia
St. Petersburg State University of Technology and Design, St. Petersburg, Russia

Received November 13, 2002

Abstract—The pore structure of filled films of xerogels of ultra-high-molecular-weight polyethylene prepared by gel-casting technique was studied by Fourier IR spectroscopy, attenuated total internal reflection spectroscopy, and optical microscopy. The influence of the filler nature, particle shape, and concentration on the pore structure formation of filled xerogels of ultra-high-molecular-weight polyethylene was examined.

Much attention is given today to development of new polymer materials, among which a special place is occupied by composite materials with a set of properties offering wide application prospects. In particular, filled composites with crystallizing polymers as binders came recently into active use. These materials can be prepared by various methods, in particular, gel casting, which enables various fillers to be combined with dilute polymer solutions. It was shown previously that this method is suitable for preparing efficient sorbents for oil products in the form of porous xerogel films of ultra-high-molecular-weight polyethylene (UHMWPE) filled with sorption-active peat [1, 2]. Mercury porometric, IR attenuated total internal reflection (ATIR) spectroscopic, and optical microscopic studies revealed the influence exerted by the hydrophilic dispersed filler (peat) on the nature of the forming pore structure of filled UHMWPE xerogels [3–5].

In this work we studied the pore structure of filled films of UHMWPE xerogels as influenced by the filler nature, particle shape, and concentration. To this end, we utilized IR Fourier and ATIR spectroscopy and optical microscopy.

EXPERIMENTAL

Our study was concerned with films of xerogels of UHMWPE with the average molecular weight of 4.0×10^6 and different contents of the filler. As fillers we used polyacrylonitrile (PAN) fibers (fibril length 2×10^3 μm, average diameter 19 μm) and talc (particle diameter 1 μm), as well as polydisperse ferrocyanide and swollen vermiculite with the particle size varying within 150–1500 and 150–3000 μm, respectively. For our studies we selected ferrocyanide and vermiculite with the particle diameter of 150–250 μm.

The fillers were combined with a 2% UHMWPE solution in paraffin at 160°C [6]. The choice of the solvent was substantiated in [3, 7]. The solution containing 5–80 wt % of fibrous or disperse filler was transferred into gel by cooling on a metal table whose surface temperature was varied from 160 to 20°C at a rate of 1.6 deg min^{-1}. The filled UHMWPE gel films were converted to filled xerogel films by removing the solvent (paraffin) via extraction with heptane in a fixed state in a Soxhlet apparatus at 70–75°C, followed by drying at room temperature.

To determine the bulk and surface porosities of the filled UHMWPE xerogel films, we recorded the IR absorption spectra of the samples on an Equinox-55 IR Fourier spectrometer and the ATIR spectra of the film surfaces on a Specord M80 spectrometer. ATIR elements were KRS-5 plates with the reflection index $n_1 = 2.4$ and the incidence angle of 62°. A combination of the IR absorption and ATIR spectroscopic methods allows separate monitoring of the structural changes occurring in the bulk and on the surface of filled film of UHMWPE xerogel. The porosity (pore concentration) of the xerogel films on the surface and in the bulk of the sample was estimated using the IR absorption band corresponding to the rocking vibrations $r_R(CH_2)$ at 730 cm^{-1} [8, 9]. The porosity of the sample (rel. units) was calculated by the formula

$$\varepsilon = D/d,$$

1070-4272/03/7603-0464$25.00

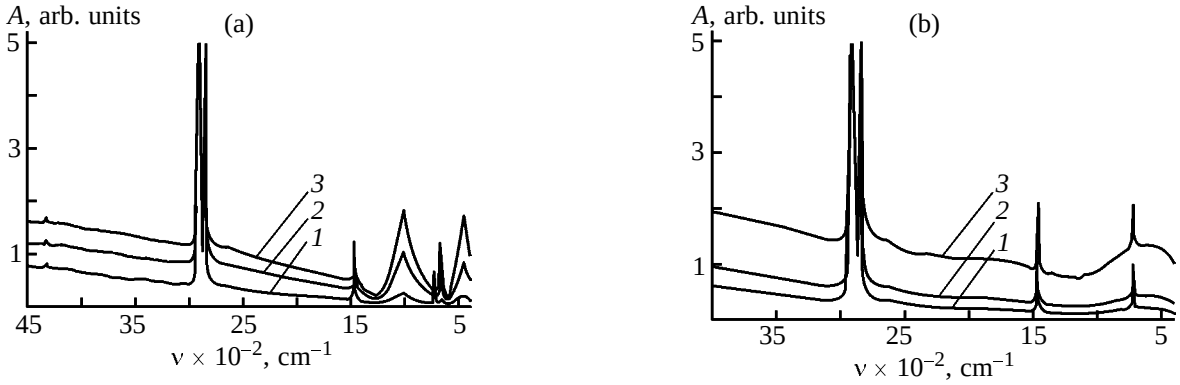

Fig. 1. IR absorption spectra of UHMWPE films filled with (a) talc and (b) PAN fibers with different degrees of filling. (*A*) Absorption and (ν) wave number. Degree of filling, %: (*1*) 10 (talc) and 20 (PAN), (*2*) 30, and (*3*) 50.

where ε is the extinction coefficient, which is a measure of the bulk porosity of the sample; *D*, the optical density at the maximum of the IR absorption band chosen; and *d*, the film thickness.

The surface of the filed films of UHMWPE xerogels was also analyzed by optical microscopy on an Neophot 30 metallographic microscope in the dark field mode with a 500 × magnification. The image was transmitted via the optical channel of the microscope to a video camera and then, via video multiplier, to the PC interface.

Figure 1 presents the IR spectra of the UHMWPE xerogel films filled with talc powder and PAN fibers. It is seen that, with increasing filler concentration, scattering by the filler particles tends to increase (the background of the IR spectrum tends to rise). Also, the absorption bands of the filler itself get more pronounced, especially in the case of the films filled with talc. Indeed, in the IR spectrum of the talc-filled UHMWPE fibers (Fig. 1a), the absorption bands with maxima at 500, 700, and 1000 cm^{-1} corresponding, most probably, to vibrations of the Si–O groups in the talc structure [10] significantly increase in intensity. Figure 2 presents the electron micrographs of films filled with talc and PAN fiber. The filler particles and fibers occurring in the UHMWPE matrix are clearly seen.

Figure 3 presents the extinction coefficient of the IR band at 730 cm^{-1} as a function of the filler type and concentration in the UHMWPE xerogel film. It is seen that the porosity of the xerogel films is strongly influenced by the filler added. For example, samples filled with swollen vermiculite, talc, and PAN fiber exhibit a decrease in the extinction coefficient with increasing filler concentration, which suggests a significant increase in the sample porosity. Similar dependence was also observed for the surface porosity of these samples (Fig. 4b). This can be due to changes in the ultra-high-molecular-weight structure of UHMWPE (spherulite size and shape) whose formation is governed by the crystallization conditions strongly

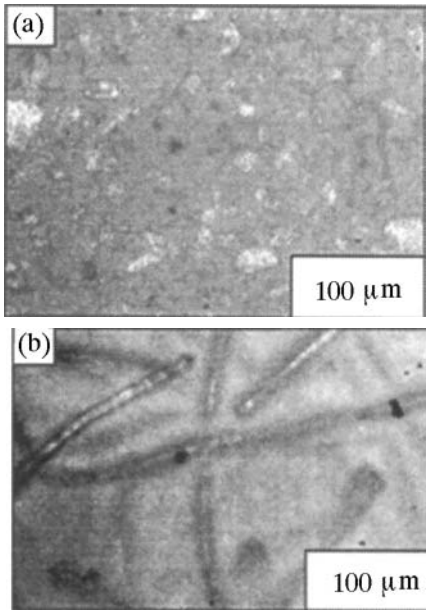

Fig. 2. Electron micrographs of the UHMWPE films with the degree of filling, %, (a) 30 (talc) and (b) 50 (PAN fibers).

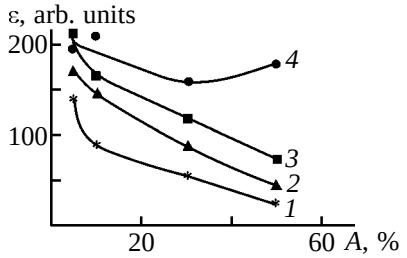

Fig. 3. Extinction coefficient ε of the IR band at 730 cm^{-1} for UHMWPE xerogel films as a function of the degree *A* of filling with (*1*) vermiculite, (*2*) PAN fibers, (*3*) talc, and (*4*) ferrocyanide.

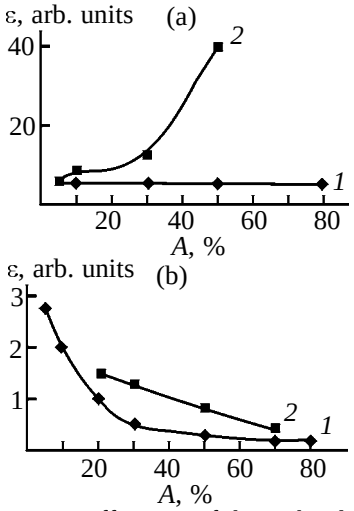

Fig. 4. Extinction coefficient ε of the IR band at 730 cm^{-1} calculated from the ATIR spectra as a function of the degree of filling *A* for UHMWPE xerogel films. Filler: (a): (*1*) talc and (*2*) ferrocyanide; (b): (*1*) vermiculite and (*2*) PAN fiber.

modified by the filler introduced. Low content of the filler favors more rapid and uniform crystallization accompanied by a decrease in the spherulite size and, in some cases, formation of the polymer structure with the highest degree of ordering. The reason for structural ordering is, probably, lower viscosity of the filled UHMWPE solution in crystallization, which is responsible for enhanced mobility of the polymer macromolecules. Further increase of the filler concentration results in formation of an excessive amount of a foreign solid phase. This precludes segmental mobility of the polymer macromolecules near the filler surface, which suppresses crystallization. This is responsible for a larger proportion of a UHMWPE amorphous phase, which yields a looser spherulite structure and, therefore, a filled UHMWPE xerogel film with a higher porosity [11, 12].

Fillers of different nature with differently shaped particles can be differently distributed within the polymer matrix and can differently affect the polymer structure. Probably, specifically these characteristics, rather than the filler concentration, govern the pore structure formation in UHMWPE films. Introduction of ferrocyanide with its spherical particles can favor structure formation, thereby increasing the packing density for the supramolecular UHMWPE structures. Ferrocyanide particles can accumulate in less ordered domains of the polymer and, acting simultaneously as nucleation centers, can exert a structurizing effect on the matrix. As a result, the surface porosity of the UHMWPE films filled with disperse ferrocyanide decreases throughout the concentration range studied, and in the bulk of the sample the porosity remains unchanged at a filler content above 30%.

Introduction of dispersed swollen vermiculite (a highly porous mineral substance) resulted in formation of a more porous structure both in the bulk (Fig. 3) and on the surface (Fig. 4) of the film, as compared to other samples. This is due to a poor wetting power exhibited by the UHMWPE solution with respect to vermiculite, which is responsible for formation of pores acting as stress concentrators and yielding additional defects [13, 14]. Also, the intrinsic pores in the structure of swollen vermiculite will contribute to the total porosity of the filled xerogel films.

A better wetting power of UHMWPE with respect to PAN fibers than to vermiculite, probably, favors formation of a more uniform adsorbed polymer microlayer on the fibrous filler surface. Further adsorption of the polymer molecules increases their packing density, though to a level still sufficient for formation of voids separating the crystallites having anisodiametric structure like spherulite tapes. Crystallites of this type are yielded by polymer crystallization in the presence of fillers with anisometric shape, as is the case of PAN fibers [11, 14]. It should also be taken into account that PAN fibers with their facial ends can also be responsible for formation of a less perfect structure of the UHMWPE films.

With introducing talc into the polymer matrix, the bulk porosity of the UHMWPE films tends to decrease as compared to the samples filled with PAN fibers or vermiculite (Fig. 3). This is probably due to aggregation of its scale-shaped particles at a high content of talc, yielding a continuous network formed by the filler. The continuous network can exert an orienting effect in the interior of the UHMWPE film, which favors formation of a less porous structure in the bulk of the sample than on its surface.

CONCLUSIONS

(1) The bulk and surface porosities of the filled xerogel films of ultra-high-molecular-weight polyethylene were determined by IR absorption and ATIR spectroscopy.

(2) The filler nature, particle shape, and concentration affect the pore structure formation in filled xerogels.

(3) For samples filled with swollen vermiculite, talc, and PAN fibers, by contrast to those filled with ferrocyanide, both the bulk and surface porosites of

filled xerogels of ultra-high-molecular-weight polyethylene tend to significantly increase with the degree of filling increasing from 5 to 80 wt %.

REFERENCES

1. Nazarova, E.V., Volkov, F.V., Anan'eva, T.A., and Choi, Yung-Su, *Fundamentals of Adsorption 7*, Nagasaki (Japan): IAS, IK International, May 20–25, 2002, pp. 848–856.
2. Anan'eva, T.A. and Nazarova, E.V., Abstracts of Papers, *Mezhdunarodnaya konferentsiya "Perspektivnye polimernye kompozitsionnye materialy. Al'ternativnye tekhnologii. Pererabotka. Primenenie. Ekologiya"* (Int. Conf. "Promising Polymer Composite Materials: Alternative Technologies, Processing, Application, Ecology"), Saratov, July 3–5, 2001, p. 362.
3. Nazarova, E.V., Anan'eva, T.A., Mikhailova, Yu.N. *et al.*, *Fizikokhim. Polim.* (Tver), 2001, no. 7, pp. 192–197.
4. Mikhailova, Yu.N., Nazarova, E.V., Khizhnyak, S.V., *et al.*, *Zh. Prikl. Khim.*, 2002, vol. 75, no. 1, pp. 107–112.
5. Nazarova, E.V., Anan'eva, T.A., and Grebennikov, S.F., *Fizikokhim. Polim.* (Tver), 2002, no. 8, pp. 28–32.
6. Volkov, F.V., Anan'eva, T.A., and Nachinkin, O.I., *Fizikokhim. Polim.* (Tver), 1996, no. 2, pp. 26–31.
7. Nazarova, E.V., Anan'eva, T.A., and Grebennikov, S.F., *Fizikokhim. Polim.* (Tver), 2001, no. 7, pp. 33–37.
8. Pakhomov, P.M., Kruglova, E.V., and Khizhnyak, S.D., *Vysokomol. Soedin., Ser. B*, 2000, vol. 42, no. 6, pp. 1081–1086.
9. Pakhomov, P.M., Khizhnyak, S.D., Malanin, M.N., and Mikhailova, Yu.N., *Zavod. Lab. Diagn. Mater.*, 2002, vol. 68, no. 5, pp. 31–33.
10. Worrall, W.E., *Clays and Ceramic Raw Materials*, New York: Halsted, 1975.
11. Solomko, V.P., *Napolnennye kristallizuyushchiesya polimery* (Filled Crystallizing Polymers), Kiev: Naukova Dumka, 1980.
12. Shangin, Yu.A., *Zh. Prikl. Khim.*, 1995, vol. 68, no. 3, pp. 484–489.
13. Lipatov, Yu.S., *Fiziko-khimicheskie osnovy napolneniya polimerov* (Physicochemical Principles of Polymer Filling), Moscow: Khimiya, 1991.
14. Andreeva, A.V., *Osnovy fizikokhimii i tekhnologii kompozitov* (Fundamentals of Physical Chemistry and Technology of Composites), Moscow: IPRZhR, 2001.

Russian Journal of Applied Chemistry, Vol. 76, No. 3, 2003, pp. 468–471. Translated from Zhurnal Prikladnoi Khimii, Vol. 76, No. 3, 2003, pp. 483–486.

MACROMOLECULAR CHEMISTRY AND POLYMERIC MATERIALS

Effect of the Structure of Oxypropylated Hydroxyl-Containing Molecules on Glycolysis of Foamed Polyurethane

I. N. Bakirova, R. R. Shagidullin, L. V. Avvakumova, I. G. Demchenko, and L. A. Zenitova

Kazan State Technological University, Kazan, Tatarstan, Russia
Arbuzov Institute of Organic and Physical Chemistry, Kazan, Tatarstan, Russia

Received February 27, 2002

Abstract—The activity of a polyether derived from ethylene and propylene oxides (Laprol 5003) and of *N*,*N*,*N*',*N*'-tetra(hydroxypropyl)ethylenediamine (Lapramol 294) in glycolytic degradation of elastic foamed polyurethane was studied.

Glycolysis is a promising route of chemical degradation of polymers; it is widely used in reprocessing of polyurethane (PU) wastes to obtain secondary raw materials [1–3]. Oxypropylated hydroxyl-containing compounds were suggested previously [4–6] as degrading agents (DAs) for polyurethanes. In this work, we consider the relationship between the structure of these compounds and their reactivity in glycolysis of elastic foamed polyurethane (FPU).

EXPERIMENTAL

Glycolysis experiments were performed with wastes of cold-molded elastic FPU. This material is produced by reaction of toluene diisocyanate with Elastofom A hydroxyl-containing component [7] (Nizhnekamskneftekhim Joint-Stock Company).

As DA we used a polyether based on ethylene and propylene oxides (Laprol 5003, molecular weight M = 5000, functionality with respect to OH groups 3) and *N*,*N*,*N*',*N*'-tetra(hydroxypropyl)ethylenediamine (Lapramol 294, M = 290, functionality with respect to OH groups 4). The weight ratio FPU : DA was 40 : 60, which is optimal for efficient degradation of FPU wastes. Degradation was performed at 180°C with stirring; finely divided waste was continuously added to the DA loaded in advance. The rate of adding FPU crumb was chosen so that it corresponded to the rate of its dissolution. In the course of glycolysis, samples were taken and analyzed for the content of OH groups, c_{OH}, by the chemical method [8]. The moment when the whole amount of FPU was added was considered as the start of degradation.

IR spectroscopic studies were performed with a Bruker Vector 22 Fourier spectrometer (resolution 4 cm^{-1}). Liquid samples were prepared as thin films between KBr plates or as solutions in CCl_4 with the layer thickness of 2 and 5 cm. Computer resolution of the absorption bands was performed using Opus software (Bruker).

Figure 1 shows that the equilibrium in degradation of FPU at the allophanate [reaction (1)], biuret [reaction (2)], and urethane [reaction (3)] groups under the action of DA hydroxy groups is 3 h for Lapramol 294 and 10 h for Laprol 5003. The degrading power of Lapramol is so high that, after certain stabilization, c_{OH} sharply decreases owing to glycolysis of more heat-resistant urea bonds in FPU with the formation of amino groups [reaction (4)]:

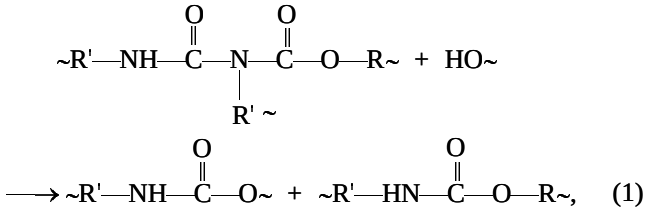

(1)

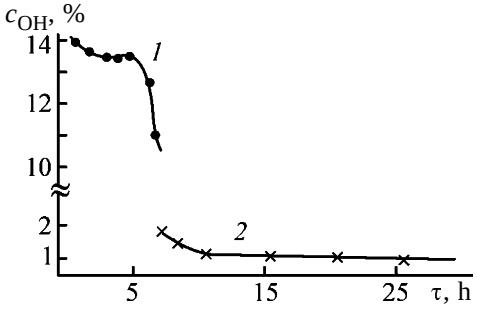

Fig. 1. Concentration of OH groups c_{OH} in products of FPU glycolysis with (*1*) Lapramol 294 and (*2*) Laprol 5003 as a function of time τ at 180°C.

1070-4272/03/7603-0468$25.00

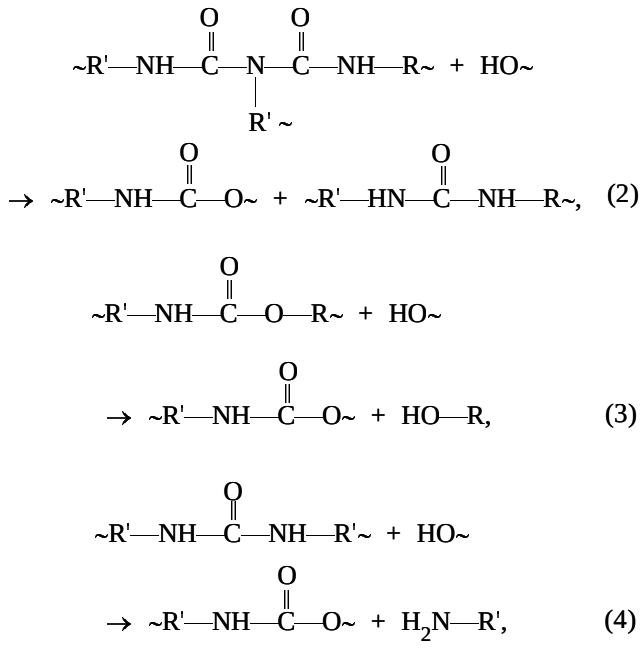

where R is the fragment of Laprol 5003 or Lapramol 2194; R' is the isocyanate fragment; OH~ denotes the hydroxy groups of Laprol 5003 or Lapramol 294.

The strong degrading power of Lapramol 294 is apparently due to the high content of OH groups: the content of OH groups is 23.2 wt % in Lapramol 294 and 1.15 wt % in Laprol 5003. Furthermore, Lapramol contains tertiary nitrogen atoms enhancing the reactivity of the OH group in glycolysis owing to formation of strong hydrogen bonds. This is indicated by the IR spectra of Lapramol 294 (Fig. 2a) and Laprol 5003 (Fig. 2b) in the range of stretching vibrations of hydroxy groups (ν_{OH}, 2200–3800 cm^{-1}). In neat films (curves *1*), broad absorption bands ν_{OH} have maxima at about 3350 (Lapramol 294) and 3480 cm^{-1} (Laprol 5003), characteristic of hydrogen-bonded hydroxyls (ν^b_{OH}). Free (not involved in hydrogen bonding) alcoholic hydroxy groups absorb above 3600 cm^{-1} (ν^f_{OH}). For secondary alcohols, ν^f_{OH} is about 3620 cm^{-1} [9, 10]. The spectra of dilute solutions (Figs. 2a and 2b, curves *2* and *3*), indeed, contain peaks at 3616 cm^{-1}. It is also known that, the stronger the hydrogen bond involving OH group, the greater the low-frequency shift, width, and intensity of the ν^b_{OH} band. The shift $\Delta\nu_{OH} = \nu^b_{OH} - \nu^f_{OH}$ is about 270 cm^{-1} for Lapramol 294 and only about 140 cm^{-1} for Laprol 5003. The corresponding hydrogen bond energies, according to the Iogansen rule, $(\Delta H)^2 = 1.92(\Delta\nu - 40)$ (kJ mol^{-1}) [11], are as follows: ΔH = 21 kJ mol^{-1} (5 kcal mol^{-1}) for Lapramol 294 and 13.9 kJ mol^{-1} (3.3 kcal mol^{-1}) for Laprol 5003. However, contrary to, e.g., amino-

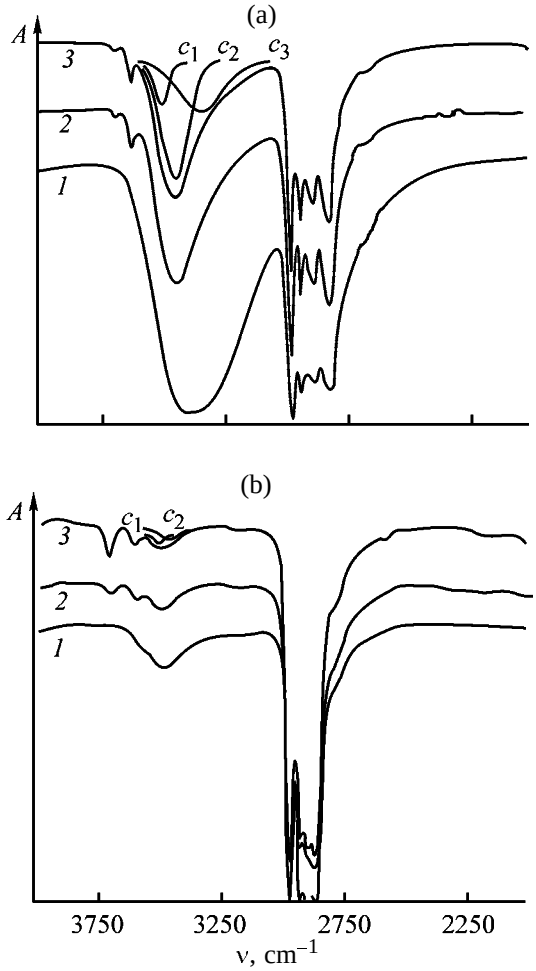

Fig. 2. IR spectra of (a) Lapramol 294 and (b) Laprol 5003: (*A*) transmission and (ν) wave number. (*1*) Thin film between KBr plates; (*2*) ~10^{-4} M solution in CCl_4, cell thickness 2 cm; and (*3*) ~5×10^{-5} M solution in CCl_4, cell thickness 5 cm. (c_1–c_3) Bands obtained by computer resolution of the experimental bands at (a) 3400 and (b) 3500 cm^{-1} into possible components.

phenols [12], the proton is not fully transferred with formation of a zwitterionic structure. Otherwise the spectra would contain a characteristic absorption band of the N^+H group at appreciably lower frequencies, less than 3000 cm^{-1} [9, 13].

Thus, the IR data show that the OH groups of the Lapramol 294 molecules are considerably more activated than the OH groups in Laprol 5003.

It is well known that tertiary amines form stronger hydrogen bonds than alcohols [9, 10, 14]. Hence, the stronger activation of OH groups in Lapramol, shown above, can be accounted for by formation of OH···N hydrogen bonds. In Laprol, apparently, only OH···O bonds can form. As seen from Figs. 2a and 2b (curves *2* and *3*), in CCl_4 solutions the maximum of the ν^b_{OH}

bands is shifted to higher frequencies. With dilution, their low-frequency component decreases in intensity (Fig. 2a, c_3; Fig. 2b, c_2), and the intensity ratio of the high-frequency components, as shown by band resolution (Fig. 2a, c_1, c_2; Fig. 2b, c_1), is preserved. On this basis, the above-given frequencies ν_{OH}^{b} of neat Lapramol and Laprol, and also the low-frequency components (3331 cm^{-1} for Lapramol and 3467 cm^{-1} for Laprol) of the bands in the solution spectra, disappearing on dilution, should be assigned to intermolecular hydrogen bonds. The peaks at 3493 and 3437 cm^{-1} for Lapramol (Fig. 2a, c_1, c_2) and at 3515 cm^{-1} for Laprol (Fig. 2b, c_1) are retained even in strongly dilute solutions. Therefore, these bands should be assigned to intramolecular hydrogen bonds OH···OH, OH···N, and OH···OH, respectively [14]. The probable molecular structures **I** and **II** of Lapramol with intramolecular hydrogen bonds are shown below:

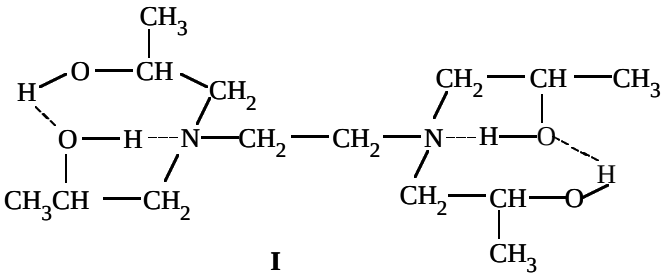

I

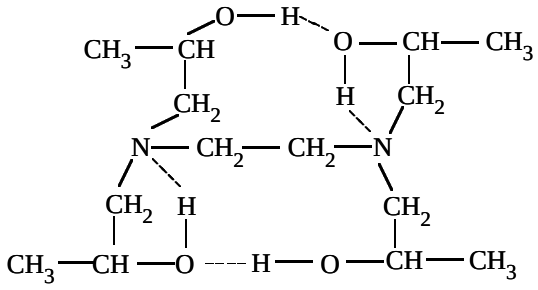

II

A cooperation of the OH···O and OH···N intramolecular hydrogen bonds in Lapramol explains the lower hydroxyl vibration frequency in its OH···O fragment, as compared to Laprol. In the condensed phase (neat film), including the reaction mixture, the intramolecular hydrogen bonnds OH···N in structures **I** and **II**, having an unfavorable geometry (five-membered ring), apparently, transform into intermolecular hydrogen bonds OH···N. Correspondingly, in neat Lapramol, structures of type **III** are probable, with the hydroxy groups activated by both weak intramolecular hydrogen bonds OH···O and relatively strong intermolecular hydrogen bonds OH···N:

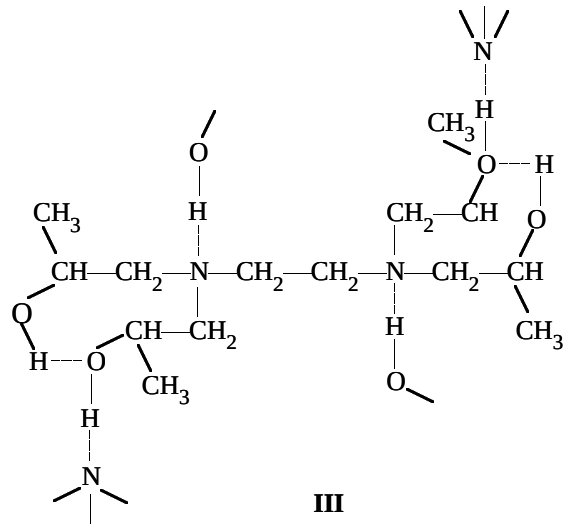

III

In Laprol, compared to Lapramol, the OH···O hydrogen bonds (both intra- and intermolecular) are less strong, which accounts for the lower activity of Laprol in glycolysis.

CONCLUSIONS

(1) In glycolytic degradation of elastic foamed polyurethane, Lapramol 294 is considerably more active than Laprol 5003.

(2) The increased degrading power of Lapramol 294 is due to the higher content of OH groups and to their activation, mainly by OH···N intermolecular hydrogen bonding. According to IR data, these bonds cause greater shifts of the OH stretching bands and correspondingly have higher enthalpies, as compared to OH···O intermolecular hydrogen bonds in Laprol 5003.

REFERENCES

1. Birkett, D., *Chem. Brit.*, 2000, vol. 36, no. 2, pp. 46–48.
2. Hemel, S., Held, S., Hisks, D., and Hart, M., *Kunststoffe*, 1998, vol. 88, no. 2, pp. 223–226.
3. Modesti, M., Simioni, F., Munari, R., and Baldoin, N., *React. Funct. Polym.*, 1995, vol. 26, nos. 1–3, pp. 157–165.
4. RF Patent 2143442.
5. RF Patent 2139313.
6. Demchenko, I.G., Bakirova, I.N., Valuev, V.I., *et al.*, *Abstracts of Papers, Rossiiskaya konferentsiya "Aktual'nye problemy neftekhimii"* (Russian Conf. "Urgent Problems of Petrochemistry"), Moscow: Ross. Akad. Nauk, 2001, p. 352.

7. RF Patent 2 117 014.
8. Siggia, S. and Hanna, J.G., *Quantitative Organic Analysis via Functional Groups*, New York: Wiley–Interscience, 1979. Translated under the title *Kolichestvennyi organicheskii analiz po funktsional'nym gruppam*, Moscow: Khimiya, 1983, p. 40.
9. Bellamy, L.J., *The Infra-Red Spectra of Complex Molecules*, New York: Wiley, 1957. Translated under the title *Infrakrasnye spektry slozhnykh molekul*, Moscow: Inostrannaya Literatura, 1963, pp. 139, 142.
10. Bellamy, L.J., *Advances in Infrared Group Frequencies*, London: Methuen, 1968. Translated under the title *Novye dannye po IK spektram slozhnykh molekul*, Moscow: Mir, 1971, pp. 104, 290.
11. Iogansen, A.V., *Spectrochim. Acta (A)*, 1999, vol. 55, pp. 1585–1612.
12. Rozdina, I.G., Tiger, R.P., Chernova, E.A., and Entelis, S.G., *Vysokomol. Soedin., Ser. A*, 1987, vol. 29, no. 8, pp. 1737–1743.
13. Colthup, N.B., Daly, L.N., and Wiberley, S.E., *Introduction to Infrared and Raman Spectroscopy*, New York: Academic, 1964, p. 381.
14. Shagidullin, Rif.R., Vibration Spectra and Molecular Structures of Hydroxyl-Containing Compounds with Intramolecular Hydrogen Bond, *Cand. Sci. Dissertation*, Kazan, 1990.

Russian Journal of Applied Chemistry, Vol. 76, No. 3, 2003, pp. 472–482. Translated from Zhurnal Prikladnoi Khimii, Vol. 76, No. 3, 2003, pp. 487–497.

MACROMOLECULAR CHEMISTRY AND POLYMERIC MATERIALS

Thermal Degradation of Polystyrene–Polydimethylsiloxane Blends

S. M. Lomakin, E. V. Koverzanova, N. G. Shilkina, S. V. Usachev, and G. E. Zaikov

Semenov Institute of Chemical Physics, Russian Academy of Sciences, Moscow, Russia
Emanuel Institute of Biochemical Physics, Russian Academy of Sciences, Moscow, Russia

Received April 9, 2002

Abstract—Specific features of thermal degradation of polystyrene–polydimethylsiloxane blends were studied, and the effect of the organosilicon polymeric additive, polydimethylsiloxane, on the heat resistance of polystyrene was examined. The thermal degradation products were analyzed by gas chromatography–mass spectrometry. A mechanism of the joint pyrolysis was suggested.

It is well known that polymer blends differ in the physical and mechanical properties from their components taken separately. Specific features of thermal degradation of polymer blends are discussed in numerous papers [1, 2]. Richard and Salter studied thermal degradation of polystyrene (PS) blended with poly-α-methylstyrene (P-α-MS) [3]. They explained the increased yield of styrene in the process by the capability of P-α-MS radicals to initiate chain propagation in depolymerization.

Mizutani *et al.* [4] suggested that degradation of polypropylene accelerates in the presence of vinyl polymers such as PS and polymethyl methacrylate (PMMA) [4]. In the course of thermal degradation, these polymers are inserted into the polypropylene chain to form block copolymers. The mechanism of their formation involves the reaction of the vinyl polymeric radical with the polypropylene chain.

Gardner *et al.* [5] studied the rate of polystyrene and P-α-MS degradation in the presence of polyacrylates. They found that the degradation rates of the blends considerably differ from those of the polymers taken separately.

Grassie *et al.* [6] compared the degradation behavior of PMMA–PS blends and methyl methacrylate (MMA)–styrene copolymers and revealed substantial differences in their behavior.

McNeill *et al.* [7–9] studied thermal degradation of various polymer blends. They suggested that the course of degradation is mainly influenced by two processes: migration of small molecules and migration of radicals. They also suggested that, in blends of polyvinyl chloride (PVC) with such polymers as PMMA, PS, and P-α-MS, the low degradation temperature of the second polymer promotes (induces) formation of $Cl^{\bullet}$ radicals.

In turn, Bate and Lehrle estimated the rate and mechanistic features of degradation of polymer blends (PMMA–PS, PMMA–HDPE, PMMA–PVC) as influenced by the following factors [10]: compatibility of polymers, physical parameters of the system (diffusion, viscosity), and cross-linking reactions. Their results show that heterogeneous blends mainly degrade within the component phases, but cross-linking due to interphase migration of small radicals or molecules is also possible. For the examined systems, cross-linking was a secondary process in most cases. It was shown that the observed rate of formation of MMA monomer in heterogeneous blends only slightly differs from the rate of its formation in a homogeneous blend. Pyrolysis of homogeneous blends involves mechanisms that can yield cross-linking products. However, it was shown that the capability to form major pyrolysis products varies significantly. These results were interpreted from the viewpoint of the thermal degradation mechanism. In partituclar, additional stages of thermal degradation were considered: cross termnation in the course of propagation of depolymerization chains results in stabilization of macroradicals; intermolecular transfer of the hydrogen atom in the course of propagation of depolymerization chains promotes the degradation of the first component and stabilizes the second component; diffusion limitations to intramolecular transfer are manifested in the case when one of the components acts as an "inert diluent," and this effect decreases the chain termination rate in depolymerization of the second component; if both components of a homogeneous blend degrade independently

1070-4272/03/7603-0472$25.00

of each other, the cross termination does not noticeably affect the overall degradation rate.

In this work, we studied the heat resistance of PS–polydimethylsiloxane (PDMS) blends, the specific features of the thermal degradation mechanism, and the possibility of controlling the heat resistance of polymeric materials by mechanical blending.

EXPERIMENTAL

The starting polymers were commercial products: PS (Aldrich), M_w 280 000, T_g 100°C; PDMS (Wacker), M_w 10^7, methyl terminal groups. Polymer blends were prepared with a laboratory extruder at 200°C.

Pyrolysis of PS, PDMS, and PS–PDMS blend (80 : 20 by weight) was performed at 300, 400, 500, 600, 700, and 800°C in a tubular cell in an air flow (flow rate about 30 ml min^{-1}). Gaseous products were condensed in a glass trap with hexane (4 ml), cooled to 0°C.

Thermogravimetric analysis (TGA) of the polymers and their blends was performed on a 950Q deriovatograph in nitrogen and in air (flow rate 100 ml min^{-1}).

Pyrolysis products were analyzed with a Tsvet 500-M gas chromatograph equipped with an electron capture detector and a glass column (4 m long, 3 mm i.d.). The stationary phase was OV-17 phenylmethylsilicone. The column and injector temperatures were 230°C, and the detector temperature, 290°C. The carrier gas was N_2 (25 ml min^{-1}). The sample volume was 2 μl.

The GC–MS analysis was performed on a Varian 3300 gas chromatograph equipped with a Finnigan MAT ITD-800 mass-spectrometric detector (ion trap). Separation was performed with a quartz capillary column (30 m long, 0.32 mm i.d.) coated with DB-5 phenylmethylsilicone (film thickness 0.25 μm). The column temperature was raised from 50 to 270°C at a rate of 10 deg min^{-1}; the injector temperature was 200°C. The carrier gas was helium (inlet pressure 0.1 MPa). Samples (1 μl) were introduced without flow division; the time before the start of purging of the sample inlet unit was 30 s.

The mass spectra were taken with ionization by electron impact (70 eV). The scanning rate was one mass spectrum per second, and the scanning range, 40–650 amu.

The kinetics of thermal degradation of PS, PDMS, and their blends was studied by dynamic TGA. The differential method (Kissinger) was used to determine the activation energy and preexponential term for thermal degradation of blends [11].

Table 1. Experimental values of the activation energy E_a and preexponential term A for thermal degradation of PS, PDMS, and their blend (heating rate 1–10 deg min^{-1})

Polymer	E_a, kcal mol^{-1}	A, min^{-1}
PDMS	26.8	0.5×10^6
PS	36.0	0.7×10^{10}
PS in PS–PDMS blend (80 : 20)	46.0	1.0×10^{11}
PDMS in PS–PDMS blend (80 : 20)	20.2	0.37×10^6

Using the equation

$$A/r = E/RT_{max}^2 \exp(E/RT_{max}),$$

where A is the preexponential term; r, heating rate, deg min^{-1}; E, activation energy; R, universal gas constant; and T_{max}, temperature corresponding to the maximal reaction rate [11], we determined the apparent activation energies and preexponential terms (Table 1).

We found that, for PS as a component of the blend, the activation energy and preexponential term for thermal degradation in a nitrogen flow are 30% higher than for pure PS. At the same time, for PDMS as a component of the blend, these parameters are 25% lower than for pure PDMS [12, 13].

The products of pyrolysis of the polystyrene component of the blend diffuse through the phase boundary and can react with the polysiloxane component.

PDMS, apparently, behaves as an inert component (diluent), decelerating the chain termination reactions with macroradicals generated by PS degradation. This stabilizes PS by intermacromolecular recombination yielding products containing styrene and siloxane fragments (cross products).

Usually dilution decelerates the chain termination reactions and increases the overall rate of thermal degradation of the PS component. As a result, the apparent activation energy of degradation of the PS component can decrease. However, actually the PS component is, on the contrary, stabilized, which can be accounted for by intermacromolecular reaction of PS with PDMS, resulting in stabilization of PS as the component degrading first.

For the second component, PDMS, the activation energy and preexponential term are 25% lower than for pure PDMS [13]. This means that the second com-

ponent becomes less heat-resistant in the blend, as compared to the pure state.

After formation of the cross-linking products in the course of pyrolysis of this polymer blend was proved by GC–MS analysis, we explained the behavior of the blend by kinetic factors. In the course of PDMS degradation, intermacromolecular reaction (recombination) terminates radical depolymerization of PS. At the same time, thermal degradation of the PDMS component is initiated by formation of PS radical fragments, which is responsible for a decrease in the PDMS heat resistance in the blend.

The chromatograms and mass spectra show that the major pyrolysis product of pure PS at 300, 400, 500, 600, 700, and 800°C is styrene (56.2, 75.6, 67.1, 58.0, 58.3, and 51.9%, respectively). Apparently, radical depolymerization initiated with oxygen remains the major pathway of PS degradation in this temperature range [14].

At 300°C, the major products of PS pyrolysis are styrene (56.2%) and benzaldehyde (30.1%); α-methylsrtyrene (2.6%) and acetophenone (2.5%) are also detected; a few other products are formed in trace amounts. At 400°C, the number of degradation products increases; styrene remains the major product (75.6%), with the other most intense peaks in the chromatogram belonging to toluene (8.3%), ethylbenzene (2.2%), benzaldehyde (3.5%), α-methylstyrene (5.4%), and styrene oligomer (1.5%). At 500°C, the number of pyrolysis products increases further; styrene is still the major product (67.1%), with the other most intense peaks corresponding to toluene (3.2%), benzaldehyde (7.2%), α-methylstyrene (4.2%), benzacetaldehyde (4.6%), and styrene oligomer (2.9%). The minor products are ethylbenzene (0.9%), phenol (0.5%), β-methylstyrene (0.9%), acetophenone (1.3%), diphenylethane (0.9%), 1,3-diphenylpropane (0.8%), and styrene pentamer (0.8%). At 600°C, the number of pyrolysis products increases further. Along with the above-mentioned products, compounds with fused benzene rings [benzofuran (0.3%) and naphthalene (0.6%)] and biphenyl (0.1%) are formed. At 700 and 800°C, the amount of compounds with fused benzene rings increases, whereas such compounds as phenol, benzaldehyde, diphenylpropane, styrene pentamer, and others disappear. The results are given in Table 2.

In pyrolysis of PDMS, the major decomposition products are oligomers (cyclic and linear methylsiloxanes). The major degradation product is octamethylcyclotetrasiloxane (OMCTS); the other most intense peaks in the chromatograms correspond to hexamethylcyclotrisiloxane (HMCTS) and decamethylcyclopentasiloxane (DMCPS). With increasing temperature, higher-molecular-weight cyclosiloxane oligomers appear, with their amount increasing: dodecamethylcyclohexasiloxane (DdMCHS), tetradecamethylcycloheptasiloxane (TdMCHpS), and tetracosamethylcyclododecasiloxane (TcMCDdS), as described in [12]. It is known that depolymerization of PDMS occurs by the molecular mechanism [12]. At 400°C and higher temperatures, along with HMCTS, we identified one more compound, 1,3,3,5,5-pentamethylcyclotrisiloxane-1-heptamethylpentasiloxane:

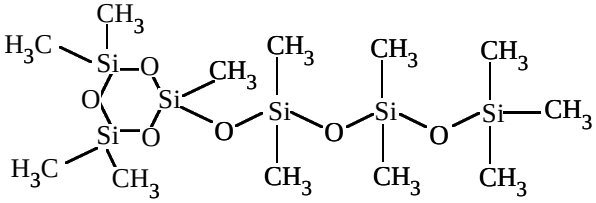

The characteristic peaks in the mass spectrum of this compound are *m*/*z* 73, 102, 193, 341, and 429. The products of thermal degradation of PDMS are listed in Table 3.

Analysis of the pyrolysis products formed from the PS–PDMS blend revealed the presence of several new products along with the degradation products of both components. At 300°C, the benzaldehyde content is abnormally high (42.9%), whereas the styrene content is as low as 13%, and the content of PDMS degradation products is insignificant. The pyrolysis products formed at 400 and 500°C have similar composition, being mixtures of degradation products of PS (toluene, 2.0 and 6.2%; ethylbenzene, 0.8 and 1.6%; styrene, 61.7 and 59.8%; benzaldehyde, 7.4 and 3.9%; α-methylstyrene, 4.4 and 3.0%, respectively) and PDMS (HMCTS, 3.7 and 6.1%; OMCTS, 3.1 and 5.0%; DMCPS, 6.0 and 7.8%; DdMCHS, 0.8 and 0.9%, respectively). At 600°C, compounds with fused benzene rings (benzofuran, 0.7%; naphthalene, 0.5%; phenanthrene, 0.1%) and biphenyl (0.2%) are formed. At this temperature, we detected two new compounds absent in pyrolysis products of PS and PDMS taken separately (retention times 8.5 and 11.0 min). The first compound, apparently formed by the cross reaction (termination) of two macroradical fragments of the PS and PDMS chains, was identified as 3-phenyl-1-(3',3',5',5',7',7',9',9'-octamethylcyclopentasiloxy)butane

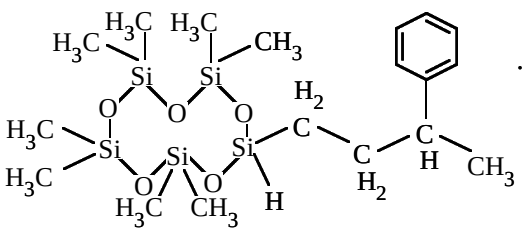

Table 2. Products of PS pyrolysis at various temperatures

Pyrolysis product	Retention time, min : s	Content, wt %, at indicated temperature, °C					
		300	400	500	600	700	800
Toluene	3:20	0.4	8.3	3.2	15.3	8.9	14.1
Ethylbenzene	4:23	0.5	2.2	0.9	7.5	6.4	2.8
Styrene	4:40	56.2	75.6	67.1	58.0	58.3	51.9
Cumene	5:15	0.1	0.1	<0.1	0.7	0.2	<0.1
Allylbenzene	5:28	1.1	0.6	0.3	0.6	0.2	0.2
Propylbenzene	5:42	0.1	0.1	0.1	0.4	0.1	<0.1
Benzaldehyde	5:46	30.1	3.5	7.2	2.6	0.3	0.3
Phenol	5:54	–	–	0.5	0.8	–	–
α-Methylstyrene	6:01	2.6	5.4	4.2	6.5	9.2	4.1
Cyclopropylbenzene	6:18	–	<0.1	0.2	0.2	0.8	0.5
Benzofuran	6:21	–	–	0.2	0.3	<0.1	0.5
β-Methylstyrene	6:42	0.3	0.2	0.9	0.5	0.8	0.4
Benzacetaldehyde	6:58	0.6	0.1	4.6	0.9	–	–
1-Propenylbenzene	7:09	–	–	0.2	0.4	2.8	2.1
1-Methylpropenylbenzene	7:18	–	0.1	0.3	0.3	0.3	0.1
Acetophenone	7:21	2.5	0.1	1.3	0.7	0.1	0.1
Isomeric diethynylbenzenes	8:13	–	–	–	0.1	0.3	0.2
	8:24	–	–	–	–	0.1	0.1
1-Butenylbenzene	8:50	–	<0.1	0.4	0.2	0.3	0.2
Naphthalene	9:18	0.1	<0.1	0.1	0.6	8.6	7.6
Isomeric methylnaphthalenes	11:08	–	–	–	<0.1	0.1	0.5
	11:24	–	–	–	–	0.1	0.4
Diphenyl	12:16	–	–	0.1	0.1	0.2	1.9
Isomeric methyldiphenyls	12:58	–	–	–	0.1	–	0.1
	13:06	–	–	–	–	<0.1	0.4
Acenaphthene	13:25	–	–	–	–	–	0.2
Isomeric diphenylethanes	14:12	0.3	<0.1	0.9	1.0	<0.1	0.3
	14:21	–	–	–	–	0.1	0.3
Fluorene	15:10	–	–	–	–	0.1	0.6
Isomeric methylfluorenes	15:27	–	–	–	<0.1	<0.1	0.3
	15:46	–	–	–	<0.1	–	0.2
1,3-Diphenylpropane	15:53	0.2	0.6	0.8	0.3	–	–
Isomeric methylfluorenes	16:36	–	–	–	0.1	<0.1	0.3
	16:43	–	–	0.3	0.3	0.1	1.6
Styrene oligomer ($2 < n < 5$)	16:48	–	1.5	2.9	0.6	0.1	0.1
Methylphenanthrene	17:29	–	–	–	–	<0.1	0.2
Phenanthrene	17:43	–	–	–	0.1	0.2	3.9
Anthracene	17:50	–	–	–	–	<0.1	0.3
1-Phenylnaphthalene	18:25	–	–	–	<0.1	0.1	0.9
Methylanthracene	18:38	–	–	–	<0.1	<0.1	0.4
2-Phenylnaphthalene	19:51	–	–	–	–	<0.1	1.2
Styrene pentamer	20:01	–	–	0.8	<0.1	–	–
Pyrene	20:56	–	–	–	–	–	0.1
Styrene oligomer ($n = 6$)	24:57	0.3	0.6	1.0	–	–	–
Unidentified compounds	–	4.5	1.0	1.1	0.6	0.9	0.4
Total		100.0	100.0	100.0	100.0	100.0	100.0

Table 3. Products of PDMS pyrolysis at various temperatures

Pyrolysis product	Retention time, min : s	Content, wt %, at indicated temperature, °C					
		300	400	500	600	700	800
Hexamethylcyclotrisiloxane	3 : 42	6.1	6.8	4.8	12.1	17.3	9.1
1,3,3,5,5-Pentamethylcyclotrisiloxane-1-heptamethylpentasiloxane	3 : 44	–	10.7	27.8	13.4	10.5	9.1
Octamethyltrisiloxane	5 : 02	–	0.1	0.5	0.1	–	0.5
Octamethylcyclotetrasiloxane	6 : 08	70.4	45.0	33.1	55.2	48.1	39.0
Heptamethylcyclotetrasiloxane	6 : 15	–	0.3	1.4	0.3	1.0	1.0
Decamethylcyclopentasiloxane	8 : 38	17.9	22.9	23.0	10.9	14.4	16.2
Nonamethylcyclopentasiloxane	10 : 16	–	0.1	<0.1	–	0.4	<0.1
Dodecamethylcyclohexasiloxane	11 : 16	1.2	1.5	1.2	2.2	1.2	3.9
Tetradecamethylcycloheptasiloxane	13 : 41	0.5	0.8	0.5	1.7	0.5	2.9
Tetracosamethylcyclododecasiloxane	15 : 52	0.3	0.3	0.3	0.6	0.1	0.8
Unidentified compounds	–	2.9	6.6	6.1	2.6	3.5	14.7
Total		100.0	100.0	100.0	100.0	100.0	100.0

Its mass spectrum is shown in Fig. 1. The second compound is probably the PS degradation product; its content in samples is low (≤0.5%), which complicates its identification. In pyrolysis at 700°C, the PDMS degradation products prevail; the contribution of HMCTS, OMCTS, and DMCPS grows (39.1, 27.4, and 12.3%, respectively), and the content of higher-molecular-weight products decreases. At 800°C, compounds with fused benzene rings are formed in increased amounts. At this temperature, a new product with the retention time of 6.33 min was detected; this product is apparently formed by the reaction of radical fragments of PS and PDMS degradation (cross reaction). The compound was identified as phenyl(3',3',5',5',7',7'-hexamethylcyclotetrasiloxy)propane

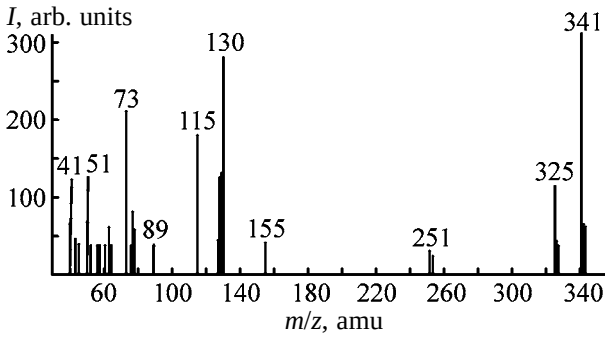

Fig. 1. Mass spectrum of 3-phenyl-1-(3',3',5',5',7',7',9',9'-octamethylcyclopentasiloxy)butane. (*I*) Intensity and (*m*/*z*) weight; the same for Figs. 2 and 6.

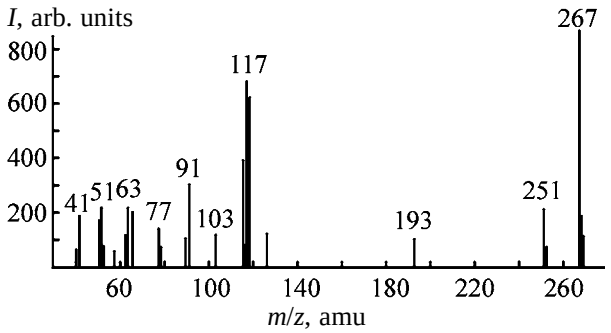

Fig. 2. Mass spectrum of phenyl(3',3',5',5',7',7'-hexamethylcyclotetrasiloxy)propane.

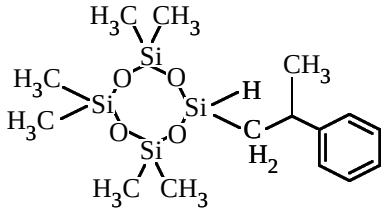

or

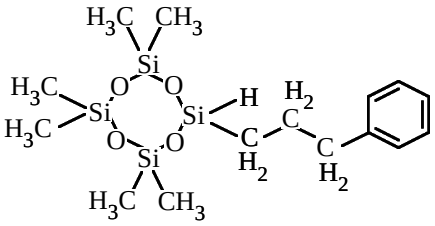

Its mass spectrum is shown in Fig. 2. The products of thermal oxidative degradation of the PS–PDMS blend are listed in Table 4.

A brief scheme illustrating the radical chain kinetic model of thermal degradation of PS in the presence of PDMS fragments was presented previously [15]. In particular, the main process includes chain initiation

with formation of primary radical (initiation at terminal groups, *e*)

$$P_n \xrightarrow{k_{ie}} R^{\bullet\bullet}_{n-1} + R^{\bullet}_1, \quad (1)$$

random initiation (*r*),

$$P_n \xrightarrow{k_{ir}} R^{\bullet}_m + R^{\bullet}_{n-m},$$

β-cleavage

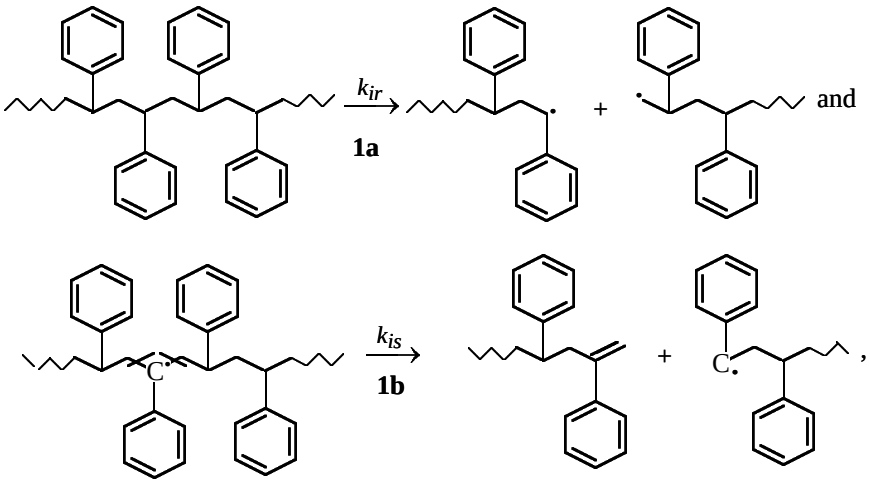

chain propagation due to intramolecular transfer

$$R^{\bullet}_n \xrightarrow{k_p} R^{\bullet}_{n-1} + P_1 \quad \text{(monomer, M)}, \quad (2)$$

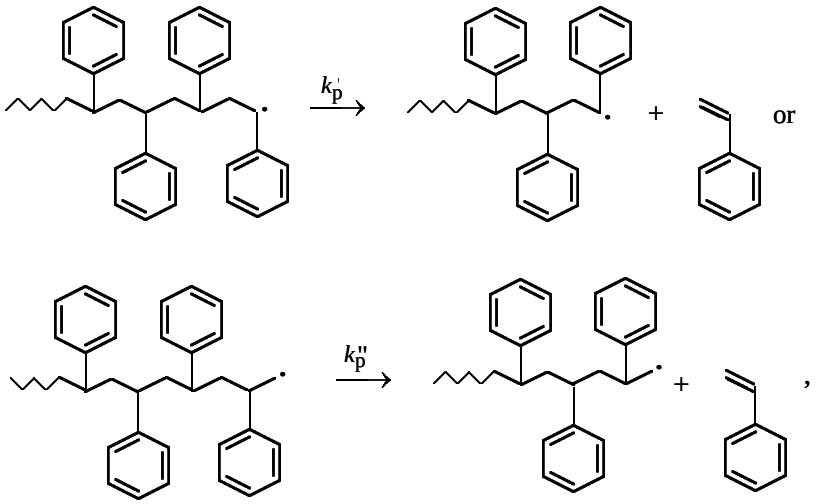

chain propagation due to intermolecular reaction

$$R^{\bullet}_n + P_s \longrightarrow R^{\bullet}_{s-r} + P_n + P_s, \quad (3)$$

intramolecular transfer (back-bitting)

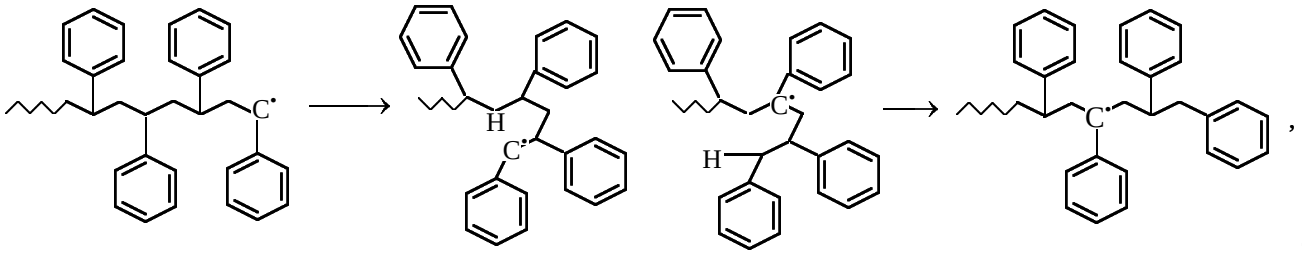

(4)

primary and(or) secondary radical termination and β-cleavage

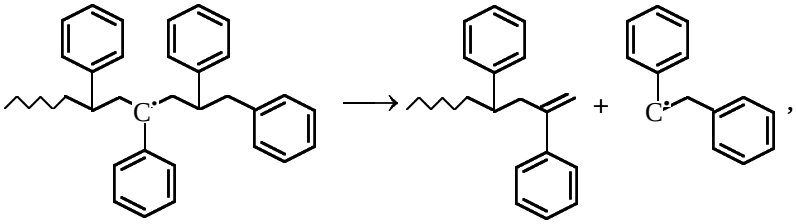

(5)

intermolecular reaction of PS and PDMS chains (cross termination), yielding cross-linking products in thermal degradation of the PS–PDMS blend

$$R_n^{\bullet} + \text{PDMS} \xrightarrow{k'_{tr}} R_{n-m}^{\bullet} + R_m\text{–PDMS}, \quad (6)$$

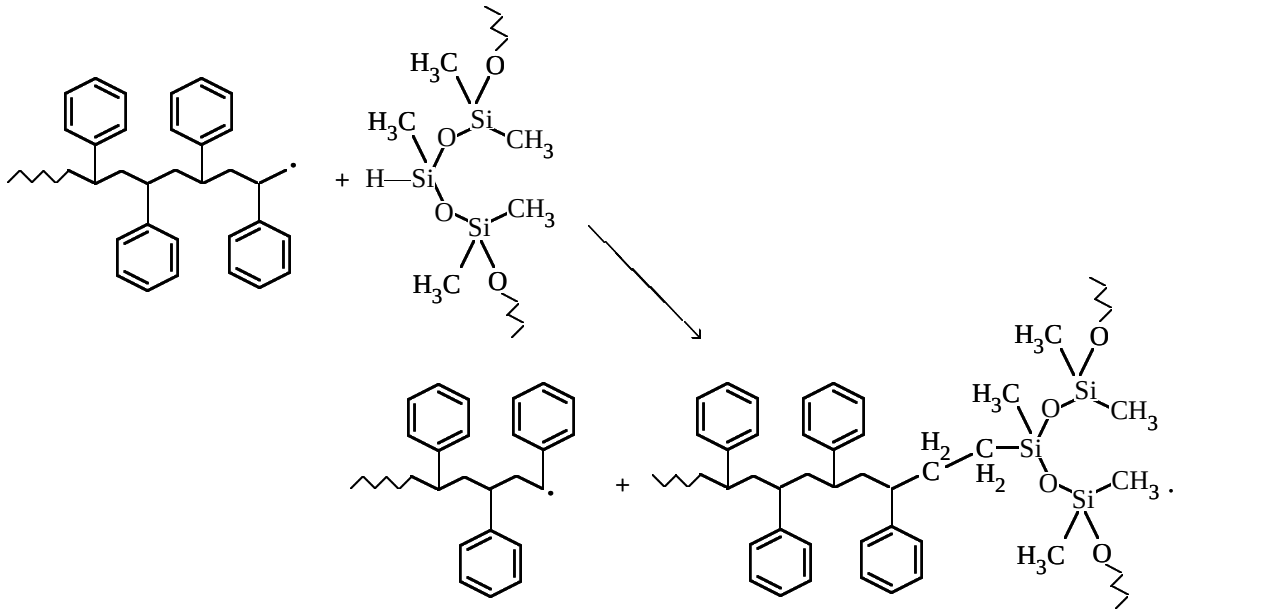

Chain termination stage: first-order

$$R_n^{\bullet} \xrightarrow{k_{tr,1}} P_n, \quad (7)$$

second-order

$$R_n^{\bullet} + R_m^{\bullet} \begin{cases} \nearrow P_n + P_m & \text{(disproportionation)} \\ \searrow P_{n+m} & \text{(recombination).} \end{cases}$$

Figures 3–5 show the differences in thermal degradation of PS, PDMS, and their blend on heating at a rate of 10 deg min^{-1} in nitrogen and in air. The effect of oxygen on the degradation is clealry seen. Thermal degradation of PDMS was studied in [12]. The two-stage pattern of PDMS degradation can be explained in terms of the mechanism involving oxygen-catalyzed depolymerization at the terminal groups, leading to random termination and cross oxidation processes

Table 4. Products of pyrolysis of PS–PDMS blend (80 : 20 by weight) at various temperatures

Pyrolysis product	Retention time, min : s	Content, wt %, at indicated temperature, °C					
		300	400	500	600	700	800
Toluene	3:20	–	2.0	6.2	7.5	3.5	5.7
Hexamethylcyclotrisiloxane	3:42	1.3	3.7	6.1	2.6	39.1	4.9
Ethylbenzene	4:23	–	0.8	1.4	3.9	0.3	0.6
Styrene	4:40	19.7	61.7	59.8	48.9	7.3	29.4
Cumene	5:15	–	<0.1	0.1	0.5	–	–
Allylbenzene	5:28	0.3	0.4	0.3	0.5	–	–
Propylbenzene	5:42	–	0.1	0.1	0.2	–	–
Benzaldehyde	5:46	42.9	7.4	3.9	3.8	0.2	0.4
Phenol	5:54	–	<0.1	0.2	0.5	–	0.1
α-Methylstyrene	6:01	2.3	4.4	3.0	5.8	0.2	1.9
Octamethylcyclotetrasiloxane	6:08	1.5	3.1	5.0	3.1	27.4	4.8
Heptamethylcyclotetrasiloxane	6:15	–	<0.1	–	–	–	–
Benzofuran	6:21	–	–	0.2	0.7	–	–
Phenyl(3',3',5',5',7',7'-hexamethylcyclotetrasiloxy)propane	6:21	–	–	–	–	–	1.0
1-Methylethylbenzene	6:29	–	–	<0.1	0.1	–	–
β-Methylstyrene	6:42	0.3	0.2	0.5	0.5	–	0.3
Benzacetaldehyde	6:58	1.4	0.3	0.4	1.0	–	0.1
1-Propenylbenzene	7:09	–	–	0.1	0.8	–	4.7
1-Methylpropenylbenzene	7:13	–	0.1	0.1	0.7	–	<0.1
Acetophenone	7:21	5.7	0.5	0.1	0.4	–	0.2
Diethynylbenzene isomer	8:13	–	–	–	–	–	0.5
3-Phenyl-1-(3',3',5',5',7',7',9',9'-octamethylcyclopentasiloxy)butane	8:25	–	–	–	0.1	0.4	0.4
Decamethylcyclopentasiloxane	8:38	3.1	6.0	7.8	7.3	12.3	2.7
Methylindene isomer	8:44	–	<0.1	–	0.1	–	–
Diethynylbenzene isomer	8:50	–	–	–	–	–	0.3
Azulene	8:58	–	–	–	<0.1	–	0.2
Methylindene isomer	8:59	–	–	–	0.1	–	0.2
Naphthalene	9:18	–	–	<0.1	0.5	0.5	18.3
Dodecamethylcyclohexasiloxane	11:16	5.9	0.8	0.9	2.8	0.8	5.5
Biphenyl	12:16	–	–	<0.1	0.2	–	1.6
2-Methylbiphenyl	12:58	–	<0.1	<0.1	0.1	–	0.2
Acenaphthene	13:25	–	–	–	–	–	0.1
Tetradecamethylcycloheptasiloxane	13:47	1.5	0.1	0.1	0.5	–	1.1
Diphenylethane	14:06	0.7	<0.1	<0.1	0.1	–	0.1
Styrene oligomer ($2 < n < 5$)	14:12	0.2	0.1	0.3	1.1	–	–
Diphenylethyne	14:21	–	–	–	–	–	0.2
Fluorene	15:10	–	–	–	–	–	0.2
Methylfluorene isomers	15:27	–	–	–	–	–	0.1
	15:46	–	–	–	–	–	0.1
1,3-Diphenylpropane	15:53	–	0.8	0.1	0.3	–	0.1
Tetracosamethylcyclododecasiloxane	15:58	–	–	–	–	–	0.2
Methylfluorene isomers	16:29	–	0.1	–	0.1	–	0.1
	16:36	–	0.1	0.6	0.4	–	0.3
Styrene oligomer ($2 < n < 5$)	16:48	–	2.6	0.3	1.2	–	0.1
Methylphenanthrene	17:29	–	–	–	–	–	<0.1
Phenanthrene	17:43	–	–	–	0.1	0.2	0.6
Anthracene	17:50	–	–	–	–	–	<0.1

Table 4. (Contd.)

Pyrolysis product	Retention time, min : s	Content, wt %, at indicated temperature, °C					
		300	400	500	600	700	800
1-Phenylnaphthalene	18 : 25	–	–	–	–	–	0.1
Methylanthracene	18 : 38	–	–	–	–	–	<0.1
2-Phenylnaphthalene	19 : 51	–	–	–	–	–	0.1
Styrene pentamer	20 : 01	–	–	–	0.2	–	–
Styrene oligomer (n = 6)	24 : 57	–	1.4	<0.1	<0.1	–	–
Unidentified compounds from PS	–	8.1	0.7	0.3	1.1	0.5	0.5
Unidentified compounds from PDMS	–	4.7	2.6	2.2	2.2	7.3	12.0
Total		100.0	100.0	100.0	100.0	100.0	100.0

[12]. The limiting stage of this process is eventually diffusion and vaporization of monomeric fragments.

Comparison of the TG and DTG curves suggests that the same PS component in a blend with PDMS degrades at a higher temperature. At the same time, PDMS as a component of the blend tends to degrade at lower temperatures. This effect is observed only when thermal degradation is performed in air.

In the PS–PDMS blend, dissolution of PS (major component) in PDMS results in stabilization of PS and destabilization of PDMS. This can be explained from the viewpoint of interpolymeric recombination. Two degradation products, phenyl(3',3',5',5',7',7'-hexamethylcyclotetrasiloxy)propane and 3-phenyl-1-(3',3',5',5',7',7',9',9'-octamethylcyclopentasiloxy)butane, were interpreted as products of interpolymeric recombination cross-linking, which may accelerate depolymerization of PDMS via radical initiation by PS fragments [13]. The possible scheme of formation of 3-phenyl-1-(3',3',5',5',7',7',9',9'-octamethylcyclopentasiloxy)butane as the product of interpolymeric cross-linking is shown below.

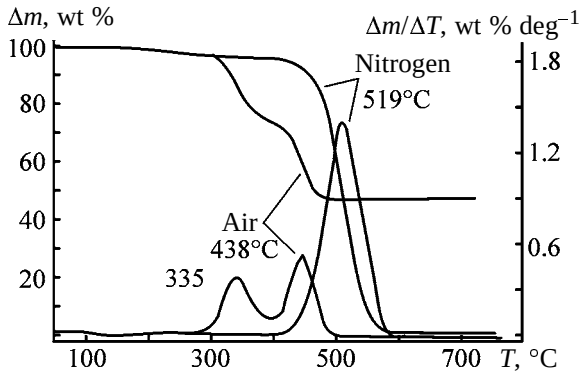

Fig. 3. TG and DTG curves of PDMS samples in nitrogen and in air. Heating rate 10 deg min^{-1}; the same for Figs. 4 and 5. (Δm) Weight loss, ($\Delta m/\Delta T$) weight loss per unit variation of temperature, and (T) temperature; the same for Figs. 4 and 5.

CONCLUSIONS

(1) Kinetic features of thermal degradation of a polystyrene–polydimethylsiloxane blend were studied. The organosilicon additive affects the heat resistance of polystyrene.

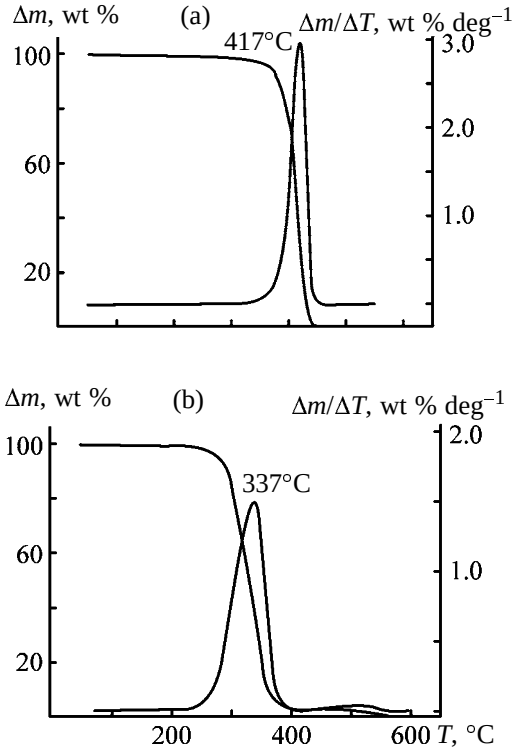

Fig. 4. TG and DTG curves of PS samples (a) in nitrogen and (b) in air.

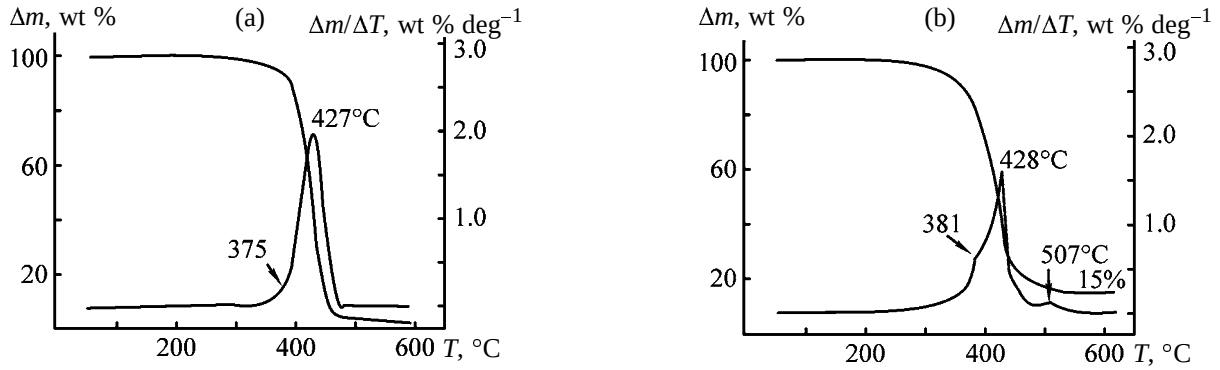

Fig. 5. TG and DTG curves of samples of 80 : 20 PS–PDMS blend, taken (a) in nitrogen and (b) in air.

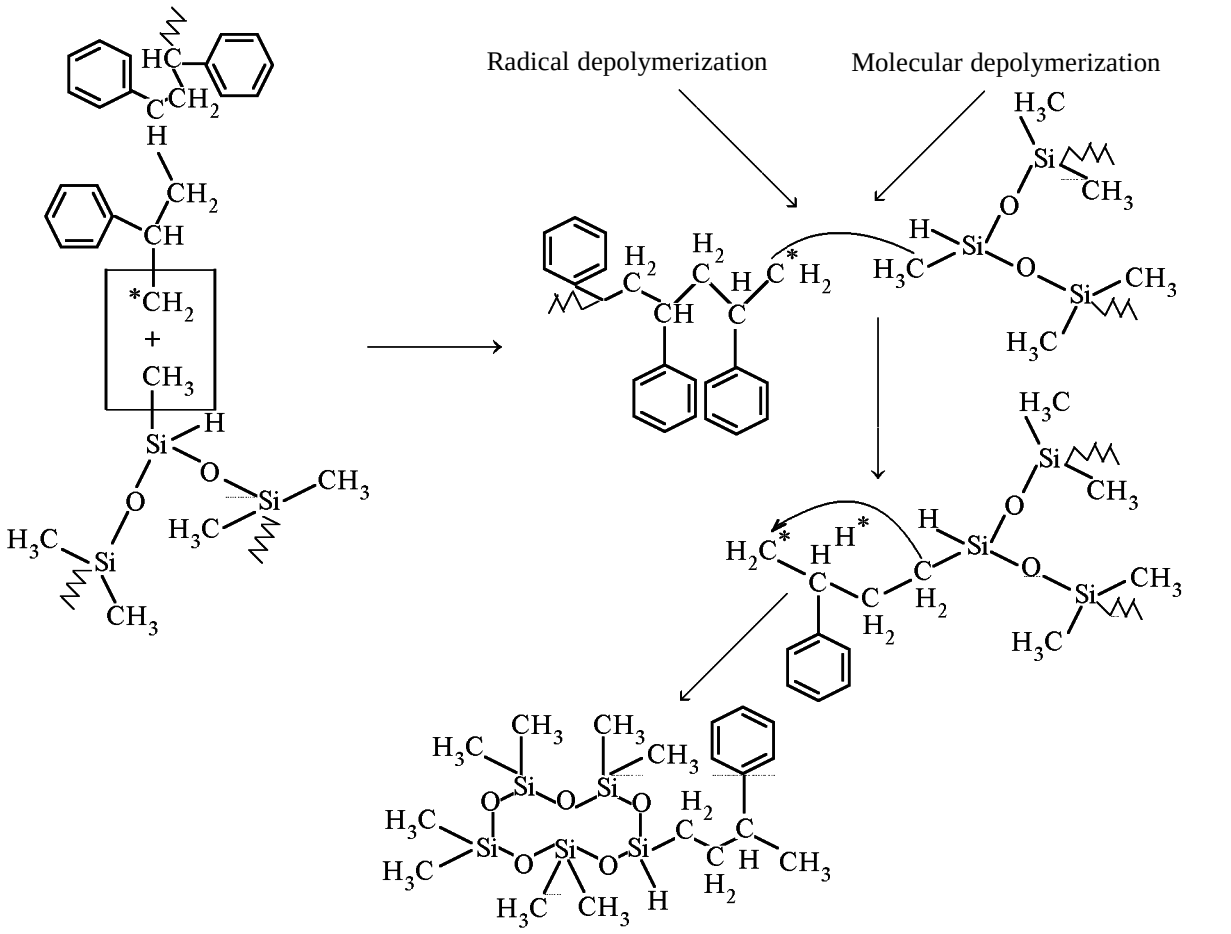

(2) In a blend with polydimethylsiloxane, polystyrene, which is less heat-resistant than polydimethylsiloxane, degrades at higher temperatures compared to pure polystyrene, i.e., it is stabilized. The stabilization in this stage is mainly due to kinetic factors. On the contrary, the subsequent stage of polydimethylsiloxane degradation starts at lower temperatures. The thermal destabilization of the system in this stage is due to cross reactions of styrene and dimethylsiloxane fragments.

(3) In the products of pyrolysis of the polystyrene–

polydimethylsiloxane blend, trace amounts of phenyl-(3',3',5',5',7',7'-hexamethylcyclotetrasiloxy)propane and 3-phenyl-1-(3',3',5',5',7',7',9',9'-octamethylcyclopentasiloxy)butane were detected.

(4) A possible mechanism of pyrolysis of the polystyrene–polydimethylsiloxane blend was suggested.

REFERENCES

1. Emanuel', N.M., Zaikov, G.E., and Maizus, Z.K., *Okislenie organicheskikh soedinenii: Vliyanie sredy* (Oxidation of Organic Compounds: Effect of the Medium), Moscow: Nauka, 1973, p. 60.
2. Krisman, V.A., Zaikov, G.E., and Emanuel', N.M., *Khimicheskaya kinetika i tsepnye reaktsii* (Chemical Kinetics and Chain Reactions), Moscow: Nauka, 1986, p. 120.
3. Richard, D.K. and Salter, D.A., *Polymer*, 1967, vol. 8, pp. 127–138.
4. Mizutani, Y., Matsuka, S., and Yamamoto, K., *Bull. Chem. Soc. Jpn.*, 1965, vol. 38, pp. 2045–2053.
5. Gardner, P., Lehrle, R.S., and Turner, D., *J. Anal. Appl. Pyrolysis*, 1993, vol. 25, p. 11.
6. Grassie, N., McNeill, I.C., and Cooke, I., *J. Appl. Polym. Sci.*, 1968, vol. 12, p. 831.
7. McNeill, I.C. and Neil, D., *Eur. Polym. J.*, 1970, vol. 6, p. 143.
8. McNeill, I.C. and Mohammed, M.A., *Eur. Polym. J.*, 1972, vol. 8, pp. 975–989.
9. McNeill, I.C. and Mohammed, M.A., *Polym. Degrad. Stab.*, 1995, vol. 50, pp. 285–295.
10. Bate, D.M. and Lehrle, R.S., *Polym. Degrad. Stab.*, 1998, vol. 62, pp. 57–66.
11. Kissinger, H.E., *Anal. Chem.*, 1959, vol. 29, pp. 1702–1706.
12. Camino, G., Lomakin, S.M., and Lazzari, M., *Polymer*, 2001, vol. 42, no. 6, pp. 2395–2402.
13. Lomakin, S.M., Koverzanova, E.V., Usachev, S.V., *et al.*, *Oxid. Commun.*, 2002, vol. 25, no. 1, pp. 51–59.
14. Guyot, A., *Polym. Degrad. Stab.*, 1986, vol. 15, pp. 219–235.
15. Bockhorn, H., Hornung, A., and Hornung, U., in *27th Symp. (Int.) on Combustion*, Combustion Inst., 1998, pp. 1343–1358.

Russian Journal of Applied Chemistry, Vol. 76, No. 3, 2003, pp. 483–486. Translated from Zhurnal Prikladnoi Khimii, Vol. 76, No. 3, 2003, pp. 498–501.

MACROMOLECULAR CHEMISTRY AND POLYMERIC MATERIALS

Influence of Process Factors on the Structure of Urea–Formaldehyde Resin

V. Z. Maslosh, V. V. Kotova, and O. V. Maslosh

Institute of Applied Chemistry, Ministry of Education and Science of the Ukraine, Rubezhnoe, Lugansk oblast, Ukraine

Received March 25, 2002

Abstract—The influence of preparation conditions on the structure of low-toxic urea–formaldehyde resins and the possibility of preparing resins of linear-branched structure and resins containing urone rings were examined.

Urea–formaldehyde resins (UFRs) are produced in large amounts and are widely used in various branches of industry depending on the properties. The reactions involved in production of UFRs have been comprehensively studied [1–3], their order and constants have been determined [4, 5], and the structure of the reaction products of urea and formaldehyde was studied in relation to the reaction conditions [6–10]. However, the relationship between the process factors and UFR structure virtually was not examined.

The reaction of urea with formaldehyde can yield a number of products whose content depends on the process factors: component molar ratio, pH, temperature, etc.

The complex structure of UFRs is also due to the high functionality of urea and formaldehyde (4 and 2, respectively), making possible formation of a large set of structures [6].

Our goal was to study the structure of low-toxic UFRs in relation to the preparation conditions. Exhaustive structural information on these materials is furnished by ^{13}C NMR spectroscopy [11].

EXPERIMENTAL

Urea–formaldehyde resins were prepared at various pH values in steps at urea : formaldehyde molar ratios of 1 : 4, 1 : 1.45, and 1 : 1.33 by two procedures.

In the first procedure, urea in each step was added in a single portion (see table, run nos. 1–4). Step I: A 250-ml three-necked flask equipped with a stirrer, a thermometer, and a condenser was charged with 58.8 g of Formalin and 29.4 g of urea; pH 9.5–10 was adjusted with NaOH (or pH 4.0–4.5, with $KHSO_4$). The stirrer was switched on, and the mixture was heated to 82–85°C and kept at this temperature for 60–90 min. Step II: $KHSO_4$ was added to adjust pH 4.0–4.5 (or NaOH, to adjust pH 9.5–10), and the mixture was kept at 82–85°C for 30–120 min. Step III: the second 51.7-g portion of urea was added, and the mixture (pH 9.5–10) was kept at 82–85°C for 120 min. Step IV: the third 7.3-g portion of urea was added, and the mixture (pH 9.5–10) was kept at 82–85°C for 90 min. Then it was cooled to 40°C, and the UFR was unloaded.

The second procedure involved addition of urea in divided portions (see table, run nos. 5–7). Step I: A 250-ml three-necked flask equipped with a stirrer, a thermometer, and a condenser was charged with 58.8 g of Formalin, and urea was added in 2.67-g portions at 10-min intervals (a total of 11 portions, pH 10, 82–85°C, total time 120 min). The total amount of the urea added was 29.4 g. After adding the 11th portion of urea, the mixture was kept for 10 min. Step II: $KHSO_4$ was added to pH 4.0–4.5 (or pH 2), and the mixture was kept for 30 min (or for 60 min at pH 9.5–10). Step III: NaOH was added to adjust pH 9.5–10, and 11 4.7-g portions of urea were added in 10-min intervals. After adding the 11th portion, the mixture was kept for 10 min. Step IV: At pH 9.5–10, nine 0.81-g portions of urea were added at 10-min intervals; the mixture was kept for 10–20 min and cooled to 40°C, after which the UFR was unloaded.

The ^{13}C NMR spectra were recorded with a Varian Gemini spectrometer (digital resolution 0.25 Hz) in a 1 : 3 water–DMSO mixture at room temperature. Samples were taken after completion of each step. The signals were assigned according to [11].

1070-4272/03/7603-0483$25.00

Conditions of UFR preparation (82–85°C)

Run no.	Step	Urea : formaldehyde molar ratio	τ, min	pH	Content of free formaldehyde, %
1	I	1 : 4	60	4–4.5	12.4
	II	1 : 1.45	120	9.5–10	1.6
	III	1 : 1.33	180	9.5–10	0.23
2	I	1 : 4	90	9.5–10	10.18
	II	1 : 4	130	4–4.5	11.3
	III	1 : 1.45	120	9.5–10	2.7
	IV	1 : 1.33	90	9.5–10	0.03
3	I	1 : 4	60	9.5–10	9.71
	II	1 : 4	30	2.0	1.82
	III	1 : 1.45	120	9.5–10	0.4
	IV	1 : 1.33	90	9.5–10	0.01
4	I	1 : 4	60	9.5–10	10.56
	II	1 : 1.45	120	9.5–10	1.86
	III	1 : 1.33	180	9.5–10	0.14
5	I	1 : 4	120	9.5–10	7.9
	II	1 : 4	30	4–4.5	4.0
	III	1 : 1.45	120	9.5–10	1.2
	IV	1 : 1.33	90	9.5–10	0.02
6	I	1 : 4	120	9.5–10	8.0
	II	1 : 4	30	2.0	6.8
	III	1 : 1.45	120	9.5–10	3.1
	IV	1 : 1.33	90	9.5–10	0.01
7	I	1 : 4	60	9.5–10	11.2
	II	1 : 4	60	9.5–10	7.0
	III	1 : 1.45	120	9.5–10	2.87
	IV	1 : 1.33	180	9.5–10	0.09

Polycondensation of urea and formaldehyde in a 1 : 4 ratio in alkaline solution at 82–85°C for 90 min yields, even in the first step, methylol groups at the secondary and tertiary nitrogen atoms (signals *p* and *n*), and also methylene ether groups at secondary nitrogen atoms (*o*) and methylenemethoxy groups at tertiary nitrogen atoms (*k*). Signals belonging to the middle groups in the polymethylene oxide chain (*h*), methylene glycol (*j*), and monosubstituted urea (*b*) are also detected.

Thus, in step I of base condensation, products of linear-branched structure are formed (see table, run no. 4, and figure, spectrum *1*). At longer (120 min) reaction time, urone rings are formed (155 ppm). However, these fragments are unstable and disappear upon further heating.

The urone rings and middle groups of the polymethylene oxide chain disappear upon loading additional portions of urea to the urea : formaldehyde molar ratio of 1 : 1.45 and 1 : 1.33 (alkaline solution). This is accompanied by formation of methylene ether groups at tertiary nitrogen atoms (*i*) and di- and trisubstituted ureas (*d*, *q*). Presumably, these processes follow the scheme

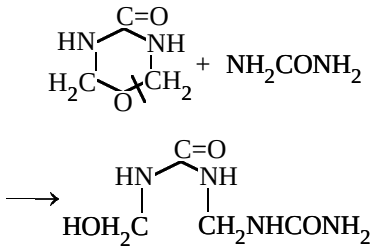

As the reaction in alkaline solution is performed further, the signals of methylene glycol and urea fully disappear, with appearance of the signals of methylenemethoxy groups at tertiary (*k*) and secondary (*m*) nitrogen atoms, methylene ether groups, disubstituted urea derivatives (*d*), methylol groups at secondary nitrogen atoms (*p*), and methylene bridges between secondary and tertiary nitrogen atoms (*v*, *g*). The final UFR obtained under base condensation conditions (see table, run no. 4, and figure, spectrum *2*) has mostly linear structure with small branchings.

When UFR is prepared under base condensation

conditions with the addition of urea in divided portions (see table, run no. 7), the products are similar in structure to those obtained in run no. 4 (see table and spectrum *2* in figure) with the addition of urea in single portions, with the only difference that, in the former case, methylenemethoxy, methylol, and methylene ether groups at tertiary nitrogen atoms (*r*, *n*, *i*) prevail, whereas in the latter case these groups are chiefly located at secondary nitrogen atoms.

These data show that, under conditions of base condensation with the addition of urea in divided portions (see table, run no. 7, and figure, spectrum *3*), more branched UFR is formed. This result is consistent with that reported in [6].

Urea–formaldehyde resins prepared at varied pH in steps (see table, run nos. 1–3, 5, 6) exhibit certain specific structural features. Polycondensation of urea and formaldehyde with the addition of urea in single portions and at pH 4–4.5 in step II (see table, run no. 2) yields products containing methylenemethoxy groups at tertiary nitrogen atoms (*r*, *k*) and terminal groups of the methylene oxide chain (*j*), along with methylol (*p*) and methoxy (*m*) groups at secondary nitrogen atoms. Urone rings (155 ppm) are also formed in this step. However, addition of the second portion of urea in alkaline solution in step III results in their disappearance. The final UFR obtained in run no. 2 with the addition of urea in single portions is a product of linear-branched structure consisting of mono-, di-, and trisubstituted urea derivatives (*b*, *c*, *d*, *q*) containing methylene ether (*j*), methylenemethoxy (*k*), and methylol (*n*) groups at tertiary nitrogen atoms, and also methylene bridges between two secondary nitrogen atoms (*v*) (see figure, spectrum *4*).

Preparation of UFR under the similar conditions but with the addition of urea in divided portions (see table, run no. 5) yields products of a more branched structure. Along with the above-mentioned groups, these resins contain methylene bridges between two tertiary nitrogen atoms (*q*), and also methylene ether and methylmethoxy groups at tertiary nitrogen atoms (*i*, *r*). Also the resins contain urone rings, which are formed in step I and are preserved upon acidification (to pH 4–4.5 or 2 in step II) and further addition of urea in alkaline solution; these rings are preserved even in the final product (see table, run nos. 5 and 6, and figure, spectrum *5*).

Thus, synthesis at varied pH and addition of urea in divided portions allows preparation of UFR of a branched structure, containing urone rings. The possibility of formation of stable urone rings in both acidic and alkaline solutions is also confirmed in other papers [12, 13].

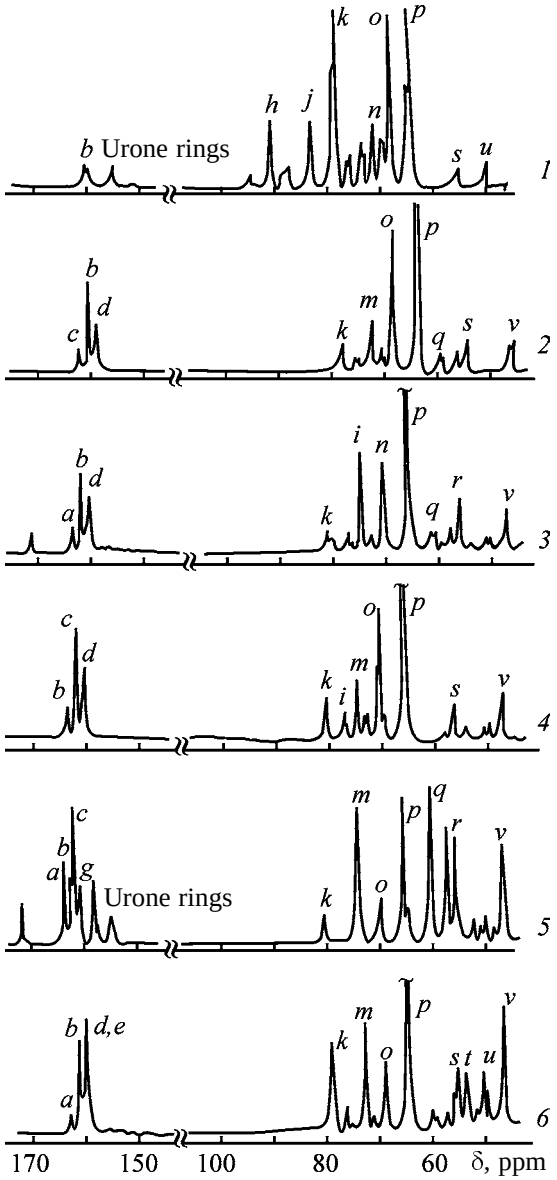

^{13}C NMR spectra of reaction products of urea and formaldehyde. (δ) Chemical shift. (*1*) step I, urea : formaldehyde 1 : 4, base condensation, urea added in single portions (run no. 4); (*2*) base condensation, final product, urea added in single portions (run no. 4); (*3*) base condensation, final product, urea added in divided portions (run no. 7); (*4*) final product obtained at varied pH and addition of urea in single portions (run no. 2); (*5*) final product obtained at varied pH and addition of urea in divided portions (run no. 6); and (*6*) final product obtained at addition of urea in single portions (run no. 1). For signal assignments, see text.

The presence of a large excess of formaldehyde is one of the necessary conditions for the formation of urone rings [7]; in our case, this is provided by the

addition of urea in divided portions in steps. Urone rings are presumably formed by intramolecular condensation of urea methylol derivatives or by their condensation with amino and imino groups. The reaction of formaldehyde with an imino group to form urone rings [14] is also possible:

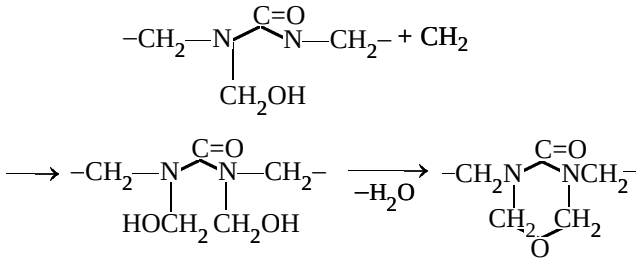

However, the UFR prepared with the addition of urea in divided portions also contains free urea (*a*).

The stronger acidity (pH 2) in step II of UFR preparation with the addition of urea in single portions (see table, run no. 3) had no appreciable effect on the structure of the final product. The structures of UFRs prepared in run nos. 2 and 3 (see table and figure, spectrum *4*) are, on the whole, identical.

Preparation of UFR with the addition of urea in single portions, acidic medium (pH 4–4.5) in step I, and alkaline medium in the subsequent steps (see table, run nol. 1) yields the resin of a linear-branched structure containing as the major structural fragments the methylene bridges between two secondary nitrogen atoms (*v*) and between secondary and tertiary nitrogen atoms (*t*). Along with methylene ether (*o*) and methylenemethoxy (*m*) groups at secondary and tertiary nitrogen atoms (*k*, *s*), the resins also contain mono- and disubstituted ureas (*b*, *d*, *e*; see table, run no. 1, and figure, spectrum *5*). Methylene bridges (*v*, *t*) are formed already in step I.

CONCLUSIONS

By varying the process parameters, it is possible to obtain urea–formaldehyde resins of both linear and branched structures with various contents of formaldehyde, and also resins containing urone rings.

REFERENCES

1. Wirpsza, Z. and Brzezinzki, J., *Aminoplasty*, Warsaw: Naukowo-Techniczne, 1970.
2. Solomon, D.G., *Khimiya organicheskikh plenkoobrazovatelei* (Chemistry of Organic Film-Forming Substances), Moscow: Khimiya, 1971.
3. Okhrimenko, I.S. and Verkholantsev, V.V., *Khimiya i tekhnologiya plenkoobrazuyushchikh veshchestv* (Chemistry and Technology of Film-Forming Substances), Leningrad: Khimiya, 1978.
4. Lipin, A.G., Ovchinnikov, L.N., Kruglov, V.A., and Kisel'nikov, V.N., *Zh. Prikl. Khim.*, 1984, vol. 57, no. 5, pp. 1169–1171.
5. Slonim, I.Ya., Alekseeva, S.G., Urman, Ya.G., *et al.*, *Vysokomol. Soedin., Ser. A*, 1978, vol. 20, no. 7, pp. 1477–1485.
6. Slonim, I.Ya., Alekseeva, S.G., Urman, Ya.G., *et al.*, *Vysokomol. Soedin., Ser. A*, 1977, vol. 19, no. 4, pp. 776–784.
7. Slonim, I.Ya., Alekseeva, S.G., Urman, Ya.G., *et al.*, *Vysokomol. Soedin., Ser. A*, 1977, vol. 19, no. 4, pp. 793–806.
8. Jong, J.I. and Jong, J., *Recl. Trav. Chim. Pays-Bas*, 1952, vol. 71, no. 6, pp. 643–660.
9. Jong, J.I. and Jong, J., *Recl. Trav. Chim. Pays-Bas*, 1952, vol. 71, no. 6, pp. 661–667.
10. Jong, J.I. and Jong, J., *Recl. Trav. Chim. Pays-Bas*, 1953, vol. 72, no. 1, pp. 88–90.
11. Slonim, I.Ya. and Urman, Ya.G., *YaMR-spektroskopiya geterogennykh polimerov* (NMR Spectroscopy of Heterogeneous Polymers), Moscow: Khimiya, 1982.
12. Kadawaki, H., *Bull. Chem. Soc. Jpn.*, 1936, vol. 11, pp. 248–251.
13. Zigeuner, G. and Fitz, H., *Monatsh. Chem.*, 1959, vol. 90, pp. 211–214.
14. Pshenitsyna, V.P., Molotkova, N.N., Drenkel', M.D., *et al.*, *Vysokomol. Soedin.*, 1979, vol. 21, no. 9, pp. 1945–1951.

Russian Journal of Applied Chemistry, Vol. 76, No. 3, 2003, pp. 487–490. Translated from Zhurnal Prikladnoi Khimii, Vol. 76, No. 3, 2003, pp. 502–505.

MACROMOLECULAR CHEMISTRY AND POLYMERIC MATERIALS

Sealants Based on Oligodiene Urethane Epoxides

A. D. Elchueva, M. M. Nazipov, A. A. Tabachkov, and A. G. Liakumovich

Kazan State Technological University, Kazan, Tatarstan, Russia

Received March 7, 2000

Abstract—Sealants in which oligodiene urethane epoxide is used as polymeric base were studied. Sulfur-containing oligomers were used for additional cross-linking via double bonds. The reaction with a polysulfide oligomer at the terminal functional groups was studied taking into account the region of thermodynamic compatibility of the reactive oligomers. Application fields were suggested for the sealants developed.

Advances in chemistry and chemical technology of oligomers open the possibilities of widely using urethane epoxy oligomers as a polymeric base for sealing compounds. Oligodiene urethane epoxide (ODUE) of PDI–ZAK brand [TU (Technical Specification) 38-10-34-10–78] based on butadiene and isoprene with terminal urethane epoxy groups exhibits good cohesion and adhesion properties and is cured with amines. In principle, any of the known mechanisms of polymerization and polycondensation via terminal epoxy groups is possible. In this work, we examined the possibility of using an amine interchange product of phenolic Mannich bases, ethylenediaminomethylphenol (aminophenol Agidol AF-2, TU 33.303340–88), for curing ODUE at room temperature to obtain elastomeric materials with satisfactory physicomechanical parameters [1].

EXPERIMENTAL

The working life of compounds was determined according to TU 38-105463–72; nominal tensile strength and relative elongation at break, according to GOST (State Standard) 21751–76; adhesion strength with metal, according to GOST 21981–76; and hardness in TIR scale, according to GOST 263–76.

The optimal curing agent dosage is 1–5 wt parts per 100 wt parts of ODUE, with active filler (carbon black, Table 1) added. At higher contents of the aminophenol, the physicomechanical parameters, especially the deformation properties of the sealants, get worse. With inert fillers (chalk, diatomite), the curing agent dosage can be increased to 6 wt parts. The maximal cohesion strength may be due to the effect of carbon black on formation of the polymer network. Fairly strong physical interactions of the oligomer and active filler make the curing more efficient.

Oligodiene urethane epoxide is an unsaturated oligomer. In this connection, the possibility of additional cross-linking via double bonds is of interest. The main parameters of sealants prepared with addition of various cross-linking agents are listed in Table 2. The enhanced cohesion strength and hardness of the composite vulcanized with a sulfur vulcanizing mixture confirms the occurrence of such cross-linking. However, the use of powdered ingredients appreciably complicates compounding, the adhesion gets worse, and sulfur particles appear on the surface of composites. These drawbacks can be eliminated by using a sulfur–styrene copolymer (SSC) containing 39 wt % chemically bound sulfur. In this case, the adhesion is enhanced. Another possible source of sulfur in sealing compounds is a copolymer of sulfur with a resin binder (SRBC), containing 15 wt % chemically bound sulfur. The compounds developed can be used for preparing corrosion-protective coatings and sealing rubber–metal articles.

To enhance the deformation and elastic properties of sealants based on ODUE, we modified the compounds with EDOS (a mixture of dioxane alcohols and formals, by-product from isoprene production), polyoxyalkylenepolyol (POAP), and polyoxyalkylene epoxide (POAE) (Table 3). POAE exerted a favorable effect: The relative elongation increased to 380–500%, and the working life decreased to 40 min. These compounds can be suggested for use in repair works when high curing rate is required. The maximal cohesion strength of the composites is observed with 20 wt parts of EDOS per 100 wt parts of ODUE. To obtain additional information on cross-linking of ODUE in the presence of EDOS, we examined the effect of heating for various times on the viscosity of the composites (Table 4).

1070-4272/03/7603-0487$25.00

Table 1. Effect of fillers on properties of composites

Parameter	Chalk (65 wt parts)		Diatomite (50 wt parts)		Carbon black (40 wt parts)	
	at indicated aminophenol content, wt parts					
	2	6	4	6	1	5
Nominal tensile strength, MPa	2.8	3.3	2.5	3.6	2.0	4.0
Relative elongation, %	210	100	100	160	240	180

Table 2. Effect of cross-linking agent on properties of composites

Parameter	Sulfur (5 wt parts)	SSC (20 wt parts)	SRBC (25 wt parts)
Working life, min	30	200	120
Nominal tensile strength, MPa	4.2	4.0	3.0
Relative elongation, %	100	200	80
Adhesion to duralumin, kN m^{-1}	0.3	2.3	2.0
Hardness, arb. units	75	65	50

Table 3. Effect of modifier on properties of composites

Parameter	EDOS			POAP			POAE		
	wt parts								
	10	20	30	10	20	30	10	20	30
Working life, min	45	75	105	35	105	125	40	60	70
Nominal tensile strength, MPa	3.3	4.2	1.4	4.1	4.0	2.7	2.1	3.0	3.2
Relative elongation, %	140	160	460	200	210	220	500	530	380

An oligomer was thermostated at 70°C for a definite time, and the time of its outflow from a Hoeppler viscometer was determined. A traditional plasticizer of sealing compounds, dibutyl phthalate (DBP), considerably reduces the viscosity of ODUE, whereas EDOS participates in formation of a three-dimensional structure: The viscosity increases by a factor of almost two. This, apparently, accounts for the increased (to 4.2 MPa) nominal tensile strength of the composites and decreased (to 160%) relative elongation.

Table 4. Viscosity of ODUE in the presence of plasticizers at 70°C

Composition	Viscosity after indicated thermostating time, h			
	0	1	2	4
ODUE	9 min 41 s	8 min 25 s	6 min	6 min
ODUE + DBP	34 s	23 s	28.6 s	40.8 s
ODUE + EDOS	1 min 23 s	45 s	1 min 15 s	2 min 13 s

Thus, curing of ODUE with ethylenediaminomethylphenol in the presence of various modifiers involves formation of a three-dimensional polymeric network enhancing the cohesion strength and hardness of the composites.

The next step in development of sealants with ODUE as polymeric base was study of its copolymerization with polysulfide oligomer (PSO, GOST 12 812–80). It was proved previously [2] that catalysis of reactive oligothiols with ethylenediaminomethylphenol and their copolymerization with oligoepoxide follow

Table 5. Results of curing with agents traditionally used for curing PSO

Parameter	Sodium dichromate			Manganese dioxide		
	at indicated ODUE content, wt parts per 100 wt parts of PSO					
	–	10	20	–	10	20
Nominal tensile strength, MPa	2.6	2.6	2.3	2.4	2.1	1.7
Relative elongation, %	240	250	260	240	260	270
Adhesion to duralumin, kN m^{-1}	1.4	1.5	1.6	1.2	1.3	1.4

Table 6. Effect of the type of the modifier on the properties of thio urethane epoxy composites

Parameter	EDOS			POAP			POAE			ODP		
	wt parts											
	10	20	30	10	20	30	10	20	30	10	20	30
Working life, min	30	90	135	75	95	175	80	100	120	120	120	120
Nominal tensile strength, MPa	4.2	3.9	3.5	3.6	3.5	3.5	4.1	4.6	3.6	3.3	3.9	4.3
Relative elongation, %	370	380	380	270	300	350	400	290	260	440	400	390

the scheme

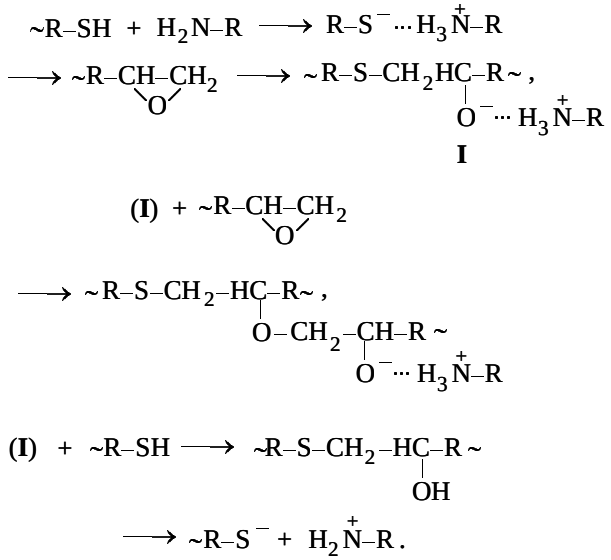

The catalytic effect of aminophenols is due not only to their capability to activate oxirane rings, but also to their proton-acceptor power, facilitating the proton detachment from the oligothiol molecule (the oxygen atom in the epoxy group is less nucleophilic than the sulfur atom in the mercapto group). This means that, at room temperature, oligothiol–ODUE block copolymers are formed first, which suggests formation of an interpenetrating polymer network, enhancing the deformation and elastic parameters of the composites. However, formation of block copolymers requires not only formation of an interpenetrating polymer network of the oligomers, but also efficient contact of terminal functional groups. In this case, the thermodynamic compatibility of the reacting groups becomes a significant factor, suppressing aggregation of the oligomers. In practice, it is advisable to use a mixture containing 10–20 wt parts of ODUE per 100 wt parts of PSO, or 25–30 wt parts of PSO per 100 wt parts of ODUE [3].

The use of traditional PSO curing agents in cocuring of the polymers does not appreciably enhance the physicomechanical parameters of the composites (Table 5).

For practical purposes, it is advisable to use the second region of thermodynamic compatibility of the polymers, i.e., 50 wt parts of PSO per 100 wt parts of ODUE; in this case, the dosage of aminophenol is 2–4 wt parts. The properties of thio urethane epoxy sealants modified with various agents, including oligodienepolyol (ODP), are listed in Table 6.

All the composites exhibit increased cohesion strength (3.3–4.6 MPa) and stable elasticity (260–440%), compared to commercial thiokol sealants

U-30MES-5 and U-30MES-10 (TU 38-10-54-62–80), characterized by the nominal strength of 2.5–3.0 MPa and relative elongation of 250–350%.

CONCLUSION

Oligodiene urethane epoxide is suitable as a polymeric base for sealing compounds if the oligomer is homocured to form a three-dimensional network and cocured with a polysulfide oligomer to form an interpenetrating polymer network, taking into account the region of thermodynamic compatibility of the reactive oligomers.

REFERENCES

1. RF Patent 2046814.
2. Elchueva, A.D., Sealants Based on Reactive Oligothiols, *Cand. Sci. Dissertation*, Kazan, 1989.
3. Polikarpov, A.P., Modification of Thiokol Sealants with Reactive Oligomers, *Cand. Sci. Dissertation*, Kazan, 1982.

Russian Journal of Applied Chemistry, Vol. 76, No. 3, 2003, pp. 491–496. Translated from Zhurnal Prikladnoi Khimii, Vol. 76, No. 3, 2003, pp. 506–511.

CHEMISTRY OF FOSSIL FUEL

Modification of Paving Asphalts with Sulfur

A. M. Syroezhko, O. Yu. Begak, V. V. Fedorov, and E. N. Gusarova

St. Petersburg State Technological Institute, St. Petersburg, Russia
Mendeleev Russian Research Institute of Metrology, State Unitary Enterprise, St. Petersburg, Russia
Kirishinefteorgsintez Production Association, Limited Liability Company, Kirishi, Leningrad oblast, Russia

Received October 31, 2002

Abstract—Sulfur dissolved in oil components of asphalt is a binder, filler, and chemical co-reagent at once. The structure of sulfur-extended asphalt depends on its formula and heating temperature. Road pavement based on sulfur-extended asphalt demonstrates higher durability as compared to that with the conventional binders.

Road pavement based on sulfur-extended asphalt demonstrates better mechanical characteristics and durability as compared to that based on the conventional binders. Recently there has been a steadily growing interest in sulfur-extended asphalts, because of the need in more rational utilization of great amounts of sulfur compounds from petroleum refining [1].

Sulfur is readily soluble in bitumen, especially in its aromatic components. The solubility of elementary sulfur in oxidized paving asphalts[1] at 120–150°C is at least 20 wt % [2].

Addition of sulfur in amount of up to 20 wt % to asphalt initiates chemical reactions whose type depends on the sulfur content and heating temperature and time of a given mixture. For example, some competing reactions can occur, including those with sulfur incorporation into the bitumen molecules or dehydrogenation with liberation of hydrogen sulfide. At heating temperature $T < 140$°C, elementary sulfur forms polysulfides in which unreacted sulfur dissolves. Along with asphaltenes, the indicated sulfur-containing compounds play a role of a structure-forming agent, i.e., they initiate formation of a network in which asphaltenes, paraffin, and sulfur stand as a dispersed phase, and molecules of resins and oils (malthenes), as a dispersion medium. Such structures differ considerably in the chemical and thermal stability from similar structures in unmodified oil asphalts.

Above 140°C, dehydrogenation of saturated components of bitumens can occur, whose depth depends on the final temperature of the reaction mixture. Also linear polysulfides can transform into stable cyclic thiophene structures. With increasing temperature, highly reactive asphaltenes and tars and also naphthene–aromatic compounds can react with sulfur through formation of the C–S bond.

It is known [3] that, at about 240°C, the reaction of sulfur with naphthene-aromatic compounds of bitumens gives asphaltenes, which play the crucial role in formation of a complex structural colloidal unit of bitumen.

Therefore, sulfur, as a chemical coreagent and filler, can have a considerable effect on the performance characteristics of paving asphalts. This effect was studied in this work.

EXPERIMENTAL

In experiments we used elementary sulfur, BND 60/90 paving asphalt and tar from the KINEF Limited Liability Company, broken granite (fraction 3–5 mm) from the Pulkovo asphaltic concrete plant, and gabbrodiorite (fraction 3–5 mm) from the Kuznechnoe deposit (Leningrad oblast).

The initial BND 60/90 paving asphalt has a softening point (T_s) of 49°C and penetration (Π_{25}) of 78 mm × 0.1.

Sulfur-extended composites were prepared as follows. A weighed portion of BND 60/90 was heated in a metallic crucible to 120°C, and then a fixed amount of elementary sulfur was added with vigorous stirring of the reaction mixture for 30 min.

The ring and ball softening point was determined according to GOST (State Standard) 9950; penetra-

[1] Paving asphalts from West-Siberian crude oil.

1070-4272/03/7603-0491$25.00

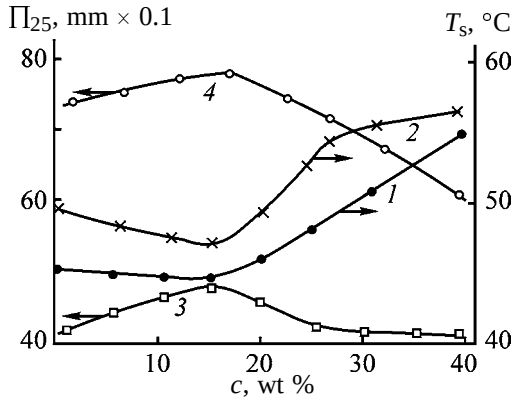

Fig. 1. Penetration Π_{25} (mm × 0.1) and softening point T_s of the composite as a function of the sulfur content (wt %): (*1*, *4*) before and (*2*, *3*) after heating.

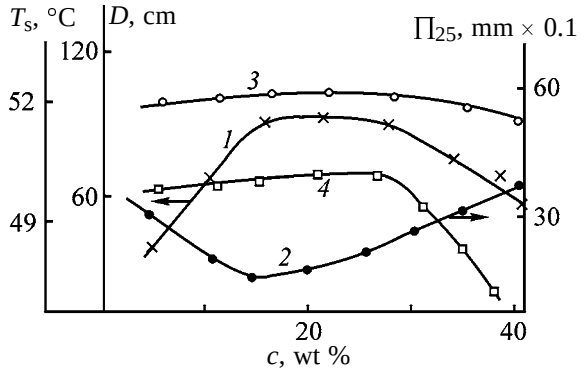

Fig. 2. (*1*) Softening point T_s, (*2*) penetration Π_{25}, and (*3*, *4*) ductility of the sulfur-extended composite *D* as functions of the sulfur content *c* during 2-month laboratory storage at 22°C: (*3*) before and (*4*) after heating.

tion, according to GOST 11508; ductility, according to ASTM D2872; and brittle point, according to GOST 11507 and also theoretically using the Gun equation [4]:

$$T_s - T_{br} = 70 - 7PI,$$

where T_s is the softening point (°C); T_{br}, brittle point (°C); and PI, penetration index (determined from a nomogram) [6].

The thermal stability of asphalts and their analogs (composites) was determined by the standard method. A weighed portion of a sample (60 ± 1 g) was placed into a stainless steel cup to form a 4-mm layer. The sample was heated at 160°C for 5 h. After heating, the softening point T_s, penetration Π_{25}, ductility *D*, and weight loss Δm (%) were measured.

The adhesion of a binder to a mineral filler was determined by the aqueous boiling method with granite and gabbrodiarite (3–5-mm fraction) at a 15 : 0.6 filler to bitumen ratio. Samples were placed onto a standard gauze and boiled for 30 min. The adhesion was estimated from the weight loss due to washing the binder off from the filler surface. Note that the 3–5-mm fraction used is the best suited to model the specific surface area of asphaltic concrete mixtures from the domestic plants.

The moisture content *W* (%) in the binder was estimated as

$$W = (W_1/W_2) \times 100,$$

where W_1 is the dry ball weight (g) and W_2, weight of the ball after saturation with water (g).

To obtain unmodified asphalt without oxidation of tar, a fixed amount of tar was placed into a metallic stirred reactor, the temperature was adjusted to 140–160°C, and powdered elementary sulfur was added. The reaction was performed for 30 min under stirring.

Evolution of properties of sulfur-extended asphalt before and after heating is shown in Fig. 1. In both cases, with small sulfur additions (5–10%), the hardness of BND 60/90 paving asphalt decreases, which is reflected in decreasing T_s and increasing penetration. The material becomes more plastic as compared to the initial material. With further increasing sulfur content, the softening point passes through a minimum and then gradually increases to the starting value. The penetration and softening point of sulfur-extended composites vary in opposite directions.

Thus, small additions (up to 10%) of sulfur to paving asphalt increase its plasticity, and large additions increase its hardness by virtue of higher degree of structuring and chemical interaction with asphalt components.

Transformation of the structure of asphalt modified with sulfur occurred not only in the preparation stage, but also in subsequent storage in the laboratory at 25°C (Fig. 2). During 2-month storage, the plasticity of sulfur-extended composites increased or decreased, depending on the sulfur content. In all cases, the penetration and softening point of sulfur-extended composites varied in opposite directions. Aging of the sulfur-extended composites is, evidently, accompanied by transformation of the micellar structure of asphalt. Here asphaltenes, paraffin, and various allotropic modifications of sulfur form a dispersed phase, and malthenes and tars form a dispersion medium. Reorganization of the solvate shell of primary micellar aggregates with formation of more compact structures proceeds slowly, being temperature-sensitive. It is of importance that, in the course of aging, T_s and pene-

tration vary within rather narrow ranges, i.e., sulfur-extended composites are relatively stable.

One more important characteristic of asphalt is the ductility reflecting the cohesion interaction between asphalt molecules. Sulfur additions (up to 20%) to paving asphalt appeared to have a positive effect on the ductility of the composites both before and after heating (Fig. 2). Note that heating at 160°C simulates the behavior of asphalt in the course of preparation of asphalt concrete hot mix.

The adhesion of the initial paving asphalt and sulfur-extended composites to a mineral filler (granite) is shown in Fig. 3 as a function of the heating time. Adhesion–cohesion interaction in both the initial paving asphalt and sulfur-extended composites depends on the contact time of the binder with granite. All the curves demonstrate the tendency to saturation at a contact time of about 2 h. It is important that, in the case of sulfur-extended composites with a sulfur content of 5–20%, the amount of asphalt retained on granite is higher as compared to the initial paving asphalt. This is consistent with the above-mentioned increase in the ductility of sulfur-extended composites.

With large sulfur additions (40%), the composite becomes loose, and its adhesion to the mineral filler is minimal.

In recent years, in laying roadbeds in the Russian Northwest, basic mineral fillers, particularly, gabbrodiorite have been widely used. This filler rapidly interacts with paving asphalt and sulfur-extended composites, so that establishment of the equilibrium takes shorter time (<30 min) as compared to granite. The composites with a sulfur content of up to 10% demonstrate higher adhesion than the initial paving asphalt. However, the composites containing 10–40% sulfur demonstrate lower adhesion than the initial material even at longer heating time. As in the case of granite, the strongest adhesion (adhesion–cohesion interaction) was observed in sulfur-extended composites containing 5% sulfur. At a heating time of 2 h, the maximal retention of the binder was 74.5 and 89% with granite and gabbrodiorite, respectively.

Based on tar from KINEF (T_s 39.3°C, $\prod_{25}$ 320 mm × 0.1), we prepared sulfur-modified composite binders (sulfur content 5, 10, and 20%). The heating temperature was 240°C, i.e., in this case sulfur was a chemical coreagent and filler. The performance characteristics of these composites (T_s, T_{br}, and $\prod_{25}$) are shown in Fig. 4. All the characteristics pass through an extremum at a sulfur content of about 10 wt %.

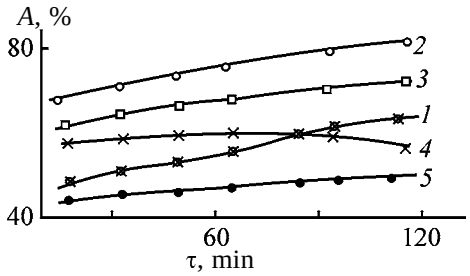

Fig. 3. Effect of the heating time τ of (*1*) paving asphalt and (*2–5*) sulfur-extended composites on the adhesion of asphalt to granite *A*. Sulfur content (%): (*2*) 5, (*3*) 10, (*4*) 20, and (*5*) 40.

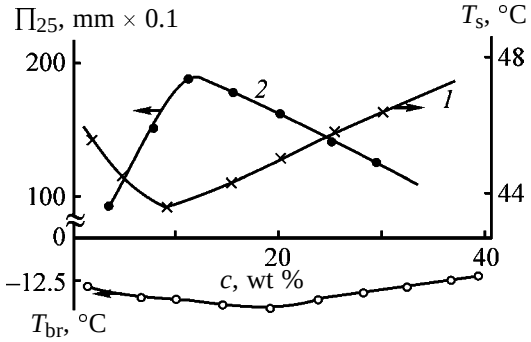

Fig. 4. Penetration $\prod_{25}$, softening point T_s, and brittle point T_{br} of sulfur-extended asphalts as functions of the sulfur content *c*.

The composite with a sulfur content of 5% meets the requirements of the GOST (State Standard) for BND 90/130 paving asphalt.

It should be pointed out that, at T < 95°C, sulfur exists as a cyclooctasulfane crown with an S–S bond length of 0.206 nm and S–S–S bond angle of 108°. At 119°C (melting point of sulfur), cyclooctasulfane turns partly into polymeric zig-zag chains (bond length 0.204 nm) [3]. At 119–159°C, molten sulfur exists essentially as cyclooctasulfane (λ-S). Above 159°C, eight-membered rings rapidly break down into biradicals [3]. In their turn, biradicals recombine to form polymeric chains with the maximal length of up to 10^6 sulfur atoms:

$$S_8 \rightleftarrows S^0\text{–}S_6\text{–}S^0$$

$$S^0\text{–}S_6\text{–}S^0 + S_8 \rightleftarrows S^0\text{–}S_6\text{–}S\text{–}S_8 \text{ etc.}$$

At 159–180°C, less stable (than S_8) cyclic structures having less or more sulfur atoms can occur in the melt. Linear sulfur biradicals are in equilibrium with large cyclic structures. The equilibrium sulfur species detected by ESR spectroscopy are as follows.

$$n\text{S}_8\text{(ring)} \rightleftarrows n\text{S}_8\text{–(chain)} \rightleftarrows (\text{S}_8)_n\text{(chain).}$$

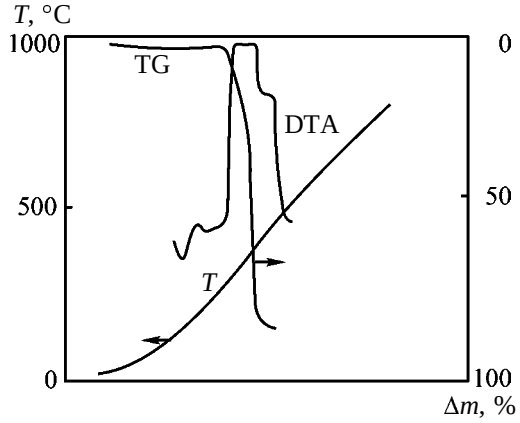

Fig. 5. TG and DTA curves of elementary sulfur. (*T*) Temperature and (Δ*m*) weight loss; the same for Fig. 6.

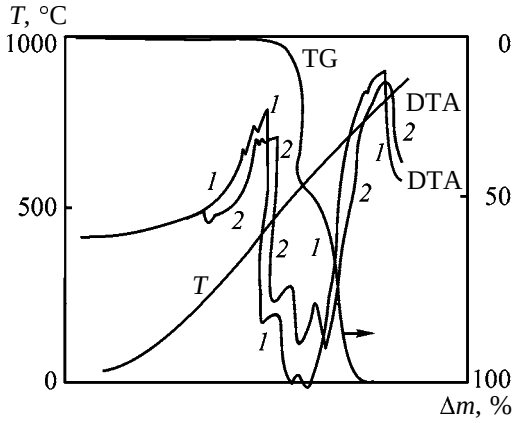

Fig. 6. TG and DTA curves of (*1*) BND 60/90 paving asphalt and (*2*) BND 60/90 + 5% S.

At T >200°C, sulfur is mahogany in color, and its melt contains S_3, S_4, and, possibly, S_2 fragments.

It was demonstrated in [5, 6] that alkanes C_7–C_{12} actively react with sulfur at lower temperatures (110–190°C) with formation of mercaptans, sulfides, and disulfides. It is known from the literature that arenes actively react with sulfur at 220–250°C, and in the presence of Lewis acids ($AlCl_3$), at 80–140°C.

Elementary sulfur was demonstrated to be the most reactive in the temperature range from 220 to 260°C (remarkable exothermic effect in the DTA curve in Fig. 5). Comparison of the DTA curves of BND 60/90 and the sulfur-extended composite (5% S) shows that at 240°C paving asphalt actively reacts with sulfur (Fig. 6). In the DTA curve, the exothermic effect of the composite is slightly weaker as compared to the initial asphalt. The maximal thermal effect due to reaction of asphalt components with sulfur was observed at 320–340°C, which was accompanied by active liberation of hydrogen sulfide. At lower temperatures, no noticeable liberation of hydrogen sulfide was observed.

At 390–425°C, active thermal decomposition of relatively thermally unstable paraffin–naphthene compounds takes place, which is reflected in clearly pronounced endothermic effect at 425°C. The IR data revealed the formation of a C–S bond at T >300°C. In this case, primarily, radical sulfur species react with unsaturated fragments of resins and alkenes (=C–S–S–C= or =C–S_{n+1}–C=).

Therefore, the major part of sulfur in asphaltic concrete mix (ACM) serves as a filler. The size of sulfur grains formed depends on the ACM preparation conditions (temperature; contacting time of tar, sulfur, and mineral filler; stirring rate; and cooling rate of the resulting composite).

It was demonstrated that the strength of sulfur-modified ACMs increases with time. Slow cooling of ACM samples results in formation of rigid mechanical contacts by virtue of sulfur crystallization. The structure of these contacts can be changed (damaged) in rapid cooling or mechanical failure (in compaction). With time, monoclinic sulfur transforms into orthorhombic sulfur, which is accompanied by increase in its strength. Therefore, structure formation in sulfur-containing organic binders is an important problem in view of development of durable sulfur organomineral materials.

It should be pointed out that, at T >100°C, the viscosity of the sulfur-extended asphaltic binder is lower by a factor of 1.6 than that of the initial paving asphalt, allowing reduction in the power consumption by virtue of decreasing temperatures of binder heating and ACM preparation by 25–30°C. Therefore, addition of 5–10% sulfur to asphalt or tar allows up to 30% saving of paving asphalt without deterioration in the characteristics of the resulting asphaltic concrete. It appeared that sulfur additions improve not only the binder ductility (Fig. 2), but also its viscosity–temperature characteristics, as clearly illustrated in Fig. 7. The T_{br}–c and D–c curves show extrema clearly pronounced at a sulfur content of 5–10%. Further increase in the sulfur content in the binder results in increasing brittle temperature and decreasing ductility. These results suggest that sulfur in the asphalt occurs in both liquid and crystalline states. Sulfur dissolved in oil components of asphalt has a plasticizing effect. Since the compounded paving asphalt based on tar and sulfur contains more oils and its dispersion medium is less structured with resins, the solubility of

sulfur in such asphalt is higher as compared to BND 60/90.

With decreasing temperature, the relative amounts of liquid and crystalline sulfur change in favor of the latter by virtue of decreasing solvency of the oil fraction. As a result, the maximal plasticizing effect is observed at low sulfur contents (Figs. 1, 2). Sulfur-extended binder has a wider operational range than the conventional paving asphalts. Additions of up to 10–15% sulfur provide such positive effect as decreasing brittle point of the binder, which is caused by improved low-temperature characteristics. At a sulfur content above 15%, the positive effect is caused by increasing T_S, i.e., as a result of increasing hardness of the paving asphalt.

Electron microscopic study of a sulfur-extended asphalt film confirmed the presence of dispersed sulfur uniformly distributed in the asphalt. This result was also supported by X-ray diffraction data (Fig. 8).

The plasticizing effect disappears in the course of prolonged storage (Fig. 4). Presumably, dissolved sulfur gradually crystallizes, thus increasing the degree of crystallinity of the material. Hence, with time, initially plastic thixotropic coagulation structure turns into rigid coagulation-crystalline structure, which is accompanied by changing properties of the binders (they turn from one rheological status into another typical of each type of the disperse structure), reflected in the binder viscosity (Fig. 7).

Note that, at T >119°C, liquid sulfur, being vigorously stirred with asphalt, is dispersed in it, forming an emulsion; and at T <119°C sulfur crystallizes. The crystallization features are affected by such factors as chemical reaction of sulfur with asphalt components and its dissolution or dispersion in the asphalt mass. The effect of newly formed structural links on properties of asphalts should largely depend on the asphalt structure. If the structure represents a maximally stabilized suspension of free asphaltenes (structure no. 11 by Kolbanovskaya), the effect of sulfur forming a crystallization network of a sort in the asphalt structure will be more distinctly pronounced than in the presence of a coagulation framework of asphaltenes (structure no. 111 by Kolbanovskaya). This effect should be reflected in increasing thermal stability, frost resistance, and elasticity of asphalt at low temperatures.

One of the features of sulfur is the manifestation of cementing properties in crystallization, i.e., in this case, sulfur is a structure-forming and binding agent simultaneously. Therefore, the desired combination of coagulation and crystallization structures in asphalt concrete and, therefore, its maximal durability can be attained by optimizing the sulfur content in asphalt.

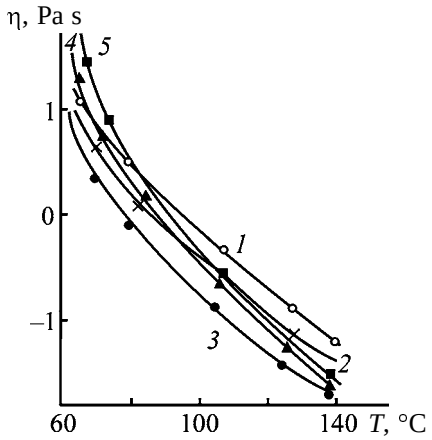

Fig. 7. Viscosity η of the binder as a function of the temperature T: (*1*) initial paving asphalt and (*2*–*5*) sulfur-extended BND 60/90. Sulfur content (wt %): (*2*) 5, (*3*) 10, (*4*) 30, and (*5*) 40.

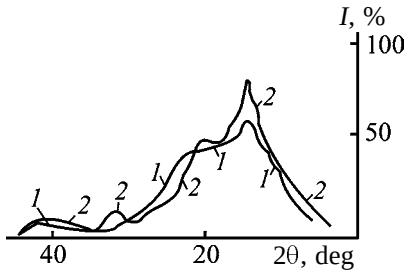

Fig. 8. X-Ray diffraction pattern of (*1*) initial paving asphalt and (*2*) sulfur-extended composite. (*I*) Relative intensity and (2θ) Bragg angle.

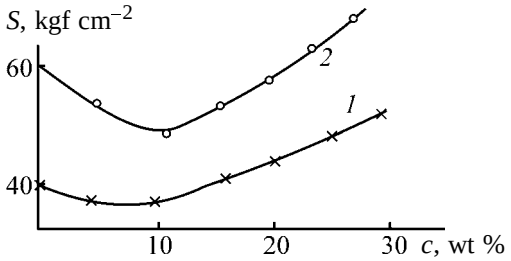

Fig. 9. Compressive strength of asphaltic concrete S as a function of the sulfur content c. Temperature (°C): (*1*) 20 and (*2*) 60.

Based on BND 60/90 paving asphalt, we prepared a cementing material by mixing the asphalt with molten sulfur at 140°C, followed by adding granite heated to the same temperature into the stirred apparatus. The strength of the resulting asphalt concrete passes through a minimum at a sulfur content of about 5% and then increases (Fig. 9). The strength is higher as compared to ACM based on conventional oil asphalt.

CONCLUSIONS

(1) With small additions of sulfur (below 10%), BND 60/90 paving asphalt becomes more plastic, and at high sulfur content, the bitumen structure becomes harder, as compared to the initial material.

(2) Adhesion–cohesion interaction of the initial paving asphalt and sulfur-extended composites depends on the time of contact of a binder with the mineral filler. The amount of paving asphalt retained on granite in a sulfur-extended composite (sulfur content 5–10%) is higher than that in the initial material.

(3) After heating for a short time (30 min), the sulfur-extended composites demonstrate higher adhesion to gabbrodiorite as compared to granite. The maximal amount of retained binder, determined by the aqueous boiling extraction method, was 74.5 and 89% on granite and gabbrodiorite, respectively, at a contact time of 120 min.

(4) Road paving based on sulfur-extended composites demonstrates better mechanical characteristics and durability as compared to the conventional binders.

REFERENCES

1. Sergienko, S.R., Taimova, B.A., and Talalaev, E.I., *Vysokomolekulyarnye neuglevodorodnye soedineniya nefti: Smoly i asfal'teny* (Macromolecular Nonhydrocarbon Petroleum Compounds: Tars and Asphaltenes), Moscow: Nauka, 1979.
2. Korgovenko, L.P., Ways to Deep Processing of Naphtha Residues of the Astrakhan Gas-Condensate Field, *Cand. Sci. Dissertation*, St. Petersburg, 2000.
3. Voronkov, M.G., Vyazankin, N.S., Deryagina, E.N., *et al*., *Reaktsii sery s organicheskimi veshchestvami* (Reactions of Sulfur with Organic Compounds), Novosibirsk: Nauka, 1979.
4. Gun, R.B., *Neftyanye bitumy* (Oil Asphalts), Moscow: Khimiya, 1973.
5. Stepan'yan, I.V., The Use of Sulfur as a Component of Asphalt Concrete, *Cand. Sci. Dissertation*, Moscow, 1988.
6. Perov, E.I., Moshchenskaya, N.V., Irkhina, E.P., and Smorodinov, V.S., *Neftekhimiya*, 2001, vol. 41, no. 5, pp. 384–388.

Russian Journal of Applied Chemistry, Vol. 76, No. 3, 2003, pp. 497–499. Translated from Zhurnal Prikladnoi Khimii, Vol. 76, No. 3, 2003, pp. 512–514.

BRIEF COMMUNICATIONS

Synthesis and Electrical Properties of Ammonium Fluorostannates(II)

N. I. Sorokin, E. G. Rakov, P. P. Fedorov, and R. M. Zakalyukin

Shubnikov Institute of Crystallography, Russian Academy of Sciences, Moscow, Russia
Mendeleev Russian University of Chemical Engineering, Moscow, Russia

Received December 5, 2001; in final form, July 2002

Abstract—With the aim of developing new fluorine-conducting solid electrolytes, the compound NH_4SnF_3 was synthesized and its electrical conductivity and thermal behavior were studied.

Tin(II) fluoride SnF_2 forms compounds $MSnF_4$ (M is Pb, Ba, or Sr) and MSn_2F_5 (M is NH_4, Na, K, Rb, Cs, or Tl), which have high unipolar electrical conductivity with respect to fluoride ions [1, 2]. Increased interest in solid electrolytes derived from SnF_2 is stimulated by prospects of their application in all-solid-state power sources, sensors, and other electrochemical apparatus. At the same time, successful application of solid electrolytes in practice requires reliable synthesis procedures to obtain materials with well reproducible chararacteristics.

In this work, ammonium trifluorostannate(II) NH_4SnF_3 was prepared and its electrical conductivity was studied.

EXPERIMENTAL

Ammonium trifluorostannate(II) was synthesized from tin(II) oxide, which, in turn, was prepared from $SnCl_2$ solution by adding a solution of $NH_3 \cdot H_2O$ to pH 9.5, separating the precipitate, repeatedly washing with distilled water, and heating the $Sn(OH)_2$ suspension for 4–5 h. The SnO and NH_4HF_2 weighed portions in a molar ratio of 1 : 1.5 were dissolved in distilled water at 60–70°C, and the solution was evaporated on a water bath until a precipitate formed, which was filtered off after cooling the solution and dried at room temperature.

Chemical analysis was performed as follows. Approximately 0.2-g portion was dissolved in hydrochloric acid, and tin(II) was determined by direct titration with an iodine solution in the presence of starch. The relative eror of the determination was less than 2%. The ammonia content was determined according to [3]. The relative determination error was less than 1%. The content of fluoride ions was not determined.

Found, mol %: NH_3 9.5; Sn(II) 59.5.
NH_4SnF_3. Calculated, mol %: NH_3 9.31; Sn(II) 61.34.

The product yield with respect to tin(II) was 92.4%. According to the X-ray phase analysis (HZG-4 diffractometer, CuK_α radiation), the samples studied are single-phase, and their structure (trigonal crystal system, a = 6.841(1) and c = 15.930(4) Å, Fig. 1a) corresponds that of NH_4SnF_3 [4]. The values available from Powder Diffraction File, Data Cards, JCPDS, no. 33–0081, are a = 6.842 Å and c = 15.92 Å.

Electrophysical properties were studied by impedance spectroscopy with a VM-507 impedansometer (frequency range 5 Hz–500 kHz, resistance range 1 Ω–10 MΩ) in a vacuum (~0.1 Pa). The electrodes were made from DAG-580 graphite paste (the Netherlands). The electrical conductivity σ was measured on pellets 5 mm diameter and 2–4 mm thick, obtained

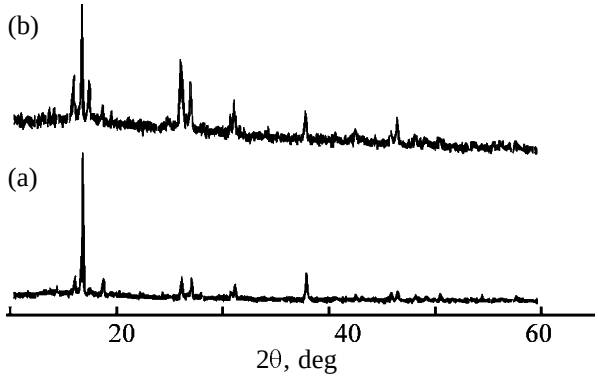

Fig. 1. X-ray diffraction patterns of ammonium fluorostannates(II). Sample: (a) initial (NH_4SnF_3) and (b) subjected to temperature measurements (NH_4SnF_3 + $NH_4Sn_2F_5$). (2θ) Bragg angle.

1070-4272/03/7603-0497$25.00

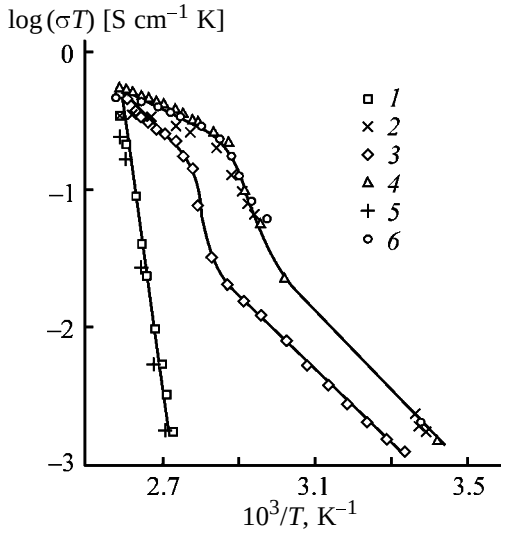

Fig. 2. log(σ*T*)–*T* plot. (σ) Conductivity of ammonium fluorostannates(II). Sample 1: (*1*) heating 1, (*2*) cooling 1, (*3*) heating 2, and (*4*) cooling 2; sample 2: (*5*) heating 1 and (*6*) cooling 1.

from thoroughly ground NH_4SnF_3 powder under a pressure of 4–5 MPa. The error in measuring σ was less than 5%. The activation energy E_a of the electrical conductivity was found from the formula

$$\sigma T = A\exp(-E_a/kT),$$

where A is the preexponential factor.

In σ measurements, the temperature was increased and decreased in steps, during each measurement it was kept constant.

The conductivity of the NH_4SnF_3 samples heated for the first time to 90°C remained lower than the sensitivity of the device (the total resistance exceeded 10^7 Ω). The low values of the NH_4SnF_3 conductivity in this temperature range are close to σ of alkali metal trifluorostannates at room temperature {σ ~ 10^{-9} S cm^{-1} [1]}. Above 90°C, σ dramatically grows (Fig. 2). On cooling and secondary heating, the compound showed a complex behavior indicative of hysteresis and phase transition. The transition region is recorded at 84±5 on heating and at 74±5°C on cooling. The temperature of the onset of the transition, as determined from both cooling and heating curves, is 78±2°C.

To interpret the results, we measured the diffraction patterns of the sample after measurements of σ at various temperatures and performed thermogravimetric analysis (Pt crucible, heating/cooling rate 10 deg min^{-1}, heating to 115°C). In addition to the NH_4SnF_3 lines, the lines due to $NH_4Sn_2F_5$ [rhombic crystal system, a = 12.4(3), b = 10.12(9), and c = 7.911(6) Å] appeared in the diffraction pattern (Fig. 1b). The values available from Powder Diffraction File, Data Cards, JCPDS, no. 16-0795, are a = 12.86, b = 10.05, and c = 7.91 Å.

Heating to 100°C is accompanied by weight loss (1.4 wt %). On cooling to 80°C, a clear endothermic peak, lacking in the heating curve, was recorded. This peak can be assigned to decomposition:

$$2NH_4SnF_3 \longrightarrow NH_4Sn_2F_5 + NH_3\uparrow + HF\uparrow.$$

This reaction is complete at a weight loss of 9.6 wt %, i.e., in the course of taking DTA curves 15% of the initial NH_4SnF_3 decomposed.

Thus, the samples were NH_4SnF_3 after the first heating to 90°C and an NH_4SnF_3 + $NH_4Sn_2F_5$ mixture after cooling and the second heating–cooling cycle. Apparently, a comparatively high electrical conductivity observed in this case in the samples studied (NH_4SnF_3 + $NH_4Sn_2F_5$) is completely determined by the formation of ammonium pentafluorostannate(II). The obtained data on the phase transition agree with the results of [2, 5, 6], according to which the phase transition in $NH_4Sn_2F_5$ occurs at 75°C [2, 5] or 70–84°C [6]. A small thermal effect accompanying this transition shows that the $NH_4Sn_2F_5$ polymorphous modifications being formed have similar structures. The conductivity value σ = 3×10^{-6} S cm^{-1} at 20°C is close to the published value (σ = 1×10^{-6} S cm^{-1} at 27°C [7]), and the activation energy E_a = 0.52 eV (20–75°C) reasonably agrees with the published values for $NH_4Sn_2F_5$ (E_a = 0.5 [2, 5] and 0.65 eV [7]).

The phase transition in $NH_4Sn_2F_5$ is accompanied by an approximately twofold increase in the activation energy of the ionic transfer and increase in the electrical conductivity by an order of magnitude. The ionic conductivity reaches 10^{-3} S cm^{-1} at 100°C. The high conductivity of $NH_4Sn_2F_5$ above 80°C was also observed in [5–7]. The obtained value of the activation energy for the high-temperature modification (E_a = 0.3 eV) is close to the published value (E_a = 0.34 eV at T > 84°C [6]).

The measurement of the transferrence numbers for electrons (t_e) in MSn_2F_5 shows that the contribution of electronic transfer to the total electrical conductivity is insignificant: for $RbSn_2F_5$ $t_e \sim 2\times10^{-5}$ at 122–168°C [7]. The structural elements of $NH_4Sn_2F_5$ are ammonium ions $[NH_4]^+$ and complex anions $[Sn_2F_5]^-$. Therefore, it was important to reveal their role in

the ionic transfer. NMR studies [1, 8] showed that reorientation of $[NH_4]^+$ ions is the main relaxation process in $NH_4Sn_2F_5$ at low temperatures, and diffusion of fluoride ions, above –20°C. In addition, according to the ^{19}F NMR data, fluoride ions occupy dynamically nonequivalent positions and this nonequivalence disappears after the phase transition. All this shows that the transfer of fluoride ions is responsible for the observed temperature dependence of the electrical conductivity in $NH_4Sn_2F_5$.

CONCLUSIONS

A study of the electrophysical properties of ammonium fluorostannate(II) shows that the NH_4SnF_3 conductivity is low ($\sigma < 10^{-6}$ S cm^{-1} below 90°C). Apparently, comparatively low values of σ in NH_4SnF_3 and alkali metal trifluorostannates(II) are due to a long distance between the $[SnF_3]^-$ complex anions in the crystal lattice. It was confirmed that at 74–84°C $NH_4Sn_2F_5$ undergoes the phase transition into the state with a high ionic conductivity ($\sigma \sim 10^{-3}$ S cm^{-1} at 114°C).

ACKNOWLEDGMENTS

The authors are grateful to V.V. Kireev for participation in the experiment.

REFERENCES

1. Murin, I.V., *Izv. Sib. Otd. Akad. Nauk SSSR, Ser. Khim. Nauk*, 1984, no. 2, pp. 53–61.
2. Reau, J.M., and Grannec, J., *Inorganic Solid Fluorides*, Hagenmuller, P., Ed., London: Academic, 1985, pp. 423–467.
3. Kreshkov, A.P., *Osnovy analiticheskoi khimii* (Fundamentals of Analytical Chemistry), Moscow: Khimiya, 1965, vol. 2.
4. Acker, E., Recker, K., and Haussuhl, S., *J. Cryst. Growth*, 1976, vol. 35, pp. 165–168.
5. Vilminot, S., Perez, G., Granier, W., and Cot, L., *Rev. Chim. Miner.*, 1980, vol. 17, no. 4, pp. 397–403.
6. Murin, I.V., Peceliunaite, A., Kezionis, A., *et al.*, Abstracts of Papers, *10th Int. Conf. on Solid State Ionics*, Singapore, December 3–8, 1995, p. 436.
7. Murin, I.V., and Chernov, S.V., *Vestn. Leningr. Gos. Univ.*, 1982, no. 10, issue 2, pp. 105–107.
8. Battut, J.P., Dupuis, J., Robert, H., and Granier, W., *Solid State Ionics*, 1983, vol. 8, pp. 77–81.

Russian Journal of Applied Chemistry, Vol. 76, No. 3, 2003, pp. 500–502. Translated from Zhurnal Prikladnoi Khimii, Vol. 76, No. 3, 2003, pp. 515–517.

BRIEF COMMUNICATIONS

Turbidimetric Titration of Ethyl Acetate Extracts of Halo- and Aminobenzoic Acids

Ya. I. Korenman, N. A. Konstantinova, and S. I. Niftaliev

Voronezh State Technological Academy, Voronezh, Russia

Received September 10, 2002

Abstract—The extraction of halo- and aminobenzoic acids from aqueous solutions with a hydrophilic solvent (ethyl acetate) was studied. Conditions for turbidimetric titration of these acids in the organic extract were optimized. Procedures for reliable nonaqueous titration of acids were developed.

Wastewaters from paint-and-varnish industry and production of chemical agents for plant protection, polymeric materials, drugs, and vitamins are contaminated with halo- and aminobenzoic acids [1, 2]. Supply of these acids into water of storage basins and sewage treatment plants affects pH, destroys microflora, and prevents biological treatment of water.

We found that these acids can be extracted from aqueous solutions with a hydrophilic solvent (ethyl acetate) and then determined in nonaqueous extract without backwashing.

The aim of this work was to develop an extraction-titrimetric method for determination of monoamino- and also mono- and polyhalo-substituted benzoic acids in aqueous solutions.

EXPERIMENTAL

The acids under consideration were extracted at pH ~ 2 and 20 ± 2°C. In order to prevent mutual dissolution of the organic and aqueous phases in extraction, ethyl acetate and water were preliminarily saturated with water and ethyl acetate, respectively. Before extraction, an aqueous solution of an organic acid to be determined was acidified with H_2SO_4, and then a prescribed amount of ethyl acetate was added. Extraction was performed at the organic to aqueous phase ratio of 1 : 10 (by volume) for 10–15 min. Under these conditions, the extraction equilibrium was attained. The equilibrium extract was quantitatively separated from the aqueous phase, transferred to titration cell, and titrated potentiometrically with 0.01 M KOH in ethanol using a glass indicator electrode and an electrochemical circuit with charge transfer

$$\mathrm{GE}\,|\,\mathrm{H^+BA}\,|\,\mathrm{AgCl}\,|\,\mathrm{KCl},$$

where GE is a glass electrode; BA, substituted benzoic acid; and AgCl/KCl, silver chloride electrode filled with saturated ethanolic solution of KCl.

The distribution factor D and degree of recovery of acids in single extraction step were calculated by known equations [3].

The concentration of substituted benzoic acid in the nonaqueous concentrate obtained by extraction of this acid with ethyl acetate was determined as follows. The concentrate, preliminarily diluted with ethyl acetate if necessary, was poured into a photometric cell and then titrated with 0.01 M KOH in ethanol. In titration, 0.02-ml portions of the titrant were added from a microburet to the titrated solution at its continuous stirring with a mechanical stirrer. The changes in the optical density of the solution in the course of titration was registered in 20 s after addition of each portion of the titrant on a KFK-2MP photocolorimeter.

The amount of acid in the solution analyzed m (mg) was calculated by the equation

$$m = 0.01cVMR,$$

where c is the titrant concentration (M); V, titrant volume (ml) consumed in titration; M, equivalent weight of acid (g mol^{-1}); and R, degree of extractive recovery of the acid (%).

It is known that the degree of extractive recovery of weak acids from aqueous solution is dependent on pH of the aqueous phase [4]. With lowering pH, ionization of weak acids in the aqueous phase is suppressed, and, as a result, the degree of their transfer into the organic solvent (i.e., the extraction efficiency) increases. To ensure favorable conditions for extrac-

1070-4272/03/7603-0500$25.00

tion of the acids under consideration, the aqueous phase was acidified to pH ~ 2. The distribution factors of acids determined in our experiments are listed in the table.

Extraction of acids with ethyl acetate is influenced by the water and ethyl acetate concentrations in both organic and aqueous phases. In going from benzoic acids with hydrophobic substituents to those with hydrophilic substituents, the distribution factors decrease.

It was found in [5] that, in extraction of acids with ethyl acetate, virtually anhydrous extracts are formed. Therefore, ethyl acetate is a poor extractant for organic acids with hydrophilic substituents (OH, NH_2).

Owing to specific steric configuration of the *meta* and *para* isomers of acids [6], these compounds are characterized by stronger hydration. As a result, their solvation with ethyl acetate weakens and the distribution factor decreases. Therefore, 3- and 4-aminobenzoic acids are extracted poorly. The increase in the distribution factor *D* of 2-aminobenzoic acid can be explained in terms of the Hildebrand theory of the regular solutions [7]. According to this theory, the intramolecular hydrogen bonding decreases both the enthalpy of vaporization and the cohesion energy density, and the latter parameter becomes close to the solubility parameter of ethyl acetate. Therefore, the solubility of 2-aminobenzoic acid in ethyl acetate increases, and, as a result, its extraction with ethyl acetate also increases.

Halobenzoic acids containing hydrophobic halide atoms are virtually completely extracted with ethyl acetate. The *ortho*-substituted halobenzoic acids are characterized by strong mesomeric conjugation between the halogen atoms and benzene ring. This effect strengthens the hydrogen bonding, which, in turn, increases the extractability of halo-substituted acids [8]. Their extractability decreases with decreasing electronegativity of halide substituents (chlorine > bromine > iodine [9]).

With increasing number of substituents, the distribution coefficient of halo-substituted acids increases owing to increase in their hydrophobicity. An exception is 2,4-dichlorobenzoic acid, which is more soluble in water than 2-chlorobenzoic acid [10].

We found that potassium 2-bromo-, amino-, and chlorobenzoates are insoluble in ethyl acetate. Therefore, the corresponding benzoic acids were titrated turbidimetrically with a KOH solution in ethanol.

To provide reliable and sufficiently accurate determination, the poorly soluble salt of the titrated acid should be formed in the course of titration and this salt should form a sol exhibiting aggregative stability and strong light scattering [11].

Distribution factors and degrees of extraction of halo- and aminobenzoic acids from aqueous solutions with ethyl acetate $r = 10$, $n = 4$, and $P = 0.95$

Acid	*D*	*R*, %
2-Aminobenzoic	510 ± 10	98.2
3-Aminobenzoic	61 ± 3	85.3
4-Aminobenzoic	10 ± 1	50.0
2-Chlorobenzoic	515 ± 8	98.1
2,4-Dichlorobenzoic	220 ± 5	95.7
2-Iodobenzoic	190 ± 4	95.0
2,5-Diiodobenzoic	273 ± 6	96.5
2,3,5-Triiodobenzoic	300 ± 7	96.8
2-Bromobenzoic	460 ± 9	97.9
5-Bromosalicylic	108 ± 6	91.4

The sols formed in titration of aminobenzoic acids with KOH do not meet these requirements. The curves of their turbidimetric titration do not show clear inflection points necessary for determining the equivalence point.

In order to choose the optimal wavelength for turbidimetric titration of the acids studied, Rayleigh spectra of their ethyl acetate extracts treated with excess KOH were registered against the initial transparent extract. These studies showed that the optimal light scattering occurs at a wavelength of 440–540 nm. To ensure the maximal accuracy, the optical density was registered in a 2-cm optical cell.

Our experiments showed that the curves of turbidimetric titration of 2-chlorobenzoic, 2,4-dichlorobenzoic, and 2-bromobenzoic acids are identical (see figure). This figure shows that, in the course of turbidimetric titration, the optical density passes through

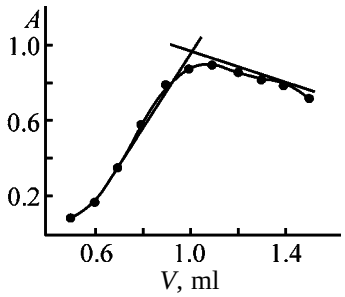

Curve of turbidimetric titration of 2,4-dichlorobenzoic acid in the ethyl acetate extract. Titrant: 0.01 M KOH solution in ethanol; $\lambda = 490$ nm. (*A*) Optical density and (*V*) titrant volume.

a maximum corresponding to the equivalence point and then decreases owing to coagulation of the sol and its dilution with excess titrant. The linear parts of the titration curve before and after the maximum were extrapolated to their interception, and the abscissa of the interception point was taken as the equivalence point. The turbidimetric titration provides fast and precise determination of substituted benzoic acids without using expensive chemicals. The determination error does not exceed 8%. The detection limit is about 0.1 mg l^{-1}. The presence of foreign mineral acids does not interfere with determination of benzoic acids.

CONCLUSIONS

Extraction of monoamino-, 2-chloro-, 2,4-dichloro-, 2-iodo-, 2,5-diiodo-, 2,3,5-triiodo-, and 2-bromobenzoic and 5-bromosalicylic acids from aqueous solutions with ethyl acetate was studied, and the optimal conditions for their turbidimetric titration in the organic extracts were found. The simple and reliable techniques for extraction-turbidimetric determination of acids in aqueous solutions at their concentration of about 0.1 mg l^{-1} were developed.

REFERENCES

1. Gorelik, M.D. and Efros, L.S., *Osnovy khimii i khimicheskoi tekhnologii aromaticheskikh soedinenii* (Fundamentals of Chemistry and Chemical Technology of Aromatic Compounds), Moscow: Khimiya, 1992.
2. Petrova, V.S., Shestakova, S.I., and Kunalenko, S.S., *Aminobenzoinye kisloty, ikh fiziko-khimicheskie svoistva i biologicheskaya aktivnost'* (Aminobenzoic Acids, Their Physicochemical Properties and Biological Activity), Ser: *Khimicheskie sredstva zashchity rastenii* (Chemical Agents for Plant Protection), Moscow: NIITEKHIM, 1989.
3. *Osnovy analyticheskoi khimii. Obshchie voprosy. Metody razdeleniya* (Fundamentals of Analytical Chemistry. General Problems. Separation Techniques), Zolotov, Yu.A., Ed., Moscow: Vysshaya Shkola, 1999.
4. Korenman, Ya.I., *Ekstraktsiya v analize organicheskikh veshchestv* (Extraction in Analysis of Organic Substances), Moscow: Khimiya, 1977.
5. Korenman, I.M., Ermolaeva, T.N., and Mishina, A.V., *Primenenie metoda sechenii dlya postroeniya troinykh diagram organicheskii gidrofil'nyi rastvoritel'–vysalivatel'–voda* (Application of Section Technique to Constructing Diagrams of Ternary Systems Organic Hydrophilic Solvent–Salting-Out Agent–Water), Available from VINITI, May 6, 1993, no. 1197-V93.
6. Cary, F.A. and Sundberg, R.J., *Advanced Organic Chemistry. Part A: Structure and Mechanisms*, New York: Plenum, 1977.
7. Fialkov, Yu.Ya., Zhitomirskii, A.N., and Tarasenko, Yu.A., *Fizicheskaya khimiya nevodnykh rastvorov* (Physical Chemistry of Nonaqueous Solutions), Leningrad: Khimiya, 1973.
8. Pliev, T.N., *Izv. Vyssh. Uchebn. Zaved., Khim. Khim. Tekhnol*., 1987, vol. 30, no. 5, pp. 29–33.
9. Neiland, O.Ya., *Organicheskaya khimiya* (Organic Chemistry), Moscow: Vysshaya Shkola, 1990.
10. *Svoistva organicheskikh soedinenii: Spravochnik* (Properties of Organic Substances: Handbook), Potekhin, A.A., Ed., Leningrad: Khimiya, 1984.
11. *Titrimetricheskie metody analiza nevodnykh rastvorov* (Titrimetric Techniques for Analysis of Nonaqueous Solutions), Bezuglyi, V.D., Ed., Moscow: Khimiya, 1986.

Russian Journal of Applied Chemistry, Vol. 76, No. 3, 2003, pp. 503–504. Translated from Zhurnal Prikladnoi Khimii, Vol. 76, No. 3, 2003, pp. 518–519.

BRIEF COMMUNICATIONS

Water Treatment To Remove Phenols in a Bubble Extractor

B. A. Alimatov and V. M. Sedov

Fergana Polytechnic Institute, Fergana, Uzbekistan
Russian Research Institute of Petrochemistry, St. Petersburg, Russia

Received June 6, 2002

Abstract—Water treatment to remove phenols using a bubble extractor is studied for specific conditions of the Fergana Refinery.

In oil-refining industry, to remove phenols, water is treated using such methods as extraction and evaporation, since the phenol concentration in wastewater is mostly high (above 3–4 g l^{-1}), and recycling of phenols completely covers the expenses for their recovery [1]. In extractive recovery, such solvents are used as carbon tetrachloride, butyl acetate, benzene, etc.

For wastewater treatment to remove phenols, a bubble extractor was proposed [2], whose design and operation are shown in the figure.

Vertical housing *1* of the extractor is divided into separate settler sections with horizontal baffle plates *2*. Mixing elements consisting of inner (*3*) and outer (*4*) concentric pipes are arranged on baffle plates *2*. The lower ends of the pipes *3* run out under the baffle plate *2*, being gas-distributing nozzles *5* with holes *6* in their sidewalls. Downpipes *7* with holes *8* at the lower blanked-off end sides are also arranged at the baffle plates *2*. The downpipes *7* are covered from above with caps *9* having cuts *10* at the lower section and holes *11* in the upper covers. Gas-intake pipes *12* are also arranged at baffle plates *2*. At the upper blanked-off ends they have holes *13* for supply of an inert gas to the annular channel between concentric pipes *3* and *4* of the mixing element.

The extractor flowsheet is as follows. A light fluid is supplied to pipe *3* through the lower section of gas-distributing nozzle *5*. A heavy fluid is supplied right there through holes *8* in downpipes *7*. Moving together bottom-up along pipe *3*, the fluids are vigorously mixed with a part of the inert bubbling gas that is fed through holes *6* and collected after mixing in a "gas bag" under baffle plate *2*. Another part of the inert gas is supplied through holes *13* of gas-intake pipes *12* to the annular channel between concentric pipes *3* and *4*. Moving bottom-up through a countercurrent flow of the fluids, the inert gas vigorously

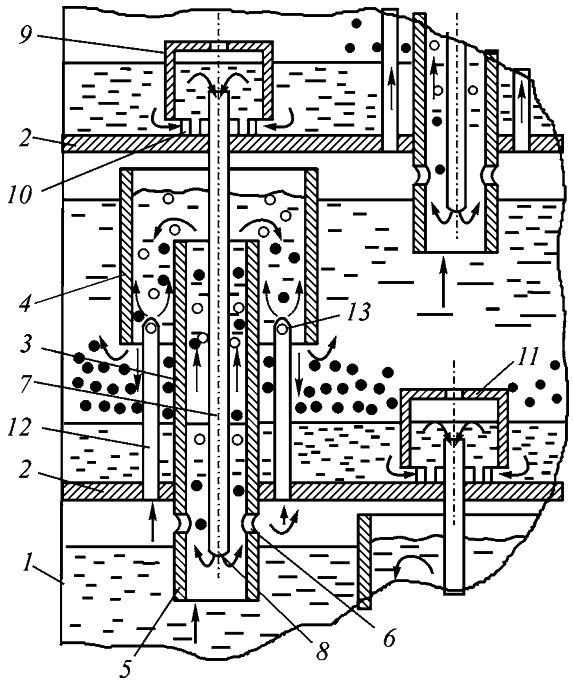

Bubble extractor (for explanation, see text).

mixes them and is then collected in a "gas bag" under baffle plate *2*.

Fluids mixed with the inert gas bubbles in pipe *3* and additionally in the annular channel between con-

Table 1. Characteristics of extractors (phenolic water–benzene liquid system)

Extractor type	Number of steps	Efficiency of step
Mixer–settler	5	0.73–0.79
Mixer–settler with a transfer pump	3	0.95
Mixer–settler with a stirrer	8	0.75
Multistep bubble extractor	3	0.93

1070-4272/03/7603-0503$25.00

Table 2. Physicochemical characteristics of liquid systems

Phase	c, g l^{-1}, for indicated extractor step			ρ, kg m^{-3}	$\mu \times 10^3$, Pa s	σ, N m^{-1}
	I	II	III			
Wastewater	0.12* 0.017	0.017 0.0037	0.0037 0.0007	1000	1.28	42.8×10^{-3}
Benzene	0 0.0015	0.0015 0.007	0.007 0.04	870	0.65	

* Initial and final concentrations are given in the numerator and denominator, respectively.

centric pipes *3* and *4* go to the settling section, where they are separated into phases. Drops of the heavy fluid settle, forming a continuous layer on baffle plate *2*, from which the heavy fluid flows through cuts *10* to downpipes *7* and then spills over to the underlying section. In this case, the position of the phase boundary between the light and heavy fluids is controlled by the position of the upper section of downpipes *7*.

The cross section of the annual channel is set so as to meet the requirement that the bottom-up fluid flow velocity is lower than the velocity of gas bubble flotation from holes *13* of pipes *12* to this channel. The arrangement of holes *13* of gas-intake pipes *12* below the lower section of pipe *4* guarantees getting of gas bubbles only to the annular channel between concentric pipes *3* and *4*.

Additional mixing of fluids in the annular channel between the concentric pipes of the mixing element is equivalent to increase in the residence time of the fluid mixture in the turbulence zone of the mixing element, thus improving the extraction efficiency.

The extractor efficiency is controlled by its diameter and the number of mixing elements per section. The desired degree of recovery of a target component is controlled by the number of sections.

We selected benzene as an extractant, because of its easy availability and relatively low distribution coefficient (according to [3], the distribution coefficient of phenols is 0.4, 2.4, and 8–12 in carbon tetrachloride, benzene, and butyl acetate, respectively).

It is of no small importance also that, because of a small phenol concentration in the extractant (benzene), the latter can be regenerated by the phenol–phenolate method [1].

Characteristics of the multistep bubble extractor proposed for wastewater treatment to remove phenols [2] are given in Table 1. The characteristics of extraction apparatuses of other types used in industry for this purpose are given for comparison.

In this work, first, we theoretically determined the overall mass transfer coefficient and single step efficiency (K_v = 0.04 s^{-1} and η = 0.92) using the relationships proposed in [4]. Then we estimated the required number of extraction steps using the grapho-analytical method [5]. This number is 3.

Experiments were conducted with industrial fluid systems from the Fergana Refinery using a model three-step bubble extractor. The benzene : water ratio was 3 : 1. The maximal water consumption was 0.13 $m^3 h^{-1}$, and that of benzene, 0.39 $m^3 h^{-1}$. The initial and final phenol concentrations in the phases are given in Table 2. The table also includes data on physicochemical characteristics of the fluid systems used (density ρ, viscosity μ, and interfacial tension σ), determined by standard methods.

Finally, it was demonstrated that treatment of 120 m^3 of wastewater with the initial phenol concentration of 0.12 g l^{-1}, to obtain the final concentration of 0.0007 g l^{-1}, requires a three-step bubble extractor with a working height of 3.2 m and a diameter of 1.96 m. The expected annual cost efficiency due to utilization of recovered phenols is 175 000 rubles.

REFERENCES

1. Proskuryakov, V.A. and Shmidt, L.I., *Ochistka stochnykh vod v khimicheskoi promyshlennosti* (Wastewater Treatment in Chemical Industry), Leningrad: Khimiya, 1977.
2. USSR Inventor's Certificate no. 1 607 859.
3. Kharlampovich, G.D. and Churkin, Yu.V., *Fenoly* (Phenols), Moscow: Khimiya, 1974.
4. Alimatov, B.A., Sokolov, V.N., and Abdurazakov, A.A., *Nauchn.-Tekh. Zh. Fergan. Politekh. Inst.*, 2000, no. 2, pp. 104–107.
5. Alimatov, B.A., Sokolov, V.N., and Karimov, I.T., *Nauchn.-Tekh. Zh. Fergan. Politekh. Inst.*, 2000, nos. 3–4, pp. 107–110.

Russian Journal of Applied Chemistry, Vol. 76, No. 3, 2003, p. 505. Translated from Zhurnal Prikladnoi Khimii, Vol. 76, No. 3, 2003, p. 520.

BRIEF COMMUNICATIONS

Mechanism of Deuterium Distribution in Ethanols

A. G. Sakhabutdinov, N. V. Kulagina, D. F. Kushnarev, A. G. Proidakov, and G. A. Kalabin

Institute of Petroleum and Coal Chemical Synthesis, Irkutsk State University, Irkutsk, Russia

Received October 10, 2002

Abstract—Deuterium distribution in ethanols produced by sulfuric acid hydration of ethylene was studied by quantitative NMR spectroscopy.

It is well known that the natural content of deuterium and the features of its distribution in structural fragments of molecules bear information on the origin of organic compounds [1]. In synthetic ethanol the deuterium content is 0.0134–0.0136%, and in food-grade ethanol its level is lower, from 0.0114 to 0.0122% [2]. However, irrespective of the ethanol origin, the deuterium content in the methyl group is higher than that in the methylene group by a factor of 1.1–1.4 in all cases [3]. Since all deuterated molecules occur in the form of d_1 isotopomer owing to minor content of deuterium, it was of interest to establish the mechanism of distribution of deuterium atoms between methyl and methylene groups of alcohol.

For this purpose, we simulated formation of ethanol by sulfuric acid hydration of ethylene and studied the deuterium distribution in this process, using deuterated sulfuric acid or [1,1-$^2H_2$]ethylene.

It was found that, in the ^2H NMR spectrum of ethanol produced by hydration of [1,1-$^2H_2$]ethylene in the presence of sulfuric acid, the intensities of signals of the methyl and methylene groups are the same. This means that proton is added to both carbon atoms of ethylene with equal probability, irrespective of deuterium substitution. Thus, the deuterium atom in the initial ethylene molecule does not affect the direction of proton addition and hence cannot be responsible for the different natural deuterium content in methyl and methylene groups of ethanol.

The ^2H NMR spectrum of ethanol produced by hydration of ethylene in deuterated sulfuric acid showed that addition of acid is accompanied by predominant deuteration of the methyl group, since the intensity of its signal is greater by a factor of more than 25 than the intensity of the signal of the methylene group. It is evident that, under the reaction conditions, the reverse decomposition of ethyl hydrogen sulfate to the initial substances proceeds to no more than 8%, and hydrogen atom of the acid mainly participates in formation of the methyl group.

The data obtained show that natural enrichment of ethanol with deuterium is caused by two sorts of deuterium atoms, deuterium of the substrate (ethylene) and reagent (acid). The deuterium content in the initial ethylene determines the amount of ethanol molecules deuterated in the methylene group, while higher fraction of molecules deuterated in the methyl group is caused by deuterium from acid.

EXPERIMENTAL

The reaction was carried out by the improved procedure in [4]. A mixture of 20 g of sulfuric acid and 0.2 g of the catalyst Ag_2SO_4 were vigorously stirred at 60°C in an ethylene medium until complete saturation. The resulting ethyl hydrogen sulfate was decomposed with a mixture of ice and water. The yield of ethanol after twofold distillation was 60%.

Ethanol was analyzed by ^2H NMR spectroscopy on a VXR-500S spectrometer operating at 76.7 MHz. The pulse length was 25 μs (90°), and delay, 8 s.

CONCLUSION

The deuterium content in methyl and methylene groups characterizes the components forming ethanol and can be used for determining its origin.

REFERENCES

1. Martin, G.J., Martin, M.L., and Mabon, F., *J. Am. Chem. Soc*., 1982, vol. 104, pp. 2658–2659.
2. Martin, G.J., Martin, M.L., Mabon, F., and Michon, M.J., *J. Agr. Food Chem*., 1983, vol. 31, pp. 311–335.
3. Martin, G.J., Martin, M.L., Mabon, F., and Michon, M.J., *Anal. Chem*., 1982, vol. 54, pp. 2380–2382.
4. Gluud, W. and Schneider, G., *Chem. Ber*., 1924, vol. 57, pp. 254–255.

1070-4272/03/7603-0505$25.00

Russian Journal of Applied Chemistry, Vol. 76, No. 3, 2003, pp. 506–507. Translated from Zhurnal Prikladnoi Khimii, Vol. 76, No. 3, 2003, pp. 521–522.

ANNIVERSARIES

Petr Anatol'evich Kirpichnikov (1913–1997)

On January 5, 2003, Petr Anatol'evich Kirpichnikov, a corresponding member of the Russian Academy of Sciences, Honorary Academician of the Academies of Sciences of the Republics of Tatarstan and Bashkortostan, Honored Scientist and Technologist of the Russian Federation and the Republic of Tatarstan, Laureate of a State Prize of the USSR, would be 90.

P.A. Kirpichnikov is a prominent scientist in the field of basic organic synthesis and macromolecular compounds. He made a major contribution to the theory and practice of development of new materials, especially rubbers and other elastomers, and to solution of problems concerning the aging and stabilization of polymers.

He was the first in the country to develop a new class of noncoloring stabilizers based on organophosphorus compounds, which effectively protect many kinds of polymers in their processing and exploitation.

He studied in detail the mechanism of their action in polymers, established the dependence of their performance on structure, determined the kinetic conditions for the appearance of a synergistic effect with organophosphorus compounds upon addition of second components. A set of investigations concerned with organophosphorus compounds resulted in that process regulations and feasibility calculations were developed and introduced into industrial practice.

Based on these studies, Kirpichnikov succeeded in solving a practically important problem of inhibiting the thermally induced polymerization of isoprene; in particular, this was done at the Nizhnekamsk combine.

An important direction in Kirpichnikov's works were studies in the field of synthesis and modification of polysulfide oligomers and polyurethane rubbers, which were used to synthesize new types of polymers, many of which are manufactured commercially and find wide application.

Kirpichnikov developed and introduced new processes into industrial practice.

Kirpichnikov was the author of more than 500 publications, 12 textbooks, manuals for higher school, monographs, and reviews; he received 330 inventor's certificates and patents. His disciples include 12 doctors and 60 candidates of science.

Kirpichnikov was an excellent pedagogue and tutor of young scientists. His services in organization of training of engineers for chemical industry are great.

When being the rector of Kazan Institute of Chemical Technology for 24 years, Kirpichnikov succeeded in making it one the most prominent higher school institutions of the country, in organizing new faculties, chairs, and branches, and in training highly skilled scientific and pedagogical workers. The institute became a center at which large conferences, symposia, workshops, schools, and All-Union, Russian, and republican schoolchildren contests were held.

Kirpichnikov was a prominent and talented science organizer, many years' head of the Kazan Branch of the Academy of Sciences of the USSR and Russian Academy of Sciences and the Tatarstan Division of the Mendeleev All-Union Chemical Society, and a member of the Editorial Board of *Zhurnal Prikladnoi Khimii* (Russian Journal of Applied Chemistry).

Kirpichnikov participated in the Great Patriotic

1070-4272/03/7603-0506$25.00

War. He served in the Air Force and was awarded orders and medals for service in battle.

Having been demobilized in 1947, Kirpichnikov was sent to Germany where he worked as chief engineer at a large chemical combine Buna, and, after Soviet plants were transferred to Germans in 1953, remained at this plant as adviser. For his contribution to the national economy of the German Democratic Republic, he received a government award "For Services in Foundation and Development of the GDR."

Kirpichnikov was a prominent public man, he was elected at member of the Supreme Soviet of the Republic of Tatarstan and Kazan City Soviet of People's Deputies, a member of the board of directors of the Soviet Foundation for Peace, and chairman of the committee for assistance to the Foundation for Peace of the Republic of Tatarstan.

The outstanding contribution of Kirpichnikov to the scientific, scientific-organization, and pedagogic activities was honored with numerous State awards and prizes.

The spirits and optimism of Petr Anatol'evich, his encyclopedic knowledge and culture in personal contacts won him deep respect of the scientific and pedagogic community, students, and industry managers.

Petr Anatol'evich was an outstanding, brilliant, and life-loving man. Despite that already 6 years have elapsed after he passed away, the pain of loss is still perceptible and the gratifying memory of him is still alive in those for whom he was a friend, co-participant in scientific creative work, and patient tutor. Petr Anatol'evich's disciples and colleagues continue to develop his ideas and hold jubilee conferences and sessions in his memory. This primarily refers to Kirpichnikov Readings, first held in 2000. These readings constitute a new tradition of the Kazan chemical school; in March 2003, Third Jubilee Kirpichnikov Readings will be held, devoted to problems of synthesis, study of properties, and processing of macromolecular compounds, and also to modern problems of education in chemical technology.

G. S. D'yakonov

Russian Journal of Applied Chemistry, Vol. 76, No. 3, 2003, p. 508. Translated from Zhurnal Prikladnoi Khimii, Vol. 76, No. 3, 2003, p. 523.

BOOK REVIEWS

Zainullin, Kh.N., Babkov, V.V., Zakirova, D.M., Chulkov, A.N., and Iksanova, E.M., *Utilizatsiya osadkov stochnykh vod gal'vanicheskikh proizvodstv* (Utilization of Sediments from Electroplating Shop Wastewater)

Moscow: Ruda i Metally, 2003, 272 pp.

Electroplating shops for various purposes are numerous in the country. According to the data presented by the authors of the monograph, about 5000 plants in Russia have such shops. However, utilization of their wastes, and sediments (sludge) formed in wastewater treatment in the first place, are far from being properly organized everywhere. This leads to pollution, significant excess over the maximum permissible concentration of heavy metals in soil and water bodies, and loss of valuable components. The monograph by Kh.N. Zainullin *et al*. is concerned with topical problems, which are important in environmental and economical regard. The authors have collected and analyzed a vast body of factual data.

The book comprises an introduction, eight chapters, conclusion, and bibliographic list. The introduction (pp. 4–16) discusses the possibility of using wastes from galvanic shops as secondary raw materials. It is noted that only 30–40% of metals and 5–20% of acids and alkalis constitutes useful expenditure. Small Chapter 1 (pp. 17–24) classifies sediments formed in wastewater at sewage treatment facilities. As examples serve typical data for electroplating shops of machine-building plants of the Republic of Bashkortostan. A practically convenient classification is that based on methods for utilization of sediments formed in wastewater of electroplating shops. Also possible are other approaches.

Chapter 2 (pp. 25–60) is devoted to the problem of waste disposal. Disposal is to be regarded as a forced measure, caused by the lack of acceptable processes for utilization of one or another kind of waste. At the same time, reliable disposal techniques are expensive and pose quite a number of environmental problems. Chapters 3 (pp. 61–83) and 4 (pp. 84–92) consider use of electroplating sludges in metallurgy. The main difficulties are posed by the pronounced inhomogeneity of composition, high moisture content, and presence of impurities hindering the recovery of the main component. A great number of flowsheets is considered. The depletion of resources of nonferrous metallurgy and the necessity for use of lean ores make processing of various kinds of secondary raw materials, including electroplating sludges, particularly topical. In their processing, both pyrometallurgical and hydrometallurgical techniques can be employed. The problems associated with recovery of valuable components from electroplating sludges by various techniques are also discussed in Chapter 5 (pp. 93–111).

Use of sludges for direct manufacture of a number of important products is the subject of Chapter 6 (pp. 112–123). As example serves production of catalysts, complex ferrites, paint-and-varnish materials, pigments, and means of corrosion protection. Chapter 7 (pp. 123–237) analyzes the possibility of utilizing wastes from electroplating shops in building-materials industry. The possibilities and prospects in this field are rather broad, but it is necessary to clearly establish the environmental safety level when using the materials thus obtained. There is no escape from mentioning that utilization of electroplating wastes by introducing them into building and pavement materials leads to irreversible loss of nonferrous metals. Chapter 8 (pp. 238–252) considers the possible organization measures for centralized utilization of electroplating wastes in cities or industrial regions. The brief conclusion (pp. 253–254) also contains organizational recommendations. The bibliographic list (pp. 255–271) includes references to 251 papers of mainly Russian authors.

The monograph gives a large number of useful recommendations concerning utilization of wastes from electroplating shops and discusses in most detail the problems associated with the use of wastes in building-materials industry. The book has technological purpose, is written in easily understandable language, and can be recommended for a very wide audience of engineers working at electroplating shops. Probably, the large number of the authors of the monograph resulted in that the text contains repetitions and the structure of the first six chapters is insufficiently clear. The book is well published and contains illustrative graphic material.

A. G. Morachevskii and I. N. Beloglazov

1070-4272/03/7603-0508$25.00 © 2003 MAIK "Nauka/Interperiodica"

Russian Journal of Applied Chemistry, Vol. 76, No. 4, 2003, pp. 509–512. Translated from Zhurnal Prikladnoi Khimii, Vol. 76, No. 4, 2003, pp. 529–532.

INORGANIC SYNTHESIS AND INDUSTRIAL INORGANIC CHEMISTRY

Calcium Phosphates Coprecipitated from Aqueous Solutions of Sodium Monophosphate and Diphosphate

V. A. Sinyaev, L. V. Levchenko, E. S. Shustikova, and J. Griggs

Institute of Chemical Sciences, Alma-Ata, Republic of Kazakhstan

Baylor College of Dentistry, The Texas A and M University System Health Science Center, Dallas, TX, USA

Received July 11, 2002

Abstract—Calcium phosphate compounds obtained by coprecipitation from sodium monophosphate and diphosphate aqueous solutions under the action of calcium chloride are described.

Materials based on crystalline hydroxyapatite are widely used in modern orthopedics and stomatology [1–3]. Recently, increasing interest has been expressed in calcium phosphate substances, which are close in composition to hydroxyapatite, but have amorphous nature. The enhanced reactivity, which results from thermodynamic instability, is an advantage of such substances over crystalline materials. Therefore, amorphous apatites can be regarded as promising compounds for regeneration of bone tissue and as precursors of bioceramics.

Crystalline hydroxyapatite is usually obtained by precipitation from aqueous solutions. This technique is based on ion-exchange reactions between soluble monophosphates and calcium salts [4]. If the precipitation is carried out in the presence of crystallization inhibitors, amorphous apatite-containing materials are formed. Various substances, such as fluorides, magnesium salts, polymeric phosphates, and calcium diphosphate can be used as inhibitors [4–7]. The last compound is of interest because it is rather close to hydroxyapatite in elemental composition and relative content of phosphorous(V) and calcium(II). An additional reason why the precipitated materials are amorphous may be formation of a nonstoichiometric hydroxyapatite

$$Ca_{(5-x/2)}(HPO_4)_x(PO_4)_{(3-x)}(OH)\cdot nH_2O,$$
$$0 < x < 1,\ n = 0\text{–}2.5,$$

which is promoted by low pH values. Since the presence of HPO_4^{2-} groups in the products is not always desirable, the acidity is usually maintained at pH 7–8 by adding an alkali in the course of precipitation or by using buffer solutions [4–7]. However, even under these conditions, a local momentary decrease in the pH value may occur at the surface of the forming particles as a result of liberation of an acid by the reaction

$$3Na_3PO_4 + 5CaCl_2 + H_2O \rightarrow Ca_5(PO_4)_3OH\downarrow + 9NaCl + HCl.$$

As a consequence, HPO_4^{2-} ions are incorporated, despite all the efforts, into the structure of the precipitated substance. To make lower the probability of this process, it is advisable to carry out precipitation in an alkaline medium where the local decrease in pH is minimized.

The aim of the study was to reveal the influence of the relative content of diphosphate ions on the nature of compounds precipitated with calcium chloride from sodium mono- (MP) and diphosphate (DP) aqueous solutions in the presence of an alkali, i.e., under conditions that hinder formation of a nonstoichiometric hydroxyapatite.

EXPERIMENTAL

Sodium hydrophosphate and diphosphate, Na_2HPO_4 and $Na_4P_2O_7$, of analytically pure grade were used in the study. Their 5% aqueous solutions were mixed in required proportions. The relative content of the salts in solutions was represented as DP/(DP + MP) ratio (MP and DF are, respectively, the numbers of moles of mono- and diphosphate in the starting solutions). Preliminarily, NaOH was added to phosphate solutions in amount sufficient to neutralize the whole

1070-4272/03/7604-0509 $25.00 © 2003 MAIK "Nauka/Interperiodica"

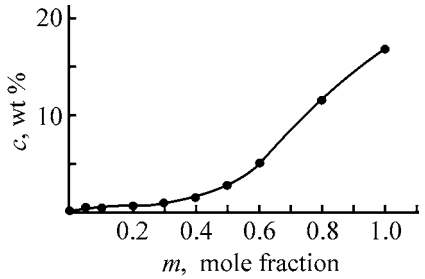

Fig. 1. Content of sodium ions *c* in precipitated phosphates vs. amount of sodium diphosphate *m* in starting solutions.

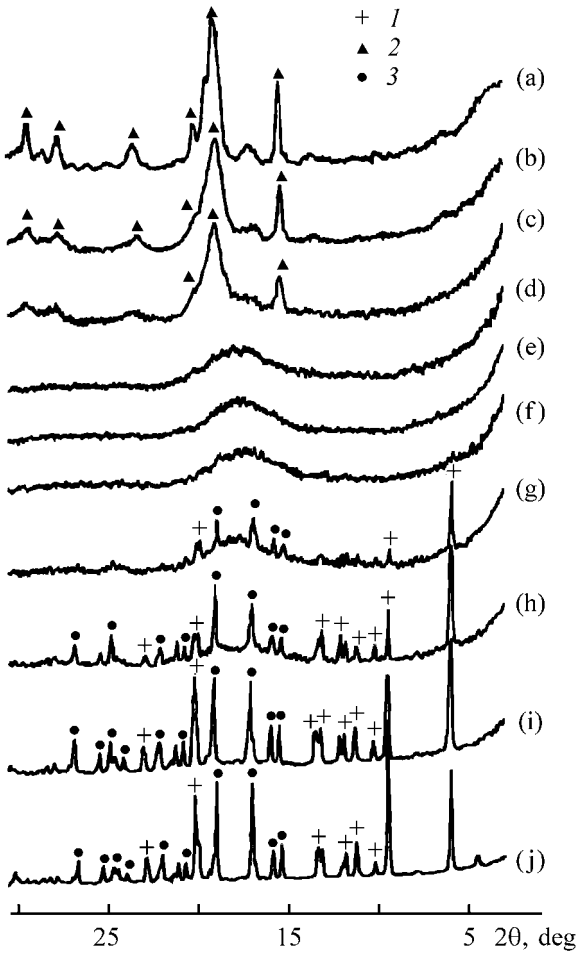

Fig. 2. X-ray diffraction patterns of precipitated products. (2θ) Bragg angle. Sodium diphosphate content in starting solutions (mol %): (a) 0, (b) 5, (c) 10, (d) 20, (e) 30, (f) 40, (g) 50, (h) 70, (i) 80, and (j) 100. (*1*) α-$Na_2CaP_2O_7 \cdot 4H_2O$, (*2*) $Ca_5(PO_4)_3OH$, and (*3*) β-$Ca_2P_2O_7$.

amount of acid liberated upon the hydroxoapitite formation. Calcium chloride (5% solution) was gradually added dropwise to the phosphate solutions under vigorous stirring. The precipitation terminated at pH 8. All the procedures were carried out at room temperature. The precipitates obtained were washed many times with a dilute NaOH solution with pH 8 until the washing water became free from chloride ions. After that the suspension was settled for 1–2 days and separated from water first by decanting and then by filtering on a porous glass filter. The substances dried at 60–80°C were studied by X-ray diffraction analysis and IR spectroscopy. A DRON-3 diffractometer (Co_{K_α} radiation) and a Jasco IR-810 IR spectrometer were employed for these purposes. KBr pellets were used to record the IR spectra. The content of sodium ions in the precipitated substances was determined by flame photometry on a FLAPHO var device.

In storage, aqueous suspensions separate into two layers: water and a more concentrated suspension. Products obtained from solutions with DP/(DP + MP) molar ratio of 0.4 separate into layers at the lowest rate. In all cases, the process is in fact complete within 5–7 h, and after that the suspensions become relatively dense precipitates which slowly loose moisture when stored in air.

The precipitates include sodium ions. It is seen from Fig. 1 that the content of sodium ions in the products obtained from solutions with molar ratios DP/(DP + MP) < 0.3–0.4 is rather small and depends on the composition of the starting solutions only slightly. The content of sodium ions in substances precipitated from solutions with higher relative DP content is higher and grows with increasing DP fraction in the starting solutions. It may be assumed that products containing sodium ions as an impurity are formed from DP-poor solutions, and calcium-sodium phosphates are precipitated from solutions with high relative content of sodium diphosphate.

According to the X-ray diffraction data, the product obtained from a solution of only sodium monophosphate is crystalline hydroxyapatite (Fig. 2a). Substances formed in the presence of even small amounts of sodium diphosphate show indications of amorphicity (Figs. 2b and 2c). The corresponding diffraction patterns suggest that these substances are based on hydroxyapatite. X-ray-amorphous products are precipitated from solutions with molar ratios $0.2 \le$ DP/(DP + MP) ≤ 0.4 (Figs. 2d–2f). If the relative content of sodium diphosphate is greater than 50%, substances containing crystalline diphosphates of calcium β-$Ca_2P_2O_7$ and calcium-sodium α-$Na_2CaP_2O_7 \cdot 4H_2O$ are formed (Figs. 2g–2j).

To elucidate the effect of the composition of starting solutions on the molecular base of the products, we studied these latter by IR spectroscopy. We found

two bands of medium intensity, which are peaked at 570 and 600 cm^{-1}, in the low-frequency region of the IR spectrum of the substance precipitated from sodium monophosphate solution, and a group of intense mutually overlapping bands peaked at 1030, 1060, and 1090 cm^{-1} in the range 950–1200 cm^{-1} (Fig. 3a). All these bands correspond to P–O stretching vibrations in hydroxyapatite monophosphate groups PO_4^{3-} [8–10]. The hydroxide ion is a structural unit of hydroxyapatite. Usually this group gives rise to a weak band ν_L(OH) at 630–640 cm^{-1} in IR spectra and also to a higher-intensity narrow band peaked at 3560–3570 cm^{-1}, which corresponds to ν_S(OH) vibrations [8–10]. In the spectrum under consideration, the first band appears as a weak peak with frequency of about 630 cm^{-1}. As for the ν_S(OH) band, it is replaced by a very broad and intense band at around 3420 cm^{-1}in the high-frequency region. This band is typical of stretching vibrations of O–H bonds in water molecules [11]. It is possible that this band and the ν_S(OH) band overlap.

When even a minor amount of diphosphate is present in a monophosphate solution, the IR spectrum of the precipitated product contains all the above-mentioned bands, but some of them become less distinct (Fig. 3b). The possible reason is the onset of disordering in the structure of the precipitate.

The IR spectrum of the substance obtained from a solution with mole ratio DP/(DP + MP) = 0.1 contains several weakly pronounced peaks, a shoulder above 1130 cm^{-1}, and a weak broadened band with frequency of about 900 cm^{-1} in addition to the group of mutually overlapping intense bands, (Fig. 3c). This shoulder becomes better pronounced in the spectrum of the product precipitated from a solution with diphosphate mole fraction of 0.2 (Fig. 3d). Among the bands typical of hydroxyapatite, only the band peaked at 1030 cm^{-1} survives, whereas all other components of the spectrum undergo changes. In particular, all the peaks within the range 500–600 cm^{-1} merge into a single broad band.

In the IR spectrum of the substance precipitated from a solution with mole ratio DP/(DP + MP) = 0.4, all the strongest bands in the range 950–1200 cm^{-1} merge into a single broad band without any clearly pronounced peaks (Fig. 3e). This band resembles in shape the IR bands of such typical amorphous phosphates as glasses [12].

Changes in the spectra of products precipitated from solutions with higher diphosphate content are caused by the appearance and growth of the fraction of calcium and calcium–sodium diphosphates (Figs. 3e–3i).

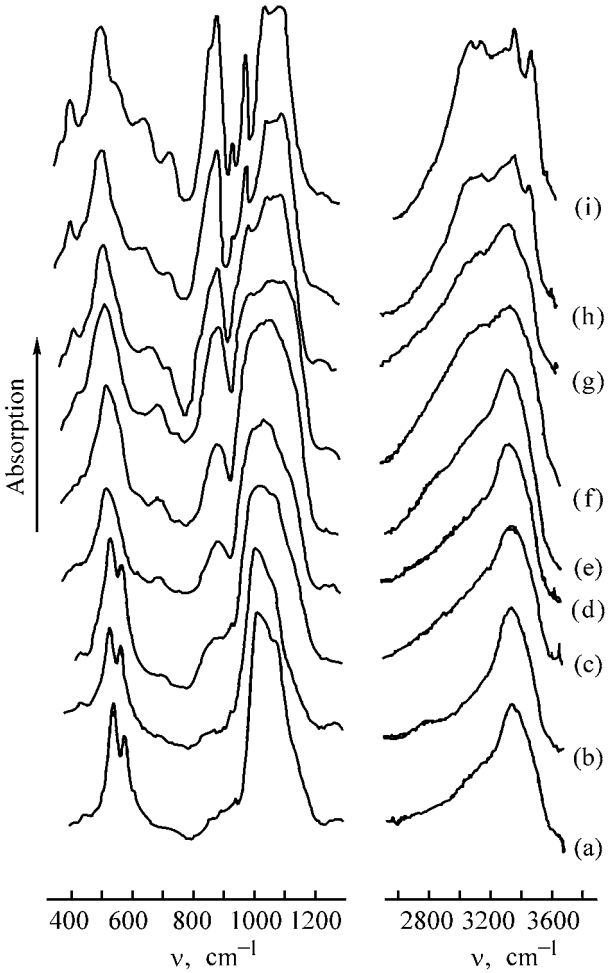

Fig. 3. IR spectra of precipitated products. (ν) Wave number. Content of sodium diphosphate in starting solutions (mol %): (a) 0, (b) 5, (c) 10, (d) 20, (e) 40, (f) 50, (g) 70, (h) 80, and (i) 100.

The IR spectra of substances precipitated from solutions with mole ratios DP/(DP + MP) = 0.2–0.4 are not a simple superposition of individual spectra of hydroxyapatite and diphosphate. In addition, the main bands are strongly broadened. As before, mono- and diphosphate groups form the molecular base of the substances, but we can assume that they have changed their nature as compared with hydroxyapatite and diphosphates. The possible reason is the mutual influence of such groups under direct contact conditions. In such a case, the amorphous substances under discussion can be regarded as an aggregate of chaotically distributed PO_4^{3-}, $P_2O_7^{4-}$ groups, and also OH^- groups, which are linked by calcium cations Ca^{2+}.

Special attention should be paid to the high-frequency range of the IR spectra, which shows stretching vibrations of O–H bonds in water molecules.

The presence of a high-intensity high-frequency band in all the spectra is attributable to strong hydration of the products. As seen from Fig. 3a, the corresponding band is asymmetric: its low-frequency wing shows a pronounced shoulder. This suggests that two forms of water are present in apatite, and one of these predominates. According to the other IR spectra, the water prevailing in hydroxyapatite is gradually replaced by the second form of water when the substance is enriched with a diphosphate.

It should be noted that none of the above-described IR spectra contains clear lines typical of nonstoichiometric hydroxyapatite [11]. This suggests that the amorphicity of substances precipitated from solutions with mole ratios DP/(DP + MP) = 0.2–0.4 is caused by the inhibiting action of diphosphate on the crystallization of hydroxyapatite.

CONCLUSIONS

(1) Crystalline or slightly amorphous products containing hydroxyapatite are precipitated with calcium chloride from alkaline sodium monophosphate solutions in the presence of minor amounts of sodium diphosphate.

(2) Crystalline calcium and calcium–sodium diphosphates are precipitated from monophosphate-lean solutions. Totally amorphous products are formed from solutions with diphosphate/(diphosphate + monophosphate) mole ratios of 0.2–0.4. These substances mainly consist of chaotically arranged discrete PO_4^{3-}, $P_2O_7^{4-}$ groups, and also OH^- groups, linked by Ca^{2+} cations. Molecular water is incorporated in the structure of all the substances precipitated.

REFERENCES

1. *Handbook of Bioactive Ceramics*, Wilson, J. and Yamamuro, T., Eds., CRC Press, 1990, vol. 2.
2. Aoki, H., *Science and Medical Applications of Hydroxyapatite*, Medico Dental Media Int., Incorp., 1992.
3. Hench, L.L., *J. Am. Ceram. Soc.*, 1998, vol. 81, no. 7, pp. 1705–1728.
4. *Neorganicheskie fosfatnye materialy* (Inorganic Phosphate Materials), Kanazava, T., Ed., Kiev: Naukova Dumka, 1998.
5. US Patent 6024985.
6. Sedunov, A.A., Kupriyanov, M.O., Batyrbaeva, A.A., *et al.*, *Probl. Stomatologii*, 2000, no. 3(9), pp. 48–50.
7. Levchenko, L.V., Batyrbaeva A.A., Kupriyanov M.O., *et al.*, *Trudy Mezhdunarodnoi konferentsii "Meditsina i obrazovanie v XXI veke"* (Proc. Int. Conf. "Medicine and Education in the XXI Century"), Almaty, 2001, pp. 263–265.
8. Stutman, J.M., Termine, J.D., and Posner, A.S., *Trans. N.Y. Acad. Sci.*, 1965, vol. 27, no. 6., pp. 669–675.
9. Baddiel, C.B. and Berry, E.E., *Spectrochim. Acta*, 1966, vol. 22, no. 8, pp. 1407–1416.
10. Blakeslee, K.S. and Condrate, R.A., *J. Am. Ceram. Soc.*, 1971, vol. 54, no. 11, pp. 559–563.
11. Joris, S.J. and Amberg, C.H., *J. Phys. Chem.*, 1971, vol. 75, no. 20, pp. 3172–3178.
12. Bertoluzza, A., Bertoluzza, M.A., Fagnano, C., and Benino G.B., *Lincei. Rend. Sc. Fis. Mat. Nat.*, 1973, vol. 54, pp. 944–956.

Russian Journal of Applied Chemistry, Vol. 76, No. 4, 2003, pp. 513–517. Translated from Zhurnal Prikladnoi Khimii, Vol. 76, No. 4, 2003, pp. 533–537.

INORGANIC SYNTHESIS AND INDUSTRIAL INORGANIC CHEMISTRY

On Reaction of Sulfur Dioxide with Aqueous Solutions of Carbamide

R. E. Khoma, V. I. Nikitin, and M. I. Gavrilenko

Mechnikov National University, Odessa, Ukraine

Received October 17, 2001; in final form, November 2002

Abstract—A mechanism of SO_2 chemisorption by aqueous solutions of carbamide was suggested. The effective rate constants of accumulation of hydrogen ions in the reaction of sulfur dioxide with aqueous solutions of carbamide in the range 278–313 K were determined.

One of the main tendencies in the use of methods for desulfurization of waste gases consists in that simple absorption purification methods of nonregenerating type with limestone, lime, or other sorbents give way to technological processes of regenerating type, which enable removal of absorbed sulfur dioxide from the system, with its subsequent utilization [1]. The possibility of generation of sulfur dioxide in the form of a virtually 100% gas can be ensured with the use of aqueous solutions of nitrogen-containing bases as sorbents [2].

The problems of SO_2 dissolution in water and aqueous solutions are widely discussed. The mechanism of sulfur dioxide dissolution in water and aqueous solutions in the ionic form was rather well described in [3–5]. This mechanism can be, in general terms, represented as follows:

gas–liquid equilibrium

$$SO_2^g \rightleftarrows SO_2^l, \quad (1)$$

specific equilibrium

$$SO_2^l + H_2O \rightleftarrows SO_2 \cdot H_2O, \quad (2)$$

$$SO_2 \cdot H_2O \rightleftarrows H^+ + HSO_3^-, \quad (3)$$

$$2HSO_3^- \rightleftarrows S_2O_5^{2-} + H_2O, \quad (4)$$

$$HSO_3^- \rightleftarrows H^+ + SO_3^{2-}, \quad (5)$$

where SO_2^g and SO_2^l stand for sulfur dioxide in the gas phase and that dissolved in water, respectively.

Also, Labutin *et al.* [6] suggested the molecular mechanism of sulfur dioxide dissolution in water

$$SO_2^g \rightleftarrows SO_2^l, \quad (6)$$

$$SO_2^l + H_2O \underset{k_2}{\overset{k_1}{\rightleftarrows}} SO_2^g \cdot H_2O, \quad (7)$$

$$SO_2^l + SO_2 \cdot H_2O \underset{k_4}{\overset{k_3}{\rightleftarrows}} H_2S_2O_5, \quad (8)$$

$$H_2S_2O_5 + H_2O \underset{k_6}{\overset{k_5}{\rightleftarrows}} SO_2 \cdot H_2O. \quad (9)$$

Based on the assumptions that the first stage of physical dissolution [Eq. (6)] is fast and obeys the Henry law and the third stage [Eq. (8)] has equilibrium nature with account of the limiting action of the second and fourth stages [Eqs. (7) and (9)], the authors of [6] note that

$$\frac{dc_{SO_2 \cdot H_2O}}{d\tau} = K_I - K_{II}c_{SO_2 \cdot H_2O} - K_{III}c^2_{SO_2 \cdot H_2O}, \quad (10)$$

where $K_I = k_1p/m$, $K_{II} = k_2 - (2k_5k_3p/k_4m)$, $K_{III} = 2k_6$, p is the partial pressure of SO_2, and m is the Henry constant. The total content of sulfurous acid, $c_{SO_2 \cdot H_2O}$, is directly proportional to the total content of the disulfurous acid, $c_{H_2S_2O_5}$:

$$c_{H_2S_2O_5} = K_{IV}c_{SO_2 \cdot H_2O}, \quad (11)$$

$$K_{IV} = k_3p/k_4m.$$

At the same time, a particular place among the existing widely diverse absorption methods for desul-

1070-4272/03/7604-0513 $25.00 © 2003 MAIK "Nauka/Interperiodica"

furization of discharged gases [1, 7–9] is occupied by the carbamide technique [2, 10, 11]. This can be accounted for by the fact that carbamide is a virtually nontoxic product manufactured on large scale and its aqueous solutions have high absorption capacity and are easily regenerated [2], which allows their further utilization. However, the mechanism of reaction between sulfur dioxide and aqueous solutions of carbamide remains poorly understood.

In the opinion of the authors of [10, 11], the reaction of SO_2 with aqueous solutions of carbamide proceeds via its acid hydrolysis to give CO_2, H_2O, and $(NH_4)_2SO_4$. However, according to [12, 13], the rate of hydrolysis of carbamide is so slow that, in actual practice, its solutions in water can be considered stable up to 80°C. Only heating to 90–100°C or presence of the urease enzyme accelerates the hydrolysis of carbamide.

In [14, 15], a mechanism of SO_2 chemisorption by aqueous solutions of carbamide was suggested. This mechanism consists in that the acid–base reaction of the generated forms of sulfurous acid with carbamide occurs via complexation. The inorganic acid neutralizes the weak organic base via protonation [Eqs. (12)–(14)] or direct addition to its molecule to give associates [Eq. (15)]:

$$[CO(NH_2)_2H]^+ + HSO_3^- \rightleftarrows [CO(NH_2)_2H]HSO_3, \quad (12)$$

$$2[CO(NH_2)_2H]^+ + S_2O_5^{2-} \rightleftarrows [CO(NH_2)_2H]_2S_2O_5, \quad (13)$$

$$2[CO(NH_2)_2H]^+ + SO_3^- \rightleftarrows [CO(NH_2)_2H]_2SO_3, \quad (14)$$

$$CO(NH_2)_2 + SO_2 + nH_2O \rightleftarrows CO(NH_2)_2 \cdot SO_2 \cdot nH_2O. \quad (15)$$

According to published data, carbamide exhibits weak basic properties ($pK_a \sim 0.5$ [16], 0.18, 0.31 [17]). This indicates that the uronium cation is a stronger acid than $SO_2 \cdot H_2O$ ($pK_a \sim 2.0$ [4]). Consequently, formation of salts [Eqs. (12)–(14)] in aqueous solutions is unlikely.

It is not improbable that donor–acceptor reaction of SO_2 with carbamide, which acts as a ligand with respect to sulfur dioxide, results in that associates are formed in water [Eq. (15)].

A model proposed by the authors of [6] can be well applied to description of the reaction of sulfur dioxide with aqueous solutions of carbamide.

The total content of sulfur dioxide in solution, Q, at temperatures higher than 278 K is given by

$$Q = c_{SO_2 \cdot H_2O} + c_{H_2S_2O_5} + [SO_2^l]. \quad (16)$$

With account of (11) and (15), Eq. (10) takes the form

$$\frac{dc_{SO_2 \cdot H_2O}}{d\tau} = K_I - K_{II}\left(\frac{Q - p/m}{1 + K_{IV}}\right) - K_{III}\left(\frac{Q - p/m}{1 + K_{IV}}\right)^2. \quad (17)$$

The total content of sulfurous acid in solution

$$c_{SO_2 \cdot H_2O} = [SO_2 \cdot H_2O] + [HSO_3^-] + [SO_3^{2-}]. \quad (18)$$

Since it is known [5] that disulfurous acid does not exist in free form, the accumulation of hydrogen ions apparently occurs mainly via dissociation of sulfurous acid by the first stage. Since sulfurous acid is a weak acid, it can be written at its low concentrations that

$$\frac{d[H^+]}{d\tau} = k\frac{dc_{SO_2 \cdot H_2O}}{d\tau}. \quad (19)$$

After rearrangements Eq. (19) can be written as

$$\frac{d[H^+]}{d\tau} = K_I' + K_{II}' Q + K_{III}' Q^2, \quad (20)$$

where K_I', K_{II}', and K_{III}' are empirical constants:

$$K_I' = kK_I + k\frac{K_{II}}{1 + K_{IV}}\frac{p}{m} - k\frac{K_{III}}{(1 + K_{IV})^2}\frac{p^2}{m^2}, \quad (21)$$

$$K_{II}' = k\frac{2K_{III}}{(1 + K_{IV})^2}\frac{p}{m} - k\frac{K_{II}}{1 + K_{IV}}, \quad (22)$$

$$K_{III}' = -k\frac{K_{III}}{(1 + K_{IV})^2}. \quad (23)$$

To verify the adequacy of the model developed, published data on the reaction of sulfur dioxide with 0.1 and 0.25 M aqueous solutions of carbamide [15, 14] were processed in terms of this model and the reaction of SO_2 with 0.5 M carbamide solutions was studied in the interval 278–313 K.

EXPERIMENTAL

The experimental procedure employed was described in detail in [15, 16].

Model solutions were prepared with distilled water and carbamide of analytically pure or pure grades, additionally purified by recrystallization. The concentration of carbamide in the systems studied was monitored by photometry [18].

Purified sulfur dioxide [19] was continuously bubbled at constant volumetric flow rate of 8 ml min^{-1} through a model solution placed in a thermostated cell (solution volume 250 ml). Together with pneumatic

agitation, mechanical stirring was also used, which ensured ideal mixing of the components. The concentration of hydrogen ions was measured in the course of experiments with an ESL-43-07 glass electrode. An EVL-1M3 silver chloride reference electrode was filled with a saturated aqueous solution of potassium chloride at 298 K.

The measurements were done at 278–313 K.

In the course of an experiment, c_{SO_2} was monitored after the reaction mixture at 15–30-s intervals by iodometry [20]. The amount of reacted SO_2 was determined by the Scheniger method [21] and calculated using the formula

$$Q = \frac{q(c^{in}_{SO_2} - c^{fin}_{SO_2})}{V_1 \cdot 64}, \quad (24)$$

where V_1 is the solution volume (ml); $c^{in}_{SO_2}$ and $c^{fin}_{SO_2}$, the SO_2 concentrations before and after the reaction (M); q, the volume of the reaction mixture (ml) passed through the reactor during a time τ.

The experiments were performed to constant determined parameters of the system. During an entire experiment, there was no sulfur dioxide at the outlet, which points to its nearly 100% absorption. It was established experimentally that raising the intensity of stirring to more than 50 rpm has no effect on the run of the pH curves, i.e., the reaction of SO_2 with aqueous solutions of carbamide proceeds under these conditions in the kinetic region. In addition, the authors of [6] maintain that, at SO_2 content in the gas phase exceeding 4 vol %, the overall rate of sulfur dioxide dissolution in aqueous solutions is limited by the rate of the SO_2 hydration stage.

As shown by the experiments, the concentration of carbamide sorbing SO_2 remains virtually constant in each set of runs over the entire range of the temperatures studied. No sulfate ions were found in the systems under study, which contradicts the model proposed in [10, 11].

The curves describing how the pH value varies with the amount of absorbed SO_2, Q (M), in solutions are shown in Figs. 1a [15], 1b [14], and 1c. Processing of these data by the least-squares method yielded dependences $[H^+] = f_{T,c_{KA}}(Q)$ in the form of third-order polynomials

$$[H^+] = A_{T,c_{KA}} + B_{T,c_{KA}}Q + C_{T,c_{KA}}Q^2 + D_{T,c_{KA}}Q^3, \quad (25)$$

where $A_{T,c_{KA}}$, $B_{T,c_{KA}}$, $C_{T,c_{KA}}$, and $D_{T,c_{KA}}$ are constants for each of the runs, which depend both on tempera-

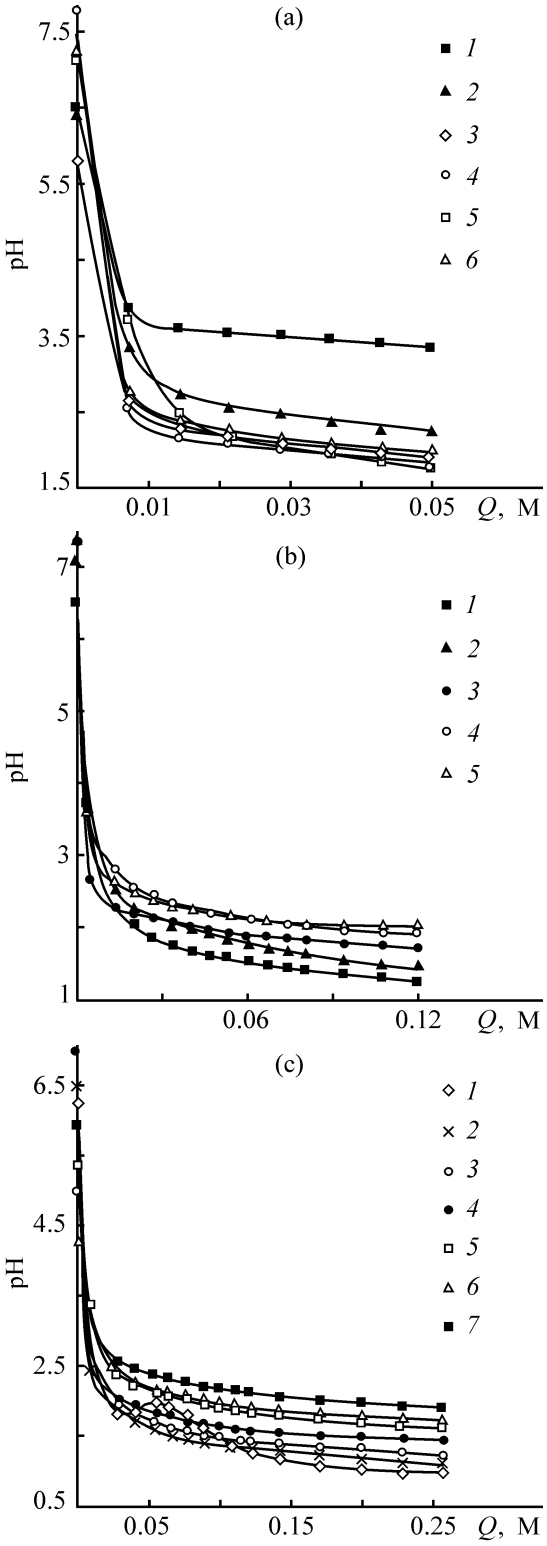

Fig. 1. Variation of the pH value with the amount Q of sulfur dioxide absorbed by (a) 0.1, (b) 0.25, and (c) 0.5 M solution of carbamide. Temperature (K): (a) (*1*) 278, (*2*) 283, (*3*) 288, (*4*) 293, (*5*) 303, and (*6*) 313; (b) (*1*) 288, (*2*) 293, (*3*) 303, (*4*) 308, and (*5*) 313; (c) (*1*) 278, (*2*) 283, (*3*) 288, (*4*) 293, (*5*) 303, (*6*) 308, and (*7*) 313.

Parameters of Eq. (20) for 0.1, 0.25, and 0.5 M carbamide solutions

T, K	c_{KA} = 0.10 M, $0 \le Q \le 0.05$ M				c_{KA} = 0.25 M, $0 \le Q \le 0.12$ M				c_{KA} = 0.50 M, $0 \le Q \le 0.25$ M			
	$K_I' \times 10^4$	$K_{II}' \times 10^3$	$K_{III}' \times 10^2$	R^2	$K_I' \times 10^4$	$K_{II}' \times 10^3$	$K_{III}' \times 10^2$	R^2	$K_I' \times 10^4$	$K_{II}' \times 10^3$	$K_{III}' \times 10^2$	R^2
278	0.39	–2.25	–3.76	0.98	–	–	–	–	–4.42	2.19	8.5	0.98
283	2.17	–1.91	0.63	0.99	–	–	–	–	8.33	–4.99	1.20	0.99
288	8.79	–43.78	76.32	0.98	8.60	–4.25	1.03	0.99	8.06	–7.53	2.30	0.99
293	7.43	–16.68	14.57	0.99	3.06	4.53	–2.95	0.99	4.91	–3.68	0.84	0.99
303	2.17	27.22	–44.97	0.99	3.95	–4.11	1.36	0.99	2.80	–1.97	0.51	0.99
313	4.99	–9.11	5.25	0.99	2.15	–2.12	0.65	0.99	1.36	–0.88	0.23	0.99

ture T and on the total content of carbamide, c_{KA}, in the reaction mixture.

With account of the fact that SO_2 was delivered during an entire run at a constant volumetric flow rate and virtually its whole amount reacted with the absorbers, it can be written that

$$Q = a\tau, \quad (26)$$

where a is a constant dependent on the gas supply rate, and τ is the time during which the gas is supplied. Substitution of (26) into Eq. (25) and subsequent differentiation with respect to time yields

$$\left(\frac{\partial[H^+]}{\partial\tau}\right)_{T,\,c_{KA}} = aB_{T,\,c_{KA}} + 2a^2C_{T,\,c_{KA}}\tau + 3a^3D_{T,\,c_{KA}}\tau^2 \quad (27)$$

or

$$\left(\frac{\partial[H^+]}{\partial\tau}\right)_{T,\,c_{KA}} = aB_{T,\,c_{KA}} + 2aC_{T,\,c_{KA}}Q + 3aD_{T,\,c_{KA}}Q^2. \quad (28)$$

If Eqs. (19) and (23) are compared, it can be written

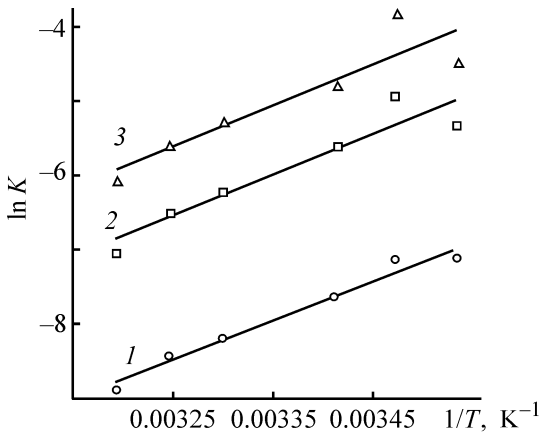

Fig. 2. Parameters of Eq. (20) for 0.5 M carbamide solution vs. temperature T. (*1*) K_I', (*2*) K_{II}', and (*3*) K_{III}'.

$$K_I' = aB_{T,c_{KA}},\ K_{II}' = 2aC_{T,c_{KA}},\ K_{III}' = 3aD_{T,c_{KA}}.$$

The processing of the data in Figs. 1a–1c made it possible to determine the average values of the empirical constants K_I', K_{II}', and K_{III}' (see table). The temperature dependences of these constants for a 0.5 M solution of carbamide can be represented in the interval 283–313 K as

$$K_I' = 8.722 \times 10^{-10}\exp(\Delta\theta_1/RT),$$

$$K_{II}' = -1.322 \times 10^{-10}\exp(\Delta\theta_2/RT),$$

$$K_{III}' = 1.106 \times 10^{-10}\exp(\Delta\theta_3/RT),$$

where $\Delta\theta_1$ = 38.94, $\Delta\theta_2$ = 41.38, and $\Delta\theta_3$ = 42.80 kJ mol^{-1}.

Analysis of the temperature dependence of the empirical constants (Fig. 2) shows that their absolute values decrease with increasing temperature, i.e., the exponents in the temperature dependences of K_I', K_{II}', and K_{III}' are positive by virtue of the relationship between the activation energies (k_1–k_6) and the exponent in the temperature dependence of the Henry constant.

However, the temperature dependences of K_I', K_{II}', and K_{III}' for 0.1 and 0.25 M solutions (see table) are more complicated and can be represented as $K_I' = f(T)$. For example, for a 0.25 M carbamide solution with sulfur dioxide concentration $0 \le Q_{SO_2} \le 0.12$ M at 288–313 K

$$K_I' = 3 \times 10^{-8}T^4 - 3 \times 10^{-5}T^3 + 0.015T^2 - 3.0189T + 228.25,$$

$$K_{II}' = -7 \times 10^{-7}T^4 + 0.0009T^3 - 0.4105T^2 + 82.672T - 6241.8,$$

$$K_{III}' = 4 \times 10^{-6}T^4 - 0.0044T^3 + 1.9847T^2 - 399.6T + 30\,162.$$

For a 0.1 M carbamide solution with sulfur dioxide concentration $0 \le Q_{SO_2} \le 0.05$ M in the range 278–313 K

$$K_I' = -2 \times 10^{-10}T^6 + 4 \times 10^{-7}T^5 - 0.0003T^4 + 0.1018T^3 - 22.129T^2 - 2565T - 123819,$$

$$K_{II}' = -3 \times 10^{-8}T^6 + 5 \times 10^{-5}T^5 - 0.0373T^4 + 14.634T^3 - 3232.7T^2 + 380754T - 2 \times 10^7,$$

$$K_{III}' = 8 \times 10^{-7}T^6 - 0.0014T^5 + 1.0154T^4 - 398.32T^3 + 87863T^2 - 10^7T + 5 \times 10^8.$$

It should be noted that in all cases the approximation is characterized by a correlation factor $R^2 > 0.97$.

Apparently, the acidity of the medium is a measure of sulfur dioxide hydration by water, since this gives $SO_2 \cdot H_2O$ [Eq. (2)] and one of products of its dissociation are hydrogen ions [Eqs. (3) and (5)].

Thus, aqueous solutions of carbamide strongly affect solvation of SO_2 by water, probably forming various associates with sulfur dioxide. The effect of carbamide on the hydration of sulfur dioxide has complex nature. For example, the acidity of the medium decreases in a 0.5 M carbamide solution with the temperature increasing from 278 to 313 K. This can be accounted for by the fact that, under the specific action of carbamide, the affinity of water for sulfur dioxide decreases in solutions with increasing temperature.

CONCLUSIONS

(1) The possibility of effective absorption of sulfur dioxide by carbamide solutions in the temperature range 278–313 K was established.

(2) It was found that the temperature of the reaction medium and its composition strongly affect the acid-base reaction in SO_2–water–carbamide systems.

REFERENCES

1. Pai, Z.P., *Khim. Interes. Ustoich. Razv.*, 1998, no. 6, pp. 367–374.
2. Khoma, R.E., Nikitin, V.I., and Gavrilenko, M.I., *Visn. Odes. Nats. Univ.*, 2000, vol. 5, no. 5, pp. 39–44.
3. Huss, A.J. and Eckert, C.A., *J. Phys. Chem.*, 1977, vol. 81, no. 24, pp. 2268–2270.
4. Romanenko, S.A., Component Composition of Aqueous Solutions of Sulfur(IV), *Cand. Sci. Dissertation*, Leningrad, 1986.
5. Pereda, S., Thomsen, K., and Rasmussen, P., *Chem. Eng. Sci.*, 2000, vol. 55, pp. 2663–2671.
6. Labutin, N.A., Batikha, M.M., Groshev, G.L. and Korotaevskii, K.N., *Khim. Khim. Tekhnol.*, 1997, vol. 40, no. 4, pp. 55–58.
7. Blokhin, P.V., Recovery of Sulfur Dioxide from Gas Discharges with Amine-containing Industrial Waste, *Cand. Sci. Dissertation*, Nizhni Novgorod, 2000.
8. Postnikova, I.N., Recovery of Sulfur Dioxide from Waste Gases with Melamine-based Polymers, *Cand. Sci. Dissertation*, Ivanovo, 1996.
9. Pavlova, I.V., Recovery of Sulfur Dioxide from Waste Gases with a Sorbent Based on Carbamido-formaldehyde Resin, *Cand. Sci. Dissertation*, Nizhni Novgorod, 1995.
10. Okhotnikova, A.P., Kostoglod, A.B., Astrelin, I.N., and Knyazev, Yu.V., *Sbornik nauchnykh trudov Mezhdunarodnoi nauchno-tekhnicheskoi konferentsii "Sovremennye problemy khimicheskoi tekhnologii neorganicheskikh veshchestv,"* Ukraina, Odessa, 2001 (Proc. Int. Sci.-Technol. Conf. "Modern Problems of Chemical Technology of Inorganic Substances," Ukraine, Odessa, 2001), vol. 2, pp. 156–159.
11. Petrovskii, V.E. and Beznosik, Yu A., *Sbornik nauchnykh trudov Mezhdunarodnoi nauchno-tekhnicheskoi konferentsii "Sovremennye problemy khimicheskoi tekhnologii neorganicheskikh veshchestv,"* Ukraina, Odessa, 2001 (Proc. Int. Sci.-Technol. Conf. "Modern Problems of Chemical Technology of Inorganic Substances," Ukraine, Odessa, 2001), vol. 2, pp. 165–167.
12. Zotov, A.T., *Mochevina* (Urea), Moscow: Goskhimizdat, 1963.
13. Kaminskaia, N.V. and Kostié, N.M., *Inorg. Chem.*, 1997, vol. 36, no. 25, pp. 5917–5996.
14. Nikitin, V.I, Khoma, R.E., and Gavrilenko, M.I., *Izv. Vyssh. Uchebn. Zaved., Khim. Khim. Tekhnol.*, 2000, vol. 43, no. 2, pp. 14–16.
15. Khoma, R.E., Nikitin, V.I., and Gavrilenko, M.I., *Izv. Vyssh. Uchebn. Zaved., Khim. Khim. Tekhnol.*, 2001, vol. 44, no. 6, pp. 24–27.
16. Adelman, R.L., *J. Org. Chem.*, 1964, vol. 29, no. 7, pp. 1837–1844.
17. Albert, A. and Serjeant, E., *Ionization Constants of Acids and Bases, A laboratory manuel*, New York: Wiley, 1962.
18. Crocker, C.L., *Am. J. Med. Technol.*, 1967, vol. 33, p. 361.
19. Voskresenskii, P.I., *Tekhnika laboratornykh rabot* (Methods of Laboratory Works), Moscow: Khimiya, 1973.
20. Kel'man, F.N., Brutskus, E.B, and Osherovich, R.Kh., *Metody analiza pri kontrole proizvodstva sernoi kisloty i fosfornykh udobrenii* (Analytical Techniques in Control over Production of Sulfuric Acids and Phosphorus Fertilizers), Moscow: Khimiya, 1965.
21. Klimova, V.A., *Osnovnye metody analiza organicheskikh soedinenii* (Basic Methods for Analysis of Organic Compounds), Moscow: Khimiya, 1975.

Russian Journal of Applied Chemistry, Vol. 76, No. 4, 2003, pp. 518–521. Translated from Zhurnal Prikladnoi Khimii, Vol. 76, No. 4, 2003, pp. 538–541.

PHYSICOCHEMICAL STUDIES OF SYSTEMS AND PROCESSES

A Study of Heat Conductivity of Methanol–*n*-Nonanol Binary Mixtures in a Wide Range of Temperatures and Pressures

M. M. Bashirov

Azerbaijani Technical University, Baku, Azerbaijan

Received May 14, 2002; in final form, November 2002

Abstract—The heat conductivity of liquid binary mixtures of the system methanol–*n*-nonanol was measured at different temperatures, pressures, and concentrations. A relationship between the heat conductivity of the binary mixtures and the concentration of their components was established.

A sufficient body of experimental data on the heat conductivity λ of neat methyl and *n*-nonyl alcohols is available in the literature. At the same time, the heat conductivities of mixtures of methyl and *n*-nonyl alcohols have only been reported once [1] for atmospheric pressure and a narrow temperature interval (20–80°C) at concentrations of 25, 50, and 75 wt %.

Results obtained in measuring the heat conductivity of neat methyl alcohol at high pressures were reported in [2–4]. Previously, the λ value has been measured for methanol [5] in a wide range of temperatures and pressures (T = 293–600 K, P = 0.1–60 MPa), and the results obtained are in good agreement with the data of [3]. The heat conductivity of *n*-nonanol was measured at high pressure in [6, 7], with the results reported being well consistent.

In the present study, the heat conductivity of liquid binary mixtures of methanol and *n*-nonanol was measured in the temperature interval 293–600 K at pressures ranging from atmospheric to 60 MPa. The experiments were carried out on a modified cylindrical high-pressure tricalorimeter [8–10].

The heat conductivity of neat methanol and *n*-nonanol and of their mixtures were measured on similar setups to eliminate systematic experimental errors constituting ~1.3% for heat conductivity (for the regular-mode method).

Basic geometric dimensions of the measuring device (mm): diameter of inner measuring cylinder 12.255, inner diameter of the outer cylinder 12.931, measuring clearance 0.338, outer diameter of the outer cylinder 37, inner diameter of the autoclave 40, length of measuring cylinders 140, length of compensating cylinders 40.

The error in determining the heat conductivity coefficient did not exceed 1.8%.

The results obtained in determining experimentally the heat conductivity for methanol–*n*-nonanol mixtures are listed in Table 1.

The scatter of experimental points around the averaging curve is less than 0.3%. Analysis of the data in Table 1 shows that the concentration dependence of heat conductivity of methanol–*n*-nonanol mixtures shows negative deviations from the additivity line and is symmetric with respect to the concentrations of the constituent components. It should be noted that the deviation δλ observed in [1] in measurements under atmospheric pressure has the same direction and magnitude. However, the effect of temperature varies. Raising the pressure and temperature makes the deviation δλ ($\delta\lambda = \lambda - \lambda_{ad}$) smaller at mass concentration x = 0.5; here, λ_{ad} is the heat conductivity of a solution, calculated using the additivity law.

On the basis of the experimental data obtained, the following empirical equation is proposed:

$$\lambda = \lambda_1 x_1 + \lambda_2 x_2 + 10^{-4} x_1 x_2 (\alpha \Delta T + \beta P - \gamma), \quad (1)$$

where λ_1 and λ_2 are the heat conductivities of the first and second components (W m^{-1} K^{-1}); x_1 and x_2 are the mass fractions of the components; α, β, and γ are constants for a given system. The following values

1070-4272/03/7604-0518 $25.00 © 2003 MAIK "Nauka/Interperiodica"

Table 1. Experimental heat conductivities of mixtures at high pressure

T, K	Heat conductivity $\lambda \times 10^4$ (W m^{-1} K^{-1}) at indicated *P*, MPa								
	0.101	1	5	10	20	30	40	50	60
	25 wt % methanol + 75 wt % *n*-nonanol								
288.7	1718	1724	1755	1786	1842	1887	1925	1961	1996
313.3	1634	1640	1670	1705	1763	1807	1850	1885	1923
344.4	1537	1547	1578	1615	1671	1717	1765	1803	1838
371.7	1460	1474	1506	1543	1600	1647	1700	1738	1774
400.0	1385	1403	1436	1474	1531	1583	1634	1675	1716
424.9		1342	1379	1419	1480	1533	1587	1629	1672
450.2		1283	1324	1365	1429	1484	1539	1586	1628
472.8		1228	1273	1320	1384	1442	1500	1548	1593
498.1			1206	1261	1334	1397	1457	1508	1553
521.7			1138	1197	1286	1354	1416	1470	1520
548.4			1040	1107	1229	1308	1375	1431	1483
570.6			962	1039	1180	1270	1342	1402	1455
599.6				978	1118	1222	1303	1367	1420
	50 wt % methanol + 50 wt % *n*-nonanol								
289.0	1801	1807	1839	1876	1929	1976	2015	2055	2092
316.2	1713	1720	1749	1787	1842	1889	1934	1974	2014
343.4	1629	1639	1670	1707	1763	1814	1860	1901	1942
370.3	1550	1568	1600	1638	1696	1746	1796	1838	1878
394.7	1485	1507	1540	1581	1639	1692	1743	1786	1829
420.0		1445	1480	1525	1587	1644	1695	1740	1786
445.9		1383	1423	1474	1538	1598	1652	1700	1745
469.3		1325	1368	1424	1495	1556	1615	1665	1712
495.6			1296	1357	1443	1510	1574	1628	1677
520.0			1208	1274	1391	1467	1537	1594	1647
546.1			1070	1156	1330	1422	1499	1560	1618
571.8				1033	1248	1374	1460	1529	1586
601.9				975	1180	1330	1429	1503	1561
	75 wt % methanol + 25 wt % *n*-nonanol								
290.3	1908	1915	1946	1976	2036	2082	2125	2165	2205
317.7	1821	1828	1855	1891	1950	1998	2040	2083	2126
340.0	1755	1762	1790	1826	1887	1936	1981	2025	2069
372.3		1678	1707	1748	1805	1855	1904	1947	1991
378.1		1662	1693	1735	1791	1841	1890	1934	1978
401.6		1603	1636	1680	1735	1792	1845	1889	1935
424.5		1550	1583	1633	1696	1755	1807	1854	1900
451.4		1485	1525	1578	1649	1711	1767	1817	1864
475.2			1461	1528	1605	1671	1733	1784	1835
500.0			1360	1454	1556	1631	1699	1754	1806
524.6			1230	1343	1501	1583	1662	1723	1781
548.5				1190	1432	1541	1630	1698	1758
569.4				1075	1360	1507	1605	1678	1740
600.5				996	1265	1456	1572	1654	1718

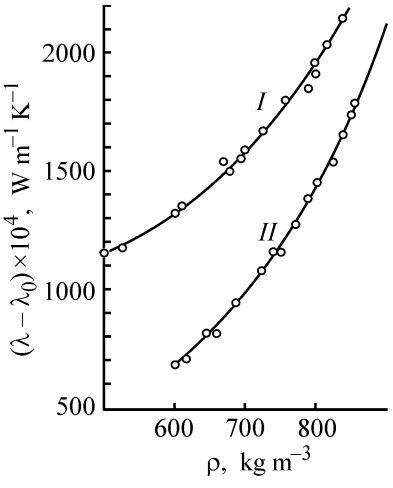

Fig. 1. ($\lambda - \lambda_0$) for (*I*) methanol and (*II*) *n*-nonanol vs. density ρ of the liquid phase.

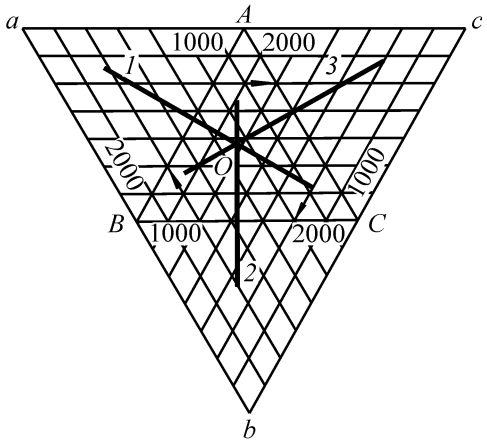

Fig. 2. Relationship between the heat conductivities $\lambda \times 10^4$ of the system methanol–*n*-nonanol at different component contents. Mixture: (*1*) *A*–*B*, (*2*) *B*–*C*, and (*3*) *C*–*A*. Methanol + *n*-nonanol (wt %): *A* = 25 + 75, *B* = 50 + 50, and *C* = 75 + 25.

were obtained: α = 0.2143, β = 0.80, γ = 215.08; $\Delta T = T - T_0$, T_0 is the base temperature, $T_0 = (T'_m + T''_m)/2$; T'_m and T''_m are the melting points of the first and second components (K), for methanol T'_m = 1 75.49 K, for *n*-nonanol T''_m = 260.60 K; *P* is pressure (MPa). The λ_1 and λ_2 values were taken from [3, 7].

Table 2. Constants a_i in Eq. (3) for methanol and *n*-nonanol

a_i	Methanol	*n*-Nonanol
a_0	890.00	–350.00
a_1	0.4167	4.1167
a_2	–0.0015	–0.0090
a_3	0.00000333	0.00000833

Equation (1) describes the experimental values of λ for binary mixtures of methyl and *n*-nonyl alcohols with an error not exceeding the experimental error.

Of practical interest is generalization of the data on heat conductivities of neat alcohols and mixtures of these. There exists a relationship between the excess heat conductivity and density of liquids and gases

$$\lambda - \lambda_0 = f(\rho), \quad (2)$$

where λ_0 is the heat conductivity of a substance at atmospheric pressure in the gas phase, λ is the heat conductivity at given *T* and *P*, and ρ is the substance density at *T* and *P*.

As seen from relation (2), a knowledge of the ρ value in a wide range of pressures and temperatures is necessary for generalization. Unfortunately, this is not the case for mixtures of methanol and *n*-nonanol. The density of neat methanol and *n*-nonanol has been determined with high accuracy [11–19]. These results enable processing of data on heat conductivities of neat liquid methanol and *n*-nonanol at high pressures. The results obtained are shown in Fig. 1, whence it can be seen that the experimental points fall on averaged parabolic curves. The maximum scatter of the points around the averaging curves is 3.5% for methanol and 3.3% for *n*-nonanol.

Processing of the data on λ_0, λ, and ρ yields the following dependence (3)

$$\lambda - \lambda_0 = \sum_{i=0}^{3} a_i \rho^i, \quad (3)$$

where a_i are constants for a given substance. The a_i values are listed in Table 2. With data on density available, relation (3) can be used to prognosticate the excess heat conductivity.

Data on λ for binary methanol–*n*-nonanol mixtures can be conveniently processed using the method of comparative calculations in a three-axis coordinate system [20], in which each axis corresponds to a mixture [three axes and three mixtures (wt %): 25, 50, and 75].

The method consists in the following. To establish a relationship between the properties of the mixtures, a closed three-coordinate system is used. The coordinate axes are arranged one after another at angles of 60° (Fig. 2). The sides of the equilateral triangle *ABC* are the coordinate axes. On each of the axes, the heat conductivities of one of the three mixtures is plotted. Here, the relationship between the three substances at once is considered. This technique makes it possible

to prognosticate the heat conductivity of a third mixture on the basis of two others and to perform interpolation and extrapolation of the λ value for the system.

The results of processing are shown in Fig. 2. It can be seen that a single curve (straight lines *1–3*) is obtained for each pair of mixtures (25 wt % methanol + 75 wt % *n*-nonanol and 50 wt % methanol + 50 wt % *n*-nonanol; 50 wt % methanol + 50 wt % *n*-nonanol and 75 wt % methanol + 25 wt % *n*-nonanol; 75 wt % methanol + 25 wt % *n*-nonanol and 25 wt % methanol + 75 wt % *n*-nonanol). All these lines intersect within the inscribed triangle at the same point. It should be noted that parts of the curves related to low heat conductivities go outside the inscribed triangle *ABC*. Therefore, the system is supplemented with a circumscribed triangle *abc*.

Each of the lines *1–3* can be described by an equation of the type $\lambda_1 = m\lambda_2 + n$, where *m* and *n* are coefficients. Correspondingly, the following empirical equations were obtained for lines *1–3*:

$$\lambda'' = 0.9812734\lambda' + 122.7266, \quad (4)$$

$$\lambda''' = 0.96473\lambda'' + 175.540, \quad (5)$$

$$\lambda' = 1.06422\lambda''' - 325.2523, \quad (6)$$

where λ', λ'', and λ''' are, respectively, the heat conductivities of the first, second, and third mixtures (25, 50, and 75 wt % methanol).

CONCLUSIONS

(1) The heat conductivities of methanol–*n*-nonanol binary mixtures were determined experimentally at content of 25, 50, and 75 wt % in the temperature interval 293–600 K and pressures ranging from 0.1 to 60 MPa. The experiments were carried out on a modified setup developed by the authors with the use of a cylindrical tricalorimeter operating in the regular mode. The results obtained are processed using the method of comparative calculations.

(2) An equation is proposed for determining the heat conductivity. This equation reflects the dependence of heat conductivity on concentration, temperature, and pressure. Experimental data for methyl and *n*-nonyl alcohols are processed using data on their densities.

REFERENCES

1. Mukhamedzyanov, G.Kh. and Usmanov, A.G., *Teploprovodnost' organicheskikh zhidkostei* (Heat Conductivity of Organic Liquids), Leningrad: Khimiya, 1971.
2. Bridgman, P.W., *The Physics of High Pressures*, London: G. Bell and Sons, 1931.
3. Golubev, I.F. and Vasil'kovskaya, T.N., *Teploenergetika*, 1969, no. 5, pp. 77–82.
4. Mukhamedzyanov, I.Kh., Mukhamedzyanov, G.Kh., and Usmanov, A.G., *Trudy Kaz. Khim.-Tekhnol. Inst.*, Kazan, 1971, no. 44, pp. 57–67.
5. Bashirov, M.M. and Naziev, Ya.M., *Probl. Energetiki*, Baku, Akad. Nauk Azerb. Rep., 2001, no. 4, pp. 133–139.
6. Vasil'kovskaya, T.N. and Golubev, I.F., *Khimiya i tekhnologiya produktov organicheskogo sinteza: Trudy GIAP* (Chemistry and Technology of Products Formed in Organic Synthesis: Coll. Works GIAP), Moscow, 1971, issue 8, pp. 102–111.
7. Naziev, Ya.M. and Aliev, N.S., *Teplofiz. Vys. Temp.*, 1987, vol. 25, no. 2, pp. 262–266.
8. Naziev, Ya.M., *Proc. 5th Symp. on Thermophys. Properties*, New York: ASME, 1970, pp. 8–14.
9. Naziev, Ya.M., Aliev, N.S., and Akhmedov, A.K., *Promyshl. Teplotekhn.*, Kiev, 1986, vol. 8, no. 4, pp. 72–76.
10. Naziev, Ya.M. and Bashirov, M.M., *Izv. Ross. Akad. Nauk, Energet.*, 2002, no. 3, pp. 157–162.
11. Zubarev, V.N., Prusakov, P.G., and Sergeeva, L.V., *Teplofizicheskie svoistva metilovogo spirta: Spravochnik* (Thermal Properties of Methyl Alcohol: Reference Book), Moscow: Izd. Standartov, 1973.
12. Zubarev, V.N. and Bagdonas, A.V., *Teploenergetika*, 1967, no. 4, pp. 79–82.
13. Ledwig, R. and Wurflinger, A.Z., *Phys. Chem.*, 1982, vol. 32, no. 1, pp. 21–26.
14. Easteal, A.J. and Woolf, L.A., *J. Chem. Thermodynamic.*, 1985, vol. 17, no. 1, pp. 49–53.
15. Golubev, I.F., *Trudy GIAP* (Coll. Works GIAP), Moscow, 1957, issue 7, pp. 57–63.
16. Naziev, Ya.M. and Gasanov, V.G., *Probl. Energet.*, Baku, Akad. Nauk Azerb. Rep., 2001, no. 2, pp. 57–60.
17. Golubev, I.F., Dobrovol'skii, O.A., and Demin, G.P., *Khimiya i tekhnologiya produktov organicheskogo sinteza. Trudy GIAP* (Chemistry and Technology of Products Formed in Organic Synthesis: Coll. Works GIAP), Moscow, 1971, issue 8, pp. 5–9.
18. Zolin, V.S., Shelkovenko, A.E., Golubev, I.F., and Vasil'kovskaya, T.N., *Proizvodstva organicheskikh produktov: Trudy GIAP* (Production of Organic Products: Coll. Works GIAP), Moscow, 1983, pp. 97–102.
19. Shakhverdiev, A.N. and Bulgan, A.T., *Teplofiz. Vys. Temp.*, 1998, vol. 36, no. 4, pp. 572–576.
20. Naziev, Ya.M., Naziev, Dzh.Ya., and Gasanov, V.G., *Teplofiz. Vys. Temp.*, 2001, vol. 39, no. 2, pp. 235–240.

Russian Journal of Applied Chemistry, Vol. 76, No. 4, 2003, pp. 522–525. Translated from Zhurnal Prikladnoi Khimii, Vol. 76, No. 4, 2003, pp. 542–545.

PHYSICOCHEMICAL STUDIES OF SYSTEMS AND PROCESSES

Heat Conductivity of Methanol–*n*-Dodecanol Binary Solutions in a Wide Range of Temperatures and Pressures

Ya. M. Naziev and M. M. Bashirov

Azerbaijani Technical University, Baku, Azerbaijan

Received May 14, 2002; in final form, November 2002

Abstract—The heat conductivity of mutual methanol–*n*-dodecanol solutions was measured at various pressures, temperatures, and concentrations. The measurements were carried out on a modified cylindrical tricalorimeter.

The heat conductivity λ is an important physicochemical property of liquids and gases. Consequently, studying the heat conductivity is of indubitable practical importance.

The already carried determinations of λ for alcohols were reviewed in [1]. Three values are known from the literature for the heat conductivity at high pressure, with the differences between these values being unacceptably large. Therefore, the heat conductivity of methyl alcohol has been measured previously at temperatures of 293–600 K and pressures in the range 0.1–60 MPa [2]. A comparison of the newly obtained data on the heat conductivity λ of methanol demonstrated that they are in satisfactory agreement only with the data of [3].

The heat conductivity of *n*-dodecyl alcohol was measured at pressures of up to 50 MPa and temperatures of 326–624 K in [4]. The present study supplements data on the λ value for the system methanol–*n*-dodecanol, which makes it possible to obtain mutual dependences of binary solutions.

The experiments were carried out on a modified setup [2, 5]. The same setup was used to measure the λ value for neat *n*-dodecyl alcohol [4] and to make a control measurement of λ for a model liquid, methanol [2].

The heat conductivity of the system methanol–*n*-dodecanol was studied in the liquid state up to 600 K and 60 MPa at component content of 25, 50, and 75 wt %.

The basic dimensions of the device were as follows (mm): diameter of inner measuring cylinder 12.255, inner diameter of the outer cylinder 12.931, annular clearance 0.338, length of measuring cylinders 40, length of compensating cylinders 40. The maximum error in determining the heat conductivity was 1.8%. In the experiments, the Rayleigh number was much smaller than 1000, and, therefore, any convection was ruled out. No corrections for heat radiation across the liquid layer were made since the alcohols are strongly absorbing media.

The results obtained in determining λ are summarized in the table. The reproducibility of the experimental points was better than 0.33%.

The heat conductivities of neat methanol and *n*-dodecanol were taken from [2, 4].

The components taken for preparing the solution had the following characteristics. For methanol: ρ_4^{20} = 791.14 kg m^{-3}, melting point T_m = 175.49 K, boiling point T_b = 337.70 K, critical temperature T_{cr} = 512.64 K, critical pressure P_{cr} = 8.096 MPa, critical density ρ_{cr} = 272 kg m^{-3}; for *n*-dodecanol, respectively: ρ_4^{20} = 829.69 kg m^{-3}, T_m = 297.07 K, T_b = 537.79 K, T_{cr} = 720 K, P_{cr} = 2.080 MPa.

The data in the table suggest that the curves describing the concentration dependence of the heat conductivity in the system methanol–*n*-dodecanol show negative deviations from additivity in the range of state parameters studied, with these curves being symmetrical with respect to the additivity line.

Analysis of the experimental data suggests the following empirical equation reflecting the dependence of the heat conductivity of solutions on concentration, pressure, and temperature:

$$\lambda = \lambda_1 x_1 + \lambda_2 x_2 + 10^{-4} x_1 x_2 (\alpha \Delta T + \beta P - \gamma), \quad (1)$$

1070-4272/03/7604-0522 $25.00 © 2003 MAIK "Nauka/Interperiodica"

Experimental heat conductivities of mixtures at high pressure

T, K	Heat conductivity $\lambda \times 10^4$ (W m^{-1} K^{-1}) at indicated *P*, MPa								
	0.101	1	5	10	20	30	40	50	60
	25 wt % methanol + 75 wt % *n*-dodecanol								
300	1774	1781	1801	1832	1882	1930	1976	2016	2056
320	1684	1692	1715	1747	1796	1846	1892	1938	1983
340	1604	1612	1636	1665	1721	1773	1818	1865	1912
360	1531	1539	1565	1595	1651	1703	1750	1795	1842
380	1464	1472	1498	1530	1586	1639	1687	1732	1778
400	1402	1410	1437	1470	1526	1580	1629	1676	1722
420	1345	1354	1382	1415	1472	1527	1577	1622	1670
440	1284	1294	1329	1369	1423	1478	1528	1576	1622
460	1230	1241	1280	1321	1378	1432	1484	1530	1578
480		1181	1228	1273	1334	1390	1442	1490	1540
500		1115	1170	1222	1294	1353	1407	1455	1503
520		1043	1105	1165	1253	1315	1372	1422	1471
540		944	1021	1099	1211	1283	1342	1393	1442
560			930	1027	1167	1249	1313	1367	1418
580			865	975	1123	1218	1289	1346	1397
600			822	937	1083	1186	1266	1326	1380
	50 wt % methanol + 50 wt % *n*-dodecanol								
300	1834	1841	1865	1898	1950	1996	2044	2085	2126
320	1755	1763	1788	1820	1873	1923	1967	2013	2060
340	1681	1689	1714	1746	1804	1856	1901	1948	1995
360	1615	1623	1651	1683	1740	1793	1840	1885	1934
380	1553	1561	1590	1625	1680	1734	1782	1828	1875
400	1494	1503	1532	1571	1624	1681	1731	1778	1826
420	1435	1445	1480	1522	1580	1637	1687	1733	1782
440		1390	1431	1476	1537	1594	1646	1693	1743
460		1334	1383	1431	1496	1554	1608	1655	1706
480		1265	1326	1383	1454	1515	1573	1622	1673
500		1191	1267	1327	1414	1481	1540	1591	1643
520			1170	1254	1371	1442	1509	1563	1615
540			1030	1164	1328	1406	1480	1537	1591
560			878	1062	1269	1375	1453	1514	1571
580			782	996	1213	1344	1432	1497	1553
600				955	1165	1314	1410	1480	1539
	75 wt % methanol + 25 wt % *n*-dodecanol								
300	1913	1920	1945	1980	2036	2083	2128	2169	2210
320	1843	1851	1876	1911	1967	2016	2059	2104	2152
340	1776	1784	1811	1844	1904	1955	1999	2045	2093
360	1716	1725	1754	1789	1847	1899	1946	1990	2038
380		1668	1698	1734	1792	1844	1893	1938	1985
400		1613	1644	1682	1740	1798	1849	1895	1942
420		1554	1595	1640	1703	1761	1812	1857	1907
440		1495	1549	1601	1666	1725	1777	1826	1874
460		1438	1501	1559	1629	1689	1746	1794	1845
480			1440	1510	1587	1654	1717	1766	1818
500			1358	1447	1548	1621	1687	1740	1793
520			1238	1357	1501	1582	1657	1715	1770
540			1015	1243	1452	1545	1629	1692	1751
560				1109	1383	1514	1601	1672	1734
580				1029	1316	1481	1583	1659	1719
600				987	1257	1450	1564	1644	1707

where, λ_1, λ_2 are the heat conductivities of the first and second components; x_1, x_2 the concentrations in mass fractions; $\Delta T = T - T_0$, $T_0 = (T'_m + T''_m)/2$, where T_0 is the base temperature; T'_m, T''_m are the melting points of the first and second components; α, β, and γ are constants for a given system, found from experimental data to be $\alpha = 0.1571$, $\beta = 0.533$, and $\gamma = 161.008$.

Equation (1) describes the experimental data with an error not exceeding the experimental error.

As seen from Eq. (1), the deviation from additivity for liquid mutual solutions of the system methanol–*n*-dodecanol depends not only on concentration, but also on temperature and pressure. Raising the temperature and pressure affects negatively the magnitude of the maximum deviation $\delta\lambda$[1]. For example, at 5 MPa and 300 K $\delta\lambda = 35.0$ W m^{-1} K^{-1} and $\delta\lambda/\lambda = 1.9\%$, and at 50 MPa and 500 K $\delta\lambda = 23.0$ W m^{-1} K^{-1} and $\delta\lambda/\lambda = 1.45\%$ ($x_1 = x_2 = 0.5$).

A theoretical expression is known, which relates the heat conductivity and the thermal pressure [6]:

$$\lambda = \lambda_0 + a(P_t/T)^n, \quad (2)$$

where λ is the heat conductivity at given T and P; λ_0 is the heat conductivity of the substance at atmospheric pressure in the gas phase; a, n are constants for the given substance; T is absolute temperature; P_t is the thermal pressure, $P_t = T\left(\frac{\partial P}{\partial T}\right)_\rho$.

The a value depends on density only slightly, and n can be considered invariable.

Expression (2) was derived from the Enskog equation [7].

The following equation can be written for determining the thermal pressure:

$$P_t = -T\left(\frac{\partial \nu}{\partial T}\right)_P \Big/ \left(\frac{\partial \nu}{\partial P}\right)_T, \quad (3)$$

where ν is the specific volume of the liquid, $\nu = 1/\rho$.

As seen from Eqs. (2) and (3), detailed experimental data on density or the equation of state is to be known for calculating the heat conductivities of liquids. Unfortunately, the density of methanol–*n*-dodecanol solutions has not been studied as a function of pressure, temperature, and concentration, and, therefore, Eq. (2) is inapplicable to the solutions.

[1] $\delta\lambda = \lambda - \lambda_{ad}$; λ_{ad} is λ value calculated on the basis of the additivity rule at $x = 0.5$.

The *PVT* dependence has been studied for *n*-dodecyl alcohol in the liquid phase in sufficient detail [8] (at $T = 308.15$–598.15 K, $P = 0.1$–50 MPa), and, therefore, Eq. (2) was tested for the case of *n*-dodecyl alcohol. Preliminarily, the thermal pressure was calculated in relation to P and T. It was found that at $a_0 = -1.0610286$, $a_1 = 0.003718$, $a_2 = -0.0000027143$, and $n = 0.992$ the error of the equation is the largest (3.0%), where $a = \sum_{i=0}^{2} a_i \rho^i$.

It has been proposed [9] to use a closed three-coordinate system in processing data on thermal properties, including heat conductivity, of solutions. However, this method allows data processing for only three solutions with different concentrations or compositions. The three-axis coordinate system is inapplicable to the case of simultaneously four solutions. Thus, a four-axis coordinate system should be used. In the present study, an attempt is made to apply such a technique to four binary systems. The use of a four-axis coordinate system will make it possible to relate in a simple way the heat conductivities of the solutions, to process these data graphically and prognosticate the heat conductivity of a solution under study on the basis of the other three solutions, and to perform, when necessary, interpolation and extrapolation. Below, the essence of the method is described.

The heat conductivities of the systems studied: methanol–*n*-hexanol, methanol–*n*-nonanol, methanol–*n*-undecanol, and methanol–*n*-dodecanol, are processed in a four-coordinate system (see figure). Four coordinate axes, *OA*, *OB*, *OC*, and *OD*, are set in the square *ABCD*. On each axis, the heat conductivity of a single solution is plotted (methanol with an alcohol). As an example serve (50 + 50%) solutions of the above alcohols. For simplicity, the heat conductivity scales are taken to be the same. For all the axes, the origin of coordinates lies at point *O*. Rectangular grids are used to find the intersection points of the heat conductivities at given P and T. Solution pairs give curves within the rectangular coordinate system. The four possible combinations of pairs give four curves *1*–*4*. It was found that, to within the experimental error, these curves are straight lines described by simple mutual-dependence equations $\lambda' = m\lambda'' + n$.

Processing gives the following equations:

$$\lambda_2 = 1.052\lambda_1 - 37.81, \quad (4)$$

$$\lambda_3 = 1.051\lambda_2 - 60.05, \quad (5)$$

$$\lambda_4 = 1.097\lambda_3 - 159.24, \quad (6)$$

$$\lambda_1 = 0.873\lambda_4 + 140.5, \quad (7)$$

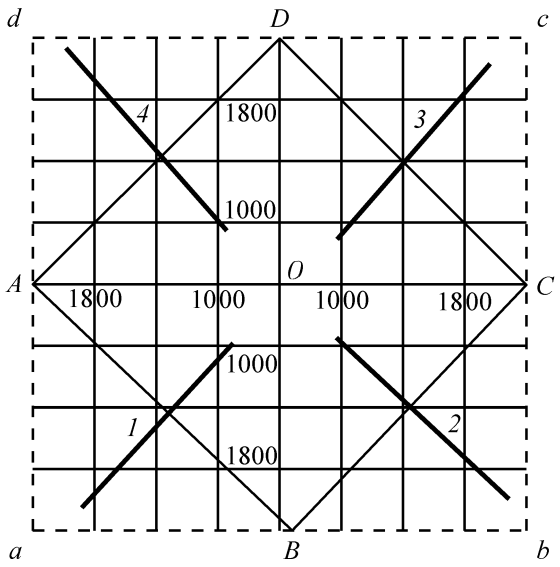

Mutual dependences of the heat conductivities of the systems methanol–*n*-hexanol, methanol–*n*-nonanol, methanol–*n*-undecanol, and methanol–*n*-dodecanol at 50 wt % methanol. Solution: (*1*) *OA–OB*, (*2*) *OB–OC*, (*3*) *OC–OD*, and (*4*) *OD–OA*, where *O*, *A*, *B*, *C*, and *D* stand for, respectively, methanol, *n*-hexanol, *n*-nonanol, *n*-undecanol, and *n*-dodecanol.

where λ_1, λ_2, λ_3, and λ_4 are the heat conductivities of the first (methanol–*n*-hexanol), second (methanol–*n*-nonanol), third (methanol–*n*-undecanol), and fourth (methanol–*n*-dodecanol) solutions. In all the solutions, the content of methanol is 50 wt %.

Equations (4)–(7) make it possible to find the heat conductivity of a given solution on the basis of the other three solutions, which is very important for mutual verification of the accuracy of calculation.

It should be noted that *P* and *T* can be used as determining parameters for the properties of solutions that are far from the saturation line and the critical region. At the same time, for the zone close to the saturation line and the pseudocritical point, the respective reduced parameters π and τ should be used, where π is reduced pressure and τ is reduced temperature.

CONCLUSIONS

(1) An experimental study of the heat conductivity of methanol–*n*-dodecanol mutual solutions at temperatures of 300–600 K and pressures in the range 0.1–60 MPa was carried out at methanol content of 25, 50, and 75 wt %. The experiments were performed on a modified setup by the regular-mode method. The results obtained were processed graphically and analytically. A four-coordinate system making it possible to calculate the heat conductivity of a solution on the basis of the three others is proposed for the first time.

(2) The heat conductivity of *n*-dodecanol was related to thermal pressure, and a corresponding equation was obtained.

REFERENCES

1. Naziev, Ya.M., Shakhverdiev, A.N., Aliev, N.S., and Bashirov, M.M., *Teplovye svoistva odnoatomnykh spirtov (teploprovodnost'): Obzory po teplofizicheskim svoi stvam veshchestv* [Thermal Properties of Monoatomic Alcohols (Heat Conductivity): Reviews of Thermal Properties of Substances], Moscow: TFTs, 1992.
2. Bashirov, M.M. and Naziev, Ya.M., *Probl. Energetiki*, 2001, no. 4, pp. 133–139.
3. Golubev, I.F. and Vasil'kovskaya, T.N., *Teploenergetika*, 1969, no. 5, pp. 77–82.
4. Naziev, Ya.M., Aliev, N.S., and Akhmedov, A.K., *Inzh.-Fiz. Zh.*, 1986, vol. 51, no. 4, pp. 685–686.
5. Naziev, Ya.M., Aliev, N.S., and Akhmedov, A.K., *Prom. Teplotekhn.*, Kiev, 1986, vol. 8, no. 4, pp. 72–76.
6. Naziev, Ya.M., A Study of Heat Conductivity of Hydrocarbons at High Pressure and Some Specific Features of Its Measurement, *Doctoral Dissertation*, Moscow, 1970.
7. Enskog, D., *Kingl. Svenska Vetenkapsakademens Hadlingar*, 1922, no. 68, p. 20.
8. Naziev, Ya.M., Shakhverdiev, A.N., Akhundov, T.S., *et al.*, *Izv. Vyssh. Uchebn. Zaved., Neft' Gaz*, 1990, no. 12, pp. 69–74.
9. Naziev, Ya.M., Naziev, Dzh.Ya., and Gasanov, V.G., *Teplofiz. Vys. Temp.*, 2001, vol. 39, no. 2, pp. 235–240.

Russian Journal of Applied Chemistry, Vol. 76, No. 4, 2003, pp. 526–530. Translated from Zhurnal Prikladnoi Khimii, Vol. 76, No. 4, 2003, pp. 546–550.

PHYSICOCHEMICAL STUDIES OF SYSTEMS AND PROCESSES

Influence of SiO_2 on the Equilibrium in the Cu–Ni–Cu_2O–NiO System

N. A. Fedorova, L. B. Tsymbulov, and L. Sh. Tsemekhman

Institut Gipronikel' Open Joint-Stock Company, St. Petersburg, Russia

Received February 11, 2003

Abstract—The equilibrium between a copper–nickel alloy and an oxide melt in the Cu_2O–NiO–SiO_2 system was studied experimentally. The distribution coefficients of nickel were determined as a function of the content of silicon dioxide, and the ratio of activity coefficients of nickel and copper oxides at 1300°C was found.

The information on thermodynamic properties of molten metallic and oxide systems makes it possible to solve a great number of problems related to the development of technological processes. The equilibrium between a metallic melt of copper with admixture of nickel and iron silicate melts with high concentration of copper and nickel oxides is of interest when analyzing pyrometallurgical processes associated with the production of copper from nickel-containing copper raw materials. To processes of this kind, in particular, belong oxidizing fusion of a copper concentrate obtained by flotation of converter matte in converters with oxygen overdraft to give nickel-containing [1, 2] and blister copper [3, 4], fusion of a similar concentrate to yield nickel-containing copper in a converter with bubbling oxygen [5], and a number of other processes.

This study is a continuation of [6], in which the equilibrium between a cooper–nickel metallic melt and Cu_2O–NiO oxide melt was analyzed. The aim of the present study was to assess the influence exerted by the main components of an industrial slag melt on the equilibrium in this system.

The equilibrium distribution of copper and nickel between metallic and oxide-silicate phases is governed by the exchange reaction

$$(Cu_2O) + [Ni] = (NiO) + 2[Cu]. \quad (1)$$

The parenthesis traditionally denote the oxide-silicate phase, and square brackets, the metallic phase.

The coefficients L_m of metal distribution between a copper–nickel alloy and an oxide-silicate melt are expressed as

$$L_m = (Ni)/[Ni]. \quad (2)$$

Since the activities of copper and nickel in metallic melts saturated with oxygen can be found in the literature [7], we can calculate the ratios of activity coefficients in Cu_2O–NiO–SiO_2 melts, using the known equilibrium constant of reaction (1):

$$\gamma_{NiO}/\gamma_{Cu_2O} = K_a/\left[\left(x_{NiO}/x_{Cu_2O}\right)\left(x_{Cu}^2/x_{Ni}\right)\left(\gamma_{Cu}^2/\gamma_{Ni}\right)\right]. \quad (3)$$

The equilibrium constant of reaction (1) was calculated from the melting heat $\Delta H_m = 50.6$ kJ mol^{-1} [8], with account of nickel oxide supercooling, to be 8.9 at 1573 K.

It was expedient to begin this study with consideration of the phase diagram of Cu_2O–NiO–SiO_2. Since this diagram could not be found in the accessible publications, we consider the available data on the binary systems Cu_2O–SiO_2 and NiO–SiO_2.

The first results obtained in studying the system Cu_2O–SiO_2 by chemical methods for determining melting points are indicative of the presence of various copper silicates: $Cu_2O \cdot SiO_2$, $2Cu_2O \cdot SiO_2$, $3Cu_2O \cdot SiO_2$, $5Cu_2O \cdot SiO_2$, and $CuO \cdot SiO_2$. However, the majority of later studies ruled out the existence of these or any other chemical compounds in the system. In particular, the systems Cu_2O–SiO_2 and CuO–SiO_2 have been studied in detail by Berezhnoi [9, 10] on quenched samples, using microscopic and X-ray methods, and then by Gadalla [11] by means of gravimetry. They also found that there are no chemical compounds in this system. In [12], the system Cu_2O–SiO_2 was subjected to X-ray diffraction analysis, and the phase diagram of the CuO–SiO_2 sys-

1070-4272/03/7604-0526 $25.00 © 2003 MAIK "Nauka/Interperiodica"

tem in air was constructed on the basis of a critical consideration of published data and the authors' own experimental data. It was found that copper(II) oxide completely dissociates at 1025°C into copper(I) oxide and oxygen and the eutectic containing 92 wt % Cu_2O + 8% SiO_2 melts at 1050°C.

The system NiO–SiO_2 belongs to eutectic systems with broad stratification region. It is seen from the phase diagram presented in [13] that a single compound, specifically, nickel orthosilicate Ni_2SiO_4 with olivine structure, exists in the system. It was shown in [14] that, unlike other olivines, which melt congruently, nickel orthosilicate dissociates in the solid state at 1545°C.

Using the EMF method, Rog and Borchardt [15] determined the standard molar Gibbs energy of Ni_2SiO_4 formation from oxides by reaction (4) and also found its temperature dependence:

$$2NiO + SiO_2 = Ni_2SiO_4, \quad (4)$$

$$\Delta G^0 = -0.0089T + 15.941. \quad (5)$$

It is seen from dependence (5) that, with increasing temperature, the Gibbs energy inevitably becomes higher and the reaction equilibrium is shifted toward the starting compounds.

The standard molar Gibbs energy of nickel orthosilicate formation by reaction (4) was determined in a similar manner in [16, 17]. The resulting Gibbs energies for Ni_2SiO_4 agree well with each other and are equal at 1300°C to –2.5 [16] and –2.6 kJ mol^{-1} [17]. These values indicate that the equilibrium constant is small and, hence, the compound obtained is rather unstable.

The available published thermodynamic data for the systems Cu_2O–SiO_2 and NiO–SiO_2 suggest that introduction of silicon dioxide into the system Cu_2O–NiO will virtually not affect the activity coefficient of copper oxide, but, in all probability, the activity coefficient of nickel oxide will decrease owing to the existence of a chemical compound in the system.

To determine the dependence of L_{Ni} on the composition of the oxide melt Cu_2O–NiO–SiO_2 and the numerical values of the $\gamma_{NiO}/\gamma_{Cu_2O}$ ratio, we performed a set of experiments by a technique similar to that described in [6], except that varied amounts of silicon dioxide were introduced into the stock. The experiments were carried out at 1300°C in an argon atmosphere. In addition to analyzing the obtained metallic alloys and oxide melts by chemical methods, part of samples of the oxide melts was quenched on a copper disc (cooling rate of about 10^3 deg s^{-1}) and studied by scanning electron microscopy and X-ray fluorescence microanalysis.

Content of nickel $[Ni]_m$ in copper and silicon dioxide (SiO_2) and nickel (Ni) in slag, and distribution coefficients of nickel L_{Ni}, as determined from experimental data

(SiO_2)	(Ni)	$[Ni]_m$	L_{Ni}	(SiO_2)	(Ni)	$[Ni]_m$
wt %				at. %		
0.12	0.25	0.10	2.50	0.28	0.47	0.10
0.26	0.73	0.22	3.32	0.61	1.38	0.24
0.32	0.28	0.09	3.11	0.76	0.53	0.10
0.78	1.93	0.68	2.84	1.80	3.57	0.74
1.18	2.44	0.66	3.70	2.69	4.47	0.71
1.26	1.90	0.64	2.97	2.88	3.50	0.69
1.28	2.50	0.79	3.16	2.92	4.57	0.85
1.70	4.29	1.06	4.05	3.77	7.65	1.15
1.90	3.07	0.75	4.09	4.26	5.53	0.81
3.06	4.20	1.01	4.16	6.67	7.37	1.09
4.81	4.51	0.87	5.18	10.23	7.72	0.94
7.00	4.72	0.87	5.43	14.74	7.85	0.94
10.49	4.30	0.76	5.66	20.89	6.89	0.82
12.39	4.20	0.80	5.25	24.17	6.59	0.86

The content of nickel in copper and silicon dioxide in nickel and slag, and also the distribution coefficients of nickel, found in our experiments, are listed in the table.

The main difficulty in studying the equilibrium between metallic and oxide melts of the system Cu_2O–NiO is that its phase diagram and, in particular, the liquidus line are unknown. Therefore, we subjected the samples obtained to chemical analysis only if we were sure that the oxide melt was homogeneous. In this case the ratio of the amounts of the starting

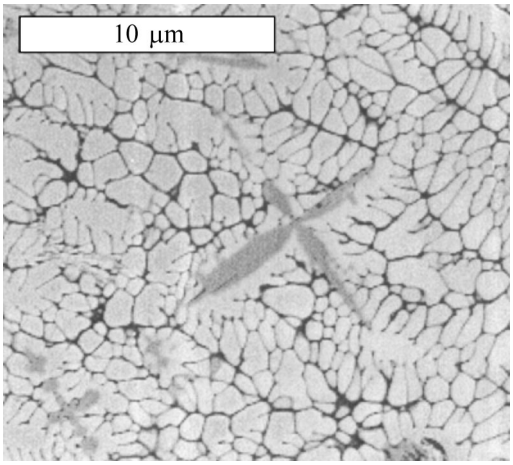

Fig. 1. Microstructure of a homogeneous oxide melt of the system Cu_2O–NiO–SiO_2.

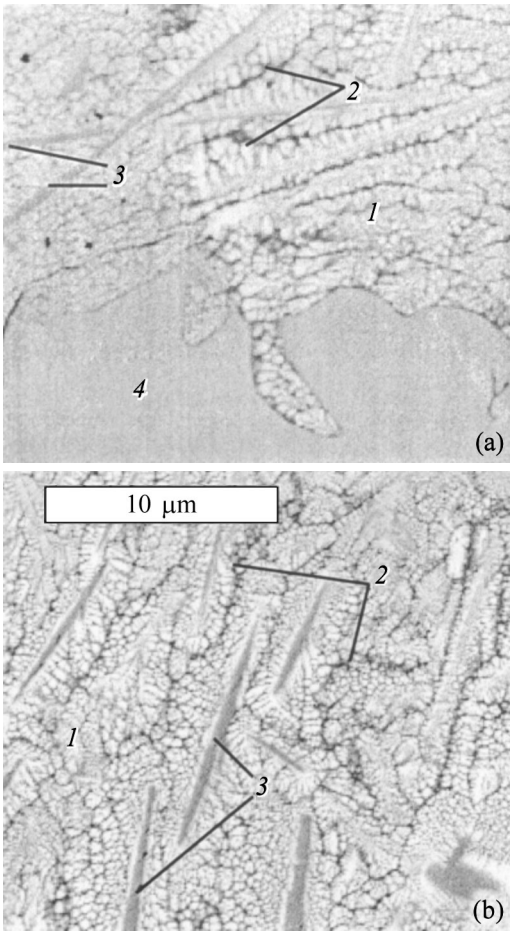

Fig. 2. Microstructure of quenched oxide melt with NiO/Cu_2O ratio of 0.13. Microstructure of (a) melt with inclusions of nickel oxide and (b) homogeneous oxide melt. Phase close in composition to (*1*) Cu_2O, (*2*) SiO_2; (*3*) nickel silicate (wt %): SiO_2 29, NiO 65.4, Cu_2O 5; (*4*) nickel oxide (wt %): SiO_2 0.2, NiO 96.7, Cu_2O 2.5. Average composition of the homogeneous part of the melt (wt %): SiO_2 6.72, NiO 6.67, Cu_2O 83.87.

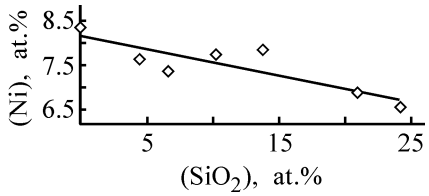

Fig. 3. Dependence of nickel content (Ni) in an oxide melt on the silicon oxide content (SiO_2) in the melt at NiO/Cu_2O ratio equal to 0.11.

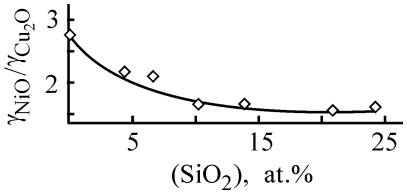

Fig. 4. Dependence of the ratio of activity coefficients of nickel and copper oxides $\gamma_{NiO}/\gamma_{Cu_2O}$ on the content of silicon dioxide (SiO_2) in an oxide melt.

materials was selected in such a way that, first, the NiO/Cu_2O ratio of molar concentrations in the oxide melt was less than 0.11 (limiting ratio of molar concentrations for a homogeneous melt in the system Cu_2O–NiO [6]) and, second, the concentration of SiO_2 was negligible (see phase diagram for Cu_2O–SiO_2 in [12]). The homogeneity of the melt was selectively monitored by its quenching.

A typical microstructure of a homogeneous oxide melt of the system Cu_2O–NiO–SiO_2 is shown in Fig. 1. It is evident that the melt is formed of copper(I) oxide on a matrix of silicon oxide with inclusions of nickel silicate. In our opinion, the phase based on nickel silicate is of secondary origin, i.e., it is formed in the course of crystallization because of the insufficient cooling rate. The size of other components of the sample also indicates that the melt is homogeneous.

When burdening involved possible going beyond the limits of the homogeneity area, the use of quenching and subsequent microanalysis to determine the phase composition and the composition of directly the homogeneous part of the melt was mandatory.

The typical microstructure of samples with inclusions of nickel silicate and oxide is shown in Figs. 2a and 2b. As a rule, these are melts with high NiO/Cu_2O ratios, in which nickel oxide crystals are irregularly distributed in the bulk of a sample. The size of these crystals is indicative of their primary origin, i.e., the crystals are present in the melt in the solid state.

We determined the concentrations of the components of the oxide melt with inclusions of nickel oxide for the subsequent calculation of L_{Ni}, with the analysis disregarding the solid phase. In this case, the maximum possible NiO/Cu_2O ratio in a slag melt at the boundary of saturation with nickel oxide in the system Cu_2O–NiO–SiO_2 was 0.13. As noted above, this ratio is 0.11 for the system Cu_2O–NiO. Thus, the introduction of silicon dioxide somewhat increased the ratio.

To assess the effect produced by raising the content of silicon dioxide on the content of nickel in a slag and on the ratio of the activity coefficients of nickel and copper oxides, we consider separately experiments in which the oxide melt was characterized by the same ratio NiO/Cu_2O (0.11) and varied SiO_2 content. The dependence of the nickel content in the oxide phase on the silicon dioxide content is shown in Fig. 3. It is seen that, with increasing concentration of silicon dioxide in a slag, the content of nickel in it decreases. However the dependence of $\gamma_{NiO}/\gamma_{Cu_2O}$ on SiO_2 shows different behavior (Fig. 4). On addition of up to 10 at.% silicon dioxide, the $\gamma_{NiO}/\gamma_{Cu_2O}$ ratio

decreases rapidly to become 1.7 times smaller than the $\gamma_{NiO}/\gamma_{Cu_2O}$ ratio in the system Cu_2O–NiO; further increase in the content of silicon oxide leaves this ratio virtually unchanged. A noticeable drop in the $\gamma_{NiO}/\gamma_{Cu_2O}$ value at small content of SiO_2 seems to be due to the fact that silicon oxide forms associates with nickel oxide, which makes lower the activity coefficient of nickel oxide, but virtually does not affect the activity coefficient of copper oxide.

At the NiO/Cu_2O ratio in an oxide melt equal to 0.11 and at silicon dioxide content in the slag exceeding 10 at.%, the whole amount of nickel oxide (in terms of the stoichiometry of the compound Ni_2SiO_4) is already associated with silicon oxide, and, therefore, an excess amount of the latter does not affect the activity coefficient of nickel oxide and, hence, the ratio of the activity coefficients.

There is good reason to believe that NiO and SiO_2 are associated in the melt in the same proportions as in Ni_2SiO_4. This is evidenced by the data of X-ray fluorescence microanalysis (Figs. 2a and 2b), which indicate that the compositions of nickel silicate and the compound in the phase diagram are close.

The coefficients of nickel distribution between an oxide melt and a metallic alloy, obtained in this study and in [6], are shown in Fig. 5a as functions of the oxide melt composition. It is seen that L_{Ni} becomes greater on addition of SiO_2 to the Cu_2O–NiO system. This is due to the fact that silicon dioxide tends to form associates with nickel. The dependence of the nickel distribution coefficient on the composition of the oxide melt in the presence of silicon dioxide is described by the equation

$$L_{Ni} = 20.285(NiO)/(Cu_2O) + 2.472. \quad (6)$$

Here (NiO) and (Cu_2O) are the concentrations (at.%).

The ratios of activity coefficients of nickel and copper oxides, found in this study, are shown in Fig. 5b. Also presented in the figure is a similar dependence obtained in [6] for the equilibrium with a binary NiO–Cu_2O melt. It is seen from Fig. 5b that the presence of silicon dioxide in a system decreases somewhat the ratio of the activity coefficients of the oxides.

As already mentioned, this is due to a drop in the activity coefficient of nickel because of its association with silica in the melt.

The dependence of the activity coefficients of nickel and copper oxides on the ratio of their concentrations in the Cu_2O–NiO–SiO_2 melts at 1300°C is described by the analytical equation

$$\gamma_{NiO}/\gamma_{Cu_2O} = 3.631 - 14.759(NiO)/(Cu_2O). \quad (7)$$

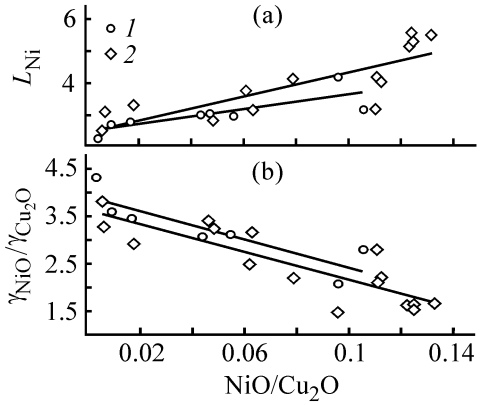

Fig. 5. Dependence of (a) nickel distribution coefficient L_{Ni} and (b) ratio of activity coefficients of nickel and copper oxides $\gamma_{NiO}/\gamma_{Cu_2O}$ on the ratio of the contents of nickel and copper oxides in an oxide melt. (*1*) Cu_2O–NiO, (*2*) Cu_2O–NiO–SiO_2.

CONCLUSIONS

(1) Silicon dioxide affects the coefficient of nickel distribution between a copper–nickel alloy and an oxide melt, which increases in proportion to the content of silicon dioxide and nickel in a slag.

(2) Addition of silicon dioxide to the NiO–Cu_2O system results in an insignificant decrease in the $\gamma_{NiO}/\gamma_{Cu_2O}$ ratio. The decrease in the $\gamma_{NiO}/\gamma_{Cu_2O}$ ratio in the Cu_2O–NiO–SiO_2 melts results from the formation of associates between NiO and SiO_2. This is confirmed by the results obtained in studying quenched oxide melts by X-ray fluorescence microanalysis.

(3) The data obtained can be used in analyzing the refinement of nickel-containing blister copper in the presence of silicon dioxide in the forming slag.

REFERENCES

1. Onishchin, B.P., Khe Khuankhua, Tsemekhman, L.Sh., *et al., Tsvetn. Met.*, 1998, no. 1, pp. 26–29.
2. Miroevskii, G.P., Golov, A.N., and Koklyanov, E.B., *Tsvetn. Met.*, 2001, no. 2, pp. 41–47.
3. Golov, A.N., A Study and Development of Ecologically Pure Autogenous Technology for Processing of Low-Iron Copper-Rich Concentrates To Obtain Copper with Prescribed Composition, *Cand. Sci. (Chem.) Dissertation*, Moscow, 2001.
4. RF Patent 2 169 202.
5. Landolt, C., Dutton, A., Fritz, A., and Segsworth, S., *Proc. Paul E. Queneau Int. Symp. Extractive Metallurgy of Copper, Nickel and Cobalt*, 1993, vol. 2, pp. 1497–1527.
6. Fedorova, N.A., Tsymbulov, L.B., and Tsemekh-

man, L.Sh., *Zh. Prikl. Khim.*, 2002, vol. 75, no. 4, pp. 535–539.

7. Kulkarni, A.D. and Johnson, R.E., *Met. Trans.*, 1973, vol. 4, pp. 1723–1727.
8. Kubaschevski, O. and Alcock, C.B., *Metallurgical Thermochemistry*, Oxford: Pergamon, 1979.
9. Berezhnoi, A.S., Karyakin, L.I., and Dudavskii, *Dokl. Akad. Nauk SSSR*, 1952, no. 83, pp. 399–401.
10. Berezhnoi, A.S. and Karyakin, L.I., *Tsvetn. Met.*, 1955, no. 2, pp. 26–33.
11. Gadalla, A.M., Ford, W.F., and White, I., *Trans. Brit. Ceram. Soc.*, 1963, vol. 62, no. 1, pp. 45.
12. Ust'yantsev, V.M., Sudakova, L.P., and Bessonov, A.F., *Zh. Neorg. Khim.*, 1966, vol. 11, no. 5, pp. 1177–1182.
13. Toropov, N.A., Barzakovskii, V.P., Lapin, V.V., *et al.*, *Diagrammy sostoyaniya silikatnykh sistem: Spravochnik* (Phase Diagrams of Silicate Systems: Reference Book), Moscow, 1970, issue 2.
14. Phillips, B., Hutta, J.J., and Warshaw, I., *J. Am. Ceram. Soc.*, 1963, vol. 46, no. 12, pp. 579–583.
15. Rog, G. and Borchardt, G., *J. Chem. Thermodyn.*, 1984, vol. 16, pp. 1103–1105.
16. Taylor, R.W. and Schmalzried, H.J., *J. Phys. Chem.*, 1964, vol. 68, pp. 2444–2449.
17. O'Neill, H.St.C., *Am. Mineralogist.*, 1987, vol. 72, pp. 280–291.

Russian Journal of Applied Chemistry, Vol. 76, No. 4, 2003, pp. 531–535. Translated from Zhurnal Prikladnoi Khimii, Vol. 76, No. 4, 2003, pp. 551–555.

SORPTION AND ION-EXCHANGE PROCESSES

A Study of Adsorption-Structural Properties of Natural and Processed Diatomites

G. G. Martirosyan, A. G. Manukyan, E. B. Ovsepyan, and K. A. Kostanyan

Institute of General and Inorganic Chemistry, National Academy of Sciences of the Republic of Armenia, Yerevan, Republic of Armenia

Received August 19, 2002

Abstract—The effect of alkaline, acid, and lime treatment on the chemical composition and sorption-structural characteristics of natural diatomites was studied. The efficiency of the lime treatment of natural diatomites for obtaining adsorbents was substantiated.

Diatomites, which belong to the group of sedimentary siliceous rocks, are composed of diatom shells having the form of an X-ray-amorphous variety of opal. Despite the large volume of mining of diatomites on the territory of CIS countries, their use is mainly limited to manufacture of cement, claydite, and bricks [1]. It is known that more promising and economically effective is use of these valuable mineral resources for manufacture of adsorbents, filter powders, fillers, and catalysts [2–5].

Synthesis of adsorbents and filter powders by lime and acid treatment of natural diatomites was studied in [3, 5–9].

The present communication reports the principal results of a study of the adsorption and structural characteristics of natural diatomites and products obtained in their alkaline, acid, and lime treatments. As objects of study were chosen typical representatives of diatomite rocks containing 44.16 to 81.00 wt % amorphous silica and 13 to 35 wt % accessory minerals (Table 1). Depending on the content of total and amorphous silica and that of accessory minerals, these rocks are conventionally termed high-quality (1), medium-quality (2), and low-quality (3) rocks.

EXPERIMENTAL

The diatomites under study were subjected to treatment with various reagents (5% NaOH solution, 6–27% HCl solution, milk of lime with CaO content of 150 g l^{-1} at $CaO : SiO_2$ molar ratio of 0.1–1.5 in the initial mixture) at 95°C and mass ratio l : s = 7. The duration of alkaline, acid, and lime treatments was 2, 4, and 1–16 h, respectively.

Washed, filtered, and dried products were subjected to comprehensive physicochemical studies.

The sorption properties of natural and processed diatomites were assessed by determining their specific surface area by the BET method [10] from low-temperature adsorption of nitrogen. For all of the samples studied, isotherms of adsorption of water and benzene vapors were measured, and porous structure param-

Table 1. Chemical composition of natural diatomites

Diatomite	Content, wt %								
	SiO_2		Fe_2O_3	Al_2O_3	CaO	MgO	$Na_2O + K_2O$	CO_2	calcination loss
	total	amorphous							
High-quality	88.26	81.00	0.49	1.26	0.58	0.42	0.22	1.82	8.60
Medium-quality	86.40	75.66	1.16	4.32	1.86	0.99	0.36	1.07	5.24
Low-quality	70.00	44.16	5.50	13.00	2.20	1.00	0.87	0.30	7.06

1070-4272/03/7604-0531 $25.00 © 2003 MAIK "Nauka/Interperiodica"

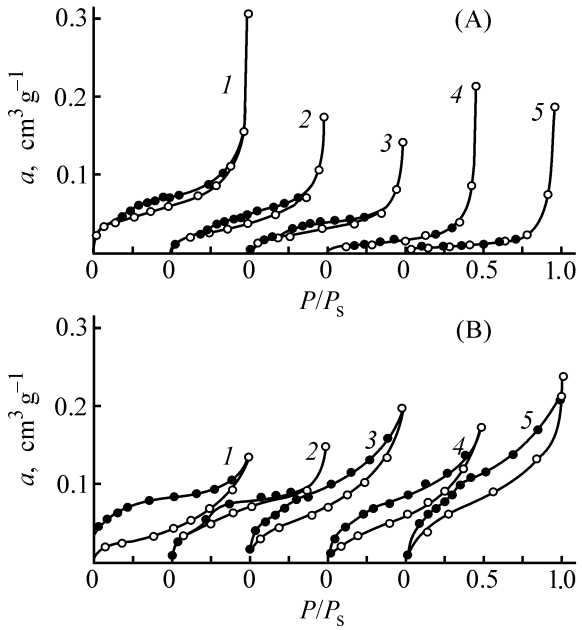

Fig. 1. Isotherms of adsorption of (A) benzene and (B) water vapor on starting diatomites at 20°C. (*a*) Adsorption and (P/P_s) relative pressure; the same for Figs. 2 and 3. Diatomite: (A) (*1*–*3*) low-quality, (*4*) medium-quality, and (*5*) high-quality; (B) (*1*) medium-quality, (*2*) high-quality, and (*3*–*5*) low-quality.

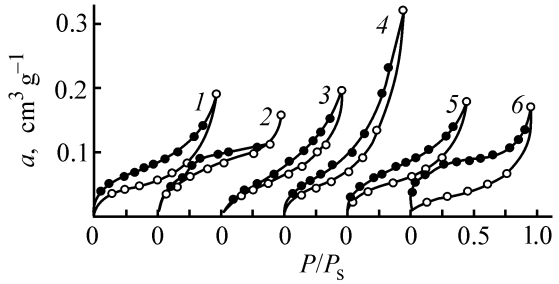

Fig. 2. Isotherms of water vapor adsorption at 20°C on diatomites treated with (*1*, *3*, *5*) alkali and (*2*, *4*, *6*) acid. Diatomite: (*1*, *2*) high-quality, (*3*, *4*) low-quality, and (*5*, *6*) medium-quality.

eters were calculated on their basis [11, 12]. A spectroscopic analysis was carried out on a Specord IR instrument in the spectral range 400–4000 cm^{-1}, and X-ray diffraction analysis, on a DRON-1,5 diffractometer [13, 14]. The chemical composition, density ρ, and volume mass m_V were found using the known procedures [15, 16].

The results obtained indicate that natural diatomites mainly possess macroporous structure with predominance of pores of the same radius, but the structure also contains intermediate pores.

As seen from Fig. 1A, the isotherms of benzene vapor adsorption on the surface of high- and medium-quality diatomites (curves *5* and *4*) have similar shapes and show hysteresis at P/P_s = 0.2–0.7. At P/P_s > 0.75, a dramatic increase in benzene adsorption is observed for all the three types of diatomites (Table 2, Fig. 1A), which points to the presence of a developed macroporous structure.

Isotherms of water adsorption (Fig. 1B) on diatomites of all types show, except in the case of sample no. 1 (curve *2*), hysteresis characteristic of swelling sorbents. The adsorption and desorption branches do not coincide in the entire range of relative pressures P/P_s (0–1). The width of hysteresis in the isotherms of water vapor adsorption in the initial region (P/P_s < 0.2) depends on the content of impurities (clayey materials). The only exception is sample no. 2 (curve *1*), whose hysteresis is wider in the initial region than that for other samples, presumably, because of the fact that the clayey component of this diatomite has an expanding structural unit (mainly of montmorillonite type) [17]. The desorption branches of the isotherms of water vapor adsorption on all the diatomites studied show a bend at P/P_s = 0.2–0.3, which corresponds to pores whose radii calculated by the Kelvin method [7] are equal to 7 Å. The presence of pores with radii of 7–8 Å in high- and medium-quality diatomites, which are nearly totally composed of intact diatom shells, suggests that pores with this radius belong to silica of organic origin.

With the content of accessory minerals increasing from 13.0 to 18.5 wt %, the density of natural diatomites grows and the porosity decreases (Tables 1 and 2). An inverse relationship between the content of diatom shells (beginning with 60–70 million shells per gram) in diatomites and their vol-

Table 2. Physicochemical properties of natural diatomites* (relative pressure P/P_s = 0.95)

Diatomite	pH of aqueous extract	m_V	ρ	S_{sp}, $m^2 g^{-1}$	Content of intact shells, million pieces per gram	Π, %	V_p ($cm\ g^{-1}$) found from adsorption of indicated vapor		r_p, Å
		kg m^{-3}					water	benzene	
High-quality	6.5	140	1620	19	60–70	91.4	0.121	0.078	89
Medium-quality	7.2	167	1700	27	50	89.8	0.122	0.085	65
Low-quality	7.6	350	2180	60	7–9	84.1	0.152	0.082	28

* Π is porosity; V_p, total pore volume; r_p, average pore radius.

Table 3. Adsorption-structural characteristics of high-quality diatomites treated with milk of lime (treatment temperature 95°C, P/P_s = 0.95)

τ, h	CaO/SiO_2 molar ratio in the initial mixture	V_p ($cm\ g^{-1}$) found from adsorption of indicated vapor		S_{sp}, $m^2\ g^{-1}$	r_p, Å	τ, h	CaO/SiO_2 molar ratio in the initial mixture	V_p ($cm\ g^{-1}$) found from adsorption of indicated vapor		S_{sp}, $m^2\ g^{-1}$	r_p, Å
		water	benzene					water	benzene		
6	0.2	0.535	0.521	191	11	6	1.25	0.775	0.745	147	13
6	0.3	0.640	0.597	–	11	1	0.4	0.591	0.540	220	11
6	0.4	0.717	0.702	257	11	2	0.4	0.656	0.603	229	11
6	0.5	0.660	0.631	237	11	3	0.4	0.703	0.680	240	11
6	0.6	0.510	0.489	160	9	4	0.4	0.710	0.688	236	11
6	0.7	0.668	0.642	–	12	6	0.4	0.717	0.702	257	11
6	0.8	0.565	0.489	160	13	10	0.4	0.705	0.681	251	10
6	1.0	–	–	140	–	16	0.4	0.974	0.965	240	10

ume mass (140–1350 $kg\ m^{-3}$) is observed, in good agreement with published data [18]. The specific surface area of all the diatomites studied is small, with high- and medium quality diatomites, in which the content of the main component (diatom shells) exceeds that in low-quality diatomites, characterized by smaller specific surface area and total pore volume than these latter (Table 2). A conclusion can be made on the basis of Tables 1 and 2 that the adsorption capacity of natural diatomites is low and they cannot be effectively used in sorption processes without preliminary treatment.

As seen from Figs. 2 and 3A and Table 3, alkaline, acid, and lime treatment of natural diatomites strongly modifies their chemical composition and physicochemical and adsorption-structural properties.

The desorption branches of the isotherms of water vapor adsorption on diatomites subjected to alkaline treatment (Fig. 2) show no bend at P/P_s = 0.2–0.3, and, consequently, there are no pores with radius of 7–8 Å. By contrast, pores with this radius are preserved in the diatomites after acid treatment. It has been shown [18] that, in the course of an alkaline treatment of the diatomites, amorphous silica contained in them is completely dissolved, whereas clayey materials remain unchanged (Table 1). Acid treatment has nearly no effect on the diatom shells and silica of chemical origin, whereas the clayey component of the diatomites partly disintegrates [18].

Reflections at 3.5–4.5 Å and absorption bands at 800 and 1100 cm^{-1}, which are characteristic of amorphous silica, disappear from X-ray diffraction patterns and IR spectra of diatomites after alkaline treatment. In the IR spectra of diatomites subjected to acid treatment, the intensity of absorption bands at 535, 430, and 3620 cm^{-1}, which are associated with montmorillonite, decreases.

The isotherms of adsorption of water and benzene vapor on diatomites subjected to lime treatment, which show hysteresis of type B according to de Boer's clas-

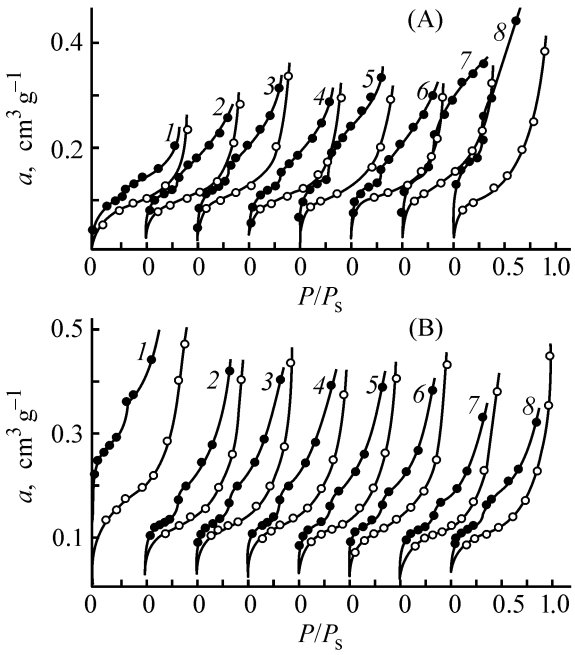

Fig. 3. Isotherms of water vapor adsorption on lime-treated high-quality diatomites at 20°C. (A) Treatment temperature 95°C and duration 6 h. CaO/SiO_2 molar ratio in the initial reaction mixture: (*1*) 0.2, (*2*) 0.3, (*3*) 0.4, (*4*) 0.5, (*5*) 0.6, (*6*) 0.7, (*7*) 0.8, and (*8*) 1.25. (B) CaO/SiO_2 molar ratio in the initial reaction mixture 0.4, treatment temperature 95°C. Treatment duration (h): (*1*) 16, (*2*) 10, (*3*) 6, (*4*) 5, (*5*) 4, (*6*) 3, (*7*) 2, and (*8*) 1.

Table 4. Chemical composition of high-quality diatomites after lime treatment (treatment temperature 95°C and duration 6 h)

CaO/SiO_2 molar ratio in the initial mixture	Content, wt %									CaO/SiO_2 molar ratio in treated diatomites	pH of aqueous extract
	SiO_2		Al_2O_3	Fe_2O_3	CaO_{tot}	MgO	$Na_2O + K_2O$	calcination loss	sum total		
	total	amorphous									
Initial diatomite	88.26	81.00	1.26	0.49	0.58	0.42	0.22	8.60	99.83	0.007	6.50
0.1	80.50	56.31	0.81	0.33	8.02	0.53	0.21	9.20	99.60	0.107	9.37
0.2	71.44	42.75	1.54	0.61	12.50	0.79	0.24	12.00	99.12	0.187	9.40
0.4	60.03	24.6	1.74	0.71	23.28	0.98	0.18	12.90	98.82	0.415	9.61
0.5	56.71	13.2	1.51	0.39	26.01	0.46	0.20	14.60	99.88	0.491	10.02
0.6	52.03	8.71	1.38	0.62	28.87	0.59	0.23	16.90	99.65	0.593	10.26
0.8	44.79	6.61	1.64	0.50	34.05	0.65	0.22	17.70	99.55	0.813	10.31
1.00	39.47	4.75	1.68	0.41	38.04	0.63	0.24	19.00	99.00	1.01	10.90
1.25	36.47	2.33	1.09	0.25	42.60	0.42	0.20	18.30	99.33	1.25	11.71
1.35	34.59	0.36	1.07	0.56	44.31*	1.04	0.21	18.00	99.78	1.37	12.3

* In addition total CaO, the sample contains 2.84 wt % free CaO.

sification, are characteristic of layered adsorbents. The bend in the desorption branches (Fig. 3A) at P/P_s 0.20–0.25 (in adsorption of benzene vapor) and 0.25–0.30 (in adsorption of water vapor) is due to adsorption of benzene and water vapors in the interlayer space of the newly formed calcium hydrometasilicates. The width of hysteresis grows with increasing CaO/SiO_2 molar ratio in the initial mixture, which points to a rise in the content of calcium hydrometasilicates of the C–S–H (1) type (according to Taylor's classification [20]) in the products obtained (Table 4). Raising the duration of the lime treatment of diatomites from 1 to 10 h at CaO/SiO_2 molar ratio in the initial mixture equal to 0.4 has virtually no effect on the run of the isotherms of water adsorption (Fig. 3A), despite the significant change in the specific surface area of the samples (Table 3). With the duration of treatment raised to 16 h, the bend in the desorption branches of the isotherms of water adsorption on the surface of diatomites treated with milk of lime and the hysteresis become more pronounced (Fig. 3B).

At CaO/SiO_2 molar ratio in the initial mixture of 0.2–0.5, the average pore radius calculated from the isotherms of benzene vapor adsorption on high-quality diatomites remains unchanged after lime treatment (11 Å), at CaO/SiO_2 = 0.6 it has the minimum value of 9 Å, and at CaO/SiO_2 molar ratios in the range from 0.7 to 1.25 it increases to 13 Å (Table 3). At constant CaO/SiO_2 molar ratio in the initial mixture (0.4), the average pore size (11–10 Å) and specific surface area remain unchanged when the treatment duration is raised from 1 to 16 h. The maximum specific surface area and pore volume are observed at CaO/SiO_2 = 0.4 (Table 3). This behavior is characteristic of all kinds of diatomites.

Analysis of the experimental data obtained and published evidence suggests that, in contrast to the other above-mentioned treatments, lime treatment of diatomites results in that active centers appear in the form of unsaturated C–S–C bonds on the surface of silica of chemical origin [20–23]. Owing to their amorphous uniform surface and structural features, diatomites treated with milk of lime have enhanced sorption capacity.

CONCLUSIONS

(1) A comprehensive study of the adsorption-structural properties of natural and treated diatomites demonstrated that, in contrast to other methods, lime treatment of diatomites leads to a pronounced increase in the specific surface and total pore volume of natural diatomites.

(2) The optimal CaO/SiO_2 molar ratios in lime treatment of diatomites were revealed, at which the treatment products have the highest adsorption capacity and most developed pore structure.

(3) It was shown that, with increasing duration of lime treatment of diatomites, the average pore radius remains virtually constant.

(4) Strong differences in the structure of diatomites subjected to treatments with different reagents were revealed.

REFERENCES

1. *Syr'evaya baza kremnistykh porod SSSR i ikh ispol'zovanie v narodnom khozyaistve* (Resources of Siliceous Rocks in the USSR and Their Use in National Economy), Petrov, V.P., Ed., Moscow: Nedra, 1976.
2. Taylor, Jr. and Harold, A., *Am. Ceram. Soc. Bull.*, 1995, vol. 74, no. 6, pp. 122–122.
3. USSR Inventor's Certificate, no. 1 599 055.
4. Fedyaev, F.F., Matveeva, L.G., Eremeev, D.N., *et al., Doklady Regional'noi konferentsii "Alyuminii Urala–96", Krasnoturinsk, 20–22 iyunya 1996 g.* (Proc. Region. Conf. "Aluminum of Urals 96", Krasnoturinsk, June 20–22, 1996), Krasnoturinsk: Izd. B. Alyum. Zavod., 1996, pp. 108–115.
5. Manukyan, A.G., Martirosyan, G.G., Kostanyan, K.A., *et al.*, *Khim. Zh. Armenii*, 1993, vol. 46, nos. 3–4, pp. 120–125.
6. Balayan, K.A., Arutyunyan, A.M., and Babayan, S.G., *Arm. Khim. Zh.*, 1976, vol. 29, no. 12, pp. 10 001–11 167.
7. USSR Inventor's Certificate, no. 1 060 567.
8. Martirosyan, G.G., Manukyan A., and Kostanyan, K.A., *Zh. Prikl. Khim.*, 2002, vol. 75, no. 2, pp. 217–220.
9. Manukyan, A.G., Martirosyan, G.G., Anakchyan, E.Kh., and Kostanyan, K.A., *Zh. Prikl. Khim.*, 1999, vol. 72, no. 11, pp. 1795–1800.
10. Gregg, S.J. and Sing, K.S.W., *Adsorption, Surface Area and Porosity*, London: Academic, 1982.
11. Dubinin, M.M., *Adsorbtsiya i poristost'* (Adsorption and Porosity), Moscow: Nauka, 1976.
12. *Eksperimental'nye metody adsorbtsii i molekulyarnoi khromatografii* (Experimental Techniques of Adsorption and Molecular Chromatography), Kiselev, A.V., Ed., Moscow: Mos. Gos. Univ., 1976.
13. Lazarev, A.I., *Kolebatel'nye spektry i stroenie silikatov* (Vibrational Spectra and Silicate Structure), Moscow: Nauka, 1968.
14. Giller, Ya.I., *Tablitsy mezhploskostnykh rasstoyanii* (Tables of Interplanar Spacings), Moscow: Nedra, 1966, vol. 2.
15. Ponomarev, A.I., *Metody khimicheskogo analiza silikatnykh i karbonatnykh gornykh porod* (Methods for Chemical Analysis of Silicate and Carbonate Rocks), Moscow: Akad. Nauk SSSR, 1961.
16. Butt, Yu.M. and Timashev, V.V., *Praktikum po khimicheskoi tekhnologii vyazhushchikh materialov* (Manual of Chemical Technology of Binders), Moscow: Vysshaya Shkola, 1973.
17. Kel'tsev, N.V., *Osnovy adsorbtsionnoi tekhniki* (Fundamentals of Adsorption Technology), Moscow: Khimiya, 1984.
18. *Kremnistye porody SSSR* (Siliceous Rocks of the USSR), Distanov, U.G., Ed., Kazan: Tatar. Kn. Izd., 1976.
19. De Boer, Y.H., Linsen, B.L., and Sondervan, G.J., *J. Catal.*, 1965, vol. 4, no. 6, pp. 949–953.
20. Taylor, F.W., *The Calcium Silicate Hydrates—The Chemistry of Cements*, London, 1964, vol. 1.
21. Dmitriev, P.P., *Izvestkovaya aktivatsiya prirodnykh mineral'nykh sorbentov dlya nefteproduktov* (Lime Activation of Natural Mineral Sorbents for Petroleum Products), Tashkent: Fan, 1975.
22. Manukyan, A.G., Martirosyan, G.G., and Kostanyan, K.A., *Khim. Zh. Armenii*, 1999, vol. 52, no. 4, pp. 3–9.
23. Liebau, F., *Structural Chemistry of Silicates: Structure, Bonding, and Classification*, Berlin: Springer, 1985.

Russian Journal of Applied Chemistry, Vol. 76, No. 4, 2003, pp. 536–540. Translated from Zhurnal Prikladnoi Khimii, Vol. 76, No. 4, 2003, pp. 556–560.

SORPTION AND ION-EXCHANGE PROCESSES

Structure and Functional Composition of the Surface of Cambrian Clay as Influenced by Modification Conditions

Yu. A. Novikova and V. G. Korsakov

St. Petersburg State Technological Institute, St. Petersburg, Russia

Received June 18, 2002

Abstract—The possibility of directed modification of the functional composition of the surface and sorption properties of a disperse Cambrian clay was examined. The concentration of donor–acceptor centers was determined and changes in the structure and composition of the adsorption centers in the course of the acid-base treatment were evaluated. The mineralogical composition of the Cambrian clay and of the products of its chemical modification was analyzed by the successive dissolution procedure.

Clays from various deposits are used as raw materials in production of ceramics and as sorbents. In these cases, the requirements to the structure and properties of clays are fundamentally different. The plasticity, phase stability, and refractoriness of clays are the most important in ceramics production, whereas the surface area, functional composition, and sorption capacity are the decisive properties for sorbents. The sorption capacity of natural clays is low and is determined by secondary porosity. The particle size and crystal structure (i.e., the nature of the clay-forming minerals) also affect the sorption capacity. The static sorption capacity of kaolins, illites, and montmorillonites is 3–15, 10–40, and 80–150 mg-equiv per 100 g dray clay, respectively [1]. The exchange capacity of natural aluminosilicates can be improved by treatment with mineral acids. The optimal activation conditions (acid concentration, activation time, liquid-to-solid phase ratio) for bentonites and zeolites from Turkmenistan were determined in [2].

To prepare inexpensive and available sorbents for treatment of soil to remove transition (heavy) metals, we examined the possibility of chemical modification of finely dispersed Cambrian clays mined in subway tunneling. The directed modification of the clay sorption properties was based on a physicochemical study of the structure and functional composition of the surface of the initial and modified samples. To study the functional composition of the clay surface and to monitor its changes in the course of modification, we used the indicator procedure for evaluation of the donor–acceptor properties, which define the possibility of using the modified clays as sorbents. The sensitivity of this procedure, proposed by Tanabe [3], was significantly improved by modern spectroscopic methods [4, 5], in particular, by diffuse reflection spectroscopy [4]. In this study we used the procedure developed by Nechiporenko [5], which allows determination of both Brønsted (protonic) and Lewis (aprotic) centers.

EXPERIMENTAL

We studied samples prepared by treatment of Cambrian clay with sulfuric acid and sodium hydroxide solutions at 20 ± 0.5 and 105 ± 0.5°C. The clay samples were ground and treated with H_2SO_4 of various concentrations (100 g clay per 100 ml acid). After that, the samples were washed with water to pH ~ 7 and then treated with NaOH solution at the same temperature as that of H_2SO_4 treatment. Our preliminarily data showed that the most pronounced differences in the structure and composition of the modified clays appear after treatment with 0.5 and 5.0 M solutions of sulfuric acid, and all further experiments on clay modification were performed using these acid concentrations.

1070-4272/03/7604-0536 $25.00 © 2003 MAIK "Nauka/Interperiodica"

Structural and surface properties of modified clays

T, °C	Modifying agent, wt %	Σq_{pK_a}, μg-mol/100 g	H_0	S_{sp}, $m^2 g^{-1}$	d, Å	B, rad	D, nm	l, μm	I,* %
Initial clay		0.19	2.8	19.3	3.2928	0.26	350	0.89	298.5
20 ± 0.5	H_2SO_4, 0.5	0.087	5.9	19.4	3.2928	0.28	325	0.88	202.1
	NaOH, 0.5	0.31	1.2	15.2	3.2928	0.30	303	1.13	217.0
105 ± 0.5	H_2SO_4, 0.5	0.023	1.3	15.7	3.2928	0.27	336	1.1	196.4
	NaOH, 0.5	0.14	0.33	16.8	3.2928	0.27	303	1.0	263.8
20 ± 0.5	H_2SO_4, 5	0.014	2.1	8.8	3.2928	0.27	336	2.0	220.9
	NaOH, 5	0.12	0.071	11.8	3.2928	0.30	336	1.5	351.0
105 ± 0.5	H_2SO_4, 5	0.017	6.6	11.0	3.2738	0.32	284	1.57	228.5
	NaOH, 5	0.030	1.6	10.5	3.2928	0.27	336	1.64	200.4
Kaolin		–	–	–	3.5797	0.45	202	–	449.1

* Total relative intensity.

The functional composition of the surface was characterized by the distribution of donor–acceptor active centers on the clay surface, which was determined by adsorption of colored acid–base indicators with pK_a varying from –4.4 to 12.8; the procedure is described elsewhere [6]. The optical density of the indicator solutions was recorded on an SF-26 spectrophotometer, then the concentration of the active centers q_{pK_a} (μg-mol g^{-1}) with given pK_a and the Hammett function of the surface acidity H_0 were evaluated. In accordance with [5], the optical density of the blank sample was also taken into account.

The specific surface area of the samples, S_{sp}, was determined by the Klyachko–Gurvich procedure (low-temperature adsorption of air), whose sensitivity was improved using the silicone oil as a pressure-gauge fluid. The particle size was tentatively evaluated from the following equation:

$$l = K_f/(\rho S_{sp}),$$

where ρ is the average density of aluminosilicates (3.5 g cm^{-3}, particle shape was disregarded) and K_f is the coefficient for the spherical and cubic particle shapes (K_f = 6).

The crystal structure of the initial and modified clays was studied by powder X-ray diffraction (XRD) on a DRON-3.0 diffractometer (Cu_{K_α} radiation, Ni filter). The samples were ground in an agate mortar and sifted with a sieve no. 004. The interplanar spacing was calculated from the Bragg equation:

$$d/n = \lambda/2\sin\theta.$$

The size of the coherent scattering regions was evaluated from the broadening of the diffraction peak, using the Selyakov equation:

$$D = k\lambda/B\cos\theta,$$

where D is the size of the coherent scattering region (nm), B is the half-width of the diffraction peak (rad), and k is the constant approximately equal to 1.

The content of heavy metals in the initial and modified Cambrian clay was analyzed on a KVANT-AFA atomic-adsorption spectrometer. The content of the majority of heavy metals in the clays of the Leningrad oblast, except iron [7, 8] (14 g per kg dray clay), is small (≤1 g kg^{-1}). Furthermore, these metals mostly occur in the form of polyanions, and only a minor fraction, in the cationic form; therefore, unchanged clay cannot act as a source of soil pollution with heavy metals.

Data on the crystal structure, composition of the surface donor–acceptor centers, and specific surface area of the initial and modified clays are listed in the table.

Figure 1a shows the distribution of the donor-acceptor centers over the sample surface in the $q_{pK_a} = f(pK_a)$ coordinates (spectra of the adsorption center distribution (ACD) [5]), where q_{pK_a} is the content of the active centers, equivalent to the amount of the sorbed indicator with the corresponding pK_a. Shifts in the entire ACD spectrum or its separate bands and variations in the band intensity indicate changes in the energy state of the modified clay surface.

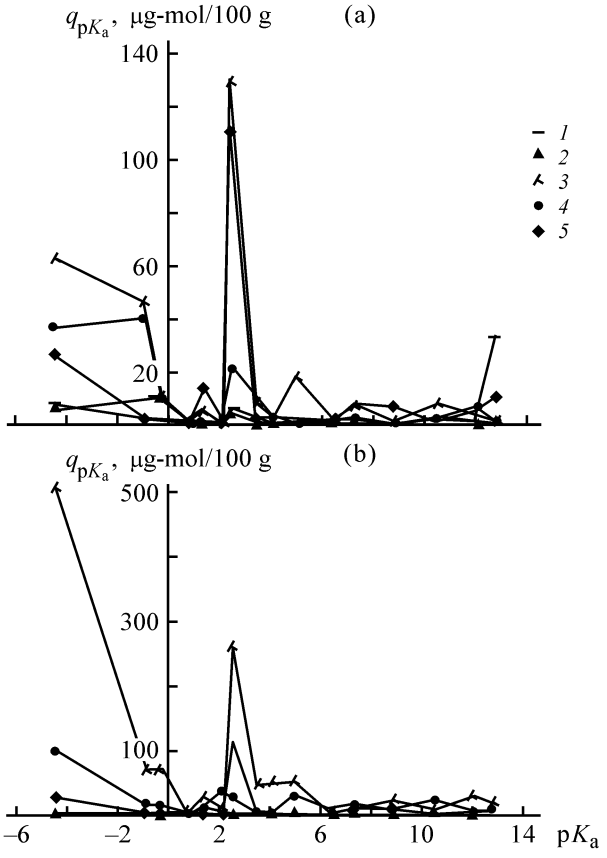

Fig. 1. Distribution of the adsorption centers in the samples treated with (a) 0.5 and (b) 5.0 M solutions of H_2SO_4 and NaOH at 20 ± 0.5 and 105 ± 0.5°C. Treatment: (*1*, *3*) acid, (*2*, *4*) base, and (*5*) initial clay. Temperature, °C: (*1*, *2*) 20 and (*3*, *4*) 105.

Since H_0 of the surface is a statistic mean value, it can be approximately evaluated from the ACD spectra, using the following equation:

$$H_0 = \Sigma\, pK_a q_{pK_a} / \Sigma\, q_{pK_a}.$$

It is known that the adsorption surface centers can be identified as Lewis and Brønsted acid and base centers. The initial clay contains both Lewis base (pK_a –4.4) and Brønsted acid (pK_a 2.5) centers; the Hammett function of the surface acidity H_0 3.9 and S_{sp} 19.3 $m^2\ g^{-1}$.

As seen from Fig. 1, after the clay treatment with 0.5 M H_2SO_4, the content of centers with pK_a –4.4 (Lewis centers providing hydrolytic adsorption of water) and 2.5 (OH groups on the anionic complex surface) strongly decreases, whereas the concentration of active centers with pK_a 10.5 (Brønsted base centers, substituted acid centers) increases.

The subsequent treatment with dilute NaOH solution makes lower the content of the active centers, and H_0 decreases from 5.9 to 1.3. The specific surface area after acid treatment slightly increases, and after base treatment it decreases to 15.2 $m^2\ g^{-1}$. When the sample is treated with 0.5 M H_2SO_4 at 105 ± 0.5°C, the specific surface area decreases to 15.7 $m^2\ g^{-1}$, and new active centers with pK_a –0.9, 5.0, and 10.5 (absent in the initial clay) appear; simultaneously, the concentration of the Brønsted acid centers increases. This is probably due to partial dissolution of the clay skeleton.

The content of the sorption centers after the base treatment decreases, although after treatment at 105 ± 0.5°C it is slightly greater, probably due to the precipitation of amorphous and finely crystalline silicates and aluminosilicates. Also possible is formation of porous crystalline aluminosilicates, zeolites [4]. Nevertheless, in all the cases, the final specific surface area does not exceed the specific surface areas of the initial Cambrian clay. The total content of the active centers increases from 0.19 (initial clay) to 0.31 mg-mol/100 g (after treatment with NaOH solution at 20°C) (see table).

After treatment of the clay with 5.0 M H_2SO_4, the content of the active centers (Fig. 1b) and specific surface area (see table) decrease appreciably; after treatment with 5 M sodium hydroxide solution, the content of the Lewis acid and base centers increases, and the content of the Brønsted centers decreases. The specific surface area after the acid treatment strongly decreases, whereas after the base treatment it increases, but remains smaller than that of the initial clay. After heating of the sample with concentrated sulfuric acid, the intensity of the bands of the Brønsted acid centers (pK_a 2.5) grows; simultaneously, the content of the other centers also increases, but to a lesser extent. After treatment with NaOH solution, the content of the active centers and the specific surface area decrease in parallel.

The powder diffraction patterns were obtained with ionization recording of the diffraction maxima at room temperature at a scanning rate of 2 deg min^{-1}. Location of the reflection maxima was determined with accuracy of 0.5 mm. The reflections were indentified using the ASTM database.

As seen from Fig. 2, the diffraction patterns of the initial and modified clays are complex and contain a series of intense reflections, which remain unchanged even after treatment of the clay with sulfuric acid and

sodium hydroxide at 20 ± 0.5 and 105 ± 0.5°C (3.29, 1.8, 1.36, 1.53, and 4.18 Å, in order of decreasing intensity). This fact suggests that the clay contains a crystalline skeleton with rather large coherent scattering regions. The most intense reflection (*d* 3.29 Å) is close to that of α-quartz (*d* 3.34 Å).

The identification of the sample structure using the database is rather difficult, because the reflections (typical of various clay-forming minerals) are shifted and superimposed. The preferred orientation of the crystals may also pead to significant error, especially in the analysis of anisotropic materials with nonspherical particles. All the defects in the crystalline sample cause diffuse scattering under angles different from the Bragg angles. Moreover, the reflections may shift owing to close atomic numbers of aluminum and silicon.

Thus, to identify the clay structure, we used the successive dissolution procedure [9]. As the amorphous fraction of the sample is dissolved in an acid, the number of reflections decreases and the diffraction pattern becomes simpler, whereas the crystalline structure represented by the reflections at 3.29, 1.8, 1.36, 1.53, and 4.18 Å remains unchanged. In particular, after treatment of the clay with 0.5 M H_2SO_4 at 20°C, the number of reflections in the XRD pattern and their intensity decrease. After subsequent treatment with 0.5 M NaOH, the intensity of the weak reflections increases somewhat. After treatment with H_2SO_4 at 105 ± 0.5°C, we obtained a sample with pronounced reflections typical of the initial clay, whereas all the other reflections disappeared. When this sample was treated with sodium hydroxide at the same temperature, the weak reflections observed in the initial clay (e.g., 2.26, 1.65 Å) appeared again. This suggests that the acid treatment removes the amorphous fraction of the clays, whereas the base treatment promotes precipitation of crystalline aluminosilicates from solutions retained in the pores after dissolution of amorphous or finely crystalline inclusions. In the course of treatment, the reflection width does not change noticeably, i.e., the size of the structural elements in the polycrystalline clay skeleton remains constant.

After subtraction of the reflections of the quartz and crystalline compounds precipitated after acid and base treatments, the spectrum contains the reflections allowing identification of kaolin with crystallite size of 202 nm (see table). Thus, in the Cambrian clay samples studied, about 33% is dispersed α-quartz (see table, 0.89/0.35). The rest contains kaolin or clay minerals and alumina. In the course of acid–base treatment, the compounds with a three-dimensional

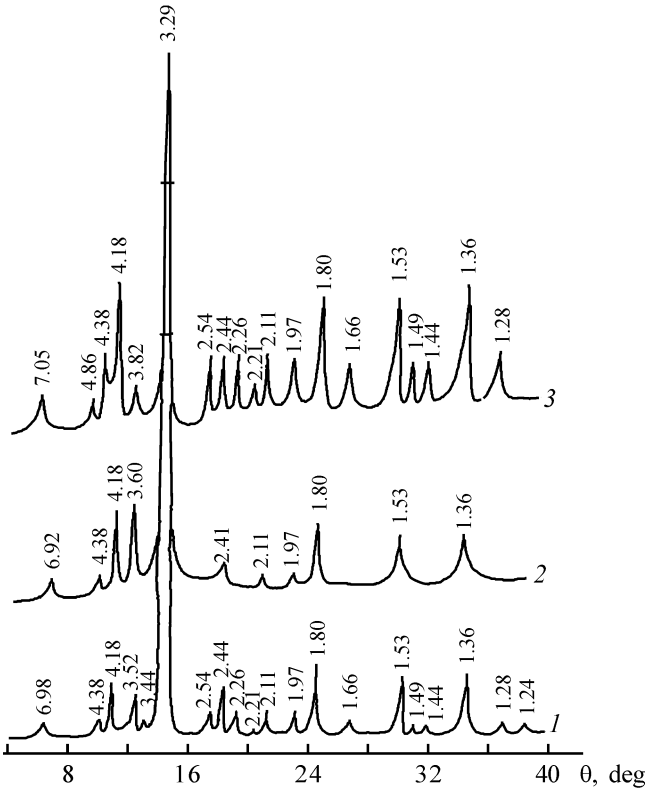

Fig. 2. Diffraction patterns of the (*1*) initial clay and (*2*, *3*) samples treated with 0.5 and 5.0 M solutions of H_2SO_4 and NaOH at 20 ± 0.5 and 105 ± 0.5°C. (θ) Bragg angle. Treatment: (*2*) 0.5 M H_2SO_4 and 105°C and (*3*) 5 M NaOH and 20°C.

skeleton (in contrast to the initial lamellar materials) precipitate. In this case, a decrease in the specific surface area is accompanied by an increase in the content of donor–acceptor centers, which increases the sorption activity of the surface in the ion-exchange stage of sorption.

The sorption capacity of the sorbents prepared was tested using lead(II) solutions (compound of hazard class I). The concentration of the initial solution was 40 mg l^{-1} and the s : l ratio was 10 g sorbent per 100 ml solution.

As seen from Fig. 3, the sorption of lead(II) cations on the modified clay samples proceeds in two steps. After the ion-exchange sorption, dissolution of the skeleton becomes predominant. The second stage includes bulk conversion of the initial silicate and aluminosilicate compounds, i.e., the degradation epitaxial transformation involving dissolved silicate polyanions proceeds. This leads to a pronounced rise in the clay sorption capacity and decrease in the residual concentration of lead(II) cations in the solution with increasing sorption time.

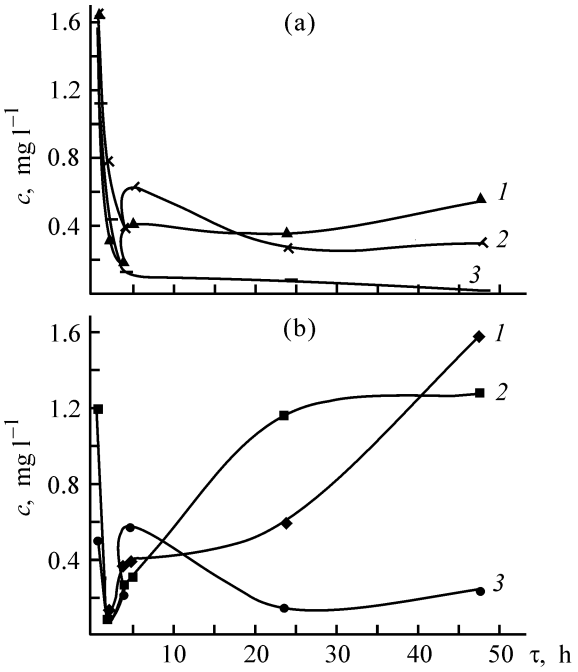

Fig. 3. Sorption of lead(II) ions on clay samples treated with (a) 0.5 and (b) 5.0 M solutions of H_2SO_4 and NaOH at 105 ± 0.5°C. (*c*) Concentration of lead(II) and (τ) time. Treatment: (*1*) first acid, (*2*) second acid, and (*3*) base.

CONCLUSIONS

(1) The possibility of directed control of the sorption properties of the Cambrian clay surface in the course of acid–base treatment was shown.

(2) The content of donor–acceptor centers on the Cambrian clay surface was studied as influenced by the conditions of chemical modifications, using the indicator procedure.

(3) The mineralogical composition of the Cambrian clay and of the products of its chemical modification was assessed by the successive dissolution method.

(4) The sorption of lead(II) cations proceeds in two steps: ion-exchange sorption and degradation epitaxial conversion.

REFERENCES

1. Grim, R.E., *Applied Clay Mineralogy*, New York: McGraw–Hill, 1962.
2. Orazmuradov, A.O., *Fizikokhimiya dispersnykh alyumosilikatov* (Physical Chemistry of Disperse Aluminosilicates), Ashkhabad: Ylym, 1988.
3. Tanabe, K., *Solid Acids and Bases. Their Catalytic Properties*, Tokio: Kadansha, 1970.
4. Gafurov, R.G., Kurbanbaeva, T., and Aripov, E.A., *Dokl. Akad. Nauk Uzb. SSR*, 1979, no. 3, pp. 46–48.
5. Nechiporenko, A.P., Burenina, T.A., and Kol'tsov, S.I., *Zh. Obshch. Khim.*, 1984, vol. 54, no. 9, pp. 1907–1912.
6. Vasil'eva, I.V., Korsakov, V.G., Myakin, S.V., and Rylova, E.V., *Zh. Fiz. Khim.*, 2002, vol. 76, no. 1, pp. 94–89.
7. Zubekhin, A.P., Strakhov, V.I., and Chekhovskii, V.G., *Fizikokhimicheskie metody issledovaniya tugoplavkikh nemetallicheskikh i silikatnykh materialov: Uchebnoe posobie* (Physicochemical Methods for Studying Refractory Nonmetallic and Silicate Materials: Manual), St. Petersburg: Sintez, 1974.
8. Zemyatchenskii, P.A., *Gliny SSSR: Obshchaya chast'* (Clays in the USSR: General Part), Moscow: Akad. Nauk SSSR, 1935.
9. Avgustinnik, A.I., *Keramika* (Ceramics), Leningrad: Stroiizdat, 1975.

Russian Journal of Applied Chemistry, Vol. 76, No. 4, 2003, pp. 541–543. Translated from Zhurnal Prikladnoi Khimii, Vol. 76, No. 4, 2003, pp. 561–563.

SORPTION AND ION-EXCHANGE PROCESSES

Gel Filtration of Model Albumin–Analgin Mixture through Sephadex To Isolate Albumin

V. V. Khasanov, K. A. Dychko, A. V. Labutin, and I. V. Ramus'

Tomsk State University, Tomsk, Russia

Received August 14, 2002; in final form, March 2003

Abstract—The preparative isolation of albumin from a model albumin–analgin mixture by filtration through Sephadex G-25 was studied. The conditions providing optimal protein decontamination to remove low-molecular-weight impurities were established, and recommendations on both laboratory and industrial application of this technique were made. Based on laboratory experiments, a commercial installation for production of refined vaccines was designed.

One of the most important applications of gel filtration through Sephadex is fast separation of organic mixtures into macromolecular (MMF) and low-molecular-weight (LMW) fractions. This technique has been successfully used for desalination of aqueous proteins, polysaccharides, and nucleic acids, replacement of buffering components, and decontamination of macromolecular compounds to remove low-molecular-weight impurities. Owing to the ease of operation, gel filtration can be successfully applied to pretreatment of multicomponent mixtures in analysis of natural objects. However, in spite of its relative simplicity, gel–chromatography requires high skill, especially in the case of preparative gel filtration involving treatment of large amounts of expensive substances.

In a common analytical version of gel chromatography, efficient separation is achieved when using long chromatographic columns, slow elution, and small samples [1]. As opposed to analytical gel chromatography, the preparative gel filtration is, as a rule, applied when it is necessary to separate macromolecular components of initial multicomponent mixture from low-molecular-weight impurities. In order to decrease the reagent consumption and accelerate the separation process, the preparative and semipreparative gel filtration should be performed under the optimal chromatographic conditions.

In this study, we analyzed gel filtration of a model aqueous analgin–albumin mixture through Sephadex G-25 to determine the conditions providing maximal decontamination of the albumin fraction to remove analgin.

EXPERIMENTAL

All experiments were carried out on a FPLC (Pharmacia-Biotech, Sweden) liquid-chromatographic device. A UV photometer (λ = 280 nm) was used as detector.

Gel filtration was performed on a column with inner diameter of 26 mm, packed with Sephadex G-25 F (Amersham Pharmacia, Sweden). At gel-bed height of 24 cm, the working volume of the column was 127 cm^3. The stock solution used in the gel filtration experiments contained albumin (5 $g\ l^{-1}$) modeling a protein (macromolecular fraction, MMF) and analgin (5 $g\ l^{-1}$) modeling a low-molecular-weight ionic component (LMWF). In gel filtration experiments, the volume of filtered albumin–analgin mixture and the eluent flow velocity were varied. Analysis of gel chromatograms allows determination of the main parameters characterizing the efficiency of separation of the filtered mixture: degree of separation R_s; degree of dilution F of the macromolecular fraction relative to its concentration in the initial mixture; separation efficiency N measured in the number of the theoretical plates (tp), determined by a common method; total eluent consumption in single separation; and content of low-molecular-weight impurity in the isolated macromolecular fraction.

The degree of separation (resolution) R_s was calculated by the formula

$$R_s = 2(\tau_{r2} - \tau_{r1})/(W_1 + W_2),$$

where τ_{r2} and τ_{r1} are the retention times of low-molecular-weight and macromolecular fractions, re-

1070-4272/03/7604-0541 $25.00 © 2003 MAIK "Nauka/Interperiodica"

Table 1. Separation parameters in relation to eluent flow velocity *v*

Parameter	Eluent flow velocity *v*, cm h^{-1}		
	60	75	90
Resolution R_S	1.08	1	1.02
Efficiency, *N*:			
MMF	392	400	432
LMWF	126	115	112
MMF volume V_{MMF}, cm^3	15	14	13
Eluent consumption in single separation, cm^3	165	172	176
Sampe volume, cm^3	5	5	5

Table 2. Separation parameters in relation to sample volume

Parameter	Volume, cm^3 (% of the working column volume)		
	5 (4)	20 (16)	30 (24)
Eluent flow velocity, *v*, cm h^{-1}	75	75	75
MMF volume V_{MMF}, cm^3	14	30	40
F (V_{MMF}/V_S)	2.8	1.5	1.33
Eluent consumption, cm^3	172	177	182
Specific eluent consumption, $cm^3\ cm^{-3}$ of the sample	34.4	9	6
Extent of separation*	C	C	P

* (C) Complete, (P) partial separation.

Table 3. Characteristics of separation of albumin from analgin by gel filtration of their mixture (sample volume 30 ml)

MMF volume, ml	Degree of recovery, %	*F*	MMF contamination with LMWF (% of LMWF content in the initial sample)
31.5	84.7	1.24	0
34.5	91.5	1.26	0
37.5	97.2	1.29	0
40.5	99.3	1.36	0.2
43.5	99.8	1.45	0.5
46.5	99.9	1.55	1.0

spectively, measured as the time elapsed from the beginning of filtration to the appearance of the elution peak; W_1 and W_2 are the widths of the elution bands of the macromolecular and low-molecular-weight fractions, respectively, measured at their bottoms.

The eluent flow velocity *v* was varied fom 60 to 90 cm h^{-1}, and the filtered sample volume *V*, from 5 to 30 cm^3, or from 4 to 24% of the working volume of column. A 0.025 M phosphate buffer solution with pH 7 was used as eluent.

The contamination of the macromolecular fraction with low-molecular-weight components was evaluated by ion-exchange chromatography on a Mono S HR5/5 column, Pharmacia-Biotech, packed with a strong cation exchanger. In elution of analgin–albumin mixture through such a column, analgin is eluted completely by the solvent, which makes the detection sensitivity the highest.

We found that, in filtering the albumin–analgin mixture, albumin is completely separated from analgin without any sorption of analgin on albumin macromolecules. Table 1 shows how the separation efficiency *N* and the degree of separation (resolution) R_S depend on the eluent flow velocity. With increasing eluent flow velocity, the efficiency of protein separation increases, whereas the band of the analgin fraction is smeared. As a result, the degree of separation of low-molecular-weight and macromolecular components (resolution) remains virtually unchanged. As expected, the eluent consumption in single separation grows somewhat with increasing eluent flow velocity. Owing to an increase in the separation efficiency, the macromolecular fraction volume decreases.

Table 2 shows how the sample volume influences the principal separation factors.

Although, with increasing sample volume, the macromolecular fraction volume grows, its dilution decreases. We found that, at the ratio of the Sephadex bed diameter to its height of 1 : 10 and the sample volume of about 1/4 of the column working volume, the bands of macromolecular and low-molecular-weight components overlap. In order to evaluate the degree of separation of the filtered mixture and choose the optimal zone of elution of the target macromolecular fraction, we determined the content of LMWF impurity in the macromolecular fraction.

Table 3 shows the main characteristics of separation of macromolecular components from low-molecular-weight impurities. It is seen that, even at a excessively large sample volume (1/4 of the Sephadex volume), approximately 99% of the macromolec-

ular component is isolated with the minimal dilution. A similar separation efficiency was obtained on a column with 1 : 10 ratio of the Sephadex bed diameter to its height.

Based on our experimental results, the following practically important conclusions can be made.

(1) In gel filtration, the eluent flow velocity is not a critical parameter. The separation efficiency grows only slightly with increasing eluent flow velocity. Therefore, gel filtration can be successfully performed using any available columns and devices for eluent feeding and sample introduction. In the case of gel filtration on the commercial scale, the eluate flow velocity should be the maximum possible. Even at minor increase in the eluent flow rate, the separation time decreases significantly and the separation efficiency increases.

(2) In order to provide efficient separation of a mixture, the sample should have the optimal volume. At approximately 1 : 10 ratio of the diameter to height of the Sephadex bed, this volume is about 20–25% of the Sephadex bed volume.

(3) In the course of gel filtration, the eluent flow velocity should not be more than 2/3 of that in the process of column packing. Under these conditions, the Sephadex bed is not compacted, and, therefore, both the separation efficiency and the adapter functioning remain stable. In filtration of more viscous solutions, still lower flow velocity should be maintained.

CONCLUSION

The most efficient decontamination of macromolecular components to remove low-molecular-weight impurities by gel filtration is achieved at the highest possible eluent flow velocity, and 1 : 10 diameter-to-height ratio of the Sephadex bed and sample volume equal to about 1/4 of the gel bed volume. Taking into account that the mechanism of gel filtration is independent of the gel nature, our recommendations can be extended to other gel materials suitable for gel filtration. The maximum permissible eluent flow velocity depends on the mechanical properties of a gel.

REFERENCES

1. Osterman, L.A., *Khromatografiya belkov i nukleinovykh kislot* (Chromatography of Proteins and Nucleic Acids), Moscow: Nauka, 1985.

Russian Journal of Applied Chemistry, Vol. 76, No. 4, 2003, pp. 544–546. Translated from Zhurnal Prikladnoi Khimii, Vol. 76, No. 4, 2003, pp. 564–566.

SORPTION AND ION-EXCHANGE PROCESSES

Calculation and Control of Solid–Liquid Extraction with Characteristic Function

E. B. Simeonov and A. D. Minchev

University of Chemical Technology and Metallurgy, Sofia, Bulgaria

Received July 8, 2002

Abstract—The kinetics of extraction of practically interesting vegetable raw materials: carsil (*Silibium marianum L.*), amorpha (*Amorpha fructicosa L.*), and coriander (*Coriandrum sativum L.*), was studied experimentally. The results obtained were represented as a characteristic function. The optimal conditions of the extraction process were studied.

The wide diversity of vegetable raw materials used for solid-phase extraction, combined with the complexity of mass transfer in the solid–liquid system, leads to a number of methodological and mathematical difficulties in describing the extraction process.

To ensure versatility of extraction apparatus, it is necessary not only to determine the extractor parameters, but also to control the process when changing the type of vegetable raw materials. This is possible with the use of the characteristic function. The method is especially valuable in the case of processing of a vegetable raw material characterized by a complex mechanism of diffusion extraction [1, 2].

The characteristic function takes into account, in an integral manner, specific structural features of the solid phase and the amount of outer-diffusion resistance. The function is derived from an experimental kinetic curve $c_1 = f(\tau)$ on the condition that the concentration c_1 is the same for all particles. The characteristic function $\Theta(\gamma)$ is most easily found with the use of kinetic curves obtained in the batch mode of the process under ideal mixing conditions [3, 4].

The aim of the present study was to demonstrate the applicability of the characteristic function to calculations and control of the extraction process.

Three solid–liquid systems were studied:

System	T, °C	ξ, $m^3\ kg^{-1}$	n, s^{-1}	c^*, $kg\ m^{-3}$
Carsil–methanol (**I**)	30	0.02	7.5	889.80
Amorpha–petroleum ether (**II**)	40	0.01	7.0	921.31
Coriander–petroleum ether (**III**)	50	0.01	7.0	735.21

Note. ξ is the specific volume; n, the rate of worm rotation; c^*, the saturation concentration.

The experiments were carried out in a batch extraction apparatus under ideal mixing conditions. The instants of sampling were varied, depending on a raw material under study. It was established experimentally that the process is limited by inner diffusion—transport within pores of the solid phase. The outer-diffusion resistance is virtually eliminated at the indicated stirring rate.

The kinetics of extraction is described by the expression

$$c_1 = A - B\exp(-H\tau), \quad (1)$$

where c_1 is the concentration of the component being extracted in the liquid ($kg\ m^{-3}$); A, B, and H are constants; τ is the process duration (s).

For systems (**I**)–(**III**), respectively,

$$c_1 = 0.980 - 0.966\exp(-2.20 \times 10^{-4}\tau), \quad (2)$$

$$c_1 = 4.600 - 4.400\exp(-3.40 \times 10^{-3}\tau), \quad (3)$$

$$c_1 = 2.050 - 1.950\exp(-1.20 \times 10^{-3}\tau). \quad (4)$$

Figures 1a–1c [respective Eqs. (2)–(4)] show the experimental data obtained. In system (**I**), silimarine (the solid phase contains silibine, silidianine, and silichrytine, with the flavolignan complex having general name silimarine) is extracted under the conditions specified. The content of the complex was analyzed by spectrophotometry. Silimarine is used in manufacture of an important pharmaceutical product Legalon (Carsil). In the case of system (**II**), the extracted solid phase contains isoflavonoids (or, more

1070-4272/03/7604-0544 $25.00 © 2003 MAIK "Nauka/Interperiodica"

precisely, rotenoids)—amorphigenine and dehydroamorphigenine. They are extracted with low-temperature fractions of petroleum ether (57°C). In system (**III**), the solid phase is a plant producing oil and essential oil. This plant contains coumarin, flavonoids, sitosterol, etc. The extraction was done with the same fraction of petroleum ether as in the case of system (**II**). The extracts obtained for systems (**II**) and (**III**) were analyzed gravimetrically with an error of 10^{-3} g.

Constants A, B, and H in Eqs. (2)–(4) were found numerically on the basis of experimental results. The statistical-average error of the experimentally determined concentrations and those calculated using Eqs. (2), (3), and (4) $\Delta = \pm 2.07$, ± 3.30, and $\pm 1.09\%$, respectively.

In [1, 2], the method of characteristic function for calculation and control of extraction from solids was described in detail. The integral (5) is a characteristic function

$$\Theta(\gamma) = -\int_i^\gamma \frac{d\gamma}{\psi(\gamma)}, \qquad (5)$$

where $\psi(\gamma) = D_e F/m_0\left(\frac{\partial c}{\partial n}\Big|_F\right)$, F is the mass-exchange surface area (m^2), and D_e is the effective diffusion coefficient ($m^2\ s^{-1}$).

The characteristic function was derived from the experimental kinetics on the condition that c_1 = const and is the same for all particles. In this case, the following sequence is observed:

$$c_1(\tau) \rightarrow \gamma(\tau) \rightarrow \Theta(\tau) \rightarrow \Theta(\gamma), \qquad (6)$$

where

$$\gamma(\tau) = 1 - \xi[c_1(\tau) - c_1(0)], \quad \Theta(\tau) = \int_0^\tau [c^* - c_1(\tau)]d\tau.$$

The calculation of continuous and batch processes with the use of $\Theta(\gamma)$ is based on the following set of equations:

$$\left.\begin{aligned} d\Theta/d\tau &= c^* - c_1 \\ \Theta &= \Theta(\gamma) \\ (1-\gamma)^{\xi^{-1}} &= c_1 - c_m \end{aligned}\right\} \qquad (7)$$

where c_m is the final concentration in the case of counterflow and initial concentration for direct flow and periodic processes in the liquid ($kg\ m^{-3}$).

Substitution of $\Theta(\gamma)$ and c_1 from the material balance equation into the differential equation of system (7) yields the dependence $\tau(\Theta)$ and, as a result, the relationship between the running time of extraction and the extractor coordinate (worm length) can be found:

$$\tau(\Theta) = \int_0^\Theta \frac{d\Theta}{c^* - c_m \pm \xi^{-1}[1-\gamma(\Theta)]} \rightarrow \gamma(\tau) \rightarrow \tau \rightarrow X = V\tau.$$

Characteristic functions were found for the three systems under study, with the kinetic equations (2)–(4) used as a basis. The method of characteristic function was used to determine for system (**I**) (Fig. 2) at a given solid-phase output capacity G and degree of extraction, η, the basic design dimensions of the worm extractor: diameter D, pitch S, and length X of the worm. The characteristic functions of systems (**II**)

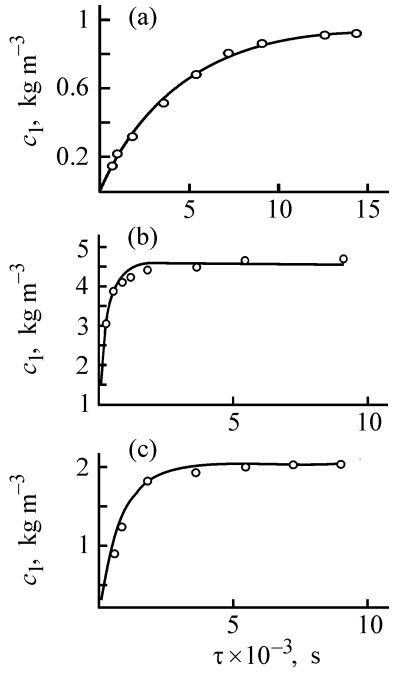

Fig. 1. Variation of the concentration c_1 in the liquid phase with time τ for systems (**I**)–(**III**). *Curve*, calculation; *points*, experiment.

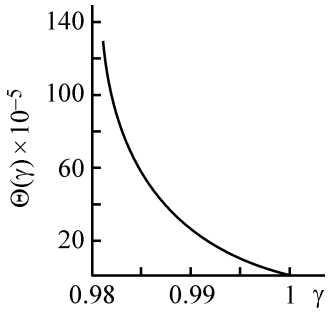

Fig. 2. Characteristic function $\Theta(\gamma)$ for system (**I**).

Parameters of the solid–liquid system (D = 0.127 m, X = 1.29 m, S = 0.057 m)

System	$G \times 10^4$, kg s^{-1}	V, m s^{-1}	$n \times 10^3$, s^{-1}	τ, s
(**I**)	6.94	2.12	3.71	6100
(**II**)	25.60	7.37	12.90	1750
(**III**)	11.70	3.30	5.79	3910

and (**III**) have been used to calculate the necessary rate n of worm rotation for the extractor designed for system (**I**) at a prescribed degree of extraction, η, and the solid-phase output capacity of the apparatus has been obtained [1, 2].

The table lists the parameters calculated for the above three solid–liquid systems.

Of interest for technological and engineering purposes is calculation of the linear motion velocity V of the solid phase in the extractor, corresponding to the rate n of worm rotation. This ensures the required time τ of extraction at which a prescribed degree of recovery, η, of a component being extracted is achieved.

CONCLUSIONS

(1) The obtained experimental data on the kinetics of the process in batch extraction from the systems constituted by carsil and methanol, amorpha and petroleum ether, and coriander and petroleum ether were used to calculate the characteristic functions $\Theta(\gamma)$.

(2) The use of $\Theta(\gamma)$ and the method of characteristic function for the carsil–methanol system yielded the basic design dimensions of the worm extractor. The same $\Theta(\gamma)$ functions were used for two other systems for calculating the rate of worm rotation and the output capacity of the apparatus at a prescribed degree of extraction.

(3) It was shown that the method of characteristic function enables not only calculation, but also control of the processes by varying certain technological parameters. In doing so, there is no need to rely upon simplifications, which are commonly inevitable in solving numerically or analytically the complicated problem of extraction from vegetable raw materials.

REFERENCES

1. Simeonov, E. and Minchev, A., *Zh. Prikl. Khim.*, 1989, vol. 62, no. 4, pp. 879–882.
2. Simeonov, E. and Minchev, A., *Zh. Prikl. Khim.*, 1990, vol. 63, no. 10, pp. 2281–2284.
3. Romankov, P.G. and Frolov, V.F., *Massoobmennye protsessy khimicheskoi tekhnologii* (Mass-Exchange Processes in Chemical Technology), Leningrad: Khimiya, 1990.
4. Aksel'rud, G.A., *Ekstragirovanie: Sistema tverdoe telo–zhidkost'* (Extraction: Solid–Liquid System), Leningrad: Khimiya, 1974.

Russian Journal of Applied Chemistry, Vol. 76, No. 4, 2003, pp. 547–549. Translated from Zhurnal Prikladnoi Khimii, Vol. 76, No. 4, 2003, pp. 567–569.

APPLIED ELECTROCHEMISTRY AND CORROSION PROTECTION OF METALS

Enhancement of the Corrosion Resistance of Aluminum–Lithium Alloys by Microalloying with Calcium

M. T. Norova, I. N. Ganiev, and Kh. M. Nazarov

Nikitin Institute of Chemistry, Academy of Sciences of the Republic of Tajikistan, Dushanbe, Republic of Tajikistan

Received September 16, 2002

Abstract—The potentiodynamic method was applied to study the corrosion-electrochemical behavior in an electrolyte (3, 0.3, and 0.03% NaCl solution), of an aluminum–lithium alloy (6% Li) alloyed with calcium (0.01–0.5%).

Alloying of aluminum alloys with lithium leads to a significant decrease in their density and increase in strength, heat resistance, and modulus of elasticity. Depending on the nature of a third alloying component, the density decreases by approximately 11% and the modulus of elasticity, by 4%, compared with the D16 alloy. Commercial alloys VAD-23, 1420, 1430, 1450, etc., which exceed in corrosion resistance the D16T alloy and approach the AMg6M alloy, have been developed on the basis of alloys of the Al–Li system. Compression-molded and rolled semifinished products are fabricated from these alloys [1–5]. To enhance the corrosion resistance of aluminum alloys with lithium, they are additionally alloyed with manganese, cadmium, and zirconium [3].

In the present study, the influence of calcium additions on the electrochemical behavior of Al–Li alloys with 6% Li was analyzed on the basis of the scientific concept assuming that the corrosion resistance of passivating alloys is enhanced by their alloying with anodic microadditives [1, 6]. As is known, Ca is an anodic additive (–2.8 V) for the aluminum–lithium alloy. The standard electrode potential of lithium is –2.87 V [7]. According to [8], minor additions of Ca make slower the rate of aluminum corrosion, with the corrosion potential shifted to the negative region, whereas major additions of calcium raise the rate of aluminum dissolution in 3% NaCl because of the formation of an intermetallic compound Al_4Ca.

EXPERIMENTAL

As object of study served aluminum of A 995 brand, LE1 lithium, and KM1 calcium. These metals were used to prepare alloys in corundum crucibles in a resistance furnace at 750°C under a layer of flux of composition (%): NaCl 32.5, KCl 32.5, LiCl 35. The chemical compositions of the alloys are listed in Tables 1–3.

The melt obtained was used to cast cylindrical samples 8–10 mm in diameter and 60–100 mm long for a study of the corrosion-electrochemical properties of the alloys. Prior to being placed in an electrochemical cell, the samples were ground and polished with fine emery paper, washed with ethanol and distilled water, and dried in a desiccator.

The measurements were done with a PI-50-1 potentiostat with LKD-4-002 recorder in a 3, 0.3, or 0.03% NaCl solution. A silver chloride reference electrode and platinum auxiliary electrode were used.

Forward and reverse potentiodynamic curves were measured at potential sweep rate of 2 $mV\,s^{-1}$. The alloy samples were polarized potentiodynamically in the positive direction from the steady-state potential attained

Table 1. Corrosion potential of Al + 6% Li alloy alloyed with calcium at different concentrations of the NaCl electrolyte

c_{Ca}, wt %	$-E_{cor}$ (V) at indicated NaCl solution concentration, wt %		
	0.03	0.3	3
–	0.830	0.930	1.020
0.01	0.800	0.800	0.875
0.05	0.730	0.730	0.870
0.10	0.690	0.700	0.800
0.50	0.690	0.700	0.780

1070-4272/03/7604-0547 $25.00 © 2003 MAIK "Nauka/Interperiodica"

Table 2. Corrosion rate K of Al + 6% Li alloy containing varied amount of calcium in NaCl solution

c_{Ca}, wt %	Concentration of NaCl solution, wt %					
	0.03		0.3		3	
	i_{cor}, A m^{-2}	$K \times 10^{-3}$, g m^{-2} h^{-1}	i_{cor}, A m^{-2}	$K \times 10^{-3}$, g m^{-2} h^{-1}	i_{cor}, A m^{-2}	$K \times 10^{-3}$, g m^{-2} h^{-1}
–	0.035	11.7	0.060	20.01	0.080	26.8
0.01	0.020	6.70	0.023	7.71	0.025	8.37
0.05	0.015	5.02	0.018	6.03	0.019	6.37
0.10	0.018	6.03	0.024	8.04	0.025	8.38
0.50	0.024	8.04	0.026	8.70	0.032	10.72

Table 3. Pitting potential E_p for alloys of the Al–Li–Ca system at varied concentration of NaCl electrolyte

c_{Ca}, wt %	$-E_p$ (V) at indicated concentration of NaCl solution, wt %			c_{Ca}, wt %	$-E_p$ (V) at indicated concentration of NaCl solution, wt %		
	0.03	0.3	3		0.03	0.3	3
–	0.650	0.680	0.680	0.10	0.460	0.570	0.670
0.01	0.540	0.580	0.680	0.50	0.460	0.560	0.660
0.05	0.480	0.580	0.670				

on submerging a sample in a solution, until a steep rise in the current was observed (to a constant current of 2 mA, and then in the reverse direction to a potential of –1600 mV), with the result that the oxide film was reduced. Finally, the samples were polarized in the positive direction to the pitting potential.

According to the phase diagram of the Al–Li–Ca system, the alloys obtained lie in the single-phase region of an aluminum–lithium solid solution or in the double-phase region of Al + Al_4Ca [9], i.e., are single-or double-phase, depending on the content of the alloying component. The results obtained in the study are shown in Figs. 1 and 2 and listed in Tables 1–3.

Figure 1 shows the time dependence of the corrosion potential of the initial Al + 6% Li alloy and alloys with various amounts of Ca. It was found that, during the first minutes after an alloy is submerged in an electrolyte solution, the potential is strongly shifted toward the positive region. In the process, a steady-state corrosion potential is reached in 40 min for an alloy without alloying additives, and in a 2 times shorter time, in 20–25 min, for alloyed alloys, which points to their relatively strong passivation under the action of calcium additions. For example, after keeping an unalloyed alloy in a 3% NaCl solution, its corrosion potential is –1.020 V, whereas for an alloy containing 0.50 wt % Ca, the potential is –0.780 V.

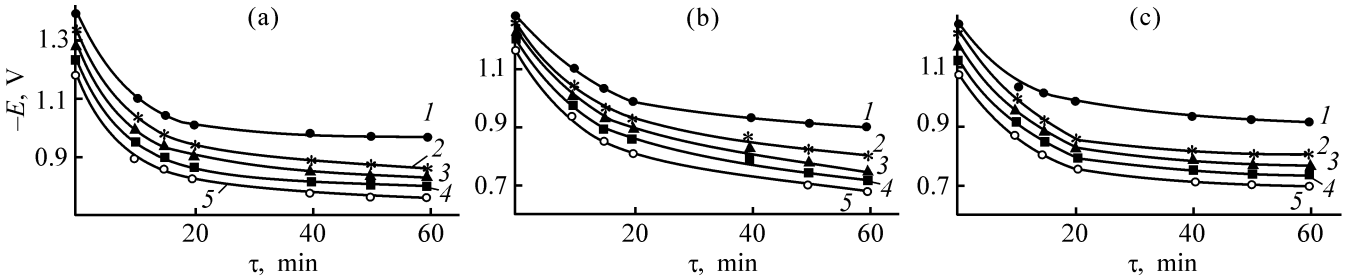

Fig. 1. Variation of the corrosion potential E with time τ for (*1*) Al + 6% Li alloys and (*2*–*5*) the same alloys with calcium. Ca content (wt %): (*2*) 0.01, (*3*) 0.05, (*4*) 0.10, and (*5*) 0.50; the same for Fig. 2. Electrolyte, NaCl solution (wt %): (a) 3.0, (b) 0.30, and (c) 0.03.

Figure 2 shows the anodic of potentiodynamic curves measured for aluminum–lithium alloys containing varied amount of Ca in a 3% NaCl solution. It can be seen that alloying with calcium shifts the corrosion potential of the alloys toward the positive region, with the pitting potential growing with the content of the alloying component increasing to 0.5 wt %.

The corrosion-electrochemical behavior of the alloys was studied at various concentrations of the NaCl electrolyte. With increasing concentration of chloride ions (Table 1), the corrosion potential decreases, which indicates that the corrosion resistance of the alloys falls. This is confirmed by studies of the rate of corrosion in NaCl solutions of alloys with varied content of Ca (Table 2).

Ca additions of up to 0.05 wt % improve the corrosion resistance of the alloys in all the solutions studied. Raising the content of the alloying component further, to 0.5 wt %, makes the corrosion rate of the alloys somewhat higher, but still lower (8.04 g m^{-2} h^{-1} in 0.03% NaCl solution) than that of the alloy without Ca (11.7 g m^{-2} h^{-1}). With increasing concentration of chloride ions, the corrosion rates of both the initial, Ca-free alloy and alloys with calcium grow. A certain increase in the corrosion resistance of alloys containing up to 0.05 wt % calcium can be accounted for by the solubility of calcium in the aluminum–lithium solid solution. According to the phase diagram of the Al–Li–Ca system, the aluminum–lithium alloys containing up to 0.05 wt % lithium lie in the single-phase region of a solid solution of lithium in aluminum. Further increase in the content of Ca leads to formation of primary crystals of an intermetallic compound, Al_4Ca, which, in all probability, acts as anode with respect to the aluminum–lithium solid solution. This, in turn, favors an increase in the corrosion rate of the alloys in the solutions studied.

The change in the pitting potential of the alloys in electrolytes with varied content of chloride ions indirectly confirms the aforesaid (Table 3). It can be seen that, with decreasing concentration of chloride ions in the electrolyte, the pitting potential grows, which indicates that the resistance of the alloys against pitting corrosion improves. Additions of the alloying component also shift the pitting potential to the positive region.

CONCLUSIONS

(1) Calcium, which is alloying anodic additive, improves the resistance of the aluminum–lithium alloy to general corrosion and pitting in 0.03, 0.3, and 3% NaCl solutions at 298 K.

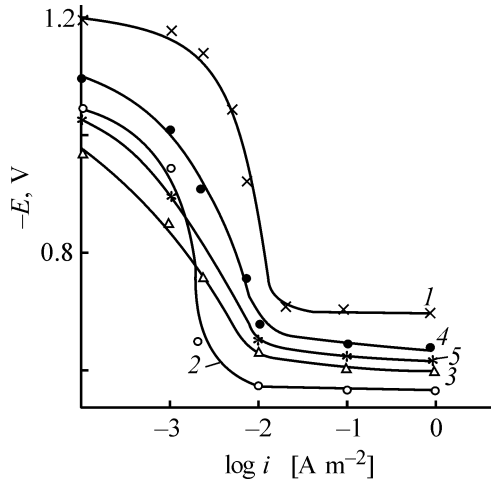

Fig. 2. Potentiodynamic anodic polarization curves (2 mV s^{-1} sweep rate) for (*1*) Al + 6% Li alloys and (*2–5*) the same alloys containing Ca. Electrolyte, 3% NaCl solution; 298 K. (*E*) Potential and (*i*) current density.

(2) The action of calcium as an effective anodic additive can be accounted for by its dissolution in the aluminum–lithium solid solution. The optimal content of calcium for improving the corrosion resistance of aluminum–lithium alloys should not exceed 0.05%.

REFERENCES

1. Fridlyander, I.N., *Alyuminievye deformiruemye konstruktsionnye splavy* (Deformable Aluminum Construction Alloys), Moscow: Metallurgiya, 1979.
2. *Promyshlennye alyuminievye splavy: Spravochnik* (Commercial Aluminum Alloys: Reference Book), Moscow: Metallurgiya, 1984.
3. *Alyuminievye splavy: Promyshlennye deformiruemye, spechennye i liteinye alyuminievye splavy: Spravochnoe rukovodstvo* (Aluminum Alloys: Commercial Deformable Sintered and Cast Aluminum Alloys: Manual), Moscow: Metallurgiya, 1972.
4. Fridlyander, I.N., Shamrai, V.F., and Shiryaeva, N.V., *Izv. Akad. Nauk SSSR, Metally*, 1965, no. 2, pp. 153–158.
5. Vyazovikina, N.V., *Zashch. Met.*, 1997, vol. 33, no. 4, p. 372.
6. Vyazovikina, N.V. and Ponomarev, S.S., Abstracts of Papers, *The 1997 Soint Int. Meeting*, Paris, 1997, vol. 97-2, no. 350, p. 428.
7. Akhmetov, N.S., *Obshchaya i neorganicheskaya khimiya* (General and Inorganic Chemistry), Moscow: Vysshaya Shkola, 1988.
8. Ganiev, I.N., Krasnoyarskii, V.V., and Zhukova, T.I., *Zh. Prikl. Khim.*, 1995, vol. 68, no. 7, pp. 1146–1149.
9. Ganiev, I.N., Nazarov, Kh.M., and Ganieva, N.I., *Izv. Ross. Akad. Nauk, Metally*, 1999, no. 6, pp. 123–125.

Russian Journal of Applied Chemistry, Vol. 76, No. 4, 2003, pp. 550–557. Translated from Zhurnal Prikladnoi Khimii, Vol. 76, No. 4, 2003, pp. 570–578.

CATALYSIS

Alkylation of Isobutane with Butenes on Zirconium Sulfate Catalysts

A. V. Lavrenov, E. V. Perelevskii, V. P. Finevich, V. I. Zaikovskii, E. A. Paukshtis, V. K. Duplyakin, and B. S. Bal'zhinimaev

Omsk Branch, Boreskov Institute of Catalysis, Siberian Division, Russian Academy of Sciences, Omsk, Russia
Boreskov Institute of Catalysis, Siberian Division, Russian Academy of Sciences, Novosibirsk, Russia

Received November 29, 2002

Abstract—Sulfated zirconia catalysts supported on silica gel and aluminum oxide were prepared by impregnation, and their structure and acid–base and catalytic properties were studied. The parameters of synthesis and characteristics of this catalyst, which ensure high activity and selectivity in liquid-phase alkylation of isobutane with butenes, were determined.

Alkylation of isobutane with butenes is one of the most important processes in production of high-quality gasolines. Industrial alkylation is performed with sulfuric and hydrofluoric acids as catalysts. Their main drawbacks are high specific consumption, toxicity, corrosion activity, and the necessity for separation of the alkylate from the catalyst-product mixture and utilization of spent acids. The progress in the technology of alkylate gasoline production is associated with passing to solid acid catalysts [1] to avoid the above problems.

The strong acidity of sulfated zirconia (SZ) allows its use as catalyst for isomerization, alkylation, acylation, and many other processes [2]. However, in spite of increased interest in this catalyst, studies of SZ catalytic properties in isobutane alkylation with butenes are few in number [3–11]. The expectancies associated with SZ as industrial alkylation catalyst have diminished in recent years because of its low stability. The studies of the synthesis of catalytic systems based on SZ, their chemical composition, and structure of active centers were systematized in [2, 12, 13]. However, the patterns established are mainly related to synthesis of catalysts for light alkane isomerization, whereas data on the chemical and phase composition, acidity, and other characteristics of such catalysts as applied to isobutane alkylation with butenes are extremely scarce [3, 6].

Dispergation of a catalytic component on the surface of a porous matrix frequently provides substantially higher activity, selectivity, and stability of the catalyst in comparison with the bulk substance. Indeed, numerous studies have shown that SZ in the form of finely divided particles fixed on the surface of porous supports is more active in isomerization [14–17] and alkylation [18].

The goal of this study was to develop a procedure for commercial synthesis of supported SZ and to analyze the texture, structural, and acid–base properties of SZ supported on silica gel and aluminum oxide, in order to understand the origin of its activity and selectivity in isobutane alkylation with butenes. In the choice of the synthesis conditions, we made an attempt to take into account the known experience, especially that concerning the support properties and conditions of zirconium hydroxide precipitation, sulfation, and calcination.

EXPERIMENTAL

Impregnation [19] is the simplest and the most practically feasible method for preparation of supported catalysts. The main stages of synthesis of "impregnated" catalysts based on SZ are shown in the scheme.

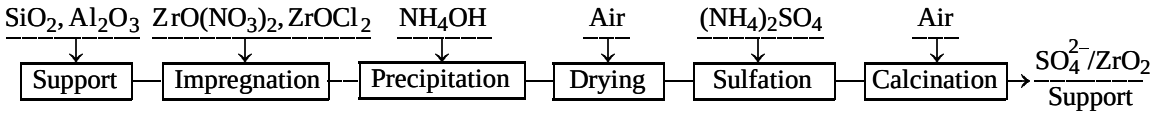

Flow sheet of the synthesis of supported zirconium sulfate catalysts.

1070-4272/03/7604-0550 $25.00 © 2003 MAIK "Nauka/Interperiodica"

Silica gel and aluminum oxide were taken as SZ supports. Their main advantages are the possibility of varying the texture characteristics, high thermal stability, low catalytic activity in side reactions of butene oligomerization, and wide experience in their industrial production and preparation of supported catalysts.

Silica gel and Al_2O_3 with specific surface area of 290 and 203 $m^2 g^{-1}$ and total pore volume of 0.95 and 0.64 $cm^3 g^{-1}$, respectively, were used. Both supports consisted of 0.4–1.0-mm particles. Silica gel was washed with 1 M HCl to remove metal impurities. Aluminum oxide was treated with 1 M H_2SO_4. This preliminary sulfation of the aluminum oxide support was performed to neutralize its basicity and thus to eliminate its influence on the subsequent precipitation of zirconium hydroxide. The thus treated supports were calcined in a muffle furnace at 600°C for 4 h.

During catalyst synthesis, both multiple and single impregnation of supports were performed (samples SZS-*X*-*Y* on silica gel, SZA-*X*-*Y* on aluminum oxide, *X* is ZrO_2 content, and *Y*, the number of impregnation runs). The supports were impregnated with $ZrO(NO_3)_2$ solutions with zirconium concentration varied from 25 to 300 g l^{-1} in terms of ZrO_2.

The above zirconium salt is a commercial product. Zirconium hydroxide formed by its hydrolysis is less contaminated with impurities, which can later uncontrollably affect the structural and acid properties of a catalyst prepared. In contrast to $ZrOCl_2$ and, the more so, to zirconium sulfate-containing compounds, which give precipitates with Cl^- or SO_4^{2-} ions virtually unremovable by washing, nitrate ions are well washed out with ammonia water at pH 8–9 and completely decompose in calcination.

The known tendency for zirconium salts to form polymeric structures in solutions complicates preparation of zirconium hydroxide with required properties [20]. Therefore, the impregnating solution was stored for a week at pH < 1 before use. After impregnation, the excess solution was separated by filtration, and the sample was dried in air at room temperature to eliminate liquid drops and then covered with the amount of ammonia water required to obtain zirconium hydroxide precipitate in the matrix pores at pH 9–10.

When preparing bulk SZ, the zirconium hydroxide precipitate is aged in some cases. The processes occurring in aging (reprecipitation, polycondensation, etc.), as a rule, favor increase in size of amorphous particles and formation of a more perfect structure and give larger specific surface area of the oxide phase after calcination. Aging of zirconium hydroxide precipitated in the support pores is hardly useful; by contrast it may lead to uncontrollable modification of the catalyst. In an alkaline mother liquor, acidic supports may break down. Silica gel will undergo partial dissolution to give ammonium silicates. The surface of sulfated aluminum oxide may also change under the action of ammonia solution. Therefore, we excluded the aging stage from the procedure for synthesis of supported catalysts.

After drying at 150°C, samples were calcined at 400°C to convert the precipitated hydroxide into zirconium oxide. Dried zirconium hydroxide actively reacts with sulfating agents already in the stage of impregnation. During the subsequent thermal treatment, the zirconium hydroxide–oxide transition is superimposed on the complex sulfation processes. From the standpoint of reproducibility and stability of synthesis, it is necessary to avoid simultaneous occurrence of these chemical processes and to subject to sulfation specifically the zirconium oxide phases obtained by calcination at 350–400°C, when dehydration and crystallization are 70–80% complete. This is confirmed by the fact that the preliminary calcination of zirconium hydroxide at 200–400°C gives catalysts with the maximal selectivity in alkylation [3]. After the formation of supported ZrO_2, each of the samples prepared was used both for further impregnation and for sulfation to obtain a finished catalyst.

It is believed that the specific kind of a sulfating agent is of no importance. Similar results were obtained when H_2SO_4, $(NH_4)_2SO_4$, $(NH_4)_2S_2O_8$, or gas mixtures $SO_2 + O_2$ and $H_2S + O_2$ were used. Probably, $(NH_4)_2SO_4$ should be preferred as the least reactive and neutral reagent. Its use allows the best control over sulfation and the highest preparation reproducibility. This is especially important in sulfation of finely dispersed supported ZrO_2 particles. Samples were sulfated with an excess of a $(NH_4)_2SO_4$ saturated solution for 1 h. Then, the samples were separated by decanting, dried, and calcined in a flow of purified air at 300°C for 1 h and then at 550°C for 2 h.

The content of SO_4^{2-} ions after sulfation followed by calcination is the most important parameter of the catalyst, since it determines the number and activity of the catalyst acid centers. In the case of bulk SZ, a monolayer coating of the ZrO_2 surface with SO_4^{2-} ions is considered to be optimal [13].

The monolayer capacity is estimated to be 4 SO_4^{2-} nm^{-2}, which gives a sulfur content of approx-

Table 1. Composition of IBF and BBF raw material fractions

Component	Content, wt %	
	IBF	BBF
Propane	0.01	0.55
Isobutane	99.81	42.64
1-Butene + isobutene	0.15	26.65
n-Butane	0.03	8.76
trans-2-Butene	0.00	12.54
cis-2-Butene	0.00	8.86

imately 2 wt % for SZ with specific surface area of 100–150 $m^2 g^{-1}$. Actually, a set of different S^{6+} coordination states exists in the catalyst [21]. Sulfate ions may be situated under the surface layer of zirconium atoms and form bulk nonstoichiometric dispersed oxysulfate phases. In addition, the surface sulfate ions may differ in denticity in complexation, and also can form disulfate ions and polymeric structures. Thus, the structure of the active center and optimal S : Zr ratio are indefinite. For a supported catalyst, the $SO_4^{2-} : ZrO_2$ molar ratio, whose optimal value can be determined only experimentally, is the most important characteristic of the active component.

For comparison, we prepared bulk sulfated zirconia under the same conditions as in the synthesis of the supported catalysts. The Zr and S content in the catalysts was monitored by X-ray fluorescence analysis on a VRA-20 spectrometer. The texture characteristics of samples were studied on a Sorptomatic-1900 device, using nitrogen adsorption–desorption isotherms at –195.6°C. The 0.4–0.6-mm fraction was used in measurements. Before the measurements, the initial samples were kept at 300°C in a vacuum, at a residual pressure of no more than 104 Pa, for 4–6 h. The adsorption measurements and data processing were performed using Milestone-200 software. The BET specific surface area, S_{sp}, was calculated at equilibrium relative nitrogen pressures of 0.05–0.33. The landing area of the nitrogen molecule in the filled monolayer was taken equal to 0.162 nm^2. The adsorption pore volume was determined from the nitrogen sorption at a relative pressure of 0.996. The molar volume of the liquid adsorbate at the temperature of the experiment was taken to be 34.68×10^{-6} $m^3 mol^{-1}$.

The X-ray diffraction analysis (XDA) was performed on a DRON-3 diffractometer (Cu_{K_α} radiation, β-filter). The phase composition and particle size were determined from X-ray diffraction patterns, using the ASTM file.

High-resolution electron microscopy (HREM) was applied to study the catalyst structure. Samples were prepared by "dry" and "wet" methods. The "wet" method involved sample grinding and preparation of suspensions in ethanol or hexane, followed by ultrasonic dispergation. The suspensions prepared were applied to perforated carbon films (supports) on copper grids. In the "dry" method, a sample was mechanically ground in an agate mortar, applied to a copper grid, and transferred into the electron microscope.

The acid centers on the catalyst surface were studied by IR spectroscopy after low-temperature adsorption of CO [22]. Carbon monoxide can form various single-ligand complexes with the surface acid centers and, depending on the center type, give H-bound states or coordinate with aprotic centers. As a rule, a spectroscopic study of adsorbed CO allows identification of the strongest Brønsted (BAC) and Lewis (LAC) acid centers, which must be primarily responsible for the catalytic properties. Samples were compacted into 4–12-mg cm^{-2}-"thick" pellets. Before CO adsorption, samples were calcined in a vacuum (0.00133 Pa) at 500°C for 1 h. Carbon monoxide was sorbed in portions at liquid nitrogen temperature and maximal pressure of 400 Pa. The IR spectra were recorded on IFS-113v Bruker and Shimadzu 8300 spectrometers within the 1000–5000 cm^{-1} range, with resolution of 4 cm^{-1} and accumulation of 50 to 128 scans. The LAC concentration c (μmol g^{-1}) was determined as $c = A/A_0$, where A is the integral intensity of the CO absorption band within the 2186–2200 cm^{-1} range, normalized to the pellet thickness, and A_0 is the integral absorption coefficient, equal to 0.8.

The catalytic properties of the samples in alkylation were studied in a 180-cm^3 stainless steel autoclave. Preliminarily purified (by treatment with solid alkali and NaA zeolite) commercial isobutane (IBF) and butane–butylene (BBF) fractions (their compositions are presented in Table 1) were used as starting reagents. A 4-g portion of a catalyst with 0.4–1-mm particle size and 40 g of IBF were loaded into the autoclave. During the experiment, BBF was introduced into the autoclave with a syringe at a rate of 0.5 to 1 g h^{-1}. The autoclave with the reaction mixture was agitated with a shaker. The alkylation was performed at a temperature of 40°C maintained by heated water circulating through the autoclave jacket. The composition of the liquid phase in the autoclave was monitored every hour by GLC, using a special syringe for sampling liquid hydrocarbons under pressure and a Hewlett–

Packard 5890 Series II chromatograph with a DB-1 capillary column and a flame-ionization detector. A Multi-Chrom computerized chromatographic system was used for recording and processing of the chromatograms.

The following parameters were determined to characterize the reaction in the autoclave: degree of butene conversion, $X_{C_{4=}}$ (%); weight yield of the C_{5+} products based on converted butenes, $Y_{C_{5+}}$ (g g^{-1}); their fractional composition. All these parameters were calculated from the material balance for every hour of the process, with subtraction of the accumulated initial substances and reaction products.

In preparing the catalysts by multiple impregnation, gradual formation of the SZ phase on the support surface allows successive monitoring of the stepwise formation of catalytically active surface state and probable reactions with the support, control over the dispersity of SZ particles, and determination of the optimal catalyst composition.

The characteristics of the texture and chemical and catalytic properties of the supported catalysts, depending on the number of impregnations, are shown in Tables 2 and 3 and in Fig. 1. Silica gel was impregnated up to ten times; the ZrO_2 content was varied from 9.5 to 39 wt %. The catalysts prepared by impregnation of aluminum oxide contained from 6.2 to 29.8 wt % ZrO_2 (1 to 5 impregnations).

At similar amounts of supported ZrO_2 and sulfation conditions, the sulfate content in the samples supported on Al_2O_3 was substantially higher than that in catalysts supported on silica gel. This is caused by the fact that sulfate ions are incorporated not only in the zirconium oxide phase but also in the aluminum oxide support during both preliminary and main sulfation. The SO_4^{2-} : ZrO_2 molar ratio in the finished catalysts varied between samples from 0.4 to 1 for the silica gel support, reaching 3 for the aluminum oxide support.

The specific surface area and pore volume of the supported catalysts are, of course, lower than those of the initial supports because of the filling or blocking of the pore space with the supported phase.

The XPA of the supported catalysts revealed no zirconium oxide or zirconium sulfate phase. The diffraction patterns of the SZS catalysts contain a broad reflection of silica gel; in the SZA catalysts, the phase of crystalline $Al_2(SO_4)_3$ with particle size (determined from the size of the coherent scattering region) of about 15 nm was identified. This suggests either high dispersity of the supported particles, exceeding the method sensitivity (~3 nm), or strong amorphization of the zirconia component, e.g., due to reaction with the support.

Table 2. Properties of silica gel–supported SZ catalysts

Sample	Number of impregnations	Composition, wt %		Pore volume, cm^3 g^{-1}	S_{sp}, m^2 g^{-1}
		ZrO_2	SO_4^{2-}		
SZS-9-1	1	9.5	5.3	–	–
SZS-15-2	2	15.2	8.2	–	–
SZS-19-4	4	19.4	15.5	0.63	270
SZS-23-5	5	22.6	15.4	0.63	–
SZS-26-6	6	25.9	12.3	0.61	265
SZS-30-7	7	29.8	11.9	0.56	266
SZS-35-8	8	34.8	10.0	0.55	–
SZS-39-10	10	39.0	14.5	0.50	–

Table 3. Composition of aluminum oxide–supported SZ catalysts

Sample	Number of impregnations	Composition, wt %	
		ZrO_2	SO_4^{2-}
SZA-6-1	1	6.2	15.6
SZS-11-2	2	11.4	19.3
SZS-18-4	3	17.8	18.0
SZS-24-5	4	24.2	–
SZS-30-5	5	29.8	–

The formation of finely divided ZrO_2 particles on the catalyst surface on the silica gel support was confirmed by HREM. It is seen on an electron micrograph of the SZS-9-1 sample (one impregnation) (Fig. 2a) that ZrO_2 forms crusts on the support particles, with

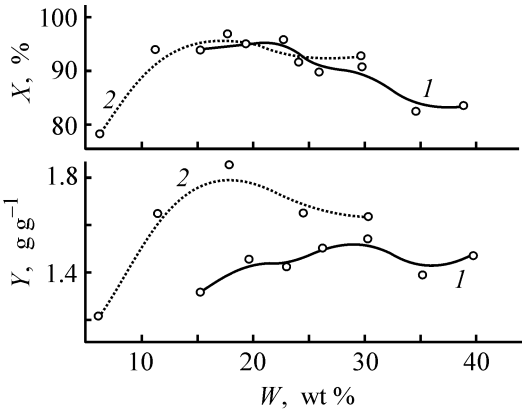

Fig. 1. Effect of the content of supported zirconium dioxide *W* on the degree of butene conversion *X* and on the yield *Y* of C_{5+} products based on converted butenes in isobutane alkylation. Support: (*1*) silica gel and (*2*) aluminum oxide.

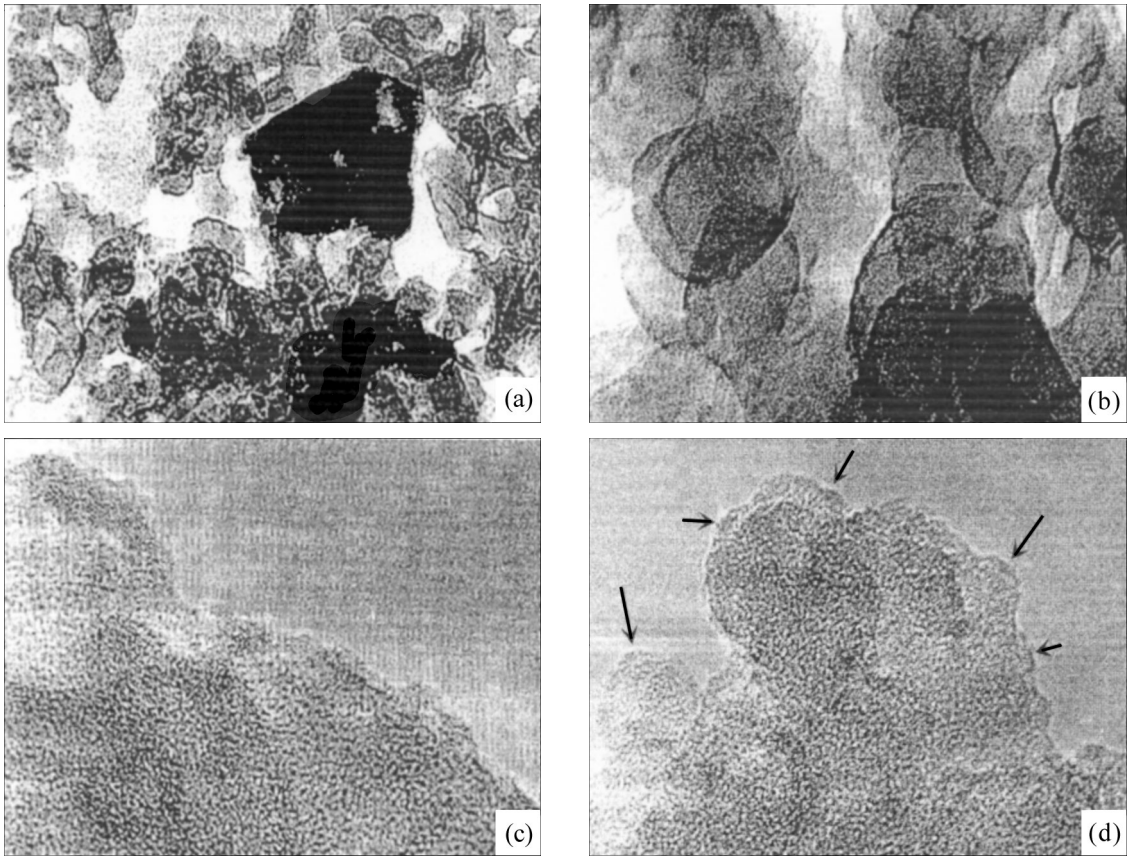

Fig. 2. Electron micrographs of samples: (a) SZS-9-1, (b) SZS-23-5, (c) SZS-35-8, and (d) SZS-19-1 (ZrO_2 particles are shown by arrows).

fairly uniform surface distribution. However, part of the zirconium oxide phase exists in the form of large aggregates (more than 100 nm), seen as a contrasting spot in the electron micrograph. The number of such particles does not grow with increasing number of impregnations (Fig. 2b, 2c), and the crust form of supported ZrO_2 remains. Flat particles of supported ZrO_2 on the surface of the silica gel globules are seen in electron micrographs of the SZS-23-5 and SZS-35-8 samples. The regions of ordered structure are 1–3 nm in size. In these formations, distorted planes of the crystal lattice with interplanar spacing of about 0.29 nm are observed. This value is characteristic of basal planes of the crystal lattice, forming the structure of known modifications of the ZrO_2 phase. For the SZS-35-8 sample (eight impregnations), the amount of such crystalline structures increases as compared with the SZS-23-5 sample, but qualitatively these samples are virtually the same.

Table 4. Properties of bulk and supported SZ catalysts

Catalyst	S_{sp}, $m^2\ g^{-1}$	Composition, wt %	
		ZrO_2	SO_4^{2-}
SZ	138	95.9	4.1
SZS-19-1	230	19.0	7.0
SZA-11-1	170	11.4	26.4

All the samples of the SZS and SZA series prepared by successive impregnation showed activity in alkylation of isobutane with butenes. The results of their tests (Fig. 1) demonstrated that satisfactory parameters of the catalytic activity (degree of butene conversion no less than 90%, yield of liquid alkylate 1.5–1.8 g per g of converted butenes) were observed beginning from the catalysts prepared by two- and three-fold impregnation. For catalysts supported on Al_2O_3, this corresponds to a ZrO_2 content of no less than 10–15 wt % and, for catalysts supported on silica gel, 15–20 wt %. Further increase in the amount of supported SZ does not affect the catalyst properties substantially. Comparison of the test results with the data of electron microscopy allows a conclusion that the alkylation catalysis is ensured by formation of highly dispersed phases of crystalline sulfated ZrO_2 on the catalyst surface.

Table 5. Vibration frequencies and concentration of CO adsorbed on LACs and BACs of catalysts

Catalyst								
SZ			SZS-19-1			SZA-11-1		
adsorption type	ν, cm^{-1}	CO content, μmol g^{-1}	adsorption type	ν, cm^{-1}	CO content, μmol g^{-1}	adsorption type	ν, cm^{-1}	CO content, μmol g^{-1}
CO-BAC	2169	91	CO-BAC	2167	75	CO-BAC	2167	116
CO-LAC (Zr^{4+})	2205	78	CO-LAC (Zr^{4+})	2204	55	CO-LAC (Al^{3+})	2223	8
CO-LAC (Zr^{4+})	2200	283	CO-LAC (Zr^{4+})	2195	283	CO-LAC (Zr^{4+})	2207	60
CO-LAC (Zr^{4+})	2191	283				CO-LAC (Zr^{4+})	2197	242

Table 6. Comparison of properties of catalysts in isobutane alkylation with butenes

Catalyst	$C_{4=}$ fed, g g^{-1} of catalyst	$X_{C_{4=}}$, %	$Y_{C_{5+}}$, g g^{-1}	Content in alkylate, wt %					TMP/DMH
				C_5–C_7	TMP	DMH	other C_8	C_{9+}	
SZ	0.11	100.00	1.75	23.10	61.02	13.77	1.13	0.98	4.43
	0.21	100.00	1.81	19.30	66.04	13.34	0.43	0.89	4.95
	0.29	94.53	1.64	19.85	65.89	11.92	1.33	1.01	5.53
	0.38	86.32	1.48	19.00	63.41	12.03	0.59	4.97	5.27
SZS-19-1	0.13	100.00	1.76	11.00	71.20	11.47	0.68	5.65	6.21
	0.22	97.20	1.84	9.95	66.90	10.55	2.20	10.40	6.34
	0.35	86.98	1.54	11.23	65.10	10.67	1.33	11.67	6.67
	0.43	78.76	1.46	10.09	59.43	9.89	1.07	19.52	6.01
SZA-11-1	0.10	100.00	2.40	19.21	47.20	22.37	8.19	3.03	2.11
	0.18	98.02	2.24	19.00	52.34	19.03	4.63	5.00	2.75
	0.28	94.15	2.07	16.67	53.24	16.48	3.09	10.52	3.23
	0.39	86.34	1.42	16.40	51.12	15.93	3.43	13.12	3.21

A single impregnation of supports also gives active alkylation catalysts (SZS-19-1 and SZA-11-1 samples) when the content of applied ZrO_2 lies within the limits of the optimal interval 10–20 wt % we found (Table 4). An HREM analysis of these samples (Fig. 2d) showed their structural identity with the catalysts prepared by multistage application of ZrO_2. Detailed data on acid-base and catalytic properties of these catalysts are listed in Tables 5 and 6. For comparison, data for bulk SZ prepared under the similar conditions are also presented.

According to XPA data, bulk sulfated ZrO_2 is a mixture of monoclinic and tetragonal modifications of zirconium dioxide in approximate ratio of 3 : 1, with ZrO_2 particle size of about 8 nm. Broadening of the peak bases in the diffraction patterns indicates the presence of an X-ray-amorphous phase (up to 10%). This phase may consist of less than 2–3-nm ZrO_2 crystallites and contain strongly disordered ZrO_2 structures.

All the catalysts are characterized by virtually the same strength and concentration of BACs. The content of strong LACs substantially exceeds the content of proton-donor centers. The greatest difference is observed for bulk SZ: the LAC concentration exceeds by approximately a factor of 7 the concentration of BACs. For SZS-19-1 and SZA-11-1 samples, the LAC-to-BAC ratio is 3–4. The total content of LACs on the surface of the bulk catalyst is also two times greater than that on supported catalysts. The 2190–2207 cm^{-1} range corresponds to CO adsorption on coordination-unsaturated Zr^{4+} ions situated at crystal defects and on more ordered surfaces [23, 24]. All the catalysts have close amounts of the strongest LACs (Zr^{4+}), which form complexes with CO with absorption at 2204–2207 cm^{-1}. The concentrations of

medium-strength centers (CO absorption at 2195–2200 cm^{-1}) are also comparable. However, bulk SZ also contains weak LACs (Zr^{4+}) with CO absorption band at 2191 cm^{-1} in approximately the same amounts (283 $\mu mol\ g^{-1}$). On the surface of the SZA-11-1 sample, there are very strong LACs (ν_{CO} = 2223 cm^{-1}) corresponding to Al^{3+} ions, but in very small amounts (8 $\mu mol\ g^{-1}$). Thus, compared with bulk SZ, the supported catalysts exhibit narrower and more uniform distribution of the surface acid centers. In accordance with [24, 25], specifically the surface LACs of the SZ catalysts directly participate in activation of alkanes. In isoparaffin alkylation, LACs can provide the so-called "hydride transfer," which determines stages of initiation and chain transfer in the course of the reaction [26].

All the catalysts are characterized by high activity in alkytation. At feeds of 0.1 to 0.2 g of butenes per gram of catalyst, they ensure complete conversion of butene and a yield of liquid alkylate (C_{5+} product) of no less than 1.7–1.8 g per gram of converted butenes, which amounts to about 80–90% of the calculated value, which is equal to 2.04 $g\ g^{-1}$. However, for the SZA-11-1 sample, the initial concentration of the catalyst is in excess with respect to the alkylation reaction, which is expressed in an overstoichiometric yield of hydrocarbons C_{5+} (up to 2.4 $g\ g^{-1}$), probably due to the so-called autoalkylation of isobutane [27].

During the reaction run, the degree of butene conversion and alkylate yield decrease rapidly on all the catalysts. At feed of 0.4 g of butenes per gram of catalyst, the butene conversion is 80–86%, and the yield C_{5+} hydrocarbons, about 1.4–1.5 $g\ g^{-1}$. The observed changes in the composition of the products are mainly associated with increasing content of heavy hydrocarbons containing more than eight carbon atoms. In accordance with the classical carbenium-ion alkylation mechanism [27], this indicates that, instead of formation of C_8 isoparaffin via abstraction of a hydride ion from the isobutane molecule, the intermediate cation C_{8+} reacts with one more or several butene molecules. This is responsible for the increased content of heavy products, decreased conversion of isobutane, and, correspondingly, lower yield of alkylation products. Thus, during deactivation of catalyst active centers, the alkylation of isobutane with butenes transforms into butene oligomerization.

The SZS-19-1 catalyst is most selective with respect to products and provides virtually the same alkylation parameters as traditional liquid acids [27]: isoparaffins C_8 constitute no less than 75–80 wt % of the liquid alkylate at average ratio of trimethylpentanes (TMP) to dimethylhexanes (DMH) of about 6, whereas the fraction of light paraffins C_5-C_7 is about 11 wt %. The samples of bulk SZ and SZ supported on aluminum oxide are characterized by elevated cracking power, which follows from the high content of the light fraction C_5–C_7. In addition, the SZA11-1 catalyst gives substantial amounts of DMH and other weakly branched octanes (20% and higher), which strongly affects the octane characteristics of the alkylate.

CONCLUSIONS

(1) Application of 10–20% sulfated zirconia (in terms of ZrO_2) on silica gel or aluminum oxide allows preparation of catalysts for isobutane alkylation with butenes. These catalysts are not inferior in activity to bulk zirconium sulfate catalysts. The activity of the supported catalysts is determined by crystalline phases of sulfated ZrO_2. Dispergation of SZ on the support surface provides attainment of the acid properties of the supported catalyst on the level of the bulk catalyst. The more uniform distribution of strong acid centers in the supported catalysts based on silica gel ensures highly selective alkylation.

(2) Despite the relatively short uninterrupted working life of the above catalysts (0.5–1 t of liquid alkylate per 1 t of the catalysts), their effective industrial exploitation in the reactor-regenerator type process with continuous catalyst circulation is possible.

ACKNOWLEDGMENTS

The authors are indebted to V.A. Drozdova for adsorption measurements.

REFERENCES

1. Gembicki, S., *Proc. 12th Int. Congr. on Catalysts, Stud. Surf. Sci. Catal.*, 2000, vol. 130, pp. 147–155.
2. Yadav, G. and Nair, J., *Microporous Mesoporous Mater.*, 1999, vol. 33, pp. 1–48.
3. Guo, C., Yao, S., Cao, J., and Qian, Z., *Appl. Catal. A*, 1994, vol. 107, no. 2, pp. 229–238.
4. Corma, A., Juan-Rajadell, M., Lopez-Nieto, J., *et al.*, *Appl. Catal. A*, 1994, vol. 111, no. 1, pp. 175–189.
5. Corma, A., Martinez, A., and Martinez, C., *J. Catal.*, 1994, vol. 149, no. 1, pp. 52–60.
6. Corma, A., Martinez, A., and Martinez, C., *Appl. Catal. A*, 1996, vol. 144, no. 1, pp. 249–268.
7. Hess, A. and Kemnitz, E., *Appl. Catal. A*, 1997, vol. 149, no. 2, pp. 373–389.

8. Das, D. and Chakrabarty, D., *Energy Fuels*, 1998, vol. 12, no. 1, pp. 109–114.
9. Gore, R.B. and Thomson, W.J., *Appl. Catal. A*, 1998, vol. 168, no. 1, pp. 23–32.
10. Zalewski, D., Alerasool, S., and Doolin, P., *Catal. Today*, 1999, vol. 53, no. 3, pp. 419–432.
11. Xiao, X., Tierney, J., and Wender, I., *Appl. Catal. A*, 1999, vol. 183, no. 1, pp. 209–219.
12. Song, X. and Sayari, A., *Catal. Rev.-Sci. Eng.*, 1996, vol. 38, no. 3, pp. 329–412.
13. Ivanov, A.V. and Kustov, L.M., *Ross. Khim. Zh.*, 2000, no. 2, pp. 21–52.
14. Luy, L., Yori, J., Castro, A., and Parera, J., *React. Kinet. Catal. Lett.*, 1988, vol. 36, no. 2, pp. 275–283.
15. Grau, J., Vera, C., and Parera, J., *Appl. Catal. A*, 1998, vol. 172, no. 2, pp. 311–326.
16. Vera, C., Pieck, C., Shimizu, K., and Parera, J., *Proc. 7th Int. Symp. on Scientific Bases for the Preparation of Heterogeneous Catalysts, Stud. Surf. Sci. Catal.*, 1998, vol. 118, pp. 369–376.
17. Lei, T., Xu, J., Tang, Y., *et al., Appl. Catal. A*, 2000, vol. 192, no. 1, pp. 181–188.
18. Guo, C. and Yu, Z., *Proc. Int. Symp. on Acid–Base Catalysis II, Stud. Surf. Sci. Catal.*, 1993, vol. 90, pp. 543–548.
19. Dzis'ko, V.A., *Osnovy metodov prigotovleniya katalizatorov* (Foundations of Methods for Catalyst Preparation), Novosibirsk: Nauka, 1983.
20. *Physical and Chemical Aspects of Adsorbents and Catalysts*, Linsen, B.G., Ed., London: Academic, 1970.
21. Laizet, J., Soiland, A., Leglise, J., and Duchet, J., *Top. Catal.*, 2000, vol. 10, no. 1, pp. 89–97.
22. Paukshtis, E.A., *Infrakrasnaya spektroskopiya v geterogennom kislotno-osnovnom katalize* (Infrared Spectroscopy in Heterogeneous Acid–Base Catalysis), Novosibirsk: Nauka, 1992.
23. Spielbauer, D., Mekhemer, G., Zaki, M., and Knozinger, H., *Catal. Lett.*, 1996, vol. 41, no. 1, pp. 101–109.
24. Morterra, C., Cerrato, G., and Pinna, F., *Spectrochim. Acta, A*, 1999, vol. 55, no. 1, pp. 95–103.
25. Morterra, C., Cerrato, G., and Bolis, E.A., *J. Chem. Soc., Faraday Trans.*, 1997, vol. 93, pp. 1179–1185.
26. Paukshtis, E.A., Duplyakin, V.K., Finevich, V.P., *et al., Proc. 12th Int. Congr. on Catalysis, Stud. Surf. Sci. Catal.*, 2000, vol. 130, pp. 2543–2548.
27. Dorogochinskii, A.Z., Lyuter, A.V., and Vol'pova, E.G., *Sernokislotnoe alkilirovanie izoparafinov olefinami* (Sulfuric Acid Alkylation of Isoparaffins with Olefins), Moscow: Nauka, 1970.

Russian Journal of Applied Chemistry, Vol. 76, No. 4, 2003, pp. 558–560. Translated from Zhurnal Prikladnoi Khimii, Vol. 76, No. 4, 2003, pp. 579–581.

Catalytic Alkylation of 1-Naphthol with Methanol

A. A. Agaev and M. K. Nazarova

Sumgait State University, Sumgait, Azerbaijan

Received January 9, 2003

Abstract—The reaction of 1-naphthol with methanol in the presence of mordenite catalysts was studied. The synthesis conditions ensuring high yields of methylnaphthols, methylnaphthalenes, or methoxynaphthalene were determined.

Catalytic methylation of naphthols with methanol has been poorly studied. Both *C*-alkylation yielding methylnaphthols and *O*-alkylation yielding methoxynaphthalenes are possible. However, it has been reported [1, 2] that the reaction of naphthol with an excess of methanol mainly yields isomeric alkylnaphthalenes. Apparently, the reaction pathway and the composition of the products depend on the reaction conditions and catalysts used.

To examine the effect exerted by zeolite composition and reaction conditions on alkylation of 1-naphthol with methanol, we studied the catalytic properties of synthetic mordenites containing 0.1–5.0 wt % Ni(II).

EXPERIMENTAL

H-Mordenite was prepared by treatment of Na-mordenite ($SiO_2 : Al_2O_3 = 10$) with 1 N NH_4Cl and then with eight portions of 2 N HCl, followed by washing and drying. The nickel-containing zeolite was prepared by impregnation of H-mordenite with a calculated amount of an $Ni(NO_3)_2$ solution. The optimal content of Ni(II) in H-mordenite was 1.5 wt %.

The catalytic activity of zeolites was evaluated on a flow-through installation at atmospheric pressure. A 10-cm^3 portion of the catalyst was charged into reactor and heated for 5 h at 450°C in a flow of dry air and then for 3 h at 450°C in a hydrogen flow. The experiments were performed at 300–425°C, molar ratio 1-naphthol : CH_3OH = 1 : 7, and space velocity of 0.8–1.4 h^{-1}. The reaction products were analyzed on a Chrom-5 chromatograph; 3600 × 4-mm columns were packed with Chromosorb W containing 15 wt % Apiezon M as the stationary phase. The relative error of the analysis did not exceed 3.0%. The IR spectra of individual reaction products were measured on an M-80 spectrometer.

In contrast to the initial Na-mordenite, on which 1-naphthol undergoes virtually no chemical transformations, the naphthol conversion on H-mordenite is significant.

The reaction of 1-naphthol with methanol follows three major pathways: etherification, ring methylation, and self-condensation. In the reaction products, we detected 1-methoxynaphthalene, 2- and 4-methyl-1-naphthols, methylnaphthalenes, and high-carbon compounds.

At low temperatures (320–380°C), the major pathway is electrophilic methylation of the 1-naphthol core at 2- and 4-positions to form the corresponding methylnaphthols. At higher temperatures (380–420°C), the contribution of dehydroxylation accompanying ring methylation increases in the presence of H-mordenite, and methylnaphthalenes become the major products. At moderate temperatures, appreciable amounts of 1-methoxynaphthalene are formed, apparently by the competing *O*-methylation pathway:

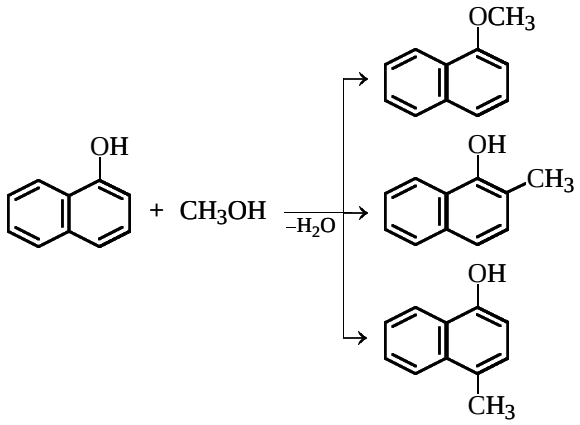

The table shows that introduction of Ni(II) into H-mordenite noticeably enhances its catalytic properties in alkylation of 1-naphthol with methanol. In the range 320–360°C, the major reaction products are 1-methoxynaphthalene and 2- and 4-methylnaphthols; the total selectivity of their formation is 91.3–96.4%.

1070-4272/03/7604-0558 $25.00 © 2003 MAIK "Nauka/Interperiodica"

Alkylation of 1-naphthol with methanol in the presence of H- and Ni,H-mordenite (molar ratio 1-naphthol : methanol = 1 : 7)

Parameter	H-Mordenite					Ni,H-Mordenite				
Temperature, °C	320	360	380	420	360	320	360	380	420	360
Space velocity, h^{-1}	1.0	1.0	1.0	1.0	1.4	1.0	1.0	1.0	1.0	1.2
Yield of reaction products based on converted 1-naphthol, %:										
1-methoxynaphthalene	26.8	10.2	4.6	–	10.0	38.5	11.1	5.0	–	12.0
2- and 4-methylnaphthols	40.0	42.1	32.4	11.7	50.3	56.2	80.2	77.7	20.5	84.4
methylnaphthalenes	17.7	44.2	55.1	77.9	36.5	–	4.7	10.0	71.1	2.0
condensation products	2.4	3.0	5.7	7.8	2.1	2.0	3.2	4.1	6.9	1.1
Conversion of 1-naphthol, %	22.2	39.0	46.5	57.7	28.5	15.0	33.8	40.0	51.1	30.0

Despite a certain decrease in the conversion of 1-naphthol, this catalytic system is more selective with respect to formation of 2- and 4-methyl-1-naphthols (56.2–84.4%).

In contrast to H-mordenite, the nickel-containing zeolite ensures highly selective (77.7%) formation of methyl homologs of 1-naphthol at 380°C. It should be noted that, above this temperature, the contribution of methylnaphthalene formation dramatically grows, and at 420°C methylnaphthalenes become the major reaction produts, as in the presence of H-mordenite. The methylnaphthalene fraction formed in the presence of both catalysts has a complex chemical composition. Its major components are 1,2-dimethylnaphthalene, 1,2,4- and 1,2,7-trimethylnaphthalenes, 1,2,4,7-tetramethylnaphthalene, and 1,2,3,4,6-pentamethylnaphthalene. Also detected are 2-methylnaphthalene, 1,2,3-trimethylnaphthalene, 1,2,3,4-tetramethylnaphthalene, and 1,2,3,4,6,7-hexamethylnaphthalene. In addition, the products contain 1-oxo-2,2-dimethyl-1,2-dihydronaphthalene and 1-oxo-4,4-dimethyl-1,4-dihydronaphthalene, which, along with naphthol methyl derivatives, may be intermediates in formation of methylnaphthalenes.

The acid centers present on the H-mordenite surface promote a number of parallel and consecutive reactions, which leads to a decrease in the selectivity with respect to the target products. The increased selectivity of Ni,H-mordenite with respect to methylnaphthols is probably due to favorable changes in the acidity of the H-mordenite surface upon modification with Ni(II). With the Ni-modified catalyst, formation of methylnaphthalenes is fully or largely suppressed. Modification with Ni(II) also makes the catalyst more stable as compared with H-mordenite (the stable working life of the catalyst increases from 5 to 50 h and more) and affects the isomeric composition of methylnaphthols.

Figures 1a and 1b show how the content of 2-methyl-1-naphthol in its mixture with 4-methyl-1-naphthol

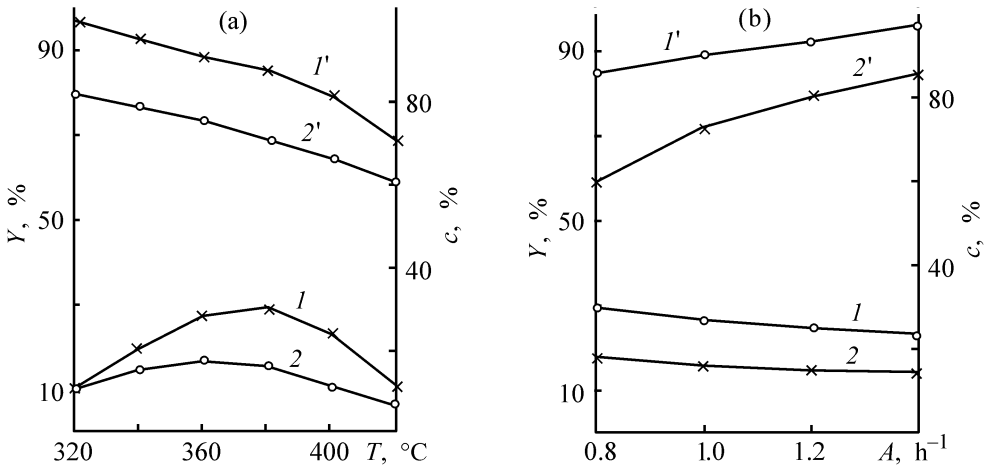

Fig. 1. Influence of (a) temperature *T* and (b) space velocity *A* on the (*1*, *2*) total yield of 2- and 4-methyl-1-naphthols, *Y*, based on the naphthol taken into the reaction and (*1*′, *2*′) content *c* of 2-methyl-1-naphthol in its mixture with 4-methyl-1-naphthol. Catalyst: (*1*, *1*′) N,H-mordenite and (*2*, *2*′) H-mordenite.

and the total yield of methyl homologs of 1-naphthol, based on the naphthol taken into the reaction, depend on the temperature and space velocity, with H- and Ni,H-mordenites as catalysts. It is seen that, as the temperature is increased from 320 to 360 (in the case of H-mordenite) or to 380°C (in the case of Ni,H-mordenite), the yield of methylnaphthols, based on the naphthol taken into the reaction, grows to become 16.4 and 31.1%, respectively. At 420°C, this parameter decreases on both catalysts. Raising the reaction temperature from 320 to 420°C also decreases the content of 2-methyl-1-naphthol in its mixture with the 4-methyl isomer. Raising the space velocity from 0.8 to 1.4 h^{-1} decreases the yield of methylnaphthols based on the 1-naphthol taken into the reaction, with the content of 2-methyl-1-naphthol in its mixture with the 4-methyl isomer growing for both catalysts. Introduction of 1.5 wt % Ni(II) into H-mordenite increases the content of 2-methyl-1-naphthol relative to 4-methyl-1-naphthol (Figs. 1a, 1b). It is seen that, in the presence of Ni,H-mordenite, the *ortho* isomer becomes prevailing in the target methylnaphthol fraction. With increasing space velocity, the content of the *ortho* isomer varies less significantly than in the presence of H-mordenite. Figure 1b shows that, with the space velocity increasing from 0.8 to 1.4 h^{-1}, the content of 2-methyl-1-naphthol in its mixture with the 4-methyl isomer grows by 24.5% on H-mordenite and by only 9.3% on Ni,H-mordenite.

Thus, our resuts suggest that the major pathway of the reaction of 1-naphthol with methanol on mordenite catalysts at 320–380°C is C-alkylation at the 2- and 4-positions. Na,H-Mordenite is more selective with respect to formation of the *ortho* isomer.

CONCLUSIONS

(1) Mordenite catalysts show high activity in reaction of 1-naphthol with methanol.

(2) By varying the reaction conditions and catalyst composition, it is possible to prepare methylnaphthols or methylnaphthalenes, and, if required, also 1-methoxynaphthalene in high yields.

REFERENCES

1. JPN Patent 56-19 332.
2. Agaev, A.A., Nazarova, M., and Mamedova, R.I., Abstracts of Papers, *2-ya Mezhdunarodnaya nauchnaya konferentsiya "Tonkii organicheskii sintez i kataliz"* (2nd Int. Scientific Conf. "Fine Organic Synthesis and Catalysis"), Baku, 2002, pp. 192–193.

Russian Journal of Applied Chemistry, Vol. 76, No. 4, 2003, pp. 561–565. Translated from Zhurnal Prikladnoi Khimii, Vol. 76, No. 4, 2003, pp. 582–585.

CATALYSIS

Plasma-Enhanced Catalytic Oxidation of Carbon Monoxide

V. I. Grinevich, N. V. Ivanova, and V. V. Kostrov

Ivanov State University of Chemical Engineering, Ivanovo, Russia

Received October 9, 2002

Abstract—Data on the kinetics of plasma-enhanced and plasma-enhanced catalytic oxidation of carbon(II) oxide with IK-1-6 catalyst are presented. The influence exerted by IK-1-6 catalyst on the conversion of carbon-containing components of the $CO–CO_2–CH_4–SO_2$–air gas mixture in barrier-discharge plasma is analyzed.

Methods using fast-electron beams or low-temperature plasma (barrier or corona discharge) to initiate oxidation are presently recognized as promising methods for purification of exhaust gases of thermal power plants and internal-combustion engines, with the plasma activation being, as a rule, more advantageous energetically [1]. Combining the action of nonequilibrium plasma on the gas mixtures with the activating properties of catalysts may lead to a decrease in energy expenditure and increase in the process rate and degree of conversion. However, data on the kinetics of plasma-enhanced catalytic oxidation, and all the more, on their mechanisms, are scarce. Therefore, a study of the conversion of the main components of real exhaust gases or model gas mixtures in barrier-discharge (BD) plasma and in a combined plasma-enhanced catalytic process is a topical task.

The aim of this study was to analyze the processes of plasma-enhanced catalytic oxidation of carbon monoxide in various gas mixtures.

EXPERIMENTAL

As test objects were chosen gas mixtures of composition (vol %): $CO–O_2$–He (CO 6, O_2 24, and He 70), $CO–CO_2–SO_2$–air (CO 5.84, CO_2 0.16, and SO_2 0.10), and $CO–CO_2–CH_4–SO_2$–air (CO 0.74, CO_2 17, SO_2 0.10, and CH_4 0.26). The initial gas mixture was fed at a certain rate into the discharge cell, where a barrier discharge was excited at atmospheric pressure. The reactor was in the form of two coaxial cylinders, one of which (outer) was made of molybdenum glass (dielectric barrier), and the other (inner electrode), of an aluminum alloy [2]. The thicknesses of the dielectric layer (S-49 glass) and air layer between the electrodes were the same in all the experiments (1.5 and 3 mm, respectively). The discharge was excited with a high-voltage transformer (ac frequency 50 Hz,) at a voltage varied within the range 12–16 kV. The discharge current was monitored with an oscilloscope.

Plasma-enhanced catalytic processes were studied with an IK-1-6 ($V_2O_5 \cdot K_2O/SiO_2$) commercial catalyst [3]. The catalyst (grain size 1.0–1.6 mm) was placed in the plasma zone and fixed there with fluoroplastic rings with holes for the gas mixture to flow. The concentration of CO, CO_2, and CH_4 in the initial gas mixture and at the reactor outlet was monitored chromatographically [4] (LKhM–80 chromatograph with heat-conductivity detector, carrier gas helium), and the SO_2 concentration, photometrically, using a standard procedure [5]. The gas flow rate was varied from 0.08 to 0.63 $cm^3\ s^{-1}$, which corresponded to 20 to 120 s of contact of the gas with the plasma. The random error in measuring the CO, CO_2, and CH_4 concentrations in a set of runs was no more than 30% at confidence probability of 0.95.

One of parameters determining the kinetics of processes occurring in BD plasma is the plasma dose D (mA s cm^{-2}), related to the current density j and to the time τ_c of contact between gas and plasma by

$$D = j\tau_c.$$

The plasma dose was varied within 0.1–2.0 mA s cm^{-2}.

It is known that use of BD leads to rather high degrees of carbon(II) oxide conversion in stoichiometric mixtures with an oxidant [6]. Measurements of the

1070-4272/03/7604-0561 $25.00 © 2003 MAIK "Nauka/Interperiodica"

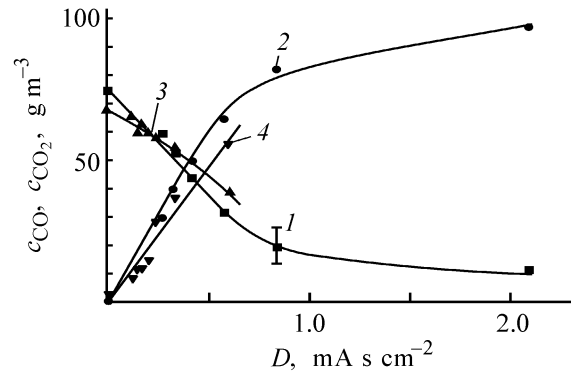

Fig. 1. CO and CO_2 concentrations c_{CO} and c_{CO_2} at the exit from the discharge zone vs. plasma dose *D*. Gas mixture: (*1*) CO (CO–O_2–He), (*2*) CO_2 (CO–O_2–He), (*3*) CO (CO–CO_2–SO_2–air), and (*4*) CO_2 (CO–CO_2–SO_2–air).

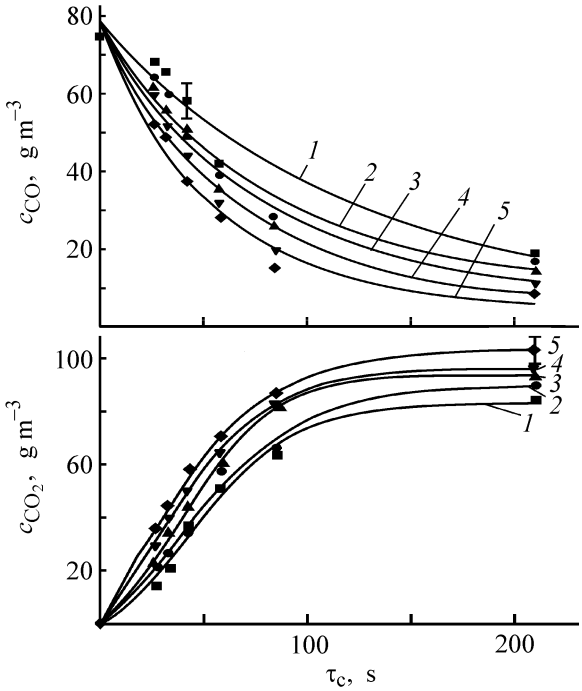

Fig. 2. CO and CO_2 concentrations c_{CO} and c_{CO_2} vs. the time of contact τ_c between gas and plasma at various voltages applied. Voltage (kV): (*1*) 12, (*2*) 13.5, (*3*) 15, (*4*) 16, and (*5*) 17.

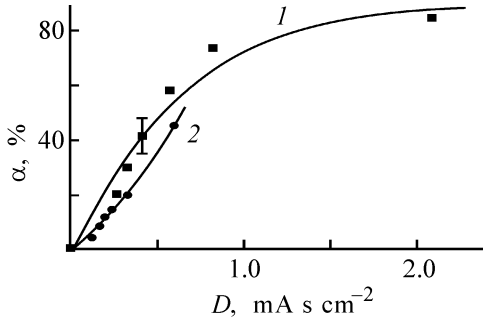

Fig. 3. Degree of CO conversion, α, at various plasma doses *D*. Gas mixture: (*1*) CO–O_2–He, and (*2*) CO–CO_2–SO_2–air.

CO and CO_2 concentrations in the CO–O_2–He mixture at the exit from the discharge zone showed that, with increasing plasma dose, the CO concentration decreases from 74.5 to 11.18 g m^{-3} (i.e., by a factor of 6), and the CO_2 concentration increases (Fig. 1). The CO_2 yield and the decrease in the CO concentration are not affected by the voltage (or power) applied within the experimental error (Fig. 2). The CO concentration in the CO–CO_2–SO_2–air mixture subjected to plasma treatment also decreases from 68 to 38.1 g m^{-3} (i.e., by a factor of 1.8), with a simultaneous increase in the CO_2 concentration (Fig. 1). The carbon monoxide treated with the BD plasma in a mixture with O_2 and He is easily converted into CO_2, with the degree of conversion as high as 80% at the maximum plasma dose (2.0 mA s cm^{-2}) (Fig. 3). In the CO–CO_2–SO_2–air mixture, the maximum degree of conversion of 44% is attained at a plasma dose of 0.63 mA s cm^{-2}. However, the degrees of the CO conversion in the gas mixtures indicated (CO–O_2–He and CO–CO_2–SO_2–air) coincide to within the measurement error at the same plasma doses.

In the CO–O_2–He mixture, the carbon balance (amount of CO converted into CO_2) is observed to within 19% at a short time of contact between gas and plasma and to within 5% at long time of contact. The fact that the carbon balance is observed with rather good accuracy shows that the CO conversion in BD plasma is mainly associated with of CO_2 formation. To a first approximation, formation of other carbon-containing compounds can be neglected. For the CO–CO_2–SO_2–air mixture, the total content of carbon in the system (before and after plasma treatment) remains constant to within 6% at all plasma doses, and the carbon balance is observed to within, on the average, 17%, which does not go beyond the measurement error.

In the general case, the CO oxidation is described satisfactorily by a first-order reaction equation with effective rate constant of 0.005 s^{-1} (for CO–CO_2–SO_2–air) or 0.016 s^{-1} (for CO–O_2–He).

In plasma treatment of CO-containing gas mixtures, the degree of dissociation and the reaction products depend on the composition of a plasma-forming gas and discharge parameters [7]. The action of BD plasma on the CO–CO_2–CH_4–SO_2–air mixture results in that the CO concentration in the mixture grows, compared with the initial concentration, with increasing plasma dose. This is due to the fact that the CO_2 concentration in the mixture exceeds the CO concen-

tration by a factor of 23. Under the action of active species (e.g., free electrons) carbon dioxide dissociates into CO (Fig. 4), and the total content of carbon in the system remains unchanged within the measurement error (no more than 7%) at any plasma dose. If it is assumed that, in the given case, the conversion of the carbon-containing compounds is described by the reactions:

$$CO_2 \rightarrow CO + O,\ CH_4 \rightarrow CO + 2H_2O,$$

then the mass of carbon in the output part of the (CO_2 + CH_4) balance equation will be considerably higher (by a factor of 2–3.5, depending on plasma dose) than the mass in the input part (CO). This means that, alongside with CO_2 conversion into CO (methane contribution to the carbon unbalance is insignificant), there exists at least one more reaction channel. In fact, the set of reactions occurring in plasma is very large. To these belong reverse processes, reactions involving electron-excited species, and those with ozone. Carbon suboxide C_2O_3, carbonyl compounds, compounds with double C=C bond, acetylene, and alcohols can be formed in BD plasma [8]. Among the intermediate products of plasma-enhanced CH_4 oxidation may be aldehydes and alcohols, the possible final products are CO_2 and H_2O. A qualitative reaction for formaldehyde demonstrated its total absence to within the detection sensitivity of the method (less than 0.01 mg m^{-3}). At the same time, appearance of other products of CO_2 and CH_4 conversion, such as carbon suboxide, carbon, and saturated hydrocarbons, cannot be ruled out. Probably, formation of intermediates in the conditions under consideration is not a rate-determining stage. The role of the latter is played by oxidation-initiating reactions, i.e., by the interaction of initial compounds with active species of the plasma.

The reactions of CH_4 oxidation, CO formation, and CO_2 dissociation are satisfactorily described by first-order equations with effective constant of 0.01, 0.004, and 0.0007 s^{-1}, respectively.

To accelerate the CO and SO_2 oxidation in air, the IK-1-6 commercial catalyst was introduced into the plasma zone. The experiments showed that, in a combined plasma-enhanced catalytic process (CO–CO_2–SO_2–air mixture), the degrees of CO conversion are the same as those observed in plasma-enhanced oxidation. This may be due to low efficiency of the given catalyst in CO and CO_2 conversion. Similarly to plasma-enhanced oxidation, combined plasma-enhanced catalytic process is characterized by carbon

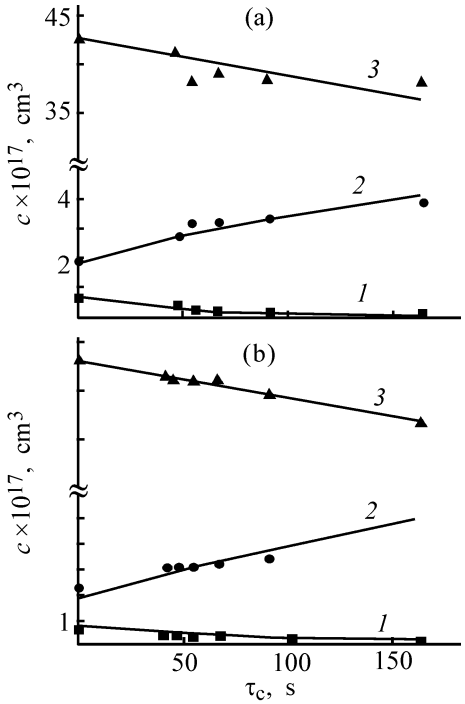

Fig. 4. Kinetics of variation of the concentrations c of carbon-containing components of the CO–CO_2–CH_4–SO_2–air gas mixture in (a) plasma-enhanced oxidation and (b) plasma-enhanced catalytic process. (τ_c) Time of contact. (*1*) CH_4, (*2*) CO, and (*3*) CO_2. Points: experimental data, lines: results of model calculation.

balance observed to within 20% for all plasma doses. The fact that the carbon balance is observed with sufficient accuracy shows that CO_2 formation is the main channel of CO conversion. For the CO–CO_2–CH_4–SO_2–air mixture, the influence of the IK-1-6 catalyst on the efficiency of CO and CH_4 oxidation and CO_2 decomposition is virtually not manifested, either (Fig. 4). The effective rate constant of CH_4 oxidation is approximately twice that of CO formation (Table 1).

Table 1. Effective rate constants of conversion reactions in plasma-enhanced oxidation and plasma-enhanced catalytic process with IK-1-6 catalyst

Mixture composition	K(CO)	K(CO_2)	K(CH_4)	K(SO_2)
	s^{-1}			
CO–CO_2–SO_2–air	0.0050* 0.0045	0.025 0.022	– –	0.039 0.105
CO–CO_2–SO_2–CH_4–air	0.040 0.0055	0.0007 0.001	0.011 0.009	0.018 0.017

* Numerator, without catalyst; denominator, with catalyst.

Table 2. Effective rate constants calculated by parametric identification of the kinetic model for the gas mixture $CO–CO_2–SO_2–CH_4–air$

Process	K_1	K_2	K_3
	c^{-1}		
Plasma-enhanced	0.014	2.6×10^{-4}	6.9×10^{-4}
Plasma-enhanced catalytic (IK-1-6 catalyst)	0.010	4.1×10^{-4}	5.4×10^{-4}

In the plasma-enhanced catalytic process, similarly to plasma-enhanced oxidation, the SO_2 concentration at the reactor outlet decreases with increasing time of contact between the gas mixture and plasma. However, the oxidation of SO_2 is more efficient. The effective rate constant of SO_2 oxidation in the plasma-enhanced catalytic process was 0.105 s^{-1}, i.e., exceeded by approximately a factor of 2.7 that in plasma oxidation (Table 1). The degree of SO_2 conversion in the heterogeneous process grows to 99% with increasing plasma dose. In the $CO–CO_2–CH_4–SO_2–air$ mixture, the rate constant of SO_2 oxidation is independent of the presence of catalyst in the plasma zone and is lower by about a factor of 2 than that in the $CO–CO_2–SO_2–air$ mixture.

The conversion of carbon-containing compounds in a mixture $CO–CO_2–CH_4–SO_2–air$ can be represented by the following simplified scheme

$$CH_4 \xrightarrow{K_1} CO \xrightarrow{K_2} CO_2 \xrightarrow{K_3} \text{products},$$

which is described by a set of differential equations:

$$\begin{cases} \dfrac{dc_{CH_4}}{d\tau} = -K_1 c_{CH_4}, \\ \dfrac{dc_{CO_2}}{d\tau} = -(K_2 + K_3) c_{CO_2}, \\ \dfrac{dc_{CO}}{d\tau} = -K_1 c_{CH_4} + K_2 c_{CO_2}. \end{cases}$$

The rate constants of the elementary processes were estimated by means of parametric identification of kinetic models specified in the form:

$$dX/d\tau = f(X, \theta),\ X_{\tau=0} = X^0,\ Y = GX + \varepsilon,$$

where X is n-dimensional vector of state, Y and ε are m-dimensional vectors of the output and random noise, and θ is p-dimensional vector of the parameters being estimated.

The most plausible estimates of the parameters $\hat{\theta}$ were obtained using the Gauss–Newton method:

$$\hat{\theta}^{k+1} + \hat{\theta}^k + \rho_k P^k,$$

where k is the iteration number, ρ_k and P^k are the step and vector of descent in k-th iteration.

The results of the calculation are in good agreement with the experimental data.

Comparison of the effective rate constants calculated in terms (Table 2) of the given model shows that the rate of plasma-enhanced oxidation of methane without catalyst exceeds by a factor of 1.4 that in the combined plasma-enhanced catalytic process and the total rate of CO_2 dissociation is independent of whether a catalyst is present in the plasma or not. The effective rate constants of methane oxidation and overall dissociation of CO_2 ($K_2 + K_3$), found using the model, coincide with those obtained from kinetic dependences graphically (with the difference not exceeding 22% for methane and 26% for CO_2).

CONCLUSION

The results of the study performed show that the kinetics of CO oxidation is affected, both in plasma-enhanced oxidation and in plasma-enhanced catalytic process, by barrier-discharge parameters and composition of the model gas mixture. The presence in the gas mixture of such carbon-containing compounds as CO_2, CH_4, and SO_2 makes the efficiency of CO oxidation lower at the same parameters of barrier discharge. The obtained data on the kinetics of CO oxidation in the gas mixtures studied confirm the known mechanism of CO oxidation in barrier-discharge plasma.

REFERENCES

1. Pikaev, A.K., *Khim. Vys. Energ.*, 2000, vol. 34, no. 1, pp. 53–57.
2. Grinevich, V.I., Ivanova, N.V., and Kostrov, V.V., *Inzh. Ekolog.*, 2002, no. 2, pp. 38–44.
3. Mukhlenov, I.P., *Tekhnologiya katalizatorov* (Technology of catalysts), Leningrad: Khimiya, 1989.
4. Kleshchev, N.F., Kostyrkina, T.D., Morgunova, E.T., and Beskova, G.S., *Analiticheskii kontrol' v osnovnoi*

khimicheskoi promyshlennosti (Analytical Monitoring in Basic Chemical Industry), Moscow: Khimiya, 1992.

5. Berlyand, M.E., *Sbornik metodik po opredeleniyu kontsentratsii zagryaznyayushchikh veshchestv v promyshlennykh vybrosakh* (Tutorial on Determination of Concentrations of Contaminants in Industrial Wastes), Leningrad: Gidrometeoizdat, 1987.
6. Alkhasov, T.G., and Margolis, L. Ya., *Glubokoe kataliticheskoe okislenie organicheskikh veshchestv* (Deep Catalytic Oxidation of Organic Substances), Moscow: Khimiya, 1985.
7. Eremin, E.N., *Trudy Pervoi Mezhvuzovskoi Konferentsii po Khimii i Fizike Nizkotemperaturnoi Plazmy: Khimiya i Fizika Nizkotemperaturnoi Plazmy* (Proc. 1st Intercollegiate Conf. on Chemistry and Physics of Low-Temperature Plasma: Chemistry and Physics of Low-Temperature Plasma), Moscow: Mos. Gos. Univ., 1971.
8. Volchenok, V.I., Egorov, N.P., Komarov, V.N., *et al.*, *Zh. Fiz. Khim.*, 1976, vol. 46, no. 12, pp. 2541–2550.

Russian Journal of Applied Chemistry, Vol. 76, No. 4, 2003, pp. 566–568. Translated from Zhurnal Prikladnoi Khimii, Vol. 76, No. 4, 2003, pp. 586–588.

CATALYSIS

Optimization of Synthesis of 2,4-Dinitrophenylhydrazones under Carbon Dioxide Pressure

A. P. Eremeev

Pod"emtransmash Open Joint-Stock Company, St. Petersburg, Russia

Received July 3, 2002; in final form, January 2003

Abstract—Catalytic synthesis of 2,4-dinitrophenylhydrazones formed in the aqueous reaction mixture of aliphatic and aromatic carbonyl derivatives with 2,4-dinitrophenylhydrazine in the presence of carbonic acid protons under pressure of the CO_2–H_2O a steam–gas mixture was studied for the example of synthesis of *p*-quinone–mono-2,4-dinitrophenylhydrazone.

Hydrazones are brightly colored (yellow to red) chemical products insoluble in water and soluble in polar organic solvents. Also, hydrazones are thermally stable up to their melting points and resistant to direct solar rays and ultraviolet radiation, acids, and oxygen, and act as microbiocides. All this makes hydrazones valuable for various chemical, chemical-engineering, medical, and hygienic applications. When introduced into protective organic-phase or water-dispersible paint-and-varnish and impregnating materials, hydrazones act as biocides and anticorrosives for wood and metals.

Previously, 2,4-dinitrophenylhydrazones have been synthesized in the presence of protons of a strong inorganic acid [1]. A drawback of this process is the need to treat ready-for-use products with an alkali solution to neutralize the residual acid and to additionally wash them with water to completely remove the forming salts, which leads to a loss of up to 10% of the target product.

In this study, we suggested to catalyze the process of interest with carbonic acid formed under carbon dioxide pressure in an aqueous pulp of the reaction mass. We expected that the product to be isolated from the reactor after the condensation of 2,4-dinitrophenylhydrazone with a carbonyl derivative is complete and the carbon dioxide pressure is relieved will not require additional treatment to remove acid, since carbonic acid decomposes and carbon dioxide volatilizes upon completion of the process.

EXPERIMENTAL

In our experiments, we used an RTsG-1.6-10-1k-01 1.6-l autoclave* [TU (Technical Specifications) 26-01-476–85] made of 12Cr18Ni10Ti steel (filling factor 0.7, working pressure up to 100 MPa, temperature up to 300°C) equipped with an impeller-type stirrer (3000 rpm). We used carbon dioxide from cylinders and the following chemicals: 2,4-dinitrophenylhydrazine DNPH (pure grade, TU 6-09-2894–72) and *p*-benzoquinone (PBQ, pure grade, TU 6-09-156–76) in a 1 : 1 molar ratio and also other carbonyl derivatives (RHCO or RR'CO with R or R' = Alk or Ar).

The condensation of DNPH with PBQ to form 2,4-dinitrophenylhydrazone (DNPHN) was studied using the design matrix of full-factorial experiment (FFE-2^3) [2] with varied physical factors: X_1 for the carbon dioxide pressure, MPa (lower level 0.5, upper level 2.5); X_2 for the reaction time, *h* (0.5, 3.5); and X_3 for the reaction mass temperature, °C (50, 80). After isolation from the reaction mass, DNPH was dried at 105°C and weighed, whereupon the yield (% of the theoretical value) was estimated.

The regression equation with the coefficients calculated by the Yates method [2] adequately describes the experimental responses for FFE-2^3 ($Y_i \pm \Delta Y_i = \hat{Y}_i \pm 1.2$ at $p = 0.95$, $f = 2$, $s^2 = 0.5$):

$$\hat{Y}_i = 44.9 + 25.3X_1 + 4.9X_2 + 14.9X_3 + 8.5X_1X_3. \quad (1)$$

In Eq. (1), the pair interaction effect X_1X_3 proved to be significant, in agreement with the local optimum of the DNPH–PBQ condensation, which is determined primarily by the concentration of protons and temperature X_3, and to a lesser extent by the reaction time X_2. This corresponds to the reaction mechanism analogous to that describing the influence of strong acid protons [1, 3] in accordance with the reactions

$$RR'CO + H^+ \rightleftarrows RR'(OH)C^+, \quad (2)$$

* Manufactured by the Staraya Russa Chemical Machine Building Plant.

1070-4272/03/7604-0566 $25.00 © 2003 MAIK "Nauka/Interperiodica"

$$Ph(NO_2)_2NHNH_2 + RR'(OH)C^+ \rightleftarrows [Ph(NO_2)_2NHNH_2C(OH)RR']^+, \quad (3)$$

$$[Ph(NO_2)NHNH_2C(OH)RR'] \rightleftarrows RR'C{=}NNHPh(NO_2) + H^+ + H_2O. \quad (4)$$

The significance of the time factor X_2 is determined by the fact that the reactions are diffusion-controlled and occur at the DNPH | DNPHN | PBQ | water interface in the pulp of the reaction mass, which is saturated with protons, after the necessary degree of hydrolysis of carbon dioxide by the reaction

$$CO_2 + H_2O \rightleftarrows H^+ + HCO_3^- \rightleftarrows 2H^+ + CO_3^{2-} \quad (5)$$

is attained under the optimal conditions as determined by the X_1 and X_3 factors.

The process becomes predominantly kinetically controlled [reactions (2)–(4)] under conditions of vigorous stirring, which continuously renew the DNPH solid particle surface, thereby making it accessible to an attack by protonated molecules of the carbonyl derivative dissolved in water. Thus, DNPHN (a loose product formed on the DNPH particle surface) is removed from the reaction zone owing to constant abrasive collisions of the DNPH particles getting overgrown with a DNPHN layer.

The behavior of the response surface was visualized as the geometric image of the pair interaction [4, 5], using the regression equation

$$\hat{Y}_i = 45 + 25X_1 + 15X_3 + 9X_1X_3, \quad (6)$$

incorporating significant effects of factors entering into the X_1X_3 pair interaction.

The 3D diagram of the response surface of the X_1X_3 pair interaction effect presented in the figure suggests the following.

(1) When the X_1 factor changes from the lower (X_1^- = 5 MPa) to upper (X_1^+ = 20 MPa) level at fixed lower level (X_3^- = 0.5 h) of the X_3 factor, the response changes by $\Delta\hat{Y}_1 = |\hat{Y}_1 - \hat{Y}_2| = 32\%$, i.e., the product yield grows by 32% when the carbon dioxide pressure is raised, owing to an increase in the concentration of protons in the reaction mass via reaction (5).

(2) When the X_1 factor changes from the lower (X_1^- = 5 MPa) to upper (X_1^+ = 20 MPa) level at fixed higher level (X_3^+ = 1 h) of the X_3 factor, the response changes by $\Delta\hat{Y}_3 = |\hat{Y}_3 - \hat{Y}_4| = |12 - 80| =$ 68%, i.e., the product yield increases by 68% (in proportion to the doubled reaction time). This suggests the rates of reactions (2)–(4) are invariable for a given chemical system under the chosen synthesis conditions.

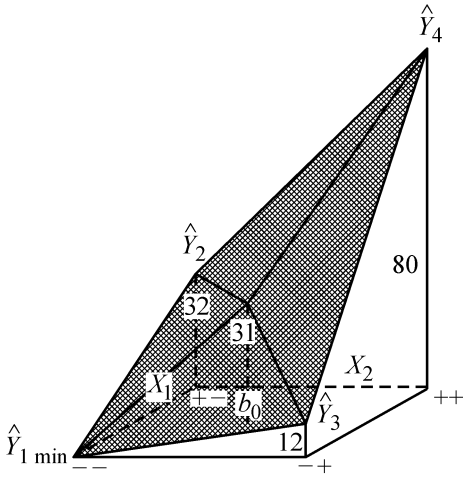

3D diagram of the response surface for X_1X_3 pair interaction. $b_0 = \hat{Y}_0 - \hat{Y}_{\min} = 45 - 14 = 31$. $\hat{Y}_i$ = 12, 32, 80.

(3) When the X_3 factor changes from the lower (X_3^- = 0.5 h) to upper (X_3^+ = 1 h) level at fixed lower level (X_1^- = 5 MPa) of the X_1 factor, the response changes by $\Delta\hat{Y}_2 = |\hat{Y}_1 - \hat{Y}_3| = |0 - 12| =$ 12%, i.e., the product yield increases by 12% only, owing to a low concentration of protons under decreased carbon dioxide pressure and to insufficient shift of equilibrium (5) to the right.

(4) When the X_3 factor changes from the lower (X_3^- = 0.5 h) to upper (X_3^+ = 1 h) level at fixed higher level (X_1^+ = 20 MPa) of the X_1 factor, the response changes by $\Delta\hat{Y}_4 = |\hat{Y}_2 - \hat{Y}_4| = |80 - 32| =$ 48%, i.e., the product yield increases by 48%, which is virtually proportional to the reaction time doubled for chemical reactions (2)–(4).

Thus, the interaction of the upper levels of factors X_1X_3 ensures the optimal influence of these factors on the product synthesis. This can be accounted for by a strong shift to the right of the equilibrium in reaction (2), owing both to an increase in the carbon dioxide pressure and, hence, in the proton concentration [reaction (5)] and to rise in temperature, which favors reactions (3) and (4). This stabilizes the shift of the equilibria of reactions (2), (3), and (5) at a level at which the main reaction (4) proceeds in the optimal regime with high yield of *p*-quinonemono-2,4-dinitrophenylhydrazone (99.95%).

The experimental results for DNPH–PBQ condensation under the optimal conditions we found were extended to some other commercial aliphatic and aromatic carbonyl derivatives. The yields of the corresponding 2,4-dinitrophenylhydrazones (% of the theoretical value) were as follows: anisaldehyde 99.7, acetone 99.2, benzaldehyde 99.5, isobutyraldehyde 99.6, methyl ethyl ketone 99.2, *m*-nitrobenzaldehyde 99.4, salicylicaldehyde 99.3, and cyclohexanone 99.5.

CONCLUSIONS

(1) A full-factorial experiment on condensation of 2,4-dinitrophenylhydrazine with *p*-benzoquinone to *p*-quinone mono-2,4-dinitrophenylhydrazone suggests that synthesis of hydrazones can be catalyzed by protons of carbonic acid formed in the aqueous pulp of the reaction mass via hydrolysis of dissolved carbon dioxide under a pressure of the CO_2–H_2O steam–gas mixture.

(2) The optimal conditions were found for synthesis of *p*-quinone mono-2,4-dinitrophenylhydrazone: pressure $P \geq 2.5$ MPa, temperature $T \geq 80$°C, condensation time $\tau \geq 1$ h.

(3) The 3D diagram of the response surface and the revealed regression effect of the X_1X_3 pair interaction (total pressure of the steam–gas mixture in the autoclave X_1 and the reaction mass temperature X_3) confirms that the proton catalysis mechanism of condensation of 2,4-dinitrophenylhydrazine with *p*-benzoquinone is similar to that revealed previously for strong inorganic and organic acids.

(4) The condensation reaction studied is suitable for synthesizing 2,4-dinitrophenylhydrazones from aliphatic and aromatic carbonyl derivatives in high yield (99.3–99.7%).

REFERENCES

1. Eremeev, A.P., Belyaeva, E.M., and Golounin, A.V., *Zavod. Lab.*, 1986, vol. 52, no. 10, pp. 61–62.
2. Hicks, Ch.R., *Fundamental Concepts in the Design of Experiments*, New York: Holt, Rinehart, and Winston, 1973.
3. Eremeev, A.P. and Belyaeva, E.M., *Kontrol' mekhanizma protsessa parnymi vzaimodeistviyami* (Control of the Mechanism of the Process by Pair Interactions), Available from ONIITEKhIM, Cherkassy, March 3, 1980, no. 865-khp-D80.
4. Eremeev, A.P., *Posledovatel'noe planirovanie khimicheskogo eksperimenta s ispol'zovaniem fiziko-khimicheskoi interpretatsii effektov parnykh vzaimodeistvii* (Successive Designing of a Chemical Experiment Using Physicochemical Interpretation of Pair Interaction Effects), Available from VINITI, Moscow: November 16, 1981, no. 5245–81.
5. Eremeev, A.P., *Zh. Prikl. Khim.*, 1980, vol. 53, no. 5, pp. 1134–1135.

Russian Journal of Applied Chemistry, Vol. 76, No. 4, 2003, pp. 569–571. Translated from Zhurnal Prikladnoi Khimii, Vol. 76, No. 4, 2003, pp. 589–591.

ENVIRONMENTAL PROBLEMS OF CHEMISTRY AND TECHNOLOGY

Low-Selective GaAs and GaSb Semiconductor Sensors for Potentiometric Analysis of Liquid Media

Yu. G. Vlasov, V. A. Burakhta, and Yu. E. Ermolenko

St. Petersburg State University, St. Petersburg, Russia

Received February 13, 2003

Abstract—The possibility of using low-selective sensors based on gallium arsenide and gallium antimonide semiconductor compounds as indicators in acid–base, precipitating, and complexometric titration in model multicomponent systems and natural water was studied.

Chemical sensors can be used as a convenient analytical tool in comprehensive ecological monitoring of the environment [1].

At present, the design of chemical sensors is heading in several directions consisting in fabrication of increasingly selective sensors, on the one hand, and development of a multisensor approach employing low-selective sensors, on the other [2]. In analysis of multicomponent systems, to which environmental objects mostly belong, high-selective sensors pose certain difficulties associated with their insufficient selective [2]. Use of a multisensor system of the "electronic tongue" type, which combines an array of various low-selective sensors with high cross sensitivity, enables successful multicomponent quantitative analysis of complex liquids, e.g., technological electrolyte solutions [3]. The created multisensor systems with chalcogenide-glass electrodes characterized by high stability and reproducibility have been tested on model solutions in order to enable their further use in determining heavy-metal cations (Cu^{2+}, Zn^{2+}, Pb^{2+}, and Cd^{2+}) and inorganic anions (Cl^-, F^-, and SO_4^{2-}) in natural and waste water [4, 5]. Use of different sensors in combination with mathematical processing of signals by the image recognition procedure employing, e.g., artificial neural networks makes it possible to overcome the problem of sensor selective, which predominates in analysis of multicomponent solutions in the presence of a great number of interfering ions.

Another promising approach to solving the low selective problem is to use a single semiconductor sensor sensitive to a number of ions for determining several components in complex aqueous systems, with the known methods of potentiometric titration employed.

This study is concerned with the possibility of applying single low-selective semiconductor sensors and methods of potentiometric titration for analyzing such complex solutions as natural water.

EXPERIMENTAL

Potentiometric titration was performed on an EV–74 ion-meter. An EVL–IM3 silver chloride electrode served as reference. As indicator electrodes were studied electrochemical sensors based on semiconductor compounds gallium arsenide (GaAs) and gallium antimonide (GaSb), fabricated in the form of solid contact electrodes. The semiconductor compounds were single crystals grown by the Czochralski technique [6]. When passing in potentiometric titration from one type of ions to another, the electrodes were polished with thin emery paper, washed with distilled water, and wiped dry with filtering paper. Between measurements, the electrodes were stored in air. It has been found previously in preliminary experiments that GaAs and GaSb semiconductor sensors are sensitive in solutions to different ions and, consequently, are low-selective sensors.

For comparison, ion-selective electrodes based on heavy-metal chalcogenides: silver-selective electrode AgSE with Ag_2S membrane, copper-selective electrode CuSE with Ag_2S–CuS membrane, chloride-selective electrode ClSE with Ag_2S–AgCl membrane, and ESL–63–07 glass electrode were also used as indicator electrodes.

1070-4272/03/7604-0569 $25.00 © 2003 MAIK "Nauka/Interperiodica"

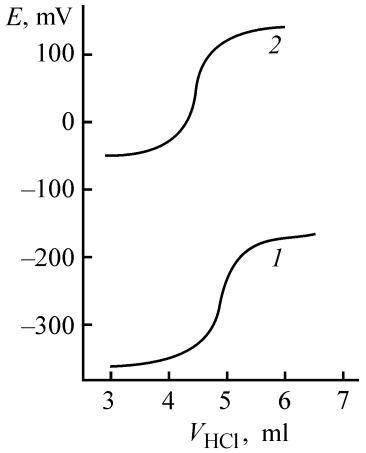

Fig. 1. Curves of potentiometric titration of a $NaHCO_3$ standard solution with a 0.1 N HCl solution (*1*) GaSb sensor and (*2*) glass electrode. (*E*) Potential and (V_{HCl}) titrant volume; the same for Fig. 2.

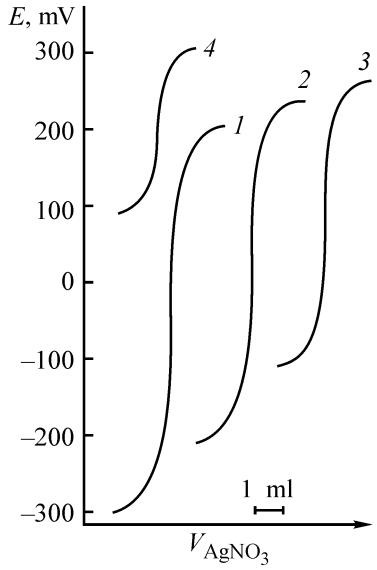

Fig. 2. Curves of potentiometric titration of KCl model solution with a 0.1 N $AgNO_3$ solution, with (*1–3*) GaAs electrode and (*4*) ClSE. Titration: (*1*) first, (*2*) second, and (*3*) third.

As model solution for potentiometric titration served 0.1 N solutions of $NaHCO_3$, KCl, and EDTA, prepared from fixanals. As titrants were used 0.1 N solutions of HCl, $AgNO_3$, and $CuSO_4$.

The possibility of using semiconductor sensors as indicators in acid–base titration was studied with standard solutions of sodium hydrocarbonate. An ESL–63–07 glass electrode served as a standard. The curves of potentiometric titration of a $NaHCO_3$ solution with a 0.1 N HCl solution, shown in Fig. 1, exhibit pronounced potential jump near the final titration point for both glass and GaSb indicator electrodes, with the titration curve measured using a GaSb electrode shifted toward negative potentials. The magnitudes of the potential jumps are the same for both types of electrodes, i.e., semiconductor sensors can be used along with the conventional glass electrodes.

It was established for gallium arsenide and gallium antimonide indicator electrodes used to determine chloride ions by precipitating titration with $AgNO_3$ solution that the end point of titration is clearly recorded with a GaAs electrode. Titration of KCl model solutions can be considered as an example (Fig. 2). As seen, the potential jump corresponding to chloride ions is the most pronounced for sensors with freshly polished surface (curve *1*). When a sensor is used for titration of chloride ions for the second time without preliminary polishing, the titration curve (curve *2*) shifts to more positive potentials, which is a characteristic of a chloride-selective electrode (curve *4*).

After third titration of a KCl solution with $AgNO_3$ solution, using a GaAs electrode having unfreshened surface, the titration curve is shifted to even greater extent to the range of positive potentials, with the magnitude of the potential jump approaching that for ClSE (curve *3*). After three or four successive titrations with GaAs electrode having unpolished surface, the magnitude of the potential jump becomes virtually constant and the titration curve remains in a strictly fixed range of potentials from –150 to +250 mV. When the surface of the semiconductor electrode is freshened with thin emery paper, the first part of the titration curve, which corresponds to the reaction $Cl^- + Ag^+ \rightarrow AgCl\downarrow$, is again markedly shifted to negative potentials to –300 mV. In the course of titration, Ag^+ and Cl^- ions are chemisorbed to give a poorly soluble compound AgCl on the surface. The thus self-modified GaAs sensor ensures a stable potential jump near the end point of titration. The magnitude of this jump exceeds that for the chloride-selective electrode by a factor of 2, which makes it possible to determine the end of titration with high accuracy.

The sensors based on GaAs and GaSb semiconductor compounds were studied in a complexometric titration. The potential jumps obtained for a standard EDTA solution titrated with 0.1 N $CuSO_4$ solution with the semiconductor sensors and the conventional copper-selective electrode do not differ significantly. The potentiometric titration curves measured for an EDTA solution with GaAs and GaSb electrodes are well reproducible, which allows reliable identification of the end point of titration.

The possibility of using GaAs and GaSb semiconductor sensors as indicator electrodes for potentiometric, acid–base, and complexometric titration, which was established on model solutions, made it possible to test them in multicomponent aqueous systems, to which belongs natural water. The determination of HCO_3^-, Cl^-, and SO_4^{2-} in natural water, which is an integral part of ecological analytical monitoring, is commonly performed in laboratory with glass, chloride-selective, and sulfate-selective electrodes, respectively [7]. GaAs and GaSb sensors were tested in determining major anions in river water. Bicarbonates and chlorides were determined by direct titration with 0.1 N solution of HCl and $AgNO_3$, respectively. Sulfate ions were determined by back titration after their precipitation with a barium salt solution and dissolution in an ammonia solution of EDTA [8]. The excess amount of EDTA solution was back-titrated with a 0.1 N solution of $CuSO_4$. The results obtained in determining the main anions in water of the Drakul River (Kazakhstan) are listed in the table. As seen, the determination of HCO_3^-, Cl^-, and SO_4^{2-} ions with sensors based on GaAs and GaSb semiconductor compounds is characterized by sufficient accuracy and good reproducibility. The results obtained with the conventional ion-selective electrodes and semiconductor sensors are in good agreement. However, in the latter case, sensors ensure a more reliable determination of the end point of titration.

Results of determination of anions in water of the Drakul River (n = 5, P = 0.95)

Anion	Titrant	Electrode	Found, mg l^{-1}
HCO_3^-	HCl	GaSb	212 ± 3
		ESL-63-07	214 ± 3
Cl^-	$AgNO_3$	GaAs	223 ± 2
		ClSE	224 ± 3
SO_4^{2-}	$CuSO_4$	GaAs	108 ± 6
		CuSE	104 ± 5

Thus, the properties of low-selective sensors based on semiconductor compounds were used to determine several components in natural water by acid–base, precipitating, and complexometric titration. Unlike direct potentiometry, the given method does not require use of highly selective sensors.

CONCLUSIONS

(1) It is established that low-selective sensors based on gallium arsenide and gallium antimonide semiconductor compounds can be used as indicators for acid–base, precipitating, and complexometric titration.

(2) The possibility of using semiconductor sensors for determining HCO_3^-, Cl^-, and SO_4^{2-} ions in multicomponent systems, including natural water, is demonstrated.

(3) It is proposed to use a single low-selective semiconductor sensor for determining several components in natural water, which is convenient from the standpoint of unification of analytical procedures.

ACKNOWLEDGMENTS

The study was supported in part by the Russian Foundation for Basic Research (project no. 02-03-32 740), Foundation of the Ministry of Education for Basic Research in the Field of Natural and Exact Sciences (project no. E02-5.0–85), and by the Russia's Federal Program "Integratsiya" (project no. B 0028).

REFERENCES

1. Afanas'ev, Yu.A., and Fomin, S.A., *Monitoring i metody kontrolya okruzhayushchei sredy* (Methods for Monitoring of the Environment), Moscow: MNEPU, 1998.
2. Vlasov, Yu.G. and Legin, A.V., Abstracts of Papers, *I Vserossiiskaya Konferentsiya "Analiticheskie pribory"* (I All-Russia Conf. "Analytical Devices") St. Petersburg, 2002, p. 69.
3. Vlasov, Yu.G. Ermolenko, Yu.E., Legin, A.V., and Murzina, Yu.G., *Zh. Anal. Khim.*, 1999, vol. 54, no. 5, pp. 542–549.
4. Vlasov, Yu.G., Legin, A.V., Rudnitskaya, A.M., *et al.*, *Zh. Anal. Khim.*, 1997, vol. 52, no. 11, pp. 1199–1205.
5. Vlasov, Yu., Legin, A., and Rudnitskaya, A., *Anal. Bioanal. Chem.*, 2002, vol. 373, no. 3, pp. 136–146.
6. *Metallurgiya i technologiya poluprovodnikovykh materialov* (Metallurgy and Technology of Semicondutor Materials), Sakharov, B.A., Ed., Moscow: Metallurgiya, 1972.
7. *Ionometriya v neorganicheskom analize* (Ionometry in Inorganic Analysis), Demina, L.A., Krasnova, N.B., Yurishcheva, B.S, and Chupakhina, M.S., Eds., Moscow: Khimiya, 1991.
8. Williams, W.J., *Handbook on Anion Determination*, London: Butterworths, 1979.

Russian Journal of Applied Chemistry, Vol. 76, No. 4, 2003, pp. 572–576. Translated from Zhurnal Prikladnoi Khimii, Vol. 76, No. 4, 2003, pp. 592–596.

ORGANIC SYNTHESIS AND INDUSTRIAL ORGANIC CHEMISTRY

High-Energy-Capacity Cobalt(III) Tetrazolates

A. Yu. Zhilin, M. A. Ilyushin, I. V. Tselinskii, A. S. Kozlov, and I. S. Lisker

St. Petersburg State Technological Institute, St. Petersburg, Russia
Agrophysical Institute, St. Petersburg, Russia

Received May 30, 2002

Abstract—Physicochemical and explosive properties of cobalt(III) tetrazolate perchlorate complexes were studied. The spectrophotometical properties of these complexes in the solid state and their sensitivity to laser radiation were examined.

Tetramminebis(5-nitrotetrazolato)cobalt(III) perchlorate **I** is used as an explosive in priming charges (PCs) initiated with a laser diode (λ = 800 nm, E_{beam} = 0.5 mJ) [1, 2]. Both **I** and its analogs are promising photosensitive compounds since they are safer than conventional primers used in laser detonators [3]. This study is concerned with a series of tetraminetetrazolato Co(III) perchlorates with the general formula

$$[Co(NH_3)_4(Tz)_n](ClO_4)_m,$$

n = 2, m = 1 (**I**–**IV**); n = 1, m = 1 (**V**); n = 2, m = 3 (**VI, VII**);

Tz = 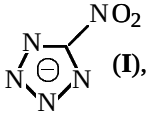 **(I)**, 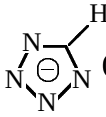 **(II)**, 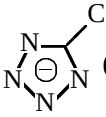 **(III)**, 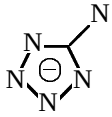 **(IV)**, 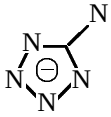 **(V)**, 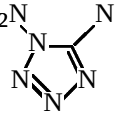 **(VI)**, 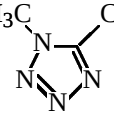 **(VII)**.

Compounds **I**–**VII** were prepared by the reaction

$$\underset{\textbf{VIII}}{[Co(NH_3)_4(H_2O)_2](ClO_4)_3} + n\text{Tz} \xrightarrow[95^\circ C,\ 4\ h]{HClO_4/H_2O,\ pH < 2,} \underset{\textbf{I–VII}}{[Co(NH_3)_4(Tz)_n](ClO_4)_m} + 2H_2O. \quad (1)$$

The complexes are crystalline compounds soluble in water, DMSO, DMF and difficulty soluble in ethanol, isopropanol, and isobutanol. Their physicochemical and explosive characteristics are summarized in the table.

The densities of Co(III) tetramine complexes were calculated as sums of molecular increments of structural fragments with average error of ±0.04 g cm^{-3}. To determine the detonation rate of **I**–**VII**, their molecules were divided into active (perchlorate anion and the ligands) and inert (metal cation) parts. The detonation rate was calculated from these increments with average error of ±140 m s^{-1} [4].

Thermolysis of **I**–**VII** was studied under nonisothermal conditions at a heating rate of 5 deg min^{-1}. These compounds are relatively thermostable since their T_{oid} temperature is higher than 230°C. In the first stage of thermolysis of tetrazolatotetrammine cobalt(III) perchlorates, the inner coordination sphere of this complex degrades with elimination of ammonia. Then tetrazole ligands are thermally decomposed with their stepwise oxidation by outer-sphere perchlorate anions [5]. The thermal analysis curves of **I** and **VII** contain a broad exothermic peak corresponding to simultaneous occurrence of these steps. Clearly, in this case, the energy liberation is at a maximum and the energy loss, at a minimum. As a result, the combustion–detonation transition for **I** and **VII** is the fastest. For **II** and **IV**, the three thermolysis steps are separated in time. The total exothermic effect is lower owing not only to endothermic elimination of ammonia, but also to removal of the fuel from the reaction zone. A nonstoichiometric ratio of the fuel and oxidizing agent may result in

1070-4272/03/7604-0572 $25.00 © 2003 MAIK "Nauka/Interperiodica"

Physicochemical and explosive characteristics of (tetramminetetrazolato)cobalt(III) perchlorates

Property	Compound						
	I	**II**	**III**	**IV**	**V**	**VI**	**VII**
Density, ρ, g cm^{-3}	1.97*	1.86	1.75	1.81	1.90	1.85	1.90*
Detonation rate D$^{\rho}$, km s^{-1}	8.1	6.9	6.8	6.7	7.1	7.3	7.5
Onset temperature of intense decomposition T_{oid}, °C	234	239	252	242	238	233	234
Shock sensitivity H_{25}/cm, %**	8	64	–	14	10	32	8
Minimal priming charge (MIC), g	0.05	0.45	0.30	0.50	0.40	0.35	0.15

* Experimental values.

** Load 2 kg, sample weight 20 mg.

additional heat loss and longer combustion–detonation transition, which is actually the case (see table). In thermolysis of **III**, **V**, and **VI**, the pattern is intermediate between those observed with **I**, **VII** and **II**, **IV**.

The kinetic parameters of thermolysis of **I**–**VII** at T_{oid} were calculated from the T–TG, T–DTG, and T–DTA curves. The preexponential factor in the Arrhenius equation, activation energy (kJ mol^{-1}), and reaction order are 18.5, 212.2, 0.5; 18.8, 228.6, 0.5; 16.7, 204.7, 1.0; 26.3, 293.3, 0.5; 17.6, 231.6, 1.0; 17.4, 204.6, 1.0; and 18.6, 218.3, 1.0, respectively. The fact that the reaction order of thermolysis is lower than unity (n = 0.5) is presumably due to occurrence of the reaction at the interface between sample and the reaction product and the influence of the crystal lattice on the diffusion of the reaction products [6]. The reaction order equal to 1.0 indicates that thermolysis is not hindered by diffusion factors.

The IR spectra of **I**–**VII** contain absorption bands associated with coordinated ammonia, substituents in the heterocyclic ring, tetrazole ring, and outer-sphere perchlorate anion.

The electronic absorption spectra of **I**–**VII** in aqueous solutions are typical of this type of compounds [7] and contain the *d*–*d* band of $^1T_{1g} \leftarrow {}^1A_{1g}$ transition. The other strong band ($^1T_{2g} \leftarrow {}^1A_{2g}$) is overlapped by the absorption of the tetrazole ligand. Clearly, these complexes contain the octahedral chromophore CoN_6.

The ^{1}H NMR spectra of all the compounds except **III** contain signals of equatorial (in low field) and ax. (in high field) ammonia ligands in the range 3.4 –4.3 ppm. In the spectrum of **III**, the ammonia ^{1}H signal is not split, probably owing to *trans* configuration of the complex. The different chemical shifts of the equatorial and ax. ammonia molecules are consistent with coordination of the heterocyclic ligands via nitrogen atoms [8]. The splitting of these signals into a doublet is due to nonequivalence of the ammonia protons. This splitting is caused by coordination of the tetrazole ring via different atoms: N^1 and N^2 in **II** and **IV** [9], N^1 and O of one of the nitro groups in **V** (5-nitroaminotetrazole is coordinated in the bidentate manner) [10], and N^3 and N^4 in **VI** and **VII** [11]. The tetrazole ligands of **I** are coordinated only via the N^2 atom [12].

We also studied the sensitivity of pressed powders of the explosives to a single pulse of neodymium solid-state laser (λ = 1.06 μm, τ_q = 2 ms, E = 1.5 J, d_{beam} = 1 mm). The results obtained are listed below.

Compound	Effect
I	Detonation
II	Combustion
III	Failure
IV	Detonation
V	Failure
VI	Detonation
VII	Failure

The modern concept of initiation of explosives with pulsed laser radiation is based on the ignition at centers formed upon hypothesis of radiation absorption by optical microheterogeneities in separate crystals [3]. In this context, a spectral study of the primers in the wavelength range used in industrial lasers (visible and near-IR region, ruby laser operating at 690 nm and neodymium laser operating at 1060 nm) is of not only theoretical, but also practical interest.

We recorded optical spectra of crystalline complexes **I**–**III** and **IV** (in pellets). First we recorded the spectra of **I** and **II**. Since the influence of the material brought in contact with primers in priming charges (PCs) is of practical interest, pellets of the compounds examined were placed on a copper support (Figs. 1, 2).

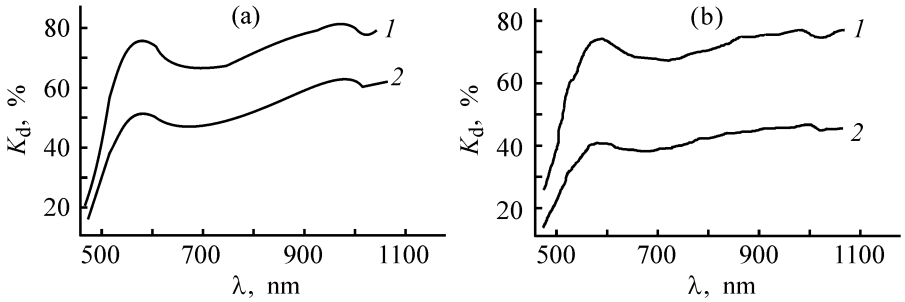

Fig. 1. Diffuse reflectance spectra of (a) **I** and (b) **II**. (K_d) Diffuse reflectance coefficient and (λ) wavelength. (*1*) No support and (*2*) on a support; the same for Fig. 2.

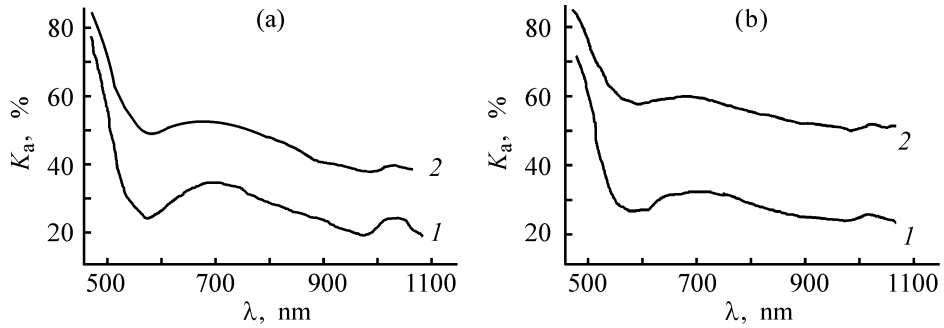

Fig. 2. Electronic absorption spectra of (a) **I** and (b) **II** (K_a) Absorption coefficient and (λ) wavelength.

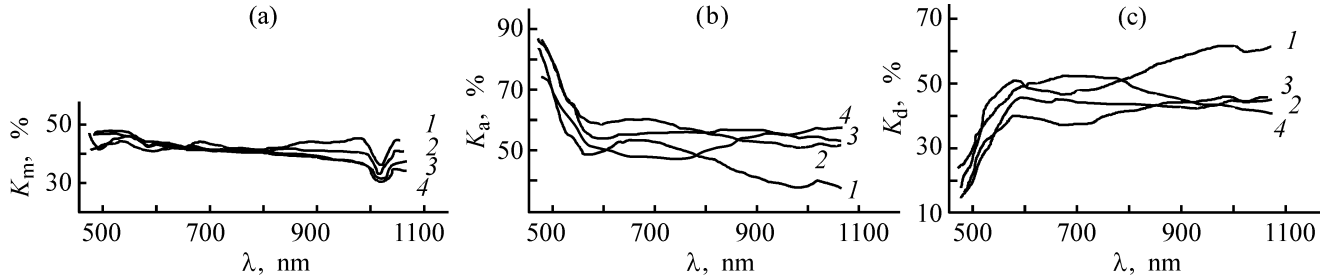

Fig. 3. (a) Mirror reflectance, (b) absorption, and (c) diffuse reflectance spectra of (*1*) **I**, (*2*) **II**, (*3*) **III**, and (*4*) **VI** on a support. (K_m, K_a, K_d) Coefficeints of mirror reflectance, absorption, and diffuse reflectance, respectively; (λ) wavelength.

As seen from Figs. 1 and 2, compounds **I** and **II** behave similarly under exposure to radiation in the whole spectral range, including the wavelength of the neodymium laser (1060 nm). In all cases, the copper support affects the spectral properties. To confirm this result, we also recorded the spectra of **III** and **VI** (Figs. 3a–3c).

As seen from Figs. 3a–3c, the initiation threshold of the crystalline primers is independent of the wavelength of the initiating light. However, it is necessary to study the influence of the particle size distribution and the type of interparticle cohesion on initiation of these explosives. Laser initiation of the complexes was performed with assistance of V.V. Blagoveshchenskii.

Thus, the (tetraminetetrazolato)cobalt(III) perchlorates can be used as primers both in conventional priming charges and in optically initiated priming charges of high safety.

EXPERIMENTAL

The IR spectra of crystalline **I**–**VII** (Nujol or fluorinated oil mulls between KBr windows) were recorded on a Perkin–Elmer M457 spectrometer.

The UV spectra were recorded on a Perkin–Elmer LAMBDA 40 spectrometer in 1-cm quartz cells (analytical concentration 10^{-1}–10^{-2} M).

The ^{1}H NMR spectra were recorded on a Bruker AC (300 MHz) spectrometer using DMSO-d_6 as solvent and hexamethyldisiloxane (HMDS) as internal reference.

Synthesis of **I**–**VII** was monitored by thin-layer chromatography on Silufol UV-254 plates, using 3%

sodium perchlorate as eluent. A thermal gravimetric analysis was performed on an MOM derivatograph (Hungary) in the range 20–500°C at a heating rate of 5 deg min^{-1}. The onset temperature of intense decomposition, T_{oid}, was determined on a thermograph at a heating rate of 5.3 deg min^{-1}. The sensitivity to shock was determined by the pile-driving procedure performed in accordance with GOST (State Standard) 1944–80. The minimal primer charge (MPC) of the complexes was determined with respect to hexogen in the geometry of detonating cap (DC) no. 8 (compaction pressures P_c of the compound and hexogen were 121 and 363 kg cm^{-2}, respectively).

The optical properties of the solid compounds were studied on SPEFOT spectrophotometric unit described in [13].

Diaquatetramminecobalt(III) perchlorate **VIII** prepared by the procedure described in [14] was used in further synthesis without isolation from the solutions.

Tetramminebis(5-nitrotetrazolato)cobalt(III) perchlorate I and **tetramminebis(1-methyl-5-aminotetrazole)cobalt(III) perchlorate VII** were prepared by the procedure described in [15] in 54 and 51% yields, respectively. Compound **I**. IR spectrum, cm^{-1}: 1588 m, 1316 m (NH_3, Tz), 1076 m (ClO_4), 1540 m (NO_2). UV spectrum, λ_{max} = 456 nm, ε = 74 l cm^{-1} mol^{-1}. ^1H NMR spectrum (DMSO-d_6), δ, ppm: 3.79, 4.29 (12H, NH_3).

Found, %: C 4.8, H 2.3, N 42.6.

$C_2H_{12}ClCoN_{14}O_8$.

Calculated, %: C 5.3, H 2.7, N 43.1.

Compound **VII**. IR spectrum, cm^{-1}: 3316 m, 1334 m (NH_3, Tz), 1118 m (ClO_4), 1628 m (C=N), 3236 w, 1616 w (NH_2), 2830 w (CH_3). UV spectrum, λ_{max} = 466 nm, ε = 77 l cm^{-1} mol^{-1}. ^1H NMR spectrum (DMSO-d_6), δ, ppm: 3.85, 3.90 (9H, NH_3 eq.); 3.75, 3.80 (3H, NH_3 ax.); 7.12 (2H, NH_2–Tz, ax.), 7.52 (2H, NH_2–Tz eq.); 4.03 (3H, CH_3–Tz ax.), 4.22 (3H, CH_3–Tz eq.).

Found, %: C 7.8, H 3.3, N 31.9.

$C_4H_{22}Cl_3CoN_{14}O_{12}$.

Calculated, %: C 7.7, H 3.6, N 31.5.

Published procedures were used to prepare tetrazole [16], 5-methyltetrazole [17], 5-nitroaminotetrazole [18], 5-aminotetrazole [19], and 1,5-diaminotetrazole [20]. The physicochemical properties of the compounds agreed with published data.

Tetramminebis(trazolato)cobalt(III) perchlorate II, tetramminebis(5-methyltetrazolato)cobalt(III) perchlorate III, tetramminebis(5-aminotetrazolato)-cobalt(III) perchlorate IV, tetrammine-5-nitroaminotetrazolatocobalt(III) perchlorate V, and **tetramminebis(1,5-diaminotetrazole)cobalt(III) perchlorate VI**. Carbonatotetramminecobalt(III) perchlorate (0.5 g) prepared by the procedure described in [21] was dissolved in 5% perchloric acid (15 ml) until CO_2 evolution stopped. The solution was filtered. An appropriate tetrazole derivative was added in 60% excess to the filtrate. The reaction mixture was heated on a boiling water bath for 4 h, cooled to 15°C, and poured into propan-2-ol (100 ml). The precipitate was filtered off and washed with two portions of ethanol (2 × 5 ml). Yield (60–65 %). Compound **II**. IR spectrum, cm^{-1}: 3320 m, 1329 m (NH_3, Tz), 3050 m (CH), 1094 ws (ClO_4). UV spectrum, λ_{max} = 454 nm, ε = 87 l cm^{-1} mol^{-1}. ^1H NMR spectrum (DMSO-d_6), δ, ppm: 4.00, 4.25 (9H, NH_3 eq.), 3.66, 3.85 (3H, NH_3 ax.), 6.90 (H, C–H, Tz ax.), 8.70 (H, C–H, Tz, eq.).

Found, %: C 6.7, H 4.1, N 45.7.

$C_2H_{14}ClCoN_{12}O_4$.

Calculated, %: C 6.6, H 3.9, N 46.1.

Compound **III**. IR spectrum, cm^{-1}: 3315 m, 1330 m (NH_3, Tz), 1101 s (ClO_4), 1450 s, 1370 s (CH_3). UV spectrum, λ_{max} = 455 nm, ε = 92 l cm^{-1} mol^{-1}. ^1H NMR spectrum (DMSO-d_6), δ, ppm: 3.74, (12H, NH_3 eq.), 2.52 (6H, CH_3–Tz ax.).

Found, %: C 6.7, H 4.1, N 45.7.

$C_4H_{18}ClCoN_{12}O_4$.

Calculated, %: C 6.6, H 3.9, N 46.1.

Compound **IV**. IR spectrum, cm^{-1}: 3318 m, 1312 m (NH_3, Tz), 3426 w, 1596 w (NH_2) 1084 m (ClO_4). UV spectrum, λ_{max} = 463 nm, ε = 80 l cm^{-1} mol^{-1}. ^1H NMR spectrum (DMSO-d_6), δ, ppm: 4.05, 4.25 (9H, NH_3 eq.), 3.45, 3.72 (3H, NH_3 ax.), 5.22 (2H, NH_2–Tz ax.), 6.87 (2H, NH_2–Tz, eq.).

Found, %: C 6.1, H 4.3, N 49.5.

$C_2H_{16}ClCoN_{14}O_4$.

Calculated, %: C 6.1, H 4.1, N 49.7.

Compound **V**. IR spectrum, cm^{-1}: 3320 s, 1308 m (NH_3, Tz), 1556 m (NO_2), 1340 m (C–N), 1110 s (ClO_4). UV spectrum, λ_{max} = 475 nm, ε = 63 l cm^{-1} mol^{-1}. ^1H NMR spectrum (DMSO-d_6), δ, ppm: 4.10, 4.50 (6H, NH_3 eq.), 3.45, 3.75 (6H, NH_3 ax.).

Found, %: C 3.8, H 3.9, N 39.6.

$CH_{12}ClCoN_{10}O_6$.

Calculated, %: C 3.4, H 3.4, N 39.5.

Compound **VI**. IR spectrum, cm^{-1}: 3321 m, 1332 m (NH_3, Tz), 1095 s (ClO_4), 1630 m (C=N), 3232 w, 1610 w (NH_2). UV spectrum, λ_{max} = 470 nm ε = 80 l cm^{-1} mol^{-1}. ^1H NMR spectrum (DMSO-d_6), δ, ppm: 4.00, 4.15 (9H, NH_3 eq.), 3.70, 3.78 (3H, NH_3 ax.), 6.20 [4H, $(NH_2)_2$–Tz ax.], 6.92 [4H, $(NH_2)_2$–Tz, eq.).

Found, %: C 3.8, H 3.6, N 35.9.

$C_2H_{20}Cl_3CoN_{16}O_{12}$.

Calculated, %: C 3.8, H 3.2, N 35.8.

REFERENCES

1. Merson, J.A., Salas, F.J., and Harlan, J.G., *Proc. Int. Pyrotech. Semin.*, 1994, vol. 19, pp. 191–206.
2. Fyfe, D.W., Fronabarger, J.W., and Bickes, R.W., Jr., *Proc. Int. Pyrotech. Semin.*, 1994, vol. 20, pp. 341–343.
3. Ilyushin, M.A., Tselinskii, I.V., and Chernai, A.V., *Ross. Khim. Zh.*, 1997, vol. 41, no. 4, pp. 81–88.
4. Ilushin, M.A., Smirnov, A.V., Kotomin, A.A., and Tselynsky, I.V., *Hanneng caliliao=Energ. Mater.*, 1994, vol. 2, no. 1, pp. 16–20.
5. Zhilin, A.Yu., Ilyushin, M.A., and Tselinskii, I.V., *Zh. Obshch. Khim.*, 2001, vol. 71, no. 5, pp. 710–713.
6. Kukushkin, Yu.N., Budanova, V.F., and Sedova, G.N., *Termicheskoe prevrashchenie koordinatsionnykh soedinenii v tverdoi faze* (Thermal Transformations of Coordination Compounds in the Solid Phase), Leningrad: Leningr. Gos. Univ., 1981.
7. Fronabarger, J., Schuman, A., Chapman, R.D., *et al.*, *AIAA Pap.*, 1995, no. 2858, pp. 1–7.
8. Sheng, D., Ma, F., Sun, F., and Lu, Q., *Hanneng caliliao=Energ. Mater.*, 2000, vol. 8, no. 3, pp. 100–103.
9. Moore, D.S. and Robinson, S.D., *Adv. Inorg. Chem.*, 1988, vol. 32, pp. 171–239.
10. Subba Rao, N.S.V., Ganorkar, M.C., Mohan Murali, B.K., and Ramaswamy, C.P., *Bull. Acad. Polon. Sci.*, 1979, vol. 27, no. 1, pp. 21–28.
11. Shilin, A.Yu., Ilyushin, M.A., Tselinskii, I.V., *et al.*, *Zh. Prikl. Khim.*, 2002, vol. 75, no. 11, pp. 1885–1888.
12. Morosin, B., Dunn, R.G., Assink, R., *et al.*, *Acta Crystallogr.*, 1997, Sect. C, vol. 53, pp. 1609–1611.
13. RF Patent no. 1673928.
14. Ilyushin, M.A., Lukogorskaya, A.S., Tselinskii, I.V., and Brykov, A.S., *Zh. Obshch. Khim.*, 1999, vol. 69, no. 3, pp. 449–451.
15. Zhilin, A.Yu., Ilyushin, M.A., Tselinskii, I.V., and Brykov, A.S., *Zh. Prikl. Khim.*, 2001, vol. 74, no. 1, pp. 96–99.
16. Gaponik, P.N. and Karavai, V.P., *Vestn. Belorus. Gos. Univ., Ser. 2*, (Minsk), 1980, no. 3, pp. 51–52.
17. Spear, R.J., *Aust. J. Chem.*, 1984, vol. 37, no. 12, pp. 2453–2468.
18. Mayants, A.G., *Khim. Geterotsikl. Soedin.*, 1969, no. 11, pp. 1569–1571.
19. Lavrenova, L.G., Larionov, S.V., Grankina, Z.A., and Ikorskii, V.N., *Izv. Sib. Otd. Akad. Nauk SSSR, Ser. Khim. Nauk*, 1983, nos. 2/1, pp. 81–86.
20. Gaponik, P.N. and Karavai, V.P., *Khim. Geterotsikl. Soedin.*, 1984, no. 12, pp. 1683–1686.
21. Novakovskii, M.S., *Laboratornye raboty po khimii kompleksnykh soedinenii* (Laboratory Works on Coordination Chemistry), Kharkov: Kharkov Univ., 1972.

Russian Journal of Applied Chemistry, Vol. 76, No. 4, 2003, pp. 577–581. Translated from Zhurnal Prikladnoi Khimii, Vol. 76, No. 4, 2003, pp. 597–601.

ORGANIC SYNTHESIS AND INDUSTRIAL ORGANIC CHEMISTRY

Thermal Reactions of Fullerene C_{60} with Iron(III) Acetylacetonate

V. G. Isakova, E. A. Petrakovskaya, A. D. Balaev, and T. A. Kolpakova

Kirenskii Institute of Physics, Siberian Division, Russian Academy of Sciences, Krasnoyarsk, Russia
Krasnoyarsk State Technical University, Krasnoyarsk, Russia

Received June 13, 2002; in final form, February 2003

Abstract—Thermal reaction of solid mixtures of fullerene C_{60} with iron(III) acetylacetonate proceeds in the combustion mode; the composition and characteristics of the reaction products are governed by the Fe : C_{60} ratio in the initial mixture. The magnetization of iron-fullerene complexes was measured.

Iron-fullerene derivatives attract the researchers' attention owing to the possibility of synthesis of new magnetic materials, catalysts, and biologically active compounds based on these derivatives. The characteristics of iron fulleride FeC_{60} and organometallic complexes of fullerene C_{60} with ferrocene and iron carbonyls have been studied most extensively [1–6]. Organometallic iron-fullerene complexes are synthesized by exchange reactions in organic solutions [5, 6]. Iron fulleride can be produced by chemical methods, e.g., by decomposition of ferrocene fullerene complexes [1], reactions in the gas phase [7], or direct synthesis of fullerene in arc discharge with the use of iron-containing graphite electrodes or $Fe(CO)_5$ medium [8]. Crystalline FeC_{60} exhibits superparamagnetic characteristics [1]. In [9], iron-fullerene complexes were produced in a flow of iron-doped carbon-helium plasma formed by a high-frequency ac electric arc. Iron powder or wire was placed in a hole of one of the electrodes. Iron-containing fullerene mixtures extracted from fullerene soot with organic solvents were used in synthesis of water-soluble iron-fullerene products having biological activity [10]. The possibility of synthesis of fullerene derivatives of *d*-transition metals by the reaction of fullerenes with metal acetylacetonates, proceeding in the combustion mode, was shown in [11, 12].

The aim of this study was to make a physicochemical analysis of characteristics of materials and compounds formed by thermal reaction of fullerene C_{60} with iron(III) acetylacetonate.

EXPERIMENTAL

Iron(III) acetylacetonate [$Fe(acac)_3$] used in this study was produced by the procedure described in [13]. Finely ground mixtures of fullerene C_{60}[1] (99.5%) with $Fe(acac)_3$ in stoichiometric ratios C_{60} : Fe 1 : 1, 1 : 2, and 1 : 5 (sample nos. 1, 2, and 3, respectively) were placed in quartz crucibles, which were closed with lids and heated to visual glowing of the substance. The clearance between the crucible and lid allowed removal of volatile products from the reaction area. After completion of the thermal reaction, the combustion products (CPs) were washed with boiling aqueous hydrochloric acid (1 : 5) and organic solvents (benzene and toluene) until colorness solutions were obtained.

Differential thermal analysis (DTA) was performed on an MOM Q-1000 derivatograph (Hungary) with heating of $Fe(acac)_3$ and sample no. 1 in air at a rate of 20 deg min^{-1} in crucibles covered with lids. The weighed portions were 40 mg. The clearance between the crucible and lid was 0.05–0.06 mm. The crucible was fully filled with a sample.

The ESR spectra were recorded on SE/X-2544 and RE-1308 spectrometers in the *X*- and *Q*-ranges at temperatures of 77–500 K. The substances were characterized by the linewidth ΔH and the position of the ESR signal (effective *g*-factor). The spectra of iron-containing products are not typical ESR spectra and differ from the spectra of ferromagnetic resonance in a bulk substance, so we used in this study the term EMR (electronic magnetic resonance). The analysis of magnetic characteristics was based on EMR data, Mössbauer spectroscopy, and measurements of magnetization of some characteristic synthesis products on a vibration magnetometer at 77–300 K. The X-ray

[1] Synthesized by A.V. Eletskii.

1070-4272/03/7604-0577 $25.00 © 2003 MAIK "Nauka/Interperiodica"

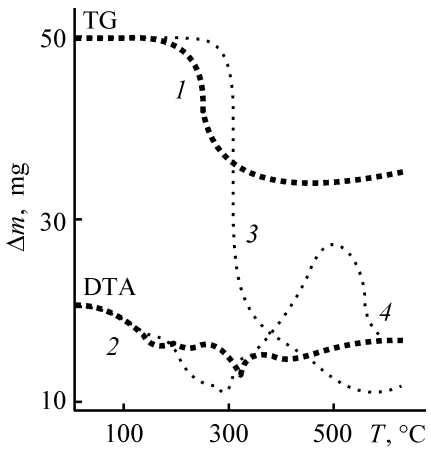

Fig. 1. TG and DTA curves of the initial C_{60}–$Fe(acac)_3$ mixture corresponding to (*1*, *2*) composition no. 1 and (*3*, *4*) $Fe(acac)_3$. (Δm) Weight change, and (T) temperature.

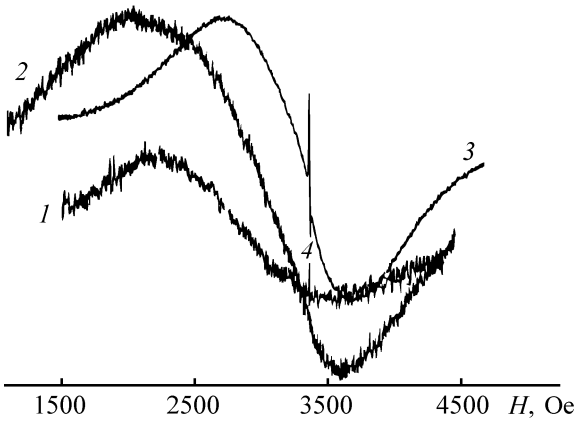

Fig. 2. EMR spectra of the samples of the initial composition 1 : 1. (*H*) Magnetic field strength, the same for Fig. 5. (*1*) C_{60}–$Fe(acac)_3$ mixture after keeping for 24 h at room temperature, (*2*) CP1, (*3*) CP1 treated with HCl, and (*4*) signal from C_{60} radical.

phase analysis was carried out on a DRON-2 equipment.

Heating of solid mixtures $C_{60}/Fe(acac)_3$ in air to 400°C and above, i.e., to temperatures exceeding the thermal decomposition point, results in ignition of reactants and is accompanied by complete loss of fullerene. Under the same conditions, free fullerene does not undergo noticeable transformations, and in the absence of fullerene, $Fe(acac)_3$ sublimes with insignificant decomposition. It is likely that combustion is a catalytic reaction. Fullerene C_{60} is able to chemisorb significant amounts of oxygen [14]; therefore, it can supply active oxygen initiating combustion. At the same time, it is well known that iron acetylacetonate exhibits catalytic ability in oxidation of organic compounds [15].

The DTA curves of sample no. 1 and $Fe(acac)_3$ are compared in Fig. 1. The experiments were carried out under conditions of limited air access. This was done by using crucibles covered with lids and filling the whole crucible volume with the substance. The thermal behavior of $Fe(acac)_3$ is typical of volatile metal acetylacetonates [13]. In the range 190–347°C, the TG and DTA curves correspond to sublimation and evaporation of $Fe(acac)_3$. At higher temperatures, there are two exothermic peaks in the DTA curves, corresponding to pyrolysis of the sample residue. At the same time, the weight loss of the reaction mixture $C_{60}/Fe(acac)_3$ begans at a temperature lower by 30°C than the temperature associated with weight loss of $Fe(acac)_3$ caused by sublimation. The weight loss at 230°C corresponds to the weight of acetylacetone released, apparently, by fullerene-catalyzed homolytic rupture of the bond of acetylacetonate ligand with Fe^{3+} ion and its reduction to Fe^{2+}. The total change in the weight of $C_{60}/Fe(acac)_3$ sample upon heating to 500°C corresponded to conversion of $Fe(acac)_3$ in the initial mixture to Fe_2O_3. With C_{60}, no noticeable weight variation was observed. The final product of heating of free $Fe(acac)_3$ to 500°C is also Fe_2O_3. However, at the temperature corresponding to the onset of thermal decomposition of $Fe(acac)_3$, the product of its pyrolysis is predominantly magnetite.

With account of the DTA data, thermal reactions of C_{60} with $Fe(acac)_3$ were carried out with limited air access. The initial mixtures $C_{60}/Fe(acac)_3$ were heated to a temperature corresponding to the onset of thermal decomposition of $Fe(acac)_3$. In this case, combustion proceeded in the nonequilibrium heterogeneous system $C_{60}/Fe(acac)_3$(solid)–$Fe(acac)_3$(vapor) without ignition, in the glowing mode. The combustion products of the initial mixture nos. 1–3 (CP1–CP3, respectively) were black magnetic powders. According to Mössbauer spectra these powders contain 83–97% magnetic heterogeneous phase similar to magnetite; the rest is paramagnetic. The amount of the paramagnetic phase and deviation of the parameters of the Mössbauer spectra from those of bulk magnetite increase with decreasing content of iron in the initial mixture.

The EMR spectrum of $Fe(acac)_3$ in the initial mixture of reactants is a broad symmetrical line with the parameters g_{eff} = 2.4 and line width 1400 Oe (Fig. 2, *1*). For fullerene C_{60}, the ESR line is characteristic of a radical center (Fig. 3, *1*); its nature was discussed, e.g., in [16]. For the C_{60} samples used in

this study, g = 2.0021 and ΔH = 1 Oe. The EMR spectra of samples CP2 and CP3 at 293 K are broad lines with effective g-factor much exceeding 2 (see table).

The spectra show that, at high content of $Fe(acac)_3$ in the initial sample, the magnetic properties of the products of the thermal reaction are determined predominantly by magnetite formed via thermal decomposition of $Fe(acac)_3$. Lowering the temperature to 77 K results in a considerable broadening of lines and a downfield shift. By contrast, heating to 500 K results in an upfield shift; in this case, the lines became narrower and more symmetrical. The variation of the resonance field and linewidth with temperature correspond to that for amorphous magnetics [17], whose magnetism is caused by the Fe^{3+} ion in octahedral positions with a typical set of nonequivalent distortions of the symmetry. Similar results were obtained for the temperature behavior of the EMR linewidth and resonance field in magnetic polymers [18]. By analogy with these data, and also with account of the results of Mössbauer spectroscopy, the products of thermal synthesis are nonequilibrium ferromagnetics. The ESR line of radical centers of fullerene C_{60} in these products is significantly broadened.

It has been shown previously [19] that the variation of the EMR linewidth with temperature in these systems is governed by fluctuations of magnetization. When the linewidth is determined by anisotropy, these fluctuations result in line narrowing with increasing temperature. The size of magnetic particles can be determined from the relationship

$$\Delta H = \Delta H_0 M_S V H_0 / 2kT,$$

where M_s is saturation magnetization; V, particle volume; k, Boltzmann constant; T, temperature; and ΔH and H_0, the linewidth of EMR signal and its position, respectively.

In the case of magnetite particles, the magnetization is 2400 G; the linewidth ΔH_0 and resonance field H_0 refer to 300 K. For the CP3 sample, the average particle size is 200 nm. Our measurements showed that an increase in the iron concentration results in line narrowing; hence, the particle size decreases and the crystal structure is disrupted. In this context, the absence of reflections characteristic of iron compounds in the X-ray patterns of samples CP1 and CP2 can be accounted for by the amorphous nature of fine particles. An X-ray phase analysis of sample CP3 revealed significantly broadened magnetite reflections.

Parameters of EMR spectra in the X-range for CPs of mixtures $C_{60}/Fe(acac)_3$ before and after treatment with HCl and C_6H_6

Combustion products of mixtures	g_{eff}	ΔH	C_{60} radical, ΔH
		Oe	
CP1	2.16	1000	2
CP2	2.2	1320	
CP3	2.4	1500	
CP1*	2.03	600	1.2
CP2*	2.04	800	2
CP3*	2.06	1300	5
CP2**	2.0337	600	1.5
CP3**	2.1	1300	4.5

* Treated with HCl.

** Treated with HCl and C_6H_6.

The EMR spectrum of sample CP1 is shown in Fig. 2, *2*. For this sample, the ESR signal from the C_{60} radical centers is observed. The transformations of this signal in the course of synthesis are shown in Fig. 3. The appearance of an additional line with g = 1.998 (Fig. 3, *2*), which corresponds to fullerene radical anion [14], suggests the formation of a complex of fullerene with iron acetylacetonate even at room temperature. Then, in the course of combustion, the organic part of the complexes burns out to form $Fe_nO_mC_{60}$.

Magnetic measurements demonstrated that, in the range 300–77 K, this substance is superparamagnetic

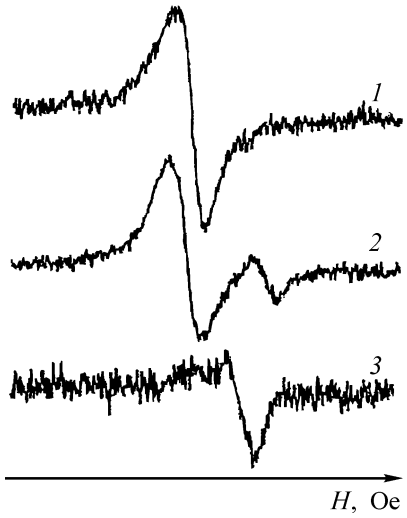

Fig. 3. ESR spectrum of C_{60} radicals in samples of the initial composition 1 : 1. (*H*) Magnetic field strength. (*1*) C_{60} radical of the initial mixture, (*2*) C_{60} radical and C_{60} radical anion after keeping the mixture for 24 h, and (*3*) mixture after thermal reaction.

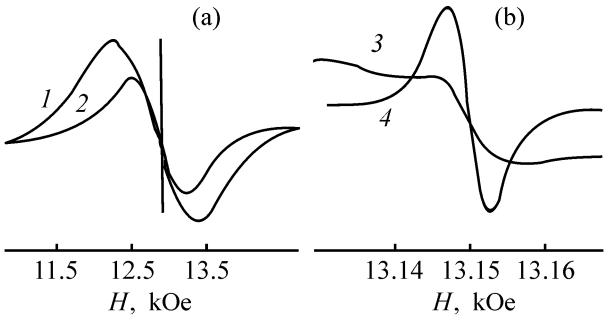

Fig. 4. Spectra of HCl-treated samples recorded in the *Q*-range. (*H*) Magnetic field strength. (a) EMR spectra and (b) single-out ESR lines of C_{60} radical. (*1*) sample CP3, (*2*) sample CP2, (*3*) C_{60} radical of sample CP3, and (*4*) C_{60} radical of sample CP2.

and its temperature and field dependences are similar to those described previously [1]. The magnetization in magnetic field of 5 kOe is 0.25 at 300 K and 0.37 G cm^3 g^{-1} at 77 K. The temperature dependence of magnetization is virtually linear.

Iron-fullerene derivatives were recovered from the combustion products CPs by prolonged (for more than 5 h) boiling of the samples in dilute HCl to dissolve Fe_3O_4 and Fe_2O_3, followed by extraction with organic solvents to remove excess C_{60}.

In treatment of the samples with boiling HCl, the solution color changed from pale green, characteristic of Fe^{2+} chlorohydroxo complexes, to yellow owing to oxidation of Fe^{2+} to Fe^{3+} in air. Iron was not completely recovered from the samples. The parameters of the EMR spectra of insoluble products are listed in the table. The EMR spectrum of sample CP1 treated with HCl is shown in Fig. 2, *3*. The trend toward a decrease in the *g*-factor and linewidth in the spectra of these products is evident.

In the ESR spectra of these samples, there is a signal of C_{60} radical, broadened as compared with that of C_{60} fullerite radical, especially in sample CP3 treated with HCl. This product is ferromagnetic in the range 500–77 K, the coercive force is approximately 250 Oe at 250 K and 50 Oe at 300 K, and the magnetization in the magnetic field of 1000 Oe is 4.5 G cm^3 g^{-1} at 77 K. Extrapolation of the magnetization to high temperatures showed that the Curie point is 427°C, which is much lower than that of bulk Fe_3O_4 (585°C) and suggests the formation of chemical bonds of particles with fullerene. The spectrum in the *Q*-range consists of a symmetrical EMR signal with g_{eff} = 2.002 and ΔH = 1000 Oe (Fig. 4, *1*) and a weak ESR signal of the C_{60} radical (Fig. 4, *3*).

The saturation magnetization of HCl-treated sample CP2 in a magnetic field of 1 kOe was 0.17 G cm^3 g^{-1} and coercive force, 250 Oe at 77 K. In the *Q*-range, there is an EMR signal with g_{eff} = 2.002 and ΔH = 570 Oe (Fig. 4, *2*), and also an ESR signal from the C_{60} radical, ΔH = 4.4 Oe (Fig. 4, *4*). The shift of the EMR line, observed for both samples with increasing frequency (see table), is due to the presence of the energy gap in the magnetic, caused by magnetic anisotropy. Comparison of the spectra of the samples shows that the dependences of the resonance characteristics on the amount of iron in the initial mixture and after treatment of CP2 and CP3 with HCl remain the same. An increase in the intensity of the ESR signal from the C_{60} radical is clearly seen in Fig. 4, *4*.

A set of narrow peaks in a magnetic field of 2000 Oe was observed in the EMR spectrum of CP3 sample treated with HCl. Similar signals were observed in the spectra of insoluble residues when the combustion products were treated with benzene. This effect can be accounted for, e.g., by the spin-wave resonance in thin films of magnetite covering fragments of the C_{60} crystalline phase. It is apparent that a decrease in the amount of iron in the samples "removes" this coating. We obtain a magnetic, which is the product of the reaction of iron(III) oxide with fullerene. The other possible explanation of these peaks is the presence of a phase similar to the Wigner glass [20].

After the reaction with hydrochloric acid, synthesis products CP2 and CP3 were treated with organic solvents (benzene, toluene). Extraction with organic solvents resulted in additional extraction of iron and changes the parameters of the EMR spectra of insoluble residues (see table). Their probable elemental composition, according to chemical analysis and IR spectra, is $Fe_xO_y(OH)_zC_{60}$. Both substances are weak ferromagnetics. The temperature shifts of the EMR lines for these samples are insignificant. In the spectra of fractions soluble in organic solvents and extracted from CPs pretreated with HCl, the ESR signal of the radical anion was observed as an individual line or an unresolved doublet with C_{60} radical. The parameters of EMR spectra were as follows: g_{eff} = 2.02–2.00 and linewidth of approximately 400 Oe. This suggests the presence of iron in the resulting extracts, and the appearance of the radical anion can serve as evidence in favor of chemical bonding between iron and fullerene.

The solid residues formed after treatment of combustion products CP1–CP3 with organic solvents are heterogeneous ferromagnetics. The EMR spectra of the residue after treatment of sample CP2 with toluene were recorded at 300 and 77 K (Fig. 5, *2* and *3*).

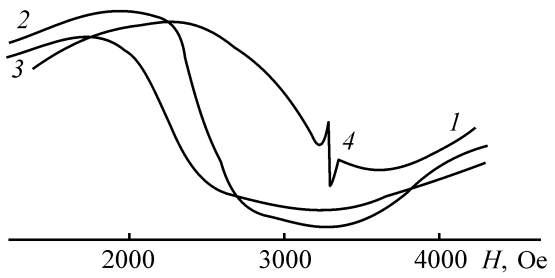

Fig. 5. EMR spectra of CP2 samples after treatment with toluene: (*1*) product soluble in toluene, (*2*, *3*) insoluble product at 300 K and 77 K, respectively, and (*4*) ESR line of C_{60} fullerene radical.

The EMR spectrum of a substance extracted from this sample is shown in Fig. 5, *1*. This substance is not ferromagnetic in the range 77–500 K; however, it differs from ordinary paramagnets. According to the preliminary data, these products are similar to superparamagnets and spin glasses.

CONCLUSION

The products formed by thermal reaction of solid mixtures of fullerene with iron(III) acetylacetonate contain complexes of iron with fullerene and a composite consisting magnetite and fullerite particles. The average size of the magnetite particles decreases with decreasing iron concentration in the initial mixture. Small particles (on the order of nanometers) can be chemically bonded to fullerene. The composition and magnetic characteristics of iron-fullerene complexes vary in purification of the thermal synthesis products to remove Fe_3O_4 and excess C_{60}, but their dependence on the Fe : C_{60} ratio in the initial mixture is retained. A set of products of the synthesis based on thermal reaction of fullerene C_{60} with $Fe(acac)_3$ can be obtained, from heterogeneous ferromagnetics to superparamagnetics and individual ironfullerene complexes.

ACKNOWLEDGMENTS

The authors are grateful to O.A. Bayukov for recording and analysis of Mössbauer spectra, A.I. Zaitsev for assistance in obtaining the DTA data, N.V. Bulina for recording of the X-ray patterns, and K.A. Sablina and G.N. Churilov for interest in the study and useful discussion.

This study was supported financially by the Ministry of Education of the Russian Federation in the framework of the State Scientific and Technical Program "Scientific Research of Highest School in Priority Directions of Science and Technology" (project no. 203.02.05.007).

REFERENCES

1. Zubov, E., Byszewski, P., Chabanenko, V., *et al.*, *J. Magn. Magn. Mater.*, 2000, vol. 222, nos. 1–2, pp. 89–96.
2. Crane, J.D., Hitchcock, P.B., Kroto, H.W., *et al.*, *Chem. Commun.*, 1992, no. 23, pp. 1764–1767.
3. Christides, C., Devlin, E., Simopoulos, A., Meidine, M.F., *et al.*, *J. Phys. Chem.*, 1994, vol. 98, no. 45, pp. 11666–11668.
4. Gorel'skii, S.I., Magdesieva, T.V., and Butin, K.P., *Izv. Ross. Akad. Nauk, Ser. Khim.*, 1996, no. 6, pp. 1453–1457.
5. Fagan, P.J. and Joseph, G., *Acc. Chem. Res.*, 1992, vol. 25, no. 5, pp. 134–142.
6. Konarev, D.V. and Lyubovskaya, R.N., *Usp. Khim.*, 1999, vol. 68, no. 1, pp. 23–29.
7. Roth, L.M., Huang, Y., Schwedler, J.T., *et al.*, *J. Am. Chem. Soc.*, 1991, vol. 113, no. 16, pp. 6298–6299.
8. Pradeep, T., Kulrarni, G.U., Kannan, K.N., *et al.*, *J. Am. Chem. Soc.*, 1992, vol. 114, no. 6, pp. 2272–2273.
9. Churilov, G.N., Bayukov, O.A., Petrakovskaya, E.A., *et al.*, *Zh. Tekhn. Fiz.*, 1997, vol. 67, no. 9, pp. 142–144.
10. Pukhova, Ya.I., Churilov, G.N., Isakova, V.G., *et al.*, *Dokl. Akad. Nauk*, 1997, vol. 335, no. 2, pp. 269–272.
11. Kolpakova, T.A., Petrakovskaya, E.A., and Isakova, V.G., *Vysokoenergeticheskie protsesy i nanostruktury: Materialy mezhregional'noi konferentsii* (High-Energy Processes and Nanostructures: Proc. Interregional Conf.), Krasnoyarsk, April 12, 2001, pp. 58–59.
12. Nevkrytova, T.A., Isakova, V.G., Petrakovskaya, E.A., *et al.*, *Materialy 6 Vserossiiskoi nauchno-tekhnicheskoi konferentsii "Perspektivnye materialy, tekhnologii, konstruktsii"* (Proc. Sixth Russian Scientific and Technical Conf. "Promising Materials, Technologies, and Structures"), Krasnoyarsk, May 25–27, 2000, pp. 114–115.
13. Joshi, K.C. and Pathak, V.N., *Coord. Chem. Rev.*, 1977, vol. 22, no. 1, pp. 37–112.
14. Pushkin, A.N., Zenin, N.N., Kuznetsova, O.A., *et al.*, *Zh. Fiz. Khim.*, 1999, vol. 73, no. 9, pp. 156–161.
15. *Problemy khimii i primeneniya β-diketonatov metallov* (Problems of Chemistry and Application of Metal β-Diketonates), Spitsyn, V.I., Ed., Moscow: Nauka, 1982.
16. Zaritskii, I.M., Ishchenko, S.S., Konchits, A.A., *et al.*, *Fiz. Tverd. Tela*, 1996, vol. 38, no. 2, pp. 419–426.
17. Petrakovskii, G.A., Sablina, K.A., Volkov, N.V., *et al.*, *Zh. Eksp. Teor. Fiz.*, 1983, vol. 85, no. 8, pp. 592–601.
18. Petrakovskii, G.A., Piskorskii, V.P., Sosnin, V.M., and Kosobudskii, I.D., *Fiz. Tverd. Tela*, 1983, vol. 25, no. 11, pp. 3256–3260.
19. Slichter, C.P., *Principles of Magnetic Resonance*, Berlin: Springer, 1980.
20. Dumas, J., Tholenc, J.L., Continentio, M., *et al.*, *J. Magn. Magn. Mater.*, 2001, vols. 226–230, part 1, pp. 468–469.

Russian Journal of Applied Chemistry, Vol. 76, No. 4, 2003, pp. 582–584. Translated from Zhurnal Prikladnoi Khimii, Vol. 76, No. 4, 2003, pp. 602–604.

ORGANIC SYNTHESIS AND INDUSTRIAL ORGANIC CHEMISTRY

Absorption and Luminescence Spectra of 1,1,3-Trimethyl-3-Phenylindan

V. N. Salimgareeva, S. S. Ostakhov, V. A. Ponomareva, S. V. Kolesov, and G. V. Leplyanin

Institute of Organic Chemistry, Ufa Scientific Center, Russian Academy of Sciences, Ufa, Bashkortostan, Russia

Received January 22, 2003

Abstract—Electronic absorption and luminescence spectra of cyclic dimer of α-methylstyrene, 1,1,3-trimethyl-3-phenylindan, were described. The quantum yield and lifetime of fluorescence were determined.

It is well known that certain individual and substituted hydrocarbons, whose molecules contain rings and conjugated double bonds, are capable of light emission, i.e., they luminesce when exposed to high-energy radiation [1]. Such compounds are distinguished by a rigid molecular structure precluding free rotation of molecular segments, thus decreasing the probability of nonradiative transitions.

Among the compounds of interest are aromatic polycyclic hydrocarbons (naphthalene, anthracene, naphthacene, phenanthrene, etc.), aromatic chain compounds (polyphenylenes, stilbene, diphenylpolyenes, aryldivinylbenzenes, etc.) [1–4]. In the molecules of luminescent compounds, the ordinary bond is located between two double bonds or between a multiple bond and an atom having unshared *p*-electron pair. This applies to, e.g., nitrogen- and oxygen-containing heterocyclic compounds (aryloxazoles, aryloxadiazoles, etc.).

Chain aromatic compounds exhibit luminescence in the case when conjugation in the molecule is disturbed by methylene groups inserted between the benzene rings like, e.g., in diphenylmethane or dibenzyl [5]. The absorption and emission spectra of compounds with Ph–X–Ph structure are close to those of the corresponding benzene derivatives.

It was of interest to study the optical properties of an aromatic compound whose molecule contains an X group rigidly linked to one of the benzene rings. An example of such a compound is 1,1,3-trimethyl-3-phenylindan (TMPI) yielded by cyclodimerization of α-methylstyrene [6]. It was termed "crystalline dimer of α-methylstyrene." This is an aromatic hydrocarbon of the following structure

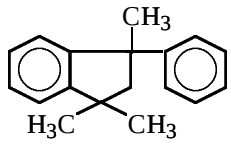

Owing to its π-electron system, TMPI is capable of fluorescence and/or intermolecular energy transfer. Linear oligomers of α-methylstyrene, prepared by its cationic polymerization, exhibit fluorescence at 270–310 nm with emission peak at 285 nm [7]. As far as we know, the luminescence properties of cyclic dimers of α-methylstyrene have not been studied previously.

A great number of luminescent compounds have been proposed recently, but a search for new luminophores with fast luminescence response and high quantum yield for designing scintillators is still a topical task. Candidate scintillators or luminescent additives for liquid or plastic scintillators must exhibit high thermal and chemical resistance and radiation hardness. This is characteristic specifically of TMPI [8, 9].

The electronic structure of the TMPI molecule composed of phenyl and indan rings must be intermediate between the conjugated (biphenyl) and nonconjugated (diphenylmethane) structures. Similarly to diphenylmethane, conjugation in the TMPI molecule is disturbed but, unlike diphenylmethane, the central carbon atom in the TMPI molecule is involved in the five-membered ring of the indan moiety. This must increase to a certain extent the rigidity of its structure, making it more similar to that of biphenyl. Also, the interest in TMPI is due to the possibility of preparing high-purity (up to 99.99%) TMPI in high yield (over 96%), as well as to its good solubility in many organic solvents and polymers (up to 60 wt %).

1070-4272/03/7604-0582 $25.00 © 2003 MAIK "Nauka/Interperiodica"

EXPERIMENTAL

Absorption spectra of TMPI solutions in heptane were recorded on a Specord UV-Vis spectrophotometer.

The luminescence spectra of TMPI in heptane and polymethyl methacrylate (PMMA) were recorded on an MPF-4 Hitachi spectrofluorimeter. Luminescence was excited at λ = 250 nm.

The quantum yield of fluorescence was determined using the procedure from [4] by comparison with the flourescence of toluene whose quantum yield is known.

The fluorescence lifetime was determined using an PRA pulse spectrofluorimeter [4].

1,1,3-Trimethyl-3-phenylindan was synthesized by the procedure from [6] and recrystallized from heptane. The product purity was monitored by gas–liquid chromatography, IR spectroscopy, and ^{1}H NMR spectroscopy (mp 51–52°C, bp 183°C/20 mm Hg).

For studying optical properties, we prepared solutions of the luminophore in heptane and PMMA. TMPI was introduced into PMMA by bulk polymerization of methyl methacrylate in the presence of an initiator, dicyclohexyl peroxodicarbonate, at 40°C. The resulting block was finally polymerized at 110°C, cut into 1-mm high disks, and polished.

The UV spectrum of TMPI contains a well-resolved band at 210–280 nm with peaks at 257, 263, and 270 nm and a stronger band at λ < 240 nm, whose intensity sharply increases with decreasing wavelength, with a peak at 204 nm (Fig. 1). Similarly to other hydrocarbons containing a benzene ring, TMPI is transparent at λ > 300 nm. The emission spectrum of TMPI at room temperature contains bands at 260–320 nm with peaks at 273 and 280 nm and a sholder at 287 nm. The electronic absorption and luminescence spectra of TMPI proved to be close to those of diphenylmethane rather than to biphenyl. Biphenyl absorbs at 220–290 nm and exhibits fluorescence at 290–380 nm [5]. Diphenylmethane absorbs and exhibits luminescence in the same regions as TMPI (240–285 and 260–310 nm, respectively) [5]. Broadening of the bands in the absorption and luminescence spectra of TMPI relative to diphenylmethane is probably due to the alkyl substituent at the central carbon atom. Evidently, TMPI should be treated as a compound with nonconjugated chain structure of the Ph–X–Ph type.

In studies of light absorption by complex molecules, of the greatest interest is the longest-wavelength

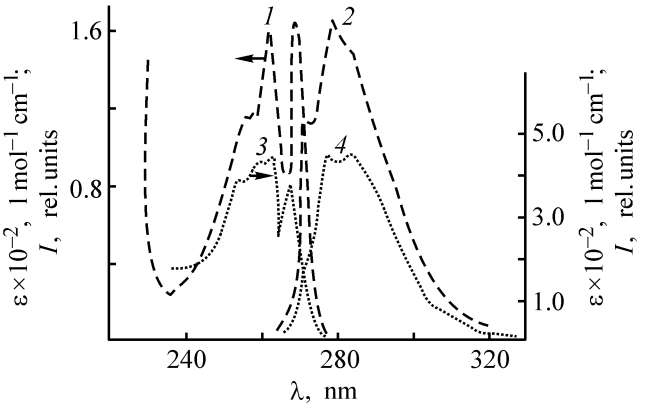

Fig. 1. (*1, 3*) Absorption and (*2, 4*) luminescence spectra of (*1, 2*) TMPI and (*3, 4*) diphenylmethane. (ε) Molar extinction coefficient, (*I*) luminescence intensity, and (λ) wavelength.

absorption band. As known, all lines of this band correspond to transitions between various vibrational sublevels of the ground and lowest-excited electronic states. The molar extinction coefficient ε at the peak of the long-wavelength absorption band of TMPI is 1.69×10^3 l mol^{-1} cm^{-1}, which significantly exceeds that of diphenylmethane (4.6×10^2 l mol^{-1} cm^{-1}). The molar extinction coefficient of TMPI falls within the region characteristic of the bands of π–π transitions [2].

The π–π^* transitions of hydrocarbon molecules are characterized by the predominance of vibrational frequencies of the carbon skeleton, and the frequencies corresponding to C–H vibrations are not very active. The vibronic structure of the TMPI spectra is better resolved than that of diphenylmethane. The increase in the intensity of the absorption and emission bands, as well as the increase in the molar extinction coefficient, in going from diphenylmethane to TMPI may be due to hindered relative rotation of the phenyl groups around the bond linking them to the central carbon atom, because of the increased rigidity of the molecular structure. In diphenylmethane, such rotation is not hindered, which favors dissipation of the electronic excitation energy.

Like the majority of aromatic compounds having Ph–X–Ph structure with conjugated π-electron systems of the benzene rings, TMPI exhibits absorption and emission spectra close to those of the corresponding alkyl-substituted benzenes and, in particular, toluene [5]. Both compounds exhibit absorption and luminescence in the same region; their luminescence can be excited at the same wavelength. The quantum yield of luminescence of TMPI proved to be 0.27, which ex-

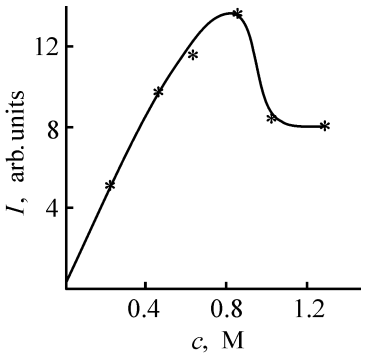

Fig. 2. Intensity I of TMPI fluorescence at λ = 282 nm vs. its concentration c in PMMA.

ceeds significantly those of diphenylmethane and biphenyl (0.16 and 0.18. respectively) [5].

The lifetime of the excited state (luminescence duration) τ for TMPI was estimated at 8 ns, which allows this luminescence to be qualified as fluorescence, for which the light emission spectrum is due to the same electronic states as the long-wave absorption band, i.e., to the transition from the singlet excited state to the ground state ($S_1^* \rightarrow S_0$ transitions). The occurrence of fluorescence suggests that the probability of nonradiative deactivation of the excited S_1^0 state is low.

Polymethyl methacrylate proved to be a good solvent for TMPI; it is characterized by high transparency in the UV and visible regions (including the regions of absorption and luminescence of TMPI). PMMA is used for fabrication of large plastic scintillators [1]. We have shown previously [10] that TMPI does not react with the propagating radical in MMA polymerization and occurs in the polymer as a dissolved substance. Incorporation of the luminophore into the solid solution must impart additional rigidity to its molecule, which will inhibit nonradiative deactivation of the electronically excited states.

Figure 2 presents the concentration dependence of the fluorescence intensity for TMPI in PMMA (Fig. 2). The plot exhibits extrema: With increasing concentration, the fluorescence is initially enhanced, passed through a maximum at 0.85 M, and then decreases owing to the concentration quenching. The electronic energy turns into the energy of vibrational or translational degrees of freedom [11], i.e., an increase in the concentration of molecules similar to the excited molecule makes more probable the nonradiative process. According to Krasovitskii and Bolotin [3], the concentration quenching is due to formation of fluorescent dimers acting as quenchers (deactivators of the excitation energy of the molecules). Concentration quenching may also be due to formation of nonfluorescent excimers yielded by collisions of an excited molecule with unexcited molecules and are stable in the excite states only.

To be suitable as luminophores or scintillator components, luminescent substances must have appropriate electronic absorption spectrum, quantum yield of luminescence, and luminescence duration. TMPI absorbs in the short-wavelength region of the spectrum, which allows more efficient capture of the incident high-energy radiation. TMPI is characterized by high quantum yield of luminescence and short scintillation time. This makes TMPI promising for fabrication of scintillators.

CONCLUSIONS

(1) Fluorescent properties of the cyclic dimer of α-methylstyrene, 1,1,3-trimethyl-3-phenylindan, were revealed.

(2) The lifetime of the excited state was estimated at 8×10^{-9} s, and the fluorescence quantum yield, at 0.27.

REFERENCES

1. Birks, J.B., *The Theory and Practice of Scintillation Counting*, Oxford: Pergamon, 1964.
2. Nurmukhametov, R.N., *Pogloshchenie i luminestsentsiya aromaticheskikh soedintnii* (Absorption and Luminescence of Aromatic Compounds), Moscow: Khimiya, 1971.
3. Krasovitskii, B.M. and Bolotin, B.M., *Organicheskie lyuminofory* (Organic Luminophores), Moscow, 1984.
4. Parker, C.A., *Photoluminescence of Solutions. With Applications to Photochemistry and Analytical Chemistry*, Amsterdam: Elsevier, 1968.
5. Berlman, J.B., *Handbook of Fluorescence Spectra of Aromatic Molecules*, New York: Academic, 1971.
6. Staudinger, H. and Brensch, F., *Chem. Ber.*, 1929, vol. 26, pp. 452–455.
7. Velichkova, R., Panayotov, J.M., Doicheva, J., *et al.*, *J. Polym. Sci., Polym. Chem. Ed.*, 1982, vol. 20, no. 10, pp. 2895–2902.
8. Vol'-Epshtein, A.B., *Neftekhimiya*, 1967, vol. 7, no. 1, pp. 13–18.
9. US Patent 3161692.
10. Salimgareeva, V.N., Sannikova, N.S., and Leplyanin, G.V., *Bashk. Khim. Zh.*, 1997, vol. 4, no. 1, pp. 32–36.
11. Stepanov, B.I., *Lyuminestsentsiya slozhnykh molekul* (Luminescence of Complex Molecules), Minsk: Akad. Nauk BelSSR, 1955, part 1.

Russian Journal of Applied Chemistry, Vol. 76, No. 4, 2003, pp. 585–590. Translated from Zhurnal Prikladnoi Khimii, Vol. 76, No. 4, 2003, pp. 605–610.

CHEMISTRY OF FOSSIL FUEL

Thermolysis of Kansk–Achinsk Coals with Varied Extent of Oxidation and Combustion of Nonvolatile Thermolysis Products: A Study by Complex Thermal Analysis

E. A. Boiko, D. G. Didichin, and P. V. Shishmarev

Krasnoyarsk State Technical University, Krasnoyarsk, Russia

Received May 27, 2002; in final form, March 2003

Abstract—Thermolysis of Berezovka coals with varied extent of oxidation and combustion of nonvolatile thermolysis products were studied by complex thermal analysis. The dynamics of thermochemical transformation of the fuel in an inert medium was evaluated, with simultaneous determination of the kinetic parameters of evaporation of various kinds of moisture. The burn-out of nonvolatile thermolysis residues obtained from Berezovka coals at various pretreatment temperatures was studied, and a correlation was revealed between the kinetic parameters of combustion of nonvolatile residues and the extent of oxidation of the initial fuel.

Kansk–Achinsk coal fields are important for the development the Russian fuel industry, and proper utilization of coals from these fields is a topical problem. At the same time, the experience of burning of Kansk–Achinsk coals at thermal power plants shows that efficient procedures for pretreatment and combustion of these coals, which could ensure reliable operation of boilers, are still lacking. This is largely due to significant variations in the main thermal characteristics and reactivity of the fuel. The quality of coal supplied to power plants tends to get worse. The coal composition and properties vary across the strata in the horizontal and vertical directions; coals from the upper layers are strongly oxidized and sooty [1].

One of the ways to improve the quality of coals with the minimal power consumption and without major degradation of the organic matter is low-temperature pretreatment of the fuel dust prior to combustion. Theoretical studies [2, 3] have shown that the optimal temperature and time of pretreatment of Kansk–Achinsk coals are, depending on their initial quality, 120–300°C and 0.8–1.2 s. These conditions ensure the required degree of drying and removal of ballast volatiles (in particular, CO_2), with the minimal power and labor consumption. However, since nonvolatile residues from heat treatment of coals with different extents of oxidation are to be utilized for the production of energy, it is of most interest to study these residues from the viewpoint of ensuring their stable ignition and burn-out in a real furnace. This is necessary for understanding the combustion mechanism and for finding the optimal conditions and pretreatment procedures for efficient combustion of Kansk–Achinsk coals of variable quality.

In this study, such experiments were performed with Kansk–Achinsk coals of the Berezovka deposit. The coals differed in the extent of oxidation and had the following characteristics: sooty coal, extent of oxidation 88%, $W_h^{\text{h}} = 18.9\%$, $A^d = 14.5\%$, $V^{\text{daf}} = 53.1\%$, $C_0^{\text{daf}} = 65.8\%$, $H_0^{\text{daf}} = 3.8\%$, $O_d^{\text{daf}} = 28.6\%$, $S_f^{\text{daf}} = 0.7\%$, $N_t^{\text{daf}} = 1.1\%$, $Q_i^r = 11766$ kJ kg^{-1}; oxidized coal lying at a depth of 15–18 m from the stripping level, extent of oxidation 63%, $W_t^h = 16.0\%$, $A^d = 6.4\%$, $V^{\text{daf}} = 48.5\%$, $C_0^{\text{daf}} = 69.3\%$, $H_0^{\text{daf}} = 4.2\%$, $O_d^{\text{daf}} = 25.1\%$, $S_t^{\text{daf}} = 0.7\%$, $N_t^{\text{daf}} = 0.7\%$, $Q_i^r = 13031$ kJ kg^{-1}; run-of-mine coal, extent of oxidation 42%, $W_t^h = 12.1\%$, $A^d = 4.1\%$, $V^{\text{daf}} = 46.0\%$, $C_0^{\text{daf}} = 72.0\%$, $H_0^{\text{daf}} = 4.6\%$, $O_d^{\text{daf}} = 22.5\%$, $S_d^{\text{daf}} = 0.3\%$, $N_t^{\text{daf}} = 0.6\%$, $Q_i^r = 15580$ kJ kg^{-1}. The extent of fuel oxidation was determined petrographically according to GOST (State Standard) 8930. To make the results representative, all samples of Berezovka coal with different extents of oxidation were taken from randomly chosen wells from different points across the coal stratum thickness [2].

Thermolysis of Berezovka coals with varied extent of oxidation and the characteristics and proper-

1070-4272/03/7604-0585 $25.00 © 2003 MAIK "Nauka/Interperiodica"

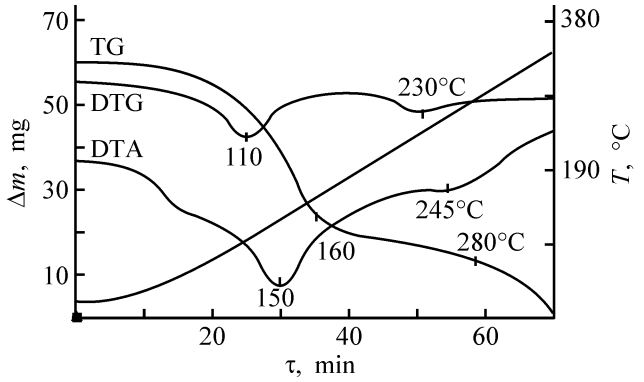

Fig. 1. Thermolysis of Berezovka coal in an inert medium (heating rate 5 deg min^{-1}): (Δm) variation of the sample weight, (T) temperature, and (τ) heating time.

ties of the nonvolatile residues were studied by complex thermal analysis [4]. Owing to the high resolving power of this method, it is possible to reveal thermal transitions corresponding to changes in the physicochemical state of a coal, evaluate the thermal effects accompanying one or another process, and obtain quantitative data for estimating the process kinetics.

EXPERIMENTAL

Complex thermal analysis of the fossil fuel was performed with an installation consisting of a *Q* derivatograph and a Soyuz-3101 chromatographic gas analyzer. With this installation, data on the dynamics of release of gaseous products (CO, CO_2, H_2, CH_4, etc.) under nonisothermal conditions are obtained along with the integral characteristics of coal thermal behavior (weight loss and its rate, thermal effects). The mode of the *Q* derivatograph operation was chosen so as to single out definite temperature ranges of the heat treatment of the material. In experiments on fuel thermolysis, the conditions were as follows: inert medium (Ar), sample weight 500 mg, and heating rate 5 deg min^{-1}. Experiments on combustion of nonvolatile thermolysis products were performed under different conditions: oxidizing medium (air), coal sample weight 50 mg, and heating rate 10 deg min^{-1}. The following conditions were common to both types of experiments: inert reference Al_2O_3; ceramic crucible; sensitivity levels (mV): TG 500, DTA 250, and DTG 250; gas flow rate 200 cm^3 min^{-1}; polydispersed coal fraction (R_{90} = 45, R_{200} = 30, R_{1000} < 1%).

In experiments on thermolysis of Berezovka coals in the inert medium, we obtained nonvolatile residues corresponding to final temperatures of 120, 150, 200, 250, and 300°C, with TG, DTG, and DTA curves recorded (Fig. 1) and the composition of gaseous products determined (see table).

Data on thermolysis of Berezovka coals in the range 120–300°C (TG curve) allow us to distinguish two steps of the process. In the range 20–160°C, the rate of the weight loss grows, but at approximately 160°C the slope of the TG curve changes and then remains constant in the range 160–280°C.

The curvilinear plot of the weight loss in the range 20–160°C is fully consistent with the pattern corre-

Composition of products formed by thermolysis of Berezovka coal samples of various extents of oxidation

Coal, extent of oxidation, %	T, °C	Composition of gaseous thermolysis products, %					
		CO_2	CO	H_2	CH_4	N_2	H_2O_{pyr}
Sooty, 88	120	81.41	–	–	–	13.17	–
	150	82.37	2.69	0.03	–	15.82	0.002
	200	93.75	5.67	0.013	0.071	–	0.015
	250	92.72	7.05	0.011	0.144	0.081	0.035
	300	90.28	9.2	0.018	0.278	0.22	0.036
Oxidized, 63	120	75.95	–	–	–	–	–
	150	82.32	11.14	0.039	–	6.54	0.001
	200	92.31	6.84	0.023	0.107	0.71	0.004
	250	90.72	7.84	0.014	0.324	1.1	0.012
	300	90.96	8.59	0.014	0.421	0.11	0.023
Run-of-mine, 39	120	85.24	–	–	–	–	–
	150	87.18	10.26	0.08	–	–	0.001
	200	88.99	6.03	0.018	0.113	4.86	0.005
	250	89.63	8.85	0.014	0.31	1.24	0.011
	300	88.21	10.77	0.022	0.53	0.23	0.022

sponding, according to Rebinder's classification, to evaporation of hygroscopic moisture. The change in the fuel mass in this range corresponds to evaporation of capillary moisture and moisture adsorbed in the monomolecular and polymolecular mode owing to hydrogen bonding with the active centers of the fuel surface [5]. Intense evaporation of moisture in this range corresponds to the period of a constant drying rate, accompanied by a pronounced endothermic effect in the DTA curve.

The subsequent weight loss at 160–280°C is associated with two competing processes: evaporation of chemically bound moisture and release of volatiles, mainly CO and CO_2 (see table). It should be noted that the content of chemically bound moisture in Berezovka coals with varied extent of oxidation is rather high, ranging from 4% for run-of-mine coal to 7% for sooty coal. It is known that the hydrophilic components of coal contain active functional groups (OH, COOH, CO, etc.) capable of hydrogen bonding with each other and with molecules of polar liquids, including water; the contribution of the hydrogen bond energy is low: about 24 kJ kg^{-1} [6]. These facts suggest that the chemically bound water, released in the range 160–280°C, is bound to coal macromolecules by secondary valence forces. The rate of evaporation of chemically bound moisture is low (W_{max} = 2.2–2.5 mg g^{-1} deg^{-1}), compared with that of hygroscopic moisture (W_{max} = 4.8–5.3 mg g^{-1} deg^{-1}), owing to the presence of ionic bonds and hydroxy groups in the fuel.

The kinetic parameters of evaporation of various forms of moisture (E_i, k_{0i}) were determined according to [7], using the following kinetic equation [8]:

$$\frac{dU_i}{d\tau} = k_{ei}(U_{0i} - U_i),$$

where $dU_i/d\tau$ is the evaporation rate of ith form of moisture; U_{0i} and U_i are the initial and final contents of the ith form of moisture in coal; k_{ei} is the rate constant of evaporation of ith form of moisture, $k_{ei} = k_0 \exp[-E_i/RT(\tau)]$.

To plot the differential curves for the periods of evaporation of hygroscopic and chemically bound moisture, we subjected the TG and DTG curves for the corresponding temperature ranges to preliminary processing with a 5°C step.

When estimating the rate of evaporation of chemically bound moisture, we took into account the release of volatiles detected with a gas chromatograph (see table). The amount of the released volatiles was subtracted from the total weight loss. The rate of release of individual gaseous components, ω_i (cm^3 g^{-1} min^{-1}), was calculated as a quantity proportional to their concentration c_i (%) [7]:

$$\omega_i = Kc_i/100,$$

where K is the proportionality coefficient taking into account the deviation of the experimental conditions (rate of gas removal, sample weight, etc.) from the standard.

After converting ω_i to the dimension of mg min^{-1}, these quantities were subtracted from the total weight losses at the corresponding temperatures, determined from the TG curves (160–280°C). The initial content U_{0i} of each form of moisture was determined from the area under the $dU_i/d\tau = f(T)$ plots. The running moisture content U_i was determined by planimetric treatment of the portions of the rate curves up to the given temperature.

It is seen that the kinetics of evaporation of hygroscopic moisture is consistent with the mechanism involving competition of the adsorption and desorption of water present in the coal as a common phase and as molecular clusters in pores of the coal structure. The statistically estimated mean binding energy of hygroscopic moisture in Berezovka coals is 12.8 kJ mol^{-1}, and the preexponential factor is 2.3 s^{-1}, which suggests the physical binding [9]. At the same time, we revealed a close correlation between the extent of oxidation of Berezovka coal and the kinetic parameters of evaporation of chemically bound moisture. Despite the high content of chemically bound moisture in sooty coals (6% and more), the binding energy was 18.7 kJ mol^{-1}. In coals oxidized to a lesser extent, the binding energy of moisture is higher: 22.9 kJ mol^{-1} in oxidized coals and 28.3 kJ mol^{-1} in run-of-mine coals. As the extent of coal oxidation grows, the temperature at which the rate of evaporation of chemically bound moisture passes through a maximum increases, which confirms that this moisture is chemically bound to the fuel [10].

The nonvolatile thermolysis residues obtained at various temperatures were subjected to combustion in a derivatograph under oxidative conditions.

The results obtained (Fig. 2) show that the temperatures at which the rate of combustion of the nonvolatile residues passes through a maximum (DTG curve) closely correlate with the extent of oxidation of Berezovka coals. The combustion rate is the highest for nonvolatile residues of the sooty coal, reaching 1.4–1.68 mg g^{-1} deg^{-1}. For nonvolatile residues of the oxidized and run-of-mine coals, the combustion rates

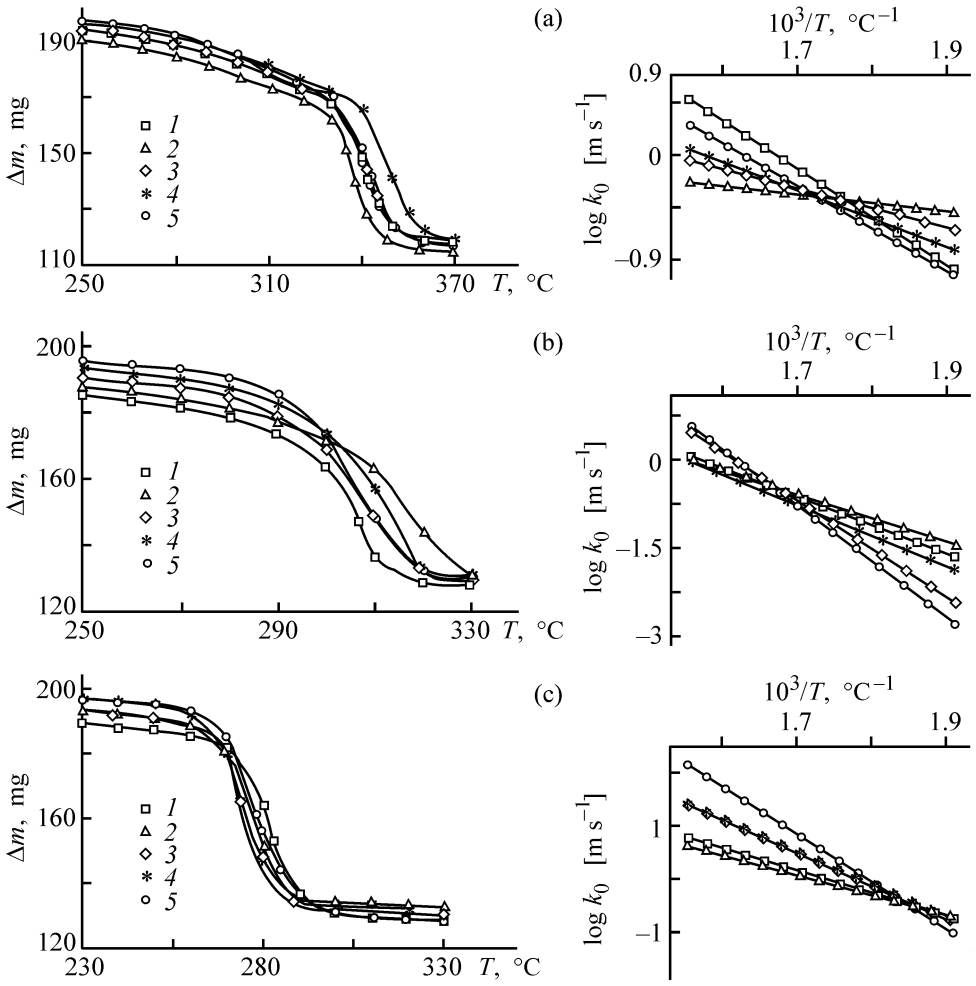

Fig. 2. Kinetics of combustion of nonvolatile residues from thermolysis of Berezovka coals with varied extent of oxidation, monitored under conditions of complex thermal analysis: (Δm) change in the sample weight and ($\log k_0$) logarithm of the rate constant. Coal: (a) run-of-mine, (b) oxidized, and (c) sooty. Final thermolysis temperature, °C: (*1*) 120, (*2*) 150, (*3*) 200, (*4*) 250, and (*5*) 300.

are close, ranging from 0.76 to 0.9 mg g^{-1} deg^{-1}. With increasing thermolysis rate the rate of combustion of the nonvolatile residue decreases by 10–12% for the sooty coal and increases by 5–7% for the oxidized and run-of-mine coals.

We evaluated the kinetic characteristics of combustion of nonvolatile residues from thermolysis of Berezovka coals with varied extent of oxidation. Since the combustion of these materials is a heterogeneous process, its rate W (kg s^{-1}) was determined as a function of the reaction surface area [11]:

$$W = kmS_{sp}\rho_{app},$$

where k is the combustion rate constant, m s^{-1}; m, amount of nonvolatile residue, kg; S_{sp}, specific surface area of the nonvolatile residue, m^2 kg^{-1}; ρ_{app}, apparent density of the nonvolatile residue, kg m^{-3}.

Since the size of nonvolatile residue particles [12], the reaction surface area, and, hence, (under equal other conditions) the combustion rate vary in the course of combustion, we calculated the rate constant k (m s^{-1}) by the equation

$$k = Wd_i/(m_0 - m),$$

where $d_i = d[(m_0 - m)/m]^{1/3}$ is the running size of nonvolatile residue particles [13], m; m_0, initial weight of the nonvolatile residue, kg; and d, mean diameter of nonvolatile residue particles, m.

Using this equation, we calculated the kinetic characteristics of the combustion, assuming that the nonvolatile residue particles are spherical, no reaction occurs within the pores, and the organic matter is fully separated from the mineral matter. After calculating the rate constants at 10°C intervals, we plotted the

Arrhenius dependences $\log k = f(10^3/T)$, which appeared to be straight lines (Fig. 2). From their slopes, we determined the activation energy E, kJ mol^{-1}:

$$E = \frac{2.303R(\log k_2 - \log k_1)}{(1/T_1 - 1/T_2) \times 10^3}.$$

The probability factor was estimated assuming that, if $T_1 \to \infty$, i.e., $k_1 \to k_0$, then

$$\log k_0 = \frac{E}{2.303R}\frac{10^3}{T_2} + \log k_2,$$

where R is the universal gas constant (kJ mol^{-1} deg^{-1}).

The kinetics of combustion of nonvolatile residues from thermolysis of Berezovka coals with varied extent of oxidation (Fig. 3) are described by the following regression equations: for run-of-mine coal, $E = 123.22 - 0.5231T + 0.0022T^2$, $\log k_0 = 10.216 - 0.0467T + 0.0002T^2$; for oxidized coal, $E = 109.56 - 0.4389T + 0.0015T^2$, $\log k_0 = 9.4414 - 0.0375T + 0.0001T^2$; and for sooty coal, $E = 101.31 - 0.3144T + 0.0013T^2$, $\log k_0 = 9.1323 - 0.0285T + 0.0001T^2$, where T is the final temperature of fuel thermolysis (°C).

For all types of the initial Berezovka coal, irrespective of their extent of oxidation, the activation energies E and probability factors k_0 as functions of thermolysis temperature pass through a minimum in the range 120–150°C. For example, for the initial samples of the run-of-mine, oxidized, and sooty coals, the activation energies of combustion are 126.32, 110.79, and 104.14 kJ mol^{-1}, respectively; after heating to 150°C, they decrease to 75.03, 70.55, and 70.2 kJ mol^{-1}; and after heating to 300°C, the activation energies grow again, reaching 154.15, 107.57, and 120.1 kJ mol^{-1}, respectively.

There is good reason to believe that the maximum in the dependence of the reactivity of the nonvolatile residues on the final temperature of thermolysis of Berezovka coals is associated with accumulation of phenolic, carbonyl, and hydroxy groups as a result of cleavage of intermolecular bonds and ether bonds in units linking aromatic rings [14]. For example, on heating the initial fuel to 150°C, the content of carbonyl and hydroxy groups grows from 3.7 to 4.33 and from 3.2 to 4.4 mg-equiv g^{-1}, respectively, which results in a 26% increase in the content of active functional oxygen. The content of carboxy groups slightly decreases (from 0.42 to 0.25 mg-equiv g^{-1}; ≤2% of the total content of functional groups).

Further heating to 300°C leads to a dramatic decrease in the content of oxygen-containing functional groups; as a result, the content of aliphatic compounds changes, and the kinetic parameters grow. Irrespective of the thermolysis temperature, the nonvolatile residues from the sooty coals are the most reactive, then follow the residues from oxidized coals, and those from the run-of-mine coals are the least reactive. This is confirmed by the values of the probability factor, ranging from 2.76×10^{10} to 7.54×10^{13} m s^{-1} for nonvolatile residues from the run-of-mine coal and from 1.09×10^6 to 5.6×10^9 m s^{-1} for those from the sooty and oxidized coals. On the whole, the functional dependence $E = f(\log k_0)$ for the combustion of nonvolatile residues from thermolysis of Berezovka coals is linear, suggesting similar and invariable combustion mechanisms for fuel samples with different extents of oxidation and with different temperatures of preliminary thermolysis.

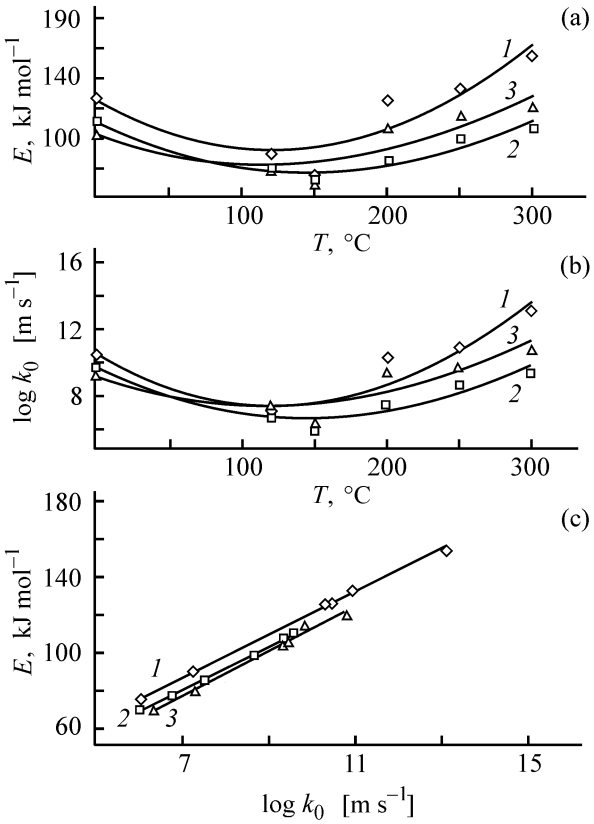

Fig. 3. (a) Activation energy E and (b) logarithm of the preexponential factor, $\log k_0$, for the combustion of nonvolatile residues from thermolysis of Berezovka coals vs. the final temperature T of the preliminary heat treatment; (c) correlation of E with $\log k_0$. Coal: (*1*) run-of-mine, (*2*) oxidized, and (*3*) sooty.

CONCLUSIONS

(1) Thermolysis of Berezovka coals with varied extent of oxidation and combustion of the nonvolatile

residues were studied by complex thermal analysis. It was found that the behavior of these materials largely depends on the extent of oxidation of the initial fuel.

(2) It was shown that the kinetic parameters of evaporation of hygroscopic moisture are independent of the extent of oxidation of the initial Berezovka coal, whereas the parameters of evaporation of chemically bound moisture grow with decreasing extent of oxidation.

(3) Regression equations describing the correlation of the kinetic parameters of combustion of nonvolatile residues from thermolysis of Berezovka coals with the temperature of the preliminary heat treatment of the initial fuel samples with varied extent of oxidation were obtained.

REFERENCES

1. Kukharenko, T.A. and Tolchinskaya, R.Ya., *Khim. Tverd. Topl.*, 1977, no. 2, pp. 20–30.
2. Potekhin, G.A., Specific Features of the Composition and Properties of Kansk–Achinsk Coals from the Oxidation Zone and Improvement of the Efficiency of Utilizing These Coals at Thermoelectric Power Plants, *Cand. Sci. Dissertation*, Tomsk, 1986.
3. Madoyan, A.A., Baltyan, V.N., and Grechatnyi, A.N., *Effektivnoe szhiganie nizkosortnykh uglei v energeticheskikh kotlakh* (Efficient Combustion of Low-Grade Coals in Boilers for Power Production), Moscow: Energoatomizdat, 1991.
4. Alaev, G.P., Development and Use of a Complex Method for Evaluating the Reactivity of Fuels for Power Engineering, *Doctoral Dissertation*, Leningrad, 1978.
5. Agroskin, A.A., Lyashchenko, V.I., and Svyatets, I.E., *Khim. Tverd. Topl.*, 1979, no. 6, pp. 79–84.
6. Wildegger-Gaismaier, A.E. and Agarwal, P.K., *Chem. Eng. Res. Des.*, 1990, vol. 68, no. 3, pp. 251–262.
7. Boiko, E.A., *Khim. Tverd. Topl.*, 1995, no. 5, pp. 31–37.
8. McIntosh, M.J., *Fuel*, 1976, vol. 55, no. 4, pp. 446–455.
9. Boiko, E.A. and Dubrovskii, V.A., *Zh. Prikl. Khim.*, 1992, vol. 68, no. 10, pp. 2350–2355.
10. Dubrovskii, V.A. and Kulikov, S.M., *Zh. Prikl. Khim.*, 1989, vol. 65, no. 4, pp. 937–939.
11. *Osnovy prakticheskoi teorii goreniya* (Principles of the Practical Combustion Theory), Pomerantsev, V.V., Ed., Leningrad: Energoatomizdat, 1986.
12. Khzmalyan, D.M., *Teoriya topochnykh protsessov* (Theory of Furnace Processes), Moscow: Energoatomizdat, 1990.
13. Boiko, E.A., *Thermochim. Acta*, 2000, no. 348, pp. 97–104.
14. Butuzova, L.F., Isaeva, L.N., Krshton', A., *et al.*, *Khim. Tverd. Topl.*, 1994, no. 1, pp. 45–52.

Russian Journal of Applied Chemistry, Vol. 76, No. 4, 2003, pp. 591–594. Translated from Zhurnal Prikladnoi Khimii, Vol. 76, No. 4, 2003, pp. 611–615.

MACROMOLECULAR CHEMISTRY AND POLYMERIC MATERIALS

Influence of the Chemical Structure of 4-Hydroxybenzylidenealkanones on Nonlinear Optical Properties of Their Complexes with Poly-1,10-Decamethyleneacetamidine

A. V. Ten'kovtsev, A. E. Trofimov, M. M. Dudkina, and V. N. Lukoshin

Institute of Macromolecular Compounds, Russian Academy of Sciences, St. Petersburg, Russia
Ioffe Physicotechnical Institute, Russian Academy of Sciences, St. Petersburg, Russia

Received December 15, 2002

Abstract—The influence exerted by the length exerted by the conjugation chain in 4-hydroxybenzylidenealkanones on the generation of the third harmonic by complexes of these chromophores with aliphatic polyamidine was studied.

At present, growing interest is aroused by materials exhibiting nonlinear optical (NLO) effects [1]. This is primarily due to their promise for optoelectronic applications. Within a large class of compounds with prominent NLO properties, of greatest importance are those with refractive indices widely varying with light intensity. This allows control over the propagation of the optical radiation in a medium in, e.g., designing optical switches, modulators, etc. Special attention is given to preparation of polymeric materials exhibiting NLO effects [2].

Polymers containing NLO-active moieties (chromophores) favorably compare with the conventionally used inorganic substances in a number of properties owing both to the polymeric nature of a substance and to the possibility of directed variation of the structure of the active component.

As known, practically acceptable NLO susceptibilities χ^3 are exhibited by compounds containing a sufficiently long π-conjugation system (e.g., β-carotene, polyacetylene, polythiophene, etc. [3]). Despite much progress achieved in the development of materials with NLO properties, preparation of film-forming macromolecular compounds of the mentioned type or of composite materials of the guest-host type encounters many difficulties because of the poor solubility and complicated synthesis of polyconjugated polymers in the former case and the thermodynamic incompatibility of the polymeric and low-molecular-weight substances, in the latter. Earlier [4], we have proposed an alternative approach to preparing polymer systems exhibiting third-order NLO effects [third harmonic generation (THG)]. It is based on preparing ionic complexes between low-molecular-weight NLO-active chromophores and polymeric carriers [4], in particular, complexes of (4-hydroxyarylidene)alkanones and poly-1,10-decamethyleneacetamidine. It was shown that, owing to formation of quinoid moieties via ionization of chromophores by highly basic poly-1,10-decamethyleneacetamidine, it is possible to prepare filmforming polymer complexes with sufficient thermal resistance, which are stable for prolonged (over 2 years) periods of time and capable of efficient generation of the third harmonic.

The aim of this study was to analuze how the specific chemical structure of chromophores containing the 4-hydroxycinnamoyl moiety, which is capable of quinoidization, affects the THG efficiency of complexes of the above-mentioned compounds with poly-1,10-decamethyleneacetamidine.

EXPERIMENTAL

We synthesized 1-(4-hydroxyphenyl)-5-arylpenta-1,4-dien-3-ones, 1-(4-hydroxyphenyl)-1-arylpropenones, and 1-(4-hydroxyphenyl)-7-phenylhepta-1,4,6-trien-3-one by the known procedures [5, 6]. Consistent analytical data and spectral characteristics were obtained for the synthesized compounds.

Poly-1,10-decamethyleneacetamidine was synthesized by the procedure described in our previous publication [6]. Analysis by gel-permeation chromatog-

1070-4272/03/7604-0591 $25.00 © 2003 MAIK "Nauka/Interperiodica"

raphy showed that the molecular weight of the poly-1,10-decamethyleneacetamidine sample used in the present study was 8000, and the polydispersity coefficient, 2.7.

Solutions of the complexes were prepared by mixing ethanolic solutions of the chromophore and poly-1,10-decamethyleneacetamidine, saturated at room temperature, in a 1 : 0.25 polymer:chromophore ratio (molar ratio of the repeating unit of the polymer to the low-molecular-weight compound). Samples for optical studies were prepared by casting the ethanolic solutions of the complexes onto a rotating glass substrate, followed by solvent vaporization at room temperature under atmospheric pressure. Prior to measurements, the resulting films were dried in a vacuum (0.1 torr) to constant weight.

Calorimetric measurements were carried out with a DSC 7 Perkin–Elmer calorimeter in the range from –50 to 250°C at a heating rate of 10 deg min^{-1}. The UV spectra were recorded on a Varian Cary 100 spectrophotometer suitable for measuring the NLO characteristics of thin films. Thermogravimetric measurements were carried out on a TGA Perkin–Elmer instrument in the range from 30 to 500°C at a heating rate of 10 deg min^{-1}.

The NLO properties of the resulting materials were estimated by the THG method. The samples were excited with a Nd-YAG pulse laser operating at a wavelength of 1.06 μm in the *Q*-switched mode with pulse duration of 15 ns. The radiation energy in the pulse was widely varied (up to 30 mJ). The Gaussian 3D profile of the laser beam was set by selecting the highest transverse modes with an intra-resonator diaphragm. The *p*-polarized radiation was focused onto a sample under study using a convex spherical lens with F = 100 mm. Part (4%) of the radiation was diverted by a beam splitter to a calibrated photodiode. The light from the sample was directed via a lens system to the entrance slit of an MDR-2 grating monochromator and further to an FEU-106 photomultiplier. The electrical signals from both the photodetectors were fed to an integrating analog-digital converter and further, via the CAMAC instrumental interface, to a PC for subsequent processing.

In view of the difficulties encountered in determining the absolute values of the intensity of exciting radiation incident on the sample, the NLO susceptibility of the materials studied was determined against a reference. As the latter served a 0.5-mm-thick fused-silica plate set to the first intensity maximum of the third harmonic (Maker fringe method) [7].

In this case, the χ^3 parameter can be estimated for the materials studied by the relation

$$\chi^{(3)} = \chi_s^{(3)}[I^{1/2}(3\omega)/l_{c,c}]/[I_s^{1/2}(3\omega)/l_{c,s}].$$

Here, $I(3\omega)$ and $I_s(3\omega)$ are the intensities of THG by the samples and reference, respectively; $I_{c,c}$ and $I_{c,s}$ are their respective coherence lengths; $\chi_s^{(3)} = 3.11 \times 10^{-14}$ CGSE units for SiO_2 at λ = 1.06 μm.

To eliminate the influence of the intrinsic absorption of the sample at the THG wavelength (355 nm), the experimental $\chi^{(3)}$ values were normalized using the equation

$$\chi_n^{(3)} = \chi^{(3)}\ln(l/T)/[(l - T)T^{0.5}].$$

Here, $\chi_n^{(3)}$ is the normalized susceptibility, and T is the transmission at the THG wavelength.

The geometry of the complexes was optimized by the STO-3-21G method (Hyperchem 7.01 software package; RSM energy gradient under 0.01 kcal mol^{-1} $Å^{-1}$). The absorption spectra were calculated by the ZINDO/S semiempirical method, taking into account the configurational interaction for 15 higher occupied and 15 lower unoccupied orbitals. The second-order hyperpolarizabilities were calculated by the AM1 (Austin Model) method (MOPAC 7.0 software package). The averaged hyperpolarizabilities were calculated by the equation

$$\gamma = \frac{\gamma_{xxxx} + \gamma_{yyyy} + \gamma_{zzzz} + 2(\gamma_{xxyy} + \gamma_{xxzz} + \gamma_{yyzz})}{5},$$

where γ_{ijkl} are the hyperpolarizability tensor components.

We have shown previously [4] that deprotonation of the chromophores from the series of 1-(4-hydroxyphenyl)-5-arylpenta-1,4-dien-3-ones and formation of quinoid moieties are necessary conditions for their complexes with highly basic polymers to exhibit third-order NLO activity. This effect is evidently due to changes in the conjugation character (transition from a cross-conjugated to a linear π system) and to an increase in the degree of delocalization of π electrons. Tykwinski *et al.* [8] demonstrated that, theoretically, the THG efficiency must be proportional to the conjugation system length raised to fifth power. Thus, it could be assumed that, in going from enol of 1-(4-hydroxyphenyl)-1-arylpropenone (**I**) to that of 1-(4-hydroxyphenyl)-5-arylpenta-1,4-dien-3-one (**II**) and further to that of 1-(4-hydroxyphenyl)-7-phenylhepta-1,4,6-tiren-3-one (**III**), which act as chromo-

phore groups in complexes of their corresponding compounds with 1,10-decamethyleneacetamidine, $\chi^{(3)}$ must obey a power law:

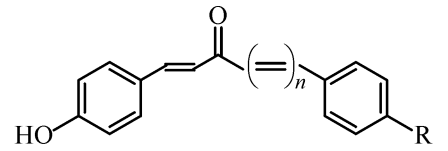

Ia–**Id**, **IIa**–**IId**, **III**

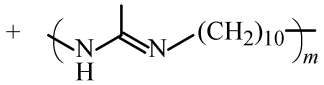

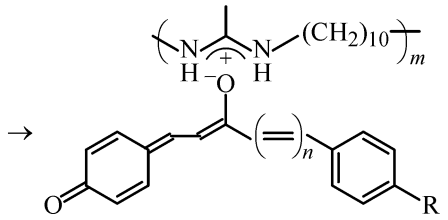

Here, **I**, n = 0, R = H (**Ia**), CH_3 (**Ib**), Cl (**Ic**), $N(CH_3)_2$ (**Id**); (**II**), n = 1, R = H (**IIa**), CH_3 (**IIb**), Cl (**IIc**), $N(CH_3)_2$ (**IId**); (**III**), n = 2, R = H.

It was found that all the chromophores are sufficiently acidic to form ionic structures when reacting with poly-1,10-decamethyleneacetamidine, which is manifested in a bathochromic shift (about 100 nm, depending on the chromophore structure) of the long-wavelength absorption band. According to quantum-chemical calculations, this band can be assigned to the π–π^* transition in the dye molecule.

The polymer reactivity toward a chromophore was found spectrophotometrically [9] (see figure). It was established that, in all cases, the chromophore is completely bound by the polymer molecule up to the polyamideto-chromophore ratio of 3 as calculated for the monomer unit of the polymer. In this context, we chose for studying the NLO properties, complexes containing 0.25 M chromophore per polyamidine unit.

The thermograms suggest that the resulting complexes are individual polymeric compounds, rather than mechanical mixtures of a polymer and a low-molecular-weight substance. The DSC curves of poly-1,10-decamethyleneacetamidine are indicative of a transition at 5°C (T_g), and those of all the complexes, only of a glass transition within 35–55°C, depending on the chemical structure of the chromophore.

As already mentioned, it could be suggested that, in going from enol **Ia** to enol **IIa** and, further, to enol **III** as chromophore groups in complexes with poly-1,10-decamethyleneacetamidene, the parameter

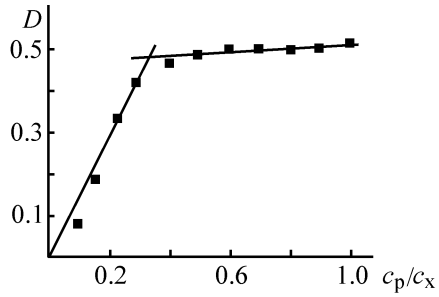

Absorption of the ethanolic solution of the complex (λ = 450 nm) vs. the polyamidine/**Ia** ratio. (D) Optical density, (c_p) concentration of 1,10-decamethyleneacetamidene, mole of unit l^{-1}, and (c_x) the concentration of **Ia**, mole of unit l^{-1}.

$\chi^{(3)}$ must increase. However, Table 1 suggests that the susceptibility is little affected by the conjugation chain length.

At the same time, it is seen that an increase in the number of ethylene units results in a minor bathochromic shift.

Table 2 lists the third-order molecular susceptibilities $\chi^{(3)}$ and the second-order hyperpolarizabilities

Table 1. Susceptibilities $\chi^{(3)}$ and peaks in long-wavelength absorption band of complexes formed by unsubstituted chromophores with poly-1,10-decamethyleneacetamidine

Chromophore	$\chi^{(3)} \times 10^{12}$, CGSE unit	λ_{max}, nm
Ia	6.3	450
IIa	4.9	451
III	7.7	467

Table 2. Experimentally determined $\chi^{(3)}$ parameters and calculated (AM1 method) γ parameters for chromophores **Ia**–**Id** and **IIa**–**IId**[*]

R	**Ia**–**Id**		**IIa**–**IId**	
	$\chi^{(3)} \times 10^{12}$	$\gamma \times 10^{38}$	$\chi^{(3)} \times 10^{12}$	$\gamma \times 10^{38}$
H	6.3	1.1	4.9	2.9
CH_3	5.7	1.3	5.1	3.0
Cl	3.2	1.5	3.5	2.2
$N(CH_3)_2$	5.9	1.6	6.5	3.6

* 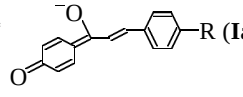 R (**Ia**–**Id**), 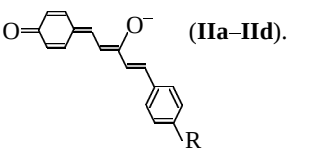 (**IIa**–**IId**).

γ for complexes containing chromophores **Ia**–**Id** and **IIa**–**IId**. Both the parameters characterize the THG efficiency, with $\chi^{(3)}$ related to the macroscopic effect, and γ, to the susceptibility of an individual molecule. Comparison of the parameters $\chi^{(3)}$ and γ for complexes from the series of substituted 1-(4-hydroxyphenyl)-1-arylpropenones and 1-(4-hydroxyphenyl)-5-arylpenta-1,4-dien-3-ones (Table 2) suggests that the length of the conjugation chain in the chromophore does not markedly affect the susceptibility. Moreover, auxochromes introduced into the molecules of 3-(4-hydroxyphenyl)-1-arylpropenone virtually do not affect $\chi^{(3)}$, whereas in the case of 1-(4-hydroxyphenyl)-5-arylpenta-1,4-dien-3-ones the susceptibilities correlate with the Hammett constants σ [6].

Our data suggest that the main contribution to the NLO effect comes from 3-(4-oxocyclohexa-2,5-dienyl)propene-1-ylate moiety, and the remaining segment of the molecule is less significant. The NLO effect, probably, results from a decrease in the degree of conjugation owing to the noncoplanar arrangement of the π bonds in the chromophore molecule. Quantum-chemical calculations of the molecular geometry of the chromophores in the complexes give the following dihedral angles φ between the "quinoid" and "nonquinoid" moieties of the chromophore molecule:

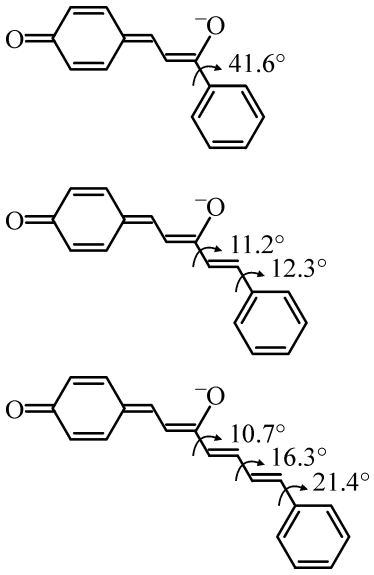

In view of the proportionality between the degree of conjugation and $\cos^2\varphi$, it can be assumed that the substituents must exert a virtually unnoticeable effect on the susceptibility in the case of 1-(4-hydroxyphenyl)-1-arylpropenones and a rather pronounced effect in the case of 1-(4-hydroxyphenyl)-5-arylpenta-1,4-dien-3-ones. The experimental data agree well with these assumptions.

Thus, the major contribution to the NLO effect manifested by quinoid forms of 4-hydroxybenzylidenalkanones comes from 4-hydroxycinnamoyl moiety, whereas the influence of the lengthening conjugation chain is largely eliminated by the noncoplanarity of the π system as a whole.

CONCLUSION

A study of the nonlinear optical properties of complexes of hydroxyphenyl-substituted unsaturated ketones with poly-1,10-decamethyleneacetamidine as influenced by the chemical structure of the ketones demonstrated that the major contribution to the NLO effect comes from the enol form of 4-hydroxycinnamoyl moiety of the chromophore.

ACKNOWLEDGMENTS

The study was supported financially by the Russian Foundation for Basic Research (project no. 01-03-32 294).

REFERENCES

1. Hulliger, J., Kaminskii, A.A., and Eichler, H.J., *Adv. Funct. Mater.*, 2001, vol. 11, no. 4, pp. 243–250.
2. Samyn, C., Verbiest, T., and Persoons, A., *Macromol., Rapid Commun.*, 2000, vol. 21, no. 1, pp. 1–15.
3. *Nonlinear Optics of Organic Molecules and Polymers*, Nalwa, H.S. and Miyata, S., Eds., Boca Raton: CRC, 1997.
4. Tenkovtsev, A.V., Yakimansky, A.V., Dudkina, M.M., *et al., Macromolecules*, 2001, vol. 34, no. 2, pp. 7100–7107.
5. Wendelin, W. and Kerbl, H., *Monatsh. Chem.*, 1984, vol. 115, no. 3, pp. 309–326.
6. Ten'kovtsev, A.V., Dudkina, M.M., Trofimov, A.E., *et al., Zh. Prikl. Khim.*, 2001, vol. 74, no. 7, pp. 1147–1151.
7. Kubodera, K. and Kobayashi, H., *Mol. Cryst. Liq. Cryst.*, 1990, vol. 182A, pp. 103–113.
8. Tykwinski, R.R., Gubler, U., Martin, R.E., *et al., J. Phys. Chem., Part B*, 1998, vol. 102, no. 23, pp. 4451–4465.
9. Bekturov, E.A. and Legkunets, R.E., *Assotsiatsiya polimerov s malymi molekulami* (Polymer Association with Small Molecules), Alma-Ata: Nauka, 1983.

Russian Journal of Applied Chemistry, Vol. 76, No. 4, 2003, pp. 595–599. Translated from Zhurnal Prikladnoi Khimii, Vol. 76, No. 4, 2003, pp. 616–620.

MACROMOLECULAR CHEMISTRY AND POLYMERIC MATERIALS

Specific Features of Cellulose Phase Transition via Knecht Additive Compound

E. V. Gert, O. V. Zubets, M. V. Shishonok, V. I. Torgashov, and F. N. Kaputskii

Research Institute of Physicochemical Problems, Belarussian State University, Minsk, Belarus

Received January 15, 2003

Abstract—The capability of cotton and wood cellulose in the common and microcrystalline forms to transform into cellulose-II under the action of 68–69% HNO_3 was studied. The influence of temperature on the course of the phase transition in cellulose samples differing in origin and morphological structure and the dynamics of concomitant hydrolytic degradation and esterification of these materials were studied.

Mercerization of cellulose (C) based on its intracrystallite swelling in solutions of alkali metal hydroxides is of great applied importance. Intracrystallite swelling of native C is also caused by HNO_3 at its concentrations close to 68.4% (concentration of the azeotropic mixture with water) [1]. As a result of swelling, the crystalline phase of the Knecht additive compound (KC) is formed [2–4]. The action of water regenerates the C-II polymorph from KC, which is similar to the behavior of alkaline C and makes it possible to speak about acid mercerization. Several examples of effective use of this process for preparing structurally and chemically modified forms of powdered C have been reported [4–6]; however, information about specific features of phase transitions of C in nitric acid medium is scarce.

Available data [7, 8] are limited to indications that the extent of the phase transition under the action of 66–69% HNO_3 at room temperature strongly depends on the parameters of the crystal structure of native C. The extent of phase transitions of C, associated with the formation of both KC and alkaline C, is determined by the transverse size $\bar{L}$ of the crystallites of the starting material [8].

Here we discuss the influence of temperature on nitric acid mercerization of C samples differing in origin and morphological structure. The concomitant chemical and physical transformations caused by the nontraditional mercerizing agent are analyzed.

EXPERIMENTAL

The main starting materials were as follows: cotton cellulose (CC) of Hercules brand [98% α-C, degree of polymerization (DP) 2000]; sulfide wood cellulose (WC) of Florenier brand (96% α-C, DP 1200); microcrystalline forms (MCC) of these kinds of cellulose (DP 200 and 160, respectively); and commercial MCC of LT Lachema brand. Preparation of cotton and wood MCC (CMCC and WMCC) involved the following steps: boiling of a fiber in 8% HNO_3 (1 h, liquid-to-solid ratio 20 ml g^{-1}), repeated washing of the slurry with water, and displacement of water with acetone. This was followed by drying at room temperature, grinding in a mortar, and collection of the fraction passing through a 100-μm-mesh sieve. The crystallinity index calculated according to [9] was 0.70 for CC, 0.74 for CMCC, 0.63 for WC, and 0.65 for WMCC. The treatment was preceded by keeping the materials in a desiccator over a saturated $NaNO_2$ solution (66% relative humidity).

Commercial 72% HNO_3 (ultrapure grade) was diluted to 68.5% concentration. The liquid-to-solid ratio in mercerization was 20 ml g^{-1}; the temperature was 20 (thermostat) or 0°C (vessel with thawing ice); the washing and drying procedure was the same as in preparation of MCC.

The degree of polymorphic transition was determined according to [9] from the X-ray diffraction patterns recorded on an HZG-4a diffractometer (Cu_{K_α} radiation, Ni filter). The results from 2–4 replicate measurements were averaged. The measurement error was ±5%.

The degree of polymerization of C was determined from the viscosity of solutions of its nitrate esters [10]. This procedure was successfully tested on samples with known DP. The content of bound nitrogen was determined by the Kjeldahl method. The physical and chemical transformations in C in the

1070-4272/03/7604-0595 $25.00 © 2003 MAIK "Nauka/Interperiodica"

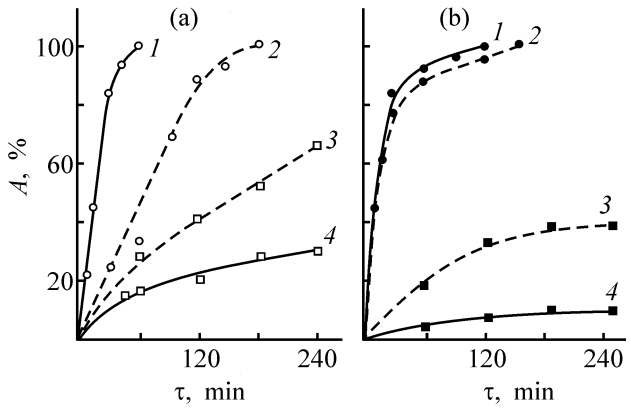

Fig. 1. Degree of conversion into C-II, *A*, of (a) fibrous and (b) microcrystalline forms of (*1*, *2*) WC and (*3*, *4*) CC vs. time τ of treatment with 68.5% HNO_3 at (*1*, *4*) 20 and (*2*, *3*) 0°C.

course of mercerization were monitored by IR spectroscopy (Specord 75-IR, KBr pellets). The water retention capacity (WRC) was determined according to [11], and the sorption power with respect to Congo Red, according to [12].

In contrast to alkali metal hydroxides, nitric acid is, relative to C, a multifunctional agent exerting complexing, estrifying, oxidizing, and hydrolyzing effects. This fact should be taken into account when choosing conditions for nitric acid mercerization. For example, the capability of HNO_3 to form an additive KC with C becomes pronounced at 68% concentration [7, 8]. At higher HNO_3 concentrations, this property is enhanced. At the same time, active accumulation of the pseudo-form of HNO_3 ($HO–NO_2$) causing *O*-nitration of C starts from approximately 69% concentration [10]. Thus, the stimulating effect of HNO_3 on the phase transitions is complicated by the esterifying effect of HNO_3 at its concentrations exceeding 69%. Therefore, we took 68.5% HNO_3.

It is known that traditional mercerization of C is better performed at low temperatures. This is due to the fact that the temperature coefficient of the rate of hydrolysis of alkaline C is higher than that of the rate of its formation. For nitric acid mercerization, such data are lacking.

Our experiments (Fig. 1) show that nitric acid mercerization of C samples of varied origin and morphology is characterized by different temperature dependences. With CC, the temperature dependence is similar to that observed in traditional mercerizartion: As the temperature of HNO_3 treatment is lowered from 20 to 0°C, the polymorphic transition is stimulated (Fig. 1). However, the conversion of the starting material into C-II is incomplete. Compared with the initial CC, the phase transitions in CMCC are considerably slower. The advantage of the common CC form over the microcrystalline form in the capability to form KC has been noted previously [7, 8]. It was presumed that structurally disordered areas of the fibers act as "mediators" facilitating access of HNO_3 to crystallites. However, this viewpoint fails to explain the following facts.

Under the conditions examined, treatment of C with HNO_3 causes complete and relatively fast conversion of sulfite WC into C-II. In contrast to CC, at 20°C the process occurs faster than at 0°C. The abnormal temperature dependence is especially pronounced in samples with common amorphous-crystalline morphology (Fig. 1a). In contrast to CMCC, microcrystalline wood cellulose undergoes mercerization at an unexpectedly high rate, virtually independent of temperature, until approximately 60% conversion is attained (Fig. 1b). The final stage of the polymorphic transition at 0°C is somewhat slower than that at 20°C. According to [8], sulfite WC also shows increased activity in mercerization with NaOH solutions, whereas CC, along with ramie cellulose, is among the least active kinds of cellulose.

Apparently, the true temperature dependence of the rate of the permutoid (according to Mark) reaction of KC can be obtained from experiments with CC, since its chemical purity is higher than that of technical-grade WC, irrespective of its production process. The content of C in the corresponding raw materials is up to 98% in cotton linters and no more than 55% in wood tissues. High concentration of lignin and hemicelluloses (including cellulosans) in wood and severe conditions of cooking, accompanied by degradation, negatively affect the capillary–poroius system and reactivity of the recovered C fibers. It is known that dense deposits of unremoved low-molecular-weight fractions, mainly hemicelluloses, alter the relative contributions of the capillary and diffusion transport of chemical agents in favor of the latter mechanism [10, 13]. Therefore, preactivation procedures are especially necessary in chemical processing of WC. As for CC fibers, concomitant substances affect their capillary-porous system to a lesser extent. The access of chemical agents to CC crystallites is facilitated by the high degree of crystallinity and presence of an internal channel in the fibers.

Thus, there is good reason to believe that, at low temperatures, the transport of HNO_3 to WC crystallites involves larger diffusion hindrance than its transport to CC crystallites. This may be associated with slow transport of the acid through hemicellulose de-

posits, because the hydrolytic activity is lower at low temperatures (Fig. 2). Correspondingly, the transformation of crystallites, detected by X-ray diffraction, is "delayed." This viewpoint is convincingly supported by the fact that WMCC is mercerized at 0°C faster than the initial cellulose. The acceleration is most probably due to weakening of the influence exerted by the diffusion factor on the process kinetics, which occurs when the crystallites get free of the structurally disordered binder. In traditional mercerization, the penetration of the chemical agent is facilitated by the solubility of hemicelluloses in alkalis. Furthermore, the equilibrium swelling of C in 68– 69% HNO_3 is lower than that in NaOH solutions [14].

The incapability of both morphological forms of CC undergoing complete mercerization in conditions at which mercerization of the same forms of WC goes to completion (Fig. 1) is consistent with the concept of Ioelovich and Veveris [8, 9, 15], which concerns the influence of the crystallite dispersity on the extent of phase transitions involving formation of additive compounds. Crystallites of Hercules CC ($\bar{L}$ = 10 nm) are considerably larger than those of Florenier WC ($\bar{L}$ = 6 nm) [15]. As a result of hydrolysis of cellulose fiber to "limiting" DP, $\bar{L}$ inevitably grows owing to recrystallization and hydrolytic breakdown of the smallest crystallites. It follows from [8, 9, 15] that, in preparation of CMCC, the increase in $\bar{L}$ is appreciably more pronounced (~35%) than that in preparation of WMCC (~20%). As the difference between the crystallite sizes of these two kinds of microcrystalline C increases, the difference between the degrees of their mercerization grows also, reaching a factor of 10 (Fig. 1b). Microcrystalline wood cellulose is mercerized at 0°C faster than the initial C, despite the coarsening of crystallites in the partial hydrolysis. However, the coarsening of crystallites is responsible for the appearance of a pronounced slow (final) stage of mercerization of the coarsest crystallites. In all probability, the crystallite size in both morphological forms of WC is smaller than the level limiting the degree of polymorphic transition under the treatment conditions examined. It is quite probable that specifically this fact is responsible for the better suitability of wood C for nitric acid mercerization.

In the course of nitric acid mercerization, common amorphous-crystalline C undergoes significant degradation (Fig. 2). A fast decrease in the DP of the starting C in the initial period of treatment with 68.5% HNO_3 is followed by slow degradation of chain molecules. The rate of hydrolytic cleavage of macromolecules strongly depends on the mercerization temperature. Complete polymorphic transition of Florenier WC at 20°C (1-h treatment with HNO_3) is accompanied by a decrease in the initial DP (1200) by approximately a factor of 3, and at 0°C (3-h treatment with HNO_3), by only a factor of 1.5. In contrast to the initial C, its microcrystalline form remains resistant to hydrolysis under conditions of intracrystallite swelling, too. A factor that possibly prevents development of degradation processes is the high stoichiometry of the interaction of 68.5% HNO_3 with C macromolecules in crystallites [3, 16]. According to [3], the Knecht compound contains one HNO_3 molecule per two anhydroglucopyranose units of C. Within the time of complete mercerization of Florenier WMCC, both at 20 and at 0°C, the initial degree of polymerization remains virtually unchanged (Fig. 2).

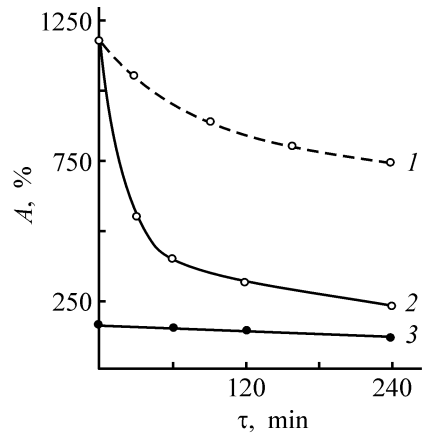

Fig. 2. DP of (*1*, *2*) initial and (*3*) microcrystalline Florenier *C* vs. mercerization time τ at (*2*, *3*) 20 and (*1*) 0°C.

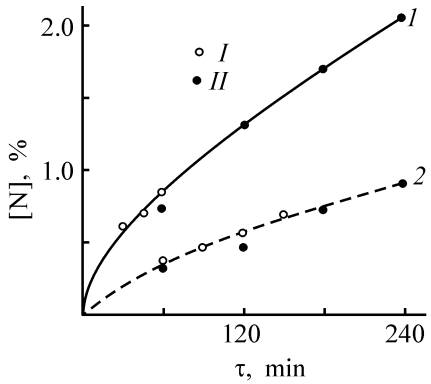

Fig. 3. Content of chemically bound nitrogen [N] in (*I*) initial and (*II*) microcrystalline Florenier C vs. time τ of treatment with 68.5% HNO_3 at (*1*) 20 and (*2*) 0°C.

Specific features distinguishing C-II from C-I [17] are clearly manifested in IR spectra of mercerized C. There is no evidence of oxidative transformations (no carbonyl absorption in the range 1700–1800 cm^{-1}), but the bands belonging to nitric acid esters (1650, 1280, 850, 750 cm^{-1}) are present. The rate of accumulation of bound nitrogen in C strongly depends on the temperature of treatment with HNO_3 (Fig. 3).

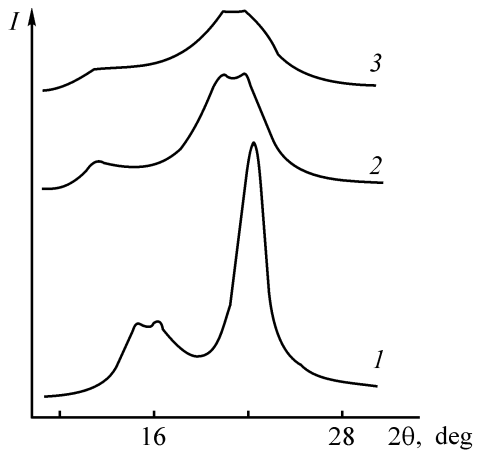

Fig. 4. X-ray diffraction patterns of Florenier MCC: (*1*) initial, (*2*) mercerized for 4 h at 0°C, and (*3*) mercerized for 3 h at 20°C. (*I*) Relative intensity and (θ) Bragg angle.

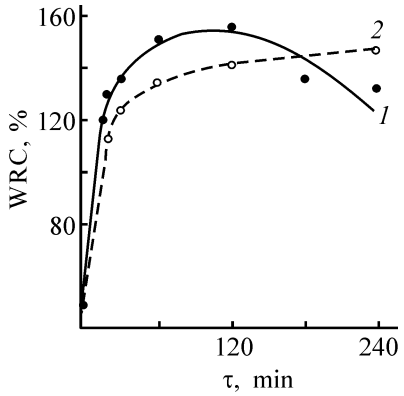

Fig. 5. Water retention capacity WRC of Florenier MCC vs. time τ of mercerization at (*1*) 20 and (*2*) 0°C.

The morphology of the starting material affects esterification with HNO_3 only slightly. Samples of Florenier C accumulate in the course of complete mercerization at 20 (1-h treatment with HNO_3) and 0°C (3-h treatment with HNO_3) approximately equal amounts of nitrogen, 0.7–0.8% (degree of substitution, DS_{ONO_2} 0.8–0.9).

In nitric acid mercerization of WMCC, the effect of esterification on the physical structure of the products is appreciable. Microcrystalline wood cellulose mercerized at 0°C (2.5-h treatment with HNO_3) considerably surpasses in crystallinity the same cellulose mercerized at 20°C (2-h treatment with HNO_3). In the latter sample, the content of bound nitrogen is almost two times higher (~1.3%, DS_{ONO_2} 0.15). Upon longer (4 h) mercerization, the nitrogen content increases to 2% (DS_{ONO_2} 0.25).

In the X-ray diffraction patterns of the products obtained, the crystallite scattering degenerates as the degree of esterification grows, and at DS ≥ 0.25 it virtually disappears. At the same time, in the X-ray diffraction pattern of the MCC sample mercerized for 4 h at 0°C, the crystallite scattering of C-II is rather well pronounced (Fig. 4), since the content of bound nitrogen is as low as 0.9% (DS_{ONO_2} 0.1). There is a clear correlation between the degrees of esterification and decrystallization of mercerized WMCC. We believe that partial esterification is the major factor responsible for the structural disordering of WMCC in the course of its nitric acid mercerization. It should be emphasized that the clearly pronounced decrystallization effect can be observed specifically in mercerization of WMCC. This effect may be favored by relatively low length of WMCC macromolecules, comparable with the segment length in common C.

The different rates of accumulation of bound nitrogen are also responsible for different trends in variation of WRC in the course of WMCC mercerization at 20 and 0°C (Fig. 5). The materials formed by the time when transformation of the native WMCC structure to the hydrated cellulose structure at 20 and 0°C is complete exhibit WRC of 155 and 143%, respectively. Apparently, the observed difference is due to nonequivalent contributions of the decrystallizing effect of *O*-nitration to the increase in WRC. At the same time, accumulation of nitric acid ester groups enhances the sample hydrophilicity owing to decrystallization until the hydrophobizing effect of the ester groups on the forming hydrated cellulose becomes prevailing. In the products of WMCC mercerization at 20°C for 3 and 4 h, the hydrophobizing effect prevails over the effect associated with decrystallization, which results in a noticeable decrease in WRC; however, WRC remains on the level characteristic of WC mercerized by the traditional procedure [13]. In the case of WMCC mercerization at 0°C, esterification is inhibited, and the corresponding effect of the forming hydrated cellulose on WRP is positive (though weakened) in the entire range of mercerization times examined.

To conclude, nitric acid mercerization of specifically WMCC enhances to the greatest extent its sorption activity owing to decrystallization. This can be judged from comparison of the kinetic curves of Congo Red sorption on commercial MCC (LT Lachema) and on the product of its 3-h mercerization at 20°C (Fig. 6). The initial MCC sample is one of the best sorbents of this class, which is used in thin-layer chromatography. As seen from Fig. 6, the limiting sorption of the dye by the mercerized sample increases by approximately 60% as compared with the initial sample, and the sorption–desorption equilibrium is attained approximately four times faster.

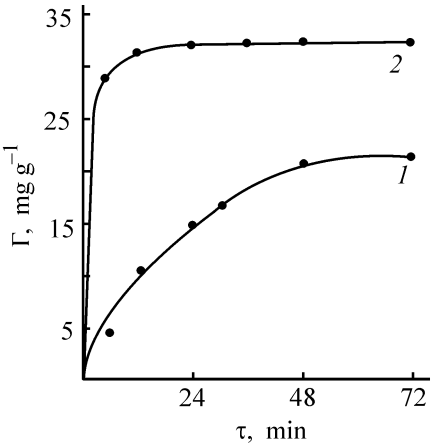

Fig. 6. Kinetic curves of Congo Red sorption from its 0.02% solution by (*1*) LT Lachema MCC and (*2*) product of its 3-h mercerization. (Γ) Sorption and (τ) sorption time.

CONCLUSIONS

(1) The rate of the polymorphic transition in wood cellulose decreases by about a factor of 3 as the temperature of treatment with 68.5% HNO_3 is lowered from 20 to 0°C, owing to the prevalence of the diffusion transport of the reagent to crystallites over the capillary transport, in contrast to cotton cellulose in which the phase transition occurs faster at lower temperature of HNO_3 treatment. The diffusion hindrance is due to weakening of the hydrolytic activity of HNO_3 at low temperatures, so that it passes more difficultly through hemicellulose deposits in capillaries and pores of wood cellulose fibers. It is quite natural that the microcrystalline form of wood cellulose, free of structurally disordered component, is mercerized under the action of HNO_3 at a rather high rate only slightly depending on temperature.

(2) The complete polymorphic transition of wood cellulose is accompanied by a decrease in the degree of polymerization by approximately a factor of 3 at 20°C and only 1.5 at 0°C. At the same time, the microcrystalline form of this cellulose is mercerized at 20 and 0°C without changes in the degree of polymerization, which is due to the high stoichiometry of interaction of HNO_3 with ordered macromolecules in crystallites (formation of the Knecht compound).

(3) Weak *O*-nitration of cellulose under the conditions of intracrystallite interaction with HNO_3 exerts a decrystallizing influence on the mercerization products, which is the stronger, the higher the temperature and the longer the treatment. This effect, which is the most pronounced in microcrystalline wood cellulose, enhances the hydrophilicity and sorption capacity of the final products.

REFERENCES

1. Atroshchenko, V.I. and Kargin, S.I., *Tekhnologiya azotnoi kisloty* (Technology of Nitric Acid), Moscow: Khimiya, 1970.
2. Knecht, E., *Ber.*, 1904, vol. 37, pp. 549–552.
3. Andress, R.K., *Z. Phys. Chem.*, 1928, vol. 136, pp. 279–288.
4. Gert, E.V., *Usp. Khim.*, 1997, vol. 66, no. 1, pp. 78–98.
5. Gert, E.V., Shishonok, M.V., Zubets, O.V., *et al.*, *Vysokomol. Soedin., Ser. A*, 1995, vol. 37, no. 7, pp. 1130–1136.
6. Gert, E.V., *Cellulose*, 1996, vol. 3, no. 4, pp. 217–228.
7. Shishonok, M.V., Gert, E.V., Filanchuk, T.I., and Kaputskii, F.N., *Zh. Prikl. Khim.*, 1987, vol. 60, no. 5, pp. 1153–1157.
8. Ioelovich, M.Ya. and Veveris, G.P., *Khimiya delignifikatsiii tsellyulozy* (Delignification and Cellulose Chemistry), Riga: Zinatne, 1991.
9. Ioelovich, M.Ya. and Veveris, G.P., *Khim. Drev.*, 1983, no. 2, pp. 10–14.
10. Nikitin, N.I., *Khimiya drevesiny i tsellyulozy* (Wood and Cellulose Chemistry), Moscow: Akad. Nauk SSSR, 1962.
11. Fahmy, Y. and Mobarak, F., *Sven. Pappererstidning. Och. Svenpappersförädlingstidskr., Ser. A*, 1971, vol. 74, no. 1, pp. 2–9.
12. Ioelovich, M.Ya., *Khim. Volokna*, 1992, no. 6, pp. 46–48.
13. Papkov, S.P. and Fainberg, E.Z., *Vzaimodeistvie tsellyulozy i tsellyuloznykh materialov s vodoi* (Interaction of Cellulose and Cellulose Materials with Water), Moscow: Khimiya, 1976.
14. Gert, E.V., Socarras Morales, A., Zubets, O.V., and Kaputskii, F.N., *Cellulose*, 2000, vol. 7, pp. 57–66.
15. Ioelovich, M.Ya. and Veveris, G.P., *Khim. Drev.*, 1985, no. 6, pp. 30–34.
16. Gert, E.V., Shishonok, M.V., Torgashov, V.I., and Kaputskii, F.N., *J. Polym. Sci., Part C: Polym Lett.*, 1990, vol. 28, pp. 163–166.
17. Nelson, M.L. and O'Connor, R.T., *J. Appl. Polym. Sci.*, 1964, vol. 8, pp. 1311–1324.

Russian Journal of Applied Chemistry, Vol. 76, No. 4, 2003, pp. 600–602. Translated from Zhurnal Prikladnoi Khimii, Vol. 76, No. 4, 2003, pp. 621–623.

MACROMOLECULAR CHEMISTRY AND POLYMERIC MATERIALS

Adsorption of Hydroxyethyl Cellulose Selenium Nanoparticles during Their Formation in Water

V. V. Kopeikin, S. V. Valueva, A. I. Kipper, L. N. Borovikova, Ya. I. Nazarkina, E. N. Khlebosolova, and A. I. Filippov

Institute of Macromolecular Compounds, Russian Academy of Sciences, St. Petersburg, Russia

Received December 23, 2002

Abstract—Two previously unknown phenomena were observed in studying the reduction of selenious acid with ascorbic acid in an aqueous hydroxyethyl cellulose solution: (1) formation of nanoparticles of amorphous Se^0 with uniform particle size distribution and mean particle radius of 15 ± 4 nm and (2) adsorption of more than 3000 macromolecules on these nanoparticles with formation of spherical nanostructures.

Thanks to its availability, permanently reproducible natural sources, and wide potentialities for chemical modification, cellulose is of indisputable scientific and practical interest as the basis for development of novel materials for biomedical and health purposes. At the same time, in view of the rapid development of nanotechnology and supramolecular chemistry, particular attention is paid to study of metal–polymer systems containing nanoparticles of metals in zero oxidation state. Such nanoparticles 1–100 nm in size in polymeric matrices demonstrate anomalous physicochemical, catalytic, and biological properties, which is caused by high energy saturation of their surface [1].

For instance, Ag^0 nanoparticles stabilized by polyvinylpyrrolidone demonstrate unique pharmacological properties [2], which are not characteristic of bulk silver. In impregnation of bacterial cellulose (BC) gel films with aqueous solutions of such nanocomposites, Ag nanoparticles are irreversibly adsorbed on the cellulose matrix. As a result, such a bandaging material acquires high antimicrobial activity [3]. Kotel'nikova [4] has succeeded in diffusion-reductive intercalation of silver nanoparticles into fibers and films of microcrystalline cellulose (MCC). In this method, the morphological structure of cellulose is modified, and silver nanoparticles are tightly bound to the cellulose matrix.

It is noteworthy that there are virtually no data on polymer-stabilized nonmetallic nanoparticles. Of particular interest are nanoparticles of amorphous selenium (nano-a-Se^0), which demonstrate not only unique photoelectric, semiconducting, and X-ray-sensing properties, but also exceptionally broad spectrum of biological activity [5].

Since BC and MCC are insoluble in most of solvents, a study of their interaction with nanoparticles in solutions is quite problematic. Here we report on the interaction of the water-soluble polysaccharide hydroxyethyl cellulose (HEC) with nano-a-Se^0.

EXPERIMENTAL

We chose as object of study a-Se^0 nanoparticles prepared by reduction of selenious acid (SA) in an aqueous ascorbic acid solution both in the presence and in the absence of HEC.

We used reagents with the main substance content of no less than 99.99%. The hydroxyethylcellulose used had a degree of substitution of 1.2 and MW 150×10^3.

The reduction kinetics was studied spectrophotometrically (Specord M40, λ = 320 nm, 20°C) at an SA concentration of 1.7 mM and pH 3.1.

Reduction of Se(IV) in its 0.01 wt % solution gives nanocomposites with HEC-to-Se^0 weight ratio of 90 : 10.

The relative viscosity η_r was determined with an Ostwald capillary viscometer (water outflow time 120 ± 0.2 s at 21°C).

Using the flow birefringence (FBR) method [6] we characterized the molecular dispersity of the ad-

1070-4272/03/7604-0600 $25.00 © 2003 MAIK "Nauka/Interperiodica"

sorbates formed. The FBR value Δn was determined as dependent on the rotor speed gradient g and the HEC concentration c at a fixed Se concentration.

In the experiments, we used a titanium dynamo-optimeter with 4-cm-high inner rotor and 0.03-cm gap between the rotor and stator. All the FBR measurements were performed with temperature control (21°C) to eliminate changes in the solution viscosity and also optical distortions induced by the temperature gradient. The measuring system was calibrated against phenylethanol, which is characterized by high FBR ($\Delta n/g = 17 \times 10^{-12}$), and the polystyrene–bromoform system. The intrinsic FBR $[n] = \lim_{g \to 0, c \to 0} (\Delta n/gc\eta_0)$, where η_0 is the solvent viscosity, was determined to within 10%. The measurements were carried out at $g < g_k$, where g_k is the speed gradient at which flow turbulence starts.

The experimental value of $[n]$ ($dn/dc \neq 0$, where dn/dc is the increment in the refractive index of the solution, which is 0.102 and 0.149 for the systems investigated, HEC–H_2O and HEC-Se^0–H_2O, respectively) is, generally, composed of three terms: $[n] = [n]_e + [n]_{fs} + [n]_f$. Here $[n]_e$ is the intrinsic anisotropy; $[n]_{fs}$, microform term; $[n]_f$, macroform term [6]. In this case, the total segment anisotropy ($[n]_e + [n]_{fs}$) is determined by the equilibrium rigidity A of the polymer chain and the polymer unit structure, and $[n]_f$ is related to the asymmetry p of the shape of a macromolecule (particle) as

$$[n]_f = [(n_s^2 + 2)/3)^2 [M_w (dn/dc)^2 f(p)]/(30\pi RTn_s)$$
$$= \text{const}\, M_w (dn/dc)^2 f(p).$$

Here M_w is the molecular weight of the adsorbate macromolecule; n_s, refractive index of the solvent; T, absolute temperature; R, gas constant; $f(p)$, tabulated function for the axis ratio of a rigid (impermeable to the solvent) ellipsoid approximating the particle shape [6].

Therefore, for flexible and moderately rigid-chain high-molecular-weight polymers ($A < 5$ nm) characterized by low optical anisotropy and low molecular weight of the polymer unit, the relationship $[n] \sim [n]_f$ is valid, allowing direct estimation of the parameter p from the experimental data on FBR [6].

The nanostructures investigated were characterized by the molecular weight M_w and size R_g, using the static light scattering method [7], and also by their solvent (water) affinity using data on the second virial coefficient A_2. The amount of adsorbed macromolecules on the surface of Se nanoparticles was determined from the relationship between the M_w values for HEC and its adsorbates. The reduced intensity of light scattering of solutions, R_θ, was determined with a Fica photogoniodiffusometer. The wavelength of vertically polarized incident light was 546.1 nm. The measurements were performed over the scattering angle range $\theta = 30°$–$150°$. The solutions and solvents were clarified by centrifugation at 15 000 rpm for 1–1.5 h. The increment in the refractive index, dn/dc, was estimated from the refractometric data (IRF23 instrument).

The experimental light-scattering data were processed by the Zimm method by double extrapolation (to $c = 0$ and $\theta = 0$) of the Kc/R_θ-vs.-[$\sin^2(\theta/2) + kc$] plot (K is the calibration constant, and k, empirical parameter).

The mean hydrodynamic size R_H of the particles was determined by the quasi-elastic (dynamic) light scattering method [8]. The parameter ρ^*, which characterizes the conformation of nanostructures was estimated from experimental R_g and R_H obtained for the HEC–Se^0 adsorbate [9–12].

The optical part of the setup for measuring the dynamic light scattering was equipped with an ALV-SP goniometer (Germany) and a Spectra-Physics He–Ne laser (λ 632.8 nm, 20 mW) as a source of light. The correlation function for the light-scattering intensity was obtained with a 288-channel Photo Cor-FC correlator (Anteks Private Company, Russia). Experimental data were processed using the cumulant and Tikhonov's regularization methods.

In SA reduction with ascorbic acid, the first-order rate constant with respect to SA was found to be 1.56×10^{-3} s^{-1}, and that in the presence of HEC, 0.42×10^{-3} s^{-1}. In the absence of the polymeric stabilizer, the Se nanoparticles appeared to be aggregatively unstable. In 3–4 days they formed conglomerates and precipitated. In the case of polymer-stabilized nano-Se^0, the aggregative stability of the particles was preserved for at least 6 months.

On passing from the initial HEC to the HEC–nano-Se^0 adsorbate, the intrinsic viscosity $[\eta]$ decreases from 5.3 to 3.6 dl g^{-1}. However, according to the static light-scattering data, the molecular weight M_w of the adsorbate is 480×10^6, which is higher by a factor of 3200 than that of free HEC.

The second virial coefficient A_2 of the HEC–Se^0–H_2O system is zero, suggesting the ideal thermodynamic state of the solution.

The mean hydrodynamic radius R_H of free HEC in aqueous solutions is 182 nm, and that of Se nanoparticles obtained in the absence of the polymeric stabilizer, 170 nm. The size of the HEC–Se^0 adsorbate, estimated by the dynamic and static light-scattering

methods, is smaller (mean-square radius of inertia R_g = 85 nm and mean hydrodynamic radius R_H = 147 nm). In this case, the parameter $\rho^* = R_g/R_H = 0.6$, which suggests an ideal sphericity of the adsorbate formed [9–12].

To determine the radius of Se particles in the adsorbate core, we employed lyophilic drying of the HEC–Se^0 aqueous solution. The resulting dry product was pelletized and studied by the low-angle X-ray scattering method. The radius of Se^0 spherical particles was determined to be 15 ± 4 nm, which is an order of magnitude smaller than that of the Se particles obtained without the polymeric stabilizer (171 nm). Therefore, in the aqueous solution, the depth of the satellite polymeric coating on the Se^0 nanoparticles is about 70 nm, i.e., adsorption results in a considerable compaction of the macromolecules.

On passing from the HEC–H_2O system to HEC–Se^0–H_2O, the optical anisotropy increases substantially from 300 to 3000 $cm^4 s^2 g^{-2}$, which is probably due to the adsorption of a huge number of macromolecules on single nano-Se^0 particles, with the hydrophobic interactions of the nonpolar fragments of the macromolecules with nano-Se^0 being the major driving force of the adsorption.

It should be pointed out that, in the HEC–H_2O and HEC–Se^0–H_2O systems, the molecular dispersion of the solutions remains unchanged over the whole c range, as demonstrated by the features of the $\Delta n = f(g)$ dependences (at $g < g_k$ they are well approximated for any c by straight lines crossing the origin of coordinates).

The parameter p estimated for the HEC–Se^0–H_2O system in the $[n] \sim [n]_f$ approximation revealed that the nanostructure takes a practically ideal spherical conformation (p = 1.4) (it is known that, in water, HEC takes a conformation of Gaussian globule [13]). Taking into account the increased rigidity of HEC (A = 15 nm) [13], one may conclude that the actual p value is even closer to unity. Therefore, the adsorbate is an ordered spherical nanostructure.

Finally, the results obtained cast light on the nature of structural and morphological transformations of cellulose in formation of metallic and nonmetallic nanoparticles in its matrix.

CONCLUSIONS

(1) Spherical nanoparticles of amorphous selenium about 15 nm in size were obtained by reduction of Se(IV) in the selenite–ascorbate redox system.

(2) In the system formed by hydroxyethyl cellulose, Se^0, and water, the viscosity of a solution falls, and the solution properties approach those of an ideal solution, which suggests the formation of compact aggregatively stable adsorbates of the macromolecules on selenium nanoparticles.

(3) The resulting adsorbate is a supramacromolecular close-packed spherical nanostructure consisting of about 3000 macromolecules, as demonstrated for the first time by methods of molecular hydrodynamics and optical methods.

REFERENCES

1. Pomogailo, A.D., *Nanochastitsy metallov v polimerakh* (Metallic Nanoparticles in Polymers), Moscow: Nauka, 1999.
2. Kopeikin, V.V. and Panarin, E.F., *Dokl. Ross. Akad. Nauk*, 2001, vol. 380, no. 2, pp. 497–500.
3. Khripunov, A.K., Tkachenko, A.A., Baklagina, Yu.G., *et al.*, Abstracts of Papers, *Vtoraya mezhdunarodnaya konferentsiya "Sovremennye podkhody k razrabotke effektivnykh perevyazochnykh sredstv, shovnykh materialov i polimernykh implantatov"* (2nd Int. Conf. "Modern Approaches to Development of Effective Bandaging and Suture Materials and Polymeric Implants"), Moscow, November 21–22, 1995, pp. 71–73.
4. Kotel'nikova, N.E., Adsorption-Chemical Modification of Cellulose with Bioactive Compounds, *Doctoral Dissertation*, St. Petersburg, 2002.
5. Zhang, J.S., Gao, X.Y., Zhang, L.D., and Bao, Y.P., *Biofactors*, 2001, vol. 15, no. 1, pp. 27–38.
6. Tsvetkov, V.N., Eskin, V.E., and Frenkel', S.Ya., *Struktura makromolekul v rastvorakh* (Structure of Macromolecules in Solutions), Moscow: Nauka, 1964.
7. Eskin, V.E., *Rasseyanie sveta rastvorami polimerov i svoistva makromolekul* (Light Scattering in Polymer Solutions and Properties of Macromolecules), Leningrad: Nauka, 1986.
8. Brown, W., *Dynamic Light Scattering: the Method and Some Application*, Oxford: Clarendon, 1993.
9. Meewes, M., Ricka, J., De Silva, M., *et al.*, *Macromolecules*, 1991, vol. 24, no. 21, pp. 5811–5816.
10. Nishio, I., Sun, Shao Thang, Swislow, G., and Tanaka, T., *Nature*, 1979, vol. 281, no. 5728, pp. 208–209.
11. Konishi, T., Yoshizaki, T., and Yamakawa, H., *Macromolecules*, 1991, vol. 24, no. 20, pp. 5614–5622.
12. Burchard, B.W., *Laser Light Scattering in Biochemistry*, Harding, S.E., Satelle, D.B., and Bloomfild, V.A., Eds., Cambridge: Royal Soc. Chem. Inform. Services, 1992, pp. 3–21.
13. Tsvetkov, V.N., *Zhestkotsepnye polimernye molekuly* (Rigid-Chain Polymeric Molecules), Leningrad: Nauka, 1986.

Russian Journal of Applied Chemistry, Vol. 76, No. 4, 2003, pp. 603–606. Translated from Zhurnal Prikladnoi Khimii, Vol. 76, No. 4, 2003, pp. 624–628.

MACROMOLECULAR CHEMISTRY AND POLYMERIC MATERIALS

Conducting Materials Based on Thermally Expanded Graphite

V. N. Gorshenev, S. B. Bibikov, and Yu. N. Novikov

Emanuel' Institute of Biochemical Physics, Moscow, Russia

Nesmeyanov Institute of Organoelemental Compounds, Russian Academy of Science, Moscow, Russia

Received August 2, 2002

Abstract—The electrical conductivity of composites produced from thermally expanded graphite, isoprene rubber, and polyvinyl chloride plastisol was studied as influenced by the process conditions.

Preparation of conducting polymers (CPs) is a topical task of modern materials science. Highly conductive polymers are extensively used to ensure reliable operation of radio equipment in, particular, to shield radioelectronic devices [1–7].

Low-resistance composites are known [6] to contain, as a filler, expensive fine silver powders in high amounts.

In this study, we prepared highly conductive polymeric composites containing thermally expanded graphite (TEG) as filler and analyzed their properties as influenced by the conditions of mixing of the filler with a binder.

EXPERIMENTAL

Thermally expanded graphite was prepared by the hydrosulfate procedure [8–10] involving the following three main steps: (1) stirring of low-ash GSM-1 graphite for 30 min in a mixture of concentrated nitric and sulfuric acids to form an intercalation compound (graphite hydrosulfate), (2) hydrolysis of the graphite intercalation compound with water and drying of oxidized graphite to a friable state, and (3) thermal expansion of oxidized graphite by rapid heating to 800–900°C to form TEG. The bulk density of the TEG was ρ_{bulk} = 16 g l^{-1}. Elemental analysis showed the presence of up to 0.5 wt% sulfur in the TEG. As determined by scanning electron microscopy with 100-nm resolution, graphite had pronounced layered structure [11].

Since TEG has the layered structure, it can be rolled to give highly conductive sheets. A porous flat 1–2-cm-thick TEG sample prepared by compacting a TEG powder was rolled on bench rolls with variable gap to thickness of 0.7–0.3 mm. The rollers were 10 cm in diameter (*D*), and their rotation rate was ν = 5–15 rpm. Dense sheets of TEG are formed by compaction of the initial porous sample; in the process, the gap between the rollers and the shearing stress arising in the course of rolling were varied.

We used SKI-3 rubber and polyvinyl chloride (PVC) plastisol as binders for prepating conducting TEG composites.

The conducting composites of TEG (50%) and SKI-3 rubber were prepared by the following procedure. A rubber solution in benzine (1 l, 15 g l^{-1} concentration) was mixed with dicumyl peroxide (1 g) and TEG (15 g). The solvent was removed on a rotary evaporator at 50°C to give a loose powder. To obtain samples for resistance measurements, the resulting formulation was pressed in a mold at 143°C and a pressure of 20 MPa for 30 min.

The plastisol technology is frequently used to produce highly filled polymeric composites [12]. This is due to low viscosity of the plastisol, simple production of the composite, and satisfactory physicomechanical properties of the plastigel.

The procedure for preparing PVC–TEG composites included the following steps. An EP-66 PVC powder was thoroughly mixed with dioctyl phthalate in the weight ratio of 2 : 1 or 1 : 1. The mixture was plasticized on a water bath at 90°C for 45 min. To inhibit dehydrochlorination, 3wt % of calcium stearate was added with vigorous stirring. Then, the conducting filler, TEG, was added. The mixture was stirred until a uniform composition was formed. The composites was prepared by pressing in a mold at 0.2–0.5 MPa. The resulting samples were rolled at 120–140°C with the gap between the rollers slowly varied.

1070-4272/03/7604-0603 $25.00 © 2003 MAIK "Nauka/Interperiodica"

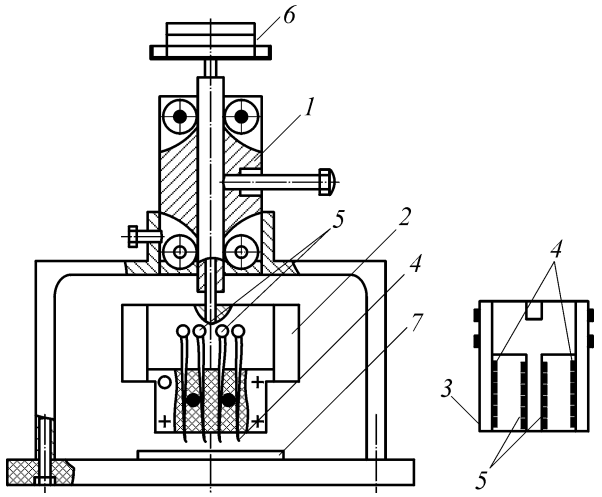

Fig. 1. Unit for measuring the electrical conductivity of the composites by the four-probe method. (*1*) pressure pad, (*2*) removable contacts with needle electrodes, (*3*) removable contacts with plate electrodes, (*4*) current electrodes, (*5*) potential electrodes, (*6*) load on the pressure pad, and (*7*) sample.

The bulk resistivity ρ_v of the composites was measured by the four-probe method [13]. To provide fast fixing of the sample, a pressure pad with removable contacts was used (Fig. 1).

The resistivity of the samples with thickness of 0.3 to 3 mm was measured with a contact unit made from Plexiglas, in which plates of current and potential electrodes were fixed (Fig. 1). The resistivity ρ_v was calculated by the common equation for the plane-parallel geometry of conducting samples

$$\rho_v = R_{av}\frac{S}{l},$$

where R_{av} is the electrical resistance of a sample (Ω), calculated by the least-squares procedure from the $I(U)$ dependence; S, the area of a cross section of the sample with the plane normal to the current direction; l, the distance between the potential electrodes.

We measured the bulk resistivity of a sample 0.3 to 3 mm thick, 25 mm wide, and 40 mm long. The distance between the potential electrodes was 5 mm.

The shielding coefficient K_{sc} (dB) of the samples was determined as the logarithm of the ratio of the power of incident microwave radiation I_{inc} to that of the radiation passed through the sample I_{pas}:

$$K_{sc} = 10\log\frac{I_{inc}}{I_{pas}},$$

This coefficient depends on the radiophysical properties (complex permittivity and magnetic permeability) and thickness of a sample. As the conductivity of a sample increases, both the reflection of the electromagnetic energy from the conductive surface and the energy dissipation in the bulk of the sample increase. Hence, the shielding coefficient K_{sc} increases. The general equation taking the interference into account is rather cumbersome [14, 15]. However, for thin conducting nonmagnetic samples it reduces to the equation

$$K_{sc} \simeq 20\log(1 + 188\sigma d),$$

where 188 (Ω) is the wave resistance of free space, σ is the electrical conductivity of the material (S cm^{-1}), and d is the sample thickness (mm).

The shielding coefficients were determined on a unit for measuring coefficients of transmission and reflection of microwave radiation in rectangular 23 × 10 mm waveguide (H_{01} mode). The unit was constructed on the basis of P2-61 panoramic standing wave-ratio meter and was modified to allow automated measurements. The measurements on this unit involve the following steps. A sample in the form of rectangular plates 0.3 to 10 mm thick was placed in a rectangular waveguide at a right angle to the direction of propagation of the electromagnetic energy. The internal cross-section (23 × 10 mm) of the waveguide was completely covered. Identical directed couplers with built-in microwave diode detectors were fixed in front of, and behind the sample. A sweep oscillator was connected to one end of the waveguide, and a matched load, which substantially decreases the reflection from the end of the line, to the other end. Both microwave detectors were connected via an amplifier-demodulator to an analog receiver-divider of the signal. The sweep oscillator and receiver were controlled by a computer. The signal from both detectors is proportional to the electromagnetic power propagating from the generator to the load. Hence, the ratio of the detector signals is proportional to the ratio of the microwave power of the incident radiation and that of the radiation passed through the sample. Analog-digital processing of this ratio gave the shielding coefficient.

It is known [16, 17] that binder-free TEG is molded owing to mechanical adhesion of the carbon layers. The folded and deformed structure of the carbon layers favors compression of the material and formation of graphite foil in the course of rolling on rollers with variable gap.

The electricalal conductivity of a material strongly depends on its production process. For example, pressed 3-mm-thick TEG sample with bulk density

ρ_{bulk} = 140 g l^{-1} has volume conductivity Σ_v = 1.5×10^2 S cm^{-1}, tensile strength γ_t = 0.05 MPa and relative elongation at rupture ε = 2%. After rolling of this sample to a thickness of 0.4 mm, these parameters changed as follows: ρ_{bulk} = 1100 g l^{-1}, σ_v = 1.5×10^3 S cm^{-1}, γ_t = 0.5 MPa, and ε = 5%.

The conductivity of graphite foil is close to the limiting value permissible for preparing TEG composites, since the conductivity of a composite composed of a conducting filler and dielectric binder must be lower than that of graphite foil because of the formation of nonconducting layers between graphite particles.

The dependence of the conductivity of TEG–SKI-3 rubber composites on the concentration of the conducting filler is shown in Fig. 2. As seen from Fig. 2, the conductivity reaches 60–80 S cm^{-1} at filler concentration of 50–60 wt %. This value is lower by a factor of 20–30 than the conductivity of a TEG foil but is sufficient for preparing antistatic materials or materials shielding high-frequency electromagnetic radiation.

After rolling of the samples at 40°C at different rotation rates of the rollers (the procedure typically used with rubber stocks), which provides more uniform distribution of the filler in the rubber, the elasticity and strength increases and the conductivity decreases. The conductivity of a sample containing 60 wt % TEG decreases by a factor of 10 (σ_v = 7.7 S cm^{-1}) and the tensile strength and relative elongation increase by a factor of 2 (γ_t = 1.2 MPa and ε = 10%) after rolling of the sample for 7 min. Probably, the conductivity decreases owing to degradation of conducting TEG aggregates in the SKI-3 polymeric matrix under high dynamic stresses arising in the course of the rolling.

We studied the conductivity of the composites based on PVC plastisol as influenced by the procedure for rolling the samples on rollers with variable gap. The conductivity of PVC composites containing initial GSM-1 low-ash graphite and TEG is higher at low TEG content.

When the content of GSM-1 graphite in the PVC composites ranges from 33 to 55 wt %, the conductivity of the samples σ_v (ρ_{bulk} = 800–870 g l^{-1} for unrolled samples) increases from 2.5×10^{-5} to 0.1 S cm^{-1}. At the filler content of 3.6 to 13 wt %, the conductivity of unrolled samples filled with TEG (ρ_{bulk} = 450–500 g l^{-1}) increases from 2.0×10^{-4} to 1.0 S cm^{-1}. The conductivity of the samples filled with TEG and rolled on rollers with variable gap grows from 3.3×10^{-3} to 25.0 S cm^{-1} as the concentration of the conducting filler is increased from 2.4 to 26 wt %.

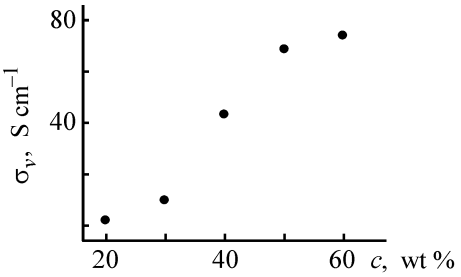

Fig. 2. Electrical conductivity σ_v of composites based on SKI-3 rubber vs. the concentration c of TEG conducting filler.

The physicochemical parameters of PVC composites with 9.1 wt % TEG rolled at 120–140°C and different gaps between the rollers, are listed in Table 1.

The rise in the conductivity of the samples after rolling is obviously due to an increase in the number of conducting chains in a unit volume owing to a change in the bulk density of the composite from 400 to 1000 g l^{-1}. The rise in the tensile strength and relative elongation of the samples may be due to strengthening of the interaction between TEG and the binder during rolling.

The volume conductivities σ_v, tensile strengths γ_t, and elongations at rupture, ε, of the composites with varied TEG content are listed in Table 2. These

Table 1. Physicomechanical parameters of PVC plastisol–TEG composites rolled at different gaps between rollers h (PVC : DOP = 1 : 1)

h, mm	σ_v, S cm^{-1}	γ_t, MPa	ε, %
3	0.47–0.53	0.6	22
1	0.56–0.67	1.1	26
0.4	0.77–0.83	1.7	30

Table 2. Physicomechnaical parameters of PVC plastisol composites with different contnet of TEG filler (PVC : DOP = 1 : 1)

TEG, wt %	σ_v, S cm^{-1}	γ_t, MPa	ε, %
0.0	–	4.0	330
2.4	2.5×10^{-3}–3.3×10^{-3}	0.5	36
4.8	0.11–0.12	0.6	33
9.1	0.59–0.67	1.3	30
13.0	1.1–1.7	1.6	29
16.7	5.6–6.7	1.9	27
20.0	7.7–9.1	2.1	16

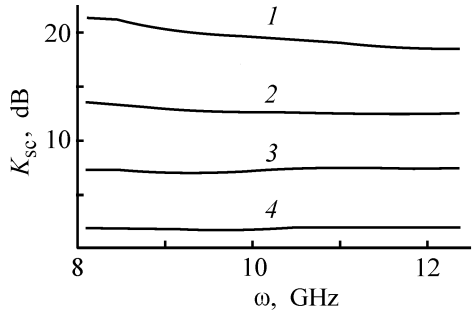

Fig. 3. Shielding coefficient K_{sc} of TEG–PVC composites vs. frequency ω. TEG content (wt %): (*1*) 25, (*2*) 26, (*3*) 14, and (*4*) 6.3. Sample thickness (mm): (*1*) 0.70, (*2*) 0.25, and (*3*, *4*) 0.30.

data confirm the advantages of composites with TEG filler, rolled at a variable gap between rollers. As seen from Table 2, the electrical conductivity σ_v of composites increases by four orders of magnitude when the filler content is raised by an order of magnitude. The tensile strength increases owing to strong interaction of TEG with the binder.

As noted above, the composites can be used for various radio engineering purposes. Experimental dependences of the shielding coefficients of radio-frequency radiation for PVC–TEG composites are shown in Fig. 3.

Having all properties of graphite, TEG exhibits new properties, such as easy molding, low bulk weight, and strong interaction with a polymeric matrix, which makes TEG promising for preparing conducting composites.

CONCLUSIONS

(1) Low-resistance composites with thermally expanded graphite as filler of the polymeric binder were prepared at lower filler content as compared with that of other graphites.

(2) The conditions for preparing polyvinyl chloride-thermally expanded graphite composites with the conductivity from 10 to 25 S cm^{-1} were determined.

(3) The mechanical and electrical properties of composites formed by polyvinyl chloride and thermally expanded graphite were determined as influenced by the rolling conditions.

(4) The possibility of using TEG composites for radio engineering purposes was demonstrated.

REFERENCES

1. Grodnev, I.I., *Elektromagnitnoe ekranirovanie v shirokom diapazone chastot* (Electromagnetic Shielding in a Wide Frequency Range), Moscow: Svyaz', 1972.
2. Polonskii, B.N., *Konstruirovanie elektromagnitnykh ekranov dlya REA* (Construction of Electromagnetic Shields for Radioelectronic Apparatus), Moscow: Sov. Radio, 1979.
3. Alimin, B.F., *Zarubezh. Elektron.*, 1989, no. 2, pp. 75–82.
4. Alekseev, A.G. and Korneev, A.E., *Magnitnye elastomery* (Magnetic Elastomers), Moscow: Khimiya, 1987.
5. Petrykhnenko, S.I., Sergeev, V.I., Katsevman, M.L., and Mironov, N.A., *Plast. Massy*, 1993, no. 2, p. 28.
6. USSR Inventor's Certificate, no. 974 416.
7. Gorshenev, V.N., Bibikov, S.B., and Spector, V.N., *Synth. Mater.*, 1997, vol. 86, pp. 2255–2256.
8. USSR Patent no. 1657474A1.
9. Titel'man, G.I., Pechkin, S.V., Gel'man, V.N., *et al.*, *Khim. Tverd. Topl.*, 1991, no. 4, pp. 79–84.
10. Chernysh, I.G., Karpov, I.I., Prikhod'ko, G.P., and Shai, V.M., *Fiziko-khimicheskie svoistva grafita i ego soedinenii* (Physicochemical Properties of Graphite and Its Compounds), Kiev: Naukova Dumka, 1990, pp. 140–152.
11. Gorshenev, V.N., Ovchinnikov, A.A., and Novikov, Yu.N., *Zh. Fiz. Khim.*, 2001, vol. 75, no. 6, pp. 1058–1062.
12. Drinberg, S.A. and Verkholantsev, V.V., *Organodispersnye lakokrasochnye materialy i pokrytiya* (Dispersed Organic Paint and Vanish Materials and Coatings), Moscow: Khimiya, 1976.
13. Levit, R.M., *Elektroprovodyashie volokna* (Conducting Fibers), Moscow: Khimiya, 1986.
14. Bibikov, S.B., Gorshenev, V.N., and Novikov, Yu.N., *The 12th Int. Conf. On Composite Materials ICSM*, Paris, July 5–9, 1999, p. 195.
15. Bibikov, S.B. and Gorshenev, V.N., *Int. Scientific and Technical Conf. "Polymaterials-2001,"* Moscow, November 26–30, 2001, p. 150–153.
16. Yurkovskii, N.M., Smirnov, T.Yu., and Malei, L.S., *Khim. Tverd. Topl.*, 1986, no. 1, pp. 127–131.
17. Avdeev, V.V., Graphite Intercalation Compounds and New Crabon Materials on Their Base: Synthesis, Physicochemical Properties, and Aplication, *Doctoral Dissertation*, Moscow: 1996.

Russian Journal of Applied Chemistry, Vol. 76, No. 4, 2003, pp. 607–609. Translated from Zhurnal Prikladnoi Khimii, Vol. 76, No. 4, 2003, pp. 629–631.

MACROMOLECULAR CHEMISTRY AND POLYMERIC MATERIALS

Specific Features of Suspension Copolymerization of Vinyl Chloride with Methyl Methacrylate

N. A. Bichuch, T. G. Ganyukhina, and Yu. D. Semchikov

Nizhni Novgorod State University, Nizhni Novgorod, Russia

Research Center, Kaprolaktam Open Joint-Stock Company, Dzerzhinsk, Nizhni Novgorod oblast, Russia

Received June 21, 2002

Abstract—Suspension copolymerization of vinyl chloride with methyl methacrylate was studied. The process is characterized by a pseudo-gel effect manifested as a sharp increase in the reaction rate after exhaustion of methyl methacrylate. The influence exerted by the monomer addition procedure on how the copolymer composition varies in the course of polymerization was examined.

Recently there has been a great deal of interest in modification of polymers by blending of macromolecular compounds of varied chemical nature. Naturally, these studies mainly concern combinations of various comprehensively studied and commercially available polymers. In particular, much attention is given to binary systems based on polyvinyl chloride (PVC) and polymethyl methacrylate (PMMA); however, most of these studies are purely scientific rather than applied. It has been shown that, in a wide range of compositions, this system exhibits two glass transition points and tends to form multiphase structures [1].

To improve the compatibility of PVC with PMMA, it seemed promising to add a third component, a copolymer of vinyl chloride (VC) and methyl methacrylate (MMA). Since the copolymerization constants of these monomers differ dramatically [2, 3], it can be expected that the resulting copolymer will be strongly nonuniform in composition and that the solubility parameters of its fractions will vary widely. This factor may be of decisive importance for improving the compatibility of PVC with PMMA. Furthermore, VC–MMA copolymers themselves may be of interest, since introduction of MMA units may improve the physicomechanical and optical properties of PVC, with the incombustibility of the material preserved. Therefore, we studied the suspension copolymerization of these monomers.

EXPERIMENTAL

Suspension copolymerization of VC with MMA was performed in a 3.5-l autoclave equipped with an impeller stirrer (180–200 rpm), a dosing unit, and a sampler. Methyl oxypropyl cellulose (F-50 brand) was used as protective colloid. The initiating system was a mixture of di-2-ethylhexyl peroxodicarbonate and lauryl peroxide. The ratio of the monomeric and aqueous phases was 1 : 2. The copolymerization was performed at 66°C until the pressure in the autoclave started to decrease. In some cases, with the aim to monitor variation of the composition and molecular weight of the copolymer, samples were taken in the course of the process. To obtain a copolymer with more uniform composition, the more active monomer, MMA, was introduced into the autoclave in small portions during the whole polymerization process. The polymer was separated from the mother liquor on a Büchner funnel, washed with distilled water, and dried in an oven at 55–60°C. The composition of the copolymers was evaluated from the chlorine content [GOST (State Standard) 25303–92], and the molecular weight (MW), from the Fickentscher constant K_F (GOST 14040–82), which varies in parallel with MW. In some cases, for PVC (control sample) and copolymers containing more than 50 wt % vinyl chloride, MW was determined from the Mark–Kuhn–Houwink equation [4] (cyclohexane, 25°C):

$$[\eta] = KM^{\alpha}, \text{ where } K = 1.37 \times 10^{-4}, \ \alpha = 0.78.$$

In synthesis of suspension copolymers VC–MMA of different compositions and approximately equal degrees of conversion, the process decelerates with increasing content of the more active component, MMA. It should be noted that approximately 80 wt % conver-

1070-4272/03/7604-0607 $25.00 © 2003 MAIK "Nauka/Interperiodica"

Rate constants of elementary chain propagation reactions K_p in copolymerization of VC with MMA

Propagation reaction, activities of components	K_p, l mol^{-1} s^{-1}	
	constant	value
~$VC^{\cdot}_{act}$ + MMA_{act}	$K_{12} = K_{11}/r_1$	(85–550) × 10^3
~$VC^{\cdot}_{act}$ + VC_{inact}	K^*_{11}	1700–11000
~$MMA^{\cdot}_{inact}$ + MMA_{act}	K^*_{22}	580
~$MMA^{\cdot}_{inact}$ + VC_{inact}	$K_{21} = K_{22}/r_2$	38.6

* K_p values for homopolymerization of the monomers [6].

sion is attained in 7.5 h in copolymerization of VC (95 wt %) with MMA (5 wt %) and in 2.5 h in homopolymerization of VC and MMA, i.e., the copolymerization rate is slower than the rate of homopolymerization of both monomers. This trend is characteristic of copolymerization of active monomers and inactive monomers in which the double bond is not conjugated with an unsaturated group of the substituent. The copolymerization constants for VC and MMA ($r_{VC,1}$ = 0.02, $r_{MMA,2}$ = 15) [5] and the rate constants of chain propagation in homopolymerization of VC and MMA allow calculation of the propagation rate constants for elementary stages of copolymerization. The table shows that the fastest elementary propagation reaction is the reaction of the VC propagation radical with MMA, and the slowest, the reaction of the MMA propagation radical with VC. This result is fully consistent with the well-known rule according to which inactive propagation radicals are formed from active monomers with π–π conjugation of the double bond and vice versa. The fastest stage involves the active VC radical and active MMA monomer, and the slowest stage, the inactive MMA radical and inactive VC monomer. The latter stage decreases the overall copolymerization rate as compared with the rates of VC and MMA homopolymerization, because the rate of a chain reaction is limited by the rate of the slowest stage.

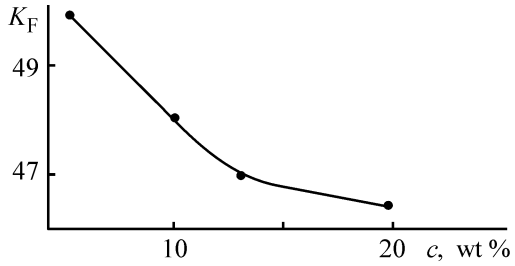

Fig. 1. Fickentscher constant K_F vs. MMA content *c* in copolymer with VC.

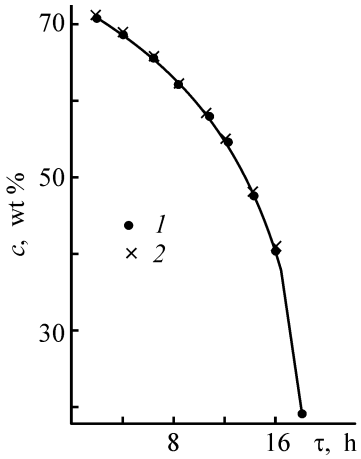

Fig. 2. Variation of the copolymer composition in the course of polymerization. MMA content in the monomer mixture 17 wt %. (*c*) Content of MMA units and (τ) reaction time; the same for Fig. 4. Copolymer samples taken (*1*) after termination of polymerization after a certain time and (*2*) directly in the course of polymerization.

Simultaneously, MW decreases, as judged from the variation of K_F (Fig. 1). The observed effects are due to a considerable difference in the copolymerization constants of VC and MMA. More active MMA monomer acts as a chain-terminating agent for the copolymer: As the MMA content in the macromolecule grows, K_F clealrly tends to decrease. Analysis of samples taken in the course of copolymerization shows that, in the initial stages, the polymer is strongly enriched in MMA, whereas in later stages, as MMA is exhausted, the composition of the copolymer becomes similar to that of the initial monomer mixture. The reliability of conclusions concerning the variation of the composition of the VC–MMA copolymer was confirmed by the consistence of composition data obtained by sampling in the course of polymerization and by stopping the polymerization at various stages by rapid cooling (Fig. 2). The dramatic changes in the copolymer composition in the course of conversion indicate that the copolymer is strongly nonuniform in composition.

A characteristic feature of copolymerization of VC with MMA is a pronounced pseudo-gel effect, specifically, sharp acceleration of copolymerization upon exhaustion of MMA. Therefore, in all the cases under consideration, the conversion in the initial stages is low, which is confirmed by kinetic curves in Fig. 3. In contrast to the true gel effect, which is due to a decrease in the rate of bimolecular termination with increasing viscosity of the reaction medium, the reaction acceleration in our case is due to a change in the apparent rate constant. It was already noted that MMA inhibits the copolymerization (addition of ~17 wt %

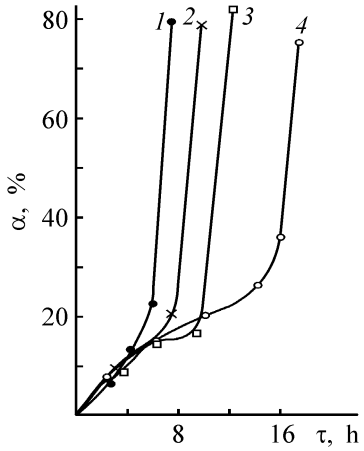

Fig. 3. Variation of the conversion α in the course of copolymerization at the MMA content in the monomeric mixture of (*1*) 5, (*2*) 9, (*3*) 13, and (*4*) 17 wt %. (τ) Reaction time.

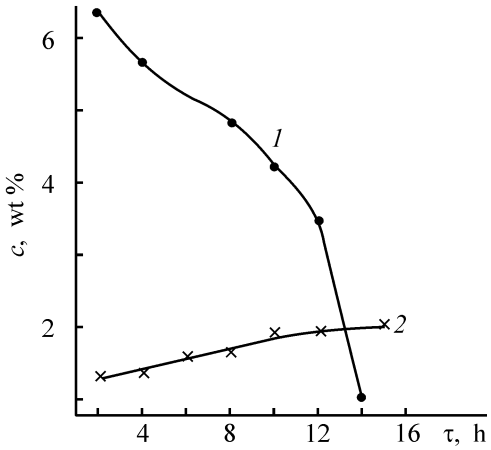

Fig. 4. Composition of copolymer vs. time for different ways of MMA introduction. MMA content in the monomer mixture 13 wt %. (*1*) Both monomers loaded simultaneously and (*2*) more active MMA added in portions.

MMA decelerates the process by more than an order of magnitude as compared with homopolymerization of VC). With increasing conversion, MMA is rapidly exhausted, the relative amount of low-active propagation radicals decreases, and, as a result, the chain propagation accelerates.

It was interesting to compare the trends in variation of the composition (monitored directly in the course of copolymerization) synthesized of VC–MMA copolymers with simultaneous addition of both monomers and with addition of more active MMA in portions (three portions at 3.5-h intervals). Figure 4 shows that, when both monomers are loaded simultaneously (curve *1*), the MMA content in the copolymer varies in a wide range (within more than 50%), whereas with addition of MMA in portions (curve *2*), this range is much narrower (about 6%), which means that the copolymer becomes much more uniform in composition, which favorably affects its solubility. It should be noted that, in the latter case, the MMA content in the copolymer is higher and its MW is somewhat lower (30 000 against 43 000) at the same composition of the monomer mixture.

CONCLUSIONS

(1) Suspension copolymerization of vinyl chloride with methyl methacrylate is characterized by the inhibiting effect of the second comonomer and significant variation of the copolymer composition with increasing conversion.

(2) Addition of more reactive methyl methacrylate in portions in the course of suspension copolymerization with vinyl chloride results in the formation of a product that is considerably more uniform in composition.

REFERENCES

1. Li, W., Shi, L., Shen, D., and Zheng, Y., *Polym. Int.*, 1992, vol. 27, no. 1, pp. 57–62.
2. Tkachenko, G.V., Stupen', L.V., Kofman, L.P., and Karacheva, L.A., *Zh. Fiz. Khim.*, 1958, vol. 32, no. 11, pp. 2492–2499.
3. *Copolymerization*, Ham, G.E., Ed., New York: Interscience, 1964.
4. Semchikov, Yu.D. and Smirnova, L.A., *Vysokomolekulyarnye soedineniya* (Macromolecular Compounds), Nizhni Novgorod: Nizhegor. Gos. Univ., 1996.
5. *Entsiklopediya polimerov* (Polymer Encyclopedia), Kargin, V.A., Ed., Moscow: Sovetskaya Entsiklopediya, 1972, vol. 1.
6. Lipatov, Yu.S., Grishchenko, T.M., and Veselovskii, R.A., *Spravochnik po khimii polimerov* (Handbook of Polymer Chemistry), Kiev: Naukova Dumka, 1971.

Russian Journal of Applied Chemistry, Vol. 76, No. 4, 2003, pp. 610–615. Translated from Zhurnal Prikladnoi Khimii, Vol. 76, No. 4, 2003, pp. 632–638.

MACROMOLECULAR CHEMISTRY AND POLYMERIC MATERIALS

Sedimentation Kinetics of Bentonitic Clay Suspension as Influenced by pH of the Medium, Chemical Nature and Concentration of Surfactants, and Molecular Properties of Cationic Acrylamide Copolymer Flocculants

V. E. Proskurina, L. A. Akhmetova, and V. A. Myagchenkov

Kazan State Technological University, Kazan, Tatarstan, Russia

Received December 6, 2002

Abstract—The kinetics of flocculation of bentonitic clay suspensions and thickening of the sediments was studied in the modes of free and hindered sedimentation as influenced by pH of the medium, chemical nature and concentration of surfactants, and molecular properties of cationic flocculants, random copolymers of acrylamide with dimethylaminoethyl methacrylate hydrochloride.

The kinetic dependences of flocculation and thickening of sediments of model disperse systems (MDs) in the presence of ionic and nonionic polyacrylamide flocculants (PAAFs) and their mixtures have been studied extensively, and the results are partially summarized in reviews [1–3]. At the same time, the effect of PAAFs on the kinetic aspects of flocculation and sedimentation stability of real DSs has been poorly studied.

Since real disperse systems are multicomponent compositions and frequently comprise involve a poorly characterized ensemble of dispersed phase (DP) particles [3, 4], a study of flocculation and thickening of real DS sediments in the presence of polymeric additives is obviously rather difficult. Thus, data on the effect of active components on the flocculation kinetics of real DSs (in particular, bentonitic clay suspensions) in the modes of their free and hindered sedimentation are of scientific and practical importance. This DS finds wide application in oil production as effective regulator of the bed permeability to aqueous and organic components of the dispersion medium, as sorbent of a wide assortment of pollutants present in wastewaters from motor-car factories, and as agent increasing the flake weight [2].

It should be particularly noted that a search for new active additives and study of sedimentation conditions both decreasing and increasing the sedimentation stability of the Bentokam clay powder are of practical importance. In oil production, a bentonitic clay suspension is added to multicomponent aqueous solutions with varied pH and containing various salt additives, wide assortment of surfactants, etc. The effect of the solution ionic strength on the kinetics of flocculation of bentonitic clay suspensions and thickening of sediments was studied in [5].

In this paper, we report on our continued studies in this direction and examination of the kinetics of flocculation of a bentonitic clay suspension in the modes of free and hindered sedimentation as influenced by the concentration and molecular weight of cationic acrylamide copolymers, solution pH, and surfactants. The cationic acrylamide copolymers in question are of particular interest owing to their high flocculating properties, which are probably related, to a certain extent, to the difference in the charge of the bentonitic clay particles and macromolecular cations. It should be noted that the pH of a dispersion medium strongly affects the macromolecule conformation and flocculation properties.

EXPERIMENTAL

In our study, we used a Bentokam bentonitic clay suspension from the Berezovo deposit (Tatarstan) [TU (Technical Specifications) 39-0147001-105–93] with average particle radius $R = 7.28 \times 10^{-6}$ m. The integral curve of the DP particle size distribution, found from data of sedimentometric analysis performed in the mode of free (unhindered) sedimentation, is shown

1070-4272/03/7604-0610 $25.00 © 2003 MAIK "Nauka/Interperiodica"

in Fig. 1. As seen, the minimal and maximal sizes of DP particles differ by nearly an order of magnitude ($\bar{R}_{min} = 0.24 \times 10^{-5}$ and $\bar{R}_{max} = 2.38 \times 10^{-5}$ m). As cationic PAAFs we used samples of a random copolymer of acrylamide and dimethylaminoethyl methacrylate hydrochloride with varied molecular weight and similar compositions of the copolymer macromolecules (weight content of ionic units β 16.3%).

Similarly to [6], the polymer samples were prepared by radical degradation of the initial macromolecular copolymer $\mathbf{K}_1$ under mild conditions. The initial copolymer $\mathbf{K}_1$ with $\bar{M} = 2.3 \times 10^6$ was prepared from acrylamide and dimethylaminoethyl methacrylate hydrochloride in an aqueous solution in the presence of potassium persulfate as initiating agent. The molecular weight of the copolymer samples studied, $\mathbf{K}_9$–$\mathbf{K}_1$, was varied in a wide range from 2.5×10^4 to 2.3×10^6. The structure of these copolymers can be represented as

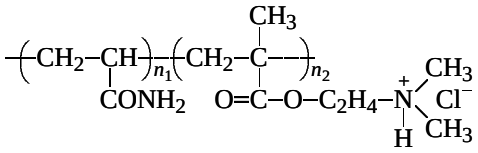

In this study, we used the following surfactants: (1) anionic surfactant (AS): disodium alkylsulfosuccinate (Surfagen S-30 brand, Vopelius Chemie GmbH, Germany)

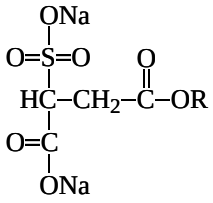

R = C_{16}–C_{18}

(2) cationic surfactant (CS): alkyldimethylbenzylammonium chloride [Katamin AB brand, Bursintez-M Joint-Stock Company, Moscow, Russia, TU (Technical Specifications) 9392-003-48 482 528–99]

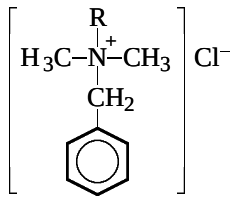

R = C_{16}–C_{18}

(3) Nonionic surfactant (NS): oxyethylated isononylphenol (Neonol AF_9-10 brand, Nizhnekamskneftekhim Joint-Stock Company, Nizhnekamsk, Russia, TU (Technical Specifications) 2483-077-05 766 801–98)

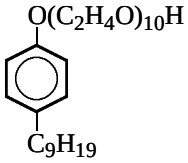

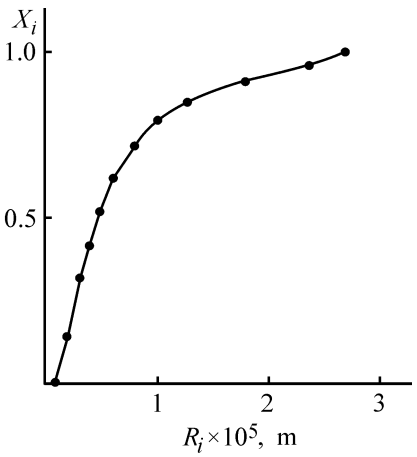

Fig. 1. Integral curve of the particle size distribution of the dispersed phase (bentonitic clay). (X_i) Integral weight fraction of the *i*th fraction and (R_i) particle radius in *i*th DP fraction.

The sedimentation kinetics of the bentonitic clay suspension was studied by sedimentometric analysis performed in the mode of free sedimentation (DP concentration c_d = 0.8%), using a VT-500 torsion balance in a 400-ml cylinder at different pH adjusted by adding required amounts of 0.1 M HCl or KOH solution to the disperse systems. Before tests, the clay suspensions were clarified for 1 day at each given pH. Then, a 200-ml portion of the flocculant solutions with concentration 2*c*, prepared by preaddition of the required volume of 0.1% solutions of copolymers $\mathbf{K}_1$–$\mathbf{K}_9$, was poured into a cylinder containing 200 ml of a bentonitic clay suspension. The resulting solution was mixed with a perforated disk stirrer, which was slowly shifted within the cylinder 10 times in the vertical direction, and then the sedimentation kinetics of the bentonite suspension was studied on a torsion balance.

The sedimentation kinetics of the bentonitic clay suspension in the mode of hindered sedimentation (DP concentration c_d = 7%) and sediment thickening was studied in a 100-ml cylinder by monitoring the shift of the boundary between the clarified and unclarified fractions of the suspension after mixing by overturning the cylinder ten times. Before tests, the clay

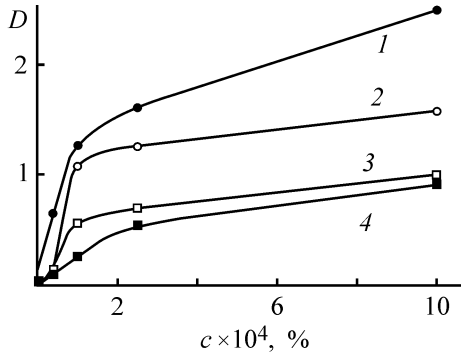

Fig. 2. Flocculation parameter D vs. concentration c of the cationic acrylamide copolymers at pH (*1*, *4*) 3.3 and (*2*, *3*) 7.0. PAAF: (*1*, *2*) $\mathbf{K}_2$ ($\overline{M} = 1.44 \times 10^6$) and (*3*, *4*) $\mathbf{K}_8$ ($\overline{M} = 0.093 \times 10^6$).

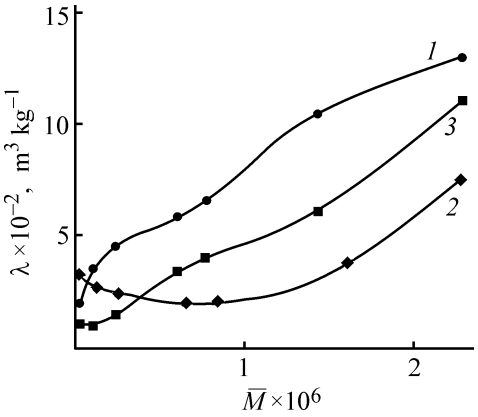

Fig. 3. Flocculation activity λ vs. the molecular weight $\overline{M}$ of cationic acrylamide copolymers at pH (*1*) 2.2, (*2*) 7.0, and (*3*) 13.2.

suspensions were clarified for 1 day at each given pH. Immediately before the tests, a required amount of 0.1% PAAF solutions (0.4–4.0 ml) was diluted with distilled water to 50 ml and then mixed with the bentonitic clay suspension (50 ml). The resulting solution was mixed by tenfold overturning of the cylinder.

Let us consider sedimentation of the bentonitic clay suspension in acidic and weakly alkaline solutions as influenced by the cationic PAAFs. Although several experiments were performed in strongly alkaline solutions, their results were ambiguous and did not allow correct conclusions on the features of sedimentation of bentonitic clay suspensions under such conditions. Therefore, only acidic and weakly alkaline mixtures were studied.

To obtain quantitative characteristics of the flocculation kinetics, we calculated the flocculation effect D and flocculation activity λ [3]:

$$D = \frac{v}{v_0} - 1, \quad (1)$$

$$\lambda = \left(\frac{v}{v_0} - 1\right)\frac{1}{c} = \frac{D}{c}, \quad (2)$$

where v and v_0 are the average rates of sedimentation of the bentonitic clay suspension in the presence of flocculant or surfactants and without them, respectively; c is the concentration of the polymeric additive or surfactant.

The positive values of D and λ indicate the flocculating effect of the additive, whereas at $D < 0$ and $\lambda < 0$ a stabilization effect is observed.

The concentration dependences of the flocculation effect D for two PAAF samples with different molecular weights are shown in Fig. 2. First of all, we should note the dependence of the parameter D on the average molecular weight $\overline{M}$: At pH 3.3 and 7.0, summarized flocculation effect was observed with the cationic PAAF $\mathbf{K}_2$ ($\overline{M} = 1.44 \times 10^6$) than that with the low-molecular-weight copolymer $\mathbf{K}_8$ ($\overline{M} = 0.093 \times 10^6$). Obviously, the comparison was performed at $[\mathbf{K}_2] = [\mathbf{K}_8] = 10 \times 10^{-4}$%. To account for the experimental dependences $D = f(\overline{M})$, we should note that the rms macromolecule size $(\overline{R}^2)^{0.5}$ varies in parallel with $\overline{M}$ [7]. Greater $(\overline{R}^2)^{0.5}$ values increase the probability of interaction of a single macromolecule with two and more DP particles (formation of bridges), and thus D values for copolymer $\mathbf{K}_2$ are greater than those for $\mathbf{K}_8$.

The quantitative data on the flocculation of the bentonitic clay suspension in the presence of cationic acrylamide copolymers with various $\overline{M}$ at various pH are summarized in Fig. 3. To determine the dependence $\lambda = f(\overline{M})$ adequately, we performed the experiments so that, except the main factor, the effect of all other factors on the sedimentation of DP particles could be neglected. In the case of a copolymer with strongly different physicochemical properties of the components (e.g., copolymers $\mathbf{K}_1$–$\mathbf{K}_9$), the effect of the copolymer composition on the flocculation parameters D and λ is probably more essential than that of $\overline{M}$ [6]. The samples with various molecular weights $\overline{M}$ were prepared by radical degradation, which allowed us to exclude *a priori* significant differences in the composition of copolymer macromolecules [8]. As seen from Fig. 3, the flocculation activity grows with increasing molecular weight of cationic PAAFs in the entire pH range studied. However, the shapes of the $\lambda = f(\overline{M})$ dependences at each pH are fundamentally different. The greatest λ values are typical of acidic media (Fig. 3, curve *1*). Naturally, we compared samples with equal molecular weights. In ac-

Table 1. Experimental data on the flocculation and thickening of a bentonitic clay suspension* in the presence of cationic copolymers $\mathbf{K}_1$ and $\mathbf{K}_9$ ([PAAF] = 4×10^{-3}%)

PAAF	pH	D	$\lambda \times 10^{-2}$, $m^3\ kg^{-1}$	Q_{max}	$\rho_s \times 10^{-3}$, $kg\ m^{-3}$	$\gamma \times 10^3$, s^{-1}
None	3.3	–	–	0.48	1.083	9.47
$\mathbf{K}_1$		20.1	5.02	0.98	1.072	2.78
$\mathbf{K}_9$		0.473	0.12	0.45	1.078	1.16
None	2.2	–	–	0.50	1.086	1.41
$\mathbf{K}_1$		19.0	4.75	0.46	1.079	2.58
$\mathbf{K}_9$		9.66	2.41	0.47	1.081	1.75
None	1.85	–	–	0.52	1.090	2.45
$\mathbf{K}_1$		22.1	5.52	0.47	1.081	2.42
$\mathbf{K}_9$		10.6	2.65	0.49	1.086	1.64

* Q_{max} is maximal clarification degree of the suspension in the cylinder, and ρ_s is the sediment density.

cordance with [9], chages in λ on varying the pH of the medium may be due not only to changes in the structure of the electrical double layer around the DP particles, but also to those in the mechanism of copolymer macromolecule adsorption on the DP particles.

Now we consider the effect of pH on the flocculation in the mode of hindered sedimentation of a bentonitic clay suspension in the presence of polymeric flocculants. The optimal concentration of the polymeric additives ($c = 4 \times 10^{-3}$%) was determined experimentally. Previously [3], we have made a general conclusion that the flocculation parameters of flexible-chain weak polyelectrolytes of the PAAF type strongly depend on pH of the medium. Therefore, this parameter must affect the conformation of the cationic copolymer macromolecules, structure of the electrical double layer (especially its electrokinetic potential ζ), and nature and concentration of the adsorption centers localized on the DP particle surface. In analyzing of the effect of pH on the flocculation, we should also take into account, that, with the DP concentration increasing by an order of magnitude (on passing from free to hindered sedimentation), the influence of pH on the balance of the attraction and repulsion forces between the bentonitic clay particles must obviously increase [10].

The kinetic curves of sedimentation and thickening of bentonitic clay suspensions at pH 1.85 in the presence of copolymers $\mathbf{K}_1$ and $\mathbf{K}_9$ with maximal and minimal molecular weights (2.3×10^6 and 0.025×10^6, respectively) are shown as example in Fig. 4. The data on the flocculation and thickening of the bentonite suspensions at three pH values studied are listed in Table 1. The resulting data were plotted in the $\ln[Q_{max} - Q(t)] = f(t)$ coordinates, which allowed us to calculate the constants of sediment thickening, γ, from the slopes of the experimental straight lines (Fig. 4b) [11].

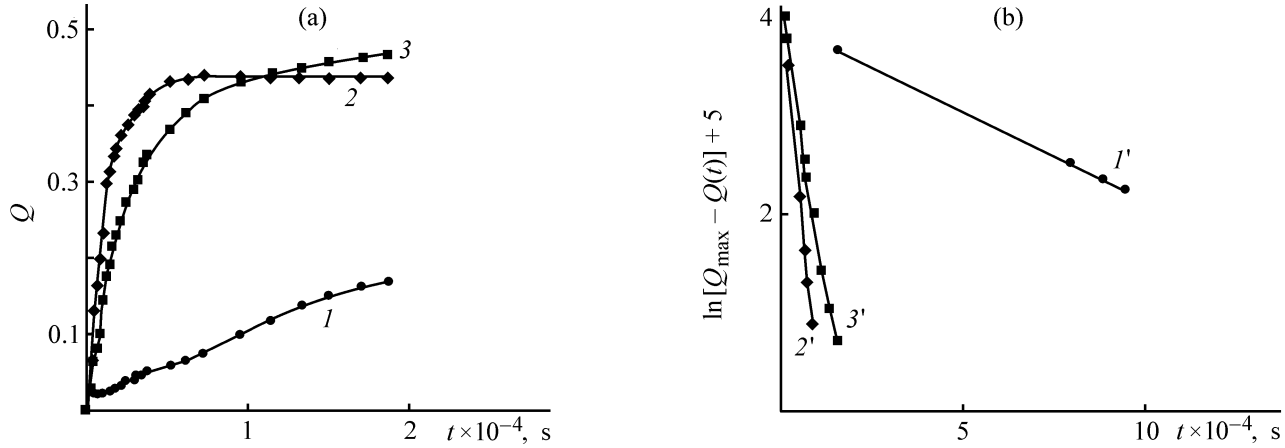

Fig. 4. Kinetic curves of sedimentation and thickening of a bentonitic clay suspension at pH 1.85 in the coordinates (a) $Q = f(t)$ and (b) $\log[Q_{max} - Q(t)] = f(t)$. $[\mathbf{K}_1] = [\mathbf{K}_9] = 4 \times 10^{-3}$%. ($Q$) Degree of clarification and (t) time; the same for Fig. 5. Flocculants: (*1*, *1'*) none, (*2*, *2'*) $\mathbf{K}_1$, and (*3*, *3'*) $\mathbf{K}_9$.

Table 2. Experimental data on the flocculation of the bentonitic clay suspension in the presence of various surfactants

Surfactant	$c \times 10^2$, %	pH	λ, $m^3\ kg^{-1}$
AS	9.9	2.2	–0.391
		7.0	–0.353
		9.6	–0.621
	19.6	2.2	–0.2
		7.0	–0.27
		9.6	–0.33
CS	9.9	2.2	0.724
		7.0	1.89
		9.6	1.67
	19.6	2.2	0.133
		7.0	0.933
		9.6	1.13
NS	9.9	2.2	–0.153
		7.0	–0.114
		9.6	–0.354

Along with Q_{max} and γ, the density ρ_s is also an important sediment characteristic, which gives information on the sediment structure and degree of its thickening and dehydration. The sediment density ρ_s depends on the weight concentration and density of the DP particles in the sediment [12]:

$$\rho_s = [m + (V_s - m/\rho)\rho_0]/V_s, \quad (3)$$

where ρ and ρ_0 are the densities of clay (2.63×10^3 kg m^{-3}) and water (1.0×10^3 kg m^{-3}), and m is the clay weight.

The sediment volume

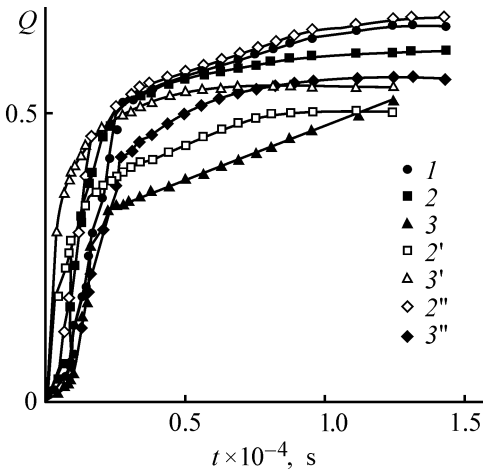

Fig. 5. Kinetic curves of sedimentation of the bentonitic clay suspension at pH 3.3 containing (*1*) no surfactant, (*2*, *3*) AS, (*2*', *3*') CS, and (*2*", *3*") NS. [SAS], %: (*1*) 0, (*2*, *2*', *2*") 0.38, and (*3*, *3*', *3*") 1.07.

$$V_s = (1 - Q_{max})V_0, \quad (4)$$

where V_0 is the volume of bentonitic clay suspension in the cylinder (V_0 = 100 ml).

Our experimental data on the kinetics of the sediment thickening, given in Table 1 and Fig. 4b, show that the sediment density ρ_s and the constant of sediment thickening, γ, decrease upon addition with polymeric flocculants $\mathbf{K}_1$ and $\mathbf{K}_2$ as compared with similar parameters of the bentonitic clay suspension in the absence of PAAF. These differences suggest changes in the structure of the resulting sediments; more friable structure of the bentonitic clay sediment is typical of systems containing PAAF additives whose macromolecules participate in the aggregation in the initial stage of sedimentation.

As a continuation of our systematic study of the effect of various active parameters of the dispersion medium on the sedimentation stability of a bentonitic clay suspension, we analyzed along with ionic strength [5] and pH, also the effect of surfactants of various types. Surfactants, depending on their type, can accelerate or decelerate sedimentation of a model kaolin disperse system [13]; certain variations in the sedimentation stability with surfactant concentration were also revealed. At low degrees of coating of the DP particle surface, hydrophobization of the particle surface was observed, which destroys the boundary water layers on the particle surface and thus promotes coagulation. With increasing surfactant concentration, the disperse system tends to stabilize owing to the secondary hydrophobization of the particle surface and appearance of the steric repulsion barrier [14].

The data on the flocculation of a bentonitic clay suspension in the presence of anionic (AS), cationic (CS), and nonionic (NS) surfactants at various solution pH are listed in Table 2.

The negative values of λ indicate that the anionic and nonionic surfactants act as stabilizers of the DP particles ($v < v_0$). Only upon addition of CS, the parameter λ slightly increases, and thus this additive accelerates sedimentation ($v > v_0$). As seen from the data on the sedimentation stability of the real DS studied in the presence of AS and CS in various concentrations, the surfactant concentration affects the sedimentation rate v only slightly. We should note that, in these experiments, the working concentrations of surfactants were several orders of magnitude higher than the concentrations of the polymeric additives.

In the mode of hindered sedimentation (c_d = 7%), a series of tests were performed with addition of various surfactants to the bentonitic clay suspension at constant pH 3.3. The kinetic curves of flocculation shown in Fig. 5 illustrate the effect of the concentra-

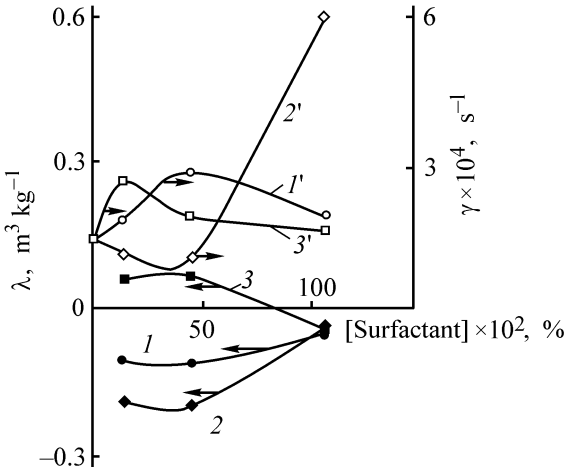

Fig. 6. Flocculation activity λ and thickening constant γ vs. the surfactant concentration at pH 3.3. (*1*, *1*') AS, (*2*, *2*') CS, and (*3*, *3*') NS.

tion and chemical nature of surfactants on the sedimentation rate of the bentonitic clay suspension. As seen, the sedimentation rate decreases with increasing content of the anionic or nonionic surfactants. This is primarily due to the excess of a surfactant in the system, which promotes stabilization of the DP particles by surfactant molecules.

The data on sedimentation and thickening of the sediments of the bentonitic clay suspension in solutions with varied pH are shown in Fig. 6. The relatively low λ parameters recorded for the samples in question may be due to the their low effect on the sedimentation rate *v*. This occurs for two reasons: (1) "deficiency" of surfactant due to the high concentration of the dispersed phase (c_d = 7%) and (2) considerably weaker effect of surfactant on the average rate of the DP sedimentation, compared with the effect of PAAFs.

Thus, our preliminarily data allow only schematic assessment of the influence exerted by the concentration and chemical nature of the surfactants on the sedimentation rate of bentonitic clay suspension.

CONCLUSIONS

(1) As found with a real disperse system (bentonitic clay suspension) as an example, the concentration and molecular parameters of the cationic acrylamide copolymer and pH of the medium strongly affect the kinetics of flocculation and thickening of the sediments in the modes of free and hindered sedimentation.

(2) The effect of pH on the flocculation parameters of the multicomponent disperse system and on the structural parameters of the resulting sediments was evaluated.

(3) The effect of the chemical nature and concentration of surfactants on the sedimentation stability, thickening constants, and density of the Bentokam clay sediments in aqueous solutions was determined.

REFERENCES

1. Zapol'skii, A.K. and Baran, A.A., *Koagulyanty i flokylyanty v protsessakh ochstki vody* (Coagulants and Flocculants in Water Treatment), Leningrad: Khimiya, 1987.
2. Veitser, Yu.I. and Mints, D.M., *Vysokomolekulyarnye flokulyanty v protsessakh ochistki prirodnykh i stochnykh vod* (Macromolecular Flocculants in Treatment of Natural and Waste Waters), Moscow: Stroiizdat, 1984.
3. Myagchenkov, V.A., Baran, A.A., Bekturov, V.A., and Bulidorova, G.V., *Poliakrilamidnye flokulyanty* (Polyacrylamide Flocculants), Kazan: Kazan Tekhnol. Univ., 1998.
4. Lebukhov, V.I., *Khim. Tekhnol. Vody*, 1992, vol. 14, no. 7, pp. 491–498.
5. Myagchenkov, V.A., Proskurina, V.E., Bulidorova, G.V., and Yakimova, E.A., *Vest. Kazan. Gos. Tekhnol. Univ.*, 2000, nos. 1–2, pp. 24–29.
6. Myagchenkov, V.A. and Frenkel', S.Ya., *Kompozitsionnaya neodnorodnost' polimerov* (Composition Heterogeneity of Polymers), Leningrad: Khimiya, 1988.
7. Rafikov, S.R., Budtov,V.P., and Monakov, Yu.B., *Vvedenie v fizikokhimiyu polimerov* (Introduction to Physical Chemistry of Polymers), Moscow: Nauka, 1978.
8. Myagchenkov, V.A., Kurenkov, V.F., and Akhmed'yanova, R.A., *Vysokomol. Soedin., Ser. B*, 1984, vol. 26, no. 5, pp. 340–343.
9. Myagchenkov, V.A., Proskurina, V.E., Bulidorova, G.V., *et al.*, *Khim. Tekhnol. Vody*, 2001, vol. 23, no. 3, pp. 285–296.
10. Baran, A.A., *Polimersoderzhashchie dispersnye sistemy* (Polymer-Containing Dispersed Systems), Kiev: Naukova Dumka, 1986.
11. Proskurina, V.E. and Myagchenkov, V.A., *Zh. Prikl. Khim.*, 1999, vol. 72, no. 10, pp. 1704–1708.
12. Lyubarskii, V.M., *Osadki prirodnykh vod i metody ikh obrabotki* (Sediments of Natural Waters and Procedures for Their Treatment), Moscow: Stroiizdat, 1980.
13. Bulidorova, G.V., Flocculation of Kaolin with Acrylamide Copolymers in the Presence of Coagulants and Surfactants, *Cand. Sci. Dissertation*, Kazan, 1996.
14. Zimon, A.D. and Leshchenko, N.F., *Kolloidnaya khimiya* (Colloidal Chemistry), Moscow: VLADMO, 1999.

Russian Journal of Applied Chemistry, Vol. 76, No. 4, 2003, pp. 616–618. Translated from Zhurnal Prikladnoi Khimii, Vol. 76, No. 4, 2003, pp. 639–641.

MACROMOLECULAR CHEMISTRY AND POLYMERIC MATERIALS

Effect of Small Additions of Stabilizer and Pigments on the Degree of Bulk Curing of a Filled Photopolymer

D. L. Starokadomskii and T. N. Solov'eva

Institute of Surface Chemistry, National Academy of Sciences of Ukraine, Kiev, Ukraine

Received June 25, 2002; in final form, February 2003

Abstract—The effect exerted by additions of stabilizer and pigments to oligoether acrylate compounds filled with finely dispersed silica on the degree of curing and its variation with depth was examined.

Photocurable compounds based on oligoether acrylates have found numerous applications in the past 15 years [1–7]. The use of filled photopolymeric materials in stomatology [6–11], microelectronics [12], and other fields tends to grow. Most of the compounds used in practice contain stabilizing additives preventing spontaneous polymerization [6–8, 9, 13, 14]. However, the effect of stabilizers on the polymerization capacity of filled photocurable compounds has been studied insufficiently. Stomatological photopolymers contain pigments as essential components [6, 7, 9]. Polymerization in the presence of pigments [15–17] has also been studied insufficiently, especially the photopolymerization of filled systems.

EXPERIMENTAL

Studies were performed by multiple attenuated total internal reflection [4] (MATIR) IR spectroscopy with a UR-20 double-beam IR spectrophotometer. A trapeziform total-internal-reflection element made of KRS-5, providing 10–20 reflections, was brought in optical contact with a millimeter-thick layer of a formulation. The degree of curing was evaluated by a decrease in the intensity of the absorption band at 1635 ± 5 cm^{-1}, associated with the vinyl bonds in the oligomers.

We used the following chemicals: OKM-2 oligomer [α,ω-bis(methacryloyloxyethyleneoxycarbonyloxy)ethyleneoxyethylene], TU (Technical Specifications) 113-03-22-65–79, fresh (subject to gradual turns yellowing in storage); UDMA oligomer (bisphenol A glycidyl methacrylate); benzoin isobutyl ether (photoinitiator), chemically pure grade; dimethylaminoethyl methacrylate, chemically pure grade; methacrylic acid, MRTU (Interrepublican Technical Specifications) 6-09-1768–64, chemically pure grade; Aerosil A-100 silica, GOST (State Standard) 14922–77, specific surface area 100 ± 7.5 m^2 g^{-1}, additionally calcined for 1 h at 400°C; pigments (yellow burnt sienna, cadmium lemon, burnt umber, TU 6-10-1320–77); and Ionol stabilizer (2,5-di-*tert*-butyl-*p*-cresol), chemically pure grade.

The formulations studied consisted of 65 wt % polymeric matrix (compound A) and 35% A-100. The composition of the polymeric matrix (wt %) was as follows: urethane dimethacrylate 35, oligocarbonate methacrylate 53, photoinitiator 1.0, dimethylaminoethyl methacrylate 0.1, and methacrylic acid 10.9. In experiments with addition of Ionol stabilizer (0.4, 1.0 wt %), the content of the major component, OKM-2, was correspondingly decreased (to 53.6 and 53.0 wt %, respectively). The degree of conversion, α, was studied in relation to the Ionol concentration *c*, irradiation time *t*, and mixture layer thickness *h*.

To examine the effect exerted by pigments, we added to the filled formulation the following pigments (with the corresponding decrease in the OKM-2 content), wt %: formulation P1, yellow sienna 0.025 and cadmium lemon 0.025; formulation P2, umber 0.05; and formulation P3, umber 0.02, cadmium lemon 0.01, yellow sienna 0.01, and black iron oxide pigment 0.01.

Figure 1A shows that, in curing the formulation without stabilizer (c = 0 wt %) at $h \le 1.5$ mm, the degree of curing, α, decreases gradually (the α–t curves slightly shift down); in the range $1.5 \le h < 2$ mm, α abruptly decreases. Addition of the stabilizer causes the degree of curing to decrease: The α–t curves in Fig. 1A for c = 0.4 and 1.0 wt % lie below the curve for c = 0 wt %). Figure 1A shows that the effect of the stabilizer depends on the layer depth h. Indeed, at $h \le 1$ mm α decreases only slightly after adding

1070-4272/03/7604-0616 $25.00 © 2003 MAIK "Nauka/Interperiodica"

the stabilizer, whereas at h = 1.5 mm the decrease is abrupt; with the thickness increasing further, to 2 mm, the effect of the stabilizer does not become appreciably stronger (Fig. 1A).

Thus, the effect of the stabilizer is manifested in a decreased α. The effect becomes stronger in going to deeper layers of the formulation. The shielding effect of the surface layers on the deeper layers is also enhanced in the presence of a stabilizer. This may be due to the ability of the stabilizer to deactivate radicals generated by UV irradiation.

It is interesting that the dependence of α on the stabilizer concentration c is nonmonotonic. For example, there is a clear minimum in curves 1–3 at c = 0.4 wt %, especially pronounced at h = 1.5 and 2 mm (Fig. 1B). At the stabilizer concentrations exceeding 0.4 wt %, its effect weakens. From the kinetic viewpoint, this trend suggests that the deactivating effect may be even stronger at lower stabilizer content. As a rule (Fig. 1B), the minimum in the α–c curves is the more pronounced, the shorter the irradiation time t and the deeper the mixture layer under examination.

Figure 2 shows that addition of even small amounts of the pigments noticeably decreases the reactivity of the formulation in polymerization and enhances the deactivating role of the upper layers relative to the lower layers. Indeed, after adding the pigments, the conversion falls by 25–30%, and the decrease in α with the depth becomes more pronounced (Figs. 2, 3). At 1 < h < 1.5 mm, the nonuniformity in curing of different layers can be leveled out by raising (e.g., doubling) the curing time; however, at h > 1.5 mm longer curing fails to produce the desired effect.

The conversion α is also influenced by the type of pigment. Comparison of the curves in Fig. 2 shows that addition of dark pigments causes a stronger decrease in α than addition of light pigments. On addition of dark and light pigments simultaneously (Fig. 2d), the effect on α is intermediate between the effects exerted by the dark and light pigments.

Let us consider the α–h dependence for the pigment-free formulations and those with pigments added. In the absence of pigments (Fig. 3a), α varies with h only slightly at 0 < h < 1.5 mm, but decreases appreciably at h > 1.5 mm. This means that, for the pigment-free formulation, photocuring is virtually complete in 7 min, and at h < 1.5 mm longer irradiation (15 min) only slightly affects α. With the dark pigment added (formulation P2), the degree of conversion is not appreciably affected by the irradiation time and layer depth at h < 1 mm. However, the dependence of α on t becomes more pronounced at h > 1 mm, and at h ≈ 1.5 mm the conversions attained in 7, 10, and 15 min differ considerably. With the light pigments added (formulation P1), the dependence of α on the irradation time (Fig. 3b) is noticeable even at h ≈ 1 mm. The α–h curves for P1 and P2 (Figs. 3b, 3c) somewhat differ in shape, which may

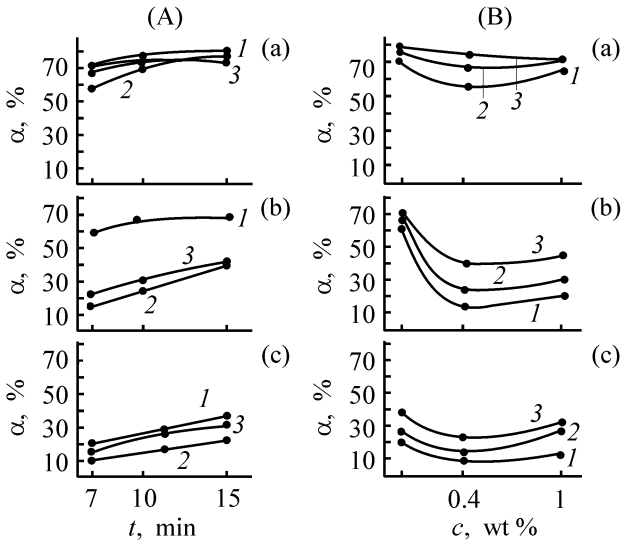

Fig. 1. Degree of conversion, α, vs. (A) irradiation time t and (B) stabilizer concentration c. (A) c, wt %: (*1*) 0, (*2*) 0.4, and (*3*) 1.0. (B) t, min: (*1*) 7, (*2*) 10, and (*3*) 15. h, mm: (a) 1.0, (b) 1.5, and (c) 2.0.

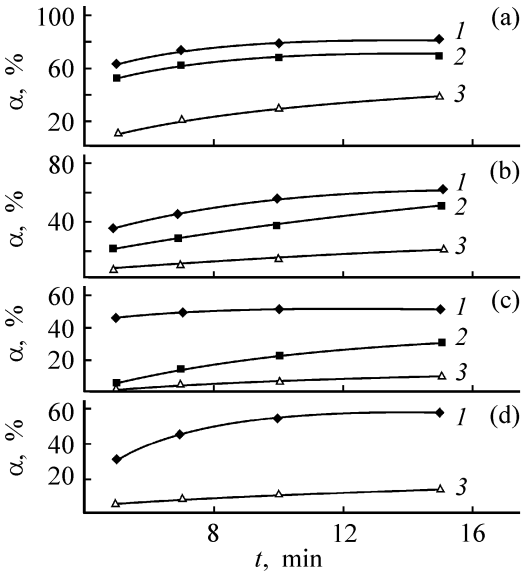

Fig. 2. Degree of conversion, α, vs. irradiation time t. h, mm: (*1*) 1.0, (*2*) 1.5, and (*3*) 2.0 mm. Formulation: (a) no pigments added, (b) P1 (yellow pigments), (c) P2 (dark pigment), and (d) P3 (2/5 yellow pigments and 3/5 dark pigments).

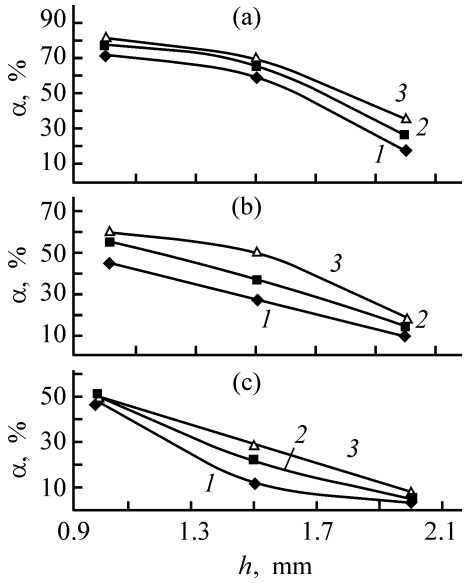

Fig. 3. Degree of conversion, α, vs. thickness *h* of the mixture layer. Irradiation time *t*, min: (*1*) 7, (*2*) 10, and (*3*) 15. Pigments added: (a) none, (b) yellow (P1), and (c) dark (P2).

be due to a faster decrease in α with increasing *h* for the formulation with the dark pigment.

CONCLUSIONS

(1) The effect exerted by small additions of a stabilizer (Ionol) and pigments (umber, cadmium lemon, black iron oxide, yellow sienna) on the photopolymerization of oligoether acrylate formulations filled with silica was studied. The stabilizer and pigments impair the quality of curing and increase the nonuniformity of curing throughout the depth. This fact should be taken into account when performing polymerization of thick layers.

(2) The dependence of the inhibiting effect of Ionol on its concentration is nonmonotonic: The curve of the degree of conversion vs. stabilizer concentration passes through a minimum.

(3) The conversion α is largely influenced by the type of the pigment added. Additions of dark pigments decrease α more significantly, compared with light pigments, and, on adding dark and light pigments simultaneously, the effect is intermediate.

ACKNOWLEDGMENTS

The authors are grateful to V.A. Khranovskii and E.N. Ostapyuk (Institute of Macromolecular Chemistry, National Academy of Sciences of the Ukraine, Kiev) for the high quality of spectroscopic measurements.

REFERENCES

1. Korolev, G.V., Mogilevich, M.M., and Golikov, I.V., *Setchatye poliakrilaty* (Network Polyacrylates), Moscow: Khimiya, 1995.
2. Maslyuk, A.F., Ageeva, V.V., Bereznitskii, G.K., *et al.*, *Vysokomol. Soedin., Ser. A*, 1997, vol. 39, no. 5, pp. 773–780.
3. Starokadomskii, D.L. and Solov'eva, T.N., *Zh. Prikl. Khim.*, 2002, vol. 75, no. 1, pp. 138–141.
4. Maslyuk, A.F. and Khranovskii, V.A., *Fotokhimiya polimerizatsionnosposobnykh oligomerov* (Photochemistry of Polymerizable Oligomers), Kiev: Naukova Dumka, 1989.
5. *Materialy 8-i Respublikanskoi konferentsii po vysokomolekulyarnym soedineniyam* (Proc. 8th Republican Conf. on Macromolecular Compounds), Kiev, September 24–26, 1996.
6. Borisenko, A.V. and Nespryad'ko, V.P., *Kompozitsionnye plombirovochnye i oblitsovochnye materialy* (Composite Filling and Facing Materials), Kiev: Kniga-Plyus, 2001.
7. Makeeva, I.M., *Vosstanovlenie zubov svetootverzhdaemymi kompozitnymi materialami* (Restoration of Teeth with Photocurable Composite Materials), Moscow: Stomatologiya, 1997.
8. Bland, M.H. and Peppas, N.A., *Biomaterials*, 1996, vol. 17, no. 11, pp. 1109–1114.
9. O'Brien, W.J., *Dental Materials and Their Selection*, Chicago: Quintessence, 1997.
10. Makeev, A.F. and Starokadomskii, D.L., *Nov. Stomatol.*, 1996, no. 1, pp. 40–44.
11. Chung, C.M., Kim, J.G., and Choi, J.H., *J. Appl. Polym. Sci.*, 2000, vol. 77, no. 8, pp. 1802–1808.
12. Baikerikar, K.K. and Scranton, A.B., *Polymer*, 2001, vol. 42, no. 2, pp. 431–441.
13. Plotnikov, V.G. and Efimov, A.A., *Usp. Khim.*, 1990, vol. 59, no. 8, pp. 1362–1386.
14. Rot, A.S., Chernyakov, E.A., Videnina, N.G., and Omel'chenko, S.I., in *Issledovaniya v oblasti sinteza polimerov* (Studies in the Field of Polymer Synthesis), Kiev: Naukova Dumka, 1978, pp. 36–45.
15. *Materialy 5-i Respublikanskoi konferentsii po vysokomolekulyarnym soedineniyam* (Donetsk, 1984) (Proc. 5th Republican Conf. on Macromolecular Compounds (Donetsk, 1984)), Kiev: Naukova Dumka, 1984.
16. Rumyantsev, L.Yu., Golovko, L.I., and Prokopchuk, E.G., Abstracts of Papers, *5-e Vsesoyuznoe soveshchanie po khimii i fizicheskoi khimii poliuretanov* (5th All-Union Meet. on Chemistry and Physical Chemistry of Polyurethanes), Kiev: Naukova Dumka, 1979, p. 68.
17. Kalinina, L.E., Terman, E.A., Korotkova, V.N., and Alekseenko, V.I., in *Stroenie i svoistva poverkhnostnykh sloev polimerov* (Structure and Properties of Polymer Surface Layers), Kiev: Naukova Dumka, 1972, pp. 89–96.

Russian Journal of Applied Chemistry, Vol. 76, No. 4, 2003, pp. 619–622. Translated from Zhurnal Prikladnoi Khimii, Vol. 76, No. 4, 2003, pp. 642–645.

MACROMOLECULAR CHEMISTRY AND POLYMERIC MATERIALS

New Heat-Resistant Polyimidates Derived from Bisphenols and Mono- and Dicarboxylic Acid Imidoyl Chlorides

D. B. Sanzhizhapov, Yu. V. Tonevitskii, D. M. Mognonov, and Yu. E. Doroshenko

Buryat State University, Ulan-Ude, Buryatia, Russia

Baikal Institute of Nature Management, Siberian Division, Russian Academy of Sciences, Ulan-Ude, Buryatia, Russia

Mendeleev Russian University of Chemical Engineering, Moscow, Russia

Received January 15, 2002

Abstract—New polyimidates were prepared from bisphenols and mono- and dicarboxylic acid imidoyl chlorides. The structures of the polymers were determined, and their physicochemical, chemical, and thermal properties were studied. The possibility of preparing film and compression materials with good mechanical characteristics from these polymers was examined.

Among the known polyheteroarylenes, nitrogen-containing aromatic polymers are of particular interest owing to their high heat resistance and high softening point in combination with good electrophysical and physicomechanical properties. However, data on aromatic polyimidates (PIDs) as a particular class of heat-resistant nitrogen-containing polymers [1, 2] are lacking. Synthesis of new polyheteroarylenes and materials thereof, combining good thermal, chemical, and physicomechanical properties, is still a topical problem.

The goal of this study was to develop synthesis procedures and analyze new PIDs derived from bisphenols and mono- and dicarboxylic acid imidoyl chlorides.

The polymers were prepared similarly to polycondensation of aromatic diamines with mono- and dicarboxylic acid imidoyl chlorides (MDAICs) [3], using bisphenols as nucleophilic agents:

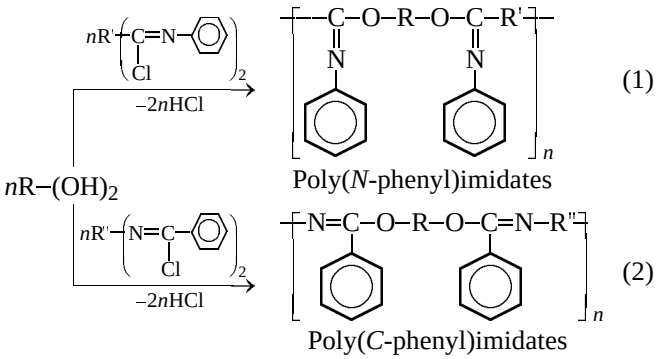

(1)

(2)

where R = 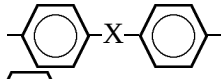 ; R' and R'' =  , 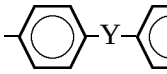 ; X = $-C(CH_3)_2-$, $-CH_2-$, –O–, σ bond; Y = $-CH_2-$, –O–, σ bond.

With the reaction of diphenylolpropane with *N*,*N*'-diphenylisophthalimidoyl chloride taken as example, we studied in detail how the reaction temperature and time, and also the concentration and ratio of monomers, affect the reduced viscosity and yield of PID. The main trends are similar to those obserbed in polycondensation with aromatic diamines, despite that the structures of MDAICs are different. Figure 1 shows that the highest yield (90%) and viscosity (η_r = 0.88–0.93 dl g^{-1}) of the polymers are attained at 140–160°C,

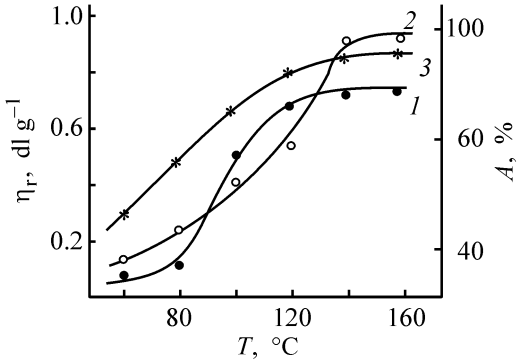

Fig. 1. Influence of temperature *T* on the (*1*, *2*) reduced viscosity η_r and (*3*) yield *A* of the polymer. Solvent: (*1*) dimethylacetamide and (*2*) *N*-methylpyrrolidone; the same for Figs. 2 and 3.

1070-4272/03/7604-0619 $25.00 © 2003 MAIK "Nauka/Interperiodica"

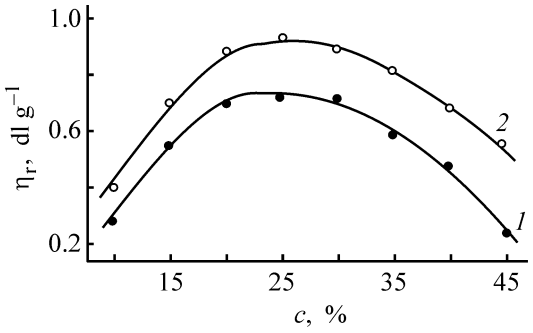

Fig. 2. Influence of the concentration *c* of the monomers on the reduced viscosity η_r of the polymer.

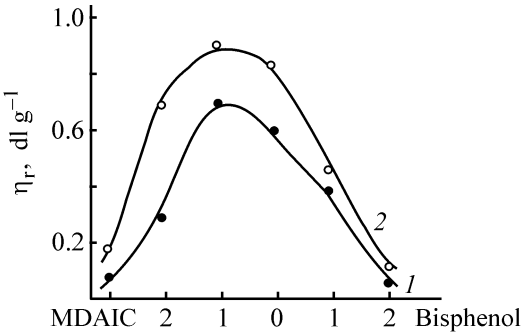

Fig. 3. Influence of the monomer ratio on the reduced viscosity η_r of the polymer. Reaction time 12 h, 160°C. *Abscissa*: relative molar excess (×10) of monomers.

reaction time of 12–14 h, and excess of imidoyl chloride (solvent *N*-methylpyrrolidone, *N*-MP).

The PID viscosity is affected by the concentration of the initial monomers (Fig. 2). At the optimal concentration (20–30%), the reaction is fast and yields polymers with better viscosity characteristics. A decrease in the η_r of the solutions of the polymers prepared at monomer concentrations exceeding the optimum value is due to slow diffusion of molecules in highly viscous reaction solutions.

Table 1. Structure, reduced viscosity,* and chemical resistance of PIDs derived from bisphenols and MDAICs

PID no.	R' and R''	R	η_r before treatment, dl g^{-1}	η_r (dl g^{-1}) after treatment with concentrated solution of indicated agent					
				H_2SO_4	HCl	HCOOH	CH_3COOH	CCl_3COOH	NaOH
	Poly(*N*-phenyl)imidates [scheme (1)]								
1		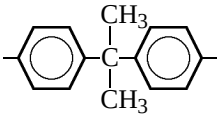	0.72	0.70	0.66	0.70	0.71	0.68	0.16
2		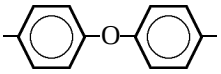	0.70	0.65	0.63	0.65	0.68	0.58	0.15
3		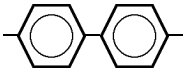	0.64	0.52	0.50	0.60	0.61	0.53	0.18
	Poly(*C*-phenyl)imidates [scheme (2)]								
4	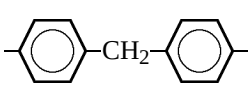	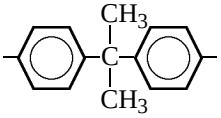	0.76	0.51	0.72	0.65	0.66	0.61	0.01
5	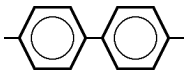	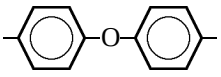	0.64	0.53	0.62	0.59	0.60	0.60	0.02
6	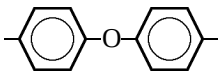	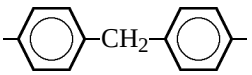	0.75	0.52	0.68	0.62	0.63	0.59	0.01

* In dimethylacetamide.

The viscosity characteristics of the polymers are also largely affected by the monomer ratio (Fig. 3). Polymers with the highest η_r are obtained at a relative molar excess of MDAIC of 0.1 mol. Such a ratio may be due to interaction of MDAIC with solvent molecules (Vilsmeier adduct, iminium complex) [4].

With respect to the capability to form high-molecular-weight polymers, MDAICs can be ranked in the following order: *p*-C_6H_4 < *m*-C_6H_4 < (1,4-C_6H_4)$_2$O < (1,4-C_6H_4)$_2$$CH_2$ (Table 1).

The PIDs were identified by elemental analysis and IR spectroscopy. The following absorption bands were detected (cm^{-1}): 3060–3010 (C–H arom.); 2950, 2870 (C–H aliph.); 2000–1790 (C_6H_5); 1665–1635 (C=N acycl.); 1600 (C–C atom.); 1420 (C–N); 1390, 1280–1260 (C–O ether), and also the bands of stretching and bending vibrations of atoms of disubstituted benzene and diphenyl ether. The characteristic bands are those of C=N acycl. and C–O, indicative of the formation of the imidate group, the unit of the macromolecules.

The polymers are readily soluble in highly polar organic solvents: DMF, dimethylacetamide, *N*-MP, DMSO, and *m*-cresol. The chemical resistance of the polymers was evaluated by the reduced viscosity before and after treatment with solutions of mineral acids and alkalis at 25–100°C for 48 h. Polyimidates are more resistant to concentrated acid solutions; their viscosity decreases only slightly. At the same time, tratment with alkali solutions decreases the reduced viscosity of PIDs [especially poly(*C*-phenyl)imidates] considerably. This fact suggests the occurrence of base hydrolysis of the polymers with cleavage of the macromolecular chain, primarily across the C–O and C=N bonds of the imidate group (Table 1).

The results of thermomechanical and thermogravimetric studies are listed in Table 2. The temperature of the plastic deformation of the polymers lies within 225–390°C. Polymers consisting of only aromatic fragments are the most resistant to thermal oxidative degradation: they decompose at 490°C. For polymers containing bridging groups in the hydrocarbon radical, the heat resistance decreases in the following order: σ bond > –O– > –CH_2– > –$C(CH_3)_2$–.

The relatively large margin between the softening and decomposition points offers good opportunities for PID processing into finished items. For example, compression materials (without filler) obtained by direct pressing at 245–400°C and 75 MPa exhibit good physicomechanical properties (Table 2).

Table 2. Thermal and physicomechanical properties of PIDs derived from bisphenols and MDAICs*

PID no.	T_s, °C	$T_{5\%}$, °C	σ_t, MPa	ε, %	*a*, kJ m^{-2}
1	230	385	43	3–4	7.5–8.0
2	315	460	40	–	–
3	365	490	35	2–3	7.5–8.5
4	225	365	44	3–4	7.5–8.5
5	390	465	42	2–4	6.5–7.0
6	325	405	43	2–3	6.5–7.5

* (T_s) Softening point corresponding to 5% deformation of PID, ($T_{5\%}$) temperature of 5% weight loss in air, (σ_t) tensile strength, and (ε) relative elongation.

EXPERIMENTAL

Dicarboxylic acid imidoyl chlorides were prepared according to [5].

Polyimidates were prepared in a three-necked flask equipped with a stirrer, and argon inlet tube, and a dropping funnel, with vigorous stirring. A solution of 0.011 mol of imidoyl chloride in *N*-MP was added in small portions from a dropping funnel to a solution of 0.01 mol of bisphenol in *N*-MP containing 0.022 mol of triethylamine. The mixture was gradually heated to 140–160°C and kept at this temperature for 13–15 h. The polymer was isolated by precipitation into water. The precipitate was filtered off, washed successively with 0.5% solutions of Na_2CO_3, HCl, and H_2O to pH 7, and dried in a vacuum oven at 80°C to constant weight.

The reduced viscosity of PIDs was determined according to GOST (State Standard) 18249–79. The IR spectra were recorded on a Specord IR-75 spectrophotometer.

A thermomechanical analysis of PIDs was performed on a modified Tsetlin device at a load of 0.33 or 1.0 MPa and heating rate of 100 deg h^{-1}. The thermal characteristics were obtained with a Q-1000 derivatograph at a heating rate of 5 deg min^{-1}. Mechanical tests were performed according to GOSTs 17036–71 and 14235–69.

CONCLUSIONS

(1) A number of new poly(*N*-phenyl)- and poly(*C*-phenyl)imidates were prepared by nonequilibrium

polycondensation of mono- and dicarboxylic acid imidoyl chlorides with bisphenols. The products were identified by elemental analysis and IR spectroscopy, and their properties were studied.

(2) Examination of the physicomechanical, thermal, and chemical properties of the polymers synthesized revealed their high heat resistance and a large margin between the softening and decomposition points.

REFERENCES

1. Korshak, V.V., *Termostoikie polimery* (Heat-Resistant Polymers), Moscow: Khimiya, 1969.
2. Buhler, K.-U., *Spezialplaste*, Berlin: Akademie, 1978.
3. Tonevitskii, Yu.V., Mognonov, D.M., Sanzhizhapov, D.B., *et al.*, *Vysokomol. Soedin., Ser. B*, 2000, vol. 42, no. 6, pp. 1054–1059.
4. Meth-Cohn, O. and Tarnowski, B., *Adv. Heterocyclic Chem.*, 1982, vol. 31, pp. 207–208.
5. Grenda, V.J., Jones, R.E., Gal, G., and Sletzinger, M., *J. Org. Chem.*, 1965, vol. 30, no. 1, pp. 259–261.

Russian Journal of Applied Chemistry, Vol. 76, No. 4, 2003, pp. 623–625. Translated from Zhurnal Prikladnoi Khimii, Vol. 76, No. 4, 2003, pp. 646–649.

MACROMOLECULAR CHEMISTRY AND POLYMERIC MATERIALS

Synthesis and Properties of Epoxy–Acrylate Polymers Prepared in the Presence of Sulfoxides and Their Complexes

G. V. Gatiyatullina, Yu. A. Prochukhan, E. M. Battalov, N. G. Afzaletdinova, and Yu. I. Murinov

Institute of Organic Chemistry, Ufa Scientific Center, Russian Academy of Sciences, Ufa, Bashkortostan, Russia

Received July 19, 2002; in final form, December 2002

Abstract—The initiating activity of some sulfoxides and their complexes in photopolymerization of epoxy–acrylate oligomer obtained by the reaction of ED-16 epoxy oligomer with acrylic acid was studied, and the degree of cross-linking of the resulting polymers was evaluated by analyzing their swelling kinetics.

The epoxy–acrylate oligomer was prepared by esterification of an epoxy oligomer with an equimolar amount of acrylic acid (AA) at 120°C in the presence of a polymerization inhibitor (hydroquinone) and a catalyst of epoxy ring opening (triethylamine), by the following scheme:

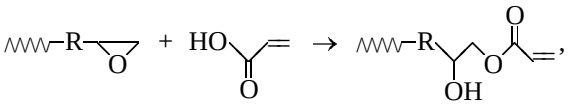

where R is the oligomeric block of the epoxy oligomer.

We used ED-16 epoxy oligomer. Acrylic acid was purified by distillation. The oligomers synthesized chiefly contain diacrylates and certain amount of epoxy acrylates (in the course of synthesis of the epoxy–acrylate oligomer, the content of epoxy groups decreases from 24 to 9 mol %). Such an oligomer was used in this work. Its structural formula

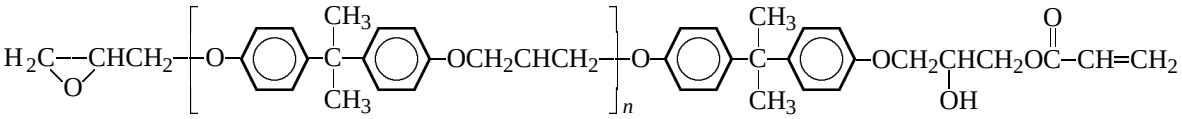

ED-16–AA

It was confirmed by the ^{13}C and ^{1}H NMR spectra. The NMR spectra were recorded on a Bruker AM-300 spectrometer (working frequency 76.46 and 300 MHz, respectively; solvent $CDCl_3$, internal reference TMS). The signals were assigned using the two-dimensional correlation technique (COSY H–H, C–H).

The degree of swelling was studied with films of ED-16–AA polymers prepared in the presence of sulfoxides and their complexes. The film thickness was about 50 μm.

Sulfoxide complexes were prepared at the Laboratory of Physical Chemistry, Institute of Organic Chemistry, Ural Scientific Center, Russian Academy of Sciences, and recrystallized from hexane; the purity was checked by IR spectroscopy and potentiometric determination of sulfoxide sulfur (98.5–99%). Petroleum sulfoxides (PSOs) were prepared from petroleum sulfide concentrates or straight-run fractions of high-sulfur oils boiling in the range 260–360°C. Petroleum sulfides were oxidized with hydrogen peroxide. In the process, the substituents at sulfur remained intact. The physicochemical constants of purified individual sulfoxides were in agreement with published data. Sulfoxide complexes have the general structure

$$R{-}S{=}O{\cdots}X{\cdots}O{=}S{-}R,$$

where R is an aliphatic or cyclic substituent; X = HCl, H_3PO_4, $VOCl_3$, $HCl \cdot FeCl_3$, etc.

1070-4272/03/7604-0623 $25.00 © 2003 MAIK "Nauka/Interperiodica"

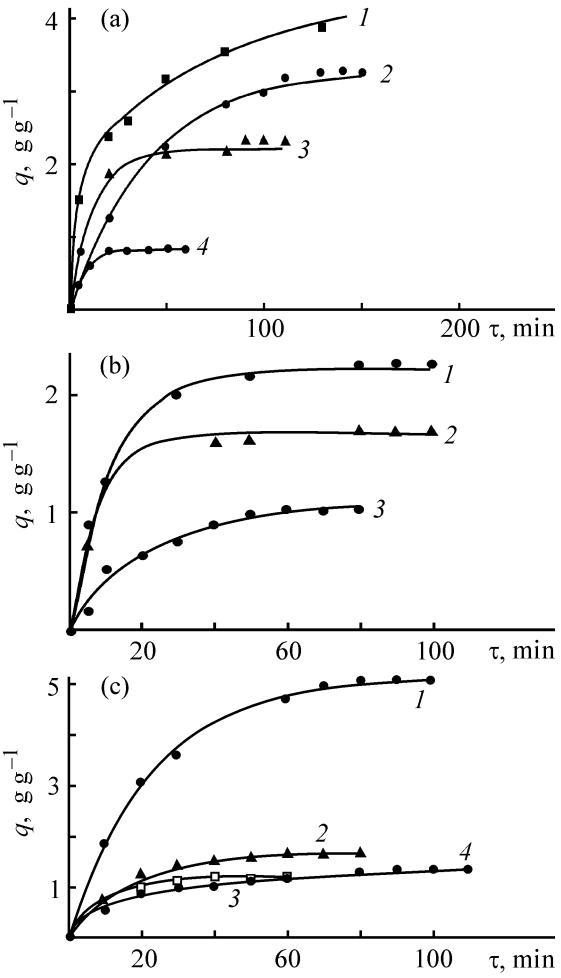

Fig. 1. Kinetic curves of swelling of polymers prepared in the presence of (a) aliphatic sulfoxides, (b) mixed sulfoxides, and (c) sulfoxide complexes. Photopolymerization time 60 min, concentration of sulfoxides and sulfoxide complexes 2.0 wt %. (*q*) Degree of swelling and (τ) time. (a) (*1*) Didodecyl sulfoxide, (*2*) dioctyl sulfoxide, (*3*) dihexyl sulfoxide, and (*4*) dimethyl sulfoxide; (b) (*1*) benzyl octyl sulfoxide, (*2*) dibenzyl sulfoxide, and (*3*) PSOs; (c) (*1*) $HCl \cdot FeCl_3 \cdot 4DHSO$, (*2*) $VOCl_3 \cdot 3DHSO$, (*3*) $HCl \cdot 2DHSO$, and (*4*) $H_3PO_4 \cdot 2DHSO$.

Photopolymerization was induced with a PRK-400 medium-pressure mercury lamp placed at a distance of 14 cm from the oligomer.

It is known that free sulfoxides affect the photopolymerization kinetics of vinyl monomers only slightly. However, sulfoxide complexes of metal chlorides and oxychlorides, HCl, and uranyl are effective photoinitiators of methyl methacrylate polymerization [1]. The sensitizing activity of sulfoxides in photochemical cross-linking of polyvinylbutyral and polyethylene was reported in [2]. In an ESR study of low-temperature radiolysis and photolysis of DMSO [3], methyl radicals were detected in photolysis of polycrystalline DMSO; further annealing resulted in the formation of sulfinyl radicals $CH_3SO^{\cdot}$. The relative concentration of methyl radicals in γ-radiolysis was considerably lower than in photolysis. It has been found previously by ESR spectroscopy that thiyl $RS^{\cdot}$, formyl $HCO^{\cdot}$, and methyl radicals are generated in prolonged photolysis of DMSO (naphthalene sensitizer, λ = 313 nm). The radicals accumulate without induction period. The mechanism of radical generation in photolysis of DMSO assumes initial generation of the $^{\cdot}CH_2SOCH_3$ radical, but the mechanism of this process is not fully understood [4]. An ESR study of thermolysis and photolysis of other sulfoxides was made in [5].

The above-cited demonstrated [1–5] show that photolysis of DMSO involves generation of free radicals. These species must be reactive in polymerization of monomers (or oligomers) and cross-linking of polymers. Without dwelling upon the mechanism of radical generation and concentration of radicals in photolysis of various sulfoxides, we can judge the efficiency of sulfoxides as photoinitiators of polymerization or cross-linking from the degree of cross-linking of the polymers formed in the presence of sulfoxides. In this context, it is of interest to study photopolymerization of an epoxy–acrylate oligomer in the presence of sulfoxides.

Below is given the time τ in which polymeric films are formed in photopolymerization of ED-16–AA epoxy–acrylate oligomer in the presence of certain sulfoxides (2.0 wt %):

Sulfoxide	τ, min
Benzophenone	10
Didodecyl sulfoxide	20
Dibenzyl sulfoxide	30
Dioctyl sulfoxide	35
Dihexyl sulfoxide (DHSO)	40
Petroleum sulfoxides	50
Dimethyl sulfoxide	60

The rate of oligomer photopolymerization in thin films on a glass support was evaluated by the time of formation of a nonsticking polymeric film.

It is seen that the initiating activity of sulfoxides is lower than that of the known photopolymerization initiator, benzophenone, but sufficient for the synthesis of epoxy–acrylate polymers.

The kinetic curves of swelling in trichloroethylene of the polymers prepared in the presence of aliphatic and mixed sulfoxides in the same reaction time are shown in Figs. 1a and 1b, and similar plots for the polymers prepared in the presence of certain sulfoxide complexes, in Fig. 1c.

The values of the limiting swelling of the polymers (Figs. 1a, 1b) show that the degree of cross-linking depends on the sulfoxide used. As the length of the alkyl substituent in an aliphatic sulfoxide is increased, the degree of cross-linking decreases (Fig. 1a). Mixed sulfoxides and PSOs favor formation of relatively more cross-linked polymer as compared with aliphatic sulfoxides. The degree of swelling (or cross-linking) of the polymeric material correlates with the rate of formation of a nonsticking polymeric film: The higher the curing rate, the lower the degree of the polymer cross-linking (Figs. 1a, 1b). The above data on the degree of cross-linking of the epoxy–acrylate polymer show that aliphatic and mixed sulfoxides effectively initiate photopolymerization of this oligomer. To compare, with benzophenone as initiator, the degree of swelling is 2–5 g g^{-1}.

The structure of the sulfoxide affects both the rate of radical generation and the intensity of their decay under the action of UV light. Figures 1a and 1b show that the most cross-linked polymers are formed in the presence of DMSO and petroleum sulfoxides. It seems probable that the common feature of DMSO photolysis, both in polycrystalline DMSO at low temperatures and in a viscous medium of the oligomer, is the low probability of the radical decay. This assumption is supported by the fact that, apparently, DMSO does not initiate photopolymerization of methyl methacrylate [1].

Sulfoxide complexes of metal chlorides, uranyl, or inorganic acids, e.g., $VOCl_3$, HCl, and H_3PO_4, also show promise as initiators of photochemical curing of epoxy–acrylate oligomers. Firstly, as shown above, the sulfoxides themselves initate photopolymerization; secondly, some metal salts and inorganic acids exhibit a photoinitiating activity [5].

Figure 1c shows the kinetic curves of swelling of polymers prepared in the presence of sulfoxide complexes. It is seen that, in almost all the cases, the resulting polymers are more cross-linked than those obtained in the presence of free sulfoxides. For example, UV-induced polymerization of the oligomer in the presence of DHSO and $H_3PO_4 \cdot 2$DHSO yields a polymer with the limiting swelling of 2.2 and 1.24 g g^{-1}, respectively. With the other sulfoxides and their complexes, the pattern is similar, i.e., the sulfoxide complexes are, on the whole, more active in photopolymerization than the free sulfoxides. The photoinitiation mechanism may be specific for each sulfoxide complex. There may be a synergism in the effect of sulfoxide and metal halide (or inorganic acid) in the complex. Similarly to the case of UV-induced polymerization of methyl methacrylate in the presence of sulfoxide complexes of metal halides and oxychlorides, the initiating radicals are probably halogen atoms.

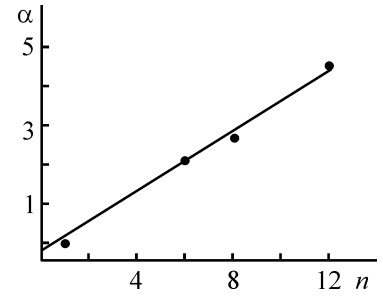

Fig. 2. Limiting swelling α of the polymers vs. the number *n* of carbon atoms in aliphatic substituent R in sulfoxides R_nSOR_n.

An interesting fact is observed in photopolymerization of the epoxy–acrylate oligomer, initiated by aliphatic sulfoxides: As the number of carbon atoms *n* in alkyl substituent R in sulfoxide R_nSOR_n is increased, the limiting swelling grows (Fig. 2). This is apparently due to a decrease in the mole fraction of SO groups with increasing *n*.

CONCLUSIONS

(1) Sulfoxides and their complexes are fairly effective and available initiators of photopolymerization of ED-16–acrylic acid oligomer.

(2) Sulfoxide complexes surpass free sulfoxides in the capability to initiate photochemical cross-linking of epoxy–acrylate oligomers and show promise for synthesis of epoxy–acrylate polymers with a prescribed degree of cross-linking.

REFERENCES

1. Rafikov, S.R., Leplyanin, G.V., Battalov, E.M., *et al.*, *Dokl. Akad. Nauk SSSR*, 1977, vol. 235, no. 6, pp. 1360–1362.
2. Kachan, A.A. and Shrubovich, V.A., *Fotokhimicheskoe modifitsirovanie sinteticheskikh polimerov* (Photochemical Modification of Synthetic Polymers), Kiev: Naukova Dumka, 1973.
3. Machado, J.C., Debuyst, R., Dejehet, F., and Apers, D., *Radiochem. Radioanal. Lett.*, 1972, vol. 9, no. 5, pp. 363–371.
4. Mardaleishvili, I.R. and Mel'nikov, M.Ya., *Vestn. Mosk. Gos. Univ., Ser. Khim.*, 1979, vol. 20, no. 2, pp. 145–147.
5. Bamford, C.H., Jenkins, A.D., and Johnston, R., *Nature*, 1956, vol. 177, pp. 992–993.

Russian Journal of Applied Chemistry, Vol. 76, No. 4, 2003, pp. 626–628. Translated from Zhurnal Prikladnoi Khimii, Vol. 76, No. 4, 2003, pp. 650–652.

MACROMOLECULAR CHEMISTRY AND POLYMERIC MATERIALS

Evaluation of the Degree of Cross-Linking of Epoxy–Acrylate Polymers with a Luminescence Probe

G. V. Gatiyatullina, E. M. Battalov, A. I. Voloshin, and Yu. A. Prochukhan

Institute of Organic Chemistry, Ufa Scientific Center, Russian Academy of Sciences, Ufa, Bashkortostan, Russia

Received July 19, 2002; in final form, December 2002

Abstract—Luminophores, 4,4'-diaminodiphenylmethane and Oxazine-17, were introduced into a photopolymerizable formulation based on an epoxy–acrylate oligomer, and their behavior in thin-film polymerization was studied.

Experiments were performed with an epoxy–acrylate oligomer derived from UP-612 cycloaliphatic epoxy resin. Epoxy–acrylate resins were prepared by esterification of epoxy oligomers with acrylic acid (AA) in the presence of a polymerization inhibitor at 120°C by the following scheme [1]:

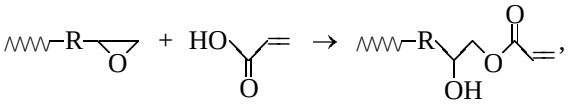

where R is the oligomeric block of the epoxy oligomer.

The oligomers were identified by ^{13}C and ^{1}H NMR spectroscopy. The NMR spectra were recorded on a Bruker AM-300 spectrometer (working frequency 76.46 and 300 MHz, respectively; solvent $CDCl_3$, internal reference TMS). The signals were assigned using the two-dimensional (2D) correlation technique (COSY H–H, C–H).

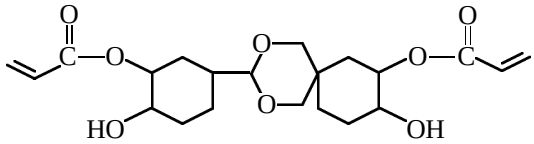

The reaction course was monitored by variation of the iodine number [1]. Acrylic acid was purified by distillation.

Epoxy–acrylate films were prepared from acetone solutions of the initial oligomer, containing 5 wt % benzophenone (BP) as photoinitiator. The film thickness was 75 μm. A 0.5-cm^2 square piece of a film was irradiated with two SVD-120 lamps (VIO-2 illuminator); the line with λ = 313 nm was picked out with ZhS-3 and UFS-2 color filters. The incident light intensity was determined with a ferrioxalate actinometer [2]. The following luminophores were chosen:

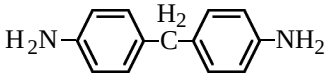

4,4'-Diaminodiphenylmethane (DAM)

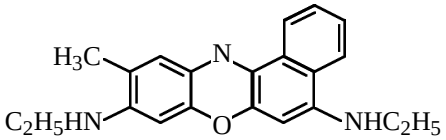

Oxazine-17

The concentration of the luminophores in the initial oligomer was 1×10^{-4} M.

The luminescence spectra were recorded with an MPF-4 device (Hitachi). The photomicrographs in polarized light were obtained with Amplival-pol and Axiolab-pol microscopes (Carl Zeiss, Germany).

It is known that the luminescence spectra of luminophores in polyethylene terephthalate, polycaproamide, and polyvinyl chloride appreciably change upon orientation extension of the polymer [3–5], which allows monitoring of changes in the polymer microstructure. Changes occurring in a polymer under mechanical action affect the state of the luminophore introduced, which allows interpretation of its spectral characteristics. It is also known that, with a luminescence probe introduced into a polymerizing system, it is possible to monitor the polymerization of monomers and curing of epoxy compounds by variation of the luminophore spectrum [6, 7]. However, studies in which various probes were used in synthesis

1070-4272/03/7604-0626 $25.00 © 2003 MAIK "Nauka/Interperiodica"

of 3D polymers are very few, and changes in the luminescence spectra were different in each particular case, irrespective of the nature of a probe used.

In this study, we monitored the photochemical curing of UP-612–AA epoxy–acrylate oligomer by introducing Oxazine-17 and DAM as luminescence probes into a photocurable system and by measuring the luminescence spectra during the process.

Figure 1 shows how the photoluminescence spectra of luminophores introduced into the epoxy–acrylate oligomer change upon curing. It is seen that the intensity of Oxazine-17 luminescence in the long-wave region (650 nm) grows upon photocuring, and that of DAM luminescence decreases. Such a behavior of the luminescence spectra of Oxazine-17 may be due to changes in the state of the luminophore molecules with increasing degree of cross-linking. The decomposition of luminophore associates (polymeric species) and formation of dimers in the course of the polymer cross-linking, as also in the course of extension of polyvinyl chloride films containing the same luminophore [5], results in a redistribution of the luminescence bands and a long-wave shift of the luminescence spectrum. The photomicrographs of UP-612–AA films, taken in polarized light after photocuring for different times (Fig. 2), illustrate changes occurring in the polymer upon UV irradiation.

Figures 2a and 2b show that, in the initial stage of photopolymerization, when the polymer is not fully cross-linked, the sample is anisotropic. After the cross-linking under the given conditions is complete, the sample becomes isotropic (Fig. 2c). As the polymer microstructure gets stabilized, the luminescence spectra of Oxazine-17 no longer change. Apparently, in cross-linked polymeric films in which there is no anisotropy of the polymer properties, the conditions are favorable for the existence of dimeric Oxazine-17 species. A decrease in the intensity of DAM luminescence in the course of the oligomer cross-linking may be due to the luminophore consumption in side reactions and to significant changes in the probe configuration in the rigid polymeric matrix.

Our results, ultimately characterizing the degree of cross-linking of the polymer being synthesized, are well consistent with the results obtained in determining the degree of cross-linking by other methods. For example, the degree of cross-linking of 3D polymers is usually determined from their swelling in a solvent [8]. The degree of swelling of the polymer derived from UP-612–AA in trichloroethylene is plotted in Figs. 3 and 4 together with the shift of the luminescence peak of Oxazine-17 and with the decay of

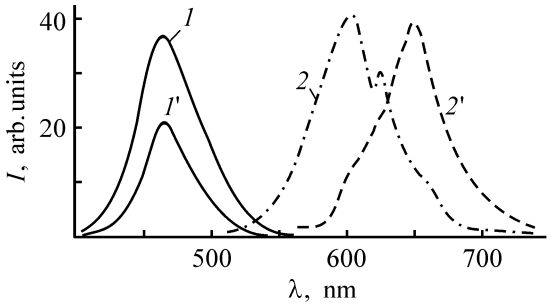

Fig. 1. Photoluminescence spectra of (*1*, *1*') DAM and (*2*, *2*') Oxazine-17 (*1*, *2*) before and (*1*', *2*') after photocuring of UP-612–AA oligomer. Excitation wavelength 365 nm. (I) Emission intensity and (λ) wavelength.

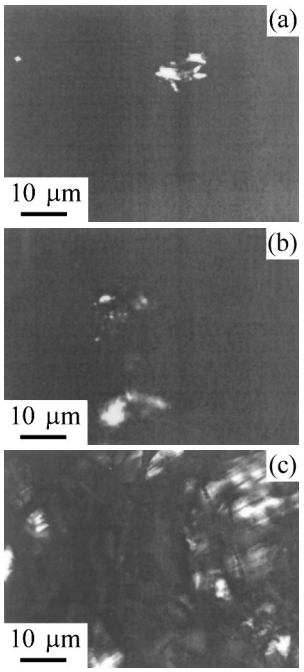

Fig. 2. Photomicrographs (polarized light) of epoxy–acrylate oligomer subjected to UV curing for different times. Exposure time, min: (a) 20 and (b) 30; (c) polymer washed to remove the sol fraction.

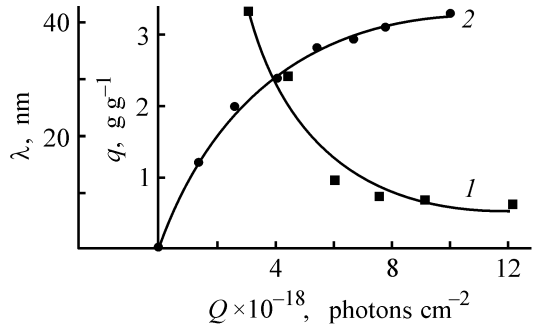

Fig. 3. (*1*) Shift λ of the luminescence peak of Oxazine-17 in the oligomer and (*2*) degree of swelling *q* of the polymer in TCE, vs. the irradiation dose *Q*. Photopolymerization of UP-612–AA with 313-nm light;the same for Fig. 4.

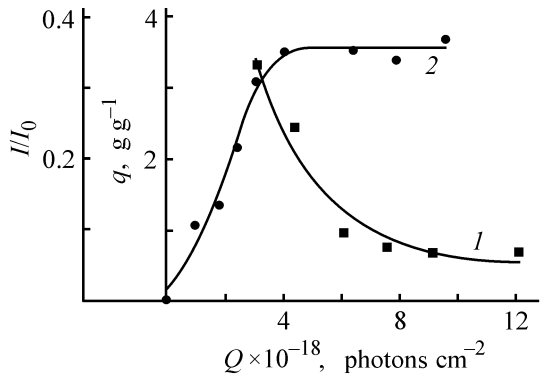

Fig. 4. (*1*) Decay of the intensity I/I_0 of DAM luminescence in the oligomer and (*2*) degree of swelling q of the polymer in TCE vs. the irradiation dose Q.

DAM luminescence in the polymeric matrix against the exposure of the oligomer to UV light. It is seen that the curves for these parameters level off at similar irradiation doses. In turn, the luminescence spectra of the polymer with these luminophores allow estimation of the degree of cross-linking. Such an approach to evaluation of the degree of cross-linking is especially important for industrial processes, as a way of prompt and nondestructive process monitoring.

CONCLUSION

Luminescence probes introduced into a photocurable oligomer show different trends in variation of the luminescence spectra in the course of polymerization. The photopolymerization of epoxy–acrylate oligomer can be to a certain extent monitored by variation of the luminescence spectra of the probe.

REFERENCES

1. *Epoksiakrilovye smoly. Khimicheskaya promyshlennost'. Ser.: "Epoksidnye smoly i materialy na ikh osnove": Obzornaya informatsiya* (Epoxy–Acrylate Resins, Chemical Industry, Ser. "Epoxy Resins and Materials Based on Them," Review), Moscow: NIITEKhIM, 1981.
2. Rabek, J.F., *Experimental Methods in Polymer Chemistry. Physical Principles and Applications*, Chichester: Wiley, 1980.
3. Kalechits, I.I., Kuz'min, M.G., Lukovkin, G.M., *et al.*, *Vysokomol. Soedin., Ser. A*, 1989, vol. 31, no. 10, pp. 2230–2233.
4. Kalechits, I.I. and Kuz'min, M.G., *Vysokomol. Soedin., Ser. B*, 1992, vol. 34, no. 10, pp. 55–58.
5. Ostakhov, S.S., Kazakov, V.P., and Voloshin, A.I., *Vysokomol. Soedin., Ser. B*, 1996, vol. 38, no. 2, pp. 352–354.
6. Strehmel, B., Strehmel, V., and Younes, M., *J. Polym. Sci. B: Polym. Phys.*, 1999, vol. 37, no. 13, pp. 1367–1386.
7. Lees, Aj., *J. Polym. Polym. Compos.*, 1998, vol. 6, no. 3, pp. 121–131.
8. Rafikov, S.R., Budtov, V.P., and Monakov, Yu.B., *Vvedenie v fizikokhimiyu rastvorov polimerov* (Introduction to Physical Chemistry of Polymer Solutions), Moscow: Nauka, 1978.

Russian Journal of Applied Chemistry, Vol. 76, No. 4, 2003, pp. 629–633. Translated from Zhurnal Prikladnoi Khimii, Vol. 76, No. 4, 2003, pp. 653–657.

MACROMOLECULAR CHEMISTRY AND POLYMERIC MATERIALS

ESR Study of Photopolymerization of Epoxy-Acrylate Oligomers

R. A. Sadykov, G. V. Gatiyatullina, E. M. Battalov, and Yu. A. Prochukhan

Institute of Petroleum Chemistry and Catalysis, Academy of Sciences of the Republic of Bashkortostan, Ufa, Bashkortostan, Russia

Institute of Organic Chemistry, Ufa Scientific Center, Russian Academy of Sciences, Ufa, Bashkortostan, Russia

Received July 22, 2002; in final form, January 2003

Abstract—Photopolymerization and thermal polymerization of epoxy-acrylate oligomers were studied by ESR at room temperature.

Epoxy-acrylate oligomers are extremely attractive materials for use as, e.g., protective and reinforcing coatings in production of waveguide fibers, adhesives, etc.

For the most of polymerizable systems based on vinyl monomers, the nature of radicals responsible for polymerization has been studied in sufficient detail [1]. At the same time, any studies of the nature of active centers for epoxy-acrylate oligomers are lacking.

This is concerned with the paramagnetic centers arising in polymerization of epoxy-acrylate oligomers.

EXPERIMENTAL

Epoxy-acrylate oligomers were synthesized by esterification of epoxy oligomers with acrylic acid at equimolar ratio of reactants in the presence of a polymerization inhibitor (hydroquinone) and a catalyst [2-(diethylamino)-1-ethanol] for opening of epoxy rings at 120°C by the scheme

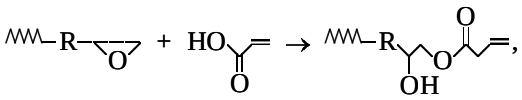

where R is the oligomer block of an epoxy oligomer.

We used epoxy oligomers UP-612 and Oksilin (ON), which is the product of reaction of glycerol with epichlorohydrin and ED-16. Acrylic acid (AA) was purified by distillation. The oligomers synthesized (UP-612–AA, ON–AA, and ED-16–AA, respectively) contain mainly diacrylates and a certain amount of epoxy acrylates (less than 5%; from here on, wt %).

The structure of the oligomers synthesized

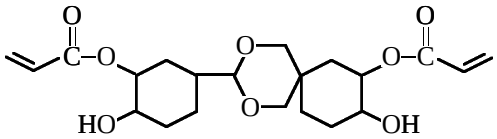

UP-612–AA

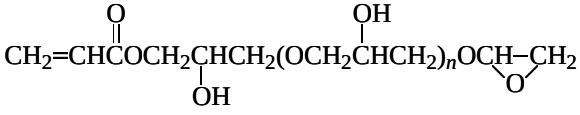

ON–AA

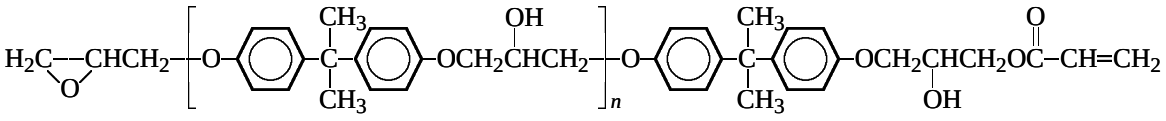

ED-16–AA

1070-4272/03/7604-0629 $25.00 © 2003 MAIK "Nauka/Interperiodica"

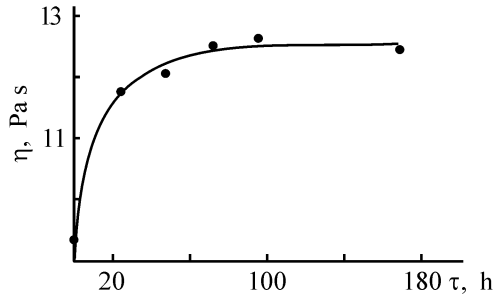

Fig. 1. Variation of dynamic viscosity η of UP-612–AA oligomer with time τ after UV irradiation for 15 s.

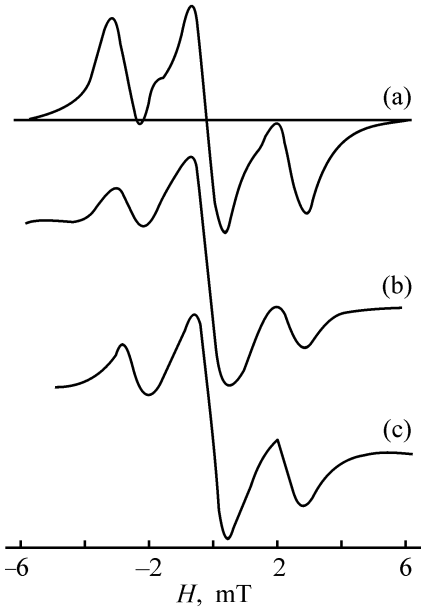

Fig. 2. ESR spectra of solid polymers at 20°C. (*H*) Magnetic field strength; the same for Figs. 3 and 4. (a) Polyacrylic acid after gamma irradiation [5], (b) oligomer UP-612–AA + 10% BP after UV irradiation for 110 min, and (c) oligomer ED-16 + 1% BP after UV irradiation for 2 h (irradiation at 20°C).

was determined by ^{13}C and ^{1}H NMR spectroscopy. The NMR spectra were recorded on a Bruker AM-300 spectrometer operating at 300 (^{1}H) and 76.46 MHz (^{13}C). $CDCl_3$ was used as a solvent, and TMS, as internal reference. The spectra were analyzed and the signals were assigned using two-dimensional H–H and C–H COSY NMR techniques.

The dynamic viscosity of epoxy acrylates was measured on a Rheotest rotary viscometer. Benzophenone (BP) was purified by the common procedure.

To detect radicals generated in thermal polymerization and photopolymerization, we used as spin trap 2-methyl-2-nitrosopropane (MNP) synthesized by the procedure described in [2]. MNP was added to the oligomer in a concentration of $(1–5) \times 10^{-2}$ M.

The ESR spectra were recorded on an SE/X 2543 spectrometer operating at 9 GHz (wavelength $\lambda = 3$ cm). The samples were placed in quartz ampules 4–5 mm in diameter. In the experiments on photopolymerization, BP (1 and 10%) was used as photoinitiator.

The experiments on thermal polymerization in the presence of a spin trap were carried out directly in the resonator of the ESR spectrometer equipped with a temperature-control unit.

Photopolymerization of oligomers was carried out by irradiation with light from high-pressure mercury lamp. To suppress the visible radiation, especially the band with $\lambda = 650$ nm, which readily causes photolysis of MNP to give di-*tert*-butylnitroxyl radical interfering with the study, we used a UFS-2 filter. The field sweep range was determined from the field marks generated by a special unit.

To determine the *g*-factors of radical centers, we used 1-1-diphenyl-2-picrylhydrazyl (DPPH) with $g = 2.0037$ [3]. The *g*-factor of the sample under study was determined by the formula

$$g_X - g_S = \frac{-\Delta H}{H_S} g_S,$$

where g_S is the *g*-factor of the reference, g_X is *g*-factor of the sample being studied; H_S, magnetic induction corresponding to the center of the reference signal; and ΔH, the distance between the centers of ESR signals from the reference and a sample studied.

Of some interest is the prolonged post-effect in studying the polymerization of epoxy oligomers. For example, after UV irradiation of an oligomer based on UP-612–AA (initiator 5% BP) for 15 s, its dynamic viscosity increases (Fig. 1), which suggests postpolymerization after cutting off the light source. A similar pattern is observed in thermal initiation. Long-lived radicals of chain propagation, which are responsible for postpolymerization and whose decay is limited owing to relatively high viscosity of the oligomer medium, must be detectable by direct methods.

It is well known that radical centers similar to the centers expected have been observed directly. For example, upon gamma irradiation of a solid polymer of acrylic acid at room temperature, a triplet signal was observed in the ESR spectrum (Fig. 2a) [4]. This signal was assigned to a terminal radical of the $–CH_2\dot{C}HCO_2H$ type; the *g*-factor of this signal is 2.0031. Upon heating of the sample irradiated at 77 K or upon irradiation at 300 K, macroradicals $–CH_2\dot{C}(COOH)CH_2–$ (quintet, $\Delta H_r = 2.4$ mT) initially predominate. At 300 K and higher temperatures, these macroradicals are irre-

versibly converted to terminal radicals $-CH_2(CO_2H)\dot{C}H$. The signal from this radical is characterized by the constants $a_{\alpha}^{H} = 2$, $a_{\alpha}^{H_1} = 2.5$, and $a_{\beta}^{H_2} = 3$ mT. It can be suggested that the terminal radicals in polyacrylic acid are formed by the reaction of macroradicals with AA. In the above examples, the radical centers became stable as a result of their fixing in the solid polymer matrix. In the liquid phase, these radicals rapidly decay. In the case in question, the propagation radical differs only in the presence of the methyl substituent, instead of the hydrogen atom, in the acid group, which does not noticeably alter the spectrum shape. We hope that, at high degrees of conversion in polymerization of oligomers, the propagation radical stabilized in the solid phase will be detected.

To verify this assumption, we carried out photopolymerization of two samples, oligomer UP-612–AA with 10% BP and ED-16–AA with 1% BP, to high degrees of conversion. The ESR spectra recorded after this procedure are shown in Figs. 2b and 2c, respectively. The ESR spectrum is similar to that reported in [5] ($g = 2.0031$). The shift of the side components of the triplet from the triplet center is 2.57 mT. The shift found previously [5] is 2.55 mT. Thus, it can be concluded that, in both cases, the observed triplet can be assigned to the same radical center, specifically, to the terminal radical or the propagation radical.

Comparison of Figs. 2a and 2b shows that the intensity of the central component of the ESR signal of gamma irradiated polyacrylic acid is lower than that in the samples of UV-irradiated oligomers. This is apparently caused by the existence of another signal coinciding with the central component of the triplet and corresponding to another radical center. With the aim to resolve this signal, we carried out photolysis of the gel fraction of the polymers produced from epoxyacrylate polymers (ED-16–AA and UP-612–AA) after removal of the residual oligomer (sol fraction). As a result, we obtained the ESR spectra shown in Figs. 3a and 3b. These spectra are superpositions of the ESR signals from several radical centers. The first is well-known propagation radical, to which two weak side lines are assigned. The triplet with components of equal intensity, separated by 0.8 mT, can be assigned to the second radical center. The singlet obscured by the triplet of the latter radical center can be assigned to an unknown third radical center. The unknown paramagnetic centers cannot be identified under these experimental conditions. The presence of other radical centers governing the cross-linking in the polymer at high degrees of conversion is indirectly confirmed by the recombination chemiluminescence in photopolymerization of these oligomers [6].

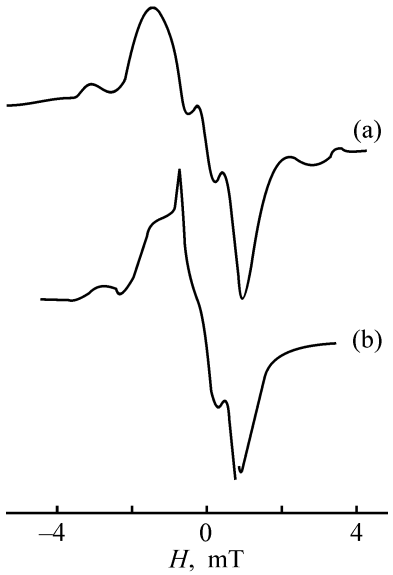

Fig. 3. ESR spectra of the gel fraction of polymers subjected to UV irradiation at 20°C: (a) ED-16–AA + 5% BP, irradiation time 40 min and (b) UP-612–AA + 5% BP, irradiation time 1 h.

With the aim to confirm the conclusion about the nature of the propagation radical, we carried out experiments on detection and identification of radical centers formed in the course of polymerization, using the well-known method of spin traps [7]. This method involves the reaction of a spin trap (MNP) with a short-lived radical to form nitroxyl radical, adduct of unstable radical with the trap, which is sufficiently stable for recording the ESR spectra:

$$(CH_3)_3CN{=}O + R^{\bullet} \rightarrow (CH_3)_3CNR,\ \ |\ O^{\bullet}$$

The presence of ESR signals not only proves the formation of paramagnetic centers in the system at hand, but also allows, in many cases, their simple identification from the hyperfine structure of the spectra. As a result of UV irradiation of UP-612–AA oligomer with 1% BP in the presence of MNP (c = 0.05 M), we obtained the ESR spectrum shown in Fig. 4a. It is believed that the spectrum is a superposition of a broadened triplet of doublets and a triplet. The triplet with characteristic coupling constant with nitrogen nucleus $a_N = 1.573$ mT is assigned to the side di-*tert*-butylnitroxyl radical formed under the action of UV irradiation [7] and has no relation to the reaction in question:

$$(CH_3)_3CN{=}O \xrightarrow{h\nu} (CH_3)C^{\bullet} + NO^{\bullet},$$

$$(CH_3)_3CN{=}O + (CH_3)_3C^{\bullet} \rightarrow (CH_3)_3C{-}N{-}C(CH_3)_3.\ \ |\ O^{\bullet}$$

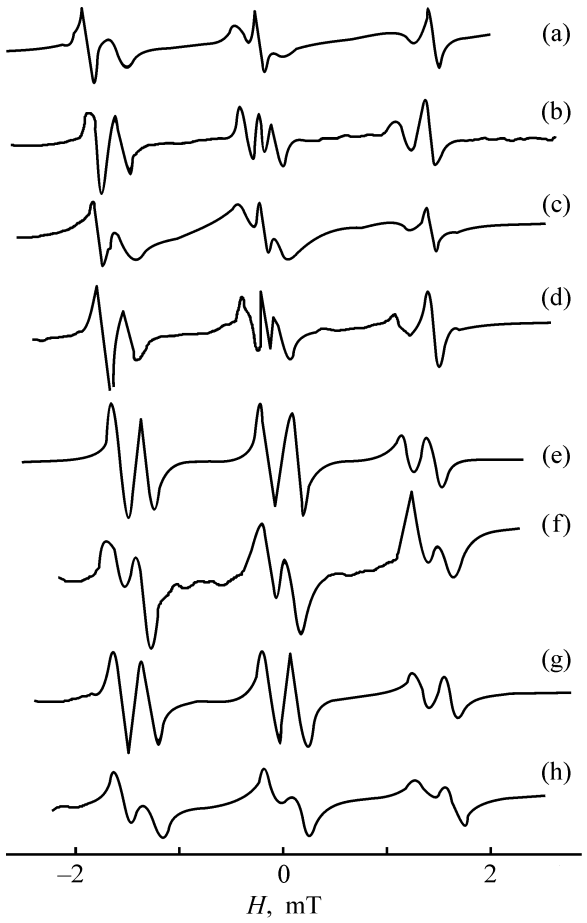

Fig. 4. ESR spectra obtained in the course of polymerization of oligomers (UV irradiation) in the presence of MNP (5×10^{-2} M): (a) UP-612–AA + 1% BP, irradiation for 10 s; (b) UP-612–AA with 1% BP (diluted with CH_2Cl_2, 1 : 1), irradiation for 2 min; (c) ON–AA + 1% BP (diluted with CH_2Cl_2, 1 : 1), irradiation for 160 s; (d) ED-16–AA + 1% BP (diluted with CH_2Cl_2, 1 : 1), irradiation for 20 s; (e) ED-16–AA + 1% BP (diluted with CH_2Cl_2, 1 : 1), irradiated for 35 s with subsequent heating of the sample for 5 min at 70°C; (f) butyl acrylate + 1% BP, irradiated for 2 min; (g) ED-16–AA after thermal polymerization, heating at 70°C for 40 min; and (h) ON–AA after thermal polymerization, heating at 60°C for 22 min.

Broadening of the lines in the triplet of doublets assigned to the adduct of the propagation radical of oligomer with MNP is caused by high viscosity of UP-612–AA. Under these conditions, the triplet lines are broadened to a significantly lesser extent, since, despite the high viscosity of the medium, di-*tert*-butylnitroxyl radicals, having significantly smaller size as compared with the oligomer radical, are more mobile. With the aim to decrease the linewidth and improve the spectrum resolution, the sample was diluted with methylene chloride. As a result of dilution and, correspondingly, more prolonged irradiation, the spectrum became better resolved (Fig. 4b).

The measured hyperfine coupling constants of unpaired electron with nitrogen and hydrogen nuclei were a_N = 1.43 and a_H = 0.27 mT.

The ESR spectra of irradiated samples of oligomers ON–AA and ED-16–AA diluted with CH_2Cl_2 are shown in Figs. 4b and 4c. Similarly, the spectra contain a triplet and a triplet of doublets. In the case of ED-16–AA, the triplet of doublets has the following parameters: a_N = 1.52 and a_H = 0.30 mT, and in the case of ON–AA, a_N = 1.45 and a_H = 0.28 mT. It is of interest that the adduct of the propagation radical of ON–AA oligomer gives a strongly broadened signal even at high dilution of the sample with CH_2Cl_2. To obtain a better resolved ESR spectrum of the adduct of the propagation radical of the oligomers with the spin trap, the sample of UV-irradiated ED-16–AA oligomer having the spectrum presented in Fig. 4b was heated at 70°C for several minutes. As a result, the interfering triplet of di-*tert*-butylnitroxyl radical disappeared and practically pure signal of the propagation radical adduct remained in the spectrum. The decay of di-*tert*-butylnitroxyl radicals can be explained as follows. Upon heating of the sample, thermal polymerization of the oligomer starts, in the course of which the forming propagation radicals of the oligomer recombine with di-*tert*-butylnitroxyl radicals as the most mobile species.

The hyperfine splitting in the form of a triplet of doublets in the ESR spectra of propagation radicals is caused by the interaction of the unpaired electron spin with the nitrogen nuclear spin and with the spin of one hydrogen nucleus at the α-carbon atom. It is believed that the adduct is formed by the scheme

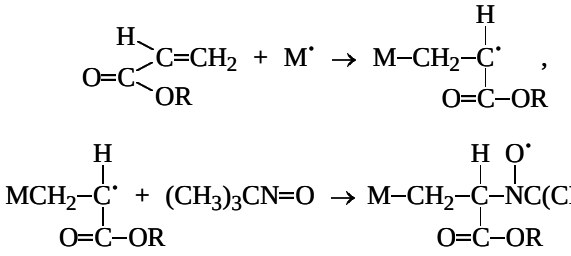

where M$^{\cdot}$ is the propagation radical or initiator.

To confirm additionally the suggested structure of the propagation radical, we performed an independent experiment on recording the propagation radical of the well-known acrylic monomer, butyl acrylate (BA). As a result of UV irradiation in the presence of MNP of the BA sample containing 1% BP for 2 min,

the ESR spectrum containing a triplet of doublets was recorded (Fig. 4f). Undoubtedly, this spectrum can be assigned to the adducts of the propagation radical of BA with MNP; it has the same parameters as the above spectra (a_N = 1.43 and a_H = 0.28 mT):

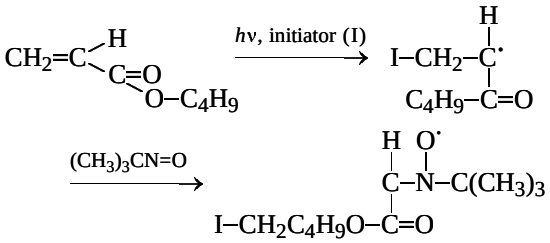

It is well known that acrylic monomers undergo thermal polymerization at elevated temperature. To identify the propagation radicals in the course of thermal polymerization of the oligomers at hand, we heated oligomers ED-16–AA and ON–AA in the presence of MNP to 60–70°C directly in the spectrometer resonator. In both cases, after heating the samples for 40 min at 70°C, we observed in the ESR spectra a triplet of doublets with parameters corresponding to the signals from the adduct of the propagation radical with MNP, recorded in photopolymerization (Figs. 4g, 4h). The triplet of di-*tert*-butylnitroxyl radical was not recorded. The ESR signals observed in thermal polymerization and photopolymerization of the adducts studied have virtually the same parameters, which suggests the similar structure of the adducts.

Unknown radicals found at high degrees of conversion suggest complex character of polymerization of epoxy-acrylate oligomers.

CONCLUSION

Thermal polymerization and photopolymerization of epoxy-acrylate oligomers based on epoxy oligomers ED-16, UP-612, and Oksilin were studied by ESR at room temperature. The ESR spectra of propagation radicals stabilized in the solid polymer matrix were recorded at high degrees of conversion and in the initial stages of polymerization. The propagation radicals have the same structure and correspond to typical propagation radicals of acrylic monomers, irrespective of the procedure of polymerization initiation.

REFERENCES

1. Stovell, J.C., *J. Org. Chem.*, 1971, vol. 36, p. 3055.
2. Wertz, J.E. and Bolton, J.R., *Electron Spin Resonance: Elementary Theory and Practical Applications*, New York: McGraw–Hill, 1972.
3. Milinchuk, V.K., Klinshpont, E.R., and Pshezhetskii, S.Ya., *Makroradikaly* (Macroradicals), Moscow: Khimiya, 1980.
4. Glay, M.R. and Charlesby, A., *Eur. Polym.*, 1975, vol. 11, pp. 187–193.
5. Ormerod, M. and Charlesby, A., *Polym.*, 1964, vol. 5, p. 67.
6. Kramer, O.L., Battalov, E.M., Voloshin, A.I., and Prochukhan, Yu.A., *Zh. Prikl. Khim.*, 2001, vol. 74, no. 7, pp. 1158–1161.
7. Zubarev, V.E., *Metod spinovykh lovushek: Primenenie v khimii, biologii i meditsine* (Spin Trap Method: Application to Chemistry, Biology, and Medicine), Moscow: Mosk. Gos. Univ., 1984.

Russian Journal of Applied Chemistry, Vol. 76, No. 4, 2003, pp. 634–638. Translated from Zhurnal Prikladnoi Khimii, Vol. 76, No. 4, 2003, pp. 658–662.

MACROMOLECULAR CHEMISTRY AND POLYMERIC MATERIALS

Synthesis, Structure, Composition, and Properties of Rolivsans

B. A. Zaitsev, G. I. Khramova, and T. S. Tsygankova

Institute of Macromolecular Compounds, Russian Academy of Sciences, St. Petersburg, Russia

Received February 17, 2002; in final form, January 2003

Abstract—Novel thermosetting resins Rolivsans were prepared, and their structure, composition, and properties were studied. The structural parameters of Rolivsans as influenced by the synthesis conditions were determined.

Novel thermosetting liquid (solvent-free) resins named Rolivsans are used for preparing polymeric and composite materials with enhanced resistance to heat and to the most aggressive agents [1–12]. They are used in various branches of engineering. Rolivsans have been prepared by acid-catalyzed reactions of bis[4-(1-hydroxyethyl)phenyl] ether with methacrylic acid [13–15].

The goals of this study were to analyze in detail the synthesis conditions, elucidate the composition and structure of Rolivsans, and reveal correlations between their structural characteristics and properties. The starting compound in the synthesis is diphenyl ether **I**, which is quantitatively converted to di(4-acetylphenyl) ether **II** by the Friedel–Crafts acylation. Compound **II** is subsequently hydrogenated in the presence of Raney nickel to obtain bis[4-(1-hydroxyethyl)phenyl] ether **III**, which is then refluxed with methacrylic acid **IV** in an aromatic solvent in the presence of an acid catalyst (e.g., *p*-toluenesulfonic acid) and a polymerization inhibitor (e.g., hydroquinone):

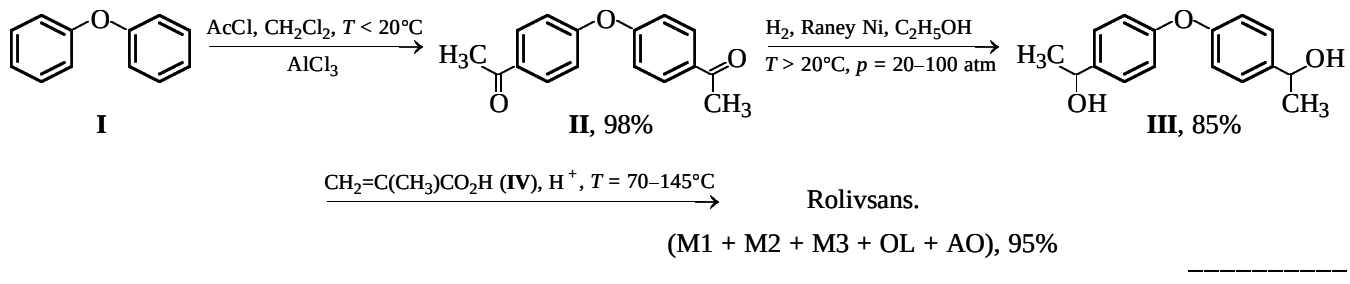

where M1–M3 are monomers, OL is an oligomer, and AO denotes antioxidants (products of alkylation of phenolic compounds with monomers M1 and M2 and with oligomer OL).

Comprehensive studies have shown that a one-pot process resembling the synthesis of oligoether acrylates and performed in the course of one or several hours at 70–110°C involves the following successive-parallel reactions: polycondensation of diol **III** [15, 16]; esterification with methacrylic acid of this diol and oligoethers containing terminal hydroxy groups and formed by polycondensation (formation of monomeric and oligomeric methacrylates [13–15]); dehydration of diol **III** and oligoethers [15, 17, 18]; cleavage of (di)methacrylates to (di)vinyl-substituted aromatic compound and methacrylic acid [13–15, 19, 20]; stepwise (co)polymerization of (di)vinyl-substituted aromatic compounds by the polyaddition mechanism with proton transfer (oligomerization) [13–15, 18, 21–23]; and alkylation of dihydric phenols (e.g., hydroquinone) with unsaturated aromatic compounds [24].

Each of these reactions was studied separately with model compounds and Rolivsan components; also, separate stages of the synthesis of Rolivsan as a system of monomers and oligomers were examined. The composition and structure of Rolivsans were studied by exclusion liquid chromatography (ELC) (Figs. 1, 2), IR and ^{1}H NMR spectroscopy, elemental analysis, and analysis for functional groups (ester and bromine numbers, ozonolysis). The IR and ^{1}H NMR

1070-4272/03/7604-0634 $25.00 © 2003 MAIK "Nauka/Interperiodica"

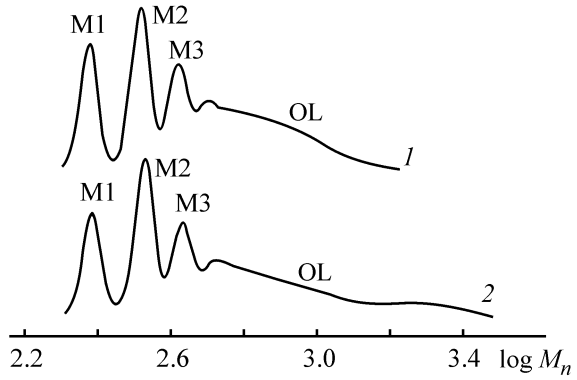

Fig. 1. Gel chromatograms of sample K (Table 2), obtained at 20°C with (*1*) one column and (*2*) six series-connected columns. Eluent tetrahydrofuran. ($\overline{M}_n$) Number-average molecular weight; the same for Fig. 3.

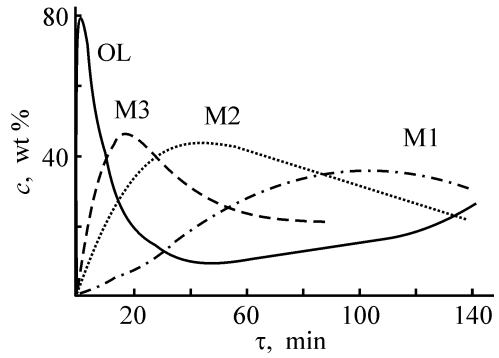

Fig. 2. Composition of Rolivsan vs. synthesis time τ (benzene, 13.5 mM sulfo acid **V**, 80°C). (*c*) Content of components.

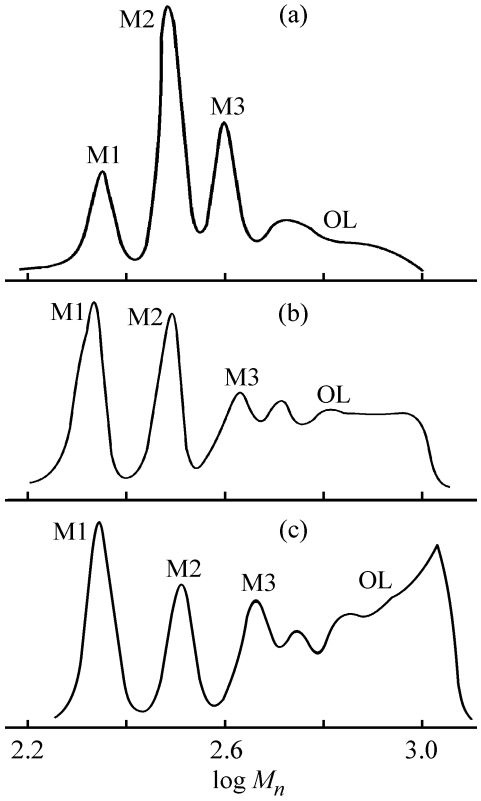

Fig. 3. Gel chromatograms of Rolivsans prepared in benzene at the ratio diol **III** : acid **IV** = 1 : 2.5. Initial concentration of sulfo acid **V** 13.5 mM. Samples were taken (a) 45, (b) 90, and (c) 120 min after the beginning of the synthesis.

spectra of model compounds and separate Rolivsan components M1, M2, M3, and OL have been discussed previously [15, 22–25]. Naturally, the spectra of Rolivsan as a system of monomers and oligomers contain a much greater number of absorption bands associated with various functional groups than the spectra of the components taken separately.

A typical IR spectrum of Rolivsan contains absorption bands of unsaturated and aromatic groups at 3080, 3060, 3030, 2975, 1630, 1600, 1500, 985, 965, 940, and 905 cm^{-1}, and also bands of methyl and methylene groups at 2960, 2925, 2870, and 2850 cm^{-1} and methine groups at 2900 cm^{-1}. The IR spectrum also contains strong absorption bands related to carbonyl groups in methacrylates (1715 cm^{-1}) and to aromatic ether groups (1240 cm^{-1}), and to other absorption bands (1170, 1100, 1060 cm^{-1}, etc.) assignable to stretching vibrations of ester and ether groups.

The ^{1}H NMR spectrum of Rolivsan contains signals typical of such related compounds as styrene, its unsaturated dimer *trans*-1,3-diphenyl-1-butene [24], and methacrylates. Protons of the substituted phenylene group give an *AA*'*BB*' pattern centered at δ = 7.25 ppm. Protons of the unsaturated groups appear as a set of signals (ppm) at δ = 6.7–5.2, namely, at 6.66 (CH= in CH_2=CH), 6.21 and 5.75 [CH_2= in CH_2=C(CH_3)], doublets at 5.63 (5.60 and 5.66; CH_2= in CH_2=CH) abd 5.23 (5.20 and 5.26; CH_2= in CH_2=CH), and a doublet of doublets at 6.45. The signal at 6.21 ppm also belongs to the *trans*-CH=CH protons, since similar signals of the internal double bond (δ 6.19, 6.24 ppm) are observed in the ^{1}H NMR spectrum of the related compound, unsaturated styrene dimer [PhCH=CHCH(CH_3)Ph]. The *tert*-H proton in the >CHPh group appears as a broad ill-resolved multiplet at 3.67 ppm and a multiplet at 4.32 ppm (PhCHPh). The methyl and methylene groups give signals at 2.01 and 1.45 (MeC=CH_2), 1.61 and 1.64 (MeCHAr), and 2.59 ppm (CH_2Ar). The ^{1}H NMR spectrum contains no signals at 2.3 ppm, which are characteristic of toluene methyl protons. This fact suggests that, under the conditions of Rolivsan synthesis, acid-catalyzed aralkylation of the solvent (toluene) with M1, M2, and OL does not occur.

Table 1. Influence of the synthesis time τ on the composition and properties of Rolivsans

τ, min	Resin composition, wt %					Unsaturation, mol >C=C</100 g product	Ester number, mg KOH/g product	n_D (T, °C)
	M1	M2	M3	OL	AO			
45	14	37	30	18	1	0.559	190	1.577 (20)
90	20	24	21	34	1	0.592	160	1.597 (40)
120	16	20	15	48	1	0.610	135	1.609 (40)

Table 2. Characteristics of Rolivsan M1

Grade	Component content, wt %					Unsaturation, mol >C=C</100 g product	$\overline{M}_n$	n_D^{20}	η^{25}, cP	d^{20}, g cm^{-3}
	M1	M2	M3	OL	Ar(OH)$_n$					
K	14	27	25	32	2	0.58	420	1.590	1620	1.09
S	12	22	18	46	2	0.55	480	1.600	3500	1.10

Figures 2 and 3 show how the composition and molecular-weight distribution (MWD, found by ELC) depend on the synthesis conditions. Initially, refluxing in benzene or toluene results in fast polycondensation of diol **III**, which results in the formation of an oligoether with terminal hydroxy groups [15, 16]. The competing reactions are esterification of the oligoether of diol **III** with methacrylic acid [15, 16] and dehydration; these reactions yield oligomeric methacrylates (OL), monomer M1 [15, 18], and water removed by azeotropic distillation. Acidolysis of the oligoether and oligomeric methacrylates yields monomeric methacrylates M2 and M3 [13–15].

It is known that the components of Rolivsans are M1, M2, M3, OL, and AO. The composition and properties of Rolivsans can be varied widely by ensuring a greater extent of oligomerization of M1 and M2 in the presence of *p*-toluenesulfonic acid **V** by the step (dimerization) addition mechanism with proton transfer to the monomer and formation of, first, dimers, then trimers [13–15, 21–23], etc. Methacrylates M2 and M3 are gradually cleaved to form acid **IV** and, respectively, monomers M1 and M2 (Table 1):

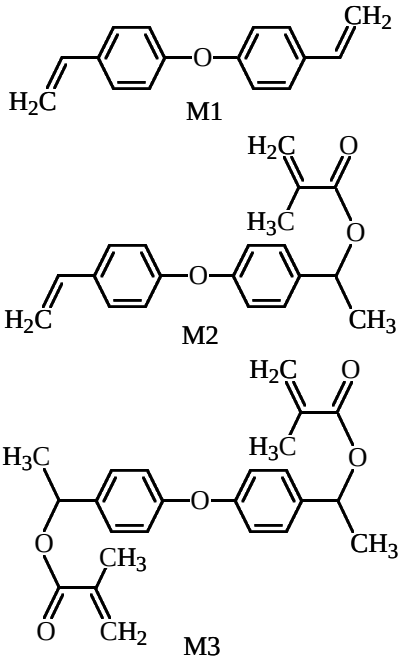

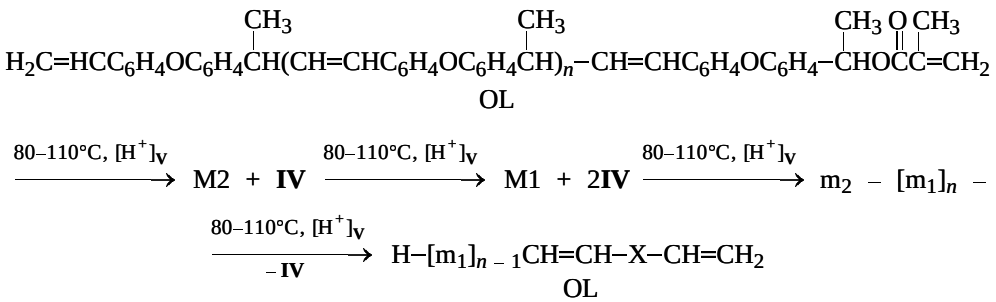

m_1 = CH=CH–X–CH(CH$_3$), m_2 = H$_2$C=CMeCO$_2$MeHC–X–CHMe, X = C$_6$H$_4$OC$_6$H$_4$.

Tables 1 and 2 show that, at relatively low conversions, when the concentrations of methacrylates M2 and M3 are relatively high and the content of oligomers (mainly dimers) is low, the refractive index n_D^{20} and viscosity η^{25} of the resin are comparatively low (1.56 and 450 cP, respectively).

Oligomerization leads to lower content of M2 and M3 and higher content of linear unsaturated oligomers with increased molecular weights (mainly dimers to pentamers); as a result, the refractive index and viscosity grow substantially (to n_D^{20} = 1.60–1.62 and η^{25} = 2500–4000 cP).

Thus, the composition and properties of Rolivsans, molecular-weight distribution of oligomeric components, and distribution of functional groups can be varied within prescribed limits by changing the synthesis conditions.

EXPERIMENTAL

The IR spectra were measured on a Specord 75-IR spectrophotometer (thin films), and the ^{1}H NMR spectra, on a JEOL C-60 HL spectrometer (60 MHz, $CDCl_3$, internal reference TMS). The ELC analysis of Rolivsans and their components was performed using a Waters gel-permeation chromatograph with columns packed with Ultrastyrogel (500 Å) at 20°C; eluent THF, $CHCl_3$, or toluene. The number-average molecular weight $\bar{M}_n$ was determined with a Hitachi–Perkin–Elmer 115 vapor osmometer. The content of unsaturated bonds was found by ozonation (ADS-3 ozonizer, 0°C, solvent CCl_4) and by the bromide–bromate method (determination of the bromine number, followed by recalculation to the iodine number). The ester number was found by dissolving the resin sample in dioxane purified by distillation from KOH and Na, adding 0.1 N solution of KOH in ethanol–dioxane, refluxing for 7 h (the reflux condenser was equipped with a tube packed with soda lime), and titrating with 0.1 N HCl.

CONCLUSIONS

(1) The mechanism of formation of Rolivsans, novel thermosetting resins whose curing yields heat-resistant network polymers, was elucidated.

(2) The composition and structure of Rolivsans were determined by IR and ^{1}H NMR spectroscopy, vapor osmometry, elemental and functional analysis, and exclusion liquid chromatography.

REFERENCES

1. Zaitsev, B.A., Khramova, G.I., Dantsig, L.L., *et al.*, *Plast. Massy*, 1981, no. 9, pp. 12–13.
2. Zaitsev, B.A., Khramova, G.I., Tsygankova, T.S., *et al., Mekh. Kompozit. Mater.*, 1982, no. 5, pp. 775–778.
3. Zaitsev, B.A., *Sintez, struktura i svoistva polimerov* (Synthesis, Structure, and Properties of Polymers), Leningrad: Nauka, 1989, pp. 66–77.
4. Zaitsev, B.A., Abstracts of Papers, *1st China–Japan–USSR Joint Symp. on Advanced Polymers*, Moscow, September 15–21, 1991, p. A-21.
5. Zaitsev, B.A., *Polym. Mater. Sci. Eng.*, 1992, vol. 66, pp. 70–71.
6. Zaitsev, B.A., Abstracts of Papers, *XVI Mendeleevskii s"ezd po obshchei i prikladnoi khimii (25–29 maya 1998 g., Sankt-Peterburg)*, (XVI Mendeleev Congr. on General and Applied Chemistry (May 25–29, 1998, St. Petersburg)), Moscow, 1998, no. 2, pp. 304–305.
7. Zaitsev, B.A., Tsygankova, T.S., and Khramova, G.I., Abstracts of Papers, *VII Mezhdunarodnaya konferentsiya po khimii i fizikokhimii oligomerov "Oligomery-2000" (4–8 sentyabrya 2000 g., Perm')*, (VII Int. Conf. on Chemistry and Physical Chemistry of Oligomers "Oligomers-2000" (September 4–8, Perm)), Moscow, 2000, p. 330.
8. Zaitsev, B.A., Abstracts of Papers, *VII Mezhdunarodnaya konferentsiya po khimii i fizikokhimii oligomerov "Oligomery-2000" (4–8 sentyabrya 2000 g., Perm')*, (VII Int. Conf. on Chemistry and Physical Chemistry of Oligomers "Oligomers-2000" (September 4–8, Perm)), Moscow, 2000, p. 122.
9. Zaitsev, B.A., Maik, V.Z., Pomerantsev, V.I., and Shvabskaya, I.D., Abstracts of Papers, *VII Mezhdunarodnaya konferentsiya po khimii i fizikokhimii oligomerov "Oligomery-2000" (4–8 sentyabrya 2000 g., Perm')*, (VII Int. Conf. on Chemistry and Physical Chemistry of Oligomers "Oligomers-2000" (September 4–8, Perm)), Moscow, 2000, p. 278.
10. Zaitsev, B.A., Elokhovskaya, N.A., Kotelyanets, N.P., *et al.*, Abstracts of Papers, *VII Mezhdunarodnaya konferentsiya po khimii i fizikokhimii oligomerov "Oligomery-2000" (4–8 sentyabrya 2000 g., Perm')*, (VII Int. Conf. on Chemistry and Physical Chemistry of Oligomers "Oligomers-2000" (September 4–8, Perm)), Moscow, 2000, p. 329.
11. Zaitsev, B.A., Khramova, G.I., Tsygankova, T.S., *et al.*, Abstracts of Papers, *VIII Mezhdunarodnaya konferentsiya po khimii i fizikokhimii oligomerov "Oligomery-2002" (9–14 sentyabrya 2002 g., Chernogolovka)*, (VIII Int. Conf. on Chemistry and Physical Chemistry of Oligomers "Oligomers-2002" (September 4–8, Chernogolovka)), Moscow, 2002, p. 252.
12. Zaitsev, B.A., Khramova, G.I., and Tsygankova, T.S., Abstracts of Papers, *VIII Mezhdunarodnaya konferentsiya po khimii i fizikokhimii oligomerov "Oligomery-2002" (9–14 sentyabrya 2002 g., Chernogolovka)*, (VIII Int. Conf. on Chemistry and Physical Chemistry

of Oligomers "Oligomers-2002" (September 4–8, Chernogolovka)), Moscow, 2002, p. 253.

13. Zaitsev, B.A., Khramova, G.I., and Dantsig, L.L., *Vysokomol. Soedin., Ser. A*, 1982, vol. 24, no. 12, pp. 2467–2474.
14. Zaitsev, B.A., Dantsig, L.L., and Khramova, G.I., *Zh. Org. Khim.*, 1983, vol. 19, no. 11, pp. 2340–2349.
15. Zaitsev, B.A., Regular Trends in Formation, Structure, and Properties of Heat-Resistant Network Polyarylenes, *Doctoral Dissertation*, Leningrad, 1983.
16. Zaitsev, B.A., Fedorova, A.V., Kiseleva, R.F., *et al.*, *Vysokomol. Soedin., Ser. A*, 1983, vol. 25, no. 5, pp. 1076–1081.
17. Zaitsev, B.A. and Dantsig, L.L., *Izv. Akad. Nauk SSSR, Ser. Khim.*, 1986, no. 1, pp. 88–94.
18. Zaitsev, B.A. and Kiseleva, R.F., *Vysokomol. Soedin., Ser. A*, 1981, vol. 23, no. 8, pp. 1783–1790.
19. Zaitsev, B.A., Khramova, G.I., Tsygankova, T.S., *et al., Acta Polym.*, 1985, vol. 36, no. 10, pp. 527–530.
20. Zaitsev, B.A., Dantsig, L.L., Gusarova, I.O., *et al.*, *Izv. Akad. Nauk SSSR, Ser. Khim.*, 1982, no. 8, pp. 1881–1883.
21. Zaitsev, B.A. and Kiseleva, R.F., *Acta Polym.*, 1983, vol. 36, no. 10, pp. 527–530.
22. Zaitsev, B.A., Kiseleva, R.F., Denisov, V.M., *et al.*, *Vysokomol. Soedin., Ser. A*, 1984, vol. 26, no. 8, pp. 1602–1609.
23. Zaitsev, B.A., Kiseleva, R.F., and Gusarova, I.O., *J. Polym. Sci., Polym. Chem. Ed.*, 1996, vol. 34, pp. 1165–1181.
24. Zaitsev, B.A., Kiseleva, R.F., Denisov, V.M., *et al.*, *Izv. Akad. Nauk SSSR, Ser. Khim.*, 1990, no. 11, pp. 2566–2574.
25. Zaitsev, B.A., Lukasov, S.V., Kiseleva, R.F., *et al.*, *Acta Polym.*, 1985, vol. 36, no. 10, pp. 521–526.

Russian Journal of Applied Chemistry, Vol. 76, No. 4, 2003, pp. 639–642. Translated from Zhurnal Prikladnoi Khimii, Vol. 76, No. 4, 2003, pp. 663–666.

MACROMOLECULAR CHEMISTRY AND POLYMERIC MATERIALS

Destruction and Hydrolysis of Proteins in Their Electrochemical Extraction

E. E. Kuprina, S. V. Vodolazhskaya, and G. G. Nyanikova

Gyprorybflot State Research and Design Institute for Fishing Fleet, St. Petersburg, Russia

Received February 26, 2002

Abstract—An electrochemical method was used to extract proteins from a dispersed protein-containing raw material. Cleavage of disulfide and peptide bonds in protein solutions in the course of electrochemical extraction and dissolution of proteins was studied.

Extraction of proteins from dispersed biological raw materials is based on successive separation of water-, salt-, and alkali-soluble proteins from various tissues. The acid and enzymic extraction and dissolution of proteins from different protein-containing raw materials are the most widely used methods for production of protein hydrolyzates for various purposes. However, in shellfish processing to separate proteins from the shell with the purpose of chitin production, base treatment is more effective as compared with the acid and enzymic methods, since, in this case, hydrolysis of β-*D*-glycoside bonds of chitin occurs to a lesser extent [1].

In the electrochemical technology[1], an aqueous salt dispersion of a raw material is processed in dc membrane electrolyzers. In this case, protein extraction and hydrolysis occur in the alkaline medium forming in the cathode cells. This technology allows virtually complete decomposition of the raw material into constituents, such as protein in the form of a protein solution, lipids, and insoluble bone tissue (in the case of a fish raw material) or cover shell tissue (for a shell-fish raw material) [2].

In the electrochemical processes, when a weakly alkaline medium (NaOH concentration 0.025 M) and reducing potential (appearing as a result of discharge of water molecules and dissolved oxygen at the cathode) act on a protein-containing raw material simultaneously, the degree of protein extraction approaches 98–99%. At the same time, with NaOH of the same concentration used alone, proteins are only partially dissolved (degree of extraction ≤40%). Deep extraction of proteins, with tissue decomposition into components, can only be achieved by raising the NaOH concentration to 1.0–2.0 M [3].

[1] Developed at Giprorybflot.

By no means all the protein transformations occurring under the action of the alkali [4] are desirable: proteins after alkaline treatment more difficultly undergo enzymic proteolysis; their nutritive value decreases; finally, they may become toxic.

It is well known that the solubility of proteins in alkaline solutions is caused by cleavage of the intermolecular disulfide bonds responsible for the stability of the protein tertiary structure [5]. In protein molecules, the S–S bonds are weak and labile, especially in reducing media, and also upon heating and in alkaline solutions [6]. At high OH^- concentrations, the cleavage of the S–S bonds proceeds mostly as β-elimination with partial racemization of amino acids [7].

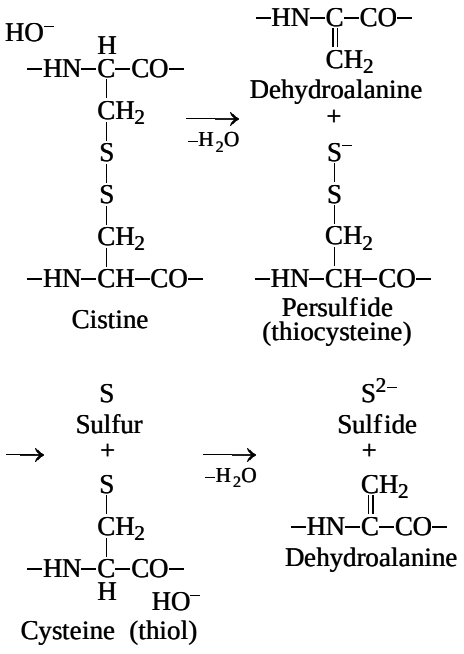

1070-4272/03/7604-0639 $25.00 © 2003 MAIK "Nauka/Interperiodica"

Table 1. Effect of protein extraction procedure on the content of −S−S− and −SH groups in BSA solutions

Sample	c_{SH}	c_{S-S}	S−S cleavage, %
	μM		
W	0	500	–
A-4	300	50	90
A-0.1	500	125	75
C-5	550	100	80
EC	500	125	75

The forming dehydroalanine demonstrates high reactivity toward a number of nucleophilic groups of proteins, yielding a spectrum of new toxic products, thus decreasing the quality of the hydrolyzates [4].

Hydrolysis of the peptide bonds in alkaline solutions is also possible [4].

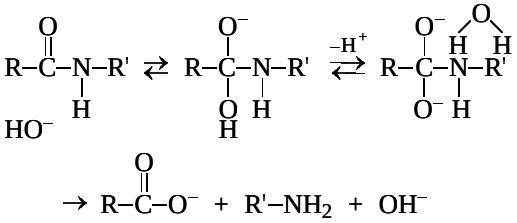

However, this process can have only insignificant effect on the dissolution of proteins. To gain better insight into the electrochemical extraction of proteins, we studied variations in the amounts of the disulfide and thiol groups and amine nitrogen in protein solutions for different methods of processing of protein-containing raw materials.

EXPERIMENTAL

In this study, we a used protein-containing muscular tissue of fish, which was dispersed to particle size of 5×10^{-3} m, and bovine serum albumin (BSA) with standard content of the S−S and SH bonds in the molecule (17 and 1, respectively) and molecular weight of 67 000.

Electrochemical treatment of aqueous salt suspensions of the protein-containing raw material was carried out in a cathode cell of a membrane electrolyzer. The cathode material was Cr18Ni9Ti stainless steel, and the anode material, platinized titanium. As membrane served MF4SK-100 ion-selective sulfonic cation-exchange fabric. The raw material was mixed with an aqueous salt solution (NaCl concentration <10%) at fixed weight ratio.

To study the effect of the treatment procedure on the content of the S−S and SH group and amine nitrogen in the course of electrochemical extraction and hydrolysis of proteins, we prepared variously processed samples referred to as EC, C-5, A-0.1, A-4, and W.

Sample EC was prepared by electrochemical treatment of a suspension of the raw material in a cathode cell of the electrolyzer. Electrolysis was carried out until reaching pH ≥ 12.0 ± 0.1 and $Eh \le -600 \pm 10$ mV. The pH and *Eh* were measured against an Ag/AgCl reference electrode with a pH-metric glass and redoxmetric Pt electrodes, respectively, on an I-120.2 ion meter [8].

Sample C-5 was prepared in a stirred reactor by treating the raw material with a catholyte solution obtained in the cathode cell of the electrolyzer. Electrolysis was performed until reaching pH ≥ 12.2 ± 0.1 and $Eh \le -850$ mV.

To elucidate the effect of electrochemical treatment, we studied protein solutions prepared by treating the raw material in water and aqueous NaOH (c_{NaOH} 0.025 and 1.0 M). The respective samples are designated as W, A-0.1, and A-4.

The content of SH and S−S group in protein solutions was determined by direct and back amperometric titration [5] to within 5%. Amine nitrogen was determined using the Formalin test according to GOST (State Standard) 7636–85, and the protein content, by the Lowry method [10] to within 0.6%. The experimental results were statistically processed at a 0.95 confidence level.

The BSA concentration in all the samples was 5 mg ml^{-1}, which is close to the protein content in the commercial hydrolyzates produced from hydrobionts. Experimental data on the content of S−S and SH group contents are listed in Table 1.

The results show the lack of cysteine SH groups in the aqueous BSA solution (sample W) in the absence of electrochemical and base treatment, which is consistent with published data [5] (native BSA contains only cystine responsible for the formation of its tertiary structure through S−S bonding).

In the case of treatment with 1.0 M NaOH (sample A-4), virtually all the S−S bonds were cleaved (their content decreased by a factor of 10). This process favors denaturation of the protein (protein molecules lose the crosslinks and the tertiary structure). However, only 40% of S−S groups of cystine are converted into SH groups of cysteine. The remaining

S–S groups, evidently, enter side reactions involving cleavage of the C–S bonds by the β-elimination mechanism and yielding rather toxic products (β-elimination is followed by nucleophilic addition) [4].

In samples A-0.1, C-5, and EC, the amount of S–S groups decreases by a factor of 4–5, i.e., the degrading effect on the protein molecule appears to be lower by a factor of 1.6–1.8, suggesting, on the one hand, weaker degradation processes and preservation of the protein native structure, and, on the other, suppression of undesired side reactions in cleavage of the S–S bonds.

Thus, the low NaOH concentration (0.025 M) in the extractant provides better quality of the extracted protein, so that it is not advisable to raise the NaOH concentration to 1.0 M. Unfortunately, the measured SH content can be underestimated because of the masking of these groups in the protein, which results from their steric inaccessibility to the $AgNO_3$ reagent and also from specific features of their ionic environment and hydrophobic interactions [5]. However, we have no information about more precise methods.

Finally, electrochemical dissolution of BSA proteins in the catholyte or directly in the cathode cell of the electrolyzer has 2 times weaker degrading effect on the S–S bonds as compared with samples treated with NaOH, promotes the favorable degradation mechanism to give SH groups of cysteine.

To confirm the observed trends, we studied the content of SH and S–S groups in protein extracts obtained from protein-containing muscular tissue of fish under conditions similar to those used for BSA, except for A-0.1 sample, since tissue proteins cannot be dissolved at such a low NaOH concentration. In the samples studied, the protein content determined by the Lowry method was 29.0 ± 0.1 mg ml^{-1}. The data obtained are listed in Table 2.

The results show that, in fish proteins extracted and dissolved electrochemically (EC and C-5 samples), the degree of protein denaturation caused by cleavage of S–S bonds is lower than that in A-4 sample prepared with 1.0 M NaOH. At the same time, in EC and C-5 samples, the SH content is higher by a factor of 2.2–2.4 as compared with A-4, which suggests lower content of by-products formed by the β-elimination mechanism through cleavage of C–S bonds [4].

Protein extraction by treating the aqueous salt suspension of the raw material in the cathode cell leads to stronger degradation with cleavage of the S–S bonds than that with the catholyte (C-5), which is probably due to the effect of reducing agents, such as

Table 2. Effect of extraction procedure on the content of S–S, SH, and NH_2 groups in protein solutions obtained from protein-containing raw material

Sample	pH	c_{SH}	c_{S-S}	c_{NH_2}
		μM		
A-0.1	12.31	1000	300	1.02
EC	11.25	2200	550	1.14
C-5	11.25	2400	700	1.09

$H^{\cdot}_{ads}$, H_2, etc., reacting with the protein just *in statu nascendi*. Cleavage of the S–S bonds in proteins under the action of reducing agents and, in particular, hydrogen was studied in [5].

$$R_1{-}S{-}S{-}R_2 \xrightarrow{\text{Reducing agent}} R_1{-}SH + HS{-}R_2.$$

It is known that dissolution of alkali-soluble proteins necessarily involves the stages of degradation of their tertiary structure and unrolling of their molecule [5]. Ashikari *et al*. have demonstrated for model immunoglobulins that degradation with cleavage of the S–S bonds and the subsequent unrolling of a protein molecule in the presence of reducing agents occur at pH 8.5. In the absence of reducing agents, unrolling of protein molecules in the solution starts only at pH > 11.6 [11]. It was demonstrated by the same authors that, at the indicated pH, no functional groups other than SH are involved in the unrolling of protein molecules.

It may be concluded that the effect of electrochemical dissolution of tissue proteins at such a low NaOH concentration as 0.025 M, observed for EC and C-5 samples (Table 2), is caused by reducing agents, whose presence is demonstrated by strongly negative redox potentials of the extractant (*Eh* = –600 to –850 mV). The dissolution is also promoted by hydrolysis of the peptide bonds increased by 10%, as estimated from the NH_2 content.

CONCLUSION

The electrochemical extraction and hydrolysis of proteins is based on the ability of extractants to reduce proteins with cleavage of mainly disulfide bonds and formation of thiol groups under the action of reducing agents formed in the course of water electrolysis. Suppression of protein destruction at the –C–S– bonds, which are responsible for formation of hazardous by-products in the course of extraction, provides high quality of the resulting hydrolyzates.

REFERENCES

1. Kuprina, E.E., Kozlova, I.Yu., and Timofeeva, K.G., *Sovremennye tendentsii v sposobakh polucheniya i primeneniya khitina i khitozana: Obzornaya informatsiya* (Modern Trends in Preparation and Application of Chitin and Chitosan: A Review), *Ser.: Obrabotka ryby i moreproduktov* (Processing of Fish and Seafood), Moscow: Vseross. Nauchno-Issled. Inst. Ekon. Razvit. Rybn. Khoz–va, 1999, no. 3(1).
2. RF Patent no. 2110926.
3. Vodolazhskaya, S.V., Electrochemical Process for Preparation of Protein Hydrolyzates for Microbiological Nutrient Media from Hydrobionts, *Cand. Sci. Dissertation*, St. Petersburg, 2001.
4. Whitaker, J.R. and Feeney, R.E., *Crit. Rev. Food Sci. Nutrition*, 1983, vol. 3, no. 19, pp. 173–212.
5. Torchinsky, J.M., *Sulfur in Proteins*, Oxford: Pergamon, 1981.
6. Volkin, D.R., Mach, H., and Middaugh, C.R., *Mol. Biotechnol.*, 1997, vol. 8, no. 2, pp. 105–112.
7. Nashet, A.S., Osuga, D.T., Lee, H.S., *et al.*, *J. Agric. Food Chem.*, 1977, no. 25, pp. 245–273.
8. Kalous, V. and Pavlíček, Z., *Biofyzikalni chemie*, Prague: Nakl. Technicke Literatury, 1980.
9. Bykov, V.P., *Izmeneniya myasa ryby pri kholodil'noi obrabotke: Avtoliticheskie i bakterial'nye protsessy* (Changes in Fish in Refrigerated Processing: Autolytic and Bacterial Processes), Moscow: Agropromizdat, 1981.
10. Baily, J.C., *Techniques in Protein Chemistry*, Amsterdam: Elsevier, 1962.
11. Ashikari, J., Arato, Y., and Hamaguchi, K., *J. Biochem.*, 1985, vol. 97, no. 2, pp. 517–528.

Russian Journal of Applied Chemistry, Vol. 76, No. 4, 2003, pp. 643–647. Translated from Zhurnal Prikladnoi Khimii, Vol. 76, No. 4, 2003, pp. 667–671.

MACROMOLECULAR CHEMISTRY AND POLYMERIC MATERIALS

Dynamics of Propyl Chitosan Solutions in Longitudinal and Shear Modes

Z. F. Zoolshoev, I. A. Strelina, V. A. Petrova, and L. A. Nud'ga

Institute of Macromolecular Compounds, Russian Academy of Sciences, St.Petersburg, Russia

Received October 18, 2002; in final form, January 2003

Abstract—Low-substituted chitosan was synthesized from shrimp chitin. The effect of the ionic strength on the dynamics of acetic acid solutions of propyl chitosan in longitudinal and shear modes was studied. The dynamic characteristics of these solutions under the action of hydrodynamic fields were estimated.

Steadily increasing requirements to the environmental safety of the use and utilization of polymeric materials stimulate interest in natural polymers. Among them a particular attention is paid to chitosan (Ch) and its derivatives, whose molecules contain ionic amino groups. Thanks to electrostatic interactions between these groups, the chitosan molecules can change their conformation and size. Processing into films and fibers is one of the advanced practical applications of these polymers. Films prepared from chitosan–cellulose composites demonstrate high sorption capacity and low toxicity and show promise as materials for wound and burn cure [1–3]. In production of fibers, chitosan solutions are exposed to strong longitudinal fields. This is the case in both the predrawplate region and orientation drawing. As a result, the molecules pass into a highly oriented state, which does provide high strength of the final product.

By now, the dynamics of uncharged macromolecules in the longitudinal mode has been rather thoroughly studied both theoretically and experimentally [4–6]. However, the dynamics of polyelectrolytes in the longitudinal mode remains to be understood yet [7].

Previously, in studying chitosan solutions, Brestkin *et al*. [8] have demonstrated that deformation effect of a longitudinal flow is stronger than that of a shear flow.

This study is concerned with a new chitosan derivative, low-substituted propyl chitosan (PrCh) containing the hydrophobic propyl substituent in addition to the hydrophilic amino and hydroxy groups. Synthesis of organo-soluble propyl cellulose was reported in [9, 10] and that of the water-soluble mixed cellulose ether, propyl methyl cellulose, in [11]. Introduction of the propyl substituent into methyl cellulose considerably shifts the hydrophilic-hydrophobic balance of the macromolecule, and, at a degree of substitution (DS) exceeding 0.3, the mixed ether no longer dissolves in water. In this context, we developed in the course of the study conditions under which the resulting propyl chitosan preserves its solubility in 0.33 M acetic acid.

The goal of this study was to analyze the effect of the ionic strength on the dynamics of weakly charged propyl chitosan chains in the longitudinal and shear modes.

EXPERIMENTAL

We studied PrCh solutions containing 0.33 M CH_3COOH and 0.01 or 0.3 M NaCl. Concentrations of the polymer, c_p, and salt, c_s, in solutions are listed in Table 1. Because of the low degrees of dissociation of acetic acid and PrCh as a polybase, the ionic strength I of the solution is controlled in the experimental c_s range mostly by the NaCl concentration ($I \approx c_{NaCl}$). In the case of acetic acid solutions of PrCh, containing low-molecular-weight chitosan, the contribution of the polymer to the ionic strength should be taken into account.

In synthesis of PrCh, we used Ch extracted from shrimp chitin (MW 1.88×10^5, degree of deacetylation 0.88). The alkylating agent, propyl bromide was distilled and the 71°C fraction was taken. The diluent, isopropanol (chemically pure grade) was used without further purification. The reaction was performed

1070-4272/03/7604-0643 $25.00 © 2003 MAIK "Nauka/Interperiodica"

Table 1. Characteristics of PrCh solutions in 0.33 M CH_3COOH

c_p, g dl^{-1}	I, M	[η], dl g^{-1}	g_{cr}, s^{-1}	$\tau \times 10^5$, c	$\Delta n/g'(\eta-\eta_0) \times 10^{-10}$, cm s^2 g^{-1}
0.06	0.3		14582	3.4	43
0.12	0.3	4.7	12820	3.9	42
0.24	0.3		6226	8.0	44
0.06	0.01		11450	4.4	91
0.12	0.01	9.8	4680	10.6	93
0.24	0.01		1470	34.0	90

Table 2. Synthesis and characterization of propyl chitosan

Sample no.	Ch : NaOH : PrBr molar ratio	Time, min	DS per a glucosamine unit	N_{am} content, %	
				calculated	found
1	1 : 0.75 : 0.5	15	0.05	7.33	7.4
2	1 : 0.75 : 0.5	30	0.1	7.24	7.25
3	1 : 3 : 2	30	0.2	7.06	6.94

as follows. A weighed portion of air-dry Ch was dispersed in 2-propanol (solid-to-liquid ratio 1 : 20). Then a calculated amount of 47% aqueous NaOH was added, the mixture was stirred for 20 min at room temperature with bubbling of N_2, and the required amount of propyl bromide was added. The reaction was performed at 70°C (glycerol bath) with stirring. After the completion of the reaction, PrCh was filtered off, washed with 80% methanol to remove NaOH, and dried at 60°C in a vacuum. The degree of substitution was estimated from data on the amine nitrogen content, obtained by conductometric titration. The synthetic procedure conditions are listed in Table 2.

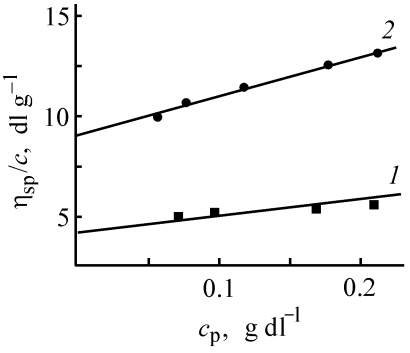

Fig. 1. Reduced viscosity η_{sp}/c of PrCh in 0.33 M CH_3COOH vs. the polymer concentration c_p. Ionic strength (M): (*1*) 0.3 and (*2*) 0.01.

To evaluate the effect of the ionic strength of the solution on the dynamics of PrCh macromolecules, we selected sample no. 2, which appeared to be quite sufficient, since the samples studied only slightly differed from one another in the degree of substitution, and the difference in the birefringence for them was within the experimental error at all.

The solution viscosity was measured at 21°C on a modified Ostwald viscometer with a spiral-shaped capillary (length 100 cm, diameter 0.06 cm). Measurements were carried out at velocity gradients of 20 to 1000 s^{-1}. The viscosity data reported here were obtained by extrapolation of the viscosity to zero velocity gradient.

The reduced viscosity of the PrCh solutions (η_{sp}/c) is given in Fig. 1 as a function of the polymer concentration c_p at various ionic strengths. As seen, the reduced viscosity is a linear function of the polymer concentration, suggesting that the size and shape of the polyions, as well as the ionic strength, remain unchanged upon dilution, so that there is no need to use the isoionic dilution method. Lowering the ionic strengh of the solution results in an increase in η_{sp}/c (Fig. 1) and intrinsic viscosity [η] (Table 1). For example, lowering I from 0.3 to 0.01 M leads to an increase in [η] by a factor of 2, suggesting increase in the size of macromolecular coils as a result of polyelectrolyte swelling.

The birefringence (BR) Δn was measured, as influenced by the velocity gradient g' and polymer concentration, using the procedure described in [12]. The shear flow velocity gradient is written as

$$g' = (\omega r)/2\Delta r, \quad (1)$$

where ω is the angular velocity of a rotor with the radius $r = r_1$; r_2, the stator radius; and $\Delta r = r_1 - r_2$. We used a titanium dynamo-optimeter with rotor height of 8.95 cm, Δr = 0.075 cm, and $2r_1$ = 7.5 cm.

Similarly to other polysaccharide solutions, PrCh solutions demonstrate positive birefringence in a flow. The dependence of Δn–g' for a shear flow was obtained at velocity gradients ranging from 200 to 2000 s^{-1}, in which the flow laminarity condition is met. Over the indicated range, this dependence is linear and passes through the origin (Fig. 2), indicating a molecular dispersity of the PrCh solutions. We also determined

the optical shear coefficient $\Delta n/g'(\eta - \eta_0)$ (Table 1). With changing polymer concentration, the optical shear coefficient remains unchanged, suggesting an insignificant contribution of the macroform anisotropy.

The longitudinal flow dynamics of the solutions was studied on the experimental setup described in [13]. The principle of its operation is similar to that of Frank–Keller's method proposed for generation of a longitudinal hydrodynamic field in a gap between coaxial capillaries. Upon suction of a solution into the capillaries along their axes, an optically anisotropic region appears as a thin luminous filament at some critical velocity gradient g_{cr}. The Δn was determined by measuring the phase difference σ of the ordinary and extraordinary waves passing along the diameter of the optically anisotropic region of the solution and the diameter d of this region:

$$\Delta n = (\delta\lambda)/(2\pi d), \quad (2)$$

where λ is wavelength. The velocity gradient is written as

$$g = Q/\pi r^2(l/2), \quad (3)$$

where Q is the volumetric flow rate of the solution through a capillary; r, radius of the capillaries; and l, distance between their end faces. The degree of uncoiling in the longitudinal flow was characterized by reduced birefringence $\Delta n/\Delta n_\infty$. Here the limiting birefringence Δn_∞ for a given solution concentration is writen as

$$\Delta n_\infty = [2\pi(n^2 + 2)^2/9n](\alpha_1 - \alpha_2)N, \quad (4)$$

where n is the refractive index of the solution; $(\alpha_1 - \alpha_2)$, optical anisotropy of the chain segment, associated with its intrinsic optical anisotropy and macroform effect; N, number of segments in the unit volume of the solution.

The results obtained in studying the effect of longitudinal hydrodynamic field on PrCh solutions of various polymer concentrations and ionic strengths are shown in Fig. 3 as the dependences of $\Delta n/\Delta n_\infty$ on the velocity gradient g in the solution flow direction. With increasing c_p, $\Delta n/\Delta n_\infty$ decreases, which is due to strengthening of intermolecular interactions and to the effect of partial uncoiling of the chains on the structure of the hydrodynamic field itself. In the velocity field, rotation components appear; the deformation effect on the molecule becomes alternating, and the

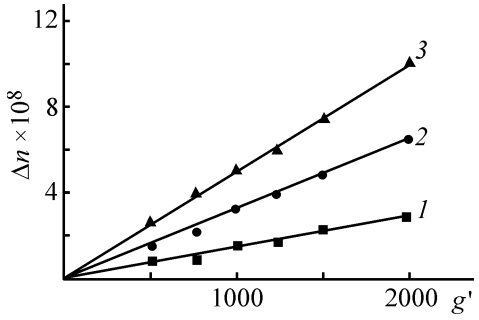

Fig. 2. Birefringence Δn of PrCh in 0.33 M CH_3COOH vs. shear flow velocity gradient g'. I = 0.3 M. c_p (g dl^{-1}): (*1*) 0.06, (*2*) 0.12, and (*3*) 0.24.

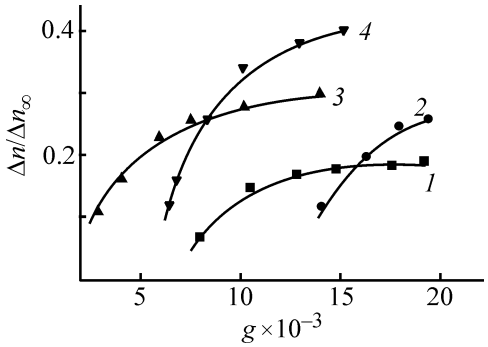

Fig. 3. Reduced birefringence $\Delta n/\Delta n_\infty$ vs. longitudinal flow velocity gradient g in PrCh solutions in 0.33 M CH_3COOH. I (M): (*1*, *2*) 0.03 and (*3*, *4*) 0.01. c_p (g dl^{-1}): (*1*, *3*) 0.24 and (*2*, *4*) 0.12.

degree of uncoiling decreases [14]. These effects become more pronounced with increasing polymer concentration. It should be pointed out that, lowering the ionic strength of the solution from 0.3 to 0.01 M at the same polymer concentration leads to an increase in $\Delta n/\Delta n_\infty$ (Fig. 3, curves *1*, *3*). This is associated with increasing length of the Kuhn segment as a result of electrostatic repulsion of the charge-bearing groups of the macromolecule. The maximal $\Delta n/\Delta n_\infty$ obtained did not exceed 0.4. It may also be noted that transition of the macromolecules to the uncoiled state takes place over a rather wide range of velocity gradients, and the $\Delta n/\Delta n_\infty$–g curves are concave down, suggesting that the orientation of molecular coils contributes significantly to the observed birefringence of the PrCh solutions [15].

It was demonstrated in [16–18] that, under the action of a longitudinal hydrodynamic field, uncharged macromolecular coils of rigid-chain polymers pass virtually completely into the uncoiled state, and $\Delta n/\Delta n_\infty$ approaches 0.95. The $\Delta n/\Delta n_\infty$–g curves are markedly concave up (toward the ordinate axis). All these cir-

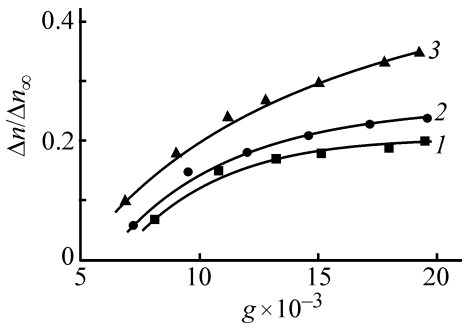

Fig. 4. Reduced birefringence $\Delta n/\Delta n_\infty$ vs. longitudinal flow velocity gradient g in PrCh solutions in 0.33 M CH_3COOH with addition of low-molecular-weight chitosan (LCh). c_p = 0.24 g dl^{-1}. I (M), c_{NCh} (g dl^{-1}): (*1*) 0.3, 0; (*2*) 0.3, 0.5; and (*3*) 0.15, 0.5.

cumstances suggest that, in the case of flexible-chain polymers, the effect of a longitudinal hydrodynamic field is of essentially the deformation nature.

Lyubina *et al*. [19] have demonstrated that, in acetic acid solutions, the chitosan macromolecules take the swollen coil conformation. The macromolecular coil loses its conformational stability in a longitudinal hydrodynamic field, and the polymer solution passes into the forced anisotropic state at a velocity gradient meeting the condition given by Eq. (5) [20, 21]:

$$g_{cr}\tau = 1/2, \quad (5)$$

where $\tau = M[\eta]\eta_0/RT$ is the time of orientation-deformation relaxation of the whole chain; η_0, solvent viscosity; R, gas constant; T, temperature (at $g < g_{cr}$, the flowing polymer solution is virtually isotropic).

The g_{cr} and τ values determined for the longitudinal flow are listed in Table 2. At a constant ionic strength of the solution, raising the c_p results in a decrease in g_{cr} and increase in τ. This effect strengthens with decreasing I. Lowering the ionic strength of the solution increases the electrostatic repulsion between the charged groups of the macromolecules. In this case, the number of monomeric units in the segment and the relaxation time τ increase, which also shifts g_{cr} to lower values.

We also studied the effect of addition of low-molecular-weight chitosan on transition of PrCh solutions to the anisotropic state. Our results showed that raising the solution viscosity by addition of the low-molecular-weight component has no significant effect on the anisotropic transition. For example, after adding low-molecular-weight Ch (c_{NCh} = 0.5%, $[\eta]$ = 1.2 dl g^{-1}) to an acetic acid solution of PrCh (c_p = 0.24 g dl^{-1}, I = 0.3 M) g_{cr} decreased from 6200 to 6000 s^{-1}. In a similar experiment, but with I = 0.1, g_{cr} decreased to 5500 s^{-1}.

In isoionic solutions, the lower the ionic strength, the higher the maximum achieved $\Delta n/\Delta n_\infty$ (Fig. 4), suggesting that the ionic strength is the crucial factor in anisotropic transition in the PrCh solutions.

CONCLUSIONS

(1) A new chitosan derivative, low-substituted propyl chitosan (DS 0.05–0.20) soluble in 0.33 M acetic acid was synthesized.

(2) It was shown that the forced optical anisotropy of the propyl chitosan solutions is caused by essentially orientational, rather than deformational effect of the hydrodynamic field. Lowering the ionic strength shifts the anisotropic transition range in propyl chitosan solutions to lower velocity gradients.

REFERENCES

1. Sakurai, K., Miyata, M., and Takahashi, T., *Fiber (Sen-i-Gak-kaishi)*, 1990, vol. 16, no. 2, pp. 79–83.
2. Wang, X.P., Zheu, Z.Q., and Zhang, F.Y., *J. Appl. Polym. Sci.*, 1998, vol. 69, pp. 2035–2039.
3. Vikhoreva, G.A., Kil'deeva, N.R., and Rogovina, S.V., *Khim. Volokna*, 2000, no. 6, pp. 14–17.
4. De Gennes, G., *J. Chem. Phys.*, 1974, vol. 60, no. 12, pp. 5030–5034.
5. Gotlib, Yu.Ya., Klushin, L.I., and Svetlov, Yu.Ya., *Vysokomol. Soedin., Ser. A*, 1989, vol. 31, no. 5, pp. 1049–1055.
6. Brestkin, Yu.V., Gotlib, Yu.Ya., and Klushin, L.I., *Vysokomol. Soedin., Ser. A*, 1989, vol. 31, no. 6, pp. 1143–1148.
7. Darinskii, A.A., and Saf'yannikova, M.G., *Vysokomol. Soedin., Ser. A*, 1996, vol. 38, no. 2, pp. 236–245.
8. Brestkin, Yu.V., Strelina, I.A., Zoolshoev, Z.F., *et al.*, *Vysokomol. Soedin., Ser. A*, 1997, vol. 39, no. 2, p. 295.
9. Nikitin, N.I. and Orlova, I.M., *Zh. Prikl. Khim.*, 1933, vol. 6, no. 6, pp. 12–16.
10. Ushakov, S.N. and Kucherenko, S.I., *Plastmassy*, 1934, vol. 3, pp. 12–14.
11. Bochek, A.M., Nud'ga, L.A., Petrova, V.A., and Petropavlovskii, G.A., *Zh. Prikl. Khim.*, 2000, vol. 73, no. 2, pp. 304–308.
12. Tsvetkov, V.N., Eskin, V.E., and Frenkel', S.Ya.,

Struktura makromolekul v rastvorakh (Structure of Macromolecules in Solutions), Moscow: Nauka, 1964.

13. Brestkin, Yu.V., Agranova, S.A., Zoolshoev, Z.F., *et al.*, *Vysokomol. Soedin., Ser. A*, 1995, vol. 37, no. 8, pp. 1319–1324.
14. Brestkin, Yu.V., Strelina, I.A., Zoolshoev, Z.F., *et al.*, Vysokomol. Soedin., Ser. A, 2000, vol. 42, no. 2, pp. 347–352.
15. Tsvetkov, V.N., *Zheskotsepnye polimery* (Rigid-Chain Polymers), Leningrad: Nauka, 1985.
16. Brestkin, Yu.V., *Acta Polymerica, Ser. B*, 1987, no. 8, pp. 470–478.
17. Keller, A. and Odell, J.A., *Colloid Polym. Sci.*, 1985, vol. 263, no. 3, pp. 181–184.
18. D'yakonova, N.E., Brestkin, Yu.V., Agranova, S.A., *et al.*, *Vysokomol. Soedin., Ser. B*, 1989, vol. 31, no. 11, pp. 845–849.
19. Lyubina, S.Ya., Strelina, I.A., Nud'ga, L.A., *et al.*, *Vysokomol. Soedin., Ser. A*, 1983, vol. 25, no. 7, pp. 1467–1472.
20. Peterlin, A., *J. Polym. Sci. Lett.*, 1966, vol. 4, no. 5, pp. 287–290.
21. Gotlib, Yu.Ya. and Klushin, L.I., *Vysokomol. Soedin., Ser. A*, 1990, vol. 32, no. 2, pp. 273–278.

Russian Journal of Applied Chemistry, Vol. 76, No. 4, 2003, pp. 648–651. Translated from Zhurnal Prikladnoi Khimii, Vol. 76, No. 4, 2003, pp. 672–675.

MACROMOLECULAR CHEMISTRY AND POLYMERIC MATERIALS

Effect of Arylamines Containing 3,5-Di-*tert*-butyl-4-hydroxyphenyl Fragment on Stability of Polypropylene, Isoprene Rubber, and Thermoelastoplastics Derived from Them

M. V. Borisova, G. N. Nugumanova, D. S. Cherezov, A. D. Khusainov, E. N. Cherezova, S. V. Bukharov, and N. A. Mukmeneva

Kazan State Technological University, Kazan, Tatarstan, Russia

Received June 4, 2002; in final form, January 2003

Abstract—The effect of arylamines containing a sterically hindered phenolic fragment on the resistance of polypropylene, synthetic isoprene rubber, and thermoelastoplastics derived from them to oxidative and thermomechanical degradation was studied in relation to the structure of the additives.

One of promising lines in extension of the range of raw materials for rubber items is utilization of thermoelastoplastic (TEP) materials based on mixtures of rubbers with thermoplastics. Such polymeric materials exhibit a wide spectrum of service properties which can be controlled by varying the type and ratio of the polymeric components. One of promising TEPs is a blend of synthetic isoprene rubber with polypropylene (SIR–PP).

Previously we have prepared a number of arylamines containing a sterically hindered phenolic (SHP) fragment. In their molecules, there are at least two functional groups (SHP and secondary amino group) potentially capable of inhibiting oxidative processes [1]. The capability of these compounds to prevent oxidation of organic substrates by scavenging peroxide radicals responsible for the aging was evaluated in model reactions of initiated oxidation of styrene and PP, and their antioxidative performance was found to be high [2].

In this study we examined the possibility of using these additives to preserve in the course of aging the physicomechanical properties of PP, SIR, and TEPs derived from them.

EXPERIMENTAL

The stabilizers, *N*,*N*'-bis(3,5-di-*tert*-butyl-4-hydroxybenzyl)-*p*-phenylenediamine **I**, mp 197–199°C; *N*,*N*'-bis(3,5-di-*tert*-butyl-4-hydroxybenzyl)ethylenediamine **II**, mp 189°C; (3,5-di-*tert*-butyl-4-hydroxybenzyl)phenylamine **III**, mp 105°C; and *N*,*N*,*N*',*N*'-tetra-(3,5-di-*tert*-butyl-4-hydroxybenzyl)-*p*-diphenylenediamine **IV**, mp 192–194°C, were prepared according to [1].

Autooxidation of polymers was performed in an installation described in [3], in an oxygen atmosphere (p_{O_2} = 250 mm Hg) at 165°C (polymer sample weight 0.1 g). The dissolved stabilizing components were added to the PP powder and thoroughly mixed at room temperature; the mixture was vacuum-dried to constant weight. SIR-3 was reprecipitated three times with acetone from toluene solution according to [4]. The stabilizer was added to a 5% (here and hereinafter, wt %) solution of SIR-3 in toluene and stirred to complete dissolution, after which the solvent was vacuum-evaporated.

The torque M_t was determined in a Brabender plasticorder [5]. The choice of the time for recording M_t was governed by the residence time of the polymer in the mixing chamber in TEP preparation.

The TEP based on SIR and PP was prepared using the formulation from [6]; the resulting TEP exhibits high physicomechanical parameters. The vulcanizate composition and the time of successive addition of ingredients are given in Table 1.

After adding all the ingredients, they were stirred for 6–7 min, with simultaneous melting of PP and vulcanization. The vulcanization was performed in the dynamic mode. The vulcanization time was determined from the maximal value of M_t in the kinetic curve. Af-

1070-4272/03/7604-0648 $25.00 © 2003 MAIK "Nauka/Interperiodica"

Table 1. Composition of the vulcanizate and time τ of ingredient addition (temperature in the chamber, °C: initial 140, final 215)

Ingredient	Content, wt parts	τ, min	Rotor rotation rate, rpm	Ingredient	Content, wt parts	τ, min	Rotor rotation rate, rpm
SIR-3	75–50	0	60	Stearic acid	2		
Stabilizer	1			Sulfenamide Ts	5	5	
Titanium dioxide	2			Sulfur	0.35	5.5	
Zinc oxide	5	4.5		Polypropylene (252-01 030)	25–50	6	90

Table 2. Comparison of the inhibiting effects of **I**–**V** in oxidation of SIR-3 (165°C, p_{O_2} = 250 mm Hg)

Stabilizer	Induction period of oxidation τ (min) at c_{AO} = 3%	AO concentration $c \times 10^4$, mol kg^{-1}		Content in molecule	
		corresponding to 3%	required to attain τ = 100 min	SHP fragments	NH_{Ar} groups
I	180	5.56	3.02	2	2
II	45	6.05	13.44	2	–
III	150	9.65	6.45	1	1
IV	100	2.84	2.84	4	–
V	130	13.32	10.20	–	2

ter reaching the maximal M_t, the stirring was continued for additional 3 min. Then the TEP was subjected to sheeting with microrolls (2-mm slit). The cooled material was extruded through a slit die head (1.5-mm slit).

The TEP samples were tested according to GOST (State Standard) 270–85 [7] to determine the tensile strength σ, relative elongation L_{rel}, and residual elongation L_{res}.

The antioxidative effects of amines **I**–**IV** on PP and SIR-3 were evaluated by the induction period of oxidation, determined in the autooxidation mode on a static oxidation unit. Such tests allow evaluation of the performance of an additive under the conditions of polymer processing [3]. Also, we examined the capability of stabilizers **I**–**IV** to prevent thermomechanical degradation of PP and SIR-3. This parameter is particularly important for dynamic TEPs whose vulcanization is combined with mixing at the temperature of the thermoplastic melt, which results in that the polymers undergo significant degradation. The degradation is manifested in a decrease of the torque in mechanical treatment of the polymer.

We evaluated the effect of **I**–**IV** on the stability of physicomechanical parameters of TEPs in the course of aging. The polymeric material is a multicomponent system whose properties depend not only on the initial mixture composition and mixing procedure, but also on possible interactions between the mixture components in the course of mixing. Therefore, the stabilizing performance of antioxidants (AOs) depends on the mixture ingredients.

The results of testing of amines **I**–**IV** as AOs for SIR-3 are listed in Table 2. The reference stabilizer was *N*-phenyl-*N*'-isopropylphenylenediamine **V** (stabilizer 4010 NA) used in industry for stabilization of dark SIR brands and their vulcanizates. When autooxidation of a polymer is performed at elevated temperature (130°C), stabilizer **V** starts to sublime; this significant drawback was noted in a number of papers [8–10]. No noticeable sublimation of **I**–**IV** was observed under the testing conditions.

As seen from Table 2, the longest induction period in oxidation of SIR-3 was observed with **I** and **III**. Comparison of **I**–**V** shows that the best stabilizing effect is achieved with the molecules that combine SHP and NH_{Ar} groups. Amine **II** combining the SHP and NH_{Alk} groups, is a poor inhibitor, probably because of the high rate of oxidation chain transfer from the $\dot{N}_{alk}$ radical generated in the course of stabilization [11]. The advantages of **I** and **II** become particularly obvious when using the molar scale (mol kg^{-1}), which reflects the molecular activity of the compounds, instead of the weight percentage scale accepted in industry (Table 2).

Table 2 shows that, with **I** and **III**, the 100-min induction period of SIR-3 oxidation is attained at a lower inhibitor concentration than with **V**.

Amine **I** also ensures the longest induction period in oxidation of PP:

Stabilizer	–	**I**	**II**	**III**	**IV**	**V**
τ, min	20	140	40	70	55	135

Table 3. Variation of M_t of SIR-3 and PP in the course of treatment in a plasticorder in the presence of stabilizers **I**–**IV** (rotor rotation rate 90 rpm)

Stabilizer	Content, %	M_t (N m^{-1}) after treatment for indicated time, min		
		4	7	10
SIR-3, t_{in} = 130°C				
–	0.40	24	17	12
I	0.40	26	18	15
II	0.40	25	17	13
III	0.40	24	21	19
IV	0.40	25	16	13
PP, t_{in} = 180°C				
–	–	15.0	13.7	12.8
I	0.10	10.2	9.6	9.1
	0.15	11.7	11.1	10.6
	0.20	11.9	10.9	10.3
	0.25	10.9	10.4	10.1
II	0.10	11.5	9.6	8.3
	0.15	12.2	11.0	9.8
	0.20	11.7	9.75	8.6
	0.25	13.2	11.9	10.8
III	0.10	13.7	12.7	12.7
	0.15	12.8	11.6	11.5
	0.20	14.8	13.0	12.3
	0.25	12.3	11.9	11.8

Table 4. Physicomechanical properties of TEP based on SIR-3 and PP at various rubber : plastic ratios

Stabilizer	SIR-3 : PP weight ratio			
	50 : 50	60 : 40	70 : 30	75 : 25
σ, MPa				
–	14	17	16	15
I	17	16	16	12
III	16	14	14	12
V	16	16	16	15
L_{rel}, %				
–	270	370	380	407
I	398	380	375	400
III	357	330	367	398
V	346	366	532	599
L_{res}, %				
–	117.3	153.3	133.3	118.7
I	194.7	129.3	88	66.7
III	173.3	122	85.3	73.3
V	143.2	158.4	136.8	90.4

Compound **I** is comparable in its antioxidative power with the commercial PP stabilizer Irganox (**VI**), ester of pentaerythritol and 2,6-di-*tert*-butyl-4-hydroxyphenylpropionic acid.

In treatment of SKI-3 in a Brabender plasticorder for 10 min at 130°C, addition of **I**–**IV** in amounts of less than 0.3% had no effect on the torque variation. In all the cases, M_t decreased by approximatelyl 50%. In the presence of **I** and **III** in a concentration exceeding 0.3%, M_t decreased to a considerably lesser extent (Table 3), i.e., these stabilizers efficiently prevent the thermomechanical degradation of the polymer.

Similar data on the performance of **I**–**IV** were obtained in experiments on thermomechanical treatment of PP (Table 3).

Amines **I** and **III**, which showed the best stabilizing performance were tested as stabilizers for TEP derived from a mixture of SIR-3 and PP (weight ratio SIR-3 : PP from 75 : 25 to 50 : 50).

Data on the influence of the stabilizer structure on the physicomechanical properties of TEPs (Table 4) show that the strength σ of the material is virtually independent of the rubber : plastic ratio in the range

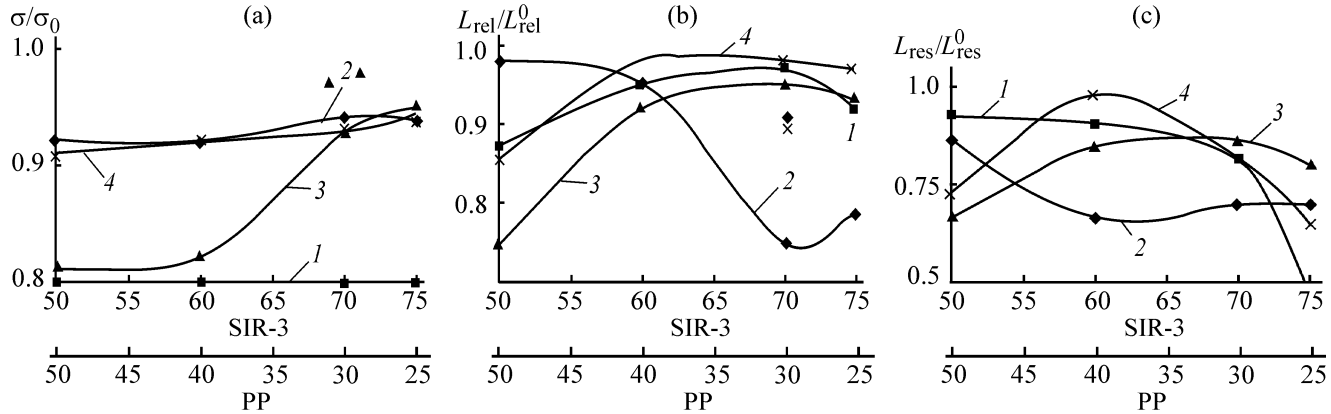

Fig. 1. Variation of TEP properties in the course of thermal aging at various ratios (mol %) of SIR-3 and PP. c_{AO} = 1%, 100°C, 72 h. (a) (σ/σ_0) tensile strength, (b) (L_{rel}/L_{rel}^0) relative elongation, and (c) (L_{res}/L_{res}^0) relative residual elongation (relative to the initial values). Stabilizer added: (*1*) none, (*2*) **V**, (*3*) **I**, and (*4*) **III**.

from 50 : 50 to 70 : 30 and of the presence and type of a stabilizer, except for amine **III** with which the strength decreases at rubber content in TEP exceeding 60%. The relative elongation L_{rel} depends on the polymer ratio only weakly in the presence of **I** and **III**, but with **V**, the relative elongation sharply increases at rubber content exceeding 60%. The relative residual elongation L_{res} of TEPs stabilized with **I** and **III** decreases approximately linearly with increasing content of SIR-3, whereas with **V**, the residual elongation as a function of the SIR-3 content passes through a maximum.

The AO effect of stabilizers in TEP was evaluated by the coefficient of resistance to thermal aging, equal to the ratio of a parameter determined after aging to that before aging. These coefficients are plotted in Fig. 1 against the ratio of the polymeric components.

Figure 1 shows that stabilizers **I** and **III** are level with V or even surpass it in the capability to preserve the properties of TEPs at the SIR-3 : PP ratio varied from 55 : 45 to 70 : 30.

CONCLUSION

Arylamines combining sterically hindered phenolic and HNAr fragments show promise as agents enhancing the resistance of isoprene rubber and polypropylene, and also of thermoelastoplastics derived from them (rubber : polypropylene ratio from 50 : 50 to 70 : 30), to oxidative and thermomechanical degradation.

REFERENCES

1. Nugumanova, G.N., Zhukova, R.S., Cherezova, E.N., and Mukmeneva, N.A., *Zh. Obshch. Khim.*, 1997, vol. 67, no. 6, pp. 993–996.
2. Mukmeneva, N.A., Cherezova, E.N., Rusina, I.F., *et al.*, *Int. J. Polym. Mater.*, 2000, vol. 47, no. 2, pp. 317–328.
3. Piotrovskii, K.B. and Tarasova, Z.N., *Starenie i stabilizatsiya kauchukov i vulkanizatov* (Aging and Stabilization of Rubbers and Vulcanizates), Moscow: Khimiya, 1980.
4. Lazarev, S.Ya., Reisfel'd, V.O., and Erkova, L.N., *Laboratornyi praktikum po sinteticheskim kauchukam* (Laboratory Manual on Synthetic Rubbers), Leningrad: Khimiya, 1986.
5. Vol'fson, S.I., Karp, M.G., Gidiyatullin, M.M., and Garifullin, F.A., *Kauchuk Rezina*, 1989, no. 9, pp. 13–16.
6. RF Patent 2 067 103.
7. Okhotina, N.A., *Osnovnye metody fiziko-mekhanicheskikh ispytanii elastomerov: Metodicheskie ukazaniya k laboratornomu praktikumu* (Main Methods for Physicomechanical Tests of Elastomers: Methodical Instructions to Practical Laboratory Course), Kazan: Kazan. Gos. Tekhnol. Univ., 1995; *GOST* (State Standard) *270–85: Method for Determining the Elastic and Strength Properties at Extension*.
8. Afanas'ev, S.V., Nazarova, F.A., Lebedeva, S.A., and Bogdanov, V.V., *Kauchuk Rezina*, 1991, no. 6, pp. 14–17.
9. Kavun, S.M., *Kauchuk Rezina*, 1994, no. 5, pp. 32–43.
10. Gerasimovich, S.P., Kavun, S.M., Masagutova, L.V., and Borzenkova, A.Ya., *Kauchuk Rezina*, 1990, no. 5, pp. 15–18.
11. Emanuel', N.M. and Buchachenko, A.L., *Khimicheskaya fizika stareniya i stabilizatsii polimerov* (Chemical Physics of Aging and Stabilization of Polymers), Moscow: Nauka, 1982.

Russian Journal of Applied Chemistry, Vol. 76, No. 4, 2003, pp. 652–655. Translated from Zhurnal Prikladnoi Khimii, Vol. 76, No. 4, 2003, pp. 676–679.

MACROMOLECULAR CHEMISTRY AND POLYMERIC MATERIALS

Recovery of Butadiene–Styrene Rubber from Latex at Low Temperature with Various Coagulants

S. S. Nikulin, I. N. Akatova, and N. A. Kondrat'eva

Voronezh State Academy of Forestry Engineering, Voronezh, Russia
Voronezh State Technological Academy, Voronezh, Russia

Received June 25, 2002; in final form, January 2003

Abstract—The influence of the charge of a metal cation and the nature of a coagulant on the recovery of butadiene–styrene rubber and properties of rubber stocks and vulcanizates was examined.

Rubbers produced by emulsion copolymerization are widely used in industry for production of tires and other rubber items [1–5]. An advantage of the emulsion copolymerization is the absence of dangerously explosive, inflammable, and harmful organic solvents. A wide variety of butadiene–styrene rubbers are produced commercially; the starting monomers for their synthesis are readily available, and the polymers are uniform in properties and have high quality.

One of the key stages in production of emulsion rubbers is their recovery from latexes with an aqueous NaCl solution acidified with H_2SO_4 [3]. The high consumption of the coagulant (180–250 kg t^{-1} rubber) results in strong contamination of the forming wastewater with NaCl, which cannot be removed at water treatment facilities. Therefore, active efforts are made to develop new processes for recovery of rubbers from latexes, including a search for new coagulants [6].

Numerous inorganic and organic coagulants have been suggested [7–10]. However, their commercial application involves serious problems. For example, aqueous solutions of protein coagulants exhibit low stability, especially at elevated temperatures. Proteins degrade with evolution of noxious substances with unpleasant odor, which results in air pollution in the working rooms. Other coagulants are expensive and are in short supply. Therefore, up to now, the main coagulant used in production of emulsion rubbers has been NaCl; recovery is performed at 50–65°C [3].

Published data and industrial experience show that multicharged metal salts are the most promising coagulants; they can be taken in considerably smaller amounts than NaCl [3]. However, the relationship between the consumption of coagulants based on multicharged metal salts and the composition of emulsifying systems is poorly understood.

The emulsifying agents that are widely used today in commercial production of emulsion butadiene–styrene rubbers are soaps based on tall oil, disproportionated rosin, and fatty acid salts, taken in various ratios.

In this study, we analyzed coagulation of SKS-30 ARK butadiene–styrene latex at low temperature, with NaCl, $CaCl_2$, $AlCl_3 \cdot 6H_2O$, and $SnCl_4 \cdot 5H_2O$ as coagulating agents.

Experiments on rubber recovery from the latex were performed in a stirred vessel placed in a thermostat. The vessel was charged with 20 ml of the latex and kept for 15–20 min to attain the required temperature, after which aqueous solutions of the coagulants acidified with H_2SO_4 were added. Coagulation was performed at pH 2.0–2.5.

Coagulants were taken as aqueous solutions containing (wt %) 24 NaCl or 10 $CaCl_2$, $AlCl_3$, or $SnCl_4$.

Data on the completeness of rubber recovery from the latex as influenced by temperature, nature of coagulant, and its consumption are given in Figs. 1 and 2.

The experimental dependences show that, in going from single- to triple-charged metal ion, the required coagulant consumption considerably decreases, which is consistent with the results of [3].

At 2–4°C, the consumption of $SnCl_4$ required for complete recovery of the rubber is lower than the con-

1070-4272/03/7604-0652 $25.00 © 2003 MAIK "Nauka/Interperiodica"

sumption of $AlCl_3$, the most active coagulant among those tested previously. At 20°C, however, the consumptions of $SnCl_4$ and $AlCl_3$, required for 100% coagulation, become approximately equal, and at 40°C $AlCl_3$ becomes even more effective. Thus, the Sn(IV) cation exhibits high coagulating power only at low temperatures. With $SnCl_4$, no acidification with H_2SO_4 is required. In aqueous solution, $SnCl_4$ undergoes hydrolysis to form HCl, stannic acid, and hexachlorostannic acid [11]:

$$SnCl_4 + 6H_2O \rightleftarrows H_2[Sn(OH)_6] + 4HCl,$$

$$3SnCl_4 + 4H_2O \rightleftarrows 2H_2[Sn(Cl)_6] + Sn(OH)_4,$$

$$SnCl_4 + 2HCl \rightleftarrows H_2[Sn(Cl)_6].$$

Hexachlorostannic acid is strong; its stable salts give a neutral reaction in aqueous solution and are not hydrolyzed even on boiling. Therefore, the surfactants present in the emulsifying system can react with hexachlorostannic acid:

$$H_2[Sn(Cl)_6] + R\text{–}COONa(K)$$

$$\rightarrow Na_2(K_2)[Sn(Cl)_6] + R\text{–}COOH.$$

Hydrolysis of $SnCl_4$ makes the content of the salt in the system lower, especially at elevated temperature [12], and may be responsible for the increase (relative to $AlCl_3$) in the consumption of $SnCl_4$ required for 100% recovery of rubber from the latex with the temperature increasing from 2–4 to 20 and then to 40°C.

A specific feature of coagulation with $SnCl_4$ is the formation of a fine rubber crumb, which results in major loss of rubber with washwater.

By computer processing of the experimental data, we obtained the following regression equations for the dependence of the coagulant consumption on the cation charge at various temperatures of rubber recovery:

$$Y_{2-4°C} = 318 - 307.33x + 100x^2 - 10.667x^3,$$

$$Y_{20°C} = 877 - 892.33x + 297.5x^2 - 32.167x^3,$$

$$Y_{40°C} = 845 - 841.17x + 275.5x^2 - 29.333x^3.$$

From the dried samples of SKS-30 ARK rubber, we prepared standard rubber stocks, which were vulcanized at 143°C.

Tests of rubber stocks and vulcanizates based on SKS-30 ARK rubber recovered from latex with salts of single- to quadruple-charged metal ions showed that the properties of these materials are not influenced appreciably by the nature of the coagulant.

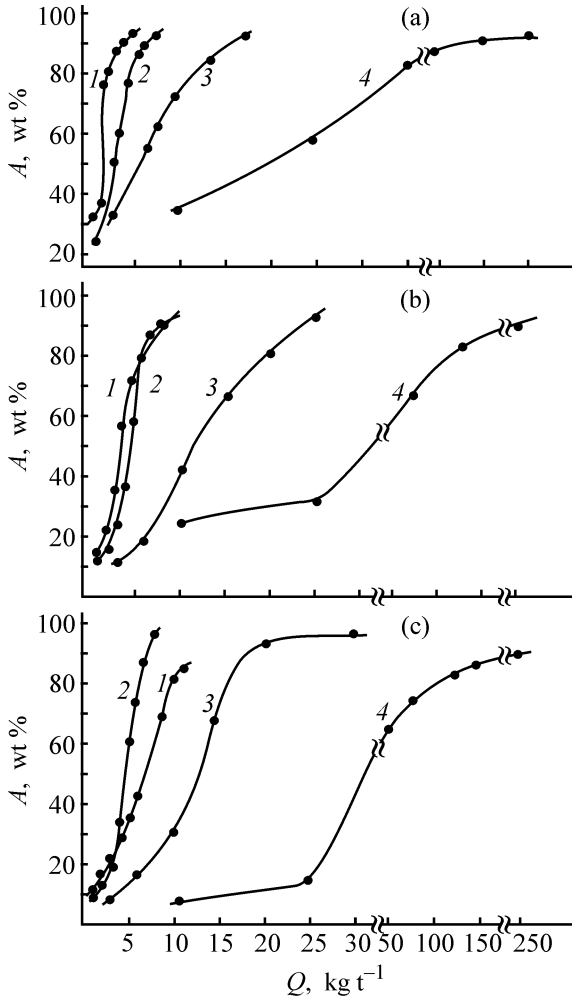

Fig. 1. Degree of recovery *A* of rubber from SKS-30 ARK lattice, as influenced by the nature and consumption *Q* of the coagulant. Temperature, °C: (a) 2–4, (b) 20, and (c) 40. (*1*) $SnCl_4$, (*2*) $AlCl_3$, (*3*) $CaCl_2$, and (*4*) NaCl.

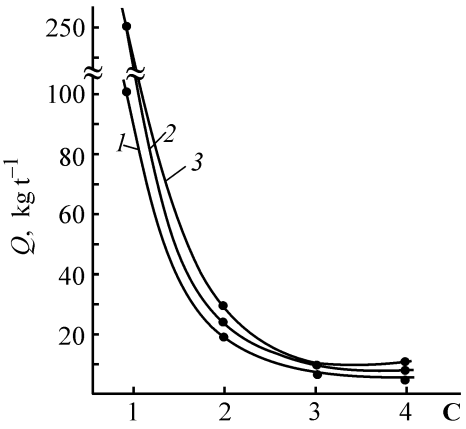

Fig. 2. Coagulant consumption *Q* required for complete coagulation of rubber from SKS-30 ARK latex vs. cation charge **C**. Temperature, °C: (*1*) 2–4, (*2*) 20, and (*3*) 40.

Table 1. Properties of rubber stocks and vulcanizates based on SKS-30 ARK rubber

Parameter	Coagulant			
	NaCl	$CaCl_2$	$AlCl_3$	$SnCl_4$
Mooney viscosity MB 1 + 4 (100°C) of rubber stock	45.0	50.0	49.0	46.0
Karrer plasticity of rubber stock, arb. units	0.39	0.37	0.37	0.42
Recovery, mm	1.46	1.69	1.65	1.38
Nominal stress at 300% elongation, MPa	9.2 / 11.1	8.3 / 8.9	8.7 / 9.8	10.3 / 12.0
Nominal tensile strength, MPa	24.7 / 24.5	25.1 / 24.4	25.0 / 25.2	26.2 / 26.4
Relative elongation at break, %	580 / 510	610 / 570	600 / 560	560 / 500
Relative set after break, %	12 / 10	20 / 16	14 / 14	14 / 12
Rebound elasticity, %	42	40	40	39
Shore hardness A, arb. units	57	59	59	61

Note. Vulcanization at 143°C for 60 (numerator) or 80 (denominator) min.

Table 2. Characteristics of vulcanization of rubber stocks based on SKS-30 ARK rubber at 160°C

Parameter	Coagulant			
	NaCl	$CaCl_2$	$AlCl_3$	$SnCl_4$
Minimal torque M_L, N m	4.8	4.6	5.1	5.1
Maximal torque M_H, N m	36.5	33.0	33.5	36.2
Time of vulcanization onset t_S, min	3.5	4.0	4.0	4.0
Time of 50% vulcanization $t_{S(50)}$, min	10.2	10.7	11.5	9.9
Optimal vulcanization time $t_{S(90)}$, min	27.5	18.5	26.0	23.0
Vulcanization rate R_v, min^{-1}	4.17	6.90	4.54	5.26

However, it should be noted that the rubber stocks based on SKS-30 ARK rubber coagulated with $SnCl_4$ show higher plasticity and lower recovery (Table 1).

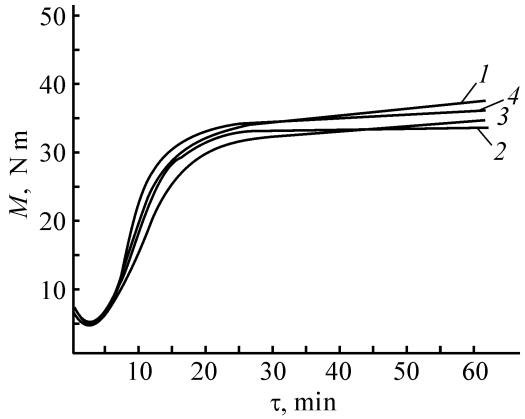

Fig. 3. Kinetics of vulcanization of rubber stocks based on SKS-30 ARK rubber recovered using (*1*) $SnCl_4$, (*2*) $AlCl_3$, (*3*) $CaCl_2$, and (*4*) NaCl. (*M*) Torque and (τ) time.

The kinetic curves of vulcanization (Fig. 3) show that the rubber stocks prepared from SKS-30 ARK rubber coagulated with $CaCl_2$ are characterized by faster vulcanization, and in the case of NaCl and $AlCl_3$ coagulants, the vulcanization is the slowest (Table 2).

CONCLUSIONS

(1) The maximal decrease in the salt consumption was observed on passing from single- to triple-charged metal ions.

(2) With $SnCl_4$ as coagulant, acidification is unnecessary.

(3) With $SnCl_4$, coagulation is more efficient at lower temperatures.

(4) The nature of the coagulant has no appreciable effect on the properties of the resulting rubbers, rubber stocks, and vulcanizates.

REFERENCES

1. Erkova, L.N. and Chechik, O.S., *Lateksy* (Latexes), Leningrad: Khimiya, 1983.
2. Eliseeva, V.I., Ivanchev, S.S., Kuchanov, S.I., and Lebedev, A.V., *Emul'sionnaya polimerizatsiya i ee primenenie v promyshlennosti* (Emulsion Polymerization and Its Use in Industry), Moscow: Khimiya, 1976.
3. Kirpichnikov, P.A., Averko-Antonovich, L.A., and Averko-Antonovich, Yu.O., *Khimiya i tekhnologiya sinteticheskogo kauchuka* (Chemistry and Technology of Synthetic Rubber), Leningrad: Khimiya, 1987.
4. Bashkatov, T.V. and Zhigalin, Ya.L., *Tekhnologiya sinteticheskogo kauchuka* (Technology of Synthetic Rubber), Leningrad: Khimiya, 1987.
5. Averko-Antonovich, Yu.A., Omel'chenko, R.Ya., Okhotina, N.A., and Ebich, Yu.R., *Tekhnologiya rezinovykh izdelii: Uchebnoe posobie dlya vuzov* (Technology of Rubber Items: Textbook for Higher Schools), Kirpichnikov, P.A., Ed., Leningrad: Khimiya, 1991.
6. Verezhnikov, V.N., Nikulin, S.S., Poyarkova, T.N., and Garshin, A.P., *Vestn. Tambov. Univ.*, 1997, vol. 2, no. 1, pp. 47–52.
7. USSR Inventor's Certificate, no. 1131883.
8. USSR Inventor's Certificate, no. 1151541.
9. US Patent 4025711.
10. Moiseev, V.V., Kosovtsev, V.V., Popova, O.K., and Markova, Z.N., *Kauchuk Rezina*, 1984, no. 7, pp. 39–41.
11. Stepin, B.D. and Tsvetkov, A.A., *Neorganicheskaya khimiya* (Inorganic Chemistry), Moscow: Vysshaya Shkola, 1994.
12. Glinka, N.L., *Obshchaya khimiya* (General Chemistry), Leningrad: Khimiya, 1988.

Russian Journal of Applied Chemistry, Vol. 76, No. 4, 2003, pp. 656–660. Translated from Zhurnal Prikladnoi Khimii, Vol. 76, No. 4, 2003, pp. 680–684.

MACROMOLECULAR CHEMISTRY AND POLYMERIC MATERIALS

Effect of Higher Fatty Acids and Their Mixtures on Interfacial and Physicomechanical Properties of Vulcanized Rubbers

A. P. Rakhmatullina, L. A. Zavarikhina, O. G. Mokhnatkina, I. L. Mikhailova, S. A. Bogdanova, R. A. Akhmed'yanova, and A. G. Liakumovich

Kazan State Technological University, Kazan, Tatarstan, Russia

Received July 9, 2002

Abstract—The interfacial characteristics of stearic and oleic acids and their mixtures were studied. The surface free energies of isoprene and butadiene–styrene rubbers and vulcanizates thereof, obtained using fatty acids and their synergistic mixture as vulcanization activators, were evaluated from the contact angles.

Surfactants play an important role in preparation and processing of rubber stocks. They are used as vulcanization activators and process additives improving the dispersion and ensuring uniform distribution of all the rubber stock components; they improve the compatibility of fillers with the polymeric matrix and control interphase interactions at phase boundaries [1, 2]. Higher fatty acids and their salts are traditional ingredients of rubber stocks exhibiting, along with the capability to affect the colloidal-chemical characteristics of the system, also the properties of structural plasticizers [2]. Active search for new, more effective surfactants and for optimal conditions of their introduction is being continued, together with studies concerned with the mechanism of the effect of surfactants on the rheological characteristics of rubber stocks, vulcanization rate, and physicomechanical parameters of the vulcanizates. Published data on the effect of unsaturated fatty acids on the density of the structural network and vulcanization characteristics show that surfactants exert a polyfunctional effect and can affect selectively and directionally the properties of elastomers [3, 4].

It is known that combinations of different surfactants can exhibit enhanced performance in complex multicomponent systems [4, 5]. For example, the synergistic effect has been revealed in studies of crystallization of isoprene rubber in the presence of a mixture of saturated and unsaturated fatty acids [6]. This opens up wide opportunities for formulating rubber stocks. In this context, the use of surfactant mixtures as process additives with a wide spectrum of activity is of scientific and applied interest.

In this study, we analyzed how mixtures of saturated and unsaturated fatty acids affect the interphase properties, vulcanization parameters, and physicomechanical parameters of vulcanized rubbers. We chose saturated stearic (St) and unsaturated oleic (Ol) acids, which are widely used in rubber and tire industry as activators of vulcanization of rubber stocks.

EXPERIMENTAL

Experiments were performed with isoprene (SKI-3) and butadiene–styrene (SKMS-30, ARKM-15) rubbers. The rubber stocks contained the following additives (wt parts per 100 wt parts rubber): vulcanizing system, technical-grade sulfur 2.1 and sulfenamide Ts 1.5; vulcanization activators, zinc oxide 3.0 and fatty acid 2.0. Samples with surfaces to be studied were obtained by compacting rubbers and rubber stocks were pressed at 100°C for 10 min. Rubber stocks with laboratory rollers and vulcanized in an electric press at 143°C for 50 min. The vulcanization kinetics was studied with a Monsanto vibrorheometer at 143°C. The vulcanometric curves were processed according to GOST (State Standard) 12535–84, and the physicomechanical properties of rubber stocks and their vulcanizates were evaluated according to GOST 270–75.

The surface tension γ of higher fatty acids and their mixtures was determined by the Wilhelmi plate method in a temperature-controlled cell. The temperature was varied from 25 to 80°C; the accuracy of the method was 0.3%. The contact angles θ were determined by the sedentary drop method with a KM-8 cathetometer modified with an ocular micrometer. The surface

1070-4272/03/7604-0656 $25.00 © 2003 MAIK "Nauka/Interperiodica"

free energy (SFE) γ_s of rubber and vulcanizate samples and its polar, γ_s^p, and dispersion, γ_s^d, constituents were determined using the Fowkes plots [7], from the contact angles with the surface wetted with test liquids at $25 \pm 1°C$. As test liquids we used water, dimethylformamide, dimethyl sulfoxide, glycerol, and α-bromonaphthalene, which were freshly distilled and purified by appropriate procedures.

The ability of surfactants to be involved in interphase interaction can be quantitatively characterized by the surface free energy; for equilibrium liquids, it is equal to the surface tension. We measured the surface tension of Ol, St, and their mixtures of definite compositions at 60, 70, and 80°C.

At any of the examined temperatures, the composition dependences of the surface tension pass through a minimum at 40 wt % St and 60 wt % Ol (Fig. 1). As the temperature is raised, the minimum shifts toward lower surface tensions, with the deepest minimum being observed at 80°C. These data reveal a synergistic effect: At definite acid ratios, the surface tension of a mixture of acids is appreciably lower than that of the acids taken separately. The temperature dependence of γ is linear for both individual acids and their mixtures, which is, on the whole, consistent with published data [8].

According to Fainerman *et al.* [9], there is a correlation between γ of a substance and its surface activity at interfaces. Therefore, it can be expected that a mixture of Ol and St in a weight ratio of 60 : 40 will affect the interfacial characteristics of rubber stocks more efficiently. The fact that the minimum of γ becomes deeper with increasing temperature suggests the hydrophobic nature of intermolecular interactions in the system Ol–St, since it is well known that hydrophobic interactions become stronger with increasing temperature [10]. Apparently, at certain ratio of the acids, St molecules form surface-active associates in the medium of Ol. We examined the effect of St additions (up to 1 wt %) on γ of Ol. Experimental data (Fig. 2) show that γ of Ol decreases in the presence of St, suggesting participation of St molecules in formation of boundary layers.

Wetting, as the most important surface phenomenon occurring at the boundary of three phases, plays an important role in preparation of polymeric composites. In this study, we examined the wetting power of Ol relative to various surfaces and the effect of St additions on the contact angle. As models we chose glass for hydrophilic surface and Teflon for hydrophobic surface. Addition of St to Ol (up to 1 wt %) results in virtually complete spill on the polar surface

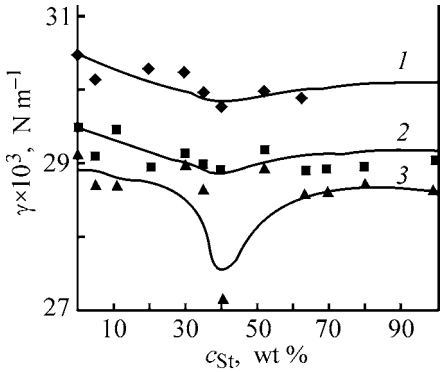

Fig. 1. Surface tension γ vs. the content of stearic acid c_{St} in its mixture with oleic acid. Temperature, °C: (*1*) 60, (*2*) 70, and (*3*) 80.

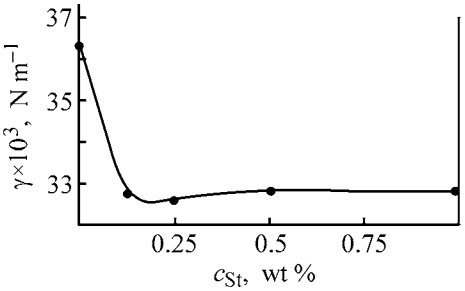

Fig. 2. Influence of the concentration of stearic acid, c_{St}, on the surface tension γ of oleic acid.

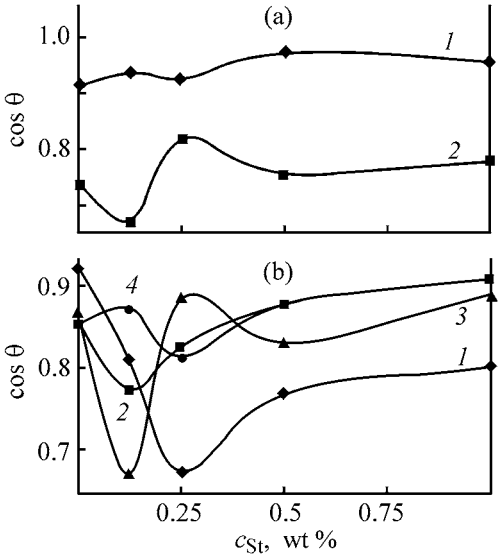

Fig. 3. Isotherms of wetting of various surfaces with oleic acid containing stearic acid. Surface: (a) (*1*) glass and (*2*) Teflon; (b) rubber: (*1*) isoprene, (*2*) butadiene–styrene, (*3*) isoprene with the vulcanizing system, and (*4*) butadiene–styrene with the vulcanizing system.

(Fig. 3a, curve *1*), which, according to the Young equation, may be due to a decrease in γ of a liquid upon adsorption of a surfactant on the liquid–air interface.

In experiments on wetting of a nonpolar Teflon surface (Fig. 3a, curve *2*), additions of St to Ol in-

Table 1. Surface energy characteristics and physicomechanical properties of rubbers and their vulcanizates*

Parameter	SKI-3	SKI-3 + VS	SKMS-30 ARKM-15	ARKM-15 SKMS-30 + VS
$\gamma_s \times 10^3$, N m^{-1}	30.50	27.56	31.25	29.66
$\gamma_s^p \times 10^3$, N m^{-1}	0.25	1.56	1.00	1.50
$\gamma_s^d \times 10^3$, N m^{-1}	30.25	26.00	30.25	28.16
σ, MPa	1.6×10^{-3}	1.5×10^{-3}	7.7×10^{-2}	7.2×10^{-2}
L, %	225	240	740	510

Parameter	SKMS-30 ARKM-15 + VS + VA (St)		SKMS-30 ARKM-15 + VS + VA(Ol)		SKMS-30 ARKM-15 + VS + VA (Ol + St)	
	1**	2**	1**	2**	1**	2**
$\gamma_s \times 10^3$, N m^{-1}	34.64	38.81	32.00	37.70	37.61	41.49
$\gamma_s^p \times 10^3$, N m^{-1}	1.00	4.00	3.50	3.06	6.25	9.00
$\gamma_s^d \times 10^3$, N m^{-1}	33.64	34.81	28.50	34.84	31.36	32.49
σ, MPa	1.10×10^{-1}	1.1	7.3×10^{-2}	1.1	1.1×10^{-1}	1.0
L, %	540	230	660	255	460	140

* (VS) Vulcanizing system, (VA) vulcanization activators, (σ) nominal tensile strength, and (L) relative elongation.

** (1) Crude and (2) vulcanized rubber stocks.

crease $\cos\theta$ to a greater extent; the wetting power of the liquid grows owing to adsorption of St on the Ol–solid interface. Thus, studies of wetting give an estimate of the intensity of adhesion interaction of fatty acids with surfaces of various polarities.

One of our goals was to study the specific features of interaction of Ol, St, and their mixtures with rubbers and ingredients of rubber stocks. We studied wetting of the surface of the rubbers tested with Ol containing additions of St.

Figure 3b shows that isoprene rubber is wetted with Ol better than does butadiene–styrene rubber. Addition of 0.125 to 0.5 wt % St sharply decreases the wetting. Probably, the effect of St adsorption at the rubber–Ol interface prevails in this concentration range; intense interactions of the molecules with the surface make the surface oleophilic. Further increase in the concentration of stearic acid results in stronger spill owing to prevailing adsorption of St at the Ol–air interface. Furthermore, chemisorption of St on the rubber surface cannot be ruled out.

With rubber containing vulcanizing agents, the results were, on the whole, similar to those obtained with pure rubber. The minimum in the curve of γ vs. c_{St} shifted somewhat (Fig. 3b). In the presence of vulcanizing agents, the amount of active centers on the surface increases, which results in the growth of the polar constituent of SFE. This, apparently, complicates adsorption of St at the interface, and $\cos\theta$ decreases to a lesser extent.

The surface and interfacial phenomena in polymeric composites largely determine their performance. The structural features of polymer macromolecules affect the formation of boundary layers and the intermolecular interactions leading to conformational transformations at phase boundaries [11]. One of the main parameters of polymer surfaces, attracting researchers' attention, is the surface free energy, often considered a response function of interactions in the system.

We determined SFE and its constituents for isoprene and butadiene–styrene rubbers and various vulcanizates based on them (Table 1).

Experiments showed that, as expected, the surface of rubbers is characterized by low energy with small polar constituent, which is somewhat higher for butadiene–styrene rubber. This is associated with the structural features of its macromolecule, apparently exhibiting an appreciable dipole moment and asymmetry. The susceptibility of the rubbers to surface oxidation may also vary. Addition of vulcanizing agents increases the polar constituent owing to the appearance of surface polar groups. These may be sulfur-containing groups or fragments of sulfur particles insufficiently well dispersed in the rubber. On the whole, however, SFE somewhat decreases, which may be due to disordering of the boundary layer.

Addition of vulcanization activators considerably increases SFE. Comparative analysis shows that, in the presence of stearic acid, the major contribution to the growth of SFE is made by the dispersion constituent, and in the presence of Ol, by the polar constituent. This fact points to specific participation of surfactants in the formation of the boundary layer. On the whole, the increase in SFE indicates that the arrangement of macromolecules in the boundary layers becomes more ordered, which may be due to significant role of surfactants in homogenization of the system and more uniform distribution of the ingredients. The highest values of SFE were obtained for the rubber stock containing a synergistic mixture of surfactants; in this case, the contribution of the polar constituent of SFE is high, suggesting increased role of polar interactions in the surface layer of the elastomers. The mechanism responsible for the increase in SFE and its polar constituent requires further study; apparently, energy barriers at boundaries of phases with different polarities become lower, strong adhesion couples are formed, and formation of a three-dimensional structure is facilitated. Vulcanization of rubbers increases SFE owing to restriction of the macromolecule mobility upon formation of a cross-linked structure and to partial oxidation of the surface. In vulcanized rubbers, the trends in the dependence of SFE on the kind of surfactant are preserved. The highest SFE is observed in the sample containing a mixture of Ol and St; in this sample, γ_s^p is also high. Our results show that the synergistic mixture of surfactants exhibiting the minimal surface tension shows the highest activity at phase boundaries.

The interfacial surface energy affects the deformation and failure of solids. The correlation between the mechanical strength of polymeric materials and SFE was repeatedly noted by Lipatov [11].

In this study, we also revealed a correlation between SFE and strength characteristics of crude unfilled rubber stocks. The nominal tensile strength of butadiene–styrene rubber decreases somewhat upon introduction of sulfur and sulfenamide Ts, which correlates with SFE of the same systems (Table 1). When vulcanization activators are added along with the vulcanizing system, the strength of crude rubber stocks grows; this trend is the most pronounced when Ol and St are taken simultaneously in the optimal ratio. The strength characteristics of vulcanized rubbers are independent of a fatty acid used; their parameters are virtually similar. However, the mixture of surfactants appreciably affects the relative elongation of both crude stocks and vulcanized rubbers.

Table 2. Vulcanization characteristics of unfilled vulcanized rubbers based on butadiene–styrene rubber*

Acid	M_L	M_{max}	t_s	$t_{s(90)}$	R_v, min^{-1}
	N m		min		
St	5.8	31.6	20.0	36.5	6.1
Ol	4.6	33.4	17.5	37.8	4.9
Ol + St	4.6	33.9	13.5	30.1	6.0

* (M_L, M_{max}) Minimal and maximal torque, respectively; (t_s, $t_{s(90)}$) time of vulcanization onset and optimal vulcanization time; (R_v) vulcanization rate.

For unfilled stocks based on butadiene–styrene rubber, the time of vulcanization onset and the optimal vulcanization time are shorter with a synergistic mixture of Ol and St than with each of these acids taken separately (Table 2), i.e., this mixture of surfactants accelerates vulcanization. This allows the power consumption for preparation of rubber stocks to be reduced. Similar results have been obtained previously for filled rubbers [12].

It has also been found previously that a mixture of Ol and St exerts a synergistic effect on the rheological and dynamic properties of filled rubbers based on SKMS-30 ARKM-15 rubber. It was found that the viscosity of the rubbers and endurance of the vulcanizates as functions of the composition of the fatty acid mixture pass through a minimum and a maximum, respectively [12]; their position corresponds to the composition at which the surface tension of the acid mixture passes through a minimum: 60 wt % Ol and 40 wt % St.

Our studies confirm that the synergistic effect of mixtures of saturated and unsaturated fatty acids, mainfested in vulcanization and physicomechanical properties of rubbers, is due to interfacial properties of these acids and specific features of intermolecular interaction.

CONCLUSIONS

(1) Measurements of the surface tension of mixtures of oleic and stearic acids as a function of their ratio revealed a minimum at a weight ratio of 60 : 40, which becomes deeper with increasing temperature.

(2) Experiments on wetting of the surfaces of glass, Teflon, isoprene rubber, and butadiene–styrene rubber with oleic acid containing additions of stearic acid showed that stearic acid is involved in formation of the boundary layer at the rubber–oleic acid interface.

(3) The surface free energy and its constituents were calculated for rubbers, unfilled rubber stocks, and vulcanizates prepared using oleic acid, stearic acid, or their synergistic mixture. An increase in the surface free energy is due to the predominant contribution of the polar constituent, which is the most pronounced for rubbers prepared with the synergistic acid mixture.

(4) The correlation revealed between the vulcanization and physicomechanical properties of unfilled rubber stocks and vulcanized rubbers, on the one hand, and the interfacial properties, on the other, opens up prospects for improving the efficiency of various processes in production and use of rubber items.

REFERENCES

1. Grishin, B.S., El'shevskaya, E.A., and Pisarenko, T.I., *Primenenie poverkhnostno-aktivnykh veshchestv dlya uluchsheniya pererabatyvaemosti rezinovykh smesei* (Use of Surfactants for Improving the Processability of Rubber Stocks), Moscow: TsNIITEneftekhim, 1987.
2. Insarova, G.V., *Vliyanie poverkhnostno-aktivnykh veshchestv na pererabotku rezinovykh smesei i svoistva rezin* (Effect of Surfactants on the Processing of Rubber Stocks and Properties of Vulcanized Rubbers), Moscow: TsNIITEneftekhim, 1980.
3. Pisarenko, T.I. and Grishin, B.S., *Kauchuk Rezina*, 1990, no. 12, pp. 6–11.
4. *Poverkhnostnye yavleniya i poverkhnostno-aktivnye veshchestva: Spravochnik* (Surface Phenomena and Surfactants: A Handbook), Abramzon, A.A., Ed., Leningrad: Khimiya, 1984.
5. Shpenzer, N.P., Antipova, L.D., and Talmud, S.L., *Zh. Prikl. Khim.*, 1980, vol. 53, no. 5, pp. 1043–1047.
6. Tanaka, Y., Kawahara, C., Nishiyama, N., and Kakubo, T., *Proc. Int. Rubber Conf.*, Kobe (Japan), 1995, pp. 31–34.
7. Fowkes, F.M., *Adv. Chem. Ser.*, 1964, vol. 43, pp. 99–111.
8. Rusanov, A.I. and Prokhorov, V.A., *Mezhfaznaya tenziometriya* (Interfacial Tension Measurements), St. Petersburg: Khimiya, 1994.
9. Fainerman, A.E., Lipatov, Yu.S., and Kulik, V.M., *Kolloidn. Zh.*, 1969, vol. 31, no. 1, pp. 140–146.
10. Pchelin, V.A., *Gidrofobnye vzaimodeistviya v dispersnykh sistemakh* (Hydrophobic Interactions in Disperse Systems), Moscow: Znanie, 1976.
11. Lipatov, Yu.S., *Mezhfaznye yavleniya v polimerakh* (Interfacial Phenomena in Polymers), Kiev: Naukova Dumka, 1980.
12. Rakhmatullina, A.P., Zavarikhina, L.A., Akhmed'yanova, R.A., *et al.*, *Kauchuk Rezina*, 2001, no. 6, pp. 44–45.

Russian Journal of Applied Chemistry, Vol. 76, No. 4, 2003, pp. 661–662. Translated from Zhurnal Prikladnoi Khimii, Vol. 76, No. 4, 2003, pp. 685–686.

BRIEF COMMUNICATIONS

Synthesis of NaA Zeolite by Mechanochemical Methods

N. E. Gordina, V. Yu. Prokof'ev, and A. P. Il'in

Ivanovo State University of Chemical Technology, Ivanovo, Russia

Received September 13, 2002

Abstract—A method for obtaining NaA zeolite by mechanochemical activation of a raw material is proposed. The method produces no wastewater in the course of zeolite synthesis.

It is known that synthesis of zeolites by their precipitation from solutions leads to formation of a considerable amount of wastewater [1]. Therefore, development of new methods for production of zeolites is a promising direction of research in the field of synthesis of these compounds.

In the present study, it is proposed to synthesize a NaA zeolite by mechanochemical treatment of raw materials, which yields the product without any liquid-phase products.

EXPERIMENTAL

To carry out mechanochemical synthesis under "mild" conditions [2, 3], it is preferable to use compounds containing constitution water. This is the reason why aluminum hydroxide $Al(OH)_3$ (hydrargillite), sodium silicate $Na_2SiO_3 \cdot 6H_2O$ and silica gel $SiO_2 \cdot nH_2O$ with $n = 0.875$ were chosen as raw material. The component ratio corresponds to the stoichiometry of the reaction producing NaA zeolite:

$$6(Na_2SiO_3 \cdot 6H_2O) + 12Al(OH)_3 + 6(SiO_2 \cdot 0.875H_2O) = 6Na_2O \cdot 6Al_2O_3 \cdot 12SiO_2 \cdot 59.25H_2O.$$

The synthesis was performed in a VM-4 roller vibrating mill with impact-shear loading, vibration frequency of 930 min^{-1}, and energy load of 5.4 kW kg^{-1}, in the course of 30 min. Then a sample obtained was calcined at 450°C for 4 h. The resulting zeolite was identified by comparing its characteristics with published data [1] and parameters of a commercial NaA zeolite [TU (Technical Specifications) 38-83-047–88]. An X-ray phase analysis was made on a DRON-3M diffractometer with Cu_{K_α} radiation, and a differential-thermal analysis, on a Q-1500D derivatograph (Hungary) in air at sample heating rate of 5 deg min^{-1}. IR spectra of samples compacted with KBr in 5% dilution were measured on a Nicolet AVATAR 360 FT-IR IR spectrometer in the 400–1250 cm^{-1} spectral range.

As shown by the experimental data obtained (Fig. 1), the X-ray diffraction pattern of the starting mixture used to synthesize the A zeolite contains diffraction peaks of hydrargillite and sodium silicate. After dispergation of the mixture for 30 min the reflections associated with sodium silicate disappear, and the intensity of reflections corresponding to hydrargillite decreases substantially (by approximately a factor of 3). New peaks appear at diffraction angles 2θ 14.0°, 24.3°, 34.4°, 42.7°, and 52.0°. Comparison of the X-ray diffraction pattern with published data suggests

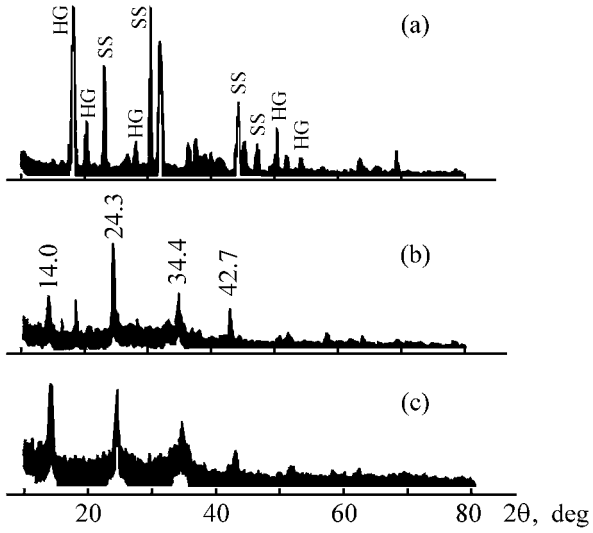

Fig. 1. X-ray diffraction patterns (Cu_{K_α} radiation) of mixtures used to synthesize NaA zeolite. (2θ) Bragg angle. HG stands for hydrargillite, and SS, for sodium silicate. Time of dispergation (min): (a) 0 and (b) 30; (c) calcined sample.

1070-4272/03/7604-0661 $25.00 © 2003 MAIK "Nauka/Interperiodica"

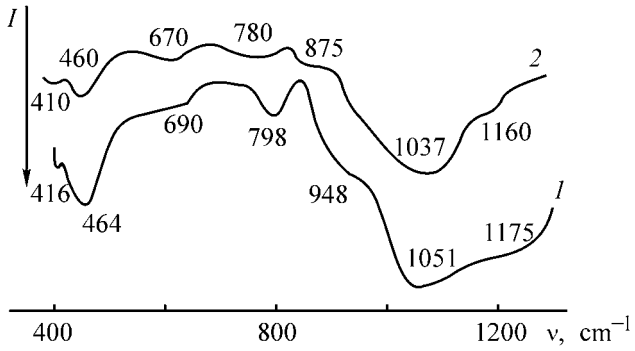

Fig. 2. IR absorption spectra of (*1*) NaA zeolite produced by mechanochemical synthesis and (*2*) commercial NaA sample. (*I*) Absorption intensity and (ν) frequency.

that the NaA zeolite is formed already in the course of mechanochemical synthesis, and calcination completes the formation of its crystal lattice.

X-ray diffraction data are confirmed by the results obtained from IR spectra. The spectrum of a sample synthesized in this study is similar to that of the commercial zeolite (Fig. 2), with only minor differences observed. For example, the bands in the spectrum of the synthesized zeolite are shifted to lower frequency, with their intensity decreasing, relative to the bands in the spectrum of the commercial sample. These differences are accounted for by the fact that the sample synthesized in this study contains a greater number of crystal structure defects. This is also confirmed by X-ray diffraction data, the diffraction peaks of the synthesized sample have relatively low intensity and large width (Fig. 1c), which is characteristic of poorly crystallized samples [4, 5].

The use of mechanochemical synthesis makes it possible to eliminate the stage of activation of zeolites to improve their reactivity [5], since their crystal structure changes already in the course of synthesis.

The presence of structural defects in the NaA zeolite synthesized in this study is also indicated by the fact that this sample is less thermally stable than commercial zeolite. The first exothermic peak (590°C) corresponds to disintegration of crystalline zeolite to the amorphous state, and the second peak at around 700°C indicates recrystallization to yield a new phase, which is of the β-crystobalite type in the given case [1]. For commercial zeolite, these temperatures are higher: 700 and 800°C, respectively.

CONCLUSION

The possibility of mechanochemical synthesis of NaA zeolite from hydrated aluminum and silicon oxides and sodium silicate is established. The sample synthesized by this method has defective crystal structure. Use of this synthesis technique eliminates formation of a liquid phase.

REFERENCES

1. Breck, D.W., *Zeolite Molecular Sieves*, New York: John Wiley & Sons, 1974.
2. Avvakumov, E.G., *Mekhanicheskie metody aktivatsii khimicheskikh protsessov* (Mechanical Methods for Activation of Chemical Processes), Novosibirsk: Nauka, 1986.
3. Il'in, A.P., Shirokov, Yu.G., and Prokof'ev, V.Yu., *Neorg. Mater.*, 1995, vol. 31, no. 7, pp. 933–936.
4. Prokof'ev, V.Yu., Il'in, A.P., and Sazanova, T.V., *Neorg. Mater.*, 2000, vol. 36, no. 9, pp. 1076–1081.
5. Sivirilova, L.I., Koval', L.M., and Vosmerikov, A.V., *Zh. Fiz. Khim.*, 1989, vol. 63, no. 11, pp. 2973–2977.

Russian Journal of Applied Chemistry, Vol. 76, No. 4, 2003, pp. 663–665. Translated from Zhurnal Prikladnoi Khimii, Vol. 76, No. 4, 2003, pp. 687–689.

BRIEF COMMUNICATIONS

Determination of the Surface Area of Minerals by Sorption of Methylene Blue and Thermal Desorption of Argon

D. E. Chirkst, I. S. Krasotkin, O. V. Cheremisina, M. I. Streletskaya, and M. V. Ivanov

St. Petersburg State Mining Institute (Technical University), St. Petersburg, Russia

Received May 30, 2002

Abstract—The specific surface area of a number of natural aluminosilicates was determined by the methods of thermal desorption of argon and limiting sorption of Methylene Blue. The correlation between the results obtained using these two techniques was discussed.

In view of the undertaken studies of the sorption properties of mineral components of soils, the specific surface area and exchange capacity of a number of minerals were analyzed. It was necessary to consider the correlation between the results obtained in determining the specific surface area by the commonly accepted methods of thermal desorption of argon [1–3] and limiting sorption of Methylene Blue (MB) [4]. Natural aluminosilicates commonly occurring in northwestern Russia: kaolinite $Al_4(OH)_8[Si_4O_{10}]$, Cambrian blue clay $K_2Al_4[Al_2Si_6O_{20}](OH,F)_4$, albite $Na[AlSi_3O_8]$, oligoclase $(Na_{0.9}Ca_{0.1})[Al_{1.1}Si_{2.9}O_8]$, and microcline $K[AlSi_3O_8]$, were chosen for the study.

Mineral samples were ground and sieved into fractions with different particle sizes. The specific surface area of the minerals was determined by gas chromatography by the method of thermal desorption of argon [1–3] and from MB sorption from solution [4]. According to the latter technique, a 0.5–2-g portion of air-dried mineral powder passed through a sieve with 0.1–0.4-mm mesh was placed in a 100-cm^3 conical vessel. A 20–50-ml portion of a 10^{-2}–10^{-3} N solution of MB was introduced with a pipette. Then the contents of the vessel were shaken and the resulting suspension was allowed to stay for 12–14 h.

The dyed suspension was twice filtered through "blue ribbon" filter. First portions of the filtrate (~10 ml) were discarded because of the sorption of MB on the filter. Pipette was used to take 1-ml samples of the filtrate and the initial MB solution. The aliquots were diluted with water to 100 ml. An SF-46 spectrophotometer was used to measure the optical density of an MB solution under study and of the initial MB solution at a wavelength of 665 nm. The MB concentration in the filtrate was calculated using the formula

$$c_f = c_{in}(D_f/D_{in}).$$

The exchange capacity E was calculated (with accuracy of 0.1 mg-equiv kg^{-1}) by the formula

$$E = \frac{\Delta cV \times 10^3}{m}, \quad (1)$$

where Δc is the difference of the concentrations of the initial MB solution and that under study (equiv l^{-1}), V is the amount of the initial solution (cm^3), and m is the mass of a mineral sample (g).

The exchange capacity of the minerals studied was used to calculate the specific surface area. The landing area of a single MB cation is 95.6 $Å^2$ according to X-ray diffraction analysis [4]. If it is assumed that the limiting sorbed amount of MB corresponds to a monomolecular layer of the dye on faces of layered minerals, then the specific surface of these minerals, S_{sp} ($m^2 g^{-1}$) can be calculated using the formula

$$S_{sp} = 10^{-6} E N_A W_0, \quad (2)$$

where E is the exchange capacity of a mineral for MB (mg-equiv kg^{-1}), N_A is the Avogadro number, and W_0 is the area occupied by an MB cation.

The results of determinations are listed in the table. As determination error is given the reproducibility of the values obtained.

The measurement results suggest the following. With the average particle diameter decreasing by

1070-4272/03/7604-0663 $25.00 © 2003 MAIK "Nauka/Interperiodica"

Specific surface area S_{sp} and exchange capacity E of minerals

Mineral	Grain size, mm	E, mg-equiv kg^{-1}	S_{sp}, $m^2\ g^{-1}$	
			from argon desorption	from MB adsorption
Kaolinite	–0.04	9.1 ± 0.2	1.80 ± 0.05	5.2 ± 0.1
	–0.4 ± 0.16	–	0.97 ± 0.03	–
Cambrian blue clay	–0.16	10.3 ± 0.1	–	5.86 ± 0.06
Oligoclase	–0.04	–	0.80 ± 0.05	–
	0.4 ± 0.16	0.14 ± 0.02	0.17 ± 0.01	0.08 ± 0.01
Albite	–0.04	–	0.67 ± 0.01	–
	0.4 ± 0.16	0.22 ± 0.02	0.20 ± 0.01	0.13 ± 0.01
Microcline	–0.04	–	0.67 ± 0.01	–
	0.4 ± 0.16	0.36 ± 0.02	0.21 ± 0.01	0.21 ± 0.01

an order of magnitude (from –0.4-mm to –0.04-mm fraction), the specific surface area increases by a factor of 2–4. In this case, the least pronounced rise in the surface area (by approximately a factor of 2) is observed for kaolinite containing no cations of alkali and alkaline-earth metals. In feldspars (oligoclase, albite, and microcline), the rise in the surface area is by a factor of 3–4, being the most pronounced for oligoclase containing calcium cations in the outer sphere. The varying rise in the surface area of the minerals upon grinding can be understood in terms of the hydration energies of the outer-sphere cations. The enthalpies of hydration were calculated from the data of [5] to be (kJ mol^{-1}) –767 for K^+, –851 for Na^+, and –2455 for Ca^{2+}. The stronger the exothermic effect of hydration of cations, the more pronounced their leaching from the surface layer of the crystals into solution, which favors the development of porosity. It should be noted that kaolinite and feldspars also have different surface microprofiles. The surface microprofile is determined by cleavage microcracks in kaolinite and by step-like cleavages in spars [6].

In spars, the S_{sp} values obtained by thermal desorption of argon, as a rule, exceed those found from MB sorption (except in the case of microcline), with this difference correlated with the magnitude of the exothermic effect of hydration of outer-sphere cations in the order microcline < albite < oligoclase. Correspondingly, in albite and, especially, oligoclase, separate fragments of the surface microprofile become inaccessible to large MB molecules. The landing areas for argon and MB are, respectively, 15.7 [7] and 95.6 $Å^2$ [4]. This can account for the difference between two S_{sp} values obtained by two independent techniques.

However, the S_{sp} value obtained for kaolinite with MB exceeds by nearly a factor of 3 that determined from thermal adsorption of argon. The reason is that the adsorption of the dye from an aqueous solution was studied after agitation of phases for many hours. As a result, kaolinite particles and clays were additionally dispersed to form a fine difficultly filterable suspension. In the given case, the S_{sp} values found from MB adsorption correspond to a finely dispersed aqueous suspension of the mineral, rather than to its sieve fraction taken for the experiment.

It may be concluded that, to evaluate the sorption capacity of minerals for metal cations, it is advisable to use the method of thermal desorption of argon, since the landing areas for argon and metal cations are close. Previously, the results obtained in studying the isotherms of sorption of Sr(II) cations on clay have been reported [8]. The limiting sorption of Sr(II) from an aqueous solution, i.e., the sorption capacity of the clay for Sr(II) cations, was found to be 68 mg-equiv kg^{-1}. The sorption of Sr(II) was studied under the conditions identical to those for MB sorption on the same clay sample. Consequently, the S_{sp} of the clay can be taken to be 5.86 $m^2\ g^{-1}$ (see table). Hence the landing area for Sr(II) cations, calculated by the formula

$$S_m = \frac{S_{sp}}{\Gamma_\infty N_A},$$

where Γ_∞ is the limiting sorption (mol kg^{-1}), equal to 28.6×10^{-20} m^2. This value corresponds to a cross-section of a hydrated cation, $Sr_{aq}^{2+} = 30.0 \times 10^{-20}$ m^2, calculated from the Stokes radius of 309 pm. Thus, in studying the sorption from aqueous solutions, it is better to characterize minerals dispersed in the course of phase convection by the sorption of MB.

The capacity of the clay for strontium cations is 6.6 times that for MB. The presumable reason is that not all exchange groups are involved in sorption of large molecules of the dye. The landing area for Sr(II) cations is smaller by a factor of 3.2, with the capacity being correspondingly higher. However, to account for the observed capacity of the clay for Sr(II),

an assumption should also be made that the capacity is proportional to the cation charge, which leads, in the case in question, to an additional increase in capacity by a factor of 2. Thus, the exchange capacity of the minerals is proportional to the ratio of the charge of a cation being sorbed to its landing area, which can be calculated from the Stokes radius. In accordance with the aforesaid, the capacity of the clay for Sr(II) cations must higher by a factor of $3.2 \times 2 = 6.4$ than that for MB, with the corresponding experimental value equal to 6.6.

CONCLUSIONS

(1) It is advisable to use for determining the specific surface area of minerals the method of thermal desorption of argon. However, in studying sorption of cations from solution on minerals dispersed in convection, the surface areas obtained from the limiting sorption of Methylene Blue under the identical conditions should be used.

(2) The exchange capacity of the minerals is proportional to the ratio between the charge of a cation being sorbed and its landing area corresponding to the Stokes radius.

ACKNOWLEDGMENTS

The study was supported financially by the Program of the Ministry of Education of the Russian Federation ("Research in Higher Schooll in Priority Fields of Science and Technology"), Subprogram 207 "Ecology and Rational Use of Natural Resources," project no. 01.01.001.

REFERENCES

1. Krasotkin, I.S. and Dubrovinskii, R.L., *Obogashch. Rud*, 1970, no. 4, pp. 62–66.
2. Krasotkin, I.S. and Dubrovinskii, R.L., *Zap. Len. Gorn. Inst.*, 1973, vol. 54, no. 3, pp. 161–167.
3. *GOST* (State Standard) *23401–78, Metal Powders, Catlysts and Supports. Determination of Specific Surface Area*, Moscow: Izd. Standartov, 1978.
4. Kul'chitskii, L.I., Ishchuk, A.R., and Koloskova, V.N., *Metodicheskie rekomendatsii po opredeleniyu fiziko-khimicheskikh svoistv glinistykh gruntov* (Methodological Recommendations on Determining Physicochemical Properties of Clayey Soils), Moscow: VNII Gidrogeol. Inzh. Geol., 1979.
5. *Termicheskie konstanty veshchestv* (Technical Constants of Substances), vol. 10, Glushko, V.P., Ed., Moscow: Akad. Nauk SSSR, 1981, part 1.
6. Kelly, A. and Groves, G.W., *Crystallography and Crystal Defects*, Harlow: Longmans, 1970.
7. Gregg, S.J. and Sing, K.S.W., *Adsorption, Surface Area and Porosity*, London: Academic, 1982.
8. Chirkst, D.E., Litvinova, T.E., Cheremisina, O.V., *et al.*, *Materialy V Vserossiiskoi konferentsii "Fundamental'nye issledovaniya v tekhnicheskikh universitetakh" SPb, 8–9 iyunya 2001 g.* (Proc. V All-Union Conf. "Basic Research at Technical Universities," St. Petersburg, June 8–9, 2001), St. Petersburg: SPb Gos. Tekhn. Univ., 2001, p. 179.

Russian Journal of Applied Chemistry, Vol. 76, No. 4, 2003, pp. 666–668. Translated from Zhurnal Prikladnoi Khimii, Vol. 76, No. 4, 2003, pp. 690–692.

BRIEF COMMUNICATIONS

Use of Mother Liquor from Fluorplastic Production for Preparing Composite Coatings

S. V. Devyaterikova, S. V. Khitrin, and S. L. Fuks

Vyatka State University, Kirov, Russia

Received November 27, 2002

Abstract—The composition and properties of mother liquor from production of F4D fluoroplastic were studied. Nickel–fluoroplastic cathodic and aluminum oxide-fluoroplastic anodic composite coatings were prepared. Aluminum oxide–fluoroplastic composite coatings were obtained by thermal treatment of aluminum oxide coatings impregnated with the mother liquor.

The mother liquor (ML) from production of emulsion fluoroplastic is presently discharged into industrial wastewater. In order to improve the environmental situation, decrease the load on sewage plants, and reduce the price of the target product, we studied the possibility of utilizing mother liquors in production of composite coatings.

EXPERIMENTAL

In our experiments, we used mother liquors from production of F4D fluoroplastic. These mother liquors containing valuable components are discharged in large amounts into industrial wastewater.

The mother liquor is a suspension of polytetrafluoroethylene (PTFE) particles with density of 1.21 g cm^{-3}, viscosity of 1.034–1.069 cSt and pH 0.45–3.9. The nephelometrically determined size of polytetrafluoroethylene particles [1] is 116–124 nm. Upon neutralization of this suspension with alkali to pH 8, the fraction of the coarsest particles decreases by more than 30% and their anionic electrophoretic activity decreases. This fact shows that neutralized ML suspensions can be used for preparation of cathodic composite coatings (CCPs).

The curve of potentiometric titration of the mother liquor with aqueous alkali has four inflection points presumably corresponding to successive neutralization of perfluoropelargonic, perfluoroenanthic, and dibasic succinic acids [2].

A chromatographic-mass spectrometric analysis showed [3] that the mother liquor contains paraffins, used as a latex stabilizer in production of PTFE, and amino and fluoro derivatives, used as PTFE emulsifiers.

The surface-active properties of PTFE particles suspended in the ML were characterized by electrocapillary curves obtained with a mercury dropping electrode. Plots of the surface tension on the mercury dropping electrode in the Na_2SO_4 + ML (F4D) mixture against the polarization voltage are given in Fig. 1 [4]. These curves show that nonionic fluoroplastic particles contained in the mother liquor are specifically sorbed on mercury at both the anodic and cathodic polarization. With increasing ML content in the Na_2SO_4 (0.1 M) + ML (F4D) mixture, the electrocapillary maximum is not shifted. These results show

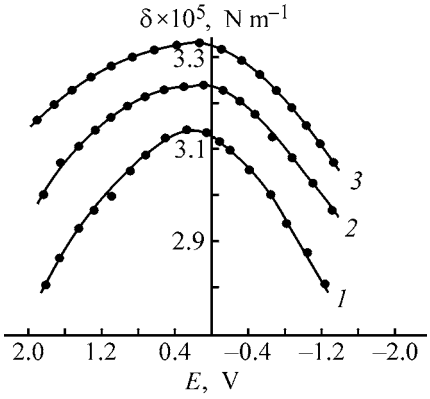

Fig. 1. Electrocapillary curves for PTFE particles in a 0.1 M Na_2SO_4 + ML (F4D) suspension. (δ) Surface tension and (*E*) voltage. ML (F4D), ml^{-1}: (*1*) 4.04, (*2*) 8.72, and (*3*) 18.52.

1070-4272/03/7604-0666 $25.00 © 2003 MAIK "Nauka/Interperiodica"

that PTFE particles can be sorbed on both positively and negatively charged surfaces.

To elucidate whether the PTFE particles can be sorbed on both anodically and cathodically polarized electrodes, we determined their electrophoretic mobility and the electrokinetic potential ξ. Figure 2 shows that PTFE particles have positive ξ potential and its value is somewhat larger at anodic polarization than at cathodic polarization. This means that the anionic contribution to the electrophoretic activity of the PTFE particles predominates. This may be due to the fact that PTFE macromolecules, owing to their helical conformation, form a cylindrical structure with an external shell containing electronegative fluorine atoms. Owing to high electrophoretic mobility of the PTFE particles, their electrodeposition must be rather fast. Thus, the mother liquors can be used for preparation of anodic composite coatings.

In order to obtain cathodic composite coatings, the negatively charged PTFE particles should be recharged to impart to them a fractional positive charge. Such recharging was performed by introducing a surfactant (SURF) [ammonium perfluoroenanthate (4 g l^{-1})] into the MLF4D) suspension [5].

Figure 2 shows that the negative ξ-potential and the corresponding electrophoretic mobility are at a maximum within the first 10 min of electromigration. In further electromigration, these parameters gradually decrease, and, after 1 h, the electrophoretic mobility decreases by a factor of 4 as compared with its maximal value. Therefore, the optimal time for preparation of the cathodic composite coatings is 15–20 min. Upon longer exposure, the initially formed composite coating is covered with a metallic film.

In the first experiments, composite cathodic coatings were obtained on a 08 kp nickel-plated steel electrode with surface area of 1 dm^2. The nickel-plating was carried out from a standard nickel-plating electrolyte-PTFE suspension. In these experiments, semilustrous and dull light gray coatings uniformly incrusted with fluoroplastic particles were obtained. We found that, irrespective of the nature and concentration of surfactant and the PTFE content, the current efficiency by nickel, evaluated by the method reported in [6], first reaches a maximum (70–99%) within the current density range 2–3 A dm^{-2} and then decreases.

The amount of PTFE incorporated into a composite coating grows with increasing PTFE content in the suspension and exhibits a complicated dependence on the surfactant concentration [5].

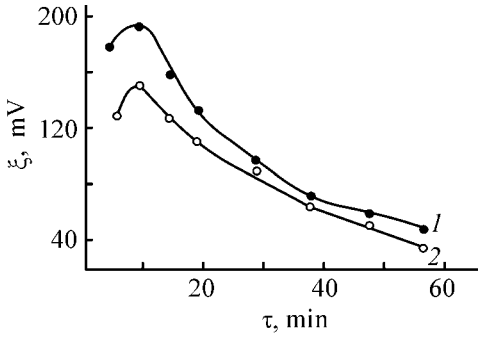

Fig. 2. ξ-potential of ML (F4D) suspension (1 : 300) vs. the electrophoresis time τ at E = 95 V.

In further experiments, the cathodic nickel-plating was performed from a standard nickel-plating electrolyte modified by adding a mother liquor containing PTFE particles with sorbed surfactant molecules. The optimal current densities were determined in a Hull cell on the basis of such coating characteristics as luster, peeling, and presence of uncoated areas.

Composite nickel–PTFE coatings were prepared in a Moler cell at current density of 0.5–7.7 A dm^{-2} and plating time of 20 min from various nickel-plating solutions whose compositions are listed in the table.

With electrolyte no.1, the current efficiency increases from 55.8 to 97.8% within the current density range 0.5–2 A dm^{-2} and gradually decreases to 90.5% at higher current densities. With nickel electrolyte no. 2 and no. 1 + ML (10 vol %) and no. 2 + ML (10 vol %), the current efficiency is lower than that with electrolyte no. 1 by 14.6–36.4%, and a sharp decrease in the current efficiency occurs already at a current density of 4 A dm^{-2}.

With electrolyte no. 3, the current efficiency is 98.5–99.0 within the current density range 1–6 A dm^{-2}. Introduction of ML (100 ml l^{-1}) into this electrolyte expands the current density range in which the highest current efficiency (79.4%) is observed to higher cur-

Compositions of nickel-plating electrolytes

Electrolyte component	Component concentration, g l^{-1}		
	no. 1	no. 2	no. 3
$NiCl_2 \cdot 6H_2O$	–	50	250
$NiSO_4 \cdot 7H_2O$	200	300	–
H_3BO_3	30	30	30
NH_4Cl	–	–	50
$C_6H_4–SO_2–CO–NH$	1	1	1

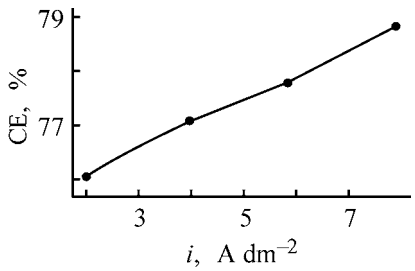

Fig. 3. Nickel + PTFE current efficiency CE vs. current density *i* in plating composite Ni–PTFE coatings from electrolyte no. 5 + 100 ml l^{-1} ML (F4D) at pH 2.8.

rent densities. As in the above experiments, the coatings formed under these conditions have uniform light gray semilustrous surface.

Figure 3 shows that, on addition of ML to nickel electrolyte no. 3 in amount of 100 ml l^{-1}, the current efficiency grows from 76.1 to 78.9% with the current density increasing from 2 to 7.7 A dm^{-2}.

The sign and value of the stretching stress in the composite coatings were determined [7]. We found that the internal stress in the coatings obtained from the nickel electrolyte is compressive and grows on adding ML. Therefore, crack formation in these coatings is unlikely.

The mother liquor was also added to electrolyte in aluminum anodic oxidation to obtain an aluminum oxide film on the surface of metallic aluminum. Anodic oxidation was performed in concentrated ML containing citric and oxalic acids. Within the current density range 10–50 A dm^{-2}, uniform gray coatings including visible incorporated PTFE particles were obtained on the surface of AD 32 aluminum.

Composite coatings with similar characteristics were obtained by thermal treatment of an aluminum oxide coating preliminarily impregnated with the mother liquor. In these experiments, uniform gray coatings with PTFE particles incorporated into aluminum oxide pores were obtained.

CONCLUSIONS

(1) The composition and properties of the mother liquor from F4D fluoroplastic production were studied; it was found that polytetrafluoroethylene particles contained in the mother liquor are adsorbed under both anodic and cathodic polarization.

(2) Polytetrafluoroethylene particles exhibit high electrophoretic mobility.

(3) Cathodic nickel–polytetrafluoroethylene coatings were obtained after recharging the surface of initial polytetrafluoroethylene particles with a surfactant. Aluminum oxide–polytetrafluoroethylene coatings were obtained on the surface of metallic aluminum both by anodic oxidation of aluminum in the mother liquor without recharging of polytetrafluoroethylene particles and by thermal treatment of the aluminum oxide coatings preliminarily impregnated with the mother liquor.

REFERENCES

l. Grigorov. O.N., *Rukovodstvo k prakticheskim rabotam po kolloidnoi khimii* (Manual on Colloidal Chemistry), Moscow: Khimiya, 1964, 2nd ed.

2. *Khimicheskaya entsiklopediya* (Chemical Encyclopedia), Knunyants, I.L., Ed., Moscow: Bol'shaya Rossiiskaya Entsiklopediya, 1992, vol. 5.

3. Khitrin, S.V., Fuks, S.L., and Devyaterikova, S.V., *Zh. Prikl. Khim.*, 2002, vol. 75, no. 1, pp. 63–66.

4. *Techniques of Electrochemistry*, Yeager, E. and Salkind, A.J., Eds., New York, vol. 1997, vol. 1.

5. Fuks, S.L., *Optimizatsiya uslovii osazhdeniya KEP nikel'–ftoroplast* (Optimization of Conditions for Plating of Composite Nickel–Fluoroplastic Coatings) Available from VINITI, August 22, 1995, no. 2481-V95.

6. Antropov, L.I., *Teoreticheskaya elektrokhimiya* (Theoretical Electrochemistry), Moscow: Vysshaya Shkola, 1984.

7. Schmeling, E., *Metalloberflache*, 1985, vol. 39, no. 4, pp. 131–134.

Russian Journal of Applied Chemistry, Vol. 76, No. 4, 2003, pp. 669–670. Translated from Zhurnal Prikladnoi Khimii, Vol. 76, No. 4, 2003, pp. 693–694.

ANNIVERSARIES

Boris Veniaminovich Gidaspov (To 70th Anniversary of His Birthday)

On April 16, 2003, Boris Veniaminovich Gidaspov, a corresponding member of the Russian Academy of Sciences and an outstanding scientist in the field of chemistry and technology of nitrogen-containing organic compounds, will be 70.

In 1955, B.V. Gidaspov graduated from Kuibyshev Industrial Institute and was left there as an assistant at the chair of explosives.

In 1954, he developed, when being a 5th-year student, an original technology for obtaining trinitrobenzene (industrial manufacture started in 1970), and later, in 1956, a technology for production of sodium azide from hydrazine.

In 1959, Gidaspov became a postgraduate student at Lensovet Technological Institute in Leningrad and, having successfully backed hid dissertation, worked at this institute from 1961 till 1977 to make a career from junior research worker to head of chair, dean of the special department of chemical engineering, and chief designer of Tekhnolog Special Designing Office. Gidaspov's outstanding organizational talent, initiative, and persistence favored the intensive development of research carried out by the Special Designing Office in the field of new technology.

The basic principle constituting the foundation of Tekhnolog Special Designing Office is the opportunity, for creative groups, to work freely beyond the limits of the administrative-command system, and, therefore, the Designing Office conforms to all requirements of the market economy and successfully operates at the present time.

Gidaspov is a leading scientist in the field of energy-intensive compounds.

He has carried out extensive studies aimed at developing new methods for synthesis of nitro- and polynitrocompounds of the aliphatic, aromatic, and heterocyclic series and polynitrous compounds of the aliphatic and heterocyclic series, and analyzed their structure, physicochemical properties, and reactivity.

He has established the mechanism of highly important chemical reactions of nitroaminoalkylation, transaminomethylation, N-nitration, and alkylation of triazoles and tetrazoles.

Foundations of a quantitative theory have been developed for these and some other reactions, and a general approach allowing prognostication of the chemical structure of reaction products and also rates and constants of equilibrium of reversible processes in relation to the properties of the starting reagents and characteristics of the reaction medium.

Based on the results of these studies, groups of researchers, headed by Gidaspov, developed technologies and created several large-tonnage continuous highly automated plants satisfying the needs of the country for special-purpose chemical materials.

For his participation in the development of a new class of organic compounds and an industrial technology for their manufacture, Gidaspov was awarded the 1976 Lenin Prize in science and technology.

From March 1977 till August 1989, Gidaspov was general director of the Gosudarstvennyi institut prikladnoi khimii (State Institute of Applied Chemistry) research-and-production association (NPO GIPKh).

1070-4272/03/7604-0669 $25.00 © 2003 MAIK "Nauka/Interperiodica"

NPO GIPKh has developed under Gidaspov's supervision new homogeneous fuels for promising power stations, energy-intensive hydrocarbon fuels, and oxidizing agents ensuring the development of new technology exceeding in basic parameters the world's best level. High-output-capacity processes for their manufacture and exploitation have been developed and put into industrial practice. For these works, Gidaspov was awarded a 1981 State Prize of the USSR in science and technology.

From 1977 till 1989, Gidaspov was the scientific supervisor of most important fields of technical chemistry in the national economy and special-purpose technology.

In 1988–1989, Gidaspov was the chairman of the board of directors of the Tekhnokhim Interbranch association, a versatile research-and-production organization comprising plants and research institutes of Leningrad and other cities of northwestern Russia, which was the first country's organizational structure that existed beyond the limits of industrial ministries and integrated plants from various industries (machinebuilding, instrument-building, petrochemical, fertilizer-producing, etc.) to solve the problem of chemicalization of the region.

From 1989 till 1991, Gidaspov was the first secretary of the Leningrad committee of the communist party of the USSR, secretary of the Central committee of this party, chairman of the Council for economical cooperation of provinces belonging to the Northwestern Region; he became the chairman of the board of directors of Aviatsionnoe vooruzhenie (Airforce Armaments) corporation in 1996, president of Interkhimprom financial-and-industrial group in 1998, and chairman of the Coordination council of Azot AKhK (Nitrogen-Chemical Combine) in 2001.

Gidaspov, a corresponding member of the Russian Academy of Sciences, developed new forms and methods for supervision and control of leading research institutes and plants of chemical industry. In the fundamentally changed conditions of management, he organized the reforming of the scientific and technological institutions of the country in order to preserve the scientific potential for development of chemical industry.

As the chairman of the board of directors of Aviatsionnoe vooruzhenie corporation he implements innovative technologies of new materials and components to develop new types of warfare.

Gidaspov made a major contribution to the coordination of the work of plants in territorially remote regions and to the development of scientifically substantiated, efficient programs for modernization and renewal of facilities for manufacture of mineral fertilizers to satisfy the needs of Russia's agriculture and to export part of the fertilizers produced.

Gidaspov's activities in the Interkhimprom Joint-Stock Company, which are concerned with the development of chemical industry and creation of scientific and technological prerequisites for its successful operation, planning and coordination of joint research of scientific institutions, industrial plants, and designing offices, and wide cooperation with foreign companies in manufacture of chemical products, make an important contribution to strengthening of the national economy.

Gidaspov's scientific activities have resulted in more than 200 publications (including two monographs) and 250 inventor's certificates, with many of his inventions implemented in industry and design developments.

At present, Gidaspov is Editor-in-chief of *Khimicheskaya promyshlennost'* (Chemical Industry) journal, deputy Editor-in-chief of *Zhurnal organicheskoi khimii* (Russian Journal of Organic Chemistry), and member of Editorial boards of *Zhurnal obshchei khimii* (Russian Journal of General Chemistry) and *Zhurnal prikladnoi khimii* (Russian Journal of Applied Chemistry).

Gidaspov has founded a highly productive scientific school: 55 candidate and 12 doctoral dissertations have been backed under his supervision, new courses of lectures have been created, and a number of textbooks and manuals have been written.

Gidaspov was awarded Lenin Order (1983) and Order of October Revolution (1969) for successful scientific and technological, organizational, and pedagogical work; Order of Labor Red Banner for his part in eliminating the consequences of the Chernobyl disaster (1987); medals; Honored Tester of Space Technology badge (2003).

Staff members of Prikladnaya Khimiya Russian Scientific Center, St. Petersburg Publishing House Nauka of the Russian Academy of Sciences, and editorial office of Zhurnal prikladnoi khimii heartily congratulate Boris Veniaminovich Gidaspov on the jubilee and wish him sound health and further creative success.

Staff members of Prikladnaya Khimiya
Russian Scientific Center
St. Petersburg Publishing House Nauka
Editorial board and editorial office of
Zhurnal prikladnoi khimii

Russian Journal of Applied Chemistry, Vol. 76, No. 4, 2003, pp. 671–673. Translated from Zhurnal Prikladnoi Khimii, Vol. 76, No. 4, 2003, pp. 695–697.

Justus von Liebig (To 200th Anniversary of His Birthday)

German scientist Justus von Liebig is among the most outstanding chemists of the XIX century. He made a major contribution to the development of organic, analytic, agronomic, and physiological chemistry and created an extensive international scientific school. At different times, such known Russian chemists as A.A. Voskresenskii (1809–1880), N.N. Zinin (1812–1880), A.I. Khodnev (1818–1883), P.A. Il'enkov (1821–1877), N.N. Sokolov (1826–1877), and F.F. Bel'shtein (1838–1906) worked at Liebig's laboratory in Gissen. Already in 1830, Liebig was elected a foreign corresponding member of the St. Petersburg Academy of Sciences.

Justus Liebig was born on May 12, 1803, in Darmstadt (Duchy of Gessen). His father manufactured and sold paints and chemical preparations. Already at early age, the youth became interested in chemistry, carried out experiments at home laboratory, gained necessary experimental skills, and read all the available chemical literature. At the age of 15, Liebig left gymnasium and worked as apprentice pharmacist in 1818. In 1819, Liebig entered Bonn University and came there under strong influence of professor of chemistry, Karl Kastner (1783–1857). Following Kastner, Liebig moved to the University of Erlangen in 1821. In 1822, he published his first scientific study concerned with the action of alkalis on fulminating silver. In October 1822, a stipend granted by the government of the Duchy of Gessen enabled Liebig to continue his education in Paris, where, in contrast to Germany, natural sciences flourished at that time. Liebig worked at laboratories and attended lectures delivered by L.J. Thenard (1777–1857) and L.J. Gay-Lussac (1778–1850), prominent French chemists members of the Paris Academy of Sciences, and honorary foreign members of the St. Petersburg Academy of Sciences (since 1826). Liebig made friends with P.L. Dulong (1785–1838), a known French chemist and physicist. Particular mention should be made of the support and help provided to the young scientist by Alexander Humboldt (1769–1858), an outstanding German natural scientist, traveler, and public figure.

In 1823, in Paris, Liebig continued, together with Gay-Lussac, an experimental study of fulminates,

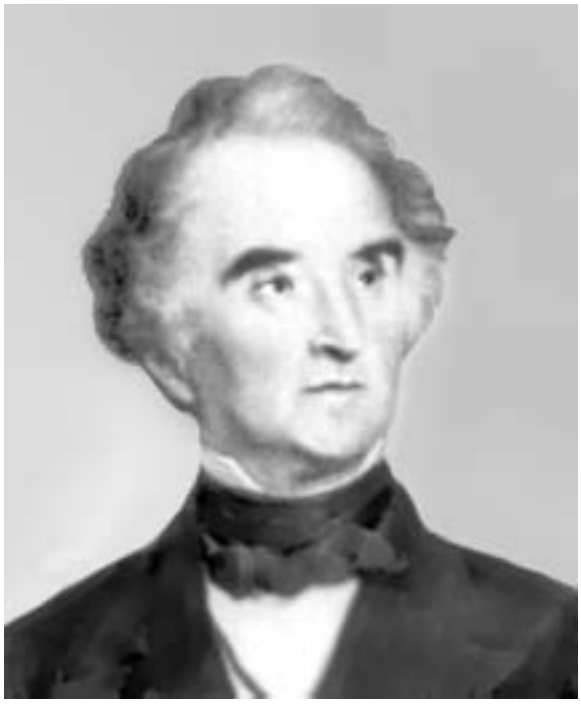

started in Bonn. A comparison of the results of this study with the data obtained by another young German chemist, Friedrich Wöhler (1800–1882), demonstrated that the scientists observed for the first time the phenomenon later named isomerism. The friendship of Liebig and Wöhler, these two prominent German chemists, continued for 45 years, till the end of Liebig's life. In 1823, the University of Erlangen conferred to Liebig, by correspondence, the degree of a doctor of philosophy for his theoretical work "On the Relationship between Mineral Chemistry and Vegetation Chemistry." In May 1824, by Humboldt's recommendation, Liebig was appointed an extraordinary professor of Gissen University. Soon, a vacancy appeared at the university and he became an ordinary professor (1826). In addition to Wöhler, Liebig was on intimate terms with another known German chemist, Karl Mohr (1806–1879).

In a short time, Liebig managed to equip a chemical laboratory at Gissen University and introduced into the curriculum laboratory works by students. The exceptional talent and diligence of the young scientist, and pupils' help allowed Liebig to perform a large

1070-4272/03/7604-0671 $25.00 © 2003 MAIK "Nauka/Interperiodica"

number of various investigations in a short time. Already by the 1830s, the small town of Gissen became one the most prominent international centers of chemical education and research. In contrast to France, where most of scientists were concentrated in Paris at that time, there was no centralization of this kind in Germany.

The main direction of the scientist's research during the first period of his activities concerned the elemental analysis of organic compounds. The methods developed by him allowed whole sets of analyses to be made during a rather short time. These methods were described in a book published by Liebig in 1831 *On a New Apparatus for Analysis of Some Organic Substances*. A Russian translation of the second German edition of this book (1853) was published in Germany under the title *Rukovodstvo k analizu organicheskikh veshchestv* (A Manual of Analysis of Organic Substances) (1858).

Experimental studies led Liebig to develop a theory of complex radicals and that of polybasic acids. When studying the composition of compounds of benzoic acid and chemical reactions involving these compounds, Liebig and Wöhler came to a conclusion (in 1832) that there exists a complex radical, named by them benzoyl. The concept of the radical was accepted by a number of leading chemists; however, there also were those opposing such an approach. In particular, the existence of complex radicals, including oxygen in addition other elements, contradicted the concept of the structure of organic acids, developed by the known Swedish scientist, Jöns Jacob Berzelius (1779–1848). Liebig became acquainted with Berzelius at a congress of natural scientists in Hamburg.

Based on a study of quite a number of organic acids, Liebig was the first to give their clear classification in basicity. The fundamentals of the theory developed by him were described in detail in his work *On the Structure of Organic Acids*, published by him in 1838. Liebig defined organic acids as compounds that contain hydrogen which can be substituted by metals. As mentioned in the monograph [1], Liebig's theory of polybasic organic acids was highly appreciated in all fundamental works on history of chemistry.

Beginning in 1839, the central place in Liebig's works was occupied by problems of feeding of plants and animals. In 1840, he completed his book *Chemistry as Applied to Agriculture and Physiology*. The book aroused strong interest and was repeatedly republished, with already its ninth edition published by 1876. This Liebig's book was published in Russia in full in the Klassiki estestvoznaniya (Classics of Natural Science) series [2]. Based on numerous analyses of plants and soils, the scientist came to a conclusion that growing plants extract mineral substances from soil, and these substances are not returned into the fields. This was, in Liebig's opinion, the reason for falling productivity. Liebig's contribution to foundations of agricultural science is of great importance. The use of artificial fertilizers in agriculture in accordance with Liebig's concepts of plant feeding made it possible not only to preserve, but also to improve the fertility of soil. Beginning in 1847, Germany did not suffer for decades any significant crop failure. Liebig's theory of rational agriculture and development of plants for manufacture of artificial fertilizers brought excellent results. In 1844 and 1845, Liebig visited Britain to organize manufacture of fertilizers recommended by him.

Of particular interest are Liebig's articles on the state of agriculture, published in Russian in 1861 [3].

In parallel, the scientist carried out studies in the field of biological chemistry. Liebig considered very important the problem of providing the mankind with food. The transition from studies of plant feeding to investigations of how animals and humans feed seems to be logical. Among the first Liebig's works in the field of biochemistry belongs *A Study of the Nature of Uric Acid*, carried out together with Wöhler (1838). In this and following studies, precise chemical investigation techniques were used. In 1842, in Germany and then in Britain, a fundamental work of the scientist was published, namely, *Organic Chemistry as Applied to Physiology and Pathology*. This study was analyzed in detail in the monograph [1].

The scientific merits of Liebig are rather diverse and great. The scientist was invited more than once to head a chair or a laboratory of universities in Germany and in other countries, including Russia. Only in 1852, Liebig considered his 28-year services to Gissen University complete and accepted an invitation to get a chair at the University of Munich, the capital of Bavaria, having made a provision that his pedagogic activities are to be limited. Nevertheless, he delivered public lectures on various parts of chemistry for all comers.

A prominent place in Liebig's scientific-organizational activities was occupied by publication of a journal, which was named *Annalen der Pharmacie* originally (beginning in 1832), *Annalen der Chemie und Pharmacie* in 1840–1873, and *Liebigs Annalen der Chemie* in memory of Liebig since 1873. The journal published papers by leading chemists of Germany, France, Britain, Russia, and other countries. The scientific authority of the journal was very high.

In 1855, Liebig was elected a member of the Berlin Academy of Sciences; in 1860, he became president of the Bavarian Academy of Sciences. In subsequent years, he was elected an honorary member or foreign corresponding member of most of the academies and scientific societies of the world, awarded various kinds of orders, and two Russian orders among these. Justus von Liebig passed away on April 18, 1873, shortly before his 70th birthday. The International committee for immortalizing the memory of the scientist included leading scientists from many countries all over the world. Russian scientists, academician Zinin and professor Beil'shtein (academician since 1886), were among these. Monuments to Liebig were erected in the tree cities in which he had lived: Darmstadt (1887), Gissen (1890), and Munich (1883). By Humboldt's words "scientific interests were above any other human interests" for Liebig.

A vast literature is devoted to the life and activities of the outstanding German scientist. Much was done by the known historian of chemistry Yu.S. Musabekov (1910–1970), professor of the Yaroslavl Technological Institute. He wrote a popular-science biography of Liebig and described in detail the life and scientific, pedagogical, and public activities of the scientist [1]. The book also presents a list of Liebig's works in chronological order, and also a list of publications about Liebig. In separate publications, Musabekov considered methodological problems in the creative work of Liebig as a chemist-thinker and philosopher [4] and scientific relationships between Russian scientists and Liebig [5].

A major contribution to making the Russian audience familiar with Liebig's works was made by Il'enkov, a known chemist-technologist and agricultural chemist, professor of Peter the Great Academy of Agriculture and Forestry in Moscow. After graduating from St. Petersburg University in 1843, Il'enkov improved his education in universities of Germany and France for about two years and worked with Liebig. Il'enkov not only popularized Liebig's ideas, but also developed them on his own. To the importance of Liebig's works for agriculture was devoted Il'enkov's report at the Annual meeting of Moscow Society for Agriculture in April 1874 [6].

The evidence concerning Liebig's life and activities can be found in books by Sharvin [7], Krasnogorov [8], article by Debu [9], etc. [10–12]. Spacious articles about Liebig can be found in known foreign reference books [13, 14].

REFERENCES

1. Musabekov, Yu.S., *Yustus Libikh* (Justus Liebig), Moscow: Akad. Nauk SSSR, 1962.
2. Liebig, Ju. Von, *Die organische Chemie in ihrer Anwendung auf Agrikulturchemie und Physiologie*, 1840.
3. *Pis'ma Libikha o nyneshnem sostoyanii sel'skogo khozyaistva* (Liebig's Letters about the Present State of Agriculture), Sovetov, A., Ed., St. Petersburg: Izd. Tovarishch. Obshch. Pol'za, 1861.
4. Musabekov, Yu.S., *Uchen. zap. Yarosl. Tekhnol. In–ta: Khim. Khim. Tekhnol.*, 1971, vol. 27, pp. 3–10.
5. Musabekov, Yu.S., *Uchen. zap. Yarosl. Tekhnol. In–ta: Khim. Khim. Tekhnol.*, 1959, vol. 3, pp. 319–342.
6. Il'enkov, P.A., *Libikh i ego znachenie dlya sel'skogo khozyaistva* (Liebig and His Importance for Agriculture), Moscow, 1874.
7. Sharvin, V.V., *Yustus Libikh* (Justus Liebig), Moscow: Gosizdat, 1925.
8. Krasnogorov, V., *Libikh* (Liebig), Moscow: Znanie, 1980.
9. Debu, K.I., *Chelovek Priroda*, 1923, no. 12, pp. 1–8.
10. Blokh, M.A., *Biograficheskii spravochnik: Vydayushchiesya khimiki i uchenye XIX i XX stoletii, rabotavshie v smezhnykh s khimiei oblastyakh nauki* (Biographic Reference Book: Outstanding Chemists and Scientists of the XIX and XX Centuries, Who Worked in Fields of Science Adjacent to Chemistry), vol. 1, Leningrad: Nauch. Khim.-Tekhn. Izd., 1929.
11. Usanovich, M.M., *Tvortsy khimii. Vydayushchiesya khimiki vsekh vekov i narodov* (Creators of Chemistry: Outstanding Chemists of All Centuries and Countries), Leningrad: Krasn. Gazeta, 1930.
12. Tuchs, G., Heinig, K., Kertscher, G. *et al.*, *Biographien bedeutender Chemiker*, Berlin: Volk und Wissen Volkseigener, 1977.
13. J.C.Poggendorff's *biographisch-literarisches Handworterbuch der exakten Naturwissenschaften*, 1971, vol. VIIa, Supplement, pp. 375–389.
14. Holmes, F.L., *Dictionary of Scientific Biography*, vol. 7, Gillespil, Ch.C., Ed., New York: Charles Scrilners & Sons, 1981, pp. 329–350.

A. G. Morachevskii

Russian Journal of Applied Chemistry, Vol. 76, No. 4, 2003, p. 674. Translated from Zhurnal Prikladnoi Khimii, Vol. 76, No. 4, 2003, p. 698.

Paderin, S.N. and Filippov, V.V., *Teoriya i raschety metallurgicheskikh sistem i protsessov* (Theory and Calculation of Metallurgical Systems and Processes), Moscow: Mosk. Inst. Stali i Splavov, 2002, 334 pp.

The book is devoted to a topical problem and is recommended by the educational-methodological association for education in metallurgy as a textbook for students of higher school institutions training bachelors and engineers specialized in metallurgy. This purpose of the book, aimed at a wide audience of specialists in metallurgy, imposes special requirements on its structure, content, manner of presentation, graphical illustrations, and choice of examples for calculations.

The textbook comprises a foreword, nine chapters, and list of recommended literature. The very brief foreword (pp. 7, 8) describes the level of cast iron and steel production and modern tendencies in the development of ferrous metallurgy. The first chapter (pp. 9–30) is devoted to the state and nearest prospects for the development of ferrous metallurgy in the world. Unfortunately, virtually no attention is given to the industry of Russia, its state and prospects.

The second chapter (pp. 31–54) contains general evidence about thermodynamic description of metallic solutions. The third chapter (pp. 55–77) considers very briefly some thermodynamic models, which are mainly based on complicated versions of the consept of regular solutions. The fourth chapter (pp. 78–114) is devoted to specific features of the thermodynamic behavior of dilute solutions. The problems associated with the choice of the standard state and the interaction parameters are discussed in detail. The objects of thermodynamic analysis in the fifth chapter (pp. 115–209) are metallurgical slags, mattes, and fluxes. The small sixth chapter (pp. 210–233) contains evidence about the solubility of oxygen in liquid iron, oxidative refining of the liquid metal, and thermodynamics of steel deoxidation. The seventh chapter (pp. 234–293) considers in detail the use of solid electrolytes with anionic conduction for determining the activity of oxygen in liquid iron and steels and discusses the electrochemical properties of solid electrolytes and the limits of electrochemical stability of transducers. The eighth chapter (pp. 294–316) analyzes the problem of steel decarbonization with gaseous oxygen, considers kinetic features of the process, and presents results of pilot meltings under industrial conditions. The ninth chapter (pp. 317–329) contains evidence about oxidation processes accompanying the decarbonization of steels. The bibliographic list gives the recommended literature for each chapter of the book separately. Unfortunately, the absence of titles of journal articles impairs its information value, the more so as no references are given in the text.

Each chapter, including the first one, which drops out of the general structure of the textbook, pays much attention to problems, some of which are worked and others are intended for independent solution. On the whole, both kinds of problems and control questions account for about 30% of the book's volume.

Analysis of the textbook by S.N. Paderin and V.V. Filippov shows that, in describing the concentration and temperature dependences of thermodynamic functions in metallic and slag melts, the authors obviously prefer "complicated" versions of the regular solution model, using such not quite clear terms as "pseudoregular" and "subregular" solutions. The terminology of this kind and the associated mathematical apparatus were first applied to metallurgical systems more than 40 years ago in publications of mostly domestic authors and are used now only by few researchers. It is hardly advisable to use models of this kind in a textbook intended for introduction of students into the thermodynamics of variable-composition phases for the example of metallurgical systems. Unfortunately, the presentation of the basic thermodynamic relationships is impaired by a number of annoying errors.

In our opinion, the book can be used in training of engineers and masters specializing in ferrous metallurgy, but there is no sufficient reason to recommend it for bachelors specializing in metallurgy or engineers of wide metallurgical profile.

A. G. Morachevskii

1070-4272/03/7604-0674 $25.00 © 2003 MAIK "Nauka/Interperiodica"

Russian Journal of Applied Chemistry, Vol. 76, No. 4, 2003, pp. 675–676. Translated from Zhurnal Prikladnoi Khimii, Vol. 76, No. 4, 2003, pp. 699–700.

BOOK REVIEWS

Denisov, V.M., Istomin, S.A., Podkopaev, O.I., Belousova, N.V., Pastukhov, E.A., Serebryakova, L.I., and Kvasova, T.O., *Germanii, ego soedineniya i splavy* (Germanium, Its Compounds and Alloys), Yekaterinburg: Ur. Otd. Ross. Akad. Nauk, 2002, 600 pp.

A group of authors from the Institute of Metallurgy, Ural Division, Russian Academy of Sciences, wrote a capital monograph devoted to analysis of experimental data on compounds and alloys of germanium, their structure and physicochemical properties. Much attention is given to the liquid state. The electrical properties of germanium-based materials are discussed.

The book comprises an introduction, ten chapters, and a bibliographic list. The very brief introduction (p. 7) notes the role of germanium and its compounds in modern technology. The first chapter (pp. 8–42) contains evidence about physical properties of germanium in solid and liquid states. Specific features of the liquid state are considered in detail with account of the fact that transition from covalent to metallic bonding occurs in melting of germanium. Special mention is made of the results obtained in studying liquid germanium by diffraction techniques.

The second chapter (pp. 43–123) is devoted to interaction of germanium with Group-I elements. Alloys with alkali metals are described very briefly, the main attention is given to interaction of germanium with copper, silver, and gold. The third chapter (pp.124–164) contains evidence about alloys of germanium with Group-II elements. Alloys of magnesium not only with germanium, but also, for comparison, with other Group-IV elements: silicon, tin, and lead, are considered in detail. Their electrical conductivity and magnetic properties in liquid and solid states, thermodynamic properties of liquid phases and methods for their assessment and description in terms of various model concepts are discussed. Less attention is given to alloys of germanium with calcium, strontium, and barium. Evince concerning the thermodynamic properties of liquid alloys of germanium with zinc and some data on solid alloys of germanium with cadmium or mercury are given.

The fourth chapter (pp. 165–247) includes a vast body of data on interaction of germanium with scandium, lanthanoids, and boron-subgroup elements. Having mentioned investigations of V.N. Eremenko and co-workers into phase diagrams of germanium alloys with rare-earth metals, the authors pay no attention to the concluding publication of this group, the book by Yu.I. Buyanov *et al*. *Fazovye ravnovesiya i termodinamika obrazovaniya faz v dvoinykh sistemakh redkozemel'nykh metallov s germaniem* (Phase Equilibria and Thermodynamics of Phase Formation in Binary Systems Formed by Rare-Earth Metals with Germanium), Kiev: Inst. Probl. Materialoved. Nats. Akad. Nauk. Ukrainy, 1998. The fifth chapter (pp. 248–304) is concerned with analysis of systems formed by germanium with Group-IV elements. There is only limited evidence about the interaction of germanium with titanium, zirconium, and hafnium and virtually no data on the system germanium–carbon. The central position in the chapter is occupied by alloys of germanium with silicon.

The sixth chapter (pp. 305–355) presents a relatively small amount of data on alloys with germanium with vanadium-subgroup metals. Most attention is given to the interaction of components in the system germanium–arsenic. The seventh chapter (pp. 356–457) contains evidence about alloys of germanium with Group-VI elements. For the chromium subgroup, the body of data on the interaction of germanium with molybdenum and tungsten is at a minimum. In most detail are discussed germanium oxides, glassy formulations with GeO_2, and various compounds and systems, including germanium dioxide. Much attention is given to the system germanium–tellurium and ternary compounds on its base.

The eighth chapter (pp. 458–471) is concerned with the interaction of germanium with Group-VII elements, manganese and halogens. Among the latter, most attention is given to bromine interacting with germanium. The ninth chapter (pp. 472–528) mainly considers alloys of germanium with iron-subgroup

1070-4272/03/7604-0675 $25.00 © 2003 MAIK "Nauka/Interperiodica"

metals. Of platinum-subgroup metals, some evidence is only given for alloys of the system germanium–palladium. The very small tenth chapter (pp. 529–530) notes that alloys of germanium with actinoids are the least studied, with phase diagrams only given for the systems germanium–thorium and germanium–uranium.

The bibliographic list (pp. 531–597) contains 1204 references to studies of predominantly domestic authors, with references to foreign investigations not exceeding 20%. The inclusion of article titles makes the list more informative.

On the whole, the book is a reference publication including various kinds of evidence concerning one or another system under consideration: phase diagram, thermodynamic characteristics and structure of predominantly liquid phases, data on electrical conductivity, magnetic susceptibility, density, surface properties, and electrical properties associated with impurity doping. In this situation, a particular attention of the authors to data sources, formulas presented, terminology, and dimension of the quantities mentioned is required. Unfortunately, this is not always the case. Let us give a characteristic example: "Heat of lithium dissolution in solid germanium, ΔH = 54.43 kJ mol^{-1}" (p. 45), with the authors referring to a low-authority publication. The phrase poses quite a number of questions. Many equations cannot be used, since the necessary dimensions of the quantities involved are not given. In a number of cases, complex equations have purely "decorative" importance, being not commented at all. The books gives in ample detail the results of thermodynamic investigations of numerous systems in liquid state, but they are not, as a rule, discussed by the authors. Not always there is the necessary unity in designations and terminology throughout the monograph.

The authors have done an extensive amount of work on collecting and systematizing a wide variety of experimental data. The monograph may be of interest for a wide audience of specialists in inorganic materials science and semiconducting materials. The book is very well printed in all respects.

A. G. Morachevskii

Russian Journal of Applied Chemistry, Vol. 76, No. 5, 2003, pp. 677–688. Translated from Zhurnal Prikladnoi Khimii, Vol. 76, No. 5, 2003, pp. 705–715.

300th ANNIVERSARY OF ST. PETERSBURG

Studying chemistry has two goals: progress of natural science and improvement of the well-being.

M. V. Lomonosov

Chemists of St. Petersburg and Development of Science and Technology in Russia

A. G. Morachevskii and V. S. Shpak

St. Petersburg was founded by Peter the Great on May 16(27), 1703, in the marshy delta of the Neva River on a small island Ennisaari (Zayachii). Having chosen this place close to an exit to open sea, for which he strove so much, Peter the Great laid there foundation of a fortress. The victory over Swedes in the Poltava battle (1709) strengthened the positions of Russia near the exit into the Baltic Sea and made it possible to begin, together with creating a defense system, the construction of the city. In 1712, St. Petersburg was finally recognized as the capital of the Russian Empire. Administrative buildings, sea-port, and shipyards were under construction. Already in 1715, the first state plant for manufacture of powder was founded near St. Petersburg, on the Okhta River. In 1720, the first chemical laboratory, in which ores were analyzed, was created at the Berg-Kollegiya (the governing body for Russia's mining and metals industry).

To the most important decisions made by Peter the Great belongs foundation on February 8, 1724, of the Academy of Sciences and Arts, and also of the university and gymnasium affiliated with the Academy. Thus, during the initial period of its existence, the Academy of Sciences (AS) was simultaneously a research and educational institution.

Chemical research in Russia was initiated by M.V. Lomonosov (1711–1765), who was elected an academician in 1745. His scientific activities were rather diverse, but his main attention was focused on the development of chemistry and physics. By the scientist's initiative, the first Russia's chemical research laboratory was created in St. Petersburg in 1748. This laboratory existed till 1793. In 1748 to 1757, Lomonosov carried out at this laboratory, nearly without any assistants, a great number of various studies. The scientist's achievements in the design of colored glasses, which served as a basis for the famous mosaics, and glasses with different refractive indices are outstanding. A glass factory was built by his design near St. Petersburg (1752). In 1752–1754, Lomonosov delivered the first world's course of lectures on physical chemistry to students of the Academy University. After Lomonosov's death, the Academy University started to die away and was abolished in 1767, having served to training of first domestic scientists.

Lomonosov made an invaluable contribution to the development of chemistry and chemical technology, which were the same science at that time. After Lomonosov, studies of Russian chemists of the second half of the XVIII century were mainly aimed to solve practical problems with relatively narrow scope. Academician I.G. Leman (1719–1767) was mainly engaged in analyses of ores and minerals, and wrote the first manual of assaying. E.G. Laksman (1737–1796) was known for the development of a new technique for manufacture of glass with the use of dehydrated sodium sulfate instead of potash. T.E. Lovits (1757–1804, academician since 1793) discovered the phenomenon of impurity adsorption from various solutions by charcoal. He also was the first to obtain glacial acetic acid, suggested a number of cooling mixtures, improved methods for chemical analysis, and was a many-sided chemist. V.M. Severgin (1765–1826) was elected an academician in mineralogy, but was also known for his studies in chemistry and technology of mineral salts and in assaying.

At the turn of the XIX century, the nature of activities of the AS changed, it ceased to execute educational functions; simultaneously increased the number of corresponding members and honorary members of the AS, who not necessarily lived in St. Petersburg. Many scientists, when elected to the AS, continued working at higher-school institutions. Thus, St. Petersburg, remaining the largest scientific center of Russia,

1070-4272/03/7605-0677$25.00

D. I. Mendeleev

took an opportunity to coordinate research in other cities of the country. This part had been played by St. Petersburg at least till the mid 1930s.

Honorary member of the AS (since 1796) A.A. Musin-Pushkin (1760–1809), vice president of the Berg-Kollegiya, carried out the first Russia's investigations in the field of chemistry and technology of platinum-group metals and suggested a method for purification of raw platinum to remove iron and iridium impurities. After the discovery of extremely rich platinum deposits in the Urals (1824–1825), the Joint laboratory of the Department of Mining and Salt Affairs, Gornyi Kadetskii Korpus (Military Mining College; later, Mining Institute), and Gornaya Apteka (Mining Repository) commenced industrial refining of platinum, which was then converted into a forgeable form. The latter procedure laid foundation of a new technology, powder metallurgy. From 1841 till 1867, platinum was refined by St. Petersburg mint. To the most important events related to studies and manufacture of platinum metals in Russia belongs the discovery of ruthenium in insoluble residues of the Ural platinum ore by C.E. Claus (1796–1864), professor of Kazan university and corresponding member of the St. Petersburg AS since 1861. Claus is one of founders of the chemistry of platinum and associated metals in Russia.

In 1808, Academician A.I. Sherer (1772–1824), professor at a number of higher-school institutions of St. Petersburg, wrote the first original textbook on chemistry in Russian, *Rukovodstvo k prepodavaniyu khimii* (Chemistry Teacher's Manual), in which the oxygen theory of H. Lavoisier (1743–1794) was popularized and much attention was given to development of the Russian chemical nomenclature. Later achievements in the field of chemistry were reflected in a textbook *Osnovaniya chistoi khimii* (Foundations of Pure Chemistry, 1831), by Academician G.H. Hess (1802–1850). The book was approved by the AS and ran through seven editions in 18 years. In the 1830s–1840s, the book served as the main textbook on chemistry and much affected the scientific concepts of the following generations of Russian chemists, among whom were N.N. Zinin (1812–1880), N.N. Beketov (1827–1911), A.M. Butlerov (1826–1886), and D.I. Mendeleev (1834–1907).

In 1831, the St. Petersburg Applied Technological Institute was opened in order to "train people who would possess theoretical and practical knowledge sufficient for managing factories or parts of these" [1]. This was the first educational institution of this kind in Russia. The training course covered three years. Hess accepted an invitation to take the position of inspector of classes (deputy director) at this institute. He composed the curricula and invited the best specialists from other civilian and military educational institutions of St. Petersburg for teaching the basic disciplines. In accordance with Hess's recommendations, a chemical laboratory was organized at the Technological Institute.

In 1832, Hess was elected professor of chemistry and technology at the Chief Pedagogical Institute, he also taught at the Military Institute of Means of Communication and Mikhail Artillery College. Particular intensive were his activities at the Mining Institute (1832–1849). He created there a chemical laboratory, introduced practical studies in chemistry for students, and paid much attention to training students in experimental work. Mainly owing to Hess's efforts, the chemical laboratory of the Mining Institute became a prominent research and pedagogical center in Russia. Such outstanding scientists as K.I. Lisenko (1836–1903), V.F. Alekseev (1852–1919), D.P. Konovalov (1856–1929), I.F. Shreder (1858–1918) and N.S. Kurnakov (1860–1941) received education and started scientific activities at this laboratory. A many-

sided scientist, one of creators of modern thermochemistry, Hess made a major contribution to training of highly skilled chemists in Russia in the first half of the XIX century.

Much was done in teaching chemistry at the University and other higher-school institutions of St. Petersburg and creating scientific schools in the field of chemistry by A.A. Voskresenkii (1809–1880, Corresponding Member of the AS since 1864). He graduated from the Chief Pedagogical Institute, where he attended Hess's lectures, in 1836. In his turn, Voskresenskii taught chemistry to Mendeleev, who entered this institute in 1850.

A prominent role was played in the development of applied electrochemistry in Russia by a St. Petersburg scientist, academician in physics, B.S. Jacobi (1801–1874). A broadly educated scientist, he made a major contribution to the development of electrical engineering and science of electromagnetic phenomena. Simultaneously, he was inventor of electroforming and did much for improvement of chemical power sources of that time. As noted by A.N. Frumkin [2], the discovery of electroforming, studies of chemical power sources, and development of techniques for measuring electrochemical parameters place Jacobi in one of the first places in the electrochemical science of the XIX century.

In the second half of the XIX century, chemistry in St. Petersburg flourished. The Academy of Sciences, St. Petersburg University, Mining Institute, Mikhail Artillery Academy, Technological Institute, and Agricultural (Forestry) Institute constituted the St. Petersburg scientific center, which exerted profound influence on the development of not only domestic, but also world science [3]. A school of chemists, characterized by one or another direction of research, formed at each of the above institutions. The scientific force accumulated in St. Petersburg constituted the basis of the scientific potential of the country. Among those who worked in St. Petersburg were Zinin, founder of the domestic school of organic chemists; Butlerov, creator of the theory of chemical structure of substances; Mendeleev, discoverer of the periodic law of chemical elements; Beketov, the first Russian physical chemist.

In the initial period of his scientific activities, Zinin worked at Kazan University. However, already in 1847, he was elected a professor at the chair of chemistry and physics of St. Petersburg Military Medical-Surgical Academy (Military Medical Academy since 1881); in 1865, he was elected ordinary academician

N. S. Kurnakov

of the St. Petersburg AS. A prominent place among Zinin's works is occupied by synthesis of primary aromatic amines (aniline, aminonaphthalene, benzidine, etc.), which are exceedingly important for synthesis of organic dyes, by reduction of nitro compounds. The reaction for synthesis of amines, which is of general character, became history as the Zinin reaction. The new method, its simplicity, and low cost of raw materials ensured manufacture of aniline in enormous quantities. Already several years after Zinin's works, a new large branch of chemical industry, manufacture of dyes, was created. In 1871, Butlerov wrote in an article "On Practical Importance of Scientific Studies in Chemistry": "Manufacture of aniline paints grew monthly, rather than yearly, and managed to occupy a prominent place in very few years. At present, this is a matter of extensive factory industry..." [3]. Zinin was among those who initiated the organization of Russian Chemical Society and was elected its first president at the organizational meeting held on December 5, 1868.

Butlerov, a graduate from Kazan University, was a professor there and became a professor of St. Peters-

St. Petersburg State Technological Institute.

burg University in 1869, and an academician in 1874. Together with creating the theory of chemical structure of organic compounds and writing a classical work "Introduction to Comprehensive Studies of Organic Chemistry" (1864–1866), Butlerov carried out a great number of experimental investigations, including synthesis of tertiary alcohols and studies of polymerization involving unsaturated compounds. The school of organic chemists founded by Butlerov and his scientific ideas exerted a profound influence on the development of organic chemistry in various cities of Russia. For example, Butlerov's disciples and followers include known chemists, founders of chemical directions of research in their own regions: V.V. Markovnikov (1837–1904), professor of Moscow University; A.M. Zaitsev (1841–1910), professor of Kazan University and corresponding member of the AS; F.M. Flavinskii (1848–1917), professor of the same university; S.N. Reformatskii (1860–1932), Professor of Kiev University, corresponding member of the AS since 1928, and founder of the Kiev school of organic chemists.

In 1869, Mendeleev discovered the periodic law of chemical elements and substantiated it experimentally and theoretically in the nearest two or three years. This greatest discovery was based on the entire body of evidence concerning the properties of elements, obtained by the middle of the XIX century, and established relationships between elements. Already in 1870, the structure of the periodic system acquired the most perfect form. The fundamental Mendeleev's work *Osnovy khimii* (Foundations of Chemistry) ran through eight editions during his life (1st in 1868–1871, 8th in 1906). The periodic law exerted profound influence on the development of research in the field of structure of substance both by physicists and by chemists. In addition to the periodic law, Mendeleev was interested during his entire scientific life in the problem of solutions. In the late 1880s, he put forward and substantiated the concept of existence of "singular points" in the curves describing the composition dependence of the solution density. In its final form, this concept was formulated by the scientist in the monograph *Issledovanie vodnykh rastvorov po udel'nomu vesu* (Study of Aqueous Solutions by Analysis of Their Density) (1887). Mendeleev's ideas in the field of variable-composition phases were further developed by two scientific schools founded in St. Petersburg by Kurnakov (physicochemical analysis) and Konovalov (thermodynamic theory of solutions). Mendeleev was engaged in pedagogical activities at St. Petersburg University (1857–1890) and, simultaneously, for several years, at the Technological Institute (1864–1872). A rather comprehensive characteristic was given to Mendeleev by L.A. Tschugaeff (1873–1922), a known chemist: "Genius chemist; first-rate physicist; fruitful researcher in the field of hydrodynamics, meteorology, geology, various branches of chemical engineering (explosives, oil, theory of fuels, etc.), and other disciplines adjacent to chemistry and physics; expert in chemical industry in general, and Russian chemical industry, in particular; original thinker in the field of domestic economy..." [4].

Mendeleev was more than once elected president of the Russian Chemical Society.

A.A. Fadeev (1810–1898), head of the chair of chemistry of Mikhail Academy, was founder of the school of chemists concerned with explosives. His disciple L.N. Shishkov (1830–1908) created there in 1860 one of the best Russia's chemical laboratories of that time. Among graduates from this educational institution were A.N. Engel'gardt (1832–1893), a professor of the St. Petersburg Agricultural Institute (1866–1870) and publisher, together with N.N. Sokolov (1826–1877), of the first Russian chemical journal (1859–1877); V.N. Ipat'ev (1867–1952, academician since 1916), one of the most outstanding chemists of the first half of the XX century.

A.A. Letnii (1848–1883), a lecture at the Technological Institute, was the first to discover decomposition of heavy oil residues at above 300°C, which served as a basis for the development of the cracking process and for production of divinyl from oil. Benzene, toluene, xylene, anthracene (1877), and butadiene (1878) were isolated by pyrolytic decomposition of Caucasus oils, and fundamental aspects of oil pyrolysis were established.

Of great importance for the development of physical chemistry, theory of solutions, and resolution of applied problems were investigations of D.P. Konovalov, a disciple and closest Mendeleev's associate and academician since 1923. As far back as 1884, he established in his classical work "On Vapor Pressure of Solutions" important relationships named Konovalov's laws. Further scientist's investigations were devoted to the development of Mendeleev's concepts of interaction between solute and solvent. In 1907–1915, Konovalov held important positions in the Russian government. To Konovalov's disciples belong, in particular, A.A. Baikov (1870–1946, academician since 1932) and M.S. Vrevskii (1871–1929, corresponding member of the AS since 1929).

In February 1899, Emperor Nicholas II approved the report by the minister of finance S.Yu. Witte on organization of the Polytechnic Institute in St. Petersburg. Mentioning the deficiency of specialists with higher technical education in a number of industries in Russia, Witte, in particular, wrote: "...with the development of those branches of industry in which chemical technology occupies the most important place, a necessity for specialization of applied science is increasingly manifested, which is exemplified by electrochemistry and metallurgy." Studies began already on October 2, 1902. The central place in the curricula of the metallurgical department, which also included

V. N. Ipat'ev

an electrochemical subdepartment, was occupied by chemical disciplines. The curricula were composed with participation of such known chemists as Mendeleev, P.I. Walden (1863–1957, academician since 1910), and D.K. Chernov (1839–1921), a prominent metallurgist. A spacious chemical building housed excellently equipped laboratories of general chemistry, analytical and organic chemistry, physical chemistry and theoretical electrochemistry, technical electrochemistry and mineral technology, mineralogy and geology, and also laboratories and cabinets of metallurgical profile [5]. As the first dean of the metallurgical department was appointed, and then elected, N.A. Menshutkin (1842–1907), a prominent scientist in the field of organic and analytical chemistry, who had been a lecturer at St. Petersburg University (1865–1901, professor since 1869). His major success was invitation to the Polytechnic Institute, for teaching the basic disciplines, of quite a number of the already well-known specialists. Later, the leading professors of the department, Baikov, F.Yu. Levinson-Lessing, V.A. Kistyakovskii, N.S. Kurnakov, and M.A. Pavlov became academicians, and V.E. Grum-

V. I. Vernadsky.

Grzhimailo and P.P. Fedot'ev, corresponding member of the AS. Among young lecturers, who later became known scientists, were S.P. Gvozdev, S.F. Zhemchuzhnyi, B.N. Menshutkin, D.N. Monastyrskii, and L.A. Rotinyants.

The opening of the Polytechnic Institute with its modern laboratories allowed training of highest-skill specialists. By Kurnakov's initiative, students of the metallurgical department were entitled, for the first time in the practice of Russia's higher-school technical institutions, to defend their experimental studies to be qualified as engineer-metallurgists. From the very first years of existence, the Polytechnic Institute became one of the best higher-school institutions of not only Russia, but also Europe.

In the early XX century, training of specialists in applied electrochemistry was commenced by the initiative of professor A.A. Krakau (1855–1909) and N.A. Pushin (1875–1947) at the St. Petersburg Electrotechnical Institute.

The chemical laboratories of the Mining, Polytechnic, and Electrotechnical institutes served as experimental base for creation by Kurnakov (academician since 1913) of the Russian school of inorganic chemists. His closest associates at these institutes were N.I. Stepanov (1879–1938, corresponding member of the AS since 1929), Zhemchuzhnyi (1873–1929), and Pushin. A great number of investigations of metallic and other systems served as a basis for formulation of general principles of physicochemical analysis (1913), a branch of general chemistry that studies by physical and geometric methods various equilibrium systems formed by two or more components. The physicochemical analysis is very important, in scientific and applied regard, for the development of chemical technology, halurgy, and metallurgy.

At the turn of the XX century, work in the field of organic chemistry were successfully developing in St. Petersburg. Of outstanding importance were investigations by representatives of Butlerov's school, A.E. Favorskii (1860–1945, academician since 1929) and V.N. Ipat'ev. Butlerov's own disciple, Favorskii (a professor of St. Petersburg University since 1896) was among those who created the chemistry of acetylene compounds, discovered and studied a great number of isomerization processes in series of unsaturated hydrocarbons, and founded his scientific school of organic chemists. V.N. Ipat'ev commenced studies of isomerization of unsaturated hydrocarbons on Favorskii's advice. In 1896–1897, when working in Munich at the laboratory of A. Bayer (1835–1917), V.N. Ipat'ev concluded studies of the isoprene structure and synthesized this monomer unit of natural caoutchouc. In autumn of 1900, the scientist started experimental studies of catalytic organic synthesis. Rather fruitful was the period of time from 1900 till 1914, which yielded original results [6, 7]. V.N. Ipat'ev was the first to apply high pressure (up to 1000 atm) and temperature (up to 700°C) in performing heterogeneous catalytic processes and to introduce into laboratory and technological practice a great number of previously unused catalysts. In 1909, the scientist made a major discovery: He demonstrated that use of mixed catalysts increases dramatically the possibilities of heterogeneous catalysis and allows directed variation of the properties of solid catalysts. V.N. Ipat'ev's studies served as a basis for a great number of industrial process, many of which are used now.

The discovery of the phenomenon of radioactivity (H. Becquerel, 1896) and radioactive elements (Pierre and Marie Curie, 1898) gave birth to a new chemical discipline, radiochemistry. Prominent Russian scientists, including V.I. Vernadsky (1863–1945, academician since 1912), a geochemist and mineralogist,

understood the importance of these discoveries. Already in 1910, the Radium committee was created in the AS. Making a report at the annual meeting of the AS in 1910, Vernadsky said: "The radioactivity phenomena open up new sources of atomic energy, which are millions of times more powerful than any sources of energy that could be imagined by the mankind... We cannot be indifferent toward how the radium ores will be studied. They should be studied by us, Russian scientists" [8]. Vernadsky organized and supervised prospecting for radioactive minerals and headed this important field of research till the end of his life.

Despite the successes of chemical science and foundation of scientific schools, World War I revealed the technological and economic backwardness of Russia and weakness of its chemical industry. Russia possessed abundant mineral wealth, but mining and processing of mineral resources were undeveloped. In 1907–1914, Russia's material production increased rapidly, but, on the whole, it remained low and the country was unready for a long war. Already in the first months of war, it was found that nitric and sulfuric acids were in short supply for satisfying the dramatically increased demand for powders and explosives, and neither benzene nor toluene were available in sufficient amounts. When the Germans started to use chemical warfare, it was found that means of protection were totally lacking and adequate means of attack were in acute deficiency. Also in short supply were pharmaceutical preparations, fuels, and lubricants. During this difficult period of time, general-lieutenant V.N. Ipat'ev, professor of the Artillery Academy, manifested his superior qualities as organizer, scientist, and technologist who supervised reforms, in the shortest time, and organization of the military chemical industry in Russia [6, 7]. V.N. Ipat'ev was appointed chairman of the committee for provision of explosives in February 1915, and head of the Chemical committee at the Main Artillery Commission, in April 1916. The committee, which comprised five departments and had numerous regional bureaus, included leading chemists of Petrograd: Academician Kurnakov, professors Favorskii, Tschugaeff, Tishchenko, G.V. Khlopin, and A.A. Yakovkin, and a number of scientists from other regions of the country. In [6, 9] were reported data characterizing the fast rise in manufacture of explosives and war gases and other important chemical products already by the end of 1916.

G.V. Khlopin (1863–1929), professor of the Clinical Institute in Petrograd, headed a special commission for problems associated with manufacture of a gas mask. Petrograd scientists headed by professor N.D. Zelinsky (1861–1953, academician since 1929) developed the schematic of a gas mask and methods for manufacture of activated carbon. A major contribution to studies of adsorption of war gases by carbon and analysis of the protective action of the gas mask was made by Professor N.A. Shilov (1872–1930), a physical chemist from Moscow. During V.N. Ipat'ev's work at the Chemical committee of the Main Artillery Commission, more than 15 million gas masks were delivered to the front lines [6]. The activities of the Chemical committee were described by V.N. Ipat'ev in 1921 [10].

Vernadsky, a prominent public figure and member of the State Council, initiated, with the support of a number of other leading scientists, organization by the AS in 1915 of the Permanent commission for investigation of natural productive forces of Russia (CNPF). Vernadsky was elected its chairman, and A.E. Fersman (1883–1945, academician since 1919), its secretary. The principal goals of the commission were to study the natural wealth and its industrial use. In the first place, it was necessary to organize throughout the country a precise and, to the maximum possible extent, comprehensive and systematic accounting of the natural resources of Russia. Already in 1916, CNPF organized 14 special expeditions to various regions of the country [11]. Relationships were established with a number of important State institutions whose activities satisfied the needs of the military industry. In addition, the Military-Chemical committee was organized in Petrograd at the Russian Physicochemical Society to "unite efforts of Russian chemists for joint and systematic work on problems associated with the needs of State defense" [12]. Kurnakov was elected the chairman, Tishchenko (1861–1941, academician since 1935), the deputy chairman, and Professor Tschugaeff, the secretary of the committee.

In 1918–1920, CNPF initiated organization in Petrograd, despite the general devastation in the country, a number of scientific institutions, which later served as a basis for prominent research centers. Kurnakov supervised organization of the Institute of Physicochemical Analysis, in which studies concerned with the theory of physicochemical analysis, salt-containing and organic systems, natural salts, and metallic alloys were carried out. It was necessary to resolve urgent problems associated with manufacture of new metals and alloys in the country and use of the mineral wealth of our salt lakes.

Prikladnaya Khimiya Russian Scientific Center

Simultaneously, in 1918, the Institute of Platinum and Other Noble Metals was organized. The institute was headed by Tschugaeff (1873–1922), a professor of Petrograd University and author of fundamental studies in the field of chemistry of coordination compounds. One of the main tasks of the institute was to improve methods for refining of platinum-group metals. Such known scientists as A.A. Grinberg (1898–1966, academician since 1958), I.I. Chernyaev (1893–1966, academician since 1943), and V.V. Lebedinskii (1888–1956, corresponding member of the AS since 1946) started their scientific careers under Tschugaeff's supervision. After the untimely death of Tschugaeff in September 1922, Kurnakov was elected director of the institute. The level of investigations of platinum-group metals, achieved in scientific institutions of Petrograd, enabled industrial-scale refining of the Ural platinum at a plant in Yekaterinburg. This involved direct participation of a Kurnakov's disciple, N.N. Baraboshkin (1880–1935), subsequently a professor of the Ural Polytechnic Institute. Later, scientists from Leningrad took part in the development of a technology for obtaining platinum-group metals from sulfide ores of the Norilsk deposit.

In 1918, a decision was made to organize a pilot plant for recovery of radium from the ore mined at the Tyuya-Muyun deposit in Central Asia. Owing to efforts of Petrograd chemists I.Ya. Bashilov (1892–1953) and V.G. Khlopin (1890–1950, academician since 1939) already in December 1921, the first Russia's high-activity radium preparations were obtained from domestic raw materials [6, 13]. In January 1922, the State Radium Institute was created in Petrograd, with a pilot plant included. Vernadsky was approved as director of the institute and held this position till 1938.

To solve the most important tasks of the national economy in the field of chemistry and chemical technology, the State Optical Institute (1918), Russian Institute of Applied Chemistry (1919; later, GIPKh, State Institute of Applied Chemistry; now, Prikladnaya Khimiya Russian Scientific Center), and other industrial institutes were founded in Petrograd [14].

The necessity for producing aluminum from domestic ores was stated by Vernadsky and Kurnakov as far back as 1915. By that time, Pushin at the Electrotechnical Institute and Fedot'ev (1864–1934, corresponding member of the AS since 1933) performed, together with V.P. Il'inskii (1885–1964), investigations into production of aluminum by electrolysis of melts. In 1916, a bauxite deposit was discovered near Tikhvin (now, Leningrad oblast). A geological survey carried out by 1923 demonstrated that the deposit can satisfy the nearest demand of the country for aluminum; also, mention was made of the low cost of bauxite mining. However, the bauxites are low-grade because of the high content of silica (up to 18%) and required development of a new technology for their processing. Several scientific institutions of

Leningrad started a search for the most feasible flowsheet. The industrial procedure for recovery of alumina from high-silica bauxites was developed at GIPKh under supervision of Yakovkin (1860–1936, corresponding member of the AS since 1925). Raw materials were processed by the pilot plant, and first aluminum was obtained in June 1929. Already a year later, construction of the first Russia's aluminum plant was commenced on banks of the Volkhov river, and the plant was put into service on May 14, 1932.

In June 1933, production of aluminum was commenced by the Dnieper aluminum plant. Alumina raw materials for this plant were manufactured from Tikhvin bauxites by a procedure developed by staff members of the Mining institute in Leningrad, A.N. Kuznetsov (1877–1946) and E.I. Zhukovskii (1892–1965). Further, major contribution to studies in the field of production of alumina, aluminum, magnesium, and titanium and to plant designing was made by staff members of the All-Union Research Institute of Aluminum, Magnesium, and Electrode Industry (VAMI), founded in Leningrad in September 1931 [15, 16]. In particular, an efficient technology for integrated processing of nepheline concentrates to produce alumina, soda, potash, and portland cement was developed for the first time in the world practice. Of particular importance for extension of the raw material resources of the aluminum industry were works of VAMI on development and implementation of a technology for processing of alunites into alumina, sulfuric acid, and potassium sulfate. In 1998, the output of the metal by the Russian aluminum industry exceeded three million tons. Russia is second only to the United States in production of primary aluminum and occupies the first place in the export of this metal.

As far back as 1917, analysis of preliminary samples of brine led Kurnakov to a conclusion that the Verkhnekamskoe deposit of potassium salts is of industrial interest and detailed geological and chemical studies are necessary for determining the limits and conditions of occurrence of salts. In 1925, an expedition headed by Leningrad geologist, Professor P.I. Preobrazhenskii (1874–1944) discovered the world's largest deposit of potassium and magnesium salts. In November 1927, in Solikamsk of Perm oblast was laid foundation of a potassium mine, and utilization of the natural wealth of upper flows of the Kama River commenced. At the beginning of 1934, construction of the potassium combine was complete, and fields started to receive a valuable fertilizer, potassium chloride [17]. In the following years, processing of carnallite and manufacture of a number of other chemical products were organized with active participation of Leningrad chemists. The problem of integrated use of potassium salts, sylvinite and carnallite, from the Verkhnekanskoe deposit was resolved during a rather short time.

The process of magnesium manufacture from carnallite was developed at GIPKh under supervision of P.F. Antipin (1860–1960, corresponding member of the AS since 1939). The magnesium plant constructed in Solikamsk produced first batches of metal in March 1936. One of the oldest cities of the Urals became a prominent center of chemical industry.

In 1931, the All-Union Research and Design Institute of Halurgy (VNIIG) was created in Leningrad. The results obtained by the institute served as a basis for organization of the industry of potassium salts in the Soviet Union and also plants for mining and processing of rock salt, sodium sulfate, phosphorites, and other halurgic and mining-and-chemical raw materials.

Kurnakov and co-workers also paid uninterrupted attention to the unique salt field, Kara-Bogaz-Gol, containing vast resources of sea-type salts in its brines and deposits. After quite a number of expeditions, industrial mining of the Karabogaz sodium sulfate, a highly important raw material for chemical industry, commenced in 1924.

Geological surveys of the Kola Peninsula had been carried out under supervision of Fersman, one of the closest Vernadsky's associates, beginning in 1920 [18]. In the 1930s, quite a number of scientific institutions from Leningrad took part in the development of apatite–nepheline deposits of the Khibiny massif, deposits of copper–nickel ores in Monche-tundra, and ores of rare metals in Lovozero tundras.

An event of worldwide importance was the development in the Soviet Union of an industrial technology for manufacture of synthetic rubber. S.V. Lebedev (1874–1934, academician since 1932), Favorskii's disciple, came, as far back as 1913, to a conclusion that the ability to polymerize is a general property of hydrocarbons possessing a conjugated system of double bonds. He also formulated general concepts concerning the nature, rate, and mechanism of polymerization processes. At the beginning of 1926, the Supreme Council of the National Economy of the USSR announced an international competition for the best process for industrial manufacture of synthetic rubber. By the end of 1927, Lebedev's group comprising seven chemists developed procedures for obtaining divinyl directly from ethanol and for polymeriza-

Institute of Macromolecular Compounds, Russian Academy of Sciences.

tion of divinyl, having chosen appropriate catalysts and process modes. The Lebedev method for production of synthetic rubber was recognized as the best. A Pilot plant was constructed in Leningrad, together with some laboratories. On February 15, 1931, the plant produced by the Lebedev technique a first block of synthetic rubber, weighing 260 kg. In basic parameters, the rubber obtained compared well with the natural product. In 1932–1933, plants for manufacture of sodium-butadiene rubber were constructed in Voronezh, Yaroslavl, and Efremov (Tula oblast). The Pilot plant in Leningrad was transformed into the Academician Lebedev All-Union Research Institute of Synthetic Rubber (VNIISK). In subsequent years, a major contribution to the development of various methods for manufacture of synthetic rubber was made by Leningrad scientists, Academician B.A. Dolgoplosk (1905–1994) and Corresponding Member of the Academy of Sciences A.A. Korotkov (1910–1967).

The achievements in the field of chemical kinetics are associated with activities of Academician N.N. Semenov and co-workers, first at the Physicotechnical Institute of the AS, and then at the Institute of Chemical Physics, organized in Leningrad in 1931. They developed a rigorous theory of branched chain reactions, which was one of the most outstanding achievements of theoretical chemistry in the first half of the XX century. For his works in the field of chain reactions, Semenov was awarded, together with a British physical chemist C. Hinshelwood (1897–1967), the 1956 Nobel Prize in chemistry.

In 1902–1904, V.A. Kistyakovskii (1865–1952, academician since 1929) created at the Polytechnic Institute the first Russia's laboratory of physical chemistry and electrochemistry, which was excellently equipped by the standards of that time. Among numerous directions of research conducted by Kistyakovskii, the central position was held by studies of the electrochemical behavior of metals in aqueous media [19]. By 1925, the concepts concerning the film theory of passivity and its relationship with corrosion processes had formed conclusively. The scientist regarded as the reason for the onset of the passive state the formation of an amorphous or glassy oxide film densely coating the metal surface. In 1930, Kistyakovskii organized in Leningrad the Colloid-Electrochemical laboratory, affiliated with the AS (now, Institute of Physical Chemistry, Russian Academy of Sciences, in Moscow). A major contribution to the understanding of corrosion and passivation phenomena was made by Leningrad scientists A.I. Shultin (1898–1978), Ya.V. Durdin (1900–1980), V.V. Skorchelletti (1902–1982), and A.M. Sukhotin (1928–2002).

In 1926, by V.N. Ipat'ev's initiative, the Laboratory of high pressures was created at the Institute of Applied Chemistry. The laboratory soon became an independent scientific institution. It served as a basis

for the organization, in 1927, of the Institute of High Pressures, at which organic catalysis, ammonia synthesis, and displacement of metals from salts were studied. Of young V.N. Ipat'ev's co-workers, B.N. Dolgov, V.V. Ipat'ev, B.L. Moldavskii, M.S. Nemtsov, A.D. Petrov, G.A. Razuvaev, A.V. Frost, and others became known scientists.

An exceedingly strong influence on the development of chemistry after World War II was exerted by the necessity for studying the chemical aspects of nuclear power engineering and creating structural materials for new technology. Somewhat later, it also became necessary to develop techniques for obtaining substances in high-purity state, synthesize materials with various valuable physical and chemical properties for radioelectronics and other purposes. The staff of research institutes and educational institutions of Leningrad made a major contribution to the solution of these problems.

Under the general supervision of Academician V.G. Khlopin, a technology for recovery of plutonium from irradiated uranium was under development at the Radium Institute of the AS. The following Leningrad scientists took part in the industrial implementation of the process at the first Russia's radiochemical plant: B.P. Nikol'skii (1900–1990, academician since 1968) and Corresponding Members of the Academy of Sciences B.A. Nikitin (1906–1952), I.E. Starik (1902–1964), and V.M. Vdovenko (1907–1978) [20]. B.P. Nikol'skii, a professor of the Leningrad University, was a representative of M.S. Vrevskii's school and an outstanding physical chemist and radiochemist.

In the late 1940s, investigations in the field of macromolecular compounds became much more extensive. In 1948, the Institute of Macromolecular Compounds, Academy of Sciences of the USSR, was organized by the initiative of Corresponding Member of the Academy of Sciences S.N. Ushakov (1893–1964) and other scientists. At this institute worked, in particular, such known scientists as P.P. Kobeko (1897–1954), a corresponding member of the AS and a specialist in the physics of amorphous substances; S.N. Danilov (1889–1978), a corresponding member of the AS, who studied both natural and synthetic macromolecular compounds, cellulose ethers and esters, and viscose; N.I. Nikitin (1890–1975), a corresponding member of the AS, specialist in chemistry of wood. The fundamental and applied studies carried out at the institute enabled synthesis a large number of polymeric products.

A major contribution to the organization of industrial manufacture of polyethylene, polystyrene, and other important materials was made by the Plastpolimer Research and Production Association.

In 1948, the Institute of Silicate Chemistry was founded in Leningrad with active participation of Academician I.V. Grebenshchikov (1887–1953). The institute's scientists carried out extensive studies in the field of structure, chemistry, and thermodynamics of glass-forming melts and glasses and created new multipurpose corrosion-protective materials. In 1953–1968, the institute was headed by N.A. Toropov (1908–1968), a corresponding member of the AS and a prominent scientist in the field of inorganic materials science and technology of silicate systems. During 1948–1961, N.N. Kachalov (1883–1961), one of those who organized the domestic manufacture of optical glass, the author of fundamental works in the field of glass-making and grinding and polishing of glasses, worked at the institute. In 1930, the scientist founded at the Technological Institute the chair of glass technology and headed this chair till the end of his life.

In the postwar period, quite a number of tasks of primary importance, mainly associated with defense, were assigned to staff members of GIPKh. To accomplish them successfully, it was, in fact, necessary to create a scientific institution of a new type, including a research complex, a designing unit, and pilot plants. In this way, GIPKh became the largest chemical institute of the country, with a number of branches and unique technological base. Mention can be made here of only some of the most important developments. Based on the institute research and designs, an industry for manufacture of fluorine and fluorine-containing compounds was created in the country. Wide application was enjoyed by organofluorine polymers, Freons, and surfactants. GIPKh took active part in the development of propellants and structural materials for rocket engines. In creating the propellants, facilities for large-scale manufacture of hydrogen peroxide, hydrazine and its derivatives, ammonium perchlorate, various oxidizing agents, corrosion inhibitors, catalysts, and other products were set up, and conditions were determined under which these substances can be stored and safely used. The results obtained were important not only for defense purposes but also for the national economy.

To the important scientific and technological achievements of GIPKh belong industrial synthesis of a great number of chemical compounds with molecules containing radioactive or certain stable isotopes and manufacture of a wide variety of luminophores for various purposes.

In all periods of its development, chemistry always

has been solving the main problem of how to obtain substances and materials with valuable properties. Decades and centuries passed by, systems of state organization and generations of scientists changed, research techniques were improved, requirements to the final product became increasingly stringent, but the basic concept remained as before. We made an attempt to reflect in a brief essay the contribution made by St. Petersburg scientists to the solution of problems encountered by chemistry and chemical technology in the XVIII–XX centuries, to demonstrate the succession of scientific schools, and to make the reader recall some most important scientific events.

REFERENCES

1. *150 let Leningradskogo tekhnologicheskogo instituta im. Lensoveta* (150 Years of Lensovet Technological Institute in Leningrad), Leningrad: Khimiya, 1978.
2. Jacobi, B.S., *Raboty po elektrokhimii* (Works on Electrochemistry), Frumkin, A.N. Ed., Moscow: Akad. Nauk SSSR, 1957.
3. Solov'ev, Yu.I., *Istoriya khimii v Rossii* (History of Chemistry in Russia), Moscow: Nauka, 1985.
4. Makarenya, A.A., *D.I. Mendeleev i fiziko-khimicheskie nauki* (D.I. Mendeleev and Physicochemical Sciences), Moscow: Atomizdat, 1972.
5. Morachevskii, A.G., *Zh. Prikl. Khim.*, 1999, vol. 72, no. 9, pp. 1574–1579.
6. Loktev, S.M., *Vestn. Akad. Nauk SSSR*, 1990, no. 1, pp. 104–118.
7. Kuznetsov, V.I. and Maksimenko, A.M., *Vladimir Nikolaevich Ipat'ev: 1867–1952*, Moscow: Nauka, 1992.
8. Pogodin, S.A. and Libman, E.P., *Kak dobyli sovetskii radii* (How Soviet Radium Was Obtained), Moscow: Atomizdat, 1977.
9. Ipat'ev, V.N., *Rabota khimicheskoi promyshlennosti na oboronu vo vremya voiny* (Work of the Chemical Industry to Satisfy Needs of Defense during the War), Petrograd, 1920.
10. Ipat'ev, V.N., *Khimicheskii komitet pri Glavnom artilleriiskom upravlenii i ego deyatel'nost' dlya razvitiya otechestvennoi khimicheskoi promyshlennosti* (Chemical Committee at Main Artillery Commission and Its Activities Aimed at Development of Domestic Chemical Industry), Petrograd: Nauchn. Khim.-Tekhnol. Izd., 1921, part 1.
11. Mochalov, I.I., *Vladimir Ivanovich Vernadsky: 1863–1945*, Moscow: Nauka, 1982.
12. Solov'ev, Yu.I., *Nikolai Semenovich Kurnakov: 1860–1941*, Moscow: Nauka, 1986.
13. Morachevskii, A.G., *Zh. Prikl. Khim.*, 1997, vol. 70, no. 11, pp. 1931–1933.
14. *Organizatsiya i razvitie otraslevykh nauchno-issledovatel'skikh institutov Leningrada (1917–1977)* (Organization and Development of Industrial Research Institutes in Leningrad (1917–1977)), Kozlov, B.I., Ed., Leningrad: Nauka, 1979.
15. Kaluzhskii, N.A., Lankin, V.P., and Shchegolev, V.I., *Tsvetn. Met.*, 2001, no. 8, pp. 63–72.
16. Morachevskii, A.G., *Zh. Prikl. Khim.*, 2002, vol. 75, no. 5, pp. 873–877.
17. Morachevskii, A.G., *Zh. Prikl. Khim.*, 1997, vol. 70, no. 11, pp. 1931–1933.
18. Morachevskii, A.G. and Beloglazov, I.N., *Zh. Prikl. Khim.*, 2000, vol. 73, no. 5, pp. 869–872.
19. Morachevskii, A.G. and Shpak, V.S., *Zh. Prikl. Khim.*, 2001, vol. 74, no. 3, pp. 516–520.
20. Nikol'skii, B.P., Recollections: History of Nuclear Industry in the Soviet Union, *Preprint of TsNIIatominform*, Moscow, 1996.

Russian Journal of Applied Chemistry, Vol. 76, No. 5, 2003, pp. 689–699. Translated from Zhurnal Prikladnoi Khimii, Vol. 76, No. 5, 2003, pp. 716–727.

REVIEWS

Fullerene-Containing Chalcogenide Glassy Materials

L. N. Blinov

St. Petersburg State Polytechnic University, St. Petersburg, Russia

Received July 15, 2002

Abstract—Possibilities of simulation and subsequent synthesis of fullerene-containing chalcogenide glasses are considered, and some characteristics of this class of semiconducting disordered materials are analyzed.

Fullerenes and fullerene-containing materials have been extensively studied recently [1–15]. The 1991 discovery of nanotubes (or tubelenes) composed of two halves of a fullerene molecule and a cylinder of hexagons in the form of a rolled-up graphite layer aroused to even greater extent the interest in carbon materials with varied hierarchy of structures [16–21]. A powerful stimulus to studies of fullerenes was the discovery of the ability of their compounds with some metals (fullerenides) to undergo, on being cooled to a certain threshold temperature T_c, a superconducting transition characteristic of other substances of varied chemical nature [22–29].

However, despite the great, and increasing, number of publications concerned with fullerenes and their derivatives, studies devoted to development of a fundamental general theoretical approach to creation of fullerene-based materials and, in particular, to determining their place (niche) among other materials exhibiting high-temperature superconductivity (HTSC) are virtually lacking. It is known that the efficiency of application of various materials and, in particular, those possessing HTSC is determined both by what, and to what extent, is known about particular substances and by the existence of a general conceptual approach, unified theory, and general criteria for a broad class of materials [30]. Development of such an approach will make it possible not only to consider and analyze from a common standpoint single-type or closely similar classes of known materials with different compositions, but also to determine the strategy of a search for new materials. However, most of studies and reviews on fullerenes and their derivatives and also materials exhibiting HTSC are, as a rule, devoted to investigation of separate properties or groups of objects and generalization of the results obtained. In this case, a "physical" or "chemical" trend in analysis and presentation of data can be clearly observed.

In the chemical part of investigations concerned with fullerenes and their derivatives, the following sections can be distinguished [1–22, 29–38]: endohedral complexes of fullerenes, chemical properties of fullerenes and their derivatives, reactions of fullerenes with metals, oxidation of fullerenes, their reactions with Lewis acids, reactions of fullerenes with free radicals, behavior of fullerenes as ligands, nanotubes (or tubelenes), etc.

Separate publications have been devoted to reaction of radical cations of the type C_{60}^{+}, C_{60}^{2+}, and C_{60}^{3+} with water, alcohols, ethers, and esters; dissolution of fullerenes in organic solvents; adsorption properties of fullerene-containing materials; host–guest complexes with fullerenes; etc. [39–45].

A large group of studies have been concerned with synthesis of fullerenes and fullerene-containing materials [20, 21, 31, 46–52].

On the whole, analysis of papers reporting on physicochemical studies of fullerenes and their derivatives shows that they are mainly concerned with reactions of fullerenes with a limited set of metals or with organic substances of varied composition. No general approach to fullerene-containing materials, including those exhibiting HTSC, has been developed; although noticeable success has been achieved in separate directions [20, 21].

At present, investigations in the field of noncrystalline materials occupy one of central positions in physics and chemistry of solids. The interest in these materials is due to their inherent specific properties (variable composition, efficient production and processing, stability in various media, etc.), which favor their wide practical application, and to importance of studying these materials for the development of fundamental science. The progress in this field is promoted, in particular, by physicochemical studies of glasses, which belong to noncrystalline materials.

1070-4272/03/7605-0689$25.00

To elucidate the nature of the glassy state, it is necessary to determine the extent to which the concept that any substance except helium can be, in principle, obtained in glassy state is correct [53]. Of particular importance for experimental verification of this hypothesis are data on synthesis of glasses containing some unconventional components. To these belong, in particular, fullerenes.

Chalcogen- and chalcogenide-based glassy materials have been known for a rather long time [54–59]. Data on existence of a glassy material based on fullerene C_{60} are also available [60]. Since new materials based on chalcogenide glasses and fullerenes show promise for diverse applications, in particular, as matrices for creation of high-temperature superconducting materials, it was of scientific and practical interest to study the possibility of obtaining fullerene-containing chalcogenide materials and to establish a correlation between the superconductivity and composition of substances [61].

Any basic property of a substance is ultimately determined by the electronic structure of its constituent atoms and nature of their chemical interaction. On determining how these characteristics, which are related to the composition of a compound, vary with the charge of the nucleus of an averaged atom ($\bar{Z}$) or with some other reliably established numerical value, e.g., number of electrons in a substance (N_e), the above question can be resolved.

In [62–65], it was established that an expression of the type

$$G_T = \bar{n}\bar{K}/\bar{Z} \quad (1)$$

can characterize the glass-forming ability of a molten substance in its spontaneous cooling.

In Eq. (1), G_T is the glass-forming ability of a melt; $\bar{n}$ and $\bar{Z}$ are, respectively, the contributions of the principal quantum numbers of valence electrons and charge numbers of nuclei of melt components; $\bar{K}$, the mean rigidity of the electronic skeleton of chemical bonds (ESCB). In the general case, the overall $\bar{K}$ value is constituted by several components [66]. Further investigations demonstrated that this qualitative approach is promising for assessing the possibility of obtaining a number of new compositions of glassy materials after performing preliminary calculations of their glass-forming ability [64–67].

A relation similar to Eq. (1):

$$S = \bar{n}_s\bar{K}_s/\bar{Z}_s, \quad (2)$$

where the parameters $\bar{n}_s$, $\bar{K}_s$, and $\bar{Z}_s$ refer to substances capable of a superconducting transition above a certain temperature T_c, and S is the ability of a substance to undergo a superconducting transition, was used to analyze the main materials under study, with widely differing compositions (metals, intermetallic compounds, oxides, chalcogenides, fullerenides), which can pass into the superconducting state at temperatures close to 0 K or at higher temperatures (Table 1).

In calculating the numerical values, account was only taken of the main contributions to the ESCB rigidity, since all other contributions in these superconductors are zero [61, 68].

Further, it was necessary to determine the dependence of the S-function on the total number of electrons (N_e) in atoms of a substance $A_xB_yC_z$..., where A, B, C are symbols denoting chemical elements and x, y, z are their indices in a substance. With this dependence established, it becomes possible to perform a purposeful search for new substances that can undergo a superconducting transition both at low and at high temperatures. Figure 1 plots such a dependence, whence it can be seen that virtually all substances considered in this paper fall, as regards their glass-forming ability, on a single smooth curve. Comparison of this curve with a similar plot describing the glass-forming ability of melts [62, 64] shows that the latter lies lower than the curve for substances capable of a superconducting transition. This leads to the following suggestions.

(1) Most of substances that can pass into the glassy state in spontaneous cooling (cooling rate <100 K s^{-1}) cannot be superconductors. A possible exception are simple bodies and chemical compounds of constant and variable composition for which the charge number of an "averaged" atom (calculated from mole fraction) is within the range $Z = 20–30$. It should be noted that the possibility of superconduction in chalcogenide glasses was mentioned in [69].

(2) Most of substances capable of a superconducting transition cannot solidify as a glass on cooling their melts at cooling rate <100 K s^{-1}. The only exception are superconductors with averaged-atom charge $\bar{Z} = 20–30$.

(3) Analysis of the data in Table 1 and Fig. 1 shows that the most appropriate chalcogenide glassy matrices for introduction of fullerenes are selenium, systems on its base, and also ternary and more complex systems based on Se, S, P, As, and some metals, in which the charge number of averaged atom is close to the range 20–30.

Table 1. Calculated characteristics of substances capable of a superconducting transition on being cooled to a superconducting transition temperature T_c, K

Composition	$\bar{K}_s$	$\bar{n}_s$	$\bar{Z}_s$	S	T_c
Pb	1.198	6.0	82	0.088	7.2
W	1.183	6.0	74	0.096	0.01
Ta	1.737	6.0	73	0.143	4.5
Re_2Si	1.572	4.333	54.667	0.125	3.8
Sn	1.141	5.0	50	0.114	3.7
Nb_3Sn	1.503	4.25	43.25	0.148	18.0
$Pb_{1.14}Se_{1.14}Nb_2Se_4$	1.335	4.396	42.300	0.139	3.4
GeTe	1.144	4.5	42	0.123	0.17
URu_2Si_2	1.33	4.367	41.6	0.140	1.3
Nb	1.099	5	41.0	0.134	9.25
$Pb_{1.14}Nb_3Se_{7.14}$	1.348	4.355	40.713	0.144	4.8
Nb_3Ge	1.225	4.75	38.75	0.150	23
$LaMo_6Se_8$	1.265	4.133	38.733	0.135	11
$(Nb_3Al)_4Nb_3Ge$	1.070	4.55	34.95	0.139	20
$PbMo_{5.1}S_6$	1.202	4.091	32.413	0.152	15
$Tl_2Ag_8Ba_2Ca_2Cu_3O_{10}$	1.160	3.859	31.741	0.141	117
UNi_2Al_3	1.661	3.333	31.167	0.178	1
$PbMo_6S_8$	1.152	3.975	30.8	0.149	14
Zn	1.069	4	30	0.143	0.88
$Ba_{0.6}K_{0.4}BiO_3$	1.508	3.44	29.64	0.178	105
$CeCu_2Si_2$	1.714	3.4	28.8	0.202	0.6
$BiBa_{0.6}K_{0.4}BiO_3$	1.247	3.867	28.355	0.170	32
$Tl_2CaBa_2Cu_2O_8$	1.387	3.467	27.733	0.173	107.11
$Bi_2Sr_{1.3}Ca_{0.7}CuO_{6.2}$	1.398	3.351	27.5	0.170	87
$TlBa_{1.6}La_{2.4}Cu_2O_9$	1.335	3.218	27.338	0.157	42
$La_2Ni_5C_3$	1.397	3.8	27.2	0.195	1.8
$Bi_3Sr_2Ca_2Cu_3O_7$	1.344	3.647	26.588	0.184	110.5
$Bi_{1.4}Pb_{0.6}Ca_2Sr_2Cu_3O_7$	1.255	3.500	26.525	0.166	110
$Sm_{1.83}Cl_{0.17}CuO_4$	1.238	3.429	26.331	0.161	20
$Nd_2CuO_{3.8}F_{0.2}$	1.202	3.619	25.886	0.168	27
$Nd_{1.86}Ce_{0.14}CuO_4$	1.234	3.429	25.8	0.164	20
$Bi_2Sr_2CaCu_2O_8$	1.378	3.333	25.6	0.179	80
$Bi_{1.5}Pb_{0.5}Sr_2CaCu_2O_8$	1.440	3.297	25.567	0.186	85
$Bi_{1.6}Pb_{0.4}Sr_2Ca_2Cu_3O_8$	1.295	3.412	25.447	0.174	113
$Bi_2Sr_2CaCu_2O_{8.16}$	1.379	3.310	25.414	0.179	91
$Bi_{1.85}Pb_{0.15}Sr_2CaCu_2O_{8.18}$	1.357	3.303	25.381	0.177	88
$Tl_2Ba_2Ca_2Cu_3O_{10}$	1.373	3.318	25.316	0.183	121
V_3Ga	1.067	4.0	25.000	0.171	14.5
$La_{1.88}Sr_{0.12}CuO_4$	1.523	3.314	24.674	0.205	20
$La_{1.8}Sr_{0.12}CuO_4$	1.234	3.301	24.457	0.167	32
$NdBa_2Cu_3O_7$	1.329	3.604	4.231	0.198	92
$Bi_2Sr_2Ca_2Cu_3O_{10}$	1.359	3.263	23.632	0.188	109.5
$Bi_{1.6}Pb_{0.4}Sr_2Ca_2Cu_3O_{10}$	1.360	3.253	23.53	0.187	108
$Bi_{1.5}Pb_{0.5}Sr_2Ca_2Cu_3O_{10}$	1.361	3.462	23.605	0.200	108
$Y_{0.7}Ca_{0.3}Ba_2Cu_3O_{6.02}$	1.351	3.370	23.333	0.195	35
$Tl_{0.5}Pb_{0.5}Sr_2Ca_{0.8}Er_{0.2}Cu_2O_7$	1.4	3.198	23.161	0.193	115
$YBa_2(Cu_{0.99}Fe_{0.01})_3O_{6.55}$	1.379	3.316	23.132	0.198	60
$YBa_2Cu_3O_{6.6}$	1.380	3.315	23.079	0.198	53
$Tl_{0.5}Pb_{0.5}Sr_2Ca_{0.8}Y_{0.2}Cu_2O_7$	1.399	3.203	22.715	0.197	107
$YBa_2Cu_{2.82}Ga_{0.18}O_7$	1.411	3.255	22.643	0.203	70
$YBa_2Cu_{2.7}Zn_{0.3}O_7$	1.420	3.234	22.638	0.203	79

Table 1. (Contd.)

Composition	$\bar{K}_s$	$\bar{n}_s$	$\bar{Z}_s$	S	T_c
$YBa_2Cu_{2.85}Zn_{0.15}O_7$	1.403	3.249	22.627	0.202	59
$YBa_2Cu_{2.86}Zn_{0.14}O_7$	1.401	3.249	22.620	0.201	68
$YBa_2Cu_3O_7$	1.418	3.349	22.615	0.204	77
$YBa_2Cu_{2.7}Fe_{0.3}O_{6.9}$	1.397	3.249	22.608	0.201	90
$Y_{0.7}Ca_{0.3}Ba_2Cu_3O_{6.85}$	1.39	3.258	22.342	0.202	88
$YBa_2Cu_3O_{6.5}$	1.337	3.333	22.279	0.200	54
NbS_3	1.405	3.25	22.25	0.205	2
$YBa_2Cu_{2.7}Al_{0.3}O_{7.07}$	1.334	3.225	22.246	0.206	98
$YBa_2Cu_4O_8$	1.354	3.215	22.067	0.197	75
$Tl_{0.5}Pb_{0.5}Sr_{0.8}Ba_{0.2}CaCu_2O_7$	1.410	3.055	21.425	0.201	90
$La_{1.87}Ca_{1.13}Cu_2O_6$	1.274	3.099	21.381	0.185	50
$Tl_{0.5}Pb_{0.5}Sr_{0.5}Ba_{0.5}Ca_2Cu_3O_9$	1.387	3.025	20.469	0.205	110
$YBaCu_{2.94}Co_{0.06}O_7$	1.290	2.975	19.823	0.194	67
$SrTiO_3$	1.45	2.9	16.8	0.250	0.4
$Cu[N(CN)_2]Br$	1.486	2.5	13.857	0.268	11.7
Al	1.508	3	13	0.348	1.2
$K_3Tl_{45}C_{60}$	2.005	2.356	11.578	0.408	17.6
Rb_3C_{60}	1.487	2.143	7.476	0.570	28
$Cu_{1.5}C_{60}$	2.036	2.037	6.561	0.632	–

(4) Evaluation calculations of S also demonstrated that, to obtain glassy compositions, the amount of fullerenes in chalcogenide matrices cannot be high. In this case, the rate of melt cooling should exceed 100 K s^{-1}. The available, by that time, experimental data on introduction of preliminarily treated shungites into chalcogenide glasses confirmed to a certain extent the suggestions made [29, 70, 71].

On the basis of the aforesaid, selenium [72] and glassy compounds of the systems P–Se, As–P–Se, and Ag–As–Se were chosen for studying the possibility of fullerene introduction into chalcogenide glasses serving as reference substrate (matrix). The choice of a procedure and mode of synthesis was determined by

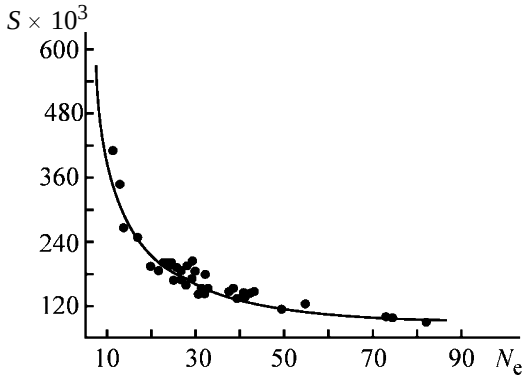

Fig. 1. Capacity S of a substance for a superconducting transition in relation to the total number of electrons in an "averaged" atom (N_e).

several factors specified below. It is known that the classical procedure for preparing a glass consists in nonequilibrium cooling of a melt preliminarily brought into thermodynamic equilibrium at a sufficiently high synthesis temperature T_s. Determining the temperature T_s and the minimum time of keeping the melt at a given temperature is an important experimental task [57]. However, there exist glasses which cannot, in principle, be obtained by the classical method, and these are not only glassy crystals for which the glass phase is obtained by cooling of the corresponding crystal [60]. It is the necessity for bringing a melt into the state of thermodynamic equilibrium that precludes synthesis of some glassy materials. In particular, such a situation is characteristic of fullerene-containing glassy materials, first synthesized in 1993 [29].

Fullerenes are big spherical molecules composed of carbon atoms. The most stable of these is the C_{60} molecule, a spherical molecular formation in the form of a truncated icosahedron. The C_{60} molecule, which resembles in its shape the surface of a soccer ball, is composed of edge-linked pentagons and hexagons, with each pentagon surrounded by hexagons only. The diameter of the C_{60} molecule is 7.2 Å. Fullerenes can be, in particular, obtained in evaporation of graphite by a special procedure [3, 73]. Naturally, such exotic molecules as C_{60} and C_{70} constitute only a minor fraction in graphite vapor mainly composed of small

clusters, mostly C_2. This is not surprising, since spontaneous formation of rather complex C_{60} and C_{70} molecules is unlikely, and their decomposition is, as a rule, irreversible. In view of this circumstance, melts containing a noticeable fraction of fullerenes are commonly thermodynamically unstable.

Since fullerenes can survive in thermodynamically unstable melts only at relatively low temperatures, it is hoped that fullerene-containing glassy materials can be obtained by relatively rapid cooling of such melts. Compared with glasses prepared by the classical technique of fast cooling of an equilibrium melt [56, 57], the given materials are characterized by lower configuration entropy [74]. Since the mutual position of atomic nuclei ultimately determines most of properties of any condensed system, the following questions are of primary importance. How are the structure R and parameters of a transition to the superconducting state related? Is it possible to increase the critical temperature T_c (R) of a superconducting phase transition by varying the structure R of a system at its invariable chemical composition? What is the structure R^{max} to which corresponds the absolute maximum

$$T_c^{max} \equiv T_c R^{(max)} = \max_{\{R\}} T_c(R) \quad (3)$$

of the function $T_c(R)$? These issues were considered in detail in [74–77].

It was shown in these publications that specific ensembles of structures with decreased configuration entropy can be distinguished in condensed systems. Systems with structures composed of these ensembles can be named systems with decreased configuration entropy. Here is meant the *a priori* (before obtaining any of the systems under consideration) configuration entropy, determined by probabilities of occurrence of the structure, which characterize a certain statistical ensemble of structures.

To systems with decreased configuration entropy belong, in particular, disordered microscopically heterogeneous materials with relatively large heterogeneity lengths λ [74]. For example, the λ value for glasses containing shungites with additions of fullerenes and fullerenides exceeds 100 Å [29, 74]. As established in [72, 74], the structurally inhomogeneous materials considered contain superconducting fragments for which T_c lies within the range 70–100 K (depending on composition).

Within the approach being developed, it becomes clear why the high-temperature superconductivity has been discovered just in structurally inhomogeneous materials, specifically, metal oxide ceramics. In all probability, the following hypothesis is valid. Most of high-temperature superconductors are structurally inhomogeneous materials with decreased configuration entropy and relatively large heterogeneity length λ(R) (Fig. 2).

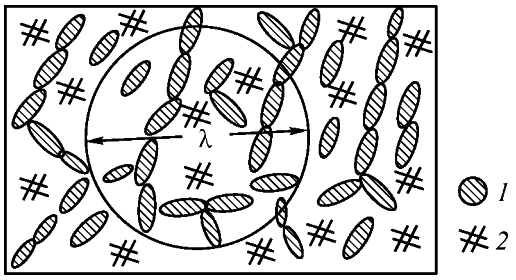

Fig. 2. A variant of the structure of a structurally inhomogeneous superconductor: (*1*) superconducting fragments and (*2*) fragments of the atomic network.

It is due to the existence of heterogeneities that the critical temperature T_c can be raised. The microscopic mechanisms responsible for this increase vary. For example, if heterogeneities are created (Fig. 2), the frequencies of atomic vibrations within them become higher. This leads [78] to an increase in the T_c values corresponding to these heterogeneities. In addition, it has been shown that, when the concentration of a certain kind of heterogeneities is raised, it may be hoped that the T_c values will increase [29, 72, 74].

It follows from the aforesaid that fullerenes of the types C_{60}, C_{70}, etc. must lead to a decrease in the structural disorder in the whole fullerene-containing system, i.e., to lowering of the configuration entropy. Naturally, preserving fullerenes in a melt in the course of synthesis requires that not only temperatures should be comparatively low, but also the chemical interaction with other components should be nondestructive. Unfortunately, the chemistry of fullerenes has not been studied sufficiently completely. Most of the presently known chemical reactions involve only chemical bonds separating two neighboring hexagons [1–15]. As a rule, mixtures of products are obtained, since multiple additions are possible. The last fact indicates that fullerene fragments are incorporated in condensed matrices by alternative mechanisms.

According to quantum-mechanical calculations, the energy of the whole system is lowered upon addition of one or two electrons to a C_{60} molecule by, respectively, 0.92 and 3.6 eV [3], and, therefore, many metals and their salts can serve as electron donors for fullerenes. For example, electron transfer from alkali

metal atoms to C_{60} occurs easily. Rubidium, potassium, and cesium fullerenides M_3C_{60} have metallic conductivity and exhibit superconductivity at low temperatures. The conductivity decreases when the composition deviates from M_3C_{60} to both higher and lower content of the alkali metal [79].

Being acceptors, C_{60} molecules form with electron donors, depending on their strength, either charge-transfer complexes or radical ion salts. Some of these show ferromagnetism or superconductivity [80]. A specific feature of the C_{60} molecule as an acceptor is its spherical shape and comparatively high negative reduction potentials. This circumstance predetermines the relatively low stability of fullerenes in air.

The criteria to be used in choosing donors for the C_{60} molecule have not been determined conclusively. It is believed [80] that the configuration flexibility is an important structural characteristic of a donor molecule as a component of a charge-transfer complex. Donors capable of changing their configuration, adjusting it to the rather rigid spherical shape of the C_{60} molecule, seem to be preferable for formation of sufficiently stable charge-transfer complexes. To such donors, in particular, belong molecules of chalcogens, e.g., sulfur molecule S_8. A complex $C_{60} \cdot 2S_8$ has been prepared [80]. It may be stated that sulfur is a sufficiently versatile donor for fullerenes.

It seems reasonable to assume that not only sulfur, but also other chalcogens (selenium, tellurium) can form charge-transfer complexes with C_{60}, and, therefore, fullerenes can, up to their certain concentrations, be incorporated in the network (structure) of some chalcogenide glasses. This is indicated by the data in Fig. 1.

Glassy fullerene-containing materials were synthesized using as a basis the temperature mode of synthesis developed for obtaining glasses containing Karelian shungites [29, 81]. The synthesis was carried out in preliminarily washed and dried (at 150°C) quartz ampules evacuated to a residual pressure of 10^{-5} torr. Ampules containing 2 g of the starting materials were kept in a furnace at 800°C for 2–3 h. For better homogenization of the melts in synthesis, they were agitated by rotating the ampules. Several parallel meltings were carried out for each composition. All measurements were done on no less than two samples from parallel meltings. As criteria of the glassy state served the shell-like fracture, absence of lines in powder X-ray diffraction patterns, and lack of heterogeneities on samples inspected using an MIK-1 IR microscope.

Fullerene-containing glassy materials were synthesized on the basis of the systems Se–C_{60}, P–Se–C_{60}, As–P–S–C_{60}, and Ag–As–S–C_{60}. It should be noted that as one of the main criteria for selecting chalcogenide matrices for introduction of fullerenes served the ability of the matrices to be donors for fullerenes, and also the configuration flexibility and diversity of structural formations. For example, glassy selenium has a rather labile polymeric skeleton based on covalently bonded structural units $SeSe_{2/2}$, which can adjust to the rigid structure of fullerenes. Matrices based on P–S and P–Se not only can be donors for fullerenes, but are also characterized by a wide diversity of structural groups, which facilitates incorporation of fullerenes in the structural network (matrix) of the glassy alloy. The choice of metals contained in glassy matrices was governed by the ability of such systems to form structurally inhomogeneous glasses.

As starting fullerenes served a mixture of 96 wt % C_{60} and 4 wt % C_{70}. In all of the systems studied, introduction of up to 2 wt % fullerenes preserved the glassy state of the initial matrices, and introduction of more than 2 wt % yielded glassy crystals.

To confirm the survival of fullerenes after synthesis, the mass spectra of the glassy samples obtained were measured. The mass-spectrometric studies were carried out with a time-of-flight mass spectrometer of the mass-reflectron type with resolution of 5000 at half-maximum of a peak at mass number of 500 amu [82]. Typical results of a mass-spectrometric study of fullerene-containing chalcogenide glassy materials are presented in Fig. 3. The presence of lines corresponding to fullerenes in the mass spectra clearly indicates that the fullerene structure is preserved in the synthesis mode used.

Some physicochemical parameters of the glassy materials obtained are listed in Table 2. The density ρ of the samples was measured by hydrostatic weighing in toluene, and their microhardness was determined on a PMT-3 device. The electrical conductivity of the samples was measured by the two-probe method at temperatures in the range 20–100°C, with the error in determining $\log\sigma$ not exceeding 0.1 order of magnitude. The glass transition temperature T_g was found from the bend in the temperature dependence of the electrical conductivity under condition of constant sample compression between the electrodes.

Analysis of the results obtained shows that the most pronounced changes in the structure and properties of a glass after introduction of fullerenes are observed for selenium-based samples. This is also indicated by the data listed in Table 3.

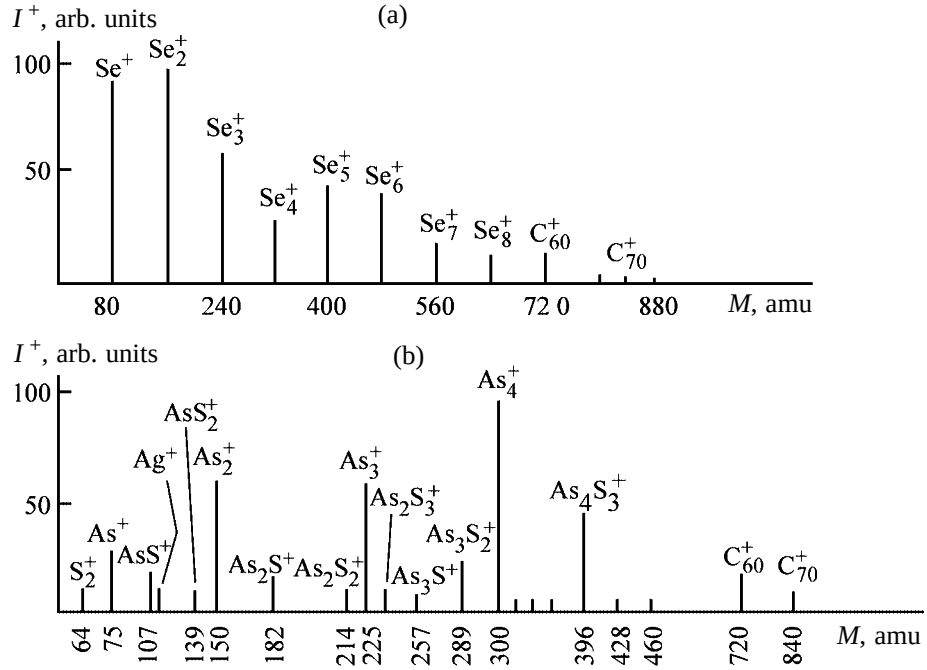

Fig. 3. Mass spectra of fullerene-containing glassy compositions: (a) Se + 2% C_{60}, T_{ev} = 200°C, U_{el} = 50 eV; (b) Ag_3AsS_3 + 2% C_{60}, T_{ev} = 350°C, U_{el} = 30 eV.

The results of examining with a metallographic microscope the polished surfaces of the alloys synthesized show that selenium-based samples are the most homogeneous. They also exhibit an increase in microhardness and a pronounced rise in glass-transition temperature. Probably, chemical interaction of carbon clusters with selenium, which leads to strengthening of the alloy structure, is manifested to the greatest extent. The temperature dependence of electrical conductivity shows clearly pronounced exponential behavior both at $T < T_g$ and in the glass-forming region (Fig. 4). The observed differences in the activation energy before and after T_g indicate that structural transformations occur in the glass network.

Table 2. Physicochemical characteristics of fullerene-containing glassy materials

System	Composition of the initial matrix	C_{60} content, wt %	ρ, g cm^{-3}	H, kg mm^{-2}	$-\log\sigma_0$, [Ω^{-1} cm^{-1}]	Type of conduction
Se–C_{60}	Se	0.9	4.27	42	12.7	Electronic
	Se	2.0	4.21	45	10.8	〃
P–Se–C_{60}	P_2Se_5	2.0	3.80	56	>12	〃
	P_2Se_5 + 0.1Fe	2.0	3.63	51	>12	〃
As–P–Se–C_{60}	AsP_3S_{10}	2.0	4.09	76	>12	〃
Ag–As–S–C_{60}	Ag_3AsS_3	2.0	5.75	62	6–7	Hole

Table 3. Parameters of selenium-based glassy materials

Composition	T_g, K	$-\log\sigma_{20}$	$-\log\sigma_{T_g}$	E_0, eV	$\log\sigma_0$	Notes
Se	314	13.8	11.0	0.90	4.0	Data of [15]
Se + 0.9 wt % C_{60}	333	12.7	10.4	0.95	3.7	$T < T_g$
				0.50	3.2	$T > T_g$
Se + 2.0 wt % C_{60}	338	10.8	10.7	1.15	6.8	$T < T_g$

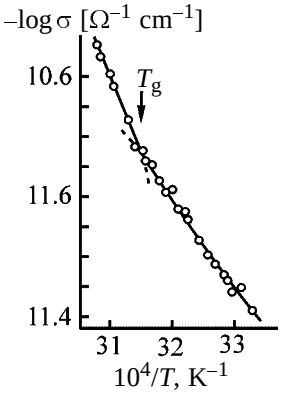

Fig. 4. Electrical conductivity of glassy selenium containing 2 wt % C_{60} vs. temperature T.

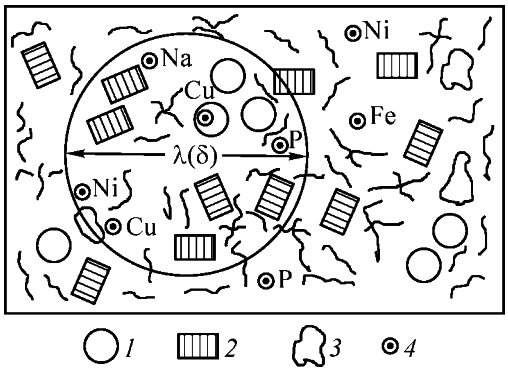

Fig. 5. Fullerene-containing selenium–carbon matrices: (*1*) fullerene molecule, (*2*) graphite fragment, (*3*) chain of selenium atoms, and (*4*) impurity atoms.

It should be noted that two characteristic regions with different activation energies of conductivity have also been observed in C_{60}-based films [83].

As already noted, the problem of glass formation in the system Se–C_{60} and other chalcogenide systems with fullerenes is far from being trivial. On the one hand, glassy selenium is a classical glass obtained by rapid cooling of an equilibrium melt [57], and on the other, the glassy phase of C_{60} is an example of a nonclassical glass obtained by nonequilibrium cooling of a C_{60} crystal from 300 to 15 K [60], with the corresponding glass transition temperature T_g equal to 90 K.

Thus, the preparation procedure is not the only factor governing the nature of the glassy state. Therefore, it is of prime importance to understand on the microscopic level the common features of all the above-considered cases (in particular, formation of Se and C_{60} glasses). This consideration can be based, to certain extent, on data in [76, 84–86]. Let us briefly discuss some conclusions following from these works.

Depending on the thermal history of a glass synthesized, the system "falls" into different potential wells. In other words, virtually infinite number of different glasses can be, in principle, obtained at fixed chemical composition. Being close in structure, most of these glasses have close properties.

The properties of the classical glasses are determined by potential wells which coincide with, or are close to those characteristic of a melt. However, there also exist an exponentially large number of potential wells grouped around the potential well of the ideal crystal. A rather great number of stationary quantum states are localized within these wells. A quantity ε_{cr}, which is similar to ε_g, can be introduced for the ensemble of these states [87]. For a C_{60} crystal, a temperature of about 90 K corresponds to the energy ε_{cr}. In other words, if the energy of a crystal exceeds ε_{cr}, then transitions between different states of the ensemble under consideration occur rather rapidly, with the result that an equilibrium is attained. If the energy is lower than ε_{cr}, such transitions are frozen.

Thus, the microscopic mechanisms of glass formation in Se and C_{60} are similar. The only difference consists in that these mechanisms operate in dissimilar ensembles of stationary quantum states, which differ fundamentally from one another.

Naturally, the exponentially large number of potential wells includes those to which correspond heterogeneous structures. In all probability, fullerenes are arranged within matrices of chalcogenide glasses statistically nonuniformly. Fullerene molecules form a kind of clusters (Fig. 5). This is confirmed by the presence of the above-mentioned superconducting fragments and absence of through superconductivity (Fig. 2). Surely, the clusters are much smaller in size (on the order of 10^{-3} cm) than the initial particles in a weighed portion. If these latter were preserved in the alloys synthesized, they would be observable under an IR microscope.

Quantitatively, the degree of heterogeneity of a system can be characterized by the value of $\lambda(\sigma)$ [88]. The length $\lambda(\sigma)$ is equal to the diameter of a sphere with minimum dimensions (Fig. 5), which isolates, irrespective of its position within a macroscopic sample, similar (to within relative fluctuation σ) regions. The similarity not necessarily means identity, it suffices that a number of integral characteristics of the regions, such as dipole moment, polarizability, overall chemical composition, etc., are close. In other words, even though regions of diameter $\lambda(\sigma)$ differ, as a rule, from one another in how the constituent fragments are linked, they are, nevertheless, closely similar.

The order of magnitude of $\lambda(\sigma)$ can be evaluated using a simple formula [88]:

$$\lambda(\delta) \approx D/(\delta^{2/3} \min_i n_i^{1/3}), \quad (4)$$

where D is the diameter of a sphere whose volume is equal to the average volume per atom in the system, and n_i is the relative concentration of atoms of ith kind.

According to Eq. (4), the values of $\lambda(0.01)$ for the alloys synthesized are on the order of 100 Å. It is fragments of this diameter that contain information about most of the properties of the materials considered. This, apparently, cannot be said about fragments with dimensions not exceeding 10 Å, since the diameter of a fullerene molecule is on the order of 10 Å.

Studies concerned with fullerene-containing glasses and with fullerenes themselves are still in the initial stage. In view of this circumstance, it is difficult to make any prognoses, but, in the author's opinion, these studies are of not only scientific, but also practical importance. In this context, it suffices to recall that the already investigated compositions of disordered materials with fullerenes possess a number of nontrivial properties, including high-temperature superconductivity [29, 72, 89]. Rather promising for studying this phenomenon in such materials is the method of microwave absorption in zero magnetic field [90]. This technique was used by the author in a study of selenium with addition of shungite (Fig. 6). A certain information about specific structural-chemical features of these materials can also be furnished by ESR spectroscopy (Fig. 7).

The main result obtained is that the possibility in principle of preparing fullerene-containing glasses by cooling the corresponding melts is established. In this case, the extent to which fullerenes interact with matrices of different compositions varies, which is, in particular, indicated by the dissimilar degrees of microheterogeneity of the compositions obtained. This is also favored by cluster formation. The fragments containing information about most of the properties of the materials under consideration have the size on the order of 100 Å and more.

It follows from the presented data on the chemical properties of fullerenes and glasses of the systems Se–C_{60}, P–Se–C_{60}, As–P–S–C_{60}, and Ag–As–S–C_{60} that the class of fullerene-containing chalcogenide glasses may be rather broad.

The microscopic mechanism by which widely diverse glasses, including glassy crystals, are obtained

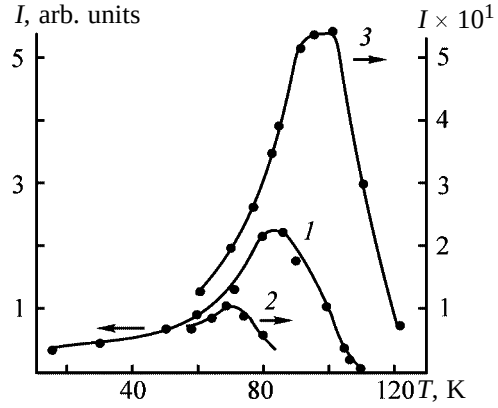

Fig. 6. Intensity of microwave absorption vs. temperature T: (*1*) glassy shungite in paraffin, (*2*) glassy selenium with 0.9 wt % shungite, and (*3*) glassy-crystalline selenium with 9 wt % shungite.

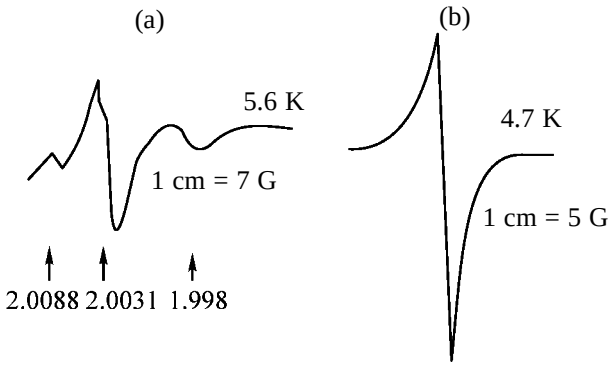

Fig. 7. ESR spectra of (a) amorphous shungite and (b) glassy selenium with 0.9 wt % shungite.

is the same. It consists in transitions between quasi-stationary quantum states with markedly different lifetimes.

The preservation of the fullerene structure in chalcogenide glass matrices also opens up new opportunities for preparation on their base of new disordered materials exhibiting high-temperature superconductivity.

ACKNOWLEDGMENTS

The author thanks M.D. Bal'makov, who participated in some parts of the study, for help in discussion of many of the results obtained.

REFERENCES

1. Bochvar, D.A. and Gal'pern, E.G., *Dokl. Akad. Nauk SSSR*, 1973, vol. 209, no. 3, pp. 610–612.
2. Sokolov, V.I., *Dokl. Ross. Akad. Nauk*, 1992, vol. 325, no. 5, pp. 991–993.

3. Sokolov, V.I., *Izv. Ross. Akad. Nauk, Ser. Khim.*, 1993, no. 1, pp. 10–19.
4. Kroto, H.W. *et al.*, *Nature*, 1985, vol. 318, pp. 162–165.
5. Curl, R.F. and Smalley, R.E., *Fullerenes, Sci. Am.*, October 1991, vol. 265, no. 4, pp. 32–41.
6. Vol'pin, M.E., *Vestn. Ross. Akad. Nauk*, 1992, no. 10, pp. 25–32.
7. Curl, R.F., *Carbon*, 1992, vol. 30, no. 8, pp. 1149–1155.
8. Kratschmer, W., *Nature*, 1990, vol. 347, pp. 354–388.
9. Smalley, R.E., *Usp. Fiz. Nauk*, 1998, vol. 168, pp. 323–330.
10. US Patent 5227038.
11. Kratschmer, W. and Huffman, D.R., *Carbon*, 1992, vol. 30, no. 8, pp. 1143–1147.
12. Sokolov, V.I. and Stankevich, I.V., *Usp. Khim.*, 1993, vol. 62, no. 5, pp. 455–473.
13. Hirsch, A., *The Chemistry of the Fullerenes*, Stuttgart: Georg Thieme, 1994.
14. Osip'yan, Yu.A. and Kveder, V.V., *Materialovedenie*, 1997, no. 1, pp. 2–6.
15. Zharikov, O.V., *Priroda*, 1992, no. 3, pp. 68–73.
16. Iijima, S., *Nature*, 1991, vol. 354, pp. 56–58.
17. Ebessen, T.W., *J. Phys. Chem. Solids*, 1997, vol. 58, no. 11, pp. 1979–1982.
18. Eletskii, A.V., *Usp. Fiz. Nauk*, 1997, vol. 167, no. 9, pp. 945–972.
19. Ivanovskii, A.L., *Kvantovaya khimiya v materialovedenii* (Quantum Chemistry in Materials Science), Yekaterinburg: Ural. Otd., Ross. Akad. Nauk, 1989.
20. *Fullereny i fullerenopodobnye struktury: Sbornik nauchnykh trudov* (Fullerenes and Fullerene-Like Structures: Coll. Sci. Works), Minsk: Bel. Gos. Univ., 2000.
21. *Fullereny i drugie uglerodnye klastery: Annotirovannyi ukazatel' patentnykh dokumentov 1988–1995 gg.* (Fullerenes and Other Carbon Structures: Annotated Index of Patent Literature for 1988–1995), St. Petersburg: Fond Intellektual'nogo Sotrudnichestva, 1995.
22. Blatt, J.L., *Theory of Superconductivity*, New York: Academic, 1964.
23. Nelson, D.L., Whittingham, M.S., and George, T.J., *Chemistry of High Temperature Superconductors, ACS Symp. Ser. 351*, Washington, DC, 1987, pp. 308–312.
24. Harrison, M.R., Hegedus, S.T., Freeman, W.G., *et al.*, *Chemistry of Oxide Superconductors*, Rao, C.N.R., Ed., Blackwell Scientific, 1988, pp. 131–146.
25. *Vysokotemperaturnye sverkhprovodniki* (High-Temperature Superconductors), Nelson, D., Wittingham, M., and George, T., Eds., Moscow: Mir, 1988.
26. Shveikin, G.P., Gubanov, V.A., Fotiev, A.A., *et al.*, *Elektronnaya struktura i fiziko-khimicheskie svoistva vysokotemperaturnykh sverkhprovodnikov* (Electronic Structure and Physicochemical Properties of High-Temperature Superconductors), Moscow: Nauka, 1990.
27. Larin, V.P., Sumarokov, V.N., Men'shenin, Yu.V., and Kuzovkina, N.N., *High-Temperature Superconducting Materials*, part 1: *Methods for Synthesis of HTSC Materials and Their Superconducting Properties, Obz. Elektron. Tekh.*, Ser. 6: *Mater.*, 1991, issue 9.1648.
28. Shabashov, V.A., *Sverkhprovodimost': Fiz., Khim., Tekh.*, 1993, vol. 6, no. 5, pp. 1043–1049.
29. Blinov, L.N., Likholit, I.L., Ananichev, V.A., *et al.*, *Pis'ma Zh. Tekh. Fiz.*, 1993, vol. 19, no. 12, pp. 47–50.
30. Blinov, L.N., Noskova, N.A., Orkina, T.N., *et al.*, *Pis'ma Zh. Tekh. Fiz.*, 1999, vol. 22, issue 9, pp. 58–63.
31. Parker, D.H., Chatterjee, K., Wurs, P., *et al.*, *Carbon*, 1992, vol. 30, no. 8, pp. 1167–1182.
32. Konarev, D.V. and Lyubovskaya, R.N., *Usp. Khim.*, 1999, vol. 69, no. 1, pp. 23–44.
33. Eletskii, A.V., *Usp. Fiz. Nauk*, 2000, no. 2, pp. 113–142.
34. Osawa, E., Yoshida, M., Ueho, H., *et al.*, *Fullerene Sci. Technol.*, 1999, vol. 7, no. 2, pp. 239–262.
35. Kratschmer, W., *Priroda*, 1992, no. 1, pp. 30–33.
36. Nagase, S., Kobayashi, K., and Acasaka, T., *Bull. Chem. Soc. Jpn.*, 1996, vol. 69, pp. 2131–2142.
37. Sueki, K., Kikuchi, K., Akiyama, K., *et al.*, *Chem. Phys. Lett.*, 1999, vol. 300, no. 1, pp. 140–144.
38. Xu, Z., Nakane, T., and Shinohara, H., *J. Am. Chem. Soc.*, 1996, vol. 118, pp. 11309–11310.
39. Kartsova, L.A. and Makarov, A.A., *Zh. Prikl. Khim.*, 2002, vol. 75, no. 11, pp. 1761–1767.
40. Belov, N.N., Sukhov, I.V., Bezmel'nitsyn, V.N., *et al.*, *Radiokhimiya*, 1994, vol. 36, no. 5, pp. 457–458.
41. Beck, M.T. and Mandi, G., *Fullerene Sci. Technol.*, 1997, vol. 5, no. 2, pp. 291–310.
42. Buvari-Barcza, A., Barcza, L., Brann, T., *et al.*, *Fullerene Sci. Technol.*, 1997, vol. 5, no. 2, pp. 311–323.
43. Bezmel'nitsyn, V.N., Eletskii, A.V., and Okun', M.V., *Phys. Usp.*, 1998, vol. 41, pp. 1091–1114.
44. Ruoff, R.S., Tse, D.S., Malhotra, R., and Lorents, D.C., *J. Phys. Chem.*, 1993, vol. 97, pp. 3379–3383.
45. Robert, D. J., Constantino, S.Y., Mattanjah, S. de Vries, *et al.*, *Nanotechnology*, 1992, vol. 3, no. 1, pp. 164–166.

46. Krestinin, A.V. and Moravskii, A.P., *Khim. Fiz.*, 1999, vol. 18, no. 3, pp. 58–66.
47. US Patent 5 300 203.
48. Bubnov, V.P., Kramnitskii, I.S., Laukhina, E.E., and Yagubskii, E.B., *Izv. Ross. Akad. Nauk, Ser. Khim.*, 1994, no. 5, pp. 805–809.
49. JPN Appl. 06-211 510.
50. WO Patent 92-20 622.
51. JPN Appl. 07-61 803.
52. Lian, Y., Shi, Z., Zhou, X., He, X., and Gu, Z., *Carbon*, 2000, vol. 38, pp. 2117–2121.
53. Turnbull, D., in *Physics of Non-Crystalline Solids*, Amsterdam: North Holland, 1965, pp. 41–65.
54. Goryunova, N.A. and Kolomiets, B.T., *Stekloobraznoe sostoyanie* (Glassy State), Moscow, 1960, pp. 71–78.
55. Myuller, R.L., *Khimiya tverdogo tela* (Solid-State Chemistry), Leningrad: Leningr. Gos. Univ., 1965, pp. 9–63.
56. Borisova, Z.U., *Khimiya stekloobraznykh poluprovodnikov* (Chemistry of Glassy Semiconductors), Leningrad: Leningr. Gos. Univ., 1972.
57. Borisova, Z.U., *Khal'kogenidnye poluprovodnikovye stekla* (Chalcogenide Semiconducting Glasses), Leningrad: Leningr. Gos. Univ., 1983.
58. Baidakov, L.A. and Blinov, L.N., *Tverdoe telo: amorfnoe sostoyanie veshchestva* (Solids: Amorphous State of Substance), Leningrad: Leningr. Politekh. Inst., 1984.
59. Feltz, A., *Amorphe und glasartige anorganische Festkorper*, Berlin: Akademie, 1983.
60. Toyoda, N., Sakaue, K., and Terauchi, H., *J. Phys. Soc. Jpn.*, 1994, vol. 63, no. 6, pp. 2025–2027.
61. Baidakov, L.A., Blinov, L.N., Kuznetsova, L.A., and Pocheptsova, N.S., *Pis'ma Zh. Tekh. Fiz.*, 1995, vol. 21, no. 6, pp. 74–78.
62. Baidakov, L.A., Blinov, L.N., and Pocheptsova, N.S., *Pis'ma Zh. Tekh. Fiz.*, 1986, vol. 12, no. 15, pp. 954–957.
63. Baidakov, L.A. and Blinov, L.N., *Novye idei v fizike stekla* (New Concepts in Physics of Glass), Moscow, 1987, pp. 59–66.
64. Baidakov, L.A., Blinov, L.N., and Baidakov, E.L., *Izv. Akad. Nauk SSSR, Neorg. Mater.*, 1989, vol. 25, no. 7, pp. 1578–1581.
65. Baidakov, L.A., Blinov, L.N., and Pocheptsova, N.S., *Pis'ma Zh. Tekh. Fiz.*, 1992, vol. 18, no. 10, pp. 11–15.
66. Baidakov, L.A., *Fiz. Khim. Stekla*, 1994, vol. 20, no. 3, pp. 69–77.
67. Baidakov, L.A. and Blinov, L.N., Abstracts of Papers, *Nekristallicheskie poluprovodniki-89* (Noncrystalline Semiconductors-89), Uzhgorod, 1989, vol. 1, pp. 160–162.
68. Blinov, L.N. and Kuznetsova, L.A., *J. Mater. Sci. Lett.*, 2002, vol. 21, pp. 165–167.
69. Mott, N.F., *J. Non-Crystalline Solids*, 1993, vols. 164–166, pp. 1177–1178.
70. Blinov, L.N., Licholit, I.L., and Baidakov, L.A., Abstracts of Papers, *Int. Workshop "Fullerenes and Atomic Clusters,"* St. Petersburg, 1993, pp. 55.
71. Blinov, L.N., Licholit, I.L., and Baidakov, L.A., Abstracts of Papers, *185 Conf. of Am. Electrochem. Soc.*, San-Francisco, 1994, p. 219.
72. Bal'makov, M.D., Blinov, L.N., and Baidakov, L.A., *Fiz. Khim. Stekla*, 1995, vol. 21, no. 4, pp. 321–329.
73. Zhu, L., Xu, Z., Iihg, Z., *et al.*, *Fullerene Sci. Technol.*, 1993, vol. 1, no. 1, pp. 45–53.
74. Bal'makov, M.D., Blinov, L.N., and Pocheptsova, N.S., *Tech. Phys. Lett.*, 1994, vol. 20, no. 6, pp. 444–445.
75. Bal'makov, M.D., *Fiz. Khim. Stekla*, 1989, vol. 15, no. 2, pp. 293–295.
76. Bal'makov, M.D., *Fiz. Khim. Stekla*, 1992, vol. 18, no. 3, pp. 1–22.
77. Bal'makov, M.D., *Stekloobraznoe sostoyanie veshchestva* (Glassy State of Substance), St. Petersburg: Sankt-Peterb. Gos. Univ., 1996.
78. Ginzburg, V.L. and Kirzhnits, D.A., *Usp. Fiz. Nauk*, 1987, vol. 152, no. 4, pp. 575–582.
79. Solodovnikov, S.P., Bashlov, V.V., and Sokolov, V.I., *Dokl. Ross. Akad. Nauk*, 1993, vol. 330, no. 2, pp. 220–222.
80. Buravov, L.I., D'yachenko, O.A., Konovalikhin, S.V., *et al.*, *Izv. Ross. Akad. Nauk, Ser. Khim.*, 1994, no. 2, pp. 262–266.
81. Kholodkevich, S.V., Bekrenev, A.V., Donchenko, V.K., *et al.*, *Dokl. Ross. Akad. Nauk*, 1993, vol. 330, no. 3, pp. 340–341.
82. Blinov, L.N. Karataev, V.I., Baidakov, L.A., *et al.*, *Fiz. Khim. Stekla*, 1990, vol. 16, no. 3, pp. 337–342.
83. Sherman, A.B., Shakin, O.V., Lemanov, V.V., *et al.*, *Pis'ma Zh. Tekh. Fiz.*, 1995, vol. 21, no. 6, pp. 19–22.
84. Nemilov, S.V., *Fiz. Khim. Stekla*, 1991, vol. 17, no. 3, pp. 511–514.
85. Bal'makov, M.D., *Fiz. Khim. Stekla*, 1992, vol. 18, no. 6, pp. 152–159.
86. Bal'makov, M.D., *Fiz. Khim. Stekla*, 1986, vol. 12, no. 5, pp. 527–535.
87. Bal'makov, M.D., *Fiz. Khim. Stekla*, 1988, vol. 14, no. 1, pp. 19–28.
88. Bal'makov, M.D., *Fiz. Khim. Stekla*, 1981, vol. 7, no. 5, pp. 535–543.
89. Blinov, L.N., Noskova, N.A., Orkina, T.N., *et al.*, *Pis'ma Zh. Tekh. Fiz.*, 1996, vol. 22, no. 9, pp. 58–63.
90. *Vysokotemperaturnaya sverkhprovodimost'* (High-Temperature Superconductivity), Kiselev, A.A., Ed., Leningrad: Leningr. Gos. Univ., 1990.

Russian Journal of Applied Chemistry, Vol. 76, No. 5, 2003, pp. 700–705. Translated from Zhurnal Prikladnoi Khimii, Vol. 76, No. 5, 2003, pp. 728–733.

INORGANIC SYNTHESIS AND INDUSTRIAL INORGANIC CHEMISTRY

Nonhydrothermal Synthesis and Properties of Saponite-Like Materials

R. V. Prikhod'ko, M. V. Sychev, I. M. Astrelin, K. Erdmann, E. J. M. Hensen, and R. A. van Santen

Kiev Polytechnic Institute, National Technical University of the Ukraine, Kiev, Ukraine
Copernicus University, Torun, Poland
Technical University of Eindhoven, Eindhoven, Netherlands

Received July 24, 2001; in final form, June 2002

Abstract—Main features of nonhydrothermal synthesis of saponite-like materials containing Zn(II) and Mg(II) cations in octahedral networks were studied. Optimal conditions for the synthesis were determined. The influence exerted by the double-charged structure-forming cation on the rate of structure formation in the synthesized materials and also on their pore structure and thermal stability was studied.

Unique catalytic and adsorption properties of natural clay minerals are known and are a subject of numerous papers [1]. However, nonuniformity of the chemical composition and pore structure and a considerable content of impurities considerably limit their application in catalysis [2]. At the same time, synthetic clays have homogenous composition and structure, and their physicochemical properties can be controlled already in the stage of their preparation [2–4]. This fact, and also the possibility for the directional synthesis of materials having no natural analogs open new prospects for catalytic applications [5–8].

Synthetic clays are usually prepared under hydrothermal conditions (5–17 MPa, 423–773 K) [9] using special expensive autoclaves, which considerably limits applications of these materials. Therefore, it is urgent to develop alternative procedures for their preparation, among which the nonhydrothermal synthesis (synthesis under normal pressure) is the most promising [5]. The applicability of this procedure to obtaining saponite-like materials was shown in [5–8]. The key moment in the process is the use of urea as a hydrolyzing agent; its thermally initiated decomposition makes it possible to smoothly vary pH of the reaction medium [10] and thus to control the hydrolysis rate and hence the formation of the target material [5–7]. However, detailed information on the features of the nonhydrothermal preparation of synthetic clays is lacking.

Clay minerals included in the group of natural layered aluminosilicates are formed mainly from two structural fragments, namely, the networks of silicon–oxygen tetrahedra SiO_4 (*T*-network) and of aluminum–oxygen octahedra $Al(O, OH)_6$ (*O*-network) [11]. These networks are joined through O^{2-} ions into layers, which form the basis of the unit cell of the minerals. The structure of smectites, including saponite, is formed by layers separated by interlayer intervals, in which two *T*-networks are joined with an *O*-network lying between them (*T*–*O*–*T* minerals). The isomorphous substitutions, e.g., Al(III)→Si(IV), in the *T*-networks give rise to an excessive negative charge which is compensated by either positive charges localized in the *O*-networks or charges of cations arranged in interlayer spaces [1, 2, 11]. The idealized formula of saponite is $M^{z+}_{x/z}[Mg_6](Si_{8-x}Al_x)\cdot O_{20}(OH)_4\cdot nH_2O$, where M are exchange (interlayer) cations; cations in the composition of the *O*-network are given in brackets; ions in tetrahedral networks are given in parentheses; $x = 1.2$ [11]. This mineral is of considerable interest for heterogeneous acid catalysis [2, 5, 6], because its surface has enhanced acidity owing to the isomorphism Al(III) → Si(IV) in the *T*-networks.

The aim of this work was to reveal the main features of the synthesis of Zn- and Mg-containing synthetic analogs of natural saponite under nonhydrothermal conditions and to study their physicochemical properties.

EXPERIMENTAL

The objects of this study were synthesized by a procedure close to that described in [5–8]. We used

1070-4272/03/7605-0700$25.00

$Na_2SiO_3 \cdot 9H_2O$ (27 wt % SiO_2), $Al(NO_3)_3 \cdot 9H_2O$, $Mg(NO_3)_2 \cdot 6H_2O$, or $Zn(NO_3)_2 \cdot 6H_2O$ as sources of Si(IV), Al(III), and double-charged cations.

The synthesis procedure is described for a sample with the atomic ratio Si(IV)/Al(III) = 12 as example. An $Al(OH)_4^-$ sol was prepared by dissolution of 4.22 g (11.25 mmol) of $Al(NO_3)_3 \cdot 9H_2O$ in 2 M NaOH (28 cm^3). Then this sol was added in portions with vigorous stirring to a solution of $Na_2SiO_3 \cdot 9H_2O$ (30.0 g, 0.135 mol) in 75 cm^3 of demineralized water. The resulting gel was kept at room temperature for 1 h without stirring, suspended with stirring in 600 cm^3 of H_2O, and heated to 363 K. Then 500 cm^3 of a separately prepared aqueous solution containing 32.60 g (0.109 mol) of $Zn(NO_3)_2 \cdot 6H_2O$ [or 28.1 g of $Mg(NO_3)_2 \cdot 6H_2O$ (0.109 mol)] and $CO(NH_2)_2$ (0.15–0.80 mol) was added to the heated gel suspension. The addition rate was selected so that the temperature of the reaction mixture did not decrease by more than 10 K. This mixture was heated at 363 K for 3–72 h with continuous stirring. The resulting solid phase was separated by filtration, washed with five portions of distilled water, and dried for 12 h at 383 K. The samples containing Zn(II) and Mg(II) cations in octahedral networks are denoted as Zn-SP and Mg-SP, respectively.

The pH of the reaction medium was monitored with a CG804 (Schott–Gerade) pH-meter with automatic data recording. The ^{27}Al NMR spectra were obtained in the magic angle spinning mode on a Bruker AMX 300 WB spectrometer (standard ZrO_2 rotor, magnetic field frequency 78.20 MHz). The ^{27}Al chemical shift was determined relative to $[Al(H_2O)_6]^{3+}$. The X-ray diffraction (XRD) patterns of the synthesized materials were taken on DRON-3 and Philips 1170 diffractometers (CuK_α radiation, λ = 0.154178 nm, Ni filter). The adsorption–desorption isotherms of nitrogen (77 K) were obtained on an ASAP 2010 (Micromeritics) adsorption installation using samples preliminarily evacuated for 5 h at 473 K and a pressure of 10^{-2} Pa. The IR spectra of samples prepared as pellets in thoroughly dried KBr (1 : 60) were recorded on Specord-M80 and FTIR Perkin–Elmer 2000 spectrophotometers.

The content of Mg(II), Zn(II), and Al(III) cations was determined by atomic absorption spectroscopy (Perkin–Elmer PE 3030 spectrophotometer). The cation-exchange capacity (CEC) of the synthesized materials was determined according to [12] by adsorption of a copper(II) ethylenediamine complex at pH 7.

The experimental dependences of pH of the medium on the synthesis time (Fig. 1) have no pronounced

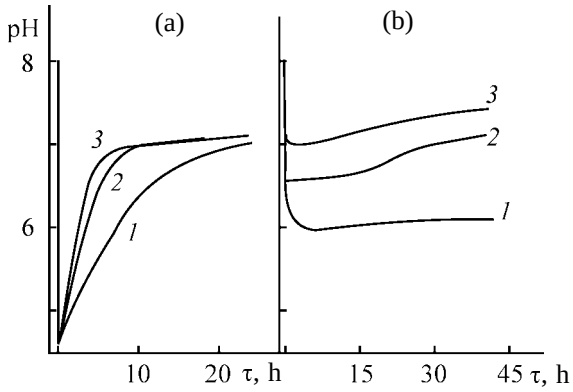

Fig. 1. Variation with synthesis time τ of pH of the reaction medium at various urea concentrations. Sample: (a) Zn-SP and (b) Mg-SP; the same for Fig. 3. $CO(NH_2)_2$ concentration, M: (*1*) 0.15, (*2*) 0.45, and (*3*) 0.80.

extrema, which suggests smooth nucleation and growth of particles of the synthesized materials. It is most probable that the decrease in pH observed in the initial moment of the reaction is due to the formation of $Zn(OH)_2$ and $Mg(OH)_2$ phases. A considerable difference in the initial pH values during the syntheses of Zn-SP and Mg-SP may be due to different solubility of these hydroxides, which is much higher in the case of $Mg(OH)_2$.

The ^{27}Al NMR spectra of the starting gels used for the synthesis of Zn-SP and Mg-SP contain a resonance of tetrahedrally coordinated Al(III) cations [Al(III)(tetr.)] with a chemical shift δ about 54 ppm (Fig. 2). At the reaction time of 3 h, a signal of octahedrally coordinated Al(III) (δ = 10 ppm) and a shoulder with δ = 64 ppm assignable to Al(III)(tetr.) are observed in the spectrum of Zn-SP. The latter signal is characteristic of Al(III) cations localized in tetrahedral networks of smectites (Al–O–Si bonds) [13]. When the syntheses time increases to 12, and especially to 24 h, the intensity of this resonance considerably increases, which is accompanied by the disappearance of the signal with δ = 24 ppm (Fig. 2a). In this case, the change in the urea concentration within these limits affects the parameters of the ^{27}Al NMR spectra only slightly. Nevertheless, the strongest signal of Al(III)(tetr.) was observed for a sample prepared in the presence of 0.45 mol of $CO(NH_2)_2$. The data obtained suggest that the incorporation of Al(III) cations into the crystal lattice of Zn-SP is practically complete within approximately 24 h. In the case of Mg-SP, this process is much slower, and a weak signal of Al(III)(tetr.) with δ about 64 ppm was detected only at the reaction time of 30 h. Its intensity considerably increases as the synthesis time is increased

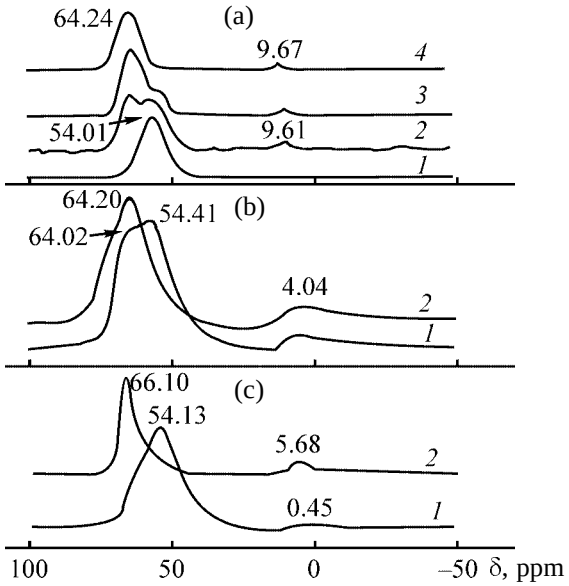

Fig. 2. ^{27}Al NMR spectra of synthesized materials. (δ) Chemical shift. Sample: (a) Zn-SP and (b, c) Mg-SP; the same for Fig. 4. Synthesis time τ (h): (a) (*1*) 0.5, (*2*) 3.0, (*3*) 12, and (*4*) 24; (b) (*1*) 30 and (*2*) 36; (c) (*1, 2*) 36. $CO(NH_2)_2$ concentration, M: (a, b) 0.45 and (c) 0.80.

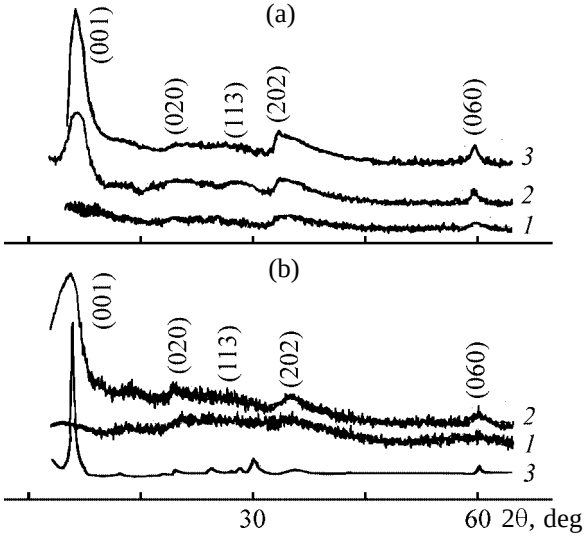

Fig. 3. Diffraction patterns of materials prepared at various synthesis times. (2θ) Bragg's angle. Synthesis time τ, h: (a) (*1*) 3.0, (*2*) 12, and (*3*) 24; (b) (*1*) 5.0; (*2*) 36, and (*3*) natural saponite (Ballarat).

to 36 h (Fig. 2b). In this case, the amount of urea and hence the pH value crucially affect the course of Al(III) incorporation into the tetrahedral network of the synthesized material (Fig. 2c).

The increase in the Si(IV)/Al(III) atomic ratio in the reaction gel from 5 to 12 results in an appreciable decrease in the content of octahedrally coordinated Al(III)., with the content of Al(III)(tetr.) remaining virtually unchanged. Therefore, we can conclude that saponite-like materials with preferential Al(III) localization in the tetrahedral networks (a characteristic feature of this smectite [3, 5]) can be obtained under non-hydrothermal conditions only at Si(IV)/Al(III) ≥ 12. Therefore, further experiments were performed using samples with the Si(IV)/Al(III) atomic ratio of 12 and Mg-containing materials synthesized in the presence of 0.80 mol of urea.

The X-ray diffraction analysis has shown that, in the case of Zn-SP, a certain amount of a saponite-like phase is formed within 3.0–3.5 h. As the synthesis time is increased to 12 h, its amount and the crystallinity of the resulting material increase (Fig. 3a), as indicated by the growth of the intensity of the long-range order basal reflections (020/110) and (113) [4, 6]. At the reaction time increased to 24 h, the X-ray peaks become narrower, and the intensity of the first basal reflection [*d*(001)] considerably increases. At the synthesis time of 36 hm the shape of X-ray diffraction patterns undergoes no significant changes, suggesting that the crystallization of Zn-SP is complete within 24 h. The macrostructure of this material is formed by crystallites with fairly large particles connected to each other predominantly by a plane–plane motif, as indicated by considerable intensity and symmetry of basal reflections [4, 5, 14, 15].

The X-ray diffraction patterns of Mg-saponite obtained at various synthesis times are given in Fig. 3b. They show that the structure of this material is formed much more slowly than that of Zn-SP. At a reaction time of 5 h only weakly pronounced reflections (060) and (201) are detected. The diffraction pattern of Mg-SP synthesized in 36 h contains all the basal reflections characteristic of saponite [4, 14]. However, the corresponding peaks remain fairly broad, with the value of *d*(001) being greater than for Zn-SP (Fig. 3b). Further prolongation of the synthesis (to 72 h) only slightly affects the intensity and width of the X-ray peaks. It should be noted that it is almost impossible to obtain X-ray patterns for Mg-SP using nonoriented samples. This fact suggests that the macrostructure of this material is formed by small particles, the majority of which are connected to each other by a plane–facet or facet–facet motif [4]. Such a structure is called "house of cards" or delaminated [2, 16]; its formation was noted earlier in the case of low-temperature syntheses of others trioctahedral Mg-containing clays [15].

The capability to swell in polar media, in particular, in ethylene glycol vapor, is a characteristic feature

Pore structure parameters, elemental composition, and exchange capacity of synthetic saponite-like materials

Sample	τ,* h	S_{BET}, $m^2\ g^{-1}$	V_{lim}	V_{micro}	SiO_2	Al_2O_3	$M^{2+}O$	CEC, mg-equiv g^{-1}
			$cm^3\ g^{-1}$		wt %			
Zn-SP	12	142.24	0.162	0.003	35.30	2.45	38.96	0.97
	24	218.72	0.183	0.004	35.25	2.49	38.86	1.20
Mg-SP	24	599.50	0.625	0.150	48.24	3.40	26.33	0.82
	36	592.14	0.323	0.280	48.20	3.43	25.10	1.25

* (τ) Synthesis time.

of smectites [1]. We found that Zn-SP samples synthesized in 3 or 24 h have this property, as seen from an increase in the size of their interlayer space Δd; in the sample prepared in 24 h, this effect is more pronounced. Among the Mg-SP materials, the swelling was detected only for samples synthesized in more than 30 h. These observations agree with the assumption that the crystallization of Zn-containing saponite is practically complete in 24 h, whereas the formation of the Mg-SP structure requires a longer time. Furthermore, the nature of the structure-forming double-charged cation appreciably affects the value of Δd. In the case of Mg-SP samples, it is greater by 0.3–0.4 nm than that in their Zn-containing analogs. This may be due to the effect of a smaller size of Mg-SP crystallites and also to weaker electrostatic interaction of its silicate layers [14]. In view of these facts, we further studied the Zn-SP samples synthesized in 12 and 24 h and the Mg-SP samples synthesized in 24, 36, and 72 h.

The isotherms of N_2 adsorption–desorption for the Zn-containing materials (Fig. 4a) can be assigned to type IV according to the IUPAC classification [17]. This is indicative of the predominantly mesoporous structure [18]. The observed shape of the hysteresis loop (mixed type H4 + H2 [17–19]) is indicative of the presence of slit- and bottle-like pores [19]. The increase in the synthesis time from 12 to 24 h only slightly affects the shape of the isotherms and the parameters of the pore structure of Zn-SP samples (see table; Fig. 4a). In the case of Mg-containing materials, these parameters, as well as the shape of the isotherms of nitrogen adsorption, strongly depend on the synthesis time (see table; Fig. 4b). The sample obtained in 24 h is mainly mesoporous (type IIb isotherm [15]). Taking into consideration the NMR and XRD data, we can explain this fact by the presence of an amorphous phase. For materials prepared in a longer time (36–72 h), the adsorption isotherms differ insignificantly, and they can be assigned to distorted type I [20], which is characteristic of microporous substances [18–20]. A narrow hysteresis loop (Fig. 4b) close to the H4 type [18] points to the presence of slit-like pores. Similar isotherms were obtained for synthetic laponite, a mineral with a delaminated structure [20]. Therefore, we can suggest that the macrostructures of Mg-SP and laponite are similar to each other, which also agrees with the above-given XRD data. Thus, we can conclude that the formation of the pore structure of Mg-containing saponite is complete in 36 h.

The nature of double-charged cations strongly affects the size and volume of pores and the specific surface area of the synthesized clays (see table). Sam-

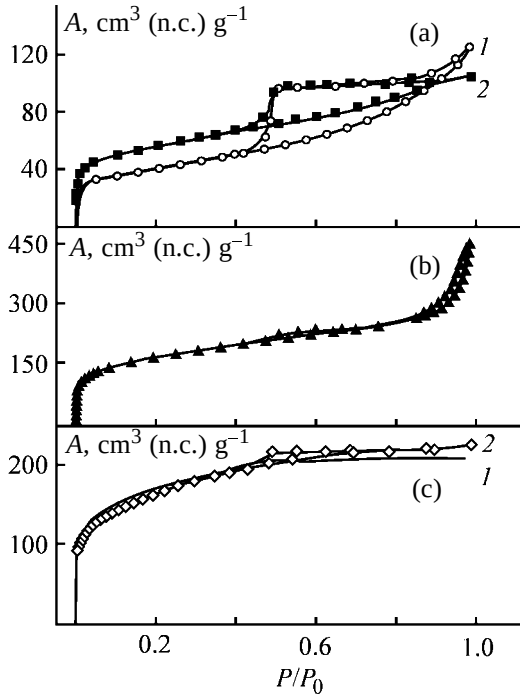

Fig. 4. Nitrogen adsorption–desorption isotherms. (*A*) Sorbed volume and (P/P_0) relative pressure. Synthesis time τ, h: (a) (*1*) 12 and (*2*) 24; (b) 24; (c) (*1*) 36 and (*2*) 72.

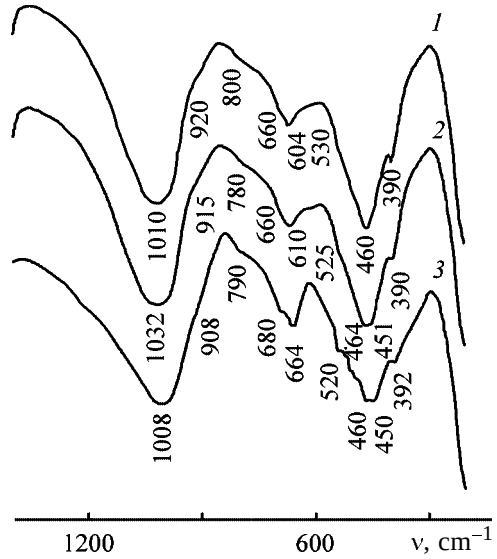

Fig. 5. IR spectra of samples. (ν) Wave number. Sample: (*1*) Zn-SP, (*2*) Mg-SP, and (*3*) natural saponite (Ballarat).

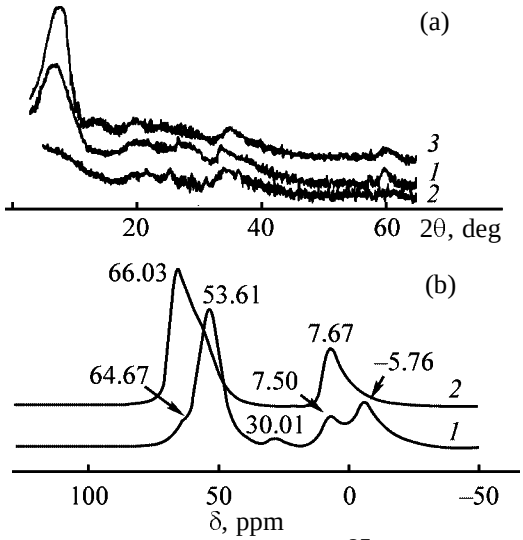

Fig. 6. (a) Diffraction patterns and (b) ^{27}Al NMR spectra of calcined samples. (2θ) Bragg's angle and (δ) chemical shift. Sample: (a) (*1, 2*) Zn-SP and (*3*) Mg-SP; (b) (*1*) Zn-SP and (*2*) Mg-SP. *T*, K: (a) (*1*) 673, (*2*) 773, and (*3*) 873; (b) (*1*) 773 and (*2*) 873.

ples of Zn-SP are mainly mesoporous, whereas Mg-containing saponite-like materials are microporous.

The IR spectra of Zn-SP and Mg-SP samples in the region of lattice vibrations are given in Fig. 5. It is seen that the nature of the structure-forming double-charged cation affects the position of the maximum of the strong band near 1020 cm^{-1} (Si–O–Al bending vibrations [13, 21]). Less intensive absorption bands at 915–920, 800–780, and 660–620 cm^{-1} are assignable to the Si(Al)–O, Si–O–Al, Al–OH–Mg, and Si–O–Mg vibrations, respectively [11, 18]. The bands of the Mg(Zn)–OH, Si–O–Mg, or Si–O–Zn vibrations (550–527 and 460–440 cm^{-1}) are also present in the IR spectra [13, 22]. All these absorption bands are characteristic of lattice vibrations of trioctahedral smectites [21, 22], including natural saponite (see spectrum of the reference sample). The chemical compositions of the synthesized materials and their cation–exchange capacities (see table) also agree with the corresponding published data for this clay mineral [14, 22].

Summarizing the data obtained, we can conclude that the optimal parameters of the Zn-SP synthesis are the time of 24 h and the urea concentration in the reaction mixture of 0.45 M, whereas for the synthesis of its Mg-containing analog these are 36 h and 0.80 M, respectively.

The thermal stability is one of the major characteristics of heterogeneous catalysts [23]. As the substances studied in this work can be potentially used in high-temperature catalytic reactions [4–8], it seemed important to study the stability of their structure at elevated temperatures. We heated the samples stepwise in an air flow in the range 298–1073 K at a rate of 5 deg min^{-1}, with keeping at selected temperatures for 18 h. The structural transformations were monitored by XRD and ^{27}Al NMR.

The results obtained are shown in Fig. 6. It is seen from the X-ray patterns (Fig. 6a) that the calcination of Zn-SP at 623 K makes its structure amorphous to a considerable extent, and at 773 K its crystallinity is virtually fully lost. The NMR spectrum appreciably changes in the process (Fig. 6b). The signal at δ = 64 ppm [Al(III)(tetr.)] becomes considerably less symmetric. The computer resolution of this signal has shown that it is a superposition of two signals with δ 62 and 56 ppm. The latter signal is assignable to the Al(III)(tetr.) resonance in an amorphous phase. Simultaneously, a weak signal appears in the NMR spectrum near 30 ppm, which is assignable to the resonance of five-coordinate Al(III) [24]. In the case of Mg-SP, the calcination at temperatures of up to 873 K does not make its structure amorphous to a noticeable extent (Fig. 6a), and the shape of the ^{27}Al NMR spectra does not change appreciably (Fig. 6b). As the temperature is increased further to 973 K, the Al(III)(tetr.) signal becomes less symmetric, suggesting partial degradation of the crystal structure. Thus, Mg-SP is more thermally stable than its Zn-containing analog. This may be due to the effect of the size of the double-charged cation forming the octahedral networks of synthetic saponite. It was

shown in the case of trioctahedral micas that the minerals containing structure-forming cations with large ionic radii have a lower thermal stability [25].

It should be specially noted that the temperatures at which the structures of the synthesized materials degrade are higher than those known for natural saponites. This fact once again demonstrates prospects for using synthetic clays as heterogeneous catalysts.

CONCLUSIONS

(1) Experiments on optimization of the conditions for preparing of Zn- and Mg-containing synthetic analogs of natural trioctahedral smectite (saponite) under conditions of nonhydrothermal synthesis showed that the preferential localization of Al(III) cations in the tetrahedral networks of these materials is possible only at the atomic ratios Si(IV)/Al(III) ≥12.

(2) The rate of formation of the structure of M(II)-containing synthetic saponites [the process is complete in 24 h for Zn(II) and 36 h for Mg(II)], the parameters of their pore structure, and the macrostructure and thermal stability depend on the nature of the structure-forming cation [Zn(II) or Mg(II)]. Synthetic Mg-saponite has a large specific surface area (650 $m^2 g^{-1}$) and a high thermal stability (up to 973 K).

ACKNOWLEDGMENTS

The authors are grateful to M. Mittelmayer-Haseleger (University of Amsterdam, Netherlands) for adsorption measurements. The work was financially supported by the Ministry of Education and Science of the Ukraine (grant 0102 U 002 191), Committee for Scientific Research of Poland (KBN), and also NWO, the Netherlands (Spinoza grant).

REFERENCES

1. Gil, A., Gandia, L.M., and Vicente, M.A., *Catal. Rev.-Sci. Eng.*, 2000, vol. 42, pp. 145–212.
2. Vaccari, A., *Appl. Clay Sci.*, 1999, vol. 14, pp. 161–198.
3. Lambert, J.-F., Chevelier, S., Frank, R., *et al.*, *J. Chem. Soc., Faraday Trans.*, 1994, vol. 90, no. 4, pp. 675–682.
4. Thomas, J.M. and Theocharis, C.R., *Perspectives in Catalysis*, Thomas, J.M. and Zamaraev, K.I., Eds., London: Blackwell Scientific, 1992, pp. 465–488.
5. Vogels, R.J.M.J., Kerkhoffs, M.J.H.V., and Geus, J.W., *Stud. Surf. Sci. Catal.*, 1995, vol. 91, pp. 1153–1161.
6. Sychev, M. and Prihod'ko, R., *Stud. Surf. Sci. Catal.*, 1998, vol. 91, pp. 967–974.
7. Sychev, M., *Proc. 12th Int. Zeolite Conf., Mater. Res. Soc.*, 1999, vol. 2, pp. 1261–1268.
8. Prikhod'ko, R.B., Enhbold, T., Astrelin, I.M., and Sychev, M.V., *Neftekhimiya*, 1999, vol. 39, no. 6, pp. 461–467.
9. Whitney, G., *Clays Clay Miner.*, 1983, pp. 1–8.
10. Geus, J.W., *Stud. Surf. Sci. Catal.*, 1983, vol. 16, pp. 1–34.
11. Rozengart, M.I., V'yunova, G.M., and Isagulyants, G.V., *Usp. Khim.*, 1988, vol. 57, no. 2, pp. 204–227.
12. Bergaya, F. and Vayer, M., *Appl. Clay Sci.*, 1997, vol. 12, pp. 275–280.
13. Li, L., Liu, X., Ge, Y., *et al.*, *J. Phys. Chem.*, 1993, vol. 97, pp. 10 389–10 393.
14. Kloprogge, J.T., *Ph.D. Thesis*, the Netherlands: Univ. of Utrecht, 1992.
15. Decarreau, A., *Sci. Geol. Mem.*, 1983, vol. 74, pp. 1–191.
16. Schoonheydt, R.A., Introduction to Zeolite Science and Practice, *Stud. Surf. Sci. Catal.*, 1991, vol. 52, pp. 201–238.
17. Sing, R.S.W., Everett, D.H., Haul, R.A.W., *et al.*, *Pure Appl. Chem.*, 1985, vol. 57, no. 4, pp. 603–619.
18. Rouquerol, F., Rouquerol, J., and Sing, K.S.W., *Adsorption by Powder and Porous Solids: Principles, Methodology, and Applications*, San Diego: Academic, 1999, pp. 439–441.
19. Gregg, S.J. and Sing, K.S.W., *Adsorption, Surface Area, and Porosity*, London: Academic, 1982.
20. Cool, P. and Vansant, E.F., *Microporous Mater.*, 1996, vol. 6, pp. 27–36.
21. Maller, H.W. van der and Beutelspacher, H., *Atlas of Infrared Spectroscopy of Clay Minerals and Their Admixtures*, Amsterdam: Elsevier, 1976.
22. Vicente, M.A., Banares-Munoz, M.A., Suarez, M., *et al.*, *Langmuir*, 1996, vol. 12, no. 21, pp. 5143–5147.
23. Kieboom, A.P.G., Moulijn, J.A., Sheldon, R.A., and Leeuwen, P.W.N.M. van, in *Catalysis: An Integrated Approach*, Amsterdam: Elsevier, 1999, pp. 29–80.
24. Engelhardt, G. and Michel, D., *High Resolution Solid State NMR of Silicates and Zeolites*, New York: Wiley, 1987.
25. Hazen, R.M. and Wanes, D.R., *Am. Mineral.*, 1972, vol. 57, pp. 103–129.

Russian Journal of Applied Chemistry, Vol. 76, No. 5, 2003, pp. 706–709. Translated from Zhurnal Prikladnoi Khimii, Vol. 76, No. 5, 2003, pp. 734–737.

INORGANIC SYNTHESIS AND INDUSTRIAL INORGANIC CHEMISTRY

Burning of Sodium Chlorate Based Formulations

O. N. Kirsanov, Yu. A. Berezuev, V. I. Ostrovskii, and V. N. Tyminskii

Prikladnaya Khimiya Russian Scientific Center, St. Petersburg, Russia
Kontekh Ltd., St. Petersburg, Russia

Received January 22, 2002

Abstract—The burning velocity of sodium chlorate based formulations with polyethylene and kerogen under atmospheric conditions was studied in relation to composition, i.e., oxygen excess factor.

The increasing prospects for use of high-energy explosive formulations (blends) in various branches of the national economy: mining, building, metal working, and manufacture of construction materials, required enhanced safety measures (including environmental safety) in use of these formulations. A necessity has arisen for development of a procedure for calculating charges of these formulations with account of specific properties of a medium to be destroyed.

This study was devoted to development and analysis of formulations based on some widely used oxidizing agents and low-cost and readily available combustibles whose burning occurs in the deflagration mode.

In the first stage, we chose a formulation based on sodium chlorate (SC) and hydrocarbons. The kinetics of burning of SC-based formulations with polyethylene (PE) or kerogene (KE) was analyzed on a laboratory setup. Our goal was to search for and develop new materials for mining of block stone (for building industry), with sparing approach to natural and artificial objects. The studies in this direction, e.g., those concerned with pastelike hydrogen peroxide [1, 2], have been limited to separate tests and are hindered now by difficulties encountered in the development of a formulation that would be stable in prolonged storage. As for blended explosives based on liquid oxygen and formulations with liquid hydrogen peroxide, their use is problematic, except in special cases, because handling them in field conditions is complicated and dangerous. Use of standard explosives based on chlorates and perchlorates [3] is undesirable because of the detonation mode of their physicochemical conversion [4]. Detonation leads to cracking and microcracking both in a block being separated and in the solid rock, which makes the yield of the finished product lower, and the time during which a deposit can be in service, shorter [4]. According to preliminary data, the necessary requirements can be satisfied by a formulation based on SC and hydrocarbons, placed in a special gas generator [5, 6]. In energy-related parameters, the formulations proposed are somewhat inferior (by $5 \pm 15\%$) to those based on hydrogen peroxide. The environmental impact of formulations of this kind exceeds that of peroxide formulations only slightly.

The aim of this study was to determine the burning rate of formulations based on SC (which is the most accessible and cheap among chlorates and perchlorates) and hydrocarbons under atmospheric conditions as a preliminary stage of works necessary for their industrial implementation.

EXPERIMENTAL

In an experimental study of the burning of an SC formulation with combustibles, the rates of burning and weight change were determined in order to analyze the manner in which the solid residue of burning products moves away from the flame zone. The combustion time of a formulation was measured on a setup similar to that described previously in [1], between two reference points spaced by $l = 55$ mm (determined when mounting the contacts). In this case, the measuring system included two electric circuits with a single dc power source ($V = 5$ V) connected to an electrically conducting casing. Each circuit had an electric contact introduced through an insulating ceramic channel to within the casing. The instants of time at which the combustion surface passed through the reference points were recorded as successive closures of contacts in two electric circuits connected to an S9-8 digital storage oscilloscope. Another setup was used to determine qualitatively how the formulation weight

1070-4272/03/7605-0706$25.00

changes in the course of burning: whether the burning rate varies with time and, if so, whether it decreases or increases as the formulation burns out. The setup was constituted by VLK-500 g electromechanical balance with an inductive displacement sensor attached to the balance beam. The tests were performed under atmospheric pressure at ambient temperature. The combustible formulation included SC oxidant of 50–150-μm fraction (50% 25–65-μm fraction) and PE of 10–180-μm fraction (71% 15–65-μ fraction) or KE of 20–150-μm fraction. Several experiments were performed with addition of Al powder of 10–25-μm fraction to make higher the energy released in the process. In each run, the SC weight was varied within the range 57–82 g. A preliminarily interspersed mixture of SC and PE (KE) of required (as regards the oxidant excess factor) composition was charged to a height of 80 mm into the experimental vessel (l = 30 mm) made of Cr18Ni9Ti steel, and the weights of the vessel and charge were measured. The scatter in bulk density did not exceed 7% for the oxidant excess factor equal to unity, and 4% otherwise. The fuel formulation was ignited in both setups with a 1-g weighed portion of the PTT paste, using a Nichrome coil (V = 12 V, R = 1 Ω). To obtain more reliable results, all the tests were replicated at least twice. The linear burning velocity (mm s^{-1}) was determined as

$$U = l/t_b,$$

where l is the distance between the reference points (mm), and t_b is the time of burning of a formulation between the reference points (s).

The overall relative error in measuring the linear velocity did not exceed ±10%.

The specific mass velocity of burning, U_m (g cm^{-2} s^{-1}), was calculated by the formula

$$U_m = mh_r/(hft_b),$$

where m is the total charge of a formulation in the casing (g); h_r, the distance between the reference points, 55 mm; h, the total height (m) to which the casing is charged with a weighed portion m of a formulation; $f = 0.785d^2$, the area of the internal cross section of the casing (mm^2).

The main results obtained in studying the influence exerted by the excess of the oxidant on the linear velocity U (mm s^{-1}) of burning of a formulation are shown in Fig. 1a. The lines represent regression equations derived by polynomial processing of experimental data by the least-squares method. For formulation no. 1 (SC + PE), the following regression equation is obtained with a correlation factor R^2 = 0.950:

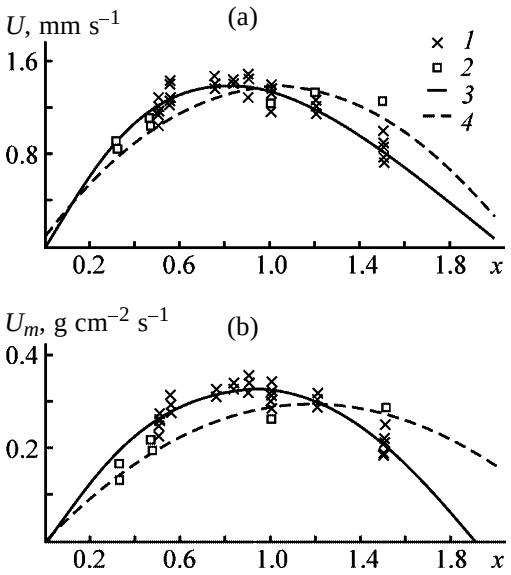

Fig. 1. (a) Linear burning velocity U and (b) U_m in relation to composition (oxidant excess factor x). Formulation: (*1*) no. 1 (SC + PE) and (*2*) no. 2 (SC + KE); (*3*, *4*) approximations for formulation nos. 1 and 2, respectively.

$$U = 0.554x^3 - 2.983x^2 + 3.797x - 0.004.$$

Consequently, the maximum linear burning velocity of the given formulation is 1.41 ± 0.01 mm s^{-1} at the oxidant excess factor x = 0.827.

For formulation no. 2 (SC + KE), the regression equation has the following form (R^2 = 0.939):

$$U = -1.206x^2 + 2.506x + 0.095.$$

The maximum linear burning velocity is 1.43 ± 0.01 mm s^{-1} at the oxidant excess factor x = 1.039.

Analysis of the data obtained shows that the maximum linear burning velocity of formulation no. 2 virtually coincides with the velocity for the stoichiometric composition, whereas for formulation no. 2 the maximum in velocity is shifted toward an excess of the combustible. Introduction into the formulations of 3 g of powdered aluminum (oxidant excess factor x = 0.93) leads to an increase in the linear burning velocity to (3.77–4.09) ± 0.01 mm s^{-1} for formulation no. 1 and to 2.17 ± 0.01 mm s^{-1} for formulation no. 2. The effect of aluminum on the burning velocity is particularly pronounced for formulation no. 1. Figure 1b shows the main results obtained in studying how the formulation composition (oxidant excess) affects the

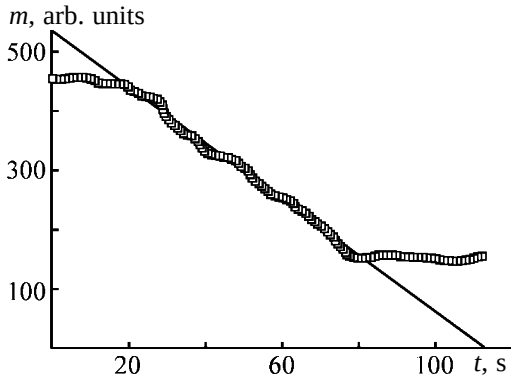

Fig. 2. Variation of the weight m of a formulation in the course of its burning-out. (t) Time. Points, experimental data; straight line, approximation.

specific mass velocity of burning, U_m (g cm^{-2} s^{-1}). The interest in this parameter can be accounted for by the fact that the rate of pressure build-up in the volume is determined just by the mass of substance burnt-out in unit time, whereas the linear burning velocity is only necessary for assessment of the mode of conversion, by deflagration or detonation. Similar processing yields the following results. For formulation no. 1 (R^2 = 0.956)

$$U_m = 0.036x^3 - 0.466x^2 + 0.761x - 0.001.$$

The maximum specific mass burning velocity, which is achieved at oxidant excess factor x = 0.913, is 0.33 ± 0.01 g cm^{-2} s^{-1}. For formulation no. 2 (R^2 = 0.821), the following dependence was obtained:

$$U_m = -0.203x^2 + 0.485x + 0.009.$$

In this case, the maximum specific burning velocity, equal to 0.30 ± 0.01 g cm^{-2} s^{-1}, is achieved at oxidant excess factor x = 1.195. Addition of aluminum to the formulations also increased the specific mass burning velocities: to (0.59–0.64) ± 0.01 g cm^{-2} s^{-1} for formulation no. 1 and to 0.34 ± 0.01 g cm^{-2} s^{-1} for formulation no. 2. Analysis of the dependences obtained shows that the maxima of specific mass burning velocities are shifted to higher oxidant excess factors, compared to the maxima of linear burning velocities.

Among the experimental results not represented in the plots, the following are worth mentioning. According to preliminary thermodynamic calculations, the burning products of the formulations under consideration contain a substantial amount of NaCl with the melting point of 1073 K and boiling point of 1713 K. For the oxidant excess factors in the interval of interest, the process temperature falls within the range 2370–3470 K. Thus, NaCl is in the gaseous state at the combustion front. Away from the front, the salt condenses, because of heat losses, either at a large distance from the front, within the flow, or at casing walls. This is manifested both in the manner in which the burning products outflow from the cylinder and in salt deposits on the inner surface of the cylinder. For example, at oxidant excess factor less than unity ($0.4 < x < 0.75$) the salt was carried by flame away from the reaction zone, the casing was heated to bright red, and no salt deposits were found on the inner surface of the cylinder after burning terminated. With the oxidant concentration increasing further, up to unity, the casing color changed, despite that the process temperature reached a maximum (3470 K), to dull cherry, instead of the expected bright white, and a 0.5–1.5-mm-thick salt deposit appeared on the inner surface of the cylinder. Larger, than before, drops of molten salt were observed in the flame trail. At oxidant excess factor of 1.5, the casing ceased to glow during burning, the salt layer became as thick as 2–8 mm, and molten salt was ejected from the cylinder as lava from a volcanic pipe (in the form of large conglomerates). In view of these specific features of the burning process under study, we studied the manner in which the weight of a formulation charged into the cylinder changes during burning. Figure 2 shows how the formulation weight (in arbitrary units) varies with time. Analysis of this dependence shows that the formulation burns out at a virtually constant rate, with the exception of transient processes at the beginning and end of burning. Only slight fluctuations of the burning rate are observed near the mean value which can be determined from the process equation (correlation factor R^2 = 0.989):

$$Y = -4.734t + 536,$$

where Y is weight (arb. units), and t is time (s).

Seemingly, when using the given technique, account should be taken of the influence exerted by the reactive force created by gases outflowing from the reaction zone. This force is proportional to the dynamic pressure created by the outflowing gases and to the flow cross-section area. However, since the dynamic pressure does not exceed 90 mm Hg even for mercury fulminate $Hg(CNO)_2 \cdot 1/2H_2O$ (mass burning velocity 5.9 g cm^{-2} s^{-1} according to data obtained by A.F. Belyaev), the influence of the reactive force can be neglected for the formulations studied.

Full-scale tests of the formulations under study (SC + PE) under the standard conditions demonstrated

complete absence of detonation and improvement of the quality of stone blocks.

CONCLUSIONS

(1) The dependence of the burning velocity of formulations based on sodium chlorate and polyethylene or kerogen under atmospheric conditions was analyzed in the preliminary stage of the study in relation to the oxidant-to-combustible ratio at oxidant excess factor varying from 0.37 to 1.5.

(2) The burning velocity depends on the composition of the formulations studied and reaches a maximum at nearly stoichiometric compositions at an excess of the combustible for sodium chlorate with polyethylene, and at an excess of oxidant for sodium chlorate with kerogen.

(3) The maximum burning velocities (linear and mass), which are virtually the same for the formulations studied, do not exceed 1.5 mm s^{-1} and 0.4 g cm^{-2} s^{-1}, respectively.

(4) In the composition range studied, the formulations burn out at a constant rate.

(5) Introduction of 3–5% aluminum into a combustible formulation raises the burning velocity by approximately a factor of 2 for the formulation composed of sodium chlorate and polyethylene and by about 12–20% for the formulation with sodium chlorate and kerogen.

(6) Full-scale tests carried out in block stone mining show that the formulations proposed are efficient and promising.

REFERENCES

1. Kirsanov, O.N., Mokeev, V.V., and Akhtyrskii, M.V., *Zh. Prikl. Khim.*, 1999, vol. 72, no. 12, pp. 2011–2017.
2. Kirsanov, O.N., Klubkova, I.N., and Mokeev, V.V., *Zh. Prikl. Khim.*, 1999, vol. 72, no. 3, pp. 391–396.
3. Blinov, I.F., *Khloratnye i perkhloratnye vzryvchatye veshchestva* (Chlorate and Perchlorate Explosives), Moscow: Oborongiz, 1941.
4. Ligotskii, D.N., in *Poteri granita pri dobyche i obrabotke: Problemy teorii proektirovaniya kar'erov, Mezhvuzovskii sbornik nauchnykh trudov* (Loss of Granite in Mining and Processing: Problems of the Theory of Quarry Design, Intercollegiate Coll. of Sci. Works), St. Petersburg, 1995, pp. 76–77.
5. RF Patent 2153096.
6. RF Patent 2152376.

Russian Journal of Applied Chemistry, Vol. 76, No. 5, 2003, pp. 710–713. Translated from Zhurnal Prikladnoi Khimii, Vol. 76, No. 5, 2003, pp. 738–741.

PHYSICOCHEMICAL STUDIES OF SYSTEMS AND PROCESSES

Activity of Components in Surface Layer of Chloride–Fluoride Mutual Melts

B. V. Patrov

St. Petersburg State Technical University, St. Petersburg, Russia

Received February 5, 2002; in final form, February 2003

Abstract—The activities of components in the bulk and surface layer of melts of chloride–fluoride ternary mutual systems were calculated in the framework of the regular solution model using surface tension values and considering the surface layer is a separate phase.

Study of the surface tension of chloride–fluoride melts is of theoretical and practical significance, because they can be used in electroslag remelting as flux and for welding of nonferrous metals. Determination of the activity of melt components is of great importance for thermodynamic calculations of salt systems [1]. The most widely used method in studying the metallurgical systems is the model of regular solutions.

A calculation of the component activity for mutual melts from experimental surface tension values has been described previously [2]. For the exchange reaction MA + NB = NA + MB, the diagonal MA–NB is stable at $\Delta G_T^0 > 0$. The mole fractions x and $(1 - x)$ of substances MA and NB in the initial mixture become $(x - y)$ and $(1 - x - y)$ in the equilibrium mixture, i.e., become lower by the value of y equal to the mole fraction of the reaction products. Within the framework of the regular solution model [3, 4], we can write

$$\ln\gamma_1 = A(1 - x - y)^2/RT, \quad (1)$$

$$\ln\gamma_2 = A(x - y)^2/RT, \quad (2)$$

where γ_1 and γ_2 are the activity coefficients of components MA and NB belonging to the stable diagonal; A is the interaction parameter determined from comparison of the experimental and calculated phase diagrams [4].

Because the concentration of the components belonging to the unstable diagonal did not exceed 6 mol %, their activities a_{NA} and a_{MB} were assumed equal to the mole fraction y. The latter was derived from the equation for the equilibrium constant of exchange reaction:

$$K_a = y^2\{(x - y)\exp[A(1 - x - y)^2/RT](1 - x - y) \times \exp[A(x - y)^2/RT]\}^{-1}. \quad (3)$$

The interaction parameter A was determined from experimental data on the surface tension described by the Burylev equation [5] for regular solutions

$$\sigma = \sigma_1 x_1 + \sigma_2 x_2 + Cx_1x_2, \quad (4)$$

where x_1 and x_2 are the mole fractions of components MA and NB ($x_1 = x$, $x_2 = 1 - x$), and σ_1 and σ_2 are the surface tensions of these components comprising a mixture, the calculated surface tension of which σ was compared with the experimental value for the mutual system.

The constant C includes the mutual exchange energy [5] and is related to the interaction parameter A from Eqs. (1) and (2). To find A, it is sufficient to multiply C by the molar surface area:

$$A = C\omega, \quad (5)$$

where $\omega = V_m^{2/3}N^{1/3}$, and N is the Avogadro number.

To a first approximation, the molar volume of the mixture is calculated by the additivity equation $V_m = xV_{MA} + (1 - x)V_{NB}$, and more exactly it is calculated from the equation

$$V_m = (x - y)V_{MA} + (1 - x - y)V_{NB} + yV_{NA} + yV_{MB}.$$

The necessary data on the density of components involved in the exchange were taken from [6].

Comparison of the component activities in LiF–NaCl and LiF–KCl systems, calculated by the Fellner

1070-4272/03/7605-0710$25.00

procedure [4] and by the method proposed, showed that the maximal difference is 0.008 at the mole fraction $x = 0.5$ and does not exceed 2%, i.e., both methods yield the similar values. Consequently, the proposed calculation method using surface tension gives reliable data on the component activity in ternary mutual systems.

From the condition [7] for equilibrium of a component in solution surface layer and bulk,

$$\mu_i^\omega - \mu_i = \sigma\omega_i, \quad (6)$$

we obtain the expression for the binary solution at the equal molar surface areas:

$$\sigma = \sigma_1 + \frac{RT}{\omega}\ln(a_1^\omega/a_1) = \sigma_2 + \frac{RT}{\omega}\ln(a_2^\omega/a_2). \quad (7)$$

This equation yields the component activities in the surface layer of mutual melts:

$$\ln a_1^\omega = \frac{\sigma - \sigma_1}{RT}\omega + \ln a_1, \quad (8)$$

$$\ln a_2^\omega = \frac{\sigma - \sigma_2}{RT}\omega + \ln a_2. \quad (9)$$

The component activities a_1 and a_2 of the systems studied have been reported elsewhere [2, 8, 9]. Assumption is made that the melt surface layer, like bulk, is a regular solution. For regular solutions, the activity coefficients of components belonging to the stable diagonal in the surface layer are as follows:

$$\ln\gamma_1^\omega = A(a_2^\omega)^2/[RT(\gamma_2^\omega)^2], \quad (10)$$

$$\gamma_2^\omega = \exp\{A(a_1^\omega)^2/[RT(\gamma_1^\omega)^2]\}, \quad (11)$$

where A is the interaction parameter determined from the experimental data on the surface tension described by the Burylev equation [5].

Substitution in Eq. (10) of the expression for the activity coefficient of the second component in the surface layer gives

$$\ln\gamma_1^\omega = \frac{A}{RT}\frac{(a_2^\omega)^2}{\{\exp[A(a_1^\omega)^2] - \exp[RT(\gamma_1^\omega)^2]\}^2}. \quad (12)$$

Thus, the activity coefficients in the surface layer of the components belonging to the stable diagonal are calculated by Eqs. (10) and (12), and the mole fractions, by the equations

$$x_1^\omega = a_1^\omega/\gamma_1^\omega, \; x_2^\omega = a_2^\omega/\gamma_2^\omega. \quad (13)$$

Table 1. Activity of components in the surface layer of the LiF (1)–CsCl (2), NaF (1)–CsCl (2), and KF (1)–CsCl (2) systems

x_1	a_1^ω	a_2^ω	γ_1^ω	γ_2^ω	x_1^ω	x_2^ω
LiF–CsCl, 1173 K						
0.1	0.0022	0.8876	0.0755	0.9972	0.0296	0.8901
0.2	0.0082	0.7152	0.1845	0.9936	0.0444	0.7198
0.3	0.0210	0.5511	0.3634	0.9892	0.0577	0.5571
0.4	0.0441	0.3891	0.5997	0.9825	0.0735	0.3960
0.5	0.0839	0.2584	0.7911	0.9640	0.1060	0.2681
0.6	0.1362	0.1464	0.9225	0.9313	0.1477	0.1572
0.7	0.2102	0.0759	0.9749	0.8593	0.2156	0.0883
0.8	0.3347	0.0364	0.9909	0.6892	0.3378	0.0529
0.9	0.4430	0.0106	0.9987	0.5263	0.4436	0.0201
NaF–CsCl, 1100 K						
0.1	0.0027	0.8692	0.184	0.9995	0.0147	0.8696
0.2	0.0094	0.7214	0.3104	0.9979	0.0303	0.7229
0.3	0.0211	0.5739	0.4753	0.9956	0.0444	0.5764
0.4	0.0402	0.4427	0.6398	0.9912	0.0628	0.4466
0.5	0.0674	0.3161	0.7937	0.9840	0.0849	0.3212
0.6	0.1163	0.2323	0.8775	0.9614	0.1325	0.2416
0.7	0.1936	0.1568	0.9355	0.9086	0.2069	0.1726
0.8	0.3275	0.0939	0.9675	0.7738	0.3385	0.1214
0.9	0.5428	0.0371	0.9882	0.5089	0.5493	0.0728
KF–CsCl, 1073 K						
0.1	0.0137	0.9072	0.5127	0.9994	0.0266	0.9077
0.2	0.0428	0.7903	0.6001	0.9959	0.0713	0.7936
0.3	0.0828	0.6581	0.6983	0.9888	0.1180	0.6656
0.4	0.1400	0.5642	0.7614	0.973	0.1839	0.5799
0.5	0.2023	0.4358	0.8445	0.9545	0.2395	0.4566
0.6	0.2926	0.3368	0.8964	0.9172	0.3264	0.3672
0.7	0.3958	0.2300	0.9446	0.8673	0.4190	0.2652
0.8	0.5080	0.1278	0.9797	0.8041	0.5185	0.1589
0.9	0.7383	0.0516	0.9947	0.6398	0.7422	0.0807

First, systems comprising cesium chloride and lithium, sodium, and potassium fluorides are considered. Their characteristics (Gibbs energy of exchange reaction, constant of the Burylev equation, molar surface area, and interaction parameter) are presented below:

System	T, K	ΔG_T^0, J	$-C$, mJ m^{-2}	ω, m^2 mol^{-1}	$-A$, J mol^{-1}
LiF–CsCl	1173	87 391	370	85 998	31 810
NaF–CsCl	1100	52 375	185	110 431	20 474
KF–CsCl	1073	30 208	65.7	110 102	7233

The calculated component activities in the surface layer of the melts are listed in Table 1.

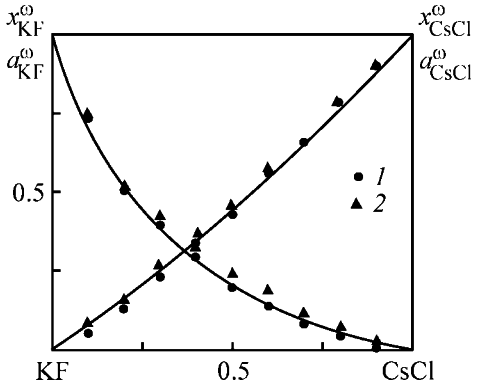

Fig. 1. (*1*) Activity a^{ω} and (*2*) mole fraction x^{ω} of components in the surface layer vs. their mole fraction in the KF–CsCl melt.

Table 2. Activity of components in the surface layer of the LiF (1)–NaCl (2), LiF (1)–KCl (2), and NaF (1)–KCl (2) systems

x_1	a_1^{ω}	a_2^{ω}	γ_1^{ω}	γ_2^{ω}	x_1^{ω}	x_2^{ω}
LiF–NaCl, 1123 K						
0.1	0.0254	0.8864	0.5605	0.9985	0.0452	0.8877
0.2	0.0607	0.7743	0.6400	0.9934	0.0949	0.7795
0.3	0.1069	0.669	0.7119	0.9836	0.1501	0.6802
0.4	0.1660	0.5671	0.7768	0.967	0.2137	0.5864
0.5	0.2407	0.4667	0.8346	0.9407	0.2884	0.4961
0.6	0.3341	0.3677	0.8848	0.9006	0.3776	0.4083
0.7	0.4499	0.2702	0.9270	0.8411	0.4853	0.3212
0.8	0.5943	0.1752	0.9612	0.7552	0.6183	0.2320
0.9	0.7724	0.0831	0.9876	0.6381	0.7821	0.1302
LiF–KCl, 1123 K						
0.1	0.0077	0.9023	0.1988	0.9971	0.0385	0.9049
0.2	0.0229	0.7956	0.2773	0.9867	0.0824	0.8064
0.3	0.0474	0.6444	0.4229	0.9755	0.1120	0.6605
0.4	0.0834	0.4906	0.5989	0.9624	0.1393	0.5098
0.5	0.1328	0.3506	0.7608	0.9417	0.1745	0.3723
0.6	0.1992	0.2363	0.8735	0.9025	0.2281	0.2618
0.7	0.2835	0.1453	0.9422	0.8365	0.3009	0.1737
0.8	0.3743	0.0750	0.9805	0.7501	0.3818	0.1000
0.9	0.5432	0.0321	0.9934	0.5544	0.5469	0.0580
NaF–KCl, 1173 K						
0.1	0.0103	0.8621	0.4729	0.9995	0.0217	0.8625
0.2	0.0301	0.7497	0.5660	0.9972	0.0532	0.7518
0.3	0.0600	0.6442	0.6538	0.9916	0.0918	0.6497
0.4	0.1029	0.5425	0.7347	0.9804	0.1401	0.5533
0.5	0.1621	0.4413	0.8084	0.9603	0.2005	0.4596
0.6	0.2433	0.3418	0.8714	0.9245	0.2792	0.3697
0.7	0.3534	0.2439	0.9227	0.8627	0.3830	0.2827
0.8	0.4985	0.1495	0.9621	0.7631	0.5181	0.1959
0.9	0.7061	0.0625	0.9891	0.5986	0.7139	0.1044

The data obtained on the component activity should be discussed taking into account the Gibbs energy of the exchange reactions. In the series of the KF–CsCl, NaF–CsCl, and LiF–CsCl systems, with increasing Gibbs energy, a eutectic phase diagram of the stable diagonal changes to a singular phase diagram with separation [8, 9]. In this series of systems comprising different fluorides and the same chloride, the cesium chloride surface activity increased simultaneously. It is noteworthy that the cesium chloride activity in the surface layer of the systems studied appeared to be equal to the mole fraction: $a_2^{\omega} \sim x_2^{\omega}$. This is clearly illustrated by the $a_2^{\omega} = f(x_2)$ and $x_2^{\omega} = f(x_2)$ plots for the KF–CsCl system in which the difference between the activities and mole fractions was the largest (Fig. 1). The activity of lithium, sodium, and potassium fluorides was also equal to the mole fraction, but at a high mole fraction of fluorides (higher than 0.5). At a lower content of fluorides, the difference between the activity and mole fraction in the surface layer ranged from 0.02 to 0.04.

The second group of chloride–fluoride mutual systems included the LiF–NaCl, LiF–KCl, and NaF–KCl systems characterized by the following values of the Gibbs energy, constant of the Burylev equation, molar surface area, and interaction parameter:

System	T, K	ΔG_T^0, J	$-C$, mJ m^{-2}	ω, m^2 mol^{-1}	$-A$, J mol^{-1}
LiF–NaCl	1123	52 109	95	72 189	6858
LiF–KCl	1123	65 392	212	86 877	18 418
NaF–KCl	1173	24 933	113	86 896	9819

With respect to the Gibbs energy, the systems of this group can be presented as a series LiF–NaCl, LiF–KCl, LiF–CsCl, with the same fluoride (LiF) and different chlorides. However, the LiF–CsCl system was considered within the first group. Replacement of this system by the system NaF–KCl should not affect the eutectic phase diagrams of the stable diagonal [10]. The calculated component activities in the surface layer of the melts are presented in Table 2.

As seen, the general conclusions made for the systems of the first group are also true for the systems of the second group. For example, the activity of chlorides in the surface layer is virtually equal to the mole fraction. The activity of fluorides is equal to the mole fraction when their content x_1^{ω} is higher than 0.6, with the activity coefficient γ_1^{ω} of fluorides exceeding 0.9.

Consequently, Eq. (7) for the surface-active com-

ponents, i.e., chlorides, takes the form

$$\sigma = \sigma_2 + \frac{RT}{\omega}\ln(x_2^{\omega}/a_2). \quad (14)$$

For the surface-inactive components, i.e., fluorides, in the concentration range x_1 = 0.5–1, this equation becomes

$$\sigma = \sigma_1 + \frac{RT}{\omega}\ln(x_1^{\omega}/a_1). \quad (15)$$

CONCLUSION

The equations were obtained for calculating the surface tension of mutual chloride–fluoride systems as a function of the concentration of fluorides and chlorides in the surface layer.

REFERENCES

1. Gorodyskii, A.V., *Termodinamicheskie svoistva rasplavov solevykh sistem: Spravochnoe posobie* (Thermodynamic Properties of Salt Systems: Handbook), Kiev: Naukova Dumka, 1985.
2. Patrov, B.V., *Zh. Prikl. Khim.*, 1998, vol. 71, no. 3, pp. 507–508.
3. Hildebrand, J.H., *Solubility of Non-Electrolytes*, New York: Reinhold, 1936.
4. Fellner, P., *Chem. Zvesti*, 1983, vol. 37, pp. 603–607.
5. Burylev, B.P. and Vasil'ev, V.V., *Fizicheskaya khimiya poverkhnostnykh yavlenii v rasplavakh* (Physical Chemistry of Surface Phenomena in Melts), Kiev: Naukova Dumka, 1971, pp. 144–149.
6. Morachevskii, A.G., *Spravochnik po rasplavlennym solyam* (Handbook on Molten Salts), Leningrad: Khimiya, 1971.
7. Popel', S.I., *Poverkhnostnye yavleniya v rasplavakh* (Surface Phenomena in Melts), Moscow: Metallurgiya, 1994.
8. Patrov, B.V., *Zh. Prikl. Khim.*, 1998, vol. 71, no. 3, pp. 508–510.
9. Patrov, B.V., *Zh. Prikl. Khim.*, 1998, vol. 71, no. 7, pp. 1206–1207.
10. Posypaiko, V.I., and Alekseeva, E.A., *Diagrammy plavkosti solevykh sistem: Troinye vzaimnye sistemy* (Fusibility Curves of Salt Systems: Ternary Mutual Systems), Moscow: Khimiya, 1977.

Russian Journal of Applied Chemistry, Vol. 76, No. 5, 2003, pp. 714–718. Translated from Zhurnal Prikladnoi Khimii, Vol. 76, No. 5, 2003, pp. 742–746.

PHYSICOCHEMICAL STUDIES OF SYSTEMS AND PROCESSES

Calculation of the Thermodynamic Properties of the Copper–Zinc System from Measured Boiling Point Values

E. B. Koklyanov, E. B. Kritskaya, G. P. Miroevskii, B. P. Burylev, and L. Sh. Tsemekhman

Gipronikel' Institute, Joint-Stock Company, St. Petersburg, Russia

Received August 23, 2001

Abstract—The temperature dependences of the saturated vapor pressure, the enthalpies of vaporization, standard boiling points, enthalpies, entropies, Gibbs energies, and component activities were calculated for liquid alloys of the copper–zinc system from the measured boiling points at various pressures. The calculation results were compared with the previous data obtained for this system by other methods.

Data on the copper–zinc system are important for production of copper–nickel alloys. It was of interest to compare the thermodynamic characteristics obtained by different methods. Data on thermodynamic properties of solutions can be obtained directly from the generalized Raoult equation if data on the vapor phase composition are available. One of versions of this method is the method of boiling points, which allows all thermodynamic functions of binary systems to be obtained for a wide range of temperatures and concentrations [1].

Based on reference data [2] and on the enthalpies and entropies of vaporization, we obtained the dependences of the saturated vapor pressure P_i^0 (Pa) of a pure liquid component i (i = Zn or Cu) on temperature T (K):

$$\log P_{Zn}^0 = -(6024/T) + 10.114, \quad (1)$$

$$\log P_{Cu}^0 = -(15\,760/T) + 10.601. \quad (2)$$

The similar dependences can be obtained from experimental data of [3, 4]:

$$\log P_{Zn}^0 = -(5962/T) + 10.074, \quad (3)$$

$$\log P_{Cu}^0 = -(15\,870/T) + 10.445. \quad (4)$$

The results of calculation of the saturated vapor pressure P_i^0 (kPa) for a pure component i (i = Zn, Cu) by Eqs. (1)–(4) at various temperatures T (K) are given in Table 1.

The saturated vapor pressure of zinc calculated by Eqs. (1) and (3) are virtually the same, whereas those for copper differ appreciably. However, this is of no importance, because, according to [2], the ideal separation coefficient

$$\alpha = P_{Zn}^0/P_{Cu}^0 \quad (5)$$

in the temperature range 1323–1523 K varies from 7.5×10^6 to 0.8×10^6, i.e., zinc vaporizes from copper–zinc alloys predominantly.

The saturated vapor pressures of copper calculated from data of [4–13] for a wider temperature range (up to 1973 K) are presented in Table 2.

It is seen that the vapor pressures calculated from data in [6] and, to a lesser extent, from data in [5, 7] exceed the values calculated from data in the other works. At the same time, all data unambiguously show that the saturated vapor pressure of zinc exceeds that of copper by several orders of magnitude.

The boiling points in the Cu–Zn system at different

Table 1. Calculated saturated vapor pressure P_i^0 of Cu and Zn at various temperatures

Temperature, K	P_i^0 calculated by Eqs. (1)–(4), kPa			
	P_{Zn}^0 (1)	$P_{Cu}^0 \times 10^3$ (2)	P_{Zn}^0 (3)	$P_{Cu}^0 \times 10^3$ (4)
1323	363.7	0.049	369.5	0.028
1373	532.8	0.133	539.1	0.077
1423	759.8	0.281	766.0	0.196
1473	1057.8	0.798	1062.9	0.469
1523	1440.9	1.791	1443.3	1.261

1070-4272/03/7605-0714$25.00

Table 2. Saturated vapor pressure of copper P^0_{Cu} at various temperatures, as calculated from data of [4–13]

P^0_{Cu}, Pa, at indicated temperature, K							References
1356	1473	1573	1673	1773	1873	1973	
0.0529	0.556	3.147	14.475	56.048	187.817	556.761	[5]
0.127	1.099	5.395	21.896	75.876	230.258	624.387	[6]
0.0934	0.836	4.202	17.414	61.481	189.705	522.169	[7]
0.0551	0.469	1.015	9.100	31.194	93.748	252.006	[4]
0.0676	0.589	2.901	11.816	41.072	124.985	339.766	[8]
0.0654	0.589	2.976	12.389	43.908	135.951	375.378	[9]
0.0561	0.514	2.626	11.040	39.480	123.221	342.675	[10]
0.0421	0.405	2.133	9.170	33.305	105.015	293.777	[11]
0.0500	0.455	2.391	10.315	37.060	112.301	290.448	[12]
0.0325	0.316	1.679	7.271	26.577	84.278	236.882	[13]

pressures, as calculated from data of [14], are presented in Table 3.

The experimental data were treated by the least-square method at the confidence level $p = 0.95$ using the equation

$$\log P = -\frac{a \pm \Delta a}{T} + b \pm \Delta b, \quad (6)$$

where P is the saturated vapor pressure (Pa), T is temperature (K), a and b are the constants determined from experimental data, and Δa, Δb, the confidence intervals.

The experimental data of [14] and the results of calculation by Eq. (6) are plotted in Fig. 1. The calculated values of the constants are given in Table 4.

According to [2], the standard boiling point of zinc is 1179.35 K. The value from Table 4 is 1178 K. The enthalpy of vaporization of 115.31 ± 0.42 kJ mol^{-1} [2] is higher by 1.4% than that in Table 4.

Using data of Table 4 and in accordance with the generalized Raoult equation, we determined the zinc activities:

$$a_{Zn} = P_{Zn}/P^0_{Zn} \quad (7)$$

or

$$\log a_{Zn} = \log P_{Zn} - \log P^0_{Zn}. \quad (8)$$

For different compositions we obtained the equation

$$\log a_{Zn} = -A/T + B, \quad (9)$$

Table 3. Pressure P and boiling point T of the copper–zinc system at various mole fractions of zinc x_{Zn} [compositions (1)–(9)]

P, kPa	T, K	P, kPa	T, K
$x_{Zn} = 1.000$ (1)		$x_{Zn} = 0.681$ (4)	
411.38	1337	224.43	1323
563.37	1380	576.54	1454
714.34	1414	733.59	1493
830.86	1436	$x_{Zn} = 0.589$ (5)	
1158.14	1487.5	226.97	1356
$x_{Zn} = 0.900$ (2)		227.98	1359
436.71	1360.5	302.96	1395
618.08	1411	425.56	1444
876.46	1461.5	426.58	1447
$x_{Zn} = 0.7955$ (3)		607.95	1500
255.84	1311.5	$x_{Zn} = 0.502$ (6)	
466.10	1391	135.27	1341
806.55	1474	135.78	1341
1093.30	1523	135.78	1342.5
162.12	1365	$x_{Zn} = 0.278$ (8)	
274.59	1434.5	60.49	1402
274.59	1435	93.32	1457
338.42	1467	101.32	1467.5
340.45	1469	102.84	1470
398.21	1492	135.27	1508
$x_{Zn} = 0.384$ (7)		143.88	1519
101.32	1377	$x_{Zn} = 0.1825$ (9)	
101.32	1378	42.25	1446
101.32	1378	52.79	1472
179.34	1452	78.73	1533
179.34	1353	101.32	1565
185.42	1458	101.32	1565
243.18	1497		
243.18	1500		

Table 4. Constants a and b in Eq. (6), enthalpies ΔH_{vap} and entropies ΔS_{vap} of vaporization, and standard boiling points T_{sb} at various concentrations of zinc x_{Zn}

x_{Zn}, mole fraction	a	$\pm\Delta a$	b	$\pm\Delta b$	ΔH_{vap}, kJ mol^{-1}	ΔS_{vap}, J mol^{-1} K^{-1}	T_{sb}, K	T, K
1.000	5943	33	10.051	0.019	113.75	96.57	1178	1337–1488
0.900	5953	329	10.014	0.233	113.94	95.86	1189	1360–1462
0.7955	5947	28	9.942	0.020	113.82	94.48	1205	1313–1523
0.681	5988	82	9.877	0.058	114.61	93.24	1229	1323–1493
0.589	6096	69	9.847	0.048	116.68	92.68	1259	1356–1500
0.502	6236	28	9.781	0.020	119.36	91.40	1306	1341–1492
0.384	6519	47	9.739	0.033	124.74	90.60	1377	1377–1500
0.278	6891	71	9.699	0.048	131.89	89.83	1468	1402–1519
0.1825	7109	217	9.544	0.143	136.07	86.86	1566	1446–1565

with the values of A and B given below:

x_{Zn}, mol. %	A	$-B$
0.9	10	0.037
0.7955	4	0.109
0.681	45	0.174
0.589	153	0.204
0.502	293	0.270
0.384	576	0.312
0.278	948	0.353
0.1825	1166	0.507

The enthalpy of vaporization ΔH_{vap} calculated by the equation from [15], and also the entropy of vaporization ΔS_{vap} and the standard boiling point T_{sb} determined from relations (10)–(12) are given in Table 4.

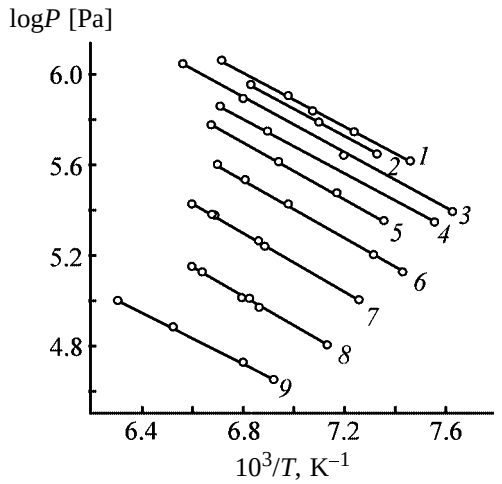

Fig. 1. Logarithm of the saturated vapor pressure P vs. reciprocal temperature $1/T$ for various compositions of the Cu–Zn system. (*1–9*) Calculation by Eq. (6) (line nos. are system nos. in Table 3); (points) experimental data [14].

$$\Delta H_{vap} = 19.14a, \quad (10)$$

$$\Delta S_{vap} = 19.14(b - 5.006), \quad (11)$$

$$T_{sb} = a/(b - 5.006). \quad (12)$$

The partial molar enthalpy of mixing of zinc $\Delta\bar{H}_{Zn}$ was determined from the expression

$$\Delta\bar{H}_{Zn} = \Delta H^0_{Zn} - \Delta H^s_{Zn}, \quad (13)$$

where ΔH^0_{Zn} is the enthalpy of vaporization of pure zinc and ΔH^s_{Zn}, the enthalpy of zinc vaporization from a solution of a given composition.

The values of $\Delta\bar{H}_{Zn}$ (J mol^{-1}) at 1450 K, obtained using data of Table 4, are as follows:

x_{Zn}, mol %	$-\Delta\bar{H}_{Zn}$	x_{Zn}, mol %	$-\Delta\bar{H}_{Zn}$
0.900	190	0.502	5610
0.7955	140	0.384	10 990
0.681	860	0.278	18 140
0.589	2930	0.1825	22 320

By integrating the Gibbs–Duhem equation, we can determine the partial molar enthalpy of mixing of copper $\Delta\bar{H}_{Cu}$ and then the enthalpy of mixing

$$\Delta H_m = \Delta\bar{H}_{Zn}x_{Zn} + \Delta\bar{H}_{Cu}x_{Cu}. \quad (14)$$

At the same time, the concentration dependence of $\Delta\bar{H}_{Zn}$ can be fitted by an interpolating polynomial [15]

$$-\frac{\Delta\bar{H}_{Zn}}{(1 - x_{Zn})^2} = a + b(1 - x_{Zn}) + c(1 - x_{Zn})^2, \quad (15)$$

in which $a = 15.117$, $b = -14.105$, and $c = 56.523$.

The results of the comparison are shown in Fig. 2.

Since an increase in the number of terms in interpolating polynomial (15) does not improve fitting to experimental data, we use the binomial equations given in [16] and taking into account the energy nonadditivity in a binary solution:

$$\Delta\bar{H}_1 = (Q_1 - Q_2)(1 - x_1)^2 + 2Q_2(1 - x_1)^3, \quad (16)$$

$$\Delta\bar{H}_2 = (Q_1 + 2Q_2)(1 - x_2)^2 + 2Q_2(1 - x_2)^3. \quad (17)$$

It follows from the dependence of $\Delta\bar{H}_{Zn}/(1 - x_{Zn})^2$ on $(1 - x_{Zn})$ (Fig. 3) that

$$\Delta\bar{H}_{Zn} = 5000(1 - x_{Zn})^2 - 55\,000(1 - x_{Zn}), \quad (18)$$

$$Q_1 = -50\,000 \text{ and } Q_2 = 27\,500 \text{ J mol}^{-1}.$$

The results of the calculations by formulas (15) and (18) are plotted in Fig. 2.

For the enthalpy of mixing, we obtain the expression

$$\Delta H_m = Q_1x_1x_2 + Q_2x_1x_2^2 = -50\,000x_{Cu}x_{Zn} + 27\,500\,x_{Cu}x_{Zn}^2. \quad (19)$$

Below we present the concentration dependence of the enthalpy of mixing ΔH_m (J mol^{-1}):

x_{Zn}	$-\Delta H_m$	x_{Zn}	$-\Delta H_m$
0.1	4252	0.6	8040
0.2	7120	0.7	6458
0.3	8768	0.8	4920
0.4	9360	0.9	2273
0.5	9062		

The data presented show the dependence to be asymmetrical, with the extremum at $x_{Zn} = 0.435$. The negative asymmetric deviations in this system were also observed in [17].

From data of Table 4 and the equation

$$\Delta\bar{S}_{Zn} = \Delta S^0_{Zn} - \Delta S^s_{Zn}, \quad (20)$$

the partial molar entropy of mixing of zinc $\Delta\bar{S}_{Zn}$ (J mol^{-1} K^{-1}) at 1450 K was found for various compositions as the difference between the entropies of vaporization of pure zinc, ΔS^0_{Zn}, and of zinc from a solution, ΔS^s_{Zn}:

x_{Zn}	$\Delta\bar{S}_{Zn}$	x_{Zn}	$\Delta\bar{S}_{Zn}$
0.90	0.037	0.502	0.2702
0.7955	0.1086	0.384	0.3123
0.681	0.1739	0.278	0.3525
0.589	0.2043	0.1825	0.5066

The results obtained can be approximated at 1450 K by the equation

$$\frac{\Delta\bar{S}_{Zn}}{(1 - x_{Zn})^2} = 4.7071 - 11.8240(1 - x_{Zn}) + 8.6535(1 - x_{Zn})^2. \quad (21)$$

The results are compared in Fig. 4.

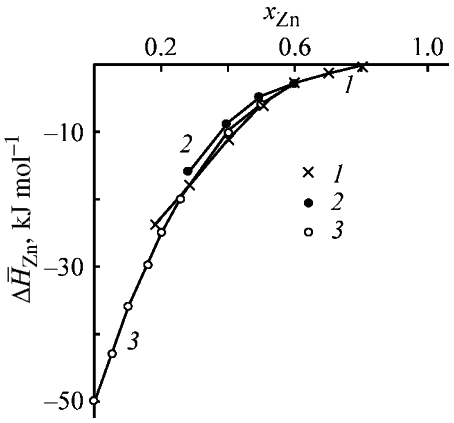

Fig. 2. Partial molar enthalpy of mixing of zinc $\bar{H}_{Zn}$ vs. zinc mole fraction x_{Zn}: (*1*) experimental data and (*2*, *3*) calculations by Eqs. (15) and (18), respectively.

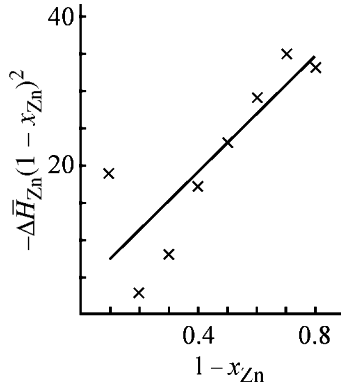

Fig. 3. Plot of $\Delta\bar{H}_{Zn}/(1 - x_{Zn})^2$ vs. $(1 - x_{Zn})$ at 1450 K. (Points) experimental data.

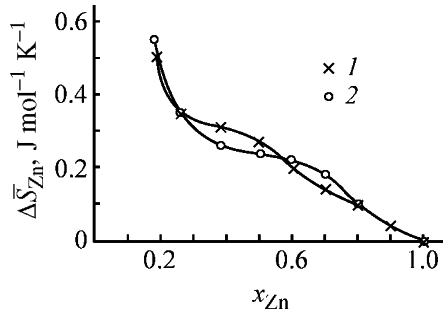

Fig. 4. Partial molar entropy of mixing of zinc $\Delta\bar{S}_{Zn}$ vs. zinc mole fraction x_{Zn}: (*1*) experimental data and (*2*) calculation by Eq. (21).

The Gibbs energy can be determined from the relationship

$$\Delta G^{ex} = \Delta H_m - T\Delta S^{ex}. \quad (22)$$

From the experimental data of [18], an expression for the activity coefficient of zinc f_{Zn} at 1200 K can be derived:

$$\frac{\ln f_{Zn}}{(1 - x_{Zn})^2} = (5.25 \pm 0.57)(1 - x_{Zn}) + (1.33 \pm 0.28). \quad (23)$$

It is recommended in a review [19] to determine f_{Zn} from the equation

$$RT \ln f_{Zn} = Q(1 - x_{Zn})^2, \quad (24)$$

where $Q = -27\,000$ J mol^{-1}, in good agreement with the results of [3].

The negative deviations from ideality were shown in [20, 21]. In [22, 23], the Krupkowski equation was used to describe the concentration dependence of the activity, and negative deviations from ideal solutions in the given system were observed.

REFERENCES

1. Burylev, B.P., Tsemekhman, L.Sh., Sryvalin, I.T., and Mironov, V.L., Abstracts of Papers, *Vsesoyuznyi seminar po teorii regulyarnykh rastvorov, ee razvitiyu i primeneniyu k rasplavam* (All-Union Seminar on Theory of Regular Solutions, Its Development, and Application to Melts), Krasnodar, April 18–21, 1972, pp. 24–25.
2. *Termicheskie konstanty veshchestv: Spravochnik* (Thermal Constants of Substances: Handbook), Moscow: VINITI, 1972, issue VI, part 1, pp. 12, 114.
3. Baker, E.H., *J. Appl. Chem.*, 1966, vol. 16, no. 11, pp. 321–324.
4. Vaisburd, S.E., Tsemekhman, L.Sh., Taberko, A.V., *et al.*, Abstract of Papers, *Vsesoyuznoe soveshchanie po primeneniyu vakuuma v chernoi i tsvetnoi metallurgii* (All-Union Meet. on Application of Vacuum in Ferrous and Nonferrous Metallurgy), Moscow: Inst. Metall., Akad. Nauk SSSR, 1979, p. 131.
5. Nikolaev, G.I., and Nemets, A.M., *Atomno-absorbtsionnaya spektrometriya v issledovanii ispareniya metallov* (Atomic-Absorption Spectrometry in Study of Metal Vaporization), Moscow: Metallurgiya, 1982.
6. Severin, V.I., Tseplyaeva, A.V., Priselkov, Yu.A., and Ryabtseva, L.P., *Teplofiz. Vys. Temp.*, 1986, vol. 24, no. 3, pp. 487–492.
7. Karasev, Yu.A., Tsemekhman, L.Sh., and Vaisburd, S.E., *Zh. Fiz. Khim.*, 1971, vol. 45, no. 8, pp. 2068–2070.
8. Morris, J.P., and Zellars, G.R., *Trans. Am. Inst. Met. Eng.*, 1956, vol. 206, pp. 1086–1090.
9. Ban-ya, S., Maruyama, N., and Fujino, S., *J. Iron Steel Inst. Jpn.*, 1982, vol. 68, no. 2, pp. 269–276.
10. Alcock, C.B., Itkin, V.P., and Horrigan, M.K., *Can. Met. Quart.*, 1984, vol. 23, no. 3, pp. 309–313.
11. Kubashewski, O. and Alcock, C., *Metallurgical Thermochemistry*, Oxford: Pergamon, 1979.
12. *Termodinamicheskie svoistva neorganicheskikh veshchestv: Spravochnik* (Thermodynamic Properties of Inorganic Substances: Handbook), Zefirov, A.P., Ed., Moscow: Atomizdat, 1965.
13. Smithells, *Metals Reference Book*, London: Butterworths, 1955, vol. 2, pp. 613–618.
14. Baker, E.H., *Inst. Min. Metall. Trans., Sect. C*, 1970, vol. 79, bull. no. 760, pp. 1–5.
15. Wagner, C., *Thermodynamik metallischen Mehrstoffsysteme*, Cambridge: Addison-Wesley, 1952.
16. Burylev, B.P., *Izv. Vyssh. Uchebn. Zaved., Tsvetn. Metall.*, 1964, no. 4, pp. 65–72.
17. Sharkey, R.L., Pool, M.J., and Hoch M., *Metall. Trans.*, 1971, vol. 2, no. 11, pp. 3039–3049.
18. Downel, D.B., *Acta Metall.*, 1964, vol. 12, no. 8, pp. 875–882.
19. Azakami, T., and Yazawa, A.U., *Can. Met. Quart.*, 1976, vol. 15, no. 2, pp. 111–122.
20. Rapperport, E.J. and Pemsler, J.P., *Met. Trans.*, 1972, vol. 3, no. 4, pp. 827–831.
21. Sugino, S., and Hadiwara, H., *J. Jpn. Inst. Met.*, 1986, vol. 50, no. 12, pp. 1068–1074.
22. Nowakowski, J., *Zesz. Nauk. AGH*, 1974, vol. 434, pp. 137–151.
23. Julian, P., Leszek, B., and Krzysztof, W.J., *Rudy Met. Niezelez.*, 1984, vol. 29, no. 6, pp. 234–238.

Russian Journal of Applied Chemistry, Vol. 76, No. 5, 2003, pp. 719–722. Translated from Zhurnal Prikladnoi Khimii, Vol. 76, No. 5, 2003, pp. 747–750.

SORPTION AND ION-EXCHANGE PROCESSES

Adsorption of Chlorobenzene on γ-Al_2O_3 Obtained by Calcination of Boehmite at Various Temperatures

L. D. Asnin and A. A. Fedorov

Institute of Technical Chemistry, Ural Division, Russian Academy of Sciences, Perm, Russia

Received July 22, 2002

Abstract—The influence exerted by the temperature of boehmite calcination in air within the range 450–600°C on the adsorption properties of the resulting γ-Al_2O_3 with respect to chlorobenzene was studied.

γ-Al_2O_3 is frequently used as support for catalysts for deep oxidation of chlorobenzene [1–4]. The concentration of surface OH groups, which largely determines the sorption properties of a support, may vary widely with synthesis and working temperatures of these catalysts (these temperatures are limited to the existence range of the γ phase, up to 900°C [5, 6]). The influence exerted by the concentration of surface OH groups on the sorption characteristics of oxide supports has been studied extensively [7–12]. For example, it is known that step-by-step removal of chemisorbed water from the Al_2O_3 surface leads to an increase in its hydrophilicity [11]. By contrast, it has been established for the example of ZnO that the heat of adsorption of benzene, toluene, and chlorobenzene decreases with decreasing number of surface OH groups [12]. A similar pattern has been observed for silica gel [13]. Presumably, such a behavior will be observed for aromatic compounds on oxides of other elements (Al, Ti). Kiselev and Lygin [3] attributed this to a decrease in the number of surface OH groups interacting with the aromatic ring. Nagao *et al*. [10, 12] pointed to a decreasing probability of two-center adsorption of chlorobenzene on the dehydroxylated surface of oxides.

Less unambiguous is the influence exerted on the sorption capacity of oxide supports by dehydration. This is so because the calcination conditions affect not only the content of structural water, but also the support texture. However, a general pattern can be revealed in this case also. For example, it was shown in [9, 10] that the fraction of aromatic compounds irreversibly sorbed on TiO_2 and ZnO is the lowest for hydrated oxides and increases for dehydrated oxides. A detailed study of the influence exerted by conditions of thermal treatment of aluminum hydroxides on the texture characteristics of the oxides obtained was reported in [14].

Thus, some aspects of the influence of calcination temperature T_{cal} on the adsorption properties of aluminum oxide can be predicted qualitatively. It is of interest to evaluate the extent of this influence on the chlorobenzene adsorption. The present study is concerned with chlorobenzene adsorption on γ-Al_2O_3 samples obtained by calcination of boehmite at 450 (OA1) and 600°C (OA2) in air for 5 h.

EXPERIMENTAL

The boehmite used to obtain aluminum oxide was synthesized by a procedure described in [15]. The phase composition of the samples was determined by X-ray phase analysis on a DRON-2 diffractometer. Adsorption isotherms were measured chromatographically [13] in the temperature range 190–300°C; the apparatus used and experimental conditions were described in [15]. The same equipment was used to determine by the method of frontal chromatography the sorption capacity of the samples for chlorobenzene at 50 and 100°C. The working gas-and-vapor mixture was prepared by saturating the carrier gas (nitrogen, flow rate 25 $cm^3\ min^{-1}$) with chlorobenzene vapor in a glass saturator with constant evaporation area at room temperature (vapor concentration 43–46 $\mu g\ cm^{-3}$). The dead time was determined for methane. The specific surface area S_{sp} of the samples was found by the method of thermal desorption of nitrogen, and the content of structural water, by calcination at 1000°C of samples preliminarily dried at 300°C. The pore volume V_p was found from the weight gain of samples after their saturation with benzene vapor in a desiccator at room temperature. The characteristics of the samples are listed in Table 1.

1070-4272/03/7605-0719$25.00

Table 1. Characteristics of γ-Al_2O_3 samples

Sample	T_{cal}, °C	S_{sp}, $m^2\ g^{-1}$	V_p, $cm^3\ g^{-1}$	n
OA1	450	160	1.07	0.18
OA2	600	150	0.86	0.10

* (n) Number of water molecules per Al_2O_3 formula unit.

Table 2. Sorption capacity of γ-Al_2O_3 samples

Sample	T = 50°C			T = 100°C		
	SC, $g\ g^{-1}$	SC', $g\ m^{-2}$	θ	SC, $g\ g^{-1}$	SC', $g\ m^{-2}$	θ
OA1	0.086	0.00054	1.3	0.028	0.00018	0.45
OA2	0.079	0.00053	1.3	0.022	0.00015	0.36

Both samples studied give similar X-ray diffraction patterns, which are characteristic of γ-Al_2O_3. The specific surface areas of the samples are about the same, in agreement with the data of [14]; a more pronounced difference is observed in the pore volumes. The samples differ strongly in the content of structural water. If it is assumed that the whole amount of water is present on the surface as OH groups (as demonstrated by recent measurements by Simonova *et al.* [16], no more than 5% of OH groups in γ-Al_2O_3 calcined at 600°C belong to intraglobular water), then the density of surface OH groups is 13.2 and 7.8 OH groups per 1 nm^2 for samples OA1 and OA2, respectively.

Table 2 lists the values of static sorption capacity per unit weight (SC) and unit surface area (SC') of the samples. The isotherms of chlorobenzene adsorption on sample OA1 were presented in [15], and those for sample OA2 are shown in Fig. 1. In all cases, the experimental data are described satisfactorily by Freundlich's adsorption isotherm equation (correlation coefficient ≥0.998).

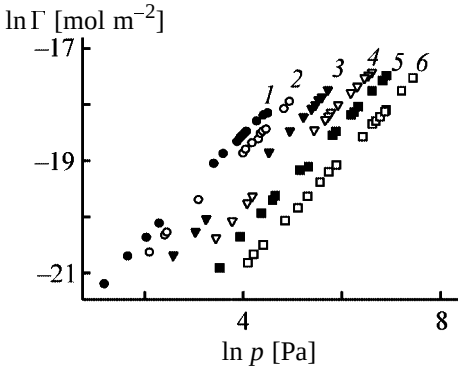

Fig. 1. Isotherms of chlorobenzene adsorption on OA2 sample. (Γ) Adsorption and (p) partial pressure of adsorbate. Adsorption temperature (°C): (*1*) 190, (*2*) 200, (*3*) 220, (*4*) 240, (*5*) 260, and (*6*) 300. Error in determining Γ and p does not exceed 7%.

The isotherms of chlorobenzene adsorption on sample OA1 lie above those for sample OA2, with the curves converging with increasing temperature. The difference in specific sorption activity between the samples at low surface fillings ($\theta \approx 10^{-4}$–10^{-3}) results from the difference in the concentration and, possibly, features of the surface OH groups. In the saturation region, these differences become insignificant, since the entire surface is involved in the adsorption process in this case. This is also confirmed by the fact that the specific surface sorption capacities are close for both samples at 50°C ($\theta > 1$). At 100°C the fraction of "working" surface area is lower ($\theta < 0.5$), and SC' is somewhat higher for sample OA1.

The isosteric heats of chlorobenzene adsorption, q_{st} (Fig. 2), were calculated from the equilibrium adsorption data obtained by the known method (by plotting adsorption isosteres) [13].

The isosteric heats of adsorption of both benzene and chlorobenzene on OA2 are somewhat lower than the respective values for OA1. Apparently, this is due to lower degree of hydration of sample OA2; a similar effect was observed on Si and Zn oxides. Commonly, it is attributed to lower probability of formation of a hydrogen bond between protons of OH groups and the aromatic molecule on a dehydrated oxide. Estimation of the upper limit of the number of OH groups per molecular area of chlorobenzene (0.465 nm^2 [10]) gives 6 and 3–4 OH groups for samples OA1 and OA2, respectively. Thus, multicenter adsorption is possible on the hydrated oxide. The involvement of several OH groups in benzene adsorption on silica gel was reported by Kiselev and Lygin [8]. A strong two-center interaction of chlorobenzene with the surface of hydrated Ti and Zn oxides through formation of hydrogen bonds OH···π electrons of the aromatic ring and OH···Cl was observed in [9, 10, 12]. The lower concentration of surface OH groups on OA2 decreases the probability of two-center adsorption and makes unlikely fixation of a chlorobenzene molecule on more than two surface centers. It is also known for the example of silica gel that, in the first place, calcination removes closely arranged OH groups, i.e., potential centers of multicenter adsorption are destroyed.

The centers present on the surface of aluminum

oxide include, in addition to OH groups (Brønsted centers), also Lewis acid and base centers, Al^{3+} cations and O^{2-} anions of varied coordination, which belong to the crystal lattice of the oxide [5, 17]. These centers will also take part in the formation of the common electrostatic field of the surface; however, their contribution to nonspecific adsorption interaction will be insignificant, since they are shielded by surface OH groups and the energy of nonspecific interaction falls rapidly with increasing distance. Moreover, it may be assumed by analogy with silica gel [8] that the contribution of nonspecific interactions to the heat of adsorption will be the same on samples with different degrees of hydroxylation.

As for specific interactions of chlorobenzene with surface Lewis centers, the contribution of these interactions to the heat of adsorption must also be not too great because of the shielding effect of surface OH groups [18]. Thus, the difference between the heats of chlorobenzene adsorption on samples OA1 and OA2 is mainly associated with the difference in the degrees of surface hydroxylation.

With a knowledge of q_{st}, the differential entropy change in adsorption can be readily calculated:

$$\Delta\bar{S}^s = -q_{st}/T_{am},$$

where T_{am} is the arithmetic mean temperature of the interval studied (T_{am} = 235°C).

The model of ideal two-dimensional gas can be used to calculate the theoretical decrease in entropy in adsorption, $\Delta\bar{S}^s_{theor}$. The procedure for calculating $\Delta\bar{S}^s_{theor}$ in the case of adsorption described by Freundlich's isotherm equation was presented in [15]. Comparison of $\Delta\bar{S}^s$ and $\Delta\bar{S}^s_{theor}$ with the use of the function $D = |\Delta\bar{S}^s| - |\Delta\bar{S}^s_{theor}|$ gives certain information about the mobility of molecules in the adsorption layer [19]. The D–Γ dependences are plotted in Fig. 3, whence it can be seen that the curves describing the D–Γ functions for the samples run virtually in parallel and are similar to the corresponding q_{st}–Γ dependences. As expected, the D–Γ function is a descending function, since molecules adsorbed in the initial stage are less mobile than those adsorbed from the subsequent portions of the adsorbate. At the same time, there is no strict localization of chlorobenzene molecules on the sample surface. Indeed, a calculation of the decrease in entropy in adsorption on the assumption of three translational degrees of freedom and absence of vibrations perpendicular to the surface [20] gives for both samples a value of about 180 J mol^{-1} K^{-1}, which is independent of Γ within the experimental error.

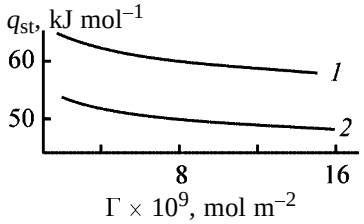

Fig. 2. Isosteric heat of chlorobenzene adsorption, q_{st}, vs. adsorption Γ for samples (*1*) OA1 and (*2*) OA2. The error in determining q_{st} does not exceed 3 kJ mol^{-1}.

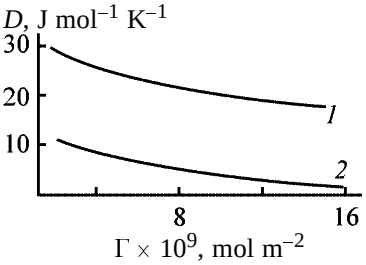

Fig. 3. Function D vs. adsorption Γ for samples (*1*) OA1 and (*2*) OA2. The error in calculating D is 7 J mol^{-1} K^{-1}.

With increasing Γ, the observed $|\Delta\bar{S}^s|$ steadily decreases within the range of partial adsorbate pressures studied from 127 to 114 J mol^{-1} K^{-1} for sample OA1 and from 106 to 95 J mol^{-1} K^{-1} for sample OA2, which is much lower than the above value.

Chlorobenzene molecules are more mobile on sample OA2. With increasing Γ, the adsorption layer on this sample becomes virtually similar to the ideal two-dimensional gas, which is not surprising in view of the high adsorption temperature.

CONCLUSION

The calcination temperature affects the adsorption properties of γ-Al_2O_3 with respect to chlorobenzene primarily by changing the concentration of surface OH groups. Under the adsorbent preparation conditions considered, oxides are formed with a hydroxide coating largely shielding Lewis acid centers on the surface. In this case, an increase in the calcination temperature, lowering the degree of surface hydroxylation, leads to a decrease in the isosteric heat of chlorobenzene adsorption and to an increase in its mobility in the adsorption layer.

ACKNOWLEDGMENTS

The study was financially supported by the Russian Foundation for Basic Research (project no. 02-03-

96405ural). The authors thank N.E. Skryabina for diffraction measurements, R.M. Yakushev for determinations of the specific surface area, and Yu.S. Chekryshkin for helpful discussions.

REFERENCES

1. Krishnamoorthy, S. and Amiridis, M.D., *Catal. Today*, 1999, vol. 51, pp. 203–214.
2. Jones, J. and Ross, J.R.H., *Catal. Today*, 1997, vol. 35, pp. 97–105.
3. Brink, R.W. van den, Mulder, P., and Louw, R., *Catal. Today*, 1999, vol. 54, pp. 101–106.
4. Yakubovich, M.N., Lazukin, V.I., Mantulo, A.P., and Novikov, I.N., *Ekotekhnol. Resursosberezh.*, 1994, no. 3, pp. 51–54.
5. *Physical and Chemical Aspects of Adsorbents and Catalysts*, Linsen, B.G., Ed., London: Academic, 1970. Translated under the title *Stroenie i svoistva adsorbentov i katalizatorov*, Moscow: Mir, 1973, pp. 190–232.
6. Trimm, D.L. and Stanislaus, A., *Appl. Catal.*, 1997, vol. 21, pp. 215–238.
7. Kiselev, A.V., *Mezhmolekulyarnye vzaimodeistviya v adsorbtsii i khromatografii* (Intermolecular Interactions in Adsorption and Chromatography), Moscow: Vysshaya Shkola, 1986.
8. Kiselev, A.V. and Lygin, V.I., *Infrakrasnye spektry poverkhnostnykh soedinenii* (IR Spectra of Surface Compounds), Moscow: Nauka, 1972.
9. Nagao, M. and Suda, Y., *Langmuir*, 1989, vol. 5, pp. 42–47.
10. Nagao, M. and Matsuoka, K., *J. Chem. Soc., Faraday Trans. 1*, 1988, vol. 84, pp. 1277–1285.
11. Gregg, S.J. and Sing, K.S.W., *Adsorption, Surface Area, and Porosity*, London: Academic, 1982.
12. Morimoto, T., Suda, Y., and Nagao, M., *J. Phys. Chem.*, 1985, vol. 89, pp. 4881–4883.
13. Kiselev, A.V. and Yashin, Ya.I., *Gazoadsorbtsionnaya khromatografiya* (Gas-Adsorption Chromatography), Moscow: Nauka, 1967.
14. Razouk, R.I., Mikhail, R.Sh., and Iskander, A.R., *J. Phys. Chem.*, 1965, vol. 69, pp. 1805–1808.
15. Asnin, L.D., Fedorov, A.A., and Chekryshkin, Yu.S., *Izv. Ross. Akad. Nauk, Ser. Khim.*, 2001, no. 1, pp. 65–69.
16. Simonova, L.G., Lapina, O.B., Krivoruchko, O.B., and Terskikh, V.V., *Kinet. Katal.*, 2000, vol. 41, no. 2, pp. 298–303.
17. Chukin, G.D. and Seleznev, Yu.A., *Kinet. Katal.*, 1989, vol. 30, no. 1, pp. 69–77.
18. Busca, G., *Phys. Chem. Chem. Phys.*, 1999, vol. 1, pp. 723–736.
19. Lopatkin, A.A., *Zh. Fiz. Khim.*, 1997, vol. 71, no. 5, pp. 916–919.
20. *Physical and Chemical Aspects of Adsorbents and Catalysts*, Linsen, B.G., Ed., London: Academic, 1970. Translated under the title *Stroenie i svoistva adsorbentov i katalizatorov*, Moscow: Mir, 1973, pp. 168–189.

Russian Journal of Applied Chemistry, Vol. 76, No. 5, 2003, pp. 723–726. Translated from Zhurnal Prikladnoi Khimii, Vol. 76, No. 5, 2003, pp. 751–754.

SORPTION AND ION-EXCHANGE PROCESSES

Adsorption of Carbon Monoxide on Oxidized Activated Lignin Carbon

L. N. Grigor'ev, T. I. Burenina, and A. M. Sukhenko

St. Petersburg State Technological University of Plant Polymers, St. Petersburg, Russia

Received December 9, 2002; in final form, April 2003

Abstract—Experimental data on the dynamics of carbon monoxide adsorption on oxidized activated lignin carbon are presented.

Flue gases of industrial installations and exhaust gases of vehicles are mostly rendered harmless by catalytic afterburning [1]. The adsorption-catalytic method is commonly regarded in recent years as an alternative means for rendering harmless low-temperature discharges [2]. In [3, 4], the possibility of using this technique for purification of wastes to remove carbon monoxide CO was demonstrated, and the direction of its modification, a search for new catalytically active materials with increased adsorption and chemical activity, was determined. As a material of this kind was proposed mordenite modified with manganese or cobalt oxide. It should, however, be noted that the results of [4] are best applicable to the case of detoxication of relatively highly concentrated wastes (CO concentration 1.25–7.50 g m^{-3}) taken in small amounts. This can be judged from the low linear velocity of the gas flow in the free cross section of the adsorption-catalytic reactor (0.03 m s^{-1}), which is lower than that in adsorbers (0.15–0.25 m s^{-1}) or catalytic reactors (0.5–1.0 m s^{-1}).

Considerable amounts of gases discharged into the atmosphere have relatively low CO concentrations (20–100 mg m^{-3}) and large flow rates [$>(10-60)\times 10^3$ m^3 h^{-1}]. These mainly include ventilation gases discharged by installations for plasma cutting of metals, oxygen bleaching of cellulose, and electric smelt furnaces, air from compressors, etc.

Deeper understanding of the adsorption-catalytic conversion of CO in detoxication of such gases could enable wider use of the method as regards the contamination sources and a search for new adsorbents-catalysts. Of interest as adsorbents-catalysts are oxidized activated lignin carbons prepared from wastes of pulp-and-paper and hydrolysis plants.

It has been shown previously [5, 6] that additional oxidation of the activated lignin carbon (ALC) enhances its chemisorption activity toward nitrogen monoxide NO. It was shown in [7] that is possible, in principle, to oxidize CO on ALC containing manganese and copper oxides. To determine the feasibility of practical application of oxidized ALC for treatment of gases contaminated with CO, it is necessary to have information about their properties in dynamic adsorption conditions.

Our goal was to analyze the equilibrium and dynamics of CO adsorption on oxidized ALC, with the aim to obtain data necessary for calculating an adsorption-catalytic reactor.

Isotherms of CO adsorption were calculated on the basis of the results of dynamic studies from full output curves.

The dynamics of adsorption was studied on a flow-through installation. As adsorber served a molybdenum glass column with inner diameter of 1.4×10^{-2} m, sealed in a column of diameter 2.6×10^{-2} m, within which water from a thermostat was circulated. Carbon monoxide was obtained in nitrogen [grade 1, GOST (State Standard) 9293–74] as described in [8]. A model gas mixture was prepared by evacuating a cylinder to residual pressure of 3.5 Pa, introducing CO with a calibrated syringe, and filling the cylinder with nitrogen to a pressure of 4.5 kPa. Metered amounts of the mixture of nitrogen and CO were introduced in an air flow delivered to the adsorber. The CO concentration c_0 in the air was 35.0–105.0 mg m^{-3}. The CO concentration was determined by gas chromatography [8] with a Chrom-5 chromatograph (heat conductivity detector) and AgNaγ zeolite as concentrator.

An ALC sample on which the best kinetic parameters were obtained in studying CO chemisorption [7]

1070-4272/03/7605-0723$25.00

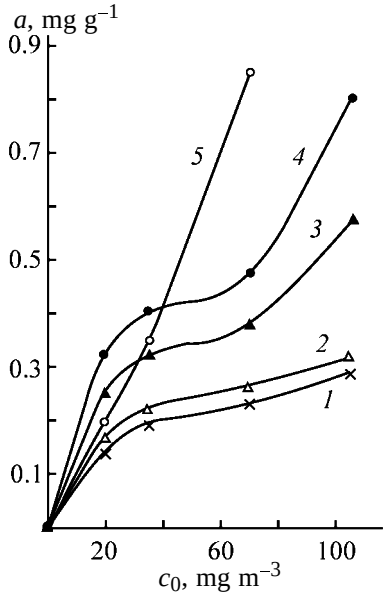

Fig. 1. CO adsorption isotherms. (a) Equilibrium adsorption and (c_0) CO concentration. Temperature (K): (*1, 2*) 293, (*3*) 323, (*4*) 353, and (*5*) 423. Relative humidity of the gas flow (%): (*1, 3–5*) 45.0 and (*2*) 5.0.

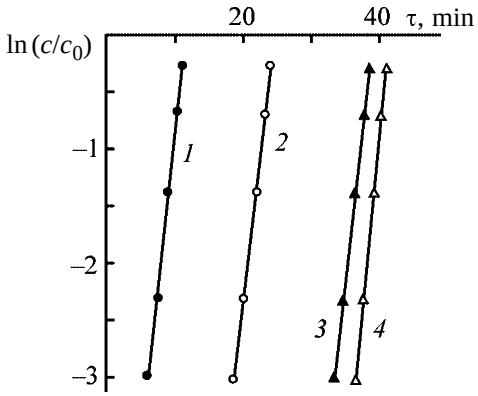

Fig. 2. Output curves of CO adsorption. (c/c_0) Relative breakthrough concentration and (τ) time of passing CO-containing gas. Temperature (K): (*1, 2*) 293, (*3*) 323, and (*4*) 353. Adsorbent bed height (m): (*1*) 0.05 and (*2–4*) 0.10.

was chosen as object of the study. Sample parameters: content of manganese 4.11%, that of copper 6.97%, specific surface area of mesopores 37.3 $m^2 g^{-1}$, and extent of sample oxidation 0.498 mg-equiv g^{-1}. It should be noted that, before treating an ALC sample with manganese and copper compounds, an air flow was passed through it at 423 K.

The overall mass-transfer coefficient β was calculated from the output curves of adsorption, using the expression [9]

$$\beta = -(\ln c_b/c_0)\omega/L,$$

where ω is the linear air flow velocity in the free section of the adsorber (m s^{-1}); L, sample bed height (m); and c_b, breakthrough concentration of CO (mg m^{-3}).

The isotherms of CO adsorption on oxidized ALC samples are shown in Fig. 1. The rise in the equilibrium CO adsorption a with increasing temperature indicates the chemisorption nature of the process. Figure 1 shows that the shape of the output curves depends on the adsorption temperature, i.e., in all probability, the type and strength of CO binding to active centers on the ALC surface change with temperature; stronger chemisorption complexes are formed at higher temperature. Figure 1 also shows that increasing humidity of the gas flow does not exert any noticeable influence on the adsorption activity of ALC.

Adsorption of CO on an ALC sample proceeds in accordance with the commonly accepted concepts: At low initial CO concentrations in the gas, the output curves in Fig. 2 are straight lines over virtually the entire range of relative breakthrough concentrations. These lines can be considered parallel at different sample bed heights, i.e., CO moves along the ALC bed at the same velocity. It could be expected that, with increasing temperature and with accumulation of intermediates and carbon dioxide CO_2 on the sorbent surface, the process would pass to the non-steady-state mode, previously observed in NO adsorption on oxidized ALC [5]. However, in the case of CO adsorption on oxidized activated carbon, the process starts to become non-steady-state only at high relative breakthrough concentrations ($c/c_0 \geq 0.95$). This is presumably due to the fact that the chemical reaction of adsorbed CO with the surface functional groups of the active centers of carbon is not accompanied by CO_2 accumulation at these centers, with CO_2 adsorption proceeding, in all probability, at other centers.

To assess the role of mass transfer in CO adsorption on a sample, the mass-transfer coefficients were calculated (Table 1). Table 1 shows that raising the temperature leads to an increase in the mass-transfer coefficient, which decreases when the CO concentration becomes lower.

In CO adsorption on ALC containing manganese and copper oxides, the coefficient β remains constant in a wide range of relative breakthrough concentrations. This fact suggests that, within the concentration range studied (straight portions of the output curves), the kinetics of adsorption is mainly determined by the external mass-exchange, and to much lesser extent by the longitudinal transfer.

The data presented in Table 1 and Fig. 1 were used

Table 1. Mass-transfer coefficient β and duration τ_b of CO adsorption as influenced by the adsorption conditions. Relative humidity 45%, $\omega = 0.15$ m s^{-1}, $c_b/c_0 = 0.05$

c_0, mg m^{-3}	L, m	T, K	β, s^{-1}	τ_b, min		ν,* %
				calculated	found	
70.0	0.10	293	18.9	15.7	18.8	12.8
		323	27.9	24.8	32.1	18.1
		353	35.7	29.4	36.7	15.6
		293	18.7	5.0	6.1	14.0
70.0	0.05	323	26.8	8.7	11.2	17.7
		353	35.1	12.5	14.1	8.5
		293	14.1	21.8	28.2	18.1
35.0	0.10	323	18.9	38.6	49.2	17.1
		353	31.8	54.0	65.1	13.2

* (ν) Relative error of calculation.

to calculate the duration of adsorption, τ_b, by the equation derived by Dubinin and co-authors [9]:

$$\tau_b = [1 - \omega \ln(c_0/c_b)/\beta]\alpha a/(c_0\omega),$$

where α is a coefficient found from the output curve, and a is the equilibrium adsorption (mg m^{-3}).

Table 1 shows that the relative error ν of calculation by the equation does not exceed 18.1%, which allows it to be recommended for determining the duration of the stage of CO adsorption on oxidized ALC in calculating the process of treatment of gases discharged into the atmosphere.

Of primary importance for practical application of oxidized ALC is the possibility of its regeneration, which assumes removal of adsorbed CO from the surface and restoration of the activity of the functional groups. The regeneration was carried out by passing an air flow through the ALC layer at 453 K, with the linear flow velocity gradually raised from 0.10 to 0.30 m s^{-1}. The regeneration efficiency was evaluated by comparing the initial CO concentration c_0 at the adsorber inlet and the breakthrough CO concentration c_b in the purified gas at the adsorber outlet at constant duration of the adsorption stage. The maximum efficiency (95%) is achieved after the first stage of adsorption (before regeneration of the adsorbent). The regeneration conditions and the change in the ALC activity (at adsorption stage duration of 20 min), evaluated by the efficiency of purification of the gas flow, in the cyclic operation mode (adsorption–regeneration–cooling) are listed in Table 2.

Table 2 shows that, under the experimental conditions, stable and efficient operation of ALC is achieved by the 3rd cycle at regeneration stage duration of 20 min. Under any particular conditions, efficient operation of ALC can be ensured by controlling the air flow rate and the temperature of ALC treatment.

In analyzing the prospects for practical use of oxidized ALC, the following can be noted. Comparison of the above data with the results of [4] shows that, under comparable conditions of CO adsorption (c_0 = 1250 mg m^{-3}, $\omega = 0.03$ m s^{-1}, $L = 0.026$ m, relative humidity of gas flow 5.0%), ALC is a material less active toward CO: at 293 K the equilibrium adsorption a of CO on ALC is 2.98 mg ml^{-1}; the amount

Table 2. Conditions of regeneration of oxidized carbon in the cyclic operation mode.* Relative humidity 45%, $c_0 = 70$ mg m^{-3}, $T = 453$ K, $L = 0.1$ m

Run no.	Cycle no.	τ, min	η, %
1	1	5.0	75.3
	3	5.0	70.1
	5	5.0	69.0
2	1	10.0	82.0
	3	10.0	80.3
	5	10.0	77.8
3	1	15.0	85.4
	3	15.0	83.8
	5	15.0	81.9
4	1	20.0	94.0
	3	20.0	93.3
	5	20.0	93.0

* (τ) Duration of regeneration and (η) adsorption efficiency; $\eta = (1 - c_b/c_0) \times 100$.

of CO adsorbed on mordenite containing 16% MnO_2 is 6.7 mg ml^{-1}. However, at 323 K the sorption activities of the materials become comparable (a = 5.88 mg ml^{-1} for ALC). It should be noted that the sorption activity of ALC can be raised not only by carrying out the purification process at higher temperatures, but also by making higher the concentration of active centers and using other oxidizing agents (mixture of oxidants) that would be more active than those contained in the ALC studied. Under real conditions of application of oxidized ALC, its advantages are lower energy expenditure for the regeneration stage, which is carried out at lower temperatures (no higher than 473 K) as compared to, e.g., mordenite modified with MnO_2 (623 K) [4], and also a weak dependence of the ALC activity on the gas flow humidity.

CONCLUSIONS

(1) Oxidized activated lignin carbon can be used as adsorbent-catalyst in treatment of low-concentration discharges of various industries to remove carbon monoxide at moderate temperatures (293–353 K).

(2) The main resistance to mass transfer in CO adsorption on oxidized activated lignin carbon is concentrated in the gas phase.

(3) The duration of CO adsorption on oxidized activated lignin carbon can be calculated using the Dubinin equation.

(4) Effective regeneration of activated lignin carbon is ensured by passing through it an air flow with a linear velocity of 0.15–0.30 m s^{-1} at 453–473 K.

REFERENCES

1. Popova, N.M., *Katalizatory ochistki gazovykh vybrosov promyshlennykh proizvodstv* (Catalysts for Purification of Gas Discharges from Various Industries), Moscow: Khimiya, 1991.
2. Toropkina, G.N., Kalinkina, L.I., and Kisarov, V.M., *Zh. Vseross. Khim. O–va.*, 1992, no. 1, pp. 33–42.
3. Solov'ev, S.A., Belokleitseva, G.M., and Vlasenko, V.M., *Zh. Prikl. Khim.*, 1992, vol. 65, no. 9, pp. 1921–1926.
4. Solov'ev, S.A., Belokleitseva, G.M., and Vlasenko, V.M., *Zh. Prikl. Khim.*, 1994, vol. 67, no. 9, pp. 1467–1470.
5. Grigor'ev, L.N., Petrova, E.V., and Cheperegin, G.G., *Zh. Prikl. Khim.*, 1995, vol. 68, no. 9, pp. 1510–1513.
6. Grigor'ev, L.N. and Petrova, E.V., *Zh. Prikl. Khim.*, 1999, vol. 72, no. 1, pp. 62–65.
7. Grigor'ev, L.N., Cherkashin, A.G., and Burenina, T.I., *Zh. Prikl. Khim.*, 1999, vol. 72, no. 10, pp. 1673–1676.
8. Peregud, E.A. and Gorelik, D.O., *Instrumental'nye metody kontrolya zagryazneniya atmosfery* (Instrumental Methods for Monitoring Atmosphere Pollution), Leningrad: Khimiya, 1981.
9. Nikolaev, K.M., Dubinin, M.M., and Polyakov, N.S., in *Kinetika i dinamika fizicheskoi adsorbtsii: Trudy Tret'ei Vsesoyuznoi konferentsii po teoreticheskim voprosam adsorbtsii* (Kinetics and Dynamics of Physical Adsorption: Proc. 3rd All-Union Conf. on Theoretical Problems of Adsorption), Moscow: Nauka, 1973, pp. 117–123.

Russian Journal of Applied Chemistry, Vol. 76, No. 5, 2003, pp. 727–730. Translated from Zhurnal Prikladnoi Khimii, Vol. 76, No. 5, 2003, pp. 755–758.

SORPTION AND ION-EXCHANGE PROCESSES

Isotherm of Strontium Sorption on Clay

D. E. Chirkst, T. E. Litvinova, O. V. Cheremisina, M. V. Ivanov, and N. A. Mironenkova

St. Petersburg State Mining Institute, St. Petersburg, Russia

Received April 3, 2002; in final form, January 2003

Abstract—Sorption of strontium(II) with soil components from model solutions was studied. Limiting sorption of strontium ions, their landing site area, and Langmuir constants were determined.

Previously, we studied the strontium(II) sorption with soil components to substantiate, develop, and optimize a process for decontamination of soils from ^{90}Sr [1, 2]. To calculate the process parameters, the thermodynamic characteristics of strontium desorption from the surface of soil components into the washing solution are required. At the equilibrium, they are equal to the thermodynamic functions of sorption with the opposite sign; therefore, we studied sorption of Sr^{2+}.

The strontium(II) sorption with soil was determined under static conditions from model strontium chloride solutions. The solution was mixed with a sample of an air-dry soil for 5–6 h to attain the equilibrium [constant Sr(II) concentration in the solution], as judged from the constancy of Sr(II) concentration in time. The liquid volume to sample weight ratio was 10 $cm^3\ g^{-1}$ at a sample weight of 3 g.

After sorption completion, the liquid was filtered through a blue tape paper filter, the filtrate (2–10 ml depending on Sr^{2+} content) was transferred into a 50-ml flask, and required pH 2.8–3.0 was adjusted with acetate buffer (10 ml). Then, 25 ml of 60% acetone in water and 1 ml of 0.1% nitroorthanil C (nitrochromazo) were added. The strontium(II) content in the solution was determined by measuring the intensity of the absorption band of the Sr(II) complex with nitrochromazo at 650 nm. This method allows determination of 2 to 20 μg of Sr(II) in 25 ml of the solution [3]. Under these conditions, 100-fold excess of Na^+ and NH_4^+, 30-fold excess of K^+, 1.5-fold excess of Ca^{2+}, and 5-fold excess of Mg^{2+} do not interfere with determination of the target cation. The Sr(II) distribution coefficient between the solid and liquid phases was calculated by the formula

$$D_{s/l} = \frac{(c_0 - c_\infty)Vd}{c_\infty m \gamma_{Sr^{2+}}}, \quad (1)$$

where C_0 and C_∞ are the initial and equilibrium strontium concentrations in the aqueous phase (M), respectively; V, solution volume (m^3); d, solution density ($kg\ m^3$); m, sample weight (kg); and $\gamma_{Sr^{2+}}$, Sr(II) activity coefficient in the initial solution calculated by the Davies equation [4].

The composition and specific surface area S_{sp} of the soil components studied are as follows [5]:

Sample	S_{sp}, $m^2\ g^{-1}$
Kaolinite $Al_4(OH)_8[Si_4O_{10}]$	5.2
Cambrian blue clay $K_2Al_4[Al_2Si_6O_{20}](OH, F)_4$	5.86
Oligoclase $(Na_{0.9}Ca_{0.1})[Al_{1.1}Si_{2.9}O_8]$	0.17
Albite $Na[AlSi_3O_8]$	0.20
Potassium feldspar $K[AlSi_3O_8]$	0.21
Dolomite $Ca(Mg, Fe)[CO_3]_2$	–

The distribution coefficients obtained are listed in Table 1.

As seen, in accordance with a decrease in $D_{s/l}$ and S_{sp}, the minerals can be ranked in the following order: Cambrian blue clay ~ kaolinite > potassium feldspar >

Table 1. Distribution coefficients of strontium ions between $SrCl_2$ solution and soil components

Mineral	pH_{init}	pH_{fin}	$c_\infty \times 10^4$, mol kg^{-1}	$D_{s/l}$
Cambrian blue clay	6.3	~7	3.0	26.5
Kaolinite	6.3	~7	2.8	32.5
Dolomite	6.3	~7	5.5	10.4
Potassium feldspar	6.3	~7	3.5	23.5
Oligoclase	3.0	4.85	8.2	2.8
	6.4	7.5	8.9	1.6
Albite	3.1	4.7	7.9	4.0

1070-4272/03/7605-0727$25.00

Table 2. Characteristics of Sr^{2+} distribution between $SrCl_2$ solution and clay

$c_0 \times 10^4$, M	pH_{eq}	$c_\infty \times 10^4$, M	$\gamma_{Sr^{2+}}$	$\Gamma \times 10^4$, mol kg^{-1}	$D_{s/l}$
1.0	4.09	0.42	0.92	5.8	15.0
2.0	3.35	1.05	0.89	9.5	10.2
4.0	3.42	2.08	0.85	19.2	10.8
6.0	3.38	3.33	0.83	26.7	9.7
8.0	3.11	4.36	0.80	36.4	10.4
10	3.68	5.55	0.80	44.5	10.0
20	3.28	11.3	0.72	87	10.7
30	3.35	18.9	0.67	111	9.8
70	3.44	50	0.56	200	7.2
90	3.32	65	0.52	250	7.4
100	3.22	73	0.51	270	7.3
200	3.54	172	0.44	280	3.7
400	3.47	371	0.34	290	0.23

albite > oligoclase. Hence, we can conclude that in contaminated soils ^{90}Sr is fixed mainly on the surface of clay minerals, which is in agreement with reference data [6, 7]. Therefore, we studied the Sr(II) sorption with clay more thoroughly.

The thermal analysis showed that Cambrian blue clay belongs to hydromicaceous type. The sorption isotherm was studied at the initial pH 3.0. The average equilibrium pH was 3.4 ± 0.2. A small increase in pH can be explained by substitution of anions of weak acids with the anion of a strong acid, Cl^-, on the mineral surface. The choice of pH value is governed by two factors. First, the soil is decontaminated from ^{90}Sr by washing with an iron(III) salt solution [1, 2]. Weakly acidic medium is required to avoid hydrolysis of Fe^{3+} ions. Second, conversion of clay into the H form allows stabilization of the mechanism of strontium ion sorption. Therefore, clay was preliminarily treated with 1 M HCl, washed with water to pH 3, and dried to air-dry state. The $SrCl_2$ solutions were also acidified to pH 3. The clay sample weight was 3 g, and the l/s ratio was 10 $cm^3\ g^{-1}$. The equilibrium was attained in 5–6 h, but actually the contact time was no less than 1 day. The data on Sr^{2+} distribution between the model $SrCl_2$ solution and clay are presented in Table 2. The sorption isotherm constructed from these data is shown in Fig. 1. The sorption Γ (mol kg^{-1}) was calculated by the formula

$$\Gamma = (c_0 - c_\infty)V/m.$$

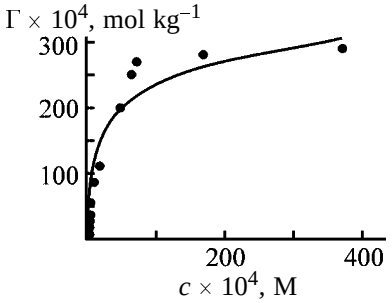

Fig. 1. Isotherm of Sr^{2+} sorption on clay: (Γ) sorption and (c) strontium(II) concentration; the same for Fig. 2.

At equilibrium pH 3.4 ± 0.2, the distribution coefficient of strontium(II) between the solid and liquid phases is 10 ± 1.8 (Table 2). A decrease in $D_{s/l}$ at high Sr^{2+} concentrations in the aqueous phase is caused by saturation of the surface. When pH is increased to 7.0–7.5, the degree of dissociation of silanol groups, negative charge of the surface, and $D_{s/l}$ increase (Table 1). A similar increase in the ^{137}Cs distribution coefficient between the model solution and kaolinite was observed in [8].

The ^{90}Sr distribution coefficients obtained in this work are lower than those obtained in [7] for certain minerals (1710 for montmorillonite and 180 for kaolinite at pH ~7). One of the probable reasons of this disagreement is the presence in the samples studied in [7] of the soil organic substance, which increases D. Another reason is the dependence of D on the degree of surface filling. In [8], the distribution coefficient of ^{137}Cs between montmorillonite and the solution decreased from 7200 to 23 as the surface was filled, since sorption primarily proceeds on crystal faces, and, as they are filled, D decreases. In [7], sorption was studied with trace amounts of ^{90}Sr; this explains high distribution coefficients. The D values obtained in our study are related to conditions of thermodynamic equilibrium with weighable amounts of Sr and agree with the concept of high strontium(II) mobility in grounds [6, 9, 10].

Sorption isotherms can be described by the Langmuir equation, as indicated by the linear dependence of reciprocal sorption on reciprocal concentration:

$$\frac{1}{\Gamma} = \frac{1}{\Gamma_\infty} + \frac{1}{\Gamma_\infty K}\frac{1}{c_\infty}, \qquad (2)$$

where Γ and Γ_∞ are equilibrium and limiting sorption values (mol kg^{-1}), K is the Langmuir constant, and c_∞ is the equilibrium concentration of strontium cations in the aqueous phase (M).

The absolute term of Eq. (2) is equal to the reciprocal value of the limiting sorption, which amounts to

0.034 mol kg^{-1} for Sr^{2+} and is consistent with the Γ_∞ value in the sorption isotherm. Since the substituting ability of strontium cations with respect to hydroxonium ions is high and clay initially was in the H form, the exchange capacity of clay can be estimated as 68 mg-equiv kg^{-1}. From data on sorption of methylene blue on this clay sample we obtain 10.3 mg-equiv kg^{-1} [5] The underestimated value of the sorption capacity can be explained by a large landing site area of methylene blue.

The landing site area of Sr^{2+} ions found by the formula

$$S_M = \frac{S_{sp}}{\Gamma_\infty N_A}, \quad (3)$$

where N_A is Avogadro number, is equal to 28.6×10^{-20} m^2. Hence, the radius of sorbed Sr^{2+}_{aq} cation is 302 pm. This value is close to the Stokes radius of Sr^{2+}_{aq}, 309 pm. This shows that strontium ions are sorbed in the hydrated state in the Stern layer on the clay surface. The constant K, determined from the slope, is 294.

In this work, we studied the thermodynamic phase equilibrium under conditions of sorption of macrocomponent ions from dilute solutions. Let us consider the correlation between the Langmuir constant and the equilibrium constant of sorption:

$$Sr^{2+}_{aq} \rightarrow Sr^{2+}_{ads}. \quad (4)$$

In contrast to the distribution coefficient, both Langmuir and equilibrium constants should not depend on the degree of filling of the mineral surface. We obtain the following correlation between them:

$$\Gamma = c_\infty \gamma_{Sr^{2+}} D_{s/l} = \Gamma_\infty \frac{Kc_\infty}{1 + Kc_\infty}, \quad (5)$$

and find the distribution coefficient:

$$D_{s/l} = \frac{\Gamma_\infty K}{\gamma_{Sr^{2+}}(1 + Kc_\infty)}. \quad (6)$$

It follows from Eq. (6) that the distribution coefficient depends on the Sr(II) concentration in the equilibrium solution and hence on the degree of surface filling (Table 2). However, at infinite dilution $D_{s/l} = \Gamma_\infty K = 10.0$, which coincides with the experimental value (Table 2). For equilibrium (4), which characterizes the sorption ability of strontium ions, we obtain

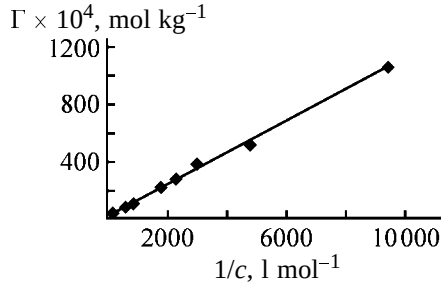

Fig. 2. Linearized form of the isotherm of Sr^{2+} adsorption on clay.

the Gibbs energy $\Delta G^0_{298} = RT \ln D_{s/l} = -5.7$ kJ mol^{-1}. Taking $\Delta_f \Delta G^0_{298}(Sr^{2+}_{aq}) = -563.9$ kJ mol^{-1} [11], we obtain the following Gibbs energy of formation of the sorbed cation: $\Delta_f G^0_{298} = -569.6$ kJ mol^{-1}.

CONCLUSION

Sorption of Sr^{2+} ions with Cambrian blue clay is described by Langmuir isotherm with the constant of 294 and limiting sorption of 0.034 mol kg^{-1}. The landing site area of Sr^{2+} is 28.6 Å^2. The radius of the hydrated cation is 302 pm, which coincides with the Stokes radius of 309 pm. The Sr^{2+} distribution coefficient between the solid and liquid phases at pH 3.4 ± 0.2 is 10, and the Gibbs energy of sorption is –5.7 kJ mol^{-1}.

ACKNOWLEDGMENTS

The work was performed in the framework of the Scientific and Technical Program of the RF Ministry of Education "Scientific Investigations of Higher School on Priority Directions of Science and Engineering", subprogram 207 "Ecology and Rational Nature Management."

REFERENCES

1. Dibrov, I.A., Chirkst, D.E., Chaliyan, K.N., and Streletskaya, M.I., *Radiokhimiya*, 2000, vol. 42, no. 3, pp. 273–276.
2. Chirkst, D.E., Litvinova, T.E., Cheremisina, O.V., and Streletskaya, M.I., *Radiokhimiya*, 2001, vol. 43, no. 5, pp. 475–478.
3. Poluektov, N.S., *Analiticheskaya khimiya strontsiya* (Analytical Chemistry of Strontium), Moscow: Akad. Nauk SSSR, 1971.
4. Vasil'ev, V.P., *Termodinamicheskie svoistva rastvorov elektrolitov* (Thermodynamic Properties of Electrolyte Solutions), Moscow: Vysshaya Shkola, 1982.

5. Chirkst, D.E., Krasotkin, I.S., Litvinova, T.E., *et al*., *Zh. Prikl. Khim*., 2003, vol. 76, no. 4, pp. 687–689.
6. Martyushov, V.V., Spirin, D.A., Bazylev, V.V., *et al*., *Ekologiya*, 1995, no. 2, pp. 110–113.
7. Benes, J., Radicheva, M., and Mishev, J., *Isotopenpraxis*, 1989, vol. 25, no. 10, pp. 441–444.
8. Kornilovich, B.Yu., Pshinko, G.N., and Spasenova, L.N., *Radiokhimiya*, 2000, vol. 42, no. 1, pp. 92–96.
9. Lisin, S.K., Simirskaya, G.P., Simirskii, Yu.N., *et al*., *Radiats. Risk*, 1993, no. 3, pp. 129–132.
10. Chuveleva, E.A., Firsova, L.A., Milyutin, V.V., *et al*., *Radiokhimiya*, 1996, vol. 38, no. 6, pp. 554–557.
11. *Termicheskie konstanty veshchestv: Spravochnik* (Thermal Constants of Substances: Handbook), Glushko, V.P., Ed., Moskow: Akad. Nauk SSSR, 1979, vol. 9.

Russian Journal of Applied Chemistry, Vol. 76, No. 5, 2003, pp. 731–735. Translated from Zhurnal Prikladnoi Khimii, Vol. 76, No. 5, 2003, pp. 759–763.

SORPTION AND ION-EXCHANGE PROCESSES

Preparation and Ion-Exchange Properties of Mixed Zirconium(IV) Phosphate–Phosphonate Sorbents

I. V. Romanova, I. A. Farbun, V. S. Aleksandrova, and S. A. Khainakov

Institute of Sorption and Endoecological Problems, National Academy of Sciences of Ukraine, Kiev, Ukraine

Received December 19, 2002

Abstract—Composite sorbents based on Zr(IV) phosphate–hydroxyethylidenediphosphonate with different phosphate–phosphonate ratio were prepared. These sorbents were characterized by elemental analysis, X-ray diffraction, and IR spectroscopy, and their ion-exchange sorption capacity for several transition metals and strontium was studied. The sorption capacity of these sorbents increases with increasing pH.

Sorbents based on hydrated oxides and phosphates of Group III and IV metals are widely used for sorption decontamination of various liquids from heavy metals and radionuclides. These sorbents are characterized by chemical, thermal, radiation, and microbiological stability; furthermore, they exhibit high selectivity for several toxic metals. The selectivity of such sorbents, in particular, those based on titanium and zirconium phosphates, is governed by the structure of their matrix and the nature of the functional groups located on the sorbent surface [1].

Different approaches were developed to improve the sorbents under consideration. With this aim, additional agents are introduced into reaction mixture in preparing these sorbents to form pores of a certain size and shape in the sorbent matrix [2]. According to another technique [3], the initially prepared sorbent is treated with an appropriate chemical agent [3] to modify the sorbent surface with the additional complexing functional groups.

In this work, the initial sorbent (zirconium phosphate) was prepared by a gel–sol technique [4] based on the reaction between a zirconium salt and phosphoric acid in an aqueous solution. It was found that thermal treatment of the initial zirconium phosphate increases its sorption capacity with respect to Sr^{2+} [2]. The reason is that the strontium cations are sorbed on zirconium phosphate mainly by their exchange for the protons of the hydrogen and dihydrogen phosphate groups of the sorbent. The thermal treatment results in condensation of the mono- and dihydrogen phosphate groups to form polymeric phosphate anions which are stronger complexing agents for alkaline-earth cations.

In order to increase the contribution of complex formation to the total sorption capacity of zirconium phosphate, the sorbent was modified with hydroxyethylidenediphosphonic acid (HEDP). This acid was chosen as a modifying agent because of its structural similarity with phosphoric acid and its strong complexation with various metal cations [6].

The synthesis of tin phosphate modified with nitrilotris(methylenetriphosphonic acid) was reported in [7]. As compared to titanium and zirconium phosphates, this sorbent shows higher selectivity for alkali, alkaline-earth, and some transition metals and exhibits higher stability to hydrolysis in both strongly alkaline and strongly acidic solutions. These features considerably widen the areas of the sorbent application.

The complexation of zirconium with hydroxyethylidenediphosphonic acid (HEDP)

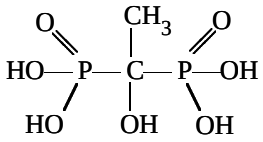

was studied in [8, 9].

It is known [6] that HEDP forms very stable complexes with alkali, alkaline-earth, and some transition metals. Long-term application of HEDP in agriculture (as a fertilizer component) and medicine (as a drug component) showed that this compound is nontoxic [6], which is important for future application of HEDP for water treatment.

The aim of this work was to prepare ion exchangers based on mixed Zr(IV) phosphate–phosphonate. The procedures used in synthesis of these sorbents and

1070-4272/03/7605-0731$25.00

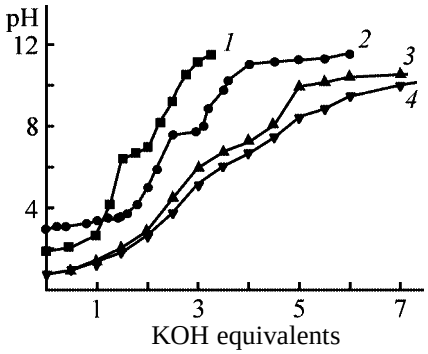

Fig. 1. Curves of potentiometric titration of (*1*) H_3PO_4, (*2*) HEDP, (*3, 4*) H_3PO_4–HEDP mixtures at (*3*) 1 : 1, and (*4*) 1 : 0.1 H_3PO_4 : HEDP ratio. For these mixtures, the KOH equivalent was recalculated to H_3PO_4.

their main physicochemical and sorption characteristics are given below.

EXPERIMENTAL

All the chemicals used in our experiments were of chemically pure or analytically pure grade. Aqueous solutions of alkaline-earth and transition metal chlorides and acetates and of potassium hydroxide were prepared by dissolution of their weighed portions in water.

Zirconium(IV) phosphate–phosphonates were prepared by adding an aqueous solution containing a mixture of phosphoric (3 M) and hydroxyethylidenediphosphonic (1.5 M) acids into an aqueous zirconium oxychloride solution (2 M) with vigorous stirring. This synthesis was carried out with varied ratios of phosphoric and hydroxyethylidenediphosphonic acids. In order to prolong the gelation process so as to obtain the uniform product, an appropriate complexing agent was added. The H_3PO_4 : HEDP ratio in the initial solution, the gel time, and some characteristics of the final sorbents are listed in the table. The Zr : P molar ratio in all the prepared sorbents was 1.5. After mixing, the reaction mixture gradually transformed into a gel. As the gel time we took the time τ after which the reaction mixture loses fluidity on inclining the reaction vessel (for 6–15 s). The gel was kept for 1 day, broken-down to small particles, washed with distilled water, and air-dried at room temperature to the moisture content of 20%. The resulting dried gel is a mechanically strong, glass-like colorless material.

The X-ray diffraction phase analysis of the sorbents was carried out on a DRON-3M diffractometer. The IR spectra (KBr pellets or mulls in Vaseline oil) were recorded in the range 400–4000 cm^{-1} on an M-80 (Carl Zeiss, Jena) IR spectrometer. The changes in the sorbent structure result in appearence of broad bands in the IR spectra in the range of the OH vibrations. In order to improve the analysis of these spectroscopic effects, the baseline was built and the absorption intensity was measured relative to the H_2O bending vibration band at ~1635 cm^{-1}, insensitive to structural changes in the sorbent matrix.

The carbon content in the sorbents was determined after their dissolution in HF-containing solution. The moisture content and the pore sorption volume W_s (with respect to water and benzene) were determined by the desiccator technique [10]. The pH was measured on an I-130.2M.1 ionometer. The initial and equilibrium copper and cobalt content in the initial solutions was determined photocolorimetrically. The strontium content in the solutions was determined on a C-115M-1 atomic-absorption spectrometer by a standard procedure.

The sorption recovery of transition metals from aqueous solutions with the sorbents prepared was studied as follows. An MCl_2 aqueous solution (M = Cu^{2+}, Co^{2+}, or Sr^{2+}) with the concentration of 1×10^{-3}–6×10^{-2} M was stirred, using a magnetic stirrer, with the sorbent sample at the solid to liquid phase ratio s : l = 1 : 100 at room temperature for 1 day. The sorption capacity of the sorbent with respect to the individual ion A (mmol g^{-1}) is expressed by the equation

$$A = (c_i - c_e)V/m,$$

where c_i and c_e are the initial and equilibrium metal concentrations in the solution (mM), m is the sorbent sample weight, and V is the solution volume.

The Zr(IV) complexation with both phosphoric acid and HEDP in aqueous solutions was studied in [8, 9] by potentiometric titration. In these works, curves of potentiometric titration of zirconium(IV) chloride, phosphoric and hydroxyethylidenediphosphonic acids, and complexes formed at various reactant ratios were also obtained. Proceeding with these studies, we prepared two series of metal-free solutions with the H_3PO_4 : HEDP ratio of 1 : 1 and 1 : 0.1 and varied their pH from 1 to 11 by adding aqueous KOH. We found that, on standing for 3 days, pH first decreased and then remained constant. Figure 1 shows the equilibrium curves of potentiometric titration of aqueous phosphoric acid, hydroxyethylidenediphosphonic acid, and their mixtures. These curves show that, in going from individual acid solutions to their mixtures, pH decreases and the inflection point shifts toward

Sorbent characteristics

Sample no.	H_3PO_4 : HEDP ratio in the reaction mixture	τ, s	W_s, $cm^3\ g^{-1}$		C, % in sorbent
			for C_6H_6	for H_2O	
1	100 : 0	6–7	0.14	0.107	0
2	99 : 1	7	0.14	0.096	1.23
3	97 : 3	7	0.13	–	1.23
4	95 : 5	8	0.12	0.090	1.23
5	93 : 7	8	0.12	–	1.31
6	90 : 10	7–8	0.01	0.090	1.48
7	70 : 30	9–10	0.01	0.090	3.07
8	50 : 50	12	0.01	0.080	4.12
9	30 : 70	14	0.01	0.079	4.22
10	0 : 100	15	0.01	0.070	5.38

higher pH. These results suggest that a common system of hydrogen bonds between different acids is formed in H_3PO_4–HEDP mixtures. The difference between the titration curves of the individual acids and their mixtures is stronger at lower HEDP content (Fig. 2). Presumably, the common system of hydrogen bonds is preferably formed at lower HEDP content.

We prepared ten samples of Zr(IV) phosphate–phosphonate sorbents at different H_3PO_4 : HEDP ratios in the reaction mixture (see table). The table shows that, with increasing HEDP content in the reaction mixture, the gelation significantly decelerates. This fact shows that in our systems the gelation is inhibited not only by zirconium(IV) complexation with the standard complexing agent added to the reaction mixture, but also by additional compexation with HEDP. Large amounts of HEDP deteriorate the gel structure. We found that both the appearance and mechanical properties of the sorbents prepared with the HEDP content in the reaction mixture less than 10% (sample nos. 2–6) are identical to those of the initial zirconium phosphate (sample no. 1). With HEDP content exceeding 10% (sample nos. 7–9), less uniform sorbents containing separate aggregates are formed. Elemental analysis showed that these sorbents incorporated HEDP.

The carbon content in the modified sorbent linearly increases with increasing HDEP content in the reaction mixture (correlation coefficient $R = 0.977$). We found that the carbon amount in the modified sorbents does not exceed 40% of that introduced into the reaction mixture with HEDP. The sorption pore volume of the sorbent determined with respect to water and benzene decreases with increasing HEDP content in the reaction mixture, which suggests condensation of phosphate and phosphonate groups in the course of formation of zirconium(IV) phosphate–phosphonate sorbents. The prepared sorbents have microporous structure. Variations of the appearance and structural characteristics of the sorbents with the HEDP content and the results of potentiometric titration show that the HEDP content in the reaction mixture must not be higher than 10%.

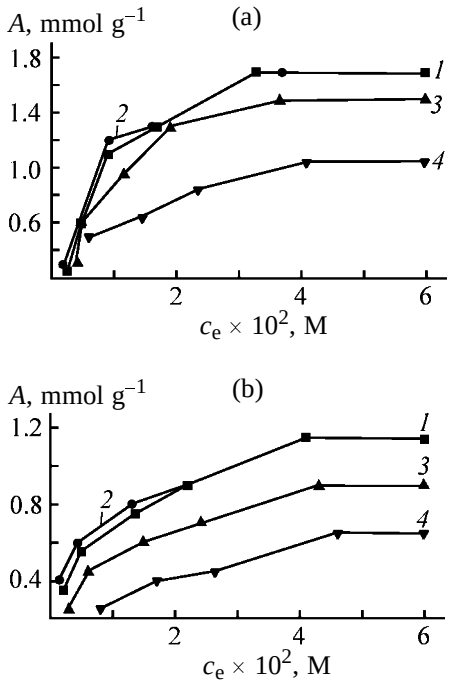

Fig. 2. Sorption isotherms of (a) cobalt and (b) copper on (*1*) unmodified zirconium phosphate and (*2–4*) zirconium phosphate modified with HEDP. (*A*) Sorption capacity and (c_e) Me^{2+} equilibrium concentration in the aqueous phase. HEDP content in the reaction mixture (%): (*2*) 5, (*3*) 50, and (*4*) 100.

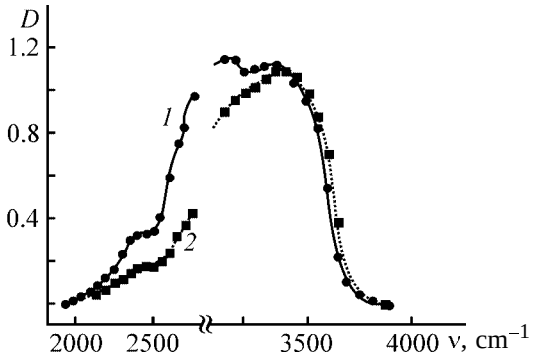

Fig. 3. IR spectrum of Zr phosphate–phosphonate (5% HEDP, sample no.4) in the range 1500–4000 cm^{-1} (*1*) before and (*2*) after strontium sorption. (*D*) Optical density and (ν) wave number.

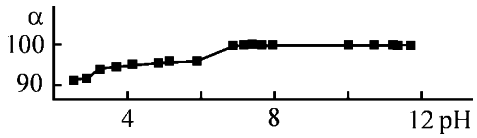

Fig. 4. Decontamination factor of solution from strontium after treatment with Zr(IV) phosphate–phosphonate sorbent (sample no. 4) as a function of pH. Initial Sr concentration $c_{Sr} = 7 \times 10^{-3}$ M.

The X-ray diffraction patterns of the prepared sorbents are indicative of their amorphous structure. With increasing HEDP content in the sorbent, the absorption bands of the ν(CO) groups (~1120 cm^{-1}) [11] becomes sharper, and absorption of the (C)–OH groups is manifested as broadening of the absorption band of the surface hydroxy groups and water molecules from its high-frequency side.

Owing to the surface (P)–OH groups, among them those belonging to HEDP, the sorbents in hand are cation exchangers. The ion-exchange properties of these sorbents were characterized by their sorption capacity with respect to copper and cobalt. Figures 2a and 2b show the sorption isotherms of copper and cobalt on both the initial zirconium phosphate and that modified with HEDP. The static exchange capacity of the tested sorbents for heavy metals varies from 1.2 to 1.75 mmol g^{-1} depending on the kind of metal and sorbent composition. On the whole, the sorption capacity of the sorbents containing 50% and more HEDP is substantially lower than that of the unmodified zirconium phosphate (sample no. 1). The sorption capacity of the sorbents containing less than 5% HEDP is considerably higher and close to that of the initial zirconium phosphate. The sorption capacity of zirconium phosphate modified with a small amount of HEDP (5×10^{-3}–2×10^{-2} M) exceeds that of the initial sorbent.

We also studied strontium sorption on modified sorbents. The following exchange capacities for strontium were obtained (mmol g^{-1}): 0.3–0.4 (sample nos. 6–10; HEDP content in the reaction mixture exceeds 10%), 0.6–0.7 [initial zirconium(IV) phosphate], 0.7–0.9 (sample nos. 3 and 4; HEDP content 3 and 5%, respectively). These results show that the relationships in sorption of transition metals and strontium are similar. It was reported [5] that Zr(IV) phosphate sorbents subjected to high-temperature treatment have sorption capacity for strontium of 0.3–0.4 mmol g^{-1}. Our sorbents, prepared without thermal treatment, exhibit higher sorption capacity for strontium.

Figure 3 demonstrates the effect of Sr sorption on the IR spectrum of the Zr(IV) phosphate–phosphonate sorbent (sample no. 4). The Sr sorption results in significant decrease in the intensity of the OH stretching band from the low-frequency side. This suggests that strontium is sorbed by the mechanism of exchange for protons of the (P)–OH groups.

The best Zr phosphate–phosphonate sorbent (5% HEDP, sample no. 4) was tested for decontamination of aqueous solutions from strontium ($c_{Sr} = 7 \times 10^{-3}$ M) within a wide pH range (1–12). The decontamination factor from strontium as a function of pH is given in Fig. 4. This plot shows that, with increasing pH from 1 to 12, the decontamination factor increases from 90 to 99.8%. The stepwise shape of this plot suggests that the zirconium phosphate–phosphonate sorbents have several kinds of sorbing sites of different acidities.

The results obtained in this work show that zirconium phosphates modified with HEDP are promising sorbents. We believe that the use of phosphonic acids with a branched bulky hydrocarbon radical as modifying agents may improve the structural and sorption characteristics of the sorbents.

CONCLUSIONS

(1) New sorbents based on zirconium phosphate modified with hydroxyethylidenediphosphonic acid (HEDP) were prepared. The elemental analysis and IR data showed that the sorbent matrix includes HEDP.

(2) With HEDP content in the reaction mixture about 5% relative to H_3PO_4, the conditions for condensation of the phosphate and phosphonate groups in the sorbent matrix are optimal. Modification of zirconium phosphate sorbents with HEDP improves

their sorption characteristics and extends the pH range of the efficient sorption. This improvement is due to both the favorable structural changes (increase in the size of channels and pores) and appearance of additional complexing groups on the sorbent surface.

REFERENCES

1. Amphlett, C.B., *Inorganic Ion Exchangers*, Amsterdam: Elsevier, 1964.
2. Bortun, A.I., A Study of Specific Ionic Mechanisms of Formation of Sorbents Based on Titanium and Zirconium Phosphates, *Cand. Sci. Dissertation*, Kiev, 1981.
3. Zaitsev, V.N., *Kompleksoobrazuyushchie kremnezemy: sintez, stroenie privitogo sloya i khimiya poverkhnosti* (Complexing Silicas: Synthesis, Graft Layer Structure, and Surface Chemistry), Kharkov: Folio, 1997, vol. 1.
4. Sharygin, L.M., Moiseev, V.E., and Pyshkin, V.P., *Izv. Akad. Nauk SSSR, Neorg. Mater.*, 1983, vol. 19, no. 11, pp. 1899–1902.
5. Bortun, A.I., Belyakov, V.N., Kvashenko, A.P., and Kuchinskaya, N.L., *Zh. Prikl. Khim.*, 1989, vol. 62, no. 4, pp. 848–851.
6. Dyatlova, N.M., Temkina, V.Ya., and Popov, K.I., *Kompleksony i komplexonaty metallov* (Complexones and Metal Complexonates), Moscow: Khimiya, 1988.
7. Bortun, A., Bortun, L., Clearfield, A., *et al.*, *Solvent Extr. Ion Exch.*, 1998, vol. 16, no. 2, pp. 651–667.
8. Strelko, V.V., Romanova, I.V., Bortun, A.I., and Khainakov, S.A., *Zh. Neorg. Khim.*, 1996, vol. 41, no. 8, pp. 1290–1293.
9. Romanova, I.V., Strelko, V.V., Khainakov, S.A., and Kostromina, N.A., *Ukr. Khim. Zh.*, 1997, vol. 63, no. 2, pp. 77–82.
10. Kel'tsev, N.K., *Osnovy adsorbtsionnoi tekhniki* (Fundamentals of Adsorption Technique), Moscow: Khimiya, 1984.
11. Nakamoto, K., *Infrared and Raman Spectra of Inorganic and Coordination Compounds*, New York: Wiley, 1986.

Russian Journal of Applied Chemistry, Vol. 76, No. 5, 2003, pp. 736–741. Translated from Zhurnal Prikladnoi Khimii, Vol. 76, No. 5, 2003, pp. 764–770.

SORPTION AND ION-EXCHANGE PROCESSES

Application of a Matrix of Piezosorption Sensors to Analysis of Ethanol-Containing Gas Mixtures

T. A. Kuchmenko, Zh. Yu. Kochetova, E. V. Fedorova, L. P. Bondareva, Yu. K. Shlyk, and Ya. I. Korenman

Voronezh State Technological Academy, Voronezh, Russia

Received December 25, 2001; in final form, March 2003

Abstract—General relationships were established for operation of piezosorption sensors when exposed to an ethanol-based multicomponent gas mixture. The operation conditions were optimized for the sensors; a matrix comprising six piezosorption elements was designed for analyzing gas mixtures containing low-boiling C_1–C_5 alcohols and ethyl acetate. The sensor matrix is suitable for foodstuff analysis.

The demand for sensors characterized by high selectivity and low detection limits, as well as by compactness, reliability, and easy exploitation, steadily grows. Development of express and test analytical methods and their wide application in analytical practice allow solution of not only certain environmental but also social problems such as deriving information on the air and water condition and foodstuff quality [1].

Ever growing importance is assigned to foodstuff identification by a number of procedures aimed at elucidating whether a foodstuff corresponds to the reference or its description.

This makes it important to design sensors suitable for identifying rude falsifications or low-quality foodstuffs at acceptable economic costs. In this case, the analytical information "carriers" are not only the foodstuffs themselves but also the equilibrium gas phases [2–4]. The presence/absence of low-boiling microimpurities (alcohols, alkyl acetates, acids) and their levels (if present) allow judging the quality and safety of certain types of the foodstuffs tested.

The aim of this work is to develop a procedure for analyzing alcohol-containing solutions by piezoelectric-quartz microweighing of the equilibrium gas phase.

EXPERIMENTAL

Gas mixtures of low-boiling compounds were analyzed with a specially designed matrix detector based on six piezoelectric quartz resonators (PQRs) of volume-acoustic waves with the intrinsic vibration frequency $F_v = 9 \pm 1$ MHz [5]. The piezoresonator electrodes were coated with receptor sorbent films by the method of static evaporation of a drop within 30 min at 40–45°C. We analyzed solutions of polyethylene glycol-2000 (PEG-2000), polyethylene glycol succinate (PEGS), polyethylene glycol sebacate (PEGSb), polyethylene glycol adipate (PEGA), Triton X-100, dinonyl phthalate (DNP) in ethanol, bees glue (propolis) in ethanol, beeswax (BW), dicyclohexano-18-crown-6 crown ether (DCH-18-C-6) in chloroform, and polystyrene (PS) in toluene. The complete removal of the solvent was ascertained by the stability of the vibration frequency of the resonator coated with a modifier film, F^f, Hz (drift $\Delta F^f \leq 3$ Hz min^{-1}).

An aqueous solution containing (ω, wt %) ethanol 40–42, ethyl acetate 0.02–0.05, C_1–C_4 alcohols 0.09–0.15, and isopentyl alcohol 0.07–0.10 was injected into the detector, and the vibration frequency was determined for each sensor (film-coated resonator) of the matrix by the appropriate algorithm. The analytical signal of the detector is the total response composed of the changes in the vibration frequency of all the sensors, Hz: $\Delta F^s_{i(i \to 1-6)} = F^f_i - F^s_i$. As the responses of each individual matrix element we took the individual kinetic and quantitative parameters of interaction between the receptor film and the mixture components. The "visual imprint" of the equilibrium gas phase of the solution was represented as a circular diagram ("aromatogram"). The final decision on the composition of the tested samples containing the components of the mixture analyzed (whether the sample corresponds to the standard and, if corresponds, to what extent) was taken using the sample identification algorithm.

1070-4272/03/7605-0736$25.00

The accuracy of determining low-boiling alcohols and ethyl acetate in the matrix of piezosorption sensors was controlled by gas chromatography (3 m × 3 mm column packed with Inerton modified with polyethylene glycol PEG-1500; helium carrier gas, flow rate 40 $cm^3\ min^{-1}$; injector, column, and flame-ionization detector temperatures 150, 80, and 200°C, respectively). The results were compared with those obtained at the accredited laboratory for foodstuff analysis and certification, Voronezh State Technological Academy.

The piezosorption matrix detector was regenerated by blowing with dry air for 15–20 min. The detector is suitable for conducting no less than 20 sorption–desorption runs in analysis of ethanol-based solutions without application of fresh receptor films.

The theoretical basis for controlling the sensitivity level of the piezoelectric sensor (resonator coated with a modifier film) in the gas phase was the Sauerbrey's microgravimetric concept of operation of a PQR [6]. The corresponding model is used for interpreting the experimental results obtained with a piezoresonator in the gas phase more frequently than the more recently developed theoretical models. This model is, essentially, represented by Eq. (1).

$$\Delta F = -2.3 \times 10^{-6} \frac{F_v^2 M_f}{A}. \quad (1)$$

Here, ΔF is the sensor response, i.e., the change in the vibration frequency of the PQR due to sorption of low-boiling compounds on the receptor films, which is calculated as the difference between the initial frequency of vibrations of the film-coated sensor F_f^0 and the equilibrium frequency of vibration of the sensor during sorption F^s, Hz; 2.3×10^{-6}, calibration constant; F_v, intrinsic frequency of vibrations of the PQR, MHz; M_f, mass of film coating on the electrodes, μg; and A, PQR electrode area, cm^2.

The change in the resonance frequency of vibrations of the PQR quantitatively correlates with the parameters of the surface wear or with the inequality of the masses of the coatings applied to both sides of the electrode. Viscous and liquid film coatings with a low kinematic viscosity are characterized by significant damping powers. Therefore, when applied to a piezoelectric quartz resonator, they cause a frequency instability of the sensor response. At the same time, the Sauerbrey model can be applied in the case of small mass increments (film thickness up to 3 μm) on electrodes without taking into account the details of the film structure and its changes on sorption [7, 8]. Upon application of film coatings thicker than 3 μm (60–80 μg), the energy losses in the film and piezoresonator tend to significantly increase and become comparable. Further thickening of the film coating tends to increase the contribution to the total response of the sensor from the component due to the wave propagation through the film rather than to the change in its mass upon sorption. Heavy coatings cause the piezoresonator vibrations to fail. The general relationships in sorption of low-boiling compounds of various classes on thin films of modifiers of the PQR electrodes with masses of up to 40 μg were described by the Sauerbrey model. The energy losses in such films can be neglected, and Eq. (1) can be taken as adequately describing the experiment.

Available data from the existing databank of kinetic and quantitative sorption parameters for the major classes of organic compounds, treated using the cluster analysis, suggest the possibility of designing a PQR-based sensor matrix for analyzing ethanol-containing gas mixtures with impurities such as C_1–C_5 alcohols and ethyl acetate [9–11].

We estimated the sorption affinities of individual sensors for low-boiling alcohols and alkyl acetates whose levels are regulated by appropriate norms and which are indicative of falsifications of certain foodstuffs (Table 1). As selectivity criteria we chose the kinetic (the time of the maximal response of the sensor τ_{max}, s) and quantitative (analytical signal ΔF_c, Hz, and sensitivity S, Hz $mol^{-1}\ dm^3$) parameters of the sensors when exposed to vapors of these compounds. Also, we took into account the stability of the operation of the modified sensor when exposed to a low-boiling compound vapor (characterized by S_r, relative rms deviation, %).

We found that the sorption efficiency tends to increase with increasing mass of the sorbent film in the range from 5 to 20 μg. With films heavier than 30 μg, the zero signal appreciably drifts and the results become poorly reproducible. Also, with PEG-2000 and DNP films the overcharges are responsible for "failures" of the resonator autovibrations. The optimal mass of the films for sorbents studied in this work is 10–20 μg.

The complementarity of the receptor films to low-boiling alcohol and alkyl acetate microimpurities is high, but the selectivity is low. The response of one sensor based on the receptor films studied does not allow identification of the microimpurities and determination of their ratio in the gas phase. This problem can be solved by using several sensors with cross sensitivities (like in "electronic nose" systems) and by

Table 1. Quantitative (S) and qualitative (τ_{max}) parameters of sorption of C_1–C_5 aliphatic alcohols on the receptor films of the PQR electrodes

Sorbent	Alcohol							Ethyl acetate
	methanol	ethanol	isopropanol	*n*-butanol	isobutanol	pentanol	isopentanol	
PEG-2000:								
S, Hz mol^{-1} dm^3	0.03	0.03	0.13	0.22	0.20	0.45	0.49	0.02
τ_{max}, s	30	60	90	120	135	225	225	45
PEGSb:								
S, Hz mol^{-1} dm^3	0.02	0.02	0.15	0.26	0.09	0.22	0.18	0.01
τ_{max}, s	30	60	90	120	135	225	225	30
PEGS:								
S, Hz mol^{-1} dm^3	0.01	0.01	0.09	0.03	0.07	0.20	0.14	0.01
τ_{max}, s	5	5	10	30	45	105	120	30
PEGA:								
S, Hz mol^{-1} dm^3	0.01	0.02	0.02	0.05	0.06	0.10	0.08	0.01
τ_{max}, s	5	15	45	45	45	60	60	30
Triton X-100:								
S, Hz mol^{-1} dm^3	0.03	0.06	0.03	0.50	0.52	0.55	0.24	0.02
τ_{max}, s	5	5	15	135	165	210	180	30
Beeswax:								
S, Hz mol^{-1} dm^3	0.01	0.02	0.06	0.01	0.02	0.07	0.08	0.01
τ_{max}, s	5	45	75	150	165	180	180	30
Propolis:								
S, Hz mol^{-1} dm^3	0.02	0.07	0.11	0.78	0.09	0.11	0.14	0.01
τ_{max}, s	15	60	105	120	150	165	180	10
DNP:								
S, Hz mol^{-1} dm^3	0.02	0.01	0.02	0.50	0.18	0.58	0.56	0.01
τ_{max}, s	≤5	10	15	15	15	10	15	10
PS:								
S, Hz mol^{-1} dm^3	0.01	0.01	0.01	0.01	0.01	0.04	0.02	0.001
τ_{max}, s	30	45	150	180	105	120	120	5

subsequent mathematical processing of the overall response [12–14].

To improve the efficiency and selectivity of analysis, we applied, for the first time, a sensor based on DCH-18-C-6 crown ether which is an efficient extracting agent for oxygen-containing substances. Preliminary assessment of the selectivity and sensitivity of the receptor films and the stability of the position of the zero signal suggest that it is appropriate to use the following set of substances in the sensor matrix intended for testing alcohol mixtures: PEG-2000, PEGA, Triton X-100, propolis, DNP, and crown ether. We established the relationships in variation of the sensor response under successive introduction of microamounts of ethanol homologs and ethyl acetate into aqueous solution with high ethanol content (Table 2). With introducing ethyl acetate and pentyl alcohols, the analytical signal from PEG-2000-, DNP-, and DCH-18-C-6-based sensors significantly changes. The same effect in the case of PEGA-, propolis-, Triton X-100-, and beeswax-based sensors is due to all the impurities occurring in aqueous ethanol (Table 2). The PS films are weakly sensitive to volatile components of the ethanol-based mixture but exhibit a minor drift of the zero signal (film instability) (Fig. 1).

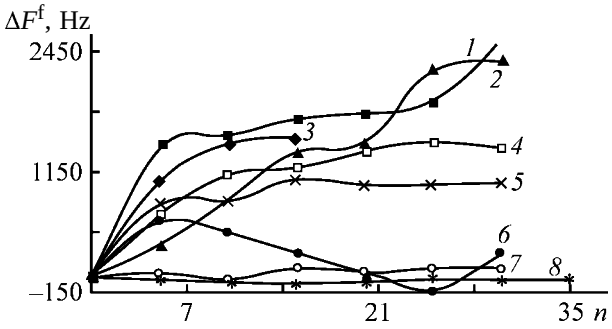

Fig. 1. Zero signal drift ΔF^f for sensors modified with (*1*) DNP, (*2*) DCH-18-C-6, (*3*) beeswax, (*4*) propolis, (*5*) PEGA, (*6*) PEG-2000, (*7*) PS, and (*8*) Triton X-100 on exposure to aqueous ethanol vapor. (*n*) Number of cycles of sorption–desorption of the analyte vapor.

Table 2. Characteristics of sorption of ethanol vapor with successively introduced C_1–C_5 alcohols and ethyl acetate (ω = 0.1 wt %) on the receptor films with the optimal mass

Characteristic	Sorbent							
	PEG-2000	PEGA	propolis	DNP	Triton X-100	DCH-18-C-6	PS	beeswax
				Ethanol (40 wt %)				
$\Delta F^c \pm \Delta$,* Hz	4100 ± 370	730 ± 85	1310 ± 65	1300 ± 220	2410 ± 80	2490 ± 80	190 ± 15	2320 ± 20
S_r, %	4.9	6.2	2.7	9.1	2.0	6.1	4.5	1.0
				Methanol				
$\Delta F^c \pm \Delta$,* Hz	5250 ± 345	1560 ± 70	2810 ± 105	2760 ± 310	4950 ± 75	2610 ± 75	320 ± 10	1040 ± 30
S_r, %	3.6	2.4	2.1	6.1	1.2	1.5	1.4	1.4
				Ethyl acetate				
$\Delta F^c \pm \Delta$,* Hz	5360 ± 370	1300 ± 65	1760 ± 80	2660 ± 320	4580 ± 85	1800 ± 60	250 ± 10	1050 ± 45
S_r, %	4.8	2.7	2.4	7.8	1.0	1.8	2.5	2.4
				Isobutanol				
$\Delta F^c \pm \Delta$,* Hz	5300 ± 290	1160 ± 60	1680 ± 60	3425 ± 422	4270 ± 115	1900 ± 80	210 ± 10	1000 ± 45
S_r, %	4.0	3.7	1.9	6.7	1.5	2.9	2.8	2.3
				Pentanol				
$\Delta F^c \pm \Delta$,* Hz	6080 ± 400	1350 ± 90	1490 ± 65	7550 ± 480	7160 ± 210	1570 ± 70	480 ± 10	930 ± 35
S_r, %	3.7	3.8	2.4	3.5	1.5	2.5	1.0	2.1
				Isopentanol				
$\Delta F^c \pm \Delta$,* Hz	5360 ± 445	1250 ± 60	1840 ± 70	7720 ± 310	4240 ± 110	2050 ± 75	270 ± 10	1035 ± 30
S_r, %	4.5	2.6	2.0	2.2	1.4	2.0	2.4	1.4

* Confidence interval for ΔF^s at the confidence level of 0.95.

Sensitive DNP and DCH-18-C-6 films exhibit a significant drift of the zero signal. It is recommended that ΔF^f be decreased by preliminarily exposing the sensors to the "analyte" vapor (film "training").

Valuable information about the operation of the sensor when exposed to single- and multicomponent gas mixtures can be derived from the frequency vs. time plots (Figs. 2, 3). Taking the sensor with a DCH-18-C-6 crown ether film as an example, we studied the geometry parameters of the frequency vs. time plot as influenced by the microimpurities (Fig. 2). To elucidate the relationships in variation of the sensor sensitivity with the compositions of the solution and the equilibrium gas phase, we successively introduced the components into the mixture analyzed. The time vs. frequency plot is strongly influenced by introduction into an aqueous ethanolic solution of microimpurities such as ethyl acetate (Fig. 2, curve *2*) and isopentanol (Fig. 2, curve *5*).

We analyzed the trends in variation of the sensor response within 5, 60, 120, and 180 s as measured from the moment of injecting the sample containing ethanol solely (curve *1*), ethanol + methanol, isopropanol, and *n*-butanol microimpurities (curve *3*), the alcohols + ethyl acetate (curve *4*), and all the above-listed components + isopentanol (curve *5*). The sensor response reaches a maximum in 5-s sorption of the

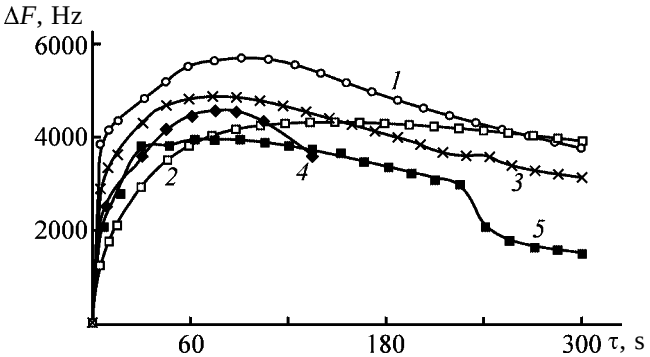

Fig. 2. Frequency vs. time plot for sorption on a DCH-18-C6 film of vapor of aqueous solution of (*1*) ethanol and ethanol mixed with (*2*) ethyl acetate, (*3*) methanol, (*4*) isobutanol, and (*5*) isopentanol. (ΔF) Sensor response and (τ) sorption time; the same for Fig. 3.

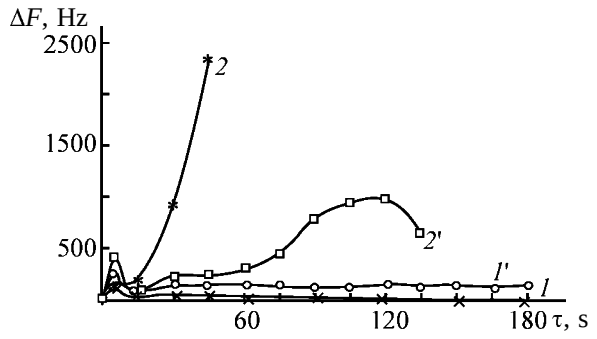

Fig. 3. Frequency vs. time plot for sorption of vapor of (*1*, *1*') aqueous ethanol and (*2*, *2*') the same with microimpurities on (*1*, *2*) DNP and (*1*', *2*') PEG-2000 films.

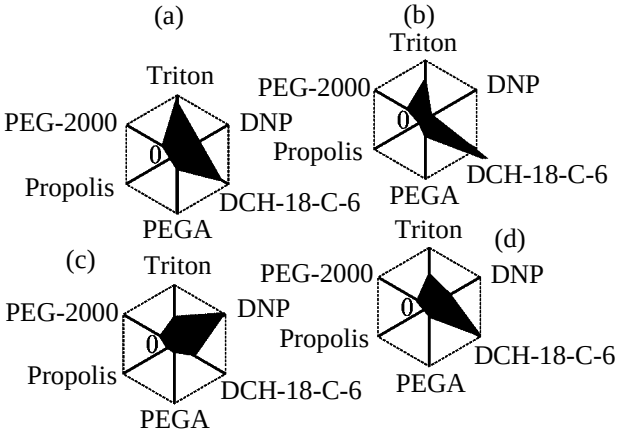

Fig. 4. Sorption diagrams for (a, c) C_1–C_4 alcohol mixture and (b, d) C_1–C_5 alcohol + ethyl acetate mixture on Triton X-100, DCH-18-C-6, propolis, PEGA, PS, and PEG-200 films. Response recorded in (a, b) 5 and (c, d) 30 s. Sensor response magnitude: (a, b) 1200 and (c, d) 4000 Hz.

equilibrium gas phase of aqueous ethanol. With introducing microamounts of more volatile methyl and isopropyl alcohols into an aqueous solution, ΔF tends to decrease (>5 s). Butyl and pentyl alcohols and their isomers affect similarly (decrease) the sensor response at the initial moment of sorption. The response from the crown-ether-based sensor was at a minimum at the moment of introducing ethyl acetate into the alcohol mixture.

Thus, by analyzing the responses of the sensor after 5-s sorption, it is possible to estimate the content of the microimpurities (isopropanol, iso- and *n*-butanol, and ethyl acetate) in aqueous ethanolic solutions with a high concentration of ethanol. Similar changes were observed in the frequency vs. time plots for 14–45-s sorption. The sensor responses recorded after 60–180-s sorption differ less significantly when microimpurities are introduced. The weakest response was observed with pentanol and butanol impurities. The responses from the crown-ether-based sensor in sorption runs longer than 15–30 s bear no information.

Prompt response was obtained from the DNP film sensor when exposed to a vapor of a solution based on ethanol with microimpurities of other alcohols and ethyl acetate (τ_{max} = 5–15 s, see curves *1*, *2* in Fig. 3). Microamounts of C_1–C_5 alcohols and ethyl acetate introduced into an aqueous ethanol affect the frequency vs. time plot (Fig. 3, curve *2*). A sharp increase in the DNP sensor response in a 15-s sorption run is due to the presence of C_4–C_5 alcohols and ethyl acetate microimpurities in the solution with a high ethanol content. The parabolic shape of the frequency vs. time plots (τ up to 15 s) suggests desorption of the components from the film surface. Sensors based on propolis, Triton X-100, and PEGA films characterized by longer desorption (over 180 s) operate similarly.

The PEG-2000 film is the site of absorption; the frequency vs. time plot is clearly indicative of the main stages of interaction between the mixture components with the receptor film (Fig. 3, curves *1*', *2*'). The first maximum (τ^1_{max} = 15 s) corresponds to adsorption of low-boiling alcohols (C_1–C_4) and ethyl acetate, and when these are partially desorbed, the sensor begins to respond to isopentanol. Accumulation of ethyl acetate by the receptor film takes much time, as the entire film is involved in sorption (absorption). The second maximum in the frequency vs. time plot is observed at τ^2_{max} = 150–180 s. Thus, prolonged sorption on the PEG-2000 receptor film and a drastic change in the signal of the DNP film sensor after 5–10-s sorption suggests the presence of isopentanol microimpurities in the equilibrium gas phase.

The mutual location of the maxima in the frequency vs. time plots for various sensors governed the order of their arrangement in the matrix, as well as the algorithms of receiving individual and forming the overall signals from the detector. The maximal response time $\tau_{max(i)}$ determines the inertia of the entire detector. Figure 4 demonstrates the overall signal from the matrix comprised of six sensors based on various films when exposed to a vapor of model mixtures containing C_1–C_4 alcohols, as well as C_1–C_5 alcohols + ethyl acetate. The overall signal is represented by a circular diagram with the sensor responses corresponding to various sorption times ($\tau_{max(i)}$ = 5 and 30 s) plotted on the axes. The changes in the geometry of the overall signal upon introducing isopentanol and ethyl acetate confirm our suggestions concerning the influence exerted by these microim-

purities on the frequency vs. time plots for sensors based on PEG-2000, DCH-18-C-6, and DNP films.

Our results were applied to analyzing solutions with a high content of ethanol, containing microamounts of other alcohols and alkyl acetates. This method was tested with foodstuffs containing such compounds. All the samples were simultaneously tested using standard techniques, gas chromatography, and the suggested method based on the use of a piezosorption matrix detector. Microamounts of acetaldehyde and ethyl formate do not affect the results of analysis by the method proposed; determination of their amounts in specimens has no priority in estimating the foodstuff quality. Based on the results of analysis by standard techniques and gas chromatography, we selected samples for compilation of the database using standard aromatograms.

Thus, we demonstrated the possibility of reliably analyzing the equilibrium gas phase of ethanol-containing solutions with a matrix detector. This method does not require sample preparation; a small sample volume (1 ml) is sufficient; the detector is simple and cheap.

CONCLUSION

Ethanol-based multicomponent gas mixtures can be analyzed using a sensor matrix. Polyethylene glycol PEG-2000, dinonyl phthalate, dicyclohexano-18-crown-6 ether, polyethylene glycol adipate, propolis, and Triton X-100 are suggested as selective coatings for the electrodes of piezoelectric quartz resonators. The optimal mass of the film applied is 10–20 μg. A specific algorithm of receiving the signals from individual sensors improves the selectivity of detecting complex mixtures of vapors of organic compounds from various classes.

REFERENCES

1. Zolotov, Yu.A., *Vestn. Ross. Akad. Nauk*, 1997, vol. 67, no. 6, pp. 508–513.
2. Lucas, Q., Guerin, Y., and Benincasa, V., Abstracts of Papers, *Pittsburgh Conf. on Analytical Chemistry and Applied Spectroscopy*, PITTCON'97, Atlanta, GA, March 16–21, 1997, p. 613.
3. US Patent 5627307.
4. US Patent 5465608.
5. Korenman, Ya.I., Kuchmenko, T.A., and Kudinow, D.A., *Ecol. Congr.* (USA), 2002, vol. 6, no. 1, pp. 15–18.
6. Malov, V.V., *P'ezorezonansnye datchiki* (Piezoresonance Sensors), Moscow: Energoatomizdat, 1989.
7. Dorozhkin, L.M., Doroshenko, V.S., and Krasilov, Yu.I., *Zh. Anal. Khim.*, 1995, vol. 50, no. 9, pp. 979–982.
8. Korenman, Ya.I., Tunikova, S.A., Bel'skikh, N.V., *et al.*, *Zh. Anal. Khim.*, 1997, vol. 52, no. 3, pp. 313–318.
9. RF Patent 2098805.
10. Kuchmenko, T.A., Korenman, Ya.I., Trivunats, K.V., *et al.*, *Zh. Anal. Khim.*, 1999, vol. 54, no. 2, pp. 178–182.
11. Kuchmenko, T.A., Semenyakina, N.V., and Korenman, Ya.I., *Zh. Prikl. Khim.*, 1999, vol. 72, no. 8, pp. 1285–1292.
12. Ganshin, V.M., Fesenko, A.V., and Chebyshev, A.V., Abstracts of Papers, *Vserossiiskaya konferentsiya "Sensor-2000. Sensory i mikrosistemy"* (Russian Conf. "Sensor-2000. Sensors and Microsystems"), St. Petersburg, 2000.
13. Vlasov, Yu.G., Legin, A.V., and Rudnitskaya, A.M., *Zh. Anal. Khim.*, 1997, vol. 52, no. 11, pp. 1199–1205.
14. Xing, Wan-Li, He, Xi-Wen, Fang, Yan-Hong, and Wei, Hong-Mei, *Acta Chim. Sci.*, 1997, vol. 55, no. 11, pp. 1130–1137.

Russian Journal of Applied Chemistry, Vol. 76, No. 5, 2003, pp. 742–744. Translated from Zhurnal Prikladnoi Khimii, Vol. 76, No. 5, 2003, pp. 771–773.

APPLIED ELECTROCHEMISTRY AND CORROSION PROTECTION OF METALS

Features of Spark Dispersion of Some Metals

R. K. Bairamov

Olimpiya Limited Liability Company, Novomoskovsk, Tula oblast, Russia
Novomoskovsk Institute, Mendeleev Russian University of Chemical Engineering, Novomoskovsk, Tula oblast, Russia

Received November 11, 2002; in final form, March 2003

Abstract—The influence exerted by the frequency of current pulses applied to the electrodes on spark erosion of some metals was studied.

Spark dispersion of metals results in formation of essentially different products depending on the process conditions [1–3]. Conventionally, metals subjected to spark dispersion can be subdivided into two groups. The first group includes metals forming surface oxide films having high contact resistance and undergoing spark erosion, and the second group includes metals that to not form such films [4]. In spark erosion of the latter metals, the probability of spark discharges is lower, and that of shorts between the electrodes and metal granules is higher, which ultimately results in cessation of the spark erosion. The spark dispersion of such metals is performed using a metal of the first group, e.g., aluminum, a certain amount of which in the form of electrodes or granules is introduced into the reactor together with the metal studied [4].

In this work we studied the influence exerted by current pulses applied to the electrodes on spark erosion of some metals. The installation and experimental procedure are described in [12]. The electrodes made of the metal studied were fixed to the edges of the reactor, and granules of the same metal were charged inside. The working solution was distilled water. The current pulses of varied frequency F (Hz) were applied to the electrodes in the course of spark erosion, and the optimal frequency was determined. The spark-erosion efficiency of the metals N (kg h^{-1}) was determined as the ratio of the weight loss of the electrodes and granules after erosion to the erosion time. The efficiency largely depends on the electrode surface area [5]. In our experiments, the total surface area of the electrodes was about 16 cm^2. The specific energy consumption W (kW h kg^{-1}) was calculated as the ratio of the consumed energy to the weight of the dispersed metal obtained from electrodes and granules.

The results obtained in studying the effect exerted by the frequency of the current pulses applied to the electrodes on the spark-erosion efficiency of the metals are plotted in Fig. 1. As known, the oxide film covers the metal surface nonuniformly and has variable thickness. Figure 1 shows that, with increasing frequency of current pulses, the spark-dispersion efficiency by zinc, which belongs to the first group, first grows sharply and then gradually approaches the limiting value (curve *1*). Such a trend in the erosion efficiency suggests that, in sites where the surface oxide film is thinner, a part of the supplied energy goes into the metal bulk [6]. At higher frequencies, the supplied energy is redistributed, with the main part accumulated on the surface. As a result, the efficiency by zinc grows sharply. When the accumulated energy attains the limiting value, the spark erosion efficiency virtually stops to vary.

In spark erosion of tungsten (curve *2*) and nickel (curve *3*), which belong to the second group, the pattern is different. As the frequency of current pulses is increased, the dispersion efficiency of both metals first grows sharply. Then, in the ranges F = 300–500 (Ni) and 600–800 Hz (W), the spark-erosion efficiency varies insignificantly. At higher F (up to 2500 Hz), the efficiency decreases (first sharply and then slowly for Ni; gradually for W).

Such a shape of the N–F curves in spark dispersion of the second-group metals is due to the different distribution of the supplied energy at the metal surface and in bulk, which affects the spark-erosion efficiency. The different positions of the maxima of the spark-erosion efficiency for Ni and W may be due to specific features of these metals and formation of the surface oxide film.

The influence exerted by the frequency of current

1070-4272/03/7605-0742$25.00

pulses applied to the electrodes on the specific energy consumption upon spark erosion of the metals is illustrated in Fig. 2. As seen, the specific consumption of the electrical energy in spark dispersion of zinc, which belongs to the first group, varies in parallel with the process efficiency. In spark erosion of the second-group metals, e.g., tungsten (curve *2*) and nickel (curve *3*), the specific energy consumption varies in opposite direction with the process efficiency. As noted above, the second-group metals undergo spark dispersion in the presence of electrodes or granules of a first-group metal. This is presumably due to the fact that a natural oxide film on their surface increases the electrical resistance of the chain.

In spark dispersion of the metals studied, in the points denoted by asterisks in Figs. 1 and 2, the spark erosion was performed using aluminum electrodes and granules of the metals studied. In spark dispersion of zinc, the use of aluminum electrodes does not noticeably affect spark erosion. It is quite natural, because both aluminum and zinc are first-group metals. For tungsten and nickel, which are second-group metals, a different pattern was observed. In this case, the spark-erosion efficiency decreased, and the specific energy consumption increased. In all probability, the fact that, without aluminum electrodes or granules, the metals of the second group do not undergo spark dispersion [4] can be due to the high frequency of the current pulses applied to the electrodes and to the low contact resistance of surface oxide films.

The influence exerted by the frequency of current pulses on the composition of the products obtained in spark erosion of aluminum is illustrated in Fig. 3. As seen, with increasing frequency the content of the metal powder increases (curves *1*, *2*) and the content of aluminum hydroxide in the erosion product decreases (curves *3*, *4*). When the frequency of current pulses applied to the electrodes is low, a part of the supplied energy goes into the metal bulk. As a result, the number of spark discharges decreases. In the process, the portion of the energy spent for the thermal decomposition of the working solution components decreases. As a result, the amount of atomic oxygen and, consequently, the fraction of the dispersed metal coated with a protective oxide film decrease. The content of the metal powder in the erosion product also decreases. The increase in the current pulse frequency results in the formation of atomic oxygen in a greater amount and, as a consequence, in the growth of dispersed metal particles coated with the protective oxide film. Ultimately, the content of the metal powder in the erosion product increases.

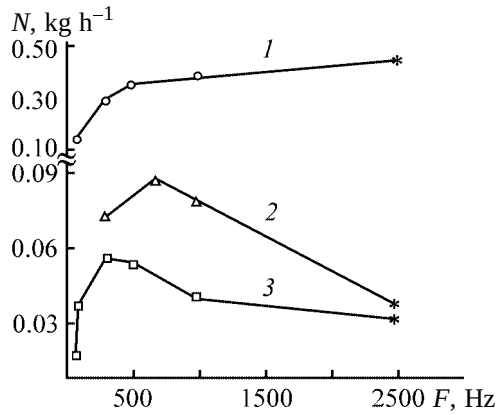

Fig. 1. Spark-erosion efficiency *N* for (*1*) zinc, (*2*) tungsten, and (*3*) nickel as a function of the frequency *F* (Hz) of the current pulses applied to the electrodes. Distilled water working medium, slurry treatment temperature 25°C, time 4 h; the same for Fig. 2.

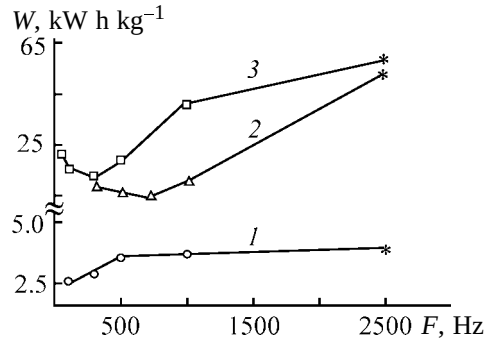

Fig. 2. Specific consumption of electrical energy *W* in the course of spark erosion of (*1*) zinc, (*2*) tungsten, and (*3*) nickel vs. the frequency *F* (Hz) of current pulses applied to the electrodes.

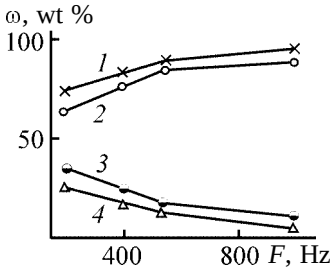

Fig. 3. (*1, 2*) Concentration ω of aluminum powder and (*3, 4*) total content of aluminum hydroxides vs. frequency *F* of current pulses applied to the electrodes. Slurry treatment temperature 25°C and time 4 h. Working medium, M: (*1, 4*) 0.19 acetic acid and (*2, 3*) 0.14 oxalic acid.

Thus, our results show that spark dispersion of second-group metals can be performed using electrodes and granules of the metal studied and current pulses of the optimal frequency.

CONCLUSION

The spark erosion of the metals studied is strongly affected by the frequency of the current pulses applied to the electrodes. The metals forming surface oxide films with low contact resistance undergo spark dispersion at the optimal frequency of the current pulses. It was shown that the amount of the metal powder in spark dispersion of aluminum increases with increasing frequency of the current pulses.

REFERENCES

1. Asanov, U.A., and Sakavov, I.E., *Izv. Akad. Nauk Kirg. SSR*, 1967, no. 4, pp. 71–75.
2. Bairamov, R.K., Vedernikova, N.P., and Ermakov, A.I., *Zh. Prikl. Khim.*, 2001, vol. 74, no. 10, pp. 1703–1705.
3. Bairamov, R.K., Ermakov, A.I., and Vedernikova, N.P., *Zh. Prikl. Khim.*, 2002, vol. 75, no. 3, pp. 419–421.
4. USSR Inventor's Certificate 833377.
5. Arenkov, A.B., *Osnovy elektrofizicheskoi obrabotki metallov* (Principles of Electrophysical Treatment of Metals), Leningrad: Mashinostroenie, 1967.
6. *Elektrotekhnologicheskie promyshlennye ustanovki* (Electrotechnological Industrial Installations), Svenchanskii, A.D., Ed., Moscow: Energoizdat, 1982.

Russian Journal of Applied Chemistry, Vol. 76, No. 5, 2003, pp. 745–750. Translated from Zhurnal Prikladnoi Khimii, Vol. 76, No. 5, 2003, pp. 774–778.

APPLIED ELECTROCHEMISTRY AND CORROSION PROTECTION OF METALS

Effect of Lithium Sulfide on Electrical Properties of Li_2S–$LiPO_3$ Glasses

I. A. Sokolov, N. A. Valova, Yu. P. Tarlakov, and A. A. Pronkin

St. Petersburg State Technological Institute, St. Petersburg, Russia

Received June 24, 2002; in final form, March 2003

Abstract—The temperature and concentration dependences of the electrical conductivity was studied in Li_2S–$LiPO_3$ glasses. The effect of lithium sulfide additions (22.5–25 mol %) to $LiPO_3$ on the electrical conductivity was studied. The nature of the conductivity was studied over the whole range of Li_2S concentrations using Tubandt's procedure, and the contribution of electronic component to the total electrical conductivity was examined by Liang–Wagner's polarization method.

Ion-conducting substances used as solid electrolytes (SELs) for chemical current sources and in producing electrochemical transducers and ion-selective sensors attract intent researchers' attention. Crystalline compounds are most commonly used as SELs; however, glassy compounds are also given a considerable attention. These latter have a number of advantages over crystalline SELs: they are weakly sensitive to impurities and convenient in processing; they allow vacuum-tight connections to be ensured. Electrical parameters of glassy compositions are highly stable and reproducible. Moreover, the electrical conductivity of glassy compositions is one or two orders of magnitude higher than the conductivity of crystalline compounds of the same composition.

In SEL, the electronic component of electrical conductivity is absent, and the total conductivity is determined by the migration of ions in an electric field. The expression for the total conductivity of SEL taking into account the contribution of both positive and negative current carriers has the form

$$\sigma = \sigma_+ + \sigma_- = qn(\mu_+ x_+ + \mu_- x_-), \quad (1)$$

where σ is the total electrical conductivity; σ_+ and σ_-, electrical conductivities determined by the migration of positive and negative current carriers, respectively; n, number of molecules per unit volume; $q = ez$, electrical charge of a carrier; x_+ and x_-, mole fractions of cations and anions; and μ_+ and μ_-, ionic mobilities.

Often one kind of the current carriers dominates in the electrical conductivity. In this case, the conductivity of glassy systems can be described by the equation [1]

$$\sigma = n\alpha(ez)\mu, \quad (2)$$

where α is the degree of dissociation.

It follows from relationship (2) that an increase in the conductivity can be achieved by increasing both the number of current carriers and their mobility.

The electrical conductivity of binary alkali oxide glasses increases as the content of an alkali metal oxide increases. Therefore, seemingly, glassy SELs should be searched for among the systems into which a maximal amount of current carriers could be introduced. However, this line is limited by the fact that glasses with a high M_2O content (M = Li, Na, K, etc.) have a low chemical stability and readily crystallize. At the same time, the number of ions participating in current transfer can be increased at the expense of decreasing the energy of their bonding with the glass matrix. This can be achieved by introducing inorganic salts with large anions (SO_4^{2-}, SO_3^{2-}, and halide ions) into the glass composition. In this case, the structure of the starting glass becomes loosened, and the electrical conductivity increases [2–4].

As believed in [5–8], the substitution of sulfur(II) ions for oxygen ions in the glass structure should also be accompanied by an increase in the ionic conductivity. In fact, sulfur(II) ions are larger than oxygen ions ($r_{S^{2-}}$ = 1.84 and $r_{O^{2-}}$ = 1.40 Å) and have a more pronounced tendency to form covalent bonds. Therefore, the energy of interaction between sulfur-containing glass fragments and alkali metal ions is lower than in oxide glasses. Consequently, the energy of dissociation of polar structural chemical units containing

1070-4272/03/7605-0745$25.00

Table 1. Chemical analysis of Li_2S–$LiPO_3$ glasses

Composition, mol %		Found, wt %			Calculated, %		
Li_2S	$LiPO_3$	S	Li	P	S	Li	P
–	100.0	–	8.08	36.07	–	7.87	35.61
5.0	95.0	1.91	8.76	35.08	1.36	5.54	34.95
10.0	90.0	3.92	9.40	34.05	3.38	9.18	34.08
15.0	85.0	6.00	10.07	32.96	5.61	9.59	33.13
20.0	80.0	8.21	10.78	31.82	7.74	10.65	31.91
25.0	75.0	10.55	11.52	30.61	9.93	11.26	30.68

sulfur(II) will be lower, and the electrical conductivity itself must increase at the expense of an increase in the number of current carriers. Thus, the substitution of sulfur for oxygen in Na_2O–GeO_2 glasses (to give the Na_2S–GeS_2 system) was shown [6–9] to result in increased conductivity. This can be accounted for by the fact that sulfur(II) compounds have a higher ionic conductivity than their oxide analogs. Indeed, the electrical conductivity of sulfide glasses considerably exceeds that of oxide glasses. At room temperature, the specific electrical conductivity of glasses, e.g., in the Na_2O–P_2O_5 system attains 7×10^{-9} S cm^{-1} at E_σ = 1.36 eV [10], and in the Na_2S–P_2S_5 system, $\sigma = 3.9 \times 10^{-6}$ S cm^{-1}, E_σ = 1.08 eV [11].

To further increase the electrical conductivity, halide salts are introduced into sulfide glasses. For example, a glass of the composition $0.477(GeS_2 \cdot Ag_2S) \cdot 0.523AgI$ with the conductivity of 4.7×10^{-3} S cm^{-1} (25°C) and E_σ = 0.50 eV was described in [12]. The study of the conductivity nature showed that glasses of these systems are ionic conductors, and the electronic component of the conductivity in silver-containing sulfide glasses is 3–4 orders of magnitude lower than the ionic component [13]. Among essential drawbacks of such glasses are their high hygroscopicity and difficult synthesis [11, 14]. We emphasize that the published data on the properties of glassy compositions mainly concern silicates and borates. The electrical properties of sulfur-containing oxide–phosphate glasses are known only for Na_2O–Na_2S–P_2O_5 glasses [15] and for silver-containing systems [16]. In this work we studied the temperature and concentration dependences of the electrical conductivity and the nature of current carriers in the Li_2S–$LiPO_3$ glasses.

EXPERIMENTAL

We synthesized the glasses in glassy carbon crucibles in a dry argon atmosphere in a laboratory electric furnace at 1100–1150°C for about 25 min. This time was sufficient for complete melting and homogenization of the melt. The charge was prepared from chemically pure grade $LiPO_3$ and lithium sulfide obtained by direct synthesis in liquid ammonia [17]. The purity of the resulting Li_2S was no worse than 99.5%, with polysulfides as impurities.

To decrease sulfur volatilization, we placed the crucible with the charge into a crucible of a larger volume; the space between the crucibles was filled with lithium sulfide, and the external crucible was covered by a lid [8]. We sampled the glasses by pouring off the melt into preheated metallic molds with the subsequent annealing for 1 h in a muffle furnace at a temperature approximately 15°C lower than T_g and cooling together with the muffle to room temperature. The glass transition point T_g was determined by the plot of the relative elongation of the sample (a glass cylinder 50.0 ± 0.5 mm long) vs. temperature. The measurements were performed on a DKV-5 vertical quartz dilatometer. The annealing quality was monitored by the polarization optical method.

The chemical analysis of the synthesized glasses showed that their compositions are close to the calculated compositions (Table 1). The phosphorus content was determined by the standard procedure involving the formation of phosphomolybdic acid [18]. Since sulfur can be in various forms in the glass structure (free, sulfide, and polysulfide), we determined the total content of sulfur by the decomposition of a glass sample and subsequent sulfur oxidation to sulfate ion [15]. The lithium content was determined by flame photometry.

We determined the density of glasses by hydrostatic weighing in carbon tetrachloride. The reproducibility of the results for glasses obtained in replicate meltings is $(3–5) \times 10^{-3}$ g cm^{-3}.

The electrical conductivity was measured with parallel-plate finely polished samples 1.50 ± 0.01 mm

Table 2. Electrical properties of $Li_2O–P_2O_5$ glasses [19]

Li_2O, mol %	$c_{Li^+} \times 10^2$, mol cm^{-3}	$-\log\sigma$ (σ, S cm^{-1}) at indicated T, °C			$\log\sigma_{O^+}$, (σ, S cm^{-1})	E_σ, eV
		25	100	200		
38.0	2.32	10.95	8.15	5.8	3.0	1.65
40.0	2.39	10.55	7.8	5.5	3.15	1.62
42.5	2.46	9.9	7.35	5.2	2.85	1.51
45.0	2.55	9.5	7.05	4.95	2.9	1.47
50.0	2.74	8.45	6.15	4.2	3.05	1.36
52.5	2.82	8.0	5.8	3.9	3.0	1.30
55.0	2.94	7.5	5.45	3.7	2.75	1.21
58.0	3.08	6.85	4.95	3.35	2.6	1.12

thick and 20 mm in diameter [19]. To exclude the possible surface conductivity, we carried out the measurements using safety electrodes [according to GOST (State Standard) 6433.2.71] in the direct current mode with active (lithium amalgam) electrodes in the range from room temperature to 270°C under heating and cooling conditions. No hysteresis phenomena were observed. We used ED-05M and ITN-7 electrodynamic electrometers as measuring devices. The obtained experimental data lied along a straight line in the $\log\sigma = f(1/T)$ coordinates. The data were processed using the equation

$$\sigma = \sigma_0 \exp(-E_\sigma/2kT).$$

Lithium metaphosphate has an electrolytic conductivity, the transport numbers of lithium ions being 0.97–1.00 depending on the conditions of its synthesis [19]. Along with lithium ions, protons formed upon dissociation of impurity water can take part in current transport. To estimate the content of water in the glasses under study, we recorded the IR transmission spectra of parallel-plate polished samples (l = 1.50 mm) in the range 2000–5000 cm^{-1}. The intensity of absorption at 2300, 2900, and 3400 cm^{-1} in the spectra of $Li_2S–LiPO_3$ glasses is substantially lower than in the spectra of $Li_2O–P_2O_5$ and $Li_2O–LiPO_3$ glasses, which indicates that the content of impurity water in the first case is small [$\sim(2–5) \times 10^{-2}$ wt %]. The introduction of lithium sulfide, which is a cationic conductor, into $LiPO_3$ should not be accompanied by a change of the nature of current carriers. The conductivity of $Li_2S–LiPO_3$ glasses will be determined by the migration of lithium ions only. To check this assumption, we determined the transport numbers of lithium ions using Tubandt's method. The amount of electricity passing through the samples during electrolysis was measured by a silver–thallium coulometer and a Kh-603 electrolytic quantity meter connected in series. We let 4–6 C of electricity pass through a stack of glasses. If more than 10 C of electricity passed, the growth of dendrites and breakdown of the samples were observed. We estimated the changes in the composition of the near-electrode and middle samples after the electrolysis by the changes in their weight. We weighed the samples on a VLAO-100/1 semimicroanalytical balance. An experiment was considered to be correct if the weight of a middle sample before and after electrolysis remained the same within the error of weighing. The contribution of the electronic component (10^{-3}%) to the total conductivity was determined using the Liang–Wagner polarization method.

It follows from Table 1 that the analytical content of lithium and phosphorus virtually corresponds to their calculated content, whereas the sulfur loss reaches 6–7%. This is due to the fact that water present in the charge as an impurity reacts with sulfide ions to give hydrogen sulfide.

It is interesting that, in the $Li_2O–P_2O_5$ system, it is possible to synthesize a glass containing 58 mol % Li_2O (Table 2) [19]. The concentration of lithium ions in this glass is 3.08×10^{-2} mol cm^{-3}, and in $LiPO_3$ it is 2.74×10^{-2} mol cm^{-3}. The activation energy at such an increase in the content of lithium ions decreases from 1.36 to 1.12 eV, and the electrical conductivity (at 200°C) increases by almost an order of magnitude (see figure; Table 2).

The addition of lithium sulfide to lithium metaphosphate is accompanied by an increase in the concentration of lithium ions by a factor of almost 1.5 (Table 3). This concentration is 3.84×10^{-2} mol cm^{-3} in the glass containing 25 mol % Li_2S. In this case, the activation energy of the electrical conductivity

Table 3. Density d, volume concentration of lithium ions c_{Li^+}, and molar volume V_{mol} of the Li_2S–$LiPO_3$ glass

Composition, mol %		d, g cm^{-3}	$c_{Li^+} \times 10^2$, mol cm^{-3}	V_{mol},* cm^3 mol^{-1}	$-\log\sigma$ (σ, S cm^{-1}) at indicated T, °C			$\log\sigma_0$, (σ, S cm^{-1})	E_σ, eV
Li_2S	$LiPO_3$				25	100	200		
0	100.0	2.37	2.75	8.45	6.1	4.15	3.2	1.38	36.26
5.0	95.0	2.35	2.96	7.55	5.55	3.9	2.35	1.17	35.72
10.0	90.0	2.33	3.175	6.6	4.9	3.45	2.0	1.02	35.17
15.0	85.0	2.33	3.40	5.95	4.4	3.05	1.9	0.93	34.31
20.0	80.0	2.32	3.62	5.7	4.15	2.9	1.85	0.89	33.59
22.5	77.5	2.32	3.75	5.45	4.05	2.95	1.5	0.82	33.17
25.0	75.0	2.31	3.84	5.65	4.2	3.0	1.45	0.84	32.88

* $V_{mol} = M/d$, where M is the molar weight of the glass.

decreases from 1.38 to 0.84 eV, and $-\log\sigma$ at 200°C changes from 4.15 to 3.0 (see figure; Table 3).

When the concentration of lithium ions increases within the limits of $(2.74–3.08) \times 10^{-2}$ mol cm^{-3}, the activation energy of electrical conductivity and the electrical conductivity itself for the Li_2O–P_2O_5 and Li_2S–$LiPO_3$ glasses almost coincide (see figure). This may be due to the fact that sulfur-containing polar structural chemical units appear to be blocked (in this concentration range of Li_2S) by the $Li^+[O^-PO_{3/2}]$ units.

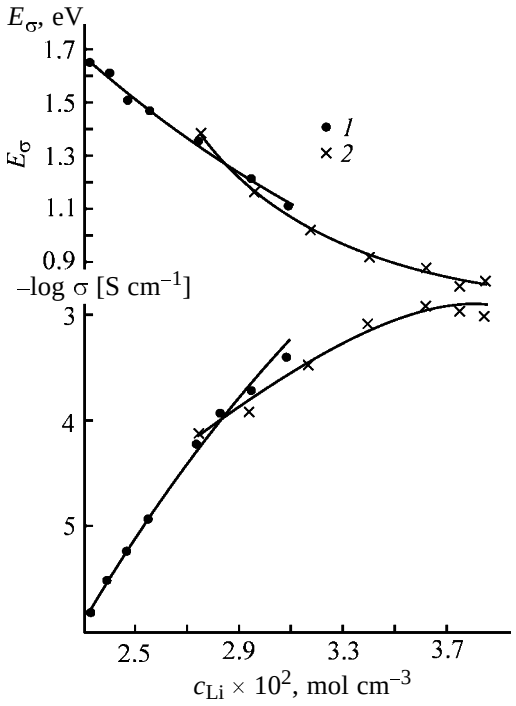

Plots of the logarithm of specific electrical conductivity $\log\sigma$ and of the activation energy of electrical conductivity E_σ of (*1*) Li_2O–P_2O_5 [19] and (*2*) Li_2S–$LiPO_3$ glasses vs. concentration of lithium ions c_{Li^+} at 200°C.

The introduction of lithium into P_2O_5 is actually accompanied by the break of bridging P–O–P bonds and by the depolymerization of polyphosphate chains to give di-, tri-, and tetraphosphate anions. Myuller [1] believes that the structure of such glasses consists of polar and nonpolar structural chemical units [1]. When [Li]/[P] < 1, the structure will be determined by a combination of polar $Li^+[O^-PO_{3/2}]$ and nonpolar $[PO_{4/2}]$ structural chemical units. As the concentration of lithium ions increases, the content of polar structural chemical units increases, and at [Li]/[P] = 1 the structure of the glass of the metaphosphate composition will consist mainly of polar $Li^+[O^-PO_{3/2}]$ structural chemical units only. In the glasses with [Li]/[P] > 1, along with polar $Li^+[O^-PO_{3/2}]$ structural chemical units, new polar $Li_2^+[O_2^-PO_{2/2}]$ units are formed. The interaction between polar $Li^+[O^-PO_{3/2}]$ structural chemical units is accompanied by the appearance of the quadrupoles

$$\begin{array}{l} O_{3/2}P–O^-Li^+ \\ \quad\vdots\quad\vdots \\ Li^+O^-–PO_{3/2}. \end{array}$$

The energy of lithium dissociation from these quadrupoles is lower than that from the polar $Li^+ \cdot [O^-PO_{3/2}]$ structural chemical units. The number of current carriers increases at this expense. The energy of activation shift, E_a, of dissociated ions in the medium of polar structural chemical units is lower than that in the medium of the nonpolar $[PO_{4/2}]$ structural chemical units. As already noted, the structure of lithium metaphosphate is formed by polar structural chemical units; hence, lithium ions migrate in a polar medium, and $E_a \approx$ const, as the migration mechanism remains unchanged. The increase in the electrical conductivity can be accounted for by a decrease in the dissociation energy of quadrupoles E_g, which results

Table 4. Transport numbers of lithium ions in the Li_2S–$LiPO_3$ glasses*

Composition, mol %		T, °C	Electricity passed		Changes in the weight of anodic glass		ν_{Li^+}
Li_2S	$LiPO_3$		Q, C	$Q' \times 10^5$, equiv	$\Delta P \times 10^3$, g	$Q'' \times 10^5$, equiv	
0	100.0	207.5	5.68	5.89	5.94	5.77	0.98
0	100.0	198.3	4.53	4.69	4.74	4.64	0.99
10.0	90.0	210.2	5.23	5.42	5.47	5.37	0.99
20.0	80.0	204.8	4.95	5.13	5.18	5.13	1.00
20.0	80.0	189.7	4.41	4.57	4.61	4.62	1.01
22.5	77.5	218.0	5.17	5.36	5.41	5.36	1.00
22.5	77.5	200.3	4.26	4.42	4.46	4.40	0.99_5

* $Q' = Q/F$, where F is the Faraday number; $\nu_{Li^+} = Q''/Q'$.

in increased number of dissociated lithium ions, which are the current carriers. As a result, the activation energy of electrical conductivity, E_σ, decreases (see figure; Table 2).

In experiments with $AgPO_3$–Ag_2S glasses, it was suggested that sulfur(II) is able to replace oxygen in the glass structure [15]. In line with this concept, introduction of lithium sulfide into lithium metaphosphate will be accompanied both by incorporation of sulfide ions in the anionic component of the structure ($O_{3/2}P$–S–$PO_{3/2}$) and by the formation of various sulfur-containing polar structural chemical units. Therefore, we assume that, along with polar oxide $Li^+[O^-PO_{3/2}]$ and $Li_2^+[O_2^-PO_{2/2}]$ structural chemical units, the $Li^+[S^-PO_{3/2}]$ units

$$\begin{array}{ccc} Li^+S^-PO_{3/2}, & & Li^+O^-PO_{3/2} \\ \vdots\ \vdots & & \vdots\ \vdots \\ O_{3/2}PS^-Li^+ & & O_{3/2}PS^-Li^+ \end{array}$$

are formed in the structure of Li_2S–$LiPO_3$ glasses.

The ionic conductivity depends on the energy of lithium binding with the glass framework. A decrease in the binding energy is accompanied by an increase in the number of current carriers at the expense of increased degree of dissociation of polar structural chemical units and, consequently, by an increase in the electrical conductivity (Tables 3, 4).

Therefore, the increase in the electrical conductivity of the Li_2S–$LiPO_3$ glasses is attributable to the fact that the replacement of oxygen in the glass structure by a more polarizable sulfur(II) ion results in the weakening of bonds between lithium ions and the glass framework. This is responsible for a decrease in the dissociation energy of polar structural chemical units and an increase in the number of current carriers and in the electrical conductivity itself.

CONCLUSION

The formation of sulfur-containing oxide polar structural chemical units in the structure of Li_2S–$LiPO_3$ glasses is accompanied by an increase in the electrical conductivity and a decrease in the activation energy of electrical conductivity. Such structural chemical units have a lower (compared to pure oxide) dissociation energy, which results in an increase in the number of current-carrying ions.

REFERENCES

1. Myuller, R.L., *Elektroprovodnost' stekloobraznykh veshchestv* (Electrical Conductivity of Glassy Substances), Leningrad: Leningr. Gos. Univ., 1968.
2. Raven, D., in *Stekloobraznoe sostoyanie* (Glassy State), Leningrad: Nauka, 1983, pp. 180–185.
3. Button, D.P., Tandon, R.F., Tuller, H.R., and Uhlman, D.R., *Solid State Ionics*, 1981, vol. 5, part 1, pp. 655–658.
4. Pronkin, A.A., Naraev, V.N., Tsoi Tong Bing, and Eliseev, S.Yu., *Fiz. Khim. Stekla*, 1992, vol. 18, no. 3, pp. 52–63.
5. Burrou, B., Ribes, M., Rovaine, D., and Satour, J.M., *Silicates Ind.*, 1979, vol. 44, no. 12, pp. 275–281.
6. Burrou, B., Ribes, M., Maurin, M., *et al.*, *J. Non-Cryst. Solids*, 1980, vol. 37, no. 1, pp. 1–14.
7. Malugani, J.P., Fanys, B., Mercier, R., *et al.*, *Solid State Ionics*, 1983, vol. 9–10, no. 1, pp. 659–665.
8. Zaretskaya, G.N., Pronkin, A.A., and Il'in, A.A., *Fiz. Khim. Stekla*, 1987, vol. 13, no. 3, pp. 464–467.
9. Carette, B., Robinel, E., and Ribes, M., *Glass Technol.*, 1983, vol. 24, no. 3, pp. 157–160.
10. Sokolov, I.A., Naraev, V.N., and Pronkin, A.A., *Fiz. Khim. Stekla*, 2000, vol. 26, no. 6, pp. 853–860.
11. Ribes, M., Burrou, B., and Souquet, J.L., *J. Non-Cryst. Solids*, 1980, vol. 38/39, part 1, pp. 103–105.

12. Robinel, E., Carette, B., and Ribes, M., *J. Non-Cryst. Solids*, 1983, vol. 57, no. 1, pp. 49–58.
13. Malugani, J.P. and Robert, G., *Solid State Ionics*, 1980, vol. 1, no. 5/6, pp. 519–523.
14. Kulkarni, A.R., Maiti, H.S., and Paul, A., *Bull. Mater. Sci*., 1984, vol. 6, no. 2, pp. 201–221.
15. Hillebrand, W.F. and Lundell, G.E.F., *Applied Inorganic Analysis with Special Reference to the Analysis of Metals, Minerals and Rocks*, Lundell, G.E.F., Bright, H.A., and Hoffman, J.I., Eds., New York: Wiley, 1963.
16. Baud, G. and Besse, J.P., *J. Am. Ceram. Soc*., 1981, vol. 64, no. 2, pp. 242–244.
17. Baudler, M., Brauer, G., Feher, F., *et al*., *Handbuch der präparativen anorganischen Chemie*, Stuttgart: Ferdinand Enke, 1975, vol. 1.
18. *Rukovodstvo po analizu fosfora, fosfornoi kisloty i udobrenii* (Handbook on the Analysis of Phosphorus, Phosphoric Acid, and Fertilizers), Mozheis, I.B., Ed., Leningrad: Khimiya, 1967.
19. Pronkin, A.A., Murin, I.V., Sokolov, I.A., *et al*., *Fiz. Khim. Stekla*, 1997, vol. 23, no. 5, pp. 547–554.

Russian Journal of Applied Chemistry, Vol. 76, No. 5, 2003, pp. 751–754. Translated from Zhurnal Prikladnoi Khimii, Vol. 76, No. 5, 2003, pp. 779–782.

APPLIED ELECTROCHEMISTRY AND CORROSION PROTECTION OF METALS

Nickel–Zinc Battery with Nickel Oxide Electrode Made of Spherical Nickel Hydroxide on Foamed Nickel Support

M. M. Loginova, T. B. Kas'yan, Z. P. Arkhangel'skaya, and L. B. Raikhel'son

Rigel' Battery Company, Open Joint-Stock Company, St. Petersburg, Russia

Received October 28, 2002; in final form, January 2003

Abstract—Electrochemical and working characteristics of a nickel–zinc battery with nickel oxide electrode made of spherical nickel hydroxide on foamed nickel support were determined.

Nickel–zinc (NZ) battery yielding high output power is known as a power supply for means of transportation, such as underwater vehicles, motor scooters, motorcycles, and hybrid automobiles. Its specific energy is as high as 75–80 W h kg^{-1}, and specific power, 250 W kg^{-1}. However, application of NZ batteries for these purposes has been limited until recently by their short service life and high cost of the positive electrode with metal–ceramic (MC) support.

New methods for fabrication of nickel oxide electrodes (NOE) of nickel–cadmium and nickel–metal hydride batteries have been developed and successfully implemented. These methods employ highly dispersed materials, which are deposited onto a foamed nickel (FN), rather than metal–ceramic, support. To materials of this kind belong spherical nickel hydroxide with addition of hydroxide compounds of cobalt and zinc [1]. Fabricated by pasting and subsequent compaction, NOE have 1.2–1.5 times better specific characteristics because of the use of a lighter support and a compact arrangement of particles of the active paste [2].

Use of spherical nickel hydroxide modified with activating additives in an NZ battery in the form of a compacted electrode with FN support may affect substantially the processes occurring in the battery. In particular, addition of cobalt hydroxide can prevent the commonly occurring in NZ batteries "poisoning" of a compacted NOE by zinc ions [3]. In addition, the dynamics of intraelectrode ("loss of shape") and interelectrode zinc transfer may change because of the densified structure of NOE with spherical nickel hydroxide, and this can affect the working capacity of the zinc electrode. The loss of shape has been attributed to various factors: phase segregation in the electrolyte upon a change in the concentrations of KOH and $Zn(OH)_4^{2-}$ [4], convection in the electrolyte [5], and nonuniform distribution of the current over the electrode surface [6]. Solution of this problem, which is of high theoretical and practical importance, cannot be considered conclusive up to now.

EXPERIMENTAL

In this study, we determined the electrical characteristics of an NTs-25 battery with compacted NOE fabricated by pasting spherical nickel hydroxide onto an FN support. Nickel hydroxide contained 5.6% cobalt and 3.2% zinc. In other respects, the design and technology of fabrication of the battery were the same as those for a battery with MC NOE. The cobalt-to-nickel ratio in the material used was close to the optimal value [Co/(Co + Ni) = 0.07] [7].

The basic parameters of batteries of several types differing in the amount of active paste in unit volume of the positive electrode and in the ratio of active paste masses in the positive and negative electrodes are given in Table 1.

The calculated capacities of positive electrodes, listed in Table 1, correspond to the transformation of Ni^{2+} to Ni^{3+}. The ratio of capacities of the negative and positive electrodes in the batteries under study is smaller than that in batteries with MC NOE, since a greater amount of the active paste is contained in the same NOE volume.

This makes it possible to obtain a higher capacity from the battery in the initial cycles, but, at the same time, creates conditions for fast accumulation of excess charged phase in the zinc electrode, especially so in view of the fact that an excess, with respect to the calculated value, capacity should be imparted to the positive electrode in battery forming.

1070-4272/03/7605-0751$25.00

Table 1. Characteristics of NTs-25 batteries. Thicknesses of positive and negative electrodes 0.95 and 1.25 mm, respectively

Battery	Calculated electrode capacity, A h		Density of active paste, g cm^{-3}		(+)-to-(–) capacity ratio	Battery weight, g
	(+)	(–)	(+)	(–)		
NTs-25:						
with MC NOE	30.8	95	–	1.7	3.0	780
with FN NOE I	46.8	95	2.5	1.7	2.0	735
with FN NOE II	54.0	95	2.7	1.7	1.74	760

The batteries were studied in cycling in the ventilated mode (with low-pressure valves). At regular intervals of time, one battery of each batch was disassembled to determine its state and make analyses; in addition, discharge was performed in separate cycles by different currents to determine the working capacity of a battery in the range from 0.1 to 2*C*.

In order to determine the extent of self-discharge, part of batteries were stored in the charged state for 1 month with the subsequent discharge.

It was found that, in contrast to the MC electrode, the active paste of the positive electrode made of spherical $Ni(OH)_2$ acquires capacity in forming cycles gradually, in 2–3 cycles (Table 2). In the first cycle, the discharge capacity of batteries of type I was only 50–55% of the capacity imparted in charging, and that in the second cycle, 83%, which corresponds to 60% of the theoretical capacity corresponding to conversion of Ni^{2+} into Ni^{3+}. Batteries of type II, with NOE possessing increased capacity, were subjected to three forming cycles, with the positive electrodes yielding in discharge 80% of the calculated capacity.

Charging was done in each stage to a final voltage of 1.98–2.0 V, and discharge, to 1.2 V.

In subsequent cycling, the initial discharge capacity of batteries with FN NOE I (25–27 A h) approximately corresponded to the capacity of batteries with the MC electrode, which allowed their comparison under comparable conditions (Fig. 1).

Table 2. Forming modes and results obtained for different types of NTs-25 batteries

Cycle no.	Charging/discharge capacity, A h		
	with FN NOE I	with FN NOE II	with MC NOE
1st	33/18	42/32	33/27
2nd	33/27.5	45/37.5	33/27
3rd	–/–	55/43	–/–

One of basic characteristics of NZ batteries, which determines the possibility of their use in means of transportation, is their working capacity in intensive discharge modes. Tests demonstrated that the voltage of batteries with FN NOE in charging was markedly lower than that in batteries with the MC electrode, and, in discharge with currents of 0.1–1*C*, their capacity and voltage are virtually identical. And only in the 2*C* mode, the batteries under study, with spherical nickel hydroxide on FN support, have somewhat lower capacity at the same electrode thickness (~1 mm). Therefore, it is advisable to use thinner compacted NOE in batteries intended for short discharge modes.

Comparison of characteristics of the batteries under study (types I and II) with different active paste densities shows that the voltage of a battery with increased amount of electrode material is higher in charging and lower in discharge, with the difference becoming more pronounced with increasing discharge current (Fig. 2). With increasing number of cycles, the achieved degree of NOE charging decreases to a greater extent for batteries of type II, although the discharge capacity of this type of batteries retains higher values up to 100 cycles (Fig. 3).

A decrease in the ratio of capacities of the negative and positive electrodes affects adversely the states of the zinc electrode. As shown by chemical analysis of the active paste from negative electrodes of disassembled batteries, the content of the reduced phase increased, and that of the oxidized phase, decreased.

Content of reduced phase in discharged negative electrode of NTs-25 battery with FM NOE

Cycle	(Zn/Zn + ZnO), %
Initial	7.4
After forming	31
63rd	78
110th	80
200th	85

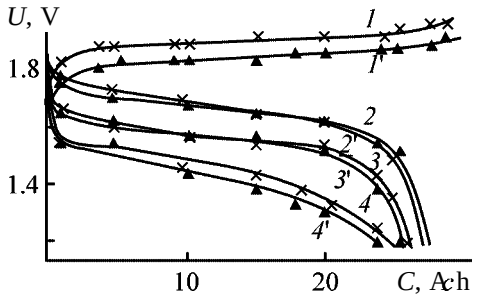

Fig. 1. Charging and discharge curves of NTs-25 batteries with positive electrodes of different designs. Electrode: (*1–4*) metal–ceramic and (*1'–4'*) fabricated by pasting nickel hydroxide on foamed nickel support. (*C*) Capacity and (*U*) voltage. (*1, 1'*) Charging; discharge with current, A: (*2, 2'*) 5, (*3, 3'*) 25, and (*4, 4'*) 50.

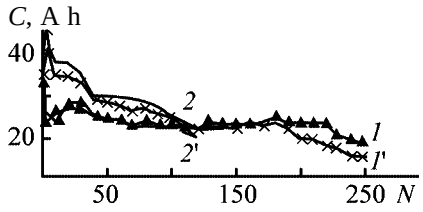

Fig. 3. Variation of (*1, 2*) charging and (*1', 2'*) discharge capacity in cycling of NTs-25 batteries with NOE on foamed nickel support with varied density of the electrode material. (*N*) Number of cycles and (*C*) discharge capacity. Density (g cm^{-3}): (*1, 1'*) 2.5 and (*2, 2'*) 2.7.

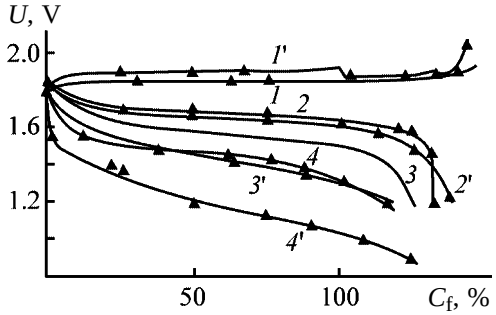

Fig. 2. Effect of density of the electrode material of NOE on foamed nickel support on the electrical characteristics of NTs-25 battery. (*U*) Voltage and (C_r) fraction of rated discharge capacity. Density of electrode material (g cm^{-3}): (*1–4*) 2.5 and (*1'–4'*) 2.7. (*1, 1'*) Charging; discharge with current of (*2, 2'*) 0.2*C*, (*3, 3'*) 1*C*, and (*4, 4'*) 2*C*.

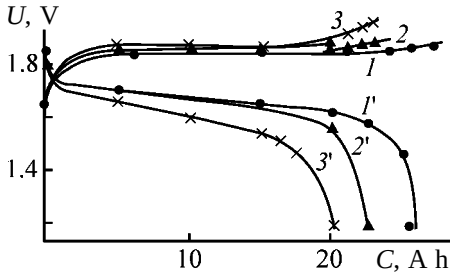

Fig. 4. Effect of service time on (*1–3*) charging and (*1'–3'*) discharge characteristics of NTs-25 battery with NOE on foamed nickel support. (*C*) Discharge capacity and (*U*) voltage; the same for Fig. 5. Cycle: (*1, 1'*) 10th, (*2, 2'*) 100th, and (*3, 3'*) 200th.

In batteries of type I, the whole amount of the oxidized phase was exhausted by the 125th cycle, and in batteries of type II, already by 70th cycle, which required deep discharge to convert the accumulated metallic zinc into the oxidized state (Fig. 3). Changes in the active paste of the negative electrode in the course of cycling lead to a decrease in discharge capacity and increase in charging voltage of the batteries (Figs. 3 and 4).

Apparently, to prevent accumulation of the charged phase in the electrode and to stabilize the discharge capacity of a battery for a longer time, it is necessary to pass to a sealed battery design. This will also ensure deeper deforming of the NOE under study without overcharging of the zinc electrode, since its active paste will be oxidized by evolving oxygen [8].

An analysis of the state of batteries disassembled after cycling demonstrated that changes in the shape of the negative electrode, which only become noticeable by 200th cycle, are manifested in a decrease in the thickness of the active paste layer in a narrow upper part of the electrode. At the same time, in a battery with metal–ceramic NOE the active paste is absent, under the same conditions, on 20% of the electrode area [6]. This is a favorable indication of longer service life of the battery under study, compared with that of the already existing battery.

A study of the influence exerted by storage of a charged battery with NOE made of nickel hydroxide on foamed nickel support demonstrated a 9% self-discharge in 30 days (Fig. 5), which virtually coincides with the degree of self-discharge of batteries with MC support [9].

Our results show that, on replacing the positive electrode with MC support by a compacted electrode with spherical nickel hydroxide, the NZ battery has similar electrical and service characteristics. In addition, the electrode under study is simpler in fabrication.

However, the practically accepted ratio of capacities of the negative and positive electrodes is violated in view of the fact that the capacity of the compacted electrode exceeds that of MC in the same volume. Raising the ratio to the optimal value will enable an increase in the discharge capacity of the NZ battery by 20–30%. Making larger the reserve of the active

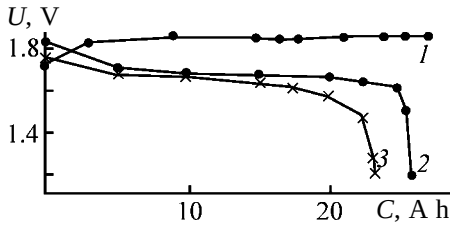

Fig. 5. Effect of storage on discharge capacity of NTs-25 battery with NOE on foamed nickel support. (*1*) Charging; discharge: (*1*) 1 h after charging and (*2*) 30 days after charging.

paste in the negative electrode is also necessary in view of the overcharging of the zinc electrode in forming and subsequent cycling of a battery and the resulting necessity for periodic "deep" discharges.

CONCLUSIONS

(1) The nickel oxide electrode made of spherical nickel hydroxide on a foamed nickel support ensures, in operation in a previously developed nickel–zinc battery, electrochemical characteristics similar to those of the metal–ceramic electrode in a wide range of current loads.

(2) To improve the characteristics of batteries with nickel oxide electrode on foamed nickel support, it is necessary to optimize the active paste ratio in the negative and positive electrodes.

REFERENCES

1. Chang Zhaorong, Li Gongan, Zhao Yujuan, *et al*., *J. Power Sources*, 1998, vol. 74, pp. 252–254.
2. Yu, C.Z., Lai, W.H., Yan, G.J., and Wu, J.Y., *J. Alloys Comp*., 1999, vols. 293–295, pp. 784–787.
3. Kuz'min, Yu.A., Mashevich, M.N., Uflyand, N.Yu., and Frolova, S.P., in *Sbornik rabot po khimicheskim istochnikam toka* (Coll. of Sci. Works on Chemical Power Sources), Leningrad: Energiya, 1972, issue 7, pp. 163–167.
4. Bazarov, S.P., Bachaev, A.A., El'kind, K.M., *et al*., in *Sbornik "Khimicheskie istochniki toka"* (Coll. "Chemical Power Sources"), Leningrad: Energoatomizdat, 1983, pp. 68–71.
5. Gunther, R.G. and Bendert, R.M., *J. Electrochem. Soc*., 1987, vol. 134, no. 4, pp. 782–791.
6. Alekseeva, M.E., Arkhangel'skaya, Z.P., Ivanova, R.P., *et al*., *Zh. Prikl. Khim*., 1998, vol. 71, no. 6, pp. 941–945.
7. Pralong, V., Delahaye-Vidal, A., Beaudoin, B., *et al*., *J. Electrochem. Soc*., 2000, vol. 147, no. 4, pp. 1306–1313.
8. Alekseeva, M.E., Arkhangel'skaya, Z.P., Ivanova, R.P., *et al*., *Zh. Prikl. Khim*., 1995, vol. 68, no. 9, pp. 1492–1497.
9. Reshetova, G.N., Kuz'min, Yu.A., and Arkhangel'skaya, Z.P., in *Khimicheskie istochniki toka* (Chemical Power Sources), Leningrad: Energoatomizdat, 1984, pp. 60–63.

Russian Journal of Applied Chemistry, Vol. 76, No. 5, 2003, pp. 755–761. Translated from Zhurnal Prikladnoi Khimii, Vol. 76, No. 5, 2003, pp. 783–790.

APPLIED ELECTROCHEMISTRY AND CORROSION PROTECTION OF METALS

Determination of Ascorbic Acid by Electrocatalytic Response of an Electrode Coated with Polyvinylpyridine Film and Palladium-Plated

L. G. Shaidarova, A. V. Gedmina, and G. K. Budnikov

Kazan State University, Kazan, Tatarstan, Russia

Received January 10, 2003

Abstract—A procedure was developed for analysis of ascorbic acid with a carbon glass electrode coated with a palladium-modified poly(2-vinylpyridine) film.

Ascorbic acid is a water-soluble vitamin which is involved in a number of biochemical processes including electron transfer, oxidative catabolism of aromatic amino acids, synthesis of precollagen and collagen, etc. Owing to reducing properties, ascorbic acid is widely used in food industry as a preservative or food additive. Pharmaceuticals containing ascorbic acid are used to prevent and treat various diseases. Therefore, determination of ascorbic acid in biological objects is an important analytical task. Ascorbic acid can be quantitatively determined by titrimetric [1, 2], spectrophotometric [1–4], and chromatographic [5, 6] procedures. Most of them are labor-consuming or have limited application. Highly sensitive electrochemical methods are also used to determine ascorbic acid. Ascorbic acid is reversibly oxidized on a mercury dropping electrode [7]. However, on solid electrodes it is irreversibly oxidized with a high overvoltage [8]. Polarographic methods were widely used to determine ascorbic acid. However, mercury toxicity prevents application of these methods in laboratory practice. Analytical potentialities of voltammetry with chemically modified electrodes (CMEs) are substantially wider. Various CMEs were proposed to increase the sensitivity and selectivity of ascorbic acid determination [9]. Advantages of CMEs in flow-injection analysis of ascorbic acid are reviewed in [10].

Chemically modified electrodes based on electron carrier materials are of special interest [9]. Wring *et al.* [11] used an epoxy–graphite composite electrode modified with cobalt phthalocyanine for determining ascorbic acid. The detection limit of amperometric determination of ascorbic acid in multivitamin preparations is 0.65 ng ml^{-1}. Disadvantages of this method are complex preparation of the electrode and limited application in flow-injection systems. Electrodes coated with a polymeric film are used in [12–14]. Electrooxidation of ascorbic acid on CMEs coated with polypyrrole [12], poly(3-methylthiophene) [13], and polyaniline [14] films was studied. Preparation of film electrodes is simple, and their catalytic activity is high. However, although the analytical signal of film electrodes has better shape and higher intensity, the detection limit of ascorbic acid does not noticeably decrease. Determination of ascorbic acid with CMEs plated with platinum group metals was studied in [15, 16]. These electrodes are highly sensitive to ascorbic acid but their analytic signal is poorly reproduced.

Inclusion of platinum metals in polymeric films is one of the pathways to improve electrocatalytic properties of platinum metals and the stability of chemical sensors on their base. Ruthenium, Rh, Pd, and Pt are electroplated on polyvinylpyridine film in the form of finely divided deposits having high catalytic activity [17–21]. The influence of the polymeric matrix on the deposit properties is provided by adsorption interaction of its fragments, in particular, pyridine rings, with the surface of metal particles.

In this work we studied electrocatalytic acidity of palladium particles plated on the surface of carbon glass (CG) and a poly(2-vinylpyridine) (PVP) film in electrooxidation of ascorbic acid.

Electrooxidation of ascorbic acid on carbon glass. Ascorbic acid is irreversibly oxidized on solid electrodes to form dehydroascorbic acid. This two-electron process is usually describe by the equation [15]

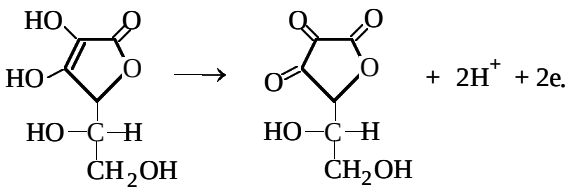

1070-4272/03/7605-0755$25.00

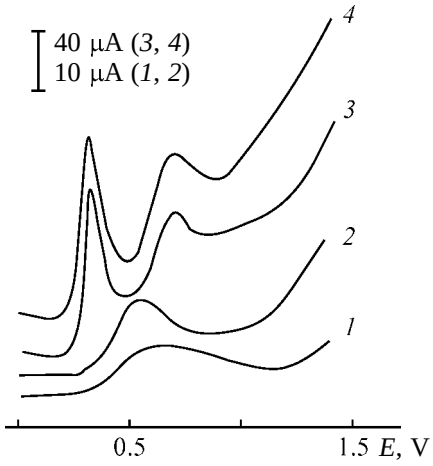

Fig. 1. Voltammogram of ascorbic acid oxidation in 0.1 M H_2SO_4 on (*1*) CG, (*2*) PVP-CG, (*3*) Pd-CG, and (*4*) Pd-PVP-CG electrodes. Ascorbic acid concentration 5×10^{-3} M; the same for Fig. 2. (*E*) Potential; the same for Fig. 2.

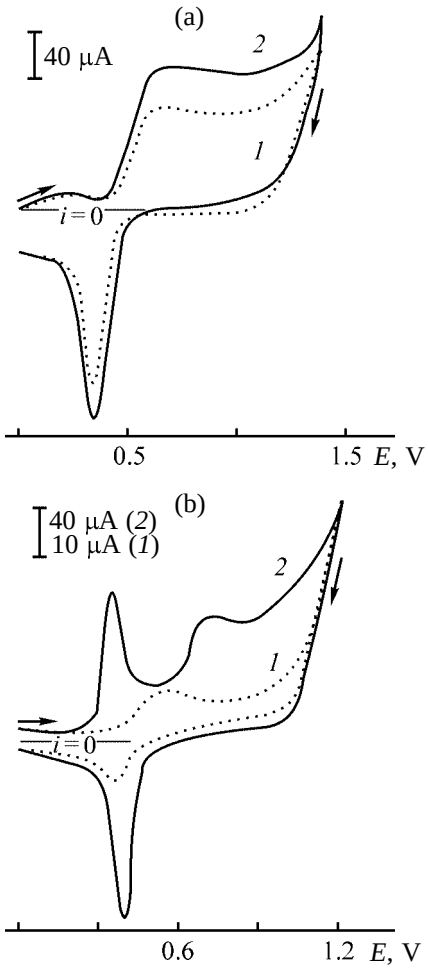

Fig. 2. Cyclovoltammogram of (a) Pd plating and (b) ascorbic acid oxidation in 0.1 M H_2SO_4 on (*1*) Pd-CG and (*2*) Pd-PVP-CG electrodes. (a) (*1*) Pd-CG and (*2*) Pd-PVP-CG; (b) (*1*) PVP-CG and (*2*) Pd-PVP-CG.

Voltammogram of ascorbic acid oxidation on CG electrode (Fig. 1, curve *1*) contains a broad irreversible peak at E_p = 0.60 V, whereas a reversible wave with $E_{1/2}$ = –0.4 V (vs. SCE) is registered on a mercury dropping electrode (m.d.e.) [7]. The overvoltage on CG electrode is more than 500 mV as compared to m.d.e. In addition, the electrochemical signal of the solid electrode is poorly reproducible owing to adsorption of products of the electrochemical reaction. All these factors affect the metrological parameters of ascorbic acid determination. The dependence of peak current on the ascorbic acid concentration is linear in a narrow concentration range from 5×10^{-4} to 1×10^{-2} M.

When electrocatalytic CMEs are used, the overvoltage decreases, the shape of the electrochemical signal is improved, and the sensitivity of determination of ascorbic acid increases.

We compared electrochemical behavior of ascorbic acid on CG, CG with electrodeposited PVP film (PVP-CG), palladium-plated CG (Pd-CG), and on GC electrode coated with PVP film and then palladium-plated (Pd-PVP-CG). Preliminarily we determined conditions for preparing these chemically modified electrodes.

Palladium electroplating of CG. Palladium electrochemistry is relatively complex and involves formation of oxo and hydroxo derivatives with various oxidation states of palladium, such as PdO, PdOH, $Pd(OH)_2$, PdO_2, and PdO_3 [22]. The cyclovoltammogram recorded on a Pd-CG electrode in 0.1 M H_2SO_4 is shown in Fig. 2. When the anodic potential is swept to the positive region, a wave with $E_{1/2}$ = 0.65 V appears due to Pd^{2+} formation:

$$Pd^0 \rightleftarrows Pd^{2+} + 2e.$$

At more positive potentials, palladium(II) oxide particles inhibiting this reaction are formed. Higher palladium oxides are formed simultaneously with oxygen liberation at E > 1.2 V [22]. A sharp peak with E_p = 0.34 V assigned to reduction of PdO to Pd^0 is observed at the reverse potential sweeping [22]. The standard potential of the Pd^{2+}/Pd^0 redox system (E^0 = 0.951 V [23]) differs from the potential of palladium electroplating on CG (E_p = 0.34 V) owing to the overvoltage of palladium electroplating of graphite support [24].

Palladium was electroplated on the surface of CG electrode by two methods: cyclic potential sweeping in a definite potential range and potentiostatic electroplating (Table 1). In both cases, palladium was plated

Table 1. Conditions for palladium plating on the CG and PVP-CG surface

Matrix	Cyclic sweeping		Electroplating			
	E_p, V	i, μA	E_e, V	i, μA	t_e, min	i, μA
CG	–0.3 to +0.3	40	+0.3	17	1	14
	–0.3 to +0.2	50	+0.1	21	3	22
	–0.3 to +0.1	53	+0.0	23	5	30
	–0.3 to +0.0	58	–0.2	26	7	32
	–0.4 to +0.0	58	–0.4	30	9	31
PVP-CG	–0.3 to +0.3	55	+0.3	30	1	32
	–0.3 to +0.2	65	+0.1	39	3	46
	–0.3 to +0.1	76	+0.0	48	5	60
	–0.3 to +0.0	87	–0.2	54	7	59
	–0.4 to +0.0	87	–0.4	60	9	60

in a stirred electrolyte. When the first method was used, the potential was swept from –0.3 to +0.3 V. At lower potential, the palladium layer was loosened by the hydrogen evolved. A shift of the polarization potentials to the positive region appreciably decreased the intensity of the palladium oxidation wave at $E_{1/2}$ = 0.65 V (Table 1).

Potentiostatic palladium electroplating was performed at E < 0.3 V, since Pd(II) is reduced to Pd(0) at E_p = 0.34 V. The working electrolysis potential was E_e = –0.3 V, and the electrolysis time was t_e = 5 min (Table 1). However, when E_e was decreased even to –0.3 V, the current of palladium oxidation was substantially lower than that in the first procedure. In the subsequent experiment, palladium was plated by potential sweeping from –0.3 to +0.3 V over five cycles. Voltammograms were recorded after keeping the electrode at the initial potential E_i = 0.0 V for 50 s.

Palladium plating on PVP film on CG support. Palladium-modified PVP film was also prepared by potential sweeping and electrolysis at a constant potential. Previously we determined conditions for depositing PVP film of CG [25]. We prepared composite electrodes under different conditions. The currents registered on the electrodes prepared by successive application of PVP film on CG and palladium plating were maximal. The preparation conditions of CMEs are summarized in Table 1. The maximal current of palladium oxidation was observed on the Pd-PVP-CG (as well as Pd-CG) electrode prepared by cyclic potential sweeping from –0.3 to +0.0 V.

The composite film was prepared as follows. First, PVP film was deposited on CG surface by electrolysis of an acetonitrile solution containing 1 mg ml^{-1} PVP and 0.1 M $LiClO_4$ at E_e = –1.5 V. Then palladium was plated on the PVP film from a 5×10^{-3} M solution of $PdCl_2$ in 0.01 M H_2SO_4 by potential sweeping from –0.3 to +0.0 V over five cycles. The voltammogram recorded on the CME contains two sharp anodic–cathodic peaks (Fig. 2, curve *2*) whose intensity is reproduced for several days. We studied the shape of the anodic–cathodic peaks registered on the CME as influenced by the pH of the supporting electrolyte. The palladium oxidation wave decreases with increasing pH and disappears at all at pH > 5.

The shapes of voltammograms recorded on Pd-CG (Fig. 2, curve *1*) and Pd-PVP-CG (Fig. 2, curve *2*) electrodes are similar. However, the peaks registered on the composite electrode are more intense and better reproducible (S_r < 1%). The peak intensity increases owing to an increase in the dispersity of the palladium deposit. Smolin *et al*. found [17] that the size of crystallites formed in the Pd-PVP-CG system was more than an order of magnitude smaller than that of Pd crystallites plated on CG. This fact was explained by the influence of porosity of the PVP film. In the first electrocrystallization steps, nucleation and initial growth of palladium crystallites occurs on the CG surface. Then crystallites grow along the pores and reach the PVP–electrolyte interface. The degree of dispersion of the deposit affects not only the size of the effective electrode surface but also the palladium electrocatalytic properties.

Electrooxidation of ascorbic acid on CME. Voltammograms of oxidation of ascorbic acid in 0.1 M H_2SO_4 on CG coated with PVP film (curve *2*), palladium-plated CG (curve *3*), and composite electrode coated with PVP film and plated with Pd particles (curve *4*) are shown in Fig. 1.

Ascorbic acid is oxidized on PVP-CG electrode at

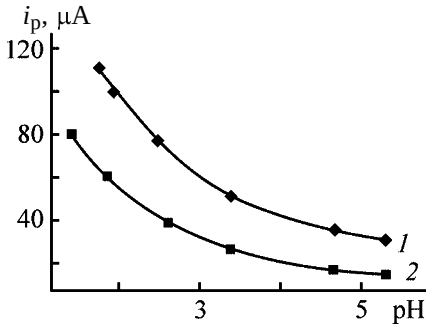

Fig. 3. Peak current i_p of ascorbic acid oxidation on Pd-PVP-CG electrode as a function of pH of the electrolyte. Peak potential E_p, V: (*1*) 0.32 and (*2*) 0.65.

E_p = 0.54 V. The anodic peak is close to that registered on the nonmodified CG (E_p = 0.06 V), i.e., the overvoltage on the CME decreases negligibly. The reaction on the film electrode is reversible, unlike the CG electrode on which irreversible peak of ascorbic acid oxidation is registered. The cyclovoltammogram on the PVP-CG electrode (Fig. 3, curve *1*) contains a couple of anodic–cathodic peaks (E_a = 0.54, E_c = 0.35 V) whose intensities are higher than those on the nonmodified electrode. Appearance of the reversible peak and an increase in the current of ascorbic acid oxidation can be due to mediator properties of the polymeric film.

The overvoltage of electrooxidation of ascorbic acid on the palladium-plated CG electrode is substantially lower than that on the PVP-CG electrode. In this case, the anodic branch of the cyclovoltammogram contains two peaks at E_p = 0.32 and 0.70 V. The peak potential of ascorbic acid oxidation on the Pd-modified electrode is lower by 300 mV than that on the nonmodified electrode. The electrochemical signals on the modified electrode have the peak shape, with the first peak being sharper. The intensity of second peak is higher by several orders of magnitude than that of the peak of ascorbic acid oxidation on CG and increases with increasing substrate concentration. The second peak appears at the palladium oxidation potentials, and its intensity decreases with increasing ascorbic acid concentration.

The logarithm of the peak current of the first and second waves is directly proportional to the logarithm of the sweeping rate of the potential with the slope of 0.40 and 0.80, respectively. This indicates that the oxidation at the potentials of the first and second peaks is complicated by chemical reaction and adsorption, respectively. The voltammograms were recorded at different initial potentials E_i and times of electrolysis at this potential t_d. We found that, as E_i decreased and t_d increased, the intensity of the first peak did not change and the limiting current of the second peak increased. This also suggests the adsorption mechanism of ascorbic acid oxidation at the second peak potential.

Probably, at the first peak potentials ascorbic acid molecules diffusing to the electrode are oxidized. The second peak appearing in the range of PdO formation is due to oxidation of ascorbic acid molecules adsorbed on the electrode surface. Weakening of the second peak with increasing ascorbic acid concentration can be explained by adsorption of the products of its electrochemical oxidation, shielding the electrode surface. However, it should be noted that adsorption of these products has no effect on the voltammogram reproducibility, which is likely due to reversibility of the electron transfer on the modified electrode.

The voltammograms of ascorbic acid oxidation, recorded on Pd-CG and Pd-PVP-CG electrodes, are similar (Fig. 1): The peak potentials are the same and the currents of the first peak are close, i.e., the palladium dispersity has virtually no effect of the electrode process. On the contrary, the current of the second peak increases in going from Pd-CG to Pd-PVP-CG, i.e., it depends on the support nature and hence on the palladium dispersity.

It should be noted that, unlike a graphite electrode, the products of the electrochemical reaction are sorbed, as in the case of Pd-CG electrode, on the surface of the modified electrode. However, the sorption products have no effect on the voltammogram reproducibility, since they are reduced in the course of the reverse potential sweeping at the reduction potentials of palladium(II) oxide and palladium(II) hydroxide.

The catalytic effect of palladium electroplated both on CG and PVP-CG can be due the modification of the support properties in the presence of the palladium catalyst. Hydrogen adsorption on the palladium surface is also possible. As also observed in [24], carbon glass is activated in the course of palladium electroplating, which favors electrooxidation of ascorbic acid. Protons formed during this process are probably sorbed on palladium particles, thus catalyzing the reaction and increasing the yield of the oxidation products. Probably, at the second peak potentials Pd is electrooxidized to Pd(II) species which oxidize ascorbic acid.

We studied electrocatalytic oxidation of ascorbic acid on the Pd-PVP-CG electrode at different pH. As pH is increased from 1.0 to 5.3, the currents of the first and second peaks decrease (Fig. 4), probably

owing to a decrease in the catalytic activity of CME and a change in the acid–base properties of the substrate. In alkali solutions, the peak potential is shifted to zero, broadened, and weakened. In the subsequent experiments, voltammetric determination of ascorbic acid on Pd-PVP-CG electrode was performed in 0.1 M H_2SO_4.

Thus, as compared to nonmodified CG electrode, the overvoltage on the Pd-modified electrode is lower by about 300 mV and the peak current is many times higher. The current of the first peak of both Pd-CG and Pd-PVP-CG electrodes is directly proportional to the ascorbic acid concentration in the range from 1×10^{-6} to 1×10^{-2} M. However, the catalytic current of the composite film electrode is better reproducible (Table 2). We used Pd-PVP-CG electrode for analytical purposes.

Ascorbic acid determination on CG electrode coated with polyvinylpyridine film and palladium-plated. To a 10-ml volumetric flask, a definite volume of standardized ascorbic acid solution or a solution of a weighed portion of a pharmaceutical in 5 ml of 0.2 M H_2SO_4 was introduced. The volume was brought to the mark with distilled water. The resulting solution was placed in an electrochemical cell. CME and auxiliary and Ag/AgCl electrodes were immersed in the solution. The voltammogram was recorded in the potential range from 0.0 to 1.2 V. The current of the oxidation peak at E_p = 0.32 V was measured.

The ascorbic acid concentration was determined by the calibration curve fitted by the regression equation $i_p = a + bc$ (I_p, μA; c, M), where $a = 5.7 \pm 0.3$, $b = (1.9 \pm 0.1) \times 10^{-4}$ and $r = 0.9999$. To illustrate the advantages of the CME, the $\log i_p$ vs. $\log C$ dependence is shown in Fig. 4. As seen from Fig. 4, the dependence of the analytical signal of CG and Pd-PVP-CG electrodes on the ascorbic acid concentration is linear in the range 5×10^{-4}–1×10^{-2} and 1×10^{-6}–1×10^{-2} M, respectively, i.e., the use of CME with electrocatalytic properties broadens the range of analytical concentrations and decreases the detection limit of ascorbic acid by two orders of magnitude.

The accuracy of the procedure was determined by the introduced–found method (Table 2). The relative standard deviation in the whole concentratin range is no more than 5%.

We used a Pd-PVP-CG electrode for voltammetric determination of ascorbic acid in some pharmaceuticals. In preliminary experiments, we studied the influence of various components of these preparations on the analysis results. The compounds exhibiting

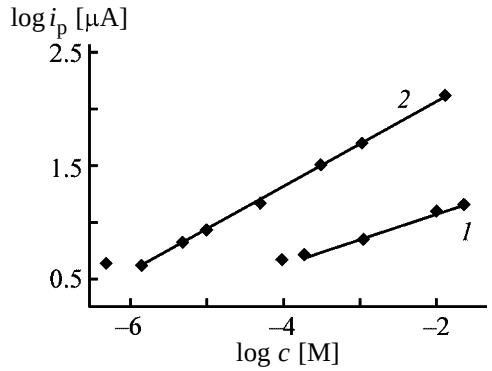

Fig. 4. Logarithm of peak current i_p of ascorbic acid oxidation on (*1*) CG and (*2*) Pd-PVP-CG electrodes as a function of the logarithm of its concentration c.

electrochemical or electrocatalytic activity at the potentials of ascorbic acid oxidation interfere with the determination. For example, the presence of iron species interferes with ascorbic acid determination, since their oxidation potentials are close. In this case, the analysis should be performed after appropriate pretreatment. The results of determination of ascorbic acid in the presence of glucose, nicotinamide, vitamins A, B_1, B_2, B_6, P, and E, as well as calcium and magnesium cations, which do not interfere with the determination, are given in Table 3. The results converge well ($S_r < 5\%$).

The results of determination of ascorbic acid in some pharmaceuticals are presented in Table 4. The content of ascorbic acid indicated in the direction for each pharmaceutical was used as the reference. Statistical treatment of these results with the use of t criterion showed the absence of significant fixed error: $t_{calc} < t_{tabl}$.

EXPERIMENTAL

The dc voltammograms were recorded with a PU-1 polarograph, and cyclovoltammograms, with a PI-50-

Table 2. Metrological parameters of ascorbic acid determination on CG electrode coated with PVP film with Pd particles (n = 6, P = 0.95)

Matrix	Substrate content, μmol		S_r
	introduced	found, $x \pm \Delta x$	
Pd-CG	5.0	4.6 ± 0.3	0.07
	10.0	9.6 ± 0.8	0.08
	100	101 ± 7	0.07
Pd-PVP-CG	5.0	4.8 ± 0.2	0.04
	10.0	10.0 ± 0.3	0.03
	100	100 ± 2	0.02

Table 3. Influence of components of pharmaceutical matrix on the results of voltammetric determination of ascorbic acid with a CG electrode coated with PVP film and palladium-plated (n = 6, P = 0.95, t_{tabl} = 2.57)

Pharmaceutical	Matrix component	Ratio	Introduced	Found	S_r
			g		
Ascorbic acid with glucose	Glucose	1 : 8	0.050	0.048 ± 0.001	0.02
Hexavit	Vitamin A	1 : 40	0.080	0.076 ± 0.004	0.05
	Vitamin B_1	1 : 35	0.100	0.097 ± 0.003	0.03
	Vitamin B_2	1 : 35	0.200	0.198 ± 0.002	0.01
	Vitamin B_6	1 : 35	0.240	0.243 ± 0.002	0.009
	Nicotinamide	1 : 4	0.080	0.077 ± 0.003	0.04
Ascorutin	Vitamin P (rutin)	1 : 1	0.025	0.253 ± 0.004	0.015
Karinat	β-Carotene	1 : 12	0.01	0.0096 ± 0.0004	0.04
	Vitamin E	1 : 6	0.15	0.147 ± 0.003	0.02
Dolmatin S	Calcium(II)	1 : 10	0.045	0.043 ± 0.002	0.04
	Magnesium(II)	1 : 20	0.03	0.029 ± 0.001	0.03
Mumivit	Mumie	1 : 10	0.3	0.297 ± 0.006	0.02

1.1 potentiostat in a three-electrode cell. Carbon glass electrode with the working surface area of 0.1 cm^2, palladium-plated CG electrode, and CG electrode coated with PVP film or palladium-plated PVP film were used as the working electrodes. A silver chloride electrode and platinum wire were used as the reference and auxiliary electrodes, respectively. The potential was swept at a constant rate of 20 mV s^{-1}, or the sweeping rate was varied from 10 to 50 mV s^{-1}.

The film electrode was prepared from PVP of pure grade (Ferak). Palladium was plated from a $PdCl_2$ solution (Aldrich). Prior to the modification of a CG electrode, its surface was pretreated by the following procedure: the electrode was polished on filter paper and tracing paper, washed with double-distilled water, and activated by repeated potential sweeping in 0.5 M H_2SO_4. PVP films were applied from acetonitrile solutions of PVP and $LiClO_4$, which, in turn, were prepared by dissolution of weighed portions of these substances in magnetically stirred acetonitrile. Acetonitrile was purified by the known procedure [26]. The polymeric film was removed from the XME surface by immersion in acetonitrile.

Table 4. Concentration of ascorbic acid in pharmaceuticals determined by voltammetry on a CG electrode coated with PVP film and palladium-plated (n = 6, P = 0.95, t_{tab} = 2.57)

Pharmaceutical	Reference value	Found	S_r	t_{calc}
	g			
Ascorbic acid with glucose	0.100	0.096 ± 0.005	0.005	2.0
Hexavit	0.030	0.026 ± 0.004	0.004	2.4
Ascorutin	0.250	0.243 ± 0.009	0.008	2.1
Karinat	0.010	0.014 ± 0.006	0.006	1.6
Dolmatin S	0.050	0.054 ± 0.008	0.008	1.2
Mumivit	0.030	0.027 ± 0.003	0.003	2.4

Solutions of ascorbic acid were prepared by dissolution of its weighed portions in water. Solutions with lower concentrations were prepared by dilution of the initial solution prior to the experiment. The supporting electrolyte was 1 M H_2SO_4. Required pH was adjusted by adding NaOH to this solution. pH was measured with a pH-150 pH-meter. Solutions of pharmaceuticals were prepared by dissolution of their weighed portions in 0.1 M H_2SO_4. When a pharmaceutical contained fillers insoluble in water, the precipitate was filtered off and the filtrate was studied.

CONCLUSIONS

(1) Palladium particles plated on carbon glass or polyvinylpyridine film catalyze oxidation of ascorbic acid.

(2) Conditions for preparing composite film on carbon glass surface and for obtaining the maximal catalytic effect of this electrode were determined. Palladium plated on poly(2-vinylpyridine) film increase the catalytic activity of the electrode and improve the

metrological parameters of voltammometric determination of ascorbic acid.

(3) A carbon glass electrode coated with poly(2-vinylpyridine) film and palladium-plated was used for voltammetric determination of ascorbic acid in some pharmaceuticals. The components of pharmaceuticals that do not interfere with ascorbic acid determination were found.

ACKNOWLEDGMENTS

This work was financially supported by the Russian Foundation for Basic Research (project no. 00-03-32 389).

REFERENCES

1. Melent'eva, G.A., *Farmatsevticheskaya khimiya* (Pharmaceutical Chemistry), Moscow: Meditsina, 1968.
2. *Farmatsevticheskii analiz lekarstvennykh sredstv* (Pharmaceutical analysis of Drugs), Shapovalova, V.A., Ed., Kharkov: IMP Rubikon, 1995.
3. Arya, S.P., Mahajan, M., and Jain P., *Anal. Sci.*, 1998, vol. 14, no. 5, pp. 889–895.
4. Thompson, R.Q., *Anal. Chem.*, 1987, vol. 59, no. 8, pp. 1119–1121.
5. *High Performance Liquid Chromatography in Bio-Chemistry*, Henschen, A., Hupe, K.-P., Lottspeich, F., and Voelter, W., Eds., Weinheim: VCH, 1985.
6. Lykkesfeldt, J., *Anal. Biochem.*, 2000, vol. 282, no. 1, pp. 89–93.
7. Heyrovsky, J. and Kuta, J., *Zaklady polarografie*, Prague: Ceskoslov. Acad. Ved, 1962.
8. Lechien, F., Valenta, P., Nurnberg, H.W., and Patriarche, G.J., *Fresenius Z. Anal. Chem.*, 1982, vol. 105, no. 2, pp. 311–315.
9. Budnikov, G.K., Maistrenko, V.N., and Murinov, Yu.I., *Voltamperometriya s modifitsirovannymi i ultramikroelektrodami* (Voltammetry with Modified and Ultramicroelectrodes), Moscow: Nauka, 1994.
10. Yebra-Biurrun, M.C., *Talanta*, 2000, vol. 52, no. 3, pp. 367–383.
11. Wring, S.A., Hart, J.P., and Birch, B.J., *Anal. Chim. Acta*, 1990, vol. 229, no. 1, pp. 63–70.
12. Gao, Z.Q., Chen, B.S., and Zi, M.X., *J. Electroanal. Chem.*, 1994, vol. 365, nos. 1–2, pp. 197–205.
13. Gao, Z., Yap, D., and Zhang, Y., *Anal. Sci.*, 1998, vol. 14, no. 6, pp. 1059–1063.
14. Xu, J.-J., Zhou, D.-M., and Chen, H.-Y., *Fresenius J. Anal. Chem.*, 1998, vol. 362, no. 2, pp. 234–238.
15. Matos, R.C., Augelli, M.A., Lago, C.L., and Angnes, L., *Anal. Chim. Acta*., 2000, vol. 404, no. 1, pp. 151–157.
16. Wang, J., Pamidi Prasad, V.A., Renschler, C.L., and White, C., *J. Electroanal. Chem.*, 1996, vol. 404, no. 1, pp. 137–142.
17. Smolin, A.V., Maksimov, Yu.M., and Podlovchenko, B.I., *Elektrokhimiya*, 1995, vol. 31, no. 6, pp. 571–576.
18. Podlovchenko, B.I., Maksimov, Yu.M., Azarchenko, T.L., and Gas'kov, A.M., *Elektrokhimiya*, 1994, vol. 30, no. 6, pp. 794–798.
19. Maksimov, Yu.M., Afanas'eva, O.V., and Podlovchenko, B.I., *Elektrokhimiya*, 1995, vol. 31, no. 2, pp. 149–153.
20. Maksimov, Yu.M. and Podlovchenko, B.I., *Elektrokhimiya*, 1997, vol. 33, no. 7, pp. 823–826.
21. Smolin, A.V., Podlovchenko, B.I., and Maksimov, Yu.M., *Elektrokhimiya*, 1997, vol. 33, no. 4, pp. 477–484.
22. Casella, I.G., *Electrochim. Acta*, 1999, vol. 44, no. 19, pp. 3353–3360.
23. Lur'e, Yu.Yu., *Spravochik po analiticheskoi khimii* (Handbook on Analytical Chemistry), Moscow: Khimiya, 1971.
24. Mayer, P. and Holze, R., *J. Solid State Electrochem.*, 2001, vol. 5, no. 2, pp. 402–411.
25. Shaidarova, L.G., Gedmina, A.V., and Budnikov, G.K., *Zh. Anal. Khim.*, 2003, vol. 58, no. 2, pp. 193–198.
26. Weissberger, A. and Proskauer, E.S., *Organic Solvents. Physical Properties and Methods of Purification*, Riddick, J.A., and Toops, E.E., Eds., New York: Interscience, 1955.

Russian Journal of Applied Chemistry, Vol. 76, No. 5, 2003, pp. 762–765. Translated from Zhurnal Prikladnoi Khimii, Vol. 76, No. 5, 2003, pp. 791–794.

ENVIRONMENTAL PROBLEMS OF CHEMISTRY AND TECHNOLOGY

Exhaustive Purification of Aqueous Solutions with Schungite Rock To Remove Phenols

I. G. Lugovskaya, S. I. Anufrieva, N. D. Gertseva, and A. V. Krylova

Fedorovskii Russian Institute of Mineral Raw Materials, Moscow, Russia
Mendeleev Russian University of Chemical Engineering, Moscow, Russia

Received July 26, 2002; in final form, March 2003

Abstract—The possibility of exhaustive purification of aqueous solutions with schungite to remove phenol to the MPC level and effects of the initial phenol concentration, sorption time, and other factors on the efficiency of phenol recovery are studied.

In wastewater treatment by sorption, diverse synthetic and natural materials are used, including activated and oxidized coals and active anthracites. Theoretical and practical aspects of the use of carbonaceous adsorbents in wastewater treatment to remove organic substances are thoroughly examined in [1, 2].

Apart from the known advantages, activated carbons have a series of drawbacks such as low abrasion resistance, thermal regeneration loss, and, finally, high cost. Furthermore, one of the significant drawbacks of activated carbons is their low selectivity with respect to many readily soluble organic compounds [3].

Recently good results were obtained with various natural sorbents and also with some combinations of sorbents, particularly, of activated carbon and mineral sorbents (silica gels etc.) [3].

Among materials showing considerable promise are Karelian schungite materials, which, thanks to their complex mineral composition (quartz, aluminosilicates, carbon, etc.) are of interest as potential integrated sorbents simultaneously having properties of carbonaceous and silicate materials. Schungite rocks are characterized by high mechanical strength and thermal and chemical resistance, and lower cost (compared to activated carbons).

Gorshtein and Baron [4} reported on sorption of phenol from aqueous solutions with modified schungite obtained by alkaline, autoclave alkaline, or basic aluminum nitrate treatment, etc. Note that most of the works on phenol sorption with various sorbents, including schungite, were performed for an initial phenol concentration of 100–500 mg l^{-1}, not covering the concentration range practically important from the exhaustive purification standpoint, i.e., with phenol concentrations lower by 2–3 orders of magnitude.

Because of extremely low maximal permissible concentration (MPC) accepted for phenol (0.001 mg l^{-1} for fishponds), finishing treatment of weakly polluted water is of particular importance. As follows from published data, exhaustive water purification to remove phenol remains till now one of the most difficult problems, since none of the existing methods provides a desired efficiency at reasonable performance characteristics [5]. Here we report data on phenol sorption from aqueous solutions (initial phenol concentration 0.1–2 mg l^{-1}) with schungite.

According to [6], Karelian schungite rocks are subdivided into five types by the free carbon content in them (wt %): I 98, II 35–75, III 20–35, IV 10–20, and V 5–10. In sorption experiments we used schungite sorbent (SchS) samples obtained by crushing type III schungite rock from the Zazhogino deposit to the 2.5–0.5 mm size grade and also that modified with aqueous NaOH. The contents of basic chemical components in SchS, obtained by the photometric ($SiO_2 \cdot Al_2O_3$, and Fe_2O_3), gasometric (C), atomic absorption (CaO and MgO), and flame photometric methods (K_2O and Na_2O), were as follows (wt %): SiO_2 56.46, C 26.26, Al_2O_3 4.05, Fe_2O_3 1.01, CaO 0.12, MgO 0.56, K_2O 1.23, and Na_2O 0.36.[1]

According to quantitative X-ray diffraction analysis data, the major rock-forming minerals of schungite rock are quartz (52%), hydromica (15%), schungite matter (20%), feldspar (10%), and pyrite (2%).

[1] Analyses were made at the Analytical Center for Certification Testing, Russian Institute of Mineral Raw Materials.

1070-4272/03/7605-0762$25.00 © 2003 MAIK "Nauka/Interperiodica"

Table 1. Static sorption capacity and surface coverage of SchS and MSchS with phenol* (sorption time 24 h)

m, g	V_l, l	V_l/V_s	c_{res},** mg l^{-1}	Sorption, mg g^{-1}	Degree, %, of	
					phenol recovery	surface coverage
Schungite sorbent						
75	0.150	2	0.017	0.004	99.10	0.13
25	0.125	5	0.077	0.009	95.93	0.31
15	0.150	10	0.320	0.015	83.07	0.52
5	0.125	25	0.995	0.022	47.35	0.76
3	0.150	50	1.690	0.010	10.58	0.34
1	0.100	100	1.790	0.010	5.29	0.34
Modified schungite sorbent						
5.000	0.050	10	0.105	0.018	94.47	0.25
2.000	0.050	25	0.390	0.038	79.47	0.52
1.000	0.050	50	0.650	0.063	65.79	0.87
0.200	0.100	500	1.700	0.100	10.52	1.39

* Initial phenol concentration c_0 was 1.89 and 1.90 mg l^{-1} for SchS and MSchS, respectively.
** Residual phenol concentration.

Among secondary minerals are carbonates (calcite and dolomite) and gypsum.

The BET specific surface area of the samples was determined by the nitrogen thermal desorption method [7]. To increase the specific surface area and sorption capacity, schungite sorbents were modified by alkaline treatment [8] (NaOH concentration 250 mg l^{-1}, liquid to solid phase ratio l : s = 10, treatment time 2 h, and temperature 80–85°C). Modification increased the specific surface area from 6.8 to 17.0 $m^2 g^{-1}$. Also the micropore structure became more developed, as judged from an increase in the sorption capacity for iodine from 2.4 to 24.1 mg g^{-1}.

The sorption of phenol was studied in both the static and dynamic modes. The phenol concentration in solutions was monitored by the fluorescence spectra. In the kinetic experiments, 15-g SchS and MSchS samples were contacted with solutions of fixed phenol concentrations in flasks with ground-glass stoppers. The flasks were shaken at 135 rpm for 5–90 min. Then the sorbent was filtered off, and the filtrate was taken for analysis.

The kinetic curves of phenol recovery with SchS and MSchS at an initial phenol concentration of 1.9 mg l^{-1} are presented in Fig. 1.

Figure 1 shows that, at such a low phenol concentration, sorption proceeded quite rapidly, especially on MSchS. In the first 5 min, the degree of phenol recovery was 50 and 40% on MSchS and SchS, respectively. Then phenol recovery decelerated with both sorbents, and practically stopped 30 min after for SchS and 60 min after for MSchS. Finally, the degree of phenol recovery was above 60 and about 80% with SchS and MSchS, respectively.

The static sorption capacity of SchS and MSchS was determined at various solution to sorbent volume ratios (V_l/V_s). The initial phenol concentration (c_0) was 1.9 mg l^{-1}. As 1 day passed, the liquid phase was decanted and analyzed for residual phenol.

From the sorption capacity a we estimated the surface coverage of the sorbents θ:

$$\theta = a/a_m, \quad (1)$$

where a_m is the amount of phenol required to saturate a monolayer (2.88 and 7.19 mg l^{-1} for SchS and MSchS, respectively), estimated previously from the Langmuir equation [9].

Conditions and results of the static experiments are summarized in Table 1.

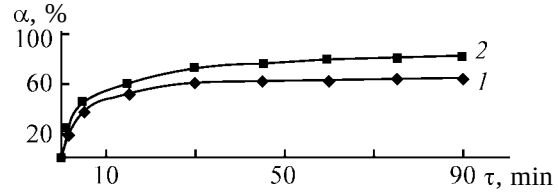

Fig. 1. Kinetic curves of the phenol recovery α with (*1*) SchS and (*2*) MSchS. Initial phenol concentration 1.9 mg l^{-1}. (τ) Time.

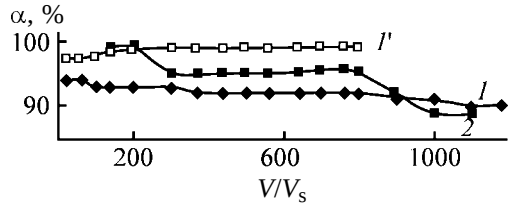

Fig. 2. Degree of phenol recovery α as a function of the ratio of the volume of the solution passed V to the sorbent volume V_s: (*1*, *1'*) SchS and (*2*) MSchS. Initial phenol concentration (mg l^{-1}): (*1*, *2*) 0.1 and (*1'*) 1.2.

Comparison of the residual phenol concentrations shows that, to attain the same degree of phenol recovery, the amount of MSchS can be about half that of SchS (94.5–96.0% recovery is reached at V_l/V_s = 10 with SchS and 5 with MSchS). The surface coverage with phenol in sorption was no more than 0.31%.

With increasing l : s, the sorption of phenol on SchS and MSchS somewhat increased, but the degree of phenol recovery decreased (in the case of MSchS, to 80% and even stronger), and the surface coverage increased to 1.4%.

With increasing sorption time from 1 to 7 days, the sorption on SchS increased to about 0.5 mg g^{-1} (θ ~ 7%), suggesting a considerable contribution of slow sorption of phenol from weak solutions. It may be suggested also that such a slow sorption reflects diffusion control of the sorption rate.

Table 2. Initial and residual phenol concentrations in dynamic sorption experiments

Sorbent	V_l/V_s	Phenol concentration, mg l^{-1}	
		initial solution	eluate
MSchS	88	0.1	<0.0005
	128	0.1	<0.0005
	168	0.1	0.0009
	238	0.1	0.0008
	298	0.1	0.0110
	368	0.1	0.0120
SchS	98	0.1	0.0060
	138	0.1	0.0060
	298	0.1	0.0060
	368	0.1	0.0090
	438	0.1	0.0100
	90	1.2	0.1900
	130	1.2	0.0200
	190	1.2	0.0100
	300	1.2	0.0100
	370	1.2	0.0100
	430	1,2	0.0100

Dynamic sorption experiments were performed with SchS and MSchS in fresh 0.1 and 1.2 mg l^{-1} aqueous phenol solutions. The solution was passed through a column 15 cm high and 3.5 cm in diameter. The sorbent volume in the column was 50 ml.

The eluate was analyzed for residual phenol at intervals of 100–200 column volumes. The solution feed rate was 3 volume parts per hour (relative to the sorbent volume).

In Figure 2 the degree of phenol recovery is plotted vs. the ratio of the volume of the solution passed to the sorbent volume (V/V_s) for the most dilute initial phenol solution (0.1 mg l^{-1}, which corresponds to 100 MPC). The curves demonstrate the possibility of practically 100% removal of phenol from 200 volumes of the solution with MShcS and of 95% removal from 800 volumes. The corresponding values for SchS are 94 and 92%.

Curve *1'* in Fig. 2 shows that, at the initial phenol concentration corresponding to 1200 MPC, 99–99.5% removal of phenol from more than 800 volumes of the solution can be realized with SchS.

The residual phenol concentration in the eluate at increasing number of the solution volumes passed through the column is given in Table 2 for two different initial concentrations of phenol.

The results show that, at an initial phenol concentration of 0.1 mg l^{-1}, the use of MSchS allows treatment of about 240 volumes of the solution to remove phenol to a level below MPC accepted for fishpond water. With further increasing volume, the residual phenol concentration remains within the limits accepted for industrial water.

After passing 300 volumes of the solution of the same initial concentration through SchS, the residual phenol concentration was found to be 0.006 mg l^{-1}, and after passing about 400 volumes, 0.01 mg l^{-1}. At the initial phenol concentration of 1.2 mg l^{-1}, the residual phenol concentration after passing 400 volumes was 0.01 mg l^{-1} also.

Adsorbed phenol cannot be removed from the surface of the sorbents by treatment with NaOH, suggesting the chemisorption mechanism.

The performance characteristics of the sorbents are summarized in Table 3.

As seen, with SchS and MSchS, at the initial phenol concentration of 0.1 mg l^{-1}, the residual phenol

Table 3. Performance characteristics of SchS and MSchS

Sorbent	c_0, mg l^{-1}	Performance characteristics
SchS	0.1	1180 volumes passed. Residual phenol concentration 0.03 mg l^{-1}. Sorption 0.152 mg g^{-1}. Surface coverage θ = 5.3%
MSchS	0.1	1094 volumes passed. Residual phenol concentration 0.020 mg l^{-1}. Sorption 0.142 mg g^{-1}. Surface coverage θ = 2.0%
SchS	1.2	801 volumes passed. Residual phenol concentration 0.028 mg l^{-1}. Sorption 1.038 mg g^{-1}. Surface coverage θ = 36.0%

concentration after passing 1100–1200 volumes of the solution was 0.030 and 0.020 mg l^{-1}, respectively, and the surface coverage was found to be not high, ranging from 2 to 5.3%.

After passing about 800 volumes of 1.20 mg l^{-1} solution through SchS, the residual phenol concentration was about 0.03 mg l^{-1} and the surface coverage, 36%. In this case, the residual phenol concentration (about 0.03 mg l^{-1}, which is lower than the initial phenol concentration in the other series of solutions) suggests the possibility of finished treatment of fishpond water to the MPC level (0.001 mg l^{-1}), if the sorbent bed will be increased or two columns will be used.

CONCLUSIONS

(1) Natural and modified schungites demonstrate high sorption characteristics in exhaustive purification of aqueous solutions to remove phenols.

(2) The use of the modified schungite sorbent allows finished treatment of more than 200 volume parts of an aqueous solution with the initial phenol concentration of 0.1 mg l^{-1} to remove phenol to the MPC level accepted for wastewaters from the fish industry.

(3) The surface coverage of the schungite sorbents with phenol in sorption from dilute solutions does not exceed 36%.

REFERENCES

1. Smirnov, A.D., *Sorbtsionnaya ochistka vody* (Sorption Treatment of Water), Leningrad: Khimiya, 1982.
2. Koganovskii, A.M., Klimenko, N.A., Levchenko, T.M., and Roda, I.G., *Adsorbtsiya organicheskikh veshchestv iz vody* (Adsorption of Organic Substances from Water), Leningrad: Khimiya, 1990.
3. Antonyuk, N.G., Karmazina, T.V., Klimenko, N.A., *et al*., *Khim. Tekhnol. Vody*, 1997, vol. 19, no. 6, pp. 617–622.
4. Gorshtein, A.E. and Baron, N.Yu., *Zh. Prikl. Khim*., 1979, vol. 52, no. 6, pp. 1279–1282.
5. Perevalov, T.M., Komarova, L.F., Smekalov, V.G., and Khotimskii, V.S., *Zh. Prikl. Khim*., 1999, vol. 72, no. 2, p. 248.
6. *Netraditsionnye vidy nerudnogo mineral'nogo syr'ya* (Unconventional Nonmetallic Mineral Raw Materials), Distanov, G.M. and Fil'ko, A.S., Eds., Moscow: Nedra, 1990.
7. Buyanova, N.E., Gudkova, G.B., and Karnaukhov, A.P., *Kinet. Katal*., 1965, vol. 6, no. 6, pp. 1085–1091.
8. Gorshtein, A.E., Baron, N.Yu., and Syrkina, M.L., *Izv. Vyssh. Uchebn. Zaved., Ser.: Khim. Khim. Tekhnol*., 1979, vol. 22, no. 6, pp. 711–716.
9. Lugovskaya, I.G., Theoretical and Experimental Support of Using Schungite Rocks for Wastewater and Gas Effluent Treatment, *Cand. Sci. Dissertation*, Moscow, 2001.

Russian Journal of Applied Chemistry, Vol. 76, No. 5, 2003, pp. 766–770. Translated from Zhurnal Prikladnoi Khimii, Vol. 76, No. 5, 2003, pp. 795–799.

ENVIRONMENTAL PROBLEMS OF CHEMISTRY AND TECHNOLOGY

Chemical Composition and Toxicity of Wastewater from Production of Chemicothermomechanical Mass

N. E. Manvelova, E. G. Sergienko, I. T. Chenib, L. V. Khramova, I. V. Vol'f, Z. P. El'nitskaya, E. I. Savel'eva, and M. A. Sinyakova

Maikop State Technological Institute, Maikop, Adygeia, Russia
St. Petersburg State Technological University of Plant Polymers, St. Petersburg, Russia
Research Institute of Human Hygiene, Professional Pathologies, and Ecology, Kuz'molovskii, Leningrad oblast, Russia
St. Petersburg State University, St. Petersburg, Russia

Received November 25, 2002; in final form, February 2003

Abstract—The article reports on the impurity composition and toxicological hazard of the wastewater from production of chemicothermomechanical mass for manufacturing pressboard and different types of paper.

Pulp and paper industry consumes large amounts of wood and fresh water. Large amounts of wastewater are discharged into water basins, thus significantly contributing to environmental pollution. Conventional pulp production procedures are characterized by $\leq 50\%$ yield of the target product. The remaining 50% of the wood matter contaminates the environment as part of gas and dust emissions and wastewater (various compounds of lignin, lignin-like substances, phenolic compounds, and various sulfur-containing substances such as sulfur dioxide, hydrogen sulfide, methyl mercaptan, etc.).

This makes urgent development and introduction in pulp and paper industry of low-waste procedures. Of special interest is development of procedures for preparation of intermediate products in high yields from deciduous wood. Large-scale application of such procedures will allow simultaneous solution of three important problems: (1) to facilitate supply of industrial enterprises with wood raw materials by utilizing wood of lower quality, (2) to meet strengthening requirements on the environmental protection, and (3) to decrease the prime cost of the products.

Recently, numerous procedures have been suggested for preparing intermediate products in high yield. These procedures are mainly based on milling chips at elevated temperature and pressure. Production of thermomechanical (TMM), chemicothermomechanical (CTMM), and chemicomechanical (CMM) masses rapidly grows. The application field for these intermediate products is steadily widening, and they replace less economical cellulose in many applications [1, 2].

The yield of the target product in wood mass production is almost twice that in pulp production, and the amount of the process emissions and discharges decreases correspondingly. Replacement of soda hemicellulose by CTMM allows reduction of the specific (per ton of the end product, pressboard) consumption of water from 80 to 13 m^3 (by a factor of 6.15) [3]. Thus, a changeover to CTMM production brings appreciable environmental and economic benefits. At the same time, the wastewater from production of high-yield intermediate products is highly toxic, which is mainly due to the extractive substances passing into wastewater from wood [4, 5].

The wastewater is generated in the following production phases: (1) chips washing; (2) CTMM thickening; and (3) pressboard production on a pressboard-making machine (PMM).

The wastewater from wood pretreatment and CTMM production comes to a sewerage system; the PMM wastewater also comes partially to a sewerage system and partially, to a local plant for wastewater treatment by pressure flotation [3]. The fibers entrapped at the plant are utilized in pressboard production (incorporated into its formulation), and the decontaminated water is used for washing chips and waste paper.

A closed-loop water use system would allow even greater reduction of the amount of the wastewater

1070-4272/03/7605-0766$25.00

discharged. However, this requires knowledge of the chemical composition of the wastewater from CTMM production. Such data are also necessary for developing the most efficient and economical system for treatment of this wastewater.

The aim of this work is to identify the impurities and to make a toxicological assessment of the wastewater from production of CTMM and multilayer pressboard thereof, as well as to propose an efficient and economical method for its treatment.

EXPERIMENTAL

Samples for determining the chemical composition and toxicity of wastewater were taken from the circulating water freed from suspended matter at the pressure flotation plant and from the wastewater generated by the CTMM production shop. The flow rate of the forming wastewater was 250 $m^3 h^{-1}$. The results of the wastewater analysis by standard procedures are given below:

pH	7.0–9.9
Suspended matter, mg l^{-1}	300
BOD_5, mg O_2 l^{-1}	600
Oxidizability, mg O_2 l^{-1}	1000–1500
Ammonia, mg l^{-1}	2.2–2.8
Nitrates, mg l^{-1}	2.3–2.5
Nitrites, mg l^{-1}	0.3–1.2
Iron, mg l^{-1}	0.6–3.3
Phosphates, mg l^{-1}	2.1–2.9
Sulfates, mg l^{-1}	158–192
Chlorides, mg l^{-1}	85–112
Oil products, mg l^{-1}	0.01–0.20
COD (single determinations), mg O_2 l^{-1}	1500

To identify toxic compounds in the samples, we determined volatile organic compounds (VOCs) by gas chromatography-mass spectrometry (CC–MS).

The GC–MS analysis was carried out on a Shimadzu (Japan) instrumental complex comprising a GC-17A gas chromatograph, a QP 5000 mass spectrometer equipped with a quadrupole analyzer, and a data processing system. Ionization was effected by electron impact (ionizing electron energy 70 eV, ion source temperature 280°C). The instrument parameters were adjusted automatically. We used a 25 m × 0.2 mm capillary column made of melted quartz (0.33-μm-thick film of the DB-5 stationary phase; helium carrier gas, flow rate 1 ml min^{-1}). Liquid samples (1 μl) were introduced in the splitless (0.3 min), and gaseous samples (1 ml), in the split mode. The injector temperature was 250°C; the column was heated in a programmed mode from 40 to 270°C at a rate of 5 deg min^{-1} and kept at 270°C for 15 min.

Table 1. Content of low-boiling organic compounds in water samples as determined by head-space GC–MS analysis

Compound	Content in the sample, mg l^{-1}	
	circulating water	wastewater
Ethanol	0.10	0.15
Acetone	–	0.06
Dimethyl sulfide	–	0.02
Carbon disulfide	0.08	–
Butyral	–	0.05
Limonene	0.34	0.48

For analyzing low-boiling organic compounds, we took a 20-ml portion of each sample, saturated with sodium chloride, placed into hermetically sealed glass flasks with Teflon stoppers, thermostated for 1 h at 40°C, and analyzed by GC–MS the equilibrium vapor phase. The results are presented in Table 1.

For analyzing moderately volatile organic compounds, we took a 1-l portion of each sample. The analytical procedure consisted of successive repeated extractions of the aqueous sample with methylene chloride at pH 8 (a basic-neutral fraction) and pH 2 (acid fraction). Next, the fractions were combined, dried, concentrated, and aliquots were analyzed by GC–MS [7]. The results (tentative, semi-quantitative data) are presented in Table 2.

Tables 1 and 2 show that the samples analyzed contain a significant amount of VOCs from various classes: alcohols, aldehydes, ketones, acids, etc. Most of them are components of natural extractive substances contained in wood or are lignin degradation products.

Though only slightly contributing to COD of the wastewater, VOCs include highly toxic compounds. Table 3 lists the maximum permissible concentrations (MPCs) for some of them [8–10].

It should be noted that not nearly all the actual or potential polluting substances have their established MPCs. For example, such substances as guaiacol and *p*-ethylphenol have no MPCs but this by no means suggests that these compounds are not toxic.

Toxicological control consisted in biotesting with two testing objects from different taxonometric groups, *D. Magna* and *Paramecium Caudatum*.

Table 2. Content of moderately volatile organic compounds in water samples as determined by head-space GC–MS

Compound	Content in the sample, mg l^{-1}		Compound	Content in the sample, mg l^{-1}	
	closed-loop water	wastewater		closed-loop water	wastewater
Propioin	–	0.01	Salicyl alcohol	0.07	0.14
2-Methyl-2-cyclopentenone	0.01	0.02	Acetylanisole*	0.03	0.13
2,4-Hexadienoic acid (Sorbistat)	–	0.02	Phenylacetic acid	–	0.05
			Dimethoxyphenol*	0.31	0.52
2,4-Hexadienal (sorbaldehyde)	–	0.008	Vanillin	0.09	0.28
			Cinnamic acid	0.007	0.14
Acetylmethylfuran*	–	0.005	Propenylguaiacol*	0.06	0.15
Phenol	0.50	0.63	Acetovanillone (apocynine)	0.06	0.18
Cyclooctane	–	0.05	Guaiacylacetone	–	0.26
Benzyl alcohol	0.11	0.19	Raspberry ketone	0.03	0.12
Dimethylcyclopentenone*	–	0.02	Acetylveratrone	0.06	0.25
Salicylaldehyde	0.02	0.03	Methoxyeugenol*	0.05	0.07
Dimethylcyclopentanedione	0.04	0.05	Homovanillic acid	0.14	0.29
Benzocatechol	0.06	0.02	Jasminaldehyde	0.22	1.7
Guaiacol (2-methoxyphenol)	0.18	0.24	Acetoxyjasmine ketone	–	0.61
Ethylresorcinol*	0.02	–	Coniferyl alcohol	0.72	1.7
Ethylresorcinol alcohol*	–	0.02	Dimethyl dimethylmucate	0.19	0.57
2,5-Xyloquinone	0.01	0.02	Verartryl alcohol	0.29	0.59
Phenylethyl alcohol	0.01	0.02	Dibutyl phthalate	0.19	0.54
Dimethylheptene	0.01	0.02	Dimethoxypropenylbenzene*	0.28	1.0
p-Ethylphenol	0.14	0.05	Dimethoxycoumaric alcohol* alcohol*	1.2	–
Benzoic acid	0.13	0.48			
p-Resorcinolcarbaldehyde	0.02	0.08	Aliphatic hydrocarbons (total)*	16.8	3.5
Hydroxycinnamic acid*	–	0.13			

* Compounds whose structures could not be established exactly due to the lack of reference samples and information about the chromatographic retention indices.

The concentration of dissolved oxygen in the samples was brought to the optimal level of 7.0–8.0 mg l^{-1}, and pH, to 7.5–8.0. The samples were filtered off using paper filters intended for biological studies. Each test took 96 h.

Table 3. MPCs of selected toxic compounds in water basins

Compound	PC, mg l^{-1}, in indicated water basins	
	sanitary and domestic	fisheries
Acetone CH_3COCH_3		0.05
Dimethyl sulfide $(CH_3)_2S$	0.01	1×10^{-5}
Carbon disulfide CS_2	1.0	1.0
Phenol C_6H_5OH	0.001	0.001
Dibutyl phthalate $C_6H_4(COOC_4H_9)_2$	0.2	0.001

The indices calculated in biotests were as follows. For *D. Magna*: A, the percentage of daphnias perished in the tested medium relative to the control water; LT_{50}, the average time within which 50% daphnias perished in the tested water; L_{dd50}, the degree of dilution at which 50% of daphnias survived in the tested water within 96 h; L_{dd0}, the minimal degree of dilution of the tested water at which daphnias survived within 96 h; and T, toxicity. For *Paramecium Caudatum*: T_{un}, the toxicity index for undiluted water; T_{16}, the toxicity index for water diluted by a factor of 16; and DT, the degree of toxicity.

The biotests performed (see Table 4) allow qualification of the water in the samples tested as moderately toxic with respect to *D. Magna* but as highly toxic with respect to *Paramecium Caudatum* cultures.

Thus, the wastewater generated by multilayer pressboard production from CTMM is characterized by a high content of suspended matter and toxic organic substances and, thus, needs treatment before discharg-

Table 4. Biotesting results

Water	pH_{in}	pH_{test}	O_{2in}	O_{2test}	*D. Magna*					*Paramecium Caudatum*		
			mg l^{-1}		A, %	L_{50}, h	L_{dd50}	LT_{dd0}	T	T_{un}	T_{16}	DT
Wastewater	12.65	7.6	2.4	7.8	100	20	5.16	20.9	Medium	0.95	0.25	High
Circulating water	6.6	7.8	3.8	7.7	100	20	4.09	16.0	Low	0.89	0.36	

ing into sewerage system for the subsequent biological treatment.

Finely dispersed suspended and soluble organic impurities can be removed from wastewater by coagulation, adsorption, and biological methods. However, the recommended aerobic and anaerobic biological methods of wastewater treatment are unsuitable for enterprises lacking their own facilities for biological treatment of wastewater.

In our opinion, electrochemical coagulation is promising in this case. This process can be run in an electrolyzer provided with a set of aluminum or iron plates where the treated water flows in the interplate spaces [10].

Electrocoagulation offers such advantages as compactness and easy operation of the setup, no need in chemicals, and low sensitivity to the changing treatmental condition, as well as good structural and mechanic properties of the resulting slurry.

A drawback of electrocoagulation is increased power and metal consumption. The amount of sheet metal consumed can be decreased by using electrodes filled with metal chips which are metal processing waste.

We studied the treatment of wastewater generated by CTMM production in a specially assembled electrocoagulation cell. The initial wastewater was supplied to the bottom of the electrocoagulator and enriched with the required portion of the coagulant. The treatment efficiency was estimated from the permanganate oxidizability of the treated wastewater. The electric scheme provided permanent control over the current strength and voltage at the electrodes. The wastewater consumption in the installation was kept constant at 3 l h^{-1}.

The optimal results were obtained for the wastewater treated with aluminum electrodes at the current density of 8.5–9.5 A dm^{-2}, voltage of 30–35 V, and preliminary dilution by a factor of 2–4. Under these conditions, the averaged treatment efficiency was estimated from the permanganate oxidizability at 94%, and the current efficiency, at 55%.

It should be noted that wastewater from CTMM production contains large amounts of low-molecular-weight organic compounds which cannot be removed from water by coagulation. Thus, the efficiency achieved in this work should be regarded as high, though insufficient for the wastewater to be safely discharged or recycled into the production process. For this reason, we finally treated the wastewater by adsorption on activated carbon.

CONCLUSIONS

(1) Wastewater from production of chemicothermomechanical mass and multilayer pressboard thereof contains over 40 dissolved organic substances.

(2) The amounts of the pollutants contained in the wastewater generated by production of chemicothermomechanical mass and their toxicities were estimated.

(3) A method was proposed for local treatment of the wastewater generated by production of chemicothermomechanical mass.

REFERENCES

1. Shamko, V.E., *Polufabrikaty vysokogo vykhoda* (High-Yield Intermediate Products), Moscow: Lesn. Prom–st., 1989.
2. Polyakov, Yu.A., *Proizvodstvo mekhanicheskoi massy* (Production of Mechanical Mass), St. Petersburg: Sankt-Peterburgskaya Lesotekhnicheskaya Akad., 1992.
3. Manvelova, N.E., Sotnikov, A.A., Matveichuk, G.P., *et al.*, *Materialy nauchno-prakticheskoi konferentsii "Inzhenernoe obespechenie resursosberegayushchikh tekhnologii vodopol'zovaniya dlya promyshlennykh, kommunal'nykh i sel'skokhozyaistvennykh proizvodstv"* (Proc. Scientific and Practical Conf. "Engineering Provision of Resource-Saving Water Use Technolo-

gies for Industrial, Municipal, and Agricultural Enterprises St. Petersburg: Sankt-Peterburgskii Gosudarstvennyi Tekhnologicheskii Univ. Rastitel'nykh Polimerov, May 18–19, 1999, pp. 126–130.

4. Azarov, V.I., Burov, A.V., and Obolenskaya, A.V., *Khimiya drevesnykh i sinteticheskikh polimerov* (Chemistry of Wood and Synthetic Polymers), St. Petersburg, Sankt-Peterburgskaya Lesotekhnicheskaya Akad., 1999.
5. Fengel, D. and Wegener, G., *Wood. Chemistry, Ultrastructure, Reactions*, Berlin: Walter de Gruyter, 1989.
6. Lur'e, Yu.Yu., *Analiticheskaya khimiya promyshlennykh stochnykh vod* (Analytical Chemistry of Industrial Wastewater), Moscow: Khimiya, 1984.
7. Soniassy, R., Sandra, P., and Schiett, C., *Water Analysis. Organic Micropollutants*, Hewlett–Packard Company, 1994.
8. *Bezopasnye urovni soderzhaniya vrednykh veshchestv v okruzhayushchei srede* (Safe Levels of Harmful Substances in the Environment), Severodonetsk, 1984.
9. *Perechen' PDK i OBUV vrednykh veshchestv dlya vody rybokhozyaistvennykh vodoemov (List of MPCs and TSPLs* (Tentatively Safe Pollutant Levels) for Harmful Substances in Water of Fisheries Basins), Moscow: Medinor, 1995.
10. *Ochistka i rekuperatsiya promyshlennykh vybrosov* (Treatment and Regeneration of Industrial Discharges), Maksimov, V.F. and Vol'f, I.V., Eds., Moscow: Lesn. Prom–st., 1989.

Russian Journal of Applied Chemistry, Vol. 76, No. 5, 2003, pp. 771–774. Translated from Zhurnal Prikladnoi Khimii, Vol. 76, No. 5, 2003, pp. 800–803.

ENVIRONMENTAL PROBLEMS OF CHEMISTRY AND TECHNOLOGY

Effect of Low-Molecular-Weight Cationic Praestols on the Efficiency of Water Pretreatment at Heat and Electric Power Plants

V. F. Kurenkov, E. L. Gogolashvili, I. V. Molgacheva, A. I. Gaisina, A. R. Garipova, and F. I. Lobanov

Kazan State Technological University, Kazan, Tatarstan, Russia
Energoprogress Engineering Center, Kazan, Tatarstan, Russia
Stockhausen Eurasia. Engineering and Environment Limited Liability Company, Moscow, Russia

Received February 11, 2003

Abstract—The efficiency of water pretreatment at heat and electric power plants using low-molecular-weight cationic Praestols (coagulants) in combination with lime, iron sulfate, and flocculant (high-molecular-weight anionic Praestol) was studied.

Desalted water for heat and electric power plants (HEPPs) is often prepared in two main stages: pretreatment to remove coarse, colloidal, and dissolved mineral and organic admixtures and demineralization with ion-exchange resins. Pretreatment is performed with mineral coagulants such as iron(II) sulfate and aluminum sulfate or chloride, with subsequent clarification of water and removal of precipitates using clarifiers and mechanical filters. As shown in [1], the pretreatment of water at about a half of heat and electric power stations in Russia is performed using iron(II) sulfate (liming and coagulation). In the recent decades, organic polymeric coagulants with low molecular weight and positive charge, providing destabilization of negatively charged colloidal particles and rapid flocculation, have found expanding application in advanced countries along with common mineral coagulants. In the presence of organic coagulants, the precipitate particles become coarser, and thus the solutions are easier clarified and filtered, whereas the mineral composition of water and its pH remain unchanged. Water pretreatment can be intensified by simultaneous use of organic and mineral coagulants and flocculants [2]. As shown in [3], iron(II) sulfate coagulant in combination with high-molecular-weight cationic and anionic Praestol flocculants shows high performance in the water pretreatment at heat and electric power plants.

In this work we studied the performance of low-molecular-weight cationic Praestol coagulants used in combination with lime, iron(II) sulfate, and flocculant (high-molecular-weight anionic Praestol) in water treatment at HEPP facilities.

EXPERIMENTAL

In the tests we used commercial[1] cationic Praestol 655 (sample K-1) [copolymer of acrylamide (AA) with *N*-acrylamidopropyl-*N*,*N*,*N*-trimethylammonium chloride (APTMAC)] and anionic Praestol 2530 (sample A) [copolymer of AA with sodium acrylate (Na-AA)]. The properties of these polymers are listed in Table 1. The samples of cationic Praestols (K-2–K-8) with various intrinsic viscosities [η] (Table 1) were prepared according to [4] by degradation of sample K-1 in 0.1% aqueous solutions in the presence of potassium persulfate (PP) radical degradation agent at [PP] = 0.06% (in water) and 50°C for various times. The above degradation conditions provided preparation of copolymers with various [η] and constant chemical composition of macromolecules [5]. The degradation process was monitored by viscometry [6]. The [η] values in the reaction mixture were calculated using the linear dependences $\eta_{sp}/c_p = f(c_p)$, obtained at isoionic dilution of the copolymer solutions with 0.5 M NaCl solution at 25°C using a VPZh-3 viscometer (d_c = 0.56 mm). The content of the APTMAC units in cationic Praestols was evaluated from the content of chloride ions, determined by mer-

[1] Produced by Moscow–Stockhausen–Perm Russian–German Joint-Stock Company.

1070-4272/03/7605-0771$25.00

Table 1. Properties of anionic and cationic Praestols*

Sample	[η], $cm^3\ g^{-1}$	Content of ionic fragments in copolymer, mol %		
		AA	Na-AA	APTMAC
A	1800	80	20	–
K-1	440	67	–	33
K-2	370	67	–	33
K-3	280	67	–	33
K-4	220	67	–	33
K-5	170	67	–	33
K-6	100	67	–	33
K-7	50	67	–	33
K-8	40	67	–	33

* Structures:

Praestol A

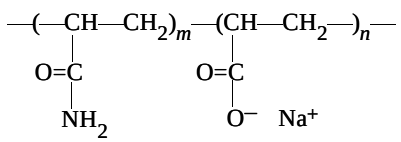

Praestols K-1–K-8

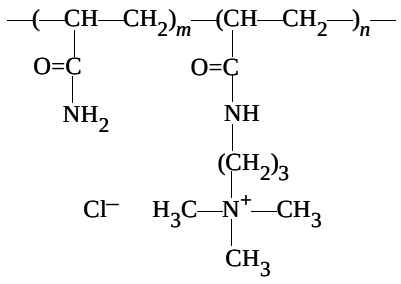

curimetry [7], and the content of the Na-AA units in the anionic Praestols, by potentiometric titration [8].

In this work, iron(II) sulfate [GOST (State Standard) 6981–75] and saturated solution of construction lime (GOST 9179–79) were used as coagulants. Solutions were prepared in distilled water. The content of suspended particles and organic compounds in the purified water was evaluated by the turbidity and permanganate oxidizability of solutions, respectively. In accordance with standards [9], after pretreatment the permanganate oxidizability of water should comprise 40–50% of that of the initial water sample. The samples of the initial and clarified water were analyzed by common procedure [10] using chemically pure and analytically pure grade reagents. The coagulation pretreatment was performed using the Volga river water sampled at the water scoop of the Kazan HEPP-2 (total hardness 3.3 mg-equiv l^{-1}, alkalinity 2.3 mg-equiv l^{-1}). The liming, coagulation, and clarification of the natural water samples were carried out in 250-ml cylinders. For this purpose, natural water was successively treated with solutions of lime, iron(II) sulfate, and cationic Praestol; in some tests, anionic Praestol was also used. In accordance with [11], the lime dosage was calculated from the following expression using the data on the chemical composition of the initial water sample:

$$D_l = [CO_2]_i + A_i + D_c,$$

where $[CO_2]_i$ is the concentration of carbon dioxide in the initial water (mM), A_i is the alkalinity of the initial water (mg-equiv l^{-1}), and D_c is the coagulant dosage (mg-equiv l^{-1}).

All the reagents were added successively at 1-min intervals. Then the mixture was stirred on a magnetic stirrer for 5 min, and variation of the optical density of the resulting suspension was monitored on an LAM-1 device (λ 670 nm, *l* 35.2 mm). The measurements were carried out in the same cylinder (at a depth of 90 mm from the surface) after its placing in the device. After sedimentation, the precipitate was settled for 20 min and filtered off on a paper filter, and the resulting filtrate was analyzed for the permanganate oxidizability.

First, we evaluated the effect of cationic Praestols

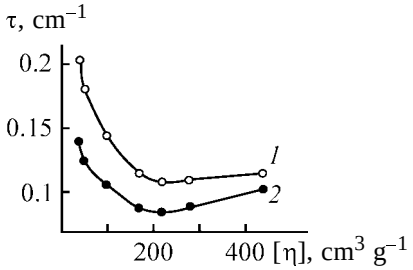

Fig. 1. Natural water turbidity τ (*1*) 5 and (*2*) 10 min after sedimentation start as a function of the intrinsic viscosity of the cationic Praestol solutions [η]. Concentration: lime 3.55 mg-equiv l^{-1} and cationic Praestol 0.4 mg l^{-1}.

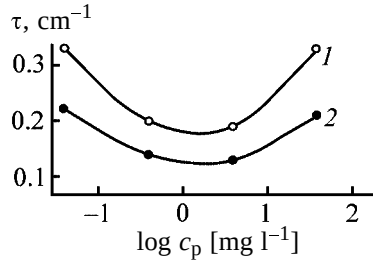

Fig. 2. Natural water turbidity τ (*1*) 5 and (*2*) 10 min after sedimentation start as a function of the cationic Praestol (sample K-4) concentration c_p. Lime concentration 3.55 mg-equiv l^{-1}.

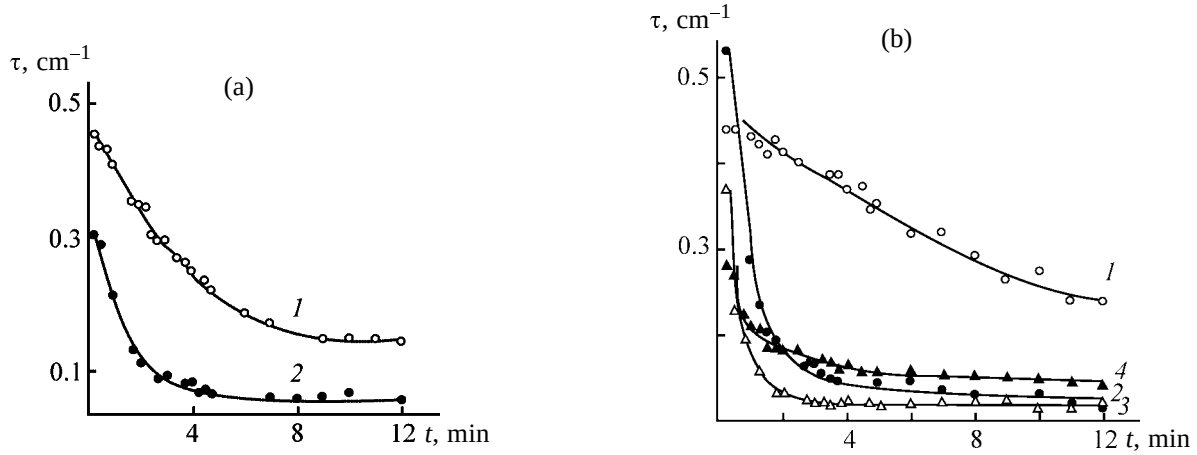

Fig. 3. Turbidity τ as a function of the sedimentation time *t* of natural water in the presence of (*1*) lime and iron(II) sulfate; (*2*) lime, iron(II) sulfate, and cationic Praestol (sample K-4); (*3*) lime, iron(II) sulfate, cationic Praestol (sample K-4), and anionic Praestol (sample A); and (*4*) lime, cationic Praestol (sample K-4) and anionic Praestol. (a) Concentrations: lime 3.8 mg-equiv l^{-1}, iron(II) sulfate 0.8 mg-equiv l^{-1}, and cationic Praestol 1 mg l^{-1}. (b) Concentrations: lime 3 mg-equiv l^{-1}, iron(II) sulfate 0.4 mg-equiv l^{-1}, cationic Praestol 1 mg l^{-1}, and anionic Praestol, 0.4 mg l^{-1}.

with various [η] on the water pretreated with lime. The data on the water turbidity, measured in 5 and 10 min after the sedimentation start, are shown in Fig. 1. As seen, the greatest decrease in the water turbidity is observed on adding cationic Praestol with [η] = 220 $cm^3 g^{-1}$, and further experiments were performed with this copolymer.

To determine the optimal dosage of the copolymer, we studied the dependence of the water turbidity 5 and 10 min after sedimentation start on the concentration of cationic Praestol with [η] = 220 $cm^3 g^{-1}$. As seen from Fig. 2, the optimal concentration of this copolymer is 1 mg l^{-1}.

Consider the effect of cationic Praestol ([η] = 220 $cm^3 g^{-1}$) additives on the turbidity (Fig. 3) and permanganate oxidizability (Table 2) after pretreatment of water with lime and iron(II) sulfate. As seen from Figs. 3a and 3b, the sedimentation rate of the precipitate particles increases with addition of cationic Praestol (curves *1*, *2*). The comparison of these curves at a given sedimentation time *t* also indicates that the degree of clarification increases with Praestol addition, which promotes more complete removal of organic impurities and decreases the permanganate oxidizability of water (Table 2). However, our attempt to decrease the dosage of mineral or organic flocculants failed, because in both cases the quality of water (with respect to the content of organic compounds) got worse.

It should be noted that water purification is noticeably improved on additional treatment of the clarified water with anionic Praestol 2530. Addition of the flocculant decreases the turbidity of water (Figs. 3a, 3b, curves *2*, *3*). This can be explained by coarsening of the aggregates due to the fact that the flocculant macromolecules form bridges between the flakes formed from colloidal and suspended particles in the course of coagulation, which, in turn, accelerates sedimentation. The content of organic compounds in water remains constant in the process (Table 3).

We also examined the possibility of excluding the mineral coagulant from the process of water treatment. The experimental data (Figs. 3a, 3b) show that high sedimentation efficiency with respect to suspended particles is retained (curves *3*, *4*), whereas the permanganate oxidizability of clarified water strongly in-

Table 2. Oxidizability of clarified water as influenced by cationic Praestol (sample K-4)

Reagent concentration			Oxidizability, % of the initial
lime, mg-equiv l^{-1}	$FeSO_4$, mg-equiv l^{-1}	Praestol, mg l^{-1}	
3.8	0.8	–	69
3.8	0.8	1.0	54
3.5	0.6	–	65
3.5	0.6	1.0	50
3.1	0.4	–	60
3.1	0.4	1.0	48
2.9	0.6	–	40
2.9	0.6	0.2	47
2.5	0.2	–	69
2.5	0.2	0.2	75

Table 3. Oxidizability of clarified water as influenced by cationic Praestol (sample K-4) and anionic Praestol (sample A)

Reagent concentration				Oxidizability, % to the initial
lime, mg-equiv l^{-1}	$FeSO_4$, mg-equiv l^{-1}	Praestol K-4, mg l^{-1}	Praestol A, mg l^{-1}	
3.0	0.4	–	–	50
3.0	0.4	0.2	–	49
3.0	0.4	0.2	0.4	47
1.8	–	1.0	–	87

creases. As seen from our experimental data (Table 3 and Figs. 3a, 3b), the best results are obtained when adding mineral and organic coagulants in combination with anionic Praestol 2530.

CONCLUSIONS

(1) Cationic Praestol with $[\eta] = 220$ cm^3 g^{-1} can be used as organic coagulant for pretreatment of water for heat and electric power plants.

(2) The combined use of mineral and organic coagulants provides more profound removal of organic compounds from purified water.

(3) With addition of organic coagulant only, the rate of precipitate sedimentation increases, but the content of organic impurities in water grows also.

(4) The most exhaustive and rapid removal of organic compounds from water is ensured by combined use of mineral and organic coagulants with a flocculant, anionic Praestol 2530.

REFERENCES

1. Popov, A.A., Blokhin, A.I., Keneman, F.E., *et al.*, *Elektr. Stantsii*, 2000, no. 8, pp. 6–15.
2. Zapol'skii, A.K. and Baran, A.A., *Koagulyanty i flokulyanty v protsessakh ochistki vody: Svoistva. Polu-chenie. Primenenie* (Coagulants and Flocculants in Water Treatment: Properties, Preparation, Use), Leningrad: Khimiya, 1987.
3. Kurenkov, V.F., Gogolashvili, E.L., and Saifutdinov, R.R., *Zh. Prikl. Khim.*, 2001, vol. 74, no. 9, pp. 1151–1154.
4. Kurenkov, V.F., Len'ko, O.A., Snigirev, S.V., and Lobanov, F.I., *Zh. Prikl. Khim.*, 2002, vol. 75, no. 7, pp. 1164–1168.
5. Kurenkov, V.F., Khartan, Kh.-G., and Lobanov, F.I., *Zh. Prikl. Khim.*, 2002, vol. 75, no. 7, pp. 1057–1068.
6. *Praktikum po khimii i fizike polimerov* (Handbook of Chemistry and Physics of Polymers), Kurenkov, V.F., Ed., Moscow: Khimiya, 1995.
7. *Rukovodstvo po khimicheskomu i tekhnologicheskomu analizu vody* (Manual on Chemical and Technological Analysis of Water), Moscow: Stroiizdat, 1973.
8. Churikov, F.I., Snegirev, S.V., and Kurenkov, V.F., *Zavod. Lab. Diagnost. Mater.*, 1998, no. 6, pp. 9–10.
9. *Tipovaya instruktsiya po obsluzhivaniyu vodopodgotovitel'nykh ustanovok, rabotayushchikh po skheme khimicheskogo obessolivaniya* (Master Guide on Maintenance of Water-Treatment Installations Operating in Chemical Demineralization Mode), Moscow: STsNTI ORGRES, 1975.
10. *Unifitsirovannye metody analiza vod* (Standard Methods of Water Analysis), Lur'e, Yu.Yu., Ed., Moscow: Khimiya, 1973.
11. *Rukovodyashchie ukazaniya po izvestkovaniyu vody na elektrostantsiyakh* (Master Guideline on Liming of Water at Heat and Electric Power Plants), Moscow: STsNTI, 1973.

Russian Journal of Applied Chemistry, Vol. 76, No. 5, 2003, pp. 775–777. Translated from Zhurnal Prikladnoi Khimii, Vol. 76, No. 5, 2003, pp. 804–806.

ENVIRONMENTAL PROBLEMS OF CHEMISTRY AND TECHNOLOGY

Consolidation and Melioration of Salted Sandy Soils Using a Compound of Acetone–Formaldehyde Resin with Silk Sericin

A. A. Kholmuminov, O. B. Avazova, Yu. N. Mirkhaidarova, I. N. Ruban, and S. Sh. Rashidova

Institute of Chemistry and Physics of Polymers, Academy of Sciences of Uzbekistan Republic, Tashkent, Uzbekistan

Received May 20, 2002; in final form, January 2003

Abstract—Curing of the compound of acetone–formaldehyde resin with natural silk sericin in the presence of inorganic salts and its effect on a salted sandy soil were studied.

Acetone–formaldehyde resin (AFR) is cross-linked to form a three-dimensional network in aqueous solutions in the presence of a base catalyst and, being an efficient binder, is used in various compounds [1]. For example, development of the AFR compounds with biologically active substances (in particular, biopolymers), which can be used for consolidation of unstable salted sandy soils and their melioration, is of practical importance [2, 3]. A wide assortment of biopolymers is available for this purpose. In this work we studied a compound of AFR with sericin (SR), a globular protein obtained as by-product at uncoiling of natural silk cocoons [4, 5].

EXPERIMENTAL

The required compound was prepared using commercial acetone–formaldehyde resin (3M) as 65% aqueous oligomer solution. This resin forms a kinetically stable system at addition of the silk sericin in moderate amounts. It is known [1, 2] that AFR cross-linked in the presence of a catalyst (NaOH) at 10 : 1 ratio is used as a binder of neutral substances. This condition was taken into account in searching for the optimal composition of a compound of AFR with silk sericin and inorganic salts (S): Na_2SO_4, NaCl, $CaCl_2$, and $MgSO_4$. In our tests we also used the salt mixture NaCl–Na_2SO_4–$CaCl_2$–$MaSO_4$ (SM) with a 0.25 : 0.25 : 0.25 : 0.25 weight ratio. We found that the optimal component weight ratios are as follows: AFR–NaOH–SR, 10 : 1 : 2; AFR–NaOH–SR–S, 10 : 1 : 2 : 2; AFR–NaOH–S, 10 : 1 : 2; AFR–NaOH–SR–SM; 10 : 1 : 2 : 2, and AFR–NaOH–SM, 10 : 1 : 2.

The initial AFR solutions and their mixtures with SR and S are transparent colorless or light brown liquids. At curing, they acquire yellowish color and lose transparency, e.g., the intensity of the light transmission decreases to the greatest extent. The process was monitored using a Spectromom-410 unit and a polarization microscope (λ 560 nm).

The degree of AFR cross-linking in the samples was determined by extraction with water of the non-cross-linked polymer fraction, SR, and S from the cured compositions in a Soxhlet apparatus. The interaction of AFR with SR and S was studied by IR spectroscopy [6]. The experiments on the sand consolidation were carried out by the direct application of the AFR compound onto the surface of model systems of salted sandy soils. These model systems were prepared from the barkhan sand, which was thoroughly mixed with the salt solutions after its washing and screening through a sieve (0.125 cm pore size). After drying, the content of salts in the samples was about 2%, which is permissible for the plant growth. The average thickness of the surface layer consolidated with AFR compound was about 0.1 cm.

The mechanical strength of the consolidated sand layer was determined directly by the critical impact load (g) providing breakdown of the sample with a surface area of 1 cm^2 [7]. The efficiency of melioration was monitored by germination and growth of wheat seeds.

Under the laboratory conditions, the AFR systems were cured with deposition of a 0.1-cm layer on the cover glass surface. It was found that the light trans-

1070-4272/03/7605-0775$25.00

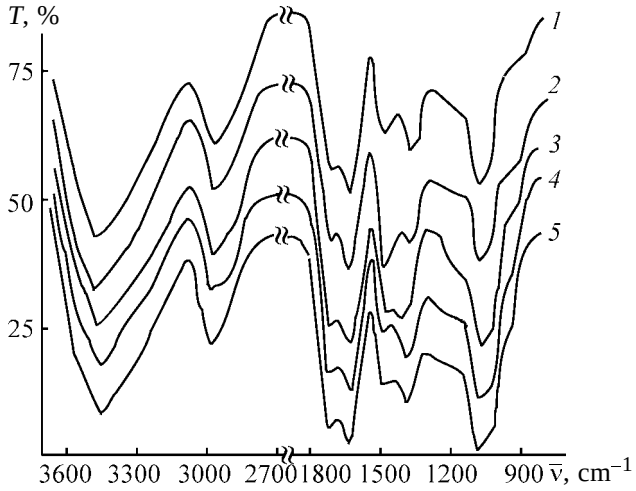

Fig. 1. IR spectra of the cured samples. (*T*) Transmission and ($\bar{\nu}$) wave number; the same for Fig. 2. (*1*) AFR, (*2*) AFR–SR, (*3*) AFR–$MgSO_4$, (*4*) AFR–$CaCl_2$, and (*5*) AFR–NaCl.

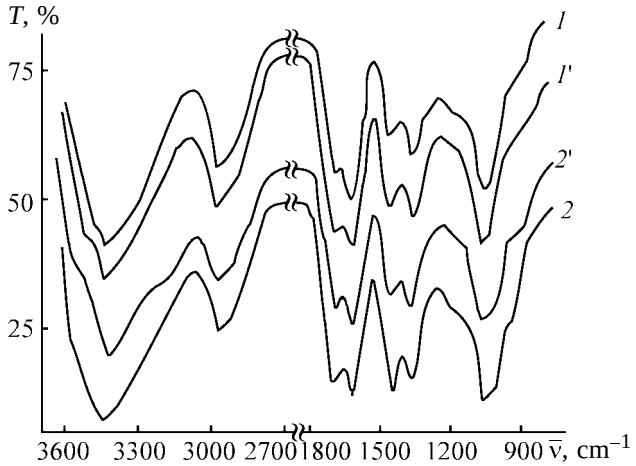

Fig. 2. IR spectra of the cured samples after water treatment: (*1*′) AFR–SM and (*2*′) AFR–SR–SM. (*1, 2*) The respective samples before water treatment.

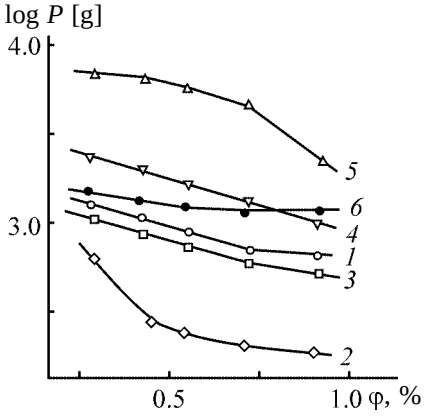

Fig. 3. Critical mechanical load *P* of the cured AFR–SR composition on consolidated salted sandy soil as a function of the volume fraction of water φ. Salt present in water: (*1*) NaCl, (*2*) Na_2SO_4, (*3*) $CaCl_2$, (*4*) $MgSO_4$, (*5*) SM, and (*6*) none.

mission through the samples strongly changes with curing. The AFR–NaOH–H_2O (10 : 1 : 2) system is cured completely in 30 min, and this time decreases to 10–15 min in the presence of Na_2SO_4 or NaCl. This is obviously due to the increasing concentration of sodium cations acting as catalyst in these systems; at the same time, the other salts or their mixtures and SR decelerate the curing. For example, the samples containing $MgSO_4$ and SR + SM mixture are cured in 90 and 80 min, respectively. This is probably due to the inhibiting effect of the corresponding ions on the AFR curing. As shown in [1], the rate of the AFR cross-linking strongly decreases in the presence of the other catalysts and fillers [1]. Based on our experimental data, the following degrees of the AFR cross-linking were determined (%): AFR, 70; AFR–SR, 65; AFR–Na_2SO_4, 60; AFR–NaCl, 62; AFR–$CaCl_2$, 72; AFR–$MgSO_4$, 75; AFR–SM, 68; and AFR–SR–SM, 66.

The reaction of AFR with SR and S was studied by IR spectroscopy. The IR spectra of the samples in question exhibit similar absorption bands at 2900 and 3400 cm^{-1}, characterizing the stretching vibrations of the CH_2, CH_3, and OH groups. The characteristic bands of the stretching vibrations of the C=O and CH_3 groups in AFR appear at 1440 and 1700 cm^{-1}. The intensity of these bands strongly depends on the additives: in the presence of SR, the intensity of the band at 1440 cm^{-1} increases, whereas in the case of inorganic salts S the intensity of these bands depends on particular metal ion. In general, these data suggest that filled AFR compounds are obtained without formation of new chemical bonds. After treatment with water, the intensity of the characteristic bands in the spectra of the cured compounds becomes close to that of the bands in the spectra of AFR cured without additives (Fig. 2). This trend is especially pronounced in the IR spectra of the samples cured in the presence of SM (Fig. 2). Our experimental data showed that the excess filler and non-cross-linked AFR fraction are efficiently removed with water.

The salted sandy soil consolidated using AFR compositions with SR exhibits certain mechanical strength. This resistance to the external effects strongly depends on the water content in the initial compound, which is confirmed by our experimental data characterizing the effect of various loads on the strength of a 0.1-cm layer of the salted sandy soil consolidated with AFR compound (Fig. 3). As seen, the strength of the consolidated soil layer decreases with increasing water content in the compound. In general, the strength characteristics of our experimental samples meet the requirements to soil-fixing agents [2].

Comparative data on the germination of wheat seeds in salted sandy soils consolidated with AFR compounds

Fixing agent	Fixing agent : product : H_2O	Germination, %
AFR : NaOH : H_2O = 5 : 0.5 : 100	1 : 5 : 10	80
SR : H_2O = 2 : 100	1 : 5 : 10	95
AFR : SR : NaOH : H_2O = 5 : 2 : 0.5 : 100	1 : 5 : 10	90
AFR : NaOH : H_2O : SM = 5 : 0.5 : 100 : 2	1 : 5 : 10	50
AFR : SR : NaOH : H_2O : SM = 5 : 2 : 0.5 : 100 : 2	1 : 5 : 10	85
No fixing agent	0 : 5 : 10	80

The sandy soil consolidated with AFR compound contains small amounts of water, which are insufficient for the crop (e.g., wheat) germination. The required water (in amounts by an order of magnitude greater than the weight of the AFR compound) was added directly into the soil. As a result, a sufficiently humid medium was formed under the consolidated soil layer (1-cm thickness), in which SR was gradually transferred. As a result, the soil was enriched with the biologically active substance.

To evaluate the melioration effect of the AFR–SR compounds, the germination and growth of wheat seeds were studied (see table). With the compound containing no SR, inorganic salts exhibit the negative affect on the dynamics of the seed germination.

It should be noted that SR, being added into the AFR compound, completely eliminates this negative effect and improves germination. It also enhances the performance of the AFR compound as a sand-fixing agent.

CONCLUSION

The strength properties of the salted sandy soil consolidated with the acetone–formaldehyde resin compound were determined, and the positive melioration effect of the compounds on the wheat seed germination was revealed.

REFERENCES

1. Kirgizbaeva, M.Yu., Amanov, A.A., and Petrov, A.I., *Uzb. Khim. Zh.*, 1990, no. 2, pp. 131–134.
2. Zaplishnyi, V.N., Zakopyan, G.A., and Pogosyan, G.M., *Plast. Massy*, 1985, no. 4, pp. 50–54.
3. Rashidova, S.Sh., Ruban, I.N., and Petrov, A.I., *Probl. Osvoen. Pustyn'*, 1998, no. 3, pp. 164–168.
4. Liu, Guanteng, *J. Text. Res.*, 1992, vol. 13, no. 1, pp. 11–14.
5. Williams, V.R. and Williams, H.B., *Basic Physical Chemistry for the Life Sciences*, San Francisco: Freeman, 1973.
6. Dechant, J., Danz, R., Kimmer, W., *et al*. *Ultrarotspektroskopische Untersuchungen an Polymeren*, Berlin: Akademie, 1972.
7. Mukhmasimov, F.N., Fedotov, I.P., and Zelenov, Yu.V., *Fizicheskie metody izmereniya* (Physical Methods of Measurements), Tashkent: Fan, 1988.

Russian Journal of Applied Chemistry, Vol. 76, No. 5, 2003, pp. 778–780. Translated from Zhurnal Prikladnoi Khimii, Vol. 76, No. 5, 2003, pp. 807–809.

ORGANIC SYNTHESIS AND INDUSTRIAL ORGANIC CHEMISTRY

Thermochemical Reactions of H Complexes

Yu. N. Sazanov, V. N. Artem'eva, G. N. Fedorova, N. V. Kukarkina, E. M. Kulikova, and V. V. Kudryavtsev

Institute of Macromolecular Compounds, Russian Academy of Sciences, St. Petersburg, Russia

Received February 14, 2003

Abstract—Thermal reactions of H complexes formed by methyl and ethyl diesters of aromatic tetracarboxylic acids with diamines were studied by thermal analysis. Some kinetic parameters of formation and degradation of polyimides during thermolysis in the self-generated atmosphere were determined.

The problems of thermal stability and thermal transformations of H complexes formed by dimethyl dihydrogen benzophenonetetracarboxylate with a series of diamines were considered previously in the context of developing a process for production of foamed polyimides [1, 2]. Dialkyl dihydrogen arenetetracarboxylates are formed by dissolving the corresponding aromatic dianhydrides in refluxing alcohols [3–5]. Addition of various diamines to the resulting alcoholic solutions at room temperature causes spontaneous formation of H complexes. Probable structures of various H complexes were determined from kinetic data and by quantum-chemical calculations [6]; a mechanism of their thermal imidization, favorable from the energetic and steric viewpoints, was suggested.

An H complex (see below), when heated at a constant rate, undergoes transformations involving virtually simultaneous release of the alcohol and water in the first step and formation of the polyimide in the final step:

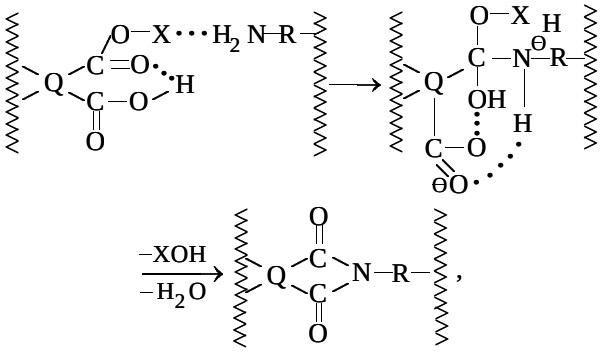

where

Q = 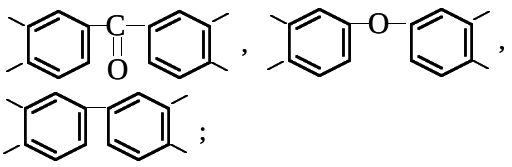

R = 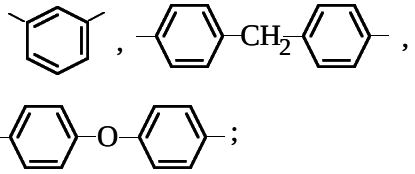

X = $-CH_3$ or $-C_2H_5$.

In this work, using thermogravimetric (TG), differential thermal (DTA), and thermovolumetric (TVA) analyses, we examined how the chemical structure of the initial H complexes affects the kinetics of their thermal cyclization (imidization).

EXPERIMENTAL

The H complexes were prepared by the procedure described in [6]. The dried samples were subjected to vacuum thermolysis on a TVA installation [7]. The heating rate was varied from 3 to 7 deg min^{-1}. Some samples were kept at a fixed temperature (250 or 400°C) for 3 h. Pyrolysis in the self-generated atmosphere (SGA) was performed by a standard procedure on a C-1500 derivatograph (Hungary) at a heating rate of 5 deg min^{-1}.

A characteristic pattern of the evolution of volatile products in the course of thermal transformation of the H complex into polyimide at linear heating in a vacuum is shown in Fig. 1. It was demonstrated by the example of the H complex of dimethyl dihydrogen diphenyltetracarboxylate with an equimolar mixture of *m*-phenylenediamine and 4,4'-diaminodiphenylmethane that volatile imidization products (methanol and water) vigorously evolve in the range 80–200°C. It is seen that the reaction occurs in two overlapping steps. As expected, at the lower heating rate the peaks

1070-4272/03/7605-0778$25.00 © 2003 MAIK "Nauka/Interperiodica"

are observed at lower temperatures (100 and 140°C). As the heating rate is increased, the peak temperatures grow and the difference between them decreases. This indicates that the rate constants of the release of volatiles in the first and second steps of imidization are different; this difference is due to structural features of the system, which is confirmed in [2].

It should be noted that curve *1* in Fig. 1 also has a noticeable peak at 78°C, assignable to evolution of residual solvent, not incorporated into the complex. At the higher heating rate, this peak coalesces with the peak due to evolution of volatiles.

Thus, lower heating rate favors better separation of the two steps of thermal imidization of the H complex. The temperature of the first step of the evolution of volatile products decreases by approximately 40°C. On further heating in the range 170–300°C (Fig. 1), no volatile products are released, suggesting imidization completion.

To confirm this, we performed experiments in which the samples were heated at the same rate to 96 and 250°C and then kept at these temperatures for 3 h. Comparison of the observed weight losses with the calculated loss for the case of complete imidization shows that the amount of the released methanol and water, relative to the calculated amount, is 75–80% at 96°C and almost 100% at 250°C. This fact suggests that, on heating to 200°C, the H complex in question fully transforms into the polyimide, which is thermally stable up to 300°C. It should be noted that agreement between the experimental and calculated weight losses is far from being a common feature for all the H complexes under consideration. For example, the complexes containing fragments of bis(dicarboxyphenyl) ether, diaminodiphenyl ether, and ethyl esters show excessive weight loss when kept at 250°C, which may be due either to the presence of the residual solvent in the H complex or to structural differences between the forming polyimides and those considered above [8].

Further heating in the range 300–400°C (Fig. 1) is again accompanied by the release of volatiles, indicative of degradation of the formed polyimide. As in the case of thermal imidization, the peak position, shape, and intensity depend on the heating rate (variation of the heating rate is actually equivalent to variation of the heat treatment time). Apparently, the heating rate is a decisive factor in initiation of degradation and cross-linking starting at approximately 400°C. As seen from curves *1* and *2* in Fig. 1, the higher heating rate favors development of degradation reactions with the evolution of a large amount of volatiles. Furthermore, the structure of the H complex also affects the degradation of polyimides. Experiments on isothermal heating of all the samples at 400°C showed that, irrespective of the chemical structures of the ester and amine components, the weight loss varies within 40–55%. This indicates that, in the range 300–400°C, polyimides partially decompose. Above 400°C, the second step of thermal degradation is observed; the weight loss is 14–35% of the total weight, with the difference apparently associated with the structural features of the H complexes. The largest weight loss is observed with the samples derived from benzophenonetetracarboxylic acid, and the smallest weight loss, in those derived from ethyl esters.

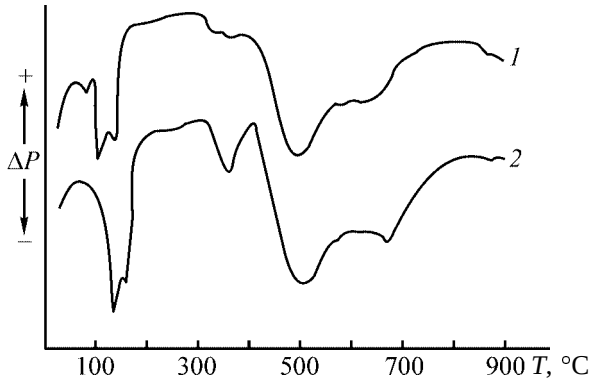

Fig. 1. TVA curves of thermolysis of the H complex formed by dimethyl dihydrogen tetracarboxylate with an equimolar mixture of *m*-phenylenediamine and 4,4'-diaminodiphenylmethane. (Δ*P*) Pressure difference in the TVA manometric system and (*T*) sample temperature. Heating rate, deg min^{-1}: (*1*) 3 and (*2*) 7.

The final products of thermal degradation of the H complexes in a vacuum are carbonized residues; their formation is complete at 800°C. Their weight does not exceed 15–20% of the initial sample weight.

In thermolysis of the H complexes in SGA, the yield of the carbonized residue is higher (~35%), demonstrating an appreciable effect of diffusion factors and certain oxidation reactions on the cross-linking of the H complexes and their imidization products. The TG and DTA data obtained under SGA conditions (Fig. 2) show that the alcohol and water are released in the range 130–200°C with a total weight loss of 16.6% (calculated weight loss 20%), showing an unresolved endothermic effect with a maximum at 143°C. In the range 270–410°C, in contrast to the TVA experiment, virtually no gases are evolved. Hence, in this range the imidization product undergoes internal rearrangement, probably with partial intermolecular cross-linking and certain ordering of the intramolecular organization. This is suggested by an endothermic

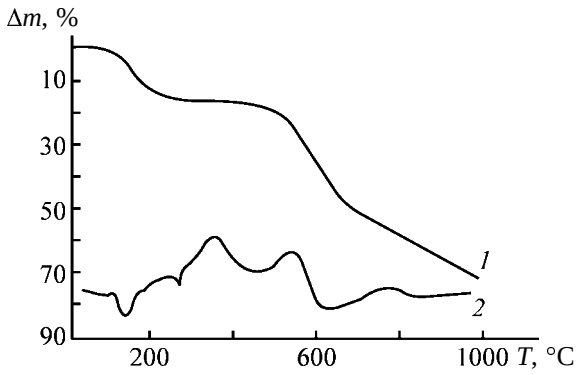

Fig. 2. (*1*) TG and (*2*) DTA curves of the same H complex as in Fig. 1. Heating rate 5 deg min^{-1}, SGA. (Δ*m*) Weight loss and (*T*) temperature.

effect at 270°C and an exothermic effect at 353°C, assignable to melting and crystallization or cross-linking of the ordered regions of the polyimide. Above 560°C, the polymer undergoes further degradation with an appreciable weight loss (~30%), followed by carbonization.

CONCLUSION

The chemical structure of H complexes formed by aromatic tetracarboxylic acid diesters with diamines affects the kinetics of their thermal imidization and of degradation and carbonization of the resulting polyimides. The yield of the carbonized product is 2–3 times higher when thermolysis is performed under the conditions of diffusion control.

ACKNOWLEDGMENTS

The study was supported by the Russian Foundation for Basic Research (project no. 00-15-97297).

REFERENCES

1. Artem'eva, V.N., Kukarkina, N.V., Samarin, V.P., *et al.*, *Zh. Prikl. Khim.*, 2000, vol. 73, no. 7, pp. 1172–1179.
2. Artem'eva, V.N., Chupans, P.I., Kukarkina, N.V., *et al.*, *Zh. Prikl. Khim.*, 2000, vol. 73, no. 5, pp. 810–815.
3. Artem'eva, V.N., Chupans, P.I., Smirnova, E.A., *et al.*, *Zh. Prikl. Khim.*, 1990, vol. 63, no. 4, pp. 655–660.
4. Koton, M.M., Artem'eva, V.N., Glumova, T.D., *et al.*, *Zh. Prikl. Spektrosk.*, 1987, vol. 47, no. 4, pp. 623–629.
5. Artem'eva, V.N., Kudryavtsev, V.V., Chupans, P.I., *et al.*, *Izv. Akad. Nauk SSSR, Ser. Khim.*, 1992, no. 11, pp. 2517–2524.
6. Artem'eva, V.N., Kudryavtsev, V.V., Chupans, P.I., *et al.*, *Izv. Akad. Nauk SSSR, Ser. Khim.*, 1995, no. 6, pp. 1060–1065.
7. Sazanov, Yu.N. and Sysoev, V.D., *Eur. Polym. J.*, 1974, vol. 10, pp. 867–869.
8. Kostereva, T.A., Artem'eva, V.N., Kukarkina, N.V., *et al.*, *Zh. Prikl. Khim.*, 2001, vol. 74, no. 9, pp. 1533–1536.

Russian Journal of Applied Chemistry, Vol. 76, No. 5, 2003, pp. 781–784. Translated from Zhurnal Prikladnoi Khimii, Vol. 76, No. 5, 2003, pp. 810–813.

ORGANIC SYNTHESIS AND INDUSTRIAL ORGANIC CHEMISTRY

Hydrolytic Copolycondensation of Ethyl Silicate with Cobalt and Manganese Salts

V. A. Sviderskii, M. G. Voronkov, S. V. Klimenko, and D. N. Bystrov

Kiev Polytechnic Institute, National Technical University of Ukraine, Kiev, Ukraine
Favorskii Irkutsk Institute of Chemistry, Siberian Division, Russian Academy of Sciences, Irkutsk, Russia

Received June 26, 2002

Abstract—Hydrolytic copolycondensation of ethyl silicate with cobalt salts and manganese chloride was studied under conditions of base (NH_4OH) catalysis.

Sol–gel process based on hydrolytic copolymerization of alkoxysilanes in aqueous–organic media is one of the most efficient methods of preparing polymetallosiloxanes [1, 2]. This reaction is difficult to control. Even when certain optimal conditions (pH, temperature, organic diluent and catalyst, reactant ratio) are followed, characteristics of the resulting cohydrolysis products are not always reproducible.

Earlier, we studied the possibility of controlling the sol–gel process, in particular, the synthesis of polycuprosiloxanes, by varying the copper salt anion [3]. Copper salts were taken because of their capability to form stable ammonia complexes within a wide pH range. Proceeding with these studies, we considered in this work the use in the sol–gel process of metals forming weaker complexes with ammonia.

EXPERIMENTAL

Commercial ethyl silicate-40 (partially hydrolyzed tetraethoxysilane), cobalt salts $Co(NO_3)_2 \cdot 6H_2O$, $CoCl_2 \cdot 6H_2O$, $CoSO_4 \cdot 7H_2O$, $Co(CH_3COO)_2 \cdot H_2O$, and manganese chloride $MnCl_2 \cdot 5H_2O$ were used as initial reagents.

Cobalt salts form ammonia complexes only with excess ammonia, and manganese salts form no ammonia complexes. The synthesis conditions were similar to those described in [3]. The products of hydrolytic copolycondensation were thoroughly washed by decanting, dried to the xerogel state at 120 ± 0.5°C for 16 h, and studied by thermal analysis (MOM derivatograph, heating rate 10 deg min^{-1} in air) and IR spectroscopy (Specord-75 IR spectrometer, KBr pellets). The sorbed water was determined gravimetrically after keeping the samples in a dessicator for 72 h at 98% relative humidity.

The hydrolytic copolycondensation of ethyl silicate with $CoSO_4$, $CoCl_2$, and $Co(NO_3)_2$ under conditions of base catalysis gives polymeric structures containing endo- and exoskeleton Si–O–Co–O and Si–O–Si groups, residual ethoxy groups, and isopropoxy groups, originating from ester interchange of the ethoxy groups.

Similar structures are probably formed with cobalt acetate and manganese chloride, but only at the reaction temperature of 45°C. This is confirmed by shift of the ν(Si–O) band relative to its frequency of 1093 cm^{-1} in the spectrum of silica xerogel containing no metal. The above shift depends of both salt cation and anion (for cobalt salts) (Table 1).

In the IR spectra of polycobaltoalkoxysiloxanes prepared from $Co(NO_3)_2$, the ν(Si–O) shift ranges from –33 to +20 cm^{-1}. This suggests formation of thermodynamically unstable structures with random distribution of mobile components in the siloxane matrix. In the case of $CoCl_2$ and $CoSO_4$, temperatures of 25 and 35°C, and reaction times of 3 and 5 h, the ν(Si–O) shift becomes approximately constant. The half-width $\Delta\nu_{1/2}$ and optical density *D* of this band, which characterize the degree of cross-linking, also show a clear trend in variation (Table 2). The shift of the band ν(Si–O) 1093 cm^{-1} and a decrease in both $\Delta\nu_{1/2}$ and optical density indicate that various polymeric structures are formed: from cross-linked to three-dimensional–cyclic or cyclic–linear structures mainly consisting of cyclic trimeric and tetrameric units bound by oxygen bridges [4]. The stabilization of the ν(Si–O) shift indicates their thermodynamic stability.

Cobalt acetate and manganese chloride at 25 and 35°C give more stable metal polysiloxane structures

1070-4272/03/7605-0781$25.00

Table 1. Shifts of absorption bands ν(Si–O) at 1093 and 800 cm^{-1}, $\Delta\nu$, in the IR spectra of polymetalloalkoxysiloxane xerogels containing cobalt or manganese heteroatoms*

Synthesis conditions		$\Delta\nu$, cm^{-1}				
T, °C	τ, h	$Co(NO_3)_2$	$CoCl_2$	$CoSO_4$	$Co(OCOCH_3)_2$	$MnCl_2$
		ν(Si–O) = 1093 cm^{-1}				
25	1	+20	+13	+15	0	0
25	3	+13	+7	+10	0	0
25	5	0	+7	+10	0	0
35	1	0	+23	23	0	0
35	3	–9	+10	+13	0	0
35	5	+13	+10	+13	0	0
45	1	–33	–6	–6	–13	–9
45	3	+10	–10	–6	–13	–12
45	5	–6	–6	–8	–16	–16
		ν(Si–O) = 800 cm^{-1}				
25	1	+6	+6	+12	0	0
25	3	0	+6	+6	0	0
25	5	–6	+6	+6	0	0
35	1	–8	+6	+12	0	0
35	3	0	+6	+6	0	0
35	5	+14	+6	+6	0	0
45	1	–7	0	0	0	–12
45	3	+6	0	0	–6	–6
45	5	+8	0	0	–6	–12

* Shift: (+) to higher frequencies and (–) to lower frequencies.

compared to $Co(NO_3)_2$, as shown by a fixed position of ν(Si–O) and by regular variation of $\Delta\nu_{1/2}$ and *D*.

The constancy of ν(Si–O) shows that exoskeleton Si–O–M groups (M = metal) are primarily formed. Increase in the temperature to 45°C in all cases promotes deeper transformations and is accompanied by a decrease in the thermodynamic stability of the structure [in this case, the optical characteristics of the ν(Si-O) band at 1093 cm^{-1} change irregularly].

The formation of thermodynamically stable structures at 25 and 35°C with $CoCl_2$, $CoSO_4$, and $Co(CH_3COO)_2$ can be explained by the lower energy barrier of the reaction as compared to $Co(NO_3)_2$. However, the nitration (oxidation) of alkoxy groups with cobalt nitrate is more probable.

The specific structure of polymanganoalkoxysiloxanes is probably due to features of $MnCl_2$ behavior in aqueous ammonia, which is described by the following reactions:

$$Mn^{2+} + 2NH_4OH \rightarrow Mn(OH)_2 + 2NH_4^+,$$

$$2Mn(OH)_2 + O_2 + (2x - 2)H_2O \rightarrow 2MnO_2 \cdot xH_2O.$$

At 25 and 35°C, manganese dioxide only partially reacts with ethyl silicate to form mixed oxides and surface Si–O–Mn groups. At 45°C, the reaction shifts toward formation of intraskeleton (endo) Si–O–Mn groups.

The structural changes in Si–O–Si groups are characterized by the band of symmetrical stretching vibrations of the SiO_4 tetrahedron at 800 cm^{-1}, which overlaps, however, with bands of two other vibrations [4].

In the IR spectra of metal polymetalloalkoxysiloxane xerogels prepared from $Co(NO_3)_2$, the shift of this band is variable in sign and value. On the contrary, in the IR spectra of the polymers prepared with $CoCl_2$ and $CoSO_4$ at 25 and 35°C, this band shifts by 6 cm^{-1} to higher wave numbers, while at 45°C this shift is absent. In the spectra of the products prepared with $Co(CH_3COO)_2$ and $MnCl_2$, the band shifts (to lower wave numbers) only in products synthesized at 45°C, while at 25 and 35°C the band shift is absent. In all the above cases, the band half-width and optical density vary only slightly (within 23–26 cm^{-1} and 0.03–0.08, respectively).

All these data show that the polysiloxane structure

Table 2. Half-width $\Delta\nu_{1/2}$ and optical density D of absorption bands ν(Si–O) at 1093 and 800 cm^{-1} in the IR spectra of polymetalloalkoxysiloxane xerogels containing cobalt or manganese heteroatoms

Synthesis conditions		$\Delta\nu_{1/2}$, cm^{-1}/D				
T, °C	τ, h	$Co(NO_3)_2$	$CoCl_2$	$CoSO_4$	$Co(OCOCH_3)_2$	$MnCl_2$
		ν(Si–O) = 1093 cm^{-1}				
25	1	103/0.82	109/0.88	113/1.17	129/0.91	198/0.64
25	3	109/0.88	103/0.82	109/1.12	123/0.86	193/0.60
25	5	120/1.18	103/0.79	109/1.07	106/0.49	173/0.54
35	1	90/0.71	113/0.87	103/0.87	159/1.74	186/0.80
35	3	86/0.69	109/0.85	91/0.84	140/0.93	172/0.79
35	5	120/1.10	100/0.83	91/0.85	116/0.72	159/0.62
45	1	80/0.68	100/0.80	117/1.08	199/1.45	173/0.67
45	3	103/0.80	93/0.79	103/0.98	123/1.21	153/0.54
45	5	113/0.97	76/0.59	86/0.86	126/0.81	146/0.54
		ν(Si–O) = 800 cm^{-1}				
25	1	26/0.07	26/0.05	26/0.07	23/0.04	26/0.05
25	3	26/0.07	23/0.09	23/0.06	23/0.05	26/0.05
25	5	26/0.08	23/0.05	26/0.06	23/0.03	26/0.04
35	1	26/0.05	26/0.06	23/0.06	26/0.08	23/0.05
35	3	26/0.05	23/0.06	23/0.06	23/0.05	26/0.04
35	5	26/0.08	23/0.03	23/0.05	23/0.08	26/0.04
45	1	25/0.05	26/0.06	26/0.06	26/0.08	23/0.04
45	3	23/0.07	26/0.04	26/0.06	26/0.07	26/0.05
45	5	26/0.06	26/0.04	26/0.06	26/0.08	23/0.04

consisting of Si–O–Si fragments in the polymers prepared with $CoCl_2$ and $CoSO_4$ at 25 and 35°C also tends to rearrangements. At 45°C, the initial siloxane structure of these polymers does not change. On the contrary, in the polymers prepared with $Co(CH_3COO)_2$ and $MnCl_2$, the basic siloxane skeleton changes only when they are prepared at 45°C (at 25 and 35°C, the structure remains unchanged). The structure of the siloxane skeleton of polymetallosiloxanes prepared with cobalt nitrate is unstable. As a whole, the structure of polymetallosiloxanes is determined by the ratio of the rates of hydrolysis and copolycondensation depending on the salt anion (and cation) and reaction conditions.

Under the experimental conditions, polymetalloalkoxysiloxane xerogels (which are mainly metal-containing silicas) are formed. As shown by thermogravimetry, the content of metal-containing silica depends on the salt cation and anion and amounts to 86.0–90.5 wt %. The presence of small amounts of alkoxy groups is confirmed by the weight loss at 200–450°C and the corresponding exothermic effects in the DTA curves (Tables 3, 4).

In all cases, the exothermic peak shifts to higher temperatures when the synthesis time and temperature are increased. The DTA curves of polymetallosiloxanes based on cobalt salts have one exothermic peak shifted to higher temperatures by 5–10°C. In the case of $MnCl_2$, two exothermic peaks are observed at 210 and 310°C. Their shift with increase in the synthesis temperature and time amounts to 60 and 140°C, respectively. Depending on synthesis conditions, polymetallosiloxanes obtained are both low- and high-molecular-weight polymers (exothermic effects at 200–210 and 310°C, respectively). The high-molecular-weight polymers are formed under more rigid synthesis conditions (temperature, synthesis time). The larger weight loss by polymetallosiloxanes based on $Co(CH_3COO)_3$ and $MnCl_2$ is probably caused by condensation of the residual alkoxy groups.

Thus, the sol–gel process based on hydrolytic copolycondensation of ethyl silicate with cobalt and manganese salts in 2-propanol under conditions of base (NH_4OH) catalysis gives polymetalloalkoxysiloxanes with three-dimensional and cyclic–linear structures. This process can be controlled by the salt anion and cation, temperature, and synthesis time. Thermodynamically stable structures containing endo- and exoskeleton Si–O–M and Si–O–Si fragments are formed when the synthesis is performed with $CoCl_2$,

Table 3. Weight loss Δm of cobalt and manganese polyalkoxysiloxane xerogels at heating within the 200–450°C range

Synthesis conditions		$\Delta m_{1/2}$, wt %				
T, °C	τ, h	$Co(NO_3)_2$	$CoCl_2$	$CoSO_4$	$Co(OCOCH_3)_2$	$MnCl_2$
25	1	2.8	2.7	2.4	3.5	2.6
25	3	2.6	2.7	1.8	3.5	2.4
25	5	2.3	2.5	1.6	3.2	2.0
35	1	2.5	2.0	2.2	4.0	2.5
35	3	2.5	2.0	1.7	4.2	2.5
35	5	2.0	1.8	1.5	3.8	2.3
45	1	2.9	3.2	2.6	4.0	3.7
45	3	3.1	3.2	2.5	3.8	3.3
45	5	3.1	2.8	2.5	3.8	2.9

Table 4. Temperature of the exothermic peak T_{max} in DTA curves of cobalt and manganese polyalkoxysiloxane xerogels*

Synthesis conditions		T_{max}, °C				
T, °C	τ, h	$Co(NO_3)_2$	$CoCl_2$	$CoSO_4$	$Co(OCOCH_3)_2$	$MnCl_2$
25	1	200 m**	210 w	210 m	200 w	210 w/310 w
25	3	205 m	215 w	210 m	200 w	210 s/310 w
25	5	200 m	215 w	210 m	200 w	230 s/370 w
35	1	200 m	210 w	210 m	200 w	220 s/405 w
35	3	200 m	210 w	210 w	200 w	230 s/410 m
35	5	210 m	215 w	215 w	200 w	230 s/410 w
45	1	205 m	215 w	210 w	200 w	250 s/410 w
45	3	210 m	210 w	210 w	200 w	270 s/440 w
45	5	210 m	215 w	215 w	210 w	270 s/450 m

* Silica xerogel, 250°C.
** Intensity of the exothermic effect: (s) strong, (m) medium, and (w) weak.

$CoSO_4$, and $Co(CH_3COO)_2$ at 25 and 35°C. In the case of cobalt acetate, Si–O–Co fragments are mainly formed on the surface by heterofunctional condensation

$$\equiv Si–OR + CH_3COOCo– \rightarrow \equiv Si–OCo– + CH_3COOR.$$

The kind of the starting salts also affects the water absorption by the polymetallosiloxanes synthesized. It amounts to 17.1, 29.4, 25.4, 28.9, and 32.5 wt % for $Co(NO_3)_2$, $CoCl_2$, $CoSO_4$, $Co(CH_3COO)_2$, and $MnCl_2$, respectively.

CONCLUSIONS

(1) The composition, structure, and properties of polymetallosiloxanes formed by hydrolytic copolycondensation of ethyl silicate with metal salts are determined by the salt anion and cation, and by the synthesis temperature and time.

(2) The synthesis of polymetallosiloxanes based on $CoCl_2$, $CoSO_4$, $Co(CH_3COO)_2$, and $MnCl_2$ in 2-propanol at 25 and 35°C under conditions of base (NH_4OH) catalysis gives thermodynamically stable polysiloxane structures with predictable characteristics. Structures with random distribution of mobile fragments of the siloxane matrix are formed when cobalt nitrate is used.

REFERENCES

1. Hench, L.L. and West, J.K., *Chem. Rev.*, 1990, vol. 90, no. 1, pp. 33–72.
2. Voronkov, M.G., Maletina, E.A., and Roman, V.K., *Geterosiloksany* (Heterosiloxanes), Novosibirsk: Nauka, 1984.
3. Sviderskii, V.A., Voronkov, M.G., Klimenko, S.V., and Bystrov, D.N., *Zh. Prikl. Khim.*, 2001, vol. 74, no. 12, pp. 2027–2030.
4. Bellamy, L.J., *The Infra-Red Spectra of Complex Molecules*, London: Methuen, 1954.
5. Lazarev, A.N. and Voronkov, M.G., *Opt. Spektrosk.*, 1958, vol. 4, no. 2, pp. 180–188.

Russian Journal of Applied Chemistry, Vol. 76, No. 5, 2003, pp. 785–790. Translated from Zhurnal Prikladnoi Khimii, Vol. 76, No. 5, 2003, pp. 814–819.

ORGANIC SYNTHESIS AND INDUSTRIAL ORGANIC CHEMISTRY

Mechanism of Methylcyclohexane Ozonolysis

A. M. Syroezhko, O. Yu. Begak, and V. A. Proskuryakov

St. Petersburg State Technological Institute, St. Petersburg, Russia
Mendeleev Russian Research Institute of Metrology, Federal State Unitary Enterprise, St. Petersburg, Russia

Received January 22, 2003

Abstract—A mathematical model of selective oxidation of methylcyclohexane with ozone–oxygen mixtures was substantiated.

The methylcyclohexane molecule has three nonequivalent C–H bonds (at primary, tertiary, and five secondary carbon atoms at the α-, β-, and γ-positions relative to the methyl substituent). Therefore, selective oxidation of this molecule at a definite C–H bond can hardly be expected, the more so as thermal oxidation of methylcyclohexane with oxygen occurs at a noticeable rate only at elevated temperatures (above 120°C) and is low-selective [1].

The procedures for oxidation and analysis of reaction products were described in [2]. Ozonolysis of methylcyclohexane is active at 20°C (Fig. 1) and yields hydroperoxides, alcohols, ketones, acids, and esters.

Among methylcyclohexyl hydroperoxides formed by oxidation of methylcyclohexane, the major isomer (95–96%) is 1-methylcyclohexyl hydroperoxide. Among methylcyclohexanols, all possible isomers are detected (Table 1), with 1-methylcyclohexanol prevailing. The yield of the tertiary alcohol decreases with increasing conversion, temperature, and ozone concentration (Table 1, Fig. 1). Among isomeric methylcyclohexanones, 2-methylcyclohexanone prevails (Table 1). As the methylcyclohexane conversion increases, the yield of the alcohols and ketones decreases, with a simultaneous slight increase in the relative yield of hydroperoxides, acids, and esters (Fig. 2). The tertiary hydroperoxide at low temperatures (20°C) is consumed in the reaction with ozone slowly (rate constant 19×10^{-3} l mol^{-1} s^{-1}); therefore, its yield increases with conversion of methylcyclohexane. Ozonolysis of methylcyclohexane is highly selective with respect to the yield of 1-methylcyclohexanol at conversions of up to 12%. An increase in the yield of acids in the developed ozonolysis of methylcyclohexane is due to further oxidation of secondary and tertiary methylcyclohexanols and isomeric methylcyclohexanones.

Among carboxylic acids, ozonolysis of methylcyclohexane yields monocarboxylic, dicarboxylic, and keto acids. The ratio of the yield of monocarboxylic acids to the total yield of keto and dicarboxylic acids in the examined temperature range (20–80°C, $[O_3]$ = 4 vol %) is 0.6–0.7 at the methylcyclohexane conversion of 12–82%. This ratio varies within a narrow range (0.4–0.7) [1] as the ozone concentration is varied within 2–4 vol %. The composition of the acids is given in Tables 2 and 3. Among monocarbox-

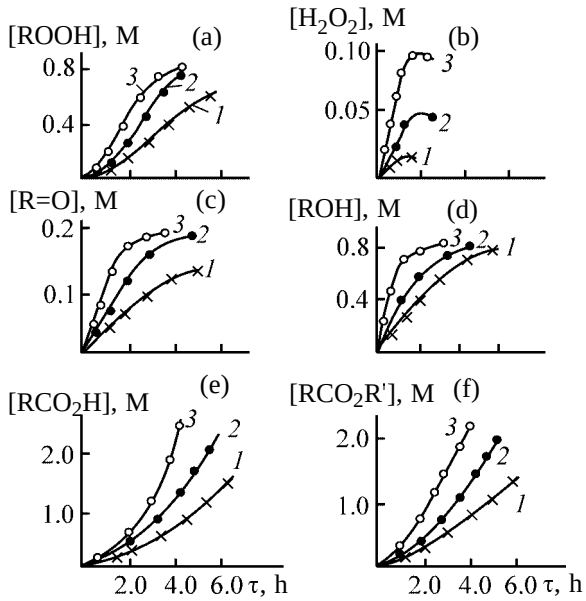

Fig. 1. Kinetic curves of accumulation of (a) hydroperoxides ROOH, (b) hydrogen peroxide H_2O_2, (c) ketones R=O, (d) alcohols ROH, (e) acids RCO_2H, and (f) esters RCO_2R' in oxidation of methylcyclohexane ($[O_3]$ = 4 vol %). (τ) Time; the same for Fig. 3. *T*, °C: (*1*) 20, (*2*) 40, and (*3*) 80; the same for Figs. 2 and 3.

1070-4272/03/7605-0785$25.00

Table 1. Composition of neutral products of methylcyclohexane ozonolysis ([O_3] = 4 vol %)*

™, °C	α**	τ,** h	Alcohols, mol %			Ketone, mol %	
			1-MCHL	2-MCHL	3- + 4-MCHL	2-MCHN	3- + 4-MCHN
20	12	2	93	5.5	1.5	95	5
	35	4	93	5.0	2.0	93	7
	57	6	90	8.0	2.0	90	10
40	20	2	85	12	3	90	10
	55	4	81	15	4	86	14
	77	6	75	16	9	80	20
80	35	2	80	15	5	85	15
	82	4	75	17	8	80	20
40***	26	6	95	4	Traces	96	4

* 1-, 2-, 3-, and 4-MCHL denote the respective isomers of methylcyclohexanol, and 2-, 3-, and 4-MCHN, the respective isomers of methylcyclohexanone.
** (α) Degree of conversion and (τ) ozonolysis time.
*** [O_3] = 2 vol %.

ylic acids, acetic acid prevails (70–87%). We also identified propionic, butyric, valeric, and capric acids. Among dicarboxylic and keto acids, we identified ε-ketoenanthic (16.2–35.1%), α- and β-methyladipic (40.7–53.2% in total), oxalic, succinic, methylsuccinic, α- and β-methylglutaric, and glutaric acids (Table 3). As the ozone concentration and temperature are increased, the yield of acetic and ε-ketoenanthic acids decreases. Keto acids are formed by ozonolysis of the tertiary hydroperoxide, 1- and 2-methylcyclohexanols, and 2-methylcyclohexanone [3–6].

Low-temperature ozonolysis of methylcyclohexane is a radical-chain reaction. Calculations show that, as in oxidation of cyclohexane, the chain-propagating species are alkoxy radicals rather than less active $RO_2^{\bullet}$ radicals. Alkoxy radicals are apparently generated by recombination of tertiary peroxy radicals and by reaction of $RO_2^{\bullet}$ radicals with ozone. The tertiary hydroperoxide is formed by cross recombination of $RO_2^{\bullet}$ and $HO_2^{\bullet}$ radicals and is mainly consumed with formation of 1-methylcyclohexanol.

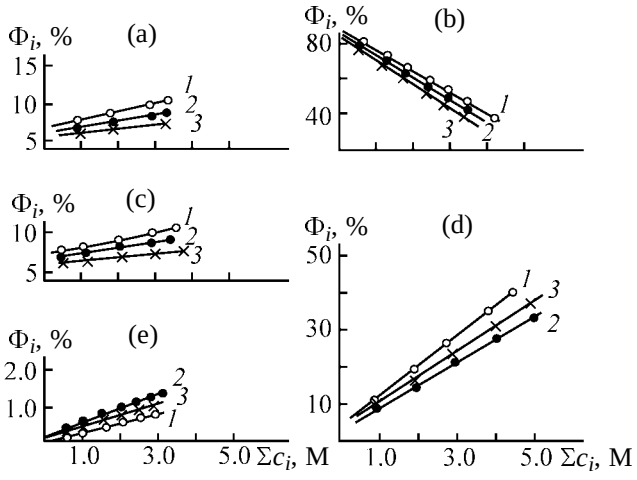

Fig. 2. Yield Φ_i of (a) hydroperoxides ROOH, (b) alcohols ROH, (c) ketones R=O, (d) acids RCO_2H, and (e) esters RCO_2R' as a fuinction of methylcyclohexanol conversion at [O_3] = 2 vol %. (Σc_i) Sum of ozonolysis products.

At low (4–7%) methylcyclohexane conversions, ozonolysis occurs to 92–93% at the tertiary C–H bond. For example, at 20°C ([O_3] = 0.5–2.5 vol %), the total yield of 1-methylcyclohexanol and 1-methylcyclohexyl hydroperoxide is 92–93%, that of other methylcyclohexanols and of methylcyclohexanones, 6–6.5%, and that of acids, 0.5–2%. The whole set of the data obtained allow us to propose the following mechanism of methylcyclohexane ozonolysis at low conversions:

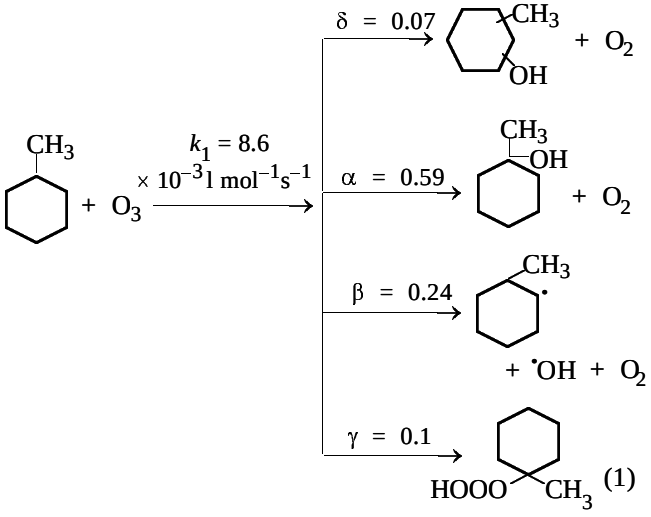

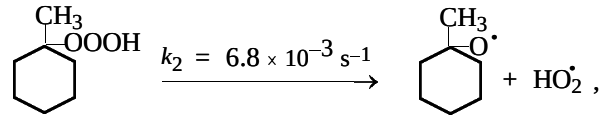

(2)

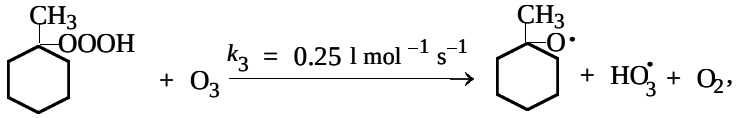

(3)

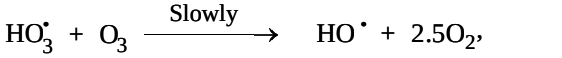

(4)

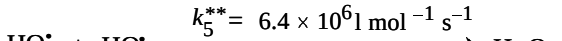

(5)

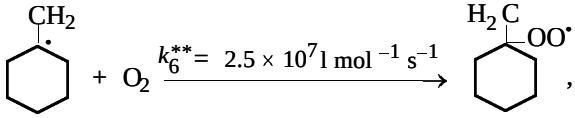

(6)

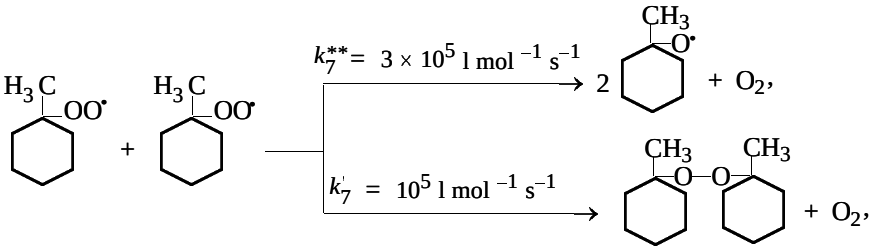

(7)

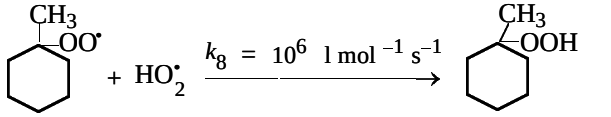

(8)

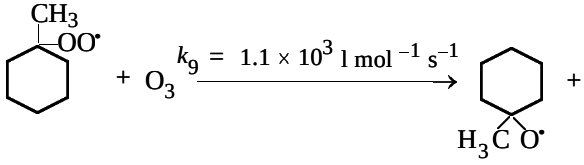

(9)

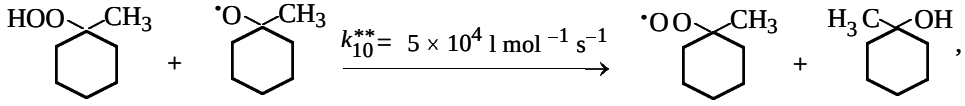

(10)

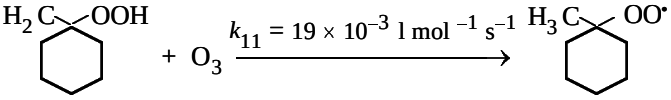

(11)

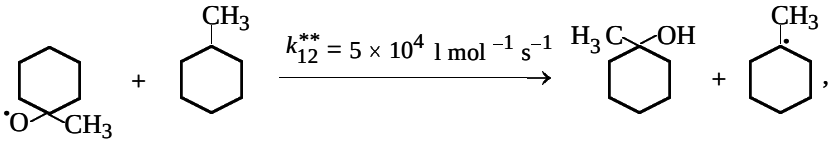

(12)

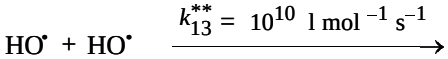

(13)

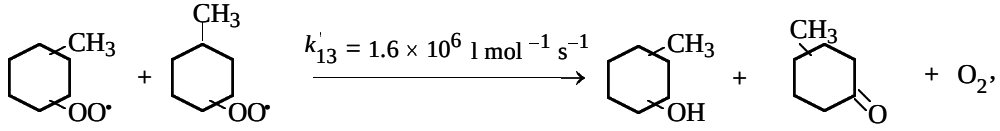

(14)

Table 2. Content of monocarboxylic acids formed by ozonolysis of methylcyclohexane ([O_3] = 4 vol %)

T, °C	α, %	τ, h	Acid, mol %				
			C_2	C_3	C_4	C_5	C_6
20	12	2	69.8	13.4	5.0	5.0	6.8
	35	4	71.0	12.5	4.7	5.0	6.5
	57	6	74.0	10.0	5.0	5.3	6.1
40	20	2	74.1	10.0	5.2	8.0	2.3
	55	4	75.0	10.0	5.1	7.0	2.9
	77	6	76.0	9.5	4.8	6.0	3.6
80	35	2	76.0	9.5	2.9	7.0	4.5
	82	4	80.0	8.3	3.5	5.0	3.0
40	26	6	87.0	1.0	Traces	Traces	12.0

Table 3. Content of keto and dicarboxylic acids formed by ozonolysis of methylcyclohexane ([O_3] = 4 vol %)

T, °C	α, %	τ, h	Acid, mol %				
			oxalic	methylsuccinic + succinic	glutaric and methylglutaric	ε-ketoenanthic	(α + β)-methyladipic
20	12	2	15.0	7.5	11.6	20.6	45.4
	35	4	13.0	7.0	12.0	18.8	49.2
	57	6	12.5	6.9	12.4	16.2	52.0
40	20	2	10.5	5.1	8.0	28.1	48.3
	55	4	8.5	4.3	10.3	27.5	49.4
	77	6	6.1	3.1	12.5	26.6	51.7
80	35	2	4.0	2.7	10.8	32.3	50.1
	82	4	2.7	2.1	11.5	30.5	53.2
40	26	6	10.0	5.9	8.3	35.1	40.7

where k^{**} are the estimated values of the constants, refined during further optimization.

The steady-state concentrations of the ith radical are determined from the condition $d[X_i]/d\tau = 0$. Taking into account the yields of products formed by the attack of ozone and radicals at the tertiary and secondary C–H bonds of the methylcyclohexane molecule, we can write

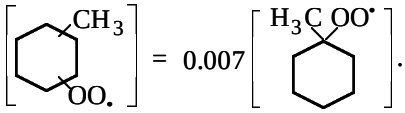

The rates of elementary reactions (1)–(14) of methylcyclohexane ozonolysis are expressed as follows: $R_1 = k_1[RH][O_3]$, $R_2 = k_2[ROOOH]$, $R_3 = k_3 \times [ROOOH][O_3]$, $R_4 = k_4[O_3][HO_3^{\cdot}]$, $R_5 = k_5[HO_2^{\cdot}] \times [HO_3^{\cdot}]$, $R_6 = k_6[O_2^{\cdot}][R^{\cdot}]$, $R_7 = k_7[RO_2^{\cdot}]^2$, $R_8 = k_8 \times [RO_2^{\cdot}][HO_2^{\cdot}]$, $R_9 = k_9[RO_2^{\cdot}][O_3]$, $R_{10} = k_{10}[ROOH] \times [RO^{\cdot}]$, $R_{11} = k_{11}[O_3][ROOH]$, $R_{12} = k_{12}[RH][RO^{\cdot}]$, $R_{13} = k_{13}[HO^{\cdot}]^2$, and $R_{14} = k_{13}[RO_2^{\cdot}]^2$.

The initial reactant concentrations are [RH] = 7.8, [O_3] = 1.3×10^{-3}, and [O_2] = 5.6×10^{-3} mol l^{-1} s^{-1}. The concentrations of the radicals are found from the following relationships:

$$[RO_2^{\cdot}] = [(2R_2 + R_4 + R_{11} + \beta R_1)/(2k_7')]^{1/2},$$

$$[R^{\cdot}] = \frac{\beta R_1 + R_{12}}{[O_2]k_6},$$

$$[^{\cdot}OH] = [(\beta R_1 + R_4 + R_{11})/(2k_{13})]^{1/2},$$

$$[HO_3^{\cdot}] = R_3/([O_3]k_4 + k_5[HO_2^{\cdot}]),$$

$$[RO^{\cdot}] = (R_2 + R_3 + 2R_7 + R_9)/(k_{10}[ROOH] + k_{12}[RH]),$$

$$[HO_2^{\cdot}] = (R_2 - R_3 + R_4)/([RO^{\cdot}]k_8).$$

The constants k_5–k_7, k_{10}, k_{12}, k_{13}, and k_{13}' were taken from [7–12], and the constants k_1, k_9, and k_{11} were measured by us in special experiments.

The rates of consumption of methylcyclohexane (RH) and accumulation of 1-methylcyclohexanol (ROH_t), 1-methylcyclohexyl hydroperoxide (ROOH), hydrogen peroxide, sum of secondary methylcyclohexanols (ROH_s), methylcyclohexanones (R=O), and hydrotrioxide (ROOOH) are described by the differential equations

$$d[RH]/d\tau = -R_1 - R_{12}, \quad d[ROH]_t/d\tau = R_{10} + R_{12} + \alpha R_1,$$

$$d[ROOH]/d\tau = R_8 - R_{10} + \alpha R_{11},$$

$$d[H_2O_2]/d\tau = R_5 + R_{13}, \quad d[ROH]_s/d\tau = \delta R_1 + k'_{13}[R'O_2^{\cdot}]^2,$$

$$d[R{=}O]/d\tau = k'_{13}[R'O_2^{\cdot}]^2, \quad d[ROOOH]/d\tau = \gamma R_1 - R_2 - R_3.$$

Integration of this sytem of differential equations allows refinement of the constants k_1–k_{13}^{**} and coefficients α, β, γ, and δ. The values of these parameters are given in the scheme of the mechanism of methylcyclohexane ozonolysis. The calculated data reasonably agree with the experiment (Figs. 1–3). The steady-state concentrations of the radicals are as follows: $[RO_2^{\cdot}] = (1.32–1.36) \times 10^{-5}$, $[RO^{\cdot}] = (3.62–3.68) \times 10^{-10}$, $[^{\cdot}OH] = (3.13–3.21) \times 10^{-8}$, $[HO_2^{\cdot}] = (5.48–5.72) \times 10^{-7}$, and $[HO] = (1.04–1.07) \times 10^{-7}$ M (τ = 10–60 min).

According to the suggested mechanism, methylcyclohexane is consumed by the nonchain and chain pathways. Linear consumption (Fig. 3) is observed only at small conversions. In the developed process, the kinetic curves of methylcyclohexane (RH) consumption are nonlinear and are described by the following equation in the entire range of reactant concentrations up to deep conversions:

$$-d\left[\text{C}_6\text{H}_{11}\text{CH}_3\right]/d\tau = k_{app}[RH] = k_{1app}[RH][O_3] + k([RH]_0 - [RH])/[RH].$$

Computer processing of the experimental data gave the following expressions: $k_{1app} = 1.25 \times 10^2 \times e^{-(25500 \pm 3500)/RT}$ l mol^{-1} s^{-1} and $k = 3.5 \times 10^{-1} \times e^{-(25500 \pm 3500)/RT}$ l mol^{-1} s^{-1}.

The bimolecular rate constant of the reaction of 1-methylcyclohexyl hydroperoxide with ozone is low. However, in the developed reaction of methylcyclohexane ozonolysis, it is possible that the associate of 1-methylcyclohexyl hydroperoxide and 1-methylcyclohexanol (their association was detected by ^{1}H NMR [13]) reacts with ozone at the same rate as does nonassociated 1-methylcyclohexyl hydroperoxide. To reveal the role of this reaction in the overall ozonolysis of methylcyclohexane, we added at the stage of the developed reaction (20°C, $[O_3]$ = 4 vol %, 30 min after the start of the experiment) ^{14}C-labeled 1-methylcyclohexyl hydroperoxide. The specific activity of the added hydroperoxide decreases (Fig. 4) owing to both its consumption and dilution with the forming nonradioactive 1-methylcyclohexyl hydroperoxide. The labeled compound transforms into the following ^{14}C-labeled products: 1-methylcyclohexanol, ε-ketoenanthic acid, and acetic acid. From variation of the specific activity of the hydroperoxide in the course of the experiment, we calculated the rates of its formation. Taking into account the experimental rates of 1-methylcyclohexyl hydroperoxide accumulation, we calculated the rates of its consumption (Fig. 4).

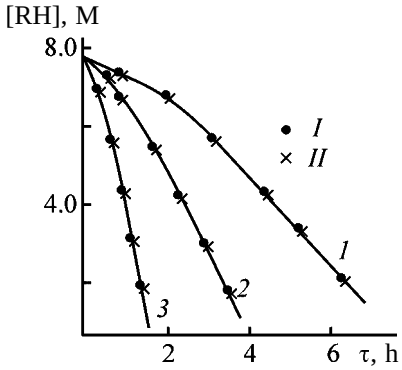

Fig. 3. Kinetic curves of consumption of methylcyclohexane RH ($[O_3] = 1.3 \times 10^{-3}$ M): (*I*) experiment and (*II*) calculation.

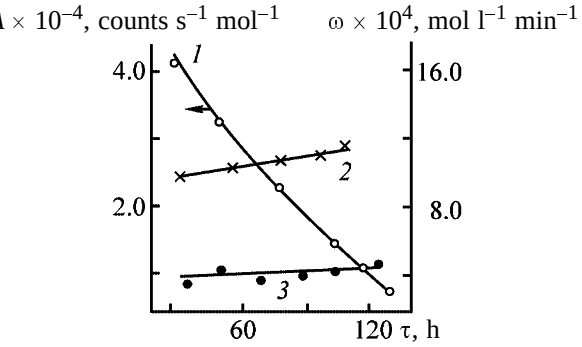

Fig. 4. Variation of the (*1*) specific activity *A* and of the rates ω of (*2*) formation and (*3*) consumption of 1-methylcyclohexyl hydroperoxide in the course of methylcyclohexane ozonolysis (20°C, $[O_3]$ = 4 vol %).

Among the products of 1-methylcyclohexyl hydroperoxide transformations, 1-methylcyclohexanol comprises only 6–7%. An increase in the rate of formation of the tertiary hydroperoxide with the conversion of

the hydrocarbon is apparently due to increase in the rate of $HO_2^{\bullet}$ generation. Unstable methylcyclohexyl hydrotrioxide may be a source of $HO_2^{\bullet}$. A decrease in the yield of hydrogen peroxide (Fig. 1), seemingly contradicting this assumption, may be due to catalysis of its decomposition with acids.

CONCLUSION

In contrast to nonselective high-temperature noncatalytic oxidation of saturated hydrocarbons containing primary, secondary, and tertiary C–H bonds, their low-temperature ozonolysis at small conversions, as demonstrated by the example of methylcyclohexane, occurs selectively at the tertiary C–H bond and yields the corresponding alcohols. The tertiary alcohols are formed by recombination of the $R^{\bullet}$ and $OH^{\bullet}$ radicals generated by primary initiation, by radical-chain transformations of tertiary hydroperoxides, and by attack of the starting substrate by $RO^{\bullet}$ radicals.

REFERENCES

1. Vikhorev, A.A., Syroezhko, A.M., and Proskuryakov, V.A., *Zh. Prikl. Khim.*, 1976, vol. 49, no. 7, pp. 1592–1597.
2. Vikhorev, A.A., Syroezhko, A.M., Proskuryakov, V.A., and Yakovlev, A.S., *Zh. Prikl. Khim.*, 1978, vol. 51, no. 11, pp. 2568–2572.
3. Vikhorev, A.A., Syroezhko, A.M., and Proskuryakov, V.A., *Zh. Prikl. Khim.*, 1977, vol. 50, no. 3, pp. 698–699.
4. Vikhorev, A.A., Syroezhko, A.M., and Proskuryakov, V.A., *Zh. Prikl. Khim.*, 1976, vol. 49, no. 3, pp. 588–592.
5. Vikhorev, A.A., Syroezhko, A.M., and Proskuryakov, V.A., *Zh. Prikl. Khim.*, 1975, vol. 48, no. 9, pp. 2059–2062.
6. USSR Inventor's Certificate 745 891.
7. Emanuel', N.M., Denisov, E.T., and Maizus, Z.K., *Tsepnye reaktsii okisleniya uglevodorodov v zhidkoi faze* (Chain Reactions of Liquid-Phase Oxidation of Hydrocarbons), Moscow: Nauka, 1965.
8. Denisov, E.T., Mitskevich, N.I., and Agabekov, V.E., *Mekhanizm zhidkofaznogo okisleniya kislorodsoderzhashchikh soedinenii* (Mechanism of Liquid-Phase Oxidation of Oxygen-Containing Compounds), Minsk: Nauka i Tekhnika, 1975.
9. Denisov, E.T., Mechanism of Liquid-Phase Homolysis of Molecules, *Itogi Nauki Tekh., Ser.: Kinet. Katal.*, 1981, vol. 9.
10. Denisov, E.T., *Konstanty skorosti gomoliticheskikh zhidkofaznykh reaktsii* (Rate Constants of Homolytic Liquid-Phase Reactions), Moscow: Nauka, 1971.
11. Emanuel', N.M., Zaikov, G.E., and Maizus, Z.K., *Rol' sredy v radikal'no-tsepnykh reaktsiyakh okisleniya organicheskikh soedinenii* (Role of the Medium in Radical-Chain Oxidation of Organic Compounds), Moscow: Nauka, 1973.
12. Antonovskii, V.L., *Organicheskie perekisnye initsiatory* (Organic Peroxide Initiators), Moscow: Khimiya, 1972.
13. Vikhorev, A.A. and Syroezhko, A.M., in *Issledovaniya v oblasti khimii i tekhnologii produktov pererabotki goryuchikh iskopaemykh* (Studies in the Field of Chemistry and Technology of Products of Fossil Fuel Processing), Leningrad: Leningr. Tekhnol. Inst. im. Lensoveta, 1977, pp. 33–37.

Russian Journal of Applied Chemistry, Vol. 76, No. 5, 2003, pp. 791–799. Translated from Zhurnal Prikladnoi Khimii, Vol. 76, No. 5, 2003, pp. 820–828.

MACROMOLECULAR CHEMISTRY AND POLYMERIC MATERIALS

Structure and Gas Separation Properties of Composite Membranes with Poly(2,2,3,3,4,4,5,5-octafluoro-*n*-amyl Acrylate) Cover Layer

S. V. Kononova, Yu. P. Kuznetsov, A. V. Shchukarev, V. N. Ivanova, K. A. Romashkova, and V. V. Kudryavtsev

Institute of Macromolecular Compounds, Russian Academy of Sciences, St. Petersburg, Russia
Mekhanobr-analit Regional Analytical Center, Close Corporation, St. Petersburg, Russia

Received November 13, 2002; in final form, March 2003

Abstract—Effect of the formation procedure on the structure and transport characteristics of poly(2,2,3,3,4,4,5,5-octafluoro-*n*-amyl acrylate)–polyamidoimide composite membranes in separation of O_2/N_2 gas mixture (air) over a wide temperature range is studied.

Studies of the structural features of multilayer polymer systems, as influencing their mass-exchange characteristics, are necessary in designing high-performance gas separation membranes. Among these systems are composite membranes (CMs) of the diffusion type, in which the surface of a microporous support with an asymmetrical cross section structure is coated from the side of a denser layer (skin layer) with a thin continuous layer of one or more polymers of different chemical nature (cover layer). If the cover layer is applied by deposition of a polymer from a dilute solution, pores of the skin layer may be partially or totally filled with this polymer. Therefore, composite membranes can be regarded as a morphologically complex multilayer object consisting of (a) polymer layer of the support with unfilled pores, (b) skin layer of the support with pores partially or totally filled with a polymer of the cover layer, and (c) cover layer over the support surface (Fig. 1).

To estimate the contribution of polymers composing a multilayer membrane to its selective transport properties, the Henis–Tripodi resistance model is used [1, 2]. According to this model, the selectivity of separation of a gas mixture (separation factor f) is controlled by the characteristics of all the nonporous layers of a composite membrane in combination (diffusion layer of a composite membrane). If the resistance of the CM cover layer to mass transfer of gases is considerably higher than that of the support, the total CM selectivity approaches that of the covering polymer. The reverse can be realized when pores of the skin layer of the support are partially or totally blocked with the covering polymer, i.e., when the support demonstrates a higher resistance to a gas flow as compared to the covering polymer. In this case, the mass transfer rate across the composite membrane is controlled by transport of gases across the support, and the separation selectivity approaches the value typical of the support polymer. As a result, the separation factor can change over a wide range from some intermediate values to those typical of the polymers composing the cover layer and the support, depending on the structure of the CM diffusion layer. Generally, the contribution of each polymer composing a composite membrane to the mass transfer can be characterized by some arbitrary parameter expressed as the product of the effective thickness of diffusion layer of this polymer (volume fraction of a given polymer in the diffusion layer) by its selectivity.

It should be pointed out that the basic principles of the resistance model were formulated without taking into account possible structural transformations in the boundary layer of the covering polymer at the support surface [3]. However, such an effect was demonstrated to occur in a series of polymer/inorganic support composites and also in polymer/polymer composites not related to membrane systems [3–5]. It was demonstrated that a polymer in such a boundary layer has a structure different from that typical of the same polymer, but in the layers more distant from the support surface. It is known also that the structural ordering in polymers, reflected in the nature of thermal (phase) transitions, has an effect on the gas permeability and selectivity of diffusion membranes [6, 7]. Par-

1070-4272/03/7605-0791$25.00

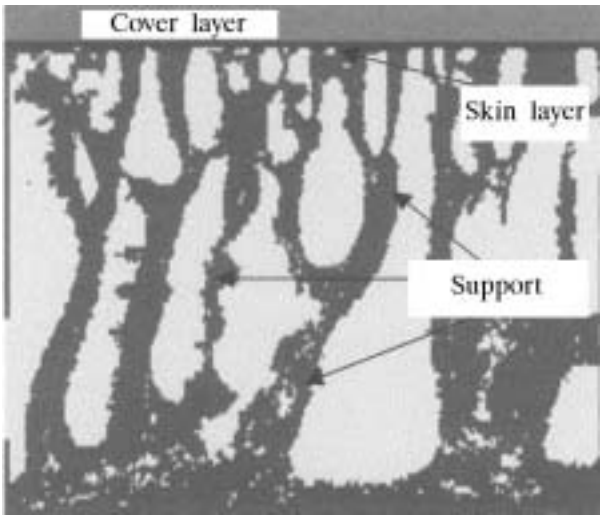

Fig. 1. Schematic representation of the cross section of a composite membrane.

ticularly, the selectivity of a diffusion membrane in separating binary gas mixtures (O_2, N_2, He, etc.) is determined by the diffusion coefficient ratio of the components to be separated, depending, therefore, on the nature of intra- and supramolecular structural organization of a polymer [8].

The selectivity of the existing diffusion CMs (gas-separation and pervaporation) is mostly consistent with that predicted by the Henis–Tripodi model [9–12]. However, for some composite membranes this was not the case [9, 11]. The most significant inconsistencies were found for CMs with cover layers from polymers having low glass transition points (T_g), especially for comb-shaped poly(2,2,3,3,4,4,5,5-octafluoro-*n*-amyl acrylate) (PFAA). Particularly, some CMs with a PFAA cover layer on the surface of an aromatic polyamidoimide (PAI) support demonstrated a higher selectivity in separating O_2 and N_2 (air) than that typical of both PFAA and the corresponding PAI taken separately. Therefore, the goal of this work is to study in more details the mechanism of selective transport of O_2/N_2 mixture across PFAA/PAI composite membranes and the effect of the structural features of a polymer of the cover layer on the transport properties.

EXPERIMENTAL

Poly(2,2,3,3,4,4,5,5-octafluoro-*n*-amyl acrylate) (T_g 248 K, MW 2.5×10^6) was synthesized according to the procedure described in [13] and used as a polymer of the cover layer. The polymer is characterized by a narrow unimodal molecular-weight distribution, as demonstrated by GPC with polystyrene as a reference.

To prepare asymmetrical porous supports, we used aromatic PAIs of the general formula

$$[–CO–R_1–CONH–R_2–NH–]_n,$$

where R_1 is a disubstituted 2-phenylisoindole-1,3-dione, and R_2 is as follows:

PAI-1

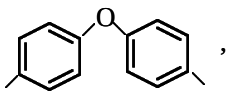

PAI-2

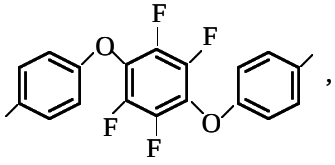

PAI-3

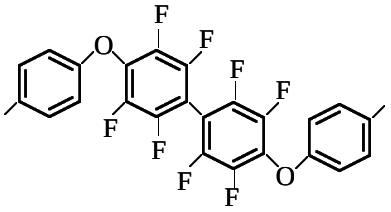

PAI-4

$–(CH_2)_3–Si(CH_3)_2–O–Si(CH_3)_2–(CH_2)_3–$
(5 mol %)

+

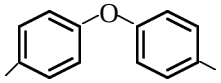

(95 mol %)

Microporous supports were prepared under similar conditions of the phase inversion process using wet molding [14]. Composite membranes were fabricated by casting a cover polymer solution on the support working surface under the conditions described elsewhere [9].

The transport properties of CMs were tested with regard to a mixture of the major components of air, O_2 and N_2, having close kinetic diameters of their molecules (3.46 and 3.64 Å, respectively) [15]. The gas permeability was determined chromatographically over the temperature range 303–393°C at a constant gas pressure loss on the membrane of 1 bar. The effective surface area of the samples was 28.3 or 5.7 cm^2.

The morphology of CMs was studied by the low-temperature chip method using scanning electron microscopy and also by the Cr–C replication of the surfaces using transmission electron microscopy [9, 15]. The cover layer thickness was estimated by

Table 1. Transport characteristics of composite membranes and polymers composing them at 303 K

Parameter	Samples formed on indicated PAI supports									no 10, PFAA**
	no. 1	no. 2*	no. 3	no. 4	no. 5	no. 6, PAI-2	no. 7, PAI-3	no. 8	no. 9	
	PAI-1 (f** = 5.1)					(f = 1.5)	(f = 2.5)	PAI-4 (f = 2.3)		
Concentration of covering polymer solution, wt %	2	2	2	5	5	2	2	2	2	
Number n of coating stages	1	1	2	1	2	2	1	1	2	–
Thickness of covering polymer layer l_1, μm	2	2	8	4	22	4	3.5	2	–	≥40
Permeability $(P/l) \times 10^6$, $cm^3\ cm^{-2}\ s^{-1}\ cm^{-1}$ Hg:										
for O_2	0.56	0.56	0.25	0.49	0.39	3.63	2.01	0.69	0.77	–
for N_2	0.19	0.16	0.05	0.09	0.04	1.04	0.44	0.13	0.09	–
$f(O_2/N_2)$	3.0	3.5	5.15	5.4	7.4	3.5	4.6	5.2	8.2	2.8
$F(O_2/N_2)$***	5.9				10.0	3.7				

* Sample is identical to sample no. 1 after heating to 393 K and keeping under normal conditions for 20 h.
** Characteristics of homogeneous films.
*** Obtained just after cycling (heating to 393 K–cooling to 303 K).

averaging values measured on various areas of the membrane.

X-ray photoelectron spectra were recorded on a PHI 5400 electron spectrometer (Perkin–Elmer) using $MgK_{\alpha_{1,2}}$ excitation. The operating vacuum in the spectrometer was 2×10^{-8} torr. The thickness of analyzable layer was 100 Å and less. The binding energy (E_b) scale was calibrated by C1*s* line of the benzene ring (E_b 284.7 eV [16]). Binding energies were determined to within 0.1 eV. The quantitative analysis was based on the integral intensities of photoelectron peaks and on the ionization cross sections included in the Perkin–Elmer software.

The SEM results revealed similar morphology of all PAI supports used [9, 14, 15]. PAI1–PAI-4 supports have finger-shaped pores in the base cross section, tapering in the direction of the skin layer surface (working surface of the support). According to the SEM data, the pores in the skin layer are no more than 200 Å in diameter. The use of the TEM surface replication method allowed more precise determination of the mean pore size on the surfaces of PAI-1 and PAI-3 supports (50 and 125 Å, respectively, at a broad spectrum of the pore size distribution) [15]. All the supports demonstrate similar surface topography. However, on passing from PAI-1 to fluorine-containing supports, the pore size somewhat increases and their profile becomes more perfect. The characteristics of pores of the surfaces, controlling the resistance of the supports to mass transfer, correlate with the gas permeability of the supports for N_2, which was found to be 4.1×10^{-3}, 95.2×10^{-3}, and 13.6×10^{-3} $cm^3\ cm^{-2}\ s^{-1}\ cm^{-1}$ Hg for PAI-1, PAI-2, and PAI-3, respectively. Similar correlation was also observed for PFAA–PAI composite membranes with close thicknesses of PFAA cover layers, whose gas permeability increased in the order PAI-1 < PAI-3 < PAI-2 (see results below). This result suggests that PFAA, having higher molecular weight, only insignificantly penetrates into pores of the skin layers of the PAI supports.

All the composite membranes under consideration have thin uniform layers of a covering polymer, characterized by a smooth surface of the PFAA layer and distinct interface with the support (with no remarkable filling of pores of the skin layer with the covering polymer). This allows application of the TEM data to estimating the effective thickness of the cover layer of composite membranes.

The transport properties of CMs in separation of the O_2/N_2 mixture (air) were analyzed in terms of the Henis–Tripodi resistance model. Characteristics of PFFA–PAI composite membranes and homogeneous films of polymers composing these membranes, determined under similar conditions, are given in Table 1. First of all, it should be pointed out that the selectivity coefficients $f(O_2/N_2)$ of all the composite membranes are higher than that typical of the covering polymer (f(PFAA) = 2.8). Increasing thickness of the cover

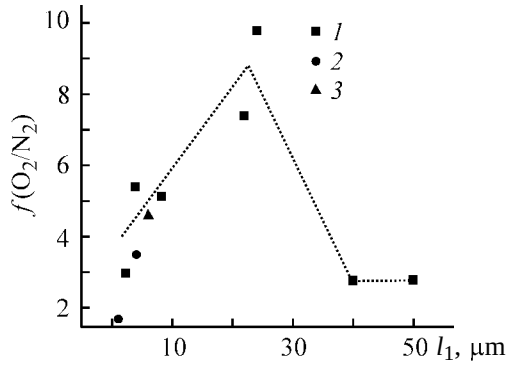

Fig. 2. Selectivity coefficient $f(O_2/N_2)$ as a function of the thickness l_1 of the cover layer of PFAA–PAI composite membranes. Support: (*1*) PAI-1, (*2*) PAI-2, and (*3*) PAI-3.

layer l_1 results in decreasing permeability of CM. In this case, for PFAA–PAI-1, PFAA–PAI-2, and PFAA–PAI-3 membranes, the nitrogen permeability decreases more rapidly than the oxygen permeability, resulting in a considerable increase in f from 3 to about 10. On the contrary, for PAI-4 coated with PFAA in n stages, increase in the selectivity is associated with increasing permeability for oxygen against the background of decreasing permeability for nitrogen.

These trends are clearly demonstrated in Fig. 2 in which f is plotted against l_1 for PFAA–PAI membranes. Analysis of this dependence is necessary not only for determining the general trend of f, but also for clarifying the question about predominant effect of the cover layer thickness on the selectivity of composite membranes. The dependence with a maximum, observed for PFAA–PAI-1, is consistent, in general, with that typical of the known composite membranes with cover layers from low-selective elastomers [1, 9, 11, 17–20]. However, the position of the maximum is remarkably different in our case. According to the resistance model, this position corresponds to the minimal effective thickness of the cover layer (sufficient for complete covering of the pores on the support surface, i.e., for formation of a diffusion layer of the composite membrane). Table 1 shows that, in the case of PFAA–PAI-1, this condition is met at l_1 = 4 μm (f > 5.1). Since for all the membranes of the PFAA–PAI-1 series, at $l_1 \geq 4$ μm, the total contribution of the support and skin layer (including pores covered by PFAA) to the total resistance of the composite membrane is constant, it should be expected that, with increasing l_1 within the experimental range, the selectivity will vary monotonically, tending to the value typical of PFAA (f = 2.8), rather than pass through an extremum. This is associated with increase in the volume fraction of the less selective polymer (PFAA) in the diffusion layer of CM and its contribution to the transport. However, actually, at l_1 = 22–30 μm the dependence has a maximum of the selectivity, whose values is considerably higher than that of PAI-1 (f = 7.4 at l_1 = 22 μm against 5.1 for PAI-1). At such a thickness of elastomer cover layers, the separating characteristics of the known CMs deteriorate, approaching those typical of the covering polymers [17–20]. At the same time, in the case of PFAA–PAI-1 composite membranes, the decrease in the selectivity to the value typical of PFAA (f = 2.8) is observed only at l_1 = 30–40 μm.

It should be pointed out that single coating of a PAI-1 skin layer with 2 wt % PFAA provides formation of a 2-μm cover layer, while two-stage coating gives approximately 8-μm cover layer. With 5 wt % PFAA, we also observed nonadditive increase in l_1 (4 μm at n = 1 and 22 μm at n = 2). Furthermore, small increase in the contact time of the support surface and the polymer solution in the course of second coating with 5 wt % PFAA results in formation of a 24-μm cover layer, the selectivity of the composite membrane being considerably increased (f = 9.8).

In the case of PAI-2, under similar conditions (n = 1, c = 2 wt %), a thicker cover layer is formed (about 1 μm, Fig. 2), which, evidently, is associated with larger pore size in the skin layer. After recoating, l_1 increases nonadditively from 1 to 4 μm, but to a lesser extent than with PAI-1. In the case of a PAI-3 support, at n = 1 and c = 2 wt %, a thicker cover layer is formed (about 3.5 μm), though the mean pore size on the PAI-3 support is larger as compared to the PAI-1 support. At the same time, PFAA–PAI-3 composite membranes are more selective than PFAA–PAI-1 membranes prepared at the same n and c.

Table 1 shows that, at close l_1 of about 4 μm, the selectivity of PFAA–PAI membranes increases in the order PAI-2 < PAI-3 < PAI-4 < PAI-1, for all the composite membranes being higher as compared to the corresponding PAI. The PFAA cover layers formed on various supports under similar conditions (same n and c, which corresponds to similar contribution of PFAA to formation of the effective diffusion layer of CM) differ from each other not only in the thickness, but also in the permeability for nitrogen (corrected for the transport characteristics of the support). Presumably, these differences are caused by the transport characteristics of the diffusion layers.

The contradictory results noted above can be interpreted with the assumption that PFAA cover layers formed on various PAI supports differ in the nature

and degree of structural organization. The observed trends are associated, evidently, not so much with participation of the polymer of the support in separation, but with the features of the supramolecular structure of PFAA in the cover layers of the composite membranes under consideration. Simultaneous considerable increase in f and l_1 on passing to two-stage coatings and also the trends in l_1 as a function of n suggest that these effects are caused not by compaction of the cover layer, but by formation of more ordered structure of the PFAA diffusion channels capable of distinguishing molecules of gases even close in size.

Evidently, in the stage of formation of the cover layer by adsorption of PFAA from a dilute solution, a structure is formed on the PAI support surface, which differs in the degree of ordering from that typical of the covering polymer in the bulk. Based on the general views of the dynamics of adsorption of macromolecules [4], it may be suggested that the structural ordering in the PFAA cover layer is controlled by just the adsorption structure formed in the course of contacting the support with a PFAA solution and fixed as a condensed cover layer (so-called primary structural effect).

This hypothesis is supported by the published data [21, 22] on structural self-organization of PFAA in both a solution and condensed state. X-ray diffraction study of PFAA showed that, despite the lack of fragments characterized by a remarkable level of nonuniformity, the X-ray diffraction pattern of amorphous PFAA demonstrates a definite order in arrangement of the backbone and side chains of the polymer. Having a considerably lower degree of ordering, the structure of amorphous PFAA in a continuous film is similar to that of its regular homologs with n 8 or 10, characterized by mutual arrangement of the side chains with formation of a hexagonal lattice in the plane perpendicular to the axis of the side difluoromethylene chain (mean diameter 5.7 Å). Based on the concept of the mesomorphic structure of comb-shaped polymers at $n = 10$, a 3D model was proposed, involving layers formed by antiparallelly arranged side groups.

Figure 3 shows the temperature dependences of the selectivity of PFAA–PAI-1 composite membranes with a 2-μm cover layer in the first (Table 1, sample no. 1) and second cycles of thermal treatment (Table 1, sample no. 2). As seen, the dependences have a maximum in both thermal cycles. The selectivity coefficients f determined for PFAA–PAI-1 composite membranes (sample nos. 1 and 5) just after the cycle heating to 393 K–cooling to the initial temperature are

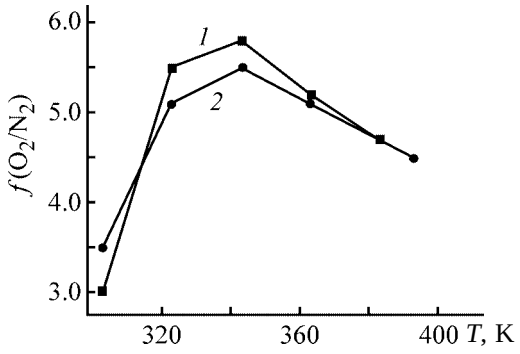

Fig. 3. Selectivity coefficient $f(O_2/N_2)$ of PFAA–PAI composite membrane (l_1 = 2 μm) as a function of the temperature T. (*1*) First and (*2*) second heating–cooling cycles.

given in Table 1. In this case we obtained the selectivity coefficients considerably higher than those before heating. At the same time, after the samples were heated, cooled, and held at 293 K for about 20 h, f returned to nearly the initial values (Fig. 3, curve *1*) [after the second thermal cycle and exposure to 293 K, f(303 K) = 3.2]. This effect is probably due to thermal transitions in the polymers composing the membrane. Since the covering polymer (PFAA) is characterized by a low glass transition point (T_g = 248 K), and that of the polymer of the support (PAI-1) (513 K) is much higher than the experimental temperature range studied in this work, one can speak of a characteristic thermal transition in just the PFAA cover layer. Evidently, the increase in the thermal mobility of the macromolecules, generally leading to regularly decreasing selectivity, in this case is compensated by some additional transformation of the supramolecular organization of PFAA in the cover layer (the secondary structural effect).

If the structuring mode in the cover layer really depends on the nature of the supporting polymer, this effect should be manifested in the temperature dependences of the selectivity of PFAA–PAI composite membranes with PAI-1–PAI-4, whose study, therefore, is of a particular interest.

The temperature dependences of $f(O_2/N_2)$ and P/l for PFAA–PAI-1 composite membranes with various l_1, and also for a PFAA continuous film formed on an inert support are given in Fig. 4A. The separating capacity of PFAA gets worse with heating, which is typical of homogeneous polymeric membranes, particularly those having a low T_g. For PFAA–PAI composite membranes, the $f(O_2/N_2)$–T curves have a maximum, and, starting from 343 K, f monotonically decreases in parallel to the curve observed for PFAA

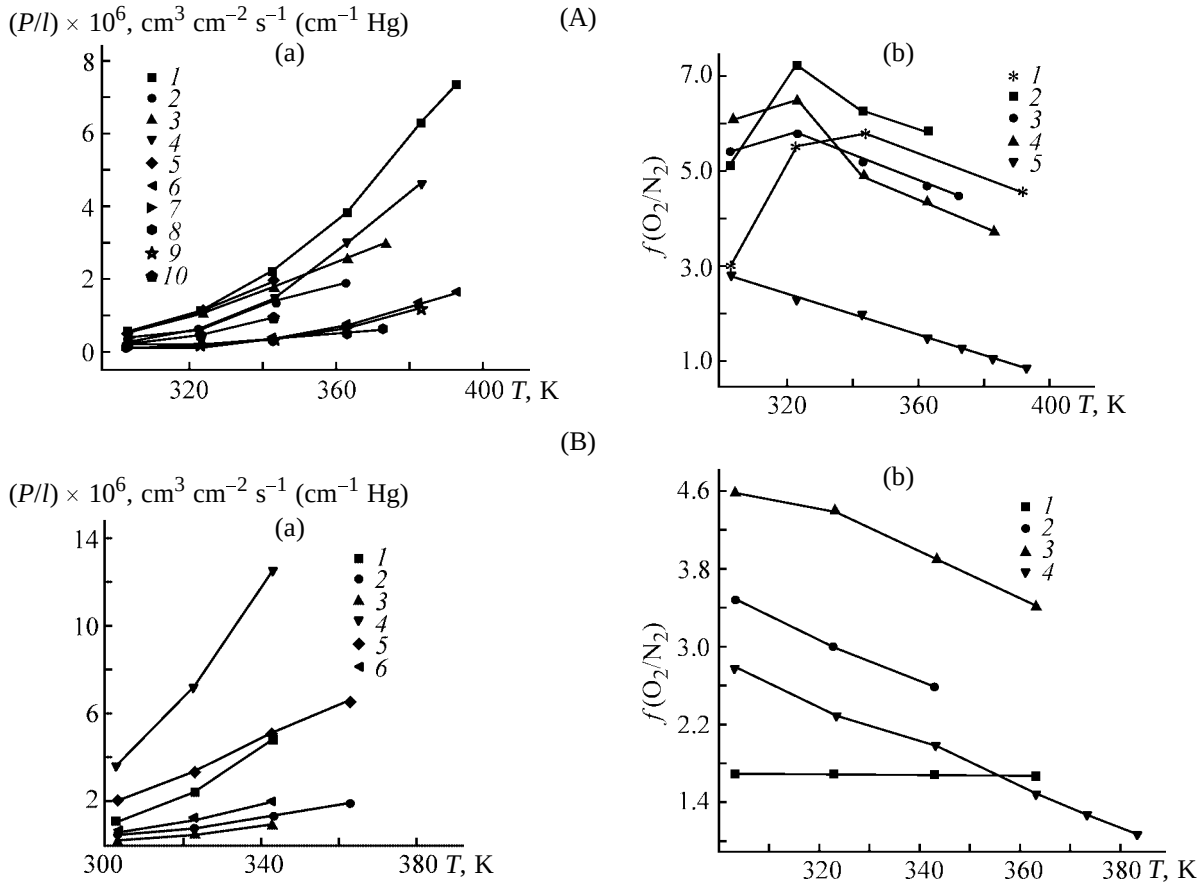

Fig. 4. Temperature dependences of (a) permeability P/l and (b) selectivity coefficient $f(O_2/N_2)$ of (A) PFAA–PAI-1 and (B) PFAA–PAI-2 and PFAA–PAI-3 having various thickness of the cover layers. (*T*) Temperature (K); the same for Fig. 5. (A) (a) P/l: (*1*–*5*) for O_2 and (*6*–*10*) for N_2; *c* (wt %): (*1, 2, 6, 7*) 2, (*3, 4, 8, 9*) 5, and (*5, 10*) continuous PFAA film; *n*: (*1, 3, 6, 8*) 1 and (*2, 4, 7, 9*) 2. (b) *c* (wt %): (*1, 2*) 2, (*3, 4*) 5, and (*5*) continuous PFAA film. (B) (a) P/l: (*1*–*3*) for N_2 and (*4*–*6*) for O_2; *c* (wt %): (*1, 2, 4, 5*) 2 and (*3, 6*) continuous PFAA film; *n*: (*1, 4*) 2 and (*2, 5*) 1; (*1, 4*) PAI-2 and (*2, 5*) PAI-3. (b) *c* (wt %) (*1, 3*) 2 and (*4*) continuous PFAA film; *n*: (*1, 3*) 1 and (*2*) 2; (*1, 2*) PAI-2 and (*3*) PAI-3.

(Fig. 4A). All the composite membranes of this series demonstrate higher selectivity as compared to the covering polymer in the bulk. The behavior of the curves in Fig. 4Ab (including the position of the maximum) reveals that heating to 343 K initiates transformation of the initial supramolecular structure of the cover layer of each CM (l_1 = 2–24 μm) into even more ordered "secondary" structure. It is clear that the observed effect cannot be related to some irreversible process, for example, removal of the residual solvent from the membrane, since the temperature dependences of *f* are similar in both the first and second heating–cooling cycles, as was demonstrated even for CM with l_1 = 2 μm, in which the pores of the skin layer are blocked with PFAA incompletely, and the selectivity at 303 K does not exceed that of PAI-1 (3.0 and 5.1, respectively) (Fig. 4).

The only conclusion that can be made from the above results is that some structural transformation of PFAA occurs in the cover layers of all the PFAA–PAI series studied (primary and secondary structural effects). However, it remains unclear whether the boundary effect is the only cause for ordering and whether the chemical nature of the supporting polymer and, therefore, the structural and energy characteristics of the support surface influence the primary and secondary effects in the PFAA cover layer. If it is the boundary effect that controls formation of the cover layer, the temperature dependences of $f(O_2/N_2)$ and P/l for PFAA–PAI-2, PFAA–PAI-3, and PFAA–PAI-4 should be similar to those for PFAA–PAI-1.

Figure 4B shows the temperature dependences of $f(O_2/N_2)$ and P/l for PFAA–PAI-2 and PFAA–PAI-3 composite membranes having practically identical thickness of the cover layer [4 and 3.5 μm, respectively, Table 1)]. On passing from PAI-2 to PAI-3, the permeability of the resulting membranes decreases, and the selectivity considerably increases. However,

generally, all the temperature dependences of the selectivity are parallel to the curve typical of PFAA (Fig. 5). Therefore, the range of thermal transformation (secondary structural effect) in lacking in the cases of PFAA–PAI-2 and PFAA–PAI-3, which, in comparison with data on PFAA–PAI-1 (Fig. 5), suggests that the structural organization of the coverung polymer depends on the chemical nature of the supporting polymer.

The same conclusion follows from comparative analysis of the transport properties of composite membranes formed on PAI-I and PAI-4 supports. Sample nos. 1 and 3 (PFAA–PAI-1) and 8 and 9 (PFAA–PAI-4) (Table 1) were prepared under similar formation conditions. Despite higher permeability and close thickness of the cover layer, PFAA–PAI-4 membranes are considerably more selective under the same conditions. The P/l–T curves (Fig. 5) show that, in contrast to PFAA–PAI-1, PFAA–PAI-4 membranes are characterized by higher permeability for oxygen. On passing from PFAA–PAI-1 to PFAA–PAI-4, the behavior of the temperature dependences of the selectivity changes. Above 343 K, the $f(O_2/N_2)$–T curves demonstrate no parallelism not only with the corresponding curves for PFAA–PAI-1, but also with the curves observed for the covering polymer. It may be suggested that membranes of the PFAA–PAI-4 type have cover layers in which the PFAA ordering mode strongly differs from that in PFAA on PAI-1–PAI-3 supports as well as in a continuous PFAA film.

Therefore, comparative analysis of the transport properties of PFAA–PAI composite membranes with PAI-1–PAI-4 supports and also of PFAA films reveals that the structural order levels in the cover layers on various supports are considerably different, in all cases differing from that characteristic of PFAA in the bulk. Formation of PFAA layers of different structural organization is reflected in the transport characteristics of the resulting composite membranes and cannot be interpreted by the boundary effect only. Evidently, changing chemical nature of the polymer on passing from PAI-1 to fluorine- and silicon-containing supports, accompanied by modification of the chemical structure of the surface, results in changes in the concentration and (or) nature of adsorption sites on this surface. The latter controls formation of the primary adsorption structure of PFAA in the boundary layer of each CM series, which, in its turn, governs the structural organization of PFAA layers more distant from the boundary.

Comparative angle-resolved XPS study of the boundary layers of PAI-1 and PAI-2 supports and

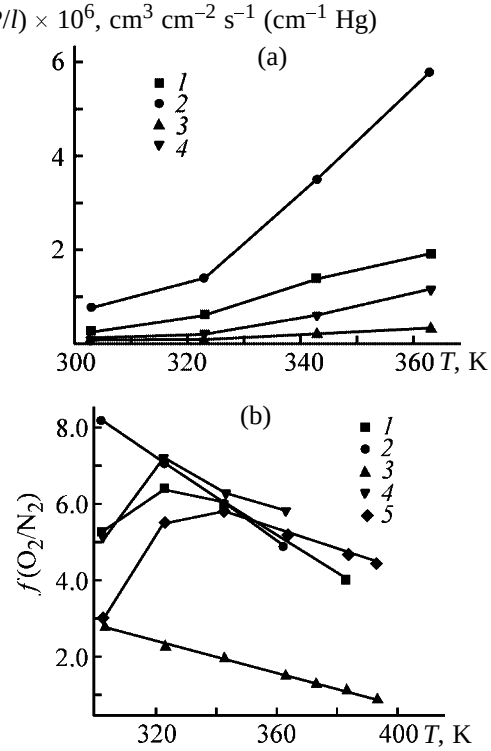

Fig. 5. Temperature dependences of (a) permeability P/l and (b) selectivity coefficient $f(O_2/N_2)$ of composite membranes with PAI-1 and PAI-4. (a) c = 2 wt %, n = 2; P/l: (*1*, *2*) for O_2 and (*3*, *4*) for N_2; (*1*, *3*) PAI-1 and (*2*, *4*) PAI-4. (b) c (wt %): (*1*, *2*, *4*, *5*) 2 and (*3*) continuous PFAA film; n: (*1*, *5*) 1 and (*2*, *4*) 2; (*1*, *2*) PAI-4 and (*4*, *5*) PAI-1.

PFAA–PAI model composite films with cover layers up to 100 Å thick allowed more accurate determination of the nature of the active sites on the working surface of the supports as well as the formation mode of the PFAA primary structure at the PAI-I surface. Varying the photoelectron sampling angle α, we performed layer-by-layer examination of the atomic composition near the surface of each sample at a depth of 96, 87, 70, and 26 Å, which correspond to sampling angles of 75°, 60°, 45°, and 15°, respectively. The chemical composition of the supports were demonstrated to be identical to that of the free surfaces, corresponding to the stoichiometry of PAI-1 or PAI-2 molecular units. As seen from Table 2, the atomic compositions of the surfaces of PAI-1 and PAI-2 supports are identical to those of deeper boundary layers (skin layers). Therefore, in the skin layers of the PAI-1 and PAI-2 supports, the macromolecules are arranged coplanarly to planes of the corresponding surfaces, which is consistent with X-ray diffraction data obtained for PAI-1-based films and supports [23].

Study of PFAA–PAI-1 film composites showed considerable differences between the state of the car-

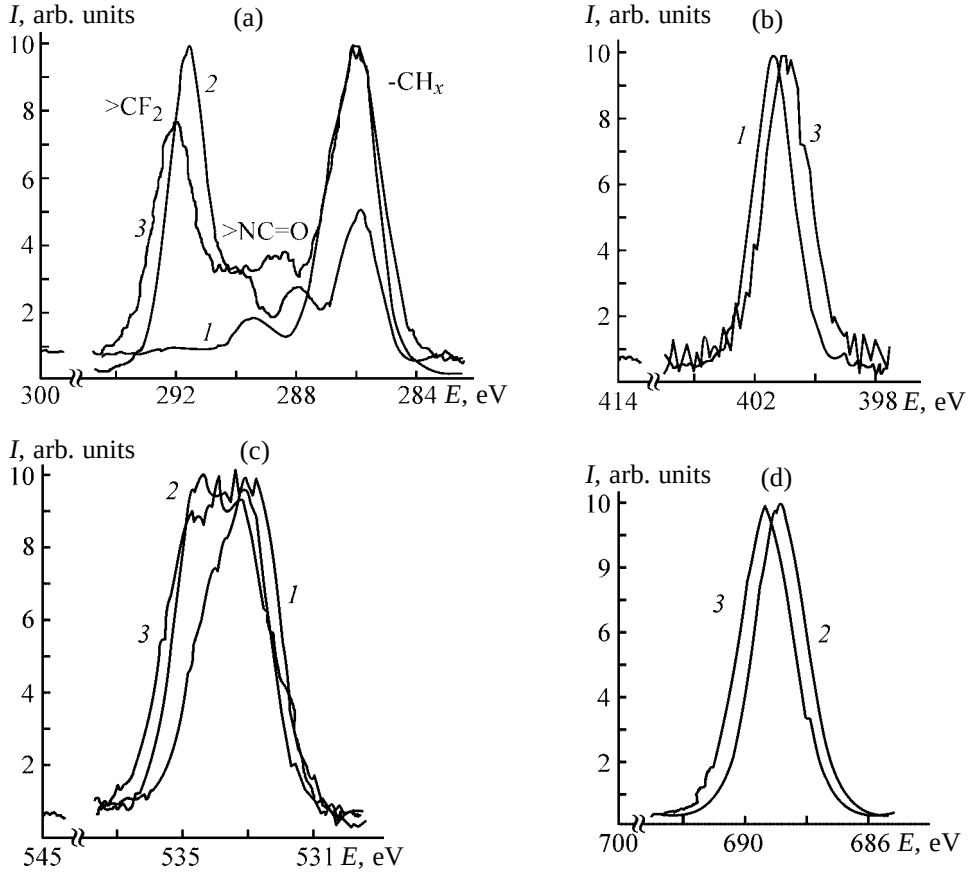

Fig. 6. X-ray photoelectron spectra of 1*s* core levels of (a) C, (b) N, (c) O, and (d) F in (*1*) PAI-1, (*2*) PFAA, and (*3*) PFAA–PAI-1 model composite. (*I*) Intensity and (*E*) binding energy.

bon atoms in both $-CF_2-$ groups of polyfluoroalkyl acrylate and –CON< groups of PAI near the PFAA/PAI-1 boundary ($\alpha = 45°$) and the state of these atoms on the surface of continuous films of the corresponding polymers. The chemical shifts of photoemission lines of these atoms are shown in Fig. 6a. The PE spectrum of nitrogen (contained in PAI-1 molecule only) (Fig. 6b) reveals that the investigated layer of the composite is at the PAI/polyfluoroacrylate boundary, as lines of the both polymers are observed. Change in the electronegativity (EN) of the nitrogen atoms of the >NC=O group (from 400.4 eV in PAI-1 to 400.0 eV in the composite) and of fluorine (from 688.8 eV in PFAA to 689.2 eV in the composite) at the cover layer/support boundary (Figs. 6b and 6d, respectively) relative to their characteristic values on the surface of PFAA and PAI-1 films is accompanied by decrease in the electron density on the carbon atoms (Fig. 6a) in $>CF_2$ groups (290.7 eV in PFAA and 292.2 eV in the composite) and also in EN of the carbonyl carbon (288.4 eV in PAI-1 and 289.2 eV in the composite). Changes in EN of the carbonyl oxygen from 531.8 eV in PAI-1 to 531.3 eV in the composite and from 532.0 eV in PFAA to 532.5 eV in the composite, and also changes in EN of oxygen in –C–O–C– (*E* 533.3 eV) and $-O-C-CF_2-$ groups (*E* 533.6 eV) to the state with *E* 534.0 eV also show that, at the interface, interaction of the electronic shells of fluorine (electron donor) and nitrogen atoms (electron acceptor), accompanied by redistribution of the electron density of neighboring atoms, is the most probable.

Table 2. Atomic composition of the boundary layers of PAI-1 and PAI-2 asymmetrical supports, determined at various photoelectron sampling angles α

PAI	α, deg	Content, %			
		C	O	N	F
PAI-1	15	76.00	15.65	8.35	–
	45	75.50	15.68	8.81	–
	75	76.22	14.72	9.06	–
PAI-2	15	68.36	12.81	5.31	13.52
	60	68.43	12.60	5.43	13.50

Finally, the results obtained reveal that (1) formation of PFAA cover layer in the course of adsorption from a dilute solution is accompanied by orientation of the fluorine-containing fragments (in the boundary layer at the support) in the direction to the PAI-1 surface; (2) the main adsorption sites on the support surface are, most likely, PAI-1 fragments containing >NC=O groups; and (3) the observed changes in the electronegativity of the fluorine and nitrogen atoms suggest the formation of stable adsorption structures, i.e., of the PFAA primary structure at the boundary with the support (primary structural effect).

CONCLUSIONS

(1) Comparative analysis of the experimental data shows that, in designing high-performance composite membranes of the diffusion type using the Henis–Tripodi resistance model, it is necessary to take into consideration not only the morphological features of the diffusion layers of membranes and selectivity and transport characteristics of polymers used, but also possible structural effects in the boundary layers of the covering polymer. The diffusion layers of composite membranes, formed in the course of adsorption interaction of a polymer from a dilute solution with the surface of a support based on another polymer, in some cases can demonstrate a structural organization different from that typical of the cover polymer in the bulk.

(2) It was demonstrated with an example of poly(2,2,3,3,4,4,5,5-octafluoro-*n*-amylacrylate)–polyamidoimide composite membranes that highly selective diffusion layers, particularly of low-selective elastomers, can be realized on the support by optimization of the chemical structure of PAI, i.e., by varying the nature and (or) concentration of adsorption sites on the support surface and, therefore, its energy characteristics. This allows manufacture of diffusion membranes whose separating characteristics differ from those predicted theoretically on the basis of the resistance model in that they surpass the selectivity of all individual polymers composing the composite membrane.

ACKNOWLEDGMENTS

The authors are grateful to D.M. Amirkhanova (Russian Research Center Kurchatov Institute) for his help in examination of the transport properties of continuous films of polyamidoimides, and also to T.E. Sukhanova and O.V. Kudasheva (Institute of Macromolecular Compounds, Russian Academy of Sciences) for providing micrographs.

REFERENCES

1. US Patent 4230463.
2. Henis, J.M.S. and Tripodi, M.K., *J. Membrane Sci.*, 1981, vol. 8, pp. 233–246.
3. Malinskii, Yu.M., *Usp. Khim.*, 1970, vol. 39, no. 8, pp. 1511–1536.
4. *Fizikokhimiya mnogokomponentnykh system* (Physical Chemistry of Multicomponent Systems), Lipatov, Yu.S., Ed., Kiev: Naukova Dumka, 1986, vol. 1.
5. Dolinnyi, A.I., *Vysokomol. Soedin., Ser. A*, 1990, vol. 32, no. 9, pp. 1938–1945.
6. Durgar'yan, S.G., Yampol'skii, Yu.P., and Plate, N.A., *Usp. Khim.*, 1988, vol. 57, no. 6, pp. 974–989.
7. Teplyakov, V.V., *Zh. Vses. Khim. O–va.*, 1987, vol. 32, no. 6, pp. 693–697.
8. Chalykh, A.E. and Zlobin, V.B., *Usp. Khim.*, 1988, vol. 57, no. 5, pp. 903–928.
9. Kononova, S.V., Kuznetsov, Yu.P., Sukhanova, T.E., *et al.*, *Vysikomol. Soedin., Ser. A*, 1993, vol. 35, no. 2, pp. 216–222.
10. Kononova, S.V., Kuznetsov, Yu.P., Apostel, R., *et al.*, *Angew. Macromol. Chem.*, 1996, vol. 237, no. 4122, pp. 45–53.
11. Kononova, S.V. and Kuznetsov, Yu.P., *Preprints of the Int. Congr. on Membranes and Membrane Processes (ICOM'93)*, Heidelberg (Germany), August 1993, pp. 2–33.
12. Kuznetsov, Yu.P., Kononova, S.V., Kruchinina, E.V., *et al., Zh. Prikl. Khim.*, 2001, vol. 74, no. 8, pp. 1302–1307.
13. Rostovskii, E.N. and Rubinovich, L.D., *Karbotsepn. Soedin.*, 1963, no. 4, pp. 140–143.
14. RF Patent 2129910.
15. Sukhanova, T.E., Kudasheva, O.V., Kononova, S.V., *et al.*, Abstracts of Papers, *2nd Int. Symp. "Molecular Order and Mobility in Polymer Systems,"* St. Petersburg (Russia), May 21–24, 1996, p. 173.
16. Beamson, G. and Briggs, D., *The XPS of Polymers. Database*, Surface Spectra, 2000.
17. Stern, S.A., Shah, V.M., and Hardy, B.J., *J. Polym. Sci., Ser. B*, 1987, vol. 25, pp. 1263–1298.
18. Karode, S.K. and Kulkarni, S.S., *J. Membrane Sci.*, 1997, vol. 127, pp. 131–140.
19. Marchese, J., Ochoa, N., and Pagliero, C., *J. Chem. Technol. Biotechnol.*, 1995, vol. 63, pp. 329–336.
20. Chen, Y., Miyano, T., Fouda, A., and Matsuura, T., *J. Membrane Sci.*, 1990, vol. 48, pp. 203–219.
21. Budovskaya, L.D., Ivanova, V.N., Oskar, L.N., *et al.*, *Vysokomol. Soedin., Ser. A*, 1990, vol. 32, no. 3, pp. 561–565.
22. Budovskaya, L.D., Boyarchuk, Yu.M., Denisov, V.M., *et al.*, *Vysokomol. Soedin., Ser. A*, 1992, vol. 34, no. 7, pp. 98–103.
23. Baklagina, Yu.G., Sidorovich, A.V., Urban, I., *et al.*, *Vysokomol. Soedin., Ser. B*, 1989, vol. 30, no. 1, pp. 38–42.

Russian Journal of Applied Chemistry, Vol. 76, No. 5, 2003, pp. 800–803. Translated from Zhurnal Prikladnoi Khimii, Vol. 76, No. 5, 2003, pp. 829–832.

MACROMOLECULAR CHEMISTRY AND POLYMERIC MATERIALS

Statistical Analysis of Microdomain Ensembles on the Surface of Poly(4,4'-oxyphenylenepyromellitimide) Films in the Course of Imidization

S. V. Bronnikov, T. E. Sukhanova, T. K. Meleshko, and M. A. Mikhailova

Institute of Macromolecular Compounds, Russian Academy of Sciences, St. Petersburg, Russia
Tver State University, Tver, Russia

Received December 15, 2002; in final form, February 2003

Abstract—The statistical ensembles of supramolecular formations (microdomains) on the surface of films of the polyamido acid derived from pyromellitic dianhydride and 4,4'-oxydiphenylenediamine and evolution of these ensembles in the course of thermal and chemical imidization were studied using the reversible aggregation model. The regular trends in variation of the distribution parameters (aggregation energy and mean microdomain size) in the course of thermal imidization were established. The distribution parameters were compared for polyimide films prepared by thermal and chemical imidization.

Aromatic polyimides (PIs) are heat-resistant polymers; they are used in various branches of engineering [1]. The most common polyimide material is that derived from pyromellitic dianhydride and 4,4'-oxydiphenylenediamine (PI PM). PI PM films are produced in Russia and the United States under the trade names Arimid and Kapton, respectively.

PI items are usually prepared in two steps. In the first step, the prepolymer, polyamido acid (PAA), is prepared in an aprotic solvent; in the second step, PAA items are heated stepwise to 300–400°C in a vacuum or in an inert medium (thermal imidization), or are kept in a dehydrating medium (chemical imidization) [1].

The morphology of PI PM films and its evolution in the course of solid-phase thermal transformation PAA → PI have been fairly well studied by X-ray scattering and electron microscopy [2, 3]. In particular, the scale-invariant nature of the supramolecular structure of the PI PM film surface was established using the fractal approach [3].

In this work, we studied by transmission electron microscopy the statistical ensembles of microdomains on the PAA PM film surface and their evolution in the course of thermal and chemical imidization.

EXPERIMENTAL

We studied films of PAA PM and its imidization product, PI PM, formed by the reaction

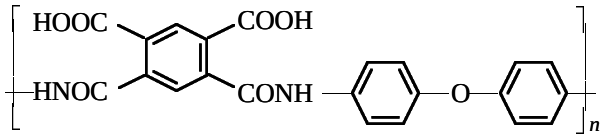

PAA PM

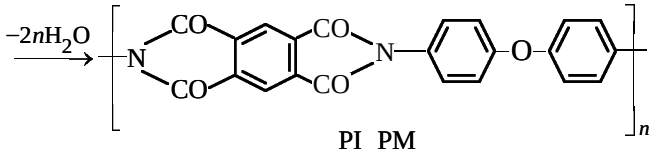

PI PM

The films (30–60 μm thick) were prepared from 12% solutions of PAA PM in dimethylformamide (DMF) by casting onto glass supports followed by drying in air at 50°C for 1 day.

Thermal imidization was performed in a vacuum by stepwise heating of PAA PM films to 400°C in a thermal cycling device at a rate of 2 deg min^{-1}. Chemical imidization was performed by keeping PAA PM films in a dehydrating mixture (solution of acetic anhydride, pyridine, and triethylamine in benzene [4]) until the *o*-carboxamide units of PAA completely cyclized. The absence of isoimide units in the cyclization product was checked by IR spectroscopy.

Electron-microscopic examination was performed with a Tesla BS-500 transmission electron microscope at a magnification from 40000 to 59000. To create a surface relief, PAA PM and PI PM films were etched from the air-contacting side with an oxygen high-

1070-4272/03/7605-0800$25.00

frequency (HF) discharge plasma, with subsequent vapor deposition of platinum and preparation of carbon–platinum (C–Pt) replicas [3, 5, 6]. A 100-W generator was the source of HF discharge. The discharge parameters were as follows: oxygen pressure 0.05 Pa, distance from the discharge gap to the film surface 0.2 m, and electron energy 4–5 eV. The etching time was varied from 15 (PAA PM) to 60 min (PI PM imidized at 350 and 400°C). Such an etching mode is considered as "mild," since the film surface is heated by no more than 50°C and the erosion of the layer surface is minimal [3, 5]. The C–Pt replicas were deposited on the etched film surface with a VUP-5 vacuum unit. The platinum shading angle was 45°, and the calculated thickness of the replicas, 5 nm.

Figure 1 shows the electron micrographs of single-step C–Pt replicas of the etched surface of films of (a) PAA PM, (b, c) PI PM prepared by thermal imidization, and (d) PI PM prepared by chemical imidization. Supramolecular formations (microdomains) of approximately spherical shape are clearly seen; their size depends on the imidization mode and conditions. The etched relief depth and distance between microdomains vary in the course of thermal imidization, reaching a maximum at 170–180°C, which may be due to removal of the disordered polymer phase with the residual solvent (DMF) and water formed in the course of thermal imidization [1].

Figure 2 shows the microdomain diameter distributions $h(y)$ obtained by statistical processing of the micrographs. In each micrograph we analyzed from 500 to 2900 structural formations. It is seen that, for both PAA PM and PI PM, in all the stages of thermal imidization and also after chemical imidization, the microdomain ensembles show monomodal asymmetric distributions which were described in terms of the reversible aggregation model [7, 8].

The model suggests that a substance in the liquid state undergoes continuous fluctuations, generating a sequence of equivalent microstructures, and only one of the set of possible configurations is realized on cooling. Structural elements (aggregates) are dynamic units characterized by a disordered internal structure. The aggregates continuously arise and disappear, giving rise to a set of optimized configuration of ensembles characterized by a steady-state aggregate size distribution. Formation of an aggregate ensemble can be represented as a set of simultaneously occurring reversible chemical reactions. The thermodynamic interpretation of the rate constant leads to the expression [7, 8]

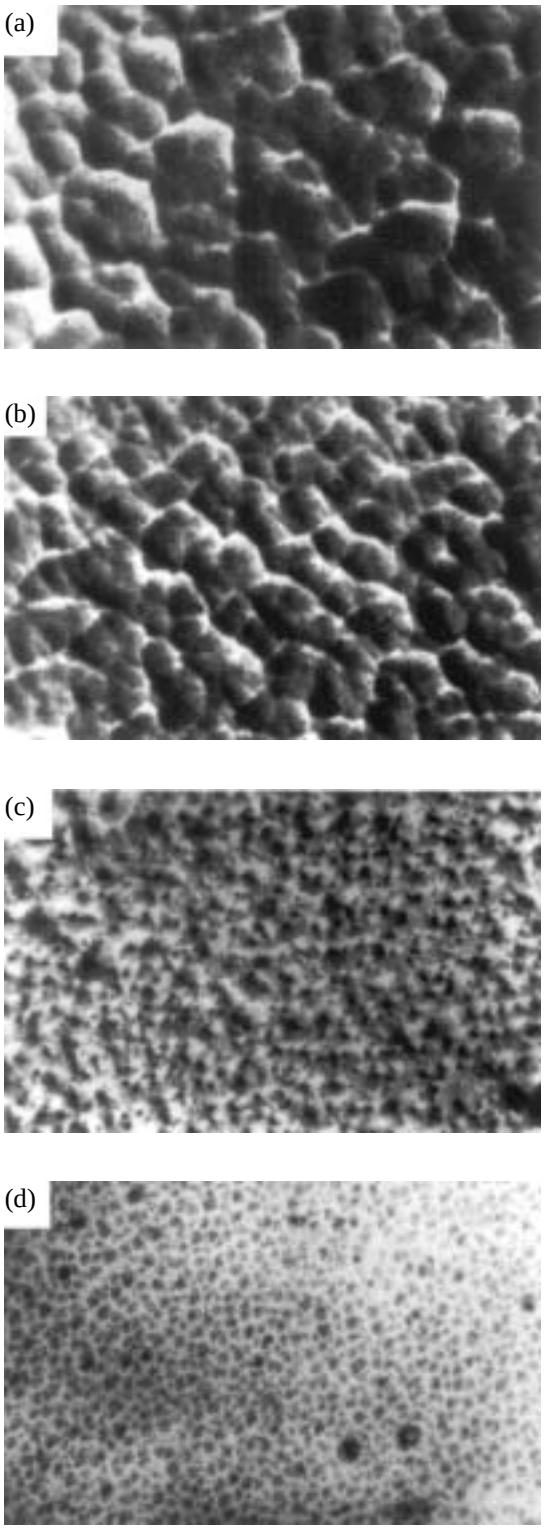

Fig. 1. Electron micrographs of C–Pt replicas taken from the surfaces of (a) PAA PM films; (b, c) PI PM films heated to 180 and 350°C, respectively; and (d) PI PM films prepared by chemical imidization. Magnification: (a, b) 44000 and (c, d) 40000.

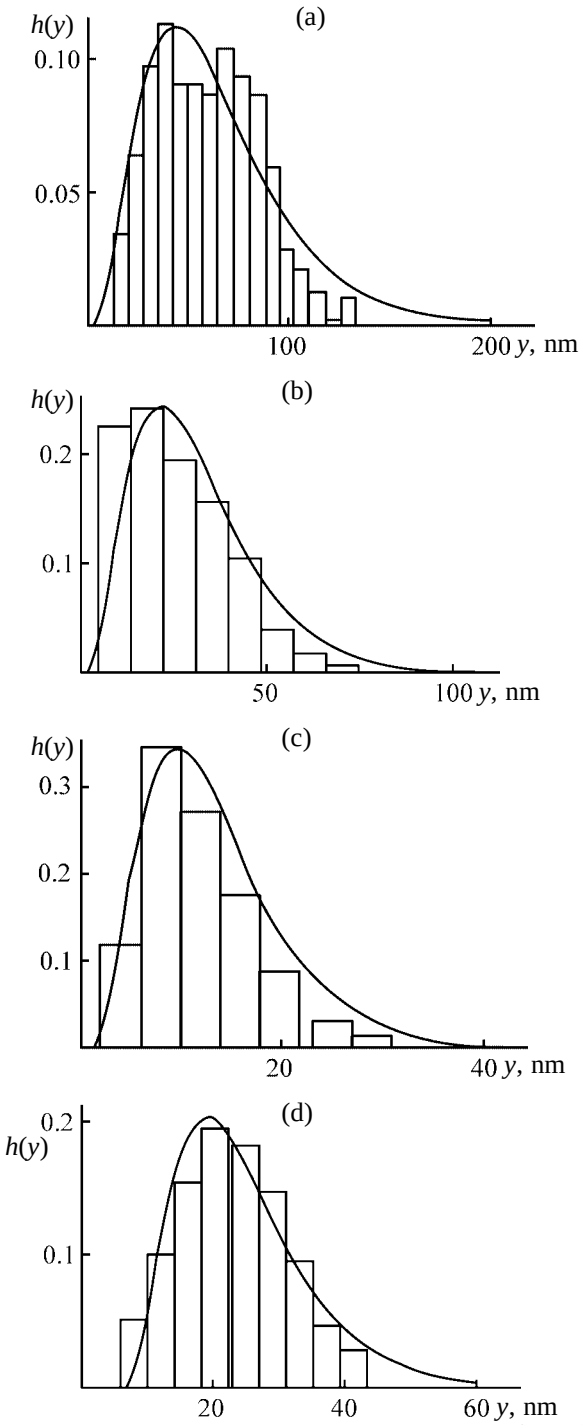

Fig. 2. Microdomain size distribution $h(y)$ on the surface of films of (a) PAA PM; (b, c) PI PM prepared at 180 and 350°C, respectively; and (d) PI PM prepared by chemical imidization.

$$h(y - y_0) = A(y - y_0)^2 \exp[-(y - y_0)\Delta U_0 (kT)^{-1}], \quad (1)$$

where A is a normalizing factor; $\Delta U \equiv (y - y_0)\Delta U_0$, energy of aggregate formation depending on the reduced linear size of the microdomain $(y - y_0)$; ΔU_0, standard aggregation energy per unit linear size of the microdomain, J m^{-1}; y_0, size of the microdomain nucleus; k, Boltzmann constant; and T, absolute temperature.

In statistical physics, Eq. (1) is a canonical distribution of the thermodynamic probability of the energy fluctuation (Gibbs distribution) at constant volume [9].

We successfully used this model previously for describing the microdomain diameter distribution on the surface of films of PAA derived from 3,3',4,4'-diphenyltetracarboxylic dianhydride and *p*-phenylenediamine (PAA DP PP) and its evolution in the course of thermal imidization, including the process in the presence of a thermal stabilizer [10, 11].

The results of calculations with Eq. (1) are shown in Fig. 2 as curves. In the calculations, the values of A, y_0, and ΔU_0 were taken as free parameters. Figure 2 shows that Eq. (1) fairly adequately describes the experimental microdomain diameter distribution on the surface of PAA PM and PI PM in all the steps of thermal imidization and after chemical imidization.

The mean microdomain diameter $\langle y \rangle$ in an ensemble was determined as the normalized population mean:

$$\langle y \rangle = \frac{\int_0^\infty (y - y_0)h(y - y_0)dy}{\int_0^\infty h(y - y_0)dy} = \frac{3kT}{\Delta U_0} + y_0. \quad (2)$$

Figure 3 shows how the distribution parameters [reduced standard aggregation energy U ($U = \Delta U_0/kT$) and $\langle y \rangle$] depend on the temperature of thermal imidization. As seen from Fig. 3a, in the initial step (50–130°C), U varies insignificantly, after which it decreases, reaching a minimum at about 160°C. It is known [1] that, in this temperature range, the PAA $\rightarrow$ PI transformation is accompanied by intense degradation with a decrease in the molecular weight of the polymer. In the range 180–200°C, the activation energy substantially grows, reaching a virtually constant level in the final step of thermal imidization (T > 300°C). In the process, the molecular weight of the polymer is restored [1]. The dependence $\langle y \rangle(T)$ in Fig. 3b shows an opposite trend. Such trends in variation of the distribution parameters were observed previously in studies of the effect exerted by thermal imidization on the morphology of PI DP PP films [10, 11].

In Fig. 3 we also compare the distribution parameters of the microdomain ensemble on the surface of

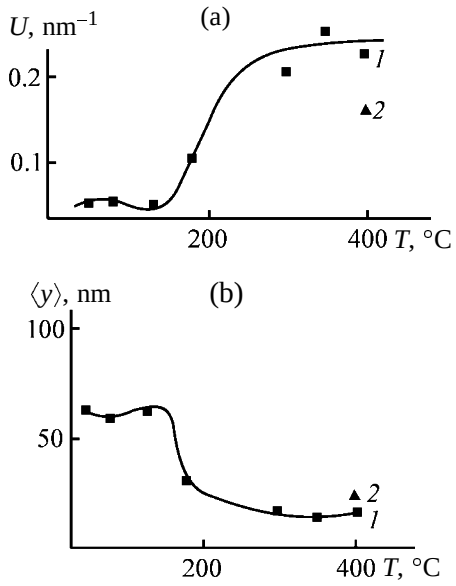

Fig. 3. (a) Reduced standard aggregation energy U and (b) mean microdomain diameter $\langle y \rangle$ as functions of the imidization temperature T. Imidization: (*1*) thermal and (*2*) chemical.

PI PM films prepared by thermal and chemical imidization. It is seen that the aggregation energy of the microdomain ensemble on the surface of a PI PM film prepared by thermal imidization is approximately 1.5 times higher compared to the film prepared by chemical imidization, i.e., the microdomain size distribution in the first case is narrower. Hence, microdomains on the surface of a PI PM film prepared by thermal imidization are more uniform in size. Furthermore, the mean size of microdomains on the surface of a PI PM film prepared by thermal imidization is approximately 1.5 times smaller compared to the film prepared by chemical imidization (15 and 23 nm, respectively). The previously revealed correlation between $\langle y \rangle$ and the mechanical strength of PI films [10, 11] suggests that the PI PM films prepared by thermal imidization will be stronger than those prepared by chemical imidization. Indeed, the strength of thermally and chemically imidized PI PM films determined in [12] appeared to be 200 and 160 MPa, respectively.

CONCLUSIONS

(1) The microdomain diameter distribution on the surface of films of a polyamido acid derived from pyromellitic dianhydride and 4,4'-oxyphenylenediamine and its evolution in the course of thermal and chemical imidization can be described in terms of the reversible aggregation model.

(2) The mechanical strength of polyimide films is inversely proportional to the mean diameter of microdomains.

(3) The surface of a polyimide film prepared by thermal imidization is characterized by the narrower microdomain size distribution and by the smaller mean microdomain diameter, as compared to the film after chemical imidization.

ACKNOWLEDGMENTS

The study was financially supported by the RF Ministry of Education (project no. T02-6.3-2706).

REFERENCES

1. Bessonov, M.I., Koton, M.M., Kudryavtsev, V.V., and Laius, L.A., *Poliimidy – klass termostoikikh polimerov* (Polyimides: A Class of Heat-Resistant Polymers), Leningrad: Nauka, 1983.
2. Sukhanova, T.E., Structurization and Morphology of Oriented Polyimides and Fibrous Composites Based on Them, *Doctoral Dissertation*, St. Petersburg, 1999.
3. Novikov, D.V., Sukhanova, T.E., Lavrent'ev, V.K., and Vylegzhanina, M.E., *Vysokomol. Soedin., Ser. A*, 1999, vol. 41, no. 8, pp. 1266–1273.
4. Sukhanova, T.E., Sidorovich, A.V., Gofman, I.V., *et al.*, *Dokl. Akad. Nauk SSSR*, 1989, vol. 306, no. 1, pp. 145–149.
5. Startsev, V.M., Chugunova, N.F., Matveev, V.V., and Chalykh, A.E., *Vysokomol. Soedin., Ser. A*, 1986, vol. 28, no. 11, pp. 2378–2381.
6. Bovenko, V.N. and Startsev, V.M., *Vysokomol. Soedin., Ser. B*, 1994, vol. 36, no. 6, pp. 1004–1007.
7. Kilian, H.G., Metzler, R., and Zink, B., *J. Chem. Phys.*, 1997, vol. 107, pp. 8697–8707.
8. Kilian, H.G., Kopf, M., and Vettegren, V.I., *Prog. Colloid Polym. Sci.*, 2001, vol. 117, pp. 172–181.
9. Lavenda, B.H., *Statistical Physics. A Probabilistic Approach*, New York: Wiley–Interscience, 1991.
10. Bronnikov, S. and Sukhanova, T., *Image Anal. Stereol.*, 2001, vol. 20, suppl. 1, pp. 133–138.
11. Bronnikov, S.V., Sukhanova, T.E., and Laius, L.A., *Vysokomol. Soedin., Ser. A*, 2002, vol. 44, no. 6, pp. 940–945.
12. Kudriavtsev, V.V., Zubkov, V.A., Meleshko, T.K., *et al.*, *Polyimides: Materials, Chemistry, and Characterization*, Feger, C., Khojasteh, M.M., and McGrath, L.E.. Eds., Amsterdam: Elsevier, 1989, pp. 419–451.

Russian Journal of Applied Chemistry, Vol. 76, No. 5, 2003, pp. 804–808. Translated from Zhurnal Prikladnoi Khimii, Vol. 76, No. 5, 2003, pp. 833–837.

MACROMOLECULAR CHEMISTRY AND POLYMERIC MATERIALS

1,1,3-Trimethyl-3-phenylindan as a Luminescent Additive to a Plastic Scintillator Based on Poly(methyl Methacrylate)

V. N. Salimgareeva, R. M. Polevoi, S. V. Kolesov, S. S. Ostakhov, V. A. Ponomareva, and G. V. Leplyanin

Institute of Organic Chemistry, Ufa Scientific Center, Russian Academy of Sciences, Ufa, Bashkortostan, Russia

Received February 4, 2003

Abstract—The luminescence and scintillation properties of poly(methyl methacrylate) containing 1,1,3-trimethyl-3-phenylindan were studied.

Plastic scintillators (PSs), i.e., solid solutions of luminophores in polymeric matrices, are widely used as components of scintillation counters for detecting ionizing radiation. Light flashes (scintillations) arising under the action of radiation [1] are detected with a photomultiplier (PM). In PSs based on polystyrene, polyvinylstyrene, and polyvinylxylene, the primary fluorescence emitter is the polymer itself, efficiently transmitting the excitation energy to luminescence additives such as polyarenes and aryl-substituted oxazoles and oxadiazoles: *p*-terphenyl (PPP), 2,5-diphenyloxazole (PPO), 1,4-di(5-phenyl-2-oxazolyl)benzene (POPOP), 2-phenyl-5-(4-biphenylyl)-1,3,4-oxadiazole (PBD), etc. [1–3]. The transparency of these PSs is low because of absorption of UV and visible radiation by benzene groups of the polymer.

The PS containing poly(methyl methacrylate) (PMMA) having no absorption bands in the UV (250–400 nm) and visible ranges is highly transparent, but PMMA, in contrast to polymers containing a system of conjugated double bonds, shows no luminescence. Therefore, large (up to 20 wt %) amounts of luminescent aromatic compounds (naphthalene, its derivatives, etc.) acting as primary luminescence emitters are added to PMMA-based PSs as an active filler. The energy incident on the luminophore (playing the role of a secondary solvent) and on the polymeric matrix is absorbed by the luminophore. A weak emission of naphthalene (fluorescence quantum yield 0.17 [4]) is sensitized by an activator, luminescent additive with a strong intrinsic luminescence, such as PPO, PPP, or PBD [1–3]. The light emitted by the activators is shifted toward the range of the highest PM sensitivity by introduction of one more luminescent additive, a spectrum shifter, the most effective of which is POPOP [3]. Furthermore, this luminophore decreases the probability of absorption of the activator fluorescence by the solvent, eliminating self-absorption and making the system more transparent.

Naphthalene in more effective as intermediate solvent than any other known solvents [3]; however, it inhibits polymerization of methyl methacrylate; it is also toxic and volatile. In this work, we attempted to use for this purpose 1,1,3-trimethyl-3-phenylindan (TMPI), a cyclic α-methylstyrene dimer exhibiting fluorescence properties [5]. This compound is highly soluble in both methyl methacrylate [up to 25 wt % at room temperature and up to 60 wt % at 40°C (temperature of the polymer synthesis)] and PMMA (up to 60 wt %). In the course of methyl methacrylate polymerization, TMPI does not react with the propagating radical and is present in PMMA as a solute [6]. Furthermore, TMPI is nontoxic, nonvolatile, and highly resistant to heat, chemicals, and radiation [7, 8].

EXPERIMENTAL

PS samples were prepared by bulk polymerization of methyl methacrylate at 40°C in the presence of various amounts of TMPI, PPP, and POPOP, with substance initiation. The upper limits of the concentrations of the additives were determined by their solubility in the polymerizing mixture. Samples for studying scintillation characteristics were prepared as polished disks 20 mm in diameter and 10 mm high, and samples for optical studies, as disks 20 mm in diameter and 1 mm high.

1,1,3-Trimethyl-3-phenylindan was prepared as described in [9] and recrystallized from heptane. The

1070-4272/03/7605-0804$25.00

product purity was checked by GLC and by IR and ^{1}H NMR spectroscopy; mp 52°C, bp 183°C/20 mm Hg. PPP and POPOP were of scintillation chemically pure grade.

The absorption spectra of the luminophores in heptane were recorded on a Specord UV-Vis spectrophotometer. The fluorescence spectra of the luminophores in heptane and PMMA were taken on a Hitachi MPF-4 spectrofluorimeter. The luminescence excitation wavelength was 250 and 280 nm. The luminescence quenching constants were calculated according to [10].

The scintillation characteristics of PS were taken in a ^{137}Cs γ-radiation field. The light output was determined according to [11] by comparison with that of samples of a reference PS: PMMA + 15% naphthalene + 0.3% PPO + 0.06% POPOP [12]. The effective transparency of PS for the own emission was measured according to [13]. The light transmission was calculated according to the Lambert–Beer equation [10].

1,1,3-Trimethyl-3-phenylindan efficiently absorbs in the range 210–280 nm ($\varepsilon = 1.69 \times 10^3$ l mol^{-1} cm^{-1} at $\lambda = 269$ nm) and shows fluorescence with a short lifetime (8 ns) and quantum yield of 0.27 in the range 260–320 nm [5]. The transparency of TMPI at $\lambda >$ 300 nm allows its large amounts (up to 60 wt %) to be introduced into PMMA, which, in combination with the short fluorescence lifetime, makes TMPI promising for development of large PSs for detecting γ-radiation and long-path high-energy particles. Another favorable property of TMPI as a primary emitter is its high boiling point, so that, in contrast to naphthalene, TMPI does not volatilize from the scintillation formulation in the course of service.

As a sensitizer of TMPI luminescence we chose PPP exhibiting high quantum yield (0.93) and short lifetime (0.95 ns) of the fluorescence. The quantum yield of the PPP fluorescence is higher compared to TMPI; in this case, according to [10], the acceptor utilizes the quanta emitted by the donor more efficiently. In such cases, the number of quanta emitted by the mixture is higher than the total number of quanta emitted by the donor and acceptor in separate solutions.

The overlap integrals between the absorption bands of the acceptor and fluorescence bands of the donor are considerably larger than those of the absorption and luminescence bands of related molecules (Fig. 1), which is due to higher molar extinction coefficients of the acceptor ($\varepsilon = 3.4 \times 10^4$ l mol^{-1} cm^{-1}) and full

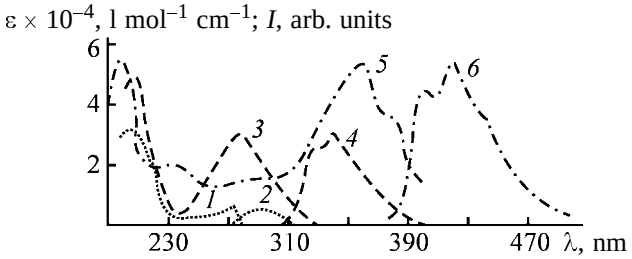

Fig. 1. (*1*, *3*, *5*) Absorption and (*2*, *4*, *6*) luminescence spectra of (*1*, *2*) TMPI, (*3*, *4*) PPP, and (*5*, *6*) POPOP. Solutions in heptane (2×10^{-2} M). (ε) Molar extinction coefficient, (*I*) luminescence intensity, and (λ) wavelength.

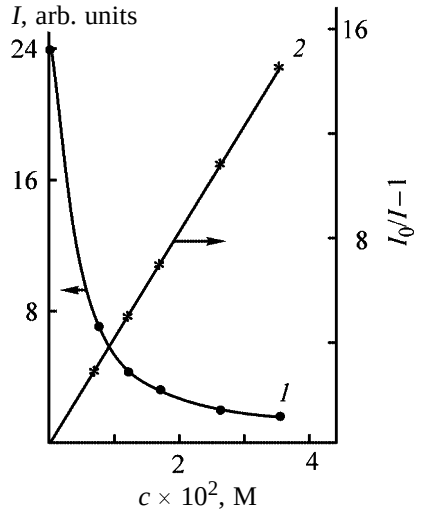

Fig. 2. (*1*) Intensity *I* of TMPI fluorescence at $\lambda = 282$ nm and (*2*) the quantity $I_0/I - 1$ as functions of the PPP concentration *c* in PMMA.

coincidence between the luminescence range of the energy donor (TMPI) and absorption range of the acceptor (PPP). As a result, the efficiency of the inductive-resonance dipole–dipole energy transfer is high.

As seen from Fig. 2, the TMPI luminescence is efficiently quenched by PPP and virtually is not observed at the PPP concentration $c \geq 3 \times 10^{-2}$ M.

The quenching effect of one luminescent additive on another may be due either to a chemical reaction between them or to energy transfer. Under the conditions of the polymer synthesis, these compounds are inert [6]. The luminescence quenching is due to the energy transfer from TMPI to PPP and, as follows from the linear dependence of $(I_0/I - 1)$ on *c* (Fig. 2, curve *2*), is described by the Stern–Volmer law [10] with the bimolecular quenching rate constant $K_q = 6.8 \times 10^9$ l mol^{-1} s^{-1} (PMMA, 298 K). To compare, in such a well-known formulation as naphthalene–PPO, the quenching rate constant appeared to be almost an order of magnitude lower: 8.7×10^8 l mol^{-1} s^{-1} (PMMA, 298 K).

Properties of PMMA-based PSs

PS components, %	Light output, %	Absorption coefficient, cm^{-1}	Block length for 41.5% transmission at 420 nm, m	Number of radiation damages in PMMA macromolecule after γ-irradiation to 5.0 Mrad	γ-Irradiation doze causing 25% decrease in light output, Mrad
TMPI, 17.0; PPP, 0.2; POPOP, 0.010; PMMA,* 98.79;	105	0.0020	2.0	3.0	11
TMPI, 30.0; PPP, 0.6; POPOP, 0.013; PMMA,* 69.27;	115	0.0020	2.0	1.9	14
TMPI, 60.0; PPP, 0.85; POPOP, 0.015; PMMA,* 39.0;	120	0.0025	1.6	1.2	15
TMPI, 40.0; PPP, 0.40; POPOP, 0.015; PMMA,* 59.59;	130	0.0020	1.9	1.4	14
Naphthalene, 15.0; PPO, 0.30; POPOP, 0.08; PMMA,** 84.62	100	0.0040	1.0	7.0	8

* PMMA molecular weight 10×10^6. ** PMMA molecular weight 2×10^6.

To shift the luminescence spectrum of the TMPI–PPP binary system toward the range of the highest PM sensitivity, it is appropriate to use POPOP exhibiting a strong fluorescence in the range 370–480 nm; its absorption spectrum efficiently overlaps with the luminescence spectrum of PPP (Fig. 1). When PMMA samples containing TMPI, PPP, and POPOP are irradiated at λ = 280 nm (with no TMPI absorption), the intensity of the PPP luminescence grows as its concentration is increased to 1.15 M (Fig. 3a). Further increase in the PPP concentration decreases the fluorescence intensity, probably owing to concentration quenching, whereas the intensity of the POPOP emission remains unchanged. Apparently, the energy transfer from PPP to POPOP occurs faster than self-quenching of the PPP fluorescence. When similar samples are irradiated at λ = 250 nm, TMPI strongly absorbs the energy along with PPP. An increase in the PPP concentration is accompanied by quenching of the TMPI luminescence (Fig. 2) and enhancement of the PPP luminescence (Fig. 3b), probably, owing to increased probability of the energy transfer from TMPI to PPP. In turn, POPOP accepts the excitation energy from both TMPI and PPP, causing the light pulse in the emission range of this luminophore to grow in intensity with increasing PPP concentration.

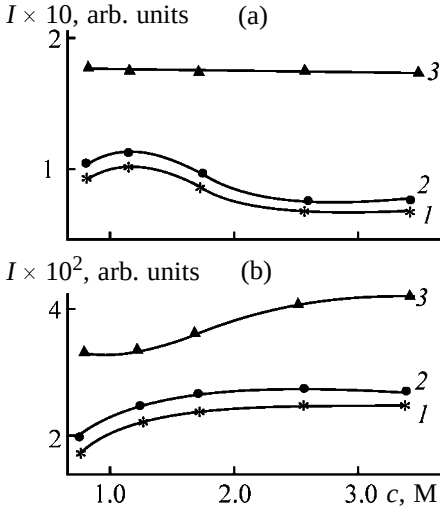

Fig. 3. Fluorescence intensity *I* of (*1*) PPP at λ = 338 nm, (*2*) PPP at λ = 323 nm, and (*3*) POPOP at λ = 415 nm as a function of the PPP concentration *c*. Excitation wavelength, nm: (a) 280 and (b) 250.

Calculations performed according to [14] show that, in the system TMPI (1.27 M, or 30 wt %)–PPP (8.5×10^{-3} M, or 0.2 wt %)–POPOP (3×10^{-4} M, or 0.01 wt %) in PMMA, the energy transfer from TMPI

to PPP occurs with 70% efficiency, and from PPP to POPOP, with 73% efficiency. As the PPP concentration is increased to 3.4×10^{-2} M, the efficiency of the energy transfer from TMPI to PPP increases to 96%.

The PMMA-based plastic scintillator containing TMPI, PPP, and POPOP is an optically uniform highly transparent block showing a high scintillation efficiency (table). The low extinction coefficients and high light transmission coefficients allow fabrication of a scintillator with the two times larger linear dimensions as compared to the scintillator containing the naphthalene–PPO–POPOP additives, with the other parameters being the same.

The scintillation efficiency of PMMA-based PS containing TMPI, PPP, and POPOP can be enhanced by introducing polystyrene fragments in the polymeric chain in the course of copolymerization of methyl methacrylate with styrene. Figure 4 shows that the PS scintillation efficiency grows with increasing content of styrene units (curve *1*). However, introduction of styrene units makes the scintillation block less transparent: The absorption coefficient of the material containing 15 wt % styrene units is as high as 0.015 cm^{-1}.

Copolymerization of α-methylstyrene with methyl methacrylate in the presence of TMPI, PPP, and POPOP yields a PS whose scintillation efficiency is even lower than that of PMMA-based PS, decreasing as the α-methylstyrene content is increased (Fig. 4, curve *2*). It is known that α-methyl groups in the polystyrene chain impair the scintillation characteristics of PSs; the scintillation efficiency of poly-α-methylstyrene is zero [2].

It should be noted that the scintillation efficiency of PMMA containing TMPI, PPP, and POPOP considerably grows with increasing TMPI content (Fig. 5, curve *1*) and only slightly grows with increasing PPP content (curve *2*).

The concentration dependence of the intensity of TMPI fluorescence passes through a maximum at 0.85 M (25 wt %) content in PMMA [5]. The scintillation efficiency of PS monotonically grows with increasing TMPI concentration; the curve is steeply ascending at TMPI content below 0.85 M and gradually flattens out at higher TMPI content (Fig. 5). The different trends in variation of the intensity of TMPI fluorescence in PMMA and of the PS scintillation efficiency suggest that the rate constant of the energy transfer from TMPI to PPP molecules in the scintillator is higher than the rate constant of self-

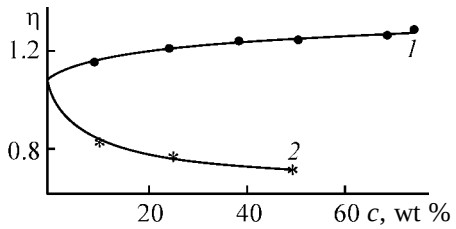

Fig. 4. PS scintillation efficiency η as a function of the content *c* of (*1*) styrene and (*2*) α-methylstyrene in the copolymer. PS composition, wt %: (*1*) 75.29 methyl methacrylate–styrene copolymer + 24.5 TMPI + 0.2 PPP + 0.01 POPOP; (*2*) 75.29 methyl methacrylate–α-methylstyrene copolymer + 24.5 TMPI + 0.2 PPP + 0.01 POPOP.

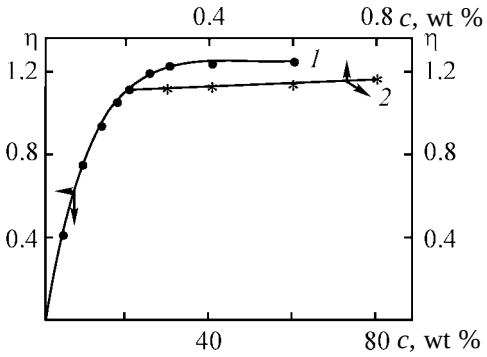

Fig. 5. PS scintillation efficiency η as a function of concentration *c* of (*1*) TMPI and (*2*) PPP. PS composition, wt %: (*1*) PMMA + 0.2 PP + 0.01 POPOP + TMPI and (*2*) PMMA + 24.5 TMPI + 0.01 POPOP + PPP.

quenching. Also, this may due to physical differences between scintillation and luminescence. In excitation with, e.g., a ^{60}Co source (γ-ray energy 1.17 and 1.33 MeV), molecules pass to a higher excited state than in UV excitation (energy about 10 eV). The subsequent energy redistribution over vibrational levels can affect the scintillation light output.

The TMPI inertness in polymerization of methyl methacrylate allows wide variation of its concentration in scintillation blocks. The presence of large amounts of this luminophore in the polymerizing mixture results in dilution of the monomer and "smearing" of the gel effect (sharp acceleration of the polymerization on reaching 15–20% conversion of the monomer), which facilitates removal of the heat released in the process and prevents overheating of the block. The molecular weight of the polymer does not decrease, and the concentration of double bonds which can form by disproportionation termination of the propagating chain (a mechanism competing with recombination) and absorb in the short-wave range does not grow. It is known that double bonds reduce the

polymer transparency and enhance its sensitivity to external effects.

The high transparency and high light output are attained owing to a combination of TMPI with PPP and POPOP. All the additives used have several functions. They transfer the energy and ensure the maximally complete conversion of the incident energy to the light energy. They exhibit high radiation resistance and show radioprotective properties [15]. Owing to absorption of the energy incident on the polymer, followed by its emission in the form of fluorescence, they protect the polymer from the radiation aging, which is seen from the table. The numbers of radiation damages in the PMMA macromolecule decrease with increasing TMPI content, and the irradiation dose causing a 25% decrease in the light output grows. Prevention of the degradation of the polymeric base favors stabilization of the scintillation characteristics of PS in the course of service.

Thus, the use of TMPI as a luminescent additive to PMMA widens the range of luminophores suitable as secondary solvents for PSs, allows fabrication of large PS blocks (more than 100 mm thick and more than 2 m long), improves their scintillation characteristics, and enhances their resistance to heat, light, and radiation.

CONCLUSIONS

(1) Since 1,1,3-trimethyl-3-phenylindan absorbs in the short-wave range only, its addition to poly(methyl methacrylate) does not deteriorate the effective transparency of the polymer.

(2) The energy transfer from the donor (1,1,3-trimethyl-3-phenylindan) to acceptor (*p*-terphenyl) occurs at a high rate, virtually without energy loss.

(3) The plastic scintillator based on poly(methyl methacrylate) and containing as luminescent additives 1,1,3-trimethyl-3-phenylindan, *p*-terphenyl, and 1,4-di(5-phenyl-2-oxazolyl)benzene is characterized by low absorption coefficient (0.0020–0.0025 cm^{-1}) and high light output (110–130%) relative to the plastic scintillator with additions of naphthalene, 2,5-diphenyloxazole, and 1,4-di(5-phenyl-2-oxazolyl)benzene.

REFERENCES

1. Birks, J.B., *The Theory and Practice of Scintillation Counting*, Oxford: Pergamon, 1964.
2. Barashkov, A.A. and Gunder, O.A., *Fluorestsiruyushchie polimery* (Fluorescent Polymers), Moscow: Khimiya, 1987.
3. Krasovitskii, B.M. and Bolotin, B.M., *Organicheskie lyuminofory* (Organic Luminophores), Moscow: Khimiya, 1984.
4. Berlman, J.B., *Handbuch of Fluorescence Spectra of Aromatic Molecules*, New York: Academic, 1971.
5. Salimgareeva, V.N., Kolesov, S.V., Ostakhov, S.S., *et al.*, *Zh. Prikl. Khim.*, 2003, vol. 76, no. 4, pp. 602–604.
6. Salimgareeva, V.N., Sannikova, N.S., and Leplyanin, G.V., *Bashk. Khim. Zh.*, 1997, vol. 4, no. 1, pp. 32–36.
7. Vol'-Epshtein, A.B., *Neftekhimiya*, 1967, vol. 7, no. 1, pp. 13–18.
8. US Patent 3 161 692.
9. Staudinger, H. and Brensch, F., *Chem. Ber.*, 1929, vol. 26, pp. 452–455.
10. Parker, C.A., *Photoluminescence of Solutions. With Applications to Photochemistry and Analytical Chemistry*, Amsterdam: Elsevier, 1968.
11. Gunder, O.A., Malinovskaya, S.A., Daich, A.R., and Teslya, A.G., *Prib. Tekh. Eksp.*, 1969, no. 3, pp. 66–69.
12. Volosyuk, G.P., Petrova, I.B., Prokof'eva, A.S., and Gunder, O.A., in *Monokristally, stsintillyatory i organicheskie lyuminofory* (Single Crystals, Scintillators, and Organic Luminophores), Kharkov: Vses. Nauchno-Issled. Inst. Monokristallov, 1972, vol. 2, pp. 293–296.
13. Tsirlin, Yu.A., *Zh. Prikl. Spektrosk.*, 1965, vol. 2, no. 4, pp. 341–343.
14. Levshin, V.P. and Grineva, Yu.I., *Zh. Prikl. Spektrosk.*, 1968, vol. 2, no. 11, pp. 630–636.
15. Salimgareeva, V.N., Leplyanin, G.V., Sannikova, N.S., and Kirichenko, G.N., *Khim. Vys. Energ.*, 1996, vol. 30, no. 6, pp. 424–427.

Russian Journal of Applied Chemistry, Vol. 76, No. 5, 2003, pp. 809–812. Translated from Zhurnal Prikladnoi Khimii, Vol. 76, No. 5, 2003, pp. 838–841.

MACROMOLECULAR CHEMISTRY AND POLYMERIC MATERIALS

Structure Formation in Carbon Fibers in the Course of Flash High-Temperature Treatment

P. V. Semenov, V. A. Tyumentsev, A. A. Sviridov, S. A. Podkopaev, and G. P. Shveikin

Chelyabinsk State University, Chelyabinsk, Russia
Chelyabinsk Electrode Plant, Chelyabinsk, Russia
Institute of Solid State Chemistry, Ural Division, Russian Academy of Science, Yekaterinburg, Russia

Received April 15, 2002

Abstract—The size of coherent scattering regions formed in carbon fibers was studied as influenced by the preparation conditions of the initial polyacrylonitrile thread and conditions of preliminary (~200°C) and flash high-temperature (~2400 and ~3200°C) thermomechanical treatments.

Carbon fibers with good mechanical properties are produced by multistep thermomechanical treatment (TMT) of polyacrylonitrile (PAN) threads at temperatures of up to 3200°C. Carbon fiber well-textured along the filament axis is formed after complex structural-chemical transformations during high-temperature treatment. The texture and average sizes L_{002} and L_{110} of the coherent scattering regions (CSRs) formed in the carbon fiber largely determine its physicochemical properties and depend on both preparation conditions of PAN threads and conditions of the thermomechanical treatment [1–6]. The dependence of the average sizes of CSRs (L_{002} and L_{110}) on the heat treatment temperature and the correlation of L_{002} and L_{110} were studied in [3–5]. Since flash thermal treatment lasts for no more than 10 s [1], CSRs are formed under strongly nonequilibrium conditions.

In this work we analyzed the average sizes of CSRs (L_{002} and L_{110}) formed in carbon PAN threads in the course of their preparation by flash thermal treatment of a braid of 7200 PAN threads at 2400 and then at 3200°C. The following experimental parameters were varied: (a) thermal stabilization conditions (extent of oxidation F of the threads determined by the procedure in [6]), (b) preparation conditions of the initial PAN thread (temperature and concentration of the precipitating solution), and (c) mechanical loading on the braid during the high-temperature treatment (variation of the relative elongation of the braid). In some experiments the time of the high-temperature isothermal treatment was also varied. The average values of L_{002} and L_{110} in carbon fibers was determined by conventional X-ray diffraction analysis (DRON-3 diffractometer, CuK_α radiation).

Experimental average sizes of CSRs (L_{002} and L_{110}) and the L_{110}/L_{002} ratio in carbon fibers prepared under different heat-treatment conditions are presented in Tables 1 and 2. Let us consider the influence of the thermal stabilization conditions on the average sizes of CSRs in the carbon fibers treated at 2400°C. The extent of oxidation F of PAN threads in the range from 0.44 to 0.7 was afforded by varying the temperature and time of the thermal stabilization. As seen from Table 1, the average sizes of CSRs in the carbon fiber prepared under these conditions appreciably differ. The L_{002} in the carbon fibers ranged from 2 to 2.5 nm, whereas L_{110} characterizing the length of carbon CRS varied in a wider range, from 4 to 11.6 nm. The minimal and maximal values of L_{110}/L_{002} were 1.9 and 5.4, respectively.

Carbon fibers with L_{002} and L_{110} in the range 1.9–2.5 and 5.9–7.4 nm, respectively, were prepared by varying in a wide range the axial mechanical loading providing 10 and 20% increase in the specific elongation as compared to the preset value. In these experiments, L_{002} and L_{110} changed to a similar extent ($L_{110}/L_{002} = 3$).

The preparation conditions of the initial PAN thread (temperature and concentration of the precipitating solution) negligibly affect L_{002} and L_{110}, which are in the range 2.1–2.3 and 3.9–5.2 nm, respectively. In these experiments, the L_{110}/L_{002} ratio varied from 1.9 to 2.4.

The average sizes $\bar{L}_{002}$ and $\bar{L}_{110}$ in all the samples prepared at 2400°C are 2.2 and 5.2 nm, respectively, and $\bar{L}_{110}/\bar{L}_{002} = 2.3$. The least-squares plot

1070-4272/03/7605-0809$25.00

Table 1. Structural parameters of carbon fiber prepared by TMT under similar conditions of the flash high-temperature treatment

Preparation conditions of carbon fiber	2400°C			3200°C		
	L_{002}	L_{110}	$\bar{L}_{110}/\bar{L}_{002}$	L_{002}	L_{110}	$\bar{L}_{110}/\bar{L}_{002}$
	nm			nm		
From braids thermally stabilized under different conditions (the extent of oxidation F of PAN thread ranged from 0.44 to 0.7)	2.4	6.2	2.6	7.0	16.6	2.4
	2.2	5.5	2.5			
	2.1	4.9	2.3	–	–	–
	2.1	4.7	2.2			
	2.5	6.5	2.6	6.6	18.7	2.8
	2.2	5.2	2.4			
	2.1	4.4	2.1	8.9	22.8	2.6
	2.1	4.0	1.9			
	2.1	5.0	2.4	8.1	24.6	3.0
	2.1	5.5	2.6			
	2.2	5.4	2.5	8.6	20.2	2.3
	2.5	6.1	2.4			
	2.0	7.6	3.8	9.7	59.0	6.1
	2.4	11.6	4.8	9.4	51.8	5.5
	2.1	10.9	5.1	9.3	52.8	5.7
	2.0	10.9	5.4	9.0	54.3	6.0
	2.0	7.8	3.9	9.6	61.3	6.4
	2.0	7.6	3.7	9.6	57.9	6.1
From PAN thread prepared at different temperatures and concentrations of the precipitating solutions and thermally stabilized under the same conditions	2.2	4.7	2.1	8.1	14.1	1.7
	2.3	4.8	2.1	6.8	12.5	1.8
	2.2	4.7	2.1	9.2	16.5	1.8
	2.1	3.9	1.9	7.5	13.5	1.8
	2.1	4.6	2.2	6.7	12.8	1.9
	2.2	5.2	2.4	6.5	12.6	1.9
	2.3	5.1	2.2	6.2	12.5	2.0
	2.3	4.7	2.0	8.8	17.3	2.0
	2.2	4.9	2.2	–	–	–
	2.3	5.1	2.2	6.6	11.8	1.8
	2.2	4.9	2.2	7.0	12.6	1.8
From PAN threads drawn under different conditions (preset elongation increased by 10 and 20%) and thermally stabilized under the same conditions	2.5	7.4	3.0	4.8	13.5	2.8
	1.9	5.9	3.1	5.0	14.2	2.8
	2.3	6.8	3.0	4.5	13.3	3.0

of L_{002} vs. L_{110} is virtually parallel to the L_{110} axis (Fig. 1a).

This indicates that the sizes of CSRs in carbon fibers thermomechanically treated at the temperatures relatively low for carbon materials increase mainly along the carbon layers.

The average sizes of $\bar{L}_{002}$ and $\bar{L}_{110}$ regions in PAN threads prepared at 2400°C and thermomechanically

Fig. 1. Correlation of L_{002} and L_{110} sizes of CSR regions in carbon fibers heated (a) at 2400 and (b) at 2400 and additionally at 3200°C.

Table 2. Structural parameters of carbon fiber prepared by flash high-temperature treatment

Preparation conditions of carbon fiber	Variable parameter	L_{002}, nm	L_{110}, nm	$\bar{L}_{110}/\bar{L}_{002}$
Prolonged isothermal high-temperature treatment, τ_1–τ_6	τ_1 = 2.2 s	6.6	22.0	3.4
		7.2	20.6	2.9
	τ_2 = 1.8 s	8.9	27.4	3.1
		8.0	26.7	3.3
		8.0	28.1	3.5
	τ_3 = 1.55 s	7.3	26.7	3.7
		8.3	27.0	3.3
	τ_4 = 1.35 s	6.9	21.7	3.1
		7.1	26.0	3.7
	τ_5 = 1.2 s	6.4	20.9	3.3
		7.3	23.7	3.2
	τ_6 = 1 s	8.9	29.7	3.3
Heating from T_1 ~3050 to T_7 ~3150°C under 1.5 kg axial loading on the braid	T_1	6.5	20.4	3.1
	T_2	7.3	26.3	3.6
	T_3	8.3	30.3	3.7
	T_4	8.3	33.6	4.0
	T_5	10.3	53.0	5.1
Heating from T_1 ~3050 to T_7 ~3200°C under 0.75 kg axial loading on the braid	T_1	7.2	25.8	3.6
	T_3	7.6	32.6	4.3
	T_5	9.4	41.7	4.4
	T_6	8.3	33.1	4.0
	T_7	9.8	50.8	5.2
Heating from T_1 ~3050 to T_7 ~3200°C under 0.375 kg axial loading on the braid	T_1	7.5	30.7	4.1
	T_3	7.5	27.1	3.6
	T_5	7.2	27.1	3.8
	T_6	7.5	31.1	4.1
	T_7	8.0	34.2	4.3
Heating from T_1 ~3050 to T_7 ~3200°C under 0.125 kg axial loading on the braid	T_1	7.0	26.1	3.7
	T_2	6.8	24.6	3.6
	T_3	7.7	29.8	3.9
	T_4	6.7	24.3	3.6
	T_5	8.2	33.1	4.0
	T_6	8.3	30.7	3.7
	T_7	8.4	35.4	4.2

treated at 3200°C reached 7.5 and 28.2 nm, respectively (i.e. they increased by a factor of 3.4 and 5.4, respectively, as compared to those in the thread treated at 2400°C), and the $\bar{L}_{110}/\bar{L}_{002}$ ratio reached 3.1 (i.e., it increased by a factor of 1.4). The sizes L_{002} and L_{110} in the carbon fibers range from 12 to 60 and from 5 to 10 nm, respectively (Tables 1, 2). As seen from Table 1, the largest CSR regions with L_{110}/L_{002} from 5.5 to 6.4 are formed in the threads pretreated at 2400°C with L_{110} exceeding 6.7 nm.

The L_{002} vs. L_{110} dependence for carbon fibers additionally heated at 3200°C can be fitted by a linear function $L_{002} = 0.065L_{110} + 6$ (see Fig. 1b). In this case, unlike carbon fibers heated at 2400°C, larger L_{002} corresponds to larger CSR size in the (110) direction. The L_{110} size in the direction along the filament axis can be substantially changed by mechanical drawing in the course of heat treatment (Table 2). The sizes of CSRs did not change when the isothermal heat treatment at 3200°C was shortened from 2.2 to 1 s.

Thus, CSRs are formed in carbon fiber upon flash high-temperature treatment. The sizes L_{002} and L_{110}

strongly and simultaneously increase upon additional heat treatment at 3200°C. The difference in the ratio of the length of CSRs to their height (L_{110}/L_{002}) for the threads heated both at 2400 and 3200°C is probably due to structural differences produced under different conditions of formation and thermal stabilization of PAN threads and different conditions of TMT.

CONCLUSIONS

(1) The L_{002} and L_{110} sizes of coherent scattering regions in the carbon fibers rapidly heated to high temperatures are determined by conditions of thermal stabilization and formation of polyacrylonitrile threads.

(2) The L_{002} and L_{110} sizes increase several times after additional high-temperature (~3200°C) thermomechanical treatment of the carbon fiber. In this case, the final structure also depends on the conditions of thermal stabilization and formation of the polyacrylonitrile thread.

ACKNOWLEDGMENTS

This work was financially supported by the Russian Foundation for Basic Research (project no. 99-03-32 696).

REFERENCES

1. Podkopaev, S.A., Semenov, P.V., Shibalenkov, D.N., *et al*., *Proc. Third Int. Conf. "Single Crystal Growth, Strength Problems, and Heat Mass Transfer,"* Obninsk, 2000, pp. 367–373.
2. Podkopaev, S.A., Shibalenkov, D.N., Tyumentsev, V.A., *et al*., *Proc. Third. Int. Conf. "Single Crystal Growth, Strength Problems, and Heat Mass Transfer,"* Obninsk, 2001, pp. 320–324.
3. Kochetkov, V.V., Rybakova, T.V., Kumok, I.L., *et al*., *Khim. Volokna*, 1991, no. 1, pp. 47–49.
4. Skripchenko, G.B., *Khim. Volokna*, 1991, no. 3, pp. 26–29.
5. Belenkov, E.A., *Zh. Prikl. Khim*., 1999, vol. 72, no. 9, pp. 1526–1530.
6. Podkopaev, S.A., Tyumentsev, V.A., Yagafarov, Sh.Sh., and Saunina, S.I., *Zh. Prikl. Khim*., 1994, vol. 67, no. 3, pp. 433–435.

Russian Journal of Applied Chemistry, Vol. 76, No. 5, 2003, pp. 813–817. Translated from Zhurnal Prikladnoi Khimii, Vol. 76, No. 5, 2003, pp. 842–846.

MACROMOLECULAR CHEMISTRY AND POLYMERIC MATERIALS

Influence of the Concentration of Ionic Acrylamide Copolymers, Ionic Strength, and Kind of the Electrolyte on the Thoms Effect

V. A. Myagchenkov and S. V. Chichkanov

Kazan State Technological University, Kazan, Tatarstan, Russia

Received January 13, 2003

Abstract—The influence exerted by the copolymer concentration, ionic strength, and kind of single- and multicharged ions on the reduced Thoms effect was examined for ionic acrylamide copolymers as additives reduciong the hydraulic resistance of turbulent aqueous-salt flows. Synergism and antagonism were detected for certain combinations of the polymer and electrolytes.

Ionic acrylamide (AA) copolymers, along with polyoxyethylene [1, 2], are relatively accessible synthetic water-soluble polymers showing much promise as additives decreasing the hydraulic resistance of turbulent water flows (Thoms effect) [3, 4]. When working with multicomponent aqueous solutions of various compositions (in particular, with aqueous-salt media), a topical problem is to find additional possibilities for enhancing the performance of ionic AA copolymers as turbulence quenchers. Available data on how the value of the Thoms effect (T) depends on the chemical nature of the electrolyte are extremely scarce: The only indication is that T decreases on introducing into the dispersion medium some 1–1 electrolytes (NaCl, KCl) [5–7].

In this work, we evaluated on the quantitative level how the chemical nature of single- and multicharged electrolytes and their binary compositions affects the performance of ionic (anionic and cationic) AA copolymers as additives decreasing the apparent viscosity of turbulent aqueous solutions. Also we determined the conditions of manifestation of the synergistic and antagonistic effects associated with the nonadditive contributions of the components (polymer and electrolyte) to the resultant macroscopic Thoms effect [8].

In the aqueous-salt solutions studied, the synergistic and antagonistic effects are highly probable owing to two facts: (1) multicharged electrolyte ions very strongly affect the conformation of flexible-chain macromolecules of ionic AA copolymers and the structure of the electrical double layer [9]; (2) capillary transport of aqueous-salt solutions of ionic AA copolymers was performed in flows of liquids with a weakly pronounced turbulence: For water, the Reynolds number $Re = 5.2 \times 10^3$ [10, 11]. It should be noted that, at low Re, the macromolecules did not undergo noticeable mechanical degradation in a turbulent flow through a capillary [12].

EXPERIMENTAL

Experiments were performed with cationic (C) and anionic (A_1 and A_2, differ in the content of ionic units) water-soluble AA copolymers. Sample A_1 was a random copolymer of AA with sodium acrylate (SA); $M = 7.3 \times 10^6$, content of ionic (acrylate) units $\beta = 41.0\%$. The copolymer was prepared by mild base hydrolysis of high-molecular-weight polyacrylamide (0.1% aqueous solution, 50°C, NaOH). Sample A_2 had a similar molecular weight ($M = 10.8 \times 10^6$) but different microstructure of macromolecules. It was purchased from Allied Colloids (the United Kingdom) under the trade name of Alcoflood 1175-A. This anionic copolymer of AA with SA ($\beta = 21.5\%$) was prepared by radical copolymerization of AA with SA in aqueous solution. Sample C was a random copolymer of AA with dimethylaminoethyl methacrylate hydrochloride; $M = 2.3 \times 10^6$, $\beta = 16.3\%$. It was prepared by radical copolymerization of the corresponding monomers in aqueous solution.

As multicharged electrolytes we used $K_4[Fe(CN)_6]$ with a quadruple-charged anion and $FeCl_3$ with a triple-charged cation, and also NaCl as a reference electrolyte.

The procedures for measuring the parameter T and the reduced Thoms effect $\gamma = T/c$ (c is the polymer concentration) are similar to those described in [8, 13].

1070-4272/03/7605-0813$25.00

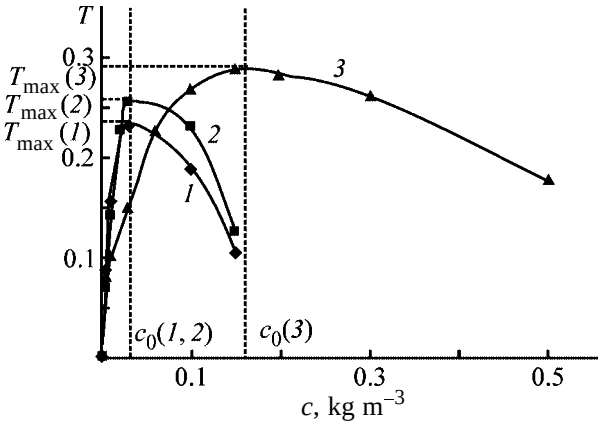

Fig. 1. Thoms effect T for nonionic AA copolymers as a function of copolymer concentration c: (*1*) A_1, (*2*) A_2, and (*3*) C.

Consider the concentration dependence $T = f(c)$ for three ionic AA copolymers: A_1, A_2, and C (Fig. 1). First, it should be noted that curves *1–3* have well-defined maxima; as the molecular weight M of the copolymers increases (going from C to A_1, A_2), the maximum shifts toward lower values of the argument: $c_0(1, 2) < c_0(3)$. The maxima in the curves $T = f(c)$ are apparently associated with the presence of a certain optimal concentration c_{opt} of ionic AA copolymers in the most active zone of quenching of turbulence waves, namely, in the near-wall zone of the capillary (zone I) [10]. In view of specific features of mass transfer of macromolecules in the turbulent mode of solution flow, the concentration c_{opt} differs from c_0, sometimes considerably, especially when strong changes in the conformational state of macromolecules (or macroions) in going from the laminar to turbulent mode of solution flow are taken into account [14]. The ascending portions of curves *1–3* at concentrations of AA copolymers below c_0 suggest that c_{opt} grows with increasing c; hence, the concentration of the most active local centers of quenching of turbulence waves, arising in the immediate vicinity of the capillary walls, varies in the same direction. The descending portions of the $T = f(c)$ curves at the concentrations $c > c_0$ suggest that the number of "effective" quenchers of the flow turbulence in zone I does not increase or increases only slightly.

In the descending portions of curves *1–3* in Fig. 1, the decisive role is played by an increase in the effective viscosity of solutions of ionic AA copolymers during transport to the capillary inlet. When viscous solutions pass along the pumping line (including the transition section at the capillary inlet), the mean velocity of the macroscopic liquid flow v decreases as compared to the similar parameter for the "internal reference," water. As a consequence of a decrease in v, the effective excess pressure in solution flow in a capillary decreases, and this trend is more pronounced at higher c. Obviously, the rate of solution transport through the capillary decreases in parallel with the excess pressure; hence, at copolymer concentrations $c > c_0$ an increase in c is accompanied by a decrease in T and γ.

In view of the inequalities $M(A_1)$, $M(A_2) > M(C)$, and $(\bar{R}^2)^{0.5}(A_1)$, $(\bar{R}^2)^{0.5}(A_2) > (\bar{R}^2)^{0.5}(C)$ [9], the relationsip between the parameters T in the region of the maxima in the $T = f(c)$ curves, namely, $T_{max}(C) > T_{max}(A_1)$, $T_{max}(A_2)$, is quite unexpected.

This apparently illogical inequality becomes understandable if we take into account specific features of electrostatic interactions of C, A_1, and A_2 macroions with the negatively charged surface of the capillary. For C macrocations, these interactions increase the potential energy of attraction U_{attr}, and for A_1 and A_2 macroanions U_{attr} decreases. As a result, the localized adsorption and the parameter c_{opt} increase for C macrocations and decrease for A_1 and A_2 macroanions, which ultimately results in increased $T_{max}(C)$ and decreased $T_{max}(A_1)$ and $T_{max}(A_2)$.

Let us then consider how the Thoms effect is manifested in more complex systems, namely, in disperse systems with added low-molecular-weight electrolyte. Preliminary experiments showed that, to obtain quantitative information on how the ionic strength J and chemical nature of the electrolyte influence the Thoms effect, it is most appropriate to keep constant the concentartion of the polymeric additive and add controlled amounts of electrolytes. For the electrolytes $K_4[Fe(CN)_6]$ and $FeCl_3$, the ionic strength was calculated as

$$J = 0.5(a_1 z_1^2 + a_2 z_2^2),$$

where a_1 and a_2, z_1 and z_2 are, respectively, the molar concentrations and charges of the first and second ions of the electrolyte in solution.

Taking into account the specific features of $T = f(c)$ dependences for the cationic (C) and anionic (A_1, A_2) AA copolymers, we chose two working concentrations, one of which corresponded to the ascending ($c < c_0$), and the other, to the descending ($c > c_0$) portion of the $T = f(c)$ dependence.

Figures 2a–2c show the $\gamma = f(J)$ dependences for all the examined ionic AA copolymers and electro-

lytes. Comparative analysis of these data allows some basic conclusions.

(1) For all the AA copolymers (C, A_1, A_2), the reduced Thoms effect γ strongly depends on particular electrolyte. This is clearly seen when comparing the γ values at fixed *J*.

(2) The shape of the $\gamma = f(J)$ curves in Figs. 2a–2c strongly depends on the copolymer concentration. At the concentrations of A_1, A_2, and C corresponding to the ascending portions of the curves $T = f(c)$, the reduced Thoms effect tends to decrease with increasing *J* (antagonistic effect), whereas at higher concentrations of the ionic AA copolymers, corresponding to the descending portions of the curves $T = f(c)$, γ tends to grow with increasing *J* (synergistic effect in the systems ionic AA copolymer–electrolyte). This difficultly predictable change in the behavior of ionic AA copolymer–electrolyte systems (transition from the synergistic to antagonistic effect) at variation of the copolymer concentration can be qualitatively understood taking into account that different functions of an electrolyte are manifested simultaneously. In particular, electrolytes participate in formation of the electrical double layer (EDL) at the capillary surface; they also affect the conformation and optimal concentration c_{opt} of macromolecules (macroions) of ionic AA copolymers in the most active zone of turbulence quenching (zone I) and the effective viscosity in the pumping line of the installation for studying the Thoms effect [13, 15].

(3) With increasing concentration of $K_4[Fe(CN)_6]$, the reduced Thoms effect for the cationic AA copolymer drastically decreases (Fig. 2c), and with $FeCl_3$ a similar trend is observed for the anionic AA copolymers (Figs. 2a, 2b). The primary cause of strong antagonistics effects observed in the systems ionic copolymer–multicharged electrolyte is associated with local electrostatic interactions of charged segments of A_1 and A_2 macroanions (or C macrocation) with Fe^{3+} cations {or $[Fe(CN)_6]^{4-}$ anions}, which sharply decrease the root-mean-square size of macromolecular coils and induce their globulization [14, 16].

This is supported by viscometric data for these systems (Fig. 3, curves *3*, *4*). When a multicharged ion has a like charge with a macroion (Fig. 3, curve *2*), and also when a 1–1 electrolyte (NaCl) is used in combination with both anionic and cationic copolymers, the decrease in the viscosity number and reduced Thoms effect with increasing *J* is appreciably less pronounced. An exception is the C–$FeCl_3$ system for which, although both the macroion and Fe^{3+} ion are positively charged, the viscosity number noticeably decreases with increasing *J*. (Fig. 3, curve *5*). Such a trend for the C–$FeCl_3$ system is due to intra- and intermolecular donor–acceptor interactions of Fe(III) with the carbonyl oxygen atom of monomeric (acrylamide) fragments of C macromolecules, which are accompanied by contraction of macromolecular coils {decrease in $(\overline{R}^2)^{0.5}$ [17, 18]}. Note that in C the concentration of nonionic (AA) units considerably exceeds the concentration of ionic units (β = 16.3%).

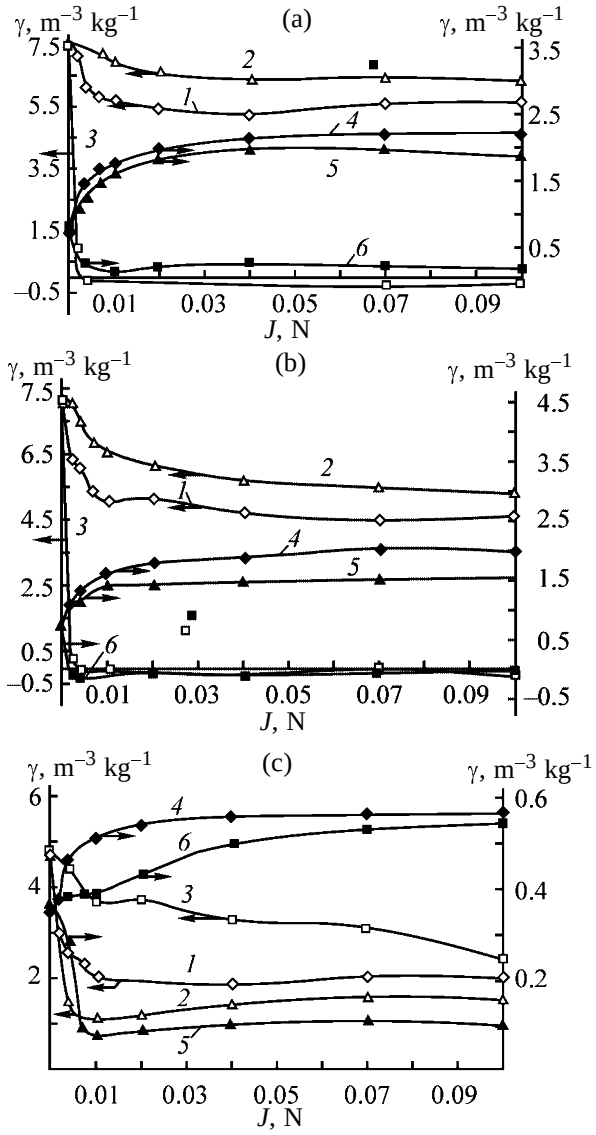

Fig. 2. Reduced Thoms effect γ as a function of the solution ionic strength *J* for ionic copolymers (a) A_1, (b) A_2, and (c) C. Polymer concentration, kg m^{-3}: (*1*–*3*) 0.03 and (*4*–*6*) 0.15. Electrolyte: (*1*, *4*) $K_4[Fe(CN)_6]$, (*2*, *5*) NaCl, and (*3*, *6*) $FeCl_3$.

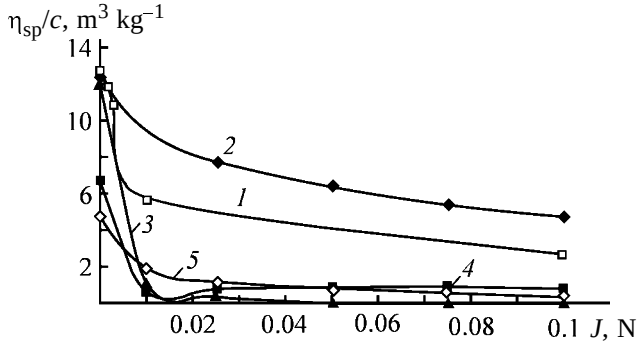

Fig. 3. Viscosity number η_{sp}/c of ionic copolymers (*1–3*) A_1 and (*4*, *5*) C as a function of the ionic strength *J*. Polymer concentration, kg m^{-3}: (*1–3*, *5*) 0.03 and (*4*) 0.1. Electrolyte: (*1*) NaCl, (*2*, *4*) $K_4[Fe(CN)_6]$, and (*3*, *5*) $FeCl_3$.

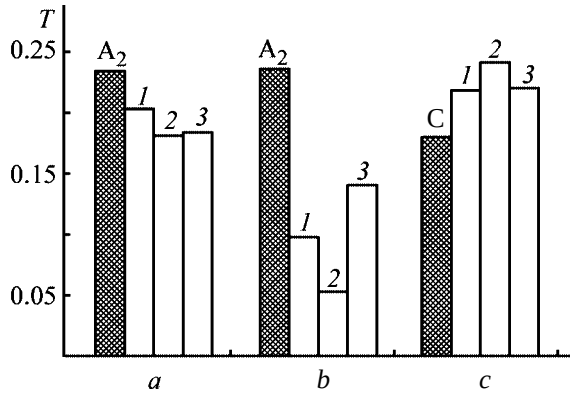

Fig. 4. Thoms effect *T* for copolymers (*a*, *b*) A_1 and (*c*) C as influenced by the order of adding binary electrolyte compositions. (A_1, A_2, C) Copolymer solution without electrolytes added. Polymer concentration, kg m^{-3}: (*a*, *b*) 0.03 and (*c*) 0.5. Electrolytes, g-equiv l^{-1}: (*a*) (E_1) 0.01 $K_4[Fe(CN)_6]$ and (E_2) 0.01 NaCl; (*b*) (E_1) 0.02 $K_4[Fe(CN)_6]$ and (E_2) 0.01 $FeCl_3$; and (*c*) (E_1) 0.01 NaCl and (E_2) 0.01 $FeCl_3$. Order of adding electrolytes: (*1*) first E_1, then E_2; (*2*) first E_2, then E_1; and (*3*) E_1 + E_2 simultaneously.

In view of the facts that *T* and γ strongly depend on particular electrolyte and interaction of active components in aqueous salt solutions involves many factors, it seemed interesting to study how binary electrolyte systems and the order of their addition affect the resultant macroscopic Thoms effect. Figure 4 shows that the parameter *T* depends on the order of adding components both for binary mixtures of multicharged and 1–1 electrolytes (Fig. 4, histograms *a*, *c*) and for a mixture of two multicharged electrolytes (Fig. 4, histogram *b*). The effect of the order of adding components was pronounced to a considerably greater extent for a mixture of $K_4[Fe(CN)_6]$ and $FeCl_3$ (Fig. 4, histogram *b*), which is quite understandable, since the interaction of the electrolytes is complicated by a redox reaction.

Thus, it is principally possible to enhance the Thoms effect by properly choosing the mode of adding binary electrolyte systems, so as to obtain a synergistic effect [8].

CONCLUSIONS

(1) The ionic strength and chemical nature of multicharged electrolytes strongly influence the reduced value of the Thoms effect.

(2) In multicomponent systems, active components (polymeric additive and electrolytes) can exhibit both synergism and antagonism with respect to the Thoms effect.

(3) With binary electrolyte systems, the value of the Thoms effect depends on the order of adding the components.

REFERENCES

1. Kulik, V.M., *Inzh.-Fiz. Zh.*, 1992, vol. 62, no. 2, pp. 228–234.
2. Pogrebnyak, V.G. and Naumchuk, N.V., *Inzh.-Fiz. Zh.*, 1995, vol. 68, no. 1, pp. 146–148.
3. Nikolaev, A.F. and Okhrimenko, G.I., *Vodorastvorimye polimery* (Water-Soluble Polymers), Leningrad: Khimiya, 1979.
4. Abramova, L.I., Baiburdov, T.A., *et al.*, *Poliakrilamid* (Polyacrylamide), Moscow: Khimiya, 1992.
5. Seo Young Hyo, Park O Ok, and Chun Miung-Suk, *J. Chem. Eng. Jpn.*, 1996, vol. 29, no. 4, pp. 611–619.
6. Muller, A.J., Saez, A.E., and Odell, J.A., *Am. Inst. Chem. Eng. J.*, 1995, vol. 41, no. 5, pp. 1333–1336.
7. Mumick, P.S., Hester, R.D., and McCormick, Ch.L., *Polym. Eng. Sci.*, 1994, vol. 34, no. 18, pp. 1429–1439.
8. Myagchenkov, V.A., Chichkanov, S.V., Proskurina, V.E., and Myagchenkov, A.V., *Zh. Prikl. Khim.*, 2002, vol. 75, no. 9, pp. 1517–1520.
9. Tsvetkov, V.N., Eskin, V.E., and Frenkel', S.Ya., *Struktura makromolekul v rastvorakh* (Structure of Macromolecules in Solutions), Moscow: Nauka, 1994.
10. Rabinovich, E.Z., *Gidravlika* (Hydraulics), Moscow: Nedra, 1980.
11. Garifullin, F.A., *Mekhanika nen'yutonovskikh zhidkostei* (Mechanics of Non-Newtonian Fluids), Kazan: Fen, 1998.
12. Baramboim, N.K., *Mekhanokhimiya vysokomolekulyarnykh soedinenii* (Mechanochemistry of Macromolecular Compounds), Moscow: Khimiya, 1971.

13. Mjagchenkov, V.A., Chichkanov, S.V., Proskurina, V.E., and Krupin, S.V., *Georesources*, 2002, no. 6, pp. 19–23.
14. Gennes, P.-G. de, *Scaling Concepts in Polymer Physics*, Ithaca: Cornell Univ. Press, 1979.
15. Myagchenkov, V.A., Chichkanov, S.V., Proskurina, V.E., and Lebukhov, V.I., in *Aziatsko-Tikhookeanskii region v global'noi politike, ekonomike i kul'ture XXI veka: Materialy dokladov mezhdunarodnoi nauchnoi konferentsii* (Asian–Pacific Region in Global Policy, Economy, and Culture of XXI Century: Proc. Int. Scientific Conf.), Khabarovsk, October 22–23, 2002, vol. 4, pp. 85–93.
16. Tanford, Ch., *Physical Chemistry of Macromolecules*, New York: Wiley, 1963.
17. Shur, A.M., *Vysokomolekulyarnye soedineniya* (Macromolecular Compounds), Moscow: Vysshaya Shkola, 1981.
18. Bekturov, E.A. and Suleimanov, I.E., *Polimernye gidrogeli* (Polymeric Hydrogels), Almaty: Gylym, 1998.

Russian Journal of Applied Chemistry, Vol. 76, No. 5, 2003, pp. 818–821. Translated from Zhurnal Prikladnoi Khimii, Vol. 76, No. 5, 2003, pp. 847–850.

MACROMOLECULAR CHEMISTRY AND POLYMERIC MATERIALS

Formation of Se^0 Nanoparticles in an Aqueous Cationic Polyelectrolyte

V. V. Kopeikin, S. V. Valueva, A. I. Kipper, A. P. Filippov, E. N. Khlebosolova, L. N. Borovikova, and V. K. Lavrent'ev

Institute of Macromolecular Compounds, Russian Academy of Sciences, St. Petersburg, Russia

Received December 23, 2002

Abstract—The nanostructures formed by reduction of Se(IV) in the selenite–ascorbate redox system in an aqueous solution of supermacromolecular polycation, poly[trimethyl(methacryloyloxyethyl)ammonium] methyl sulfate, were studied by static and dynamic optical scattering and flow birefringence.

Formation of uncharged metal nanoparticles of 1–100 nm size, which have energy-saturated surface and exhibit certain anomalies in physicochemical properties, is extensively studied [1].

However, such metal nanoparticles are unstable in aqueous solutions in the absence of stabilizing agents. One of the most promising procedures for preparing stable metal nanoparticles is reduction of their ionic species in polymer solutions. In the course of the pseudo-template synthesis, macromolecules and forming nanoparticles recognize each other, which allows control of the nanoparticle size by varying the structure and molecular weight of the polymer [2].

Such polymer-stabilized nanoparticles are of particular importance as highly selective catalytic systems and adsorption matrices for immunoassay, and, due to the rapid development of the biological nanotechnologies, as active components of drugs and transport systems for biologically active compounds [3–5].

However, much less attention was given to nonmetal nanoparticles, especially those of amorphous selenium(0) (nano-a-Se^0), which, in contrast to metal nanoparticles, can be described as an inorganic polymer containing predominantly the Se_6 and Se_8 ring fragments bound by the Se–Se covalent bonds [6]. Nano-a-Se^0 exhibits unique photoelectric and semiconductor properties and X-ray sensitivity; it is used as highly sensitive biological sensor for immunoassay [7] and chromatographically mobile affine reagent [8].

Moreover, selenium is an imperative element for normal vital activity, it exhibits antioxidantive, antimutagenic, immunnostimulating, and detoxication activity [9]. Therefore, selenium and its compounds are of particular interest as potential drugs.

As shown in [10], the reduction of sodium selenite with glutathione in aqueous solution of bovine serum albumin (BSA) yields red nano-a-Se^0, which is weakly toxic but retains the biologically active properties typical for ionic selenium species. It was found that these nano-a-Se^0 particles are predominantly stabilized by adsorption processes, in which the noncovalent (poorly understood at present) interactions of the BSA macromolecules with nanoparticles play the decisive role.

To reveal the nature of these interactions and their contribution to stabilization of nano-a-Se^0, we studied formation of selenium(0) nanoparticles in the presence of a synthetic polybase and analyzed the morphological characteristics of the resulting adsorbates by various optical methods.

EXPERIMENTAL

In our work we studied nanoparticles of a-Se^0 prepared by reduction of selenious acid (SA) with ascorbic acid in the presence of a polymer and without it.

The reagent purity was no less than 99.99%. The reduction kinetics was studied at the SA concentration of 1.7 mM at 20°C on a Specord M40 spectrophotometer (λ 320 nm).

As a polymeric stabilizer we used supermacromolecular poly[trimethyl(methacryloyloxyethyl)ammonium] methyl sulfate [polybase (PB)] with M_w 9×10^6 and intrinsic viscosity in 1 M $NaNO_3$ $[\eta]^{21} = 4.5$ dl g^{-1}:

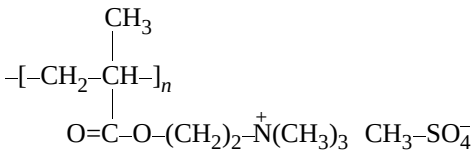

1070-4272/03/7605-0818$25.00

The nanocomposites of PB and elemental Se in the 90 : 10 weight ratio were prepared by reduction of Se(IV) in solutions with a selenium concentration of 0.01%.

The variation of the apparent viscosity of PB solution with time in the course of SA reduction was monitored on a Brookfield rheoviscometer at a rotor rotation rate of 12 rpm.

The relative viscosity η_r was determined on an Ostwald capillary viscometer with a water outflow time of 120 ± 0.2 s at 21°C.

Using the flow birefringence (FBR) procedure [11], we evaluated the molecular dispersity of the resulting adsorbates in solutions using the gradient dependence of the FBR value Δn.

The FBR value Δn was determined in relation to the gradient of the rotor rotation rate g and PB concentration c at fixed concentration of selenium. We used a titanium dynamo-optimeter equipped with an internal rotor (4 cm high, with a 0.3 mm gap between the rotor and stator). All the measurements were carried out in the temperature-controlled solutions at 21°C to exclude changes in the viscosity and optical density due to the temperature gradient. The experimental setup was calibrated using phenylethyl alcohol with high FBR ($\Delta n/g$ 17×10^{-12}) and the polystyrene–bromoform system. The error in the FBR determination $[n] = \lim_{g \to 0, c \to 0} (\Delta n/gc\eta_0)$ (η_0 is the solvent viscosity) did not exceed 10%. The measurements were performed at $g < g_k$, where g_k is the velocity gradient at which the flow becomes turbulent.

In the general case ($dn/dc \neq 0$, where dn/dc is an increment of the solution refraction index, which comprised 0.155 and 0.214 for PB–H_2O and PB–Se^0–H_2O systems, respectively), the experimental $[n]$ value includes three effects: $[n] = [n]_e + [n]_{fs} + [n]_f$, where $[n]_e$ is the intrinsic anisotropy and $[n]_{fs}$ and $[n]_f$ are the micro- and macroform effects, respectively [11]. The total segmental anisotropy $[n]_e + [n]_{fs}$ is determined by the equilibrium rigidity of the polymer chain A and by the structure of a polymer unit, whereas $[n]_f$ is related to the asymmetry of the macromolecule (or particle) p by the following expression:

$$[n]_f = [(n_s^2 + 2)/3]^2[M_w(dn/dc)^2 f(p)]/(30\pi RTn_s)$$

$$= \text{const} M_9 (dn/dc)^2 f(p),$$

where M_w is the molecular weight of the adsorbate macromolecule; n_s, refractive index of the solvent; T, absolute temperature; R, universal gas constant; and $f(p)$, tabulated function of the ratio of axes of a rigid (impermeable for solvent) ellipsoid approximating a particle [11].

Thus, for macromolecular flexible-chain and moderately rigid-chain polymers ($A < 5$ nm) with insignificant optical anisotropy and low molecular weight of the monomeric unit, $[n] \sim [n]_f$, which allows direct determination of the parameter p from the experimental FBR values [11].

Using the elastic (static) light scattering method [12], we evaluated the molecular weight M_w and the size R_g of nanoparticles in question, and also their affinity for water solvent (from the second virial coefficient A_2). The amount of macromolecules adsorbed on the selenium nanoparticle surface was determined from the ratios of M_w for PB and its adsorbates. The reduced intensity of the solution scattering R_θ was determined using a Fica photogoniodiffusometer. The wavelength of the incident vertically polarized light was 546.1 nm. The measurements were performed at the scattering angles $\theta = 30°$–$150°$. The solutions and solvents were purified by centrifuging at 15×10^3 rpm for 1.0–1.5 h. The refractive index increments dn/dc were determined with an IRF-23 refractometer.

The experimental data on the light scattering were treated with the Zimm procedure by double extrapolation (to $c = 0$, $\theta = 0$) of the dependences of Kc/R_θ on $\sin^2(\theta/2) + kc$ (K is the calibration constant, and k is a numerical constant).

The average hydrodynamic parameters of the particles R_H were determined by the quasi-elastic (dynamic) light scattering method [13]. The parameter ρ^* characterizing the nanostructure conformation [14–17] was determined from the experimental ratio of R_g and R_H for the PB–Se^0 adsorbate.

The optical section of the unit for measurements of the dynamic light scattering was equipped with an ALV-SP goniometer (Germany) and an He–Ne laser (λ 632.8 nm, 20 mW). The correlation function of the scattered light intensity was evaluated with a 288-channel Photo Cor-FC correlator (Anteks Joint-Stock Company, Russia). The experimental data were treated by the Tikhonov's methods of cumulants and normalization using appropriate software.

In reduction of SA with ascorbic acid, the first-order rate constant with respect to SA was 1.56×10^{-3} s^{-1}, and it increased to 2.1×10^{-3} s^{-1} in the presence of PB. Without PB, the resulting Se^0 nanoparticles were unstable and formed aggregates in 3–4 days, which then precipitated. In the presence of

the polymer stabilizer, the nano-a-Se^0 particles were aggregation-stable for at least 6 months.

The apparent viscosity of the PB solution remained constant for 1 day, comprising about 200 cPs, and then it sharply decreased to 30 cPs, which suggests that the total number of the particles in the solution decreased owing to the adsorption of macromolecules on the surface of selenium nanoparticles. As seen from the comparison of the intrinsic viscosity of the initial PB and PB–nano-a-Se^0 adsorbate, the estimated [η] value decreased from 55 to 12 dl g^{-1}. At the same time, M_w for the adsorbate determined from the data of the static light scattering was 100×10^6, i.e., it increased by a factor of 11 as compared to the free PB macromolecules.

The second virial coefficient A_2 for this system is very small (0.1×10^{-4} cm^3 mol g^{-1}); it shows that the thermodynamic state of solution is close to ideal.

In aqueous solutions, the average hydrodynamic radius R_H for free PO macromolecules is 540 nm, whereas for selenium nanoparticles prepared in the absence of polymeric stabilizer it comprises 170 nm. The size of the PB-Se^0 adsorbate, evaluated from the dynamic and static light scattering data, is considerably smaller [R_g (rms radius of inertia) 70 nm, R_H 70 nm]. In this case, $\rho^* = R_g/R_H = 1$, which suggests almost ideal spherical shape of the adsorbate formed [14–17].

To determine the radius of the core selenium nanoparticles in the adsorbate, the aqueous PB-Se^0 solution was lyophilically dried, and the dry product was pelletized and studied by small-angle X-ray diffraction analysis. It was found that the radius of the spherical Se^0 particle was about 15 nm, i.e., it was smaller by nearly an order of magnitude than that of the particles prepared without polymeric stabilizer. Thus, in aqueous solution the thickness of the polymeric coating on the Se^0 nanoparticles is about 55 nm, i.e., macromolecules are strongly compacted upon adsorption.

The data on the optical properties of PB suggest that in aqueous solutions it is an impermeable strongly asymmetric swollen ball with asymmetry $p > 2$ [18]. On passing from the PB–H_2O system to the PB–Se^0–H_2O system, the optical anisotropy decreased from 10 000 to 6000 cm^4 s^2 g^{-2}, which is probably due to the changes in the macromolecule conformation.

It should be noted that, in the entire concentration (c) range studied, the PB–H_2O and PB–Se^0–H_2O systems retain the molecular-dispersion state of solutions. This is confirmed by the $\Delta n = f(g)$ dependences: at $g < g_k$, for any c, these dependences are well approximated by straight lines passing through the origin.

In the $[n] \sim [n]_f$ approximation for the PB–Se^0–H_2O system, our calculations of the parameter p showed nonspherical conformation of the nanostructure; $p = 2.1$, which corresponds to the conformation of the Gaussian ball [11]. However, the absence of the concentration dependence of the reduced optical anisotropy in the PB–Se^0–H_2O system indicates that the parameter p tends to 1, i.e., the conformation tends to spherical [11]. Since, even in the case of such rigid macromolecule as DNA, the shape of macromolecule adsorbates on metal nanoparticles is close to spherical [19], the $[n] \sim [n]_f$ approximation for the PB–Se^0–H_2O system is inadequate. In this case, a major contribution to the observed optical anisotropy is made by the segmental optical anisotropy probably related to high hydrophobicity of the PB monomer unit [20], and specifically the hydrophobic interactions of nonpolar macromolecule fragments with nano-Se^0 are responsible for adsorption.

Assuming nearly spherical conformation of the nanostructure, its packing coefficient k can be described by the following equation [21]:

$$k = NM_w^* \Sigma_i \Delta V_i / v^* M_0, \quad (2)$$

where $\Sigma_i \Delta V_i = 253$ Å^3 [21] is the van der Waals volume of the monomeric unit, which is the sum of the van der Waals volume increments of the separate atoms in this unit; M_w^*, molecular weight of the particle; N, number of the adsorbed polymer macromolecules; M_0, molecular weight of the monomeric unit; and v^*, adsorbate volume $[4\pi/3(R^*)^3]$.

The R^* value is the rms radius of inertia or the average hydrodynamic radius of an adsorbate, which are equal under the experimental conditions studied.

The parameter k was 0.7, which is typical for globular proteins (k 0.6–0.8). Thus, the adsorbate can be described as a compact approximately spherical nanostructure.

Our data are of particular interest for deeper understanding of the biological and catalytic processes occurring in the nature with participation of nanoparticles of elements. We found that such nanoparticles are adsorption matrices for biological polymers and chemical reagents, which provides high local concentrations of these compounds and can strongly accelerate biochemical and catalytic processes.

CONCLUSIONS

(1) Spherical particles of amorphous selenium about 15 nm in size were obtained by reduction of selenium(IV) in the presence of the selenite–ascorbate redox system in aqueous solution of a cationic polyelectrolyte.

(2) Sharp decrease in the intrinsic and apparent viscosity of the resulting polymer–Se^0–water solution indicates that the thermodynamic properties of this system become close to ideal, which suggests formation of aggregation-stable macromolecule adsorbates on selenium nanoparticles.

(3) As shown by the molecular hydrodynamics and optical data, the resulting adsorbate can be described as a supermacromolecular close-packed ($k \approx 0.7$) spherical nanostructure of nearly 70 nm size, containing about 11 macromolecules whose hydrodynamic radius in the free state would be 540 nm.

REFERENCES

1. Pomogailo, A.D., *Nonochastitsy metallov v polimerakh* (Metal Nanoparticles in Polymers), Moscow: Nauka, 1999.
2. Litmanovich, A.A. and Papisov, I.M., *Vysokomol. Soedin., Ser. B*, 1997, vol. 39, no. 2, pp. 313–326.
3. Kopeikin, V.V. and Panarin, E.F., *Dokl. Ross. Akad. Nauk*, 2001, vol. 243, no. 2, pp. 497–500.
4. Balogh, L., Swanson, D.R., Tomalia, D.A., *et al*., *Nano Lett*., 2001, vol. 1, no. 1, pp. 18–21.
5. Connelly, S. and Fitzmaurice, D., *Adv. Mater*., 1999, vol. 11, no. 14, pp. 1202–1205.
6. *Handbook of Chemistry and Physics*, Lide, R.D., Ed., Cleveland: Chapman and Hall, 2001, 81-st ed.
7. US Patent 4954452.
8. US Patent 5120643.
9. *Selenium in Biology and Human Health*, Burk, R.F., Ed., New York: Springer, 1994.
10. Zhang, J.S., Gao, X.Y., Zhang, L.D., and Bao, Y.P., *Biofactors*, 2001, vol. 15, no. 1, pp. 27–38.
11. Tsvetkov, V.N., Eskin, V.E., and Frenkel', S.Ya., *Struktura makromolekul v rastvorakh* (Structure of Macromolecules in Solutions), Moscow: Nauka, 1964.
12. Eskin, V.E., *Rasseyanie sveta rastvorami polimerov i svoistva makromolekul* (Light Scattering in Polymer Solutions and Properties of Macromolecules), Leningrad: Nauka, 1986.
13. Brown W., *Dynamic Light Scattering: The Method and Some Applications*, Oxford: Clarendon, 1993.
14. Meewes, M., Ricka, J., De Silva, M., *et al*., *Macromolecules*, 1991, vol. 24, no. 21, pp. 5811–5816.
15. Nishio, I., Shao, Thang Sun, Swislow, G., and Tanaka, T., *Nature*, 1979, vol. 281, no. 5728, pp. 208–209.
16. Konishi, T., Yoshizaki, T., and Yamakawa, H., *Macromolecules*, 1991, vol. 24, no. 20, pp. 5614–5622.
17. Burchard, B.W., *Laser Light Scattering in Biochemistry*, Harding, S.E., Satelle, D.B., and Bloomfild, V.A., Eds., Cambridge: Royal Soc. Chem. Inform., 1992, pp. 3–21.
18. Valueva, S.V., Kipper, A.I., Rumyantseva, N.V., and Klenin, S.I., *Vysokomol. Soedin., Ser. A*, 2000, vol. 42, no. 7, pp. 1152–1157.
19. Storhoff, J.J., Lazaorides, A.A., Mucic, R.C., *et al*., *J. Am. Chem. Soc*., 2000, vol. 122, no. 19, pp. 4640–4650.
20. Valueva, S.V., Conformation Properties of Macromolecular Diphilic Polyanions and Polycations in Aqueous Salt and Aqueous Acetone Solutions, *Cand. Sci. Dissertation*, St. Petersburg, 1997.
21. Askadskii, A.A. and Matveev, Yu.I., *Khimicheskoe stroenie i fizicheskie svoistva polimerov* (Chemical Structure and Physical Properties of Polymers), Moscow: Khimiya, 1983.

Russian Journal of Applied Chemistry, Vol. 76, No. 5, 2003, pp. 822–826. Translated from Zhurnal Prikladnoi Khimii, Vol. 76, No. 5, 2003, pp. 851–855.

MACROMOLECULAR CHEMISTRY AND POLYMERIC MATERIALS

Synthesis of Polypyrrole Nanoparticles by Dispersion Polymerization

A. Yu. Men'shikova, B. M. Shabsel's, and T. G. Evseeva

Institute of Macromolecular Compounds, Russian Academy of Sciences, St. Petersburg, Russia

Received December 24, 2002; in final form, January 2003

Abstract—The influence of pyrrole, oxidant ($FeCl_3$), and polymeric stabilizer (polyvinyl alcohol) concentrations and of temperature on the rate of redox dispersion polymerization of pyrrole, diameter of the forming particles, and their size distribution was studied with the aim to prepare polypyrrole nanoparticles.

Development of methods for controlling the size and surface properties of polypyrrole (PP) nanoparticles in the course of their synthesis by redox dispersion polymerization is an urgent problem, since PP shows promise as a conducting polymer. However, its mechanical strength and adhesion to other materials are poor, and it is virtually insoluble in common organic solvents, which complicates its processing. Therefore, it was suggested to prepare colloidal dispersions of PP nanoparticles and then to use them in formation of composite materials [1–6]. Conjugates of PP particles with biospecific ligands can be used for development of biosensors with an electric response on variation of the concentrations of biologically active substances [7]. The black color of PP particles also allows their use instead of colloidal gold as markers of linked bioligands for imaging of immunochemical reactions [7, 8].

Polypyrrole dispersions can be prepared by pyrrole polymerization effected by an oxidant in the presence of soluble polymers which are adsorbed on precipitating PP particles and stabilize them, preventing further aggregation [1–5]. The nature of the polymeric stabilizer, its molecular weight, and concentration in the reaction mixture can appreciably affect both the size of the forming PP nanoparticles and the stability of PP dispersions in the course of their synthesis and subsequent storage. In preparation of composites, the polymeric stabilizer coating the PP nanoparticles can also take part in formation of interface structures, affecting thus the adhesion, interfacial electrical conductivity, and characteristics of the composite materials obtained.

The size of PP particles determines the structure of the composites and the thickness of interface layers. Therefore, the control of the size and size distribution of PP particles in the course of their preparation is an urgent problem. With the aim to solve this problem and to prepare aqueous PP dispersions differing in the particle size and concentration of the polymeric stabilizer in them, we examined the influence exerted by the concentrations of pyrrole, oxidant ($FeCl_3$), and polymeric stabilizer (polyvinyl alcohol, PVAl) and by the reaction temperature on the kinetics of redox dispersion polymerization of pyrrole and on the diameter and size distribution of the forming PP particles.

EXPERIMENTAL

Pyrrole and DMF were purified by vacuum distillation. As a dispersion medium we used double-distilled water. $FeCl_3$, $NaHSO_3$, and standard HCl solution (analytically pure grade) were used without additional purification. As a polymeric stabilizer we used two PVAl samples (Plastpolimer Research and Production Association, St. Petersburg) containing 11 [PVAl(I)] and 10 [PVAl(II)] mol % residual acetate groups. The batch of PVAl(I), 5/9 grade, was produced according to GOST (State Standard) 10779–81, and PVS(II), 13/16 grade, was a pilot batch. The viscosity-average molecular weight M of PVAl(I) and PVAl(II), calculated by the Mark–Kuhn–Houwink equation with the parameters $K = 2.0 \times 10^{-4}$ and $\alpha = 0.76$ [9] from the intrinsic viscosity in water at 25°C, was 1.7×10^4 and 5.0×10^4, respectively.

The compositions of the reaction mixtures in redox dispersion polymerization of pyrrole,

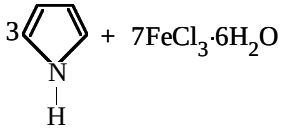

1070-4272/03/7605-0822$25.00

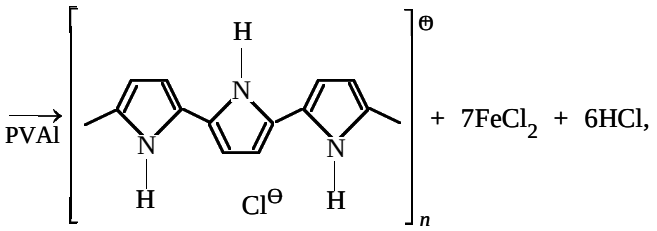

are listed in the table. The concentration of PVAl aqueous solutions was varied within 0.3–1.6 wt %. The oxidant ($FeCl_3$) concentration was calculated from the stoichiometric ratio $FeCl_3$: pyrrole = 7 : 3 for the monomer concentration in the aqueous phase of 1.0–2.7 wt %. In run nos. 1 and 2 it was 0.65; in run nos. 3 and 8–10, 0.32; and in run no. 6, 0.85 M.

Polymerization was performed both at room temperature (296 K) and at 277 K in a refrigerator. The diameters of PP particles were determined by electron microscopy (JEM 100 S electron microscope, JEOL, Japan).

The degree of pyrrole conversion in samples withdrawn in the course of the synthesis was determined by gas chromatography with *n*-amyl alcohol as internal reference. Polymerization was stopped by adding the sample into a solution containing 0.5 M $NaHSO_3$ and 0.1 M HCl. The conversion was determined with 5% accuracy.

In the course of polymerization, the initially transparent solution transformed into an intensely colored black PP dispersion; therefore, we could monitor how its optical density varies in the course of the synthesis. The electronic absorption spectrum of the PP dispersion in the visible and near-IR range (SF-26 spectrophotometer) is shown in Fig. 1. The PP dispersions prepared to determine the degree of pyrrole conversion chromatographically (25 μl) were diluted with water to 3 ml, and the light absorption at 1000 nm was measured (Fig. 1).

To study the seed polymerization of pyrrole in acid solution on Fe_3O_4 particles according to [10], we prepared a magnetic fluid by the reaction

$$FeCl_2 \cdot 4H_2O + 2FeCl_3 \cdot 6H_2O + 8NH_4OH = Fe_3O_4\downarrow + 8NH_4Cl + 20H_2O.$$

As a polymeric stabilizer of Fe_3O_4 particles we used PVAl(II) of 5 wt % concentration. In the magnetic fluid obtained, the Fe_3O_4 concentration was also 5 wt %, and the prevailing particle diameter, about 10 nm (Fig. 2f). However, coarser particles of irregular (not spherical) shape are also seen in the electron micrographs. This is due to aggregation of magnetic Fe_3O_4 particles.

Influence of the reaction mixture composition and temperature in redox dispersion polymerization of pyrrole on the diameter *d* of the forming PP nanoparticles

Run no.	PVAl* (wt %)	Pyrrole (wt %)	*T*, K	*d*, nm
1	0.6	2.0	296	Coagulation
2	0.6	2.0	296	80
3	0.9	1.0	296	60–100
4	0.8	2.7	277	60–100
5	0.3	1.0	277	90
6	0.5	1.0	277	90
7	0.8	1.0	277	70
8	1.6	1.0	277	70
9	0.8	1.0	296	60
10	1.6	1.0	296	50–70
11	0.7	1.4	296	30–50
12	0.7	1.4	296	20–40

* Run no. 1 was performed with PVAl(I), and the other runs, with PVAl(II).

The seed polymerization of pyrrole on Fe_3O_4 particles stabilized with PVAl is initiated by back dissolution of the magnetite particles in an acid medium

$$Fe_3O_4 + 8HCl = 2FeCl_3 + FeCl_2 + 4H_2O$$

and by oxidation of pyrrole with the forming Fe(III). The HCl concentration was 0.28 M, and content of Fe_3O_4 particles, 0.70 wt %; in the case of complete oxidation and dissolution of Fe_3O_4 particles, this corresponds to the Fe(III) concentration of 0.057 M. To localize the pyrrole oxidation on the surface of Fe_3O_4 particles, the monomer was added in a concentration of 0.21 M, which corresponds to its 16-fold excess

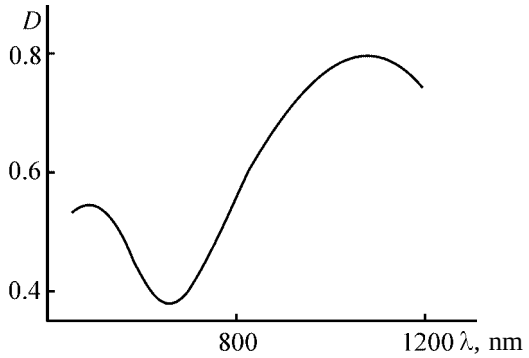

Fig. 1. Electronic absorption spectrum of PP dispersion: (*D*) optical density and (λ) wavelength.

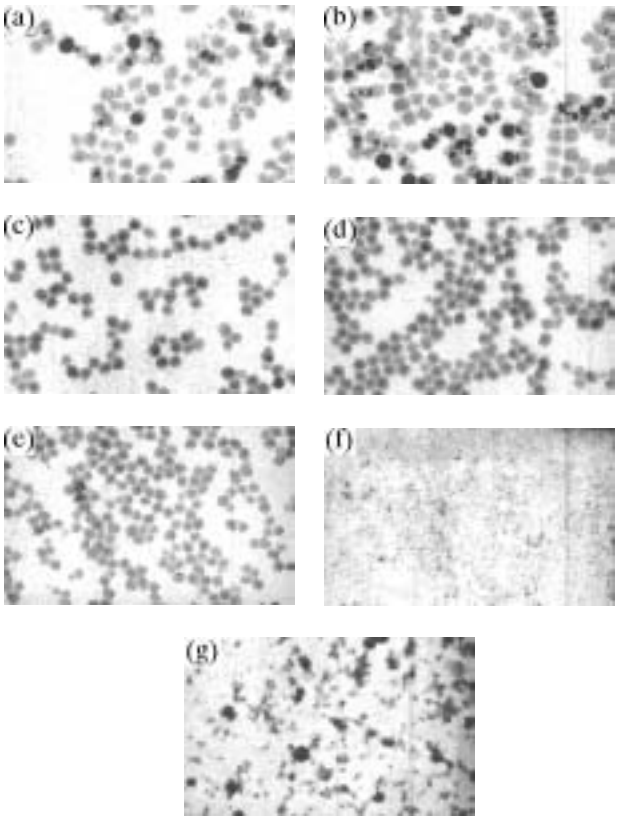

Fig. 2. Electron micrographs of PP particles prepared at PVAl(II) concentration of (a) 0.3, (b) 0.5, (c) 0.8, and (d) 1.6 wt %, and those of (f) magnetic fluid and (g) PP dispersion prepared with this fluid under argon. Polymerization temperature, K: (a–d) 277 and (e, g) 296. Magnification ×50 000.

over the oxidant, Fe(III). In run nos. 11 and 12, the reaction mixture composition was the same (see table), but run no. 12 was performed in an argon atmosphere to restrict oxidation of Fe(II) to Fe(III) with atmospheric oxygen in the bulk of the aqueous phase.

The influence of the redox dispersion polymerization of pyrrole in aqueous PVAl solutions on the size of the forming PP nanoparticles is illustrated by the table and Fig. 2. It is seen that the capability of PVAl to stabilize aqueous PP dispersion largely depends on the PVAl molecular weight. With PVAl(I), we have not obtained a stable PP dispersion; it coagulated in the course of the synthesis (run no. 1). On the contrary, PVAl(II) at the same concentration efficiently stabilized the PP dispersion. The dispersions obtained were characterized by a narrow particle-size distribution, and in some cases they could be regarded as monodisperse. This difference is presumably due to the higher molecular weight of PVAl(II). Owing to the high content of acetate groups, the PVAl(II) chain is diphilic, and the polymer, being surface-active, is efficient as a steric stabilizer.

We found that, at room temperature (296 K), the redox polymerization of pyrrole occurs at a high rate at its content in the aqueous phase of 1.0–2.7 wt %. However, as the pyrrole concentration is increased, the forming PP particles become coarser, with broadening of the particle-size distribution (see table, run nos. 9, 2, 4). Particles of irregular (nonspherical) shape were detected (run no. 4). This is due to increase in the $FeCl_3$ concentration (in stoichiometric proportion with the pyrrole concentration) and decrease in the surface charge of particles with increasing ionic strength, which results in certain destabilization of the dispersion [11]. Therefore, further experiments were performed at a pyrrole concentration in the aqueous phase of 1.0 wt %.

We examined how the reaction temperature affects the polymerization kinetics and particle-size distribution of PP. The polymerization time increased by a factor of 3–5 in going from 296 to 277 K (Fig. 3a). The mean diameters of the forming nanoparticles are similar at both temperatures, but in the samples prepared at room temperature the particle-size distribution is somewhat broader (see table). The increase in the PVAl concentration resulted in faster polymerizatiuon (Fig. 3a) and formation of finer PP particles (see table; Figs. 2a–2d). This may be due to strengthening of the structural-mechanical barrier formed by the water-soluble polymer at the particle surface, and also to an increase in the viscosity of the aqueous phase, preventing aggregation of PP particles in the stage of seeding. Thus, redox polymerization of pyrrole in aqueous PVAl solutions allows preparation of PP dispersions with the particle size ranging from 50 to 100 nm and narrow particle-size distribution.

Monitoring of the optical density of reaction mixtures in the course of pyrrole polymerization showed that the dependences obtained (Fig. 3b) run in parallel with the conversion curves (Fig. 3a). To evaluate the extent of correlation of the optical density and conversion, we calculated the degrees of conversion of pyrrole into PP as the ratios of the optical density of the reaction mixture at the instant of sampling in the course of the synthesis to the optical density of the ready PP dispersion. The degrees of conversion evaluated spectrophotometrically and determined chromatographically are compared in Fig. 4. The correlation coefficients of these quantities as functions of the time from the start of polymerization at PVAl concentration of 0.8 and 1.6 wt % are 0.93 at 296 K and 0.86 and 0.98, respectively, at 277 K. The satisfactory cor-

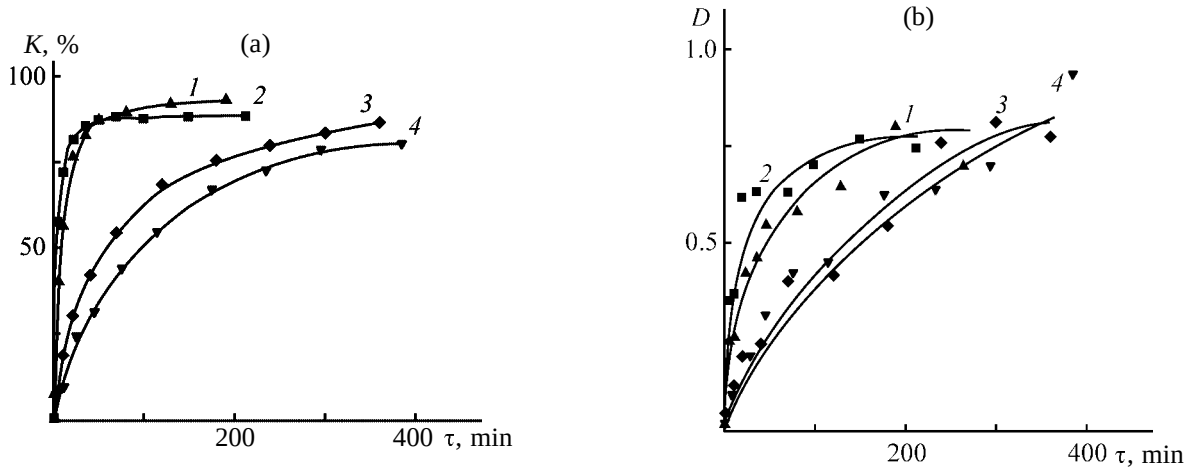

Fig. 3. (a) Degree of pyrrole conversion *K* determined by gas chromatography and (b) optical density *D* of the reaction mixture as functions of time τ from the start of polymerization at (*1*, *2*) 296 and (*3*, *4*) 277 K. Pyrrole concentration in water 1.0 wt %. PVAl(II) concentration, wt %: (*1*, *3*) 0.8 and (*2*, *4*) 1.6.

relation between the optical density of the reaction mixture and degree of polymerization of the monomer determined chromatographically allows spectrophotometric evaluation of the PP conversion in the course of dispersion polymerization, which is a simpler procedure than gas chromatography.

A promising procedure for preparing composite particles is polymerization of various monomers, in particular, pyrrole in the presence of dispersions of metal oxides, silica gel, or polymeric microspheres having a narrow particle-size distribution [8, 12, 13]. Usually the size of seed particles varies in the submicrometer or micrometer range and considerably exceeds the thickness of the polymer layer formed on the particle surface. Here we used this approach for decreasing the size of the PP particles formed. As seeds we used nanoparticles of Fe_3O_4 magnetic fluid 10 nm in diameter, stabilized by PVAl (Fig. 2f). In the presence of HCl, these particles slowly dissolve to form $FeCl_3$. In this case, the redox polymerization of pyrrole occurs under the action of Fe(III) formed *in situ*. In the process, the reaction mixture changes the color from orange-yellow to black, which also allows spectrophotometric evaluation of the pyrrole conversion into PP.

It should be noted that the rate of seed polymerization of pyrrole may be limited by diffusion, because the Fe^{3+} ions and pyrrole molecules should diffuse toward each other through a PP layer arising on the surface of the growing particles. Under these conditions, the pyrrole polymerization proceeded until Fe_3O_4 nanoparticles dissolved completely, as indicated by the fact that the formed PP particles had no magnetic properties, and also by a considerable increase in their size as compared to the Fe_3O_4 seed nanoparticles.

Thus, seed redox polymerization of pyrrole on Fe_3O_4 nanoparticles in acid solutions allowed preparation of PP particles with the minimal size as small as 30 nm (run no. 11). However, at room temperature,

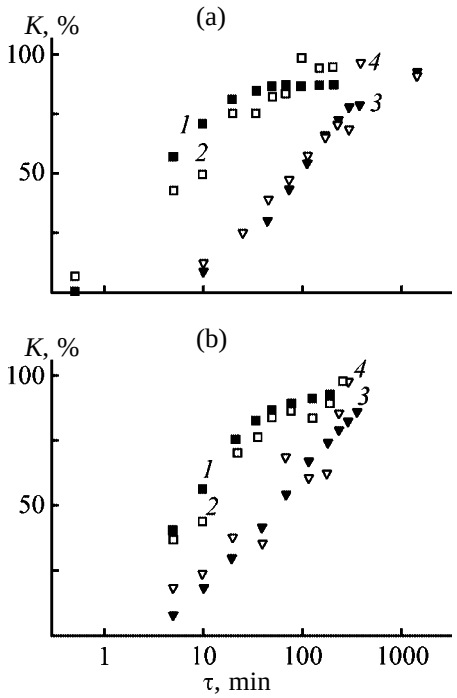

Fig. 4. Comparison of the degrees of pyrrole conversion *K* at (*1*, *2*) 296 and (*3*, *4*) 277 K, determined (*1*, *3*) by gas chromatography and (*2*, *4*) spectrophotometrically, as functions of the time τ from the start of polymerization. PVAl(II) concentration, wt %: (a) 0.8 and (b) 1.6.

coarser PP particles were also obtained. This may be due to too fast dissolution of Fe_3O_4 and diffusion of the Fe^{3+} ions to the bulk of the aqueous phase, where pyrrole could also polymerize. To prevent oxidation of the monomer with atmospheric oxygen, the reaction mixture was purged with argon before adding pyrrole (run no. 12). In this case, the diameter of the major fraction of the formed PP nanoparticles was decreased to 20–30 nm (see table), which may be due to more compact packing of the PP chains. However, the electron micrograph of this dispersion revealed also the presence of coarser particles of nonspherical shape (Fig. 2g). Apparnetly, these particles originate from pyrrole polymerization on aggregates of Fe_3O_4 particles present in the magnetic fluid. The impurity of these coarse particles can be separated from 20–30-nm PP nanoparticles by ultrafiltration.

CONCLUSIONS

(1) The main features of redox polymerization of pyrrole in aqueous solutions of polyvinyl alcohol were determined, and the conditions were found for preparing monodiserse polypyrrole particles 60–90 nm in diameter. A spectrophotometric method was suggested for evaluating the conversion of pyrrole into polypyrrole in the dispersions.

(2) Seed dispersion redox polymerization of pyrrole on Fe_3O_4 nanoparticles allows preparation of polypyrrole particles with the diameter as small as 20 nm.

ACKNOWLEDGMENTS

The study was financially supported by the Russian Foundation for Basic Research, project no. 01-03-32414.

REFERENCES

1. Armes, S.P., Miller, J.F., and Vincent, B., *J. Colloid Interface Sci.*, 1987, vol. 118, no. 2, pp. 410–416.
2. Markham, T.M. and Vincent, O.B., *Colloids Surf.*, 1990, vol. 51, no. 1, pp. 239–253.
3. Beaman, M. and Armes, S.P., *Colloid Polym. Sci.*, 1993, vol. 271, no. 1, pp. 70–75.
4. Pelster, R. and Simon, U., *Colloid Polym. Sci.*, 1999, vol. 277, no. 1, pp. 2–14.
5. Zelenev, A., Sonnenberg, W., and Matijevic, E., *Colloid Polym. Sci.*, 1998, vol. 276, no. 6, pp. 838–841.
6. Wang, L.X., Li, X.G., and Yang, Y.L., *React. Funct. Polym.*, 2001, vol. 47, no. 2, pp. 125–139.
7. Tarcha, P.J., Misun, D., Finley, D., *et al.*, *Polymer Latexes: Preparation, Characterization, and Applications*, Daniels, E.S., Sudol, E.D., and El-Aaser, M.S., Eds., *ACS Symp. Ser.*, Washington, DC, 1992, vol. 492, pp. 347–367.
8. Partch, R.E., Gangolli, S.G., Owen, D., *et al.*, *Polymer Latexes: Preparation, Characterization, and Applications*, Daniels, E.S., Sudol, E.D., and El-Aaser, M.S., Eds., *ACS Symp. Ser.*, Washington, DC, 1992, vol. 492, pp. 367–386.
9. *Polymer Handbook*, Brandrup, J., Immergut, E.H., and Grulke, E.A., Eds., New York: Wiley, 1999, 4th ed.
10. Berkovskii, B.M., Medvedev, V.F., and Krakov, M.S., *Magnitnye zhidkosti* (Magnetic Fluids), Moscow: Khimiya, 1989.
11. Men'shikova, A.Yu., Evseeva, T.G., Ivanchev, S.S., *et al.*, *Zh. Prikl. Khim.*, 2002, vol. 75, no. 12, pp. 2029–2035.
12. Laselles, S.F., McCarthy, G.P., Butterworth, M.D., and Armes, S.P., *Colloid Polym. Sci.*, 1998, vol. 276, no. 6, pp. 893–902.
13. Laselles, S.F. and Armes, S.P., *J. Mater. Chem.*, 1997, vol. 7, no. 8, pp. 1339–1347.

Russian Journal of Applied Chemistry, Vol. 76, No. 5, 2003, pp. 827–830. Translated from Zhurnal Prikladnoi Khimii, Vol. 76, No. 5, 2003, pp. 856–859.

MACROMOLECULAR CHEMISTRY AND POLYMERIC MATERIALS

Thermal Oxidation of Polyethylene Films Containing Dispersed Copper and Amine Antioxidant

D. G. Lin and E. V. Vorob'eva

Skorina Gomel State University, Gomel, Belarus

Received January 29, 2003

Abstract—Thermal oxidation of polyethylene filled with dispersed copper and containing an amine antioxidant was studied. The concentration ranges in which the catalytic effect of the metal on the polymer oxidation or the stabilizing effect of the antioxidant prevails were determined. Under certain conditions, dispersed copper enhances the stabilizing effect of the antioxidant.

It was found previously [1–3] that an amine oxidant (AO) Neozon D inhibits oxidation of polyethylene (PE) more efficiently when the polymer is in contact with metallic copper. For example, the induction period of oxidation (IPO) of PE films inhibited with Neozon D is longer when the films are in contact with a copper support, as compared to the films that are in contact with inert (e.g., glass) supports. This result is quite unexpected, since the copper support catalyzes oxidation of noninhibited PE [4–6] and accelerates the consumption of phenolic AOs acting by a similar mechanism, thus shortening the IPO [7]. Enhancement of the inhibiting activity of amine AO is observed not only in oxidation of PE films on copper supports [4, 7] but also in oxidation of PE films filled with dispersed copper [8]. This effect was attributed to a reaction of Neozon D with copper, yielding a more effective AO [1–3].

At the same time, the mechanism responsible for enhancement of the inhibiting power of the amine AO under conditions of contact of PE with copper is poorly understood. In particular, the relationship between the catalytic effect of copper on oxidation of PE and enhancement of the performance of Neozon D is unclear. These factors, apparently, affect IPO in opposite directions.

In this work, with copper-filled PE as example, we studied how the concentrations of the dispersed metal and Neozon D influence the inhibiting effect.

EXPERIMENTAL

Experiments were performed with powdered nonstabilized high-density PE prepared at low pressure on complex organometallic catalysts [GOST (State Standard) 16338–85, base grade 20306-005]. Copper powder (M1 grade) and Neozon D (β-phenylnaphthylamine, GOST 39–79) were introduced by mechanical blending. From blends of the polymer with the additives, we prepared by hot pressing (150°C, 30–90 s) films 30–200 μm thick, which were subsequently oxidized on KBr supports. In some cases, M1 copper foil was used as support. Oxidation was performed in air in ovens at 150°C.

The extent of oxidation was estimated from the IR transmission spectra. If oxidation was performed on a copper support, the film was separated from the support; with KBr supports, transparent in the IR range, this was unnecessary. The IR spectra were recorded on a Specord 75-IR spectrophotometer. The extent of PE oxidation was evaluated from the optical density of the carbonyl absorption band at 1720 cm^{-1}, using the band at 1460 cm^{-1} as internal reference. The IPO duration was determined from the kinetic curves of accumulation of carbonyl groups; the moment at which the extinction parameter (ratio of the optical density to the film thickness) reached 3–4 cm^{-1} was taken as the end of IPO.

When studying samples of inhibited and unfilled PE films oxidized on a copper support, we determined, along with the extent of PE oxidation, also the content of the transferred metal in the bulk of the polymer. Using ac voltammetry, we measured the metal concentration in solutions prepared from the ash residues of the polymer samples, with the subsequent recalculation to the metal content in the polymer. The procedure is described in more detail in [9].

Figure 1a shows data on oxidation of inhibited PE

1070-4272/03/7605-0827$25.00

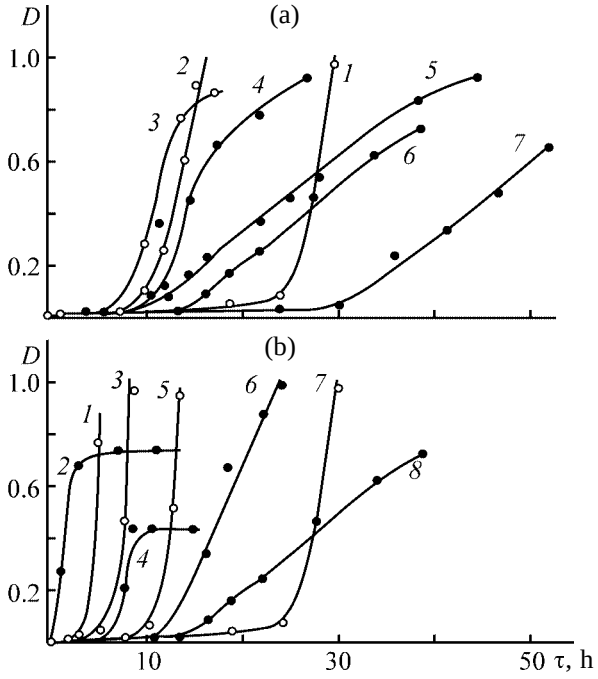

Fig. 1. Variation with oxidation time τ of the optical density D of the 1720 cm^{-1} band in the IR spectra of PE films containing various amounts of (a) copper filler and (b) AO. Film thickness 100 μm, oxidation temperature 150°C; the same for Fig. 2. (a) AO concentration 0.5 wt %; Cu concentration, wt %: (*1*) 0, (*2*) 1, (*3*) 3, (*4*) 5, (*5*) 7, (*6*) 10, and (*7*) 20. (b) Cu concentration 10 wt %; AO concentration, wt %: (*1*, *2*) 0, (*3*, *4*) 0.1, (*5*, *6*) 0.3, and (*7*, *8*) 0.5; polyethylene: (*1*, *3*, *5*, *7*) unfilled and (*2*, *4*, *6*, *8*) filled.

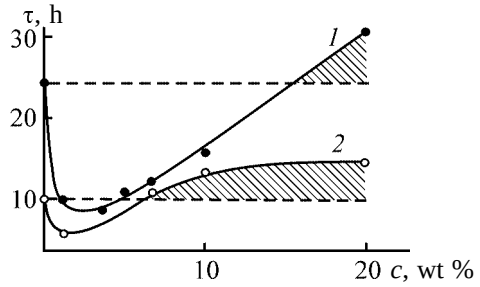

Fig. 2. Duration τ of IPO of PE films as a function of concentration c of dispersed copper in the polymer. AO concentration in the polymer, wt %: (*1*) 0.5 and (*2*) 0.3.

films (AO concentration 0.5 wt %) containing various amounts of the copper filler. As judged from IPO, at a filler concentration of up to 10 wt % the polymer oxidation is accelerated (Fig. 1a, curves *1*–*6*), and only at a higher copper content (e.g., 20 wt %) the inhibiting power of the amine AO is enhanced: IPO of the filled PE becomes longer than that of the unfilled polymer (Fig. 1a, curves *1*, *7*).

Data in Fig. 1a can be summarized by plotting the IPO duration vs. copper concentration in the polymer at an AO concentration of 0.5 wt % (Fig. 2, curve *1*). This dependence has a minimu at a filler concentration of about 3 wt %. As noted above, IPO is determined by two competing processes: catalysis of the polymer oxidation with copper and transformation of amine AO into a more effective product, also under the action of copper. Both these processes occur in the polymer layer adjacent to the filler particle surface. Apparently, at the Cu concentration from 0 to 3 wt %, the catalysis prevails (IPO decreases), whereas at higher Cu concentrations the transformation of AO becomes the major factor (IPO increases). At a Cu concentration exceeding 16 wt %, the IPO of the filled PE exceeds that of the unfilled PE, i.e., introduction of copper powder into inhibited PE enhances rather than lowers the oxidation resistance of the polymer. This range of the filler concentration is cross-hatched in Fig. 2 (curve *1*). As the copper concentration is increased above 16 wt %, the inhibiting effect becomes stronger.

It should be noted that the IPO duration measured in the experiment is an arbitrary characteristic of the oxidation resistance of the polymer. Actually we determine the time in which a certain small (comparable with the measurement sensitivity) amount of oxidation products is accumulated in PE under the experimental conditions (the extinction parameter of the 1720 cm^{-1} band reaches 3–4 cm^{-1}). By the end of this time, certain oxidative transformations have already occurred in the polymer, and therefore IPO, more precisely, characterizes the rate of these transformations. In other words, if IPO is longer, accumulation of the oxidation products in this step is slower. These reasonings are confirmed by the experimental results. For example, as the copper concentration in the polymer is increased from 3 to 20 wt %, the IPO duration increases (Fig. 2, curve *1*), and the oxidation rate evaluated from the kinetic curves of accumulation of carbonyl groups (Fig. 1a, curves *3*–*7*), on the contrary, decreases. Correspondingly, in the range of filler concentrations from 1 to 3 wt %, as IPO becomes shorter, the polymer oxidation accelerates.

Figure 1b shows how the AO concentration affects the PE oxidation at a constant concentration of the Cu filler (10 wt %). As seen, the effect of Cu becomes weaker with increasing AO concentration. For example, at an AO content of 0.3 wt %, addition of Cu increases the IPO from 8 to 11 h (Fig. 1b, curves *5*, *6*). On the contrary, addition of the same amount of Cu to PE containing 0.5 wt % AO shortens the IPO from 24 to 13 h, i.e., the filler apparently behaves as a catalyst (Fig. 1b, curves *7*, *8*). However, in any case an

increase in the AO concentration in PE filled with the same amount of Cu makes IPO longer, which is primarily due to slower accumulation of carbonyl groups in the initial step of the polymer oxidation (Fig. 1, curves *4*, *6*, *8*).

The effect of AO on oxidation of unfilled PE can be evaluated most accurately by comparing the plots of IPO duration vs. Cu filler concentration for different AO concentrations (Fig. 2, curves *1*, *2*). As the AO concentration is decreased from 0.5 to 0.3 wt %, the Cu concentrations corresponding to the minimum of the plot and to the point in which the IPO duration coincides with that for the unfilled polymer decrease.

Shortening of IPO on introducing dispersed copper (oxidation catalyst) into inhibited PE (Fig. 2, descending portions of curves *1*, *2*) is quite expected. It is known [10] that, as the concentration of the Cu filler in uninhibited PE is increased, IPO becomes shorter and the polymer oxidation accelerates. However, we found that in some cases filling of inhibited PE with copper makes IPO longer rather than shorter (Fig. 2, ascending portions of curves *1*, *2*). Such a trend may be due to more active reaction of Neozon D with the filler, yielding a more effective AO, at higher filler concentrations.

To check this assumption, we performed additional experiments. Inhibited PE films of various thicknesses were oxidized on copper supports, which in this case modeled the surface of the filler particles. Therefore, decreased film thickness was equivalent to decreased distance between the filler particles, i.e., to increased concentration of the filler in the polymer.

In the course of the experiment, we obtained the kinetic curves of accumulation of carbonyl groups in polymer films of various thickness. In parallel, we performed studies in which PE films were oxidized on an inert support (KBr plates) [10]. Figure 3 shows that the dependences of the IPO duration on the film thickness are opposite for the Cu and KBr supports (curves *1*, *2*). For PE films oxidized on a KBr support, IPO becomes longer with increasing film thickness, and with a Cu support it becomes shorter. Apparently, extension of the IPO with increasing concentration of Cu powder (Fig. 2, curve *1*) and with decreasing thickness of unfilled PE film oxidized on a Cu support (Fig. 3, curve *2*) are due to the same factor: increase in the specific area of the metal–polymer contact surface (ratio of the contact surface area to the polymer weight). Assuming that the copper particles used in the experiment (particle size about 6 μm) have a spherical shape, the presence of 5 to 33 wt % filler in a 100-μm-thick film will be equivalent, from the viewpoint of the contact surface area, to contact of a copper support with an unfilled PE film of the thickness from 200 to 30 μm, respectively.

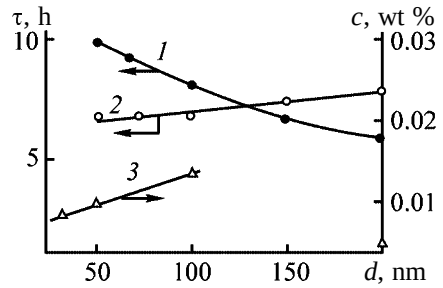

Fig. 3. IPO duration τ for unfilled PE films as a function of their thickness *d*. Support: (*1*) Cu and (*2*) KBr. AO concentration in the polymer 0.1 wt %, oxidation temperature 150°C. (*c*) Cu concentration. (*3*) Accumulation of Cu in PE films oxidized on Cu supports by the end of IPO.

It is known [4, 6] that the catalysis of PE oxidation in contact with Cu is due to transfer into the polymer of catalytically active Cu-containing compounds, products of contact reactions. Since the measured IPO duration is an arbitrary characteristic (in this step slow polymer oxidation already occurs), it was interesting to find whether variation of IPO duration for thin films is related to the rate of transfer of copper compounds. For this purpose, we studied how the thickness of a PE film correlates with the amount of copper compounds accumulated by the end of IPO. The results are shown in Fig. 3, curve *3*. It is seen that, as the film thickness is increased from 30 to 100 μm, the concentration of Cu transferred into the polymer grows. Apparently, in thin films Neozon D transforms into a more effective AO faster. As a result, the rate of oxidative transformations in the adhesion contact zone decreases, which results in decelerated transfer of copper compounds into the bulk of the polymer and in extension of the IPO.

CONCLUSION

Extension of the induction period of oxidation on introducing an oxidation catalyst, dispersed copper, into inhibited polyethylene is due to a decrease in the thickness of the polymer layer between the filler particles. As the layer of the polymer oxidized on a copper support surface is made thinner, transformation of Neozon D into a more effective antioxidant accelerates, which results in slower transfer of copper-containing compounds into the bulk of the polymer and in longer induction period of oxidation.

REFERENCES

1. Lin, D.G. and Vorob'eva, E.V., *Plast. Massy*, 2002, no. 1, pp. 9–11.
2. Vorob'eva, E.V., Lin, D.G., and Mironovich, L.L., Abstracts of Papers, *Mezhdunarodnaya nauchno-tekhnicheskaya konferentsiya "Polimernye kompozity 2000"* (Int. Scientific and Technical Conf. "Polymeric Composites 2000"), Gomel, 2000, pp. 33–34.
3. Vorob'eva, E.V. and Lin, D.G., Abstracts of Papers, *Mezhdunarodnaya nauchno-prakticheskaya konferentsiya "Kompozitsionnye materialy v promyshlennosti"* (Int. Scientific and Practical Conf. "Composite Materials in Industry"), Yalta, 2001, pp. 27–28.
4. Lin, D.G., Scientific Principles for Development of Layered Metal–Polymer Machine-Building Materials Using Thermoplastics and Elastomers, *Doctoral Dissertation*, Gomel, 1993.
5. Lin, D.G., *J. Appl. Polym. Sci.*, 1994, vol. 54, pp. 1789–1793.
6. Lin, D.G. and Vorob'eva, E.V., *Zh. Prikl. Khim.*, 2001, vol. 74, no. 6, pp. 998–1002.
7. Lin, D.G., *Izv. Akad. Nauk Bel. SSR, Ser. Fiz.-Tekh. Nauk*, 1978, no. 3, p. 126.
8. Egorenkov, N.I., Lin, D.G., and Belyi, V.A., *J. Therm. Anal.*, 1976, vol. 10, pp. 357–362.
9. Lin, D.G. and Vorob'eva, E.V., *Zh. Prikl. Khim.*, 2002, vol. 75, no. 5, pp. 836–839.
10. Lin, D.G. and Vorobieva, E.V., *J. Appl. Polym. Sci.*, 2001, vol. 80, pp. 2047–2052.

Russian Journal of Applied Chemistry, Vol. 76, No. 5, 2003, pp. 831–834. Translated from Zhurnal Prikladnoi Khimii, Vol. 76, No. 5, 2003, pp. 860–862.

MACROMOLECULAR CHEMISTRY AND POLYMERIC MATERIALS

A Micromethod of Estimating the Reactivity of Cellulose to Acetylation

R. Z. Pen, P. V. Mironov, and O. A. Kolmakova

Siberian State Technological University, Krasnoyarsk, Russia

Received October 23, 2002; in final form, March 2003

Abstract—A micromethod was developed for estimating the reactivity of cellulose to acetylation by monitoring temperature variation in the process.

Since acetylation of cellulose with acetic anhydride is an exothermic process, a series of methods for determining the acetylation rate and estimating the cellulose reactivity are based on temperature measurements, with the reaction being carried out under adiabatic conditions [1]. According to generally accepted analysis methods, cellulose acetylation is carried out by the homogeneous procedure in a Dewar vessel. For analysis, 10 g of air-dry cellulose and 239 ml of acetylating mixture are taken [2]. In the reaction of cellulose with the acetylating mixture, the temperature of the reaction mixture increases from 20°C to 36°C.

To carry out of the process in a calorimeter, 3.5 g of cellulose and 365 ml of the acetylating mixture are taken. Cellulose placed in the calorimeter shaft is ejected into the acetylating mixture. In the process, the temperature of the reaction mixture increases by 10–15°C [3].

Among the most significant drawbacks of this procedure are considerable increase in the temperature of the reaction mixture, which distorts the kinetic parameters of the process. In addition, relatively large amounts of cellulose required for measurements are inconvenient for laboratory studies.

Here we studied the possibility for estimating the rate of cellulose acetylation using a non-adiabatic microcalorimeter under the conditions close to isothermal.

EXPERIMENTAL

The measuring system consists of two batteries of thermocouples connected by the differential scheme and attached to an emf amplifier, which allows recording of the temperature difference in the cells of microcalorimetric blocks. The signal from the emf amplifier is recorded on a diagram tape in the form of the plot time τ (s)–temperature difference ΔT (°C). The nominal sensitivity of the device (from the diagram) was 7.5×10^{-5} W mm^{-1}.

Cellulose was activated before acetylation. For this purpose, 0.5 g of pulverized air-dry cellulose was uniformly moistened in 0.5 cm^3 of glacial acetic acid in a 15 cm^3 bottle and placed in a thermostat at 80°C for 1 h, after which it was kept at room temperature for 2 h.

The acetylating mixture was prepared by mixing acetic anhydride, acetic acid, and concentrated sulfuric acid in the volume ratio of 50 : 100 : 1, respectively. A 2 cm^3 portion of this mixture was placed into the reaction vessel of the measurement cell of the device. Activated cellulose (5–10 mg) was attached to the end of the sample holder with a very thin wire and placed into the acetylating mixture. The instant of immersion was considered as the reaction start (τ = 0).

A typical diagram of temperature variation in the reaction mixture is shown in Fig. 1. The ascending

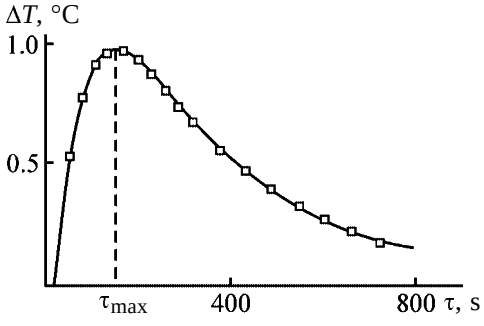

Fig. 1. Variation of temperature of the reaction mixture ΔT in time τ. The points were transferred from the recorder, and the solid line is calculated by Eq. (12).

1070-4272/03/7605-0831$25.00

branch of the curve reflects increase in the temperature due to the heat released in exothermic reactions, and the descending branch, decrease in the temperature due to heat diffusion.

Acetylation of cellulose (C) with formation of cellulose acetate (CA) can be described by the scheme

$$C + (CH_3CO)_2O \rightarrow CA + CH_3COOH + Q, \quad (1)$$

where Q is the total heat effect of cellulose acetylation and reaction of acetic anhydride with water.

Since acetic aldehyde is in a large excess, we can assume zero partial kinetic order of reaction (1) with respect to this reactant and the first order with respect to cellulose. Then, the equation for the reaction rate can be written in the form

$$d[CA]/d\tau = k_1([C]_0 - [CA]), \quad (2)$$

where $[C]_0$ is the cellulose concentration (weight fraction) in the reaction mixture in the beginning of the reaction (at $\tau = 0$), [CA] is the current concentration of cellulose acetate, and k_1 is the reaction rate constant (s^{-1}).

The solution of Eq. (2) is known:

$$[CA] = [C]_0[1 - \exp(-k_1\tau)]. \quad (3)$$

The amount of the released heat Q is in direct proportion to the amount of the formed cellulose acetate, i.e., the following relationship is valid:

$$Q = a[1 - \exp(-k_1\tau)], \quad (4)$$

where a is a coefficient taking into account the amount of the reaction mixture and the thermal effect of the reaction.

When considering the weight m and heat capacity C of the reaction mixture as constants, we can pass from Eq. (4) to the equation for increase in temperature ΔT due to the heat released in the reaction, in which coefficient A_1 includes, along with a, also m and C values.

$$\Delta T_1 = A_1[1 - \exp(-k_1\tau)]. \quad (5)$$

If the temperature of the device and surrounding before the reaction was T_0, the temperature in the measuring cell should increase to T_1 owing to the heat released in the reaction:

$$T_1 = T_0 + \Delta T_1. \quad (6)$$

The rate of cooling of the reaction mixture is in direct proportion to the difference in temperature between the measuring cell and the surrounding [4]:

$$\frac{d}{d\tau}(\Delta T_2) = -k_2(T_1 - \Delta T_2 - T_0), \quad (7)$$

where ΔT_2 is decrease in temperature in the measuring cell due to heat emission, and k_2 is a coefficient.

After substitution of expressions (5) and (6) in relationship (7), we obtain

$$\frac{d}{d\tau}(\Delta T_2) = -k_2\{T_0 + A_1[1 - \exp(-k_1\tau)] - \Delta T_2 - T_0\}$$

$$= k_2\Delta T_2 - k_2A_1[1 - \exp(k_1\tau)]. \quad (8)$$

The equation similar to Eq. (8) describes the rate of variation of the final product concentration in two successive first-order reactions. The solution of Eq. (8) is [5]

$$\Delta T_2 = A_1[1 + k_1(k_2 - k_1)^{-1}\exp(-k_2\tau) - k_2(k_2 - k_1)^{-1}\exp(-k_1\tau)]. \quad (9)$$

Subtracting Eq. (9) from Eq. (5), we obtain

$$\Delta T = \Delta T_1 - \Delta T_2 = A_1k_1(k_2 - k_1)^{-1}[\exp(-k_1\tau) - \exp(-k_2\tau)]. \quad (10)$$

The device records the dependence

$$y = f(\tau), \quad (11)$$

where y is the deviation of the recorder pen, proportional to ΔT.

According to Eq. (10), this dependence can be approximated by the equation

$$\hat{y} = Ak_1(k_2 - k_1)^{-1}[\exp(-k_1\tau) - \exp(-k_2\tau)], \quad (12)$$

where A is a compensating factor proportional to the initial amount of cellulose in the measuring cell.

Dependence (12) has a maximum at time τ_{max} (Fig. 1) determined from the condition

$$(dy/d\tau)_{\tau=\tau_{max}} = 0, \quad (13)$$

from which we obtain

$$\tau_{max} = (k_2 - k_1)^{-1}\ln(k_2/k_1). \quad (14)$$

Table 1. Parameters of Eq. (12)

Sample no.	A	k_1, s^{-1}	k_2	R^2	$1/\tau_{max}$, s^{-1}
1	1.0	0.0133	0.00294	0.995	0.00690
2	0.6	0.0186	0.00241	0.998	0.00781
3	1.6	0.0050	0.00366	0.987	0.00417
4	0.9	0.0099	0.00283	0.989	0.00562
5	0.9	0.0109	0.00242	0.998	0.00571
6	0.6	0.0176	0.00230	0.998	0.00741
7	0.7	0.0104	0.00232	0.992	0.00555
8	0.8	0.0104	0.00200	0.984	0.00526
9	0.5	0.0110	0.00228	0.984	0.00555
10	1.5	0.0146	0.00342	0.998	0.00741
Average	0.91	0.0122	0.00266	0.992	0.00614
Variance	0.14	1.59×10^{-5}	2.92×10^{-7}	–	1.38×10^{-6}

The best least-squares estimates for A, k_1, and k_2 are determined from the condition of minimization of the functional

$$\Psi = \Sigma(y - \hat{y})^2 \rightarrow \min. \quad (15)$$

The minimum of Ψ was found by the Marquardt method (StatGraphics Plus 5.0 package, Nonlinear Regression software, Marquardt method). The quality of approximation was characterized by the coefficient of determination (the square of estimated coefficient of Spirman multiple correlation R^2):

$$R^2 = 1 - \Sigma(y - \hat{y})^2/\Sigma(y - \bar{y})^2. \quad (16)$$

The results of analysis of ten different samples of unbleached pulp, significantly different in the yield from wood and degree of delignification, are given in Table 1. High coefficients of determination (close to 1) show that Eq. (12) satisfactorily approximates experimental curves.

For comparison, a sample of prehydrolyzed cellulose of cold elevation [GOST (State Standard) 21 101–83] was acetylated by the procedure described in [3] and by the proposed procedure. The reactivity of cellulose was characterized by the rate constant of acetylation with the correction for the reaction temperature [3]. The results of comparison are as follows: by the existing procedure, $k_1 = 0.0108\ s^{-1}$ and by the proposed procedure, $k_1 = 0.0103\ s^{-1}$.

In the physical sense, the coefficient k_2 is equivalent (within a constant factor) to the coefficient of heat transfer from the reaction mixture, i.e., under conditions of the specific analysis it can be considered as a device constant. The results of evaluation of the parameters of Eq. (12) with the average $k_2 = 0.00266$ confirm the validity of this assumption. In this case, Eq. (14) unambiguously relates k_1 to τ_{max} (Fig. 2).

Hence, the reactivity of cellulose to acetylation can be characterized by the τ_{max} value, determined directly from the process diagram (Fig. 1). For comparison of the cellulose samples with respect to this characteristic, it is more convient to use the reciprocal value $1/\tau_{max}$, since its dimension (s^{-1}) coincides with the dimension of the reaction rate constant k_1.

It should be noted that τ_{max} is independent of the amount of cellulose (it is not nexessary to weigh activated cellulose introduced into the measuring cell), which significantly simplifies the analytical procedure. It is only essential that the weight of cellulose

Table 2. Parameters of Eq. (12) under condition k_2 = constant = 0.00266

Sample no.	A	k_1, s^{-1}	R^2	$1/\tau_{max}$, s^{-1}
1	0.9	0.0141	0.995	0.00696
2	0.6	0.0161	0.993	0.00757
3	1.3	0.0066	0.987	0.00441
4	0.9	0.0101	0.990	0.00567
5	0.9	0.0096	0.995	0.00549
6	0.7	0.0146	0.989	0.00712
7	0.8	0.0088	0.988	0.00522
8	0.9	0.0075	0.975	0.00475
9	0.6	0.0090	0.980	0.00529
10	1.3	0.0182	0.989	0.00820
Average	0.89	0.0115	0.988	0.00607
Variance	0.06	1.57×10^{-5}	–	1.67×10^{-6}

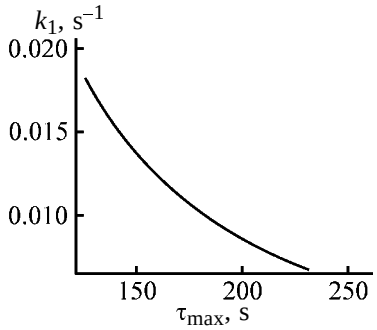

Fig. 2. Rate constant of the reaction k_1 as a function of time in which the maximal difference in temperature is attained, τ_{max}.

should be considerably (by 2–3 orders of magnitude) lower than the total weight of the reaction mixture, since, in this case, the influence of small variation in temperature ΔT in the measuring cell can be neglected and the process conditions can be considered as isothermal.

CONCLUSION

The proposed procedure of cellulose acetylation in a non-adiabatic microcalorimeter and mathematical processing of the results allow fast and accurate estimation of the reactivity of cellulose microamounts to acetylation. The convenient characteristic for comparison of the samples is $1/\tau_{max}$, reciprocal time in which the maximum in the τ–ΔT diagram is attained.

REFERENCES

1. Rogovin, Z.A., *Khimiya tsellyulozy* (Chemistry of Cellulose), Moscow: Khimiya, 1972.
2. Obolenskaya, A.V., Shchegolev, V.P., Akim, G.L., *et al*., *Prakticheskie raboty po khimii drevesiny i tsellyulozy* (Practical Works on Chemistry of Wood and Cellulose), Moscow: Lesn. Prom–st., 1965.
3. Kozlov, N.A., Medved', Z.N., Chernousov, V.O., and Kiselev, Yu.I., *Efiry tsellyulozy* (Cellulose Esters), Perepechkin, L.P., Ed., Vladimir: Vladimir. Nauchno-Issled. Inst. Sint. Smol, 1969, pp. 96–116.
4. Batuner, L.M. and Pozin, M.E., *Matematicheskie metody v khimicheskoi tekhnike* (Mathematical Methods in Chemical Practice), Leningrad: Khimiya, 1968.
5. Eremin, E.N., *Osnovy khimicheskoi kinetiki* (Principles of Chemical Kinetics), Moscow: Vysshaya Shkola, 1976.

Russian Journal of Applied Chemistry, Vol. 76, No. 5, 2003, pp. 835–839. Translated from Zhurnal Prikladnoi Khimii, Vol. 76, No. 5, 2003, pp. 863–867.

MACROMOLECULAR CHEMISTRY AND POLYMERIC MATERIALS

A Conducting Composite of Polyaniline and Wood

I. Yu. Sapurina, V. I. Frolov, B. M. Shabsel's, and J. Stejskal

Institute of Macromolecular Compounds, Russian Academy of Sciences, St. Petersburg, Russia
Institute of Macromolecular Chemistry, Academy of Sciences of Czechia, Prague, Czechia

Received March 12, 2003

Abstract—Production of a new conducting composite material based on polyaniline and wood by simple one-stage synthesis from aniline and wood sawdust is described. The material characteristics were studied in relation to the synthesis conditions and composition.

Antistatic materials are the most important application of conducting polymeric composites. The required level of the specific conductivity is low, 10^{-5}–10^{-6} S cm^{-1}. These composites are also used for electric heaters, conducting adhesives, and radiation-shielding coatings [1]. Traditional conducting composites are produced with carbon black or metallic fillers. However, the main problems of these materials are deterioration of the mechanical characteristics of the polymeric matrix on addition of the required amount of a conducting additive and also aging of composites, i.e., decrease in the conductivity caused by phase segregation of the material or oxidation of conductive additive.

In recent years, much more attention is given to production of conductive materials based on polyconjugated polymers having intrinsic specific conductivity of 10^{0}–10^{2} S cm^{-1} in the doped state [2]. Although the mechanical characteristics of conjugated polymers are relatively poor, procedures were developed for combining these polymers with classical dielectric polymers and for producing of conductive composites with the required mechanical characteristics. Addition of polyconjugated polymers imparts new useful properties to a composite. Unique optical, magnetic, and oxidative characteristics of these materials significantly extend their fields of application in comparison with traditional antistatic substances. New materials are used for electromagnetic screening, corrosion protection of ferrous and non-ferrous metals, and nonlinear optics; they are used for production of electrochromic devices and gas-distributing and pervaporation membranes [3].

Polyaniline (PA) is characterized by the resistance to the action of the environment, ready availability of raw materials, and the simplicity and low cost of synthesis. Therefore, it was the first commercially produced polyconjugated polymer. Fairly high conductivity and the possibility of varying the molecular weight of the polymer over a wide range make this polymer the most suitable for production of conductive composite materials. In recent years, numerous PA composites with synthetic polymers, inorganic substances, and natural compounds were produced [4].

Among natural materials, wood is of great importance. The interaction of PA with the main components of wood, cellulose and lignin, was the subject of recent studies. Based on water-soluble forms of cellulose, stable aqueous colloids of PA with the conductivity of 10^{-2} S cm^{-1} were prepared [5]. Flexible and transparent films produced from the composite with cellulose acetate have a conductivity of 10^{-1} S cm^{-1} even at PA content less than 5 wt %. The specific conductivity of 10^{-1} S cm^{-1}, more than sufficient for antistatic materials, is reached even at a PA content of 0.5 wt % [6–11]. The PA composites with cross-linked cellulose having the conductivity of 10^{-2} S cm^{-1} were produced. The compatibility of the polymers is good, which may be due to formation of hydrogen bonds between hydroxy groups of cellulose and amino groups of PA [12].

Blends and composites of PA with lignin and its derivatives were studied. Polyaniline is compatible with lignin owing to the interaction of the –NH– fragments with hydroxy and carbonyl groups of the natural polymer [13, 14]. The use of lignosulfonate for doping of PA results in formation of self-organizing polyelectrolyte complexes generating films with alternating layered structure [15, 16]. The use of similar structures for corrosion inhibition is suggested.

Data on composites of PA with wood are lacking. At the same time, sawdust is a material with valuable

1070-4272/03/7605-0835$25.00

consumer characteristics; it is a porous matrix suitable for production of composites with bulk conductivity. It is a cheap and readily available product; as a rule, it is a waste from woodworking industry whose utilization is an urgent problem. Here we describe the production of a conducting composite based on PA and milled wood and the characteristics of the composite material depending on its composition and synthesis conditions.

EXPERIMENTAL

In the experiments we used milled spruce wood (sawdust fraction 0.25–1.00 mm); aniline and ammonium persulfate $(NH_4)_2S_2O_8$ purchased from Aldrich; and 75% orthophosphoric acid purchased from Vekton.

The composite was synthesized as follows. Spruce sawdust (2 g) was added at 20°C with gentle stirring to 100 ml of a polymerization mixture containing aqueous aniline and ammonium persulfate. The molar ratio of the oxidizing agent and monomer was kept equal to 1.25. The polymerization mixture was acidified with orthophosphoric acid, since the rate of cellulose hydrolysis in this acid is the lowest. Acidic medium is required for the synthesis and subsequent efficient doping of PA. The resulting composite material was filtered off and dried in air and then in a vacuum at 40°C for 48 h.

To determine the amount of PA bonded to the wood surface, the composite was dispersed in a large volume of aqueous H_3PO_4 and washed on a fine (0.2-mm) sieve to remove free PA.

The progress of exothermic polymerization of aniline was monitored by variation of the temperature of the polymerization mixture with a THERMO TM-120 Sigma digital thermometer.

The composition of the material was determined from its yield and checked by elemental analysis.

The conductivity of the samples in the form of pellets 13 mm in diameter and 1 mm thick, produced by pressing in a vacuum at 700 MPa, was determined at 20°C. For the samples with the specific conductivity more than 10^{-3} S cm^{-1}, we used the four-point method modified by van der Pauve at direct current, and for the samples with lower conductivity we used the bridge method with alternating current.

Thermal gravimetric analysis of the composite was carried out on a MOM C derivatograph at a heating rate of 1 deg min^{-1} in an air flow of 50 cm^3 min^{-1} in corundum crucibles; weighed portion 50 mg.

Absorption spectra of aniline solutions were recorded on a Lambda 20 Perkin–Elmer spectrometer.

Polyaniline produced in the absence of wood at the initial concentration of the monomer of 0.2 M had the conductivity of 3.38 S cm^{-1} and contained 11 wt % nitrogen and 12 wt % phosphorus. Spruce wood had the conductivity of 6.3×10^{-15} S cm^{-1}, and within the experimental error, contained no nitrogen and phosphorus, while according to published data [17] spruce wood contains 0.1 wt % nitrogen and 0.02 wt % phosphorus. The conductivity of spruce wood kept in 0.2 M acidic aniline solution for 2 days was 1.15×10^{-14} S cm^{-1}.

Polyaniline is a powder with extremely low solubility; its melting point exceeds the temperature of polymer degradation. Therefore, production of composite materials based on polyaniline by the standard procedures such as mixing in melt or solution, as a rule, is impossible. In such cases, polymerization *in situ* finds growing application. The procedure consists in the direct polymerization of a monomer at the surface of a composite matrix. A comprehensive study of this procedure showed that, in the course of synthesis, PA forms tightly sorbed layers at various types of surfaces immersed in the polymerization mixture. Porous milled wood having developed surface can serve as suitable dielectric matrix carrying the conducting polymer layer.

The composite was synthesized by immersion of spruce sawdust into an aqueous polymerization solution containing aniline, H_3PO_4, and $(NH_4)_2S_2O_8$. As a result of aniline oxidation, the conducting form of PA is formed:

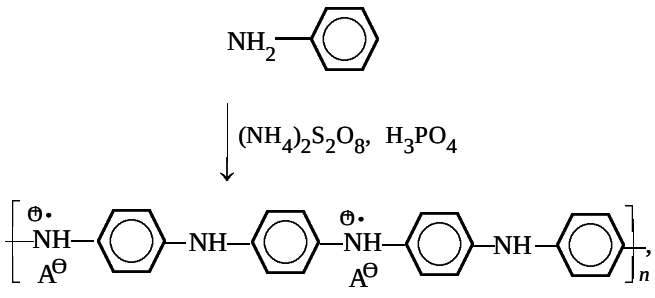

where A^- is $1/3\,PO_4^{3-}$, $1/2\,HPO_4^{2-}$, or $H_2PO_4^-$.

However, wood is a complicated natural material hydrolyzable in acidic medium and oxidizable in the presence of strong oxidizing agents such as $(NH_4)_2S_2O_8$. It was necessary to check whether the synthesis of the composite is complicated by side

processes decreasing the yield of the polymer or resulting in degradation of the wood material.

A contact of spruce wood with acidified aqueous solution of aniline results in instantaneous bright yellow coloration of wood. It was found that coloration is caused by the reaction of aniline with functional groups of lignin, whose content in spruce wood is 28 wt % [17]. Under these conditions, cellulose produced from spruce wood gave no coloration. The reactions carried out with model compounds showed that similar yellow coloration appears in the reaction of acidic solutions of aniline with cinnamaldehyde, one of the main structural units of lignin. Thus, the most probable explanation of the product coloration is the reaction of aniline with conjugated aldehyde groups of lignin:

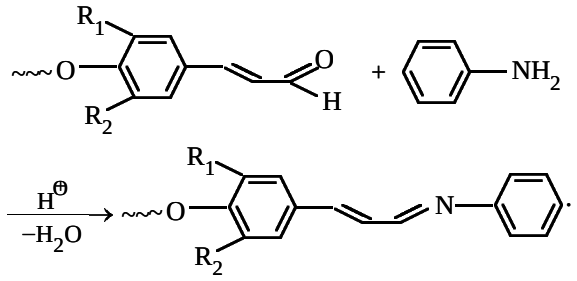

Formation of Schiff bases with further extension of the conjugated chain shifts the absorption band to the visible range and gives rise to coloration. However, the fraction of aniline participating in this reaction is low. The spectral analysis of polymerization solutions of aniline before and after addition of sawdust showed that the loss of the monomer, monitored by the strong absorption bands of aniline in the range 250–300 nm, did not exceed 10^{-5} mol per 2 g of wood. Hence, the color reaction can noticeably contribute to the process only at low aniline concentrations. In other cases, it is not competitive with polymerization.

It was found that the polymerization rate and characteristics of the resulting material were independent of the order in which the components of polymerization solution were added to the sawdust (Table 1). Preliminary keeping of wood in solution of aniline or ammonium persulfate for 1 h gave the same results as in the case of addition of sawdust directly to the prepared polymerization mixture. This suggests that wood is not hydrolyzed or oxidized in the system.

Polymerization of aniline is an exothermic process. The reaction rate and degree of conversion of the monomer can be evaluated from the rate of temperature variation in the polymerization mixture and the heat effect of the reaction [18]. Variation of the temperature in time during aniline polymerization both in the presence and in the absence of wood material is shown in Fig. 1. Close location of the curves suggests that the presence of spruce wood does not substantially affect the mechanism and degree of conversion of the monomer. Thus, we can conclude that the components of the polymerization mixture do not affect the wood material, and, vice versa, aniline in the presence of wood polymerizes as in the presence of an inert matrix.

Table 1. Polymerization of aniline in the presence of wood at various orders of mixing the reactants*

Procedure of mixing the reactants**	τ, min	α, %	æ, S cm^{-1}
(An + Ox) + W	22	97	0.41
(An + W) + Ox	21	100	0.52
(Ox + W) + An	25	98	0.39

* (τ) Polymerization duration and (α) degree of PA conversion.
** (An) Aniline, (Ox) ammonium persulfate, and (W) milled wood.

The results of synthesis of the composite at various molar concentrations of the monomer (aniline) are listed in Table 2. With decreasing concentration of aniline c_a, the process duration increases and the yield of PA and its content in the composite decrease. The conductivity of the samples increases with increasing content of PA in the composite material from 6×10^{-15} for pure spruce wood to 5.1×10^{-1} S cm^{-1} for the composite containing 64 wt % PA (composite 1). At a high concentrations of polyaniline, the conductivity of the composite (Fig. 2) is close to that of pure PA (3.38 S cm^{-1}) produced under the similar conditions.

Starting from the existing concepts of the PA polymerization mechanism, we can distinguish two processes: so-called "surface" and "bulk" growth of polymer chains [19, 20]. The surface process is responsible for formation of a polymer layer at the surface

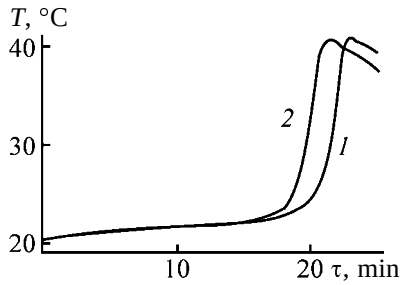

Fig. 1. Variation of the temperature of aniline polymerization T in time τ (*1*) in the absence and (*2*) in the presence of sawdust. Aniline concentration 0.2 M.

Table 2. Polymerization of aniline in the presence of wood

c_a, M	τ, min	α, %	Composite 1		Composite 2	
			PA, wt %	æ, S cm^{-1}	PA, wt %	æ, S cm^{-1}
0.25	18	100	64	5.1×10^{-1}	28	1.8×10^{-1}
0.2	22	93	57	3.4×10^{-1}	15	5.2×10^{-2}
0.1	58	85	37	7.1×10^{-2}	10	3.3×10^{-2}
0.05	140	79	22	5.2×10^{-3}	5	1.9×10^{-3}
0.01	>300	36	2	8.4×10^{-6}	1	4.5×10^{-9}
0.005	>300	0	0	3.1×10^{-10}	0	8.0×10^{-11}
0.001	>300	0	0	1.0×10^{-10}	0	7.0×10^{-12}

of a matrix immersed in polymerization solution. Depending on the polymerization conditions, these layers have thickness from tens to hundreds of nanometers and are characterized by high adhesion of the polymer to the matrix. The bulk process is polymerization of aniline in the solution bulk with formation of a PA precipitate, whose adhesion to various materials is as low as that of the polymer powder. The ratio of contributions of surface and bulk processes is governed by the polymerization conditions and surface type.

To estimate the contribution of both processes in production of the wood composite, the composite material was washed on a fine sieve to remove PA nonbonded to the surface. As seen from data listed in Table 2 (composite 2), in this process the fraction of PA in the composite decreases, on the average, by 2/3 as compared to the initial value. In this experiment, the PA content was determined not only from the weight loss but also by elemental analysis of the composite for nitrogen. Under these conditions, the ratio of weight fractions of PA formed by the bulk and surface processes is 2/1 (Table 2). This ratio of contributions of the two reactions is kept at all the initial concentrations of the monomer.

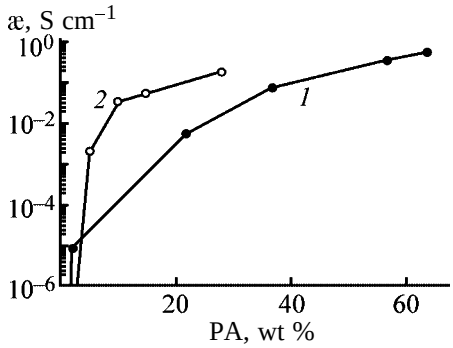

Fig. 2. Specific conductivity æ of (*1*) composite 1 and (*2*) composite 2 as a function of PA content.

The conductivities of the samples containing only surface-bonded PA (composite 2) are listed in Table 2. Despite the fact that the total amount of the conductive polymer substantially decreased, the conductivity of the composite decreased insignificantly. This suggests that the composite conductivity is mainly governed by the PA layer formed by surface polymerization. Addition of a powder-like PA precipitate, increasing the amount of PA in the composite by a factor of 2, only slightly improves its conductivity. According to the dependence of the conductivity on composition (Fig. 2), the conductive paths in the composite begin to form even at the PA content of 1–2 wt %. This low percolation limit is typical for composites consisting of dielectric particles coated with a conducting polymer [21, 22]. The results obtained suggest that special procedures of synthesis of composite materials based on PA are more efficient than addition of PA powder to a dielectric matrix.

In the course of synthesis of the composite material, we used orthophosphoric acid. It is incorporated in the composite as PA dopant. According to elemental analysis, the phosphorus content in neat PA is 12 wt %, and in the composite it varies from 6.0 wt % to several tenths of per cent depending on the content of the conductive polymer. It is well known that addition of phosphorus even in the amount of several per cents substantially improves the fire resistance of wood and items thereof [23]. A fairly high content of phosphorus in the form of phosphate anions incorporated into the composite will surely improve the fire resistance of the material.

The results of thermal gravimetric analysis of spruce wood and composite containing 28 wt % PA are shown in Fig. 3. In the first stage of thermal degradation of spruce wood (up to 120°C), the weight loss is 10%, which corresponds to removal of sorbed water and volatile substances. With further heating, after a small plateau of thermal stability (150–250°C),

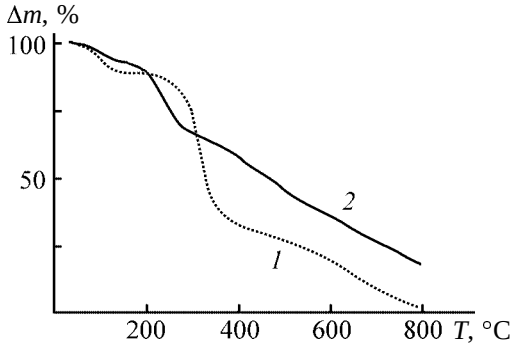

Fig. 3. Thermal gravimetric analysis of (*1*) spruce wood and (*2*) composite containing 28 wt % PA. (Δ*m*) Weight loss and (*T*) temperature.

the main weight loss proceeds at a high rate up to 360°C. Further burning of the pyrolysis residue (approximately 40%) proceeds more slowly up to complete decomposition of the sample at 800°C.

Thermal decomposition of the composite proceeds differently. The initial weight loss (up to 130°C) is caused by removal of water and volatile substances of wood. The subsequent stage of thermal degradation (200–300°C) involves several processes, one of which is dedoping of PA (240–270°C), responsible for the loss of the composite conductivity in this temperature range. Abrupt weight loss (30%) observed in spruce wood in the range from 250 to 360°C does not occur in the composite. The remaining 70% of the composite weight is lost at a constant rate comparable with the rate of burning of the pyrolysis residue. However, 18 wt % of the material remains at 800°C.

CONCLUSIONS

(1) A new conductive composite material based on polyaniline and milled wood with the specific conductivity of approximately 10^{-1} S cm^{-1} was obtained.

(2) The composite is prepared by one-stage polymerization of aniline in the presence of sawdust, i.e., the wastes from wood working can be used as main raw materials.

(3) The conductivity of the composite is mainly governed by the layer of polyaniline sorbed at the wood surface in the course of synthesis and only slightly depends on the presence of the powder-like precipitate of polyaniline.

(4) The study of the thermal stability and measurements of the sample conductivity at elevated temperature showed that the composite loses conductivity in the range 240–270°C, which is caused by thermal dedoping of polyaniline.

REFERENCES

1. Nikolaev, A.F., *Plastmassy s povyshennoi elektroprovodimost'yu* (Plastics with Increased Conductivity), Leningrad: Leningr. Tekhnol. Inst., 1991.
2. MacDiarmid, A.G., *Angew. Chem. Int. Ed.*, 2001, vol. 40, pp. 2581–2590.
3. *Handbook of Organic Conductive Molecules and Polymers*, Nalwa, H.S., Ed., Chichester: Wiley, 1977, vols. 1–4.
4. Malinauskas, A., *Polymer*, 2001, vol. 42, pp. 3957–3972.
5. Stejskal, J., *J. Polym. Mater.*, 2001, vol. 18, pp. 225–238.
6. Pron, A., Zagorska, M., Nicolau, Y., Genoud, F., and Nechtschein, M., *Synth. Met.*, 1997, vol. 84, pp. 89–90.
7. Pron, A., Nicolau, Y., Genoud, F., and Nechtschein, M., *J. Appl. Polym. Sci.*, 1997, vol. 63, pp. 971–977.
8. Wolter, A., Banka, E., Genoud, F., *et al.*, *Synth. Met.*, 1997, vol. 84, pp. 753–754.
9. Planes, J., Cheguettine, Y., and Samson, Y., *Synth. Met.*, 1999, vol. 101, pp. 789–790.
10. Cheguettine, Y., Planes, J., and Samson, Y., *Synth. Met.*, 1999, vol. 101, pp. 787–788.
11. Laska, J., Zak, K., and Pron, A., *Synth. Met.*, 1997, vol. 84, pp. 117–118.
12. Yin, W., Li, J., Li, Y., *et al.*, *Polym. Int.*, 1997, vol. 42, pp. 276–280.
13. Rodrigues, P.C., Cantao, M.P., Janissek, P., *et al.*, *Eur. Polym. J.*, 2002, vol. 38, pp. 2213–2217.
14. Rodrigues, P.C., Muraro, M., and Garsia, C.M., *Eur. Polym. J.*, 2001, vol. 37, pp. 2217–2223.
15. Paterno, L.G., Constantino, C.J.L., Oliviera, O.N., and Mattoso, L.H.C., *Colloids Surf., Ser. B*, 2002, vol. 23, pp. 257–262.
16. Roy, S., Fortier, J.M., Nagarajan, R., *et al.*, *Biomacromolecules*, 2002, vol. 3, pp. 937–941.
17. Blazej, A., *Rastlinné fenolové zlúceniny*, Bratislava: Alfa, 1973.
18. Sapurina, I., Riede, A., and Stejskal, J., *Synth. Met.*, 2001, vol. 123, pp. 503–507.
19. Orlov, A.V., Kiseleva, V.G., Yurchenko, O.Yu., and Karpacheva, G.P., *Polym. Sci., Ser. A*, 2000, vol. 42, pp. 1292–1297.
20. Fedorova, S. and Stejskal, J., *Langmuir*, 2002, vol. 18, pp. 5630–5631.
21. Omastova, M., Pavlinec, J., Pionteck, J., and Simon, F., *Polym. Int.*, 1997, vol. 43, pp. 109–112.
22. Khan, M.A. and Armes, S.P., *Langmiur*, 1999, vol. 15, pp. 3469–3473.
23. Rogovin, Z.A., *Khimiya tsellyulozy* (Chemistry of Cellulose), Moscow: Khimiya, 1972.

Russian Journal of Applied Chemistry, Vol. 76, No. 5, 2003, pp. 840–841. Translated from Zhurnal Prikladnoi Khimii, Vol. 76, No. 5, 2003, pp. 868–869.

BRIEF COMMUNICATIONS

Niobium(V) Recovery from Titanium-Containing Sulfate Solutions

V. G. Maiorov and A. I. Nikolaev

Tananaev Institute of Chemistry and Technology of Rare Elements and Mineral Raw Materials, Kola Scientific Center, Russian Academy of Sciences, Apatity, Murmansk oblast, Russia

Received January 10, 2003

Abstract—The separation of niobium(V) from titanium(IV) by extraction with tributyl phosphate containing an amine, followed by precipitation from sulfate media with organic coagulants, was studied.

The problem of niobium(V) and titanium(IV) separation arises in treatment of some types of secondary raw materials, e.g., alloys and intermediate solutions, from sulfuric acid processing of titanoniobates [1]. The most efficient separation is attained in the fluoride extraction system. However, along with undoubted advantages, the fluoride system has significant drawbacks (corrosiveness, toxicity, short supply and high cost of hydrofluoric acid, and environmental problems associated with utilization of fluorine-containing wastes). In this work we studied separation of niobium(V) from titanium(IV) in a system containing sulfuric acid only.

Tributyl phosphate (TBP) is one of the most widely used neutral organic solvents. From sulfuric solutions Nb(V) is extracted with TBP better than Ti(IV). According to [2, 3], the degrees of extraction of Nb(V) and Ti(IV) from 8 M H_2SO_4 are about 50 and 15%, respectively, which is insufficient for the recovery of Nb(V) and its separation from Ti(IV). Tri-*n*-octylamine (TOA) is known [3] to extract Nb(V) much better than TBP. Therefore, it was of interest to test TBP with small additions of technical-grade trialkylamines (TAA), analogs of TOA, as extractant (especially as such a system is expected to show a synergistic effect [3]). The initial sulfuric acid solution contained (M) 0.06 Nb(V), 0.45 Ti(IV), and 0.25 $(NH_4)_2SO_4$. Pure-grade TBP and TAA containing about 70 vol % TOA were used. The extraction was performed for 30 min. The distribution of Nb(V) and Ti(IV) was monitored by chemical analysis.

The experimental data are shown in Table 1. As seen, the separation of Nb(V) and Ti(IV) is improved as both the concentration of H_2SO_4 and the amount of TAA in the system are increased [at the expense of growth of the TAA content in the extractant and of the volume ratio of the organic and aqueous phases ($V_o : V_{aq}$)]. Upon threefold successive treatment of the aqueous solution (8.5 M H_2SO_4) with fresh portions of the extractant (30 vol % TAA in TBP; $V_o : V_{aq}$ = 2 : 1), the total extraction of Nb(V) was about 90%, and the coextraction of Ti(IV) was less than 10%. Washing of the extract with an H_2SO_4 solution ensures additional removal of Ti(IV) from Nb(V) (Table 2). Niobium hydroxide, which contained after

Table 1. Extraction of Nb(V) and Ti(IV) with a mixture of TBP and TAA

$c_{H_2SO_4}$, M	Content of TAA in TBP, vol %	$V_o : V_{aq}$	Recovery, %	
			Nb(V)	Ti(IV)
8.5	15	1.4 : 1	70.2	10.8
8.5	25	1.4 : 1	69.6	7.9
8.5	35	1.4 : 1	69.1	9.0
8.5	15	2 : 1	74.7	9.7
8.5	25	2 : 1	73.9	6.0
8.5	35	2 : 1	73.1	–
8.0	30	2 : 1	68.6	8.0
8.5	30	2 : 1	73.5	≤7
9.0	30	2 : 1	76.1	7.0

Table 2. Distribution of Nb(V) and Ti(IV) upon sulfuric acid washing of the organic phase containing 30 vol % TAA in TBP

$c_{H_2SO_4}$ in washing solution, M	Washing run no.	Total washout, %	
		Nb(V)	Ti(IV)
7	1	7.5	–
	2	13.4	~100
6	1	7.5	–
	2	12.5	~100
5	1	6.5	–
	2	10.3	~100

1070-4272/03/7605-0840$25.00

Table 3. Selective precipitation of niobium(V) with organic coagulants from titanium-containing sulfuric acid solutions

Starting solution, M			Coagulant	Coagulant consumption, g per g Nb_2O_5	Degree of precipitation, %		
Nb	Ti	H_2SO_4			Nb	Ti	Fe
0.07	0.044	3.5	PAA	1.7	~94	16	0.8
0.10	0.81	2.6	PAA*	3.0	90	22	0.5
0.08	0.14	3.9	PEI	0.8	97.9	55	5.6
0.10	0.81	2.6	PEI*	1.2	99.3	18	3.2

* With preliminary reduction of Ti(IV) to Ti(III) with metallic iron.

calcination less than 2 wt % TiO_2, was obtained by back extraction with ammonia water.

Similar data were obtained when using another organic additive to TBP, tetranaphthenylthiuram disulfide

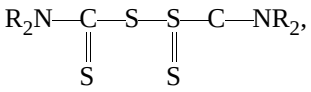

where R is a naphthenic radical (n + m = 8–14)

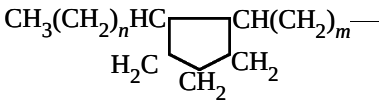

After extraction of niobium(V), titanium(IV) can be isolated by known methods, e.g., by hydrolysis.

We also studied the selective precipitation of niobium(V) from titanium-containing sulfuric acid solutions with organic coagulants like polyacrylamide (PAA)

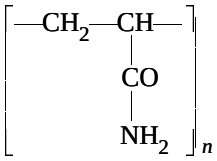

and polyethylenimine (PEI) [4]

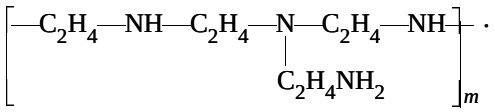

The experimental data are given in Table 3. Organic coagulants allow efficient separation of niobium(V) from titanium(IV). Presumably, the process involves a chemical reaction rather than coagulation proper. Anionic sulfate complexes of the elements are bonded by nitrogen-containing groups of coagulant (by analogy with amine extraction) to form compounds that are precipitated. A disadvantage of using coagulants is the necessity to take them as dilute aqueous solutions (~0.5 wt % PAA and 2–10 wt % PEI), which inevitably leads to dilution of sulfuric acid solutions of titanium.

If sulfuric acid solution contains tantalum(V) in addition to niobium and titanium, then in the extraction process tantalum remains in the aqueous phase along with Ti(IV), whereas in the process with coagulants it selectively coprecipitates with niobium(V). Preliminary experiments showed that, in hydrochloric acid solutions, the target components behave similarly.

CONCLUSIONS

(1) Nb_2O_5 containing less than 2 wt % TiO_2 can be obtained by extraction of niobium(V) from titanium-containing sulfuric acid solutions with tributyl phosphate containing an amine.

(2) Niobium(V) can be separated from titanium(IV) by selective precipitation with organic coagulants, namely, polyacrylamide and polyethylenimine.

REFERENCES

1. Sklokin, L.I., Zots, N.V., Shestakov, S.V., *et al*., *Tsvetn. Met*., 2000, no. 10, pp. 48–53.
2. Maiorov, V.G., Skabichevskaya, G.I., Babkin, A.G., and Kopkov, V.K., *Zh. Prikl. Khim*., 1981, vol. 54, no. 1, pp. 151–153.
3. Nikolaev, A.I. and Maiorov, V.G., *Ekstraktsiya niobiya i tantala* (Extraction of Niobium and Tantalum), Apatity: Kol'skii Nauchnyi Tsentr Ross. Akad. Nauk, 1995.
4. Gembitskii, P.A., Zhuk, D.S., and Kargin, V.A., *Polietilenimin* (Polyethylenimine), Moscow: Nauka, 1971.

Russian Journal of Applied Chemistry, Vol. 76, No. 5, 2003, pp. 842–843. Translated from Zhurnal Prikladnoi Khimii, Vol. 76, No. 5, 2003, pp. 870–871.

BRIEF COMMUNICATIONS

Synthesis of Cyclic Organic Carbonates from C_3–C_{16} Epoxides

G. V. Rybina, S. S. Srednev, and L. I. Bobyleva

Yaroslavl State Technical University, Yaroslavl, Russia

Received October 28, 2002; in final form, March 2003

Abstract—Cyclic organic carbonates were prepared from epoxides (derivatives of C_3–C_{16} olefins, C_4 and C_8 dienes, styrene; epichlorohydrin) in the presence of a catalytic system consisting of $CoCl_2 \cdot 6H_2O$ and dimethylformamide.

Cyclic organic carbonates are used in oil refining as extractants of aromatic hydrocarbons, and also in synthesis of drugs and plant protection agents. Of particular interest for industrial organic synthesis is preparation of nitrogen-containing polymers from cyclic carbonates [1].

Cyclic organic carbonates are prepared in industry by reactions of epoxides with CO_2 in the presence of alkali metal halides:

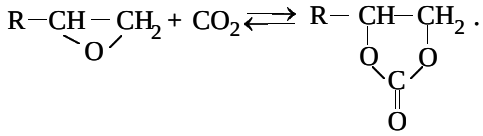

This process, however, requires high pressures (3–10 MPa) and temperatures (180–220°C) [2].

It was suggested previously [3] to perform this reaction in the presence of a Co(II) or Ni(II) halide and dimethylformamide (or dimethylacetamide). With this catalytic system, it appeared possible to decrease the reaction temperature (to 120–130°C) and pressure (to 1.0–1.5 MPa), and also to prepare vinylethylene carbonate by carboxylation of divinyl oxide at a high rate and with a high selectivity with respect to the target product [4].

Our goal was to test the suggested catalytic system for synthesis of cyclic carbonates from epoxides of various structures, containing aliphatic (saturated and unsaturated), aromatic, and other substituents.

Carboxylation was performed at 130°C and CO_2 pressure of 1.5 MPa; the starting mixture contained 25.0 wt % epoxide and 2.50 wt % $CoCl_2 \cdot 6H_2O$. The reaction time was 120 min. The results are listed in the table.

The cyclic carbonates were isolated by vacuum fractionation; their purity was no less than 98.5%. The purity, composition, and structure of the target products were confirmed by chromatography, chemical analysis, and ^{13}C NMR spectroscopy.

EXPERIMENTAL

The starting epoxides were prepared by hydroperoxide oxidation of appropriate olefins and isolated by distillation. The main substance content was no less than 98.5%. The solvent, catalyst, and auxiliary substances met the requirements of the corresponding State Standards. Carboxylation of epoxides was performed in a temperature-controlled stirred metallic vessel.

The reaction products were analyzed by gas–liquid chromatography on an LKhM-8 MD device (3000 × 3-mm steel column, stationary phase 15% diisooctyl sebacate + 1.5% sebacic acid on Chromaton N AW-DMCS). 1-Propanol was used as internal reference. Chemical analysis was performed according to [5]. The ^{13}C NMR spectra were recorded on a Tesla BS-576A spectrometer (25.142 MHz, internal reference HMDS).

CONCLUSION

A catalytic system consisting of $CoCl_2 \cdot 6H_2O$ and dimethylformamide is effective in synthesis of cyclic carbonates from various saturated and unsaturated epoxides.

ACKNOWLEDGMENTS

The study was financially supported by the program "Research at Higher Schools in Priority Fields of Science and Engineering," 2001.

1070-4272/03/7605-0842$25.00

Synthesis of cyclic carbonates from epoxides in the presence of $CoCl_2 \cdot 6H_2O$ and dimethylformamide

Epoxide	Conversion, %	Cyclic carbonate				
		selectivity, %	state of aggregation	T_b, °C	P, kPa	content, wt % [5]
Propylene oxide	97.4	95.7	Liquid*	–	–	–
1-Pentene oxide	95.0	91.1	″	127.0–127.5	0.93	98.81 ± 0.16
1-Heptene oxide	92.7	89.8	″	125.5–126.0	0.27	99.1 ± 0.13
1-Octene oxide	88.9	89.1	″	131.0–131.5	0.27	98.5 ± 0.14
1-Nonene oxide	84.8	84.5	″	148.0–149.0	0.27	98.68 ± 0.27
1-Undecene oxide	81.0	81.4	Amorphous	163.0–163.5	0.40	99.01 ± 0.11
1-Dodecene oxide	78.1	80.4	″	176.0–178.0	0.27	99.23 ± 0.08
1-Tetradecene oxide	67.2	85.1	″	181.5–182.0	0.27	98.96 ± 0.22
1-Hexadecene oxide	51.8	72.5	″	199.0–199.5	0.40	99.17 ± 0.09
1,3-Butadiene oxide	92.4	91.4	Liquid	121.0–121.5	1.33	99.41 ± 0.03
1,7-Octadiene oxide	96.9	94.2	″	156.0–156.6	1.33	98.78 ± 0.19
3-Methyl-1-butene oxide	86.1	91.1	″	96.0–96.5	0.27	99.06 ± 0.12
Epichlorohydrin	96.6	94.9	″	128.5–129.0	0.27	98.56 ± 0.22
Styrene oxide	85.2	80.0	Liquid*	–	–	

* Not isolated from the reaction mixture.

REFERENCES

1. Koren'kova, O.P. and Kvasha, V.V., *Khim. Prom–st.*, 1961, no. 9, pp. 33–38.
2. Ufimtsev, A.V. and Kuzora, I.E., *Khim. Prom–st.*, 1993, no. 11, pp. 555–557.
3. RF Patent 2 128 658.
4. Bobyleva, L.I., Rybina, G.V., and Srednev, S.S., *Khim. Prom–st.*, 2002, no. 7, pp. 1–5.
5. Bobyleva, L.I., Kozlova, O.S., Rybina, G.V., and Moskvichev, Yu.A., *Zh. Anal. Khim.*, 2000, vol. 55, no. 10, pp. 1102–1104.

Russian Journal of Applied Chemistry, Vol. 76, No. 5, 2003, pp. 844–846. Translated from Zhurnal Prikladnoi Khimii, Vol. 76, No. 5, 2003, pp. 872–874.

INFORMATION

Fifth Chemical Forum "Tekhnokhimiya-2003"

The Fifth Chemical Forum "Tekhnokhimiya-2003" (Technical Chemistry 2003) was held in St. Petersburg on March 19–23, 2003. The forum was organized by Lenekspo Open Joint-Stock Company, Prikladnaya Khimiya Russian Scientific Center (PKhRSC), Prometei Central Research Institute of Structural Materials (PCRISM), and All-Union Research Institute of Corrosion (Moscow), with the support of Ministry of Industry and Science of the Russian Federation, Administration of St. Petersburg, and Russian Chemical Society. Within the framework of the forum were held Fifth Conference "Teknokhimiya" and Sixth International Scientific and Technical Conference "New Materials and Technology for Corrosion Protection," and also thematic exhibitions "New Materials and Technologies for Corrosion Protection," "Chemical Industry," "Industrial Ecology and Safety," and "Instruments, Equipment, and Apparatus." Simultaneously, the Tenth International Exhibition "Ecology of a Large City" was held within the framework of the International Ecological Forum.

At present, the chemical industry is one of the most rapidly developing branches of the domestic economy. The appearance of a great number of new plants with different kinds of property and the tendency toward replacement of imported goods by home-made products make necessary an intensive information exchange between participants of the market of chemical technologies and separate plants. At the same time, the development of chemical industry is closely associated with introduction of environmentally safe technologies, raw material processing, and utilization of wastes.

The Program of the Fifth Conference "Tekhnokhimiya" included reports devoted to technological reequipment and modernization of chemical plants and solution of problems associated with industrial ecology and safety. All the reports can be divided into two groups: "High Technologies, Technological Equipment, and Analytical Monitoring in Manufacture of Chemical Products" and "Ecology and Industrial Safety in Chemical Industry." In both groups, most of reports were presented by staff members of PKhRSC. At present, this is the leading Russian scientific center in the field of chemistry and chemical technology. It is aimed to formulate the scientific and technological policy in chemistry-related branches of industry and to develop and implement the most important state programs. The main avenues of research at PKhRSC are as follows: chemistry and technology of fluorine-containing compounds, basic and fine organic synthesis, products of inorganic synthesis, membranes, sorbents and catalysts for technological and ecological purposes, ultrapure substances, composites and polymeric materials, isotopically labeled compounds, processes and apparatus of chemical technology, scientific foundations of design of versatile chemical shops on the basis of modular equipment, and means of control and automation. A prominent place is occupied by studies in the field of chemistry of the defense and aerospace complex of Russia, conversion of defense industries, and utilization of military products. The main avenues of research were reflected in reports presented by participants of the "Tekhnokhimiya" conference.

V.S. Leont'ev and P.Yu. Smykalin discussed physicochemical and mathematical foundations for intensification and modernization of processes and apparatus for reequipment of chemical industries. The authors noted that the problems of modernization of industrial processes and apparatus are multilevel and many-parametric. Models of the first (lower), second (medium), and third (upper) levels are analyzed. V.S. Shpak and co-authors considered chemical and technological problems associated with internal-combustion engines and means of transportation in Russia. V.G. Barabanov, B.N. Maksimov, G.I. Kaurova, *et al.* summarized the results of studies in the field of chemistry and technology of fluorine compounds, carried out at PKhRSC. The applied research is done in the following directions: Freons for various purposes (refrigerants, solvents, fire-extinguishing agents, etc.); fluorine-containing monomers for fluoroplastics; thermally and chemically stable oils, lubricants, dielectric liquids; fluoroaromatic compounds. Much success has been achieved in all of these directions.

D.S. Pashkevich and V.G. Barabanov reported on the development of a process for synthesizing fluorine-containing compounds using elemental fluorine in order to perform conversion of fluorine plants. At present, elemental fluorine is available commercially. The processes developed at PKhRSC served as

1070-4272/03/7605-0844$25.00

a basis for creating a number of works at Russia's plants manufacturing elemental fluorine. There are large-tonnage shops for production of fluorine compounds at major fluorine-manufacturing plants, such as Galogen Open Joint-Stock Company (SF_6, WF_6, BF_3, C_3F_8), Kirovo-Chepetsk Chemical Combine (SF_6, $C_{10}F_{18}$), and Angarsk Electrolysis Chemical Combine (CF_4).

E.E. Gusarov, Yu.P. Malkov, and M.A. Rotinyan discussed in their report an integrated process for plasmochemical elimination of organohalogen substances and wastes and cleaning of industrial equipment to remove these contaminants. The authors noted that many halogen-containing compounds, which had been widely used in the industry and are still stored in large amounts, and also industrial wastes containing these compounds, are highly hazardous for humans and the environment. To compounds of this kind belong, in the first place, ozone-destroying Freons, polychlorobiphenyls, and toxic halogen-containing wastes from chemical industries. For example, according to the authors' data, about 2 million tons of various ozone-destroying Freons have been accumulated in the world and require environmentally safe elimination. The world's stock of polychlorobiphenyls, which are one of the main sources of such superecotoxicants as dioxins, is estimated at 760 million liters. Also reported were advantages and high efficiency of the plasmochemical process in elimination of organohalogen substances.

An important issue associated with the development of new effective adsorbents and localizers for recovering and eliminating spills and preventing contamination of the environment with petroleum products and other inflammable and toxic liquids was considered in the report presented by S.V. Polyakov and co-authors.

Together with staff members of PKhRSC, representatives of other institutions also presented a number of reports. B.V. Gidaspov and V.G. Dedukh (Azot-Vzryv Closed Joint-Stock Company) considered problems associated with manufacture of explosives for industrial purposes. Ammonium nitrate is the most widely used oxidizing agent in substances of this kind. It is produced in Russia on a rather large scale (more than 8 million tons was manufactured in 2002). The present-day economic situation in Russia's industry and agriculture leads to the following distribution of the whole manufactured amount of ammonium nitrate: 70–80% exported, 10–15% used in agriculture as fertilizer, and 5–10% used in manufacture of industrial explosives. The authors analyze the requirements to the quality of ammonium nitrate used to produce explosives and assess the state of affairs at plants manufacturing ammonium nitrate. The proposed liberalization of the market of natural gas may lead to a significant rise in its price. At the same time, average expenditure of natural gas for manufacture of 1 ton of ammonium nitrate at Russia's plants exceeds the average world's level by a factor of 1.8–2.0, and the overall expenditure of electric power, by a factor of more than 2. The factory cost price of ammonium nitrate has already become close to the disbursing price, and the profitability is as low as 5–10%.

The report by E.A. Vlasova and N.V. Mal'tseva (St. Petersburg State Technological Institute) was devoted to development of sorbents and catalysts for solving environmental problems.

Domestic developers of anticorrosion materials and technologies and representatives of some foreign companies took part in sessions of the International Scientific and Technological Conference "New Materials and Technology for Corrosion Protection." The reports they presented covered a wide variety of problems: new protective coatings and technologies of their application, inspection of the corrosion state of equipment and structures, economical and environmental aspects of means and methods of corrosion protection, licensing and certification of means and techniques of corrosion protection, corrosion risk insurance, and methods for monitoring and diagnostics of corrosion.

Modern problems of corrosion resistance of steels and corrosion protection of equipment in oil refining and petrochemical industries were considered in the report presented by Yu.I. Archakov (VNIIneftekhim Open Joint-Stock Company, St. Petersburg). The author noted that, in view of the substantial scale of the industries and large dimensions of the equipment employed, wide use of special stainless steels and alloys is impossible for economic reasons. At the same time, the working media used in various stages of oil processing are corrosion-active. Particularly complicated is corrosion protection at elevated temperatures and high pressures. The author analyzed a complex of promising techniques for corrosion protection of equipment for various working conditions and types of corrosion-active media. V.V. Burlov and G.F. Palatik (VNIINeftekhim Open Joint-Stock Company, St. Petersburg) reported the results obtained in studying the efficiency of industrial amide–imidazoline inhibitors for corrosion protection of installations for primary oil processing.

The report by S.S. Vashchilova (Emlak Closed

Joint-Stock Company) was devoted to new paint-and-varnish materials offered by Emlak Company for protection of various kinds of oil processing equipment working under standard atmospheric conditions and in corrosive media. V.L. Zhak, M.D. Sarachuk, and V.S. Rammo (Gamma Ltd., St. Petersburg) reported on the development of water-dilutable epoxy paint-and-varnish materials. Coatings based on the materials manufactured by the company are intended for protection of steel, aluminum–magnesium, and zinc-plated surfaces under atmospheric conditions, at increased humidity, in saline and alkaline media, and also in oils and petroleum products. The problems associated with raising the longevity of paint-and-varnish coatings were considered in the report by V.D. Pirogov and M.A. Mikhailova (PCRISM, St. Petersburg).

G.Yu. Kalinin and co-authors (PCRISM) reported on the development of a high-strength austenite nitrogen-containing steel. The steel shows good characteristics as regards corrosion cracking and intergranular and pitting corrosion. S.Yu. Mushnikova *et al.* (PCRISM) reported the results obtained in a comparative study of resistance to pitting, crevice, and intergranular corrosion, and also to corrosion cracking, of high-nitrogen (05KhAN4B, 0.13N) and carbon (07Kh16R4B) steels. It was found that replacement of carbon with nitrogen in a moderately alloyed chromium–nickel steel 05Kh16AN4B improves significantly its resistance to pitting and crevice corrosion in chloride solutions, compared with the 07Kh16N4B steel unalloyed with nitrogen and containing about 0.07% C.

I.A. Susorov and co-authors (Kronos-SPb Open Joint-Stock Company, St. Petersburg) reported on the development and commercial production of a number of new anticorrosion materials for various industries and presented their basic technical characteristics. The products manufactured by Kronos-SPb St. Petersburg paint-and-varnish plant have been known for more than 60 years. Together with production of new materials, the company continues to manufacture the conventional alkyd, acryl, and perchlorovinyl enamels and primers. Susorov *et al.* presented data on application-ready primer-paint Surik Svintsovyi (Red Lead), whose industrial use was allowed by the State Sanitary and Epidemic Control Commission. The same company offers Germokron-ZhD corrosion-protective coating stable in mineralized corrosive media.

V.I. Trusov (Notekh Research and Production Plant, St. Petersburg) noted the advantages of a new rust converter Notekh-K (concentrate) and described fields of its application.

In this brief journal review, it was only possible to dwell on selected, most characteristic reports. Extended abstracts of all reports presented at both conferences and the official alphabetic catalog of exhibitors, participants of thematic exhibitions, can be found in a special publication by Lenekspo.

In view of the subject fields and goals of the Teknokhimiya-2003 chemical forum, it seems quite reasonable that the Tenth International Exhibition "Ecology of Large City" was held on the same days (March 19–22, 2003). The main goal of the exhibition was to demonstrate the best examples of domestic and foreign products, equipment, services, technologies, and scientific and applied developments in the field of ecology. In accordance with these circumstances, the subject of the exhibition covered the following directions: environment protection and restoration, wastewater purification, water treatment and supply, waste management, recycling industry, methods for monitoring of air contaminants and systems for air purification, protection and restoration of arable lands, efficient use of energy. More than 50 companies from Russia and Poland took part in the exhibition.

Simultaneously with the exhibition, two scientific and applied symposia were held: "Water Treatment and Water Supply, Topical Problems and Experience of Their Solution" and "Improvement of Water Quality as a Source of Health for Population."

A. G. Morachevskii

Russian Journal of Applied Chemistry, Vol. 76, No. 5, 2003, p. 847. Translated from Zhurnal Prikladnoi Khimii, Vol. 76, No. 5, 2003, p. 875.

BOOK REVIEWS

Surzhko, O.A., *Resurso-tekhnologicheskie problemy elektroliticheskogo polucheniya binarnykh splavov s nevzaimodeistvuyushchimi komponentami* (Resource-Related and Technological Problems Associated with Electrolytic Production of Binary Alloys with Noninteracting Components)

Rostov-on-Don, 2001, 108 pp.

Despite the complicated title, the brief monograph actually presents results of an experimental study of electrolytic production of cobalt–lead alloys and data on properties of the alloys obtained. The introductory chapters contain general evidence. The book comprises an introduction, six chapters, conclusion, and a bibliographic list with 96 references to works of mainly domestic authors.

The introduction (pp. 4–6) notes a certain interest aroused by the properties of alloys belonging to systems with noninteracting components. Very brief Chapter 1 (pp. 6–10) discusses the possibility of replacing rare and expensive components with lower-cost formulations having similar properties. Naturally, such a replacement requires detailed substantiation in each particular case. Chapter 2 (pp. 10–23) considers specific features of the structure and properties of electrolytic alloys with noninteracting components. The author focuses attention on alloys with magnetic properties. Chapter 3 (pp. 23–42) is devoted to theoretical foundations of formation of electrolytic alloys. Chapter 4 describes the experimental techniques applied by the author to study the cobalt–lead system: chemical, spectral, and X-ray structural analyses and measurement of magnetic characteristics. Chapter 5 (pp. 50–76) contains evidence about electrodeposition of a cobalt–lead alloy from a pyrophosphate electrolyte with rather complex composition. The interaction of the electrolyte components was studied by measuring electronic absorption spectra. Chapter 6 (pp. 76–94) presents data on the phase composition and magnetic and corrosion properties of an electrolytically prepared cobalt–lead alloy.

The conclusion (p. 94–99) summarizes the main results of the study performed. It is shown that the pyrophosphate electrolyte with various additives, proposed by the author, can be used to obtain alloys in the cobalt–lead system in a wide range of compositions (14 to 91 wt %). A suggestion is made, concerning the possible mechanism by which pyrophosphate complexes of cobalt and lead are discharged at the cathode. A study of the phase composition demonstrated that lead-based solid solutions with cobalt content of up to 10–12 wt % can be formed. Also noted is the formation of a new phase whose nature could not be identified so far. The obtained cobalt–lead alloys possess ferromagnetic properties.

The main importance of the monograph is, in my opinion, in its second part (Chapters 4–6) which presents experimental results. Unfortunately, the general theoretical chapters (Chapters 1–3) are written without due clarity, the equations presented are virtually not commented at all, and a number of annoying inaccuracies can be found.

The book may be of interest for specialists in electroplating.

A. G. Morachevskii

1070-4272/03/7605-0847$25.00

Russian Journal of Applied Chemistry, Vol. 76, No. 5, 2003, pp. 848–849. Translated from Zhurnal Prikladnoi Khimii, Vol. 76, No. 5, 2003, p. 876.

BOOK REVIEWS

Nikitin, M.K. and Mel'nikova, E.P., *Khimiya v restavratsii* (Chemistry in Restoration)

St. Petersburg: Tekhinform, 2002, 304 pp.

The original and needed reference book considers chemical processes occurring in restoration of architectural monuments, paintings, sculptures, pieces of art made of stone, wood, metal, glass, ceramics, fabrics, paper, and leather, and presents a vast body of evidence concerning materials used in restoration work. The first edition of the reference book was published by Khimiya publishing house in 1990 and was met with lively interest by readers both in Russia and other countries. The authors of the book are known specialists in the field of restoration.

The reference book comprises an introduction, ten chapters, and appendix. In the brief introduction (pp. 5–7), the authors, in particular, mention the importance of carrying out conservation work, which neutralizes the detrimental action of numerous damaging factors associated with the general environmental situation. Chapter 1 (pp. 8–40) presents criteria to be used in choosing materials for restoration of historical and cultural monuments. Particular attention is given to polymeric materials (both synthetic and natural), organosilicon compounds (polyorganosiloxanes, polyorganosilazanes). Also presented are data on organic solvents that can be used in restoration works.

Chapter 2 considers chemical materials used in restoration of paintings in oil or distemper on canvas, fresco on lime plaster, paintings in distemper on wood (restoration of icons), polychromic wooden sculpture, and wax articles. Chapter 3 (pp. 73–98) is devoted to restoration of stone articles, sculptures in museums and stone buildings and structures, ant to protective-decorative dressing of facades. The set of necessary chemical materials to be used, depending on a particular task to be accomplished, is very wide. Prominent place among such materials is occupied by polymeric solutions and epoxy resins. Small Chapter 4 (pp. 99–108) contains evidence about chemical materials used in restoration of concrete and armored-concrete buildings and structures. Polymeric cements, composites containing fast-cured mineral binders with polymers, are widely used to reinforce buildings, glue together fragments of sculptures, and for other purposes. Concrete and armored-concrete surfaces are hydrophobized and reinforced with solutions of polyalkylhydridosiloxanes in organic solvents or corresponding emulsions. Surfaces of concrete structures can also be reinforced by impregnation with epoxy or polyester resins.

Chapter 5 (pp. 107–127) describes chemical materials used in restoration of wooden objects or articles. It considers measures for integrated protection of wood in historical buildings and structures, articles found in archaeological excavations, sculpture, furniture, and museum exhibits. Fire and biological protection of wood, its conservation and reinforcement, and deposition of protective-decorative coatings are envisaged. Various polymeric materials are widely used in these procedures.

Chapter 6 (pp. 126–201) discusses chemical materials used to conserve and restore articles made of metals: copper, bronze and other copper alloys, iron, cast iron, tin, lead, and noble metals. A wide variety of processes are considered for each of the metals. These include cleaning of metals to remove corrosion products, choice of solders and fluxes for soldering, use of polymeric materials in gluing, chemical or electrochemical deposition of coatings, and inhibition of corrosion processes. A great number of different formulations are presented. Chapter 7 (pp. 202–214) contains information about chemical materials used in restoration of enamels, glass articles, porcelain, and ceramics. Chapter 8 (pp. 215–233) is devoted to chemical materials used in restoration of various kinds of fabrics. Chapter 9 discusses restoration of paper and paper documents. The authors note that the difficulties encountered in restoration of works of art on paper consist in the wide diversity of the materials used, their varied degree of preservation, and different ways of creating images on paper. Detergents, bleaching agents, reagents for removing spots from paper,

1070-4272/03/7605-0848$25.00

antimicrobial means, paper stabilization, and reinforcing formulations for decrepit paper are described. Chapter 10 (pp. 247–269) presents evidence concerning chemical materials used in restoration of articles made of bone, leather, and semiprecious stones.

The appendix (pp. 270–285) presents in the form of tables the basic characteristics of chemical substances used in restoration: inorganic acids, organic acids and salts, organic solvents, cellulose ethers and esters, synthetic polymers, biocides of various kinds. The book is supplied with a list of recommended literature, summary in Russian and English, and index.

The reference book is written by expert scientists and creates rather good impression. As regards manner of presentation, the book is understandable for a wide audience of readers, irrespective of their professional training.

A. G. Morachevskii and I. N. Beloglazov

Russian Journal of Applied Chemistry, Vol. 76, No. 6, 2003, pp. 851–858. Translated from Zhurnal Prikladnoi Khimii, Vol. 76, No. 6, 2003, pp. 881–887.

REVIEWS

New Methods for Controlled Chain Growth in Polymerization of Vinyl Chloride

L. L. Semenycheva and D. F. Grishin

Research Institute of Chemistry, Lobachevsky Nizhni Novgorod State University, Nizhni Novgorod, Russia

Received November 27, 2002; in final form, February 2003

Abstract—Published data concerning the ways to control the kinetic parameters of vinyl chloride polymerization and molecular-weight characteristics of polyvinyl chloride through directed modification of the reactivity of the growing macroradical are considered.

Polyvinyl chloride (PVC) is one of the most important large-scale polymers. In the world production volume, it ranks second to low-density polyethylene, standing far ahead of polypropylene and high-density polyethylene [1–3]. The reason is that, depending on a synthetic procedure (polymerization in the bulk, suspension, microsuspension, or emulsion), temperature, modifiers, and processing conditions, PVC can be used for manufacture of a wide variety of plastics (rigid or soft, transparent or colored). PVC goods find wide application in manufacture of artificial leather, pipes, plastisols, glues, insulating and construction materials, etc. [1, 3–5].

The basic method for PVC production is radical polymerization of vinyl chloride (VC) [1, 4, 6–10], whose obvious advantages are good reproducibility and technological simplicity. However, synthesis of high-quality PVC under heterogeneous conditions poses a number of problems. First of all, this is the low initial rate of polymerization, whose spontaneous increase in the course of the process gives rise to the so-called gel effect. Nonuniform course of polymerization has negative effect on the formation of macromolecules and supramolecular structures, and, therefore, on the performance characteristics of the resulting polymer. It has been demonstrated that the gel effect results in lower thermal stability and composition inhomogeneity and higher polydispersity of the polymer [1, 4, 9–15]. The process conditions also influence the quality of the polymer. Among them are temperature, choice of necessary additives (emulsifiers and modifiers in suspension and emulsion polymerization and also chain transfer agents) [1, 11, 17–19], stirring mode, crust and "fish eye" formation [1, 10, 13], etc.

Devising advanced methods for controlling polymeric chain growth in radical polymerization of, in particular, VC is among the priority lines of the development of the macromolecular chemistry. It is well known that the gel effect and molecular-weight characteristics can be controlled using methods based on reactions competing with the main process. These methods include, first of all, direct introduction of chain transfer agents (mercaptans, halogenated hydrocarbons, etc.) and inhibitors (quinones, phenols, allyl derivatives, and dithiocarbamates) in the polymerizate [4, 10, 12]. Among ather methods are optimization of the temperature mode [4, 9, 19–22], addition of compounds promoting decomposition of peroxides [14, 23, 24], and use of new initiators or intiator mixtures [19, 22, 24–32].

Recently, methods of other kind have been proposed for chain growth control, based on coordination of a growth radical to organoelement compounds or stable radicals. These methods allow effective control of both the VC polymerization kinetics and formation of the polymer macromolecule. In this review, we examine new approaches to control of the VC polymerization kinetics and molecular-weight characteristics of PVC.

RADICAL POLYMERIZATION OF VC IN THE PRESENCE OF ORGANOELEMENT COMPOUNDS

Organic compounds of nontransition elements in combined with oxidants, have long been known as initiators of low-temperature polymerization of vinyl monomers, among them VC [4]. The reason is that reactions of alkyl and mono- and dialkoxy derivatives

1070-4272/03/7606-0851 $25.00 © 2003 MAIK "Nauka/Interperiodica"

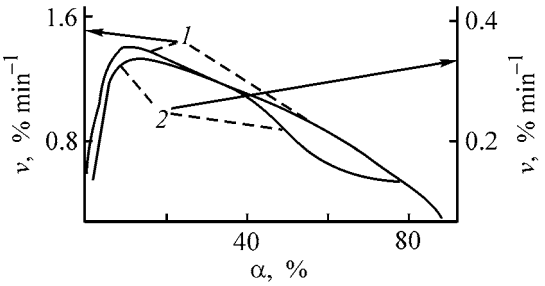

Fig. 1. Kinetic curves of VC polymerization: (*1*) in the bulk and (*2*) in suspension at 20°C in the presence of the triisobutylborane–organoelement peroxide initiator [22]. (v) Polymerization rate and (α) conversion; the same for Fig. 2. Triisobutylborane concentration (mol %): (*1*) 0.8 and (*2*) 0.06. (*1*) *tert*-Butylperoxyphenyldimethylsilane (0.2 mol %) and (*2*) di(*tert*-butylperoxy)triphenylantimony (0.2 mol %).

of Group II–IV nontransition elements with oxygen and peroxides mostly proceed homolytically [33–37]. The performance of the indicated initiator systems is largely governed by the structure of an organoelement compound used. It has been demonstrated that, in the case of diethylzinc and diethylcadmium, the conversion in 6 h does not exceed 5–7%, whereas with triisobutylborane it is about 40% [4] (this compound shows promise as the most efficient initiator of polymerization of vinyl monomers [19, 22, 34, 36, 38–41].

In the early 1980s, G.A. Razuvaev and coworkers proposed systems based on trialkylboranes and thermally stable organic peroxides, containing Group IV–V elements as efficient initiators for polymerization of vinyl monomers, which allow the process to be performed to high conversions over a wide temperature range [19, 22, 38–55]. A specific feature of polymerization in the presence of the indicated compounds is that a monomer directly participates in the chain initiation stage [34, 39–41].

In the case of VC, polymerization proceeds by an uncommon mechanism. It is characterized by high initial rate, which approaches a maximum at 15–20% conversion; after that the process goes quite smoothly (Fig. 1) until virtually complete (90–98%) conversion of the monomer [22, 42].

Taking into account the observed high chain propagation rate and certain trends in physicochemical characteristics of the homo- and copolymers synthesized in the presence of an initiator system constituted by alkylboron and organoelement peroxide, Grishin and Moikin [56–60] suggested that the components of the initiator not only participate in the initiation stage, but also, being weak Lewis acids, have a direct effect on the propagation and termination of the chain by virtue of coordination of the growth radical to the organoelement additive [61, 62].

Such interaction can occur directly at the reactive center (with participation of an unpaired electron) or at a functional group [scheme (1)], or at both centers simultaneously (with delocalization of the unpaired electron) [scheme (2)]:

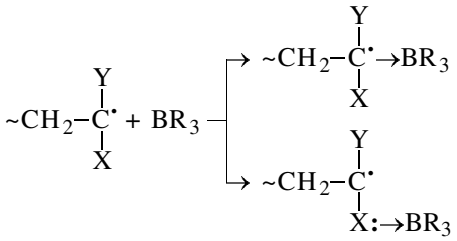

(1)

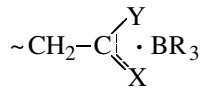

(2)

where X is the functional group, and Y, a hydrogen atom or methyl group.

This enhances the electron-acceptor capacity (electrophilicity) of a growing macroradical and also its reactivity toward the multiple bond of the monomer. Quantum chemical calculations and ESR data [58, 59, 63] confirm the possibility of such an interaction. Similar complexes of vinyl monomers with metal halides (Lewis acids) have been well known for a long time and studied in detail (see, e.g., the monograph [64]).

Direct involvement of organic compounds of boron, aluminum, and some other coordination-unsaturated elements in chain propagation has been demonstrated for a wide variety of monomers [57–60, 65, 66], with organic peroxides and azobis(isobutyronitrile) (AIBN) used as initiators, and organoelement compounds added in concentrations comparable with that of the initiator.

In the case of VC, introduction of an trialkylborane into a system polymerizing in the presence of dicyclohexyl peroxydicarbonate (DCPD) leads to a considerable increase in the initial polymerization rate and weakening of the gel effect: in the presence of the organoelemental additive, the initial rate of VC polymerization at 30°C is nearly twice that in the case of initiation with DCPD but without additive [67]. It has been demonstrated that PVC formed in the presence of trialkylboranes is characterized by high syndiotacticity index [19, 67], increased softening point [19, 22, 43, 44], and enhanced heat resistance [22, 68].

Semenycheva [22] and Dodonov *et al*. [48] reported synthesis of C-90 high-molecular-weight PVC under favorable temperature and time conditions (20–30°C, 7–8 h) with a binary initiator system, triisobutylborane–di(*tert*-butylperoxy)triphenylantimony. Addition of catalytic amounts of aluminum alkoxides (diethylaluminum ethoxide and ethylaluminum dietoxide) to a system with AIBN also decreases the autoacceleration, providing smooth polymerization of VC [67, 69].

Results on copolymerization of VC with alkenes (Table 1) under conditions typical of VC polymerization (50°C, 3–5 atm) [67, 69] give additional evidence in favor of the coordinated radical mechanism of VC polymerization in the presence of organoelement additives. It should be pointed out that VC copolymers with ethylene and α-olefins show promise as plastics: they are easily workable and have high elongation at break, impact resilience, etc. Furthermore, addition of even a small amount (5–10%) of alkene units to PVC considerably decreases the cost of the polymer. The unavailability of effective initiators hinders large-scale production of the copolymers indicated. It follows from Table 1 that, in the presence of organoaluminum compounds raising the electrophilicity of the growth radical by virtue of its coordination to an aluminum alkoxide, it is possible to obtain in high yield a polymer containing alkene (ethylene and propylene) units. The presence of propylene units in PVC has been confirmed by IR spectroscopy [67].

Initiator systems based on alkylboranes and Group IV organoelement peroxides enable copolymerization of VC with ethylene and α-olefins over wide composition range at high rate and product yield under mild conditions [50, 53, 70]. The use of systems constituted by trialkylborane and organoelement peroxide leads to pronounced equalization of the copolymerization constants. For example, in copolymerization of VC with ethylene and other olefins, the composition curve is S-shaped, and the copolymer composition in the monomer mixture is virtually constant over the olefin concentration range from 30 to 70 mol %, irrespective of the monomer mixture composition [53, 70]. It should be pointed out that raising the initiator concentration at constant monomer ratio in the mixture leads to a decrease in the viscosity of the resulting copolymers and a slightly (by 5–6%) increase in conversion [50].

It has been demonstrated that PVC containing alkene units differs from ordinary PVC in its physicochemical characteristics. In particularly, the intrinsic viscosity and molecular weight M of the VC/ethylene copolymer decrease with increasing mole fraction of ethylene. The Fickentscher constant characterizing the molecular weight of this polymer (K_f = 40–70 [4]) is also considerably lower as compared to PVC synthesized with the indicated initiators (Table 1) [22, 67, 69]. Decreased K_f of PVC makes its plasticity better [4, 7], which is important from the practical standpoint.

Table 1. Copolymerization of VC with alkenes in the presence of organoaluminum compounds (0.2 mol %) [67] [initiator AIBN (0.2 mol %), T = 323 K]

Additive	Alkene, wt %	Content, %, in polymer		K_f
		alkene units	chlorine	
–	–	0	57.6	71–72
$EtOAlEt_2$	Ethylene			
	3	2	54.9	55–57*
	10	7	52.5	52–54*
	Propylene			
	5	5	53.7	56–58
	10	10	51.0	52–54
$(EtO)_2AlEt$	Ethylene			
	5	5	53.8	66–68
	10	10	52.6	67–69

* Organoelement compounds were added as benzene solutions (benzene content in the polymerizate was 15 wt %).

Therefore, the use of coordination-unsaturated organoelement compounds directionally affecting the reactivity of macroradicals is an effective method for control of polymer chain growth in radical polymerization of VC.

Another possible way to control the polymer chain lifetime, aimed at synthesis of compositionally uniform polymers, is use of stable radicals.

"LIVING" POLYMERIZATION OF VC

In recent years, a new concept of controlled radical polymerization through the "living" mechanism is intensively developed. The essence of the "pseudoliving polymerization" (term "living polymerization" is used as well) is as follows [53, 71–75]. Catalytic amounts of specific reactive additives are added to the polymerizate. Among them are, for example, stable radicals or their sources, complex ions of variable-valence metals, and other chain-terminating agents ($X^{\bullet}$) capable of reversibly interacting with growing radicals ($R^{\bullet}$) to give a labile adduct (R–X), which then de-

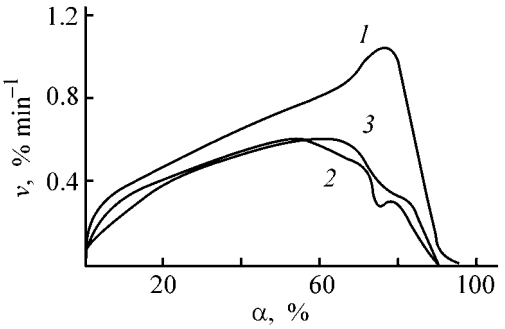

Fig. 2. Kinetic curves of VC polymerization in the presence of BPN at 50°C. BPN concentration (%): (*1*) 0, (*2*) 0.005, and (*3*) 0.1. Initiator DCPD (0.1 mol %) [80].

composes under certain conditions to regenerate the same growing radical.

Despite that "pseudoliving" radical polymerization is a relatively new line in the chemistry of controlled radical processes, quite a few organic and organometallic compounds allowing realization of radical polymerization through the "living-chain" mechanism have been proposed. However, the absolute majority of relevant studies is devoted to polymerization of styrene and its homologs and also of acrylates and methacrylates. Only few reports deal with controlled radical polymerization of VC. First of all, this is caused by the fact that stable carbon-centered and nitroxyl radicals are mostly used as grows regulators, most often, 2,2,6,6-tetramethyl-1-piperidinyloxyl (TEMPO) and its analogs; nitrogen- and sulfur-containing iniferters {term "iniferter" is composed of English abbreviations for the elementary stages of radical polymerization, namely, initiation (ini), transfer (fer), and termination (ter) [72]}; and also transition metal halides [53, 72–75]. Most of the known regulators effectively operate only at relatively high temperatures (100–130°C), being, therefore, absolutely impracticable in polymerization of VC as a gaseous monomer.

Table 2. Characteristics of PVC synthesized in the presence of BPN [81] ([DCPD] = 0.1 mol %, T = 50°C)

Sample no.	[BPN], mol %	α, %	[η]	$M_n \times 10^{-3}$	$M_w \times 10^{-3}$	M_w/M_n
1	0.01	4	0.4	19	33	1.7
2	0.01	13	0.6	28	53	1.9
3	0.01	23	0.7	32	60	1.9
4	0.01	48	0.8	40	71	1.8
5	0.01	62	0.8	41	81	2.0
6	0.01	89	0.9	44	97	2.2
7	0.01	94*	1.1	49	114	2.3
8	0.01	114**	1.1	48	108	2.3
9	0.05	6	0.2	8	15	2.0
10	0.05	12	0.5	18	40	2.3
11	0.05	31	0.6	19	49	2.6
12	0.05	41	0.7	30	62	2.0
13	0.05	63	0.8	35	74	2.1

* Sample obtained by postpolymerization, with fresh portion of the monomer added on reaching 58% conversion.

** Sample obtained by postpolymerization, with fresh portion of the monomer added on reaching 52% conversion.

Therefore, those regulators show promise for controlled polymerization of VC which, being taken in combination with peroxides and azo compounds serving as common radical initiators, are capable of generating stable radicals directly in a polymerization system (*in situ*) at a temperature of PVC synthesis (about 50°C). For example, we have proposed previously to use the well-known spin trap, *N-tert*-butyl-α-phenylnitrone (BPN) as an effective regulator of the polymer chain lifetime in polymerization of a series of vinyl monomers, including VC [76–80].

Polymerization of VC in the presence of BPN demonstrates all the most significant signs of pseudoliving polymerization: (1) the gel effect degenerates (Fig. 2); (2) the process goes to high conversion (~90%); (3) the molecular weight of the resulting PVC linearly increases with conversion {Table 2, see the intrinsic viscosity [η] and weight-average (M_w) and number-average (M_n) molecular weights} (4) the molecular-weight distribution (MWD) of PVC is unimodal and the mode is regularly shifted toward the high-molecular-weight region with increasing conversion; and, finally, (5) the polydispersity (M_w/M_n) of the polymer remains virtually unchanged over the conversion range 4–48%, being equal to 1.7–1.8 (Table 2).

With the conversion increasing further, the polydispersity of PVC grows, but remains considerably lower than that in ordinary radical polymerization [77, 80]. In this case, M_w/M_n = 2.2 at 89% conversion (Table 2). A similar increase in the polydispersity has been observed at a conversion of 50% and more in polymerization of acrylic monomers through the pseudoliving chain mechanism in the presence of triphenylmethyl radicals [81, 82], suggesting a decrease in the contribution of pseudoliving polymerization to the polymer formation at high degrees of conversion. It is known that, in the case of ordinary radical polymerization of VC, the molecular weight of PVC remains unchanged throughout the process [4, 7], and no shift of the molecular-weight distribution mode toward higher molecular weights is observed [4, 7, 83].

To obtain additional evidence in favor of the pseudoliving mechanism of VC polymerization in the presence of BPN, we performed postpolymerization of VC [80]. A fresh portion of VC was added to PVC obtained in the presence of BPN, and polymerization was carried out in the same mode. The MWD patterns of the samples obtained by postpolymerization were unimodal, as in the case of PVC synthesized in the presence of BPN, and, with the conversion increasing in the course of postpolymerization, the mode continued to shift steadily toward higher molecular weights. Table 2 shows that, in this case, the molecular weight of PVC increases, and the polydispersity of the polymer obtained by postpolymerization in the presence of BPN (sample nos. 7 and 8) is well comparable with that of PVC at high degree of conversion (sample no. 6). The results obtained on polymerization of VC in the presence of BPN open the door for controlled chain growth and production of PVC with prescribed molecular-weight characteristics under ordinary industrial conditions. It is well known [73] that, in postpolymerization and synthesis of block and star copolymers, living cationic and anionic polymerization processes are used. Using the pseudoliving chain mechanism in radical polymerization of VC is the tool for extension of its practical use to, e.g., synthesis of PVC with wide range of M under ordinary industrial conditions.

On the basis of the available experimental data, the following scheme of chain propagation in the presence of BPN has been suggested [76, 80]. In the first stage, BPN reacts with the growing macroradicals (~$P_n^{\bullet}$) to form stable nitroxyl radicals ($A^{\bullet}$):

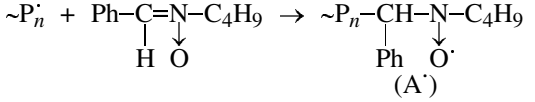

$$\sim P_n^{\bullet} + Ph{-}C(H)=N(\downarrow O){-}C_4H_9 \rightarrow \sim P_n{-}CH(Ph){-}N(\downarrow O^{\bullet}){-}C_4H_9 \quad (A^{\bullet})$$

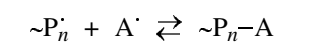

$$\sim P_n^{\bullet} + A^{\bullet} \rightleftarrows \sim P_n{-}A$$

Then the nitroxyl spin adducts ($A^{\bullet}$) react with growing radicals (~$P_n^{\bullet}$) to give labile terminal groups. This reversible reaction causes alteration of the "sleep" and "watch" periods in the "life" of the polymeric radical. In this case, chain growth proceeds through successive addition of monomer molecules to the macroradical (radical initiation). By analogy with polymerization of acrylic monomers through the living-chain mechanism [84], synthesis of PVC in the presence of nitroxyl spin adducts or their sources can be represented as

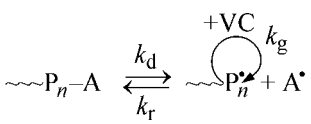

$$\sim\sim P_n{-}A \underset{k_r}{\overset{k_d}{\rightleftharpoons}} \sim\sim P_n^{\bullet} + A^{\bullet} \quad (+VC,\ k_g)$$

where k_d is the dissociation rate constant of the adduct ~P_n–A; k_r, the recombination rate constant of the radials $P_n^{\bullet}$ and $A^{\bullet}$; k_g, the growth rate constant.

CONCLUSION

The above analysis revealed the considerable recent progress in directed synthesis of PVC. Addition of ultralow concentrations of reactive additives allows significant and, what is the most important, directed modification of the reactivity of macroradicals and control of polymer chain growth. It is of primary importance that some organoelement compounds and spin traps are reactive under mild temperature conditions, being taken in a concentration comparable with that of the initiator.

ACKNOWLEGMENTS

The work was supported financially by the Russian Foundation for Basic Research (project no. 02-03-32427).

REFERENCES

1. *Polivinilkhlorid* (Polyvinyl Chloride), Ul'yanov, V.M., Rybkin, E.P., and Gutkovich, A.D., Eds., Moscow: Khimiya, 1992.
2. *Polyvinyl Chloride Resin, Khim. Kompl. Ros.*, 1998, vol. 1, pp. 7–9.
3. Gallari, J., *Plast. World*, 1995, vol. 25, pp. 65–71.
4. *Poluchenie i svoistva polivinilkhlorida* (Preparation and Properties of Polyvinyl Chloride), Zil'berman, E.N., Ed., Moscow: Khimiya, 1968.
5. Roder, H., *Polimery*, 1996, nos. 11–12, pp. 663–668.
6. Gladyshev, V.P. and Popov, V.A., *Radikal'naya polimerizatsiya na glubokikh stepenyakh prevrashcheniya* (Radical Polymerization at Deep Conversion), Moscow: Nauka, 1974.
7. Sangalov, Yu.A., Yasman, Ya.B., Romanko, T.V., and Krasulina, N.A., *Bashk. Khim. Zh.*, 1999, vol. 6, no. 1, pp. 12–17.
8. Kolegov, V.I., Potapov, V.N., Sorokina, T.M., *et al.*, *Plast. Massy*, 1982, no. 12, pp. 36–40.
9. Minsker, K.S. and Fedoseeva, G.T., *Destruktsiya i stabilizatsiya polivinilkhlorida* (Degradation and Stabilization of Polyvinyl Chloride), Moscow: Khimiya, 1979.
10. Ivanchev, S.S., *Radikal'naya polimerizatsiya* (Radical Polymerization), Leningrad: Khimiya, 1985.
11. Titova, V.A., Zegel'man, V.I., Pessina, A.Ya., *et al.*, *Vysokomol. Soedin, Ser. A*, 1982, vol. 24, no. 6, pp. 1207–1211.

12. Ganyukhina, T.G., Modification of Properties of PVC in Synthesis, *Cand. Sci. Dissertation*, Nizhni Novgorod, 1999.
13. Titova, V.A., Defective Structures and Thermal Stability of Polyvinyl Chloride, *Cand. Sci. Dissertation*, Dzerzhinsk, 1989.
14. Kanakov, A.E., Effect of the Nature of Initiator System on Suspension Polymerization of Vinyl Chloride and Properties of the Polymer, *Cand. Sci. Dissertation*, Nizhni Novgorod, 1998.
15. Bort, D.N., *Vysokomol. Soedin, Ser. A*, 1980, vol. 22, no. 12, pp. 2641–2648.
16. Shvarev, E.P., Suchkova, N.A., and Romanov, V.D., *Plast. Massy*, 1999, no. 6, pp. 18–20.
17. Sharetskii, A.M., Svetozarskii, S.V., Kotlyar, I.B., and Zil'berman, E.N., *Plast. Massy*, 1968, no. 3, pp. 6–8.
18. Schmidt, M.J., Farbe, J.N., and Valies, E.M., *Polym. Eng. Sci.*, 1994, vol. 34, no. 6, pp. 532–540.
19. Ivanova, Yu.A., Initiator Systems Based on Group II and III Organometallic Compounds and Peroxides, *Cand. Sci. Dissertation*, Gor'kii, 1975.
20. Zvereva, Yu.A., Kotlyar, I.B., Ol'nev, N.N., *et al.*, *Plast. Massy*, 1969, no. 2, pp. 5–7.
21. Kolegov, V.I., Potapov, V.N., Sorokina, T.M., *et al.*, *Plast. Massy*, 1982, no. 12, pp. 36–40.
22. Semenycheva, L.L., Alkylborane–Organometallic Peroxide Systems as Low-Temperature Initiators of Radical Polymerization of Vinyl Chloride, *Cand. Sci. Dissertation*, Gor'kii, 1989.
23. Dodonov, V.A., Semenycheva, L.L., Grishin, A.N., *et al.*, Abstracts of Papers, *Vsesoyuznaya nauchno-tekhnicheskaya konferentsiya "Polivinilkhlorid-91"* (All-Union Scientific and Technical Conf. "Polyvinyl Chloride-91"), Dzerzhinsk, 1991, p. 39.
24. Kanakov, A.E., Kronman, A.G., Semchikov, Yu.D., *et al.*, *Zh. Prikl. Khim.*, 1997, vol. 70, no. 8, pp. 1375–1379.
25. Kolesnikov, V.Ya., Popov, V.A., and Zvereva, Yu.A., *Plast. Massy*, 1983, no. 8, pp. 7–9.
26. Bogdanov, O.S. and Rakhimov, A.I., Abstracts of Papers, *Pervaya vsesoyuznaya konferentsiya po polimernym materialam ponizhennoi goryuchesti* (First All-Union Conf. on Low-Combustibility Polymeric Materials), Volgograd, 1995, pp. 56–57.
27. Kronman, A.G., Semchikov, Yu.D., Groshev, G.L., and Kanakov, A.E., *Vysokomol. Soedin, Ser. A*, 1997, vol. 39, no. 12, pp. 1588–1592.
28. Zvereva, Yu.A., Baramonova, G.L., Popov, V.A., and Shvarev, E.P., Abstracts of Papers, *Vsesoyuznaya nauchnaya konferentsiya "Sostoyanie issledovanii i perspektivy razvitiya tekhnologii polucheniya i pererabotki polivinilkhloridnykh materialov"* (State of Research and Prospects for the Progress in Technologies of Production and Utilization of PVC Materials), Dzerzhinsk, 1986, p. 10.
29. Naumov, V.A., *O kinetike protsessov radikal'noi polimerizatsii* (On the Kinetics of Radical Polymerization), Moscow: Gos. Komitet RF po Vysshemy Obrazovaniyu, 1993.
30. Kolesnikov, V.Ya., Improvement and Intensification of the Process for Production of Suspension Polyvinyl Chloride, *Cand. Sci. Dissertation*, Dzerzhinsk, 1984.
31. Rakhimov, A.I., Butkovskaya, L.A., Baklanov, A.V., and Zegel'man, V.I., Abstracts of Papers, *Vsesoyuznaya nauchno-tekhnicheskaya konferentsiya "Polivinilkhlorid-91"* (All-Union Scientific and Technical Conf. "Polyvinyl Chloride-91"), Dzerzhinsk, 1991, pp. 37–38.
32. Sharetskii, A.M., Study of Process for Production of Polyvinyl Chloride with Increased Softening Point, *Cand. Sci. Dissertation*, Gor'kii, 1971.
33. Aleksandrov, Yu.A., *Zhidkofaznoe avtookislenie* (Liquid-Phase Autooxidation), Moscow: Nauka, 1978.
34. Grishin, D.F., Homolytic Reactions of Organic and Organoelement Peroxides with Some Organometallic Compounds and Coordinated Radical (Co)polymerization with Their Participation, *Doctoral Dissertation*, Nizhnii Novgorod, 1994.
35. Milovskaya, E.B., *Usp. Khim.*, 1973, vol. 42, no. 5, pp. 881–895.
36. Ivanychev, S.S., Shumnyi, L.V., and Konovalenko, V.A., *Vysokomol. Soedin., Ser. A*, 1980, vol. 22, no. 12, pp. 2735–2740.
37. Dodonov, V.A., Sofronova, S.M., Stepovik, L.P., and Semenycheva, L.L., *Vysokomol. Soedin., Ser. B*, 1986, vol. 28, no. 12, pp. 906–908.
38. Razuvaev, G.A., Dodonov, V.A., and Ivanova, Yu.A., *Dokl. Akad. Nauk SSSR*, 1980, vol. 250, no. 1, pp. 119–122.
39. Dodonov, V.A., Grishin, D.F., Morozov, O.S., and Cherkasov, V.K., *Zh. Obshch. Khim.*, 1981, vol. 52, no. 11, pp. 2494–2500.
40. Razuvaev, G.A., Dodonov, V.A., Tsvetkov, V.G., *et al.*, *Vysokomol. Soedin., Ser. A*, 1988, vol. 30, no. 2, pp. 144–150.
41. Razuvaev, G.A., Dodonov, V.A., Grishin, D.F., and Cherkasov, V.K., *Dokl. Akad. Nauk SSSR*, 1980, vol. 253, no. 1, pp. 113–118.
42. Semenycheva, L.L., Bort, D.N., and Dodonov, V.A., in *Fizikokhimicheskie osnovy sinteza i pererabotki polimerov: Mezhvuzovskii sbornik* (Physicochemical Principles of Synthesis and Utilization of Polymers: Intercollegiate Collection of Works), Gor'kii: Gor'k. Gos. Univ, 1983, pp. 36–39.
43. Dodonov, V.A. and Semenycheva, L.L., Abstracts of Papers, *Vsesoyuznaya konferentsiya "Radikal'naya*

polimerizatsiya" (All-Union Conf. "Radical Polymerization"), Gor'kii, 1989, pp. 73–74.

44. Razuvaev, G.A., Dodonov, V.A., Ivanova, Yu.A., *et al.*, in *Novye initsiiruyushchie sistemy na osnove boralkilov i elementoorganicheskikh mono- i diperoksidov pri polimerizatsii vinilkhlorida* (New Initiator Systems Based on Alkylboranes and Organoelement Mono- and Diperoxides in Vinyl Chloride Polymerization), Dzerzhinsk: Nauchno-Issled. Inst. Polimerov, 1981, pp. 8–20.
45. Dodonov, V.A., Ivanova, Yu.A., Grishin, D.F., and Semenycheva, L.L., in *Novye initsiiruyushchie sistemy na osnove boralkilov i elementoorganicheskikh mono- i diperoksidov pri polimerizatsii vinilkhlorida* (New Initiator Systems Based on Alkylboranes and Organoelement Mono- and Diperoxides in Vinyl Chloride Polymerization), Dzerzhinsk: Nauchno-Issled. Inst. Polimerov, 1981, pp. 53–70.
46. Dodonov, V.A., Semenycheva, L.L., Sazonova, E.V., and Ivanova, Yu.A., *Vysokomol. Soedin., Ser. B*, 1983, vol. 25, no. 4, pp. 235–237.
47. Dodonov, V.A., Semenycheva, L.L., and Gorshkova, M.B., *Vysokomol. Soedin., Ser. B*, 1984, vol. 26, no. 2, pp. 101–104.
48. Dodonov, V.A., Semenycheva, L.L., Ovchinnikov, Yu.V., and Titova, V.A., *Izv. Vyssh. Uchebn. Zaved., Khim. Khim. Tekhnol.*, 1993, vol. 36, no. 3, pp. 90–92.
49. Zhuravlev, M.A., Semenycheva, L.L., and Ivanov, V.B., *Khim. Fiz.*, 1989, vol. 8, no. 6, pp. 790–797.
50. Grishin, D.F. and Zhislina, V.B., *Izv. Vyssh. Uchebn. Zaved., Khim. Khim. Tekhnol.*, 1992, vol. 35, no. 1, pp. 47–52.
51. Grishin, D.F. and Dodonov, V.A., *Plast. Massy*, 1992, no. 2, pp. 5–6.
52. Grishin, D.F. and Dodonov, V.A., Abstracts of Papers, *Vsesoyuznaya nauchno-tekhnicheskaya konferentsiya "Polivinilkhlorid-91"* (All-Union Scientific and Technical Conf. "Polyvinyl Chloride-91"), Dzerzhinsk, 1991, pp. 10–11.
53. Grishin, D.F. and Semenycheva, L.L., *Usp. Khim.*, 2001, vol. 70, no. 5, pp. 486–510.
54. Grishin, D.F. and Chinyaeva, O.Yu., *Vysokomol. Soedin., Ser. B*, 1993, vol. 35, no. 6, pp. 156–158.
55. Grishin, D.F., Dodonov, V.A., Zolotova, O.V., and Cherkasov, V.K., *Vysokomol. Soedin., Ser. A*, 1992, vol. 34, no. 7, pp. 33–37.
56. Grishin, D.F. and Razmaev, P.S., *Izv. Vyssh. Uchebn. Zaved., Khim. Khim. Tekhnol.*, 1992, vol. 35, no. 8, pp. 47–49.
57. Moikin, A.A., Control of Radical Polymerization of Vinyl Monomers Using Organoelement Compounds, *Cand. Sci. Dissertation*, Nizhnii Novgorod, 1998.
58. Grishin, D.F. and Moikin, A.A., *Vysokomol. Soedin., Ser. B*, 1996, vol. 38, no. 11, pp. 1909–1912.
59. Grishin, D.F. and Moikin, A.A., *Vysokomol. Soedin., Ser. B*, 1997, vol. 39, no. 5, pp. 880–885.
60. Grishin, D.F. and Moykin, A.A., *Mendeleev Commun.*, 1998, no. 1, pp. 34–36.
61. Abakumov, G.A., *Zh. Vses. Khim. O–va*, 1979, no. 24, pp. 156–159.
62. Golubev, V.B., Zubov, V.P., Valuev, L.I., *et al.*, *Vysokomol. Soedin., Ser. A*, 1969, vol. 11, no. 7, pp. 2689–2701.
63. Ignatov, S.K., Razuvaev, A.G., Grishin, D.F., and Kuznetsov, M.V., *Vysokomol. Soedin., Ser. A*, 1999, vol. 41, no. 10, pp. 1587–1592.
64. Kabanov, V.A., Zubov, V.P., and Semchikov, Yu.D., *Kompleksno-radikal'naya polimerizatsiya* (Coordinated Radical Polymerization), Moscow: Khimiya, 1987.
65. Grishin, D.F., Moikin, A.A., and Yashpertov, A.N., *Izv. Vyssh. Uchebn. Zaved., Khim. Khim. Tekhnol.*, 1998, vol. 41, no. 1, pp. 69–73.
66. Grishin, D.F., Moikin, A.A., Semyonycheva, L.L., and Kolyakina, E.V., *Polimery*, 2000, vol. 35, no. 10, pp. 680–686.
67. Semenycheva, L.L., Sokolov, K.V., Liogon'kaya, T.A., and Grishin, D.F., *Izv. Vyssh. Uchebn. Zaved., Khim. Khim. Tekhnol.*, 2001, vol. 44, no. 6, pp. 24–29.
68. Dodonov, V.A. and Semenycheva, L.L., *Plast. Massy*, 1988, no. 11, pp. 40–41.
69. Semenycheva, L.L., Abstracts of Papers, *Pervaya mezhdunarodnaya nauchnotekhnicheskaya konferentsiya "Aktual'nye problemy khimii i khimicheskoi tekhnologii (Khimiya-97")* [1st Int. Scientific and Technical Conf. "Topical Problems of Chemistry and Chemical Technology (Chemistry-97")], Ivanovo (Russia), 1997, p. 45.
70. Grishin, D.F. and Dodonov, V.A., *Plast. Massy*, 1992, no. 2, pp. 5–7.
71. Smirnov, B.R., *Vysokomol. Soedin., Ser. A*, 1990, vol. 32, no. 3, pp. 583–589.
72. Otsu, T. and Matsumoto, A., *Adv. Polym. Sci.*, 1998, vol. 136, no. 1, pp. 75–127.
73. Zaremskii, M.Yu. and Golubev, V.B., *Vysokomol. Soedin., Ser. C*, 2001, vol. 43, no. 9, pp. 1689–1728.
74. Matyjaszewski, K., *Controlled/Living Radical Polymerization*, Oxford: Univ., 2000.
75. Korolev, G.V. and Marchenko, A.P., *Usp. Khim.*, 2000, vol. 69, no. 3, pp. 447–475.
76. Grishin, D.F., Semenycheva, L.L., Sokolov, K.V., and Kolyakina, E.V., *Vysokomol. Soedin., Ser. B*, 2000, vol. 42, no. 7, pp. 1263–1265.
77. Kolyakina, E.V., Grishin, D.F., Semenycheva, L.L., and Sokolov, K.V., Abstracts of Papers, *Vtoroi vse-*

rossiiskii karginskii simpozium "Khimiya i fizika polimerov v nachale XXI veka" (Second Russian Kargin Symp. "Chemistry and Physics of Polymers in the Beginning of the 21st Century"), Chernogolovka, Moscow oblast (Russia), 2000, pp. 2–56.

78. Grishin, D.F., Abstracts of Papers, *38th Macromol. IUPAC Symp., World Polymer Congr. "IUPAC MACRO 2000"*, Warsaw, 2000, vol. 1, p. 172.
79. Kolyakina, E.V., Grishin, D.F., and Semenycheva, L.L., *38th Macromol. IUPAC Symp., World Polymer Congr. "IUPAC MACRO 2000"*, Warsaw, 2000, vol. 1, p. 227.
80. Grishin, D.F., Semenycheva, L.L., Pavlovskaya, M.V., and Sokolov, K.V., *Zh. Prikl. Khim.*, 2001, vol. 74, no. 9, pp. 1546–1550.
81. Chernikova, E.V., Pokataeva, Z.A., Garina, E.S., *et al.*, *Vysokomol. Soedin., Ser. A*, 1995, vol. 37, no. 8, pp. 1638–1643.
82. Chernikova, E.V., Pokataeva, Z.A., and Garina, E.S., *Vysokomol. Soedin., Ser. B*, 2000, vol. 42, pp. 1530–1533.
83. Kolegov, V.I., *Plast. Massy*, 1978, no. 5, pp. 31–34.
84. Le Mercierc, C., Lutz, J.F., Marque, S., *et. al.*, *Am. Chem. Soc.*, Washington, DC, 2000, ch. 8, pp. 108–122.

Russian Journal of Applied Chemistry, Vol. 76, No. 6, 2003, pp. 859–862. Translated from Zhurnal Prikladnoi Khimii, Vol. 76, No. 6, 2003, pp. 888–891.

INORGANIC SYNTHESIS AND INDUSTRIAL INORGANIC CHEMISTRY

Separation of Alkali Metals

I. A. Tikhomirov, A. A. Orlov, and D. G. Vidyaev

Tomsk Polytechnic University, Tomsk, Russia

Received April 26, 2002

Abstract—A new gallam-exchange technique for separation of alkali metals was developed. The alkali metal separation factors were determined for the gallam-exchange systems LiGa–NaOH, LiGa–KOH, and KGa–NaOH. The effect of temperature and concentration of the exchanging phases on the separation factors were studied for the systems LiGa–NaOH and LiGa–KOH. Kinetic parameters of lithium, sodium, and potassium element exchanges were determined. The properties of gallam-exchange and amalgam-exchange systems were compared.

At present, special-purity materials find increasing use in technology; the requirements to these materials are growing steadily. Special purity is necessary in certain cases for alkali metals.

In practice, alkali metals are separated and purified by the amalgam-exchange technique [1, 2]. Its main disadvantage consists in that it uses large amounts of highly toxic mercury, which results in environment contamination and makes more complicated the equipment and safety measures in the separation industry. In this context, studies aimed to develop high-performance and environmentally safe methods for separation of alkali metals become topical.

An environmentally safe gallam-exchange technique for purification and separation of alkali metals, in which an intermetallic compound of gallium and alkali metal, gallam, is used instead of amalgam, was developed in [3].

The present study is concerned with separation of alkali metal pairs, Li and Na, Li and K, Na and K, in exchange between a gallam and a hydroxide solution of one of these metals.

Typical parameters of the efficiency of one or another separation technique and, in particular, of the gallam exchange, are the separation factor α and kinetic parameters of the exchange and decomposition of an intermetallic compound (gallam) brought in contact with aqueous solutions of an alkali metal hydroxide. The exchange rate depends on the rate of interfacial electrochemical reactions and on the rate of reagent supply from the bulk of the phases to the interface. Therefore, the aim of the study was to determine the separation factors for the indicated pairs of alkali metals and the kinetic parameters of the exchange process and thus to evaluate the efficiency of gallam-exchange systems in separation and purification of alkali metals.

EXPERIMENTAL

The gallam used in the experiments was obtained by direct dissolution of metallic lithium of LE-1 brand in chemically pure gallium (99.99% of the main substance) [3]. Hydroxide solutions were prepared from chemically pure NaOH and KOH and distilled water.

The experimental laboratory installation is shown schematically in Fig. 1. The exchange was studied in

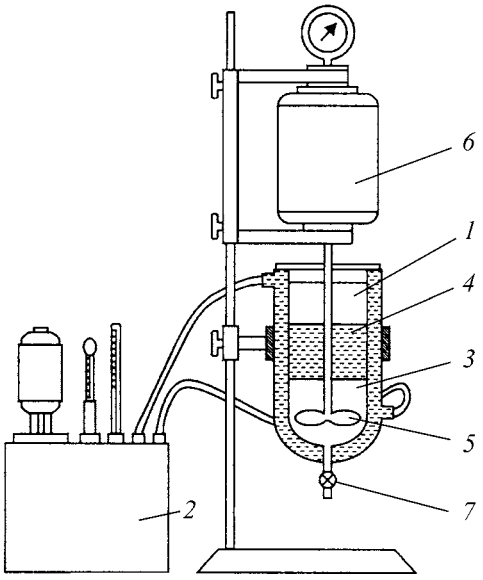

Fig. 1. Schematic of experimental laboratory installation.

1070-4272/03/7606-0859 $25.00 © 2003 MAIK "Nauka/Interperiodica"

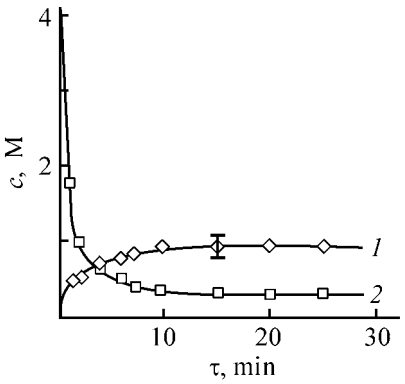

Fig. 2. Variation of sodium content c in (*1*) lithium gallam and (*2*) sodium hydroxide solution in the course of the exchange. Initial concentration of gallam 0.95 M, and that of hydroxide solution 4.0 M; temperature 40°C. (τ) Time.

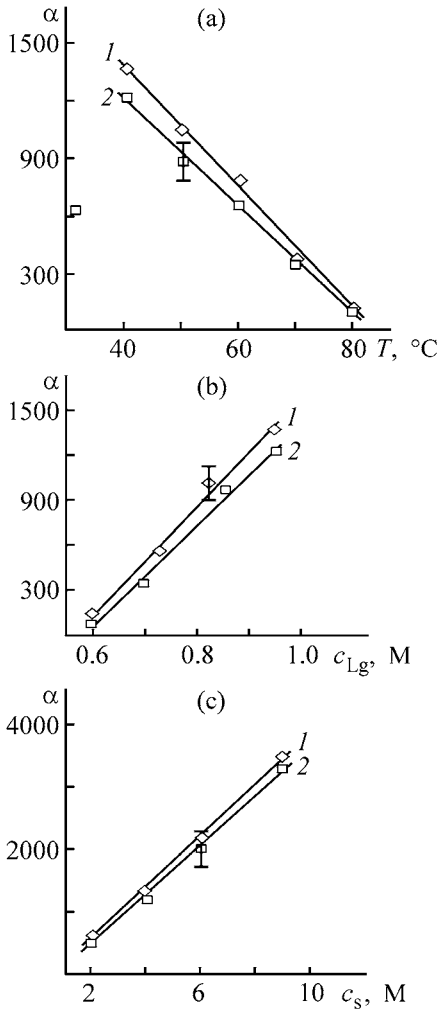

Fig. 3. Separation factor α vs. (a) temperature T, (b) concentration c_{Lg} of lithium gallam, and (c) concentration c_s of hydroxide solutions. Initial concentration of gallam (a, c) 0.95 M, (a, b) that of hydroxide solutions 4.0 M, (b, c) temperature 40°C. System: (*1*) LiGa–NaOH and (*2*) LiGa–KOH; the same for Fig. 4.

a cylindrical cell *1* 30 mm in diameter, equipped with a water-jacket. Thermostat *2* maintained a constant temperature. In the course of the experiments, gallam *3* was poured in a beaker and then hydroxide solution *4* was added. Phases were mixed by a propeller stirrer *5* rotated by electric motor *6* at a rate of 750–800 rpm. The gallam was not dispersed in the course of stirring. The phase contact area was calculated as the area of the cone formed in stirrer rotation at the gallam–solution interface.

After a run was complete, the hydroxide solution was sampled from the upper part of the exchange cell, and the gallam was discharged through a stop-cock *7* and decomposed with distilled water. The content of the components being separated was determined using an FPA-2 flame photometer in the solution obtained upon the gallam decomposition and in the hydroxide solution sampled from the exchange cell.

The experiments have shown that the equilibrium in the LiGa–NaOH, LiGa–KOH, and NaGa–KOH systems is attained within ca. 15 min. The typical shape of curves characterizing the kinetics of equilibration in the LiGa–NaOH system is shown in Fig. 2. The separation factor α was calculated for all the systems from the results of experiments performed under varied initial conditions. Each experiment was carried out in two replications. The separation factors for the Li and Na and Li and K pairs in the corresponding gallam-exchange systems were found to depend on temperature and on concentrations of the gallam and the alkali solution. The influence of these factors is shown in Figs. 3a–3c.

The experiments with the KGa–NaOH system were carried out only at 40°C and the following starting concentrations of the reacting phases (M): potassium gallam 0.92 and sodium hydroxide solution 4.0. The value of α was 1.7 under these conditions.

The kinetic parameters (rate constant of the exchange reaction, exchange current density, and half-exchange time) of the alkali metal (lithium, sodium, and potassium) exchange processes were calculated for all the systems by the known technique [2, 4, 5].

The experimental values of the kinetic parameters of the exchange processes for the LiGa–NaOH and LiGa–KOH systems are shown in the table.

The following values of the kinetic parameters were obtained for the KGa–NaOH system: τ_e = 39 s, I_e = 30.22 kA m^{-2}, and K_e = 1.51 × 10^{-2} cm s^{-1}.

The plots in the ln K_e–$10^3/T$ coordinates are straight lines (Fig. 4). Consequently, the rate constant of el-

Kinetic parameters of exchange between lithium gallam and aqueous solutions of sodium and potassium hydroxide at various temperatures

Parameter*	Temperature, °C					Parameter*	Temperature, °C				
	40	50	60	70	80		40	50	60	70	80
LiGa–NaOH						LiGa–KOH					
τ_e, s	27	24	19	14	10	τ_e, s	25	22	18	13	9
I_e, kA m^{-2}	35.74	40.58	46.97	57.89	69.31	I_e, kA m^{-2}	37.58	42.46	50.35	62.68	74.10
$K_e \times 10^2$, cm s^{-1}	1.83	2.08	2.41	2.97	3.55	$K_e \times 10^2$, cm s^{-1}	1.90	2.15	2.55	3.18	3.76

* (τ) Half-exchange time, (I_e) exchange current density, and (K_e) rate constant of exchange.

ement exchange is expressed within the temperature range under study by the Arrhenius equation

$$\ln K_e = -\frac{E_e}{RT} + K'_e,$$

Here E_e is the activation energy of the element exchange reaction (J mol^{-1}); R, the gas constant (J mol^{-1} K^{-1}); K_e, the exchange rate constant (cm s^{-1}); K'_e, the integration constant (cm s^{-1}); T, the absolute temperature.

For the LiGa–NaOH and LiGa–KOH systems, we determined the activation energies of the exchange reactions, E_e (kJ mol^{-1}), and integration constants K'_e (cm s^{-1}) to be 13.44 ± 0.76, 1.18 and 14.13 ± 1.10, 1.48, respectively.

Comparison of the rate constants of the element exchange in the LiGa–NaOH, LiGa–KOH, and KGa–NaOH systems suggests that the exchange rates in all the systems are approximately equal at 40°C. In addition, the exchange current densities in all the systems under study are rather high, up to tens of kiloamperes per square meter.

A comparison of the results obtained with the data [3, 6] on the kinetics of decomposition of a gallam brought in contact with hydroxide aqueous solutions showed that the ratio K_e/K_d (K_d is the rate constant of gallam decomposition) for the LiGa–NaOH and LiGa–KOH systems varies within the temperature range under study from 40.9 and 39.9 at 80°C to 77.2 and 76.3 at 40°C, respectively. For the KGa–NaOH system, the K_e/K_d ratio was 70.6. Consequently, the rate of exchange in these systems is much higher than the rate of decomposition, which allows us to maintain that a manyfold multiplication of the single-stage separation effect is possible in this case.

Comparison of the kinetic parameters of alkali metal exchange in the gallam-exchange systems LiGa–NaOH, LiGa–KOH, and KGa–NaOH with similar data for amalgam-exchange systems [1, 2] shows that the rates of element exchange in the gallam and corresponding amalgam systems are approximately equal.

In the gallam systems LiGa–NaOH and LiGa–KOH, the values of α at 40°C are nearly an order of magnitude lower than those in similar amalgam systems at 20°C [1]. However, the high separation factors in gallam systems make it possible to achieve an appreciable separation of alkali metals (95–99%) even in a single exchange process.

The separation factor for the gallam system KGa–NaOH at 40°C is approximately half that in the corresponding amalgam system at 20°C [2]. However, the rate of the element exchange in this system is significantly higher than the rate of potassium gallam decomposition, which allows a manyfold enhancement of the single-stage separation effect.

On the whole, the good kinetics of the element exchange, high separation factors of alkali metals (lithium, potassium, and sodium) in the gallam-ex-

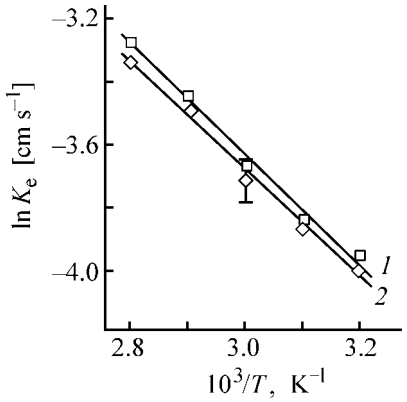

Fig. 4. Dependence of exchange rate constant K_e on temperature T. Starting concentration of gallam 0.95 M, that of hydroxide solutions 4.0 M.

change systems under study, and the environmental safety of the gallam technique show its promise for separation and purification of alkali metals (lithium, sodium, and potassium).

CONCLUSIONS

(1) Separation factors of alkali metals in the gallam systems investigated decrease with increasing temperature. Raising the concentrations of exchanging phases leads to higher α.

(2) The rate of exchange of alkali metals increases with temperature and significantly exceeds the rate of their decomposition within the temperature range investigated, which allows manyfold enhancement of the single-stage separation effect.

(3) The separation factors of alkali metals in gallam systems at 40°C are approximately an order of magnitude lower than those in similar amalgam systems at 20°C.

(4) The exchange rate of alkali metals in gallam systems is comparable with that of the same metals in amalgam systems.

ACKNOWLEDGMENTS

This study was supported financially by the Ministry of Education of the Russian Federation (grant TO-07.2-692).

REFERENCES

1. Konstantinov, A.P. and Alimova, I.A., *Zh. Prikl. Khim.*, 1962, vol. 35, no. 10, pp. 2266–2271.
2. Konstantinov, A.P., and Alimova, I.A., *Zh. Prikl. Khim.*, 1962, vol. 35, no. 9, pp. 1908–1916.
3. Tikhomirov, I.A., Orlov, A.A., Vidyaev, D.G., and Chumakov, D.N. *Razdelenie shchelochnykh metallov v gallamno-obmennykh sistemakh* (Separation of Alkali Metals in Gallam-Exchange Systems), Available from VINITI, 1999, Tomsk, no. 669–B99.
4. Konstantinov, A.P., Kiselev A.P., and Skrebtsov, G.P., *Radiokhimiya*, 1960, vol. 2, no. 1, pp. 44–49.
5. Tsivadze, A.Yu., Levkin, A.V., Knyazev, D.A., and Klinskii, G.D., *Zh. Neorg. Khim.*, 1987, vol. 32, no. 7, pp. 1757–1758.
6. Tikhomirov, I.A., Lavrenyuk, P.I., Orlov, A.A., and Vidyaev, D.G., *Zh. Prikl. Khim.*, 2002, vol. 75, no 1, pp. 30–33.

Russian Journal of Applied Chemistry, Vol. 76, No. 6, 2003, pp. 863–866. Translated from Zhurnal Prikladnoi Khimii, Vol. 76, No. 6, 2003, pp. 892–895.

INORGANIC SYNTHESIS AND INDUSTRIAL INORGANIC CHEMISTRY

Composition and Physicochemical Properties of Cobalt Molybdophosphates

N. I. Radishevskaya, L. A. Egorova, and V. V. Kozik

Department of Macrokinetics, Tomsk Scientific Center, Siberian Division, Russian Academy of Sciences, Tomsk, Russia

Received June 19, 2002; in final form, January, 2003

Abstract—Cobalt molybdophosphates were synthesized. The composition of the compounds was confirmed by IR spectral, thermogravimetric, X-ray phase, and atomic-emission analyses. The influence of the composition on the thermochromic properties of the compounds was demonstrated.

Recently, the interest in iso- and heteropoly compounds, whose structural features and nature of chemical bonding govern a wide variety of physicochemical and functional properties, has increased considerably. Their structure and conditions of their preparation are being studied intensively.

Heteropoly compounds of transition metals are of scientific and practical interest. Introduction of a cation with variable oxidation state makes it possible to obtain new inorganic materials with charge transfer [1].

The present communication reports the results obtained in studying preparation conditions and thermal stability of cobalt molybdophosphates.

Cobalt heteropoly molybdates were synthesized from weakly acid aqueous solutions by methods: from 12-molybdophosphoric acid and from molybdenum(VI) oxide (alkaline fusion), sodium hydrophosphate, and cobalt(II) chloride.

The composition and structure of the obtained substances were identified by differential thermal [Q 1500 derivatograph (Hungary), heating rate 10 deg min^{-1}] and X-ray phase (DRON-3M installation) analyses. The incorporation of phosphorus in the composition of the salts was confirmed by atomic emission analysis (ISP-30 spectrograph). The content of chloride ions in the solid phase was determined by mercurimetry. The type of heteropoly anions was established by IR spectroscopy in the range 4000–400 cm^{-1} (Specord M-80, KBr pellets). The energy gap was calculated from reflection spectra (Specord M-40).

The reaction of 12-molybdophosphoric acid with a minor excess of cobalt(II) chloride at pH 5–6 results in precipitation of a lilac-colored lacunar form of cobalt(II) 11-molybdophosphate $Co_2H_3[PMo_{11}O_{39}] \cdot 11H_2O \cdot 2HCl$ from solution, with a dark gray substance formed at the solution–air boundary. The compound obtained by the reaction of MoO_3 with $CoCl_2$ in a nearly neutral medium can also be identified as cobalt(II) 11-molybdophosphate with composition $Co_2H_3[PMo_{11}O_{39}] \cdot 20H_2O \cdot 3HCl$. The results obtained in studying the effect of the pH of the medium, nature of initial components, and synthesis conditions on the formation of cobalt heteropoly compounds are listed in Table 1.

Cobalt molybdophosphates obtained by the two methods described have similar IR absorption spectra (Fig. 1). The stretching and bending vibrations ν(Mo=O), ν(P–O), ν(Mo–O), ν(Mo–O–Mo), ν(–O–),

Table 1. Effect of the nature of initial reagents and synthesis conditions on the product composition P : Mo = 1 : 12, pH 5–6

Reagent	Product composition
$H_3[PMo_{12}O_{40}] \cdot nH_2O$, $CoCl_2 \cdot 6H_2O$ (under a mother liquor)	$Co_2H_3[PMo_{11}O_{39}] \cdot 11H_2O \cdot 2HCl$
$H_3[PMo_{12}O_{40}] \cdot nH_2O$, $CoCl_2 \cdot 6H_2O$ (solution–air)	MoO_2Cl_2, $NaCo^{2+}Co^{3+}(MoO_4)_3 \cdot 4H_2O$
MoO_3, Na_2HPO_4, $CoCl_2 \cdot 6H_2O$	$Co_2H_3[PMo_{11}O_{39}] \cdot 20H_2O \cdot 3HCl$

1070-4272/03/7606-0863 $25.00 © 2003 MAIK "Nauka/Interperiodica"

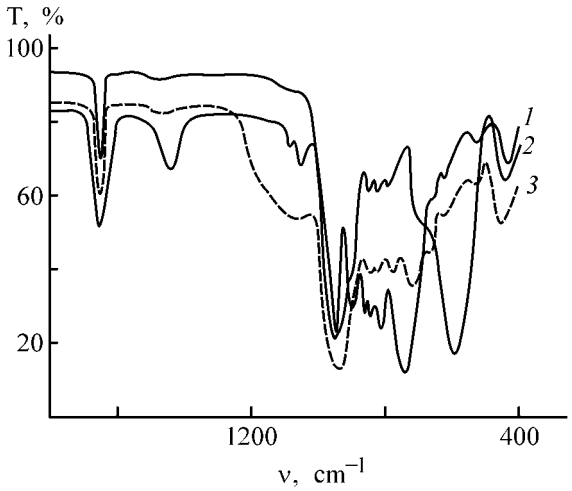

Fig. 1. IR spectra of cobalt(II) 11-molybdophosphates: (*1*) before and (*2*, *3*) after annealing. (T) Transmission and (ν) wave number. Sample synthesized from: (*2*) 12-molybdophosphoric acid (*3*) MoO_3.

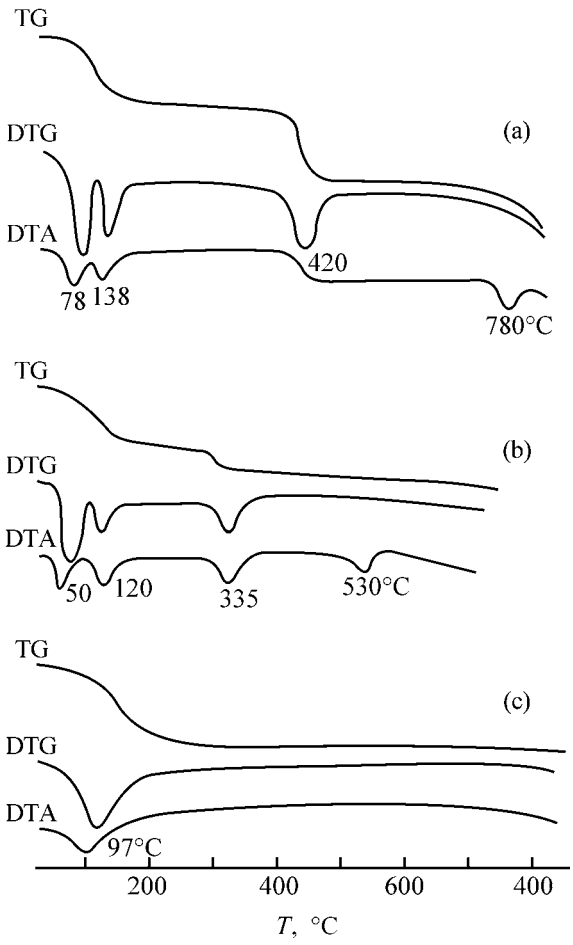

Fig. 2. Thermograms of (a) 12-molybdophosphoric acid and cobalt(II) 11-molybdophosphate obtained from (b) 12-molybdophosphoric acid and (c) MoO_3. (*T*) Temperature.

and δ(P–O) at 960, 910, 870, 815, 720, 510 cm^{-1}, respectively, characterize the formation of Keggin-type structures [2].

The stretching P–O vibration, which appears in the IR spectrum of $[PMo_{12}O_{40}]^{3-}$ as a high-intensity band at 1060 cm^{-1}, is split into two components (1080, 1050 cm^{-1}) in the case of the lacunar form $[PMo_{11}O_{39}]^{7-}$ [3].

The bands at 845, 670, and 620 cm^{-1} correspond to stretching vibrations ν(Co–O) bond, and the band at 420 cm^{-1}, to ν(Co–Cl).

Vibrations ν(–OH) of surface OH groups bound to cobalt are observed at 3710 cm^{-1} [4, 5].

Cobalt salts obtained by precipitation with cobalt(II) chloride from molybdophosphoric acid solutions decompose under heating in the same way as $H_3[PMo_{12}O_{40}] \cdot nH_2O$ acid does. Two endothermic effects corresponding to loss of adsorbed and crystallization water are observed in the range 50–150°C (Fig. 2). According to our calculations, the loss of substance corresponds to 11 mol of water per 1 mol of the compound. The activation energy of dehydration is 53 kJ mol^{-1}, the reaction is first-order. An endothermic effect accompanied by removal of water from the inner coordination sphere is observed at 335°C. This is confirmed by the shift of the characteristic frequencies in the IR spectra of samples annealed at 500°C as compared with the initial sample (Fig. 1). After thermolysis, a strong absorption band at 940 cm^{-1} and a high-intensity peak at 600 cm^{-1}, which correspond to, respectively, stretching vibrations of the MoO_2^{2+} group and bending vibrations δ(O–P–O) in the $P_2O_7^{4-}$ group, appear in the IR spectrum of the salt. Also, a slight rise in the intensity of the peak at 420 cm^{-1}, associated with stretching vibrations ν(Co–Cl), is observed. The absorption band ν(Co–O) at 845 cm^{-1} is retained. The absorption bands at 820 and 780 cm^{-1} are attributable to asymmetric stretching vibrations ν(Mo–O) of the tetrahedral $[MoO_4]^{2-}$ group. The intensity of the peak associated with vibrations of the bridging oxygen in the octahedral group decreases substantially and the peak is shifted from 740 to 700 cm^{-1} (shoulder at 700 cm^{-1}). This points to thermal decomposition of the original structure of the heteropoly salt.

The cobalt salt obtained from MoO_3, Na_2HPO_4, and $CoCl_2$ decomposes in a single stage, which apparently involves loss of water. The salt is a mixture of cobalt and dioxomolybdenum(VI) chlorides, phosphates, and molybdates. Thermogravimetric calcula-

tion shows that the salt contains 20 H_2O molecules. The activation energy of dehydration is 110 kJ mol^{-1}, the reaction is first-order. The decomposition yields mostly the $(MoO_2)(HPO_4)$ and $CoMoO_4$ phases. This is confirmed by analysis of the characteristic frequencies in the IR spectral range. A strong absorption band of the MoO_2^{2+} group is observed at 940 cm^{-1}. Broad peaks corresponding to stretching and bending vibrations of the HPO_4^{2-} group appear at 1000–1200 and 550–650 cm^{-1}. The intensity of the absorption band ν(Co–Cl) at 420 cm^{-1} slightly increases. The intensity of the absorption band associated with vibrations of the bridging oxygen decreases and the band is shifted from 740 to 710 cm^{-1}. The spectra of cobalt(II) molybdophosphates synthesized by the two methods show a significant decrease in the intensity of the peak at 3600–3000 cm^{-1}, which is characteristic of stretching vibrations of adsorbed and crystallization water, after annealing. The absorption band ν(OH) at 3700 cm^{-1} is shifted to 3680 cm^{-1}. The intensities of the peaks corresponding to bending vibrations of OH groups [4–6] change as follows: that of the peak at 1640 cm^{-1} decreases considerably, and the absorption at 1450 cm^{-1} disappears completely. The data obtained are in agreement with the results of [7].

The differences observed in thermal decomposition of salts of cobalt 12-molybdophosphates synthesized in the two ways are clearly seen in the DTA curves. In the first case, absorbed and crystallization water is lost in two stages, and in the second, in a single stage. However, when the salt synthesized from 12-molybdophosphoric acid is subjected to thermolysis, loss of water is observed at 350–400°C. Presumably, this water is removed from the inner coordination sphere. An X-ray phase analysis demonstrated that cobalt 11-molybdophosphates prepared in different ways have virtually identical X-ray diffraction patterns.

When molybdophosphoric acid reacts with cobalt(II) chloride, a dark gray substance is formed at the solution–air boundary, which is due to a redox reaction in air, in which the oxidation states change from Co^{2+} to Co^{3+} and from O_2^0 to O^{2-}. MoO_2Cl_2 and $NaCo^{2+}Co^{3+}(MoO_4)_3 \cdot 4H_2O$ are formed, which was confirmed by X-ray phase analysis.

The content of chloride ions in cobalt 11-molybdophosphates, determined by mercurimetry, is listed in Table 2.

The results of atomic-emission analysis of cobalt 11-molybdophosphates obtained by the two methods indicate that phosphorus does enter into the composition of the salts (approximately 1.5 wt %).

Table 2. Content of chloride ions in cobalt molybdophosphates (pH 5–6)

Salt	Cl^-, mg l^{-1}	Cl^- in heteropoly salt, mol
$Co_2H_3[PMo_{11}O_{39}] \cdot 11H_2O \cdot 2HCl$ (from acid)	3.5	2
$Co_2H_3[PMo_{11}O_{39}] \cdot 20H_2O \cdot 3HCl$ (from MoO_3)	5.3	3

The cobalt salts obtained possess thermochromic properties and have a Keggin-type lacunar structure, with their color varying from lilac to dark gray. The temperature at which the salts change their color before and after annealing is 400–450°C.

The thermally reversible change of color by the compounds obtained is attributable to the previously suggested mechanism of charge transfer via the inner-sphere redox process

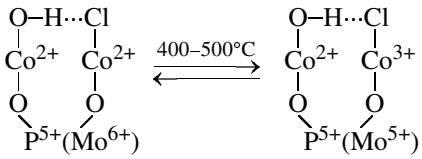

Thus, the reversible change of color of the compounds under consideration, which is observed at 400–450°C, is associated with electron transfer along the chain

$$Co^{2(3)+}—O—Mo^{6(5)+}.$$

When the temperature is raised, Co^{2+} is oxidized to Co^{3+}, and Mo^{6+}, reduced to Mo^{5+}. In the case when the temperature is lowered, a reverse electron transfer takes place.

Compounds obtained under similar conditions from cobalt(II) salts with another anion exhibit no thermochromic properties, which may result from different positions of the chloride and other ligands in the spectrochemical series for Co(II)/Co(III). The cobalt(II) molybdophosphates obtained belong to wide-bandgap semiconducting materials. The energy gap calculated from reflection spectra in the visible spectral range is 2.55 eV for molybdophosphoric acid and varies for cobalt salts from 3.23 (salts obtained from the acid) to 3.47 eV (salts obtained from MoO_3). The structure indicated undergoes irreversible destruction above 500°C, with loss of thermochromic properties.

CONCLUSIONS

(1) Cobalt heteropoly salts $Co_2H_3[PMo_{11}O_{39}] \cdot 11H_2O \cdot 2HCl$ and $Co_2H_3[PMo_{11}O_{39}] \cdot 20H_2O \cdot 3HCl$ synthesized in aqueous solutions at nearly neutral pH have a Keggin-type lacunar structure.

(2) The compounds obtained are wide-bandgap semiconductors and can be used as thermochromic materials. Cobalt(II) molybdophosphates change coloration reversibly. The thermochromic properties of cobalt 11-molybdophosphates are preserved after multiple annealing of the salts.

RERERENCES

1. Radishevskaya, N.I., Egorova, L.A., and Kozik, V.V., *Zh. Prikl. Khim.*, 2000, vol. 73, no. 7, pp. 1066–1068.
2. Bielanski, A., Matecka, A., and Kubelkova, L., *J. Chem. Soc. Faraday Trans. I*, 1989, vol. 85, no. 9, pp. 2847–2856.
3. Pope, M.Th., *Heteropoly and Isopoly Oxometalled*, Berlin: Springer, 1983.
4. Nakamoto, K., *Infrared and Raman Spectra of Inorganic and Coordination Compounds*, New York: Wiley, 1986.
5. Davydov, A.A., *IK-spektroskopiya v khimii poverkhnosti okislov* (IR spectroscopy in Chemistry of Oxide Surfaces), Novosibirsk: Nauka, 1984.
6. Petrov, K.I., Poloznikova, M.E., Sharipov, Kh.T., and Fomichev, V.V., *Kolebatel'nye spektry v neorganicheskoi khimii* (Vibrational Spectra in Inorganic Chemistry), Tashkent: Fan, 1990.
7. Maksimovskaya, R.I., Bondareva, V.M., and Litvak, G.S., *Zh. Neorg. Khim.*, 1996, vol. 41, no. 7, pp. 1173–1180.

Russian Journal of Applied Chemistry, Vol. 76, No. 6, 2003, pp. 867–870. Translated from Zhurnal Prikladnoi Khimii, Vol. 76, No. 6, 2003, pp. 896–899.

INORGANIC SYNTHESIS AND INDUSTRIAL INORGANIC CHEMISTRY

A Study of Structure and Surface Properties of Cleaved Mica Particles

M. V. Maslova, L. G. Gerasimova, V. N. Makarov, V. Naidenov, and W. Forsling

Tananaev Institute of Chemistry and Technology of Rare Elements and Mineral Raw Materials, Kola Scientific Center, Russian Academy of Sciences, Apatity, Russia

Luleo Technical University, Luleo, Sweden

Received October 9, 2002; in final form, February 2003

Abstract—The structure of cleaved mica particles and the influence of cleavage conditions on surface properties of mica were studied by IR spectroscopy.

In recent years, there has been considerably increased interest in processing of mining tailings, whose utilization frequently yields products that are in short supply.

The consumption of raw mica is mainly limited to large-plate phlogopite and muscovite, which are starting materials for radio electronics and radio engineering. At the same time, demand for fine (small-size) mica is virtually absent.

The problem of full utilization of mica raw materials can be solved solely by developing new technologies for utilization of small mica fractions, now going to wastes. It is known that the crystal size is not an important parameter for pigments used in manufacture of paint-and-varnish materials, rubber fillers, and plastics [1]. The finer the initial mica, the lower the amount of energy consumed for its cleavage and grinding, and the cheaper the final product obtained.

Splitting and grinding of mica is accompanied by destruction of the interlayer space, with deformation or destruction of the crystal lattice and the resulting change in the surface properties of mica, owing to the appearance of an uncompensated structural charge [2]. These changes determine the quality of ground micas and the possible field of their use.

The aim of this study was to analyze structural changes and surface properties of phlogopite and muscovite cleaved by different methods.

EXPERIMENTAL

Phlogopite used in the study was obtained from mica-ore-dressing tails of the Kovdor deposit, and and muscovite was a by-product of mica production in Karelia. The starting material consisting of 1×2-cm^2 plates was subjected to chemical and electrochemical cleavage and then ground on a ball mill in wet mode. The <63-μm fraction was used in the study.

In chemical cleavage, mica was treated with 0.5 M sulfuric acid for 120 h [3]. Leaching of the structure-forming (cross-linking) elements disturbs the neutral charge of a mica pack and leads to its cleavage. Electrochemical cleavage [4] is based on leaching of potassium ions into the liquid phase on applying a potential difference to an aqueous mica suspension, with the mica pack disrupted by the uncompensated charge of the cleavage planes.

The cleaved mica was studied by the diffusion reflection IR Fourier spectroscopy. The chemical composition of the samples was determined with an ICP–QMS mass-spectrometer. The crystallinity of structure was characterized using a Siemens D 5000 diffractometer, and the specific surface area was measured by the BET method on a Micrometric 2000 instrument. The liquid phase was analyzed with a Perkin–Elmer 3100 atomic-adsorption spectrometer, and the degree of recovery of the components into solution was calculated.

The data presented in Fig. 1 give insight into the behavior of the main cross-linking cations of mica in its splitting. Evidently, the degree of cation leaching is higher in chemical treatment, compared with electrochemical treatment in a neutral medium. Irrespective of a cleavage method, the degree of leaching of octahedral cations exceeds that for tetrahedral cations. The decrease in the specific surface area S_{sp} of

1070-4272/03/7606-0867 $25.00 © 2003 MAIK "Nauka/Interperiodica"

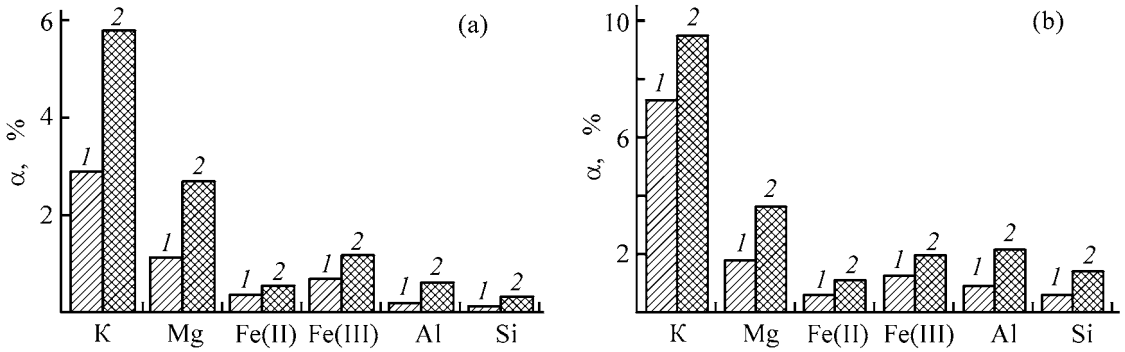

Fig. 1. Leaching diagram for the main components of mica in (*1*) electrochemical and (*2*) chemical cleavage. (α) Degree of leaching. (a) Muscovite and (b) phlogopite.

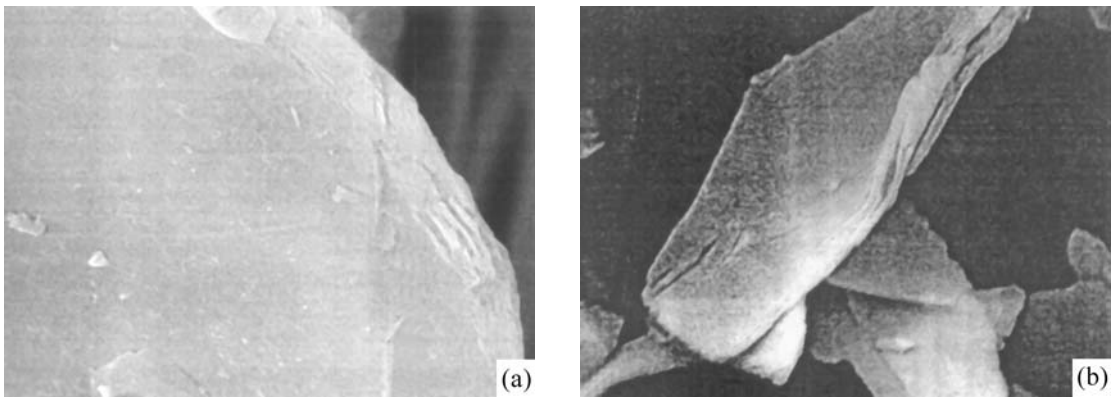

Fig. 2. Micrograph of phlogopite particles after (a) chemical and (b) electrochemical cleavage.

the electrochemically cleaved particles (see table) is due to a decrease in their thickness, which results from more complete splitting and smoothening of their surface. S_{sp} of the chemically cleaved samples increases twofold as compared with the initial value. Micrographs of particles of this kind (Fig. 2b) indicate that their edges are corroded because of the partial splitting and the resulting formation of new basal surfaces.

Chemical composition and specific surface area of mica

Component	Content	
	Muscovite	Phlogopite
SiO_2	46.4 ± 0.1	40.0 ± 0.1
Al_2O_3	34.0 ± 0.1	13.5 ± 0.1
MgO	1.32 ± 0.01	23.2 ± 0.1
Fe_2O_3	2.32 ± 0.01	8.35 ± 0.01
K_2O	10.5 ± 0.1	9.53 ± 0.01
CaO	<0.1	0.158 ± 0.001
MnO	0.029 ± 0.0001	0.0901 ± 0.0001
Na_2O	0.625 ± 0.001	0.439 ± 0.001
P_2O_5	0.0081 ± 0.0001	0.0187 ± 0.0001
TiO_2	0.371 ± 0.001	0.694 ± 0.001
Specific surface area of mica ($m^2\ g^{-1}$):		
initial	7.34	7.06
after electrochemical cleavage	4.5	2.13
after chemical cleavage	12.67	14.65

A spectroscopic study demonstrated that the loss of large cations into the liquid medium is closely related to changes in the octahedral and tetrahedral layers of mica. For cleaved muscovite (Fig. 3a), the intensity of vibrations at 3600 cm^{-1}, associated with intrasphere bonds, e.g., AlOH, grows [5]. It has been confirmed that the intensity of this band is independent of crystal orientation [6]. Muscovite cleavage in an aqueous medium as a result of deformation distortions and loss of potassium ions facilitates proton incorporation into the structure to give a hydroxonium ion for compensating the charge in a tetrahedron. For chemically cleaved muscovite, the band due to low-frequency stretching vibrations of OH^- groups at 3315 cm^{-1} is revealed more clearly, and the set of peaks in the 1800–1537 cm^{-1} range is due to bending vibrations of adsorbed water molecules.

Strong adsorption bands in the 1000–1025 cm^{-1} range belong to Si–O stretching vibrations and are

weakly related to the lattice vibration bonds. By contrast, the Si–O vibration bonds characterized by bands at 400–550 and 750 cm^{-1} are strongly related to other vibration bonds [7]. The rise in the intensity of the 750 cm^{-1} band and the low-frequency shift of the 536 cm^{-1} band, which are associated with Si–O–Al tetrahedral vibrations [8], result from an increase in the Si–O–Al bond length and point to deformation of the tetrahedral layer. The increase in the intensity of the 930 cm^{-1} band results from a decrease in the magnesium(II) content in the octahedral environment. The appearance of a clearly pronounced band at 1062 cm^{-1} is due to asymmetric vibrations of the Si–O–Si bond. Evidently, fast exchange reactions between the potassium ions and the proton in chemical cleavage are accompanied by hydroxylation of the tetrahedron vertex and rupture of the bond between the oxygen atom of silicon-oxygen tetrahedron and the octahedral cation. Leaching of octahedral magnesium(II) cations and aluminum(III) leads to weakening of siloxane bonds and promotes loss of silicon(IV) from the tetrahedral layers. In electrochemical cleavage in neutral media, the mobility of octahedral cations and aluminum(III) decreases, and loss of silicon(IV) into solution is hindered by slow rupture of aluminum bonds in the lattice. On the whole, it was noted that, irrespective of muscovite cleavage conditions, formation of hydrated forms of the starting layered structure is observed, with all basic structural characteristics of the starting phase retained. This is confirmed by the X-ray diffraction pattern demonstrating only a slight redistribution of the reflection intensities, which is associated with the defectiveness of the structure (Fig. 4).

For cleaved phlogopite (Fig. 3b), no significant changes in the range of OH^- group vibrations was observed. This is so because the loss of K^+ from the mineral is commonly accompanied by oxidation $Fe^{2+} \rightarrow Fe^{3+}$ [9], and there is no need for protonation of surface groups to neutralize the negative charge. The weak band at 3664 cm^{-1} in the spectra of the starting and cleaved phlogopite reflects the presence of Fe(III) in the octahedral position. For electrochemically cleaved mica, an increase in the intensity of the 1650 cm^{-1} peak corresponding to bending vibrations of water was observed. In chemical cleavage, changes in the tetrahedral layer manifest themselves in a low-frequency shift of the Si–O stretching vibration band at 985 cm^{-1}, resulting from the increase in the Si–Al–O bond length and appearance of a new band at 1041 cm^{-1}, associated with asymmetric vibrations of the Si–O–Si bond. The band at 456 cm^{-1} can be ascribed to the $Si–O–M^{2+}_{tetr}$ (M = Mg, Fe) bond

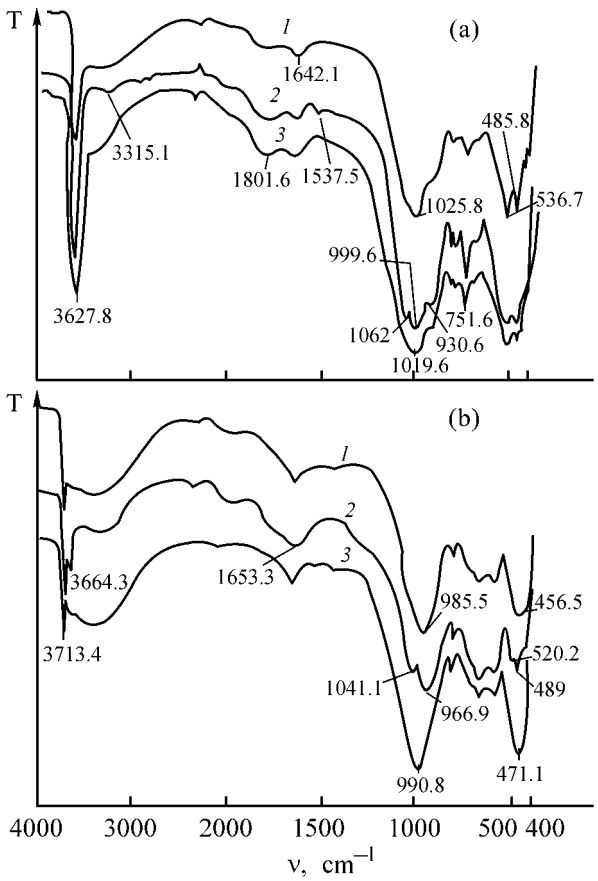

Fig. 3. IR spectra of (a) muscovite and (b) phlogopite. (T) Transmission and (ν) wave number. Mineral: (*1*) initial and after (*2*) electrochemical and (*3*) chemical cleavage.

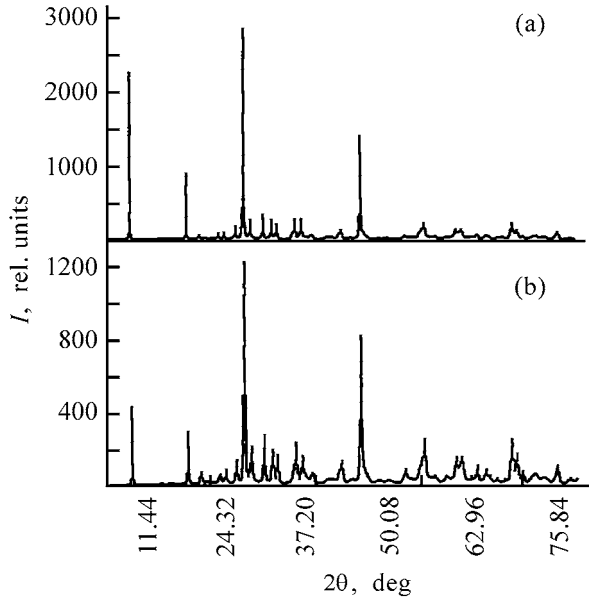

Fig. 4. X-ray diffraction patterns of muscovite. (*I*) Intensity and (2θ) Bragg angle. Mineral: (a) initial and (b) after electrochemical cleavage.

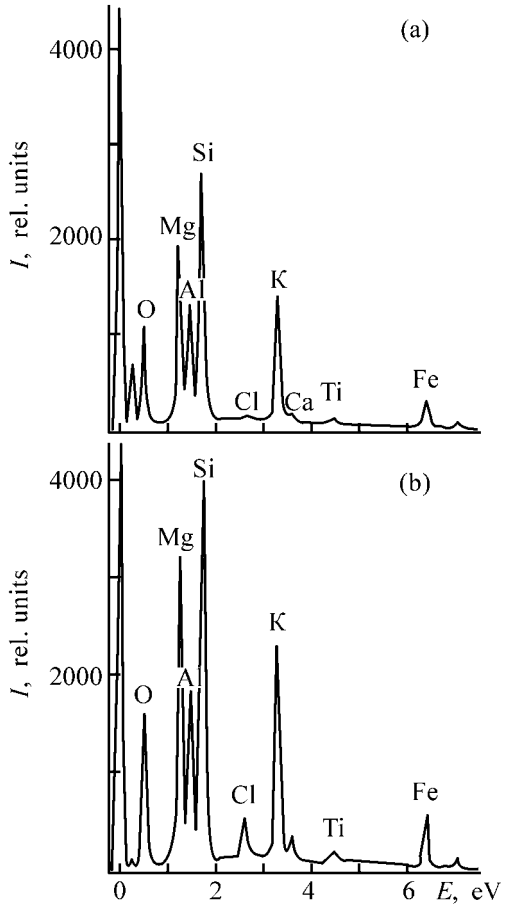

Fig. 5. Scanning spectral analysis of the phlogopite surface after chemical cleavage. (*I*) Intensity and (*E*) binding energy. Surface: (a) lateral and (b) basal.

[10]. In iron(III) oxidation, this band is observed at 520 cm^{-1}, and the Si–O–Mg bond is manifested at lower frequencies, which is due to the increased length of the M^{2+}–O–Si bond and to its more polar character.

Thus, the cleavage of mica leads to the structural changes in mica particles (formation of hydrated forms, isomorphic substitutions in octahedral layers, and deformation distortion in tetrahedral layers), which can affect mica properties. In particular, the appearance of an uncompensated structural charge on the basal surface as a result of isomorphic substitution enhances the ion-exchange and sorption properties of such minerals.

Use of finely ground mica as a pigment imposes stringent requirements upon the state of the surface of mica particles [11]. A scanning spectral analysis of the mica surface demonstrated that nonuniform dissolution of the basal and lateral surfaces of minerals occurs in chemical cleavage (Fig. 5). This leads to defect formation and edge corrosion. Deposition of a titanium coating onto such particles yields pigments that are nonuniform across their thickness, which impairs their optical properties and, consequently, quality.

CONCLUSIONS

(1) The crystal structure of mica cleaved by different methods was studied by IR spectroscopy. Cleavage of mica leads to changes in the octahedral and tetrahedral layers. In addition, protonation of aluminum bonds, caused by leaching of interlayer potassium ions, was observed for muscovite.

(2) Chemical treatment causes corrosion of edges of cleaved particles. This results from different rates of dissolution of their basal and lateral surfaces.

ACKNOWLEDGMENTS

The study was supported financially by the Swedish Institute (Stockholm).

REFERENCES

1. Gerasimova, L.G., *Pigmenty i napolniteli iz prirodnogo titansoderzhashchego syr'ya i tekhnogennykh otkhodov* (Pigments and Fillers Prepared from Titanium-containing Mineral Raw Materials and Technologica Wastes), Apatity: Kol'sk. Nauchn. Tsentr Ross. Akad. Nauk, 2001.
2. *Strukturnye prevrashcheniya mineralov* (Structural Transformations in Minerals), Kukovskii, E.G., Ed., Kiev: Naukova Dumka, 1984.
3. Ferro, Z.D., *J. Mining Eng.*, 1988, vol. 40, no. 6, pp. 428–429.
4. RF Patent 1 640 894.
5. Farmer, V.C., *Infrared Spectra of Minerals*, London: Mineral Soc., 1974.
6. Stubican, V. and Roy, R., *Am. Mineralogist*, 1961, vol. 46, pp. 32–51.
7. Vedder, W., *Am. Mineralogist*, 1964, vol. 49, pp. 736–768.
8. Plyusnina, I.I., *Infrakrasnye spektry silikatov* (IR Spectra of Silicates), Moscow: Mos. Gos. Univ., 1967.
9. Kukovskii, E.G., *Prevrashchenie sloistykh silikatov* (Transformation of Layered Silicates), Kiev: Naukova Dumka, 1973.
10. Plyusnina, I.I., *Infrakrasnye spektry mineralov* (IR Spectra of Minerals), Moscow: Mos. Gos. Univ., 1977.
11. Gershenzon, A.Sh., Gerasimova, L.G., Khokhulya, M.S., *et al., Neorg. Mater.*, 2001, vol. 37, no. 5, pp. 631–635.

Russian Journal of Applied Chemistry, Vol. 76, No. 6, 2003, pp. 871–874. Translated from Zhurnal Prikladnoi Khimii, Vol. 76, No. 6, 2003, pp. 900–903.

INORGANIC SYNTHESIS AND INDUSTRIAL INORGANIC CHEMISTRY

Preparation of Stable Copper Dispersions by Redox Reactions of Cu(II) Salts with Sulfur-containing Reducing Agents and Properties of the Dispersions

I. N. Terskaya, V. V. Budanov, and L. V. Ermolina

Ivanovo State University of Chemical Engineering, Ivanovo, Russia

Received November 13, 2002

Abstract—A procedure was developed for preparing copper dispersions that can be used as catalytic systems in electroless metallization of insulators by chemical reduction of Cu(II) salts with sodium hydroxymethanesulfinate (rongalite) or thiourea dioxide in aqueous-alcoholic media.

Chemical precipitation of metals is widely used to obtain sols [1, 2]. Conventional reducing agents used for this purpose are aluminum hydride, borohydride, aminoborane, and hypophosphite [3, 4]. However, sols of metals obtained with the use of these reducing agents contain significant amounts of impurities and have a broad particle size distribution. It is known [3, 5, 6] that colloids of most metals are rapidly oxidized by atmospheric oxygen, water, and other oxidants. This impairs the stability and catalytic activity of colloid solutions and makes difficult their practical use.

It has been found previously that sodium hydroxymethanesulfinate (HMS) $HOCH_2SO_2Na$ and thiourea dioxide (TUDO) $(NH_2)_2CSO_2$ are effective reducing agents for metal ions [7]. Chemical reactions of HMS or TUDO with Cu^{2+} and Ni^{2+} ions yield high-purity (up to 99.9% metal) precipitates of the metals with particle size of up to 1 μm for Cu and 0.5 μm for Ni, with the introduction of an alcohol (butanol or decanol) into the reaction system increasing the degree of dispersion of the resulting powders. In this context, it was of interest to study the possibility of improving the aggregative stability of the above-mentioned dispersions with the purpose of obtaining stable systems. This communication reports the results obtained in a study of HMS and TUDO application for obtaining metal dispersions with rather high aggregative stability and controllable degree of dispersion.

EXPERIMENTAL

Copper dispersions were prepared as follows. An aqueous solution of $CuSO_4$ was added to an aqueous solution of TUDO or HMS (chemically pure salts). Thiourea dioxide was prepared from chemically pure thiourea by oxidation with hydrogen peroxide according to the known technique [8], or a commercial-grade product was used after twofold recrystallization from water. Sodium hydroxymethanesulfinate was also obtained from a commercial-grade product by twofold recrystallization from water. The concentration of a metal salt was varied within the limits 5×10^{-3}–5×10^{-2} M, and the concentration of a reducing agent was selected so that its 10–20-fold excess was provided. The reduction reaction was carried out in glass temperature-controlled vessels at fixed temperature (40–80°C). To stabilize the resulting dispersions, protective colloids (gelatin, agar-agar, polyvinyl alcohol, glycerol, and also alcohols, such as butanol and decanol) were added to a solution in various proportions (from 0.5 up to 10 vol %).

Spectra of the copper dispersions were taken on a Specol-210 spectrophotometer. The particle size was determined by turbidimetry [9], using the theory of light scattering in disperse systems, for which Rayleigh's equation does not hold. The particle radii were calculated by Heller's empirical equation [9]. The sizes and amounts of particles were also determined using a Tesla BS-300 electron microscope. Both the methods yielded average sizes of particles coinciding to the first significant digit.

The formation of a copper dispersion was judged from the appearance of a characteristic red-brown coloration and from the presence of Tyndall's cone. The stability of the dispersion was characterized by the period of time from the instant of its prepara-

1070-4272/03/7606-0871 $25.00 © 2003 MAIK "Nauka/Interperiodica"

Table 1. Effect of stabilizing agents, alcohol, and reagent concentrations on stability of copper dispersions (concentration of copper(II) 5×10^{-2} M, content of stabilizing additive 3%; T = 313 K)

Reducing agent, M	Solvent	Additive	Dispersion stability
TUDO:			
0.1	H_2O	Gelatin	30 min
	H_2O : butanol:		
	9 : 1	–	50 min
	1 : 1	–	35 min
	9 : 1	Gelatin	25 day
	9 : 1	Agar-agar	12 day
0.5	9 : 1	Gelatin	25 day
HMS:			
0.1	H_2O	"	35 min
	H_2O : butanol = 9 : 1	–	65 min
	The same	Gelatin	19 day
	"	Agar-agar	9 day
0.5	"	Gelatin	5 day

tion to that of the onset of sedimentation. The variation of the degree of dispersion and that of the particle size of a dispersed phase with time were monitored in parallel.

It is known [3] that colloid solutions can be formed in organic media, and use of microemulsions is a promising way to obtain colloids with controllable degree of dispersion.

Table 1 lists data on the effect of solvent composition and reducing agent (HMS and TUDO) concentrations on the stability of the dispersions[1] under study. It can be seen that the dispersion of Cu^0, which retains stability for 25 days, is formed when Cu^{2+} is reduced in an aqueous-alcoholic medium (butanol concentration not exceeding 10 vol %) in an excess of a reducing agent (concentrations 0.1 and 0.5 M) at 313 K and in the presence of stabilizing additives. The thus obtained solutions have intense red-brown color and a typical absorption spectrum shown in Fig. 1, curves *4* and *5*. It was noted in [5] that a monodispersed colloid solution shows an absorption peak at wavelengths in the range 550–650 nm. Therefore, the presence of an absorption band at λ = 570 nm in the spectra (Fig. 1) indicates that the method suggested makes it possible to obtain a copper dispersion with rather narrow range of degrees of dispersion.

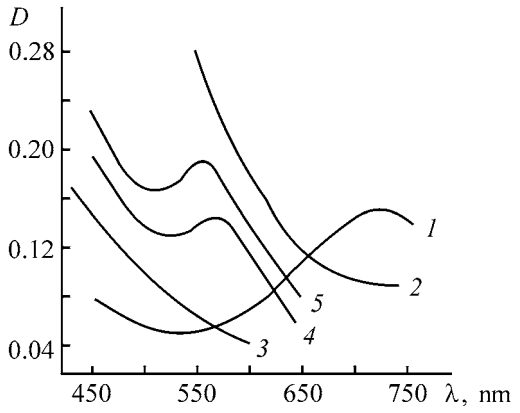

Fig. 1. Absorption spectra. D is optical density and λ is wavelength. Concentration: copper(II) 5×10^{-2}, TUDO 0.1 M; T = 298 K. (*1*) $CuCl_2$, aqueous solution; (*2*) TUDO, aqueous solution; (*3*) gelatin, aqueous solution (3 wt %); (*4*) solution of colloid copper in water–butanol medium (9 : 1); (*5*) solution of colloid copper in water–butanol (9 : 1)–gelatin (3 wt %) medium.

The electron-microscopic data (Figs. 2a and 2b) show that the use of gelatin additions allows the average size of dispersed phase particles to be decreased by an order of magnitude. In this case, the fraction of particles with average size of 1.5 μm constitutes approximately 90% of the dispersed phase weight, whereas in the absence of these additives (glycerol-water medium), the average size of copper particles is 20–30 μm, and the precipitate itself is more polydispersed (Fig. 2b).

It is necessary to note that the copper dispersions are stable up to 373 K; however, they abruptly lose aggregative stability upon dilution with water. With increasing HMS concentration, the stability of copper dispersions decreases, whereas the excess of TUDO does not affect its stability (Table 1). This is attributable to the fact that, unlike TUDO, HMS is a strong electrolyte (sodium salt of hydroxymethanesulfinic acid) [9].

Copper dispersions were found to change red-brown color for green under the action of light (λ = 350–780 nm). It is known that monodispersed systems are less stable against photooxidation than polydispersed systems [10]. The following processes are possible in solution under the action of light:

$$Cu^0(\text{polydispersed}) \overset{h\nu}{\rightleftharpoons} Cu^0(\text{monodispersed}), \quad (1)$$

$$Cu^0(\text{polydispersed}) \overset{h\nu}{\rightleftharpoons} Cu^+ + e. \quad (2)$$

The reversibility of process (2) is confirmed by the fact that the absorption spectrum of the solution

[1] Within the indicated life time of a system, the average size of dispersed phase particles, determined by electron microscopy, remained virtually constant.

obtained upon exposure of a copper dispersion to light is identical to that of a true Cu(I) solution. When the solution subjected to the action of light is placed in the dark, the red-brown color is not restored. However, heating of this solution yields a solution of dispersed copper again. Conceivably, this transition occurs either as a result of disproportionation

$$2Cu^{+} \xrightarrow{t} Cu^{0} + Cu^{2+}, \quad (3)$$

or under the action of a reducing agent

$$Cu^{+} + TUDO\,(HMS) \xrightarrow{t} Cu^{0}. \quad (4)$$

It is necessary to note that the rate of photooxidation of copper dispersions is essentially reduced when butanol is added to them, together with gelatin, during preparation. Probably, the stabilizing role of alcohols is due not only to specific solvation and suppression of diffusion processes, but also to their reducing properties.

It was noted in [10] that copper colloid solutions have high catalytic activity in oxidation of CO, various hydrocarbons, and methanol, and also in chemical metallization of fiber-glass laminate in manufacture of printed circuit boards and elastic screening and microwaves-reflecting materials based on metallized fabrics. Despite that solutions of colloid copper rank somewhat below palladium activators, they have several advantages: the number of operations is reduced because the intermediate stages of article washing after activation and the necessity for palladium recovery from sewage are eliminated, and also the possibility of decomposition of chemical-metallization solutions upon introduction of palladium-activated samples into a bath is ruled out.

Copper dispersions obtained by reduction of Cu(II) salts with HMS or TUDO were studied as activators for electroless nickel plating on carbon fibers and glass articles. The procedures are based on the reduction of Ni^{2+} ions from an ammine complex by the sulfur-containing reducing agents HMS and TUDO [11, 12]. The surface of samples was activated by various methods: by treatment with standard [based on palladium(II) or tin(II) salts] and copper colloid solutions stabilized with gelatin additions and also by treatment with low-temperature atmospheric plasma. It was found that that the activation of samples with a copper colloid solution yields metallic films with high adhesion strength: it was rather difficult to detach a film from the substrate surface by mechanical force (with a steel trowel). A comparative estimate of the effect of the activator nature on the strength of

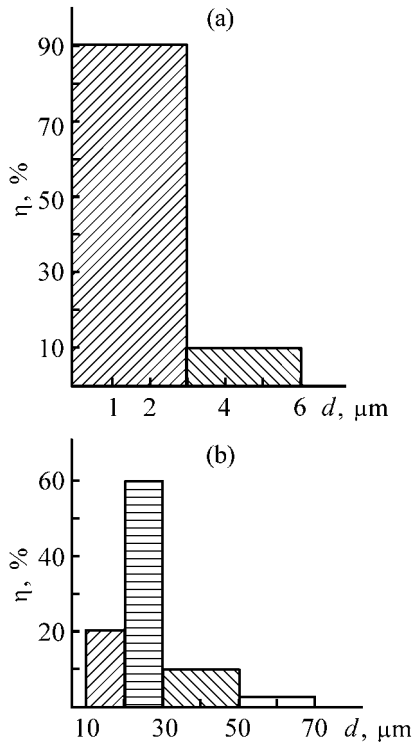

Fig. 2. Distribution of copper particles, η, with respect to size *d*. Medium: (a) 3% gelatin solution, (b) 50% glycerol solution.

adhesion of nickel films to a substrate was made using the "ultrasonic" method (UD-20 ultrasonic disintegrator). Nickel-plated samples were placed in a vessel with distilled water, so that the focusing attachment of the vibrator was at a distance of 10 mm from the sample surface. The instants τ_1 and τ_2 of, respectively, the destruction onset and final destruction of a nickel film on a sample under the action of ultrasound were determined. As the conditional time of complete destruction was chosen that when the diameter of a destruction zone reached 5 mm and more. The thickness *h* of a metal coating was determined in parallel for each sample by gravimetry. The metallization stage was performed under the same conditions: nickel(II) concentration 0.1 M, TUDO concentration 0.2 M; T = 343 K; τ = 15 min.

The results obtained in studying silicate-glass samples are listed in Table 2. It can be seen that activation with solutions of palladium(II) and tin(II) chlorides and with a copper colloid solution in gelatin provides virtually the same thickness of a metal film (~1.7 μm). However, the highest adhesion strength is achieved for samples activated with a copper colloid solution stabilized with gelatin (destruction time as long as 20 min). Similar results were obtained when studying the efficiency of various methods for activation of

Table 2. Effect of a method for activation of silicate glass samples on thickness and adhesive properties of nickel coating

Activation method	τ_1, min	τ_2, min	*h*, μm
$PdCl–2H_2O$, 0.5 g l^{-1} HCl_{conc}, 10 ml l^{-1}	6	9	1.77
$SnCl_2–2H_2O$, 0.25%, HCl_{conc}, up to 1 ml l^{-1}	9	12	1.72
Copper colloid solution in gelatin (3 vol %)	8	19.5	1.77
Treatment in atmospheric plasma	3	6	0.05
and with copper colloid solution in gelatin	12	20	1.25

carbon fiber and molybdate glass. The plasma activation of the glass, both by itself and in combination with activation with a copper colloid solution, does not yield any appreciable positive results (Table 2). Thus, the combination of butanol additives (up to 10 vol %) with gelatin in preparation of dispersed copper makes it possible to obtain monodispersed systems, which are stable for up to a month and have high activating capacity in electroless copper plating.

REFERENCES

1. Creiqhton, J.A., Alvarez, M.S., *et al.*, *J. Phys. Chem.*, 1983, vol. 87, no. 24, pp. 4793–4799.
2. Anqel, S.M., Katz, L.F., *et al.*, *Appl. Spectrosc.*, 1989, vol. 43, no. 3, pp. 367–372.
3. *Khimicheskoe osazhdenie metallov iz vodnykh rastvorov* (Chemical Deposition of Metals from Aqueous Solutions), Sviridov, V.V,, Ed., Minsk: Universitetskoe, 1987, pp. 98–127.
4. Mal'tseva, N.I. and Khain, V.S., *Borogidrid natriya: Svoistva i primenenie* (Sodium Borohydride: Properties and Application), Moscow: Nauka, 1985, pp. 142–190.
5. Loginov, A.V., Alekseeva, L.V., Gorbunova, V.V., *et al.*, *Zh. Prikl. Khim.*, 1994, vol. 67, no. 5, pp. 803–808.
6. Frolov, Yu.S., *Kurs kolloidnoi khimii: Poverkhnostnye yavleniya i dispersnye sistemy* (Course of Colloid Chemistry: Surface Phenomena and Disperse Systems), Moscow: Khimiya, 1982.
7. Ermolina, S.V., Makarov, S.V., Terskaya, I.N., and Budanov, V.V., *Zh. Neorg. Khim.*, 1995, vol. 40, no. 9, pp. 14–69.
8. Budanov, V.V. and Makarov, S.V., *Khimiya serosoderzhashchikh vosstanovitelei (rongalit, ditionit, dioksid tiomocheviny)* [Chemistry of Sulfur-containing Reducing Agents (Rongalite, Dithionite, Thiourea Dioxide)], Moscow: Khimiya, 1994.
9. *Laboratornye raboty i zadachi po kolloidnoi khimii* (Laboratory Works and Problems in Colloidal Chemistry), Frolov, Yu.S., Ed., Moscow: Khimiya, 1986, pp. 11–29.
10. Alekseeva, L.V., Photochemical Preparation and Properties of Colloids Based on Transition Metal Complexes, *Cand. Sci. (Chem.) Dissertation*, St. Petersburg, 1994.
11. RF Patent 2063461.
12. RF Patent 2167113.

Russian Journal of Applied Chemistry, Vol. 76, No. 6, 2003, pp. 875–878. Translated from Zhurnal Prikladnoi Khimii, Vol. 76, No. 6, 2003, pp. 904–908.

INORGANIC SYNTHESIS AND INDUSTRIAL INORGANIC CHEMISTRY

Sol–Gel Synthesis of Monodispersed SiO_2 Nanoparticles in the Presence of Organic Amines

N. N. Khimich, Yu. V. Zvyagil'skaya, A. N. Zhukov, and O. G. Us'yarov

Institute of Silicate Chemistry, Russian Academy of Sciences, St. Petersburg, Russia
St. Petersburg State University, St. Petersburg, Russia

Received December 24, 2002

Abstract—Preparation of monodispersed SiO_2 nanoparticles of varied size by hydrolysis of tetramethoxysilane and polycondensation of the hydrolysis products was studied as influenced by the basicity and nucleophilicity of organic amines.

In 1967, Stöber and Fink [1] showed that hydrolysis of silicon alkoxides in the presence of ammonia yields SiO_2 nanoparticles with narrow particle size distribution. Since that time, suspensions of particles of this kind became commercially available and found wide application in electronics and for preparing composites, monolithic glasses for optics, etc. [2, 3]. It is also known that hydrosols of these particles yield colloids with alternating structure (colloidal crystals), which are unique models for fundamental study of various types of interparticle interactions [4, 5] and crystallization from solution [6].

Although obvious progress has been achieved in the synthesis of SiO_2 nanoparticles, the results obtained are poorly reproducible [7]. To enhance the reproducibility, the effect of various factors on the size of SiO_2 nanoparticles was examined. In particular, the type of the initial alkoxysilane and alcohol used as the solvent, temperature of the sol–gel process, alkoxysilane concentration, alkoxysilane-to-water ratio, ammonia concentration, and rate of alkoxysilane addition were varied [1, 7–9]. However, there is one more factor affecting formation of a SiO_2 dispersion in the course of a sol–gel process: nature of the base catalyst, not examined in previous papers. Let us consider chemical reactions involved in this process [10]:

$$\equiv Si{-}OR + H_2O \underset{\text{Etherification}}{\overset{\text{Hydrolysis}}{\rightleftarrows}} \equiv Si{-}OH + ROH, \quad (1,2)$$

$$\equiv Si{-}OR + HO{-}Si\equiv \underset{\text{Alcoholysis}}{\overset{\text{Condensation}}{\rightleftarrows}} \equiv Si{-}O{-}Si\equiv + ROH, \quad (3,4)$$

$$\equiv Si{-}OH + HO{-}Si\equiv \underset{\text{Hydrolysis}}{\overset{\text{Condensation}}{\rightleftarrows}} \equiv Si{-}O{-}Si\equiv + H_2O. \quad (5,6)$$

Hydrolysis of silicon alkoxide yields silanols [reaction (1)] which can condense by reactions (3) and (5). When the sol–gel process is performed in an alkaline solution, reactions of alcoholysis (4) and hydrolysis (6), which are responsible for growth of SiO_2 particles with a definite size distribution, prevail. The rate of all of these reactions is acceptable only in the presence of catalysts. However, the mechanism of the base catalysis was reduced in the literature and, in particular, in a comprehensive monograph [11] to a bimolecular nucleophilic attack (S_N2–Si) of the hydroxide anion at the silicon atoms of alcoxysilane to give a five-coordinate intermediate which eliminates the alcohol molecule ROH (hydrolysis) or the RO^- anion (condensation). Thus, it is assumed that the sol–gel process involving hydrolysis of a silicon alcoxide and condensation of the hydrolysis products is controlled exclusively by the concentration of OH^- anions. Any organic base, in particular a nitrogen-containing compound, can be considered a proton acceptor. Its strength can be estimated from the pK_a of the conjugated acid:

$$:NR_3 + H_2O \rightleftarrows HN^+R_3 + OH^-. \quad (7)$$

However, the processes occurring in the sol–gel system incompletely fit in the logical path: (i) increase in the strength of the organic base, (ii) increase in the concentration of OH^- anions, and (iii) acceleration of the hydrolysis and condensation. For example, it is known that, although F^- is a weaker base than NH_3,

1070-4272/03/7606-0875 $25.00 © 2003 MAIK "Nauka/Interperiodica"

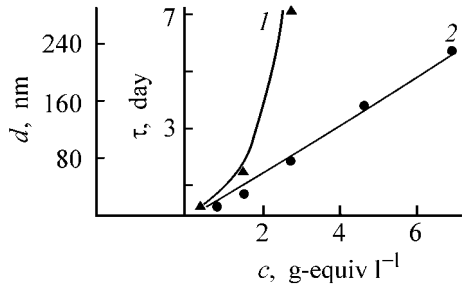

Fig. 1. (*1*) Average size *d* of SiO_2 particles and (*2*) gelation time τ vs. the 4-(dimethylamino)pyridine **V** concentration *c* in sol–gel systems 1–4 and 5b.

gelation of tetraethoxysilane solutions in the presence of KF is substantially faster than in the presence of the same amount of ammonia [11]. It is believed in this case that the F^- anion is close in size to the OH^- anion and can increase the coordination of the silicon atom in alkoxysilane [12]. In other words, not only proton affinity of the catalyst [Eq. (7)] but also its nucleophilicity (attack of its lone electron pair at the silicon atom of alkoxysilane) should be taken into account when describing the mechanism of the sol–gel process.

The nucleophilicity of a Lewis base depends on many factors, including the type of the chemical reaction involving this base [13]. In this study, we analyzed hydrolysis of tetramethoxysilane (TMOS) and polycondensation of the hydrolysis products in an alkaline solution in the presence of amines whose nucleophilicity was varied by changing the steric and electronic environment of the nitrogen atom.

Thus, the present study was concerned with conditions for obtaining monodispersed SiO_2 nanoparticles and development of methods for preparative synthesis of this material.

EXPERIMENTAL

Base hydrolysis of TMOS and polycondenstaion of the hydrolysis products were studied in the presence of the following thermally and chemically stable organic amine cata lysts: pyridine (**I**), 4-methylpyridine (**II**), 3-ethyl-4-methylpyridine (**III**), 2,6-dimethylpyridine (**IV**), 4-(dimethylamino)pyridine (**V**), *N*-methylmorpholine (**VI**), piperidine (**VII**), *N*-methylpiperidine (**VIII**), and ethyldiisopropylamine (**IX**):

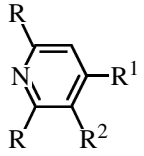

I–V

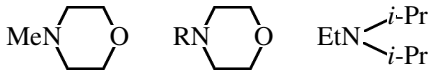

VI **VII, VIII** **IX**

Here R = R^1 = R^2 = H (**I**); R = R^2 = H, R^1 = Me (**II**); R = H, R^1 = Me, R^2 = Et (**III**); R = Me, R^1 = R^2 = H (**IV**); R = R^2 = H, R^1 = NMe_2 (**V**); R = H; (**VII**); R = Me (**VIII**).

TMOS and amines **I**–**IX** were distilled on a 10 TP column at atmospheric and reduced (15–760 mm Hg) pressure, with fractions boiling in the 0.5°C range collected. Amine **V** was recrystallized from alcohol. Sol–gel synthesis of SiO_2 nanoparticles was performed in a glass reactor equipped with a double water jacket, magnetic stirrer, dropping funnel, and reflux condenser. Appropriate amine, ethanol, and water were placed in the reactor. An ethanolic solution of TMOS (25 ml) was added with vigorous stirring at 70°C within 3 min. We prepared 13 sol–gel systems with TMOS : water : ethanol = 1 : 25 : 110. The mole fraction of amines is given below:

Sol–gel system	1	2	3	4	5a	5b	5c
Amine	**I**	**II**	**III**	**IV**	**V**	**V**	**V**
Mole fraction	7.0	1.4	1.4	1.4	0.35	1.4	2.8

Sol–gel system	5d	5e	6	7	8	9
Amine	**V**	**V**	**VI**	**VII**	**VIII**	**IX**
Mole fraction	4.9	7.0	1.4	1.4	1.4	1.4

The particle size was determined with an EM-125 electron microscope at accelerating voltage of 75 kV. The samples were prepared by applying the suspension (in some cases, diluted by a factor of 2–3 with alcohol) to a carbon-reinforced collodion support.

The organic amines were chosen so that the acidity constants of their conjugated acids and their boiling points varied widely:

Amine	**I**	**II**	**III**	**IV**	**V**
bp, °C [15]	115	145	198*	143–145	
pK_a, 20°C [16]	5.20	6.02	6.46	6.77	9.70

Amine	**VI**	**VII**	**VIII**	**IX**	Ammonia
bp, °C [15]	115–116**	124	106	127	
pK_a, 20°C [16]	7.38	11.3	10.20	10.50	9.25

* At 25°C [1, 5]. ** At 750 mm Hg.

All the experiments can be divided into three groups. In the first group, we varied the concentration of 4-(dimethylamino)pyridine **V** (sol–gel systems 5a–5d, Fig. 1). In the second, we varied the sub-

stituients in the pyridine ring (sol–gel systems 1–4 and 5b). Electron micrographs of SiO_2 particles formed in these systems are shown in Fig. 2. In experiments of the third group, we used strong organic bases **V**–**IX**.

Prior to discussing the results obtained, the following should be noted. First, the resolution of the microscope used does not allow determination of particles smaller than 10 nm in diameter. Second, separate SiO_2 nanoparticles can be obtained only when TMOS is strongly diluted with ethanol and water, which promotes hydrolysis and alcoholysis of the Si–O–Si bonds in the sol–gel systems [Eqs. (4), (7)] [17]. Otherwise gelation of the sol is complete in less than 10 min in the presence of pyridine catalyst and is almost instantaneous in the presence of bases **V**–**VIII**.

The size of silica particles prepared by hydrolysis of TMOS and polycondensation of the hydrolysis products in the presence of 4-(dimethylamino)pyridine grows linearly with increasing amine concentration (Fig. 1). At amine concentration of 0.35 g-equiv l^{-1}, the particle size is close to the detection limit, whereas at amine concentration of 7 g-equiv l^{-1}, it is 210–240 nm. Since particles formed in alkaline solution are negatively charged and repel one another [18], they grow by the condensation mechanism through dissolution of smaller particles. These smaller particles are not perfectly spherical, with pointed projections and irregularities (Fig. 2b). It is these projections and irregularities that have an excess energy and initiate, in the first place, rupture of the Si–O–Si bonds. Hence, as silica particles grow, their shape becomes more spherical (Figs. 2c, 2d).

It should be noted that the dissolution and condensation to form an ensemble of spherical particles compete with polymerization gelation. Each of these processes prevails at a definite base concentration. Heating of sol–gel system 5b for 30 min does not cause particle coarsening but accelerates the gelation. Thus, at low catalyst content, small silica particles susceptible to polycondensation with inclusion of a solvent and to gelation are formed owing to insufficiently fast rupture–formation of Si–O–Si bonds. At high catalyst content (Fig. 2e, 7 g-equiv l^{-1}), large particles are formed. In this case, the sol degrades by sedimentation and subsequent coagulation. Sols prepared at a catalyst content of about 0.5 g-equiv l^{-1} are stable for many days (Figs. 2d, 2d).

It should be noted that all the above processes of silica nanoparticle formation in sol–gel systems 5a–5e are fast. Electron micrographs taken immediately after the reaction completion, i.e., several minutes after the onset of hydrolysis of TMOS and polycondensation of the hydrolysis products, are shown in Figs. 2a–2e. Such a high rate is provided by high basicity and nucleophilicity of 4-(dimethylamino)pyridine. When amines **I**–**IV** having a similar structure and lower basicity are used as catalysts, all these processes are strongly decelerated. Hardly visible particles are formed on heating at 70°C for 4 h in the presence of 4-methylpyridine (Fig. 2g). Silica particles generated in the presence of 3-ethyl-4-methylpyridine **III** within the same time are slightly larger. When the least basic amine, pyridine, was used, visible particles (Fig. 2f) were formed only after keeping the sol–gel system at 70°C for 8 h and then at room temperature for 8 days. The behavior of sol–gel systems 1–3 correlates with an increase in the amine basicity. However, no visible particles appear when sol–gel system 4 containing 2,6-dimethylpyridine is heated for 4 h, although the basicity of this amine is substantially higher than that of amines **I**–**III**.

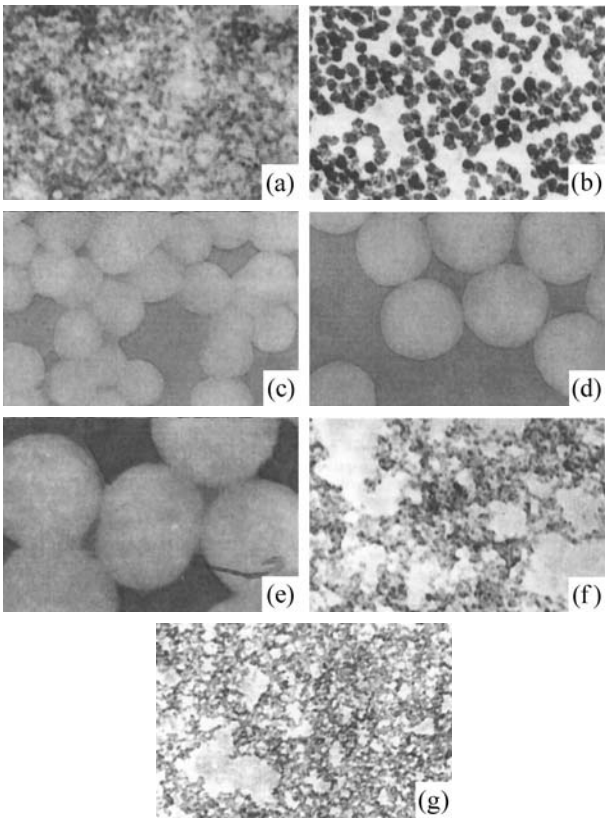

Fig. 2. Electron micrographs of SiO_2 particles prepared in sol–gel systems (a) 5a, (b) 5b, (c) 5c, (d) 5d, (e) 5e, (f) 1 and (g) 2. Magnification ×100 000 (100 nm in 1 cm); the same for Fig. 3.

Thus, the mechanism of formation of silica nanoparticles in the presence of organic amines must involve an attack on the silicon atoms by the lone elec-

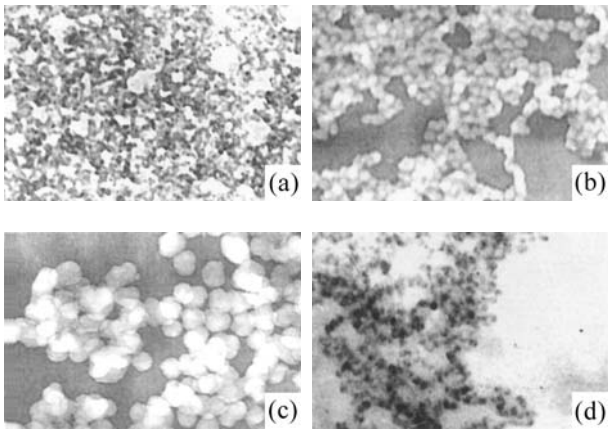

Fig. 3. Electron micrographs of silica particles formed in sol–gel systems (a) 6, (b) 8, (c) 7, and (d) 9.

tron pare of the nitrogen atom. If the electron pair is less accessible, as in, e.g., amine **IV**, owing to steric hindrance caused by two methyl groups, the sol–gel process is decelerated, i.e., it is controlled by the nucleophilicity, rather than basicity of the catalyst.

Clearly, this assumption is true when strongly basic amines **V**–**IX** are used as catalysts. Electron micrographs of SiO_2 particles prepared by the sol–gel process catalyzed with these amines are shown in Fig. 3. Hardly visible silica particles about 10 nm in diameter are formed in the presence of *N*-methylmorpholine (Fig. 3a). The diameter of silica particles grows with increasing amine basicity in the order *N*-methylmorpholine **VI** < 4-(dimethylamino)pyridine **V** (Fig. 2b) ~ *N*-methylpiperidine **VIII** (Fig. 3b) << piperidine **VII** (Fig. 3c). However, when less nucleophilic sterically hindered ethyldiisopropylamine is used, the particle size sharply decreases despite the high basicity of the amine (Fig. 3d).

CONCLUSIONS

(1) The procedure developed for preparative synthesis of monodispersed SiO_2 nanoparticles gives well-reproducible results and requires simple equipment.

(2) When a strongly basic amine ($pK_a > 9$) is used as catalyst, the particle size grows almost linearly with its increasing concentration.

(3) Catalytic hydrolysis of TMOS and polycondensation of the hydrolysis products to form SiO_2 nanoparticles are governed not only by the concentration of hydroxide anions in a solution (i.e., by basicity of an amine), but also by the nucleophilicity of the amine.

ACKNOWLEDGMENTS

We are grateful to I.A. Drozdova for performing electron microscopic studies.

This study was supported financially by the Russian Foundation for Basic Research (project no. 02-03-32730).

REFERENCES

1. Stöber, W. and Fink, A., *J. Colloid Interface Sci.*, 1968, vol. 26, pp. 62–69.
2. Petrovskii, G.T., Shashkin V.S., Yakhkind, A.K., *Fiz. Khim. Stekla*, 1997, vol. 23, no. 1, pp. 43–53.
3. So, J.-H., Oh, M.-H., Lee, J.-D., and Yang, S.-M., *J. Chem. Eng. Jpn.*, 2001, vol. 34, no. 2, pp. 262–268.
4. Efremov, I.F., *Periodicheskie kolloidnye struktury* (Periodical Colloid Structures), Leningrad: Khimiya, 1971.
5. Hunter, R.J., *Foundations of Colloid Science*, Oxford: Univ. Press, 2001.
6. Okubo, T. And Ishiki, H., *J. Colloid. Interface Sci.*, 1999, vol. 211, p. 151–159.
7. Bogush, G.H., Tracy, M.A., and Zukoski, C.F., *J. Non-Cryst. Solids*, 1988, vol. 104, pp. 95–106.
8. So, Jae-Hyun, Yang, Seung-Man, Kim, C., and Hyn, J.C., *Colloids Surf. A: Physicochem. Eng. Aspects*, 2001, vol. 190, pp. 89–98.
9. Sung Kyoo Park, Ki Do Kim, and Hee Taik Kim, *Colloids Surf. A: Physicochem. Eng. Aspects*, 2002, vol. 197, pp. 7–17.
10. Brinker, C.I. and Scherer, G.W., *Sol–Gel Science*, New York: Academic, 1990.
11. Pope, E.J.A. and Mackenzie, J.D., *J. Non-Cryst. Solids*, 1986, vol. 87, pp. 185–198.
12. Corriu, R.J.P. and Young, J.C., *The Chemistry of Organic Silicon Compounds*, Patai, S. and Rappoport, Z., Eds., New York: Wiley, 1989, ch. 20, pp. 1241–1288.
13. Carey, F.A. and Sundberg, R.J., *Advanced Organic Chemistry, Part A: Structure and Mechanisms*, New York: Plenum, 1977.
14. *Aldrich Catalog Handbook of Fine Chemicals*, Sigma-Aldrich, 2000.
15. *Beilstein Handbook of Organic Chemistry: Fifth Suppl. Ser.*, Berlin: Springer, 1989, vol. 20, part 6.
16. Perrin, D.D., *Dissociation Constants of Organic Bases in Aqueous Solutions*, London: Butterworths, 1965.
17. Klein, L.C., *Ann. Rev. Mater. Sci.*, 1985, vol. 15, pp. 227–248.
18. Iler, R.K., *The Chemistry of Silica*, New York: Wiley–Interscience, 1979.

Russian Journal of Applied Chemistry, Vol. 76, No. 6, 2003, pp. 879–883. Translated from Zhurnal Prikladnoi Khimii, Vol. 76, No. 6, 2003, pp. 909–913.

PHYSICOCHEMICAL STUDIES OF SYSTEMS AND PROCESSES

Saturated Vapor Pressure in a System Constituted by Anthranilic Acid and Hydrogen Fluoride

A. P. Murlyshev, Yu. F. Kobzar', V. V. Lazarchuk, Yu. Ya. Tomash, A. G. Krupin, V. D. Filimonov, I. I. Zherin, V. V. Gordienko, and S. N. Gerasimenko

Siberian Chemical Plant, Seversk, Russia,

Tomsk Polytechnic University, Tomsk, Russia

Received August 22, 2002; in final form, December 2002

Abstract—The saturated vapor pressure in a system constituted by anthranilic (*o*-aminobenzoic) acid and hydrogen fluoride was studied by the static method in the temperature range 0–90°C. The isotherms of vapor pressure as a function of solution composition were approximated using the least-squares method.

Synthesis of *o*-fluorobenzoic acid by the diazotization method involves a stage in which a solution of anthranilic acid (AA) in hydrogen fluoride is prepared, with the subsequent diazotization and thermal decomposition of a diazonium salt formed. To preclude loss of hydrogen fluoride in the above stages and to study the kinetics of diazonium salt decomposition, data on saturated vapor pressure in the AA–HF system are necessary.

EXPERIMENTAL

The saturated vapor pressure in the AA–HF system was measured on an installation including the following units (Fig. 1):

(1) Vessel *1* for charging a mixture under study and a calibration vessel *2* for vapor sampling are mounted within heat-insulating jackets *3* and *4*, in which an ethylene glycol solution, fed from a SZhML-19/2,5-I1-9

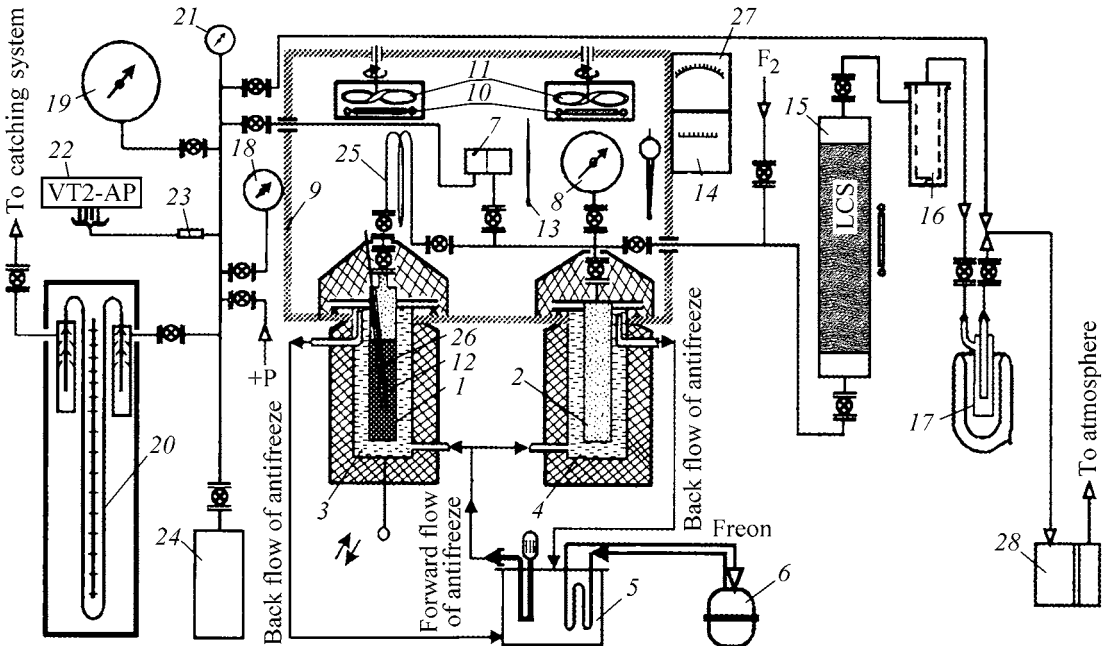

Fig. 1. Schematic of the experimental setup. (*23*) Pressure gage, (*24*) calibration vessel, (*25*) helical compensator, (*26*) thermocouple pocket, (*27*) secondary gage, (*28*) rough-pressure pump; for the remaining notations see text.

1070-4272/03/7606-0879 $25.00 © 2003 MAIK "Nauka/Interperiodica"

thermostat *5*, is circulated. Ethylene glycol is cooled by a refrigerating compressor *6* or heated by heaters built in the thermostat *5* to ensure the required range of working temperatures. The vessels *1* and *2* are connected to a pressure measurement system.

(2) The system for vapor-pressure measurements consists of two DP-5 pressure reducers *7* with measurement ranges 0–50 and 0–300 mm Hg and an MO-11202 reference gage *8* (0.4 accuracy rating), mounted within an air thermostat *9*. The thermostat *9* is equipped with heaters *10*, fans *11*, Chromel–Copel thermocouple *12*, mercury thermometer *13*, and KSP-4 control potentiometer *14*.

(3) The vacuum system includes a pump protection unit, a unit for measuring the pressure in the reference chamber, and a 2NVR-5DM rough-vacuum pump. The first unit consists of a sorption column *15* filled with granulated sorbents [sodium fluoride, lime chemical sorbent (LCS)], porous-metal filter *16*, and freezing trap *17* cooled with liquid nitrogen. The pressure in the reference chamber of DP-5 is measured with an MO-11202 reference gage *18* (0.4 accuracy rating), V-1227 reference vacuum gage *19* (0.25 accuracy rating), open mercury pressure gage *20*, OBMB-1-160 vacuum gage *21* (1.5 accuracy rating), and VT-2AP thermocouple vacuum gage *22* with a PMT-4 lamp *23*.

The error in pressure measurement was ±0.5, ±1.5, and ±5 for pressures of up to 50, 300, and 6500 mm Hg, respectively. The temperature in the thermostat was maintained constant to within ±0.05°C.

As main construction materials were used nickel, stainless steel, and copper, with fluoroplast-4 serving as laying material. The inner surfaces of the vessels *1* and *2* were preliminarily polished mechanically and chemically.

Prior to tests, all the surfaces of the pipelines and valves contacting with the corrosive medium were passivated with elementary fluorine for 24, h with gradual heating to 100°C.

We used AA [GOST (State Standard) 14310–78] and anhydrous hydrogen fluoride of A brand satisfying the requirements of GOST 14022–88, which corresponds to 99.95 wt % pure substance and more. The purity of AA was verified by the melting point method (mp 143°C).

Initial samples were prepared in a sealed cell in argon dried by circulation in a column packed with LCS and NaA zeolite.

Prescribed amounts of AA and HF were weighed on an analytical balance in a thoroughly washed and dried Teflon flask and placed in vessel *1*. The vessel was sealed, cooled with liquid nitrogen, and evacuated to residual pressure of less than 0.1 mm Hg. Vessel *1* with a mixture of prescribed composition was placed in a jacket *3* and connected to a pressure measurement system. Ethylene glycol with required temperature was fed into the jacket, with the temperature in the air thermostat maintained at 5–8°C above that in the jacket. The vessel *1* was subjected to vibration treatment. As the instant of time at which equilibrium was attained in the system was taken that when the vapor pressure reached a constant value. The pressure was indicated by readings of the reducers *7* and reference gage *8*.

The saturated vapor pressure in the AA–HF system was studied by the static method in the temperature range 0–20°C at a step of 5°C and 30–90°C at a step of 10°C for solutions containing 8.79, 17.41, 21.70, 23.41, 28.08, 32.74, and 36.03 wt % AA. The contents above 36.03 wt % were not studied, because the AA solubility at 20°C does not exceed 40 wt %.

The experimental data on the dependence of saturated vapor pressure on solution composition in the temperature range 0–90°C are presented in Table 1.

Table 1. Saturated vapor pressure at different solution compositions

AA		Saturated vapor pressure (mm Hg) at indicated temperature, °C											
mol %	wt %	0.0	5.0	10.0	15.0	20.0	30.0	40.0	50.0	60.0	70.0	80.0	90.0
0.00*	0.00	364	443	535	645	773	1093	1516	2069	2778	3677	4801	6191
0.015	8.79	320	375	445	530	645	930	1275	1795	2430	3160	3850	5130
0.029	17.41	283	318	385	455	535	780	1070	1565	2185	2905	3630	4920
0.036	20.28	242	275	310	360	455	700	975	1360	1930	2595	3340	4205
0.043	23.41	205	240	280	325	405	595	865	1245	1800	2410	3110	3780
0.049	28.08	160	183	218	265	345	515	720	1025	1470	2050	2650	3410
0.066	32.74	123	142	168	210	280	455	650	870	1260	1865	2285	2870
0.072	36.03	85	102	120	145	205	345	520	725	1010	1480	1920	2420

* The saturated vapor pressures of pure solvent (hydrogen fluoride) in relation to temperature [1].

The AA–HF system consists of components with strongly different saturated vapor pressures (standard boiling point of HF is 19.5°C, and AA sublimation temperature, 143°C). Therefore, the vapor phase is considerably enriched in hydrogen fluoride in the entire temperature range studied, and the AA vapor pressure can be neglected.

The dependence of saturated vapor pressure over a solution of solid substances in volatile solvents is expressed by Raoult's law:

$$\frac{p_i^0 - p_i}{p_i^0} = \frac{\Delta p}{p_i^0} = \frac{n_2}{n_1 - n_2} x_2, \qquad (1)$$

where p_i^0 is the saturated vapor pressure over pure solvent; p_i, the solvent vapor pressure over a solution of given concentration; $\Delta p/p_i^0$, the relative decrease in the solvent vapor pressure; n_2 and n_1, the number of moles of the solute and solvent, respectively.

The values of the relative decrease in the vapor pressure of the solvent for given compositions, as calculated by Eq. (1) and averaged over the temperature range 0–90°C, are presented below:

AA, mole fraction	$\Delta p/p_i^0$	AA, mole fraction	$\Delta p/p_i^0$
0.015	0.159	0.049	0.504
0.029	0.233	0.066	0.855
0.036	0.319	0.072	0.883
0.043	0.395		

It can be seen that the $\Delta p/p_i^0$ ratio grows with increasing solute concentration. This indicates that the solvent interacts with the solute.

The experimental data presented in Table 1 were processed by means of the least-squares method, using the Clausius–Clapeyron equation [2] in integral form

$$\log p = A - B/T, \qquad (2)$$

where A is a constant; $B = \Delta H_{vap}/2.3R$; $R = 1.986$ cal mol^{-1} deg^{-1}, the universal gas constant; ΔH_{vap}, the molar heat of vaporization (cal); T, temperature (K).

Figure 2 shows the temperature dependence of the vapor pressure on temperature, as calculated by Eq. (2) for different solution compositions.

The dependence of the boiling point of the AA–HF solution on composition at 760 mm Hg is presented in Fig. 3.

In addition, the experimental data were processed using the Kirchhoff–Eigen equation (3), Kirchhoff–Rankine–Du'pre equations (4, 5), and Antoine's equation (6) [3]:

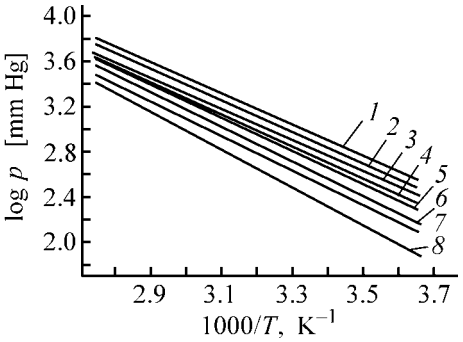

Fig. 2. Hydrogen fluoride vapor pressure p vs. temperature T for different compositions of the AA–HF system. (*1*) HF; AA content (mol %): (*2*) 0.015, (*3*) 0.029, (*4*) 0.036, (*5*) 0.043, (*6*) 0.049, (*7*) 0.066, and (*8*) 0.072.

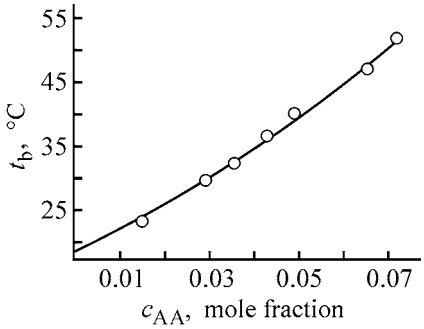

Fig. 3. Standard boiling point t_b of the AA–HF solution vs. composition. (c_{AA}) AA content; the same for Fig. 4.

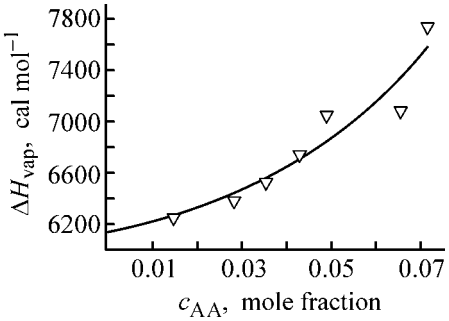

Fig. 4. Molar heat of vaporization ΔH_{vap} of the solvent vs. solution composition in the AA–HF system.

$$\ln p = A_2 - B_2 \ln T + C_2 T - H/T, \qquad (3)$$

$$\ln p = A_3 - B_3 \ln T + C_3 T, \qquad (4)$$

$$\log p = A_4 - B_4 \log T + C_4 T, \qquad (5)$$

$$\log p = A_5 - B_5(t + C_5 T). \qquad (6)$$

The numerical values of the coefficients in Eqs. (2)–(6) and the molar heats of vaporization,

Table 2. Coefficients of Eqs. (2)–(6)

Equation	Coefficient	Coefficients at indicated AA content, mole fraction						
		0.015	0.029	0.036	0.043	0.049	0.066	0.072
(2)	A	7.4206	7.5237	7.5732	7.6237	7.7082	7.8342	8.0352
	B	1348.8398	1398.1618	1432.8990	1463.2546	1515.0294	1578.4450	1676.5015
	r*	0.99476	0.99638	0.99351	0.98917	0.99441	0.98798	0.99025
(3)	A_2	–1158.836	–1717.835	–1711.043	–3084.838	–1711.073	–2039.965	–2320.721
	B_2	–204.1324	–299.9803	–299.7517	–538.3592	–299.7571	–358.4233	–407.7439
	C_2	–0.3206	–0.4599	–0.4676	–0.8438	–0.4676	–0.5736	–0.6557
	H	–29223.95	–45398.58	–44304.53	–82070.02	–44305.37	–52081.34	–59214.31
	r	0.99871	0.99883	0.99986	0.99994	0.99978	0.99838	0.99935
(4)	A_3	4.3238	–49.3884	–32.2585	–23.7155	–14.8144	41.0688	58.0289
	B_3	1.8907	9.8829	7.3621	6.1137	4.8240	–3.4116	–5.8556
	C_3	2514.1964	126.9011	995.6700	1456.1928	1978.9970	4702.0533	5692.5784
	r	0.99794	0.99744	0.99954	0.99925	0.99877	0.99768	0.99866
(5)	A_4	1.8776	–49.3884	–14.0097	–10.2996	–25.3308	17.8362	25.2019
	B_4	–1.8907	9.8829	–7.3621	–6.1138	11.3058	3.4117	5.8557
	C_4	1091.8922	126.90113	432.4113	632.4113	–8.4306	2042.0906	2472.2712
	r	0.99783	0.99754	0.99932	0.99943	0.99862	0.99756	0.99821
(6)	A_5	7.927604	11.53989	10.0246	9.5279	9.0983	7.3026	7.1449
	B_5	1686.1084	5056.2230	3385.5670	2903.3819	2513.8837	1262.0419	1163.6271
	C_5	309.9434	554.8940	440.8348	400.6633	363.0267	240.2186	221.2471
	r	0.99866	0.99875	0.99984	0.99991	0.99969	0.99848	0.99921
$\Delta H_{vap} \pm 5$, cal mol^{-1}		6227	6386	6520	6723	7035	7055	7732

* (r) Correlation coefficient.

ΔH_{vap}, for fixed compositions in the temperature range 0–90°C are listed in Table 2, along with the correlation factors calculated for each of the above equations.

The average relative error of experimental data processing for Eqs. (2), (3), (4), (5), and (6) was 4, 3, 3.5, and 3.5%, respectively.

Figure 4 shows the dependence of the molar heat of vaporization of the solvent on solution composition, as calculated by the Clausius–Clapeyron equation [4]:

$$\Delta H_{vap} = 0.95RB\left(\frac{T}{T - 43}\right)^2, \quad (7)$$

$$B = \frac{\ln (p_2^0/p_1^0)}{\frac{1}{t_1 + 230} - \frac{1}{t_2 + 230}}, \quad (8)$$

where p_1^0 and p_2^0 are the vapor pressures at temperatures t_1 and t_2, respectively.

The molal rise in the boiling point (ebullioscopic constant, or boiling constant) for the AA solutions in HF was 7.059 ± 0.012 deg mol^{-1}.

CONCLUSIONS

(1) The saturated vapor pressure in the anthranilic acid–hydrogen fluoride system was studied by the static method for solutions containing 8.79, 17.41, 21.70, 23.41, 28.08, 32.74, and 36.03 wt % anthranilic acid at 0–90°C. It was shown that, in the concentration range studied, the system is not azeotropic and exhibits negative deviations from Raoult's law.

(2) The experimental data obtained were processed using the Clausius–Clapeyron, Kirchhoff–Eigen, Kirchhoff–Rankine–Du'pre, and Antoine's equations, with average relative error of 4, 3, 3.5, and 3.5%, respectively. It was found that the Kirchhoff–Eigen equation describes the temperature dependence of the saturated vapor pressure with the highest precision.

(3) The molar heats of vaporization, ΔH_{vap}, were determined for fixed compositions in the temperature range 0–90°C.

(4) The molal rise in the boiling point of the anthranilic acid solution in hydrogen fluoride was 7.059 ± 0.012 deg mol^{-1}.

REFERENCES

1. Sheft, I., Perkins, A.J., and Hyman, H.H., *J. Inorg. Nucl. Chem.*, 1973, vol. 35, no. 11, pp. 3677–3679.
2. Kogan, V.B., *Geterogennye ravnovesiya* (Heterogeneous Equilibria), Moscow: Khimiya, 1968.
3. Moelwyn-Hughes, E.A., *Physical Chemistry*, London: Pergamon, 1961, 2nd ed. Translated by *Fizicheskaya khimiya, Kniga 1*, Moscow: Inostrannaya Literatura, 1962.
4. Hala, E., Pick, I., Fried, V., and Vilim, O., *Vapor–Liquid Equilibrium*, London: Pergamon, 1958. Translated by *Ravnovesie mezhdu zhidkost'yu i parom*, Moscow: Inostrannaya Literatura, 1962.

Russian Journal of Applied Chemistry, Vol. 76, No. 6, 2003, pp. 884–887. Translated from Zhurnal Prikladnoi Khimii, Vol. 76, No. 6, 2003, pp. 914–917.

PHYSICOCHEMICAL STUDIES OF SYSTEMS AND PROCESSES

Distribution of Microimpurities among Phases of Converter Matte from Pechenganikel' Combine

L. N. Ertseva, O. V. Korotkova, P. S. Seregin, and I. G. Fokeeva

Institut Gipronikel' Open Joint-Stock Company, St. Petersburg, Russia

Received April 8, 2003

Abstract—Scanning electron microscopy and X-ray fluorescence microanalysis were applied to study the distribution of zinc, lead, arsenic, antimony, and tin among phases of the converter matte from the Pechenganikel' combine.

In manufacture of nonferrous metals at plants of the Kola Mining and Smelting Company (KGMK), it is possible to process secondary raw materials containing considerable amounts of impurities, such as Zn, Pb, Sn, As, and Sb. In waste processing, these impurities pass into various half-products (matte, dusts, return slag). Owing to the high content of nonferrous metals, return materials are recycled into various stages of the smelting process, which results in gradual accumulation of impurities in some metallurgical half-products and, in the end, in that these impurities pass into commercial products. In this context, it becomes important to study the behavior of microimpurities in different stages of metallurgical processes at KGMK.

The main source from which the microimpurities under study come into the smelting process is the metallic copper waste processed in vertical converters at the copper shop of the Severonikel' combine [1]. The converter slag, into which a large amount of microimpurities passes, is a return material processed in ore-thermal furnaces and horizontal converters at the smelting shop. This is how Pb, Zn, As, Sb, and Sn impurities find way into the converter matte of the Pechenganikel' combine.

Further ingress of the microimpurities into nickel and copper concentrates depends on their distribution among phases of the converter matte delivered to flotation separation.

The real content of the impurities under study in industrial converter mattes is rather low (wt %): As 0.13; Pb 0.03; Zn, Sn, and Sb up to 0.01. In view of this circumstance, increased amounts of these metals were introduced in laboratory into the copper matte in order to elucidate the mechanism of microimpurity distribution among the concentrates. Zinc, lead, arsenic, antimony, and tin (in metallic form) were introduced (0.1 and 0.5 wt %) into a weighed portion of the converter matte.

Experiments were done in an induction furnace in the atmosphere of argon. A weighed portion was melted in a crucible (heating rate of 1 deg min^{-1}) and then kept at 1300°C for 15–20 min and slowly cooled with the furnace. The system for control over the furnace heater allowed programmed cooling.

A sample of a typical converter matte from the Pechenganikel' combine was chosen for study [2]. Converter matte composition (wt %): S 22.2, Fe 2.9, Co 0.7, Ni 39.9, and Cu 30.6.

The converter matte samples with introduced impurities were studied using scanning electron microscopy (SEM) and X-ray fluorescence microanalysis (CamScan scanning electron microscope with ED spectrometer and LINK ISIS 200 processing unit). Under the chosen analytical conditions, the minimum determinable content of Ni, Cu, Co, Fe, Zn, Pb(M_α), As(L_α), Sb(L_α), and Sn(L_α) was 0.03–0.04 wt %. (M_α and L_α are the characteristic lines of X-ray emission for the elements under study).

It was established that solid converter matte has a structure typical of such products (Fig. 1a): the matrix of the sample is constituted by nickel sulfide, which is close in composition to heazlewoodite Ni_3S_2 (Hz_{SS}) and contains structures formed in eutectic or eutectoid decomposition (Fig. 1b). Rounded copper

1070-4272/03/7606-0884 $25.00 © 2003 MAIK "Nauka/Interperiodica"

sulfide inclusions, which are typical of the converter matte structure, were found in the matrix of the heazlewoodite solid solution. Copper sulfide has a structure typical of the case of decomposition of a solid solution and corresponds in its average composition to a chalcosine–bornite solid solution Cu_2S–Cu_5FeS_4 $(Cc–Bn)_{SS}$. The sample contains virtually no well-formed crystals of the metallic phase.

The general view of a sample with 0.1 wt % impurities is shown in Fig. 1a.

The sample contains (Fig. 1c) minor amounts of metallic copper in the form of typical lens-like inclusions at the boundaries of nickel and copper sulfide phases, minute inclusions of lead sulfide (also at the phase boundaries between nickel and copper sulfides), and rounded inclusions of zinc sulfide in the bulk of the chalcosine–bornite solid solution (Fig. 1d).

The compositions of all the structural constituents of the sample (with the exception of lead sulfide) are listed in the table. Analysis of these data shows the following.

(1) Lead is contained in the sample as a separate PbS phase; other structural constituents contain no lead impurities.

(2) Zinc is distributed among the chalcosine–bornite solid solution and metallic copper. In view of the small volume of metallic copper, it can be concluded that the main part of zinc is contained in the chalcosine–bornite solid solution. It is noteworthy that the zinc sulfide phase is precipitated within the bulk of the copper solid solution, which is, in all probability, due to a decrease in its solubility in copper sulfide at lower temperatures.

(3) Arsenic, tin, and antimony are concentrated in nickel sulfide, with the maximum content of these impurities observed in the structural constituents formed in eutectoid decomposition, especially in the metallic phase. This means that the impurities are concentrated in crystallization of the residual melt. The metallic phase, which is present in the form of regular crystals, has composition typical of converter mattes and does not contain any of these impurities, since its crystallization occurs in early stages of cooling.

Figure 2a shows the general view of a sample containing 0.5 wt % impurities. As regards the main constituents, the sample differs from the preceding one only slightly. The differences are as follows: the content of metallic copper is much lower, the metallized

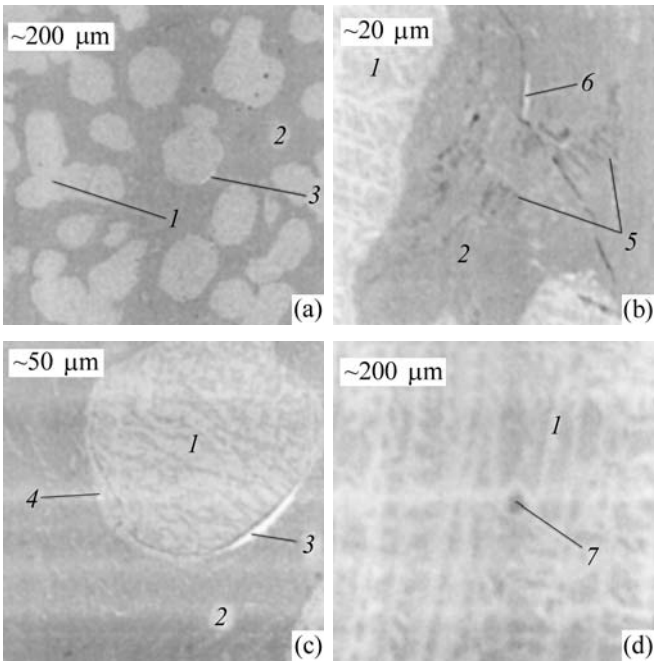

Fig. 1. Structure of a converter matte sample containing 0.1 wt % microimpurities. (a) General view, (b) structures formed in decomposition of a heazlewoodite solid solution, (c) inclusions of metallic copper and lead sulfide, (d) inclusions of zinc sulfide. (*1*) Chalcosine–bornite solid solution, (*2*) heazlewoodite solid solution, (*3*) metallic copper, (*4*) lead sulfide, (*5*) monosulfide solid solution (M_{SS}), (*6*) metallic component, and (*7*) lead sulfide.

phase in the structure formed in decomposition of nickel sulfide has the form of thin needle-like inclusions oriented in a certain direction (Figs. 2b, 2c); rounded and dendritic zinc sulfide crystals and inclusions of the metallic copper–silver phase are observed within the globules of the chalcosine–bornite solid solution; no separate phases of lead are observed in the sample; an iron–zinc oxide phase not associated with any other phase is found in the sample.

Needle- or thread-like inclusions of the metallized phase (Fig. 2b) are untypical of copper–nickel converter mattes cooled in equilibrium or nearly equilibrium mode. Introduction of an additional impurity even in amount of 0.1% can strongly affect the composition and shape of crystals growing from the melt. According to Saratovkin [3], if even at least a single atom of an impurity substance is present at a distance of 1000 interatomic spacings from the face of a growing crystal and the lattice constant is about 5 Å, then, when the face moves over a distance of 0.5 μm, it encounters a monomolecular layer of the impurity component, which hinders further crystal growth. The blocking layer can be removed via convection or diffusion. As is known, convection only exists in

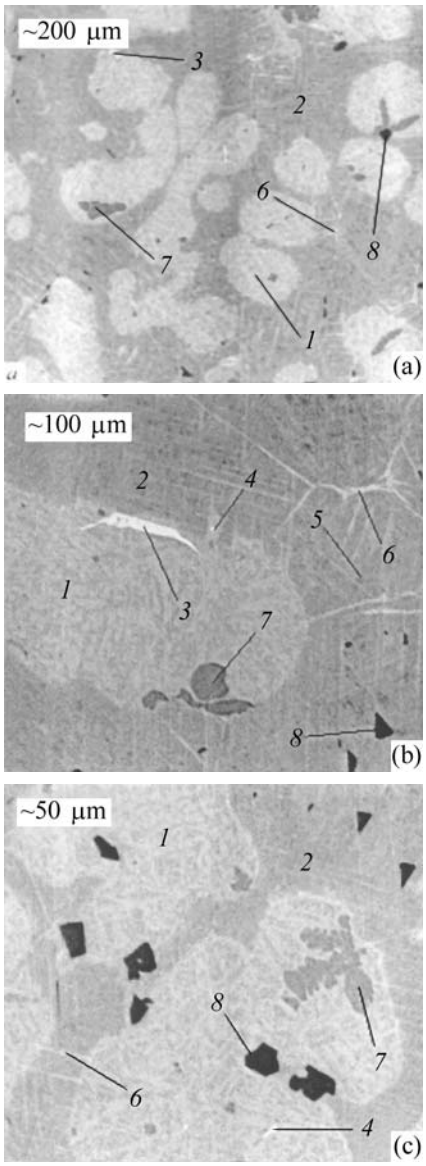

Fig. 2. Structure of a converter matte sample containing 0.5 wt % microimpurities. (a) General view; (b, c) structures formed in decomposition of a heazlewoodite solid solution and precipitation of metallic copper, lead and zinc sulfides, and oxide phase. (*1*) Chalcosine–bornite solid solution, (*2*) heazlewoodite solid solution, (*3*) metallic copper, (*4*) copper–silver metallic phase, (*5*) monosulfide solid solution (M_{SS}), (*6*) metallic component, (*7*) lead sulfide, and (*8*) oxide phase.

the case when different layers in the system under study have different densities, and at sufficiently slow cooling of the converter matte, the convection flows are insignificant.

Now, diffusion is considered for the case when the impurity component does not form a solid solution with the substance of the growing crystal. As a rule, the diffusion rate is insignificant as compared with the crystal growth rate, and the crystal can only grow so as to move over the maximum possible distance at the minimum possible expenditure of the building material in the direction where this material is available. The crystal starts to form thin outgrowths and takes a thread- or needle-like shape.

If an impurity is a surfactant with respect to a crystal growing from solution or forms a solid solution with the substance of the crystal, then a change in surface tension at the solution–crystal interface necessarily affects the type of the crystal growth mechanism and the kinetics of crystal growth. This also refers to the case when a crystal of a new phase is formed from a solid solution in, e.g., an eutectoid transformation.

The compositions of all the structural constituents of the samples are listed in the table. In crystallization of converter mattes under nearly equilibrium conditions, the eutectoid decomposition of the high-temperature form of nickel sulfide in the presence of iron and cobalt is complete at 470–480°C. The product formed in this stage of decomposition is (Fe, Ni, Co)S_{SS}, which contains, in accordance with the crystallization rules [4, 5], the main part of "unassimilated" impurity elements (see table).

Analysis of the data in the table shows that none of the structural constituents contains lead, and zinc is distributed among zinc sulfide, oxide phase, metallic copper, and chalcosine–bornite solid solution. Zinc sulfide, which contains virtually no copper, can be formed both in direct sulfidization of metallic zinc introduced into the matte, with the zinc sulfide phase remaining heterogeneous (mp > 1600°C), and on lowering the melt temperature. Arsenic is associated with nickel phases: heazlewoodite solid solution, monosulfide solid solution, and metallized phase from the structure formed in decomposition of nickel sulfide. Antimony and tin are also associated with nickel phases, with the main part of these impurities contained in the metallized component formed in decomposition of the heazlewoodite solid solution. The oxide phase is, in all probability, formed in the course of remelting, since it contains considerable amounts of zinc and tin impurities. The absence of zinc in a sample that is richer in microimpurities can be accounted for by the ingress of particles from the upper part of the ingot into the sample. This conclusion is also confirmed by the presence in the composition of the given sample of iron oxide particles, which can only be formed on the ingot surface. By contrast, the sample with microimpurity content of 0.1% contains particles from the lower part of the ingot, which is enriched in the lead phase.

Composition of structural constituents of converter matte samples with varied impurity content

Impurity content, wt %	Structural constituent of converter matte	Composition, wt %										
		S	Fe	Co	Ni	Cu	Zn	As	Ag	Sn	Sb	Pb
0.1	Converter matte*	22.7	2.9	0.7	40.0	31.3	0.3	0.1	–	0.1	0.2	0.1
	$(Cc–Bn)_{SS}$	21.5	4.7	–	1.9	69.4	0.8	–	–	–	–	–
	Hz_{SS}	26.2	0.7	1.3	70.7	1.3	–	–	–	–	–	–
	Metal (eutectic)	8.5	9.6	1.4	62.6	13.2	–	Up to 0.5	–	Up to 4.6	0.9	–
	Metal (crystal)	1.4	9.5	1.4	79.9	7.6	–	–	–	–	–	–
	Eutectoid*	25.2	4.6	1.6	65.5	2.3	–	–	–	0.3	0.3	–
	M_{SS}	29.9	25.6	5.6	35.8	1.0	–	Up to 0.4	Up to 0.2	Up to 0.4	Up to 0.4	–
	Metallic Cu	0.4	0.7	Up to 0.3	2.0	95.7	0.9	–	0.8	–	–	–
	Zinc sulfide	27.6	5.0	0.4	0.3	21.7	42.7	–	–	–	–	–
0.5	Converter matte*	21.9	2.9	0.8	39.8	30.1	0.8	0.4	–	0.6	0.7	0.1
	$(Cc–Bn)_{SS}$	20.7	4.0	–	0.9	70.9	0.8	–	–	–	–	–
	Hz_{SS}	23.9	0.6	1.1	69.5	1.9	–	0.6	–	0.6	0.7	–
	M_{SS}	28.0	22.6	4.8	39.0	0.9	–	1.1	–	0.5	1.0	–
	Metallized phase	14.9	2.5	0.9	54.3	11.0	–	0.7	–	10.0	3.6	–
	Metallic Cu	–	0.6	–	0.4	95.3	0.8	–	Up to 1.1	–	–	–
	Zinc sulfide	31.1	1.7	0.3	1.0	1.9	64.0	–	–	–	–	–
	Oxide phase**	–	54.7	0.5	3.6	1.6	10.3	–	–	2.1	–	–

* Average value.

** Oxygen content 28–29 wt %.

Thus, a study of the microstructure of the converter matte samples revealed that, at the content used in the experiments, antimony, tin, and arsenic form no independent phases and are virtually entirely concentrated in the nickel-containing phase of the converter matte. Zinc is present in the chalcosine–bornite solid solution as an independent sulfide phase within the copper-containing phase. Lead is sulfidized to form an independent phase at the boundary of chalcosine–bornite globules.

It would be expected that, in flotation separation of the converter matte from the Pechenganikel' combine, arsenic, antimony, and tin must mostly pass into the nickel concentrate, and zinc, into the copper concentrate, with the question as to how lead is distributed remaining open, since the behavior of zinc depends to the greatest extent on the flotation process parameters.

REFERENCES

1. Miroevskii, G.P., Koklyanov, E.B., Ermakov, I.G., *et al., Tsvet. Met.*, 2001, no. 2, pp. 51–55.
2. Miroevskii, G.P., Golov, A.N., Ertseva, L.N., *et al., Tsvet. Met.*, 2001, no. 2, pp. 30–35.
3. Saratovkin, D.D., *Dendritnaya kristallizatsiya* (Dendritic Crystallization), Moscow: Metallurgizdat, 1953.
4. Flemings, M., *Protsessy zatverdevaniya* (Hardening Processes), Moscow: Mir, 1977.
5. Pfann, W.J., *Zonnaya plavka* (Zone Melting), Moscow: Metallurgizdat, 1960.

Russian Journal of Applied Chemistry, Vol. 76, No. 6, 2003, pp. 888–891. Translated from Zhurnal Prikladnoi Khimii, Vol. 76, No. 6, 2003, pp. 918–921.

PHYSICOCHEMICAL STUDIES OF SYSTEMS AND PROCESSES

Effect of Method Used for Synthesis of Silica Sols on Pore Characteristics of Silica Gels on Their Base

S. S. Airapetyan and A. G. Khachatryan

Yerevan State University, Yerevan, Armenia

Received December 3, 2002; in final form, May 2003

Abstract—Problems associated with synthesis of silica gels with prescribed pore characteristics from stabilized silica sols with controlled colloid particle size, obtained in the metastable solubility region of the system SiO_2–H_2O (8.5–9.5), are considered.

Conventionally, silica gels are synthesized from alkali metal silicates by precipitation with an acid [1–5]. The silica gels prepared using this technique have a number of disadvantages: poor reproducibility of pore characteristics, impossibility to control growth of primary structure-forming colloid particles in the course of gelation, necessity for removal of a considerable amount of alkali metal cations, etc.

Strict requirements (narrow pore size distribution, reproducible pore characteristics, high mechanical strength, etc.) are imposed on sorbents and supports for high-efficiency liquid chromatography. However, silica gels prepared from soluble silicates cannot satisfy these requirements completely.

Directed synthesis of sorbents with prescribed pore characteristics has always been and still is a topical task. Therefore, a search for methods that could solve the problem of control and reproducibility of pore characteristics is an important issue.

A possible way to control the porous structure of silica gels is to use sols of silicic acid as starting material [1, 6–8]. The size distribution of colloid particles of a silica sol determines, in the end, the pore size distribution (in gelation without precipitation), and the size of particles themselves determine the specific surface area of the silica gels obtained.

There exist various methods for obtaining silica sols [9–17]. These methods use polysilicic acid (PSA) prepared by ion-exchange conversion of a liquid glass solution (3.5–4.0 wt % SiO_2, SiO_2/Na_2O = 3.25) as starting material [9].

To gain better understanding of how SiO_2 colloid particles grow in the SiO_2–H_2O system, it is necessary to consider some questions associated with nucleation of a new phase. A silica solution is subjected to homogeneous nucleation. At high pH values, associates of silicate ions, which contain up to 5–10 SiO_2 units, are mostly present in silicate solutions. For silica, there exists a certain possibility of formation of a dense octameric structure, which can form colloid particles about 1 nm in size. As the $SiO_2 : M_2O$ ratio becomes greater than 2 : 1, three-dimensional corpuscular "colloid species" start to form in solution, which eventually become nuclei [1].

It has been shown that nucleation of a new phase in early stages of polycondensation, with the number and size of nuclei depending on the initial supersaturation in the system, results in that, further, this process starts to occur by the heterogeneous mechanism [18, 19].

Nucleation occurs in the SiO_2–H_2O system at low supersaturation values. The equilibrium solubility of silica in water at room temperature is 0.007 wt % (in terms of SiO_2) [1]. Consequently, to ensure growth of colloid particles of silicon dioxide, it is necessary to clearly delineate the metastable solubility region in the SiO_2–H_2O system. Particles grow in the metastable state, and both the particle growth and nucleation occur at high degree of supersaturation [20–22].

The polysilicate fraction is characterized by narrow polyion size distribution, which is due to the fact that small particles are more soluble than large particles. This leads to fast change in particle size distribution, to the point of total homogeneity [1].

Nucleation and further growth of colloid SiO_2 particles at high pH values make it possible to work with more concentrated solutions, easily control the metastable region by varying the pH of the medium (which

1070-4272/03/7606-0888 $25.00 © 2003 MAIK "Nauka/Interperiodica"

yields colloid particles more uniform in size), and suppress secondary nucleation.

When SiO_2 particles grow without formation of secondary growth centers, the supply rate of feeding sol becomes important. In this case, the particle surface on which further growth proceeds without secondary nucleation, becomes the rate-determining factor [15].

EXPERIMENTAL

SiO_2 colloid particles grow upon addition of freshly prepared PSA (3–4 wt % SiO_2) to the starting alkali solution under stirring. The process is carried out in a vacuum-evaporation installation at boiling temperature of 80–85°C [16, 17]. The acid is introduced at a rate equal to the evaporation rate of the system in such a way that the volume of the system remains invariable during the entire growth stage.

Figure 1a shows the pH value of the system as a function of the PSA feed factor in sol synthesis by the first scheme. In this case, the volume of the initial solution was 50% of the total PSA volume. As growth criterion served the final pH value, which must not be lower than 6.5 to preclude gelation of the system.

Figure 1b shows the pH value of the system as a function of the PSA feed factor in sol synthesis by the second scheme. In this case, the volume of the initial solution was 25% of the total PSA volume. According to this scheme, the pH of the medium in which colloid particles grow is well-controlled by periodic addition of a 0.1 M NaOH solution. Four growth modes were studied, with the lower limit of the pH of the growth medium controlled: (1) pH 8.0, (2) pH 8.5, (3) pH 9.0, and (4) pH 9.25.

All silica sol samples were gelated by addition of a 0.1 M HNO_3 solution to pH 6.0–6.2. After aging of the samples obtained, they were washed with distilled water, dried at 150°C for 2 h, and calcined at 500°C for 4 h.

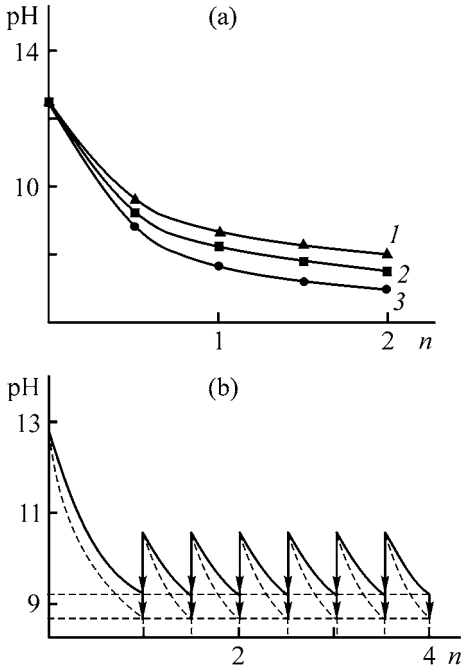

Fig. 1. pH of the system vs. PSA feed factor n. SiO_2 sol obtained by (a) first and (b) second scheme. (a) *Digits at curves* correspond to sample numbers in the table.

The size of colloid particles of the silica gels was determined by titration by the Searce method [1]. The pore characteristics of silica gel samples were determined by the methods of thermal desorption (TD) [23, 24], benzene sorption [25], and mercury porosimetry (MP) (on Pore-Sizer 9300 porosimeter).

All the reagents used (NaOH, HNO_3, HCl, NaCl) were of chemically pure grade.

The table lists colloid particle sizes of silica sols synthesized by the first scheme (Fig. 1a) at dif-

Characteristics of silica sols and silica gels

Sample no.	S_{sp}, $m^2 g^{-1}$				Average size of silica sol particles, nm	Pore volume, $cm^3 g^{-1}$	Average pore diameter in silica gel, nm	pH_{fin}
	TD	MP	Searce	$S_{sp.av}$				
First scheme of synthesis								
1	380	390	430	385	6.0	0.60	6.2	7.0
2	360	370	400	375	7.0	0.57	6.1	7.4
3	330	340	360	340	8.0	0.55	6.5	7.8
Second scheme of synthesis								
4	275	252	260	262	10.6	0.60	9.0	8.0
5	248	220	235	234	11.7	0.58	10.0	8.5
6	192	201	195	196	10.6	0.56	12.0	9.0

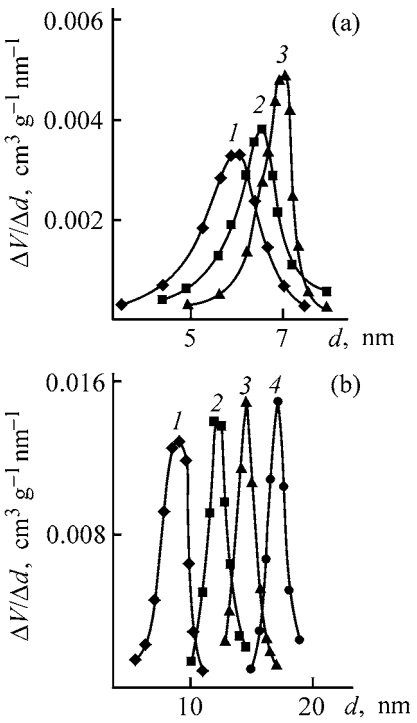

Fig. 2. Pore size (d) distribution for silica gels obtained from silica sols by (a) first and (b) second schemes. Final pH value: (a) (*1*) 6.8, (*2*) 7.2, and (*3*) 7.8; (b) (*1*) 8.0, (*2*) 8.5, (*3*) 9.0, and (*4*) 9.25.

ferent final pH values, and also pore characteristics of silica gels obtained on their base.

Figure 2a shows the pore size distributions of the silica gels studied. It can be seen that, in the case when SiO_2 colloid particles cease to grow at comparatively high pH values of 7.8, the silica gel obtained from such a silica sol possesses a narrower pore size distribution (curve *3*). At lower pH values (6.8 and 7.2), mainly secondary nucleation occurs, with the result that the pore size distribution for silica gels prepared from such silica sols becomes broader (curves *1*, *2*). It follows from the table and Fig. 2a that silica sols with colloid particles not larger than 8 nm in size can be obtained. Synthesis of silica sols with larger colloid particles by this scheme becomes impossible, since part of PSA is to be added to the system outside the metastability region (pH < 8.0), which leads to polydispersity of the system owing to formation of new growth centers.

Figure 2b shows the pore size distribution for silica gels obtained from silica sols synthesized by the second scheme. The table lists sizes of colloid particles of these silica sols obtained at different pH values and pore characteristics of silica gels synthesized on their base.

Raising substantially the pH of the medium at regular intervals (Fig. 1b) not only prevents formation of secondary growth centers, but also leads to dissolution of minute nuclei formed via fluctuation aggregation. The comparatively high pH values of the medium (> 8.5) favor predominant growth of the already existing nuclei without formation of new growth centers. This makes it possible to obtain silica sols with prescribed particle size.

It follows from Fig. 2b and the table that silica gels with rather narrow pore size distribution can be obtained from these silica sols. It should also be noted that this method of silica sol preparation allows growth of SiO_2 colloid particles to 15 nm and more.

CONCLUSIONS

(1) The most favorable conditions for growth of SiO_2 colloid particles without secondary nucleation are created at pH 8.5–9.5.

(2) Silica sols with prescribed particle size can be obtained and silica gels with reproducible pore characteristics can be synthesized on their base.

REFERENCES

1. Iler, R.K., *The Chemistry of Silica*, New York: Wiley–Interscience, 1979.
2. Roland, E.M., *LC–GC International*, 1998, April, pp. 7–21.
3. Titulaer, M.K., Exter, M.J., Talsma, H., *et al., J. Non-Cryst. Solids*, 1994, vol. 170, pp. 113–127.
4. Neimark, I.E., *Sinteticheskie mineral'nye adsorbenty i nositeli katalizatorov* (Synthetic Mineral Adsorbents and Catalyst Supports), Kiev: Naukova Dumka, 1982.
5. *Physical and Chemical Aspects of Adsorbents and Catalysts*, Linsen, B. G., Ed., London: Academic, 1970.
6. Dobruskin, V.Kh., Belotserkovskii, G.M., and Plachenov, T.G., *Zh. Prikl. Khim.*, 1967, vol. 40, no. 11, pp. 2443–2451.
7. Belotserkovskii, G.M., Dobruskin V.Kh., and Plachenov, T.G., *Zh. Prikl. Khim.*, 1971, vol. 44, no. 6, pp. 1380–1388.
8. Shabanova, N.A. and Trukhanova, N.V., *Kolloid. Zh.*, 1989, vol. 51, no. 6, pp. 1157–1163.
9. US Patent 2 244 325.
10. US Patent 2 574 902.
11. US Patent 3 789 009.
12. Australian Patent 418 170.
13. US Patent 3 374 180.
14. US Patent 3 440 175.
15. US Patent 3 538 015.

16. USSR Inventor's Certificate, no. 1 174 376.
17. USSR Inventor's Certificate, no. 1 258 017.
18. Frolov, Yu.G., Shabanova, N.A., and Popov, V.V., *Kolloid. Zh.*, 1983, vol. 45, no. 1, pp. 179–182.
19. Frolov, Yu.G., Shabanova, N.A., and Popov, V.V., *Kolloid. Zh.*, 1983, vol. 45, no. 2, pp. 382–386.
20. Nyvlt, J., *Krystalizacia z roztokov*, Bratislava: Slov. vydavat. techn. literatury, 1967.
21. Laudise, R.A., *The Growth of Single Crystals*, Englewood Cliffs, New Jersy: Prentice Hall, 1970; Parker, R.L., *Crystal Growth Mechanisms: Energetics, Kinetics and Transport,* New York: Academic, 1970. Translated under the title Lodiz, R. and Parker, R., *Rost kristallov*, Moscow: Mir, 1974.
22. Flemings, M.C., *Solidification Processing*, New York: McGraw–Hill, 1974.
23. Kiselev, A.F. and Yashin, N.A., *Gazoadsorbtsionnaya khromatografiya* (Gas-Adsorption Chromatography), Moscow: Nauka, 1967.
24. Karnaukhov, A.L. and Buyanov, M.E., *Fiziko-khimicheskoe primenenie gazovoi khromatografii* (Physicochemical Applications of Gas Chromatography), Moscow: Khimiya, 1973.
25. Galimov, Zh.B., Dubinina, G.K., and Masagurov, R.N., *Metody analiza katalizatorov neftepererabotki* (Methods for Analysis of Catalysts for Oil Processing), Moscow: Khimiya, 1973.

Russian Journal of Applied Chemistry, Vol. 76, No. 6, 2003, pp. 892–895. Translated from Zhurnal Prikladnoi Khimii, Vol. 76, No. 6, 2003, pp. 922–925.

SORPTION AND ION-EXCHANGE PROCESSES

Thermodynamic Study of Iron(III) Sorption on Clay

D. E. Chirkst, T. E. Litvinova, O. V. Cheremisina, M. V. Ivanov, and N. A. Mironenkova

St. Petersburg State Mining Institute, St. Petersburg, Russia

Received April 8, 2002; in final form, January 2003

Abstract—Sorption of Fe(III) cations on Cambrian blue clay is discussed in term of the Langmuir isotherm. The thermodynamic characteristics of sorption were determined. The Gibbs energies of formation of sorbed Fe(III) aqua and hydroxo cations were calculated. The role of hydroxo complexes in sorption was considered.

Earlier, we proposed a method for deactivation of soils by washing with iron(III) salt solutions [1]. The Fe^{3+} cation has high charge and relatively small radius. Owing to the high ionic potential (z/r), iron(III) replaces other cations, including ^{137}Cs and ^{90}Sr radionuclides, in ion-exchange reactions on the mineral surface. A process was developed for decontamination of soil to remove ^{90}Sr under natural conditions [2, 3], but comprehensive physicochemical data are required for its optimization. It was shown in [4] that ^{90}Sr is fixed mainly by the clay. In this study, we analyzed sorption of Fe^{3+} on Cambrian blue clay $K_2Al_4[Al_2Si_6O_{20}](OH, F)_4$ with specific surface area of 5.86 $m^2\ g^{-1}$ [5]. A thermal analysis showed that this clay belongs to the hydromicaceous type.

The sorption Γ (mol kg^{-1}) was determined under static conditions at V/m 10 ml g^{-1} and clay sample weight of 3 g as the difference between the concentrations of the initial (c_0) and equilibrium (c_∞) solutions by the formula $\Gamma = (c_0 - c_\infty)V/m$. Initially, the clay was treated with 1 M HCl, washed with water to pH 3, and dried to air-dry state. A solution of $FeCl_3$ was also acidified to pH 3. The time of equilibrium attainment, in which the iron(III) concentration in the solution became constant, amounted to 5–6 h; in the experiments the time of phase contact was no less than 1 day. The iron(III) content was determined from the intensity of the absorption band of the thiocyanate complex at 480 nm. The sorption isotherm obtained from the experimental data listed in Table 1 is shown in Fig. 1. The distribution coefficient of iron(III) between the solid and liquid phases was calculated by the formula

$$D_{s/l} = \frac{(c_0 - c_\infty)Vd}{c_\infty m \gamma_{Fe^{3+}}},$$

where c_0 and the c_∞ are initial and equilibrium Fe^{3+} concentrations in the aqueous phase, respectively (M); V, solution volume (m^3); d, solution density (kg m^{-3}); m, clay sample weight (kg); and $\gamma_{Fe^{3+}}$, Fe^{3+} activity coefficient in the equilibrium solution calculated by the Davies equation [6].

It follows from Table 1 that the Fe^{3+} distribution coefficient at equilibrium pH 3.1 ± 0.3 is 27 ± 4. The sorption isotherm can be described by the Langmuir equation, as indicated by the linear relationship between reciprocal sorption and reciprocal concentration in accordance with equation

$$\frac{1}{\Gamma} = \frac{1}{\Gamma_\infty} + \frac{1}{\Gamma_\infty K}\frac{1}{c_\infty},$$

where Γ_∞ is the limiting sorption (mol kg^{-1}) and K is the Langmuir constant.

The absolute term of the equation is equal to inverse limiting sorption, 0.026 mol kg^{-1} for Fe^{3+}, which is consistent with Γ_∞ in the sorption isotherm.

Table 1. Data for building the iron(III) sorption isotherm on clay

$c_0 \times 10^4$, M	pH_{eq}	$c_\infty \times 10^4$, M	$\Gamma \times 10^4$, mol kg^{-1}	$D_{s/l}$	$\gamma_{Fe^{3+}}$
1.54	3.42	1.28	2.6	2.8	0.73
4.78	3.34	1.84	29.4	27.5	0.58
6.4	3.44	2.38	40.2	31.3	0.54
6.7	3.35	2.53	41.7	31.1	0.53
14.6	3.14	5.24	93.6	43.6	0.41
28.3	2.85	16.9	114	22.5	0.30
43	2.72	27.9	151	23.5	0.23
55	2.62	35.5	195	27.4	0.20
61.4	2.56	46.1	153	18.5	0.18

1070-4272/03/7606-0892 $25.00 © 2003 MAIK "Nauka/Interperiodica"

The landing site area of Fe^{3+}, calculated by the formula

$$S_M = \frac{S_{sp}}{\Gamma_\infty N_A},$$

where N_A is the Avogadro number, is equal to 38×10^{-20} m^2. Hence, the radius of the sorbed iron(III) cation is 348 pm. This value should be regarded as the average effective radius of sorbed $Fe^{3+} \cdot nH_2O$, $Fe(OH)^{2+} \cdot mH_2O$, and $Fe(OH)_2^+ \cdot qH_2O$ cations, which is greater than that for Sr_{aq}^{2+} 302 pm [4] (309 pm by Stokes), since the ionic potential and, correspondingly, the degree of hydration of iron(III) cations are higher.

The Langmuir constant K was determined from the slope of the linear dependence in Fig. 2 to be 731.

The distribution coefficient and K found by us, describe the set of the following equilibria:

$$Fe_{aq}^{3+} \rightleftarrows Fe_{ads}^{3+}, \quad (1)$$

$$Fe(OH)_{aq}^{2+} \rightleftarrows Fe(OH)_{ads}^{2+}, \quad (2)$$

$$Fe(OH)_{2\ aq}^{+} \rightleftarrows Fe(OH)_{2\ ads}^{+}. \quad (3)$$

Here, account is taken of the main iron(III) species (with known thermodynamic parameters) existing in the solution at pH 3.1. The sorption of polymeric iron(III) species was neglected. Sorption of iron(III) in the above approximation is described by Eqs. (1)–(3) with coefficients m, n, and p:

$$\frac{n}{m} = \frac{[Fe(OH)^{2+}]}{[Fe^{3+}]} = \frac{K_{h,1}}{[H^+]}, \quad (4)$$

$$\frac{p}{m} = \frac{[Fe(OH)_2^+]}{[Fe(OH)^{2+}]} = \frac{K_{h,2}}{[H^+]}, \quad (5)$$

$$m + n + p = 1. \quad (6)$$

The hydrolysis constants of iron(III) cations are $K_{h,1} = 6.74 \times 10^{-3}$ and $K_{h,2} = 3.09 \times 10^{-3}$ [7]. The concentration of hydroxonium cations was determined from the experimental pH value of 3.1. Then, $m = 0.024$, $n = 0.20$, and $p = 0.776$. The overall equation of iron sorption is as follows:

$$0.024Fe_{aq}^{3+} + 0.2Fe(OH)_{aq}^{2+} + 0.776Fe(OH)_{2\ aq}^{+}$$
$$\rightleftarrows 0.024Fe_{ads}^{3+} + 0.2Fe(OH)_{ads}^{2+} + 0.776Fe(OH)_{2\ ads}^{+}. \quad (7)$$

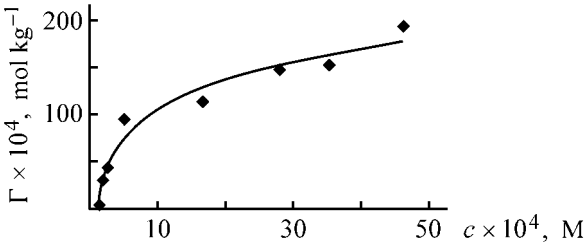

Fig. 1. Isotherm of Fe(III) sorption on Cambrian blue clay: (Γ) sorption and (c) iron(III) concentration; the same for Fig 2.

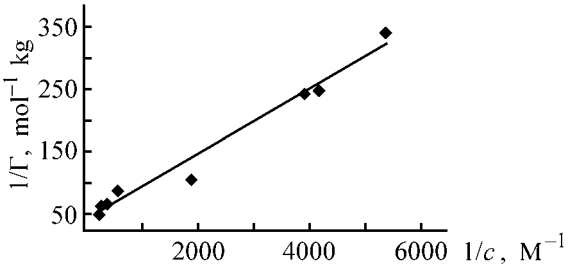

Fig. 2. Linearized form of the isotherm of iron(III) adsorption on clay.

The Gibbs energy of reaction (7) was determined from the overall distribution coefficient

$$\Delta_7 G_{298}^0 = -RT \ln D_{s/l} = -8.2 \pm 0.3 \text{ kJ mol}^{-1}.$$

Let us calculate the equilibrium constants of equilibria (1)–(3):

$$\Delta_7 G_{298}^0 = m\Delta_1 G_{298}^0 + n\Delta_2 G_{298}^0 + p\Delta_3 G_{298}^0. \quad (8)$$

Hence,

$$D = D_1^m D_2^n D_3^p, \quad (9)$$

where D is the experimental overall distribution coefficient of iron(III) and D_n are partial distribution coefficients of particular iron species among reactions (1)–(3), equal to

$$D_1 = \frac{[Fe_{ads}^{3+}]}{[Fe_{aq}^{3+}]}, \quad (10)$$

$$D_2 = \frac{[Fe(OH)_{ads}^{2+}]}{[Fe(OH)_{aq}^{2+}]}, \quad (11)$$

$$D_3 = \frac{[Fe(OH)_{2\ ads}^{+}]}{[Fe(OH)_{2\ aq}^{+}]}, \quad (12)$$

$$D = \frac{[Fe(OH)_{ads}^{2+}] + [Fe(OH)_{2\ ads}^{+}]}{c}. \quad (13)$$

Table 2. Thermodynamic characteristics of sorption of iron(III) cations on clay

Reaction	$\Delta_f G^0_{298}(Cat^{z+}_{aq})$ [7]	$\Delta_f G^0_{298}(Cat^{z+}_{ads})$	$\Delta_f G^0_{298}$	K_{eq}
	kJ mol^{-1}			
$Fe^{3+}_{aq} \rightleftarrows Fe^{3+}_{ads}$	–4.52	–22.1	–17.6	1200
$Fe(OH)^{2+}_{aq} \rightleftarrows Fe(OH)^{2+}_{ads}$	–229.37	–239.6	–10.2	60
$Fe(OH)^{+}_{2\ aq} \rightleftarrows Fe(OH)^{+}_{2\ ads}$	–452.29	–459.7	–7.4	20
$Sr^{2+}_{aq} \rightleftarrows Sr^{2+}_{ads}$ [4]	–563.9	–569.6	–5.7	10

In (13), the contribution of Fe^{3+} to the sorption was neglected because of its small concentration. The solution of system (9)–(13) gives D_2 and D_3:

$$D_3 = \frac{Dc - [Fe(OH)^{2+}_{ads}]}{[Fe(OH)^{+}_{2\ aq}]} = \frac{Dc - K_2[Fe(OH)^{2+}_{aq}]}{[Fe(OH)^{+}_{2\ aq}]}. \quad (14)$$

Substituting in (14) $D = 27$, $[Fe(OH)^{+}_{2\ aq}] = 0.2c$, and $[Fe(OH)^{2+}_{aq}] = 0.776c$ and assuming the exchange constant of various iron(III) species to be approximately unity (in this case, $D_1 \approx D_2^{1.5}$, $D_2 \approx D_3^2$, and $D_1 \approx D_2D_3$), we obtain $D_1 = 1200$, $D_2 = 60$, and $D_3 = 20$. Hence, $\Delta_1G^0_{298} = -17.6$, $\Delta_2G^0_{298} = -10.2$, and $\Delta_3G^0_{298} = -7.4$ kJ mol^{-1}. The thermodynamic characteristics of reactions (1)–(3) allow calculation of the Gibbs energies of formation of sorbed iron(III) cations and of the sorption equilibria (Table 2).

Consider the thermodynamics of ion exchange of iron(III) and strontium(II) cations on the clay surface. In this case, three exchange reactions proceed simultaneously:

$$1/3Fe^{3+}_{aq} + 1/2Sr^{2+}_{ads} \rightleftarrows 1/3Fe^{3+}_{ads} + 1/2Sr^{2+}_{aq},$$
$$\Delta_{15}G^0_{298} = -3.02 \text{ kJ equiv}^{-1},\ K_{15} = 3.4, \quad (15)$$

$$1/2Fe(OH)^{2+}_{aq} + 1/2Sr^{2+}_{ads} \rightleftarrows 1/2Fe(OH)^{2+}_{ads} + 1/2Sr^{2+}_{aq},$$
$$\Delta_{16}G^0_{298} = -2.25 \text{ kJ equiv}^{-1},\ K_{16} = 2.5, \quad (16)$$

$$Fe(OH)^{+}_{2\ aq} + 1/2Sr^{2+}_{ads} \rightleftarrows 1/2Fe(OH)^{+}_{2\ ads} + 1/2Sr^{2+}_{aq},$$
$$\Delta_{17}G^0_{298} = -4.55 \text{ kJ equiv}^{-1},\ K_{17} = 6.3. \quad (17)$$

The Gibbs energy of the overall reaction of iron(III) ion-exchange with strontium can be calculated by the equation

$$\Delta_\Sigma G^0_{298} = 0.072\Delta_{15}G^0_{298} + 0.4\Delta_{16}G^0_{298} + 0.776\Delta_{17}G^0_{298} = -4.65 \text{ kJ mol}^{-1}.$$

Then, the overall constant of the ion exchange equilibrium is 6.5. Hence, we can conclude that Sr^{2+} cations pass into the solution when washing soil with an iron(III) salt solution. The constants obtained can be used for calculating the volume of washing solution and the number of washing cycles required for achieving the necessary degree of soil deactivation [2, 3].

The average dynamic charge of iron(III) cations in the ion-exchange reaction with strontium cations on the clay surface was calculated by the method of Gamayunov *et al.* [8] by the formula

$$K_{ex} = \frac{\sqrt[z]{D_{Fe}}}{\sqrt{D_{Sr}}}.$$

After substitution in Eq.(1) of $K_{ex} = 6.5$, $D_{Sr} = 10$, and $D_{Fe} = 27$, we obtained $z = 1.1$. In [8], $z = 0.72$–0.98 was obtained for Fe(III) sorption by humic acids. The z value calculated in the present study is somewhat greater, which can be accounted for by acidification of the solution to pH 3 and clay transformation into the H form.

CONCLUSIONS

(1) Sorption of iron(III) by Cambrian blue clay is described by a Langmuir isotherm with a constant of 731. The maximum sorption is 0.026 mol kg^{-1}. The landing site area of iron(III) cations is 38.0 Å, and the effective radius of the hydrated cation is 348 pm. The distribution coefficient of iron(III) between the solid and liquid phases at equilibrium pH 3.1 ± 0.3 is 27 ± 4.

(2) The constant of strontium(II) substitution with iron(III) on the clay surface is 6.5. This shows that ^{90}Sr can be displaced from contaminated soils by washing with iron(III) salt solutions.

ACKNOWLEDGMENTS

The study was performed in the framework of Scientific and Technical program of the RF Ministry of Education "Scientific Investigations at Higher School in Priority Directions of Science and Engineering," subprogram 207 "Ecology and Rational Nature Management."

REFERENCES

1. RF Patent 2 050 029.
2. Dibrov, I.A., Chirkst, D.E., Chaliyan, K.N., and Streletskaya, M.I., *Radiokhimiya*, 2000, vol. 42, no. 3, pp. 273–276.
3. Chirkst, D.E., Litvinova, T.E., Cheremisina, O.V., and Streletskaya, M.I., *Radiokhimiya*, 2001, vol. 43, no. 5, pp. 475–478.
4. Chirkst, D.E., Litvinova, T.E., Cheremisina, O.V., *et al.*, *Zh. Prikl. Khim.*, 2003, vol. 76, no. 6, pp. 755–758.
5. Chirkst, D.E., Krasotkin, I.S., Litvinova, T.E., *et al.*, *Zh. Prikl. Khim.*, 2003, vol. 76, no. 4, pp. 687–689.
6. Vasil'ev, V.P., *Termodinamicheskie svoistva rastvorov elektrolitov* (Thermodynamic Properties of Electrolyte Solutions), Moscow: Vysshaya Shkola, 1982.
7. *Termicheskie konstanty veshchestv: Spravochnik* (Thermal Constants of Substances: Handbook), Glushko, V.P., Ed., Moskow: Akad. Nauk SSSR, 1973, vol. 6.
8. Gamayunov, N.I. and Maslennikov, B.I., *Pochvovedenie*, 1992, no. 3, pp. 146–151.

Russian Journal of Applied Chemistry, Vol. 76, No. 6, 2003, pp. 896–900. Translated from Zhurnal Prikladnoi Khimii, Vol. 76, No. 6, 2003, pp. 926–930.

SORPTION AND ION-EXCHANGE PROCESSES

Sorption of Methylene Blue Dye by Activated Carbon Fibers

O. Yu. Mukhina, I. A. Piskunova, and A. A. Lysenko

St. Petersburg State University of Technology and Design, St. Petersburg, Russia

Received March 15, 2002; in final form, February 2003

Abstract—The sorption of Methylene Blue on carbon fibers with various pore structures was studied. The dye sorption was analyzed as influenced by the initial concentration, temperature, time, and solution pH.

Activated carbons and carbon fibers are widely used as sorbents for purification of wastewaters and for fine treatment of drinking water [1, 2]. The sorption volume and pore size distribution primarily determine the adsorption capacity of carbon materials. Microporous materials effectively sorb small molecules, whereas mesoporous materials are the most efficient in sorption of large molecules, especially from liquid media. Moreover, the size, shape, charge, and concentration of sorbate species, solution pH, concentration of other compounds in solution, and the protonation of the ionic groups on the sorbent surface (if present) and its surface charge should be taken into account in studying sorption processes. In many cases, sorption is influenced by temperature and flow velocity of the solution from which the sorption is performed [3].

Although the sorption of dyes and, in particular, Methylene Blue (MB) on activated carbons has been long studied, the mechanisms of diffusion and retention of such large organic molecules in the sorbent structure are still poorly understood [4–6]. It should be noted that the experimental dependences of the dye adsorption would allow prediction of the adsorption behavior of other large organic molecules, such as pesticides, organochlorine compounds, humic acids, and proteins [7–9].

The practical goal of the study was to determine (for the example of Methylene Blue) the feasibility and rate of rendering harmless wastewaters containing dyes [4–6, 10].

EXPERIMENTAL

In our study we used activated carbon fibers (ACFs) prepared by carbonization of hydrated cellulose fibers at 700°C with subsequent steam activation of the carbonized products at 800°C. The resulting fibers have different sorption volumes and pore structures; the ACF properties are listed in Table 1.

To study the pore structure of the samples, we measured the isotherms of benzene sorption–desorption. The pH of the aqueous extract was determined after keeping the ACF sample in distilled water at room temperature (ACF : H_2O ratio 1 : 200) for 1 day in a sealed vessel; then the fiber was separated and the solution pH was determined.

Methylene Blue was used in the form of quaternary ammonium chloride; its structure is given below:

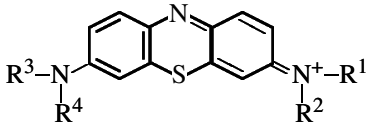

$R^1 = R^2 = R^3 = R^4 = CH_3$.

The molecular weight of the dye is 284 (without hydrochloric acid), and the molecular size, 14.3 ×

Table 1. Properties of activated carbon filers

Parameter	ACF-1	ACF-2	ACF-3
Sorption volume for benzene, $cm^3\ g^{-1}$	0.28	0.50	0.63
Volume of micropores, $cm^3\ g^{-1}$	0.27	0.39	0.48
Volume of mesopores, $cm^3\ g^{-1}$	0.01	0.11	0.15
Sorption activity for iodine, % [2, 11]	104	118	149
pH of aqueous extract	9.1	7.4	7.0

1070-4272/03/7606-0896 $25.00 © 2003 MAIK "Nauka/Interperiodica"

Table 2. Parameters of MB sorption on ACF

Initial solution		Parameter	Sorbent		
c, mM	pH		ACF-1	ACF-2	ACF-3
1.5	4.2	Sorption, mmol g^{-1}	0.20	0.78	0.80
		Degree of recovery, %	22.0	97.8	98.0
		Solution pH after sorption	6.1	8.8	5.7
3.1	3.6	Sorption, mmol g^{-1}	0.29	1.42	1.58
		Degree of recovery, %	18.3	95.9	97.5
		Solution pH after sorption	4.1	4.1	3.8
4.7	3.5	Sorption, mmol g^{-1}	0.35	1.65	1.86
		Degree of recovery, %	15.3	68.0	75.3
		Solution pH after sorption	3.9	3.8	3.5
6.3	3.2	Sorption, mmol g^{-1}	0.37	1.81	1.96
		Degree of recovery, %	12.4	57.4	58.4
		Solution pH after sorption	3.3	3.25	3.3
9.4	2.5	Sorption, mmol g^{-1}	0.43	1.99	2.05
		Degree of recovery, %	9.3	42.6	43.3
		Solution pH after sorption	3.4	3.5	3.3

6.1 × 4 Å. The dye is well soluble in water, the solution is stable in the pH 2–11 range, and the maximum light adsorption is observed at 597 nm [6, 12, 13].

The MB sorption was carried out under static conditions (sorbent: solution ratio 1 : 500, agitation by rocking at a rate of 125 min^{-1}) from solutions with different initial concentrations of the dye and, in some cases, at different temperatures and pH values. The amount of the sorbed dye was determined from the difference of the dye concentrations in the initial solution and in solution after sorption, evaluated using an MKMF-1 spectrophotometer (l 10 mm) [14].

The influence of the initial concentration c and initial acidity of the solution on the dye recovery, equilibrium pH values, and actual sorption is illustrated in Table 2. In this experimental series, the sorption time t was 24 h.

As seen from Table 2, all the initial MB solutions were acidic. With increasing initial concentration of the dye from 1.5 to 9.4 mM, pH decreases from 4.2 to 2.5. This decrease in the solution pH is probably due to the hydrolysis of MB as a quaternary ammonium chloride. In sorption of MB, the solution pH often increases owing to a decrease in the dye concentration in solution and to sorption (neutralization) of hydrochloric acid on the carbon fibers. In the presence of oxygen in aqueous solutions, the activated carbon fibers can generate hydroxy ions [15], which can increase the solution pH.

The isotherms of MB sorption on the ACF samples are shown in Fig. 1; these isotherms are plotted in the coordinates of the linear Langmuir equation [16]:

$$c_i/a_i = 1/(a_\infty K) + c_i/a_i, \quad (1)$$

where a_i and a_∞ are the actual and limiting sorption capacities (mmol g^{-1}); c_i, the equilibrium MB concentration in the external solution (mM); K, adsorption equilibrium constant.

As seen from Fig. 1, a linear dependence of the sorption capacity is observed in the entire range of equilibrium concentrations, which indicates the formation of an ideal adsorption solution. The equation constants (limiting sorption capacity and equilibrium

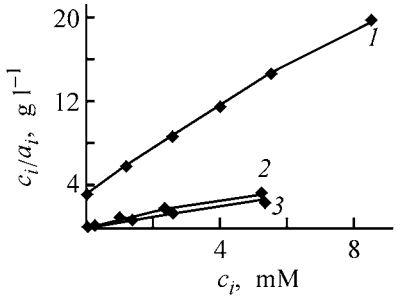

Fig. 1. Isotherms of MB sorption on fibers with various pore structures at 20°C. (c_i) Equilibrium concentration of MB and (a_i) sorption capacity. Sorbent: (*1*) ACF-1, (*2*) ACF-2, and (*3*) ACF-3; the same for Fig. 2.

Table 3. Langmuir equation constants

Sorbent	a_∞, mol l^{-1}	K
ACF-1	0.49	0.60
ACF-2	1.92	8.68
ACF-3	2.08	24.04

constant), determined graphically, increase steadily from ACF-1 to ACF-3 (Table 3).

As seen from Table 3, a_∞ and K rapidly increase with the appearance of mesopores in ACF-2 and ACF-3 (Table 1); this trend can also be related to increasing radius of the micropores.

In the crude approximation, we can calculate the volume of adsorbed MB molecules at their closest packing in a single monolayer on the sorbent surface:

$$V_\infty = a_\infty N_A V_m, \quad (2)$$

where N_A is the Avogadro constant and $V_m = 14.3 \times 6.1 \times 4 \times 10^{-24}$ cm^3 is the MB molecule volume.

Thus, we can evaluate the volumes of the adsorbed MB molecules for the ACF-1, ACF-2, and ACF-3 samples to be 0.10, 0.40, and 0.44 cm^3 g^{-1}, respectively. As seen from a comparison with the data given in Table 1, micropores in ACF-2 and ACF-3 samples are almost completely filled with sorbed MB molecules, whereas in ACF-1 nearly half of the volume of micropores is used. This fact indicates that the geometric size of micropores in ACF-1 does not allow accommodation of the MB molecules simultaneously on two pore surfaces, if we assume that dye molecules are arranged on the carbon surface as washers (4 Å high) and the width of the micropore is comparable with this value. Thus, the pore structure of the carbon sorbents can be easily determined from the sorption capacity for MB [3].

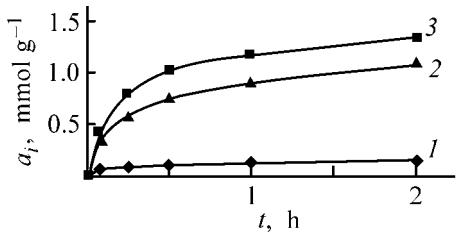

Fig. 2. Kinetic curves of MB sorption on fibers with various pore structures, initial MB concentration 4.7 mM, 20°C. (a_i) Sorption and (t) time; the same for Fig. 4.

The limiting sorption capacities a_∞ of ACF-2 and ACF-3 sorbents are approximately equal, although the total sorption volume and the volume of micropores in the ACF-3 sample are greater. This fact suggests that, owing to the features of size distribution of micropores in ACF-3 sample, certain micropores are inaccessible to MB molecules. Hence, sorbents with high content of micropores are not appropriate in some cases for sorption of large organic molecules. Moreover, ACFs containing only micropores whose size is comparable with the size of organic molecules (ACF-1) are also inefficient, because the sorption proceeds slowly owing to the absence of transport mesopores and to steric hindrance, and some micropores do not participate in sorption. This is confirmed by our data on the sorption kinetics (Fig. 2).

The diffusion coefficients were evaluated using the method of the kinetic curve moments [17], which allows estimation of the diffusion coefficients without solving a of system of kinetic equations. These moments are defined as areas over the kinetic curve which are commonly found graphically. To eliminate this approximate operation, the following kinetic equation was proposed in [18] can be used:

$$\gamma = 1 - \exp(-\delta t^n), \quad (3)$$

which gives analytical expressions for the first moment of the kinetic curve:

$$M_1 = \delta^{-1/n}\Gamma(1 + 1/n) \quad (4)$$

and for the effective diffusion coefficient in an infinite cylinder (fiber) of radius R:

$$D_{eff} = 0.125R^2/M_1, \quad (5)$$

where δ and n are constants, $\Gamma(x)$ is the tabulated gamma function, and $\gamma = a_i/a_\infty$.

The δ and n constants were determined graphically, by plotting the experimental data in the coordinates corresponding to the linear forms of Eq. (3): $\ln(1-\gamma) = f(t^n)$ and $\ln\ln(1-\gamma)^{-1} = f(\ln t)$.

The experimental data are satisfactorily described by Eq. (3) at $n = 0.3$. The effective diffusion coefficients (D_{eff}) calculated from Eqs. (4) and (5) are 0.39×10^{-17}, 2.3×10^{-17}, and 6.0×10^{-17} m^2 s^{-1} for ACF-1, ACF-2, and ACF-3, respectively. At the same time, the effective diffusion coefficient depends on the equilibrium solution concentration. The dependence of the effective diffusion coefficient of the concentration of the equilibrium solution for ACF-2 is shown in Fig. 3 (curve *1*). With increasing concentration, D_{eff}

decreases, which may be due to the aggregation of the molecules in solution.

Temperature strongly affects the dye sorption. The kinetic curves of MB sorption on the ACF-2 fiber at various temperatures are shown in Fig. 4. The temperature dependence of the effective diffusion coefficient for ACF-2 is shown in Fig. 3 (curve *2*).

As seen from Fig. 4, with the temperature increasing from 20 to 95°C, the sorption grows from 1.09 to 1.74 mmol g^{-1} (t = 2 h); the sorption rate increases simultaneously: at 20°C the half-sorption time is 25 min, at 65°C, 5 min, and at 95°C, 3 min. These results are in good agreement with published data [9].

The activation energies for temperature ranges 20–65 (E_a = 48.8 kJ mol^{-1}) and 65–95°C (E_a = 20.3 kJ mol^{-1}) were estimated from the temperature dependence of the effective diffusion coefficient (Fig. 3, curve *2*), approximated by the Arrhenius equation. It is known that dye molecules are solvated in solution and can form aggregates of several molecules in dilute solutions and in the sorbent phase [19]. With increasing temperature, the rate of diffusion grows, probably owing to breakdown of the solvation shells of the molecules and their aggregates. This is confirmed by a significant decrease in the activation energy (Fig. 3, curve *2*).

Our experimental data showed that sorption is almost independent of the solution acidity (or basicity) in the pH 2.4–11 range.

At 20°C, only up to 25% of the MB dye can be desorbed from the fiber with water. Subsequent treatment with NaCl solution did not provide dye desorption, and further treatment with 0.1 N HCl for 24 h allowed additional recovery of only 1% of MB.

Our experimental data suggest that at least 25% of the dye is weakly sorbed on the sorbent surface (physical bonding [3]). The absence of additional desorption of the dye upon treatment with NaCl and HCl solutions and the stability of sorption in a wide pH range show that ion exchange does not contribute to the sorption process.

CONCLUSIONS

(1) The sorption capacity and sorption rate were found to grow with increasing sorption volume of the sorbents.

(2) The limiting sorption capacities and constants of adsorption equilibrium with Methylene Blue for all the carbon fiber samples studied were calculated from the adsorption isotherms using the Langmuir equation.

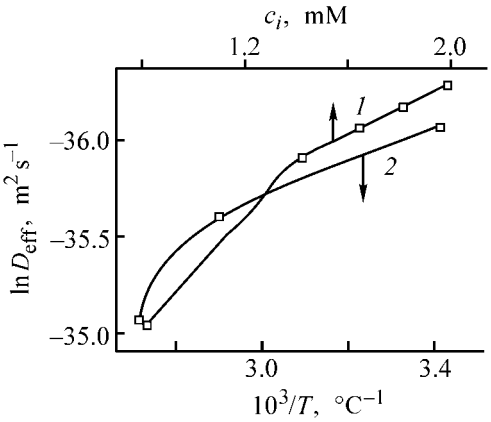

Fig. 3. Effective diffusion coefficient D_{eff} vs. (*1*) concentration c_i and (*2*) temperature T of the equilibrium MB solution for ACF-2 sorbent.

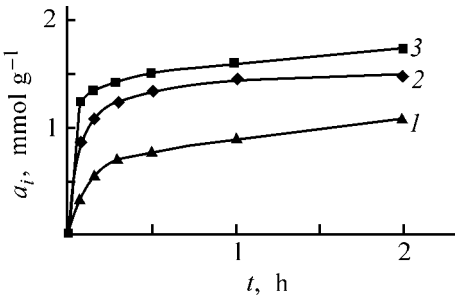

Fig. 4. Kinetic curves of MB sorption on ACF-2 fiber at various temperatures. Temperature (°C): (*1*) 20, (2) 65, and (*3*) 95.

(3) The effective diffusion coefficients in the 20–65 and 65–95°C range were calculated. These data allowed determination of the activation energies and gave insight into the mechanism of dye sorption in the fiber structure.

(4) It was established that sorption of Methylene Blue is approximately constant in the pH 2.4–11 range.

(5) Treatment of the carbon fiber with water resulted in approximately 25% desorption of the dye. Upon subsequent treatment with NaCl and HCl solutions, further desorption of the dye was insignificant.

REFERENCES

1. *Uglerodnye materialy i ugleplastiki: Katalog* (Carbon Materials and Carbon Reinforced Plastics: Catalog), St. Petersburg: PANTEKS, 1999.
2. *Aktivnye ugli: Elastichnye sorbenty. Katalizatory. Osushiteli. Khimicheskie poglotiteli: Katalog* (Activated Carbons: Elastic Sorbents, Catalysts, Desiccants, Chemical Absorbents: Catalog), Cherkassy: NIITEKhIM, 1996.

3. Polyanskii, N.G., Gorbunov, G.V., and Polyanskaya, N.L., *Metody issledovaniya ionitov* (Methods for Analysis of Ion Exchangers), Moscow: Khimiya, 1976.
4. Meshko, V., Markovska, L., and Minceva, M., Abstracts of Papers, *7th Int. Conf. on Fundamentals of Adsorption*, Nagasaki (Japan), May 20–25, 2001, p. 188.
5. Tamai, H., Yoshida, T., and Sosaki, M., *Carbon*, 1999, vol. 37, pp. 983–989.
6. Pelekani, C. and Snoeyink, V.L., *Carbon*, 2000, vol. 38, pp. 1423–1436.
7. Lysenko, A.A., Timoshenko, S.I., Astashkina, O.V., *et al.*, Abstracts of Papers, *III Natsional'nyi simpozium "Teoreticheskie osnovy sorbtsionnykh protsessov"* (III Nat. Symp. "Theoretical Bases of Sorption Processes"), Moscow, 1997, p. 76.
8. Lysenko, A.A., Medvedeva, N.G., Gridneva, Yu.A., and Sukhareva, S.V., *Biotekhnologiya*, 2001, no. 5, pp. 51–57.
9. Katorgina, E.Yu., Development of Fiber Sorbents for Biologically Active Compounds, Analysis of Properties and Application Areas, *Cand. Sci. Dissertation*, St. Petersburg, 1996.
10. *Ochistka stochnykh vod v tekstil'noi i legkoi promyshlennosti* (Treatment of Wastewaters from Textile and Light Industry), Moscow: Legkaya Prom–st., 1979, issue 4.
11. *GOST* (State Standard) *6217–74: Activated Crushed Charcoal: Technical Specifications*, 1974.
12. Emel'yanov, A.G., *Pryamye krasiteli i ikh primenenie v tekstil'noi promyshlennosti* (Direct Dyes and Their Use in Textile Industry), Moscow: Legkaya Prom–st., 1936.
13. Gordon, P.F. and Gregory, P., *Organic Chemistry in Colour*, Berlin: Springer, 1983.
14. *GOST* (State Standard) *4453–74: Activated Fining Powdered Charcoal: Technical Specifications*, 1974.
15. Frumkin, A.N., *Potentsialy nulevogo zaryada* (Zero-Charge Potentials), Moscow: Nauka, 1982.
16. Koganovskii, A.M., *Adsorbtsiya i ionnyi obmen v protsessakh vodopodgotovkiib ochistki stochnykh vod* (Adsorption and Ion Exchange in Water Treatment and Purification of Wastewaters), Kiev: Naukova Dumka, 1983.
17. Zolotorev, P.P. and Ugrozov, V.V., in *Adsorbtsiya i adsorbenty* (Adsorption and Sorbents), Moscow: Nauka, 1987, pp. 127–132.
18. Suzdal', V.G., Grebennikov, S.F., Kombikova, R.A., and Adonts, A.M., *Izv. Vyssh. Uchebn. Zaved., Khim. Khim. Tekhnol.*, 1986, vol. 29, no. 2, pp. 45–47.
19. Movshovich, I.M., *Kinetika protsessov krasheniya tekstil'nykh materialov* (Kinetics of Dyeing of Textile Materials), Moscow: Legkaya Prom–st., 1979.

Russian Journal of Applied Chemistry, Vol. 76, No. 6, 2003, pp. 901–905. Translated from Zhurnal Prikladnoi Khimii, Vol. 76, No. 6, 2003, pp. 931–935.

SORPTION AND ION-EXCHANGE PROCESSES

Sorption of Fulvic Acids from the Neva River on Anion Exchangers Based on Styrene–Divinylbenzene Copolymer

G. V. Slavinskaya

Voronezh State University, Voronezh, Russia

Received February 10, 2003

Abstract—Sorption of fulvic acids (FA) on anion exchangers based on styrene–divinylbenzene copolymer was studied.

All the surface and underground waters contain humic substances, among which fulvic acids (FAs) prevail. The FA content exceeds that of humic acids (HA) by a factor of 10–30 [1–4]. Fulvic acids are undesirable impurities in potable and industrial waters. The coagulation and sorption on activated carbon remove humic substances unefficiently. More efficient purification can be achieved by water treatment with porous anion exchangers [4–6]. In order to improve preparation of ultrapure water, a wide variety of sorbents should be tested to find the anion exchangers with the maximum selectivity with respect to organic pollutants and, especially, fulvic acids.

EXPERIMENTAL

In this study, we tested the following anion exchangers based on styrene–divinylbenzene copolymer (DVB): widely used strongly basic AV-17P resin with quaternary ammonium base sorbing sites, medium-basic ANT-511 anion exchanger (Research Institute of Plastics, Moscow, Russia), and Wofatit AD-41-anion exchanger with tertiary amino groups (St. Bitterfeld Chemiekombinat, Germany). We also tested weakly basic IA-1 and IA-2 polycondensation ion exchangers derived from *m*-phenyldiamine with primary and secondary amino groups (Research Institute of Plastics, Nizhni Tagil, Russia) [5].

Before use, all the anion exchangers were conditioned by alternating treatment with 1 M NaOH and HCl [7]. The amount of removed impurities was determined by the optical density of the filtrates at 220 nm. The conditioning was performed until the optical densities (D_{220}) of the washing solution at the inlet and outlet of the column became equal. In the course of conditioning, the IR spectra of anion exchangers were recorded.

The quarternary ammonium bases have ionization constants $K_b \approx 10^{-1}$–10^{-2} (pK_b = 1–2). The tertiary amino groups are less ionized: $K_b \approx 10^{-3}$–10^{-5} (pK_b = 3–5). The basicity of primary and secondary amino groups depends on their location in the anion-exchanging polymer. When linked with aliphatic chains, they have $K_b \approx 10^{-3}$–10^{-5} (pK_b = 3–5); when bound to aromatic rings (directly or through a methylene group), they have considerably lower ionization constants: $K_b \approx 10^{-6}$–10^{-9} (pK_b = 6–9) [8, 9].

The ionization constants of low-basic amino groups of IA-1 and IA-2 anion exchangers were refined by potentiometric titration with 0.1 M HCl at constant ionic strength (0.1 M KCl). Upon adding each portion of the titrant, the mixture was allowed to stay for 14 days. We found that the ionization constants of different batches of weakly basic anion exchangers, calculated by the Henderson–Hasselbach method [10], are close to 2×10^{-8} (pK_b = 7.8).

In this study, we used fulvic acids recovered from the Neva River by the technique reported in [3]. These FAs were purified to remove mineral impurities and then identified by physicochemical methods. The FA content in the aqueous solutions was determined specrophotometrically, using the calibration plot of $D_{205} - D_{250}$ vs. FA concentration. The calibration solutions were prepared by dissolving weighed portions of ash-free FA. It is known that the optical density of aqueous solutions of FA in the ultraviolet range decreases with increasing wavelength [1, 3]. Therefore, the cal-

1070-4272/03/7606-0901 $25.00 © 2003 MAIK "Nauka/Interperiodica"

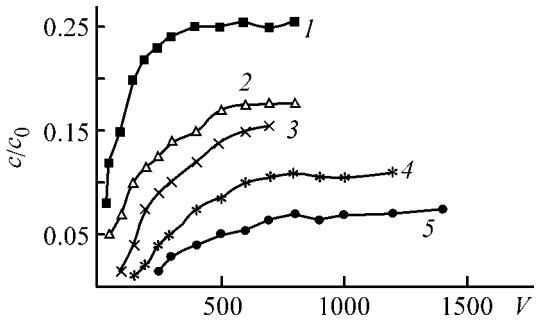

Fig. 1. Output curves of FA sorption on anion exchangers (*1*) AV-17-2P, (*2*) ANT-511, (*3*) IA-1, (*4*) IA-2, and (*5*) Wofatit AD-41. (c/c_0) FA concentration ratio in the filtrate and initial solution and (V) number of column volumes of the initial FA solution passed through the column; the same for Figs. 3 and 4.

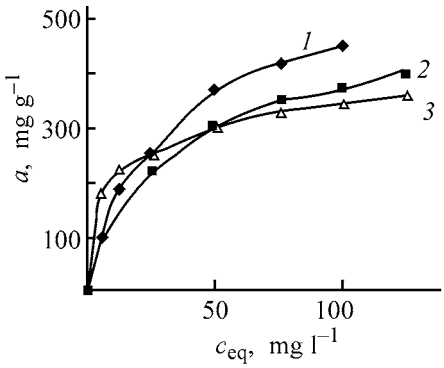

Fig. 2. Sorption isotherms of FA on (*1*) Wofatit AD-41, (*2*) AV-17-2P, and (*3*) ANT-511. (a) Sorption and (c_{eq}) equilibrium FA concentration in the aqueous phase.

ibration curves were constructed at different wavelengths. Such calibration curves allow determination of the FA concentration (c_{FA}) over a wide range without dilution of the samples.

Taking into account that the shape of the output curve of ion-exchange sorption is a function of both the equilibrium and kinetic sorption characteristics [11, 12], the FA sorption on the anion exchangers was studied under dynamic conditions. In these experiments, a sorbent was placed in a column with cross section of 0.92 cm^2. The sorbent bed height was 18–20 cm; the flow velocity, 10 ± 1 m h^{-1}; initial FA concentration, 17 ± 0.5 mg l^{-1}; and pH, 3.2 ± 0.1.

The mutual arrangement of the output curves (Fig. 1) of FA sorption shows that the strongly basic anion exchanger sorbs FAs somewhat more weakly than the less ionizable resins. On filtering 700 column volumes of the FA solution, the FA content in the filtrate was $(0.1–0.15)c_0$ and $0.25c_0$ for weakly basic and strongly basic anion exchangers, respectively.

The isotherms of FA sorption on anion exchangers based on styrenedivinylbenzene copolymer were obtained under static conditions. The sorbent and liquid phases were brought in contact for 15 days at 20 ± 1°C with intermittent stirring for 8 h, followed by standing for 16 h. The sorption isotherms (Fig. 2) have a convex shape and are fairly well described by the Freundlich equation [13]

$$a = \beta c_\alpha,$$

where a is sorption; c, sorbable substance concentration in the liquid phase; β, parameter characterizing sorption of the sorbable substance at its concentration 1 mg l^{-1}; α, empirical parameter varying from 0.1 to 0.5 [14].

It is known that tap water contains up to 10 mg l^{-1} FA [1, 3, 4], i.e., it is a dilute FA solution. As seen from the above equation, the efficiency of sorption treatment of water to remove FA is governed by the β parameter at low FA concentrations. The values of β and limiting FA sorption after 15-day contact with different anion exchangers are given below:

Anion exchanger	β(±3), mg g^{-1}	a_∞(±5), mg g^{-1}
ANT-511	122	375
Vofatit AD-41	41	610
AV-17-2P	62	485

Comparison of these results and those in Fig. 2 shows that the highest sorption activity is exhibited by ANT-511 anion exchanger in dilute solutions, despite its lowest sorption capacity for FA.

The sorption of large organic molecules decreases the moisture content of the anion exchangers, which hinders transfer of the sorbable components into a granule [15]. This steric hindrance deteriorates the sorption kinetics. Furthermore, the pore water volume and transfer of sorbable components into the sorbent granule depend on the degree of cross-linking.

In order to elucidate how the cross-linking agent (DVB) affects the sorption capacity of the anion exchanger for FA, we obtained the output curves of FA sorption on AV-17-P anion exchangers containing 2, 12, and 20% DVB. We also studied the FA sorption on AV-17-8 gel-like anion exchanger, which is a nonporous analogue of AV17P. The total exchange capacity (TEC), content of weakly and strongly basic amino groups, moisture content of AV-17 anion exvaried with varied DVB content, determined by standard techniques [16], are listed in the table.

Characterization of AV-17 anion exchanger madifications

Anion exchanger	TEC (±0.02), mg-equiv g^{-1}	Basic group content (±0.02), mg-equiv g^{-1}		Moisture content, g H_2O/g	FA sorption (±0.05), mg cm^{-3}
		strongly basic	weakly basic		
AV-17-2P	4.53	2.98	1.55 (34.2)*	3.44	3.01
AV-17-8	3.12	2.38	0.74 (23.8)	1.41	2.11
AV-17-12P	2.84	2.03	0.81 (28.5)	1.20	1.08
AV-17-20P	2.13	2.00	0.13 (6.1)	1.13	0.61

* Content of weakly basic amino groups, %.

These results show that all the sorbents tested contain both weakly and strongly basic amino groups, and the amount of weakly basic amino groups decreases with increasing content of the cross-linking agent (DVB). The most cross-linked AV-17-20P anion exchanger contains predominantly strongly basic amino groups. For all of the anion exchangers, the TEC and moisture content decrease with increasing DVB content. Thus, our sorption experiments failed to establish an unambiguous correlation between the sorption capacity with respect to FA and the degree of cross-linking.

The output curves of FA sorption were obtained using a 17.2 ± 0.5 mg l^{-1} FA aqueous solution at pH ~4.2. As seen from the table and Fig. 3, the sorption capacity decreases in the order AV-17-2P > AV-17-8 > AV-17-12P > AV-17-20P with increasing degree of cross-linking. It should be noted that, although AV-17-8 is a nonporous anion exchanger, its TEC and the shape of the output sorption curve follow the general relationships typical of the sorbent series under consideration.

We found that the maximum sorption capacity for FA is exhibited by AV-17-2P anion exchanger with the minimum DVB content (2%). This sorbent is characterized by the highest moisture content and TEC. The more cross-linked anion exchangers AV-17-12P and AV-17-20P, which contain, respectively, 12 and 20% DVB, have virtually the same moisture content (1.20 and 1.13 g H_2O/g anion exchanger). However, AV-17-12P contains a considerably larger amount of weakly basic groups, which increases its sorption capacity as compared to AV-17-20P. However, it is not improbable that the sorption capacity of the anion exchangers under consideration is governed not only by ionic groups, but also by the pore size. Although the data on the moisture content show that the total pore volume of AV-17-12P and AV-17-20P are close, we can expect that the pores of more strongly cross-linked AV-17-20P anion exchanger are narrower than those of AV-17-12P. This factor hinders transfer of FA molecules into AV-17-20P globules, and, therefore, FAs are predominantly sorbed on the sorbent surface.

The sorption service life of ANT-511 (Fig. 4a) and AV-17-2P (Fig. 4b) in water treatment to remove FA

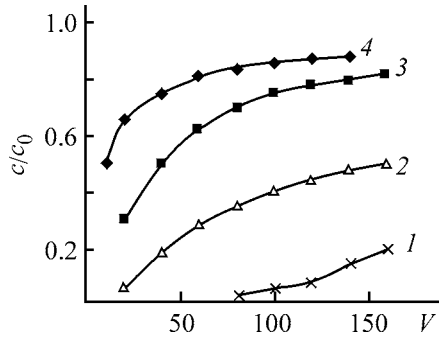

Fig. 3. Output curves of FA sorption on AV-17 anion exchangers with varied cross-linking agent content. Cross-linking agent content, %: (*1*) 2, (*2*) 8, (*3*) 12, and (*4*) 20.

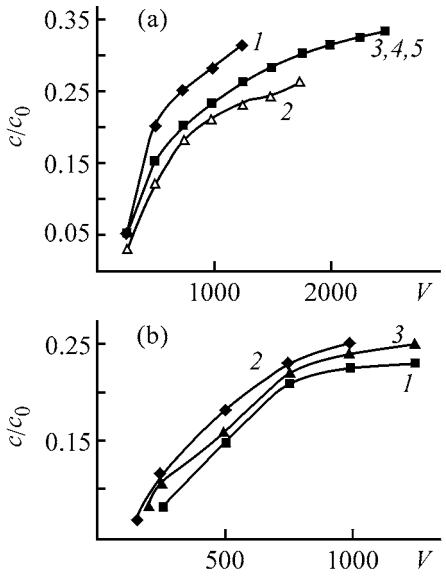

Fig. 4. Output curves of FA sorption on (a) ANT-511 and (b) AV-17-2P anion exchangers. *Digits at curves* are numbers of the filtration cycle.

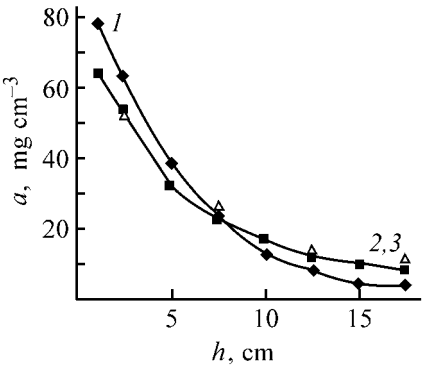

Fig. 5. FA distribution along a column packed with (*1*) IA-2, (*2*) Wofatit AD-41, and (*3*) ANT-511 anion exchangers. (*a*) FA content in the anion exchanger and (*h*) bed length.

was determined under dynamic conditions with sorption–desorption filtration cycles. In these experiments, 800 to 2500 column volumes of FA aqueous solution was passed through a column. We found that, after the first filtration cycle, the sorption efficiency of AV-17-2P anion exchanger slightly decreases, presumably owing to incomplete FA desorption. By contrast, the sorption efficiency of ANT-511 anion exchanger remains unchanged even after treatment of 11000 column volumes of water to remove FA in five successive filtration cycles.

The IR spectra of a dry residue of FA-containing water filtered through an anion exchanger showed that the chemical nature of the organic matter sorbed on the anion exchanger depends on the kind of a sorbent. With a strongly basic anion exchanger, the dry residue of the filtrate contains no FA carboxy groups but shows the presence of the aliphatic chains. At the same time, on filtering through ANT-511 and IA-2 resins, the filtrates are depleted of aliphatic components, but the carboxy groups appear. These results show that water treatment to remove organic impurities should be carried out by successive filtration through strongly, medium, and weakly basic anion exchangers.

In water treatment with two-stage sorption, the weakly basic anion exchangers were used and regeneration was carried out with 2% NaOH. The strongly basic anion exchangers were regenerated with an alkaline–salt solution (2% NaOH + 10% NaCl) [4]. Upon successive filtering through ANT-511 (Wofatit AD-41) and AV-17-P at a filtration velocity of 10 m h^{-1}, the FA content in the initial model solution decreases from 21.8 to 4.6–5.1 mg l^{-1}.

Similar results were obtained in successive filtration of water through polymerization anion exchangers of different basicities and weakly basic condensation anion exchangers. After successive filtration of an aqueous solution (800 column volumes) through IA-1 (IA-2)–AV-17-P and IA-1 (IA-2)–Wofatit AD-41 column systems, the average FA content in the filtrate did not exceed 4.8 mg l^{-1}. Our results show that the weakly and medium-basic anion exchangers remove FA to a similar extent. We studied also FA distribution along an anion-exchange column. In these experiments, column was saturated with fulvic acids and then divided into 3-cm parts. These fragments were treated with an alkaline solution to desorb FAs. Figure 5 demonstrates the FA distribution along the column. This figure shows that saturation of IA-1 weakly basic anion exchanger with FA is stronger in the upper layer and weaker in the lower layer; this resin is more effective than strongly basic anion exchangers. With strongly basic resins, the FA sorption is lower, and the sorption front is more diffuse.

The long-term bench tests showed that successive filtration through IA-2 weakly basic condensation and AV-17-2P strongly basic polymerization anion exchangers ensures efficient purification of Neva water to remove FAs and HAs. Taking into account these results, an anion-exchange sorption unit was installed into an industrial desalination device with output capacity of 2 m^3 h^{-1}. Installation of such a unit eliminates the need for coagulation water treatment. The chemical oxygen demand of desalinated water prepared by this technique does not exceed 1 mg O_2 l^{-1}, which meets the requirements to industrial water.

CONCLUSIONS

(1) The sorption capacity of anion exchangers based on styrene–divinylbenzene copolymer with respect to fulvic acids increases with decreasing degree of ionization of ionic groups or the content of the cross-linking agent.

(2) Strongly basic anion exchangers predominantly sorb the fulvic acid fractions containing ionic carboxylate groups; the medium and weakly basic anion exchangers sorb nonionic organic impurities.

(3) Two-stage sorption treatment of water to remove fulvic acids by successive filtering through columns packed with anion exchangers of different basicities decreases the organic impurity content to a level corresponding to deionized water with chemical oxygen demand less than 1 mg O_2 l^{-1}.

REFERENCES

1. Shevchenko, M.A., *Organicheskie veshchestva v prirodnoi vode i metody ikh udaleniya* (Organic Sub-

stances in Natural Water and Techniques for Their Removal), Kiev: Naukova Dumka, 1966.

2. Kul'skii, L.A. and Strokach, P.P., *Tekhnologiya ochistki prirodnoi vody* (Techniques for Natutal Water Purification), Kiev: Vishcha Shkola, 1986.
3. Slavinskaya, G.V. and Selemenev, V.F., *Ful'vokisloty prirodnykh vod* (Fulvic Acids of Natural Waters), Voronezh: Voronezh. Univ., 2001.
4. Grebenyuk, V.D., and Mazo, A.A., *Obessolivanie vody ionitami* (Water Desalination with Ion Exchangers), Moscow: Khimiya, 1980.
5. Vakulenko, V.A., Kuznetsova, E.P., and Samborskii, I.V., *Teor. Prakt. Sorb. Prots.* (Voronezh), 1973, no. 8, pp. 58–61.
6. Slavinskaya, G.V., Zeleneva, L.A., and Shkol'nyi, A.K., *Khim. Tekhnol. Vody*, 1990, vol. 12, no. 3, pp. 245–249.
7. Slavinskaya, G.V. and Shchedrina, V.B., Abstracts of Papers, *IV Vsesoyuznoe Nauchno-Tekhnicheskoe Soveshchanie "Sovremennye Aspecty Sinteza i Proizvodstva Ionnoobmennykh Materialov"* (IV All-Union Meet. "Modern Aspects of Synthesis and Production of Ion-Exchange Materials"), Cherkassy, 1990, p. 57.
8. Lur'e, A.A., *Sorbenty i khromatograficheskie nositeli* (Sorbents and Chromatographic Supports), Moscow: Khimiya, 1972.
9. Ashirov, A., *Ionoobmennaya ochistka stochnykh vod, rastvorov i gazov* (Ion-Exchange Treatment of Wastewater, Solutions, and Gases), Leningrad: Khimiya, 1983.
10. Helfferich, F., *Ionenaustaucher*, Weinheim: Chemie, 1959.
11. Venitsianov, E.V. and Rubinshtein, R.N., *Dinamika sorbtsii iz zhidkikh sred* (Dynamics of Sorption from Liquid Media), Moscow: Nauka, 1983.
12. Kokotov, Yu.A., Zolotarev, P.P., and El'kin, G.E., *Teoreticheskie osnovy ionnogo obmena* (Theoretical Fundamentals of Ion Exchange), Leningrad: Khimiya, 1986.
13. Fridrikhsberg, D.A., *Kurs kolloidnoi khimii* (Course of Colloidal Chemistry), Leningrad: Khimiya, 1984.
14. Dubinin, M.M., *Fiziko-khimicheskie osnovy sorbtsionnoi tekhniki* (Physicochemical Fundamentals of Adsorption Technique), Moscow: ONTI, 1935.
15. Samsonov, G.V., Trostyanskaya, E.B., and El'kin, G.E., *Ionnyi obmen: sorbtsiya of organic substances* (Ion Exchange: Sorption of Organic Substances), Leningrad: Khimiya, 1969.
16. Polyanskii, N.G., Gorbunov, G.V., and Polyanskaya, N.L., *Metody issledovaniya ionitov* (Methods for Study of Ion Exchangers), Moscow: Khimiya, 1976.

Russian Journal of Applied Chemistry, Vol. 76, No. 6, 2003, pp. 906–908. Translated from Zhurnal Prikladnoi Khimii, Vol. 76, No. 6, 2003, pp. 936–938.

SORPTION AND ION-EXCHANGE PROCESSES

Sorption of Industrial Oil by Expanded Graphite

M. V. Savos'kin, A. P., Yaroshenko, V. N. Mochalin, and B. V. Panchenko

Litvinenko Institute of Physicoorganic Chemistry and Coal Chemistry, National Academy of Sciences of Ukraine, Donetsk, Ukraine

Received May 13, 2002; in final form, April 2003

Abstract—Sorption of industrial oil by expanded graphite prepared from residual graphite hydrosylfate at 300–900°C was studied. The sorption isotherms of both neat oil and oil from its aqueous suspension were measured. The sorption capacity for oil was studied as influenced by the specific surface area and specific volume of expanded graphite sorbent.

As previously shown by the method of direct sorption, expanded graphite is a highly efficient sorbent for petroleum (1 g of the sorbent sorbs up to 80 g of petroleum) [1–5]. Expanded graphite has also been proposed [6, 7] as a sorbent of various fats and oils; however, no quantitative sorption parameters were reported in these studies and the dependenes of the sorption on the sorbent properties were not evaluated. In this study we analyzed sorption of industrial oil by expanded graphite as influenced by the properties and preparation conditions of the graphite. For this purpose we used pure industrial oil (direct sorption) or aqueous oil emulsions.

We used residual graphite hydrosulfate prepared by the procedure described in [8]. The sorbent was prepared by flash heating of residual graphite hydrosulfate in a muffle furnace at temperature ranging from 300 to 900°C. The samples were kept at 300–500°C for 5 min and then at 600–900°C for 2 min. We measured the specific surface area S_{sp} ($m^2\ g^{-1}$), specific volume V_{sp} ($cm^3\ g^{-1}$), and specific sorption of industrial oil W_{sp} ($g\ g^{-1}$) for all samples of expanded graphite. The BET specific surface area was determined by low-temperature argon adsorption in accordance with GOST (State Standard) 13 144–79. The specific volume was calculated as the reciprocal of the bulk density of the sorbent, which, in turn, was determined in accordance with GOST (State Standard) 14 922–77.

Sorption of neat I-20 industrial oil and sorption of this oil from an aqueous emulsion were studied at 20°C. In the first case, a weighed portion of the sorbent was placed in a glass vessel, carefully wetted with excess oil (25 g), and kept for 30 min to complete the sorption. Then the vessel was covered with perforated metal foil and unsorbed oil was allowed to drain down for 1 day. The oil sorption was determined gravimetrically [9].

Oil sorption from an aqueous emulsion was performed by the following procedure. An oil emulsion was prepared by stirring a mixture of oil with 1 dm^3 of distilled water with a magnetic stirrer. The oil concentration c_{oil} ($g\ dm^{-3}$) was varied from 0.08 to 20 $g\ dm^{-3}$. A weighed portion of the sorbent was added to the emulsion and the mixture was stirred for 15 min. The sorbent was then quantitatively separated by filtration through a paper filter, dried at 100°C, and weighed. The oil sorption on the paper filter was determined in a blank experiment. In special experiments, we found that there are no losses of sorbed oil during drying of the sorbent.

The properties of the sorbents prepared at temperatures from 300 to 900°C are presented in the table.

We measured the sorption isotherm of I-20 industrial oil from neat oil and its aqueous emulsion on

Properties of expanded graphite sorbent prepared at different temperatures

T_{exp}, °C	S_{sp}, $m^2\ g^{-1}$	V_{sp}, $cm^3\ g^{-1}$
300	9.6	52
400	12.1	122
500	30.7	149
600	41.2	179
700	55.4	222
800	47.8	250
900	66.7	278

1070-4272/03/7606-0906 $25.00 © 2003 MAIK "Nauka/Interperiodica"

the sorbent prepared at 900°C. We used this sorbent since it is characterized by the maximum specific surface area, maximum specific volume and, as previously shown [9], by the maximal sorption capacity for petroleum. The sorption isotherms are shown in Figs. 1a and 1b.

Both isotherms are typical of sorption processes. The specific sorption of neat oil grows almost linearly with increasing oil-to-sorbent weight ratio up to values slightly exceeding 40 (Fig. 1a). The slope of the isotherm in this range is close to unity, i.e., the whole amount of oil is sorbed by the expanded graphite. At a ratio of about 100, the isotherm flattens out. The sorption capacity of the expanded graphite for industrial oil W_{sp}^{max} (g g^{-1}), determined from the sorption isotherm, is about 70 g g^{-1}. It should be noted that this value is close to the sorption capacity of expanded graphite for petroleum, determined by the direct sorption procedure [9].

When the oil is sorbed from its aqueous emulsion, the specific sorption grows linearly with the oil concentration increasing up to 4 g dm^{-3} and then flattens out. The maximum sorption of oil from the emulsion (the sorption capacity), determined by cubic interpolation of the experimental data, is about 20 g g^{-1} at oil concentration of 6.7 g dm^{-3}.

We studied how the temperature at which expanded graphite was prepared affects the oil sorption from an aqueous emulsion. In these experiments, the oil concentration (6.7 g dm^{-3}) was close to that at which the isotherm of oil sorption by expanded graphite prepared at 900°C starts to flatten out. Since the sorption capacity of graphite expanded at 900°C is highest among the samples prepared in the range from 300 to 900°C, the above choice of emulsion concentrations ensures that the values obtained for all the samples studied fall on the plateaus of the sorption isotherms, i.e., allows determination of their sorption capacities.

As seen from Fig. 2a, the sorption capacity of expanded graphite determined in the experiment with an oil emulsion grows linearly with increasing sorbent preparation temperature. This is due to a linear rise in the specific surface area and specific volume of the sorbent with increasing preparation temperature (see table; Figs. 2a, 2b). The influence exerted by the specific surface area and specific volume of the samples on the sorption capacity of graphites expanded at 300–900°C for oil from an aqueous emulsion is described by the following two-parameter linear regression equation $W_{sp} = 0.592S_{sp} + 0.415V_{sp}$ ($r = 0.995$). As determined from Student's t-test at the confidence level of 0.95, the coefficient at parameter S_{sp} is significant and the significance of the coefficient

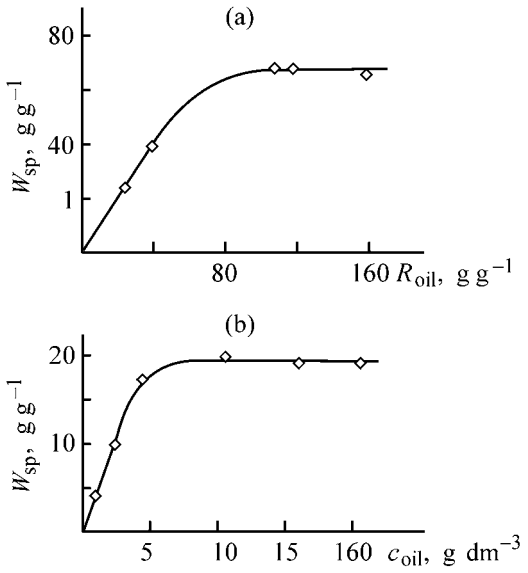

Fig. 1. Isotherms of sorption of I-20 industrial oil at 20°C by expanded graphite prepared from residual graphite hydrosulfate at 900°C. (W_{sp}) Sorption capacity of expanded graphite, (R_{oil}) initial oil/sorbent ratio, (c_{oil}) oil concentration in aqueous emulsion. (a) Direct sorption and (b) sorption from aqueous emulsion.

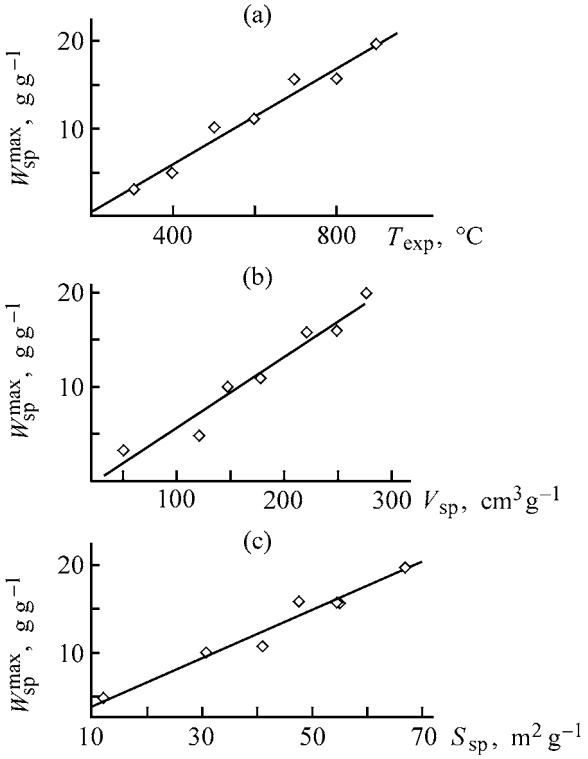

Fig. 2. Sorption capacity of expanded graphite, W_{sp}^{max}, for oil from an aqueous oil emulsion vs. (a) sorbent preparation temperature T_{exp}, (b) specific volume of the sorbent V_{sp}, and (c) specific surface area of the sorbent, S_{sp}.

at V_{sp} is close to the limiting significance value. The latter fact is probably due to strong correlation between S_{sp} and V_{sp} ($r = 0.95$). Our results show that oil sorption from an aqueous emulsion depends on both the specific volume and the specific surface area of the sorbent. As determined from the regression equation, 60% of oil is sorbed on the sorbent surface, and 40%, in the bulk of the sorbent.

It should be noted that the sorption capacity of expanded graphite for oil from an aqueous emulsion is lower by a factor of 3.5 than that for neat oil. This difference cannot be due to higher oil concentration in neat oil, since the sorption capacity levels off at 6.7-g dm^{-3} oil concentration in the emulsion. This cannot be accounted for by preferential sorption of water, either, since the surface of the expanded graphite is hydrophobic. Even if water is sorbed in the first steps, it will be desorbed from the sorbent by hydrophobic oil. The lowering of the sorption capacity in an aqueous emulsion as compared to the direct sorption experiment is presumably due to structural transformations of expanded graphite under the action of water. Indeed, the specific surface area and specific volume (parameters responsible for the sorption capacity of expanded graphite) of the samples wetted with water and then dried decrease by a factor of 2–3.

CONCLUSION

Expanded graphite is an efficient sorbent for industrial oil. The sorption is controlled by both the specific volume and the specific surface area of the sorbent. Graphite expanded at 900°C has the maximum sorption capacity and can be used in practice. The capacity of this sorbent for neat oil is about 70 g g^{-1}. When oil is sorbed from its aqueous emulsions, the sorption capacity decreases to 20 g g^{-1}, but remains sufficient for effective application of the sorbent.

REFERENCES

1. Toyoda, M., Moriya, K., and Inagaki, M., *EUROCARBON 2000, 1st World Conf. on Carbon: Abstracts and Programme*, Berlin (Germany), July 9–13, 2000, vol. 2, pp. 697–698.
2. Toyoda, M. and Inagaki, M., *Carbon*, 2000, vol. 38, no. 2, pp. 199–210.
3. Toyoda, M., Moriya, K., Aizawa, J., *et al.*, *Desalination*, 2000, vol. 128, no. 3, pp. 205–211.
4. Tryba, B., Kalenczuk, R.J., and Morawski, A.W., *11th Int. Symp. on Intercalation Compounds: Program and Abstracts*, Moscow (Russia), May 27–31, 2001, p. 104.
5. US Patent 6 306 264.
6. UK Patent 2 149 769.
7. US Patent 5 282 975.
8. Ukrainian Patent 34 777.
9. Savoskin, M.V., Yaroshenko, A.P., Shologon, V.I., *et al.*, *EUROCARBON 2000, 1st World Conf. on Carbon: Abstracts and Programme*, Berlin (Germany), July 9–13, 2000, vol. 2, pp. 673–674.

Russian Journal of Applied Chemistry, Vol. 76, No. 6, 2003, pp. 909–911. Translated from Zhurnal Prikladnoi Khimii, Vol. 76, No. 6, 2003, pp. 939–941.

SORPTION AND ION-EXCHANGE PROCESSES

Nondestructive Surface Sampling with Polymethyl Methacrylate Doped with Alkali Metal Cations

G. V. Lyamina, E. P. Knyazeva, and G. M. Mokrousov

Tomsk State University, Toms, Russia

Received June 20, 2002

Abstract—Sorption of copper and copper oxide from the alloy surface by poly(methyl methacrylate) doped with alkali metal cations was studied with the aim to develop nondestructive sampling of metals from the surface. The sampling efficiency was studied as influenced by the content of alkali metal cations and water in the polymeric matrix.

Nondestructive methods for studying and analyzing the surface require, as a rule, complex equipment, are expensive, and cannot be used for express analysis on the site. Therefore, development of a nondestructive express analysis of various objects for the content of metals and their compounds is a topical problem.

The aim of this study was to demonstrate the possibility of using a polymeric formulation based on polymethyl methacrylate and alkali metal trifluoroacetates (MPMMA) [1, 2] as a sorbent for nondestructive express sampling of metals and their oxides from the surface of an alloy containing 74 wt % silver and 26 wt % copper.

EXPERIMENTAL

In chemical analysis, polymers are mainly used in the form of solutions and films immobilized on the surface of a conducting material [3, 4]. In this study, we used MPMMA in the form of plates (organic glasses) pre- pared by bulk polymerization of methyl methacrylate (MMA) mixed with an appropriate alkali metal trifluoroacetate [1]. The salt concentration was varied from 1 to 6 mol per 1 kg of MMA. Some of the samples were kept for 1 day in desiccators at a humidity ω of 47, 58, and 80%; the water content in the samples depended on the nature and content of a modifier (Table 1). We studied sampling from the surface of a copper-containing alloy. The polymers were mechanically pressed against the surface with a 5 kg cm^{-2} force for 20 min. The contact time was determined experimentally (Fig. 1).

The sorption of copper and its oxides by MPMMA was determined voltammetrically with mercury and amalgam (HgNa) electrodes (contact time 5 min) by the procedure described in [5, 6]. The copper sorption was measured with the first electrode, and the sorption of copper and its oxides, with the second. After a contact of the mercury or amalgam electrode with the polymer surface, a differential voltammogram was recorded in 0.1 M KCl at potential sweeping in the range from –0.8 to 0.0 V at a rate w = 30 mV s^{-1}. The potential was measured relative to 0.1 M silver chloride electrode.

The copper sorption by the polymer depends on the nature of metal cations introduced into the poly-

Table 1. Dependence of water content in polymethyl methacrylate modified with CF_3COOM on the relative humidity ω

CF_3COOM, mol kg^{-1}	Water content (wt %) at indicated ω, %		
	47	58	80
CF_3COOK:			
2	2.3	2.9	4.0
6	2.4	4.5	6.5
CF_3COONa:			
2	2.5	3.6	4.8
6	2.7	6.8	8.3
CF_3COOLi:			
2	3.5	4.9	7.4
6	5.2	10.0	13.8

1070-4272/03/7606-0909 $25.00 © 2003 MAIK "Nauka/Interperiodica"

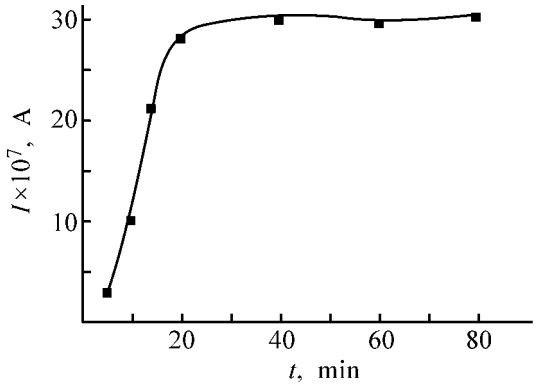

Fig. 1. Voltammetric signal I characterizing the sorption capacity of MPMMA(K^+) as a function of the time t of contact with the sample.

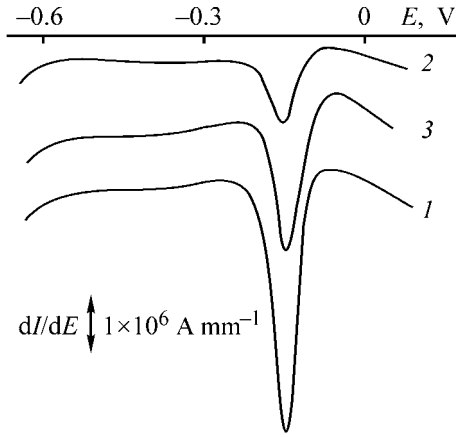

Fig. 2. Voltammogram recorded with the amalgam electrode and characterizing copper sorption on MPMMA containing (*1*) potassium, (*2*) sodium, and (*3*) lithium trifluoroacetates. (*E*) Potential.

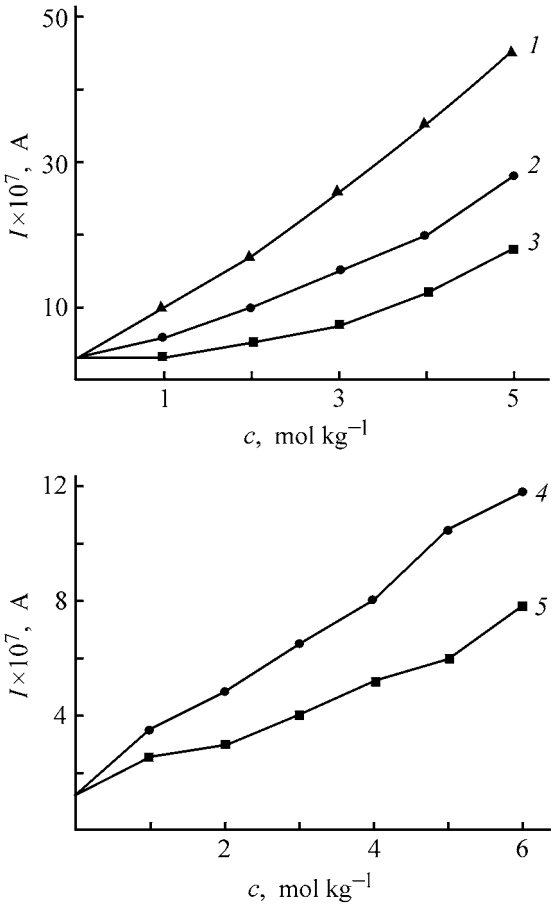

Fig. 3. Voltammetric signal I of amalgam electrode, characterizing the copper sorption by MPMMA, vs. the content c of (*1–3*) CF_3COOK, (*4*) CF_3COONa, and (*5*) CF_3COOLi in the polymer. Polymers were kept in desiccators with humidity (%) of (*1, 4, 5*) 80, (*2*) 58, and (*3*) 47.

mer (Fig. 2) and on their hydration properties (Fig. 3, Table 1). The activity of alkali metal cations grows in the order $Li^+(Na^+) < K^+$, which is probably due to the difference in their ionic radii. As the ionic radius increases, the positive charge is shielded, the bonding of the cation with the terminal groups of the polymeric matrix is weakened, and the mobility of the cation grows.

The sorption activity of MPMMA samples containing Li^+ and Na^+ cations increases after keeping the samples in a humid atmosphere. This is due to an increase in the radius of the hydration shell of the alkali metal cations, which is the most pronounced for lithium. Correlation analysis of the results of voltammometric determination of copper shows that the sorption capacity of MPMMA depends on the content of alkali metal trifluoroacetate. The sorption grows with increasing CF_3COOK concentration in the polymer (Fig. 3, curves *1–3*). The sorption capacity of the CF_3COOK-modified polymer for copper oxides increases after keeping the polymer in a humid atmosphere. This is also the case for elemental copper, but the analytical signal is lower by an order of magnitude. The sorption of both forms of copper by the polymer kept at $\omega = 80\%$ is the strongest, and by the polymer kept at $\omega = 47\%$, the weakest.

In the case of a polymer containing CF_3COONa, the rise in the sorption of elemental and oxidized copper species with increasing modifier content is observed for the polymer kept at 80% humidity (Fig. 3, curve *4*) and not observed for a polymer kept at 58% humidity.

The sorption of copper oxides by MPMMA containing CF_3COOLi grows with increasing modifier content only for the samples kept at 80% humidity (Fig. 3, curve *5*). The content of the lithium salt has virtually no effect on the sorption of copper oxide. Thus, the polymers modified with lithium and so-

dium salts and kept in a humid atmosphere are characterized by copper sorption dependent on the modifier content and by improved reproducibility of the analytical results (Table 2).

The copper sorption was determined gravimetrically. CF_3COOLi-doped MPMMA (modifier content 5 mol kg^{-1}) sorbs 0.0011 ± 0.0002 g of copper after contact with a 1-cm^2 surface of a copper plate for 7 days.

Sorption of elemental copper and its oxides by MPMMA is probably due to potential difference across the polymer/sample interface, which is confirmed by emf generation in the Cu | MPMMA | Pt system. After a contact of the polymer with a sample, the absorption band of water sorbed by alkali metal cations (ν = 3500 cm^{-1}) broadens and becomes unsplit, which indicates hydrogen bonding between water molecules. The bands of the functional groups of the polymer and those of alkali metal trifluoroacetates incorporated in the polymeric matrix are not shifted. These facts suggest that copper sorbed by MPMMA is in the form of an aqua complex weakly bound to the polymer matrix. After prolonged contact of MPMMA with a copper-containing sample (60 days), the polymer turns blue. The sorption properties of MPMMA with respect to copper and its oxides do not change for up to 4 years.

CONCLUSIONS

(1) Polymethyl methacrylate doped with potassium cations exhibits the best sorption properties with respect to copper. The sorption of copper and its compounds from the sample surface by this polymer is the strongest. The reproducibility of analysis of the sample surface for copper with a polymeric formulation composed of polymethyl methacrylate and CF_3COOK, kept in a humid atmosphere, is the best.

(2) The formulation composed of polymethyl methacrylate and alkali metal salts is promising for nondestructive analysis of the surface of copper-containing samples.

Table 2. Variation coefficients S_r (n = 3) of the voltammometrically determined content of copper sorbed by MPMMA kept in desiccators at various humidities

CF_3COOM, mol kg^{-1}	S_r (%) at indicated ω, %					
	58	80	58	80	58	80
	CF_3COOK		CF_3COONa		CF_3COOLi	
1	24	19	28	24	29	25
2	23	18	27	22	26	22
3	20	16	23	19	22	18
4	15	12	20	15	17	13
5	12	7	16	11	13	9

ACKNOWLEDGMENTS

This study was supported finacially by the Russian Foundation for Basic Research (p98Siberia, no. 98-03-03 052) and Ministry of Education, grant for natural sciences.

REFERENCES

1. USSR Patent no 1 806 152.
2. Mokrousov, G.M. and Gavrilenko, N.A., *Zh. Fiz. Khim.*, 1996, vol. 10, no. 1, pp. 159–163.
3. Budnikov, G.K., Maistrenko, V.N., and Murinov, Yu.I., *Vol'tamperometriya s modifitsirovannymi i ul'tramikroelektrodami* (Voltammetry with Modified and Ultramicroelectrodes), Moscow: Nauka, 1994.
4. Zolotov, Yu.A. and Kuz'min, N.M., *Kontsentrirovanie mikroelementov* (Concentration of Microelements), Moscow: Khimiya, 1982.
5. Mokrousov, G.M., Knyazeva, E.P., and Volkova, V.N., *Zavod. Lab.*, 1995, no. 3, pp. 7–9.
6. Mokrousov, G.M., Knyazeva, E.P., Volkova, V.N., and Alifanova, I.A., *Zh. Anal. Khim.*, 1994, vol. 49, no. 9, pp. 1013–1016.

Russian Journal of Applied Chemistry, Vol. 76, No. 6, 2003, pp. 912–916. Translated from Zhurnal Prikladnoi Khimii, Vol. 76, No. 6, 2003, pp. 942–946.

APPLIED ELECTROCHEMISTRY AND CORROSION PROTECTION OF METALS

Voltammetric Determination of Tin(II) and Iron(II) on Mechanically Renewed Graphite Electrode in Tin-Plating Electrolyte

L. I. Skvortsova and A. Zh. Medvedev

Institute of Solid-State Chemistry and Mechanochemistry, Siberian Division, Russian Academy of Sciences, Novosibirsk, Russia

Received January 22, 2003

Abstract—The analytical properties of the cathodic peak of tin(II) reduction and the anodic peak of iron(II) oxidation on a graphite electrode were studied with the electrode surface mechanically renewed directly in a solution before applying a potential in each measurement. The influence of the organic components of the phenolsulfonic tin-plating electrolyte on the cathodic current of tin(II) reduction and anodic current of iron(II) oxidation was studied. A dc voltammetric method was proposed for determining tin(II) directly in the phenolsulfonic tin-plating electrolyte, and iron(II) after the electrolyte is diluted tenfold with a 0.5M H_2SO_4 supporting solution.

Tin is one of the few metals, whose compounds are not harmful to humans. For this reason, it is used to coat any items associated with storage and manufacture of food products. Tin coatings are also used for electrochemical protection of steels and for imparting good electrical conductivity to contact surfaces. Tin is electroplated in both acid and alkaline solutions. Acid electrolytes are prepared by dissolving tin(II) salts in sulfuric, hydrofluoric, tetrafluoroboric, phenolsulfonic, and sulfamic acids. The most widely used in industry are sulfate electrolytes containing a 0.5–1.0 N solution of $SnSO_4$ in 1.5–2 N sulfuric acid, which hinders tin(II) hydrolysis and raises the electrical conductivity of the solution [1]. Dense, compact, finely grained tin deposits with structure relatively uniform across the thickness are obtained from acid electrolytes in the presence of some surfactants.

Electrolytes based on tin(II) phenolsulfonate in *n*-phenolsulfonic acid are less subject to tin(II) oxidation than sulfate electrolytes [2]. The stability of this electrolyte and the coating quality at high current densities are also markedly improved upon addition of a surfactant.

In this study, we verified the possibility of monitoring the content of tin(II) and iron(II) by dc voltammetry in a phenolsulfonic tin-plating electrolyte. This electrolyte is used for tin coating of steel tape in the Ferrostan technology. Its standard composition is (g l^{-1}): Sn^{2+} ions (in the form of $SnSO_4$) 30, *n*-phenolsulfonic acid 75.8 (66%), and ESNA (ethoxylated α-naphtholsulfonic acid) as surfactant additive 6.7. Since the Ferrostan technology uses anodes made of metals other than tin, the content of tin(II) in the electrolyte decreases continuously. According to the technical regulations, the tin(II) concentration in electrolyte is maintained within 30 ± 1 g l^{-1}. For this reason, it is necessary to monitor its content at regular intervals of time and adjust it by adding a concentrated $SnSO_4$ solution. The most common industrial method for determining tin(II) is volume iodatometric or iodometric titration [3].

A method is known for direct voltammetric determination of tin(II) in chloride solutions [4]. This technique is based on recording the anodic peak of tin(II) electrooxidation on a graphite electrode at a potential $E_p = 0.3$ V. It was noted in [4] that a peak of Sn^{4+} reduction is observed in addition to the cathodic peak of Sn^{2+} reduction at $E_p = -0.68$ V, and, therefore, the latter cannot be used for determining tin(II) content in a chloride medium. Tin(II) is reduced to metal in a 1M H_2SO_4 solution on mercury electrode at a half-wave potential $E_{1/2} = -0.46$ V [5].

When in use, tin-plating electrolyte continuously accumulates Fe^{2+} ions, which affect adversely the coating quality at concentrations higher than 10 g l^{-1}.

1070-4272/03/7606-0912 $25.00 © 2003 MAIK "Nauka/Interperiodica"

This necessitates monitoring of the iron(II) concentration in tin-plating electrolytes on regular basis. Electrooxidation of Fe^{2+} to Fe^{3+} on a mercury electrode in a sulfate supporting electrolyte occurs at $E_{1/2}$ = +0.54…+0.60 V [6]. Among organic supporting solutions, the oxalate solution is more commonly used for voltammetric determination of Fe^{2+}, since the half-wave potential of iron(II) oxidation in this solution is ±0.24 V [7].

The method of direct voltammetric determination of Sn^{2+} and Fe^{2+} ions on a graphite indicator electrode served as basis for developing a procedure for monitoring the content of these ions in a phenolsulfonic tin-plating electrolyte. The influence of all electrolyte components on the peak currents of each ion to be determined was studied and conditions of microelectrode polarization were chosen.

EXPERIMENTAL

Voltammograms were recorded with a PA-2 polarograph and N-307 plotter in a three-electrode cell with a saturated calomel reference electrode and auxiliary graphite electrode. The graphite indicator electrode was in the form of a cylindrical rod made of cured epoxy resin (external diameter 4 mm). Its electrically active part (2 mm in diameter) made of a hardened graphite formulation was situated along the rod axis. The working surface of the indicator electrode (rod edge) was renewed at regular intervals directly in the test solution by cutting-off mechanically a 0.5-μm surface layer on a special device [7, 8]. The surface was always renewed before applying the electrode potential. The potential sweep rate was varied from 10 to 100 mV s^{-1}.

Model electrolyte solutions were prepared according to prescription by dissolving organic components in distilled water and adding a calculated weighed portion of $SnSO_4$ and $FeSO_4 \cdot 7H_2O$. Preliminarily, the tin content in the reagent (pure grade) was found by iodatometric titration (starch indicator) [1], and the iron(II) content in a freshly recrystallized reagent, by theoretical calculation. Since tin(II) and iron(II) are easily oxidizable, all solutions were prepared from separate weighed portions of a reagent in a deoxygenated supporting solution.

As supporting solutions were chosen sulfuric, hydrochloric, oxalic, and phenolsulfonic acids. The voltammogram of a sulfate supporting electrolyte shows in the cathodic region a peak due to reduction of dissolved oxygen, which completely disappears after argon is passed through the solution for 5 min. The polarization curve of cathodic reduction of tin(II) to metal on a graphite electrode in a 0.2M H_2SO_4 supporting solution shows a clearly pronounced and well-resolved peak at E_p = –0.66 V. A study of the influence exerted by phenolsulfonic acid, ENSA surfactant, and iron(II) compound on the cathodic peak of tin(II) reduction demonstrated that the qualitative and quantitative characteristics of the tin(II) peak in a sulfate supporting electrolyte are not affected by these components. The calibration plot of the peak current of tin(II) reduction against its concentration in a 0.2M H_2SO_4 solution is a straight line emerging from the origin. However, at Sn^{2+} content exceeding 10 g l^{-1}, the slope of the calibration plot changes somewhat.

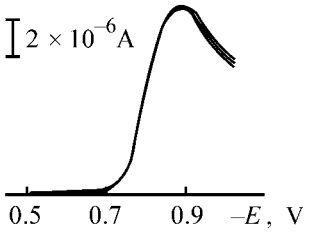

Fig. 1. Voltammograms of Sn^{2+} cathodic reduction on mechanically renewed graphite electrode in phenolsulfonic electrolyte for tin plating. $c_{Sn^{2+}}$ = 10 g l^{-1}, V = 50 mV s^{-1}, and n = 5. (E) Potential; the same for Figs. 2 and 3.

Compared with the sulfate supporting electrolyte, the potential of the Sn^{2+} reduction peak in a phenolsulfonic electrolyte containing 76 g l^{-1} *n*-phenolsulfonic acid and 6.7 g l^{-1} ENSA is shifted to the negative region and, depending on the bulk concentration of tin(II), falls within E_p = –0.90…–0.95 V. The linear run of the $I_p = f(c_{Sn^{2+}})$ calibration plot for Sn^{2+} reduction in a phenolsulfonic electrolyte is preserved. The reproducibility of voltammograms of tin(II) oxidation is demonstrated in Fig. 1 for five curves. The relative standard deviation of the peak current for tin(II) concentration of 30 g l^{-1} in this electrolyte at n = 8 and P = 0.95 does not exceed 0.006.

As is known, Sn^{2+} ions are easily oxidized by atmospheric oxygen, so the Sn^{4+} ions are always accompanying. A study of the electrochemical behavior of Sn^{2+} ions in a 0.5M sulfate supporting solution demonstrated that Sn^{4+} ions are cathodically reduced on a graphite indicator electrode at potentials E_p = –0.80…–0.87 V. The difference between the potentials of tin(II) and tin(IV) peaks in this supporting solution is insignificant (–0.15…–0.2 V). In those cases, when Sn^{2+} and Sn^{4+} are present simultaneously, an overall voltammogram is recorded in a sulfate supporting solution. Another situation is observed in a phenolsulfonic supporting solution. Addition of a tin(IV) com-

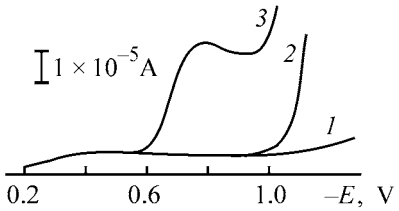

Fig. 2. Voltammograms of cathodic reduction of Sn^{2+} and Sn^{4+} in phenolsulfonic electrolyte for tin plating. V = 100 mV s^{-1} and $I = h \times 10^{-5}$ A cm^{-1}. (*1*) Supporting solution of phenolsulfonic electrolyte, (*2*) supporting solution with addition of Sn^{4+} ($c_{Sn^{4+}}$ = 0.17 g l^{-1}), (*3*) solution 2 with addition of Sn^{2+} compound ($c_{Sn^{2+}}$ = 0.28 g l^{-1}).

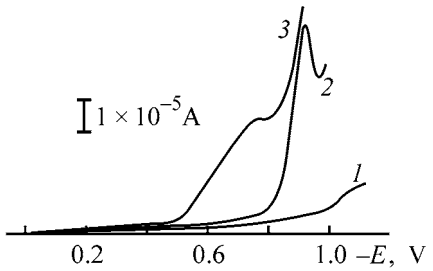

Fig. 3. Voltammograms of supporting solutions and iron(II) oxidation on renewed graphite electrode V = 50 mV s^{-1} and $I = h \times 10^{-5}$ A cm^{-1}. (*1*) 0.5 M H_2SO_4 solution with addition of Sn^{2+} ($c_{Sn^{2+}}$ = 3 g l^{-1}), (*2*) phenolsulfonic electrolyte diluted tenfold with 0.5 M H_2SO_4 solution, (*3*) supporting solution *2* with addition of Fe^{2+} ($c_{Fe^{2+}}$ = 2 g l^{-1}).

pound to the phenolsulfonic supporting solution shifts somewhat the onset potential of hydrogen evolution in the voltammogram, but the peak of the Sn^{4+} cathodic electroreduction is not recorded before the region of hydrogen evolution (Fig. 2, curve *2*). At the same time, the peak of Sn^{2+} reduction is preserved without any change in its shape (Fig. 3, curve *3*).

It should be noted that the reproducibility of the current and potential of the tin(II) reduction peak depend on the state of the surface of the graphite electrode. In the absence of mechanical renewal, with the deposit on the surface of the graphite electrode dissolved electrochemically, the potential of the subsequent peak of tin(II) reduction shifts to the cathodic region by approximately 0.10 V. In addition, the reproducibility of the peak current decreases by an order of magnitude and more. After the mechanical renewal of the graphite electrode is resumed, all the parameters of the peak of tin(II) reduction are restored.

Thus, the experiments on model solutions showed that the content of tin(II) can be determined by voltammetry rapidly, and in a simple way, directly in a phenolsulfonic tin-plating electrolyte from the current of its reduction peak in the cathodic region of polarization of the graphite electrode.

Fe^{2+} ions are oxidized to Fe^{3+} on a graphite electrode in all the supporting solutions chosen for the experiment. In a sulfate solution (0.2–0.5 M H_2SO_4), Fe^{2+} is oxidized anodically at +0.33 V. The peak of tin(II) oxidation is not recorded in this potential range in sulfate solutions (Fig. 3, curve *3*), in contrast to chloride solutions, i.e., the presence of tin(II) in a solution does not affect the current of the iron(II) oxidation peak. In the $I_p = f(c_{Fe^{2+}})$ calibration plot, the current of iron(II) oxidation in a sulfate supporting solution is proportional to bulk concentration of iron(II) within the range 0.1–15 g l^{-1}.

In the voltammogram measured in freshly prepared phenolsulfonic supporting electrolyte, two current peaks are recorded in the anodic region, with the first of these observed at E_p = +1.05 V. Apparently, oxidation products of organic compounds are accumulated in the supporting electrolyte during its storage, which leads to an increased number of the anodic peaks observed. In a solution of phenolsulfonic electrolyte, i.e., in the presence of the organic compounds mentioned above, the potential of the iron(II) oxidation peak is shifted by 0.45 V to the positive region, reaching a value E_p = +0.78 V. Voltammetric determination of iron(II) directly in a phenolsulfonic electrolyte is complicated by the presence of a neighboring peak of phenolsulfonic acid oxidation (Fig. 3, curve *2*). The shape of the iron(II) oxidation peak is distorted somewhat (flattened), since there is no portion of current drop after the maximum because of an increase in the current, associated with the subsequent peak of oxidation of organic compounds (phenolsulfonic acid and SAA). This fact makes it difficult to measure the current of the iron(II) oxidation peak. A tenfold dilution of phenolsulfonic acid with sulfuric acid is sufficient for obtaining an analytical signal of iron(II) that is suitable for measurements (Fig. 3, curve *3*). In such a supporting solution, tin(II) does not affect the current of iron(II) oxidation peak, either. The linear calibration plot for the current of the iron(II) peak was obtained in a phenolsulfonic electrolyte diluted with 0.5 M sulfuric acid within the range 1–15 g l^{-1} iron(II).

To improve the peak parameters, electrochemical oxidation of iron(II) was studied in a 0.2 M solution of oxalic acid (pH ≈ 3). The peak of iron(II) oxidation in this supporting electrolyte is shifted somewhat to the cathodic region and has a more clearly pronounced shape than that in the sulfate solution. Unfortunately, tin(II) is also oxidized in the oxalate supporting solution in the anodic region. For this reason, oxalic acid

Results of voltammetric determination of Sn^{2+} and Fe^{2+} on renewed graphite electrode in phenolsulfonic electrolyte for tin plating

Fed, g l^{-1}		Found by voltammetry, g l^{-1}		S_r		Volumetric analysis, g l^{-1}	
Sn^{2+}	Fe^{2+}	Sn^{2+}	Fe^{2+}	Sn^{2+}	Fe^{2+}	Sn^{2+}	Fe^{2+}
25.4	7.99	25.2 ± 0.4	8.01 ± 0.16	0.021	0.028		
29.4	10.01	29.5 ± 0.3	9.98 ± 0.08	0.016	0.008		
34.8	15.05	35.1 ± 0.2	15.1 ± 0.2	0.011	0.013		
		26.6 ± 0.6	1.0 ± 0.1	0.019	0.039	27.8	Not found
		13.0 ± 0.3	1.3 ± 0.1	0.022	0.036	11.8	″
		30.0 ± 0.4	3.5 ± 0.1	0.011	0.014	30.2	3.8
		28.0 ± 0.6	5.2 ± 0.1	0.021	0.016	29.2	6.5

cannot be used as supporting solution in determining iron(II) in tin-plating electrolytes. To obtain reliable results in voltammetric determination of iron(II), it is important to renew mechanically the surface of the graphite electrode in the solution being analyzed each time before recording a voltammogram, similarly to the case of tin(II). This makes it possible to obtain peaks with well-reproducible intensities (see table). Presumably, electrochemical renewal of the electrode surface without cutting off a spent layer is insufficient, since such a renewal changes the shape of the iron(II) peak, with the peak becoming flattened and disappearing completely in the subsequent tests. Probably, iron(II) oxidation is hindered in this case by adsorption of organic components (phenolsulfonic acid, surfactant, and products of their oxidation) of the solution on the graphite electrode.

To determine tin(II), phenolsulfonic tin-plating electrolyte (25–30 cm^3) was charged into an electrolyzer with electrodes, the surface of the graphite indicator electrode was renewed by cutting off a 1–2-μm layer, the potential of polarization onset was set at –0.4 V relative to a saturated Calomel electrode, and the cathodic peak of tin(II)was recorded in the potential range –0.9 … –0.95 V at a sweep rate of 100 mV s^{-1}. The peak current was measured and the tin(II) concentration in the electrolyte was found from the calibration plot.

To determine iron(II), 5 cm^3 of phenolsulfonic electrolyte was placed in a 50-cm^3 volumetric flask, and 0.5 M H_2SO_4 was added to the marker. The mixture was stirred and part of it was poured into the electrolyzer. The surface of the graphite indicator electrode was renewed by cutting off a ~1–2-μm layer, the onset potential of polarization was set at 0.0 V, and the peak of the anodic oxidation of iron(II) was recorded at a potential sweep rate of 50 mV s^{-1}. The current of the iron(II) peak at +0.78 V was determined, and the iron(II) concentration was found from the calibration plot.

The results obtained were verified by the "fed–found" method on model solutions of phenolsulfonic electrolyte, and also on technological electrolytes taken from a working electrolyzer, by comparing the results of voltammetric determination with the previously obtained data of chemical analysis. Table lists the results of a voltammetric determination of tin(II) and iron(II) on a renewed graphite electrode.

The good reproducibility and correctness of the results obtained in model solutions can be attributed to the fact that the analysis was done in freshly prepared solutions. Apparently, a slight deviation of the results of voltammetric determination in technological solutions from the previous data of chemical analysis stems from the fact that they were obtained at different times. Oxidation processes permanently occur in an electrolyte, which results in that the concentration of the cations being determined varies somewhat.

The voltammetric method has the following advantages: it is fast, simple, and can be automated. The time necessary for analyzing a single sample for the content of two components is less than 10 min.

CONCLUSION

A fast instrumental method for determining on-line the content of tin(II) and iron(II) by dc voltammetry on a graphite mechanically renewed electrode in phenolsulfonic tin-plating electrolyte with linear potential sweep was developed.

REFERENCES

1. Kudryavtsev, N.T., *Elektrokhimicheskie pokrutiya metallami* (Electroplated Metal Coatings), Moscow: Khimiya, 1979.

2. Golikov, N.S., and Simonova, M.E., *Zashch. Met.*, 1965, vol. 1, no. 4, pp. 447–449.
3. Il'in, V.A., *Khimicheskie i elektrokhimicheskie protsessy v proizvodstve pechatnykh plat* (Chemical and Electrochemical Processes in Manufacture of Printed-Circuit Boards), Moscow: Khimiya, 1995.
4. Kiryushov, V.N., and Kopylova, N.S., *Zavod. Lab.*, 1998, no. 8, pp. 3–5.
5. Kryukova, G.A., Sinyakova, S.I., and Aref'eva, G.V., *Polyarograficheskii analiz* (Polarographic Analysis), Moscow: Goskhimizdat, 1959.
6. Vinogradova, E.N., Gallai, Z.A., and Finogenova, Z.M., *Metody polyarograficheskogo i amperometricheskogo analiza* (Methods of Polarographic and Amperometric Analysis), Moscow: Mos. Gos. Univ., 1963.
7. Kletenik, Yu.B., Bek, R.Yu., Kiryushov, V.N., *et al.*, *Izv. Sib. Otd. Akad. Nauk SSSR, Ser. Khim. Nauk.*, 1985, vol. 2, no. 1, pp. 85–92.
8. Kletenik, Yu.B., and Aleksandrova, T.P., *Zh. Anal. Khim.*, 1997, vol. 52, no. 3, pp. 280–284.

Russian Journal of Applied Chemistry, Vol. 76, No. 6, 2003, pp. 917–922. Translated from Zhurnal Prikladnoi Khimii, Vol. 76, No. 6, 2003, pp. 947–952.

APPLIED ELECTROCHEMISTRY AND CORROSION PROTECTION OF METALS

Joint Electrodeposition of Tellurium(IV) and Cadmium(II) from Acid Solutions in the Presence of 2,2'-Dipyridyl

M. B. Dergacheva, V. N. Statsyuk, L. A. Fogel', and N. V. Pen'kova

Sokol'skii Institute of Organic Catalysis and Electrochemistry, Ministry of Education and Science of the Republic of Kazakhstan, Almaty, Kazakhstan

Received September 26, 2002; in final form, March 2003

Abstract—Cyclic voltammetry was applied to study the effect of addition of 2,2'-dipyridyl on joint electroreduction of Te(IV) and Cd(II) from sulfuric acid solutions on glassy carbon and titanium electrodes. The optimal potentials of electrodeposition of CdTe films were determined and the structure of these films was studied by means of X-ray phase analysis.

The method of electrochemical deposition of thin films of semiconducting compounds, with underpotential deposition of the second component (UPD method) was described by Stickney *et al.* [1]. Later, this technique has been used to obtain very thin films of a semiconducting compound, CdTe [2–6]. This method can be conveniently applied to obtain a photosensitive material at common pressures and temperatures.

Cadmium telluride is a semiconductor with energy gap of 1.44 eV and one of the best suitable materials for use in devices for solar energy conversion.

The known method for obtaining CdTe films includes electrodeposition from sulfuric acid solutions containing 0.5 M $CdSO_4$ and 4.5×10^{-3} M K_2TeO_3 at pH 1.4–1.6 and temperatures of 85–90°C [3, 5]. A low rate of CdTe deposition from these solutions, which results from the low concentration of tellurium(IV) in the electrolyte, has been noted. Therefore, a number of researchers suggested to use complex compounds of tellurium in nonaqueous electrolytes [7] or ammonia media [8]. The choice of an electrolyte and electrodeposition conditions strongly affects the structure and phase composition of the deposits obtained [4, 5].

The present study is concerned with conditions of CdTe electrodeposition from sulfuric acid solutions, with addition of 2,2'-dipyridyl as a complexing agent for cadmium and a surfactant. Account is taken of the fact that, in acid solutions, 2,2'-dipyridyl is adsorbed on the electrode in the form of protonated molecules [9].

EXPERIMENTAL

The experimental procedure was described in detail in [10, 11]. As working electrodes served glassy carbon and titanium disk-shaped electrodes with apparent surface area of 0.07 cm^2. A platinum coil with large surface area (1.5 cm^2) was used as auxiliary electrode. All the potentials obtained experimentally in this study are given relative to a silver chloride reference electrode. Before carrying out an experiment, the surface of working electrodes was subjected to mechanical treatment with finely dispersed Al_2O_3 and then washed with distilled water. The structure of cadmium telluride films was studied using a DRON-4 instrument with Co-radiation. For this purpose, cadmium telluride films were deposited onto 1×1 cm glassy carbon or titanium plates.

As supporting electrolyte served 0.45 M Na_2SO_4 + 0.05 M H_2SO_4 solution.

To reveal specific features of the electrochemical reactions leading to the formation of CdTe compound, cyclic voltammetric curves of joint reduction of Cd(II) and Te(IV) ions in a sulfuric acid solution at a glassy carbon electrode were measured (Fig. 1a). In the first reduction cycle (curve *1*), the voltammetric curve shows a Te(IV) ion reduction wave (E_{max} = –0.26 V) by the reaction

$$Te(IV) + 4e \rightarrow Te^0 \quad (1)$$

and a Cd(II) ion reduction wave (E_{max} = –0.8 V) by the reaction

$$Cd(II) + 2e \rightarrow Cd^0. \quad (2)$$

1070-4272/03/7606-0917 $25.00 © 2003 MAIK "Nauka/Interperiodica"

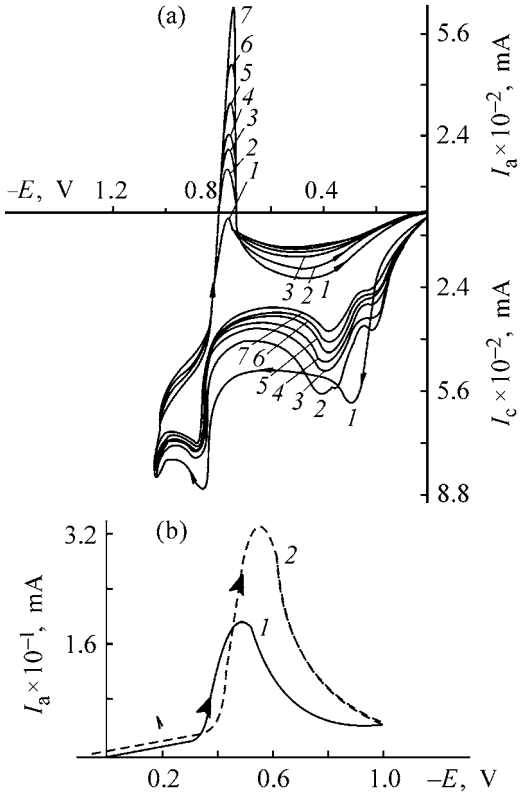

Fig. 1. Voltammetric curves of joint discharge–ionization of Te(IV) and Cd(II) ions on a glassy carbon electrode in sulfate electrolytes of various compositions. (*I*) Current and (*E*) potential; the same for Figs. 2–4. (a) $c_{Te(IV)} = c_{Cd(II)} = 1 \times 10^{-3}$ M. (b) $c_{Te(IV)} = 0.98 \times 10^{-3}$ M; $c_{Cd(II)}$ (M): (*1*) 0 and (*2*) 0.5×10^{-3}.

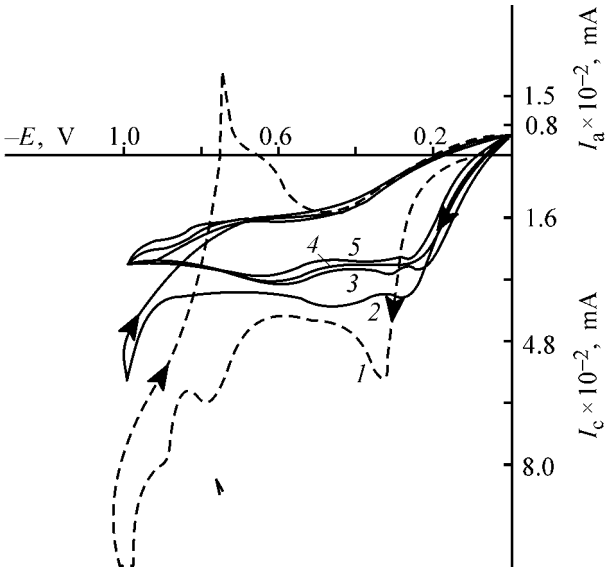

Fig. 2. Cyclic voltammetric curves of CdTe reduction on a glassy carbon electrode in the presence of 2,2'-dipyridyl. Cycling range 0…–1.1 V, $c_{Te(IV)} = c_{Cd(II)} = c_{dipy} = 1 \times 10^{-3}$ M. *Digits at curves* correspond to cycle numbers.

The peak of reduction of metallic tellurium to telluride ions

$$Te^0 + 2e \rightarrow Te^{2-}, \quad (3)$$

which is characteristic of reduction of elementary tellurium and commonly appears at the limiting current of Te(IV) reduction at negative potentials, is not observed. In the second reduction cycle (Fig. 1a, curve *2*), the Te(IV) reduction wave in the voltammetric curves is shifted to more positive potentials, the current of Te(IV) reduction decreases, and an additional reduction wave with characteristic peak ($E_{max} = -0.35$ V) appears. The height of the Cd^{2+} reduction wave increases with respect to the limiting current of Te(IV) reduction. When the potential sweep direction is changed, the anodic voltammetric curves show a rise in the height of the peak corresponding to oxidation of metallic cadmium ($E_p = -0.7$ V).

In the subsequent reduction cycles (curves *3–7*), the Te(IV) reduction current and the current of the additional wave decrease, but the Cd(II) reduction wave becomes more pronounced [the difference of the limiting current of Te(IV) and the current corresponding to the Cd(II) peak grows], which leads to an increase in the amount of metallic cadmium on the electrode surface and to a rise in the oxidation current of metallic cadmium in the reverse run of the voltammetric curves.

Figure 1b (curve *2*) shows that formation of the CdTe compound shifts the anodic peak of tellurium oxidation to Te(IV) to more positive potentials to $E = 0.56$ V. The shift is 0.06 V.

Figure 2 shows cyclic voltammetric curves of joint reduction of Te(IV) and Cd(II) on a glassy carbon electrode in a sulfuric acid electrolyte in the presence of 1×10^{-3} M of 2,2'-dipyridyl. In the first cycle (Fig. 2, curve *1*), the voltammetric curve shows a Te(IV) reduction wave, which is peaked at $E_{max} = -0.3$ V, a peak of Cd(II) reduction ($E_p = -0.8$ V), and a wave of 2,2'-dipyridyl reduction ($E_{1/2} = -0.85$ V). A peak corresponding to Cd^0 oxidation to Cd^{2+} ($E_p = -0.73$ V) appears in the anodic region. In the second and subsequent cycles (Fig. 2, curves *2–5*), the cathodic curves show a shift of the Te(IV) reduction wave to less negative potentials and a significant decrease in the current of Te(IV) reduction. An additional Cd(II) reduction wave, which is clearly observed in an acid solution containing no 2,2'dipyridyl at potentials more negative than –0.3 V [12–16], is weakly manifested in the presence of 2,2'-dipyridyl. In the absence of 2,2'-dipyridyl, the anodic peak of Cd^0 oxidation to Cd^{2+} grows with increasing number of deposition cycles

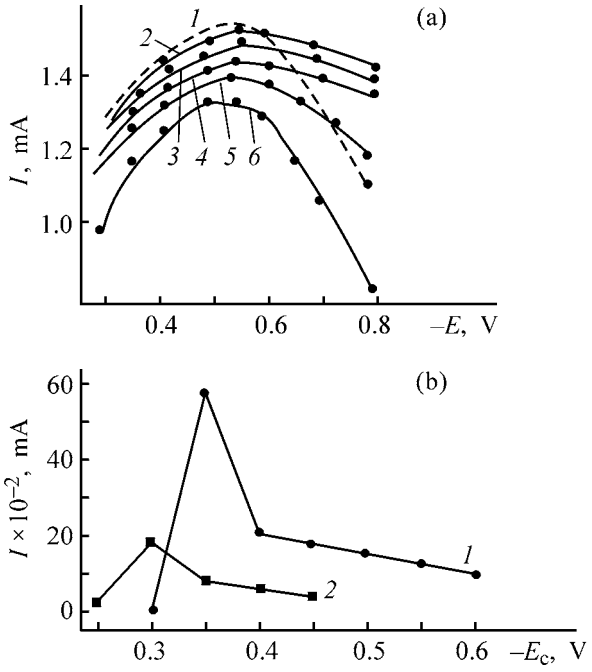

Fig. 3. Effect of CdTe deposition potential on the current of anodic peaks of oxidation (a) in the presence of 2,2'-dipyridyl and (b) without it on (a) glassy carbon and (b) titanium electrodes. (a) c_{dipy} (M): (*1*) 0, (*2*) 1.7×10^{-4}, (*3*) 3.4×10^{-4}. (*4*) 6.7×10^{-4}, (*5*) 1×10^{-3}, and (*6*) 2.7×10^{-3}. (b) Concentration (M): (*1*) 1×10^{-3} Te(IV) and 1×10^{-3} Cd(II), (*2*) 1×10^{-3} Te(IV) and 1×10^{-2} Cd(II).

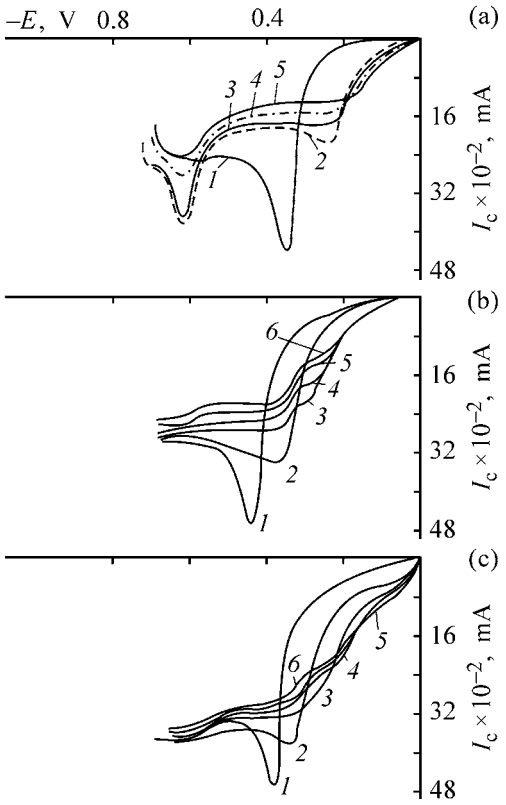

Fig. 4. Voltammetric curves of cathodic deposition of Te(IV) and Cd(II) on an unrenewed titanium electrode. Potential sweep rate V_s = 10 mV s^{-1}. Concentration (M): (a–c) 1×10^{-3} Te(IV), (b, c) 1×10^{-3} Cd(II), (c) 2.5×10^{-4} dipy.

(Fig. 1a), whereas in the presence of this compound, this peak is virtually not observed at all (Fig. 2). This indicates that electrodeposition of cadmium is hindered in the presence of 2,2'-dipyridyl.

Also, the influence exerted on the height of anodic peaks of CdTe oxidation by the potential of CdTe deposition onto a glassy carbon electrode in a sulfuric acid electrolyte at various 2,2'-dipyridyl concentrations was studied. The concentrations of tellurium(IV) and cadmium(II) were 1×10^{-3} M, and that of 2,2'-dipyridyl was varied from 1.7×10^{-4} to 2.7×10^{-3} M. The deposition potentials were in the range from –0.3 to –0.8 V. Before measuring anodic voltammetric curves, CdTe was deposited onto the electrode surface at the chosen cathodic potentials with electrolyte stirring for 30 s. With increasing 2,2'-dipyridyl concentration, the heights of anodic peaks of cadmium telluride oxidation decrease, i.e., the amount of CdTe deposit on the electrode surface becomes lower (Fig. 3a). At low 2,2'-dipyridyl concentrations (up to 1×10^{-3} M), the range of cadmium telluride electrodeposition expands. Deposition of cadmium telluride on the surface of the glassy carbon electrode is possible at these 2,2'-dipyridyl concentrations at potentials ranging from –0.2 to –0.8 V. However, at higher 2,2'-dipyridyl concentration (2.7×10^{-3} M), the range of electrodeposition becomes markedly narrower. The maximum amount of cadmium telluride electrodeposited from a sulfuric acid electrolyte in the presence of 2,2'-dipyridyl is observed at electrodeposition potential E = –0.5 V (Fig. 3a).

Joint electrodeposition of tellurium(IV) and cadmium(II) at their equal concentrations in the electrolyte (1×10^{-3} M) was also studied by analyzing cyclic voltammetric curves of cathodic deposition onto the titanium electrode. In Figs. 4a–4c, these curves are compared with cyclic curves of tellurium(IV) electrodeposition onto a titanium electrode. As in all of the above-described experiments, the second and subsequent curves of Te(IV) reduction (Fig. 4a) show a significant shift of the reduction potential in the positive direction, which is due to reduction of Te(IV) at the surface of an electrode partly covered with metallic tellurium and to a gain in the crystallization energy. In the absence of cadmium(II),

two stages of tellurium(IV) reduction to tellurium(0) and then to tellurium(–2) is clearly observed in all deposition cycles. The decrease in the height of the first Te(IV) reduction wave with increasing number of cycles may be associated with the possible decrease in the amount of $HTeO_2^+$ cations at the electrode surface in unstirred solutions because of the reaction between Te(IV) and Te(–2) to give finely dispersed Te(0) or with a change in the conductivity of the tellurium-coated electrode.

The half-wave potential for the first stage of reduction changes from second to sixth cycle only slightly (Fig. 4a). It may be assumed that adsorption of dispersed tellurium formed by reaction (1) at the electrode has virtually no effect on the reduction potential.

The general appearance of the first wave in the voltammetric curve of electroreduction is preserved when there occurs joint reduction of tellurium(IV) and cadmium(II) (Fig. 4b). However, the second peak of tellurium(0) reduction to telluride ions in the range of negative potentials under study (up to –0.8 V) disappears in this case. This points to firm binding of telluride into a compound with cadmium. The cadmium reduction wave, which must have appeared at a potential of –0.7 V at the titanium electrode, is also absent at the chosen relative concentrations of Te(IV) and Cd(II). Preliminary experiments revealed that the cadmium reduction wave is observed at this potential if the cadmium(II) concentration exceeds severalfold the concentration of tellurium(IV).

It can be seen from Fig. 4b that a clearly pronounced additional wave appears in the third and subsequent reduction cycles. Additional reduction current appears at a potential of –0.3 V. The limiting current of this wave preserves its value as far as –0.75 V. The nature of this additional wave has been discussed previously [14, 17]. This wave is due to underpotential reduction of cadmium at a tellurium-coated electrode by the so-called UPD reduction mechanism. The potential of cadmium(II) reduction is shifted by approximately 0.470 V because of the high Gibbs energy of CdTe compound formation, which is equal to –92.8 kJ mol^{-1} [1]. Therefore, the reaction of reduction at potentials of the additional wave can be written as

$$Cd^{2+} + 2e + Te^0_{surf} \rightarrow CdTe. \quad (4)$$

Despite that the subsequent reduction cycles occur at the electrode surface partly covered with a CdTe deposit, the additional reduction wave remains well pronounced. Analysis of the reduction potentials (Fig. 4b) shows that the potential of the additional wave of cadmium(II) reduction virtually coincides, in the first and second cycles, with the potential of the tellurium(IV) reduction wave, which occurs with substantial overvoltage at the clean surface of the titanium electrode.

Introduction of 2,2'-dipyridyl additive raises the limiting current of the additional reduction wave (Fig. 4c). This effect may be due to adsorption on the electrode of complexes formed by cadmium and 2,2'-dipyridyl, which act as additional source of cadmium ions in reaction (4). The amount of CdTe deposit accumulated on the electrode surface was determined from the oxidation current of this compound under assumption that the current is proportional to the amount of the substance on the electrode.

The oxidation peak height grows with accumulation of CdTe on the titanium electrode. The heights of oxidation peaks of CdTe accumulated during 120 s with stirring at different potentials without 2,2'-dipyridyl were used to choose the potential at which the greatest amount of CdTe is deposited. The deposition was done on a titanium electrode at potentials in the range $E = -0.30\ldots-0.60$ V. Figure 3b (curve *1*) shows that the highest oxidation current is observed if the CdTe deposit is accumulated at $E = -0.35$ V.

Deposition of CdTe at this potential in the presence of 2,2'-dipyridyl in different concentrations demonstrated that the greatest amount of CdTe is deposited at 2,2'-dipyridyl concentration of 2.5×10^{-4} M. Deposition of CdTe with accumulation for 120 s at different potentials in the presence of 2.5×10^{-4} M 2,2'-dipyridyl confirmed that the highest current of CdTe oxidation corresponds to potential $E = -0.35$ V.

Also, the effect of varying the ratio of initial cadmium and tellurium concentrations on conditions of CdTe deposition onto a titanium electrode was studied. On raising the concentration of cadmium by a factor of 10 (1×10^{-3} M K_2TeO_3 + 1×10^{-2} M $CdSO_4$), the height of the peak of tellurium(IV) reduction to tellurium(0) decreases as compared with that in the voltammetric curve for Cd : Te = 1 : 1, and the currents of cadmium oxidation and reduction increase in proportion to its concentration in solution. In this case, the peak of CdTe oxidation at the titanium electrode is not observed in the anodic region. At high content of cadmium in the electrolyte, the peak of CdTe oxidation becomes noticeable when the oxidation curve is measured after accumulation of cadmium telluride for 120 s ($E = -0.30$ V) under stirring, which indicates that the amount of CdTe electrodeposited in the presence of a large excess of Cd(II) ions in the

electrolyte is smaller. Figure 3b (curve *2*) shows that the maximum current of CdTe oxidation corresponds to a deposition potential $E = -0.30$ V, i.e., the optimal potential of CdTe deposition is shifted to less negative values in the presence of an excess amount of cadmium ions in the electrolyte. In this case, the current of CdTe oxidation is much lower than the oxidation currents observed at equal Cd and Te concentrations in the electrolyte.

On the basis of the results obtained, the following electrolytes and potentials for electrodeposition of CdTe compound in 0.45 M Na_2SO_4 + 0.05 M H_2SO_4 as supporting electrolyte were chosen: 1×10^{-3} M $CdSO_4$ + 1×10^{-3} M K_2TeO_3 and 1×10^{-3} M $CdSO_4$ + 1×10^{-3} M K_2TeO_3 + 3.4×10^{-4} M dipy at $E = -0.50$ V on glassy carbon electrode; 1×10^{-3} M $CdSO_4$ + 1×10^{-3} M K_2TeO_3 and 1×10^{-3} M $CdSO_4$ + 1×10^{-3} M K_2TeO_3 + 2.5×10^{-4} M dipy at $E = -0.35$ V on titanium electrode.

These electrolytes were used to obtain CdTe deposits on large planar electrodes with surface area of 1 cm^2. An X-ray phase analysis of these deposits was made.

Figure 5 shows X-ray diffraction patterns of cadmium telluride films on a glassy carbon electrode. It can be seen that the film obtained at 90°C (Fig. 5b) is characterized by more distinct reflections of the CdTe compound. The reflections from the substrate are poorly pronounced. This means that the electrodeposition process yielded a film whose crystal structure is well formed. By contrast, electrodeposition at a temperature of 30°C (Fig. 5a) gives a more amorphous film whose X-ray pattern is complicated by reflections associated with carbon mainly constituting the glassy carbon electrode. This confirms the conclusion that electrodeposition should be carried out in conventional electrolytes at elevated temperatures to ensure better crystallization conditions.

In the case of electrodeposition of cadmium telluride from a sulfuric acid electrolyte containing 2,2'-dipyridyl, the X-ray diffraction pattern changes. Figures 5c and 5d show diffraction patterns of CdTe films deposited at 30 and 90°C and $E = -0.5$ V. It can be seen that addition of 2,2'-dipyridyl favors crystallization and makes it possible to obtain a crystalline film with well-pronounced structure at low temperature and the optimal electrodeposition potential equal to –0.5 V.

The shift of the electrodeposition potential to the negative direction has unfavorable effect on the structural characteristics of a film. When this potential

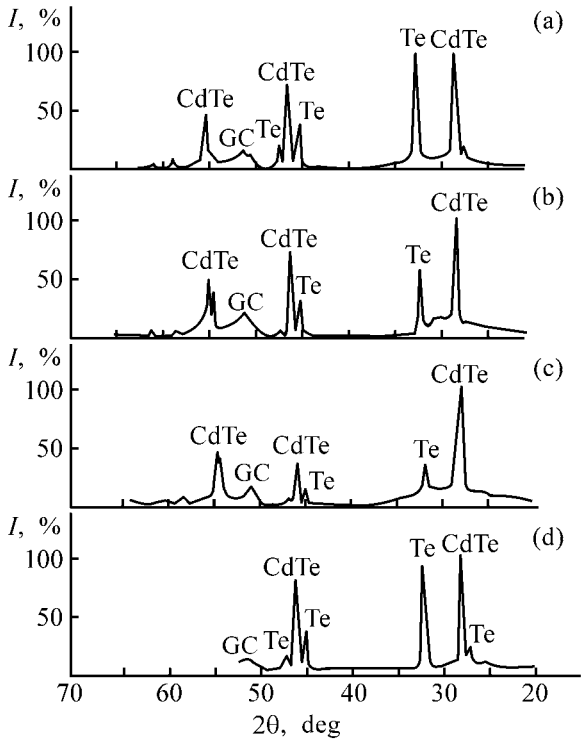

Fig. 5. X-ray diffraction patterns of CdTe films on glassy carbon electrode. (I) Intensity and (2θ) Bragg angle; the same for Fig. 6. Concentration (M): (a–d) 1×10^{-3} Te(IV) and 1×10^{-3} Cd(II) and (c, d) 3.4×10^{-4} dipy. Temperature (°C): (a, c) 30 and (b, d) 90.

approaches the electrodeposition potential of cadmium (–0.8 V), the X-ray diffraction pattern is affected adversely. The films obtained are thin, the reflections are unclear, and the whole pattern is complicated by carbon reflections.

Raising the concentration of 2,2'-dipyridyl changes the X-ray diffraction pattern: CdTe films become thinner, but the density and adhesion of these films are higher than those in films obtained without addition of 2,2'-dipyridyl.

Tellurium is present in the form of a separate phase in all of the X-ray diffraction patterns, with a decrease in the intensity of tellurium peaks in comparison with CdTe peaks observed when electrodeposition onto a glassy carbon electrode is performed at 30°C, 2,2'-dipyridyl concentration of 3.4×10^{-4} M (Fig. 5c), concentration ratio Cd : Te = 1 : 1 ($c_{Cd(II)} = c_{Te(IV)} = 1 \times 10^{-3}$ M), and electrodeposition potential $E = -0.5$ V.

Thus, it was established that, by introducing minor concentrations of 2,2'-dipyridyl into an electrolyte, one can obtain a well-formed crystalline deposit as a CdTe film with lowered content of the free tellurium phase at low temperatures.

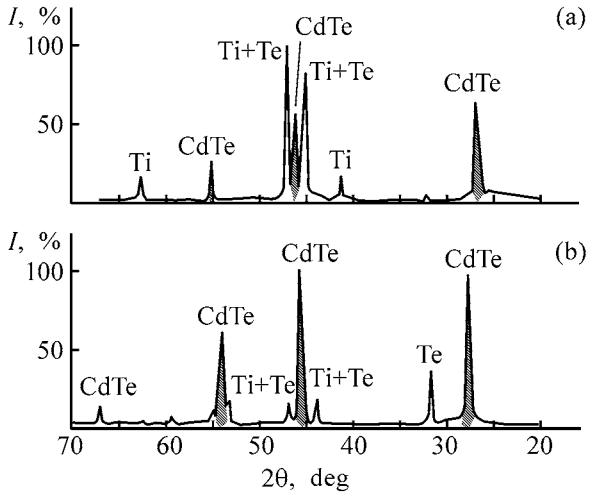

Fig. 6. Effect of 2,2'-dipyridyl on X-ray diffraction patterns of CdTe films on titanium electrode. Deposition conditions: $E = -0.35$ V, $t = 90$°C. 2,2'-dipyridyl concentration (M): (a) 0 and (b) 2.5×10^{-4}.

Figure 6 shows X-ray diffraction patterns of CdTe films deposited at 90°C onto a titanium electrode at $c_{Te(IV)} = c_{Cd(II)} = 1 \times 10^{-3}$ M without 2,2'-dipyridyl (Fig. 6a) and with addition of 2.5×10^{-4} M 2,2'-dipyridyl at the choses optimal deposition potential $E = -0.35$ V (Fig. 6b).

It can be seen from Fig. 6 that a significant decrease in the content of the free tellurium phase and predominance of CdTe reflections are observed under these conditions. The results obtained suggest that the titanium substrate exerts a specific influence on the deposit structure. The favorable effect of 2,2'-dipyridyl addition on the structure of the CdTe deposit on titanium is only observed in the case of deposition at 90°C and a 1 : 1 ratio of the cadmium and tellurium concentrations in the electrolyte. (Fig. 6b). The X-ray diffraction pattern in Fig. 6b characterizes the formation of a well-structured CdTe film with 100% main peak intensities and a pronounced decrease in the relative content of the tellurium phase to 20%.

CONCLUSIONS

(1) In joint electrodeposition of cadmium(II) and tellurium(IV), cadmium is reduced at more positive potentials than its standard potential, with the CdTe compound formed.

(2) Introduction of 2,2'-dipyridyl into a sulfuric acid electrolyte makes higher the limiting current of the additional cadmium reduction wave.

(3) Use of an electrolyte containing equal amounts of cadmium(II) and tellurium(IV) and minor addition of 2,2'-dipyridyl [$(2.5–3.4) \times 10^{-4}$ M] makes it possible to obtain CdTe deposits at 30°C and to diminish the content of the free tellurium phase.

REFERENCES

1. Gregory, B.W. and Stickney, J.Z., *J. Electroanal. Chem.*, 1991, vol. 300, pp. 543–561.
2. Gregory, B.W., Suggs, D.W., and Stikney, J.Z., *J. Electrochem. Soc.*, 1991, vol. 138, no. 5, pp. 2–1284.
3. Youu, J.K., Yang, Y., Chen, X.G., *et al., J. Electroanal. Chem.*, 1996, vol. 305, nos. 1–2, pp. 233–237.
4. Danaher, W.J. and Zyons, Z.E., *Aust. J. Chem.*, 1983, vol. 36, pp. 1011–1016.
5. Peter, Z.M. and Wang, R.Z., *Electrochem. Commun.*, 1999, no. 1, pp. 544–558.
6. Saraby-Reintjes, A., Peter, Z.M., Özsan, M.E., *et al., J. Electrochem. Soc.*, 1993, vol. 140, no. 10, pp. 2880–2888.
7. Rastogi, A.C. and Balakrishnan, K.S., *J. Electrochem. Soc.*, 1989, vol. 136, no. 5, pp. 2–1506.
8. Murase, Watanabe, H., Mori, S., *et al., J. Electrochem. Soc.*, 1999, vol. 146, no. 12, pp. 4477–4484.
9. Zhdanov, S.I., Abilova, M.U., Shaldybaeva, A.M., and Mambetkaziev, E.A., in *Sbornik MV i SSO KazSSR "Fizikokhimicheskoe issledovanie slozhnykh sistem"* (Coll. of Works of the Ministry of Higher and Special Secondary Education "Physicochemical Study of Complex Systems"), Alma-Ata: KGU, 1981, pp. 48–56.
10. Dergacheva, M.B., Statsyuk, V.N., and Fogel', L.A., *Elektrokhimiya*, 2001, vol. 37, no. 6, pp. 734–737.
11. Dergacheva, M.B., Statsyuk, V.N., Fogel', L.A., and Abdrakhimova, A.R., *Zh. Prikl. Khim.*, 1998, vol. 41, no. 4, pp. 616–619.
12. Panicker, M.P.R., Knaster, M., and Kröger, F.A., *J. Electrochem. Soc.*, 1978, vol. 125, no. 4, pp. 566–572.
13. Engelken, R.D. and Van Doren, T.P., *J. Electrochem. Soc.*, 1985, vol. 132, no. 12, pp. 2904–2909.
14. Sella, C., Boncorps, P., and Vedel, J., *J. Electrochem. Soc.*, 1986, vol. 133, no. 12, pp. 2043–2047.
15. Dergacheva, M.B., Statsyuk, V.N., Fogel, L.A., *et al., IV Int. Symp. of "New Electrochemical materials,"* Canada, 2001, p. 103.
16. Fogel', L.A., Elecrochemical Reactions Involving Tellurium(IV) Ions and Their Role in Electrodeposition of Semiconducting Compounds, *Cand. Sci. Dissertation*, Almaty, 2002.
17. Abdrakhimova, A.R., Electrochemical Processes in Deposition of $Cd_xHg_{1-x}Te$ Semiconducting Formulation, *Cand. Sci. Dissertation*, Almaty, 2000.

Russian Journal of Applied Chemistry, Vol. 76, No. 6, 2003, pp. 923–928. Translated from Zhurnal Prikladnoi Khimii, Vol. 76, No. 6, 2003, pp. 953–958.

APPLIED ELECTROCHEMISTRY AND CORROSION PROTECTION OF METALS

Processes in a Nickel-Zinc Battery with Nickel Oxide Electrode Fabricated from Spherical Nickel Hydroxide

Z. P. Arkhangel'skaya, T. B. Kas'yan, M. M. Loginova, and L. B. Raikhel'son

Akkumulyatornaya Kompaniya Rigel' Open Joint-Stock Company, St. Petersburg, Russia

Received January 15, 2003

Abstract—Processes occurring in a cycled nickel-zinc battery with positive nickel oxide electrode fabricated from spherical nickel hydroxide on foamed-nickel support and the influence exerted by its physicochemical parameters on changes in the electrolyte composition and on inter- and intraelectrode mass transfer of zinc was studied.

Until recently, positive electrodes with metal-ceramic (MC) support have been predominantly used in nickel-zinc (NZ) batteries, because, in contrast to compacted electrodes, they are not "poisoned" by zinc ions. The successful use of electrodes made of spherical nickel hydroxide in nickel-cadmium (NC) and nickel-metal-hydride (NMH) batteries posed the question of their suitability for NZ batteries, too. First, use of spherical nickel hydroxide could help in solving the problem of poisoning of a compacted nickel oxide electrode (NOE), since introduction of hydroxide compounds of cobalt into the electrode stabilizes the electrode capacity in the presence of zinc [1]. Second, use of an active paste composed of spherical particles, which can be well compacted, and lightweight foamed support could improve the energy-related characteristics of a battery [2, 3]. In addition, a study of processes occurring in NZ batteries with compacted NOE is of particular interest for revealing the influence of its physicochemical parameters on processes occurring in the electrode itself and at the zinc electrode.

It seems impossible to use for this purpose, for prognosticating the characteristics and service life of NZ batteries, data obtained for NC and NMH batteries, since processes in NOE in the nickel–zinc system occur under different conditions.

This study is concerned with prototype NTs-25 batteries differing from previously developed batteries only in the positive electrode: in these batteries the NOE with MC support onto which nickel hydroxide is deposited is replaced with NOE with compacted active mass composed of spherical nickel hydroxide on foamed-nickel support at the same number of electrodes and same apparent surface area.

The advantage of spherical nickel hydroxide prepared by the technology developed in [2] over the materials previously used in compacted electrodes is due not only to the possibility of denser (by a factor of 1.2–1.5) packing of its particles, but also to its higher conductivity. Cobalt hydroxide introduced into the electrode during its fabrication is transformed, in the course of NOE forming, into a compound with conductivity of 10^{-2} S cm^{-1}, which is several orders of magnitude higher than the conductivity of $Ni(OH)_2$, equal to 10^{-5} S cm^{-1} [4].

In the case of dense packing of nickel hydroxide particles modified with cobalt, a rather high solid-phase conductivity is ensured in NOE. Simultaneously, the conditions of ion transport in the liquid phase change fundamentally. The pore size in the active paste of the electrode in question are of the same order of magnitude as particle size, but the pores are closed. Therefore, their role in transport of electrolyte ions within the electrode is insignificant. By contrast, nickel hydroxide particles are distributed in the electrode of the MC type over the inner surface of coarser and deeper pores, which creates conditions for involvement of electrolyte ions in current transport deep inside the electrode.

EXPERIMENTAL

The electrodes for the batteries under study were fabricated by the technology described in [2, 3]. As starting material served nickel hydroxide composed

1070-4272/03/7606-0923 $25.00 © 2003 MAIK "Nauka/Interperiodica"

Table 1. Parameters of NTs-25 battery with NOE made of spherical nickel hydroxide on foamed-nickel support

Parameter	Electrode	
	positive*	negative
Active paste of electrodes, %	Ni 53.9, Co 5.1–5.6, Zn 3.2, fluoroplastic, carboxymethyl cellulose	ZnO, Zn_{met}, CdO, PbO, polyethylene oxide, fluoroplastic
Separator	Polypropylene	1. Polypropylene 2. Alkali-resistant paper 3. Hydrated cellulose film 101
Capacity ratio of active pastes (+/–)	1/2.3	
Battery mass, g	735	
Number of electrode assemblies	7(+)/8(–)	

* Positive electrode used in doubled form.

of 1–30-μm particles with predominant radius of about 10 μm. The active mass was pasted onto a foamed-nickel support and then the electrodes were compacted to a required thickness. The electrode parameters (amount and composition of paste, electrode thickness) were calculated in such a way that the prototype electrode should have capacity comparable with that of the MC electrode used in the NTs-25 battery. This made it possible not only to compare the parameters of the batteries under study with those of the existing batteries, but also to reveal specific features of processes occurring in compacted electrodes with foamed-nickel support.

Table 1 lists the initial parameters of the batteries under study.

The batteries were tested in a ventilated variant with low-pressure valves (0.4×10^2 kPa). In choosing the conditions of fabrication of prototype NOE and in performing tests, account was taken of the possible influence exerted by specific structural features of the active paste under study and by an additive introduced on the occurring processes and the electrochemical parameters of the NZ battery.

Nickel hydroxide with structure of the β type, used in the experiments, was chosen as optimal after testing several batches. It contained 5.6% Co and 3.2% Zn, which corresponds, for cobalt, to the range of optimal values (5–7%) found in [5] in an electrochemical and Raman study of nickel hydroxide of β type, $Ni_{1-x}Co_x(OH)_2$ [or $Ni_{1-x}Co_xOOH$].

Spherical nickel(II) hydroxide commonly contains, in addition to cobalt, 2–4% Zn(II), which is introduced to prevent formation in the electrode of the gamma phase of NiOOH, which has irregular and easily destructible structure. The presence of such an amount of zinc does not impair the service characteristics of NOE.

According to [6], up to 10 mol % zinc(II) can be introduced into NOE, with the structure of the β type preserved, and this does not affect adversely the parameters of the electrode. The solubility of the zinc component of the forming intercalation compound in alkaline solutions is approximately 2 orders of magnitude lower than the solubility of zinc oxide [7], i.e., the intercalating zinc remains in the active paste.

In cycling of NZ batteries with metal-ceramic NOE, more than 20% zinc(II) is accumulated in the electrodes. In battery charging, zinc is deposited within NOE pores as an independent ZnO phase [8]. It was observed that accumulation of zinc oxide in such great amounts does not affect adversely the parameters of MC NOE.

The tests were carried out with account of the data obtained in [4], where the mechanism of the activating action of cobalt compounds on the electrochemical activity of $Ni(OH)_2$ was studied and the composition of the oxide compound, which has electronic conduction and serves as active component, was determined. The charging was done in the rather intensive mode [with a current of 0.1–0.2 *C*] recommended in [4], which favors formation of the $Ni_{1-x}Co_xOOH$ phase on the basis of β-CoO_2H. In discharges, the potential was not allowed to decrease below 0.1 V relative to the mercury oxide reference electrode (in 7 M KOH solution) in order to preserve the activity of this compound. The potential only decreased below this value when performing two deep discharges, with no more than 20% of the total capacity taken off, in view of the necessity for oxidation of the reduced phase accumulated in the zinc electrode.

The extent to which an electrode fabricated from spherical $Ni(OH)_2$ is charged in forming depends on the excess capacity imparted in the course of charging. At a capacity of 150% in terms of the $Ni(OH)_2 \rightarrow Ni(OH)_3$ conversion, a degree of charging equal to 90–95%, which is preserved in subsequent cycling, can be achieved in 2 or 3 cycles [2]. However, such a charging mode was found to be unacceptable for

Table 2. Modes of NTs-25 battery testing

Mode	Charging				Discharge	
	I (A) in indicated stage		U_c, V	C, A h	I, A	U_c, V
	I	II				
Forming cycles:						
1st	3	–	1.98–2.05	33	3	1.2
2nd	3	–	1.98–2.05	33	3	1.2
Cycling	7–5	1.5–1	1.98–2.05	28–20	5	1.2
Deep discharge (126th cycle)	5	1	1.98–2.05	22	5	0.1–0.0

a ventilated NZ battery with 2.3/1 capacity ratio of the negative and positive electrodes.

The NTs-25 batteries studied were formed in two cycles. The charging current was 3 A, and 120% of capacity calculated for the conversion of $Ni(OH)_2$ into $Ni(OH)_3$ was imparted to the positive electrode in each cycle. The nickel use factor was 0.6.

In the subsequent working cycles, the batteries were charged with a current of 7–5 A in stage I and 1.5–1.0 A in stage II, without allowing the voltage to rise above 2.05 V in each stage, and discharged with a current of 5 A to final voltage of 1.2 V. In some cycles, the electrode potentials were measured relative to a mercury oxide electrode. The tests were done at room temperature.

Because of the increase in the amount of reduced phase in the zinc electrode in the process of cycling, its content became so high by 125th cycle that subsequent complete charging of the batteries was impossible. Therefore, they were subjected to deep discharge with a current of 5 A to a final voltage of 0.1–0 V, after which the battery capacity again stabilized at 24–22 A h (Table 2).

In cycling for 200 cycles, one battery of each batch was disassembled at regular intervals of time to inspect the state of the electrodes and to analyze the active paste and the electrolyte. The data obtained were compared with similar results of tests of NTs-25 batteries with MC NOE. It was found that the charging voltage of the batteries under study is somewhat lower than that of batteries with MC NOE (Fig. 1). This reflects the specificity of the processes at the NOE, which mostly occur in the inner-diffusion mode at low concentration of OH^- ions in the reaction zone in a battery with MC electrode, and in the outer-diffusion mode in the batteries with spherical nickel hydroxide, which are the subject of this study. The distribution of current within the MC electrode is largely due to the low conductivity of nickel hydroxides. In view of the high conductivity of the $Ni_{1-x}Co_xOOH$ compound contained in the positive electrode, the current in the batteries under study mostly flows in the solid phase and the electrochemical process occurs at the surface.

The difference in current distribution between the electrodes being compared is particularly pronounced in the case of deep discharge (Fig. 2). In the NOE

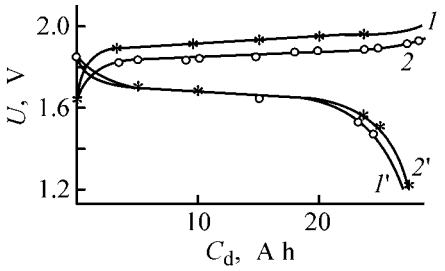

Fig. 1. Variation of the voltage U during (*1, 2*) charging and (*1'*, 2') discharge of NZ batteries with (*1, 1'*) NOE made of spherical nickel hydroxide on foamed-nickel support and (*2, 2'*) metal-ceramic electrode. (C_d) Discharge capacity; the same for Fig. 2.

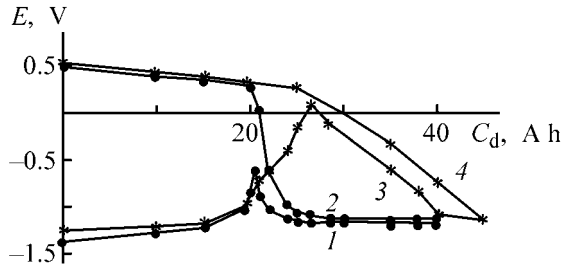

Fig. 2. Variation of the potentials E of (*1, 3*) negative and (*2, 4*) positive electrodes of NZ batteries with NOE on (*1, 2*) foamed-nickel and (*3, 4*) MC supports in deep discharge in the 126th cycle.

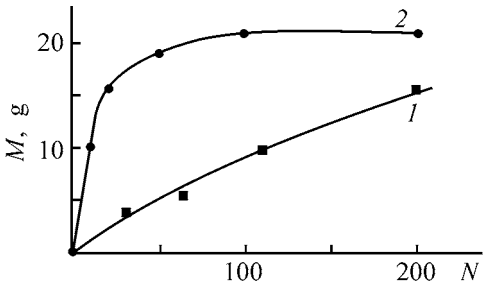

Fig. 3. Variation of the amount M of zinc accumulated in (*1*) NOE made of spherical nickel hydroxide on foamed-nickel support and (*2*) in metal-ceramic electrode in the course of cycling of NZ batteries. (N) Number of cycles; the same for Figs. 4 and 5.

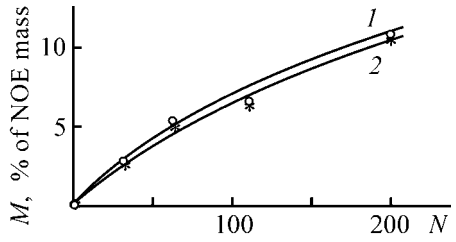

Fig. 4. Variation of the amount M of zinc (*1*) lost from the zinc electrode and (*2*) introduced into NOE made of spherical nickel hydroxide with foamed-nickel support in the course of cycling of NZ batteries.

with spherical nickel hydroxide, studied here, the potential rapidly shifts toward negative values, as far as the potential of hydrogen evolution, after the main part of the active paste is reduced. The discharge of a zinc electrode with excess capacity continues, after a short-time shift of the potential toward positive values, with simultaneous evolution of hydrogen at the NOE, until the charged phase contained in it is exhausted.

In additional discharge of MC NOE, the potential shifts more slowly. This indicates that, as the potential decreases, the process involves surface area with undischarged active paste, on which additional discharge of nickel hydroxide occurs at decreasing potential of the zinc electrode. The subsequent evolution of hydrogen at the NOE is accompanied by a similar gradual reverse shift of the potential of the zinc electrode toward negative values (Fig. 2).

The specific features of the processes occurring at NOE made of spherical nickel hydroxide give rise to differences in how the state of the active paste of the electrodes and the electrolyte composition vary in cycling of the batteries being compared. This, in the first place, refers to the inter- and intraelectrode mass transfer of zinc.

In NOE with MC support, zinc accumulates in pores, mainly as ZnO, through decomposition of the zincate complex under conditions of anodic polarization and incomplete chemical dissolution of zinc in the case of cathodic polarization [8].

In view of the increased conductivity of the solid spherical nickel hydroxide and hindered current transport in the electrolyte in pores, the electrochemical process in electrodes made of spherical $Ni(OH)_2$ is concentrated at the electrode surface and is accompanied by less pronounced changes in concentration in the diffusion layer. Therefore, accumulation of zinc in the electrode is slow and has another dynamics. In contrast to the MC electrode, in which mass transfer ceases after 50–60 cycles, the content of zinc in the NOE under study grows at a constant rate (Fig. 3). It is noteworthy that there exists a virtually complete correspondence between the mass of zinc lost by the negative electrode and that accumulated in the NOE (Fig. 4). The difference of these quantities approximately corresponds to the amount of zinc that passed into the electrolyte.

The difference in dynamics between the processes under consideration may be due to the following. In the absence of conditions for decomposition of the zincate complex in the diffusion layer of the electrode, accumulation of zinc may occur as a result of its introduction into the nickel hydroxide structure. The occurrence of this process and the degree of its involvement in zinc transport can be judged from the solubility of zinc contained in NOE in KOH solutions [7]. A chemical analysis of the positive electrode made of spherical nickel hydroxide, performed after 200 cycles, demonstrated that zinc accumulated in the electrode does not dissolve in a 5 M KOH solution (this concentration is established in the battery electrolyte in the course of cycling). After keeping the electrodes in KOH, 85.5% of the total amount of zinc accumulated in the NOE in cycling remains in the electrodes. Thus, loss of zinc from the negative electrode and its accumulation in NOE are due to introduction of zinc into the nickel hydroxide structure by intercalation.

Simultaneously with the decline in interelectrode transport of zinc in batteries with spherical NOE, compared with the MC electrode, the intraelectrode mass transfer of zinc within the negative electrode itself also decreases. This follows from the distribution of phases of the active paste along the electrode height in the course of cycling (Table 3).

It can be seen that no loss of zinc is observed in the upper part of the electrode. There only occurs

Table 3. Phase distribution in the active paste of the zinc electrode in NZ battery with NOE made of spherical nickel hydroxide in the course of cycling*

Phase of active paste	Phase content, %											
	1st cycle			63rd cycle			110th cycle			200th cycle		
	1	2	3	1	2	3	1	2	3	1	2	3
Zn	33	33	33	31	37	31	30.5	35	34	31	26.1	42.5
ZnO	33	33	33	37	38	28	35.6	33	30	36.5	32.7	30.3
Zn + ZnO	33	33	33	34	37.5	29.5	33.5	34	32	34	29.4	36.4
Total Zn + ZnO in the electrode	96.5			95.8			90.5			83.3		

* 1, 2, and 3 stand for upper, middle, and lower parts of the electrode, respectively.

its insignificant redistribution into the middle part of the electrode. Under similar conditions of cycling of the MC NOE, only about 60% of the active paste is retained in the upper part of the zinc electrode already by 100th cycle. The comparison performed suggests that redistribution of zinc over the surface of the negative electrode is largely due to redistribution of current in NOE. In the course of cycling of the MC electrode, the extent to which its upper part is charged grows, since the conductivity of the active paste is higher in this region. This also leads to gradual overcharging of the upper part of the zinc electrode and the resulting loss of its shape [9].

In electrodes with spherical nickel hydroxide the distribution of current is more uniform, since the difference in conductivity between $Ni(OH)_2$ and NiOOH is compensated for by the influence of the electrically conducting cobalt compound.

The concentrations of KOH and K_2CO_3 vary in the initial period of cycling of the battery under study (up to 30 cycles) (Fig. 5). Then the content of KOH and K_2CO_3 stabilizes. Such a kind of variation of the electrolyte composition indicates that this variation is due to gradual transfer to the electrolyte of carbonates originally contained in the active paste of the electrodes and in separators. As shown by previous studies [10], the KOH concentration established in the battery (4.5 M) is sufficient for ensuring stable operation in cycling conditions of the NOE under study.

CONCLUSIONS

(1) Electrodes fabricated from spherical nickel hydroxide with addition of electrically conducting cobalt compounds ensure effective current transport in the solid phase and occurrence of the anodic process in the outer-diffusion mode. In this case, the charging of the electrode is accompanied by less pronounced, compared with that in the inner-diffusion mode, decrease in the concentration of OH^- ions in the reaction zone, which does not impair the stability of the zincate complex. Zinc mainly accumulates in the nickel oxide electrode fabricated from spherical nickel hydroxide as a result of its introduction into the structure of the positive electrode. The resulting disturbance of equilibrium in the reversibly operating system is compensated for by loss of the corresponding amount of zinc from the negative electrode.

(2) Use of spherical nickel hydroxide in nickel-zinc batteries makes it possible to markedly decelerate the deshaping of the zinc electrode owing to increased uniformity of current distribution in the nickel oxide electrode in the presence of cobalt compounds and, correspondingly, in the zinc electrode, too.

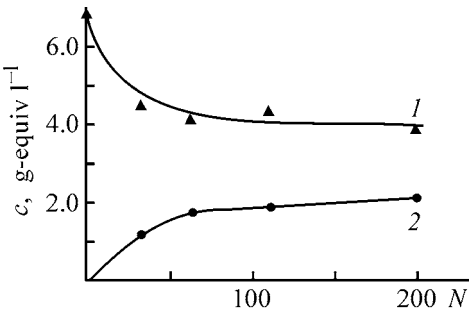

Fig. 5. Variation with cycling of the concentration c of (*1*) KOH and (*2*) K_2CO_3 in the electrolyte of NZ battery with NOE made of spherical nickel hydroxide on a foamed-nickel support.

ACKNOWLEDGMENTS

The authors thank G.A. Tal'yanova and N.V. Vinogradova with co-workers for developing experimental procedures and making analyses.

REFERENCES

1. Kuz'min, Yu.A., Mashevich, M.N., Uflyand, N.Yu., and Frolova, S.P., in *Sbornik rabot po khimicheskim istochnikam toka* (Coll. of Works on Chemical Power Cells), Leningrad: Energiya, 1972, issue 7, pp. 163–167.
2. Yu, C.Z., Lai, W.H., Yan, G.J., and Wu, J.Y., *J. Alloys Compounds*, 1999, vols. 293–295, pp. 784–787.
3. Loginova, M.M., Kas'yan, T.B., Arkhangel'skaya, Z.P., and Raikhel'son, L.B., *Zh. Prikl. Khim.*, 2003, vol. 76, no. 5, pp. 779–782.
4. Pralong, V., Delahaye-Vidal, A., Beaudoin, B., *et al., J. Electrochem. Soc.*, 2000, vol. 147, no. 4, pp. 1306–1313.
5. Audemer, A., Delahaye, A., Farhi, R., *et al., J. Electrochem. Soc.*, 1997, vol. 144, no. 8, pp. 2614–2620.
6. Ezhov, B.B., Egorova, S.A., and Goryainova, T.I., *Zh. Prikl. Khim.*, 1992, vol. 65, no. 1, pp. 11–15.
7. Ezhov, B.B. and Kamnev, A.A., *Zh. Prikl. Khim.*, 1997, vol. 70, no. 1, pp. 73–78.
8. Arkhangel'skaya, Z.P., Ivanova, R.P., Kas'yan, T.B., and Raikhel'son, L.B., *Zh. Prikl. Khim.*, 2001, vol. 74, no. 4, pp. 589–592.
9. Alekseeva, M.A., Arkhangel'skaya, Z.P., Ivanova, R.P., *et al., Zh. Prikl. Khim.*, 1998, vol. 71, no. 6, pp. 941–946.
10. Arkhangel'skaya, Z.P., Ivanova, R.P., Kas'yan, T.B., and Raikhel'son, L.B., *Zh. Prikl. Khim.*, 2001, vol. 74, no. 9, pp. 1438–1442.

Russian Journal of Applied Chemistry, Vol. 76, No. 6, 2003, pp. 929–931. Translated from Zhurnal Prikladnoi Khimii, Vol. 76, No. 6, 2003, pp. 959–961.

APPLIED ELECTROCHEMISTRY AND CORROSION PROTECTION OF METALS

Current Density Distribution as Parameter of Electroionite Process

N. N. Zubets

Voronezh State University, Voronezh, Russia

Received January 29, 2003

Abstract—The effect of artificially preset current density distribution in an electroionite apparatus on the extent of water demineralization is considered. The change in the extent of demineralization on varying the distribution of one and the same current between parts of apparatus at the inlet and outlet of diluate is explained.

In [1], specific features of current density distribution along the height of an electroionite apparatus, i.e., electrodialyzer with ion-exchange filler in its chambers, were considered and the following was shown. In an electrodialyzer with inert separators, the local current density decreases in the direction of diluate supply. By contrast, in an electroionite apparatus, the tendency toward a decrease in the local current density becomes less pronounced, and this parameter may even grow with increasing current strength and electrical conductivity of the ion-exchange filler. In the present study, the effect of current density distribution on the efficiency of the electroionite apparatus and, in particular, on the degree of demineralization is considered.

In all the known studies concerned with the current density distribution in an electrodialyzer, this distribution has only been considered under natural conditions and special provisions were made to prevent disturbance of this natural distribution. In [2], it was noted that, in principle, an artificial current density distribution can be created, but it was only meant to create conditions under which certain model concepts can be implemented. In the present study, an artificial current density distribution is regarded and used as a preset process parameter.

EXPERIMENTAL

A three-chamber electrodialyzer with MK-40 cation-exchange membrane on the cathode side and MA-41I anion-exchange membrane on the anode side was used. The depth of the diluate chamber was 1 mm, and that of electrode chambers, 10 mm; the width of all the chambers was 10 mm, and the height, 120 cm. A grid woven from alternating bands with cation- and anion-exchange properties and bulk conductivity was placed in the diluate chamber [3, 4]. Tap water subjected to back osmosis treatment and having electrical resistivity of 30 kΩ cm was fed from below upwards into all the chambers at a rate of 2 cm s^{-1}. The anode was made of platinum. A stainless steel cathode was separated, along its height, into two equal parts. A variable resistor was switched into the circuit of each of these parts in series with an ammeter. The average, over the entire apparatus area, current density was always set to a constant value of 0.1 mA cm^{-2}. The electrical resistivity of the diluate was measured with a Tesla BM 484 semiautomatic bridge in a thermostated flow-through cell at a temperature of 20°C.

Dividing the electrode into only two parts allows characterization of the current distribution by only a single dimensionless parameter α defined as the ratio between the strength of the current flowing through the upper part of the apparatus to the total current strength.

Without additional resistors, i.e., in the case of a natural current distribution, the value of α was 0.47 for the ion-exchange filler used [1]. When resistors of up to 20 kΩ were switched into the circuit of the upper part of the apparatus, α decreased to 0.08, and on switching the same resistors into the circuit of the lower part, α increased to 0.96. The limiting values of α (0 and 1) can be formally obtained by entirely switching off, respectively, the upper or lower part of the cathode.

The figure shows the dependence of the electrical resistivity ρ of the diluate on the α value set with resistors. With increasing load on the upper part of

1070-4272/03/7606-0929 $25.00 © 2003 MAIK "Nauka/Interperiodica"

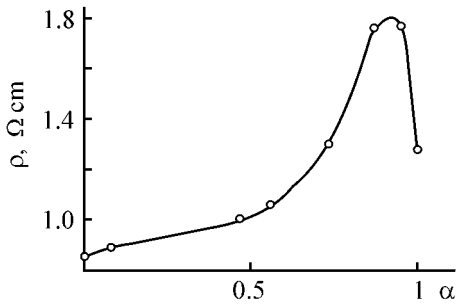

Electrical resistivity ρ of demineralized water vs. preset value of α. Average current density 0.1 mA cm^{-2}, diluate flow velocity 2 cm s^{-1}.

the apparatus, the electrical resistivity grows, and only in the case of completely switched-off lower part, ρ decreases somewhat. The direct dependence of ρ on α shows that more favorable conditions for deep desalination are created when the zones of the lowest diluate concentration and highest current density coincide, i.e., when the probability of exceeding manyfold the limiting diffusion current density is the highest. According to the conventional concepts of electrodialysis, this must have led to a decrease in current efficiency; however, the rise in ρ actually points to a more effective action of the current.

This behavior can be accounted for by specificity of deep electrodialysis demineralization. When the electrical conductivity of a solution approaches, because of the presence of dissolved salts, the background value determined by the electrical conductivity of the medium, the remaining salt ions mostly pass from solution into the ion-exchange resin as a result of ion exchange, rather than under the action of the electric field. For this to occur, it is necessary that a sufficient fraction of the ion-exchange material filling the diluate chamber should be present in the hydrogen and hydroxide forms. Just this objective is achieved when most part of the current is passed through the upper, lying closer to the diluate outlet, part of the apparatus. Thus, it may be concluded that, at least in the outlet part of the apparatus, the following demineralization mechanism is operative at a sufficiently high current density: decomposition of water at the heteropolar contact of ion-exchangers, sorption of hydrogen ions and hydroxy ions by ion-exchangers, ion exchange of these ions for dissolved salt ions, and removal of salt ions across unipolar contacts of ion exchangers and membranes and, through the latter, into the concentrate. This charge transfer mechanism does not lead to a decrease in the current efficiency, since ions of the medium, which are involved in the transport, do not find way into the concentrate, with the transfer chain ending there with transfer of salt ions. Presumably, the energy expended for dissociation of water is not lost completely, since hydrogen ions an hydroxy ions are returned into the diluate and, upon molization, release energy, which heats the diluate and thereby facilitates dissociation of other water molecules.

Such a demineralization mechanism is not new and may be operative for mixed ion-exchange filler of any kind. However, for the woven grid used in the experiment, it is the most probable mechanism for two reasons. First, ions of the medium, which arrive at the ion-exchange grid and move within it, may traverse a relatively long path, with high probability of their exchange for salt ions. Second, the heteropolar contacts of ion exchangers are abundant and virtually do not include contacts that could serve as a source of mineralization.

The point is that, both in the case of multilayer charging of the chamber with a mixed bed of granulated ion exchangers and with a grid woven from bands with ion-exchange properties and different polarities of counterions, there exist equal numbers of heteropolar contacts with "diluate" and "concentrate" geometric arrangement. However, in the case of a grid there is a good, multiple electrical contact between all parts of each monopolar part of the grid and the corresponding membrane. Since the ion exchanger has immeasurably higher electrical conductivity than the surrounding demineralized water, the electric voltage applied to the diluate chamber must drop nearly entirely across the solution. In this case, the electric potentials of all parts of a monopolar half of the grid and of the corresponding membrane must be nearly the same. Consequently, the electric potentials of all points of the cation-exchange part of the grid must be more negative than the potentials of all points of the anion-exchange part, since just this relationship is observed between the electric potentials of the corresponding membranes delimiting the diluate chamber. In this case, it is of no importance on which sides of a heteropolar contact are the cation- and anion-exchanger. In other words, when the diluate chamber is filled with a mixed bed of ion-exchangers in the form of a woven grid, all the numerous heteropolar contacts operate as diluate contacts, irrespective of their geometric orientation.

When most of the current flows through the inlet zone of the apparatus, in which the diluate concentration is higher, the ratio of the current density to solution concentration becomes more uniform over different points of the chamber. In this case, the probability of appearance of zones in which the limiting

diffusion current density is much exceeded becomes lower, with the correspondingly decreasing probability of ion-exchange absorption of salt ions from solution and diminishing share of charge transfer by the mechanism described above.

Further analysis of the data in the figure poses a question as to why the diluate quality is not the same at the limiting values of the distribution factor (0 and 1). Formally, it must have been of no importance which half of the apparatus, upper or lower, is working. However, it is apparent that at different electric potentials of two neighboring, but separated from each other, parts of the cathode, a current will flow between them across the electrode solution. In this case, the electric charge passing through the ammeter must be partly transferred to the switched-off part of the cathode, and then to the anode through the switched-off part of the electrodialyzer. A certain amount of charge transfer between the two zones of the apparatus necessarily occurs on connecting an additional resistor to one of them.

This means that the real α deviates somewhat from that found from ammeter readings toward its natural value corresponding to a normally connected electrode with equal electric potentials in all of its parts. Consequently, the whole apparatus actually works on switching-on any of the two halves of the cathode, but the operation modes are somewhat different in two limiting cases ($\alpha = 0$ and $\alpha = 1$). At $\alpha = 0$, a greater part, even though not the whole of the current is concentrated in the inlet part of the apparatus. A noticeable desalination of the solution occurs in the inlet part, whereas the diluate quality in the upper part of the apparatus is nearly not improved at all, since the current density in this zone is insufficient for the ion-exchange mechanism of deep desalination to be operative. By contrast, at $\alpha = 1$, a low current density at the inlet is sufficient for preliminary desalination through electromigration, which is common with electrodialysis, and high current density at the outlet converts ion exchangers into the hydrogen and hydroxide forms, thereby favoring deep desalination with intense ion exchange. As a result, the electrical resistivity of the diluate at $\alpha = 1$ much exceeds that at $\alpha = 0$. This confirms, to a certain extent, the feasibility of the above mechanism of deep desalination.

Apparently, the optimal value of α corresponds to such a process in which there occurs pronounced preliminary desalination in the inlet zone of the apparatus and, at the same time, the current density in the outlet zone is sufficiently high for converting a required amount of ion exchangers into the hydrogen and hydroxide forms. In the case in question, this optimum corresponds to $\alpha = 0.85–0.90$.

CONCLUSIONS

(1) The degree of demineralization of water in its electroionite treatment depends on how the preset current density is distributed over the electroionite apparatus along the direction of dilate feed.

(2) The degree of demineralization can be raised substantially by artificially redistributing the current density.

(3) There exists a certain optimal ratio of current densities at the diluate entry into, and exit from the apparatus.

REFERENCES

1. Zubets, N.N., Shaposhnik, V.A., Mill', B.E., and Strygina, I.P., *Zh. Prikl. Khim.*, 1995, vol. 68, no. 10, pp. 1657–1661.
2. Shaposhnik, V.A., *Kinetika elektrodializa* (Inetics of Electrodialysis), Voronezh: Vor. Gos. Univ., 1989.
3. Shaposhnik, V.A., Strygina, I.P., Zubets, N.N., and Mill', B.E., *Zh. Prikl. Khim.*, 1991, vol. 64, no. 9, pp. 1942–1946.
4. Shaposhnik, V.A., Zubets, N.N., Mill, B.E., and Strigina, I.P., *Desalination*, 2001, no. 133, pp. 211–214.

Russian Journal of Applied Chemistry, Vol. 76, No. 6, 2003, pp. 932–935. Translated from Zhurnal Prikladnoi Khimii, Vol. 76, No. 6, 2003, pp. 962–965.

APPLIED ELECTROCHEMISTRY AND CORROSION PROTECTION OF METALS

Specific Features of Porous Silicon Synthesis in Aqueous-Alcoholic Solutions

I. L. Baranov, L. V. Tabulina, and L. S. Stanovaya

Belarussian State University of Information Science and Radio Electronics, Minsk, Belarus

Received July 18, 2002; in final form, April 2003

Abstract—The uniformity of growth of porous silicon layers, electrochemical parameters of their synthesis, surface resistance, and morphology of porous structure in aqueous and aqueous-alcoholic electrolytes (H_2O–$C_nH_{2n+1}OH$, n = 1, 3–5) was studied.

Porous silicon (PS) formed in electrochemical anodic treatment of single-crystal silicon in HF-based electrolytes has been studied extensively [1]. However, its use in semiconductor electronics is restricted by high nonuniformity of its morphological structure. This is particularly characteristic of lightly doped *n*-type silicon [2, 3]. Nevertheless, the interest in PS, demonstrated by specialists developing designing-and-technological variants of semiconductor electronic circuits with varied degree of integration, is unwaning [4, 5]. Studying the specific features of PS film formation in relation to properties of the employed electrolytes is a topical task.

In continuation of previously commenced investigations [6], the present study is concerned with the influence exerted by the properties of alcohol components of the electrolytes on the uniformity of growth of PS layers, their porosity, and surface resistance, and also on electrochemical characteristics of pore formation processes, such as effective valence and current efficiency. The study is aimed to determine what electrolytes with alcohol solvents of HF are the most appropriate for synthesis of PS films in semiconductor microelectronics.

EXPERIMENTAL

PS layers were formed in darkness at current density of 10 mA cm^{-2} in the course of 60 min on lightly doped KEF-20 (100)Si substrates. The electrochemical cell used for this purpose was described in [6]. As starting electrolyte served 48% hydrofluoric acid. As organic solvents of HF were used alcohols $C_nH_{2n+1}OH$ (n = 1, 3–5). The influence of ethanol on PS synthesis was described in [6]. The concentration of alcohol ingredients of the electrolytes used in the study was varied within the range 0.5–15.0 M. The uniformity of PS film formation on the surface of the silicon anode, the corresponding porosities, pore morphology, effective valence, and current efficiency were deterined using procedures described in [6–8]. The surface resistance of PS layers was measured using a four-probe ac technique. The electrodes of the four probe measuring device, spaced by 1 mm, were made of titanium.

To gain better understanding of how the alcohol components of the electrolyte affect the pore morphology and uniformity of PS film growth on the surface of silicon substrates, similar studies were carried out for solutions with HF diluted with water. In calculating the dilution, it was taken that 48% hydrofluoric acid corresponds to a solution with zero amount of added water.

The growth rate of PS layers and uniformity of their distribution over the surface of the silicon anode in aqueous electrolytes is illustrated by Fig. 1. It can be seen that dilution of HF with water leads first to gradual, and then to fast decrease in the growth rate of PS films. The scatter of PS layer thicknesses is wide (±30 μm) in all cases (Fig. 1, curve *1*). The variation of their porosity indicates that the most pronounced rise in this parameter occurs when electrolytes with water concentration exceeding 30 M are used (Fig. 1, curve *2*). As revealed by an electron-microscopic study, this tendency is due to abundant formation of branches on walls of the growing pores. As a result, the morphology of the porous structure of PS layers synthesized in aqueous electrolytes can be interpreted as tree-like.

1070-4272/03/7606-0932 $25.00 © 2003 MAIK "Nauka/Interperiodica"

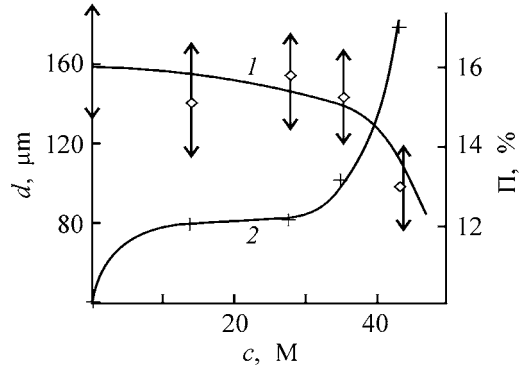

Fig. 1. Effect of dilution of HF with water on (*1*) thickness *d* and (*2*) porosity Π of PS layers. (*c*) HF concentration.

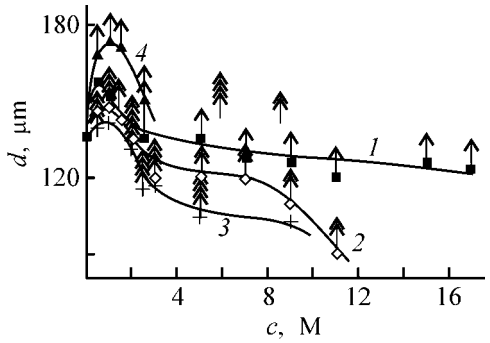

Fig. 3. Effect of concentration *c* of alcohols on thickness *d* of PS layers. (*1*) Methanol, (*2*) 2-propanol, (*3*) 1-butanol, and (*4*) 1-pentanol; the same for Figs. 4 and 5. *Vertical arrows* show scatter of thicknesses over the anode surface (shown in + direction).

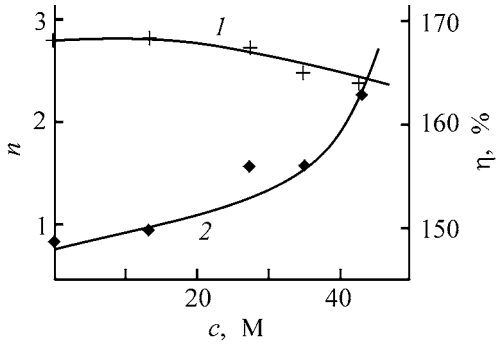

Fig. 2. (*1*) Effective valence *n* and (*2*) current efficiency η of electrochemical dissolution of silicon vs. water concentration *c* in electrolyte.

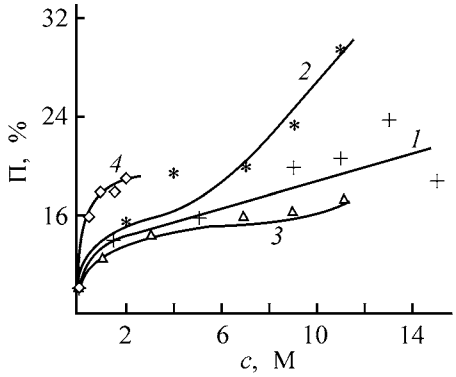

Fig. 4. PS layer porosity Π vs. alcohol concentration *c* in electrolyte.

The effect of dilution of HF with water on the process of pore formation in PS synthesis is due to a certain weakening of the influence exerted on it by electrochemical factors. This is indicated by changes in the effective valence and current efficiency (Fig. 2). As follows from the dependences presented here, the effective valence decreases within the range 2.8–2.6, i.e., only slightly (Fig. 2, curve *1*). The current efficiency changes more substantially, with its values growing steadily. The limiting value exceeds 160% in the given case (Fig. 2, curve *2*). This means that dilution of HF with water favors chemical dissolution of silicon. However, since no acceleration of SiF_2 (intermediate product of electrochemical dissolution of silicon) formation is observed, this points to weak influence of chemical reactions on the arrival of charge carriers (holes) at the Silelectrolyte interface. This gives rise to a nonuniform front of silicon etching on the anode surface and a tendency toward formation of narrow side channels on pore walls, probably, because of spontaneous dissolution of silicon. The occurrence of electroless processes of this kind in water on the surface of PS was also reported in [9].

It should be noted that the surface resistance R_s of PS layers synthesized in electrolytes of the system H_2O–HF is independent of the dilution of HF with water and equals 15–20 $\Omega\,cm^{-2}$. The order of magnitude of R_s points to high ion mobility on the PS surface, which can be accounted for both by sorption of H_2F^+ or H_3O^+ ions on the surface and by its hydrophilic properties.

When PS is synthesized using electrolytes with alcohol components, film formation depends on the molecular weight of the organic additives (Fig. 3, curves *1–4*). In a narrow range of concentrations (0–1 M), the growth rate of PS layers increases. In subsequent dilution of HF with the alcohol components, the intensity of PS formation decreases. The rate of PS film growth changes to a greater extent for alcohols with $n \geq 3$ (Fig. 3, curves *2–4*). The scatter of PS film thicknesses over the surface of the silicon anode does not exceed ±16 μm in all of the aqueous alcoholic electrolytes used. The highest uniformity of their distribution is achieved in the case of solutions with addition of 2-propanol (Fig. 3, curve *2*). These same layers show the highest porosity (Fig. 4, curve *2*).

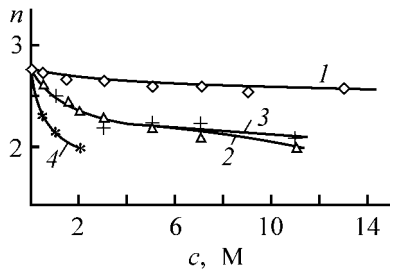

Fig. 5. Effect of alcohol concentration c in electrolyte on effective valence n of silicon dissolution.

The alcohol components with $n \geq 3$ strongly affect the variation of the effective valence (Fig. 5, curves *2–4*). The value of this electrochemical parameter of the process of PS formation in electrolytes belonging to the system HF–H_2O–*i*-C_3H_7OH decreases from 2.8 (for 48% hydrofluoric acid) to 2.0 when the concentration of the organic component reaches a value of 11 M (Fig. 5, curve *2*). The corresponding current efficiencies grow to 200%. This indicates that chemisorption of the alcohol components of the electrolytes favors formation on the PS surface of additional positive charge carriers, which accelerate the SiF_2 formation.

Thus, chemical dissolution of silicon in aqueous-alcoholic electrolytes is more intimately related to electrochemical processes occurring in PS synthesis. Electron-microscopic studies demonstrated that the morphology of the porous structure of PS layers synthesized in electrolytes of the system H_2O–HF–$C_nH_{2n+1}OH$ is not represented by system of branching channels. The diameter of their voids is approximately 1.3–1.5 times that in PS layers synthesized in aqueous electrolytes at the same dilution of HF. Raising the molecular weight of the alcohol components of the electrolytes favors expansion of the pore voids. Their orientation coincides to a greater extent with the direction of the flowing current, compared with the case of PS layers synthesized in aqueous electrolytes. This is particularly pronounced for the porous structure of PS layers synthesized in electrolytes with 2-propanol, with concentration exceeding 1 M. In this case, the shape of pore voids can be interpreted as needle-like.

The R_s values for PS layers synthesized in electrolytes with alcohol components are approximately 3 to 4 orders of magnitude higher than the corresponding values for PS films of the same thickness, synthesized in aqueous electrolytes. In this case, the higher the molecular weight of an organic substance, the greater R_s. This indicates that chemisorption of the alcohol ingredients of the electrolyte on the PS surface is due to formation of coordination bonds between hydroxy groups in their molecules and atoms in the solid phase.

It was noted in [10] that a similar adsorption mechanism changes the electrical parameters of adjacent defects on the semiconductor surface and the field effect of these defects extends as far as several lattice constants. This shifts the Fermi level of semiconducting silicon toward the valence ?band and creates positive charge on the silicon surface. It should be noted that this process may also be favored by formation in electrolytes of the system H_2O–HF–$C_nH_{2n+1}OH$ of $C_nH_{2n+1}OH_2^+$ cations, as it occurs in alcoholic solutions of hydrochloric acid [11]. These cations possess abnormally high mobility [11] and raise by an order of magnitude the mobility of Cl^-, H_3O^+, and OH^- ions, thereby making much higher the electrical conductivity of the solutions. In the $C_nH_{2n+1}OH_2^+$ group, the highest mobility is observed for cations formed from *i*-C_3H_7OH. These data reveal, probably, one of the major reasons why all characteristics of pore-formation on the surface of the silicon anode are changed to the greatest extent in electrolytes of the system H_2O–HF–*i*-C_3H_7OH (Figs. 4 and 5, curves *2*).

In view to the presence of $C_nH_{2n+1}OH_2^+$ cations in alcoholic electrolytes with HF, account should also be taken of the particular specificity of the influence exerted by the cations on the state of the solid surface, which is commonly covered with a hydrated oxide film. This influence is manifested in that, despite having the charge of the same sign as the solid phase, organic cations are adsorbed on its surface owing to their high adsorption potential. This leads to hydrophobization of the surface, shielding of the electrical double layer, and the resulting decrease in the electrokinetic potential in electrolytes [12].

In processes occurring in electrochemical treatment of materials in aqueous-alcoholic electrolytes with HF, these factors make the current distribution of the matrix substance surface more uniform and accelerate the mass-exchange of reagents within the forming pores. In synthesis of PS films, this creates conditions for their formation with more uniform, over the anode surface, porous structure morphology [13] with pore voids oriented along the current flow direction, which is actually the case in electrolytes with 2-propanol.

Thus, the presence of alcohol components in solutions with HF favors formation on the surface of a silicon wafer of PS films with uniform thickness and more regular porous structure. The best suitable for this purpose are electrolytes containing 2-propanol. Their use makes it possible to obtain PS films best

satisfying the requirements of the technology of semiconductor integrated circuits.

CONCLUSIONS

(1) In aqueous-alcoholic electrolytes, the growth rate of porous silicon films and their porosity depend on the concentration of the alcohol components and their molecular weight. The most uniform distribution of porous silicon films with thickness of 80 μm and more on a lightly doped *n*-type silicon is achieved in their synthesis in electrolytes containing more than 1 M of 2-propanol.

(2) Introduction of alcoholic complexes into electrolytes changes the effective valence and current efficiency of porous silicon synthesis. In electrolytes containing 2-propanol, the current efficiency increases to 200%, and the effective valence decreases to 2.

(3) The morphology of the porous structure of porous silicon layers synthesized in electrolytes with 2-propanol is represented by needle-like pores whose voids are oriented along the direction of the flowing current.

(4) The positive influence of the alcohol components on synthesis of porous silicon layers is due to the formation in the electrolytes with HF of $C_nH_{2n+1}OH_2^+$ ions whose chemisorption and high adsorption potential favor uniform distribution of the current over the surface of the silicon anode and intensify the mass-exchange of reagents in the forming pores.

REFERENCES

1. *Porous Silicon*, Canham, L., Ed., INSPEC, The Institution of Electrical Engineers, London, UK, 1997.
2. Gershinskii, A.E. and Mironova, L.V., *Elektrokhimiya*, 1989, vol. 25, no. 10, pp. 1374–1380.
3. Buchin, E.Yu. and Prokaznikov, A.V., *Mikroelektronika*, 1998, vol. 27, no. 2, pp. 107–113.
4. Kostishko, B.M., Atazhanov, Sh.R., Puzov, I.P., *et al., Pis'ma Zh. Tekh. Fiz.*, 2000, vol. 26, no. 5, pp. 42–48.
5. Makara, V.A., Boltovets, N.S., Vakulenko, O.V., *et al., Zh. Prikl. Spektrosk.*, 1999, vol. 66, no. 3, pp. 423–427.
6. Baranov, I.L., Stanovaya, L.S., Tabulina, L.V., *et al., Elektrokhimiya*, 1998, vol. 34, no. 6, pp. 588–592.
7. Baranov, I.L., Stanovaya, L.S., Tabulina, L.V., *et al., Zh. Prikl. Khim.*, 1998, vol. 71, no. 11, pp. 1813–1817.
8. Baranov, I.L., Stanovaya, L.S., Tabulina, L.V., *et al., Elektrokhimiya*, 2000, vol. 36, no. 12, pp. 1511–1513.
9. Kompan, M.E. and Shabanov, I.Yu., *Fiz. Tekh. Poluprovodn.*, 1995, vol. 29, no. 10, pp. 1859–1869.
10. Kiselev, V.F., *Poverkhnostnye yavleniya v poluprovodnikakh i dielektrikakh* (Surface Phenomena in Semiconductors and Insulators), Moscow: Nauka, 1970.
11. Gezalov, A.A., Mutalenko, A.A., Krasnov, B.P., *et al., Elektrokhimiya*, 1986, vol. 22, no. 10, pp. 1313–1318.
12. Komarov, V.S. and Dubnitskaya, I.B., *Fiziko-khimicheskie osnovy regulirovaniya poristoi struktury adsorbentov i katalizatorov* (Physicochemical Foundations of Control over Porous Structure of Adsorbents and Catalysts), Minsk: Nauka Tekhnika, 1981.
13. Gavrilov, S.A., Zavaritskaya, T.N., Karavanskii, V.A., *et al., Elektrokhimiya*, 1997, vol. 33, no. 9, pp. 1064–1068.

Russian Journal of Applied Chemistry, Vol. 76, No. 6, 2003, pp. 936–938. Translated from Zhurnal Prikladnoi Khimii, Vol. 76, No. 6, 2003, pp. 966–968.

APPLIED ELECTROCHEMISTRY AND CORROSION PROTECTION OF METALS

Potentiometric Method for Evaluation of Protective Properties of Polymeric Coatings

V. S. Kolosnitsyn, I. F. Gladkikh, N. M. Cherkasov, and L. V. Sheina

Institute of Organic Chemistry, Ufa Scientific Center, Russian Academy of Sciences, Ufa, Bashkortostan, Russia
Poisk Research Center, Ufa, Bashkortostan, Russia

Received February 11, 2003

Abstract—A new method is proposed for evaluation of protective properties of polymeric coatings. The method allows evaluation of the corrosion rate of a coated metal by means of potentiometric indication.

One of the main difficulties encountered in developing new polymeric coatings is rapid evaluation of their protective properties. Several methods have been proposed, which allow prognostication, with varying reliability, of the service life of protective coatings. These methods include impedance meagerment and impedance spectroscopy, conductometry, and some others [1–4]. However, none of these techniques enables unambiguous assessment of protective properties of coatings.

The method developed in this study, which makes it possible to evaluate the rate of metal corrosion under a protective coating, is based on measuring the time of destruction by corrosion of a metal layer of known thickness under a protective coating. It is proposed to use potentiometric indication for determining the instant of time at which the corrosion process is complete. Potentiometric indication can be applied in those cases when the electrochemical potential of an electrode made of a metal under study changes dramatically after its destruction by corrosion. This can be achieved by using two-layer bimetallic indicator electrodes. The surface layer of the indicator electrode is to be fabricated from the metal under study, and the inner layer, from a metal whose potential in the corrosive medium is more positive than the potential of the metal under study. The most convenient support is copper, since its potential in corrosive media is more positive than the potentials of the majority of construction metals and alloys. In a test, the potential of the indicator electrode is first determined by the potential of a metal under study, e.g., iron, and after its destruction by corrosion, by the potential of the support metal.

The aim of this study was to assess the possibility of applying the potentiometric method to study properties of protective coatings.

EXPERIMENTAL

To ensure rapid evaluation of protective properties of coatings, it is very important to choose correctly the thickness of the surface layer of the bimetallic indicator electrode. Use of electrodes with thick surface layer makes longer the testing time. Small thickness of the surface layer may give rise to rather significant errors because of the possible scatter of its thickness. In most cases, the rate of metal corrosion under a coating must not exceed 0.1 mm/yr (~1.14×10^{-2} μm h^{-1}), which ensures a 20–30-year service life of a technical structure, e.g., pipeline. If it is taken that the acceptable duration of corrosion studies must not exceed 500–1000 h, then the most convenient thickness of the layer of metal under study is 5–10 μm.

In this study, iron, which is the most widely used construction material, was chosen as the metal of the surface layer. Copper was used as the material of the support. To rule out edge effects, the study was carried out with cylindrical electrodes having spherical lower end. The electrode area was 15 cm^2. An iron layer 10 μm thick was deposited onto the surface of the copper electrode by electroplating from a chloride electrolyte [5]. Corrosion studies were performed in glass cells communicating with the atmosphere. The electrode potential was measured with a V7-23 digital voltmeter relative to a silver chloride reference electrode. As corrosive medium served 0.5 M (3%)

1070-4272/03/7606-0936 $25.00 © 2003 MAIK "Nauka/Interperiodica"

aqueous solution of NaCl. As protective coating was used Asmol varnish [TU (Technical Specification) 5623-002-16 802 026–94].

The experiments were done as follows. Electrolyte was poured into a glass cell in which the electrode under study and reference electrode were placed. The cell communicated with the atmosphere through a special aperture. The tests were done at temperatures ranging from 18 to 25°C. All the potentiometric measurements were made after thermostating the cells at 25°C in an air thermostat.

To assess the reliability of the results obtained, the corrosion rate of a steel St.3 electrode was studied in parallel under similar conditions. In studying the corrosion behavior of steel electrodes, each test was interrupted after stable potential was attained and corrosion products were accumulated in amounts sufficient for analysis. The corrosion products were carefully removed from an electrode under study and transferred to solution, together with the corrosion products accumulated in the electrolyte. Then the resulting solution was subjected to complexometric titration to determine the content of iron ions [6]. The results obtained in analysis were used to calculate the corrosion rate. Further, the experiment was continued, following the same procedure. The electrodes were again placed in the cell, poured over with fresh electrolyte, and the cycle described above was repeated. The experiment was done several times, until stable results were obtained. To assess their reproducibility, 3 to 4 parallel runs were performed.

The study was carried out for the example of two-layer bimetallic electrodes with and without a protective coating. The potential of metallic electrodes in a corrosive medium is determined by several simultaneously occurring chemical and electrochemical processes. To determine the steady-state potentials, the variation of the potential of steel and copper electrodes was studied in preliminary experiments. The data obtained are shown in Fig. 1. It can be seen that, during first hours after bringing the steel and copper electrodes in contact with a corrosive solution, their potentials shift into the cathodic region. This can be accounted for by a change in the pH value and composition of the near-electrode layer of the electrolyte in the course of corrosion. The potentials of both the copper and steel electrodes stabilize in 25–30 h. The stabilized potentials remain invariable within several thousand hours.

Because of the difference between the properties of electroplated deposits of iron and steel, it could be expected that they should behave differently in electrochemical regard, too. However, as shown by the results of the study, the manners in which the potentials of a steel electrode and a two-layer bimetallic "iron-on-copper" electrode vary are virtually the same.

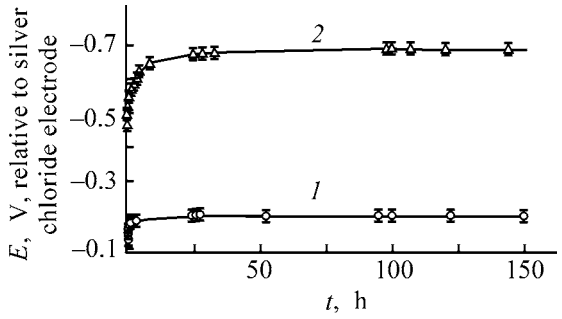

Fig. 1. Chronopotentiograms of (*1*) copper and (*2*) iron electrodes in 3% NaCl solution. (*E*) Potential and (*t*) time; the same for Fig. 2.

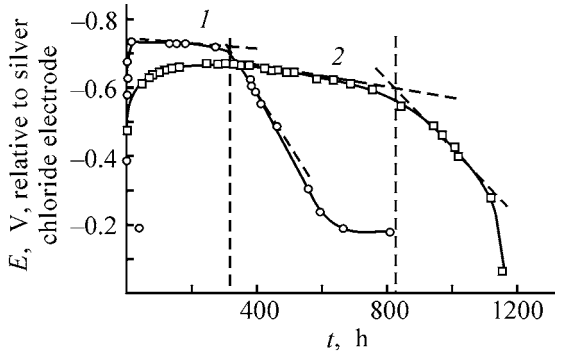

Fig. 2. Chronopotentiograms of two-layer bimetallic "iron-on-copper" electrodes in 3% NaCl solution. (*1*) Without coating and (*2*) with a single-layer coating with Asmol varnish.

Chronopotentiograms of two-layer bimetallic electrodes with and without a protective coating are shown in Fig. 2. It can be seen that the electrode potentials start to shift, in 310 h for an electrode without coating and 830 h for a coated electrode, toward the anodic region, reaching in the end the potential of the copper electrode. The instant of time at which the potentials start to shift, found as an intersect of two tangents to linear portions of the chronopotentiograms, points to the time of the through damage of the iron layer. The time of complete iron dissolution can be found from the intersect of tangents to the transition and final portions of the chronopotentiograms.

To determine the true corrosion rate of a coated metal by the method of the thin-layer electrode, it is necessary to correctly determine the time of corrosion destruction of the indicator layer of the metal. With account taken of the roughness of this layer and the positive and negative deviations from its integral-

Analytically determined corrosion rates v_c

t, h	Amount of corrosion products, g		$v_c \times 10^5$, g cm^{-2} h^{-1}		$v^*_{c.av}$	
	sample no. 1	sample no. 2	sample no. 1	sample no. 2	10^5 g cm^{-2} h^{-1}	10^2 μm h^{-1}
190	0.0319	0.0282	1.12	0.99	1.06	1.38
96	0.0218	0.0210	1.51	1.45	1.48	1.92
71	0.0185	0.0133	1.74	1.25	1.50	1.95
109	0.0189	0.189	1.16	1.16	1.16	1.51
96	0.0194	0.0277	1.35	1.93	1.64	2.13

* ($v_{c.av}$) Average corrosion rate.

average thickness considered to be equiprobable, it may be assumed that, in the middle of the transition portion, the actual dissolution depth of the layer is, to a first approximation, close to its integral-average thickness.

To assess the reliability of the data obtained, corrosion rates of iron, found by analysis of the amount of corrosion products (see table) and yielded by chronopotentiometry, were compared. The corrosion rates v_c found from the results of potentiometric studies are presented below:

Time of completion of a corrosion process	$v_c \times 10^2$, μm h^{-1}
Appearance of through damage	3.23
Time found at the middle of the transition portion	2.00
Completion of corrosion destruction	1.61

It can be seen that the corrosion rates obtained by different methods are in satisfactory agreement.

The relative error of the analytically found mean-arithmetic value of the average corrosion rate, with respect to the corrosion rate calculated at the middle point of the transition portion of the chronopotentiogram, was about 10%. The corrosion rate found from the time corresponding to the middle of the transition portion of the chronopotentiogram is the closest to the corrosion rate found analytically.

The time of destruction of the uncoated and coated metal under study can be used to calculate the coefficient of protective action of a coating, K_{pr} (cm^{-1}):

$$K_{pr} = \frac{t_{mc} l_m}{t_m l_{mc} l_c},$$

where t_m is the time of dissolution of the layer of an uncoated metal under study (h); t_{mc}, the time of dissolution of coated metal (h); l_c, the coating thickness (cm); l_m, the thickness of the metal electrode under study (cm); l_{mc}, the thickness of the coated metallic electrode under study (cm).

The service life of a metal under protective coating, T (h), can be found as

$$T = T_m K_{pr} l_{pr},$$

where T_m is the service life of uncoated metal (h); K_{pr}, the coefficient of protective action of a coating, (cm^{-1}); l_{pc}, the thickness of the protective coating (cm).

The average corrosion rate of St.3 steel was 1.37×10^{-5} g cm^{-2} h^{-1}.

The linear velocity of steel dissolution can be readily calculated from the data in the table to be 1.78×10^{-6} cm h^{-1} or 1.78×10^{-2} μm h^{-1}.

CONCLUSION

The potentiometric method using a two-layer bimetallic electrode can be successfully applied to evaluate the protective properties of polymeric coatings.

REFERENCES

1. Rozenfel'd, I.L. and Zhigalova, K.A., *Uskorennye metody korrozionnykh ispytanii metallov* (Methods for Rapid Corrosuion Tests of Metals), Moscow: Metallurgiya, 1966, p. 347.
2. Fokin, M.N., Emel'yanov, Yu.V., Strochkova, E.M., *et al., Lakokras. Mater. Ikh Primen.*, 1980, no. 1, p. 33.
3. Fomin, M.N. and Zhigalova, K.A., *Metody korrozionnykh ispytanii metallov* (Methods for Corrosion Tests of Metals), Moscow: Metallurgiya, 1986, p. 11.
4. Kuzmak, A.E., Agasyan, P.K., and Kozheurov A.V., *Zashch. Met.*, 1989, vol. 25, no. 2, pp. 179.
5. *Gal'vanotekhnika: Spravochik* (Electroplating: Reference Book), Ginberg, A.M., Ed., Moscow: Metallurgiya, 1987, p. 202.
6. Vol'f, L.A., *Vvedenie v teoriyu i praktiku kompleksonometricheskogo metoda* (Introduction to Theory and Practice of Complexometry), Leningrad: Goskhimizdat, 1963, p. 50.

Russian Journal of Applied Chemistry, Vol. 76, No. 6, 2003, pp. 939–942. Translated from Zhurnal Prikladnoi Khimii, Vol. 76, No. 6, 2003, pp. 969–972.

CATALYSIS

Properties of Mixed Polyfunctional Fluoride Catalysts for Synthesis of Pyridine Bases from Acetylene and Ammonia (Methanol)

R. A. Khamidullaev and D. Yusupov

Tashkent Chemical Engineering Institute of Uzbekistan Republic, Tashkent, Uzbekistan

Received March 5, 2003

Abstract—New catalysts based on cadmium, zinc, chromium, iron, and aluminum compounds were synthesized and their properties were studied. A pilot catalyst batch was obtained and tested on a pilot installation.

Pyridine and its homologs are widely used in production of chemicals and pharmaceuticals and in agriculture [1, 2]. The interest in these compounds increased after the appearance of pesticides of selective and total action such as Reglon, Fusilad, Parskvat, Lontrel, etc. [3].

Among the known methods for preparing pyridine bases, their synthesis from acetylene and ammonia (methanol) is the most promising [4–7]. Wide industrial use of this method is impeded by the lack of highly active and stable catalysts. The available catalysts for synthesis of pyridine bases from acetylene and ammonia work with constant activity for 72 h at best [8, 9].

Formation of pyridine bases from acetylene and ammonia or acetylene, ammonia, and methanol is a result of complex combination of parallel-successive reactions accompanied by vinylation, dehydrocyclization, isomerization, trimerization, etc.

In the gas phase, this is only possible with polyfunctional catalysts.

An analysis of published data on the mechanism of acetylene and amine activation showed that *d*-metal (zinc, cadmium, chromium, iron, cobalt, etc.) compounds, which are also active in reactions of addition of various molecules to acetylene can catalyze ammonia and amine vinylation in the gas phase. Such compounds are typical catalysts for dehydrogenation and dehydration [10, 11].

Studies of promotion of cadmium and zinc compounds with metal fluorides and X-ray diffraction analysis of other polyfunctional catalytic systems showed that, during catalyst preparation, zinc, cadmium, iron, and aluminum form hydroxofluorides Cd(OH)F, Zn(OH)F, $Al(OH)_2F$, $Al(OH)F_2$, etc., which are, probably, responsible for the high catalytic activity of the catalysts [12, 13].

The zinc and cadmium ions favor activation of acetylene and ammonia molecules, and the basic centers on the catalyst surface (O^-, F^-, OH^-) favor formation of amide groups from ammonia and amines:

$$M(OH)F(NH_3) \begin{cases} \nearrow MF(NH_2) + H_2O \\ \searrow M(OH)(NH_2) + HF \end{cases}$$

where M is Zn^{2+}, Cd^{2+}, Fe^{2+}, etc.

An X-ray diffraction study showed that the catalysts are fairly active in the semiamorphous-crystalline state, in which they contain chemically bound water. With the calcination temperature from 450 to 650°C, the fraction of the crystalline phase grows, the content of chemically bound water decreases, and hydroxofluorides start to decompose. As a result, the specific surface area and activity of the catalyst decrease.

We found that, when catalysts contain, along with zinc, cadmium, and aluminum hydroxofluorides, also 3.0–5.0 wt % zinc and chromium(III) [or iron(III)] oxides, they are fairly active, selective, and stable in synthesis of pyridines from acetylene, and ammonia (methanol). Taking this circumstance into account, we synthesized more than 30 catalysts; their compositions and properties are listed in Table 1.

As seen, the KTsZhKhA-5 catalyst is the most active and stable in synthesis of 2- and 4-methylpyridines, while the KTsKhZhA-6 catalyst is the best in synthesis of pyridine and a mixture of isomeric

1070-4272/03/7606-0939 $25.00 © 2003 MAIK "Nauka/Interperiodica"

Table 1. Comparative characteristics of catalysts

Catalyst	Composition, wt %	Run before regeneration, h	Specific surface area, $m^2 g^{-1}$	Mechanical strength, MPa	Productivity, g kg^{-1} of cat. h^{-1}	Acetylene conversion, %	Catalyzate (organic layer) composition, %		
							pyridine	2-methyl-pyridine	3- and 4-methylpyridines
KTsA-1	CdF_2 3.0, ZnO 5.0, AlF_3 3.0, Al_2O_3 89.0	96.0	172.0	4.2	96.0	85.0	–	42.0	24.0 (4-methylpyridine)
KTsKhA-2	CdF_2 3.0, ZnO 3.0, Cr_2O_3 3.0, AlF_3 3.0, Al_2O_3 88.0	120.0	165.0	4.8	112.0	88.0	30.0	31.0	18.0
KTsKhA-3	CdF_2 3.0, ZnO 5.0, Cr_2O_3 3.0, AlF_3 5.0, Al_2O_3 86.0	96.0	165.0	4.6	96.0	85.0	–	44.0	24.0
KTsZhA-4	CdF_2 5.0, ZnO 7.0, ZnF_2 3.0, AlF_3 3.0, Fe_2O_3 3.0, Al_2O_3 80.0	120.0	203.0	5.6	132.0	90.1	32.1	28.0	22.0
KTsZhKhA-5	CdF_2 2.0, Cr_2O_3 3.0, ZnF_2 3.0, ZnO 3.0, Fe_2O_3 3.0, Al_2O_3 86.0	144.0	232.0	6.1	152.0	92.0	–	52.0	34.0
KTsKhZhA-6	CdF_2 1.5, Cr_2O_3 2.0, ZnF_2 1.5, AlF_3 3.0, ZnO 3.0, Fe_2O_3 3.0, Al_2O_3 86.0	180.0	196.0	6.4	163.0	92.0	34.0	22.0	24.0

methylpyridines. Promotion of zinc-chromium-aluminum and zinc-chromium-iron-aluminum catalysts with 1.5–3.0 wt % cadmium, zinc, and aluminum fluorides raises the acetylene conversion and catalyst productivity by a factor of 1.5–2.0. In the process, the loss of cadmium metal from the catalyst is probably prevented by introduction of cadmium fluoride into the defective spinel structure characteristic of γ-Al_2O_3 and by its fixation in this structure.

To determine the dependence of the activity of catalysts on their texture properties, we measured the specific surface area, acidity, pore radius and volume, phase composition, and mechanical strength of the catalysts. The acidity of the KtsKhZhA-6 catalyst strongly differs from that of the other catalysts. It acidifies water within the first 20 s by 1.2 pH units; after 40 min, the pH value stabilizes. The other catalysts acidify water by 0.4 to 0.8 pH units within the first 20–30 s (see figure).

Probably, it is hydroxofluorides that produce acidic centers on the catalyst surface. The presence of hydroxofluorides on the catalyst enhances sorption of acetylene, ammonia, and methanol molecules, with the result that their molecules are polarized.

Table 2. Characterization of synthesis of pyridine bases on KTsKhZhA-6 catalyst [T 280–360°C, W_{tot} 150–180 h^{-1}, $C_2H_2 : NH_3 = 1 : 2$ (vol : vol)]

Synthesis time, h	T, °C	Acetylene conversion, %	Catalyzate composition, wt %			
			2-methylpyridine	4-methylpyridine	acetonitrile	sum of by-products
0–30	280	98.0	35.5	16.4	32.0	15.0
30–60	290	95.0	39.6	23.2	26.0	13.0
60–90	300	92.0	42.0	21.0	21.0	10.0
90–120	310	90.0	44.0	24.0	16.0	25.0
120–150	320	86.0	47.0	22.0	12.0	19.0
150–160	330	82.0	51.0	25.0	8.0	26.0
180–200	340	70.0	53.0	27.0	3.0	17.0

It was found that, in the first 60 h, the selectivity of a fresh catalyst with respect to pyridine yield is unstable; the major products are acetonitrile, benzene, propionitrile, etc. After 70 h, the process selectivity becomes stable, and the acetonitrile content in the catalyzate gradually decreases (Table 2).

After 180 h of work and subsequent regeneration, the catalyst becomes completely ripened. In this case, the content of acetonitrile, by-products, and tars in the catalyzate does not exceed 20–25%.

We found that the specific surface area of the catalyst decreases with time by 30 $m^2 g^{-1}$ on the average. Simultaneously, its mechanical strength increases by approximately 0.8–1.0 MPa. It should be noted that, in the course of catalyst operation, a new crystalline phase is formed, which makes the catalyst more stable.

The KTsKhZhA-6 catalyst was tested in the continuous mode for 1500 h in synthesis of pyridine and isomeric methylpyridines from acetylene, ammonia, and methanol. The following optimal process parameters were found: temperature 360–440°C; acetylene : ammonia : methanol molar ratio 1.0 : 2.0 : 0.8; total space of the velocity 100–200 h^{-1}. The catalyzate (organic layer) obtained under these conditions has the following composition (wt %): pyridine 28.0–33.0, 2-methylpyridine 12.0–25.0, 3-methylpyridine 18.0–21.0, 4-methylpyridine 12.0–15.0, with the remainder being higher pyridines, acetonitrile, and tars.

Thus, new catalysts based on cadmium, zinc, chromium, iron, and aluminum oxides and fluorides were developed and tested in synthesis of pyridine bases from acethylene, ammonia, and methanol.

The catalysts were prepared by suspending, followed by molding, drying, and calcination. Aluminum hydroxide (calcination loss 33.0%) was used as support.

X-ray diffraction patterns of the catalysts were recorded on a DRON-2 diffractometer (Cu_{K_α} radiation). The specific surface area was measured by the BET method. The catalyst acidity was determined pH-metrically with a pH-673 pH-meter equipped with an ESL-43-07 glass electrode. The pore structure of the catalyst was studied by mercury porosimetry.

The catalytic condensation of acethylene with ammonia and methanol was performed in a 25 × 1000 mm cylindrical stainless steel flow-through reactor. The temperature, space velocity, and ratio of the initial components were varied.

The reaction products were analyzed by GLC [Chrom-5 chromatograph, Apiezon-M (12–15 wt %) on Celite 545 as stationary phase, column temperature 120°C, toluene as internal reference, carrier gas helium, flow rate 2.4 $l\,h^{-1}$].

The products were separated by catalyzate fractionation on a 30-TP column and identified by their physical constants and also by obtaining their picrates and chloroplatinates.

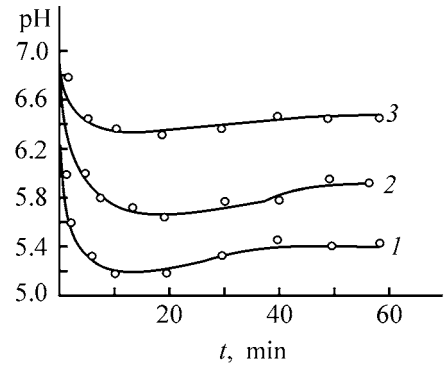

Variation with time t of pH of water contacting with the catalyst surface. Catalyst: (*1*) KTsKhZhA-6, (*2*) KTsZhKhA-5, and (*3*) KTsMA-4.

REFERENCES

1. Mel'nikov, N.N., Novozhilov, K.V., and Pylova, T.N., *Khimicheskie sredstva zashchity rastenii* (Chemical Agents for Plant Protection), Moscow: Khimiya, 1980.
2. Petrenko, D.S., *Piridinovye i khinolinovye osnovaniya* (Pyridine and Quinoline Bases), Moscow: Metallurgiya, 1973.
3. Kuklenko, S.S., Shestakova, S.I., and Shulaeva, E.Yu., *Khim. Sel'sk. Khoz.*, 1980, no. 4, pp. 51–54.
4. Chumakov, Yu.I., *Piridinovye osnovaniya* (Pyridine Bases), Kiev: Tekhnika, 1965.
5. Vereshchagin, L.I. and Kotlyarevskii, I.L., *Usp. Khim.*, 1961, vol. 30, no. 8, pp. 982–1012.
6. Moll. K., *Chem. Technol.*, 1967, vol. 19, pp. 528–539.
7. Lazdin'sh, I.Ya. and Avot, S.S., *Khim. Geterotsikl. Soedin.*, 1979, no. 8, pp. 1011–1026.
8. Yusupov, D., Babadzhanov, D.K., Kuchkarov, A.B., and Akhmerov, K.M., *Zh. Prikl. Khim.*, 1984, vol. 57, no. 11, pp. 2631–2633.
9. Yusupov, D., Kuchkarov, A.B., Khamidullaev, R.A., *et al., Zh. Prikl. Khim.*, 1988, vol. 61, no. 5, pp. 1089–1093.
10. Chistozvonov, D.B., Sobolevskii, V.S., Kozlov, L.I., and Livshits, V.D., in *Nauchnye osnovy podbora i proizvodstva katalizatorov* (Scientific Fundamentals of Selection and Production of Catalysts), Novosibirsk: Nauka, 1964, pp. 174–177.
11. Fridshtein, I.L. and Zimina, N.A., in *Nauchnye osnovy podbora i proizvodstva katalizatorov* (Scientific Fundamentals of Selection and Production of Catalysts), Novosibirsk: Nauka, 1964, pp. 267–279.
12. Yusupov, D. and Akhmerov, K.M., *Kataliticheskaya geterotsiklizatsiya atsetilenovykh soedinenii* (Catalytic Heterocyclization of Acethylene Derivatives), Tashkent: Fan, 1985.
13. Yusupov, D., Promonenkov, V.K., Kuchkarov, A.B., and Kolyada, G.G., *Itogi Nauki Tekhn., Ser.: Org. Khim.*, 1990, vol. 16, pp. 49–103.

Russian Journal of Applied Chemistry, Vol. 76, No. 6, 2003, pp. 943–945. Translated from Zhurnal Prikladnoi Khimii, Vol. 76, No. 6, 2003, pp. 973–975.

PRODUCTION AND USE OF NEW MATERIALS

Experience of Control over Process of Chemical-Informational Synthesis

V. B. Aleskovskii, S. G. Klochev, A. D. Misharev, and A. I. Romanychev

Research Institute of Chemistry, St. Petersburg State University, St. Petersburg, Russia

Received February 26, 2003

Abstract—Conditions under which various kinds of carbon nanoparticles are obtained by thermal oxidative conversion of methane in chlorine in the temperature range 20–500°C were studied. The influence exerted by conditions of synthesis of nanodispersed carbon on the properties of its samples was analyzed.

According to the theory of chemical-informational synthesis [1–6], desired products can be obtained with minimum energy expenditure and maximum productivity by performing synthesis far from equilibrium, with programmed departure from equilibrium, and "quenching" these metastable products with minimum possible delay. Experience shows that mostly low-molecular-weight products are formed in one mode of methane burning [7, 8], and supramolecular products of oxidative condensation of methane, in another [9]. Use of flame as a reaction zone bounded on all sides allows localization of a high-temperature chemical process, which enables sufficiently fast quenching, and allows control over its rate by varying not only hydrodynamic, but also thermal conditions, e.g., by changing one method of cooling of burning products for another.

EXPERIMENTAL

This paper presents the results obtained in experiments on fine control over the process of oxidative condensation of methane, which makes it possible to preset not only the degree of condensation of hydrocarbon chloroderivatives, but also parameters of supramolecules of these highly condensed synthesis products. Pipeline methane (98% methane, 0.7 ethane, 0.2 propane, 0.07 butane) and oxidizing gas "khlor" Cl_2^* obtained by reacting calcium hypochlorite with hydrochloric acid were used in the experiments. This gas contained (vol %): chlorine 46.5, HCl 24.4, nitrogen 20.8, oxygen 5.5, water 0.85, and CO_2 1.95. The oxidative conversion of methane was performed in a tubular reactor by burning the gas in a flow of chlorine. Solid reaction products were separated from gaseous products in a separator. The elemental analysis of the resulting solid products was made by their burning in oxygen in the presence of a catalyst and by ESCA; the specific surface area was measured by the method of low-temperature adsorption of nitrogen; IR spectroscopy, mass spectrometry, and electron microscopy were also employed.

A study of solid products of methane conversion demonstrated that they are composed of nanosize carbon particles enveloped with a shell composed of a solid solution or layers of benzene chloroderivatives [9]. These derivatives are rather easily evaporated on heating to 300–350°C in a vacuum, with the organic shell removed and the carbon core of the particles stripped. Carbon samples were studied on an MS-1301 mass spectrometer, in which a sample was heated from room temperature to 1200°C. On heating a sample to 300°C, the mass spectrum shows high-intensity lines corresponding to $C_6Cl_4^+$, $C_6Cl_4H^+$, $C_6Cl_5^+$, $C_6Cl_5H^+$, $C_6Cl_6^+$ and higher-molecular-weight substances (up to $C_{28}H_{14}$), with hexa- and pentachlorobenzene being the main desorption products; the intensity ratio for $C_6Cl_6^+$ and $C_6Cl_5H^+$ is approximately 1.5 : 1. In the temperature range 300–1200°C, desorption of organic products from a sample terminates virtually completely. Thus, thermal treatment at 300°C and higher results in that a sample is completely freed of a shell and becomes pure carbon at 1200°C.

As objects of further investigation served samples subjected to thermal treatment in a vacuum at 300°C for 1–1.5 h, with 25–30% of their mass lost. A study of these samples with a Tesla BC-613 electron microscope (at magnification of 80 000) demonstrated that they are composed of particles 100 to 300 Å in size, which form chain-like structures.

1070-4272/03/7606-0943 $25.00 © 2003 MAIK "Nauka/Interperiodica"

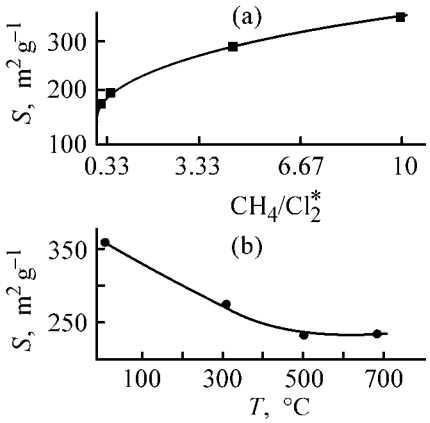

Fig. 1. Specific surface area S of a carbon sample vs. (a) flow rate ratio CH_4/Cl_2^* and (b) reactor heating temperature T.

One of the most important characteristics of carbon products is their specific surface area. The specific surface area of the samples under study depends both on the ratio of reagent flow rates and on the synthesis temperature.

Figure 1a shows the dependence of the specific surface area of the samples (after removal of a shell composed of organic products) on the flow rate ratio of methane and "khlor" (Cl_2^*, a mixture of chlorine, oxygen, HCl, nitrogen, etc.).

It can be seen that the specific surface area of carbon samples grows with increasing excess of methane; however, the yield of carbon black particles decreases. The results obtained were used to choose the optimal flow rates of gases fed into the conversion process (ml min^{-1}): CH_4 230 and Cl_2^* 68. Under these conditions, a rather large amount of carbon particles with specific surface area of about 300 $m^2 g^{-1}$ is formed.

The specific surface area of carbon samples is strongly affected by the temperature of external heating of the reactor. In some experiments, the reaction zone was preliminarily heated with an electric furnace to 20–680°C, and then oxidative conversion of methane was performed under the same conditions in a Cl_2^* flow. The experiments were done at the previously chosen optimal ratio of methane and Cl_2flow rates (see Fig. 1b).

Elemental composition of carbon-containing sample

Element	Content, wt %	
	ESCA	burning in oxygen
C	72.7	72.5
Cl	16.5	–
O	8.8	–
N	0.7	–
H	–	1.2

It can be seen from Fig. 1b that, on raising the reactor temperature, the specific surface area of the carbon samples obtained decreases. The maximum specific surface area of samples obtained without additional heating was 360 $m^2 g^{-1}$. The size of particles, calculated from their specific surface area, is approximately 10 nm, and that following from electron-microscopic data falls within the range 10–30 nm. The difference can be accounted for by particle aggregation.

Industrial carbon black, which has specific surface area exceeding 100 $m^2 g^{-1}$, retains such a high degree of dispersity for short time only [6]. The specific surface area of the carbon samples synthesized in the present study remained unchanged for 20 days. After 100 days, it decreased somewhat, but still remained rather high (250–270 $m^2 g^{-1}$). The highest specific surface area was observed for carbon samples stored for a long time in the initial state (without removing the organic shell) and subjected to temperature treatment in a vacuum immediately before measuring the specific surface area. Apparently, the shell composed of benzene chloroderivatives, which is formed in the course of synthesis and covers the carbon particles, prevents their aggregation. In "encapsulated form," dispersed particles retain high specific surface area for a long time. It follows from the aforesaid that a reproducible method for obtaining and stabilizing carbon nanoparticles, with their physicochemical properties long preserved, has been found.

The elemental composition of the carbon samples was studied by burning them in a flow of oxygen and by ESCA. Analysis for the content of carbon, hydrogen, and nitrogen was made on a Hewlett Packard 185B Carbon Hydrogen Nitrogen Analyzer. However, this technique yielded understated values of carbon content in the samples, probably, because of the incomplete burning of carbon in a flow of oxygen during the time of analysis (50 s). In further studies, the content of carbon was determined by burning a sample in a flow of oxygen in the presence of a catalyst (in the course of 20 min), using a procedure described in [10]. The content of other elements in the samples synthesized was determined by ESCA. This technique does not record hydrogen, and, therefore, the concentrations of elements were corrected with account of the content of hydrogen. The thus obtained elemental composition of carbon-containing samples is listed in the table.

Both these analytical techniques yield data on the content of carbon in the samples under study, which are in rather good agreement. Studying the mechanism of transformations occurring in the course of synthesis is complicated by the wide variety of possible chemical reactions involving free radicals. However, analysis of the products formed in oxidative condensation of methane burning in a chlorine flow confirms the validity of the scheme suggested in [7]. Chlorine removes from methane all its four hydrogen atoms to form carbons

$$CH_4 + 2Cl_2 \rightarrow C + 4HCl.$$

Carbon atoms immediately combine to form carbon nanoparticles:

$$nC \rightarrow [C]_n.$$

The nanoparticles react with chlorine to give chlorine-containing carbon

$$[C]_n + 0.5mCl_2 \rightarrow [C]_nCl_m.$$

On the surface of $[C]_nCl_m$ particles, there occur reactions yielding an organic shell composed of benzene chloroderivatives

$$6CH_4 + 15Cl_2 \rightarrow C_6Cl_6 + 24HCl$$

(it is known that synthesis of hexachlorobenzene is performed in the presence of activated carbon.) In view of the fact that the shell of nanoparticles synthesized in oxidative conversion of methane in its burning in a "khlor" flow is composed of organic benzene derivatives, it may be assumed that, before being subjected to thermal treatment at above 300°C, the carbon-containing particles themselves are constituted by partly chlorinated aromatic structures.

CONCLUSIONS

(1) It is confirmed by a new experiment that monodisperse "technical-grade carbon"—nanodispersed carbon, can be obtained in the temperature range 20–500°C. A homologous series of supramolecules of nanodispersed carbon is formed in the given temperature range.

(2) The synthesis can be guided in a desired direction by changing the mode of diffusion burning, i.e., it can be controlled by varying the synthesis conditions.

(3) The efficiency of chemical-informational synthesis is high: it occurs in high yield at moderate temperatures, needs no catalysts, and makes it possible to prescribe properties of target products.

ACKNOWLEDGMENTS

The authors thank V.M. Smirnov and Yu.G. Kol'tsova for much help in the study.

The study was supported financially by the Russian Foundation for Basic Research (grant no. 02-03-32 710) and by the Program "Leading Scientific Schools."

REFERENCES

1. Aleskovskii, V.B., *Vestn. SPb. Gos. Univ.*, 1992, no. 25, series 4, issue 4, pp. 75–76.
2. Aleskovskii, V.B., *Zh. Obshch. Khim.*, 1995, vol. 65, no. 11, pp. 1928–1929.
3. Aleskovskii, V.B., Abstracts of Papers, *1-ya Mezhdunarodnaya konferentsiya "Khimiya vysokoorganizovannykh veshchestv i nauchnye osnovy nanotekhnologii" Sankt-Peterburg, 25–28 iyunya 1996 g.* (1st Int. Conf. "Chemistry of Highly Organized Substances and Scientific Foundations of Nanotechnology," St. Petersburg, June 25–28, 1996), St. Petersburg, 1996, pp. 4–7.
4. Aleskovskii, V.B., Abstracts of Papers, *2-ya Mezhdunarodnaya konferentsiya "Khimiya vysokoorganizovannykh veshchestv i nauchnye osnovy nanotekhnologii" Sankt-Peterburg, 22–26 iyunya 1998 g.* (2nd Int. Conf. "Chemistry of Highly Organized Substances and Scientific Foundations of Nanotechnology," St. Petersburg, June 22–26, 1998), St. Petersburg, 1998, pp. 5–6.
5. Aleskovskii, V.B., Abstracts of Papers, *3-ya Mezhdunarodnaya konferentsiya "Khimiya vysokoorganizovannykh veshchestv i nauchnye osnovy nanotekhnologii" Sankt-Peterburg, 26–29 iyunya 2001 g.* (3rd Int. Conf. "Chemistry of Highly Organized Substances and Scientific Foundations of Nanotechnology," St. Petersburg, June 26–29, 2001), St. Petersburg, 2001, pp. 7–14.
6. Aleskovskii, V.B., *Zh. Obshch. Khim.*, 2002, vol. 72, no. 4, pp. 611–616.
7. Aleskovskii, V.B. and Sulimov, O.K., *Vestn. SPb. Gos. Univ.*, 1999, no. 25, series 4, issue 4, pp. 135–136.
8. Aleskovskii, V.B., Sulimov, O.K., and Misharev, A.D., *Vestn. SPb. Gos. Univ.*, 2001, no. 4, series 4, issue 1, pp. 46–54.
9. Aleskovskii, V.B., Gorshkova, Yu.G., Romanenko, E.K., and Romanychev, A.I., *Vestn. SPb. Gos. Univ.*, 2001, no. 28, series 4, issue 4, pp. 145–147.
10. Klimova, V.A., *Osnovnye mikrometody analiza organicheskikh soedinenii* (Basic Microscopic Methods for Analysis of Organic Compounds), Moscow: Khimiya, 1975.

Russian Journal of Applied Chemistry, Vol. 76, No. 6, 2003, pp. 946–948. Translated from Zhurnal Prikladnoi Khimii, Vol. 76, No. 6, 2003, pp. 976–978.

PROCESSES AND EQUIPMENT OF CHEMICAL INDUSTRY

Prognostication of Pneumatic Fractionation of Free-flowing Bulk Materials

V. A. Kirsanov

Southern-Russian State Technical University, Novocherkassk, Russia

Received January 22, 2003

Abstract—A mathematical method for prognostication of results obtained in fractionation of free-flowing bulk materials with account of the input particle concentration is described. Using this method makes it possible to substantiate the choice of the optimal design of contact units in cascade pneumatic classifiers for various technological conditions.

Of particular importance for ensuring efficient separation of free-flowing bulk materials in cascade pneumatic classifiers is prognostication of the results of the process. Solution of this problem reduces to substantiation of the optimal separation boundary ensuring the maximum yield of the target product with account of the technological requirements to quality. The previously developed mathematical models for prognostication of the optimal parameters of the process in question have been constructed without considering the input concentration of particles in an apparatus, which governs its output capacity [1, 2].

Let us consider a process of separation of a polydisperse mixture, which is aimed to obtain a coarse fraction of a certain granulometric composition, the product in the given case. Technological requirements, as a rule, restrict the maximum content of contaminating fractions and the minimum content of the commercial fraction; the output of the commercial product must be the highest. Thus, the constraint on the content of contaminating fractions in the product can be written as

$$\sum_{i=1}^{m} r_{\mathrm{k}i}^{\mathrm{cont}} \le k,$$

where i and m are the initial and final numbers of the contaminating fractions in the product; $r_{\mathrm{k}i}^{\mathrm{cont}}$, the content of ith contaminating fraction in the product; k, the maximum content of contaminating fractions in the product.

The constraint on the content of valuable fractions in the product is written in a similar way

$$\sum_{i=a}^{b} r_{\mathrm{k}i}^{\mathrm{val}} \ge L,$$

where a and b are the initial and final numbers of the valuable fractions in the product; $r_{\mathrm{k}i}^{\mathrm{val}}$, the content of ith valuable fraction in the product; L, the minimum content of the valuable fraction in the product.

To these constraints should be added the condition ensuring the maximum yield of the product, γ_{k}, which has the form $\gamma_{\mathrm{k}} \to \max$. Then, with account of the relations

$$r_{\mathrm{k}i} = \Phi_{\mathrm{k}i} r_i / \gamma_{\mathrm{k}}, \quad \gamma_{\mathrm{k}} = \sum_{i=1}^{n} \Phi_{\mathrm{k}i} r_i,$$

(where $\Phi_{\mathrm{k}i}$ is the degree of fractionation recovery of ith fraction from the initial mixture into the product, and r_i is the content of ith fraction in the initial mixture), the following system, which is a mathematical model applicable to solution of the problem at hand, can be written:

$$\begin{gathered} \sum_{i=1}^{m} r_{\mathrm{k}i}^{\mathrm{cont}} = \sum_{i=1}^{m} \left(\Phi_{\mathrm{k}i} r_i \Big/ \sum_{i=1}^{n} \Phi_{\mathrm{k}i} r_i \right) \le k, \\ \sum_{i=a}^{b} r_{\mathrm{k}i}^{\mathrm{val}} = \sum_{i=a}^{b} \left(\Phi_{\mathrm{k}i} r_i \Big/ \sum_{i=1}^{n} \Phi_{\mathrm{k}i} r_i \right) \ge L, \\ \gamma_{\mathrm{k}} = \sum_{i=1}^{n} \Phi_{\mathrm{k}i} r_i \to \max. \end{gathered} \tag{1}$$

The degree of fractionation recovery is sufficiently well approximated with the Plitt function [3]

1070-4272/03/7606-0946 $25.00 © 2003 MAIK "Nauka/Interperiodica"

$$\Phi_{ki} = 1 - \frac{100}{1 + (x_i/x_b)^P}, \quad (2)$$

where x_i is the average grain size of ith class, and P is the efficiency factor characterizing the steepness of the fractionation separation curve $\Phi_k(x)$.

As optimization parameters in solving the given problem serve the separation boundary x_b and the Eder–Mayer number $\chi = x_{25}/x_{75}$, where x_{25} and x_{75} are sizes, according to the separation curve, of particles 25 and 75% recovered into the coarse product. The Eder–Mayer number and the efficiency factor are related by $\chi = (1/9)^{1/P}$ [4]. The parameters characterizing the efficiency of the separation process depend both on the design of contact units (CU) of cascade pneumatic classifiers and on the input particle concentration μ.

Figure 1 shows experimental dependences $P = f(\mu)$ for pneumatic classifiers with CU of various designs [5]. This dependence is approximated by an equation of the following type

$$P = c_1\mu^2 + c_2\mu + c_3. \quad (3)$$

The values of the coefficients c_1–c_3 are listed in the table for all the apparatus under study. Substituting the $P = f(\mu)$ dependence in Eq. (2), we obtain an expression for Φ_k for each apparatus design in relation to the input particle concentration μ.

For example, for a pneumatic classifier with triple-flow CU, the degree of fractionation recovery can be calculated using the equation

$$\Phi_{ki} = 1 - \frac{100}{1 + (x_i/x_b)^{-0.004\mu^2 - 0.21\mu + 5.01}},$$

The problem in question is tackled with by determining the optimal separation boundary x_b at which the condition (1) is valid, by solving by computerized marching method with preset step the system of inequalities (1) at different P in relation to the input particle concentration μ.

The given mathematical model was applied to prognosticate the results obtained in separation of filling materials (stock) of roasting furnaces[1] in order to make recommendations concerning the choice of the optimal CU design. The CU were mounted in the separation chamber of pneumatic classifiers with output capacity of 15 ton h^{-1}. The technological conditions required that a certain granulometric composition of the stock should be ensured, with the content of particles less than 500 μm in size not exceeding 5%. In this case, the content of valuable fractions must not be less than 70%. The averaged granulometric composition of the stock is given below:

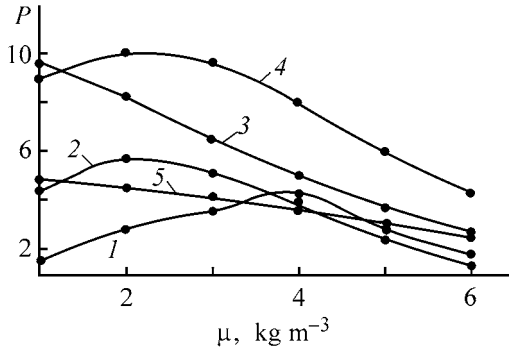

Fig. 1. Efficiency factor P of pneumatic classification vs. particle concentration μ in the apparatus. Apparatus: (*1*) hollow; with contact units: (*2*) lamellar, (*3*) double-flow, (*4*) steplike, and (*5*) triple-flow.

Sieve mesh, μm	1000	630	400	
Partial residues	24.6	10.7	8.5	
Sieve mesh, μm	315	200	160	
Partial residues	6.6	11.2	9.4	
Sieve mesh, μm	100	63	50	Tray
Partial residues	12.9	10.3	1.8	4.0

The mathematical model was used to compute parameter values in order to solve the problem mentioned above for the given composition of the filling material. The separation efficiency was preset using the Eder–Mayer number and the P factor (in Plitt's approximation) for particle concentration in the flow, μ, varying from 0.5 to 6.5 kg m^{-3} with a step of 0.5 kg m^{-3}.

Coefficients in Eq. (3)

Apparatus	c_1	c_2	c_3
Pneumatic classifier:			
hollow	–0.33	2.33	–0.45
with lamellar CU	–0.34	1.54	3.45
with double-flow CU	0.04	–1.67	11.20
with steplike CU	–0.40	1.74	7.74
with triple-flow CU	–0.04	–0.21	5.01

[1] Vyazemskii zavod grafitovykh izdelii Open Joint-Stock Company (VZGI).

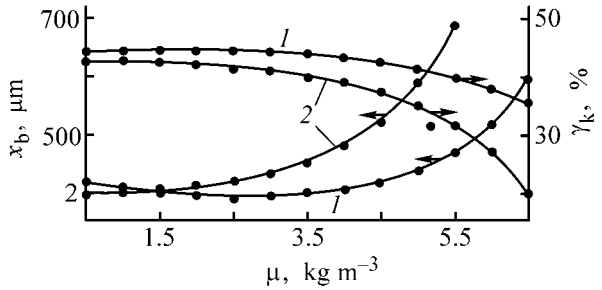

Fig. 2. Yield γ_k of coarse product and boundary particle size x_b vs. particle concentration in the apparatus. Apparatus with (*1*) steplike and (*2*) double-flow CU.

Figure 2 shows the results of calculation as a dependence of the yield of the finished product, γ_k, and boundary particle size x_b on the concentration μ for apparatus with steplike and double-flow CU. It can be seen that the maximum yield for the given pneumatic classifiers is 42%. Such a low yield of the stock of required granulometric composition can be accounted for by the fact that the content of valuable fractions in the initial filling material is 43.8%, and that of contaminating fractions, 56.2%. In this case, the limiting particle concentration μ = 5 kg m^{-3}, since, for a steplike unit, an increase in particle concentration from 0.5 to 5 kg m^{-3} has virtually no effect on the value of γ_k. The optimal parameters are, in this case, γ_k = 41.2% and x_b = 450 μm (P = 6.8, χ = 72.5%). Raising the concentration of the solid phase leads to a decrease in the yield of the finished product, steep rise in loss of valuable fractions, and increase in the boundary size of particles. Use of double-flow CU for solving the problem in question is inefficient since the yield of the finished product decreases dramatically when μ exceeds 3 kg m^{-3}. The optimal parameters for apparatus with double-flow CU are as follows: γ_k = 40.1% and x_b = 410 μm (at P = 7.4 and χ = 74.2%).

CONCLUSION

It is advisable to use, to separate filling materials with boundary particle size of 500 μm, a pneumatic classifier with steplike contact units, which ensures somewhat higher yield of stock with required granulometric composition and prescribed quality restrictions and has higher output capacity. The latter is particularly important, since the yield of stock is relatively low because of the increased content of contaminating fractions in the initial material.

REFERENCES

1. Barskii, M.D., *Fraktsionirovanie poroshkov* (Fractionation of Powders), Moscow: Nedra, 1980.
2. Danilov, V.L., Optimization of Dry Separation of Sands, *Cand. Sci. Dissertation*, Sverdlovsk, 1991.
3. Rozin, E. and Rammler, P., *Podgotovka, sushka, razmol, szhiganie nizkosortnykh topliv NKTP* (Treatment, Drying, Grinding, and Burning of Low-Grade Fuels at People's Commissariat of Heavy Industry), Moscow: Gosenergoizdat, 1933.
4. Govorov, A.V. and Barskii M.D., *Affinnye svoistva krivykh razdeleniya, approksimatsii i kombinirovannye razdelitel'nye kaskady* (Affine Properties of Separation Curves, Approximations, and Combined Separating Cascades), 1983, Sverdlovsk, Available from ONII-TEKhIM, 1983, Cherkassy, no. 1082khp D83.
5. Kirsanov, V.A. and Novoselov, A.M., in *Razrabotka i issledovanie novykh konstruktsii kontaktnykh elementov kaskadnykh pnevmoklassifikatorov: Sbornik nauchnykh trudov NGTU* (Development and Study of New Designs of Contact Units for Cascade Pneumatic Classifiers: Coll. of Sci. Works of NGTU), Novocherkassk: Novocherk. Gos. Tekh. Univ., 1997, pp. 101–104.

Russian Journal of Applied Chemistry, Vol. 76, No. 6, 2003, pp. 949–952. Translated from Zhurnal Prikladnoi Khimii, Vol. 76, No. 6, 2003, pp. 979–981.

PROCESSES AND EQUIPMENT OF CHEMICAL INDUSTRY

Kinetic Characteristics of Back-Osmosis Separation of Aqueous-Organic Solutions

V. L. Golovashin, S. I. Lazarev, and O. A. Abonosimov

Tambov State Technical University, Tambov, Russia

Received April 9, 2002; in final form, November 2001

Abstract—Back-osmosis separation of aqueous solutions of morpholine and hydroquinone on an industrial back-osmosis installation was studied in relation to the concentration and flow velocity of a solution in the intermembrane channel. The behavior of the main kinetic characteristics of separation as influensed by physical conditions of the separation process was analyzed and accounted for.

An important problem of industrial organic synthesis is utilization of waste industrial solutions and wastewater with low concentration of dissolved substances. The most promising methods for purification and concentration of these aqueous solutions are membrane separation techniques and, in particular, back osmosis. In a number of reports [1–4], results obtained in separation of aqueous solutions of low-molecular-weight organic substances by back osmosis were presented. However, the experiments described were carried out on laboratory installations, without due account of the concentration polarization, which strongly affects the separation process under industrial conditions.

The present communication reports the results obtained in studying separation of aqueous solutions of morpholine and hydroquinone on an industrial back-osmosis installation. These data are necessary both for analyzing mass-transfer processes and constructing mathematical models of the process and for developing engineering procedures for calculation of back-osmosis installations.

The experiments were done on an MRR 5-21K-01 industrial back-osmosis installation equipped with ERO-E-950/6.5 back-osmosis units of the roll type, with an MGA-95K composite cellulose acetate membrane.

The installation is shown schematically in Fig. 1. The roll units were preliminarily washed to remove glycerol impurities formed in storage and fabrication and mounted in the back-osmosis apparatus (Fig. 2) in the following sequence: the first ERO unit 7 was fixed in the cover *1* with a seal *2*. Then the cover was mounted in the apparatus case *3*, and the joint was tightened with a seal *4* and fixed with a locking ring *5*. A second ERO unit was connected to the first with adapter *6* and fixed in the apparatus case similarly to the first one. Then the feed liquid tank E1 (Fig. 1) was filled with 200 l of water and the valve Vr1 was opened. The pump P was switched on and the pressure in the system was gradually raised to 4.0 ± 0.5 MPa with a throttle valve Th. The mem-

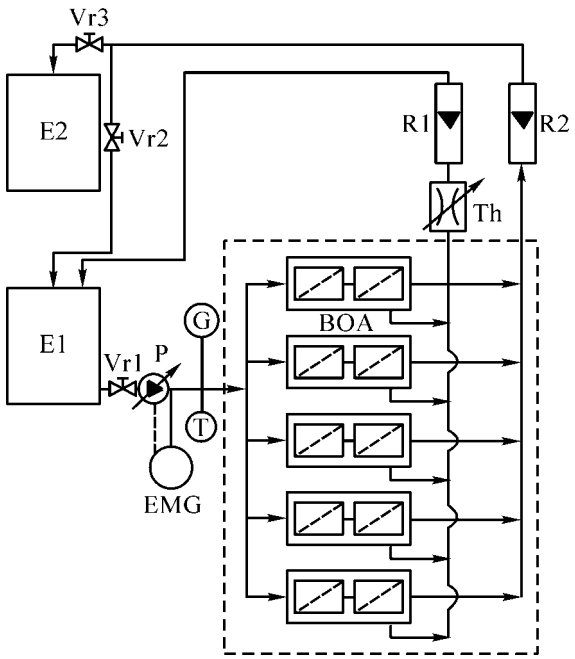

Fig. 1. Schematic of industrial back-osmosis installation. For explanation see text; the same for Fig. 2.

1070-4272/03/7606-0949 $25.00 © 2003 MAIK "Nauka/Interperiodica"

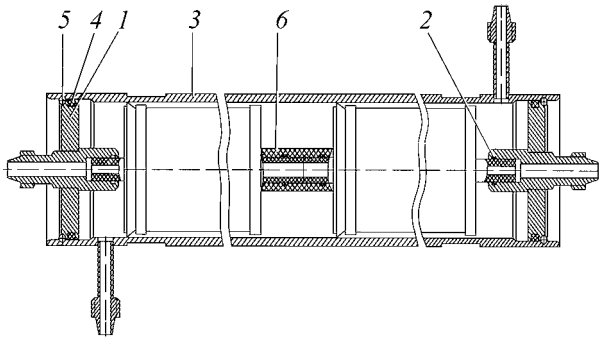

Fig. 2. Back-osmosis apparatus.

branes in the roll units were pressurized for 4 h at 4.0 ± 0.5 MPa in a flow-through mode to constant throughput. Then water was discharged from vessel *3* and the installation. The feed liquid tank E1 was filled with 200 l of an aqueous solution of a substance under study. The necessary flow rate of the feed liquid was set on the basis of readings of the rotameter R1. On switching-on the pump P and raising the pressure in the hydraulic system of the installation to the working value with the throttle valve Th, a control run was performed in the course of 4 h. The permeate and retentate were discharged into the feed liquid vessel E1. The pressure in the system was monitored with pressure gage G and electromechanical pressure gage EMG. Then the installation was switched off and kept filled with the solution for a long time (10–12 h).

The technique described above was also used to perform the working run with varied flow rate of the feed liquid. The solute concentrations (concentrations of dissolved substances) were determined by photometry [5]. The readings of the rotameters R1 and R2 were used to calculate the volumetric flow rates of the retentate and permeate.

On the basis of the experimental results, the retention factor k (%) and specific flow rate J ($m^3\ m^{-2}\ s^{-1}$) of the solvent were calculated for the membranes

$$k = (1 - c_{per}/c_f), \quad (1)$$

$$j = V/(F\tau), \quad (2)$$

where c_{per} and c_f are the solute concentrations in the permeate and feed solution (kg m^{-3}); V, the volume of permeate obtained during a run (m^3); F, the working surface area of the membranes (m^2); τ, the run duration (s).

The influence exerted by the solute concentration on the separation process was studied. To analyze the effect of mode parameters on the separation process, additional experiments were carried out at solution flow velocity in the intermembrane channel varied from 0.036 to 0.18 m s^{-1}. The results obtained (Tables 1 and 2) give insight into the relationship between the solubility of substances and the sorption capacity of a membrane.

Let us consider the effect of the solution flow velocity in the intermembrane channel on the specific flow rate of the solvent across the membrane. It can be seen from Table 1 that the solution flow velocity strongly affects the specific flow rate of the solvent. The increase in the specific flow rate of the solvent is due to a weaker influence of the concentration polar-

Table 1. Back-osmosis separation of aqueous solutions on an industrial back-osmosis installation at varied solution flow velocity (feed solution concentration 1.0 kg m^{-3})

Solution	Solution flow velocity, m s^{-1}	Concentration in permeate, kg m^{-3}	$J \times 10^6$, $m^3\ m^{-2}\ s^{-1}$	k, %
Morpholine	0.036	0.53	4.05	47.52
	0.06	0.4	4.54	60.39
	0.077	0.3434	4.93	66.00
	0.135	0.28	5.82	72.27
	0.18	0.24	5.92	76.23
Hydroquinone	0.036	0.87	3.4	13.0
	0.06	0.86	4.0	14.0
	0.077	0.85	4.3	15
	0.108	0.83	4.7	17
	0.135	0.81	4.7	19
	0.18	0.8	4.9	20

Table 2. Back-osmosis separation of aqueous solutions on an industrial back-osmosis installation at varied solution concentration

Solution	Concentration, kg m^{-3}			$J \times 10^6$, $m^3\ m^{-2}\ s^{-1}$	k, %
	in feed solution	in retentate	in permeate		
Morpholine	0.86	1.01	0.2	5.92	80.00
	1.06	1.26	0.22	5.87	82.29
	1.24	1.46	0.26	5.83	82.38
	1.52	1.79	0.31	5.74	82.40
	1.84	2.13	0.44	5.49	79.51
Hydroquinone	1.045	1.1	0.909	4.3	13
	1.064	1.12	0.924	4.25	13.1
	1.425	1.5	1.232	4.1	13.5
	2.185	2.3	1.879	4	14
	2.28	2.4	1.915	3.98	16

ization [6]. It should also be noted that, in the case of morpholine, the osmotic flow of the solvent across the membrane is an important factor. When the solution flow velocity in the intermembrane channel is raised, the agitation in the near-membrane layers is improved, with the result that the osmotic flow rate decreases and, consequently, the specific flow rate of the solvent increases.

Raising the solution concentration leads to a decrease in the specific flow rate of the solvent. This is a consequence of two effects: the increase in the solution concentration in the near-membrane region leads, on the one hand, to clogging of pores in the membrane as a result of interaction of the solute with the material of the active layer of the membrane [7, 8], and, on the other, to an increase in the osmotic pressure of the solvent at the membrane surface [9] and, as a consequence, to a decrease in the specific flow rate of the solvent.

Let us consider the effect of concentration and flow velocity of the solution on the retention factor of the membrane for dissolved substances. Morpholine and hydroquinone are polar substances and can form hydrogen bonds with the membrane material [10]. In this case, three-dimensional polymolecular structures composed of solute and solvent molecules can be formed both in the near-membrane region and in the solution bulk. Also, sorption of solutes by the active layer of the membrane causes partial clogging of pores, with the result that the membrane permeability to the solute decreases. It is these effects that lead, combined, to a rise in the retention factor of the membrane with increasing concentration of dissolved substances.

The fact that the membrane has different retention factors for the solutes can be explained as follows. The solute is transferred across the membrane by two flows: convective (with the solvent) and diffusion [11]. The amount of substance transported by any of these flows depends on the sorption capacity of the membrane [7, 8]. The membrane has different sorption capacities for morpholine and hydroquinone. The latter is strongly sorbed by the membrane, and the former, in smaller amounts. The following pattern is observed in adsorption from solutions: a substance is sorbed from solution the better, the lower its solubility in the solvent (water) [12]. Hydroquinone, being a weak acid, shows limited solubility in water [10] (P_{max} = 67 kg m^{-3} at 20°C) and, therefore, is well sorbed by the membrane surface. As a result, the retention factor for morpholine exceeds that for hydroquinone.

Raising the solution flow velocity over the membrane leads to better agitation of near-membrane layers, with the result that the solute concentrations in the flow core and in the near-membrane region become equal and, as a consequence, the amount of substance transferred by the convective flow decreases. The decrease in the solute concentration in the near-membrane region also leads to a fall in the concentration gradient on both sides of the membrane, with the transmembrane diffusion flow decreasing. Acting together, these effects result in that the retention factor of the membrane grows with increasing velocity of solution flow over the membrane.

CONCLUSIONS

(1) The retention factor of the membrane and the specific flow rate of the solvent across it are higher for well-water-soluble morpholine, compared with the poorly soluble hydroquinone. At morpholine concentrations of 0.86–1.84 kg m^{-3}, the specific flow rate of the solvent is (5.92–5.49) × 10^{-6} m^3 m^{-2} s^{-1}, and the retention factor, 80–79%. At hydroquinone concentrations of 1.045–2.28 kg m^{-3}, the specific flow rate of the solvent is (4.25–3.98) × 10^{-6} m^3 m^{-2} s^{-1}, and the retention factor, 13–16%.

(2) With the solution flow velocity in the intermembrane channel increasing within the range 0.036–0.18 m s^{-1}, both the retention factor and the specific flow rate of the solvent grow [k = 47.52–76.23% and J = (4.05–5.92) × 10^{-6} m^3 m^{-2} s^{-1}, for an aqueous solution of morpholine and k = 13–20% and J = (3.4–4.9) × 10^{-6} m^3 m^{-2} s^{-1} for an aqueous solution of hydroquinone].

REFERENCES

1. Lazarev, S.I., Korobov, V.B., Kliot, M.B., and Pirogov, P.A., *Izv. Vyssh. Uchebn. Zaved., Khim. Khim. Tekhnol.*, 1993, vol. 36, no. 5, pp. 76–80.
2. Korobov, V.B. and Lazarev, S.I., *Izv. Vyssh. Uchebn. Zaved., Khim. Khim. Tekhnol.*, 1995, vol. 38, nos. 4–5, pp. 73–79.
3. Golovashin, V.L., Lazarev, S.I., and Korobov, V.B., *Izv. Vyssh. Uchebn. Zaved., Khim. Khim. Tekhnol.*, 1999, vol. 42, no. 5–6, pp. 126–128.
4. Golovashin, V.L., Lazarev, S.I., and Korobov, V.B., *Izv. Vyssh. Uchebn. Zaved., Khim. Khim. Tekhnol.*, 1999, vol. 42, nos. 5–6, pp. 129–131.
5. Peregud, E.A., *Khimicheskii analiz vozdukha (novye i usovershenstvovannye metody)* [Chemical Analysis

of Air (New and Modified Methods)], Leningrad: Khimiya, 1976.

6. Bryk, M.T. and Tsapyuk, E.A., *Ul'trafil'tratsiya* (Ultrafiltration), Kiev: Naukova Dumka, 1989.
7. Tone, S., Shinohara, K., Igorashi, Y., and Otake, T., *J. Membrane Sci.*, 1984, vol. 19, pp. 195–208.
8. Sourirajan, S., *Pure Appl. Chem.*, 1978, vol. 50, pp. 593–615.
9. Nikolaev, N.N., *Diffuziya v membranakh* (Diffusion in Membranes), Moscow: Khimiya, 1980.
10. Petrov, A.A., Bal'yan, Kh.V., and Troshchenko, A.T., *Organicheskaya khimiya: Uchebnik dlya vuzov* (Organic Chemistry: Textbook for Higher School Institutions), Moscow: Vysshaya Shkola, 1981.
11. Chalykh, A.E., *Diffuziya v polimernykh sistemakh* (Diffusion in Polymeric Systems), Moscow: Khimiya, 1987.
12. Koganovskii, A.M., Klimenko, I.A., Levchenko, T.M., *et al., Adsorbtsiya organicheskikh veshchestv iz vody* (Adsorption of Organic Substances from Water), Leningrad: Khimiya, 1990.

Russian Journal of Applied Chemistry, Vol. 76, No. 6, 2003, pp. 953–957. Translated from Zhurnal Prikladnoi Khimii, Vol. 76, No. 6, 2003, pp. 982–986.

ORGANIC SYNTHESIS AND INDUSTRIAL ORGANIC CHEMISTRY

Synthesis of 4-Amino-4'-nitrodiphenyl Sulfide

V. S. Pilyugin

Research and Technological Institute of Herbicides and Plant Growth Regulators, Academy of Sciences of Bashkortostan Republic, Ufa, Bashkortostan, Russia

Received January 9, 2003

Abstract—The possibility of preparing 4-amino-4'-nitrodiphenyl sulfide by reaction of chlorobenzene with sodium sulfide in a two-phase system composed of water and organic solvent in the presence of a phase-transfer catalyst under continuous hydroacoustic treatment was examined.

4-Amino-4'-nitrodiphenyl sulfide **I** is an intermediate in production of 3,4,4'-triaminodiphenyl sulfide, the synthetic precursor of antihelminth agents of the 5(6)-(4'-aminophenylthio)-2-aminobenzimidazole series [1].

Thioethers (sulfides) are prepared by condensation of alkyl halides or nitro-substituted aryl halides with sodium sulfide [2–4].

Synthesis of thioethers by reaction of thiocyanates with alcohols under heating in the presence of stoichiometric amounts of alkali or alkaline-earth metal hydroxides or alcoholates or those of tertiary amines is described in a patent [5].

Dialkyl sulfides can also be prepared by reaction of alkyl chlorides with an aqueous or aqueous-alcoholic solution of alkali metal sulfide in an autoclave at high pressure [6]; diaryl sulfides are synthesized by reaction of appropriate nitrochlorobenzenes in dimethylformamide (DMF) with an aqueous solution of sodium sulfide in the presence of finely divided sulfur [7] or in refluxing alcohol with fine powder of a preliminarily fused mixture of sodium sulfide and sulfur [8].

There are numerous procedures for reducing nitro compounds to the corresponding amines [9]; in some cases, it is possible to selectively reduce one of the nitro groups of polynitro compounds with a calculated amount of sodium (or ammnonium) sulfide (or hydrosulfide) [9].

A procedure has been developed for preparing 4,4'-diaminodiphenyl sulfide **I** by reaction of 4-nitrochlorobenzene **II** with sodium sulfide in DMF, followed by reduction of the resulting 4,4'-dinitrodiphenyl sulfide with iron powder in aqueous alcohol in the presence of ammonium chloride under heating [10].

Hodson and Wilson [11] prepared diphenyl sulfide **I** as follows. A solution of **II** in absolute ethanol is heated almost to reflux, and an aqueous solution of sodium sulfide is added in small portions. The resulting mixture is refluxed with stirring for 10 h. Yield of **I** is about 20% (mp 138–142°C).

According to Radulova and Tapalova's procedure [12], a mixture of **II** with water and sodium sulfide is heated, an additional portion of **II** is added, and, after prolonged heating, toluene is added; the yield of **I** is about 68% (mp 143–144°C).

Zasosov and Gal'chenko prepared sulfide **I** by adding a portion of **II** to a boiling aqueous solution of sodium sulfide. After stirring for a certain time, the next portion of **II** is added, and the mixture is refluxed with stirring. Then an additional small amount of aqueous sodium sulfide solution is introduced, and the mixture is refluxed with stirring. The resulting mixture is steam-distilled to remove unchanged **II**; yield of **I** 77–80% (mp 145–147°C, from toluene).

Raiziss *et al.* [14] refluxed a mixture of Na_2S, water, and a part of the required amount of **II**, after which they added the remaining part of **II**, with the refluxing continued. The resulting mixture was steam-distilled; yield of **I** 80% (mp 141–413°C, from ethanol).

Aminonitrodiphenyl sulfides can also be prepared by reaction of alkaline solutions of substituted aminothiophenols with alcoholic solutions of halonitrobensenes [15–20].

All the above procedures for preparing sulfides **I** are time- and labor-consuming; the yield and quality of the target product are poor. The procedures involve

1070-4272/03/7606-0953 $25.00 © 2003 MAIK "Nauka/Interperiodica"

Table 1. Variation with time of the concentrations of *p*-nitrochlorobenzene **II**, c_{II}, and *p*-chloroaniline **V**, c_V, in the organic phase in the course of synthesis of **I**

Sampling time (from the reaction start) τ, h	c_{II}	c_V
	M	
0	3.16	–
0.5*	2.10	0.10
1.0	1.66	0.12
1.5**	1.56	0.11
2.0	1.50	0.12
2.5	1.50	0.11
3.0	1.46	0.12
3.5	1.06	0.12
4.0	0.67	0.12
5.0	0.42	0.12
6.0	0.23	0.12
7.0	0.08	0.12
8.0	0.01	0.12

* Completion of loading Na_2S.

** Addition of PEG-400.

numerous auxiliary operations or require difficultly available chemicals. Therefore, none of these procedures has been introduced on the commercial or semicommercial scale.

In this study, we developed an improved procedure for preparing sulfide **I**, based on the reaction of nitrochlorobenzene **II** with sodium sulfide in a two-phase system constituted by water and organic solvent (chlorobenzene, toluene, chloroform, etc.) under heating in the presence of a phase-transfer catalyst (PTC: quaternary alkylammonium salts, polyethylene glycol PEG-400, etc.), with simultaneous hydroacoustic treatment of the reaction mixture.

Reaction of **II** with sodium sulfide involves a number of steps: formation of sodium 4-nitrothiophenolate **III** and its successive reduction with sodium sulfide to the nitroso, hydroxylamino, and finally, amino derivatives. Sodium 4-aminothiophenolate **IV** mainly accumulates in the aqueous phase.

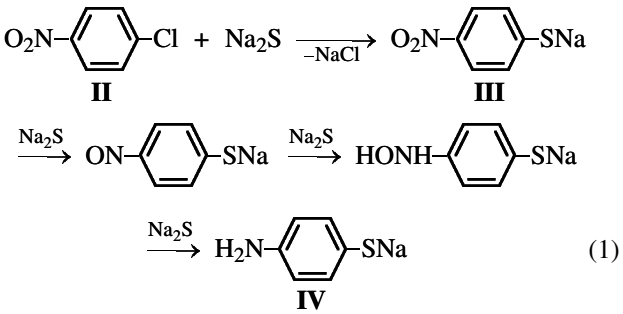

(1)

Sulfide **I** is formed by the reaction of **IV** with the remaining part of **II**:

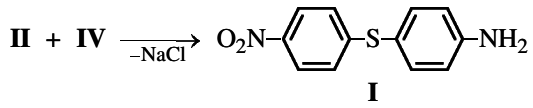

(2)

An impurity of *p*-chloroaniline **V** is formed by reduction of the nitro group via a series of intermediates:

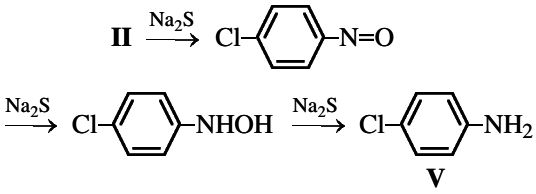

(3)

An impurity of 4,4'-dinitrodiphenyl sulfide **VI** is formed by the reaction of **III** with **II**:

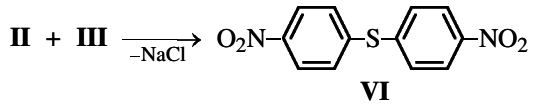

(4)

Thiophenolate **III** and products of its sequential reduction to **IV** are water-soluble and, when formed, pass to the aqueous phase. The compounds mainly occurring in the organic phase are sulfide **I**, chloronitrobenzene **II**, chloroaniline **V**, and also dinitrodiphenyl sulfide **VI** formed in small amounts.

The optimal parameters of sulfide **I** preparation (temperature, reaction time before adding phase-transfer catalyst, water : organic solvent and **II** : Na_2S ratios) are those at which, before adding the phase-transfer catalyst, the amount of **V** is the smallest, compound **VI** is virtually absent, approximately half of **II** is converted to salt **IV** and passes to the aqueous phase, and the other half remains in the organic phase (Table 1).

When a phase-transfer catalyst (PEG-400 etc.) is added at this instant of time to the reaction mixture and the mixture is subjected to intense hydroacoustic treat ment, the transfer of salt **IV** from the aqueous to organic phase and its reaction with chloronitrobenzene **II** in the organic phase to form sulfide **I**, also dissolving in the organic phase, are sharply accelerated. In most cases, in synthesis of **I**, chlorobenzene (Table 2) or toluene (Table 3) is used as organic solvent.

The advantage of chlorobenzene is that, in contrast to toluene, this solvent (and solution of **I** in it) can be subsequently used for preparing 4-amino-3,4'-dinitrodiphenyl sulfide. Furthermore, as follows from

Table 2. Synthesis of sulfide **I** in chlorobenzene under various conditions and at various reactant ratios (phase-transfer catalyst PEG-400,* reaction time before adding PEG-400 1 h**)

II : Na_2S molar ratio	Water–chlorobenzene volume ratio	**II** : chlorobenzene weight ratio	Amount of PEG-400 relative to **II**, %	*T*, °C	τ (h) after adding PEG-400	Yield of crude product, %	Content of **I** in crude product, wt %
1.00 : 1.74	2.50 : 1.00	1.00 : 0.56	3.125	98	6	93	91
1.00 : 1.74	2.50 : 1.00	1.00 : 0.56	3.125	95	7	93	90
1.00 : 1.74	2.50 : 1.00	1.00 : 0.56	3.125	104	6	93	94
1.00 : 1.74	2.50 : 1.00	1.00 : 0.56	3.125	90	7	70	72
1.00 : 1.74	Water	1.00 : 0.00	3.125	100	7	76	85
1.00 : 1.74	2.50 : 1.00	1.00 : 0.56	No	102	8	52	74
1.00 : 1.74[a]	2.50 : 1.00	1.00 : 0.56	3.125	98	6	75	86
1.00 : 1.74[b]	2.50 : 1.00	1.00 : 0.56	3.125	98	6	90	91
1.00 : 1.74[c]	2.50 : 1.00	1.00 : 0.56	2.50	102	6	92	93
1.00 : 1.74[d]	2.50 : 1.00	1.00 : 0.56	3.125	100	6	90	91
1.00 : 1.74	2.00 : 1.00	1.00 : 0.69	3.125	98	6	91	95
1.00 : 1.74	3.00 : 1.00	1.00 : 0.46	3.125	100	6	93	93
1.00 : 1.74	6.00 : 1.00	1.00 : 0.23	3.125	100	6	79	94
1.00 : 1.74	1.50 : 1.00	1.00 : 0.93	3.125	100	6	92	93
1.00 : 1.74	1.00 : 1.00	1.00 : 1.38	3.125	100	6	81	93
1.00 : 1.74	2.50 : 1.00	1.00 : 0.48	3.125	102	6	93	93
1.00 : 1.74	2.50 : 1.00	1.00 : 0.69	3.125	100	6	92	93
1.00 : 1.74	2.50 : 1.00	1.00 : 1.01	3.125	102	6	91	93
1.00 : 1.74	2.50 : 1.00	1.00 : 1.37	3.125	102	6	77	91
1.00 : 1.74	2.50 : 1.00	1.00 : 0.29	3.125	100	6	71	94
1.00 : 1.74	2.50 : 1.00	1.00 : 0.56	2.500	102	6	92	93
1.00 : 1.74	2.50 : 1.00	1.00 : 0.56	2.000	100	6	92	93
1.00 : 1.74	2.50 : 1.00	1.00 : 0.56	1.000	100	7	92	92
1.00 : 1.74	2.50 : 1.00	1.00 : 0.56	0.520	100	6	78	88
1.00 : 1.74	2.50 : 1.00	1.00 : 0.56	4.000	100	6	93	92
1.00 : 1.74	2.50 : 1.00	1.00 : 0.56	5.200	100	6	95	68
1.00 : 1.74	2.79 : 1.00	1.00 : 0.50	2.600	102	6	93	93
1.00 : 1.74[e]	2.79 : 1.00	1.00 : 0.50	2.600	102	6	82	85
1.00 : 1.74[f]	2.79 : 1.00	1.00 : 0.50	2.600	102	7	94	71
1.00 : 1.74	2.79 : 1.00	1.00 : 0.50	2.600	102	5	87	78
1.00 : 1.40	2.79 : 1.00	1.00 : 0.50	2.600	102	6	92	93
1.00 : 1.03	2.79 : 1.00	1.00 : 0.50	2.600	102	6	81	78
1.00 : 2.00	2.79 : 1.00	1.00 : 0.50	2.600	102	6	92	93
1.00 : 2.50	2.79 : 1.00	1.00 : 0.50	2.600	102	6	84	85
1.00 : 1.74	2.79 : 1.00	1.00 : 0.50	2.600	102	8	93	93
1.00 : 1.74	2.79 : 1.00	1.00 : 0.50	2.600	102	9	92	93

* Specific features of particular experiments: [a] a mixture of water, chlorobenzene, and sodium sulfide was charged, after which compound **II** was added; [b] Katamin AB used instead of PEG-400; [c] Tetraethylammonium iodide used instead of PEG-400; [d] toluene used instead of chlorobenzene.

** Unless otherwise indicated ([e], 2 h; [f], 0.67 h).

Table 3. Synthesis of sulfide **I** in toluene (molar ratio **II** : Na_2S = 1.0 : 1.7, volume ratio water : toluene = 2.5 : 1.0, weight ratio **II** : toluene = 1.17 : 1.00, phase-transfer catalyst PEG-400)

Amount of PEG-400 relative to **II**, %	Reaction time after completion of adding Na_2S, h		Yield of crude product, %	Content of **I** in crude product, wt %
	before adding PEG-400	after adding PEG-400		
3.00	1.00	6	91	90
3.12	1.00	6	90	91
2.15	1.00	7	89	90
1.50	1.50	7	90	90
4.00	1.50	6	89	90
3.12	1.5	6	89	90
3.12	1.0	7	90	90

Tables 2 and 3, chlorobenzene, compared to toluene, ensures higher yield and quality of **I**.

Laboratory experiments on development of a procedure for preparing **I** (Table 2) show that the best synthesis conditions are as follows. Temperature schedule: 80–85°C in the stage of adding Na_2S, keeping for 0.5 h at 80–85°C after adding the whole amount of Na_2S; heating to 96–102°C for 0.5–1.0 h before adding phase-transfer catalyst (PEG-400); addition of PEG-400 and subsequent reaction at 96–102°C. Ratios: water : chlorobenzene (by volume) 2.5 : 1.0, chlorobenzene : **II** (by weight) 1.00 : 1.17, **II** : Na_2S (molar) 1.0 : 1.7, and **II** : PEG-400 (by weight) 1.000 : (0.014–0.017). Under these optimal conditions, sulfide **I** is prepared relatively simply in a yield of no less than 92%, with the main substance content of no less than 93 wt %. The process was developed on a semicommercial scale (160-l reactor with immersed device for hydroacoustic treatment [21]).

EXPERIMENTAL

The reaction mixtures and crude products in the stage of preparation of **I** were analyzed qualitatively by TLC and quantitatively by HPLC, and identified by IR and ^{13}C NMR spectroscopy.

The IR spectra were recorded with a Jasco 810-IR spectrometer in the 4000–400 cm^{-1} range using CCl_4 solutions or mulls in mineral oil. The ^{13}C NMR spectra were measured on a Bruker CXP-100 spectrometer at a working frequency of 22.63 MHz under conditions of total proton decoupling or without it; solvent DMSO, internal reference HMDS. The signal assignment was based on the chemical shifts, coupling constants, multiplicities, and relative intensities; data for related model compounds and results of calculation of magnetic shielding in an aromatic ring were also taken into account.

The TLC analysis was performed on Silufol plates; the development involved reduction with an $SnCl_2$ solution, diazotization of the resulting anilines, and azo coupling with 1-naphthol; eluent C_6H_6 : C_2H_5OH, 10 : 1 by volume.

Quantitative HPLC analysis was performed with an Altex model 330 liquid isocratic chromatograph equipped with a model 110 pump, a model 153 detector, model 210 20-μl loop dosing units, and 30-, 50-, and 100-μl SNR Hamilton microsyringes. Separation and analysis of a mixture of nitrobenzene **II**, sulfide **I**, dinitro sulfide **VI**, and chloroaniline **V** were performed on a stainless steel column (25 cm × 4.6 mm i.d.) packed with Ultraspher ODS phase (grain size 5 μm). The products were analyzed and identified using water–acetonitrile (20 : 80 to 30 : 70 by volume) eluent and diphenyl as internal reference.

A glass reactor equipped with a reflux condenser was charged with the required amounts of water and organic solvent (chlorobenzene, toluene, chloroform, etc.), after which crystalline chloronitrobenzene **II** was added. The mixture was vigorously stirred with a hydroacoustic device mounted on the reactor lid and heated to 65–70°C; in so doing, chloronitrobenzene **II** gradually dissolved in the organic phase. Then crystalline $Na_2S \cdot 9H_2O$ (or its aqueous solution prepared in advance) was added in small portions so as to keep the reaction temperature within 80–85°C. When solid sodium sulfide was added, the temperature first noticeably decreased owing to endothermic dissolution of Na_2S and then sharply increased owing to fast exothermic reaction (with the Na_2S solution prepared in advance, the temperature variations are weaker). Therefore, Na_2S should be added carefully, since overheating of the reaction mixture (above 80–85°C) causes side reactions.

After adding the whole amount of Na_2S, the mixture was vigorously stirred at 80–85°C with a built-in device for hydroacoustic treatment for an additional 30 min, after which it was heated to 96–102°C and stirred at this temperature for 0.5–1 h. Then, a phase-transfer catalyst (PEG-400 or quaternary alkylammonium salt) was added in the amount of 1–4% relative to the charged chloronitrobenzene **II**, and the mixture was vigorously stirred at 96–102°C with the hydroacoustic treatment for 6–7 h.

After reaction completion and phase separation, the lower aqueous salt solution was separated and discarded, and the organic layer was washed with hot water with vigorous stirring to remove the inorganic salts and organic intermediates more completely. After phase separation, the lower organic layer (a solution of crude sulfide in chlorobenzene, toluene, or chloroform) was poured into a crystallizer and cooled to 0°C. The precipitated crystals of **I** were filtered off, washed with water, and dried at 60–70°C.

CONCLUSION

The reaction of 4-nitrochlorobenzene with sodium sulfide in a two-phase system constituted by water and organic solvent (chlorobenzene, toluene, chloroform, etc.) in the presence of a phase-transfer catalyst (PEG-400, quaternary alkylammonium salts, etc.) added after a definite period of time, under vigorous hydroacoustic treatment and at temperature maintained

in the ranges 80–85 (addition of Na_2S, before adding phase-transfer catalyst) and 96–102°C (phase-transfer step), gives 4-amino-4'-dinitrodiphenyl sulfide in a yield of no less than 92%, with the main substance content of no less than 93%.

ACKNOWLEDGMENTS

The study was supported by the Russian Foundation for Basic Research (project no. 02-03-97911).

REFERENCES

1. USSR Inventor's Certificate, no. 1246563.
2. Neniţescu, C.D., *Chemie Organica*, Bucharest: Tehnica, 1960, vol. 1.
3. Nesmeyanov, A.N. and Nesmeyanov, N.A., *Nachala organicheskoi khimii* (Fundamentals of Organic Chemistry), Moscow: Khimiya, 1969, book 1.
4. UK Patent 1498410.
5. FRG Patent 1193047.
6. Polish Patent 56199.
7. USSR Inventor's Certificate, no. 230133.
8. Krulikovskaya, E.A., Kirilova, V.G., and Bykova, L.B., *Tr. Tomsk. Univ.*, 1968, vol. 192, pp. 13–19.
9. Fieser, L.F. and Fieser, M., *Advanced Organic Chemistry*, New York: Reinhold, 1962.
10. USSR Inventor's Certificate, no. 491624.
11. Hodson, H.H. and Wilson, J., *J. Chem. Soc.*, 1912, vol. 101, no. 9, pp. 1693–1696.
12. Radulova, S. and Tapalova, E., *Vet. Mid. Nauki* (Sofia), 1965, vol. 2, no. 9, pp. 873–877.
13. Zasosov, V.A. and Gal'chenko, M.I., *Zh. Prikl. Khim.*, 1946, vol. 19, nos. 5–6, pp. 580–584.
14. Raiziss, G.W., Clemence, L.W., Sevarac, M., and Maetsch, J.C., *J. Am. Chem. Soc.*, 1939, vol. 61, no. 12, pp. 2763–2768.
15. Gupta Satya Prokash and Gara Devendra Mohan Lal, *Indian J. Appl. Chem.*, 1966, vol. 29, nos. 2–3, pp. 51–56.
16. Sharma, H.L., Sharma, V.N., and Mital, A.L., *Aust. J. Chem.*, 1968, vol. 21, no. 21, pp. 3081–3084.
17. Sharma, H.L., Sharma, V.N., and Mital, A.L., *Tetrahedron Lett.*, 1967, no. 17, pp. 1657–1662.
18. Davis, F.A. and Wetzel, R.B., *Tetrahedron Lett.*, 1969, no. 51, pp. 4483–4487.
19. Sevbo, D.P. and Ginzburg, O.F., *Zh. Org. Khim.*, 1970, vol. 6, no. 2, pp. 345–348.
20. Jain, S.M., Chandra, D., and Mital, R.L., *Indian J. Chem.*, 1971, vol. 9, no. 11, pp. 1236–1241.
21. USSR Inventor's Certificate, no. 1477458.

Russian Journal of Applied Chemistry, Vol. 76, No. 6, 2003, pp. 958–961. Translated from Zhurnal Prikladnoi Khimii, Vol. 76, No. 6, 2003, pp. 987–989.

ORGANIC SYNTHESIS AND INDUSTRIAL ORGANIC CHEMISTRY

Distribution of Functional Groups in Carboxymethyl Rhodexman

O. V. Sibikina, A. A. Iozep, and B. A. Ershov

St. Petersburg State Academy of Pharmaceutical Chemistry, St. Petersburg, Russia
Research and Technological Institute of Antibiotics and Enzymes, St. Petersburg, Russia

Received December 10, 2002; in final form, March 2003

Abstract—The distribution of functional groups in the monomeric unit of carboxymethyl rhodexman was studied by periodate oxidation and ^{13}C NMR.

Rhodexman, linear β-1,3-β-1,4-*D*-mannan produced by *Rhodotorula rubra* yeast culture, occupies a particular place among polysaccharides. It is virtually nontoxic; it normalizes the blood coagulation system, exhibits pronounced antilipidemic and radiation-protective activity, and enhances the nonspecific resistance of a living body [1]. A semisynthetic pharmaceutical Rhonasan exhibiting antisclerotic effect and hypoglycemic activity was developed on the basis of sulfated rhodexman. Its surpasses the analogs produced beyond Russia in safety (low toxicity) and other properties [2]. It seems also promising to develop physiologically active polymers based on carboxymethyl rhodexman (CMR). In this study we analyzed the distribution of carboxymethyl groups in CMR with the aim to find conditions for preparing the standardized product and elucidate factors affecting its reactivity. Rhodexman was alkylated with monochloroacetic acid in isopropyl alcohol in the presence of an alkali [3]. CMR samples were isolated and purified as described in [4] and were characterized by the degree of carboxymethylation C_{cm} (number of carboxymethyl groups per monomeric unit of the polysaccharide), which was calculated from the results of conductometric and volumetric titration [4]. The CMR samples used in this study had C_{cm} = 0.18–1.07.

To determine the predominant alkylation direction in CMR samples with various degrees of substitution, the number of α-glycol groups was determined by periodate oxidation:

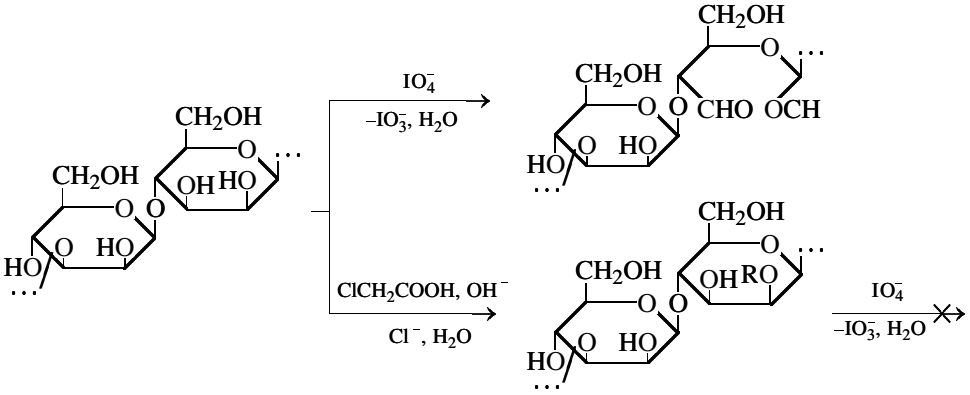

We took into account that the number of α-glycol groups in the CMR sample decreases by 1 mol only when the alkylation occurs in the 1,4-linked monosaccharide fragment at the C^2–O and/or C^3–O positions. Carboxymethylation at the other positions of the rhodexman polymeric chain does not affect the results of periodate oxidation. Examination of the correlation between the number of α-glycol groups and C_{cm},

1070-4272/03/7606-0958 $25.00 © 2003 MAIK "Nauka/Interperiodica"

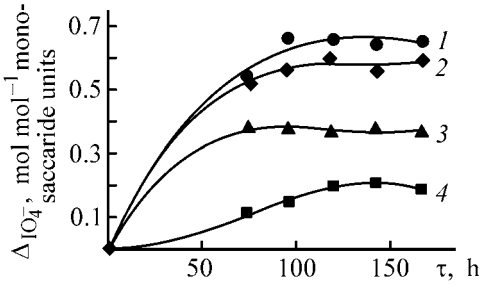

Fig. 1. Consumption of periodate $\Delta_{IO_4^-}$ vs. reaction time τ in oxidation of CMR. C_{cm}: (*1*) 0, (*2*) 0.18, (*3*) 0.7, and (*4*) 1.07.

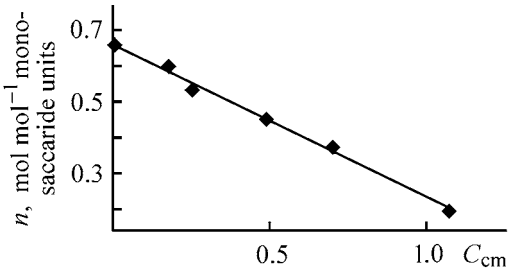

Fig. 2. Content of α-glycol groups *n* in rhodexman vs. the degree of its carboxymethylation, C_{cm}. Correlation equation: $y = -0.4192x + 0.6566$; $R^2 = 0.992$.

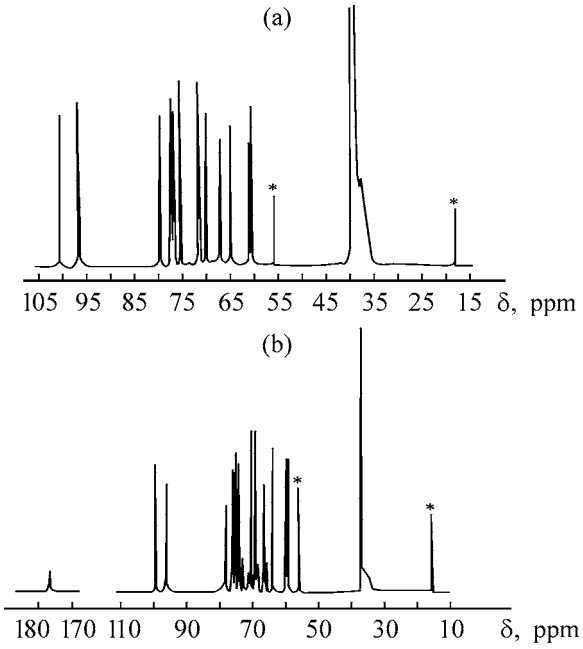

Fig. 3. ^{13}C NMR spectra of (a) rhodexman and (b) CMR (C_{cm} = 0.25). (δ) Chemical shift. The signals belonging to residual ethanol used for precipitation of rhodexman or CMR are marked with an asterisk.

provided that the substituents are distributed over the polysaccharide chain uniformly, allows evaluation of the relative reactivities of various monosaccharide fragments of rhodexman.

Oxidation of polysaccharide samples was performed with sodium metaperiodate in acetate buffer solution (pH 4.1) [5]. The oxidant consumption was monitored spectrophotometrically (λ 222.5 nm) [3].

We found that, in CMR samples with C_{cm} = 0.2–1.0, as compared to the initial rhodexman, the content of α-glycol groups decreases by 0.42 mol per mole of introduced carboxy groups (Figs. 1, 2).

Since only 66% of rhodexman units linked by the β-1,4-glycoside bond are oxidized with periodate, it seems that the polysaccharide is alkylated randomly. At C_{cm} = 1.0, there is 0.66 mol of the substituent per 0.66 mol of 1,4-linked monosaccharide fragments, including 0.42 mol of carboxymethyl groups at the C^2–O and/or C^3–O positions (in the case of purely random distribution, the content of such groups would be 0.44 mol). However, there are indications in the literature that, among two vicinal secondary hydroxy groups of cellulose, only one is substituted by the carboxymethyl group, and the probability of substitution at C^2–O is two times higher than at C^3–O [6]. This fact is due to repulsion between the negatively charged chloroacetate ions and carboxymethyl groups at position 2 or 3 [7]. Experiments on dextran carboxymethylation also showed that monosubstitution decreases the reactivity of the remaining OH groups: by approximately 50% at the β-position and 30% at the γ-position [8]. It is also known that, in 1,4-glucans, the primary hydroxy groups are alkylated almost as readily as the groups at the C^2 position. Published data on the direction of carboxymethylation of cellulose, dextran, and other polysaccharides [9–11] suggests that carboxymethyl groups in CMR are located at the C^2–O position in 1,4-linked monosaccharide units of rhodexman and at the C^6–O position in 1,3- and 1,4-linked units.

To determine the direction of rhodexman carboxymethylation, we measured the ^{13}C NMR spectra of samples of the initial polysaccharide and carboxymethylrhodexman with C_{cm} = 0.25 and 0.7 (Figs. 3a, 3b). The assignments are given in the table.

As shown in [12, 13], alkylation of the OH groups of the pyranose ring shifts the signals of the carbon atoms linked to these groups downfield by 6–12 ppm, which is due to conformational changes in the carbohydrate chain and mannose units. In our case, the signals of the C^6 and $C^{6'}$ atoms linked to OH groups decrease in intensity, and new, less strong signals appear at 71.0 and 73.1 ppm, assignable to the C^6 and

Signal assignment for carbon atoms of mannopyranose units of rhodexman and carboxymethyl rhodexman samples

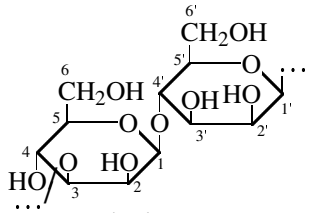

Rhodexman

Carbon atom	δ_C (ppm) at indicated C_{cm}			Carbon atom	δ_C (ppm) at indicated C_{cm}		
	0	0.25	0.7		0	0.25	0.7
1	96.7	98.3	98.0	4	65.0	66.7	66.4
1'	100.3	101.7	101.4	4'	77.2	78.4	78.1
2	66.9	69.0	68.7	5	76.9	77.7	77.5
2'	70.0	73.1 (76.5)*	71.9 (75.2)	5'	75.5	76.5	76.3
3	79.5	80.6	80.4	6	61.1	62.6 (73.1)	61.7 (72.4)
3'	71.8	73.8	72.9	6'	60.6	61.07 (71.0)	61.3 (71.2)

* The signals of carbon atoms at which the O atoms underwent carboxymethylation are given in parentheses.

$C^{6'}$ atoms linked to the carboxymethylated O atoms. Thus, the C^6 and $C^{6'}$ signals are shifted by 9–10 ppm. Also, the signal of the $C^{2'}$ atom linked to the OH group decreases in intensity, and new signals appear at 75.2–76.5 ppm, assignable to the $C^{2'}$ atom linked to the carboxymethylated O atom; the $C^{2'}$ signal is thus shifted by 3–4 ppm (see table).

The small shift of the signals of the carbon atoms bearing nonalkylated OH groups, relative to the spectrum of the initial rhodexman, is due the fact that, when recording the CMR spectrum, the chemical shift scale was not corrected by the DMSO signal. Comparison of the spectra of the initial and modified rhodexman reveals new signals in the carboxymethylated sample at 176–179 ppm, assignable to the carboxyl carbon atom. This signal is split, suggesting two different positions of the carboxy groups. From the intensity ratio of these signals, it is possible to estimate the ratio of carboxymethyl groups in positions 6, 6', and 2'.

Thus, in alkylation of rhodexman, about 60–70% of carboxymethyl groups appear at the C^6–O position of both monosaccharide units, and 30–40%, at the C^2–O position of the β-1,4-linked units, which is consistent with the results of periodate oxidation. Carboxymethylation does not occur at the C^3–O and C^4–O positions, and at the C^2–O atom of the β-1,3-linked unit the alkylation probability is low.

CONCLUSION

The ^{13}C NMR spectra and results of periodate oxidation show that, in alkylation of rhodexman with monochloroacetic acid in isopropyl alcohol in the presence of 30% NaOH, about 60–70% of carboxymethyl groups appear at the C^6–O position in both kinds of monosaccharide units, and 30–40%, at the C^2–O position of the β-1,4-linked units.

REFERENCES

1. Alyushin, M.T., Gritsaenko, I.S., and Kamenskaya, M.V., *Nauchn. Tr. Vses. Nauchno-Issled. Inst. Farm.*, 1990, no. 28, pp. 5–11.
2. Ryzhenkov, V.E., Abstracts of Papers, *V Rossiiskii natsional'nyi kongress "Chelovek i lekarstvo"* (V Russian National Congr. "Human and Drug"), Moscow, April 21–25, 1998, p. 612.
3. *Methods in Carbohydrate Chemistry*, Whistler, R.L. and Wolfrom, M.L., Eds., New York: Academic, 1962–1965.
4. Iozep, A.A., Kupriyanova, L.N., Ponomarenko, M.N., *et al., Zh. Prikl. Khim.*, 1996, vol. 69, no. 9, pp. 1537–1542.
5. Zakharova, I.Ya. and Kosenko, L.V., *Metody izucheniya mikrobnykh polisakharidov* (Methods for Studying Microbial Polysaccharides), Kiev: Naukova Dumka, 1982.

6. Sokolov, V.B., Matyushichev, I.Yu., and Passet, B.V., *Zh. Prikl. Khim.*, 1999, vol. 72, no. 2, pp. 333–332.
7. Petropavlovskii, G.A., *Gidrofil'nye chastichno zameshchennye efiry tsellyulozy i ikh modifikatsiya putem khimicheskogo sshivaniya* (Hydrophilic Partially Substituted Cellulose Ethers and Esters and Their Modification by Chemical Cross-Linking), Leningrad: Nauka, 1988.
8. Krentsel', L.B., Ermakov, I.V., Yashin, V.V., *et al., Vysokomol. Soedin., Ser. A*, 1997, vol. 39, no. 1, pp. 83–89.
9. Zeller, S.G., Griesgraber, G.W., and Grau, G.R., *Carbohydr. Res.*, 1991, vol. 211, pp. 41–45.
10. Niemela, K. and Sjostrom, E., *Carbohydr. Res.*, 1988, vol. 180, pp. 43–52.
11. Kragten, E.A. and Kamerling, J.P., *J. Chromatogr.*, 1992, vol. 623, no. 1, pp. 49–53.
12. Shashkov, A.S. and Chizhov, O.S., *Bioorg. Khim.*, 1976, vol. 2, no. 4, pp. 437–496.
13. Breitmaier, E. and Voelter, W., ^{13}C-*NMR Spectroscopy*, New York: Chemie, 1978.

Russian Journal of Applied Chemistry, Vol. 76, No. 6, 2003, pp. 962–966. Translated from Zhurnal Prikladnoi Khimii, Vol. 76, No. 6, 2003, pp. 990–994.

ORGANIC SYNTHESIS AND INDUSTRIAL ORGANIC CHEMISTRY

Ozonolysis of 1-Methylcyclohexanol

A. M. Syroezhko and O. Yu. Begak

St. Petersburg Technological Institute, St. Petersburg, Russia

Mendeleev Russian Research Institute of Metrology, Federal State Unitary Enterprise, St. Petersburg, Russia

Received January 30, 2003

Abstract—The kinetic features and composition of products of 1-methylcyclohexanol ozonolysis were studied.

In low-temperature selective ozonolysis of methylcyclohexane involving cleavage of the C–H bond, 1-methylcyclohexanol (MCHl) is formed by recombination of $R^{\cdot}$ and $^{\cdot}OH$ radicals after primary initiation, radical-chain transformations of 1-methylcyclohexyl hydroperoxide, and attack of $RO^{\cdot}$ radicals at the starting substrate [1].

In the developed process, the forming MCHl is consumed, and the selectivity with respect to MCHl decreases. In this study, we analyzed the features of MCHl transformation in ozonolysis. The substrate was oxidized and the products analyzed by the procedures described in [2].

An examination of the kinetic features (Fig. 1) and composition of products of MCHl ozonolysis (40–115°C, $[O_3]$ = 1–4 vol %) [2–8] showed that oxidation of this alcohol yields hydrogen peroxide, MCHl α-hydroperoxide, mono- and dicarboxylic acids, ε-ketoenanthic acid (Table 1), and esters. The ratio of monocarboxylic and steam-undistillable acids is within 0.25–0.30, being virtually independent of temperature, ozone content in the oxidizing gas, and reaction time.

The selectivity of MCHl ozonolysis with respect to acids (Fig. 2) grows with increasing conversion and temperature.

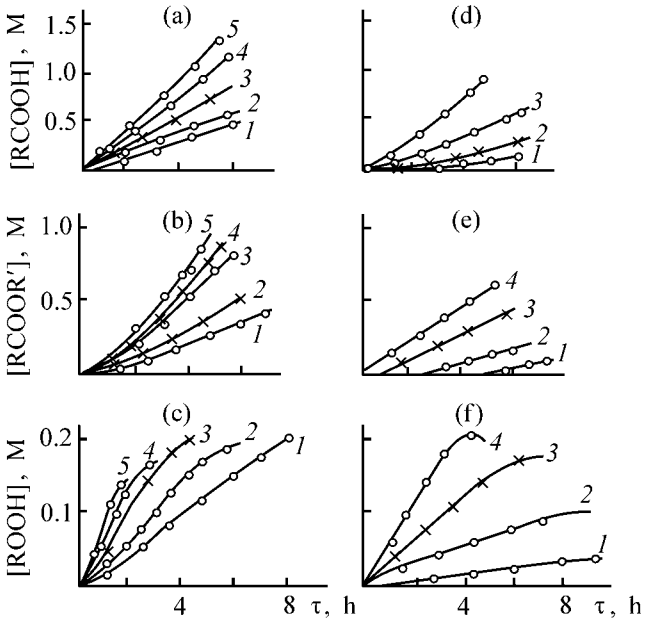

Fig. 1. Kinetic curves of accumulation of (a, d) acids RCOOH, (b, e) esters RCOOR', and (c, f) peroxides ROOH in ozonolysis of MCHl. (τ) Time. (a–c) $[O_3]$ = 4 vol %; *T*, °C: (*1*) 40, (*2*) 60, (*3*) 70, (*4*) 100, and (*5*) 115. (d–f) *T* = 100°C; $[O_3]$, vol %: (*1*) 1, (*2*) 2, (*3*) 3, and (*4*) 4.

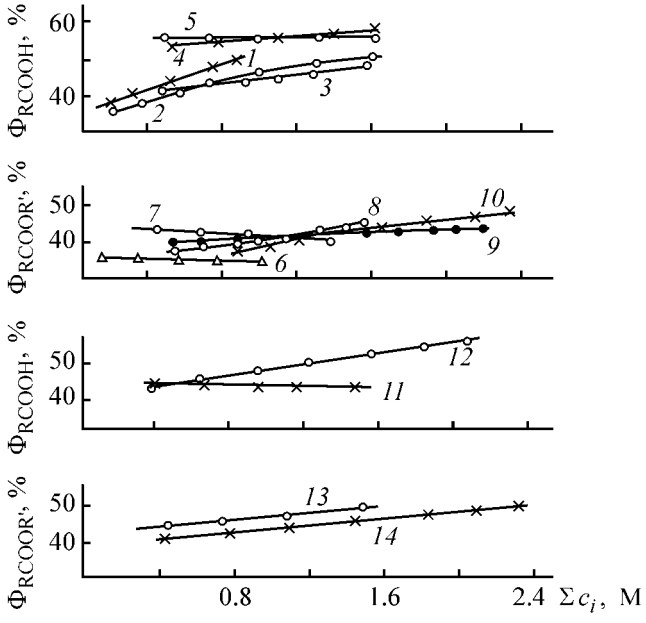

Fig. 2. Yields Φ of acids RCOOH and esters RCOOR' vs. MCHl conversion at (*1–10*) various temperatures and (*11–14*) various ozone concentrations. (Σc_i) Total content of MCHl conversion products. (*1–10*) $[O_3]$ = 4 vol %; (*11–14*) *T* = 100°C. *T*, °C: (*1*, *6*) 40, (*2*, *7*) 60, (*3*, *8*) 70, (*4*, *9*) 100, and (*5*, *10*) 115. $[O_3]$, vol %: (*11*, *13*) 3 and (*12*, *14*) 4.

1070-4272/03/7606-0962 $25.00 © 2003 MAIK "Nauka/Interperiodica"

Table 1. Composition of monocarboxylic, dicarboxylic, and keto acids formed in MCHl ozonolysis

T, °C	τ, min	Acid content, mol % based on the sum of acids									
		acetic	propionic	butyric	valeric	caproic	methylsuccinic	succinic	glutaric	α-methyladipic	ε-ketoenanthic
10% conversion											
10	–	–	–	–	–	–	6.3	7.0	23.5	29.2	35.0
40	360	75	10.3	5.2	6.5	3.0	–	–	–	–	–
70	240	78.3	9.7	4.2	5.5	2.3	6.5	11.5	18.2	20.5	44.3
80	210	79.7	9.5	3.7	5.1	2.0	5.0	6.1	33.7	10.0	45.2
100	180	81.9	9.3	3.0	4.3	1.5	7.2	9.0	30.5	15.3	38.0
115	120	83.2	8.6	2.5	3.7	1.8	6.3	6.8	24.5	20.4	42.0
25% conversion											
40	540	75.5	10.6	4.7	6.3	4.0	1.5	9.5	25.5	32.0	31.5
70	420	77.0	10.0	4.5	5.7	2.8	1.5	9.0	20.0	27.0	42.5
80	300	78.0	9.8	4.1	5.6	2.5	2.2	7.8	35.0	12.5	42.5
100	300	80.0	9.5	3.5	5.0	2.0	4.6	9.5	32.0	19.0	35.0
115	240	81.5	9.0	3.1	4.5	1.9	4.8	7.3	30.2	20.6	37.1

At low temperatures (40–60°C) the selectivity with respect to esters weakly decreases with increasing MCHl conversion, apparently, owing to their consumption. At higher temperatures (70–115°C), the rates of both MCHl esterification by monocarboxylic acids (primarily acetic acid) and ozonolysis of esters increase [1]. However, the esterification rate is higher; therefore, with increasing conversion, the yield of esters weakly grows. The selectivity of peroxide formation decreases with increasing MCHl conversion.

The ozone concentration (Fig. 1) affects only slightly the ratio of acids and esters accumulating in MCHl oxidation products. Table 1 shows that, with increasing temperature (at the same conversion), the content of acetic acid grows, and that of propionic, butyric, valeric, and caproic acids decreases. In the course of MCHl ozonolysis, the C_3–C_6 acids undergo decarboxylation and oxidation with cleavage of the C–C bond, as judged from experiments with labeled acids [1].

Tables 1 and 2 show that, with increasing ozone content, the yields of ε-ketoenanthic and glutaric acids grow and that of α-methyladipic acid decreases. The parallel variation of the content of methylsuccinic and methyladipic, and of glutaric and ε-ketoenanthic acids suggests their genetic relationship: lower carboxylic acids are formed by ozonolysis of higher dicarboxylic acids and ε-ketoenanthic acid. This has been confirmed in experiments with labeled acids [9].

Thus, the major products of MCHl ozonolysis are ε-ketoenanthic and α-methyladipic acids. ε-Ketoenanthic acid is formed in isomerization of 2-hydroxy-2-methyl-1-cyclohexyloxy and 1-methyl-1-cyclohexyloxy radicals with ring opening, accompanied by oxidation by oxygen and ozone, and also in ozonolysis of MCHl α-hydroperoxide (at elevated temperatures) or α-hydrotrioxide (at 10–70°C).

Table 2. Composition of dicarboxylic and keto acids formed in MCHl ozonolysis (100°C, 300 min)

Acid	Content, mol %, at indicated ozone concentration, vol %			
	1	2	3	4
Methylsuccinic	10.5	6.0	4.5	4.6
Succinic	23.5	17.0	12.1	9.5
Glutaric	13.0	19.0	23.2	32.0
α-Methyladipic	41.5	38.5	36.4	19.0
ε-Ketoenanthic	11.5	19.5	24.2	35.0

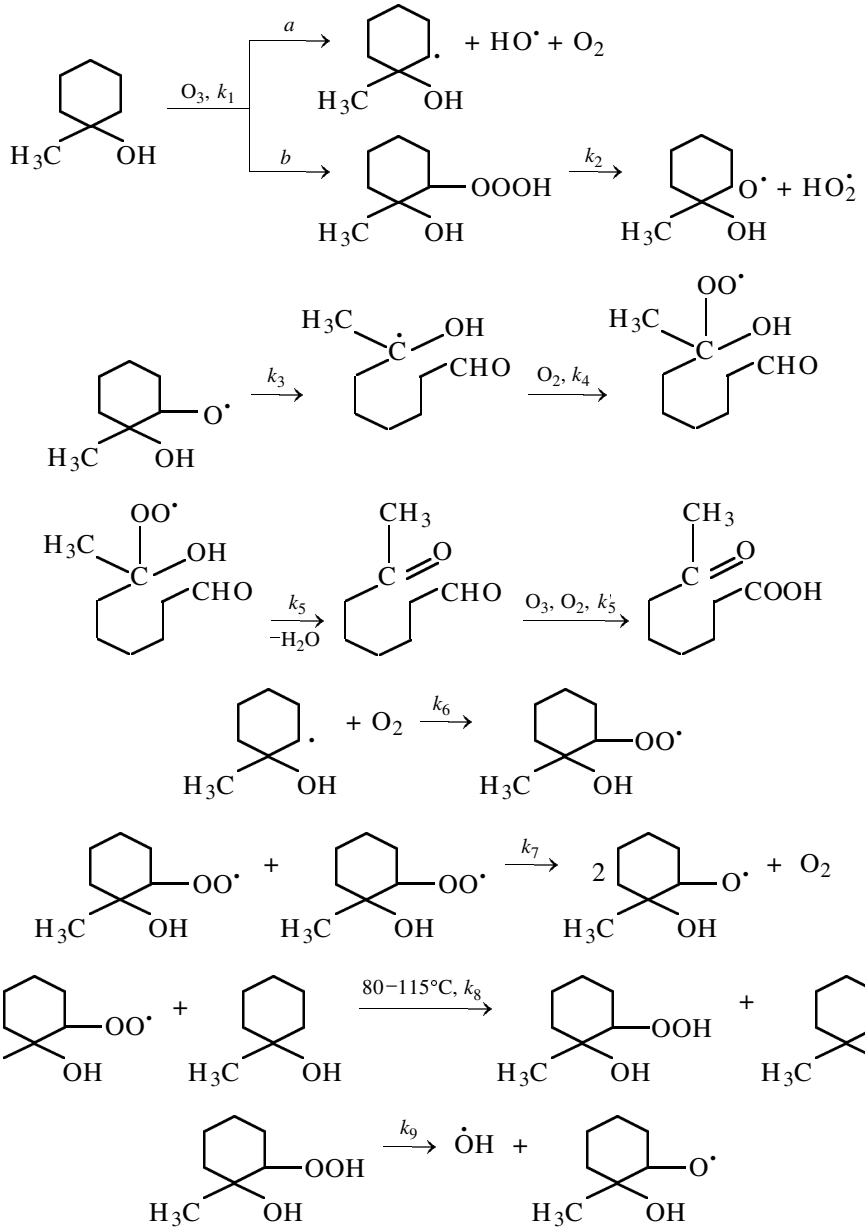

The probability of ozone attack at the O–H bond in MCHl, which is stronger than the C–H bond, is low. However, the alkoxy radical formed by this and other pathways [10] also contributes to formation of ε-ketoenanthic acid by ring opening, followed by reaction with oxygen and ozone:

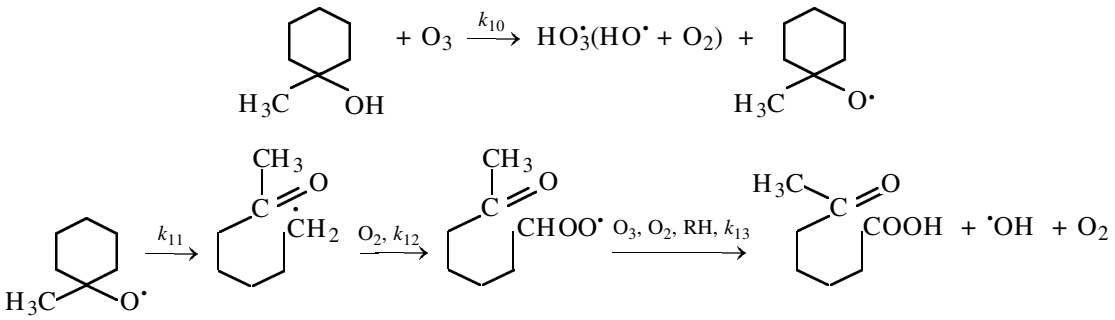

It has been shown [10] that the source of the 1-methyl-1-cyclohexyloxy radical at high temperatures is the adduct of hydrogen peroxide with MCHl [10]. 2-Hydroxy-2-methyl-1-cyclohexyloxy radical can also form by decomposition of unstable MCHl hydrotrioxide and recombination of the 2-hydroxy-2-methyl-1-peroxycyclohexyl radical.

α-Methyladipic acid is presumably formed in ozonolysis of MCHl by the following pathway:

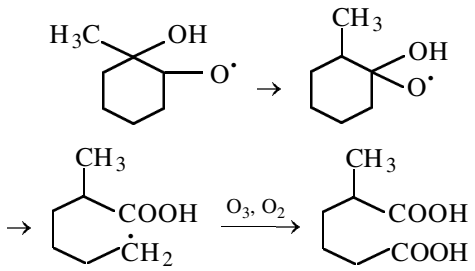

Lower mono- and dicarboxylic acids are partially formed by further ozonolysis of ε-ketoenanthic and α-methyladipic acids.

Figure 3 shows the typical kinetic curves of MCHl consumption in ozonolysis. The tertiary alcohol is consumed with autoacceleration. The experimental results were fitted with the equation

$$-d[ROH]/d\tau = k_1[ROH]_0[O_3]_0 + k_2([ROH]_0 - [ROH])[ROH] = k_{app}[ROH], \quad (1)$$

where [ROH] and $[ROH]_0$ are the running and initial MCHl concentrations, respectively (M); k_{app} is the apparent rate constant (min^{-1}).

The first reaction order with respect to MCHl and ozone was found from the initial reaction rates. Thus, the first term in Eq. (1) is determined by bimolecular reaction of MCHl with ozone, and the second implicitly takes into account the reactions of the products with ozone and radicals with MCHl. The constants k_1 and k_2 were determined by computer fitting for each particular dependence at different initial con centrations of the reactants and were then refined by numerical integration of the set of differential equations in the whole range of the initial concentrations of the alcohol and ozone.

The consumption of MCHl in ozonolysis in the examined range of temperatures and ozone concentrations is described by Eq. (1) at the following constants k_1 and k_2, $l\ mol^{-1}\ s^{-1}$:

$$k_1 = (1.2 \pm 0.1)\exp[-(16500 \pm 2500)/RT], \quad (2)$$

$$k_2 = (1.42 \pm 0.11)\,10^{-3}\exp[-(16500 \pm 2500)/RT]. \quad (3)$$

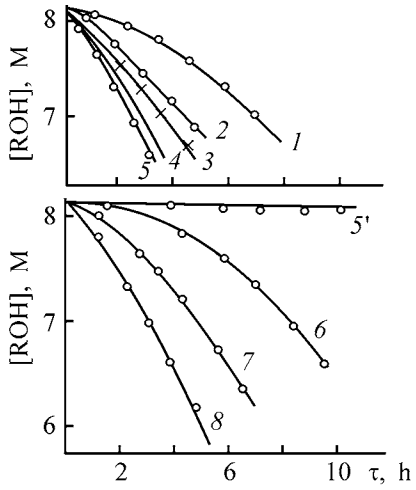

Fig. 3. Kinetic curves of MCHl (ROH) consumption. (*1–5*) $[O_3]$ = 4 vol %; (*5'*, *6–8*) T = 100°C. T, °C: (*1*) 40, (*2*) 60, (*3*) 70, (*4*) 100, and (*5*) 115. $[O_3]$, vol %: (*5'*) 1, (*6*) 2, (*7*) 4, and (*8*) 4.

When discussing the mechanism of MCHl ozonolysis, we disregarded the MCHl association [10].

CONCLUSIONS

(1) Consumption of 1-methylcyclohexanol in ozonolysis at 10–115°C and ozone concentrations in the range 1–4 vol % is described by Eq. (1), with the constants k_1 and k_2 calculated from Eqs. (2) and (3).

(2) 1-Methylcyclohexanol is oxidized by ozone to form hydrogen peroxide, 1-methylcyclohexanol α-hydroperoxide, C_2–C_6 monocarboxylic acids, dicarboxylic acids (succinic, methylsuccinic, glutaric, α-methyladipic), ε-ketoenanthic acid, and esters of these acids with the starting alcohol.

REFERENCES

1. Syroezhko, A.M., Liquid-Phase Oxidation of Alkanes, Cycloalkanes, and Their Oxygen-Containing Derivatives with Oxygen and Ozone in the Presence of *s*- and 3*d*-Metal Compounds, *Doctoral Dissertation*, Leningrad, 1985.
2. Vikhorev, A.A., Syroezhko, A.M., and Proskuryakov, V.A., *Zh. Prikl. Khim.*, 1975, vol. 48, no. 9, pp. 2059–2062.
3. USSR Inventor's Certificate, no. 555084.
4. Dobinson, F., *Chem. Ind.*, 1959, vol. 26, no. 1, pp. 853–854.

5. Vikhorev, A.A., Syroezhko, A.M., and Proskuryakov, V.A., *Zh. Prikl. Khim.*, 1977, vol. 50, no. 3, pp. 698–699.
6. Vikhorev, A.A., Syroezhko, A.M., and Proskuryakov, V.A., *Zh. Prikl. Khim.*, 1976, vol. 49, no. 7, pp. 1592–1597.
7. Vikhorev, A.A., Syroezhko, A.M., and Proskuryakov, V.A., *Zh. Prikl. Khim.*, 1976, vol. 49, no. 3, pp. 588–592.
8. Vikhorev, A.A., Syroezhko, A.M., and Proskuryakov, V.A., *Izv. Vyssh. Uchebn. Zaved., Khim. Khim. Tekhnol.*, 1976, vol. 19, no. 3, pp. 1499–1503.
9. Vikhorev, A.A., Syroezhko, A.M., and Proskuryakov, V.A., *Zh. Prikl. Khim.*, 1977, vol. 50, no. 6, pp. 1310–1314.
10. Vikhorev, A.A. and Syroezhko, A.M., in *Issledovaniya v oblasti khimii i tekhnologii produktov pererabotki goryuchikh iskopaemykh* (Studies in the Field of Chemistry and Technology of Products of Fossil Fuel Processing), Leningrad, 1977, issue 1, pp. 33–37.

Russian Journal of Applied Chemistry, Vol. 76, No. 6, 2003, pp. 967–971. Translated from Zhurnal Prikladnoi Khimii, Vol. 76, No. 6, 2003, pp. 995–999.

MACROMOLECULAR CHEMISTRY AND POLYMERIC MATERIALS

Evolution of Statistical Ensembles of Microdomains on the Surface of Films of Rigid-Chain Polyimide during Thermal Imidization

S. V. Bronnikov, T. E. Sukhanova, and M. Ya. Goikhman

Institute of Macromolecular Compounds, Russian Academy of Sciences, St. Petersburg, Russia

Received March 19, 2003

Abstract—Statistical ensembles of microdomains formed on the surface of polyimide films based on pyromellitic dianhydride and 2,7-diaminofluorene during thermal imidization were described in terms of the model of reversible aggregation using the electron-microscopic data. Parameters of the statistical distribution were determined for each ensemble depending on the film heating temperature.

The supramolecular structure of rigid-chain polyimide based on pyromellitic dianhydride and 2,7-diaminofluorene (PI PMF), which was prepared by thermal imidization (TI), has been studied earlier by small-angle X-ray scattering [1] and electron microscopy [2]. These studies have shown that the ordered phase of the polymer heated to 400°C is constituted by crystallites which are part of larger supramolecular formations, microdomains [1]. Electron micrographs of ultrathin cross sections and low-temperature chips confirmed the domain structure of PI PMF films upon TI [2]. More recent studies based on the fractal approach [3] revealed the scale-invariant nature of the PI PMF film surface.

In this study, we continue the electron-microscopic investigations of the supramolecular structure or the PI PMF film surface by analyzing the statistical ensembles of microdomains evolving in the course of TI.

EXPERIMENTAL

The objects of our study were films of PAA PMF (PAA is polyamido acid) and films of the product of its TI, PI PMF, formed by the reaction [4]

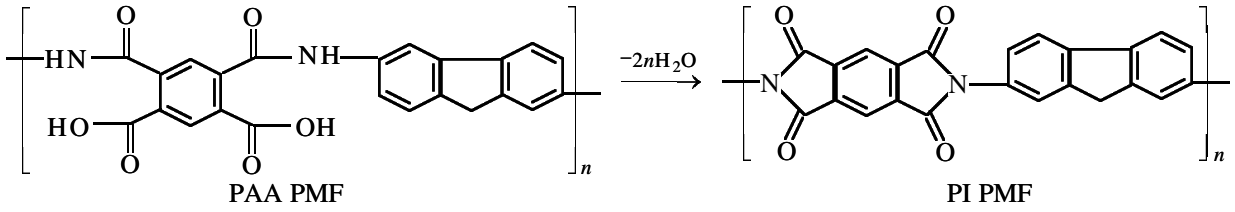

The PAA PMF films with thickness of 40 ± 5 μm were prepared from a 10% solution of the polymer in dimethylformamide (DMF) by casting onto glass substrates followed by drying in air at 50°C for 1 day to constant weight.

Thermal imidization was carried out by stepwise heating of the PAA PMF films to 400°C at a rate of 2 deg min^{-1}. Each step was followed by film detachment from the substrate and etching on the air-exposed side in a plasma of oxygen high-frequency glow discharge [5]. The etching conditions were as follows: electron energy 5 eV; oxygen pressure 0.05 Pa; ionization angle 90°; distance between the discharge zone and the film surface 0.2 m; etching time 15 (PAA PMF), 30 (PI PMF heated to 125 and 250°C), and 60 min (PI PMF heated to 350 and 400°C). These are "mild" ionization parameters: Etching leads to heating of the film surface to ≤50°C and a minimal ero-

1070-4272/03/7606-0967 $25.00 © 2003 MAIK "Nauka/Interperiodica"

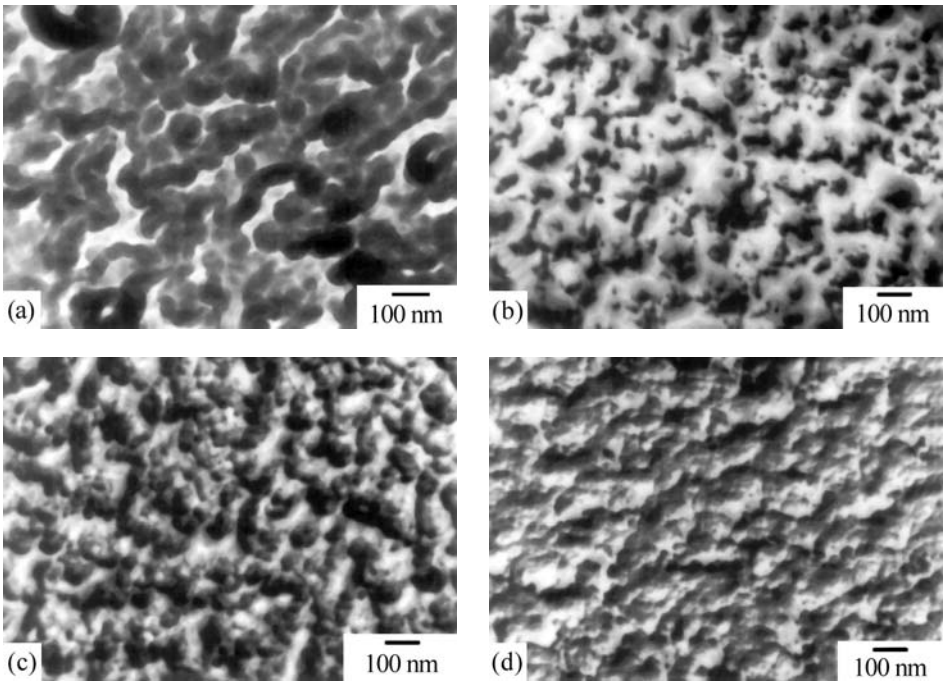

Fig. 1. Electron micrographs of carbon-platinum replicas of the surface of (a) PAA PMF films and PI PMF films heated to (b) 125, (c) 250, and (d) 400°C.

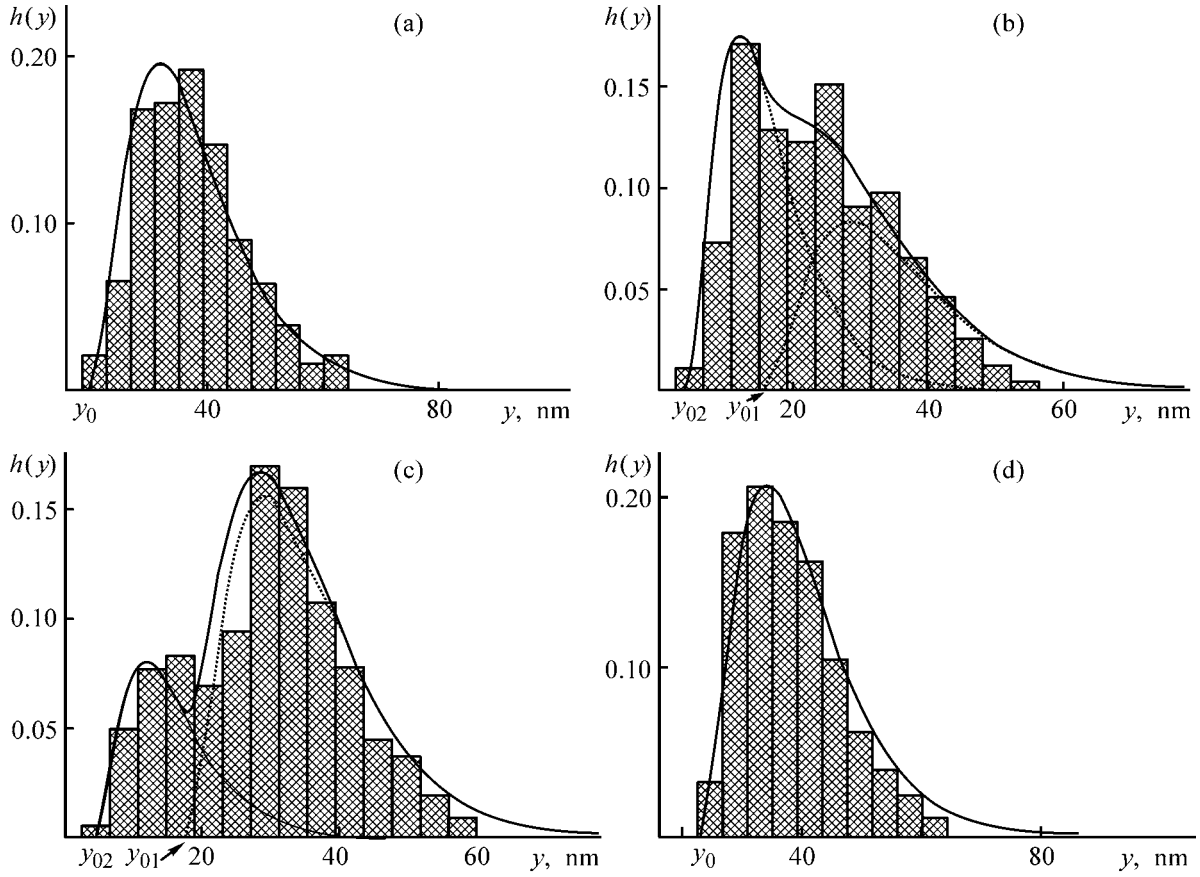

Fig. 2. Distribution $h(y)$ with respect to diameter y of the microdomains on the surface of (a) PAA PMF films and PI PMF films heated to (b) 125, (c) 250, and (d) 400°C.

sion of the surface layers [3, 6]. Platinum was deposited by sputtering on the etched film surface at an angle of 45°, whereupon one-stage carbon-platinum replicas were prepared. Micrographs of the replicas were obtained with a BS-500 (Tesla) transmission electron microscope at a $\times 40\,000$ magnification.

Figure 1 presents the electron micrographs of the carbon-platinum replicas from the etched surface of the PAA PMF and PI PMF films heated to 125, 250, and 400°C. It is seen that the film surface is constituted by nearly spherical microdomains. Comparative analysis of these micrographs revealed changes (most profound in the films heated to 250–300°C) in the depth of the etched profile. This may be due to removal of the disordered phase of the polymer with the residual DMF and water formed during TI.

Figure 2 presents the results of statistical processing of the micrographs as a plot of distribution of the microdomains with respect to their diameter $h(y)$. From 960 to 1500 microdomains were analyzed on each micrograph.

The histograms for the PAA PMF film (Fig. 2a) and the PI PMF film heated to 400°C (Fig. 2d) demonstrate a monomodal size distribution for the microdomain ensemble on the surface, with a maximum near 30 nm. In the histograms of the PI PMF films heated to 125 and 250°C (Figs. 2b, 2c), two superimposing ensembles of microdomains can be distinguished, one of which (major) preserves a size distribution maximum near 30 nm, and the other (additional) exhibits a maximum near 12 nm.

The monomodal distributions were analytically described by the following expression, derived in terms of the reversible aggregation model [7, 8] and resulting from the canonical distribution of the energy fluctuations at a constant volume [9]:

$$h(y - y_0) = A(y - y_0)^m \exp\left[-\frac{(y - y_0)\Delta U_0}{kT}\right], \quad (1)$$

where, A is the normalization factor; $(y - y_0)\Delta U_0$, the aggregation energy, which is a product of the reduced size of the aggregate in the ensemble $(y - y_0)$ and the standard aggregation energy ΔU_0, J m^{-1}; y_0, size of the smallest aggregate; k, Boltzmann constant; T, absolute temperature; m, dimensionality of the space in which the aggregate grows ($m = 2$ for the surface).

The key parameter in expression (1) is ΔU_0 which governs the equilibrium size distribution pattern for the aggregates. Obviously, the bimodal distributions should be described by an equation which is the sum

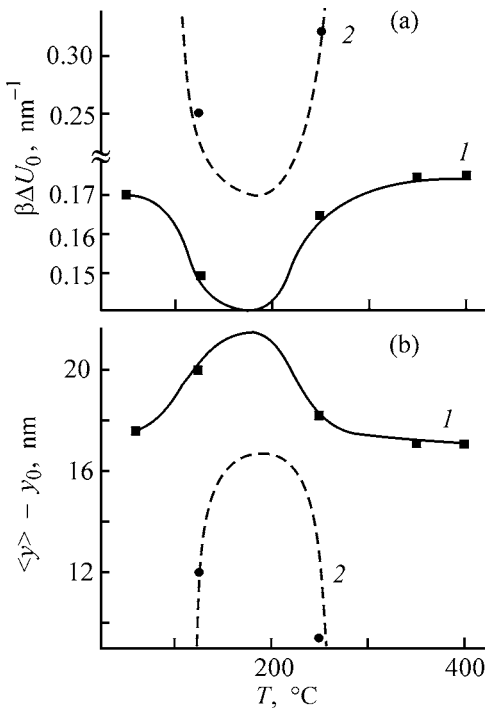

Fig. 3. (a) Reduced standard aggregation energy $\beta\Delta U_0$ and (b) average reduced diameter of microdomains, $\langle y\rangle - y_0$, vs. the film heating temperature T. Ensemble: (*1*) major and (*2*) additional.

of two expressions (1) with different A, y_0, and ΔU_0 parameters.

The lines in Fig. 2 represent the results of calculations by Eq. (1). For bimodal distributions, dashed lines show the distributions for each mode. The numerical values of the parameters A, y_0, and ΔU_0 (for bimodal distribution, A_1, A_2, y_{01}, y_{02}, ΔU_{01}, and ΔU_{02}) were used in calculations as free quantities. Our results suggest that the size distribution of the microdomains, both monomodal (at 50 and 400°C) and bimodal (at 125 and 250°C), can be described in terms of the reversible aggregation model. Therefore, the condition for optimization of the size of the aggregate ensemble is met in the course of TI [7, 8].

A practically important characteristic of the distribution is the average size of the aggregate in the ensemble. It is defined as the normalized expectancy

$$\langle y\rangle - y_0 = \frac{\int_0^\infty (y - y_0)\,h(y - y_0)\,\mathrm{d}y}{\int_0^\infty (y - y_0)h\,\mathrm{d}y} = \frac{(m + 1)kT}{\Delta U_0}. \quad (2)$$

Figure 3 presents the reduced standard aggregation energy $\beta\Delta U_0$ ($\beta \equiv 1/kT$) and the reduced average diameter ($\langle y\rangle - y_0$) of the microdomains as functions

of the film heating temperature for both statistical ensembles of microdomains. Let us consider first the temperature dependences of these parameters for the case of the major ensemble, namely, $\beta\Delta U_{01}(T)$ and $(<y_1> - y_{01})(T)$.

When the films are heated to 125°C, $\beta\Delta U_{01}$ tends to decrease, and $(<y_1> - y_{01})$, correspondingly, to increase. As known, imidization at temperatures within 100–180°C involves active chemical transformation PAA PMF → PI PMF, which is accompanied by evolution of water and degradation products of the DMF associates [4]. These processes are responsible for a decrease in the molecular weight of the polymer, which is at a minimum near 180°C [4].

This suggests the existence of extrema near 180°C, namely, a minimum for $\beta\Delta U_{01}(T)$ and a maximum for $(<y_1> - y_{01})(T)$. At this temperature, aggregation is the most active, and the aggregates in the ensemble have the largest average size.

Within 125–180°C, a second (additional) ensemble is formed, whose reduced standard aggregation energy $\beta\Delta U_{02}$ at 125°C exceeds $\beta\Delta U_{01}$ by nearly a factor of 1.7. Therefore, the microdomains in the second ensemble have smaller average size than those in the main ensemble. At 125°C, the peak height in the distribution pattern for the second ensemble is more than twice that for the first ensemble. This means that the number of microdomains in the second ensemble exceeds that in the first.

Under further heating (>180°C), the forming imide moieties decelerate aggregation in both ensembles. At 250°C, the number of microdomains in the first (major) ensemble exceeds that in the second ensemble. At high temperatures, within 350–400°C, $\beta\Delta U_{01}$ attains a constant value which slightly exceeds the initial value (at 50°C), and the second ensemble of microdomains disappears: The aggregation energy of the second ensemble becomes infinitely large, and the average diameter of the microdomains in it, infinitely small (Fig. 3).

Similar trends in variation with heating temperature of the standard aggregation energies and average diameters of the microdomains in the major ensemble were observed in our previous studies of statistical ensembles of microdomains in the surface layers of films of polyimides derived from 3,3',4,4'-diphenyltetracarboxylic dianhydride and *p*-phenylenediamine [10, 11], as well as from pyromellitic dianhydride and 4,4'-oxyphenylenediamine [12]. However, the microdomains of these polymers form only one statistical ensemble throughout the TI temperature range of 50–400°C. It can be assumed that the bimodal distribution of the microdomains in the partially imidized PI PMF films is due to specific features of the chemical structure of the polymer.

Bell [13] showed that, in the course of drying and TI, polyamido acids containing fluorene units in the backbone undergo cross-linking, primarily, via oxidation of the methylene group of the fluorene unit into carbonyl fluorenone group. In the case of PAA PMF, this yields the following macromolecules

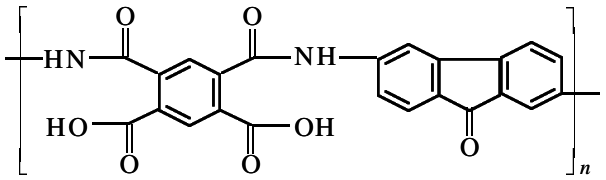

Under heating to 125–180°C, the polymer chain in the PAA PMF macromolecules actively degrades into oligomeric fragments [4]. This significantly increases the concentration of the terminal amino groups, which react with fluorenone units yielding 3D cross-linked structures with azomethine bonds at the cross-linking sites:

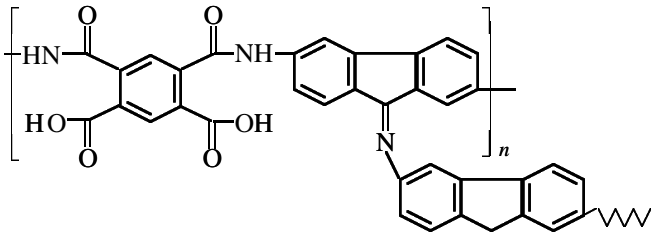

Such structures, probably, form the second statistical ensemble whose microdomain size distribution pattern is illustrated by the histograms in Figs. 2b and 2c.

Further heating of the films within the 180–300°C range leads to active TI in the polymers, accompanied by water elimination. The easily hydrolyzable azomethine intermolecular bonds degrade into amine and fluorenone groups, and the polymer structure becomes linear again. These processes, along with the reactions of resynthesis and increase in the molecular weight of he polymer, are responsible for the specific features of the distribution of the microdomain size in PI PMF in early TI stages.

CONCLUSIONS

(1) The reversible aggregation model was used to describe how the distribution of the microdomains with respect to diameter on the surface of films of

the polyimide derived from pyromellitic dianhydride and 2,7-diaminofluorenone varies during thermal imidization.

(2) The microdomains on the surface of films of polyamido acid and completely imidized poyamide form one statistical ensemble, and in the case of a partially imidized polyamide, two ensembles, one of which is probably constituted by intermediate cross-linked structures.

(3) Regular trends were revealed in variation of the parameters of the microdomain distribution with respect to diameter in the course of imidization.

ACKNOWLEDGMENTS

This study was supported financially by the RF Ministry of Education, project no. T02-6.3-2706.

REFERENCES

1. Lavrent'ev, V.K. and Sidorovich, A.V., *Vysokomol. Soedin., Ser. B*, 1984, vol. 26, no. 1, pp. 3–9.
2. Pogodina, T.E. and Sidorovich, A.V., *Vysokomol. Soedin., Ser. A*, 1984, vol. 26, no. 5, pp. 974–980.
3. Novikov, D.V., Sukhanova, T.E., Lavrent'eva, V.K., and Vylegzhagina, M.E., *Vysokomol. Soedin., Ser. A*, 1999, vol. 41, no. 8, pp. 1266–1273.
4. Bessonov, M.I., Koton, M.M., Kudryavtsev, V.V., and Laius, L.A., *Poliimidy – klass termostoikikh soedinenii* (Polyimides: A Class of Thermally Stable Compounds), Leningrad: Nauka, 1983.
5. Startsev, V.M., Chugunova, N.F., Matveev, V.V., and Chalykh, A.E., *Vysokomol. Soedin., Ser. A*, 1986, vol. 28, no. 11, pp. 2378–2381.
6. Casperson, G., Haensel, H., and Hoffmann, G., *Faserforsch. Textiltechnik*, 1967, vol. 18, pp. 455–459.
7. Kilian, H.G., Metzler, R., and Zink, B., *J. Chem. Phys.*, 1997, vol. 107, pp. 8697–8714.
8. Kilian, H.G., Köpf, R., and Vettegren, V.I., *Prog. Colloid Polym. Sci.*, 2001, vol. 117, pp. 172–181.
9. *The Collected Works of J.W. Gibbs: In two volumes*, New York: Logmans, 1928. *A Commentary on the Scientific Writings of J. Willard Gibbs: In Two Volumes*, Donnan, F.G. and Haas, A., Eds., New Haven: Yeala Univ., 1936.
10. Bronnikov, S. and Sukhanova, T., *Image Anal. Stereol.*, 2001, vol. 20, suppl. 1, pp. 133–138.
11. Bronnikov, S.V, and Sukhanova, T.E., *Vysokomol. Soedin., Ser. A*, 2002, vol. 44, no. 6, pp. 940–945.
12. Bronnikov, S.V., Sukhanova, T.E., Meleshko, T.K., and Mikhailova, M.A., *Zh. Prikl. Khim.*, 2003, vol. 76, no. 5, pp. 829–832.
13. Bell, V.L., *J. Polym. Sci., Polym. Chem. Ed.*, 1976, vol. 14, no. 1, pp. 225–235.

Russian Journal of Applied Chemistry, Vol. 76, No. 6, 2003, pp. 972–977. Translated from Zhurnal Prikladnoi Khimii, Vol. 76, No. 6, 2003, pp. 1000–1005.

MACROMOLECULAR CHEMISTRY AND POLYMERIC MATERIALS

Precondensation of a Mixture of Epoxy-4,4'-Isopropylidenediphenol and Phenol-Formaldehyde Oligomers in Solution

A. N. Krasovskii and V. N. Filippov

Pigment Open Joint-Stock Research and Production Company, St. Petersburg, Russia

Received January 31, 2003

Abstract—Kinetic viscosity curves $\eta(t)$ for solutions of a mixture of epoxy-4,4'-isopropylidenediphenol and phenol-formaldehyde resins in Cellosolve at 333 K were studied. The optimal precondensation time t was determined for the oligomer mixture in solution in the presence of orthophosphoric acid.

In [1–4], various mechanisms of thermal precondensation of a mixture of epoxy-4,4'-isopropylidenediphenol oligomer (EO) and phenol-formaldehyde oligomer (PFO) in Cellosolve solution were considered. The kinetic curve of the viscosity of the EO–PFO mixture during thermal precondensation has an extremum. The EO and PFO molecules form polymolecular complexes via hydrogen bonding.

Sukhareva *et al*. [5] demonstrated that the corresponding sizes of the oligomer aggregates during precondensation of the EO–PFO mixture in solution pass through an extremum. An electron-microscopic examination [6] showed that, with increasing precondensation time t, the radius of the particle aggregate in the epoxy-phenol coatings cured at 483 K first decreases from 500 to 50 nm and then increases to 100 nm. This allowed Sukhareva *et al.* to suggest that the optimal precondensation time t of the oligomer mixture corresponds to the minimum size of the particle aggregates in solution.

It is known [1, 3, 4, 7, 8] that curing of epoxy-phenol formulations involves concurrent reactions between methylol (butoxy) groups in PFO and epoxy (hydroxy) groups of EO and formation of dimethyl ether bridges between the methylol groups in PFO. In the presence of orthophosphoric acid H_3PO_4, the epoxy groups in EO are consumed at a high rate, yielding mono-, di-, and triphosphates [9]. On the whole, thermal precondensation of the oligomer mixture in solution improves the compatibility of EO and PFO, yielding a uniform chemical network of epoxyphenol polymer upon curing of an oligomer formulation [1, 2].

In [10, 11], we suggested a cluster mechanism of aggregation of oligomers during their thermal precondensation in solution. The cluster model [12, 13] distinguishes three main kinetic stages of thermal precondensation of the EO–PFO mixture in solution and the corresponding three topological types of surface structure of the cross-linked epoxy-phenol polymer in various kinetic stages of precondensation of oligomers [11]. Also, this approach allows a wellfounded choice of the molecular parameters and concentrations of the oligomers in solution for precondensation [10, 11].

The principles of the cluster lattice model [12–14] can be useful in quantitative description of the thermal precondensation kinetics of the oligomer mixture in solution. In this context, we studied the kinetic viscosity curves $\eta(t)$ for solutions of the oligomer mixture under shear flow during thermal precondensation. We analyzed the precondensation time of the oligomers as influenced by the N_1(EO)/N_2(PFO) molar ratio and the content of orthophosphoric acid in the EO–PFO mixture and the shear rate g.

EXPERIMENTAL

The molecular weight distributions for oligomer sample nos. 1 and 2 were determined by viscometry and gel-permeation chromatography (Shodex KF-803 column; solvent tetrahydrofuran; 5–10-μl samples; eluent flow rate 1 ml min^{-1}; spectrophotometric detector, λ = 250 nm) [15]. The number-average molecular weight M_n and the M_w/M_n ratios (M_w is the weight-average molecular weight) for sample nos. 1

1070-4272/03/7606-0972 $25.00 © 2003 MAIK "Nauka/Interperiodica"

Table 1. Characterization* of oligomer samples, 298 K

Sample no.	Oligomer	EN, %	[η], dl g^{-1} ±5%	DP	M_n ±10%	$\frac{M_w}{M_n}$ ±10%	Sample no.	Oligomer	EN, %	[η], dl g^{-1} ±5%	DP	M_n ±10%	$\frac{M_w}{M_n}$ ±10%
1	E-05	1.8	0.134	10–17	2850	2.70	2	DFFr	–	0.061	2–5	1030	3.85

* EN is the epoxy number, and DP is the degree of polymerization.

Table 2. Composition of the E-05–DFFr mixtures in C solution*

N_1/N_2	c (E-05)	c (DFFr)	[η], g dl^{-1}	N_1/N_2	c (E-05)	c (DFFr)	[η], g dl^{-1}	N_1/N_2	c (E-05)	c (DFFr)	[η], g dl^{-1}
	dl g^{-1}				dl g^{-1}				dl g^{-1}		
0.7	26.7	15.2	0.115	1.0	26.7	9.12	0.140	1.5	26.7	6.08	0.154

* [η] is the intrinsic viscosity of the E-05–DFFr mixture (or precondensate) in solution at 298 K [11], and N_1 and N_2 are the numbers of moles of E-05 and DFFr, respectively.

and 2 are listed in Table 1. The intrinsic viscosities [η] of sample nos. 1 and 2 in C solution were determined by the procedure from [16].

The time dependences of the viscosity, η(t), for the mixture of epoxy-4,4'-isopropylidenediphenol (E-05) and phenol-formaldehyde (based on 4,4'-isopropylidenediphenol and formaldehyde) (DFFr) resins (Pigment Research and Production Company) in Cellosolve solution were studied at N_1(E-05)/N_2(DFFr) ratios within 0.7–1.5.

The viscosity of the oligomer mixture in solution was measured on a Rheotest-2 rotary viscometer with a coaxial-cylinder working unit at 333 K and shear rate g = 27–81 s^{-1}. The viscosity η was measured accurately to within 5 mPa s, and temperature, to within 0.5 K. The choice of the specific dynamic modes for measuring the viscosity η was governed by the dependences of the shear rate g on the shear stress τ for E-05 and the E-05–DFFr mixture in C solutions (Fig. 1).

We estimated the concentrations c of E-05 and DFFr in C solutions for N_1/N_2 = 1 at 26.7 and 9.12 g dl^{-1}, respectively (Table 2), from the concentration dependences of the relative viscosity, η_{rel}-vs.-c, for the oligomers in solution by the algorithm proposed by us in [11]. For example, the concentration c = 26.7 g dl^{-1} calculated for N_1/N_2 = 1 corresponds to formation of a continuous network of intermolecular contacts in E-05 in solution, and c(DFFr) = 9.12 g dl^{-1}, to a fractal transition $D_1 \rightarrow D_2$ or to formation of discrete aggregates of DFFr molecules [11]. Orthophosphoric acid was introduced into the E-05–DFFr mixture as a 25% H_3PO_4 solution in C 40 min after the onset of precondensation of the oligomers at 333 K. The orthophosphoric acid concentration in the oligomer mixture was varied from 14 to 500% (with the concentration corresponding to 0.25 g H_3PO_4 per 36 g of the E-05–DFFr mixture taken as 100% [17]) (Table 3). The measurement of the precondensation time was started 20–30 min after mixing the oligomers. The precondensation time t was 90 min at a minimum and ca. 400 min at a maximum.

Thermal precondensation of the oligomer mixture in solution is described by nonmonotonic viscosity curves [η](t) comprising descending, ascending, and leveling-off sections. The η-vs.-t curves retain their extrema with varying molar ratio N_1/N_2, H_3PO_4 concentration in the oligomer mixture (or $N_3/(N_1 + N_2)$ ra-

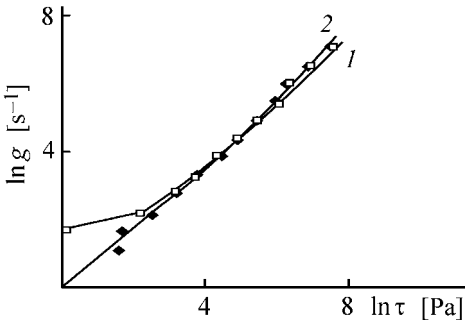

Fig. 1. Logarithmic flow curves for (*1*) E-05 and (*2*) E-05–DFFr mixture in Cellosolve solutions. c(E-05) = 26.7 and c(DFFr) = 12.5 g dl^{-1}; N_1/N_2 = 0.8; $N_3/(N_1 + N_2)$ = 0.07 (N_3 is the number moles of H_3PO_4); 333 K. (g) Shear rate, and (τ) shear stress.

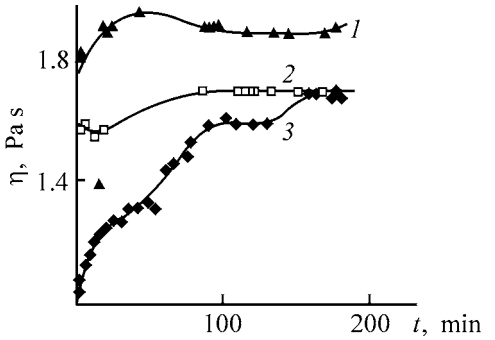

Fig. 2. Kinetic curves of viscosity η, of the E-05–DFFr mixture in Cellosolve solution at the N_1/N_2 ratio of (*1*) 1.5, (*2*) 1, and (*3*) 0.7. Shear rate g = 27 s^{-1}, 333 K. (*t*) Time; the same for Figs. 3 and 4.

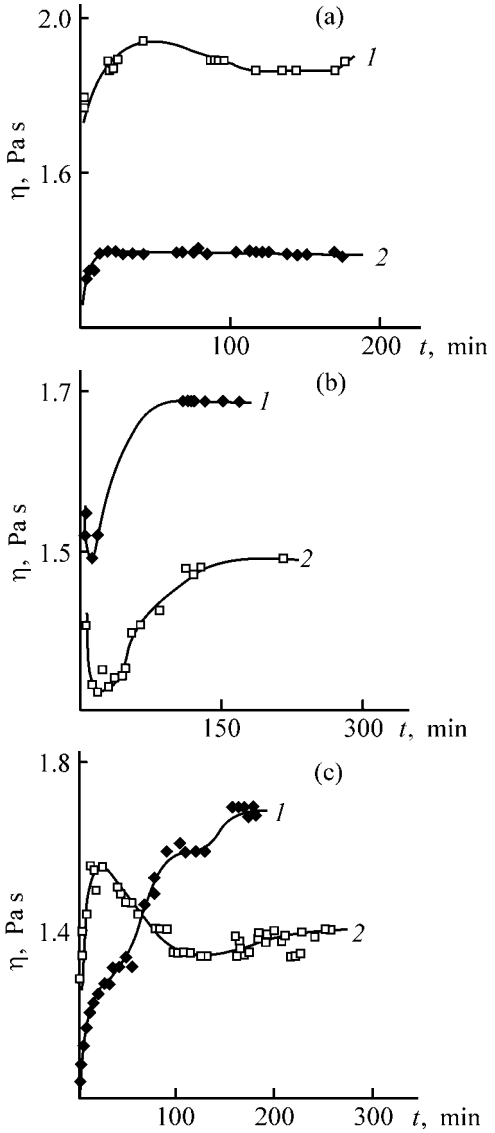

Fig. 3. Kinetic curves of the viscosity η, of the E-05–DFFr mixture in Cellosolve solution at the N_1/N_2 ratio of (a) 1.5, (b) 1, and (c) 0.7 (333 K). Shear rate g, s^{-1}: (*1*) 27 and (*2*) 81.

tio), and shear rate g. However, the positions of these extrema and sections vary with N_1/N_2, $N_3/(N_1 + N_2)$, and g (Figs. 2–4, Table 3).

The η(*t*) curves can be described, to a first approximation, by a scaling relation for the viscosity η as a function of the reduced time $\tau = \gamma t$ [14]:

$$\ln \eta \sim [\eta]c[w(1 + \gamma t)]^{(3-2D)/D}. \quad (1)$$

Here, γ is the kinetic constant depending on the particle concentration, shear rate g, and temperature, as well as on the H_3PO_4 content; D, the fractal dimension of the oligomer aggregates; and w = 0.637, a random packing coefficient for hard spheres [12].

According to expression (1), the viscosity η of the oligomer mixture in solution varies with the fractal dimension D of the mixed aggregates of the oligomer molecules. The position of the maximum (or minimum) in the η(*t*) curves is determined by the kinetic constant γ, which, in turn, varies with the N_1/N_2 molar ratio, orthophosphoric acid concentration in the mixture, and shear rate g.

The density ρ of the aggregates of E-05 and DFFr molecules can be represented as a function of the precondensation time t [14]:

$$\rho(t) \sim w^{(3-D)/D}([\eta]c/\ln \eta)^{(3-D)/(3-2D)}. \quad (2)$$

The density of the mixed aggregates of the oligomer molecules varies nonmonotonically along the η(*t*) curve (Table 4). One can distinguish four kinetic stages of variation of the density ρ and the fractal dimension D of the oligomer aggregates. In the initial and intermediate precondensation stages, ρ and D decrease, and in the final stage, increase.

The plots of the viscosity η vs. precondensation time t at varied N_1/N_2 ratios (without orthophosphoric acid in the oligomer mixture at g = 27 s^{-1}) have a minimum at $N_1/N_2 = 1$ and a maximum at $N_1/N_2 > 1$ (Fig. 2). In the former case, the viscosity of the oligomer mixture in solution attains a limiting value at $t > 100$ min, and in the latter, at $t > 150$ min. For $N_1 = N_2$, the extremum in the η(*t*) curve is reached in shorter times t than those for $N_1 \neq N_2$. Near the minimum in the η(*t*) curve, the mixed elementary oligomer aggregates have a fractal dimension D equal to 1.5 ($N_1/N_2 = 1$), and the maximum in the η(*t*) curves at $N_1/N_2 > 1$ corresponds to $D < 1.5$ (Fig. 2).

The time in which the viscosity η of the oligomer mixture takes a limiting value is also strongly dependent on g. For example, at g = 27 s^{-1} ($N_1/N_2 = 1$), the limiting viscosity is attained within $t \approx 100$ min, and

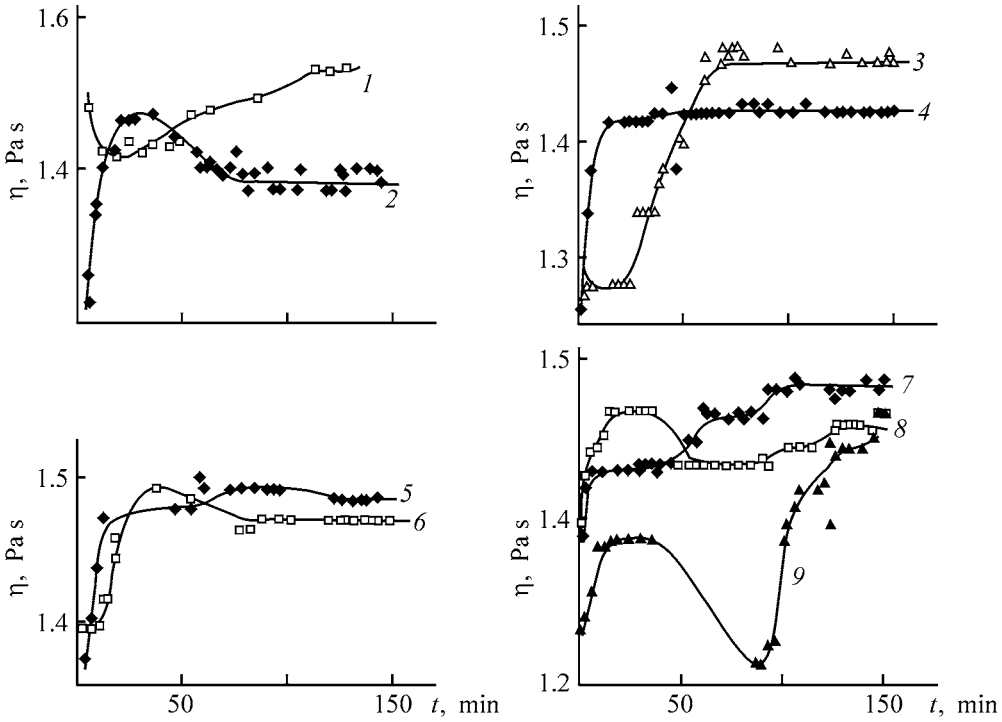

Fig. 4. Kinetic curves of viscosity η of the E-05–DFFr mixture in Cellosolve at different concentrations of orthophosphoric acid in the mixture. N_1/N_2 = 1, g = 81 s^{-1}, 333 K. H_3PO_4 concentration, %: (*1*) 0, (*2*) 100, (*3*) 14, (*4*) 30, (*5*) 50, (*6*) 75, (*7*) 125, (*8*) 150, and (*9*) 490.

at g = 81 s^{-1}, within $t \geq 200$ min (Fig. 3). For g = 81 s^{-1} and N_1/N_2 = 0.7, the viscosity η attains a limiting value at t = 150 min, and for g = 27 s^{-1}, does not attain it at $t \geq 200$ min (Fig. 3). At relatively small g values, the time of attainment of the limiting viscosity η in the oligomer mixture is the shortest at N_1/N_2 = 1.

Thus, without H_3PO_4 in the oligomer mixture in solution, the time of attainment of a limiting value of the viscosity η is the shortest at N_1/N_2 = 1. For small g values, the kinetic constant g at N_1/N_2 exceeds that at N_1/N_2 = 0.7 or under excess of DFFr in solution (Figs. 2, 3).

Orthophosphoric acid is a cross-linking agent for EO [9]. Therefore, with H_3PO_4 introduced into the oligomer mixture (N_1/N_2 = 1) in the early precondensation stage, the kinetic constant γ increases relative to that in the oligomer mixture containing no H_3PO_4 (Fig. 4, curves *1*, *2*). In this case, the extremum in the η(t) curves shifts to smaller times t, and the time corresponding to attainment of the limiting viscosity η in the oligomer mixture varies with the H_3PO_4 concentration (Fig. 4, curves *1*–*9*).

The η(t) curves obtained on introducing H_3PO_4 into the oligomer mixture at $N_3/(N_1 + N_2) < 0.07$ are identical to those obtained in the absence of H_3PO_4. A viscosity maximum in the η(t) curve is observed at $N_3/(N_1 + N_2) \approx 0.1$, and the limiting value of the viscosity η is attained at t = 90–120 min. At $N_3/(N_1 + N_2) \approx$ 0.7, the viscosity η of the oligomer mixture does not attain a limiting value at t > 240 min.

The data in Table 3 suggest a correlation between the limiting viscosity η of the oligomer mixture in

Table 3. Time of attainment of the limiting viscosity η(t) for the E-05–DFFr mixture in C solution* (N_1/N_2 = 1, g = 81 s^{-1}, 333 K)

$c(H_3PO_4)$, %	$N_3/(N_1 + N_2)$	η ± 0.01, Pa s	t, min	$c(H_3PO_4)$, %	$N_3/(N_1 + N_2)$	η ± 0.01, Pa s	t, min
0	0	1.54	180	100	0.13	1.38	90
14.3	0.019	1.47	150	125	0.17	1.59	150
30	0.04	1.43	120	150	0.20	1.56	>180
50	0.07	1.51	120	490	0.66	1.53	>240
75	0.09	1.47	120				

* The concentration $c_{H_3PO_4}$ is expressed in percent of the relative value (100% = 0.25 g of H_3PO_4 per 36 g of the E-05–DFFr mixture [17]); N_3 is the number of H_3PO_4 moles.

Table 4. Kinetic parameters of the E-05–DFFr mixture in C solution in various precondensation stages [N_1/N_2 = 1, $N_3/(N_1 + N_2)$ = 0.13, g = 46.6 s^{-1}, 333 K]

Precondensation stage	t, h	γ	$\alpha^* = (3-D)/D$ ±10%	D ±7%	ρ^{**} ±0.01
Initial	0.1	<0	~0.5	~2.0	~0.66
Viscosity growth and formation of mixed E-05–DFFr aggregates	0.16–0.5	≈0	~1.0	1.54	~0.52
Viscosity decrease and size growth for E-05–DFFr aggregates	1–2	<0	~0.8	>1.7	~0.60
Viscosity saturation and formation of infinite cluster from E-05 and DFFr molecules	2–2.5	→0	0.5	2.0	~0.69

* Analogous to the power index in the Mark–Kuhn–Houwink relation for intrinsic viscosity [16].

** The density was calculated by the expression $\rho = w^{(3-D)/D}([\eta]c/\ln \eta_{rel})^{(3-D)/(3-2D)}$, where $\eta_{rel} = \eta/\eta_0$ is the relative viscosity of the oligomer mixture in solution, and η_0, solvent viscosity.

solution and the time of its attainment, as well as between the optimal precondensation time t and the H_3PO_4 concentration (N_3) in the mixture, when the acid is introduced 40 min after mixing the oligomers. These data suggest that the precondensation time t is at a minimum at $N_3/(N_1 + N_2) \approx 0.1$; in this case, the limiting viscosity η of the oligomer mixture in C solution is also at a minimum.

In other cases like, e.g., at relative deficiency of H_3PO_4 [$N_3/(N_1 + N_2) < 0.1$] in the oligomer mixture, the precondensation time increases. At orthophosphoric acid concentrations appreciably exceeding the optimal value in the oligomer mixture [$N_3/(N_1 + N_2)$ = 0.2–0.7], the $\eta(t)$ curve oscillates, and the mixture viscosity η does not attain a limiting value within a fairly long period of time t (Table 3; Fig. 4, curves *7*–*9*). Under these conditions, the oligomers are not fully compatible.

The cluster mechanism of thermal precondensation of oligomers in solution accounts for a decrease in the mixture viscosity due to degradation of the particle aggregates and formation of mixed oligomer aggregates in the initial and intermediate stages, as well as the viscosity growth and saturation in the final stages of the process due to formation of an infinite cluster from EO and PFO molecules [18] (Table 4). These precondensation stages are characterized by a change in the fractal dimension D of the particle aggregate and in the kinetic constant γ which is also dependent on g.

CONCLUSIONS

(1) The kinetic viscosity curves $\eta(t)$ of the mixture of epoxy-4,4'-isopropylidenediphenol and phenol-formaldehyde oligomer mixture in Cellosolve are described by a scaling relation for reduced time and exhibit an extremum. The positions of the extrema and of the sections corresponding to decrease, growth, and leveling-off of the viscosity η in the $\eta(t)$ curves are determined by the molar ratio N_1/N_2 of the oligomers, concentration of orthophosphoric acid in the mixture, and shear rate g.

(2) The thermal precondensation time of the oligomers in solution can be determined as the time t of attaining the limiting viscosity of the mixture, whose plot against the H_3PO_4 concentration has an extremum. The corresponding time t is at a minimum at H_3PO_4 concentration in the mixture close to $N_3/(N_1 + N_2) \approx 0.1$. The optimal concentration of H_3PO_4 in the oligomer mixture is primarily governed by the formation of dihydrogen phosphate esters of epoxy-4,4'-isopropylidenediphenol oligomer.

(3) The precondensation time can be made shorter by introducing orthophosphoric acid in the initial stage of the process, which involves formation of mixed aggregates of oligomer molecules.

REFERENCES

1. Markevich, M.A., Kuzaev, A.I., Vladimirov, L.V., *et al.*, *Vysokomol. Soedin., Ser. A*, 1985, vol. 27, no. 5, pp. 1000–1008.
2. Nizhnik, I.N., Aleksandrov, V.N., Fartunin, V.I., and Rozenberg, B.A., *Lakokras. Mater. Ikh Primen.*, 1989, no. 2, pp. 16–18.
3. Kochnova, Z.A., Khrisanova, T.A., and Sorokin, M.F., *Lakokras. Mater. Ikh Primen.*, 1989, no. 2, pp. 82–89.
4. Solov'ev, A.G. and Butaeva, A.B., *Lakokras. Mater. Ikh Primen.*, 1991, no. 2, pp. 6–8.
5. Sukhareva, L.A., Sorokin, M.F., Kochnova, Z.A., and Svetlakova, T.N., *Lakokras. Mater. Ikh Primen.*, 1982, no. 1, pp. 10–11.
6. Sukhareva, L.A., Sorokin, M.F., Kochnova, Z.A., *et al.*, *Lakokras. Mater. Ikh Primen.*, 1982, no. 4, pp. 30–31.

7. Aleksandrov, V.N., Tarasov, A.N., and Rozenberg, B.A., *Lakokras. Mater. Ikh Primen.*, 1985, no. 6, pp. 35–38.
8. Aleksandrov, V.N., Tarasov, A.N., and Rozenberg, B.A., *Lakokras. Mater. Ikh Primen.*, 1986, no. 2, pp. 16–19.
9. Sorokin, M.F., Kochnova, Z.A., Nikolaev, L.P., *et al.*, *Tr. Khim.-Tekhnol. Inst. im. D.I. Mendeleeva*, 1980, issue 110, pp. 63–67.
10. Krasovskii, A.N., Novikov, D.V., Krasheninnikov, V.A., *et al.*, *Zh. Prikl. Khim.*, 2001, vol. 74, no. 1, pp. 124–134.
11. Krasovskii, A.N., Novikov, D.V., Filippov, V.N., *et al.*, *Zh. Prikl. Khim.*, 2003, vol. 76, no. 2, pp. 304–312.
12. Feder, J., *Fractals*, New York: Plenum, 1988.
13. Gennes, P.-G. de, *Scaling Concepts in Polymer Physics*, Ithaca: Cornell Univ., 1979.
14. Krasovskii, A.N. and Belousova, I.A., *Zh. Prikl. Khim.*, 1996, vol. 69, no. 10, pp. 1735–1744.
15. Gorshkov, A.V., Verenish, S.S., Evreinov, V.V., and Entelis, S.G., *Chromatographia*, 1988, vol. 26, pp. 338–342
16. Tsvetkov, B.N., Eskin, V.E., and Frenkel, S.Ya., *Struktura makromolekul v rastvorakh* (Structure of Macromolecules in Solutions), Moscow: Nauka, 1964
17. *Lakokrasochnye materialy dlya zashchity konservnoi tary* (Paint and Varnish Materials for Can Protection), Lyalyushko, S.M., Ed., Moscow: NIITEKhim, 1981.
18. Krasovsky, A.N., Novikov, D.V., Philippov, V.N., *et al.*, Abstracts of Papers, *4th Int. Symp. "Molecular Order and Mobility in Polymer Systems,"* St. Petersburg, 2002, p. 257.

Russian Journal of Applied Chemistry, Vol. 76, No. 6, 2003, pp. 978–980. Translated from Zhurnal Prikladnoi Khimii, Vol. 76, No. 6, 2003, pp. 1006–1008.

MACROMOLECULAR CHEMISTRY AND POLYMERIC MATERIALS

^{13}C NMR Study of the Structure of Products Formed in Base Hydrolysis of Nitron D Polyacrylonitrile Fiber

L. P. Krul', E. I. Nareiko, D. V. Krakodeev, E. V. Grinyuk, A. S. Rybak, E. D. Skakovskii, and L. Yu. Tychinskaya

Research Institute of Physicochemical Problems, Belarussian State University, Minsk, Belarus

Institute of Physicoorganic Chemistry, Belarussian National Academy of Sciences, Minsk, Belarus

Received February 11, 2003

Abstract—The composition and structure of the products formed in base hydrolysis of Nitron D polyacrylonitrile fiber were studied by ^{13}C NMR.

Hydrolysis of acrylonitrile polymers and copolymers yields water-soluble polymers widely used in various branches of industry and agriculture [1]. Recently, the interest in structural studies of hydrolysis products has increased, and, along with traditional IR spectroscopy and elemental analysis [2–5], the ^{13}C NMR spectroscopy finds growing use [6].

The products of base hydrolysis of polyacrylonitrile fibers are used in production of adhesives, polyelectrolyte hydrogels, and binders for composite polymeric materials [7]. However, up to now, their structure has not been studied by ^{13}C NMR.

The aim of this study was to analyze by ^{13}C NMR the products of base hydrolysis of Nitron D polyacrylonitrile fiber, terpolymer of acrylonitrile, methyl acrylate, and 2-acrylamido-2-methylpropanesulfonic acid with the weight ratio of acrylnitrile, methyl acrylate, and 2-acrylamido-2-methylpropanesulfonic acid units equal to 89.4 : 9.3 : 1.3. Base hydrolysis of Nitron D was performed at the boiling temperature of the solution for 3 h. According to published data [2–5], under these conditions the nitrile group of the initial polyacrylonitrile fiber is completely hydrolyzed, and the ratio of the concentrations of the acrylamide and carboxylate units in the resulting copolymer depends on the weight ratio of alkali and polyacrylonitrile fiber. In the experiments, the ratio of the amounts of NaOH and Nitron D was varied from 1.38 to 2.50 mol per 100 g of dry fiber.

EXPERIMENTAL

Base hydrolysis was performed in a 1-l round-bottom flask with a reflux condenser. The amount of Nitron D in the flask, recalculated to dry fiber, was 100 g. Sodium hydroxide was preliminarily dissolved in distilled water. The total weight of water in the flask was 550 g, and the amount of added alkali, 55, 75, and 100 g (1.38, 1.88, and 2.50 mol, respectively).

The ^{13}C NMR spectra of hydrolyzates, shown in Fig. 1, confirm published data on the chemical composition of products formed in base hydrolysis of polyacrylonitrile fibers and allow more precise determination of the ratio of acrylamide and carboxylate units in

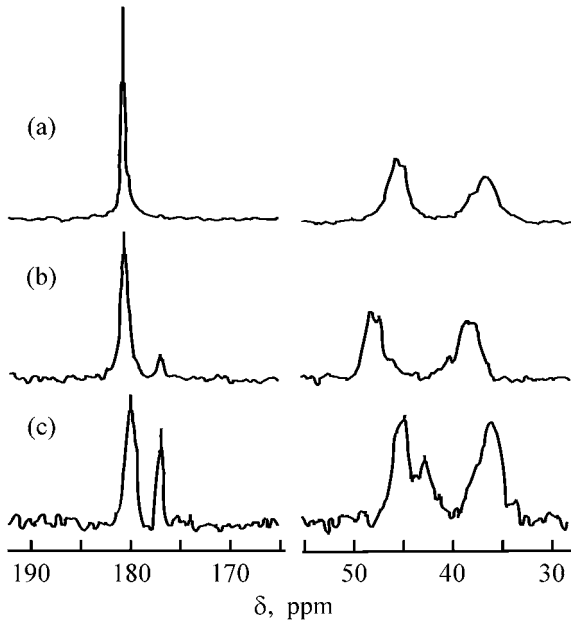

Fig. 1. ^{13}C NMR spectra of base hydrolyzates of Nitron D fiber. (δ) Chemical shift. Amount of NaOH per 100 g of dry fiber (mol): (a) 1.38, (b) 1.88, and (c) 2.5.

1070-4272/03/7606-0978 $25.00 © 2003 MAIK "Nauka/Interperiodica"

the copolymer formed in base hydrolysis. The ^{13}C MNR spectrum of the hydrolyzate produced at a NaOH to Nitron D ratio equal to 1.38 mol per 100 g of dry fiber is shown in Fig. 1a. There are lines of the copolymer containing acrylamide and carboxylate units. These units were identified from the spectra of polyacrylamide (PAA) and sodium polyacrylate (PANa) with the use of published data [8] and the spectra of specially synthesized homopolymers. The spectral lines were assigned as follows: δ 179.7 (CO, PANa), 176.6 (CO, PAA), 44.8 (CH, PANa), 42.5 (CH, PAA), and 36.2 ppm (CH_2, PAA and PANa). Analysis of the integral intensities of the lines corresponding to carboxamide and carboxylate carbon atoms and also of the lines of methine carbon atoms gives the ratio of molar concentrations of acrylamide and carboxylate units equal to 33 : 67, in good agreement with data obtained by IR spectroscopy and elemental analysis [2–4].

The spectrum of the hydrolyzate produced at a NaOH to Nitron D ratio equal to 1.88 mol per 100 g of dry fiber (Fig. 1b) contains, similarly to the previous case (Fig. 1a), lines of acrylamide and carboxylate units. However, their ratio is different 17 : 83. Along with the integral intensities, chemical shifts are also diffrent, which suggests the formation of a copolymer.

Only PANa is formed at a NaOH to Nitron D ratio equal to 2.50 mol per 100 g of dry fiber (Fig. 1c). This result is the most interesting, since it fundamentally differs from published data [2–4]. Contrary to results of IR spectroscopy and elemental analysis [2–4], the ^{13}C NMR spectra do not reveal the presence of acrylamide units in the hydrolyzate produced at high NaOH to Nitron D ratio (2.50 mol per 100 g of dry fiber). It is evident that NMR data are the most reliable, since the signals of acrylamide and carboxylate units are clearly separated, which allows determination of the concentration ratio of these units with high accuracy. IR spectroscopy is significantly less accurate in this respect: with increasing ratio of concentrations of carboxylate and acrylamide units in the copolymer, the characteristic bands begin to overlap, which gives high error in quantitative estimation. The results of elemental analysis revealing the presence of nitrogen in the hydrolyzate cannot prove the presence of acrylamide units in macromolecules, either, since nitrogen can belong to ammonium carboxylate present in the hydrolysis product along with sodium carboxylate. In none of the cases were detected signals of nitrile groups (δ = 120 ppm) in the soluble copolymer. This suggests that, under the conditions of the experiment, nitrile groups were completely hydrolyzed.

The solutions of hydrolyzates whose characteristics are illustrated by data shown in Fig. 1 had pH > 9, i.e., in all cases carboxylate groups had negative electric charge and acrylamide groups had no charge. Under these conditions, the interaction of acrylamide and carboxylate groups of copolymer, possible only at low pH values and affecting the positions and intensities of the ^{13}C NMR signal [9], could not affect the obtained concentration ratios of these functional groups.

Thus, the ^{13}C NMR spectra show that, at a alkali to Nitron ratio equal to 2.5 mol per 100 g of dry fiber, the molar content of acrylamide groups in the hydrolyzate of Nitron D polyacrylonitrile fiber decreases virtually to zero, i.e., the polymeric part of the hydrolyzate is nearly pure sodium polyacrylate, rather than a copolymer of acrylamide with sodium acrylate.

The process was carried out at the boiling point of the reaction mixture for 3 h. During this period, all nitrile groups of the initial polymer entered into the reaction at any concentration of sodium hydroxide within the range examined, and the fiber was completely converted into a water-soluble product.

Polyacrylamide and sodium polyacrylate were synthesized by radical polymerization in solution at 50°C. The standard redox system constituted by ammonium persulfate and *N*,*N*,*N*',*N*'-tetramethylethylenediamine in the equimolar ratio (concentration 4.4×10^{-3} M) was used as initiator. The synthesis of PAA was carried out in 10% aqueous solution of acrylamide. PANa was synthesized in 20% aqueous solution of acrylic acid in the presence of an equimolar amount of NaOH. The samples for analysis were prepared by drying in a desiccator at 60°C to constant weight.

The ^{13}C NMR spectra were recorded on a BS-587A (Tesla) spectrometer operating at 20 MHz. Approximately 10% solutions of copolymers in D_2O were placed in standard ampules (10 ml). The spectra were recorded without NOE; the pulse delay exceeded $7T_1$, where T_1 is the longest spin-lattice relaxation time. The signals were assigned by the DEPT technique [8] using model compounds. Chemical shifts were measred relative to acetone-d_6 used as internal reference (δ = 30.2 ppm).

The relative error in quantitative determination of the content of acrylamide and acrylate units did not exceed 7%.

CONCLUSION

A ^{13}C NMR study showed that base hydrolysis of Nitron D polyacrylonitrile fiber under conditions

providing complete conversion of nitrile functional groups of the initial polymer is accompanied by formation of either copolymer of acrylamide with sodium acrylate or pure sodium polyacrylate, depending on the ratio of sodium hydroxide and the polymer.

REFERENCES

1. Nikolaev, A.F. and Okhrimenko, T.I., *Vodorastvorimye polimery* (Water-Soluble Polymers), Leningrad: Khimiya, 1979.
2. Shmelev, A.L., Fedosov, S.V., Zaitsev, V.A., *et al*. Available from ONIITEKhIM, April 2, 1988, no. 362-khp-88.
3. Krul', L.P., Yakimtsova, L.B., Brazhnikova, M.M., *et al., Vestsi Nats. Akad. Navuk Bel., Ser. Khim. Navuk*, 1999, no. 4, pp. 95–97.
4. Krul', L.P., Yakimtsova, L.B., Matusevich, Yu.I., and Krakodeev, D.V., *Vestsi Nats. Akad. Navuk Bel., Ser. Khim. Navuk*, 2000, no. 1, pp. 103–105.
5. Martinovich, V.I., Elinson, I.S., and Soldatov, V.S., *Vestsi Nats. Akad. Navuk Bel., Ser. Khim. Navuk*, 2001, no. 4, pp. 39–43.
6. Krentsel, L.B., Kudryavtsev, Y.V., Rebrov, A.I., *et al., Macromolecules*, 2001, no. 34, pp. 5607–5610.
7. Krul', L.P., Absracts of Papers, *Polymernye kompozity-2000* (Polymer Composites-2000), Gomel: Inst. Makromol. Soed., Nats. Akad. Nauk Belarusi, 2000, pp. 10–16.
8. Derome, A.E., *Modern NMR Techniques for Chemistry Research*, Oxford: Pergamon, 1987.
9. Garces, F.O., Sivadasan, K., Somasundaran, P., and Turro, N.G., *Macromolecules*, 1994, vol. 27, no. 1, pp. 272–278.

Russian Journal of Applied Chemistry, Vol. 76, No. 6, 2003, pp. 981–984. Translated from Zhurnal Prikladnoi Khimii, Vol. 76, No. 6, 2003, pp. 1009–1012.

MACROMOLECULAR CHEMISTRY AND POLYMERIC MATERIALS

Degradation of Copolymers of *N*-Vinylpyrrolidone with Sodium 2-Acrylamido-2-Methylpropanesulfonate in Aqueous Solutions

V. F. Kurenkov, N. N. Zaitseva, T. A. Zhelonkina, and F. I. Lobanov

Kazan State Technological University, Kazan, Tatarstan, Russia
Stockhausen Eurasia Co., Moscow, Russia

Received October 22, 2002; in final form, February 2003

Abstract—The kinetics of controllable degradation of *N*-vinylpyrrolidone–sodium 2-acrylamido-2-methylpropanesulfonate copolymers in aqueous solutions under the action of degrading agents at 25–50°C were studied by viscometry. The efficiency of controlling the molecular weight of copolymer was estimated.

Degradation of water-soluble polymers in solutions under the action of degrading agents is a promising method for chemical modification of polymers, which allows control of their molecular weight and performance [1]. To elucidate the possibility of producing partially degraded copolymers of *N*-vinylpyrrolidone (N-VP) with sodium 2-acrylamido-2-methylpropanesulfonate (Na-AMS), with controllable molecular weight (MW), we studied the features of degradation Na-VP–Na-AMS copolymers in aqueous solutions in the presence of radical initiators at 20–50°C. This study was stimulated by the lack of data on degradation of these copolymers and by their practical significance as effective flocculants [2] and adhesion and antistatic agents [3]. These copolymers also attract attention as thickeners, stabilizers, and complexing agents for various branches of industry and medicine [4, 5].

EXPERIMENTAL

In this study, we used copolymers of N-VP with Na-AMS with the content of N-VP and Na-AMS units equal to 50 mol % and varied intrinsic viscosity:

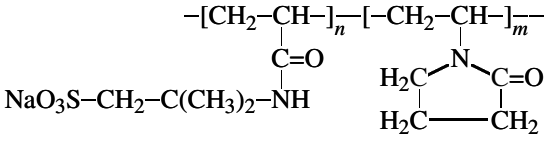

Sample	no. 1	no. 2	no. 3	no. 4
$[\eta]$, $cm^3\ g^{-1}$	120	410	360	300

Copolymer sample no. 2 was produced by copolymerization of monomers in aqueous solutions at low degree of conversion (less than 4%) by the procedure similar to that described in [6]. The copolymer samples nos. 1, 3, and 4 were prepared by degradation of copolymer no. 2 under mild conditions in 0.1% aqueous solutions in the presence of potassium persulfate (PS) at 60°C, which provided the identity of the composition of the copolymers.

PS, hydrogen peroxide (HP), and a redox system constituted by PS and sodium sulfite (SS) were used as degradation initiators. All the reagents used were of chemically pure grade. Solutions were prepared in distilled water [GOST (State Standard) 6709–72].

Degradation was carried out in aqueous solutions of N-VP–Na-AMS copolymers under the action of radical initiators. The course of degradation was monitored viscometrically [7]. The process was carried out in a glass reactor with a jacket for thermal stabilization, magnetic stirrer, thermometer, connecting pipe for sampling, and VPZh-3 capillary viscometer for monitoring the viscosity of the reaction mixture [7]. The viscometer was equipped with a jacket for thermostatic control at the same temperature as that in the reactor.

The prepared aqueous solution of the copolymer was charged into the reactor and brought to the required temperature, after which a degrading agent was added, with this instant of time taken as the start of degradation. In the course of degradation, we measured at certain intervals the outflow time of the copolymer solution in the reactor, t_1, with a viscometer and determined the reduced viscosity η_{sp}/c_p, where c_p is the copolymer concentration. The values of η_{sp}/c_p

1070-4272/03/7606-0981 $25.00 © 2003 MAIK "Nauka/Interperiodica"

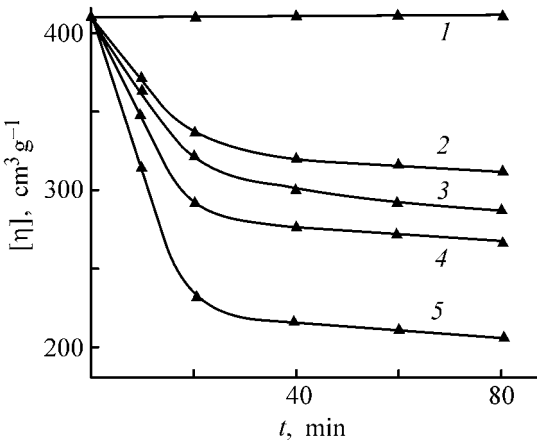

Fig. 1. Variation of [η] with time t in the course of degradation of N-VP–Na-AMS copolymer (sample no. 2) at different concentrations of PS. c_p = 0.1%, 50°C. [SP]/[copolymer]: (*1*) 0, (*2*) 0.01, (*3*) 0.02, (*4*) 0.04, and (*5*) 0.08.

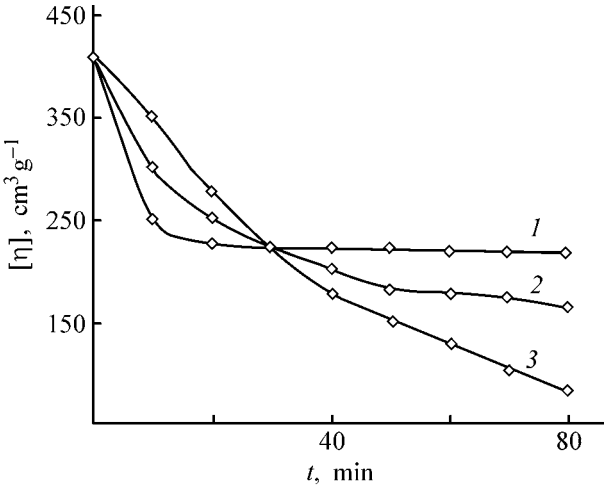

Fig. 2. Variation of [η] with time t in the course of degradation of N-VP–Na-AMS copolymer (sample no. 2) under the action of different degrading agents. [Degrading agent]/[copolymer] = 0.08, c_p = 0.1%, 50°C. Degrading agent: (*1*) PS, (*2*) HP, and (*3*) PS–SS, 1 : 2 (by weight).

were referred to the instant of time $t = t_2 + t_1/2$, where t_2 is the time elapsed from the onset of degradation to the start of measuring t_1. Then we plotted the dependence $\eta_{sp}/c_p = f(t)$. In the course of degradation, the reaction solution was sampled at certain intervals to determine [η].

The measurements of [η] were carried out in a VPZh-3 viscometer (d = 0.56 mm) in 0.5 M NaCl at 30°C. The values of [η] were determined from the linear dependence $(\eta_{sp}/c_p) = f(c_p)$ as $[\eta] = \lim(\eta_{sp}/c_p)$ at $c_p \to 0$. From the [η] values measured at constant copolymer composition, solvent, and temperature for copolymers with identical molecular characteristics, we evaluated MW of the copolymer, since, according to the Mark–Houwink–Kuhn equation, $[\eta] \sim MW$.

The content of ionic units in the copolymer composition was evaluated by elemental analysis for sulfur [8].

For potentiometric measurements we used a pH meter (pH-121) with a measuring glass electrode (ESL 65-07) and an auxiliary silver chloride electrode (EVL 1M3).

With the aim to prevent deterioration of the performance of N-VP–Na-AMS copolymers, commonly observed at high extents of degradation, we selected as optimum such degradation conditions which provided formation of partially degraded copolymers and allowed viscosimetric monitoring of degradation. The optimal degradation conditions were established based on previous studies [1]. Degradation was carried out in 0.1–1% aqueous solutions of copolymers at 25–60°C in the presence of radical degrading agents, taken in the amount of 1–8% relative to the copolymer weight. To exclude the complicating effect of the difference between the molecular characteristics of N-VP–Na-AMS copolymers, all experiments were carried out on sample no. 2, produced at a low degree of conversion, which provided the constancy of the molecular weight, average composition, and composition heterogeneity of the copolymer.

Let us consider the effect of degrading agents on degradation of N-VP–Na-AMS copolymer (sample no. 1). The experiments were carried out in 0.1% solutions of the copolymer at 50°C. The influence of PS concentration on the variation of [η] in the course of copolymer degradation is shown in Fig. 1. Without initiator, the [η] values do not vary with time (curve *1*), suggesting the absence of noticeable degradation of the copolymer. Variation of [η] values on adding PS suggests that degradation occurs. Its intensity grows with increasing concentration of degrading agent and reaction duration (curves *2–4*). Similar variations in [η] were observed in degradation of the copolymer under the action of another initiator, HP.

Under experimental conditions, degradation of the copolymer under the action of radicals $R^{\bullet}$ generated by decomposition of initiators proceeded with the rupture of carbon–carbon bonds in the backbone of the macromolecule, which occurred by the random law without depolymerization. In this case, the initiating centers could be monomer units joined "head to head." The general scheme of degradation of N-VP–Na-AMS copolymer under the action of radicals $R^{\bullet}$ is similar to that described in [1].

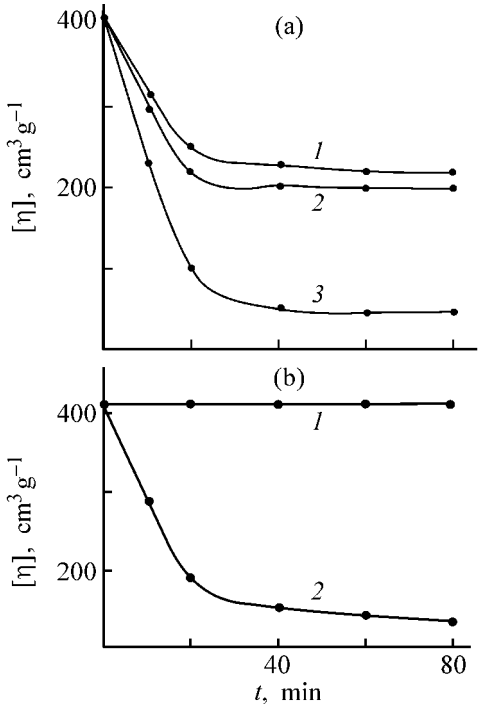

Fig. 3. Variation of [η] with time t in the course of degradation of N-VP–Na-AMS copolymer (sample no. 2) at different temperatures (c_p = 0.1%). (a) [PS]/[copolymer] = 0.08. T (°C): (*1*) 40, (*2*) 50, and (*3*) 60. (b) [PS]/[SS] = 1 : 2 (by weight), 25°C. [PS + SS]/[copolymer]: (*1*) 0 and (*2*) 0.24.

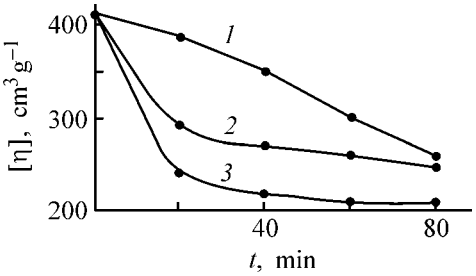

Fig. 4. Variation of [η] with time t in the course of degradation of N-VP–Na-AMS copolymer (sample no. 2) at different copolymer concentrations. [PS]/[copolymer] = 0.08, 50°C. c_p (%): (*1*) 1, (*2*) 0.5, and (*3*) 0.1.

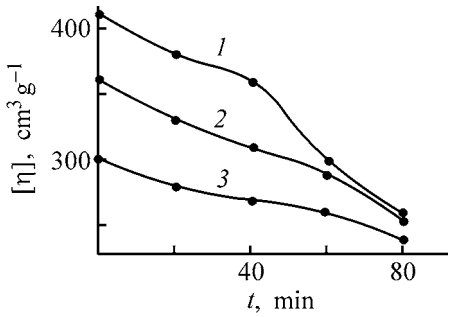

Fig. 5. Variation of [η] with time t in the course of degradation of N-VP–Na-AMS copolymer with the same composition and different initial values of [η]. [PS]/[copolymer] = 0.08, c_p = 1%, 50°C. [η], cm³ g^{-1}: (*1*) 410 (sample no. 2), (*2*) 360 (sample no. 3), and (*3*) 300 (sample no. 4).

The results of degradation of N-VP–Na-AMS copolymer in 0.1% solutions at 50°C under the action of different degrading agents at their equal concentrations in the solution are shown in Fig. 2. As seen, the initial degradation rate decreases in the order PS > HP > PS–SS, and the limiting degree of the copolymer degradation in 80 min varies in the reverse order.

The influence of temperature on the variation of [η] of the copolymer in the course of degradation was estimated in the range 40–60°C, with other reaction conditions fixed (Fig. 3a). Figure 3a shows that the initial rate and the limiting degree of degradation increase with temperature. This is caused by an increase in the concentration of radicals generated by decomposition of the initiator and including degradation of the copolymer.

To elucidate the possibility of low-temperature degradation of the N-VP–Na-AMS copolymer in 0.1% solution, we carried out experiments at 25°C using the PS–SS redox system as degrading additive. The results of these experiments (Fig. 3b) show that degradation of the copolymer is not observed without the PS–SS initiating system (curve *1*), and in the presence of this system degradation proceeds efficiently (curve *2*). The possibility of degradation of copolymer macromolecules at 25°C is caused by intensification of the PS decomposition under the action of SS reducing agent and rise in the concentration of free radicals in the system.

With the aim to elucidate how the concentration of N-VP–Na-AMS copolymer affects degradation, experiments were carried out in 0.1–1% solutions, other degradation conditions being the same. The results of this series of experiments are shown in Fig. 4. At all of the copolymer concentrations studied, the [η] values drastically decrease as a result of rupture of the C–C bonds in the macromolecular backbone. It also follows from Fig. 4 that, with increasing copolymer concentration, the intensity of its degradation decreases. This is caused by an increase in the viscosity of the reaction medium, which results in a slower diffusion of the degrading agent to the macromolecule.

The influence of MW of the initial N-VP–Na-AMS copolymer on degradation process is illustrated in Fig. 5. The experiments performed with the copolymer samples of the same chemical composition and under the same conditions suggest intensification of

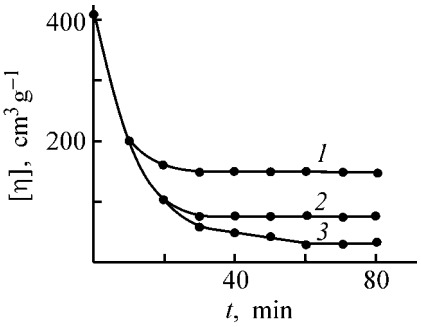

Fig. 6. Variation of [η] with time *t* in the course of degradation of N-VP–Na-AMS copolymer (sample no. 2) (*1, 2*) in the presence of KI and (*3*) without it. [PS]/[copolymer] = 0.08, [PS]/[KI] = 1 : 1 (by weight), 60°C. Time of KI addition (min): (*1*) 10 and (*2*) 20.

degradation with increasing [η] of the initial copolymer samples. These results are in good agreement with published data [9] on variation of MW of polyacrylamide in the course of degradation. It is evident that, with increasing MW, the content of weak bonds (e.g., abnormally "head to head" bonded units) subjected to rupture grows. This is in good agreement with the general features of polymer degradation [10]. In addition, at the same number of ruptures per macromolecule, the decrease in the MW is more significant for a copolymer with higher molecular weight.

We also evaluated the effect of KI additions on degradation of N-VP–Na-AMS copolymer in 0.1% solution in the presence of PS at 60°C. Figure 6 shows that addition of KI at various degradation stages results in weaker decrease in [η] (curves *1*, *2*) as compared to the run without addition of KI (curve *3*). This is apparently caused by the reaction of KI with the radical $R^{\bullet}$, generated from the initiator, according to the scheme

$$2KI + 2R^{\bullet} + 2H_2O \rightarrow 2KOH + 2RH + I_2.$$

These data suggest that KI is a stabilizer for solutions of N-VP–Na-AMS copolymer and can be used for controlling MW of the copolymer in its degradation. The data on stabilizing characteristics of KI in the system studied are in good agreement with the possibility of stabilization of hydrolyzed PAA solutions under the action of KI, shown previously in [11].

The above results give grounds to believe that controllable degradation of N-VP–Na-AMS copolymer in aqueous solutions in the presence of radical initiators can be used as a facile route to copolymers with controllable MW.

CONCLUSIONS

(1) Partially degraded copolymers of *N*-vinylpyrrolidone and sodium 2-acrylamido-2-methylpropanesulfonate, with molecular weight controllable in a wide range (an order of magnitude and more), can be produced by degradation of macromolecular copolymers in aqueous solutions under the action of radical degrading agents at 25–50°C.

(2) The initial rate of copolymer degradation increases with temperature, reaction duration, and concentration of various degrading agents, and decreases in the order potassium persulfate > hydrogen peroxide > system potassium persulfate–sodium sulfite. Addition of KI inhibits the degradation.

(3) Degradation is intensified with decreasing concentration of the copolymer and its increasing molecular weight.

ACKNOWLEDGMENTS

This work was supported financially by the R&D Foundation of the Republic of Tatarstan (project no. 07-7.1-104/2002).

REFERENCES

1. Kurenkov, V.F., Hartan, H.-G., and Lobanov, F.I., *Zh. Prikl. Khim.*, 2002, vol. 75, no. 7, pp. 1057–1068.
2. Kurenkov, V.F., Sharapova, Z.F., and Khairullin, M.R., *Zh. Prikl. Khim.*, 1999, vol. 72, no. 8, pp. 1374–1378.
3. Shevtsova, S.A., Zaitseva, O.A., and Kurenkov, V.F., *Vestn. Kazan. Tekhnol. Univ.*, 2000, nos. 1–2, pp. 126–128.
4. Lisovtsev, V.V., Rostokin, G.A., and Kulikov, A.E., in *Khimicheskaya Promyshlennost, Ser.: Akrilaty i polivinilkhlorid* (Chemical Industry, Ser.: Acrylates and Polyvinyl Chloride), Moscow: NIITEKHIM, 1984, pp. 1–20.
5. Sidel'kovskaya, F.P., *Khimiya N-vinilpirrolidona i ego polimerov* (Chemistry of *N*-Vinylpyrrolidone and Its Polymers), Moscow: Nauka, 1970.
6. Kurenkov, V.F., Sirotkin, O.S., Beryachkova, E.A., and Khairullin, M.R., *Zh. Prikl. Khim.*, 1999, vol. 72, no. 8, pp. 1374–1378.
7. *Praktikum po khimii i fizike polimerov* (Practical Works on Polymer Chemistry and Physics), Kurenkov, V.F., Ed., Moscow: Khimiya, 1995.
8. Charlot, G., *Les Methods de la Chemie Analytique. Analyse quantitative Minerale*, Quatrieme Edition, Paris: Masson, 1961.
9. Kurenkov, V.F. and Tazieva, E.D., *Zh. Prikl. Khim.*, 1994, vol. 67, no. 7, pp. 1162–1166.
10. Grassie, N. and Scott, G., *Polimer Degradation and Stabilisation*, Cambridge: Cambridge Univ., 1985.
11. Nakonechnyi, I.I., Baiburdov, T.A., and Kurenkov, V.F., *Zh. Prikl. Khim.*, 1991, vol. 64, no. 5, pp. 1062–1065.

Russian Journal of Applied Chemistry, Vol. 76, No. 6, 2003, pp. 985–988. Translated from Zhurnal Prikladnoi Khimii, Vol. 76, No. 6, 2003, pp. 1013–1016.

MACROMOLECULAR CHEMISTRY AND POLYMERIC MATERIALS

Sorption Interaction of Lysozyme with Carboxylic Cation Exchangers

A. T. Melenevskii, K. P. Papukova, V. S. Yurchenko, and E. B. Chizhova

Institute of Macromolecular Compounds, Russian Academy of Sciences, St. Petersburg, Russia

Received October 29, 2002; in final form, February 2003

Abstract—A comparative study is made of sorption interaction of individual lysozyme and lysozyme as component of chicken egg white with KMDM-6-5 carboxylic cation exchanger.

Among problems arising in studying interactions of biologically active compounds with charge-bearing surfaces of polymers, the effect of the composition of a multicomponent mixture on the sorption is of a particular importance. The same problem arises in developing processes of chromatographic separation and purification of biologically active compounds on polymeric sorbents.

It is known that ion-exchange chromatography is among the most efficient and cost-effective methods used for primary recovery of target components from complex biological raw materials. In some specific cases, the use of selective high-capacity sorbents [1] allows separation of a target component from a complex mixture in a single stage. Even at a target component concentration of about fractions of a percent or several percent, proper choice of an ion-exchange sorbent and sorption conditions can provide increase in the component concentration in the eluate to several tens of percent [1].

At the same time, the result of sorption depends on the component concentration in the mixture, as demonstrated by experiments with model mixtures of proteins [2, 3]. Helfferich and Klein proposed a mathematical model that takes into account the mutual influence of components in sorption. They introduced the concept of the competitive and synergistic sorption mechanisms [4]. If proteins interact with the pore surface of a sorbent by the synergistic mechanism with multilayer sorption of the proteins, separation of the components in a dynamic column experiment is virtually impossible. By the optimal conditions of sorption are meant those under which sorption of proteins proceeds in competition for sites on the sorbent pore surface, but not by the synergistic mechanism. In this case, proper choice of the desorption mode will allow elution of the target component only.

The goal of this study was to optimize the conditions of ion-exchange sorption/desorption of lysozyme from a multicomponent mixture on a carboxylic cation exchanger, using the competitive sorption mechanism.

EXPERIMENTAL

In the study, we used chicken egg white (CEW) lysozyme from the Ferrein Joint-Stock Company. The product contains 97% protein (MW 14 600). Lysozyme has isoelectric point at pH 10.7–11.2 and maintains its activity in neutral solutions [5–7]. As a lysozyme-containing multicomponent mixture we used CEW (preliminarily frozen and then warmed to room temperature).

As cation exchangers we used SGK-7 and KMDM-6-5 cross-linked carboxylic polyelectrolytes. The former was obtained by copolymerization of acrylic acid with divinylbenzene in the presence of a modifying solvent [8]. The sorbent is composed of white spherical granules with macroporous structure. The static exchange capacity of SGK-7 for Na^+ is 9.0 mg-equiv g^{-1} dry sorbent; specific volume, 4.7 ml g^{-1}; apparent ionization constant, pK 6.4. The pK was determined by potentiometric titration [9]. The KMDM-6-5 carboxylic cation exchanger (from the Institute of Macromolecular Compounds, Russian Academy of Sciences) is a copolymer of methacrylic acid and *N*,*N*'-hexamethylenedimethacrylamide. It is a cross-linked heteropolymer. Its total exchange capacity for Na^+ is 9.5 mg-equiv g^{-1} dry sorbent; specific volume, 10.5 ml g^{-1}; 1 g of wet sorbent occupies a volume of 1.02 ml; pK 6.7. The moisture content of the swollen polymer is 90%. The grain size of the swollen sorbents (both SGK-7 and KMDM-6-5) ranges from 315 to 500 μm.

1070-4272/03/7606-0985 $25.00 © 2003 MAIK "Nauka/Interperiodica"

Parameters of sorption of lysozyme from egg white on KMDM-6-5 carboxylic cation exchanger at 20°C

Form of sorbent	pH	τ, h	Lysozyme concentration in indicated phase		Specific activity of eluate, lA ml^{-1}
			CEW, lA ml^{-1}	sorbent, lA g^{-1}	
H-	6.4	2	0.6	385	3.6
	6.3	3	0.3	468	1.5
Na-	9.3	2	0.6	470	9.6
	9.0	3	0.3	540	6.5
H–Na-	7.3	3	0.3	468	2.3

The lysozyme concentration was determined spectrophotometrically (λ = 274 nm, molar extinction coefficient of lysozyme 38.9 [10]) and also by the method described in [11].

Before sorption experiments, egg white was fourfold diluted with 0.1 N phosphate buffer, to decrease the solution viscosity. Sorption of lysozyme from egg white was performed by the static method in a vessel with stirrer rotation at 30–50 rpm. The activity of lysozyme expressed in lA units was determined by the turbidimetric method based on the ability of lysozyme to destroy cell walls of *Micrococcus lysodeikticus* [5]. A suspension of cells of *Micrococcus lysodeikticus* was prepared in an 0.066 M phosphate buffer (pH 6.2), to obtain an optical density of 0.6–0.7 at a wavelength of 570 nm. To 3 ml of the substrate was added 0.5 ml of the enzyme solution with lysozyme concentration of up to 1 mg ml^{-1}. After 15-min incubation at 37°C, the optical density at 570 nm was measured again. Preliminarily, we plotted a calibration curve for a standard sample of lysozyme (at lysozyme concentration of 1 mg ml^{-1}, the activity was 19 ± 1 lA ml^{-1}).

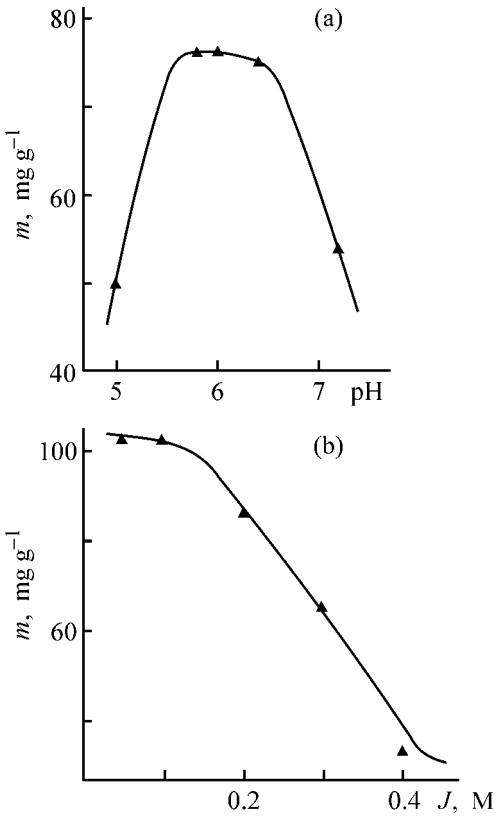

Fig. 1. Sorption *m* of individual lysozyme vs. (a) pH and (b) ionic strength *J*.

Chicken egg white itself is a buffer solution with high buffer capacity. Therefore, not attempting to adjust the pH of CEW, we studied the influence exerted by the sorbent preparation thechnique on the sorption of lysozyme from two CEW samples on various forms of KMDM-6-5.

Data in the table show that the lysozyme concentration in the sorbent phase, specific activity of the eluate, and the lysozyme yield increase on passing from the H form to the H–Na and Na forms. This can be interpreted as follows. It has been demonstrated previously [1] that the maximum sorption of proteins, having the isoelectric point in the acidic region, on carboxylic cation exchangers is observed near the isoelectric point of the protein, whereas that of proteins having the isoelectric point in the alkaline region, near the p*K* of the cation exchanger (p*K* 6.7 for KMDM-6-5). We have demonstrated that the maximum sorption of individual lysozyme occurs at pH 5.8–6.4 (Fig. 1a). Sorption of egg albumen (macrocomponent of egg white) is at a maximum at pH 5.0 (sorption occurs in the pH range from 3.5 to 5.5). Since the content of egg albumen in CEW is several times that of lysozyme (lysozyme content in CEW is 2–4% [10]), in sorption at pH 6 (optimal pH for sorption of lysozyme), albumen is also considerably sorbed, which, evidently, decreases the sorption of lysozyme At pH 7.2–7.5, the sorption of individual lysozyme decreases by no more than 30–35% (Fig. 1a), and that of egg albumen is negliigble under these conditions.

In the alkaline range, i.e., on passing from the H to Na form of the sorbent, the synergistic mechanism changes for the competitive one (although, in this case, there is nothing for lysozyme to compete with), and purely ion-exchange sorption of lysozyme (alkaline protein) occurs, whereas acidic proteins are not sorbed, forming no second sorption layer on the surface of the already sorbed protein. The lack of the second sorption layer allows subsequent elution of individual lysozyme.

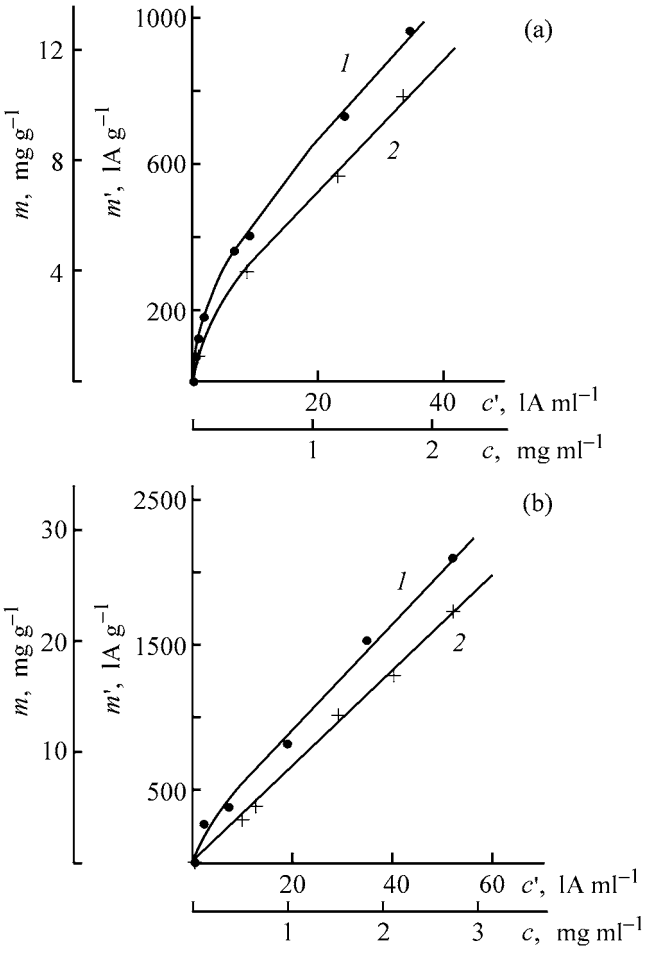

Fig. 2. Sorption isotherms of lysozyme from CEW on (a) KMDM-6-5 and (b) SGK-7. (m, m') Concentration and activity of lysozyme in the sorbent phase; (c, c') concentration and activity of lysozyme in the solution. Temperature (°C): (*1*) 20 and (*2*) 8.

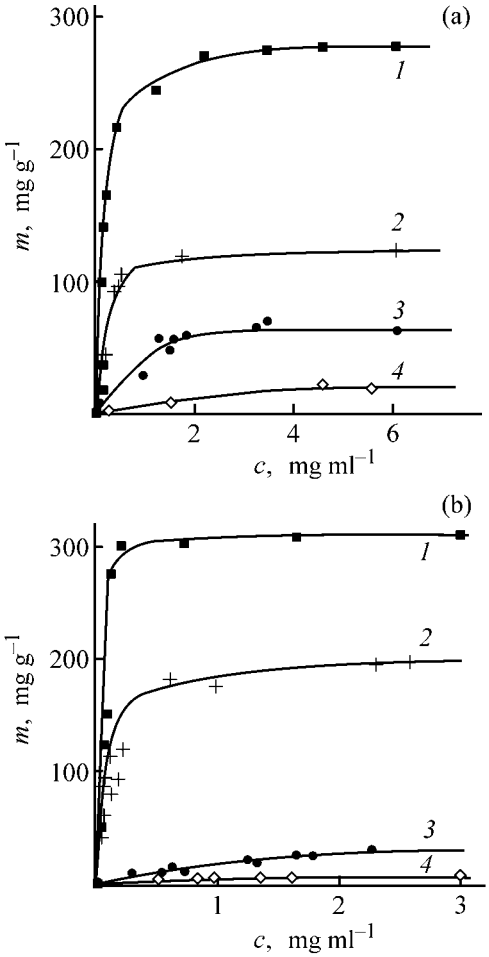

Fig. 3. Sorption isotherms of individual lysozyme on (a) KMDM-6-5 and (b) SGK-7. (m) Lysozyme concentration in the sorbent phase and (c) lysozyme concentration in the solution. Ionic strength (M): (*1*) 0.1, (*2*) 0.15, (*3*) 0.25, and (*4*) 0.5.

A study of the effect of the ionic strength on the sorption of individual lysozyme revealed that, over the NaCl concentration range 0–0.1 M, the sorption capacity of the sorbent remains virtually unchanged, but decreases with J increasing further. Taking these results and data given in the table into account, all further experiments were carried out with KMDM-6-5 and SGK-7 sorbents in the H–Na form. The sorbents were preliminarily treated with 0.05 M phosphate buffer (pH 7.2). This pH value was selected because lysozyme loses its biological activity at higher pH [5, 6].

The sorption isotherms of lysozyme directly from CEW on KMDM-6-5 and SGK-7 are shown in Fig. 2 for the above-indicated conditions at two different temperatures. The results indicated that temperature has only slight effect on the sorption. Therefore, the experiments could be carried out without temperature control. The temperature effect was studied because in most cases, sorption was performed from solutions obtained after defrosting an initially frozen CEW. The sorption isotherms of lysozyme at room temperature were then used to determine the sorbent volume required for sorption of the maximum amount of the protein from CEW.

Figure 3 shows the sorption isotherms of individual lysozyme at pH 7.2 on KMDM-6-5 and SGK-7 cation exchangers at different ionic strengths. As seen, the ionic strength strongly influences the sorption, with the sorption decreasing by a factor of up to several tens. Comparison of Figs. 2 and 3 reveals that the overal effect of all the components contained in CEW on the sorption is comparable with that exerted by the ionic strength in the range from 0.25 to 0.5 M.

Evidently, under these conditions, the efficiency of sorption of lysozyme from CEW is small. Nevertheless, raising the sorbent to CEW ratio allows recovery of up to 85% of lysozyme contained in the initial mixture.

Desorption of lysozyme from both KMDM-6-5 and SGK-7 was performed at ionic strength increased to 1 M. Comparison of the compositions of the eluates obtained after sorption of CEW on the sorbents in the H and H–Na forms shows that, in the case of the H forms, the eluate contained 30–35% lysozyme, 20–25% other proteins, and nonprotein matter the balance. In sorption on the H–Na forms, the eluate contained 50–60 lysozyme, traces of other proteins, and nonprotein matter the balance.

CONCLUSION

In sorption of proteins from complex multicomponent mixtures, it is not always advantageous to carry out the process under conditions ensuring the maximum sorption efficiency with respect to a target component. It was demonstrated for the example of lysozyme that less tight binding of the protein to the sorbent can provide a gain in the sorption selectivity.

REFERENCES

1. Shataeva, L.K., Kuznetsova, N.N., and El'kin, G.E., *Karboksil'nye kationity v biologii* (Carboxylic Cation Exchangers in Biology), Leningrad: Nauka, 1979.
2. Melenevskii, A.T., Chizhova, E.B., and Papukova, K.P., *Zh. Fiz. Khim.*, 1999, vol. 73, no. 9, pp. 1693–1696.
3. Melenevskii, A.T., Chizhova, E.B., and Papukova, K.P., *Zh. Fiz. Khim.*, 2000, vol. 74, no. 8, pp. 1464–1467.
4. Helfferich, F. and Klein, G., *Multicomponent Chromatography*, New York, 1970.
5. Bukharin, O.V. and Vasil'ev, I.V., *Lizotsim i ego rol' v biologii i meditsine* (lysozyme and Its Role in Biology and Medicine), Tomsk: Tomsk. Gos. Univ., 1974.
6. White, A.W., Handler, P., Smith, E.L., Hill, R.L., and Lehman, I.R., *Principles of Biochemistry*, New York: McGraw–Hill, 1978.
7. Margoliash, E. and Schejter, A., *Adv. Protein Chem.*, 1966, vol. 58, pp. 593–595.
8. *Ionoobmennye materially dlya protsessov gidrometallurgii, ochistki stochnykh vod i vodopodgotovki* (Ion-Exchange Materials for Hydrometallurgy, Wastewater Treatment, and Water Preparation), Laskorin, B.N., Ed., Moscow: Vses. Nauchn.-Issled. Inst. Khim. Tekhnol., 1983.
9. Polyanskii, N.G., Gorbunov, G.V., and Polyanskaya, N.A., *Metody issledovaniya ionitov* (Methods for Studying Ion Exchangers), Moscow: Khimiya, 1976.
10. *Farmakopeinaya stat'ya* (Pharmacopoeia Article) FS-42-2585-88, Moscow: Ferrein Joint-Stock Company, 1993.
11. Demin, A.A., Dynkina, I.M., Yurchenko, V.S., and Melenevskii, A.T., *Zh. Anal. Khim.*, 1997, vol. 52, no. 4, pp. 422–424.

Russian Journal of Applied Chemistry, Vol. 76, No. 6, 2003, pp. 989–996. Translated from Zhurnal Prikladnoi Khimii, Vol. 76, No. 6, 2003, pp. 1017–1024.

MACROMOLECULAR CHEMISTRY AND POLYMERIC MATERIALS

Structural Parameters of Cellulose Produced by *Acetobacter Xylinum* and Their Variation in the Course of Drying of Gel Films

Yu. G. Baklagina, A. K. Khripunov, A. A. Tkachenko, S. V. Gladchenko, V. K. Lavrent'ev, A. Ya. Volkov, V. K. Nilova, V. M. Denisov, T. E. Sukhanova, I. S. Zanaveskina, V. V. Klechkovskaya, and L. A. Feigin

Institute of Macromolecular Compounds, Russian Academy of Sciences, St. Petersburg, Russia

St. Petersburg State University, St. Petersburg, Russia

Institute of Cytology, Russian Academy of Sciences, St. Petersburg, Russia

Institute of Crystallography, Russian Academy of Sciences, Moscow, Russia

Received March 14, 2003

Abstract—The cellulose-producing power of the VKM V-800 *Acetobacter xylinum* strain under conditions of static culture was studied. The culture medium was optimized with the aim to increase the cellulose yield and obtain highly crystalline cellulose I with molecular weight of about 5×10^5.

A considerable progress in studies of cellulose biosynthesis, development of the concepts of structural hierarchy of cellulose, and discovery of two crystalline modifications, CI_α and CI_β, in native cellulose samples stimulated in the past decade active studies of evolutionarily different celluloses on the molecular and supramolecular levels. The structure of native celluloses is extensively studied by biochemical, genetic, physicochemical, and also theoretical methods [1–12].

The most success has been gained in studies of cellulose produced by *Valonia ventricosa* alga and of bacterial cellulose produced by *Acetobacter xylinum* (CAX) [3].

Two polymorph families of crystalline cellulose I are distinguished: that rich in the I_α form (algal and bacterial celluloses) and that rich in the I_β form (cellulose of higher plants and animal cellulose) [7–10]. Electron diffraction studies showed that, in the metastable I_α phase, cellulose chains are packed to form a triclinic cell (space group $P1$) with a single tie chain, and under certain conditions, this phase transforms into the thermodynamically stable monoclinic I_β structure (space group $P2_1$) with two macrochains in the unit cell [7, 10]. The I_α/I_β ratio for celluloses of various origins forms in the course of biosynthesis and is not directly related to the degree of crystallinity of a polymeric sample. For example, in the cellulose produced by *Valonia ventricosa* alga (degree of crystallinity 100%) I_α/I_β = 60/40, and in the animal cellulose produced by *Halocynthia*, with the same degree of crystallinity, this ratio is 10/90 [12].

It has been found [9] that the degree of transformation of structures I_a and I_b during heat treatment of cellulose samples is independent of the initial crystallinity. In this context, a fundamental question arises concerning exact ultrastructural localization of each phase. This question was answered to certain extent in recent papers [13, 14]; the procedure used was based on different reactivities of the I_α and I_β phases. The conclusion of [13, 14] that the I_α phase is situated on the surface of microcrystals or microfibrils was also confirmed by the data of high-resolution atomic-force microscopy [15].

Numerous papers published in the past five years show that the ratio and sizes of structural modifications I_α and I_β and their mutual arrangement depend both on the evolutionary origin of cellulose samples and on the biosynthesis conditions, varying from one sample to another [16].

The efforts of many research teams are aimed today at revealing the factors responsible for variation of the I_α/I_β ratio in the course of cellulose biosynthesis.

1070-4272/03/7606-0989 $25.00 © 2003 MAIK "Nauka/Interperiodica"

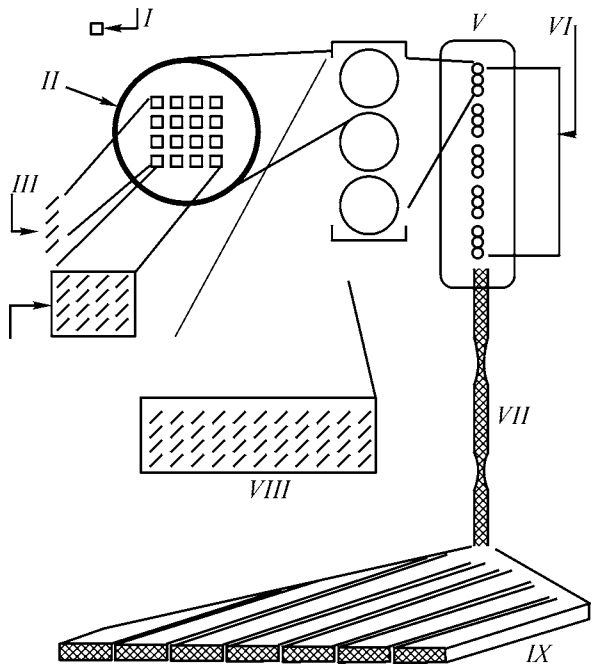

Fig. 1. Scheme of the structure of linear TC of *A. xylinum* bacterium, illustrating the formation of a mini-sheet from four glucan chains and of a mini-crystal from 16 chains by a subunit: (*I*) catalytic site of a glucan chain, (*II*) TC subunit, (*III*) mini-sheet, (*IV*) mini-crystal of one TC subunit, (*V*) TC triplet, (*VI*) linear series of Acetobacter TC triplets, (*VII*) ribbon of microfibrils, (*VIII*) crystalline microfibril of three TC subunits, and (*IX*) 10–100 microfibrils/ribbon. Three TC subunits form a crystalline microfibril, and 10–100 subunits form a ribbon.

Particular attention is given to crystallization of bacterial CAX as a model system for which the I_α/I_β ratio varies with strain and cultivation conditions (e.g., addition of chemicals to culture medium, variation of temperature) [3, 4, 16].

The interest in fine details of biosynthesis and structure of CAX is due to the possibility of preparing chemically pure cellulose by an environmentally acceptable procedure and using it in diverse branches of medicine [17] and engineering [18]. Various structural levels of CAX are discussed: the structure of the terminal complex (TC) itself; its subunit; fine structural elements formed: mini-sheet, mini-crystal, microfibril, and ribbon [3, 11]. Brown [3] suggested a scheme (Fig. 1) illustrating the shape and size of a linear TC and their correlation with the microfibril size. Each TC subunit includes 16 catalytic sites forming four mini-sheets, which, in turn, form a mini-crystal. A microfibril is formed from three TC subunits, and a ribbon, from 10–100 microfibrils. Experiments on CAX cultivation with addition of Tinopoal dye showed that the macrochain packing varies with dye concentration. At low dye concentrations, the microfibril formation is disturbed. At high dye concentrations, only mini-sheets of glucan chains are obtained in the form of tubular cellulose; in the course of washing or photoisomerization, this structure can transform into a microfibril [11].

Attempts are made to affect, via the composition of the culture medium, the capability of *A. xylinum* strains to produce ribbons and their aggregates with more perfect structural characteristics. It has been shown [19] that addition to the culture medium of antimetabolites, such as nalidixic acid and chloramphenicol, makes bacterial cells longer and, as a consequence, results in production of wider ribbon aggregates.

The effect of polymeric additives on the formation of CAX microfibrils of various sizes and the mechanism of crystallization of cellulose I_α and I_β in them are discussed in [20–22]. It was found that addition of carboxymethyl cellulose or xyloglucan to the culture medium reduces formation of the I_α phase, increasing the I_β fraction; according to an electron-microscopic examination, this is associated with a decrease in the width of CAX microfibrils. Similar effects have also been observed by other authors [23] upon introduction of oligo- and polysaccharides into the culture medium. Samples of CAX and its composites have been prepared under various synthesis conditions with addition of lignin–carbohydrate complexes or specific polysaccharides to the culture medium; an X-ray diffraction study of these samples has shown that some additives increase the content of the I_β phase, and, in some cases, the crystal structure does not change (the I_α phase remains) or low-crystalline composites are obtained [23].

Our goal was to reveal a correlation between the structural organization of CAX macrochains in the course of the syntheses, suggested in [3] (Fig. 1), and structural parameters of cellulose macrosamples in the course of drying of CAX gel films. Here, we report the results of optimization of the CAX synthesis by the VKM V-880 *A. xylinum* strain and the structural features of CAX samples, which were evaluated by X-ray diffraction analysis and dielectric spectroscopy.

EXPERIMENTAL

The cellulose synthesis by the VKM V-880 *A. xylinum* strain maintained at the Microbiology Chair, St. Petersburg State University, was performed in a culture medium containing aqueous solutions of yeast extract (YE), glucose, peptone, ethanol, and

wort in optimized concentrations, at pH 5.9–6.0. The seed was a 48-h *A. xylinum* culture grown in a medium containing YE and wort (6° Baling scale) in 1 : 1 ratio, with 2 wt % glucose and 1 vol % ethanol. Cultivation was performed at 29–30°C for 6–7 days, after which CAX was separated and intermittently washed with boiling 0.5–1% aqueous NaOH to remove *A. xylinum* cells. Then CAX was washed to remove NaOH with distilled water, 0.5% acetic acid solution, and again distilled water to neutral reaction. The resulting CAX was stored either as a gel film (in distilled water at 5°C) or (after autoclave sterilization) at room temperature, or it was dried in a vacuum at 40°C and stored in the dry state. The procedure was optimized by additive-lattice experimental design [24]; the five varied factors were concentrations of the components of the medium, and the cellulose yield was determined at different factor values.

X-ray diffraction patterns (DRON-2 diffractometer and RKV-86 X-ray camera, Ni-filtered Cu_{K_α} radiation) were measured for the initial CAX gel films cleaned to remove the culture medium, and also for the films from which a certain amount of water was removed (before and after drying in air at room temperature to the air-dry state). The dielectric properties of CAX were measured with a TR-9701 device in the frequency range 1–100 kHz at temperatures from –140 to 120°C. A two-electrode cell with chrome-plated brass electrodes and Teflon insulation was used. The measurements were performed in dry air with 30–60-μm-thick film samples dried in a vacuum at 60°C.

It is known that *A. xylinum* well develops in culture media containing glucose and some other monosaccharides as carbon sources, and also yeast extract as growth factor and source of nitrogen [25]. To determine the cellulose-producing power of the VKM V-880 *A. xylinum* strain, the culture medium based on the initial medium containing glucose, YE, and peptone was optimized. The effect of organic additives, wort and ethanol, on the biosynthesis of cellulose was elucidated [26]. Determination of the cellulose yield from culture media of 25 different compositions showed that, at the optimal combination of the components (7 wt % glucose, 0.3 wt % YE, 30 vol % wort, 0.3 wt % peptone, 3 vol % ethanol), up to 50 g of air-dry cellulose is obtained from 1 m^2 of the reactor surface.

It has been found previously that CAX can be synthesized on culture media with various cheap sources of carbon: industrial wood hydrolyzates, peat hydrolyzates, molasses, and other media containing monosaccharides [27, 28]. To determine the structural characteristics of CAX synthesized by the VKM V-880 strain, we used gel films prepared in a medium containing 2% glucose, 0.2% peptone, 0.3% YE, and 2 vol % ethanol. The IR absorption bands and X-ray reflections of these samples were found in the ranges characteristic of cellulose I. Determination of the molecular weight of CAX by sedimentation and diffusion in cadoxen gave an M_{SD} value of 5×10^5. The polydispersity index M_z/M_w determined by correlation laser spectroscopy in cadoxen [26] was approximately 1.1. All these data are nicely consistent with the CAX characteristics available from the literature [29].

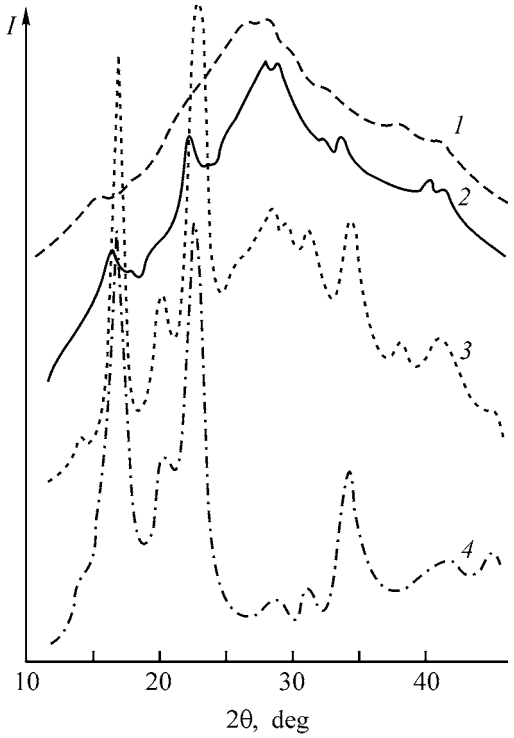

Fig. 2. Diffraction patterns of CAX in various steps of gel film drying. (*I*) Intensity and (2θ) Bragg angle; the same for Figs. 4–6. (*1*) Initial gel films with the dry polymer : water ratio of 1 : 100; (*2*) CAX sample squeezed to remove 50% of water; (*3*) sample dried at 20°C for 3 h; (*4*) sample dried in a vacuum at 40°C.

Since the X-ray diffraction patterns obtained from CAX gel films dried under various conditions differed from those reported in [23, 30], it seemed appropriate to study in more detail the kinetics of water removal from the CAX gel film in the course of drying.

The diffraction pattern of the initial gel film with the dry polymer : water ratio of 1 : 100 (Fig. 2, curve *1*) is characterized by a broad maximum at 2θ =

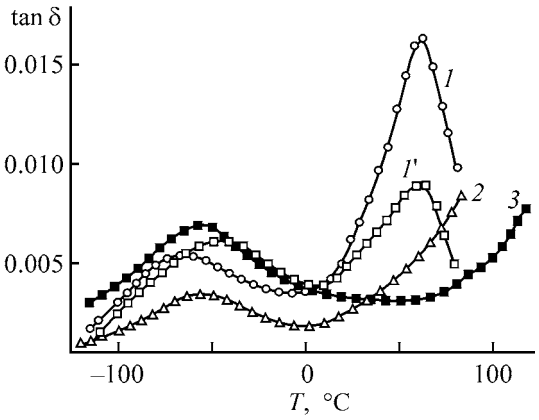

Fig. 3. Temperature dependence of the dielectric loss tangent tan δ for (*1*, *1*') CAX, (*2*) CAX heated to 100°C in a vacuum in the course of measurement, and (*3*) dried cotton linter. Measurement frequency, kHz: (*1–3*) 1 and (*1*') 10.

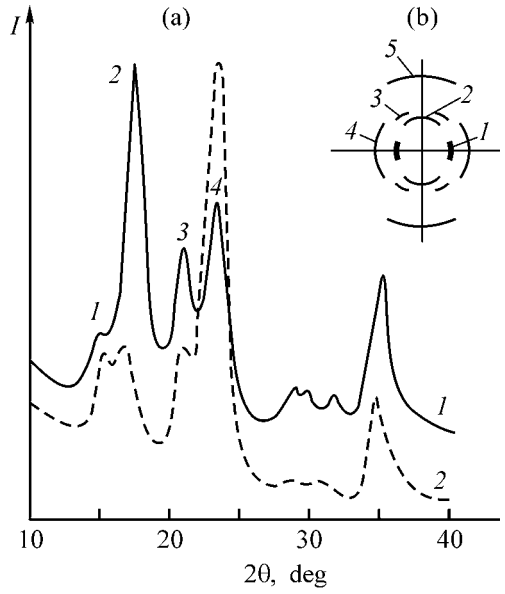

Fig. 4. (a) Diffraction patterns and (b) scheme of X-ray pattern obtained at (a) perpendicular and (b) parallel incidence of the X-ray beam relative to the plane of the dry sample. Sample: (a) (*1*) CAX and (*2*) LC; (b) CAX.

20°–40°. When 40–50% of the initial water is removed from the gel film, clear reflections appear against the background of this halo at 2θ 15°–16°, 23°, 27°, 32°–34°, and 40°–42°, with the broad maximum in the range 25°–30° being preserved (Fig. 2, curve *2*). After drying this sample in air at 20°C for 2–3 h, the reflection positions and intensities changed (Fig. 2, curve *3*). A noticeable diffuse background remained in the range 2θ = 20°–40°, and the reflections corresponding to *d* 0.532, 0.435, 0.390, and 0.259 nm became the strongest. In the X-ray patterns of the CAX films dried in a vacuum at 40°C (Fig. 2, curve *4*), the positions of these four reflections remained unchanged, whereas the diffuse halo virtually disappeared.

However, the samples dried under these conditions still contained water molecules, as suggested by the CAX relaxation properties determined by dielectric spectroscopy [31]. Figure 3 shows the temperature dependence of the dielectric loss tangent, $\tan\delta = f(T)$, for samples of CAX and, for comparison, cotton linter cellulose (LC). For samples of both CAX and LC, $\tan\delta_m$ passes through a maximum at negative temperatures (about –60°C, 1 kHz). According to the concept of the relaxation properties of cellulose [31–33], this range of dielectric loss in CAX must be associated with relaxation of the dipole polarization and mobility of primary hydroxy groups of cellulose molecules. Above 0°C, the dielectric loss increases. At 60–70°C, the loss decreases irrespective of the measurement frequency (curves *1*, *1*'); heating in a vacuum enhances this trend (curves *1*, *2*). This fact suggests removal of compounds increasing the electrical conductivity from the sample bulk (in the given case, this is, most probably, water [33]).

Simultaneoulsy, $\tan\delta_m$ decreases, and the maximum shifts from –60°C to higher temperatures. This suggests disappearance of the plasticization effect associated with the presence of water molecules forming hydrogen bonds with primary hydroxyls. The break-down of the hydroxyl–water complexes does not cause the peak of $\tan\delta_m$ to grow in intensity, which may be due to involvement of the released OH groups in a new system of intermolecular hydrogen bonds. Comparison of the dependences $\tan\delta = f(T)$ for CAX and LC samples (Fig. 3, curves *2*, *3*) shows that the maximal value of $\tan\delta_m$ at –60°C for CAX is two–three times lower than for LC. Since the height of the peak at –60°C is determined by the amount of primary OH groups that can participate in thermal motion and this motion can occur in defective areas only, it can be presumed that bacterial cellulose, compared to linter cellulose, is characterized by a more regular network of hydrogen bonds and a more regular structure [31–33]. Indeed, the X-ray diffraction patterns of CAX and LC samples showed that CAX films were more ordered (Fig. 4a, curve *1*); all the reflections of CAX were indexed in the monoclinic system of modification I, which is a two-phase system of CI_α and CI_β.

Particular attention should be given to the range 2θ = 13°–18° in the diffraction pattern of CAX. It is seen that the $\bar{1}10$ reflection (2θ = 15°) of the CAX

film (Fig. 4a, curve *1*) is considerably weaker as compared to LC (Fig. 4a, curve *2*). At the same time, the intensity of the reflection at $2\theta = 16°50'$ [sum of (110) and (002) reflections] is many times higher as compared to LC and varies from one sample to another.

To reveal a planar texture in CAX films, we measured the X-ray patterns with the plane of the dried sample arranged in parallel with the incident X-ray beam. Figure 4b shows the scheme of the five major reflections of CAX, denoted by the corresponding numerals in Fig. 4a.

We revealed an appreciable redistribution of the reflection positions and intensities. A reflection with $d = 0.607$ nm ($2\theta = 15°$), corresponding to the reflection from the $\bar{1}10$ planes, is clearly seen in the equatorial region. A reflection in the meridional region at $d = 0.523$ nm [reflection from the (002) planes] is clearly seen against the background of a weak ring reflection at $2\theta = 17°$. The (110) reflection in the equator is absent; only a weak "ring" reflection from (110) planes with $d = 0.532–0.535$ nm is observed.

As for the other reflections, the weak third reflection at $2\theta = 20°40'$ is detected in the vicinity of the meridional region and is undoubtedly a sum of reflections from the (102) and (012) planes of the monoclinic lattice with $d = 0.437$ and $d = 0.432$ nm. In the equatorial region, there is a fairly strong fourth reflection with $d = 0.389–0.392$ nm, corresponding to the reflections from the (200) planes in which hydrogen-bonded cellulose chain molecules are arranged to form parallel layers. Finally, the fifth reflection with $d = 0.259–0.260$ nm, which is a superposition of moderately strong reflections from the system of planes (004), (220), (031), and (023), is clearly seen in the meridional region of the X-ray pattern of a CAX film taken from the end side, i.e., it characterizes the periodicity along the polymeric chain.

Thus, aggregates of CAX microfibrils are arranged in the plane of the dried film, forming an axial texture whose axis is perpendicular to the film plane. Since the (110) reflection ($2\theta = 15°$) is only manifested in the majority of samples when the X-ray beam is parallel to the sample surface, it can be concluded that, in the crystallites constituting CAX ribbons, the ($\bar{1}10$) planes of the monoclinic cell are arranged parallel to the macrosample, i.e., an axial-planar texture arises [34].

Comparison of the diffraction patterns of CAX films (VKM V-880 strain) prepared in this study and CAX samples produced by the ATCC 53524 strain

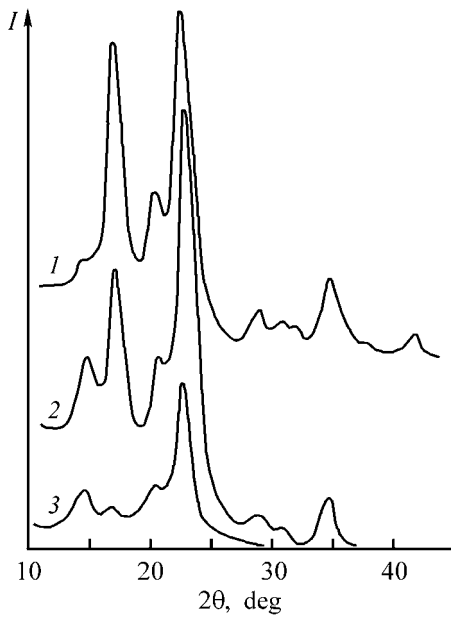

Fig. 5. Diffraction patterns of CAX samples dried (*1*) at 40°C and (*2*) lyophilically after freezing the gel film at –30°C; (*3*) CAX sample (ATCC 53524 strain) dried in the course of freezing [23].

[23] reveals differences in the intensities of some reflections (Fig. 5). This may be due to different procedures of sample preparation. The films were dried on glass supports at room temperature or at 40°C in a vacuum; they had an axial-planar texture. The CAX sample dried in the course of freezing [23] had an isotropic polycrystalline structure (Fig. 5, curve *1*). To eliminate the texturing effect, we changed the drying procedure: A gel film was first frozen at –30°C and then dried lyophilically. However, after such a treatment, the axial-planar texture of the CAX film was preserved, even though to a considerably lesser extent (Fig. 5, curve *2*).

The use of isotropic polycrystalline samples for X-ray diffraction analysis allowed resolution of reflections at 2θ 15° and 17° and their assignment to the I_α and I_β modifications [23]. For the textured samples under consideration, this is impossible. However, the presence of the (002) reflection on the meridian of the diffraction pattern (Fig. 4b) obtained at parallel arrangement of the CAX sample plane relative to the incident X-ray beam indicates that the gel film contains an appreciable amount of the monoclinic I_β phase with the parameters $a = 0.801$, $b = 0.817$, $c = 1.036$ nm (macromolecular axis), and $\beta = 97°$, suggested in [10].

The diffraction patterns of CAX films prepared using, in the biosynthesis step, such carbon sources as industrial hydrolyzates of wood, peat, and liquors

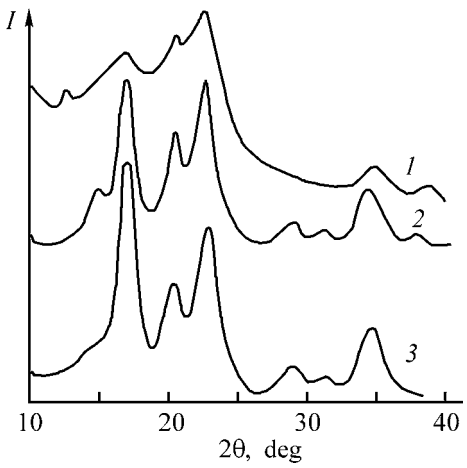

Fig. 6. Diffraction patterns of CAX samples prepared using different carbon sources. Medium: (*1*) containing wood hydrolyzate, (*2*) standard [26], and (*3*) containing glycerol.

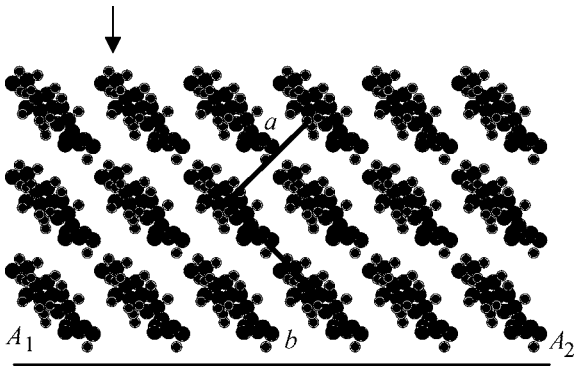

Fig. 7. Model of cellulose chain packing (projection onto the *ab* plane) in the monoclinic cell. (A_1–A_2) Orientation of ribbon microfibrils in the macrofilm plane. The arrow shows the direction of mini-sheets in the course of biosynthesis.

from pulp-and-paper and fruit-and-berry productions [27, 28] show that, depending on conditions of cultivating *A. xylinum*, the CAX produced does not always have the cellulose I structure (Fig. 6, curve *2*); in some cases, it is a mixture of the cellulose I and cellulose II modifications (Fig. 6, curve *1*). The biosynthesis conditions also govern the extent of microfibril orientation in the plane of the CAX film. For example, using glycerol as the carbon source, we observed in CAX samples a clear axial-planar texture (Fig. 6, curve *3*).

Thus, comparison of the diffraction patterns of the CAX gel films dried by different procedures or prepared under different cultivation conditions with the data given in [23, 30] shows that, under conditions of our experiments, a texturing effect arises. Furthermore, the previously published electron diffraction data [35] in combination with the X-ray diffraction patterns for CAX of the VKM V-880 strain suggest that, in the textured samples, the content of the I_β modification exceeds that of the I_α modification.

The possibility of obtaining different I_α/I_β ratios in CAX ribbon formations depending on the conditions of cultivating *A. xylinum* was discussed in [15, 23]. These papers consider the shear stresses in thin planar ribbon ensembles of CAX in the course of simultaneous crystallization and twisting. The ribbons are twisted owing to rotation of bacteria during their forward motion in a culture medium. Aggregation of microfibrils yields wide (40–60 nm) ribbons; their twisting gives rise to end stresses, inducing formation of the I_α structure. On the contrary, the I_β structure is formed in the central parts of the ribbons. If the ribbons are less twisted or microfibrils have smaller transverse size, the number of the stressed regions is considerably smaller, which favors formation of the I_β structure in CAX. Bowling *et al.* [36] observed untwisting of CAX ribbons during degradation of cellulose chains effected by fungus cellulases. This rotary motion was explained by lifting of bending stress and formation of relaxing conformations.

Presumably, in our case the CAX ribbons, orienting on the surface of the culture medium, form a network of hydrogen bonds via primary hydroxy groups, which can prevent twisting of ribbon ensembles and result in a higher content of the I_β structure, compared to I_α, in textured CAX samples.

Proceeding with the concept suggested in [4], we propose a model of cellulose chain packing in the projection onto the *ab* plane for the monoclinic cell with two macromolecules (Fig. 7). The A_1–A_2 line denotes the directing defining the orientation of microfibrillar ribbons on the surface of the culture medium. Such an orientation of glucoside fragments on the microfibril surface explains the presence of a large amount of water molecules hydrogen-bonded with primary hydroxyls. As seen from Fig. 7, the C^6–OH groups are arranged at the phase boundary along the A_1–A_2 line; according to the theoretical calculations [6], these groups have the *tg* conformation in the triclinic I_α structure and the *gt* conformation in the monoclinic structure, participating in the latter case in the hydrogen bonding between the mini-layers. The direction of mini-layers (this concept was suggested in [3]; Fig. 1) is marked in the scheme with an arrow. It is seen (Fig. 7) that the mini-layers are perpendicular to the culture medium surface.

It is known that CAX gel films can retain from 100 to 200 g of water per gram of dry polymer, preserving

a high intrinsic tensile strength (up to 2 kgf mm^{-2}) [26]. The X-ray patterns suggest that the microfibrillar ribbons oriented on the film surface act not only as a reinforcing network but also as hydrophilic layers capable of interacting with a large amount of water molecules. According to electron-microscopic data [35], the diameter of the aggregates is about 50 nm, and their length is extremely large. Microfibrillar aggregates occupy an insignificant part of the gel film volume, which allows introduction depending on the degree of film drying, of diverse systems into gel films. For example, it has been shown that a CAX gel film is an excellent carrier of such antiseptics as Catapol and Poviargol containing silver clusters [37, 38].

CONCLUSIONS

(1) The composition of the culture medium was optimized with the aim to attain the maximal yield of cellulose produced by *Acetobacter xylinum*. The VKM V-880 strain of *A. xylinum* is capable of synthesizing high-molecular-weight cellulose in a static culture using a wide range of carbon sources.

(2) The kinetics of structural transformations that occur in this cellulose when water is removed from gel films in the course of drying was studied by X-ray diffraction and dielectric spectroscopy. It was shown that, in the dried films of highly crystalline cellulose, an axial-planar texture is formed in which crystallographic planes ($\bar{1}10$) of the monoclinic cell (d = 0.61 nm) are arranged parallel to the sample plane.

(3) To describe the packing of ribbon aggregates in the plane of a cellulose film, a model was suggested according to which the mini-sheets constituting the aggregates are arranged in the perpendicular direction relative to the phase boundary between the culture medium and air.

ACKNOWLEDGMENTS

The study was supported financially by the Russian Foundation for Basic Research (project no. 01-03-33158) and NWO (grant no. 047.009.015).

REFERENCES

1. Delmer, D.P., *Ann. Rev. Plant Physiol. Plant Mol. Biol.*, 1999, vol. 50, pp. 245–276.
2. Brown, R.M., Jr. and Saxena, J.M., *Plant Physiol. Biochem.*, 2000, vol. 38, nos. 1/2, pp. 57–67.
3. Brown, R.M., Jr., *J.M.S.–Pure Appl. Chem.*, 1996, vol. 33A, no. 10, pp. 1345–1373.
4. Ranby, B., *Cellulose Chem. Technol.*, 1997, vol. 31, pp. 3–16.
5. O'Sullivan, A.C., *Cellulose*, 1997, vol. 4, pp. 173–207.
6. Vietor, R.J., Mazeau, K., Lakin, M., and Perez, S., *Biopolymer*, 2000, vol. 54, pp. 342–354.
7. Wada, M., Okano, T., and Sugiyama, J., *Cellulose*, 1997, vol. 4, pp. 221–232.
8. Wada, M., Okano, T., and Sugiyama, J., *J. Wood Sci.*, 2001, vol. 47, pp. 124–128.
9. Debzi, E.M., Chanzy, H., Sugiyama, J., *et al.*, *Macromolecules*, 1991, vol. 24, no. 25, pp. 6816–6822.
10. Sugiyama, J., Young, R., and Chanzy, H., *Macromolecules*, 1991, vol. 24, no. 14, pp. 4168–4175.
11. Cousins, S.K. and Brown, R.M., Jr., *Polymer*, 1997, vol. 38, no. 4, pp. 897–912.
12. Yamamoto, H. and Horii, F., *Macromolecules*, 1993, vol. 26, no. 6, pp. 1313–1317.
13. Sassi, J.-F., Tekely, P., and Chanzy, H., *Cellulose*, 2000, vol. 7, pp. 119–132.
14. Wada, M. and Okano, T., *Cellulose*, 2001, vol. 8, pp. 183–188.
15. Baker, A.A., Helbert, W., Sugiyama, J., and Miles, M.J., *Biophys. J.*, 2000, vol. 79, pp. 1139–1145.
16. Hirai, A. and Horii, F., *JCR Annual Rep.*, 1999, vol. 6, pp. 28–29.
17. US Patent 4655758.
18. EP Patent O 197748 B1.
19. Yamanaka, S., Ishihara, M., and Sugiyama, J., *Cellulose*, 2000, vol. 7, pp. 213–225.
20. Yamamoto, H., and Horii, F., *Cellulose*, 1994, vol. 1, pp. 57–66.
21. Yamamoto, H., Horii, F., and Hirai, A., *Cellulose*, 1996, vol. 3, pp. 229–242.
22. Hirai, A., Tsuji, M., Yamamoto, H., and Horii, F., *Cellulose*, 1998, vol. 5, pp. 201–213.
23. Iwata, T., Indrarti, L., and Azuma, J.-I., *Cellulose*, 1998, vol. 5, pp. 215–228.
24. Biryukov, V.V., Kantere, V.M., in *Optimizatsiya periodicheskikh protsessov mikrobiologicheskogo sinteza* (Optimization of Batch Processes of Microbiological Synthesis), Moscow: Nauka, 1985, ch. 3, pp. 18–54.
25. Whister, R.L., in *Methods in Carbohydrate Chemistry*, vol. 3: *Cellulose*, New York: Academic, 1963, pp. 4–9.
26. Khripunov, A.K., Tkachenko, A.A., Moskvicheva, Yu.B., *et al.*, in *Biotekhnologiya i genetika: Mezhvuzovzkii sbornik nauchnykh trudov* (Biotechnology and Genetics: Intercollegiate Coll. of Scientific Works), Nizhni Novgorod: Nizhegorod. Gos. Univ., 1991, pp. 54–64.
27. RF Patent 2141530.
28. RF Patent 2189394.

29. Nevell, T.P. and Zeronian, S.H., in *Cellulose Chemistry and Its Application*, New York: Ellis Horwood, 1985, pp. 67–73.
30. Watanabe, K., Tabuchi, M., Morinaga, Y., and Yoshinaga, F., *Cellulose*, 1998, vol. 5, pp. 187–200.
31. Gladchenko, S.V., Khripunov, A.K., Tkachenko, A.A., and Borisova, T.I., Abstracts of Papers, *II Mezhdunarodnyi simpozium "Stroenie, svoistva i kachestvo drevesiny"* (II Int. Symp. "Structure, Properties, and Quality of Wood"), Moscow–Mytishchi, October 21–24, 1996, p. 48.
32. Borisova, T.I., Petropavlovskii, G.A., and Kotel'nikova, N.E., *Vysokomol. Soedin., Ser. A*, 1979, vol. 21, no. 9, pp. 2031–2037.
33. Gladchenko, S.V., Borisova, T.I., Larina, E.I., and Petropavlovskii, G.A., *Vysokomol. Soedin., Ser. B*, 1992, vol. 34, no. 3, pp. 21–23.
34. Tsvankin, D.Ya., *Vysokomol. Soedin.*, 1963, vol. 5, no. 1, pp. 123–128.
35. Zanaveskina, I.S., Stiopina, N.D., Khripunov, A.K., *et al.*, Abstracts of Papers, *8th European Conf. on Organized Films*, Otranto (Italy), September 3–7, 2001, paper 11.12.
36. Bowling, A.J., Amano, Y., Lindstron, R., and Brown, R.M., Jr., *Cellulose*, 2001, vol. 8, no. 1, pp. 91–97.
37. Kopeikin, V.V. and Panarin, E.F., *Dokl. Ross. Akad. Nauk*, 2001, vol. 380, no. 4, pp. 497–500.
38. Khripunov, A.K., Tkachenko, A.A., Baklagina, Yu.G., *et al.*, *II Mezhdunaropdnaya konferentsiya "Sovremennye podkhody k razrabotke effektivnykh perevyazochnykh sredstv, shovnykh materialov i polimernykh implantantov": Materialy konferentsii* (Proc. II Int. Conf. "Modern Approaches to Development of Effective Dressings, Suture Materials, and Polymeric Implantants"), Moscow: November 21–22, 1995, pp. 71–73.

Russian Journal of Applied Chemistry, Vol. 76, No. 6, 2003, pp. 997–1001. Translated from Zhurnal Prikladnoi Khimii, Vol. 76, No. 6, 2003, pp. 1025–1029.

MACROMOLECULAR CHEMISTRY AND POLYMERIC MATERIALS

Rate of Acid Hydrolysis of Starch as Influenced by Intensive Mechanical Effects

N. V. Losev, L. I. Makarova, and I. M. Lipatova

Institute of Chemistry of Solutions, Russian Academy of Sciences, Ivanovo, Russia

Received July 16, 2002; in final form, March 2003

Abstract—The influence of ultrasonic cavitation on the rate of acid hydrolysis of gelatinized starch under the action of ultrasonic field or strong mechanical stresses in a rotary-pulsating activator is discussed. The dependences of the hydrolysis rate on the starch concentration, acid content, temperature, and intensity of mechanical action on the system are analyzed.

Hydrolytic degradation with rupture of the glycoside bond is one of the most practically significant reactions involving starch. The intensification of starch hydrolysis is an urgent problem; it is of theoretical and practical importance. The possibility of enhancing the reactivity of gelatinized starch by intensive mechanical treatment in a rotary-pulsating activator (RPA) [1] has been poorly studied as yet. In such devices, a material is exposed to combined action of ultrasonic vibrations and strong shear stresses. Some features of the effect of such treatment in RPA on the state of starch hydrogels have been reported previously [2, 3]. The possibility of accelerating reactions of starch hydrogel with low-molecular-weight reagents by mechanical treatment was studied in [4] for the example of permanganate oxidation. Previously, it has been considered that shear strains are decisive factor in the enhancement of the starch reactivity. However, our new experimental data on the effect of both shear-free ultrasonic field [5] and RPA treatment on the state of starch hydrogels suggest that the role of the shear and ultrasonic action in the course of mechanical intensification of chemical processes in the gelatinized starch should be revised.

In this study, we examined the possibility of intensifying acid hydrolysis of starch under the influence of ultrasonic field and combined ultrasonic and shear treatment in a rotary-pulsating activator.

EXPERIMENTAL

In this study, we used corn starch [GOST (State Standard) 7697–82]. Starch hydrogels to be mechanically treated were prepared by cooking a starch suspension on a water bath at 90°C for 15 min.

The acid hydrolysis of gelatinized starch was performed by three methods: in a temperature-controlled vessel with ordinary stirring, in a temperature-controlled beaker with ultrasonic treatment (UZDN-2T ultrasonic pulverizer), and in a temperature-controlled RPA chamber.

Starch hydrogels were treated in a UZDN-2T ultrasonic pulverizer at 22 kHz; the volume density of the acoustic energy, determined by calorimetry, was 1.34 W cm^{-3}.

Starch hydrogels were also treated in a laboratory RPA. The working chamber of the activator is formed by a rotor and a stator, which are equipped with special fittings. The gap between the rotating and fixed elements of the working chamber in a given operation mode determines the tangential stresses in the liquid-phase material treated. The rotor rotation rate was varied in the 1000–5000 rpm range, and the gradients of the shear rate, within $(0.5–17.4) \times 10^4$ s^{-1}.

To confirm the occurrence of ultrasonic cavitation in the RPA working chamber, we used the standard test reaction $Fe^2 \rightarrow Fe^{3+}$ in an acidic medium. This reaction does not occur in the absence of ultrasonic cavitation [6]. The same reaction was used to determine the amount of ultrasonic energy absorbed by the material (using chemical dosimetry).

The starch concentration in the gels was 2–8%, and the process temperature, 20–70°C; the sulfuric acid concentration was varied within 0.03–0.15 M, and the time of mechanical treatment was 10–90 s.

1070-4272/03/7606-0997 $25.00 © 2003 MAIK "Nauka/Interperiodica"

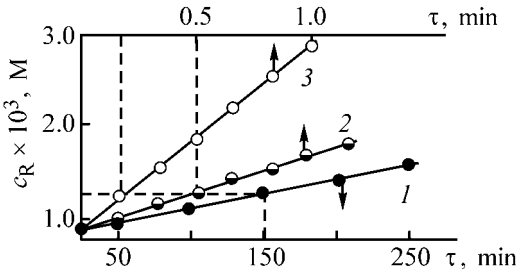

Fig. 1. Concentration c_R of the reducing groups accumulated in the starch hydrogel in the course of hydrolysis performed in (*1*) thermostat, (*2*) UZDN-2T, and (*3*) RPA vs. time τ; starch concentration 2 wt %, acid concentration 0.03 M.

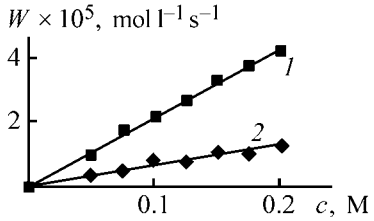

Fig. 2. Average rate W of accumulation of the reducing groups in the starch hydrogel vs. the sulfuric acid concentration c in the course of hydrolysis performed in (*1*) RPA and (*2*) UZDN-2T.

The rate of starch hydrolysis was determined from the data on accumulation of reducing groups [7]. In our case, the standard procedure to monitor the hydrolysis rate by a decrease in the solution viscosity, used under the common reaction conditions [8], is inapplicable, because hydrolysis under strong mechanical stresses is accompanied by mechanical dispersion of the starch (crushing of grains and their parts) and, thus, by a significant decrease in the viscosity, even in the absence of chemical reagents.

To analyze the origin of the mechanical (including ultrasonic) effect on the starch hydrolysis, we studied the dependences of the hydrolysis rate on temperature and concentrations of starch and acid and compared the results obtained for all the three treatment procedures.

It was found that, at the same temperatures and acid concentrations, application of a mechanical stress strongly accelerates the accumulation of the reducing groups. As seen from Fig. 1, one and the same concentration of the reducing groups, 1.25×10^{-3} M, is reached in 150 min in the case of the ordinary stirring, and in 30 and 13 s, respectively, in an ultrasonic field and after the RPA treatment. Before the experiments, we carried out blank tests in which the starch hydrogels were exposed to mechanical treatment without addition of acid. In this case, no increase in the concentration of the reducing groups was found. This fact indicates that the cavitation itself does not produce any significant amount of the reducing groups under the experimental conditions studied.

It is known that, under the conventional conditions (no mechanical stresses), the rate of the acid hydrolysis of starch is described by a first-order equation. The reaction rate is directly proportional to the acid concentration and is independent of the starch concentration [9]. Upon application of an ultrasonic field or upon RPA treatment, the accumulation rate of the reducing groups is a linear function of the acid concentration (Fig. 2).

To determine the kinetic order of the reactions proceeding in starch hydrogels under mechanical stress, we should take into account the features of the concurrent mechanically induced structural transformations. The kinetic dependences $\ln(c_0/c) = f(\tau)$, obtained for these reactions, are linear only up to a certain degree of hydrolysis, i.e., at some instant of time the rate constants calculated from the first-order kinetic equations begin to decrease. A decrease in the reaction rate constants with increasing degree of starch hydrolysis has been found previously for common reaction conditions [8]. This is probably due to the accumulation in solution of linear dextrins forming compact structures with higher energy of intermolecular interaction, which increases their hydrolytic stability. For comparative evaluation of the effect of various mechanical stresses on the reaction rate, we used the rate constants corresponding to the linear portions of the $\ln(c_0/c) = f(\tau)$ curves. The rate constants of the reactions performed in RPA and in an ultrasonic field are (on the average) higher by three orders of magnitude than those recorded for reactions performed under the ordinary reaction conditions at the same temperature and acid concentration.

Under the ordinary conditions, the hydrolysis rate of gelatinized starch is independent of the starch concentration in the hydrogel. The initial viscosity of these hydrogels varied within a wide range (0.01–1000 Pa s). The independence of the starch hydrolysis rate from the solution viscosity suggests that the process is kinetically controlled, and thus a strong decrease in the solution viscosity during the mechanical treatment cannot lead to pronounced changes in the hydrolysis rate under mechanical stress.

To evaluate how the mechanical degradation of the initial structure of the starch hydrogel affects the reaction rate, we performed a series of tests with pretreatment of hydrogels in RPA and UZDN-2T at 20°C. Immediately after such a treatment, the samples were

placed in a temperature-controlled flask, the required amount of acid (0.15 M) was added, and the hydrolysis as performed under the ordinary conditions at 60°C.

As seen from the table, after mechanical activation of the starch hydrogels the rate of its hydrolysis increases by nearly an order of magnitude, and this effect significantly decreases with increasing starch concentration. The dependence of the degree of reaction acceleration on the intensity and time of mechanical pretreatment is ambiguous. For example, after ultrasonic treatment of the starch hydrogel for 30 s, the increase in the reaction rate is greater than that after treatment for 60 s. This is probably related to the fact that [3], under strong mechanical stress, the breakdown of the initial gel structure is accompanied by formation of new compact structures through orientation and aggregation processes.

The above processes probably account for the dependence of the hydrolysis rate of starch on its concentration in the course of the reaction in an ultrasonic field or under ultrasonic treatment combined with mechanical shear stress in RPA (Fig. 3). Under ultrasonic treatment, the hydrolysis rate slightly decreases with increasing starch concentration, which is due to a decrease in the efficiency of the ultrasonic degradation of starch with its increasing concentration. The increase in the rate of the reaction performed in the RPA chamber with starch concentration decreasing to 2–3 wt % can be accounted for by the fact that the static pressure in the working chamber sharply grows with decreasing hydrogel viscosity, which, in turn, increases the erosion activity factor [10]. In other words, the degradation of the starch hydrogel structures is more profound at small concentrations. The rise in the rate of hydrolysis performed in RPA with growing starch concentration is due to an increase in the contribution of the shear stresses to the breakdown of the initial gel structure, and also to general activation of the system with simultaneous decrease in the contributions of the orientation and aggregation processes.

Without mechanical treatment, no hydrolysis of gelatinized starch is observed at acid concentration of 0.15 M and 20°C; in any case, no increase in the concentration of reducing groups was observed, at least, in the first 2–3 h. At 60°C and the same acid concentration, the hydrolysis rate is appreciable. The activation energy of the reaction without mechanical activation was calculated to be 206 kJ mol^{-1}.

The effect of temperature on the rate of acid hydrolysis of starch under high-intensity mechanical treatment (RPA and UZDN-2T) is ambiguous. For example, at 20–45°C the reaction rate is almost independent of temperature, which is typical of mechanochemical and, in particular, sonochemical reactions. At 60°C, the process appreciably accelerates. However, the activation energy is still significantly smaller (34 kJ mol^{-1}) than that of the reaction under the ordinary conditions. Above 50°C, the temperature dependence becomes stronger with decreasing rotor rotation rate n (Fig. 4a). The higher the rotation rate n,

Rate of starch hydrogel hydrolysis as influenced by mechanical pretreatment (temperature 60°C, acid concentration 0.15 M)

Treatment	τ, s	$k \times 10^4$ (s^{-1}) at indicated starch content, wt %	
		2	5
–	–	0.298	0.286
UZDN-2T	30	1.28	0.345
	60	0.925	0.306
RPA, n^*, rpm:			
3000	5	0.925	–
5000	5	0.745	0.493
5000	30	1.64	–

* Rotation rate in RPA.

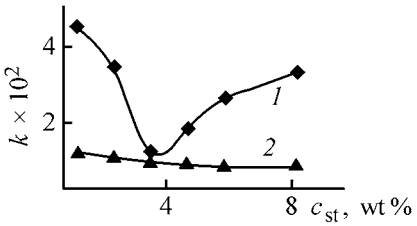

Fig. 3. Rate constant k of the acid hydrolysis of starch vs. the concentration c_{st} of starch in hydrogel at 60°C in the course of its treatment using (*1*) RPA and (*2*) UZDN-2T; acid concentration 0.03 M.

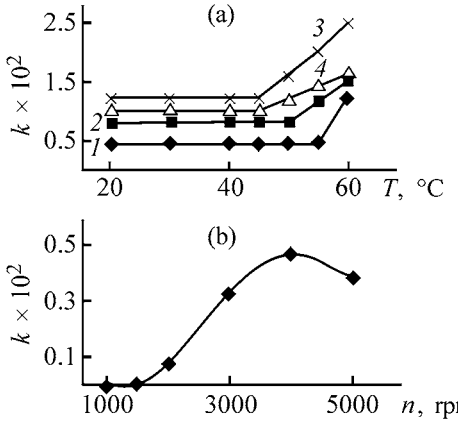

Fig. 4. Rate constant k of the acid hydrolysis of starch vs. (a) temperature T and (b) intensity n of mechanical treatment in RPA. (a) Rotation rate: (*1*) 2000, (*2*) 3000, (*3*) 4000, and (*4*) 5000.

the smaller the contribution of temperature to the rate acceleration. Thus, we obtain above 50°C a combined thermomechanical intensification of the process, and this is not a mechanochemical reaction in pure form. At lower temperatures, when the reaction does not occur at a given acid concentration under ordinary conditions and the reaction rate in RPA is independent of temperature, we can regard this process as mechanochemical, which allows calculation of the mechanochemical yield of the reducing groups (namely, the terminal hemiacetal carbon atoms C_1) formed in the course of hydrolysis.

In our calculations, we took into account that formation of a single terminal reducing group corresponds to a single event of hydrolytic cleavage of the glycoside bond. The second terminal carbon atom C_4, situated before degradation on the other side of the glycoside bond, is not a reducing group. The number of reducing groups formed per 100 eV of absorbed energy E was calculated from the equation [6]:

$$F = \frac{\Delta c N_A}{1000 W_{ac}} \frac{100}{6.25 \times 10^{18} \tau},$$

where Δc is the change in the concentration of the reducing groups (CHO) in time τ; N_A, Avogadro number; W_{ac}, acoustic power density (W cm^{-3}); τ, time of mechanical treatment (s).

The acoustic power was measured by the method of chemical dosimetry, using a standard test system ($FeSO_4$ in 0.8 N H_2SO_4). For RPA and UZDN-2T, the acoustic power density was 2.57 and 1.34 W cm^{-3}, respectively. The sonochemical yields for UZDN-2T were 0.07–0.10 and the mechanochemical yields (RPA), 0.034–0.152 reducing group per 100 eV of absorbed energy. The close sonochemical (ultrasonic treatment) and mechanochemical (RPA) yields indicate that the acceleration of the acid hydrolysis under mechanical treatment in RPA is primarily related to the ultrasonic component of the combined treatment or, more precisely, to ultrasonic cavitation, because specifically the ultrasonic cavitation is the origin of the chemical effects in the ultrasonic field [11]. The contribution of the shear strains to the intensification of the hydrolysis of gelatinized starch in RPA is probably smaller than the cavitation effect.

The role of cavitation in aqueous solutions consists only in the decomposition of water molecules in cavitation voids to give H$^\cdot$ and OH$^\cdot$ radicals. The hydrolytic degradation of polysaccharides in the presence of acids proceeds by the following scheme: (1) protonation of the oxygen atom in the glycoside bond with formation of an oxonium ion, (2) dissociation of the oxonium ion with rupture of the glycoside bond and formation of the glycosyl cation, and (3) reaction of this cation with water:

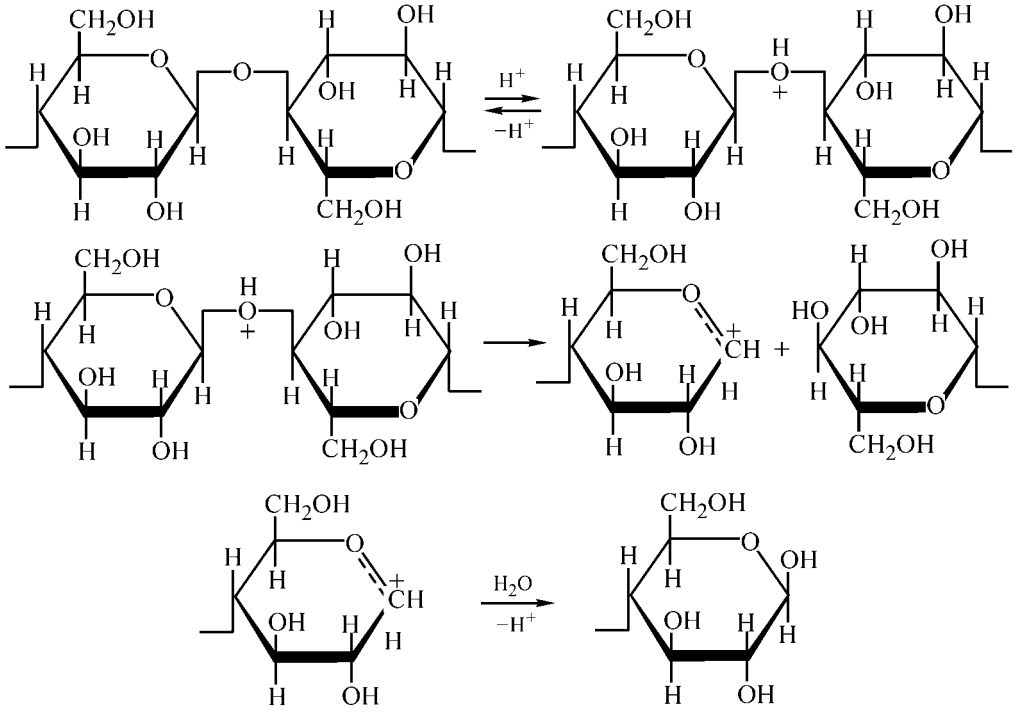

Under the cavitation conditions, the limiting stage of formation of the glycosyl radical-cation and its further reaction with water are probably accelerated due to participation of the free radicals formed in water sonolysis.

As seen from Fig. 4b, the maximum reaction rate is observed at rotor rotation rate of 4000 rpm, whereas at 5000 rpm, the hydrolysis rate decreases. With increasing rotation rate, the frequency of ultrasonic vibrations in the RPA working chamber grows, and such an increase in frequency can decrease the rate of the sonochemical reactions [6].

CONCLUSIONS

(1) Under strong mechanical stresses (including ultrasonic treatment), the rate of acid hydrolysis of gelatinized starch increases, on the average, by three orders of magnitude. In this case, the acoustic cavitation is a decisive factor in the system activation, whereas the mechanically induced structural changes in starch hydrogels lead to an increase in the reaction rate by nearly an order of magnitude.

(2) The sonochemical yields of the reducing groups formed during the acid hydrolysis of starch under the ultrasonic filed and mechanical treatment in the rotary-pulsating activator were, respectively, 0.07–0.10 and 0.034–0.152 group per 100 eV.

REFERENCES

1. Lipatova, I.M., Padokhin, V.A., Moryganov, A.P., *et al.*, *Tekstil. Prom–st.*, 1998, no. 5, pp. 32–33.
2. Lipatova, I.M., Yusova, A.A., and Moryganov, A.P., *Zh. Prikl. Khim.*, 2000, vol. 73, no. 8, pp. 1372–1376.
3. Lipatova, I.M., Yusova, A.A., and Blokhina, S.V., *Zh. Prikl. Khim.*, 2001, vol. 74, no. 9, pp. 1517–1521.
4. Lipatova, I.M., Yusova, A.A., and Ermolaeva, N.A., *Tekstil. Prom–st.*, 1995, no. 2, pp. 85–89.
5. Lipatova, I.M., Losev, N.V., and Yusova, A.A., *Zh. Prikl. Khim.*, 2002, vol. 75, no. 4, pp. 540–544.
6. Margulis, M.A., *Osnovy zvukokhimii (khimicheskie reaktsii v akusticheskikh polyakh)* [Fundamentals of Sonochemistry (Chemical Reactions in Acoustic Fields)], Moscow: Vysshaya Shkola, 1974.
7. Richter, M., Augustat, S., and Schierbaum, F., *Ausgewahlte Methoden der Starkechemie*, Leipzig: Fachbuchverlag, 1968.
8. Kadykova, E.L. and Gubina, S.M., *Zh. Prikl. Khim.*, 1992, vol. 65, no. 4, pp. 891–895.
9. Senakhov, A.V., Koval', V.V., and Sadov, F.I., *Zagustki, ikh teoriya i primenenie* (Bunches, Their Theory and Use), Moscow: Legkaya Prom–st., 1972, p. 73.
10. *Ul'trazvukovaya tekhnologiya* (Ultrasonic Technology), Agranat, B.A., Ed., Moscow: Metallurgiya, 1974.
11. *Chemistry with Ultrasound*, Mason, T.J., Ed., London: Elsevier Applied Science, 1990.

Russian Journal of Applied Chemistry, Vol. 76, No. 6, 2003, pp. 1002–1005. Translated from Zhurnal Prikladnoi Khimii, Vol. 76, No. 6, 2003, pp. 1030–1033.

MACROMOLECULAR CHEMISTRY AND POLYMERIC MATERIALS

Swellability of ASMOL Protective Coating in Water and Aqueous Salt Solutions

I. F. Gladkikh, V. S. Kolosnitsyn, N. M. Cherkasov, L. V. Sheina, and E. V. Karaseva

Institute of Organic Chemistry, Ufa Scientific Center, Russian Academy of Sciences, Ufa, Bashkortostan, Russia
Poisk Research Center, Ufa, Bashkortostan, Russia

Received March 5, 2003

Abstract—The swellability of a new material for protective coatings, ASMOL (asphalt–resin oligomer), in water and aqueous salt solutions was studied gravimetrically and by thermogravimetric analysis.

Pipelines are today the main means of transportation of crude oil, petroleum products, and natural gas. Various protective coatings are used for preventing pipeline corrosion. The reliability of protective coatings largely determines the failure-proof operation of pipelines. For example, almost 40% of all pipeline failures are due to corrosion damage.

The diversity of soil and climatic conditions under which pipelines are exploited, and also high mechanical and thermal loads impose stringent requirements upon protective coatings. The insufficient assortment of corrosion-protective materials produced in Russia and the growing requirements to their quality call for development and production of new insulating coatings suitable for diverse service conditions.

The first representative of a new generation of protective coatings is ASMOL (asphalt–resin oligomer) [1, 2]. ASMOL is a product of catalytic reaction of propane-precipitated asphalt with bottom residues from regeneration of dimethylformamide in isoprene production. ASMOL is a uniform product incorporating compounds of varied chemical nature. The main difference between ASMOL and asphalt is the presence in ASMOL of compounds containing highly polar functional groups and exhibiting chemical and surface activity: amide, sulfone, and sulfonic acid groups. Therefore, ASMOL has high adhesion to metals.

An important service parameter of polymeric protective coatings, determining the rate of metal corrosion, is their swellability in water and aqueous salt solutions. Therefore, we analyzed in this study the swellability of ASMOL in water and aqueous NaCl solutions.

EXPERIMENTAL

The swellability of ASMOL was determined in water and in 3, 6, and 9% NaCl solutions gravimetrically and by thermogravimetric analysis.

Two types of ASMOL samples were tested. Samples of the first type were neat 1.2–1.3-mm-thick ASMOL plates of the area 6 cm^2, and samples of the second type, St.3 steel plates coated on both sides with a 1.2–1-3-mm layer of ASMOL. The surface area of the ASMOL-coated steel plates was also 6 cm^2. In fabrication of samples of the second type, the coating continuity was checked visually.

Samples prepared for tests were placed in hermetically sealed vessels filled with water or aqueous salt solution and kept at room temperature (20–25°C) for a prescribed time. To determine the amount of absorbed water, samples were removed from the vessel, water drops were removed from the surface with filter paper, and the samples were weighed on an analytical balance. For thermogravimetric studies, a piece of the swollen material was separated from one of replicate samples. After weighing, the samples were returned to the same vessels. The swollen samples were weighed at 20–60-h intervals depending on the moisture absorption rate.

Thermogravimetric experiments with ASMOL were performed on an MOM derivatograph (Hungary). The sample weight was 100–200 mg. Thermal degradation of ASMOL samples was performed in open corundum crucibles in air. With the aim of uniform heating, the crucibles were placed in a quartz beaker. Aluminum oxide was used as reference. The heat-

1070-4272/03/7606-1002 $25.00 © 2003 MAIK "Nauka/Interperiodica"

ing rate was 5 deg min^{-1}. Samples were heated to 500°C. The error in determination of the weight loss did not exceed 0.2%.

To obtain reproducible results, we performed no less than three replicate runs. The experimental error did not exceed 5%.

Usually the parameter set by standards is the swellability of a protective material in water in 24 h. Although this parameter does characterize the tendency of a protective material to interact with water, it does not fully reflect the true protective properties of coatings based on this material, because such a short testing time is insufficient for the thermodynamic equilibrium to be attained. Therefore, we performed longer tests, for up to 5000 h.

The results of ASMOL swellability tests are shown in Figs. 1–3. It is seen that the ASMOL swellability is appreciably affected by two factors: time elapsed after ASMOL fabrication and concentration of salt solution. Therefore, the tests were performed in solutions with various NaCl concentrations, using ASMOL samples stored for 3 and 8 months after fabrication.

The water absorption in 24 h by ASMOL samples stored for 3 months after fabrication was 2.4% from water, 1.45% from 3% NaCl, 1.25% from 6% NaCl, and 1.12% from 9% NaCl solution. That is, the swellability of ASMOL is somewhat higher than that of asphalts [the swellability (water absorption) of asphalts under similar conditions is about 0.2%].

The swellability of ASMOL largely depends on the salt concentration (Fig. 1). In all the media, the kinetic curves of swelling do not flatten out. It should be noted that the ASMOL swelling curve in water differs essentially in shape from the curves obtained in salt solutions. In salt solutions, the water absorption rate considerably decreases in the initial period, becomes constant after 1000–1500 h, and remains on this level till the end of the tests. In distilled water, the curve has a complex shape. Its initial portion is similar to the initial portions of the water absorption curves in salt solutions. However, in contrast to salt solutions, the water absorption rate does not become constant. After 2500 h, the water absorption rate starts to grow sharply. After a 4500-h test, the water absorption was as large as 100% relative to the initial sample weight.

The complex shape of the water absorption curve suggests that the process is multistage. A microscopic examination showed that, in ASMOL samples kept in distilled water for 1500–2000 h, micropores and microcracks appear, which grow in size during longer tests. In 4000–4500 h, the samples break down.

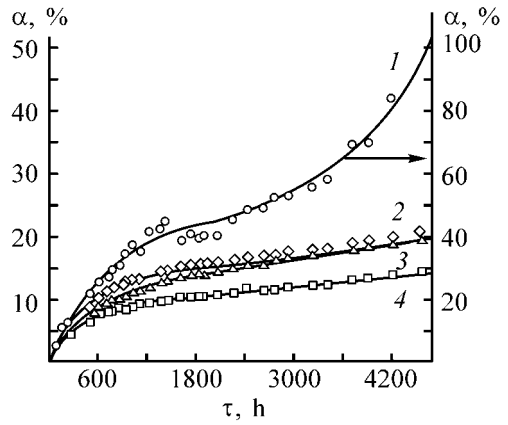

Fig. 1. Swellability of ASMOL protective coating in various media. Time interval between ASMOL fabrication and start of the tests 3 months; the same for Fig. 3. (α) Swellability and (τ) time; the same for Figs. 2 and 3. (*1*) Distilled water, (*2*) 3% NaCl, (*3*) 6% NaCl, and (*4*) 9% NaCl; the same for Fig. 3.

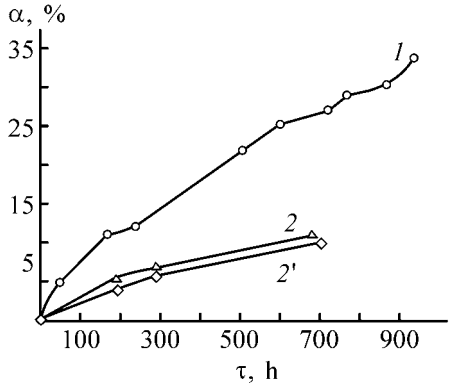

Fig. 2. Influence of the time elapsed after ASMOL fabrication on its swellability in distilled water. Time from ASMOL fabrication, months: (*1*) 3 and (*2*, *2'*) 8. Determination procedure: (*2*) gravimetric and (*2'*) thermogravimetric.

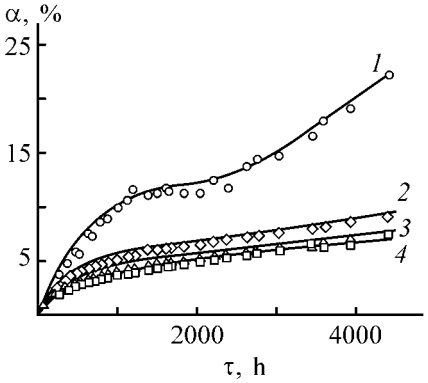

Fig. 3. Swellability of ASMOL protective coating on a steel support in various media.

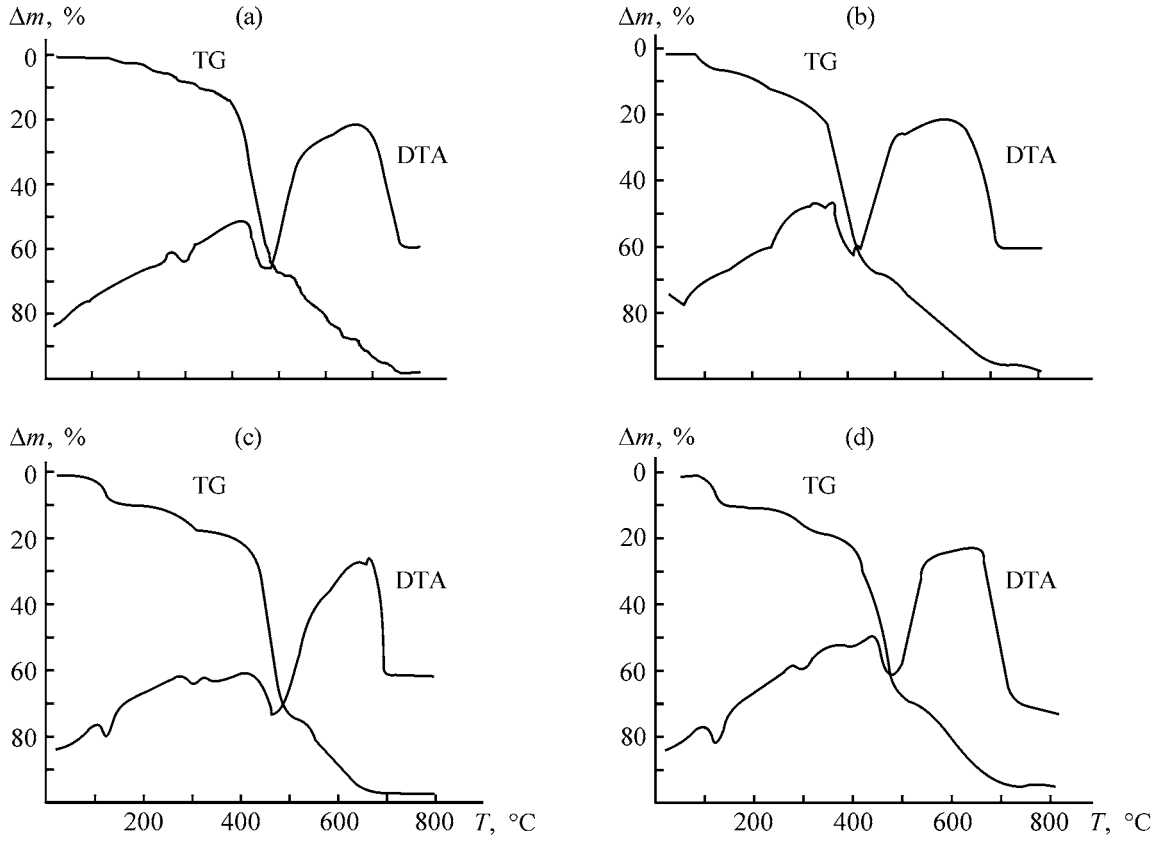

Fig. 4. Thermograms of an ASMOL protective coating: (a) unswollen and (b–d) swollen in distilled water for 312, 480, and 768 h, respectively. (Δm) Weight loss and (T) temperature.

The water absorption by ASMOL in salt solutions is by a factor of 5–6 lower than that in distilled water, decreasing as the salt concentration is increased. According to a microscopic examination, even after 4500-h tests the sample structure is not altered appreciably.

The swellability in water of ASMOL samples stored for 8 months after fabrication was lower than that of the samples stored for 3 months (Fig. 2) and amounted to 1.9% in 24 h. In 1000 h, the swellability of the former samples was lower by a factor of 3.

Experiments on water absorption of ASMOL on a steel support were performed with the samples stored for 3 months after fabrication.

We found that the swellability of ASMOL on a steel support was considerably lower than that of the neat sample (Fig. 3) and amounted in 24 h to 0.7% in water, 0.65% in 3% NaCl, 0.5% in 6% NaCl, and 0.4% in 9% NaCl solution. In 5000 h, the swellability of ASMOL on a steel support in distilled water was about 25%, i.e., it was four times lower than the swellability of the neat ASMOL sample. The swellability of ASMOL on a steel support in salt solutions is approximately half that of neat ASMOL. It should be noted that, despite different water absorption values, the curve of water absorption by ASMOL samples on a steel support is similar in shape to the curves obtained with neat ASMOL samples.

An examination of ASMOL samples on a steel support after 4500-h exposure to water and salt solutions showed that their external surface, initially lustrous black, became dark gray and dull (to 0.1–0.2-mm depth). The internal layers of ASMOL remained virtually unchanged in appearance. The ASMOL layer contacting the metal was harder than the initial ASMOL and had a brownish tint. The adhesion of ASMOL to the steel surface was very high; ASMOL could be separated only by cutting with a scalpel. Thermogravimetric studies showed that water is distributed in the ASMOL coating nonuniformly. The highest moisture content is observed in external ASMOL layers. The layers adjacent to the metal surface contain virtually no water.

To confirm the results of gravimetric studies of the ASMOL swellability and elucidate the character of water binding with ASMOL, we performed thermo-

gravimetric experiments. The curves obtained gravimetrically and thermogravimetrically (Fig. 2) virtually coincide.

The thermograms of ASMOL kept in distilled water for various periods of time are shown in Fig. 4. It is seen that the shape of the TG curves depends on the time of contact with water.

The TG curves of ASMOL samples kept in water have portions assignable to water removal. According to the TG curve of an ASMOL sample kept in water for 312 h, the weight loss occurs in a single stage at 70–100°C. The ASMOL samples kept in distilled water for 480 and 768 h lose weight in two stages: at 70–100 and 280–300°C. The presence of two portions of the weight loss in the TG curves suggests the two-stage mechanism of water removal. Apparently, in the first stage, at 70–100°C, physically adsorbed water located in ASMOL micropores is removed. The second stage, at 280–300°C, involves removal of water tightly bound to ASMOL components. This may be water that hydrates the sulfo groups of aromatic sulfonic acids present in ASMOL.

The IR studies confirmed this assumption. In the IR spectra of samples kept in water for 480 and 768 h, the stretching and bending absorption bands of water molecules had a complex shape.

Our studies showed that, in contrast to asphalt, a traditional material widely used for corrosion protection of pipelines, ASMOL absorbs more water. This is due to the presence of polar components such as sulfonic acids, sulfones, carboxylic acids, amines, amides, etc. The presence of these compounds imparts to ASMOL, on the one hand, high adhesion to metals and, on the other, increased swellability in water and salt solutions. However, our studies showed that increased swellability of ASMOL in water does not affect negatively its protective properties. By contrast, certain water absorption by ASMOL may be a favorable factor.

In the presence of small amounts of water at the steel–ASMOL interface, the sulfonic acids of ASMOL react with oxide films and corrosion products inevitably present on the metal surface, to form iron sulfonates. Chemical etching of the metal enhances the adhesion of ASMOL to the metal surface. Iron sulfonates partially dissolve in ASMOL and partially form a separate finely dispersed phase. Finely dispersed solid products of ASMOL reaction with steel are uniformly distributed in the surface layer of the coating, reinforcing it and thus enhancing the protective properties. Since sulfonic acid salts are hydrated considerably more weakly than free sulfonic acids, the swellability of ASMOL in water decreases as these salts are formed. This was confirmed by the thermogravimetric studies which showed that the ASMOL layer adjacent to the metal surface contains virtually no moisture.

Active sulfonic acids present in ASMOL gradually react with aromatic compounds to form sulfones, which are inert and highly stable. As the content of free sulfonic acids decreases, the swellability of ASMOL in water decreases, with the material becoming similar in this property to petroleum asphalts.

CONCLUSIONS

(1) ASMOL, a new corrosion-protective material, efficiently protects steel.

(2) Aromatic sulfonic acids and water present in ASMOL ensure formation of a strong protective layer at the steel–ASMOL interface.

(3) Active sulfonic acids present in ASMOL undergo spontaneous chemical transformations in the course of several months, yielding inert compounds; as a result, the swellability of ASMOL-based coatings decreases.

REFERENCES

1. *TU* (Technical Specifications) *5623-002-05 111 644–96: ASMOL Mastic Formulation for Corrosion-Protective Coatings*.
2. *TU* (Technical Specifications) *4859-001-05 211 644–95: Coating Based on ASMOL Mastic for Corrosion Protection of Underground Pipelines.*

Russian Journal of Applied Chemistry, Vol. 76, No. 6, 2003, pp. 1006–1007. Translated from Zhurnal Prikladnoi Khimii, Vol. 76, No. 6, 2003, pp. 1034–1035.

BRIEF COMMUNICATIONS

Thermodynamic Characteristics of Ni_3S_2 Compound Formation

A. G. Morachevskii and L. B. Tsymbulov

St. Petersburg State Polytechnic University, St. Petersburg, Russia
Gipronikel' Institut Open Joint-Stock Company, St. Petersburg, Russia

Received May 6, 2003

Abstract—Published data on thermodynamic properties of the Ni_3S_2 compound in the liquid and solid states are compared and discussed.

Compounds and melts of the nickel–sulfur system play important role in the technology of processing of copper–nickel sulfide ores. Procedures performed at relatively high temperatures with liquid and solid phases require detailed analysis. The nickel–sulfur system is characterized by complex phase diagram; at least five compounds, Ni_3S_2, Ni_7S_6, NiS, Ni_3S_4, and NiS_2, are formed, with the first three having two (low- and high temperature) modifications each. In the sulfur-rich part of the system, a separation region is observed [1].

The compound Ni_3S_2 containing 26.7 wt % S is of particular interest in technological regard. Its low-temperature phase is, to within error of analysis, a stoichiometric compound, known as heazlewoodite mineral contained in copper–nickel sulfide ores and other natural formations. The high-temperature phase, $Ni_3S_{2\pm x}$, having wide region of homogeneity, is stable above 823 ± 10 K. Alloys of the Ni–S system, corresponding to the composition Ni_3S_2, are in liquid state above 1073 K.

All the publications considered here are concerned with the standard Gibbs energy of formation of the Ni_3S_2 compound in solid or liquid states from solid nickel and diatomic molecular sulfur vapor (S_2, 1 atm) as a function of temperature. First data on the thermodynamics of Ni_3S_2 formation were obtained by Vol'skii and summarized in a monograph [2]. On the basis of these data, the standard Gibbs energy of Ni_3S_2 formation was estimated in the reference book by Gerasimov' *et al.* [3] to be (kJ mol^{-1}):

T, K	773	973	1173	1373	1573
ΔG_T^0, kJ mol^{-1}	–96.36	–80.00	–58.32	–47.36	–37.71

A ΔG_T^0 value of –177.6 kJ mol^{-1} for Ni_3S_2(s) at 1000 K was reported later by Rosenqvist [4], also on the basis of a study of the solid–vapor equilibrium.

Lin *et al.* [5] studied the thermodynamic properties of alloys belonging to the Ni–S system in the solid state in the central region of compositions in ample detail by the method of heterogeneous equilibrium. For the Ni_3S_2 compound, the following $\Delta G_T^0 = f(T)$ (kJ mol^{-1}) dependence was obtained within the temperature range 845–1040 K:

$$\Delta G_T^0 = -279.47 + 0.1028T. \quad (1)$$

Correspondingly, $\Delta G_{100}^0 = -176.67$ kJ mol^{-1} at 1000 K, which virtually coincides with the results of [4]. Mehrotra *et al.* [6] determined the standard Gibbs energy of N_3S_2 formation in solid (973–1089 K) and liquid (1089–1173 K) states by measuring the EMF in a cell with $ZrO_2 + Y_2O_3$ solid oxygen-conducting electrolyte. In contrast to the liquidus temperature of 1073 K, obtained previously for a composition corresponding to the Ni_3S_2 compound, a value of 1089 K was found in [6], which is, however, of no fundamental importance. The following results were obtained (kJ mol^{-1}):

$$\Delta G_T^0(Ni_3S_2, s) = -312.71 + 0.1297T, \ 973–1089 \text{ K}, \quad (2)$$

$$\Delta G_T^0(Ni_3S_2, l) = -252.80 + 0.0747T, \ 1089–1173 \text{ K}. \quad (3)$$

The enthalpy of melting of the phase of stoichiometric composition Ni_3S_2 is 59.91 kJ mol^{-1}. For alloys in the solid state

T, K	973	1000	1050	1089
ΔG_T^0, kJ mol^{-1}	–186.5	–183.0	–176.5	–171.4

1070-4272/03/7606-1006 $25.00

For alloys in the liquid state:

T, K	1089	1100	1150	117
ΔG_T^0, kJ mol^{-1}	–171.4	–170.6	–166.4	–165.2

The ΔG_T^0 values reported in [6] are close to the results obtained in [4, 5] at comparable temperatures. The above enthalpy of melting differs significantly from that (24.27 kJ mol^{-1}) reported by Kubashewski and Alcock [7], but is close to the value of 47.28 kJ mol^{-1}, obtained by Nagamori and Ingraham [8].

Hsieh and Chang [9] used the EMF method with zirconium dioxide solid electrolyte to study the equilibrium in the system Ni–S–O at $P(SO_2)$ = 1 atm. The constituents of such an equilibrium are the equilibria in the corresponding binary systems. Based on an analysis of published data, the authors of [9] recommended Eq. (1) for calculating ΔG_T^0 of Ni_3S_2(s). The error involved was estimated to be ±6 kJ mol.

Osadchii *et al.* [10] also demonstrated the possibility of using a solid electrolyte with anionic conductivity in a study of equilibria in the Ni–S–O system (at 850–1050 K). The data obtained were used to estimate, in particular, the ΔG_T^0 values for Ni_3S_2(s). In [10], these values were compared with those obtained previously by studying the heterogeneous equilibrium [5] (kJ mol^{-1}):

T, K	850	900	950	1000	1050
ΔG_T^0, kJ mol^{-1} [10]	–186.0	–181.9	–176.6	–170.2	–162.7
ΔG_T^0, kJ mol^{-1} [5]	–192.1	–187.0	–181.8	–176.7	–171.5

Let us consider data obtained in determining ΔG_T^0 for liquid Ni_3S_2. Nagamory and Ingraham [8] used the method of heterogeneous equilibria for studying the thermodynamic properties of the Ni–S system ($0.22 \le x_{Ni} \le 0.46$) at 973–1373 K. According to the data of [8], the standard Gibbs energy, ΔG_T^0, of Ni_3S_2(l) formation from solid nickel and gaseous sulfur (S_2, 1 atm) is expressed as a function of temperature by the equation (kJ mol^{-1}) [8]:

$$\Delta G_T^0 = -242.3 + 0.0665T \pm 0.8. \quad (4)$$

Equation (4) yields the following values of ΔG_T^0 (kJ mol^{-1}):

T, K	1073	1173	1273	1373
ΔG_T^0, kJ mol^{-1}	–170.6	–164.6	–156.3	–150.7

The $\Delta G_T^0 = f(T)$ dependence is plotted in the figure, according to the data of [5, 6, 8, 10]. With account of inaccuracies ranging from ±6.0 to ±8 kJ mol, the disagreement between results of these studies is not too pronounced. It seems reasonable to recommend use of the data presented in [5] for calculating equilibria involving solid Ni_3S_2 at 850–1050 K and the results of [8] for Ni_3S_2(l) in the temperature range from T_m to 1373 K. In this case, account should be necessarily taken of the standard states for nickel and sulfur, chosen in [5, 8]. According to [3], the ΔG_T^0 values from the monograph [2] are in error. This monograph presents data for heterogeneous equilibria involving Ni–S melts and $H_2S + H_2$ vapor, with equilibrium constants expressed in the ideal form.

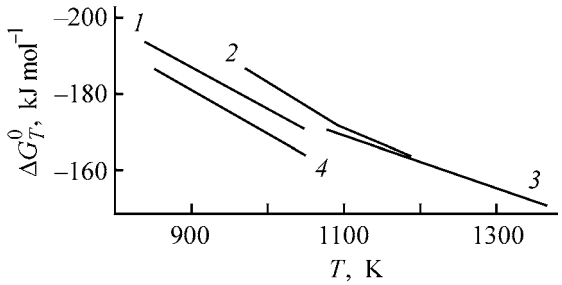

Standard Gibbs energy ΔG_T^0 of Ni_3S_2 formation vs. temperature T, according to the data of different studies. Standard state: solid nickel and diatomic S_2 vapor at P = 1 atm. Data: (*1*) [5], (*2*) [6], (*3*) [8], and (*4*) [10].

REFERENCES

1. *Diagrammy sostoyaniya dvoinykh metallicheskikh sistem: Spravochnik* (Phase Diagrams of Binary Metallic Systems: Reference Book), Lyakishev, N.P., Ed., Moscow: Mashinostroenie, 1999.
2. Vol'skii, A.N., *Osnovy metallurgicheskikh plavok* (Principles of Metallurgical Fusing), Moscow: Metallurgizdat, 1943.
3. Gerasimov, Ya.I., Krestovnikov, A.N., and Shakhov, A.S., *Khimicheskaya termodinamika v tsvetnoi metallurgii: Spravochnik* (Chemical Thermodynamics in Non-Ferrous Metallurgy: Reference Book), Moscow: Metallurgiya, 1966, vol. 4.
4. Rosenqvist, T., *J. Iron Steel Institute*, 1954, vol. 176, January, pp. 37–57.
5. Lin, R.Y., Hu, D.C., and Chang, Y.A., *Met. Trans. B*, 1978, vol. 9B, December, pp. 531–538.
6. Mehrotra, G.M., Tare, V.B., and Wagner, J.B., *J. Electrochem. Soc.*, 1985, vol. 132, no. 1, pp. 247–250.
7. Kubashewski, O. and Alcock, C., *Metallurgical Thermochemistry*, Oxford: Pergamon, 1979.
8. Nagamori, M., and Ingraham, T.R., *Met. Trans.*, 1970, vol. 1, July, pp. 1821–1825.
9. Hsieh, K.-Ch., and Chang, Y.A., *Met. Trans., B*, 1986, vol. 17B, March, pp. 133–146.
10. Osadchii, E., Rosen, E., and Saitton, B., *Acta chem. scand.*, 1990, vol. 44, pp. 476–480.

Russian Journal of Applied Chemistry, Vol. 76, No. 6, 2003, pp. 1008–1010. Translated from Zhurnal Prikladnoi Khimii, Vol. 76, No. 6, 2003, pp. 1036–1038.

BRIEF COMMUNICATIONS

Synthesis of Intermetallic Compounds $LaNi_5$ and $NdNi_5$ from Mixed Basic Carbonates of Lanthanum or Neodymium and Nickel

A. G. Burlakova, L. S. Volkov, and S. P. Shilkin

Institute for Problems of Chemical Physics, Russian Aacademy of Sciences, Chernogolovka, Moscow oblast, Russia

Received January 17, 2003

Abstract—The possibility of obtaining powdered $LaNi_5$ and $NdNi_5$ intermetallic compounds by reaction of mixed basic carbonates $La_2Ni_{10}(CO_3)_8(OH)_{10} \cdot 54H_2O$ and $Nd_2Ni_{10}(CO_3)_8(OH)_{10} \cdot 14H_2O$ with calcium hydride in a hydrogen flow at 1073 K and 10^5 Pa was studied.

Powdered intermetallic compounds of rare-earth and 3*d*-transition metals are used as hydrogen-sorbing materials [1] and materials for fabrication of magnets with high magnetic characteristics [2]. The production of such materials includes the stage of alloying of appropriate metals in electric-arc or vacuum induction furnaces with the subsequent grinding of the alloys under the action of hydrogen [1, 3, 4] or under exernal mechanic action in various ball-type activating mills [5, 6].

Presently, attention is attracted in laboratory and industrial practice to reduction-diffusion methods for obtaining intermetallic compounds containing rare-earth and 3*d*-transition elements. These techniques include reduction of mixtures of metal oxides, hyroxides, chlorides, carbonates with various reducing agents in hydrogen or an inert medium [2, 7, 8]. The advantage of this method is that it yields powdered intermetallic compounds with narrow fraction distribution and controlled chemical composition without stages of alloying and mechanic grinding of the alloys.

This communication describes synthesis of basic carbonates $La_2Ni_{10}(CO_3)_8(OH)_{10} \cdot (H_2O)_x$ and $Nd_2Ni_{10}(CO_3)_8(OH)_{10} \cdot (H_2O)_y$ and their reduction with calcium hydride in hydrogen with the aim of obtaining the intermetallic compounds $LaNi_5$ and $NdNi_5$.

To prepare mixed basic carbonates of lanthanum(III) [or neodymium(III)] and nickel(II), we dissolved starting $Ni(OH)_2$ in a solution of $LnCl_3 + 10HCl$ (Ln–La, Nd) in the ratio Ln : Ni = 1 : 5 under heating without boiling. Then we filtered the solution, added a solution of Na_2CO_3 to the filtrate in the ratio $Ln^{3+} : CO_3^{2-} = 1 : 4$, and added, in the course of 0.5 h under conditions of vigorous stirring, a 1.2 N solution of NaOH in the amount corresponding to the ratio $Ln^{3+} : OH^- = 1 : 5$. The suspension was allowed to settle for 15–20 h, then filtered, and the precipitate was dried in air at room temperature for 20–30 h. The powders obtained were X-ray-amorphous. According to IR spectral and chemical analysis data, their empirical composition corresponded to the formulas: $La_2Ni_{10}(CO_3)_8(OH)_{10} \cdot (H_2O)_x$ ($x \approx 54$) and $Nd_2Ni_{10}(CO_3)_8(OH)_{10} \cdot (H_2O)_y$ ($y \approx 14$).

To elucidate the role of molecular hydrogen and calcium hydride in reduction of mixed basic carbonates of La(III) [or Nd(III)] and Ni(II) with the abovementioned composition, we carried out the reaction in two stages. In the first stage, we placed a molybdenum container with a weighed portion of a mixed basic carbonate in a quartz reactor 20 mm in diameter and 600 mm in length, the reactor was purged with argon, the temperature in the hot zone of the reactor was raised to 1023 K for La(III) and Ni(II) basic carbonate and to 873 K for Nd(III) and Ni(II) basic carbonate, and the reactor was kept at these temperatures with flowing hydrogen for 2.5–3 h. The completion of the reaction was judged from termination of water drop formation in the cold part of the reactor. Thereafter the heating was switched off and the reaction mixture was cooled to room temperature in flowing hydrogen, then the reactor was purged with argon for 0.25 h, and the reaction products were discharged in an inert atmosphere. According to the results of X-ray phase analysis, the powders obtained were mix-

1070-4272/03/7606-1008 $25.00 © 2003 MAIK "Nauka/Interperiodica"

tures of nickel with lattice constant a_0 = 0.3521 nm and hexagonal modifications of La_2O_3 with a_0 = 0.4000, c_0 = 0.6340 or Nd_2O_3 with a_0 = 0.3963, c_0 = 0.6301 nm, which is in good agreement with published data and points to the absence of reaction between these compounds in the solid phase.

In the second stage, powders of Ni and La_2O_3 or Ni and Nd_2O_3 were mixed with CaH_2, placed in the same reactor, and kept in flowing hydrogen for 2.5–3 h at 1273 K. After cooling the reaction mass first in flowing hydrogen and then in argon, the reactor was discharged. In the case of lanthanum, the powder was washed first with distilled water cooled to 273 K, and then with ethanol and diethyl ether. The resulting dried powder was composed of the intermetallic compound $LaNi_5$. According to the results of chemical analysis:

Found (wt %): La 31.95, Ni 68.00.
$LaNi_5$.
Calculated (wt %): La 32.12, Ni 67.88.

An X-ray phase analysis of the powder indicated that only a single phase is present, which corresponds to the intermetallic compound $LaNi_5$ crystallizing to give hexagonal crystals with lattice constants a_0 = 0.5010 and c_0 = 0.3970 nm.

According to the results of reaction gas chromatography, the content of oxygen in the sample obtained was 0.2 wt %; a chemical analysis demonstrated that the content of calcium and chlorine did not exceed 0.1 wt %.

Since neodymium salts are more susceptible to hydrolysis than lanthanum salts, the desired compound was isolated from the reaction mixture using magnetic separation [9]. According to the results of chemical analysis:

Found (wt %): Nd 32.87, Ni 66.96.
$NdNi_5$.
Calculated (wt %): Nd 32.95, Ni 67.05.

As indicated by reaction gas chromatography, the content of oxygen in the sample obtained was about 0.2 wt %. The compound $NdNi_5$ crystallizes to give hexagonal crystals with lattice constants a_0 = 0.4963 and c_0 = 0.3974 nm, which is in reasonable agreement with published data for the reference intermetallic compound $NdNi_5$ obtained in an electric arc furnace (a_0 = 0.4926 and c_0 = 0.3957 nm) [10].

The size of powder particles, calculated in the approximation of their spherical shape, is about 220 nm for $LaNi_5$ and 400 nm for $NdNi_5$.

The powders of intermetallic compounds, obtained by the above procedure absorb about 6 mol of hydrogen per 1 mol of intermetallic compound in the reaction with hydrogen. The enthalpies of hydrogenation of the samples under study in the region of the $\beta \rightarrow \alpha$ transition, calculated from the experimental dependence of $\log(P[H_2])$ on inverse temperature, are (kJ mol^{-1} H_2): ΔH = –33.0 for $LaNi_5$ (ΔH = –32.9 for a molten alloy) and ΔH = –30 for $NdNi_5$ (ΔH = 30.1 for a molten alloy).

Thus, the reactions of mixed basic carbonates of composition $La_2Ni_{10}(CO_3)_8(OH)_{10} \cdot 54H_2O$ and $Nd_2Ni_{10}(CO_3)_8(OH)_{10} \cdot 14H_2O$ with calcium hydride in flowing hydrogen yield $LaNi_5$ and $NdNi_5$ powders without stages of alloying of the corresponding metals or their mechanic grinding.

EXPERIMENTAL

In this study, we used commercial pure-grade $Ni(OH)_2 \cdot 0.25H_2O$, basic nickel carbonate containing 47.6% nickel(II), chemically pure-grade Na_2CO_3, NaOH, hydrochloric acid, metallic lanthanum of 99.9% purity, 99.85% pure neodymium, 99.99% pure nickel, and calcium hydride of purity 99.9% with respect to H_2. Hydrogen-sorption characteristics of $LaNi_5$ and $NdNi_5$ powders were studied on a high-pressure installation by plotting isotherms of hydrogen pressure against the composition of the hydride phase at various temperatures [11].

We used a metal-hydride battery [12] as a source of high-purity hydrogen. The composition of the hydride phases formed in the reactions of intermetallic compounds with hydrogen, calculated from pressure changes in a calibrated system, was refined by a standard procedure of sample combustion in flowing oxygen. The thermodynamic characteristics of hydride formation were determined from the dependence of the equilibrium pressure of H_2 in the regions of the $\beta \rightarrow \alpha$ transition on inverse temperature.

We prepared the reference intermetallic compounds $LaNi_5$ and $NdNi_5$ by alloying calculated amounts of La or Nd with Ni in an electric arc furnace with a permanent tungsten electrode in the atmosphere of high-purity argon. The alloy samples were subjected to threefold remelting and then to homogenizing annealing at 950–1000 K for 500 h with the subsequent quenching in water at 273 K. The X-ray studies were carried out using the powder technique on an ADP-1 diffractometer (Cu_{K_α} radiation) equipped with a microcomputer controller. The error in determining the lattice constants did not exceed 0.0004 nm. The elemental chemical analysis of mixed basic carbonates

of La(III) or Nd(III) with Ni(II) and analysis of the final products of their reactions with CaH_2 and H_2 were carried out by the standard procedures.

All the operations involving loading and discharging of reactors, including sampling for analysis, were carried out in the atmosphere of argon.

CONCLUSION

Powders of the intermetallic compounds $LaNi_5$ and $NdNi_5$ were obtained without stages of high-temperature alloying and mechanic grinding of alloys. The compounds crystallize to give hexagonal crystals with lattice constants $a_0 = 0.5010$, $c_0 = 0.3970$ and $a_0 = 0.4963$, $c_0 = 0.3974$ nm, respectively.

REFERENCES

1. Kuijpers, F., *Philips Res. Repts. Suppl.*, 1973, vol. 28, no. 2, pp. 1–18.
2. *Postoyannye Magnity* (Permanent Magnets), Pyatin, Yu.M., Ed., Moscow: Energiya, 1980.
3. Matsubara, E., Waseda, Y., and Lix, G., *J. Mater. Sci. Lett.*, 1990, vol. 9, no. 9, p. 1017.
4. Fokin, V.N., Tarasov, B.P., Korobov, I.I., Shilkin, S.P., *et al.*, *Koord. Khim.*, 1992, vol. 18, no. 5, pp. 526–534.
5. Andrievskii, R.A., Tarasov, B.P., Korobov, I.I., *et al.*, *Zh. Neorg. Khim.*, 1996, vol. 41, no. 8, pp. 1295–1289.
6. Chu, B.-L., Lee, S.-M., and Perng, T.-P., *Int. J. Hydrogen Energy*, 1991, vol. 16, no. 6, p. 413.
7. Wang, X. and Wang, G., *Z. Phys. Chem. (BRD)*, 1989, vol. 164, no. 2, pp. 1207–1212.
8. Tarasov, B.P., Burlakova, A.G., Volkova, L.S., *et al.*, *Zh. Neorg. Khim.*, 1997, vol. 42, no. 2, pp. 209–212.
9. Karmazin, V.V. and Karmazin V.I., *Magnitnye metody obogashcheniya* (Magnetic Methods of Enrichment), Moscow: Nedra, 1984.
10. Gladyshevskii, E.I. and Bodak, O.I., *Kristallokhimiya intermetallicheskikh soedinenii redkozemel'nykh metallov* (Crystal Chemistry of Intermetallic Compounds of Rare-Earth Metals), Lvov: Vysshaya Shkola, 1982.
11. Burnasheva, V.V. and Tarasov, B.P., *Zh. Neorg. Khim.*, 1984, vol. 29, no. 5, pp. 1136–1141.
12. Tarasov, B.P., Fokin, V.N., Korobov, I.I., and Shilkin, S.P., Abstracts of Papers, *4th Eur. East-West Conf. and Exhibition on Materials and Process*, St. Petersburg, 1993, p. 92.

Russian Journal of Applied Chemistry, Vol. 76, No. 6, 2003, pp. 1011–1013. Translated from Zhurnal Prikladnoi Khimii, Vol. 76, No. 6, 2003, pp. 1039–1041.

BRIEF COMMUNICATIONS

Mechanochemical Treatment of Electrolytic Manganese Dioxide

Yu. S. Kononov, A. M. Zhizhaev, and V. V. Patrushev

Institute of Chemistry and Chemical Technology, Siberian Division, Russian Academy of Sciences, Krasnoyarsk, Russia

Received February 13, 2003

Abstract—The influence exerted by mechanical activation of electrolytic manganese dioxide under conditions ensuring insulation of the system from a reducing agent on parameters of chemical batteries based on the Zn–MnO_2 electrochemical system was studied.

Mechanochemical treatment of solid phases used as components of chemical power cells must change parameters of the power cells themselves because of the activation of components of the electrochemical system. However, the previously obtained data demonstrated a dramatic decrease in electric energy output for a Zn–MnO_2 power cell based on mechanically activated electrolytic manganese dioxide (EMD) [1]. The reason is that MnO_2 is partly reduced to Mn_2O_3 by iron from drum walls and grinding bodies in the course of grinding. As one more reducing agent in joint activation serves amorphous carbon (carbon black) added to improve the conductivity of the solid phase in fabrication of a manganese-zinc power cell. As a result, the cathode paste is virtually completely deactivated. Of interest is a study of the influence exerted on cell parameters by mechanical activation of EDM-2, with the activating system insulated from the reducing agent. This can be achieved by using drums lined with agate (or nephrite, or jasper) and the corresponding ball charge.

EXPERIMENTAL

As object of study served manganese dioxide synthesized electrolytically from sulfate media by a procedure described previously in [1]. The mechanical activation was done in dry mode in agate drums with agate grinding balls (diameter 10 mm) in a Fritch Pulverizette-5 mill (Germany). A weighed portion of EMD was 10 g, and the ball charge, 100 g. The mill worked in the batch mode, with acceleration factor of 12g [2]. Since this device is less energy consuming than the previously used M-3 centrifugal-planetary mill, the treatment duration was raised to 1, 5, and 10 min. The samples were subjected to X-ray phase analysis (XPA) on a DRON-3 diffractometer with Cu_{K_α} radiation at a scanning rate of 1 deg min^{-1}.

The prototype manganese-zinc power cell was fabricated from the initial and activated EMD fractions by a procedure also described in [1]. A 2.5-g weighed portion of initial or activated EMD powder was mixed with 0.3 g of carbon black to improve the electrical conductivity. The mixture was wetted in a measuring cell with 5 ml of electrolyte (10% $ZnCl_2$ + 20% NH_4Cl) and a zinc electrode was pressed against it. The discharge curve was recorded with a load of 10 Ω to U_{fin} = 750 mV.

Figure 1 shows discharge curves for samples based on the initial EDM-2 and that subjected to mechanical activation under the indicated conditions for 1, 5, and 10 min. The initial sample is characterized by a discharge curve with U_0 = 1810 mV and specific capacity of the active paste of 84 A h kg^{-1}. Discharge to U_{fin} = 750 mV occurs in 2.5 h (Fig. 1, curve *1*), which conforms to standard requirements to manganese-zinc power cells [3]. The discharge curves of activated samples are characterized by higher open-circuit voltage (with difference of up to hundreds of millivolts) and more prolonged discharge (Fig. 1, curves *2–4*), which, combined, give an increased specific capacity. Already after 1 min of mechanical activation, the discharge duration of a manganese-zinc power cell to 750 mV increases to 3 h. For manganese dioxide activated during 5 min, the discharge continues for nearly 4 h (Fig. 1, curve *3*). The specific capacity of the given EMD sample is as high as 122 A h kg^{-1}, which exceeds by nearly a factor of 1.5 that in the control sample (without activation). For power cells based on EDM-2 activated for 10 min, the parameters are somewhat inferior to those in the initial period of

1070-4272/03/7606-1011 $25.00 © 2003 MAIK "Nauka/Interperiodica"

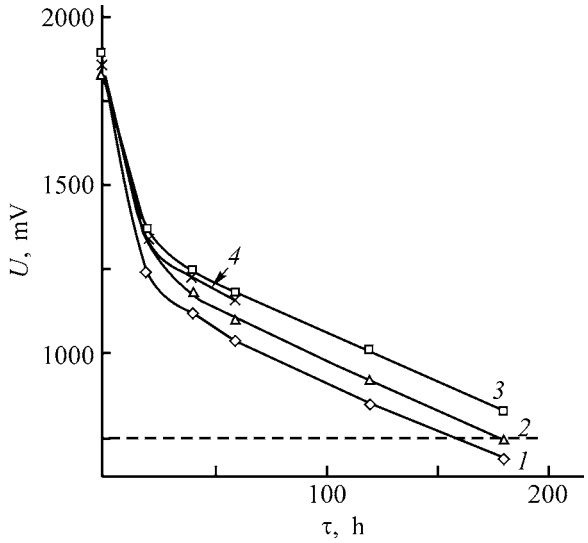

Fig. 1. Discharge curves of prototype manganese-zinc power cells fabricated from (*1*) initial and (*2–4*) mechanically treated MnO_2 powders. (*U*) Voltage and (τ) time. Duration of mechanical treatment (min): (*2*) 1, (*3*) 5, and (*4*) 10; the same for Fig. 2.

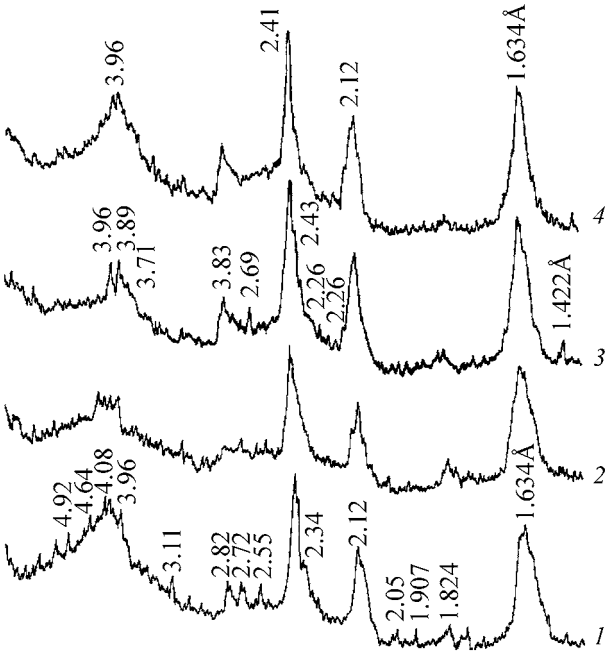

Fig. 2. X-ray diffraction pattern of (*1*) initial and (*2–4*) mechanically activated MnO_2 samples.

activation (Fig. 1, curve *4*). In further recording the discharge curve, a wide scatter of data obtained in parallel runs was observed, with, however, the parameters remaining, on the whole, better than those of the control samples. The irreproducibility of results is probably associated with heating of the material in prolonged mechanical activation. Heat elimination cannot be achieved because of the low heat conductivity of the agate material of the mill. A local rise in temperature leads to oxygen elimination from the crystal lattice of manganese dioxide to give a continuous series of nonstoichiometric manganese oxides, extending as far as bixbyite Mn_2O_3, with the fraction of the electrically active material decreasing [3, 4].

A certain role in the improvement of parameters of a manganese-zinc power cell can be played by surface renewal and by decrease in EMD particle size. However, additional experiments demonstrated that grinding of an initial sample in an agate mortar, with particle size decreasing from 0.16 to 0.063 mm, does not lead to any noticeable changes in the amount of electric energy produced. The contribution of the dimension factor is insignificant in the given case. In all probability, the electric energy output can be raised in the given conditions because of the higher manganese dioxide utilizing factor [3].

According to XPA (Fig. 2, curve *1*), the initial EMD sample is composed of a mixture of electrically active γ- and ε-MnO_2 (*d* 3.96, 2.41, 2.12, 1.634 Å JCPDS, 14–644, 30–820) with admixture of ramsdellite α-MnO_2 (*d* 4.64, 4.08, 2.55, 1.907 Å, JCPDS, 7–222) and pyrolusite β-MnO_2 (*d* 3.11 Å, JCPDS, 24–735) [3, 4]. Present in minor amounts are $Mn(O,OH)_2$ (*d* = 2.34 Å, JCPDS, 17–510) and oxide of the MnO_x series with $x < 2$ (e.g., $MnO_{1.88}$, *d* = 4.92 Å etc., JCPDS, 5–673). The presence of inert constituents is also seen from the shape of the peak at *d* = 1.634 Å, since closely spaced high-intensity lines of several forms of manganese dioxide overlap in this region. These lines show, however, a sufficient noncoincidence and form a broad serrate peak.

After mechanical activation for even 1 min, the amount of inert impurities becomes smaller, which is seen from a decrease (to the background level) in the intensity of peaks at *d* 2.40–3.00 and 4.20–6.00 Å (Fig. 2, curve *2*). Also decreases the intensity of reflections on the right-hand shoulder of the peak at *d* = 2.41 Å. After mechanical activation for 5 min, the amount of impurities falls to the lowest level. Only a weak peak of β-MnO_2 at *d* = 3.11 Å is observed (Fig. 2, curve *3*). Also seen are a number of lines at *d* 3.89, 3.71, 2.83, 2.69, 2.26 Å, which are identified as belonging to ε-MnO_2 (JCPDS, 30–820, 12–141). The shape of the peak at *d* = 1.63 Å, which has the highest intensity for this phase, is changed. Presumably, homogenization and redistribution of water molecules in the dioxide lattice leads to recrys-

tallization of the inactive α- and β-forms into γ-MnO_2. Simultaneously, long ε-MnO_2 channels are formed [3, 4]. Longer activation leads to partial disintegration of the superstructure, which is manifested in diffraction line intensity redistribution in favor of γ-MnO_2 (Fig. 2, curve *4*). No new phase formation is revealed in the given stage.

Thus, XPA shows that the main difference of the phase activated for 5 min from the initial EMD consists in decreased content of α- and β-MnO_2, which are inert in the manganese-zinc power cell, and increased content of ε-MnO_2, which is responsible for discharge duration. The specific capacity of EMD activated under the optimal conditions is as high as 122 A h kg^{-1}, which is 145% of that for the control sample. Such an increase in capacity should be regarded as rather good, since mechanical activation is not labor-consuming and can be done in a short time. It should be noted that the theoretical specific capacity of the EMD active paste is 308 A h kg^{-1} [3]. The increase achieved in this study constitutes only a minor fraction of the maximum possible value.

CONCLUSIONS

(1) Mechanical activation of electrolytic manganese dioxide in a centrifugal-planetary mill, with the system isolated from reducing agents, leads to an increase in the specific capacity of manganese dioxide by 20–45%.

(2) The improvement of parameters of manganese-zinc power cells fabricated from electrolytic manganese dioxide mechanically activated under these conditions is due to partial recrystallization of inert impurities into the electrically active form.

REFERENCES

1. Kononov, Yu.S., Zhizhaev, A.M., and Kulebakin, V.G., *Zh. Prikl. Khim.*, 1998, vol. 71, no. 4, pp. 396–398.
2. Kamenskii, Yu.D. and Musatov, V.V., *Nauka Proizvodst.*, 2002, no. 2, pp. 47–51.
3. Andersen, T.N., *Modern Asp. Electrochem.*, 1996, no. 30, pp. 313–413.
4. Kondrashev, Yu.D. and Zaslavskii, A.I., *Izv. Akad. Nauk SSSR, Ser. Fiz.*, 1951, vol. 15, no. 2, pp. 179–186.

Russian Journal of Applied Chemistry, Vol. 76, No. 6, 2003, pp. 1014–1016. Translated from Zhurnal Prikladnoi Khimii, Vol. 76, No. 6, 2003, pp. 1042–1044.

BRIEF COMMUNICATIONS

Preparation of Solder Powders and Properties of Low-Temperature Solder Creams Based on a Polyester Resin and Dimethylethylphenylammonium Iodide

N. I. Polezhaeva, I. V. Polezhaeva, V. A. Levdanskii, and B. N. Kuznetsov

Institute of Chemistry and Chemical Technology, Siberian Division, Russian Academy of Sciences, Krasnoyarsk, Russia

Received January 10, 2003

Abstract—Solder powders were prepared, and properties of solder creams based on rosin-modified polyester resin and dimethylethylphenylammonium iodide were studied. The possibility of using dimethylethylphenylammonium iodide as a flux in low-temperature solder creams was examined.

Solder creams consist of a powdered solder and an organic binder containing a flux [1]. Particles of the solder powder should have definite size and shape and should not be oxidized. The best results are obtained with particles 3–25 μm in size [2].

The functioning of a solder cream depends on the size of solder powder particles: The smaller the particles, the higher the probability of their oxidation. Oxidation can occur in the course of cream fabrication, after fabrication (before use), and during application. Oxidation of the solder powder is undesirable, since additional power is required to remove the oxide film.

Procedures for pulverizing solids are numerous [3]. The simplest procedure is mechanical grinding in special installations (mills or crushers). However, this procedure is unsuitable for grinding solders because of their high plasticity. Ultrasonic spraying of a molten solder is performed as follows. A molten solder is slowly poured onto the vibrating end of the concentrator of an ultrasonic atomizer and is sprayed in the form of drops, which are deposited after cooling as a powder in a special collector. The drawback of this procedure is that it requires sophisticated equipment; furthermore, it is difficult to prevent the powder oxidation in the course of the process. Spraying of a molten solder in a special sprayer with compressed gas also requires sophisticated equipment to obtain a high-quality powder.

This work continues our studies aimed at development of formulations of low-temperature corrosion-inactive solder creams with different melting points, using quaternary ammonium salts as fluxes [4–6].

EXPERIMENTAL

The solder powder was prepared as follows. The solder was placed in a glass reaction vessel, and VM-1S industrial oil was added. The mixture was heated to a temperature exceeding by 30–50°C the melting point of the solder, after which the electric stirrer was switched on. The mixture was cooled with stirring to a temperature below the melting point of the solder. Then the stirrer was switched off, and the powder was separated after sedimentation by decanting and washed with benzine and acetone.

From the obtained powders of various compositions, we prepared low-temperature solder creams based on the following solders: POSK 50-18, mp 160–180°C; solder of the composition 45% Sn, 29% Pb, 17% Cd, and 9% In, mp 160–180°C; and POIN-52, mp 120°C [7].

To determine the optimal particle size of the solder, we separated the powder by sieving into fractions with particle size of 1–10, 10–50, and 50–100 μm.

From these powder fractions, we prepared solder formulations applied onto contact areas of test printed-circuit boards. The contact areas were prepared by thick-film technology from Ag-containing and Ag–Pd conductor formulations, and also from thin-film copper conductors with a protective tin or gold coating. No significant catalytic effect of metals entering into

1070-4272/03/7606-1014 $25.00 © 2003 MAIK "Nauka/Interperiodica"

solder powder formulas on thermal oxidative degradation of the polyester resin was detected.

To prepare a solder cream, the chosen solder powder should be mixed with a binder containing a flux. As a flux we chose dimethylethylphenylammonium iodide (DMEPAI). A 2-g portion of DMEPAI was added to 15 g of a polyester resin prepared according to [4], and the components were thoroughly mixed.

The parameters of thermal oxidative degradation of the mechanical mixture of polyester resin with DMEPAI flux were determined by dynamic thermogravimetry [8]. To determine the temperature of the decomposition onset more accurately, we recorded not only TG, but also DTG (Fig. 1a) and DTA (Fig. 1b) curves. Experiments were performed with an MOM Q-1000 derivatograph (Hungary) in the programmed heating mode. A 0.03-g sample was heated in a platinum crucible in air at a rate of 10 deg min^{-1}. The sensitivity parameters were as follows: balance, 50 mg; DTA, 1/3; and DTG, 1/10.

The heat resistance of the polyester resin with DMEPAI was judged from the temperature of degradation onset (T_d^{DTG}, temperature at which the DTG curve starts to deviate from the baseline; T_d^{DTA}, temperature of the onset of the exothermic peak in the DTA curve, corresponding to the start of the oxidation) [9]. The results are listed in the table.

The degradation temperature T_d^{av} of a mixture of the polyester resin with DMEPAI is lower than T_d^{av} of the straight polyester resin; the shift is due to both enhanced chemical activity and increased specific surface area [8].

According to the TG and DTA curves, the DMEPAI flux degrades at 140–200°C. This means that DMEPAI is suitable as a component of solder cream formulations with melting point below 200°C.

To study the properties of solder creams, we prepared three formulations containing 15% polyester resin, 2% DMEPAI, and 83% one of the solder powders.

We found that the powder with particle size of 50 to 100 μm is too coarse; the cream with this powder is applied through templates badly and quickly undergoes phase separation in storage. The cream based on the finest powder (1–10 μm) is well applied through templates but requires increased amount of the organic binder; furthermore, in the course of tinplating, many fine particles remain suspended in the organic binder layer and do not form a continuous solder layer.

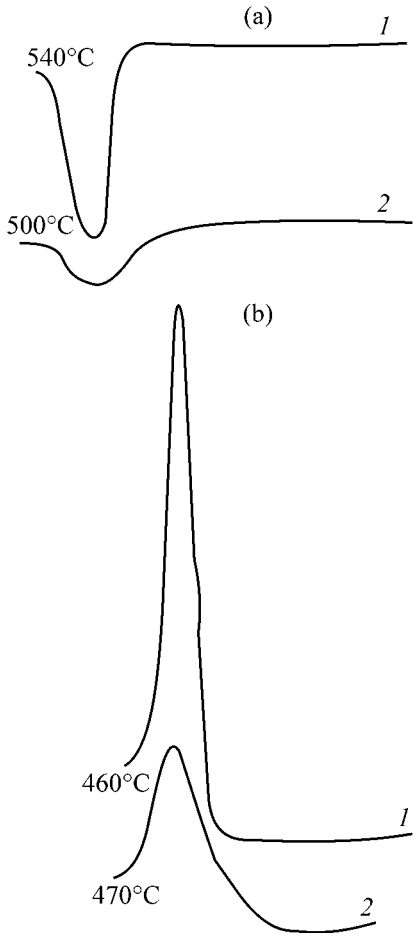

Fig. 1. (a) DTG and (b) DTA curves of (*1*) rosin-modified polyester resin and (*2*) mixture of the polyester resin with DMEPAI.

The optimal particle size is 10 to 50 μm. The solder creams based on this powder are well applied through bimetallic templates and ensure high-quality soldering upon fusion.

The quality of tinplating with solder creams was examined with an MBS-9 microscope at 8–16-fold magnification, following the procedure described in [6].

Parameters of the heat resistance of the samples, according to dynamic thermogravimetry

Sample	T_d^{DTG}	T_d^{DTA}	T_d^{av}
	°C		
Polyester resin	540	460	500
Polyester resin + DMEPAI	500	470	485

* $T_d^{av} = (T_d^{DTG} + T_d^{DTA})/2$ is the degradation temperature defined as the half-sum of the temperatures evaluated from the DTG and DTA data.

The adhesion of the solder cream layers to the contact areas after fusion was evaluated by the procedure involving detachment of the film from the contact area of the test printed-circuit board with an MR-05 tensile-testing machine [6].

With the contact areas prepared by the thick-film technology, the adhesion was no less than 50 kg cm^{-2}, and with those prepared by the thin-film technology, no less than 25 kg cm^{-2}. In most cases, the strength of the solder joint exceeded the adhesion of the contact area to the support.

CONCLUSIONS

(1) A procedure was developed for preparing solder powders for low-temperature solder creams, ensuring the required particle size and protection from oxidation in the course of fabrication.

(2) Formulations of low-temperature solder creams were developed, containing a polyester resin as an organic binder and dimethylethylphenylammonium iodide as a flux.

(3) With respect to the heat resistance, tinplating quality, and adhesion, the formulations developed meet the requirements to solder creams.

REFERENCES

1. Taylor, B.E., Slutsky, J., and Larry, J.R., *Solid-State Technol.*, 1981, Sept., pp. 127–135.
2. Trizna, Yu.P., Panov, L.I., Koretskii, V.N., and Rogovskii, V.F., *Tekh. Sredstv Svyazi, Ser. TPO*, 1979, no. 2, pp. 61–64.
3. Krasov, V.G., Petrauskas, G.B., and Chernozubov, Yu.S., *Tolstoplenochnaya tekhnologiya v SVCh mikroelektronike* (Thick-Film Technology in UHF Microelectronics), Moscow: Radio i Svyaz', 1985.
4. Polezhaeva, N.I., Polezhaeva, I.V., Levdanskii, V.A., *et al., Zh. Prikl. Khim.*, 2001, vol. 74, no. 4, pp. 684–685.
5. Polezhaeva, N.I., Polezhaeva, I.V., Levdanskii, V.A., and Kuznetsov, B.N., Abstracts of Papers, *IX konferentsiya "Destruktsiya i stabilizatsiya polimerov"* (IX Conf. "Polymer Degradation and Stabilization"), Moscow, April 16–20, 2001, pp. 150–151.
6. Polezhaeva, N.I., Polezhaeva, I.V., Levdanskii, V.A., *et al., Zh. Prikl. Khim.*, 2002, vol. 75, no. 4, pp. 689–690.
7. *OST* (Branch Standard) *4GO 033000: Fluxes and Solders: Composition, Properties, Application Fields*.
8. Wendlandt, W.Wm., *Thermal Methods of Analysis*, New York: Interscience, 1964.
9. Prokopchuk, N.R., *Vestn. Akad. Nauk Bel. SSR, Ser. Khim. Nauk*, 1984, no. 4, pp. 119–121.

Russian Journal of Applied Chemistry, Vol. 76, No. 6, 2003, pp. 1017–1018. Translated from Zhurnal Prikladnoi Khimii, Vol. 76, No. 6, 2003, pp. 1045–1046.

INFORMATION

XI Enikolopov Symposium

XI Enikolopov Symposium (March 13, 2003, Moscow) was held at the Enikolopov Institute of Synthetic Polymeric Materials (ISPM) (Moscow), Russian Academy of Sciences (RAS). The symposium was organized by RAS [Department of Chemistry and Materials Science, ISPM, Scientific Council for Macromolecular Compounds, Semenov Institute of Chemical Physics (Moscow), Institute for Problems of Chemical Physics (Chernogolovka, Moscow oblast)] and Moscow Physicotechnical Institute (Dolgoprudnyi, Moscow oblast).

The symposium program included four plenary lectures devoted to further progress of concepts formulated in his time by Academician Enikolopov.

N.Z. Lyakhov (Institute of Solid Fuel Chemistry and Mechanochemistry, Siberian Division, RAS, Novosibirsk) reported in his lecture the mechanism of formation of nanocomposites in mechanical alloying, including data on the initial stages of formation of nanocomposites in metallic systems. The lecturer gave analysis of general features of alloying and specific features of phase interaction in miscible (producing intermetallic compounds) and immiscible systems. It was illustrated by numerous examples that the resulting mechanocomposites are precursors of a new type for subsequent solid-phase reactions occurring in self-propagating high-temperature synthesis and also for synthesis of oversaturated solid solutions, etc.

From the standpoint of synthesis of practically important compounds and materials, an attempt was made to expand the previously developed approaches to systems of different types, including metal–oxide, metal–polymer, and layered systems.

Considerable interest was aroused in the audience by the lecture delivered by S.N. Chvalun (ISPM RAS), devoted to nanostructured polymeric hybrid materials. Nanostructured polymer–inorganic composites constitute one of the most important class of new synthetic hybrid materials. Directed design and manufacture of such materials with preset supramolecular nanostructure is a topical problem of modern science. The lecture covered preparation methods, major properties, and possible application areas of nanocomposites based on various ceramics, polymers, and oligomers. Special emphasis was made on the new class of layered ceramic-polymeric nanocomposites showing promise for practical use. Also, the lecture were considered various methods for preparation of metal–semiconductor–polymer nanomaterials in which inorganic nanoparticles demonstrate unique size-dependent electronic, photophysical, sensor, and catalytic properties.

The lecture given by O.A. Serenko (ISPM RAS) was devoted to composite materials based on plastic matrix and rubber particles. The lecturer considered deformation behavior of elastic particles in a plastic polymer and their effect on the stability of a composite material. He demonstrated that filled composites based on thermoplastics are characterized by definite critical content of rubber particles at which the materials abruptly lose their deformability, failing even at low ultimate elongations. By contrast, composite materials based on a plastic polymer demonstrate deformation without neck propagation and embrittlement.

In composites based on a plastic matrix and rubber particles, raising the filler content leads to successive change of the fracture mechanism, specifically, from neck propagation to brittle fracture and then from brittle fracture to macrouniform deformation. The first transition is accompanied by loss of deformability, and the second, by its increase. The increase in deformability in highly filled materials is due to localization of plastic flow of the matrix polymer in the microzones whose characteristic feature is their orientation. For example, it was demonstrated that the microzones are oriented perpendicularly to the stretching axis.

The fourth lecture given by V.A. Zhorin (Institute of Chemical Physics, RAS) was devoted to the effect of electrical factors on chemical and physical processes occurring in plastic deformation under high pressure. Exposure of solids of varied chemical nature to high pressure leads to a change in their electrical properties. In the case of organic insulators, at pressures of about 2 GPa, 2–3-fold increase in the permittivity was observed, and for some metal oxides this increase was as large as 50-fold. The conductivity of insulators decreases with increasing pressure, and

1070-4272/03/7606-1017 $25.00 © 2003 MAIK "Nauka/Interperiodica"

that of organic semiconductors increases by 3–4 orders of magnitude. Electron injection from a metal of the anvil has a strong effect on the conductivity of insulators. In the course of plastic deformation, the conductivity of different materials may increase 3 to 4–5 orders of magnitude. Applying magnetic and electric fields to compounds under investigation in the course of their high-pressure processing or introducing some functional additives, i.e., changing the electrical conditions of high-pressure experiments, allows control both over the course of chemical reactions and over structuring processes.

The results of the symposium demonstrate that Enikolopov's ideas are being successfully developed by his disciples and other scientists both in Russia and in other FSU countries.

G. E. Zaikov

Russian Journal of Applied Chemistry, Vol. 76, No. 6, 2003, pp. 1019–1022. Translated from Zhurnal Prikladnoi Khimii, Vol. 76, No. 6, 2003, pp. 1047–1050.

Nikolai Nikolaevich Kachalov (To 120th Anniversary of His Birthday)

Nikolai Nikolaevich Kachalov, a scientist, engineer, and pedagogue, made an outstanding contribution to the technology of manufacture and processing of glasses for various purposes, to the development of domestic glass industry, and to the science of glass.

N.N. Kachalov was born on June 21, 1883, in a cultured, high-born family of noblemen. His father, also Nikolai Nikolaevich Kachalov (1852–1909), was educated as naval officer and worked at the St. Petersburg Technical College of Telegraph Engineers with three-years education term from the time of its foundation, first as inspector (deputy director) and later, in 1895–1898, as director. He was honored engineer-electrician. It is during these years that the College was reorganized into Institute of Electrical Engineering with five-years education term (1898) and the construction of new building for the Institute was complete. The grandfather of the scientist-to-be, Nikolai Aleksandrovich Kachalov (1818–1891), a naval officer at the beginning of his career, later held high State posts and had a rank of privy councilor. His mother, Ol'ga L'vovna Kachalova (1859–1900), née Blok, was sister of A.L. Blok (1852–1909), professor of state law at Warsaw University, father of poet A.A. Blok (1880–1921). The Kachalov and Blok families were on intimate terms.

In 1900, after finishing secondary school, N.N. Kachalov entered the Mining Institute in St. Petersburg, one of the oldest higher school institutions of Russia (founded in 1773). At the beginning of the XX century, quite a number of prominent Russian scientists were among lecturers at the institute, including a specialist in mining mechanics I.A. Time (1838–1920), chemists I.F. Shreder (1857–1918) and N.S. Kurnakov (1860–1920), metallurgist V.N. Lipin (1858–1930), and electrical engineer M.A. Shatelen (1866–1957). When studying at the institute, N.N. Kachalov worked, in different years, at mining plants of Urals and Donetsk basin. This particularly refers to the period from 1904 till 1907, when studies at the institute were interrupted for a long time.

In 1911, having graduated from the Mining Institute, N.N. Kachalov went to work at the Imperial

Porcelain and Glass Factory at St. Petersburg (later Lomonosov Porcelain Factory) where he successively occupied positions of laboratory assistant, junior technician, and senior technician. In summer of 1910, N.N. Kachalov married Elizaveta Ivanovna Time (1884–1968), younger daughter of I.A. Time, professor of the Mining Institute. N.N. Kachalov's wife was an actor at Aleksandrinskii Theater in St. Petersburg and was already widely popular. For this reason the young family could not move to industrial regions of Russia, where graduates from the Mining Institute traditionally went to work.

N.N. Kachalov's activities at the factory were quite successful, and, in 1916, he became its technical director. World War I (1914–1918) posed a wide variety of important tasks to be accomplished by Russia's industry. To these belonged the necessity for organizing domestic manufacture of optical glass [1]. By N.N. Kachalov's initiative, a special board was created,

1070-4272/03/7606-1019 $25.00 © 2003 MAIK "Nauka/Interperiodica"

N.N. Kachalov. Sculpture (in glass) by V.I. Mukhina.

already in August 1914, for solving this complicated problem. The board included a number of leading scientists from St. Petersburg: academician N.S. Kurnakov and professors V.E. Grum-Grzhimailo, N.A.Pushin, D.S. Rozhdestvenskii, and V.E. Tishchenko [2]. On the suggestion of N.A. Pushin (1875–1947), a professor of the Institute of Electrical Engineering, direct supervision of work on melting was entrusted to his pupil, young lecture at the same institute, I.V. Grebenshchikov (1887–1953, academician since 1932). V.E. Grum-Grzhimailo (1864–1928), a professor of Polytechnic Institute, was charged with furnace design. Professor of physics, D.S. Rozhdestvenskii (1876–1940, academician since 1929) was a known specialist in the field of optics; V.E. Tishchenko (1861–1941, academician since 1935), a professor of St. Petersburg University, was the only member of the academic board who was experienced in glass melting. In 1896–1900, he developed stock formulations for 28 different brands of glass for chemical glassware. The problem of optical glass melting could not be solved in a short time without using the know-how of foreign companies. Pushin was sent to a business trip to London for difficult negotiations with British; N.N. Kachalov also went to Great Britain for completion of the negotiations. Grebenshchikov was the last to visit Great Britain with a group of master craftsmen for ascertaining details of meltings. The vigorous activities of N.N. Kachalov and Grebenshchikov, in which all the members of the academic board took an active part, resulted in that manufacture of optical glass was for the first time started in Russia. By the beginning of 1917, more than 8 tons of glass of satisfactory quality was manufactured [2].

Under N.N. Kachalov's supervision, manufacture of a new brand of porcelain (soft porcelain) was brought to a commercial level at the factory and technical porcelain was started to be produced for the first time. By scientist's initiative, a special building was erected on the territory of the factory for organizing in it a research center for glass and ceramics. During the civil war and the resulting period of collapse of the national economy, the manufacture of optical glass on the territory of the porcelain factory was closed down temporarily. However, an optical glass factory was created on its base already in 1923. N.N. Kachalov was appointed the technical supervisor of this factory, and Grebenshchikov and Rozhdestvenskii became consultants.

In 1918, State Optical Institute (GOI) was organized in Petrograd. Rozhdestvenskii was appointed its director and held this position till 1932. Grebenshchikov organized at this institute a chemical laboratory and headed it till the end of his life. In 1921, Grebenshchikov was sent to a business trip to Germany to purchase necessary materials and equipment and to visit German factories manufacturing optical glass. Later, during the period from 1932 till 1946, N.N. Kachalov also worked at GOI as deputy director, head of laboratory, and (beginning in 1937) consultant.

In 1923, work on refining of technology and improvement of optical glass quality was continued at Leningrad factory of optical glass. Unfortunately, not all members of the original academic board could take part in these activities. It happened so that, in the following years, Grum-Grzhimailo was a professor at Sverdlovsk (Yekaterinburg) University, and Pushin, a professor of the Zagreb University (Yugoslavia). However, Rozhdestvenskii's colleagues from the Optical Institute, known physicists A.A. Lebedev (1893–1969), A.I. Tudorovskii (1875–1963), and I.V. Obreimov (1894–1981), were among the participants. In 1926, a new rapid melting technology was developed, which differed significantly from the original method. Key experiments were performed in June 1926; these experiments were described in detail by journalist Yu.L. Alyanskii in his book devoted to the life and activities of N.N. Kachalov [3]. The duration of each melting was decreased (from 100 to 25 h), the output

capacity of the factory increased by a factor of 2, and the quality of the optical glass obtained conformed to most stringent requirements. The main contribution to the development of the domestic technology for glass manufacture for optical instruments was made by N.N. Kachalov, Grebenshchikov, and Rozhdestvenskii. The import of optical glass to the USSR was completely terminated in 1927 [4, 5].

During many years (from 1918 till 1930), N.N. Kachalov's activities were associated with the State Ceramic Institute. This institute was organized with his participation, and he held there a number of important positions. Under his supervision, extensive studies aimed to improve the technology of manufacture of refractory materials used in glass-making and investigations of the properties of high-quality domestic clays were carried out [4, 6]. The results obtained were summarized in a collective publication "Fireclays" (*Trudy Gos. Issled. Inst.*, 1929, issue 16).

In 1930, N.N. Kachalov was appointed head of the research sector of the All-Union Association of the optical-mechanical industry, where he was engaged in organization of research in the field of manufacture of optical-mechanical instruments. (till 1932) [7].

In 1930, N.N. Kachalov's pedagogical activities commenced at the Leningrad Technological Institute (LTI), where he organized the first chair of glass in the USSR and remained its head till the end of his life. Exceedingly important is N.N. Kachalov's contribution to training of high-skill engineers, many of his pupils became known specialists in the field of technology of inorganic materials and the glassy state. The chair of glass has always been rather popular with students of LTI.

The research activities at the chair developed in three directions: grinding and polishing of glass, manufacture of art glass and enamels, and development of new glass formulations and study of their properties. In 1935, a pilot glass-melting installation was constructed at the chair. This installation served as a basis for practical studies of students, experimental meltings, and execution of orders for manufacture of valuable brands of glass and enamels. At the same year, the laboratory of cold glass processing was organized at the chair. In 1935–1937, an extensive series of investigations carried out under N.N. Kachalov's supervision was devoted to development of a technology for mass production of polished sheet glass. The general theoretical concepts of glass polishing mechanism, developed by Grebenshchikov, served as a basis for extensive experimental studies of the influence exerted by various technological factors on the polishing process. Further, the results obtained in the study, in which a large group of laboratory staff members took part, were summarized by N.N. Kachalov in the monograph *Osnovy protsessov shlifovki i polirovki stekla* (Fundamentals of Glass Grinding and Polishing) (Moscow: Akad. Nauk SSSR, 1946). The monograph was awarded a State Prize in 1947.

In 1948, N.N. Kachalov organized the laboratory of cold processing of silicate materials at the Institute of Silicate Chemistry, Academy of Sciences of the USSR. The equipment of the laboratory with modern high-precision instruments and special devices made it possible to extend the scale of investigations into the physical and physicochemical essence of processes occurring in grinding and polishing of glass and other brittle materials.

A prominent place within the sphere of N.N. Kachalov's scientific interests was occupied by art glass and development of a technology for manufacture of large glass articles. In 1940, he initiated transformation of the Leningrad Mirror Factory into Plant of Art Glass, with an affiliated scientific laboratory. The main part of investigations was transferred from the chair of glass at LTI to the new laboratory and directly to the plant. The artistic supervision of plant was entrusted to a known sculptor, V.I. Mukhina (1889–1953), and the scientific and technological supervision, to the chair of glass at LTI. As plant's consultant was invited professor V.V. Vargin, a specialist in enamel manufacture.

The last N.N. Kachalov's capital work was the unique monograph *Steklo* (Glass) (Moscow: Academy of Sciences of the USSR, 1959), which unveiled the many-century history of glass, technology of its manufacture, and its application in technology, architecture, and art.

Among N.N. Kachalov and E.I. Time's friends were quite a number of prominent writers and artists. They included: A.N. Tolstoy (1882–1945), one of the most prominent Russian writers of the first half of the XX century; L.N. Sobinov (1872–1934), an exceedingly widely known singer; in later time, ballerina G.S. Ulanova (1910–1998). Unfortunately, N.N. Kachalov had no time to write recollections of his life, meetings, and nearest friends. To some extent this is compensated for by the book of E.I. Time's recollections *Dorogi iskusstva* (Avenues of Art) (Moscow: Vses. Teatr. O–vo, 1967), which was written with active participation of Nikolai Nikolaevich.

N.N. Kachalov's scientific, engineering, and pedagogical activities were highly appreciated. Already in 1933, he was elected a corresponding member of the Academy of Sciences of the USSR, Department of Chemical Science; in 1935, he was awarded an honorary title of Honored Scientist and Technologist of the Russian Soviet Federative Socialist Republic. N.N. Kachalov was honored with quite a number of State awards.

Nikolai Nikolaevich Kachalov passed away on June 19, 1961, and was buried in Leningrad at *Literatorskie mostki* (Writers' Footpath) at Volkovo Cemetery. In 1965, one of streets in Leningrad was named after professor N.N. Kachalov. In scientist's memory, memorial boards were mounted on the house where he lived from 1911 till 1961 (Vosstaniya ul., 6), in a hall at the Institute of Silicate Chemistry, and on the building of the Plant of Art Glass. The memory of the scientist is preserved by his numerous pupils.

REFERENCES

1. Bakhrakh, A.M., *Iz istorii opticheskogo priborostroeiya: Ocherki* (Essays on the History of Optical Instrument Building), Moscow: Mashgiz, 1951, vol. 1.
2. Rozhdestvenskii, D.S., *Tr. Gos. Optich. In–ta*, 1932, vol. 8, no. 84, pp. 1–22.
3. Alyanskii, Yu.L., *Magicheskii kristall professora Kachalova* (Professor Kachalov's Magic Crystal), Leningrad: Lenizdat, 1966.
4. *Nikolai Nikolaevich Kachalov: Materialy k biobibliografii uchenykh SSSR, Seriya khimicheskikh nauk* (Nikolai Nikolaevich Kachalov: Materials on Biobibliography of Scientists of the USSR), Moscow: Akad. Nauk SSSR, 1953, issue 18.
5. Barzakovskii, V.P. and Korelova, A.I., *Trudy LTI im. Lensoveta*, 1958, issue 49, pp. 5–10.
6. *Steklo Keram.*, 1958, no. 9, pp. 46–47.
7. Bokin, P.Ya., *Opt.-Mekh. Prom–st.*, 1961, no. 11, pp. 55–56.

A. G. Morachevskii

Russian Journal of Applied Chemistry, Vol. 76, No. 6, 2003, p. 1023. Translated from Zhurnal Prikladnoi Khimii, Vol. 76, No. 6, 2003, p. 1051.

BOOK REVIEWS

Barbin, N.M., Kazantsev, G.F., and Vatolin, N.A., *Pererabotka vtorichnogo svintsovogo syr'ya v ionnykh solevykh rasplavakh* (Processing of Secondary Lead in Ionic Salt Melts), Yekaterinburg: Ur. Otd. Ross. Akad. Nauk, 2002, 178 pp.

The monograph is authored by N.A. Vatolin, academician of the Russian Academy of Sciences, and N.M. Barbin and G.F. Kazantsev, experienced researchers in the field of high-temperature electrochemical technologies. During quite a number of years, all of them have been paying much attention to processing of various technological wastes and, in particular, to utilization of secondary lead and search for ecologically safe technologies.

The book comprises a brief foreword and two parts, each constituted by chapters, conclusion, and bibliographic list. The foreword (pp. 5–6) notes that more than 50% of world's lead is manufactured by processing scrap lead and wastes. The authors point to a number of advantages offered by use of ionic melts in various technological processes.

The first part of the monograph, which comprises five chapters, is devoted to electrometallurgical processing of lead-containing wastes in a carbonate melt. The first chapter (pp. 10–30) briefly characterizes mainly pyrometallurgical methods for processing of lead-containing raw materials. The second chapter (pp. 31–53) describes physicochemical foundations of electrometallurgical processing of lead-containing compounds in a carbonate melt. Much attention is given to thermodynamic modeling of reduction of lead compounds in molten carbonates. The third chapter (pp. 54–80) contains evidence on processing of lead battery scrap and wastes from battery manufacture in a carbonate melt. The process is carried out at temperatures of 800–1050°C in electric furnaces with the use of various reducing agents. The fourth (pp. 81–99) and fifth (pp. 100–130) chapters are devoted to rather specific issues: processing of dust from shaft furnaces of Verkh-Neivinskii plant of secondary nonferrous metals and lead-containing wastes from copper-smelting plants. In the latter case, fine dusts caught by bag filters after shaft furnaces and converters (lead content 24–33 wt %) and products formed in hydrochemical processing of dusts, lead cakes (up to 42 wt % Pb) serve as objects of study. In all cases, molten carbonates are used as the reaction medium.

The second part of the monograph, which is smaller in volume, comprises four chapters considering the physicochemical foundations (pp. 142–160) and technology (pp. 161–172) of electrochemical processing of lead-containing wastes in hydroxide melts.

The bibliographic lists for the first and second parts of the book contain, respectively, 99 and 30 references to publications of mainly domestic authors. About 30% of all the published sources belong to the authors of the monograph.

Unfortunately, the book makes no attempt to analyze the present state of the problem of lead battery scrap, which is the most important, in economic and ecological regards, kind of secondary lead. The processing of battery scrap has nearly escaped the authors' attention. The monograph primarily presents the results of many-year authors' investigations, which are interesting and original, but are mainly devoted to minor kinds of lead-containing raw materials, dusts of shaft furnaces and wastes from battery manufacture.

The book summarizes a vast experimental material, evidence obtained in laboratory and pilot-plant studies, and results of mathematical modeling. All these data may be of interest for scientists, engineers, and technicians working in the field of utilization of secondary lead. The book is well published and contains a large number of tables and figures.

A. G. Morachevskii

1070-4272/03/7606-1023 $25.00 © 2003 MAIK "Nauka/Interperiodica"

Russian Journal of Applied Chemistry, Vol. 76, No. 7, 2003, pp. 1025–1030. Translated from Zhurnal Prikladnoi Khimii, Vol. 76, No. 7, 2003, pp. 1057–1062.

INORGANIC SYNTHESIS AND INDUSTRIAL INORGANIC CHEMISTRY

Effect of Alloying Elements on the Temperature Dependence of the Rate Constants and on the Activation Energy of Oxidation of Titanium Alloys

V. I. D'yachkov

St. Petersburg State University, St. Petersburg, Russia

Received December 6, 2002

Abstract—The influence exerted by the nature and concentration of alloying elements on the temperature dependence of the rate constants and on the activation energy of oxidation of titanium alloys in air at 823–1473 K was considered.

Available literature on oxidation of titanium alloys contains no systematic data on the effects of alloying elements on such important characteristics of the process as the temperature dependence of the rate constants and the activation energy of oxidation. The authors often restrict the consideration to the estimation of the effect exerted by alloying elements on the heat resistance of alloys, without identification of the oxidation kinetic law. At the same time, the knowledge of these characteristics is useful for comprehensive understanding of the complicated oxidation mechanism.

Such studies are also appropriate in view of the fact that, according to previous data [1–10], in contrast to the data of other authors and partly of [11], the oxidation of titanium and all its alloys indicated below proceeds in a nonstationary (transient) mode in which diffusion and interphase reactions exert comparable effects on the total rate of the process. The validity of the Evans equation supports this conclusion [12]:

$$K_l q^2 + K_p q + K_l K_p \tau = C,$$

where q is weight; τ, time; C, a constant; K_l and K_p, rate constants of the oxidation by the linear and parabolic laws, respectively.

In this study we analyze the effects exerted by the nature and concentration of alloying elements and by the temperatures and duration of tests on the temperature dependence of the rate constants and on the activation energy of oxidation of titanium alloys in air at 823–1473 K.

The corresponding data on the temperature dependence of K_l and K_p were obtained for titanium (purity 99.93%) and alloys with the following contents of alloying elements (wt %): Ti–0.6, 2.2, 3.4, 4.7, 5.9 Al; Ti–1.9, 7.4, 14.2 Zr; Ti–2.0 Al–2.5 Zr (PT-7M); Ti–1.5, 5.0, 10.0 Fe; Ti–0.5, 0.9, 3.0 V; and Ti–5.2 Al–1.2 V–1.1 Mo. The experimental technique and the process for preparing alloys were published earlier [1, 4].

According to [1–10], the Evans equation virtually adequately describes the oxidation rate (3 h) of titanium and its alloys at 923(973)–1373(1473) K. It is valid also in the initial stage of the test at 723–898 K, being replaced then by a cubic or approximately cubic law. When the above-mentioned materials are oxidized (3 h) at $T \geq 973(1023)$ K, two Evans equations with different K_l and K_p values are usually followed sequentially. For reasons given in [10], to increase the descriptiveness of the data on the temperature dependence of these constants, in this work we used their values for the initial and subsequent periods of oxidation, $K_l^{(1)}$, $K_p^{(1)}$ and $K_l^{(2)}$, $K_p^{(2)}$, respectively.

The temperature dependences of $K_l^{(1)}$ and $K_p^{(1)}$ for titanium and some of its alloys are shown in the figure, and the apparent activation energy E of the oxidation calculated by the linear (E_l) and parabolic (E_p) laws for the initial ($E_l^{(1)}$, $E_p^{(1)}$) and the subsequent ($E_l^{(2)}$, $E_p^{(2)}$) stages of the test are given in the table. For each combination of $E_l^{(1)}$, $E_l^{(2)}$ and $E_p^{(1)}$, $E_p^{(2)}$, the corresponding temperature ranges of their validity are indicated. When the boundaries of the temperature ranges for the both periods of oxidation mismatch, their values for the second stage of the test are given in parentheses. The accuracy of the determination of E for titanium is ~(3–5)%, and that for alloys is

1070-4272/03/7607-1025$25.00

Influence of the material composition, temperature, and test duration on the apparent activation energy of oxidation calculated by the linear (E_l) and parabolic (E_p) laws

Material composition, wt %	T, K	$E_l^{(1)}$	$E_l^{(2)}$	T, K	$E_p^{(1)}$	$E_p^{(2)}$
		kJ mol^{-1}			kJ mol^{-1}	
Ti refined	823–973	125	–	823–973	155	–
	973–1173	71	65	973–1173(1073)	235	203
	1173–1423(1373)	199	180	1123(1073)–1223(1173)	510	530
				1223(1173)–1373	159	158
Ti–0.6 Al	823(948)–1173	117	114	873(948)–1223(1173)	280	325
	1173–1423	206	240	1223(1173)–1423	110	171
Ti–2.2 Al	823(1023)–1223	121	133	873–1223	260	275
	1223–1473(1373)	217	237	1223–1473	156	168
Ti–3.4 Al	823–973	80	–	823(973)–1173	221	290
	973–1173	161	156	1173–1373	192	133
	1173–1373	150	208			
Ti–4.7 Al	823–973	50	–	823(1073)–1223(1273)	267	273
	973–1073	268	254	1223(1273)–1423	169	120
	1073–1273	123	102			
	1273–1373(1473)	234	276			
Ti–5.9 Al	823–923	82	–	873(973)–1273	269	295
	923–1023(1073)	334	270	1273–1473	169	132
	1023(1073)–1273	116	100			
	1273–1473	215	241			
Ti–1.9 Zr	823(973)–1123	75	75	823–973	147	–
	1123–1473	175	125	973–1173	290	293
				1173–1473	277	320
Ti–7.4 Zr	823–973	95	–	823–973	101	–
	973–1173	109	67	973–1073	189	202
	1173–1473	212	213	1073–1473	354	368
Ti–14.2 Zr	823–973	102	–	823–973	132	–
	973–1173	40	90	973–1423(1473)	248	271
	1173–1473	180	228			
PT-7M	823–923	79	–	823–923	137	–
	923–1173	159	156	923–1073(1123)	385	386
	1173(1123)–1473	159	132	1073(1123)–1273	172	152
				1273–1473	219	295
Ti–1.5 Fe	973(1023)–1173	64	30	973(1073)–1173	96	213
	1173–1223	345	331	1173–1273(1223)	610	780
	1223–1373	152	102	1273(1223)–1423(1473)	129	153
Ti–5.0 Fe	1023–1123(1173)	40	31	1023–1173	96	223
	1123(1173)–1223(1273)	240	290	1173–1223	550	640
	1223(1273)–1473	45	97	1223–1473	225	117
Ti–10.0 Fe	1023–1123	54	52	1023–1123	189	302
	1123–1173	193	52	1123–1173	460	500
	1173–1373	85	141	1173–1423	215	189
Ti–0.5 V	1073–1173	150	142	1073–1223	291	385
	1173–1373	229	215	1223–1373	291	143
Ti–0.9 V	1073–1173	134	112	1073–1223	315	398
	1173–1323	237	265	1223–1323	315	147
Ti–3.0 V	1073–1173	102	88	1023–1223	327	342
	1173–1323	203	217	1223–1323(1373)	92	135
Ti–5.2 Al–1.2 V–1.1 Mo	973–1473(1423)	145	128	973–1473	210	223

±(3–7)%. The E_l and E_p values were calculated from the slopes of the linear portions of the temperature dependences of therate constants.

It follows from the table and figure that the temperature dependence of K_l and K_p in both stages of oxidation for the majority of compositions is characterized by bends in the range 1123–1173 K, and in the case of titanium, PT-7M, and some alloys of the systems Ti–Al and Ti–Zr, oxidized at 823–1473 K, also in the range 923–973 K. Moreover, for Ti there are two bends in the $\log K_p = f(1/T)$ curve: at 1123(1073) and 1223(1173) K, and in the case of Ti–Fe, also in the $\log K_l = f(1/T)$ curve at 1123(1173) and 1223(1273) K. It should be noted that, in [13], three zones with different values of the activation energy were detected for the oxidation of technical-grade titanium in air in the range 1073–1373 K. At the same time, the Ti–0.5, 0.9 V and Ti–7.4, 14.2 Zr alloys have no bend in the $\log K_p = f(1/T)$ curve in the range 1123–1223 K. Similar trends are observed for PT-7M in the case of $\log K_l = f(1/T)$ and for Ti–5.2 Al–1.2 V–1.1 Mo in the case of both dependences. However, the temperature coefficients of $K_l^{(2)}$ and $K_p^{(2)}$ for all the alloys, except for Ti–5.2 Al–1.2 V–1.1 Mo and for Ti–7.4, 14.2 Zr ($K_p^{(2)}$), undergo the corresponding changes.

For the majority of compositions, the temperature coefficients $K_l^{(1)}$ and $K_l^{(2)}$ increase in going to the region above the temperatures of the bend T_{bend}, in contrast to the PT-7M alloy and partly to the Ti–Fe alloy. On the contrary, the dependence $\log K_p = f(1/T)$ in both stages of oxidation is characterized by a decrease in the slope at the last bend in the range 1023–1473 K, except for the alloys Ti–Zr, Ti–0.5, 0.9 V, and Ti–5.2 Al–1.2 V–1.1 Mo, for which this dependence is linear in the first or in both stages of the test.

The table shows that the T_{bend} values for the $\log K_l = f(1/T)$ and $\log K_p = f(1/T)$ dependences in both stqages of the oxidation ($T_{bend}^{l_1}$, $T_{bend}^{l_2}$ and $T_{bend}^{p_1}$, $T_{bend}^{p_2}$) above 973(1023) K are equal for the majority of compositions within the limits of each dependence. In the first case, the exceptions are Ti–5.9 Al, Ti–5.0 Fe, and PT-7M alloys, whereas in the second case these are Ti and Ti–0.6, 4.7 Al, Ti–1.5 FE, PT-7M, and conventionally Ti–0.5, 0.9 V, owing to a change in the shape of the dependence $\log K_p = f(1/T)$ in going from the initial to the subsequent periods of oxidation. A feature of pure Ti is that, in going from the initial to the subsequent periods of oxidation, the boundaries of the 1123–1223 K range shift by 50 K toward lower temperatures (1073–1173 K), with retention of the dependence type.

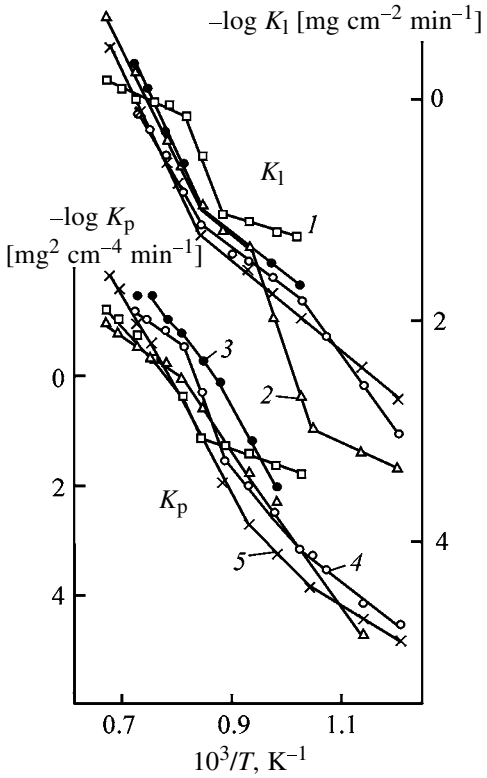

Temperature dependence of K_l and K_p for titanium and its alloys. (K_l, K_p) rate constants of the oxidation calculated by the linear and parabolic laws, respectively; (T) temperature. Alloy (wt %): (*1*) Ti–5.0 Fe, (*2*) Ti–4.7 Al, (*3*) Ti–3.0 V, (*4*) Ti and (*5*) Ti–7.4 Zr.

As K_l and K_p characterize mutually dependent processes, it was natural to expect that T_{bend}^{l} and T_{bend}^{p} for both oxidation stages of oxidation will coincide. In fact, in the initial stage of the test of the Ti–2.2, 3.4, 5.9 Al and Ti–Fe alloys, $T_{bend}^{l_1}$ and $T_{bend}^{p_1}$ fully coincided. For the other compositions (Ti–0.6 Al, Ti–1.9 Zr, Ti–V, and PT-7M) $T_{bend}^{l_1}$ is less than $T_{bend}^{p_1}$, and in the case of Ti–4.7A1 and Ti–7.4 Zr, on the contrary, $T_{bend}^{l_1}$ is higher than $T_{bend}^{p_1}$. In the second oxidation stage, titanium and Ti–Al, Ti–Fe alloys have virtually equal values of $T_{bend}^{l_2}$ and $T_{bend}^{p_2}$, whereas for PT-7M and Ti–V $T_{bend}^{l_2}$ is lower than $T_{bend}^{p_2}$. However, the difference between T_{bend}^{l} and T_{bend}^{p} usually do not exceed 50 K, which in many cases is the temperature interval between separate experiments.

The changes in the slope of the dependences $\log K_l = f(1/T)$ and $\log K_p = f(1/T)$ in the range 1123–1223 K, apart from other reasons, are associated with

the effect exerted on the oxidation by the allotropic $\alpha \leftrightarrows \beta$ transition in the metallic phase. This transition takes place in pure titanium at 1155 K. It is accompanied by weakening of interatomic bonds in the metallic lattice, by excitation of atoms, and, therefore, by changing conditions for occurrence of an interphase reaction on the metal–gas boundary and for diffusion. The rate constants K_l and K_p of these processes characterize the nonstationary oxidation at $\tau \to 0$ and $\tau \to \infty$, respectively, since an α-layer with a constant surface concentration of oxygen, close to the equilibrium concentration for pure titanium, is formed in the outer zone of the matrix even in the initial stage of the test [14].

The effect of the $\alpha \to \beta$ transition on the oxidation is manifested not only at the equilibrium temperature, but also in a certain temperature range. In particular, this is due to the fact that the equilibrium temperature of the $\alpha \to \beta$ transition on the metal surface is much lower (by 80 K) than in the bulk metal [15]. A considerable increase in the slope of the dependence $\log K_p = f(1/T)$ in the range 1073–1173 K can be also associated with this phenomenon. Above 1173(1223) K, the surfaces and volumes of matrices of all the materials under consideration have the same β-structure [16]. The corresponding decrease in the temperature coefficient K_p is due, at least partly, to a smaller energy consumption for the diffusion of oxygen in the β-phase compared to the α-modification [17], and, according to [18], the transition to the range of $T > 1173$ K is accompanied by a considerable decrease in the temperature coefficient of the total oxygen uptake by the metal. These features of the temperature dependence of K_p largely result also from changes with temperature in the contributions of bulk and intercrystallite diffusion, scaling, and growth of the diffusion oxygen layer (DOL) to the total oxidation process, and also in the equilibrium of defects in the oxide.

According to the table and figure, the T^{l}_{bend} value (1173 K) remains practically unchanged above 1073 K in going from titanium to the Ti–0.6 Al, Ti–7.4, 14.2 Zr, PT-7M, Ti–1.5, 10.0 Fe, and Ti–V alloys. However, T^{l}_{bend} increases to 1273 K as c_{Al} increases, whereas it tends to decrease as compared to titanium when c_{Fe} increases. To a first approximation, this is attributable to the effect of these elements on the temperature of the $\alpha \to \beta$ transition in the metal. Thus, aluminum as an α-stabilizer increases the temperature of the $\alpha \to \beta$ transition, which is higher by almost 100 K than for pure titanium [16] at c_{Al} = 5.9%, whereas iron, on the contrary, stabilizes the β-phase. The dependence of T^{p1}_{bend} on c_{Al} and c_{Fe} is similar, though it is less pronounced for the Ti–Al alloys. It should also be noted that T^{p1}_{bend} decreases as c_{Zr} increases in alloys at $T > 973$ K.

In most cases, $T^{l1}_{bend} = T^{l2}_{bend}$ and $T^{p1}_{bend} = T^{p2}_{bend}$, except for Ti, PT-7M, Ti–0.6, 4.7 Al, and Ti–1.5, 5.0 Fe.

According to the table, three temperature zones with different E_l and E_p values can be distinguished for titanium in the range 823–1473 K: 823–973, 973–1173(1223), and above 1173(1223) K. In going from the first zone to the second zone, $E_l^{(1)}$ decreases, and $E_p^{(1)}$, on the contrary, increases. Approximately a half of the alloys demonstrate a similar variation of $E_p^{(1)}$ and an opposite variation of $E_l^{(1)}$, whereas in the remaining cases their values within the limits 823–1173(1223) K remain virtually constant. The absence of data for $E_l^{(2)}$ and $E_p^{(2)}$ at 823–973 K in the table results from the fact that the Evans equation is usually valid in this range only in the initial stage of the test. The transition to temperatures higher than 1173(1223) K, as already noted, is accompanied by an increase in E_l and a decrease in E_p in both stages of the oxidation of titanium and majority of the alloys. The exceptions with respect of E_l are mainly Ti–Fe alloys, and in the case of E_p, Ti–Zr and PT-7M alloys.

The values of E_l are lower than the values of E_p for all the compositions in the range 823–1173 K. At the same time, in many cases (Ti–Al and Ti–V) at $T >$ 1223 K, especially in the second stage of the oxidation, the relationship is opposite. It can be treated as growth of the relative contribution of interphase processes to the control of the overall oxidation rate with temperature, which does not contradict the existing theoretical concept of the temperature effect on the energy consumption for diffusion and interphase processes [19].

Let us consider the effect of material composition on E_l and E_p in various temperature ranges. In the range 823–973 K, the alloying of titanium with up to 2.2 wt % aluminum leaves E_l practically unchanged, and at $c_{Al} > 2.2$ wt % it gives rise to its decrease. In this case, as c_{Al} increases, E_l tends to decrease, whereas as c_{Zr} grows, E_l clearly tends to increase. Titanium and Ti–Al alloys with a low Al content have the maximal values of E_l, and Ti–1.9 Zr and PT-7M, the minimal values. In the range 973–1173 K, $E_l^{(1)}$ and $E_l^{(2)}$ for the majority of alloys, except for Ti–Fe, are

higher than those of titanium. As c_M in the Ti–Al alloys increases, $E_l^{(1)}$ and $E_l^{(2)}$ clearly tend to increase, as well as $E_l^{(2)}$ in the case of Ti–Fe, whereas in the case of the Ti–Zr and Ti–V alloys they decrease, as well as $E_l^{(1)}$ in the oxidation of Ti–Fe. The highest values of $E_l^{(1)}$ and $E_l^{(2)}$ in the range 973–1173 K are observed for the Ti–Al ($c_{Al} > 3.4\%$) and PT-7M alloys, and the lowest, for titanium and Ti–Fe. At $T >$ 1173(1223) K, the alloying of titanium with vanadium increases $E_l^{(1)}$, and in most of the remaining cases it is accompanied by its decrease. With respect of $E_l^{(2)}$, a similar behavior is observed for the Ti–Fe, Ti–1.9 Zr and PT-7M alloys, whereas its values for the remaining compositions are higher than for titanium. As c_M in the Ti–Al [c_{Al} = 0.6–2.2%] and Ti–Zr alloys increases, $E_l^{(1)}$ tends to increase, and in the case of Ti–Fe and Ti–V it tends to decrease. The same pattern is observed for $E_l^{(2)}$ in the oxidation of the Ti–Al and Ti–Fe alloys, in contrast to Ti–Zr and Ti–V. At $T >$ 1173(1223) K the most energy-consuming interphase processes occur in both stages of the oxidation of Ti–V and partly of Ti–Al alloys, whereas Ti–5.0, 10.0 Fe has the minimal $E_l^{(1)}$ value and Ti–1.9 Zr and PT-7M, the minimal $E_l^{(2)}$ value.

In the initial stage of the oxidation at 823–973 K, the energy consumption for diffusion processes in Ti–Al alloys is higher, and in the case of Ti–Zr and PT-7M, lower than for titanium, and it tends to decrease as c_{Al} (<4.7 %) and c_{Zr} increase. In the range 973–1123 K, the alloying of titanium with iron (up to 5.0%) decreases $E_p^{(1)}$. For the other compositions, $E_p^{(1)}$ and $E_p^{(2)}$ are mostly higher than for titanium. As C_M in the Ti–Al ($c_{Al} \le 3.4\%$) and Ti–Zr alloys increases, $E_p^{(1)}$ and $E_p^{(2)}$ tend to decrease, and in the case of Ti–Fe and Ti–Al ($c_{Al} > 3.4$ %) they clearly increase. In this case, the PT-7M and Ti–V alloys have the highest $E_p^{(1)}$ and $E_p^{(2)}$ values, and Ti–1.5, 5.0 Fe, the lowest $E_p^{(1)}$ values.

In the range 1123(1073)–1223(1173) K, all the alloys under consideration (except partly Ti–Fe) are characterized by the lower energy consumption for diffusion processes in both stages of oxidation, as compared to titanium. As c_{Al} and c_{Zr} increase within certain limits, $E_p^{(1)}$ and $E_p^{(2)}$ decrease, whereas with increasing c_V and c_{Fe} they tend to grow.

In the range $T >$ 1223 K, the alloying of titanium mostly increases $E_p^{(1)}$. The alloys Ti–Zr and PT-7M have higher $E_p^{(2)}$ values than titanium, whereas in the case of Ti–V, Ti–3.4, 4.7, 5.9 Al, and Ti–5.0 Fe the relationship is reverse. As c_{Al} and c_{Zr} increase, $E_p^{(1)}$ and $E_p^{(2)}$ tend to decrease, and in the case of increasing c_{Fe} they tend to grow. As c_V increases, $E_p^{(1)}$ decreases nonmonotonically, and changes in $E_p^{(2)}$ do not exceed the experimental error. The Ti–Zr alloys are characterized by the greatest energy consumption for diffusion processes in both oxidation stages at $T >$ 1223 K, and the Ti–Al alloys, by the lowest energy consumption.

The comparison of E_l and E_p values for the Ti–2.2 Al and Ti–1.9 Zr alloys with the data for PT-7M (Ti–2.0 Al–2.5 Zr) having the same total atomic concentration of Al and Zr (4.8 at %) shows that zirconium affects the oxidation of the PT-7M alloy to a greater extent than aluminum, though its atomic concentration in the alloy (1.3 at. %) is much lower.

The established dependences of E_l and E_p on the material composition, temperature, and duration of oxidation are associated with the effects of these factors on the composition and structure of metallic and oxide phases. In particular, the alloying of titanium results in a change in the energy of interatomic bonds in the matrix lattice and changes in conditions and, therefore, growth rates of DOL, for example, upon redistribution of alloying elements in oxidation products [20, 21]. It also affects the temperature of $\alpha \leftrightarrows \beta$ transitions in the metal and the type and concentration of point defects, which form on penetration of alloying elements into the rutile lattice and determine the diffusion mechanism of scaling.

The extent of changes in the oxidation mechanism and rate depend on the nature and concentration of alloying elements. The degree and the form of their participation in scaling and DOL growth can change not only with temperature, but also with duration of the oxidation, which is confirmed by the established effects of these factors on E_l and E_p. The Ti–Al and Ti–Fe alloys are remarkable in this respect. For example, aluminum, being an α-stabilizer and having a smaller atomic radius than titanium, enhances the strength of the α-Ti lattice [22]; strengthening of this effect with increasing c_{Al} should result in the growth of E_l. The data in the table for $T >$ 973 K do not contradict this conclusion. When titanium is alloyed with iron stabilizing the β-phase, the strength of interatomic bonds in the matrix lattice decreases, and we can expect that E_l will decrease, which is actually observed in the experiment.

Nonmonotonic and unclear dependence of E_l and E_p on the nature and concentration of alloying elements is attributable, apart from other reasons, to their low content in the alloys and also to inaccuracy of

the experiment. These circumstances and the extraordinary complexity of the oxidation of titanium and its alloys, affected by oppositely acting factors, do not always allow clear interpretation of the effect of these factors on the process parameters.

CONCLUSIONS

(1) The slope of the temperature dependence of K_l for nonstationary oxidation of titanium and the majority of the considered alloys increases, and that of K_p, decreases in going to the range $T >$ (1123–1223) K. The temperatures T^l_{bend} and T^p_{bend} of bends in these dependences remain practically unchanged on alloying of titanium and in going from the initial to the subsequent stages of the oxidation.

(2) In most cases, alloying of titanium results in increase in E_l and E_p in both stages of the test at 973–1373(1473) and 973–1123(1073) K, respectively, and also at temperatures higher than 1223 K. The exceptions are several Ti–Al, Ti–V (E_p), Ti–5.2. Al–1.2 V–1.1 Mo (E_l), and Ti–Fe (E_l, E_p) alloys. The diffusion processes for all the alloys (except partly for Ti–Fe) in the range 1123(1073)–1223(1173) K are less energy-consuming than in the case of titanium.

(3) The growth of c_M in Ti–Al and Ti–Zr alloys is accompanied by the tendency to a nonmonotonic increase in $E_l^{(1)}$ and $E_l^{(2)}$ above 973 K, and in the case of Ti–Fe and Ti–V their decrease is observed. Under these conditions, $E_p^{(1)}$ and $E_p^{(2)}$ tend to decrease with increasing c_{Zr}; for the Ti–Al alloys this is true only with respect to $E_p^{(2)}$. At the same time, when c_{Fe} (outside the 1173–1223 K range) and c_V (≤0.9%) increase, and also (as far as $E_p^{(1)}$ is concerned) when c_{Al} grows, the trend is opposite.

(4) In going to the range 973–1173(1223) K, $E_l^{(1)}$ for titanium decreases and $E_p^{(1)}$ increases. The changes in $E_p^{(1)}$ for the majority of alloys of the systems Ti–Al and Ti–Zr and also for the PT-7M alloy are similar to this pattern, whereas $E_l^{(1)}$ values change in opposite directions, being constant for certain compositions in the range 823–1223 K. In the case of titanium and majority of the alloys, heating above 1173–1223 K results in an increase in E_l and a decrease in E_p.

(5) Passing from the initial to the subsequent periods of titanium oxidation is accompanied by a decrease in E_l at 973–1373 K and a decrease in E_p at 973–1123(1073) K, whereas above 1223(1173) K $E_p^{(1)}$ is equal to $E_p^{(2)}$. For the majority of the alloys, this transition results in the opposite change in E_l (T 1173 K) and E_p (T 1223 K).

REFERENCES

1. D'yachkov, V.I., *Zh. Prikl. Khim.*, 1990, vol. 63, no. 4, pp. 752–757.
2. D'yachkov, V.I., Privol'neva, A.S., Syshchikov, V.I., and Tikhomirov, V.I., *Zh. Prikl. Khim.*, 1977, vol. 50, no. 12, pp. 2657–2660.
3. D'yachkov, V.I., Lemke, N.G., and Syshchikov, V.I., *Zashch. Met.*, 1990, vol. 26, no. 3, pp. 426–432.
4. D'yachkov, V.I., *Zh. Prikl. Khim.*, 1990, vol. 63, no. 4, pp. 763–769.
5. D'yachkov, V.I., *Zh. Prikl. Khim.*, 1991, vol. 64, no. 5, pp. 978–983.
6. D'yachkov, V.I., *Zh. Prikl. Khim.*, 1990, vol. 63, no. 10, pp. 2156–2162.
7. D'yachkov, V.I., *Zh. Prikl. Khim.*, 1991, vol. 64, no. 2, pp. 249–257.
8. D'yachkov, V.I., *Zh. Prikl. Khim.*, 1992, vol. 65, no. 6, pp. 1244–1253.
9. D'yachkov, V.I., *Zh. Prikl. Khim.*, 1996, vol. 69, no. 2, pp. 192–198.
10. D'yachkov, V.I., *Zh. Prikl. Khim.*, 2002, vol. 75, no. 1, pp. 10–14.
11. Bai, A.S., Lainer, D.I., Slesareva, E.N., and Tsypin, V.I., *Okislenie titana i ego splavov* (Oxidation of Titanium and its Alloys), Moscow: Metallurgiya, 1970.
12. Evans, U.R., *Trans. Electrochem. Soc.*, 1924, vol. 46, no. 1, pp. 247–274.
13. Takayama, I., *J. Iron Steel Inst. Jpn.*, 1986, vol. 72, no. 3, pp. 1639–1645.
14. D'yachkov, V.I. and Tikhomirov, V.I., *Fiz. Met. Metalloved.*, 1969, vol. 27, no. 4, pp. 655–661.
15. Fukuda, Y., Lancaster, G.M., Honda, F., and Rabalais, W.J., *Phys. Rev.*, 1978, vol. 18, no. 11, pp. 1691–1694.
16. Molchanova, E.K., *Atlas diagramm sostoyaniya titanovykh splavov* (Atlas of Phase Diagrams of Titanium Alloys), Moscow: Mashinostroenie, 1964.
17. Ignatov, D.V., Model', M.S., Sokiryanskii, L.F., and Shinyaev, A.Ya., *Khimiya metallicheskikh splavov* (Chemistry of Metal Alloys), Moscow: Nauka, 1973, pp. 208–213.
18. Tikhomirov, V.I. and D'yachkov, V.I., *Zh. Prikl. Khim.*, 1967, vol. 40, no. 11, pp. 2405–2413.
19. Hauffe, K., *Reaktionen in und an festen Stoffen*, Berlin: Springer, 1955, vol. 2.
20. Voitovich, R.F. and Golovko, E.I., *Vysokotemperaturnoe okislenie titana i ego splavov* (High-Temperature Oxidation of Titanium and Its Alloys), Kiev: Naukova Dumka, 1984.
21. D'yachkov, V.I., *Zh. Prikl. Khim.*, 1998, vol. 71, no. 11, pp. 1761–1766.
22. Glazova, V.V., *Legirovanie titana* (Alloying of Titanium), Moscow: Metallurgiya, 1966.

Russian Journal of Applied Chemistry, Vol. 76, No. 7, 2003, pp. 1031–1034. Translated from Zhurnal Prikladnoi Khimii, Vol. 76, No. 7, 2003, pp. 1063–1066.

INORGANIC SYNTHESIS AND INDUSTRIAL INORGANIC CHEMISTRY

Subsolidus Phase Relationships in the Er_2O_3–Rh_2O_3 System

V. N. Skrobot, S. K. Kuchaeva, D. P. Romanov, and R. G. Grebenshchikov

Grebenshchikov Institute of Silicate Chemistry, Russian Academy of Sciences, St. Petersburg, Russia

Received March 18, 2003

Abstract—The Er_2O_3–Rh_2O_3 system was studied by the annealing and quenching method using X-ray phase, thermal, and chemical analyses. A schematic subsolidus diagram of phase relationships was constructed.

In recent decades, there has been a great deal of interest in multicomponent oxide systems [1–3] owing to the fact that phases of various chemical compositions and structures, existing in such systems, have practically important properties. In particular, it was found that complex oxides existing in the systems Ln–M–Rh–O [4–6] (Ln is a rare-earth element and M, an alkaline-earth element) have interesting electrical, magnetic, and catalytic properties. The purposeful search for new mixed oxides in these and even more complicated similar systems should be based on the physicochemical analysis of simpler oxide systems M–Rh–O and Ln–Rh–O along with development of synthetic methods. Of prime importance are the phase diagrams in the subsolidus region.

This work continues the study of phase relationships in systems containing rare-earth and rhodium sesquioxides [7–10]. Our goal was to study in detail the subsolidus phase relationships in the Er_2O_3–Rh_2O_3 system in air at temperatures of up to 1600°C and to construct the corresponding phase diagram.

The fact that the mixed oxide $ErRhO_3$ is formed in the system Er–Rh–O was first reported in 1964 [11]. Later the synthesis and crystal-chemical and certain physicochemical properties of this compound were repeatedly studied [12–15]; however, phase relationships in the Er–Rh–O system were not studied.

EXPERIMENTAL

The initial reagents were erbium oxide Er_2O_3 containing no less than 99.9% main substance and pure-grade rhodium trichloride crystal hydrate $RhCl_3 \cdot 4H_2O$. The prolonged oxidation of the latter compound with atmospheric oxygen in the temperature range 650–700°C yields the metastable polymorph α-Rh_2O_3 with a classic hexagonal corundum-type structure [16]. The high-temperature stable polymorphic form β-Rh_2O_3 [17] was obtained by two following ways. The first method consisted in heat treatment of the metastable form of α-Rh_2O_3 at 800–950°C in air. The second method consisted in the oxidation of finely dispersed metallic rhodium at 950–1000°C in air or in an oxygen flow for no less than 20 h. Finely dispersed rhodium (metallic rhodium black) was obtained by the reduction of rhodium trichloride hydrochloric acid solution with metallic zinc.

The initial compositions for studying phase relationships were prepared from the mixtures of Er_2O_3 and α-Rh_2O_3 in the molar ratios of 9 : 1, 4 : 1, 3 :1, 2 : 1, 3 : 2, 1 : 1, 3 : 5, 1 : 2, 1 : 3, 1 : 4, and 1 : 9. When studying the equimolar composition, we also used a mixture of Er_2O_3 and finely dispersed rhodium. These mixtures were triturated in a jasper mortar with ethanol, dried in air, and then annealed in corundum crucibles at temperatures from 600 to 1600°C at 100°C intervals. In certain cases, e.g., for the equimolar composition, the annealing and quenching were carried out at 10–20°C intervals. The duration of annealing at temperatures of up to 1000°C reached 150 h, and above 1000°C it was up to 75 h. After intermediate annealings for more than 20 h, samples were homogenized by trituration. Up to 1000°C, annealings were performed in a SNOL-I4 electric furnace. In the experiments at higher temperatures, we used an electric furnace with a heater made from a platinum–rhodium, Pt/Rh (30%), wire. Annealing and quenching were performed in air. During the isothermal annealing, the temperature was held constant with an accuracy of no less than ±10°C.

The phase composition of the initial reagents and mixtures and also of samples after annealing and quenching was determined with DRON-3 and Siemens D 500 HS X-ray diffractometers. We used CuK_α radiation with a nickel filter. Scanning was carried

1070-4272/03/7607-1031$25.00

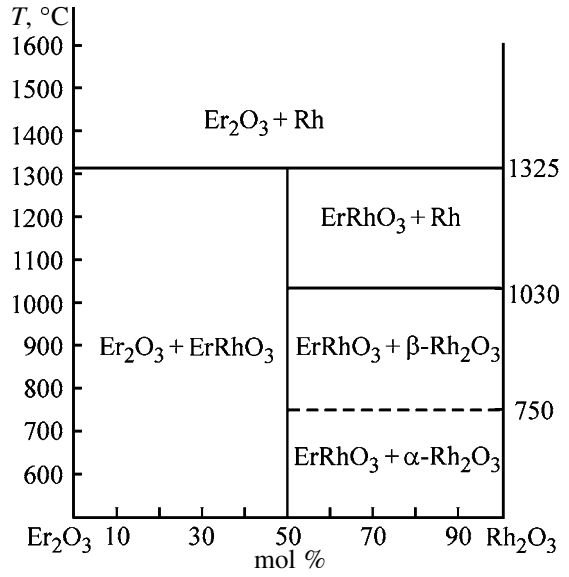

Schematic diagram of phase relationships for the subsolidus region of the system Er_2O_3–Rh_2O_3 in air. (*T*) Temperature. Irreversible polymorphic transition of Rh_2O_3 is shown by a dashed line.

out in the range of 2θ angles 10°–95°, scan rate 2 deg min^{-1}, scanning step 0.02°.

Thermal and chemical analyses, and also some other details of experiments were described earlier [9, 10].

The schematic diagram of phase relationships for the subliquidus region of the system Er_2O_3–Rh_2O_3 is shown in the figure as a combination of diagrams for two pseudo-binary systems Er_2O_3–Rh and Er_2O_3–Rh_2O_3 in the ternary system Er–Rh–O. This way of representation of phase equilibria is characterized by the fact that the reversible dissociation of solid oxide phases is considered conventionally as a phase transition at which a gas phase (oxygen) is not taken into consideration. Then the phase equilibria in a ternary system can be represented using a combination of binary systems, which allows a pictorial schematic diagram of phase relationships to be obtained on a plane. First, such a technique of representation of phase relations was used by Muan [18] when he studied systems involving iron oxides. Later Schneider and Roth applied it to the systems containing other transition metal oxides, including platinum metal oxides [19, 20].

According to the suggested phase diagram (see figure), there are four stable solid phases in the subliquidus region of the system Er_2O_3–Rh_2O_3: Er_2O_3 (C-form of Er_2O_3), β-Rh_2O_3, Rh, $ErRhO_3$, and also one metastable phase α-Rh_2O_3. When three solid phases and a gas phase (oxygen) coexist in equilibrium in the ternary system Er–Rh–O, the system is monovariant. In this case, three condensed phases coexist at a fixed partial pressure of oxygen and a unique value of temperature. Therefore, three-phase equilibria are shown in the phase diagram by horizontal continuous lines. The dashed line in the figure corresponds to the monotropic polymorphic transition

$$\alpha\text{-}Rh_2O_3 \longrightarrow \beta\text{-}Rh_2O_3. \quad (1)$$

In the course of this transition, the metastable polymorph α-Rh_2O_3 with a classic hexagonal corundum-type structure [16] irreversibly transforms to the stable polymorphic form β-Rh_2O_3, the rhombic structure of which is also a derivative of the corundum-type structure [17]. The main features of this monotropic polymorphic transition were studied earlier [15, 21–26]. The temperature range and rate of transformation (1) depend on the composition, structure, and dispersity of the initial α-Rh_2O_3. All these characteristics are determined by the way and conditions of the synthesis of the metastable form α-Rh_2O_3. It is possible to identify unambiguously polymorphic transition (1) of α-Rh_2O_3 synthesized in this work and the formation of β-Rh_2O_3 by X-ray technique after annealing of the initial α-Rh_2O_3 at temperatures above 750°C, but not higher than 1030°C. The reversible thermal dissociation by Eq. (2) is observed above 1030°C:

$$\beta\text{-}Rh_2O_3 = 2Rh + 3/2O_2. \quad (2)$$

Equilibrium (2) and its certain thermodynamic features have been studied fairly well [22–28]. Using the data from [22, 28], we have calculated the dissociation temperature of β-Rh_2O_3 in air at normal atmospheric pressure, i.e., at the partial pressure of oxygen of 0.21 atm. The obtained values of 1034 and 1033°C reasonably agree with the value of 1042°C given in [27]. According to the data from [25, 26], obtained by differential thermal and high-temperature X-ray phase analyses, equilibrium (2) is established in air at 1030 ± 5°C.

Only one phase transition was established also for the binary oxide $ErRhO_3$ at temperatures of up to 1600°C. It is the reversible thermal dissociation by the equation

$$ErRhO_3 = 1/2Er_2O_3 + Rh + 3/4O_2. \quad (3)$$

The thermal dissociation of erbium rhodite is detected in X-ray patterns starting from 1325°C as

an endothermic effect and an abrupt weight loss of 7.42%. This value agrees well with the theoretical value of 7.54% calculated by Eq. (3). In the X-ray patterns of single-phase samples of $ErRhO_3$ after their annealing at temperatures above 1325°C, well-pronounced narrow diffraction peaks appear, which correspond to well-crystallized coarse-grained metallic rhodium and the low-temperature polymorphic form of erbium(III) oxide (so-called C-form of Er_2O_3) crystallizing in the cubic system [29]. These substances do not react with each other and with atmospheric oxygen at 1325–1600°C. But specifically the reaction yielding the double oxide $ErRhO_3$ was detected by the X-ray phase analysis after prolonged calcination (for more than 100 h) of a mixture of Er_2O_3 with finely dispersed rhodium at 1300°C in air. Thus, the results of our annealing–quenching experiments in combination with the data of X-ray and thermal analyses unambiguously prove the validity of Eq. (3) and determine the temperature at which this equilibrium is attained in air, 1325 ± 10°C.

It should be noted that $ErRhO_3$ and β-Rh_2O_3 undergo a similar decomposition by Eqs. (3) and (2), respectively. The reversible dissociation with the formation of metallic rhodium and oxygen is characteristic for these oxides, the decomposition temperature of the double rhodium erbium oxide $ErRhO_3$ being much higher than that of the simple rhodium oxide Rh_2O_3.

Therefore, we have found that only one double oxide $ErRhO_3$ is formed in the system Er_2O_3–Rh_2O_3. The data of the chemical analysis of $ErRhO_3$ agree well with the corresponding calculated values (differences do not exceed 0.2%). The X-ray diffraction study confirmed the data [12–15] on the crystallization of $ErRhO_3$ in the structure of orthorhombically distorted perovskite such as $GdFeO_3$. Single-phase samples of the double oxide $ErRhO_3$ are brown homogeneous polycrystal powders insoluble in water, inorganic acids (hydrochloric, nitric, sulfuric, and phosphoric), and alkalis (NaOH and KOH).

It should be noted that high resistance to the action of acids and alkalis is also characteristic of the simple rhodium(III) oxide.

The offered subsolidus diagram of phase relationships for the system Er_2O_3–Rh_2O_3 is topologically equivalent to the corresponding phase diagrams for the systems Ln_2O_3–Rh_2O_3 (Ln = La, Yb, Lu) studied earlier [7–10]. The phase diagrams of these systems differ only in the dissociation temperatures of $LnRhO_3$ compounds, which decrease from 1450 to 1275°C in going from $LaRhO_3$ to $LuRhO_3$ [7–10]. The offered diagram for the subsolidus region demonstrates phase relationships in air at normal atmospheric pressure, i.e., at the oxygen partial pressure of 0.21 atm. However, variation of the oxygen partial pressure will affect the dissociation temperatures of β-Rh_2O_3 and $ErRhO_3$. According to [22], the increase in the oxygen partial pressure from 0.01 to 0.96 atm results in the increase from 900 to 1126°C in the equilibrium temperature of the dissociation of rhodium(III) oxide. Such experimental studies were not carried out for $ErRhO_3$, but it was found [8] that the dissociation temperature of the similar perovskite-like oxide $LaRhO_3$ increases from 1455 to 1570°C as the partial pressure of oxygen is increased from 0.21 to 1.00 atm. Apparently, the behavior of $ErRhO_3$ will be similar.

Thus, as repeatedly noted earlier [2, 7–10, 22–28], the dissociation temperatures of rhodium oxides in similar systems strongly depend on the partial pressure of oxygen, and its variation will affect the position of the temperature–concentration boundaries of phase fields in the diagrams.

The results of this work confirm certain previous experimental observations and conclusions [2, 7–10, 13–15, 19, 20, 22–28].

CONCLUSIONS

(1) Subliquidus phase relation in binary oxide systems involving oxides of platinum metals are determined mainly by the nature of the corresponding initial simple oxide of a noble metal irrespective of the physicochemical nature of the second component (oxide of a base metal).

(2) The double oxides formed in systems base metal–platinum metal–oxygen inherit physicochemical properties of simple oxides formed in the systems platinum metal–oxygen. In particular, high chemical and thermal stability of simple oxides of platinum metals corresponds to that of the mixed oxides.

(3) The majority of simple and double oxides of platinum metals, when heated, undergo reversible thermal dissociation but not melting. Simple oxides of platinum metals reversibly decompose to give the corresponding platinum metal and oxygen. The dissociation into a platinum metal, oxygen, and a base metal oxide is characteristic, as a rule, for double oxides containing a platinum metal and a base metal. In this case, double oxides dissociate at higher temperatures than the corresponding simple platinum metal oxides.

(4) There is a deep physicochemical analogy between the systems platinum metal–oxygen and base metal–platinum metal–oxygen.

ACKNOWLEDGMENTS

The authors are grateful to A.E. Lapshin for the help in performing the experiments.

REFERENCES

1. Bazuev, G.V. and Shveikin, G.P., *Slozhnye oksidy elementov s dostraivauyshchimisya d- i f-obolochkami* (Complex Oxides of Elements with Incomplete *d* and *f* Shells), Moscow: Nauka, 1985.
2. Lazarev, V.D., Krasov, V.G., and Shaplygin, I.S., *Elektroprovodnost' oksidnykh sistem i plenochnykh struktur* (Electrical Conductivity of Oxide Systems and Film Structures), Moscow: Nauka, 1979.
3. Rao, C.N.R. and Raveau, B., *Transition Metal Oxides: Structure, Properties, and Synthesis of Ceramic Oxides*, New York: Wiley, 1998.
4. Shimura, T., Itoh, M., Inaguma, Y., and Nakamura, T., *Phys. Rev*., 1994, vol. 49B, no. 8, pp. 5591–5598.
5. Layland, R.C., Kirkland, S.L., and Loye, H.C. zur, *J. Solid State Chem*., 1998, vol. 139, no. 1, pp. 79–84.
6. Watson,, P.R. and Somorjai, G.A., *J. Catal*., 1982, vol. 74, no. 2. P. 282–295.
7. Shevyakov, A.M., Skrobot, V.N., and Fedorov, N.F., *Dokl. Akad. Nauk SSSR*, 1978, vol. 241, no. 2, pp. 423–425.
8. Jacob, K.T. and Waseda, Y., *J. Am. Ceram. Soc*. 1995, vol. 78, no. 2, pp. 440–444.
9. Skrobot, V.N. and Grebenshchikov, R.G, *Zh. Prikl. Khim*., 1999, vol. 72, no. 8, pp. 1247–1250.
10. Skrobot, V.N. and Grebenshchikov, R.G, *Zh. Prikl. Khim*., 2000, vol. 73, no. 11, pp. 1767–1769.
11. Chazalon, R., Bertaut, E.F., and Tran Qui Duc, *Bull. Soc. Fr. Miner. Crist*., 1964, vol. 87, no. 1, pp. 88–89.
12. Shannon, R.D., *Acta Crystallogr., Sect. B*, 1970, vol. 26, no. 4, pp. 447–449.
13. Lazarev, V.D. and Shaplygin, I.S., *Zh. Neorg. Khim*., 1978, vol. 23, no. 2, pp. 291–303.
14. Lazarev, V.D. and Shaplygin, I.S., *Izv. Akad. Nauk SSSR, Neorg. Mater*., 1978, vol. 14, no. 11, pp. 1942–1949.
15. Shaplygin, I.S., Prosychev, I.I., and Lazarev, V.D., *Zh. Neorg. Khim*., 1986, vol. 31, no. 11, pp. 2870–2875.
16. Coey, J.M.D., *Acta Crystallogr., Sect. B*, 1970, vol. 26, no. 11, pp. 1876–1877.
17. Biesterbos, J.W.M. and Hornstra, J., *J. Less-Common Met*., 1973, vol. 30, no. 1, pp. 121–125.
18. Muan, A. and Gee, C.L., *J. Am. Ceram. Soc*., 1956, vol. 39, no. 6, pp. 207–214.
19. Schneider, S.J., Waring, J.L., and Tressler, R.E., *J. Res. Nat. Bur. Stand*., 1965, vol. 69A, no. 3, pp. 245–254.
20. Negas, T. and Roth, R.S., *J. Res. Nat. Bur. Stand*., 1969, vol. 73A, no. 4, pp. 431–442.
21. Wold, A., Arnott, R.J., and Croft, W.J., *Inorg. Chem*., 1963, vol. 2, no. 5, pp. 972–974.
22. Bayer, G. and Wiedemann, H.G., *Thermochim. Acta*., 1976, vol. 15, no. 2, pp. 213–226.
23. Muller, O. and Roy, R., *J. Less-Common Met*., 1968, vol. 16, no. 2, pp. 129–146.
24. Skrobot, V.N. and Grebenshchikov, R.G., *Zh. Neorg. Khim*., 1989, vol. 34, no. 8, pp. 2127–2130.
25. Skrobot, V.N., Romanov, D.P., Kuchaeva, S.K., and Grebenshshikov, R.G., Abstracts of Papers, *Int. Conf. "Powder Diffraction and Crystal Chemistry,"* St. Petersburg, June 20–23, 1994, p. 81.
26. Skrobot, V.N. and Grebenshchikov, R.G., *Zh. Neorg. Khim*., 1997, vol. 42, no. 11, pp. 1908–1911.
27. Jacob, K.T. and Sriram, M.V., *Metall. Mater. Trans*., 1994, vol. 25A, no. 7, pp. 1347–1357.
28. Schmahl, N.G. and Minzl, E., *Z. Phys. Chem*., 1964, vol. 41, no. 1–2, pp. 78–96.
29. Glushkova, V.B., *Polimorfizm okislov redkozemel'nykh elementov* (Polymorphism of Oxides of Rare-Earth Elements), Leningrad: Nauka, 1967.

Russian Journal of Applied Chemistry, Vol. 76, No. 7, 2003, pp. 1035–1038. Translated from Zhurnal Prikladnoi Khimii, Vol. 76, No. 7, 2003, pp. 1067–1070.

INORGANIC SYNTHESIS AND INDUSTRIAL INORGANIC CHEMISTRY

Behavior of Metal Particles Formed in Electric-Spark Dispersion of Aluminum in Aqueous Solutions

R. K. Bairamov

Olimpiya Open Joint-Stock Company, Novomoskovsk, Tula oblast, Russia
Novomoskovsk Institute, Mendeleev Russian University of Chemical Engineering, Novomoskovsk, Tula oblast, Russia

Received December 27, 2002

Abstract—The effect of additives introduced into the working solution on the behavior of dispersed aluminum particles obtained in electric erosion was studied.

The electric-spark dispersion of a metal is strongly affected by the conditions under which the electric erosion process is carried out, with formation of various products possible [1–3]. It can be conventionally taken that electric erosion occurs in two stages. The first stage, which occurs in the electric discharge zone characterized by high temperatures, leads to melting of the metal, its partial evaporation, and removal of the liquid–vapor phase in the form of congealed metal particles [4, 5]. In the second stage, which occurs in the sludge-collecting tank, dispersed metal particles enter or do not enter into the reaction with the working solution. The stages under consideration are strongly affected by additives introduced into the working solution. Thermal decomposition of the working solution in the spark discharge zone yields atomic oxygen whose amount largely depends on the nature and concentration of an additive [3]. When present in a sufficient amount, oxygen reacts with dispersed aluminum to form on its surface a protective oxide film which protects the metal from reacting with the working solution. If, however, oxygen is formed in an insufficient amount, surface oxidation of the dispersed metal is only partial, and it reacts with the working solution to form aluminum hydroxides (AH).

This study proceeded with investigations of how additives introduced into the working solution affect the behavior of the forming dispersed aluminum particles; also the dispersity of the products obtained was determined. The experiments were carried out on an installation, and by a procedure, described previously in [1].

Electron-microscopic studies of samples were performed on an EMV-100LM electron microscope with accelerating voltage of 75 kV and beam current of 40 μA. The samples were preliminarily prepared with a UZDN-1 ultrasonic disperser in isopropyl alcohol with subsequent deposition on an organic substrate.

To exclude the influence exerted by the first stage of the electric erosion process and by the resulting change in the concentration of the additive on the nature of processes occurring in the second stage, electric erosion of aluminum was carried out until complete filling of the sludge-collecting tank. Further, 3-l sludge samples were taken from the collecting tank and subjected to thermal treatment at 90°C. The time of thermal treatment of the samples was varied: 3 h for the first sample, 5 h for the second, 7 h for the third, etc. Thus, the initial composition of the sludge was invariable at different times of its thermal treatment.

The influence exerted by the duration of the thermal treatment on the composition of the products obtained with various additives is illustrated in Fig. 1.

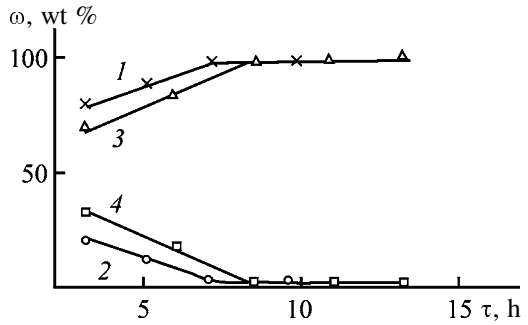

Fig. 1. Content ω of (*1, 3*) boehmite and (*2, 4*) bayerite AH in products of electric-spark dispersion of aluminum in a working solution vs. duration τ of thermal treatment of sludge. Sludge treatment temperature 90°C. Working solution (M): (*1, 2*) 0.039 ammonium acetate and (*3, 4*) 0.22 urea.

1070-4272/03/7607-1035$25.00 © 2003 MAIK "Nauka/Interperiodica"

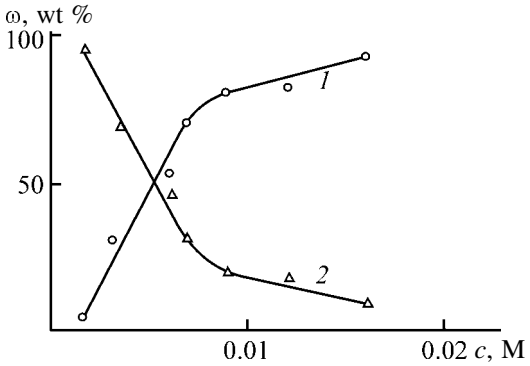

Fig. 2. Content ω of (*1*) aluminum powder and (*2*) AH in electric erosion products vs. concentration *c* of nitric acid in a mixture with 0.025 M working solution of ammonium nitrate. Sludge treatment temperature 25°C, treatment duration 4 h; the same for Fig. 4.

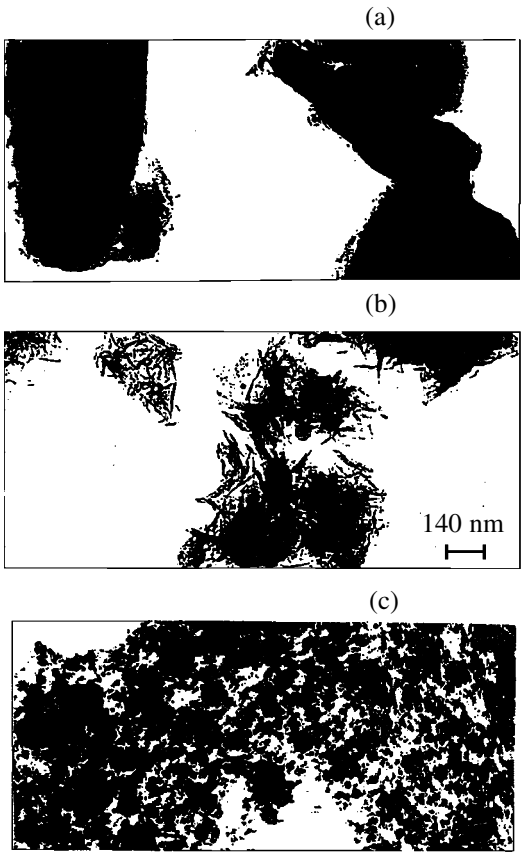

Fig. 3. Electron micrographs of (a) bayerite and (b) boehmite AH and (c) aluminum powder, products formed in electric-spark dispersion of aluminum in a working solution. Working solution (M): (a) distilled water, (b) 0.039 ammonium acetate, and (c) 0.028 nitric acid.

It can be seen that the content of boehmite AH in the erosion product grows and that of bayerite AH decreases with increasing duration of thermal treatment. The observed difference in how the content of boehmite AH grows (and, correspondingly, the content of bayerite AH decreases) in the presence of ammonium acetate and urea in the working solution is probably due to their different adsorption onto the surface of dispersed aluminum. Compared to urea, ammonium acetate presumably forms stronger complexes with oxide areas on the surface of dispersed aluminum particles and shields these areas, thus protecting dispersed aluminum from further hydration. This suggests that an increased amount of less hydrated form, boehmite AH, and decreased amount of bayerite AH are formed. As a result, the initial content of boehmite AH in an ammonium acetate solution exceeds that in an urea solution, and, therefore, the limiting product ratio is reached faster in the presence of ammonium acetate, compared to the case of urea.

Figure 2 shows how nitric acid introduced into a working solution containing ammonium nitrate affects the composition and amount of products obtained in the course of electric erosion. At 0.002 M concentration of nitric acid in an ammonium nitrate solution, the erosion products mainly contain aluminum hydroxide. With increasing concentration of nitric acid in the working solution, the content of powdered aluminum in the product first grows steeply and then varies slowly, approaching a limiting value (curve *1*). Such a behavior of the metal powder content in the product indicates that the amount of atomic oxygen grows in the course of the process. As a result, the fraction of dispersed metal particles with a surface oxide film protecting them from interaction with the working solution increases. Raising further the concentration of nitric acid in the solution affects the amount of forming oxygen only slightly; correspondingly, the fraction of dispersed metal with surface occupied by the oxide film remains nearly constant. As a result, the content of powdered metal in the product grows slowly. Since the working solution contains substances with the same anion, nitrate ion, the effect of the working solution on the composition of the erosion products is largely associated with a change in the concentration of hydrogen (hydroxonium) ions. Thus, the experimental data obtained confirm the previous assumption that the mechanism of aluminum powder formation involves hydroxonium ions.

Electron micrographs of samples obtained in electric-spark dispersion of aluminum under varied conditions are shown in Fig. 3. Three types of products are formed in electric erosion. Figure 3 shows that crystallites of bayerite AH have the shape of parallelepipeds 400 nm and less in size (Fig. 3a), and crystals of boehmite AH are needles about 150 nm long and

Effect of additives introduced into the working solution on composition of products formed in electric-spark dispersion of aluminum

Ammonium salt	*c*, M	*T*,* °C	τ,* h	Product composition, wt %	
				aluminum powder	total content of all AH forms
Acetate	0.039	90	8	–	100
Oxalate	0.030	25	5	91	9
Tartrate	0.024	25	5	93	7
Citrate	0.032	25	5	94	6

* *T* and τ are, respectively, the temperature and duration of sludge treatment.

20 nm wide (Fig. 3b). In both cases, the crystallites subsequently coagulate to form secondary aggregates. Crystallites in aluminum powder, which are mostly spherical, also coagulate into secondary aggregates, with only their minor part remaining uncoagulated (Fig. 3c). The size of uncoagulated metal particles varies within 10–50 nm.

Figure 4 shows the results of a morphological analysis of a metal powder obtained in electric erosion of aluminum in a nitric acid solution. Several days after being obtained, dispersed metal particles are mainly represented by secondary aggregates with average size of 3.8 μm and very narrow distribution.

The influence exerted by the concentration of the ammonium acetate and oxalate working solutions on the composition and amount of electric erosion products is illustrated in Fig. 5. With increasing concentration of the working solution, the content of boehmite AH in the product grows (and, correspondingly, the content of bayerite AH falls) (Fig. 5, curves *1* and *2*). Electric erosion of aluminum with ammonium oxalate as the working solution yields AH and metal powder. Raising the concentration of the ammonium oxalate solution leads to a steep rise in the content of aluminum powder, which further becomes slower, with the optimal value reached (Fig. 5, curve 3). Correspondingly, the content of AH in the erosion product decreases (Fig. 5, curve *4*). The observed difference in the composition of products obtained in electric erosion in working solutions containing ammonium acetate or oxalate is due to different types of "primary" processes occurring in the spark-discharge zone. In the first case, thermal decomposition of acetate ions yields an insufficient amount of atomic oxygen, which leads to only partial surface oxidation of the dispersed metal, which further reacts with the working solution to give various forms of AH. In the second case, thermal decomposition of oxalate ions yields atomic oxygen in sufficient amounts, with the result that the fraction of dispersed metal particles having protective oxide film on their surface increases. At the end, the content of metal powder in the erosion product becomes higher. As seen from the table, the increased content of metal powder in the erosion product is also observed in electric-spark dispersion of aluminum in solutions of salts of polybasic carboxylic acids.

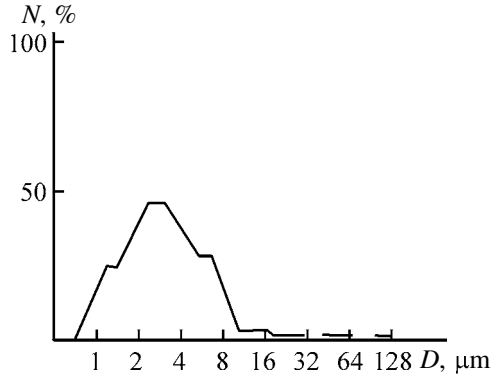

Fig. 4. Content *N* of aluminum particles obtained in electric-spark dispersion of aluminum in a 0.028 M solution of nitric acid vs. their size *D*.

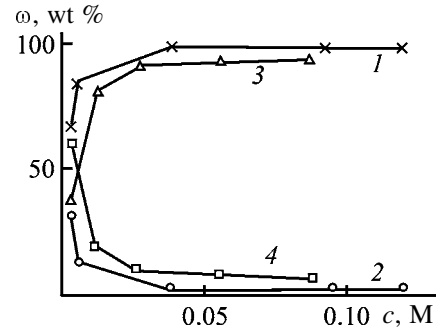

Fig. 5. Content ω of (*1*) boehmite and (*2*) bayerite AH, (*3*) aluminum powder, and (*4*) total AH vs. concentration *c* of the additive in the working solution. Additive: (*1, 2*) ammonium acetate and (*3, 4*) ammonium oxalate. Sludge treatment temperature (°C): (*1, 2*) 90 and (*3, 4*) 25. Sludge treatment duration (h): (*1, 2*) 8 and (*3, 4*) 5.

It is known that temperature strongly affects the stability of organic substances [6]. In electric erosion in the spark-discharge zone, in which temperature becomes as high as several thousands of degrees [5], carboxylic acid residues can be broken down. This conclusion is supported by the data of [7, 8]. The formation of atomic oxygen in the spark-discharge zone in thermal decomposition of carboxlic acid residues can be represented as follows:

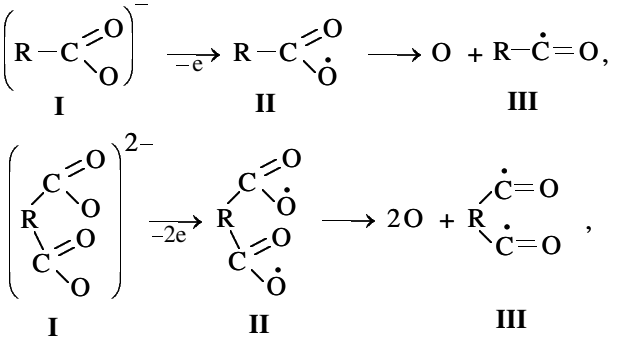

I **II** **III**

I **II** **III**

where **I** are carboxylic acid residues; **II**, acyloxy radicals; **III**, acyl radicals; and O, atomic oxygen.

In the course of thermal decomposition, acyl radicals may undergo further transformations.

CONCLUSION

Secondary processes occurring in the sludge collector in electric-spark dispersion of aluminum are affected by adsorption of components of the working solution on the surface of dispersed particles of the metal and its oxidized phase. The previously suggested mechanism, which suggests involvement of hydroxonium ions in the formation of a protective oxide film on the surface of dispersed metal, was confirmed experimentally. It was established that most part of dispersed metal particles and products of their reaction with the working solution coagulate to form secondary aggregates. Introduction of ammonium salts of polybasic carboxylic acids promotes formation of aluminum powder in electric erosion.

REFERENCES

1. Bairamov, R.K., Vedernikova, N.R., and Ermakov, A.I., *Zh. Prikl. Khim.*, 2001, vol. 74, no. 10, pp. 1703–1705.
2. Bairamov, R.K., Ermakov, A.I., and Vedernikova, N.R., *Zh. Prikl. Khim.*, 2001, vol. 74, no. 10, pp. 1708–1710.
3. Bairamov, R.K., Ermakov, A.I., and Vedernikova, N.R., *Zh. Prikl. Khim.*, 2002, vol. 75, no. 3, pp. 419–421.
4. *Elektrotekhnologicheskie promyshlennye ustanovki* (Electric Technological Installations), Svenchanskii, A.D., Ed., Moscow: Energoizdat, 1982.
5. Arenkov, A.B., *Osnovy elektrofizicheskikh metodov obrabotki metallov* (Foundations of Electric Methods for Metal Working), Leningrad: Mashinostroenie, 1967.
6. Nonhebel, D.C., Tedder, J.M., and Walton, J.C., *Radicals*, Cambridge: Cambridge Univ. Press, 1979.
7. Asanov, U.A. and Sakavov, I.E., *Izv. Akad. Nauk Kirg. SSR*, 1967, no. 4, pp. 71–75.
8. Asanov, U.A., Bazilova, S., and Sakavov, I.E., *Mekhanoemissiya i mekhanokhimiya tverdykh tel* (Mechanoemission and Mechanochemistry of Solids), Frunze: Ilim, 1974, pp. 174–175.

Russian Journal of Applied Chemistry, Vol. 76, No. 7, 2003, pp. 1039–1044. Translated from Zhurnal Prikladnoi Khimii, Vol. 76, No. 7, 2003, pp. 1071–1076.

INORGANIC SYNTHESIS AND INDUSTRIAL INORGANIC CHEMISTRY

Formation of Texture Characteristics of SiO_2 Xerogels Prepared from a Spent Film-Forming Formulation

A. N. Murashkevich, V. G. Vashina, and I. M. Zharskii

Belarussian State Technological University, Minsk, Belarus

Received December 27, 2002

Abstract—The possibility of obtaining silica gels with controllable porosity by using various methods for accomplishing a structural transformation in hydrogels was studied.

At present, the sol–gel process with controlled hydrolysis of silicon alkoxides is one of the most promising methods for silica gel preparation [1]. It is important to have, for use in catalysis and chromatography, xerogels with certain physicochemical characteristics. In particular, the highest demand is for silica gels with large sorption volume and prescribed pore size, used as adsorbents and catalyst supports [2]. The structure and properties of a final product obtained by hydrolytic polycondensation of tetraethoxysilane (TEOS) are mainly determined by the initial composition of a mixture being hydrolyzed, conditions under which hydrolysis and polycondensation occur, water : alkoxide molar ratio, presence of catalysts and modifiers in the system, amount and nature of solvents present in the system, and mode of drying of the forming gel [2–8].

The effect of surfactants as active forming agents controlling the pore structure of silica gels obtained from aqueous solutions of sodium silicate was analyzed in [3]. In accordance with the results obtained in [3], surfactants suppress the influence of pH on the particle size and hinder densification of a hydrogel in its drying, which makes it possible to obtain silica gels with large specific surface area and large pore volume: up to 960 $m^2 g^{-1}$ and 2.05 $cm^3 g^{-1}$ for cetylpyridinium chloride, and up to 844 $m^2 g^{-1}$ and 1.71 $cm^3 g^{-1}$ for cetyltrimethylammonium bromide, respectively. However, the largest sorption volumes were obtained at rather high (up to 5 wt %) surfactant concentrations.

The effect of the solvent and water : alkoxide molar ratio was studied in [4, 5]. The dependence of the pore size distribution on the nature and length of the organic radical of the solvent was established. Gels obtained in solvents with shorter organic radicals, which cause weaker steric hindrance, are characterized by smaller pores and narrower pore size distribution. In the presence of methyl ethyl ketone, the maximum sorption volume was 1.68 $cm^3 g^{-1}$ at average effective pore radius of 25 nm and specific surface area of 257 $m^2 g^{-1}$. With ethanol used as a solvent, the samples obtained had specific surface area of 580 $m^2 g^{-1}$ at average effective pore radius of 1.5 nm. The effect of the amount of solvent or solvents introduced remained unclear, although the solvents present affect the particle aggregation and, ultimately, also the internal state of hydrogels, because of the dilution of the formulation.

The drying conditions, which are mainly characterized by kinetics of removal of moisture and solvents present in a hydrogel, also affect the structure of the xerogels obtained. For example, it has been shown [6–8] that, with microwave radiation, the sample drying time can be made considerably shorter. According to [6, 7], the concentration of fluorine-containing ions is a key factor affecting the sorption characteristics of samples prepared under the conditions of microwave drying. With the ammonium hexafluorosilicate concentration raised to 4×10^{-2} M, the pore radius increased to 2.6 nm at specific surface area of 106 $m^2 g^{-1}$. It should be noted that the studies [6–8] were carried out in a rather narrow concentration range at constant water : alkoxide : solvent molar ratio and pore diameters evaluated only approximately from the bulk volume of the powder.

The microporous structure of the samples obtained gives no way of anticipating any significant decrease in diffusion limitations in heterogeneous reactions with a reactant immobilized in a silica gel of this kind: the time of equilibration increases to 47 min when the pore diameter decreases to 1.1 nm [6]. It was noted

1070-4272/03/7607-1039$25.00

that the time of equilibration is independent of the concentration of an immobilized component, being rather diffusion-controlled. Thus, elimination of diffusion limitations, which consists in raising the pore number and volume, is a factor governing the service characteristics of xerogels of this kind. Moreover, of interest is the influence exerted by microwave radiation on the structural-sorption characteristics of xerogels, which have been studied insufficiently.

The aim of this study was to analyze the conditions of formation of the silica gel pore structure by varying the initial conditions of the process and the state of a structure-forming component (tetraethoxysilane), and by introducing modifying additives and subsequent stages of ripening and drying of the hydrogel.

EXPERIMENTAL

Xerogels were synthesized using an organosilicon film-forming formulation based on TEOS. At present, this formulation is employed in manufacture of LCD indicators for depositing protective dielectric layers of SiO_2. The formulation contains, in addition to silicon alkoxide, water in amount necessary for the hydrolysis, HCl catalyst, ethanol, and ethyl acetate. The formula is adapted to obtaining dense nonporous dielectric SiO_2 coatings.

The moderate content of SiO_2 (3 wt %) and the large amount of organic solvents are due to necessity for depositing dielectric films of prescribed thickness. HCl present in the system acts as a catalyst which accelerates TEOS hydrolysis and formulation ripening in the initial stage and as a peptizing agent which prevents coagulation by stabilizing the system. Tetraethoxysilane is present in the formulation in partly hydrolyzed (by 60–70%, on the average) state [9], which specifies a number of characteristic features of the given system, since coatings are deposited using formulations in which the amount of polymeric ethers with large molecular weight and branched 3D structure is not high as yet.

After a certain service time of a formulation, coatings deposited from it no longer satisfy requirements to protective dielectric coatings and the formulation is regarded as spent. At the same time, it is sufficiently stable and remains in this state for several months without introduction of gelation-stimulating additives. Of interest is development of techniques for utilization of the given formulation to obtain high-purity xerogels with developed internal surface.

To obtain xerogels, gelation-accelerating additives were introduced into the formulation in the form of aqueous solutions of prescribed concentration. As these additives served ammonium bifluoride (ABF), ammonium silicofluoride (ASF), diethylamine (DEA), triethanolamine (TEA), ammonia NH_3, hexamethylenetetramine (HMTA), and polyethylene glycol (PEG) with average molecular weight of 6000. Introduction of an additional amount of water may lead to polycondensation and fast gelation with pore closure. Consequently, an additive introduced must promote by itself a change in the ratio of hydrolysis and polycondensation rates, i.e., it must enhance polycondensation.

This requirement is satisfied by fluorine-containing ions which exert a strong catalytic action on the polycondensation rate through formation of a fluorosilicon transition complex [10], are strong coagulants, and favor formation of a developed porous structure. When an above-critical concentration of fluorine-containing ions is used, a precipitated product is obtained [10].

Introduction of a number of organic amines and a cationic surfactant stabilizes particles formed in the sol stage, with their dimensions preserved in the gel structure, i.e., prevents densification of a humid hydrogel precipitate in the course of its drying [3]. Introduction of ammonia and a number of organic amines makes it possible to change the acidity of the medium, since the formulation itself contains HCl originally and an alkaline medium is characterized by a tendency toward formation of silica gels with developed system of pores at a certain decrease in the specific surface area. Thus, choosing the optimal amounts of additives introduced and process conditions may favor formation of a developed porous texture of the gel, which is preserved after drying.

Since the reaction medium plays an important part in hydrolytic polycondensation of alkoxides, changing the composition of this medium is a good method for controlling the porosity. In this study, the substitution of the dispersion medium was done by multiple treatment of hydrogels with aqueous ammonia. This favors deeper extent and more intensive course of the polycondensation through dissolution–reprecipitation reactions and leads to formation of a rigid porous gel skeleton [11].

The large amount of organic solvents in the formulation requires a sufficient time for their removal. Solvents can inhibit polycondensation and affect structure-forming processes because of the formation of hydrogen bonds with silanol groups [4, 5]. Therefore, it is of interest to compare various methods for hydrogel drying. In this study, the recently proposed

Table 1. Preparation conditions and structural characteristics of silica gels. Samples dried at 900 W for 20 min

Sample no.*	Active additive	Concentration		H_2O : TEOS molar ratio	Ripening time, days	V_s, $cm^3\ g^{-1}$		S_{sp}, $m^2\ g^{-1}$		r_{eff}, nm
		$c \times 10^3$, M	wt %**			static	dynamic	for benzene	for phenol	
1	HCl	1.17	–	10	1	0.66	0.64	443	372	2.9
2	HMTA	8.5	–	19.1	1	0.29	0.23	384	–	1.2
3	NH_3	–	2.4	11.3	1	0.32	0.27	423	219	1.3
4	ABF	11	–	15	1	0.83	0.82	405	407	4.0
5	DEA	–	33	19.6	1	0.46	0.47	454	263	2.1
6	ABF	11	–	15	1	0.65	0.56	443	262	2.5
7	ASF	2	–	15	1	0.25	0.27	105	–	4.3
8	–	–	–	6.4	>60	0.26	0.27	510	–	1.1
9	–	–	–	6.4	>60	0.69	0.78	500	376	3.1
10	TEA	–	50	12.7	1	0.57	–	–	493	–
11	PEG	–	10	13.3	3	0.16	–	–	–	–

* Sample nos. 1, 4, and 9 treated with 2 N ammonia solution in the hydrogel stage.
** In terms of SiO_2.

drying procedure employing microwave radiation [6–8] was used together with the conventional drying at elevated temperature. The new technique makes it possible to make the drying time as short as several minutes and positively affects formation of mesoporosity in xerogels.

The pore structure parameters of xerogels were determined using the standard procedure from isotherms of adsorption–desorption of benzene vapor and calculated by the BET technique [12]. Also, the sorption volume for benzene under static conditions and the specific surface area for phenol adsorbed from a solution in heptane [13] were determined, which yields more comprehensive information about the real structure of the samples.

The influence exerted by preparation conditions and by the nature of active additives on the structural characteristics of silica gels is illustrated in Table 1 and in the figure. Introduction of fluorine-containing additives yields, in most cases, samples with developed mesoporosity: the largest sorption volume and effective radii were obtained with ABF. Treatment in the hydrogel stage with aqueous ammonia of samples modified with ABF made it possible to raise the sorption volume and pore radius by a factor of 1.5 at invariable specific surface area, which indicates that the given treatment method is promising for modification of the silica gel surface. With ASF, samples with small specific surface area were obtained, but their effective radii indicate that the optimal amount of additive introduced is to be chosen for making larger the specific surface area of the silica gels.

Introducing an additional, compared with that in the initial spent formulation, amount of HCl, i.e., performing the process in a strongly acidic medium with subsequent treatment of the hydrogel with aqueous ammonia yields samples with developed interconnected and accessible surface area: the effective pore radius is 2.9 nm and the sorption capacities in the static and dynamic modes are virtually identical. The isotherms of benzene vapor sorption on the silica gels obtained (see figure) are isotherms of physical sorption of types I and IV according to the IUPAC classification, which points to, respectively, micro- and mesoporous structure of the samples obtained.

With ABF (sample no. 4), ASF, and DEA as active additives, and also with an additional amount of HCl introduced, mesoporous samples could be obtained. The shape of the hysteresis loop of the isotherms is characteristic of cylindrical mesopores or bottle-like

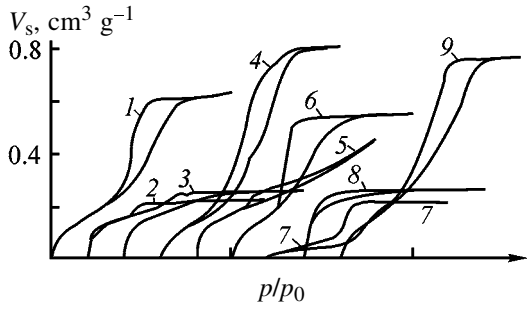

Isotherms of benzene vapor adsorption–desorption for SiO_2 xerogels. (V_s) Volume and (p/p_0) vapor pressure relative to saturated vapor pressure. Digits at curves correspond to sample nos. in Table 1.

Table 2. Effect of ABF concentration and ripening and drying conditions on sorption volume of xerogels

$c \times 10^3$, M	Ripening time, h	Drying conditions			V_s static, $cm^3\ g^{-1}$
		N,* W	τ, min	*T*, °C	
2	168	900	20	–	0.20
5	168	900	20	–	0.22
8.5	168	900	20	–	0.65
11	168	900	20	–	0.84
8.5	24	900	10	–	0.20
8.5	24	900	20	–	0.21
8.5	24	900	40	–	0.47
8,5	2	–	120	120	0.50
11	2	–	120	120	0.75
8.5	2	900	40	–	0.38
8.5	24	900	40	–	0.47
8.5	168	900	40	–	0.65

* *N* is microwave power.

mesopores with very wide entrances into voids [14]. The run of the isotherms is characteristic of agglomerates and globules that are sufficiently uniform in size and are uniformly packed. Samples containing ABF (sample no. 4) and HCl contain a certain amount of very large pores, which are only filled at p/p_0 close to unity (see figure, isotherms *1* and *4*).

With a number of organic amines, silica gels with good sorption characteristics could also be obtained, but, in some cases (HMTA), the amount of the modifier introduced was presumably insufficient for a structural transformation to occur, since HCl is present in the formulation from the very beginning. Introduction of ammonia into the formulation yielded samples with developed microporosity: the sorption volume of the silica gels was 0.32 $cm^3\ g^{-1}$ in the static mode and the pore radius was 1.3 nm at specific surface area of 423 $m^2\ g^{-1}$.

In the case when HMTA or NH_3 are used, the sorption isotherms of the samples belong to a hybrid type I + IV. The samples obtained are composed of mesoporous grains and contain micropores whose total volume gives rise to a plateau in the isotherm. Microporous samples have a rather large external surface area or a pronounced microporosity, or both [12]. It may be assumed that the amount of ammonia additionally introduced into the formulation is insufficient for structural modification and treatment of the hydrogel obtained with ammonia is more promising. With this method of synthesis, the hydrogel formation proceeds in the first stage in a strongly acidic medium with fluorine-containing modifiers, which gives rise to a well-developed surface. Use of a preset excess of ammonia in the second stage leads to roughening of the structure, which makes it possible to obtain samples with controllable porosity.

Treatment with aqueous ammonia of a spontaneously gelated spent formulation yielded samples with large sorption volume and large effective pore radius (sample no. 9). Mention should be made, however, of a too long time of hydrogel ripening and difficult reproducibility of the results obtained. Microwave drying of a spent formulation that gelated spontaneously without introduction of a modifier or treatment with aqueous ammonia yields microporous samples.

Introduction of PEG as modifier did not affect substantially the porosity of silica gels. It is known that PEG introduction in early stages of hydrolysis and condensation affects the morphology of the gels obtained and, in particular, the early development of a gel. Addition of PEG to a formulation in which TEOS is largely hydrolyzed does not cause any significant changes in xerogels.

Table 2 illustrates, for a xerogel modified with ABF as example, the influence exerted by the concentration of an additive introduced and by the conditions of ripening and drying on the sorption volume of the samples obtained. It can be seen that raising the concentration of an additive introduced or making longer the time of hydrogel ripening leads to an increase in the sorption volume of the xerogels obtained. Use of microwave radiation makes it possible to vary, by influencing the liquid evaporation processes, the porous structure of the samples obtained. A large amount of solvents present in the spent and initial

Table 3. Effect of treatment and drying conditions on sorption volume of xerogels. Ripening time 1 week

Active additive	Concentration		Drying conditions			V_s static, $cm^3\ g^{-1}$
	$c \times 10^3$, M	wt *	N, W	τ, min	T, °C	
ABF	8.5	–	900	20	–	0.64
	8.5	–	–	–	450	0.65
ABF**	8.5	–	900	20	–	0.74
	8.5	–	–	–	450	0.76
ABF	11	–	900	20	–	0.84
	11	–	–	–	450	0.65
ABF**	11	–	900	20	–	0.82
	11	–	–	–	450	0.84
PEG	–	10	900	20	–	0.16
PEG**	–	10	900	20	–	0.27
HCl	0.40	–	900	20	–	0.18
HCl**	0.40	–	900	20	–	0.62
HCl	1.17	–	900	20	–	0.23
HCl**	1.17	–	900	20	–	0.66

* In terms of SiO_2.
** Samples treated with 2 N ammonia solution in the hydrogel stage.

formulations is removed rapidly and simultaneously from the gel bulk, which gives rise to a well-developed surface of the silica gels. The structural rearrangement occurring in the course of prolonged ripening results in formation of a rather loose structure in which the intraand intermolecular condensation proceeds to the greatest extent because of the presence of fluorine-containing ions. The open porosity does not prevent removal of solvents from the bulk of the matrix, and the gel skeleton has enough time in the course of ripening to acquire a rigidity sufficient to withstand shrinkage.

The sorption volumes of the xerogels obtained with or without their treatment in the hydrogel stage with aqueous ammonia and subjected to drying in different ways are compared in Table 3. It can be seen that the sorption volumes of the samples upon microwave drying coincide with, or, in some cases, even exceed the values obtained after drying at elevated temperature. This indicates that a skeleton not subject to further shrinkage is formed in the course of gel ripening, processes of relaxation, condensation, and collapse of pores are complete, and pores in the gels are large enough for free removal of large amounts of organic solvents.

Changing the nature of the reaction medium by replacing the intrapore liquid in the course of synthesis is one more way to control the porosity of xerogels. Treatment of hydrogels with aqueous ammonia actually provides two-stage catalysis in the system, i.e., enables finer, compared with that in a single-stage process, control over gelation stages.

It is known that silica is rather well soluble in the presence of considerable amounts of hydroxide ions, and the originally poorly cross-linked macromolecules may dissolve and repeatedly precipitate at highly condensed surface centers. As a result, the gel skeleton is transformed to take the form of large clusters and relatively large pores in between. Moreover, the aqueous solution itself favors more complete course of the hydrolysis of ethoxy groups, which also promotes formation of a high porosity. The excess of aqueous ammonia results in that the clusters grow rather rapidly and have enough time to become sufficiently large to form a coarsely porous structure after drying.

The strongest influence (Table 3) on the sorption volume is exerted (within a factor of 3–3.5) by ammonia treatment of samples obtained in the presence of an additional amount of HCl, i.e., performing the process in the two-stage catalysis mode strongly affects the porosity formation. In the case of a partly hydrolyzed TEOS, when the initial formation of the gel skeleton is already initiated by introduction of fluorine-containing ions, the condensation proceeds to the greatest extent in the first stage and further treatment with aqueous ammonia raises the porosity to a lesser extent.

CONCLUSIONS

(1) Spent film-forming formulation can be used to obtain mesoporous SiO_2 xerogels by intensive technology.

(2) An important part in formation of structural features is played by organic solvents and methods of their removal in xerogel drying. Raising the concentration of a fluorine-containing additive, making longer the ripening time, and using microwave drying favor formation of a well-developed surface in the samples obtained. Replacing the dispersion medium by treatment in the hydrogel stage makes a greater contribution to porosity formation than use of a number of modifiers introduced into the initial formulation.

(3) The rapidity of the microwave drying, leading to local disintegration and shrinkage of the silica gel skeleton, puts in the forefront the problems associated with the skeleton strengthening. These problems can be resolved by making longer the ripening time and choosing the optimal amounts of modifying additives.

REFERENCES

1. Lev, O., Tsionsky, M., Rabinovich, L., *et al*., *Anal. Chem*., 1995, vol. 67, no. 1, pp. 22–29.
2. Kuznetsova, T.F. and Barkatina, E.N., *Izv. Ross. Akad. Nauk, Neorg. Mater*., 1994, vol. 30, no. 7, pp. 988–991.
3. Kuznetsova, T.F. and Barkatina, E.N., *Zh. Prikl. Khim*., 1989, vol. 62, no. 5, pp. 965–968.
4. Sviderskii, V.A., Klimenko, V.S., and Klimenko, S.V., *Kolloidn. Zh*., 1996, vol. 58, no. 3, pp. 395–397.
5. Sviderskii, V.A., Klimenko, V.S., and Klimenko, S.V., *Izv. Ross. Akad. Nauk, Neorg. Mater*., 1998, vol. 34, no. 10, pp. 1185–1188.
6. Morosanova, E.I., Velikorodnyi, A.A., Zolotov, Yu.A., and Skornyakov, V.I., *Zh. Anal. Khim*., 2000, vol. 55, no. 12, pp. 1265–1270.
7. RF Patent 2139244.
8. Morosanova, E.I., Velikorodnyi, A.A., Nikulin, I.V., *et al*., *Zh. Anal. Khim*., 2000, vol. 55, no. 5, pp. 539–545.
9. Murashkevich, A.N., But'ko, M.S., and Zharskii, I.M., *Zh. Prikl. Spektrosk*., 2001, vol. 68, no. 5, pp. 605–611.
10. Murashkevich, A.N. and Zharskii, I.M., *Kremniisoderzhashchie produkty kompleksnoi pererabotki fosfatnogo syr'ya* (Silicon-Containing Products of Integrated Processing of Phosphate Raw Materials), Minsk: Bel. Gos. Tekh. Univ., 2002.
11. Murashkevich, A.N., Vashina, V.G., and Zharskii, I.M., *Sol–Gel Sci. Technol*., 2001, vol. 20, pp. 7–12.
12. Gregg, S.J. and Sing, K.S.W., *Adsorption, Surface Area, and Porosity*, London: Academic, 1982.
13. *GOST* (State Standard) *18307–78: Silica Filler*, Moscow: Izd. Standartov, 1984.
14. Kuznetsova, T.F. and Eremenko, S.I., *Kolloidn. Zh*., 2002, vol. 64, no. 4, pp. 503–508.

Russian Journal of Applied Chemistry, Vol. 76, No. 7, 2003, pp. 1045–1047. Translated from Zhurnal Prikladnoi Khimii, Vol. 76, No. 7, 2003, pp. 1077–1079.

INORGANIC SYNTHESIS AND INDUSTRIAL INORGANIC CHEMISTRY

Thermal Stability of Limestone

A. A. Kabanov

Krasnoyarsk Pedagogical State University, Krasnoyarsk, Russia

Received November 4, 2002; in final form, February 2003

Abstract—Thermal stability of limestones and effects of various impurities on their stability were discussed.

The thermal stability of limestones and factors affecting it are of scientific and applied interest, because limestones are widely used in various industries. A number of interesting effects of impurities on the thermal stability of $CaCO_3 \cdot 17H_2O$ samples was established earlier [1–3], and testing natural limestones with respect to these effects has become urgent.

In this work, we used limestone from the Solomensk deposit (Kemerovo oblast). Its –0.08-mm fraction was sifted after dispersion and kept over P_2O_5 for 10 days. Then the sample was degassed at 200°C for 6 h and again kept over P_2O_5 for no less than 10 days. The limestone sample thus pretreated was considered as the starting sample.

The quantitative analysis of the samples was carried according to GOSTs (State Standards) 4530–76 and 5382–91. The X-ray analysis was performed on a DRON-3 diffractometer. The mass spectra were obtained on an MI-1305 ionization spectrometer. Thermal measurements were performed in air on a Q-1500D derivatograph. Magnetic susceptibility was measured on a pendular magnetic balance with automatic equilibration. The sensitivity of measuring specific magnetic susceptibility was 10^{-7} $cm^3\ g^{-1}$. The Mössbauer spectra were obtained on an electrodynamic spectrometer based on an AI-5006-3M-V100 analyzer operating in the constant acceleration mode. The spectra were processed on an ES-1022 computer. γ-Radiation was emitted by a ^{57}Co source of 0.5 GBq activity in a chromium matrix.

Analytical data for limestone (wt %): main substance $CaCO_3$ 95.08, Fe 0.81, (K + Na) 0.08, Si 0.52, Al 0.70, and others 2.81. The X-ray phase analysis (Fig. 1) shows that the starting sample contained $CaCO_3$ in the form of calcite, α-Fe_2O_3, and ferrigaluasite $(Fe^{III}, Al_4)(OH)_8(Si_4O_{10}) \cdot 1.74H_2O$. It is known that the X-ray diffraction patterns of α-Fe_2O_3 and α-$Fe_2O_3 \cdot xH_2O$ are identical. Taking into account the signal intensity and sensitivity of the X-ray diffractometer, we can conclude that the concentration of both iron(III) compounds in limestone is 0.10%.

Thermogravimetric analysis shows (Fig. 2) that the weight of the limestone sample starts to change noticeably in air at 130°C. The highest rate of the sample

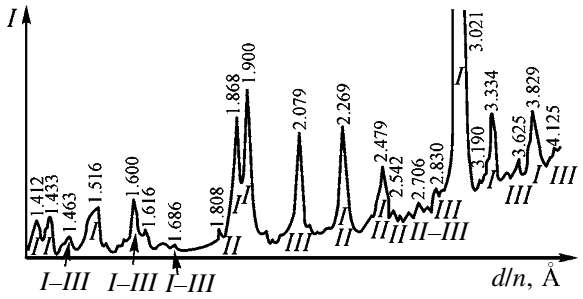

Fig. 1. X-rray diffraction pattern of the starting limestone: (*I*) absorption intensity and (*d*/*n*) interplanar spacing. (*I*) $CaCO_3 \cdot 0.06H_2O$, (*II*) hydrohematite α-$Fe_2O_3 \cdot 0.38H_2O$, and (*III*) ferrigaluasite $(Fe^{III}, Al_4)(OH)_8(Si_4O_{10}) \cdot 1.74H_2O$.

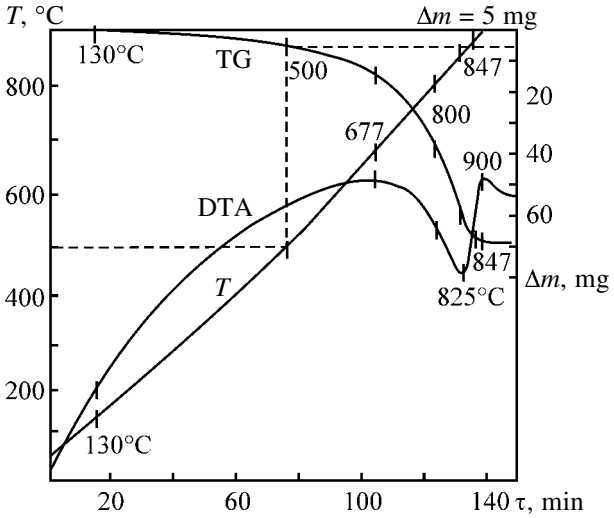

Fig. 2. Derivatogram of the starting limestone. *m* 0.2 g, $dT/d\tau$ = 6 deg min^{-1}. (*T*) Temperature and (Δm) weight loss.

1070-4272/03/7607-1045$25.00 © 2003 MAIK "Nauka/Interperiodica"

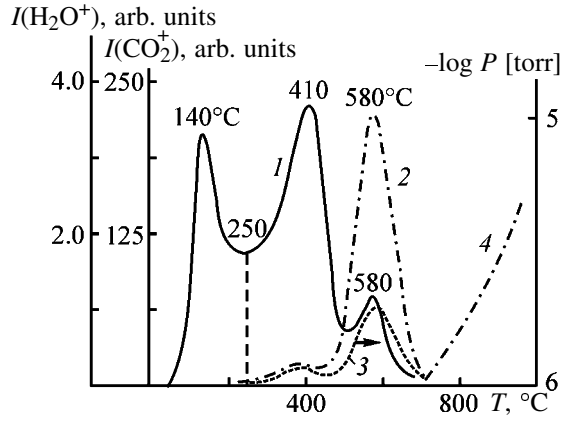

Fig. 3. Mass spectrometric monitoring of thermal decomposition of the starting limestone: (*I*) intensity and (*T*) temperature. (*1*) H_2O, (*2*) CO_2, (*3*) pressure in the reactor, and (*4*) H_2O from vessel glass. m = 0.01 g, $dT/d\tau$ = 18.0 deg min^{-1}, 10^{-6} torr.

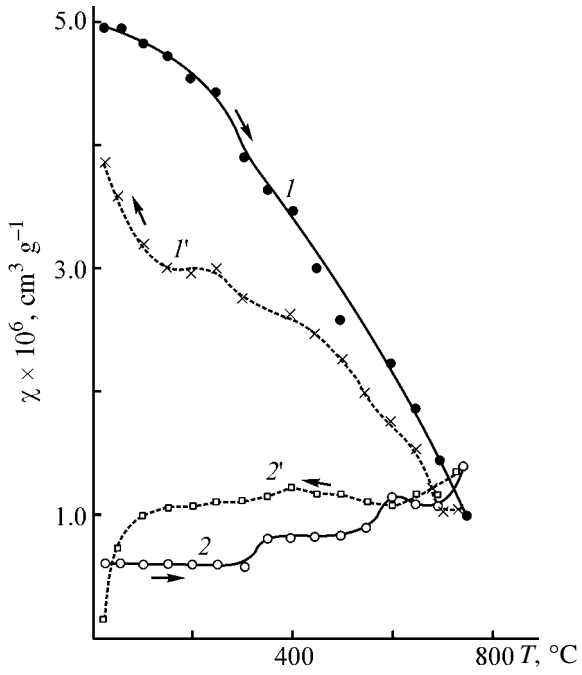

Fig. 4. Specific magnetic susceptibility χ of (*1*, *1*') starting powdered limestone and (*2*, *2*') $CaCO_3 \cdot 0.17H_2O$ (analytically pure grade reagent) vs. temperature T. (*1*', *2*') Cooling. m = 0.2 g, $dT/d\tau$ = 2 deg min^{-1}.

decomposition is observed at 852 ± 2°C, and the sample weight gets stabilized at about 900°C. According to the mass-spectrometric data (Fig. 3), the maximal decomposition rate of limestone in a vacuum of 10^{-6} torr is observed at 580 ± 2°C. A significant difference between the maximal decomposition rates in air and in a vacuum is typical for calcite [1].

Three experimental maxima of limestone dehydration rate (Fig. 3) are indicative of the presence of at least three centers of water localization in limestone. It is known [5] that the hydrohematite dehydration starts at 136°C. Therefore, the first maximum (140°C) in curve *1* (Fig. 3) can be assigned to this process. By analogy with $CaCO_3 \cdot 0.17H_2O$ [1, 2], the third maximum (580°C) probably originates from the presence of calcite. Then the second maximum (410°C) is caused by the dehydration of ferrigaluasite. In contrast to $CaCO_3 \cdot 0.17H_2O$ [1], a small maximum of the rate of CO_2 evolution was found for limestone near 410°C, which agrees with an increase in the pressure in the reactor (Fig. 3, curve *3*). It suggests a certain correlation between the dehydration of ferrigaluasite and the partial decomposition of calcite, which seems to result from the bonds in the crystalline calcite phase through polarized H_2O dipoles.

Limestone and $CaCO_3 \cdot 0.17H_2O$ on heating and cooling show principally different temperature dependences of the specific magnetic susceptibility (Fig. 4). On heating, the magnetic susceptibilities are determined for limestone, by ferrigaluasite (it seems to be ferrimagnetic), and for $CaCO_3 \cdot 0.17H_2O$, by van Vleck paramagnetism [1]. On cooling, the magnetic susceptibility seems to be determined in both cases by hematite, which is completely separated from the calcite phase upon dehydration. In all the cases (Fig. 4), we deal with paramagnetism and possibly with ferrimagnetism (for the initial state of ferrigaluasite).

According to the mass-spectrometric data [1] for $CaCO_3 \cdot 0.17H_2O$, its dehydration rate has a small temperature maximum at 235°C, which is not yet understood. In [6], its origin was specially studied by quantitative analysis, mass spectrometry, and Mössbauer spectrometry. It was found that the analytically pure grade reagent $CaCO_3 \cdot 0.17H_2O$ contains about 0.014% α-$Fe_2O_3 \cdot 0.04H_2O$ (which does not contradict the requirements of GOST 4530–76 to the reagent purity). Consequently, the calcite binds only 0.13 mol, but not 0.17 mol of H_2O [1, 2]. The results of this work allow us to supplement the conclusions of [6] by an assumption that the α-$Fe_2O_3 \cdot 0.04H_2O$ phase is linked to the calcite phase through H_2O molecules. The difference between the temperatures of maximal dehydration rate of α-$Fe_2O_3 \cdot 0.38H_2O$ in limestone (Fig. 3, 140°C) and of α-$Fe_2O_3 \cdot 0.04H_2O$ in the $CaCO_3 \cdot 0.17H_2O$ can be explained by different (by nearly an order of magnitde) H_2O content.

According to our data, the iron(III) content in limestone is 0.81%. To make a rough estimate of the iron(III) fractions in hydrohematite and ferrigaluasite, we recorded the Mössbauer spectrum of the starting limestone (Fig. 5). It contained six bands typical for

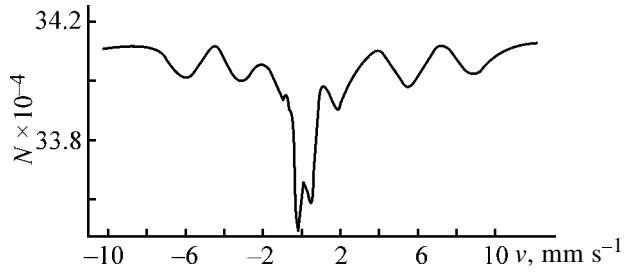

Fig. 5. Mössbauer spectrum of the starting limestone: (*N*) Counts per channel and (*v*) velocity of the γ-source.

hematite [7]. Hydrohematite should have the same spectrum (because of similarity of their X-ray diffraction patterns [4]). The isomer shift $\delta E = 0.2 \pm 0.1$ mm s^{-1} and the quadrupole splitting $\Delta E_Q = 0.5 \pm 0.1$ mm·s^{-1} were calculated from the spectrum. Their values confirm the presence of hematite (or hydrohematite). The absence of ferrigaluasite signals from the Mössbauer spectrum suggests [7] that the concentration of this impurity is at the least by an order of magnitude lower than that of hematite. Therefore, the iron(III) content can be divided into fractions of hematite (0.73%) and ferrigaluasite (0.08%). Let us then calculate the total concentration of H_2O in limestone and its three components (corresponding to three localization centers [1]) on the basis of Figs. 2 and 3 with the calibration of H_2O bands (Fig. 3) by the TG curve (Fig. 2) for 500°C. Under vacuum conditions, it corresponds to the temperature of 250°C [1] at which there is no CO_2 interference (Fig. 3).

Calculations based on the gravimetric calibration of the first band area (Fig. 3, curve *1*; up to 5°C) allow us to make the following conclusions. After thermal treatment at 200°C, the total content of water in the starting limestone sample is 7.52%. The fractions of H_2O in calcite, hydrohematite, and ferrigaluasite are 1.12, 2.50, and 3.90%, respectively. It corresponds to the following formulas of the compounds: $CaCO_3 \cdot 0.06H_2O$, α-$Fe_2O_3 \cdot 0.38H_2O$, and $(Fe^{III}, Al_4)(OH)_8 \cdot (Si_4O_{10}) \cdot 1.74H_2O$. The concentrations of iron-containing impurities can be calculated taking into account the iron(III) content in them. The content of ferrigaluasite and hydrohematite in limestone is 1.47 and 1.06%, respectively. These values are within the framework of the sensitivity of the X-ray diffractometer in use and, consequently, they agree with the X-ray diffraction data (Fig. 1).

CONCLUSIONS

(1) Water in limestone (7.52%) is in three states: in the base substance (calcite) and in hematite and ferrigaluasite impurities.

(2) The chemical composition of limestone is as follows (%): $CaCO_3 \cdot 0.06H_2O$ 96.20, α-$Fe_2O_3 \cdot 0.38H_2O$ 1.06, $(Fe^{III}, Al_4)(OH)_8(Si_4O_{10}) \cdot 1.74H_2O$ 1.47, and impurities 1.17.

(3) The impurity of H_2O in calcite enhances the limestone thermal stability, whereas impurities of iron(III) compounds reduce it.

(4) The available data suggest that calcite is bound to impurities of iron(III) compounds in limestone through H_2O molecules.

REFERENCES

1. Kabanov, A.A., *Zh. Fiz. Khim.*, 2001, vol. 75, no. 4, pp. 746–748.
2. Kabanov, A.A., *Zh. Fiz. Khim.*, 2002, vol. 76, no. 2, pp. 227–232.
3. Kabanov, A.A., *Zh. Fiz. Khim.*, 2002, vol. 76, no. 9, pp. 1719–1721.
4. Remy, H., *Lehrbuch der anorganischen Chemie*, Leipzig: Geest und Portig, 1961, vol. 2.
5. Ivanova, V.P., Kasatov, B.K., Krasavina, T.N., and Rozinova, E.L., *Termicheskii analiz mineralov i gornykh porod* (Thermal Analysis of Minerals and Rocks), Leningrad: Nedra, 1974.
6. Kabanov, A.A., State of Water in Calcium Carbonate, *Nauchn. Ezhegodn. Krasnoyarsk. Pedagog. Univ.*, 2002, vol. 1, issue 3.
7. Kündig, W., Lindquist, R., and Constabaris, G., *Magnetic Resonance and Relaxation*, Amsterdam: North-Holland, 1967.

Russian Journal of Applied Chemistry, Vol. 76, No. 7, 2003, pp. 1048–1051. Translated from Zhurnal Prikladnoi Khimii, Vol. 76, No. 7, 2003, pp. 1080–1083.

PHYSICOCHEMICAL STUDIES OF SYSTEMS AND PROCESSES

Determination of Solid-Phase Composition in Alcohol–Water–Salt Systems from Data on Vapor–Saturated Solution Equilibrium

A. N. Marinichev

St. Petersburg State University, St. Petersburg, Russia

Received January 30, 2003

Abstract—A thermodynamic method is proposed for calculating the composition of the solid phase crystallizing from a three-component saturated solution occurring in equilibrium with a two-component vapor phase. The method is illustrated by an example of the methanol–water–salt systems under the isothermal and isobaric conditions.

Systems of inorganic salts in aqueous–organic solvents are widely used in chemical technology for salt extraction and distillation, which are suitable for separation and purification of substances. Recently, much attention has been given to the interaction of ions in a solution with solvent molecules, salting-in and salting-out phenomena. Various multiparametric models describing solvation and hydration in mixed solvent are described in the literature. At the same time, if the vapor phase is assumed to be an ideal gas mixture, it becomes possible to obtain in a comparatively simple form a number of thermodynamic relations for calculating the composition of the coexisting one-, two-, or three-component solid phase from the data on two-phase equilibrium (for example, between two-component vapor and three-component saturated solution). This was the subject of our study. Note also that the treatment of experimental data to reveal how the temperature or pressure at which the phases coexist depends on the vapor phase composition was made previously in [1] to predict the composition of the liquid phase (or liquid phases) in systems consisting of volatile components only.

Let us present the fundamental equation describing under isothermal conditions (T = const) a change in the state of a salt-saturated solution in the form

$$V_l dP = x_1 d\mu_2 + x_2 d\mu_2 + x_3 d\mu_3, \qquad (1)$$

where V_l is the molar volume of a solution; P, pressure at which the phases coexist; x_i and μ_i, mole fraction and the chemical potential of the ith component in solution.

Let alcohol be the first component, water, the second, and salt, the third. If the solid phase in equilibrium with a three-component solution is a compound of constant composition containing ν_1 alcohol molecules and ν_2 water molecules per salt formula unit, then the isothermal variations of the chemical potentials of components are related as

$$0 = \nu_1 d\mu_1 + \nu_2 d\mu_2 + d\mu_3. \qquad (2)$$

Let us consider how ν_1 and ν_2 can be calculated from data on the saturated solution–vapor equilibrium, and thus how the actual composition of the solid phase can be determined without additional experimental study.

If the vapor phase containing solely volatile components (alcohol and water) is assumed to be an ideal gas mixture, then for isothermal conditions the following relationship is valid:

$$d\mu_i = RT\ln(Py_i), \qquad i = 1,2, \qquad (3)$$

where y_i is the mole fraction of the ith component in the vapor phase (hereafter, $y \equiv y_1$).

Since $PV_l/RT \ll 1$, the expression in the left-hand side of the inequality can be neglected compared to unity. After simple transformations of (1)–(3) are performed, the final relationship becomes as follows:

$$\tilde{x} \equiv \frac{x_1 - \nu_1 x_3}{1 - (1 + \nu_1 + \nu_2)x_3} = y\left[1 - (1 - y)\frac{d\ln P}{dy}\right]. \qquad (4)$$

Let us illustrate the applicability of (4) to analysis of the isothermal data on the solid salt–salt-

1070-4272/03/7607-1048$25.00

Table 1. Pressure and compositions of saturated solution and vapor coexisting at 25°C in the system methanol–water–calcium chloride, for the $CaCl_2 \cdot 6H_2O$ crystallization branch [2]

Test no.	x_3	x_1	P, mm Hg	y	$\tilde{P}$	$\tilde{x}$	Z
1	0.1166	0	6.85	0	6.81	0	0
2	*0.1197*	*0.0127*	*8.64*	*0.229*	8.68	0.014	–0.106
3	*0.1212*	*0.0179*	*9.76*	*0.342*	9.79	0.020	0.198
4	0.1221	0.0202	10.30	0.393	10.33	0.023	0.683
5	*0.1226*	*0.023*	*10.49*	*0.43*	10.74	0.026	0.956
6	*0.1246*	*0.0283*	*11.46*	*0.484*	11.37	0.032	1.140
7	*0.1269*	*0.0345*	*12.00*	*0.527*	11.90	0.040	1.457
8	0.1281	0.0373	12.37	0.54	12.07	0.043	1.761
9	*0.1292*	*0.0389*	*12.54*	*0.57*	12.46	0.045	1.841
10	0.1326	0.0435	12.85	0.592	12.75	0.050	2.012
11	*0.1331*	*0.0441*	*12.89*	*0.603*	12.90	0.051	2.194
12	0.1362	0.0462	12.96	0.613	13.04	0.053	2.226
13	0.1372	0.0468	12.82	0.615	13.07	0.054	2.295

* Additional data from [3] are printed italic.

saturated solution–vapor equilibrium in the system methanol–water–calcium chloride at 25°C. Fairly extensive data are available for this system [2, 3]; these data show that the solubility line contains four branches of crystallization of solid phases: $CaCl_2 \cdot 6H_2O$, $CaCl_2 \cdot 4H_2O$, $CaCl_2 \cdot 2CH_3OH$, and $CaCl_2 \cdot 4CH_3OH$. The saturated vapor pressures and compositions of the coexisting phases for the crystallization branch of the hexahydrate are presented in Table 1. The calculated values of the saturated vapor pressure $\tilde{P}$ as a function of composition can be determined with a high correlation coefficient (0.996) by treatment of the experimental data by the correlation equation (hereafter, the standard deviations of the left-hand side values are given with the ± sign in parentheses).

$$\tilde{P} = \exp[1.918(\pm 0.010) + 1.060(\pm 0.021)y]. \quad (5)$$

After the $\tilde{x}$ values were calculated from Eqs. (4) and (5), ν_1 and ν_2 were determined from the evident linear relationship easily derived from (4):

$$Z = \nu_1 + (1 + \nu_1 + \nu_2)\tilde{x}, \text{ where } Z \equiv \frac{\tilde{x} - x_1}{x_3}. \quad (6)$$

The values of the required coefficients [obtained from linear regression using Eq. (6) with the correlation coefficient of 0.979] are as follows: $\nu_1 = 0.28(\pm 0.08)$ and $1 + \nu_1 + \nu_2 = 6.9(\pm 0.3)$. Because the dispersion of the sum of the coefficients approached the ν_1 value, it can be accepted with assurance that $\nu_1 = 0$ and $\nu_2 = 5.9 \approx 6$, which is confirmed by the results obtained by the Schreinemaker's method of wet residues, as applied to the experimental data on the gross compositions of the prepared mixture and on the composition of the saturated solution. The proposed method using the dependence of the saturated vapor pressure on the vapor composition and Eqs. (4) and (6) for determining the liquid-phase composition has also been successfully applied to other crystallization branches of solid phases in the system considered.

Data on the vapor–saturated solution equilibrium for a large number of alcohol–water–salt ternary systems under isobaric conditions (P = const) are presented in a handbook [4]. As in [1], for these cases relationship (4) can be presented in the form

$$\tilde{x} = y\left\{1 + (1 - y)\frac{[L_1 y + L_2(1 - y)]}{R}\frac{\mathrm{d}(1/T)}{\mathrm{d}y}\right\}, \quad (7)$$

where T is the boiling point of the solution saturated with the corresponding salt; L_1 and L_2, molar heats of vaporization (J mol^{-1}) of the first and second components (methanol and water, respectively; L_1 = 35300 and L_2 = 40680 [5]); R, gas constant (8.31451 J mol^{-1} K^{-1}).

The data on the boiling points and compositions of the coexisting phases in the system methanol–water–potassium chloride at normal pressure are presented in Table 2. The calculated values of the boiling point $\tilde{t}$ (°C) as a functions of the vapor composition y were determined with a high correlation coefficient (0.998) by treatment of the experimental data (run nos. 1–7) using the correlation equation

Table 2. Data on boiling points and compositions of saturated solution and vapor coexisting at normal pressure in the system methanol–water–potassium chloride [4]

Test no.	x_3	$x_1/(1 - x_3)$	t, °C	y	$\tilde{t}$, °C	$\tilde{x}$	Z
1	0.122	0	108.8	0	108.4	0	0
2	0.105	0.024	99.0	0.245	100.0	0.008	–0.125
3	0.091	0.062	91.6	0.47	90.9	0.101	0.489
4	0.082	0.106	85.5	0.593	85.5	0.210	1.376
5	0.066	0.190	80.8	0.69	81.0	0.334	2.369
6	0.057	0.250	78.4	0.723	79.5	0.384	2.606
7	0.043	0.335	76.6	0.759	77.7	0.444	2.880
8	0.03	0.444	73.8	0.798	73.7	0.498	2.255
9	0.021	0.541	72.0	0.83	72.0	0.569	1.871
10	0.017	0.593	71.2	0.849	71.1	0.612	1.738
11	0.011	0.694	69.0	0.884	69.3	0.696	0.857
12	0.007	0.806	67.4	0.925	67.3	0.798	–0.271
13	0.004	0.905	65.3	0.963	65.4	0.898	–0.749
14	0.003	1	63.8	1	63.6	1	1

$$\tilde{t} = 10^3[2.62(\pm0.005) + 0.213(\pm0.026)y + 0.117(\pm0.029)y^2]^{-1} - 273.2. \quad (8)$$

After $\tilde{x}$ was calculated from Eqs. (7) and (8), ν_1 and ν_2 were determined, as previously, from linear equation (6). The values of these parameters appeared to be $\nu_1 = 0.11(\pm0.07)$ and $1 + \nu_1 + \nu_2 = 6.99(\pm0.26)$. Consequently, we can consider that $\nu_1 = 0$ and $\nu_2 = 5.99 \approx 6$. For run nos. 8–14, the following correlation equation is valid (with the correlation coefficient of 0.998):

$$\tilde{t} = 10^3[2.544(\pm0.008) + 0.425(\pm0.009)y]^{-1} - 273.2. \quad (9)$$

It should be noted that the $\tilde{x}$ values calculated using Eq. (9) for run nos. 9–14 are close to the relative mole fractions $x_1/(1 - x_3)$. This fact shows that, for this range of solution concentrations, the solid phase is KCl. The similar cases have been considered previously [6]. Run nos. 8 and 9 (Table 2) can be assigned to the transition region in which anhydrous KCl starts to crystallize instead of KCl hexahydrate.

Table 3 presents the experimental data and results of their treatment by relationship (7) for the system ethanol–water–mercury iodide at a pressure of 755 ± 3 mm Hg. Unfortunately, for this system the mole fractions of the salt in a saturated solution are not reported. Therefore, relationship (6) cannot be used. At the same time, the crystallization regions of various solid phases can be qualitatively predicted using relationship (7). In contrast to the previous system, the dependence of the boiling point t (°C) on the vapor composition y was derived using the orthogonal Chebyshev polynomials of the first kind [7]. The equation for calculating the boiling points with the correlation coefficient of 0.994 has the form

$$\tilde{t} = 10^3[2.86(\pm0.06) - 0.11(\pm0.09)y + 0.18(\pm0.05)T(2,y) + 0.08(\pm0.02)T(3,y)]^{-1} - 273.2,$$

where $T(2,y) = 2y^2 - 1$ and $T(3,y) = 4y^3 - 3y$ are the Chebyshev polynomials (higher polynomials did not noticeably improve the interpolation equation). The value of 34 000 J mol^{-1} [5] was taken for the molar heat of vaporization of ethanol.

As follows from Table 3, the differences between the experimental and calculated relative mole fractions of alcohol in solution reflect four concentration ranges: the first range covers run nos. 1–3; the second, run nos. 4 and 5; the third, run nos. 7–10; and the fourth, run nos. 11–13. In the first concentration range, crystallization of anhydrous mercury iodide can be assumed, whereas the second, third, and fourth ranges must correspond to solid phases containing different amounts of crystallization molecules of water and (or) alcohol. Therefore, in the concentration triangle the line of the saturated salt solutions would have four crystallization intervals corresponding to different solid phases.

CONCLUSIONS

The thermodynamic relations for calculating the composition of a solid phase crystallizing from a

Table 3. Experimental and calculated boiling points and compositions of the saturated solution and vapor coexisting at a pressure of 755 ± 3 mm Hg in the system ethanol–water–mercury iodide [4]

Test no.	$x_1/(1 - x_3)$	t, °C	y	$\tilde{t}$, °C	$\tilde{x}$	$\tilde{x} - x_1/(1 - x_3)$
1	0	99.8	0	99.87	0	0
2	0.011	95.6	0.157	95.84	0.004	–0.007
3	0.051	90.5	0.356	89.10	0.058	0.007
4	0.134	84.2	0.488	84.62	0.193	0.059
5	0.230	82.2	0.543	82.92	0.274	0.044
6	0.344	81.2	0.587	81.67	0.348	0.004
7	0.461	80.2	0.633	80.49	0.431	–0.030
8	0.562	79.4	0.677	79.51	0.514	–0.048
9	0.684	78.7	0.741	78.36	0.639	–0.045
10	0.799	78.2	0.819	77.50	0.783	–0.016
11	0.895	77.7	0.89	77.31	0.896	0.001
12	0.951	77.6	0.948	77.65	0.964	0.013
13	1	77.9	1	78.36	1	0

three-component saturated solution in equilibrium with a two-component vapor (phase) were derived and tested with the methanol–water–salt system as example.

REFERENCES

1. Marinichev, A.N., *Zh. Prikl. Khim.*, 1995, vol. 68, no. 4, pp. 542–546.
2. Storonkin, A.V., and Simanavichus, L.E., *Vestn. Leningr. Gos. Univ.*, 1957, vol. 22, no. 4, pp. 103–110.
3. Simanavichus, L.E., Thermodynamic Study of the Solid Phase–Solution–Vapor Three-Phase Equilibrium in the System $CaCl_2$–CH_3OH–H_2O, *Cand. Sci. Dissertation*, Leningrad, 1958.
4. Tsiparis, I.N., *Sbornik dannykh po vliyaniyu solei na fazovoe ravnovesie mezhdu zhidkost'yu i parom* (Collection of Data on the Effect of Salts on the Liquid–Vapor Phase Equilibrium), Kaunas: Lit. Sel'skokhoz. Akad., 1966.
5. Reid, R.C., Prausnitz, J.M., and Sherwood, T.K., *The Properties of Gases and Liquids. Their Estimation and Correlation*, New York: McGraw-Hill, 1958.
6. Marinichev, A.N., in *Materialy II Vserossiiskoi Internet-Konferentsii* (Proc. II Russian Internet Conf.), Tambov, April–May 2001, issue 7, pp. 57–58.
7. Bateman, H., and Erdölyi, A., *Higher Transcendental Functions*, New York: McGraw-Hill, 1953, vol. 2.

Russian Journal of Applied Chemistry, Vol. 76, No. 7, 2003, pp. 1052–1054. Translated from Zhurnal Prikladnoi Khimii, Vol. 76, No. 7, 2003, pp. 1084–1087.

SORPTION AND ION-EXCHANGE PROCESSES

Synthesis and Properties of Expandable Residual Graphite Hydrosulfate Obtained in the System CrO_3–H_2SO_4

A. P. Yaroshenko, M. V. Savos'kin, A. N. Magazinskii, and G. E. Vaiman

Litvinenko Institute of Physical Organic and Coal Chemistry, National Academy of Sciences of Ukraine, Donetsk, Ukraine

Received July 24, 2002; in final form, March 2003

Abstract—The fundamental aspects of synthesis of expandable residual graphite hydrosulfate with the use of an oxidizing system CrO_3–H_2SO_4 at ultralow consumption of the reagents and their separate introduction into the reaction mass were studied. The dependence of the expansion ratio of the samples obtained on the content of intercalant and expansion temperature was analyzed.

It has been shown previously that successive treatment of natural graphite with a concentrated aqueous solution of chromium(VI) oxide, sulfuric acid, and water yields expandable residual graphite hydrosulfates (RGH) of high quality [1–7]. The products obtained are characterized by high expansion ratios at relatively low expansion temperature (500°C), stability of properties in prolonged storage, and convenient use.

The method developed differs from the conventional techniques in that the graphite oxidation stage is carried out at ultralow consumption of the oxidizing agent and acid and the components of the intercalating solution are introduced into the reaction mass separately. The mass ratio of the total amount of liquid components and graphite does not exceed unity. Interaction of the liquid components to give active species executing the intercalation process occurs *in situ* in the adsorption layer on the surface of graphite particles. This study is concerned with the effect of synthesis conditions on the properties of the RGH obtained.

Natural flaked graphite of the GT-1 brand from the Zaval'evskoe deposit (Ukraine) with ash content of 5.68 wt % was subjected to oxidation. The graphite is mainly composed of two fractions: 74.3 wt % 0.630–0.315-mm particles and 22.1 wt % 0.315–0.200-mm particles. A 50% aqueous solution of chromium(VI) oxide (ρ = 1.501 g cm^{-3}) and concentrated (95%) sulfuric acid of chemically pure grade (ρ = 1.835 g cm^{-3}) were used.

Graphite was oxidized in a cylindrical glass reactor equipped with a T-shaped stainless still rabble. The reaction mass was stirred at room temperature without forced heating or cooling. The reactor was charged with 25 g of graphite, stirring was switched on, and the aqueous solution of chromium(VI) was added. After 10 min of stirring, sulfuric acid was introduced into the mixture and stirring was continued for an additional 10 min. Then 750 cm^3 of water was added to the oxidized graphite, and the resulting mixture was allowed to stand for 24 h for the hydrolysis to occur. During this period of time, continuous evolution of fine gas bubbles from the solid-phase layer was observed. Then the solid phase was filtered off in a water-jet-pump vacuum and washed on the filter with water to pH 5–6. The washed product was dried at 100–110°C to constant weight (moisture content not exceeding 1.0 wt %).

The consumption of the aqueous solution of CrO_3 was varied from 2 to 20 cm^3 per 100 g of graphite, and that of H_2SO_4, from 20 to 48 cm^3 per 100 g of graphite. For all of the 80 RGH samples obtained, the yield, expansion ratio in impact heating mode in the range 400–900°C, and weight loss in expansion at temperatures of 500–900°C were determined. The data on product yield were used to calculate the intercalant content m_i (wt %) in a compound obtained with account of the fact that the contribution from the phase oxidation of graphite under the synthesis conditions was negligible [8, 9].

The expansion ratio of the products obtained was determined as follows. A weighed portion of the product (m = 0.2–0.3 g) was placed in a stainless steel cell preliminarily mounted in a muffle furnace heated to a required temperature. The expansion was done for

1070-4272/03/7607-1052$25.00

5 min at 400–600°C and for 2 min at 700–900°C. The cell with expanded graphite was extracted from the furnace, its contents were carefully transferred to a glass volumetric vessel, and the volume V (cm^3) occupied by the expanded graphite was measured. The expansion ratio was found using the relationship $K_e = V/m$ as arithmetic mean of three replicate measurements.

The process involves graphite oxidation with chromium(VI) oxide and intercalation of the resulting positively charged graphite matrix with hydrosulfate anions solvated by sulfuric acid molecules to give graphite hydrosulfate. In the reagent consumption range used in this study, a compound of the second intercalation stage, $C_{48}^{+}\cdot HSO_4^{-}\cdot(2.0–2.5)H_2SO_4$, is formed.[1] Hydrolysis of this compound gives residual graphite hydrosulfate, in which sulfuric acid molecules solvating hydrosulfate anions in the interlayer space of the graphite matrix are replaced by water molecules.

We found that, with the reagent consumption in the graphite oxidation stage raised, the content of the intercalant in the final product grows. The RGH expansion ratio grows with increasing intercalant content and expansion temperature. The mass loss by RGH samples in their expansion in the temperature range 500–900°C depends linearly on the intercalant content m_i in the initial samples. A typical example of a dependence of this kind is shown for an expansion temperature of 500°C in Fig. 1. The dependences for the other temperatures are similar. For all these dependences, the intercept is virtually zero and the slope is close to unity. This indicates that the expansion in the specified temperature range occurs without burnout of the carbon matrix and is accompanied by virtually total removal of intercalant species.

It was found unexpectedly that, whereas the dependences of the weight loss on the intercalant content in RGH are linear for all the expansion temperatures, the dependences of the expansion ratio on the intercalant content are exponential. For all the expansion temperatures studied, these dependences are expressed by an equation of the type

$$K_e = A\exp(bm_i), \quad (1)$$

where A and b are constants.

A typical semilog plot of the expansion ratio at 500°C vs. the intercalant content m_i in RGH is shown in Fig. 2.

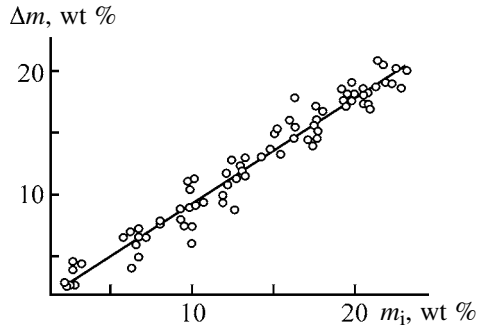

Fig. 1. Weight loss Δm from RGH samples in their expansion at 500°C vs. intercalant content m_i in the samples. $Y = 0.86x + 0.63$; $R^2 = 0.96$.

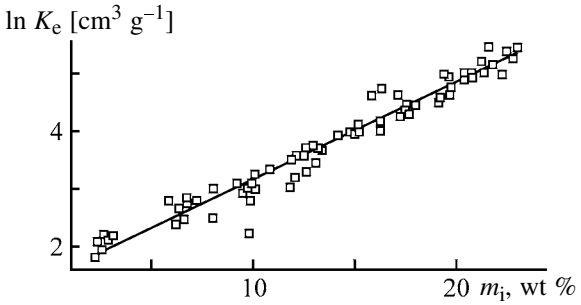

Fig. 2. Semilog plot of the expansion ratio K_e of RGH samples at 500°C vs. intercalant content m_i in the samples. $Y = 0.17x + 1.49$; $R^2 = 0.96$.

The dependences obtained at other expansion temperatures are similar and can also be described by Eq. (1). The parameters of Eq. (1) for expansion of RGH samples at 400–900°C are listed in the table.

It can be seen that, for all the expansion temperatures, parameter b remains virtually invariable, whereas parameter A grows linearly with increasing expansion temperature (Fig. 3).

Figure 4 shows the dependences of the expansion ratio of RGH samples on the content of the intercalant in them and on the expansion temperature. The entire

Parameters of Eq. (1) in relation to expansion temperature T of RGH samples

T, °C	A	b
400	2.36	0.136
500	4.44	0.167
600	7.48	0.156
700	9.17	0.158
800	10.75	0.160
900	14.47	0.146

[1] The general formula of graphite hydrosulfate is $C_{24n}^{+}\cdot HSO_4^{-}\cdot mH_2SO_4$, where n is the stage number of a graphite intercalation compound, designating the number of graphite layers between the two nearest layers of the intercalant.

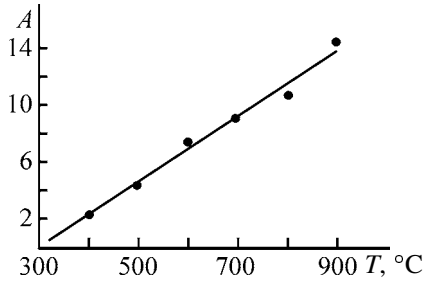

Fig. 3. Parameter A in Eq. (1) vs. expansion temperature. $Y = 0.0232x - 6.97$; $R^2 = 0.985$.

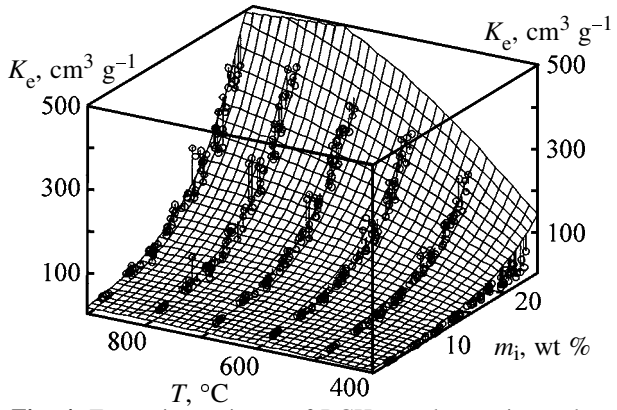

Fig. 4. Expansion ratio K_e of RGH samples vs. intercalant content m_i in the samples and expansion temperature T.

body of data is fairly well described ($R^2 = 0.94$) by the following two-parameter equation:

$$\ln K_e = a + bm_i + c/t^2, \quad (2)$$

where $a = 3.150$, $b = 0.143$, and $c = -285\,600$.

Analysis of the response surface shows that its sections parallel to the temperature axis are near linear at small m_i and take the form of flat, leveling-off curves at higher values of this parameter. The sections parallel to the axis of intercalant content m_i, which are described by the bm_i term in Eq. (2), are exponential dependences, in agreement with a description by a single-parameter equation (1).

The observed exponential dependence of the expansion ratio on the intercalant content is unconventional, since a linear relationship between these parameters is observed for graphite nitrate and other compounds obtained on the basis of graphite hydrosulfate with nitric acid as oxidizing agent [10]. Indeed, the linear dependence can be readily accounted for assuming that the chemical nature and composition of the intercalant remain unchanged when its content grows. In this case raising the intercalant content at constant expansion temperature must lead, in accordance with the Mendeleev–Clapeyron equation, to a linear rise in K_e, and this behavior is indeed observed experimentally [10].

As compared to graphite intercalation compounds, which exhibit a linear relationship between K_e and m_i, with RGH the pattern is different. In all probability, the chemical nature of the intercalant changes with its increasing content in RGH. Species having higher efficiency in RGH expansion are accumulated in the layer introduced. It may be assumed that structural fragments similar to those in the case of graphite oxide act as species of this kind. Such structural fragments may be accumulated as a result of oxidative-hydrolytic processes occurring in the stage of hydrolysis of graphite hydrosulfate [9, 11].

The products obtained under the optimal synthesis conditions are characterized by expansion ratios of 300–400 cm^3 g^{-1} at 900°C and 200 cm^3 g^{-1} at 500°C.

CONCLUSIONS

(1) It was found that the expansion ratio of a product at a given temperature is determined by the content of intercalant in it.

(2) An exponential dependence of the expansion ratio on the intercalant content was observed for the first time for the products obtained.

(3) An assumption was made that the possible reason for such an unusual behavior is a change of the chemical nature of intercalant species.

REFERENCES

1. Yaroshenko, A.P., Shapranov, V.V., and Kucherenko, V.A., *Khim. Tverd. Topl.*, 1994, no. 2, pp. 91–96.
2. Yaroshenko, A.P., Popov, A.F., and Shapranov, V.V., *Zh. Prikl. Khim.*, 1994, vol. 67, no. 2, pp. 204–211.
3. Yaroshenko, A.P. and Savos'kin, M.V., *Zh. Prikl. Khim.*, 1995, vol. 68, no. 8, pp. 1302–1306.
4. RF Patent 2058261.
5. Ukrainian Patent 30796.
6. Ukrainian Patent 30797.
7. Ukrainian Patent 34777.
8. Horn, D. and Boehm, H.-P., *Z. Anorg. Allg. Chem.*, 1979, vol. 456, no. 9, pp. 117–129.
9. Chernyshev, I.G., Karpov, I.I., Prikhod'ko, G.P., and Shai, V.M., *Fiziko-khimicheskie svoistva grafita i ego soedinenii* (Physicochemical Properties of Graphite and Its Compounds), Kiev: Naukova Dumka, 1990.
10. Yaroshenko, A.P., Savos'kin, M.V., Magazinskii, A.N., *et al.*, *Zh. Prikl. Khim.*, 2002, vol. 75, no. 6, pp. 881–885.
11. Monyakina, L.A., Avdeev, V.V., Nikol'skaya, I.V., *et al.*, *Zh. Fiz. Khim.*, 1995, vol. 69, no. 5, pp. 926–930.

Russian Journal of Applied Chemistry, Vol. 76, No. 7, 2003, pp. 1055–1058. Translated from Zhurnal Prikladnoi Khimii, Vol. 76, No. 7, 2003, pp. 1088–1091.

SORPTION AND ION-EXCHANGE PROCESSES

Synthesis and Sorption Properties of Filled Fibrous Sorbents with Immobilized Hetarylformazan Groups

I. G. Pervova, G. N. Lipunova, T. A. Mel'nik, I. N. Lipunov, and G. I. Sigeikin

Ural State Forestry Engineering University, Yekaterinburg, Russia
Ural State Technical University, Yekaterinburg, Russia
Interdepartmental Center of Analytical Research in the Field of Physics, Chemistry, and Biology, Presidium of the Russian Academy of Sciences, Moscow, Russia

Received February 10, 2003

Abstract—New sorbents were prepared by immobilization of structurally different sulfur-containing hetarylformazans on nonwoven polyacrylonitrile fiber filled with AV-17 anion exchanger. Sorption of some heavy metals on these materials was studied as influenced by various factors. Sorbents for selective recovery of copper(II) in the presence of nickel(II), zinc(II), and cadmium(II) cations were found.

Fibrous ion-exchange sorbents widely used for recovering metal ions from solutions attract growing attention [1, 2]. Introduction of complexing groups into fibrous materials increases their selectivity with respect to some metals. These modified sorbents are used for selective recovery of valuable elements of multicomponents solutions and for removal of toxic metals from natural waters [3, 4]. Filled fibrous materials are the most promising [5] since they exhibit good sorption and kinetic properties and can be used for recovery of metals under dynamic conditions. A finely divided complexing sorbent is used as a filler.

Previously we showed [6–8] that immobilization of complexing formazan groups on AN-20, AN-18, and AV-17 anion exchangers substantially improved their sorption activity and selectivity with respect to some metals. In this work, sulfur-containing hetarylformazans were immobilized on nonwoven polyacrylonitrile fiber filled with AV-17 anion exchanger, and the properties of the resulting sorbents were studied.

EXPERIMENTAL

Nonwoven polyacrylonitrile fiber filled with AV-17 anion exchanger was prepared by the special procedure (Russian Research Institute of Manmade Fibers, Tver). The thickens of a swollen fiber thread was 30–100 μm; the filler content was 50%. The fiber was modified with various formazans with different heterocyclic fragments containing different substituents at the aromatic ring (Table 1). The possible structure of the resulting sorbents is shown below:

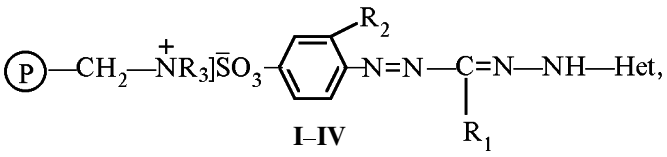

I–IV

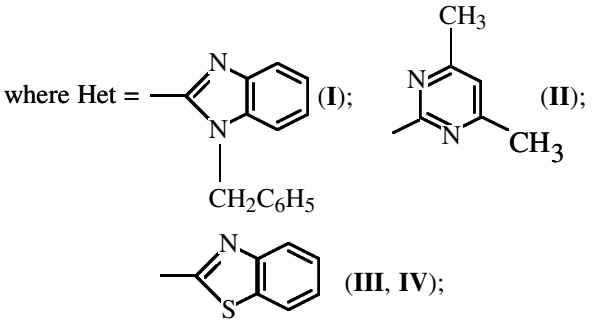

where Het = (**I**); (**II**);

(**III**, **IV**);

$R_1 = CH_3$ (**I, II**), C_2H_5 (**III, IV**); R_2 = H (**I**–**III**), OH (**IV**).

The content of formazans (*A*) in **I** and **II** was 0.15 and 0.09 mmol g^{-1}, respectively, and that in **III** and **IV** was 0.10 mmol g^{-1}.

The formazan groups were immobilized by the following ion-exchange procedure. To a weighed portion of the fiber filled with AV-17 anion exchanger in the OH^- form (0.4 g), an aqueous–ethanolic solution (1 : 1) (100 ml) of formazan (0.05 g) was added. The mixture was stirred with a vibrator for 4–6 h. The sorbent was filtered off, washed with distilled water, and dried in air. The residual formazan concentration

1070-4272/03/7607-1055$25.00 © 2003 MAIK "Nauka/Interperiodica"

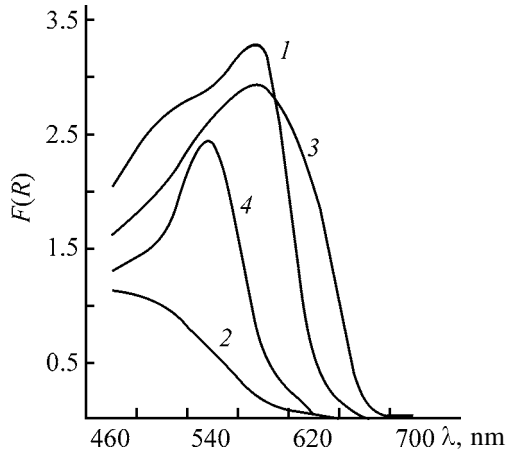

Fig. 1. Diffuse reflectance spectra of modified fibrous sorbents (*1*) **I**, (*2*) **II**, (*3*) **III**, and (*4*) **IV** filled with AV-17. (λ) Wavelength.

in the filtrate was determined photocolorimetrically. Immobilization of formazan was indicated by a change in the fiber color from colorless to yellow or red-violet depending on the formazan structure. Diffuse reflectance spectra of modified sorbents **I**–**IV** are shown in Fig. 1. As seen from Fig. 1, sorbents **I, III**, and **IV** strongly absorb in the range 530–640 nm. In the spectrum of sorbent **II** containing pyrimidinylformazan, a hypsochromic shift of λ_{max} to 500 nm is observed. The content of formazan groups A in modified fibers **I**–**IV** was 0.09-0.15 mmol g^{-1}.

We studied sorption of Cu(II), Ni(II), Zn(II), and Cd(II) cations on the initial and modified fibers. The sorption under static conditions was performed for 3 days by intermittent stirring of a mixture of aqueous solutions of copper(II) sulfate, nickel(II) nitrate, zinc(II) chloride, and cadmium(II) chloride with the sorbent at the solution volume–sorbent weight ratio of 500 : 1. The metal concentration in the electrolytes was 100 and 1000 mg l^{-1}; pH was 3.5 and 6.9. The contact time in the sorption kinetic experiments varied from 10 to 90 min.

Sorption capacity of modified fibrous sorbents. Contact time 3 days, $V : m = 500$

Fiber	c_M, mg l^{-1}	pH	SC, mg-equiv g^{-1}			
			Cu(II)	Ni(II)	Zn(II)	Cd(II)
Initial	100	6.9	0	0.09	0.25	0
I	100	6.9	0.32	0.10	0.13	0
II	100	6.9	0.91	0.10	0.08	0
III	100	6.9	0	0	0.59	0.60
IV	100	6.9	0	0.08	0.69	0.60
I	1000	6.9	0.62	0	0.39	0.90
II	1000	6.9	0.50	0	0.39	0.90
I	1000	3.5	1.09	0.31	0.47	0.78
II	1000	3.5	0	1.38	0.60	1.00

The sorption under dynamic conditions was performed by passing an electrolyte solution at a 0.5 ml min^{-1} flow rate through a 50-mm sorbent bed packed in a glass column 10 mm in diameter.

The metal concentration in model solutions of pure salts, solutions after the sorption, and eluates was determined photocolorimetrically, and in mixed electrolyte solutions, by atomic absorption analysis.

To determine the sorption capacity of the fibers (SC), we measured sorption of heavy metal cations from 100 mg l^{-1} aqueous solutions of their salts at pH 6.9 (see table).

The sorption capacities for Cu(II) of fibers filled with AV-17 anion exchanger and modified with benzimidazolyl and pyrimidinylformazan groups (sorbents **I** and **II**, SC 0.32 and 0.91 mg-equiv g^{-1}, respectively) are higher than those of the initial fiber.

Fibers modified with benzothiazolylformazans (sorbents **III** and **IV**) have high sorption capacity for Zn(II) and Cd(II) and do not sorb Cu(II) and Ni(II).

Not only Cu(II) but also Zn(II) and Cd(II) are sorbed on **I** and **II** from 1000 mg l^{-1} solutions of salts of these metals at neutral pH. In acidic solutions (pH 3.5) the sorption of all the examined metals on **I** and **II** increases [except for sorption of Cu(II) on **II**] as compared to that at pH 6.9. In acidic solutions sorbent **II** sorbs Ni(II), Zn(II), and Cd(II), and its sorption capacity for Cu(II) and Cd(II) is lower than that of **I**.

The study of sorption of heavy metal ions on the modified fibrous sorbents filled with AV-17 anion exchanger showed that immobilization of hetarylformazans on the fiber enhances not only the sorption capacity but also selectivity with respect to some metals.

Thus, sorbent **II** can be used for concentration and recovery of Cu(II) from neutral solutions containing Ni(II), Zn(II), and Cd(II) at the total metal concentration of up to 100 mg l^{-1}, and sorbents **III** and **IV**, for joint recovery of Zn(II) and Cd(II) in the presence of Cu(II) and Ni(II) under the same conditions.

With polyacrylonitrile fiber **I** filled with AV-17 anion exchanger and modified with formazan with benzylbenzimidazole groups was example, we studied in more detail how the sorption of heavy metal ions

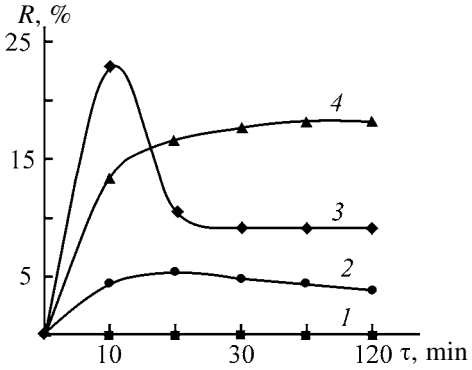

Fig. 2. Degree of sorption R of (*1*) Cd^{2+}, (*2*) Ni^{2+}, (*3*) Zn^{2+}, and (*4*) Cu^{2+} (the same for Fig. 3) on fiber **I** from model solutions of their pure salts under static conditions as a function of the phase contact time. Concentration c_M, mg l^{-1}: Ni^{2+} 25; Cd^{2+}, Cu^{2+}, and Zn^{2+} 75; pH 5.5–6.9; $V : m$ = 500; the same for Fig. 3.

depends on the phase contact time. The sorption kinetics on this sorbents was studied under the static conditions (R is the degree of sorption of metal ions) on the sorbent. The kinetic curves of sorption of Cd(II), Ni(II), Zn(II), and Cu(II) ions from model solutions of pure salts of these metals are shown in Fig. 2. Sorption of Zn(II) and Cu(II) cations on fiber **I** is characterized by good kinetic parameters favorable for recovery of these metals from multicomponent solutions.

Selective sorption on **I** of Zn(II) in the presence of Ni(II) and Cd(II) (Fig. 3a) and Cu(II) in the presence of Ni(II) and Cd(II) (Fig. 3b) confirms the good kinetic properties.

To find whether Zn(II) and Cu(II) cations can be selectively recovered under dynamic conditions, we compared the dynamics of sorption of these cations on fiber **I**.

As seen from the outlet curves for Zn(II) and Cu(II) (Fig. 4), Cu(II) can be completely recovered from Zn(II)-containing aqueous solutions under dynamic conditions. The time during which a filter based on sorbent **I** ensures protective effect with respect to Cu(II) cations is longer than that with respect to Zn(II) cations.

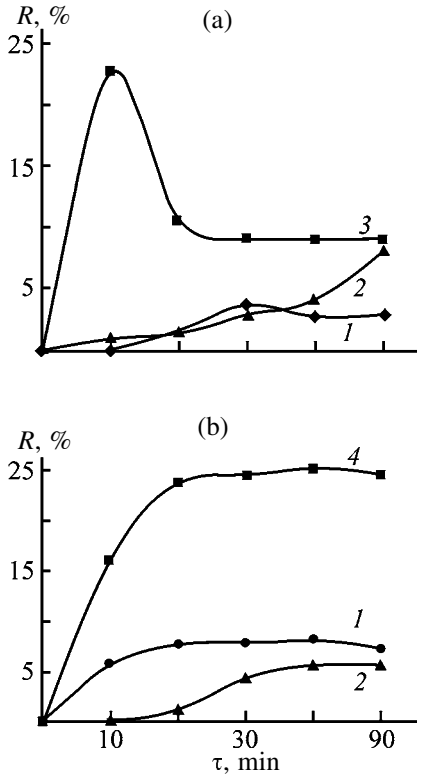

Fig. 3. Degree of sorption of the metal ions R on fiber **I** from model solutions containing a mixture of (a) Cd^{2+}, Ni^{2+}, and Zn^{2+} and (b) Cd^{2+}, Ni^{2+}, and Cu^{2+} ions under static conditions as a function of phase contact time.

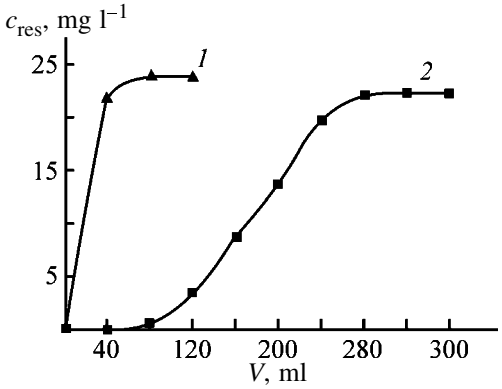

Fig. 4. Outlet curves characterizing sorption of (*1*) Zn^{2+} and (*2*) Cu^{2+} on sorbent **I**. (c_{res}) Residual metal concentration in the solution and (V) solution volume.

CONCLUSIONS

(1) The prepared fibrous polymers with hetarylformazan groups are promising sorbents for recovering Cu(II) cations from solutions containing nickel(II), zinc(II), and cadmium(II) cations.

(2) Sorbents modified with fragments of benzothiazolylformazans can be used for concentrating Zn(II) and Cd(II) cations from dilute solutions and for separating these cations from Cu(II) and Ni(II); sorbents modified with pyrimidinylformazan, for concentrating and separating Cu(II) from solutions containing Ni(II), Zn(II), and Cd(II); and sorbents modified with benzylbenzimidazolylformazans, for concentrating Cu(II) from dilute solutions and for separating Cu(II) from Ni(II) and Cd(II).

ACKNOWLEDGMENTS

This work was financially supported by the Russian Foundation for Basic Research (project no. 02-03-96424-p2002 Ural and no. 03-03-32044).

The authors are grateful to G.V. Myasoedova for kindly supplying fibrous sorbent samples.

REFERENCES

1. Soldatov, V.S. and Sergeev, G.I., *Zh. Vses. Khim. O–va.*, 1990, no. 1, pp. 101–135.
2. Andreeva, I.Yu., Min'ko, I.A., and Kazakevich, Yu.I., *Zh. Prikl. Khim.*, 1991, no. 6, pp. 1276–1280.
3. Myasoedova, G.V., Shcherbinina, N.I., and Savvin, S.B., *Zh. Anal. Khim.*, 1983, vol. 38, no. 8, pp. 1503–1514.
4. Simanova, S.A. and Kukushkin, Yu.N., *Izv. Vyssh. Uchebn. Zaved., Khim. Khim. Tekhnol.*, 1986, vol. 39, no. 5, pp. 3–15.
5. Myasoedova, G.V., Nikashina, V.A., Molochnikova, N.P., and Lileeva, L.V., *Zh. Anal. Khim.*, 2000, vol. 55, no. 6, pp. 611–615.
6. Lipunova, G.N., Pervova, I.G., and Lipunov, I.N., *Vysokomol. Soedin., Ser. B.*, 1997, vol. 39, pp. 1523–1526.
7. Lipunov, I.N., Pervova, I.G., Lipunova, G.N., *et al.*, *Koord. Khim.*, 1997, vol. 23, no. 12, pp. 934–937.
8. Pervova, I.G., Yushkova, O.G., Lipunova, G.N., and Lipunov, I.N., *Persp. Razv. Est. Nauk Vyssh. Shkole*, 2001, vol. 1, pp. 258–261.

Russian Journal of Applied Chemistry, Vol. 76, No. 7, 2003, pp. 1059–1066. Translated from Zhurnal Prikladnoi Khimii, Vol. 76, No. 7, 2003, pp. 1092–1098.

APPLIED ELECTROCHEMISTRY AND CORROSION PROTECTION OF METALS

Manganese-Containing Anodic Layers on Titanium

V. S. Rudnev, M. S. Vasil'eva, L. M. Tyrina, T. P. Yarovaya, V. G. Kuryavyi, N. B. Kondrikov, and P. S. Gordienko

Institute of Chemistry, Far-Eastern Division, Russian Academy of Sciences, Vladivostok, Russia

Far-Eastern State University, Vladivostok, Russia

Received August 8, 2002; in final form, December 2002

Abstract—Data on formation of anodic layers containing $MnTiO_3$, β-Mn_2TiO_4, Mn_2O_3, Mn_3O_4, and $Mn_3(BO_3)_2$ on titanium from aqueous electrolytes at sparking voltages are presented.

Transition metals oxides and, in particular, manganese oxides are used in catalysis because of their thermal stability and relatively high activity [1, 2]. A conventional method for fabrication of oxide catalysts is thermal decomposition of salts or hydroxides of the corresponding metals on the surface of pretreated supports [3]. Salts or hydroxides are deposited on a substrate by impregnation or precipitation from solutions, by solution spraying, deposition from the gas phase, etc.

Certain opportunities in synthesis of various high-temperature oxide structures, including those promising for catalysis [4–6], on metal surfaces are furnished by anodic-spark deposition. It could be expected that coatings formed on the surface of rectifying metals from aqueous electrolytes with manganese salts should contain manganese oxides, manganese-containing oxide solid solutions, or spinels [7]. For example, coatings containing $MnTiO_3$ spinel [7, 8] have been obtained on titanium from an electrolyte containing Na_2SO_4 and $Mn(CH_3COO)_2$.

It is practically important that, in this technique, high-temperature oxides are synthesized at the surface of the metallic anode in the bulk of the aqueous electrolyte at an average temperature not exceeding 100°C. As additional advantages of the technique can be regarded the following: (i) formation, between the metal and the active layer, of a sublayer composed of the oxide of a metal being anodized, which can serve as a support; (ii) possibility of processing articles with complex geometric shape; and (iii) restoration of the catalyst properties by repeated treatment of an article. However, insufficient attention has been given to application of this technique for preparing oxide catalyst supports on metals and catalytically active structures [4–6].

It has been shown previously that anodic layers containing a thermally stable rutile modification of TiO_2 are formed on titanium in an aqueous tetraborate electrolyte [9]. The aim of this study was to analyze the influence exerted by addition of manganese-containing salts on the formation and the elemental and phase composition of anodic-spark layers on titanium.

EXPERIMENTAL

For surface standardization, samples ($25 \times 5 \times 1$ mm) of VT1-0 titanium were ground mechanically, polished chemically in a 1 : 3 mixture of concentrated HF and HNO_3 at 60–80°C for 2–3 s [10], washed with distilled water, and dried in air.

Electrolytes were prepared from distilled water and commercial reagents $Na_2B_4O_7 \cdot 10H_2O$, $Na_3PO_4 \cdot 12H_2O$, $KMnO_4$, $Mn(CH_3COO)_2 \cdot 4H_2O$, $MnSO_4 \cdot 5H_2O$, and 96% C_2H_5OH, all of chemically pure grade. Electrolytes containing $KMnO_4$ were prepared by adding the required weighed portions of the salt to a 0.1 M solution of $Na_2B_4O_7$. The remaining electrolytes were prepared by combining solutions of sodium tetraborate or orthophosphate and an appropriate manganese(II) salt. Ethanol was added either to a mixture of solutions or to an $Mn(CH_3COO)_2$ solution.

Anodic films were formed in the mode of spark and microarc electric breakdowns. As power source served a TEP4-100/46OH thyristor converter generating pulsed unipolar current. The treatment was done both in the galvanostatic mode at i = 0.2 A cm^{-2} and

1070-4272/03/7607-1059$25.00

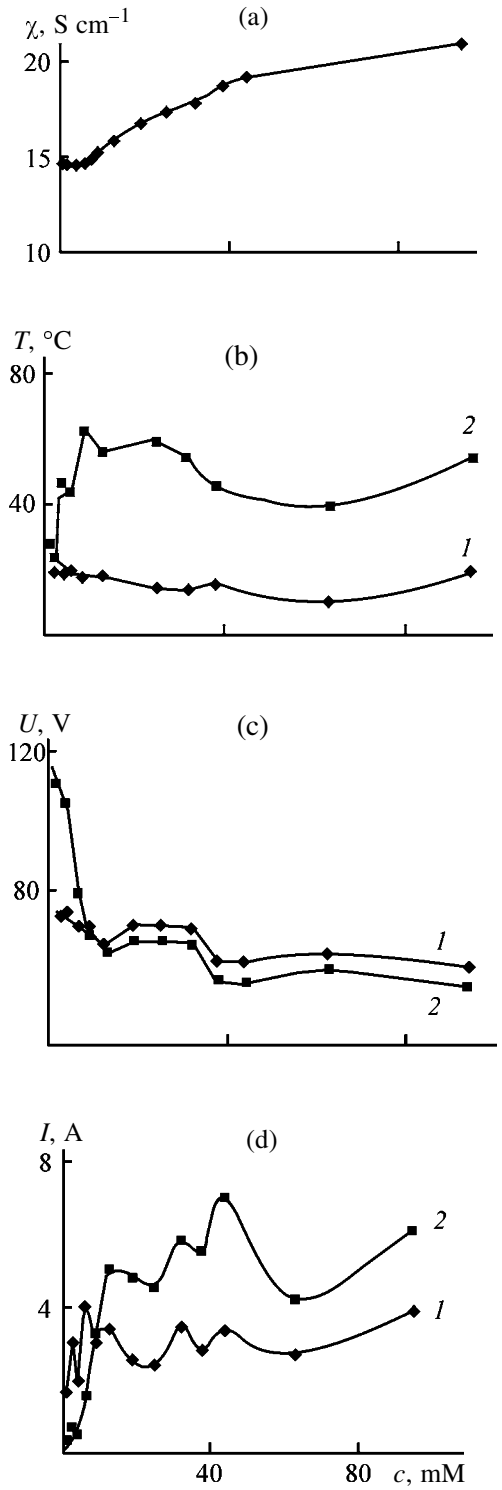

Fig. 1. Effect of the concentration c of $KMnO_4$ additive in 0.1 M tetraborate aqueous electrolyte on (a) electrical conductivity χ of the solution, (b) temperature T of the electrolyte, (c) voltage U across the electrodes, and (d) current I flowing through the cell. Coatings formed in the falling-power mode, U_s = 450 V, treatment duration 4 min. Parameter values: (*1*) initial and (*2*) final.

in the falling-power mode. In the latter case, voltage was set to U_s = 450 or 500 V in the open-circuit mode and then the power source was connected to the electrochemical cell.

Anodic-spark deposition was carried out in a 500-ml vessel made of heat-resistant glass. As cathode served a pipe coil made of Cr18Ni9Ti stainless steel and cooled with tap water. The cooling conditions (flow rate and temperature of water) were the same in all the experiments. The initial temperature of the electrolytes was 13–18°C. Oxidized samples were washed with distilled water and dried in air.

The phase composition of the coatings was determined on a DRON-2.0 X-ray diffractometer (CuK_α radiation), and the elemental composition, on a JXA-5A X-ray fluorescence microanalyzer which gave no way of determining light elements, including boron and oxygen. Electron-microscopic studies were performed on an LEO 430 microscope.

Data on the influence of $KMnO_4$ additive on the electrical conductivity of the tetraborate electrolyte, formation parameters (voltage across the electrodes, current flowing through the cell, temperature in the solution bulk), and elemental and phase composition of the anodic layers formed are shown in Figs. 1 and 2. The results obtained make it possible to distinguish three $KMnO_4$ concentration ranges in which variations of the process parameters under study, electrolyte characteristics, and composition of the surface layers formed are observed (M): $c < 9 \times 10^{-3}$ (I), $9 \times 10^{-3} < c < 40 \times 10^{-3}$ (II), and $c > 40 \times 10^{-3}$ (III).

In region I, the content of titanium in the coatings formed decreases and that of manganese increases with growing $KMnO_4$ concentration. The content of sodium is 0.1–0.2 wt %. The oxide layers contain crystalline TiO_2 phases (rutile, anatase). In the course of time, as films are formed in the falling-power mode, the final voltage across the electrodes increases and the current flowing through the cell decreases.

In contrast to the situation in region I, the voltage across the electrodes decreases and the current flowing through the cell increases in the course of oxide layer formation in regions II and III. Also, the electrolyte warms up to a much greater extent. The films obtained contain 1–2 wt % sodium. In region II, the content of titanium in the anodic layers increases (up to 60 wt %) and that of manganese decreases. The layers contain, together with titanium oxides, crystalline $TiBO_3$. In region III, as also in region I, the content of manganese in the surface part of the films, which is analyzed, increases and that of titanium decreases.

The films formed contain crystalline phases $MnTiO_3$ and β-Mn_2TiO_4. Raising the treatment duration and the initial voltage across the electrodes leads to higher crystallinity of the oxide structures obtained (Fig. 2).

The experimental data indicate that, in the above-considered ranges of $KMnO_4$ concentration in the tetraborate electrolyte, the processes of solution component incorporation into the anodic-spark coatings are different.

As $KMnO_4$ is added to the tetraborate electrolyte, the solution becomes dark violet (a coloration typical of permanganate ions), and the color intensity grows. Before carrying out the oxidation process, no precipitates are formed in the solutions, and the pH value of the solutions under study is independent of the $KMnO_4$ concentration and equals 9.48–9.52. A change in the electrical conductivity of the electrolytes is observed in concentration range II (Fig. 1a). This is due to a change in the charge, number, and mobility of charge carriers, i.e., to a change in the ionic composition of the electrolyte. In the course of electrolysis, a dark brown MnO_2 precipitate is gradually accumulated in the cell, and metallic manganese is deposited at the cathode.

Reasoning from the results described above, known concepts of the mechanism of anodic-spark deposition [11–14], and chemistry of boron and manganese, the processes associated with the influence exerted by the components of the tetraborate–permanganate electrolyte on the formation parameters and composition of oxide layers can be represented schematically as follows. The composition of an anodic-spark layer is determined by two basic concurrent processes: (a) electrochemical oxidation of the anode metal on parts free of the influence of electric breakdowns and (b) interaction between the electrolyte components and the substrate, thermolysis and partial melting of the precipitate formed from the electrolyte, and phase transitions near electric breakdown channels. In a single-component tetraborate electrolyte, anodic-spark layers formed at the titanium anode contain TiO_2 in the rutile modification [9]. Being an oxidant, $KMnO_4$ presumably additionally initiates in the tetraborate electrolyte oxidation of the titanium substrate in areas free of breakdowns. This assumption is confirmed by the presence of a low-temperature anatase modification of TiO_2 in coatings formed in concentration ranges I and II. At the same time, formation of MnO_2 via redox reactions at the anode, in the near-anode region, and in the solution bulk and through permanganate decomposition near the breakdown channels under the action of elevated temperature leads to incorporation of manganese compounds into coatings and to formation of an MnO_2 precipitate in the electrolyte. The reducing medium at the anode and in the near-anode region is created by thermolysis of water under the action of electric breakdowns [15, 16]. Areas of frozen melt, separated by cracks, are

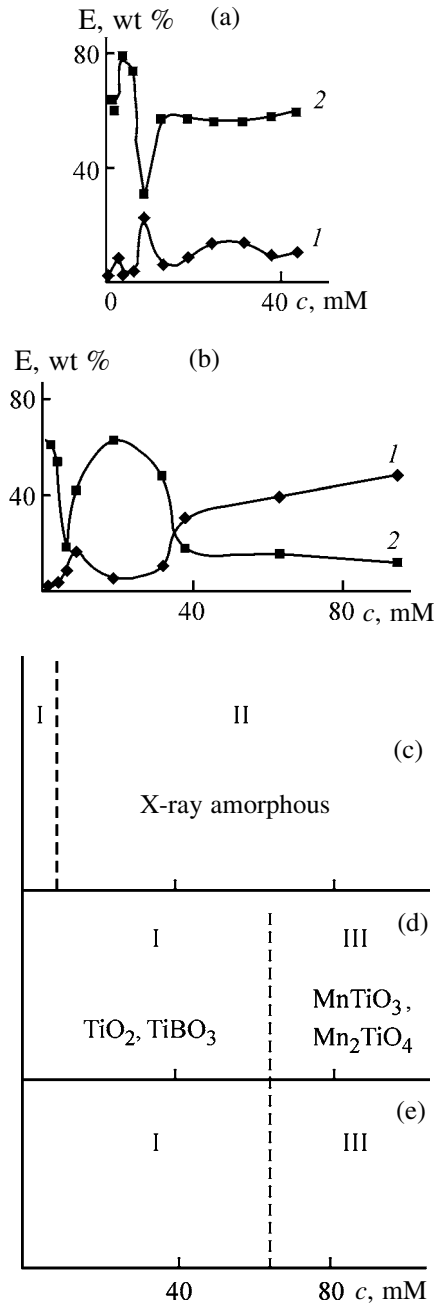

Fig. 2. Effect of the $KMnO_4$ concentration in aqueous electrolyte containing 0.1 M $Na_2B_4O_7$ on (a, b) elemental (E) and (c–e) phase composition of coatings on titanium. Falling-power mode; U = 450 V, (a, c) τ = 4 min and (d) 10 min; (b, e) U_s = 500 V, τ = 4 min. Elemental content: (*1*) Mn and (*2*) Ti.

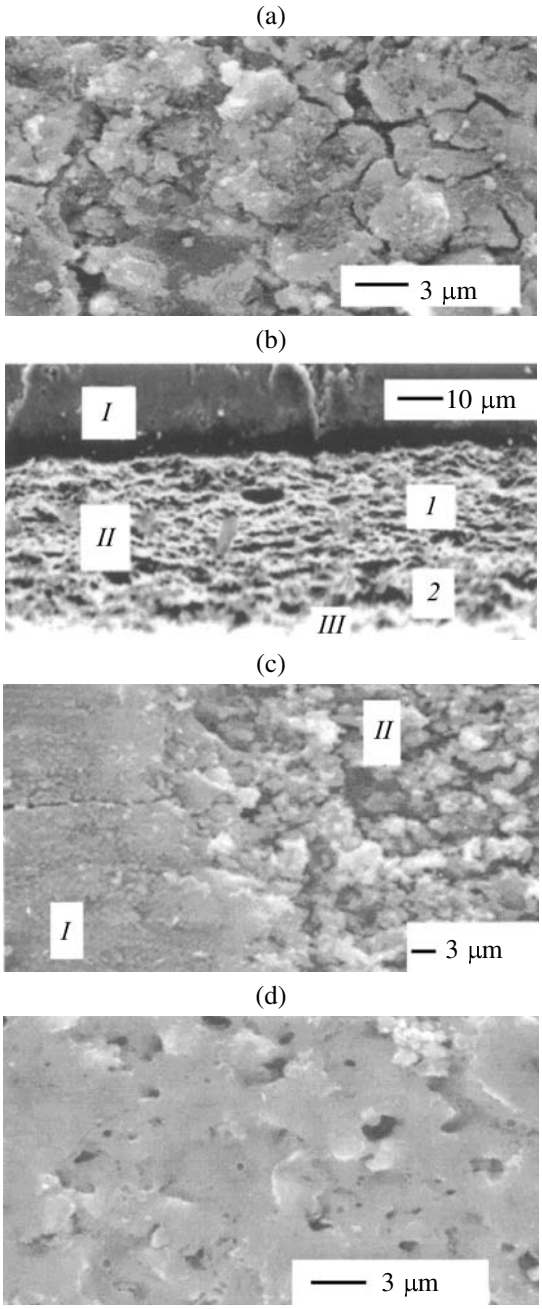

Fig. 3. (a, c, d) Plan-view and (b) cross-sectional electron micrographs of a sample with coating. Coatings contain the following phases: (a) $MnTiO_3$, β-Mn_2TiO_4; (b, c) Mn_2O_3, Mn_3O_4; and (d) $Mn_3(BO_3)_2$. (b) (*I*) Titanium and (*II*) anodic layer; (*1*) inner and (*2*) outer part; (c) (*I*) dense part and (*II*) part containing loosely packed particles.

seen on the surface of coatings formed in region III (Fig. 3a). Presumably, $MnTiO_3$ and β-Mn_2TiO_4 are formed by interaction of titanium and manganese oxides in the melt with its subsequent crystallization.

The scheme described is in agreement with the composition of anodic layers formed in concentration ranges I and III, i.e., at low and high $KMnO_4$ concentrations in the tetraborate electrolyte. In the intermediate region II, the content of manganese in the anodic layers formed is insignificant and the coatings contain titanium borate. This means that, in region II, a change in the ionic composition of the electrolyte near the breakdown channels results in that boron-containing compounds are mainly deposited, undergo thermolysis, and interact with titanium oxide.

The warming-up of electrolytes, decrease in the voltage across the electrodes, and increase in the current flowing through the electrochemical cell in the course of anodic-spark deposition of oxide layers in concentration ranges II and III are interrelated phenomena. They may be due to occurrence of exothermic reactions at the anode, formation of structures with low electrical resistance in the oxide, or changes in energy-related parameters of separate electric breakdowns.

On combining aqueous solutions of 0.1 M $Na_2B_4O_7$ and $Mn(CH_3COO)_2$ (with the concentration in the range 18.1×10^{-3}–90.5×10^{-3} M), a jelly-like pinkish white precipitate was formed. The pH value changed from 8.89 to 8.68. When coatings were formed with stirring by a magnetic stirrer, the precipitate was in the electrolyte bulk in the form of a suspension.

The elemental and phase composition of the coatings formed in these electrolytes are listed in Table 1. In contrast to the previously considered processes in an electrolyte with $KMnO_4$, a decrease in the current flowing through the cell and increase in the voltage across the electrodes is observed in coating formation for all the $Mn(CH_3COO)_2$ concentrations studied. With increasing $Mn(CH_3COO)_2$ concentration in the electrolyte, the content of manganese in the surface part of the anodic layers formed grows, and that of titanium falls, to 60–70 and 2–6 wt %, respectively. At $c > 45 \times 10^{-1}$ M, the crystalline phases of Mn_2O_3 and Mn_3O_4 are present in the coatings formed. The surface of the coatings is colored dark brown. Figure 3b shows a cross-sectional electron micrograph of a titanium sample with coating no. 11 (Table 1). The coating has nonuniform thickness, varying from 50 to 60 μm. A 10–20-μm-thick layer with relatively poor adhesion lies on the outer part of the coating. On its surface, dense areas alternate with areas composed of loosely packed particles 9 μm and less in size (Fig. 3c). It is noteworthy that films obtained in the galvanostatic mode are denser and show better adhesion to the substrate than films formed in the falling-power mode.

Table 1. Effect of $Mn(CH_3COO)_2$ concentration c in 0.1 M $Na_2B_4O_7$ solution on the elemental and phase composition of anodic-spark layers

Coating no.	$c \times 10^3$, M	τ,* min	Elemental composition, wt %			Phase composition**
			Mn	Ti	Na	
Falling-power mode, U_s = 450 V						
1	18.1	0.5	11.3	57.4	0.7	X/a
2	18.1	4	28.2	30.0	0.4	TiO_2(r)
3	18.1	10	20.3	30.0	0.44	TiO_2(r)
4	45.3	4	49.8	6.2	1.0	Mn_2O_3, Mn_3O_4
5	90.5	4	58.2	2.3	0.14	Mn_2O_3, Mn_3O_4
Galvanostatic mode, i = 0.2 A cm^{-2}						
6	18.1	4	19.7	30.6	0.24	TiO_2(r)
7	18.1	10	11.4	39.8	0.21	Mn_2O_3, Mn_3O_4?
8	45.3	4	41.2	27.7	0.18	Mn_2O_3, Mn_3O_4
9	45.3	10	55.8	13.0	0.4	Mn_2O_3, Mn_3O_4
10	90.5	4	63.0	6.02	0.16	Mn_2O_3, Mn_3O_4
11	90.5	10	68.0	2.8	0.18	Mn_2O_3, Mn_3O_4

* τ is the coating formation duration.
** X/a, X-ray-amorphous; r, rutile; ?, possible presence of a phase.

The effect of the precipitate in the bulk of the tetraborate–acetate electrolyte on the formation and the elemental and phase composition of coatings was analyzed. For this purpose, the precipitate from electrolyte no. 4 (Table 1) was filtered off. In the surface layers formed under the same conditions in an electrolyte with the precipitate removed, the content of manganese decreased to 10 wt %, and that of titanium increased to 50 wt %. In their elemental and phase composition and outward appearance, these layers correspond to coatings no. 1 (Table 1).

As follows from the data obtained, coatings containing crystalline manganese oxides can be formed, in the systems and conditions under study, in a colloid electrolyte. It could be expected that the precipitate formed in a tetraborate–acetate aqueous electrolyte at pH 9 should contain manganese hydroxides [17] and manganese borates [18] simultaneously. In addition, borate ions are coprecipitated, together with metal hydroxides, from solutions of this kind at pH 8–10 [19]. Apparently, particles containing manganese hydroxides and borates are deposited at the anode in the experimental conditions under the action of spark and microarc electric breakdowns. The high temperature in the vicinity of breakdown channels causes decomposition of manganese hydroxides to manganese oxides. At temperatures of 600–800°C, metal borates undergo a "borate rearrangement," crystallization and decomposition with partial liberation of B_2O_3 [18]. Since no crystalline boron-containing compounds were found in the layers formed, the precipitate deposited at the anode is presumably mainly composed of manganese hydroxide with minor amount of manganese and sodium borates.

An assumption was made that addition of organic compounds, e.g., ethanol, to an electrolyte will favor formation of coatings containing oxides with varied degree of manganese oxidation. Ethanol was added either to a colloid electrolyte containing 0.1 M solution of $Na_2B_4O_7$ and $Mn(CH_3COO)_2$ (scheme 1, Table 2, coating nos. 1–4) or to a solution with manganese acetate before combining it with an $Na_2B_4O_7$ solution (scheme 2, Table 2, coating nos. 7 and 8). Adding ethanol in accordance with scheme 1 affects the composition of the coatings obtained (Table 2, nos. 1–6; Table 1, nos. 4 and 5), with the manganese content decreasing substantially. Raising the amount of alcohol or the treatment duration leads to crystallization of boron-containing compounds, including Mn(II) borate, in the coatings. Partly melted glassy formations can be seen on the coating surface around breakdown craters (Fig. 3d). Addition of ethanol to an $Mn(CH_3COO)_2$ solution before combining it with a 0.1 M $Na_2B_4O_7$ solution (scheme 1) has no effect on the composition of the coatings obtained (Table 1, no. 5; Table 2, nos. 7 and 8).

The effect of the order of adding chemicals on the

Table 2. Effect of ethanol addition to electrolytes on the phase and elemental composition of anodic layers on titanium. Coatings obtained in the falling-power mode, U_s = 500 V

Coating no.	τ, min	$c^* \times 10^3$, M	C_2H_5OH, vol %	Elemental composition, wt %			Phase composition**
				Mn	Ti	Na	
1	4	45.3	2	26.4	29.6	0.5	TiO_2(r)
2	4	45.3	20	12.0	50.4	0.1	TiO_2(r)
3	10	45.3	20	6.6	44.9	0.2	TiO_2(r), $Mn_3(BO_3)_2$
4	4	45.3	30	1.5	67.2	0.2	TiO_2(r), TiO_2(a)
5	4	90.5	5	23.3	51.1	0.5	TiO_2(r), $TiBO_3$?, MnO?
6	4	90.5	20	20.6	36.4	0.6	TiO_2(r), $Mn_3(BO_3)_2$
7	1	90.5	30	52.7	15.1	0.1	Mn_2O_3, Mn_3O_4
8	4	90.5	30	50.8	9.4	0.1	Mn_2O_3, Mn_3O_4

* c is the $Mn(CH_3COO)_2$ concentration in 0.1 M $Na_2B_4O_7$ solution.
** r is rutile, and a, anatase.

Table 3. Effect of $MnSO_4$ and $Mn(CH_3COO)_2$ additions to 0.1 M tetraborate electrolyte on the elemental and phase compositions of the anodic layers. The coatings were prepared in the falling-power mode, U_s = 450 V, τ = 4 min

Coating no.	$c \times 10^3$, M	Elemental composition, wt %				Phase composition
		Mn	Ti	Na	S	
1	45 $Mn(Ac)_2$	49.8	6.2	1.0	–	Mn_2O_3, Mn_3O_4
2	41.5 $MnSO_4$	6.4	37.2	0.3	1.2	TiO_2(r)
3	45 $Mn(Ac)_2$ + 20.7 $MnSO_4$	5.9	44.3	0.4	0.3	TiO_2(r)
4	45 $Mn(Ac)_2$ + 41.5 $MnSO_4$	22.5	47.8	0.2	0.3	$MnTiO_3$

composition of anodic layers can be accounted for as follows. It was established experimentally that addition of ethanol to a 0.1 M solution of $Na_2B_4O_7$ leads to salting-out of borates from the solution. Presumably, addition of C_2H_5OH in deposition of coatings from electrolytes prepared by scheme 1 makes higher the concentration of poorly soluble boron-containing compounds in the deposit formed at the anode. High temperatures in the vicinity of breakdown channels lead to a reaction between manganese oxides and boron-containing compounds to give titanium or manganese borates.

Addition of C_2H_5OH to an $Mn(CH_3COO)_2$ solution leads to formation of manganese(II) alcoholates [17]. When such a solution is combined with an aqueous solution of $Na_2B_4O_7$ (scheme 2), ethanol presumably has no effect on the state of $Na_2B_4O_7$ in solution, i.e., it does not affect the amount of boron-containing compounds arriving at the anode in the course of any particular breakdown.

Partial replacement of $Mn(CH_3COO)_2$ in a tetraborate electrolyte with $MnSO_4$ leads to lower content of manganese in the coatings formed and to synthesis of the $MnTiO_3$ spinel (Table 3). Previously, films with $MnTiO_3$ have been obtained in an electrolyte containing Na_2SO_4 together with $Mn(CH_3COO)_2$ [7, 8]. Apparently, the formation of spinels in the presence of the SO_4^{2-} ion in the electrolyte is determined by occurrence of redox reactions in the solution bulk, near the anode, and at the electrodes. The pH value of the solutions under study, which contain $Na_2B_4O_7$, $Mn(CH_3COO)_2$, and $MnSO_4$, is, depending on the relative concentrations of Mn(II) salts, within the range 8.7–9.3. The solutions give a jelly-like precipitate. With increasing concentration of $MnSO_4$, the precipitate changes its color from pinkish white to dark brown. Presumably, the content of manganese oxides or borates in the precipitate grows. Possibly, the formation of a spinel in the coatings is due, as in the case of tetraborate electrolytes with $KMnO_4$, to the influence of boron compounds. It is known that molten boron(III) oxide (mp 450°C [20]) can dissolve many metal oxides, transferring them to the active state. Molten boron oxide makes looser the lattices of titanium and manganese oxides, favors defect formation in these lattices, and intensifies solid-phase reactions at lower temperatures [21].

Table 4. Elemental composition of anodic layers formed in the electrolyte containing 0.1 M Na_3PO_4 and $Mn(CH_3COO)_2$. The coatings were prepared in the falling-power mode, U_s = 450 V; phase composition TiO_2(a)

Coating no.	τ, min	$c^* \times 10^3$, M	Elemental composition, wt %			
			Mn	Ti	Na	P
1	4	4.1	2.8	42.1	1.1	10.2
2	4	22.7	4.6	27.6	1.2	12.1
3	4	45.3	9.5	27.6	1.5	12.1
4	10	45.3	11.7	28.3	1.5	14.1

* $Mn(CH_3COO)_2$ concentration.

The influence exerted by replacing $Na_2B_4O_7$ with Na_3PO_4 in an electrolyte on the composition of the anodic layers formed was also studied. On adding $Mn(CH_3COO)_2$ to an Na_3PO_4 solution, the solution turns dark brown and a brown flaky precipitate is formed, which is presumably composed of manganese phosphates [19, 22] with impurity of Mn(II) and Mn(IV) oxides and hydroxides; the solution pH is 10. In contrast to tetraborate electrolytes, an insignificant amount of manganese is incorporated into the coatings in the given case on the background of a high content of phosphorus(V) (Table 4). The latter is generally observed in anodic-spark treatment of titanium in phosphate electrolytes [7, 8, 13]. PO_4^{3-} anions are incorporated into anodic titanium oxide to form complexes of the type $(TiO)_x(PO_4)_y$ [23]. Under the action of high temperature in the vicinity of breakdown channels, complexes of this kind may be converted into titanium phosphates and interact, similarly to titanium oxide, with manganese-containing compounds. However, an X-ray phase analysis did not reveal crystalline compounds of titanium or manganese with phosphorus. Possibly, the forming anodic layers contain, similarly to coatings obtained in aqueous electrolytes with sodium polyphosphates and $Mn(CH_3COO)_2$ [24], X-ray amorphous manganese titanophosphates.

CONCLUSIONS

(1) Aqueous electrolytes based on sodium tetraborate are promising for obtaining anodic-spark layers containing various manganese compounds on titanium.

(2) The elemental and phase compositions of the coatings and their surface structure depend on the nature and concentration of a manganese(II) salt introduced into solution and on addition of ethanol.

(3) In aqueous electrolytes containing 0.1 M $Na_2B_4O_7$ and more than 18×10^{-3} M of $Mn(CH_3COO)_2$, anodic films with Mn_2O_3 and Mn_3O_4 in the surface layer can be obtained.

ACKNOWLEDGMENTS

The authors are grateful to T.A. Kaidalova and E.S. Panin for assistance in determining the phase and elemental composition of coatings.

The study was supported in part by the programs "New Materials" (project no. 02.02.032) and "Universities of Russia" (project no. UR-05.01.018).

REFERENCES

1. Zaki, M.I., Hasan, M.A., Pasupulety, L., and Kumari, K., *Thermochim. Acta*, 1998, vol. 311, pp. 97–103.
2. Zaki, M.I., Hasan, M.A., Pasupulety, L., and Kumari, K., *Thermochim. Acta*, 1997, vol. 303, pp. 171–191.
3. Boreskov, G.K., *Geterogennyi kataliz* (Heterogeneous Catalysis), Moscow: Nauka, 1988.
4. Gordienko, P.S., Rudnev, V.S., Gnedenkov, S.V., *et al.*, *Zh. Prikl. Khim.*, 1995, vol. 68, no. 6, pp. 971–974.
5. GDR Patent 273364.
6. GDR Patent 248064.
7. Gordienko, P.S. and Khrisanfova, O.A., *Vliyanie ionnogo sostava elektrolita i rezhima oksidirovaniya na fazovyi i elementnyi sostav pokrytii, poluchennykh na metallakh* (Effect of the Ionic Composition of Electrolyte and the Mode of Oxidation on Phase and Elemental Composition of Coatings Obtained on Metals), Available from VINITI, Vladivostok, May 6, 1989, no. 2986V83.
8. Khrisanfova, O.A., Volkova, L.M., Gnedenkov, S.V., *et al.*, *Zh. Neorg. Khim.*, 1995, vol. 40, no. 4, pp. 558–562.
9. Vasil'eva, M.S., Rudnev, V.S., Tyrina, L.M., *et al.*, *Zh. Prikl. Khim.*, 2002, vol. 75, no. 4, pp. 583–586.
10. Grilikhes, S.Ya., *Obezzhirivanie, travlenie i polirovanie metallov* (Degreasing, Etching, and Polishing of Metals), Leningrad: Mashinostroenie, 1977.
11. Bakovets, V.V., Polyakov, O.V., and Dolgovesova, I.P., *Plazmenno-elektroliticheskaya anodnaya obrabotka metallov* (Plasma-Electrolytic Anodic Treatment of Metals), Novosibirsk: Nauka, 1991.
12. Chernenko, V.I., Snezhko, L.A., and Papanova, I.I., *Poluchenie pokrytii anodno-iskrovym elektrolizom* (Coating Deposition by Anodic-Spark Electrolysis), Leningrad: Khimiya, 1991.
13. Gordienko, P.S., *Obrazovanie pokrytii na anodno-polyarizovannykh elektrodakh v vodnykh elektrolitakh*

pri potentsialakh iskreniya i proboya (Formation of Coatings on Anodically Polarized Electrodes in Aqueous Electrolytes at Sparking and Breakdown Potentials), Vladivostok: Dal'nauka, 1996.

14. Yerokhin, A.L., Nie, X., Leyland, A., *et al.*, *Surf. Coat. Technol.*, 1999, vol. 122, pp. 73–93.
15. Gordienko, P.S. and Yarovaya, T.P., Gas Evolution on Metal Alloys, *Preprint of Inst. of Chemistry*, *Far-Eastern Division, USSR Acad. Sci.*, Vladivostok, 1989.
16. Ragalyavichus, R. and Yusis, Z., *Chemija* (Lithuania), 1992, no. 2, pp. 45–50.
17. Lavrukhina, A.K. and Yukina, L.V., *Analiticheskaya khimiya margantsa* (Analytical Chemistry of Manganese), Moscow: Nauka, 1974.
18. Keshan, A.T., *Sintez boratov v vodnom rastvore i ikh issledovanie* (Synthesis of Borates in Aqueous Solution and Their Study), Riga: Akad. Nauk Latv. SSR, 1955.
19. Mun, A.I., Radionova, M.A., and Lukonina, Z.N., *Tr. Inst. Khim. Nauk Akad. Nauk Kaz. SSR*, 1973, vol. 36, pp. 70–75.
20. *Fiziko-khimicheskie svoistva okislov: Spravochnik* (Physicochemical Properties of Oxides: Reference Book), Samsonov, G.V., Ed., Moscow: Metallurgiya, 1978.
21. Pishch, I.V., *Khimiya kislorodnykh soedinenii bora* (Chemistry of Boron Compounds with Oxygen), Riga: Latv. Gos. Univ., 1981, pp. 108–110.
22. Konstant, Z.A. and Dindune, A.P., *Fosfaty dvukhvalentnykh metallov* (Phosphates of Bivalent Metals), Riga: Zinatne, 1987.
23. Badekas, H. and Panagopoulos, Chr., *Surf. Coat. Technol.*, 1987, vol. 31, no. 3, pp. 381–388.
24. Tyrina, L.M., Rudnev, V.S., Abozina, E.A., *et al.*, *Zashch. Met.*, 2001, vol. 37, no. 4, pp. 366–369.

Russian Journal of Applied Chemistry, Vol. 76, No. 7, 2003, pp. 1067–1069. Translated from Zhurnal Prikladnoi Khimii, Vol. 76, No. 7, 2003, pp. 1099–1102.

APPLIED ELECTROCHEMISTRY AND CORROSION PROTECTION OF METALS

Thin-Film Cathode Materials Based on Chromium Oxides

N. D. Ivanova, S. V. Ivanov, E. I. Boldyrev, I. S. Makeeva, and G. V. Sokol'skii

Vernadsky Institute of General and Inorganic Chemistry, National Academy of Sciences of Ukraine, Kiev, Ukraine
National Aviation University, Kiev, Ukraine

Received April 25, 2002; in final form, May 2003

Abstract—The possibility of cycling of thin (8–10 μm) films of chromium oxide compounds was studied. The charging–discharge conditions were optimized.

In the recent decade, much attention has been given to thin-film materials for primary and secondary chemical power sources (CPS) [1, 2]. Such materials are promising electrodes for unconventional (flexible) CPS. Flat CPS are used in laptops, credit cards, optical displays, solar batteries, etc. Also, thin-film electrodes have aroused specific interest for rechargeable power sources. In such sources, protons or ions diffuse for a short distance, and the charging–discharge processes are short compared to pelletized electrodes.

Many materials are used as CPS electrodes: metal oxides, chalcogenides, and some polymers. Among them, the oxide materials are the most environmentally acceptable and convenient in use; they also have high specific electrical characteristics [3].

When choosing the oxide compound for CPS electrode, it should be taken into account that the incorporation of the corresponding ion (Li^+, Na^+, or H^+) must change the unit cell volume of the oxide by no more than approximately 20%. If this value exceeds 20% (as, e.g., 38% for CrO_2 and 33% for MnO_2), then the ion incorporation is irreversible [4] (this also refers to lithium ion).

A cathode material for secondary CPS must be capable of recovery, i.e., discharge in the cathodic cycle and charging in the anodic cycle. Thus, in the ideal case, the lithium ion incorporation into, and removal from the crystal lattice must be reversible to the extent as maximal as possible. As shown in [5], the higher the diffusion rate, the easier are the charging–discharge processes in the system. The mass-transfer rate is considerably higher in oxide compounds with the disordered structure [4–7]. For this reason, nonstoichiometric oxide compounds are of undoubted interest [6, 7]. It was shown that, in such compounds, the rate of electrochemical processes is considerably higher (sometimes by several orders of magnitude) than in stoichiometric compounds. For example, stoichiometric chromium oxide CrO_2 is unsuitable for secondary power sources [4], whereas the nonstoichiometric oxide is a promising electrode material [8].

Powders and films of nonstoichiometric oxide compounds of a series of transition metals can be prepared by an electrochemical procedure developed previously [9]. Use of such compounds as a cathode of primary CPS increases the rate of electrochemical processes, which is manifested as a considerable increase in the current density of pelletized electrodes [5].

The goal of the work was to examine the possibility of using thin-film chromium oxide compounds as cathodes and to find how the extent of reversibility of the charging–discharge process depends on the compound composition (degree of nonstoichiometry).

EXPERIMENTAL

The test objects were chromium oxide compounds differing in the degree of nonstoichiometry. Films of chromium oxide compounds were prepared from an electrolyte containing 2.5 M CrO_3. To vary the compound composition, 0.1, 0.2, 0.3, or 0.4 M fluoride ions were introduced as ligands. The electrolyte temperature did not exceed 30 ± 0.1°C, and the current density was 50 A dm^{-2}.

Films of different compositions were deposited onto electrodes made of 1Cr18Ni10Ti stainless steel. The electrode area was 0.25 cm^2. The film thickness was 8–10 μm depending on the electrolysis time. A film more than 4 μm thick is nonporous, which excludes the contact of the support with the electrolyte.

As electrolyte, we used 1 M KOH. The tests were performed at room temperature. Platinum (surface

1070-4272/03/7607-1067$25.00

Table 1. Composition of samples of chromium oxide compounds

Sample no.	c_F in electrolyte, M	Content, wt %						
		Cr_{tot}	OH	H_2O	O	Cr^0	Cr^{2+}	Cr^{3+}
1	0.1	70.0	6.0	5.0	19.0	13.1	1.12	0.96
2	0.2	73.0	5.0	4.5	17.5	11.5	1.06	0.93
3	0.3	75.0	4.5	4.0	9.5	10.7	1.05	0.92
4	0.4	83.0	4.0	4.0	7.0	10.2	1.03	0.89

area 4 cm^2) was the counterelectrode, and saturated calomel electrode was the reference electrode. The cyclovoltammograms (CVA) and charging–discharge curves were recorded on a PI-50-1 potentiostat (potential scanning rate 2 mV s^{-1}) with an LKD-4 recorder.

The ionic component of the conductivity and the composition of the chromium samples were determined by the procedures described previously [9]. Table 1 presents the composition of the samples of the chromium oxide compounds obtained at various concentrations of fluoride ions in the electrolyte.

The reversibility of the process can be judged from the CVA. Figure 1 shows the typical CVAs for a sample of a chromium oxide compound. As seen, both

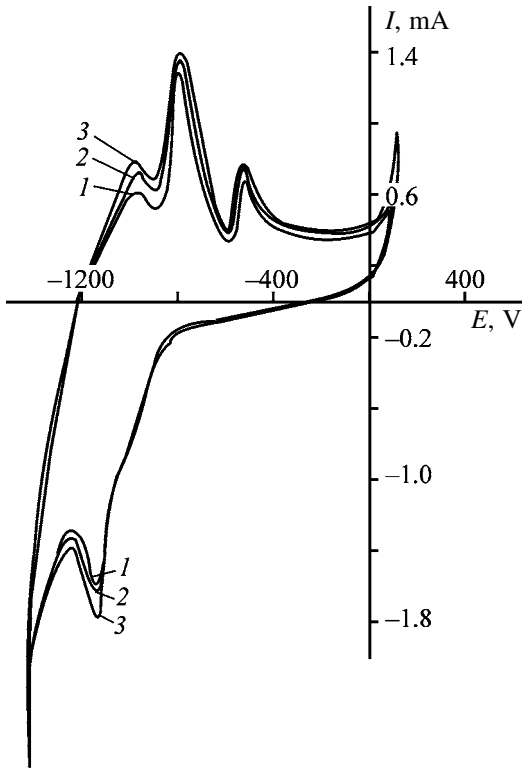

Fig. 1. Cyclovoltammogram of the chromium oxide compound (sample no. 1). Scanning rate 2 mV s^{-1}. (*I*) Current and (*E*) potential. Curve numbers are cycle numbers.

direct and reverse processes occur. The extent of reversibility of the given process can be determined from CVA as the ratio of the current peaks in the second cycle to that in the first cycle [8]. The results are given in Table 2.

Table 2 shows that the extent of reversibility I_{p2}/I_{p1} of the process depends on the sample composition and increases as the deviation from the stoichiometric composition grows.

It should be noted that the degree of conversion in the system is higher in the second cycle. The same is true for the process rate, as seen from the currents of the direct and reverse processes. In both the anodic and the cathodic cycles, the samples are ranked in the following order with respect to the current values: no. 1 > no. 2 > no. 3 > no. 4. In going from sample no. 1 to sample no. 4, the content of total chromium grows, and the content of oxygen, water, and hydroxy groups decreases (Table 1).

It should be noted that the ionic conductivity of the samples correlates with the ratio of the peak currents in the second (I_{p2}) and first (I_{p1}) cycles (Fig. 2). The extent of reversibility of the electrochemical process increases with increasing ionic conductivity (Table 2).

The charging–discharge curves of the chromium samples studied are shown in Fig. 3. They allow evaluation of the reversibility of the charging–discharge processes. The first and the last charging–discharge curves are similar (to the 10th cycle inclusive), indicating that the proton incorporation is fairly reversible and fast.

The values of the given capacity correlate with the total content of chromium in the samples. The voltage efficiency for sample nos. 1 and 2 is 81 and 76%, respectively. The efficiency (discharge-to-charging capacity ratio) is about 97–98%. The specific capacities are fairly high (Table 2); in this respect, nonstoichiometric chromium oxide compounds are comparable with other oxides, e.g., manganese dioxide [10].

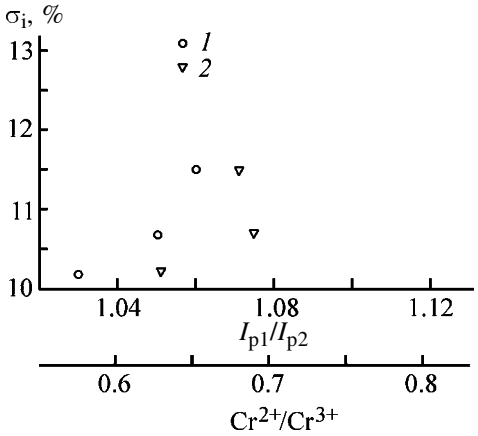

Fig. 2. Dependence of the ionic conductivity σ_i of the chromium oxide compounds on the (*1*) extent of reversibility of the charging–discharge process I_{p2}/I_{p1} and (*2*) Cr^{2+}/Cr^{3+} ratio.

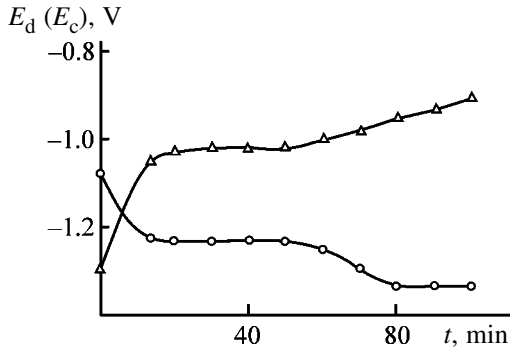

Fig. 3. Charging–discharge curves (sample no. 2). Current 0.7 mA, active paste weight 5 mg. (E_d, E_c) Potential and (*t*) time.

At the same time, the main advantage of chromium oxide compounds is the possibility of depositing then as thin (8–10 μm) films with high adhesion onto virtually any structural material intended for flexible cathode.

It was shown [9, 11] that the ionic conductivity characterizes the amount of defects in the compound; their increase can considerably accelerate electrode processes. This effect was also observed previously [5] on pelletized samples, in line with the published data [6, 7, 12] on the role of structural defects in electrochemical processes. Compared to stoichiometric compounds, nonstoichiometric compounds, including the chromium compounds under consideration, contain a large number of defects and have more disordered structure. They contain M^{n+}/M^{n+1} pairs differing in charges [12, 13] and OH^- groups binding structural defects.

Table 2. Extent of reversibility of charging–discharge processes C_d/C_c, capacity C_{sp}, and ionic conductivity σ_i of the samples of chromium oxide compounds

Sample no.	C_d/C_c	C_{sp}, mA h g^{-1}	σ_i, %	I_{p2}/I_{p1} in indicated region	
				cathodic	anodic
1	0.985	276	13.1	1.12	0.96
2	0.981	268	11.5	1.06	0.93
3	0.964	217	10.7	1.05	0.92
4	0.959	210	10.2	1.03	0,89

CONCLUSION

The possibility of cycling of chromium oxide compounds was demonstrated. These compounds show promise for thin-film batteries with aprotic electrolytes. The optimal charging–discharge conditions are realized on samples (nos. 1 and 2) having the strongest deviation from the stoichiometry.

REFERENCES:

1. Passerini, S., Scarmino, J., and Scrosati, B., *J. Appl. Electrochem.*, 1993, vol. 23, pp. 1187–1195.
2. Ho, C., Raistrik, I.D., and Huggins, R.A., *J. Electrochem. Soc.*, 1980, vol. 127, no. 2, pp. 343–350.
3. Nizhnikovskii, E.A., *Elektrokhimiya*, 1998, vol. 34, no. 7, pp. 722–726.
4. Kedrinskii, I.A., Dmitrenko, V.E., and Grudyanov, I.I., *Litievye istochniki toka* (Lithium Power Sources), Moscow: Energoizdat, 1992.
5. Ivanova, N.D., Ivanov, S.V., Boldyrev, E.I., and Sokol'skii, G.V., *Elektrokhimiya*, 1999, special issue, pp. 133–134.
6. Oshe, E.K., *Elektrokhimiya*, 1994, vol. 30, no. 4, pp. 499–505.
7. Kellerman, D.G. and Gorshkov, V.S., *Elektrokhimiya*, 2001, vol. 37, no. 12, pp. 1413–1423.
8. Jacubes, I., Vondrac, J., and Brudsca, J., *J. Power Sources*, 1992, vol. 39, pp. 133–145.
9. Ivanova, N.D., and Ivanov, S.V., *Usp. Khim.*, 1993, vol. 62, no. 10, pp. 907–918.
10. Mondoloni, C., Laborde, M., Rioux, J., *et al.*, *J. Electrochem. Soc.*, 1992, vol. 139, no. 4, pp. 954–960.
11. Ivanova, N.D., Filatov, K.V., Boldyrev, E.I., *et al.*, *Dokl. Akad. Nauk Ukr.*, 1992, no. 11, pp. 136–139.
12. Brenet, J.P., *J. Power Sources*, 1979, vol. 4, pp. 183–189.
13. Abbas, H., and Nasser, S.A., *J. Power Sources*, 1996, vol. 58, pp. 15–21.

Russian Journal of Applied Chemistry, Vol. 76, No. 7, 2003, pp. 1070–1075. Translated from Zhurnal Prikladnoi Khimii, Vol. 76, No. 7, 2003, pp. 1103–1108.

APPLIED ELECTROCHEMISTRY AND CORROSION PROTECTION OF METALS

Kinetics of Hydrogen Peroxide Accumulation in Electrosynthesis from Oxygen in Gas-Diffusion Electrode in Acidic and Alkaline Solutions

G. A. Kolyagin and V. L. Kornienko

Institute of Chemistry and Chemical Technology, Siberian Division, Russian Academy of Sciences, Krasnoyarsk, Russia

Received February 13, 2003

Abstract—Accumulation of H_2O_2 in aqueous solutions with various pH values in electroreduction of oxygen in carbon-black gas-diffusion hydrophobized electrodes was studied. The effect of various parameters of the process on its electrochemical component and decomposition rate of the H_2O_2 formed was analyzed.

In the last 20 years, much interest has been shown in indirect oxidation of organic and inorganic substances with hydrogen peroxide generated electrochemically from oxygen [1–3]. This interest stems from the wide use by modern chemical industries of principles of conjugated processes [4] involving environmentally safe reagents, such as electric current and chemically bound forms of oxygen (O_3, H_2O_2, ROOH, etc.).

Hydrogen peroxide as oxidizing agent has a number of unique properties. It is well soluble in water and is nontoxic. Use of hydrogen peroxide does not yield dangerous wastes, only water and oxygen being products of its decomposition. Hydrogen peroxide shows a pronounced oxidizing power and allows oxidation of various organic and inorganic compounds both in alkaline and in acidic media. The range of its applicability is exceedingly wide: aqueous H_2O_2 solutions are used in pulp-and-paper industry, in manufacture of detergents, in hydrometallurgy, in wastewater purification, and in many other industries requiring an environmentally safe oxidizing agent [5, 6].

It is known that hydrogen peroxide can be comparatively easily obtained by cathodic reduction of oxygen on graphitic carbon electrodes in alkaline solutions. Since the solubility of oxygen in aqueous electrolyte solutions is low, hydrophobized gas-diffusion electrodes are presently used for intensifying its reduction process. This method is waste-free and enables production of H_2O_2 at its consumption site in the form of aqueous solutions and use of these solutions as a commercial product without preliminary isolation of H_2O_2, which makes the cost of hydrogen peroxide much lower [7, 8].

It is known that the rate of H_2O_2 accumulation in the electrolyte in electroreduction of oxygen is described by the equation [9]

$$V_a = dc/d\tau = V_s - V_d = A\gamma I/v - V_d, \quad (1)$$

where V_a is the rate of H_2O_2 accumulation (mol l^{-1} h^{-1}); V_s, rate of H_2O_2 electrosynthesis; V_d, rate of H_2O_2 decomposition; A, electrochemical equivalent of H_2O_2 (mol A^{-1} h^{-1}); I, electrolysis current (A); v, catholyte volume (l); γ, fraction of current consumed for O_2 reduction to H_2O_2; c, H_2O_2 concentration in the catholyte (M); and τ, electrolysis time (h).

Decomposition of hydrogen peroxide is a complex process which depends on numerous factors, including the degree of dissociation in aqueous solutions. In acidic solutions, H_2O_2 molecules are little dissociated and the decomposition process follows the equation [5, 6]

$$2H_2O_2 = 2H_2O + O_2. \quad (2)$$

In alkaline solutions, H_2O_2 is largely dissociated [10, 11]:

$$H_2O_2 + OH^- = HO_2^- + H_2O. \quad (3)$$

When perhydroxide ions appear in considerable amounts, decomposition of H_2O_2 may involve these ions [7, 11, 12]:

$$2HO_2^- = 2OH^- + O_2, \quad (4)$$

$$HO_2^- + H_2O_2 = H_2O + OH^- + O_2. \quad (5)$$

1070-4272/03/7607-1070$25.00

Table 1. Effect of electrolyte composition on coefficients of Eqs. (6), (7), and (9) and on electrolysis parameters*

Run no.	Agitation mode	Electrolyte, M	k	V_d, mol l^{-1} h^{-1}, at $c_{H_2O_2}$ = 0.6 M	γ_{av}	$c_{H_2O_2}$, M	η
1**	I	0.25 NaOH	0.12 h^{-1}	0.072	0.96	0.93	0.69
2**	II	0.25 NaOH	0.17 h^{-1}	0.10	0.97	0.8	0.59
3	II	0.25 NaOH	0.34 mol l^{-1} h^{-1}	0.122	0.97	0.68	0.52
4	I	0.5 NaOH	1.54 mol l^{-1} h^{-1}	0.086	0.97	0.72	0.55
5	I	1.0 NaOH	8.0 mol l^{-1} h^{-1}	0.027	0.98	0.89	0.68
6	I	1.0 NaOH + 0.017 Na_2SiO_3	0.05 h^{-1}	0.03	0.98	1.13	0.86
7	II	0.1 H_2SO_4	0.05 h^{-1}	–	0.4	0.25	0.32
8	II	0.05 K_2SO_4 + 0.15 H_2SO_4	0.085 h^{-1}	0.051	0.75	0.83	0.63

* $c_{H_2O_2}$ and η are the concentration and current efficiency by H_2O_2 after 7 h of electrolysis.
** Experiments carried out with electrodes fabricated from paste heated at 340°C.

Among the factors affecting the rate of H_2O_2 decomposition [3, 5, 6, 10–20], the composition and pH value of solutions are among those most important [5, 10–12, 19, 20]. The rate of decomposition in alkaline solutions can be formally described using various equations:

$$V_d = kc_{H_2O_2} \text{ [9]}, \quad (6)$$

$$V_d = kc^{ud}_{H_2O_2}c_{HO_2^-} \text{ [12]}, \quad (7)$$

$$V_d = kc^{ud}_{H_2O_2} + k_0 \text{ [11]}, \quad (8)$$

where $c_{H_2O_2}$ is the total concentration of H_2O_2; $c^{ud}_{H_2O_2}$, concentration of the undissociated H_2O_2 species; $c_{HO_2^-}$, concentration of perhydroxide anions; and k and k_0, constants.

In acidic solutions, the decomposition rate is commonly described by Eq. (6) [8], whereas in alkaline solutions, each particular case should be considered separately.

The known studies concerned with H_2O_2 electrosynthesis from O_2 paid little attention to kinetics of H_2O_2 accumulation and did not consider as a whole the wide variety of factors affecting the process simultaneously. Revealing the fundamental aspects of the process of H_2O_2 accumulation is an important and necessary stage as regards practical application of the electrochemical method for obtaining H_2O_2 in solutions with varied pH value.

This study is concerned with the effect of the composition, concentration, and pH of the electrolyte on the kinetics of accumulation of H_2O_2 in its synthesis from O_2 in gas-diffusion electrodes.

EXPERIMENTAL

The experimental conditions and the electrolyzer design were similar to those described in [4, 7, 8]. Preparative electrolysis was carried out in the galvanostatic mode at 20°C for 7 h at a current density of 50 mA cm^{-2}, as calculated per unit apparent frontal surface area (5 cm^2). The catholyte volume was 0.023 l. Oxygen was fed into the electrode from its back surface under atmospheric pressure. To reveal the influence exerted by the mass transfer of substances involved in the process, the catholyte was agitated by bubbling of argon through a tube 1.5 mm in diameter at a rate of 10 ml min^{-1} continuously (agitation mode I) or at a rate of 38 ml min^{-1} for 1 min before sampling a solution to determine the content of H_2O_2 every hour (agitation mode II).

The catholyte and anolyte were separated by an MF-4SK-100 cation-exchange membrane. The electrodes were prepared from A-437E acetylene carbon black containing 40 wt % Ftoroplast-4D (Teflon), with 65 vol % porosity, and sintered in air at 360°C for 10 min [17]. The electrode paste was preliminarily heated at a temperature of up to 300°C. Part of electrodes were prepared from a paste heated at 340°C. The results obtained with these electrodes are listed in Table 1 and shown in Fig. 1, curves *3* and *4*.

The fraction of current consumed for synthesis of H_2O_2 was determined by gasometry, or, when possible, calculated from experimental data [16]. The rate of H_2O_2 decomposition was found using Eq. (1) by differentiating graphically the curves of H_2O_2 accumulation. The electrode potential was measured relative to a silver chloride reference electrode. In acidic and alkaline solutions, oxygen is reduced to H_2O_2 in the same range of potentials 0.4–0.6 V,

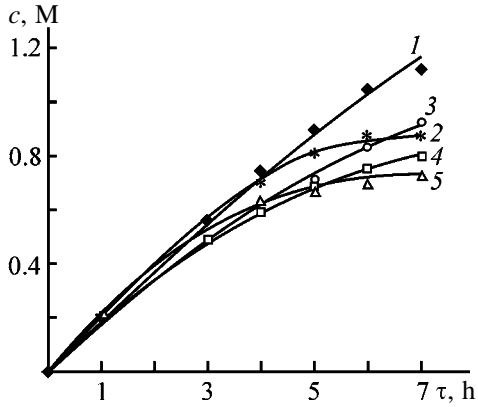

Fig. 1. Curves of hydrogen peroxide accumulation in alkaline electrolytes. (*c*) H_2O_2 concentration and (τ) time; the same for Figs. 4 and 5. Electrolyte (M): (*1*) 1.0 NaOH + 0.017 Na_2SiO_3, (*2*) 1.0 NaOH, (*3, 4*) 0.25 NaOH, and (*5*) 0.5 NaOH. Agitation mode (*1–3, 5*) I and (*4*) II. Points, experiment; lines, calculation.

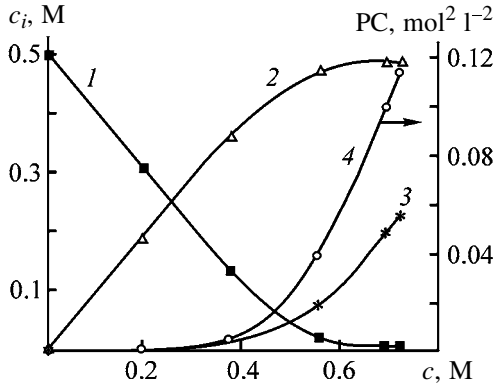

Fig. 2. Concentrations c_i of (*1*) OH^- and (*2*) HO_2^- ions, (*3*) undissociated H_2O_2, and (*4*) product of concentrations PC, $c^{ud}_{H_2O_2} c_{HO_2^-}$, vs. hydrogen peroxide concentration *c* in 0.5 M NaOH solution.

despite that the zero-current potential is about –0.2 V in alkaline solutions and is shifted to the anodic region in acidic solutions. As in [21], the potential is independent of $c_{H_2O_2}$. For example, the potential remained within 0.56–0.58 V at H_2O_2 concentrations in the range from 0.54 to 0.024 M at pH 0.9 (0.05 M K_2SO_4 + 0.15 M H_2SO_4) and shifted in the negative direction to 0.53 V with pH increasing to 2.1. The overvoltage of O_2 reduction to H_2O_2 in acidic solutions much exceeds that in alkaline solutions. No evolution of hydrogen occurs under the given conditions because of the high overvoltage of its reduction on carbon black.

Figure 1 shows curves of H_2O_2 accumulation in the cathode chamber in solutions with various NaOH concentrations and with sodium silicate added as H_2O_2 stabilizer. Table 1 lists constants *k* for Eqs. (6), (7), and (9), current efficiencies by H_2O_2, and its concentrations after 7 h of electrolysis. Also listed for comparison are rates of H_2O_2 decomposition at a concentration of 0.6 M.

As seen from Fig. 1 (curves *1, 2, 5*) and Table 1 (run nos. 4–6), raising the concentration of alkali and adding sodium silicate to the solution make higher the H_2O_2 concentration and the current efficiency by H_2O_2, which can be accounted for by a decrease in the rate of H_2O_2 decomposition [12, 19, 20]. At $c_{H_2O_2}$ = 0.6 M, the action of the stabilizing agent is not manifested yet; when, however, the content of H_2O_2 is raised further, the decomposition rate decreases.

The accumulation rate is strongly affected by the technology of electrode fabrication (Table 1, run nos. 2 and 3). Raising the temperature to which the electrode paste is heated leads to a change of the run of the $V_d = f(c_{H_2O_2})$ dependence, presumably owing to more complete removal of surfactants and other adsorbed substances [18] and to partial oxidation of the carbon black [16]. These electrodes have lower electrolyte porosity (0.5 vol %). The potential of these electrodes in electrolysis is shifted, compared with the other electrodes, to the cathodic region by 0.2–0.3 V. In experiments with electrodes fabricated from a paste heated at 340°C, the rate of H_2O_2 decomposition is described by Eq. (6). With the other electrodes, the rate of H_2O_2 decomposition in 0.5 and 1.0 M NaOH solutions is described by Eq. (7), that in a solution with addition of sodium silicate, by Eq. (6), and that in a 0.25 M NaOH solution, by the equation

$$V_d = k(c_{H_2O_2})^2. \quad (9)$$

Figure 2 shows as an example the influence of $c_{H_2O_2}$ in a 0.5 M NaOH solution on the values of $c^{ud}_{H_2O_2}$, $c_{HO_2^-}$, and c_{OH^-}, calculated using equations taken from [10]. The equilibrium constant of reaction (3) at 20°C is 261.4 [10]. Despite the fact that concentrations were taken instead of activities in the calculations, the resulting products of $c_{HO_2^-}$ and c_{OH^-} were in good agreement with the values reported in [12].

As seen from Fig. 2, the concentration of hydroxide ions decreases and the concentrations of perhydroxide ions and undissociated H_2O_2, and the product of these, grow with increasing total concentration of H_2O_2. In a 0.5 M NaOH solution, at $c_{H_2O_2}$ of up to approximately 0.5 M, when H_2O_2 is mainly in the

form of perhydroxide ions, the decomposition rate can be described using Eq. (6) with $k = 0.05$ h^{-1}. This value is equal to that for a solution with sodium silicate, which must be the case, since the accumulation curves coincide up to 0.5 M of H_2O_2 at equal γ. When a considerable amount of undissociated H_2O_2 is additionally present in the solution, the decomposition rate is described by Eq. (7) in the whole concentration range.

Figure 3 shows the dependence of the H_2O_2 decomposition rate in 0.5 and 1.0 M NaOH solution on the product $c^{ud}_{H_2O_2} c_{HO_2^-}$. The slope of the straight line, i.e., the value of k, grows with increasing alkali concentration, but the product decreases, as also does the decomposition rate.

Figure 1 (curves *2, 5*) shows the accumulation curves calculated using Eqs. (1) and (7) and values of k and γ from Table 1. These curves are in good agreement with experimental data.

Depending on the type of the equations $V_d = f(c_{H_2O_2})$ and $\gamma = f(c_{H_2O_2})$, solutions to Eq. (1) are also different:

$$c = g[\exp(2gk\tau) - 1][1 + \exp(2gk\tau)]^{-1},$$
$$g = [A\gamma I/(kv)]^{1/2} \quad (10)$$

at $V_d = k(c_{H_2O_2})^2$ and γ = const;

$$c = AI\gamma[1 - \exp(-k\tau)]/(kv) \quad (11)$$

at $V_d = kc_{H_2O_2}$ and γ = const [8];

$$c = \frac{AIb\{\exp[(AIa/v - k)\tau] - 1\}}{[AIa/v - k]v} \quad (12)$$

at $V_d = kc_{H_2O_2}$ and $\gamma = b - ac_{H_2O_2}$ [4].

Equation (12) was used to calculate curves *1, 3*, and *4* in Fig. 1.

In alkaline electrolytes, γ is large and virtually independent of $c_{H_2O_2}$ and other electrolysis parameters, even though it tends to decrease somewhat (linearly) with increasing H_2O_2 concentration, as is also the case in [22]. For example, $\gamma = 1 - 0.085c_{H_2O_2}$ in a 0.25 M NaOH solution (Table 1, run no. 1). In acidic solutions, γ depends on the solution composition, but also is a linear function of $c_{H_2O_2}$ [8]. For example, $\gamma = 1 - 0.39c_{H_2O_2}$ in a solution containing 0.05 M K_2SO_4 + 0.15 M H_2SO_4.

In alkaline and acidic solutions, changes in γ are associated both with H_2O_2 decomposition in the electrode, when the appearing oxygen undergoes repeated reduction, and with further reduction of H_2O_2. In alkaline solutions, H_2O_2 is reduced on graphitic carbon materials at high overvoltage, whereas in acidic solutions this process is markedly facilitated. Therefore, the insignificant decrease in γ in alkaline solutions is only due to a rise in the rate of H_2O_2 decomposition in the electrode with increasing H_2O_2 concentration, whereas in acidic solutions the decrease in γ is mainly due to an increase in the rate of H_2O_2 reduction.

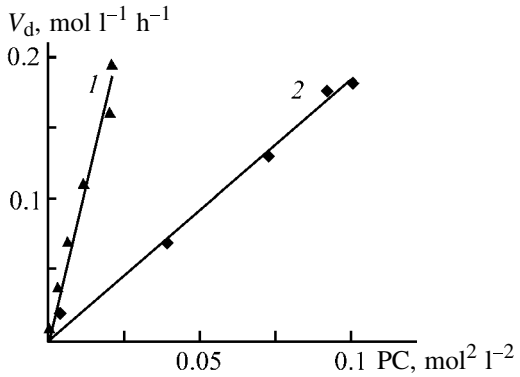

Fig. 3. Effect of the product of concentrations, PC, $c^{ud}_{H_2O_2} \times c_{HO_2^-}$, on the decomposition rate V_d of H_2O_2 in (*1*) 1.0 M NaOH solution and (*2*) 0.5 M NaOH. Agitation mode I; the same for Fig. 5.

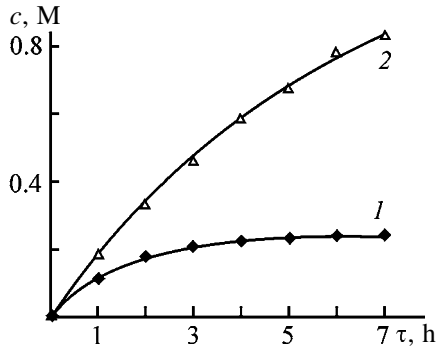

Fig. 4. Curves of H_2O_2 accumulation in solutions with pH 0.9. Electrolyte (M): (*1*) 0.1 H_2SO_4 and (*2*) 0.05 K_2SO_4 + 0.15 H_2SO_4. Points, experiment; lines, calculation by Eq. (2).

Thus, the process occurring in an electrode are strongly affected by H_2O_2 removal from the electrode and by the activity of hydrogen ions, which depends on the electrolyte composition and electrolysis conditions [8], within the electrode. Compared to acidic solutions, removal of H_2O_2 from the pore volume of the electrode is somewhat facilitated in alkaline solutions, since perhydroxide ions are removed not only by diffusion, but also via migration under the action of the electric field. Figure 4 illustrates the influence of the composition of an acidic solution by the exam-

Table 2. Electrolysis parameters* used to calculate curves of H_2O_2 accumulation, shown in Fig. 6

Curve no.	I, A	Catholyte volume, l	b	a, l mol^{-1}	k, h^{-1}	τ, h	η
1	0.25	0.023	1	0	0	2.47	1.00
2	0.25	0.01	1	0.5	0.1	1.33	0.81
3	0.50	0.023	1	0.5	0.1	1.55	0.80
4	0.25	0.023	1	0.01	0.1	2.85	0.86
5	0.25	0.023	1	0.5	0.05	3.10	0.80
6	0.25	0.023	1	0.5	0.1	3.43	0.72
7	0.25	0.023	0.6	0.5	0.1	8.78	0.28

* τ and η are the time of electrolysis, necessary for the H_2O_2 concentration of 0.5 M to be reached, and the resulting current efficiency, respectively.

ple of the curves of H_2O_2 accumulation in solutions with pH 0.9 (Table 1, run nos. 7 and 8).

The aforesaid is also confirmed by the fact that the agitation mode affects differently the values of γ and $c_{H_2O_2}$ in acidic and alkaline solutions. Raising the intensity of agitation in alkaline solutions leads to a decrease in the rate of decomposition because of the change in $c_{H_2O_2}$ in the near-electrode space (Table 1, run nos. 1 and 2) and has virtually no effect on γ, whereas in acidic solutions, a decrease in γ is observed because of the increasing supply to the electrode of hydrogen ions involved in H_2O_2 reduction to water. For example, in a solution containing 0.05 M K_2SO_4 + 0.15 M H_2SO_4, γ decreases by a factor of nearly 2 in going from agitation mode I to mode II, whereas already at pH 3.2 (0.495 M K_2SO_4 + 0.005 M H_2SO_4) the agitation mode has virtually no effect, since the activity of hydrogen ions decreases by a factor of more than 100.

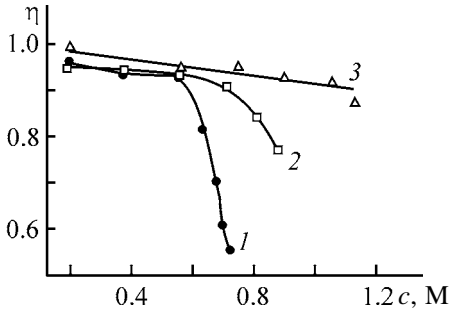

Fig. 5. Current efficiency η vs. H_2O_2 concentration c in various electrolytes. Electrolyte (M): (*1*) 0.5 NaOH, (*2*) 1.0 NaOH, and (*3*) 1.0 NaOH + 0.017 Na_2SiO_3.

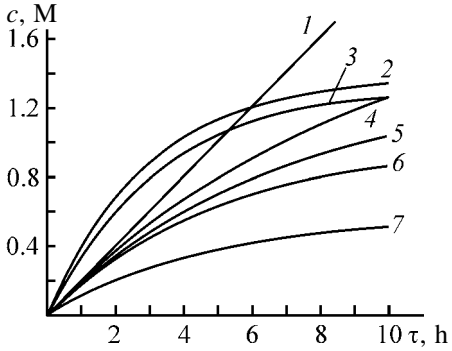

Fig. 6. Effect of electrolysis parameters (Table 2) on the run of curves of H_2O_2 accumulation, calculated by Eq. (2).

The linear dependence of the current efficiency η on $c_{H_2O_2}$ (Fig. 5) is preserved at higher H_2O_2 concentrations on raising the concentration of alkali and on introducing a stabilizer, i.e., in the case when the decomposition rate depends on $c_{H_2O_2}$ linearly [23]; further, the current efficiency falls dramatically because of an increase in the rate of H_2O_2 decomposition. In acidic electrolytes, in contrast to alkaline solutions, the type of the equation $V_d = f(c_{H_2O_2})$ is independent of the electrolyte composition and the dependence $\eta = f(c_{H_2O_2})$ is linear during the whole time of electrolysis [4]. For example, $\eta = 0.97 - 0.37c_{H_2O_2}$ for a solution containing 0.05 M K_2SO_4 + 0.15 M H_2SO_4 (Table 1, run no. 8).

To evaluate the influence exerted by the electrolysis parameters on the run of an accumulation curve and to predict the current efficiency, which is one of the most important electrosynthesis parameters, it is necessary to analyze Eq. (12), which turns into Eq. (11) at $a = 0$ ($\gamma = b$). Figure 6 shows curves of H_2O_2 accumulation for various values of the electrolysis parameters (Table 2). Table 2 also lists for comparison the times required for solutions with $c_{H_2O_2}$ = 0.5 M to be obtained and the resulting current efficiencies. For clarity, the values of the parameters are chosen so that curves do not overlap. All the comparisons are made relative to curve *6* (Fig. 6). Curve *1* is calculated using the equation $c_{H_2O_2} = A\gamma I\tau/v$.

As seen from Fig. 6 and Eq. (12), the multiplier

AIb/v determines the initial slope of an accumulation curve, i.e., the rate of H_2O_2 accumulation, which decreases with increasing H_2O_2 concentration because of a decrease in γ and rise in the decomposition rate. The highest H_2O_2 concentration is obtained when the accumulation rate becomes equal to the rate of H_2O_2 decomposition. When the decomposition rate is described by Eq. (6), the maximum concentration is given by the expression $c_{H_2O_2} = A\gamma I/(kv)$.

The rate of H_2O_2 accumulation is strongly affected by coefficient b (Fig. 6, curve *7*). The decrease in k and a starts to affect the accumulation rate at higher H_2O_2 concentrations (curves *4* and *5*). The quantity I/v is the volume current density and, consequently, the rate of H_2O_2 accumulation may become higher with increasing current density or decreasing catholyte volume (Fig. 6, curves *2* and *3*). This may give, during the first hours of electrolysis, an H_2O_2 concentration exceeding the concentration that would be observed at a decomposition rate close to zero and $\gamma = 1$ (Fig. 6, curve *1*).

CONCLUSIONS

(1) The rate of subsequent electroreduction of H_2O_2 to water in an alkaline electrolyte in hydrophobized carbon black electrodes is low. The accumulation rate of hydrogen peroxide is determined under these conditions by the rate of its chemical decomposition in the cathode chamber.

(2) In acidic solutions, the rate of hydrogen peroxide accumulation is mainly determined by the rate of subsequent H_2O_2 reduction to water, which depends on the concentration of H_2O_2 and hydrogen ions in the volume of the gas-diffusion electrode.

(3) The equations relating $c_{H_2O_2}$ and electrolysis duration, presented in the communication, well describe experimental curves of H_2O_2 accumulation. All the other parameters being the same, the initial rate of H_2O_2 accumulation is determined by the volume current density; with increasing electrolysis duration and H_2O_2 concentration, the rate of hydrogen peroxide decomposition in an alkaline medium and reduction to water in an acidic medium starts to exert steadily increasing influence on the accumulation rate.

REFERENCES

1. Vasil'eva, I.S., Kornienko, V.L., and Kolyagin, G.A., *Khim. Inter. Ustoich. Razv.*, 2001, vol. 9, no. 4, pp. 529–532.
2. Pletcher, D., *Acta Chem. Scand.*, 1999, vol. 53, p. 745.
3. Brillas, E., Bastida, R. M., Llosa, E., and Casado, J., *J. Electrochem. Soc.*, 1995, vol. 142, no. 6, pp. 1733–1741.
4. Nagiev, T.M., *Usp. Khim.*, 1985, vol. 54, no. 10, pp. 1654–1673.
5. Schumb, W.C., Satterfield, Ch.N., and Wentworth, R.L., *Hydrogen Peroxide*, New York: Chapman and Hall, 1955.
6. *Khimiya i tekhnologiya perekisi vodoroda* (Chemistry and Technology of Hydrogen Peroxide), Serysheev, G.A., Ed., Leningrad: Khimiya, 1984.
7. Kornienko, V.L., Kolyagin, G.A., and Saltykov, Yu.V., *Zh. Prikl. Khim.*, 1999, vol. 72, no. 3, pp. 353–361.
8. Kolyagin, G.A. and Kornienko, V.L., *Khim. Inter. Ustoich. Razv.*, 2000, vol. 8, no. 6, pp. 803–807.
9. Vert, Zh.L. and Pavlova, V.F., *Zh. Prikl. Khim.*, 1988, vol. 61, no. 5, pp. 1148–1150.
10. Balej, J. and Spalek, O., *Coll. Czech. Chem. Commun.*, 1979, vol. 44, no. 2, pp. 488–494.
11. Spalek, O., Balej, J., and Paseka, I., *J. Chem. Soc., Faraday Trans. 1*, 1982, vol. 78, pp. 2349–2359.
12. Duke, F.R. and Haas, T.W., *J. Phys. Chem.*, 1961, vol. 65, no. 2, pp. 304–306.
13. Moiseev, I.I., *Izv. Akad. Nauk, Ser. Khim.*, 1995, no. 3, pp. 578–588.
14. Gyenge, E.L. and Oloman, C.W., *J. Appl. Electrochem.*, 2001, vol. 31, no. 2, pp. 233–243.
15. Chaenko, N.V., Kornienko, G.V., Vasil'eva, I.S., and Kornienko, V.L., *Zh. Prikl. Khim.*, 1996, vol. 69, no. 5, pp. 792–794.
16. Kenova, T.A., Abolin, O.E., and Kornienko, V.L., *Zh. Prikl. Khim.*, 1991, vol. 64, no. 3, pp. 792–794.
17. Kolyagin, G.A. and Kornienko, V.L., *Zh. Prikl. Khim.*, 1989, vol. 62, no. 9, pp. 2082–2087.
18. Chaenko, N.V., Kornienko, G.V., Kenova, T.A., *et al.*, *Zh. Prikl. Khim.*, 2000, vol. 73, no. 1, pp. 51–54.
19. Kanter, M.Ya., Raskina, I.Kh., Bogdanov, G.A., and Koziv, Yu.N., *Zh. Prikl. Khim.*, 1977, vol. 50, no. 4, pp. 724–731.
20. Raskina, I.Kh., Sadov, F.I., and Bogdanov, G.A., *Zh. Prikl. Khim.*, 1977, vol. 39, no. 1, pp. 35–39.
21. Anurova, A.I., Daniel'-Bek, V.S., and Rotinyan, A.L., *Elektrokhimiya*, 1968, vol. 4, no. 7, pp. 815–821.
22. Malyshev, V.A. Abolin, O.E., and Kornienko, V.L., *Zh. Prikl. Khim.*, 1991, vol. 64, no. 10, pp. 2181–2183.
23. Khomutov, N.E., Khachaturyan, O.B., and Khokhlov, M.I., *Zh. Prikl. Khim.*, 1987, vol. 60, no. 1, pp. 31–34.

Russian Journal of Applied Chemistry, Vol. 76, No. 7, 2003, pp. 1076–1078. Translated from Zhurnal Prikladnoi Khimii, Vol. 76, No. 7, 2003, pp. 1109–1111.

APPLIED ELECTROCHEMISTRY AND CORROSION PROTECTION OF METALS

Electrochemical Synthesis of 2,5-Dichloroaniline

V. R. Islamgulova, A. P. Tomilov, S. G. Akhmerova, V. T. Gil'mkhanova, and Yu. E. Sapozhnikov

Research and Technological Institute of Herbicides and Plant Growth Regulators, Ufa, Bashkortostan, Russia
State Research Institute of Organic Chemistry and Technology, Moscow, Russia

Received February 26, 2003

Abstract—A procedure was proposed for electrochemical reduction of 2,5-dichloronitrobenzene to 2,5-dichloroaniline in aqueous-ethanolic solution of sulfuric acid. The procedure for preparing 2,5-dichloroanilinium sulfate was optimized. The influence exerted by the cathode material, nature and amount of the organic solvent, sulfuric acid concentration, and electrolysis temperature on the yield and quality of the target product was discussed.

2,5-Dichloroaniline (2,5-DCA) is an intermediate in synthesis of pesticides. The existing methods of reduction of nitro compounds with metals do not meet modern environmental requirements, because the arising wastes are difficult to utilize. Therefore, electrochemical reduction of aromatic nitro compounds attracts much attention [1–5]. However, we found no data on cathodic reduction of 2,5-dichloronitrobenzene (2,5-DCNB) to 2,5-DCA. This process was the subject of the present study.

We tested two procedres for electrochemical reduction of 2,5-DCNB: a classical procedure based on electroreduction of the nitro compound in a sulfuric acid medium, yielding the amine in the salt form, and a recently suggested procedure of reduction in a two-phase system [5] involving the use of a solvent immiscible with water and a buffer solution with the pH close to pK of the forming amine. The second procedure allows preparation of the free amine in one step.

Classical reduction was performed in aqueous solfuric acid with addition of an organic solvent miscible with water to obtain a homogeneous solution.

The first series of experiments on choosing the optimal cathode material was performed in an aqueous-alcoholic solution of sulfuric acid at a cathodic current density of 750 A m^{-2} and temperature of 48–50°C. The catholyte had the following composition (wt %): 2,5-DNCB 7.6, H_2SO_4 7.0, and C_2H_5OH 50.

Table 1 shows that the chemical yield of reduction of 2,5-DCNB to 2,5-DCA on copper is low (69%). The reduction on brass and nickel is also inefficient. Addition of an Sn(II) salt has no appreciable effect on the 2,5-DCA yield, whereas in the presence of zinc sulfate the yield of 2,5-DCA based on 2,5-DCNB increases to 87%. Reproducibly high yield of 2,5-DCA (up to 88%) was obtained on a lead cathode in an aqueous-ethanolic solution of sulfuric acid.

Then, using the lead cathode, we examined how the 2,5-DCA yield depends on the nature and amount of the organic solvent and on the concentrations of 2,5-DCNB and sulfuric acd. We found (Table 2) that such solvents as acetone and acetonitrile affect the reaction negatively. This is manifested in the decreased yield of 2,5-DCA (3.6–6.0%) as compared to reduction in water without organic solvent added (39%). Apparently, these solvents prevent adsorption of 2,5-DCNB on the cathode. Addition of about 50 wt % of aliphatic alcohol increases the yield of 2,5-DCA to 88.4–88.9%.

Variation of the 2,5-DCNB concentration in the reaction mixture from 5.5 to 10% has virtually no

Table 1. Influence of the cathode material on the yield of the reaction products

Cathode	2,5-DCA yield based on 2,5-DCNB, %
Cu	69.0
Cu*	71.0
Cu**	87.1
Brass	63.0
Ni	58.0
Pb	88.0
Pb + 4%Sb	80.0

* $SnCl_2$ added to 0.1 M concentration.
** $ZnSO_4$ added to 0.1 M concentration.

1070-4272/03/7607-1076$25.00

Table 2. Effect of organic solvent on the 2,5-DCA yield. Lead cathode, 48–50°C, cathodic current density 750 A m^{-2}

Organic solvent	Content in catholyte, wt %			2,5-DCA yield based on 2,5-DCNB, %
	organic solvent	2,5-DCNB	H_2SO_4	
Acetone	50	5.3	7.0	3.6
Acetonitrile	50	5.2	6.8	6.0
Methanol	50	5.4	6.9	88.5
Isopropanol	50	5.3	6.9	88.4
Ethanol	50	5.3	7.0	88.9
	80	5.4	6.8	66.0
	30	5.2	6.9	58.0
No organic solvent	–	5.5	7.0	39.0

effect on the process (Table 3). When the 2,5-DCNB content is increased to 10%, the target product starts to crystallize on the cathode, which may disturb the process. Therefore, to ensure the homogeneous medium, it is not advisable to increase the 2,5-DCNB concentration above 8%.

An increase in the sulfuric acid concentration in the reaction mixture above 13% favors the Gattermann rearrangement, and the yield of 2,5-DCA decreases. At the H_2SO_4 concentration of 6.8–10.3%, the yield of 2,5-DCA is 86.3–88.3%, whereas at 20.7 wt % concentration of H_2SO_4 it is as low as 61%.

The optimal reaction temperature is 48–50°C. At lower temperatures, the solubility of 2,5-DCNB in the catholyte decreases; above 50°C, by-products are formed. In particular, the Gattermann rearrangement occurs, yielding dichloro-*p*-aminophenol.

The 2,5-DCNB molecule contains reducible functional substituents, chlorine atoms. Therefore, it seemed appropriate to study how the 2,5-DCA yield based on 2,5-DCNB depends on the amount of the electricity passed. We found that the highest yield of 2,5-DCA is attained after passing 150% amount of electricity relative to the amount required by the stoichiometry. At longer electrolysis, the 2,5-DCA yield based on 2,5-DCNB does not decrease, i.e., the product is resistant to further electrochemical reduction.

Thus, the optimal conditions for electrochemical synthesis of 2,5-DCA sulfate in the cathodic chamber of a diaphragm electrolyzer are as follows. Catholyte composition, wt %: 7.7 2,5-DCNB, 6.8–8.7 sulfuric acid, and 50 aliphatic alcohol; lead cathode; current density 750 A m^{-2}; 48–50°C; amount of the electricity passed 150%. Under these conditions, the 2,5-DCA yield based on 2,5-DCNB is 88.6–88.7%, and the current efficiency is 59.1%. Reuse of the electrolyte solution after adjustment of its composition does not impair the process but considerably reduces the amount of wastes and the consumption of auxiliary materials.

Our next goal was to examine the feasibility of preparing free 2,5-DCA directly from 2,5-DCNB by electrolysis in a two-phase system with a cadmium cathode [5]. The catholyte was a phosphate buffer solution (pH 5.0). Toluene was taken as a solvent immiscible with water. After electrolysis, the organic layer of the catholyte was separated, and the solvent was distilled off. Yield of 2,5-DCA 80%.

Thus, 2,5-DCNB can be electrochemically reduced both in an acid solution to obtain the 2,5-DCA salt and in a weakly acidic medium to obtain the free base. In both procedures, the yield of the target product based on 2,5-DCNB exceeds 80%.

EXPERIMENTAL

2,5-DCNB was prepared from 2,5-dichlorobenzene by nitration with a mixture of sulfuric and nitric acids.

Table 3. Influence of the concentrations of 2,5-DCNB and sulfuric acid in the catholyte on the 2,5-DCA yield. Lead cathode, 48–50°C, cathodic current density 750 A m^{-2}, ethanol content 50 wt %

Loaded, wt %		H_2SO_4 : 2,5-DCNB molar ratio	2,5-DCA yield based on 2,5-DCNB, %
2,5-DCNB	H_2SO_4		
5.8	5.0	1.7 : 1	87.1
5.8	7.5	2.4 : 1	88.7
7.7	6.8	1.7 : 1	88.3
7.0	8.6	2.4 : 1	88.5
10.0	8.7	1.7 : 1	88.0
7.0	10.3	3.0 : 1	86.3
7.0	13.1	3.6 : 1	73.0
7.0	20.7	6.8 : 1	61.0

The main substance content was 90%. Potassium phosphate, sulfuric acid, phosphoric acid, and other chemicals (pure or analytically pure grade) were used without additional purification.

Electrolysis was performed in the galvanostatic mode in a 150-ml temperature-controlled cell equipped with a reflux condenser, a ceramic diaphragm, and a platinum spiral anode. The cathode (several materials were tested) was treated with an acid solution and washed with a large amount of water before the experiment.

Reduction in an aqueous-ethanolic solution of sulfuric acid was performed as follows. The cathode compartment (with a lead cylinder as cathode) was charged with 100 ml of a solution containing 7.5 wt % sulfuric acid and 50 wt % ethanol. Then 7.9 g (0.0402 mol) of 2,5-DCNB was added. The anolyte was 25% aqueous H_2SO_4.

The mixture was heated to 50°C, and reduction with a current of 6.5 A (cathodic current density 750 A m^{-2}) was performed for 1 h 29 min with vigorous stirring. After electrolysis completion, the mixture was unloaded and kept for 30–40 min at 3–5°C. The precipitate of 2,5-DCA sulfate was filtered off and dried at room temperature; 9.2 g of 2,5-DCA sulfate was obtained. The product contained about 62.8% DCA and 34% sulfate ions. Yield based on 2,5-DCNB 88.7%, current efficiency 59.1%.

Reduction in the two-phase system was performed with a cadmium cathode (working surface area 87 cm^2). The cathodic compartment was charged with 70 ml of a 1 N potassium phosphate solution (pH 5), 10 g (0.052 mol) of 2,5-DCNB, and 30 ml of toluene. The anolyte was 20% aqueous H_3PO_4. Electrolysis was performed with a current of 6 A (cathodic current density 700 A m^{-2}) for 1 h 20 min and then with a current of 3 A for an additional 1 h 20 min. In the course of the electrolysis, the mixture in the cathodic compartment was vigorously stirred; pH 5.0 was adjusted at regular intervals by dropwise addition of phosphoric acid. The temperature was kept in the range 50–52°C. Yield of 2,5-DCA 7.3 g (main substance content 92%, yield based on 2,5-DCNB 80%, current efficiency 56%).

The content of 2,5-DCNB and 2,5-DCA in the reaction mixtures and isolated products was determined by GLC. The content of sulfate anions was determined by a standard procedure (titration with a $BaCl_2$ solution). The structure of the product was proved by ^{13}C NMR spectroscopy.

REFERENCES

1. Tomilov, A.P., Fioshin, M.Ya., and Smirnov, V.Ya., *Elektrokhimicheskii sintez organicheskikh veshchestv* (Electrochemical Synthesis of Organic Substances), Leningrad: Khimiya, 1976.
2. Izgaryshev, N.A. and Fioshin, M.Ya., *Dokl. Akad. Nauk SSSR*, 1953, vol. 90, pp. 189–190.
3. *Technique of Organic Chemistry*, vol. 2: Komarewsky, V.I., Riesz, C.H., and Moritz, F.L., *Catalytic Reactions*; Masson, C.R., Boekelheide, V., and Noyes, W.A., *Photochemical Reactions*; Swann, Sh., *Electrolytic Reactions*, New York: Interscience, 1956.
4. Gul'tyai, V.P. and Leibzon, V.N., *Elektrokhimiya*, 1996, vol. 32, pp. 65–74.
5. Tomilov, A.P. and Smirnov, Yu.D., *Elektrokhimiya*, 1997, vol. 33, pp. 1260–1261.

Russian Journal of Applied Chemistry, Vol. 76, No. 7, 2003, pp. 1079–1082. Translated from Zhurnal Prikladnoi Khimii, Vol. 76, No. 7, 2003, pp. 1112–1115.

CATALYSIS

A Study of the Surface of Mo-Containing Phosphorus-Modified Catalysts Supported by γ-Al_2O_3 Using Probe Molecules (CO_2 and O_2)

M. A. Lur'e, K. P. Zhdanova, I. Z. Kurets, and F. K. Shmidt

Institute of Oil- and Coal-Chemical Synthesis, Irkutsk State University, Irkutsk, Russia
Favorskii Institute of Chemistry, Siberian Division, Russian Academy of Sciences, Irkutsk, Russia

Received March 5, 2003

Abstract—The possibility is considered of using probe molecules to estimate the effect exerted by addition of phosphorus to supported Mo-containing catalysts on the dispersion of the active component and the support coverage.

Phosphorus modification of Mo-containing catalysts, which are widely used in hydrosupply of oil fractions, is one of the most common methods to enhance the process efficiency [1]. The addition of P to the catalyst strongly affects the physicochemical and service characteristics, such as dispersion of the active component, its reducibility and susceptibility to sulfiding, phase composition, surface acidity, activity in target reaction, the ratio of different types of activities, resistance to coking, and service life of a catalyst.

To understand such a complex effect of P, it is necessary to study in detail all aspects of its action on the catalytic system, including such important parameter as the dispersion of Mo-containing particles. Raman, IR, and X-ray photoelectron spectroscopic studies revealed an increase in the degree of dispersion of Al–Mo [1–4] and Al–Ni(Co)–Mo [3, 5, 6] catalysts at a certain concentration of P, irrespective of the sequence of deposition of components onto Al_2O_3.

To perform a more accurate quantitative estimation of the active component dispersion and to ascertain how P influences it in catalysts of different compositions, it is reasonable to use selective adsorption of probe molecules along with the above methods. This method can yield additional information on the dispersion, active surface area, and coverage of the support. Molecular oxygen, which is not noticeably adsorbed by the support, is a common probe molecule for studying Al_2O_3-supported Mo-containing oxide catalysts. The adsorption is performed on preliminarily reduced samples.

The fact that the amount of chemisorbed O_2 depends on the degree of the Mo reduction makes the use of this sorbate insufficiently reliable. Therefore, it is appropriate to use some additional probe reacting solely with the free surface of the support. The fact that the catalyst additives can appreciably affect the reducibility of the active component makes the use of such a procedure still more necessary.

Carbon dioxide, which interacts with the basic OH groups of Al_2O_3 to form $(CO_3H)^-$-like structures [7, 8], is not adsorbed on Mo-containing catalyst particles.

No data are available on simultaneous adsorption of O_2 and CO_2 on modified Mo-containing catalysts.

In this work, the results of the CO_2 and O_2 chemisorption were used to estimate the effect exerted by P additive on the coverage of the support by the active component and its dispersion in catalysts differing in the composition and sequence of the Mo and P deposition onto Al_2O_3.

EXPERIMENTAL

The test objects were samples of A-64 γ-Al_2O_3 catalysts, aluminum–molybdenum and aluminum–molybdenum–nickel, phosphorus-free (Al_2O_3, Al–Mo, and Al–Ni–Mo) and containing various amounts (0–0.8 mmol g^{-1}) of P (Al–P, Al–P–Mo, and Al–Ni–Mo–P).

P was introduced into Al_2O_3 by impregnation with a solution of ammonium dihydrogen phosphate. The Al–P–Mo catalysts were prepared by impregnating Al–P samples with a solution of ammonium paramolybdate. The Mo concentration in the catalyst was 0.7 mmol g^{-1}. To ensure introduction of the pre-

1070-4272/03/7607-1079$25.00

Amount of chemisorbed CO_2, V_{CO_2}, in different samples

Sample	V_{CO_2}, ml g^{-1}, at indicated c_P, mmol g^{-1}										
	0	0.6	0.15	0.16	0.29	0.32	0.48	0.60	0.65	0.75	0.81
Al–P	2.0	1.69	–	1.64	–	1.20	–	–	0.75	–	0.80
Al–P–Mo	1.1	0.90	0.80	–	0.63	–	–	0.55	–	0.55	–
Al–Ni–Mo–P	0.57	1.0	–	1.0	–	1.0	0.75	–	0.70	–	0.70

scribed amounts of P and Mo, the impregnation was performed under saturation conditions. To synthesize the Al–Ni–Mo–P samples, P was introduced by the above method into the commercial Al–Ni–Mo catalyst ready for use, which contained 0.5 mmol g^{-1} Ni and 0.9 mmol g^{-1} Mo.

The catalytic mass was air-dried for 24 h, then dried at 110–120°C, and calcined at 400°C for 6 h in air after each impregnation.

The amount of the chemisorbed CO_2 and O_2 was determined on a pulsed chromatographic installation. The preparation of samples to chemisorption included oxidation in an O_2 flow at 500°C for 1 h, reduction in an H_2 flow at 500°C for 3 h, blowing at 300°C for 15 min, and cooling to room temperature in an He flow. Then, CO_2 or O_2 was fed to complete saturation. The above conditions for the preliminary treatment ensured reproducible results.

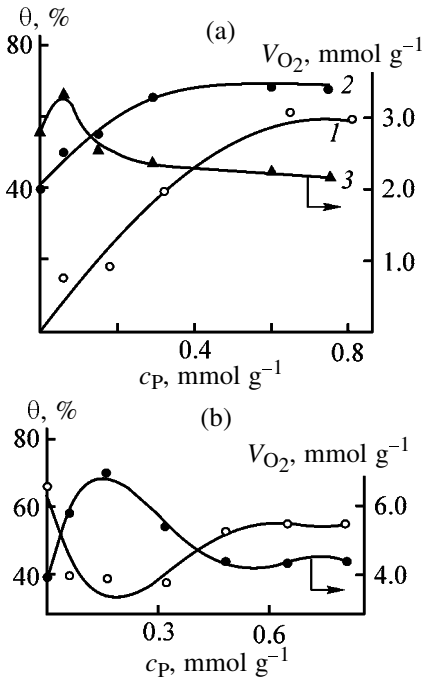

Fig. 1. Degree of exchange of basic OH groups for phosphate anions θ and amount of the chemisorbed oxygen V_{O_2} vs. phosphorus concentration c_P. Sample: (a) (*1*) Al–P and (*2, 3*) Al–P–Mo; (b) Al–Ni–Mo–P.

The amounts of chemisorbed gases were determined, and the coverage of the Al_2O_3 surface with the components was estimated by the formula [7]

$$\theta = n/mf,$$

where n is the CO_2 amount adsorbed on Al_2O_3 containing deposited components; m, CO_2 amount adsorbed on free Al_2O_3; and f, weight fraction of Al_2O_3 in the sample.

The results for the Al_2O_3, Al–P, Al–Mo, and Al–P–Mo samples are presented in the table and in Fig. 1a.

As P is introduced into Al_2O_3 and its concentration is increased, the amount of the chemisorbed CO_2 decreases and, correspondingly, θ grows (table, Fig. 1a). This phenomenon is primarily due to the fact that the phosphate anions interact with the basic OH groups at the surface to form an $AlPO_4$ layer [3, 9–13]. At a P concentration of about 0.6 mmol g^{-1}, the replacement of such OH groups reaches approximately 60% (Fig. 1a). The remaining OH groups (40%) are inactive in exchange for phosphate anions. Thus, with growing P concentration, a considerable portion of P can be attached to the surface by another mechanism. It is possible that phosphate anions interact with other sites of the Al_2O_3 surface. Also, agglomeration of phosphate structures in an impregnating solution or on the Al_2O_3 surface at higher concentrations as well as migration of certain its amount into the bulk should not be ruled out.

Fixation of molybdenum on the Al_2O_3 surface is also a result of its exchange interaction, mostly with basic OH groups [2, 13–15]. According to the results obtained, in the Al–Mo catalyst containing 0.7 mmol g^{-1} Mo, θ is about 40% (Fig. 1a). Such a coverage in the Al–P system is attained even at 0.3 mmol g^{-1} P (Fig. 1a). This confirms the greater aggregation of Mo-containing particles and weaker

adsorption of molybdate anions compared to phosphate anions, which is in line with the data of [16].

In the case of Al–P–Mo catalysts containing a small amount of the deposited P (0.06 and 0.16 mmol g^{-1}), θ is virtually equal to the sum of the θ values in the Al–P sample with the same P concentration and in the Al–Mo catalyst (Fig. 1a). Evidently, at low P concentrations, a sufficient amount of OH groups capable of exchanging for molybdate anion remains in Al–P. As a result, in the weakly phosphated Al–P–Mo system, θ is an additive quantity.

With an increase in the P content, the extent to which θ in Al–P–Mo exceeds that in Al–P decreases, reaching a minimum at 0.6–0.8 mmol g^{-1} P; at a higher P content, θ flattens out at a level of about 70% (Fig. 1a). After Mo is deposited onto Al_2O_3, 40% of OH groups interacting with CO_2 disappear. At the same time, when Mo is deposited onto Al_2O_3 containing 0.6 mmol g^{-1} P, the loss is smaller, only 10%. Apparently, certain amount of OH groups detected by CO_2 chemisorption are incapable of exchanging with molybdate anions.

Thus, only a part of basic OH groups can exchange for phosphate and molybdate anions. Gishti *et al*. [17] discussed their competition in adsorption onto Al_2O_3 and a decrease in the chemisorption capacity of the support as the P content in it grows relative to the content of molybdate anions capable of exchanging for OH groups.

The observed fact that θ in the Al–P–Mo samples stops to grow (Fig. 1a) shows that, at a certain P concentration, fixation of a part of Mo ions on the support occurs by a mechanism other than the exchange with basic OH groups, e.g., by interaction of molybdate anions with other sites of the Al_2O_3 surface, polymerization and aggregation of adsorbed anions, or adsorption on Al–O–P structures. The presence of P–OH groups on the surface of phosphated Al_2O_3 was revealed in [12, 13]. At the P concentration of 0.3 mmol g^{-1}, the molybdate anions react not only with Al–OH, but also with P–OH groups [2].

These facts suggest that, in the system containing certain amounts of P and Mo, the P–O–Mo structures must arise even in the stage of the support impregnation. The presence of these structures in calcined Al–P–Mo catalysts has been clearly confirmed in [3].

Let us consider how the amount of O_2 chemisorbed on Al–P–Mo catalysts varies with the P concentration (see Fig. 1a). The maximum at the P concentration of 0.06 mmol g^{-1} suggests an increase in the degree of Mo dispersion after a given amount of P is introduced into the support. With increasing P concentration, the amount of chemisorbed O_2 decreases to a lower level than in the modified sample. This suggests that a decrease in the O_2 chemisorption is due to the suppression of the Mo reducibility under the action of P additives, rather than by a decrease in the degree of its dispersion. The similar effect of P was found in [1, 3].

The data on CO_2 and O_2 chemisorption on samples synthesized by introducing P into the Al–Ni–Mo catalyst, i.e., into the already formed catalytic system, are presented in the table and in Fig. 1b.

In the case of the Al–Ni–Mo system, the character of the dependence of θ on the P concentration differs markedly from that for Al–P–Mo samples. For the Ni-containing catalyst, a pronounced minimum is observed. Apparently, the observed difference is due to the system composition and the sequence of introducing P and active component. Presumably, when P is added into the Al–Ni–Mo catalyst being formed, the structural rearrangement occurs even in the impregnation stage owing to the passage of certain amounts of Ni and Mo into the dissolved state. Since the impregnating solution is acidic and its acidity increases in the course of P addition, the fraction of Ni cations passed into the solution must be larger than that of Mo ions. On the contrary, in the course of the catalytic mass drying, the molybdate anions should "return" to the surface more readily than the Ni cations. Apparently, structural rearangements of the Al–Ni–Mo system may continue in the course of the subsequent thermal treatment. Small (0.35 Å) P ions can be incorporated into tetrahedral voids, replacing Ni ions [18]. Moreover, P impedes the Ni^{2+} diffusion into Al_2O_3 [5]. Its addition into an Ni-containing system hampers formation of $NiAl_2O_4$ spinel and decreases the content of this phase, increasing the content of octahedral Ni^{2+} ions [6, 19–21].

Thus, presumably, introduction of P into the already formed Al–Ni–Mo catalyst results in the breakdown of Al–Ni compounds, hydroxylation of the "released" aluminum oxide structures, and, as a consequence, appearance of OH groups capable of adsorbing CO_2. As a result, θ decreases. Apparently, when the Ni amount in the system is constant and the amount of phosphate anions increases, these anions (as well as molybdate anions) can enter into exchange reaction with the newly formed OH groups, i.e., the effect produced on θ will be opposite. Consequently, it is reasonable to expect that θ would increase after attaining a certain P concentration, which was indeed observed at a P concentration of about 0.4 mmol g^{-1} (Fig. 1b).

On the whole, the trends in variation of the amount of O_2 chemisorbed on Al–Ni–Mo–P and Al–P–Mo samples are similar (Figs. 1a, 1b). With increasing P concentration, an increase and then a decrease were observed. As for the Al–P–Mo system, the decrease may be due to the predominant formation of structures with the difficultly reducible Mo ions [3, 18]. At the same time, the dispersion effect is more pronounced than in the Al–P–Mo system. The maximal increase in the amount of chemisorbed O_2 is about 75% (compared to about 15% in the Al–P–Mo system), and the range of P concentrations at which the chemisorption is enhanced is considerably wider. Moreover, the chemisorption is never lower than that on the initial sample. These differences can result from the rearrangement of the Al–Ni–Mo structure. Apart from the direct influence exerted by P on Mo-containing particles, breakdown of Al–Ni compounds and formation of OH groups, which can interact with Mo oxide structures, can also affect the Mo dispersion. The released Ni ions can also produce an additional dispersion effect on the Mo-containing particles. The validity of this explanation can be indirectly confirmed by the fact that the dependences of θ and the amount of chemisorbed O_2 on the P concentration show opposite trends (Fig. 1b).

CONCLUSIONS

(1) Use of CO_2 and O_2 as probe molecules revealed that the hydroxy groups interacting with CO_2 are nonuniform with respect to activity in exchange with phosphate and molybdate anions.

(2) The addition of P into Al–Mo and Al–Ni–Mo catalysts increases the dispersion of Mo-containing particles.

(3) The extent of the dispersion effect in the above catalysts is different owing to the different compositions and sequences of introducing the components. Evidently, the introduction of P into the already formed Al–Ni–Mo catalyst appreciably affects its structure and produces a stronger dispersing effect.

REFERENCES

1. Bouwens, S.M.A., Vissers, J.P.R., De Beer, V.H.J., and Prins, R., *J. Catal.*, 1988, vol. 112, no. 2, pp. 401–410.
2. Lewis, J.M. and Kydd, R.A., *J. Catal.*, 1992, vol. 136, no. 2, pp. 478–486.
3. Mangnus, P.J., Van Veen, J.A.R., Eijsbouts, S., *et al.*, *Appl. Catal.*, 1990, vol. 61, no. 1, pp. 99–122.
4. Ramires, J., *Appl. Catal.*, 1992, vol. 83, no. 2, pp. 251–261.
5. Atanasova, P., Uchytil, J., Kraus, M., and Halachev, T., *Appl. Catal.*, 1990, vol. 65, no. 1, pp. 53–68.
6. Morales, A. and Ramires de Agudelo, M.M., *Appl. Catal.*, 1986, vol. 23, no. 1, pp. 23–34.
7. Zmeirczak, W., Muralidhar, G., and Massoth, F.F., *J. Catal.*, 1982, vol. 77, no.2, pp. 432–439.
8. Zhdanova, K.P., Rychagova, O.A., Ishchenko, E.D., *et al.*, *Zh. Fiz. Khim.*, 1992, vol. 66, no. 11, pp. 2939–2946.
9. McMillan, M., Brinen, J.S., and Haller, G.L., *J. Catal.*, 1986, vol. 97, no. 1, pp. 243–247.
10. Busca, G., Ramis, G., Lorenzelli, V., *et al.*, *Langmuir*, 1989, vol. 5, no. 4, pp. 911–916.
11. Lewis, J.M. and Kydd, R.A., *J. Catal.*, 1991, vol. 132, no. 2, pp. 465–471.
12. Shmachkova, V.P., Kotsarenko, N.S., and Mastikhin, V.M., *Kinet. Katal.*, 1994, vol. 35, no. 2, pp. 314–319.
13. Kraus, H. and Prins, R., *J. Catal.*, 1996, vol. 164, no. 2, pp. 260–267.
14. Iannibello, A., Marengo, S., and Trifiro, F., *Chim. Ind.*, 1975, vol. 57, no. 10, pp. 676–677.
15. Lur'e, M.A., Kurets, I.Z., Krasnopol'skaya, S.M., *et al.*, *Kinet. Katal.*, 1994, vol. 35, no. 3, pp. 444–449.
16. Souza, G.L.M., *Catal. Today*, 1989, vol. 5, no. 4, pp. 451–461.
17. Gishti, R., Iannibello, A., Marengo, S., *et al.*, *Appl. Catal.*, 1984, vol. 12, no. 3, pp. 382–393.
18. Rushala, F., Shiryaev, P.A., Kutyrev, N.Yu., *et al.*, *Kinet. Katal.*, 1981, vol. 22, no. 5, pp. 1307–1312.
19. Somogyvari, A.F., Oballa, M.C., and Herrera, P.S., in *Proc. 10th Int. Congr. on Catalysis*, Budapest, 1993, part C, pp. 1903–1906.
20. Ramires de Agudelo, M.M. and Morales, A., in *Proc. 9th Int. Congr. on Catalysis*, Ottawa, 1988, vol. 1, pp. 42–49.
21. Atanasova, P. and Halachev, N., *Appl. Catal.*, 1989, vol. 48, no. 2, pp. 295–306.

Russian Journal of Applied Chemistry, Vol. 76, No. 7, 2003, pp. 1083–1088. Translated from Zhurnal Prikladnoi Khimii, Vol. 76, No. 7, 2003, pp. 1116–1121.

CATALYSIS

Transformations of Straight-Run Naphthas on Indium-Modified Pentasils

V. I. Erofeev and L. V. Adyaeva

Department of Scientific and Technical Development, Tomsk Petrochemical Plant, Joint-Stock Company, Tomsk, Russia
Institute of Petroleum Chemistry, Siberian Division, Russian Academy of Sciences, Tomsk, Russia

Received January 14, 2003

Abstract—The influence exerted by the procedure of introducing indium into high-silica zeolite of the Pentasil type on its acid properties and catalytic activity in transformation of straight-run naphthas into lower olefins and aromatic hydrocarbons was studied.

Catalytic pyrolysis is one of the most promising procedures for commercial production of lower olefins. Zeolite-containing catalysts based on high-silica zeolites (HSZs) of the Pentasil type are widely used in oil refining and petroleum chemistry. It is known [1–3] that the activity and selectivity of HSZs of the Pentasil type in transformations of various classes of hydrocarbons are determined not only by acid properties, but also by unique molecular-sieve properties of these zeolites. It was shown previously [4–8] that the acid properties of any zeolite-containing catalyst correlate with its catalytic activity in transformation of hydrocarbon raw materials into definite target products. One of the possible ways of controlling the acid and catalytic properties, along with appropriate pretreatment, is introduction of modifying elements into the zeolite matrix.

In this work we studied how the procedure of introducing indium affects the acid properties of HSZs of the Pentasil type in transformation of straight-run naphthas into lower olefins and arenes.

EXPERIMENTAL

Experiments were performed with straight-run naphtha (SRN) from the Surgut Gas-Processing Plant. This raw material belongs to the paraffin-naphthenic type (onset of boiling at 131°C, density at 20°C 0.684 $cm^3\ g^{-1}$). The hydrocarbon composition of the SRN is as follows (wt %): *n*-paraffins 29.7, branched paraffins 27.2, and naphthenic hydrocarbons 32.8.

High-silica zeollites of the ZSM-5 type with the silicate ratio $SiO_2/(Al_2O_3 + M_2O_3) = 30$ were prepared by hydrothermal synthesis from alkaline aluminosilica gels by the procedure described in [9]. The substances were identified by IR spectroscopy and X-ray phase analysis (Mo anode, Ni filter).

The modifier, In(III) (1 wt % in terms of the metal), was introduced by the following procedures: impregnation of the zeolite matrix with an indium nitrate solution (In-HSZ-1), ion exchange of H-HSZ with In(III) (In-HSZ-2), mechanical mixing of ultradispersed indium powder with H-HSZ followed by the heat treatment (In-HSZ-3), mechanical mixing of indium nitrate with H-HSZ followed by heat treatment (In-HSZ-4), and hydrothermal crystallization of a mixture containing aluminum and indium nitrates. By the latter method, we prepared Pentasils with the framework Al atoms isomorphously substituted by In(III) to 10 (IAS-10 sample) and 20 wt % (IAS-20 sample).

The acid properties of HSZ samples modified with In(III) were studied by temperature-programmed desorption of ammonia. This method furnishes information about the content and strength distribution of acid centers [10].

The catalytic properties of In(III)-modified HSZs in transformation of straight-run naphthas were studied in a flow-through installation with a fixed catalyst bed (3 cm^3) at atmospheric pressure in the temperature range 500–700°C; the feed space velocity was 3 h^{-1}. The hydrocarbon composition of the starting SRN and reaction products was determined by gas chromatography. The error in gas-chromatographic determination of the yield of SRN transformation products and of the content of acid centers in the catalysts was ±2.5%.

All the HSZ samples synthesized, according to IR

1070-4272/03/7607-1083$25.00

Table 1. Acid properties of indium-modified zeolite-containing catalysts

Catalyst	T_{max}, °C		Content of acid centers, μmol g^{-1}		
	form I	form II	form I	form II	total
H-HSZ	203	380	615	343	958
In-HSZ-1	184	330	563	331	894
In-HSZ-2	203	360	605	221	826
In-HSZ-3	194	330	477	258	735
In-HSZ-4	198	330	469	269	738
IAS-10	194	357	524	302	825
IAS-20	194	Shoulder up to 350	–	–	742

spectra and X-ray diffraction patterns, have 90–95% degree of crystallinity and belong to the ZSM-5 type.

The spectrum of temperature-programmed ammonia desorption from the initial H-HSZ (Fig. 1a) has

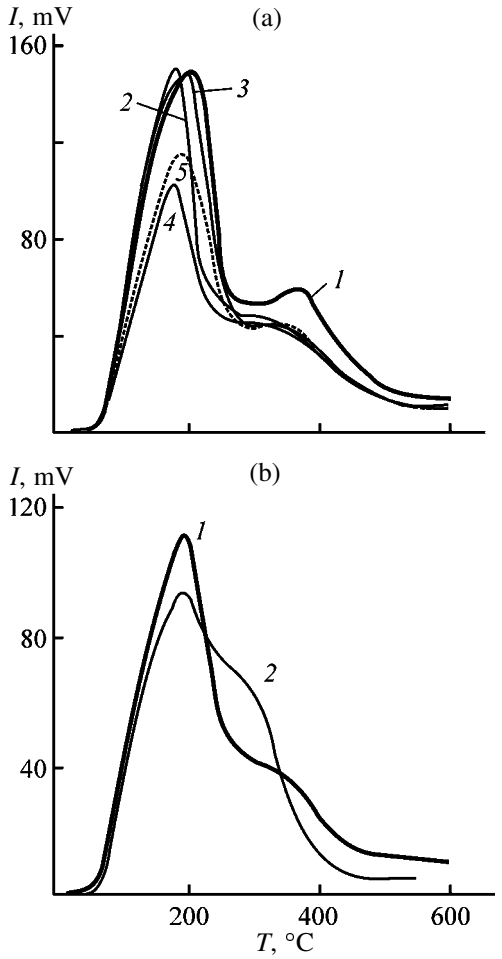

Fig. 1. Spectra of temperature-programmed desorption of ammonia from the surface of zeolites: (*I*) intensity and (*T*) temperature. Sample: (a) (*1*) H-HSZ, (*2*) In-HSZ-1, (*3*) In-HSZ-2, (*4*) I-HSZ-3, and (*5*) I-HSZ-4; (b) (*1*) IAS-10 and (*2*) IAS-20.

two peaks. The low-temperature peak in the range 110–220°C (T_{max} = 203°C) is due to ammonia desorption from weak Lewis acid centers, and the high-temperature peak (310–600°C, T_{max} = 380°C) characterizes the ammonia desorption from strong Brønsted and Lewis acid centers [11, 12]. The concentrations of the weak Lewis acid and strong acid centers in H-HSZ, determined from the amount of the desorbed ammonia, are 530 and 420 μmol g^{-1}, respectively (Table 1).

Modification of H-HSZ with In^{3+} appreciably affects the strength and concentration of acid centers in zeolite-containing catalysts. For example, modification of H-HSZ with 1 wt % In(III) by impregnation of the zeolite matrix with an indium nitrate solution (In-HSZ-1) decreases the strength of both weak (low-temperature) and strong (high-temperature) acid centers. The T_{max} values for the ammonia desorption peaks are shifted to lower temperatures: from 203 to 184 and from 380 to 330°C (Table 1). Modification of H-HSZ with 1 wt % In(III) by impregnation decreases also the concentrations of both weak (from 615 to 563 μmol g^{-1}) and strong (from 343 to 331 μmol g^{-1}) acid centers. Apparently, the In^{3+} ions not only appreciably block the strong acid centers but are also localized in channels and on the external surface of zeolite crystals, forming Lewis acid centers.

Introduction of In^{3+} into H-HSZ by ion exchange (In-HSZ-2) considerably decreases the concentration of strong acid centers (from 343 to 221 μmol g^{-1}), whereas the concentration of the weak acid centers remains virtually unchanged (Table 1). In this catalyst, the concentration ratio of the weak and strong acid centers is the highest, 2.7; in the other catalysts, it varies within a narrow range, 1.7–1.8.

Modification of H-HSZ by mechanical mixing with ultradispersed indium (In-HSZ-3) decreases the strengths and concentrations of both weak and strong

acid centers. For the high-temperature form of ammonia desorption, T_{max} decreases to 330°C. Similar changes in the acid properties are observed upon modification of H-HSZ by mechanical mixing with indium nitrate, followed by a heat treatment. Such a trend in variation of the acid properties of In(III)-modified HSZ are attributable to the fact that indium cations, being arranged on the surface of zeolite crystals, block a part of the active centers, so that the amount of acid centers accessible for the adsorbate molecules decreases.

In modification by ion exchange, impregnation, or dry mixing, the zeolite behaves as a salt of a poly acid in which the macroanion remains unchanged and only the cations compensating the negative charge of the framework are substituted. The anionic part of the Si–O framework can be controlled by adding multicharged M^{n+} cations, in paticular, In^{3+}, into the starting silica gel before its hydrothermal crystallization.

On the IAS-10 catalyst, ammonia is adsorbed in two forms. Form I (low-temperature desorption, T_{max} 194°C) corresponds to weak acid centers and form II (T_{max} 357°C), to strong acid centers (Fig. 1b). Incorporation of the In(III) ions in the stage of the hydrothermal synthesis decreases the total acidity of the catalyst to 825 μmol g^{-1} (IAS-10), with the strength of the weak acid centers remaining virtually unchanged and that of strong acid centers decreasing, as judged from the shift of T_{max} from 380 to 357°C. This is due to the fact that the In(III) ions are weaker acids than the aluminum cations.

As the In(III) concentration in HSZ is increased (IAS-20), the temperature-programmed desorption spectrum changes: There is a single maximum with a high-temperature shoulder, and different types of acid centers are not clearly resolved. The large peak width suggests a fairly broad spectrum of the acid centers, i.e., formation of energetically nonuniform centers. This may be due to the fact that the state of the multicharged M^{n+} ions in the crystallization products may be different, depending both on the composition of the starting mixture and on the nature of M^{n+}, which will affect the acidity of the catalyst and give rise to nonuniform distribution of acid centers with respect to the strength and concentration [3, 13].

Thus, the strength and concentration of acid centers and their distribution in the catalyst are largely influenced by the zeolite modification procedure, state of indium cations, and their arrangement in the zeolite.

The results of experiments on transformation of straight-run naphtha on HSZ samples modified with In(III) by various procedures are listed in Table 2.

High-silica zeolites (H-HSZs) of the ZSM-5 type show high activity in transformation of straight-run naphthas. For example, on the initial H-HSZ sample, the yield of lower (C_2–C_4) olefins increases from 8.1 to 23.6%, and the yield of aromatic hydrocarbons, from 22.3 to 39.9% as the reaction temperature is increased from 500 to 700°C.

Introduction of In^{3+} ions by impregnation of the zeolite matrix (H-HSZ) with an indium nitrate solution (In-HSZ-1) results in a substantial growth of the yield of C_2–C_4 olefins as compared to H-HSZ. The yield of lower olefins on the initial H-HSZ at 650 and 700°C is 16.0 and 23.6%, and on In-HSZ-1, 32.5 and 41.5%, respectively (Table 2). At relatively low temperatures (550–600°C), the yield of aromatic hydrocarbons on In-HSZ-1 is considerably higher (50.7%) than on H-HSZ (22–33%).

Introduction of In^{3+} ions by ion exchange (In-HSZ-2) results in a further increase in the yield of lower olefins as compared to In-HSZ-1. The maximal yield of C_2–C_4 olefins is 47.6% at 700°C. Such a trend may be due to the fact that the ion-exchange procedure ensures more complete substitution of protons in the bridging OH groups of the zeolite by the In^{3+} ions, as suggested by the temperature-programmed desorption spectra.

Modification of HSZ by mechanical mixing of ultradispersed In powder with H-HSZ followed by heat treatment (In-HSZ-3) results in increased conversion of SRN. As the reaction temperature is increased from 550 to 700°C, the yield of lower olefins on the In-HSZ-3 catalyst increases from 4.7 to 33.6 wt %. It should be noted that, at 600–650°C, the yield of aromatic hydrocarbons on this catalyst is maximal (60–61%), especially that of benzene (28–32%) and toluene (24–26%).

Mechanical mixing of indium nitrate with H-HSZ followed by the heat treatment (In-HSZ-4) increases the activity of the catalyst: The yield of aromatic hydrocarbons at 550°C becomes as high as 56.2%, and at higher temperatures the yield of lower olefins increases from 11.7 to 42.5%.

Thus, modification of H-HSZ with indium by dry mixing enhances the activity of the catalyst and increases the selectivity of formation of aromatic hydrocarbons, which may be due to formation on the catalyst surface of additional Lewis acid centers capable of abstracting the hydride ion from a saturated hydrocarbon molecule, and also to fairly high concentration

Table 2. Influence of temperature on the composition of products formed by transformation of straight-run naphtha on indium-modified HSZ

T, °C	Content of indicated products of straight-run naphtha transformation, wt %											
	C_{2+} alkanes	ethylene	propylene	butylene	C_{4-} alkenes	total of C_{4-}	C_{5+} *n*-alkanes	C_{5+} isoalkanes	benzene	toluene	*o*-, *m*-, *p*-xylenes	arenes
H-HSZ												
550	17.1	1.5	4.2	2.4	8.1	66.3	3.7	4.8	4.6	8.5	7.4	22.3
600	23.2	3.6	5.7	2.6	11.9	60.1	1.7	1.5	8.1	13.9	9.3	33.6
650	24.5	6.8	6.7	2.5	16.0	52.1	1.4	4.1	10.9	15.7	9.8	38.7
700	11.2	11.4	9.4	2.8	23.6	54.5	1.4	2.5	14.5	16.9	7.2	39.9
In-HSZ-1												
550	22.6	10.1	5.1	0.5	15.7	44.2	0.9	0.9	22.9	20.8	7.0	50.7
600	18.4	13.4	6.2	0.6	20.3	42.8	1.1	1.1	24.0	20.5	6.3	50.7
650	14.4	16.1	13.1	3.3	32.5	52.1	3.2	1.9	18.1	16.0	5.2	39.2
700	13.9	18.1	15.6	7.8	41.5	61.7	4.0	2.4	13.1	11.8	3.6	28.6
In-HSZ-2												
550	27.2	12.2	8.3	1.2	21.8	64.3	1.5	1.8	12.6	16.7	1.3	30.9
600	25.4	14.8	9.9	1.3	26.0	59.6	0.9	1.5	15.9	13.6	6.1	35.8
650	16.8	19.1	15.1	2.5	36.7	70.1	1.4	1.1	11.1	9.7	5.1	26.1
700	16.0	21.1	21.9	4.7	47.6	70.0	1.9	1.8	9.0	9.2	4.7	24.9
In-HSZ-3												
550	23.7	3.3	1.4	–	4.7	38.0	1.5	3.0	20.2	24.4	8.9	53.5
600	23.1	4.8	1.7	–	6.6	32.6	1.0	1.5	27.8	25.6	6.9	60.4
650	23.8	6.4	1.9	–	8.3	33.8	0.8	0.8	31.8	23.9	5.5	61.3
700	21.8	16.7	14.4	2.6	33.6	58.9	0.6	0.3	20.7	14.8	3.7	39.3
In-HSZ-4												
550	24.6	8.7	2.8	0.2	11.7	39.3	0.7	0.6	25.3	23.6	7.1	56.2
600	21.1	13.4	4.9	0.3	18.7	43.4	0.8	0.8	24.5	20.9	5.9	51.5
650	16.6	19.1	11.8	3.8	34.7	58.6	2.3	0.9	15.8	14.3	4.9	35.6
700	16.4	21.9	15.9	4.7	42.5	65.6	2.2	0.8	13.5	11.6	3.6	28.9
IAS-10												
550	20.8	8.7	7.2	1.7	17.6	51.5	1.8	2.4	13.6	19.7	9.6	42.9
600	19.5	13.2	9.6	2.5	25.3	54.4	1.7	2.8	14.7	17.7	7.5	39.9
650	13.6	16.9	16.4	5.3	36.6	61.3	3.5	3.4	11.3	13.3	5.9	30.6
700	14.1	15.7	16.4	9.4	41.6	61.7	6.9	4.7	6.7	7.4	3.4	17.6
IAS-20												
550	1.2	1.3	1.7	0.7	3.7	5.8	20.6	28.1	2.1	2.5	2.2	6.8
600	2.2	2.4	2.8	1.3	6.5	10.1	19.7	26.9	2.0	2.4	2.2	6.6
650	4.8	5.6	7.4	5.4	18.4	26.3	17.6	19.4	2.8	2.6	2.1	7.6
700	7.1	7.9	9.9	8.6	26.4	37.9	13.6	17.5	3.9	2.7	1.8	8.4

of Brønsted acid centers on which the radical cation can be adsorbed to form aromatic hydrocarbons.

On indioaluminosilicate IAS-10, as the reaction temperature is increased from 550 to 700°C, the yield of C_2–C_4 olefins from SRN increases from 17.6 to 41.6%, whereas the yield of aromatic hydrocarbons decreases from 42.9 to 17.6% (Table 2). Apparently, isomorphous substitution of Al(III) by In(III) in the zeolite gives rise to Lewis acid centers capable of abstracting hydride ions from the initial hydrocarbons of SRN to give radical cations. Their subsequent

transformations occur both on Brønsted acid centers to give aromatic hydrocarbons or in the bulk to give lower olefins. The radical centers Si–O*, Si–O*–Al, and Si–O*–In, as well as the In^{3+} ions occluded on the catalyst surface can act as Lewis acid centers [14].

As the degree of aluminum substitution by indium ions is further increased to 20 wt % (IAS-20 sample), the activity of the catalyst in SRN transformation drastically decreases. As the reaction temperature is increased from 550 to 700°C, the yield of lower olefins from SRN increases from 3.7 to only 26.4%, with the yield of aromatic hydrocarbons being as low as 7–8%. This may be due to fixation of the In^{3+} ions in the framework positions isomorphous with Si^{4+}; according to [13], only a certain part of In^{3+} is fixed in these positions. When the In^{3+} content is increased further, the In^{3+} ions become occluded (in the form of salts and oxides) on the crystal surface and inside the channels and become localized in the vicinity of groups containing oxygen ions with the noncompensated charge (in cationic positions), blocking the Brønsted acid centers.

Also, we studied by DTA the coking of the catalyst surface in the course of SRN transformation. On all the "coked" catalyst samples, a small endothermic effect at 110°C is due to removal of physically adsorbed water. The shift of the peak of the coke deposit combustion in the DTA curve of In(III)-modified HSZ toward higher temperatures (520–740°C) suggests formation of more "condensed" coke on the catalyst surface in the course of SRN transformation (Table 3).

The DTG and DTA curves show that the coke deposits are removed from the zeolite-containing catalyst in the range of burn-out of coke formed from polycondensed aromatic hydrocarbons [15]. In the DTA curves of coked In-HSZ-3 and In-HSZ-4 samples, a second strong maximum appears in the range 520–740°C, suggesting formation of a broader spectrum of coke deposits. The content of coke deposits on these samples is the highest, which is well consistent with their higher activity (maximal yield of aromatic hydrocarbons in transformation of straight-run naphtha).

On the IAS-20 sample, the coke deposits burn out at low temperatures (DTA peak at 420°C), which suggests their nonaromatic nature. This may be due to the absence of strong acid centers in this sample, which results in a low yield of aromatic hydrocarbons from straight-run naphthas.

It is known [16] that the coking in the course of transformation of hydrocarbons on zeolite-containing catalysts follows a consecutive scheme involving polymerization and condensation of alkenes, and also condensation and dehydrocondensation of aromatic hydrocarbons. The consecutive scheme of formation of coke residues from alkenes is as follows [17]: olefins–cycloolefins–benzene–alkylbenzene–condensed polyaromatic hydrocarbons–coke.

Table 3. Differential thermal analysis of coke deposits on indium-modified zeolite-containing catalysts

Catalyst	T of thermal effect, °C	T_{max}, °C	Coke content, %
H-HSZ	500–580	560	7.2
In-HSZ-1	520–710	700	11.0
In-HSZ-2	520–700	680	9.8
In-HSZ-3	520–740	660, 700	19.9
In-HSZ-4	520–710	600, 670	17.9
IAS-10	520–700	670	9.6
IAS-20	300–500	420	4.6

However, the coking may involve, along with polycondensation of aromatic hydrocarbons, also radical polymerization, i.e., a contact of a hydrocarbon with an active center of the catalyst may result in cleavage of aromatic hydrocarbons across the C–C bonds and nonaromatic hydrocarbons across the C–H bonds. The hydrogen atoms generated in the process can react with the carbonaceous deposits on the catalyst surface to give low-molecular-weight hydrocarbon radicals, which behave as active centers effecting propagation of the polymeric chain.

Thus, on zeolite-containing catalysts, the coking can occur by several mechanisms depending on the composition of the hydrocarbon raw material and on the type, strength, and concentration of active centers on the catalyst surface. By varying the procedure for introducing the modifier, in particular, In(III), it is possible to control the ratio of strong and weak acid centers and hence the direction of hydrocarbon transformation toward predominant formation of lower C_2–C_4 olefins or aromatic hydrocarbons. For selective formation of lower olefins, the best procedure for introducing In^{3+} into the zeolite matrix is incorporation of In(III) into the zeolite structure in hydrothermal synthesis, whereas for selective formation of aromatic hydrocarbons from straight-run naphtha it is advisable to introduce In by dry mixing of the zeolite-containing catalyst with an indium salt.

CONCLUSION

A correlation was revealed between the acid properties of In(III)-modified Pentasil-type zeolitic catalysts and their catalytic activity in transformation of straight-run naphtha. For selective production of lower olefins from straight-run naphtha, it is advisable to add In(III) in the stage of the hydrothermal synthesis, whereas for selective production of aromatic hydrocarbons dry mixing of an indium salt with the zeolitic catalyst is preferable.

REFERENCES

1. Bondarenko, T.N. and Tyurin, A.A., *Dokl. Akad. Nauk SSSR*, 1991, vol. 317, no. 2, pp. 378–381.
2. Minachev, Kh.M. and Dergachev, A.A., *Izv. Akad. Nauk SSSR, Ser. Khim.*, 1993, no. 6, pp. 1018–1027.
3. Vosmerikov, A.V., Korobitsyna, L.L., and Arbuzova, N.V., *Kinet. Katal.*, 2002, vol. 43, no. 2, pp. 299–304.
4. Erofeev, V.I., Adyaeva, L.V., and Ryabov, Yu.V., *Zh. Prikl. Khim.*, 2001, vol. 74, no. 2, pp. 231–234.
5. Erofeev, V.I., Adyaeva, L.V., and Kukharenko, O.A., *Zh. Prikl. Khim.*, 2001, vol. 74, no. 11, pp. 1791–1794.
6. Vosmerikov, A.V. and Erofeev, V.I., *Zh. Prikl. Khim.*, 1994, vol. 67, pp. 1152–1156.
7. Trofimova, A.S., Koval, L.M., and Erofeev, V.I., *Russ. J. Phys. Chem.*, 2000, vol. 74, suppl. 3, pp. 537–540.
8. Zainuddin, Z., Guersoni, F.N., and Abbot, J, *J. Catal.*, 1993, vol. 140, no. 1, pp. 150–167.
9. RF Patent 1 527 154.
10. Vosmerikov, A.V. and Erofeev, V.I., *Zh. Fiz. Khim.*, 1995, vol. 69, no. 5, pp. 787–790.
11. Topsoe, N.-Y. and Pedersen, K., *J. Catal.*, 1981, vol. 70, no. 1, pp. 41–52.
12. Hydalgo, C.V., Itoh, H., Hattory, T., *et al.*, *J. Catal.*, 1984, vol. 85, no. 2, pp. 362–369.
13. Ione, K.G. and Vostrikova, L.A., *Usp. Khim.*, 1987, vol. 56, no. 3, pp. 393–426.
14. Zhlobenko, V.L., Kustov, L.M., and Kazanskii, V.B., Abstracts of Papers, *Primenenie tseolitov v katalize: IV Vsesoyuznaya konferentsiya* (Use of Zeolites in Catalysis: IV All-Union Conf.), Moscow, 1989, pp. 33–35.
15. Slinkin, A.A., Bragina, G.O., Nissenbaum, V.D., and Kucherov, A.V., *Kinet. Katal.*, 1995, vol. 3, pp. 440–449.
16. Dmitriev, V.M., *Khim. Tekhnol.*, 1991, no. 6, pp. 3–25.
17. Buyanov, R.A., *Zakoksovyvanie katalizatorov* (Coking of Catalysts), Novosibirsk: Nauka, 1983.

Russian Journal of Applied Chemistry, Vol. 76, No. 7, 2003, pp. 1089–1093. Translated from Zhurnal Prikladnoi Khimii, Vol. 76, No. 7, 2003, pp. 1122–1126.

ENVIRONMENTAL PROBLEMS OF CHEMISTRY AND TECHNOLOGY

Water Pretreatment To Remove Organic Impurities and Desalination with Ion Exchangers

G. V. Slavinskaya

Voronezh State University, Voronezh, Russia

Received February 10, 2003

Abstract—Treatment of Neva water to remove organic and mineral impurities on an ion-exchange industrial installation with the resins produced in Russia was studied.

Many of the modern productions use a high-resistivity desalinated water prepared by treatment of natural water [1–5]. The most urgent problem in water treatment is removal of organic contaminants. The reason is that natural waters contain a wide variety of both organic and mineral impurities in diverse combinations and ratios. Therefore, the technique suited for preparation of deionized water with the minimal content of organic pollutants must be adapted to features of water to be treated [1].

The aim of this work was to analyze the efficiency of removal of organic pollutants from Neva water in the course of its pretreatment and ion-exchange desalination on an industrial ion-exchange installation.

EXPERIMENTAL

Neva water belongs to low-mineralized natural waters. It has a yellowish color caused by the significant amounts of humic (HA) and fulvic (FA) acids [1–3]. As a rule, the plant facilities use municipal tap water. This water contains variable amounts of humic substances and other undesirable impurities. Karmazinov and Gumen [6] believe that this is due to insufficient efficiency and overload of the head facilities installation and periodical deterioration of the water quality in the Neva–Ladoga water system.

Data on seasonal variations of both the permanganate oxidizability (PO) (hereinafter referred to as oxidizability) of Neva water and the content of several organic compounds averaged throughout three-year period are listed in Table 1. This table shows that, among organic impurities, fulvic acids prevail.

It is known that the most efficient procedure for water treatment [1, 3] is distillation. The laboratory experiments showed (Table 2) that distillation of Neva water removes about 95% of humic acids. However, this power-consuming technique cannot be used for a large-scale industrial water treatment. As a rule, before water desalination it is pretreated by reagent coagulation, sorption, or combination of these techniques [1]. In preparation of desalinated water for semiconductor production, aluminum sulfate is used as the most efficient coagulant [1, 7]. Upon such a treatment, the aluminum content in the purified water does not exceed 3×10^{-7}%.

Table 2 shows that HA is removed by coagulation to a greater extent than FA. Upon coagulation, the content of oxidizable compounds decreases by 40–50% only, and the residual water oxidizability exceeds 5 mg O/l. Thus, Neva water pretreatment by coagulation only does not decrease its oxidizability to 2.5 mg O/l, which is required for preparation of high-resistivity water by ion-exchange methods.

In order to increase the degree of removal of organic impurities, the tap water treated by coagulation was additionally clarified in a mechanical filter and then filtered through weakly basic IA-1 (IA-2, IA-3) polycondensation anion exchangers derived from *m*-phenylenediamine [7]. Since natural waters contain a wide variety of impurities, their ion-exchange decontamination should be performed with resins containing different functional groups [8]. It was found that anion exchangers of IA type in a salt form exhibit the maximal sorption capacity for humic substances and their sorption increases with increasing temperature and decreasing pH [1, 7]. As seen from Table 3, IA-1 resin exhibits high sorption capacity for all the organic substances present in water of different rivers: Neva (Leningrad oblast), Nevezhis and Panevezhis (Lithuania), and Usman (Voronezh oblast). These data show

1070-4272/03/7607-1089$25.00

Table 1. Content of organic substances in Neva water (St. Petersburg water supply)

Water characteristic	Sampling time		
	winter	summer	autumn
Color index, Cr–Co scale, degree	20	30	25
Permanganate oxidizability (±0.2), mg O l^{-1}	9.6	7.5	6.2
Humic acids (±0.02), mg l^{-1}	0.49	0.54	0.34
Fulvic acids (±0.05), mg l^{-1}	10.00	13.20	9.90
Amino acids (±2), μg N l^{-1}	11	6	8
Protein-like substances (±5), μg N l^{-1}	40	125	40
Sugars* (±20), μg g^{-1}	780	260	570
Esters (±10), μg-equiv l^{-1}	75	100	100
Carboxylic acids (±3), μg-equiv l^{-1}	20	22	21
Total hardness (±0.03), mg-equiv l^{-1}	0.5	0.5	0.5
HCO_3^- (±0.03), mg-equiv l^{-1}	0.5	0.5	0.5
Silicic acids (±0.01), mg l^{-1}	3.0	2.8	3.0
Total salt content (±0.03), mg-equiv l^{-1}	1.0	1.0	1.0

* Recalculated to glucose.

Table 2. Effect of Neva water treatment with distillation and coagulation on its characteristics

Water characteristic	Purification technique			
	distillation		coagulation	
	before	after	before	after
Oxidizability (±0.2), mg O l^{-1}	7.8	0.4	9.7	5.7
Impurities:				
humic acids (±0.02), mg l^{-1}	0.38	0.04	0.67	0.27
fulvic acids (±0.05), mg l^{-1}	13.20	0.19	13.60	8.05
amino acids (±2), μg N l^{-1}	16	7	–	–
sugars (±20), μg g^{-1}	266	56	–	–
esters (±10), μg-equiv l^{-1}	100	100	85	85
carboxylic acids (±3), μg-equiv l^{-1}	22	<3	80	72

that all the organic substances except esters are efficiently sorbed on IA resins. Taking into account that esters are not removed from river water by distillation, coagulation, and filtration through anion-exchange resins, a new technique suited for solution of this problem is required.

To evaluate the contribution of coagulation, sorption, and desalination steps to the total purification of Neva water to remove organic impurities, their concentrations at the inlet and outlet of the corresponding units of an industrial ion-exchange installation with the performance of 6.5 $m^3 h^{-1}$ were monitored during 20 labor shifts (160 h). These experiments were carried out in the spring flood.

In water treatment, the following sequential procedures were performed: heating of the initial water to 20–25°C, coagulation treatment with aluminum sulfate (0.5 mg-equiv l^{-1}), clarification with a mechanical filter packed with quartz sand and anthracite, filtration through strongly acidic KU-2 cation exchanger in the H form, decarbonation, filtration through an adsorber packed with IA-1 anion exchanger in the Cl form, filtration through AN-31 weakly basic anion exchanger in the OH form, and filtration through a combined sorbent (CS) consisting of KU-2-8 strongly acidic cation exchanger in the H form and AV-17-8 strongly basic anion exchanger in the OH form at their volume ratio of 1 : 1.4 and the filtration velocity of 6–7 m h^{-1}.

Under such conditions, one volume of IA-1 resin purifies up to 900–1000 volumes of Neva water. The variations of water characteristics at the inlet of the

Table 3. Effect of river water filtration through porous anion exchanger on the content of organic impurities

Water characteristic	River					
	Neva		Usman		Nevezhis	
	initial	filtrate	initial	filtrate	initial	filtrate
Oxidizability (±0.2), mg O l^{-1}	6.2	1.7	7.0	2.6	6.2	1.9
Impurities:						
humic acids (±0.02), mg l^{-1}	0.34	0.12	0.36	0.05	0.10	<0.02
fulvic acids (±0.05), mg l^{-1}	9.85	1.20	3.80	1.05	2.50	0.46
sugars (±20), μg l^{-1}	–	–	630	360	–	–
amino acids (±2), μg N l^{-1}	8	4	39	29	–	–
carboxylic acids (±3), μg-equiv l^{-1}	21	9	23	19	–	–
esters (±10), μg-equiv l^{-1}	100	100	90	90	120	120

Table 4. Effect of Neva water treatment on its characteristics

Water characteristic	Initial water	Treatment step			
		coagulation	sorption	desalination	
				AN-31	CS
Oxidizability (±0.2), mg O l^{-1}	9.7	5.6	2.1	1.1	0.8
Impurities::					
humic acids (±0.02), mg l^{-1}	0.68	0.30	0.06	0.04	<0.02
fulvic acids (±0.05), mg l^{-1}	10.50	7.90	1.90	1.00	0.40

desalinating device were as follows: oxidizability from 8.6 to 11.2 mg O l^{-1}, HA content from 0.30 to 1.50, and FA content from 8.10 to 11.5 mg l^{-1}. Taking into account that these variations are appreciable, we determined not only the mean-shift water composition (Table 4) but also water composition in separate treatment stages (Figs. 1a–1c).

Table 4 shows that the degree of HA removal from Neva water by coagulation (60%) considerably exceeds that of FA removal (25%). At the same time,

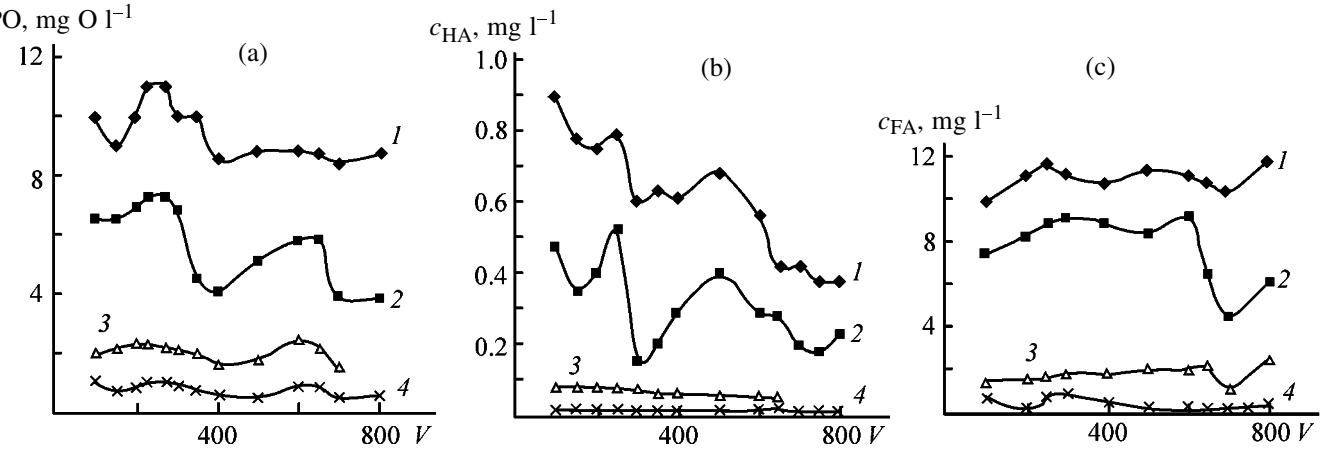

Fig. 1. Variation of the (a) permanganate oxidizability, (b) HA content c_{HA}, and (c) FA content c_{FA} (*1*) in the initial Neva water, (*2*) after coagulation treatment, (*3*) after filtration through IA-1 porous anion exchanger, and (*4*) after filtration through the combined sorbent throughout the process period. (*V*) Volume of purified water (number of IA-1 volumes); the same for Fig. 2.

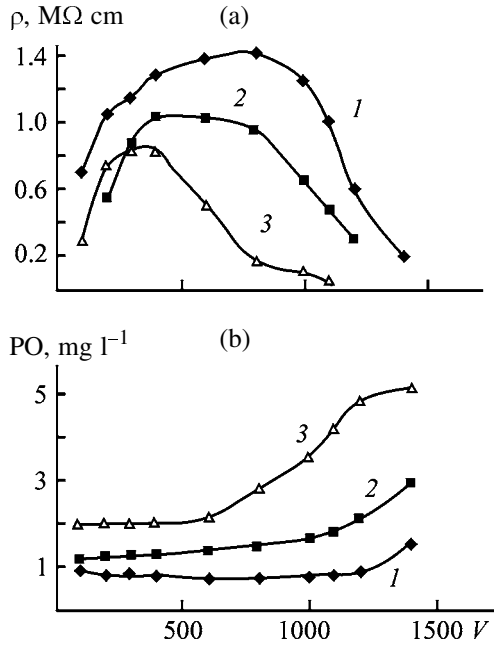

Fig. 2. (a) Specific electrical resistivity ρ and (b) water oxidizability PO as functions of the water volume filtered through the ion exchanger. Figures at curves are numbers of the filtration cycles.

the water oxidizability reflecting the total content of organics in water decreases by 40% only. Upon filtration through the porous anion exchanger, the HA and FA content decreases, on the average, by 90% and 80%, respectively. In the subsequent filtration through AN-31 and CS anion exchangers, a additional amount of organic impurities (13–15%) is removed from water. We found that, after completion of water treatment, humic acids (3–4%) and the organic matter oxidizable with $KMnO_4$ (about 10%) remain in water.

Figures 1a–1c show variations in the content of organic substances in Neva water (single samples) at different stages of its treatment (in the initial water, after coagulation treatment, and after filtration through IA-1 and CS ion exchanger). It is seen that, irrespective of the treatment procedure, the variations in the oxidizability (Fig. 1a) have similar wave-like shape. At the same time, the humic acid content remains virtually constant (Fig. 1b), and the fulvic acid breakthrough gradually increases (Fig. 1c). These facts show that Neva water contains some amount of easily oxidizable nonhumic impurities which are not removed in the course of water treatment. These impurities do not affect the electrical resistivity of deionized water ρ, i.e. they are nonelectrolytes.

We found that, during a three-year process period, the porous anion exchanger retains high sorption power and levels out the variations in the HA and FA content in the clarified water (Figs. 1b, 1c). These figures show also that the FA breakthrough exceeds that of HA. However, we failed to determine a time when IA-1 exhausts its sorption capacity for HA and FA by measuring the filtrate oxidizability, because the oxidizability characterizes the total content of easily oxidizable impurities and is insensitive to a breakthrough of difficultly oxidizable HA and FA.

This is confirmed by Fig. 2 in which the specific electrical resistivity and oxidizability of the filtrate are plotted vs. the water volume sequentially passed through IA-1 anion exchanger and desalinating filters containing KU-2-8 cation exchanger and AV-17-8 anion exchanger (total volume of the ion exchangers 1000 cm^3, filtration velocity through the adsorber and ion exchangers 7 and 20 m h^{-1}, respectively, the performance of the ion-exchange installation 100 l h^{-1}).

Figure 2 shows that a breakthrough of the organic electrolytes (HA and FA) is detected by the electrical resistivity at the smaller filtrate volume than it is detected by the oxidizability. Since the quantitative determination of HA and FA requiring their preconcentration is a prolonged procedure [9], it is difficult to unambiguously determine the time when an adsorber is exhausted and must be replaced by a fresh one.

Based on the fact that HA and FA absorb UV radiation [10], their breakthrough into filtrate was detected by measuring the optical density at 205 nm D_{205}. In order to increase the detection sensitivity, a long optical cell (100 mm) was used. In developing this technique, we found that there is an inverse correlation between the optical density D_{205} (i.e., HA and FA breakthrough into filtrate) and the electrical resistivity of the desalinated filtrate ρ.

A sharp decrease in the specific electrical resistivity of a filtrate flowing out of an adsorber packed with the CS combined deionizing sorbent shows that this sorbent is saturated with mineral ions. At this point, the adsorber must be put out of operation and replaced by a fresh one. However, the electrical resistivity of the filtrate can decrease owing to breakthrough of not only mineral but also organic electrolytes. Among them the FAs contribute maximally into the electrical conductivity, since fulvic acids of Neva water are characterized by a fairly high ionization constant, pK_a 4.3 [11]. If this is the case, the porous anion exchanger rather than the CS combined sorbent must be replaced or regenerated. In practice, upon replacing

the adsorber, the electrical resistivity of the filtrate increased to the initial level.

To meet the growing requirements of certain productions to the quality of deionized water, water treatment to remove organic impurities must be more efficient. In order to develop such an efficient technique, a wide variety of approaches should be tested: sorption treatment with synthetic sorbents selectively removing organic contaminants from natural water, sorption on combined anion–cation exchangers, oxidation under UV irradiation, with ozone, hydrogen peroxide, with combination of these, etc. [12].

CONCLUSIONS

(1) The seasonal variations in the content of organic substances in Neva water were studied. Fulvic acids were found to prevail in all the seasons.

(2) Long-term operation of an ion-exchange installation showed that Neva water pretreatment (reagent coagulation, sorption of organic impurities on porous polycondensation anion exchangers derived from *m*-phenylenediamine in the salt form, preheating of water to 20–25°C, acidification to pH 3–4) followed by desalination on a combined sorbent allows preparation of the deionized water with the specific electrical resistivity of up to 18 MΩ cm and the permanganate oxidizability lower than 1.0 mg O/l.

(3) The combined desalinating sorbent is exhausted and must be replaced by a fresh one when the optical absorption of the final filtrate at 205 nm (a 100-mm cell) caused by breakthrough of the organic impurities starts to grow.

REFERENCES

1. Grebenyuk, V.D. and Mazo, A.A., *Obessolivanie vody ionitami* (Water Desalination with Ion Exchangers), Moscow: Khimiya, 1980.
2. Kul'skii, L.A. and Strokach, P.P., *Tekhnologiya ochistki prirodnykh vod* (Processes for Natural Water Purification), Kiev: Vishcha Shkola, 1986.
3. *Vodopodgotovka* (Water Treatment), Martynova, O.I., Ed., Moscow: Atomizdat, 1977.
4. Grebenyuk, V.D., *Elektrodializ* (Electrodialysis), Kiev: Tekhnika, 1976.
5. Dytnerskii, Yu.I., *Obratnyi osmos i ul'trafil'tratsiya* (Reverse Osmosis and Ultrafiltration), Moscow: Khimiya, 1978.
6. Karmazinov, F.B. and Gumen, S.G., *Nauchnye i tekhnicheskie aspekty okhrany okruzhayushchei sredy. Obzornaya informatsiya*. (Scientific and Technical Aspects of the Environmental Protection: Review). Available from VINITI, 1995, no. 3, pp. 24–28.
7. Slavinskaya, G.V., Zeleneva, L.A., and Shkol'nyi, A.K., *Khim. Tekhnol. Vody*, 1990, vol. 12, no. 3, pp. 245–249.
8. Vakulenko, V.A., Kuznetsova, E.P., and Samborskii, I.V., *Teor. Prakt. Sorbts. Prots.* (Voronezh), 1973, no. 8, pp. 58–61.
9. Lur'e, Yu.Yu., *Unifitsirovannye metody analiza vod* (Standard Methods for Water Analysis), Moscow: Khimiya, 1971.
10. Orlov, D.S., *Khimiya pochv* (Soil Chemistry), Moscow: Mosk. Gos. Univ., 1985.
11. Slavinskaya, G.V. and Selemenev, V.F., *Ful'vokisloty prirodnykh vod* (Fulvic Acids of Natural Waters), Voronezh: Voronezh. Univ., 2001.
12. Schwarzer, H., *Chim. Oggi*, 1996, vol. 13, no. 6, pp. 17–19.

Russian Journal of Applied Chemistry, Vol. 76, No. 7, 2003, pp. 1094–1098. Translated from Zhurnal Prikladnoi Khimii, Vol. 76, No. 7, 2003, pp. 1127–1131.

PROCESSES AND EQUIPMENT OF CHEMICAL INDUSTRY

Effect of Design Parameters of the Centrifuge Rotor on Separation of Supensions

N. V. Pavlova, F. F. Spiridonov, S. A. Svetlov, I. N. Pavlov, and Yu. P. Volkov

Biisk Technological Institute, Altai State Technical University, Biisk, Altai krai, Russia

Received September 16, 2002

Abstract—Centrifugal separation of low-concentration suspension in a biconical rotor of a centrifuge was modeled numerically. A system of equations describing the motion of solid particles in a fluid flow was constructed and solved. The effect of geometric parameters of the centrifuge rotor on the separation efficiency was demonstrated.

Centrifugation is rather frequently used for separating low-concentration suspensions containing a finely dispersed solid phase. The choice of the type of a centrifuge and its design features is governed by physical characteristics of the media being separated: size and shape of particles, difference between the densities of the dispersed and continuous phases, and viscosity of the continuous phase.

Despite the sufficiently good understanding of methods used for separating suspensions and wide variety of centrifuges employed in practice, developing a theory of settling of the finely dispersed phase and precise methods for calculating the equipment to be involved is an important task. The data necessary for calculating centrifugation of a particular suspension or emulsion can be obtained from experiments concerned with separation on an experimental centrifuge modeling the design of the centrifuge to be calculated. However, this approach is not always justified.

By now, basic patterns characterizing centrifugal separation and yielding information about the optimal conditions of centrifuge operation have been established [1]. In view of the wide application of numerical methods to solution of various technical problems and simulation of industrial processes, it is possible to pass from formal approximation of experimental operation characteristics of equipment and apparatus for centrifugal separation to mathematical simulation that takes into account the hydrodynamic and kinetic characteristics of the process. In settling centrifugation, two processes occur simultaneously [2]: fluid flow within the rotor (internal problem) and motion of settling particles relative to the fluid (external problem).

Specific features of the distribution of fluid flows in a centrifuge and type of their motion within the rotor largely determine the true time of particle residence in different zones of the field of centrifugal forces, i.e., the actual output capacity of a centrifuge at a given sinking velocity of particles to be separated. In a turbulent flow of a suspension, the settling of solid particles may be strongly affected by turbulent pulsations of the fluid. In addition, the particles in the flow acquire rotatory motion. The transverse forces arising because of the rotation of particles exert influence on the nature of their motion and, consequently, on the settling rate. This rate is also affected by the lagging of the fluid behind the rotor motion. The factors mentioned above result in that a certain amount of particles with size exceeding the separation size is lost with the centrifugate.

The centrifugation of suspensions involves simultaneously occurring processes of fluid flow within the rotor, motion of settling particles relative to the fluid and to the rotor walls, formation of a sediment layer, and its densification.

The results obtained in studying the separation of suspensions in a cylindrical settling centrifuge and a centrifuge with a biconical rotor demonstrated a higher efficiency of separation of low-concentration suspensions in a biconical rotor (Fig. 1) at relatively high centrifugate output capacity of the centrifuge [3].

When describing the motion of a fluid within the rotor with account of the complexity of solution of a system of flow continuity equations and hydrodynam-

1070-4272/03/7607-1094$25.00

ic equations, the vortex strength ω and flow function ψ are introduced as main dependent variables:

$$rw = \partial\psi/\partial r, \quad rv = -\partial\psi/\partial z, \tag{1}$$

$$\omega = \partial v/\partial z - \partial w/\partial r, \tag{2}$$

where w and v are the fluid velocity components along the z and r axes, respectively. The following assumptions are made: the fluid is incompressible; effective viscosity is invariable; gravitational, electric, magnetic, and other fields are weak.

Equations for variables (1) and (2) are reduced to the form [3]

$$a_\phi\left[\frac{\partial}{\partial z}\left(\phi\frac{\partial\psi}{\partial r}\right) - \frac{\partial}{\partial r}\left(\frac{\partial\psi}{\partial z}\right)\right] - \frac{\partial}{\partial z}\left[b_\phi\frac{\partial}{\partial z}(c_\phi\phi)\right]$$

$$- \frac{\partial}{\partial r}\left[b_\phi\frac{\partial}{\partial r}(c_\phi\phi)\right] + rd_\phi = 0, \tag{3}$$

where ϕ is a dependent variable; a_ϕ, b_ϕ, c_ϕ, and d_ϕ are functions.

The values of a_ϕ, b_ϕ, c_ϕ, and d_ϕ were given, depending on the type of a function used, in [4].

The system of equations under study was solved by the finite-difference method, with a finite number of points chosen so that they are distributed in accordance with a certain pattern in the flow field; these points being mesh nodes. The values of the variables were calculated at the nodes and found by interpolation at intermediate points.

An iteration method of successive shifts was developed for solving the system of nonlinear algebraic equations. This method takes into account the specificity of the following boundary conditions for fluid flow within the centrifuge rotor.

Boundary conditions at the inlet cross section. The parameters of the flowing-in fluid are known, the streamlines are considered to be parallel to the symmetry axis in this region. This condition also determines the distribution of the vortex strength. The processes occurring within the centrifuge affect the distribution of quantities over the inlet cross section only slightly.

Boundary conditions at the wall. The wall is impermeable to the fluid and, consequently, the flow function is constant all over the wall. The circumferential velocity of the fluid in the immediate vicinity of the solid wall is equal to the velocity of the wall at any of its points.

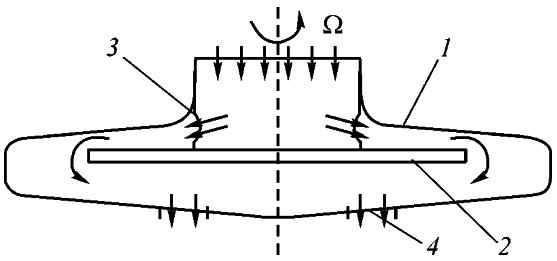

Fig. 1. Schematic of the centrifuge rotor: (*1*) rotor, (*2*) disc, (*3*) inlet opening, and (*4*) discharge opening.

Boundary conditions at the outlet cross section. The boundary conditions at the outlet cross section are set by extrapolation of the values of the sought-for variables from the flow.

Boundary conditions at the symmetry axis. The radial component of velocity at the symmetry axis is zero.

The calculation algorithm of the chosen solution method was implemented using the Maple 6 software package including procedures for data input, mesh construction, solution of the system of equation, and output of the information obtained. Numerical simulation of the flow of a fluid containing the solid phase was done for the example of separation of a suspension of microcrystalline cellulose (MCC) in water, with solid phase content of less than 5%. In doing so, the solid phase was taken to be monodisperse and to contain spherical particles of a certain size. In simulating the separation of an aqueous suspension of MCC, the average particle size d_p was chosen, which varies within the range 1–120 μm in the pulverized product. The preset parameters in studying the process of centrifugal separation were the solid phase particle diameter and the angular rotational velocity Ω of the centrifuge rotor.

Differential equations for finding the trajectory of particle motion in the centrifuge rotor were derived on the assumption that a low-concentration suspension is being separated. The particle motion in a field of centrifugal forces is described by the general law of the drag force [5]

$$m_p = \mathrm{d}w_p/\mathrm{d}t = F_d, \quad m_p = \mathrm{d}v_p/\mathrm{d}t = F_c + F_d, \tag{4}$$

where F_d is the drag force (N); F_c, centrifugal force (N); m_p, particle mass (kg); w_p and v_p, horizontal and vertical components of the particle velocity, respectively (m s^{-1}); and t, time (s).

The z and r components of the drag force F_d are given by

$$F_z = 0.5\rho(\Delta w)^2\xi(\pi d_p^2/4), \quad F_y = 0.5\rho(\Delta v)^2\xi(\pi d_p^2/4), \tag{5}$$

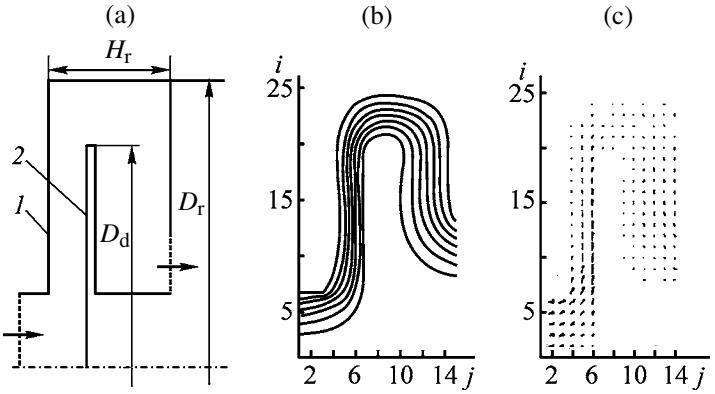

Fig. 2. Suspension flow structure in the contour. (a) Schematic of the contour: (*1*) rotor and (*2*) disc; (b) streamlines; and (c) vector filed of velocities. (D_r) Rotor diameter (m), (D_d) disc diameter (m), and (H_r) rotor height.

where ρ is the fluid density (kg m^{-3}); $\Delta w = w - w_p$, $\Delta v = v - v_p$, the differences of longitudinal and transverse components of the velocities of the fluid and dispersed phases (m s^{-1}); and ξ, the drag coefficient.

The centrifugal force can be found using the formula

$$F_c = m_p \Omega^2 r, \tag{6}$$

where r is the radius of the particle trajectory (m).

Finally, Eqs. (4) of particle motion, supplemented with kinetic relations, are represented as

$$\left.\begin{aligned} S(\mathrm{d}w_p/\mathrm{d}t) &= w - w_p, \\ S[(\mathrm{d}v_p/\mathrm{d}t) - \Omega^2 r] &= v - v_p, \\ \mathrm{d}z/\mathrm{d}t &= w_p, \\ \mathrm{d}r/\mathrm{d}t &= v_p, \end{aligned}\right\} \tag{7}$$

where S is the Stokes number, $S = \rho_p d_p^2/18\mu$ (s); ρ_p, particle density (kg m^{-3}); and μ, fluid viscosity (Pa s).

The system (7) of equations describing the motion of solid particles in the centrifugal filed of the centrifuge was solved by the single-step Gear method. The flow velocity of the fluid was determined by finding numerically the velocity profile in the centrifuge at varied geometric parameters of the centrifuge rotor. The particle velocity at the entry into the centrifuge rotor was taken to be equal to the fluid flow velocity, which is well justified for small particles. In solving the equations, the maximum rate of rotor rotation at which all particles reach the rotor wall was determined.

To study the process in more detail, the separation was simulated at varied geometric characteristics of the contour of the centrifuge rotor. The presented model of the suspension flow in the centrifuge rotor and its numerical solution were used to obtain data on the flow structure of the fluid and particles in various contours of the rotor under consideration.

Figure 2 shows streamlines and vector field of velocities in a contour with rectangular cross section, which has parameters close to those of a laboratory centrifuge with a biconical rotor.

Numerical simulation yielded data on the suspension flow structure in various contours of the centrifuge in question. These data were analyzed in studying the influence exerted by the main operation parameters of the centrifuge on the separation efficiency. In doing so, the extent to which the suspension was separated, amount of particles contained in the centrifugate, and fraction of particles settling in the centrifuge were evaluated from the trajectories of particle motion within the rotor. Therefore, to estimate the data obtained more accurately, the spectrum of particle motion trajectories was considered.

Analysis of the fluid flow structure and trajectories of particle motion in contours of different sizes shows that, at a constant rate of rotor rotation, the structure of particle motion depends on the radius of particle entry into the inlet cross section of the rotor. The influence exerted by the rate of rotor rotation on the degree of suspension separation was studied for contours with rectangular cross sections. The results obtained are shown in Fig. 3. The rate n of centrifuge rotor rotation should be noted as the basic parameter affecting the efficiency of suspension separation. The content of solid particles in the centrifugate, c_ϕ, markedly decreases when the rate of rotor rotation is raised at constant initial concentration c_{in} of the suspension and its flow rate Q.

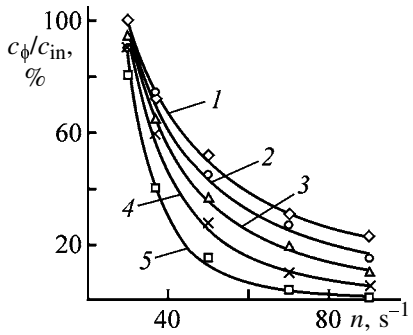

Fig. 3. Relative fraction of particles in the centrifugate, c_ϕ/c_{in}, vs. rate n of rotor rotation. Q = 9000 l h^{-1}, H = 0.045 m, D_r = 0.16 m. Particle diameter d_p (μm): (*1*) 5, (*2*) 10, (*3*) 15, (*4*) 20, and (*5*) 25.

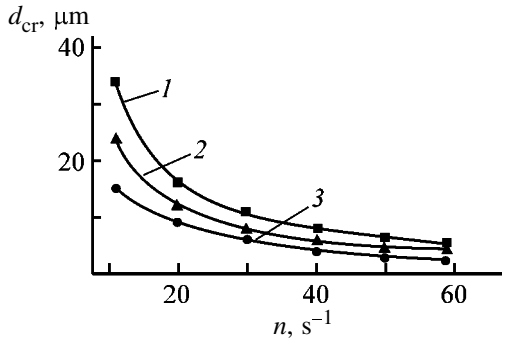

Fig. 4. Maximum particle diameter d_{cr} in the centrifugate vs. rate n of rotor rotation. Suspension flow rate Q (l h^{-1}): (*1*) 300, (*2*) 150, and (*3*) 70.

In the next stage of the study, suspension separation in the rotor of an experimental centrifuge was simulated numerically. For this purpose, the calculation algorithm was applied to the biconical rotor of the centrifuge. The trajectories of motion of solid particles within the rotor largely depend on the flow rate of the initial suspension.

The results obtained in the theoretical analysis were compared with the data furnished by experimental studies of suspension separation in a centrifuge with a biconical rotor at the same process and design parameters. The comparison demonstrated that the results of numerical and experimental studies at identical modes of centrifuge operation (flow rate of the initial suspension, rate of rotor rotation, particle diameter, concentration of the solid phase) are in reasonable agreement.

For a contour with dimensions corresponding to those of the biconical rotor, we examined the influence exerted by the rate of rotor rotation and suspension flow velocity at the centrifuge inlet on the maximum diameter of solid particles in the centrifugate. In the case of separation of a suspension with polydisperse composition of the solid phase, the maximum size d_{cr} of solid particles in the centrifugate decreases with increasing rate of centrifuge rotor rotation and decreasing rate of suspension supply into the rotor (Fig. 4).

The model of the process, presented here, was also used to study the efficiency of particle settling at varied geometric parameters of the centrifuge. The main variable parameters were rotor height, disc thickness, and rotor and disc diameters.

The influence exerted by the height of the rotor on the efficiency of suspension separation was considered with all other design parameters of the centrifuge fixed. In this case, the optimal height of the centrifuge rotor, at which particles of a certain diameter settle onto the inner surface of the rotor, was determined. Figure 5a shows the dependence of the degree of separation $\eta = (c_{in} - c_\phi)/c_{in}$ on the height H of the centrifuge rotor at different diameters of particles of the dispersed phase in the suspension at constant suspension flow rate and rate of rotor rotation. As seen from Fig. 5a, settling of particles with smaller diameters requires that the distance traversed by the fluid in the field of centrifugal forces should increase sub-

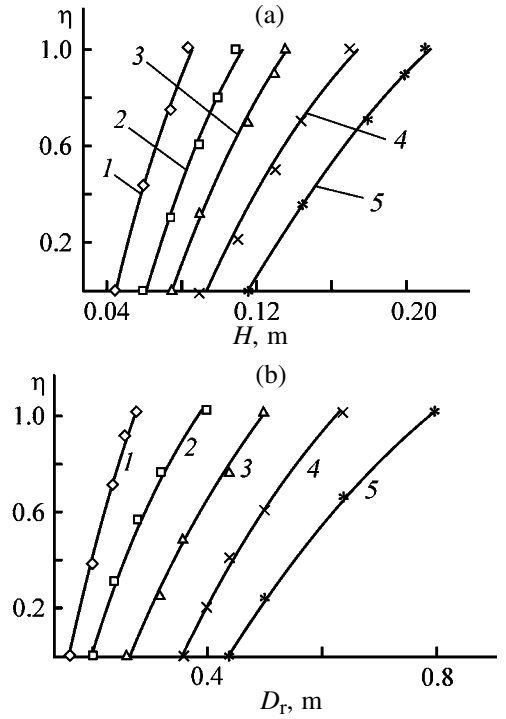

Fig. 5. Degree of suspension separation, η, vs. (a) height H and (b) diameter D_r of the rotor. n = 50 s^{-1}, Q = 9000 l h^{-1}. (a) D_d = 0.115 and D_r = 0.16 m; (b) D_d/D_r = 0.7 and H = 0.045 m. Particle diameter d_p (μm): (*1*) 25, (*2*) 20, (*3*) 15, (*4*) 10, and (*5*) 5.

stantially, which ensures finer separation of the suspension.

Since the separation is affected not only by the rotor height, but also, possibly, by other parameters, their influence was considered with other design parameters of the centrifuge rotor fixed. The influence of the rotor diameter on the efficiency of settling of solid particles was studied. It was found that, when only the rotor diameter is raised at invariable disc diameter, the separation is insufficiently efficient. This may be due to the following: particles move around an obstacle in those regions where the centrifugal force is weak; as a result, they have not enough time to settle on the rotor and find their way into the centrifugate. If the disc diameter is changed in proportion to the rotor diameter, the efficiency of the process increases substantially. Increasing the rotor diameter at constant disc diameter affects the efficiency of settling of solid particles to a lesser extent, which requires that the rotor diameter and, consequently, the overall dimensions of the centrifuge should be made much larger.

The plot representing the dependence of the degree η of suspension separation on the rotor diameter in the case of a proportional increase in the rotor and disc diameters is shown in Fig. 5b.

Simultaneous increase in the rotor and disc diameters at their optimal ratio makes it possible to substantially improve the efficiency of suspension separation at small rotor height. Depending on the requirements to the quality of isolation of the dispersed phase from a suspension, the optimal dimensions of the centrifuge rotor can be found.

To separate suspensions containing finely dispersed particles less than 5 μm in size, it is necessary to make larger the geometric dimensions of the centrifuge rotor, specifically, its height, and raise the rate of its rotation, on the basis of the flow rate and concentration of a suspension fed into the centrifuge.

CONCLUSIONS

(1) Centrifugal separation of a low-concentration aqueous suspension of microcrystalline cellulose in the biconical rotor of a centrifuge was simulated numerically on the basis of a mathematical description.

(2) The results of numerical simulation reasonably agree with experimental data.

(3) The mathematical model was used to study the influence exerted by the operation modes of the centrifuge and geometric parameters of its rotor on the efficiency of separation of suspensions containing particles of microcrystalline cellulose 5 to 25 μm in size. The efficiency of suspension separation can be improved by raising the diameter and height of the rotor.

REFERENCES

1. Sokolov, V.I., *Tsentrifugirovanie* (Centrifugation), Moscow: Khimiya, 1976.
2. Shkoropad, D.E. and Novikov, O.P., *Tsentrifugi i separatory dlya khimicheskikh proizvodstv* (Centrifuges and Separators for Chemical Industries), Moscow: Khimiya, 1987.
3. Volkov, Yu.P. and Svetlov, S.A., *Zh. Prikl. Khim.*, 2001, vol. 74, no. 11, pp. 1812–1814.
4. Gosman, A.D., Pun, W.M., Runchal, A.K., *et al.*, *Heat and Mass Transfer in Recirculating Flows*, London: Academic, 1969.
5. Fortier, A., *Mecanique des suspensions*, Paris: Masson, 1967.

Russian Journal of Applied Chemistry, Vol. 76, No. 7, 2003, pp. 1099–1103. Translated from Zhurnal Prikladnoi Khimii, Vol. 76, No. 7, 2003, pp. 1132–1136.

PROCESSES AND EQUIPMENT OF CHEMICAL INDUSTRY

Control over Extraction Rate by Means of Forced Marangoni Flows

V. V. Tarasov, Zhang Dong Xiang, Huang Hung-Ching, and K. V. Dudko

Mendeleev Russian University of Chemical Technology, Moscow, Russia
Chongqing University, China

Received May 23, 2003; in final form, December 2002

Abstract—The influence of surfactants and temperature on the intensity of interphase mass transfer in back extraction under conditions of forced Marangoni flows was studied.

Spontaneous interphase convection arising at mobile interfaces in fluid–gas and fluid–fluid systems is a powerful tool for intensifying absorption and extraction processes [1, 2]. Several mechanisms of spontaneous interphase convection are known, but the principal one is the c–σ mechanism, or the Marangoni effect [3].

This effect is a consequence of the presence at the phase boundary of places with different concentrations of surfactants and the resulting different surface tensions σ. As a result, there arise surface flows from places with lower surface tension to those with higher σ. Commonly, this process is sporadic and is difficult to control without changing the initial properties of a system. Nevertheless, further intensification of mass transfer across mobile boundaries is largely associated with a search for methods to control the surface convection.

Commonly, studies were concerned with fundamental aspects of mass transfer in systems agitated by the "classical" method in which energy is introduced into the bulk of liquids by stirrers of various types. In this case, only a negligible fraction of energy dissipated by a stirrer reaches the interfacial region in which the main resistance to substance transfer from one phase into another is concentrated.

In [4, 5], another method for energy introduction was proposed. Energy is fed directly into the interfacial region by a flexible band moving across the phase boundary, which can serve not only as a new, rather efficient method for controlling the rate of substance transfer, but also as an effective technique for detection of surface structures and study of the influence exerted by surfactants on the process kinetics.

With the use of the method proposed in [4, 5], a rather interesting type of surface flows, named "tension" flows, was discovered [6]. These flows could have also be named the mechanically induced [7] or forced Marangoni effect. Forced Marangoni flows are readily controllable. They arise upon adsorption of surfactants onto mobile boundaries or upon formation of dynamic dispersed interphase layers [8], across which solid bodies (bands, plates, threads, discs, etc.) move.

It was found that even relatively slow motions of solid bodies may lead to pronounced acceleration of mass transfer. For example, mass transfer could be accelerated by a factor of 30–40 in fluid–fluid systems in the case of formation of dynamic dispersed interphase layers [4, 5]. Despite that this way to control the rate of mass transfer is rather promising, the fundamental aspects of mass transfer under conditions of forced Marangoni flows are poorly understood. For example, there is no evidence concerning the influence exerted by the type and concentration of a surfactant and by temperature on the rate of mass transfer in the case of mechanical perturbation of the phase boundary.

The aim of this study was to determine the effect of surfactants and temperature on the intensity of interphase mass transfer in back extraction under conditions of forced Marangoni flows.

EXPERIMENTAL

We studied the kinetics of nitric acid back extraction from extracts containing solutions of hydrate solvates of tri-*n*-butyl phosphate (TBP) and nitric acid, $TBP(H_2O)_x \cdot HNO_3$, in carbon tetrachloride. Tri-

1070-4272/03/7607-1099$25.00

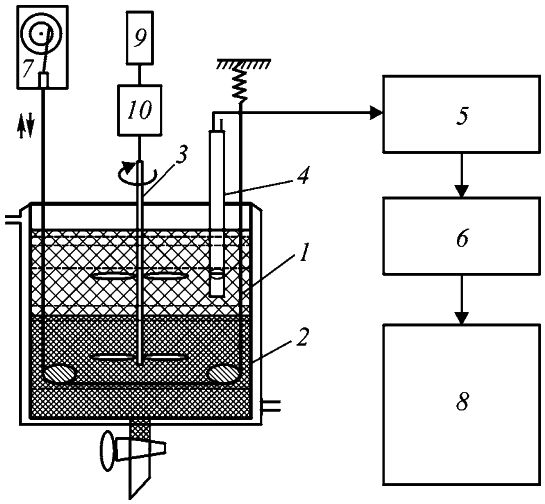

Fig. 1. Schematic of modified Gordon cell: (*1*) band, (*2*) temperature-controlled cell, (*3*) stirrer, (*4*) electrical conductivity pickup, (*5*) conductometer, (*6*) analog-to-digital converter, (*7*) band reciprocating gear, (*8*) computer, (*9*) tachometer, (*10*) dc electric motor.

n-butyl phosphate was preliminarily vacuum-distilled and contained more than 99% main substance. Carbon tetrachloride was of chemically pure grade. The surfactants used: sodium dodecyl sulfate (SDDS, an anionic surfactant) and cetyltrimethylammonium bromide (CTMAB, a cationic surfactant) were of analytically pure grade.

Back extraction of nitric acid from an organic into an aqueous phase is accompanied, as established in [8], by an instantaneous diffusion-controlled reaction (1) and a physical process (2) of phase formation:

$$\mathrm{TBP(H_2O)}_x\cdot\mathrm{HNO_3}_{\mathrm{org}} \rightarrow \mathrm{TBP}_{\mathrm{aq}} + x\mathrm{H_2O} + \mathrm{H^+(H_2O)}_y + \mathrm{NO_3^-}, \quad (1)$$

$$\mathrm{TBP}_{\mathrm{soln}} \rightarrow \mathrm{TBP}_{\mathrm{disp}}. \quad (2)$$

Reaction (1) occurs in aqueous phase layers adjacent to the phase boundary. The reaction ends in the formation of an oil-in-water emulsion from dissolved TBP [8]. This gives reason to suggest that the forced Marangoni effect may strongly affect the kinetics of back extraction, and addition of the surfactants mentioned above must markedly weaken or enhance the effect.

The installation for kinetic studies has been described previously [5]. Its modified design is shown in Fig. 1. The phase boundary is perturbed using a polyethylene band *1* which reciprocates perpendicularly to the phase boundary in the temperature-controlled cell *2* of diameter 50 mm. The fluid at phase cores was agitated with propeller stirrers *3*. The acid concentration in the aqueous (top) phase was determined using an electrical conductivity pickup *4*, conductometer *5*, analog-to-digital converter *6*, and Pentium PC-AT. The band was reciprocated perpendicularly to the phase boundary by a camshaft gear *7*.

The use of the reciprocal motion has certain methodological advantages: here, there is no need to take into account changes in the interface area or complications associated with loss of the bottom phase toward the interface with air, as it would be in the case of a continuous unidirectional motion of an "infinite" band or rotation of discs in the direction perpendicular to the phase boundary.

The kinetics of back extraction of nitric acid was studied under the following conditions: TBP concentration in the organic phase 10 vol %, nitric acid concentration 0.06 M, fixed rate of rotation (1.7 s^{-1}) of propeller stirrers, two fixed frequencies of band motion (0 and 0.8 s^{-1}), band width 2 cm, and fluid temperature in the cell varied in the range 287–308 K.

The experiments were done as follows. A 100 cm^3 portion of a 10% TBP solution in CCl_4 and the same volume of distilled water were placed in cell *2*. The stirrers were switched on, and 1 cm^3 of a solvate (10% $TBP\cdot HNO_3$ in CCl_4, c_{HNO_3} = 0.06 mol dm^{-3}) was introduced into the organic phase under stirring. It was established preliminarily that 8–10 s is necessary for complete agitation of the solvate in the bulk of the organic phase. Therefore, the first 50 s were excluded from consideration, which determined the lower limit of integration in expression (4). Since there existed a one-to-one correspondence between the electrical conductivity of the aqueous solution and the amount of acid transferred from the organic into the aqueous phase (linear relation), calculating the variation of the concentration was rather a simple task.

The experimental data obtained were processed as follows. Kinetic curves $c = f(t)$ are well approximated by the dependence

$$c_t = \sum_{i=l}^{n} a_i t^i + A\ln t \quad (l = -2, -1, 0; n = 0, 1, 2, \ldots), \quad (3)$$

where a_i and A are constants, and c_i is the HNO_3 concentration in the aqueous phase at ith instant of time t.

Differentiation of expression (1) gives

$$dc_t/dt = i\sum_{i=l}^{n} a_i t^{i-1} + A/t. \quad (4)$$

The differential mass-transfer coefficient at instant of time t was calculated using the formula

$$k_t = \frac{dc_t/dt}{(c_{eq} - c_t)(s/v)}, \quad (5)$$

where c_{eq} is the acid concentration in the aqueous phase in equilibrium (since the process is irreversible and the volumes of the organic and aqueous phases are the same and equal to v, c_{eq} is equal to the initial concentration of the acid in the organic phase), and s is the interface area.

Since the mass-transfer coefficients k_i are generally time dependent, the integral, averaged over a period of time equal to 20–200 s, mass-transfer coefficient k was calculated by the formula

$$\bar{k} = \int_{50}^{1000} k_t dt/950, \quad (6)$$

and the factor F_a of mass transfer acceleration (deceleration) upon introduction of a surfactant, by the formula

$$F_a = \bar{k}/k. \quad (7)$$

The coefficients of mass transfer of nitric acid from organic into aqueous phase and errors in determining these coefficients are listed in the table.

It can be seen that relative errors are, on the average, 6% in the case of a perturbed boundary and 11% without perturbation, which well confirms the previous conclusion [3, 4] that random errors in determining the mass-transfer coefficients decrease in the case of agitation of the interfacial layer. The data in the table also confirm the conclusion that the mass-transfer process is strongly (by a factor of 2–3) intensified under agitation of the interfacial layer because of the appearing surface flows [3–6].

Processing a large array of mass-transfer coefficients obtained without perturbation of the phase boundary with a band and in the absence of intentionally introduced surfactants yields the following value of the mass-transfer coefficient averaged over time and over the array itself: $\bar{k} = (0.760 \pm 0.084) \times 10^{-5}$ m s^{-1}. Introduction of 10^{-4} M of a cationic surfactant, CTMAB, into the system leads to a twofold decrease in this value to $\bar{k} = (0.390 \pm 0.043) \times 10^{-5}$ m s^{-1}. Almost the same is the effect of an anionic surfactant, SDDS, added in the same molar amount [$\bar{k} = (0.366 \pm 0.040) \times 10^{-5}$ m s^{-1}]. In other words, the classical case of suppression of the turbulence that comes to the phase boundary from phase cores because of the appearance of Gibbs elasticity of interfacial layers (suppression of capillary waves) is observed in the presence of "strong" surfactants.

Averaged mass-transfer coefficients and errors in determining these coefficients with and without phase boundary perturbation

Without perturbation		With perturbation	
$\bar{k} \times 10^5$, m s^{-1}	Δ, %	$\bar{k} \times 10^5$, m s^{-1}	Δ, %
0.72	9	2.0	9
0.69	13	1.8	2
0.84	6	1.9	3
0.91	15	1.6	10

If the boundary is perturbed not only by propeller stirrers, but also by band movements (f = 0.8 s^{-1}, A = 2 cm), the pattern changes fundamentally (Fig. 2). Introduction of a surfactant into the system under the same conditions leads not to deceleration, but even to a 2–3-fold acceleration of the mass transfer of nitric acid. The mass-transfer coefficients averaged over a period of 950 s are the following: $(1.67 \pm 0.100) \times 10^{-5}$ without surfactant, $(4.04 \pm 0.242) \times 10^{-5}$ in the presence of 10^{-3} M of CTMAB, and $(2.63 \pm 0.159) \times 10^{-5}$ in the presence of the same amount of SDDS. Thus, introduction of CTMAB into the system accelerates back extraction by a factor of approximately 2.8, whereas in the case of SDDS introduction, the acceleration factor is about 1.6, which much exceeds the experimental error.

The table shows that boundary perturbation accelerates the mass transfer even in the absence of special surfactant additives. However, it should be

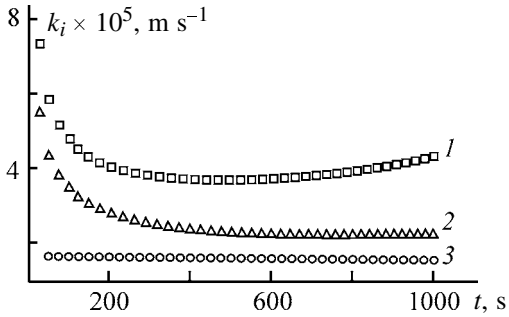

Fig. 2. Effect of surfactants on the differential mass-transfer coefficients k_i of nitric acid in the case of a phase boundary perturbed with a band (f = 0.8 s^{-1}, A = 2 cm). Surfactant concentration 10^{-3} M. (t) Process duration. (*1*) CTMAB, (*2*) SDDS, and (*3*) without surfactant.

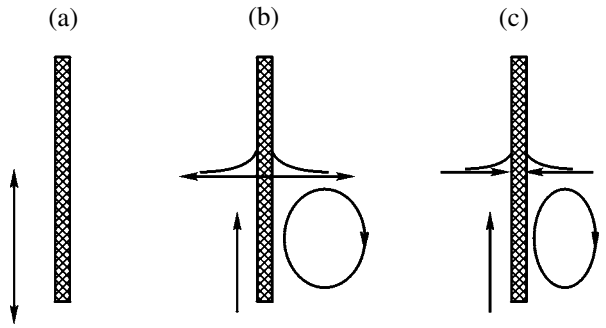

Fig. 3. Schematic of flows in the core and at the surface in band reciprocation.

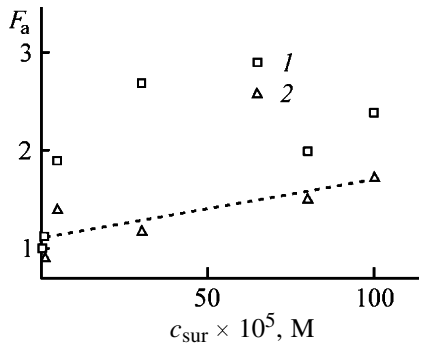

Fig. 4. Effect of surfactant concentration c_{sur} on the mass transfer acceleration factor F_a: (*1*) CTMAB and (*2*) SDDS.

kept in mind that extraction systems actually always contain surfactants. For example, surfactant properties are exhibited in the case in question by the extracting agent (TBP) itself.

The presence of special surfactants gives rise to the already mentioned Marangoni effect, i.e., surface tension flows accelerating the mass transfer, induced by band movements. The effect of a surfactant in the case of a perturbed boundary should be regarded as nonspecific. Characteristic features of these flows were described in [6, 7]. We believe that additional information is necessary for understanding of the pattern observed.

Let us consider only a single part of an infinite band. Here are meant movements induced by such a band in the case of its reciprocal motion. Landau and Lifshits [9] demonstrated that movements of entrained fluid decay fast within the hydrodynamic layer adjacent to the band. In this case, no flows are observed far away from the band (Fig. 3a). If, however, two phases are present with a phase boundary across which a band moves, the theory developed is insufficient for understanding of the arising flows. Experiment shows that two types of flows, which are different not only in nature and intensity, but also in direction (Fig. 3), can arise [5, 7]. These flows cover the entire phase boundary area between the ascending and descending parts of the band and layers adjacent to the phase boundary, in which the main resistance to mass transfer is concentrated. Therefore, even sluggish movements of the band lead to substantial effects. Movements in the bulk of the phases are the most pronounced at places of triple contact (two phases and a solid).

Figure 3b considers the case of a "clean" boundary in the form of a meniscus. Surface flows are of inertial nature: the fluid adhering to the band surface is detached from it when the band is lifted to a certain height and moves by inertia and under the action of gravity forces, spreading at the phase boundary. Thus, there appears a flow directed away from the ascending band.

In Fig. 3c, the surface is contaminated with a surfactant. In view of surfactant adsorption on the band, its motion shifts the entire surface layer of the surfactant. The reason is that there appears a gradient of surfactant concentration and a gradient of interphase tension. The phase boundary and the adjacent fluid layers move toward an ascending band, since its ascending motion is accompanied by simultaneous adsorption of the surfactant onto the band. This leads to a decrease in the surfactant concentration directly at the place where the band traverses the boundary and to an increase in surface tension at this place. This gives rise to a surface flow of molecules toward the band, and just this effect is the forced Marangoni flow.

Forced Marangoni flows can be readily observed visually. Indeed, fine particles of aluminum dust (~1–10 μm) move synchronously with the band along the phase boundary. The amplitude of these movements decreases away from the band, as if the phase boundary possessed both viscosity and mechanical elasticity simultaneously. The velocity of surfactant motion over the surface near the band in almost equal to the velocity of band motion. Moreover, intense vortices appear near the triple contact perimeter even in the case of sluggish motion of the band. Therefore, pronounced intensification of mass transfer occurs upon introduction of soluble surfactants, and even upon deposition of thick insoluble films on the phase boundary, as shown for the case of carbon dioxide absorption by water [6, 7].

One more reason for intensification of mass transfer is settling of microparticles from a dispersed layer onto the moving phase boundary. A mechanism of this kind was considered in [10]. Particles settling

from the dispersed layers onto the phase boundary entrain the substance under study, thus intensifying its transfer. The acceleration upon introduction of a surfactant into a system with perturbed boundary depends on the type of surfactants and their concentration.

Figure 4 shows the dependence of the mass-transfer acceleration factor on the concentration of a surfactant introduced into the system. Even though a wide scatter of experimental data is observed in the case of CTMAB, the tendency toward a rise in the acceleration factor with increasing concentration is clearly pronounced (at least at low surfactant concentrations).

A study of the influence of temperature on the kinetics of HNO_3 back extraction yielded additional information about the mechanism of forced Marangoni flows. The apparent activation energy was 40 kJ mol^{-1} with only propeller stirrers in the absence of surfactants. Perturbation of the phase boundary with a moving band leads to a twofold decrease in the activation energy (E_a = 20 kJ mol^{-1}). If 10^{-4} M of CTMAB is introduced into the system under these conditions, the apparent activation energy becomes negative (E_a = –23 kJ mol^{-1}), i.e., the back extraction rate decreases, rather than grows (as usual), with increasing temperature. A reasonable explanation of this fact is as follows. When the temperature is raised, the surfactant adsorption both at the phase boundary and on the band decreases. Consequently, the conditions of surfactant adhesion to the band and the entrainment of the surface layer by the band must be adversely affected by increasing temperature. This is equivalent to deterioration of the conditions of agitation of the interfacial layer and leads to a decrease in the mass-transfer coefficients with increasing temperature.

CONCLUSIONS

(1) The previous conclusion that introduction of surfactants into a system leads to acceleration, rather than to deceleration (as it commonly occurs), of mass transfer in the case of mechanical perturbation of the phase boundary with solid bodies moving across it is confirmed.

(2) The influence exerted by perturbation of the phase boundary with a solid body on the rate of mass transfer becomes more pronounced with increasing concentration of surfactants.

(3) Raising the temperature may lead, in the presence of surfactants, to deceleration of the mass transfer because of the deteriorating conditions of mixing of interphase layers.

ACKNOWLEDGMENTS

The study was supported by the Foundation "To Best Young Lecturers" of the Ministry of Education of the People's Republic of China (no. 1999-5).

REFERENCES

1. Davies, J.T. and Rideal, E.K., *Interfacial Phenomena*, New York: Academic, 1963.
2. Savistovskii, G., *Poslednie dostizheniya v oblasti zhidkostnoi ekstraktsii* (Recent Advances in the Field of Liquid Extraction), Hanson, K., Ed., Moscow: Khimiya, 1974, pp. 204–253.
3. *Gidrodinamika mezhfaznykh poverkhnostei: Mekhanika* (Hydrodynamics of Phase Boundaries: Mechanics), Ishlinskii, A.Yu. and Chernyi, G.G., Eds., Ser. 34 of *Novoe v zarubezhnoi nauke* (News of Foreign Science), Moscow: Mir, 1984.
4. Tarasov, V.V. and Chzhan Dun Syan, *Dokl. Ross. Akad. Nauk*, 1996, vol. 350, no. 5, pp. 647–649.
5. Tarasov, V.V., Chzhan Dun Syan, and Larin, G.G., *Teor. Osn. Khim. Tekhnol.*, 2000, vol. 34, no. 2, pp. 188–196.
6. Tarasov, V.V. and Larin, G.G., *Dokl. Ross. Akad. Nauk*, 1998, vol. 360, no. 4, pp. 503–506.
7. Tarasov, V.V. and Larin, G.G., *Teor. Osn. Khim. Tekhnol.*, 2000, vol. 34, no. 1, pp. 3–10.
8. Tarasov, V.V., *Russ. J. Phys. Chem.*, 2000, vol. 74, suppl. 1, pp. S118–S127.
9. Landau, L.D. and Lifshits, E.M., *Teoreticheskaya fizika* (Theoretical Physics), vol. 6: *Gidrodinamika* (Hydrodynamics), Moscow: Nauka, 1988.
10. Adamczuk, Z., Dabros, T., and Van De Ven, T.G.M., *Chem. Eng. Sci.*, 1982, vol. 37, no. 10, pp. 1513–1522.

Russian Journal of Applied Chemistry, Vol. 76, No. 7, 2003, pp. 1104–1106. Translated from Zhurnal Prikladnoi Khimii, Vol. 76, No. 7, 2003, pp. 1137–1139.

PROCESSES AND EQUIPMENT OF CHEMICAL INDUSTRY

Ultrafiltration of Aqueous Solutions of Bromocresol Purple in the Presence of Dispersed Carbon

S. V. Kozlov

Ochakovo Center of Science and High-Tech, Karpov Research Physicochemical Institute, Moscow, Russia

Received October 22, 2002

Abstract—Ultrafiltration of solutions of Bromocresol Purple on a UFM-50M membrane in the presence of dispersed carbon was studied. The variation of the flow rate through unit surface area of the membrane and of the dye retention factor with time was traced. The influence exerted on the ultrafiltration by dye adsorption on dispersed carbon and by formation of a dynamic membrane was determined. For the initial stage of filtration, the dependence of the retention factor on the dye concentration in solution was found and accounted for.

Ultrafiltration is an effective method for concentrating solutions of synthetic dyes. Ultrafiltration of solutions of this kind has been studied previously [1–3]. The influence exeted by the dye concentration and electrolyte additives on retention of azo dyes on cellulose acetate membranes has been analyzed [1]. In ultrafiltration separation of aqueous and aqueous–salt solutions of Acid Black S, it was found that the retention factor is affected by orientation of anisodiametric dye molecules in a convergent flow at membrane pore mouths [2].

This study is concerned with ultrafiltration of aqueous solutions of Bromocresol Purple in the presence of dispersed carbon. In the absence of the dispersion, the retention of the dye is very low.

EXPERIMENTAL

Bromocresol Purple $C_{21}H_{19}BrNO_5S$ is a water-soluble dye. The concentrations of the dye of analytically pure grade, determined by photometry (λ = 400 nm), were 0.065 to 0.4 g l^{-1}. Dispersed carbon (5 g l^{-1}) was added to a solution 90 min before filtration. This time was sufficient for the adsorption equilibrium of the dye to be established at carbon particles. According to electron microscopy, the average size of carbon dispersion particles was 200 nm. A UFM-50M membrane based on aromatic polyamide with average pore diameter of 30 nm was used in experiments. Different UFM-50M membranes were used in studying the influence exerted by the dye concentration.

Ultrafiltration was carried out on a non-flow-through DKRI-021 installation without agitation, with pressure created by compressed air. The surface area of the membrane was 0.0117 m^2. The ultrafiltration was done at 298 K. The scatter of the experimental data obtained was 6%, and the variance, 0.7%.

In the course of filtration, the dye is adsorbed on the surface and pore walls of the ultrafilter; carbon particles with adsorbed dye are accumulated on the ultrafilter and form a dynamic membrane layer. In the course of time, the thickness of the dynamic membrane layer grows, which leads to a decrease in the flow rate through unit surface area of the membrane. The variation of this parameter is determined by the formula [4]

$$\frac{1}{J_2} = \frac{(R_m\eta)^2}{(\Delta P)^2} + \frac{2ac_s\eta R(1-K)}{\Delta P}t, \qquad (1)$$

where J is the flow rate through unit surface area of the membrane; R_m, hydrodynamic resistance of the ultrafilter; ΔP, pressure difference; η, filtrate viscosity; a, specific resistance of filtration; c_s, substance concentration in solution; R, retention factor; K, fraction of substance transferred from the membrane surface into solution as a result of back diffusion; and t, time.

The hydrodynamic resistance of the membrane was found using the formula

$$R_d = [2ac_sVR(1-K)]A^{-1}, \qquad (2)$$

where V is the filtrate volume, and F is the membrane area.

According to formula (1), the slope of the linear

1070-4272/03/7607-1104$25.00

dependence $1/J^2 - t$ is

$$q = [2ac_s\eta R(1 - K)]\Delta P^{-1}. \quad (3)$$

From formulas (2) and (3) follows that

$$R_d = \frac{V\Delta P}{2A\eta}q. \quad (4)$$

Figure 1 shows dependences of the flow rate through unit surface area of the membrane and of the retention factor on the filtration time at dye concentration of 0.25 g l^{-1} and pressure of 0.05 MPa on a UFM-50M membrane. The retention factor was calculated using the initial concentration of the dye. The flow rate and the retention factor decrease with time. The decrease in the flow rate is accounted for by an increase in the thickness of the dynamic membrane layer composed of carbon particles having adsorbed dye on their surface. The high retention factor of the dye is determined by its adsorption on carbon particles in solution and on the surface of the dynamic membrane and walls of its pores. Without dispersed carbon, the retention factor is 3.8% at dye concentration of 0.25 g l^{-1} and pressure of 0.05 MPa.

Figure 2 shows the time dependence of $1/J^2$. This plot is a straight line which intercepts on the ordinate axis a portion equal to 5.65×10^8 $s^2\,m^{-2}$. At $\eta = 0.894 \times 10^{-3}$ N cm^{-2} and $\Delta P = 5 \times 10^4$ N m^{-2}, formula (1) gives the hydrodynamic resistance of the ultrafilter, $R_m = 1.33 \times 10^{12}$ m^{-1}.

Figure 3 shows the time dependence of the hydrodynamic resistance of the dynamic membrane at dye concentration of 0.25 g l^{-1} and pressure of 0.05 MPa. The quantity q and the volume of the filtrate obtained in a given time were used to determine, using formula (2), the hydrodynamic resistance of the dynamic membrane, which increases linearly with time.

Figure 4 shows the isotherm of dye adsorption on dispersed activated carbon at carbon concentration of 5 g l^{-1}. The initial dye concentrations were in the range from 0.05 to 0.4 g l^{-1}. With increasing equilibrium concentration, the mass of adsorbed dye grows first steeply and then only slightly.

Figure 5 shows the dependence of the retention factor on the initial concentration of the dye in solution at a pressure of 0.05 MPa on the UFM-50M membrane at instant of time t = 60 s (curve *1*). With increasing concentration, the retention of the dye decreases. This is attributed to saturation of the surface of carbon particles with adsorbed dye with its increasing concentration. Previously, a decrease in the retention of azo dyes on cellulose acetate membranes with increasing dye concentration in solution was observed in [1].

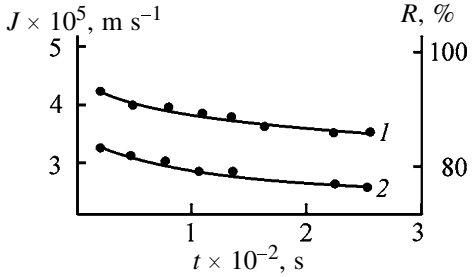

Fig. 1. (*1*) Flow rate through unit surface area of the membrane J and (*2*) dye retention factor R vs. time t on a UFM-50M membrane. Dye concentration 0.25 g l^{-1}, pressure 0.05 MPa; the same for Figs. 2 and 3.

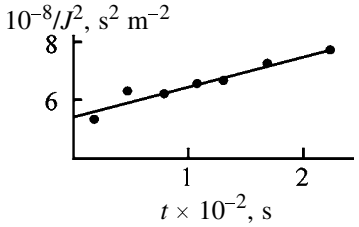

Fig. 2. $1/J^2$ vs. time t on a UFM-50M membrane.

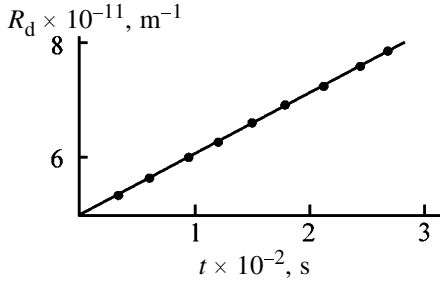

Fig. 3. Hydrodynamic resistance of dynamic membrane, R_d, vs. time t.

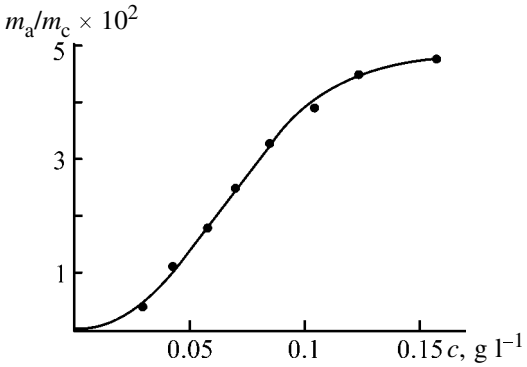

Fig. 4. Adsorbed dye to carbon mass ratio m_a/m_c vs. equilibrium dye concentration c.

Figure 5 also shows the dependence of the retention factor on the dye concentration, which was determined from the adsorption isotherm (curve *2*). Comparison of curves *1* and *2* in Fig. 5 indicates that a

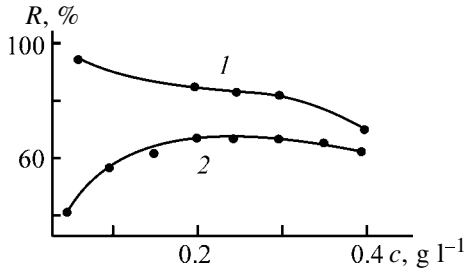

Fig. 5. Dependences of the retention factor R on the dye concentration c, obtained (*1*) in ultrafiltration and (*2*) from adsorption isotherm.

pronounced adsorption of the dye in the dynamic membrane layer occurs in the course of filtration. The enhanced adsorption of the dye on the dynamic membrane, compared with that on the surface of carbon particles, is due to an increase in the adsorption capacity in the narrow pores of the carbon layer because of the additivity of dispersion forces.

CONCLUSIONS

(1) In the presence of dispersed carbon, the retention factor of Bromocresol Purple increases manyfold.

(2) The dye retention factor decreases with increasing dye concentration.

(3) The high retention factor is due to dye adsorption on carbon particles in solution and in filtration through a carbon layer formed on the ultrafilter.

ACKNOWLEDGMENTS

The author is grateful to A.I. Bon for the provision of a membrane.

REFERENCES

1. Kukushkina, L.Ya., Migalatii, E.V., Nikiforova, A.F., and Pushkarev, V.V., *Zh. Prikl. Khim.*, 1977, vol. 50, no. 8, pp. 1847–1852.
2. Tsapyuk, E.A., Bryk, M.T., and Sapon, I.P., *Kolloidn. Zh.*, 1989, vol. 51, no. 1, pp. 197–203.
3. Schulze, B. and Dytnerskij, J.A., *Chem. Technol.*, 1980, vol. 32, no. 9, pp. 468–470.
4. Kozlov, S.V., *Kolloidn. Zh.*, 1996, vol. 58, no. 6, pp. 791–794.

Russian Journal of Applied Chemistry, Vol. 76, No. 7, 2003, pp. 1107–1111. Translated from Zhurnal Prikladnoi Khimii, Vol. 76, No. 7, 2003, pp. 1140–1144.

MACROMOLECULAR CHEMISTRY AND POLYMERIC MATERIALS

Synthesis of Branched Chemodegradable Homopolymers of *N*-(2-Hydroxypropyl)methacrylamide

M. V. Solovskii, N. V. Nikol'skaya, V. M. Denisov, A. V. Adamov, E. B. Tarabukina, and S. I. Klenin

Institute of Macromolecular Compounds, Russian Academy of Sciences, St. Petersburg, Russia

Received April 4, 2003

Abstract—Branched water-soluble *N*-(2-hydroxypropyl)methacrylamide homopolymers containing interchain urethane links were prepared. The hydrodynamic and molecular-weight characteristics of the branched homopolymers and the rate of their hydrolysis under the conditions close to those of a living body (saline, pH 7.0, 37°C) were determined.

Much attention is given today to synthesis and study of biologically active polymers (BAPs) for their use as medicinals. Biologically active polymers, as compared to low-molecular-weight drugs, ensure prolonged effect of a drug and alter its biodistribution, reducing sometimes its toxicity and giving other positive effects. Synthetic BAPs are prepared by radical copolymerization of unsaturated derivatives of existing drugs with hydrophilic copolymers and by binding drugs to a reactive hydrophilic polymeric carrier to form polymer–drug links of various types. The second route to BAPs is the most widely applied, since it allows the use of commercially available drugs; in this case, the major problem is development of a suitable polymeric carrier.

Copolymers of *N*-(2-hydroxypropyl)methacrylamide (HPMA) are widely used as polymeric carriers for drugs and biologically active substances [1–6]. It should be noted that the HPMA homopolymer contains a reactive hydroxy group via which it is possible to link various drugs and biologically active substances. This approach, however, is used relatively seldom [7].

However, since poly-HPMA as a carbon-chain polymer is not biodegradable, its molecular weight M and molecular-weight distribution (MWD) should be strictly limited to ensure easy elimination of BAPs derived from this polymer. With nonfractionated ^{14}C-poly-HPMA as example, it was shown [8] that the radioactivity level originating form this polymer (M = 28000) at single intravenous administration in rabbits decreases by half in 8 h, and in 17 days the circulatory system gets free of the polymer. Accumulation of ^{14}C-poly-HPMA with M = 33000 is temporary: After 6 months, the polymer is detected in none of the eight examined organs. It can be expected that the polymer with $M \geq 100000$ will be retained in the living body for several years, and its deposition can cause diseases. One of the ways to overcome these undesirable side effects is synthesis of high-molecular-weight (M = 70000–100000) branched copolymers containing chemically labile covalent bonds between short backbone chains. These bonds undergo gradual chemical (hydrolysis) or biological cleavage to give low-molecular-weight fragments ($M \leq 40000$) which can be readily eliminated from the living body with kidneys. Preliminary binding of a drug to such chemodegradable polymers will ensure its prolonged effect.

The goal of this study was to prepare and study as drug carriers new branched chemodegradable HPMA homopolymers containing interchain chemically labile urethane links.

N-(2-Hydroxypropyl)methacrylamide is an active monomer. Therefore, the initial linear HPMA homopolymers were prepared by polymerization of HPMA in isopropanol, which is an active transfer agent for the propagating polymeric chain [9] and decreases M of the forming polymer, and in the presence of *p*-nitrophenol (*p*-NP), which is the polymerization inhibitor and chain-terminating agent. The results are listed in Table 1.

It is seen that, under these conditions, we were able to prepare HPMA homopolymers with $\overline{M}_v$ = 7000–30000. The higher was the *p*-nitrophenol content in

1070-4272/03/7607-1107$25.00

Table 1. Polymerization of HPMA in isopropanol at 65°C in the presence of *p*-nitrophenol ([AIBN] = 4.5 wt %)

Polymerization conditions		Poly-HPMA	Yield in 24 h, %	[η],* dl g^{-1}	$\overline{M}_v$
[M], wt %	[*p*-NP], wt %				
10	–	**Ia**	99.2	0.10	26000**
15	4.25	**Ib**	63.4	0.09	22000
15	4.75	**Ic**	65.6	0.08	19000
15	5.50	**Id**	61.3	0.07	14000
15	6.90	**Ie**	54.3	0.04	7000
15	5.00***	**If**	70.2	0.07	14000
15	3.50	**Ig**	68.7	0.11	30000

* Determined in 0.1 M aqueous KCl at 25°C; the same for Tables 2 and 3.
** M_{SD} = 27000.
*** *p*-Nitrophenoxyacetic acid was used as chain-terminating agent.

Table 2. Reaction of poly-HPMA with HMDIC

Initial poly-HPMA			Conditions of the reaction with HMDIC			Chemodegradable poly-HPMA			
no.	[η], dl g^{-1}	$\overline{M}_v$	c_{cop}, wt %	[HMDIC]/[OH], mol/mol	τ, h	no.	yield, %	[η], dl g^{-1}	M_{SD}
Id	0.07	14000	12	0.09 : 1	1	**IIa**	70.4	0.11	26000
			12	0.095 : 1	1	**IIb**	58.2	0.13	–
			10	0.115 : 1	7	**IIc**	71.0	0.16	–
			12	0.10 : 1	7	–		Gelation	
Ic	0.08	19000	12	0.01 : 1	6	**IId**	90.3	0.11	–
			12	0.04 : 1	6	**IIe**	66.7	0.19	–
			12	0.08 : 1	2	–		Gelation	
Ib	0.09	22000	12	0.075 : 1	3	**IIf**	68.6	0.12	–
			12	0.075 : 1	10	**IIe**	55.2	0.17	–
Ia	0.10	26000	10	0.04 : 1	24	**IIh**	71.3	0.15	53000
			12	0.065 : 1	7	**IIi**	80.9	0.17	–
Ig	0.11	30000	12	0.045 : 1	6.5	**IIj**	79.8	0.18	71000

the initial monomeric mixture, the lower was *M* of the forming poly-HPMA.

Figure 1 shows the UV spectrum of poly-HPMA **Ib** in DMSO. The absorption band at λ_{max} = 322 nm belongs to the product of the reaction of *p*-nitrophenol with the propagating macroradical under the conditions of HPMA polymerization. As in the case of polymerization of vinyl monomers in the presence of nitrobenzene, this process leads to the chain termination [10]. The lack of absorption at 427 nm proves the absence of free *p*-nitrophenol in the polymers.

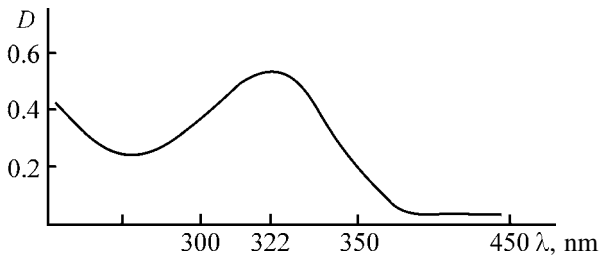

Fig. 1. UV spectrum of poly-HPMA **Ib** in DMSO, *c* = 815 μg ml^{-1}: (*D*) optical density and (λ) wavelength.

The results of the experiment on the synthesis of **If** show that *p*-nitrophenoxyacetic acid, like nitrobenzene and *p*-nitrophenol, can also be used as inhibitor of HPMA polymerization and chain-terminating agent.

It is known [5, 6] that copolymers of HPMA with *p*-nitrophenyl esters of oligopeptide *N*-methacryloyl derivatives and unsaturated phenoxyacetic acids have low *M* and narrow MWD ($\overline{M}_w/\overline{M}_n$ = 1.3–1.8) owing to the fact that the polymerizing system always contains *p*-nitrophenol impurities originating from hydrolysis of activated *p*-nitrophenoxy groups. Therefore, it can be expected that HPMA homopolymers prepared in isopropanol in the presence of *p*-nitrophenol will also have narrow MWD.

Branched HPMA homopolymers were prepared by reaction of linear poly-HPMA with a bifunctional

agent, hexamethylene diisocyanate (HMDIC), in DMF at 130°C in an argon atmosphere, i.e., under the conditions of synthesis of linear polyurethanes [11]. The results of the experiments on the reaction of the initial HPMA homopolymers with HMDIC are given in Table 2. It is seen that [η] and M_{SD} of the branched polymers are by a factor of 1.5–2 higher than those of the initial linear polymers **I**. This result suggests formation of urethane links between the polymeric chains of the initial poly-HPMA in the course of the reaction with HMDIC. The reaction conditions were determined under which the gelation is avoided and water-soluble polymers are obtained. The reaction of linear HPMA homopolymers with HMDIC is characterized by the following trends. An increase in the [HMDIC] : [OH] molar ratio at a constant initial concentration of the polymer results in increased [η] of the reaction product (polymers **IId** and **IIe**). Longer reaction, at equal other conditions, also results in increased [η] of the reaction products (polymers **IIf** and **IIg**). The hydrodynamic characteristics ([η], diffusion and sedimentation coefficients) of branched HPMA homopolymers **IIa**, **IIh**, and **IIj** are given in Table 3.

The presumed scheme of the reaction of linear poly-HPMA with HMDIC to give interchain (structure **A**) and intrachain (structure **B**) urethane links is shown below.

The presence of urethane links in the resulting branched HPMA homopolymer **IIb** was proved by ^{1}H NMR spectroscopy. Figures 2a and 2b show, respectively, the upfield and downfield parts of the spectrum of poly-HPMA **IIb** in dimethylacetamide-d_9. In the range 0.8–2.2 ppm, there are signals of the methylene protons of the backbone, four methylene protons of the cross-linking chain, and two methyl groups (one in the backbone and another in the cross-linking chain). The signal at 3.0–3.3 ppm can be assigned to the $CH_2NHC(O)$ fragment.

The richest information is apparently furnished by the signal at about 4.8 ppm. It can be assigned to the methine proton of the urethane group, –$CH(CH_3)$–OC(O)NH. Comparison of its relative intensity (0.11) with that of the sum of upfield signals (8.63) allows estimation of the content of the –$CH(CH_3)$–OC(O)NH fragments in **IIb** at 8.9 mol %. This value includes both interchain and intrachain urethane links. The content of intrachain links is apparently higher, since the initial homopolymer brought into the reaction with the bifunctional reagent contained a large amount of reactive hydroxy groups. According to [12], the probability of formation of intrachain cross-links is the lower, the smaller the content of reactive groups in the copolymer.

Table 3. Hydrodynamic characteristics of branched HPMA homopolymers

Polymer	[η], dl g^{-1}	$S \times 10^{13}$, Sv	$D \times 10^7$, cm^2 s^{-1}	M_{SD}
IIa	0.11	1.6	6.6	26 000
IIh	0.15	2.3	4.9	53 000
IIj	0.18	3.1	4.8	71 000

The hydrolysis of branched poly-HPMA **IIj** (M_{SD} = 71 000) in saline (pH 7.0) at 37°C was monitored viscometrically. Figure 3 shows that, under these mild conditions, hydrolysis of the interchain urethane links

Scheme

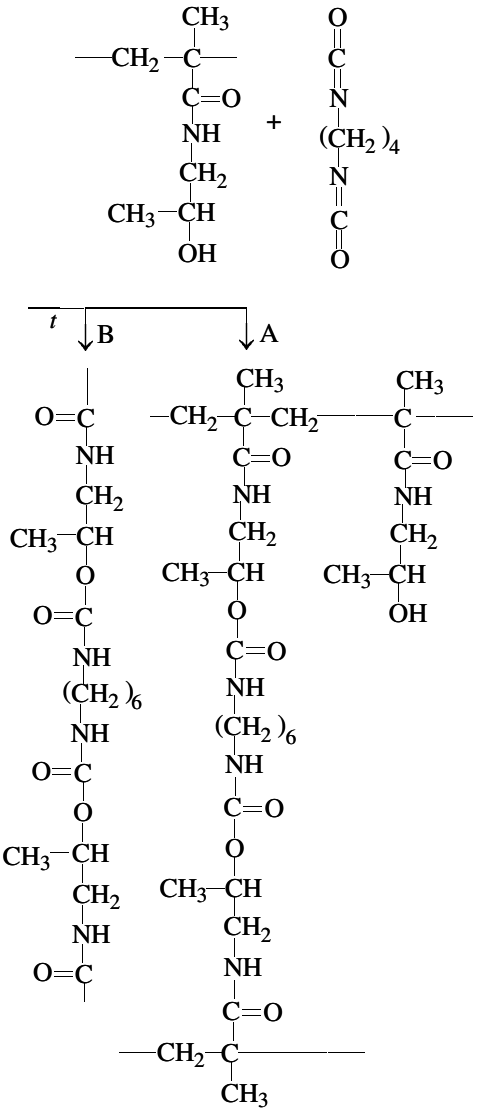

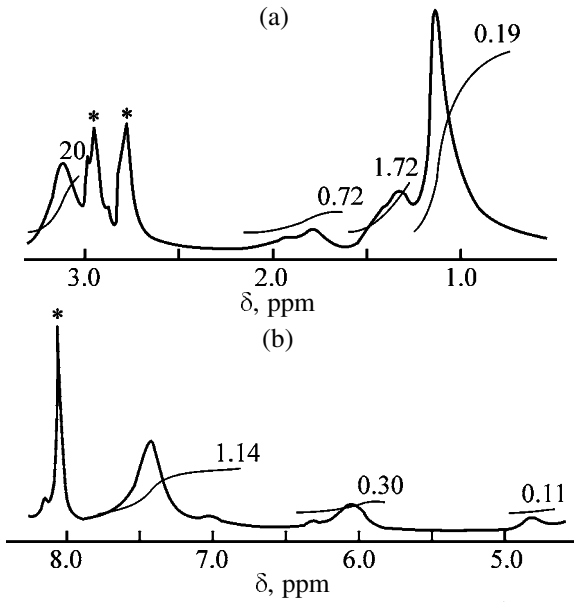

Fig. 2. (a) Upfield and (b) downfield parts of the ^{1}H NMR spectrum of poly-HPMA **IIb** in dimethylacetamide-d_9. The solvent signal is marked with an asterisk. (δ) Chemical shift.

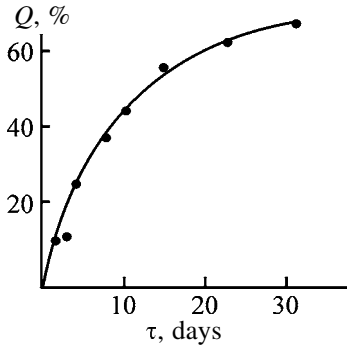

Fig. 3. Hydrolysis of branched poly-HPMA **IIj** (M_{SD} = 71 000) in saline (pH 7.0) at 37°C. (Q) Degree of hydrolysis and (τ) hydrolysis time.

in **IIj** is fairly fast. The degree of hydrolysis Q is 53% in two weeks and 68% in a month. Such a hydrolysis rate can ensure elimination of **IIj** from a living body. On the basis of chemodegradable (**IIj**) and, for comparison, initial (**Ig**) poly-HPMA, we prepared polymeric esters of a β-lactam antibiotic oxacillin.

EXPERIMENTAL

***N*-(2-Hydroxypropyl)methacrylamide** was prepared by acylation of 1-amino-2-propanol with methacrylic anhydride [13]. The elemental analysis of the monomer was consistent; mp 67°C.

AIBN was recrystallized three times from chloroform–methanol (1 : 3) at a temperature no higher than 40°C; mp 103°C.

Hexamethylene diisocyanate was purified by double vacuum distillation. The fraction boiling at 111°C (2 mm Hg) was collected. Found: n_D^{20} = 1.4535, d_4^{20} = 1.0472 g cm^{-3}; published data [14]: bp 127°C (10 mm Hg), n_D^{20} = 1.4530, d_4^{20} = 1.0460 g cm^{-3}. Calculated MR_D = 43.40; found MR_D = 42.65.

***p*-Nitrophenol** (Fisher Biotech. N.Y.) for peptide synthesis was used without additional purification.

Linear low-molecular-weight poly-HPMA Id. A glass ampule was charged with 0.09 g (4.5 wt %) of AIBN. Then a mixture of 2 g of HPMA and 0.1131 g of *p*-nitrophenol (5.5 wt %) was dissolved in 14 ml of 2-propanol in a 50-ml flat-bottomed flask. The resulting solution was added to the ampule through a funnel. The ampule was purged with argon, sealed, and placed in a thermostat maintained at 65 ± 0.5°C. After 24 h, the ampule was cooled and opened; the viscous solution from the ampule was poured dropwise with stirring into 250 ml of dry acetone. The precipitated polymer was collected on a glass frit and vacuum-dried. Yield of poly-HPMA 1.39 g (69.5%), [η] = 0.07 dl g^{-1}, $\overline{M}_v$ = 14 000. The intrinsic viscosity of the polymer was measured in 0.1 M aqueous KCl at 25°C. The viscosity-average molecular weight $\overline{M}_v$ was determined by the Mark–Kuhn–Houwink equation for poly-HPMA [15]. Other poly-HPMA samples were prepared similarly.

Branched poly-HPMA IIg. In a 20-ml conical flask, we dissolved 0.50 g of poly-HPMA ([η] = 0.09 dl g^{-1}, $\overline{M}_v$ = 22 000) in 3.88 ml of DMF, and to the resulting solution we added 42.12 μl of HMDIC, [HMDIC]/[OH] = 0.075 : 1. The reaction mixture was transferred into a glass ampule, which was purged with argon, sealed, and placed in an oil bath heated to 130°C. After 10 h, the ampule was cooled and opened; 0.5 ml of ethanol was added, and the mixture was poured into 200 ml of diethyl ether. The precipitated polymer was filtered off and dried to constant weight. We obtained 0.276 g (55.2%) of a water-soluble product; intrinsic viscosity 0.17 dl g^{-1}.

The ^{1}H NMR spectrum of branched homopolymer **IIb** was recorded on a Bruker AC-200 spectrometer in dimethylacetamide-d_9 (5% solution). The diffusion and sedimentation coefficients and the sedimentation-average molecular weight M_{SD} of branched poly-HPMA samples were determined as described in [16]. The floatability factor (1 – $v\rho_0$) fot poly-HPMA, required for determining M_{SD} by the Svedberg formula, was taken from [17]. Hydrolysis of branched HPMA homopolymer **IIj** was studied as described in [18].

CONCLUSIONS

(1) Low-molecular-weight ($\overline{M}_v$ = 7000–30000) *N*-(2-hydroxypropyl)methacrylamide homopolymers were prepared by radical polymerization in isopropanol in the presence of *p*-nitrophenol.

(2) The reaction of the linear homopolymers prepared with hexamethylene diisocyanate in dimethylformamide at 130°C under argon yielded branched homopolymers, M_{SD} = 53000–71000, containing interchain urethane links. These links are hydrolyzed at a fairly high rate in saline (pH 7.0) at 37°C.

ACKNOWLEDGMENTS

The study was financially supported by the Ministry of Science (program of support of leading scientific schools, project no. 00-1597318).

REFERENCES

1. Dunkan, R. and Kopeček, J., *Adv. Polym. Sci.*, 1984, vol. 57, pp. 53–101.
2. Chytry, V., Vrana, A., and Kopeček, J., *Makromol. Chem.*, 1978, vol. 179, no. 2, pp. 329–336.
3. Seymour, L.W., Dunkan, R., Kopečkova, P., *et al.*, *Cancer Treatment Rev.*, 1987, vol. 14, pp. 319–327.
4. Dunkan, R., Kopečkova-Reimanova, P., Strohalm, J., *et al.*, *Brit. J. Cancer*, 1987, vol. 55, pp. 165–174.
5. Solovskij, M.V., Ulbrich, K., and Kopeček, J., *Biomaterials*, 1983, vol. 4, no. 1, pp. 44–48.
6. Ulbrich, K., Nazarova, O., Panarin, E., *et al.*, *Coll. Czech. Chem. Commun.*, 1988, vol. 53, pp. 1078–1085.
7. Laane, A., Chytry, V., Haga, M., *et al.*, *Coll. Czech. Chem. Commun.*, 1981, vol. 46, no. 6, pp. 1466–1473.
8. Sprincl, L., Exner, J., Sterba, O., *et al.*, *Biomed. Mater. Res.*, 1976, vol. 10, pp. 953–963.
9. Bagdasar'yan, Kh.S., *Teoriya radikal'noi polimerizatsii* (Theory of Radical Polymerization), Moscow: Nauka, 1966.
10. Odian, G., *Principles of Polymerization*, New York: McGraw-Hill, 1970.
11. Braun, D., Cherdron, H., and Kern, W., *Praktikum der makromolekularen organischen Chemie*, Heidelberg: Alfred Huthig, 1971.
12. Kopeček, J., *Makromol. Chem.*, 1977, vol. 178, pp. 2169–2183.
13. Solovskii, M.V., Denisov, V.M., Ryadinskaya, N.Yu., *et al.*, *Zh. Prikl. Khim.*, 1999, vol. 72, no. 8, pp. 1368–1374.
14. Toroptseva, A.M., Belogorodskaya, K.V., and Bondarenko, V.M., *Laboratornyi praktikum po khimii i khimicheskoi tekhnologii vysokomolekulyarnykh soedinenii* (Laboratory Course of Chemistry and Chemical Technology of Macromolecular Compounds), Leningrad: Khimiya, 1972.
15. Bohdanecky, M., Bazilova, H., and Kopeček, J., *Eur. Polym. J.*, 1974, vol. 10, no. 5, pp. 405–410.
16. Solovskii, M.V., Nikol'skaya, N.V., Denisov, V.M., *et al.*, *Zh. Prikl. Khim.*, 2003, vol. 76, no. 2, pp. 284–288.
17. Solovskij, M.V., Panarin, E.F., Gorbunova, O.P., *et al.*, *Eur. Polym. J.*, 2000, vol. 36, no. 6, pp. 1127–1135.
18. Solovskii, M.V., Nikol'skaya, N.V., Korneeva, E.V., *et al.*, *Zh. Prikl. Khim.*, 2001, vol. 74, no. 4, pp. 643–648.

Russian Journal of Applied Chemistry, Vol. 76, No. 7, 2003, pp. 1112–1116. Translated from Zhurnal Prikladnoi Khimii, Vol. 76, No. 7, 2003, pp. 1145–1149.

MACROMOLECULAR CHEMISTRY AND POLYMERIC MATERIALS

Influence of the Structure of (Meth)acrylamides on Their Spontaneous Polymerization in Concentrated Aqueous Solutions

O. A. Kazantsev, A. V. Igolkin, K. V. Shirshin, S. A. Kazakov, N. A. Kuznetsova, and A. P. Malyshev

Dzerzhinsk Branch, Nizhni Novgorod State Technical University, Dzerzhinsk, Nizhni Novgorod oblast, Russia

Received March 18, 2003

Abstract—A study was made of spontaneous polymerization of (meth)acrylamides of different structures in concentrated aqueous acid solutions, in particular, as influenced by the monomer association.

(Co)polymerization in concentrated aqueous solutions is widely used for preparing polymers from (meth)acrylamides. It was found earlier that, in such solutions, acrylamide [1, 2] and 2-acrylamido-2-methylpropanesulfonic acid (AMPSA) [3] can undergo spontaneous polymerization. Kurlyankina *et al*. [2] demonstrated the radical mechanism of this process, with monomer molecules acting as radical sources. The detailed mechanism is, however, unknown. In this connection, it was of theoretical and practical interest to study the capability of (meth)acrylamides with different structures for spontaneous polymerization in aqueous solutions and to elucidate how the structure of the amide groups affects this process.

The choice of the monomers for the study was determined by their high solubility in water (we studied solutions with concentrations of 50 wt %) and resistance to hydrolysis. Under the experimental conditions (70°C, 3.5 h), the hydrolysis proceeds to no more than 3%.

First, we found that spontaneous polymerization in concentrated aqueous acid solutions is typical not only for acrylamide and AMPSA but also for methacrylamide and a number of N- and N,N-substituted (meth)-acrylamides with alkyl, amine, and carboxy substituents at the amide nitrogen atom. The resulting polymeric products differed in solubility, but in all the kinetic runs the mixtures were homogeneous, at least up to 15–20% conversion.

The process was run both in the presence of oxygen and in a nitrogen atmosphere. There were no peroxy compounds in the initial purified reactants, i.e., initiation of the process was not connected with degradation of the accumulated peroxides. This was emphasized by Kurlyankina *et al*. [2] who studied spontaneous polymerization of acrylamide in an argon atmosphere. The process was suppressed by introducing a sufficient amount of radical polymerization inhibitors.

Figures 1a and 1b illustrate how the structure of (meth)acrylamides affects their spontaneous polymerization in water. Comparative study of the kinetics of homogeneous polymerization of acrylic and methacrylic compounds was difficalt: With methacrylamide, the resulting polymer was insoluble in water, and the process was heterophase even at low conversions; methacrylamides disubstituted at the nitrogen atom (e.g., *N,N*-dimethylmethacrylamide) did not polymerize under the chosen conditions. In the case of monosubstituted amide monomers, we succeeded in comparing the data for *N*-methylacrylamide and *N*-methylmethacrylamide (Fig. 1a, curves *2, 4*). As in polymerization in the presence of initiators [4], the methacrylic monomer is less active than its acrylic analog.

We analyzed how the structure of the amide group affects polymerization of a series of acrylamide derivatives. As seen from the table, the acrylamides studied are characterized by similar initial rates and effective rate constants of polymerization k_{eff}. The calculations of the constants took account of the reaction orders with respect to the monomer, which varied with the amide from 1.8 to 3.6. It should be noted that the orders differed also in a study of spontaneous polymerization of *N,N*-dimethylaminoethyl methacrylates in concentrated aqueous solutions [5].

1070-4272/03/7607-1112$25.00

Influence of the structure of acrylamides CH_2=CHCONR^{1}R^2 on the initial rate v_0 and the effective rate constant k_{eff} of spontaneous polymerization in water* ($[M]_0$ = 50 wt %, 70°C, $[H_2SO_4]_0$ = 0.4 mg-equiv g^{-1})

Monomer no.	NR^1R^2	$-\log v_0$	$-\log k_{eff}$	σ*	$-R_s$
1	NH_2	3.80	3.78	0.870	0.985
2	$NHCH_3$	3.77	3.72	0.870	1.329
3	NHC_2H_5	3.79	3.80	0.870	1.615
4	$NHCH_2COOH$	3.97	3.86	0.696	1.727
5	$NHC(CH_3)_2CH_2SO_3H$	4.20	4.08	0.953	2.337
6	$NH(CH_2)_3N(CH_3)_2$	3.95	4.00	1.055	2.171
7	$NHC(CH_3)_2CH_2CH_2N(C_2H_5)_2$	4.13	4.06	0.985	2.434
8	$N(CH_3)_2$	3.52	3.48	0.835	1.719
9	$N(C_2H_5)_2$	3.86	3.79	0.883	2.199
10	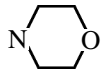	3.75	3.70	0.992	2.070

* σ* and R_s are the induction and steric constants of the NR^1R^2 groups, respectively.
** For monomer no. 5, $[H_2SO_4]_0$ = 0, $[NaOH]_0$ = 1.95; no. 6, $[H_2SO_4]_0$ = 3.52; and no. 7, $[H_2SO_4]_0$ = 2.73 mg-equiv g^{-1}.

The acrylamides studied can be ranked in the following order in accordance with their activities in spontaneous polymerization as characterized by k_{eff} (we show only the amide nitrogen atoms with the substituents):

$N(CH_3)_2$ > 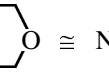 ≅ $NHCH_3$ > NH_2 ≅ $N(C_2H_5)_2$ ≅ NHC_2H_5 > $NHCH_2COOH$ > $NH(CH_2)_3N(CH_3)_2$ > $NHC(CH_3)_2CH_2CH_2N(C_2H_5)_2$ > $NHC(CH_3)_2CH_2SO_3H$. (A)

The structure of acrylamides exerts a much stronger influence on the rate of the previously studied homopolymerization of these compounds in water (at the initial concentration of 1 M) in the presence of an azo initiator [4]. According to their effective rate constants, the acrylamides studied were ranked in the following order:

$NHCH_3$ > $N(CH_3)_2$ > NH_2 > 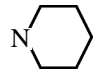 > NHC_2H_5 > $NH(CH_2)_5COOH$ > $N(C_2H_5)$ > 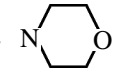 . (B)

The succession of the amides in series A and B is different. To analyze how the activity of the acrylamides in initiated and spontaneous polymerization is influenced by the structure of the amide groups, we initially used the modified Taft correlation equation

$$\log k_{eff} = \log k_0 + \rho\sigma^* + \delta R_s, \quad (1)$$

where σ* are the induction constants of the NR^1R^2 groups; R_s, steric constants of the same groups; and

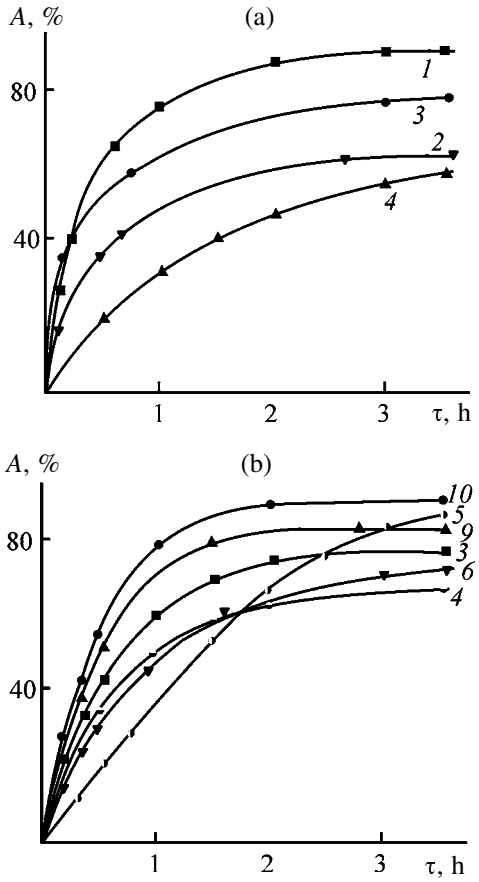

Fig. 1. Degree of conversion A of (a) CH_2=$CR^1CONR^2R^3$ and (b) CH_2=$CHCONR^1R^2$ monomers as a function of the time τ of spontaneous polymerization in water. $[M]_0$ = 50 wt %, 70°C. (a) R^1: (*1–3*) H and (*4*) CH_3; NR^2R^3: (*1*) NH_2, (*2, 4*) $NHCH_3$, and (*3*) $N(CH_3)_2$. (b) Figures at curves correspond to the monomer nos. in the table.

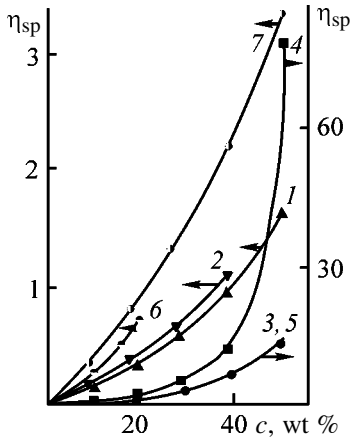

Fig. 2. Specific viscosity η_{sp} of aqueous solutions as a function of the concentration *c* of (meth)acrylamides $CH_2=CR^1CONR^2R^3$ at 25°C. R^1: (*1–5*) H and (*6–7*) CH_3; NR^2R^3: (*1, 6*) NH_2, (*7*) $NHCH_3$, (*2*) $N(CH_3)_2$, (*3*) $NHCH_2CH_2CH_2N(CH_3)_2$, (*4*) $NHCH_2COONa$, and (*5*) $NHC(CH_3)_2CH_2SO_3Na$.

ρ and δ, parameters characterizing the sensitivity of the reaction to the corresponding effects of the amide groups.

In our calculations of the induction and steric constants of the substituents, we took the carbon atom of the carbonyl groups as the reaction center; the σ* parameters were calculated by the procedures from [6, 7] (for nonionic and ionic monomers, respectively); the R_s parameters, by the procedure form [8]; and the bond lengths, using the HyperChem program by the MNDO method.

Using the experimental data from [4] (for initiated polymerization of the series B acrylamides), we obtained an unsatisfactory correlation with Eq. (1) (the correlation coefficient $r = 0.86$). It was shown in [9] that, for many nonradical reactions of (meth)acrylamides in aqueous media, a significant role is played by the hydrogen-bonding capability of the monomers. We introduced into Eq. (1) an additional parameter *n* corresponding to the number of the hydrogen atoms at the amide nitrogen atom and obtained an equation with a good correlation coefficient:

$$\log k_{eff} = 3.100 - 2.009\sigma^* + 1.465R_s - 0.508n, \quad (2)$$

$$r = 0.990, \ s = 0.006.$$

Thus, the rate of initiated polymerization of acrylamides in relatively dilute solutions tends to decrease with increasing *n*, increasing size of the amide groups, and strengthening accepting power of the substituents at the amide nitrogen atom. The first two factors are probably associated with decreases in the molecular mobility and in the accessibility of the reaction centers, respectively, and the third factor, with a decrease in the activity of the radicals due to stronger delocalization of the unpaired electrons and to an additional decrease in the electron density of the C=C bond (which strengthens the electrostatic repulsion of the monomer and propagating radicals having the partial charges of the same sign).

In the case of spontaneous polymerization of acrylamides, such correlation analysis also yielded a poor correlation coefficient with a two-parameter equation of the type (1) ($r = 0.682$) and a good, with the three-parameter equation

$$\log k_{eff} = -2.950 + 0.045\sigma^* + 0.375R_s - 0.286n, \quad (3)$$

$$r = 0.980, \ s = 0.002.$$

Appreciably smaller coefficients at all the three parameters in Eq. (3) compared to Eq. (2) confirmed that, in the monomer series studied, the influence of the structure of the amide on spontaneous polymerization is substantially smoothened compared to polymerization in the presence of initiators. The steric and hydrogen-bonding factors for both processes are unidirectional, and the inductive effect of the amide substituents is not essential for spontaneous polymerization.

Our results suggest the following mechanism of spontaneous polymerization of arcylamides. Egorov and Zubov [10] showed that initiated or spontaneous polymerization of a number of ionic vinyl monomers (salts of vinylpyridines and aminoethyl methacrylates and dimethyldiallylammonium chloride) in concentrated aqueous solutions is affected by their association. This yields precursor structures with the C=C bonds oriented in a favorable for polymerization way.

The association can be verified by a nonlinear plot of the viscosity of solution vs. monomer concentration. Indeed, the viscometric data for (meth)acrylamides of different structures confirmed association at concentrations characteristic for spontaneous polarization (the characteristic plots of viscosity vs. concentration are shown in Fig. 2).

Initiated polymerization of acrylamides was carried out at a moderate concentration of the monomers, which makes association of much smaller importance in this case. This can be responsible for a decrease in the corresponding coefficients in Eq. (3) compared to Eq. (2). For example, increased size of the alkyl substituents at the amide nitrogen atom complicated poly-

merization at moderate concentrations of the monomers, though favors association in concentrated solutions (Fig. 2, curves *3, 5*). Introduction of charged accepting groups into amides has a similar effect (strengthening of the association in such molecules is consistent with aggregation of organic ions in water [11]). Replacement of the hydrogen atoms at the amide nitrogen atom by alkyl groups, on the one hand, decreases the capability of the monomers for association by hydrogen bonding and, on the other, increases the hydrophobicity of the molecules and strengthens their aggregation.

The kinetic curves in Figs. 1a and 1b show that, in the initial stage of the process (series A), the order of the monomer activities significantly differs from the order based on data on conversion in 3.5 h (series C):

$$NH_2 \cong N\langle\rangle O > NHC(CH_3)_2CH_2SO_3H > N(C_2H_5)_2 > N(CH_3)_2 > NHC_2H_5 > NH(CH_2)_3N(CH_3)_2 > NHCH_2COOH > NHCH_3. \quad (C)$$

This may be due to the fact that, upon accumulation of a large quantity of products, the polymerization rate also depends on other factors (excluding those governing the process at low conversions). For example, a nonuniform growth of viscosity of the reaction mixtures affects the mobility of the macroradicals and the chain termination reaction in different ways. In polymerization of ionic monomers, an essential role is played by a change in the ionic strength of solutions due to decrease in the concentration of free ions in the system on changing from the monomer to polymer molecules [12]. Lastly, an important role is played by different solubilities of the products in water: Some systems remain homogeneous during the process and other become heterogeneous. For example, polymers based on disubstituted acrylamides, aminoalkylacrylamides, and AMPSA are well soluble in water, and those based on acrylamides and *N*-methylacrylamides have very limited solubilities.

EXPERIMENTAL

The initial acrylamide, methacrylamide, and AMPSA were recrystallized before use from benzene, 1 : 1 benzene–isopropanol, and acetic acid, respectively. *N*-(1,1-Dimethyl-3-diethylaminopropyl)acrylamide was synthesized by the Ritter reaction [13]; the other monomers were prepared by the Schotten–Baumann reaction [9]. 2-Acrylamidoacetic acid was recrystallized from ethyl acetate, and the other (meth)acrylamides were double-distilled in a vacuum.

The kinetics of polymerization of N- and N,N-substituted (meth)acrylamides in the presence of protic acids were studied in water at 70°C, at the initial concentrations of the reactants of 50 wt %. The polymerization was monitored by determining the concentration of the C=C bonds during the process and by isolating the products formed. The products were isolated by precipitation in acetone or by vacuum distillation of water (followed by separation of the unchanged initial substances by repeated washing with acetone). After purification, the polymers were dried in a vacuum (20°C, 2 mm Hg) to constant weight.

The concentration of the C=C bonds was determined by bromide–bromate titration. The ^{13}C NMR spectra were taken at a frequency of 75 MHz on a Varian Gemini-300 Fourier spectrometer (solvent D_2O, reference DMSO).

Poly-*N,N*-dimethylacrylamide. To 10.0 g (0.101 mol) of *N,N*-dimethylacrylamide in 8.0 ml of water, 1.96 g of 20% aqueous sulfuric acid (0.008 mol) was added. The resulting solution was kept for 4 h at 70°C, whereupon water was vacuum-distilled; the resulting polymer was washed with acetone to remove the unchanged initial monomer and sulfuric acid; the precipitate was filtered off and dried in a vacuum (20°C, 2 mm Hg). Yield 8.2 g (82%). The isolated product contained no double bonds. ^{13}C NMR spectrum, δ, ppm: 175.7–176.1 (–CON), 36.1 (CH_3–), 37.3–37.7 (–CH_2–), 34.4–35.4 (–CH–).

CONCLUSIONS

(1) (Meth)acrylamides with different structures (unsubstituted, N-, and N,N-substituted, nonionic, anionic, and cationic) undergo spontaneous polymerization in concentrated weakly acidic aqueous solutions.

(2) Correlation analysis demonstrated that the amide groups affect spontaneous and azo-initiated polymerization of acrylamides in different ways.

(3) A weak dependence of the spontaneous polymerization rate on the structure of the amide groups is presumably due to association of the monomers. The latter was confirmed by nonlinear concentration dependences of the viscosity of aqueous solutions of (meth)acrylamides.

REFERENCES

1. USSR Inventor's Certificate no. 648565.
2. Kurlyankina, V.I., Ushakova, I.L., Molotkov, V.A.,

et al., *Zh. Obshch. Khim*., 1999, vol. 69, no. 1, pp. 97–100.

3. Kazantsev, O.A., Igolkin, A.V., Shirshin, K.V., *et al*., *Zh. Prikl. Khim*., 2002, vol. 75, no. 3, pp. 476–480.
4. Kazantsev, O.A., Kazakov, S.A., Shirshin, K.V., *et al*., *Izv. Vyssh. Uchebn. Zaved., Khim. Khim. Tekhnol*, 2001, vol. 44, no. 1, pp. 62–65.
5. Efimova, D.Yu., Shibalovich, V.G., and Nikolaev, A.F., *Zh. Prikl. Khim*., 2000, vol. 73, no. 5, pp. 815–819.
6. Galkin, V.A., Cherkasov, A.R., Sayakhov, R.D., *et al*., *Zh. Obshch. Khim*., 1995, vol. 65, no. 3, pp. 458–468.
7. Galkin, V.A., Cherkasov, A.R., Sayakhov, R.D., *et al*., *Zh. Obshch. Khim*., 1995, vol. 65, no. 3, pp. 477–479.
8. Galkin, V.A., Sayakhov, R.D., and Cherkasov, A.R., *Usp. Khim*., 1991, vol. 60, no. 8, pp. 1617–1644.
9. Kazantsev, O.A., Synthesis and Properties of Nitrogen-Containing (Meth)acrylic Monomers, *Doctoral Dissertation*, Yaroslavl, 1998.
10. Egorov, V.V. and Zubov, V.P., *Usp. Khim*., 1987, vol. 56, no. 12, pp. 2076–2097.
11. Kessler, Yu.M. and Zaitsev, A.L., *Sol'vofobnye effekty: Teoriya, eksperiment, praktika* (Solvophobic Effects: Theory, Experiment, Practice), Moscow: Khimiya, 1989.
12. Kabanov, V.A. and Topchiev, D.A., *Polimerizatsiya ioniziruyushchikhsya monomerov* (Polymerization of Ionizable Monomers), Moscow: Nauka, 1975.
13. Shirshin, K.V., Kazantsev, O.A., Danov, S.M., *et al*., *Izv. Vyssh. Uchebn. Zaved., Khim. Khim. Tekhnol*., 1992, vol. 35, no. 2, pp. 23–27.

Russian Journal of Applied Chemistry, Vol. 76, No. 7, 2003, pp. 1117–1120. Translated from Zhurnal Prikladnoi Khimii, Vol. 76, No. 7, 2003, pp. 1150–1153.

MACROMOLECULAR CHEMISTRY AND POLYMERIC MATERIALS

Hydrolysis of *N*,*N*-Dimethylaminoethyl Methacrylate and Its Salts in Concentrated Aqueous Solutions

N. A. Kuznetsova, O. A. Kazantsev, K. V. Shirshin, T. A. Khokhlova, and A. P. Malyshev

Dzerzhinsk Branch, Nizhni Novgorod State Technical University, Dzerzhinsk, Nizhni Novgorod oblast, Russia

Received January 17, 2003

Abstract—The influence exerted by the structure of the ammonium group and anion, pH, and surfactant and polymeric additives on hydrolysis of *N*,*N*-dimethylaminoethyl methacrylate and its salts in concentrated aqueous solutions was studied.

N,*N*-Dimethylaminoethyl methacrylate (DMAEM) is the most widely used amine-containing (meth)acrylic monomer; polymers derived from its salts are used for wastewater treatment, in oil extraction, and in paper production [1]. Many industrial processes involve preparation of DMAEM salts in aqueous solution, followed by their (co)polymerization. Therefore, the resistance of DMAEM and its salts to hydrolysis is an important parameter which should be taken into account when choosing conditions for processes involving these monomers.

Hydrolysis of DMAEM and its acrylic analog, *N*,*N*-dimethylaminoethyl acrylate, was studied previously in relatively dilute aqueous solutions [2–4]. It was shown that, at concentrations of 0.5–2.0 M, hydrolysis of amino (meth)acrylates readily occurs at pH > 7 and sharpy accelerates upon quaternization of ammonium groups. Hydrolysis of DMAEM and its salts in more concentrated solutions was not studied, although these monomers are often used as highly concentrated solutions. The goal of this study was to reveal and explain the features of DMAEM hydrolysis in concentrated aqueous solutions.

Hydrolysis of esters can be catalyzed with both bases (the reaction in most cases occurs by the $B_{AC}2$ mechanism) and acids (in most cases, by the $A_{AC}2$ mechanism) [5]. In the absence of added acids or bases, hydrolysis of DMAEM is catalyzed by the amino group present in the molecule. As the DMAEM concentration is increased, the degree of ionization of the amino groups decreases, which should affect the hydrolysis. Furthermore, the hydrolysis yields methacrylic acid:

$$CH_2{=}C(CH_3)COOCH_2CH_2N(CH_3)_2 + H_2O \rightarrow CH_2{=}C(CH_3)COOH + HOCH_2CH_2N(CH_3)_2, \quad (1)$$

which makes lower the solution pH and thus affects the hydrolysis rate also. In base hydrolysis, the catalyst concentration decreases in the course of the reaction, and in acid hydrolysis it grows. Solutions of DMAEM quaternary salts in the absence of added acids or alkalis are neutral and do not undergo noticeable hydrolysis.

When considering the features of DMAEM hydrolysis in concentrated solutions, it should be borne in mind that the free amino ester, in contrast to its tertiary and quaternary ammonium salts, has a substantial range of phase separation in the system with water above 20°C (Fig. 1). Therefore, experiments with free DMAEM were performed at 15–20°C, so as to cover a wider concentration range. As seen from Fig. 2, at this temperature the hydrolysis is fairly slow, and its rate noticeably decreases as the initial concentration of the monomer is made higher. In 90% solutions in 10 days, no hydrolysis was observed at all (at 70%

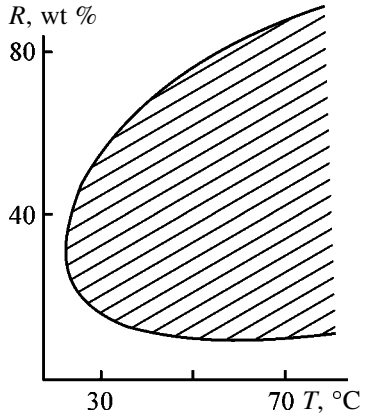

Fig. 1. Solubility diagram of the DMAEM–water system: (*R*) DMAEM content and (*T*) temperature. The phase separation region is cross-hatched.

1070-4272/03/7607-1117$25.00

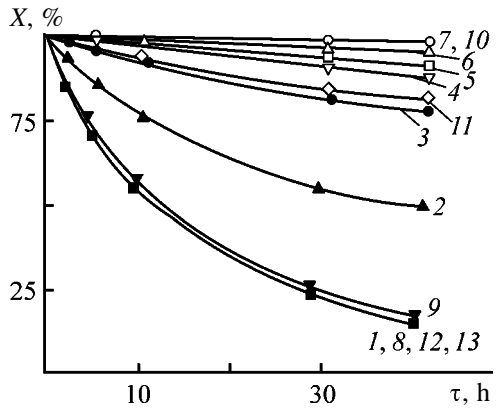

Fig. 2. Degree of DMAEM hydrolysis X as a function of time τ. 20°C. Initial DMAEM concentration, wt %: (*1*, *8*–*13*) 10, (*2*) 20, (*3*) 30, (*4*) 40, (*5*) 50, (*6*) 70, and (*7*) 90. Polymer added (5.0 wt % relative to DMAEM): (*8*) sodium 2-acrylamido-2-methylpropanesulfonate polymer and (*9*) DMAEM · $0.5H_2SO_4$ polymer. Surfactant added, M: (*10*) 5×10^{-5} cetyltrimethylammonium bromide, (*11*) 3×10^{-3} tetrabutylammonium bromide, (*12*) 5.3×10^{-4} Emul'sit 100, and (*13*) 3.13×10^{-4} M Neogen R.

concentration, the degree of hydrolysis in 10 days was 13%).

Hydrolysis of ammonium salts derived from DMAEM (*N*,*N*,*N*-trimethylammonioethyl methacrylate methyl sulfate, DMAEM · DMS; *N*,*N*,*N*-trimethylammonioethyl methacrylate chloride, DMAEM · MC; *N*-benzyl-*N*,*N*-dimethylammonioethyl methacrylate chloride, DMAEM · BC) was fast in alkaline medium (with NaOH added) and stopped on reaching the neutral medium. Therefore, the maximal degree of hydrolysis in these experiments corresponded to the amount of the initially added alkali. In particular, even at a high concentration of DMAEM · MC (70 wt %) at 20°C and NaOH concentration of 2 wt %, the solution became neutral within several minutes.

In acid solutions, the pattern changed. No hydrolysis of tertiary and quaternary salts of DMAEM, both in moderately (30 wt %) and highly (80 wt %) concentrated solutions, was detected at 20°C in several days even at pH 1–2. At 70°C, the hydrolysis became noticeable (Figs. 3, 4). As expected, the hydrolysis accelerated with decreasing initial pH. As in alkaline solutions, the hydrolysis was noticeably slower at higher initial concentrations of the monomer, and quaternary DMAEM salts were more active than the tertiary salts. Also, the consumption of ester groups in the presence of HCl was noticeably faster than in the presence of H_2SO_4 (Fig. 4, curves *7*, *9*). The degree of hydrolysis was also influenced by the structure of the ammonium group (Fig. 4, curves *3*, *4*, *6*). The quaternary salts can be ranked in the following order with respect to activity: DMAEM · MC > DMAEM · BC > DMAEM · DMS. It should be noted that, in DMAEM · DMS, both the carboxylate and sulfate ester groups undergo hydrolysis [reactions (2), (3)], and data are given for the sum of these processes:

$$CH_2=C(CH_3)COOCH_2CH_2\overset{+}{N}(CH_3)_3 + H_2O$$

$$\rightarrow CH_2=C(CH_3)COOH + HOCH_2CH_2\overset{+}{N}(CH_3)_3, \quad (2)$$

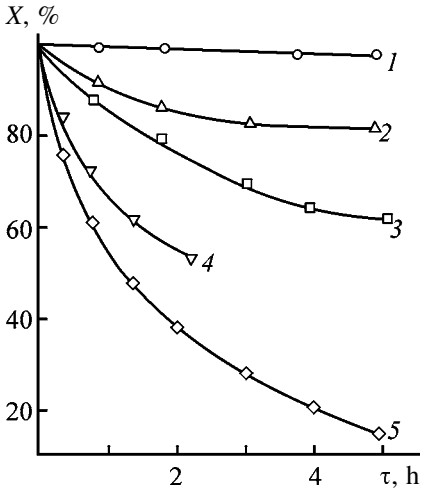

Fig. 3. Degree of hydrolysis X of DMAEM · $0.5H_2SO_4$ (40 wt %) in acid solution as a function of time τ. 70°C; the same for Figs. 4 and 5. H_2SO_4 concentration, wt %: (*1*) 2.5, (*2*) 7.4, and (*3*–*5*) 1.3. Polymer added (5.0 wt % relative to DMAEM): (*4*) sodium 2-acrylamido-2-methylpropanesulfonate polymer and (*5*) DMAEM · $0.5H_2SO_4$ polymer.

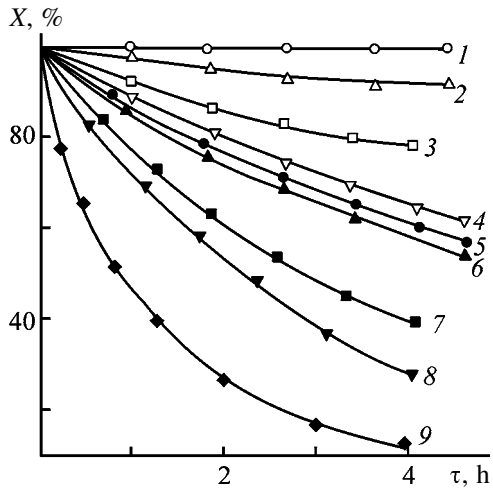

Fig. 4. Degree of hydrolysis X of (*1*, *2*, *5*, *6*–*9*) DMAEM · MX, (*3*) DMAEM · DMS, and (*4*) DMAEM · BC in acid solution as a function of time τ. Monomer concentration, wt %: (*1*, *3*–*6*) 70, (*2*) 85, (*7*, *9*) 40, and (*8*) 20. Acid: (*1*–*6*, *8*, *9*) HCl and (*7*) H_2SO_4. Acid concentration, M: (*1*) 0.01, (*2*, *5*, *8*) 0.4, (*3*, *4*, *6*) 0.5, and (*7*, *9*) 2.5.

$$CH_3SO_4^- + H_2O \rightarrow CH_3OH + HSO_4^-. \quad (3)$$

However, this does not affect the above-given order of activities of monomeric quaternary ammonium salts. For example, in 2.5 h the total degree of hydrolysis of DMAEM·DMS was 8.75% (12.3% of ammonioethyl methacrylate and 5.2% of methyl sulfate groups were hydrolyzed), compared to 27.2% for DMAEM·MC and 23.1% for DMAEM·BC.

It is known [6] that, in concentrated aqueous acidic solutions, DMAEM salts tend to spontaneous radical polymerization. To suppress this process, we added inhibitors. We revealed an interesting feature: When the amount of the inhibitor added was insufficient and spontaneous polymerization started, it accelerated the hydrolysis. Special experiments were made to evaluate the activating effect of polymerization (Fig. 3). It was shown that addition of polymers (cationic, DMAEM·0.5H_2SO_4 polymer; or anionic, sodium 2-acrylamido-2-methylpropanesulfonate polymer) to the solutions of DMAEM salts acidified with H_2SO_4 leads to faster consumption of the monomers (Fig. 3, curves *4*, *5*). It should be noted that the effect of additions of the anionic or cationic polymers on the base hydrolysis of DMAEM was insignificant (Fig. 2, curves *8*, *9*).

Thus, hydrolysis of DMAEM and its salts in highly concentrated aqueous solutions has certain features manifested in specific dependences of the reaction rate on the structure and concentration of the monomer, pH of solution, and additions of polymers. Our results can be explained using concepts of the behavior of monomers associating in aqueous solution.

It was assumed [7] that the influence of the concentration of amino methacrylate salts on features of their radical polymerization in aqueous solutions is due to association of the monomers.

Shibalovich *et al.* [8] measured the surface tension of aqueous solutions of DMAEM and its tertiary salts (monomer concentration ≤10 wt %) and concluded that these compounds exhibit surface activity.

To evaluate the influence exerted by association of DMAEM and its salts on their hydrolysis in concentrated solutions, we measured the concentration dependences of the viscosity (Fig. 6). As certain concentrations of all the DMAEM salts are exceeded, the plots start to strongly deviate from linearity, which is indicative of association. The capability of the monomers for association can be evaluated by the minimal concentration at which the viscosity starts to steeply grow.

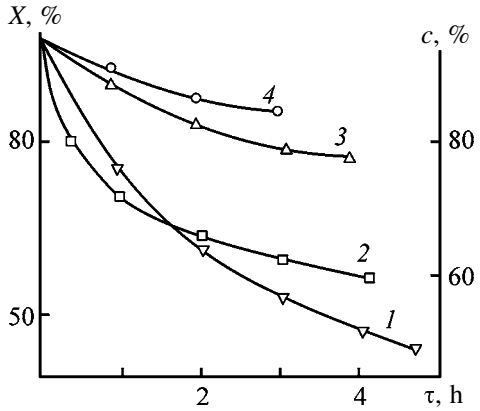

Fig. 5. Degree of (*1*, *2*) hydrolysis *X* and (*3*, *4*) consumption of C=C bonds *c* in DMAEM·0.5H_2SO_4 (40 wt %) in acid solution as a function of time τ. H_2SO_4 concentration, wt %: (*1*, *3*) 11.3 and (*2*, *4*) 8.3.

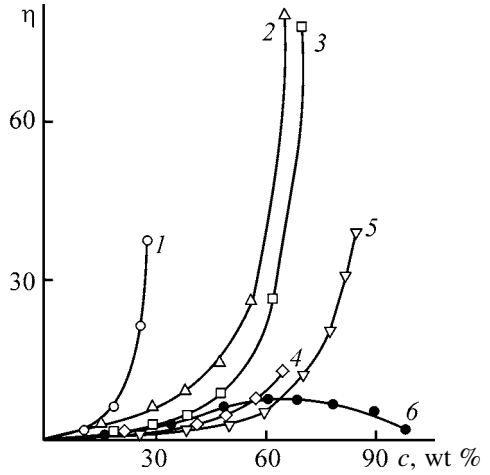

Fig. 6. Specific viscosity η of aqueous solutions of the monomers as a function of concentration *c*. 25°C. Monomer: (*1*) DMAEM·0.5H_2SO_4, (*2*) DMAEM·MC, (*3*) DMAEM·BC, (*4*) DMAEM·HCl, (*5*) DMAEM·DMS, and (*6*) free DMAEM.

Formation of associates should result in the steric shielding of the reaction centers and deceleration of the hydrolysis. Another important factor is the size of the ammonium groups and anions present in the system; apparently, the anions are mainly located on the external surface of the associates, preventing approach of the water molecules to the reaction centers. These factors may be responsible for the difference between the activities of DMAEM salts of different structures.

Polymeric molecules appearing in the system may "loosen" the monomeric associates. This was noted in experiments on addition of poly-2,5-nonene to a solution of a monomeric cationic surfactant [9]. As the molecular "packing" in the associate becomes less dense, the carbonyl carbon atom becomes more ac-

cessible, and hydrolysis should accelerate. This is apparently the case in acid solutions of DMAEM in which the monomer salts are strongly associated. In alkaline solutions, DMAEM is associated to a lesser extent (Fig. 6), and the effect of adding polymers is insignificant.

The presumed role of association of DMAEM and its salts was confirmed by experiments with addition of surfactants (Fig. 2). Cationic surfactants added to 10% DMAEM solutions noticeably decelerated (tetrabutylammonium bromide) or fully suppressed (cetyltrimethylammonium bromide) the hydrolysis. Anionic and nonionic surfactants did not noticeably affect the reaction rate. Thus, cationic micelles appearing in solutions prevent the hydrolysis, which is probably due to the capability of the cationic monomer to be "incorporated" into such micelles. In the case of anionic and nonionic micelles, penetration of the monomer inside the micelles is hindered, and, therefore, these surfactants do not affect the hydrolysis of DMAEM and its salts.

EXPERIMENTAL

Tertiary salts of DMAEM were prepared by addition of equivalent amounts of appropriate acids to aqueous solutions of the monomer. Quaternary salts were prepared in acetone or benzene by alkylation of DMAEM with dimethyl sulfate, methyl chloride, or benzyl chloride.

The hydrolytic stability of the monomers was studied at 15–70°C at a monomer concentration of 10–90 wt %. The spontaneous polymerization was excluded by adding hydroquinone (0.5 wt % relative to the monomer). The progress of hydrolysis was monitored by alkali titration, and the content of C=C bonds was determined by bromide–bromate titration. The specific viscosity of aqueous solutions of the monomers was determined with an Ubbelohde viscometer (d_c 0.56, 0.73, or 0.99 mm depending on the viscosity of the initial solution) at 25°C. When studying the hydrolysis of DMAEM·DMS, the methanol concentration was estimated by gas–liquid chromatography (Tsvet-100 device, flame-ionization detector, 2000 × 3-mm steel column, stationary phase 10% PEGA on Chromaton N-AW, carrier gas nitrogen, flow rate 2×10^{-3} $m^3 h^{-1}$, vaporizer temperature 200°C, column temperature 100°C).

CONCLUSIONS

(1) An increase in the monomer concentration and addition of cationic surfactants result in sharp deceleration of the base hydrolysis of *N*,*N*-dimethylaminoethyl methacrylate.

(2) Acid hydrolysis of *N*,*N*-dimethylaminoethyl methacrylate salts is decelerated with increasing solution concentration and accelerated on adding anionic and cationic polymers; quaternary salts are hydrolyzed more readily than tertiary salts, and their activity decreases in the order *N*,*N*,*N*-trimethylammonioethyl methacrylate chloride > *N*-benzyl-*N*,*N*-dimethylammonioethyl methacrylate chloride > *N*,*N*,*N*-trimethylammonioethyl methacrylate methyl sulfate.

(3) The hydrolysis data and concentration dependences of the viscosity of *N*,*N*-dimethylaminoethyl methacrylate salt solutions suggest that association of the monomers exerts a passivating effect on the hydrolysis.

REFERENCES

1. Askarov, M.A., Mukhitdinova, N.A., and Nazarov, A., *Polimerizatsiya aminoalkilakrilatov* (Polymerization of Aminoalkyl Acrylates), Tashkent: Fan, 1977.
2. Kazantsev, O.A., Zil'berman, E.N., Salov, V.N., and Krasnov, V.L., *Zh. Prikl. Khim.*, 1987, vol. 60, no. 9, pp. 2142–2145.
3. Kazantsev, O.A., Shirshin, K.V., Danov, S.M., and Kazakov, S.A., *Zh. Prikl. Khim.*, 1998, vol. 71, no. 2, pp. 304–307.
4. Tur'yan, Ya.I., Ignat'eva, F.K., Korshunov, M.A., and Mikhlin, V.S., *Usp. Khim.*, 1976, vol. 45, no. 2, pp. 224–250.
5. Ingold, C.K., *Structure and Mechanism in Organic Chemistry*, Ithaca: Cornell Univ. Press, 1969.
6. Efimova, D.Yu., Shibalovich, V.G., and Nikolaev, A.F., *Zh. Prikl. Khim.*, 2000, vol. 73, no. 5, pp. 815–819.
7. Egorov, V.V., Zaitsev, S.Yu., and Zubov, V.P., *Vysokomol. Soedin., Ser. A*, 1991, vol. 33, no. 8, pp. 1587–1608.
8. Shibalovich, V.G., Efimova, D.Yu., and Nikolaev, A.F., *Plast. Massy*, 2000, no. 3, pp. 25–27.
9. Egorov, V.V., *Kolloidn. Zh.*, 1992, vol. 54, no. 1, pp. 47–51.

Russian Journal of Applied Chemistry, Vol. 76, No. 7, 2003, pp. 1121–1126. Translated from Zhurnal Prikladnoi Khimii, Vol. 76, No. 7, 2003, pp. 1154–1159.

MACROMOLECULAR CHEMISTRY AND POLYMERIC MATERIALS

Influence of the Reaction Medium on the Kinetics of Copolymerization of *N*-Vinylsuccinimide with Butyl Acrylate

N. A. Lavrov, E. V. Sivtsov, and A. G. Pisarev

St. Petersburg State Technological Institute, St. Petersburg, Russia

Received April 4, 2003

Abstract—Radical copolymerization of *N*-vinylsuccinimide with *n*-butyl acrylate in pyridine and the influence of donor characteristics of the solvent on the reaction kinetics were studied. The kinetics of copolymerization in various solvents (dichloroethane, dimethyl sulfoxide, and pyridine) were studied.

It is well known that the reaction medium can significantly affect the kinetics of radical (co)polymerization [1–3] and characteristics of the resulting (co)polymers. The presence in monomer molecules of atomic groups capable to interact with medium components provides conditions for control of the reactivity of monomers and for directed synthesis of polymers. Variation of the relative activity of monomers in copolymerization allows production of copolymers of definite structure, which is of great importance in synthesis of polymers for medical purposes.

Copolymers of *N*-vinylsuccinimide (VSI) with *n*-butyl acrylate (BA) are of interest for production of flexible films for medical and biological purposes [4, 5]. With the aim to obtain soluble VSI–BA copolymers suitable for production of films, the copolymerization is carried out in organic solvents.

It was found [6] that the reactivity of monomers can be affected by using solvents with variable electron-donor power. According to data obtained in studying the kinetics of copolymerization in electron-donor solvent, dimethyl sulfoxide (DMSO), this solvent {Gutmann donor number (DN) 124.7 kJ mol^{-1} [7]} decreases the relative activity of VSI. Variation of the reactivity of VSI is caused by complexation of monomer molecules and solvent, which was confirmed by IR spectroscopy [8] and X-ray diffraction [9].

The results of studying the kinetics of copolymerization of VSI with BA in DMSO [10] suggest the possibility of controlling the relative activity of VSI in copolymerization with acrylic monomers. In view of the fact that the interaction of monomer with the solvent is considerably stronger with VSI than with an acrylic monomer [8, 9], it was suggested that the use of electron-donor solvents will increase the electron density on the double bond of the vinyl group of the VSI molecule, enhance the activity of radicals, and decrease the relative activity of the VSI monomer. To confirm experimentally this suggestion, we studied copolymerization of VSI with BA in pyridine (DN = 138.49 kJ mol^{-1} [7]). Here we report the results of this study.

Monomers and azobis(isobutyronitrile) (AIBN) were prepared by the procedure similar to that described in [10]. We used double-distilled pyridine of analytically pure grade. Copolymerization of monomers was carried out in ampules under argon at 60°C. The total concentration of monomers in pyridine was 0.7, and the concentration of AIBN, 0.0165 M. The reaction kinetics were monitored gravimetrically. After completion of the process, the contents of ampules were poured into distilled water; the precipitated copolymer was filterred off and dried to constant weight at 20°C (660 Pa). The composition of copolymers (Table 1) was determined from IR spectra, namely, from the ratio of the optical density of the band at 1700 cm^{-1}, D_{VSI}, to that of the band at 1735 cm^{-1}, D_{BA}, using the calibrating plot [10].

Copolymerization in pyridine proceeds to high degrees of conversion. The kinetic curves (Fig. 1) show no gel effect characteristic of copolymerization in the bulk. The synthesized copolymers are soluble in organic solvents, which allows production of films from these copolymers by casting from a solution.

Owing to higher reactivity of BA monomer, its concentration in the reaction mixture decreases more rapidly than the VSI concentration (Fig. 2, curves *1, 2*). The curves in Fig. 2 are similar to those describing copolymerization in DMSO [10], but the ratio of

1070-4272/03/7607-1121$25.00

Table 1. Composition of copolymers VSI (M_1)–BA obtained in pyridine at 60°C

M_1,* mole fraction	Degree of conversion, %	Mole fraction of VSI in copolymer
0.25	6	0.13
	21	0.15
	56	0.17
	67	0.19
0.50	7	0.28
	34	0.32
	44	0.41
	85	0.45
0.75	8	0.50
	30	0.52
	36	0.57
	98	0.74

* M_1 is the content of VSI in the mixture of monomers.

Table 2. Ratio of rates of BA and VSI consumption in the reaction mixture A as influenced by the solvent and by the content of VSI in the mixture of monomers M_1

M_1, mole fraction	A in copolymerization	
	in DMSO	in pyridine
0.25	43.5	19.1
0.50	10.8	8.1
0.75	1.4	1.3

the rates of BA and VSI consumption depends on the nature of the solvent. Table 2 shows that, in pyridine, this ratio is lower in all the cases than that in DMSO; therefore, the copolymers prepared in pyridine should be more uniform in composition than those prepared in DMSO.

The ratio of the rates of BA and VSI consumption in the reaction mixture also depends on the ratio of the monomers: it decreases with increasing mole fraction of VSI in the mixture of the monomers from 0.25 to 0.75, and at the VSI mole fraction of 0.75 the rates of entering of VSI and BA monomers into copolymerization are very close and almost independent of the solvent (Table 2, A = 1.3–1.4). This suggests that, at the molar ratio VSI : BA = 3 : 1, the probability of formation of copolymers with regular alternation of units is the highest.

To estimate the reactivity of VSI and BA monomers as influenced by the solvent, we evaluated the constants of copolymerization of VSI with BA using the modified Ezrielev–Brokhina–Roskin (EBR) [11] and Kelen–Tüdös (KT) methods [12], considering conversion of monomers, and also computer treatment of experimental data [13]. The calculated values were compared with the results obtained in studying co-

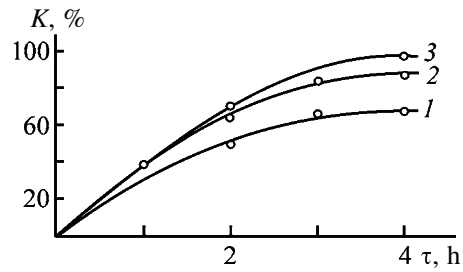

Fig. 1. Degree of conversion of monomers K as a function of duration τ of copolymerization of VSI with BA. Solvent pyridine; concentration (M): total of monomers 0.7, AIBN 0.0165; 60°C; the same for Fig. 2. Mole fraction of VSI in the mixture of monomers: (*1*) 0.25, (*2*) 0.50, and (*3*) 0.75.

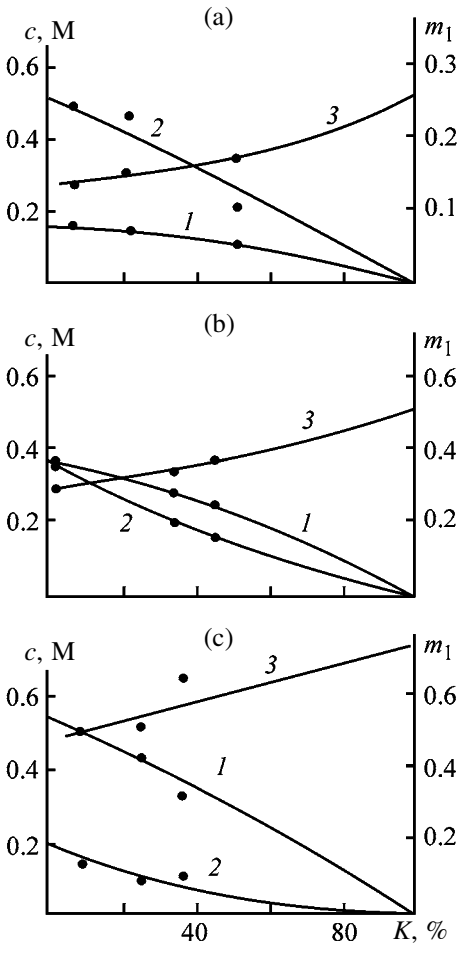

Fig. 2. Dependences of the concentration c of (*1*) VSI and (*2*) BA in the reaction mixture and (*3*) of the mole fraction of VSI units in copolymer m_1 on the degree of conversion of monomers K. Mole fraction of VSI in the mixture of monomers: (a) 0.25, (b) 0.50, and (c) 0.75.

Table 3. Constants of copolymerization of VSI (M_1) with BA (M_2). Initiator AIBN, 60°C

Solvent	r_1	r_2	$1/r_1$	$1/r_2$	r_2/r_1	r_1/r_2	Calculation procedure
Dichloroethane	0.15 ± 0.02	1.55 ± 0.08	6.67	0.645	10.3	0.232	UM
Pyridine	0.26 ± 0.05	1.86 ± 0.11	3.85	0.538	7.15	0.484	EBR
	0.29 ± 0.05	1.86 ± 0.11	3.45	0.538	6.41	0.539	KT
DMSO	0.18 ± 0.08	3.68 ± 0.79	5.55	0.272	20.4	0.662	EBR
	0.20 ± 0.08	3.79 ± 0.80	5.00	0.264	18.9	0.758	KT

Table 4. Probability of formation of diads f and average length of blocks L in chains of VSI–BA copolymers in copolymerization in various solvents. Initiator AIBN, 60°C

Solvent	M_1, mole fraction	f_{11}	f_{22}	$f_{12} = f_{21}$	L_1	L_2
Dichloroethane	0.1	0.001	0.874	0.063	1.02	15.0
	0.2	0.005	0.753	0.121	1.04	7.20
	0.3	0.011	0.637	0.176	1.06	4.62
	0.5	0.041	0.419	0.270	1.15	2.55
	0.7	0.116	0.220	0.332	1.35	1.66
	0.9	0.383	0.049	0.284	2.35	1.17
DMSO	0.1	0.0006	0.943	0.028	1.02	34.1
	0.2	0.003	0.878	0.060	1.05	15.7
	0.3	0.007	0.805	0.094	1.08	9.59
	0.5	0.031	0.628	0.171	1.18	4.68
	0.7	0.105	0.395	0.250	1.42	2.58
	0.9	0.402	0.101	0.248	2.62	1.41
Pyridine	0.1	0.002	0.892	0.053	1.03	17.7
	0.2	0.007	0.782	0.105	1.07	8.44
	0.3	0.019	0.672	0.155	1.12	5.34
	0.5	0.068	0.449	0.242	1.28	2.86
	0.7	0.189	0.231	0.290	1.65	1.80
	0.9	0.533	0.044	0.212	3.52	1.21

polymerization of VSI with BA in DMSO [10] and also with copolymerization constants in an inert solvent, dichloroethane [14], determined using the universal method (UM) [15]. It can be noted that the solvents used differ dramatically in their influence on the relative activity of the monomers (Table 3), probability of formation of diads, and average length of blocks in copolymer chains (Table 4).

Comparison of the copolymerization constants in an inert solvent, dichloroethane, and in an electron-donor solvent, DMSO, shows that the relative activity of VSI in DMSO decreases. This is caused by the interaction of VSI molecules with DMSO molecules via carbonyl groups of VSI and sulfoxide groups of DMSO, resulting in redistribution of the electron density in VSI molecule, increase in the electron density on the double bond, enhancement of the activity of macroradicals with terminal VSI unit, and decrease in the activity of VSI monomer.

The electron-donor power of pyridine is higher than that of DMSO [7]. Therefore, it can be expected that, in copolymerization of VSI with BA in pyridine, the relative activity of VSI should be decreased further. However, the copolymerization constants in pyridine, on the contrary, are closer to each other than those in DMSO. This is caused by steric factors hampering access of bulky pyridine molecule to the electrophilic centers of VSI molecule.

The evaluated copolymerization constants show that the rate constant of the reaction of the macroradical having the BA terminal unit with BA monomer exceeds the rate constant of the reaction of VSI macroradical with VSI monomer in all of the solvents used (Table 3). Evaluation of the relative activities of monomers in the reaction with macroradicals ($1/r$) shows that VSI monomer reacts with the radical having terminal BA unit more rapidly than with the own radical. In this case, the r_2/r_1 values increase in the

Table 5. Mole fraction of VSI M_1 in a mixture of monomers in copolymerization with BA in various solvents

Solvent	M_1, at indicated degree of conversion, %				
	0	10	20	40	50
DMSO	0.25	0.28	0.31	0.39	0.46
	0.50	0.54	0.59	0.71	0.75
	0.75	0.76	0.77	0.79	0.83
Pyridine	0.25	0.27	0.29	0.32	0.34
	0.50	0.52	0.55	0.59	0.62
	0.75	0.77	0.79	0.81	0.83

series of solvents pyridine < dichloroethane < DMSO, and the $1/r_1$ values increase in the series pyridine < DMSO < dichloroethane, i.e., when the reaction is carried out in pyridine, the rate constants K_{11} and K_{12} become close. Hence, in synthesis of VSI–BA copolymers in pyridine, the probability f_{11} of addition of VSI monomer to the radical with VSI terminal unit to form diads M_1M_1 is higher than that in the reactions in the other solvents (Table 4).

The value of $r_1r_2 < 1$ suggests the possibility of alternation of units in the copolymer, but the effect of cross addition of monomers to macroradicals is insignificant. The tendency for formation of alternating copolymers is pronounced only at VSI mole fraction in a mixture of monomers of 0.70–0.75 (Table 4), which is in good agreement with the conclusion made from Table 2.

The influence of an electron-donor solvent, pyridine, on the cross addition and probability of formation of diads M_1M_2 and M_2M_1 is similar to the influence of another electron-donor solvent, DMSO, on these processes. The probability $f_{12} = f_{21}$ increases in the order DMSO < pyridine < dichloroethane. This confirms validity of the hypothesis that electron-donor solvents (DMSO, pyridine) decrease the relative activ-

Table 6. Probability of formation of diads f and average length of blocks L in the chains of VSI–BA copolymers in copolymerization in various solvents at various degrees of conversion of the monomers

Solvent	M_1, mole fraction	Degree of conversion, %	f_{11}	f_{22}	$f_{12} = f_{21}$	L_1	L_2
DMSO	0.25	0	0.005	0.843	0.076	1.06	12.0
		10	0.006	0.821	0.087	1.07	10.5
		20	0.008	0.797	0.097	1.08	9.19
		40	0.015	0.731	0.127	1.12	6.76
		50	0.024	0.667	0.154	1.15	5.32
DMSO	0.50	0	0.031	0.628	0.171	1.18	4.68
		10	0.040	0.586	0.187	1.21	4.14
		20	0.054	0.531	0.208	1.26	3.56
		40	0.112	0.381	0.254	1.44	2.50
		50	0.143	0.326	0.265	1.54	2.23
DMSO	0.75	0	0.143	0.326	0.265	1.54	2.23
		10	0.153	0.311	0.268	1.57	2.16
		20	0.163	0.297	0.270	1.60	2.10
		40	0.185	0.268	0.274	1.68	1.98
		50	0.242	0.207	0.275	1.88	1.75
Pyridine	0.25	0	0.012	0.727	0.130	1.09	6.58
		10	0.015	0.705	0.140	1.10	6.02
		20	0.017	0.683	0.150	1.11	5.55
		40	0.022	0.650	0.164	1.13	4.95
		50	0.025	0.627	0.174	1.14	4.61
Pyridine	0.50	0	0.068	0.449	0.242	1.28	2.86
		10	0.075	0.427	0.249	1.30	2.72
		20	0.089	0.394	0.259	1.34	2.52
		40	0.109	0.350	0.271	1.40	2.29
		50	0.134	0.306	0.280	1.48	2.09
Pyridine	0.75	0	0.243	0.179	0.289	1.84	1.62
		10	0.268	0.159	0.286	1.94	1.56
		20	0.297	0.139	0.282	2.05	1.49
		40	0.329	0.120	0.275	2.19	1.44
		50	0.365	0.110	0.267	2.37	1.38

Table 7. Relative variation of the probability of diad formation and average length of blocks in the chains of VSI–BA copolymers with increasing degree of conversion from 0 to 50%

Solvent	M_1, mole fraction	Relative variation of indicated parameter*				
		f_{11}	f_{22}	f_{21}	L_1	L_2
DMSO	0.25	↑4.8	↓1.3	↑2.0	↑1.08	↓2.3
	0.50	↑4.6	↓1.9	↑1.5	↑1.3	↓2.1
	0.75	↑1.7	↓1.6	↑1.03	↑1.2	↓1.3
Pyridine	0.25	↑2.1	↑1.2	↑1.3	↑1.04	↓1.4
	0.50	↑2.0	↓1.5	↑1.2	↑1.2	↓1.4
	0.75	↑1.5	↓1.6	↑1.02	↑1.3	↓1.1

* (↓) Increase and (↑) decrease.

ity of VSI in copolymerization with BA as compared to an inert solvent. However, as compared to DMSO, pyridine is favorable for preparing copolymers more uniform in composition.

Taking into account variation of the VSI content in the mixture of monomers with increasing conversion (Table 5), we determined the probability of formation of diads and the average length of blocks in the copolymer chains in various solvents (Table 6). Calculation was carried out by the formulas from [16, 17] using computer software [18].

Tables 5 and 6 show that the high reactivity of BA, responsible for the higher rate of its consumption in the reaction mixture, results in enrichment of the monomer mixture in less active VSI. Therefore, with increasing conversion, the probability of formation of diads M_1M_2 and M_2M_1 increases and the probability of formation of diads containing BA units (M_2M_2) decreases. To estimate the composition uniformity of the copolymers, it is also important to know how the probability of formation of these structures will change with increasing degree of conversion. Table 7 shows that the weaker changes are observed in copolymerization in pyridine: as the degree of conversion of the monomers increases from 0 to 50% (at VSI mole fraction in the monomer mixture of 0.50), the probability of formation of diads M_1M_1 increases by a factor of only 2, that of diads M_1M_2 and M_2M_1, by a factor of 1.2, and that of diads M_2M_2 decreases by a factor of 1.5. When the reaction is carried out in DMSO, these changes are significantly stronger (Table 7).

Therefore, performing the reaction in pyridine allows synthesis of compound whose microstructure depends on conversion of monomers to the least extent, i.e., of copolymers more uniform in composition.

CONCLUSIONS

(1) Experiments on copolymerization of *N*-vinylsuccinimide with *n*-butyl acrylate confirm the influence of the electron-donor power of solvents on the relative activity of monomers and show that electron-donor solvents decrease the relative activity of *N*-vinylsuccinimide.

(2) When the reaction is carried out in pyridine, the relative variations of the probability of diad formation and of the average length of blocks with increasing conversion are the weakest. This allows synthesis of copolymers more uniform in composition, whose microstructure varies less significantly with conversation.

REFERENCES

1. Kabanov, V.A., Zubov, V.P., and Semchikov, Yu.D., *Kompleksoradikal'naya polimerizatsiya* (Complex-Radical Polymerization), Moscow: Khimiya, 1987.
2. Ivanchev, S.S., *Radikal'naya polimerizatsiya* (Radical Polymerization), Leningrad: Khimiya, 1985.
3. Lavrov, N.A., Sivtsov, E.V., and Nikolaev, A.F., *Reaktsionnaya sreda i kinetika polimerizatsionnykh protsessov* (Reaction Medium and Kinetics of Polymerization Processes), St. Petersburg: Sintez, 2001.
4. Shal'nova, L.I., Chudnova, V.M., and Trofimova, E.A., *Plast. Massy*, 1989, no. 11, pp. 29–34.
5. Lavrov, N.A., Shal'nova, L.I., and Nikolaev, A.F., *Plast. Massy*, 2001, no. 10, pp. 5–9.
6. Lavrov, N.A., Sivtsov, E.V., and Nikolaev, A.F., *Plast. Massy*, 2001, no. 10, pp. 43–45.
7. Reichardt, C., *Solvents and Solvent Effects in Organic Chemistry*, Weinheim: VCH, 1988.
8. Bondarenko, S.G., Nikolaev, A.F., Baranova, S.A., *et al.*, *Vysokomol. Soedin., Ser. A*, 1981, vol. 23, no. 12, pp. 2639–2651.

9. Sivtsov, E.V., Lavrov, N.A., and Nikolaev, A.F., *Plast. Massy*, 2001, no. 10, pp. 20–25.
10. Lavrov, N.A., Sivtsov, E.V., and Nikolaev, A.F., *Zh. Prikl. Khim.*, 1998, vol. 71, no. 12, pp. 2055–2056.
11. Ezrielev, A.I., Brokhina, E.L., and Roskin, E.S., *Vysokomol. Soedin., Ser. A*, 1969, vol. 11, no. 8, pp. 1670–1680.
12. Kelen, T. and Tüdös F., *J. Macromol. Sci., Ser. A*, 1979, vol. 9, no. 1, pp. 1–27.
13. Lavrov, N.A. and Dracheva, O.A., *Raschet kineticheskikh parametrov radikal'noi polimerizatsii i sopolimerizatsii s ispol'zovaniem EVM: Metodicheskie ukazaniya* (Computer Evaluation of Kinetic Parameters of Radical Polymerization and Copolymerization: Methodical Instructions), St. Petersburg: Sankt-Peterburg. Gos. Tekhnol. Inst., 1995.
14. Nikolaev, A.F., Bondarenko, V.M., and Lopukhinskii, L.M., *Sopolimerizatsiya N-vinilsuktsinimida s butilakrilatom* (Copolymerization of *N*-Vinylsuccinimide with Butyl Acrylate), Available from VINITI, November 17, 1975, no. 3271–75.
15. Glushchenok, I.N., *Universal'nyi metod rascheta konstant sopolimerizatsii: Uchebnoe posobie* (Universal Method of Evaluation of Copolymerization Constants: A Manual), Leningrad: Leningr. Tekhnol. Inst., 1975.
16. Gindin, L.M., Abkin, A.D., and Medvedev, S.S., *Dokl. Akad. Nauk SSSR*, 1947, vol. 56, no. 2, pp. 177–180.
17. Gindin, L.M., Abkin, A.D., and Medvedev, S.S., *Zh. Fiz. Khim.*, 1947, vol. 21, no. 11, pp. 1269–1287.
18. Lavrov, N.A., *Raschet cheredovaniya zven'ev v sopolimerakh: Metodicheskie ukazaniya* (Calculation of Alternation of Chains in Copolymers: Methodical Instructions), Leningrad: Leningr. Tekhnol. Inst., 1988.

Russian Journal of Applied Chemistry, Vol. 76, No. 7, 2003, pp. 1127–1133. Translated from Zhurnal Prikladnoi Khimii, Vol. 76, No. 7, 2003, pp. 1160–1166.

MACROMOLECULAR CHEMISTRY AND POLYMERIC MATERIALS

Aggregation of Macromolecules in Solution and Cluster Structure of the Surface of Films of Aromatic Polyetherimide

D. V. Novikov, A. N. Krasovskii, V. N. Filippov, T. E. Sukhanova, and V. M. Svetlichnyi

Institute of Macromolecular Compounds, Russian Academy of Sciences, St. Petersburg, Russia
St. Petersburg State University of Motion Pictures and Television, St. Petersburg, Russia

Received April 9, 2003

Abstract—The structural parameters of the aggregates of macromolecules of linear flexible-chain poly{*N*,*N*'-bis[4,4'-sulfonylbis(4,4'-phenoxyphenyl)][4,4'-(1,3-phenylenedioxy)bis(phthalimide)} in *N*-methyl-2-pyrrolidone solution and of the clusters of macromolecules on the surface of polyetherimide films formed from the solution were calculated from the capillary-viscometric and electron-microscopic data using the cluster model.

Substantiated choice of the concentration regimes of preparing films and coatings from solutions of polymers is topical for polymer processing technology. Of special interest are aromatic polyetherimides suitable for preparing high-strength and heat-resistant materials [1]. It is known that solution or melts of meltable polyetherimides can be processed directly, yielding thin and ultrathin films and coatings [2]. However, the factors governing the polyetherimide structure in solids at varied concentration c of the polymer in solution are studied inadequately.

As known [3], the structure of the physical network of macromolecules in films and coatings prepared from polymer solutions depends on the macromolecule concentration. The physical network sites are the aggregates or clusters of macromolecules forming in solution [4]. Such clusters have a fractal nature [4] and are characterized by enhanced density of packing of the macromolecules compared to the average density of the polymer. The cluster density and the volume fraction of the polymer occupied by the clusters are governed, in turn, by the parameters of the physical network of intermolecular contacts of the macromolecules [5]. Formation of aggregates of macromolecules in solution and in the course of film formation can be revealed experimentally. By introducing spin markers into a polymer and studying the behavior of the solution in an alternate magnetic field, it is possible to reveal the resonance absorption at low frequencies due to specific convective movements of the macromolecular aggregates. This resonance absorption is lacking in dilute solutions; it appears when a supramolecular structure (aggregates or clusters of macromolecules) arises and persists until complete solvent evaporation [4].

Importantly, during formation of films and coatings from polymer solutions, the mobility of the macromolecular aggregates sharply decreases as the solvent is removed from the system, and the fundamental time of relaxation of the macromolecules and their aggregates increases exponentially in concentrated solutions of polymers with increasing $[\eta]c$ ($[\eta]$ is the intrinsic viscosity) [6]. In this case, the time of the structural relaxation of the clusters, owing to their large size, should substantially exceed the characteristic film formation time [7]. This suggests that the topology of the cluster structure of the polymer films is predetermined by the hydrodynamic parameters of the macromolecular aggregates in solution.

Correlations between the hydrodynamic parameters of the macromolecular aggregates in solutions and the structural parameters of the clusters in a solid can be studied using the fractal cluster model [8]. This model predicts how the cluster density will vary depending on the polymer concentration in solution n [9], which is essential for the substantiated choice of the optimal concentrations for forming polymer films and coatings from solutions.

In terms of the cluster model, formation of a continuous network of intermolecular contacts of macromolecules in solution (an infinite cluster) involves successive formation of finite aggregates (clusters) and cluster–cluster aggregation of macromolecules. The relative density ρ of the sites of the fractal cluster for the Euclidean space with the dimensionality $E = 3$ varies [8] as

1070-4272/03/7607-1127$25.00

$$\rho = sV/\langle V\rangle \sim (\langle V\rangle/V)^{D/3-1}. \quad (1)$$

Here, V is the effective hydrodynamic volume of the macromolecule; $\langle V\rangle$, volume of the aggregate of macromolecules; D, fractal dimension; and s, degree of aggregation.

A transition from finite clusters to infinite cluster or to a continuous fluctuation network of intermolecular contacts of macromolecules near the threshold concentration of the polymer in solution c_{thr} is accompanied by a change in the fractal dimension D of the particles [3, 9].

In [10], we studied the hydrodynamic behavior and aggregation of the macromolecules of amorphous poly{*N*,*N*'-bis[4,4'-sulfonylbis(4,4'-phenoxyphenyl)]-[4,4'-(1,3-phenylenedioxy)bis(phthalimide)} (PEI) in an *N*-methyl-2-pyrrolidone (MP) solution. Interpretation of the viscometric data in terms of the cluster model showed that the density of the macromolecular aggregates in solution decreases with increasing $[\eta]c$. We showed that a transition from a moderately concentrated ($[\eta]c$ = 3–7) to concentrated ($[\eta]c > 7$) PEI solution corresponds to the threshold concentration c_{thr} of 13.5 ± 0.5 g dl^{-1} for linear PEI. At $c >$ 13.5 g dl^{-1} or $[\eta]c > 7$, the degree of aggregation of the macromolecules unlimitedly grows and the concentration of the clusters decreases. This suggests formation of a continuous fluctuation network of intermolecular contacts of the macromolecules in solution [9]. In [10], we also predicted a relatively higher density of the macromolecular clusters in the PEI films obtained at $c < c_{thr}$; the most uniform distribution of the cluster density in the PEI films should be achieved at c_{thr}.

According to the cluster model, the correlation radius ξ of the macromolecular clusters in films should be of the same order of magnitude as the radius $\langle R\rangle$ of the aggregates in solution near c_{thr}; on the scale of the correlation radius ξ, the fractal dimension D and the lattice density ρ_f of the macromolecular clusters in the film should coincide, respectively, with the parameters D and ρ of the aggregates in solution [3, 10, 11].

In our previous works [12, 13], we studied the relationships between the structure of the macromolecular clusters in polymer films and the concentrations of polymers in solution during film preparation. Taking the films obtained from solutions of gelatin [12] and epoxy–4,4'-isopropylidenediphenol oligomers [13] as examples, we found that the density of the physical network of macromolecules on the surface of films and coatings depends on the polymer concentration in solution, and the correlation radius ξ of the clusters is close to the hydrodynamic radius $\langle R\rangle$ of the macromolecular aggregates in solution near the threshold concentration c_{thr}.

In this work we continue our previous studies [10] with an electron-microscopic examination of the surface of the PEI films formed from solutions of different concentrations. We applied the cluster model for interpreting the viscometric and electron-microscopic data and calculated the hydrodynamic characteristics of the macromolecular aggregates in solution and the parameters of the cluster structure of the polymer on the film surface.

The aim of this work was to reveal correlations between the hydrodynamic characteristics of the macromolecular aggregates in solution and the parameters of the cluster structure of the film surface at varied polymer concentration.

EXPERIMENTAL

The subject of our study was a sample of amorphous [14] linear flexible-chain aromatic PEI containing in the diamine fragment of the backbone a four-ring 4,4'-sulfonylbis(4,4'-phenoxyphenyl) moiety

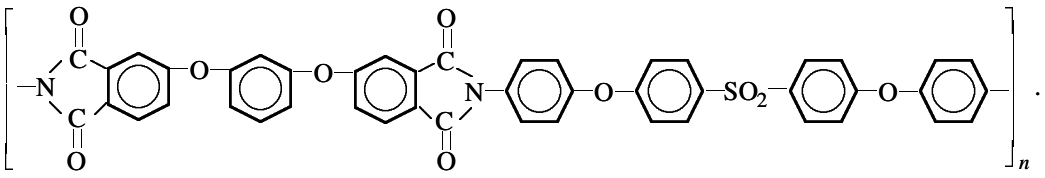

PEI was synthesized in two steps by polycondensation of the aromatic diamine and dianhydride in an MP solution, yielding polyamido acid (PAA) in the first stage. The second stage at 120–180°C involved dehydrocyclization of PAA in solution and distillation of the water released in imidization (as a toluene–water azeotrope) [2, 14]. According to the light-scattering and viscometric data [15], the molecular weight of PEI was ca. 5×10^4 Da.

The initial PEI and MP solutions had a concentration of 20.5 g dl^{-1}. The polymer solutions with con-

centrations from 0.1 to 15 g dl^{-1} were prepared by diluting the initial solution.

Films with a thickness of 10–15 μm were prepared from the PEI solutions in MP of the concentrations of 6, 14, 18, and 20.5 g dl^{-1} by casting onto glass substrates followed by vacuum drying at 80°C for 24 h. The degree of imidization of the PEI films was estimated by IR spectroscopy at 93–95% [10].

In the electron-microscopic study of the topological structure of the PEI film surface, we used the technique of gold decoration with bromine preactivation of the surface [14]. The molecular complexes of bromine with electron-donating functional groups of the polymer [16] on the film surface served as active centers for formation of gold particles in decoration [14]. The segments of the surface with enhanced local density of distribution of the decorating particles correspond topologically to the clusters of macromolecules [13, 14]. We proposed this technique in [14] for studying the cluster structure of the surface of PAA and polyimide films.

We studied the PEI film surface formed at the film–air interface. The bromine-activated film surface was subjected to vacuum (0.00133 Pa) sputtering of gold at the flux density of 10^{15}–10^{16} cm^{-2} s^{-1} to an effective layer thickness of 4 Å. The gold particles were separated from the polymer film with a supporting carbon replica and examined on an EMV 100L electron microscope at a ×30 000 magnification.

The topography of distribution of individual gold particles was analyzed using the radial distribution function $g(R)$ obtained by a step-by-step (with a step of $\delta = 3$ nm) scanning of the density ρ_s of distribution of the particles in the micrographs [14]. The scanning area of the micrographs with a ×150 000 magnification during processing on a PC was 2–2.5 μm^2.

The accumulations of the decorating gold particles on the film surface were represented as lattice clusters on the 2D lattice with the intersite distance corresponding to the most probable distance r between the particles and with the coordination number m_s determined using the average number m of the particles in the "coordination" sphere limited by the first minimum of the $g(R)$ function [14].

The average lattice density $\rho_f(R)$ of the clusters on the scale of radius R was calculated by the formula [14] $\rho_f(R) = \rho(R)/\rho'$, where $\rho(R)$ is the average density of distribution of the particles in a circumference with radius R and the center in an arbitrarily chosen particle, and ρ', density of the lattice sites determined by the formulas [17] $\rho' = 0.77/r^2$ for $m_s = 3$ and $\rho' = 1/r^2$ for $m_s = 4$.

The degree of the surface filling with the clusters ρ_f was calculated by the relation [14] $\rho_f = \rho_s/\rho'$ and also as the fraction ω of the surface covered with circumferences with the radius $R = r/2$ and centers in the decorating particles. It should be noted that the parameter ω is a more precise approximation for ρ_f, as it does not require knowledge of the lattice type.

The correlation radius of the clusters ξ was estimated from the position of the inflection point in the $\rho_f(R)$ plot constructed in the logarithmic coordinates [14]. The fractal dimension of the clusters D on the $R \le \xi$ scale was calculated from the slope of this plot using the relation $\rho_f(R) \sim R^{D-2}$ valid for $E = 2$ [8].

The order in the spatial distribution of the clusters was studied using the $g(R)$ function obtained by scanning the distribution density of the decorating particle with a step of $\delta > r$ [14].

The degree of spatial nonuniformity of the cluster density distribution was assessed using the relative fluctuation of the density $\delta\rho = (\Delta\rho^2/\rho)^{1/2}$, which was calculated by the relationship

$$\Delta\rho^2/\rho^2 = 1 + 2\pi\rho_s \int_0^\infty [g(R) - 1)]R\,dR, \qquad (2)$$

where $g(R)$ is the radial distribution function of the cluster density.

The $g(R)$ function was approximated on the $R < \xi$ scale by the power dependence $g(R) \approx R^{D-2}$ valid for fractal clusters [8].

The density ρ of the aggregates and the degree of aggregation s of the macromolecules in solution were calculated using the concentration dependence of the relative viscosity η_{rel} of PEI in MP solution [10] and also the relations from [18]:

$$\rho = (a[\eta]/[\eta]_c)^{a/(a-1)} = (x/\ln\eta_{rel})^{a/(a-1)}, \qquad (3)$$

$$s = (a[\eta]/[\eta]_c)^{a/(1-a)}, \qquad (4)$$

where $[\eta]_c$ is the running intrinsic viscosity [6] calculated from the relationship $[\eta]_c = a[\eta]([\eta]c)^{1-a}$ [18]; a, exponent in the expression $\ln\eta_{rel} = ([\eta]c)^a$, which is equal to $(3 - D)/D$ (D is the fractal dimension of the macromolecule [6]); and $x \equiv [\eta]c$.

For PEI in MP solution, the slope of the three linear portions in the $f(x)$ plot constructed in the $\ln f$–$\ln x$ coordinates (Fig. 1), where $f(x) = [\eta]c/\ln\eta_{rel} =$

Table 1. Parameters of the macromolecular aggregates in PEI solutions in MP at 298 K

c, g dl^{-1}	$[\eta]c \pm 0.1$	c_s, g dl^{-1}	$s \pm 0.2$	$D \pm 0.05$	$\rho \pm 0.02$, $E = 3$ ($E = 2$)	$\langle R \rangle$,* nm
1.0	0.5	0.78	1.31	1.60	0.78	26.9
2.5	1.3	1.37	1.83	1.60	0.59	39.7
4.1	2.1	1.83	2.24	1.60	0.51 (0.85)	43.9
6.1	3.2	2.16**	2.83	1.75	0.48 (073)	48.0
13.5***	7.0	1.07	12.6	1.75	0.15 (0.51)	126
14.7	7.6	0.58	25.3	1.45	0.06 (0.46)	155

* The $\langle R \rangle$ parameters were calculated by the expression $\langle R \rangle = Rw^{-1/D}([\eta]c/\ln \eta_{rel})^{1/(2D-3)}$, where $w = 0.673$ is the packing coefficient, and $R = 20.4$ nm, the macromolecule radius.
** Maximum of the concentration of the aggregates c_s.
*** Threshold concentration c_{thr} of PEI in solution.

$([\eta]c)^{1-a}$, varies in a such way that, in the first portion, $D_1 = 1.60$ ($[\eta]c < 3$), in the second, $D_2 = 1.75$ ($[\eta]c = 3$–7), and in the third, $D_3 = 1.45$ ($[\eta]c > 7$).

To a first approximation, the $\rho([\eta]c)$ plot for PEI in solution can be divided into two portions (Table 1) corresponding to the moderately concentrated and concentrated solutions of the polymer, respectively. A transition from the former ($[\eta]c = 3$–7) to the latter ($[\eta]c > 7$) corresponds to the threshold concentration $c_{thr} = 13.5 \pm 0.5$ g dl^{-1} (Table 1) with $D = 1.75$ in the $6 < c < 13.5$ g dl^{-1} region.

Two stages can be distinguished in the growth of aggregates in the PEI solutions. At $[\eta]c = 3$–7, the degree of aggregation s of the macromolecules tends to slowly increase with increasing concentration c (Table 1), since the probability of formation of the aggregates is primarily determined by pair collisions of the macromolecules. A rapid growth of s at $[\eta]c > 7$ is probably due to the cluster–cluster mechanism of aggregation [9].

The concentration of the aggregates $c_s = c/s$ is at a maximum below the point of transition from finite clusters to infinite cluster at $c < c_{thr}$ [8]. Our data suggest that the plot of the concentration c_s of the macromolecular aggregates vs. the concentration c of PEI in solution passes through a maximum at $c \approx 6$ g dl^{-1} (Table 1). At $c > 13.5$ g dl^{-1} (or $[\eta]c > 7$), the degree of aggregation s increases unlimitedly and c_s decreases, which suggests formation of a continuous network of intermolecular contacts of the macromolecules in solution [9].

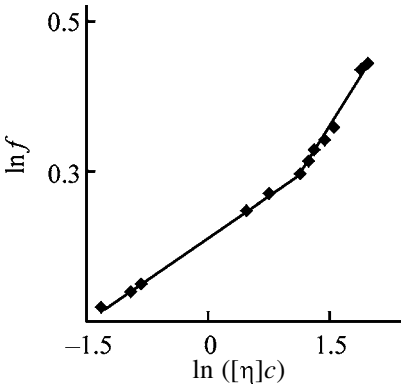

Fig. 1. Plot of $f = [\eta]c/\ln \eta_{rel}$ vs. $[\eta]c$ for PEI in MP solution in the logarithmic coordinates.

Figure 2 presents the electron micrographs of the carbon replicas with gold particles taken from the PEI film surface. The spatial distribution of the decorating particles is nonuniform; the film surface comprises areas characterized by enhanced local density of the particles, which correspond to clusters of macromolecules [14] separated by larger gold particles that are formed by coalescence of the "point" particles [17]. The predominant coalescence of the particles in the space separating the macromolecular clusters is known to be due to intensive chemisorption of bromine in looser areas of the polymer matrix.

The distribution of the cluster density is the most uniform in the case of the film obtained from the PEI solution of the concentration $c = 14$ g dl^{-1} (Fig. 2b). The films obtained from the solutions with $c = 6$ and $c = 20.5$ g dl^{-1} are characterized by major spatial fluctuations of the density (Figs. 2a, 2c).

The computer analysis of the micrographs showed that the decorating gold particles on the surface of the studied PEI films form a continuous spatial network corresponding to the infinite cluster of the PEI macromolecules [14].

Table 2 lists the spatial distribution parameters for the decorating gold particles on the surface of the PEI films. The parameters r and m were derived from analysis [14] of the radial distribution functions $g(R)$ of individual decorating particles on the surface of

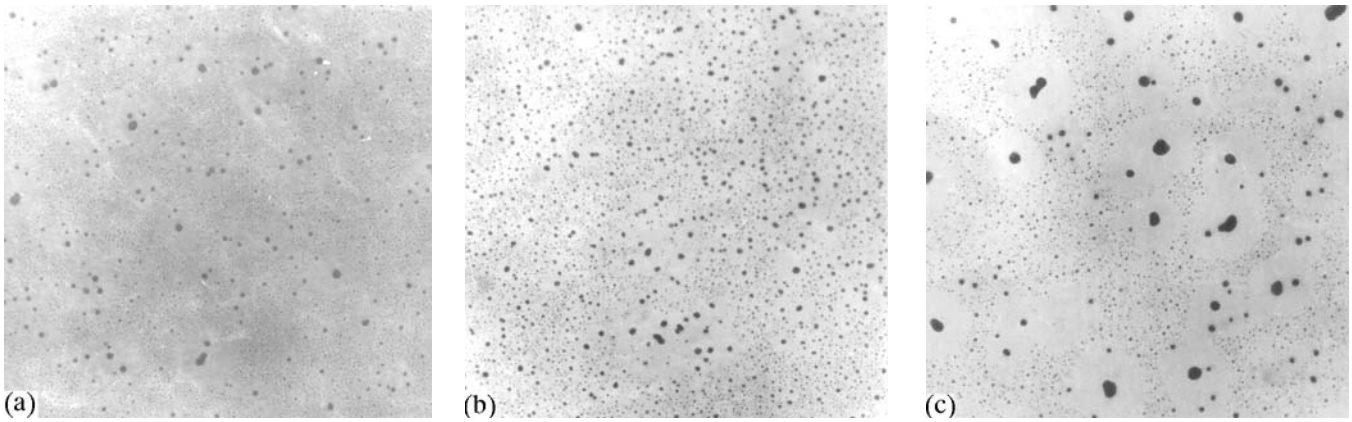

Fig. 2. Electron micrographs of the decorating gold particles on the surface of the PEI films obtained from the MP solution with the concentration c (a) 6, (b) 14, and (c) 20.5 g dl^{-1}. Magnification ×20 000.

the films formed from solutions of different concentrations. Our experimental data suggest that the densest packing of the macromolecular clusters is achieved at the maximal m value corresponding to c = 6 g dl^{-1} (Table 2).

Figure 3 shows the logarithmic plots of the lattice density $\rho_f(R)$ of the clusters of the decorating particles (or PEI macromolecules) vs. the R scale. The parameters ρ_f for the clusters were calculated using a hexagonal lattice with m_s = 3. This choice was correct, as evidenced by good agreement between the degrees of filling of the lattice with gold particles ρ_f and the fraction w of the surface covered by the circumferences representing the particles (Table 2).

For the PEI films formed from the solutions with concentrations c of 14, 18, and 20.5 g dl^{-1}, these plots consist of two linear portions (Fig. 3, curves *2* and *3*). The inflection point in the $\ln \rho_f$ vs. $\ln R$ plots, corresponding to a transition to the portion with a fractal dimension $D \approx 2$, determines the correlation radius ξ of the clusters. The lattice density of the clusters $\rho_f(\xi)$ at $R = \xi$ corresponds to the degree of the surface filling with the clusters ρ_f.

For the PEI film obtained from the solution at c = 6 g dl^{-1}, the plot of $\ln \rho_f$ vs. $\ln R$ consists of three portions (Fig. 3, curve *1*). The first portion ($R \le \xi_1$) corresponds to the fractal dimension of the clusters D = 1.84 ± 0.03, the second ($\xi_1 < R < \xi_2$), to D = 1.7, and $R = \xi_2$ is the point of transition to the portion with $D \approx 2$. Such a run of the $\rho_f(R)$ plot suggests a nonuniform structure of the percolation cluster network. It can be assumed that the skeleton of such a cluster is composed by macromolecular aggregates with the correlation radius $\xi_1 \approx 130$ nm. These aggregates are characterized by a higher local density and D = 1.84 (Table 2).

The lattice density ρ_f of the clusters in the films tends to decrease with increasing concentration c of PEI in solution (Table 2). Importantly, near the threshold concentration c_{thr} the density ρ of the aggregates of the PEI macromolecules in solution as calculated from the viscosity data for E = 2 is virtually identical to the lattice density ρ_f of the clusters on the film surface. Notably, the fractal dimension and the effective size $\langle R \rangle$ of the macromolecular aggregates in solution are close to the parameters D (at $R \le \xi$) and ξ for the cluster in the film (Tables 1, 2).

Figure 4 presents the density distribution functions $g(R)$ for the clusters on the surface of the PEI films. On the $R < \xi$ scale, the $g(R)$ plots obey the power law

Table 2. Parameters of the spatial distribution of the decorating gold particles and the cluster structure of the PEI film surface

c, g dl^{-1}	r, nm	m	$\rho_p(R = \xi) \pm 0.03$	ω	ξ, nm, ±10%	L, nm, ±10%	$D(R \le \xi) \pm 0.03$	$\delta\rho \pm 0.05$
6	21	3.2	0.62	0.66	130	–	1.84	0.62
			0.51		270		1.72	
14	21	1.7	0.47	0.42	130	260	1.70	0.47
18	21	1.2	0.37	0.32	130	250	1.70	0.57
20.5	23	1.4	0.30	0.28	130	250	1.73	0.68

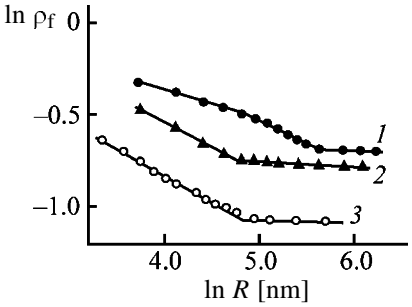

Fig. 3. Logarithmic plot of the lattice density ρ_f of the cluster distribution vs. the scale of radius R on the surface of the PEI films obtained from the MP solutions of the concentration c (*1*) 6, (*2*) 14, and (*3*) 20.5 g dl^{-1}.

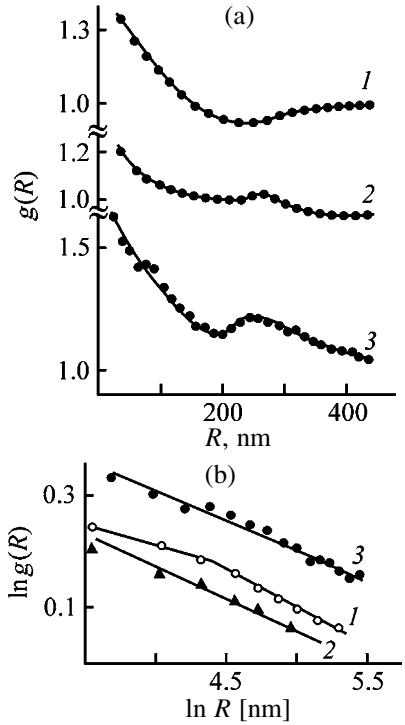

Fig. 4. (a) Density distribution function $g(R)$ for the clusters on the surface of the PEI films obtained from the MP solution of the concentration c of (*1*) 6, (*2*) 14, and (*3*) 20.5 g dl^{-1}, and (b) the same, plotted in logarithmic coordinates. (a) Step of scanning the density of distribution of the decorating gold particles δ = 40 nm; the function values were determined accurately to within 0.02. (*R*) Radius scale, nm.

$g(R) \sim R^{D-2}$ valid for fractal clusters, and in the logarithmic coordinates they are linear (Fig. 4b). These plots suggest that, near the threshold concentration c_{thr} of the polymer in solution, the fluctuations of the spatial distribution of the cluster density in the film are at a minimum. This is also evidenced by the relative fluctuation of the density $\delta\rho$ (Table 2) calculated by formula (2).

In the case of the PEI film obtained from the concentrated solution of the polymer ($c > c_{thr}$), the $g(R)$ function is characterized by a local maximum near $R \approx 250$ nm corresponding to the period L of the spatial alternation of the cluster density or of the network structure of the film surface (Fig. 4a, curve *3*). The parameter L (Table 2) is related to the correlation radius of the clusters ξ as $L \approx 2\xi$ for a hexagonal network (m_s = 3) [14]. Such an order of the topological structure of the film surface may be due to phase segregation in concentrated solutions of polymers, responsible for formation of microdomains differing in the local density of packing of the macromolecules.

CONCLUSIONS

(1) The lattice density ρ of the macromolecular clusters in films tends to decrease with increasing concentration c of the polymer in solution. A spatially uniform network of the percolation cluster characterized by the smallest density fluctuations is formed in the films obtained from solutions near the threshold concentration c_{thr} corresponding to formation of a continuous fluctuation network of intermolecular contacts of macromolecules. Formation of the continuous network of intermolecular contacts in solutions of poly{*N*,*N*'-bis[4,4'-sulfonylbis(4,4'-phenoxyphenyl)]-[4,4'-(1,3-phenylenedioxy)bis(phthalimide} near $[\eta]c$ = 7 is due to unlimited growth of the degree of aggregation s of the macromolecules.

(2) Discrete aggregates of the macromolecules in solutions of poly{*N*,*N*'-bis[4,4'-sulfonylbis(4,4'-phenoxyphenyl)][4,4'-(1,3-phenylenedioxy)bis(phthalimide} at $[\eta]c$ = 3–7 ($c < c_{thr}$) correspond to a nonuniform network of the percolation cluster in the film. The sites of such network are macromolecular aggregates with a relatively higher local density. The network of the percolation cluster in films formed from solutions at $c > c_{thr}$ is characterized by major spatial fluctuations of the density and a decrease in the density due to phase segregation in concentrated polymer solutions.

(3) The established trends in evolution of the cluster structure of the films allow a substantiated choice of the optimal concentrations of the polymer in solution for formation of polymer films and coatings.

REFERENCES

1. Bessonov, M.I., Koton, M.M., Kudryavtsev, V.V., and Laius, L.A., *Poliimidy – klass termostoikikh polimerov* (Polyimides: A Class of Heat-Resistant Polymers), Leningrad: Nauka, 1983.

2. Svetlichnyi, V.M., Arkhipova, E.V., Denisov, V.M., *et al*., *Vysokomol. Soedin., Ser. A*, 1990, vol. 32, no. 10, pp. 2075–2080.
3. Grosberg, A.Yu. and Khokhlov, A.R., *Statisticheskaya fizika makromolekul* (Statistical Physics of Macromolecules), Moscow: Nauka, 1989.
4. Bartenev, G.M. and Frenkel, S.Ya., *Fizika polimerov* (Polymer Physics), Leningrad: Khimiya, 1990.
5. Perepechko, I.I., *Vvedenie v fiziku polimerov* (Introduction to Polymer Physics), Moscow; Khimiya, 1978.
6. Baranov, V.G., Amribakhanov, D.Kh., Agranova, S.A., and Frenkel, S.Ya., *Vysokomol. Soedin., Ser. B*., 1988, vol. 30, no. 5, pp. 384–387.
7. Papkov, S.P., *Fiziko-khimicheskie osnovy pererabotki rastvorov polimerov* (Physicochemical Principles of Processing of Polymer Solutions), Moscow: Khimiya, 1971.
8. Feder, J., *Fractals*, New York: Plenum, 1988.
9. Krasovskii, A.N., Nikolaev, V.P., Shlyakov, A.M., and Mnatsakanov, S.S., *Vysokomol. Soedin., Ser. A*, 1995, vol. 37, no. 2, pp. 273–282.
10. Krasovskii, A.N., Svetlichnyi, V.M., Filippov, V.N., *et al*., *Zh. Prikl. Khim*., 2000, vol. 73, no. 12, pp. 2007–2013.
11. Gennes, P.-G. de, *Scaling Concepts in Polymer Physics*, Ithaca: Cornell Univ. Press, 1979.
12. Novikov, D.V., Krasovskii, A.N., Andreeva, A.I., and Basov, S.V., *Kolloidn. Zh*., 1999, vol. 61, no. 2, pp. 240–245.
13. Krasovskii, A.N., Novikov, D.V., Krasheninnikov, V.A., *et al*., *Zh. Prikl. Khim*., 2001, vol. 74, no. 1, pp. 124–134.
14. Novikov, D.V., Sukhanova, T.E., Svetlichnyi, V.M., *et al*., *Vysokomol. Soedin., Ser. A*, 2001, vol. 43, no. 4, pp. 634–642.
15. Bel'nikevich, N.G., Svetlichnyi, V.M., Kurenbin, O.I., *et al*., *Vysokomol. Soedin., Ser. A*, 1995, vol. 37, no. 8, pp. 1357–1360.
16. *Molecular Interactions,* Ratajczak, H. and Orville-Thomas, W.J., Eds., Chichester: Wiley, 1981, vol. 2.
17. Novikov, D.V. and Varlamov, A.V., *Poverkhnost'*, 1992, no. 6, pp. 117–121.
18. Krasovskii, A.N., Novikov, D.V., and Filippov, V.N., *Zh. Prikl. Khim*., 2003, vol. 76, no. 2, pp. 304–312.

Russian Journal of Applied Chemistry, Vol. 76, No. 7, 2003, pp. 1134–1138. Translated from Zhurnal Prikladnoi Khimii, Vol. 76, No. 7, 2003, pp. 1167–1171.

MACROMOLECULAR CHEMISTRY AND POLYMERIC MATERIALS

Thermal Transformations of Polyethylene Film and Porous Membrane on Its Basis

Yu. N. Sazanov, V. L. Ugolkov, O. E. Praslova, I. S. Kuryndin, and G. K. Elyashevich

Institute of Macromolecular Compounds, Russian Academy of Sciences, St. Petersburg, Russia
Institute of Silicate Chemistry, Russian Academy of Sciences, St. Petersburg, Russia

Received April 29, 2003

Abstract—Chemical and structural transformations in heating of extrusion and porous polyethylene films in air and an inert atmosphere are studied by thermal analysis and differential scanning calorimetry.

In recent years, microporous polymeric films have found wide application for filtration and separation of liquid mixtures and also as separation membranes in chemical power sources. The process for preparation of microporous polyethylene (PE) films by melt extrusion was reported in [1, 2]. The resulting porous films contain through-flow channels, being permeable to fluids and gases. Polyethylene is resistant to organic solvents, acids, and alkalis. Therefore, such films can be used in various media as filters and separators for chemical power sources.

Preparation of porous films involves the extrusion, annealing, and uniaxial extension stages. It is the last stage that provides formation of pores and through channels. The pore structure is stabilized by thermal fixation of samples at elevated temperature, which provides removal of stresses formed in extension of samples in the pore formation stage at room temperature. As a result of the indicated deformation and thermal treatment, porous samples are formed, having an oriented structure and highly developed relief-like surface.

The oriented structure of the films provides good mechanical characteristics, and the relief-like surface, high adhesion to deposited layers and coatings (both polymeric and nonpolymeric), allowing their use as porous supports in composite membrane systems. For example, composite membranes were obtained by polymerization of conducting polymers (polyaniline, polypyrrole) on the surface of porous PE films [3, 4]. Such systems can be used as ion-exchange and gas-separation membranes, and also as gas sensors and active elements in various electrochemical processes.

Wide potentialities of practical use of porous polymeric films initiate the need in comprehensive study of their thermal and deformation behavior. We have performed thermomechanical tests of composite membranes representing polypyrrole layers on a porous PE support [5]. The results showed that, when heated, these systems seem to be mechanically stable at temperatures much above the melting point of PE. To interpret this strange result, it appeared advisable to analyze in detail the behavior of PE supports on heating.

In this work, we studied the chemical and structural transformations occurring in porous PE films on heating in various atmospheres. We used as initial samples extruded PE films which were made porous by appropriate treatment.

EXPERIMENTAL

Extruded PE films were prepared by molding commercial HDPE ($M_w = 1.4 \times 10^5$ and $M_w/M_n = 6–8$). The extruded PE films and porous films obtained from them were studied by thermal analysis with a Netzsch STA 429 differential thermoanalyzer. Samples were heated in air or an inert atmosphere (CO_2) from room temperature to 400°C at a heating rate of 1 and 5 deg min^{-1}.

Structural transformations in cyclic heating were studied by differential scanning calorimetry (DSC) with a DSM-2 microcalorimeter at a heating rate of 16 deg min^{-1}.

Photographs of the samples after heating were obtained with an MPB-2 optical microscope at a magnification of 24.

1070-4272/03/7607-1134$25.00

Thermal behavior of the extruded PE films was studied by heating in the dynamic mode in the static air atmosphere (sample weight about 10 mg, heating rate 1 and 5 deg min^{-1}) (Fig. 1, curves *1* and *2*).

The thermal effects over the temperature range 20–300°C reflect melting of the polymer (endothermic peaks with the maxima at 127.7 and 130.5°C at a heating rate of 1 and 5 deg min^{-1}, respectively). With further heating of the melt from 183.6 and 193.1°C (respectively to the indicated heating rates), structural transformations in the polymer start, accompanied by a considerable exo effect but with no weight loss. Moreover, even some weight gain is observed at the temperature corresponding to the onset of the exo peak. Only in the next stage, on reaching 206.9 or 231.3°C (maxima of the exo peaks at a heating rate of 1 and 5 deg min^{-1}, respectively), the first signs of degradation are observed, accompanied by liberation of volatile products, as demonstrated by the TG data.

Experiments on programmed cooling of the sample from 300 to 70°C revealed the lack of weight loss and a distinctly pronounced exo effect of crystallization with the maximum at 113.9°C (Fig. 1, curve *3*).

The observed small weight gain at the onset temperature of the exothermic process can be attributed to thermal oxidation, which was observed previously in the TG curves [6]. Based on general knowledge [7], a quite substantiated hypothesis was put forward that solid oxidation products are formed via hydroperoxides. However, this phenomenon has not been analyzed in the literature yet. The TG curve obtained at a heating rate of 1 deg min^{-1} (Fig. 2, curve *1*) shows 0.5–0.8% weight gain over the temperature range 180–205°C, which is probably due to surface oxidation of the melt with formation of unstable solid products of thermal oxidation in the initial stage of cross-linking. It was demonstrated in the subsequent experiments that the value of this effect is in proportion to the sample weight and in inverse proportion to the heating rate.

These results suggest that the first section of the exothermic peak in the DSC curve is associated with oxidation and formation of hydroperoxides, whereas the second section, most likely, with subsequent cross-linking, since, as known [8], organic peroxides can initiate this process. This conclusion is also supported by the microscopic data obtained in the course of melting of the PE film. In this case, we observed loss in the melt fluidity above 240°C.

It is quite clear that oxidation and cross-linking are

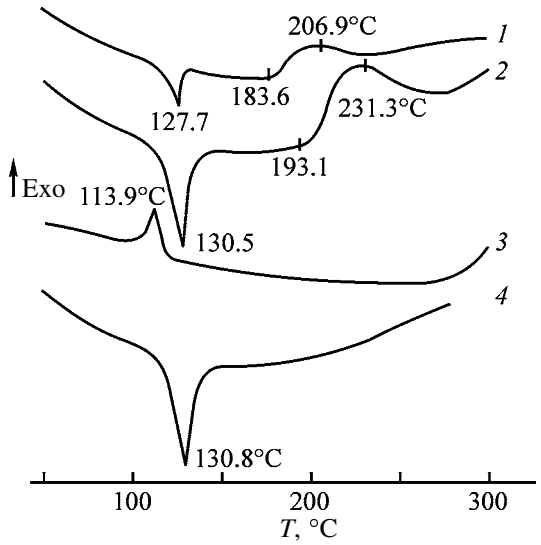

Fig. 1. DSC curves of extruded PE films in (*1–3*) air and (*4*) CO_2. Heating rate (deg min^{-1}): (*1*) 1 and (*2, 4*) 5. (*3*) Cooling at a rate of 5 deg min^{-1}. Netzsch STA 429 thermoanalyzer, sample weight about 10 mg; the same for Figs. 2 and 3. (*T*) Temperature; the same for Figs. 3 and 4.

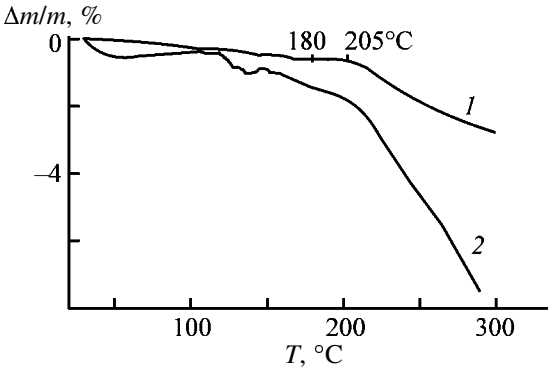

Fig. 2. TG curves in air at a heating rate of 1 deg min^{-1}: (*1*) extruded PE film and (*2*) membrane. ($\Delta m/m$) Weight loss and (*T*) temperature.

irreversible processes. They are completed after the first heating, so that no transformations accompanied by some thermal effects, other than melting and crystallization, are observed in the DSC curves on cooling and repeated heating of the samples.

The sample heated to 300°C and then cooled to room temperature represents a quite regular drop without appreciable signs of surface degradation. Its density is comparable with that of the initial PE granules.

When the experiment was carried out under similar conditions but in the inert CO_2 atmosphere, the endothermic peak caused by melting is identical to that observed in the oxidative atmosphere (Fig. 1, curve *4*). However, in this case, we observed no oxidation and

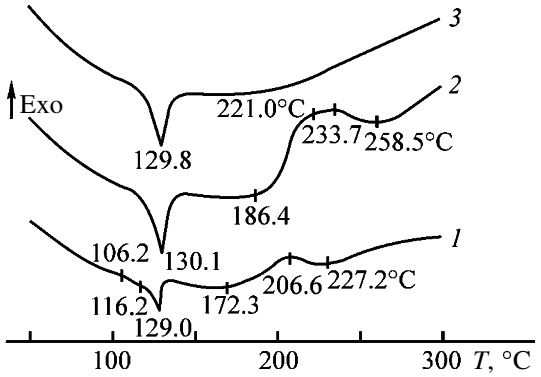

Fig. 3. DSC curves of PE membranes in (*1, 2*) air and (*3*) CO_2. Heating rate (deg min^{-1}): (*1*) 1 and (*2, 3*) 5.

cross-linking effects in the DSC curve over the above-indicated temperature range. Our thought is that this result supports the interpretation offered above for the thermal transformations in the extruded PE samples on heating in air.

On heating of a PE film membrane, we observed the effects similar to those found in studying the extruded films. However, analysis of the results obtained reveals a considerable contribution of the pore structure.

A distinctive feature of the porous samples is the change in their heat capacity at low rates of heating to the melting point. Characteristics knees in the DSC curve of the PE membranes at 101.2, 106.2, and 116.2°C (Fig. 3, curve *1*) can be attributed to changing ordering of particular domains whose relaxation time is comparable with the experimental heating rates. It is known that, above 100°C, the motion of chains in PE crystallites starts, resulting in partial disordering. At a heating rate of 5 deg min^{-1} and higher, these effects are not observed (Fig. 3, curve *2*). It may be suggested that these effects become more pronounced in heating of porous films in which the degree of orientation, size, and structural perfection of crystallites are much higher than in the extruded films, where an ordering loss is not reflected in remarkable thermal effects at temperatures below the melting point.

Figure 2 shows irregular 0.5–1% changes in the sample weight, suggesting thermal oxidation of the sample in the presence of oxygen adsorbed in pores of the membrane. In this case, the amount of adsorbed oxygen is considerably higher as compared to the extruded (nonporous) sample, since the specific surface area of the porous membrane is higher by four orders of magnitude than that of the initial PE film. Correspondingly, the increase in the sample weight caused by oxidation is higher in the membrane too. This is especially pronounced over the temperature range 70–150°C, and, initially, the oxidation is accompanied by increasing weight by virtue of temporary adsorption of primary products of PE oxidation in the membrane pores.

As the melt homogenizes in the course of heating, oxidation is extinguished, and the major changes in the weight are caused by liberation of volatile products of thermal degradation. As for the initial extruded film, in heating of the membrane, the onset of degradation with a remarkable weight loss at 250–300°C is also preceded by PE oxidation and cross-linking starting at 170–180°C. This is supported by the exo effect with the maximum at 206.6 and 221°C at a heating rate of 1 and 5 deg min^{-1}, respectively. It is clearly seen in the curve obtained at a heating rate of 5 deg min^{-1} that the exothermic peak splits into two components with maxima at 221 and 233.7°C.

Structural transformations in PE melt in melting of both films and membranes depend also on the thermal treatment conditions. Figure 4 shows the DSC curves of the extruded film (Fig. 4a) and membrane (Fig. 4b), which were heated in the cycling mode (heating–cooling–reheating). It is clearly seen that no exothermic effects typical of the initial oxidation and cross-linking stages are observed in reheating, and the repeated endo effect of melting is noticeably lower as compared to the initial sample (205 and 175 J g^{-1} in the film and 180 and 150 J g^{-1} in the membrane). Decreasing heat of melting in the second cycle is associated with the orientation loss in the sample in the first heating and also with decrease in its crystallinity, since crystallization conditions in cooling after the first heating differ from those under which the initial samples were obtained, including the lack of orientation. The lack or at least abrupt decrease in the exothermic effects, associated with the oxidation and cross-linking, in the repeated heating cycle suggests that these irreversible processes were practically completed in the first heating cycle.

In heating the membranes in CO_2, we observed no signs of oxidation in the melt as well as no concomitant exothermic effects and weight change (Fig. 2, curve *3*).

The results obtained allow interpretation of the thermodeformation behavior of composite systems based on microporous PE films in which a coating of rigid-chain polypyrrole provides preservation of the sample shape upon heating. In these systems, we

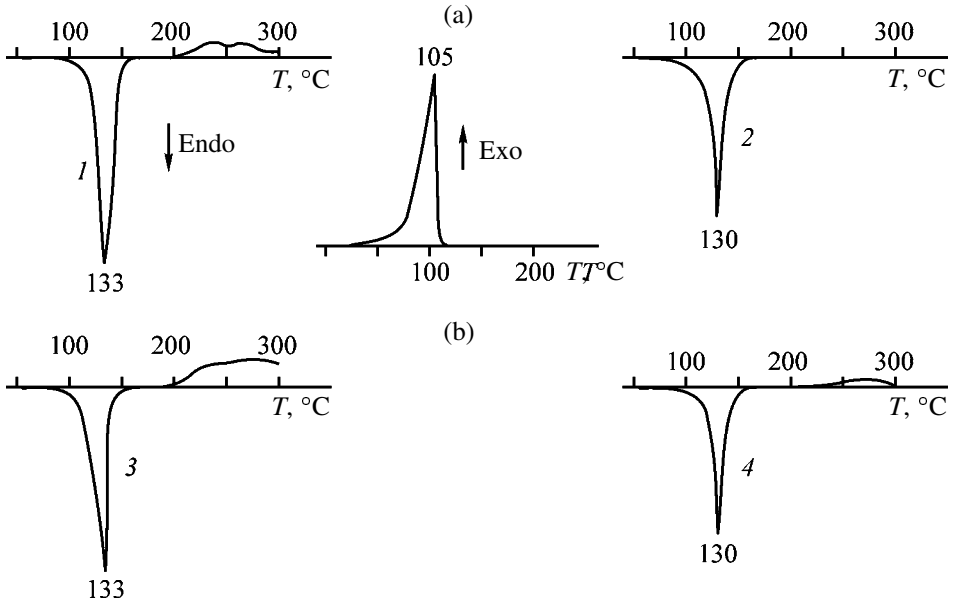

Fig. 4. DSC curves at a heating rate of 16 deg min^{-1} (DSM-2 thermoanalyzer; heating–cooling–heating cycling): (a) extruded PE film and (b) PE membrane. ΔH (J g^{-1}): (*1*) 205, (*2*) 175, (*3*) 180, and (*4*) 150.

observed maintained orientation and good mechanical characteristics of the PE support after heating in air to 200°C [5, 6]. However, irreversible transformations caused by oxidation and cross-linking result in considerable increase in the brittleness after heating to higher temperatures.

In the thermomechanical testing, we monitored evolution of the geometrical size of composite samples in the course of heating under stress in a vacuum (anaerobic conditions). Because of the lack of oxidative degradation in PE melt under these conditions, the systems maintain their dimensions, take a load upon heating, and even preserve their elasticity after heating above 300°C [5].

Above 300°C, degradation and subsequent carbonization proceed similarly in both extruded films and membranes. As demonstrated previously [4, 6] and confirmed in this work, heating above 300°C results in starting degradation with formation of volatile products. Above 400°C, the process becomes avalanche-like, coming to nearly total removal of the polymer chain residues at 500°C and burning out of the 5% solid carbonized residue at 700°C.

The optical micrograph of the PE membrane after heating in air to 400°C demonstrates a strongly carbonized material with an anthracite luster, suggesting high degree of thermal degradation. However, the typical relief-like surface and porous structure of the membrane are still clearly seen.

CONCLUSIONS

(1) Thermal analysis of PE films and porous membranes on their basis in air and inert CO_2 atmosphere showed that their structural characteristics and thermal behavior are controlled by the thermal treatment history.

(2) The surface carbonization effect was observed, controlling some performance characteristics of PE materials.

ACKNOWLEDGMENTS

The authors are grateful to V.S. Papkov and Yu.K. Godovskii for valuable discussions.

The work was financially supported by the Russian Foundation for Basic Research (gram no. 01-03-32290) and the Program of the Chemistry and Materials Science Division, Russian Academy of Sciences "Development and Study of Macromolecules and Macromolecular Structures of New Generations—Conducting and Electroactive Polymers."

REFERENCES

1. Elyashevich, G.K., Bitskii, A.E., Kozlov, A.G., and Rosova, E.Yu., *Zh. Prikl. Khim.*, 1997, vol. 70, no. 7, pp. 1175–1179.

2. Elyashevich, G.K., Kozlov, A.G., and Rosova, E.Yu., *Vysokomol. Soedin., Ser. A*, 1998, vol. 40, no. 6, pp. 956–963.
3. Rosova, E.Yu., Polotskaya, G.A., Kozlov, A.G., *et al.*, *Vysokomol. Soedin., Ser. A*, 1998, vol. 40, no. 6, pp. 914–920.
4. Elyashevich, G.K., Terlemezyan, L., Sazanov, Yu.N., *et al.*, *Zh. Prikl. Khim.*, 2000, vol. 73, no. 7, pp. 1164–1169.
5. Elyashevich, G.K., Rosova, E.Yu., Sidorovich, A.V., *et al.*, *Eur. Polym. J.*, 2003, vol. 39, no. 4, pp. 647–654.
6. Elyashevich, G.K., Sazanov, Yu.N., Rosova, E.Yu., *et al.*, *Vysokomol. Soedin., Ser. A*, 2001, vol. 43, no. 9, pp. 1548–1554.
7. *Entsiklopediya polimerov* (Encyclopedia of Polymers), Moscow: Sov. Entsiklopediya, 1977, vol. 3, p. 624.
8. *Entsiklopediya polimerov* (Encyclopedia of Polymers), Moscow: Sov. Entsiklopediya, 1972, vol. 1, p. 533.

Russian Journal of Applied Chemistry, Vol. 76, No. 7, 2003, pp. 1139–1142. Translated from Zhurnal Prikladnoi Khimii, Vol. 76, No. 7, 2003, pp. 1172–1175.

MACROMOLECULAR CHEMISTRY AND POLYMERIC MATERIALS

Polyelectrolyte Hydrogels Based on Hydrolyzed Polyacrylonitrile Fiber

L. P. Krul', A. S. Rybak, E. I. Nareiko, A. P. Polikarpov, and T. G. Klimets

Research Institute of Physicochemical Problems, Belarussian State University, Minsk, Belarus
Institute of Physical Organic Chemistry, Belarussian National Academy of Science, Minsk, Belarus

Received February 19, 2003

Abstract—Cross-linking of hydrolyzed Nitron D polyacrylonitrile fiber on exposure to ionizing radiation was studied as influenced by its concentration in the solution, dose rate, and the presence of oxygen in the system. Preparation conditions of polyelectrolyte hydrogel with maximal water absorption by radiochemical cross-linking at the minimal dose were determined.

Polyelectrolyte hydrogels (PEHGs), which can absorb water in amounts hundreds times higher than their weight, are widely used in medicine and in various branches of industry and agriculture [1–3]. Water-soluble acrylamide–sodium acrylate copolymer prepared by radiation cross-linking of base hydrolysis product of polyacrylonitrile fibers can be used as ionic hydrophilic polymer for preparing PEHG [4]. Previously we studied the influence of foreign ions, their concentration, and pH of the solution on synthesis of PEHG by irradiation of the hydrolysis product. The influence of other factors (dose rate, concentration of the hydrolysis product in the solution, and the presence of oxygen) on radiochemical cross-linking of hydrolyzed polyacrylonitrile fiber was not examined.

The aim of this work was to determine the conditions for radiochemical cross-linking of base hydrolysis product of Nitron D polyacrylonitrile fiber to form PEHG with the maximal water absorption at the minimal radiation dose.

EXPERIMENTAL

The main factors affecting radiation cross-linking of polymers in solutions are as follows: the nature of the solvent and polymer (thermodynamic parameters of the solvent as compared to those of the polymer, chemical composition and molecular weight of the polymer, the presence of impurities), solution properties (viscosity, polymer concentration, pH), and irradiation conditions (dose rate, the presence of oxygen in the system) [6]. It is known [7] that water absorption by a polymer depends on its chemical composition, in particular, on the content of ionized groups [7]. When the content of acrylate groups in acrylamide–sodium acrylate copolymer prepared by hydrolysis of polyacrylamide increases, the water absorption by the copolymer and the dose required for its cross-linking increase.

In this work we studied acrylamide–sodium acrylate copolymer with 33 : 67 molar ratio of the units. This is the maximal content of acrylamide units in the copolymer prepared by hydrolysis [8]. Taking our previous results [7] into account, we suggested that this copolymer should be cross-linked at the minimal dose.

The copolymer was prepared by base hydrolysis of Nitron D polyacrylonitrile fiber [9]. The alkali to dry fiber and water to dry fiber ratios in the reaction mixture were 0.55 and 5.5, respectively. The molecular weight of the copolymer was about 10^5 [10]. The reaction mixture was neutralized with acetic acid.

Oxygen was removed by purging solutions with argon. Deoxygenated solutions were irradiated in sealed glass ampules. The polymers were cross-linked by exposure to ^{137}Cs γ-radiation on an LMB-γ-1M unit at the dose rate P = 0.33 Gy s^{-1}. The influence of the dose rate was studied on an RKhM-γ-20 unit with a ^{60}Co source at the dose rates P 0.056 and 0.58 Gy s^{-1}. The absorbed dose was varied from 15 to 120 kGy. The gel fraction content and the water absorption were determined gravimetrically by the procedure in [5]. The results were calculated as average of three measurements.

The dependences of the (a) gel fraction content δ in cross-linked hydrolyzate of Nitron D fiber and

1070-4272/03/7607-1139$25.00

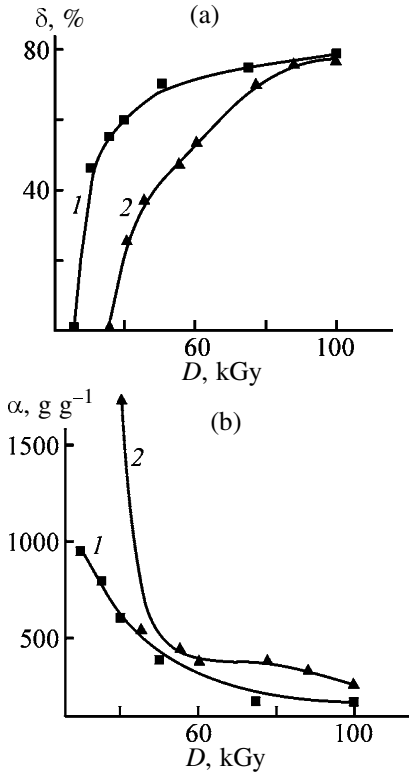

Fig. 1. (a) Gel fraction content δ and (b) water absorption α for Nitron D fiber hydrolyzate cross-linked by irradiation of its 20% aqueous solutions (*1*) in the presence of (*2*) in the absence of atmospheric oxygen as a function of absorbed dose *D*.

(b) water absorption by this sample on the absorbed dose *D* are shown in Fig. 1. The polymer concentration in these solutions was 20 wt %. As seen from Fig. 1, radiochemical cross-linking of the polymer in a solution in the presence of atmospheric oxygen (Fig. 1a, curve *1*) is more efficient (higher yield of the gel fraction at lower doses) than in a deoxygenated solution of the same concentration (Fig. 1a, curve *2*). The water absorption by 1 g of the polymer cross-linked in the presence of oxygen at a 30 kGy dose is about 1000 g (Fig. 1b, curve *1*), whereas, to reach the same water absorption for the sample prepared in a deoxygenated solution, no less than 40 kGy dose is required (Fig. 1b, curve *2*).

In deoxygenated aqueous solutions, the gel fraction is formed by recombination of macromolecular radicals generated by irradiation of these solutions. The copolymer exposed to radiation contains mainly carboxylate units. In the absence of oxygen, sodium polyacrylate is cross-linked by recombination of macromolecular radicals **1** (α-radicals) and **2** (β-radicals) formed by reaction of water radiolysis products with the polymer [11]:

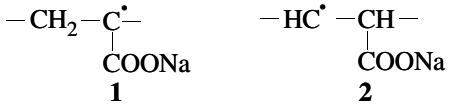

In the presence of oxygen, α- and β-radicals are converted into peroxy radicals. The rate constant of this reaction (10^8 mol ml^{-1} s^{-1}) is close to that of reaction of sodium polyacrylate with hydroxy radical, the most reactive product of water radiolysis. Liberated peroxy radicals are unstable and transform into carbon-centered radicals by the reaction [10]

More efficient cross-linking of the polymer in the presence of oxygen is likely due to an increase in the current concentration of the carbon-centered macromolecular radicals, since their generation on irradiation of the polymer in a deoxygenated solution is faster than that of α- and β-radicals.

Since the gelation in the presence of oxygen is more efficient than in deoxygenated solutions, the subsequent experiments were performed in the presence of atmospheric oxygen.

Another factor affecting formation and properties of PEHG is the dose rate. The dependence of (a) δ and (b) α on the absorbed dose for a solution of hydrolyzate of polyacrylonitrile fiber cross-linked at various dose rates is shown in Fig. 2. As seen from Fig. 2, the dose rate does not affect the shape of these dependences but changes the minimal absorbed dose causing gelation. When the dose rate increases from 0.056 to 0.58 Gy s^{-1}, the absorbed dose required for formation of the gel fraction increases (28 kGy at P = 0.056 Gy s^{-1} and 38 kGy at P = 0.58 Gy s^{-1}, all other conditions being the same). The samples with the maximal water absorption (750–1100 g of water per gram of cross-linked polymer) were prepared at the absorbed doses close to the doses of gelation onset (Fig. 2b).

As in [11], an increase in the dose of gelation onset with increasing dose rate is due to the fact that bimolecular recombination of macromolecular radicals is accelerated to a lesser extent than side monomolecular chain termination by reaction of the macromolecular radicals with low-molecular-weight radiolysis products. Hence, for the degree of cross-linking at a higher dose rate to be equal to that at a lower dose rate, higher absorbed doses are required. Another

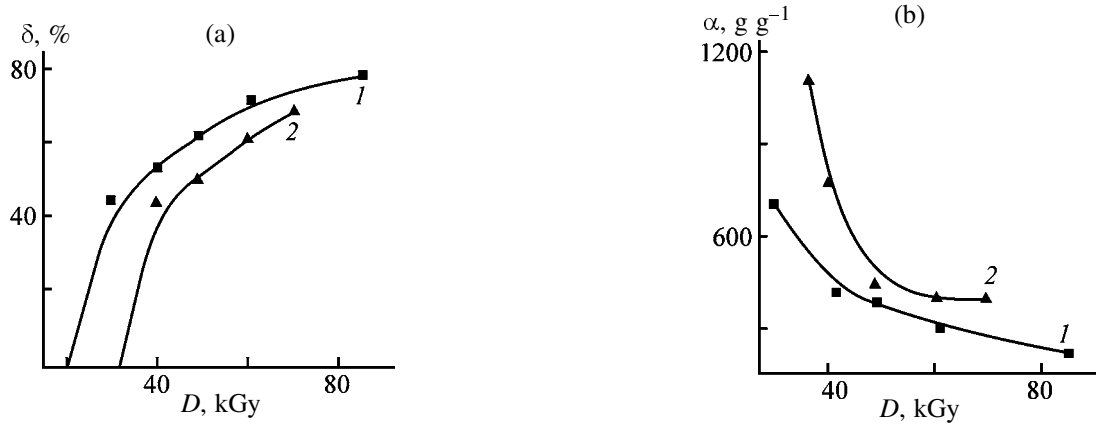

Fig. 2. (a) Gel fraction content δ and (b) water absorption α for Nitron D fiber hydrolyzate cross-linked by irradiation of its 20% aqueous solutions at the dose rate of (*1*) 0.056 and (*2*) 0.58 Gy s^{-1} as a function of the absorbed dose *D*.

factor decreasing the efficiency of radiation cross-linking of the hydrolyzate in a solution at higher dose rates may be degradation of the macromolecule, which is initiated by $OH^{\cdot}$ radicals formed by radiolysis of water.

The depedences of the gel fraction content δ on the dose absorbed by solutions with various concentrations of hydrolyzate of Nitron fiber are shown in Fig. 3. As seen from Fig. 3, the gel fraction is formed on exposure of solutions with 5–30% hydrolyzate content to γ-radiation of the ^{137}Cs source to doses of 18–35 kGy. Solutions with the concentration of 1–2% are not cross-linked up to the dose of 120 kGy. In the whole dose rate range, the gel fraction content and hence the efficiency of radiation cross-linking increase with increasing the hydrolyzate concentration in the solution.

More efficient radiation cross-linking of concentrated aqueous solutions of the copolymer can be due to high probability of recombination of the macromolecular radicals, which, in turn, increases with shortening of the intermolecular distance in more concentrated solutions.

Data on water absorption of PEHG prepared by irradiation of hydrolyzate solutions with different concentrations are presented in the table. As seen from the table, the maximum of water absorption is virtually independent of the hydrolyzate concentrations and is reached at the dose of gelation onset.

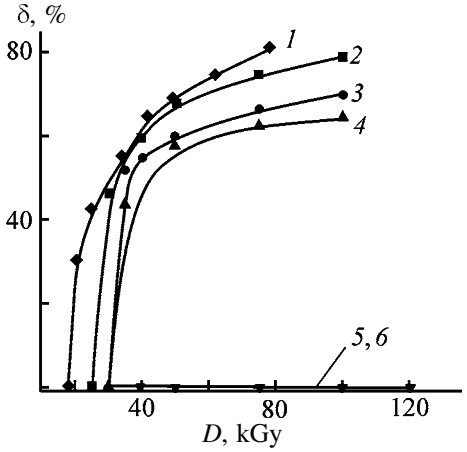

Fig. 3. (a) Gel fraction content δ in Nitron D fiber hydrolyzate cross-linked by irradiation of its (*1*) 30, (*2*) 20, (*3*) 10, (*4*) 5, (*5*) 2, and (*6*) 1% aqueous solutions as a function of the absorbed dose *D*.

CONCLUSIONS

(1) The efficiency of radiation cross-linking in an aqueous solution of acrylamide–sodium acrylate copolymer prepared by base hydrolysis of Nitron D polyacrylonitrile fiber increases in the presence of

Water absorption by Nitron D fiber hydrolyzate cross-linked by irradiation of its aqueous solutions of various concentrations

Dose, kGy	Water absorption, g g^{-1}, at indicated concentration, wt %			
	30	20	10	5
20	850	s*	s	s
25	650	s	s	s
30	–	960	s	s
35	–	713	1200	820
40	470	610	830	650
50	380	390	480	230
75	205	180	230	290
100	–	175	200	260

* (s) The sample dissolved.

oxygen, with increase in the copolymer concentration, and with decrease in the dose rate.

(2) The water absorption by polyelectrolyte hydrogels prepared from hydrolyzate of Nitron D fiber at the dose of gelation onset is maximal (1000 g of water per gram of dry polymer).

REFERENCES

1. Bekturov, E.A. and Suleimenov, I.E., *Polimernye gidrogeli* (Polymeric Hydrogels), Almaty: Gylym, 1998.
2. Peppas, N.A., *Hydrogels in Medicine and Pharmacy*, Boca Raton: CRC, 1987.
3. Budtova, T.V., Suleimenov, I.E., and Frenkel', S.Ya., *Zh. Prikl. Khim.*, 1997, vol. 70, no. 4, pp. 529–539.
4. Krul', L.P. and Nareiko, E.I., Abstracts of Papers, *XV Mendeleevskii s"ezd po obshchei i prikladnoi khimii: Khimicheskie probelmy ekologii* (XV Mendeleev Congr. on General and Applied Chemistry: Chemical Problems of Ecology), Minsk, May 24–29, 1993, Minsk: Navuka i Tekhnika, 1993, vol. 2, pp. 152–153.
5. Krakodeev, D.V. and Krul', L.P., *Mater. Tekhnol. Instrum.*, 2001, vol. 6, no. 2, pp. 39–43.
6. Pikaev, A.K., *Sovremennaya radiatsionnaya khimiya: Tverdye tela i polimery* (Modern Radiation Chemistry: Solids and Polymers), Moscow: Nauka, 1985, vol. 3.
7. Krul, L.P., Nareiko, E.I., Matusevich, Yu.I., *et al.*, *Polym. Bull.*, 2000, vol. 45, no. 2, pp. 159–165.
8. Krul', L.P., Yakimtsova, L.B., Matusevich, Yu.I., and Krakodeev, D.V., *Vestsi Nats. Akad. Navuk Bel., Ser. Khim. Navuk*, 2000, no. 1, pp. 103–105.
9. Krul', L.P., Brazhnikov, M.M., Matusevich., Yu.I., *et al.*, *Vestsi Nats. Akad. Navuk Bel., Ser. Khim. Navuk*, 2000, no. 2, pp. 90–93.
10. Matusevich, V.Yu., Zeeber, V., Yakimtsova, L.B., *et al.*, *Vestn. Belarus. Gos. Univ.*, *Ser. 2*, 2001, pp. 13–16.
11. Ulanski, P., Bothe, E., Hildenbrand, K., *et al.*, *Radiat. Phys. Chem.*, 1995, vol. 46, nos. 4–6, pp. 909–912.

Russian Journal of Applied Chemistry, Vol. 76, No. 7, 2003, pp. 1143–1151. Translated from Zhurnal Prikladnoi Khimii, Vol. 76, No. 7, 2003, pp. 1176–1184.

MACROMOLECULAR CHEMISTRY AND POLYMERIC MATERIALS

Interaction of Photographic Gelatins with Various Hardeners in the Aqueous Phase

M. A. Sakvarelidze, V. N. Izmailova, S. M. Levachev, V. V. Rodin, G. P. Yampol'skaya, A. E. Kharlov, P. V. Nuss, and I. G. Chezlov

Moscow Movie and Video Institute (Division of St. Petersburg State University of Motion Pictures and Television), Moscow, Russia
Moscow State University, Moscow, Russia
Institute of Eye Diseases, Russian Academy of Medical Sciences, Moscow, Russia
St. Petersburg State University of Motion Pictures and Television, St. Petersburg, Russia

Received December 2, 2002; in final form, March 2003

Abstract—The properties of photographic gelatins in the aqueous phase were studied as influenced by hardeners of various types. The effect of molecular-weight distribution of gelatins, reagent ratios, and temperature on hardening was analyzed.

Gelatin plays various functions in production and operation of light-sensitive materials; in particular, it acts as an active medium in generation of photographic and physicochemical properties of emulsion layers.

In various stages of generation of a photographic material, it is often necessary to change colloidal and chemical properties of gelatin by its chemical modification with hardeners [1]. Therefore, it is urgent to study the effect of various hardeners on the properties of gelatin macromolecules in the bulk [2, 3] and at the phase boundary [4, 5].

In this work we continued our studies of the mechanism of gelatin interaction with hardeners in aqueous medium. We analyzed the relative reactivity of some gelatin fractions with respect to hardeners of various types using high-performance liquid chromatography (HPLC), the molecular mechanism of interaction of gelatin with hardener (high-resolution ^{1}H NMR spectroscopy), the size of gelatin macromolecules chemically modified with hardeners (photon-correlation spectroscopy), and hydrodynamic parameters of macromolecules (capillary viscometry).

Gelatin is a product of thermal, acidic, alkaline, or enzymatic denaturation of collagens. Non-fractionated gelatin is a mixture of α-, β, and γ-chains; two last components are the fragments linked with chemical bonds, double and triple α-chains, or their fragments. These fractions are different in their molecular weight, colloidal, chemical, physicochemical, conformation, and configuration parameters, and reactivity [6].

In [7], the molecular-weight distribution (MWD) of a series of domestic and imported photographic gelatins was studied by gel electrophoresis in polyacrylamide gel and HPLC. Based on these results, a database on the gelatin MWD as influenced by raw materials and treatment procedures was developed.

Using HPLC, we studied the selectivity of interaction of various type of hardeners with separate gelatin fractions as influenced by the contact time, temperature, and reagent concentration. We used a PL gel 10^3 nm Mixed-B column (Hewlett–Packard) with the corresponding precolumn, a PUMP P-500 pump (Pharmacia), and an HP (λ = 630 nm) differential flow refractometer as detector (Hewlett–Packard) [3]. The column was calibrated with respect to water-soluble collagen. The molecular weight M of the gelatin fractions was determined from the following expression:

$$\log M = 3 - 0.057\tau, \quad (1)$$

where τ is the retention time.

In our work we studied polydisperse bone gelatin prepared by alkaline denaturation (sample no. 1) and low-molecular-weight gelatin obtained by acidic treatment of pigskin (sample no. 2); the molecular-weight distribution of the gelatins studied is illustrated in Fig. 1 and Table 1.

In our study we used the hardeners of various types: protected formaldehyde [tetra(hydroxymethyl)-urea (LIKI-1) and *N, N, N, N*-tetra(hydroxymethyl)-

1070-4272/03/7607-1143$25.00

Table 1. Molecular-weight distribution of gelatin

Sample no.	Characteristics of gelatin samples	Content of fraction, %				
		>γ (>285)	γ (285)	β (190)	α (95)	<α (<95)
1	Bone, alkaline treatment, Kazan, Tatarstan, Russia	3.4	16	16	60.4	4.2
2	Leather, acidic treatment, Kazan, Tatarstan, Russia	–	–	–	16	84
3	Bone, alkaline treatment, Kazan, Tatarstan, Russia	–	–	47.17	32.5	20.49
4	K-13016 leather, acidic treatment, the United States	2	23	33	22	20
5	Pigskin, sorption, Svema Research and Production Association, Ukraine	2.5	15	16	54	12.5
6	For color negative materials, Belgium	5	18	19	53	5

malondiamide (LIKI-19)]; epoxy [triglycidylamine (LIKI-9, TGA) and diglycidyl mono(propylene chlorohydrin) ether of glycerol (DU-652)]; acid chloride [4,6-dichloro-2-hydroxy-1,3,5-triazine (DU-679)]; acryloyl [1,3,5-triacryloylhexahydro-1,3,5-triazine (DU-801)]; and polymeric with hydroxymethyl groups [copolymer of vinylpyrrolidone and *N,N*-di(hydroxymethyl)vinylamine (SPF-1)].

The tests were performed as follows. First, a 2% aqueous solution of gelatins was prepared by the standard procedure; then the hardeners were added [0.01 and 0.001 mol per 100 g of air-dry gelatin (ADG)], and the mixture was heated at 40°C for 1 or 3 h.

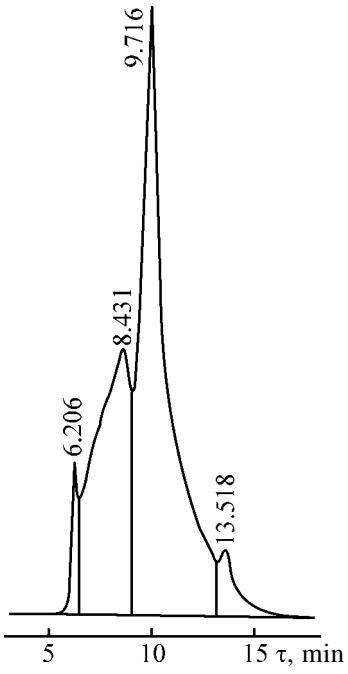

Fig. 1. Chromatogram of bone gelatin prepared by alkaline denaturation (Table 1, sample no. 1). (τ) Retention time (correlates with the molecular weight of the fraction); the same for Fig. 2.

The quantitative changes in the gelatin composition were studied by chromatography. The chromatograms of gelatin (sample no. 1) of alkaline treatment chemically modified with LIKI-19 and TGA hardeners are shown as examples in Fig. 2.

It should be noted that, in all the cases, after hardening the content of gelatin α-fraction decreases, and the greatest consumption of α-fraction is observed in reaction of gelatin with SPF-1 hardener. At the same time, consumption of α-fraction in reaction with LIKI-19 and DU-679 is similar. The trends in the decrease of the content of the α-fraction at hardening with DU-679 and LIKI-9 oxirane compounds are similar. Thus, the trends in variation of the content of the α-fraction clearly depend on the type of the hardener.

In many systems in the course of hardening, a new macromolecular fraction with the molecular weight greater than that of the γ-fraction is formed, and its content in gelatin often increases. The system cross-linking as influenced by the hardener nature, i.e., the total content of the gelatin fractions with molecular weights equal to or greater than that of γ-fraction (%), decreases in the following order: LIKI-19 (45) > SPF-1 (36) > DU-652 = LIKI-9 (30) > DU-679 (22).

Simultaneously with cross-linking, low-molecular-weight fragments of polypeptide chain with molecular weights smaller than that of the α-fraction are formed in all the systems studied. This effect is especially pronounced with DU-679 hardener. The results are summarized in Table 2.

The data on the interaction of hardeners with low-molecular-weight acidic gelatin are shown in Table 3. As seen from the data listed in Tables 2 and 3, hardening depends on the initial fraction composition of gelatins. For low-molecular-weight acidic gelatins, the selectivity of hardeners is more profound, and the most efficient cross-linking agents for the gelatin samples studied are SPF-1, DU-679, and LIKI-19.

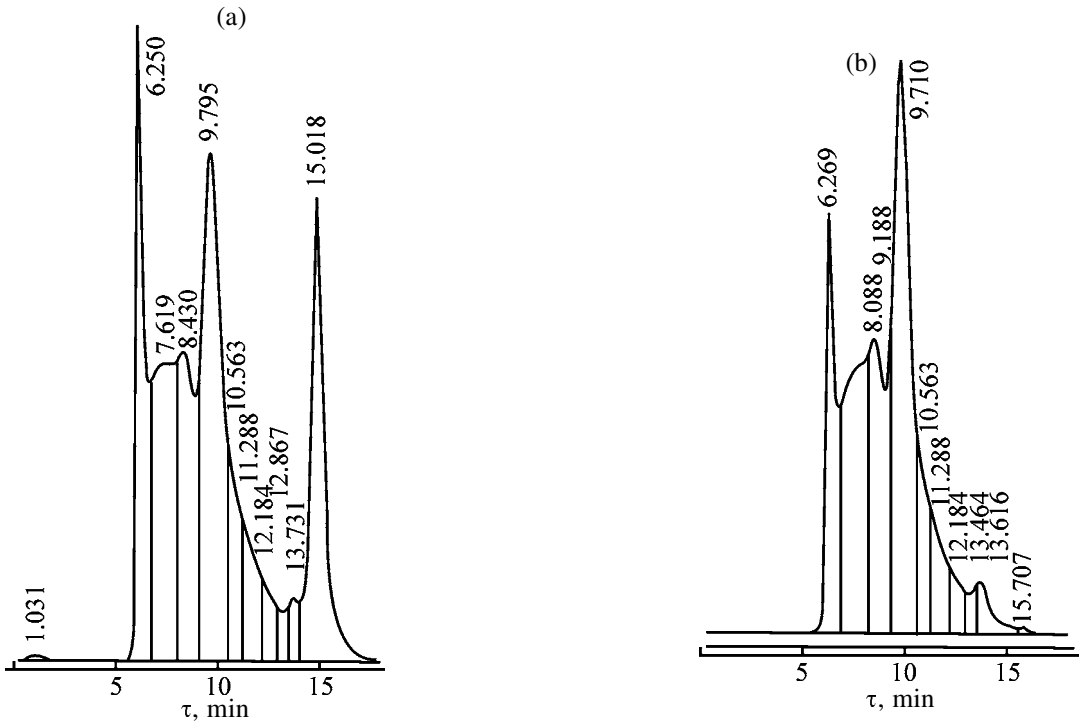

Fig. 2. Chromatograms of bone gelatin (Table 1, sample no. 1) modified with hardeners of various types; contact time with gelatin 3 h, hardener content 0.01 mol per 100 g of ADG, 40°C. Hardener: (a) LIKI-19 and (b) TGA.

Table 2. Changes in gelatin MWD (sample no. 1) at hardening

Hardener, mol per 100 g of ADG	τ, h	Content of fractions, %				
		>γ (>285)	γ (285)	β (190)	α (95)	<α (<95)
–	–	3.4	16	16	60.4	4.2
LIKI-19:						
0.001	3	4.53	–	33.26	57.56	4.64
0.01	1	4.24	–	32.51	55.7	7.55
	3	31.3	14.6	–	22.51	32.07
TGA:						
0.001	3	5.77	–	33.06	57.27	3.9
0.01	1	4.59	34.12	–	57.54	3.75
	3	12.92	19.96	–	45.59	16.03
DU-679:						
0.001	3	4.5	–	32.85	58.2	4.41
0.01	1	4.03	–	33.67	57.28	5.4
	3	5.24	21.09	17.7	32.9	19.54
SPF-1:						
0.001	3	4.01	–	33.7	58.2	4.09
0.01	1	4.3	–	36.8	49.27	4.01
	3	35.74	–	17	22.92	22.61
DU-652:						
0.001	3	4.98	–	34.12	57.03	3.87
0.01	1	4.08	–	32.08	58.85	5
	3	11.68	18.98	–	50.03	19.05
DU-801, 0.01	3	2.27	16	–	15.5	66.23

Table 3. Changes in gelatin MWD (sample no. 2) at hardening; hardener content 0.01 mol per 100 g of ADG, contact time 3 h

Hardener	Gelatin MWD, %					
	>γ (>285)	γ (285)	β (190)	α (95)	<α (<95)	<5000
–	–	–	–	16	84	–
LIKI-19	4.56	15.86	13.06	–	50.13	16.39
LIKI-9	3.52	–	–	33.41	63.08	–
DU-652	0.76	18.08	–	15.58	65.6	–
DU-679	30.77	14.75	–	–	–	53.94
SPF-1	36.51	12.93	–	–	–	49.57
DU-801	2.27	16	–	15.5	66.23	–

The temperature also appreciable affects hardening. Gelatin macromolecules in solution can occur in two conformations: globule and collagen-like spiral. At temperatures ≥35°C, gelatin occurs in a globule conformation, and on cooling to temperatures lower than 35°C a collagen-like spiral structure appears.

Hardeners, when added into the gelatin solution, fix the macromolecular conformation typical for the given temperature. Hardening of gelatin at temperatures above 35°C fixes the globule conformation, which remains unchanged at subsequent cooling [8, 9].

To evaluate the temperature dependences of hardening, we studied the interaction of gelatin with hardeners at room temperature by polyacrylamide gel electrophoresis (PAAGE). The fraction composition of gelatin begins to change only on the fifth day after the reagent mixing [3]. The hardening is probably hindered by the partial restoration of the collagen-like spirals and shielding of the reaction centers.

The interaction of various compounds with amino acid groups in the gelatin polypeptide chain can be studied by high-resolution NMR spectroscopy. Interaction of gelatin at 40–45°C in aqueous (D_2O) solution with ionic and nonionic surfactants at wide variation of the component ratio (physical modification) was studied by this method in [10]. Chemical modification of gelatin with LIKI-19 and DU-679 in the globule and spiral conformations was analyzed in [11].

Table 4. Amino acid composition of gelatin

Amino acid	ω_{am}, mol %	Amino acid	ω_{am}, mol %
Aspartic (Asp)	4.6	Threonine (Thr)	1.5
Glutamic (Glu)	7.2	Proline (Pro)	12.4
Lysine (Lys)	2.8	Glycine (Gly)	32.0
Arginine (Arg)	4.8	Alanine (Ala)	11.7
Histidine (His)	0.4	Valine (Val)	1.2
Tyrosine (Tyr)	0.1	Isoleucine (Ile)	1.1
Hydroxylysine (H-Lys)	0.4	Leucine (Leu)	2.4
Hydroxyproline	9.3	Phenylalanine	1.4
(H-Pro)		(Phe)	1.4
Serine (Ser)	3.3	Methionine (Met)	3.9

In this work we continued our studies initiated in [10, 11] and, using high-resolution ^1H NMR spectroscopy, analyzed the features of interaction of the LIKI-1 protected formaldehyde hardener with amino acid fragments of the gelatin polypeptide chains at 40°C, when the gelatin macromolecules occur in the globule conformation. The effect of the degree of linking between the gelatin and LIKI-1 hardener was also evaluated.

In these tests, we used the gelatin prepared by alkaline treatment of cattle bones (Kazan Gelatin Plant, Tasma Production Association, Kazan, Tatarstan, Russia). The MWD of the gelatin sample was studied by HPLC (Table 1, sample no. 3).

The 0.3% gelatin solutions in D_2O were prepared by the standard procedure; hardening of the gelatin with LIKI-1 reagent was performed at 60°C for 3 h, the hardener : gelatin ratio was from 10^{-2} to 10^{-4} mol per 100 g of ADG.

The high-resolution ^1H NMR spectra were recorded on a Bruker AC-200 spectrometer (200 MHz) with sodium 2,2-dimethyl-2-silapentane-5-sulfonate [$(CH_3)_3SiCH_2CH_2CH_2SO_3Na$, CSS] as internal reference. The spectra we recorded in a single-pulse mode with suppression of the water signal; sufficiently high signal/noise ratio was obtained after 100–300 scans.

The NMR spectra were analyzed taking into account the chemical composition of the gelatin. The data on the composition of amino acid fragments ω_{am} in gelatin are given in Table 4.

As seen from published ^{1}H NMR data [12], the macromolecules in the globule conformation give high-resolution spectra (Fig. 3, Table 5), which is probably due to the high mobility of the amino acid fragments. In this case, the resonance signals of protons at various carbon atoms (β-C, γ-C, and δ-C) in the side chain are well resolved.

The spectra of unmodified gelatin in D_2O (Table 1, sample no. 3) at 40°C (Fig. 4a) are similar to those recorded previously [11, 12]. The chemical shifts of protons of individual amino acid residues and the intensity of signals well agree with published data. In the general case, the integral intensity is proportional to the number of hydrogen atoms contributing to the ^{1}H NMR signal.

Figure 4b shows the high-resolution ^{1}H NMR spectrum of LIKI-1. The resonance lines are well resolved. The signals (Table 6) were assigned on the basis of their relative intensities.

A high-resolution ^{1}H NMR spectrum of the gelatin solution modified with LIKI-1 hardener is shown in Fig. 4c, and the assignment and integral intensities of the signals are listed in Table 7. The interaction of the components at chemical modification was characterized by changes in the intensities ΔI of the signals in the NMR spectrum of the modified gelatin as compared to the initial gelatin solution in D_2O:

$$\Delta I = I_g - I_m, \quad (2)$$

$$\Delta = (\Delta I / I_g) \times 100, \quad (3)$$

where I_g and I_m are the integral intensities of the signals in the spectrum of unmodified and modified gelatin, respectively, in the region of a given chemical shift and Δ is the ratio characterizing changes in the

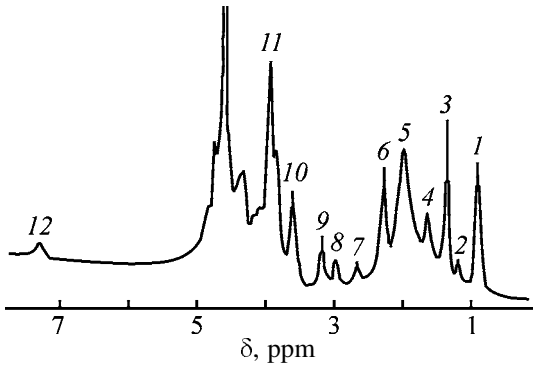

Fig. 3. High-resolution ^{1}H NMR spectra of gelatin solution in D_2O, gelatin concentration 0.5%, pD 5.0, 50°C, 500 scans. (δ) Chemical shift; the same for Fig. 4. (*1–12*) For assignment, see Table 5.

Table 5. High-resolution ^{1}H NMR spectra of gelatin solution in D_2O

Signal no. (Fig. 3)	δ ppm	Amino acid	Proton type
1	0.93	Val, Leu, Ile	γ- and δ-CH_3
2	1.22	Thr	γ-CH_3
3	1.41	Ala	γ-CH_3
4	1.65	Arg	β- and γ-CH_2
		Lys	β-, γ-, δ-CH_2
5	2.01	Pro	β- and γ-CH_2
		Met	β-CH_2 and -CH_3
6	2.30	Glu	β- and γ-CH_2
		H-Pro	β-CH_2
7	2.70	Asp	β-CH_2
8	2.99	Lys	ε-CH_2
9	3.20	Arg	δ-CH_2
		His	β-CH_2
10	3.62	Pro	δ-CH_2
11	3.94	Gly	α-CH_2
		H-Pro	γ-CH_2
12	7.20	Phe	Ar–H

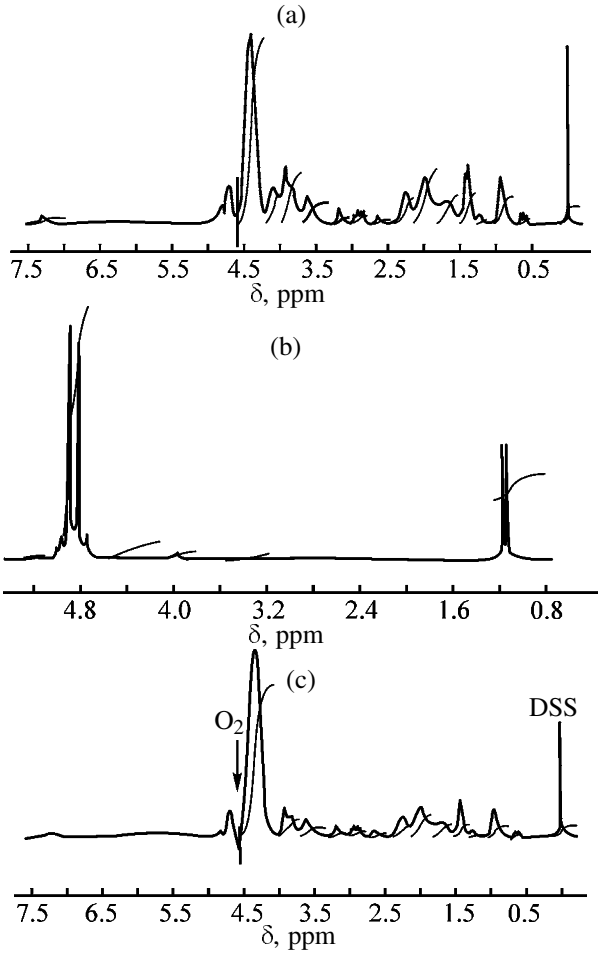

Fig. 4. ^{1}H NMR spectra of gelatin solution in D_2O. Solution: (a) 0.3% gelatin (Table 1, sample no. 3), (b) 5% LIKI-1, and (c) gelatin modified with LIKI-1.

Table 6. Signal assignment in the ^{1}H NMR spectrum of LIKI-1 solution in D_2O, LIKI-1 concentration 5%, 40°C

δ, ppm	Group*	Number of groups	Integral intensity
4.01–4.88	–(CH_2)	4	775.67
1.1	–(OH)	4	238.07

* $(HOCH_2)_2N–\underset{\underset{O}{\|}}{C}–N(CH_2OH)_2$.

integral intensity due to the chemical modification of gelatin (%).

As seen from Table 7, the most pronounced weakening of the signals of all the amino acid fragments studied is observed at the LIKI-1 content of 10^{-4} mol per 100 g of ADG.

At LIKI-1 content of 10^{-3} and 10^{-2} mol per 100 g of ADG, the spectral lines become broader and the resonance signals of all the side gelatin chains become weaker, but this effect is less pronounced. This is probably due to the reaction of LIKI-1 molecules with each other with increasing hardener concentration. As a result, the effect of hardener on the mobility of the gelatin protons is greater at its content of 10^{-4} mol per 100 g of ADG.

The effect of LIKI-1 hardener on the parameters of gelatin macromolecules in the aqueous phase was studied by photon-correlation spectroscopy. The particle size distribution was determined on a Malvern device at 40°C (λ 632.8 nm, scattering angle 90°); the results are listed in Table 8.

The reaction of gelatin with LIKI-1 protected formaldehyde hardener changes the average and most probable radii of the gelatin macromolecules; average R_1 and most probable R_2 radii increase from 11 and 22 to 18 and 32 nm, respectively. We assume that the arising intermolecular covalent bonds hinder compaction of the gelatin macromolecules.

The viscometric data for gelatin macromolecules were published previously in [13–16]; and the hydrodynamic parameters of the gelatin macromolecules modified with hydroxysuccinimide ester of lauric acid and with sodium dodecyl sulfate (SDS) were evaluated in [17].

In this work we determined the limiting viscosity

Table 7. Integral intensities of the resonance signals I and their changes ΔI in the ^{1}H NMR spectra of solutions containing the initial gelatin and that hardened with LIKI-1; gelatin concentration 0.3%, 40°C

δ, ppm	Amino acid	Proton type	I				ΔI (Δ, %)		
			gelatin	gelatin + LIKI-1*			1	2	3
				1	2	3			
0.9	Val Leu Ile	γ-, β-CH_3	16.58	10.26	17.47	13.08	6.31 (38)	–0.90 (–5)	3.50 (21)
1.2	Thr	γ-CH_3	2.54	1.74	1.73	2.35	0.80 (31)	0.81 (32)	0.19 (8)
1.4	Ala	β-CH_3	18.54	11.44	15.89	14.35	7.10 (38)	2.65 (14)	4.19 (23)
1.65	Arg Lys	β-, γ-CH_2 β-, γ-, δ-CH_2	17.65	11.45	13.87	14.20	6.18 (35)	3.77 (21)	1.45 (20)
2.0	Pro Met	β-, γ-CH_2 β-CH_2, δ-CH_3	33.66	20.39	32.07	27.67	13.27 (39)	1.59 (5)	5.99 (18)
2.3	Glu H-Pro	β-, γ-CH_2 β-CH_2	15.69	9.97	15.93	13.35	5.72 (36)	–0.24 (–2)	2.34 (15)
2.67	Asp	β-CH_2	2.59	1.76	2.74	2.03	0.82 (32)	–0.15 (–6)	0.56 (22)
3.0	Lys	ε-CH_2	4.32	4.03	5.92	4.53	0.30 (7)	–1.59 (–37)	–0.20 (–5)
3.2	Arg His	δ-CH_2 β-CH_2	3.77	2.88	5.59	3.57	0.89 (24)	–0.82 (–23)	0.23 (5)
3.62	Pro	δ-CH_2	12.34	7.32	10.74	10.25	5.02 (41)	1.59 (13)	2.09 (17)
3.9	Gly H-Pro	α-CH_2 γ-CH	31.29	15.14	24.49	19.13	16.15 (52)	6.80 (22)	12.15 (39)
7.3	Phe Tyr	Ar–H	3.41	1.99	3.09	2.90	1.42 (42)	0.31 (9)	0.51 (15)

* Molar ratio of gelatin and hardener (mol per 100 g of ADG): (1) 10^{-4}, (2) 10^{-3}, and (3) 10^{-2}.

Table 8. Effect of LIKI-1 hardener on the parameters of gelatin macromolecules determined by photon-correlation spectroscopy; gelatin concentration 0.3%, 40°C, λ 632.8 nm, scattering angle 90°

Content of LIKI-1, mole per 100 g ADG	Diffusion coefficient $D \times 10^7$ of ADG, $cm^2\ s^{-1}$	Radius, nm	
		average R_1	most probable R_2
0	2.0±0.1	11.4±0.5	22.1±0.01
10^{-4}	2.2±0.1	15.2±0.6	28.0±0.01
10^{-3}	2.1±0.1	16.4±0.9	31.9±0.01
10^{-2}	2.0±0.1	17.3±1.2	32.2±0.01
10^{-1}	1.9±0.1	18.2±0.9	31.9±0.01

number, the viscosity increment, and the axial ratio of gelatin macromolecules modified with various hardeners.

The molecular-weight distribution of the gelatin sample (Table 1, sample no. 3) was studied by HPLC. We used aqueous systems containing 0.3% gelatin modified with LIKI-1 in amounts from 10^{-4} to 10^{-1} mol per 100 g of ADG at 60°C and contact time of 3 h. The viscosity of the resulting solutions was measured with a VPZh-4 capillary viscometer placed in a temperature-controlled cell at 40.0±0.1°C. The internal capillary diameter was 0.37 mm, the outflow time of water was 185 s, and the maximal shear rate near the capillary wall was 204 s^{-1} at 40°C. The solutions were thermostated before the test for 40 min. In viscometric experiments, the gelatin concentration was 3×10^{-1}–4×10^{-3} g cm^{-3}, sample volume 5 cm^3, and solution pH 5.6–6.1.

For our modified gelatin systems, the relative viscosity η/η_0 (where η and η_0 are the viscosities of the solution and solvent, respectively), intrinsic viscosity $[\eta]$, viscosity increment ν, and the axial ratio f of gelatin macromolecules in solution were determined. The intrinsic viscosity was determined by extrapolation of the concentration dependence $[\ln(\eta/\eta_0)]/c$ to zero concentration:

$$\lim [\ln(\eta/\eta_0)]/c\Big|_{c\to 0} = \lim [(\eta/\eta_0 - 1)/c]\Big|_{c\to 0} = [\eta]. \quad (4)$$

The intrinsic viscosity $[\eta]$ and viscosity increment ν are expressed through the weight and volume concentrations, and these quantities are related by the following expression:

$$[\eta] = \nu V, \quad (5)$$

where V is the specific partial volume at infinite dilution, i.e., it is the increase in the solution volume on adding a weight unit (1 g) of anhydrous protein to a large volume of solution.

If the protein dissolution proceeds without changes in the solution volume, then the partial specific volume is equal to the reciprocal density of the dry protein [18]. Busol [18] determined the concentration dependence of the density of aqueous gelatin-containing systems. The density of anhydrous gelatin is 1.35 g cm^{-3}, and it decreases with increasing water fraction in the system. In the air-dry state, gelatin contains 10–13% water (ρ 1.32 g cm^{-3}), and the specific partial volume $V = 1/\rho$ was taken as 0.75 $cm^3\ g^{-1}$.

In accordance with the Simha equation,

$$\lim [(\eta/\eta_0 - 1)/\Phi]\Big|_{\Phi\to 0} = \nu, \quad (6)$$

where ν is the viscosity increment, which depends on the axial ratio f of the ellipsoid of revolution; it is equal to 2.5 for spheres and is greater for all the ellipsoids [19].

The intrinsic viscosity $[\eta]$, viscosity increments ν, and axial ratio f for gelatin macromolecules, calculated from these dependences, are listed in Table 9.

As seen from these data, the conformation state of the gelatin macromolecules in dilute solutions at 40°C is the ellipsoid of revolution with the axial ratio of 33 for the given sample. Upon reaction with the hardener, the axial ratio of the gelatin macromolecule increases with increasing degree of modification.

Table 9. Properties of gelatin modified with LIKI-1 protected formaldehyde hardener in aqueous solutions; contact time 3 h, gelatin concentration 0.3%

LIKI-1 content, mol per 100 g of ADG	$[\eta]$	ν	f
0	66	88.1	33
10^{-4}	68	90.6	33.5
10^{-3}	70	93.3	34
10^{-2}	73	97.3	35
10^{-1}	77	102.6	36

Table 10. Characteristics of modified gelatins with various MWD; hardener concentration 10^{-2} mol per 100 g of ADG, 60°C

Sample no.	Hardener	Contact period of gelatin with hardener, h					
		1			3		
		[η]	ν	*f*	[η]	ν	*f*
4	–	51	68	29			
	LIKI-19	68	91	34	72	96	35
	DU-679	61	81	31	62	83	32
5	–	45	60	26			
	LIKI-19	55	73	29	60	80	31
	DU-679	57	76	30	57	76	30
6	–	49	65	28			
	LIKI-19	58	77	30	63	84	32
	DU-679	60	80	31	61	81	31

The dependences of hydrodynamic parameters of modified gelatin on the hardener type and gelatin MWD are of particular importance. For this study, we chose LIKI-19 and DU-679 hardeners and samples of photographic gelatin differing in MWD (Table 1, sample nos. 4–6). The contact time of the gelatin and hardener was 1–3 h at 60°C. The hardener was added into the 0.1% gelatin solutions in amount of 10^{-2} mol per 100 g of ADG. The viscometric measurements were performed at 40°C; the results are given in Table 10.

As seen, in all the cases studied, with increasing contact time the intrinsic viscosity, viscosity increment, and axial ratio of the gelatin macromolecules increase; and this increase is the most pronounced at hardening of the gelatin sample rich in high-molecular-weight fractions (Table 1, sample no. 4). It should be noted that, at hardening of this gelatin sample with LIKI-19 protected formaldehyde hardener, the increase in the hydrodynamic parameters of macromolecules is greater as compared to DU-679 hardener.

The reaction of polydisperse gelatins rich in α-fractions (Table 1, sample nos. 5, 6) with LIKI-19 and DU-679 hardeners also increases the intrinsic viscosity, viscosity increment, and axial ratio of the gelatin macromolecules, but this increase is smaller and depends to a lesser extent on the hardener type.

The contact time of gelatin and hardener also strongly affects the properties of macromolecules. On addition of LIKI-19, the axial ratio of macromolecules increases with time, whereas in the case of DU-679 the properties of macromolecules only slightly change with time.

CONCLUSIONS

(1) Hardening of gelatin as influenced by the molecular-weight distribution, hardener type, temperature, and reagent ratio was studied.

(2) α-Chains of gelatin are the most reactive in hardening.

(3) Based on high-resolution ^{1}H NMR data, the molecular mechanism of reaction between the modifying agent and gelatin was proposed; the decrease in the integral intensity of the resonance signals of the gelatin protons depends on the degree of modification.

(4) The average and most probable radii of macromolecules increase in the course of hardening.

(5) The gelatin macromolecules in dilute solutions at 40°C in the globule conformation state are ellipsoids of revolution (oblate ellipsoid). At chemical modification with hardeners of various types, the axial ratio increases, and the gelatin macromolecule becomes more asymmetrical.

REFERENCES

1. Zavlin, P.M. and D'yakonov, A.N., *Organicheskie soedineniya v proizvodstve i obrabotke svetochuvstvitel'nykh materialov. Dubiteli* (Organic Compounds in Production and Development of Light-Sensitive Materials. Hardeners), Leningrad: Leningr. Inst. Kinoinzhenerov, 1984.
2. Denisova, N.E., Zavlin, P.M. Levachev, S.M., *et al.*, *Zh. Prikl. Khim.*, 1990, vol. 63, no. 5, pp. 1104–1108.
3. Zavlin, P.M., Nuss, P.V., Ovchinnikov, A.N., *et al.*,

Zh. Nauchn. Prikl. Fotogr., 1997, vol. 42, no. 1, pp. 27–31.

4. Izmailova, V.N., Levachev, S.M., Sakvarelidze, M.A., *et al.*, *Zh. Nauchn. Prikl. Fotogr.*, 2002, vol. 47, no. 1, pp. 29–35.
5. Kharlov, A.E., Levachev, S.M., Sakvarelidze, M.A., *et al.*, *Zh. Nauchn. Prikl. Fotogr.*, 2002, vol. 47, no. 1, pp. 44–57.
6. Hermal, H. and Seeboth, A., *J. Photogr. Sci.*, 1990, vol. 38, pp. 70–78.
7. Zavlin, P.M., Nuss, P.V., Ovchnnikov, A.N., *et al.*, *Zh. Prikl. Khim.*, 1993, vol. 66, no. 35, pp. 615–621.
8. Izmailova, V.N. and Rebinder, P.A., *Strukturoobrazovanie v belkovykh sistemakh* (Cross-Linking in Protein Systems), Moscow: Nauka, 1976.
9. Izmailova, V.N., Derkach, S.R., Zotova, K.B., *et al.*, *Kolloidn. Zh.*, 1993, vol. 55, no. 3, pp. 54–90.
10. Izmailova, V.N., Derkach, S.R., and Rodin, V.V., *Zh. Nauchn. Prikl. Fotogr.*, 2000, vol. 45, no. 1, pp. 34–45.
11. Izmailova, V.N., Naryshkina, E.P., and Yampol'skaya, G.P., *Tr. GosNIIkhimfotoproekt* (Moscow), 1989, pp. 22–25.
12. Izmailova, V.N., Yampol'skaya, G.P., and Summ, B.D., *Poverkhnostnye yavleniya v belkovykh sistemakh* (Surface Phenomena in Protein Systems), Moscow: Khimiya, 1988.
13. Krasovskii, A.N., Mnatsakanov, S.S., Belousova, I.A., *et al.*, *Kolloidn. Zh.*, 1994, vol. 56, no. .4, pp. 528–534.
14. Krasovskii, A.N., Nikolaev, B.P., Shlyakov, A.M., *et al.*, *Vysokomol. Soedin., Ser. A*, 1995, vol. 37, no. 2, pp. 273–279.
15. Krasovskii, A.N., and Andreeva, A.I., *Zh. Nauchn. Prikl. Fotogr.*, 1996, vol. 41, no. 3, p. 7.
16. Krasovskii, A.N., Andreeva, A.I., Belousova, I.A., *et al.*, *Zh. Prikl. Khim.*, 1994, vol. 67, no. 8, pp. 1351–1359.
17. Derkach, S.R., Dyakina, T.A., Kharlov, A.S., *et al.*, *Zh. Nauchn. Prikl. Fotogr.*, 2002, no. 47, no. 1, pp. 58–65.
18. Busol, T.F., Study of the Interphase Adsorption Layers of Gelatin by Internal Reflection Spectroscopy, *Cand. Sci. Dissertation*, Moscow, 1980.
19. *A Laboratory Manual of Analytical Methods of Protein Chemistry*, Alexander, P. and Block, R.I., Eds., London: Pergamon, 1960–1961. Vols. 1–3.

Russian Journal of Applied Chemistry, Vol. 76, No. 7, 2003, pp. 1152–1155. Translated from Zhurnal Prikladnoi Khimii, Vol. 76, No. 7, 2003, pp. 1185–1188.

MACROMOLECULAR CHEMISTRY AND POLYMERIC MATERIALS

Modification of Styrene-Containing Oligomer Based on Bottoms from Toluene Distillation in Production of Polybutadiene

S. S. Nikulin, O. N. Filimonova, and O. N. Oleinikova

Voronezh State Academy of Forestry Engineering, Voronezh, Russia
Voronezh State Technological Academy, Voronezh, Russia

Received November 27, 2002; in final form, April 2003

Abstract—Chemical modification of styrene-containing oligomer with maleic anhydride was studied. The process conditions and content of maleic anhydride were optimized.

The main avenue in processing and utilization of organic and polymeric wastes [1–5] is preparation from them of oligmers by polymerization or degradation. However, low-molecular-weight polymers prepared from petrochemical wastes and by-products, as a rule, do not have the required set of properties, which largely limits their application. Some characteristics of substances obtained from petrochemical wastes and by-products can be improved by modification [6]. An example of such modification can be reaction with maleic anhydride (MA) [7, 8], allowing introduction into oligomers of additional reactive groups and imparting new properties to the products.

The goal of this work was to modify with maleic anhydride the styrene-containing oligomer prepared from bottoms of distillation of recycled solvent, toluene (TDB), in production of polybutadiene, and also to examine the possibility of using the modified oligomer as impregnating material for improving the properties of wood-fiber boards.

Modification experiments were performed with TDB oligomer containing units of styrene (~75%), 4-vinylcyclohexene (VCH), 1,5,9-cyclododecatriene (CDT), and *n*-2,4,6,10-dodecatetraene (NDT). The viscosity-average molecular weight $\overline{M}_v$ of the oligomer was about 1663.

Experiments were performed as follows. A steel ampule was charged with a styrene-containing TDB-based oligmer containing no more than 5 wt % residual low-molecular-weight products (dry residue ≥95 wt %) and with MA. The reaction temperature was 160°C. The MA content was varied from 3 to 7 wt % relative to the oligomer.

The reaction of MA with the oligomer was monitored by intermittent sampling from the ampule, followed by determination of the viscosity-average molecular weight of the product $\overline{M}_v$ and of the acid number (titration with alcoholic alkali to determine the content of anhydride and carboxy groups [9]).

Experimental studies showed that the course of modification of the TDB-based styrene-containing oligomer depends on the MA content in the reaction mixture (Fig. 1a). By computer treatment of the results, we obtained second-order equations describing the influence of the process time and MA content on the viscosity-average molecular weight $\overline{M}_v$ of the modified oligomers:

$$y_1 = 1578 - 34.43x + 0.92x^2, \quad c_{MA} = 3.0 \text{ wt \%};$$

$$y_2 = 1572 - 42.26x + 1.16x^2, \quad c_{MA} = 5.0 \text{ wt \%};$$

$$y_3 = 1634 - 69.38x + 2.06x^2, \quad c_{MA} = 7.0 \text{ wt \%}.$$

All the curves pass through a minimum at the reaction time of 17–19 h. Then the molecular weight of the oligomer starts to grow.

At a low content of MA in the reaction mixture (up to 3.0 wt % relative to the oligomer), in the initial stage of the process the viscosity and hence $\overline{M}_v$ slightly decrease. This trend is particularly pronounced at the reaction time of 17–19 h. Longer (>19 h) reaction results in the growth of the viscosity and hence $\overline{M}_v$.

At the MA content increased to 5–7 wt % relative to the oligomer, the degradation processes in the initial stage become less pronounced (Fig. 1a), as indicated by the less pronounced decrease in the molecular weight of the modified oligomer.

The acid number (Fig. 1b) grows with increasing synthesis time and MA dosage. This suggests predom-

1070-4272/03/7607-1152$25.00

inant occurrence of degradation processes which primarily involve macromolecules with a high molecular weight and also highly unsaturated VCH, CDT, and NDT units. This is also indicated by an increase in the acid number of successively taken samples of the modified oligomer (Fig. 1b). However, increased content of MA causes formation of a precipitate. At an MA content of 3.0 wt %, no precipitate is formed.

The reaction of MA with the TDB-based styrene-containing oligomer can follow several pathways, of which the major pathways are (a) Diels–Alder addition of MA to double bonds [10], decreasing the extent of unsaturation, and (b) copolymerization (or cross-linking) of oligomer molecules with MA, increasing the molecular weight of the resulting product. The relative contributions of these pathways depend on the modification conditions and MA content.

At a low content of MA, the number of the cross-links formed is small, and the modified oligomer remains soluble. At increased MA content, a precipitate forms, which may be due both to formation of insoluble three-dimensional structres and to limited solubility of unchanged MA:

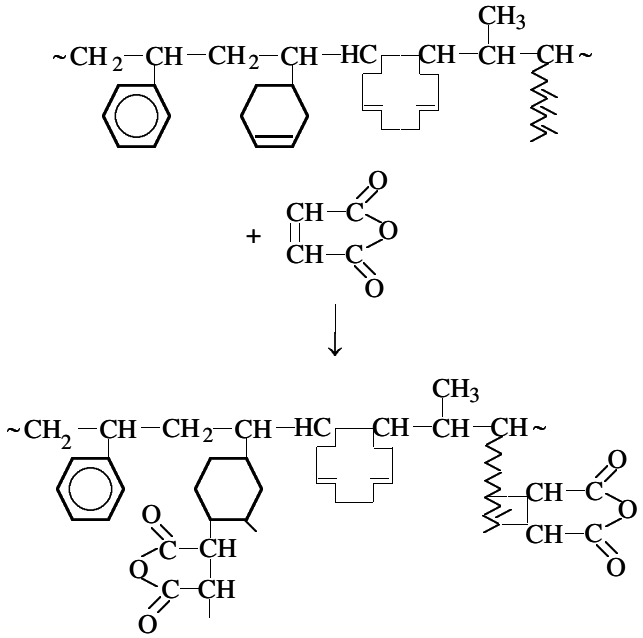

Thus, our results show that the MA content should not exceed 3.0 wt %, since the precipitate formed at a higher MA content causes the loss of the oligomers and gives rise to problems with utilization of this new kind of waste.

The IR spectrum of the MA-modified styrene-containing oligomer based on TDB (Fig. 2) contains characteristic absorption bands of the monosubstituted benzene ring at 700, 760, 1490, and 1600 cm^{-1}. Also,

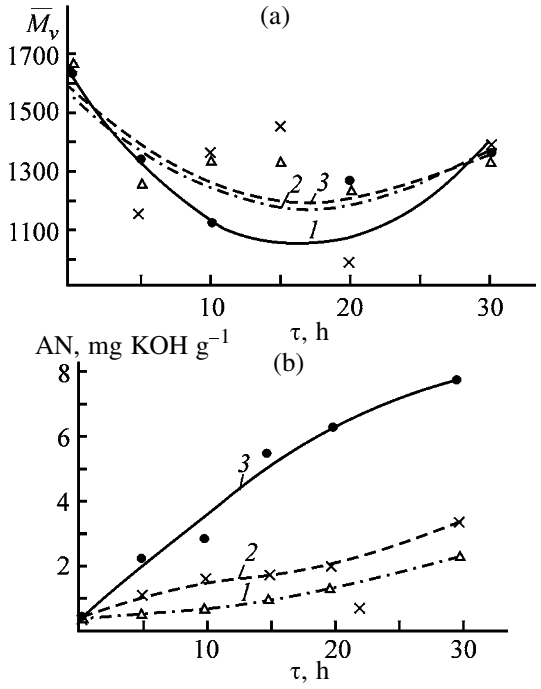

Fig. 1. (a) Viscosity-average molecular weight $\overline{M}_v$ and (b) acid number as functions of the modification time τ. MA concentration, wt %: (*1*) 3.0, (*2*) 5.0, and (*3*) 7.0.

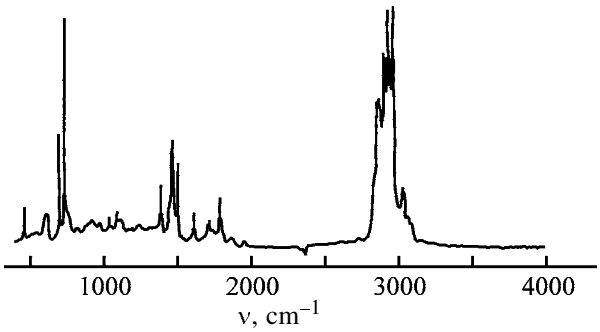

Fig. 2. IR spectrum of modified styrene-containing oligomer based on TDB. (ν) Wave number.

the ν(CO) bands appear at 1710, 1780, and (for the anhydride ring) 1840 cm^{-1}. These bands confirm addition of MA to the oligomer.

Published data suggest that the modified styrene-containing oligomer based on TDB may be promising for protective treatment of wood and wood-fiber boards. For these purposes, it will be possible to utilize substandard oligomers unsuitable for use in paint-and-varnish materials, polymeric formulations, etc. [11, 12].

However, the applicability of styrene-containing low-molecular-weight compounds prepared from petrochemical wastes is limited by the necessity of using an organic solvent, because the products are highly viscous or solid under normal conditions. An

Experimental and calculated parameters of the strength and water resistance of wood-fiber boards

Parameter	Calculation	Experiment	Control*
Ultimate bending strength, MPa	34.3	32.1	15.2
Swelling with respect to thickness in 24 h, %	17.5	17.9	26.0
Water absorption in 24 h, %	20.1	19.5	40.1

* Unmodified wood-fiber boards.

interest in the MA-modified styrene-containing oligomer based on TDB is due the fact that this product remains liquid under normal conditions after distillation of the solvent and other low-boiling components. This allows elimination of solvents from the impregnation process, significant improvement of the environmental characteristics of the process, and its simplification. Thus, the process becomes more promising for commercial implementation.

The process optimization was performed using the 4×4 Latin square experimental plan [13]. As the main factors exerting the major influence on the water resistance and strength of wood-fiber boards, we chose the impregnation temperatre (60, 80, 100, 120°C; factor A), heat treatment temperature (70, 100, 130, 160°C, factor B), and heat treatment time (1, 3, 5, 7 h, factor C). The copolymer content in the wood-fiber boards was evaluated from the weight gain of the sample. After conditioning, the boards were tested according to GOST (State Standard) 19 592–80. The content of the modified oligomer in the wood-fiber boards depended on the process conditions and varied from 12.6 to 19.4 wt %.

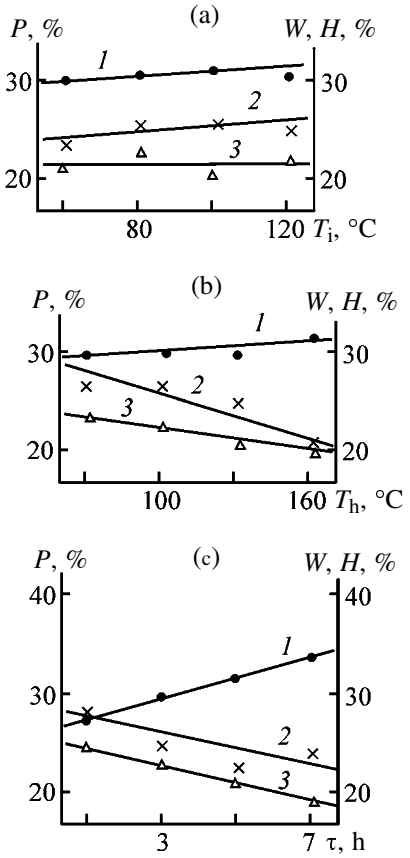

Fig. 3. Properties of modified wood fiber boards as functions of (a) impregnation temperature T_i, (b) heat treatment temperature T_h, and (c) heat treatment time τ. (*P*, *1*) Bending strength, (*W*, *2*) water absorption, and (*H*, *3*) swelling with respect to thickness.

Figure 3 shows the results of testing wood-fiber boards for the strength and water resistance. It is seen that the strongest influence on the properties of the modified wood-fiber boards in exerted by the heat treatment time; the influence of the impregnation and heat treatment temperature is weaker.

The optimal conditions for impregnation of wood-fiber boards with the modified TDB-based oligomer are as follows: impregnation temperature 60°C, heat treatment temperature 160°C, and heat treatment time 7 h. The strength and water resistance of the modified wood-fiber boards, calculated for these conditions, are compared with the experimental values in the table. These values show good agreement.

CONCLUSIONS

(1) A study of chemical modification with maleic anhydride of the styrene-containing oligomer based on the bottoms from toluene distillation showed that the optimal content of maleic anhydride is 3.0 wt %. At a higher content of maleic anhydride, a precipitate is formed.

(2) One of the promising applications of the modified oligomer obtained is treatment of wood-fiber boards.

REFERENCES

1. *Otkhody i pobochnye produkty neftekhimicheskikh proizvodstv – syr'e dlya organicheskogo sinteza* (Wastes and By-Products from Petrochemical Industry

as Raw Materials for Organic Synthesis), Cherkashin, M.I., Ed., Moscow: Khimiya, 1989.

2. Shein, V.S., Ermakov, V.I., and Norkhin, Yu.G., *Obezvrezhivanie i utilizatsiya vybrosov i otkhodov pri proizvodstve i pererabotke elastomerov* (Rendering Harmless and Utilization of Effluents and Wastes from Production and Processing of Elastomers), Moscow: Khimiya, 1987.
3. Rivin, E.M., *Novye napravleniya ispol'zovaniya otkhodov neftekhimii* (New Avenues in Utilization of Petrochemical Wastes), Moscow: TsNIITEneftekhim, 1994.
4. Nikulin, S.S., Butenko, T.R., Ryl'kov, A.A., *et al.*, *Perspektivy ispol'zovaniya kubovykh ostatkov proizvodstva vinilaromaticheskikh monomerov* (Prospects of Utilization of Bottoms from Production of Vinylaromatic Monomers), Moscow: TsNIITEneftekhim, 1996.
5. Petykhin, Yu.M. and Kontsova, L.V., *Otkhody neftekhimicheskikh proizvodstv – syr'e dlya sinteticheskikh produktov* (Petrochemical Wastes as Raw Materials for Synthetic Products), Moscow: TsNIITEneftekhim, 1991.
6. Tutorskii, I.A., Potapov, E.E., and Shvarts, A.G., *Khimicheskaya modifikatsiya elastomerov* (Chemical Modification of Elastomers), Moscow: Khimiya, 1993.
7. Rzaev, Z.M., *Polimery i sopolimery maleinovogo angidrida* (Polymers and Copolymers of Maleic Anhydride), Baku: Elm, 1984.
8. Moldavskii, V.L. and Kerpos, Yu.D., *Maleinovyi angidrid i maleinovaya kislota* (Maleic Anhydride and Maleic Acid), Moscow: Khimiya, 1976.
9. Toroptseva, A.M., Belogorodskaya, K.V., and Bondarenko, V.M., *Laboratornyi praktikum po khimii i tekhnologii vysokomolekulyarnykh soedinenii* (Laboratory Course of Chemistry and Technology of Macromolecular Compounds), Nikolaev, A.F., Ed., Leningrad: Khimiya, 1972.
10. Wassermann, A., *Diels–Alder Reactions. Organic Background and Physico-Chemical Aspects*, Amsterdam: Elsevier, 1965.
11. Nikulin, S.S., Sakhokiya, I.A., Dmitrenkov, A.I., and Filimonova, O.N., *Lakokras. Mater. Ikh Primen.*, 2001, no. 6, pp. 22–24.
12. Nikulin, S.S., Filimonova, O.N., Dmitrenkov, A.I., and Sakhokiya, I.A., *Zh. Prikl. Khim.*, 2000, vol. 73, no. 9, pp. 1565–1567.
13. Akhnazarova, S.L. and Kafarov, V.V., *Metody optimizatsii eksperimenta v khimicheskoi tekhnologii* (Methods for Experiment Optimization in Chemical Technology), Moscow: Vysshaya Shkola, 1985.

Russian Journal of Applied Chemistry, Vol. 76, No. 7, 2003, pp. 1156–1163. Translated from Zhurnal Prikladnoi Khimii, Vol. 76, No. 7, 2003, pp. 1189–1196.

MACROMOLECULAR CHEMISTRY AND POLYMERIC MATERIALS

Fullerene-Modified Polyimide Derived from 3,3',4',-Benzophenonetetracarboxylic Acid and 3,3'-Diaminobenzophenone for Casted Items and Its Use in Tribology

G. N. Gubanova, T. K. Meleshko, V. E. Yudin, Yu. A. Fadin, Yu. P. Kozyrev, V. I. Gofman, A. A. Mikhailov, N. N. Bogorad, A. G. Kalbin, Yu. N. Panov, G. N. Fedorova, and V. V. Kudryavtsev

Institute of Macromolecular Compounds, Russian Academy of Sciences, St. Petersburg, Russia
Institute of Machine Science Problems, Russian Academy of Sciences, St. Petersburg, Russia

Received October 3, 2002; in final form, April 2003

Abstract—The possibility was examined of processing into a casted item (molding) of the crystallizing thermoplastic polyimide derived from 3,3'-diaminobenzophenone and 3,3',4,4'-benzophenonetetracarboxylic dianhydride and of composites of this polyimide with fullerenes. The tribological characteristics of the moldings were studied.

The demand for structural materials with enhanced properties stimulates active studies of thermoplastic ("fusible") crystallizing polyimides (PIs) [1]. Materials based on these polyimides, in particular, composite materials [2], combine high levels of mechanical properties, heat resistance, and resistance to cracking. The above-noted properties of polyimide materials attract the interest of tribologists whose efforts are aimed at enhancing the antifriction and antiwear characteristics of friction units in machines and mechanisms, in particular, of dry friction units [3].

A promising way to improve the performance of polymeric materials, attracting growing researchers' interest, is modification with fullerenes. For example, it was reported that fullerenes improve the tribological characteristics of polymeric materials in sliding friction [4].

It was shown previously [2] that the crystallizable PI derived from 3,3',4,4'-benzophenonetetracarboxylic dianhydride and 3,3'-diaminobenzophenone (PI BZP–3,3'BZP) can exist in two crystalline modifications: CM-1 with the melting point T_{m1} = 275–290 and CM-2 with T_{m2} = 330–350°C. The structural features of this polyimide are determined by the conditions of its preparation [5]. It was found [5, 6] that formation of amorphous or partially crystalline PI BZP–3,3'BZP is mainly governed by the solvent used in synthesis and imidization of the prepolymer. The partially crystalline PI with the higher melting point T_{m2} is formed under conditions of thermal imidization, whereas chemical imidization in solution in an amide solvent yields the low-melting crystalline modification CM-1. In this case, the viscosity of the polymer melt η (Pa s) at 300–320°C is fairly low ($\log\eta$ = 2.8–3.5), which allows its processing into a matrix of a composite at temperatures close to the glass transition point T_g (245–250°C).

In this work we examined the possibility of processing of various structural modifications of PI BZP–3,3'BZP into a cast item (molding) and studied the mechanical and tribological characteristics of the resulting material. Our goal was also to develop fullerene-containing PI BZP–3,3'BZP composites, prepare moldings from them, and assess the prospects of using fullerene-containing PIs in dry friction couples with steel.

EXPERIMENTAL

Synthesis of 3,3'-diaminobenzophenone and purification of 3,3',4,4'-benzophenonetetracarboxylic dianhydride were described in [5]. The polyamido acid (PAA) was prepared by adding a stoichiometric amount of the dianhydride at 50°C into a solution of the diamine in a solvent suitable for obtaining the

1070-4272/03/7607-1156$25.00

required structural modification according to [5]. The concentration of the PAA solution was 25% (here and hereinafter, wt %), and the synthesis time, 4 h.

Powdered PI samples were prepared by thermal and chemical imidization of PAA. To obtain thermally imidized powdered PI, a 1% solution of PAA was precipitated in benzene, and the precipitate was filtered off and vacuum-dried at 60°C. Imidization was performed by successively heating the PAA powder at 100, 200, 230, and 250°C for 30 min at each temperature. For chemical imidization, the reaction solution of PAA was diluted to 5% concentration with the same solvent as that used for PAA synthesis. Then the imidizing mixture consisting of triethylamine and acetic anhydride (2 and 3 mol, respectively, per mole of elementary units of the polymer) was added. After stirring for 4 h at 50°C, the mixture was cooled to room temperature and allowed to stand for 20 h. The precipitated polymer was filtered off, washed, and dried as described in [5].

To obtain fullerene-containing polymeric samples, we used a mixture of fullerenes C_{60} and C_{70} (weight ratio 78 : 22).[1]

The viscosity of melts obtained from PI powders was determined on a PIRSP rheogoniometer (Russia) with a cone–plate working unit (cone angle 1°, diameter 40 mm) in the constant shear rate mode (10^{-2} s^{-1}) at a preset temperature.

By differential scanning calorimetry (DSC), we determined the glass transition (T_g) and melting (T_m) points (°C) and the enthalpies of melting (ΔH, J g^{-1}) of the PI samples obtained, which were subsequently used for preparing moldings. The measurements were performed with a DSM-2M microcalorimeter at a scanning rate of 10 deg min^{-1}.

The TG curves were taken on a modified (model C) MOM derivatograph (Hungary) in air at a heating rate of 10 deg min^{-1}.

The mechanical characteristics of films were determined in the uniaxial extension mode with samples in the form of 2-mm-wide bands with the working part length of 20 mm. The tests were performed on a UTS 10 universal mechanical testing installation (UTStestsysteme, Germany) at an extension rate of 20 mm min^{-1} (100% of initial length per minute). From the testing results, we determined the modulus of elasticity E (MPa), tensile strength σ_t (MPa), and elongation at break ε_b (rel. %).

[1] The mixture was provided by the Fullerene Technologies Company, Ltd. (St. Petersburg).

The glass transition points of polyimide films were determined thermomechanically on a UMIV-3 installation in the mode of uniaxial extension with a tensile stress of 0.5 MPa under conditions of linear heating at a rate of 5 deg min^{-1}.

Cast samples (moldings) based on PI powders were prepared as follows. Pellets 2–3 mm thick and 20 mm in diameter were pressed from PI powders at room temperature and a pressure of 200 atm. The pressed pellets were heated in a press mold without pressing at 320°C for 1 h. After heating, the mold was removed from the oven and finally pressed for 2–3 min at 150 atm. The mold was then cooled to 60–70°C over a period of 40 min under a pressure of 100–150 atm.

From the pellets thus prepared, we cut $5 \times 2 \times$ 18-mm flat samples for three-point bending tests at a loading rate of 1.3 mm min^{-1} and base length of 15 mm. The bending strength σ_b (MPa), Young's modulus E (MPa), and breaking strain ε_b (rel. %) were determined according to [7].

The tribological parameters and surface characteristics of moldings were studied on a friction installation described in detail in [8]. The face scheme of friction was realized. A rotating steel counterbody (in the form of a ring) was in contact with the flat surface of a polymeric disk 20 mm in diameter and 3 mm thick. The contact pressure was varied within 1.7–6.7 MPa, and the sliding velocity, within 0.047–0.138 m s^{-1}. The following main tribological parameters were determined: coefficient of dry sliding friction f, weight wear Δm (mg), and the dimensionless quantity, linear wear intensity I_w, defined as $I_w = V/(SL)$, where V is the volume (m^3) of the material removed from the contact surface in a definite time (10 min); S, minimal contact surface area (m^2); and L, sliding path (m) equal to 100 m.

In this work we also collected and analyzed polymer particles formed during the test, using a Videolab 2 automated image processing system [9]. With this system and software supplied with it, it is possible to determine the total number of particles in the visual field of the microscope, the area enclosed by the paritcle contour, and perimeter and form factor of each particle. Electron-microscopic examination of the wear particles was performed with a JSM-35 electron microscope (Japan).

By varying the conditions of PI BZP–3,3'BZP synthesis (according to [5]), we obtained powdered PI samples of the same chemical composiiton but different supramolecular structures. We compared the vis-

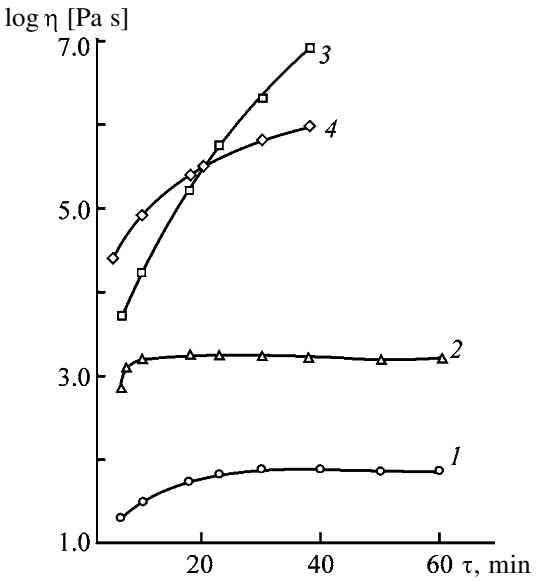

Fig. 1. Viscosity η of the PI BZP–3,3'BZP melt as a function of time τ. Sample: (*1*, *3*) amorphous and (*2*, *4*) partially crystalline. Imidization procedure: (*1*, *2*) chemical and (*3*, *4*) thermal.

cosities of their melts. In these experiments, we used PI samples prepared from PAA with the terminal amino groups protected by treatment with phthalic anhydride. This was done in order to exclude the decrease in the melt flowability caused by an increase in the molecular weight due to condensation of terminal functional groups at temperatures corresponding to the viscous-flow state of the polymer.

The method used allowed us to compare at the same temperature (330°C) the time dependences of the apparent viscosity of the polymer melts for four samples of PI BZP–3,3'-BZP (Fig. 1): amorphous samples prepared by chemical and thermal imidization and partially crystalline samples differing in the melting point. It is seen that the amorphous and partially crystalline samples prepared by chemical imidization have relatively low melt viscosity (Fig. 1, curves *1*, *2*), and the viscosity does not noticeably grow over a period of 60 min, which is particularly important for practice. These data show that such PI BZP–3,3'-BZP samples can be successfully processed into a cast item under conditions of hot pressing. The polymer samples prepared by thermal imidization (Fig. 1, curves *3*, *4*) exhibit a high initial apparent viscosity of the melt, and this parameter rapidly grows with time.

Table 1. Strength characteristics of moldings from PI BZP–3,3'BZP

Sample	σ_b, MPa	*E*, MPa	ε_b, %
Partially crystalline, CM-1:			
no. 1	118	2150	5.5
no. 2	137–160	2540–2960	5.4
Partially crystalline, CM-2	9	820	1.1
Amorphous (chemical imidization)	6	670	0.9

Three of the four structural modifications of PI BZP–3,3'BZP appeared to be suitable for casting at moderate temperatures (300–350°C), substantially lower than the temperatures of the onset of PI thermal degradation (450–500°C). From these three modifications of PI, we prepared samples of moldings and compared their strength characteristics. The results of bending tests for this series of moldings are given in Table 1. We failed to prepare a molding under the chosen conditions (320°C) from the amorphous PI BZP–3,3'BZP sample obtained by thermal imidization of the PAA powder. This is apparently due to the high viscosity (low flowability) of the polymer melt at the process temperature (Fig. 1, curve *3*).

Table 1 shows that the sample prepared from partially crystalline PI of the high-melting crystalline modification CM-2 is brittle and has a very low bending strength. This may be due to the low flowability of the polymer melt at the pressing temperature (320°C), resulting in the nonmonolithic structure of the material. At the same time, our results show that the high melt flowability (Fig. 1, curve *1*) is a necessary but insufficient condition for obtaining cast items of high strength. The molding obtained from the amorphous PI BZP–3,3'BZP sample (the least viscous at the pressing temperature, Fig. 1, curve *1*) also has a poor strength. This is apparently due to the low molecular weight of the sample. According to [5], PI prepared by chemical imidization of PAA in diglyme or *m*-cresol has a lower molecular weight.

The moldings prepared from partially crystalline PI BZP–3,3'BZP of the low-melting crystalline modification CM-1 show high levels of bending strength, modulus of elasticity, and breaking strain (Table 1). Sample no. 2 differs from sample no. 1 (Table 1) in partial protection of terminal amino groups, ensured by adding at the end of PAA synthesis 0.013 mol of phthalic anhydride per mole of PAA elementary unit. Apparently, the increased strength in this case is due to extension of the melt "life" provided by such protection.

It is interesting that the strength characteristics of these moldings are comparable to those of a PI

Table 2. Characteristics of films of fullerene-containing PI BZP–3,3'BZP

Sample no.	T_g, °C	σ_b, MPa	E, MPa	ε_b, %
2 (run no. 2)	242	142	4130	4.5
3 (run no. 3)	243	128	3150	4.5
5 (fullerene-free)	242	84	3150	3.0

Table 3. Glass transition points, melting points, enthalpies of melting, and heat resistance characteristics of samples of fullerene-containing PI BZP–3,3'BZP

Sample no.	T_g	T_m	ΔH, J kg^{-1}	τ_0	τ_5	τ_{10}
	°C			°C		
1 (run no. 1)	245	285	28.0	465	568	606
2 (run no. 2)	237	270	17.2	480	585	620
2' (run no. 2')	237	290	9.0	486	550	570
3 (run no. 3)		273	29.3	470	555	575
4 (run no. 4)	237	282	13.7	480	550	575
5 (fullerene-free)	250	290	28.0	450	532	553

BZP–3,3'BZP film prepared by thermal imidization of a PAA film (Table 2, fullerene-free sample). Thus, the bulk cast material obtained from partially crystalline PI BZP–3,3'BZP of the low-melting crystalline modification CM-1 acquires the properties characteristic of a film material obtained by traditional thermal imidization of the PAA film. Thus, proper choice of the structural modification of PI BZP–3,3'BZP and hence of the procedure for preparing the initial press powder allows realization of the intrinsic characteristics of the material.

In view of these results, we chose PI BZP–3,3'BZP of the low-melting crystalline modificatoin CM-1 for further experiments on development of a fullerene-containing polymeric composite. The PI BZP–3,3'BZP chains contain structural fragments (carbonyl groups and terminal amino groups) exhibiting certain affinity for fullerenes [10]. Therefore, we can expect that finely dispersed uniformly distributed fullerene will be bound with the polymeric matrix by complexing interactions.

Fullerene-containing samples of partially crystalline press powder of PI BZP–3,3'BZP (T_{m_1} = 275–290°C) were prepared by introducing a mixture of fullerenes C_{60} and C_{70} into the polymer using several procedures. For more uniform distribution of the fullerene, a solution of the fullerene mixture was mixed with the polymer solution in various stages of PI preparation.

In run no. 1, fullerenes were preliminarily dissolved in dimethylacetamide (DMAA) to a concentration of 0.05 mg ml^{-1}, and the entire subsequent process of preparing partially crystalline PI BZP–3,3'-BZP of the CM-1 modification was performed in this solution as described above. It is known [11] that the solubility of fullerenes in *o*-dichlorobenzene is considerably higher than in DMAA. Therefore, with the aim to introduce larger amounts of fullerenes into the polymer, we used in run nos. 2–4 a 20 mg ml^{-1} solution of the fullerene mixture in *o*-dichlorobenzene.

In run no. 2, we first kept fullerenes and the diamine in a 5 : 1 (by weight) mixture of DMAA and *o*-dichlorobenzene for 1 h at room temperature and then performed synthesis of PAA and imidization as described above. A check experiment showed that synthesis of PAA in such a solvent mixture is not accompanied by a decrease in the molecular weight of the polymer. The reduced viscosity of a 0.5% PAA solution prepared in DMAA and in a 5 : 1 mixture of DMAA with *o*-dichlorobenzene was 0.56 and 0.55 dl g^{-1}, respectively. In run no. 2' (Table 3), the terminal functional groups were partially protected similarly to sample no. 2 from Table 1 (treatment with 0.013 mol of phthalic anhydride per mole of PAA elementary units).

In run no. 3, we added a solution of fullerenes in *o*-dichlorobenzene into a reaction solution (25%) of the synthesized PAA and kept the resulting mixture at room temperature for 2 h. Then, as in the prevoius cases, PAA was imidized with the imidizing mixture after preliminary dilution wiht DMAA to 5% concentration. The weight ratio of DMAA and *o*-dichloro-

benzene in the mixture thus obtained was 40 : 1. In the course of imidization, the polymer lost solubility and precipitated from the reaction mixture in the form of a finely dispersed fullerene-containing powder of PI BZP–3,3'BZP.

In run no. 4, a solution of fullerenes in *o*-dichlorobenzene was added to a polymer solution 3 h after adding the imidizing mixture, i.e., in the course of PAA imidization but before the onset of PI precipitation. With *o*-dichlorobenzene, we introduced into the polymer 0.1% fullerenes (relative to the dry polymer weight), and with DMAA only, 0.015% fullerenes.

The uniform distribution and fixation of fullerenes in the bulk of the polymer can be confirmed by transparency and optical uniformity of films obtained from fullerene-containing PI BZP–3,3'BZP. To obtain such films, we prepared films from fullerene-containing PAAs using the composition of PAA, BZP–3,3'BZP, and fullerenes obtained in run nos. 2 and 3 and performed thermal imidization of these films. For this purpose, before adding the imidizing mixture, we cast films on glass supports from fullerene-containing composition nos. 2 and 3. The films were dried and successively heated for 1 h at 100, 200, and 300°C. As a result, we obtained transparent dark brown optically uniform films from fullerene-containing PI and determined their strength characteristics (Table 2) and T_g. For comparison, we give in Table 2 the characteristics of a fullerene-free PI BZP–3,3'BZP film prepared from PAA that was obtained in run no. 3.

It is known [5] that the PI studied in this work does not itself exhibit good film-forming properties; PAA films break after chemical imidization. Films prepared by thermal imidization of PAA films are fairly brittle (Table 2, sample no. 5). In this connection, noticeable enhancement of the deformation and strength characteristics of fullerene-containing PI BZP–3,3'BZP films is a positive result of our study (Table 2, sample nos. 2 and 3).

The next stage of our study involved preparation of fullerene-containing PI BZP–3,3'BZP press powders by the above-described procedures. We prepared sample nos. 1–4 and compared them to fullerene-free samples of partially crystalline PI BZP–3,3'BZP using differential scanning calorimetry (to determine the glass transition point, melting point, and enthalpy of melting) and thermal gravimetric analysis (to determine the temperatures of the onset of weight loss and of 5 and 10% weight loss: τ_0, τ_5, and τ_{10}, respectively) (Table 3).

Table 3 shows that addition of fullerene to the reaction solution in various stages of PI preparation has no significant effect on structure formation in PI. All the samples of fullerene-containing powdered PI exhibit well-defined softening and melting points in the DSC curves (Table 2) and belong to the low-melting crystalline modification CM-1, i.e., they show promise for casting at 300–350°C. It can be only noted that the enthalpy of melting in some cases decreases, suggesting certain decrease in the degree of crystallinity of the polymer.

Comparison of the heat resistance parameters (Table 3) shows that addition of fullerenes to PI results in a noticeable growth of the thermal degradation temperatures. Presumably, fullerenes acting as radical scavengers inhibit the radical thermal degradation of the polyimide [10].

From the fullerene-containing compositions of partially crystalline PI BZP–3,3'BZP, we prepared moldings as described above and compared their tribological characteristics. The sample prepared from fullerene-containing composition no. 1 was similar in the color (yellow-brown) to the fullerene-free PI BZP–3,3'BZP sample, apparently because of the low fullerene content (0.015%). Moldings prepared from fullerene-containing composition nos. 2–4 were black.

Figure 2a shows the pressure dependences of the sliding friction coefficient f (dimensionless quantity) in the tribocontact with the moldings under consideration. At pressures below 5 MPa, the friction coefficients are virtually constant for all the compositions, ranging from 0.15 to 0.2. At contact pressures above 5 MPa, the friction coefficient does not noticeably increase only with the molding based on the composition from run no. 2; hence, this composition is the most promising for using in friction units at tribocontact pressures of up to 10 MPa. Moldings based on the other compositions show stable operation only at pressures below 5 MPa.

Figure 2b shows the pressure dependences of the weight wear in a tribocontact at a sliding velocity of 0.14 m s^{-1} and sliding path of 100 m. It is seen that the molding sample prepared by the scheme of run no. 2 is the best with respect to the second tribological characteristic, weight wear, also. It is interesting that the weight wear of the fullerene-free moldings and of those with the minimal fullerene content, 0.015% (Fig. 2b, curves *1*, *5*), exceeds the weight wear of the moldings prepared from composition no. 2 by a factor of 15–25.

In separate experiments at low sliding velocities we studied how the linear wear intensity I_w of the

moldings depends on the sliding velocity v (m s^{-1}). We chose the moldings with the minimal (0.015%, sample no. 1), intermediate (0.1%, sample nos. 3 and 4), and maximal (1%, sample no. 3' prepared similarly to sample no. 3 but containing more fullerenes) fullerene content. Figure 3 clearly demonstrates enhancement of the wear resistance of the moldings with increasing fullerene content. It is noteworthy that the wear intensity is a linear function of the sliding velocity for all the moldings and that the moldings containing 0.1–1% fullerenes show an inflection in this dependence at a sliding velocity of 0.12 m s^{-1}.

The mechanism of wear in a friction couple is determined by processes occurring in a surface layer within a depth of several tens of micrometers. Friction of polymers induces structural rearrangements in the surface layers of the contacting materials; the temperature grows, the intermolecular interaction weakens, and, as a result, subsurface cracks and then wear particles are formed. The parameters of wear particles bear information about the surface degradation, changes in the wear mechanism, and, in particular, about the shear strength of a material.

In this work, we studied the physical processes occurring in a surface layer by collecting and analyzing the wear particles formed in the course of friction. The experiments performed at a sliding velocity of 0.14 m s^{-1} and a sliding path of 100 m showed that appreciable changes in the mean particle size occur in the same pressure range, 2.5–5 MPa, for different compositions. The mean area of wear particles is within several hundreds of square micrometers for the moldings based on composition no. 2 and within 10^3 μm^2 in the other cases. Thus, along with the low friction coefficient, moldings based on composition no. 2 also exhibit a high shear strength, which is a very important parameter for applying materials in friction units.

The presence of an inflection point in the curves of the friction coefficient vs. tribocontact pressure (Fig. 2a) can be attributed to changes in the polymer structure occurring as the temperature in the thin contact layer grows owing to an increase in the tribocontact pressure. It is known that friction can cause the temperature in the contacting materials to grow up to the melting point.

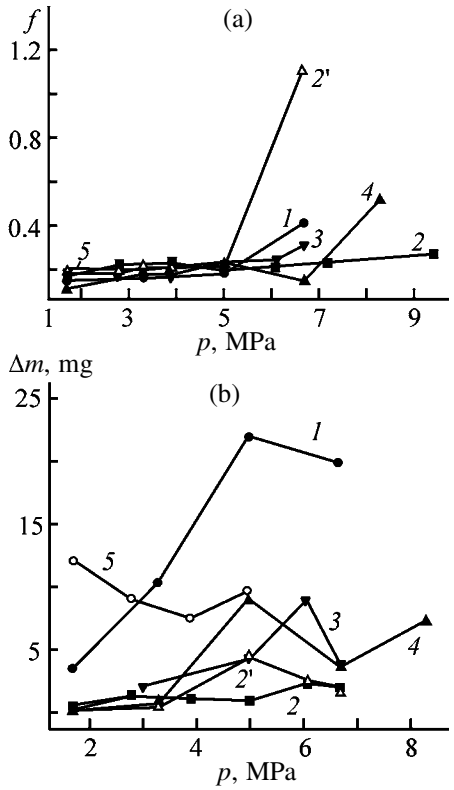

Fig. 2. (a) Sliding friction coefficient f and (b) weight wear Δm as functions of pressure in the tribocontact p with moldings prepared from fullerene-containing compositions. Figures at curves are sample nos. in Tables 2 and 3.

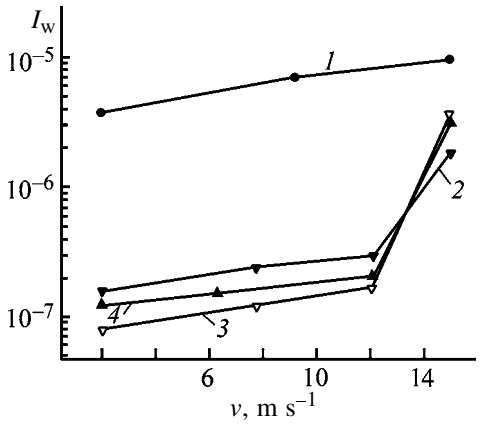

Fig. 3. Linear wear intensity I_w as a function of sliding velocity v for moldings prepared from fullerene-containing compositions that were obtained in run nos. (*1*) 1, (*2*, *3*) 3, and (*4*) 4. Tribocontact pressure 3.9 MPa. (*3*) Sample with the maximal fullerene content.

Structural changes that occur in BZP–3,3'BZP materials with increasing temperature alter the mechanism of the material failure. This is suggested by a number of facts, in particular, by changes in the shape (fractal dimensionality) of wear particles [12] observed before the point at which the properties abruptly change (Fig. 2a). Calculation of the edge of the wear particles (observed with an optical microscope) gives the fractal dimensionality D of 1.13 for low pressures ($p < 5$ MPa) and 1.07 for $p > 5$ MPa. Thus, the wear particles before the inflection point in Fig. 2a seem to have a larger surface area than those after the

(a)

(b)

Fig. 4. Electron micrographs of wear particles formed at (a) low (p < 5 MPa) and (b) high (p > 5 MPa) pressures in the tribocontact. Magnification 6000.

inflection point. Electron microscopic examination shows that actually the wear particles obtained at low pressures (before the inflection point in Fig. 2a) are lumps with a branched surface (Fig. 4a). These particles formed in a contact gap by agglutination of finer particles. At higher pressures (and hence higher temperatures), the particles become coarser, and their surface, smoother (Fig. 4b).

The polymer wear occurs when the stress in the surface layer exceeds its strength. The major wear mechanism is determined by the ratio between the acting stress and strength at a given temperature. If the stress is lower than the yield point, fatigue wear is the most probable. If the stress exceeds the yield point but does not exceed the ultimate strength, plastic ploughing becomes the most probable. In the process, the polymer on the friction surface is pressed out at the edges of friction furrows under the indentor. If the stress exceeds the ultimate strength, abrasive wear prevails, and wear particles are formed immediately, without any incubation period. Electron microscopic examination shows that the critical contact pressure of 5 MPa, apparently, characterizes the transition from wear with plastic flow elements to abrasive wear.

CONCLUSIONS

(1) The polyimide synthesized by chemical imidization from 3,3',4,4'-benzophenonetetracarboxylic dianhydride and 3,3'-diaminobenzophenone can be processed into a cast item at 320–330°C, which allows preparation of moldings with the bending strength of up to 160 MPa, Young's modulus of up to 3000 MPa, and breaking strain of 5–6%. The moldings prepared by a similar procedure from the similar polyimide syntherized by thermal imidization are very brittle and have poor mechanical properties.

(2) In all the cases, the fullerene-containing polyimide studied in this work occurs in a low-melting crystalline modification, which allows its processing into cast items or matrices of composites at 320–330°C.

(3) The optimal procedure for introducing fullerene into the polyimide derived from 3,3',4,4'-benzophenonetetracarboxylic dianhydride and 3,3'-diaminobenzophenone is addition of a solution of fullerene in *o*-dichlorobenzene to a solution of the diamine in dimethylacetamide. The molding prepared from the resulting composition exhibits decreased levels of the friction coefficient, weight wear, and linear wear intensity.

(4) The wear resistance of moldings prepared from the examined polyimides grows with increasing content of fullerenes.

ACKNOWLEDGMENTS

The study was financially supported by the Russian Foundation for Basic Research (project nos. 01-03-32415 and 00-15-97297).

The authors are grateful to M.G. Krakovyak and T.D. Anan'eva for the assistance in the studies.

REFERENCES

1. Sroog, C.E., in *Proc. 4th European Technical Symp. on Polyimides and High Performance Polymers*, Montpellier (France), May 13–15, 1996, pp. 266–297.
2. Yudin, V.E., Kalbin, A.G., Meleshko, T.K., *et al.*, *Zh. Prikl. Khim.*, 2001, vol. 74, no. 7, pp. 1151–1157.
3. Anderson, J.C., *Friction and Wear of Polymer Composites*, Friedrich, K., Ed., Amsterdam: Elsevier, 1986, pp. 329–362.

4. Ginzburg, B.M. and Tochil'nikov, D.G., *Zh. Tekh. Fiz.*, 2001, vol. 71, no. 2, pp. 120–124.
5. Kudryavtsev, V.V., Meleshko, T.K., Kalbin, A.G., *et al.*, *Zh. Prikl. Khim.*, 1998, vol. 71, no. 12, pp. 2035–2040.
6. Lukasov, S.V., Baklagina, Yu.G., Kalbin, A.G., *et al.*, *Polyimides: Trend in Materials and Applications*, Feger, C., Ed., New York: Soc. Plast. Eng., Mid-Hadson Sect., 1996, pp. 251–256.
7. Nielsen, L., *Mechanical Properties of Polymers and Composites*, New York: Marcel Dekker, 1974.
8. Fadin, Yu.A., Polevaya, O.V., and Popov, I.N., *Pis'ma Zh. Tekh. Fiz.*, 1993, vol. 19, no. 22, pp. 62–65.
9. Sasov, A.Yu. and Sokolov, V.M., *Izv. Akad. Nauk SSSR, Ser. Fiz.*, 1984, vol. 48, no. 12, pp. 2389–2396.
10. Sokolov, V.I., *Izv. Ross. Akad. Nauk, Ser. Khim.*, 1999, no. 7, pp. 1211–1218.
11. Bezmel'nitsyn, V.N., Eletskii, A.V., and Okunev, M.V., *Usp. Fiz. Nauk*, 1998, vol. 168, no. 11, pp. 1195–1220.
12. Fadin, Yu.A. and Kozyrev, Yu.P., *Pis'ma Zh. Tekh. Fiz.*, 2000, vol. 26, no. 13, pp. 46–50.

Russian Journal of Applied Chemistry, Vol. 76, No. 7, 2003, pp. 1164–1166. Translated from Zhurnal Prikladnoi Khimii, Vol. 76, No. 7, 2003, pp. 1197–1199.

MACROMOLECULAR CHEMISTRY AND POLYMERIC MATERIALS

Low-Temperature Curing of Poly[*N*-methyl(allyl)-5-vinyltetrazole]

A. M. Belousov, E. A. Paznikov, G. Ya. Petrova, and P. I. Kalmykov

Biisk Technological Institute, Branch of the Polzunov Altai State Technical University, Biisk, Altai krai, Russia

Received December 23, 2003; in final form, May 2003

Abstract—Low-temperature curing of poly[*N*-methyl(allyl)-5-vinyltetrazole) with 1,3-dicyano-2,4,6-triethylbenzene *N*,*N*'-dioxide was studied.

Thermodynamic calculations show that binders based on heterocyclic compounds can be promising components of high-energy-capacity condensed systems thanks to their high enthalpy of formation, increased nitrogen content, chemical compatibility with other components, and low sensitivity to mechanical actions. The most interesting among such compounds are poly(vinyltetrazoles) [1, 2].

In this work we studied low-temperature curing of poly[*N*-methyl(allyl)-5-vinyltetrazole], PMVT-A.

Low-temperature curing was effected by 1,3-dicyano-2,4,6-triethylbenzene *N*,*N*-dioxide (ODTB). In the experiments we used PMVT-A plasticized with various plasticizers (polymer : plasticizer weight ratio 15 : 85). As plasticizers we used a mixed nitrate ester (a mixture of glycerol trinitrate and diethylene glycol dinitrate) (binder 1) and a mixture based on 1-alkyl-3-nitro-1,2,4-triazole (binder 2). The performance of the curing agents was evaluated by changes in the gel fraction content P_g (%) and mean molecular weight of the segment between cross-links M_s.

First we examined the influence of the hardener concentration on the curing of the binders, to determine the optimal hardener concentration.

Curing was performed at 40°C with various ODTB concentrations. The results are shown in Fig. 1. It is seen that, starting from the ODTB concentration of 0.45 wt %, the gel fraction content reaches a stable level of 98–99 wt %. This ODTB concentration can be recommended as optimal.

The next stage of our work was a kinetic study of the binder curing at the optimal ODTB concentration of 0.45 wt %. Curing of binders 1 and 2 was performed at 25, 30, 35, 40, 50, and 60°C. Figure 2 shows that, below 40°C, the kinetic curves have an inflection at the gel fraction content of 85–90 wt %.

Calculation of the apparent activation energies and entropies of curing from the kinetic curves for the temperature range 25–40°C revealed significant differences between the process characteristics before and after the inflection point. The final stage of curing (P_g > 90%) is characterized by the higher activation energy and different activation entropy (see table). With the nitrotriazole plasticizer, the activation energy is lower than with the nitro ester plasticizer. This may

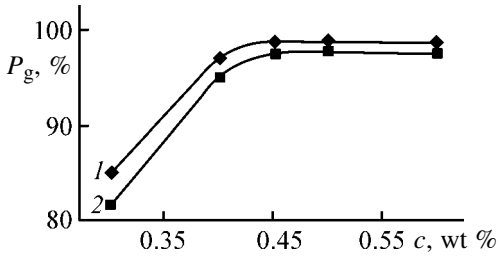

Fig. 1. Gel fraction content P_g as a function of ODTB concentration c. Binder: (*1*) 1 and (*2*) 2.

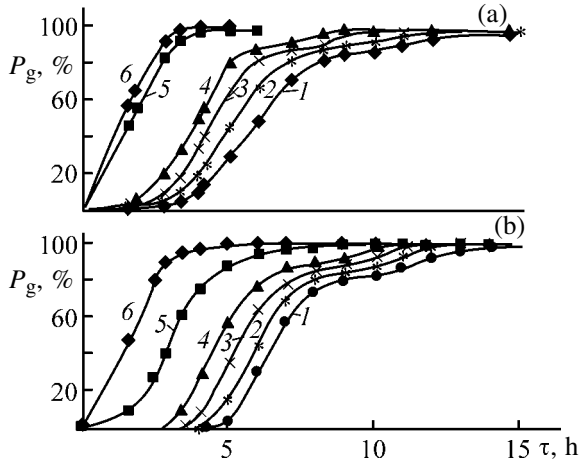

Fig. 2. Kinetic curves of curing of binders (a) 1 and (b) 2 with ODTB at (*1*) 25, (*2*) 30, (*3*) 35, (*4*) 40, (*5*) 50, and (*6*) 60°C. (P_g) Gel fraction content and (τ) time.

1070-4272/03/7607-1164$25.00

Apparent activation energy E_a and entropy ΔS of curing of PMVT-A with ODTB

Binder	E_a, kJ mol^{-1}	ΔS, cal deg^{-1} mol^{-1}	E_a, kJ mol^{-1}	ΔS, cal deg^{-1} mol^{-1}
	$P_g < 90\%$		$P_g > 90\%$	
1	19	–49.3	26.8	–52.7
2	15	–52.7	12.5	–55.9

be due to selective complexation processes characteristic of 1,2,4-triazoles [3, 4]. Determination of the mean molecular weight of the segment between cross-links M_s (Fig. 3) shows that M_s decreases with temperature, i.e., the cross-linking is more efficient at elevated temperatures. A minor difference between the M_s values for binders 1 and 2 suggests that a part of the curing agent in the nitrotriazole binder is consumed in side processes, other than formation of the three-dimensional network.

On the whole, our results can be interpreted as follows. First, the stable yield of the gel fraction at the hardener content of 0.45 wt % corresponds to the molar ratio of double bonds to ODTB of 2 : 1. This fact suggests that the curing involves the C=C bonds. This is confirmed by a considerable decrease in the intensity of the IR absorption band corresponding to the double bonds (1638–1648 cm^{-1}). Second, the inflection in the kinetic curves and, correspondingly, different activation energies of the initial and final steps of the low-temperature curing indicate that the reactivities of double bonds are different. Since the transfer of electronic effects in tetrazole compounds largely depends on the substituent position [5], the difference between the reactivities of double bonds can be attributed to the different position in the allyl groups in the tetrazole ring (at N^1 or N^2).

Published data show that units with the N^2-allyl group prevail in PMVT-A [6]. This fact suggests that the cross-linking first involves the N^2-allyl groups, and this process has a lower activation energy. As the N^2-allyl groups are exhausted, further cross-linking involves the N^1-allyl groups. With increasing temperature, the difference between the reactivities of the two kinds of allyl groups levels out, and at 50 and 60°C no inflection can be seen in the kinetic curves.

The low activation energies and high negative activation entropies of curing suggest that the [3+2]-cycloaddition of ODTB occurs via highly ordered cyclic transition state [7].

In view of these facts and taking into account data from [7], we suggest the following mechanism of PMVT-A curing with ODTB:

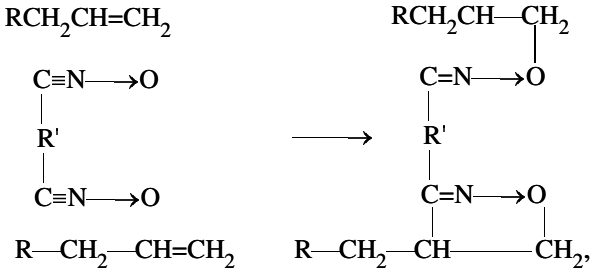

where R = [–CH$_2$—CH—]$_n$, [–CH$_2$—CH—]$_m$;

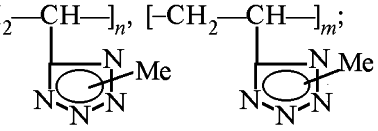

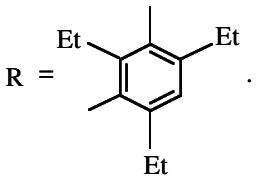

The content of allylvinyltetrazole fragments n in PMVT-A is 2–4 wt %, and the content of methylvinyltetrazole fragments m, 98–96 wt %.

EXPERIMENTAL

Experiments were performed with commercial PMVT-A samples (Sibreaktiv Joint-Stock Company, Angarsk; batch 9/91). The polymer was ground, sieved through a 100-μm sieve, and dried at 60°C for 2 h. The dried polymer was stored in a desiccator over

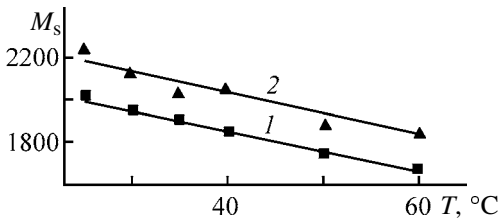

Fig. 3. Mean molecular weight of the segment between cross-links M_s in PMVT-A samples as a function of curing temperature T. Binder: (*1*) 1 and (*2*) 2.

calcined calcium chloride. As curing agent we used commercial ODTB (Tekhnolog Special Designing and Technical Bureau, St. Petersburg), which was dried for a day at 25°C before use. As dispersant we used triacetin (ODTB : triacetin = 1 : 1). The binder was prepared by direct mixing of the polymer with the plasticizer at room temperature, followed by evacuation to constant weight to remove volatiles. Curing was performed in closed aluminum weighing bottles in an oven. By sampling at regular intervals, we determined the time of the onset of curing and the parameters of the vulcanization network. The quantities P_g and M_s were calculated as described in [8]. The correlation coefficient in the calculations was 0.96–0.98.

CONCLUSIONS

(1) Low-temperature curing of poly[*N*-methyl(allyl)-5-vinyltetrazole] with 1,3-dicyano-2,4,6-triethylbenzene *N*,*N*'-dioxide yields the cross-linked polymer with the gel fraction content of 98–99% in a wide temperature range.

(2) The possible mechanism of the reaction of the hardener with the tetrazole polymer, involving addition of nitrile oxide groups to the double bonds of allyl groups to form a three-dimensional structure, was suggested.

REFERENCES

1. Tsutsuran, V.I., Petrukhin, N.V., and Gusev, S.A., *Voenno-tekhnicheskii analiz sostoyaniya i perspektivy razvitiya raketnykh topliv* (Military Engineering Analysis of the State and Prospects of Development of Propellants), Moscow: Ministerstvo Oborony RF, 1999.
2. Ostrovskii, V.A. and Koldobskii, G.I., *Ross. Khim. Zh.*, 1997, vol. 63, nos. 2–4, pp. 84–98.
3. Annenkov, V.V., Mazer, N.L., and Kruglova, V.A., *Vysokomol. Soedin., Ser. A*, 2001, vol. 43, no. 8, pp. 1308–1314.
4. Lebedeva, O.V., Kanitskaya, L.V., Pirogova, G.A., *et al.*, *Zh. Prikl. Khim.*, 2001, vol. 74, no. 9, pp. 1557–1558.
5. Shchipanov, V.P., *Khim. Geterotsikl. Soedin.*, 1983, no. 8, pp. 1130–1132.
6. Kizhnyaev, V.N., Kruglova, V.A., Ratovskii, G.V., *et al.*, *Vysokomol. Soedin., Ser. A*, 1986, vol. 28, no. 4, pp. 765–770.
7. *Comprehensive Organic Chemistry. The Synthesis and Reactions of Organic Compounds*, Barton, D. and Ollis, W.D., Eds., vol. 2: *Nitrogen Compounds*, Sutherland, I.O., Ed., Oxford: Pergamon, 1979.
8. Belousov, A.M., Lochkanova, N.A., Petrova, G.Ya., *et al.*, *Polzunovskii Al'manakh*, 2001, nos. 1–2, pp. 41–47.

Russian Journal of Applied Chemistry, Vol. 76, No. 7, 2003, pp. 1167–1173. Translated from Zhurnal Prikladnoi Khimii, Vol. 76, No. 7, 2003, pp. 1200–1206.

MACROMOLECULAR CHEMISTRY AND POLYMERIC MATERIALS

Synthesis and Flocculating Power of Pyridinium Polyelectrolytes

I. A. Novakov, A. V. Navrotskii, Ya. M. Starovoitova, M. V. Orlyanskii, S. S. Dryabina, Yu. V. Shulevich, and V. A. Navrotskii

Volgograd State Technical University, Volgograd, Russia

Received October 14, 2002; in final form, March 2003

Abstract—Synthesis of poly(1,2-dimethyl-5-vinylpyridinium methyl sulfate) and its copolymers with hydrophilic monomers by (co)polymerization initiated with water-soluble peroxides is studied. The flocculating activity of polyelectrolytes is determined in aqueous kaolin suspensions and also in dewatering of an active sludge.

Cationic polyelectrolytes are widely used as flocculants for separating various dispersions [1]. Based on the chemical nature of the cationic center of a macromolecule, two major classes of cationic polyelectrolytes can be distinguished. The first class includes polymers containing ammonium cations. In this case, introduction of cationic groups is realized by using aminoalkyl acrylates and their salts such as (2-acrylamidopropyl)trimethylammonium chloride and dialkyldiallylammonium halides as starting monomers. The second class covers pyridinium polyelectrolytes formed in polymerization of vinylpyridinium salts of various structures. One of the most active among them is poly(1,2-dimethyl-5-vinylpyridinium methyl sulfate) (poly-1,2-DM-5-VPMS) whose primary advantages are high environmental compatibility and efficiency in dispersion separation [2, 3].

In this work we studied synthesis of high-molecular-weight poly-1,2-DM-5-VPMS and its copolymers with hydrophilic monomers having high flocculating activity.

EXPERIMENTAL

Polymerization of 1,2-DM-5-VPMS was carried out in an aqueous solution at 20±0.5°C using the ampule method. A 0.001–0.01 M aqueous solution of an initiator was added to a monomer solution of a fixed concentration. The initial 1,2-DM-5-VPMS was purified by recrystallization from methanol. As initiators we used hydrogen peroxide (HP), *tert*-butyl hydroperoxide $CH_3C(CH_3)_2OOH$ (TBHP), 2-*tert*-butylperoxy-1-ethanol $CH_3C(CH_3)_2OO(CH_2)_2OH$ (TBPE), and 1-*tert*-butylperoxy-2-propanol $CH_3 \cdot C(CH_3)_2OOCH_2CH(OH)CH_3$ (TBPP). TBPE and TBPP were synthesized according to the procedure described in [4]. The organic peroxides were purified by vacuum distillation.

Copolymerization of 1,2-DM-5-VPMS with acrylic (AA) and maleic (MA) acids, acrylonitrile (AN), acrylamide (AAm), *N*-vinylpyrrolidone (VP), and vinyl acetate (VA) was performed in an aqueous solution at 20±0.5°C and various initial comonomer ratios. As an initiator we used TBPP. AAm and MA were purified by recrystallization from acetone, and AN, AA, VP, and VA were distilled prior to polymerization. Physicochemical characteristics of the monomers used were well consistent with the reference data. Copolymerization was carried out to 96–98% conversion. Then the polymerizate was dissolved in methanol and precipitated by diethyl ether. The resulting polymers were additionally purified by reprecipitation from methanolic solutions with diethyl ether and vacuum-dried (p_{res} = 1.5–2.0 mm Hg, T = 20±0.5°C) to constant weight.

The copolymers were analyzed for the carboxy group content by potentiometric titration and for quaternary pyridinium units by titration of the copolymer–polyacrylic acid complex.

The viscosity of dilute polymer solutions was measured with an Ubbelohde viscometer at 30°C in 2 M NaCl or at 25°C in 0.05 M KBr. The intrinsic viscosity was estimated by linear extrapolation of η_{sp}/c and $\ln \eta_{rel}/c$ to zero concentration (η_{sp} and η_{rel} are the specific and relative viscosities, respectively). The viscosity-average molecular weight M_η of the

1070-4272/03/7607-1167$25.00

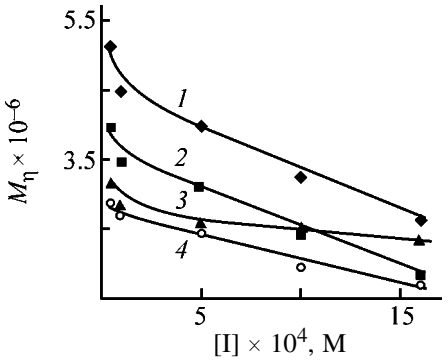

Fig. 1. Molecular weight M_η of poly-1,2-DM-5-VPMS as a function of the initiator concentration [I]: (*1*) TBPP, (*2*) HP, (*3*) TBPE, and (*4*) TBHP. $[M]_0$ = 2.3 M, 20°C.

homopolymer was estimated by Eq. (1) [5]

$$[\eta] = 0.295 \times 10^4 M_\eta^{0.8}, \quad (1)$$

where [η] is the intrinsic viscosity in 0.05 M KBr at 25°C. As a dispersion phase in the flocculation experiments we used kaolin (KSD brand) with a mean particle size of 7 μm. To 0.8% kaolin suspension a flocculant was added in amount of 0–5 mg l^{-1}. The experiments were carried out in 250-ml glass cylinders. After addition of a polyelectrolyte, the suspension was stirred with a rotary stirrer for 2 min (180 rpm) without air access. After an hour, the supernatant was sampled and its optical density A was measured on a KFK-3 instrument at a wavelength of 400 nm against water as a reference. The turbidity of the supernatant τ was estimated by Eq. (2)

$$\tau = 2.3A/l, \quad (2)$$

where l is the path length (cm).

From the experimental data thus obtained we determined the optimal concentrations of the polyelectrolytes c_{opt} providing the minimal turbidity of the supernatant. The clarification factor D_τ was estimated by Eq. (3):

$$D_\tau = \tau_0/\tau - 1, \quad (3)$$

where τ_0 and τ are the supernatant turbidities, respectively, without and with the polyelectrolyte added in a fixed concentration.

In sludge dewatering experiments, we used active sludge from biological treatment plant for sewage water (Volgogradvodokanal Municipal Enterprise). Active sludge (200 ml) was mixed with a 0.1 wt % flocculant suspension. The mixture was agitated by tenfold pouring, filtered after 30-s settling, and the filtrate was analyzed for the residual suspended matter. A filter with the precipitate was additionally dewatered under a 5-kg press. The moisture content in the cake was determined gravimetrically.

The common method for synthesis of soluble polyelectrolytes is radical polymerization of the corresponding monomers in solution or dispersion [6, 7]. In aqueous solutions of monomers, polymerization proceeds mostly at a high rate, and high-molecular-weight polymers are formed. In this case, after completion of the process, the polymerizate can be used directly for preparation of working solutions of polyelectrolytes, eliminating the isolation stage.

Persulfate-initiated polymerization of 1,2-DM-5-VPMS in aqueous solutions became a base for semicommercial production of PPS flocculant [6]. Polymers formed in the process have relatively low molecular weight [$M_\eta = (1.5–1.8) \times 10^6$] and contain some insoluble fractions. Available data on the reactivity of sulfate radical anions and their transformation products [8] and also on the reaction of persulfates with cationic polymers [9] suggest that gelation could be caused by two factors. The first factor is branching and cross-linking of the macromolecules in transfer of a radical center from the sulfate radical anions or hydroxy radicals to the macromolecules. The second possible factor is realization of ionic "pseudo-cross-links" between the macromolecules via the sulfate anions. As a result, the persulfate initiation did not allow synthesis of high-molecular-weight totally soluble polymers.

In searching for initiators providing synthesis of a high-molecular-weight readily soluble polymer in a high yield, we tested HP, TBHP, TBPE, and TBPP.

Polymerization of 1,2-DM-5-VPMS with any of the indicated initiators proved to occur even at 20°C, and the polymers formed had a fairly high molecular weight ($M_\eta = 8.0 \times 10^5–5.1 \times 10^6$). The effect of the peroxide structure on M_η is demonstrated in Fig. 1. The highest-molecular-weight poly-1,2-DM-5-VPMS was obtained with TBPP [$M_\eta = (2.96–5.13) \times 10^6$]. Regardless of the initiator structure, increasing its concentration results in decreasing M_η of the polyelectrolyte (Fig. 1).

The effect of the initiator structure can be attributed to differences in the rate of radical generation from peroxides and, correspondingly, in the initiation rate. It is obvious that decomposition of the peroxides in polymerization (T = 20°C) is an activated process. Most likely, the activating factor is the peroxide–monomer interaction with formation of a complex

with considerably decreased peroxide bond strength, as demonstrated for systems peroxide–ammonium salt [10]. It may be suggested that, in this case, the initiation rate is lower with TBPP, providing formation of a higher-molecular-weight polymer.

The differences in the qualitative and quantitative compositions of disperse systems make it necessary to extend the spectrum of flocculating agents. In this connection, it seemed advisable to study copolymerization of 1,2-DM-5-VPMS with other monomers with the purpose of modifying the structural, electrochemical, and adsorption characteristics of the polyelectrolytes, so as to enhance their flocculating activity. Of particular interest was to synthesize polyelectrolytes containing anionic active centers or nonionic elementary units. Therefore, we synthesized copolymers of 1,2-DM-5-VPMS with AA, MA, AN, AAm, VP, and VA:

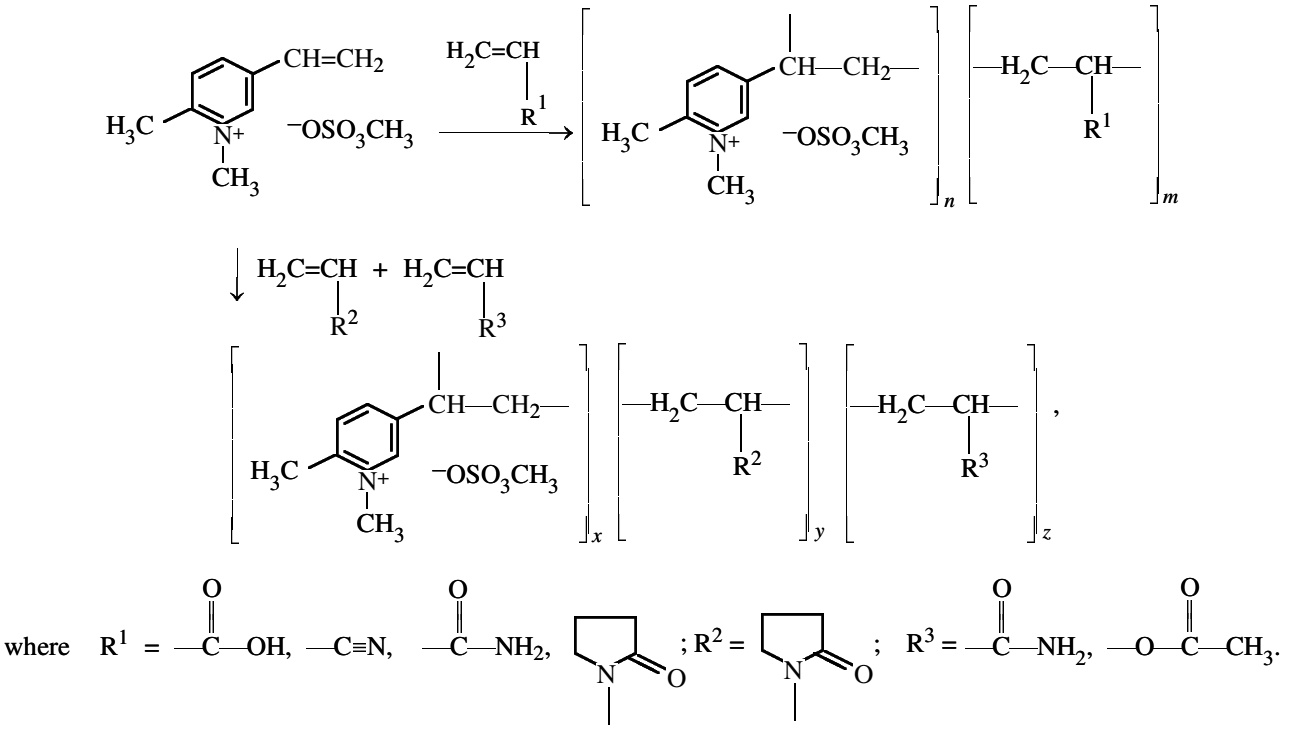

Copolymerization was carried out in aqueous solutions at 20±0.5°C with TBPP as an initiator. The copolymerization conditions and characteristics of the resulting products are summarized in Table 1. The products obtained with some of the monomers studied were high-molecular-weight copolymers ([η] = 0.5–2.5 dl g^{-1}) soluble in water, methanol, DMSO, and DMF.

Copolymerization of 1,2-DM-5-VPMS with all the monomers studied, except for MA, is characterized by high product yield (96–98%). In some cases (at certain total concentration ΣM_i and ratio f_2/f_1 of comonomers), we observed phase separation in systems with AA and AN, which is probably due to formation of copolymer fractions enriched with the second monomer and insoluble in the reaction mass. Therefore, to realize homogeneous copolymerization of 1,2-DM5-VPMS with AA or AN, it necessary to limit the content of the second monomer in the reaction mixture to 20 mol %.

Note that, in the systems with AN, the intrinsic viscosity of the resulting copolymer is practically independent of its composition, whereas with other monomers, increasing content of the second monomer somewhat decreases [η].

In the system with MA, increasing fraction of the second monomer in the reaction mixture considerably decreases the yield and molecular weight of the copolymer. For example, at an MA concentration of up to 15 mol %, the molecular weight of the resulting copolymer is rather high ([η] = 2.05–1.45 dl g^{-1}), and the product yield is 96–98%. With increasing MA fraction, the viscosity of copolymers decreases to 0.54 dl g^{-1}, and the yield, to 55%, which is caused by

Table 1. Copolymerization of 1,2-DM-5-VPMS (M_1) (ΣM_i = 2 M; initiator 10^{-3} M TBPP; 20°C)

Comonomer	Monomer mixture composition, mol %		Copolymer yield, %	Copolymer composition, mol %		[η], dl g^{-1}
	f_1	f_2		F_1	F_2	
AA	95	5	98	96.7	3.3	2.43
	90	10	97	93.1	6.9	2.04
	85	15	96	89.8	10.2	1.90
MA	95	5	99	98.6	1.4	2.05
	90	10	99	97.0	3.0	1.71
	85	15	97	95.7	4.3	1.45
	75	25	72	94.0	6.0	0.81
	65	35	67	93.0	7.0	0.73
	50	50	55	84.7	15.3	0.54
AN	95	5	98	96.2	3.8	2.40
	90	10	98	92.5	7.5	2.36
	85	15	98	89.6	10.4	2.37
	75	25	98	82.4	17.0	2.35
AAm	95	5	98	95.0	5.0	2.31
	90	10	97	90.0	10.0	2.10
	75	25	95	74.0	26.0	1.82
	60	40	95	56.0	44.0	1.80
	50	50	94	47.0	53.0	1.73
VP	95	5	98	96.5	3.5	1.65
	90	10	98	88.2	11.8	1.62
	75	25	97	77.9	22.1	1.42
VP + AAm	90	5 + 5	99	87.3	12.7*	1.81
	90	7 + 3	98	87.6	12.4*	1.72
	90	9 + 1	97	88.5	11.5*	1.60
VP + VA	90	9 + 1	98	89.6	10.4*	1.70
	80	18.5 + 1.5	96	81.5	18.5*	1.52
	75	22.5 + 2.5	96	77.6	22.4*	1.30

* $F_2 + F_3$.

low polymerization activity of MA. Therefore, to obtain high-molecular-weight copolymer, it necessary to limit the MA content in the reaction mixture to 15 mol %.

As expected, decreasing initiator concentration increases the intrinsic viscosity of the resulting copolymers (Table 2). Simultaneously, the yield decreases, remaining, however, above 90% at an initiator concentration of 10^{-4} M.

Table 2. Influence of the initiator (I) concentration on the yield and intrinsic viscosity of 1,2-DM-5-VPMS copolymers (f_1 = 90 mol %, f_2 = 10 mol %; 20°C)

Comonomer	$[I]_0$, M	Copolymer yield, %	[η], dl g^{-1}
AAm	0.0001	96	2.33
	0.001	98	1.84
	0.01	99	1.61
VP	0.0001	92	2.39
	0.001	99	1.62
	0.01	99	1.26

It appears more technologically advantageous to increase the molecular weight through increasing monomer concentration. Table 3 shows that, for different compositions of the reaction mixture, increase in the total concentration of monomers results in formation of polymers with higher intrinsic viscosity in nearly theoretical yield.

The results of studying the flocculating effect of poly-1,2-DM-5-VPMS in separation of model systems revealed high activity of this polyelectrolyte [2, 3, 11]. However, in the case of the homopolymer, the charge density is independent of its molecular weight, since each elementary unit contains the ionic group. Without question, introduction of nonionic units into the

polymer structure should influence its electrochemical and adsorption characteristics and the flocculating action as well. Therefore, in this work we made a comparative study of the flocculating activity of the copolymers obtained.

The results showed that introduction of some acidic groups into the polyelectrolyte structure decreases the flocculating activity of the copolymers. Copolymers of 1,2-DM-5-VPMS with nonionic monomers such as AAm (samples 1AAm, 2AAm, 3AAm, and 4AAm), VP (samples 1VP, 2VP, and 3VP), VP + AAm or VA [samples 1VP(AAm), 2VP(AAm), 1VP(VA), and 2VP(VA)] seem to be the most promising flocculants.

Figure 2 shows that the dependences of the supernatant turbidity on the polyelectrolyte concentration have extrema. At low flocculant concentration (up to 0.4 mg l^{-1}), the residual turbidity decreases (flocculation branch). With increasing c_f (0.4–2 mg l^{-1}), the range of dispersion destabilization is observed, and with further increasing c_f, the supernatant becomes somewhat more turbid. The latter is commonly interpreted as stabilization of the dispersion through formation of protective layers of the adsorbed polymer. The results show that higher clarification factors are realized when copolymers containing vinylpyrrolidone units are added as flocculants.

The optimal flocculation parameters for kaolin suspension with copolymers of 1,2-DM-5-VPMS with nonionic monomers are given in Table 4. As seen, the flocculating activity of the copolymers depends on their composition. Copolymers containing AAm units are close to poly-1,2-DM-5-VPMS in their flocculation activity and optimal concentration. With increasing AAm content in the copolymer, the flocculating activity decreases, and the optimal concentration increases to 1.2 mg l^{-1}.

The copolymers of 1,2-DM-5-VPMS with VP demonstrate higher flocculating activity than poly-1,2-DM-5-VPMS and the copolymers with AAm. The optimal flocculant concentrations in this case are practically the same, ranging from 0.5 to 1.2 mg l^{-1}. The highest flocculating effect was observed for sample 1VP (D_τ = 174.7).

Simultaneous introduction of VP and VA units in the amounts of 9 and 1 mol %, respectively, results in formation of a copolymer providing a 1.5-fold increase in the clarification factor as compared to the homopolymer. However, in this case, the optimal flocculant concentration increases to 0.8 mg l^{-1}.

Study of the flocculating activity of the terpoly-

Table 3. Influence of the comonomer concentration on synthesis of terpolymers of 1,2-DM-5-VPMS (M_1) with VP (M_2) and AAm (M_3) ($[I]_0 = 10^{-3}$ M; 20°C)

Composition of monomer mixture, mol %			$\Sigma[M]_0$, M	Yield, %	$[\eta]$, dl g^{-1}
f_1	f_2	f_3			
90	9	1	2.0	97	1.62
75	22	3	2.0	95	1.13
90	9	1	3.3	99	2.24
75	22	3	3.9	98	1.91
90	9	1	4.3	99	3.51
75	22	3	5.1	99	2.83

Table 4. Optimal flocculation parameters for 0.8% kaolin suspension with copolymers of 1,2-DM-5-VPMS with nonionic monomers

Flocculant	$[\eta]$, dl g^{-1}	F_2, mol %	c_{opt}, mg l^{-1}	D_τ
Poly-1,2-DM-5-VPMS	2.3	0	0.4	123.8
1AAm	2.3	5.0	0.5	117.6
2AAm	2.1	10.0	0.4	127.2
3AAm	1.8	26.0	0.6	111.9
4AAm	1.6	53.0	1.2	92.0
1VP	1.6	11.8	0.5	174.7
2VP	1.4	22.1	1.2	162.6
1VP(AAm)	1.6	12.7*	0.8	323.6
2VP(AAm)	1.1	23.5*	1.0	93
1VP(VA)	1.7	10.4*	1.0	196.4
2VP(VA)	1.3	22.4*	1.8	162.6

* $F_2 + F_3$.

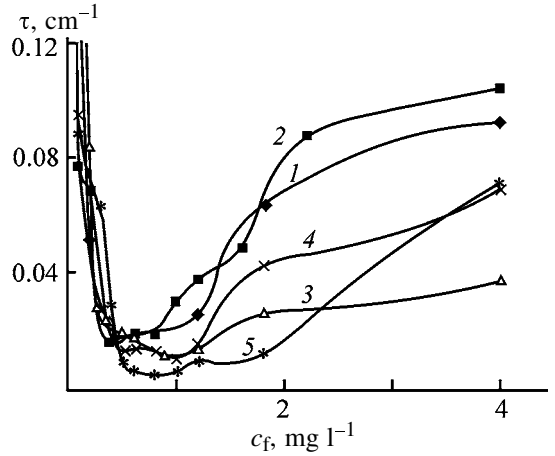

Fig. 2. Supernatant turbidity τ as a function of the flocculant concentration c_f: (*1*) poly-1,2-DM-5-VPMS, (*2*) 2AAm, (*3*) 1VP, (*4*) 1VP(VA), and (*5*) 1VP(AAm).

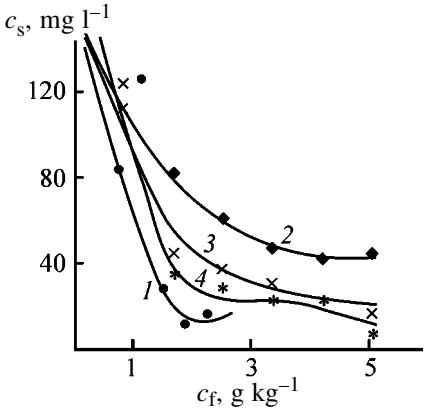

Fig. 3. Effect of the flocculant concentration c_f on the suspended matter concentration in the filtrate c_s: (*1*) poly-1,2-DM-5-VPMS, (*2*) 2AAm, (*3*) 1VP, and (*4*) 1VP(AAm).

mers of 1,2-DM-5-VPMS with VP and AAm showed that the samples containing 9 mol % VP and 1 mol % AAm provide the maximal efficiency of treatment of the kaolin suspension. In their performance these copolymers surpass the homopolymer by a factor of 2.6. In this case, the optimal concentration is 0.8 mg l^{-1}. As for the copolymers described above, with further increasing fraction of the nonionic units in the copolymer structure, the flocculant activity decreases and the optimal concentration increases.

Without question, the sedimentation rate of the kaolin suspension increases in the presence of the copolymers. Determination of the flocculation mechanism requires a thorough study of floccule and precipitate formation as well as the conformation state of copolymers of various compositions with allowance for composition nonuniformity. However, some conclusions can be made from comparison of the results obtained on the flocculating power of copolymers with various hydrophilic monomers.

Table 5. Activity of cationic flocculants in dewatering of excess sludge

Initial sludge moisture content, %	Flocculant	Concentration, g kg^{-1}	Cake moisture content, %	c_s, mg l^{-1}
99.34	KF-91	1.5	87.4	28.0
		1.9	88.6	11.7
		2.3	89.9	16.3
99.7	2AAm	1.7	90.9	81.6
		2.5	91.5	60.6
		3.4	91.9	46.6
99.7	1VP	1.7	88.8	44.3
		2.5	87.5	37.3
		3.4	89.7	30.7
99.7	1VP(AAm)	1.7	91.2	34.9
		2.5	88.0	28.0
		3.4	84.9	22.3

The results show that the flocculating power increases only with VP as a comonomer. It is unlikely that VP units are involved in hydrogen bonding and ion–dipole interactions with sites on the particle surface, because of steric hindrances resulting in shielding of the carbonyl group. Most likely, the increase in the flocculating power is associated with changing the coil conformation in the surface layer of particles and also with increasing probability of association of the coils with participation of the nonionic units, accompanied by formation of bridging bonds through two and more coils.

Based on the results obtained on the flocculating power of copolymers of 1,2-DM-5-VPMS with nonionic monomers, a series of samples were selected for testing in dewatering of excess activated sludge formed in the water treatment plant (Volgogradvodokanal Municipal Enterprise). The processes of water treatment and subsequent dewatering of excess sludge mostly involve the flocculation and filtration stages allowing removal of excess suspended material from the biological treatment zone and also regeneration of activated sludge in aeration tanks [12]. In this case, the residual moisture content of the sediment and the suspended matter content in the filtrate are the parameters characterizing the flocculant performance.

Evaluation of the flocculating efficiency requires data on the effect of the flocculant concentration on the suspended matter concentration in the filtrate c_s. As seen from Fig. 3, the suspended matter concentration abruptly decreases wit increasing flocculant concentration to 2 g kg^{-1}. With further increasing c_f, the range of sludge suspension destabilization is observed. The secondary stabilization range has not been realized under the experimental conditions, since, evidently, it occurs at higher c_f. Thus, the effective flocculant concentration falls into the range 1.5–3 g kg^{-1}. From the dependence of the moisture content of the resulting cake on the reagent concentrations, we can determine the optimal flocculant concentration. The criterion was the minimal moisture content in the cake. The flocculants studied demonstrated high performance in dewatering the sludge and decreasing suspended matter content in the filtrate (Table 5). In the experiments we used activated sludge without preconcentration, i.e., with low suspended matter content (0.3–0.7 wt %), which complicated flocculation with polymers. Nevertheless, the use of the copolymers allowed highly efficient dewatering of the activated sludge.

Table 5 shows that 1VP and 1VP(AAm) samples are more effective flocculants as compared to KF-91 homopolymer, 1VP(AAm) being especially active, having the dewatering effect higher by a factor of 1.3.

CONCLUSIONS

(1) Study of homo- and copolymerization of 1,2-dimethyl-5-vinylpyridinium methyl sulfate initiated by water-soluble peroxides revealed that the polyelectrolytes obtained using 1-*tert*-butylperoxy-2-propanol have the highest molecular weight and solubility in water. Copolymerization initiated with *tert*-butylperoxy-2-propanol allows preparation of high-molecular-weight poly(1,2-dimethyl-5-vinylpyridinium methyl sulfate) [M_η = (2.8–5.1) × 10^5] and its copolymers in nearly theoretical yield at room temperature (~20°C). Decreasing fraction of 1,2-dimethyl-5-vinylpyridinium methyl sulfate in a copolymer results in somewhat decreasing intrinsic viscosity, the effect being more pronounced in copolymers with maleic acid and *N*-vinylpyrrolidone.

(2) Copolymers of 1,2-dimethyl-5-vinylpyridinium methyl sulfate with *N*-vinylpyrrolidone and its terpolymers with *N*-vinylpyrrolidone and acrylamide or vinyl acetate demonstrate higher flocculating performance than the homopolymer. Evidently, this is due to optimal concentration and arrangement of the cationic centers in the polymer chain, and also to direct participation of the nonionic units in floccule formation.

(3) The polymers studied can be recommended as reagents for treatment of industrial reused water and wastewater.

REFERENCES

1. Zapol'skii, A.G. and Baran, L.A., *Koagulyanty i flokulyanty v protsessakh ochistki vody: Svoistva. Poluchenie. Primenenie* (Coagulants and Flocculants in Water Treatment: Properties, Manufacture, and Applications), Leningrad: Khimiya, 1987.
2. Navrotskii, A.V., Novakov, I.A., Makeev, S.M., *et al*., *Zh. Prikl. Khim*., 2001, vol. 74, no. 3, pp. 487–489.
3. Navrotskii, A.V., Dryabina, S.S., Malysheva, Zh.N., *et al*., *Zh. Prikl. Khim*., 2000, vol. 73, no. 12, pp. 1940–1944.
4. Navrotskii, A.V., Novakov, I.A., Lotov, V.V., and Navrotskii, V.A., in *Khimiya i tekhnologiya elementoorganicheskikh monomerov i polimernykh materialov: Mezhvuzovskii sbornik nauchnykh trudov* (Chemistry and Technology of Organoelement Monomers and Polymeric Materials: Intercollegiate Coll. of Scientific Works), Volgograd: Volgograd. Gos. Tekh. Univ., 1995, pp. 13–19.
5. Roganov, V.V., Bimendina, L.A., and Bekturov, E.A., *Izv. Akad. Nauk Kaz. SSR, Ser. Khim*., 1970, no. 3, pp. 24–30.
6. Zubakova, L.B., Tevlina, A.S., and Davankov, A.B., *Sinteticheskie ionoobmennye materially* (Synthetic Ion-Exchange Materials), Moscow: Khimiya, 1978.
7. *Poliakrilamid* (Polyacrylamide), Kurenkov, V.F., Ed., Moscow: Khimiya, 1992.
8. Kislenko, V.N. and Berlin, Ad.A., *Zh. Obshch. Khim*., 1989, vol. 59, no. 1, pp. 3–26.
9. Pameditite, V.V., Makushka, R.Yu., and Baeras, G.I., *Vysokomol. Soedin., Ser. A*, 1992, vol. 34, no. 9, pp. 130–138.
10. Turovskii, N.A., Tselinskii, S.Yu., Opeida, I.A., *et al*., *Dokl. Akad. Nauk Ukr. SSR, Ser. B*, 1991, no. 3, pp. 131–134.
11. Malysheva, Zh.N., Dryabina, S.S., Navrotskii, A.V., *et al*., *Izv. Vyssh. Uchebn. Zaved., Khim. Khim. Tekhnol*., 2001, vol. 44, no. 2, pp. 38–42.
12. Turovskii, I.S., *Obrabotka osadkov stochnykh vod* (Treatment of Wastewater Sludge), Moscow: Stroizdat, 1982.

Russian Journal of Applied Chemistry, Vol. 76, No. 7, 2003, pp. 1174–1175. Translated from Zhurnal Prikladnoi Khimii, Vol. 76, No. 7, 2003, pp. 1207–1209.

BRIEF COMMUNICATIONS

Recovery of Gold from Cyanide Solutions Using Activated Carbon Sorbent Based on Lignite

Yu. S. Kononov, G. L. Pashkov, and A. G. Kholmogorov

Institute of Chemistry and Chemical Technology, Siberian Division, Russian Academy of Sciences, Krasnoyarsk, Russia

Received November 21, 2002

Abstract—Recovery of gold cyanide complexes was studied using sorbents prepared from Kansk–Achinsk lignite.

To recover finely ingrained gold, the ore is often leached with a sodium cyanide solution with subsequent preparation of the concentrate or metallic gold. Gold is recovered from solutions and suspensions (in the last 2–3 decades) using predominantly carbon sorbents [1].

Gold is fairly selectively sorbed on carbon sorbents, being concentrated to a level of 1% of the sorbent weight. Concentrates or metallic gold are prepared from the gold-containing solutions obtained after sorbent treatment by various procedures.

Sorption is a decisive step of such procedure, and thus sorbent properties should meet certain requirements. It was found that the specific surface area of sorbents strongly affects the gold sorption [2]. The specific surface area of commercial sorbents prepared from coconut shells reaches 1000 $m^2 g^{-1}$, and their capacity for gold in sorption from solutions with a gold concentration of 1 $mg l^{-1}$ is about 1%.

Sorbents should be abrasion-resistant, and high mechanical strength is important, because in the course of treatment the coarse sorbent (~2 mm particle size) is stirred with finely ground ore (0.07 mm) in a sodium cyanide solution with the content of the solid matter of up to 50%. After prolonged stirring, gold dissolves and passes into the sorbent, and then the gold-containing sorbent is separated from the ground ore using a 0.5-mm gauze. Thus, with a fragile easily grindable material, the loss of gold-containing sorbent with ore will be intolerably high.

All modern procedures employ sorbents prepared from coconut shells, which exhibit acceptable capacity for gold and the required mechanical strength.

Attempts are made to prepared alternative sorbents from liquid products of shale treatment and petroleum residues, technical hydrolytic lignin, furfural, and also from wastes of production of phenol–formaldehyde resins, coal-tar raw materials, petroleum coke, and wood residue with carbonization and ultra-high-frequency activation. However, the mechanical strength of the above sorbents [in accordance with GOST (State Standard) 16-188–70] is insufficient and comprises up to 90%. The demand of the gold-mining industry in Russia is about 1000 t of sorbent per year (data are as of 1990) [2].

At the same time, the use of sorbents prepared from coconut shells in the gold hydrometallurgy has its own disadvantages, because the expenses related to the sorbent loss due to the abrasion at suspension stirring and to its periodical regeneration are nearly 50% of the sorbent cost [1]. Thus, the use of cheap disposable sorbents to recover gold from solutions seems to be advisable.

In this work, we studied the sorption capacity of ABG activated sorbent for gold cyanide complexes. Since the mechanical strength of the ABG sorbent does not allow its use in the pulp process, it was used to recover gold from solutions. Due to low cost, it was planned to ash the gold-containing sorbent with subsequent recovery of gold from the ash residue.

EXPERIMENTAL

The carbon sorbents were tested using industrial solutions from a gold-recovery enterprise with a gold content of 1.32–1.52 $mg l^{-1}$. The following carbon sorbents were used: ABG commercial product (Sorbentugol' Joint-Stock Company, Krasnoyarsk, Russia) prepared from Kansk-Achinsk lignite with the specific surface area of 560–800 $m^2 g^{-1}$ and ash content of 18–25%, commercial coconut coal (Du Pont, the United States) designed for gold recovery from the pulp (nearly 1000 $m^2 g^{-1}$), and GRC-22 commercial coconut coal (Calgon Carbon, the United States)

1070-4272/03/7607-1174$25.00

designed for gold recovery from the pulp (nearly 1000 $m^2 g^{-1}$).

The aim of the work was to study the completeness of gold recovery using the above sorbents.

Gold was recovered using the following procedure. Weighed portions of sorbents (100 mg) were placed into the solutions (100 ml), i.e., 1 g of sorbent per liter of solution (the commercial charge in the pulp is 20 $g l^{-1}$). The mixture was intermittently stirred, and then, after extraction concentration, the residual content of gold in solution was determined using the atomic absorption method, and the sorption ratios were evaluated to compare the sorbent samples. The results are listed in Table 1.

As seen from Table 1, the highest recovery of gold, 99%, is reached with coconut sorbents, and the recovery of gold by ABG sorbents is lower (96%). The lower (by 3%) gold recovery is probably due to the higher ash content and smaller specific surface area of the ABG sorbent, and this disadvantage can be overcome by taking larger amounts of the sorbent, which is acceptable for the production process because of the low cost of the ABG sorbent.

The sorption capacity under the dynamic conditions was determined in a flow of the process solution, and in each case the fresh solution was used. The average content of gold in solution was 1.32 $mg l^{-1}$, and it varied depending on its content in the ore. 1-g portions of sorbents (about 2 mm particle size) in cotton-cloth containers were placed into a column. The solution was supplied from the bottom upwards at a rate of 0.5 $l h^{-1}$; the containers were wetted uniformly. The contact periods of 40 h, 100 h, and 7 days are not related to the rate of the sorbent saturation and can be associated with the diffusion problems in sorption of gold, arising with sorbents placed in containers to simplify analytical control of the gold content. The content of gold in the sorbent was determined by the spectral method; the results are listed in Table 2.

As seen from Table 2, for both coconut and ABG sorbents, the degree of the sorbent saturation with gold is similar. The capacity of the ABG sorbent for gold of 0.5–1.0% relative to the sorbent weight is close to the capacity of the best coconut sorbents, and thus it can be used to develop a process based on the use of the ABG sorbent as disposable material to recover gold from solutions. Taking into account the average ash content of the ABG sorbent of 20%, the calculated content of gold in the ash will reach 5%. Such concentrates are utilized at refining plants; the recovery of gold on the ABG sorbent is competitive with precipitation of gold with a zinc dust, also yielding a 5% concentrate.

Table 1. Equilibrium distribution of gold in sorption on carbon sorbents under the static conditions; initial concentration of gold in solution 1.52 $mg l^{-1}$, solution volume 100 ml, sorbent weighed portion 100 mg

Sorbent	Equilibrium concentration of gold, $mg l^{-1}$	Degree of recovery, %	Ash content, %
ABG	0.06	96	18–25
	0.06	96	18–25
	0.06	96	18–25
Coconut:			
Du Pont	0.02	99	5
GRC-22	0.02	99	5
Calgon Carbon			

Table 2. Capacity of sorbents for gold under the dynamic conditions

Sorbent	Gold content in sorbent, %, at indicated contact time		
	40 h	100 h	7 days
ABG-1	0.1	0.20	0.5
	0.1	0.19	0.5
	0.1	0.20	0.5
	0.2	0.42	1.0
	0.2	0.42	1.0
	0.2	0.42	1.0
Coconut:			
Du Pont	0.2	0.44	1.0
GRC	–	0.44	1.0
Calgon Carbon			

CONCLUSION

The capacity of the ABG sorbent for gold is 0.5–1.0%, which is acceptable for developing a process based on the use of the ABG sorbent as disposable material to recover gold from solutions.

REFERENCES

1. Meretukov, M. A. and Orlov, A. M., *Metallurgiya blagorodnykh metallov: zarubezhnykh opyt* (Metalurgy of Noble Metals: Foreign Experience), Moscow: Metallurgiya, 1991.
2. Chernov, V.K., Abstracts of Papers, *Soveshchanie Irkutskogo oblastnogo pravleniya Vsesoyuznogo tekhnicheskogo obshchestva tsvetnoi metallurgii* (Conf. of Irkutsk Oblast Management of All-Union Technical Society of Non-Ferrous Metallurgy), Irkutsk, 1990.

Russian Journal of Applied Chemistry, Vol. 76, No. 7, 2003, pp. 1176–1178. Translated from Zhurnal Prikladnoi Khimii, Vol. 76, No. 7, 2003, pp. 1210–1212.

BRIEF COMMUNICATIONS

Behavior of Cross-Linked Copolymers of Acrylic Acid and 5-Vinyltetrazole in Aqueous Media

M. M. Kabakova, M. V. Uspenskaya, N. V. Sirotinkin, and E. V. Sanatin

St. Petersburg State Technological Institute, St. Petersburg, Russia
St. Petersburg State Institute of Precision Mechanics and Optics, St. Petersburg, Russia

Received October 16, 2002; in final form, April 2003

Abstract—The equilibrium swelling of new hydrogels based on sodium acrylate and *N,N*-methylenebisacrylamide modified with 5-vinyltetrazole in water and aqueous solutions of nickel salts in the stage of radical polymerization was studied. The influence of 5-vinyltetrazole concentration in the monomer mixture on the characteristics of the resulting copolymers was studied.

The influence of various modifying copolymers on the characteristics of acrylic hydrogels has been extensively studied in the past ten years, since slight changes in the copolymer composition can result in significant changes in characteristics of the new polymeric materials. Progress in synthesis of tetrazole derivatives gave opportunities for production of new macromolecular compounds, which significantly stimulated an interest in this class of (co)polymers, since introduction of tetrazole-containing monomers into copolymers expanded the application of acrylic hydrogels [1, 2]. For example, copolymers based on salts of acrylic acid (AA) and 2-methyl-5-vinylterazole can be used as a medium for growth of plants at elevated ambient temperature [3].

In this work we studied the behavior of cross-linked copolymers based on salts of acrylic acid, 5-vinyltetrazole (VT), and *N,N*-methylenebisacrylamide (MBAA) in electrolyte solutions and also the kinetics of swelling of the synthesized polymers in distilled water.

EXPERIMENTAL

Hydrogels based on sodium acrylate, VT, and MBAA used as a cross-linking agent were prepared by polymerization in aqueous solution at room temperature; the initiating system was ammonium persulfate (APS)–tetramethylethylenediamine (TMEDA). The degree of neutralization of AA with sodium hydroxide was 0.9. The concentration of acrylate monomers in the reaction mixture was 30, VT, from 10 to 50, and APS, 0.8 wt %. The concentration of cross-linking agent was varied from 0.1 to 0.7 wt % relative to the sum of the monomers. 5-Vinyltetrazole was recrystallized before polymerization.[1] The characteristics and procedures of purification of the other chemicals, and also the copolymerization procedure were described previously [2].

The degree of equilibrium swelling was measured by the standard gravimetric method and evaluated by the equation

$$Q = (m_s - m_d)/m_d,$$

where m_s and m_d are the weights of swollen and dried samples, respectively (g).

In calculations, the results obtained in measurement of swelling of five similar samples were averaged.

The kinetic dependences of the degree of swelling in distilled water with variation of the concentration of the cross-linking agent and VT in the reaction mixture are presented in Figs. 1a and 1b. The experiments were carried out at 50°C. It is seen that, with increasing content of MBAA cross-linking agent, the equilibrium degree of swelling decreases. The results obtained allow preparation of tetrazole–acrylic hydrogels with preset characteristics in a definite time interval, which is significant for specific applications. This problem can be solved, e.g., by properly choosing concentrations of the initial components in the reaction mixture.

Both hydrogen bonds involving tetrazole rings and carboxy groups and hydrophobic interactions between units affect conformation of macromolecules of N–H-

[1] 5-Vinyltetrazole was synthesized at the St. Petersburg State Technological Institute.

1070-4272/03/7607-1176$25.00 © 2003 MAIK "Nauka/Interperiodica"

acidic tetrazole-containing copolymers in solution. As a rule, interactions of both types participate in formation of compact structures. It was shown previously [4] that macromolecules of unsubstituted poly-*C*-vinyltetrazoles have the conformation of double-stranded regular chains with the outer hydrophobic hydrocarbon surface; therefore, 5-VT copolymers are poorly soluble in water.

Figures 1a and 1b show that, with increasing content of VT in the reaction mixture, the equilibrium degree of swelling decreases.

At VT concentration less than 30 wt % relative to AA and 0.1–0.7 wt % content of MBAA, the resulting hydrogels hold their shape in the swollen state and have sufficient elasticity.

As known, hydrogels in electrolyte solutions behave as three-dimensional semipermeable membranes. Depending on the solution composition (e.g., concentration and nature of polyvalent metal salt), various distributions of ions in the system hydrogel–solution can occur [5].

Variation of the degree of swelling with time in nickel chloride solutions of various concentrations is shown in Fig. 2. It is seen that the hydrogels exhibit high degrees of swelling in solutions of salts of polyvalent metals with the concentration less than 10^{-2} M. In this case, the degree of equilibrium swelling of tetrazole-containing hydrogel is higher in a solution with a very low concentration of salt (10^{-5}–10^{-4} M) than in distilled water. This can be explained by the structured state at the interface of the salt solution and hydrogel [6].

Along with sorption of water molecules, the hydrogel forms complexes with metal ions, as suggested by coloration of the swollen copolymer. Complex formation of tetrazole-containing hydrogels with metal ions involves deprotonation of the NH group of the heterocycle [7]. It can be assumed that, in complex formation of tetrazolate ions with nickel chloride, polychelate complexes are formed.

With increasing salt concentration to 10^{-1} M, the gels studied are collapsed, which is explained by additional cross-linking of the polymeric chains by the metal ions. It was shown previously that, with excess metal ions in the solution surrounding the copolymer, a complex with three tetrazole units per metal ion is formed.

The complex formation and sorption characteristics of tetrazole-containing copolymers make them promising as flocculants in treatment of wastes from various

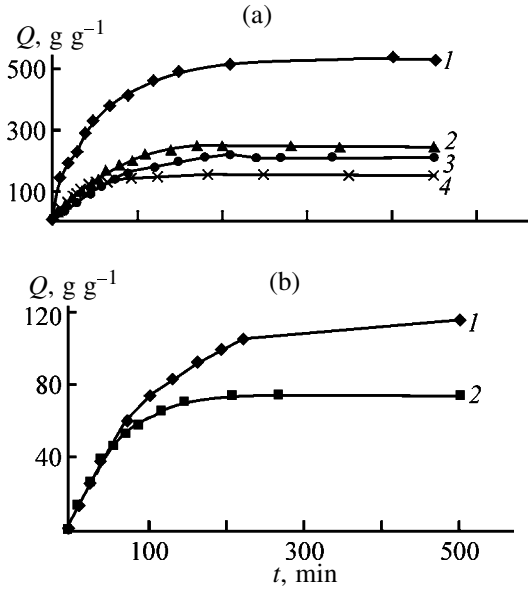

Fig. 1. Degree of swelling Q of hydrogels based on AA and VT in distilled water as a function of time t at 20°C. VT concentration in the reaction mixture, wt %: (a) 10 and (b) 30. Concentration of MBAA cross-linking agent, wt %: (*1*) 0.1, (*2*) 0.3, (*3*) 0.5, and (*4*) 0.7.

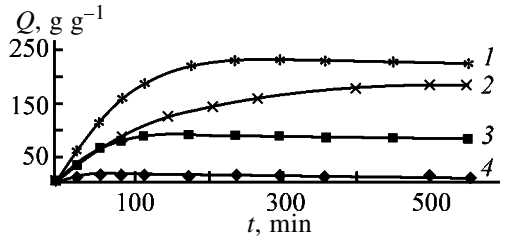

Fig. 2. Degree of swelling Q of hydrogels based on AA, VT (30 wt %), and MBAA (0.1 wt %) in nickel chloride solutions as a function of time t at 20°C. Concentration of $NiCl_2$, M: (*1*) 10^{-5}, (*2*) 10^{-4}, (*3*) 10^{-3}, and (*4*) 10^{-2}.

branches of chemical industry and in agriculture as "artificial soil" for young growth and young sowings.

ACKNOWLEDGMENTS

This work was financially supported by the Foundation for Basic Technical Sciences of the Education Ministry of the Russian Federation (project no. TOO-9.2-2078).

CONCLUSIONS

(1) The kinetic features of swelling of new hydrogels based on sodium acrylate and *N,N*-methylenebisacrylamide modified with 5-vinyltetrazole in the stage of radical polymerization in distilled water at 20°C show that the concentrations of the cross-linking

agent and 5-vinyltetyrazole in the monomer mixture affect the equilibrium degree of swelling of the resulting copolymers.

(2) Tetrazole-containing hydrogels in nickel salt solutions with the concentration less than 10^{-2} M exhibit a high water-absorbing power (up to 300 g per gram).

(3) High sorption power of the gels makes them promising for treatment of industrial wastewaters and in agriculture.

REFERENCES

1. Kruglova, V.A., Annenkov, V.V., and Saraev, V.V., *Vysokomol. Sordin., Ser. B*, 1997, vol. 39, no. 7, pp. 1257–1259.
2. Igrunova, A.V., Sirotinkin, N.V., and Uspenskaya, M.V., *Zh. Prikl. Khim.*, 2001, vol. 74, no. 5, pp. 793–797.
3. Igrunova, A.V., Sirotinkin, N.V., and Uspenskaya, M.V., *Zh. Prikl. Khim.*, 2001, vol. 74, no. 7, pp. 1170–1173.
4. Kizhnyaev, V.N., Gorkovenko, O.P., Safronov, A.P., and Adamova, L.V., *Vysokomol. Soedin., Ser. A*, 1997, vol. 39, no. 3, pp. 527–532.
5. Budtova, T.V., Sichetskii, D.A., Kuranov, A.L., and Suleimanov, I.E., *Zh. Prikl. Khim.*, 1997, vol. 71, no. 3, pp. 511–513.
6. Kizhnyaev, V.N. and Kruglova, V.A., *Zh. Prikl. Khim.*, 1990, vol. 63, no. 12, pp. 2721–2724.
7. Starikov, A.S., Dzhardimalieva, G.I., Uflyand, I.E., *et al.*, *Ross. Izv. Akad. Nauk, Ser. Khim.*, 1993, no. 1, pp. 76–80.
8. Annenkov, V.V., Kruglova, V.A., and Mazuar, N.L., *J. Polym. Sci., Part A: Polym. Chem.*, 1996, vol. 34, no. 4, pp. 597–602.

Russian Journal of Applied Chemistry, Vol. 76, No. 7, 2003, pp. 1179–1181. Translated from Zhurnal Prikladnoi Khimii, Vol. 76, No. 7, 2003, pp. 1213–1215.

BRIEF COMMUNICATIONS

Influence of Pretreatment of Expanded Graphite on Its Sorption Properties with Respect to Petroleum

M. V. Savos'kin, A. P. Yaroshenko, V. I. Shologon, and L. Ya. Galushko

Litvinenko Institute of Physical Organic Chemistry and Coal Fuel Chemistry, National Academy of Sciences of Ukraine, Donetsk, Ukraine

Received August 13, 2002

Abstract—Petroleum sorption on expanded graphite prepared from residual graphite hydrosulfate at 300–900°C was studied as influenced by pretreatment of the sorbent with water.

Expanded graphite is a highly efficient sorbent for petroleum and its derivatives; its sorption capacity for petroleum and industrial oil determined by the direct sorption procedure is about 80 [1–5] and 70 g g^{-1} [6, 7], respectively. The sorption capacity for petroleum and industrial oil form their aqueous emulsion is about 20 g g^{-1} [7, 8], i.e., it is lower by a factor of 3.5–4.

This sharp decrease in the sorption capacity cannot be due to competitive water sorption, since expanded graphite surface is mainly hydrophobic. Even if water is sorbed in the first steps, it should be desorbed from the sorbent by such a hydrophobic liquid as oil or petroleum. The lowering of the sorption capacity in an aqueous emulsion as compared to the direct sorption experiment is likely due to structural transformations of expanded graphite under the action of water. To check this assumption, in this work we studied the influence of pretreatment of expanded graphite with water on its sorption properties with respect to petroleum.

We used residual graphite hydrosulfate prepared from GT-1 natural flake graphite with the ash content of 5.68 wt % (Zaval'evskoe deposit). The graphite consists of mainly 0.630–0.315- (74.3 wt %) and 0.315–0.200-mm fractions (22.1%). The sample was treated with stirring with a 50% aqueous solution of chromium(VI) oxide (13 cm^3/100 g graphite) for 10 min and then with 95.8% sulfuric acid (42 cm^3/100 g graphite) for 10 min. After that, water (500 cm^3 per 100 g of the initial graphite) was added at room temperature and the reaction mixture was kept for 24 h. The crude product was filtered off and washed on the filter with water (8 dm^3 per 100 g of the initial graphite). The product was dried at 105°C to constant weight. Two batches of expanded graphite were prepared from the resulting graphite hydrosulfate.

The samples of the first batch were prepared by flash heating of residual graphite hydrosulfate in a muffle at a temperature ranging from 300 to 900°C. The samples were kept at 300–500°C for 5 min and then at 600–900°C for 2 min. The samples of the second batch were prepared by keeping samples of the first batch in water for 30 min. Then the liquid phase was carefully removed by filtration and drying at 105°C to constant weight.

We measured the specific surface area S_{sp} (m^2 g^{-1}), specific volume V_{sp} (cm^3 g^{-1}), and specific sorption of industrial oil W_{sp} (g g^{-1}) for all the samples of expanded graphite. The latter parameter was determined by the direct sorption method. The BET specific surface area was determined by low-temperature argon adsorption. The specific volume was calculated as the reciprocal of the bulk density of the sorbent.

We measured the sorption capacity of the expanded graphites for heavy oil [ρ = 0.873 g cm^{-3} (20°C)] from Lisichansk refinery. To a weighed portion of expanded graphite (~0.2 g) in a glass vessel, excess oil (25 g) was carefully added and the system was kept for 60 min to complete the sorption. Then the vessel was covered with a perforated metal foil and nonsorbed oil was allowed to drain down for 1 day. The oil sorption was determined gravimetrically. The sorption capacity of each sample was calculated as arithmetic mean of seven measurements.

When expanded graphite was treated with water, the following transformations were visually observed. Expanded graphite nonwetted with water was gradually saturated with water for 10 min, with its volume decreasing sharply. However, the vermiculite structure of graphite particles was retained. After drying, the black color of the initial expanded graphite changed to

1070-4272/03/7607-1179$25.00

Properties of expanded graphite samples prepared from residual graphite hydrosulfate

T, °C	S_{sp}, $m^2\ g^{-1}$		V_{sp}, $cm^3\ g^{-1}$		W_{sp}, $g\ g^{-1}$	
	batch 1	batch 2	batch 1	batch 2	batch 1	batch 2
300	9.6	5.0	52	35	17.9	14.8
400	12.1	7.3	122	66	28.2	18.5
500	30.7	12.7	149	74	31.3	23.2
600	41.2	15.1	179	75	38.5	24.7
700	55.4	22.4	222	79	48.2	26.4
800	47.8	21.9	250	86	57.1	28.0
900	66.7	26.0	278	90	60.5	29.2

gray with metallic luster. Separation of a negligible amount of small particles up to 0.1 mm in diameter was observed after both aqueous treatment and drying.

The specific surface area, specific volume, and sorption capacity for oil of the initial graphite samples expanded at T = 300–900°C (batch 1) and those of water-treated samples (batch 2) are summarized in the table. The influence of water treatment on the properties of expanded graphite is shown in Figs 1a–1c.

As seen from the table and Figs. 1a–1c, the specific surface area, specific volume, and sorption capacity for oil of all the samples linearly increase with increasing the preparation temperature. The parameters of all the samples decrease by a factor of 1.6–2.7, 1.5–3.0, and 1.2–2.0, respectively, after the samples were wetted with water and dried. The higher the preparation temperature of the samples, the more pronounced is the decrease. The temperature dependences of the specific surface area, specific volume, and sorption capacity for oil for the water-treated samples remain linear but their slopes decrease by factors of 2.5, 5, and 3.5, respectively.

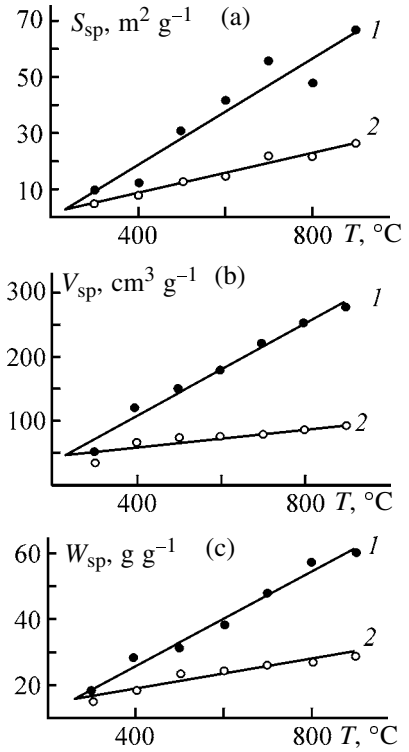

Fig. 1. (a) Specific surface area S_{sp}, (b) specific volume V_{sp} and (c) sorption capacity for petroleum W_{sp} of (*1*) the initial expanded graphite samples (batch 1) and (*2*) the samples treated with water (batch 2).

Thus, the morphology of expanded graphite particles profoundly changes after the water treatment, probably owing to a transformation of the honeycombed structure of expanded graphite under the action of forces of surface tension of water. This is confirmed by the fact that, as the preparation temperature of expanded graphite decreases and hence the strength of its honeycombed structure increases, straight lines shown in Figs. 1a–1c approach each other and cross at the point corresponding to the onset temperature of expansion of the residual graphite hydrosulfate (230–250°C).

The reasons for decrease in the specific surface area of expanded graphite are not so apparent. This cannot be due to collapse of water-filled pores during drying, since collapsed graphite layers will be expanded again with liberated water vapor. This also cannot be explained by collapse of empty pores when the specific volume of expanded graphite decreases under the action of forces of surface tension of water. This assumption is confirmed by the facts that the specific volume of expanded graphite decreases by a factor of 3 and its specific surface area remains the same after gentle mechanical treatment in the absence of water (mechanical stirring of dry expanded graphite for 45 min). We suggest that the specific surface area decreases owing to removal from the graphite structure of small fragments with the most developed surface.

A strong decrease in the sorption capacity for petroleum of expanded graphite treated with water is due to a decrease in its specific volume and specific surface area (Fig. 1c).

Thus, the substantial decrease in the sorption capacity for petroleum of expanded graphite treated with water is caused by morphological transformation of graphite particles, decreasing the specific surface area and specific volume of expanded graphite. These transformations can also be responsible for a sharp decrease in the sorption capacity of expanded graphite for petroleum and oil in going from direct sorption to sorption from an aqueous emulsion.

REFERENCES

1. Toyoda, M., Aizawa, J., and Inagaki, M., *Desalination*, 1998, vol. 115, no. 2, pp. 199–201.
2. Toyoda, M. and Inagaki, M., *Carbon*, 2000, vol. 38, no. 2, pp. 199–210.
3. Toyoda, M., Moriya, K., Aizawa, J., *et al*., *Desalination*, 2000, vol. 128, no. 3, pp. 205–211.
4. Inagaki, M., Konno, H., Toyoda, M., *et al*., *Desalination*, 2000, vol. 128, no. 3, pp. 213–218.
5. Inagaki, M., Shibata, K., Setou, S., *et al*., *Desalination*, 2000, vol. 128, no. 3, pp. 219–222.
6. US Patent 5 282 975.
7. Savos'kin, M.V., Yaroshenko, A.P., Mochalin, V.N., *et al*., *Zh. Prikl. Khim*., 2003, vol. 76, no. 6, pp. 936–938.
8. Cao, N.Z., Shen, W.C., Wen, S.Z., *et al*., Extended Abstracts, *Carbon'96*, Newcastle upon Tyne (the United Kingdom): The British Carbon Group, July 7–12, 1996, vol. 1, pp. 114–115.

Russian Journal of Applied Chemistry, Vol. 76, No. 7, 2003, pp. 1182–1184. Translated from Zhurnal Prikladnoi Khimii, Vol. 76, No. 7, 2003, pp. 1216–1218.

BRIEF COMMUNICATIONS

Structure of Asphaltene Compounds Formed by Homogeneous Pyrolysis of 2-Naphthol

V. V. Platonov, A. N. Kudrya, and S. V. Proskuryakov

Leo Tolstoy Tula State Pedagogical University, Tula, Russia
St. Petersburg State Technological Institute, St. Petersburg, Russia

Received April 24, 2002; in final form, April 2003

Abstract—The structure of asphaltene compounds formed by homogeneous pyrolysis of 2-naphthol was studied.

Although asphaltenes of various origins were studied in numerous works [1–15], their nature is not understood in detail. At the same time, asphaltenes play an important role in formation of liquid products of high-temperature coking of coals; they largely affect the structure and reactivity of coke and also of pyrocarbon prepared by pyrolysis of individual hydrocarbons and their mixtures.

To optimize processing of fossil fuels and high-temperature pyrolysis, it is quite necessary to study in detail the thermal degradation of the raw materials, including asphaltenes whose content in tars from "primary" decomposition of the organic matter of fuels reaches 30 wt %.

In this work we studied the structure of asphaltene compounds formed by homogeneous pyrolysis of 2-naphthol (800°C, 4.5 s).

EXPERIMENTAL

Asphaltenes were isolated as described in [16]. The molecular structure of asphaltenes was characterized by IR, UV, ^{1}H NMR, and ^{13}C NMR spectroscopy, elemental and quantitative functional analysis, and cryoscopy.

We found that the asphaltenes are a complex mixture of relatively high-molecular-weight polyfunctional compounds in which the prevailing structural fragments are fused aromatic rings and heterocomponents. Oxygen is present, in particular, in the forms of five-membered heterocycles inside fused aromatic structures [like naphtho(benzo)furans] and of quinoid groups (mainly 1,4-quinones). Phenolic hydroxyls are present, but alcoholic hydroxyls are not detected at all. Methoxy groups are present in small amounts. Among alkyl substituents in the rings, methyl groups prevail, but the degree of substitution is low. The mean size of fused systems is four rings.

To elucidate the structural features of asphaltene compounds in detail, we separated them into fractions by extraction with acetone, adsorption liquid chromatography, and preparative thin-layer chromatography (TLC).

Preparative TLC of asphaltene fractions was performed on standard Silufol plates (20 × 20 cm). The optimal separation of asphaltene fractions was attained in the following systems (the volume ratio is given in parentheses): fraction 1.1.1, hexane–diethyl ether–acetone (5 : 5 : 1); fraction 1.2, hexane–diethyl ether–ethyl acetate (10 : 10 : 1); fraction 2.1, heptane–diethyl ether (1 : 1); and fraction 2.2, hexane–diethyl ether (1 : 1).

The bands were developed under UV light (λ 254 and 366 nm). The nonluminescent bands were developed by treatment with solutions of various agents and also by chromatography on Silufol UV-254 plates in which the sorbent contained a luminescent additive, 0.05% sodium fluorescein. In this case, the nonluminescent bands were revealed by quenching of the green luminescence of sodium fluorescein.

The extracts, close-cut fractions, and even individual asphaltene compounds were characterized by a set of physicochemical methods.

We found that fractions 1.1.1 and 1.2 have a mixed hydroaromatic nature; they contain aromatic rings and heterocyclic groups. Their spectra exhibit absorption bands ν characteristic of fused aromatic systems (3030–3080, 1500–1600, 1450–1525 cm^{-1}). The aromatic rings are bonded with hydrogenated groups,

1070-4272/03/7607-1182$25.00

as suggested by strong bands at 2925, 2850, 1470, and 720–725 cm^{-1}.

It should be noted that the degree of aromaticity of fraction 1.1.1 is lower compared to 1.2. The content of cycloalkanes (ν 1611 cm^{-1}) in these fractions is similar and low. The content of methoxy groups (ν 2815–2830, 3050–3150 cm^{-1}) is also similar. However, in the quantitative content of other functional groups, fractions 1.1.1 and 1.2 differ appreciably. Fraction 1.2 is characterized by higher, compared to 1.1.1, intensity of the bands of phenolic hydroxyls (3850–3670, 1140–1230, 1410–1310 cm^{-1}) and heterocyclic oxygen (845–870, 3125–3165, 1030–1075 cm^{-1}). The shape and position of the quinoid bands (1600–1670, 1635–1655 cm^{-1}) suggest the presence of one (on the average) quinoid group in the ring.

The IR spectra of fractions 2.1 and 2.2 show that their major structural elements are fused aromatic rings and heterocycles (3030–3080, 1500–1600, 1450–1525 cm^{-1}), and also hydrogenated rings, as indicated by the absorption bands of the CH_2 group (2925, 2850, 1470, 720–725 cm^{-1}). The degree of aromaticity of fraction 2.2 is higher than that of 2.1. The bands at 3580–3670, 1140–1230, and 1310–1410 cm^{-1} suggest the presence of phenolic hydroxyls in both fractions, with their content in fraction 2.1 being higher by a factor of 15. The presence of quinoid groups is confirmed by the bands at 1660–1670 and 1635–1655 cm^{-1}; on the average, one quinoid group is present per ring. Quinoid groups have the structure of conjugated cyclohexanones and cyclopentanones. The content of alkoxy groups (2815–2830, 3050–3150 cm^{-1}) is low, and heterocyclic oxygen (845–870, 3125–3165, 1030–1075 cm^{-1}) prevails in fraction 2.1. It is localized in five-membered heterocycles fused with aromatic fragments to form structures of the benzo(naphtho)furan type (3125–3165, 1015–1030, 845–870, 740–810 cm^{-1}). Among alkyl substituents in rings, methyl groups prevail (2910, 2850, 1450, 1380 cm^{-1}). The pattern in the range 700–820 cm^{-1} suggests that the "acene" mode of fusion prevails over the "phene" mode.

Studies of the asphaltene compounds isolated by preparative TLC showed the following.

Fraction 1.1.1 was separated into 14 components, with their yield ranging from 3.2 to 14.3%. The content of elements (%) varies in the following ranges: C, from 80.0 to 88.1; H, from 6.4 to 7.6; and O, from 5.5 to 25.6%. The content of functional groups (g-equiv mol^{-1}) varies in the following ranges: quinone groups (QG), from 0.08 to 0.21; phenolic groups (PG), from 0.06 to 0.21; alkoxy groups (AG), from 0.01 to 0.16; and heterocyclic oxygen (O_c), from 0.04 to 0.48. The molecular formulas are $C_{11.75}H_{12.92}O_{1.00}$–$C_{18.81}H_{25.06}O_{5.39}$.

Fraction 1.2 was separated into 14 components, with their yield ranging from 4.3 to 12.8%. The content of elements (%) varies in the following ranges: C, from 63.6 to 93.0; H, from 6.3 to 9.1; and O, from 0.1 to 30.1%. The molecular weight *M* varies from 169 to 394. The content of functional groups (g-equiv mol^{-1}) varies in the following ranges: QG, from 0.01 to 0.40; PG, from 0.02 to 0.40; AG, from 0.05 to 0.22; and O_c, from 0.09 to 0.33. The molecular formulas are $C_{12.94}H_{18.35}O_{0.74}$–$C_{20.87}H_{24.80}O_{7.43}$.

Fraction 2.1 was separated into six components. Their yield varies from 2.8 to 28.3%. The content of elements (%) varies in the following ranges: C, from 80.3 to 87.5; H, from 6.0 to 9.5; and O, from 4.8 to 10.6%. *M* varies from 236 to 295. The content of functional groups (g-equiv mol^{-1}) varies in the following ranges: QG, from 0.65 to 1.00; AG, from 0.30 to 0.60; and O_c, from 0.27 to 0.35 g-equiv mol^{-1}. The molecular formulas are $C_{16.06}H_{21.79}O_{1.59}$–$C_{20.95}H_{18.10}O_{1.41}$.

Fraction 2.2 was separated into 14 components. Their yield varies from 2.0 to 18.6%. The content of elements (%) varies in the following ranges: C, from 77.6 to 90.6; H, from 5.7 to 15.2; and O, from 0.5 to 10.0%. *M* varies from 189 to 496. The content of functional groups (g-equiv mol^{-1}) varies in the following ranges: QG, from 0.12 to 0.37 and O_c, from 0.07 to 0.14. The molecular formulas are $C_{14.44}H_{11.15}O_{0.28}$–$C_{38.56}H_{30.75}O_{0.16}$.

Additionally we found that the components of fraction 1.2 have a hybrid naphthenoaromatic nature, with the cycloalkane structures prevailing. In fraction 1.1.1, aromatic structures and oxygen-containing heterocycles prevail. Fraction 2.1 mainly contains fused aromatic structures with the linear fusion mode, substituted by phenolic, methoxy, and methyl groups. Oxygen is also present in the form of cyclohexanone, cyclopentanone, and furan rings. The total number of rings in structures is 3–5.

Components of fraction 2.2, as those of fraction 2.1, consist mostly of three or four rings fused mainly in the linear mode; only one compound contains eight rings. The degree of aromaticity of the components is high, as confirmed by the C : H ratio. The calculation results obtained using the Van Krevelen [17] and Lillard [18] structural-group analysis procedures are well consistent with the suggested formulas.

CONCLUSIONS

(1) The structure of asphaltene compounds formed by homogeneous pyrolysis of 2-naphthol was studied in detail by IR, UV, ^{1}H NMR, and ^{13}C NMR spectroscopy, elemental and quantitative functional and structural-group analyses, cryoscopy, extraction, and adsorption liquid and preparative thin-layer chromatography.

(2) Asphaltene compounds have a hybrid naphthenoaromatic nature. The linear fusion mode prevails; the number of rings varies from 2 to 8. The rings contain phenolic, quinoid, alkoxy, and methyl substituents. The content of heterocyclic oxygen is high.

REFERENCES

1. Platonov, V.V., Valdez, J.C., and Vol'-Epshtein, A.B., *Neftekhimiya*, 1988, vol. 28, no. 2, pp. 225–231.
2. Platonov, V.V., Valdez, J.C., and Klyavina, O.A., *Khim. Tverd. Topl.*, 1989, no. 4, pp. 102–108.
3. Platonov, V.V., Klyavina, O.A., and Prokof'ev, E.E., *Khim. Tverd. Topl.*, 1983, no. 6, pp. 75–85.
4. Platonov, V.V., Proskuryakov, V.A., and Klyavina, O.A., *Zh. Prikl. Khim.*, 1994, vol. 67, no. 3, pp. 487–491.
5. Platonov, V.V., Proskuryakov, V.A., and Ryl'tsova, S.V., *Zh. Prikl. Khim.*, 1998, vol. 71, no. 10, pp. 1729–1736.
6. Eliseev, V.E., Comprehesive Study of the Structure of Petroleum Asphaltenes Using Ozonolysis, *Cand. Sci. Dissertation*, Moscow, 1979.
7. Bronfin, I.B., Study of Processes and Products of the Fraction of Resin–Asphaltene Concentrates, *Cand. Sci. Dissertation*, Moscow, 1975.
8. Petersen, J.C., *Fuel*, 1967, vol. 46, nos. 4–5, pp. 295–305.
9. Snyder, L.R. and Buell, B.E., *Anal. Chem.*, 1968, vol. 40, no. 8, pp. 1295–1316.
10. Magaril, R.Z. and Svintitskikh, L.E., *Tr. Tyumen. Ind. Inst., Ser. Khim. Khim. Tekhnol.*, 1972, p. 305.
11. Pokonova, Yu.V., *Khimiya vysokomolekulyarnykh soedinenii nefti* (Chemistry of Macromolecular Compounds of Oil), Leningrad: Leningr. Gos. Univ., 1980.
12. Lapik, V.V. and Kruzhinova, L.V., *Khim. Tverd. Topl.*, 1974, no. 4, pp. 54–58.
13. Platonov, V.V., Ivleva, L.N., Klyavina, O.A., and Prokof'ev, E.E., *Khim. Tverd. Topl.*, 1982, no. 5, pp. 89–99.
14. Platonov, V.V., Proskuryakov, V.A., Ryl'tsova, S.V., and Popova, Yu.N., *Zh. Prikl. Khim.*, 2001, vol. 74, no. 6, pp. 1024–1028.
15. Platonov, V.V., Proskuryakov, V.A., and Rozental', D.A., *Zh. Prikl. Khim.*, 2001, vol. 74, no. 5, pp. 858–862.
16. Kamneva, A.I. and Korolev, Yu.G., *Laboratornyi praktikum po khimii topliva* (Laboratory Course of Fuel Chemistry), Moscow: Mosk. Khimiko-Tekhnol. Inst., 1976.
17. Van Krevelen, D.V. and Chermin, N.A., *Fuel*, 1957, vol. 36, no. 2, pp. 313–320.
18. Lillard, J.G., Jones, C.J., and Anderson, J.A., *Ind. Eng. Chem.*, 1952, vol. 44, no. 11, pp. 2623–2631.

Russian Journal of Applied Chemistry, Vol. 76, No. 7, 2003, p. 1185. Translated from Zhurnal Prikladnoi Khimii, Vol. 76, No. 7, 2003, p. 1219.

OBITUARIES

Karl Samoilovich Minsker (1929–2003)

On May 23, 2003, Karl Samoilovich Minsker, an outstanding scientist, prominent specialist in chemistry of macromolecular compounds, petrochemistry, and technical chemistry, doctor of chemistry, professor, academician of the Academy of Sciences of the Republic of Bashkortostan, and Honored Scientist of the Russian Federation and the Republic of Bashkortostan, died in the age of seventy-three.

K.S. Minsker graduated from the Lomonosov Institute of Fine Chemical Technology in Moscow. He started working at the chemical plant in Dzerzhinsk, Gor'kii oblast, as head of shift. From 1953 till 1967, he worked at Dzerzhinsk Chemical Research Institute (now Kargin Research Institute of Polymer Chemistry and Technology), where made a career from junior researcher to head of laboratory. The initial period of Minsker's scientific activities is closely associated with Academician G.A. Razuvaev. In 1968, Minsker was invited to Ufa to organize at Bashkir State University a chair of macromolecular compounds. Simultaneously, from 1968 till 1983, he headed laboratory of ionic polymerization at the Institute of Chemistry, Bashkir Branch of the USSR Academy of Sciences. In 1978, Minsker organized and headed the Problem Research Laboratory of Degradation and Stabilization of Halogen-Containing Polymers at Bashkir State University.

Under Minsker's supervision, a quantitative theory of degradation of chlorine-containing polymers was set up, and quite a number of high-performance additives to polymers and formulations for materials and articles, mainly based on polyvinyl chloride, were developed. A fundamental phenomenon of modification of Ziegler–Natta catalysts with electron-donor compounds in polymerization of olefins was described for the first time, which is presently the main classical way to control the activity and selectivity of industrial catalytic systems. An original theory of the mechanism of stereoregulation in polymerization of olefins and dienes on Ziegler–Natta catalysts was developed. Important fundamental aspects of the mechanism of cationic polymerization of olefins were revealed. A new section of chemical physics and theoretical technology, concerned with occurrence of fast processes in turbulent flows, was developed, which made it possible to create and put in industrial practice a number of resource- and energy-saving highly efficient processes based on small-size tubular turbulent reactors.

Among Minsker's disciples are 54 candidates and 11 doctors of science. He published more than 1100 printed works, including 16 monographs and books, and was holder of 25 foreign patents and more than 300 inventor's certificates and RF patents. Minsker was honored with titles "Man of the Year 1994–1995" (American Biographic Institute) and "International Man of the Year 1995–1996" in science and education (International Biographic Centre, Cambridge, England). He was awarded a medal "For Achievements in the XX Century, 1999–2000" (International Biographic Centre, Cambridge, England), a State Prize of the Republic of Tatarstan in Science and Technology (2001), and Academician Kargin Prize of the Russian Academy of Sciences, and was more than once a laureate of the All-Union Exhibition Center (VDNKh) and the Russian Exhibition Center.

The blessed memory of Karl Samoilovich Minsker will be forever preserved in the hearts of his numerous disciples and colleagues and his people.

A. A. Berlin, G. E. Zaikov, V. P. Zakharov, R. Akhmetkhanov, and staff members of the Chair of Macromolecular Compounds, Bashkir State University

1070-4272/03/7607-1185$25.00

Russian Journal of Applied Chemistry, Vol. 76, No. 7, 2003, pp. 1186–1190. Translated from Zhurnal Prikladnoi Khimii, Vol. 76, No. 7, 2003, pp. 1220–1223.

HISTORY OF CHEMISTRY AND CHEMICAL TECHNOLOGY

Academician Pavel Ivanovich Walden (on 140th Anniversary of His Birthday)

In the early XX century, two positions were provided at the St. Petersburg Academy of Sciences for ordinary academicians in chemistry. Since 1886 these positions were occupied by F.F. Beilstein (1838–1906) and N.N. Beketov (1827–1911). After Beilstein's death, his position remained vacant for a certain time, and in 1916, P.I. Walden, professor of chemistry of Riga Polytechnic Institute, was elected member of the Academy of Sciences. In a representation signed by a number of scientists, including Beketov, V.I. Vernadsky, and A.P. Karpinsky, Walden's achievements were noted, in the first place, in stereochemistry of organic compounds. As an exception, Walden was allowed to temporarily remain in Riga and to come to St. Petersburg only to take part in sessions of the Academy of Sciences. World War I, which began in August 1914, resulted in that Walden did not move to Petrograd.

Walden's life and scientific activities have been the subject of a great number of publications, including a detailed scientific biography [1], and other studies and recollections [2–9]. In a brief essay, only the main events of the scientist's life and his close association with St. Petersburg colleagues will be recalled.

Pavel Ivanovich (Paul) Walden was born on July 26, 1863, in a peasant's family in Latvia, not far from the town of Cecis. In 1876, he graduated with distinction from the Cecis regional school, and in 1882, finished with the same amount of success his secondary education at Riga modern school. In December 1882, Walden became a student of Riga Polytechnic School (Riga Polytechnicum), founded in 1862. The teaching was in German, actually Walden's native language, even though he is commonly considered to be a Latvian [2, 8]. Later, in 1896, the school was reorganized into State Riga Polytechnic Institute with teaching in Russian. Riga Polytechnicum had reputation of an exemplary educational institution with high level of specialist training and was a prominent research center.

Nearly simultaneously with Walden's entry into Riga Polytechnicum, the position of a professor of chemistry at this institution was occupied by young

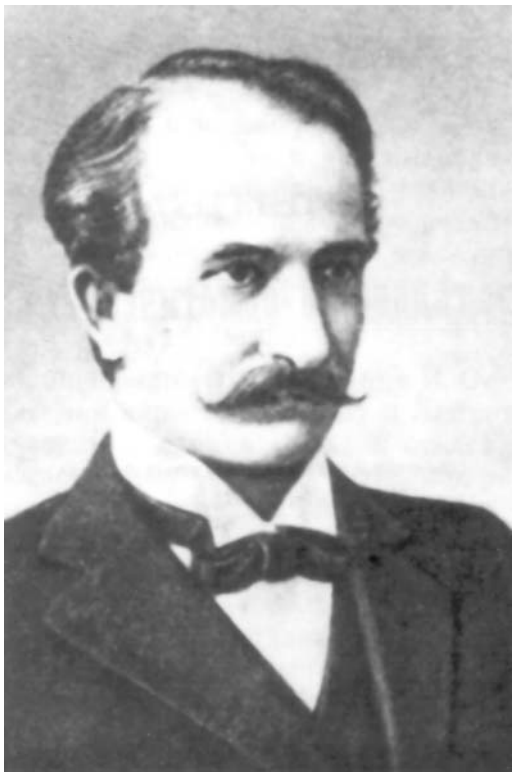

Wilhelm Ostwald (1853–1932, 1909 Nobel Prize laureate), who returned to his native city from Derpt (now Tartu, Estonia) where he studied, and then taught chemistry. Ostwald started to deliver all courses of theoretical and technical chemistry, much extended the volume of laboratory works; he demanded that students should present and defend a degree thesis devoted to research. In September 1885, having become an assistant (not on permanent staff) of a professor of physics, T. Grönberg (1845–1910), Walden found an opportunity to do experimental research. By that time, he, following Ostwald's example, decided to prepare himself to work as chemist researcher.

In 1887, the first Walden's scientific publication, concerned with comparative assessment of reactions proposed for qualitative detection of nitric acid, appeared in *Zhurnal Russkogo Fiziko-Khimicheskogo Obshchestva* (*Zh. Russ. Fiz.-Khim. O–va.*, 1887, vol. 19, no. 5, pp. 274–1295). By recommendation of

1070-4272/03/7607-1186$25.00 © 2003 MAIK "Nauka/Interperiodica"

N.S. Kurnakov, N.A. Menshutkin, and I.F. Schroeder, the young scientist was made a member of the Russian Physicochemical Society. In the same year appeared joint publication by Ostwald and Walden, which was devoted to variation of the molar electrical conductivity of acids and bases with their dilution (*Z. Phys. Chem.*, 1887, vol. 1, no. 10, pp. 529–549).

In 1888, Walden graduated with distinction from the Department of Chemical Technology, Riga Polytechnicum, and was given a rank of chemist-engineer. By that time, Ostwald moved to Leipzig, to become head of the chair of physical chemistry at Leipzig University. Professor K.A. Bischof (1855–1908), who replaced Ostwald in Riga, was an organic chemist. Walden accepted his proposition to remain assistant at the chair of chemistry (senior assistant since 1890 and associate professor since 1892) [9]. He commenced his rather intensive pedagogical and scientific activities at the Riga Polytechnicum (Polytechnic Institute), which continued till 1919.

Walden took the most active part in studies in the field of stereochemistry of organic compounds, the scientific direction developed by Bishof. A detailed analysis of the stereochemical research carried out in those years at the Riga Polytechnic Institute and other scientific centers of Russia has been made by Stradins [6]. During the period of time from 1889 till 1900, Walden published 57 papers concerned with stereochemistry in German journals and in *Zhurnal Russkogo Fiziko-Khimicheskogo Obshchestva*. He, in particular, was the first to demonstrate the possibility of spatial displacement of atomic groups about an asymmetric carbon atom, which leads to transition from one state to a mirror-opposite state (Walden inversion) [1, 6, 10, 11]. In other words, according to Walden, an optically active compound may be transformed into the corresponding isomeric antipode, bypassing the optically inactive form.

Despite his extensive and labor-consuming studies in organic chemistry and stereochemistry, Walden did not terminate research in the field close to Ostwald's interests, did not break off scientific relations with him, and more than once went to Leipzig. In September 1891, he defended with excellence at Leipzig University his doctoral dissertation "On Affinities of Certain Organic Acids and Relationship of the Affinities with the Constitution of the Acids." The thesis contained material on dissociation constants of a great number of organic acids. In summer of 1892, Walden was appointed lecturer (associate professor) of physical chemistry at the Riga Polytechnicum. His further career required a scientific degree from a Russian university. After passing the appropriate examinations, Walden defended in spring of 1893 his master's dissertation "An Experience of Study of Osmotic Phenomena on Sediment Films" at Novorossia University (Odessa), where known chemists, such as P.G. Melikishvili (1850–1927) and N.D. Zelinsky (1861–1953), were working at that time. Already in 1894, the young scientist obtained an established position of a professor of analytical chemistry at the Riga Polytechnicum. Also, Walden continued intensive research both in organic chemistry and in physical chemistry. In these same years, the scientist actively extended his scientific contacts, visited a large number of scientific centers, including St. Petersburg, Derpt (Tartu), Kiev, and universities in German cities (Freiberg, Halle, Göttingen). His scientific and personal relations with Ostwald remain especially close. In 1903, Walden wrote the first Ostwald's biography [12].

Studies in the field of stereochemistry served as a basis for Walden's doctoral dissertation, defended by him on March 7, 1899, at St. Petersburg University. Professors D.P. Konovalov (1856–1929) and N.A. Menshutkin (1842–1907) were his official opponents. After defending the dissertation, Walden focused his entire attention on physicochemical research: He studied the electrical conductivity of solutions of various substances in highly polar solvents. This direction of the scientist's research was considered in detail in [1, 13–16]. During the period from 1900 till 1934, Walden studied the ionizing capacity of about 50 solvents, introduced into scientific practice the concepts of solvation and solvolysis, established a relationship between the equivalent electrical conductivity at infinite dilution and viscosity (Walden rule), and revealed a number of other dependences. The Walden rule stimulated construction of models of solutions, based on the concept of ion motion in a continuous medium [16].

The experience of work of the Riga Polytechnic Institute, the first Russia's higher-school institution of this type, was of interest for organization of the Polytechnic Institute in St. Petersburg. Walden was invited to become a member of the Chief Commission, headed by the minister of finance S.Yu. Witte (1849–1915) and dealing with building schedule and curricula. It was also assumed that Walden would take positions of the dean of the metallurgical department and a professor of general chemistry. As noted by a known historian of chemistry, B.N. Menshutkin (1874–1938), Walden was confirmed as dean on July 27, 1901, but already in October of the same year reported that he could not accept this appointment and recommended that N.A. Menshutkin should be ap-

pointed the dean, which was done on November 1, 1901. Already at the beginning of 1902, Walden was elected director of the Riga Polytechnic Institute and confirmed in this position for four years, beginning on April 15, 1902. In view of student disturbances in autumn of 1905, Walden resigned as director and was appointed dean of the chemical faculty beginning in January 1, 1906.

As already noted, Walden was elected ordinary member (academician) of St. Petersburg Academy of Sciences in "technology and chemistry adapted to art and handicraft." After the death of Academician Beketov in November 1911, Walden was appointed head of the Chemical Laboratory, which was the only chemical research institution of the Academy of Sciences at that time. With the beginning of World War I, regular Walden's visits to Petrograd became difficult, and N.S. Kurnakov (1860–1941, elected academician in December 1913) became the actual head of laboratory.

In *Izvestiya Imperatorskoi Akademii Nauk* (Transactions of Imperial Academy of Sciences), Walden published, as an academician, 14 papers on electrochemistry of nonaqueous solutions and related problems. In December 1907, he took part in meetings of the First Mendeleev Congress and presented a report "On Mendeleev's Works Concerned with Solutions." Walden's reports at the Second Mendeleev Congress in December 1911 were devoted to the problem of mass conservation in chemical reactions and to the development of chemistry in Russia. During the period of time from 1907 till 1914, Walden took part in quite a number of large-scale Russian and international conferences and was elected honorary member of numerous academies and scientific societies. Walden's friendship with Ostwald continued and scientific relations with prominent chemists of that time, S. Arrhenius (1859–1927, 1903 Nobel Prize winner), J. van't Hoff (1852–1911, 1901 Nobel Prize winner), E. Fischer (1852–1919, 1902 Nobel Prize winner), W. Ramsay (1852–1916, 1904 Nobel Prize winner), and H. Tammann (1861–1938), were maintained. Twice, in 1913 and 1914, Walden was nominated for Nobel Prize. As noted in the monograph [1], the years of Walden's life preceding World War I were the summit of his scientific career and scientific creative activities.

In July 1915, the Riga Polytechnic Institute, and Walden together with it, were evacuated to Moscow. During the period from 1915 till 1918, the scientist had no laboratory of his own in Moscow and had virtually no opportunity to carry out research. He finished the book *Ocherk istorii khimiii v Rossii* (Study in the History of Chemistry in Russia) (1915) and delivered lectures on physical chemistry and history of chemistry not only to students in Riga, but also to those at Moscow University and other metropolitan educational institutions. During these years, Walden took part in the work of the Commission for Study of Natural Productive Forces (KEPS), organized in February 1915 by the initiative of Academician V.I. Vernadsky (1863–1945) and a number of other scientists. In the same year, the Military-Chemical Committee, presided by Kurnakov, was organized at the Russian Physicochemical Society. Walden was appointed head of the Moscow department of the Committee. The Committee and its Moscow department carried out much work on development of means for military-chemical protection and organization of manufacture of a number of chemical products.

On January 1, 1917, Walden was confirmed as rector of the Riga Polytechnic Institute. Brest peace treaty (March 1918) envisaged return of the institute to Riga occupied by German troops. Part of lecturers and students decided to remain in Russia, to become the basis of a new institute in Ivanovo-Voznesensk (now Ivanovo). The main part of professors and students of the Riga Polytechnic Institute, led by Walden, returned to Riga in August 1918.

The political instability in Latvia, nationalistic tendencies exhibited by the authorities, and lack of conditions for scientific work of full value, all this resulted in that, in early summer of 1919, Walden sent his family to Germany and soon himself accepted the invitation of Rostock University to take a position of professor of inorganic chemistry. However, Walden's relationships with Latvia and Russia were not terminated at once. In summer of 1924, he came to Riga by invitation of the Latvian University to deliver lectures on the most recent advances in chemistry. Despite the propositions made, Walden had not dared to move back to Latvia. He also declined an invitation to take the chair of inorganic chemistry at Petrograd University, which became free because of the death of L.A. Chugaev (1873–1922). Nevertheless, his scientific contacts with Russian scientists continued, and quite a number of Walden's works were published in Russian, including the monograph *Teorii rastvorov v ikh istoricheskoi posledovatel'nosti* (Theories of Solutions in Their Historical Succession) (Petrograd, 1921) and brochures *Iz istorii khimicheskikh otkrytii* (Excerpts from History of Chemical Discoveries) (Leningrad, 1925), *Proshloe i nastoyashchee stereokhimii* (Past and Present of Stereochemistry) (Leningrad, 1925), and *Khimiya i zhizn'* (Chemistry and Life) (Petrograd, part I, 2nd ed., 1922; part II, 1919; part III,

1921). The publication of Walden's works was initiated by Professor M.A. Blokh (1882–1941), a known chemist and historian of chemistry, who graduated from the Riga Polytechnic Institute in 1908 [1].

In December 1927, Walden was unanimously elected honorary member of the Academy of Sciences of the USSR. His personal meeting with Russian colleagues occurred only in September 1934, when Walden came to Leningrad to the VII Jubilee Mendeleev Congress devoted to 100th anniversary of Mendeleev's birthday as head of a representative German delegation. The delegation included H. Wieland (1877–1957, 1927 Nobel Prize winner), A. Stock (1876–1946), O. Hahn (1879–1968, 1944 Nobel Prize winner), and other known scientists. Walden made a report "Electrolytes and Solvents" and delivered speech of welcome on behalf of all foreign participants of the Congress. In his report on the trip, Walden highly appreciated the success in chemical education and industrial development, achieved in the Soviet Union by that time [1, 5].

In Rostock, Walden continued his studies of nonaqueous solutions and processes of association in these solutions, commenced in Riga in the prewar years. During the period of time from 1923 till 1934, he published, together with his disciples, more than 50 original papers; however, the interest of physical chemists in classical investigations into the nature of solutions diminished, with the main attention given to other problems. Nevertheless, Walden rather actively delivered lectures and reports in various cities of Germany and other countries. He spent the entire academic year of 1927/28 in the United States, mainly delivering lectures at the Cornell University (Ithaca, NY).

In 1934, at the age of seventy, Walden resigned and concentrated his entire attention on studies in history of chemistry [1, 4]. He made a great effort to write a monograph devoted to history of organic chemistry, covering the period from 1880 till 1940. The book was published in Germany in 1941. After that the monographs *Three Millennia of Chemistry* (1944) and *History of Chemistry* (1947) were published. As noted in [4], a historical analysis of a problem served to Walden as substantiation of the concepts developed by him.

During the night of April 24/25, 1942, as a result of bombardment of Rostock by British aircraft, Walden's house was burnt, with a large library, archive materials, manuscripts, and scientists' letters lost. After that, Walden moved to Berlin, and then to Frankfurt am Main. The town of Tübingen and Tübingen University became the scientist's last refuge. In 1950, Walden became honorary doctor of the Tübingen University and honorary professor. The scientist delivered lectures on history of chemistry to the age of 90, till July 1953.

Pavel Ivanovich (Paul) Walden died on January 22, 1957, at the age of ninety-three. The world scientific community lost a first-rate scientist who had been honored with a great number of honorary titles and awards, made an outstanding contribution to the development of chemical science, and was a prominent historian of chemistry.

REFERENCES

1. Stradins, J.P. and Solov'ev, Yu.I., *Pavel Ivanovich Val'den: 1863–1957* (Paul Walden: 1863–1957), Moscow: Nauka, 1988.
2. Stradins, J.P., in *Iz istorii estestvoznaniya i tekhniki Pribaltiki* (Excerpts from the History of Natural Science and Technology in Baltic Countries), Riga: Zinatne, 1968, vol. 1, pp. 157–167.
3. Makarenya, A.A. and Pozdysheva, V.A., in *Iz istorii estestvoznaniya i tekhniki Pribaltiki* (Excerpts from the History of Natural Science and Technology in Baltic Countries), Riga: Zinatne, 1972, vol. 4, pp. 123–135.
4. Solov'ev, Yu.I. and Stradins, J.P., in *Iz istorii estestvoznaniya i tekhniki Pribaltiki* (Excerpts from the History of Natural Science and Technology in Baltic Countries), Riga: Zinatne, 1976, vol. 5, pp. 111–133.
5. Walden-Khollo, I.P., in *Iz istorii estestvoznaniya i tekhniki Pribaltiki* (Excerpts from the History of Natural Science and Technology in Baltic Countries), Riga: Zinatne, 1976, vol. 5, pp. 286–298.
6. Stradins, J.P., in *Iz istorii estestvoznaniya i tekhniki Pribaltiki* (Excerpts from the History of Natural Science and Technology in Baltic Countries), Riga: Zinatne, 1984, vol. 7, pp. 22–54.
7. Virt, U., in *Iz istorii estestvoznaniya i tekhniki Pribaltiki* (Excerpts from the History of Natural Science and Technology in Baltic Countries), Riga: Zinatne, 1984, vol. 7, pp. 63–72.
8. Pijola, S., in *Iz istorii estestvoznaniya i tekhniki Pribaltiki* (Excerpts from the History of Natural Science and Technology in Baltic Countries), Riga: Zinatne, 1984, vol. 7, pp. 73–79.
9. Volkov, V.A., Raskin, N.M., and Stradins, J.P., *Izv. Akad. Nauk Latv. SSR*, 1987, no. 9, pp. 56–64.
10. Sheptunova, E.I., *Khim. Shkole*, 1999, no. 6, pp. 89–92.

11. Solov'ev, Yu.I. and Stradins, J.P., *Vestn. Akad. Nauk SSSR*, 1988, no. 10, pp. 112–121.
12. Stradins, J.P., *Izv. Akad. Nauk Latv. SSR*, 1979, no. 7, pp. 33–44.
13. Solov'ev, Yu.I., *Istoriya ucheniya o rastvorakh* (History of the Theory of Solutions), Moscow: Akad. Nauk SSSR, 1959.
14. Solov'ev, Yu.I., *Ocherki po istorii fizicheskoi khimii* (Studies in History of Physical Chemistry), Moscow: Nauka, 1964.
15. Izmailov, N.A., *Iz istorii otechestvennoi khimii* (Excerpts from the History of Domestic Chemistry), Kharkov: Khar'k. Univ., 1952, pp. 282–323.
16. Fialkov, Yu.Ya. and Zhitomirskii, A.N., *Izv. Akad. Nauk Latv. SSR*, 1987, no. 9, pp. 65–70.
17. Menshutkin, B.N., *Zhizn' i deyatel'nost' Nikolaya Aleksandrovicha Menshutkina* (Life and Activities of Nikolai Aleksandrovich Menshutkin), St. Petersburg, 1908.

A. G. Morachevskii

Russian Journal of Applied Chemistry, Vol. 76, No. 8, 2003, pp. 1191–1196. Translated from Zhurnal Prikladnoi Khimii, Vol. 76, No. 8, 2003, pp. 1233–1237.

INORGANIC SYNTHESIS AND INDUSTRIAL INORGANIC CHEMISTRY

Specific Features of Acid Decomposition of Eudialyte and Certain Rare-Metal Concentrates from Kola Peninsula

V. N. Lebedev, T. E. Shchur, D. V. Maiorov, L. A. Popova, and R. P. Serkova

Tananaev Institute of Chemistry and Technology of Rare Elements and Mineral Raw Materials, Kola Scientific Center, Russian Academy of Sciences, Apatity, Russia

Received April 18, 2003

Abstract—Specific features of decomposition of eudialyte concentrate by acids were studied. The structure of eudialyte crystals was analyzed by processing the kinetic characteristics obtained.

Eudialyte $Na_{12}Ca_6Zr_3Fe_3[Si_3O_9]_2 \cdot [Si_9O_{24}(OH)_3]_2$, i.e., sodium zirconosilitate with complex structure, means, in translation, "readily decomposable"; however, as a rule, the degree of its decomposition by various acids is 65–75% [1–3]. It is only possible to extract zirconium(IV) into solution rather completely under rigorous conditions with a manyfold excess of an acid or with fluoride ions introduced [4–6]. This is attributable to blocking of the mineral by silica, formation of secondary zirconium(IV) compounds, presence of "acid-insoluble zirconium," etc. A high degree of extraction with a minor excess of an acid has been reported [7]; however, no details of the procedure used were given (it may be assumed that readily decomposable forms of eudialyte containing a minimum amount of niobium and titanium were subjected to treatment).

The aim of the present study was to analyze reasons for the low degree of breakdown of the eudialyte concentrate (EC) from the Novozero deposit.

Eudialyte found in various deposits is, presumably, inhomogeneous not only in its composition, but also in structure of a unit crystal. This is rather probable because the coefficients of impurity cocrystallization in the formation of the mineral are different, and the strength of a crystal depends on its structural perfection. To verify this assumption, we obtained kinetic characteristics of decomposition of eudialyte concentrates of varied origin by diferent acids.

EXPERIMENTAL

Eudialyte concentrates from two batches[1] were used in the experiments. The composition of the concentrates is listed in Table 1.

The decomposition was carried out in a temperature-controlled beaker with a stirrer at a stoichiometric acid consumption, with its initial concentration maintained constant in each stage of decomposition. Narrow fractions of the concentrates were decomposed with 2 N H_2SO_4 at 40°C under the conditions in which no coagulation of silicic acid occurred within the recorderd intervals of time. The main monitoring parameter was the weight of dry undecomposed residue, and in certain experiments, zirconium(IV) content was determined. In sampling, a precipitate was filtered off and washed with water on a filter and by repulping under vigorous stirring. The precipitate was dried also with stirring to destroy the possible silica films. Then, weighed precipitate was treated under the initial conditions, i.e., with a new portion of the acid with the same concentration at the same consumption. The decomposition rate was estimated by the ratio of the weight loss to weight under decomposition within a unit time in relation

[1] EC-1 batch was obtained on a pilot installation of the Mining Institute, Kola Scientific Center, Russian Academy of Sciences, from the ore of the rock deposit Kedykvyrpakh, and EC-2, at GIREDMET, "Sevredmet" site from the ore from the Alluaiv deposit.

1070-4272/03/7608-1191 $25.00 © 2003 MAIK "Nauka/Interperiodica"

Table 1. Elemental composition of eudialyte concentrates

Batch	Contents of oxides, wt %										
	Zr + Hf*	Si	Na	Ca	Sr	Fe^{3+}	Fe^{2+}	Mn	Ti	Nb	Ln
EC-1	10.5–12.5	51.4	13.8	5.8	1.6	3.7	0.9	2.0	1.1	0.68	2.4
EC-2	9.8–12.2	45.7	12.8	5.1	1.7	3.8	0.9	2.0	1.9	0.5	1.8

* For other components, average values are given.

to the amount of the decomposed mineral. The content of the components in the concentrates and insoluble residues were determined by X-ray fluorescence analysis, and that in solutions, by the atomic-absorption method.

The data obtained in the experiments on decomposition are presented in Figs. 1 and 2. The specific decomposition rate W (g g^{-1} h^{-1}) and mass loss Δm (%) were found using the formulas

$$W = (m_n - m_{n+1})/\tau m_n,$$

$$\Delta m = (m_0 - m_n)/m_0.$$

Here m_0, m_n, and m_{n+1} are, respectively, the masses of the initial and current samples during decomposition (g), and τ is the time of decomposition (h).

The specific rate of zirconium(IV) transfer into solution is given, also as a function of mass loss, in

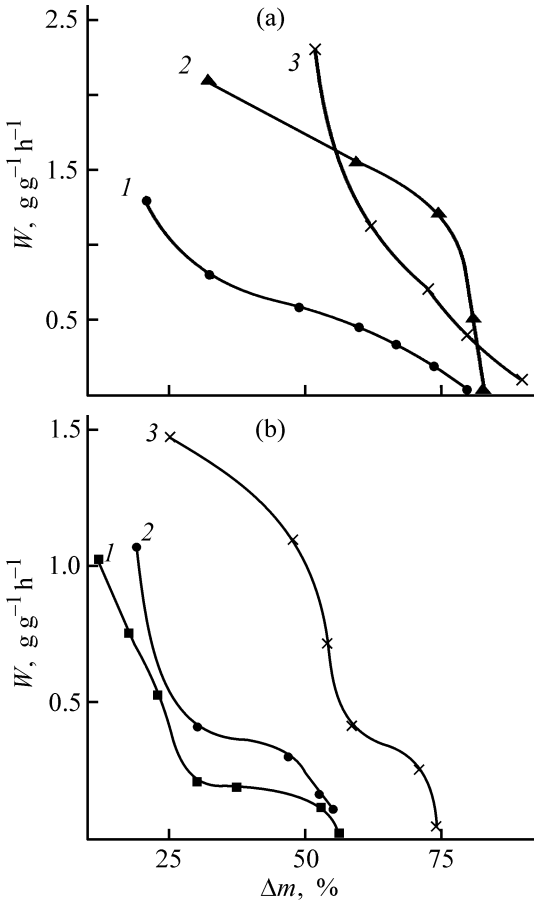

Fig. 1. Specific rate W of (a) EC-1 and (b) EC-2 decomposition with acids vs. the degree of decomposition. Fraction +0.063–0.16 mm. (Δm) Mass loss; the same for Figs. 2 and 3. Acid: (*1*) HNO_3, (*2*) H_2SO_4, (*3*) HCl.

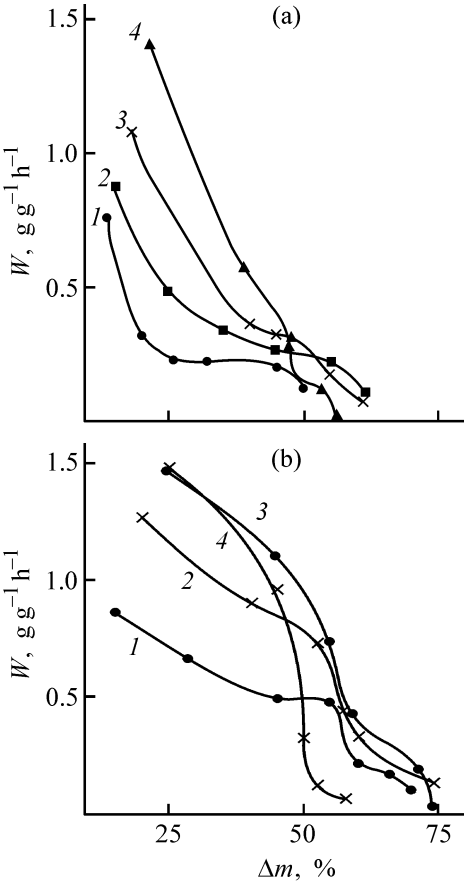

Fig. 2. Specific rate W of EC-2 decomposition with (a) HCl and (b) H_2SO_4 vs. the grain size and degree of decomposition. Fraction size (mm): (*1*) >0.315, (*2*) 0.2–0.16, (*3*) 0.06–0.16, (*4*) <0.06.

Table 2. Characteristics of EC-2 decomposition in 2 N solution of sulfuric acid

Stage	V, ml	τ, min	m_n, g	δm, g	W, g g^{-1} h^{-1}	Δm, %	ZrO_2		$W^{EC-2}_{ZrO_2}$, g ZrO_2 g^{-1} h^{-1}	$W^{EC-1}_{ZrO_2}$, g ZrO_2 g^{-1} h^{-1}
							g l^{-1}	g		
0	140	10	25							
1	110	15	19.7	4.3	1.03	21.2	5.3	0.74	0.18	–
2	83	20	15.0	4.7	0.95	40	8.0	0.88	0.18	0.2
3	63	30	11.4	3.6	0.72	54.4	7.2	0.6	0.12	0.14
4	48	30	8.8	2.6	0.46	65	7.1	0.45	0.08	0.1
5	40	60	7.4	1.4	0.32	70.4	4.0	0.19	0.04	0.05
6	35	60	6.5	0.9	0.12	74	4.0	0.16	0.02	0.03
7			6.1	0.4	0.06	76	1.6	0.056	0.008	0.01

Table 3. Content of components in insoluble residues from decomposition with sulfuric acid

Residue of EC	Content of oxides, wt %					Mass ratio of oxides		Residue of EC	Content of oxides, wt %					Mass ratio of oxides	
	Zr	Si	Nb	Ti	Fe	Nb/Zr	Ti/Zr		Zr	Si	Nb	Ti	Fe	Nb/Zr	Ti/Zr
EC-1	6.9	52.5	1.2	0.69	2.6	0.17	0.1	EC-2	8.3	54.2	1.2	4.5	4.6	0.18	0.54

Fig. 3. An example of how the mass loss rate and the rate of zirconium(IV) transfer into solution in an experiment on decomposition of the EC-2 fraction –0.3 + 0.2 mm with sulfuric acid are calculated is given in Table 2.

Since we studied concentrates, rather than a monomineral fraction, a correction for ballast impurities was made when determining zirconium in the insoluble residue (Fig. 3). It follows from Table 2 that the mass of the insoluble residue was 6.1 g, and the ZrO_2 content, 8.1 wt %. Consequently, the content of insoluble impurities is 32.5 wt % (on assumption that eudialyte contains 12 wt % ZrO_2) or 2 g per 25 g of a portion being decomposed. As follows from the run of the curves, the error associated with ballast impurities is small. Thus, the following conclusions can be made on the basis of the kinetic characteristics.

(1) The decomposition rate decreases in the course of decomposition with acids irrespective of the grain size, which confirms the heterogeneity of the eudialyte structure.

(2) For both the concentrates and all the fractions, decomposition occurs the most readily in the experimental conditions under the action of sulfuric acid, with the decomposition rate of EC-1 being higher in the case of hydrochloric acid only in the initial stage. The decomposition parameters are the worst in the case of nitric acid. The concentrate from the Alluaiv deposit is more stable against acids, probably because of an increased content of titanium(IV), presumably strengthening the crystal lattice, in the concentrate. Hydrochloric acid and, the more so, nitric acid show poorer performance in decomposition of a concentrate with increased titanium(IV) content, since compounds with titanium are less characteristic of these acids.

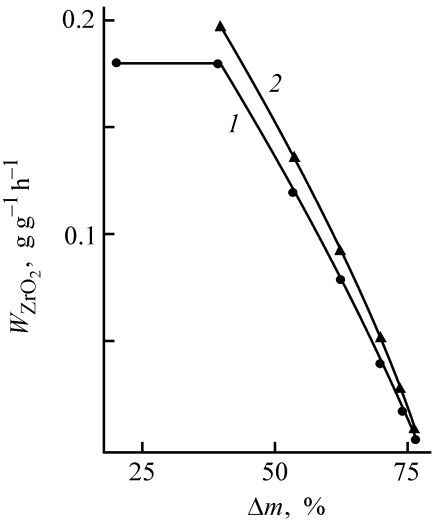

Fig. 3. Specific rate of zirconium(IV) transfer into solution W_{ZrO_2} from (*1*) EC-2 and (*2*) eudialyte vs. the degree of decomposition.

Table 4. Composition of solutions obtained by EC decomposition

Acid, EC, batch	Content of oxides, g l^{-1}								
	Zr	Na	Ca	Mn	Fe	Ln	Si	Ti	Nb
H_2SO_4:									
EC-1, 2nd	5.9	7.1	2.95	0.8	0.77		17.6	0.27	0.31
		1.2*	0.5	0.14	0.14		3.1	0.048	0.054
EC-1, 6th	2.4	2.1	1.4	0.3	0.25		4.9	0.064	0.14
		0.87	0.58	0.12	0.1		2.0	0.027	0.058
EC-2, 2nd	7.0	5.6	2.1		0.85	1.2	24	0.275	0.24
		0.8	0.3		0.12	0.16	3.4	0.04	0.03
EC-2, 7th	1.0	0.85	0.32		0.26	1.3	2.8	1.1	0.025
		0.85	0.32		0.26	0.18	2.8	1.1	0.025
EC-2, 8th**	7.0	3.9	0.37		0.9	0.27		1.1	0.124
		0.56	0.05		0.13	0.04		0.15	0.018
HCl:									
EC-2, 2nd	2.65	2.25	0.9		0.43	0.48	9.35	0.11	0.09
		0.85	0.34		0.16	0.18	3.5	0.04	0.03
EC-2, 7th	1.05	0.85	0.36		0.16	0.21	3.15	0.05	0.025
		0.8	0.34		0.15	0.2	3.0	0.05	0.02

* Ratio of the content of an oxide to that of ZrO_2. ** Treatment at 90°C.

The irregularity of the mineral structure is confirmed by the composition of insoluble residues. The mass ratio of niobium and titanium oxides to ZrO_2 in the insoluble residues from EC decomposition with hydrochloric acid is 2–3 times that in the initial concentrate (Table 3). In spite of a prolonged treatment with acids, the insoluble residues retain the eudialyte structure. Their complete decomposition with sulfuric acid at 40°C only occurs at a concentration of 4 M; at 80°C the process is more intense, but is complete at a concentration of 3 M (Fig. 4). Therefore, the residues should be decomposed separately under more rigorous conditions, probably with introduction of fluoride ions into the reaction system. The processing technology of such concentrates must involve double decomposition: first, the secondary precipitate is treated under rigorous conditions with a concentrated acid, and then this solution is used to decompose the readily soluble part of eudialyte.

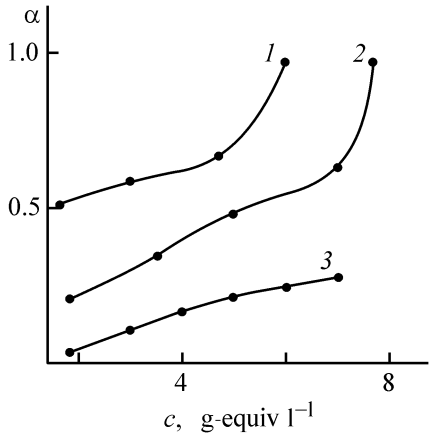

Fig. 4. Degree $\alpha = c/c_0$ of decomposition of insoluble residue vs. acidity of medium and temperature. c and c_0 are current and initial concentrations of acid. Acid: (*1, 2*) H_2SO_4, (*3*) HCl. Temperature (°C): (*1*) 80, (*2*) and (*3*) 40.

The irregularity of structure is also confirmed by the composition of the leaching solution. The contents of components in the second and the last portions of leaching solutions are listed in Table 4 (the first portion was not analyzed because of the primarily dissolving nepheline). With the decomposition of the concentrate, the ratio of the main (by mass) eudialyte components (silicon and sodium) to zirconium in solutions decreases; however, sodium is presumably leached first, with silicon retained in the eudialyte structure to a greater extent. Titanium is leached from EC-2 with hydrochloric acid in minor amounts under the experimental conditions, which is also confirmed by its increasing concentration in the insoluble residue. The leaching of titanium and niobium with sulfuric acid varies between batches. Presumably, part of these elements can strengthen the structure of the mineral, and part, be sorbed on a zeolite. The other components are leached to almost the same extent as zirconium.

Table 5. Distribution of elements in decomposition of rare-metal concentrates

Product	Decomposition technique	Degree of decomposition, %	Content of oxides, wt %					Ta/Ti(Zr) mass ratio
			Ti	Nb	Ta	Ca	Zr	
Loparite	HNO_3 + HF	80	39.6	8.8	0.62	4.5	–	0.016
Residue			38.6	8.7	0.77	4.4		0.02
Loparite	H_2SO_4 + $(NH_4)_2SO_4$	95.2	39.6	8.8	0.62	4.5		0.016
Residue			37.9	8.9	0.91	4.5		0.024
Perovskite	HCl + HF	90	48.3	1.0	0.03	31.1		0.0006
Residue			43.4	0.86	0.04	25.3		0.0009
Sphene	H_2SO_4	83	29.2	0.29	–	31.1		
Residue			31.8	0.28	–	25.3		
Baddeleyite	H_2SO_4	87	0.12	0.54	0.3		98.9	0.003
Residue			0.14	1.8	0.51		96.7	0.005
Weighed residue			0.16	2.53	0.69		84.2	0.008
Baddeleyite	CaO + $CaCl_2$	95	0.12	0.54	0.3		98.9	0.003
Residue			0.1	0.36	0.23		97.3	0.002

When other rare-metal concentrates (loparite, perovskite, sphene, and baddeleyite) are treated with acids, 5–20% of the concentrate occasionally remains undecomposed in spite of the rigorous conditions of the process. This is the most pronounced in the case of loparite, whose sulfuric acid processing resulted in extraction of the most valuable product tantalum by no more than 90%. This was attributed to hydrolysis of tantalum or its binding into phosphates. We assumed the same irregularity of the concentrate composition and checked whether the composition of insoluble deposits coincides with that of the initial concentrate. Undecomposed deposits were analyzed after separation of hydrolyzed forms by decantation and treatment of the insoluble residue with a mixture of hydrofluoric and sulfuric acids.

It was found (Table 5) that, in most cases, the content of tantalum in the insoluble residue is increased, which seems to strengthen the crystal lattice of the mineral. The only exceptions are sphene and baddeleyite residue from sintering. Stronger structural units seem to be present in sphene [8], and in the case of baddeleyite, the pretreatment and quality of stock are more important, since the decomposition conditions are rather rigorous.

CONCLUSIONS

(1) It was found by analyzing kinetic characteristics of acid decomposition of eudialyte concentrates that the structure of eudialyte crystals is irregular, and the presence of niobium and titanium in it is a probable reason for the low degree of decomposition. This also accounts for the lower degree of decomposition with nitric and hydrochloric acids, compared with sulfuric acid. The eudialyte concentrate from the Alluaiv deposit, containing 1.9 wt % TiO_2 is decomposed with hydrochloric acid to an extent of 65–70% under the chosen conditions, whereas the concentrate containing 1.1 wt % TiO_2 (with loparite accounting for about 50% of this amount) is decomposed by 95–97%. In all probability, the increase in the efficiency of eudialyte decomposition upon introduction of fluoride ions is to greater extent due to lattice destruction via binding of such strong acceptors of fluoride ions as titanium(IV), niobium(V), and tantalum(V).

(2) An analysis of residues formed in decomposition of other rare-metal concentrates, such as loparite, perovskite, and baddeleyite, demonstrated that the fraction of tantalum in relation to the main substance is increased. To improve the efficiency of processing of such concentrates, it is necessary to create a separate line for treatment of insoluble residues.

REFERENCES

1. Zakharov, V.I., Masloboev, V.A., Ponomarev, N.L., *et al., Khimicheskaya tekhnologiya redkikh elementov i mineral'nogo syr'ya* (Chemical Technology of Rare Elements and Mineral Raw Materials), Apatity: Kol'sk. Nauchn. Tsentr Ross. Akad. Nauk, 1986, pp. 8–12.
2. Zakharov, V.I., Kislykh, V.V., Masloboev, V.A., *et al., Khimicheskaya tekhnologiya redkikh elementov i mi-*

neral'nogo syr'ya (Chemical Technology of Rare Elements and Mineral Raw Materials), Apatity: Kol'sk. Nauchn. Tsentr Ross. Akad. Nauk, 1986, pp. 5–7.

3. Chekmarev, A.M., Chizhevskaya, S.V., Ponomarev, N.L., *et al., Khimiya i tekhnologiya redkikh metallov: Sbornik nauchnykh trudov MKhTI im. D.I. Mendeleeva* (Chemistry and Technology of Rare Metals: Coll. of Sci. Works of Mendeleev Chemical-Engineering Institute, Moscow), Moscow, issue 143, pp. 3–7.
4. Tishchenko, V.E. and Sidorkina, A.P., *Zh. Prikl. Khim.*, 1935, vol. 8, no. 7, pp. 1117–1125.
5. Zakharov, V.I., Kislykh, V.V., Masloboev, V.A., *et al., Khimiya i metallurgiya redkikh i tsvetnykh metallov* (Chemistry and Metallurgy of Rare and Nonferrous Metals), Apatity: Kol'sk. Nauchn. Tsentr Ross. Akad. Nauk, pp. 58–62.
6. Dibrov, I.A., Chirkst, D.E., and Litvinova, T.E., *Tsvet. Met.*, 2002, no. 12, pp. 38–43.
7. Yashnikova, O.M., Kolenkova, M.A., Sazhina, V.A., and Romantseva, T.I., *Izv. Vyssh. Uchebn. Zaved., Tsvet. Met.*, 1982, no. 1, pp. 118–120.
8. Motov, D.L. and Maksimova, G.K., *Sfen i ego khimicheskaya pererabotka* (Sphene and Its Chemical Processing), Moscow: Nauka, 1983.

Russian Journal of Applied Chemistry, Vol. 76, No. 8, 2003, pp. 1197–1200. Translated from Zhurnal Prikladnoi Khimii, Vol. 76, No. 8, 2003, pp. 1238–1240.

INORGANIC SYNTHESIS AND INDUSTRIAL INORGANIC CHEMISTRY

Fabrication of Low-Dimension CdSe Structures by Atomic Layer Epitaxy

D. P. Mikhaevich and Yu. K. Ezhovskii

St. Petersburg State Technological Institute, St. Petersburg, Russia

Received November 25, 2002; in final form, June 2003

Abstract—Formation of thin cadmium selenide films on semiconductor and dielectric matrixes of (100) and (111) orientation from atomic-molecular beams was considered. Temperature ranges in which thin CdSe films are formed were determined. Conditions for layer-by-layer growth of nanostructures were established.

The development of new synthesis techniques and study of the formation of thin layers are among first-priority problems in the development of controlled synthesis of surface nanostructures. It is of importance, for theoretical and applied purposes, to have an opportunity to predict the results of a synthesis and the structural perfection of layers being formed.

Recently, the atomic-layer epitaxy (ALE) [1, 2], which makes it possible to obtain high-quality submicrometer dielectric layers, has attracted special interest abroad. This technique, which in better known in Russia as the method of chemical assembling, is based on macromolecular concepts of solids [3]. The method enables synthesis of thin film structures and nanostructures, in particular, by chemical reactions of surface functional groups of a matrix with gaseous reagents, to give surface chemical compounds.

Monomolecular or thicker layers of a compound to be synthesized can be grown by a series of successive chemical reactions on the matrix surface. To perform chemical assembling, it is necessary that the substrate temperature T_s should satisfy the relationship: $T_A, T_B < T_s < T_{AB}$, where T_A, T_B, and T_{AB} are, respectively, the critical condensation temperatures of components A, B, and compound AB.

It is necessary to note that such a layer can be grown without formation of three-dimensional nuclei, which allows synthesis of rather thin (<10 nm) solid films. Performing the process under nonequilibrium conditions, which can be easily attained by using a significant excess of a reagent and rapidly removing gaseous reaction products, yields a stable structure. The reaction of polycondensation and addition from atomic-molecular beams (molecular layering and atomic layer epitaxy, respectively) can be used as surface reactions [4]. In the latter case atomic or molecular beams of components in a vacuum are used. The most suitable for this purpose are $A^{II}B^{VI}$ compounds, owing to the sufficiently high vapor pressure at elevated temperatures and low critical condensation temperatures of their components [5]. Among compounds of this kind, cadmium selenide, which exhibits high photoconductivity and the shortest photoresponse time, is of special interest. Ultrathin CdSe films (nanostructures) are also of interest for fabrication of various optoelectronic systems.

EXPERIMENTAL

Low-dimension structures were fabricated by successive exposures of a substrate to molecular beams of cadmium and selenium, obtained by evaporation of the respective substances from Knudsen cells in an oil-free vacuum at a residual pressure of 5×10^{-3} Pa. Single-crystal (100) GaAs wafers of AGChT-23-17 brand, glass, and (0001) mica were used as substrates. The exposure duration was varied for each reagent within the range of 0.5–6 s. The calculated component fluxes across the support plane were determined from evaporation temperatures [5] and geometric parameters of the evaporator–substrate system. At fluxes R of 5×10^{14}–5×10^{16} $cm^{-2}\ s^{-1}$ and exposure duration exceeding 0.5 s, the layer thickness was determined only by the number of cycles and substrate temperature. It is seen from Fig. 1 that the duration of exposure to component beams, required to ensure the maximal filling of the surface under fixed condi-

1070-4272/03/7608-1197 $25.00 © 2003 MAIK "Nauka/Interperiodica"

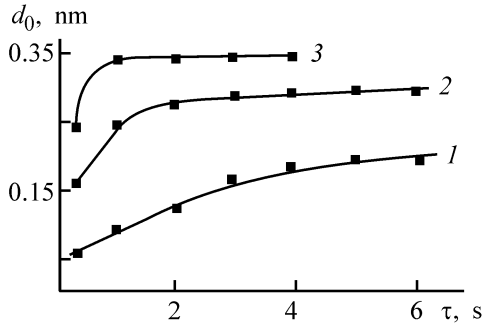

Fig. 1. Growth constant d_0 of CdSe films synthesized on (100) GaAs surface at 373 K vs. duration τ of exposure to components. R_{Cd}, R_{Se} (cm^{-2} s^{-1}): (*1*) 2.79×10^{14}, 1.38×10^{14}; (*2*) 9.3×10^{14}, 4.6×10^{14}; (*3*) 3.72×10^{15}, 1.84×10^{15}.

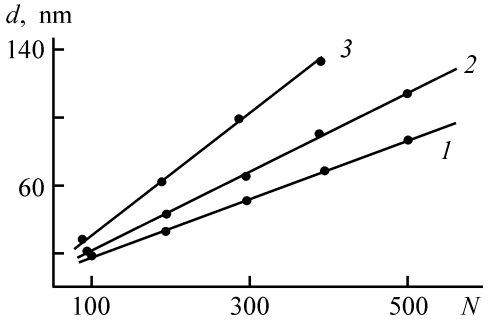

Fig. 2. Thickness of CdSe films d on mica surface vs. the number of exposure cycles N. $R_{Cd} = 9.3 \times 10^{14}$, $R_{Se} = 4.6 \times 10^{14}$ cm^{-2} s^{-1}; $\tau = 3$ s. T_s (K): (*1*) 458, (*2*) 423, and (*3*) 373.

tions of component evaporation ($R_{Cd} = 3.72 \times 10^{15}$ and $R_{Se} = 1.84 \times 10^{15}$ cm^{-2} s^{-1}) should be no less than 3 s. Therefore, the time of 3 s was chosen as exposure duration.

The thickness of the films synthesized was measured by the interference method and ellipsometry. Layer thicknesses less than 100 nm were determined from the results of ellipsometric measurements of the polarization parameters Δ and Ψ. These parameters, which characterize the surface properties, were recorded on a laser ellipsometer at a wavelength λ = 623.8 nm and light beam incidence angle θ = 68°30′. The thickness was computed in terms of the single-layer model by Drude's equation [6]. The measurement inaccuracy was no greater than 3%. Layer thicknesses exceeding 100 nm were measured by the interference method on an MII-4 interferometer.

An analysis of the experimental data on the kinetics of surface filling demonstrated that the curves covering both monomolecular and polymolecular sorption are well described by the equation

$$d_0 = d_{0(\max)}[1 - \exp(-\tau/t)] + \alpha t. \quad (1)$$

Here d_0 is a proportionality factor corresponding to the averaged layer thickness per exposure cycle; $d_{0(\max)}$, the maximum increase in layer thickness per exposure cycle; τ, the duration of contact with a reagent; t, the time constant of the process; α, a coefficient characterizing the contribution of the polymolecular adsorption, which is very close in its meaning to the condensation coefficient, $\alpha = f(R, T_s)$.

A comparison of the experimental data obtained with the calculated amount of a component, which is necessary for monomolecular filling of the surface of a given crystallographic orientation, demonstrated that the latter value is exceeded by more than a factor of 10. This points to the occurrence of a chemical reaction between the chalcogen and the metal by the Ridil–Ili mechanism. In this case, the surface reaction rate V depends on the surface filling θ and is given by the expression

$$V = k\theta R_+. \quad (2)$$

Here k is a dimensionality coefficient.

At nearly limiting filling ($\theta \to 1$), $V \to kR$, i.e., the rate of a reaction occurring under discrete exposure conditions depends only on fluxes of the substances being evaporated.

A study of the dynamics of layer growth demonstrated that, at fixed substrate temperature, the layer thickness increases in proportion to the number of cycles of exposure to molecular flows of the components. For all the substrates used, the dependences are linear (Fig. 2) and well described by the equation

$$d = d_0 N. \quad (3)$$

Here d is the film thickness, and N is the number of cycles of substrate exposure to component flows.

In atomic layer epitaxy, d_0 is named the growth parameter. It characterizes the structure of a growing layer and depends on the mechanism of its formation.

The linearity of the dependence $d = f(N)$ indicates that equal amounts of the surface compound are synthesized in each reaction cycle and, hence, the nanostructure grows uniformly. This allows control of the layer by only by the number of cycles of support surface exposure to component vapors.

Analysis of how the growth parameter depends on the substrate temperature, $d = f(T_s)$ (Fig. 3), gives

a notion of the layer formation mechanism. For example, three characteristic portions can be distinguished in Fig. 3 for all substrate types. In the low-temperature region, in which d_0 is large, the selenium vapor pressure is comparable with the cadmium vapor pressure, and the critical condensation temperatures of these substances at fixed flux are higher than the experimental temperatures, which results in the condensation of the metal and the chalcogen [7]. In this case, CdSe layers are formed through reaction between components within an adsorbed polymolecular layer. This is also indicated by values of the d_0 parameter, which significantly exceed interlayer spacings for various orientations of the crystal structure of this material. Such a film growth mechanism is accompanied by the formation of fragments of the crystalline phase of the compound, which gives polycrystalline layers [8].

At higher temperatures the value of d_0 is virtually constant, falling within the range $(0.29-0.33) \pm 0.01$ nm for the substrates under study. The calculated interlayer spacings for the sphalerite structure of CdSe are 0.303 and 0.349 nm for the (100) and (111) orientations, respectively. Comparison of the experimental d_0 values with the above-indicated calculated interlayer spacings suggests that the predominant orientation is (100) for GaAs and (111) for the glass substrate. These conclusions were confirmed by an electron-diffraction study of the structure of the layers being formed, with thickness exceeding 100 nm. It was shown that, with increasing temperature, a predominant orientation (texture) appeared in the films and transformed into a well-oriented structure. Thus, it may be assumed that the films grow by the layer mechanism with limiting, nearly monolayer filling of the surface in the indicated temperature range through chemisorption of each of the components.

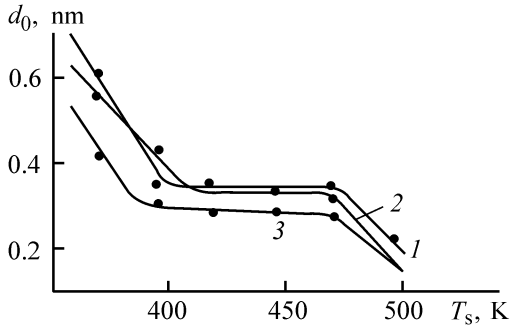

Fig. 3. CdSe film growth constant d_0 vs. substrate temperature T_s (K). Substrate material: (*1*) glass, (*2*) (100) GaAs, (*3*) mica.

With account taken of the significant degree of hydroxylation of the matrices indicated [7–9], the formation of a chalcogenide layer can be represented as the following surface reactions:

$$\begin{array}{l}=A-OH\\ \quad|\\ =A-OH\end{array} + Cd \rightarrow \begin{array}{l}=A-O-Cd\\ \quad|\\ =A-O-Cd\end{array} + 0.5Se \rightarrow \begin{array}{l}=A-O-Cd\\ \quad|\\ =A-O-Cd\end{array}\!\!\diagdown\!\!Se + 2Cd \rightarrow \begin{array}{l}=A-O-Cd\diagdown\\ \quad|\\ =A-O-Cd\diagup\end{array}\!\!Se\!\!\begin{array}{l}\diagup Cd\\ \diagdown Cd\end{array} \quad \text{etc.},$$

where A stands for surface atoms of GaAs and Si substrates.

It should be noted that, when chalcogenide structures are formed by alternating exposures of the matrix surfaces to metal and chalcogen vapors, the chemisorption of the metal on the surface hydroxy groups is predominant. The chemisorption of a chalcogen is of the dissociative nature and, as established for the case of growth of zinc sulfide nanostructures [10], is the rate-determining stage of the process.

A sharp decrease in d_0 values with increasing substrate temperature is due to partial surface filling, resulting from significant desorption of the compound components. In this case, the film growth in the initial stage may occur with the formation of two-dimensional nuclei on surface hydroxy clusters and their subsequent three-dimensional development to give a layer with critical thickness. Comparison of the calculated and experimental d_0 values allows evaluation of the degree of surface filling. It is about 0.7 for gallium arsenide at 523K, which corresponds to the degree of surface hydroxylation for this material [8]. Under these conditions, well-oriented structures were formed.

CONCLUSION

Analysis of the pattern of formation of cadmium selenide layers on the matrices under study suggests that, in all the cases, the layers grow by mechanisms successively replacing one another. These mechanisms are typical of all cyclic processes of chemical assembling. The component vapor pressure is a key factor in the low-temperature region, in which condensation processes predominate, and the degree of surface hydroxylation, at the high temperatures.

REFERENCES

1. Ming, X., *Solid State Technol.*, 2001, vol. 44, no 1, pp. 70–74.
2. Gelatos, J., *Solid State Technol.*, 2003, no 2, pp. 44–48.
3. Aleskovskii, V.B., *Stekhiometriya i sintez tverdykh soedinenii* (Stoichiometry and Synthesis of Solid Compounds), Leningrad: Nauka, 1976.
4. Suntola, T., *Materials Sci. Reports*, 1989, vol. 4, no. 7, pp. 261–312.
5. Shalimova, K.V., Voronkov, E.N., and Nikitina, N.S., *Elektron. Tekhnika, Ser. 14, Mat.*, 1970, issue. 2, pp. 31–37.
6. *Osnovy ellipsometrii* (Principles of Ellipsometry), Rzhanov, A.V., Ed., Novosibirsk.: Nauka, 1979.
7. Ezhovskii, Yu.K. and Murashev, S.V., *Zh. Prikl. Khim.*, 1987, vol. 60, no. 10, pp. 2361–2363.
8. Dmitruk, N.L., *Izv. Vyssh. Uchebn. Zaved., Fiz.*, 1980, no. 1, pp. 2103–2106.
9. Kiselev, V.F. and Krylov, O.V., *Adsorbtsionnye protsessy na poverkhnosti poluprovodnikov i dielektrikov* (Adsorption Processes on Semiconductor and Insulator Surfaces), Moscow: Nauka, 1978.
10. Ezhovskii, Yu.K., Klyuikov, A.I., and Pyatkovskaya, A.V., *Izv. Akad. Nauk, Ser. Neorg. Mater.*, 2001, vol. 37, no. 3, pp. 274–277.

Russian Journal of Applied Chemistry, Vol. 76, No. 8, 2003, pp. 1201–1204. Translated from Zhurnal Prikladnoi Khimii, Vol. 76, No. 8, 2003, pp. 1241–1244.

INORGANIC SYNTHESIS AND INDUSTRIAL INORGANIC CHEMISTRY

Optical Properties of Porous Glass Modified with Vanadium(V) Oxide

V. N. Pak and S. V. Sukhanov

Hertzen Russian State Pedagogical University, St. Petersburg, Russia

Received May 22, 2003

Abstract—Porous glasses modified with vanadium(V) oxide were obtained by impregnation with aqueous NH_4VO_3 solutions and by subsequent thermal decomposition of the salt. Changes in the charge-transfer spectra, resulting from an increase in the content of the deposited oxide and from water sorption, and also the possibility of using vanadium-containing glass for visual monitoring of air humidity were considered.

A wide variety of optical materials can be obtained from xerogels of silicic acid by introducing transition metal ions into these materials [1–6]. In particular, procedures for synthesizing transparent silica films including V(IV) and V(V) oxo anions have been studied [4–6]. Optical media of this kind can also be obtained on the basis of porous glasses (PG) modified with appropriate additives [7]. One of advantages gained in this case is the accessibility of components introduced into the porous space of the glasses to gases and vapors, and, consequently, the possibility of using modified PG as optical sensors. Also important is the problem of controlling the light absorption in the visual and UV regions by selecting a modifier and varying the size of particles introduced into open (through) pores of a glass. In this study, we analyzed the possibility of solving these problems for the example of PG modified with vanadium(V) oxide.

The porous glass used in this study was obtained by leaching a sodium-borosilicate glass of composition (mol %): $0.07Na_2O \cdot 0.23B_2O_3 \cdot 0.70SiO_2$, which was subjected to thermal pretreatment (3 days at 530°C with subsequent annealing for 3 h at 480°C) [8, 9]. The specific surface area of the PG (80 $m^2\ g^{-1}$) was determined from low-temperature adsorption of argon, and the pore volume (0.16 $cm^3\ g^{-1}$) and the predominant pore radius (4.5 nm), from the isotherm of water adsorption and parameters of the adsorption hysteresis loop [8–10]. Glass plates 1.0–1.2 mm thick were subjected to additional polishing; the resulting light transmission in the visual and near UV spectral ranges is shown in Fig. 1.

It should be noted that the possibility of obtaining transparent PG plates is limited not only by the range of small pore radii, but also by difficulties in ensuring optical homogeneity and, in particular, a constant refractive index across the plate thickness. Vanadium(V) oxide was deposited on the walls of through channels in PG by impregnating the glass with aqueous solutions of ammonium vanadate and by subsequent dehydration at 120°C and thermal decomposition of the

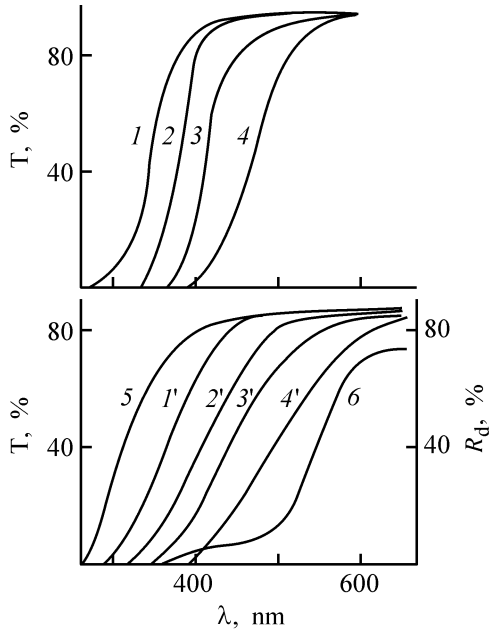

Fig. 1. Transmission spectra of (*1*–*4*) aqueous solutions of NH_4VO_3, (*1*'–*4*') PG plates impregnated with these solutions and dried at 120°C, (*5*) starting glass; (*6*) spectrum of diffuse reflection from polycrystalline V_2O_5. (T) Transmission, (R_d) the coefficient of diffuse reflection, and (λ) wavelength. NH_4VO_3 concentration (M): (*1*, *1*') 0.001, (*2*, *2*') 0.005, (*3*, *3*') 0.025, and (*4*, *4*') 0.05.

1070-4272/03/7608-1201 $25.00 © 2003 MAIK "Nauka/Interperiodica"

salt by calcination at 400°C. The transmission spectra of impregnation solutions and modified glasses were recorded on an SF-56 automated spectrometer. When studying the dependence of the spectra on the air humidity, we placed glass samples in desiccators over sulfuric acid solutions with concentrations providing a relative water vapor pressure $p/p_0 = 0.2–0.8$. The spectrum of polycrystalline vanadium oxide V_2O_5 was recorded on an SF-16 spectrometer with a spherical photometer, relative to MgO as optical reference.

The transmission spectra of aqueous solutions of NH_4VO_3 (Fig. 1), obtained in quartz cuvettes with optical thickness $l = 1$ cm, are uniformly shifted to longer wavelengths with the concentration increasing from 0.001 to 0.05 M. It appears impossible to determine the peak positions of the bands observed (even with l decreased to 1 mm), since the extinction coefficients in the charge-transfer spectra of anionic oxo vanadium species in solutions are on the order of $\varepsilon_{max} \approx 10^4$ [11].

The observed shift of the bands has been rather reliably interpreted qualitatively [11, 12] as resulting from stepwise association of the VO_4^{3-}, HVO_4^{2-}, and VO_3^- monomers into polynuclear vanadate anions under the action of increasing concentration and changing pH of solution. However, attempts to establish particular anionic species and their proportions meet substantial difficulties even under strong dilution conditions [11, 12]. The "concentration" sequence of the solution spectra (Fig. 1, curves *1–3*) is also reproduced in the case of PG plates impregnated with the solutions and dried to constant weight at 120°C. In this case, however, a noticeable long-wavelength shift of band edges is observed, which results in that modified glasses turn weak to intense yellow.

To a first approximation, it would be expected that thermal decomposition of ammonium vanadate on the silica surface of the glass in air must yield small-size particles of the higher oxide V_2O_5. Experiments with powdered polycrystalline NH_4VO_3 showed that the thermolysis of the salt is complete only at temperatures close to 400°C. The spectrum of the thus obtained orange-red V_2O_5, recorded in reflected diffusely scattered light, is shown in Fig. 1.

In this context, it is rather significant that the spectra of modified glasses treated in the range 120–400°C remain almost unchanged. This suggests that the decomposition of small salt particles on the silica surface is complete even at the temperature of glass dehydration and yields small-size vanadium oxide particles having the form of clusters with individual features of their electronic structure. These features differ from those of bulk V_2O_5 and are to some extent "inherited" from their precursors, anions in the impregnating solutions.

The recorded charge transfer spectra are formed as a result of electron excitation from nonbonding (pseudoatomic) $2p$ orbitals of oxygen to vacant $3d$ orbitals of vanadium(V). With a certain probability, their red shift is determined by the build-up of negative effective charge on oxygen with increasing size of vanadium oxide clusters. Indeed, in this case, the donor $2p$ orbitals of oxygen must be destabilized and the splitting of acceptor $3d$ states of vanadium(V) must increase, which results, in the end, in a decrease in the energy of $2p^n(O) \rightarrow 3d(V)$ transitions.

The content of vanadium(V) oxide in the glass is too small for reliable quantitative determination and can only be estimated using the glass porosity. The amount of NH_4VO_3 in PG, provided by impregnation, is found in this case as $Q = c\varepsilon\gamma$, where c is the solution concentration; ε, the volume of glass pores; γ, the coefficient characterizing the filling of the pore space, which usually does not exceed 0.9 [9, 13]. Therefore, to the concentrations of the impregnating solutions used (0.001, 0.005, 0.025, and 0.05 M) correspond the estimated $VO_{2.5}$ contents in the glass, equal to 0.14, 0.70, 3.5, and 7.0 μmol g^{-1}, respectively. With account of the well-developed PG surface (80 $m^2 g^{-1}$), it follows that its filling with small-size particles of vanadium(V) oxide is vanishingly small. For example, for a set of modified glasses, the free "landing area" per vanadium atom is $20–10^3$ nm^2.

Let us consider spectral consequences of water adsorption by modified PG (Fig. 2). Samples containing 0.14, 0.70, and 3.5 μmol g^{-1} of vanadium(V) oxide are similar in their behavior, which shows itself in a uniform shift of bands and visually observed intensification of the yellow coloration of the plates in transmitted light with increasing humidity. The changes in the electronic spectra definitely point to the coordination (ligand) character of water sorption by vanadium oxide clusters. Strong hindrance to desorption serves as additional evidence in favor of the coordination mechanism. For example, pure PG looses adsorbed water completely after 2 h of heating at 120°C, whereas the dehydration of modified glasses, which sorbed water at $p/p_0 = 0.8$, requires heating for the same period at a temperature not lower than 250°C. Only in this case, it becomes possible to restore the initial spectrum corresponding to the dehydrated state. The observed spectral shifts, accompanying water sorption, are, therefore, due to an in-

crease in the coordination number of a part of vanadium(V) atoms in oxide clusters. This results in that the splitting of 3*d* states increases to form lower states, to which electrons from oxygen are transferred.

The twofold increase in the content of vanadium oxide, from 3.5 to 7.0 μmol g^{-1}, results in a sharp change in the properties of modified glasses. Exposure of a sample to a humid atmosphere results in this case not only in a substantial shift of the spectral band, but also in a sharp loss of transparency in the range 500–800 nm (Fig. 2). So serious consequences, determined by the coordination addition of water, may be related to partial reduction of vanadium(V) in the oxide clusters to vanadium(IV). A process of this kind has been observed earlier [14, 15] on the surface of vanadium containing silica gels obtained by the molecular deposition method. A substantial transfer of the electron density of an unshared electron pair of oxygen of water to vacant 3*d* orbitals of vanadium is the reason why the V(V) → V(IV) transition occurs. The stabilization of the V(IV) valence state is believed [14, 15] to be attained in this case through cation interactions leading to delocalization of $3d^1$ electrons. This is the reason for the absence of the EPR signal and "leveling-off" of the band associated with the *d*–*d* transition (λ_{max} = 750–760 nm) typical of V(IV) in a pseudo-octahedral oxygen environment [14, 15]. It is this factor that, in all probability, determines the possibility of mild reduction of vanadium oxide clusters in PG. The increase in the size of these clusters, achieved by raising the content of vanadium oxide in PG to 7.0 μmol g^{-1}, makes the reduction process thermodynamically possible. It is important in this case that the nature and magnitude of the absorption in the visible range are clearly controlled by humidity (Fig. 2).

At pressures p/p_0 = 0.2–0.6, a relatively uniform shift of the band and a decrease in transmission in the range 500–800 nm are observed (Fig. 2). A substantial decrease in transparency is achieved by raising the humidity to p/p_0 = 0.8, which ensures water condensation in pores with predominant radius of 4.5 nm. The observed spectral consequences of water sorption are completely reversible. As in the preceding cases, complete dehydration requires raising the temperature to 250°C. However, in this case, the time expended for restoration of the initial spectrum is almost twice that necessary for dehydration of glasses with lower content of vanadium oxide. The fact that, with increasing humidity, the color of modified PG containing 7.0 μmol g^{-1} of vanadium changes rather uniformly from bright yellow to brown, and further to dark brown and the possibility of multiple thermal regeneration of the glass open up certain prospects for its use as a visual indicator of humidity.

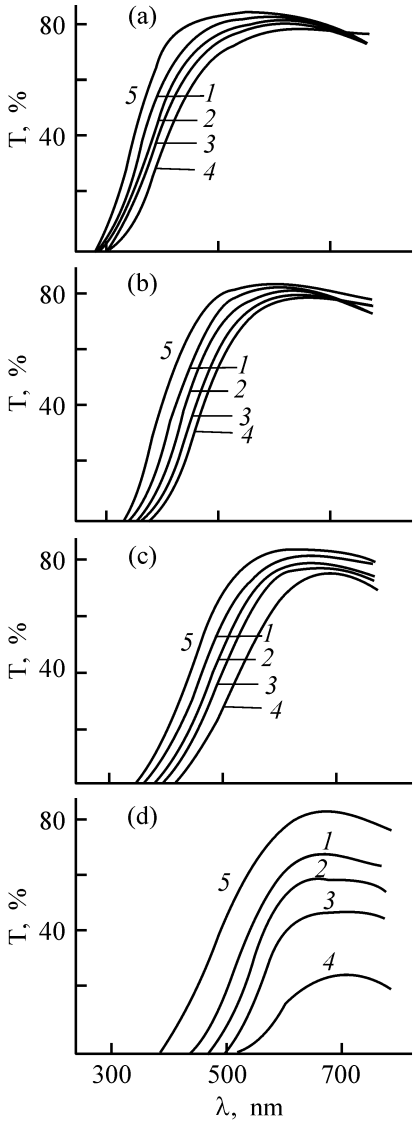

Fig. 2. Long-wavelength shift of bands and a decrease in the transparency of modified glasses with varied content of vanadium(V) oxide as a result of water vapor adsorption. (T) Transmission and (λ) wavelength. V_2O_5 content (μmol g^{-1}): (a) 0.14, (b) 0.70, (c) 3.5, and (d) 7.0. p/p_0: (*1*) 0.2, (*2*) 0.4, (*3*) 0.6, (*4*) 0.8; (*5*) spectra of dehydrated glasses.

ACKNOWLEDGMENTS

The authors are grateful to T.M. Burkat for the provision of porous glass samples.

REFERENCES

1. Roy, S. and Ganguli, D., *J. Non-Cryst. Solids*, 1997, vol. 212, no. 2, pp. 299–302.

2. Dutoit, D.C.M., Schneider, M., Fabrizioli, P., and Baiker, A., *Mater. Chem.*, 1997, vol. 7, no. 1, pp. 27–34.
3. Devi, P.S. and Ganguli, D., *J. Non-Cryst. Solids*, 1998, vol. 240, no. 1–3, pp. 50–54.
4. Hutter, F., Schmidt, H., and Scholze, H., *J. Non-Cryst. Solids*, 1986, vol. 82, no. 1–3, pp. 373–377.
5. Tran, K., Hanning-Lee, M.A., Biswas, A., *et al.*, *J. Am. Chem. Soc.*, 1995, vol. 117, no. 9, pp. 261–262.
6. Bogomolova, L.P., Yashkin, V.A., and Krasilnikova, N.A., *J. Non-Cryst. Solids*, 1998, vol. 241, no. 1, pp. 13–26.
7. Roskova, T.P. and Tsekhomskaya, T.S., *Fiz. Khim. Stekla*, 1981, vol. 7, no. 5, pp. 513–534.
8. Burkat, T.M. and Dobychin, D.P., *Fiz. Khim. Stekla*, 1992, vol. 19, no. 5, pp. 129–140.
9. Verezhinskaya, R.L., Burkat, T.M., and Pak, V.N., *Zh. Obshch. Khim.*, 2000, vol. 70, no. 3, pp. 403–407.
10. *Eksperimentalnye metody v adsorbtsii i khromatografii* (Experimental Methods in Adsorption and Chromatography), Nikitin, Yu.S., Ed., Moscow: Mos. Gos. Univ., 1990.
11. Shveikin, G.P., *Khimiya pyativalentnogo vanadiya v vodnykh rastvorakh* (Chemistry of Pentavalent Vanadium in Aqueous Solutions), Sverdlovsk: Akad. Nauk SSSR, 1971.
12. Goncharenko, A.S., *Elektrokhimiya vanadiya i ego soedinenii* (Electrochemistry of Vanadium and Its Compounds), Moscow: Metallurgiya, 1969.
13. Pak, V.N., Verezhinskaya, R.L., and Burkat, T.M., *Zh. Fiz. Khim.*, 2002, vol. 76, no. 7, pp. 1324–1327.
14. Pak, V.N., *Zh. Fiz. Khim.*, 1976, vol. 50, no. 6, pp. 1404–1407.
15. Pak, V.N., Boldyreva, A.M., Malygin, A.A., *et al.*, *Zh. Fiz. Khim.*, 1975, vol. 49, no. 2, pp. 517–3519.

Russian Journal of Applied Chemistry, Vol. 76, No. 8, 2003, pp. 1205–1210. Translated from Zhurnal Prikladnoi Khimii, Vol. 76, No. 8, 2003, pp. 1245–1250.

INORGANIC SYNTHESIS AND INDUSTRIAL INORGANIC CHEMISTRY

Composite Layers as Means of Lowering the Intensity of Scale Deposition on Elements of Power Units of Ships

S. V. Gnedenkov, S. L. Sinebryukhov, A. N. Minaev, A. N. Kovryanov, D. V. Mashtalyar, and P. S. Gordienko

Institute of Chemistry, Far-Eastern Division, Russian Academy of Sciences, Vladivostok, Russia
Far-Eastern State Technical University, Vladivostok, Russia

Received April 17, 2003

Abstract—The influence exerted by composite layers formed by microarc oxidation with subsequent treatment with polymers (ultradispersed polytetrafluoroethylene and polytrifluorochloroethylene) on the intensity of salt deposition was studied.

Scaling is a problem common to widely diverse fields of technology, which deal with heating, cooling, and evaporation of water and brines. Formation of a deposit layer with low heat conductivity coefficient on heat-transfer surfaces makes lower the overall heat transfer coefficient. This, in turn, diminishes the thermal load. With seawater used as cooling agent and heat flux of 0.2–1 MW m^{-2}, a salt layer is deposited onto the surface of heat exchanger tubes. This layer markedly lowers the heat conductivity and, consequently, impairs the operation efficiency and makes shorter the service life of heat-exchange apparatus.

The main components of scale precipitating from seawater are calcium carbonate $CaCO_3$, magnesium hydroxide $Mg(OH)_2$, and calcium sulfate in the form of gypsum $CaSO_4 \cdot 2H_2O$, semihydrate $CaSO_4 \cdot 1/2H_2O$, and anhydrite $CaSO_4$. The chemical composition of salt deposits is largely determined by the temperature of a heat-exchange surface: mainly $CaCO_3$ is deposited at 60–70°C, $Mg(OH)_2$ at 70–100°C, and anhydrous $CaSO_4$ or its crystal hydrates at temperature exceeding 100°C.

Especially difficult to remove is scale composed of $CaSO_4$. $CaSO_4$ precipitates on heating surfaces at virtually any wall temperature. The solubility of $CaSO_4$ is strongly affected by seawater components. It increases in the presence of chloride ions, compared with that in distilled water, and evaporation of water in the evaporator makes higher the concentration of Ca^{2+} and SO_4^{2-} ions, i.e., leads to an increase in the probability of formation of sulfate deposits.

Despite the pronounced scientific interest in this problem [1–5], no sufficiently effective method for protecting heat exchanger apparatus from salt deposition has been developed so far. The chemical composition of salt deposits is largely determined by the tube surface temperature. In the opinion of the author of [4], service and design measures play only an auxiliary role an cannot eliminate scale deposition completely. However, the state of the surface (chemical composition, roughness, electrical and semiconducting properties) may strongly affect the intensity of salt deposition. Since the surface layers obtained on metals and alloys by microarc oxidation (MAO) in aqueous electrolyte solutions markedly modify the state of the surface [6–14], there is good reason to believe that the effect of MAO layers on the rate of salt deposition will be discovered.

As is known, phosphates are used to diminish the permanent and temporary hardness of water with the aim of making lower the amount of scale. This leads to formation of poorly soluble compounds, which precipitate and take no part in scale formation. MAO layers obtained in phosphate electrolytes contain 4 to 10 wt % phosphorus. According to X-ray photoelectron spectroscopy [9], the state of phosphorus in coatings formed in a phosphate electrolyte is close to that in PO_4^{3-}. In seawater, phosphate ions pass into solution, which lowers the hardness of water in the near surface layer and may affect the intensity of scale formation. The above process occurs at a low rate, which may ensure a prolonged protection.

1070-4272/03/7608-1205 $25.00 © 2003 MAIK "Nauka/Interperiodica"

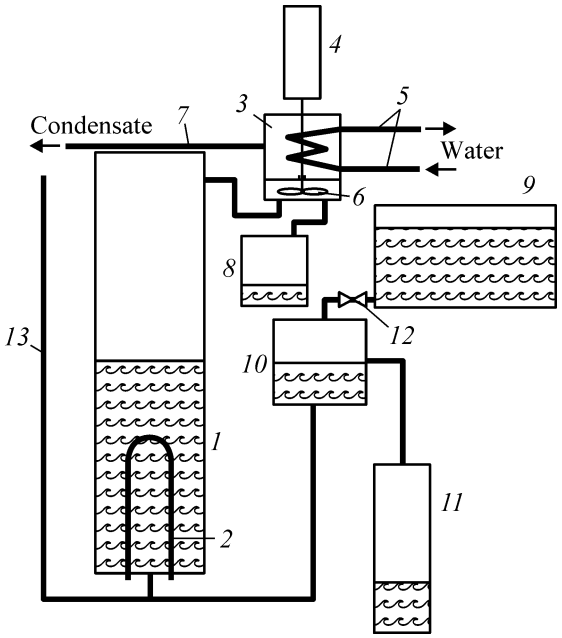

Fig. 1. Schematic of the evaporator installation.

As shown in [10, 12], the charge carrier concentration in a film may strongly affect the process of salt sorption, which is the initial and, occasionally, the key stage of salt deposition. At the same time, there is no published evidence (with the exception of several papers published by the authors of the present study) that MAO coatings affect scale formation.

In particular, the influence exerted by MAO and composite layers (fabricated on the basis of MAO coating with subsequent deposition of polytetrafluoroethylene, PTFE) on heat-exchange surfaces on the intensity of scale formation both in the case of electric heating and on a real heat-exchange installation. According to the results obtained, MAO coatings have virtually no effect on the heat conductivity of walls of a tube in a heat-exchange apparatus, but diminish substantially the rate of salt deposition onto its surface. The best protective properties are exhibited by an MAO layer treated with PTFE. After 96 h of operation of the installation, the scale layer on such a coating is 2 times thinner than that on the unprotected material, and the heat flux increases by 16% over the level for untreated titanium. The protective properties of MAO layers untreated with a polymer are weaker, but the scale layer on such coatings is more friable, compared with that on unoxidized tubes, and can be easily removed by the flow of a cooling agent [12]. In the authors' opinion, the method of combined protection (MAO + PTFE) is practically promising and requires further development.

EXPERIMENTAL

In this study, the antiscale properties of MOA coatings were tested on an evaporator installation intended for desalination of seawater.[1] The electric heater of the installation is subject to scale formation on its surface and, consequently, requires an appropriate protection.

During the experiment, natural seawater was taken from Amur Bay (Sea of Japan). The salinity of the water was approximately 30‰.

The evaporator installation is shown schematically in Fig. 1. In a steam generator *1*, seawater is heated to the boiling point by an electric heater *2* (ac feed voltage 220 V) mounted on the removable part of the heat generator's casing. Steam is fed into the bottom part of the foam disintegrator constituted by a casing *3* and motor *4*. In the upper cavity of the disintegrator casing, there is a coil *5* serving for steam condensation. In the lower cavity, there is an impeller *6* serving to separate the steam and liquid (foam). Steam arrives from the lower cavity, through the annular clearance between the impeller shaft and the partition edge, into the upper cavity of the disintegrator, and condenses there on the coil. The calculated velocity of steam upflow in a steam generator of the given design does not exceed 0.1 m s^{-1}, which corresponds to carry-over of drops less than 0.2×10^{-3} mm in diameter. This evaporation mode ensures a sufficient degree of purification. The distillate is collected in the pan and delivered therefrom through a pipe *7* into a collector vessel for the distillate. Coming in contact with the rotating impeller, the moisture and sludge contained in the steam are thrown by the centrifugal force to the walls and then flow down into a depression on the bottom, and then arrive through a tube with a siphon trap into the collecting tank *8*. Cooling tap water is fed through tubes *5* into the coil of the foam disintegrator and is then discharged into the drain.

Seawater is delivered from a tank *9* into the feeding-compensating tank *10* and arrives therefrom into the steam generator. The excess amount of water is discharged into the collecting tank *11*. The water level in the steam generator is maintained by means of its free supply from the tank *10* by the principle of communicating vessels. A fine-adjustment valve *12* is introduced into the feeding line between the tank for seawater and the feeding-compensating tank in

[1] Manufactured by Kaluzhskii turbinnyi zavod Open Joint-Stock Company.

order to minimize the discharge of excess seawater into the tank *11*. As seawater is consumed, its fresh portions are introduced into the tank *9* from an additional vessel.

All the basic members of the steam generator, foam disintegrator, compensating-feeding tank, and electric heater, which come in contact with one another and also with steam and water, are made of titanium alloys. This precludes corrosion processes and, consequently, ensures that no foreign substances capable of changing the scale formation pattern are produced and come into the heating zone. A glass tube serves as level indicator *13*. All elements of the installation are assembled on a stand made of construction steel.

The tests were carried out using an electric heater with rated power of 5.5 kW ($R \approx 8.7 \pm 0.1$ ohm) and varied state of the working surface: with natural oxide layer (without surface treatment), sample no. 1; with MAO coating formed in a phosphate electrolyte, no. 2; with MAO coating formed in a phosphate electrolyte and treated with finely dispersed PTFE with subsequent heat treatment, sample no. 3; with MAO coating formed in a phosphate electrolyte and treated with finely dispersed polytrifluorochloroethylene (PTFCE), no. 4. A PTFCE powder was dissolved in mesitylene at its boiling point (~165°C) in amount of about 260 g l^{-1}. Then the resulting solution was deposited onto the electric heater in two layers with a brush, with subsequent drying in air at room temperature for 24 h. This yielded a solid transparent polymeric coating of thickness not exceeding 20 μm. As a result of thermal treatment of a MOA layer with deposited PTFCE, a thin polymeric film was formed on the surface. This film raised the hydrophobicity of the coating and diminished its roughness. The preparation procedures and the quality of the sample nos. 1–3 under study were in complete correspondence with those in the case of surface layers studied previously in [12].

According to an estimate made, the heat flux across the heat-exchange surfaces was 0.2 MW m^{-2}. The time of testing of an electric heater in the boiling mode, with boiled-out water replenished with "fresh" seawater, was 27 h. In testing a single electric heater, 220 l of seawater was consumed. The degree of evaporation was approximately 10. Electrical conductivity measurements with an OK 102/1 conductometer demonstrated that G of the initial seawater was 25×10^{-3} S cm^{-1}, whereas the electrical conductivity of the brine formed in the steam generator after the tests was $(130–145) \times 10^{-3}$ S cm^{-1}. The change in electrical conductivity by more than a factor of 10 can be attributed to transfer of a part of salts responsible for the value of G from the dissolved state into scale and sludge.

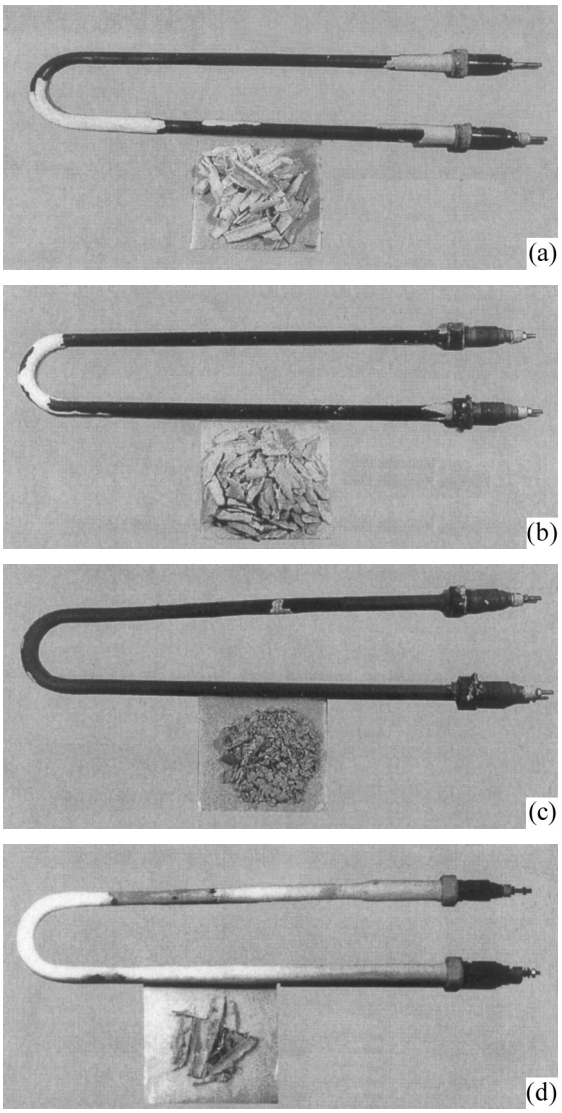

Fig. 2. Amount of scale formed on the surface of the electric heater in 27 h of operation of the evaporator installation. Total mass of scale (g): (a) 218, (b) 197, (c) 30, and (d) 171. Electric heater: (a) no. 1, (b) no. 2, (c) no. 3, and (d) no. 4.

On dismounting the electric heater after the tests, it was found that most part of scale (especially in the case of a sample with an MAO coating) fell off to the bottom of the removable part of the steam generator. The outward appearance of electric heater nos. 1–4 after tests for salt deposition is shown in Figs. 2a–2d. After drying the salt deposits (in air at 100°C for 1 h), the total mass and thickness of scale were measured and its phase composition was evaluated. Gravimetric measurements were done on an analytical balance with an error not exceeding 0.5%. The thickness was measured with a thickness gage. The sludge formed during the experiment and

Table 1. Scale formation on electric heaters with various types of protective layers on the surface (phase composition of sludge from the steam generator and disintegrator)

Electric heater no.	Scale mass		Scale layer thickness, mm	Phase composition
	total, g	specific, g cm^{-2}		
1	218	0.59	1.3–4.4	$CaSO_4$, $2CaSO_4 \cdot H_2O$
2	197	0.53	1.2–2.6	$CaSO_4$, $2CaSO_4 \cdot H_2O$, $CaCO_3^*$
3	30	0.08	0.2–1.4	$CaSO_4$, $2CaSO_4 \cdot H_2O$, $CaCO_3^*$
4	171	0.46	0.2–5	$CaSO_4$, $2CaSO_4 \cdot H_2O$, $Mg(OH)_2^*$, $CaCO_3^*$ (trace amounts)

* Component found only on the inner surface of the scale layer, adjacent to the surface of the electric heater.

present in the brine in the steam generator and in the boil-over from the foam disintegrator (sludge tank *8*) was also studied after filtering and drying. An X-ray phase analysis was performed on a DRON-2.0 diffractometer (Cu_{K_α} radiation). Fragments of scale were taken for study from the inner (adjacent to the electric heater) surface of the deposit and its outer surface. Also, scale was studied in the form of powder, which is a thickness-averaged sample. The measurement results are listed in Table 1 and shown in Fig. 2.

The experimental data obtained in this study confirm the conclusion [12] that MAO coatings affect the salt deposition process. The strongest protective effect is exhibited by an MAO layer treated with PTFE. The amount of scale formed on its surface is only 14% of that on an unprotected (with natural oxide layer) electric heater. An MAO coating untreated with PTFE lowers the rate of scale formation by approximately 10%.

The protective properties of layers obtained by the MAO method in phosphate electrolytes are due to several factors. On the one hand, the low concentration of charge carriers ($N_D = 9.8 \times 10^{17}$ cm^{-3}) in the coating material ensures its low sorption activity and, consequently, low concentration of crystallization centers. On the other hand, the egress of phosphate ions from an MAO coating into seawater, with the subsequent formation of poorly soluble salts removed as sludge from the heat-exchange zone, also leads to a decrease in the rate of salt deposition onto the coating surface.

According to the results of an X-ray fluorescence analysis, the in sludge collected in the steam generator after tests of electric heaters with MAO coatings contains trace amounts of phosphorus, which are absent in a similar sample taken after tests of an unprotected electric heater. A phase analysis confirmed the previously obtained data [4], which indicate that $CaSO_4$ is present in scale formed on the heating surface of desalting installations under virtually any temperature conditions. A minor amount of $CaCO_3$ in an aragonite crystal modification, which was found on the inner surface of the scale layer adjacent to the surface of electric heater treated by the MAO method, is, in all probability, a result of heat loss on MAO layers in the initial stage of scale formation. $Mg(OH)_2$, present in the sludge as a suspension, is actually not contained in scale at all.

Owing to its morphology, an MAO coating acts as a container retaining in its pores particles of finely dispersed PTFE, thereby creating the effect of an unwettable (hydrophobic) surface and making less pronounced its roughness. According to the experimental results obtained, this factor markedly diminishes the rate of scale formation (Table 1, Fig. 2c). Treatment of unoxidized titanium with PTFE is inefficient because of the poor adhesion of the polymer to the metal.

The mass of scale deposited onto the surface of an electric heater with an MAO layer treated with PTFCE is 171 g. This amount is smaller than that on an electric heater without a coating (m = 218 g), but much exceeds the mass of scale on an electric heater with an MAO coating obtained in a phosphate electrolyte and treated with ultradispersed PTFE (m = 30 g). The inner surface of the scale layer has dark coloration, which is probably due to destruction of PTFCE in the tests (as a result of scale formation the electric heater overheats, with fluoroplastic-3 melting and decomposing).

The experimental data obtained in this study, combined with the results of an analysis of physicochemical properties of PTFCE (Table 2), suggest that the protecting capacity of the given polymer is low when it is used as a component of a composite scale-protecting layer formed by the method described above.

The low melting (T_m) and decomposition (T_d) points of PTFCE, compared with PTFE (Table 2), are responsible for partial destruction of the polymer. This leads to carbonization of the inner surface of

Table 2. Basic physicochemical properties of PTFE and PTFCE [16–18]

Compound	M, thousand	ρ, g cm^{-3}	T_m	T_d	T_w^*
			°C		
PTFE $(-CF_2CF_2-)_n$	50–10 000	2.15–2.24	270–327	425	–260…260
PTFCE $(-CF_2CFCl-)_n$	50–200	2.09–2.16	210–215	320	–195…190

* Working temperature.

Table 3. Material balance of the evaporation process with respect to main elements

Component	m, g	V, l	Content									
			Ca		Mg		Na		K		Cl	
			g l^{-1}	g	g l^{-1}	g	g l^{-1}	g	g l^{-1}	g	g l^{-1}	g
Initial seawater	–	220	0.38	84	1.26	277	10	2200	0.4	88	17.3	3806
Brine from steam generator	–	23	0.7	16	10	230	66	1518	3.2	74	136.5	3140
Water from foam disintegrator	–	11	0.59	7	5	55	36	396	1.7	19	71.6	788
Distillate	–	180	–	–	–	–	–	–	–	–	–	–
Scale from electric heater	218	–	–	55	–	1	–	8	–	1	–	–
Δ^*		–6 (3)		–1 (1)		+8 (3)		–286 (13)		+5 (6)		+121 (3)

* Δ, the magnitude and sign ("–" deficiency, "+" excess) of unbalance (its magnitude in % is given in parentheses).

the polymer layer and its subsequent swelling, which results in a higher rate of scale formation.

To confirm the correctness of the study and to verify the conclusions concerning the effect of composite layers on the rate of scale formation, the content of the main scale-forming elements distributed in the liquid and solid phases and present in different parts of the evaporator installation was determined.

The material balance of the evaporation process for the main chemical elements (Ca, Mg, Na, K, Cl) contained in seawater was calculated for an uncoated electric heater. The content of an element in scale (on the surface of electric heater no. 2), in the distillate, in the brine from the steam generator *1*, and in the fraction from the foam disintegrator (sludge tank *8*) was determined. The content of Ca, Mg, Na, and K was determined by atomic-absorption analysis with a Nippon Jarrell Ash AA-780 atomic-absorption and flame-emission spectrophotometer. The results obtained in studying the distribution of the main elements contained in seawater among material flows are listed in Table 3.

The convergence of the material balance demonstrates the reliability results obtained by various methods, including X-ray phase analysis, according to which the main compound contained in scale is $CaSO_4$ and its semihydrate (Ca content of about 30%).

CONCLUSIONS

(1) Composite layers strongly affect the rate of salt deposition at tenfold evaporation of seawater and heat flux of 0.2 MW m^{-2}. With polytetrafluoroethylene contained in a protecting layer deposited onto the surface of titanium electric heaters preliminarily subjected to microarc oxidation, the rate of scale formation can be lowered by 86%.

(2) Polytetrafluoroethylene deposited onto a layer formed by microarc oxidation changes the surface

morphology (diminishes the surface roughness) and raises its hydrophobicity. Owing to its branched porous structure, the resulting coating acts as a sublayer improving the polymer adhesion to the substrate. At the same time, this layer itself exhibits scale-protecting properties owing to its specific semiconducting and electrochemical properties, which diminishes the rate of salt deposition by approximately 10%.

REFERENCES

1. McKenzie, C., *Mech. Inc. Eng.*, 1993, no. 6(5), pp. 134–137.
2. Weltz, R. and Hodel, A., *Chem. Process.*, 1992, no. 9(55), pp. 71–72.
3. Fitzgerald, J.H., *Werkst. und Korros.*, 1994, no. 1(45), p. 3.
4. Minaev, A.N., Process of Scale Formation and Corrosion in Elements of Marine Power Units Operating on Seawater, *Doctoral Dissertation*, Vladivostok, 1993.
5. Kovalenko, V.F. and Lukin, G.Ya., *Sudovye vodoopresnitel'nye ustanovki* (Marine Desalting Installitions), Leningrad: Sudostroenie, 1970.
6. Gordienko, P.S. and Gnedenkov, S.V., *Mikrodugovoe oksidirovanie titana i ego splavov* (Microarc Oxidation of Titanium and Its Alloys), Vladivostok: Dal'-nauka, 1997.
7. Gnedenkov, S.V., Sinebryukhov, S.L., and Gordienko, P.S., *Vestn. Dal'nevost. Otd. Ross. Akad. Nauk*, 2002, no. 3(103), pp. 21–39.
8. Gordienko, P.S., Gnedenkov, S.V., Sinebryukhov, S.L., *et al.*, *Elektrokhimiya*, 1993, vol. 29, no. 8, pp. 1008–1012.
9. Vovna, V.I., Gnedenkov, S.V., Gordienko, P.S., *et al.*, *Elektrokhimiya*, 1998, vol. 34, no. 10, pp. 1208–1211.
10. Gnedenkov, S.V., Sinebryukhov, S.L., Skorobogatova, T.M., and Gordienko, P.C., *Elektrokhimiya*, 1998, vol. 34, no. 9, pp. 1046–1051.
11. Gordienko, P.S., Gnedenkov, S.V., Khrisanfova, O.A., *et al.*, *Vestn. Dal'nevost. Otd. Ross. Akad. Nauk*, 1995, no. 2(60), pp. 56–61.
12. Gnedenkov, S.V., Gordienko, P.S., Lysenko, L.V., *et al.*, *Fiz. Khim. Obrab. Mater.*, 1997, no. 2, pp. 65–69.
13. Khrisanfova, O.A., Volkova, L.M., Gnedenkov, S.V., *et al.*, *Zh. Neorg. Khim.*, 1995, vol. 40, no. 4, pp. 558–562.
14. RF Patent 2075872.
15. Gnedenkov, S.V., Gordienko, P.S., Sinebrukhov, S.L., *et. al.*, *Corrosion*, 2000, no. 1(56), pp. 24–31.
16. Panshin, Yu.A., Malkevich, S.G., and Dunaevskaya, V.S., *Ftoroplasty* (Fluoroplastics), Leningrad, 1978.
17. *Ftoroplasty: Katalog* (Fluoroplastics: Catalogue), Cherkassy, 1983.
18. Rabinovich, V.A. and Khavin, Z.Ya., *Kratkii khimicheskii spravochnik* (Concise Handbook of Chemistry), Lenngrad: Khimiya, 1977.
19. *Metody gidrokhimicheskikh issledovanii okeana* (Methods for Ydrochemical Studies of the Ocean), Bordovskii, O.K. and Ivanenkov, V.N., Eds., Moscow: Nauka, 1978.

Russian Journal of Applied Chemistry, Vol. 76, No. 8, 2003, pp. 1211–1213. Translated from Zhurnal Prikladnoi Khimii, Vol. 76, No. 8, 2003, pp. 1251–1253.

PHYSICOCHEMICAL STUDIES OF SYSTEMS AND PROCESSES

Kinetics of Reaction between Magnesium Hydroxide and Dimethyl Phosphite

O. I. Tuzhikov, M. P. Lyabin, T. V. Khokhlova, S. N. Bondarenko, and S. M. Moskvichev

Volgograd State Technical University, Volgograd, Russia

Received June 6, 2002; in final form, January 2003

Abstract—The kinetic of the reaction between magnesium hydroxide and dimethyl phosphite in nitrobenzene was studied.

Analysis of the patent and technical literature shows that metal hydroxides and, in particular, aluminum and magnesium hydroxides are widely used as fire-retardant additives in developing polymeric composites with lowered combustibility. However, introduction of such additives impairs the physicomechanical properties of composites [1].

In order to diminish the influence of this important disadvantage and, simultaneously, to enhance the flame-quenching properties of a fire retardant, aluminum hydroxide has been modified with dimethyl phosphite and the kinetics of this reaction has been studied [2]. In continuation of these investigations, the kinetics of the reaction of modification of magnesium hydroxide with dimethyl phosphite in the liquid phase with nitrobenzene used as solvent:

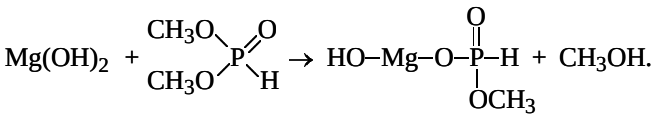

EXPERIMENTAL

The kinetics was studied in the temperature range 126–146°C in a three-neck reactor with rabble, thermometer, and condenser to remove methanol. The ±0.2°C accuracy of temperature control was provided by an ultrathermostat. The reaction course was monitored by sampling at certain intervals of time, with the concentration of dimethyl phosphite determined by titration with 0.1 N alkali solution on a pH-340 pH-meter. The reaction was stopped by cooling a sample to 2–5°C.

The overall and partial reaction orders were determined by graphical differentiation of the kinetic curves at the initial instant of time (see table). The results of kinetic studies were processed using the least-squares method.

Since magnesium hydroxide entering into the reaction is in the solid state, its concentration is determined by solubility and remains constant during the entire process. It is impossible to determine the true reaction order with respect to $Mg(OH)_2$ under these conditions. The apparent reaction order with respect to this reactant is zero.

The kinetic curves obtained in a set of experiments in which the initial concentration of dimethyl phosphite and the amount of solvent used remained constant and that of $Mg(OH)_2$ in the reaction mass varied are virtually identical (Fig. 1a). The deviations observed lie within the experimental error. This con-

Kinetic characteristics of the reaction of (1) magnesium hydroxide with (2) dimethyl phosphite in nitrobenzene

Amount of reagents, mole		(1) : (2) molar ratio	c_2^0, M	T, °C	$V_0 \times 10^3$, M s^{-1}	$k_{app} \times 10^3$, s^{-1}
(1)	(2)					
0.050	0.050	1.00	0.994	146	1.052	1.046
0.050	0.049	1.02	0.989	146	1.070	
0.050	0.038	1.32	0.752	146	0.699	
0.050	0.025	2.00	0.501	146	0.499	
0.100	0.100	1.00	2.004	146	2.348	1.012
0.025	0.025	1.00	0.506	146	4.152	
0.050	0.050	1.00	0.994	136	0.854	0.866
0.050	0.045	1.11	0.902	126	0.637	0.715

1070-4272/03/7608-1211 $25.00 © 2003 MAIK "Nauka/Interperiodica"

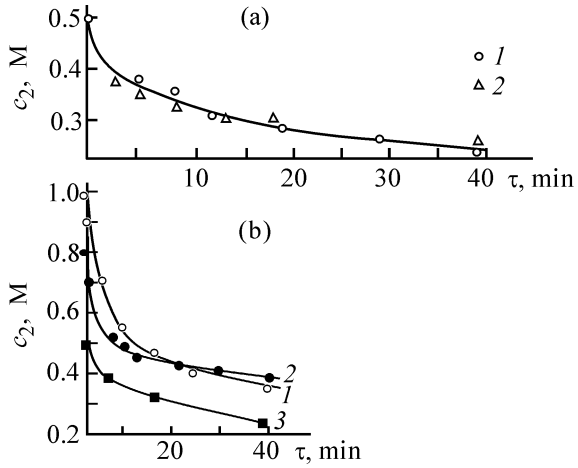

Fig. 1. Variation with time τ of the concentration c_2 of dimethyl phosphite in its reaction with magnesium hydroxide in nitrobenzene. Ratio between amounts of reactants, $\nu_1:\nu_2$ (mol:mol): (a) (*1*) 1.00 and (*2*) 2.00; (b) (*1*) 1.02, (*2*) 1.32, and (*3*) 2.00. (a) $c_1^0 = c_2^0$; (b) c_2^0 (M): (*1*) 0.989, (*2*) 0.752, and (*3*) 0.501.

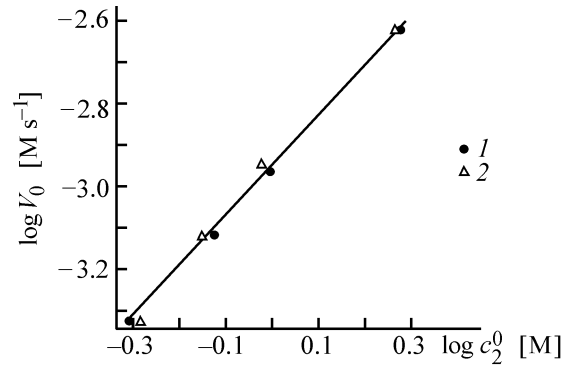

Fig. 2. $\log V_0$–$\log c_2^0$ dependence for reaction of magnesium hydroxide with dimethyl phosphite. (*1*) The partial reaction order with respect to dimethyl phosphite and (*2*) the overall reaction order with respect to the same reactant are determined.

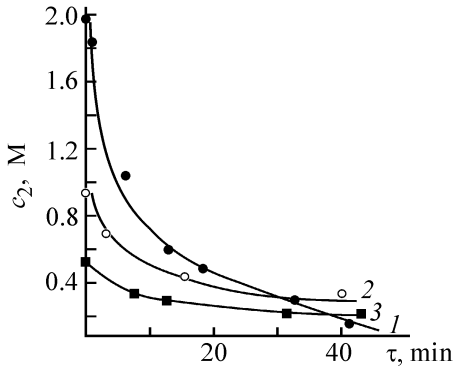

Fig. 3. Variation with time τ of the concentration c_2 of dimethyl phosphite in its reaction with magnesium hydroxide in nitrobenzene at equimolar ratio of the reactants and temperature of 146°C. c_2^0 (M): (*1*) 2.004, (*2*) 0.989, and (*3*) 0.506.

firms the zero apparent reaction order with respect to magnesium hydroxide and also indicates that the reaction occurs in solution, rather than on the surface of the solid reagent, since raising the content of $Mg(OH)_2$ in the reaction mass would accelerate the process because of the larger contact area.

The reaction order with respect to $(CH_3)_2HPO_3$ was determined by measuring the initial reaction rates at fixed amounts of magnesium hydroxide and varied (within 0.5–1.0 M) initial concentration of dimethyl phosphite (Fig. 1b). A knowledge of the partial reaction order with respect to dimethyl phosphite makes it possible to plot the dependence $\log V_0 = f(\log c_2^0)$ (Fig. 2), where V_0 is the initial reaction rate and c_2^0 is the initial concentration of dimethyl phosphite. It can be seen from Fig. 2 that the slope of the dependence of the logarithm of the initial rate on the logarithm of the initial dimethyl phosphite concentration is close to unity, which indicates the first reaction order with respect to this reagent. With account of the pseudo-zero order with respect to magnesium hydroxide, the overall reaction order is unity.

The calculations performed yielded the parameters of the linear equation

$$\log V_0 = \log k + n_1 \log c_1^0 + n_2 \log c_2^0, \qquad (1)$$

where k is the reaction rate constant, and n_1 and n_2 are the reaction orders with respect to magnesium hydroxide and dimethyl phosphite.

Under the experimental conditions, the $Mg(OH)_2$ concentration in solution, c_1^0, was maintained constant, and, consequently, $n_1 \log c_1^0 = \text{const}$. Then Eq. (1) takes the form

$$\log V_0 = (-2.9805 \pm 0.0200) + (1.1198 \pm 0.12304)\log c_2^0.$$

Consequently, the more accurate partial reaction order with respect to dimethyl phosphite is $n_2 = 1.12 \pm 0.12$.

The overall reaction order was confirmed in a set of experiments in which the initial concentration of dimethyl phosphite was varied within 0.5–2.0 M at fixed equimolar ratio of the starting reagents (Fig. 3). The calculations performed yielded the dependence

$$\log V_0 = \log k_{app} + n \log c_2^0 = (-2.9947 \pm 0.23) + (1.16 \pm 0.10)\log c_2^0,$$

which confirms the overall first reaction order under the experimental conditions and makes it possible to

find the apparent rate constant k_{app}, which is a function of the concentration of magnesium hydroxide in the liquid phase.

To determine the activation energy of the reaction, kinetic curves were measured at temperatures of 126, 136, and 146°C. In these experiments, the initial concentrations of the starting reagents remained constant (see table).

Using the method of graphical differentiation of kinetic curves at the initial instant of time in studying the kinetics of the chemical reaction at low solubility of $Mg(OH)_2$ in nitrobenzene makes it possible to state that the contribution from the heat effect of hydroxide dissolution is insignificant.

The reaction rate constant is described by the Arrhenius equation: the dependence $\log k_{app} = f(1/T)$ is described by a linear equation in integral form

$$\log k_{app} = (0.406 \pm 0.066) + (1417.79 \pm 26.89)/T;$$

$$r = 0.999, \quad S = 0.012.$$

CONCLUSIONS

(1) The reaction of magnesium hydroxide with dimethyl phosphite in nitrobenzene is first-order with respect to dimethyl phosphite, with the overall reaction order close to unity; the process occurs in solution, rather than on the surface of magnesium hydroxide.

(2) The reactions of magnesium and aluminum hydroxides with dimethyl phosphite have equal partial and overall orders.

REFERENCES

1. Tuzhikov, O.I., Bondarenko, S.N., Khokhlova, T.V., *et al., Issledovanie svoistv epoksidnykh kompozitsionnykh materialov, soderzhashchikh modifitsirovannuyu gidrookis' alyuminiya: Sbornik nauchnykh trudov* (A Study of Properties of Epoxy Composite Materials Containing Modfified Aluminum Hydroxide: Coll. of Sci. Works), Volgograd: Volg. Gos. Tekhn. Univ., 1993, pp. 86–90.
2. Bondarenko, S.N., Khokhlova, T.V., Tuzhikov, O.I., *et al., Zh. Prikl. Khim.*, 2002, vol. 74, no. 12, pp. 2059–2061.

Russian Journal of Applied Chemistry, Vol. 76, No. 8, 2003, pp. 1214–1220. Translated from Zhurnal Prikladnoi Khimii, Vol. 76, No. 8, 2003, pp. 1254–1259.

PHYSICOCHEMICAL STUDIES OF SYSTEMS AND PROCESSES

Kinetics of Oxidation of Organic Acids by Ammonium Nitrate

A. I. Kazakov, Yu. I. Rubtsov, D. B. Lempert, and G. B. Manelis

Institute for Problems of Chemical Physics, Russian Academy of Sciences, Chernogolovka, Moscow oblast, Russia

Received January 10, 2003

Abstract—Kinetics of oxidation of some organic acids by ammonium nitrate was studied. Temperature dependences of the rate constants of acid oxidation were determined.

Gas-generating formulations for household purposes have been intensively developed in recent years. Systems of this kind can be created using the principles on which design of solid mixture fuels is based. The fuel system proposed must have an acceptable thermal stability and retain its working properties during a rather prolonged test at elevated temperatures. A possible way to solve this problem is to use mixtures of ammonium nitrate (AN) with organic substances and, in particular, oxalic acid.

It has been established previously that thermal decomposition of AN into ammonia and nitric acid proceeds via its equilibrium dissociation. The rate of the process in decomposition of a pure salt is determined by the rate of oxidation of the NH_4^+ ion by a molecule of nitric acid [1]: the rate grows with increasing content of nitric acid in the system. The content of HNO_3 in molten pure AN does not exceed 0.1% of the total content of NO_3^- ions in the salt, and, therefore, the stability of pure AN is sufficiently high for this compound to be used in the mixtures under consideration. Introduction of organic acids into AN can raise the equilibrium concentration of HNO_3 and, correspondingly, impair the stability of AN. However, organic acids in aqueous solutions are much weaker than nitric acid, with the difference in p*K* values between nitric and organic acids constituting 3 units and more [2]. Therefore, it would be expected that the increase in the concentration of HNO_3 will be small, and the thermal stability of the mixture, sufficient.

The aim of the present study was to analyze the kinetics and mechanism of the reaction of oxidation of various organic, mainly dibasic acids by ammonium nitrate in order to elucidate the general pattern and distinctions of this reaction for different acids and to assess the possibility of practical use of mixtures of this kind.

EXPERIMENTAL

The kinetic pattern of heat release in thermal interaction of AN mixtures with oxalic, malonic, succinic, pimelic, malic, tartaric, citric, maleic, and benzoic acids in a 1 : 1 molar ratio was studied. Also, separate experiments were carried out for mixtures of AN with decane and polyethylene for comparison purposes. The 1 : 1 ratio of the amounts of oxalic acid and AN corresponds to equivalent of the oxidizing agent and the fuel. For all other mixtures there exists an excess of the fuel, but the equal number of moles allows easier comparison of the positions of acid–base equilibria. For a mixture of AN with succinic acid, additional experiments were carried out at the stoichiometric ratio of the components for the oxidation reaction. Chemical reagents of chemically pure and analytically pure grades were used.

The experiments were performed on a DAK-1-1 automated dynamic microcalorimeter [3] in sealed glass ampules having no cool parts, which allows preservation of all the products in the reaction zone. If not specified otherwise, a two-component mixture of the compositions mentioned above exists in the form of a homogeneous liquid phase at any of the temperatures studied. The rate of the reaction between the solid phases is below the detection limit of the calorimeter. The mixture of AN with oxalic acid shows a sufficiently high reaction rate even at 70°C, and that with malonic acid, at 85°C; for other acids the rate becomes comparable only above 100°C, when the liquid phase appears in the system.

Figure 1 shows as an example kinetic curves of heat release for the mixture of AN with oxalic acid; for malonic, succinic, pimelic, tartaric, and benzoic acids the curves are mainly similar and differ only in the heat release rate and the range of temperatures

1070-4272/03/7608-1214 $25.00 © 2003 MAIK "Nauka/Interperiodica"

studied. The rate is the highest at the beginning of the process and then decreases fast; the reaction order much exceeds the second order. The kinetic equation has the form

$$dQ/dt = k_1 Q_f(1 - \eta)^2,$$

where Q and Q_f are the running and full heats of reaction ($J\ mol^{-1}$), and $\eta = Q/Q_f$ is the extent of the process.

The running heat of the process, Q, was found by integrating numerically the obtained time dependence of the heat release rate. Since the reaction was not brought to complete termination of heat release because of its extremely long duration, the full heat of the process, Q_f, was determined by extrapolation of the $(dQ/dt)^{0.5}$ dependence from Q to zero value of dQ/dt. For most of the acids studied, the Q_f values are close to 4200 $J\ g^{-1}$. For pure AN, the heat of thermal decomposition is much lower, 1460–1670 $J\ g^{-1}$ under the experimental conditions. Oxidation of the organic component makes a major contribution to the full heat of the process. In this case, NH_4^+ ions also become involved in the oxidation reaction under the action of more active intermediate reaction products, e.g., nitrogen oxides. At the same time, in the case when the reaction proceeds to completion to give CO_2, H_2O, and N_2 in a mixture of AN with oxalic acid, more than 5430 $J\ g^{-1}$ must be released, i.e., the oxidation under the experimental conditions is incomplete. In this series of acids, a strong difference in the experimental heat of oxidation is only observed for malonic acid: the heat of its oxidation by AN is approximately 830 $J\ g^{-1}$.

In the case of deviation from the equimolar ratio of the components, the two-component mixture exists at certain temperatures in the form of solutions of constant composition, which are saturated either with organic acid or with AN, in equilibrium with the corresponding solid phase. The apparent heat release rate dQ/dt is, in the general case, given by the formula

$$dQ/dt = k_{eff} Q_f \alpha V c_{RCOOH} c_{NH_4NO_3},$$

where k_{eff} is the effective rate of oxidation of an organic acid by AN ($M^{-1}\ s^{-1}$); Q_f, the full heat effect ($J\ mol^{-1}$); V, the mixture volume (l); α, the fraction of the melt volume relative to the total volume of the mixture; c_{RCOOH}, $c_{NH_4NO_3}$, the concentrations of organic acid and AN in the melt, respectively (M).

Figure 2 shows the dependence of the initial heat release rate by 1 g of a mixture of oxalic acid and AN at 89.2°C as a function of the mole fraction of oxalic acid. At small mole fractions of oxalic acid, the system is two-phase, the product of reagent concentrations in solution is constant, the volume fraction of the melt grows with increasing mole fraction of oxalic acid, and, correspondingly, the initial heat release rate grows somewhat. On reaching a certain mole fraction of oxalic acid in a mixture, the system becomes homogeneous, which corresponds to α equal to unity.

The heat release rate grows with increasing product $c_{RCOOH} c_{NH_4NO_3}$ at approximately constant V. The maximum of $c_{RCOOH} c_{NH_4NO_3}$ is reached in the equimolar

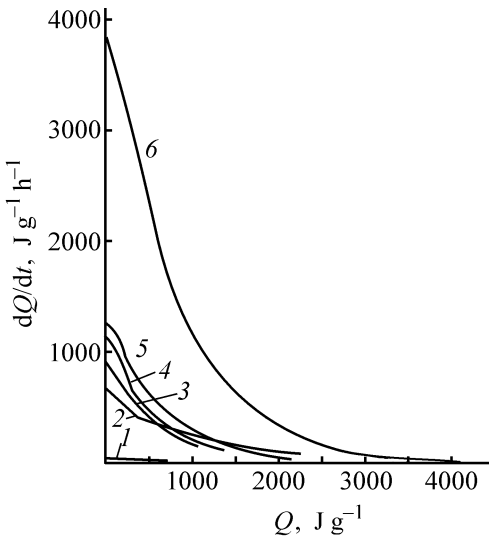

Fig. 1. Heat release rate dQ/dt vs. Q in equimolar mixture of oxalic acid with AN. T (°C): (*1*) 70.4, (*2*) 86.2, (*3*) 89, (*4*) 91, (*5*) 100, and (*6*) 106.

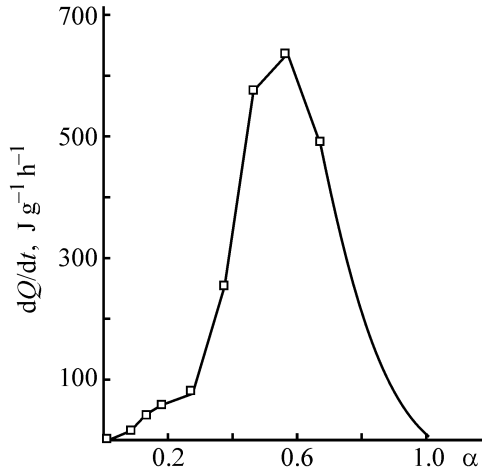

Fig. 2. Initial heat release rate dQ/dt in a mixture of oxalic acid with AN vs. mole fraction α of $(COOH)_2$ at 89.2°C.

mixture; with the mole fraction of oxalic acid increasing further, the product of concentrations starts to decrease, which leads to fall in the heat release rate. Then the mixture again becomes two-phase; the subsequent fall in the melt volume at constant product of the reactant concentrations leads to further decrease in the heat release rate.

Oxidation of maleic, malic, and citric acids by AN obeys a kinetic law different from that described by an equation of a second-order reaction. Oxidation of maleic acid is described by an equation of a first-order autocatalityc reaction with full heat of the process, Q_f, approximately equal to 5230 J g^{-1}:

$$dQ/dt = k_1 Q_f(1 - \eta) + k_2 Q_f(1 - \eta)\eta.$$

In oxidation of malic acid by AN, the heat release rate varies in the course of the process in a complicated way (Fig. 3). In the first stage, whose duration grows with increasing temperature, self-acceleration by the equation of a first-order autocatalytic reaction is observed. After the maximum rate is reached, it starts to fall by the equation of a first-order reaction to a certain level, which remains virtually constant until the conversion becomes 0.8–0.85, and then the rate again falls to complete termination of heat release.

Oxidation of citric acid by AN follows the first-order reaction law to conversion of 0.9–0.95?, after which the rate also falls abruptly to virtually zero value. The full heats of oxidation of malic and citric acids by AN are approximately equal to 4180 J g^{-1}.

The following values of $k = (dQ/dt)_{t=0}/Q_f V c_{NH_4NO_3} = k_{eff} c_{RCOOH}$ were obtained at different temperatures for all of the AN mixtures with organic acids, analyzed in this study:

Oxalic acid

T, °C	33	70.4	86.2	89	91	100	106.6
$k_1 \times 10^6$, s^{-1}	0.9	3.1	44	77	60	84	260

Malonic acid

T, °C	89.1	106	112.4	117.2	123.6	128.5
$k_1 \times 10^6$, s^{-1}	3.6	42	68	100	130	170

Succinic acid

T, °C	158.5	171.7	180	188.5	196
$k_1 \times 10^6$, s^{-1}	1.5	6.5	11	27	70

Pimelic acid

T, °C	158.5	171.7	180	188.5	196
$k_1 \times 10^6$, s^{-1}	8.1	24	47	83	120

Tartaric acid

T, °C	127	131	139	145	151
$k_1 \times 10^6$, s^{-1}	4.1	15	34	69	57

Benzoic acid

T, °C	151.5	180	188.5	196
$k_1 \times 10^6$, s^{-1}	0.058	1.6	3.5	6.8

Maleic acid

T, °C	100	138	145	148	151	152	165
$k_1 \times 10^6$, s^{-1}	2.6	40	78	91	180	180	360

Malic acid

T, °C	122.4	127.2	131.7	139	145	158.5
$k_1 \times 10^6$, s^{-1}	1.9	2.5	3.7	8.6	17	69

Citric acid

T, °C	122.4	127.2	131.7	139	145
$k_1 \times 10^6$, s^{-1}	8.7	11	21	57	110

Rate constants of interaction between AN and organic acids

Acid	pK	k_1, s^{-1}	$k_{1,\,100°C}$, s^{-1}	$t_{0.01\%\ at\ 100°C}$, s
Oxalic	1.27	$5.2 \times 10^{12} \exp(-14.2 \times 10^3/T)$	1.4×10^{-4}	72
Malonic	2.86	$4.9 \times 10^{11} \exp(-14.2 \times 10^3/T)$	1.5×10^{-5}	6.8×10^2
Succinic	4.21	$1.0 \times 10^{14} \exp(-19.7 \times 10^3/T)$	1.1×10^{-9}	9.2×10^6
Pimelic	4.51	$2.9 \times 10^9 \exp(-14.4 \times 10^3/T)$	5.1×10^{-8}	2.0×10^5
Tartaric	2.98	$4.0 \times 10^{14} \exp(-18.2 \times 10^3/T)$	2.7×10^{-7}	3.7×10^4
Benzoic	4.18	$5.8 \times 10^{14} \exp(-21.5 \times 10^3/T)$	5.7×10^{-11}	1.8×10^8
Maleic	1.92	$1.3 \times 10^9 \exp(-12.7 \times 10^3/T)$	2.3×10^{-6}	3.0×10^4
Malic	3.4	$2.5 \times 10^{13} \exp(-17.5 \times 10^3/T)$	1.0×10^{-7}	
Citric	3.13	$3.8 \times 10^{16} \exp(-19.7 \times 10^3/T)$	4.8×10^{-7}	2.1×10^4

Temperature dependences of k_1 are presented in the table. Owing to strong differences in the rates of heat release by the mixtures studied, different temperature ranges were used in the experiments. For convenience of comparison, rate constants are given for all the mixtures at 100°C, together with published values of pK for the acids studied, determined in aqueous solutions at room temperature [2]. The table also lists the times in which the reactions proceed to 1% extent, calculated using the dependences corresponding to the established kinetic pattern of the process. The temperature dependence of the constant k_2 (s^{-1}) of the autocatalytic stage, which is necessary for calculating the time of oxidation of maleic acid, is given by the expression

$$k_2 = 1.3 \times 10^8 \exp(-10.8 \times 10^3/T).$$

T, °C	100	138	145	148
k_2, s^{-1}	2.7×10^{-5}	5.7×10^{-4}	9.4×10^{-4}	7.7×10^{-4}
T, °C	151	152	165	
k_2, s^{-1}	1.9×10^{-8}	1.1×10^{-3}	1.5×10^{-3}	

The rate of thermal decomposition of pure AN at 200–250°C is determined by the rate of oxidation of the NH_4^+ ion by a molecule of nitric acid formed in dissociation of the onium salt [4]:

$$dQ/dt = k_{NH_4^+} Q_f V c_{NH_4^+} c_{HNO_3},$$

where $k_{NH_4^+}$ is the rate constant of oxidation of the ammonium ion by nitric acid, and V is the volume of the system.

In principle, the NH_4^+ ion is difficult to oxidize, with rather high temperatures necessary for achieving fast rates of AN decomposition. The temperature dependence of the initial heat release rate in decomposition of pure AN can be obtained from the data of [5]:

$$(dQ/dt)_{t=0} = 3.2 \times 10^{18} \exp(-23.8 \times 10^3/T).$$

Previously, it has been established in studying the possible ways to oxidize NH_4^+ ions with concentrated solutions of nitric acid that, at temperatures below 150–160°C and NHO_3 content exceeding that in an AN melt, the mechanism of the oxidation reaction undergoes a change. Oxidation by molecular nitric acid is replaced by oxidation by nitrogen(V) oxide formed in the equilibrium

$$2HNO_3 \rightleftarrows N_2O_5 + H_2O;$$

$$K_{deh} = a_{H_2O} a_{N_2O_5} / a_{HNO_3}^2. \quad (1)$$

Because of the lower activation energy of oxidation by nitrogen(V) oxide, the reaction rate decreases more slowly than in the case of oxidation by nitric acid, with the result that N_2O_5 makes major contribution to the apparent heat release rate in the low-temperature region. At the same time, in decomposition of AN proper, the low equilibrium concentration of HNO_3, which is additionally lowered because of the ioniza-

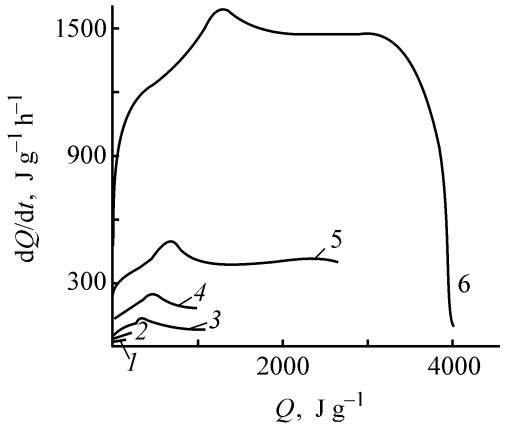

Fig. 3. Heat release rate dQ/dt vs. Q in equimolar mixture of malic acid with AN. T (°C): (*1*) 122.4, (*2*) 127.2, (*3*) 137.1, (*4*) 139, (*5*) 145, and (*6*) 158.5.

tion by impurity water, results in that the mechanism of AN decomposition with oxidation of ammonium ions by molecular HNO_3 is preserved in the entire temperature range studied, above and below the melting point [6].

In two-component systems constituted by AN and an organic acid, the rates of heat release much exceed those in thermal decomposition of pure AN. Extrapolation of the temperature dependence of the heat release rate in thermal decomposition of an AN melt [5] to 100°C yields a value of 8.1×10^{-10} W g^{-1}. In a mixture of AN with oxalic acid, the heat release rate at 100°C exceeds by 9 orders of magnitude the extrapolated value. The difference between the heat release rate in decomposition of crystalline AN, which is more stable than the melt, and the heat release rate in decomposition of a two-component mixture at this temperature will be even more pronounced.

Comparison of the rate constants of interaction between AN and various acids shows that the differences in the rates of heat release are very significant and constitute several orders of magnitude under analogous conditions. They are mainly associated with differences in the pK_a values in aqueous solution. The lower this value and, correspondingly, the higher the constant of proton ionization, the higher the oxidation rate. The highest heat release rate is observed for a mixture with oxalic acid, and the lowest, for that with benzoic acid.

The increase in the reaction rate in the two-component mixture is accounted for by two factors: (1) oxidation of an acid molecule, which occurs with much higher rate constant as compared with oxidation of the NH_4^+ ion; (2) increase in the content of nitric acid upon addition of an organic acid to AN. Mixtures of AN with polyethylene or decane, which do not affect the position of the acid equilibrium in the system, are oxidized at higher rate than NH_4^+ because of their higher intrinsic rate constant of oxidation.

The dependence of the heat release rate by a mixture of AN with an organic acid on the pK value of the acid is probably determined by the reaction of protonation of the NO_3^- anion by organic acid, which leads to an increase in the concentration of HNO_3:

$$NO_3^- + RCOOH \rightleftarrows HNO_3 + RCOO^-;$$

$$K_{ch} = a_{HNO_3} a_{RCOO^-} / a_{NO_3^-} a_{RCOOH}, \qquad (2)$$

where K_{ch} is the equilibrium constant equal to the ratio between the constants of proton ionization of an organic acid, K, and nitric acid, K_{HNO_3} in a melt; a_{HNO_3}, a_{RCOO^-}, $a_{NO_3^-}$, a_{RCOOH}, the activities of the respective species; $RCOO^-$, the anion of the organic acid.

It follows from the pK_a values of the acids, determined in aqueous solutions, that occurrence of reaction (2) in the forward direction is thermodynamically unfavorable: the pK value for HNO_3 in aqueous solution is 1.64 [2], whereas that for the weakest of the organic acids considered, oxalic acid, is higher by three units. The increase in the concentration of HNO_3 molecules cannot be significant at such pK values, and the oxidation rate must be independent of pK. It has been shown previously [7] that introduction of orthophosphoric acid (pK 2.1 in aqueous solution) into AN makes higher the HNO_3 concentration in the melt and the rate of AN decomposition, which the constant of the equilibrium

$$H_3PO_4 + NO_3^- \rightleftarrows HNO_3 + H_2PO_4^-$$

in an AN melt at 233.5°C found to be approximately 60. Such a change in the relative strength of HNO_3 may be due to the low dielectric constant of the ionic melt of AN and to selective complexation between HNO_3 molecules and ions of the melt (complex ion $2HNO_3 \cdot NO_3^-$ has been described in the literature [8]).

Apparently, a similar situation occurs in melts of AN with organic acids. The pK values for organic acids and HNO_3 must change as compared with those in aqueous solutions, and the strength of organic acids must increase with respect to that of HNO_3. The relative pK values of organic acids are mainly preserved, which is manifested in the rates of their interaction with AN, although the absolute values themselves are probably changed.

In a mixture system, the rates of heat release that are close to those in decomposition of pure AN are observed at much lower temperatures and higher HNO_3 concentrations than those in decomposition of pure AN. Such conditions probably favor occurrence of an oxidation reaction involving N_2O_5, as is the case in oxidation of the NH_4^+ ion with concentrated HNO_3 solutions. Thus, introduction of an organic acid, which is oxidized at lower temperatures than those in decomposition of an AN melt and makes higher the HNO_3 concentration, leads to a difference in the mechanisms by which are oxidized pure AN, in which HNO_3 is oxidizing agent, and a two-component system, with N_2O_5 acting as oxidant:

$$dQ/dt/Q_f V = k_{eff} c_{RCOOH} c_{NH_4NO_3}$$
$$= k'_{N_2O_5} a_{RCOOH} a_{N_2O_5} / \gamma^*_{TS}, \qquad (3)$$

where $k'_{N_2O_5}$ is the rate constant of the reaction of oxidation of an organic acid by nitrogen(V) oxide in the gas phase, and γ^*_{TS} is the activity coefficient of the activated complex in the melt [9].

At small degrees of protonation of nitrate ions, at which the activities a_{RCOO^-} and a_{HNO_3} can be considered equal, the following expression is obtained for a_{HNO_3} from equilibrium (2):

$$a_{HNO_3} = (Ka_{RCOOH}a_{NO_3^-}/K_{HNO_3})^{1/2}. \quad (4)$$

Expressing $a_{N_2O_5}$ in terms of the constants of dehydration equilibrium (1) with the use of (4) and substituting it into expression (3) for the rate yields an equation which has, after its logarithm is taken, the form

$$\log(dQ/dt/Q_fVc_{NH_4NO_3}) = \log k_1 = \log k(k_{eff}c_{RCOOH})$$
$$= \log k_{N_2O_5} + \log K_{deh} + pK_{HNO_3} - pK$$
$$+ \log(a_{RCOOH}a_{NO_3^-}/a_{H_2O}\gamma_{N_2O_5})$$
$$+ \log(c_{RCOOH}/c_{NH_4NO_3}),$$

where $k_{N_2O_5} = k'_{N_2O_5}\gamma_{RCOOH}\gamma_{N_2O_5}/\gamma^*_{TS}$ is the rate constant of oxidation of an organic acid by nitrogen(V) oxide in a melt [9], and γ_{RCOOH} and $\gamma_{N_2O_5}$ are the activity coefficients of RCOOH and N_2O_5 in the melt.

In accordance with the mechanism of oxidation by nitrogen(V) oxide, the rate must increase in proportion to the constant of proton ionization of the organic acid if the term with activity ratio is assumed to be constant. Figure 4 shows the logarithm of the rate constant of interaction between various organic acids and AN at 100°C as a function of the pK value of these acids. The relationship observed between the logarithm of the rate constant of heat release in the reaction of AN with organic acids and their pK value in aqueous solutions is close (with only a certain scatter of experimental data, caused by difference in chemical structure between the acids studied) to that assumed for the given mechanism, with a slope of the straight line approximately equal to –1. The constant of proton ionization of organic acids in aqueous solutions decreases, in going from oxalic to pimelic acid, by a factor of $10^{3.2}$, and heat release rate, by a factor of $10^{3.4}$.

Probably, owing to the higher activation energy, the rate constant of oxidation of organic acids by molecular HNO_3 will exceed the rate constant of oxidation by nitrogen(V) oxide at temperatures much higher than those used in the experiments, and, as

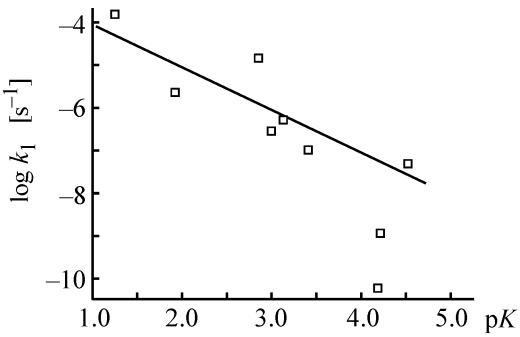

Fig. 4. log k_1 vs. pK value of organic acids. (k_1) Rate constant of interaction between AN and organic acids and (K) constant of acid dissociation of organic acid.

in the case of AN decomposition, HNO_3 will play the part of an oxidizing agent.

Thus, the main factor responsible for the difference in the rates of oxidation of organic acids by AN is their strength. At the same time, certain differences associated with the chemical structure of an acid are observed. The oxidation rate of an organic acid is determined by presence in it of fragments that can sufficiently rapidly react with a N_2O_5 molecule. In the compounds under study, these are hydrogen atoms of $–CH_2–$ groups and hydrogen atoms in α position in the –OH group. The rate of heat release by a mixture of AN with pimelic acids is 7 times that for a mixture with succinic acid, although the constant of proton ionization of pimelic acid is 2 times smaller, which is due to the presence in its molecule of a greater number of oxidizable $–CH_2–$ groups. The pK values of benzoic and succinic acids are close, and the rates differ by a factor of 18, with benzoic acid exhibiting the lowest heat release rate because of the high stability of hydrogen atoms in the benzene ring against oxidation.

The mixtures studied, constituted by AN and organic acids, strongly differ in stability, with equimolar mixtures of AN with succinic or benzoic acid being the most stable. For succinic acid, the rates of its interaction with AN were measured for the mixture components taken in stoichiometric ratio, which corresponds to mole fraction of AN equal to 0.875:

T, °C	191	195.8	200.6	204.4	214.4	221.6
$k_1 \times 10^6$, s^{-1}	7.5	14	18	25	53	78

The activation energies of reactions in equimolar and stoichiometric mixtures are the same, and the preexponential factor in the stoichiometric is 2.2 times lower. At the temperatures studied, the stoichiometric mixture of AN with succinic acid is a homogeneous

solution, and the decrease in the rate in this mixture is due to deviation from equimolarity of the amounts of AN and succinic acid.

CONCLUSIONS

(1) The thermal stability of two-component liquid mixtures of ammonium nitrate and an organic acid is determined both by the ability of an acid (determined by its strength) to transfer a proton to a nitrate ion and thereby to make higher the HNO_3 concentration in the system and by the rate constant of oxidation of the organic acid.

(2) In contrast to thermal decomposition of pure ammonium nitrate, the role of oxidizing agent in mixed systems constituted by ammonium nitrate and an organic acid is played by N_2O_5 formed in dehydration of nitric acid.

(3) Of the whole set of systems under study, constituted by ammonium nitrate and an organic acid, the most stable are mixtures with succinic and benzoic acids.

ACKNOWLEDGMENTS

The study was supported by the International Center for Science and Technology, project no. 1882-2001.

REFERENCES

1. Manelis, G.B., Nazin, G.M., Rubtsov, Yu.I., *et al.*, *Termicheskoe razlozhenie i gorenie vzryvchatykh veshchestv i porokhov* (Thermal Decomposition and Combustion of Explosives and Powders), Moscow: Nauka, 1996.
2. Albert, A. and Serjeant, E., *Ionization Constants of Acids and Bases. A Laboratory Manual*, New York: Wiley, Methuen, 1962.
3. Gal'perin, L.N., Kolesov, Yu.R., Mashkinov, L.B., *et al.*, Abstracts of Papers, *VI Vsesoyuznaya konferentsiya po kalorimetrii* (VI All-Union Conf. On Calorimetry), Tbilisi: Metsniereba, 1973, pp. 539–543.
4. Kazakov, A.I., Andrienko, L.P., and Rubtsov, Yu.I., *Izv. Akad. Nauk SSSR, Ser. Khim.*, 1980, no. 5, pp. 972–977.
5. Rubtsov, Yu.I., Kazakov, A.I., Morozkin, S.Yu., *et al.*, *Zh. Prikl. Khim.*, 1984, vol. 57, no. 9, pp. 1926–1929.
6. Rubtsov, Yu.I., Kazakov, A.I., Strizhevskii, I.I., *et al.*, Abstracts of Papers, *VIII Vsesoyuznyi simpozium po goreniyu i vzryvu* (VIII All-Union Symp. On Combustion and Explosion), Tashkent, 1986, pp. 91–94.
7. Rubtsov, Yu.I., Strizhevskii, I.I., Kazakov, A.I., *et al.*, *Zh. Prikl. Khim.*, 1989, vol. 62, no. 10, pp. 2169–2174.
8. Karavaev, M.M., *Issledovaniya v oblasti neorganicheskoi tekhnologii* (Studies in the Field of Inorganic Technology), Leningrad: Nauka, 1972, pp. 10–14.
9. Entelis, S.G. and Tiger, R.P., *Kinetika reaktsii v zhidkoi faze* (Kinetics of Reactions in Liquid Phase), Moscow: Khimiya, 1973.

Russian Journal of Applied Chemistry, Vol. 76, No. 8, 2003, pp. 1221–1224. Translated from Zhurnal Prikladnoi Khimii, Vol. 76, No. 8, 2003, pp. 1260–1263.

PHYSICOCHEMICAL STUDIES OF SYSTEMS AND PROCESSES

Properties of Systems $Ba(HCOO)_2$–$M(HCOO)_2$–H_2O (M = Ca or Mg) at 25°C

V. Z. Vasileva

Institute of General and Inorganic Chemistry, Bulgarian Academy of Sciences, Sofia, Bulgaria

Received December 6, 2002

Abstract—The systems $Ba(HCOO)_2$–$Ca(HCOO)_2$–H_2O and $Ba(HCOO)_2$–$Mg(HCOO)_2$–H_2O were studied at 25°C by the solubility method. The effect of the ionic radii of doubly charged metals on the formation of double salts containing barium formate was considered.

Barium formate and its binary compounds possess interesting physical and chemical properties: $Ba(HCOO)_2$ and $BaCd(HCOO)_4 \cdot 2H_2O$ are nonlinear optical materials [1, 2], $Ba_2Cu(HCOO)_6 \cdot H_2O$ is paramagnetic material [3], and $BaY(HCOO)_5 \cdot 4H_2O$ and $Ba_2Cu(HCOO)_6 \cdot 4H_2O$ are suitable starting compounds for synthesis of superconductors [4, 5]. A study of salt systems containing barium formate is of interest because they show promise for practical application.

Barium formate is known to form double salts with formates of some doubly charged metals. $Ba_2M(HCOO)_6 \cdot 4H_2O$ (where M is Ni, Co, Cu, or Zn) (2 : 1 : 4) and $BaM(HCOO)_4 \cdot 2H_2O$ (where M is Cd) (1 : 1 : 2) [6, 7] were obtained by the preparative method. All these double salts (except that containing cobalt) were separated from the corresponding ternary water–salt systems [4, 8–10]. The double salt $Ba_2Fe(HCOO)_6 \cdot 4H_2O$ was separated from the $Ba(HCOO)_2$–$Fe(HCOO)_2$–H_2O system at 25°C. It was established that it is isostructural to the double salts of the isomorphic series. It is also known that manganese formate does not form a compound with barium formate. The $Ba(HCOO)_2$–$Mn(HCOO)_2$–H_2O system at 25°C is simple eutonic [11]. It was of interest to elucidate whether or not barium formate forms double salts with calcium and magnesium formates.

To determine the mutual solubility of the components and the possibility of formation of new phases from barium, calcium, and magnesium formates, we studied the systems $Ba(HCOO)_2$–$Ca(HCOO)_2$–H_2O and $Ba(HCOO)_2$–$Mg(HCOO)_2$–H_2O at 25°C. The systems have not been studied previously. Data on the solubility of barium, calcium, and magnesium formates were taken from [12, 13].

EXPERIMENTAL

The starting substances were obtained by reacting barium, calcium, and magnesium carbonates (all analytically pure) with a 50% solution of analytically pure formic acid, followed by recrystallization. According to chemical, derivatographic, and X-ray phase analyses, the resulting compounds have the compositions $Ba(HCOO)_2$ [14], α-$Ca(HCOO)_2$ [15], and $Mg(HCOO)_2 \cdot 2H_2O$ [16].

The solubility was studied by Khlopin's method of isothermal elimination of supersaturation [17]: aqueous solutions of two components of the system, taken in various proportions, were prepared at 80–90°C. Then the solution was cooled in a thermostat to the working temperature and vigorously stirred to constant concentration of a saturated solution (i.e., to attainment of equilibrium). The temperature was maintained constant to within ±0.1°C. The equilibration time was 15–20 h. After the suspension was filtered, the resulting liquid phase and the wet solid phase (residue) were analyzed. The Ba^{2+}, Ca^{2+}, and Mg^{2+} content in the liquid phases and residues was determined complexometrically [18]: the sum of Ba^{2+} and Ca^{2+} ions and of Ba^{2+} and Mg^{2+} ions was determined by back titration with zinc sulfate solution in ammonia solution in the presence of Eriochrome Black T indicator, Ca^{2+} was analyzed at pH 11 (NaOH solution) in the presence of calcone indicator, Mg^{2+} was analyzed in ammonia buffer solution after precipitating barium sulfate with a sulfuric acid solution, and the Ba^{2+} content was calculated as the difference between the two determinations. The solid phase composition was determined

1070-4272/03/7608-1221 $25.00 © 2003 MAIK "Nauka/Interperiodica"

Table 1. Solubility and solid phase composition in the systems $Ba(HCOO)_2$–$M(HCOO)_2$–H_2O (M is Ca or Mg) at 25°C

Liquid phase				Residue, wt %		Solid phase composition
wt %		mol %				
$Ba(HCOO)_2$	$M(HCOO)_2$	$Ba(HCOO)_2$	$M(HCOO)_2$	$Ba(HCOO)_2$	$M(HCOO)_2$	
			$Ba(HCOO)_2$–$Ca(HCOO)_2$–H_2O system			
23.21	–	2.34	–	–	–	$Ba(HCOO)_2$
20.59	3.25	2.09	0.58	71.17	1.55	″
18.05	6.35	1.84	1.13	76.13	2.23	″
16.38	8.50	1.67	1.52	74.25	3.10	″
14.93	10.66	1.54	1.92	70.54	3.50	″
15.03	10.23	1.54	1.83	52.06	37.11	Eutonic
15.14	10.38	1.56	1.86	16.43	70.15	$Ca(HCOO)_2$
13.25	10.08	1.33	1.76	70.45	4.30	″
8.90	10.67	0.85	1.79	68.75	2.80	″
4.92	11.29	0.45	1.82	66.12	1.94	″
3.02	12.37	0.28	1.98	73.09	2.10	″
–	14.12	–	2.23	–	–	″
			$Ba(HCOO)_2$–$Mg(HCOO)_2$–H_2O system			
23.21	–	2.34	–	–	–	$Ba(HCOO)_2$
21.11	1.92	2.12	0.38	71.33	0.80	″
20.28	3.40	2.05	0.68	72.55	0.80	″
18.56	6.11	1.89	1.24	81.72	1.80	″
17.45	7.30	1.78	1.48	80.12	1.37	″
17.27	7.39	1.76	1.5	44.07	36.52	Eutonic
14.86	7.55	1.47	1.49	4.03	59.88	$Mg(HCOO)_2 \cdot H_2O$
11.45	7.63	1.09	1.45	3.25	51.79	″
7.80	8.32	0.72	1.53	2.27	55.32	″
4.20	9.80	0.38	1.76	1.57	60.38	″
–	11.99	–	2.10	–	–	″

by Schreinemaker's method of residues [19] and confirmed by chemical, thermal, and X-ray phase analyses. Thermal analysis was performed on an MOM-12 derivatograph (Hungary), and X-ray phase analysis, on a DRON-3 diffractometer (Cu_{K_α} radiation, Ni filter).

The results of a study of the system $Ba(HCOO)_2$–$Ca(HCOO)_2$–H_2O at 25°C are presented in Table 1, and the solubility isotherm is plotted in Fig. 1a. The system is simple eutonic at this temperature. The crystallizing solid phases are $Ba(HCOO)_2$ [14] and α-$Ca(HCOO)_2$ [15]. The composition of the eutonic solution is (wt %) 15.03 barium formate and 10.23 calcium formate. As either of the components is added, the solubility of the other decreases owing to salting-out.

Data on the solubility in the $Ba(HCOO)_2$–$Mg(HCOO)_2$–H_2O system are presented in Table 1 and Fig. 1b. The solubility isotherm is represented by the crystallization branches of anhydrous barium formate [14] and magnesium formate dihydrate [16], which intersect at the eutonic point of compositions (wt %): 17.27 $Ba(HCOO)_2$ and 7.39 $Mg(HCOO)_2$. The components exert the mutual salting-out effect. For example, the solubility of barium formate in the system decreases from 23.21 to 17.27 wt %, and that of manganese formate, from 11.99 to 7.39 wt %.

A study of the two systems showed that neither double salts nor mixed crystals are formed at 25°C. Thus, when barium formate is crystallized, the zinc and magnesium impurities are concentrated in the mother liquor. Barium formate free of calcium and

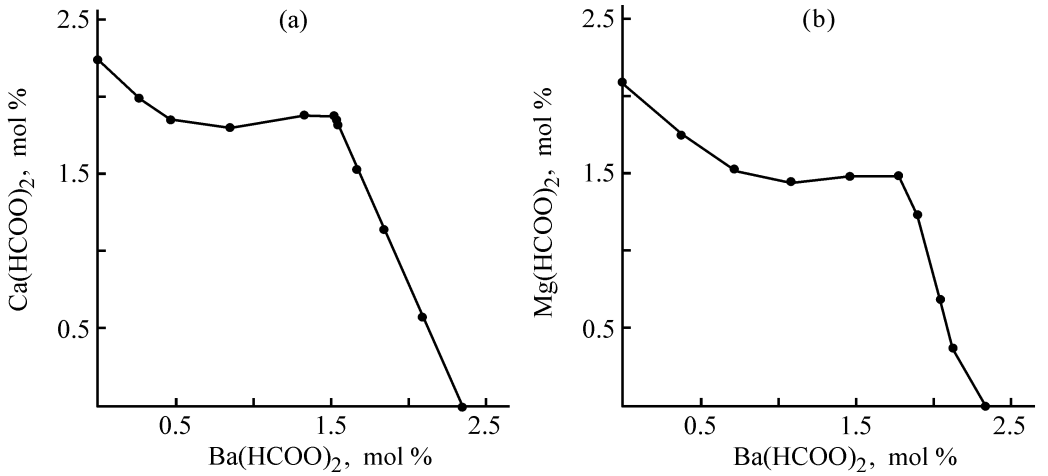

Fig. 1. Solubility isotherms of the systems (a) $Ba(HCOO)_2$–$Ca(HCOO)_2$–H_2O and (b) $Ba(HCOO)_2$–$Mg(HCOO)_2$–H_2O at 25°C.

magnesium impurities can probably be prepared by recrystallization.

Table 2 summarizes data on the compositions of double salts formed in the $Ba(HCOO)_2$–$M(HCOO)_2$–H_2O system (where M is Ni, Co, Cu, Zn, Fe, Mn, Cd, and Ca) at 25°C and lists the M^{2+} ionic radii [20]. As can be seen, barium formate yields double salts of stoichiometric composition $Ba_2M(HCOO)_6 \cdot 4H_2O$ (2 : 1 : 4) and $Ba_2M(HCOO)_4 \cdot 2H_2O$ (1 : 1 : 2) with formates of doubly charged metals. Barium formate gives the first structural type (2 : 1 : 4) with Ni, Co, Cu, Zn, and Fe formates. Only the double salt of copper has crystal structure [3]. All these double salts crystallize in the triclinic system, space group $P\bar{1}$, and have close unit cell parameters, i.e., they are isostructural.

The composition of a double salt and the M^{2+} ionic radius correlate. The structural type (2 : 1 : 4) is formed at ionic radii larger than 0.69 and smaller than 0.75Å. These conditions are satisfied by nickel(II), cobalt(II), copper(II), zinc(II), and iron(II) ions. In the systems $Ba(HCOO)_2$–$Mg(HCOO)_2$–H_2O (this study) and $Ba(HCOO)_2$–$Mn(HCOO)_2$–H_2O [11] no double salts are formed. This is because the Mg^{2+} radius (0.65Å) is probably too small, whereas the Mn^{2+} radius (0.80Å) is too large to make this structure stable. Apparently, the decisive factor influencing the formation of double compounds of the (2 : 1 : 4) structural type containing barium formate is the M^{2+} radius. The double salt of the second type [(1 : 1 : 2)] (only $BaCd(HCOO)_4 \cdot 2H_2O$ is known) crystallizes from aqueous solution at 25°C with the ionic radius increasing further. According to the data obtained in this study, no double salt is formed in the $Ba(HCOO)_2$–$Ca(HCOO)_2$–H_2O system. The ionic radii of Cd^{2+} and Ca^{2+} are very close (0.97 and 0.99Å, respectively). All the data presently available for the water–formate systems, including calcium formate, confirm the formation of anhydrous salts [21]. This fact is accounted for by strong dehydrating action of calcium formate. Probably, no double salt containing crystallization water is formed between barium and calcium formates for this reason.

Table 2. Composition of double salts formed in the $Ba(HCOO)_2$–$M(HCOO)_2$–H_2O systems

M^{2+}	Ionic radius, Å	Double salt composition
Mg^{2+}	0.65	Pure salts
Ni^{2+}	0.69	$Ba_2Ni(HCOO)_6 \cdot 4H_2O$ [6–8]
Co^{2+}	0.72	$Ba_2Co(HCOO)_6 \cdot 4H_2O$ [6, 7]
Cu^{2+}	0.72	$Ba_2Cu(HCOO)_6 \cdot 4H_2O$ [4, 6, 7]
Zn^{2+}	0.74	$Ba_2Zn(HCOO)_6 \cdot 4H_2O$ [6, 7, 9]
Fe^{2+}	0.75	$Ba_2Fe(HCOO)_6 \cdot 4H_2O$
Mn^{2+}	0.80	Pure salts [11]
Cd^{2+}	0.97	$Ba_2Cd(HCOO)_6 \cdot 2H_2O$ [6, 7, 10]
Ca^{2+}	0.99	Pure salts

CONCLUSIONS

(1) The systems $Ba(HCOO)_2$–$M(HCOO)_2$–H_2O (where M is Ca or Mg) were studied at 25°C and the formation of pure salts was established.

(2) Barium formate can be prepared by crystallization from an aqueous solution of impurity-free magnesium and calcium salts.

(3) A correlation between the composition of double barium salts and the M^{2+} ionic radius was estab-

lished. Double salts of the (2 : 1 : 4) type are formed at the ionic radii within 0.69–0.75Å. Above 0.80Å, another structural type (1 : 1 : 2) is formed.

REFERENCES

1. Bechthold, P.S. and Haussühl, S., *Appl. Phys.*, 1977, vol. 14, no. 4, pp. 403–410.
2. Feliksinski, T. and Kolasinski, W., *Mat. Res. Bull.*, 1982, vol. 17, pp. 1557–1561.
3. Sundara Rao, R.V.C., Sundarama, K, and Sinankara Rao, G., *Z. Kristallogr.*, 1958, vol. 110, nos. 3–4, pp. 231–240.
4. Portnova, S.M., Krasilov, Yu.I., Kuznetsov, N.T., and Balakaeva, I.V., *Zh. Neorg. Khim.*, 1990, vol. 35, no. 1, pp. 237–240.
5. Vega, D., Polla, G., Leyva, A.G., *et al., J. Solid State Chem.*, 1999, vol. 147, no. 2, pp. 545–551.
6. Lossen, W. and Voss, G., *Annalen der Chemie*, 1891, vol. 266, pp. 30–52.
7. Groth, P., *Chem. Cryst.*, 1910, vol. 3, pp. 11–15.
8. Fakeev, A.A., Samofalova, N.N., Iskhakova, L.D., and Zhadanov, B.V., *Zh. Prikl. Khim.*, 1999, vol. 72, no. 8, pp. 1262–1266.
9. Fakeev, A.A., Samofalova, N.N., Iskhakova, L.D., and Zhadanov, B.V., *Zh. Prikl. Khim.*, 2000, vol. 73, no. 2, pp. 180–184.
10. Nadzharyan, A.K., Itkina, L.S., and Lepeshkov, I.N., *Zh. Neorg. Khim.*, 1980, vol. 25, no. 6, pp. 1676–1679.
11. Fakeev, A.A., Iskhakova, L.D., and Samofalova, N.N., *Zh. Prikl. Khim.*, 2000, vol. 73, no. 4, pp. 532–536.
12. Ashton, F.W., Houston, D.F., and Saylor, C.P., *J. Res. U.S. Bur. Stand.*, 1933, vol. 11, pp. 233–253.
13. Balarew, Chr., Stoilova, D., and Vassileva, V., *Commun. Depart. Chem. Bulg. Acad. Sci.*, 1981, vol. 14, no. 1, pp. 57–62.
14. Watanabe, T. and Matsui, M., *Acta Crystallogr., B.*, 1978, vol. 34, no. 9, pp. 2731–2736.
15. Burger, N. and Fuess, H., *Acta Crystallogr., B.*, 1977, vol. 33, no. 6, pp. 1968–1970.
16. De With, G., Harkema, S, and van Hummel, C.J., *Acta Crystallogr. B.*, 1976, vol. 32, no. 7, pp. 1980–1983.
17. Khlopin, V.G., *Izbrannye trudy* (Selected Works), Moscow: Akad. Nauk SSSR, 1957, vol. 1.
18. Schwarzenbach, G. and Flaschka, H., *Complexometric Titrations*, London: Methuen, 1969.
19. Schreinemakers, F.A.H., *Z. Phys. Chem.*, 1906, vol. 55, p. 73.
20. Pauling, L., *The Nature of the Chemical Bond and the Structure of Molecules and Crystals*, New York: Cornell Univ., 1960.
21. Vasileva, V.Z., *Zh. Prikl. Khim.*, 2000, vol. 73, no. 3, pp. 381–383.

Russian Journal of Applied Chemistry, Vol. 76, No. 8, 2003, pp. 1225–1229. Translated from Zhurnal Prikladnoi Khimii, Vol. 76, No. 8, 2003, pp. 1264–1268.

SORPTION AND ION-EXCHANGE PROCESSES

Demineralization of Industrial Activated Carbons in an Extractor for Removing Components from Solid Materials

A. I. Loskutov, I. S. Slepchenkov, A. A. Kopyrin, and N. L. Medvedskii

St. Petersburg State Technological Institute, St. Petersburg, Russia

Received December 30, 2003; in final form, May 2003

Abstract—The possibility of exhaustive demineralization of industrial carbon sorbents by multiple treatment in the sequences acid–water–ammonia and alkali–water–acid–water was assessed. The influence exerted on the degree of demineralization by the process mode and composition of the alkaline solution was studied.

All the industrial activated carbons contain inorganic components in varied, and occasionally significant amounts. They pass into carbons from a starting material or are introduced into the charge before activation, which is carried out to improve the capacity and selectivity of sorbents or catalytically active carbons. The content of these mineral components [determined as ash according to the GOST (State Standard) 12596–67] may be as high as 20% of the carbon weight, and thus they can strongly affect the properties of the material [1–7]. Certain fraction of mineral components can leave the sorbent, strongly polluting the solution. Ash components affect the total porosity of the material [4, 8], creating nonuniform sorption profile in its bulk and, thus, changing the sorption of various (e.g., organic) compounds [7]. Therefore, the requirements to the sorbent purity are very stringent in some application fields (such as medicine, production of ultrapure compounds, nuclear industry, and drinking water supply).

Demineralization of carbon sorbents is of particular scientific and practical importance; it can be described as extraction in a solid–liquid system. Moreover, demineralization of carbon sorbents is (to some extent) similar to leaching of rocks that are difficult to break down. Acidic procedures are often used in demineralization of graphite carbon materials; for partial leaching the material is treated with nitric, hydrochloric, or sulfuric acids; for exhaustive leaching, with hydrofluoric acid or its mixtures with other mineral acids [3, 4, 8, 9]; which is followed by washing with hydrochloric acid and water.

Extraction in the solid–liquid system can be intensified by changing temperature, pressure, and particle size of the material and by applying external force fields [10–12].

We studied demineralization of carbon sorbents by their treatment with boiling reagents in the sequences acid–water–alkali–water and alkali–water–acid–water in several cycles and analyzed the effect exerted on the demineralization by intermittent and continuous stirring of a solid granular material.

EXPERIMENTAL

In this study we used SKT-6A activated carbon, because its sorption capacity is the highest among the Russian commercial activated carbons. We also studied AG-3 carbon, which is widely used in solvent recuperation and drinking water treatment. The reagents were 20% NH_4OH, KOH, and NaOH aqueous solutions, distilled water, and azeotropic hydrochloric acid. The treatment in the sequences acid–water–alkali–water and alkali–water–acid–water was performed using NH_4OH and KOH (or NaOH), respectively. The treatment time with each reagent was 4 h, so that the total cycle took 16 h. Since the multiple treatment is more efficient than a single-cycle treatment, we performed several complete treatment cycles in each sequence and with each sample.

Demineralization was carried out in a modified Soxhlet extractor [13–16] with water or acid condensates. The acid (as well as wash waters) can be distilled and recycled; as a result, the discharge of waste water would be only 1–2 volumes per sorbent volume, which is smaller than that in the existing flowsheets by a factor of 20 [3, 7, 9].

1070-4272/03/7608-1225 $25.00 © 2003 MAIK "Nauka/Interperiodica"

Table 1. Degree of demineralization of SKT-6A carbon upon treatment in the sequence HCl–H_2O–NH_4OH–H_2O without stirring

Parameter	Treatment cycle		
	no. 1	no. 2	no. 3
Content of mineral components in the starting sample c_{st}, wt %	5.57	3.87	2.89
Degree of demineralization, α, after acid and water treatment, %	13.27	1.8	8.12
Purification coefficient K_{pur}	1.15	1.46	2.14
Content of mineral components after acid and water treatment, c_{res}, wt %	4.83	3.81	2.60
Degree of demineralization, α, after alkali and water treatment, %	19.67	24.15	11.23
Purification coefficient K_{pur}	1.44	1.93	2.42
Content of mineral components after alkali and water treatment, c_{res}, wt %	3.87	2.89	2.3

* $\alpha = [(c_{st} - c_{res})/c_{res}] \times 100$, $K_{pur} = c_{st}/c_{res}$.

To break the stagnation zones in the large-scale pilot extractor and to diminish the effect of filtration, the bed of the solid sorbent was intermittently or continuously fluidized with bubbling nitrogen. In the case of intermittent fluidization, the gas was bubbled through the sorbent bed for 5–10 min after every hour of unit operation. Both the intermittent and continuous fluidization were performed in the three-phase spouted bed mode [13, 15, 19]. In the course of treatment, the ash content in the solid phase was determined according to the GOST 12596–67; the samples were taken after each cycle of water treatment. The liquid phase was also sampled for microscopic dispersion analysis of particles carried away from the carbon sorbent by a liquid flow.

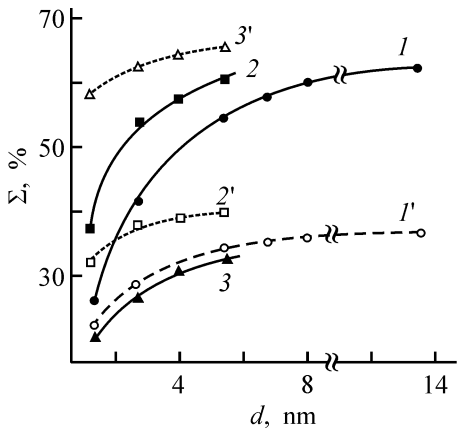

Integral size distribution curves of dispersed (*1*–*3*) carbon and (*1'*–*3'*) mineral particles. (Σ) Total content of the dispersed particles and (*d*) dispersed particle size. Sorbent treatment with: (*1*, *1'*) water, (*2*, *2'*) azeoropic hydrochloric acid, and (*3*, *3'*) aqueous ammonia.

The data on the degree of demineralization after each cycle of treatment of SKT-6A carbon with ammonia (alkali) without stirring are listed in Table 1. As seen, for SKT6A carbon, the alkaline demineralization is more efficient than the acid treatment. It should be noted, however, that acid pretreatment improves alkaline demineralization (and alkaline, vice versa, promotes acidic demineralization), because these reagents remove different mineral components from the aluminosilicate crystallites. The high efficiency of the alkaline treatment is also confirmed by data of microscopic dispersion analysis, which also indicate that some fraction of the mineral components is removed as disperse particles without dissolution (see figure).

A microscopic examination of the SKT-6A ash after three complete treatment cycles showed that the residual inclusions mainly consist of 30–90-nm coarse transparent plate-like crystals (resembling silica) and smaller steel-gray crystals.

An analysis of the wastewater after the alkali–water–acid–water treatment using KOH or NaOH showed that, after 12-h settling a carbon dust sediment was formed on the chamber bottom, and its layer was covered with a layer of light-colored mineral particles. The solution after filtration was dark green. With pH decreasing from 14 to 12–11, a significant amount of a white jelly-like precipitate appeared with significant decolorization of the solution. With pH decreasing further, to 6–4, the solution color was restored with partial dissolution of the precipitate. The residual fraction of this precipitate is probably silicic acid. This suggests that the compounds forming hydroxo complexes {$[Ni(OH)_3]^-$, $[Fe(OH)_4]^-$, $[Mn(OH)_3]^-$, $[Al(OH)_4]^-$, etc.} and fulvic acids, which are not precipitated with alkalis, are removed from activated carbons along with hydroaluminosilicates. This can account for the incomplete decolorization of the solution. Humic acids should be removed from carbon sorbents in preparing ultrapure compounds, especially ultrapure alkali metal hydroxides and salts, and also substances eluted with alkali solutions [19].

Table 2. Degree of demineralization of SKT-6A carbon samples upon treatment in the sequence $HCl–H_2O–NH_4OH–H_2O$

Cycle no.	Parameter	Stirring		
		none	intermittent	continuous
		c_{st} = 5.57 wt %		c_{st} = 10.7 wt %
1	α, %	30.33	37.7	36.5
	K_{pur}	1.44	1.61	1.58
2	α, %	46.67	57.26	49.35
	K_{pur}	1.88	2.34	1.97
3	α, %	58.7	60.50	59.13
	K_{pur}	2.42	2.50	2.45
4	α, %	–	64.63	67.94
	K_{pur}	–	2.83	3.12
c_{res} after third treatment cycle, wt %:				
extractor top		2.3	2.2	3.4
extractor bottom		3.8	2.8	3.4

Table 3. Demineralization of industrial activated carbons upon treatment in the sequence $KOH–H_2O–HCl–H_2O$

Carbon	Initial ash content (c_{st}), wt %	Acid treatment	Cycle						Residual ash content (c_{res}) after third treatment cycle, wt %
			no. 1		no. 2		no. 3		
			α, %	K_{pur}	α, %	K_{pur}	α, %	K_{pur}	
AG-3	14.3	Dynamic	65.91	2.93	77.56	4.46	80.42	5.11	2.8
SKT-6A	6.9	″	74.86	3.98	82.34	5.66	–	–	1.22
	9.47	Static	65.36	2.89	69.27	3.25	73.54	3.78	2.51
	9.47	Dynamic	66.29*	2.97	70.75*	3.42	74.85*	3.98	2.38*
	5.57	″	32.28**	1.49	56.9**	2.32	67.68**	3.10	1.8**

* Treatment with NaOH solution.

** Treatment with NH_4OH solution.

The degree of demineralization of the SKT-6A activated carbon, as influenced by the number of extraction cycles in various treatment modes, is given in Table 2. As seen, the content of mineral components in an extractor with a fixed sorbent bed, operating in the plug-flow mode, strongly changes along the apparatus height. This may be due to filtration of the washed-out dispersed particles in the sorbent bed and by the fact that, when flowing within the sorbent bed, the reagents are saturated with reaction products and thus the driving force of the extraction process becomes weaker. In the absence of fluidization, the ash content of the sorbent at the top and bottom of the extractor differed by a factor of 1.5; with intermittent stirring, by a factor of 1.15, whereas at continuous fluidization no difference was observed. Thus, stirring ensures uniform treatment of the sorbent in the apparatus volume. As seen from Table 2, at intermittent and continuous fluidization, the main fraction of mineral components (probably from the transport pores) are removed in the first two cycles. Upon subsequent treatment, the degree of demineralization increases to a lesser extent, because the process rate is limited by the rate of internal diffusion in the micropores, with decreasing total amount of the mineral inclusions. In this case, the process rate is almost independent of pulsation and fluidization.

Demineralization with KOH solution in various modes of acid treatment was studied with SKT-6A and AG-3 carbons; in the case of NaOH solution, only SKT-6A carbon was used. In all the cases, the sorbent was treated with boiling alkali solutions; the solid : liquid ratio (s : l) was 1 : 5. The results obtained are listed in Table. 3

As seen from Table 3, positive results of the alkaline treatment are manifested both in subsequent boiling in the acid and in the acid treatment in the inter-

Table 4. Total pore volume of SKT-6A carbon as influenced by the degree of demineralization in static treatment in the sequence KOH–H_2O–HCl–H_2O

Cycle no.	c_{st}, wt %	α, %	K_{pur}	V_s	ΔV_s
				$cm^3\ g^{-1}$	
0	9.47	0	0	1.08	
1	3.28	65.36	2.89	1.25	0.17
2	2.91	69.27	3.25	1.27	0.19
3	2.51	73.54	3.77	1.30	0.22
				1.37*	0.29

* After thermal treatment.

mittent washing mode; the results of treatment with NaOH are nearly similar to those with KOH (within experimental error), with subsequent boiling in the HCl solution. Alkali solution removes only 20–25% of the ash in a single cycle, and its main fraction is recovered with acid. In alkali treatment, mineral components are converted into acid-soluble compounds; without this preliminary treatment no more than 27% of the ash are removed with acid in a single cycle.

In the experiments, the carbon sorbent bed came to a boil when treated with acid with the maximum gas evolution observed in the starting period, which is due to heat release in dissolution of the mineral components. Since liquid does not flow in micropores (molecular diffusion mechanism), the main fraction of this heat is consumed for steam generation, and, due to low thermal conductivity of the carbon, only insignificant heat fraction is transferred to the particle surface and dissipated in the core of the liquid flow. The decline in the gas evolution in the course of demineralization is due to a decrease in the amount of reacting compounds (impurities) and difficult access of acid to them.

In high-temperature treatment of the carbon (carbonization, graphitization, activation), the structure of mineral inclusions may undergo partial transformation with displacement of some ions (e.g., Na^+, K^+, Ca^{2+}, Mg^{2+}) to the surface of the resulting crystallites. In the course of demineralization, these elements are removed first. The main body of the crystallites loses contact with pore walls and can be damaged by the disjoining hydraulic pressure, especially when blast waves arise upon detachment of gas bubbles from the pore ends. As a result, mineral particles are removed into the solution in a finely dispersed state; this process is also promoted by peptization.

Our experimental data on the total pore volume determined according to GOST 17219–71 well agree with published data and show that, with decreasing ash content in the SKT-6A activated carbon by 70–80%, the total pore volume increases by 0.17–0.30 cm^3 per gram carbon (Table 4).

CONCLUSIONS

(1) Multiple treatment in the sequence alkali–water–acid–water ensures demineralization of industrial carbon sorbents; the efficiency decreases in the order KOH > NaOH > NH_4OH.

(2) Demineralization of carbon sorbents involves both dissolution of mineral components and their removal as finely dispersed particles.

(3) The three-phase fluidized bed mode provides more uniform treatment of the sorbent in the apparatus volume and is especially efficient in the first two treatment cycles.

REFERENCES

1. Dubinin, M.M., in *Poverkhnostnye khimicheskie soedineniya i ikh rol' v yavleniyakh adsorbtii: Sbornik trudov po adsorbtsii, posvyashchennyi 200-letiyu MGU im. M.V. Lomonosova* (Surface Chemical Compounds and Their Role in Adsorption: Coll. of Works Devoted to Bicentenary Anniversary of the Lomonosov Moscow State University), Moscow: Mosk. Gos. Univ., 1957, pp. 9–33.
2. Hassler, J.W., *Activated Carbon*, New York: Chemical, 1963.
3. Koganovskii, A.M., Levchenko, T.M., and Kirichenko, V.A., *Adsorbtsiya rastvorennykh veshchestv* (Adsorption of Dissolved Compounds), Kiev: Naukova Dumka, 1977.
4. Loskutov, A.I., Preparation and Properties of Nitrogen-Containing Activated Carbons, *Cand. Sci. Dissertation*, Leningrad, 1968.
5. Kuzin, I.A., *Zh. Vses. Khim. O-va im. D.I. Mendeleeva*, 1969, vol. 13, no. 5, pp. 551–558.
6. Kuzin, I.A. and Loskutov, I.A., *Zh. Prikl. Khim.*, 1966, vol. 39, no. 1, pp. 100–104.
7. Ermolenko, N.F., Ulazova, A.R., and Yatsevskaya, M.I., *Uchen. Zap. Bel. Gos. Univ.*, 1955, no. 24, pp. 70–73.
8. Dubinin, M.M. and Zaverina, E.D., *Izv. Akad. Nauk SSSR*, 1961, no. 2, pp. 201–205.
9. Loskutov, A.I., Kuznetsov, M.S., Plachenov, T.G., and Ivanova, E.V., *Poluchenie, struktura i svoistva adsorbentov: Mezhvuzovskii sbornik trudov* (Preparation, Structure, and Properties of Adsorbents: Intercollegiate Collection of Works), Leningrad, Leningr. Tekhnol. Inst., 1988, pp. 15–22.

10. Romankov, P.G. and Kurochkina, M.I. *Ekstragirovanie is tverdykh materialov* (Extraction from Solids), Leningrad: Khimiya, 1983.
11. Beloglazov, I.N., *Tverdofaznye ekstraktory* (Solid-Phase Extractors), Leningrad: Khimiya, 1985.
12. Slepchenkov, I.S., Loskutov, A.I., Yankovskii, A.A., and Kopyrin, A.A., in *Sbornik nauchnykh trudov instituta* (Coll. of Scientific Works of the Inst.), Vologda: Vologod. Politekh. Inst., 1996, pp. 133–140.
13. Loskutov, A.I., Kopyrin, A.A., Slepchenkov, I.S., *et al.*, Abstracts of Papers, *Mezhdunarodnaya konferentsiya "Fundamental'nye i prikladnye problemy okhrany okruzhayushchei sredy"* (Int. Conf. "Fundamental and Applied Problems of Environmental Protection"), Tomsk, September 12–16, 1995, vol. 3, p. 193.
14. Loskutov, A.I., Parshina, E.A., Lanin, O.V., *et al.*, Abstracts of Papers, *I Mezhdunarodnyi simpozium "Problemy kompleksnogo ispol'zovaniya rud"* (I Int. Symp. "Problems of Complex Utilization of Ores"), St. Petersburg, May 10–14, 1994, pp. 82.
15. Loskutov, A.I., Slepchenkov, I.S., and Kopyrin, A.A., Abstracts of Papers, *II Mezhdunarodnyi simpozium "Problemy kompleksnogo ispol'zovaniya rud"* (II Int. Symp. "Problems of Complex Utilization of Ores"), St. Petersburg, May 19–24, 1996, pp. 286–287.
16. Loskutov, A.I., Slepchenkov, I.S., Murashkin, Yu.V., *et al.*, *Zh. Prikl. Khim.*, 1999, vol. 72, no. 11, pp. 1790–1795.
17. Matur, K. and Epstain, N., *Fontaniruyushchii sloi* (Gush Layer), Leningrad: Khimiya, 1978.
18. RF Patent 2131767.
19. Tarkovskaya, I.A., *Okislennyi ugol'* (Oxidized Carbon), Kiev: Naukova Dumka, 1981.

Russian Journal of Applied Chemistry, Vol. 76, No. 8, 2003, pp. 1230–1233. Translated from Zhurnal Prikladnoi Khimii, Vol. 76, No. 8, 2003, pp. 1269–1272.

SORPTION AND ION-EXCHANGE PROCESSES

Synthesis and Thermal Swelling of Residual Graphite Hydrosulfates Obtained Using the $Na_2Cr_2O_7$–H_2SO_4 System

A. P. Yaroshenko, M. V. Savos'kin, A. N. Magazinskii, and O. B. Savsunenko

Litvinenko Institute of Physicoorganic and Coal Chemistry, Ukrainian National Academy of Sciences, Donetsk, Ukraine

Received August 13, 2002; in final form, March 2003

Abstract—The influence exerted by the conditions of synthesis of residual graphite hydrosulfate in a system constituted by concentrated sulfuric acid and saturated aqueous solution of sodium dichromate on the properties of the final product was studied in a wide range of reagent consumptions. The swelling coefficient and the loss of the product were analyzed as functions of the intercalate content in the product.

Previously, method for preparing high-quality residual graphite hydrosulfate, including treatment of natural flaky graphite with a 50-wt % aqueous solution of CrO_3 and then with H_2SO_{4con}, hydrolysis of the obtained graphite hydrosulfate, and washing and drying of the final product, has been developed [1–7]. The product obtained effectively swells at a relatively low temperature (500°C) and is used for fire prevention and in metallurgy.

However, this method uses an aqueous solution of CrO_3, which is an extremely volatile and toxic compound. In addition, this aqueous solution is highly corrosive, even with respect to stainless steel.

In this study, we analyzed the possibility of replacing CrO_3 with less toxic sodium dichromate and the properties of the residual graphite hydrosulfates obtained in this case.[1]

Natural flaky graphite of GT-1 brand[2] with ash content of 5.68 wt % was subjected to oxidation. Mainly two graphite fractions were present: 0.630–0.315 mm (74.3 wt %) and 0.315–0.200 mm (22.1 wt %). We used a solution in distilled water, containing 67.7 wt % $Na_2Cr_2O_7$ (ρ = 1.65 g cm^{-3}), as oxidant and chemically pure H_2SO_4 with concentration of 95.8 wt % (ρ = 1.835 g cm^{-3}).

The residual graphite hydrosulfate was synthesized at room temperature by the following procedure. An aqueous solution of $Na_2Cr_2O_7$ was added to 25 g of the starting graphite under agitation. After 10 min, H_2SO_4 was introduced into the reactor, and the reaction mass was agitated for another 10 min. Then, water (500 cm^3) was added and the mixture obtained was agitated and allowed to stay for 24 h to be hydrolyzed. During this period, small gas bubbles (CO_2 and probably CO) continuously evolved from the solid-phase layer. Then, the solid phase was filtered off on a paper filter in a water-jet-pump vacuum and washed with 2 l of water. The wet product was dried at 100–110°C to humidity not exceeding 1.0 wt %. The consumption of the aqueous solution of $Na_2Cr_2O_7$ per 100 g of graphite was varied within the range 2–20 cm^3, and that of H_2SO_{4con}, within 20–48 cm^3. The coefficient of swelling at 500°C in a shock heating mode, K_s^{500} (cm^3 g^{-1}), and the mass loss at 500°C were determined for all the 92 samples synthesized. The intercalate m_i (wt %) in the product was calculated from the values of the product yield on the assumption that no phase oxidation of graphite occurs at room temperature [8, 9], i.e., the whole amount of carbon is transferred from the graphite skeleton to the final product.

To determine the swelling coefficient of the products obtained, a weighed portion (m = 0.2–0.3 g) of the product was introduced into a stainless steel cell, preliminarily placed in a muffle furnace heated to 500°C, and kept there for 5 min to complete swelling. The cell with swollen graphite was withdrawn from the furnace and its contents were carefully transferred from the cell to a glassy volumetric flask and the volume V (cm^3) occupied by swollen graphite was measured. The swelling coefficient was determined as

[1] The term "residual graphite hydrosulfate" is used in this study for nonstoichiometric compounds formed upon modification of graphite hydrosulfate with water.

[2] Graphite from the Zaval'evsk deposit, Ukraine.

1070-4272/03/7608-1230 $25.00 © 2003 MAIK "Nauka/Interperiodica"

arithmetic mean of the ratio $K_s^{500} = V/m$ in three parallel runs.

The synthesis method developed in this study allows preparation of high-quality residual graphite hydrosulfate even at total consumption of the reagents of 60–80 mass fractions per 100 mass fractions of graphite.

The process involves graphite oxidation by chromium(VI) and intercalation of the resulting positively charged graphite matrix by hydrosulfate anions solvated by sulfuric acid molecules. In the limiting case, graphite hydrosulfate of the second degree of intercalation, with composition $C_{48}^{+} \cdot HSO_4^{-} \cdot (2.0–2.5)H_2SO_4$, is formed in this stage.[3] The content of sulfur(VI) in the residual graphite hydrosulfate obtained can be diminished from 11 wt % in the starting graphite hydrosulfate to 2.0 wt % by hydrolysis and washing with water. Apparently, this is due to the replacement of sulfuric acid molecules, solvating the hydrosulfate anion, with water molecules. In this case, the total content of the intercalate in the product obtained is as high as 25–35 wt %. The product obtained effectively swells at relatively low temperature, which makes it especially attractive for use as fire retardant. At 500°C, the swelling coefficient is as high as 250 $cm^3\ g^{-1}$.

Figure 1 shows how the swelling coefficient of the residual graphite hydrosulfates obtained depends on the consumption of oxidant (sodium dichromate aqueous solution) and concentrated sulfuric acid. This dependence is a hilly surface with a small plateau at the vertex at K_s^{500} = 200 $cm^3\ g^{-1}$, at oxidant and sulfuric acid consumptions per 100 g of graphite equal to, respectively, 11–13 and 40–44 cm^3. Outside the plateau, at lower and higher reagent consumptions, a decrease in the swelling coefficient is observed.

At oxidant consumption lowered to 8 cm^3/100 g graphite, the swelling coefficient of graphite is only about 20 $cm^3\ g^{-1}$, i.e., decreases by an order of magnitude. The decline in the swelling coefficient with decreasing consumption of sulfuric acid is described by a more gently sloping dependence, which, to a first approximation, is linear. Outside the plateau, at higher reagent consumption, a slight decrease in the swelling coefficient is observed. However, this decrease has a different origin. The decrease in K_s^{500} with increasing sulfuric acid consumption is due to the formation of a difficultly agitated viscous mass, whereas that with increasing oxidant consumption is associated with a decrease in the acidity of the intercalating solution because of its dilution with water introduced with the oxidant solution.

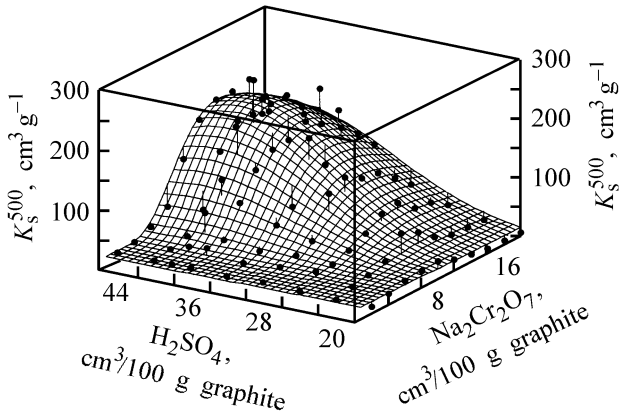

Fig. 1. Swelling coefficient of residual graphite hydrosulfate at 500°C, K_s^{500}, vs. the consumptions of $Na_2Cr_2O_7$ aqueous solution and concentrated H_2SO_4 in the synthesis stage.

The multiple parametric regression method was used to demonstrate that, at the reagent consumptions studied, the surface shown in Fig. 1 is described (with correlation coefficient r = 0.915) by the following empirical equation containing only two quadratic terms:

$$K_s^{500} = -23.24 + 0.4805AB - 0.4944A^2, \quad (1)$$

where A and B are, respectively, the oxidant and H_2SO_4 consumptions.

In setting-up Eq. (1), data corresponding to 10 samples obtained at the maximum consumption of sulfuric acid (48 cm^3/100 g graphite) were excluded from the regression because of the formation of a difficultly agitated viscous mass and the resulting uncontrollable conditions of product synthesis.

According to Student's t criterion, all the regression coefficients of Eq. (1) are significant. It is noteworthy that the regression analysis revealed nonsignificance of the linear terms, i.e., the swelling coefficient is determined by the product of the reagent consumptions, rather than by the consumptions themselves. This is due to a rise in the Cr(VI) oxidation potential with increasing solution acidity [10].

In all probability, the last, negative term of Eq. (1) reflects a decrease in the oxidation potential of dichromate ions in the intercalating mixture owing to its dilution with water introduced into the reaction mass together with the oxidizing solution.

[3] Graphite hydrosulfate has general formula $C_{24n}^{+} \cdot HSO_4^{-} \cdot mH_2SO_4$, where n is the degree of intercalation of the graphite compound, indicating the number of graphite layers between the adjacent intercalate layers.

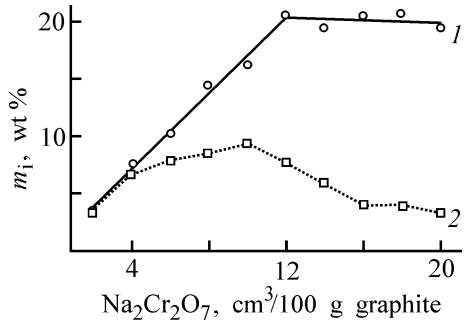

Fig. 2. Intercalate content m_i in residual graphite hydrosulfate vs. the consumption of $Na_2Cr_2O_7$ aqueous solution at constant consumption of H_2SO_4. Sulfuric acid consumption (cm^3/100 g graphite): (*1*) 44 and (*2*) 20.

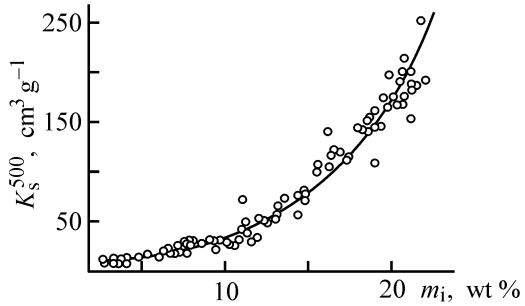

Fig. 3. Swelling coefficient of residual graphite hydrosulfate at 500°c K_S^{500} vs. intercalate content m_i. $K_S^{500} = 6.96\exp(0.160\,m_i)$, $r^2 = 0.968$.

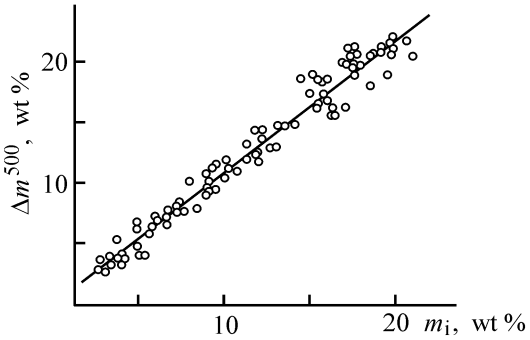

Fig. 4. Mass loss in swelling of residual graphite hydrosulfate at 500°C Δm^{500} vs. intercalate content m_i. $\Delta m^{500} = 1.099\,m_i - 0.061$; $r^2 = 0.966$.

The dependences of the intercalate content in the product synthesized at sufficiently high and relatively low acidities of the intercalating solution on the oxidant consumption (Fig. 2) clearly show that the stage of oxidation of the graphite skeleton governs the composition of the residual graphite hydrosulfate formed.

Raising the consumption of the aqueous oxidizing solution from 2 to 12 cm^3/100 g graphite at high acidity of the intercalating solution leads to a linear increase in the intercalate content in the final product (Fig. 2, curve *1*). In this case, the oxidation potential of the intercalating solution is so high that it ensures synthesis of a compound of the second degree of intercalation at 12 cm^3 of oxidizing solution consumed per 100 g of graphite, despite that the amount of the water introduced into the reaction mass with oxidizing solution grows. Raising the consumption of the aqueous oxidizing solution further does not lead to any increase in the intercalate content, which is indicated by a sharp bend and the following leveling-off of the dependence. This can be accounted for by an insufficient, despite the oxidant accumulation in the system, oxidation potential of the intercalating solution to give an intercalation compound of the first stage. Apparently, at lower consumption of the oxidizing solution, the graphite intercalation compounds of higher stages, which contain less intercalate, are formed.

At low amount of sulfuric acid in the reaction mass, raising the consumption of the oxidizing solution leads initially to an increase in the parameter m_i. However, the dilution of the intercalating solution with water introduced together with the oxidant results in a deviation from the linear dependence and gives rise to a maximum at a consumption of the oxidizing solution of 10 cm^3 per 100 g graphite (Fig. 2, curve *2*). Further increase in the oxidant consumption leads to a steady decrease in the intercalate content in the final product.

It follows from Fig. 2 that the intercalate content m_i in the final product can serve as a general characteristic of the efficiency of graphite intercalation, despite its being a complex process depending on a wide variety of parameters. It is the intercalate content that determines, in the end, the capacity of the final product for swelling under heating (Fig. 3).

The swelling coefficient of the residual graphite hydrosulfate depends on the intercalate content in it exponentially over the entire range of the reagent consumptions, with a correlation coefficient $r^2 = 0.968$. Such a behavior shows that the intercalate efficiency grows in the course of swelling, as its content in the product increases. This may be due to a change in the degree of intercalation of the residual graphite hydrosulfate with increasing intercalate content or to a change in the nature of the intercalate in the filled layers of the skeleton of residual graphite hydrosulfate.

It was found that, in swelling of the resulting products at 500°C, virtually the whole amount of the intercalate is removed from the structure of the residual graphite hydrosulfate, as evidenced by the linear relationship between the mass loss in swelling and the intercalate content m_i, with a slope close to unity (Fig. 4).

CONCLUSIONS

(1) High-quality residual graphite hydrosulfate can be obtained at extremely low consumption of the reagents by oxidation of graphite with a concentrated aqueous solution of sodium dichromate in the presence of sulfuric acid, with the subsequent hydrolysis of graphite hydrosulfate. The product obtained can be effectively swollen at relatively low temperature, which makes it especially attractive for use as fire retardant.

(2) An empirical equation, according to which the swelling coefficient is primarily determined by the product of the reagent consumptions, was suggested on the basis of an analysis of the experimental dependence of swelling coefficient on the reagent consumption in synthesis.

(3) Its was shown that the intercalate content in the final product is the general characteristic of the intercalation efficiency, and it is this value that determines, in the end, the swelling efficiency.

REFERENCES

1. Yaroshenko, A.P., Shapranov, V.V., and Kucherenko, V.A., *Khim. Tverd. Tela*, 1994, no. 2, pp. 91–96.
2. Yaroshenko, A.P., Popov, A.F., and Shapranov, V.V., *Zh. Prikl. Khim.*, 1994, vol. 67, no. 2, pp. 204–211.
3. Yaroshenko, A.P. and Savos'kin, M.V., *Zh. Prikl. Khim.*, 1995, vol. 68, no. 8, pp. 1302–1306.
4. RF Patent 2058261.
5. Ukranian Patent 30796.
6. Ukranian Patent 30797.
7. Ukranian Patent 34777.
8. Horn, D. and Boehm, H.-P., *Z. anorg. allgem. Chem.*, 1979, vol. 456, no. 9, pp. 117–129.
9. Chernysh, I.G., Karpov, I.I., Prikhod'ko, G.P., and Shai, V.M., *Fiziko-khimicheskie svoistva grafita i ego soedinenii* (Physicochemical Properties of Graphite and Its Compounds), Kiev: Naukova Dumka, 1990.
10. Rudakov, E.S., *Reaktsii alkanov s okislitelyami, metallokompleksami i radikalami v rastvorakh* (Reactions of Alkanes with Oxidants, Metal Complexes, and Radicals in Solutions), Kiev: Naukova Dumka, 1985.

Russian Journal of Applied Chemistry, Vol. 76, No. 8, 2003, pp. 1234–1237. Translated from Zhurnal Prikladnoi Khimii, Vol. 76, No. 8, 2003, pp. 1273–1276.

SORPTION AND ION-EXCHANGE PROCESSES

Composition and Physicochemical Properties of Schungite Sorbent as Influenced by Thermal Treatment

I. O. Krylov, I. G. Lugovskaya, S. I. Anufrieva, and A. V. Krylova

Fedorovskii Russian Institute of Mineral Raw Materials, Moscow, Russia
Mendeleev Russian University of Chemical Engineering, Moscow, Russia

Received July 26, 2002; in final form, February 2003

Abstract—The chemical composition, specific surface area, and pore structure of a schungite sorbent were studied as influenced by the conditions of thermal treatment.

It is known [1–3] that schungite rocks from Karelia are used as sorbents in treatment of waste and reused water. Schungite rocks consist of various minerals (e.g., quartz, aluminosilicates, carbon, etc.) and show promise as complex sorbents combining the properties of carbon and silicate materials.

The sorption properties of schungite rock can be improved by thermal treatment [4]. However, data on how the heating conditions affect the schungite properties are scarce, the possible modes of thermal treatment for schungite modification have not been substantiated.

Samples of schungite sorbents (SSs) were prepared by crushing and sieving a schungite rock from Zazhoginskoe deposit to size grade of 2.5–0.5 mm. The thermal transformations were studied in air in the 20–1000°C temperature range using a 3434-S (model 907) derivatograph (10 deg min^{-1} heating rate, 50-mg sample weight, platinum crucibles, and α-Al_2O_3 reference).

The thermal oxidative treatment of the schungite sorbent was performed at three temperatures corresponding to the characteristic points in the DTA curve of the initial sample (Fig. 1): maximum of the exothermic peak at 528°C and two inflection points of the curve at 411 and 750°C at which structural transformations of the material occur. As seen from the TG curve, a pronounced weight loss by the material begins at about 500°C.

The thermal treatment of the SS samples (35–40 g) were performed in a muffle furnace in air for 1, 2, 3, 4, and 8 h. The rate of heating of the muffle furnace to a given temperature was 5 deg min^{-1}; the temperature was controlled with an accuracy of ±3°C.

The treated samples are denoted as SS-411, SS-528, and SS-750, in accordance with heat treatment temperatures.

Data on the effect of thermal treatment on the chemical composition of schungite sorbents are listed in Table 1.

As seen, the content of carbon in the samples decreases with increasing temperature, whereas the content of silicon and aluminum oxides grows. We assume that the rapid weight loss at temperatures higher than 500°C (Fig. 1) is due to burning-out of carbon, whose content decreases by a factor of 1.4 and 3.4 for SS-528 and SS-750, respectively.

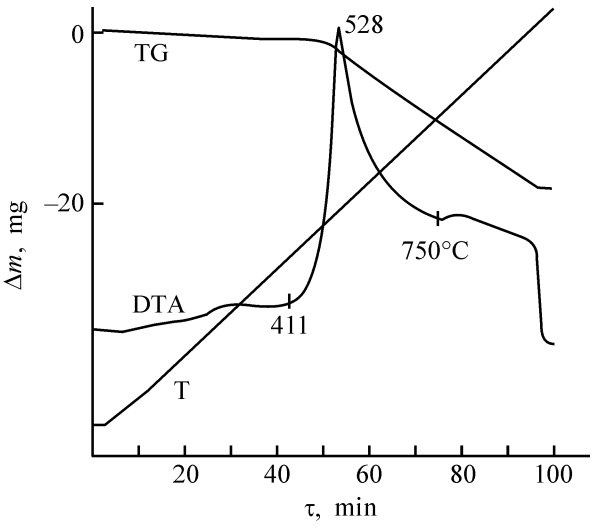

Fig. 1. TG and DTA curves of the initial schungite sorbent: (Δm) weight change and (τ) time.

1070-4272/03/7608-1234 $25.00 © 2003 MAIK "Nauka/Interperiodica"

Table 1. Chemical composition of the initial and thermally treated SS samples

Sample	Composition, wt %									
	C	SiO_2	Al_2O_3	Fe_2O_3	CaO	MgO	MnO	K_2O	Cr_2O_3	TiO_2
Initial	31.00	54.50	4.62	2.04	1.50	0.66	0.02	1.15	0.03	0.22
SS-411	28.10	59.10	4.87	0.89	0.28	0.66	0.01	1.40	<0.02	<0.02
SS-528	21.80	64.81	5.00	0.79	0.28	0.64	<0.01	1.37	<0.02	<0.02
SS-750	9.12	77.35	6.74	1.84	0.28	0.88	0.01	1.90	<0.02	<0.02

The dependences of the sample weight loss on the duration of thermal treatment at the chosen temperatures are shown in Fig. 2.

For SS-411 sample, the weight loss is insignificant (about 3%) and occurs during the first hour of thermal treatment. SS-528 loses up to 6% of its weight during the first hour, on further heating the rate of weight loss decreases, and after 4-h annealing the total weight loss reaches 15% relative to the initial weight of the sample. The dependence for SS-750 sample is steeper: the weight loss in 1 and 4 h is 8 and 20%, respectively.

As seen from Table 2, the duration of thermal treatment at various temperatures affects the specific surface area S_{sp} of the sorbents, determined by the BET procedure from thermal desorption of argon adsorbed at low temperature [5]. Annealing of schungite at 411 and 528°C makes S_{sp} greater, and its value depends on the heating time. For example, the specific surface area of schungite increases by a factor of 1.5 and 3 after heating at 411°C for 1 and 8 h, respectively.

After heating the schungite sorbent at 528°C for 1 h, S_{sp} was the greatest; with increasing annealing time at this temperature, S_{sp} gradually decreased. On heating the schungite sorbent at 750°C for 1 h, S_{sp} remained unchanged and decreased by nearly a factor of 3 after a 4-h treatment.

The pore structure of the sorbent was studied using the samples with the largest specific surface area at each treatment temperature: SS-411 (8 h), SS-528 (1 h), and SS-750 (1 h).

It is known that the micro-, meso-, and macropores on the surface of solids affect their sorption, diffusion, mechanical, capillary, and other properties and determine the features of sorption processes. According to the IUPAC classification [6], pores with average size smaller than 2 nm, 2–50 nm, and greater than 50 nm are micro-, meso-, and macropores, respectively.

Real solids may contain a set of pores ranging from macropores through meso- and micropores to "subatomic" pores as gaps between the cleavage planes or dislocations and point defects.

Table 2. Specific surface area of the SS samples as influenced by thermal treatment duration τ (S_{sp} of the initial sample 9.0 $m^2 g^{-1}$)

Sample	S_{sp} ($m^2 g^{-1}$) at indicated heating time τ, h				
	1	2	3	4	8
SS-411	13.8	20.3	24.2	25.2	28.0
SS-528	29.3	22.8	16.4	17.2	
SS-750	9.0			3.2	

Data on the pore structure, obtained by sorption of iodine and acetone using known procedures [7, 8], are listed in Table 3.

As seen, the sorption capacity for iodine increases at 411 and 528°C, which indicates that the micropore structure of the material is developed by thermal treatment; in the case of SS-411, nearly a two-fold increase in comparison with the initial sample is observed. With the temperature increasing to 528 and 750°C, the interpore partitions break down and mesopores are formed. As a result, the sorbent porosity increases by a factor of 1.5 (acetone sorption). In the case of SS-750 sample, the sorption capacity for iodine (i.e., the content of micropores) decreases.

Mercury porosimetry is the best suitable for evaluating the size of macro- and coarse mesopores. The measurements were performed on a 2000 Macropore Unit Model 120 high-pressure mercury porosimeter,

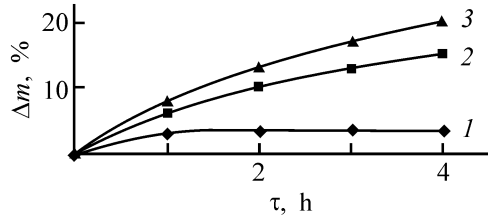

Fig. 2. Weight loss by the samples (Δ*m*) vs. the annealing time τ. (*1*) SS-411, (*2*) SS-528, and (*3*) SS-750.

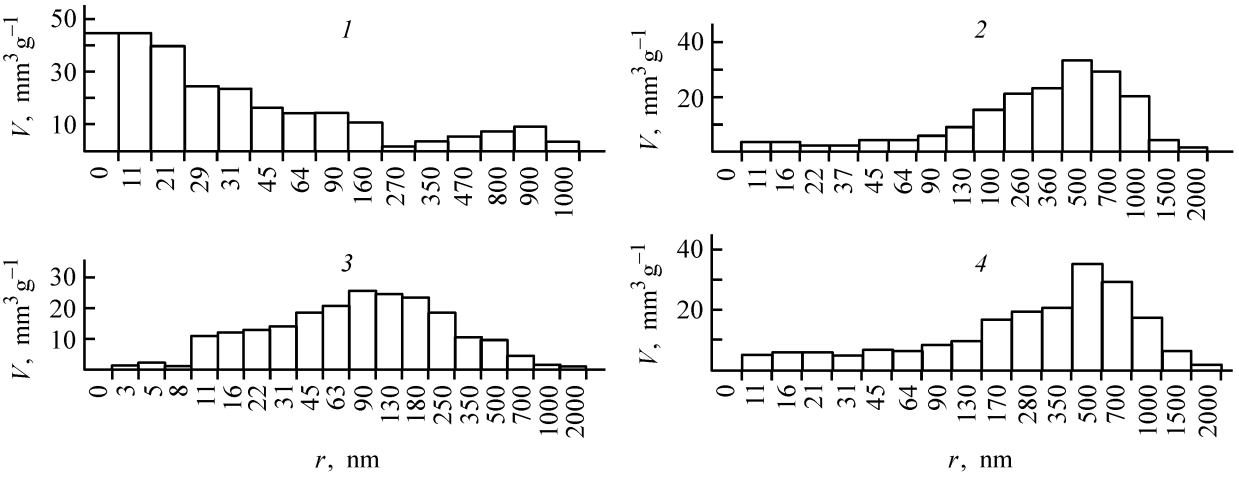

Fig. 3. Pore volume V distribution with respect to pore radius r. (*1*) Initial SS, (*2*) SS-411, (*3*) SS-528, and (*4*) SS-750.

using the procedures described in [9]. The principle of operation of this unit is based on the behavior of a nonwetting liquid (mercury) in the sample capillaries (bottles and cylinders).

The total pore volume and typical pore size in the initial and thermally modified samples, determined by mercury porosimetry, are listed in Table 3.

These data show that the total pore volume of SS-411 and SS-750 sorbents is greater by more than an order of magnitude than that of the initial sample, and a macroporous structure is formed. In SS-528 sorbent, the mesopore structure is predominant, and its total pore volume is smaller by almost a factor of 2.

The distribution of pore volumes with respect to the pore radius is illustrated by histograms Fig. 3.

Table 3. Properties of the SS samples after thermal treatment.

Properties	Initial SS	SS-411	SS-528	SS-750
Treatment temperature, °C	–	411	528	750
Treatment duration h	–	8	1	1
Sorption capacity for iodine, mg g^{-1}	11.4	23.17	16.07	9.84
Porosity for acetone, vol %	33.9	21.05	33.58	31.33
Total pore volume, cm^3 g^{-1}	0.025	0.289	0.175	0.300
Typical pore size, nm	13	596	106	596

The initial SS sample is characterized by approximately bidisperse structure with the first maximum in the mesopore range (11–21 nm), extending as a shoulder to the macropore range (64–160 nm) and the second diffuse maximum at 800 nm covering the 350–1000 nm macropore range.

As seen from Fig. 3, SS-411 and SS-750 have similar pore volume distributions in the 500–700 nm range, with a shoulder at 130–350 nm and a small maximum in the mesopore range (11–16, 21 nm). These data suggest that prolonged heating (8 h) of the SS sample at 411°C yields the same macro- and mesopore structure as treatment for 1 h at 750°C.

At a smaller total pore volume, the pore size distribution in SS-528 is more symmetrical with a maximum at 90–180 nm, a broad shoulder at 31–11 nm, and insignificant amount of fine 3–8-nm mesopores.

The development of the sorbent pore structure in the course of thermal treatment and its rather complex variation with heating may be probably due to removal of water vapor from sorbent pores at low temperatures and burning-out of schungite carbon at high temperatures. To understand in detail the mechanism of formation of the pore structure upon thermal treatment of a schungite sorbent, additional studies are required.

As seen from the above data, the schungite sorbent can be modified by thermal oxidative treatment in air, which raises the specific surface area and allows control of the pore structure. The changes in the chemical composition, specific surface area, and pore structure on heating of the schungite sorbent should be taken into account when choosing the modes of thermal oxidative modification and thermal regeneration of the sorbents.

CONCLUSIONS

(1) Thermal oxidative treatment of schungite sorbents in air raises the specific surface area and allows development of the sorbent pore structure.

(2) During thermal oxidative treatment at 528 and 750°C, the content of carbon in the schungite sorbent decreases by a factor of 1.4–3.4.

(3) The specific surface area of the schungite sorbents increases upon heating at 411 and 528°C and depends on the treatment duration.

(4) The total pore volume at any temperature of thermal treatment of the schungite sorbent increases by an order of magnitude (mercury porosimetry), and the pore size distribution depends on the treatment temperature.

REFERENCES

1. Gorshtein, A.E. and Baron, N.Yu., *Zh. Prikl. Khim.*, 1979, vol. 52, no. 6, pp. 1279–1282.
2. Lugovskaya, I.G. Theoretical and Experimental Validation of Utilization of Schungite Rocks for Treatment of Industrial Solutions and Gas Effluents, *Cand. Sci. Dissertation*, Moscow, 2001.
3. Krylov, I.O., Anufrieva, S.I., and Isaev, V.I., *Ekol. Prom-st. Rossii*, 2002, no. 6, pp. 17–20.
4. Gospodinov, D.G., Pronin, V.A., and Shkarin, A.V., *Ekol. Sist. Prib.*, 1999, no. 1, pp. 59–60.
5. Buyanova, N.E., Gudkova, G.B., and Karnaukhov, A.P., *Kinet. Katal.*, 1965, vol. 6, no. 6, pp. 1085–1091.
6. Gregg, S.J. and Sing, K.S.W., *Adsorption, Surface Area and Porosity*, London: Academic, 1982.
7. Smirnov, A.D., *Sorbtsionnaya ochistka vody* (Sorption Treatment of Water), Leningrad: Khimiya, 1982.
8. Kolyshkin, D.A. and Mikhailov, K.K., *Aktivnye ugli, svoistva i metody ispytanii* (Activated Carbons, Properties and Testing Procedures), Leningrad: Khimiya, 1972.
9. *Eksperimental'nye metody v adsorbtsii i molekulyarnoi khromatografii* (Experimental Procedures in Adsorption and Molecular Chromatography), Kiselev, A.V. and Dreving, V.P., Eds., Moscow: Mosk. Gos. Univ., 1973.

Russian Journal of Applied Chemistry, Vol. 76, No. 8, 2003, pp. 1238–1241. Translated from Zhurnal Prikladnoi Khimii, Vol. 76, No. 8, 2003, pp. 1277–1280.

SORPTION AND ION-EXCHANGE PROCESSES

Sorption of Hexacyanoferrate(II, III) Anions on Nickel(II) Hydroxide

O. V. Nagornyi, A. S. Kolyshkin, and V. V. Vol'khin

Perm State Technical University, Perm, Russia

Received April 17, 2003

Abstract—$Fe(CN)_6^{3-}$ and $Fe(CN)_6^{4-}$ anions are sorbed from aqueous solutions of their potassium and cesium salts on β-$Ni(OH)_2$ by the mechanism of anion exchange with hydroxy groups. Alkali metal cations (K^+, Cs^+) are also partly sorbed on nickel(II) hydroxide in the form of anionic complexes $(K,Cs)_zFe(CN)_6^{(n-z)-}$, where $n = 3$ or 4 ($0 < z < n$). The chemical composition of the new phase appearing in contact of nickel(II) hydroxide with aqueous potassium and cesium hexacyanoferrates(II, III) was determined by X-ray phase analysis and IR spectroscopy.

Inorganic ion exchangers are successfully used for treatment of industrial wastewater and natural waters to remove toxic metal ions and radionuclides [1, 2]. As compared to organic ion exchangers, these sorbents exhibit higher selectivity and have lower price [1, 3]. However, all the commercially available inorganic sorbents are mainly cation exchangers. Only a few types of inorganic anion exchangers have been prepared up to now [4], and the mechanism of their sorption activity is poorly understood. These factors hinder progress in the practical use of these sorbents.

In this study, we analyzed sorption of $Fe(CN)_6^{3-}$ and $Fe(CN)_6^{4-}$ anions on β-$Ni(OH)_2$. Toxic hexacyanoferrate(II, III) anions get into wastewater from units for treatment of industrial wastes to remove cyanides [5].

EXPERIMENTAL

Nickel(II) hydroxide has two crystalline modifications: α-$Ni(OH)_2$ and β-$Ni(OH)_2$ [6, 7]. The α-$Ni(OH)_2$ modification has the hydrotalcite lattice with the interplanar spacing d_{003} from 0.7 to 0.8 nm. The interlayer space in this structure is occupied by H_2O molecules and anions (e.g., NO_3^-, CO_3^{2-}). In the β-$Ni(OH)_2$ lattice, the interplanar spacing decreases to $d = 0.46$ nm which hinders penetration of foreign anions into the interlayer space. Therefore, the mechanism of anion-exchange sorption on β-$Ni(OH)_2$ is simpler, and we chose this modification of nickel hydroxide as a sorbent. In our experiments, β-$Ni(OH)_2$ was prepared by hydrolysis of $Ni(NO_3)_2$ in aqueous solution by the method reported in [8]. However, we failed to obtain nickel hydroxide free of foreign anions.

The initial nickel hydroxide and that after treatment with aqueous solutions containing hexacyanoferrate(II, III) anions were characterized by powder X-ray diffraction and IR spectroscopy. The X-ray diffraction measurements were carried out on a DRON-2.0 X-ray diffractometer with monochromatic radiation (Cu_{K_α}, primary beam). The IR spectra (KBr pellets) were recorded on Specord 75-IR and UR-20 spectrometers. The chemical composition of solid samples (after preliminary dissolution) was determined on an AAS-30 atomic-absorption spectrophotometer. The content of hexacyanoferrate(II, III) anions in solutions was determined by volumetric titration [8, 9].

Sorpion of hexacyanoferrate(II, III) anions on nickel hydroxide from aqueous solutions was studied by a common technique under both dynamic and static conditions [10]. The sorption kinetics was studied at constant $Fe(CN)_6^{n-}$ and OH^- concentrations. These studies were carried on a laboratory setup including a pH meter (an IPL-102 ionometer), a buret for automatic titration, and a controlling computer. In the course of sorption experiments, the solid and liquid phases were vigorously stirred to ensure their uniform distribution in the reaction vessel. The sorption rate was estimated by the titration time.

Sorption of $Fe(CN)_6^{3-}$ and $Fe(CN)_6^{4-}$ on β-$Ni(OH)_2$ under dynamic conditions was studied on a column about 10 cm high. The $K_3[Fe(CN)_6]$ and $K_4[Fe(CN)_6]$ content in the initial solutions was 1.0×10^{-3} M. The maximal total sorption capacity of the sorbent in our experiments was 0.33 mg-equiv g^{-1} for $Fe(CN)_6^{3-}$ and 0.32 mg-equiv g^{-1} for $Fe(CN)_6^{4-}$. In

1070-4272/03/7608-1238 $25.00 © 2003 MAIK "Nauka/Interperiodica"

the course of sorption, the pH of the sorbate increases, which shows that the sorption occurs by the mechanism of anion exchange $Fe(CN)_6^{n-} \rightleftarrows OH^-$. Hexacyanoferrate(II, III) anions were desorbed from nickel hydroxide by passing 1 M NaOH through the column. The degree of desorption was 70–80%.

The equivalence of the anion-exchange sorption was studied under the came conditions, taking into account the joint sorption of anions and cations. We found no significant difference in the sorption characteristics of $Fe(CN)_6^{3-}$ and $Fe(CN)_6^{4-}$ anions and, therefore, only the data on sorption of $Fe(CN)_6^{4-}$ are listed in the table. In the first experimental series, the sorption was studied from a 1.0×10^{-3} M $K_4[Fe(CN)_6]$ solution. In the second experimental series, the liquid phase additionally contained $CsNO_3$ (4×10^{-3} M). The data on sorption of anions and cations, obtained by the chemical analysis of two first 50-ml fractions of the solution, are listed in the table.

These results show that not only $Fe(CN)_6^{4-}$ anions, but also alkali metal cations are sorbed on $Ni(II)(OH)_2$. Sorption of these cations (especially Cs^+) decreases the amount of OH^- anions displaced from nickel hydroxide by $Fe(CN)_6^{4-}$. As can be seen from the table, in both the experimental series, the difference in the first filtrate fraction between the amounts of $Fe(CN)_6^{4-}$ and alkali metal cations sorbed on nickel(II) hydroxide is approximately equal to the amount of the OH^- anions displaced from the sorbent. At the same time, in the second filtrate fraction, the amount of displaced OH^- anions was considerably less than this difference. We believe that this is due to the fact that, in the course of sorption, not only OH^- groups, but also other foreign anions entering into the composition of the sorbent are displaced by $Fe(CN)_6^{4-}$ into the filtrate. In our numerous experiments, we found that the molar ratios of desorbed OH^- anions and sorbed hexacyanoferrate(II, III) anions $OH^-/Fe(CN)_6^{4-}$ and $OH^-/Fe(CN)_6^{3-}$ do not exceed 3.4 and 2.2, respectively.

The kinetic curves of sorption of $Fe(CN)_6^{3-}$ on nickel(II) hydroxide at pH 9 and 10 are shown in Fig. 1.

The kinetic curve of sorption of $Fe(CN)_6^{3-}$ at pH 10 is typical of diffusion-controlled ion-exchange sorption with diffusion in transport pores of granules as the limiting stage. This kinetic curve shows that the sorption rate is high initially and then decreases virtually to zero. In the kinetic curve obtained at pH 9, an inflection point appears, after which the sorption rate becomes constant. Such a shape of the kinetic curve suggests that, in the initial stage of ion-exchange sorption, nuclei of a new phase originate, and further sorption gives a separate phase.

Joint sorption of $Fe(CN)_6^{4-}$ anions and K^+, Cs^+ cations on nickel(II) hydroxide

Experimental series no.	Sorbed ions, mg-equiv				Desorbed OH^-, mg-equiv
	$Fe(CN)_6^{4-}$	K^+	Cs^+	$(I^+ + I^-)^*$	
First	0.180	0.093	–	0.087	0.073
	0.180	0.068	–	0.112	0.085
Second	0.180	0.084	0.069	0.027	0.025
	0.180	0	0.062	0.118	0.045

* $(I^+ + I^-)$ Difference between the amounts of sorbed $Fe(CN)_6^{4-}$ and alkali metal cations

To elucidate the nature of this new phase and conditions of its formation, the sorption was studied at a solid to liquid phase ratio of 1 : 50 and hexacyanoferrate(II, III) concentration of 0.1 M under static conditions. In these experiments, the effect of sorption on the structure and chemical composition of nickel(II) hydroxide was studied by X-ray phase analysis (Fig. 2) and IR spectroscopy (Fig. 3).

The powder X-ray diffraction pattern (Fig. 2, curve *1*) shows that the initial sorbent mainly consists of β-$Ni(OH)_2$. This result is confirmed by the IR spec-

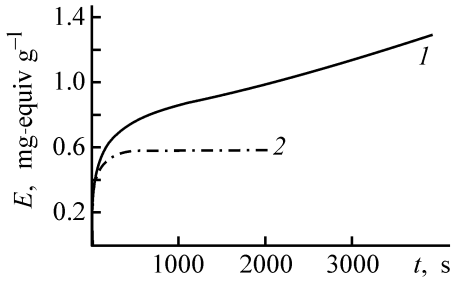

Fig. 1. Kinetic curves of sorption of $Fe(CN)_6^{3-}$ on nickel(II) hydroxide at (*1*) pH 9 and (*2*) pH 10. (*E*) Sorption of $Fe(CN)_6^{3-}$ on nickel(II) hydroxide and (*t*) time.

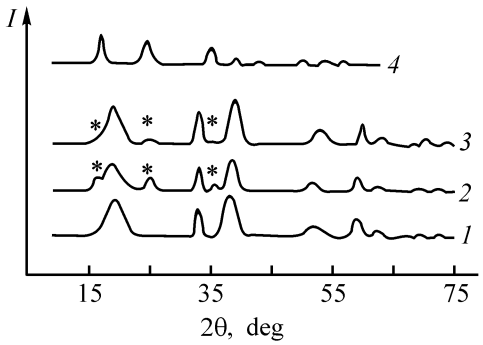

Fig. 2. Powder X-ray diffraction patterns of (*1*) initial nickel(II) hydroxide and that upon sorption of (*2*) $Fe(CN)_6^{4-}$, (*3*) $Fe(CN)_6^{3-}$, and (*4*) mixed Ni, K hexacyanoferrate(III) (*I*) intensity and (2θ) Bragg angle.

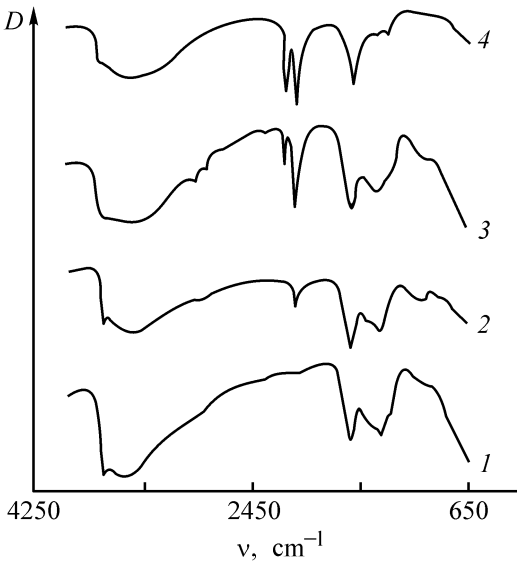

Fig. 3. IR spectra of (*1*) initial nickel(II) hydroxide and that upon sorption of (*2*) $Fe(CN)_6^{3-}$ at pH ≥ 10 (static conditions), (*3*) $Fe(CN)_6^{3-}$ at pH ≥ 9 (static conditions) and (*4*) mixed Ni, K hexacyanoferrate(III). (*D*) Transmission and (ν) wave number.

trum of a Ni(II) hydroxide sample (Fig. 3, curve *1*). The spectra of the initial sorbent contain the band of OH stretching vibrations ν(OH) at 3640 cm^{-1}, the band of the stretching vibrations of hydrogen-bonded OH groups at 3425 cm^{-1}, and the band of OH bending vibrations $\nu_2(H_2O)$ at 1635 cm^{-1}. The band at 1460 cm^{-1} is apparently due to $\nu_3(CO_3)$ vibrations. The bands at 1350 and 1000 cm^{-1} can be assigned to $\nu_3(NO_3)$ (D_{3h}) and N–O (C_{2v}) vibrations. These spectroscopic data show that the initial nickel hydroxide contains foreign CO_3^{2-} and NO_3^- anions. However, the powder X-ray diffraction pattern of our sample of nickel(II) hydroxide (Fig. 2, curve *1*) shows no changes in the interplanar spacing (00*l*) as compared to the standard values. This fact suggests that the foreign anions present in our nickel(II) hydroxide are impurities.

The powder X-ray diffraction patterns in Fig. 2, (curves *2* and *3*) show that sorption of $Fe(CN)_6^{4-}$ and $Fe(CN)_6^{3-}$ anions on nickel hydroxide is accompanied by formation of a new phase, mixed Ni, K hexacyanoferrate(II, III) with cubic structure (*Fm*3*m* space group). For comparison, Fig. 2 (curve *4*) shows an X-ray diffraction pattern of mixed Ni, K hexacyanoferrate prepared by a common technique [12]. These results show that, upon sorption of $Fe(CN)_6^{4-}$ and $Fe(CN)_6^{3-}$ anions, all the main reflections of mixed Ni, K hexacyanoferrate appear in the powder X-ray diffraction pattern of nickel(II) hydroxyde. At the same time, the initial β-$Ni(OH)_2$ phase is retained in significant amount even after contact of the sorbent with a hexacyanoferrate(II, III) solution for several days.

A study of the sorption of $Fe(CN)_6^{4-}$ and $Fe(CN)_6^{3-}$ anions from aqueous solutions of their potassium salts on β-$Ni(OH)_2$ under static conditions showed that mixed Ni, K hexacyanoferrate(II) and Ni, K hexacyanoferrate(III) phases are formed only at pH < 11.0 and <9.7, respectively. These processes are accompanied by an increase in pH, and, when alkalization reaches the above-noted levels, the formation of new phases stops. Although the phase formation stops, sorption of hexacyanoferrate(III) under these conditions continues by a common anion-exchange mechanism. This process can be observed, e.g., under dynamic conditions.

The IR spectrum of nickel(II) hydroxide containing sorbed $Fe(CN)_6^{3-}$ anions (pH > 10) (Fig. 3, curve *2*) shows an absorption band at 2100 cm^{-1} which can be assigned to ν_6 vibrations of "free" $Fe(CN)_6^{3-}$ anions with terminal N atoms. At the same time, in sorption at pH < 9.7 (Fig. 3, curve *3*), two separate bands appear at 2170 and 2100 cm^{-1}, which are typical of the bridging –CN– groups in the structure of Ni, K hexacyanoferrate(III) [12] (Fig. 3, curve *4*). The bands of the bridging –CN– groups are also observed in the IR spectra of nickel(II) hydroxide containing sorbed $Fe(CN)_6^{4-}$ anions. However, this spectrum is characterized by more complicated splitting of the absorption bands, pesumably due to partial oxidation of hexacyanoferrate(II) to hexacyaoferrate(III) by atmospheric oxygen.

Thus, $Fe(CN)_6^{4-}$ and $Fe(CN)_6^{3-}$ anions are sorbed from aqueous solutions of their potassium and cesium salts by a complicated mechanism involving anion exchange and formation of a new phase. The contribution of anion exchange to the overall sorption of $Fe(CN)_6^{4-}$ can be described by the reaction equation

$$Ni(OH)_{2-x}(CO_3)_{x/2} + y\,Fe(CN)_6^{4-} \rightleftarrows Ni(OH)_{2-x-4y}(CO_3)_{x/2}[Fe(CN)_6]_y + 4y\,OH^-. \quad (1)$$

The exchangeable OH^- anions are located on both the surface planes of β-$Ni(OH)_2$ crystals and in defective sites in which the interlayer spaces at the surface of crystallite blocks are expanded [6]. Along with anions, K^+ and Cs^+ cations are also sorbed on nickel hydroxide. We believe that these cations are sorbed in the form of $K_z[Fe(CN)_6]^{(n-z)-}$ anionic complexes, where $n = 3$ or 4 and $0 < z < n$. The possibility of joint ion-exchange sorption of Na^+ and SO_4^{2-} on double Zn–Cr(III) hydroxide was reported in [13]. Thus, ion-exchange sorption of $Fe(CN)_6^{4-}$ anions from aqueous solutions of their potassium and cesium salts on

nickel(II) hydroxide gives a new multicomponent phase whose chemical composition can be expressed by the formula

$$Ni(OH)_{2-x-(4-z)y}(CO_3)_{x/2}[K_zFe(CN)_6^{4-}]_y$$

This formula shows that the sorption is accompanied by displacement of $(4-z)y$ OH^- anions from the sorbent into the liquid phase.

As the anion-exchange capacity of nickel hydroxide is exhausted owing to a decrease in the amount of the OH^- anions available for ion exchange, the foreign anions present in nickel(II) hydroxide can get involved in the exchange. It should be noted that nitrate anions of $Ni_2(OH)_3NO_3$ basic salt are strongly bound to the nickel cation by covalent bonds and, therefore, are unexchangeable [11], so these anions are not included into the formula reflecting the sorbent composition. At the same time, it is known that carbonate anions of the basic salts are typical exchangeable groups [14]. Since the diffusion coefficient of CO_3^{2-} is considerably lower than that of OH^- anions, carbonate anions must be displaced from the sorbent after exhaustion of hydroxy anions.

Sorption of $Fe(CN)_6^{3-}$ and $Fe(CN)_6^{4-}$ is accompanied by formation of nuclei of a mixed Ni, K(Cs) hexacyanoferrate(II, III) phase. At K(Cs) hexacyanoferrate(II, III) concentration in the initial aqueous phase equal to 1.0×10^{-1} M, these initial nuclei are converted into separate phases at pH < 9.7 and <11.0 for $Fe(CN)_6^{3-}$ and $Fe(CN)_6^{4-}$, respectively. The main mechanism by which the new phase is formed (e.g., in sorption of $Fe(CN)_6^{4-}$) can be described by the following chemical reaction:

$$(2-x)Ni(OH)_2 + 2xM^+ + Fe(CN)_6^{4-} \longrightarrow M_{2x}Ni_{2-x}[Fe(CN)_6] + 2(2-x)OH^-, \quad (2)$$

where M is K^+ and Cs^+, $0 < x < 2$ (predominantly $x = 1.3$–1.5).

In going from Na^+ to Cs^+, the formation of mixed Ni, M hexacyanoferrates(II, III) increases with strengthening of the ion-exchange sorption of these cations [12]. Although the new phase is formed very slowly, it has time to build its own structure, e.g., when the sorption is performed in the batch mode. To ensure the most favorable conditions for phase formation under these conditions, pH must be lower than its maximum permissible level.

CONCLUSIONS

(1) $Fe(CN)_6^{3-}$ and $Fe(CN)_6^{4-}$ anions are sorbed on nickel(II) hydroxide mainly by ion-exchange substitution of hydroxy groups. Sorption of hexacyanoferrate(II, III) anions is accompanied by ion-exchange sorption of alkali metal cations present in the sorbate and ion exchange of the foreign anions present as impurities in nickel(II) hydroxide.

(2) In sorption of hexacyanoferrate(II, III) anions on nickel(II) hydroxide, a new phase of Ni-M hexacyanoferrate(II, III) is formed, where M is alkali metal cation. At the initial hexacyanoferrate(II, III) concentration of 1.0×10^{-1} M, this phase is formed at pH lower than 9.7 and 11.0 for $Fe(CN)_6^{3-}$ and $Fe(CN)_6^{4-}$, respectively.

REFERENCES

1. Belinskaya, F.A., in *Ionnyi obmen i ionometriya: Mezhvuzovskii sbornik* (Ion Exchange and Ionometry): Intercollegiate Coll. of Scientific Works), St. Petersburg: Sankt-Peterb. Gos. Univ., issue 10, 2000, pp. 7–49.
2. Kornilovich, B.Yu., Abstracts of Papers, *XV Mendeleevskii S"ezd po obshchei i prikladnoi khimii: Obninskii Simposium* (XV Mendeleev Congr. on General and Applied Chemistry: Obninsk Symp.), Obninsk: Fiziko-Energ. Inst., 1993, vol. 2, p. 104.
3. Sokolova, M.M., Vol'khin, V.V., and Tomchuk, T.K., in *Ochistka vody i stokov: Mezhvuzovskii sbornik* (Decontamination of Water and Discharges: Intercollegiate Coll. of Scientific Works), Tomsk: Nauchno-Issled. Inst. Vysokikh Napryazhenii, 1994, pp. 78–83.
4. Kapustin, A.E., *Usp. Khim.*, 1991., vol. 60, no. 12, pp. 2685–2717.
5. Kjeldson, P., *Water, Air Soil Pollution*, 1999, vol. 115, pp. 279–307.
6. Nishizava, H., Kishikawa, T., and Minami, H., *J. Solid State Chem.*, 1999, vol. 146, pp. 39–46.
7. Scheinost, A.C. and Sparks, D.L., *J. Colloid Interface Sci.*, 2000, vol. 223, pp. 167–178.
8. Lur'e, Yu.Yu., *Spravochnik po analiticheskoi khimii* (Handbook on Analytical Chemistry), Moscow: Khimiya, 1979.
9. Kolthoff, I.M., Belcher, R, Stenger, V.A., and Matsuyama, G., *Volumetric Analysis, vol. III: Titration Methods: Oxidation-Reduction Reactions*, New York: Interscience, 1957.
10. Polyanskii, N.G., Gorbunov, G.V., and Polyanskaya, N.L., *Metody issledovaniya ionitov* (Techniques for Studying of Ion Exchangers), Moscow: Khimiya, 1976.
11. Newman, S.P. and Jones, W., *J. Solid State Chem.*, 1999, vol. 148, pp. 26–40.
12. Tananaev, I.V., Seifer, G.B., Kharitonov, Yu.Ya., *et al.*, *Khimiya ferrotsianidov* (Chemistry of Ferrocyanides), Moscow: Nauka, 1971.
13. Khaldi, M., De Roy A., Chaouh, M., and Besse, J.P., *J. Solid State Chem.*, 1997, vol. 130, pp. 66–73.
14. Houri, B., Legrouri, A., Barroug, A., *et al.*, *Coll. Czech. Chem. Commun.*, 1998, vol. 63, pp. 732–740.

Russian Journal of Applied Chemistry, Vol. 76, No. 8, 2003, pp. 1242–1245. Translated from Zhurnal Prikladnoi Khimii, Vol. 76, No. 8, 2003, pp. 1281–1284.

APPLIED ELECTROCHEMISTRY AND CORROSION PROTECTION OF METALS

Anodic Oxidation and Contact Corrosion of Silver and Copper in Pores of Palladium Coating

E. P. Grishina

Institute for Chemistry of Solutions, Russian Academy of Sciences, Ivanovo, Russia

Received December 3, 2002; in final form, June 2003

Abstract—Cyclic voltammetry and graphical calculation of corrosion currents in short-circuited systems Ag–Pd and Cu–Pd in a 38% H_2SO_4 solution were applied to study the mechanism and evaluate the intensity of corrosion of silver and copper anodes at base of pores of a cathode coating, palladium black, in an aqueous solution of sulfuric acid.

Silver and copper are used as cathode materials in manufacture of tantalum electrolytic capacitors (TEC) [1–3]. These two metals have high electrical conductivity and corrosion stability in unoxidizing acids [4]. Palladium or platinum black is deposited onto the inner surface of the case (cathode) [2, 3], which results in that the anode capacity of the capacitor is utilized to fuller extent [1]. The resulting bimetallic system, which is constituted by the metal and the porous coating in sulfuric acid (working electrolyte of TEC), is a short-circuited galvanic cell.

Theoretically, in comparison of the standard potentials E^0 of the metals, a contact of silver with palladium can be characterized as corrosion-safe, since $\Delta E^0 = 0.987 - 0.799 < 0.400$ mV [5]. A contact of copper with palladium is inadmissible ($\Delta E^0 = 0.987 - 0.337 > 0.400$ mV). In both cases, the support metal, being more electropositive than palladium, may suffer corrosion destruction, which leads to changes in the working parameters of a capacitor or to its failure [6, 7].

Since irreversible steady-state potentials E_{st} of these metals are established in the working electrolyte of a capacitor (38% H_2SO_4 solution), the actual pattern of the process and the risk run in using one or another cathode material may differ significantly from those predicted. Experimental studies of short-circuited electrochemical systems of this kind are scarce, and there is no published evidence concerning the corrosion-electrochemical behavior of Ag–Pd and Cu–Pd systems.

The aim of this study was to analyze the mechanism and evaluate the intensity of corrosion of silver and copper anodes at base of pores of a cathode coating, palladium black, in a 38% aqueous solution of sulfuric acid.

EXPERIMENTAL

As objects of study were used stationary silver [Sr999 GOST (State Standard) 6836–80] and copper (M0b, vacuum-smelted, GOST 859–78) electrodes. Palladium plating electrolytes were prepared from $PdCl_2$ (30 g l^{-1}, for coating of silver) or $PdSO_4$ (0.64 g l^{-1}, for coating of copper) from pure or chemically pure reagents and twice-distilled water.

Potentials were measured and polarization measurements performed as in [8]. A 38% H_2SO_4 solution served as working electrolyte, the working temperature range was 20–60°C (temperature control accuracy ±0.1°C). The electrode capacity C was measured with an R 5021 ac bridge at a frequency of 1 kHz in a 38% H_2SO_4 solution, with platinum-plated platinum as counter electrode. The loss of mass from the electrode, Δm, was determined gravimetrically on a VLR 200 balance. The corrosion currents of the short-circuited electrochemical system constituted by a metal and porous coating were found graphically by a procedure described in [5].

The values of E_{st} of silver and palladium, measured at 20°C in a 38% H_2SO_4 solution, are 0.44–0.45 and 0.82–0.83 V, respectively; with ΔE_{st} close to the critical value ΔE_{cr}. At the same time, the potential of Pd with palladium black deposited on it electrochemically (Pd/Pd) is less positive and, depending on the current density j_{Pd} of palladium plating, falls with-

1070-4272/03/7608-1242 $25.00 © 2003 MAIK "Nauka/Interperiodica"

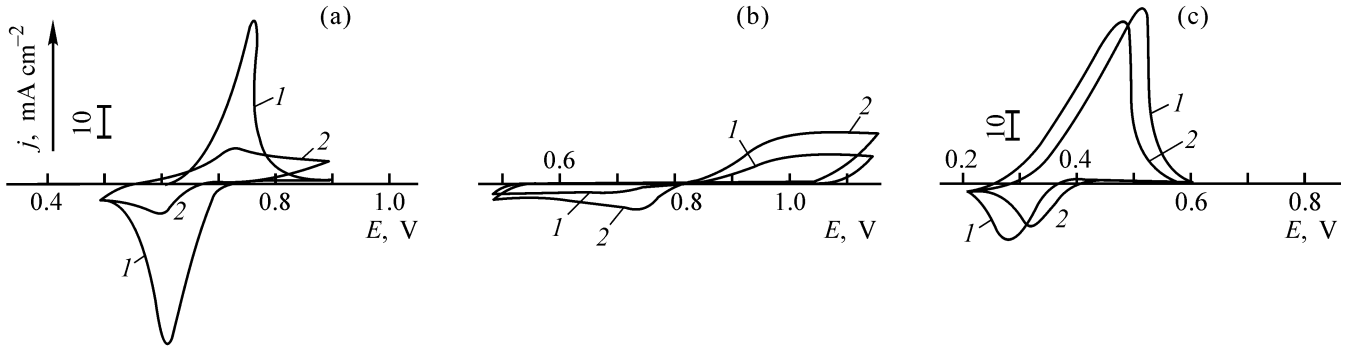

Fig. 1. Cyclic voltammograms of (a) (*1*) silver and (*2*) silver palladium plated at j = 10 mA cm^{-2}, (b) (*1*) copper and (*2*) copper with plated palladium for 60 s, and (c) (*1*) palladium and (*2*) palladium plated with palladium at j = 10 mA cm^{-2}. Electrolyte 38% H_2SO_4 solution. T = 20°C, V = 10 mV s^{-1}. (j) Current density and (E) potential.

in the range 0.675–0.690 V. Under the conditions of contact between a silver substrate and palladium black, comparison of E_{st} of silver and Pd/Pd electrodes is more adequate.

The steady-state potential of palladium-plated silver, $E_{Ag/Pd}$, depends on j_{Pd} (Table 1). $E_{Ag/Pd}$ occupies an intermediate position between E_{st} for Ag and Pd because of the presence of through pores in the coating and low voltage drop in these pores [5]. The rise in $E_{Ag/Pd}$ with increasing j_{Pd} points to a decrease in the number of through pores. Simultaneously decreases the surface capacity C, and the color of palladium black changes from gray to black. Presumably, finely crystalline palladium deposits having much more developed structure and weakly shielding the substrate surface are formed at low current densities.

The mechanism of the anodic process on Ag and Cu was studied by cyclic voltammetry, since this method allows recording of the electrochemical response of the substrate metal in the presence of through pores in a coating.

In anodic polarization of silver in sulfuric acid, there occurs an EC process [8]

$$2Ag + SO_4^{2-}(HSO_4^-) \rightleftarrows Ag_2SO_4 + 2e\ (+H^+) \quad (1)$$
$$\downarrow$$
$$2Ag^+ + SO_4^{2-}$$

This process is manifested in a cyclic voltammogram (CVA) as two conjugated current peaks: anodic in electrochemical formation of a resistive porous Ag_2SO_4 layer, and cathodic in its reduction. Figure 1 shows CVA of Ag and Ag/Pd electrodes in a 38% H_2SO_4 solution. These voltammograms are characterized by identical positions of the anodic and cathodic current peaks, with the electrochemical response of Pd not distorting the pattern of a redox process involving Ag. At any temperatures and potential sweep rates V, the main features of the anodic behavior of silver in sulfuric acid [8, 9]: number and position of anodic and cathodic peaks in CVA and linear dependence of the current density j_m^a and anodic peak potential E_m^a on $V^{0.5}$, are preserved for the bimetallic system. This indicates that the mechanisms of anodic oxidation of

Table 1. Effect of palladium-plating modes on capacity of silver and copper electrodes and on their electrochemical properties in 38% H_2SO_4 solution at 20°C

Palladium-plating mode	C, μF cm^{-2}	E_{st}, V	j_m^a, mA cm^{-2}	$\frac{j_m^a(M/Pd)}{j_m^a(M)}$	j_{cor}, μA cm^{-2}
Silver Sr999					
j,* A cm^{-2}:					
0	–	0.45	21.4	–	–
3	8.0	0.51	1.1	0.05	–
5	5.7	0.53	1.7	0.08	–
7	4.9	0.56	1.8	0.08	2.8
10	4.2	0.60	2.1	0.10	3.8
20	1.8	0.62	–	–	4.2
30	1.6	0.65	2.6	0.12	4.6
40	0.6	0.66	3.4	0.16	–
50	0.5	0.67	3.6	0.17	–
Copper M0b					
τ, s:					
0	–	0.24	105	–	–
30	24.4	0.24	97	0.92	9.6
60	18.3	0.245	96	0.91	9.6
90	16.3	0.245	92	0.88	9.6
120	17.0	0.245	92	0.88	9.6

* Q = 1.25 A s cm^{-2}.

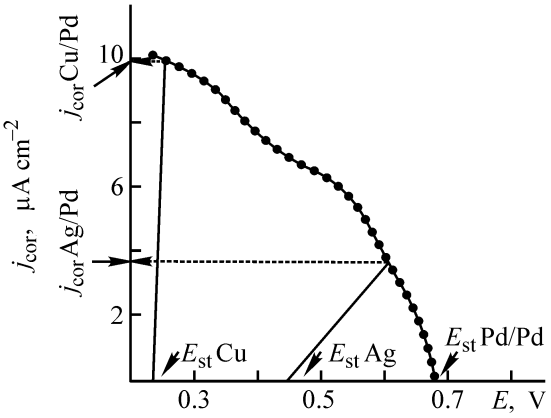

Fig. 2. Polarization corrosion diagrams of short-circuited electrochemical systems constituted by silver and palladium black and by copper and palladium black. Palladium black deposited at current density of 10 mA cm^{-2}, corrosion medium 38% H_2SO_4 solution. T = 20°C. (j_{cor}) Corrosion current density and (E) potential.

silver as individual metal and silver in contact with a porous palladium coating coincide.

The decrease in j_m^a in polarization of the Ag/Pd electrode can be attributed to two factors. The first and, presumably, foremost is the shielding of a part of the silver surface by palladium, since the current is a function of the potential and the electrochemically active part of the electrode surface under potentiodynamic conditions of polarization. The second factor is the appearance of additional hindrance to migration of the reacting anions (SO_4^{2-}, HSO_4^-) within pores of the palladium coating (limiting stage of the process [9]).

The intensity of Ag corrosion in a short-circuited Ag/Pd system is characterized by the corrosion current, which can be determined from polarization corrosion diagrams (Fig. 2). In the given case, cathodic potentiostatic polarization curves reflect the polarization behavior of palladium black. The anodic portion of the polarization diagram is obtained by connecting the point on the potential axis, which corresponds to E_{st} of Ag, and that on the cathodic polarization curve of palladium, corresponding to E_{st} of Ag/Pd.

Table 2. Loss of metal, Δm, in anodic polarization of silver and palladium-plated (at j = 10 mA cm^{-2}) silver electrodes (Q = 1.5 A s cm^{-2})

Metal	Δm (mg cm^{-2}) at j^a, mA cm^{-2}			
	0.5	5	50	250
Ag	1.55–1.60	1.45–1.60	0.75–1.0	0.80–0.85
Ag/Pd	0.55–1.15	0.75–1.15	0.45–1.15	0.35–0.45

In the system constituted by silver and palladium black, the support metal is polarized to a greater extent than the coating metal, which may be due to the significant difference between E_{st} and the equilibrium potential of the anodic reaction (1) on silver. The value of j_{cor} grows with increasing current density of palladium plating (Table 1) because the potential of the coating becomes more positive and the polarization of the cathodic process is enhanced. The cathodic process occurs in the kinetic mode (effective activation energy A_{eff} = 36.6 kJ mol^{-1}), and the rate of the anodic process is limited by the transport stage (A_{eff} = 14.4 kJ mol^{-1}), which is, presumably, migration of the salt-forming anion into the reaction zone [9].

The shielding action of the Pd coating also tells upon the cathodic loss of metal, Δm, making it much smaller (Table 2). Under these conditions, a potential corresponding to the occurrence of process (1) is established at the anode. The decrease in the loss of metal is due to an increase in the anodic current density on the silver surface not shielded by palladium and to passivation of this surface.

Thus, the safest in regard to corrosion is the contact of silver with palladium coatings deposited at low current densities. However, account should be taken of the circumstance that TEC must remain in working state at elevated temperatures (up to 85°C) and under the action of anodic currents. Palladium black formed at lower cathodic current densities is more subject to anodic dissolution than that deposited at the potentials of hydrogen ion discharge [10]. Therefore, in choosing the palladium-plating mode, preference should be given to medium current densities in the J range considered.

Change of silver for copper in TEC is rather attractive because of the comparatively low cost of the latter metal [2, 3, 11]. The rather significant difference between the steady-state potentials of Cu and Pd results in contact deposition of the more noble palladium on copper in the form of a black. The black deposited in this way does not have sufficient adhesion to the substrate, which reflects on the electrochemical characteristics of the bimetallic system.

The difference of E_{st} of Cu and Pd in a 38% H_2SO_4 solution is 0.44 V, which is much lower than the theoretical value, but exceeds somewhat ΔE_{cr}.

Figure 1 shows CVA of copper and palladium-plated copper electrodes in 38% H_2SO_4 solution. As also in the case of silver, redox processes on both

the electrodes coincide. In contrast to silver, anodic oxidation of copper in H_2SO_4 solutions is a more complex multistage process including electrochemical and chemical stages. For example, depending on the concentration of acid and dissolved oxygen, anodic oxidation of copper may proceed by an ECC or EEC mechanism (E and C stand for, respectively, electrochemical and chemical stages of the electrode process), but the primary product of electrochemical reaction is, invariably, copper(I) oxide forming a resistive porous layer [12]:

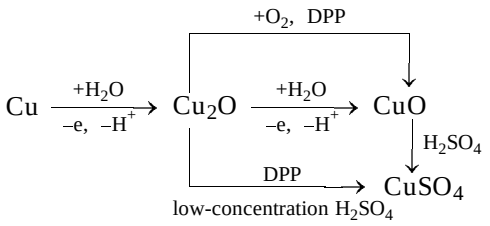

(2)

where DPP is the disproportionation process.

In potential cycling, the palladium coating flakes off the copper substrate, which is due to the formation of a Cu_2O layer. The large number of through pores reflects on the experimental values of the capacity C and E_{st} (Table 1), and the E_{st} of the Cu/Pd electrode remains inchanged.

When in contact with palladium, copper undergoes corrosion oxidation with very low polarization, whereas the cathode of the galvanic pair is strongly polarized (Fig. 2). The corrosion currents exceed by approximately a factor of 3 that in the Ag/Pd system. The A_{eff} in corrosion of copper in the given system is 16.3 kJ mol^{-1}. Apparently, the primary product of copper oxidation in corrosion will be Cu_2O, whose further chemical conversion into soluble products will proceed at a rate depending on external factors, temperature and concentration of acid, presence of dissolved oxygen.

CONCLUSIONS

(1) According to the results obtained, the anodic processes occurring in pores of the palladium coating at the Ag–electrolyte and Cu–electrolyte phase interfaces are virtually identical to those on individual metals and consist in anodic formation of, respectively, Ag_2SO_4 and Cu_2O passivating films.

(2) Combined, the contact coating with poor adhesion and the more negative value of E_{st} make the Cu/Pd system less reliable than the Ag/Pd system, as regards their use as cathodes in tantalum electrolytic capacitors. At the same time, the reliability of the Cu/Pd system can be, undoubtedly, much improved by using a number of technological procedures, and its corrosion stability can be made close to that of Ag/Pd.

REFERENCES

1. Zakgeim, L.N., *Elektroliticheskie kondensatory* (Electrolytic Capacitors), Moscow: Gosenergoizdat, 1963.
2. PNR Patent 79442.
3. US Patent 4466841.
4. Tomashov, N.D. and Chernova, G.P., *Passivnost' i zashchita metallov ot korrozii* (Passivity and Corrosion Protection of Metals), Moscow: Nauka, 1965.
5. Rozenfel'd, I.L., *Korroziya i zashchita metallov: Lokal'nye korrozionnye protsessy* (Corrosion and Protection of Metals: Local Corrosion Processes), Moscow: Metallurgiya, 1970.
6. Gordeeva, T.V., Krasikov, L.A., Kostel'ova, L.A., and Zakharova, S.E., *Elektron. Tekh., Ser. 5, Radiodet. Radiokomp.*, 1986, no. 1, pp. 6–9.
7. Jackson, N.F. and Campbell, D.S., *Thin Solid Films*, 1976, vol. 36, no. 2, pp. 331–333.
8. Grishina, E.P. and Rumyantsev, E.M., *Elektrokhimiya*, 2001, vol. 37, no. 4, pp. 474–478.
9. Grishina, E.P. and Rumyantsev, E.M., *Elektron. Obrab. Mater.*, 1999, no. 3, pp. 29–35.
10. Chevillot, J.-P., Hinnen, C., Koehler, C., and Rousseau, A., *C. r. Acad. sci.*, 1969, vol. 269, no. 15, pp. 799–802.
11. Grishina, E.P., Eremenko, D.V., Tsyplakova, L.N., *et al.*, *Izv. Vyssh. Uchebn. Zaved., Khim. Khim. Tekhnol.*, 1990, vol. 33, no. 9, pp. 65–71.
12. Grishina, E.P., Udalova, A.M., and Rumyantsev, E.M., *Elektrokhimiya*, 2002, vol. 38, no. 9, pp. 1155–1158.

Russian Journal of Applied Chemistry, Vol. 76, No. 8, 2003, pp. 1246–1252. Translated from Zhurnal Prikladnoi Khimii, Vol. 76, No. 8, 2003, pp. 1285–1291.

APPLIED ELECTROCHEMISTRY AND CORROSION PROTECTION OF METALS

Corrosion Resistance of Construction Materials in Liquid Bromine Trifluoride

G. N. Amelina, I. I. Zherin, and S. N. Lozhkomoev

Tomsk Polytechnic University, Tomsk, Russia

Received October 16, 2002; in final form, June 2003

Abstract—Results obtained in studying gravimetrically and electrochemically the corrosion resistance of the most widely used construction metals and alloys in liquid bromine trifluoride BrF_3 under steady-state conditions are presented.

Halogen fluorides are rather strong oxidizing and fluorinating agents, which can be used in gas and liquid phases both individually and in mixtures with one another. Therefore, corrosion of construction materials is a topical problem in working with this class of compounds. Among liquid halogen fluorides, BrF_3 is one of the most corrosive. This is mainly due to its susceptibility to self-ionization and high electrical conductivity ($8.02 \times 10^{-3}\ \Omega^{-1}\ cm^{-1}$), which exceeds by many orders of magnitude that of other halogen fluorides. For this reason, BrF_3 is a strong ionizing solvent and complexing agent [1]. The whole set of these properties indicates that not only chemical, but also electrochemical corrosion may occur in solutions containing BrF_3. Consequently, a contact with an electrochemically different material can strongly affect the corrosion rate, i.e., contact corrosion may occur.

Published data on this issue are rather incomplete and refer only to the gravimetric method for determining the corrosion rates of steels and alloys not manufactured in Russia [2]. It was of interest to study in sufficient detail the corrosion resistance of various widely used stainless steels in liquid BrF_3. Particular attention is required by corrosion of metals brought in contact, which depends of the potentials of the metals in the given medium.

In this context, the aim of this study was to determine the rates and potentials of corrosion of a number of construction metals that are of particular practical interest: NP2 nickel, GOST (State Standard) 492–73; M2 copper GOST 859–66; steels: 12Kh18N10T, 08Kh18N10T, 14Kh17N2, 08Kh18N11M3G2F [metal for EA-400/10U electrodes, TU (Technical Specification) 5.965-4027–72], 04Kh20N9 (metal for OZL-36 electrodes, GOST 9466–75), 04Kh19N11M3 (GOST 2246–70, wire for welding). Also, their electrochemical compatibility was to be assessed.

The stability of construction materials brought in contact with fluorinating agents is based on the formation of a dense passivating film on the surface of a material. Nickel and copper–nickel and chromium–nickel alloys are materials the most resistant to BrF_3. The results of corrosion tests of metals in liquid bromine trifluoride, reported by the Argonne National Laboratory [2], indicate that nickel, monel, *K*-monel, and inconel exhibit enhanced corrosion resistance and can be used in BrF_3. Copper is less stable than nickel or monel. Static tests for 20 weeks at 125°C and dynamic tests for 650 h at 70°C demonstrated that, in the second case, the corrosion rate of a number of materials increases by a factor of 4–20. High-alloy chromium-nickel steels with austenitic structure (such as Kh18N10T) are widely used in chemical machine building [3]. Their suitability for operation in BrF_3 is difficult to judge, but experience shows that their corrosion rate much exceeds that of nickel, monel, *K*-monel, and inconel.

Metal corrosion may proceed, in the overwhelming majority of corrosive media, by the chemical and electrochemical mechanisms [4–6].

A real corrosion process is characterized by steady-state or corrosion potential E_c [7]. The current density i_c and the potential of corrosion can be found graphically from a polarization diagram in the form of a dependence of the rates of anodic and cathodic processes on potential [4]. The processes occurring when two dissimilar metals are brought in contact in an ionizing

1070-4272/03/7608-1246 $25.00 © 2003 MAIK "Nauka/Interperiodica"

solvent with relatively high electrical conductivity can be represented as processes in a galvanic cell in which a more negative metal starts to act as anode, and the more positive, as cathode. The rate of contact corrosion of the anode in the pair is determined by polarization characteristics of the contacting metals, ratio of their areas, and the ohmic resistance of the system [3, 4]. The corrosion potentials of construction metals and alloys and their polarization characteristics in liquid BrF_3 could not be found in the literature.

EXPERIMENTAL

When gravimetric or electrochemical methods are used to determine the corrosion resistance of metals, the metal surface should be subjected to standard pretreatment and thoroughly polished. The strongest smoothing of the surface microprofile is achieved with electrochemical polishing [8]. Preliminarily, samples were polished with fine emery paper, washed, degreased, and dried.

As cathode in electrochemical polishing served a hollow perforated lead cylinder with height of 50 mm, inner diameter of 30 mm, and wall thickness of 5 mm. Electrically polished samples were washed with 3% phosphoric acid solution, degreased with acetone, and dried. To rule out the possibility of formation of an oxide film on the surface of electrically polished samples in storage, the polishing was done immediately before the beginning of each corrosion test.

Table 1. Polishing modes and electrolyte compositions

Material	i_a, A cm^{-2}	T, °C	τ, min	Electrolyte composition, wt %
Steel:				
08Kh18N10T	0.30	80	20	60 H_3PO_4, 20 H_2SO_4, 20 H_2O
12Kh18N10T	0.45	80	15	
04Kh19N11M3	0.45	80	15	
04Kh20N9	0.45	80	15	
08Kh18N11M3G2F	0.45	80	15	
14X17H2	0.30	80	20	
M2 copper	0.35	35	15	70 H_3PO_4, 6 CrO_3, 24 H_2O
NP2 nickel	0.30	30	20	

The polishing modes and electrolyte compositions chosen in the study are listed in Table 1.

The steady-state (corrosion) potentials and corrosion rates were found from polarization characteristics of the metals and alloys using the potentiostatic

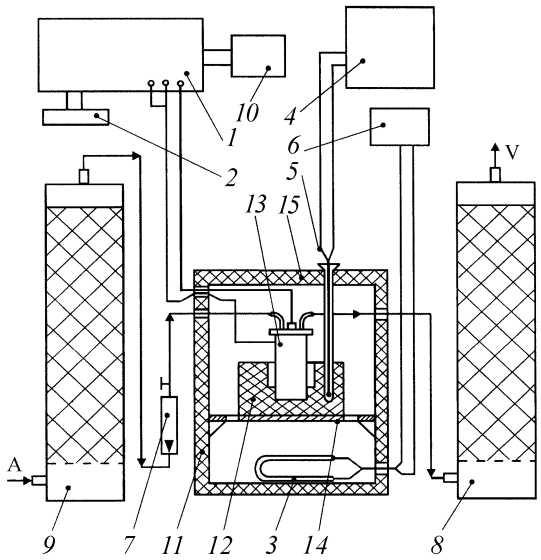

Fig. 1. Schematic of setup for determining the polarization characteristics of metals and alloys in liquid BrF_3. (*9*) Column with NaA zeolite for argon drying, (*10*) voltage stabilizer, (*11*) thermostat, (*12*) cell holder and, simultaneously, external vessel, (*13*) electrolytic cell, (*14*) perforated steel support plate, (*15*) thermostat cover; A, feed of argon from a cylinder; V, discharge of gas into ventilation system; for other designations, see text.

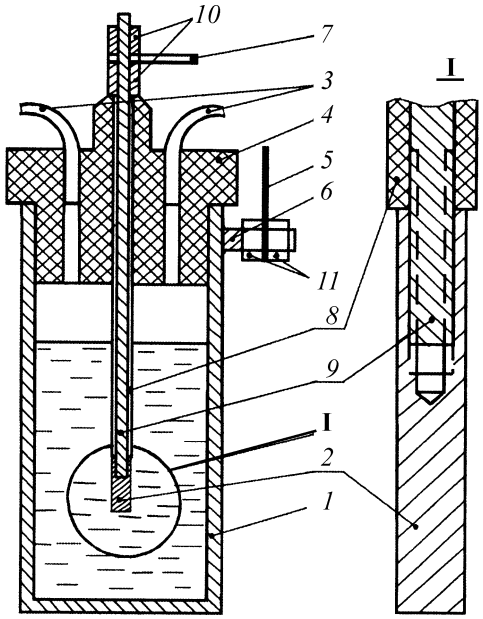

Fig. 2. Electrolytic cell for determining polarization characteristics of metals and alloys in liquid BrF_3. (*1*) Case of electrolytic cell, (*2*) working electrode, (*3*) fluoroplastic tubes for gas inlet and outlet, (*4*) fluoroplastic cover–holder of the working electrode, (*5–7*, *9*) current leads, (*8*) current lead insulation, and (*10*, *11*) nuts.

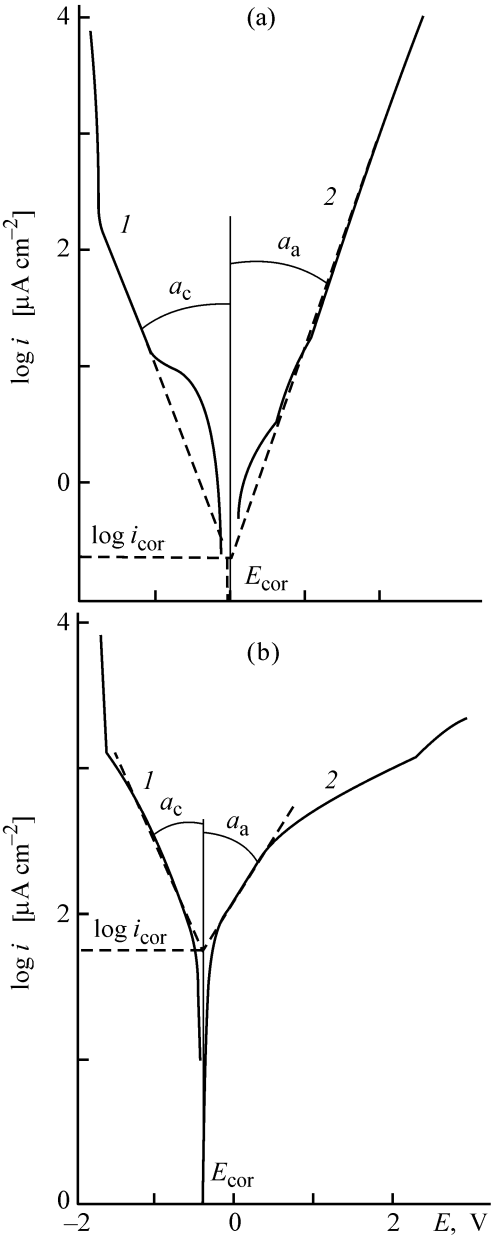

Fig. 3. (*1*) Cathodic and (*2*) anodic E–log i dependences obtained on (a) nickel and (b) 08Kh18N10T steel in liquid BrF_3 (16 ± 1°C). (a) log i_{cor} = –0.73, E_{cor} = 0.00 V; (b) log i_{cor} = 1.76, E_{cor} = –0.42 V.

method for measuring steady-state polarization curves. The potentials were measured by the Nernst–Glazer method [9]. As reference and, simultaneously, auxiliary electrode served the nickel case of the electrolytic cell. The experimental setup is shown schematically in Fig. 1.

A certain potential was applied to a working electrode under study and the current was monitored with a P-5827M potentiostat *1* and F136 microvoltnanoammeter *2*. The prescribed temperature in the thermostat was maintained with an electric heater *3*, KSM3 automatic bridge *4*, resistance thermometer *5*, and attachment *6* for position control. The argon feed was controlled with an RM-A 0.063G UZ rotameter *7*; discharged argon was purified to remove fluorine-containing gases on a column with lime chemical absorber *8*. To eliminate the influence exerted on the sample corrosion products by products of decomposition of bromine trifluoride (Br_2, BrF), the space over the surface of liquid BrF_3 was purged, through pipes (Fig. 2) with argon dried on an NaA zeolite in the column *9* to the dew point of –50°C.

The electrolytic cell is shown schematically in Fig. 2. The cylindrical case *1*, serving simultaneously as auxiliary and reference electrodes is made of NP2 nickel. Polarization characteristics were determined for working electrodes *2* having the form of cylinders 3 mm in diameter and 20 mm high.

Potentiostatic standardization of the initial state of the surface was done by keeping the working electrode in BrF_3 at a constant anode potential. This potential was chosen experimentally: if the anode current did not stabilize for a long time, the potential was raised to a value at which sufficiently fast current stabilization was observed (0.5–1.0 h). Then the working electrode was subjected to electrochemical aging to improve the reproducibility of electrochemical measurements [10]. After the measurement results became reproducible, the polarization characteristic of the working electrode was determined. The current was measured beginning with potentials of potentiostatic standardization +2…+4 V (depending on a material), with the potential shifted in discrete steps to negative values (–1.8…–2.4 V). Each time the potential of the working electrode was changed after the current attained a steady-state value. The duration of a run in which the polarization characteristic of a working electrode was determined was 6–20 h.

The polarization characteristics of construction materials (typical dependences are shown in Fig. 3) were used to find graphically the steady-state potential of the corrosion process and the corresponding logarithm of the current density of anodic dissolution.

The relationship between the corrosion current density i_{cor} (A cm^{-2}, steady-state current density of anodic dissolution) and the mass factor of the corrosion rate, K_m (g cm^{-2} h^{-1}) is described by the equation

$$i_{cor} = K_m nF/A, \quad (1)$$

where n is the degree of oxidation of a metal; F = 26.8 A h mol^{-1}, the Faraday number; A, the atomic mass of the metal (g mol^{-1}).

Table 2. Results of electrochemical and gravimetric* studies of the corrosion resistance of construction materials in liquid BrF_3 (temperature $16 \pm 1°C$)

Material	E_{cor}, V	i_{cor}, μA cm^{-2}	K_p, mm yr^{-1}	Corrosion resistance on a ten-point scale, GOST (State Standard) 13819–68	
				point	resistance group
NP2 nickel	0.00	1.86×10^{-1}	$\frac{2.0 \times 10^{-3}}{2.3 \times 10^{-3}}$**	2	Highly resistant
M2 copper	–1.12	4.07	$\frac{4.7 \times 10^{-2}}{4.9 \times 10^{-2}}$	4	Resistant
Steel:					
12Kh18N10T	–0.46	2.29	$\frac{1.8 \times 10^{-2}}{2.1 \times 10^{-2}}$	4	〃
08Kh18N10T	–0.42	57.54	$\frac{4.5 \times 10^{-1}}{–}$	6	Lower-resistant
14Kh17N2	–0.82	9.55	$\frac{7.5 \times 10^{-2}}{–}$	5	Resistant
04Kh19N11M3	–0.4	1.38×10^{-1}	$\frac{1.1 \times 10^{-3}}{–}$	2	Highly resistant
04Kh20N9	–0.29	1.38×10^{-1}	$\frac{1.1 \times 10^{-3}}{1.6 \times 10^{-3}}$	2	〃
08Kh18N11M3G2F	–1.05	1.10×10^{-2}	$\frac{8.6 \times 10^{-5}}{–}$	1	Perfectly resistant

* Gravimetric measurements were done for NP2 nickel, M2 copper, and 12Kh18N10T and 04Kh19N11M3 steels.

** K_p found electrochemically, numerator, and gravimetrically, denominator.

The corrosion depth factor K_p (m yr^{-1}, corrosion permeability) is related to K_m and i_{cor} by

$$K_p = \frac{K_m \times 8.76 \times 10^4}{\rho_M} = \frac{i_{cor} A \times 8.76 \times 10^4}{n \times 26.8 \rho_M} = \frac{i_{cor} A}{n \rho_M} \times 3268.7, \quad (2)$$

where ρ_M is the metal density, and 8.76×10^4 is the conversion factor.

The values of E_{cor} and i_{cor}, determined for metals and alloys from their polarization characteristics (Fig. 3), and the corresponding values of K_p are listed in Table 2.

Among the alloyed construction steels studied, 12Kh18N10T steel has the highest corrosion resistance. The corrosion rate K_p of this steel is 4 times smaller than that of 14Kh17N2 steel and 25 times smaller than that of 08Kh18N10T steel. The corrosion resistance of 04Kh19N11M3 and 04Kh20N9 steels in liquid BrF_3 exceeds that of 12Kh18N10T and 08Kh18N11M3G2F steels by respectively, factors of 16 and 450. For alloyed steels, intercrystallite and pitting corrosion in an electrically conducting liquid is not improbable. This kinds of corrosion were beyond the scope of this study.

The corrosion rate of NP2 nickel is an order of magnitude lower than that of 12Kh18N10T steel, and, therefore, this brand of nickel is the most preferable construction material to be used in liquid BrF_3. The corrosion rate of copper in BrF_3 exceeds that of nickel and 12Kh18N10T steel by factors of 20 and 2.5, respectively.

To verify the electrochemically obtained data and to distinguish the electrochemical component in the overall corrosion process, the corrosion rates of the metals and alloys were determined in liquid bromine trifluoride under steady-state conditions by means of gravimetry in the course of 152 days.

NP2 nickel, M2 copper, 12Kh18N10T steel, and 04Kh20N9 steel (metal of OZL-36 welding electrode) were chosen for gravimetric determination of the cor-

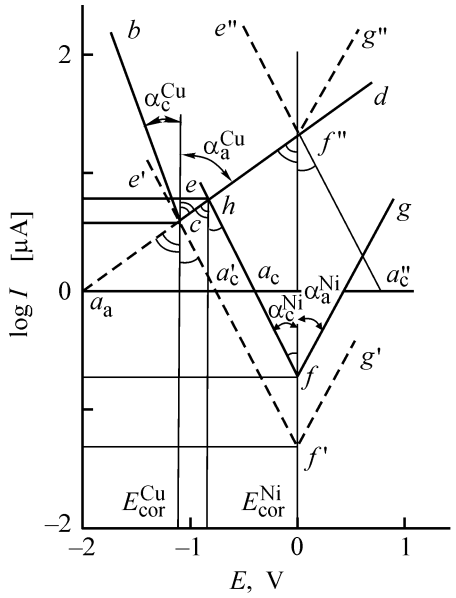

Fig. 4. Schematic E–log I dependences obtained in liquid BrF_3 (16 ± 1°C) on M2 copper at S = 1 cm^2 (*bcd*) and NP2 nickel with varied surface area. S^{Ni} (cm^2): (*e'f'g'*) 0.25, (*efg*) 1, (*e"f"g"*) 24.

rosion rate. Cylindrical samples 20 mm long and 3 mm in diameter (15 samples) were used. The temperature of bromine trifluoride was 16 ± 1°C. The results obtained are listed in Table 2.

It can be seen from Table 2 that the corrosion rates determined by gravimetry are somewhat higher than those found electrochemically, which points to the existence of a chemical component in the overall corrosion process. The average conversion factor of electrochemically determined corrosion rates with respect to the true corrosion rates is 1.2. Such an increase in corrosion permeability (Table 2) does not change the corrosion characteristics (corrosion severity and group of corrosion resistance) of the materials in question.

The compatibility of construction materials brought in contact in liquid bromine trifluoride can be judged from the corrosion potentials determined relative to a nickel (NP2) reference electrode (Table 2). Corrosion becomes stronger in contact with a more electronegative metal or alloy, and weaker or zero, in contact with a more electropositive material.

The most corrosion resistant 12Kh18N10T steel can be welded using 04Kh19N11M3 welding wire and OZL-36 electrode made of 04Kh20N9 steel. The weld metal will be protected from corrosion by the construction metal. The increase in corrosion of the construction itself will be insignificant because its surface area is many times the weld area. The corrosion rate of the metal of EA-400/10U electrodes is more than an order of magnitude lower under steady-state conditions than that of the welding wire and the metal of OZL-36 electrodes (Table 2), and the corrosion potential is more negative than that of 12Kh18N10T steel by 0.59 V, i.e., the weld metal will undergo anodic dissolution. The dissolution rate will be low in the case of a uniform corrosion over the weld surface, but occurrence of pitting and intercrystallite corrosion cannot be ruled out.

The polarization dependences obtained by extrapolation of real polarization curves can be used to determine the current of the anodic component of corrosion for a pair of contacting metals at any ratio of their surface areas. The steady-state potentials E_{cor} (V), necessary for graphical construction, and the corresponding current densities i_{cor} (μA cm^{-2}) of anodic dissolution are listed in Table 2. The constants appearing in the Tafel equation for the cathodic and anodic processes, b_c = tan α_c and b_a = tan α_a (Fig. 3), found from the polarization curves for the metals are given below:

Material	b_c, V	b_a, V
NP2 nickel	0.57	0.55
M2 copper	0.42	1.45
Steel:		
12Kh18N10T	0.52	1.42
08Kh18N10T	0.82	1.17
14Kh17N2	0.52	1.72
04Kh20N9	0.79	0.52
08Kh18N11M3G2F	0.41	0.98
04Kh19N11M3	0.90	0.69

The dependences of the logarithm of current on potential, obtained for both the constituents of a pair of contacting metals, were recalculated in accordance with their areas and plotted in a common polarization diagram as logarithm of current against potential.

Figure 4 shows polarization curves for copper and nickel samples with surface area S^{Cu} = 1 cm^2 (*bcd*) and S_1^{Ni} = 1 (*efg*), S_2^{Ni} = 0.25 (*e'f'g'*), and S_3^{Ni} = 24 cm^2 (*e"f"g"*). At area ratios of the contacting metals S^{Cu} : S^{Ni} = 1 : (0.25–24), the anodic process occurs at copper, and cathodic, at nickel. The corrosion rate and the common corrosion potential of the system were determined from the intersect of the anodic component for copper and cathodic component for nickel, i.e., the corrosion potential changed from point *c* to point *f"* on varying the nickel area.

At $S^{Cu} : S^{Ni} = 1 : (<0.25)$ the common corrosion potential of the system takes the value equal to the corrosion potential of copper ($E_{cor}^{Cu} = -1.12$ V). The current of the anodic process of copper dissolution remains invariable and equal to I_{cor}^{Cu}. For the condition of equality of the rates of the anodic and cathodic processes to be satisfied at decreasing nickel area, it is necessary to take into account the current of the cathodic process occurring at copper (at $S^{Ni} < 0.25$ cm^2, $\Sigma I_c = I_c^{Ni} + I_c^{Cu} = I_a^{Cu} = I_{cor}^{Cu}$).

At $S^{Cu} : S^{Ni} = 1 : (>24)$, the common potential of the system takes a value equal to the nickel corrosion potential ($E_{cor}^{Cu-Ni} = 0.00$ V). For the condition of equality of the rates of anodic and cathodic corrosion processes to be satisfied in this case with increasing nickel area, it is necessary to take into account the anodic dissolution of nickel, since the current of the cathodic process on nickel remains invariable and equal to I_{cor}^{Ni}.

Graphical construction (Fig. 4) yielded an equation for calculating the logarithm of the current of the anodic component of corrosion for a pair of contacting metals. For example, at $S^{Cu} : S^{Ni} = 1 : 1$ (dependences *bcd* and *efg*), $\log I^{Cu}$ is determined by the altitude of the triangle $a_a h_a c$:

$$\log I^{Cu} = \frac{a_c - a_a}{\tan\alpha_a^{Cu} + \tan\alpha_c^{Ni}} = \frac{a_c - a_a}{b_c^{Ni} + b_a^{Cu}}, \quad (3)$$

where a_c and a_a are constants equal numerically to the potentials at current density equal to unity for the cathodic process occurring at nickel (*ef*) and anodic process at copper (*cd*).

The constants were found from the equations

$$E_{cor}^{Cu} - a_a = \log I_{cor}^{Cu} \tan\alpha_a^{Cu}, \quad (4)$$

$$a_a = E_{cor}^{Cu} - \log I_{cor}^{Cu} \tan\alpha_a^{Cu}, \quad (5)$$

$$E_{cor}^{Ni} = a_c - \log I_{cor}^{Ni} \tan\alpha, \quad (6)$$

$$a_c = E_{cor}^{Ni} + \log I_{cor}^{Ni} \tan\alpha_c^{Ni}. \quad (7)$$

The current densities of anodic dissolution in steady state, i_{cor}, necessary for determining the current $I_{cor} = i_{cor}S$ and E_{cor} are listed in Table 2, and the values $\tan\alpha_a^{Cu} = b_c^{Cu}$ and $\tan\alpha_c^{Ni} = b_c^{Ni}$ are given in text. Use of these data and Eqs. (5) and (7) at $S^{Cu} : S^{Ni} = 1 : 1$ yielded $a_a = -1.12 - \log(0.186 \times 1) \times 1.45 = -2.00$ V and $a_c = 0.00 + \log(4.07 \times 1) \times 0.57 = -0.42$ V. According to Eq. (3),

$$\log I^{Cu} = \frac{-0.42 + 2.00}{0.57 + 1.45} = 0.782, \quad I^{Cu} = 6.06\ \mu A,$$

$$i_{Cu} = I^{Cu}(S^{Cu})^{-1} = 6.06 \times 1^{-1} = 6.06\ \mu A\ cm^{-2}.$$

At $S^{Cu} : S^{Ni} = 1 : (\leq 0.25)$, $i^{Cu} = i_{cor}^{Cu} = 4.07\ \mu A\ cm^{-2}$, at $S^{Cu} : S^{Ni} = 1 : (\geq 24)$, $i^{Cu} = 24.00\ \mu A\ cm^{-2}$).

Thus, at area ratio $S^{Cu} : S^{Ni} = 1 : (0.25–24)$, the current density of anodic dissolution of copper grows on bringing the metals in contact from the steady-state value ($4.07\ \mu A\ cm^{-2}$) to the maximum value ($24.00\ \mu A\ cm^{-2}$) by a factor of 6.

For an arbitrary pair of contacting metals, Eq. (3) takes the form

$$\log I^a = \frac{a_c^c - a_a^a}{b_c^c + b_a^a}. \quad (8)$$

The limiting conditions for the area ratio of the metals for expression (8) are determined from graphical constructions similar to those in Fig. 4. The internal resistance of a system in contact was taken to be zero. The given calculation procedure is inferior in precision to that using the real polarization dependences, but is much simpler and sufficiently reliable.

CONCLUSIONS

(1) Polarization characteristics of the most widely used construction materials in liquid BrF_3 were determined. These characteristics make it possible to calculate the rate of contact corrosion of the materials studied at varied ratio of contacting surface areas.

(2) It was found that nickel and copper can be recommended as construction materials that can work in liquid BrF_3, but contact between these materials is inadmissible because of their electrochemical incompatibility. Among high-alloy steels, 12Kh18N10T steel, which is compatible with 04Kh20N9 and 04Kh19N11M3 steels, is the most resistant. However, the alloyed steels studied can only be recommended for work in liquid BrF_3 after carrying out additional tests for pitting and intercrystallite corrosion.

REFERENCES

1. Nikolaev, N.S., Sukhoverkhov, V.F., Shishkov, Yu.D., and Alenchikova, I.F., *Khimiya galoidnykh soedinenii ftora* (Chemistry of Fluorine Halides), Moscow: Nauka, 1968.

2. *Reactor Handbook*, 2nd ed., Vol. II, *Fuel Reprocessing*, Stoller, S.M. and Richards, R.B., Eds., New York: Interscience, 1961.
3. Vorob'eva, G.Ya., *Korrozionnaya stoikost' materialov v agressivnykh sredakh khimicheskikh proizvodstv* (Corrosion Resistance of Materials in Corrosive Media of Chemical Industry), Moscow: Khimiya, 1975.
4. Tomashov, N.D. and Chernova, G.P., *Teoriya korrozii i korrozionnostoikie konstruktsionnye splavy* (Theory of Corrosion and Corrosion-Resistant Construction Alloys), Moscow: Metallurgiya, 1986.
5. Tomashov, N.D., *Teoriya korrozii i zashchity metallov* (Theory of Corrosion and Metal Protection), Moscow: Akad. Nauk SSSR, 1959.
6. Kolotyrkin, Ya.M. and Florianovich, G.M., *Zashch. Met.*, 1984, vol. 20, no. 1, pp. 14–24.
7. Shluger, M.A., Azhogin, F.F., and Efimov, E.A., *Korroziya i zashchita metallov* (Corrosion and Metal Protection), Moscow: Metallurgiya, 1981.
8. Grilikhes, S.Ya., *Polirovanie, travlenie i obezzhirivanie metallov* (Polishing, Etching, and Degreasing of Metals), Moscow: Mashinostroenie, 1971.
9. Rotinyan, A.L., Tikhonov, K.I., and Shoshina, I.A., *Teoreticheskaya elektrokhimiya* (Theoretical Electrochemistry), Leningrad: Khimiya, 1981.
10. Novakovskii, V.M., Trusov, G.N., and Fandeeva, M.F., *Zashch. Met.*, 1966, vol. 5, no. 5, pp. 503–510.

Russian Journal of Applied Chemistry, Vol. 76, No. 8, 2003, pp. 1253–1259. Translated from Zhurnal Prikladnoi Khimii, Vol. 76, No. 8, 2003, pp. 1292–1297.

CATALYSIS

Catalytic Activity of Complex-Oxide Perovskite-containing Compositions in Reactions of Oxidation of CO and Organic Compounds

A. A. Ostroushko, E. Shubert, A. M. Makarov, V. I. Minyaev, A. E. Udilov, L. V. Elokhina, and V. I. Aksenova

Research Institute of Physics and Applied Mathematics, Ural State University, Yekaterinburg, Russia

Higher School of Technology and Economy, Dresden, Germany

Institute of Solid-State Chemistry, Ural Division, Russian Academy of Sciences, Yekaterinburg, Russia

Institute of Metal Physics, Ural Division, Russian Academy of Sciences, Yekaterinburg, Russia

Received April 10, 2003

Abstract—The catalytic activity of composites constituted by a porous metallic or ceramic support, intermediate layers of oxide nature, and perovskite coatings, including those doped with silver, was studied in reactions of deep oxidation of CO and organic compounds of various classes. The relationship between the catalytic activity of a composite and its composition and nature of substances being oxidized was analyzed.

Reactions of deep oxidation of organic substances and carbon monoxide CO are used in developed countries to protect the environment, prevent discharge of toxic wastes formed in chemical industry, fuel and energy industry, etc. Catalysts based on platinum metals, and also lower-cost complex-oxide catalysts of, e.g., perovskite type, containing lanthanum, transition metals (manganese, cobalt, iron, chromium), and other elements are widely used for this purpose.

One of techniques for effective use of catalysts consists in developing composite catalysts including a foamed, e.g., foamed-metal, support [1], an intermediate, or transition layer, and a complex-oxide coating [2–7]. In contrast to compact elements, catalytic elements of this kind allow economic use of materials, ensure good contact with a gas flow at moderate gasdynamic resistance, and exhibit fire-extinguishing properties.

An important issue in the development and use of catalysts is that the properties of the composites obtained are rather closely associated with the mutual influence of their components, which is manifested in mechanical and chemical-thermal stabilization of the systems. Among the possible effects are mutual doping via diffusion interaction of components, formation of new phases, and promotion of the catalytically active layer by underlying surfaces [8].

The present study is concerned with the relative activities of composite catalysts of varied composition and platinum-containing catalysts on foamed-nickel or mullite-silica supports in reactions of oxidation of CO and organic substances of varied nature: *n*-heptane, benzene, ethanol.

EXPERIMENTAL

The catalysts were prepared by impregnating supports with solutions of polymer-salt formulations [9, 10]. As starting substances served lanthanum(III) nitrate hexahydrate and silver nitrate of chemically pure grade, manganese(II) nitrate hexahydrate and strontium nitrate of analytically pure grade, "pure" cobalt(II) nitrate hexahydrate, and polyvinyl alcohol of 11/2 brand. Solutions of salts necessary for synthesizing the catalysts were prepared, and then a solution of polyvinyl alcohol was added. Supports made of K-20 foamed-nickel supports with thickness of 20 mm, pore diameter in the range 1.8–3.5 mm, density of 0.3–0.4 g cm^{-3}, and air permeability of 5.5×10^{-8} m^2 were submerged in the resulting working solution. Then the supports were removed from the solution, excess amounts of the solution were allowed to flow down, and the supports were dried and subjected to pyrolysis and thermal treatment at 650°C for 4 h. The procedure was repeated again and again until

1070-4272/03/7608-1253 $25.00 © 2003 MAIK "Nauka/Interperiodica"

Table 1. Crystallographic data for complex oxides with perovskite structure

Sample	Temperature of annealing and normalizing aging, °C	*a*	*c*	Occupation number of lanthanum sublattice with silver	Bragg's *R* factor
		Å			
$La_{0.9}MnO_{3\pm y}$	1100/600	5.5105(7)*	13.337(2)	0.913(18)**	6.02
$La_{0.9}Ag_{0.1}MnO_{3\pm y}$	1100/600	5.5032(3)	13.307(1)	0.108(14)	6.77
$La_{0.9}Ag_{0.1}MnO_{3\pm y}$	650***	5.4975(6)	13.322(2)	0.071(7)	2.49
$La_{0.7}Ag_{0.3}MnO_{3\pm y}$	650***	5.4999(10)	13.349(4)	0.263(10)	2.85
$La_{0.7}Ag_{0.3}MnO_{3\pm y}$	1100/600	5.5031(1)	13.3235(4)	0.262(10)	3.90
$La_{0.75}Ag_{0.5}MnO_{3\pm y}$	650***	5.4987(8)	13.342(3)	0.198(10)	4.93

* Error in determining the last significant digit of a parameter is given in parentheses.

** Occupation number is given for lanthanum.

*** Slow cooling to indicated temperature instead of normalizing annealing.

the required amount of a catalyst was obtained on a support. Coatings on mullite-silica foamed materials with about the same porosity and permeability were deposited in a similar way. The specific surface area of the composite catalysts was monitored by the method of low-temperature sorption of nitrogen with thermal desorption, using Sorpty-1750 and Sorptomatic-1900 instruments. Part of supports were preliminarily covered with aluminum oxide deposited from an alkaline aluminate solution and stabilized with lanthanum oxide. The mass fraction of such an intermediate layer was 10–12%. An X-ray phase analysis was made on a standard DRON-3 diffractometer with Cu_{K_α} radiation. Local analysis of the distribution of element concentrations was performed with a Jeol-Super-probe 733 microanalyzer.

The catalytic activity in oxidation of carbon monoxide (CO) to carbon dioxide was studied on a setup comprising a gas tank, furnace, and system for uniform supply of the gas mixture into a catalytic reactor. The gas tank was filled with a gas mixture of air, carbon monoxide, and inert carrier-gas (nitrogen or argon). The oxidizing and reducing agents were taken in a ratio 1 vol % O_2 : 0.3 vol % CO, with the inert gas the rest. This mixture was passed at a rate of 30 l h^{-1} through a quartz tube with a catalyst at a prescribed temperature (measured with a ChA_{68} thermocouple directly in the reaction zone). Preliminarily, the content of CO in the mixture was monitored, the gas mixture was also analyzed at the outlet of the catalytic unit with an IMR-3000P gas analyzer or with indicator tubes of the TI SO-1.0 type, combined with an AM-5.M aspirator.

The catalytic activity in oxidation of organic compounds (*n*-heptane, benzene, and ethanol) was determined at their content of 5 g m^{-3} and gas flow rate of 15 l h^{-1} through the reactor with a catalyst. The specific load on the catalytic reactors did not exceed 1000 h^{-1}. The mass fraction of the active component in the catalytic compositions was 4–10%. As reference samples served Pt–Pd–Rh samples with content of 0.7–1.3 wt % on foamed-nickel supports with a sublayer of aluminum oxide stabilized with lanthanum oxide.

Heterogeneous catalysts of the system La–Ag–Mn–O [10–13], in which perovskite phases are formed and a minor amount of metallic silver is contained, are rather active in reactions of oxidation of CO and organic substances [2–7]. In particular, catalysts with empirical formula $La_{0.75}Ag_{0.25}MnO_{3\pm y}$ stand out. These catalysts were chosen as an object of study. It was found that the perovskite phases obtained in the above system do contain silver [11] even upon annealing at temperatures exceeding its melting point. This is confirmed by processing of the results of an X-ray phase analysis of samples annealed at 600–1100°C and having an empirical formula $La_{1-x}Ag_xMnO_{3\pm y}$ (x in the range from 0.1 to 0.3) by full-profile Ritwild's analysis (Fullprof software) with calculation of the occupation numbers of the lanthanum sublattice (Table 1).

For equilibrium with respect to oxygen to be attained, the samples were subjected to normalizing annealing (Table 1), since oxygen nonstoichiometry strongly affects characteristics of the samples. Raising the total content of silver in the system to, e.g., $x = 0.5$, does not increase its content in the perovskite. Above the melting point of silver, there occurs evaporation of the existing metallic form; silver contained in the perovskite is not removed in the process,

which is confirmed by chemical analysis of the samples. At 1100–1200°C, depending on composition, the perovskite phase starts to decompose, with secondary silver appearing and possing into the gas phase [11]. After annealing at 1400°C for 24 h with slow cooling, a diffusion zone is present around silver grains, in which the metal is contained in a complex oxide (Fig. 1).

The contradiction between the low magnetic moment of the manganese ion and the occurrence of doping of the lanthanum sublattice with silver, noticed in [10], is eliminated, since it is more correct to compare properties of silver-doped samples not with samples of composition $LaMnO_{3\pm y}$, as it has been done previously, but with lanthanum-deficient $La_{1-x}MnO_{3\pm y}$, where x corresponds to the amount of silver introduced into the system. Such a composition would be formed upon consumption in the course of synthesis of the whole amount of lanthanum and manganese if silver were not incorporated in the perovskite. It can be seen that silver-substituted and lanthanum-deficient kinds of perovskite have different lattice constants (Table 1). The constants were calculated in terms of the $R\bar{3}c$ space group (hexagonal packing). Also of interest are perovskite catalysts containing no silver; the most active of these are compositions containing manganese and cobalt. Their activity increases because of the substitution of lanthanum by, e.g., strontium ions.

The efficiency in CO oxidation of four variants of catalysts on foamed nickel, with the complex-oxide coating constituting 3–4% of the total mass of the composite catalyst, was studied. The results obtained are presented in Fig. 2 and Table 2. The highest efficiency was observed for composite no. 1. This fact can be explained as follows. The active complex-oxide in the system La–Ag–Mn–O is a heterogeneous mixture, and catalysts for heterogeneous reactions, which have complex composition, frequently exhibit higher activity. Presence of silver in the perovskite structure favors generation of additional defects, which makes higher the catalytic activity of the perovskite phase itself in oxidation-reduction processes.

The composition $La_{0.84}Sr_{0.16}Mn_{0.8}Co_{0.2}O_{3\pm y}$ also exhibited high efficiency under the positive influence exerted by the presence of cobalt ions characterized by low energy of bonding to oxygen [8, 14]. Doping of the perovskite $LaMnO_{3\pm y}$ with strontium also gives rise to additional defects of the type $[M^{4+}]$, with, however, one defect of this type formed per each Sr^{2+} ion, and two defects, per Ag^{+} ion. Composite

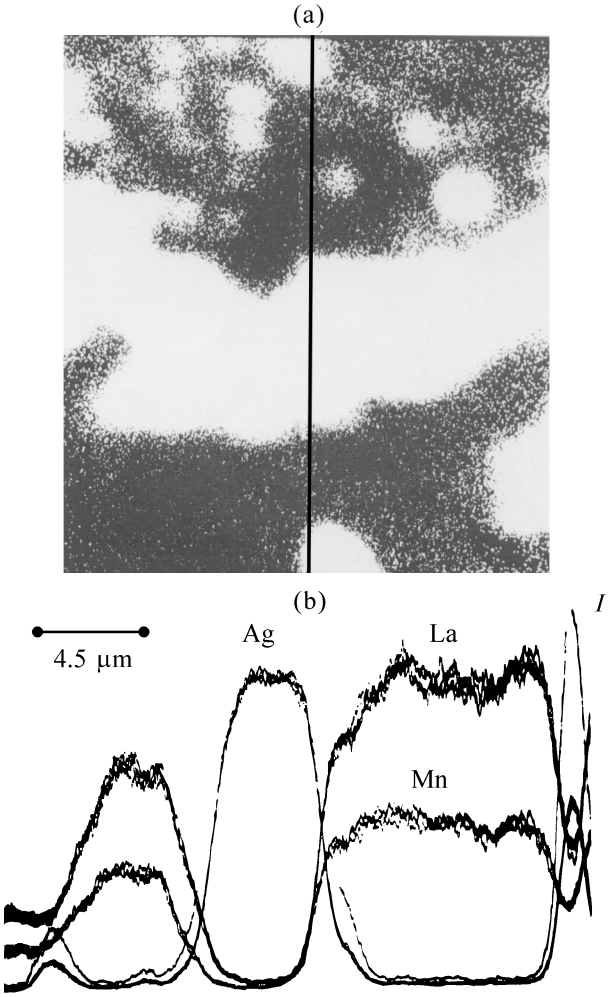

Fig. 1. Element concentration profile in $La_{0.75}Ag_{0.25}MnO_{3\pm y}$ samples after annealing at 1400°C. (a) Microphotograph taken in characteristic X-ray emission of silver. To light areas corresponds the maximum concentration of silver; the diffusion zone possibly corresponds to secondary dissolution of silver in perovskite. (b) Ag, Ln, and Mn content profiles in arbitrary units of characteristic emission intensity along the scanning line shown in Fig. 1a. (*I*) Current of electron discharge on the sample.

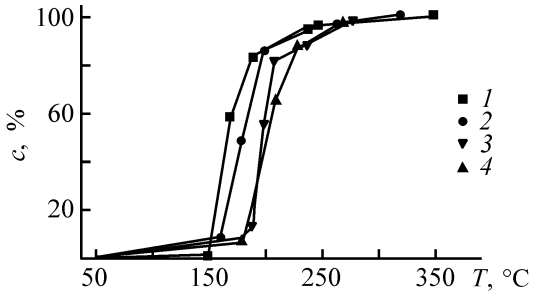

Fig. 2. Conversion c vs. temperature T in the reaction of CO afterburning (initial concentration 700 mg m^{-3}) for catalysts on foamed nickel. *Digits 1–4* correspond to catalyst numbers in Table 2.

Table 2. Characteristics of catalysts on foamed nickel in oxidation of carbon monoxide

Catalyst no.	Coating/sublayer	Total specific surface area, $m^2 g^{-1}$	Combustion temperature, °C
1	$La_{0.75}Ag_{0.25}MnO_{3\pm y}/Al_2O_3$	3.0	150
2	$La_{0.84}Sr_{0.16}Mn_{0.8}Co_{0.2}O_{3\pm y}/Al_2O_3$	2.6	160
3	$La_{0.75}Ag_{0.25}MnO_{3\pm y}/LaMnO_{3\pm y}$	1.9	185
4	$La_{0.75}Ag_{0.25}MnO_{3\pm y}/–$	0.5–0.8	180

no. 2 contains a virtually homogeneous perovskite phase. For this reason, it is somewhat inferior in efficiency to composite no. 1.

Efficiency measurements at relatively low specific load on the catalysts and temperatures close to the combustion point demonstrated that an Al_2O_3 sublayer (intermediate support) strongly affects the efficiency. The possible reason is that the specific surface area of the composites grows, also possible are other mechanisms of this effect. The aluminum oxide layer isolates the perovskite from the nickel substrate and hibnders the mutual diffusion of nickel and manganese ions between the support and the complex-oxide layer [15].

The possibility of a diffusion interaction was confirmed by modeling the system $LaMnO_{3\pm y}$ by means of contact annealings (850°C, 20 h) of ground-together plates of the corresponding materials. The component exchange between the support and coating occurs within a zone comparable in thickness with the zone of nickel oxide formation via oxidation (Fig. 3), being equal in this case to about 4–6 μm. At the same time, this value is comparable with the layer thickness of the catalytic coating.

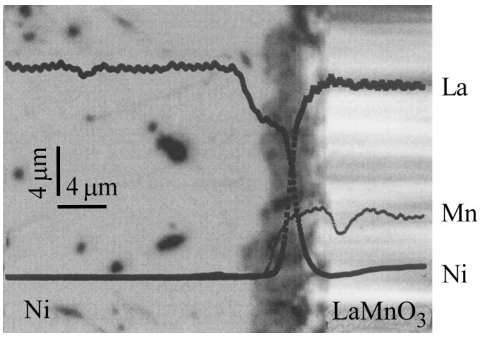

Fig. 3. Element concentration profile in the zone of contact between nickel and $LaMnO_{3\pm y}$ along a line perpendicular to the interface in arbitrary units of characteristic X-ray emission intensity.

Perovskites containing manganese and cobalt are the most active catalysts in CO oxidation, since the bonding energy of oxygen in the structure of oxides is the lowest for these metals [8, 14], which facilitates oxygen desorption from the catalyst surface and accelerates the oxidation process. For this reason, doping of a catalyst with nickel in synthesis and operation of this catalyst may presumably depress its activity (sample no. 3). Use of an intermediate $LaMnO_{3\pm y}$ layer (economically doped sample no. 4) is less effective than that of an Al_2O_3 layer. The properties of sample nos. 3 and 4 are about the same (Fig. 2), despite the differences in specific surface area, which, in the authors' opinion, does not play a key role. In this case, no reliable diffusion barrier appears (compared with the case of aluminum oxide), and the total amount of silver on the surface of sample no. 4 may be lower because of the equalization of its concentration in perovskite layers. Also possible, in the presence of an Al_2O_3 layer, is a promoting effect of aluminum oxide on the catalyst [8].

The promoting influence can also be exerted by a spinel of the $MnAl_2O_4$ type, formed in the zone of contact between compounds containing Mn, Co, and Al_2O_3. The formation of this complex oxide of brown color was recorded by X-ray phase analysis in modeling two methods for obtaining a catalytic coating on an aluminum oxide sublayer. The spinel appeared upon annealing between 650 and 850°C if the aluminum oxide powder was impregnated with a manganese oxide solution with addition of polyvinyl alcohol or upon pyrolysis (with subsequent annealing) of similar solutions containing manganese and aluminum nitrates simultaneously. A similar compound of blue color ($CoAl_2O_4$) is formed in the cobalt-containing system.

Compositions without Al_2O_3 sublayer were advantageous from the standpoint of mechanical strength of the catalytic coatings. The adhesion strength of a coating was evaluated by compressing a catalyst on foamed-nickel support, with its volume decreasing by a factor of 2–4, and then subjecting it to vibration. Up to 5–10% of the deposited composite detached from catalysts with an Al_2O_3 sublayer at the interface between the sublayer and the support. For sample nos. 3 and 4, the loss of deposited composite was no more than 1–2%. Thus, direct interaction of the catalytic layer with the support ensured its better adhesion. This result is important for catalysts intended for operation under nonsteady conditions, e.g., for neutralization of automobile exhaust gases.

The problem of deep oxidation of organic substances is frequently encountered under conditions of

Table 3. Relative activities of composite catalysts in oxidation of organic substances*

Catalyst no.	Coating/sublayer	Oxidation of substances	Activity of composites		
			A	H	B
1	$La_{0.75}Ag_{0.25}MnO_{3\pm y}$ on Ni/–	A > H > B	3 ≥ 1 > 2 > 5 > 4	1 > 2 ≥ 3 > 4 > 5	4 ≥ 3 > 2 ≥ 1 > 5
2	$La_{0.75}Ag_{0.25}MnO_{3\pm y}$ on ceramic/Al_2O_3	A > H ≥ B			
3	$La_{0.84}Sr_{0.16}Mn_{0.8}Co_{0.2}O_{3\pm y}$ on Ni/Al_2O_3	A > B > H			
4	Pt, Pd, Rh** on ceramic/Al_2O_3	B > A > H			
5	$La_{0.75}Ag_{0.25}MnO_{3\pm y}$ on Ni/Al_2O_3	A > H > B			

* A stands for ethanol; B, for benzene; H, for *n*-heptane.

** Mass ratio Pt : Pd : Rh 2 : 10 : 2 or 3 : 10 : 1.

stationary arrangement of thermocatalytic devices, when it is possible to use as catalyst supports ceramic foamed materials having somewhat lower mechanical strength than foamed metals. In oxidation of organic substances, the catalytic activity strongly depended on the nature of these compounds and on the composition of composite catalysts. As an example, Fig. 4 shows temperature dependences of the efficiency of some samples. The data obtained can be summarized to give the corresponding series in Table 3.

Complex-oxide catalysts were in all cases more efficient in alcohol oxidation than the samples containing noble metals. The highest activity was observed for the sample containing no silver. Benzene is the most readily oxidized on catalyst no. 4 (Table 3). Of the compounds studied, it is aromatic hydrocarbon that is the most readily oxidized on noble metals. Such a situation may be due to different abilities of organic substances to be sorbed on the catalyst surface: noble metals tend to adsorb aromatic compounds, whereas the oxygen-containing alcohols show higher affinity for oxide materials.

The activity of the catalysts in oxidation of heptane is intermediate, but this compound better reacts with oxygen in the presence of silver-containing catalysts. Catalysts of this type are also sufficiently active in oxidation of natural gas components [6]. Sample no. 1 (Table 3, Fig. 4) exhibits higher activity than no. 2 in oxidation of alcohol and heptane and is comparable with sample no. 2 in oxidation of benzene, despite the smaller total specific surface area of catalyst no. 1. Catalysts of composition $La_{0.75}Ag_{0.25}MnO_{3\pm y}$ on foamed nickel without a sublayer were more active than the same composition with an intermediate aluminum oxide layer (Fig. 4, Table 3). Probably, the effect of promotion by aluminum oxide is absent, and, by contrast, doping a catalyst with silver is favorable, in the case of oxidation of organic substances. Moreover, it is known that nickel exerts strong catalytic influence on those reactions of organic compounds, which involve addition or elimination of a hydrogen atom.

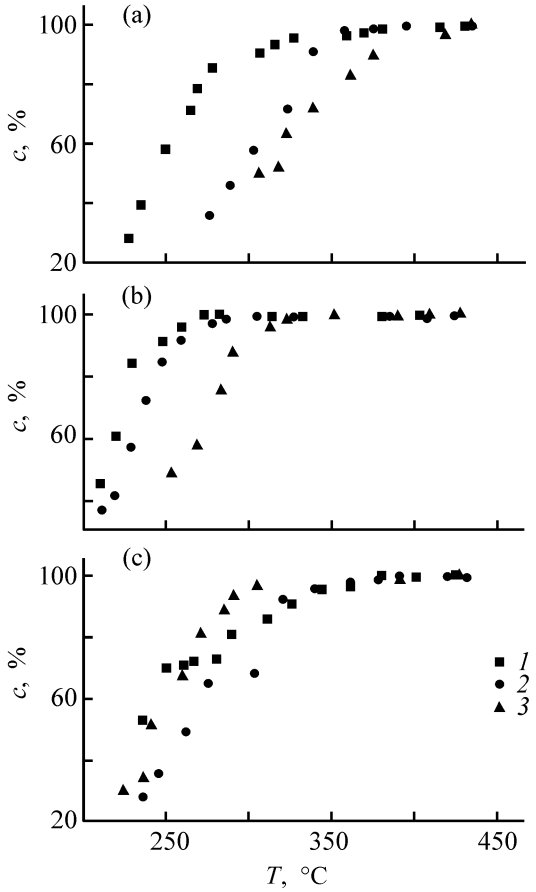

Fig. 4. Conversion *c* vs. temperature *T* in reactions of deep oxidation of organic substances on various catalysts. (*1*) Ethanol, (*2*) *n*-heptane, and (*3*) benzene. (a) $La_{0.75}Ag_{0.25}MnO_{3\pm y}$ catalyst on nickel support with Al_2O_3 sublayer, (b) the same without sublayer, and (c) catalyst based on platinum metals.

The data in Table 2 support the assumption that, in CO oxidation, too, the difference in specific surface area between the catalysts may be not a decisive factor at relatively low loads on a catalyst. Surely, it is desirable to compare catalysts with the same surface area for making more correct conclusions. It can be seen that, depending on the nature of compounds being oxidized and catalysts, manifestations of selectivity in the corresponding reactions in mixtures would be expected. To improve the efficiency of oxidation of a sum of toxic compounds, catalytic elements of different types and compositions can be combined [16].

It should be noted, to conclude, that one more type of perovskite catalysts with a silicon carbide SiC support was tested. This catalyst is of interest for developing elements heated by electric current to the working temperature because of their intrinsic electrical resistance. Measurements demonstrated that their activity is comparable with that of sample nos. 2 and 5 (Table 3) in oxidation of alcohol, sample nos. 4 and 5 in oxidation of heptane, and sample nos. 1 and 2 in oxidation of benzene.

CONCLUSION

Catalysts constituted by a porous support, intermediate oxide layer, and complex-oxide coating are proposed for use to protect the atmosphere from noxious substance discharges. Their activity is comparable with that of catalysts based on platinum-group metals. The catalytic activity is strongly affected by the nature and composition of the substances being oxidized and the catalysts, with an important role played by the interaction between the underlying surface with a catalytic coating. In particular, the perovskite structure is doped with silver in silver-containing perovskite compositions. Oxidation of CO is the most efficient just on perovskite catalysts of this kind with a sublayer of aluminum oxide, and that of *n*-heptane, on a similar catalyst without aluminum oxide sublayer. Alcohol and benzene are more readily oxidized, on a catalyst based on a mixture of cobaltite, manganite, lanthanum, and strontium.

ACKNOWLEDGMENTS

The study was supported by the Ministry of Education of the Russian Federation and also by the Russian Foundation for Basic Research (grant Ural 02-03-96443) and CDRF (project REC-005).

REFERENCES

1. Antsiferov, V.N. and Porozova, S.E., *Vysokoporistye pronitsaemye materialy na osnove alyumosilikatov* (High-Porosity Permeable Materials Based on Aluminosilicates), Perm: Perm. Gos. Tekh. Univ., 1996.
2. Ostroushko, A.A., Makarov, A.M., Porozova, S.E., *et al., The First Int. Conf. "Automobile & Technosphere (ICATS'99),"* Kazan, June 16–20, 1999, vol. 3, p. 71.
3. Ostroushko, A.A. and Makarov, A.M., Abstracts of Papers, *Nauchno-tekhnicheskaya konferentsiya "Ekologicheskie problemy promyshlennykh regionov. Uralekologiya-Tekhnogen-2000," Ekaterinburg, 4–6 aprelya 2000 g.* (Scie.-Technol. Conf. "Ecological Problems of Industrial Regions, Urarekologiya-Tekhnogen-2000," Yekaterinburg, April 4–6, 2000), p. 92.
4. Ostroushko, A.A., Udilov, A.E., Makarov, A.M., *et al,. The Second Int. Conf. "Automobile & Technosphere (ICATS'01),"* Kazan, June 13–15, 2001, pp. 175–176.
5. Ostroushko, A.A., Makarov, A.M., Budnikov, V.I., *et al., Trudy regional'nogo nauchno-prakticheskogo seminara RFFI "Puti kommertsializatsii fundamental'nykh issledovanii v oblasti khimii dlya otechestvennoi promyshlennosti" Kazan', 26–28 noyabrya 2002 g.* (Proc. Reg. Sci.-Pract Symp. of the Russian Foundation for Basic Research "Ways of Commercialization of Basic Research in the Field of Chemistry for Domestic Industry," Kazan', November 26–28, 2002), pp. 107–108.
6. Ostroushko, A.A., *Tekhnologiya izgotovleniya katalizatorov: Termokataliticheskaya ochistka otkhodyashchikh gazov v promyshlennosti, energetike, na transporte: Nauchno-prakticheskoe izdanie* (Technology of Catalyst Fabricationm: Thermocatalytic Purification of Waste Gases in Industry, Power Engineering, and Transportation: Sci.-Pract. Publication), Yekaterinburg: Ural'sk. Univ., 2002.
7. Ostroushko, A.A., Makarov, A.M., Nechaev, V.A., *et al.*, Abstracts of Papers, *Mezhdunarodnaya nauchn-tekhnicheskaya konferentsiya "Ekologicheskaya bezopasnost' Urala," Ekaterinburg, 27–29 marta 2002 g.* (Int. Sci.-Pract. Conf. "Ecological Safety of Urals," Yekaterinburg, March 27–29, 2002), p. 100.
8. Popova, N.M., *Katalizatory ochistki gazovykh vybrosov promyshlennykh proizvodstv* (Catalysts for Purification of Industrial Waste Gases), Moscow: Khimiya, 1991.
9. Ostroushko, A.A., *Ross. Khim. Zh., (Zh. Vses. Khim. O–va)*, 1998, vol. 42, no. 1–2, pp. 123–133.
10. Ostroushko, A.A., Shubert, E., Zhuravleva, L.I., *et al., Zh. Prikl. Khim.*, 2000, vol. 73, no. 8, pp. 1311–1320.
11. Udilov, A.E. and Ostroushko, A.A., Abstracts of Papers, *7-e Vserossiiskoe soveshchanie "Vysokotemperaturnaya khimiya silikatov i oksidov" Sankt-Peterburg, 19–21 noyabrya 2002 g.* (7th All-Russia Symp.

"High-Temperature Chemistry of Silicates and Oxides," St. Petersburg, November 19–21, 2002), St. Petersburg: Inst. Khim. Siliikatov, Ross. Akad. Nauk, Yanus, 2002, p. 175.

12. Heinze, R., Nobst, S., Graf, Th., *et al.*, Abstr. *Book 4 of 5 Eur. Congr. on Catalysis*, Limeric, Ireland, 2–7 Sept. 2001, pp. 7–P–57.
13. Kwang-Sup, S., Hao, X.C., Sang, D.K., and Sung-Kyu, K., *Catal. Today*, 1999, vol. 47, pp. 155–160.
14. Golodets, G.I., *Geterogenno-kataliticheskoe okislenie organicheskikh veshchestv* (Heterogweneous-Catalytic Oxidation of Organic Substances), Kiev: Naukova Dumka, 1978.
15. Ostroushko, A.A., Kvasnitsa, K., Vidmer, K., *et al.*, *Zh. Neorg. Khim.*, 1993, vol. 38, no. 3, pp. 436–438.
16. Ostroushko, A.A., Shubert, E., Makarov, A.M., *et al.*, Abstracts of Papers, *Nauchno-tekhnicheskaya konferentsiya "Ekologicheskie problemy promyshlennykh regionov," Ekaterinburg, 19–21 marta 2003 g.* (Sci.-Technol. Conf. "Ecological Problems of Industrial Regions," Yekaterinburg, March 19–21, 2003), pp. 66–67.

Russian Journal of Applied Chemistry, Vol. 76, No. 8, 2003, pp. 1260–1263. Translated from Zhurnal Prikladnoi Khimii, Vol. 76, No. 8, 2003, pp. 1298–1301.

CATALYSIS

Conjugated Oxidation of Carbon Monoxide and Reduction of Nitrogen(II) Oxide on Pt-containing Ceramic Catalyst with Modifying Additives

Yu. A. Aleksandrov, K. E. Ivanovskaya, and I. A. Vorozheikin

Lobachevskii State University, Nizni Novgorod, Russia

Received March 20, 2003

Abstract—A Pt-containing catalyst for conjugated oxidation of CO and reduction of NO was developed with the use of a synthetic porous ceramic as a support. The catalyst is modified with oxides of a number of metals to improve its efficiency.

The presently topical problem of catalysis is a search for effective catalysts for purification of exhaust gases of combustion engines [1]. The most promising are catalysts for conjugated oxidation of CO and hydrocarbons and reduction of nitrogen oxides. As shows analysis of published data, most of catalysts for the given process, containing no noble metals, have been tested only in laboratory and are rapidly deactivated in prolonged operation even under these conditions [2]. Cu- and Co-containing zeolites, intensively developed in Japan in recent years, have also proved inefficient when tested under industrial conditions [1]. In this context, development of new Pt-, Pd, or Rh-containing catalysts optimized by making lower the content of noble metals, simplifying the technology of catalyst manufacture, and using modifiers [3] remains a topical task.

Previously, catalysts for deep oxidation of CO have been obtained on supports in the form of a synthetic porous ceramic (SPC) with large specific surface area (~90 $m^2 g^{-1}$). The catalysts based on SPC are distinguished by simplicity of fabrication.

The aim of this study was to develop SPC-based Pt-containing catalysts modified with some promising additives and to test the activity of the catalysts in reaction of conjugated oxidation of CO and reduction of NO. To compare the activities of catalysts on SPC and conventional supports, a catalyst with equivalent amount of platinum supported by γ-Al_2O_3 was prepared. The activities of the catalysts studied were also compared with that of Pt-containing catalysts for the process in question, fabricated on various alumina-borosilicate and silica supports [7].

Since published evidence points to the positive influence exerted by addition of alkaline-earth, rare-earth, and transition metals on the activity of catalysts for purification of exhaust gases of combustion engines, Pt-containing catalysts modified with equal amounts of Na, Ce, and V compounds were prepared. Vanadium was introduced directly into SPC in the form of V_2O_5 in preparing a ceramic, since it was established earlier [8] that catalysts based on SPC + V_2O_5 exhibit higher activity than SPC-based catalysts.

EXPERIMENTAL

The catalysts were prepared by impregnating a support with aqueous solutions of H_2PtCl_6, $NaNO_2$, and $Ce(NO_3)_3 \cdot 6H_2O$ in amounts (percent relative to support mass) Pt 0.7 and 1.4, Ce 8, and Na 8. The impregnation was repeated 3 or 4 times. First, Pt(IV) was deposited, and then modifying additives were deposited onto a dried and calcined Pt catalyst. As mentioned above, vanadium(V) was introduced directly into SPC in the form of V_2O_5 in amount of 8% relative to the support mass. All the catalysts prepared in this way were dried in air at 100°C and then calcined in a flow of helium at 500–650°C.

The catalytic activity of the samples was studied in reactions of conjugated oxidation of CO and reduction of NO to N_2 in a pulsed microcatalytic installation (pulse volume 2 cm^3, flow rate F of carrier gas 1 $cm^3 s^{-1}$). The reaction products were analyzed by gas chromatography, with katharometer as detector and carrier-gas helium. N_2, NO, and CO were separated on a column with 5-Å NaX molecular sieves (200 × 3 mm, 50°C). IR spectra of samples of the

1070-4272/03/7608-1260 $25.00 © 2003 MAIK "Nauka/Interperiodica"

1.4% Pt/(SPC + V_2O_5) catalyst in Vaseline oil were recorded on a Specord 75-IR spectrophotometer. The spectra in Fig. 1 were obtained by subtracting the base absorption spectrum of Vaseline oil.

The compositions of the catalysts prepared are listed in Table 1.

The activity of the catalysts in the reaction of conjugated oxidation of CO and reduction of NO was studied using the pulsed method with chromatographic analysis of the reaction products. The temperature dependence of the conversion α of CO into CO_2 and NO into N_2 on the catalysts studied is shown in Fig. 2.

Complete reduction of NO to N_2 could not be observed on any of the catalysts. Complete reduction of NO with propane has not been achieved, either, on industrial catalysts [9], which is probably due to incomplete reduction of NO to N_2O.

As a comparative characteristic of catalyst activity was chosen the temperature at which a conversion of 0.5 is achieved. The following activity series of the catalysts studied in oxidation of CO and reduction of NO were obtained for α = 0.5: IV > VI = II > I > V > III and IV > VI > II > III ≈ I > V, respectively.

It can be seen that the highest activity in the reaction of conjugated oxidation-reduction of a CO + NO mixture is exhibited by catalysts IV and VI, i.e., V(V) and Ce(III) are effective modifying additives. Raising the amount of Pt from 0.7 to 1.4% also makes higher the activity of the SPC-based catalyst. Introduction of Na ions into an SPC-based Pt-containing catalyst impairs its activity.

Thus, the results obtained suggest that metal oxides with low oxygen– metal bonding energy are effective additives to catalysts for conjugated oxidation of CO and reduction of NO. However, the bonding energy in a modifying oxide must exceed the energy of bonding between oxygen and a noble metal (in the given case, the oxygen–sodium bonding energy is lower than that for oxygen and platinum, and, therefore, addition of sodium ions is inefficient).

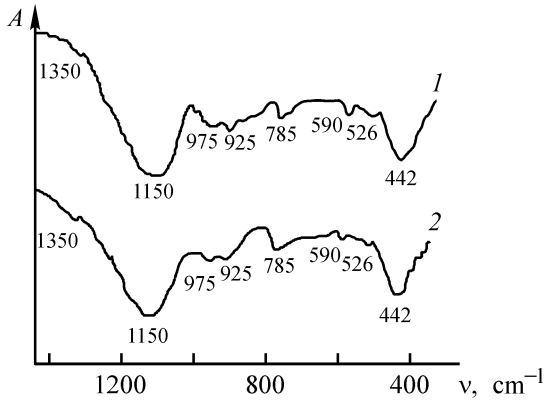

Fig. 1. IR spectra of (*1*) catalyst IV and (*2*) catalyst IV treated with CO at 500°C. (*A*) Absorption and (ν) wave number.

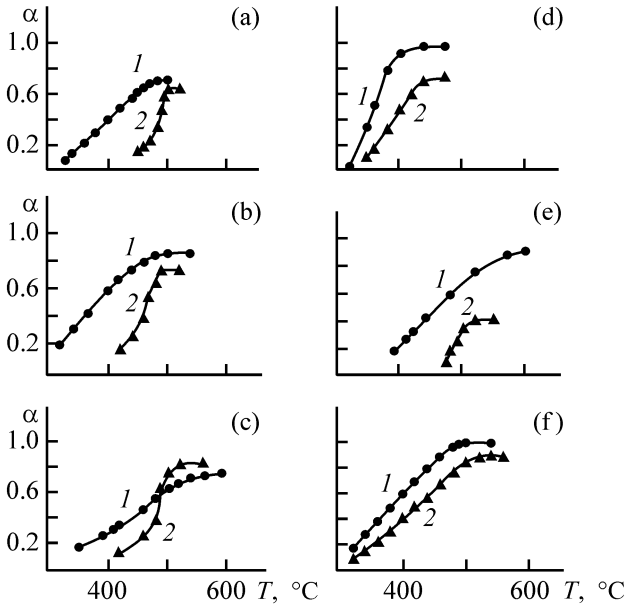

Fig. 2. Conversion α of (*1*) CO into CO_2 and (*2*) NO into NO_2 on the catalysts vs. temperature *T*. *M* = 0.5 g, starting mixture (vol %): 6NO + 12CO + 82He. Catalyst: (a) I, (b) II, (c) III, (d) IV, (e) V, and (f) VI.

The activity of the Al_2O_3-supported catalyst being tested was found to be lower than that of the SPC-supported catalysts. Comparison of the activities of the SPC-based catalysts and those supported by Al_2O_3

Table 1. Composition of catalysts for conjugated oxidation of CO and reduction of NO

Catalyst	Catalyst composition, wt %	Catalyst	Catalyst composition, wt %
I	SPC + 0.7 Pt	IV	(SPC + V_2O_5) + 1.4 Pt
II	SPC + 1.4 Pt	V	SPC + 1.4 Pt + 8 Na
III	γ-Al_2O_3 + 1.4 Pt	VI	SPC + 1.4 Pt + 8 Ce

Table 2. Kinetic parameters of the reaction of CO oxidation to CO_2 and NO reduction to N_2 on Pt-containing catalysts.

Catalyst	CO oxidation to CO_2			NO reduction to N_2		
	T, °C	E_a^{app}, kJ mol^{-1}	ln k_0^{eff}	T, °C	E_a^{app}, kJ mol^{-1}	ln k_0^{eff}
I	330–484	64.6 ± 2.9	0.43 ± 0.02	450–500	176.1 ± 12.4	17.02 ± 1.24
II	320–480	45.9 ± 1.8	–2.23 ± 0.09	460–520	130.0 ± 9.6	10.48 ± 0.79
III	420–522	107.4 ± 18.1	6.41 ± 1.11	350–540	45.39 ± 0.8	–3.29 ± 0.07
IV	320–400	185.2 ± 29.9	24.41 ± 4.01	348–438	103.0 ± 12.6	7.68 ± 0.99
V	390–600	55.6 ± 2.6	–1.26 ± 0.06	472–520	139.6 ± 35.3	10.33 ± 2.77
VI	320–490	65.6 ± 1.8	1.45 ± 0.04	320–540	59.6 ± 2.8	–0.39 ± 0.01

and various fiber glass supports [7] shows that SPC-based catalysts compare well in efficiency with the latter in the comparable temperature range.

Table 2 lists kinetic parameters of the reaction of CO oxidation to CO_2 and NO reduction to N_2 on Pt-containing catalysts. The parameters were calculated using the procedure described in detail in [8].

To determine the composition of a catalyst and elucidate the mechanism of reactions occurring at its surface, the IR spectrum of one of the most active catalysts [1.4% Pt/(SPC + V_2O_5)] was analyzed before and after its treatment with carbon monoxide at 500°C (Fig. 1).

The IR spectrum of the catalyst (Fig. 1, curve *1*) contains a strong broad band and several low-intensity bands in the frequency range 800–400 cm^{-1}. These latter can be assigned to vibrations of silicate groups contained in the ceramic. The low-intensity band peaked at 900 cm^{-1} and broad bands in the range 1700–1200 cm^{-1} are associated with vibrations of phosphate groups, and the strong band at 1200–900 cm^{-1} most probably results from superposition of vibrations of phosphate and silicate groups. The bands peaked at 1000, 955, 915, 880, and 840 cm^{-1} correspond to vibrations of the V=O bond (spectrum of vanadium-containing catalyst was compared with that of SPC).

Figure 1 (curve *2*) also shows the spectrum of a Pt-containing catalyst pretreated with carbon monoxide at 500°C. This temperature corresponds to the maximum conversion of CO into CO_2 and NO into N_2 on the given catalyst at the following composition of the reaction mixture (vol %): 6NO + 12CO + 82He. When a reaction mixture containing 12 vol % CO and 88 vol % He was passed through the 1.4% Pt/(SPC + V_2O_5) catalyst, complete oxidation of CO to CO_2 by oxygen contained in the catalyst was observed initially, but then the conversion of CO into CO_2 started to decrease gradually. The run was terminated when CO ceased to oxidize completely. Comparison of curves *1* and *2* shows that passing carbon monoxide through the catalyst at 500°C leads to a decrease in the intensity of the band corresponding to vibrations of the V=O bond. The data obtained suggest that CO is oxidized by oxygen from V_2O_5. This hypothesis is also supported by a change in the catalyst color on passing CO through it from red-yellow to dark gray, which corresponds to transition of V(V) to a more reduced form.

Thus, it may be assumed that, in passing a CO + NO mixture through a 1.4% Pt/(SPC + V_2O_5) catalyst, CO is adsorbed on active centers of the catalyst and is oxidized by their oxygen. NO is adsorbed on the same centers, but subsequent dissociation of NO to give a nitrogen molecule requires a sufficient number of active centers reduced by carbon monoxide. Experiments with catalysts based on SPC and SPC + V_2O_5 demonstrated that the key role in the reactions of conjugated oxidation-reduction is played by a noble metal, since only oxidation of CO occurs in its absence. It may be assumed that the function of a noble metal is to catalyze dissociation of an adsorbed NO molecule.

CONCLUSIONS

(1) A Pt-containing catalyst supported by an original synthetic porous ceramic was developed and tested in the reaction of conjugated oxidation of CO and reduction of NO.

(2) The catalyst was modified with oxides of a number of metals. It was found that the Pt-containing catalysts developed compare well in efficiency with the known Pt-containing catalysts on various supports.

(3) An analysis of IR spectra of one of the catalysts yielded data on its composition and allowed an assumption concerning the mechanism of the reaction of conjugated oxidation of CO and reduction of NO.

REFERENCES

1. Krylov, O.V., *Ross. Khim. Zh.*, 2000, vol. 44, part 1, no. 4, pp. 53–57.
2. Savenkov, A.S., Syu Yunlun, and Sibirtseva, M.A., *Zh. Prikl. Khim.*, 2000, vol. 73, no. 8, pp. 1339–1343.
3. Gutierrez, L.B., Boix, A.V., and Petunchi, J.O., *J. Catal.*, 1998, vol. 179, no. 1, pp. 179.
4. Aleksandrov, Yu.A., Tsyganova, E.I., Shekunova, V.M., *et al.*, *Zh. Obshch. Khim.*, 2001, vol. 71, no. 1, pp. 46–50.
5. Aleksandrov, Yu.A., Vorozheikin, I.A., Ivanovskaya, K.E., and Tsyganova, E.I., *Zh. Obshch. Khim.*, 2001, vol. 71, no. 6, pp. 881–883.
6. Aleksandrov, Yu.A., Vorozheikin, I.A., and Ivanovskaya, K.E., *Zh. Fiz. Khim.*, 2001, vol. 75, no. 11, pp. 2099–2100.
7. Barelko, V.V., Khrushch, A.P., Cherashev, A.F., *et al.*, *Kinet. Katal.*, 2000, vol. 41, no. 5, pp. 719–727.
8. Aleksandrov, Yu.A., Tsyganova, E.I., Ivanovskaya, K.E., and Vorozheikin, I.A., *Zh. Obshch. Khim.*, 2002, vol. 72, no. 1, pp. 17–20.
9. Tret'yakov, V.F., Burdeinaya, T.N., Matyshak, V.A., *et al.*, *Kinet. Kataliz*, 2000, vol. 41, no. 2, pp. 261–266.

Russian Journal of Applied Chemistry, Vol. 76, No. 8, 2003, pp. 1264–1267. Translated from Zhurnal Prikladnoi Khimii, Vol. 76, No. 8, 2003, pp. 1302–1305.

PROCESSES AND EQUIPMENT OF CHEMICAL INDUSTRY

Unconventional Method for Obtaining Homogeneous Highly Dispersed Suspensions

V. P. Zakharov, K. S. Minsker, I. V. Sadykov, A. A. Berlin, and Yu. B. Monakov

Bashkir State University, Ufa, Bashkortostan, Russia

Semenov Institute of Chemical Physics, Russian Academy of Sciences, Moscow, Russia

Institute of Organic Chemistry, Ufa Scientific Center, Russian Academy of Sciences, Ufa, Bashkortostan, Russia

Received February 21, 2003

Abstract—The possibility of obtaining suspensions with very small particle radius and low polydispersity coefficient in tubular turbulent apparatus though specific hydrodynamics of reagent motion in fast chemical reactions was studied.

Chemical technology widely employs processes for obtaining suspensions by the condensation method in the course of a chemical reaction involving precipitation. In many cases, it is necessary to obtain homogeneous finely dispersed suspensions, in particular, in preparing highly active heterogeneous and microheterogeneous Ziegler–Natta catalytic systems for polymerization of olefins and dienes, antiagglomeration agents for synthetic caoutchoucs, pigments for paints, etc.

Under industrial conditions, fast chemical reactions are frequently carried out with suspensions obtained by mixing starting homogeneous reagents in the turbulent mode effected by blades of centrifugal pumps. However, this may lead, with high probability, to failure of moving elements of the pumps and to their clogging, and in the case of corrosive media, special corrosion-protective coatings are to be deposited the working surfaces of apparatus.

Chemical reactions used to prepare finely dispersed suspensions are commonly of ion-exchange type and, as a rule, proceed at high rate. Therefore, it is apparently advisable to use in this case a new type of chemical technological apparatus: small-size high-throughput tubular turbulent apparatus of jet type [1]. The specific features of operation of these apparatus have been studied sufficiently well, and they are widely used in industry [2] to perform fast homogeneous chemical reactions. However, there have been no publications concerned with the possibility of their use for carrying out fast chemical reactions combining homogeneous fluid flows with suspension formation.

The aim of this study was to analyze the possibility of using tubular turbulent apparatus of diffuser-confuser design for obtaining homogeneous finely dispersed suspensions by the condensation method in a fast chemical reaction and to compare their efficiency with that of volume apparatus with mechanical agitation.

As model served the following fast chemical reaction

$$H_2SO_4 + BaCl_2 \rightarrow BaSO_4\downarrow + 2HCl.$$

Three methods were used to synthesize suspensions: (1) reaction of barium chloride with sulfuric acid in a volume mixing apparatus (70%-filled 500-cm^3 three-necked vessel) with a rotating rabble operating as a centrifugal pump and creating high-intensity turbulent flows in the axial direction of the reaction volume (Fig. 1a); (2) method similar to variant 1 but differing in that a deflector partition is installed within the volume of the reaction mixture (Fig. 1a), which results in higher power consumed for agitation and intensifies the turbulent mixing of flows [3]; (3) reaction of the starting reagents (aqueous solutions of H_2SO_4 and $BaCl_2$) directly in a six-section tubular turbulent apparatus of diffuser-confuser design (diameter of diffuser 24 mm, that of confuser 10 mm, section length 48 mm) at linear flow velocity of the reagents $V \approx 0.5$ m s^{-1} (Fig. 1b). In order to make greater the ratio of nucleation and crystal growth rates, so that systems as finely dispersed as possible could be obtained, concentrated (0.52 M) and diluted (0.03 M)

1070-4272/03/7608-1264 $25.00 © 2003 MAIK "Nauka/Interperiodica"

aqueous solutions of, respectively, $BaCl_2$ and H_2SO_4 were used.

Dispersion analysis of the $BaSO_4$ suspensions obtained was made by the method of sedimentation in a gravitational field on a torsion balance by the conventional procedure [4]. To diminish the probability of particle interaction in the course of sedimentation, diluted solutions of $BaSO_4$ suspensions were obtained (~0.35 wt %). The results of sedimentation analysis were processed by means of graphical differentiation of the sedimentation curves (Fig. 2). For this purpose, the sedimentation dependences of the mass of precipitate, m, on time τ were approximated with a sigmoid three-parameter function of the type

$$m(\tau) = \frac{a}{1 + \exp\left(-\frac{\tau - x_0}{b}\right)}. \quad (1)$$

The coefficients a, b, and x_0 in Eq. (1) and the error in approximation of the experimental sedimentation curves (Fig. 2) are listed in the table.

In this case, in accordance with the Svedberg–Oden equation [4], the mass m_i of a fraction of suspension particles with radius $r > r_i$, sedimented by instant of time τ_i, was calculated as

$$m_i = \frac{a}{1 + \exp\left(-\frac{\tau_i - x_0}{b}\right)} - \tau_i \frac{\exp -\frac{\tau_i - x_0}{b} \; a}{b\left[1 + \exp\left(-\frac{\tau_i - x_0}{b}\right)\right]^2}. \quad (2)$$

A microscopic analysis of the suspensions obtained demonstrated that $BaSO_4$ particles show clearly pronounced anisometry (have the form of rods with length to diameter ratio of about 4, which accounts for the sigmoid shape of sedimentation curves with an inflection). At the initial instant of sedimentation, rotation of a rod-like particle is possible, which gives rise to an additional resistance to its motion and leads to slowing down of sediment accumulation. In addition, nonspherical particles are oriented in the motion direction in free sedimentation in such a way that the highest resistance to motion is created. This also makes slower the sedimentation of solid particles in a fluid and hinders determination of their true dimensions. Because of this circumstance, the equivalent radius r_e (radius of a spherical particle sedimenting at the same velocity) was determined from the results of sedimentation analysis.

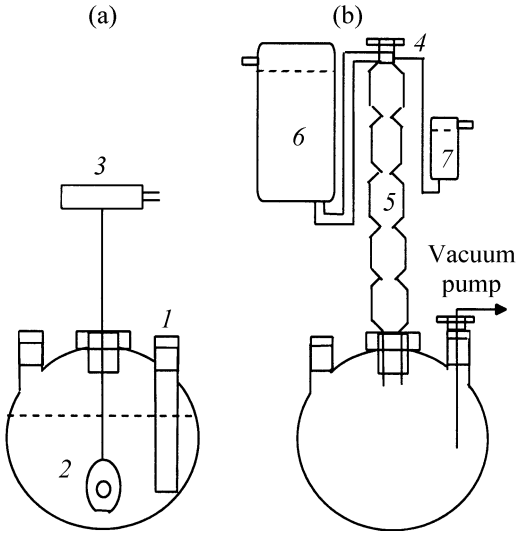

Fig. 1. Schematic of experimental setup. Suspension synthesis: (a) in a volume apparatus of mixing (variants 1 and 2) and (b) in tubular turbulent apparatus. (*1*) Deflector partition; (*2*) rabble operating as centrifugal pump; (*3*) electric drive of rabble; (*4*) three-way valve; (*5*) tubular turbulent apparatus; (*6*, *7*) vessels for, respectively, H_2SO_4 and $BaCl_2$ solutions.

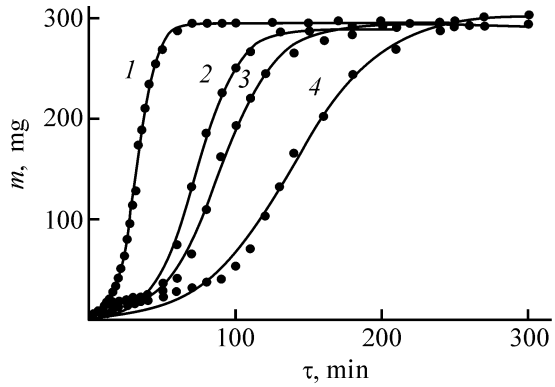

Fig. 2. Sedimentation curves for $BaSO_4$ particles. (m) Sediment mass and (τ) time. Agitation rate N (rpm): (variant 2) (*1*) 300, (*2*) 1500, and (*3*) 2500; (*4*) tubular apparatus. Points, experiment; lines, approximating function.

It can be seen from Fig. 2, that, with increasing agitation rate, the sedimentation curves shift to the range of smaller particles (longer sedimentation time), i.e., the mean particle radius decreases with increasing intensity of turbulent mixing in the reaction zone. In view of the fact that the differential particle size distribution of the dispersed phase, $F(r_e)$, is a typical distribution function of a random variable, the most

Approximation characteristics (correlation factor $R = 0.99$)

N, rpm	a	b	x_0
Volume apparatus of mixing (variant 2)			
300	295.1 ± 2.1	6.6 ± 0.2	32.4 ± 0.2
1500	289.8 ± 3.2	14.2 ± 0.6	72.8 ± 0.8
2500	293.3 ± 1.8	19.1 ± 0.6	88.9 ± 0.8
Tubular turbulent apparatus			
	303.2 ± 2.6	30.7 ± 1.1	138.7 ± 1.4

probable (integral-average) radius r_{mp} of suspension particles was calculated using the relation

$$\tau_{mp} = \frac{\int_0^\infty r_e F(r_e) dr_e}{\int_0^\infty F(r_e) dr_e}. \quad (3)$$

It can be seen (Fig. 3) that, in the case when volume apparatus of mixing (variants 1 and 2) are used to obtain suspensions, r_{mp} decreases with increasing agitation rate N (from $r_{mp} = 4.6$ μm without agitation to $r_{mp} = 1.2$ μm at $N = 5000$ rpm). In the given case, the reaction mixture is sufficiently diluted under the experiment conditions and raising the intensity of turbulent agitation cannot intensify significantly the mass transfer and, as a consequence, make higher the growth rate of crystals and, in the end, their size. A noticeable decrease in the particle radius of the dispersed phase occurs because of the high rate of micromixing, whose intensity grows when dissipation of the specific kinetic energy of turbulence, ε, becomes stronger with increasing agitation rate [5].

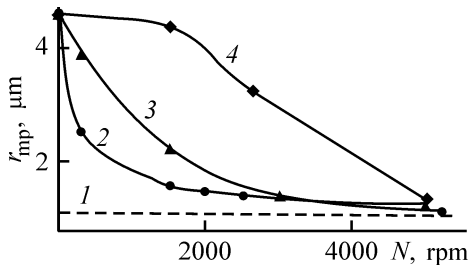

Fig. 3. Most probable radius r_{mp} of $BaSO_4$ particles vs. agitation rate N. (*1*) Tubular turbulent apparatus; volume apparatus of mixing: (*2*) variant 1, (*3*, *4*) variant 2, (*4*) after preliminary forming without agitation and aging for 90 min; the same for Fig. 4.

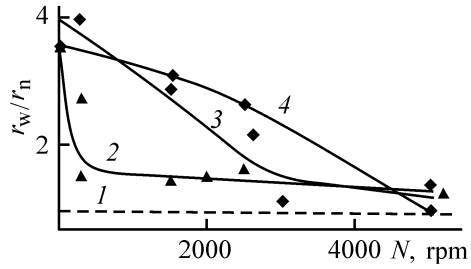

Fig. 4. Polydispersity coefficient r_w/r_n of $BaSO_4$ particles vs. agitation rate N.

At high rate of micromixing, the ratio of nucleation and crystal growth rates grows, which leads to an increase in the number of nuclei of the new phase and to a decrease in r_{mp}. This is, in particular, observed with the deflection partition (variant 2), which makes higher the intensity of turbulent mixing in the volume apparatus. In this case, the relative rate at which r_{mp} decreases with increasing rotation rate N of the rabble is higher than that in variant 1. It is noteworthy that, with the agitation rate in the volume apparatus (variants 1 and 2) increasing up to the maximum possible in laboratory ($N \approx 5000$ rpm), r_{mp} approaches the particle size ($r_{mp} \approx 1.1$ μm) of a suspension obtained in a tubular turbulent apparatus with high intensity of turbulent agitation ensured exclusively by the channel geometry and hydrodynamic energy of the flow [1].

In order to evaluate the degree of polydispersity of the suspensions obtained on the basis of the sedimentation curve (Fig. 2), the weight-average (r_w) and number-average (r_n) radii of particles were calculated:

$$r_w/r_n = \frac{\Sigma r_i n_{wi}}{\Sigma r_i n_{ni}}, \quad (4)$$

where n_{wi} and n_{ni} are the weight and number fractions of particles with radius r_i.

For a homogeneous suspension, the polydispersity coefficient $r_w/r_n = 1$. With increasing intensity of agitation in formation of solid particles in the system by variant 1, the polydispersity coefficient decreases from $r_w/r_n = 2.8$ without agitation to $r_w/r_n = 1.55$ at $N = 5000$ rpm (Fig. 4). The homogeneity of the suspension obtained by variant 2 remains virtually unchanged ($r_w/r_n \approx 1.77$) with increasing intensity of turbulent agitation. Carrying out a fast reaction with precipitation in a tubular turbulent apparatus makes it possible to obtain suspensions with rather high homogeneity: $r_w/r_n \approx 1.48$ (Fig. 4).

Naturally, it seemed appropriate to analyze the characteristics of suspensions subjected to hydrodynamic treatment after preliminary aging without agitation, rather than at the instant of formation. For this pur-

pose, the starting reagents (aqueous solutions of H_2SO_4 and $BaCl_2$) were brought into reaction in the absence of agitation, with aging for 90 min and subsequent turbulent agitation of the resulting suspensions by variant 2 in a tubular turbulent apparatus.

It was found that, in this case, the mean particle radius does not grow with suspension aging (Fig. 3, curve *4*). No sharp decrease in the radius of solid particles obtained without agitation (Fig. 3, curve *4*) with respect to that in suspensions obtained at varied rotation rates of the rabble (Fig. 3, curves *2* and *3*) is observed with increasing intensity of turbulent agitation of a mixture containing the preliminarily formed suspension. This was also demonstrated in [6]. However, highly dispersed particles with $r_{mp} = 1.2$ μm are formed under high-intensity hydrodynamic treatment in a volume apparatus (N = 5000 rpm). Use of a tubular turbulent apparatus for treatment of a mixture aged for 90 min yields dispersed systems with even smaller particles with $r_{mp} \approx 1.1$ μm (Fig. 3, curve *1*).

A similar situation is observed for the polydispersity coefficient r_w/r_n of the suspensions obtained (Fig. 4). Use of a tubular turbulent apparatus both at the instant of suspension synthesis and in treatment of a preliminarily obtained, and aged for 90 min, dispersed system yields rather uniform particles with polydispersity coefficient $r_w/r_n \approx 1.48$ (Fig. 4, curve *1*).

Thus, it was found that it is advisable to use small-size high-throughput tubular turbulent apparatus when performing fast chemical reactions to obtain homogeneous highly dispersed suspensions. In this case, the residence time of the reaction mixture in the apparatus is 2–3 s, which makes lower the probability of secondary processes. As a result, it is necessary to use tubular turbulent apparatus for obtaining Ti–Al, V–Al, Nd–Al, and other highly active microheterogeneous Ziegler–Natta catalytic systems in (co)polymerization of olefins and dienes (*cis*-1,4-isoprene, ethylene-propylene, *cis*-1,4-butadiene, and other caoutchoucs), antiagglomeration agents (M^{2+} stearates) for synthetic caoutchoucs, pigments (in particular, those based on TiO_2), and other homogeneous highly dispersed suspensions formed in interaction of homogeneous fluid flows. Apparently, apparatus of this type compare well in efficiency of suspension synthesis with pump-type or other energy-intensive equipment.

CONCLUSION

Use of tubular turbulent apparatus of diffuser-confuser design both directly in synthesis and in treatment of a finished $BaSO_4$ suspension makes it possible to obtain finely dispersed systems with mean equivalent particle radius of the dispersed phase, $r_{mp} \approx 1.1$ μm, and polydispersity coefficient $r_w/r_n \approx 1.48$, which is ensured in a volume apparatus with mechanical stirrer only at agitation rates exceeding 2000 rpm.

ACKNOWLEDGMENTS

The study was supported financially by the Russian Foundation for Basic Research (project no. 02-01-97913) and by the program "Leading Scientific Schools" (project no. 00-15-97322).

REFERENCES

1. Minsker, K.S., Zakharov, V.P., and Berlin, A.A., *Teor. Osn. Khim. Tekhnol.*, 2001, vol. 35, no. 2, pp. 172–177.
2. Berlin, A.A. and Minsker, K.S., *Nauka Proizv.*, 2002, no. 3(53), pp. 7–12.
3. Kasatkin, A.G., *Osnovnye protsessy i apparaty khimicheskoi tekhnologii* (Basic Processes and Apparatus of Chemical Technology), Moscow: Khimiya, 1971.
4. *Laboratornye raboty i zadachi po kolloidnoi khimii* (Laboratory Works and Problems in Colloid Chemistry), Frolov, Yu.G. and Grodskii, A.G., Eds., Moscow: Khimiya, 1986.
5. Kim, W.S. and Tarbell, J.M., *Chem. Eng. Commun.*, 1999, vol. 176, pp. 89–113.
6. Sung, M.H., Choi, I.S., Kim, J.S., and Kim, W.S., *Chem. Eng. Sci.*, 2000, vol. 55, pp. 2173–2184.

Russian Journal of Applied Chemistry, Vol. 76, No. 8, 2003, pp. 1268–1270. Translated from Zhurnal Prikladnoi Khimii, Vol. 76, No. 8, 2003, pp. 1306–1308.

PROCESSES AND EQUIPMENT OF CHEMICAL INDUSTRY

A Study of Radial Mixing in a Continuous Flow-through Apparatus

N. A. Dul'kina, A. B. Golovanchikov, G. V. Ryabchuk, and E. A. Selezneva

Volgograd State Technical University, Volgograd, Russia

Received May 22, 2003

Abstract—The structure of flows was studied experimentally in continuous flow-through apparatus in various flow modes.

In studying the structure of flows in continuous flow-through apparatus and reactors, it is commonly assumed that there is no concentration gradient in the radial direction [1, 2], i.e.,

$$\partial c/\partial r = 0. \quad (1)$$

However, this assumption is only valid for low-viscous media in the case of a turbulent flow and geometric simplex [3]

$$l/d > 100. \quad (2)$$

In industrial tubular apparatus and reactors, the media being processed have considerable viscosity and the length of the tubes commonly exceeds their diameter by only an order of magnitude, since these geometric dimensions are chosen in accordance with the results obtained in solving simultaneously the equations of material and heat balance [4]. The authors of the present communication studied experimentally the dependence of the indicator concentration on tube radius.

The experimental setup had the form of a hollow tube with inner diameter of 58 mm and length of 1 m, i.e., with a geometric simplex $l/d = 17.3$ (Fig. 1). Service water with kinematic viscosity $\nu = 1.1 \times 10^{-6}$ m^2 s^{-1} was pumped through the tube. Three concentration transducers were mounted in the middle of the tube at $x = l/2$ (at the flow axis $r = 0$, in the middle of the radius $r = R/2$, and at the inner wall $r = R$).

The experiments were carried out as follows. Water was fed into the tube inlet at a prescribed flow rate. Then, at instant of time $\tau = 0$, an indicator, 1 ml of a concentrated solution of common salt, was introduced into the flow in pulsed mode. Preliminarily, the concentration transducers were calibrated using balance resistance bridges. The ratio between the volume of the indicator and that of the fluid in the tube was less than 0.04, i.e., satisfied the requirement that the indicator should not affect the structure of the main flow [1, 2]. The concentration curves obtained are shown in Fig. 2.

As seen from the concentration curves, no concentration equalization occurs in the laminar flow. Molecular diffusion cannot ensure, even for such a low-viscous fluid as water, a uniform distribution of the reaction mass along the radius. In the intermediate mode (Fig. 2b), the influence of convective mass transfer on the concentration equalization along the radius is noticeable. Turbulent pulsations and vortices (Fig. 2c) well equalize the concentration along the radius. In this case, there is no need for static or dynamic mixers, even though the longitudinal mixing gives no way of describing the concentration curve of the turbulent flow by the "one-seventh" law valid for a developed turbulent flow with Re > 10^5 [5]:

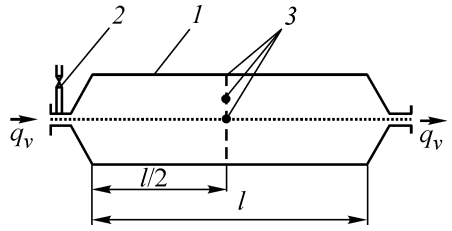

Fig. 1. Schematic of the setup used to determine the dependence of the indicator concentration on radius. (*1*) Tube, (*2*) pipe for introduction of indicator, and (*3*) concentration transducer. l = 1 m is the pipe length.

1070-4272/03/7608-1268 $25.00 © 2003 MAIK "Nauka/Interperiodica"

$$\left.\begin{aligned} v &= v_0(1 - r/R)^{1/7}, \\ C &= 14(\theta_0^7/\theta^9)[1 - (\theta_0/\theta)^7], \end{aligned}\right\} \quad (3)$$

where $v_0 = (120/98)v_{av}$; v_{av}, the average flow velocity; C, the response function of the turbulent flow; $\theta = \tau/\tau_{av}$, dimensionless time; τ, running time; τ_{av}, the average residence time equal to the ratio of the apparatus volume to the flow rate through the apparatus; $\theta_0 = \tau_0/\tau_{av}$, the relative residence time at the flow axis; τ_0, the residence time at the flow axis.

At the same time, in the case of Poiseuille's velocity profile, the response function [second equation in the system (4)] is "broadened" for the laminar flow, too, by molecular diffusion in a low-viscous fluid. This occurs both in the longitudinal and in the radial directions:

$$\left.\begin{aligned} v &= 2v_c[1 - (r/R)^2], \\ C &= 1/(2\theta^3). \end{aligned}\right\} \quad (4)$$

To equalize the concentrations in the radial direction and to diminish the effect of reverse mixing, it is necessary to decelerate the flow along the axis of an apparatus or reactor and to raise the velocity in the peripheral zone. In addition radial mixing is to be simultaneously ensured in both the zones.

Both these tasks can be accomplished in a continuous ribbon screw mixer (Fig. 3). This mixer comprises a cylindrical casing *1*, drive *2*, charging orifice *3* displaced toward the drive *2*, discharging unit *4* at the opposite end of the casing *1*, ribbon screw actuator in the form of a twin screw mixing element with internal coil *5* and external ribbon coils *6*. A planetary mechanism *7* with central tooth gear *8* and pinions *9* engaged with the gear is mounted coaxially with the drive and with the internal ribbon coil *5*. The pinions *9* are mounted in line with the external ribbon coils *6*.

The rotation of the ribbon coils gives no way of mounting static concentration transducers within the casing. However, comparison of the response function of a tubular apparatus with that of the apparatus with the ribbon screw mixer described here shows that, at an adequate choice of the ratio of the angular velocities ω_1 and ω_2, the variance of the response function decreases by a factor of 3–4 in the case of a laminar flow (Fig. 4). A characteristic feature of the flow structure in the apparatus of the design proposed is the presence of two concentration peaks, which is accounted for by the existence of a central and peripheral zones. Undoubtedly, the reduction gear and three

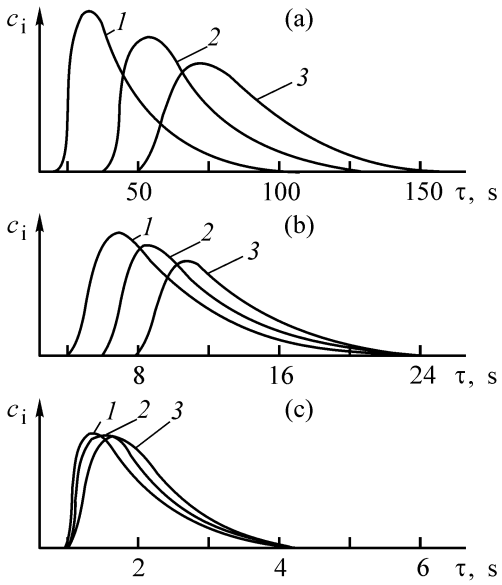

Fig. 2. Indicator concentration c_i vs. time τ after indicator introduction. Flow type: (a) laminar (Re = 530), (b) intermediate (Re = 5300), and (c) turbulent (Re = 21 100). Flow line radius r (*1*) 0, (*2*) 0.5R, and (*3*) R; the same for Fig. 6.

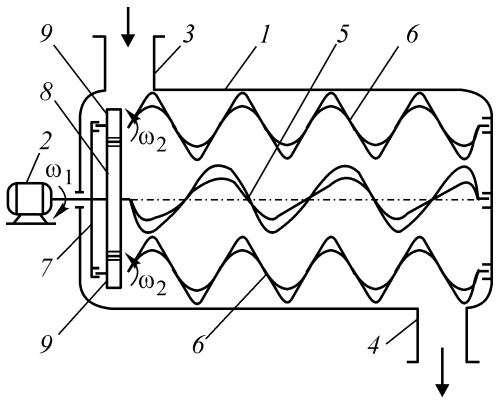

Fig. 3. Schematic of a continuous ribbon screw mixer.

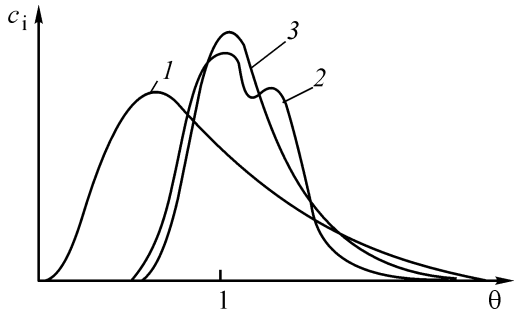

Fig. 4. Response curves of (*1*) hollow apparatus, (*2*) apparatus with continuous ribbon mixer at $\omega_1 = 15$ and $\omega = 45$ s^{-1}, and (*3*) mixing reactor. (c_i) Indicator concentration and (θ) relative dimensionless time. Apparatus scheme: (*1*) Fig. 1, (*2*) Fig. 3, (*3*) Fig. 5.

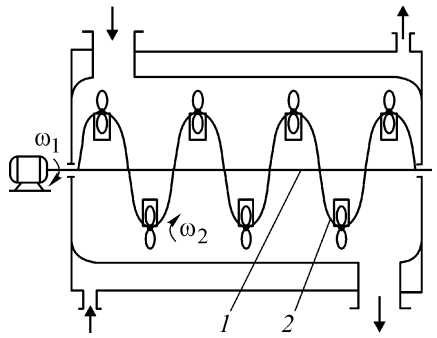

Fig. 5. Schematic of mixing reactor.

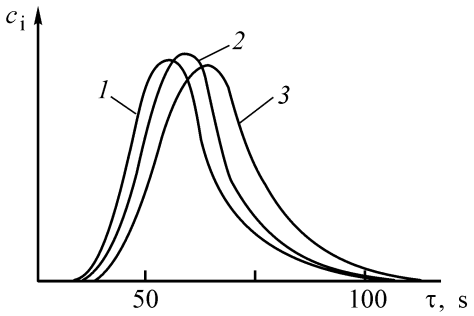

Fig. 6. Indicator concentration c_i vs. time τ after indicator introduction in the case of a laminar flow (Re = 530) and Reynolds number of the stirrer, Re_s = 340.

ribbon screws make the apparatus design more complex.

To simplify the design, a mixing reactor with a single screw, ensuring longitudinal flow with good radial mixing, can be used. The schematic of the design suggested is shown in Fig. 5 [6]. Analysis of the response curve of this apparatus shows (Fig. 4, curve *3*) that the variance decreases by a factor of 1.2–1.3, i.e., is lower than that in the ribbon screw mixer described above. However, the last design is simpler in fabrication and operation. Moreover, with a radial slit cut in the ribbon of screw *2* as far as the shaft *1*, concentration transducers can be easily mounted in accordance with Fig. 1.

The result obtained in studying the dependence of the indicator concentration on the flow line radius are shown in Fig. 6. Comparison of the concentration curves in Fig. 6 with similar curves for a hollow tube shows that a screw with propeller agitators at coil crests equalized the concentrations along the radius and makes the variance of the curves lowr by a factor of 1.6–1.8.

Compared with the screw of the conventional design, the variance of the response curves is virtually unchanged, but the dependence of the concentration curves on radius is preserved (as shown in Fig. 2a, even though the curves themselves become narrower and higher).

Thus, in the case of a turbulent flow, auto-equalization of the flow concentrations along the radius is caused by pulsations and vortices, but ideal plug flow cannot be ensured at $l/d \approx 20$.

Mounting screw mixers of special design in continuous apparatus makes it possible to make the flow close to the ideal plug flow (variance < 0.1) and to ensure the ideal mixing along the radius in the case of a laminar flow.

CONCLUSIONS

(1) Analysis of experimental response curves obtained for the internal volume of the apparatus shows that, to intensify the radial mixing and to level the velocity profile along the radius, it is necessary to mount additional mixing devices, especially at low flow velocities of the reaction mass and its high viscosity.

(2) On the basis of analysis of the response curves obtained, new designs of flow-through continuous apparatus are suggested.

REFERENCES

1. Levenspiel, O., *Chemical Reaction Engineering*, New York: Wiley, 1965.
2. Kafarov, V.V., *Metody kibernetiki v khimii i khimicheskoi tekhnologii* (Methods of Cybernetics in Chemistry and Chemical Technology), Moscow: Khimiya, 1976.
3. Zhernovaya, I.N. and Kafarov, V.V., *Protsessy peremeshivaniya v zhidkikh sredakh: Itogi nauki i tekhniki. Ser. "Protsessy i apparaty khimicheskoi tekhnologii"* (Mixing Processes in Fluid Media: Advances of Science and Technology, Ser. "Processes and Apparatus of Chemical Technology"), Moscow: VINITI, 1975, no. 3, pp. 5–44.
4. Dul'kina, N.A., Golovanchikov, A.B., and Ryabchuk, G.V., *Reologiya, protsessy i apparaty khimicheskoi tekhnologii: Sbornik nauchnykh trudov VolgGTU* (Rheology, Processes, and Apparatus of Chemical Technology: Coll. of Sci. Works of Volgograd State Techn. Univ.), Volgograd, 1999, pp. 8–15.
5. Tyabin, N.V. and Golovanchikov, A.B., *Metody kibernetiki v reologii i khimicheskoi tekhnologii: Uchebnoe posobie* (Methods of Cybernetics in Rheology and Chemical Technology: Textbook), Volgograd: Volgogradskaya Pravda, 1983.
6. RF Patent 2168351.

Russian Journal of Applied Chemistry, Vol. 76, No. 8, 2003, pp. 1271–1273. Translated from Zhurnal Prikladnoi Khimii, Vol. 76, No. 8, 2003, pp. 1309–1311.

PROCESSES AND EQUIPMENT OF CHEMICAL INDUSTRY

A Study of Drop Size Distribution in Multistage Bubble Extractor

B. A. Alimatov, V. N. Sokolov, Z. S. Salimov, and B. Zh. Khursanov

Fergana Polytechnical Institute, Republic of Uzbekistan

St. Petersburg State Technological Institute, St. Petersburg, Russia

Institute of General and Inorganic Chemistry, Academy of Sciences of Uzbekistan, Tashkent, Uzbekistan

Received June 6, 2002; in final form, January 2003

Abstract—Results obtained in determining experimentally the mean volume-surface drop diameter of the dispersed phase in a multistage bubble extractor are presented.

The experience gained in designing and introducing into industrial practice fluid extractors with pneumatic agitation shows that bubble extractors of the mixing-settling type are the most efficient under the conditions of multistage counterflow extraction [1]. Particularly important for apparatus of this kind is that data obtained on pilot installations and even in laboratory are quite reliable and can be used to pass to industrial conditions [2].

In carrying out extraction processes in bubble extractors, one of liquid phases is dispersed into drops under the action of the inert gas used for agitation. As a rule, the dispersed phase is a polydisperse system of drops whose size distribution (or interfacial area) affects, first, the rate of mass exchange across the phase boundary and, second, the rate and extent of phase separation in the settling part of each stage of the extractor.

Theoretical description of mass transfer in a polydisperse system of drops involves severe difficulties, and, therefore, to simplify calculations, most of researchers replace the polydisperse system with a monodisperse one, with particle size equal to mean particle size of the polydisperse system. This allows relations obtained for a single drop to be used when calculating the mass-transfer coefficients [3].

Passing from a polydisperse to monodisperse system for calculating the coefficients of mass transfer from drops into the continuous medium was substantiated in [4], where it was shown theoretically that relations for an isolated drop can be used if the drop diameter is replaced with a volume-surface mean drop diameter in the polydisperse system.

The specific area of the phase boundary can be calculated using the relation [5]

$$F_{sp} = 6\varphi/d_{vs}, \quad \varphi = V_d/(V_c + V_d), \qquad (1)$$

where φ is the volume fraction of the dispersed phase; V_c and V_d, the flow rates of the continuous and dispersed phases ($m^3\ s^{-1}$); d_{vs}, the mean volume-surface drop diameter (m).

The severity of difficulties encountered in attempts to describe analytically the disintegration of drops in fluid–fluid systems for any method used to supply external energy forced authors of numerous studies to take an empirical approach to this problem [6].

The mean volume-surface drop diameter was determined under the conditions of pneumatic agitation in a particular industrial process of double extraction of caprolactam [7] on a three-stage model bubble extractor. The drop diameters were found photographically [8] on a special-purpose laboratory installation.

The model extractor had the following geometric dimensions (mm): inner diameter of the glass casing 104, diameter of the external pipe of the mixer 50, diameter of the internal pipe of the mixer 33, section (extraction stage) height 400.

In the experiments, the flow rates of fluids and the inert gas were varied within the following ranges

1070-4272/03/7608-1271 $25.00 © 2003 MAIK "Nauka/Interperiodica"

Table 1. Physicochemical properties of fluids

Model section no.	Continuous phase		Dispersed phase		σ, N m^{-1}	φ
	ρ_c, kg m^{-3}	$\mu_c \times 10^3$, Pa s	ρ_d, kg m^{-3}	$\mu_d \times 10^3$, Pa s		
1	880	0.88	1036	2.8	2.77	0.193
2	868	0.62	1028	1.4	5.6	0.138
3	859	0.53	1023	1.00	10.8	0.096

(l h^{-1}): light fluid 80–240, heavy fluid 25–80, inert gas (nitrogen) 77–306. The physicochemical properties of the fluids studied are listed in Table 1.

The sizes of all drops were measured using a microscope, with a calibrated wire 1 mm in diameter, placed in the settling zone of an extractor stage, serving as a scale for determining the true sizes of drops.

In each run, data for 250–600 drops were calculated, depending on dispersity.

The whole range of drop sizes obtained was divided into intervals of 10 μm and the mean diameter d_i and number of drops in each interval were determined. Further, the total volume of drops in a group, volume of drops smaller than d_i in size, and, finally, volume fraction of drops smaller than d_i were determined.

The figure shows the drop size distributions, depending on physicochemical properties of fluids and conditions of their dispersion in a stage of the bubble extractor.

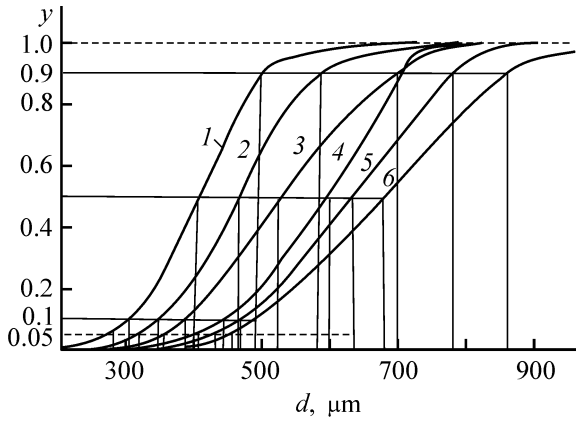

Distribution y of drops over sizes d in pneumatic dispersion. $\bar{w}_g$ (m s^{-1}): (*1, 4*) 0.1, (*2, 5*) 0.05, and (*3, 6*) 0.025. τ_{av} (s): (*1–3*) 10.6 and (*4–6*) 5.3.

Previously, a relation for determining the admissible diameter of drops carried away from the settling zone, in calculating the diameter of a bubble extractor, has been obtained by processing of experimental data [9]:

$$d_5 = 4.96 \times 10^{-6} (\sigma^{0.35} \varphi^{0.8}) / (\bar{w}_g^{0.2} \tau_{av}^{0.45} \mu_c^{1.1}), \quad (2)$$

where d_5 is the drop diameter corresponding to relative drop volume fraction of 5%; σ, the interfacial tension (N m^{-1}); $\bar{w}_g$, the reduced gas flow velocity in the mixer (m s^{-1}); τ_{av}, the average residence time of fluids in the mixer (s); μ_c and μ_d, the viscosities of the continuous and dispersed phases (Pa s); ρ_c and ρ_d, the densities of the continuous and dispersed phases (kg m^{-3}).

Analysis of the type of variation of the parameters appearing in relation (2) shows that they are totally dependent on the mechanism of drop disintegration [5, 6, 8].

The mean volume-surface drop diameter d_{vs} from the logarithmic probability equation for the upper limit is given by the expression [10]

$$d_{vs} = d_{max} / [1 + a \exp(0.25\beta \cdot \beta)], \quad (3)$$

where d_{max} is the maximum drop diameter in the emulsion (m); a and β are constant distribution parameters.

According to [11], it is recommendable to take β = 0.725 and to determine the distribution parameter a from the equality

$$a = (d_{max} - d_{50}) / d_{50}, \quad (4)$$

where d_{50} is the drop diameter corresponding to relative drop volume fraction of 50%.

In its turn, d_{max} can be found from the relation

$$d_{max} / d_{50} = [d_{50}(d_{90} + d_{10}) - 2 d_{90} d_{10}] / (d_{50}^2 - d_{90} d_{10}), \quad (5)$$

where d_{90} and d_{10} are the drop diameters corresponding to volume drop fractions of 90 and 10%.

The results obtained in processing the experimental data from the figure by relations (3)–(5) are listed in Table 2.

The data in Table 2 suggest that the mean volume-surface drop diameter d_{vs} in a multistage bubble ex-

Table 2. Results of experimental data processing

Parameter	Curve no. in figure					
	1	*2*	*3*	*4*	*5*	*6*
d_{90}, μm	490	585	690	710	780	870
d_{50}, μm	400	470	530	600	640	682
d_{10}, μm	305	350	395	438	465	490
d_{max}, μm	730	870	980	816	975	1360
a	0.825	0.85	0.9	0.36	0.52	1.0
d_{vs}, μm	376	442	480	578	610	635
d_5, μm	278	310	360	420	435	470
K	1.35	1.35	1.34	1.37	1.37	1.35

tractor can be calculated using the dependence obtained for d_5 [9] with a constant $K = 1.35$ introduced:

$$d_{vs} = 1.35\,d_5 = 6.7 \times 10^{-6}\left(\sigma^{0.35}\varphi^{0.8}\right)/\left(\overline{w}_g^{0.2}\tau_{av}^{0.45}\mu_c^{1.1}\right) \quad (6)$$

Thus, the experimentally determined curve of the drop volume distribution over drop size can be used to determine with sufficient accuracy important parameters of a fluid–fluid system, such as the admissible diameter of carried-away drops, d_5, necessary for calculating the dimensions of the settling zone of an apparatus, and the mean volume-surface drop diameter d_{vs}, depending on physicochemical properties of fluids and conditions of pneumatic agitation in the mixing zone of the bubble extractor.

REFERENCES

1. Alimatov, B.A. and Salimov, Z.S., *Nauch.-Tekh. Zh. Fergan. Politekhn. In–ta*, 2001, no. 3, pp. 84–88.
2. Ritcey, G.M. and Ashbrook, A.W., *Solvent Extraction. Principles and Applications to Process Metallurgy*, Amsterdam: Elsevier, 1979.
3. Moryakov, V.S., Nikolaev, N.A., and Nikolaev, A.M., *Izv. Vyssh. Uchebn. Zaved., Khim. Khim. Tekhnol.*, 1973, vol. 16, no. 10, pp. 1580–1583.
4. Gal-Or, B. and Hoelscher, H.E., *Am. Inst. Chem. Eng. J.*, 1966, no. 12, pp. 499–502.
5. Sokolov, V.N. and Yablokova, M.A., *Apparatura mikrobiologicheskoi promyshlennosti* (Apparatus for Microbiological Industry), Leningrad: Mashinostroenie, 1988.
6. Ermakov, S.B., Multistage Gas-Lift Apparatus for Polymer Washing), *Cand. Sci. Dissertation*, Leningrad, 1986.
7. *Proizvodstvo kaprolaktama* (Manufacture of Caprolactam), Ovchinnikov, V.M. and Ruchinskii, V.R., Eds., Moscow: Khimiya, 1977.
8. Alimatov, B.A., Design and Study of Extractor with Pneumatic Agitation for Caprolactam Extraction, *Cand. Sci. Dissertation*, Leningrad, 1977.
9. Alimatov, B.A., *Nauch. Tekh. Zh. Fergan. Politekhn. In–ta*, 1998, no. 1(2), pp. 86–89.
10. Mugele, R.H. and Evans, H.D., *Ind. Eng. Chem.*, 1951, vol. 43, no. 6, pp. 1317–1320.
11. Popov, V.F. and Vinogradova, N.V., *Khim. Prom–st'.*, 1984, no. 1, pp. 53–55.

Russian Journal of Applied Chemistry, Vol. 76, No. 8, 2003, pp. 1274–1279. Translated from Zhurnal Prikladnoi Khimii, Vol. 76, No. 8, 2003, pp. 1312–1316.

ORGANIC SYNTHESIS AND INDUSTRIAL ORGANIC CHEMISTRY

Optimization of Oxidative Method for Synthesis of 1,3-Diformyl-2,4,6-triethylbenzene

S. B. Apel'chugin, I. B. Krauklish, A. E. Punin, and G. I. Tsypin

Tekhnolog Federal State Unitary Enterprise, Special Bureau of Design and Technology, St. Petersburg State Technological Institute, St. Petersburg, Russia

Received February 13, 2003

Abstract—Oxidation of 1,3-diformyl-2,4,6-triethylbenzene with chromium anhydride in diluted H_2SO_4 to form 1,3-di(hydroxymethyl)-2,4,6-triethylbenzene was studied.

Synthesis of nitrile oxides [1], which are used as efficient cross-linking agents, has become industrially important for production of polymeric formulations containing porophore-like compounds. 1,3-Di(nitrile oxide)-2,4,6-triethylbenzene, whose stability is ensured by three alkyl substituents screening the nitrile oxide groups, is among such compounds.

The synthesis of the above compound includes the stage of preparation of 1,3-diformyl-2,4,6-triethylbenzene (**I**) as an intermediate [1]. This stage may proceed with the formation of the largest amount of impurities and is, in the end, responsible for the quality and yield of the target product. Industrially, compound **I** is commonly obtained by oxidation of 1,3-di(hydroxymethyl)-2,4,6-triethylbenzene (**II**) with Cr(VI) in an aqueous solution of sulfuric acid, with the yield of the reaction product not exceeding 50–55% [2].

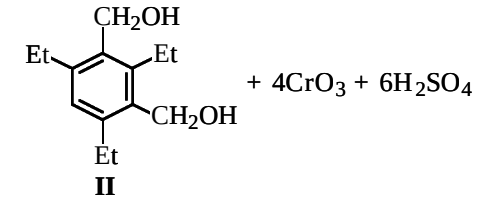

II

$$+ 4CrO_3 + 6H_2SO_4 \rightarrow 3$$

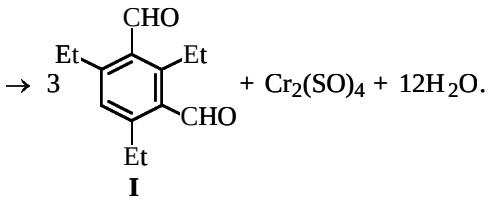

I

$$+ Cr_2(SO)_4 + 12H_2O.$$

As is known [3], transformation of a hydroxymethyl compound into a formyl compound can be accompanied by further oxidation of aldehyde groups to carboxy groups [3]. Dimerization and polymerization, involving the initial and final products of this stage [4], and also oxidation of alkyl groups to aldehyde and carboxy groups, may proceed simultaneously [5]. The rates of the above reactions are comparable, and their extent depends on the reaction conditions, i.e., component ratio, temperature, and time.

Therefore, when formylation is performed under nonoptimal conditions, the reaction product may contain a wide variety of impurities, from the starting diformyl compound to dicarboxylic acid and triethylbenzene. In addition, Cr(VI) is apparently transformed not only into chromium(II) sulfate removable by washing with water, but also into water-insoluble chromium(III) oxides. The presence of these latter in the reaction mass hinders isolation of the target product and results in its contamination.

In this study, the optimal conditions of formylation of compound **I** were determined to obtain the target product in maximum yield with high content of the main substance.

The complex composition and instability of the final reaction product make a kinetic study of the process difficult. For this reason, we solved this problem using the mathematical experiment design [7–9], which allows construction of a mathematical model of the process and its optimization with minimum experimental effort [10–12].

EXPERIMENTAL

The whole set of tests was performed under identical conditions on an installation consisting of a 500-ml

1070-4272/03/7608-1274 $25.00 © 2003 MAIK "Nauka/Interperiodica"

jacketed glass reactor with bottom drain (see figure). The apparatus was equipped with a four-blade high-speed agitator, thermometer, and a thermocouple connected to a KSP-4 recorder. The jacket of the reactor was connected to a U-2 thermostat and a cold-water line by two heat-transfer-agent circuits, which ensured control of the reactor temperature in the range from 10 to 90°C. The volume of the reaction mass was constant in all the tests (400 ml). Calculated amounts of compound **II** and diluted H_2SO_4 were charged into the reactor. The mixture was agitated for 30 min to create a uniform suspension and warmed to 25°C (fixed temperature of the reaction onset), and then a 50% aqueous solution of CrO_3 was added. After that, the reaction mass was heated to the required temperature for 5–10 min and kept at 53–55°C for 60 min.

In the first stage of the study, the reaction mass was allowed to stay for 1 h. In the second stage, the reaction mass was heated, on adding a CrO_3 solution, to a temperature determined from the disign matrix of a full factorial experiment (FFE) and kept at this temperature for a time also determined by the FFE matrix. Then, cold water was fed into the reactor jacket to cool the reaction mass to 15–20°c, and the target product **I** was extracted with carbon tetrachloride. The extraction was done with three portions of the solvent: the volume of the first portion was numerically equal to the mass of compound **II** taken for the reaction. The volumes of the second and third portions were half the above mass. The extraction time was 10–15 min, and the separation time, 20–30 min. The layers were separated in a separating funnel. Since the target product **I** is unstable, the joint extract was immediately used for preparing 1,3-diformyl-2,4,6-triethylbenzene dioxime (**III**) (reaction proceeds in quantitative yield [5, 6]) by the known procedure [3]. The oximes were formed in a 1000-ml three-necked flask equipped with a high-speed agitator rotating at fixed rate and a thermometer.

Water was poured into the reactor, and NaOH (sol) was added under agitation. After NaOH was dissolved, the extract containing aldehyde **I** and then $(NH_2OH_2) \cdot H_2SO_4$ were added. The pH of the reaction mass was measured every 10–15 min and adjusted to 6.5–7.0 with NaOH(sol) or $(NH_2OH_2) \cdot H_2SO_4$. The reaction mass was heated to 45–50°C and kept at this temperature for 1 h. After that, NaOH(sol) was added in an amount necessary for oxime **III** to be transformed into the corresponding disodium salt. The reaction mass was kept at 45–50°C for another 1 h, cooled to 20–25°C, poured into a separating funnel, and allowed to settle for 0.5 h. The lower

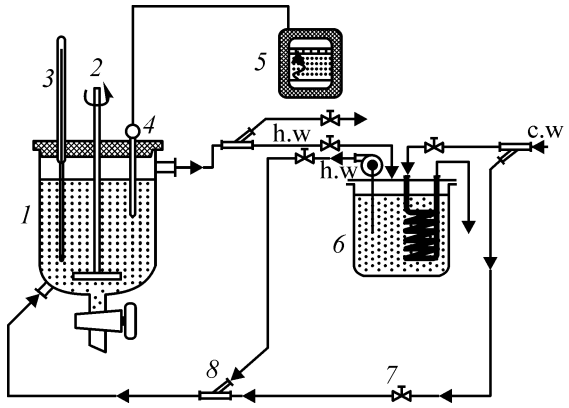

Schematic of the formylation set-up: (*1*) reactor; (*2*) agitator; (*3*) thermometer; (*4*) thermocouple; (*5*) KSP-4 recorder; (*6*) U-2 thermostat; (*7*) valve; (*8*) T-joint;, h.w and c.w stand for hot and cold water, respectively.

(organic) layer was separated, whereas the aqueous solution of disodium salt of oxime **III** was placed in the reactor again and its pH was adjusted to 6.5–7.0. For a sediment of product **III** to be formed, the solution was kept at room temperature for 1 h. The sediment was filtered off, washed with water, and dried at 50–55°C in a thermostat to constant mass. The mass of the substance, its boiling point, and the content of the main substance were determined by liquid chromatography (LC).

A quantitative analysis was done on a Milikhrom liquid chromatograph with a 64 × 2-mm KAKh-2 column packed with Separon-C_{18} (grain size 5 μm). As eluent served a mixture of dioxane, acetonitrile, and water (volume ratio 1 : 4.5 : 4.5).

An analysis of an *a priory* information about formylation made it possible to reveal a number of influencing factors (independent variables), examine them, and arrange them in order of increasing priority for the problem to be solved. To these factors we assigned, in the first place, the relative amounts of the starting components and the process temperature and time.

As optimization criterion (response function) served the yield of the target product, with account taken of the content of main substance in the target product, i.e., its quality.

In the first stage of the study, a FFE was carried out (Table 1, run nos. 1–8). To eliminate, to the maximum possible extent, the effect of interaction, the following three factors, determining the relative amounts of the starting components, were used originally: x_1, the excess of CrO_3 with respect to its amount re-

Table 1. Results of realization of OCCD matrix*

Run no.	Concentration of main substance (%) in parallel runs	Yield, %
1	99	63
2	99	63
3	98	66
4	98	65
5	97	56
6	81	48
7	92	51
8	86	55
9	98	57
10	100	64
11	98	59
12	100	61
13	82	58
14	88	54
15	99	62

* Values averaged over two parallel runs.

Table 2. Estimate of the experiment reproducibility*

Characteristic	Value of criterion
Maximum of the estimated reproducibility variances, S_{sp}	31.75
Sum of estimated reproducibility variances, S_i^2	15.82
Cochran criterion, G_{cal} [8, 9]	0.50
Cochran criterion G_{tab} for $P = 0.95$ and $N = 8$	0.68
Estimated reproducibility	$G_{tab} > G_{cal}$
Number of runs N	8
Number of parallel runs k	2
Number of degrees of freedom f for S_j^2 ($f = k - 1$)	1
Estimated reproducibility variance S_y^2	3.97
Number of degrees of freedom for S_y^2 [$f = N(k - 1)$]	8
Estimated variance of the mean S_y^2 value	1.98
Number of degrees of freedom	15

* Calculations were based on the data of Table 1.

quired by stoichiometry (%); x_2, the H_2SO_4 amount [mol mol^{-1} of initial compound **II**]; x_3, the acidity of the reaction mass in terms of H_2SO_4 concentration in the total amount of water used in the process (%).

The levels of factors and their variation ranges were chosen on the basis of an *a priory* information. The other formylation factors, i.e., the temperature of the beginning of introduction of a Cr_2O_3 solution, time of introduction, and also exposure temperature and time, were also fixed on the basis of *a priory* information at the levels considered to be optimal. The systematic experimental error was compensated for by the randomization method. The reproducibility of the experiment was estimated (Table 2), the coefficients of the regression equation (1) were calculated, the significance of the regression coefficients was determined, and the adequacy of the model was verified:

$$y = 58.31 + 0.83x_1 - 0.94x_2 + 5.94x_3 + 1.36x_1x_2 - 1.59x_1x_2x_3. \quad (1)$$

The high value (5.94) of the coefficient of x_3 shows that the factor x_3 (H_2SO_4 concentration) strongly affects the optimization parameter, i.e., the yield of the target product **I**. The sign "+" means that, with the given factor increasing, the optimization parameter increases too, in good agreement with the data of [13, 14], according to which the oxidizing capacity of Cr(VI) strongly depends on the acidity of the reaction mass and on the ability of Cr(VI) ions to form complex compounds. Thus, the sulfuric acid concentration in the oxidizing system affects rather strongly the oxidation direction and the purity of the target product.

Application of the steep-ascent method failed to find a maximum in the region studied. This may be a consequence of the possible curvature of the response surface, which is indicated, despite the formal adequacy, by the significance coefficients of the double and triple interaction terms. For adequate mathematical description of the process, we used the second-order regression equation derived using the orthogonal central composition design (OCCD). The OCCD matrix is standard for all the three factors [8] and is not randomized. The design of the first order, the FFE matrix, was completed to the OCCD plan by runs carried out at the center points (Table 1, run nos. 10–15). The results of its realization are listed in Table 1. These data were used to determine the coefficients of the second-order regression equation (2) and to estimate the significance of the equation coefficients and its adequacy.

$$y = 60.43 - 0.95x_2 + 4.69x_3 + 1.36x_1x_2 - 1.59x_1x_2x_3 - 2.77x_3^2. \quad (2)$$

Table 3. Results of tests of potentially optimal modes

Run no.	x_1	x_2	x_3	Product		Product yield, %		
				T_{mp},*	content of main substance, %	experimental		Box's calculation
						raw	recalculated to 100% content	
1	19.7	2.0	15.0	105	<60	–	–	72
2	0.3	2.0	15.0	110.5	74	67	50	67
3	0.3	3.0	15.0	115.5	87	69	60	66
4	3.5	3.0	15.0	120	100	69	69	70
5	3.5	3.0	22.0	113	81	67	54	77
6	3.5	3.0	26.4	109	69	67	47	79

* The melting point of recrystallized sample is 121°C.

The equation is adequate to the experimental data within the range of the influencing parameters, studied here.

The second-order model developed was optimized using Box's complex method [12], which made it possible to calculate the coordinates of the maximum of the target function.

The data of Table 3 show that the maximal yield is achieved at the boundary of the factor space. An attempt to perform the experiment at the point obtained in optimization (Table 3, run no. 1) failed owing to the impossibility to separate the reaction mass in extraction.

Apparently, at large excess of chromium anhydride and stoichiometric amount of sulfuric acid (Table 3, run no. 1), we presumably obtain a considerable amount of water-insoluble chromium(III) oxide, which serves as emulsifier, facilitates formation of a stable emulsion, and impedes layer separation.

As a result, only inconsiderable portion of a poor-quality final product could be separated from the reaction mass in this run (Table 3, run no. 1). With the amount of chromium anhydride diminished to a nearly stoichiometric value under otherwise invariable conditions (Table 3, run no. 2), the yield of the raw product increased, but its quality remained poor (content of the main substance 74%).

In the next run (Table 3, run no. 3), at a minimum excess amount of chromium anhydride and the same x_3 factor (H_2SO_4 concentration), the amount of sulfuric acid increased [to x_2 = 3.0 mol mol^{-1} of initial compound **II**] with respect to stoichiometric amount (2.0 mole). The comparatively poor quality of the raw product at its sufficiently high (69%) yield can be apparently accounted for by the insufficient amount of chromium anhydride, which is confirmed by the presence of unreacted bishydroxymethyl derivative of triethybenzene in the reaction mass.

In the next run (Table 3, run no. 4), chromium anhydride was taken in a 3.5% excess with respect to the stoichiometry at the same amount of sulfuric acid and its same concentration in the reaction mass. As a result, a 99.5% pure product was obtained in 69% yield (recalculated to 100% content of the main substance). In run nos. 5 and 6 (Table 3), we studied whether an increase in the x_3 factor (H_2SO_4 concentration) outside the factor space to, respectively, 22 and 26% affects the yield of the target product. The raw product was obtained in rather high yield, but with drastically impaired quality. This result can be accounted for by the fact that, under these conditions, the rate of side oxidation reactions and the fraction of their products in the raw product grow, in good agreement with the data on how the oxidation depth and the purity of the target product depend on the sulfuric acid concentration [13, 14].

The first stage of the study resulted in the following conclusion: to perform formylation with high yield and to obtain a high-quality product, it is necessary to use CrO_3 in a 3–4% excess with respect to the stoichiometry, and H_2SO_4 in an amount of 3 mole per 1 mole of initial compound **II**, and to maintain its concentration in the reaction mass within the range 14–15 wt %.

In the second stage, a mathematical model of formylation was constructed, which describes the relationship between the process temperature and time, on the one hand, and the optimization parameter (response function), i.e., the yield of the target product, on the other (with account taken of the content of initial substance in it).

Table 4. Results of realization of FFE design matrix

Run no.	Content of main substance, %	Yield, %
1	91	56
2	90	49
3	87	56
4	89	41
5	94	60

The FFE was also performed. As indicated above, the yield of the target product was used as response function, with account taken of the content of main substance in it. We chose two influencing parameters, z_1 and z_2, i.e., the reaction temperature (°C) and reaction time (min), respectively. The level of factors and their variation range were chosen on the basis of an *a priory* information. The FFE standard matrix for two factors was randomized.

The results of FFE are listed in Table 4. These data were used to calculate the coefficients of the regression equation, determine their significance, and verify the adequacy of the model. A first-degree regression equation adequately describing the response surface was obtained:

$$y = 61.57 + 5.47z_1 + 2.06z_2 - 2.25z_1z_2. \quad (3)$$

Analysis of Eq. (3) shows that the coefficient of the z_1 factor exceeds that of z_2, which confirms the positive effect exerted by a rise in temperature. The significant coefficient of the pair-interaction term, having "minus" sign, indicates that for the optimization parameter to grow, the z_1 factor must increase, rather than decrease.

To optimize the process, we used the steep-ascent method. However, it failed to find a maximum in the region studied. This may be a consequence of the curvature of the response surface, as evidenced, despite the formal adequacy, by the significant coefficients of the pair-interaction term and by the difference between the free term of the regression equation and the yield at the center of the design (Table 4, run no. 5).

The use of Box's complex method for optimizing the resulting first-order equation made it possible to avoid additional experiments to search for local extrema. This enabled calculation of the coordinates of the maximum of the target function.

The maximum yield is achieved at the boundary of the factor space. An experiment with factors calculated by Box's method, a 10-min exposure time and a 69.5–70.0°C temperature, were carried out. As a result, the product containing 99.5% main substance was obtained in 70% yield, which is rather close to Box's value (71%).

The recommended relative amounts of the reagents, and the process temperature and time worked very well under pilot plant conditions: oxime **III** was obtained with high content of the main substance (95–98%) in good yield (66–68%), close to the expected value. This result shows that the process conditions chosen ensure predominant oxidation of the initial compound **II** to dialdehyde **I**.

CONCLUSIONS

(1) Synthesis of 1,3-diformyl-2,4,6-triethylbenzene from 1,3-di(hydroxymethyl)-2,4,6-triethylbenzene by oxidizing the latter with CrO_3 in diluted H_2SO_4 was studied using a mathematical method of experiment design. The model of the process was constructed and optimized.

(2) Under the optimal process conditions [CrO_3 taken in 3–4% excess with respect to stoichiometry, and H_2SO_4 in an amount of 3.0 mol mol^{-1} of initial compound **II**, 14–15 wt % H_2SO_4 concentration in the reaction mass, and 10-min keeping of the reaction mass at 69.5–70°C the yield of the final product is as high as 67–70%.

REFERENCES

1. Yakubov, A.P., Tsyganov, D.V., Belen'kii, L.I., and Krayushkin, M.M., *Izv. Akad. Nauk SSSR, Ser. Khim.*, 1991, no. 5, pp. 1201–1203.
2. Krauklish, I.V., Apel'chugin, S.B., Tsypin, G.I., and Chernyshova, E.Yu., Abstracts of Papers, *Konferentsiya po khimii i khimicheskim produktam* (Conf. on Chemistry and Chemical Products), Moscow: Ross. Khim-Tekhnol. Univ. im. D.I. Mendeleeva, 2002, p. 102.
3. Weygand, K. and Hilgetag, G., *Organischchemische Experimentierkunst*, Leipzig: Barth, 1970.
4. Buehler, C.A. and Pearson, D.E., *Survey of Organic Syntheses*, New York: Wiley-Interscience, 1970.
5. Becker, H., Berger, W., and Domschke, G., *Organikum. Organisch-chemisches Grundpraktikum*, Berlin: Deutscher Verlag der Wissenschaften, 1967.
6. Houber, J. and Weyl, W.A., *Methoden der organischen Chemie*, Stuttgart: Tieme, 1953.
7. Charykov, A.K., *Matematicheskaya obrabotka rezul'tatov khimicheskogo analiza* (Mathematical Proces-

sing of Chemical Analysis Data), Leningrad: Khimiya, 1984.

8. Sautin, S.N., *Planirovanie eksperimentov v khimii i khimicheskoi tekhnologii* (Experiment Design in Chemistry and Chemical Engineering), Leningrad: Khimiya, 1975.
9. Ruzinov, L.P., *Statisticheskie metody optimizatsii khimicheskikh protsessov* (Statistical Methods for Optimization of Chemical Processes), Moscow: Khimiya, 1972.
10. Sautin, S.N. and Punin, A.E., *Mir komp'yuterov i khimicheskaya tekhnologiya* (Computer World and Chemical Engineering), Leningrad: Khimiya, 1991.
11. Markova, E.V. and Rokhvarger, A.E., *Matematicheskoe planirovanie khimicheskogo eksperimenta* (Mathematical Design of Chemical Experiments), Moscow: Znanie, 1971.
12. Box, M., *Comp. J.*, 1965, vol. 8, no. 1, pp. 42–52.
13. Dickerson, R.E., Gray, H.B., and Haight, G.P., *Chemical Principles*, New York: de Gruyter, 1988.
14. Horton, A., Terrll, K., Haffman, J.C., *et al.*, *J. Inorg. Chem.*, 1997, vol. 36, no. 21, pp. 4875–4882.

Russian Journal of Applied Chemistry, Vol. 76, No. 8, 2003, pp. 1280–1283. Translated from Zhurnal Prikladnoi Khimii, Vol. 76, No. 8, 2003, pp. 1317–1320.

ORGANIC SYNTHESIS AND INDUSTRIAL ORGANIC CHEMISTRY

Synthesis and Antimicrobial Activity of *N,N*-Disubstituted 3-Allyloxy-1-amino-2-propanethiols

M. A. Allakhverdiev and A. B. Askerov

Baku State University, Baku, Azerbaijan
Sumgait State University, Baku, Azerbaijan

Received March 25, 2003

Abstract—3-Allyloxy-1,2-epithiopropane was synthesized; its treatment with amines yielded *N,N*-disubstituted 3-allyloxy-1-amino-2-propanethiols, which were tested for antimicrobial activity.

Among products of thiirane ring opening, 1,2-amino thiols are of great practical importance [1–5]. For example, an aminoethanethiol moiety is a structural fragment of coenzyme A, playing a major role in the vital activity of living bodies [6]. Amino thiols and their derivatives are physiologically active compounds; they are widely used in medicine. Also they find growing application as effective components of polymeric materials enhancing the radiation resistance of polymers, suppressing oxidation and corrosion processes, etc.

In this context, we prepared in this study *N,N*-disubstituted 3-allyloxy-1-amino-2-propanethiols and tested them as antimicrobial additives to lubricating oils. As starting compound we used 3-allyloxy-1-chloro-2-propanol which, in turn, was prepared in 73% yield by treatment of epichlorohydrin with allyl alcohol; this yield is appreciably higher than that with concentrated sulfuric acid as catalyst (54%) [7]:

$$CH_2{=}CHCH_2OH + \underset{\diagdown O \diagup}{CH_3CHCH_2Cl} \xrightarrow{ZnCl_2} CH_2{=}CHCH_2OCH_2\underset{OH}{\underset{|}{C}}HCH_2Cl.$$

I

Dehydrochlorination of **I** in the presence of KOH gave 3-allyloxy-1,2-epoxypropane **II** in 85% yield:

$$\mathbf{I} + KOH \xrightarrow[-KCl\ -H_2O]{} CH_2{=}CHCH_2OCH_2\underset{\diagdown O \diagup}{CH{-}CH_2}.$$

II

Treatment of **II** with thiourea in the presence of sulfuric acid gave thiirane **III** in 79% yield:

$$\mathbf{II} + \underset{\underset{S}{\|}}{NH_2CHNH_2} \xrightarrow[-(NH_2)_2CO]{H_2SO_4} CH_2 + CHCH_2OCH_2\underset{\diagdown S \diagup}{CHCH_2}.$$

III

Previously thiirane **III** has been prepared in 30% yield by the reaction of 1,2-epithio-3-chloropropane with allyl alcohol in the presence of KOH [8]. Apparently, an oxathiolane ring is readily formed in the presence of sulfuric acid, which increases the yield of the target product.

We found that, with catalytic amounts of sulfuric acid, the procedure is simplified and the yield of **III** is increased.

Reactions of thiirane **III** with various primary and secondary amines yielded *N,N*-disubstituted 3-allyloxy-1-amino-2-propanethiols **IV**–**XII** (see table):

$$\mathbf{III} + HNR^1R^2 \rightarrow CH_2{=}CHCH_2OCH_2\underset{SH}{\underset{|}{C}}HCH_2NR^1R^2,$$

IV–**XII**

where $R^1 = R^2 = C_2H_5$ (**IV**); $R^1 = R^2 = C_4H_9$ (**V**); $R^1R^2 = (CH_2)_5$ (**VI**); $R^1R^2 = (CH_2)O$ (**VII**); $R^1R^2 = (CH_2)_2O(CH_2)_2$ (**VIII**); $R^1 = H$, $R^2 = C_6H_5$ (**IX**); $R^1 = H$, $R^2 = C_6H_5CH_2$ (**X**); $R^1 = R^2 = H$ (**XI**); $R^1 = H$, $R^2 = C_3H_7$ (**XII**).

The yields of the target products increase when the amine is taken in excess (i.e., when it acts also as a solvent). Access of air decreases the yield of amino thiols because of the oxidation and polymerization of the starting thiirane **III**. Therefore, amino thiols **IV**–**XII** were prepared in sealed ampules at a thiirane : amine ratio of 1 : 2.

1070-4272/03/7608-1280 $25.00 © 2003 MAIK "Nauka/Interperiodica"

Yields, constants, and elemental analyses of allyloxy-substituted amino thiols IV–XII

Compound	Yield, %	bp, °C (*P*, mm Hg)	n_D^{20}	Found, %/Calculated, %				Formula	R_f
				C	H	N	S		
IV	68	94–95 (2)	1.4735	59.23/59.07	10.24/10.41	6.78/6.89	15.49/15.77	$C_{10}H_{21}NOS$	0.63
V	61	100–101 (1.5)	1.4817	64.98/64.81	11.06/11.27	5.57/5.40	12.43/12.36	$C_{14}H_{29}NOS$	0.51
VI	74	97 (1.2)	1.4855	61.62/61.35	9.58/9.83	6.65/6.50	14.71/14.89	$C_{11}H_{21}NOS$	0.72
VII	80	108 (1)	1.4919	62.49/62.83	11.26/10.11	6.28/6.11	13.78/13.98	$C_{12}H_{23}NOS$	0.46
VIII	85	105 (0.9)	1.5073	55.05/55.27	8.67/8.81	6.63/6.44	14.92/14.75	$C_{10}H_{19}NO_2S$	0.69
IX	82	128 (1.0)	1.5495	64.72/64.54	7.48/7.67	6.41/6.27	14.65/14.36	$C_{12}H_{17}NOS$	0.58
X	74	130 (0.8)	1.5297	65.57/65.78	8.33/8.07	5.67/5.90	13.67/13.51	$C_{13}H_{19}NOS$	0.41
XI	38	80 (0.8)	1.4719	48.73/48.95	8.78/8.90	9.43/9.51	21.93/21.78	$C_6H_{13}NOS$	0.62
XII	75	95 (0.9)	1.5417	57.22/57.10	10.05/10.12	7.56/7.40	16.79/16.94	$C_9H_{19}NOS$	0.39

Amino thiols **IV**–**XII** are colorless liquids turning yellow on storage. The purity of all the compounds was checked by thin-layer chromatography; the composition was confirmed by elemental analysis, and the structure was determined by IR and ^{1}H NMR spectroscopy.

The IR spectra of compounds **IX**–**XII** containing a secondary amino group exhibit narrow absorption bands at 3375–3395 cm^{-1}, characteristic of the N–H bond. A very weak band at 2560–2580 cm^{-1} in the spectra of **IV**–**XII** is due to S–H stretching vibrations, and a band at 1060–1070 cm^{-1}, to C–N vibrations. The stretching vibrations of the C=C bonds in the aromatic ring and allyloxy group are manifested at 1420–1440, 1490–1500, 1600–1610, and 1650–1680 cm^{-1}.

The ^{1}H NMR spectra of **IV**–**XII** in the range 4.15–5.90 ppm contain multiplets from allyloxy group protons. In the range 6.9–8.1 ppm, compounds **IX** and **X** have signals due to nonequivalent protons of the aromatic rings. The proton signals of methylene groups bound to the nitrogen atom (amino thiols **IV**–**VIII**) are observed at 2.25–2.40 ppm. The methine proton appears as a broadened multiplet at 2.8–3.4 ppm due to coupling with the adjacent methylene protons. The two methylene groups at the oxygen atom give signals at 4.1–4.3 ppm.

It is known [9] that reactions of asymmetric thiiranes with amines follow the Krasuski rule, i.e., the ring opening occurs so that the thiol group in the 1,2-amino thiol molecule appears at the most substituted carbon atom. In the reactions of **III** with amines, this reaction pathway was confirmed by ^{1}H NMR spectroscopy. Namely, the ^{1}H NMR spectra of amino thiol **VI** were recorded before and after benzoylation. In the spectrum of **VI**, the methine proton appears as a quintet at 2.9 ppm due to coupling with the two adjacent methylene groups. Benzoylation of **VI** with benzoyl chloride (to give 3-allyloxy-1-piperidino-2-benzoylthiopropane **XIII**) shifts the methine proton signal down-field by 1.3 ppm (to 4.25 ppm) owing to the inductive effect of the benzoyl group.

A similar benzoylation experiment was performed with a primary thiol, 1-octanethiol. In the ^{1}H NMR spectrum of 1-octanethiol, the protons of the methylene group bound to the SH group appears as a triplet at 2.55 pm, and, upon benzoylation to give benzoyl octyl sulfide **XIV**, this triplet is shifted downfield to 3.00 ppm ($\Delta\delta$ 0.45 ppm). Published data [10] on acylation of primary and secondary hydroxy groups show that, upon acylation, the signals of the α-CH protons are shifted downfield by 0.5 ppm in primary alcohols and by 1.0–1.15 ppm in secondary alcohols. The 1.35 ppm shift observed in **VI** suggests that, in 1,2-

amino thiols **IV**–**XII**, the thiol groups are located at the secondary carbon atom.

The amino thiols obtained were tested as antimicrobial additives to DS-II lubricating oil and to Solidol (lubricating grease). We found that all compounds **IV**–**XII** added in amount of 0.5–1.0 wt % ensure long-term protection of DS-II and Solidol from biodamage. The width of the suppression zone, with industrially used sodium pentachlorophenolate taken as reference, was 0.7–1.3 cm for bacteria and 0.7–1.4 cm for fungi, i.e., the compounds exhibit antibacterial and fungicidal activity, with the fungicidal properties being somewhat more pronounced.

We revealed no clear correlation between the structure and antimicrobial activity of **IV**–**XII**. However, we found that phenyl and benzyl substituents (compounds **IX** and **X**) appreciably enhance the antimicrobial activity.

EXPERIMENTAL

The IR spectra were recorded on a Specord 75-IR spectrophotometer; liquid samples were prepared as thin films, and solid samples, as KBr pellets. The ^{1}H NMR spectra were recorded at 27°C on a Bruker AV spectrometer (300 MHz, CCl_4, internal reference HMDS).

3-Allyloxy-1-chloro-2-propanol I. A mixture of 7.2 g (0.12 mol) of allyl alcohol, 7.2 g (0.08 mol) of epichlorohydrin, and 0.2 g of zinc chloride was heated for 4 h at 95–100°C, after which it was cooled and vacuum-distilled. Yield of alcohol **I** 9 g (73%); bp 105–106°C (20 mm Hg), n_D^{20} 1.4619. Published data [7]: bp 86.5°C (9 mm Hg), n_D^{20} 1.4635.

3-Allyloxy-1,2-epoxypropane II. Finely ground KOH (11.2 g, 0.2 mol) was added to a solution of 15 g (0.1 mol) of alcohol **I** in 50 ml of anhydrous diethyl ether; the reaction mixture warmed up. After heating at 30°C for 2 h, the mixture was cooled, the ether layer was separated, and the residue was treated with three portions of anhydrous diethyl ether. The ether solutions were combined, the solvent was distilled off, and the reaction product was distilled at ambient pressure. Yield of oxirane **II** 9 g (79%), bp 122–123°C, n_D^{20} 1.1476. Published data [11]: bp 121–123°C, n_D^{20} 1.4159.

3-Allyloxy-1,2-epithiopropane III. A 3-ml portion of dilute sulfuric acid (0.5 mol of H_2SO_4 in 350 ml of water) was added to 7.6 g (0.1 mol) of thiourea. The mixture was cooled to 5–10°C, and 11.4 g (0.1 mol) of oxirane **II** was added dropwise over a period of 30 min with vigorous stirring, with the reaction temperature maintained at 5–10°C. After that, the mixture was stirred for an additional 1 h at room temperature and hydrolyzed with a solution of 10.6 g (0.1 mol) of sodium carbonate in 45 ml of water. The aqueous layer was separated from the organic layer and treated with two 20-ml portions of diethyl ether. The combined organic phases were dried over sodium sulfate. The solvent was distilled off, and the product was vacuum-distilled. Yield of thiirane **III** 10.3 g (73%), bp 79–81°C (12 mm Hg), n_D^{20} 1.4892, d_4^{20} 1.0215.

Found, %: S 24.56; MR_D 36.80.
$C_6H_{10}OS$.
Calculated, %: S 24.63; MR_D 36.88.

3-Allyloxy-1-diethylamino-2-propanethiol IV. A mixture of 14.6 g (0.2 mol) of diethylamine and 13 g (0.1 mol) of thiirane **III** was heated in an ampule at 80–90°C for 8 h. The ampule was cooled and opened; excess diethylamine was distilled off in a water-jet-pump vacuum. The reaction product was vacuum-distilled. Yield of amino thiol **IV** 14 g (68%), bp 94–95°C (2 mm Hg), n_D^{20} 1.4735. TLC: R_f 0.68 (hexane–isopropyl alcohol, 5 : 1).

Found, %: C 59.23, H 10.24, N 6.78, S 15.49.
$C_{10}H_{21}NOS$.
Calculated, %: C 59.07, H 10.41, N 6.89, S 15.77.

Amino thiols **V**–**XII** were prepared similarly.

3-Allyloxy-2-benzoylthio-1-piperidinopropane hydrochloride XIII. Freshly distilled benzoyl chloride (14 g, 0.1 mol) was added dropwise with cooling to 0–5°C to a solution of 10.7 g (0.05 mol) of 3-allyloxy-1-piperidino-2-propanethiol **VI** in 50 ml of anhydrous diethyl ether. The colorless crystalline precipitate was filtered off, washed several times with anhydrous diethyl ether (total volume 100 ml), and recrystallized from anhydrous acetone. Yield of **XIII** 14.7 g (83%), mp 96–97°C.

Found, %: C 61.27, H 6.42, N 3.68, S 9.27.
$C_{18}H_{21}NO_2S \cdot HCl$.
Calculated, %: C 61.44, H 6.30, N 3.98, S 9.11.

CONCLUSIONS

(1) 3-Allyloxy-1,2-epithiopropane was prepared by the reaction of 3-allyloxy-1,2-epoxypropane with thiourea in the presence of sulfuric acid. This compound was brought into reactions with amines to

obtain *N,N*-disubstituted 3-allyloxy-1-amino-2-propanethiols. The yields were high in all the steps.

(2) The *N,N*-disubstituted 3-allyloxy-1-amino-2-propanethiols prepared exhibit antibacterial and fungicidal activity in lubricating materials.

REFERENCES

1. Fokin, A.V. and Kolomiets, A.F., *Khimiya tiiranov* (Chemistry of Thiiranes), Moscow: Nauka, 1978.
2. Fokin, A.V., Allakhverdiev, M.A., and Kolomiets, A.F., *Usp. Khim.*, 1990, vol. 52, no. 5, pp. 705–737.
3. Allakhverdiev, M.A., Farzaliev, V.M., Guseinova, T.M., *et al.*, *Zh. Prikl. Khim.*, 1994, vol. 67, no. 11, pp. 1872–1876.
4. Allakhverdiev, M.A., Guseinova, T.M., and Farzaliev, V.M., *Zh. Org. Khim.*, 1995, vol. 31, no. 4, pp. 532–534.
5. Nadim, Kh.A., Guseinova, T.M., Magerramov, A.M., and Allakhverdiev, M.A., *Zh. Prikl. Khim.*, 2002, vol. 75, no. 8, pp. 1306–1308.
6. Lehninger, A.L., *Biochemistry. The Molecular Basis of Cell Structure and Function*, Mew York: Worth, 1972. Translated under the title *Biokhimiya*, Moscow: Mir, 1974, pp. 292–293.
7. Smirnov, V.V., Antonova, N.G., Zotov, S.B., *et al.*, *Khim. Geterotsikl. Soedin.*, 1970, no. 3, pp. 318–320.
8. Sadykhzade, S.I., Dzhafarov, V.A., and Kyazimov, Sh.K., *Uch. Zap. Azerb. Gos. Univ., Ser. Khim.*, 1971, no. 3, pp. 42–44.
9. Hakiuchi, H., Ijima, T., and Horie, H., *Tetrahedron*, 1979, vol. 35, no. 3, pp. 303–308.
10. Matias, A., *Anal. Chim. Acta*, 1964, vol. 31, no. 6, pp. 598–601.
11. Ponomarev, F.G., *Dokl. Akad. Nauk SSSR*, 1956, vol. 108, no. 4, pp. 648–650.

Russian Journal of Applied Chemistry, Vol. 76, No. 8, 2003, pp. 1284–1287. Translated from Zhurnal Prikladnoi Khimii, Vol. 76, No. 8, 2003, pp. 1321–1324.

ORGANIC SYNTHESIS AND INDUSTRIAL ORGANIC CHEMISTRY

Synthesis and Antioxidative Effect of Aromatic Disulfides

V. M. Farzaliev, M. A. Allakhverdiev, Sh. R. Aliev, R. M. Babai, I. A. Rzaeva, A. Z. Khalilova, and E. Z. Ismailov

Kuliev Institute of Chemistry of Additives, National Academy of Sciences of Azerbaijan, Baku, Azerbaijan
Baku State University, Baku, Azerbaijan

Received February 27, 2003

Abstract—Bis(4-hydroxy-3-formylphenyl) and bis[3-alkyl(aryl)iminomethyl-4-hydroxyphenyl] disulfides were prepared. Their reaction with cumylperoxy radicals was studied, and the inhibiting effect on the cumene oxidation was examined.

We has show previously [1] that bis[3-alkyl(aryl)-aminomethyl-4-hydroxyphenyl] sulfides effectively inhibit cumene oxidation. Proceeding with studies aimed at preparing various classes of organosulfur compounds and elucidating the mechanism of their inhibiting effect [2–4], we prepared in this work aromatic disulfides with azomethine fragments and evaluated their antioxidative performance in oxidation of cumene.

The starting compound, bis(4-hydroxy-3-formylphenyl) disulfide, was prepared by the reaction of salicylaldehyde with S_2Cl_2 in the presence of zinc as catalyst:

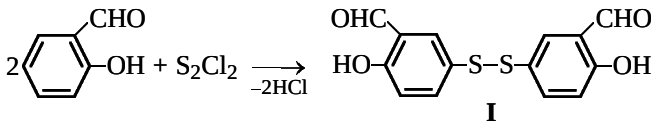

I

Subsequent condensation of **I** with primary aliphatic and aromatic amines gave the corresponding bis[3-alkyl(aryl)iminomethyl-4-hydroxyphenyl] disulfides **II**–**V** in high yields:

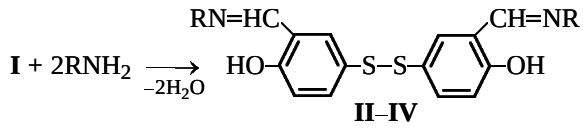

II–**IV**

where R = CH_3 (**II**), *tert*-C_4H_9 (**III**), C_6H_5 (**IV**), $C_6H_5CH_2$ (**V**).

The purity of **II**–**V** was checked by thin-layer chromatography, and the composition and structure were confirmed by elemental analysis and by IR and ^1H NMR spectroscopies.

The IR spectrum of **I** contains characteristic absorption bands of the hydroxy group at 3320 cm^{-1}. The IR spectra of **II**–**V** contain azomethine bands at 1639–1640 cm^{-1}, and the hydroxyl band is shifted to 3165 cm^{-1}.

In the ^1H NMR spectra of **II**–**V**, we have not revealed, in contrast to the spectrum of **I**, the broadened signal of the formyl proton (10.37 ppm). The spectra contain proton signals of radicals R at the N atom; the signals of nonequivalent protons of two symmetrically arranged benzene rings give a doublet at 7.0 and 7.4 ppm. The signals of the hydroxyl protons are shifted downfield by 0.4 ppm relative to **I**, giving a doublet at 10.9–11.6 ppm. This may be due to weaker intramolecular hydrogen bonding between the hydroxy group and azomethine nitrogen atom, compared to the carbonyl oxygen atom in **I**.

To evaluate the antioxidative performance of **I**–**V** in elementary steps of inhibition of cumene oxidation, we studied the reactions of these compounds with cumylperoxy radicals (CPR) and cumyl hydroperoxide (CHP).

The capability of disulfides **II**–**V** to terminate oxidation chains in reactions with peroxy radicals was evaluated for the example of cumene oxidation at 60°C, initiated by azobis(isobutyronitrile) (AIBN), in the presence of **II** (Fig. 1).

From the induction period, we calculated the stoichiometric coefficient of inhibition, *f*, equal to the number of oxidation chains terminating in molecule of the inhibitor and its transformation products:

$$f = \tau v_i / [In]_0,$$

where v_1 is the initiation rate (under the examined conditions, $v_1 = 2 \times 10^{-7}$ l mol^{-1} s^{-1}, and $[In]_0$ is the initial inhibitor concentration.

1070-4272/03/7608-1284 $25.00 © 2003 MAIK "Nauka/Interperiodica"

From the kinetics of oxygen uptake, we calculated the rate constants of the reactions of the inhibitors with CPR, k_7 [5, 6]. For this purpose, the kinetic curves of oxygen uptake were transformed from the coordinates $[O_2]$–τ to the coordinates $[O_2]^{-1}$–τ^{-1}:

$$k_7 = \tan\alpha\, k_2[RH]v_i/f[In]_0,$$

where $\tan\alpha$ is the slope of the straight line in the coordinates $[O_2]^{-1}$–τ^{-1}; k_2 = 1.51 l mol^{-1} s^{-1}, rate constant of chain initiation [1, 2]; [RH] = 6.9 M, concentration of the substance subject to oxidation; and v_i, initiation rate (under our conditions, $v_i = 2 \times 10^{-7}$ l mol^{-1} s^{-1}).

The high antioxidative performance of **II**–**V** was also confirmed by experiments on cumene autooxidation at 110°C (Fig. 2), and the kinetic parameters of the reaction were determined (Fig. 2). As seen from Table 1, the parameters f for **II**–**V** vary in the range from 1.8 to 2.4, and the rate constant k_7 of the reaction of inhibitors with peroxy radicals, from 1.92×10^4 to 2.72×10^4 l mol^{-1} s^{-1}. The products of transformations of **II**–**V** in reaction with CPR also show a certain inhibiting effect: The oxidation rate after the induction period is somewhat lower than the rate of uninhibited oxidation (Fig. 1).

We found that all the compounds **I**–**V** actively decompose CHP.

The kinetic curve of CHP decomposition in the presence of **I**–**V** is typical of autocatalytic reactions (Fig. 3). The autocatalytic character of the kinetic curves shows that decomposition of CHP is effected not by compounds **I**–**V** themselves, but by products of their transformation in the first, slow, step of the reaction with CHP.

To determine the reaction order, we studied how the initial rate of catalytic decomposition of CHP depends on the reactant concentrations. We found that the reaction is first-order with respect to both inhibitor and CHP.

To determine the reaction stoichiometry, CHP was taken in excess. The stoichiometric coefficient ν was calculated by the formula

$$\nu = \frac{[ROOH]_0 - [ROOH]_\infty}{[In]_0},$$

where $[ROOH]_0$ and $[ROOH]_\infty$ are, respectively, the initial and final CHP concentrations, and $[In]_0$ is the initial inhibitor concentration.

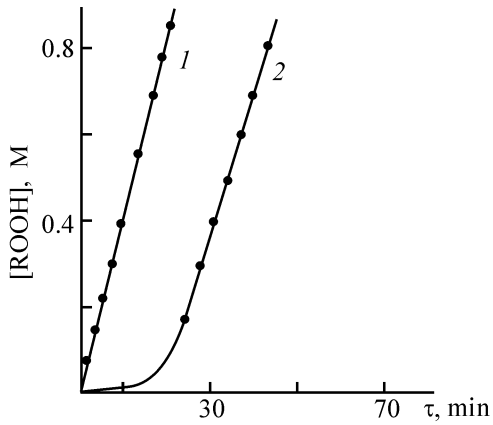

Fig. 1. Variation of CHP concentration [ROOH] with time τ in initiated oxidation of cumene (*1*) in the absence and (*2*) in the presence of **II**. [AIBN] = 2×10^{-2}, [In] = 3×10^{-4} M; 60°C.

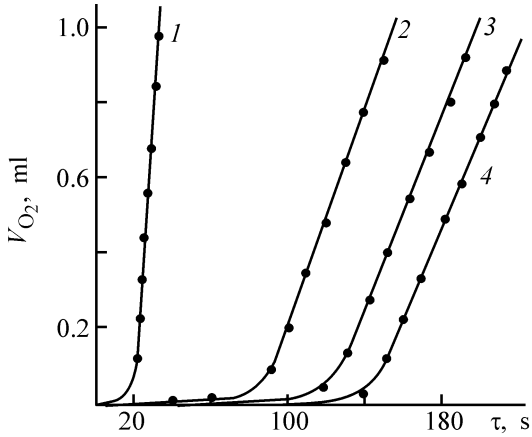

Fig. 2. Volume V_{O_2} of oxygen taken up in autooxidation of cumene at 110°C vs. time τ. Inhibitor added ([In] = 5×10^{-6} M): (*1*) none, (*2*) **II**, (*3*) **III**, and (*4*) **V**.

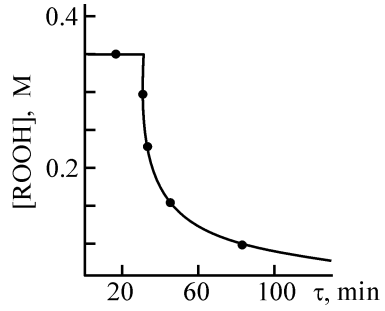

Fig. 3. Variation with time τ of the CHP concentration [ROOH] in the course of decomposition in the presence of inhibitor **I** ([In] = 5×10^{-5} M, 110°C).

As seen from Table 1, one inhibitor molecule (with its transformation products) decomposes more than 10^4 CHP molecules.

Table 1 shows that the coefficient f increases from 1.6 to 1.8–2.4 in going from disulfide **I** to **II**–**V**.

Table 1. Parameters of reactions of **I**–**V** with CPR and those of catalytic decomposition of CHP

Compound	f	$k_7 \times 10^{-4}$, l mol^{-1} s^{-1}	ν	Compound	f	$k_7 \times 10^{-4}$, l mol^{-1} s^{-1}	ν
I	1.6	1.92	18000	**IV**	2.2	2.5	26000
II	2.4	2.72	24000	**V**	2.1	2.4	20000
III	1.8	2.12	38000				

Table 2. Characteristics of compounds **II**–**V**

Compound	Yield, %	mp, °C	Found, %/Calculated, %				Formula
			C	H	S	N	
II	55	144–145	57.42/57.81	5.19/4.85	19.80/19.29	8.91/8.43	$C_{16}H_{16}N_2O_2S_2$
III	60	127–128	63.72/63.44	6.46/6.77	15.79/15.39	7.25/6.73	$C_{22}H_{28}N_2O_2S_2$
IV	75	119–120	68.10/68.41	4.67/4.41	13.60/14.05	6.39/6.14	$C_{26}H_{20}N_2O_2S_2$
V	80	131–132	62.65/69.40	5.15/4.99	13.61/13.23	5.33/5.78	$C_{28}H_{24}N_2O_2S_2$

This may be due to the presence of the N=C bond, which also terminates oxidation chains. A similar trend is observed with the parameter ν. The highest ν, 38000, is exhibited by *tert*-butyl-substituted disulfide **III**.

Table 1 shows that f and k strongly depend on the radical R in **II**–**V**. As compared to the related sulfides (ν = 5680–9000), disulfides **II**–**V** have higher ν, i.e., their inhibiting power is considerably higher; the k_7 and f values are, by contrast, somewhat higher for sulfides [f = 1.36–6.00, k_7 = (1.99–7.96) × 10^{-4} l mol^{-1} s^{-1}] [1].

EXPERIMENTAL

The IR spectra were recorded on a Specord 75-IR spectrophotometer, and the ^{1}H NMR spectra, on a Bruker spectrometer (300 MHz); the chemical shifts (ppm) are given in the δ scale relative to internal TMS.

Cumyl hydroperoxide was purified as described in [7], with the subsequent distillation; chlorobenzene and cumene were purified by a common procedure based on sulfonation of impurities with concentrated sulfuric acid [8, 9]. The CHP concentration was determined by iodometric titration [7] of intermittently taken samples. Experiments on CHP decomposition were performed in chlorobenzene at 110°C in a glass bubbler in an inert gas atmosphere; the CHP concentration was varied within 0.16–0.64 M, and the concentrations of **I**–**V**, within 10^{-5}–5×10^{-3} M.

Experiments on initiated oxidation of cumene were performed on a manometric unit [9]; as initiator served AIBN (initiation rate constant at 60°C 10^{-5} l mol^{-1} s^{-1} [10]). The initiator concentration was 2×10^{-2} M in all the experiments, and the concentration of **I**–**V**, (1–5) × 10^{-4} M.

Bis(4-hydroxy-3-formylphenyl) disulfide I. A solution of 6.7 g (0.05 mol) of S_2Cl_2 in 20 ml of CCl_4 was added with stirring to a solution of 12.2 g (0.1 mol) of salicylaldehyde in 30 ml of absolute CCl_4. The mixture was allowed to stand for 24 h, after which the solvent was distilled off and the residue was triturated with benzene. Yield of disulfide **II** 6.5 g (72%), mp 105°C.

Found, %: C 54.49, H 3.68, S 20.56.
$C_{14}H_{10}O_2S_2$.
Calculated, %: C 54.90, H 3.29, S 20.93.

Bis[3-alkyl(aryl)iminomethyl-4-hydroxyphenyl] disulfides II–**V**. A three-necked 100-ml flask equipped with a stirrer, reflux condenser, and dropping funnel was charged with a solution of 0.05 mol of disulfide **I** in 30 ml of anhydrous CCl_4, and 0.1 mol of appropriate amine was added dropwise over a period of 5 h

with stirring and cooling with ice. Then the mixture was stirred for 5 h at 30–40°C. The reaction product was washed with water and dried over Na_2SO_4; the solvent was distilled off, and the residue was recrystallized. The yields, melting points, and elemental analyses of **II**–**V** are listed in Table 2.

CONCLUSION

Bis(4-hydroxy-3-formylphenyl) disulfide was prepared; its reactions with primary amines gave the corresponding bis[3-alkyl(aryl)iminomethyl-4-hydroxyphenyl] disulfides. These disulfides inhibit cumene oxidation and catalytically decompose cumyl hydroperoxide.

REFERENCES

1. Allakhverdiev, M.A., Babai, R.M., Farzaliev, V.M., *et al.*, *Neftekhimiya*, 2001, vol. 41, no. 2, pp. 153–157.
2. Farzaliev, V.M., Allakhverdiev, M.A., Sattarzade, R.I., *et al.*, *Zh. Prikl. Khim.*, 2001, vol. 74, no. 12, pp. 2083–2086.
3. Farzaliev, V.M., Allakhverdiev, M.A., Magerramov, A.M., *et al.*, *Zh. Prikl. Khim.*, 2001, vol. 74, no. 1, pp. 114–118.
4. Farzaliev, V.M., Allakhverdiev, M.A., Rzaeva, I.A., *et al.*, *Zh. Prikl. Khim.*, 1994, vol. 67, no. 6, pp. 1025–1028.
5. Emanuel', N.M., Denisov, E.T., and Maizus, Z.K., *Tsepnye reaktsii okisleniya uglevodorodov v zhidkoi faze* (Chain Reactions of Liquid-Phase Oxidation of Hydrocarbons), Moscow: Nauka, 1965.
6. Emanuel', N.M. and Denisov, E.T., *Neftekhimiya*, 1976, vol. 16, no. 13, pp. 366–368.
7. Karnojitzki, V., *Les peroxides organiques*, Paris: Hermann, 1958.
8. Weissberger, A. and Proskauer, E.S., *Organic Solvents. Physical Properties and Methods of Purification*, Riddick, J.A. and Toops, E.E., Eds., New York: Interscience, 1955.
9. Emanuel', N.M., Gladyshev, G.P., and Denisov, E.T., Order of Testing Chemical Compounds as Stabilizers for Polymeric Materials, *Preprint of the Inst. of Chemical Physics, USSR Acad. Sci.*, Chernogolovka, 1976.
10. Denisov, E.T., *Konstanty skorosti gomoliticheskikh zhidkofaznykh reaktsii* (Rate Constants of Homolytic Liquid-Phase Reactions), Moscow: Nauka, 1972.

Russian Journal of Applied Chemistry, Vol. 76, No. 8, 2003, pp. 1288–1291. Translated from Zhurnal Prikladnoi Khimii, Vol. 76, No. 8, 2003, pp. 1325–1328.

MACROMOLECULAR CHEMISTRY AND POLYMERIC MATERIALS

Structure and Properties of the Surface Layers of Thin Films of Poly(1-trimethylsilylpropyne)

A. E. Grishchenko, V. S. Khotimskii, N. A. Mikhailova, I. I. Zaitseva, and E. G. Litvinova

Fock Research Institute of Physics, St. Petersburg State University, St. Petersburg, Russia

Topchiev Institute of Petrochemical Synthesis, Russian Academy of Sciences, Moscow, Russia

Received October 15, 2002; in final form, May 2003

Abstract—The birefringence of thin films of poly(1-trimethylsilylpropyne) with 55 : 45 ratio of units with *trans* and *cis* configurations of the –C=C– bonds was studied by the method of an oblique polarized beam. The surface birefringence coefficients were determined for films of various thicknesses. A theory of birefringence in the surface layers of polymer films was suggested, based on the assumed exponential decrease in the orientation order parameters of the molecular chain fragments with increasing distance from the film surface.

Recent studies suggest that polymers hold much promise for preparation of membranes. The relationships between the permeability coefficients of membranes, on the one hand, and the chemical structure, preparation and treatment conditions, free polymer volume, etc., on the other, have been studied. However, correlations often exhibit deviations inconsistent with the generally accepted views [1–4].

Published data show that studies of polymer membranes pay little attention to the scaling effect, i.e., the difference in the physical properties of polymers in the bulk and surface layers [5, 6]. The influence of the orientation ordering of the molecular chains relative to the surface on the membrane and film permeability has also been studied inadequately.

In this study, we analyzed the structure and properties of the surface layers of poly(1-trimethylsilylpropyne) (PTMSP) films by the method of oblique polarized beam [5–7]. It is known that PTMSP membranes are highly permeable to gas and liquid molecules. However, there are no published data on the factors responsible for the unprecedentedly high permeabilities.

Here, we studied, with the aim to explain these effects, the structure and orientation order of the chain molecules of PTMSP in the surface layers of thin polymer films.

The PTMSP samples were prepared in the presence of $TaCl_5$ catalyst, using an alkylating agent [8]. Polymerization was performed in a glass reactor equipped with a magnetic stirrer under argon atmosphere. All manipulations (drying the monomer and solvent, dosing the catalyst, charging the reactants, and performing the polymerization) were carried under high-purity argon. Powdered tantalum pentachloride (0.1–0.4-g portions) was sealed into glass ampules under argon. The sealed ampules containing the catalyst were kept at $\leq +4°C$. The catalyst was charged by opening the glass ampule. The amount of catalyst was determined as the difference between the weights of the ampule with and without the catalyst. Based on the weighed portion of the catalyst, we calculated the weights of the other components. After charging the catalyst, the solvent was introduced, and the resulting mixture was stirred for 30 min until complete dissolution of the catalyst at the polymerization temperature. Next, the monomer, 1-trimethylsilylpropyne, was added under vigorous stirring, and the resulting mixture was stirred for 24 h. When the polymerization was complete, a sixfold (by volume) excess of methanol was added to the jelly-like reaction mass. The precipitated polymer was washed with straight methanol, dissolved in toluene, and reprecipitated with methanol. The polymer was filtered off on a Schott filter and dried in air for 24 h at room temperature, whereupon the polymer dissolution, reprecipitation, and drying runs were repeated. The resulting polymer was additionally vacuum-dried at room temperature for 8 h to constant weight, and then the polymer yield was determined.

1070-4272/03/7608-1288 $25.00

The chemical structure of the polymer macromolecule was studied by ^{13}C NMR spectroscopy of PTMSP solutions in $CDCl_3$, whose signal served as reference for assigning the chemical shifts of the carbon atoms (the ^{13}C NMR spectra were recorded on a Bruker MSh-300 instrument at 75.47 MHz, with accumulation for 12 h).

According to the ^{13}C NMR data, PTMSP is a random copolymer with 55 : 45 ratio of units with *trans* and *cis* configurations of the –C=C– bonds.

An X-ray diffraction study showed the glassy structure of the sample studied.

The molecular weight of the PTMSP sample was determined by the method of molecular hydrodynamics. The hydrodynamic measurements were carried out in hexane at 25°C (density $\rho_0 = 0.774$ g cm^{-3}, viscosity $\eta_0 = 0.859 \times 10^{-2}$ P), and viscosity measurements of the PTMSP solution, in cyclohexane in an Ostwald viscometer; the solvent flow time was 105 s. The intrinsic viscosity $[\eta] = 1.3 \times 10^3$ cm^3 g^{-1} was determined by extrapolating the experimental η_{sp}/c values to zero concentration.

The forward diffusion coefficient $D_0 = 0.55 \times 10^{-7}$ cm^2 s^{-1} was estimated from the time dependence of the smearing of the diffusion boundary formed by layering of the solution under the solvent in a glass cell. The measurements were carried out at polymer concentrations c of $(3–5) \times 10^{-4}$ g cm^{-3}.

High-speed sedimentation was studied on an MOM-3180 analytical centrifuge in a two-sector cell; an artificial boundary was created. The sedimentation coefficient was determined from the shift of the sedimentation boundary with time. The measurements were carried out in the polymer concentration range $(6–8) \times 10^{-4}$ g cm^{-3}. The sedimentation coefficient $S_0 = 5.6 \times 10^{-13}$ s^{-1} was determined by plotting the concentration dependence of $1/S$.

Using the S_0, D_0, and $[\eta]$ values obtained, we calculated the molecular weight $M_{SD} = 10.5 \times 10^5$ by the Svedberg formula

$$RTS_0/[D_0(1 - \nu\rho_0)].$$

Here, ρ_0 is the solvent density; R, gas constant; $T = 298$ K, absolute temperature; and $(1 - \nu\rho_0) = 0.24$, floatability factor.

To study the birefringence of the PTMSP sample, we produced films with various thicknesses by casting a polymer solution (in toluene and CCl_4) on cellophane, followed by drying to constant weight. The film thickness was determined by the geometric method, with the density taken to be $\rho = 0.82$ g cm^{-3}.

The properties of the surface layers of the polymer films are determined not only by the chemical composition of the surface but also by its physical structure, including the orientation order of the chain molecules near interfaces. As quantitative measure of the orientation order of the molecular fragments relative to the surface serves the orientation order parameter

$$S = \frac{1}{2}\left(3\overline{\cos^2\vartheta} - 1\right). \quad (1)$$

Here, ϑ is the angle between the direction of the chain molecule fragment and the normal to the film surface.

In the case of the lacking predominant orientation of the molecular chains relative to the film surface, $\overline{\cos^2\vartheta} = 1/3$ and $S_0 = 0$. For $S \neq 0$, when the polarized beam passes at an angle i to the film normal, a birefringence arises in the film, with the phase difference between the ordinary and extraordinary beams [5–7] given by

$$\delta = B(1 - \cos 2i). \quad (2)$$

Here, B is the surface birefringence coefficient.

It can be shown that, when S is independent of the film thickness, the surface birefringence coefficient is [7]

$$B = -\frac{\pi N_A \rho}{n\lambda}\frac{a_{\parallel} - a_{\perp}}{M_0}\left(\frac{n^2+2}{3}\right)^2 SH. \quad (3)$$

Here, ρ is the polymer density; n, refractive index; N_A, Avogadro number; λ, wavelength; $(a_{||} - a_{\perp})$, difference between the main polarizabilities of the monomer unit; and M_0, molecular weight of the monomer unit.

It is seen that, in terms of the model of a film characterized by a uniform orientation order, the coefficient B is proportional to the film thickness H. However, in real films, the local value of the orientation order parameter decreases with increasing distance from the surface [6, 9, 10]. It can be shown that this decrease is described by the exponential law [10]

$$S = S_0 \exp(-H/H_0). \quad (4)$$

Here, S_0 is the order parameter near the surface, and H_0, the effective thickness of anisotropic surface layer of the polymer film.

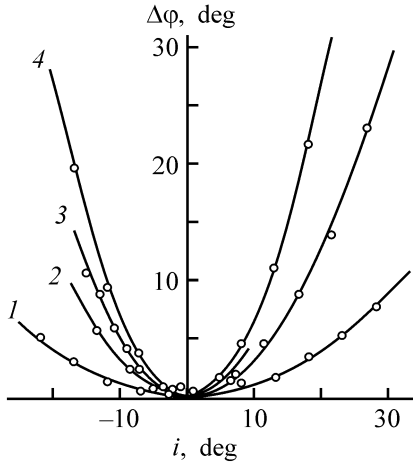

Fig. 1. Variation of φ with the beam incidence angle *i* onto the polymer film surface. Film thickness $H \times 10^3$, cm: (*1*) 0.48, (*2*) 1.55, (*3*) 2.78, and (*4*) 3.28; the same for Fig. 2.

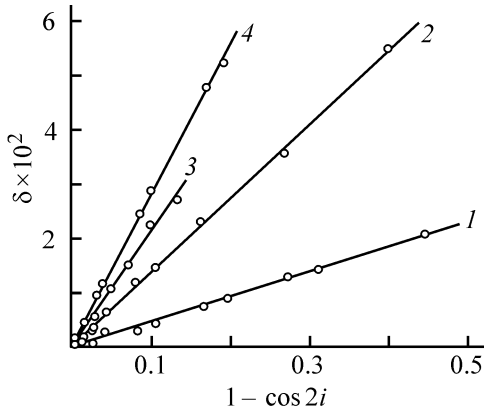

Fig. 2. Variation of the optical phase difference δ with $(1 - \cos 2i)$.

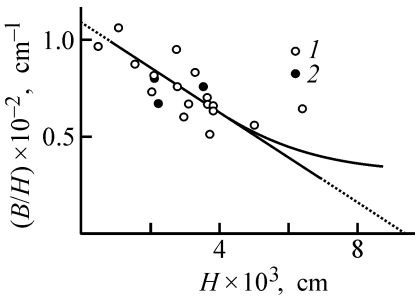

Fig. 3. Variation of the experimental *B*/*H* values with the film thickness *H*. The films were prepared from solutions in (*1*) toluene and (*2*) CCl_4.

In this case, the surface birefringence coefficient is given by [10]

$$B = B_0(1 - \exp(-H/H_0), \qquad (5)$$

where

$$B_0 = -\frac{\pi N_A \rho}{n^3 \lambda} \frac{a_\parallel - a_\perp}{M_0} \left(\frac{n^2 + 2}{3}\right)^2 S_0 H_0. \qquad (6)$$

By expanding the exponent into a series and retaining two terms, we obtain

$$\frac{B}{H} = -\frac{\pi N_A \rho}{n^3 \lambda} \frac{a_\parallel - a_\perp}{M_0} \left(\frac{n^2 + 2}{3}\right)^2 S_0 \left(1 - -\frac{H}{H_0}\right). \qquad (7)$$

Based on formula (7), we can propose a new method for determining the orientation order parameter S_0 near the film surface and the effective thickness H_0 of the anisotropic surface layer from the experimental *B*/*H*-vs.-*H* dependence.

Formula (7) suggests that $S_0 \sim \lim(B/H)$ at $H \to 0$, and $H_0 = 1/2 \lim H$ at $B/H \to 0$.

The birefringence in the PTMSP films was measured using a visual scheme of recording the optical phase difference δ [5, 6]. The film was inserted between crossed polarization prisms. For determining the optical phase difference δ created by the polymer film, we placed the compensator (by rotating the limb) in the position corresponding to equal illuminances of the two halves of the vision field (penumbra asimuth). In this case, $\delta = \delta_0 \sin 2\Delta\varphi$, where $\Delta\varphi = \varphi - \varphi_0$ is the difference in the readings of the compensator at normal incidence of the polarized beam onto the film and at an angle *i*, and $\delta_0 = 0.076$ is the phase difference created by the compensator.

By way of example, Fig. 1 presents typical experimental dependences of Δφ on the angle *i* of beam incidence onto the polymer film surface, and Fig. 2, the dependences of δ on $(1 - \cos 2i)$ for the same films. The latter dependences are described by straight lines; from their slope, we determined the magnitude and sign of the surface birefringence coefficient for each film.

Figure 3 shows how the experimental *B*/*H* values vary with film thickness *H*. With increasing film thickness, *B*/*H* tends to decrease, and the *B*/*H* vs. *H* dependence asymptotically approaches the abscissa axis.

For thin PTMSP films ($H < H_0$), the *B*/*H*-vs.-*H* dependence can be described by a portion of a straight line, in accordance with formula (7). Extrapolation of this plot to $H = 0$ yields $B/H = 1.15 \times 10^2$ cm^{-1}. Using this value, we estimated S_0 by formula (7) at –0.49. Extrapolation of the *B*/*H*-vs.-*H* plot at small *H* values to $B/H \to 0$ gives the effective thickness of the anisotropic surface layer $H_0 = 1/2 \lim H = 4.7 \times 10^{-3}$ cm.

The parameter of the orientation order near the interface of the PTMSP polymer film is characterized by $S_0 = -0.49$, which is close to the analogous value $S = -0.5$ corresponding to ideal planar ordering of the chain molecule fragments relative to the surface.

This is a characteristic feature of the structure of the surface layers formed by rigid-chain polymers at interfaces. The conclusion about enhanced thermodynamic rigidity of the molecules studied is consistent with the results of independent hydrodynamic [11] and optical [12] studies of PTMSP.

Notably, the anisotropic surface layer characterized by high degree of orientation order is very thick. The H_0 thickness exceeds by 4 orders of magnitude the transverse dimensions of the PTMSP molecules.

The negative sign of the orientation order parameter $S_0 = -0.49$ suggests that the fragments of the chain molecules of PTMSP at interfaces are predominantly oriented parallel to the film surface. The revealed characteristics will presumably exert a decisive effect on the structure and permeability of PTMSP membranes.

CONCLUSIONS

(1) The birefringence of films of poly(1-trimethylsilylpropyne) with 55 : 45 ratio of units with *trans* and *cis* configurations of the –C=C– bonds was determined by the method of oblique polarized beam. The fragments of the chain molecules of poly(1-trimethylsilylpropyne) are predominantly oriented parallel to the film surface. The orientation order parameter S_0 was estimated at –0.49, which corresponds to the ideal planar order of the fragments of poly(1-trimethylsilylpropyne) molecules at interfaces.

(2) The effective thickness of the surface layers of thin films of poly(1-trimethylsilylpropyne) H_0 was estimated at 4.7×10^{-3} cm, which exceeds by 4 orders of magnitude the thickness of the chain molecule.

ACKNOWLEDGMENTS

This study was supported financially by INTAS (project no. 2000-00230).

REFERENCES

1. Nagai, K., Masuda, T., Nakagawa, T., *et al., Prog. Polym. Sci.*, 2001, vol. 26, pp. 721–798.
2. Odani, H. and Masuda, T., *Polymer for Gas Separation*, Toshima, N., Ed., New York: VCH, 1991.
3. Takada, K., Matsuya, H., Masuda, T., and Higashimura, T., *J. Appl. Polym. Sci.*, 1985, vol. 30, no. 4, pp. 1605–1616.
4. Bokarev, A.K., Volkov, V.V., Kalyuhznyi, N.E., *et al., Dokl. Akad. Nauk SSSR*, 1989, vol. 305, no. 1, pp. 117–121.
5. Grishchenko, A.E. and Cherkasov, A.N., *Usp. Fiz. Nauk*, 1997, vol. 167, no. 3, pp. 269–285.
6. Grishchenko, A.E., *Mekhanooptika polimerov* (Mechanooptics of Polymers), St. Petersburg: Sankt-Peterb. Gos. Univ., 1996.
7. Cherkasov, A.N., Vitovskaya, M.G., and Bushin, S.V., *Vysokomol. Soedin., Ser. A*, 1976, vol. 18, no. 7, pp. 1628–1634,
8. USSR Patent 1690365.
9. Grishchenko, A.E., Kulichikhin, V.G., Ryumtsev, E.I., *et al., Vysokomol. Seodin., Ser. B*, 1996, vol. 38, no. 9, pp. 1593–1597.
10. Grishchenko, A.E., Pavlov, G.M., and Vikhoreva, G.A., *Vysokomol. Soedin., Ser. B*, 1999, vol. 41, no. 8, pp. 1347–1350.
11. Shtennikova, I.N., Kolbina, G.F., Khotimskii, V.S., *et al., Vysokomol. Soedin., Ser. A*, 1998, vol. 40, no. 10, pp. 1569–1576.
12. Shtennikova, I.N., Kolbina, G.F., Yakimanskii, A.V., *et al., Vysokomol. Soedin., Ser. A*, 1998, vol. 40, no. 12, pp. 1973–1978.

Russian Journal of Applied Chemistry, Vol. 76, No. 8, 2003, pp. 1292–1295. Translated from Zhurnal Prikladnoi Khimii, Vol. 76, No. 8, 2003, pp. 1329–1332.

MACROMOLECULAR CHEMISTRY AND POLYMERIC MATERIALS

Properties of Poly(methyl Methacrylate) Containing Metal Sulfoxide Complexes

G. V. Leplyanin, E. M. Battalov, and Yu. I. Murinov

Institute of Organic Chemistry, Ufa Scientific Center, Russian Academy of Sciences, Ufa, Bashkortostan, Russia

Received January 28, 2003

Abstract—The uniformity, light fastness, heat resistance, radiation hardness, and antistatic properties of poly(methylmethacrylate) prepared in the presence of metal sulfoxide complexes were studied.

Synthesis of polymers, in particular poly(methyl methacrylate) (PMMA) containing metal compounds is of both scientific and practical interest. Introduction of metals substantially broadens the field of polymer application. Kinetic features of MMA polymerization in the presence of sulfoxides and their metal complexes, oxychlorides, and mineral acids were well understood [1]. At the same time, properties of poly(methyl methacrylate) containing various metal sulfoxide complexes have been studied insufficiently.

EXPERIMENTAL

To remove stabilizer, methyl methacrylate was shaken with 10% KOH, washed with water to neutral reaction, dried over calcined calcium chloride, and distilled twice in a vacuum [2]. Poly(methyl methacrylate was prepared from a fraction with bp 42°C (100 mm Hg), d_4^{20} = 0.936, and n_D^{20} = 1.4130.

Azobis(isobutyronitrile) (AIBD) was recrystallized repeatedly from methanol and dried in a vacuum at room temperature to constant weight (mp 103°C, dec.). The initiator was stored at 5°C.

Sulfoxides[1] were recrystallized from hexane. Their purity was monitored by IR spectroscopy and elemental analysis for sulfoxide sulfur (potentiometric titration). The content of the main compound was 98.5–99%. Physicochemical properties of purified sulfoxides agreed well with published data. Petroleum sulfoxides (PSOs) are a mixture of mono-, bi-, and tricyclic, mainly saturated, sulfoxides.

The concentration of paramagnetic centers was determined on an RE-1301 radiospectrometer at liquid nitrogen temperature. The light fastness was estimated by a change in the color intensity of organic glass exposed for 20 h to the light of a PRK-2 lamp at a distance of 14 cm. Antistatic properties were de-

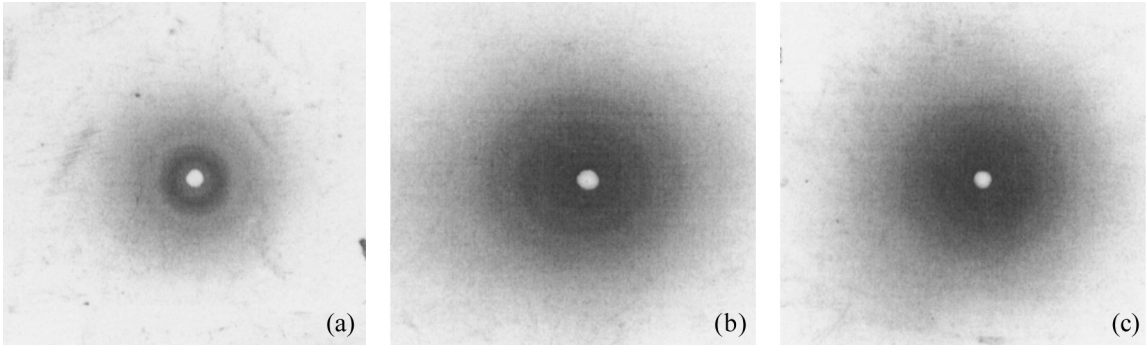

Fig. 1. Debye patterns of organic glass prepared (a) without additives and (b, c) in the presence of 1×10^{-3} M uranyl nitrate complex.

[1] Sulfoxides and their metal complexes were prepared at the laboratory of Physical Chemistry, Institute of Organic Chemistry, Ufa Scientific Center, Russian Academy of Sciences.

1070-4272/03/7608-1292 $25.00 © 2003 MAIK "Nauka/Interperiodica"

Table 1. Heat resistance and light fastness of PMMA containing some metal sulfoxide complexes

PMMA	Heat resistance, °C		Light fastness	
	thermolysis onset	intense thermolysis	time of exposure to UV radiation from mercury lamp, h	change of color intensity after irradiation
No additives	240	287	–	
Colored with anthraquinone dye	240	282	5	Decreased by a factor of 2
Containing sulfoxide complexes (2 mol %) of:				
$Co(NO_3)_2$	290	350	20	Remained the same
$Bi(NO_3)_3$	270	340		
$Cr(NO_3)_3$	240	360		
$Ni(NO_3)_2$	240	360		
$Th(NO_3)_3$	240	362		

termined by measuring the discharge rate of an electroscope connected to a plate of organic glass containing a radioactive isotope and charged with static electricity. To study thermal oxidative degradation, a sample was heated in air at a rate of 5°C min^{-1} in an MOM derivatograph (Hungary).

The organic glasses prepared in the presence of the metal sulfoxide complexes are X-ray-amorphous. The Debye patterns of the organic glass (a) with no additives and (b, c) containing uranyl nitrate sufoxide complex are shown in Fig. 1. Polymers modified with other metal complexes are also X-ray-amorphous. Hence, the distribution of the metal compounds in PMMA is uniform and the organic glass is optically homogeneous. The physicochemical properties of plates and blocks of organic glass modified with the metal compounds meet the existing requirements to organic glass. However, the softening point of the glass with high content of metal complexes (5–10 wt %) is 5–10°C lower than that of the unstabilized glass, owing to the plasticizing effect of the additive.

Metal sulfoxide complexes turned out to be effective stabilizers of photochemical and thermal oxidative degradation. The degradation temperature in air of a PMMA sample with additive concentration of 2.5–3.0 wt % is 20–50°C higher than that of an unstabilized glass. Data on heat resistance and light fastness of PMMA samples modified with metal complexes are listed in Table 1. It can be seen that, modification of organic glass with metal complexes noticeably increases the service life of these materials.

A study of the radiation hardness of the organic glasses modified with the metal complexes showed that the number of paramagnetic centers in the polymer decreases at high radiation doses (Fig. 2).

Good dielectric properties of most of plastics favor ectrostatic charging of their surface. To decrease static electrization of polymers, antistatic agents are introduced into the bulk of these materials or applied on their surface. Conducting materials, film-forming compounds, and surfactants are used as these agents.

However, introduction of antistatic agents strongly deteriorates the physicochemical properties, in particular, dielectric properties, of the polymers. Introduction of antistatic agents in the course of polymerization substantially deteriorates the most important properties of polymers, such as high electrical resistance, moisture and weather resistance, and transparency. The optical properties of optically homogeneous organic glasses are most strongly affected by antistatic agents. As a result, only a few compounds are used as antistatic additives to polymers. Among them are substances based on soaps, sulfonated organic compounds (cyclohexylammonium dodecyl sulfate), and alkylammonium salts of organic and mineral acids (e.g., triethanolammonium phenylcarboxylates). The use of phosphates as antistatic agents has also been reported.

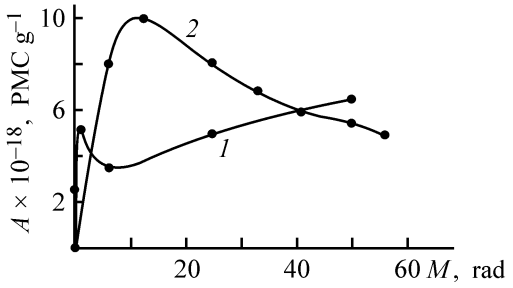

Fig. 2. Number of paramagnetic centers, *A*, in PMMA prepared (*1*) without additives and (*2*) in the presence of cobalt sulfoxide complex vs. radiation dose *M*.

Table 2. Dielectric properties of PMMA glass prepared in the presence of complexes of uranium and thorium salts

Ionizing additive	*c*, mol %	Electrical resistivity		Rate of electroscope discharge, points h^{-1}
		surface $\rho_s \times 10^{-11}$, Ω	bulk $\rho_v \times 10^{-12}$, Ω cm	
$UO_2(NO_3)_2 \cdot 2DASO$	0.01	9.4	1.90	0.04
	0.05	2.8	1.64	0.53
	0.74	5.7	0.50	1.0
$Th(NO_3)_3 \cdot 2DASO$	0.015	7.7	4.60	0.04
$Th(NO_3)_3 \cdot [(C_4H_9O)_2PO]_2$	0.050	9.4	7.0	0.20
$Th(NO_3)_3 \cdot 2[(C_{10}H_{20})_2SO]$	0.217	11.4	1.41	0.40
No additive	–	80.6	–	0.01

Polymers with antistatic properties can be prepared by polymerization of MMA in the presence of sulfoxide complexes of salts of radioactive metals. The concentration of radioactive compounds has no effect on the physicochemical properties of an organic glass and should be at the level providing safe handling of polymeric articles. Salts of α- and β-emitters, e.g., uranium, thorium, plutonium, zinc, cobalt, etc., can be used for this purpose.

Introduction of radioactive compounds into PMMA provides fast electrostatic leakage from the polymer surface owing to external and internal ionization, which is confirmed by electrization experiments.

We took the rate of electroscope discharge as a measure of ionization. A plate of organic glass charged with a definite quantity of static electricity by friction against a cloth was connected to the contact of an electroscope. The rate of electroscope discharge was proportional to the rate of charge leakage from the polymeric plate. The measurements were performed at 60% relative humidity of air and 18–21°C (Table 2). As seen from Table 2, introduction of metal complexes

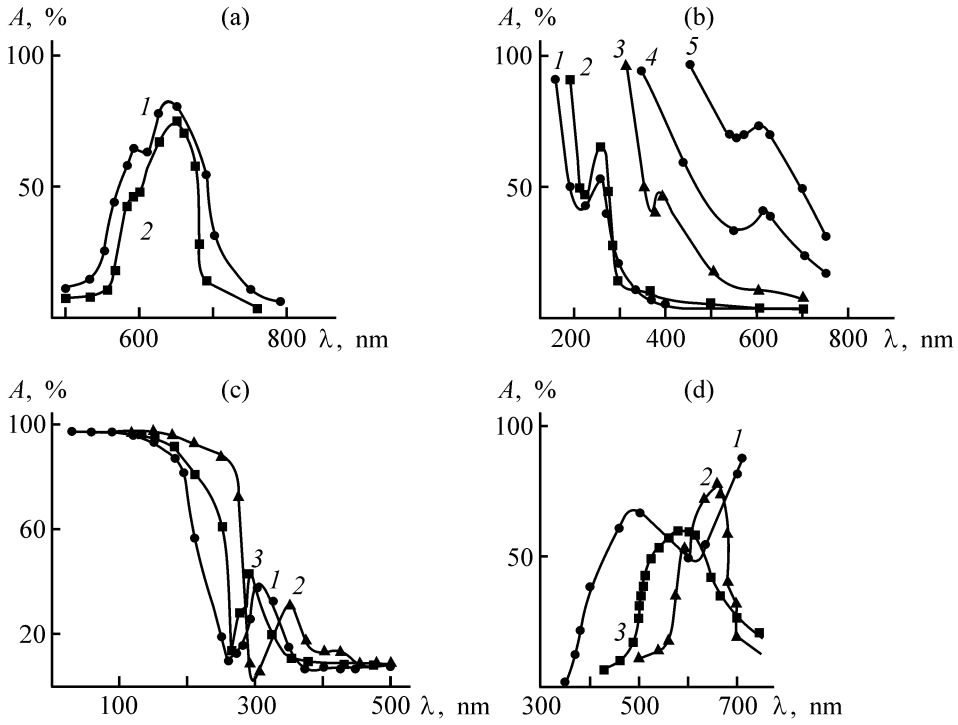

Fig. 3. Transmission spectra of PMMA containing metal sulfoxide complexes: (*A*) transmission and (λ) wavelength. (a) (*1*) MMA + $CoCl_2 \cdot 2PSO$, (*2*) PMMA + $CoCl_2 \cdot 2PSO$ (8.0×10^{-3} M); (b) PMMA + additive ($3.0 \cdot 10^{-2}$ M): (*1*) $Tb(NO_3)_4 \times 3DPSO$, (*2*) $Dy(NO_3)_3 \cdot 3PSO$, (*3*) $TeCl_4 \cdot 2PSO$, (*4*) $ZrOCl_2 \cdot 2PSO$, and (*5*) $CdCl_2 \cdot 2PCO$; (c) (*1*) $CuCl_2 \times 2DPSO$, (*2*) $CuCl_2 \times 2DCPSO$, and (*3*) $CuCl_2 \cdot 2DBSO$; (d) (*1*) $Cu(NO_3)_2 \cdot 2PSO$, (*2*) $CoCl_2 \cdot 2PSO$, and (*3*) $CoCl_2 \cdot 2PSO$ + $Co(NO_3)_2 \cdot PSO$ (8.0×10^{-2} M).

slightly decreases the surface and bulk resistivity of the organic glass. Only the bulk resistivity is proportional to the additive concentration. The rate of electrostatic leakage is proportional to the concentration of radioactive element in a sample.

The proposed metal complexes can be used as effective antistatic agents for preparing optically homogeneous transparent organic glasses with good antistatic properties and high softening points. Clearly, these glasses should be used under conditions excluding prolonged contact with human body).

The electronic spectra of polymers modified with the metal complexes are similar to those of the same complexes in the initial monomer, which indicates stability of these complexes to peroxide initiators. The transmission spectra of PMMA samples containing some of these complexes are shown in Fig. 3. The transmission depends on the nature of metal and sulfoxide. It should be noted that most of metal sulfoxide complexes are readily soluble in MMA and negligibly affect MMA polymerization.

CONCLUSION

Colored organic glasses containing metal sulfoxide complexes are transparent and resistant to heat, light, and radiation; they exhibit good antistatic properties meeting the existing requirements. Introduction of these additive does not affect the process of organic glass production.

REFERENCES

1. Leplyanin, G.B., Battalov, E.M., Murinov, Yu.I., *et al.*, *Vysokomol. Soedin.*, 1984, vol. 26, no. 2, pp. 132–134.
2. *Monomery* (Monomers), Korshak, V.V., Ed. Moscow: Inostrannaya Literatura, 1951, vols. 1, 2.

Russian Journal of Applied Chemistry, Vol. 76, No. 8, 2003, pp. 1296–1298. Translated from Zhurnal Prikladnoi Khimii, Vol. 76, No. 8, 2003, pp. 1333–1335.

MACROMOLECULAR CHEMISTRY AND POLYMERIC MATERIALS

Hydrolysis of 2-Hydroxyethyl Methacrylate in Concentrated Aqueous Solutions

O. A. Kazantsev, K. V. Shirshin, A. P. Sivokhin, S. V. Tel'nov, I. V. Zhiganov, A. E. Kuznetsov, and Yu. L. Mironycheva

Dzerzhinsk Branch, Nizhni Novgorod State Technical University, Dzerzhinsk, Nizhni Novgorod oblast, Russia

Received April 1, 2003

Abstract—Hydrolysis of 2-hydroxyethyl methacrylate in aqueous solutions, as influenced by pH, temperature, and substrate concentration, was studied. In concentrated solutions, the monomer forms associates, which promotes its hydrolysis.

(Co)polymers derived from 2-hydroxyethyl methacrylate (HEM) are used in production of coatings, adhesives, membranes, and eye contact lenses thanks to such valuable properties as nontoxicity, biocompatibility, transparency, etc. In some cases, these (co)polymers are prepared in aqueous solutions at various pH values [1]. It is known that amino-containing analogs of HEM, in particular, *N*,*N*-dimethylaminoethyl methacrylate (DMAEM), are prone to hydrolysis, especially in alkaline solutions. Studies of hydrolysis of such compounds revealed some specific features [2–4]. Lavrov *et al.* [5] showed that polymers derived from HEM also undergo base hydrolysis at elevated temperatures.

In this study, we examined the influence of pH, temperature, and concentration of HEM on its hydrolysis. We found that the monomer is hydrolytically stable in neutral solutions in a broad range of concentrations (10–90%) and temperatures (20–90°C). In acidic or alkaline solutions, HEM undergoes gradual hydrolysis to methacrylic acid and ethylene glycol:

$$CH_2{=}C(CH_3)COOCH_2CH_2OH + H_2O \rightarrow CH_2{=}C(CH_3)COOH + HOCH_2CH_2OH.$$

Accumulation of methacrylic acid alters the pH of the medium, which affects the hydrolysis rate. In base hydrolysis, the catalyst concentration decreases in the course of the process, and in acid hydrolysis it grows.

In alkaline solutions, hydrolysis is very fast even at room temperature in both dilute and concentrated HEM solutions. For example, at the initial monomer content of 20 or 80 wt % (20°C), the solution becomes neutral within several minutes after adding NaOH (0.4–1.0 mg-equiv g^{-1}), and the maximal degree of hydrolysis corresponds to the amount of the initially added alkali.

In acidic solutions, the pattern is quite different: The reaction is considerably slower, and its rate depends on temperature and on the concentrations of the monomer and catalyst. Figure 1 shows the characteristic kinetic curves illustrating how the HEM concentra-

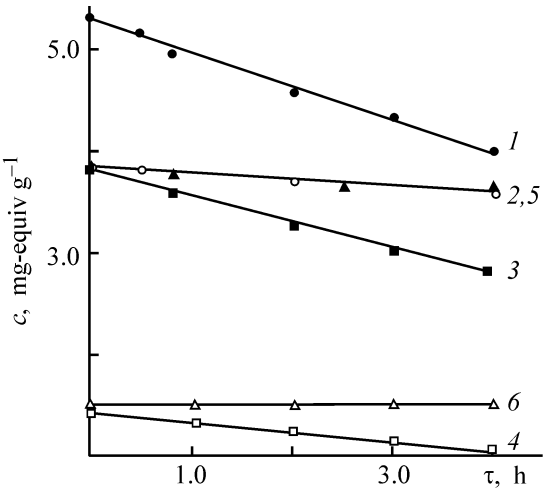

Fig. 1. Variation with time τ of the concentration *c* of monomers in water in the presence of sulfuric acid. Monomer: (*1*–*5*) HEM and (*6*) DMAEM · $0.5H_2SO_4$. $[H^+]$, mg-equiv g^{-1}: (*1*–*4*, *6*) 0.4 and (*5*) 0.1. *T*, °C: (*1*, *3*–*6*) 80 and (*2*) 60.

1070-4272/03/7608-1296 $25.00 © 2003 MAIK "Nauka/Interperiodica"

tion varies in the course of acid hydrolyhsis. Figure 2a illustrates the influence of the catalyst (H_2SO_4) concentration on the initial hydrolysis rate v_0. As expected, v_0 is a linear function of the acid concentration, and the reaction order with respect to acid is close to unity. Figure 2b illustrates the temperature dependence of the initial reaction rate. The slope of the straight line in Fig. 2b corresponds to an activation energy of 65.14 ± 1.54 kJ mol^{-1}.

An increase in the initial monomer content results in a noticeable acceleration of the acid hydrolysis (Fig. 2c). It is interesting to compare the concentration dependences of the hydrolysis rates for the hydroxyl- and amino-substituted methacrylic acid esters: HEM and DMAEM. These monomers differ only in the kind of acceptor substituents in the alcoholic moiety. The inductive constants σ^* of the –OH and $-N^+H(CH_3)_2$ groups are 1.60 and 4.38, respectively [6, 7]. Therefore, it could be expected that acid hydrolysis of protonated DMAEM would be faster than that of HEM. However, actually in moderately concentrated solutions at equal molar concentrations of the monomers and equal acidity, hydrolysis of HEM was considerably faster. For example, at 80°C, free acid concentration of 0.4 mg-equiv g^{-1}, and DMAEM · $0.5H_2SO_4$ concentration of 1.5 mg-equiv g^{-1}, there was no appreciable hydrolysis in 4 h, whereas the degree of hydrolysis of HEM under the same conditions was 30% (Fig. 1, curves *4*, *6*). Furthermore, previous studies of DMAEM hydrolysis [4] have shown that, as the amino ester concentration is increased, the hydrolysis rate in both acidic and alkaline solutions decreases. In acidic aqueous solutions of HEM, the hydrolysis, by contrast, accelerates with increasing HEM concentration, with an inflection observed in the concentration dependence of the initial hydrolysis rate at a conte4nt of approximately 40% (Fig. 2c).

Analysis of the viscosity–concentration relationship for DMAEM [4] revealed association of the monomer in concentrated solutions. To evaluate the tendency for HEM to associate, we examined the concentration dependence of the viscosity of its aqueous solutions (Fig. 3). The nonlinear growth of the viscosity with concentration suggests association of the monomeric molecules, and inflections observed in some cases are apparently due to rearrangements of the associates. In acidic solutions, the ester shows a stronger tendency toward association. It should be noted that, under similar conditions of hydrolysis and viscosity measurements (80°C, $[H^+]$ = 0.4 mg-equiv g^{-1}), the concentration at which the hydrolysis sharply accelerates corresponds to one of the two inflections in the concentra-

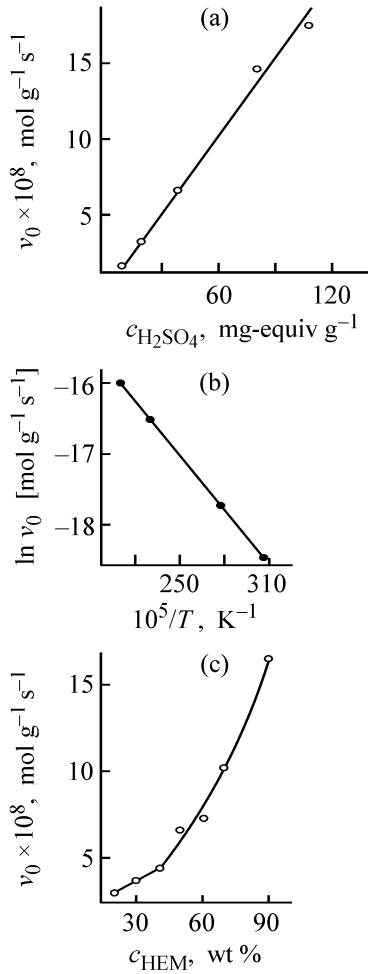

Fig. 2. Influence of the (a) H_2SO_4 concentration $c_{H_2SO_4}$, (b) temperature T, and (c) HEM content c_{HEM} on the initial rate of HEM hydrolysis v_0. (a) $[HEM]_0$ = 50 wt %, 80°C; (b) $[HEM]_0$ = 50 wt %, $[H^+]$ = 0.4 mg-equiv g^{-1}; and (c) $[H^+]$ = 0.4 mg-equiv g^{-1}, 80°C.

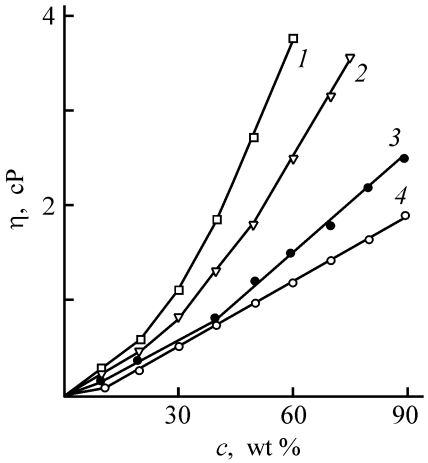

Fig. 3. Viscosity η of aqueous solutions of HEM vs. the monomer content c at various acidities. (*1*, *3*) $[H^+]$ = 0.4 mg-equiv g^{-1} and (*3*, *4*) no acid added. T, °C: (*1*, *2*) 25 and (*3*, *4*) 80.

tion dependence of the viscosity (Fig. 2c; Fig. 3, curve *3*). Thus, our results suggest that, similarly to DMAEM, the specific features of HEM hydrolysis are related to association of the monomer. In associates of DMAEM and its salts, charged and fairly bulky ammonium groups hinder access to the ester reaction center, and association decreases the hydrolysis rate. In electrically neutral HEM containing hydrophilic OH groups, the associates of the monomer must be less hydrophobic and must incorporate more water molecules. Presumably, packing of HEM and water molecules in the associates leads to higher accessibility of the carbonyl carbon atom as compared to dilute HEM solutions in which HEM, apparently, has a cyclic structure with an intramolecular hydrogen bond:

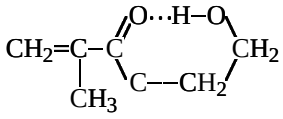

EXPERIMENTAL

The hydrolytic stability of HEM was studied at 20–90°C and monomer content of 10–90 wt %. Radical polymerization was prevented by adding hydroquinone (0.5 wt % relative to the monomer). The reaction course was monitored by alkalimetric titration and gas–liquid chromatography. The content of C=C bonds was determined by bromide–bromate titration. Gas–liquid chromatography was performed on a Tsvet-100 chromatograph equipped with a flame-ionization detector; a 1000×3-mm stainless steel column was packed with Chromaton N-AW + 8% dioctyl sebacate; the carrier gas was N_2 (flow rate 2×10^{-3} $m^3 h^{-1}$); the vaporizer temperature was 180°C, and the column temperature, 120°C. The viscosity of aqueous solutions of monomers was measured with an Ubbelohde viscometer (d_c 0.56 and 0.34 mm) at 25 and 80°C.

CONCLUSIONS

(1) Hydrolysis of 2-hydroxyethyl methacrylate in alkaline solutions is very fast at both low and high concentrations of the monomer.

(2) Acid hydrolysis of 2-hydroxyethyl methacrylate is considerably slower, and its rate grows with increasing temperature and monomer and acid concentrations.

(3) Viscosity–concentration dependences for aqueous solutions of 2-hydroxyethyl methacrylate suggest association of the monomeric molecules. Sharp acceleration of the hydrolysis in concentrated acidic solutions is presumably due to association.

REFERENCES

1. Asadov, Z.G. and Aliev, V.S., *Usp. Khim.*, 1992, vol. 61, no. 5, pp. 1002–1019.
2. Kazantsev, O.A., Zil'berman, E.N., Salov, V.N., and Krasnov, V.L., *Zh. Prikl. Khim.*, 1987, vol. 60, no. 9, pp. 2142–2145.
3. Kazantsev, O.A., Shirshin, K.V., Danov, S.M., and Kazakov, S.A., *Zh. Prikl. Khim.*, 1998, vol. 71, no. 2, pp. 304–307.
4. Kuznetsova, N.A., Kazantsev, O.A., Shirshin, K.V., *et al.*, *Zh. Prikl. Khim.*, 2003, vol. 76, no. 7, pp. 1150–1153.
5. Lavrov, N.A., Chudnova, V.M., and Nikolaev, A.F., *Zh. Prikl. Khim.*, 1986, vol. 59, no. 7, pp. 1554–1558.
6. Galkin, V.A., Cherkasov, A.R., Sayakhov, R.D., *et al.*, *Zh. Obshch. Khim.*, 1995, vol. 65, no. 4, pp. 458–468.
7. Galkin, V.A., Cherkasov, A.R., Sayakhov, R.D., *et al.*, *Zh. Obshch. Khim.*, 1995, vol. 65, no. 4, pp. 477–479.

Russian Journal of Applied Chemistry, Vol. 76, No. 8, 2003, pp. 1299–1303. Translated from Zhurnal Prikladnoi Khimii, Vol. 76, No. 8, 2003, pp. 1336–1340.

MACROMOLECULAR CHEMISTRY AND POLYMERIC MATERIALS

Synthesis and Polymerization of Unsaturated Phthalides

Yu. I. Puzin, T. V. Chebaeva, A. E. Egorov, and E. A. Khatchenko

Ufa State Petroleum Technical University, Ufa, Bashkortostan, Russia
Institute of Organic Chemistry, Ufa Scientific Center, Russian Academy of Sciences, Ufa, Bashkortostan, Russia

Received October 9, 2002; in final form, March 2003

Abstract—Procedures were developed for preparing unsaturated phthalides: phthalideneacetic acid and methylene phthalide, which are promising monomers for radical polymerization. The structures of the monomers were studied, and their copolymerization with methyl methacrylate was performed.

Much attention is given today to polymeric materials whose components change the structure and physicochemical properties, depending on external conditions (pressure, temperature, acidity of the medium, etc.). Of particular interest in this respect are phthalides showing ring–chain isomerism [1]. Phthalide-containing polymers exhibit unique electrical [2] and optical [3] properties, high heat resistance, and high softening points [4]. These polymers are most often prepared by polycondensation. However, their high heat resistance is combined with high glass transition and flow points, and also with poor solubility in the majority of industrially used organic solvents.

In contrast to phthalide-containing polymers, many vinyl polymers, in particular, polyacrylates have low glass transition and flow points and good solubility, but poor heat resistance. These polymers are most often prepared by radical polymerization. Therefore, it seems appropriate to modify vinyl polymers, such as poly(meth)acrylates, polystyrene, etc., with phthalides, and development of procedures allowing modification in the stage of synthesis is an urgent problem.

Phthalides can be incorporated into a polymeric molecule in the course of radical polymerization both via their involvement in chain initiation or transfer [3] and through (co)polymerization of unsaturated phthalides. With the aim to prepare poly(methyl methacrylate) modified with phthalide-containing compounds, we prepared two phthalide-containing monomers: phthalideneacetic acid **I** and methylene phthalide **II**:

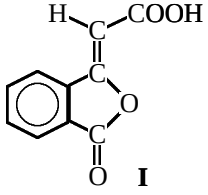
I

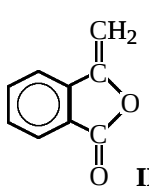
II

The monomeric purity is the necessary condition for their application.

EXPERIMENTAL

Phthalic anhydride was recrystallized from absolute ethanol before use; mp 239°C. Acetic anhydride was distilled; bp 140°C. The polymerization initiators, azobis(isobutyronitrile) (AIBN) and benzoyl peroxide (BP), were repeatedly recrystallized from methanol and vacuum-dried to constant weight.

Methyl methacrylate (MMA) was purified to remove the stabilizer by shaking with 5–10% KOH, washed with water to neutral reaction, dried over $CaCl_2$, and double-distilled in a vacuum. The fraction with bp 42°C (13.3 kPa) was used for polymerization.

Phthalideneacetic acid. Published data on synthesis of **I** and **II** are contradictory. Phthalideneacetic acid was prepared for the first time at the end of the XIX century [5–8], but its properties have been studied poorly. In this study, we prepared **I** by the Perkin–Gabriel reaction from phthalic and acetic anhydrides in the presence of a metal acetate:

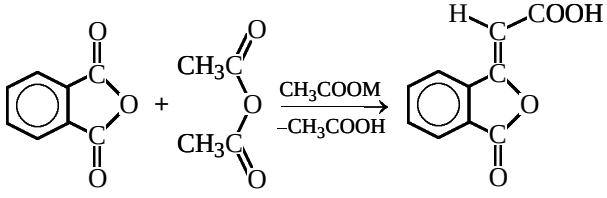

The reaction was performed in several steps. First, a flask was charged with phthalic anhydride (2–3% excess relative to the reaction stoichiometry), acetic anhydride, and potassium acetate (20–30% excess relative to phthalic anhydride). The mixture was heated for 1.5 h on a boiling water bath. Then a tenfold vol-

1070-4272/03/7608-1299 $25.00 © 2003 MAIK "Nauka/Interperiodica"

Table 1. Properties of **I** and **II**

Compound	Found, % / Calculated, %		mp, °C	UV spectrum, λ, nm	IR spectrum, ν, cm^{-1}	NMR spectrum, δ, ppm	
	C	H				^1H	^{13}C
I	63.47 / 63.16	3.02 / 3.18	280	282 (C=C)	1705 (COOH) 1800 (C=O)	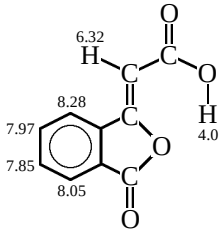	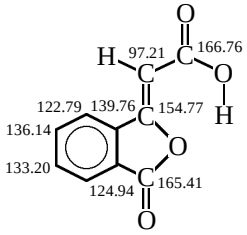
II	74.16 / 73.97	4.02 / 4.14	56	311 (C=O and Ar)	1780 (C=O)	4.80 (*cis*-H) 5.25 (*trans*-H)	94.86 ($C=CH_2$)

Table 2. Geometries of **I** and **II**

Bond	**II**		**I**	
	bond length, Å	bond angle, deg	bond length, Å	bond angle, deg
C=C	1.3	130.2 108.7*	1.3	122.7 108.8*
=C–H	1.1	130.2	1.1	119.6 115.6
=C–CO	–	–	1.5	115.8 124.8**
=C–O–	–	–	1.4	116.5
–O–H	–	–	1.0	109.9
Deviation from plane		No		–COOH, 58

* In the ring. ** Relative to the C=C bond.

ume of hot water was added, and the hot mixture was filtered. The precipitate was washed with hot water and ethanol. A light brown product was obtained; it was washed with a small amount of hot glacial acetic acid. After cooling and filtration, a yellow substance was obtained; its melting point, 249°C, is reasonably consistent with published data [6, 7]. The product was repeatedly recrystallized from glacial acetic acid in the presence of activated carbon. Colorless lustrous plates were obtained; mp 280°C (with decomposition). Further recrystallizations did not increase the melting point. The product was identified by IR, ^{13}C NMR, and ^1H NMR spectroscopy and by elemental analysis (Table 1).

Methylene phthalide. Synthesis of methylene phthalide and its polymers has been attempted by numerous researchers. However, either the suggested procedures gave the monomer in low yield (10–15%) or the product was unsuitable for polymerization because of the presence of inhibiting impurities.

In this study, to prepare and purify methylene phthalide, we chose the procedure described in [9]. It involved high-vacuum dehydration of acetophenone-*o*-carboxylic acid:

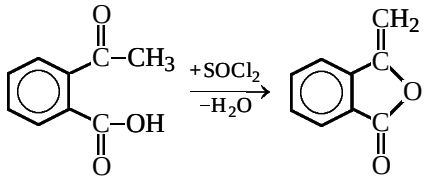

The product sublimes and is condensed as colorless needles, mp 56°C (yield about 60%); it is hygroscopic and sublimes in a vacuum at about 300°C (1–5 mm Hg). Some characteristics of **II** are listed in Table 1.

The kinetics of bulk polymerization was monitored gravimetrically [10]. The temperature was maintained at 60 ± 0.5°C. The composition was calculated from the analytical data.

The UV spectra (solutions in CH_3COOH) were recorded on a Shimadzu UV–VIS–NIR 3100 spectrometer using a 1-cm quartz cell. The IR spectra (mulls in mineral oil) were recorded on a Specord M-80 spectrophotometer (Germany). The ^1H and ^{13}C NMR spectra were taken on a Bruker AM-400 spectrometer (300 MHz, CD_3OD, internal reference hexamethyldisiloxane).

The temperature of the decomposition onset was determined by the method of tangents with an MOM Q-1500D derivatograph (Hungary); sample weight 100 mg, heating rate 5 deg min^{-1}.

The probabilities of addition of propagating radicals with different structures of terminal units to comonomer molecules were calculated as described in [10].

The overwhelming majority of studies concerned phthalideneacetic acid are limited to its synthesis. In most cases, the acid was immediately subjected to thermal decarboxylation in a vacuum to obtain methylene phthalide [7, 8]. The properties and structure of the acid remained unknown, like those of methylene phthalide. Therefore, we first examined the structures of these compounds.

The ^1H NMR spectrum of **II** (Table 1) shows that the methylene hydrogen atoms (α-position relative to the phthalide ring) are nonequivalent (*cis* and *trans* arrangement relative to the oxygen atom of the phthalide ring).

In the case of phthalideneacetic acid, two isomers with the *cis* and *trans* arrangement of the carboxy group relative to the oxygen atom of the phthalide ring are possible. The nuclear Overhauser effect (η = 8%) observed on the aromatic proton (8.28 ppm, 3-position) upon irradiation at the frequency of the olefinic proton signal (6.32 ppm) unambiguously suggests steric proximity of these protons, i.e., the *cis* structure of the product. In other words, the synthesized phthalideneacetic acid is a pure *cis* isomer. Furthermore, the chemical shift of the carboxyl proton signal is unusually small, which may be due to interaction of this proton with the oxygen atom of the phthalide ring. Unfortunately, we failed to follow the changes in the chemical shift of this signal depending on the solvent polarity because of extremely low solubility of **I** in other solvents. However, the chemical shift varies with temperature: 25°C, 4.00 ppm; 30°C, 4.72 ppm; and 40°C, 5.73 ppm. This indicates that the intramolecular hydrogen bond in the acid molecule becomes weaker.

Table 3. Characteristics of copolymerization of MMA with unsaturated phthalides at 70°C [initiator azobis(isobutyronitrile), 0.5 wt %] and decomposition (onset) temperatures of the copolymers

Phthalide content in monomer mixture, mol %	Initial copolymerization rate, % min^{-1}	Phthalide content in copolymer, mol %	T_{dec}, °C
Phthalideneacetic acid			
0	0.0950	0	190
10	0.0925	1.8	218
20	0.0800	3.3	226
30	0.0540	4.2	235
40	0.0220	6.9	230
60	0.0067	18.0	220
Methylene phthalide			
0	0.1070	0	190
10	0.1098	4.2	220
15	0.1064	7.0	228
20	0.1002	9.6	235
40	0.0891	21.6	240
60	0.0788	37.6	238
80	0.0745	60.2	242
90	0.0704	77.7	240

The molecular geometry of **I** and **II** was optimized by PM3 calculations. The results (Table 2) show that the oxygen atom deviates from the ring plane by approximately 2°; the bond angle at the ring oxygen atom is 108°, and the C–O bond length, 1.44 Å. An important result is that the phthalideneacetic acid molecule, in contrast to the methylene phthalide molecule, has functional groups that extend from the molecular plane; this must affect the electrical properties of **I** at elevated pressures and temperatures.

Unfortunately, we failed to prepare the homopolymer of phthalideneacetic acid by radical polymerization. However, we obtained copolymers of **I** with MMA. Some data on the reaction and copolymer compositions are listed in Table 3. It is seen that the copolymerization rate decreases with increasing content of **I** in the reaction mixture. This may be due to the fact that the purity of **I** is insufficient for radical polymerization. Therefore, we additionally performed repeated chromatographic purification of the mono-

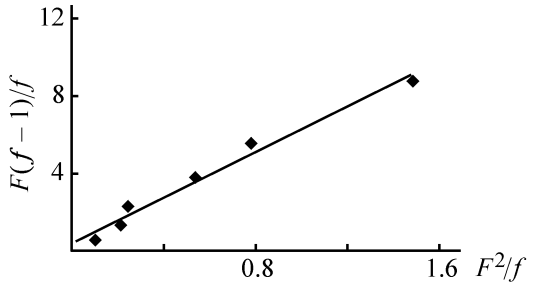

Fig. 1. Determination of the constants of MMA copolymerization with phthalideneacetic acid by the Fineman–Ross method.

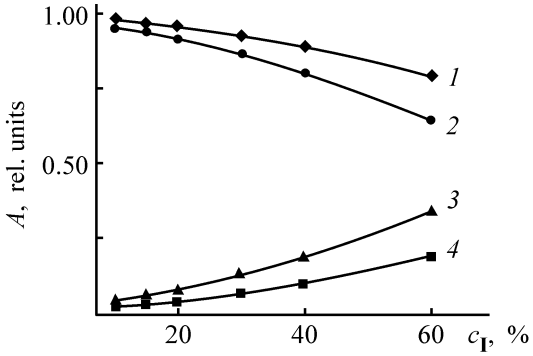

Fig. 2. Probability A of addition of a propagating radical with the of terminal unit (*1*, *2*) MMA and (*3*, *4*) phthalideneacetic acid to (*1*, *3*) MMA and (*2*, *4*) phthalideneacetic acid molecule. ($c_{\mathbf{I}}$) Concentration of **I**.

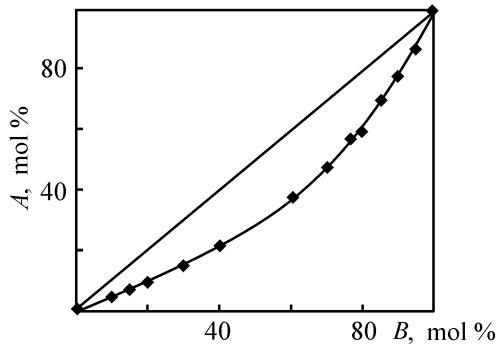

Fig. 3. Content *A* of methylene phthalide units in the copolymer vs. the content *B* of methylene phthalide in the initial monomer mixture.

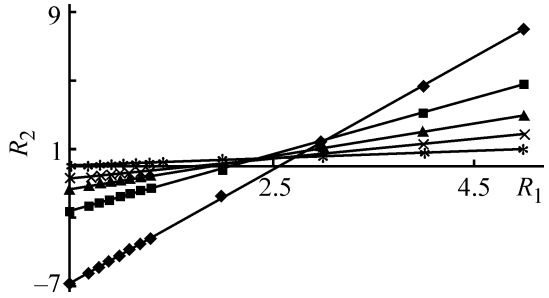

Fig. 4. Determination of the constants of MMA copolymerization with methylene phthalide by the Mayo–Lewis method.

mer. A certain increase in the copolymerization rate was, indeed, observed but attempted preparation of the homopolymer failed.

The constants of copolymerization of MMA with **I** were determined by the Fineman–Ross method [10] (Fig. 1) to be 0.36 ± 0.06 and 5.80 ± 0.08, respectively. Calculation of the probabilities of monomer addition to propagating radicals of various structures shows (Fig. 2) that incorporation of MMA into the chain is much more probable than incorporation of **I**.

At the same time, the copolymerization constants show that the monomers interact with each other (the product of the constants is significantly greater than unity), probably owing to their high polarity. Using the *Q*–*e* scheme, we calculated the parameters $e = 1.26$ (parameter characterizing the polarity of **I**) and $Q = 0.79$ (parameter characterizing the conjugation in the propagating radical with the radical center localized in the phthalideneacetic acid unit) [10]. Phthalideneacetic acid is close to MMA in the value of *Q* ($Q_{\mathrm{MMA}} = 0.74$) but significantly exceeds it in polarity ($e_{\mathrm{MMA}} = 0.40$), being in this respect close to acetonitrile ($e = 1.20$).

In contrast to phthalideneacetic acid **I**, methylene phthalide polymerizes in the presence of radical initiators, such as BP or AIBN. The reaction was performed in DMF in the presence of 3.7×10^{-3} M BP. The polymerization noticeably accelerated after reaching 30% conversion of the monomer (gel effect), suggesting the radical mechanism of the reaction. The polymer was precipitated with acetone and reprecipitated several times. Dry poly(methylene phthalide) has a high glass transition point (305°C), and its softening is accompanied by decomposition (as indicated by significant weight loss). We failed to prepare films from this polymer (under conditions similar to those used with other polymers) for studying electrical properties; therefore, it seems necessary to prepare copolymers of **II**, primarily with MMA.

A study of copolymerization of MMA with **II** showed that, with increasing content of **II**, the process decelerates but does not fully stop (Table 3), which allows preparation of the copolymer with different monomer ratios. Figure 3 shows that the copolymer is enriched in MMA units at any composition of the monomer mixture, and the ratio of the copolymerization constants meets the condition $r_1 > 1$ and $r_2 < 1$.

The copolymerization constants were determined by the Mayo–Lewis method [10] (Fig. 4) to be 2.69 ± 0.05 (for MMA) and 0.70 ± 0.07 (for **II**). In this case, too, the product of the copolymerization constants is

greater than unity, suggesting mutual interaction of the monomers; however, it is apparently weaker than that with **I**.

Methylene phthalide is characterized by $Q = 1.35$ and $e = +1.20$. It is somewhat more polar than **I**, but its growing radical is more active in chain propagation.

As expected, the copolymers show higher heat resistance, compared to poly(methyl methacrylate) (Table 3). However, with increasing content of phthalideneacetic acid, the decomposition onset temperature starts to decrease, probably owing to decarboxylation.

CONCLUSIONS

(1) Procedures were developed for synthesis and purification of phthalideneacetic acid and methylene phthalide, promising monomers for radical polymerization.

(2) The structures of the phthalides were studied; phthalideneacetic acid has the *cis* structure.

(3) (Co)polymerization of unsaturated phthalides with methyl methacrylate was performed; the copolymerization constants and *Q*–*e* parameters were calculated; the activity of **I** and **II** as monomers was evaluated.

(4) The methyl methacrylate copolymers obtained show enhanced heat resistance.

ACKNOWLEDGMENTS

The authors are grateful to S.N. Salazkin (Nesmeyanov Institute of Organometallic Compounds, Russian Academy of Sciences, Moscow) for valuable advices.

The study was supported financially by the Russian Foundation for Basic Research (project no. 98-03-33 322).

REFERENCES

1. Valter, R.E., *Kol'chato-tsepnaya izomeriya v organicheskoi khimii* (Ring–Chain Isomerism in Organic Chemistry), Riga: Zinatne, 1978.
2. Lachinov, A.N., Zherebov, A.Yu., and Kornilov, V.M., *Pis'ma Zh. Eksp. Teor. Fiz.*, 1990, vol. 52, p. 742.
3. Puzin, Yu.I., Egorov, A.E., Khatchenko, E.A., *et al.*, *Vysokomol. Soedin., Ser. A*, 2000, vol. 42, no. 9, p. 1461.
4. Buhler, K.-U., *Spezialplaste*, Berlin: Akademie, 1978.
5. Gabriel, S. and Michael, A., *Ber.*, 1877, vol. 10, p. 391.
6. Gabriel, S. and Neuman, A., *Ber.*, 1893, vol. 26, p. 951.
7. Gabriel, S., *Ber.*, 1884, vol. 17, p. 2521.
8. Iale, H., *J. Am. Chem. Soc.*, 1947, vol. 69, p. 1547.
9. Vinogradova, S.V., Salazkin, S.N., Korshak, V.V., *et al.*, *Vysokomol. Soedin., Ser. A*, 1970, vol. 12, no. 1, p. 205.
10. Gladyshev, G.P., *Polimerizatsiya vinil'nykh monomerov* (Polymerization of Vinyl Monomers), Alma-Ata: Nauka, 1964.

Russian Journal of Applied Chemistry, Vol. 76, No. 8, 2003, pp. 1304–1309. Translated from Zhurnal Prikladnoi Khimii, Vol. 76, No. 8, 2003, pp. 1341–1345.

MACROMOLECULAR CHEMISTRY AND POLYMERIC MATERIALS

p-Xylylenediamine and New Polyimides Derived from It

K. A. Zhubanov, T. S. Abil'din, N. B. Bizhanova, B. A. Zhubanov, and V. D. Kravtsova

Research Institute of New Chemical Technologies and Materials, Almaty, Kazakhstan
Bekturov Institute of Chemical Sciences, Ministry of Education and Science of the Republic of Kazakhstan, Almaty, Kazakhstan

Received November 27, 2002; in final form, May 2003

Abstract—*p*-Xylylenediamine was prepared by hydrogenation of terephthalodinitrile; the conditions ensuring high yield of this monomer were found. The influence exerted by the catalyst and solvent on the diamine yield was examined. Single-step polycondensation of *p*-xylylenediamine with tricyclodecenetetracarboxylic dianhydrides in the presence of catalytic amounts of isonicotinic acid gave a series of new polyimides consisting of aliphatic and aromatic fragments.

Polyalkanimides show promise as materials for electrical and radio engineering [1, 2]. The interest in these polymers is not occasional. Occupying an intermediate position between aromatic and aliphatic derivatives, they combine the advantages of both. Introduction of methylene units into the backbone decreases the melting point, enhances the resistance to hydrolysis, and imparts to the polymers other valuable properties allowing their processing with commercially available equipment [2].

A series of polyalkanimides (PAIs) derived from pyromellitic dianhydride and aliphatic diamines (deca- and dodecamethylenediamines, and also their mixtures) have been prepared; these materials shown long service life at temperatures of up to 200°C [2, 3]. At the same time, PAIs can also be prepared from *p*-xylylenediamine (*p*-XDA) and other anhydrides.

In this study, we prepared dianhydrides of cyclodecenetetracarboxylic acids: tricyclo[4.2.2.$0^{2,5}$]dec-7-ene-3,4,9,10-tetracarboxylic dianhydride (product of photochemical addition of maleic anhydride to benzene, AB) and its 7-fluoro (AFB) and 7-chloro (ACB) derivatives, which are starting compounds for preparing a wide set of heat-resistant polymers, including polyimides [4, 5]:

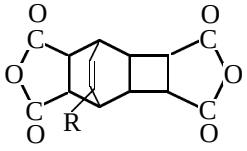

where R = H (AB), F (AFB), Cl (ACB).

It is known that the prospects for application of polymeric materials are determined by numerous factors, with the availability of the starting monomers being of major importance. We have developed a procedure for preparing *p*-XDA in quantitative yield, which allowed us to begin studies of synthesis of new PAIs derived from *p*-XDA and alicyclic dianhydrides.

Here we report the features of synthesis of *p*-XDA and polyimides derived from it.

EXPERIMENTAL

The starting compounds and solvents were purified by common procedures. The IR spectra were recorded on a Specord IR-25 spectrometer. The monomer samples were prepared as KBr pellets, and the polymer samples, as 3–5-μm films. The reduced viscosities of 0.5% solutions of polyimides were measured with an Ubbelohde viscometer at 25°C in DMSO. The TG and DTA curves were recorded simultaneously on an MOM derivatograph (Hungary) at a heating rate of 8 deg min^{-1}. From the TG curves, we calculated the temperatures of the onset of weight loss and of 5, 10, and 50% weight loss (T_0, T_5, T_{10}, and T_{50}, respectively).

The physicomechanical (tensile strength σ, relative elongation *l*) and dielectric (dielectric loss tangent tan δ, relative dielectric permittivity ε') characteristics were studied under standard conditions by published procedures [6, 7].

1070-4272/03/7608-1304 $25.00 © 2003 MAIK "Nauka/Interperiodica"

p-Xylylenediamine was prepared by catalytic reduction of terephthalodinitrile (TDN)[1] in a high-pressure kinetic unit [8] allowing monitoring of the hydrogen uptake in unit time [9]. As catalysts we used promoted catalytic alloys whose base component was Raney nickel; the catalysts were prepared by leaching of the corresponding alloys with Ni : Al ≈ 1 : 1. A 0.5-l long-necked stainless steel vessel was shaken at a frequency of 600–700 one-side rockings per minute. A 0.5-g portion of the catalyst was loaded under the layer of the solvent (50 ml of methanol preliminarily saturated with ammonia under cooling; nitrile : ammonia ratio 1 : 3). Then 1.43 g of TDN was added. Hydrogenation was performed until the H_2 uptake stopped.

p-XDA was identified by elemental analysis, melting point, and IR spectra.

Found, %: C 70.26, H 8.84, N 19.92.
$C_8H_{12}N_2$.
Calculated, %: C 70.60, H 8.09, N 20.57.

IR spectrum, ν, cm^{-1}: 1500 (benzene ring); 1670, 3420 (–NH_2 groups); 2920 (–CH in –CH_2 group); mp 34.5–35°C (published data [8]: 35°C).

AB, AFB, and ACB were prepared by published procedures [10, 11] and purified by three- or fourfold 1.5–2.0-h treatment with hot acetone under stirring. The precipitate of the monomers was filtered off and vacuum-dried in an oven to constant weight at 80–90°C.

AB: equivalent weight 68.5 (calculated 68.5), mp 250–252°C; AFB: equivalent weight 73.04 (calculated 73.04), mp 312–314°C; ACB: equivalent weight 77.12 (calculated 77.12), mp 302–304°C. The elemental analyses were consistent; the melting points agreed with published data [10, 11]. The solvents [dimethylformamide, DMF; dimethylacetamide, DMA; *N*-methyl-2-pyrrolidone, MP; dimethyl sulfoxide, DMSO] were dried over 4-Å molecular sieves.

The polyimide derived from AB and *p*-xylylenediamine was prepared as follows. A three-necked flask equipped with a stirrer and an inlet tube for inert gas was charged with 13.71 g (0.05 mol) of AB, 5.20 g (0.05 mol) of *p*-XDA, 0.09 g (5 wt % relative to the sum of the monomers) of isonicotinic acid, and 56.9 ml of DMA. The mixture was heated on an oil bath (50°C) for 15 min with stirring, after which the temperature was raised to 110°C over a period of 20 min, and the mixture was stirred for additional 2 h. After cooling to room temperature, the polyimide was precipitated with chemically pure acetone, and the precipitate was washed with two portions of acetone and vacuum-dried in an oven at 80–90°C to constant weight.

Table 1. Conditions of TDN hydrogenation on Raney nickel catalysts (H_2 pressure 4.0 MPa; 60°C)

Composition of starting alloy before leaching (weight ratio)	τ, min	*p*-XDA yield, wt %
Ni : Al = 50 : 50	140	73–75
Ni : Ti : Al commercial (TU*-59-83–75), prescribed content: Al, 50–53.5; Ni, 44–46.5; Ti, 2.2–2.8	50	90–92
N-5 catalyst		
Ni : M : Al:		
47.5 : 2.5 : 50.0	41	94–95
45.0 : 5.0 : 50.0	32	97–98

* Technical Specifications.

Table 2. Conditions of TDN hydrogenation in various solvents (H_2 pressure 4.0 MPa; 60°C)

Solvent (saturated with NH_3)	Ni–Ti catalyst (~3% Ti)		N-5 catalyst	
	τ, min	*p*-XDA yield, wt %	τ, min	*p*-XDA yield, wt %
Methanol	50	90–92	32	97–98
Ethanol	62	89–91	41	96–97
Propanol	69	90–91	48	96–97
Butanol	71	90–91	53	96–97

The elemental composition of the precipitated polymer corresponds to the theoretical value. Polyimide films were prepared by casting 25% solutions of the polyimides in DMA on glass plates. To remove the solvent, the films were predried by vacuum heating in an oven at 80°C for 0.3 h, after which they were heated to constant weight at 150°C for 1 h.

Polyimides derived from *p*-XDA and halogenated dianhydrides were prepared similarly. Yield 98.5–99.0%, degree of imidization about 100%.

Catalytic hydrogenation of nitriles involves a set of parallel-consecutive reactions [8, 12–14]. The reduction of TDN was performed on the catalysts listed in Table 1. The results are given in Tables 1 and 2.

[1] Terephthalodinitrile was kindly submitted by P.B. Vorob'ev and L.F. Gabdullina (Bekturov Institute of Chemical Sciences, Ministry of Education and Science of the Republic of Kazakhstan).

Table 1 shows that Ni–Ti and N-5 catalysts are more active, compared to straight Raney nickel. The yield of the target product is 90–92% on Ni–Ti and as high as 97–98% on N-5. Therefore, the subsequent experiments were performed with N-5 catalyst.

Published data on hydrogenation of aromatic dinitriles demonstrate a significant solvent effect on the process; the best results are attained in alcohols [14].

In this study, we examined the influence exerted by the nature of a solvent on hydrogenation of TDN on N-5 catalyst in the presence of ammonia. The results are listed in Table 2. It is known that the highest rate of formation and highest yield of the product are attained at the stoichiometric ratio of the reactants on the catalyst surface [15]; this fact was taken into account in our experiments.

Table 2 shows that the most favorable ratio of the reactants on the catalyst surface in alcohol is attained at the nitrile : ammonia ratio of 1 : 3.

It is known that the products of hydrogenation of phthalonitriles contain amino nitriles [14, 16, 17]. This fact suggests consecutive reduction of the nitrile groups. The hydrogenation rate on N-5 catalyst decreases with time; the hydrogen uptake corresponds to the reaction stoichiometry [18]. Hydrogenation starts and proceeds at a high rate until 2 mol of H_2 is taken up per mole of the dinitrile; after that, the rate of hydrogen uptake somewhat decreases, and the remaining 2 mol of H_2 is added at a lower rate [17, 18].

Hydrogenation of TDN can be described by the following scheme:

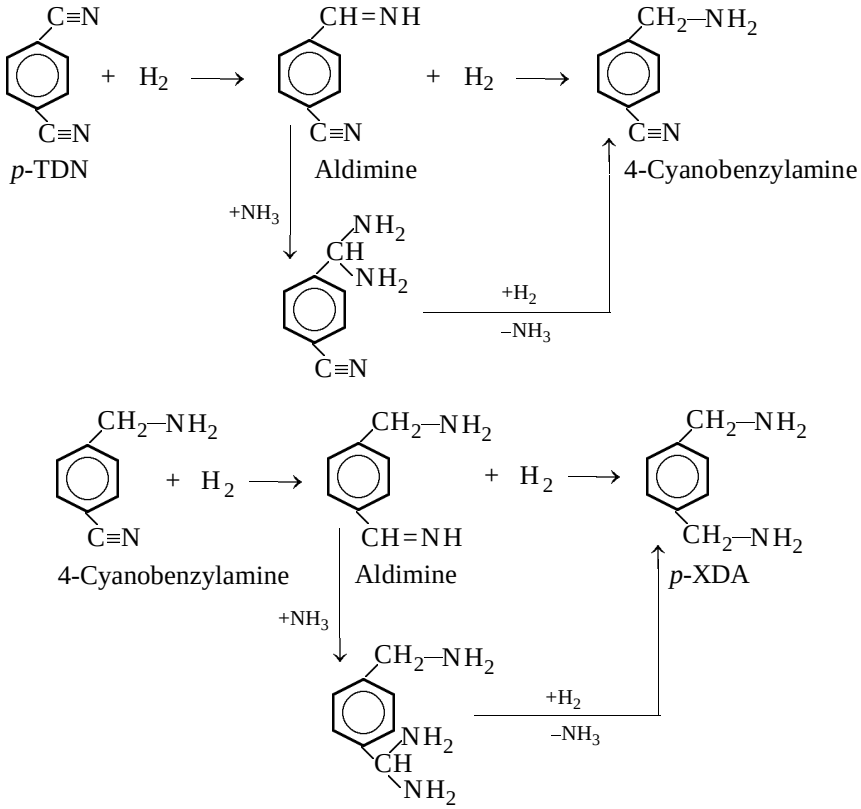

This scheme suggests that, initially, one of the nitrile groups is hydrogenated to give the amino nitrile (cyanobenzylamine), and only after that *p*-XDA is formed.

Bizhanov [19] believes that the growth of activity of Raney nickel catalysts is associated with an increase in the content of the $NiAl_3$ phase relative to the Ni_2Al_3 phase. Thus, the yield of the target product and the reaction rate depend on both the synthesis conditions and the catalyst used. The activity and selectivity of N-5 catalyst may be due to its high enrichment in firmly bound adsorbed hydrogen; its amount is 2–3 times higher than that on straight Raney nickel [19].

Tricyclodecenetetracarboxylic dianhydries are the starting monomers for preparing various heat-resistant

Table 3. Optimal conditions for preparing polyalkanimides

Polymer no.	Dianhydride	c_{mon}, wt %/c_{INA}, wt %	T, °C	τ, h	η_r (0.5% solution in DMSO, 25°C), dl g^{-1}
1	AFB	40/2.0	120	2.2	1.23
2	AB	40/2.5	120	2.5	1.10
3	ACB	40/2.5	110	2.5	0.94
4	AFB	20/0	25	2.5	0.32

Table 4. Thermal characteristics of PAI

Polymer no.	T_g, °C	Temperature of weight loss, °C							
		in air				under Ar			
		T_0	T_{15}	T_{10}	T_{50}	T_0	T_{15}	T_{10}	T_{50}
1	270	340	380	420	530	380	440	470	580
2	280	325	350	400	500	360	415	450	545
3	265	335	365	415	510	355	435	460	560

polymers, including polyimides [20, 21]. No data are, however, available on synthesis of high-performance polyimides from *p*-XDA and the above dianhydrides, because of the lack of efficient synthesis procedures. In this study, we developed such procedures. The polyimides were prepared by single-stage polycondensation of the components in polar aprotic solvents (amides) in the presence of catalytic amounts of isonicotinic (pyridine-4-carboxylic, INA) acid, which is known [5] to appreciably intensify polycondensation, like other pyridinecarboxylic acids.

It is known that polyheterocycles prepared in solution are more soluble than the same polymers prepared by solid-phase imidization of polyamido acids. Among the chosen solvents (DMF, DMA, MP, DMSO), the best results were obtained with DMA; the polyimides prepared in this solvent have the highest viscosity. For example, η_r of 0.5% solution of the fluorinated polyimide prepared in various solvents under the optimal conditions is as follows (dl g^{-1}): 0.45 in DMF, 0.53 in MP, 0.75 in DMSO, and 1.23 in DMA. Therefore, all the subsequent syntheses were performed in DMA.

A study of the reactions of *p*-XDA with alicyclic dianhydrides showed that the fluorinated dianhydride (AFB) is more reactive in acylation, which is due to the high electronegativity of the fluorine atom at the endocyclic double bond; as a result, the anhydride groups become more electrophilic. AB and ACB are less reactive [10].

It should be noted that PAIs with fairly good characteristics, derived from an alicyclic dianhydride, were prepared for the first time. The syntheses were performed at 110–120°C for 2.0–2.5 h. All the reactions occurred under homogeneous conditions and gave PAIs in almost quantitative yields, with degrees of imidization of about 100%. The viscosity of the polymers was as high as 0.94–1.23 dl g^{-1}.

The optimal conditions for preparing PAIs are listed in Table 3; for comparison, we also give data for the two-stage synthesis of the polyimide from AFB and *p*-XDA (polymer no. 4). Table 3 shows that the single-stage procedure ensures higher η_r of the polyimide.

The compositions and structures of the polyimides were confirmed by elemental analysis and IR spectroscopy. The IR spectra of the polyimides contain absorption bands at 1775 and 1715 (carbonyl groups of imide rings), 1365–1370 (>N–), and 715–725 cm^{-1} (imide ring); the PAI derived from AFB also exhibits C–F vibration band at 1260–1300 cm^{-1}, and the PAI derived from ACB, a C–Cl band at 860 cm^{-1}. No bands characteristic of uncyclized amido acid fragments were detected.

The structural features of polyimides derived from tricyclodecenetetracarboxylic dianhydrides (presence of the alicyclic structure and, in the case of AFB and ACB, also of halogen atoms) are responsible for some specific properties; for example, the glass transition points T_g decrease somewhat. Comparison of the glass transition points of PAIs, determined by dielectric measurements [22], showed that they are within 265–280°C; T_g of the halogenated polymers is 10–15°C lower, compared to the PAI derived from AB; introduction of Cl decreases T_g to a greater extent, compared to F (Table 4, polymer nos. 1, 2).

We evaluated the heat resistance of the new polymers. As seen from Table 4, decomposition of all the three PAIs in air (onset temperature T_0) starts at 325–340°C, with the nonhalogenated polymer being somewhat less heat-resistant. Decomposition under Ar starts at higher temperatures.

Table 4 shows that, for the polyimides prepared, the interval between T_g and T_0 is 45–70°C, which allows processing of the polymers by pressure molding.

The relatively high viscosity characteristics and good solubility of the polymers in DMA allowed us to prepare films with strength of 70–80 MPa and 30–40% elongation. The modulus of elasticity ranges from 2700 to 3400 MPa depending on the modifying additive (triphenyl phosphate, dimethyl phthalate, dibutyl phthalate, dimethyl terephthalate, etc.).

The dielectric loss tangent at f = 1 kHz, T = 25°C, and zero moisture content is 0.002–0.004; relative dielectric permittivity, 3.22–3.35. The relative dielectric permittivities of the new PAIs are relatively low, especially of those containing an F atom, which is due to the alicyclic structure of the anhydride ring and to the effect of the electronegative halogen atom. The relative dielectric permittivities of aromatic polyimides containing aliphatic and aromatic fragments are higher.

CONCLUSIONS

(1) Conditions were found for preparing *p*-xylylenediamine in quantitative yield by hydrogenation of terephthalodinitrile in lower aliphatic alcohols in the presence of promoted catalysts containing Raney nickel as base component and obtained by leaching of the corresponding alloys with Ni : Al ≈ 1 : 1. The catalysts used in this study are 3–4 times more active than straight Raney nickel.

(2) A series of new (including fluoro and chloro derivatives) polyimides were prepared by condensation of *p*-xylylenediamine with tricyclodecenetetracarboxylic dianhydrides in polar aprotic solvents (amides). These polymers exhibit high, for this class of materials, physicomechanical and dielectric characteristics and high heat resistance.

REFERENCES

1. Kazaryan, L.G., Azriel', A.E., Vasil'eva, V.A., *et al.*, *Vysokomol. Soedin., Ser. A*, 1988, vol. 30, no. 3, pp. 644–648.
2. Kalugina, E.V., Blyumenfel'd, A.B., Novotortsev, V.M., and Savina, M.E., *Plast. Massy*, 1996, no. 3, pp. 4–6.
3. RF Patent Appl. 93 009 681/04.
4. Zhubanov, B.A., Almabekov, O.A., Boiko, G.I., *et al.*, *Vysokomol. Soedin., Ser. A*, 1989, vol. 31, no. 12, pp. 2652–2656.
5. Zhubanov, B.A., Arkhipova, I.A., and Almabekov, O.A., *Novye termostoikie geterotsiklicheskie polimery* (New Heat-Resistant Heterocyclic Polymers), Alma-Ata: Nauka, 1979.
6. Kalinina, L.S., Motorina, M.A., Nikitina, N.I., and Khachapuridze, N.A., *Analiz kondensatsionnykh polimerov* (Analysis of Condensation Polymers), Moscow: Khimiya, 1984.
7. Bradulina, L.G., Gavrilova, N.D., Vygodskii, Ya.S., and Matieva, A.M., *Vysokomol. Soedin., Ser. B*, 1999, vol. 41, no. 5, pp. 901–905.
8. Bizhanova, N.B., Abil'din, T.S., Zhubanov, K.A., *et al.*, *Izv. Akad. Nauk Kaz. SSR, Ser. Khim.*, 1981, no. 4, pp. 68–71.
9. Chegolya, A.S., *Doctoral Dissertation*, Moscow, 1968.
10. Zhubanov, B.A., *Polym. Yearbook*, 1987, vol. 4, pp. 149–157.
11. Zhubanov, B.A. and Kravtsova, V.D., *Izv. Nats. Akad. Nauk Resp. Kaz., Ser. Khim.*, 1999, no. 6, pp. 64–70.
12. *Spravochnik khimika* (Chemist's Handbook), Nikol'skii, B.P., Ed., Leningrad: Khimiya, 1971, vol. 2.
13. Golodets, G.I., Pavlenko, N.V., and Prokhorenko, E.V., *Kinet. Katal.*, 1987, no. 3, pp. 625–631.
14. Freidlin, L.Kh. and Sladkova, T.A., *Usp. Khim.*, 1964, vol. 33, no. 6, pp. 664–686.
15. Sokol'skii, D.V., *Gidrirovanie v rastvorakh* (Hydrogenation in Solutions), Alma-Ata: Akad. Nauk Kaz. SSR, 1962.
16. UK Patent 814 631.
17. Shcheglov, N.I., Sokol'skii, D.V., Andreeva, A.A.,

et al., *Sb. Tr. Inst. Khim. Nauk Akad. Nauk Kaz. SSR*, 1966, vol. 14, pp. 167–191.

18. Abil'din, T.S., Batmanova, K.B., and Zhubanov, K.A., *Proc. 5th Int. Symp. of Science of Turkic Languages Countries on Polymers and Composites*, Almaty, 1999, pp. 217–219.
19. Bizhanov, F.B., *Doctoral Dissertation*, Alma-Ata, 1976.
20. Kravtsova, V.D. and Zhubanov, B.A., *Proc. KIEEME Summer Annual Conf.*, Korea, 2000, vol. 1, no. 1, pp. 255–258.
21. Zhubanov, B.A. and Kravtsova, V.D., *Sbornik materialov mezhdunarodnoi nauchno-prakticheskoi konferentsii "Khimiya: nauka, obrazovanie, promyshlennost'. Vozmozhnosti i perspektivy razvitiya"* (Coll. of Papers of Int. Scientific and Practical Conf. "Chemistry: Science, Education, Industry. Possibilities and Prospects of Development"), Pavlodar, 2002, pp. 143–147.
22. Voishchev, V.S., Mikhant'ev, B.I., Sazhin, B.I., *et al.*, *Vysokomol. Soedin., Ser. B*, 1973, vol. 14, no. 5, pp. 361–365.

Russian Journal of Applied Chemistry, Vol. 76, No. 8, 2003, pp. 1310–1314. Translated from Zhurnal Prikladnoi Khimii, Vol. 76, No. 8, 2003, pp. 1346–1350.

MACROMOLECULAR CHEMISTRY AND POLYMERIC MATERIALS

Degradation of Metal 2-Acrylamido-2-methylpropanesulfonate-*N*-Vinylpyrrolidine Copolymers in Aqueous Solutions Containing Different Cations

V. F. Kurenkov, T. A. Zhelonkina, N. A. Ryabysheva, and F. I. Lobanov

Kanan State Technological University, Kazan, Tatarstant, Russia
Stockhausen Eurasia. Industry and Environment Joint-Stock Company, Moscow, Russia

Received April 14, 2003

Abstract—The influence of single- and double-charged cations on degradation of metal 2-acrylamido-2-methylpropanesulfonate-*N*-vinylpyrrolidine copolymers in aqueous solutions in the presence of potassium peroxodisulfate, $K_2S_2O_8$, at 50 and 70°C was studied by viscosimetry.

Degradation of polymers in solutions in the presence of radicals is used to control the molecular weight (MW) and molecular-weight distribution (MWD) of polymers and to prepare partially degraded polymers with the best molecular characteristics, providing their best performance [1]. Previously [2] we have studied the main features of radical degradation of copolymers of sodium 2-acrylamido-2-methylpropanesulfonate (Na-AMS) with *N*-vinylpyrrolidine (N-PV) in aqueous solutions. These polymers exhibit good flocculating [3], adhesion, and antistatic activity [4] and have cross-linking and complexing properties.

As shown previously [1], degradation of polyelectrolytes in aqueous solutions is strongly affected by electrostatic interaction between charged macromolecules and the product of persulfate decomposition, SO_4^{-*} radical ions. Since the strength of such electrostatic interactions depends on the degree of binding of cations with polyanions, the cation nature must affect degradation of copolymers of H-AMS salts with N-VP in aqueous solutions containing persulfate anions. In this study, we analyzed the influence of M cations (M = Li^+, Na^+, K^+, Mg^{2+}, Ca^{2+}, and Ba^{2+}) on the degradation of M-AMS–N-VP copolymers in aqueous solutions in the presence of potassium peroxodisulfate (PP).

EXPERIMENTAL

We studied Na-AMS–N-VP copolymers prepared by radical coplymerization of the monomers in aqueous solutions.

We used H-AMS (Lubrizol 2404) purchased from Lubrizol Corporation (UK), mp 185°C; N-VP purchased from Merck (Germany) and purified by vacuum sublimation in the presence of 0.1% KOH, n_D^{20} = 1.5119; and distilled water. Other chemicals were of chemically pure and analytically pure grades. Potassium peroxodisulfate $K_2S_2O_8$ was twice recrystallized from water. The main compound, determined by redox titration was 97.8%. Sodium 2-acrylamido-2- methylpropanesulfonate (Na-AMS) was prepared by neutralization of an aqueous solution of H-AMS with NaOH.

Copolymerization of Na-AMS with N-VP was performed by the procedure described in [6]. The copolymer was precipitated from an aqueous solution with acetone, filtered off, washed with acetone, and dried in a vacuum at 50°C to constant weight. The parameters of the copolymers studied are listed in the table.

Properties of H-AMS–N-VP copolymers

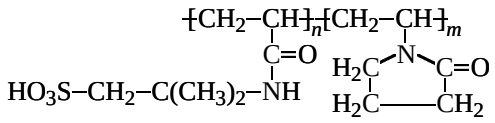

Sample no.	[η], $cm^3\ g^{-1}$	Content of indicated units, mol%	
		H-AMS	N-VP
1	180	89.0	11.0
2	380	78.1	21.9
3	120	50.0	50.0
4	410	50.0	50.0

1070-4272/03/7608-1310 $25.00 © 2003 MAIK "Nauka/Interperiodica"

The content of ionic groups in the copolymer was calculated from the sulfur content [7]. The intrinsic viscosity of polymer solutions, [η], was determined on a VPZh-3 viscometer (d_c = 0.56 mm) by isoionic dilution of a 0.5 M NaCl solution at 30°C.

To convert Na-AMS–N-VP copolymer into the H-form, its solution was passed through a column packed with KU-2 × 8 cation exchanger. The cation exchanger was pretreated in accordance with GOST (State Standard) 10896–78. Single- and double-charged metal salts of the copolymers were prepared by potentiometric titration of solution of H-AMS–N-VP copolymers with KOH or LiOH solution, or by treatment of the copolymer solution with an $Mg(OH)_2$, CaO, or $Ba(OH)_2$ suspension to pH 7 with cooling and stirring. The insoluble residue was filtered off.

Degradation in 0.1% aqueous solutions was initiated by thermolysis of PP initiator at 50 and 70°C. The reaction kinetics was monitored by viscometry [8]. The degradation was performed in a glass reactor equipped with a jacket for temperature control, a magnetic stirrer, a thermometer, a connecting pipe for sampling to measure [η], and a VPZh-3 capillary viscometer (d_c = 0.56 mm) for determining the viscosity of the reaction mixture [8]. A polymer solution placed in the reactor was brought to the required temperature, and PP initiator was added. This time was taken as the degradation onset. The time τ_1 of efflux of the reaction solution was measured intermittently. The reduced viscosity of the solution η_{sp}/c_c, where c_c is the copolymer concentration, was calculated. The $\eta_{sp}/c_c = f(\tau)$ curve, where $\tau = \tau_2 + \tau_1/2$ and τ_2 is the time elapsed from the onset of degradation till the beginning of measurements of the viscosity of the reaction solution, was plotted.

The acidity of the solution was measured with a pH-121 pH meter using an ESL-65-07 glass working electrode and an EVL 1M3 silver chloride reference electrode.

The dependence of the reduced viscosity η_{sp}/c_c of aqueous solutions of Na-AMS–N-VP copolymer (sample no. 3) and various PP concentrations at 50°C on the degradation time is shown in Fig. 1. The fact that the viscosity of the copolymer solution prepared in the absence of the initiator does not change with time indicates that the copolymer is stable under the experimental conditions. Introducing PP and raising its concentration lead to formatiom of SO_4^{-*} radical anions in the reaction solution to deincrease in η_{sp}/c_c owing to macromolecular degradation (curves *2*–*4*). As seen from Fig. 1, the initial η_{sp}/c_c (τ = 0) decreases with increasing PP concentration. This is due

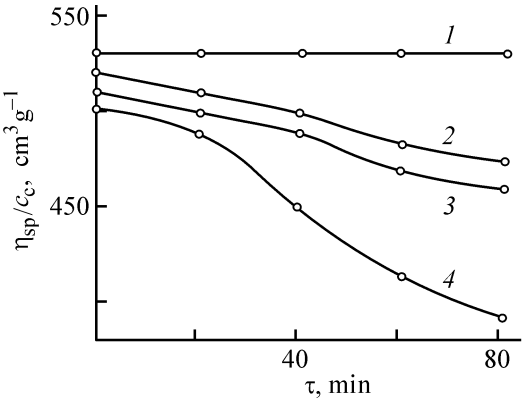

Fig. 1. Reduced viscosity η_{sp}/c_c of aqueous solutions of Na-AMS–N-VP copolymer (sample no. 3) with different PP concentrations vs. the degradation time τ. c_c = 0.1%, 50°C; the same for Fig. 4. [PP]/[copolymer]: (*1*) 0, (*2*) 0.04, (*3*) 0.06, and (*4*) 0.08.

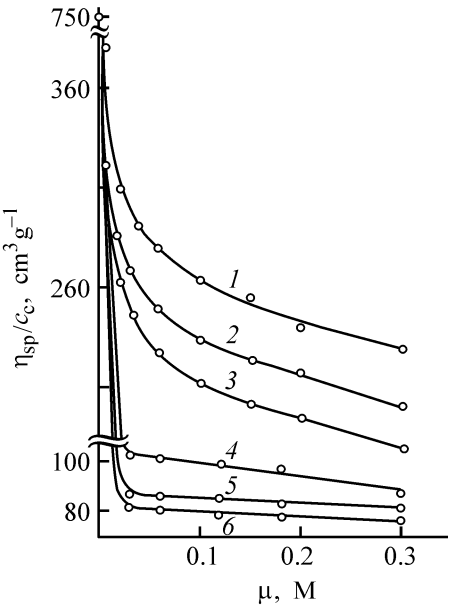

Fig. 2. Reduced viscosity η_{sp}/c_c of aqueous solutions of H-AMS–N-VP copolymer (sample no. 1) vs. the ionic strength μ produced by (*1*) KCl, (*2*) NaCl, (*3*) Li_2CO_3, (*4*) $BaCl_2$, (*5*) $CaCl_2$, and (*6*) $MgCl_2$. c_c = 0.1%; 30°C.

to a dual effect of PP additive: on the one hand, it initiates the copolymer degradation, and, on the other hand, it is a salt making higher the ionic strength μ of the solution.

The dependence of η_{sp}/c_c (c_c = const) of aqueous solutions of H-AMS–N-VP copolymer (sample no. 1) on μ produced by various salts is shown in Fig. 2. It can be seen that η_{sp}/c_c decreases with increasing μ. This is due to weakening of electrostatic repulsion of sulfonate groups along the polymeric chain, which decreases the effective size of macromolecular glob-

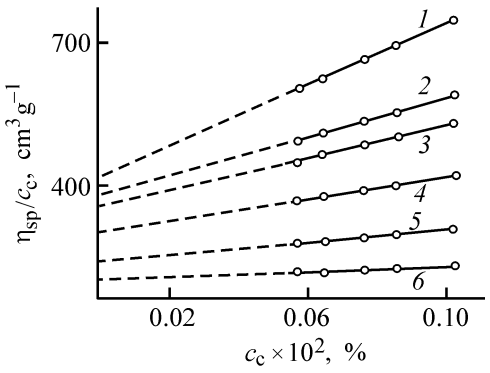

Fig. 3. Reduced viscosity η_{sp}/c_c in 0.5 M NaCl at 30°C of samples taken (*1*) 0, (*2*) 20, (*3*) 40, (*4*) 60, (*5*) 90, and (*6*) 120 min after the onset of degradation of the Na-AMS–N-VP copolymer (sample no. 4) vs. copolymer concentration c_c. Degradation conditions c_c = 0.1 %, 50°C, [PP]/[copolymer] = 0.08.

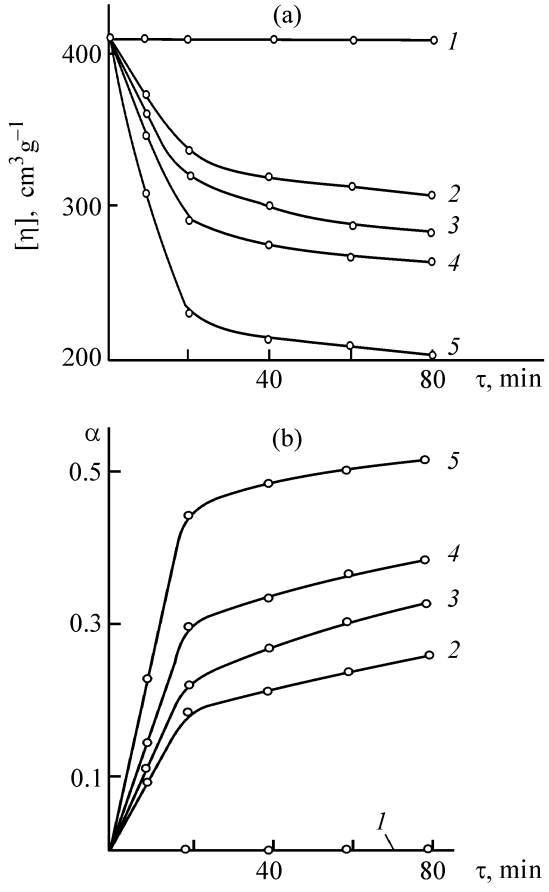

Fig. 4. Viscosity [η] vs. (a) number of ruptures per single macromolecule α and (b) degradation time τ of Na-AMS–N-VP copolymer (sample no. 4) at different PP concentrations. [PP]/[copolymer]: (*1*) 0, (*2*) 0.01, (*3*) 0.02, (*4*) 0.04, and (*5*) 0.08.

ules $(r^2)^{1/2}$. The decrease in η_{sp}/c_c of copolymer solutions at the instant of PP addition (τ = 0) with increasing PP concentration (Fig. 1) has a similar origin.

To estimate the MW of the copolymers in the course of their degradation, we determined [η], since, in accordance with the Mark–Houwink equation, MW ~ [η]. The viscosity was determined from the $\eta_{sp}/c_c = f(c_c)$ dependence obtained by isoionic dilution (0.5 M NaCl, 30°C) of samples of the reaction solution taken in the course of copolymer degradation. Typical $\eta_{sp}/c_c = f(c_c)$ dependences shown in Fig. 3 are linear. The viscosity was determined by extrapolation of these curves to c_c = 0, i.e., $[\eta] = \lim(\eta_{sp}/c_c)$.

The dependence of [η] on the time of Na-AMS–N-VP copolymer degradation is shown in Fig. 4a. In the absence of PP, [η] is constant with time (curve *1*). As the PP concentration and the reaction time increase, the viscosity falls owing to a decrease in the MW of the copolymer, caused by rupture of the macromolecule backbones (Fig. 4a, curves *2*–*5*). The number of ruptures per macromolecule was calculated from the data presented in Fig. 4a by the equation

$$\alpha = ([\eta]_0 - [\eta]_\tau)/[\eta]_\tau, \quad (1)$$

where $[\eta]_0$ and $[\eta]_\tau$ are viscosities of Na-AMS–N-VP copolymer before degradation and after degradation for time τ, respectively.

The dependence of α on the time of Na-AMS–N-VP copolymer degradation is shown in Fig. 4b. The number of ruptures grows with increasing initiator concentration and reaction time. However, the fact that the maximum α does not exceed 0.5 indicates that no low-molecular-weight products are formed.

We studied the influence of the cation nature on the degradation of Na-AMS–N-VP copolymer. These experiments were performed with samples no. 2 (see table) under the same degradation conditions at 70°C. The dependence of [η] in the presence of metal cations on the degradation time is shown in Fig. 5. The viscosity of all the samples decreases with time owing to macromolecular degradation. The viscosity at definite degradation time becomes lower with decreasing cationic radius in the following order: $K^+ > Na^+ > Li^+$ and $Ba^{2+} > Ca^{2+} > Mg^{2+}$. Similar dependences were obtained for degradation at 50°C and with copolymer samples having another ratio of AMS and N-VP units.

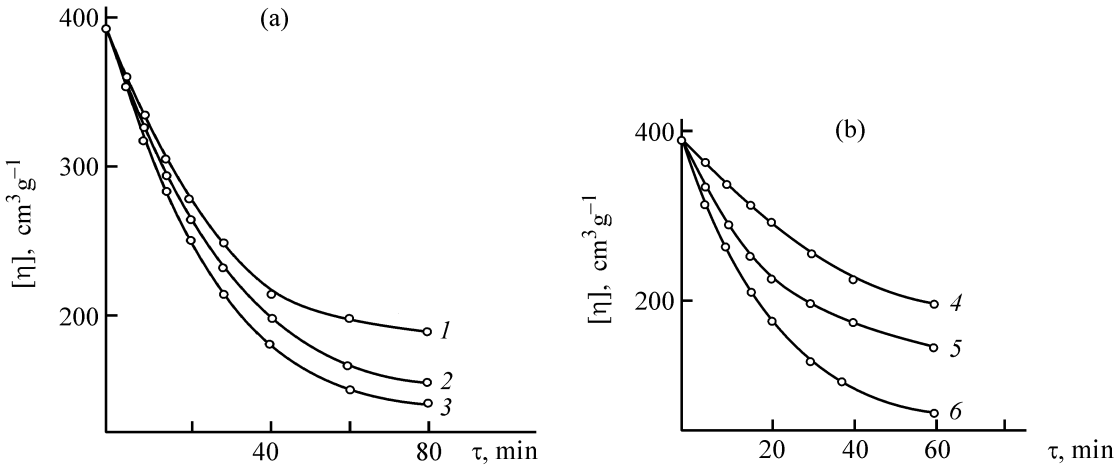

Fig. 5. Viscosity [η] of H-AMS–N-VP copolymer solution (sample no. 2) containing (*1*) K^+, (*2*) Na^+, (*3*) Li^+, (*4*) Ba^{2+}, (*5*) Ca^{2+}, and (*6*) Mg^{2+} ions vs. degradation time τ. c_c = 0.1%, 70°C. [PP]/[copolymer]: (a) 0.005 and (b) 0.02.

To understand the influence of metal cations on the degradation of copolymers of H-AMS salts with N-VP, we considered the following ionic equilibria in aqueous solutions:

$$\underset{\mathbf{I}}{A^-X^+} \rightleftarrows \underset{\mathbf{II}}{A^-} \;||\; \underset{\mathbf{III}}{X^+} \rightleftarrows A^- + X^+. \qquad (2)$$

where A^- is sulfonate anion of the macromolecule; X^+ is the cation; **I**, **II**, and **III** are the contact ion pair, solvent-separated ion pair, and free ions, respectively.

Previously we have found that the degree of binding of cations with polyanions of H-AMS– N-VP copolymers in aqueous solutions increases in the following order: $K^+ < Na^+ < Li^+$ [9] and $Ba^{2+} > Ca^{2+} > Mg^{2+}$ [9, 10]. Ionic equilibrium (2) is shifted to the left with increasing μ and degree of binding of the cations with the polysulfonate anions. This weakens the strength of intra- and intermolecular interactions between similarly charged species in the reaction system, thus changing the reactivity of the charged macromolecules with respect to SO_4^{-*} radical anions. The weakening of electrostatic repulsion between similarly charged groups fixed along the polymeric chain makes smaller the effective size of macromolecular globules $(r^2)^{1/2}$, thus decreasing η_{sp}/c_c (μ = const) in the order $K^+ > Na^+ > Li^+$ and $Ba^{2+} > Ca^{2+} > Mg^{2+}$ (Fig. 2). An increase in the degree of binding of cations with polysulfonate anions in the course of degradation of H-AMS–N-VP copolymers weakens the electrostatic repulsion between SO_4^{-*} radical anions and sulfonate groups of the macromolecules. As a result, the degradation of the macromolecules becomes more pronounced and [η] of copolymer solutions (τ = const) decreases in the order $Li^+ > Na^+ > K^+$ (Fig. 5a) and $Mg^{2+} > Ca^{2+} > Ba^{2+}$ (Fig. 5b).

CONCLUSIONS

(1) The viscosity [η] of aqueous solutions of metal 2-acrylamido-2-methylpropanesulfonate-*N*-vinylpyrrolidine copolymers subjected to radical degradation at 50 and 70°C can be controlled by varying the nature of metal cations, initiator concentration, and degradation time.

(2) The viscosity of degraded copolymers [η] decreases in the order $Li^+ > Na^+ > K^+$ and $Mg^{2+} > Ca^{2+} > Ba^{2+}$ owing to a decrease in electrostatic repulsion of SO_4^{-*} radical anions of the initiator, with charged macromolecules, with the degree of binding of the cations with the macromolecular anions increasing in the order $K^+ < Na^+ < Li^+$ and $Ba^{2+} < Ca^{2+} < Mg^{2+}$.

ACKNOWLEDGMENTS

This study was supported financially by Research and Development Foundation of the Tatarstan Republic (project code 07-7.1-104/2002).

REFERENCES

1. Kurenkov, V.F., Khartan, Kh.-G., and Lobanov, F.I., *Zh. Prikl. Khim.*, 2002, vol. 75, no. 7, pp. 1057–1068.
2. Kurenkov, V.F., Zaitseva, N.N., Zhelonkina, T.A., and Lobanov, F.I., *Zh. Prikl. Khim.*, 2003, vol. 76, no. 6, pp. 1009–1012.
3. Kurenkov, V.F., Sharapova, Z.F., and Khairullin, M.R., *Zh. Prikl. Khim.*, 1999, vol. 72, no. 8, pp. 1374–1378.

4. Shevtsova, S.A., Borkhanova, T.A., Zhelonkina, T.A., and Kurenkov, V.F., Abstracts of Papers, *Tret'i Kirpichnikovskie chteniya* (Third Kirpichnikov Reading), Kazan, March 25–27, 2003, pp. 308–311.
5. Morawetz, H., *Macromolecules in solution*, New York: Wiley, 1965.
6. Kurenkov, V.F., Khabibullina, G.Z., and Zaitseva, N.N., *Zh. Prikl. Khim.*, 2002, vol. 75, no. 11, pp. 1892–1895.
7. Charlot, G., *Les Methods de la Chemie Analytique. Analyse quantitative Minerale*, Quatrieme Edition, Paris: Masson, 1961.
8. *Praktikum po khimii i fizike polimerov* (Practical Course of Polymer Chemistry and Physics), Kurenkov, V.F., Ed., Moscow: Khimiya, 1990.
9. Kurenkov, V.F., Kolesnikova, I.Yu., and Solov'ev, D.A., *Zh. Prikl. Khim.*, 2001, vol. 74, no. 3, pp. 490–493.
10. Kurenkov, V.F., Kolesnikova, I.Yu., and Antonovich, O.A., *Zh. Prikl. Khim.*, 2002, vol. 75, no. 9, pp. 1521–1524.

Russian Journal of Applied Chemistry, Vol. 76, No. 8, 2003, pp. 1315–1318. Translated from Zhurnal Prikladnoi Khimii, Vol. 76, No. 8, 2003, pp. 1351–1354.

MACROMOLECULAR CHEMISTRY AND POLYMERIC MATERIALS

Low-Waste Process for Preparing Ketopantolactone, with Electrochemical Recovery of Bromine

L. V. Kaabak, N. P. Stepnova, A. V. Khudenko, and A. P. Tomilov

State Research Institute of Organic Chemistry and Technology, Moscow, Russia

Received January 17, 2003

Abstract—The process parameters of dehydrogenation of pantolactone with bromine in chloroform and the possibility of bromine recycling by electrolysis of hydrogen bromide formed in the synthesis of ketopantolactone were studied.

Ketopantolactone (KPL) shows promise for pharmaceutical industry. The known methods for its preparation are based on oxidative dehydrogenation of pantolactone (PL).

There are published data on oxidation of PL with oxygen in the presence of a catalyst [1, 2], as well as with calcium hypochlorite [3–5], potassium bromate [6, 7], bromine [8–10], and organic peroxides [11]. These data show that PL is catalytically oxidized at 180–300°C and elevated pressure, which requires complex equipment; the target product undergoes partial tarring. With chlorine or calcium hypochlorite, abundant nonutilizable wastewater is formed. The reaction with bromine as dehydrogenating agent proceeds by the scheme:

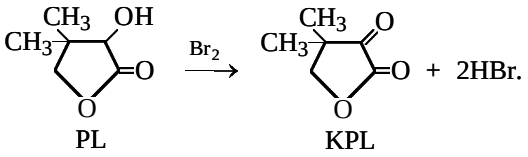

PL KPL

This scheme suggests formation of an equivalent amount of hydrogen bromide, which is suitable for high-yield recovery of recyclable bromine. This option was recognized as the most promising and was technologically developed.

In [10], dehydrogenation of PL with bromine in refluxing carbon tetrachloride was recommended; the reaction is complete within 5–8 h. In [9], this period was reduced to 1 h by adding a minor amount of water to the reaction mixture.

Presently, carbon tetrachloride is considered unsuitable as solvent for environmental reasons and its production is to be closed [12]. Therefore, we replaced carbon tetrachloride with chloroform in our experiments. Next, the possibility of recovery of bromine from an aqueous solution of hydrogen bromide formed in the synthesis was analyzed.

The initial experiments on dehydrogenation of PL in chloroform failed. The reaction was incomplete even after refluxing the PL solution in chloroform with bromine for 14 h, probably because of the lower boiling point of $CHCl_3$, compared to CCl_4. The situation was substantially improved by introducing minor amounts of water to the reaction mixture: When 10 ml of water was added to 60 ml of chloroform, the reaction was complete after heating for 3.5 h. However, further increase in the content of water decreased the weight of the target product. For example, upon adding 60 ml of water, the yield of KPL after refluxing for 5 h was only 48%, and at water content below 10% the reaction was decelerated and HBr evaporated.

An important role is also played by the PL concentration in chloroform. Table 1 shows that, at the PL : chloroform ratio of 1 : 7.5, the KPL yield remains fairly high, but falls dramatically with the amount of chloroform decreasing further; the reaction does not go to completion despite longer heating time. Thus, we developed a procedure for preparing KPL in 92–95% yield.

All the above-described experiments were performed in a 150-ml reactor charged with 4 g of PL. To test the suitability of the process for large-scale application, we carried out an experiment in a 2-l reactor charged with 100 g of PL, 900 ml of chloroform, 160 ml of water, and 137 g of bromine. The very first run showed that, on passing to a larger reactor,

1070-4272/03/7608-1315 $25.00 © 2003 MAIK "Nauka/Interperiodica"

Table 1. Influence of the PL concentration in chloroform on the yield of KPL (4 g of PL, 5.27 g of Br_2)

$CHCl_3$, ml	Water, g	PL : $CHCl_3$ ratio	Yield of KPL, %
40	1.0	1 : 10	82.8*
30	5.5	1 : 7.5	91.8
20	5.0	1 : 5.0	80.0
10	2.5	1 : 2.5	30.0**

* 7-h refluxing. ** The reaction was incomplete in 8 h.

Table 2. Influence of the electrolysis mode on the degree of bromine recovery (anolyte volume 500 ml)

HBr charge, g	*I*, A	*Q*, A h	Br_2 obtained	
			g	%
196	10	58	112	64
217	10 → 5	78	197	87
213	10 → 5	71	176	86
213	10 → 5 → 2	72	194	91

the reaction is significantly decelerated: Upon refluxing of the mixture for 3 h 50 min, only 47% of the charged PL reacted. Upon further refluxing for 3 h 30 min, PL was 75% converted. Our attempt to accelerate the reaction by illuminating the reaction mixture with a 300-W incandescent lamp was successful: Upon 45-min illumination, PL fully entered into the reaction, and the yield of isolated KPL was 85%.

Further experiments showed that, under intensive illumination, the reaction was complete within 15–20 min, but the yield of KPL decreased to 70–79%. Thus, illumination intensifies not only oxidative dehydrogenation but also side reactions, which have, most probably, the radical nature. By varying the power of the light source and the distance separating it from the reactor, we empirically chose the conditions at which the reaction was complete within 2 h and the yield of KPL based on the reacted PL was within 82–85%.

To free the HBr solution from organic impurities, the aqueous layer was distilled on a film evaporator. First, water containing unchanged bromine and chloroform dissolved in the aqueous layer was distilled off at 100–102°C. Then the vapor temperature increased, and the HBr–H_2O azeotrope containing 48% hydrogen bromide was distilled off at 123–124°C. The bottoms contained ca. 8 g of a thick tar composed, most probably, of the products of side reactions accompanying the dehydrogenation of PL. The distilled-off aqueous phase, containing bromine and chloroform, was recycled, and the HBr–H_2O azeotrope was subjected to electrolysis for recovery of bromine.

Bromine was recovered in the cathode chamber of a filter-press electrolyzer under permanent extraction of the evolving bromine with chloroform. Electrolysis was performed in the batch mode, the current lowered stepwise. The initial current density was 0.25 A cm^{-2}; after 50% of the calculated amount of electricity *Q* was passed, it was decreased to 0.10 A cm^{-2}, and the remaining 15% of the electricity was applied at a current density of 0.05 A cm^{-2}. In this mode, it is possible to recover over 90% of the bromine present in solution in the form of bromide ions. The effect of a stepwise decrease in the current density is clearly illustrated by Table 2. It is reasonable to utilize the depleted anolyte containing 3–5% HBr instead of water in further KPL synthesis.

In the experiments utilizing the generated bromine-containing solutions, the yield of KPL was 83 and 88%. A control run with pure reactants under the identical conditions gave an 85% yield.

The general flowsheet of the suggested process is shown below.

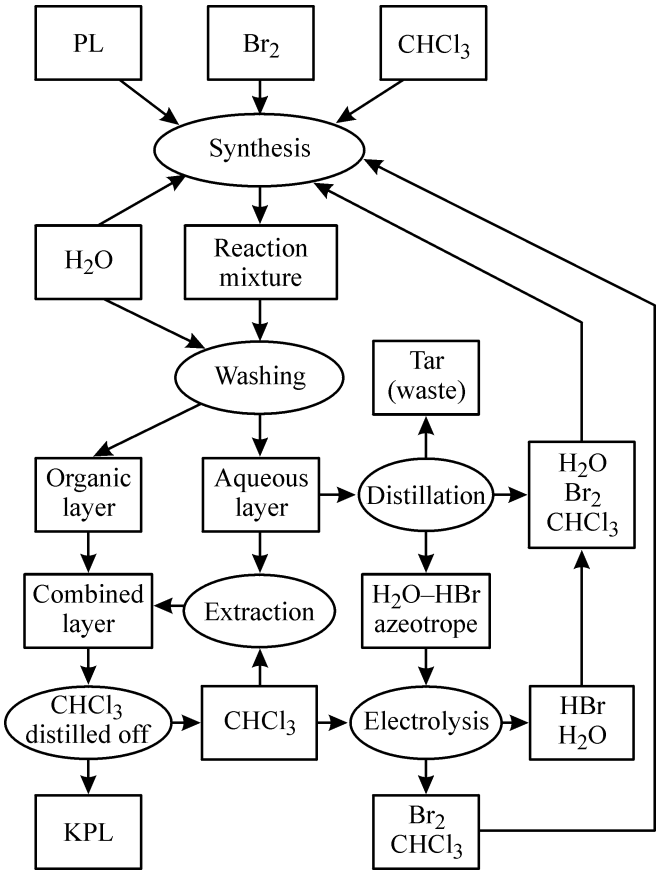

Flowsheet of the KPL synthesis involving bromine recovery.

EXPERIMENTAL

In this study, we used *DL*-pantolactone (mp 74–77°C). The other reactants (bromine and chloroform) were of chemically pure grade.

Into a 2-l flask equipped with a reflux condenser and a stirrer, 100 g of PL, 960 ml of chloroform (870 ml of recycled and 90 ml of fresh), 150 ml of water (or depleted anolyte), and 137 g of bromine were introduced. The reaction mixture was illuminated with a 300-W incandescent lamp and refluxed for 2 h. The reaction was regarded as complete when no traces of PL were revealed by gas chromatography. The reaction mixture was transferred into a separatory funnel; for better separation of the aqueous layer, 40 ml of water was added. The separated organic layer was washed with 40 ml of water. This water was combined with the separated aqueous layer, which was a concentrated solution of hydrogen bromide. The resulting aqueous layer was treated with chloroform (2 × 30 ml). The extract was combined with the organic layer, and chloroform was distilled off. The hot bottoms were transferred into a beaker for crystallization. After 1 h, the crystalline KPL precipitate had a constant weight of 83.7 g, mp 64–66°C. The waste was ca. 350 ml of an aqueous hydrogen bromide solution containing 127 g of HBr and 11.7 g of bromine.

Distillation of the aqueous layer on the film evaporator yielded 84 ml of a fraction containing water, bromine, and chloroform, 255 ml of the HBr–H_2O azeotrope, and 8 g of the bottoms containing the reaction by-products.

The HBr–H_2O azeotrope mixture was electrolyzed in a filter-press electrolyzer with the anode and cathode spaces separated by a NAFFION-403 membrane. A stainless-steel plate served as cathode, and DEZ-3 graphite used in chlorine production, as anode. Prior to being used, graphite was impregnated with a paraffin–polyethylene melt. The electrodes and the membrane were separated by 4 mm. The catholyte circulation was effected by a gas lift system, and anolyte circulation, by a rotary pump. The solution leaving the anolyte entered a backup reservoir where it passed through a chloroform layer. The bromide formed on the anode was dissolved in a chloroform layer. When the required concentration was reached, the solution of bromine in chloroform was fed to synthesis of KPL. The figure presents the general view of the setup for bromine recovery.

The anode chamber of the electrolyzer was charged with 500 ml of a 33.4% solution of HBr containing

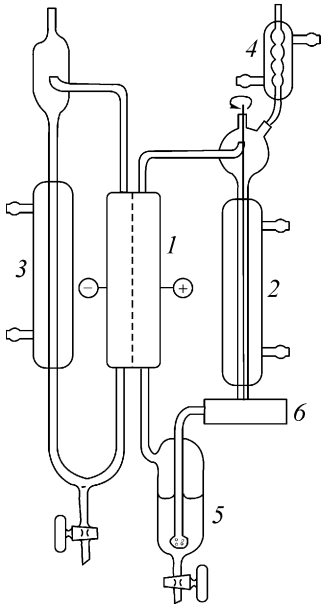

Schematic of the setup for electrochemical recovery of bromine: (*1*) electrolyzer, (*2*) anode circuit cooler, (*3*) cooler at the cathode off-gas line, (*4*) reflux condenser, (*5*) backup reservoir, and (*6*) rotary pump.

213.4 g of the bromide ion. As anolyte was used 150 ml of a HBr solution of the same concentration. Chloroform (80 ml) was poured into the backup reservoir. Electrolysis was performed in three steps at current densities of 0.25, 0.10, and 0.05 A cm^{-2}, respectively. The anolyte temperature during electrolysis was kept within 12–15°C. After each step, the solution of bromine in chloroform was discharged from the backup reservoir, and a fresh portion of chloroform (88 ml) was added. A total of 188.4 g of bromine dissolved in 240 ml of chloroform was obtained in our experiment. Waste anolyte consisted of 490 ml of the aqueous solution of HBr containing 24.7 g of HBr. Bromine was recovered to 88%. The waste anolyte

Table 3. Major parameters of a typical run*

Step no.	*I*, A	*I*/*S*, A cm^{-2}	τ, h	*V*, V	*Q*, A h	Br_2 obtained, g	CE, %
1	10	0.25	3.6	7.5	36.0	100.3	93.3
2	5	0.124	4.4	5.0	22.0	55.4	84.4
3	2	0.05	6.8	3.2	13.6	32.6	80.5
Total						188.4	88.0

* *S* is the electrode surface area; *V*, voltage; and CE, current efficiency.

was used in the synthesis instead of water. The electrolysis mode and bromine yields in each step are presented in Table 3.

CONCLUSIONS

(1) Pantolactone can be dehydrogenated with bromine in chloroform.

(2) At the pantolactone : chloroform : water ratio of 1 : 7.5 : (0.85–0.90) in the reaction mixture, ketopantolactone can be prepared in 82–85% yield. The process can be accelerated 3–4-fold by illuminating the reaction mixture.

(3) A method for electrochemical recovery of bromine and its recycling was developed. Three percent of bromine is lost in the developed scheme.

REFERENCES

1. JPN Patent 58 126 880.
2. EEC Patent 86 322.
3. FRG Patent 3 242 560.
4. EEC Patent 109 625.
5. EEC Patent 6145.
6. Abc, F., *Kagaku*, 1991, vol. 84, no. 4, pp. 151–152.
7. JPN Patent 01 305 053.
8. Ojima, J., Kugure, T., and Yodo, Y., *Org. Synth.*, 1985, vol. 6, no. 1, p. 18.
9. JPN Patent 5 927 882.
10. JPN Patent 7 988 257.
11. Tanaka, M., *Angew. Chem., Int. Ed.*, 1984, vol. 96, no. 7, pp. 519–523.
12. Zanaveskin, L.N. and Aver'yanov, V.N., *Khim. Prom–st.*, 2002, no. 9, pp. 4–21.

Russian Journal of Applied Chemistry, Vol. 76, No. 8, 2003, pp. 1319–1322. Translated from Zhurnal Prikladnoi Khimii, Vol. 76, No. 8, 2003, pp. 1355–1358.

MACROMOLECULAR CHEMISTRY AND POLYMERIC MATERIALS

2,2,4-Trimethyl-1,2-Dihydroquinoline Hydrochloride as Coagulant for Butadiene-Styrene Latices

S. S. Nikulin, V. N. Verezhnikov, T. N. Poyarkova, and Zh. V. Shmyreva

Voronezh State University, Voronezh, Russia

Voronezh State Academy of Forestry Engineering, Voronezh, Russia

Received April 16, 2003

Abstract—Coagulating action of 2,2,4-trimethyl-1,2-dihydroquinoline hydrochloride in separating butadiene-styrene rubber from latex is studied, and the properties of vulcanizate based on rubbers prepared by this procedure are examined.

The use of nitrogen-containing compounds in separation of rubber prepared by emulsion copolymerization allows, in some cases, a considerable decrease in the consumption of coagulating agents [1]. Of special interest in this regard are polymeric quaternary ammonium salts and, in particular, poly(*N*,*N*-dimethyl-*N*,*N*-diallylammonium chloride) (PDDAC), which, as shown in a series of publications [2–4], demonstrates high performance in separating rubber from latices when taken both separately and in combination with other coagulating agents.

The possibility of using PDDAC in a real process was confirmed in pilot tests [3]. However, industrial application of this reagent is limited by its short supply and considerably higher cost as compared to such commonly used coagulant as NaCl. Therefore, searching for new more readily available coagulants allowing not only reduction of the mineral salt consumption or its exclusion from the process at all, but also improvement of the performance characteristics of the resulting products (rubbers, rubber stocks and vulcanizates) is a topical task.

Desired nitrogen-containing compounds for separating rubber from latex must have a dual function, operating as a coagulant and antioxidant (stabilizer of polymer), provided that, in the course of coagulation, they will enter the composition of the resulting rubber crumb and will not be removed from the system. The antioxidant properties of a coagulant will allow lower consumption or complete elimination of expensive antioxidants, which are introduced into the latex prior to the coagulation stage in production of emulsion rubber. This should compensate to a considerable extent for the expenses for acquisition of an expensive nitrogen-containing coagulant, making rubber separation from the latex more cost-efficient.

In [5], it was suggested to use for salt-free coagulation of latices of butadiene-styrene and butadiene-acrylonitrile rubbers, a coagulant, poly(*N*-3,5-di-*tert*-butyl-4-hydroxytolyl) ethylenimine synthesized by the Mannich reaction, which also exhibits stabilizing properties for rubber. A similar bifunctional polymeric coagulant was also described in [6].

In this context, low-molecular-weight cationic reagents, such as 2,2,4-trimethyl-1,2-dihydroquinoline (DHQ), which can inhibit oxidation processes [7] and increase the stability of polymers against ozone aging [8], may be promising. The initial dihydroquinoline is a condensation product of such readily available organic compounds as aniline and acetone [9, 10].

Previously [11] we reported on a study of the kinetics of coagulation and coagulating performance of DHQ hydrochloride (DHQHC) in separating rubber from latex of emulsion polybutadiene (EPB) produced by the industry in limited amounts. It was of interest to assess the efficiency of DHQ salts in separating butadiene-styrene rubber as the most widely used rubber of general purpose.

The goal of this study was to estimate the coagulating efficiency of the water-soluble organic ammonium salt, DHQHC, in separating commercial butadiene-styrene rubbers from latices.

DHQ salts were prepared as in [9, 10].

1070-4272/03/7608-1319 $25.00 © 2003 MAIK "Nauka/Interperiodica"

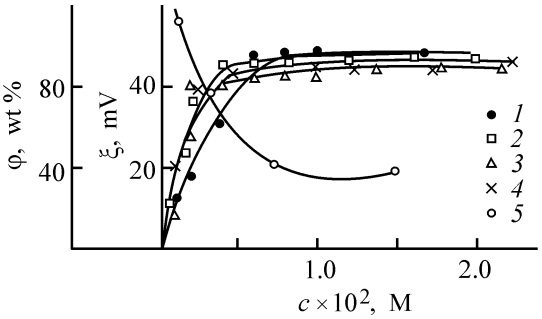

Fig. 1. (*1–4*) Rubber yield φ and (*5*) electrokinetic potential of latex particles, ξ, vs. the DHQHC concentration *c*. Disperse phase concentration (g l^{-1}): (*1*) 100, (*2*) 50, (*3*) 20, and (*4*, *5*) 7.

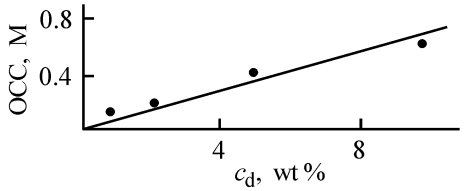

Fig. 2. Optimal coagulation concentration OCC vs. the disperse phase concentration in the latex c_d.

In coagulation experiments, we used SKS-30 ARK and SKS-30 ARKPN commercial latices. As emulsifier in synthesis of latices we used suing soap based on tall oil. The characteristics of the latices were as follows.

Latex	SKS-30 ARK	SKS-30 ARKPN
Bound styrene content, %	21.9	22.2
Polymer content, wt %	21.2	18.5
Surface tension, 10^3 J m^{-2}	63.7	56.5
Radius*, nm	50.8	46.7

* Radius of the latex globules was estimated by the Rayleigh equation from optical data [12].

Rubbers were separated from latices in a coagulation unit comprising a stirred vessel placed in a thermostat. The vessel was filled with a latex (25 ml) and allowed to stand for 10–15 min at a prescribed temperature. Then calculated amount of aqueous DHQHC (c = 3.0–5.0 wt %) was introduced with continuous stirring into the latex, and the system was acidified with aqueous sulfuric acid (c = 1.0–2.0 wt %). The coagulation efficiency was monitored visually by the transparency of serum (aqueous phase remaining after rubber separation from latex) and also by the weight of the resulting coagulum.

A reference sample was separated from the latex by coagulation with NaCl (200–250 g kg^{-1} rubber). The reference and test rubber samples were separated from the serum and dried in an oven at 75–80°C.

In the first stage, it was appropriate to make a preliminary estimate of the coagulation performance of one of the above-indicated salts. Therefore, we studied the influence of the DHQHC concentration on the amount of coagulum at various concentrations of the disperse phase. The results obtained are given in Fig. 1.

The results show that, if DHQHC is used as a coagulant, the disperse phase concentration affects the rubber separation from the latex only slightly over the investigated concentration range. With increasing c_d, the rubber separation curves shift to higher DHQHC concentrations. The optimal coagulation concentration (OCC), defined as the DHQHC concentration corresponding to flattening out of the curve, grows insignificantly with increasing c_d (Fig. 2). At the same time, as demonstrated earlier [13], c_d is one of the most important parameters in coagulation with NaCl. In this case, decreasing the concentration of the disperse phase in the latex results in abruptly increasing coagulant consumption. The lack of a significant effect of c_d on the coagulation is an important advantage of DHQHC as a coagulant, since, in real processes, c_d may vary over a rather wide range, which, naturally, is reflected in the coagulant consumption.

With DHQHC as a coagulant, rubber separation from the latex must proceed preferentially by the neutralization mechanism through DHQHC interaction with anionic emulsifiers and latex stabilizer (Leukanol) to give insoluble complexes. In this case, the precipitation curves must have extrema caused by recharging of particles at concentrations exceeding the optimal value, corresponding to neutralization of their surface charge [13, 14]. At the same time, the precipitation curves in Fig. 1 show no peak or latex restabilization branch corresponding to the assumed recharging of the particles and increase in the positive surface charge at an excess of the coagulant.

To clarify the question of particle recharging upon introduction of excess DHQHC into the latex, we measured the electrophoretic mobility of the latex as influenced by the DHQHC concentration. The electrophoretic velocity was determined by the moving boundary technique, using a Chaikovskii apparatus [15]. The electrokinetic potential ξ was estimated by the Helmholtz–Smoluchowski equation

$$\xi = \eta U/\varepsilon\varepsilon_0 H,$$

where η is the viscosity of water (1×10^{-3} Pa s); U, mean electrophoretic velocity (m s^{-1}); ε, dielec-

Table 1. Chemical composition of SKS-30 ARK and SKS-30 ARKPN rubbers

Characteristic	Reference (NaCl)	Test samples (DHQHC)
Organic acids, wt %	4.50/5.40	4.95/5.58
Organic acid soaps, wt %	0.13/0.15	Absent
Weight loss for drying, %	0.21/0.23	0.19/0.15
Ash content, wt %	0.28/0.26	0.10/0.09
Iron, wt %	0.0023/0.0021	0.0029/0.0026
Copper, wt %	0.00011/0.0001	0.0001/0.0001
Bound styrene, wt %	22.7/23.1	22.7/23.1

Table 2. Mechanical characteristics of vulcanizates based on SKS-30 ARK and SKS-30 ARKPN rubbers

Characteristic	Reference (NaCl)	Test samples (DHQHC)
Nominal tensile strength, MPa	27.5/28.1	27.9/28.7
Relative elongation at break, %	590/570	610/585
Relative residual deformation after break, %	14/12	12/12
Heat aging resistance coefficient (by strength)	0.57/0.61	0.62/0.65

tric constant; ε_0, permittivity of free space (8.85×10^{-12} F m^{-1}); H, electric gradient (V m^{-1}).

The results of the electrophoretic measurements suggest no recharging of the latex particles near OCC, and, therefore, the lack of the latex restabilization effect (no maximum in the φ–c curves).

Previously, we have reported a similar phenomenon observed in coagulation of latex of emulsion polybutadiene with DHQHC [11]. In both cases, the lack of the latex restabilization effect in the presence of an excess coagulant is, evidently, an indication of a small adsorption activity of DHQHC at the aqueous phase–polymer interface (in the absence of the electrostatic interaction with anions of the emulsifier). This is indirectly confirmed by the fact that such an anomaly was not observed with colloidal cationic surfactants as coagulants, for example, with cetylpyridinium bromide [13, 14] demonstrating high surface activity. However, the suggested interpretation requires further experimental verification.

A chemical analysis of rubbers separated from latices with DHQHC showed that the reference and test samples are identical in all basic parameters. However, it should be pointed out that the test rubber samples contain virtually no organic acid soaps, which is an important advantage. Also, these samples are characterized by lower weight loss for drying and lower ash content (Table 1).

Mechanical tests of vulcanizates based on SKS-30 ARK and SKS-30 ARKPN rubbers showed that the test rubber samples separated from the latex with DHQHC are close in all the basic parameters to the reference samples separated with NaCl (Table 2).

It follows from Table 2 that the vulcanizates based on the rubber separated from the latex with DHQHC demonstrate a slight increase in the heat aging resistance, suggesting that DHQHC and products of its interaction with components of the emulsion system, remaining in the rubber after its separation from the latex, act as antioxidants, even though to a small extent.

CONCLUSIONS

(1) It was demonstrated in studying the coagulation effect of 2,2,4-trimethyl1,2-dihydroquinoline in separating butadiene-styrene rubbers from latices that the disperse phase concentration affects only slightly the rubber separation from the latex over the range investigated.

(2) Properties of rubbers, rubberstocks, and vulcanizates obtained in this study from the experimental samples differ only slightly from those of reference samples obtained by the conventional procedure using NaCl.

REFERENCES

1. Verezhnikov, V.N., Nikulin, S.S., Poyarkova, T.N., and Garshin, A.P., *Vestn. Tambov. Univ.*, 1997, vol. 2, no. 1, pp. 47–52.
2. Garshin, A.P., Nikulin, S.S., Shapovalova, N.N., *et al.*, *Proizv. Ispol'z. Elastom.*, 1994, no. 11, pp. 2–6.
3. Garshin, A.P., Nikulin, S.S., Shapovalova, N.N., *et al.*, *Proizv. Ispol'z. Elastom.*, 1994, no. 12, pp. 9–14.
4. Nikulin, S.S., Verezhnikov, V.N., Poyarkova, T.N., and Dankovtsev, V.A., *Zh. Prikl. Khim.*, 2000, vol. 73, no. 5, pp. 833–836.
5. USSR Inventor's Certificate, no. 859377.
6. Ponomareva, I.V., Tsarev, O.P., Podalinskii, A.V., and Yurchuk, T.E., *Kauchuki emul'sionnoi polimerizatsii. Sintez i modifikatsiya: Materialy I Vsesoyuznoi konferentsii po emul'sionnym kauchukam* (Emul-

sion Rubbers. Synthesis and Modification: Proc. 1st All-Union Conf. on Emulsion Rubbers), Moscow: TsNIITEneftekhim, 1983, pp. 29–31.

7. *Khimicheskie dobavki k polimeram: Spravochnik* (Chemical Additives for Polymers: A Handbook), Maslova, I.P., Ed., Moscow: Khimiya, 1981.
8. *Khimikaty dlya polimernykh materialov: Spravochnik* (Chemicals for Polymeric Materials: A Handbook), Gorbunov, B.N., Ed., Moscow: Khimiya, 1984.
9. *Organic Synthesis. An Annual Publication of Satisfactory Methods for the Preparation of Organic Chemicals*, New York: Wiley, 1946–1952, vols. 26–32.
10. Creig, D.J., *J. Am. Chem. Soc.*, 1952, vol. 74, no. 18, pp. 4512–4520.
11. Nikulin, S.S., Verezhnikov, V.N., Poyarkova, T.N., and Shmyreva, Zh.V., *Zh. Prikl. Khim.*, 2000, vol. 73, no. 1, pp. 144–148.
12. *Kolloidnaya khimiya sinteticheskikh lateksov* (Colloid Chemistry of Synthetic Latices), Neiman, R.E., Ed., Voronezh: Voronezh. Gos. Univ., 1984.
13. Verezhnikov, V.N., Nikulin, S.S., Poyarkova, T.N., and Vostrikova, G.Yu., *Zh. Prikl. Khim.*, 2000, vol. 73, no. 10, pp. 1720–1724.
14. Verezhnikov, V.N., Poyarkova, T.N., Nikulin, S.S., and Kurbatova, N.A., *Kolloidn. Zh.*, 2000, vol. 62, no. 1, pp. 26–30.
15. Neiman, R.E., Kiseleva, O.G., Egorov, A.K., and Vasil'eva, T.M., *Kolloidnaya khimiya sinteticheskikh lateksov: Uchebnoe posobie* (Colloid Chemistry of Synthetic Latices: A Textbook), Voronezh: Voronezh. Gos. Univ., 1984.

Russian Journal of Applied Chemistry, Vol. 76, No. 8, 2003, pp. 1323–1326. Translated from Zhurnal Prikladnoi Khimii, Vol. 76, No. 8, 2003, pp. 1359–1362.

MACROMOLECULAR CHEMISTRY AND POLYMERIC MATERIALS

Effect of Sodium Chloride and Temperature on the Efficiency of Rubber Separation from Butadiene-Acrilonitrile Latex with Cationic Polyelectrolyte

V. N. Verezhnikov, G. Yu. Vostrikova, and T. N. Poyarkova

Voronezh State University, Voronezh, Russia

Received January 15, 2003

Abstract—Initial flocculation rate of SKN-26SM butadiene-acrylonitrile rubber and the polymer yield are studied in relation to the concentration of the cationic polyelectrolyte, poly(dimethyldiallylammonium chloride), at various NaCl concentrations and, in experiments on rubber separation, also at various temperatures.

In previous studies [1, 2] we have demonstrated that, in separating polymers from synthetic latices with a cationic polyelectrolyte (CPE), the maximum flocculating effect, typical of high-molecular-weight flocculants, is observed only at relatively low rubber concentrations (c_d < 10–50 g l^{-1}). At higher c_d, the flocculation curves φ–c_{CPE} (φ is the polymer coagulation efficiency, wt %) no longer show a restabilization branch, so that the initial rise in φ with increasing c_{CPE} ends in attainment of a constant limiting value corresponding to complete polymer separation. A similar effect was observed in [3] when studying flocculation of kaolin suspensions with copolymers of acrylamide and quaternary ammonioalkyl acrylates. Such a behavior is associated with the observed adsorption layers of the flocculant macromolecules are formed on the surface of disperse phase particles [1–3] and with processes occurring in these layers [4–7].

It may be suggested that the occurrence (or lack) of the latex flocculation optimum depends not only on the disperse phase concentration, but also on other factors influencing the flocculation conditions, such as ionic strength and temperature. There are only a few experimental studies concerned with this problem. Gregory [8] measured the flocculation rate of a polystyrene latex under the action of a cationic polyelectrolyte and demonstrated that introduction of an inorganic salt extends the flocculation range as a result of decreased range of electrostatic repulsive forces. Matsumotu and Adachi have shown [9] that, at high ionic strength, flocculation in emulsifier-free polystyrene latex under the action of a cationic polyelectrolyte proceeds by the nonequilibrium flocculation mechanism [6, 7]. Finally, there is no information in the literature concerning the effect of temperature on the flocculation efficiency in colloid dispersions and, in particularly, in latices.

In this study, we analyzed the effects of the NaCl concentration and temperature on the flocculation rate and the efficiency of rubber separation from butadiene-acrylonitrile latex under the action of the cationic polyelectrolyte, poly(dimethyldiallylammonium chloride) (PDDAC). This reagent shows promise for industrial production of rubber from synthetic latices [10, 11]. It has been demonstrated that its flocculating performance is influenced by inorganic electrolytes [10, 11], but the mechanism of this effect has not been considered yet.

EXPERIMENTAL

In the study, we used commercial latex of SKN-26SM butadiene-acrylonitrile rubber (content of bound acryloacrylonitrile in the copolymer 30.5%). As emulsifier in the synthesis of latex, we used suing soap based on tall oil. The polymer content in the latex was 27.5 g l^{-1}; surface tension, 36.7 mJ m^{-1}; and pH 8.5.

As flocculants we used the PDDAC sample described in [2] and also its two fractions separated by

1070-4272/03/7608-1323 $25.00 © 2003 MAIK "Nauka/Interperiodica"

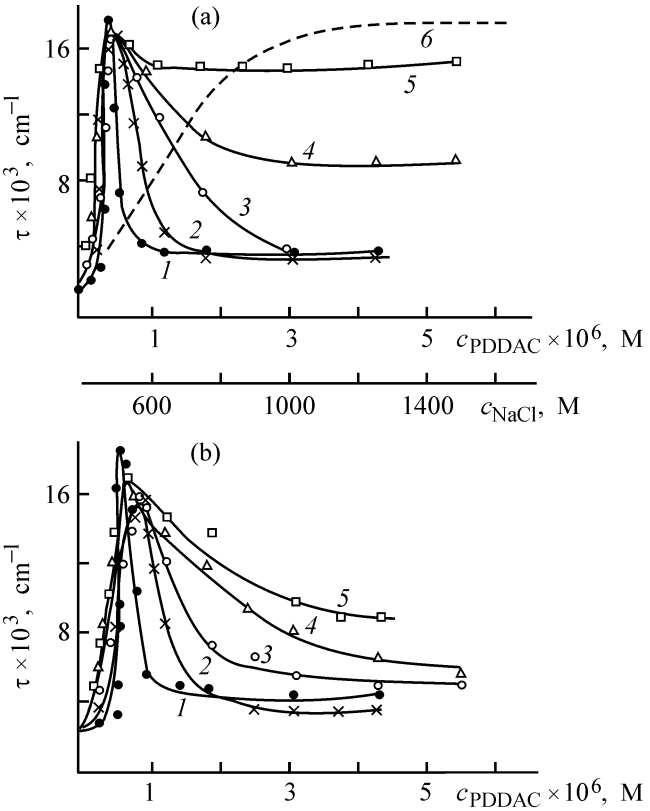

Fig. 1. Initial flocculation rate τ_1 vs. (*1*–*5*) PDDAC concentration c_{PDDCA} and (*6*) NaCl concentration c_{NaCl} in the absence of PDDAC. c_{NaCl} (M): (*1*) 0, (*2*) 0.02, (*3*) 0.05, (*4*) 0.1, and (*5*) 0.2. PDDAC mean molecular weight $M_v \times 10^{-4}$: (a) 2.3 and (b) 17.4.

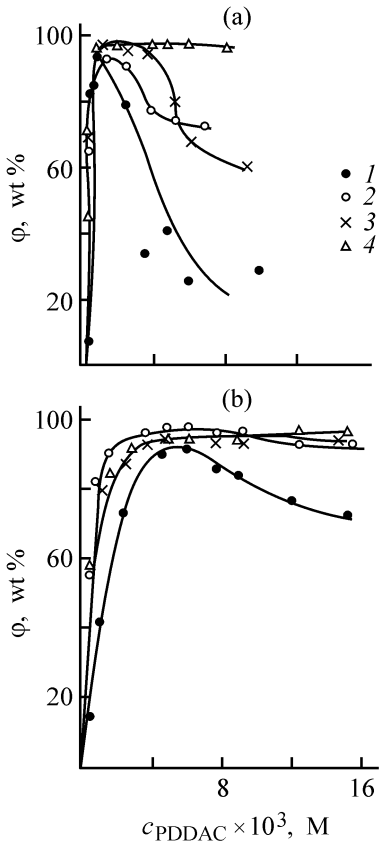

Fig. 2. Polymer separation efficiency φ vs. the PDDAC concentration c_{PDDAC}. c_{NaCl} (M): (*1*) 0, (*2*) 0.1, (*3*) 0.2, and (*4*) 0.4. Disperse phase concentration in latex ($g\ l^{-1}$): (a) 10 and (b) 30.

fractional precipitation from an aqueous solution with acetone. The viscosity-average molecular weights M_v of the initial sample and two fractions were 11.5×10^4, 2.3×10^4, and 17.4×10^4, respectively. Sodium chloride (chemically pure grade) was used without additional purification.

The viscosity of PDDAC solutions was determined in 0.1 M NaCl using an Ostwald viscometer. The M_v was estimated by the Mark–Houwink equation with $K = 1.12 \times 10^4$ and $\alpha = 0.82$ [12]. The turbidity of dilute latex solutions was measured at room temperature with an NFM nephelometer. The procedures for nephelometric determination of the initial rates of flocculation and rubber separation from the latex under the action of a flocculant were described elsewhere [2, 13].

The dependences of the initial flocculation rate of 10^4-fold diluted latex on the flocculant concentration at various NaCl concentrations are shown in Fig. 1. The initial flocculation rate was estimated as the turbidity 1 min after flocculation was started (τ_1) [6].

Figure 1 also shows τ_1 as a function of the NaCl concentration in the absence of PDDAC. The bend in this curve at $c_{NaCl} = 0.2$ M corresponds to the threshold of rapid coagulation of the latex [14].

In the absence of NaCl, the flocculation curves τ_1–c_{CPE} show clearly pronounced peaks (flocculation optimum) typical of the flocculating action of polyelectrolytes. The occurrence of flocculation optimum is caused by neutralization of the surface charge of the particles by adsorbed macrocations of the reagent, followed by recharging and restabilization of the sol through adsorption of the excess polymer and increase in the positive charge on the particles and also via formation of sufficiently thick layers of a hydrophilic polymer [15]. The occurrence of recharging of latex particles in flocculation with cationic polyelectrolytes has been more than once confirmed by measuring the electrophoretic mobility of the particles [1, 2, 16].

It should be pointed out that the flocculation rate at the optimum virtually coincides with the rate of

rapid coagulation of the latex by NaCl (Fig. 1). Therefore, at the optimal flocculating concentration (OFC) of the polyelectrolyte, flocculation must proceed as rapid coagulation.

With increasing NaCl concentration, the flocculation rate tends to grow, which is the most clearly pronounced in the restabilization range. For the lower-molecular-weight PDDAC sample, this results in virtually total suppression of the restabilization effect (at c_{NaCl} = 0.2 M). In this case, the flocculation rate approaches a value close to that with NaCl, although the coagulation rate is lower by about a factor of 3 at the indicated NaCl concentration in the absence of the polyelectrolyte,.

The NaCl concentration has a similar effect on the rubber separation efficiency in flocculation (Fig. 2). The flocculation curves have peaks which become less pronounced with increasing c_{NaCl}, virtually disappearing on reaching some critical value c^{∞}_{NaCl}. With increasing disperse phase concentration c_d, the peak in the flocculation curves disappears at lower salt concentration: at c_d of 10 and 30 g l^{-1} c^{∞}_{NaCl} is about 0.4 and 0.1 mM, respectively. Therefore, raising the ionic strength suppresses the latex restabilization effect in the course of flocculation, which is reflected in an increase both in the flocculation rate and in the efficiency of rubber separation from the latex.

This phenomenon can be interpreted taking into account two possible contributions to latex stabilization after reaching the flocculation optimum. One of these is enhancement of electrostatic stabilization, caused by increasing positive charge on the particles at concentrations above OFC [1, 2, 16]. Raising the NaCl concentration results in compaction of the diffuse electric double layer and also in weakening of the electrostatic repulsive forces, which impede agglutination of the particles upon collisions.

It should be pointed out that the range of electrostatic stabilization is restricted to relatively low salt concentrations. Simple calculation shows that, for a 1–1 electrolyte, the thickness of the electrical double layer decreases to about 1 nm even at a concentration of about 0.1 M and it loses its diffuse nature and, therefore, the electrostatic stabilization. At the same time, as seen from Figs. 1 and 2, further rise in c_{NaCl} makes the flocculation rate and rubber separation efficiency still higher. Evidently, this is a result of action of another factor, namely, nonelectrostatic interaction (repulsion) between the latex particles [17, 18]. The origin of this interaction is associated with the formation of hydrate shells of considerable thickness on the surface of latex particles, modified with the adsorption layer of the emulsifier. This phenomenon is known as secondary hydration [19]. The overlap of these shells controls the structural component of the disjoining pressure [20, 21]. In the case of the investigated butadiene-acrylonitrile latex under study, not only the secondary hydration, but also direct interaction of the polar acrylonitrile groups of the polymer with the environment may contribute significantly to the increase in the latex stability against the coagulating action of the electrolyte. This conclusion is confirmed by the industrial practice: NaCl consumption for separating acrylonitrile rubbers is higher by a factor of 3–5 than that for butadiene-styrene rubbers, the composition of the aqueous phase being nearly the same [22].

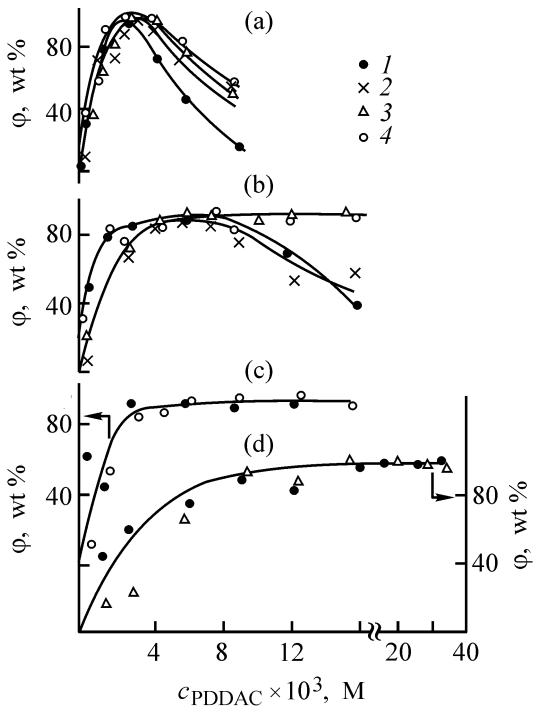

Fig. 3. Polymer separation efficiency φ vs. the PDDAC concentration c_{PDDAC}. $M_v = 17.4 \times 10^4$. T (°C): (*1*) 20, (*2*) 40, (*3*) 60, and (*4*) 80. Disperse phase concentration in latex (g l^{-1}): (a) 20, (b) 30, (c) 50, and (d) 80.

It is known [23, 24] that the thickness of hydrate shells of latex particles considerably decreases with increasing electrolyte concentration. Therefore, the observed increase in the flocculation efficiency at high NaCl concentrations (c_{NaCl} > 0.05–0.1 M) is associated with progressive breakdown and thinning of the hydrate shells under the action of the electrolyte. This allows the particles to approach one another more closely, thus increasing the probability of bridging between them.

Figure 3 shows the rubber separation curves (under the effect of PDDAC with $M_v = 17.4 \times 10^4$) at a tem-

perature of 20 to 80°C and various rubber concentrations in the latex. At relatively low disperse phase concentrations (c_d 20 and 30 g l^{-1}), raising the temperature provides an effect similar to that produced by increasing ionic strength: in the restabilization range, the rubber separation efficiency tends to grow. At c_d = 30 g l^{-1}, the restabilization effect is totally suppressed starting from 60°C, and the flocculation curves flatten out, which corresponds to complete separation of the rubber from the latex. At higher latex concentrations (c_d 50 and 100 g l^{-1}), when the restabilization effect is lost, temperature has no effect on the flocculation efficiency.

Finally, raising the temperature or ionic strength weakens the restabilization effect to the point of its elimination, provided that the disperse phase concentration is sufficiently high (c_d = 30 g l^{-1} in our case).

One of possible reasons for the observed effect is, evidently, a rise in particle mobility and in frequency and energy of their collisions with increasing temperature. In this context, heating is similar to raising the disperse phase concentration.

To conclude, the efficiency of rubber separation from a latex through flocculation with a cationic polyelectrolyte can be raised by adding an inorganic salt and elevating the temperature. In both cases, the net effect consists in weakening of the restabilization effect at flocculant concentrations exceeding OFC. From the practical standpoint, this suggests, among other things, the possibility of making less stringent the requirements to the precision of flocculant dosage as compared to that commonly needed for dilute dispersions, when efficient separation of the dispersed phase is only achieved in a narrow range of flocculant concentrations in the vicinity of OFC.

CONCLUSION

Raising the ionic strength by adding NaCl results in higher flocculation rate and completeness of coagulation of SKN-26SM butadiene-acrylonitrile rubber through weakening of the restabilization effect in the system with excess flocculant. For dilute latices, similar effect is observed at elevated temperature.

REFERENCES

1. Verezhnikov, V.N., Poyarkova, T.N., Nikulin, S.S., and Kurbatova, N. A., *Kolloidn. Zh.*, 2000, vol. 62, no. 1, p. 26.
2. Verezhnikov, V.N., Nikulin, S.S., Poyarkova, T.N., and Vostrikova, G.Yu., *Zh. Prikl. Khim.*, 2000, vol. 73, no. 10, pp. 1720–1724.
3. Baran, C. and Gregory, J., *Kolloidn. Zh.*, 1996, vol. 58, no. 1, p. 13.
4. Pelssers, E. and Cohen, S.M., *J. Chem. Soc., Faraday Trans.*, 1990, vol. 86, no. 9, pp. 1355–1361.
5. Adachi, Y. and Cohen S.M., *J. Colloid Interface Sci.*, 1994, vol. 165, no. 2, p. 310.
6. Gregory, J., *Coll. Surf.*, 1988, vol. 31, nos. 2–3, p. 231.
7. Pelssers, E., Cohen, S.M., and Fleer, G., *Colloid Surf.*, 1989, vol. 38, no. 1, p. 15.
8. Gregory, J., *J. Colloid Interface Sci.*, 1973, vol. 42, no. 2, p. 448.
9. Matsumotu, J. and Adachi, Y., *J. Colloid Interface Sci.*, 1998, vol. 204, no. 2, p. 328.
10. Garshin, A.P., Nikulin, S.S., Shapovalova, N.N., *et al., Proizv. Ispol'z. Elastom.*, 1994, no. 11, pp. 2–6.
11. Garshin, A.P., Nikulin, S.S., Shapovalova, N.N., *et al., Proizv. Ispol'z. Elastom.*, 1994, no. 12, pp. 9–14.
12. Wandrey, C., Jaeger, W., and Reinish, G., *Acta Polym.*, 1982, vol. 33, no. 2, pp. 156–159.
13. Verezhnikov, V.N., Nikulin, S.S., Krutikov, M.Yu., and Poyarkova, T.N., *Kolloidn. Zh.*, 1999, vol. 61, no. 1, pp. 37–41.
14. Neiman, R.E., *Ocherki kolloidnoi khimii sinteticheskikh lateksov* (Studies in Colloid Chemistry of Synthetic Latices), Voronezh: Voronezh. Gos. Univ., 1984.
15. Baran, A.A. and Solomentseva, I.M., *Khim. Tekhnol. Vody*, 1983, vol. 5, no. 2, pp. 120–127.
16. Solomentseva, I.M., Tusupbaev, N.K., Baran, A.A., *et al., Ukr. Khim. Zh.*, 1980, vol. 46, no. 9, pp. 929–933.
17. Golikova, E.V. and Chernoberezhskii, Yu.M., in *Voda v dispersnykh sistemakh* (Water in Disperse Systems), Moscow: Khimiya, 1989, p. 169.
18. Neiman, R.E., in *Voda v dispersnykh sistemakh* (Water in Disperse Systems), Moscow: Khimiya, 1989, p. 188.
19. Pashley, R.M., *Adv. Colloid Interface Sci.*, 1982, vol. 16, p. 57.
20. Derjaguin, B.V. and Churaev, N.V., *J. Colloid Interface Sci.*, 1974, vol. 49, p. 249.
21. Churaev, N.V., *Kolloidn. Zh.*, 1984, vol. 46, no. 2, p. 302.
22. Kirpichnikov, P.A., Averko-Antonovich, L.A., and Averko-Antonovich, Yu.O., *Khimiya i tekhnologiya sinteticheskogo kauchuka* (Chemistry and Technology of Synthetic Rubber), Leningrad: Khimiya, 1987.
23. Lebedev, A.V., *Kolloidnaya khimiya sinteticheskikh lateksov* (Colloid Chemistry of Synthetic Latices), Leningrad: Khimiya, 1976.
24. Kiseleva, O.G. and Neiman, R.E., *Kolloidn. Zh.*, 1985, vol. 47, no. 4, p. 799.

Russian Journal of Applied Chemistry, Vol. 76, No. 8, 2003, pp. 1327–1330. Translated from Zhurnal Prikladnoi Khimii, Vol. 76, No. 8, 2003, pp. 1363–1367.

MACROMOLECULAR CHEMISTRY AND POLYMERIC MATERIALS

Synthesis and Properties of 2-Vinylphenothiazine Polymers

S. S. Nikulin, V. M. Misin, V. M. Komarov, and M. V. Misin

Voronezh State Academy of Forestry Engineering, Voronezh, Russia
Institute of Biochemical Physics, Russian Academy of Sciences, Moscow, Russia
Moscow Academy of Fine Chemical Technology, Moscow, Russia

Received April 10, 2003

Abstract—2-Vinylphenothiazine was prepared, and its polymerization was studied. The possibility of using 2-vinylphenothiazine and its polymer as antioxidant in industrial rubber formulations was examined.

Nitrogen- and sulfur-containing heterocyclic compounds attract much researchers' attention. Among these compounds, phenothiazine and its diverse derivatives found extensive applications. Many phenothiazine derivatives have valuable properties and are used in pharmacy, in photographic and polygraphic industry for fabricating photographic materials, as inhibitors, antioxidants, etc. [1–5].

Vinyl derivatives of phenothiazine, especially 2-vinylphenothiazine (2-VPT), are of particular interest. However, their synthesis and preparation of polymeric materials from them have been studied poorly. First experiments on radical polymerization of 2-VPT failed, which was due to easy abstraction of hydrogen from the amino group and inhibition of the polymeric chain propagation by the resulting radical [6, 7]. Therefore, experiments on preparation of polymeric materials from 2-VPT were initially performed in an acylating solvent (acetic anhydride) and resulted in preparation of poly-2-vinyl-10-acetylphenothiazine. Saponification of this compound with an alcoholic alkali yielded poly-2-VPT. Later studies demonstrated the feasibility of preparing poly-2-VPT by direct radical polymerization of monomeric 2-VPT. However, it remains unclear from the available data how the polymerization conditions affect the degree of conversion of 2-VPT into the polymer.

In this study, we analyzed radical polymerization of 2-VPT in the bulk and in solution, evaluated the resistance of the polymer to thermal oxidative degradation, and examined the properties of polymeric compounds containing 2-VPT and its polymers.

EXPERIMENTAL

2-Vinylphenothiazine was prepared from phenothiazine (mp 182–184°C) as follows [6, 8, 9]:

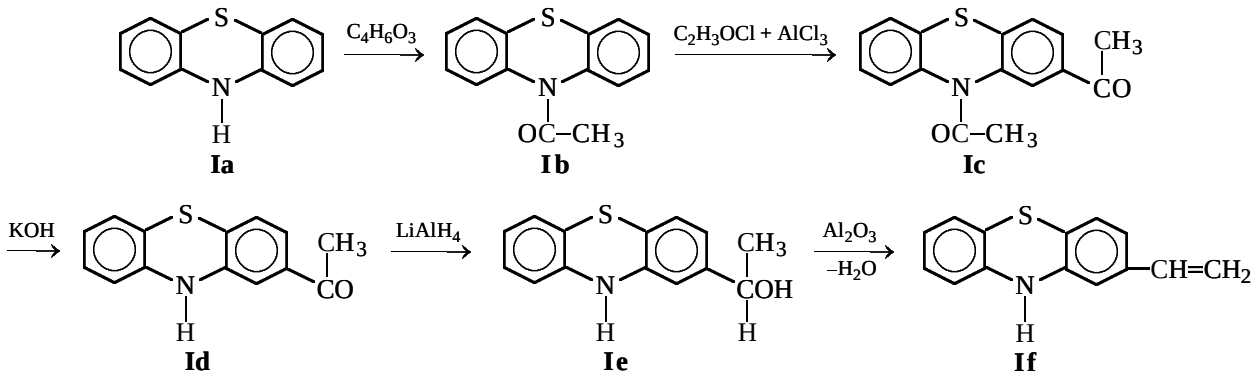

Scheme 1.

1070-4272/03/7608-1327 $25.00 © 2003 MAIK "Nauka/Interperiodica"

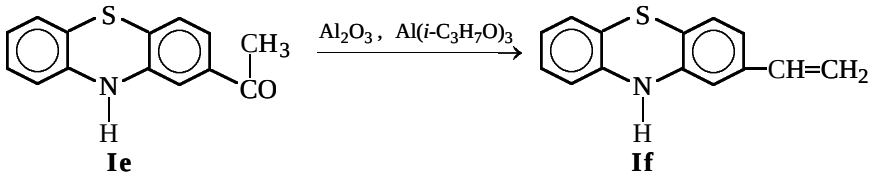

Scheme 2.

Acylation of phenothiazine (**Ia**) with refluxing acetic anhydride at 140°C for 5 h gave 10-acetylphenothiazine **Ib** in 97% yield [6]. Acylation of **Ib** with acetyl chloride in the presence of $AlCl_3$ produced 2,10-diacetylphenothiazine **Ic** [8, 9], which was then saponified with an alcoholic solution of KOH to give 2-acetylphenothiazine **Id** [6, 8]. The yield of 2-acetylphenothiazine after recrystallization from ethyl acetate was 80–95%. Compound **Id** was reduced with $LiAlH_4$ in ether within 12 h to 2-(1-hydroxyethyl)phenothiazine **Ie** in 65–74% yield [8, 10]. Dehydration of **Ie** in the presence of Al_2O_3 in a vacuum at 220–240°C gave 2-VPT (**If**) in 20–30 wt % yield (Scheme 1).

According to Scheme 2, 2-VPT can be prepared in 15–23 wt % yield in a single step under conditions of high-vacuum (10^{-3} mm Hg) high-temperature (220°C) sublimation of a mixture of 2-acetylphenothiazine (**Id**), triisopropoxyaluminum, and Al_2O_3.

The structure of the product (mp 178–180°C) was confirmed by IR, UV, and ^1H NMR spectroscopy, and also by elemental analysis.

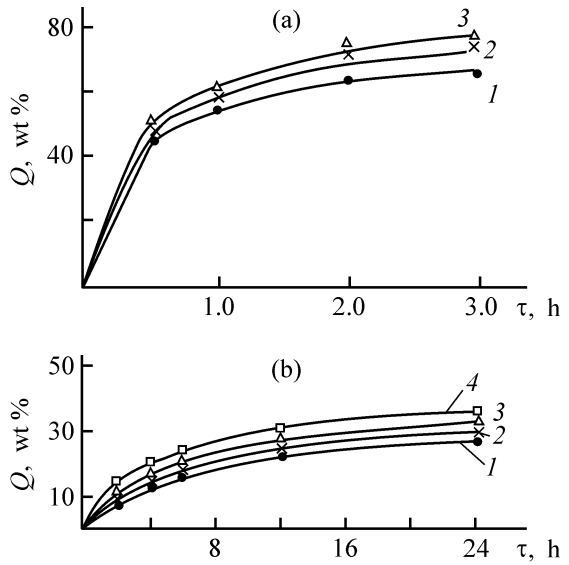

Fig. 1. Yield of poly-2-VPT *Q* vs. the time τ of polymerization (a) in the bulk and (b) in solution at various temperatures. *T*, °C: (a) (*1*) 185, (*2*) 210, and (*3*) 245; (b) (*1*) 70, (*2*) 80, (*3*) 90, and (*4*) 100.

Found, %: C 74.60; H 4.95; N 6.20.
$C_{14}H_{11}NS$.
Calculated, %: C 74.67; H 4.90; N 6.20.

High-temperature radical polymerization of 2-VPT was performed in the bulk in evacuated (10^{-3} mm Hg) and sealed glass ampules. The product was dissolved in THF or benzene and precipitated with a 5–10-fold amount of ethanol.

Radical polymerization of 2-VPT in benzene was performed in the presence of azobis(isobutyronitrile) at 70–100°C. The initial concentrations of the monomer and initiator in solution were 3.4×10^{-1} and 1.04×10^{-2} M, respectively.

We found (Fig. 1a) that, in the examined range of reaction times, the yield of poly-2-VPT steadily grows with temperature. The optimal reaction time is 2–3 h. Heating above 240°C is not appropriate, because the polymer yield does not increase further, but degradation becomes noticeable.

According to gel permeation chromatography, the synthesized poly-2-VPT had $\overline{M}_n$ = 2040, $\overline{M}_w$ = 4280, $\overline{M}_z$ = 9950, and $\overline{M}_w/\overline{M}_z$ = 2.1. Elemental analysis gave consistent results for the C, N, and H content, suggesting the absence of degradation in the course of high-temperature polymerization.

Found, %: C 74.6; H 4.95, N 6.2.
$(C_{11}H_{14}NS)_n$.
Calculated, %: C 74.7; H 4.9; N 6.2.

In polymerization in solution, the polymer yield also increased with temperature (Fig. 1b); however, it remained much lower than in that bulk polymerization in the same period of time. This is most probably due to easy abstraction of hydrogen from the amino group of the monomer or polymeric unit with the formation of a free radical terminating the polymeric chain and thus decreasing the yield and molecular weight of the polymer:

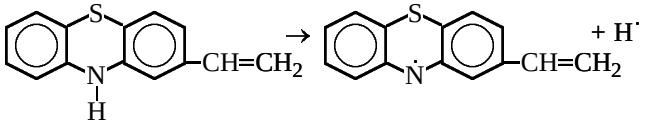

The low molecular weights of the polymers prepared by various procedures are due to the presence of the labile N–H bond in the phenothiazine group. It should be noted, however, that poly-2-VPT prepared in solution has a somewhat higher molecular weight ($\overline{M}_n$ = 3000–4000). This may be due to the fact that generation of radicals is more intense in thermal polymerization in the bulk, performed at higher temperature (185–245°C) than polymerization in solution (70–100°C). This results in higher concentration of initiating species, higher initiation rate, and hence increased conversion of the monomer, especially in the initial step. However, the high concentration of radicals in high-temperature bulk polymerization, on the other hand, results in more active chain termination, compared to polymerization in solution at a lower temperature. Therefore, the molecular weight of the polymer prepared in the bulk is lower.

Poly-2-vinylphenothiazine prepared by polymerization of 2-VPT in solution was largely similar to poly-2-VPT prepared in the bulk.

The structure of the poly-2-VPT samples obtained was confirmed by IR, UV, and ^{1}H NMR spectroscopy. The IR spectrum of poly-2-VPT (Fig. 2) shows no bands at 900 and 990 cm^{-1}, characteristic of monomeric 2-VPT. The UV spectrum of the polymer is similar to that of the starting 2-VPT. The spectrum contains a band at 258 nm (ε = 28100) characteristic of the π→π* transition in the conjugated system and a band at 320 nm (ε = 3500) related to the lone electron pairs of the N and S atoms. In the ^{1}H NMR spectrum of the polymer (Fig. 3), the signals at 5.15, 5.65, and 6.62 ppm, belonging to the vinyl protons of the monomer, disappear, and a broad unresolved signal of the CH and CH_2 protons of the polymeric chain appears at 0.75–2.7 ppm. The spectrum also contains signals from aromatic protons at 6.75–7.72 ppm and NH proton at 8.2 ppm.

The X-ray diffraction patterns of the polymers show that they are X-ray-amorphous.

The inhibition of radical polymerization by phenothiazine suggests that thermal oxidative degradation of polymers can be hindered by introduction of phenothiazine fragments into macromolecules. Also, a study of thermal oxidative degradation of poly-2-VPT prepared at low temperature in solution could show whether or not thermal degradation of poly-2-VPT can occur directly in the course of high-temperature polymerization of the monomer in the bulk. Figure 4 shows that poly-2-VPT starts to degrade in air only at high temperatures (350–380°C) exceeding by more than 100°C the polymerization temperature (≤250°C). A minor weight loss at lower temperatures is due to desorption of low-molecular-weight compounds (water, solvent, monomer). At 500°C, the weight loss slightly exceeds 30 wt %.

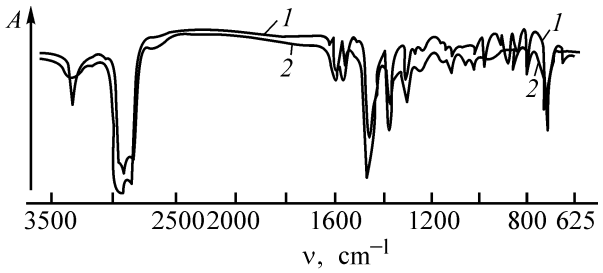

Fig. 2. IR spectra of (*1*) 2-VPT and (*2*) poly-2-VPT: (*A*) transmission and (ν) wave number.

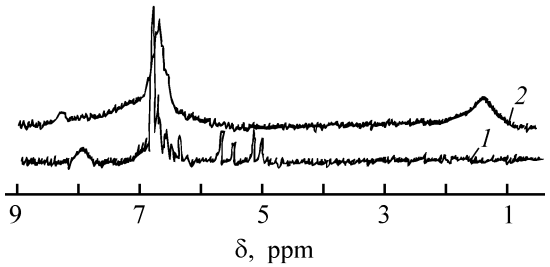

Fig. 3. ^{1}H NMR spectra of (*1*) 2-VPT and (*2*) poly-2-VPT. (δ) Chemical shift.

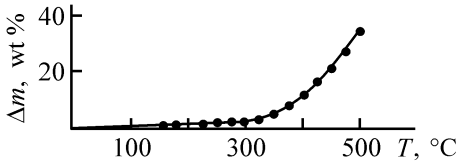

Fig. 4. Weight loss Δ*m* of poly-2-VPT on heating in air vs. temperature *T*.

The absence of degradation in poly-2-VPT at temperatures of up to 350°C confirms the possibility of high-temperature polymerization of monomeric 2-VPT in the temperature range examined. The high resistance of poly-2-VPT to thermal oxidative degradation is due to the presence, in each unit of the polymer, of the phenothiazine substituent containing the labile N–H group whose homolysis products inhibit degradation of polymeric molecules.

Fedotova *et al.* [10] has shown that introduction of phenothiazine and its derivatives into various polymers by mechanical blending enhances their resistance to thermal oxidative degradation. However, phenothiazine and its alkyl derivatives tend to exude on the surface of finished industrial rubber items, which is a major drawback, since this decreases the stability and may promote cleavage of multilayered articles. To minimize exudation, it is appropriate to modify the phenothiazine molecule with a reactive functional group capable of forming valence bonds with rubber

Properties of vulcanized rubbers based on SKD butadiene rubber

Parameter	Parameter value with indicated additive (content in wt %)						
	Neozon D, 1.5	Quinol ED, 1.5	phenothiazine, 1.5	2-VPT			poly-2-VPT, 2.5
				1.0	1.5	3.0	
Nominal tensile strength, MPa	16.3	17.6	16.9	16.9	17.9	17.3	19.8
Relative elongation at break, %	360	390	385	430	440	460	590
Relative residual deformation after break, %	8	8	8	8	8	8	8
Aging coefficient with respect to relative elongation	0.74	0.58	0.67	0.68	0.70	0.69	0.75
Resistance to repeated extension, thousands of cycles	9.2	6.9	7.5	4.8	9.8	5.0	16.0
Ozone resistance, h	1.0	1.2	1.5	1.5	1.5	2.0	–

macromolecules in the course of stock preparation and vulcanization. It can be expected that 2-VPT will be grafted via its vinyl group to polymeric chains and will act as a nonexuding chemically bound antiaging agent. To verify this assumption, we introduced 2-VPT and poly-2-VPT into the polymeric matrix in the course of rubber stock preparation, with the subsequent vulcanization.

Rubber stocks were prepared on 320×160-mm laboratory rollers at 65 ± 5°C by common procedures and vucalnized in a mold at 143°C. Tests were performed by standard procedures. The results obtained with 2-VPT and poly-2-VPT additives were compared with those obtained using known antiaging agents: Neozon D, Quinol ED, and phenothiazine.

The resistance of vulcanized rubbers to three kinds of aging was evaluated. The resistance to thermal aging was determined at 100°C over a period of 72 h by the aging coefficients with respect to relative elongation. The resistance to ozone aging was determined at 50°C, working ozone concentration of 5×10^{-5} vol %, and static elongation of 10%. The resistance to dynamic loads was evaluated under conditions of repeated extension (dynamic strain 200%) from the number of cycles till failure.

The experimental results listed in the table show that, in all the main parameters, the vulcanized rubbers containing 2-VPT and poly-2-VPT are not inferior to those containing Neozon D and Quinol ED and even surpass them in the resistance to dynamic loads and to ozone.

Thus, phenothiazine, 2-VPT, and poly-2-VPT are good agents against ozone aging. However, in vulcanizates based on SKD rubber, 2-VPT at its high content is more active than unsubstituted phenothiazine. This is due to weaker exudation of 2-VPT on the surface and to its better compatibility with the rubber, since it can add to the diene rubber molecules via vinyl group in the course of compounding.

CONCLUSIONS

(1) Experiments on radical polymerization of 2-vinylphenothiazine in the bulk at high temperatures and in solution in the presence of azobis(isobutyronitrile) as radical initiator demonstrated an inhibiting effect of phenothiazine-containing units on the degradation processes in the polymers.

(2) 2-Vinylphenothiazine and its polymer can be used as antioxidants in industrial rubber formulations.

REFERENCES

1. Ivanovskii, V.I., *Khimiya geterotsiklicheskikh soedinenii* (Chemistry of Heterocyclic Compounds), Moscow: Vysshaya Shkola, 1978.
2. *Heterocyclic Compound*, Elderfield, R.C., Ed., New York: Wiley, 1957, vol. 5.
3. Jerae, S., *Wiodem. Chem.*, 1966, vol. 20, no. 1, pp. 1–23.
4. Bodea, C. and Silkerg, J., *Adv. Heterocycl. Chem.*, 1968, vol. 9, pp. 321–460.
5. Simov, D., Georgiev, G., and Sofianski, W., *Ann. Univ. Sof. Fac. Chem.*, 1976, vol. 67, pp. 233–241.
6. Kamogawa, H., Jorkin, J.M., Toci, K., and Cassicly, H.G., *J. Polym. Sci., Part A*, 1964, vol. 2, no. 8, pp. 3603–3614.
7. Kamogawa, H., *Bull. Text. Res. Just.*, 1964, no. 68, pp. 61–68.
8. Gorlach, G.A. and Dykhanov, N.I., *Med. Prom–st. SSSR*, 1959, vol. 13, no. 4, pp. 35–37.
9. Georgiev, G., *Dokl. Bolg. Akad. Nauk*, 1964, vol. 17, no. 3, pp. 267–270.
10. Fedotova, T.V., Senatorskaya, L.G., Eitingon, I.I., *et al.*, in *Sintez rezin i ikh khimicheski aktivnykh komponentov* (Synthesis of Vulcanized Rubbers and Their Reactive Components), Moscow, 1977, pp. 189–195.

Russian Journal of Applied Chemistry, Vol. 76, No. 8, 2003, pp. 1331–1336. Translated from Zhurnal Prikladnoi Khimii, Vol. 76, No. 8, 2003, pp. 1368–1374.

MACROMOLECULAR CHEMISTRY AND POLYMERIC MATERIALS

A Composite Hardener for Epoxy Adhesives

S. L. Selektor, M. Yu. Semyachkin, and V. V. Arslanov

Institute of Physical Chemistry, Russian Academy of Sciences, Moscow, Russia

Received December 26, 2002; in final form, April 2003

Abstract—A new composite hardener for epoxy adhesives, based on a heteropoly acid, was suggested, and its formula was optimized. The curing kinetics and the physicomechanical and adhesion properties of the cured material were studied. The advantages of the new material over traditional epoxy adhesives were demonstrated, and the ways to control its characteristics were found.

Wide use of binary epoxy adhesives cured by polyamines is due to the possibility of room-temperature curing. However, the high toxicity of polyamines makes topical a search for new, less toxic and more environmentally safe, hardeners. Among such hardeners are heteropoly acids (HPAs) and their salts, which are active catalysts for polymerization of epoxy oligomers [1, 2]. The problem is that, in the presence of even small amounts of such compounds introduced as aqueous solution, the polymerization is so vigorous that the formulation warms up to temperatures exceeding the decomposition point of epoxy materials [2]. Furthermore, it should be noted that even dilute HPA solutions are aggressive liquids with low pH. These facts have prevented application of aqueous HPA solutions as initiators of curing of epoxy adhesives.

In this study, to solve these problems, we suggest a composite hardener containing, along with HPA and water, an additional third component introduced to dissipate the excess heat, decelerate the initiated polymerization, and improve the compatibility of the oligomer and hardener. As such "inhibiting" component we chose high-molecular-weight polyvinyl alcohol (VRP-1), a polymer forming stable highly viscous aqueous solutions well compatible with heteropoly compounds (HPCs).

EXPERIMENTAL

To verify our suggestions, we chose a formulation of ED-20 epoxy resin, phosphotungstic acid (HPW), and a gel-like aqueous solution of VRP-1; the weight ratio of the resin and VRP-1 solution was 9 : 1 in all the systems.

To optimize the adhesive formula and curing conditions, we studied the curing kinetics in the range 18–90°C at varied content of the initiator (HPW, 1.5–6.8 wt %). The curing kinetics was monitored by sol–gel analysis and by microhardness measurements. The sol–gel analysis was performed by extraction with acetone at room temperature to constant weight (for no less than 18 h). The microhardness of polymeric films was measured with a PMT-3 hardness gage with a pyramidal diamond indenter.

The adhesion strength was evaluated by exfoliation of A99 aluminum foil at an angle of 180° with an Instron-1121 universal tensile-testing machine. Immediately before applying the adhesive, the surface of the aluminum support was etched with 10% NaOH at 60°C for 2 min, with subsequent brightening in 20% HNO_3 and washing with distilled water. Similar tests were performed with the same ED-20 epoxy resin cured with traditionally used polyethylenepolyamine (PEPA) added in amounts of 10 wt parts per 100 wt parts of the resin. The films formed were cured for a day at 18–20°C ("cold" curing), or for 30 min at 90°C (formulations with HPW) or 3 h at 100°C (formulations with PEPA) ("hot" curing). Cold curing was continued until the sol fraction content no longer decreased.

The deformation and strength properties of the composites were studied with an Instron-1121 machine in the extension mode at a clamp velocity of 10 mm min^{-1}. Samples were prepared as strips of aluminum foil with an applied adhesive layer [3, 4]. The strength characteristics of the foil itself were determined in preliminary experiments. The modulus of elasticity E_{met}, calculated from the initial linear

1070-4272/03/7608-1331 $25.00 © 2003 MAIK "Nauka/Interperiodica"

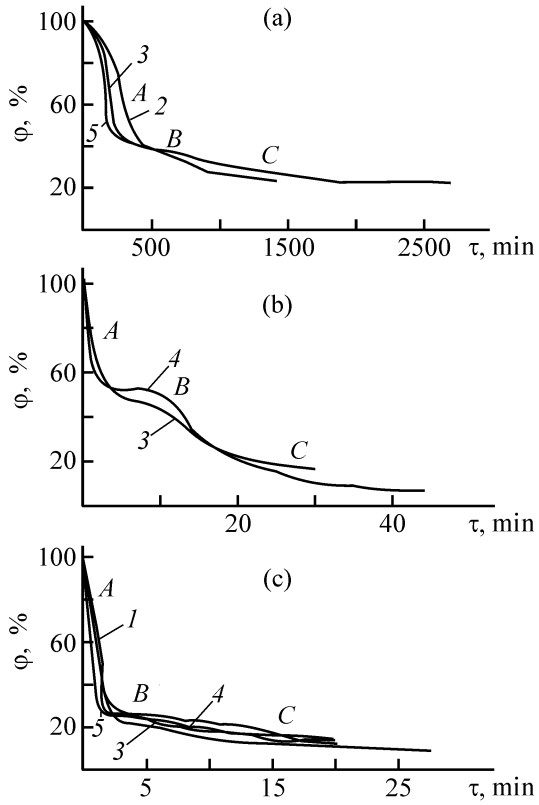

Fig. 1. Sol fraction content φ vs. the curing time τ of epoxy resins at (a) 20, (b) 60, and (c) 90°C. Initiator content, wt %: (*1*) 2.4, (*2*) 3.2, (*3*) 3.8, (*4*) 4.1, and (*5*) 4.8. (*A*–*C*) Steps of gelation.

portion of the σ–ε diagram (σ is the specific load, kg cm^{-2}; ε, relative elongation) was 3.43 MPa; the breaking load σ_{met}^{lim} was 2.6 kg per centimeter of the sample width at the place of break.

Similar measurements performed with a two-layered system showed that the sample is broken at loads considerably exceeding the strength of the metallic support, but, at the onset of failure, the deformations correspond to the portion of the σ–ε curve in which the support behaves according to the Hooke law (range of elastic strain), rather than to the range of plastic strain [5]. In this case, the stress distribution in the two-layer system can be regarded as additive, and the breaking load of the polymer layer can be calculated as the difference between the breaking load for the coated sample and the load required for extension of the uncoated foil of the same width to the extent at which the coating failed:

$$P_{pc} = P_s - P_{met} = P_s - \varepsilon_s E_{met} S_{met}.$$

Here P_{pc} is the breaking load for the polymer coating, N; P_s, ultimate load on the failure diagram for the two-layered sample, N; P_{met}, load required to deform the metal sample to ε_s, N; E_{met}, modulus of elasticity of the metal, Pa; ε_s, relative deformation of the two-layered sample at break; and S_{met}, cross section of the metal sample, m^2.

The influence of the curing time and temperature on the sol fraction content φ (%) in the formulations containing various amounts of the initiator is shown in Fig. 1. As expected, with increasing curing temperature, the gelation considerably accelerates: its duration decreases from several hours in cold curing to several minutes at 90°C. The kinetic curves (Fig. 1) can be divided in several portions corresponding to various steps of gelation. In cold curing, the sol–gel analysis reveals a short incubation period preceding the avalanche-like autocatalytic process. Such a delay is indicative of a slow diffusion of the initiator from the bulk of an emulsion drop to the phase boundary. At elevated temperatures, this step is complete in several seconds. In the next step, in all the cases, the sol fraction content rapidly decreases, which is characteristic of the relay mechanism of initiated gelation in the bulk of the material (Fig. 1, region *A*).

The influence of the initiator content on the curing kinetics is manifested to the greatest extent at room temperature: As the HPW concentration is raised from 3.3 to 5.0 wt %, the rate at which the sol fraction content decreases ($-d\varphi/d\tau$) in the initial linear portions of the curves (Fig. 1, region *A*) grows by approximately a factor of four (from 0.31 to 1.18). At 90°C, the rate ratio does not exceed 2, and gelation is mostly complete within 1.5–2 min.

In region *C*, the sol fraction content decreases very slowly at all the temperatures, which may be due to diffusion hindrance preventing further curing in the bulk of the material.

In the transition region *B* between regions *A* and *C*, the rate at which the sol fraction content decreases first falls abruptly and then grows again. This may be due to significant conformational limitations arising in the material and to the high level of internal stresses accompanying fast cross-linking; after their relaxation, the gelation slightly accelerates again.

The multistep course of network polymer formation is noted by Irzhak *et al.* [6]; they believe that the process rate in each particular step is governed by the ratio of the rate constant of the proper chemical reaction between the functional groups and those of various relaxation processes (local or segmental) involving these groups. Ivanov [2] believes that the decisive factor affecting the cross-linking kinetics of

an epoxy oligomer in the presence of an emulsified aqueous HPA solution is the HPA concentration in this solution, rather than the total amount of the solution. Unfortunately, this conclusion was based on data for a relatively narrow range of concentrations and curing temperatures. For the emulsions in question, the dependence of the gelation rate on the concentration of the initiator solution is determined by the ratio of the rates of the chemical step (polymerization) and HPW diffusion. The HPW diffusion should be considered in an emulsion drop, in the non-cross-linked resin, and in cured regions of the forming polymer. The last factor is the most important for high curing temperatures.

A comparative analysis of the sol fraction content in fully cured formulations showed that, although the gelation accelerates with increasing initiator concentration in cold curing (Fig. 1a), the degree of curing as a function of the initiator content passes through a maximum. As the HPW content is raised from 3.2 to 4.8%, the residual sol fraction content first decreases from 23 to 17% and then grows to 24%. The degree of curing in the case of hot curing varies similarly.

Such a behavior of the system confirms the existence of considerable diffusion limitations arising directly in the course of gelation. Apparently, at high initiator concentrations, fast polymerization in the regions adjacent to the phase boundaries in the emulsion (between epoxy resin and thickened aqueous HPW solution) results in formation of a densely cross-linked network preventing the initiator diffusion into the bulk of the resin. Such a concept accounts for the revealed [2] increase in the degree of polymerization of the formulations with decreasing HPA concentration in the initial solution and with increasing total amount of this solution in the system. The role of diffusion limitations decreases in the first case owing to lower initial rate of the chemical reaction at the phase boundary between the epoxy oligomer and the aqueous solution of the initiator, and in the second, owing to the increased contact surface area. The weaker influence of the initiator concentration on the curing rate at elevated temperatures suggests that, as expected, the activation energy of polymerization considerably exceeds that of diffusion. As a result, the rate of the chemical reaction of polymerization grows with increasing temperature faster than the diffusion rate, so that the diffusion limitations become more significant.

Evaluation of the activation energy of polymerization from the results of a sol–gel analysis for the formulation containing 3.8 wt % HPW gives a value of 60 kJ mol^{-1}, consistent with data of [2]. As the HPW concentration is raised, the activation energy decreases somewhat.

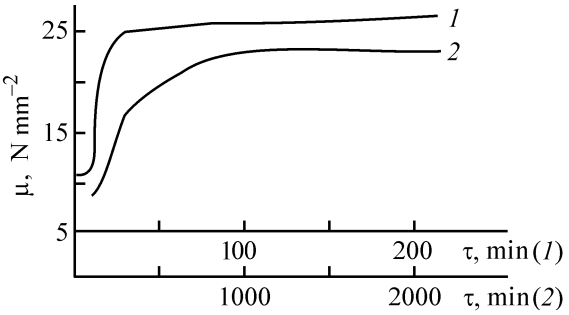

Fig. 2. Variation of the microhardness μ of the formulation containing 3.8 wt % HPW with curing time τ. Curing temperature, °C: (*1*) 20 and (*2*) 90.

The validity of the suggested curing scheme is supported by the results of the microhardness measurements. Figure 2 shows that, at both curing temperatures, there are intervals in which the microhardness grows steeply. In cold curing, the interval of the steep growth of microhardness (Fig. 2, curve *1*; up to 200 min) corresponds to completion of fast gelation (Fig. 1a). In hot curing, the microhardness starts to grow steeply only after fast gelation is complete. Such a "delay" in the microhardness growth at elevated temperatures may be due to the increasing role of diffusion limitations in both curing and extraction of the sol fraction. Deceleration of the diffusion is due to formation of densely cross-linked zones around drops of the emulsified initiator solution. These zones must appreciably hinder the cross-linking in the bulk of the nonpolymerized resin and also the extraction of the sol fraction from this volume during tests. At the same time, the presence of separate densely cross-linked zones does not affect noticeably the microhardness of the material. For the microhardness to increase, such zones must grow together to form a rigid framework.

To reveal the influence of the HPW concentration on the structure of the forming polymeric material, we analyzed how the microhardness of the fully cured films depends on the initiator content. We found that the microhardness of the films cured at 90°C decreases with increasing HPW concentration, whereas for the films cured at 20°C the dependence passes through a minimum.

The dependences observed may be due to the fact that, at low HPW concentrations, the growth of local polymerization zones noticeablly accelerates as the HPW content is raised. This considerably restricts the

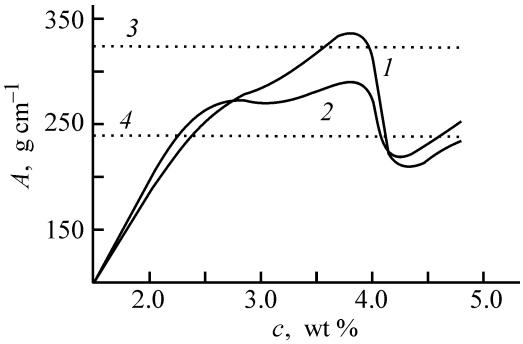

Fig. 3. Strength *A* of adhesion joints epoxy polymer–aluminum vs. the HPW content *c* in compounds cured at (*1*) 90 and (*2*) 20°C. (*3, 4*) Epoxy polymer cured with PEPA at 100 and 20°C, respectively.

conformational mobility of the cross-linking macromolecules and results in formation of a more defective polymer structure with decreased microhardness. In hot curing, this trend keeps in the entire concentration range, whereas in cold curing the microhardness starts to increase at an HPW concentration of 4.0 wt %. This growth is due to the fact that, at high concentrations of the hardener and relatively low reaction rates, the increase in the density of cross-linking of the gel fraction acquires decisive importance. In this case, apparently, the structure of the polymer becomes still less uniform, since in the entire examined range of curing temperatures the sol fraction content grows with increasing initiator concentration.

It is notable that, at all the temperatures, the sol fraction content passes through a minimum at an HPW concentration ot 3.8–4.1 wt %, i.e., at the concentration at which the microhardness also passes through a minimum. This is due to the fact that the microhardness is determined not by the overall gel fraction content but by the uniformity of distribution of the chemical bonds in the three-dimensional network of the polymer. The coincidence of the characteristic points in the concentration dependences of the microhardness and residual sol fraction content suggests that there is a threshold in the concentration region in the vicinity of these points.

It should be noted that epoxy materials cured with amines show strong structural nonuniformity, too [6–8]. Some authors speak of clusters with a high degree of ordering [8], and other authors, of a developed globular structure consisting of more densely packed regions (globules) and regions with nonuniform packing and taut chains (interglobular space) [7]. These are, however, different descriptions of the same fact: nonuniform distribution of network points in the bulk of the epoxy material.

In addition, Nielsen [8] indicates that, in some ranges, the dependence of the elastic characteristics of network polymeric materials in the glassy state on the mean concentration of network points is inverse. This is attributed to weakening of intermolecular physical interactions in formation of a rigid chemically cross-linked three-dimensional network significantly restricting the segmental mobility of macromolecules. Although Nielsen discusses the dynamic modulus of elasticity of thickly cross-linked polymers [8], it is commonly believed [9] that the microhardness also belongs to parameters characterizing the elastic properties of polymeric materials. Furthermore, in many studies, attempts are made to calculate the modulus of elasticity from the results of microhardness measurements with indenters of various shapes [9].

Thus, the study of the curing kinetic showed that it is possible to control the gelation rate, degree of gelation, and properties of the resulting material by varying the temperature and initiator concentration.

Since the main criteria in evaluating the service properties of an adhesive formulation are the strength and durability of the adhesion joint, the adhesive formula was optimized on the basis of adhesion tests. Figure 3 shows that the adhesion strength is a nonmonotonic function of the initiator concentration. At both curing temperatures, the highest adhesion strength was attained with 3.8 wt % HPW. In both cases, the adhesion strength at the maximum exceeds that attained with the amine hardener. The same formulation appeared to be the most stable in tests in water; its performance in the case of hot curing appeared to be similar to that of the aminecured compound, and in the case of cold curing it showed much better performance.

The increase in the strength of adhesion joints in the ascending branch of the strength-vs.-initiator concentration dependence is due to a rise in the cohesion strength and plasticity of the adhesive material and also to activation of the aluminum surface under the action of the HPW solution having low pH. The descending branch of the curve may be associated with acceleration of polymerization involving functional groups of the epoxy oligomer and taking them out of adhesion interaction with the polar surface of the metal. Furthermore, fast gelation largely restricts the conformational mobility of the macromolecules and segments of the polymeric network, preventing their interaction with active centers of the surface. Thus, the best service properties are shown by the adhesive containing 13.5 wt % HPW solution in VRP-1,

at a 29 wt % content of HPW in this solution (i.e., 3.8 wt % HPW in the formulation).

To refine the parameters of preparation and application of the adhesive suggested, we studied the properties of the material with the optimal initiator content in more detail. The results of a detailed sol–gel analysis for various curing temperatures are shown in Fig. 1, curve *3*. As already noted, the curing occurs in distinct steps (transition region *B*), which is due to relaxation of stresses arising in the material in the first step of gelation. A prolonged experiment showed that the sol fraction content in the samples cured at 90°C became ultimately the same as that upon curing at 60°C. Presumably, the initiated polymerization reaches the co-called topological limit in both cases [7, 8].

To confirm the significant role of relaxation of internal stresses in the curing kinetics and formation of the supramolecular structure of the adhesive, we studied its physicomechanical properties and their variation on adding the plasticizer. A calculation of the strength characteristics of the adhesive with the optimal HPW content from the results of mechanical tests showed that the material cured at room temperature has an approximately three times greater relative elongation than the hot-cured compound. The modulus of elasticity differs by approximately a factor of 5. For the cold-cured compound, E was as low as 670 MPa. For the hot-cured compound, $E = 3.1 \times 10^3$ MPa, which is close to E for the amine-cured compound. However, the breaking stress of the amine-cured compound appeared to be almost twice that of the HPW-cured compound. The fact that the modulus of elasticity of the hot-cured compound virtually coincides with that of the PEPA-cured epoxy resin suggests similar structures of these network polymers, and the different strength parameters may be due to increased defectiveness of the network formed by fast polymerization in the presence of the catalyst (HPW).

It is known that the density n_c of the chemical points of a polymeric network can be evaluated from the modulus of elasticity measured in the absence of intermolecular interactions; theoretically, this is the case in the hyperelastic state only. Therefore, the minimum in the microhardness of the considered formulation at a 3.8 wt % HPW content was due to substantial weakening of such interactions; this allowed us to estimate n_c from the measured tensile modulus of elasticity. Such approaches are widely used [10]. The mean density of network points was calculated from the formula [6]

$$n_c = 3E/\gamma RT,$$

where γ is the front factor taking into account the deviation of the network from the ideal state.

For epoxy materials, the experimentally determined value of γ is 1.4–1.9 [6]. We assumed a value of 1.9 (the most defective structure). The density of the network points in the hot-cured compound, determined by this procedure, was 2.3×10^3 m^{-3}, which virtually coincides with the n_c values obtained for epoxy polymers cured with amines under the same conditions.

As a rule, addition of a plasticizer to a polymeric material must increase its elasticity but decrease the strength and the modulus of elasticity [11]. However, plasticizers added in low concentrations make the material less defective and decrease the concentration of stresses at microcrack apices [1, 3, 7, 12–14]. This, in turn, must enhance the fatigue strength and durability. The relatively low cohesion strength of the compound in hand is apparently due to the high level of internal stresses arising from nonuniform gelation in slow relaxation. In this case, it can be expected that the presence of a plasticizer facilitating relaxation of stresses and enhancing the conformational mobility will strengthen the material under static conditions, too. As in [12], the dependence of the material strength on the amount of the additive must pass through a maximum, since weakening of intermolecular interactions at high plasticizer content will result in a gradual decrease in the strength characteristics. We emphasize that, in a system with a high level of internal stresses, the increase in the strength of the plasticized material relative to the initial material would be expected at relatively high plasticizer concentrations, too.

To check the validity of these assumptions, we measured the strength and relative deformation of a plasticized adhesive. As plasticizer we used glycerol, which, being a low-molecular-weight polar organic compound, is well compatible with the epoxy resin and VRP-1. Glycerol was added simultaneously with the curing agent; the glycerol : resin weight ratio was 1 : 10. The resulting compound appeared to be heterophase, which was manifested in the turbidity of the cured films (without plasticizer, the material became transparent upon curing).

As expected, the results of mechanical tests showed that the strength and modulus of elasticity of the material increased by more than a factor of 3 upon plasticization; for the hot-cured compound, the modulus of elasticity was 9.3×10^3 MPa, and the breaking stress, 11.1 MPa. The relative deformation of the films remained approximately the same. Note that the

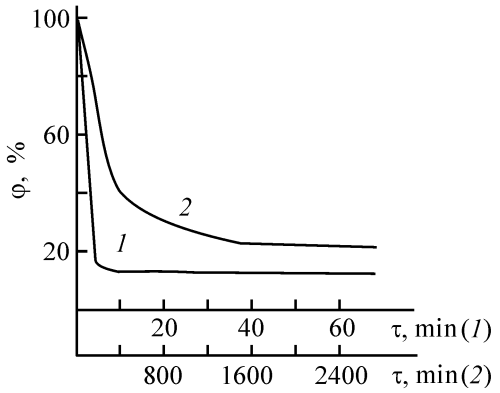

Fig. 4. Sol fraction content φ vs. time τ of curing of a compound containing 3.8 wt % HPW and glycerol. Curing temperature, °C: (*1*) 20 and (*2*) 90.

similarly measured strength of ED-20 resin cured with PEPA appeared to be 15.4 MPa, i.e., the strength of the plasticized formulation approaches that of traditional compounds.

Furthermore, the results of sol–gel analysis (Fig. 4) and microhardness measurements made with the plasticized adhesive in the course of curing show that the plasticizer inhibits somewhat the gelation and, what is especially important, smoothens inflections in the kinetic curves (Fig. 4), associated with relaxation of internal tensions (Fig. 1, range *B*). It is interesting that the residual content of the sol fraction in plasticized compounds virtually coincides with that in the glycerol-free compounds, i.e., addition of the plasticizer affects the uniformity of sol fraction distribution in the polymer bulk, rather than the overall gel fraction content.

CONCLUSIONS

(1) Introduction of a water-soluble polymer into epoxy resin hardeners based on aqueous solutions of heteropoly acids appreciably inhibits curing, decreases the heat release, and allows preparation of adhesives ensuring high strength and stability of adhesive joints; this approach opens up prospects for development of a new generation of hardeners.

(2) Curing of ED-20 epoxy resin under the action of phosphotungstic acid occurs in steps: the three-dimensionally cross-linked network is formed by intergrowth of the initially formed densely cross-linked local zones, with the transition (intergrowth) zones being the most defective and the least densely cross-linked.

(3) The mechanical properties of the adhesive developed can be controlled by introducing plasticizing additives.

REFERENCES

1. Kardashov, D.A. and Petrova, A.P., *Polimernye klei* (Polymeric Adhesives), Moscow: Khimiya, 1983.
2. Ivanov, D.A., Formation and Physicochemical Properties of a Compound Based on an Epoxy Oligomer and Heteropolymolybdic and Heteropolytungstic Acids, *Cand. Sci. Dissertation*, Moscow, 1991.
3. Arslanov, V.V., Physical Chemistry of Formation and Breakdown of Transition Composite Zones in Polymer/Metal Adhesive Joints, *Doctoral Dissertation*, Moscow, 1989.
4. Arslanov, V.V. and Ogarev, V.A., *Fiz. Khim. Obrab. Mater.*, 1977, no. 3, pp. 73–78.
5. Sanzharovskii, A.T., *Fiziko-mekhanicheskie svoistva polimernykh i lakokrasochnykh pokrytii* (Physicomechanical Properties of Polymeric and Paint-and-Varnish Coatings), Moscow: Khimiya, 1978.
6. Irzhak, V.I., Rozenberg, B.A., and Enikolopyan, N.S., *Setchatye polimery* (Network Polymers), Moscow: Nauka, 1979.
7. Chernin, I.Z., Smekhov, F.M., and Zherdev, Yu.V., *Epoksidnye polimery i kompozitsii* (Epoxy Polymers and Compounds), Moscow: Khimiya, 1982.
8. Trostyanskaya, E.B. and Babaevskii, P.G., *Usp. Khim.*, 1971, vol. 40, nos. 1–2, pp. 117–132.
9. Nielsen, L.E., *Mechanical Properties of Polymers and Composites*, New York: Marcel Dekker, 1974.
10. Lipson, G.A., Colloid-Chemical Properties of Heterogeneous Systems Based on an Epoxy Oligomer and Reactive Modifiers, *Cand. Sci. Dissertation*, Moscow, 1985.
11. *Spravochnik po plasticheskim massam* (Handbook of Plastics), Kataev, V.M., Popov, V.M., and Sazhin, B.I., Eds., Moscow: Khimiya, 1975.
12. Yakovlev, A.D., *Khimiya i tekhnologiya lakokrasochnykh pokrytii* (Chemistry and Technology of Paint-and-Varnish Coatings), Leningrad: Khimiya, 1981.
13. Funke, W. and Arslanov, V.V., *Prog. Org. Coat.*, 1988, vol. 15, no. 3, pp. 365–372.
14. Arslanov, V.V., *J. Adhesion*, 1994, vol. 44, no. 3, pp. 257–269.

Russian Journal of Applied Chemistry, Vol. 76, No. 8, 2003, pp. 1337–1343. Translated from Zhurnal Prikladnoi Khimii, Vol. 76, No. 8, 2003, pp. 1375–1381.

MACROMOLECULAR CHEMISTRY AND POLYMERIC MATERIALS

Nitric Acid Procedure for Production of Powdered Cellulose II Forms with Various Morphologies and Comparison of Their Structural and Sorption Characteristics

E. V. Gert, A. V. Matyul'ko, M. V. Shishonok, O. V. Zubets, and F. N. Kaputskii

Research Institute of Physicochemical Problems, Belarussian State University, Minsk, Belarus

Received April 14, 2003

Abstract—A two-stage procedure for production of powdered cellulose II, based on polymorphous transformation of native cellulose I and hydrolytic dispersion of the fiber with a single reagent, nitric acid, was proposed.

A search for new procedures for production of powdered cellulose (PC) forms with improved characteristics is an urgent task. The most commonly used modification of PC is microcrystalline cellulose (MCC) produced by partial acid hydrolysis of cellulose fiber to the so-called limiting degree of polymerization (DP). The vast majority of studies in this field are aimed to improve the conditions of hydrolytic cleavage of native fiber (cellulose I), characterize the recovered MCC-I, and determine the fields of its application [1–3].

At the same time, some publications [4, 5] reported similar data on cellulose II produced in the form of powder from the native fiber, using hydrolytic dispersion. According to [5], the polymorphous transition from cellulose I to cellulose II results in increased dispersity and whiteness of the final products, which is important, e.g., for pharmaceutical applications. The polymorphous transformation is usually effected by mercerization of native cellulose with 15–20% aqueous sodium hydroxide. Thus, to produce powdered cellulose II from native fiber, both alkaline and acidic reagents are used, which is inconvenient for technology.

Here, we discuss the possibility of polymorphous transformation and hydrolytic dispersion of cellulose with a single reagent, nitric acid. The structural and sorption characteristics of powdered samples of various morphologies, prepared by the acidic process, are presented in comparison with the similar characteristics of the samples produced by the traditional procedure and also of MCC-I.

EXPERIMENTAL

Purified wood sulfite cellulose of the Raikord brand (96% α-cellulose, DP = 1500) was used as the starting material for production of powdered forms.

The working 68.5% HNO_3 solution was prepared from commercial 72% HNO_3 of ultrapure grade. The acid concentration was checked by the solution density at 20°C. Along with the acid, 18% NaOH was used. Production of all powdered forms of cellulose was completed by repeated washing of the final products to neutral reaction of the wash waters, removal of water with acetone, and drying at room temperature. After drying, the samples were additionally milled in a mortar to a dispersity allowing sifting through a 100-μm sieve.

Variations of physical and chemical characteristics of cellulose in polymorphous transformation by the nitric acid procedure were judged from the IR spectra recorded on a Specord 75-IR spectrophotometer. Samples were prepared as described in [6]. The content of bound nitrogen in the samples was determined by the Kjeldahl procedure [7].

The degree of polymerization of powdered cellulose forms was estimated from the viscosity of nitrate ester solutions according to the procedure [8] tested on the samples of cellulose with known DP.

X-ray diffraction patterns were recorded on an HZG-4a diffractometer (Cu_{K_α} radiation, Ni filter). The samples in the form of flat discs were prepared by cold pressing. The crystallinity index of the samples

1070-4272/03/7608-1337 $25.00 © 2003 MAIK "Nauka/Interperiodica"

was determined from the diffraction patterns obtained under similar conditions [9].

The morphology of structural elements of the powders was studied with an EM-125K transmission electron microscope. PC particles were dispersed by ultrasonic treatment (UZDN-2T unit, 22 kHz, maximum power). As a result, a slightly opalescent suspension was obtained. A drop of this suspension was applied to the surface of freshly painted mica, and the dispersion medium was evaporated. The samples for microscopic examination were prepared using platinum-carbon replicas.

The surface of powder particles and cross sections of the fibers were studied using an S-520 Hitachi scanning electron microscope. The cross sections were obtained on a manual microtome using a razor blade. The surfaces to be studied were gold-plated in a gas-plasma discharge.

The procedure for determining the water-retaining capacity (WRC) of cellulose was described in [10]. The sorption of iodine was evaluated by the procedure described in [11], and that of Congo Red, by the procedure described in [12].

The nitric acid procedures for production of powder forms of cellulose II, discussed here, are based on the ability of HNO_3 to form the Knecht addition compound (KC) with cellulose at a concentration of 68–69%, and also to promote hydrolysis of cellulose fiber at low concentrations and elevated temperature.

KC has been known for a long time [13], but up to now its chemical composition and structure have not been determined reliably. Under the action of water, cellulose is regenerated from KC produced on the basis of native cellulose, which enables a purely acidic scheme for processing of native fiber to powdered forms of cellulose II.

HCl, as a rule, and, less commonly, H_2SO_4 are used for hydrolytic cleavage of cellulose fiber [14]. Among published data, there are only a few evidences for the use of HNO_3 for this purpose [15, 16], although its catalytic activity is rather high. When studying sucrose hydrolysis in solutions of some acids, Ostwald revealed the highest catalytic activity of HCl, which was then taken as a reference. According to similar experimental data on hydrolysis of cellulose in 2 N solutions of various acids, the catalytic activity of HNO_3 at 100°C is close to the activity of HCl (0.95 against 1), while that of H_2SO_4 is 0.57 [17]. Apparently, the development of studies on using HNO_3 for production of MCC has been restrained by the well-known ability of this acid to chemically modify cellulose.

Two samples of cellulose II in the powdered form were prepared by the unconventional procedure using nitric acid only. In production of a sample with microcrystalline structure (MCC-IIn), wood cellulose was first treated for 3 h at the temperature of thawing ice and a liquid-to-solid ratio of 20 ml of 68.5% nitric acid per gram. This treatment must provide complete intracrystallite swelling of native cellulose, so that under subsequent action of water it must completely transform via KC into cellulose II. It is wood cellulose with its inherent moderate crystallinity that is the most appropriate material for completion of these transformations under the action of 68–69% HNO_3 and then water. In the case of cotton cellulose characterized by relatively coarse and perfect crystallites, phase transitions cellulose I $\rightarrow$ KC and KC $\rightarrow$ cellulose II occur partially [18].

Nitric acid at a concentration of 68–69% exerts a weak nitrating effect on cellulose [18, 19]. To decrease the nitrating activity of nitric acid, the treatment was carried out at low temperature, which, however, increased the duration of complete conversion of cellulose into KC [19]. Cellulose swollen in 68.5% HNO_3 was squeezed out to approximately three fold overweight. In squeezing, no less than 60% of the initial amount of HNO_3 is released. After appropriate concentrating and loss compensation this acid can be reused for the polymorphous transformation of cellulose. Water was added in amount required for formation of 2.0–2.5 N HNO_3 from the concentrated acid sorbed with the fiber to the squeezed pulp. As a result of dilution, cellulose II is regenerated from KC. It was hydrolyzed to the limiting DP with boiling 2.0–2.5 N HNO_3 for 1 h at a liquid-to-solid ratio of approximately 10 ml g^{-1}.

The second sample (PC-IIn) was prepared by the purely acidic scheme based on cellulose prehydrolyzed to the limiting DP. Hydrolysis was performed with boiling 2.5 N HNO_3 at a liquid-to-solid ratio of 10 ml g^{-1} for 1 h. The resulting MCC-I was washed and dried by the above procedure. A part of this material was converted into cellulose II with 68.5% HNO_3.

With the aim to compare the characteristics of powdered forms of cellulose II produced by the purely acidic scheme, we also prepared MCC-IIt and PC-IIt samples of similar structure by the conventional scheme. In the conventional scheme, the polymorphous transformation of native cellulose was carried out by usual mercerization with 18% aqueous NaOH for 1 h at the temperature of thawing ice and liquid-to-

solid ratio of 20 ml g^{-1}. The conditions of hydrolysis, washing, and drying of all the prepared samples were the same, with only the procedures for transformation of cellulose I to cellulose II being different.

The yield of the final products is governed mainly by the loss of the material in hydrolysis of cellulose fiber to the limiting DP. This loss is the most noticeable in the case of hydrolysis of cellulose II, whose crystal structure is less perfect that that of cellulose I. The MCC-IIn and MCC-IIt samples are produced in 72–75% yield, based on the weight of the initial cellulose, with the yield of MCC-1, PC-IIn, and PC-IIt samples being 83–85%.

The IR spectra of all the prepared samples show signs of oxidative transformations (range 1700-1800 cm^{-1}). Weak absorption bands of nitrate ester groups (1650, 1280, 850, and 750 cm^{-1}) appear only in the spectrum of the PC-IIn sample produced by treatment with 68.5% HNO_3 in the final stage of the process. According to the results of chemical analysis, this sample contains approximately eight nitrate ester groups in 100 cellulose units. In production of MCC-IIn, hydrolytic cleavage of the cellulose fiber follows its treatment with HNO_3. As a result of hydrolysis, most of nitrate ester groups added in the first stage are removed from the fiber together with amorphous binder [18]. Comparison of the spectrum of MCC-I with the spectra of the other samples shows that the intensities of the absorption bands at 1430, 1111, and 890 cm^{-1} vary in conformity with the well-known manifestations of cellulose I and cellulose II in the IR spectra [20].

The X-ray diffraction patterns of the samples are shown in Fig. 1. Comparison of the reflection positions in powder patterns 2 and 4 with those in the powder patterns of similar samples subjected to the conventional mercerization (3 and 5) shows that, under the action of 68.5% HNO_3, the polymorphous transition is virtually complete. However, some "residual nativity" apparently remains in MCC-IIn, since in its powder pattern the reflection (002) is the strongest, which is not characteristic of cellulose II (powder patterns 3 and 5) and is characteristic of cellulose I (powder pattern 1). This conclusion can also be made on the basis of electron microscopic data, which are considered below.

If account is taken of the fact that, the polymorphous transformation of fibrous cellulose in 18% aqueous NaOH occurs under conditions of much stronger swelling than that in 68–69% HNO_3 [19], the retention of some elements of structural organization typical of native cellulose after acid treatment seems to be quite logical. In polymorphous transformation under the action of HNO_3, the cellulose fiber undergoes decrystallization to a noticeably greater extent than in usual mercerization with an NaOH solution. This difference in crystallinity is preserved after hydrolysis of cellulose to the limiting DP. The crystallinity index of MCC-IIn is 0.44, while that of MCC-IIt is 0.57 (see table). Polymorphous transformation of MCC-I under the action of HNO_3 is accompanied by the deepest decrystallization, whose plausible reasons were discussed in [18]. PC-IIn is characterized by powder pattern 4 typical of cellulose II with very low degree of structural ordering (crystallinity index 0.23 against 0.45 in PC-IIt).

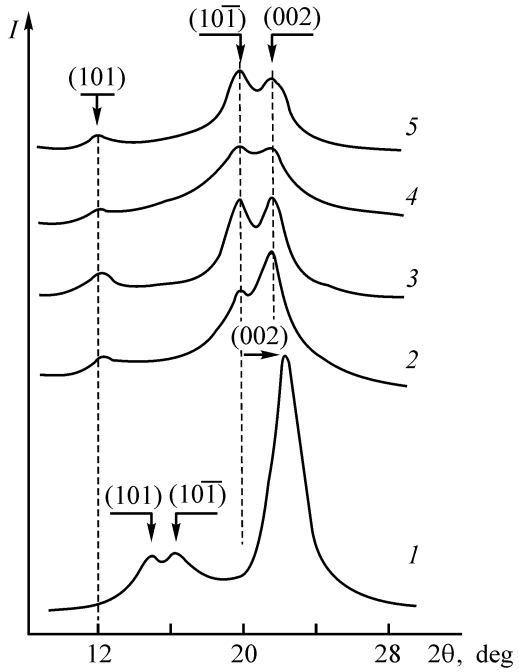

Fig. 1. X-ray diffraction patterns of powdered forms of cellulose. (*I*) Relative intensity and (2θ) Bragg angle. (*1*) MCC-I, (*2*) MCC-IIn, (*3*) MCC-IIt, (*4*) PC-IIn, and (*5*) PC-IIt.

Some characteristics of powdered forms of cellulose

Sample	DP	Crystallinity index	WRC	WRC*	Sorption of I_2, mg g^{-1}
			%		
MCC-I	170	0.67	58	56	19.9
MCC-IIn	50	0.44	107	73	76.3
MCC-IIt	50	0.57	105	65	27.0
PC-IIn	150	0.23	155	83	261.4
PC-IIt	160	0.45	208	100	119.1

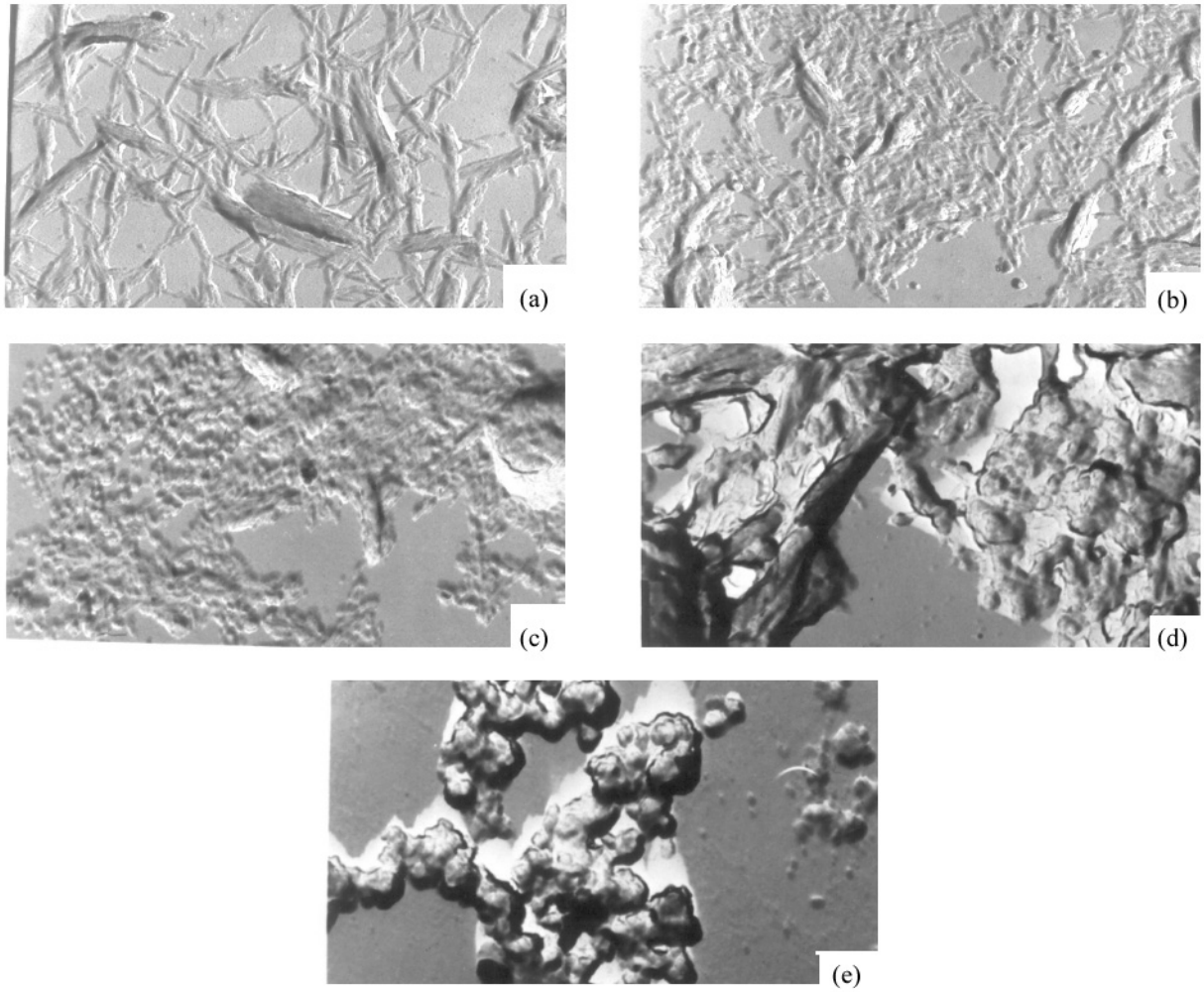

Fig. 2. Electron micrographs of fragments produced by ultrasonic dispersion of powdered forms of cellulose. Magnification 11 000. (a) MCC-I, (b) MCC-IIn, (c) MCC-IIt, (d) MCC-IIn, and (e) PC-IIt.

Figure 2 shows electron micrographs of fragments formed after desintegration of the prepared samples by ultrasonic dispersion. In the case of MCC-I (Fig. 2a), the well-known asymmetric aggregates of needle-shaped microcrystallites are well defined. At present, it is well established that this "needle morphology" is typical of microcrystallites recovered from native cellulose fiber [14]. Based on the average limiting DP of MCC-I equal to 170, the length of anhydroglucose unit of cellulose (5.15 Å), and elongated conformation of macromolecules in microcrystals, we can conclude that the average longitudinal size of microcrystals of this native material is approximately 900 Å.

In passing from cellulose I to cellulose II, the dispersity and morphology of crystallites change significantly (Figs. 2b, 2c). The average limiting DP of both MCC-IIn and MCC-IIt is approximately 50 (see table), which suggests a more than threefold decrease in the length of crystallites, compared to MCC-I. Because of the small sizes and increased tendency to aggregation during preparation of suspensions, individual microcrystals of MCC-IIn and MCC-IIt are difficult to distinguish.

Micrographs of the sample prepared through the stage of intensive swelling of the initial cellulose in alkaline solution (MCC-IIt) show no clearly pronounced indications of the asymmetric shape of microcrystals. A similar electron micrograph of cellulose II microcrystals obtained by acid hydrolysis from viscose fiber can be found in [14]. At the same time, comparison of micrographs 2b and 2c shows that, despite the equality of the limiting DP and, hence, the equality of the microcrystal lengths MCC-IIn show, in contrast to MCC-IIt, clearly pronounced elements of asymmetric aggregation of microcrystals,

characteristic of native MCC. In our opinion, this morphologic feature of MCC-IIn is due to relatively weak swelling of the initial cellulose when polymorphous transformation is performed with 68–69% HNO_3 instead of the conventionally used NaOH solution. We believe that, after the phase transition under the action of HNO_3, crystallites of the cellulose fiber keep "elements of memory" about the morphology of its native precursor.

In production of PC-IIn and PC-IIt (Figs. 2d, 2e) by polymorphous transformation of MCC-I (Fig. 2a) by both alkaline and acidic reagents, the average DP (170) characteristic of native microcrystals remains virtually the same, while the crystallite size and crystallinity of the material as a whole decrease significantly (see table). The length of crystallites is not governed by DP (DP is greater). Microcrystalline structure of cellulose I is transformed into the usual amorphous crystalline structure of cellulose II with low DP. This leads to an abrupt change in the morphology of fragments (compare Figs. 2a–2c with Figs. 2d, 2e). The extremely strong tendency for PC-IIn and PC-IIt particles to aggregate results mainly in the formation of coarse friable fragments in the form of micrometer-sized islets with irregular shape. In the case of PC-IIn, coarse fragments are composed of smaller aggregates of, as a rule, fibril-like type (Fig. 2d), and in the case of PC-IIt, of lump-like type (Fig. 2e). This is also due to different degrees of MCC-I swelling in acidic and alkaline media used for the phase transformation.

The prepared powdered forms of cellulose II differ from native MCC in the significantly higher hydrophilicity and sorption activity (see table). The hydrophilicites of cellulose powders was evaluated by two characteristics. One of these, WRC, characterizes a sample of the final product, washed to neutral reaction and not subjected to drying, and corresponds to the maximum attainable value of WRC. The second characteristic, WRC*, characterizes the ability of a dried sample in the usual air-dry state to retain water. For MCC-I, whose crystallites are similar to crystallites of the initial fiber not subjected to significant transformations in recovery, these characteristics are close. For MCC-II and, especially, PC-II samples, these characteristics are significantly different, which reflects the negative influence of drying on the hydrophilicity of cellulose II.

Microcrystalline forms of cellulose II, produced by both procedures, have comparable hydrophilicities, being markedly inferior in this regard to amorphous-crystalline forms. The most hydrophilic is the sample

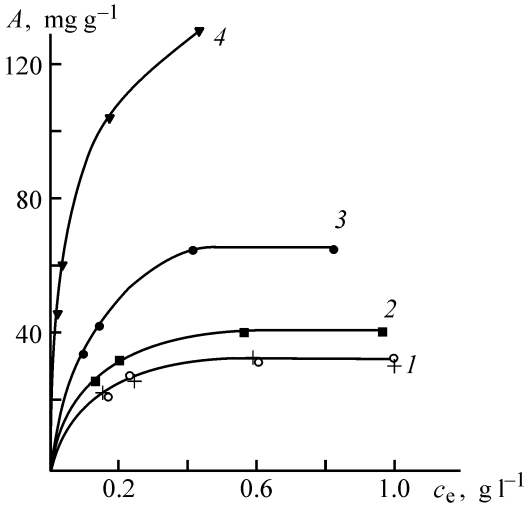

Fig. 3. Isotherms of sorption of Congo Red with powdered cellulose forms. (*A*) sorption and (c_e) equilibrium concentration. (*1*) MCC-I and MCC-IIt, (*2*) MCC-IIn, (*3*) PC-IIt, and (*4*) PC-IIn.

prepared by the conventional procedure and having amorphouscrystalline morphology (PC-IIt), despite that its crystallinity index is greater than that of the similar sample prepared by the purely acidic scheme (PC-IIn). There is no strict correlation between the crystallinity index and hydrophilicity of the samples, whereas the influence of the morphology factor of the water-retaining capacity is appreciable. This influence is especially noticeable in the case of moistening of samples during preparation (WRC characteristic). Drying of the final products even at room temperature noticeably levels out the differences in hydrophilicity between the samples of microcrystalline and amorphous-crystalline morphology (WRC* characteristic).

Powdered forms of cellulose II, prepared by the purely acidic procedure, surpass the conventional analogs in the ability to sorb iodine by more than a factor of 2 (see table). Here, the samples of amorphous-crystalline morphology have the highest sorption power. The sorption of iodine by these samples is 3–4 times greater than that of the samples of microcrystalline morphology. Similar features are observed in the case of sorption of Congo Red (Fig. 3). The isotherms of Congo Red sorption by MCC-I and MCC-IIt coincide within the measurement error (Fig. 3, curve *1*). It should be noted that the values of iodine sorption by these samples are very close. The MCC-IIn sample sorbs the dye somewhat more actively than the two above-mentioned dyes; however, the difference in the values of limiting sorption is small (Fig. 3, curves *1* and *2*). Thus, with respect to sorption of bulky molecules, the microcrystalline forms of cellu-

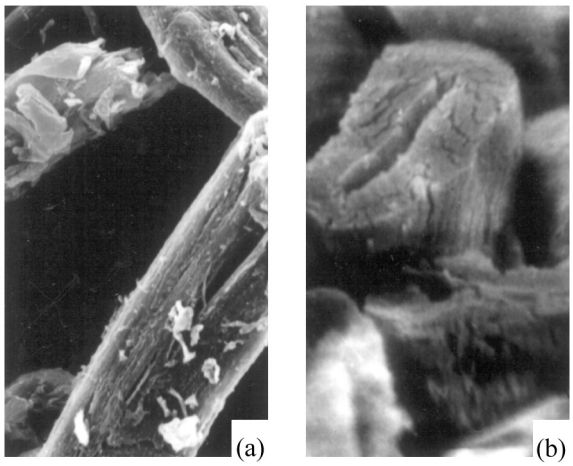

Fig. 4. SEM micrographs of (a) surface of PC-IIn particles and (b) cross section of cotton fibers after treatment with 68.5% HNO_3. Magnification 1250.

lose I and cellulose II produced by various procedures are characterized by close values of limiting sorption. Congo Red, as well as iodine, is most efficiently sorbed by PC-IIn (Fig. 3, curve *4*), which considerably exceeds all the other samples in this respect.

Within the same morphological form of the powdered material, there is a correlation between its crystallinity index and sorption capacity for both iodine and Congo Red. The lower the sorbent crystallinity, the higher its activity (see table, Fig. 3). However, the highest sorption characteristics of PC-IIn, compared to the other samples, are apparently caused by not only its low crystallinity. It was found that, in contrast to the conventional procedure, polymorphous transformation of cellulose by nitric acid is accompanied by appearance of a great number of longitudinal microcracks. These microcracks are readily seen on both the side surface and cross sections of fibrous fragments (Fig. 4). The formation of microcracks must enhance the sorption power of the material. In preparation of the MCC-IIn sample, the effect of microcracking is eliminated in hydrolytic degradation of fiber to aggregates of microcrystals in the final stage of the process. In the case when the final stage of the process is polymorphous transformation of preliminarily dispersed fiber (PC-IIn) with 68.5% HNO_3, this effect is observed. Apparently, along with low crystallinity of PC-IIn, this effect is responsible for the high sorption power of this sample.

CONCLUSIONS

(1) The ability of native cellulose to undergo phase transformation through formation of a Knecht compound in the reaction with 68.5% HNO_3 and the hydrolytic activity of boiling dilute solutions of this acid allow production of powdered forms of cellulose II without the conventional mercerization of cellulose with alkali solutions. The order of procedures performed with the same reagent governs the morphology of the final products, their degree of polymerization, hydrophilicity, and sorption power.

(2) Contrary to similar samples subjected to the conventional mercerization, powdered forms of cellulose prepared by the acidic procedure retain some elements of structural organization typical of the native cellulose. This is accounted for by the fact that the phase transition of cellulose in nitric acid occurs at considerably lower swelling than that in an alkaline medium.

(3) The discussed powdered forms of cellulose II have considerably lower crystallinity than their analogs, and values of sorption of Congo Red and iodine by these samples are more than 2 times greater, which is especially noticeable for the amorphous-crystalline samples. The phase transformation of cellulose in nitric acid is accompanied by the formation of a developed system of longitudinal microcracks in the fiber, which, in combination with the lowered crystallinity of the samples, provides their high sorption power.

REFERENCES

1. US Patent 5543511.
2. US Patent 5554287.
3. US Patent 4645541.
4. Romanian Patent no. 76116.
5. Sarybaeva, R.I., Vasil'kova, T.V., Sultankulova, A.S., and Trushkina, N.I., *Tsellyuloza v vide poroshka: Poluchenie, svoistva, primenenie* (Cellulose in Powdered Form: Production, Properties, Application), Frunze: Ilim, 1986.
6. *Metody issledovaniya tsellyulozy* (Methods of Studying Cellulose), Karlivan, V.P., Ed., Riga: Zinatne, 1981.
7. Cheronis, N.D. and Ma, T.S., *Organic Functional Group Analysis by Micro and Semimicro Methods*, New York: Wiley, 1964.
8. Nikitin, N.I., *Khimiya drevesiny i tsellyulozy* (Chemistry of Wood and Cellulose), Moscow: Izd. Akad. Nauk SSSR, 1962.
9. Iolovich, M.Ya. and Veveris, G.P., *Khim. Drev.*, 1983, no. 2, pp. 10–14.
10. Fahmy, Y. and Mobarak, F., *Sven. Papperestidning*, 1971, vol. 74, pp. 2–9.
11. Aziz, K. and Amine Abou-State, M., *Cellulose Chem. Technol.*, 1974, vol. 8, no. 5, pp. 433–447.

12. Iolovich, M.Ya., *Khim. Volkna*, 1992, no. 6, pp. 46–48.
13. Andress, R.K., *Z. Phys. Chem.*, 1928, vol. 136, pp. 279–288.
14. Battista, O.A., *Microcrystal Polymer Science*, New York: McGraw–Hill, 1975.
15. Sato, D. and Nagishi, S., *J. Jpn. Tech. Assoc. Pulp Paper Ind.*, 1966, vol. 20, pp. 427–434.
16. Usmanov, Kh.U., An, A.P., Zaripova, A.M., *et al.*, Abstracts of Papers, *V Vsesoyuznaya konferentsiya po khimii i fizike tsellyulozy* (V All-Union Conf. on Chemistry and Physics of Cellulose, Tashkent: Fan, 1982, Part 2, p. 113.
17. Sharkov, V.I., *Gidroliznoe proizvodstvo* (Hydrolysis Industry), *part 1: Teoriya osakharivaniya razbavlennymi kislotami* (Theory of Saccharification with Dilute Acids), Moscow: Gos. Lit. Tekh. Izd., 1945.
18. Gert, E.V., *Cellulose*, 1996, vol. 3, no. 4, pp. 217–228.
19. Gert, E.V., Sacarras Marales, A., Zubets, O.V., and Kaputskii, F.N., *Cellulose*, 2000, vol. 7, pp. 57–66.
20. Nelson, M.L. and O'Connor, R.T., *J. Appl. Polym. Sci.*, 1964, vol. 8, pp. 1311–1324.

Russian Journal of Applied Chemistry, Vol. 76, No. 8, 2003, pp. 1344–1347. Translated from Zhurnal Prikladnoi Khimii, Vol. 76, No. 8, 2003, pp. 1382–1385.

MACROMOLECULAR CHEMISTRY AND POLYMERIC MATERIALS

Oxidative Delignification of Flax Fiber[1]

S. N. Petrova, I. Yu. Volkova, and A. G. Zakharov

Institute of Chemistry of Solutions, Russian Academy of Sciences, Ivanovo, Russia

Received March 12, 2003

Abstract—Oxidative delignification of flax fiber at 98°C was studied. The intermediate material was produced in moderate yield with high degree of delignification. The optimum conditions of the process were determined.

Use of annual plants as a raw material for production of cellulose is highly promising, since plant resources, renewable every year, contain as well as wood material, a sufficient amount of cellulose (Table 1). This does not exert any negative influence on the environment and assists to preservation of woodland. Here, we studied delignification of intermediate flax fiber, which can serve as an excellent source of cellulose, since, as regards its chemical composition, it occupies an intermediate position between long-stemmed flax (high-grade flax fiber) and wood.

As a rule, alkaline and alkaline-peroxide treatments are used for refining of cellulose-containing materials. Hydrogen peroxide is an efficient oxidizing agent and modifier of chromophore groups of lignin. It is well known [5, 6] that transition metal compounds catalyze oxidative delignification by H_2O_2. They react with H_2O_2 to form intermediate peroxo complexes Cat–O, which, in turn, transport active oxygen from hydrogen peroxide to the substratum by the scheme

$$H_2O_2 + Cat \rightleftarrows H_2O + Cat\text{–}O,$$

$$L + Cat\text{–}O \rightleftarrows L_{ox} + Cat,$$

where L and L_{ox} are lignin and products of its oxidation, respectively [5, 7].

Sulfuric acid promotes the activity of peroxo complexes and stabilizes the peroxide solution, but, simultaneously, it causes noticeable hydrolytic degradation of polysachharides [8]. At the same time, oxidized lignin is poorly soluble in acid medium; therefore, alkaline extraction is necessary for its complete recovery.

EXPERIMENTAL

Flax fiber was subjected to two-stage treatment: oxidative treatment with an H_2O_2 solution in the presence of $(NH_4)_2MoO_4$ and H_2SO_4 as catalyst (for 60 min) and alkaline extraction with 4% NaOH (120 min). Both stages were carried out at 98°C. The H_2O_2 con-

Table 1. Chemical composition of various cellulose-containing materials

Plant material	Content, wt %					Reference
	cellulose	hemicellulose	lignin	wax	ash	
Flax fiber	88–96	0.5–1.0	0	0.4–1.3	0.7–1.6	[1]
Long-stemmed flax	65–80	12–17	3–5	1.4	1.06	[1]
Coniferous wood	45–52	10–23	28–30	2–7	0.2–1.0	[2]
Deciduous wood	37–47	22–33	19–23	1.3–7	0.2–0.4	[2]
Rye straw	37.9	36.9	17.6	2.0	3.0	[3]
Wheat straw	36.0	35.0	16.5	–	–	[4]
Intermediate flax fiber	72	8.7	11.04	1.4	2.91	This study

[1] Intermediate (low-grade) flax fibers having no practical application were subjected to delignification.

1070-4272/03/7608-1344 $25.00 © 2003 MAIK "Nauka/Interperiodica"

Table 2. Experimental data

Sample no.	Solution composition in the 1st stage, wt %			Yield of the intermediate product, %	Content of Classon lignin L, %	DP
	H_2O_2	Catalyst				
		$(NH_4)_2MoO_4$	H_2SO_4			
Initial flax	–	–	–	–	11.04	4000
1	8	–	–	63.5	4.25	1430
2		1.04	0.625	54.0	1.58	1120
3		2.08	1.25	54.0	0.22	800
4		4.16	2.5	54.5	0.80	600
5	4	–	–	54.5	6.73	2900
6		1.04	0.625	54.0	2.15	930
7		2.08	1.25	55.0	0.95	890
8		4.16	2.5	53.5	1.06	530
9	2	–	–	67.5	7.11	2800
10		1.04	0.625	56.5	3.25	1040
11		2.08	1.25	54.5	0.96	800
12		4.16	2.5	53.0	1.92	710
13	1	–	–	68.5	7.32	3300
14		1.04	0.526	58.0	3.35	1050
15		2.08	1.25	57.0	1.12	710

tent was varied from 1 to 8 wt %, and $(NH_4)_2MoO_4$ content, from 0 to 4 wt %. The H_2SO_4 content was varied in direct proportion to that of $(NH_4)_2MoO_4$. The following characteristics of the process were evaluated: degree of delignification (DD), degree of carbohydrate removal (DCR), characteristic of process selectivity (PS), and extent the process optimization (PO) [9].

In the sample produced we determined the content of Classon lignin by sulfuric acid procedure with 72% H_2SO_4 [10], and the degree of polymerization (DP), by viscometric method [11]. Changes in the structure of flax fiber during treatment were studied by IR spectroscopy. The IR spectra were recorded on an Avatar E.S.P. IR Fourier spectrometer in the range 4000–400 cm^{-1}. The samples were prepared from milled fibers in KBr pellets.

Preliminary tests showed that, in treatment of flax fiber in alkaline and alkaline-peroxide solutions, an intermediate product with residual lignin content of 6 and 4%, respectively, can be obtained. For more exhaustive delignification, the fiber was treated in two stages, using a catalytic additive. Samples of flax cellulose were obtained with average yield of 53–68%, with the residual lignin content of 0.22–7.3% (Table 2). The evaluated characteristics of the process are listed in Table 3 and shown in Fig. 1. With increasing content of the catalyst in the solution and constant concentration of H_2O_2, the degree of delignification grows and degree of polymerization decreases. For example, with the content of $(NH_4)MoO_4$

Table 3. Evaluated parameters

Sample no. (Table 2)	DD	DCR	PS
	%		
1	75.55	31.65	69.28
2	92.27	40.26	60.12
3	98.92	39.43	60.62
4	96.05	39.23	60.96
5	66.78	42.86	58,84
6	89.48	40.60	59.92
7	95.27	38.76	61,46
8	94.86	40.50	59,76
9	56.53	29.52	71.99
10	83.37	38.55	62.23
11	95.26	39.32	60.91
12	90.78	41.57	58.90
13	54.58	28.64	72.89
14	82.40	36.99	63.80
15	94.22	36.64	63.62

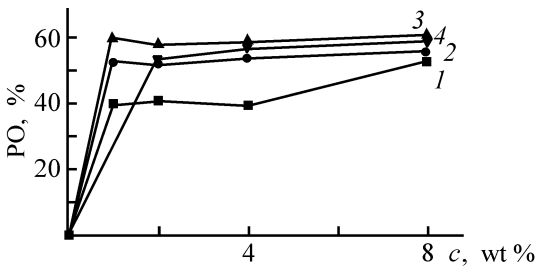

Fig. 1. Extent of the process optimization PO vs. the content c of hydrogen peroxide. Content of $(NH_4)_2MoO_4$ (wt %): (*1*) 0, (*2*) 1.04, (*3*) 2.08, and (*4*) 4.16.

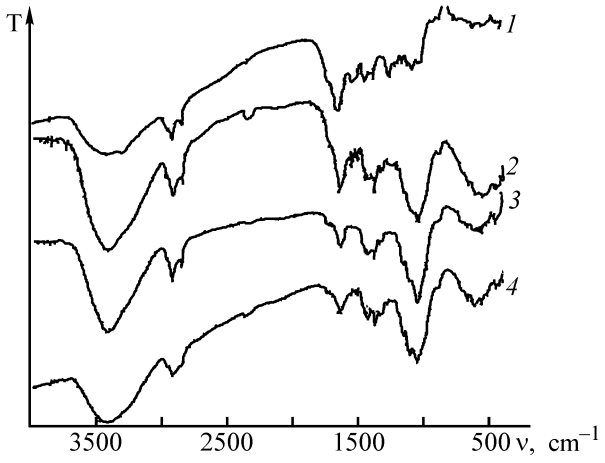

Fig. 2. IR spectra of the samples: (T) transmission and (ν) wave number. (*1*) Alkaline lignin, (*2*) initial flax fiber, (*3*, and *4*) flax fiber after chemical treatment (Table 2, sample nos. 2 and 4).

increasing from 0 to 4 wt % at 4 wt % content of H_2O_2, the degree of delignification increases from 66 to 95%, the degree of carbohydrate removal is about 40%, and DP decreases from 2900 to 530. At constant content of the catalyst, the degree of delignification grows with increasing content of H_2O_2. In this case, the degree of polymerization remains virtually constant (Table 3). Addition of the catalyst significantly accelerates the delignification of the flax fiber. For example, in treatment of a cellulose-containing material with a 1% H_2O_2 solution at the lowest content of the catalyst (1.04 wt %), the degree of delignification may reach 82.5%, while in refining without a catalyst, even in a 8% H_2O_2 solution, the degree of delignification is only 75%.

The most favorable conditions of refining of cellulose-containing material are those at which the removal of lignin is at a maximum and dissolution of carbohydrates is at a minimum. In this context, we evaluated the extent of the process optimization PO = DD PS/100 (Fig. 1). It is seen that, even at H_2O_2 content in the solution of 1 wt %, the extent of the process optimization is high. The dependence of this characteristic on the catalyst concentration passes through a maximum and, at the $(NH_4)_2MoO_4$ content higher than 2 wt %, PO decreases. This is apparently caused by predominance of dissolution of carbohydrates over degradation of lignin with a parallel increase in the H_2SO_4 concentration in the solution.

Structural transformations of flax fiber in the course of delignification were also judged from IR data (Fig. 2). For comparison, we recorded the IR spectrum of alkaline lignin produced by precipitation from the solution after alkaline extraction (Fig. 2, curve *1*). In the course of delignification, the intensities of the bands at 1050 (bending vibrations of OH groups of cellulose) and 1160 cm^{-1} (vibrations of the pyranose ring of cellulose) [3, 12, 13] increase, whereas the intensity of absorption in the range of 1450–1600 cm^{-1}, related to skeleton vibrations of the aromatic ring, and that of the band at 1270 cm^{-1}, characterizing guaiacyl structural units of lignin [14], decrease. A decrease in the splitting of the band in the range of stretching vibrations of CH bonds of methyl and methylene groups (2850–2920 cm^{-1}) also suggests removal of lignin-like structures. From the ratio of the optical densities of the absorption bands D_{1370}/D_{2900}, we estimated the crystallinity index [15, 16], which was equal to 0.84, 0.87, and 0.90 for the initial flax and purified fibers (Fig. 2), respectively. This is apparently caused by the fact that chemical modification of the plant material involves, along with removal of lignin, dissolution of the low-molecular-weight fractions of cellulose and hemicellulose.

REFERENCES

1. Krichevskii, G.E., *Khimicheskaya tekhnologiya tekstil'nykh materialov* (Chemical Technology of Textile Materials), Moscow: Khimiya, 2000, vol. 1.
2. Nikitin, V.M., Obolenskaya, A.V., and Shchegolev, V.P., *Khimiya drevesiny i tsellyulozy* (Chemistry of Wood and Cellulose), Moscow: Lesn. Prom–st., 1978.
3. Fang, J.M., Sun, R.C., and Tomkinson, J., *Cellulose*, 2000, vol. 7, pp. 87–107.
4. Iolovich, M.Ya., Tupureine, A.D., and Veveris, G.P., *Khim. Drev.*, 1989, no. 5, pp. 3–9.
5. Pen, R.Z. et al., *Khim. Rast. Syr'ya*, 2001, no. 1, pp. 43–48.
6. Deineko, I.P. and Loginova, N.M., *Khim. Drev.*, 1986, no. 3, pp. 48–52.

7. Vol'nov, I.I., *Peroksokompleksy khroma, molibdena, vol'frama* (Peroxo Complexes of Chromium, Molybdenum, and Tungsten), Moscow: Nauka, 1989.
8. Pen, R.Z. *et al.*, *Khim. Rast. Syr'ya*, 2001, no. 3, pp. 5–10.
9. Simkhovich, B.E., Zil'bergleit, M.A., and Reznikov, V.M., *Khim. Drev.*, 1986, no. 3, pp. 34–38.
10. Obolenskaya, A.V., *Laboratornye raboty po khimii drevesiny i tsellyulozy: Uchebnoe posobie dlya vuzov* (Laboratory Manual on Chemistry of Wood and Cellulose), Textbook for Higher School Institutions, Moscow: Ekologiya, 1991.
11. *Analiticheskii kontrol' proizvodstva iskusstvennykh volokon: Spravochnoe posobie* (Analytical Monitoring of Production of Synthetic Fibers: Handbook), Dibrov, A.K. and Matveeva, V.S., Eds., Moscow: Khimiya, 1986.
12. Ermolenko, I.N., *Spektroskopiya v khimii okislennykh tsellyuloz* (Spectroscopy in Chemistry of Oxidized Celluloses), Minsk: Akad. Nauk Bel. SSR, 1959.
13. Zhbankov, R.G., *Infrakrasnye spektry tsellyulozy i ee proizvodnykh* (IR Spectra of Cellulose and Its Derivatives), Minsk: Nauka i Tekhnika, 1964.
14. *Lignins: Occurrence, Formation, Structure, and Reactions*, Sarkanen, K.V. and Ludwig, C.H., Eds., New York: Wiley, 1971.
15. *Cellulose and Cellulose Derivatives*, Bikales, N. and Segal, L., Eds., New York, 1971, vol. 1.
16. Zavadskii, A.E. *et al.*, *Izv. Vyssh. Uchebn. Zaved., Tekhnol. Tekstil. Prom–sti.*, 1986, no. 2, pp. 81–84.

Russian Journal of Applied Chemistry, Vol. 76, No. 8, 2003, pp. 1348–1350. Translated from Zhurnal Prikladnoi Khimii, Vol. 76, No. 8, 2003, pp. 1386–1388.

CHEMISTRY OF FOSSIL FUEL

Transformations of Acids in the Course of Ozonolysis of Oxygen-containing Derivatives of Cycloparaffins

A. M. Syroezhko and O. Yu. Begak

St. Petersburg State Technological Institute, St. Petersburg, Russia

Mendeleev Russian Research Institute of Metrology, Federal State Unitary Enterprise, St. Petersburg, Russia

Received March 20, 2003

Abstract—Transformations of monocarboxylic, dicarboxylic, and keto acids in the course of low-temperature ozonolysis were studied using the corresponding ^{14}C-labeled compounds.

Deep oxidation of cyclohexane [1], methylcyclohexane [2], and their oxygen-containing derivatives (alcohols, ketones, esters, lactones) [2] results in accumulation of monocarboxylic, dicarboxylic, and keto acids, which are actively oxidized by ozone–oxygen mixtures.

In this study, we analyzed transformations of [2,3-^{14}C]succinic, [2,4-^{14}C]glutaric, [1,2-^{14}C]-α-ketoglutaric, and [1-^{14}C]caproic acids in 2-methylcyclohexanol under conditions of its oxidation at 80°C ([O_3] = 4 vol %).

Procedures for radiochromatographic analysis of the acids are described in [3, 4]. Calculations [2] show that, under these conditions, the hydroxy peroxy radical derived from 2-methylcyclohexanol does not react with the C–H bonds of the acids in hand and of 2-methylcyclohexanol. However, alkyl and alkoxyl radicals and ozone abstract the most labile hydrogen atoms from 2-methylcyclohexanol, labeled acids under consideration, and intermediate oxidation products, including radicals. The radioactive products of ozonolysis of [2,3-^{14}C]succinic acid are [2,3-^{14}C]propionic acid, [2-^{14}C]acetic acid, and $^{14}CO_2$.

[2,3-^{14}C]Succinic acid is 21.5% decarboxylated in 3 h at 32.5% overall conversion. Ozone attacks the acid at both the methylene chain and the functional group:

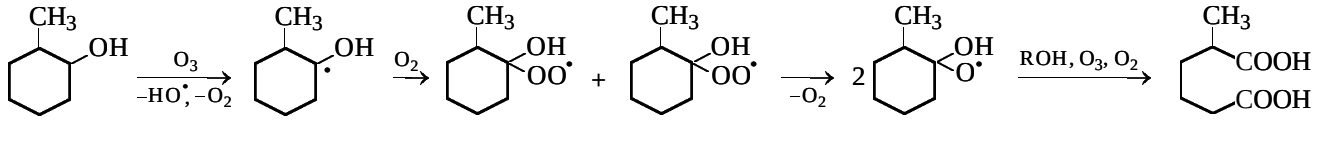

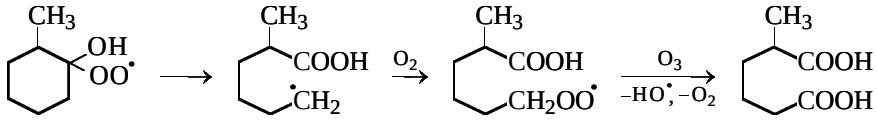

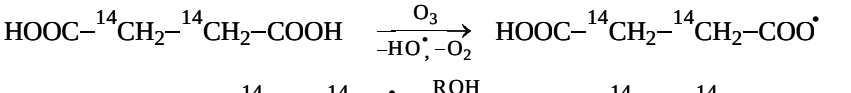

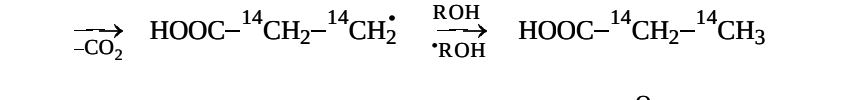

1070-4272/03/7608-1348 $25.00 © 2003 MAIK "Nauka/Interperiodica"

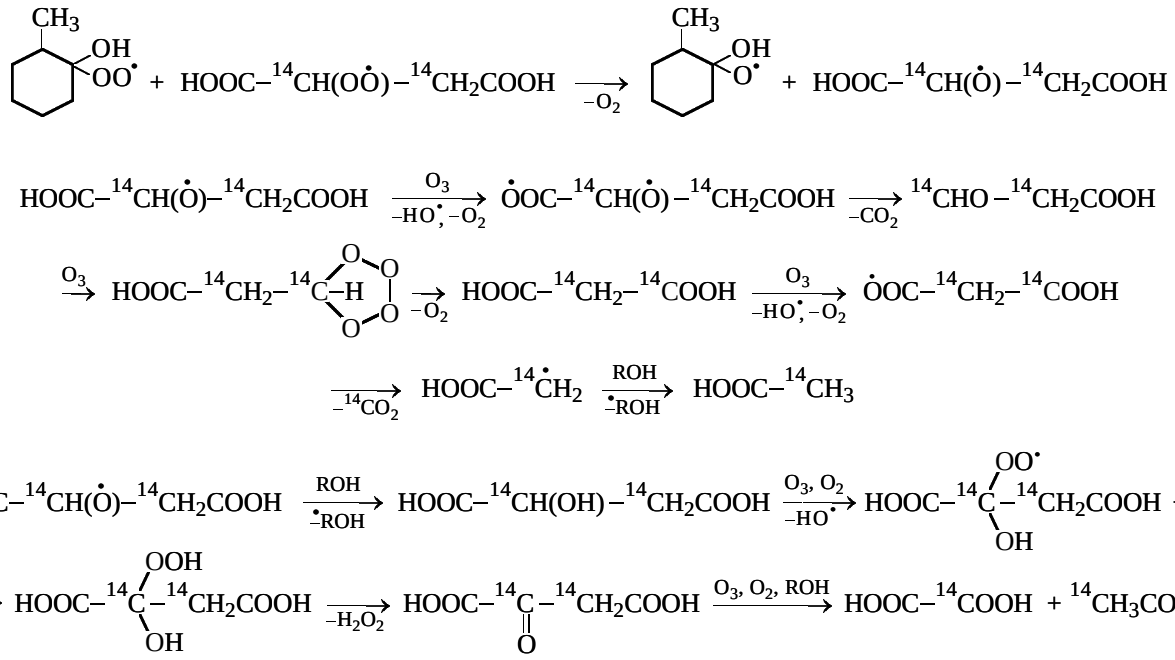

At 32.5% conversion of [2,3-^{14}C]succinic acid, the total activity of acetic and propionic acids is 10.1%. Hence, the major amount of $^{14}CO_2$ is formed in further ozonolysis of [^{14}C]oxalic acid:

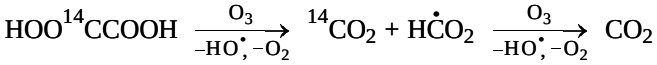

The probability of recombination of the alkoxyl and hydroxy radicals to form intermediate hydroperoxide is low. However, 2-methylcyclohexanol reacts with ozone to form unstable 1-hydroxy-1-hydrotrioxy-2-methylcyclohexane whose thermolysis generates hydroperoxy radical $HO_2^{\cdot}$ [5, 6]. Recombination of the hydroperoxy and peroxy radicals yields α-hydroperoxysuccinic acid. Its decomposition generates the corresponding α-oxyl radical:

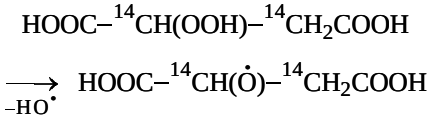

The probability of reaction of this radical with the ozone molecule via O–H bond in the carboxy group is low, since this radical reacts with a high rate constant [7] with alcohol molecules present in excess. However, occurrence of the reaction of the radical with ozone to even a small extent will result in formation of CO_2 by oxidation of the intermediately formed malonic acid:

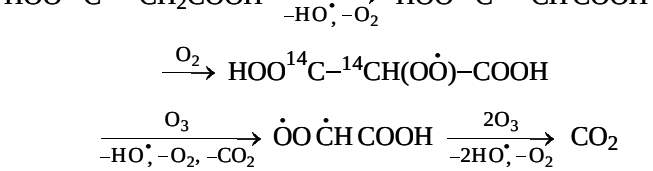

[2,4-^{14}C]Glutaric acid transforms with 30.2% conversion into $^{14}CO_2$ and [2,4-^{14}C]butyric (1.2%), [1,3-^{14}C]succinic (13%), [1-^{14}C]oxalic (0.41%), [1-^{14}C]acetic (0.8%), and [1-^{14}C]propionic (0.45%) acids within 180 min. The composition and activity ratio of the acids show that all the methylene groups of glutaric acid are attacked by ozone. However, the α-methylene groups are attacked predominantly. Note that CH and OH acids can also be attacked by alkoxyl radical.

Under the ozonolysis conditions, [1,2-^{14}C]-α-ketoglutaric acid is 42.5% consumed in 180 min; $^{14}CO_2$ and ^{14}CO are formed in 18.1 and 2.1% yields, respectively. The liquid radioactive products are [1-^{14}C]acetic (0.3%), [1-^{14}C]propionic (1.8%), [1-^{14}C]succinic (13.0%), and [1-^{14}C]oxalic (7.1%) acids. Ozone attacks α-ketoglutaric acid at the α-positions to the carbonyl and carboxy groups and also directly at the O–H bond of the carboxy group. Detection of ^{14}CO shows that ozonolysis involves cleavage of C–C bonds throughout the carbon chain of the keto acid. Experiments with [1-^{14}C]caproic acid showed that it transforms in 180 min with 30.5% conversion into

$^{14}CO_2$, [1-^{14}C]acetic acid (7%), [1-^{14}C]proionic acid (3.5%), [1-^{14}C]butyric acid (3.4%), and small amounts of formic acid:

$$CH_3(CH_2)_4{-}{}^{14}CO_2H \xrightarrow[-HO^{\bullet},\,-O_2]{O_3} CH_3(CH_2)_4{}^{14}CO\dot{O}$$

$$\xrightarrow[-{}^{14}CO_2]{} CH_3(CH_2)_3\dot{C}H_2 \xrightarrow[-\dot{R}OH]{ROH} CH_3(CH_2)_3CH_3$$

$$CH_3(CH_2)_3CH_2{}^{14}CO_2H \xrightarrow[-HO^{\bullet},\,-O_2]{O_3} CH_3(CH_2)_3\dot{C}H{-}{}^{14}CO_2H$$

$$\xrightarrow{O_2} CH_3(CH_2)_3{-}\underset{\displaystyle OO^{\bullet}}{\underset{|}{C}}H{-}{}^{14}CO_2H + \text{ 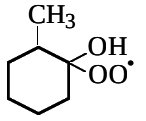 }$$

$$\xrightarrow[-O_2]{} CH_3(CH_2)_3{-}\underset{\displaystyle O^{\bullet}}{\underset{|}{C}}H{-}{}^{14}CO_2H + \text{ 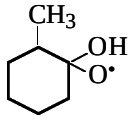 }$$

$$\xrightarrow[-HO^{\bullet},\,-O_2,\,-{}^{14}CO_2]{O_3} CH_3(CH_2)_3CHO \xrightarrow{O_3} CH_3(CH_2)_3{-}\text{ 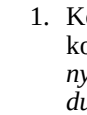 }$$

$$\xrightarrow[-O_2]{} CH_3(CH_2)_3CO_2H$$

By a similar scheme, ozone attacks the remote (β, γ, and δ relative to the carboxy group) methylene groups of caproic acid.

The ratio of the amounts of pentane and valeric acid shows that the probability of ozone attack at the α-position to the carboxy group is 3.6 times higher compared to the attack at the O–H bond of [1-^{14}C]caproic acid. [^{14}C]Formic acid and $^{14}CO_2$ can be formed from the intermediate hydroperoxide by the scheme

$$CH_3(CH_2)_3CH(O\dot{O}){-}{}^{14}CO_2H + HO_2^{\bullet}$$

$$\xrightarrow[-O_2]{} CH_3(CH_2)_3{-}CH(OOH){-}{}^{14}CO_2H$$

$$\xrightarrow[-\dot{O}H]{} CH_3(CH_2)_3{-}\underset{\displaystyle O^{\bullet}}{\underset{|}{C}}H{-}{}^{14}CO_2H$$

$$\xrightarrow[-HO^{\bullet},\,-O_2,\,-{}^{14}CO_2]{O_3} CH_3(CH_2)_3{-}CHO \xrightarrow{O_3} CH_3(CH_2)_3{-}\text{ 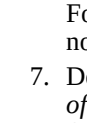 }$$

$$\xrightarrow[-O_2]{} CH_3(CH_2)_3{-}CO_2H$$

$$CH_3(CH_2)_3{-}CH(OOH){-}{}^{14}CO_2H$$

$$\xrightarrow{T,\,O_3,\,ROH} H{}^{14}COOH + CH_3(CH_2)_3COOH$$

CONCLUSIONS

(1) In ozonolysis (80°C) of [2,3-^{14}C]succinic, [2,4-^{14}C]glutaric, [1,2-^{14}C]-α-ketoglutaric, and [1-^{14}C]-caproic acids, ozone attacks the O–H bond of the carboxy groups and all the methylene groups of the aliphatic chain, predominantly those in the α-position relative to functional groups.

(2) Under the conditions examined, peroxy radicals are inactive in cleavage of the C–H and O–H bonds. The reactions involve ozone, oxygen, and alkyl, alkoxyl, hydroxy, and hyroperoxy radicals.

REFERENCES

1. Korotkova, N.P., Syroezhko, A.M., and Proskuryakov, V.A., *Okislenie tsiklogeksana i ego promezhutochnykh kislorodsoderzhashchikh soedinenii ozonovozdushnymi smesyami* (Oxidation of Cyclohexane and Its Intermediate Oxygen-Containing Derivatives with Ozone–Air Mixtures), Available from ONIITEKhIM, Moscow, June 23, 1978, no. 1805-78.
2. Syroezhko, A.M., Liquid-Phase Oxidation of Alkanes, Cycloalkanes, and Their Oxygen-Containing Derivatives with Oxygen and Ozone in the Presence of s- and d-Element Compounds, *Doctoral Dissertation*, Leningrad, 1985.
3. Syroezhko, A.M., Selivanov, N.T., Potekhin, V.M., and Proskuryakov, V.A., *Radiokhimiya*, 1970, vol. 12, no. 4, pp. 677–680.
4. Syroezhko, A.M. and Selivanov, N.T., *Zh. Prikl. Khim.*, 1973, vol. 46, no. 9, pp. 2066–2070.
5. Vikhorev, A.A., Syroezhko, A.M., and Proskuryakov, V.A., *Zh. Prikl. Khim.*, 1977, vol. 50, no. 6, pp. 1310–1314.
6. Vikhorev, A.A., Syroezhko, A.M., and Yakovlev, A.S., in *Issledovaniya v oblasti khimii i tekhnologii produktov pererabotki goryuchikh iskopaemykh* (Studies in the Field of Chemistry and Technology of Products of Fossil Fuel Processing), Leningrad: Leningrad. Tekhnol. Inst. im. Lensoveta, 1975, issue 2, pp. 39–43.
7. Denisov, E.T., *Mechanism of Homolytic Cleavage of Molecules in the Liquid Phase, Itogi Nauki Tekh., Ser.: Kinet. Katal.*, 1981, vol. 9.

Russian Journal of Applied Chemistry, Vol. 76, No. 8, 2003, pp. 1351–1353. Translated from Zhurnal Prikladnoi Khimii, Vol. 76, No. 8, 2003, pp. 1389–1391.

CHEMISTRY OF FOSSIL FUEL

Improving the Cetane Number of Diesel Fuels

O. Yu. Begak and A. M. Syroezhko

St. Petersburg State Technological Institute, St. Petersburg, Russia

Mendeleev Russian Research Institute of Metrology, St. Petersburg, Russia

Received March 27, 2003

Abstract—Effect of paraffins C_{10}–C_{13}, C_{14}–C_{17}, C_{18}–C_{23}, *tert*-butyl hydroperoxide, cumyl hydroperoxide, and isopropyl nitrate as cetane number improvers for summer- and winter-grade diesel fuels[1], added in amount of 0.4–5 wt %, is studied.

In recent years, the share of diesel fuel (DF) and, correspondingly, its total annual production volume have been growing steadily [1]. This is associated, in particular, with the fact that, in diesel engines, the compression ratio is higher, and the fuel consumption, lower by 25–30%, than in carburetter engines [2].

The cetane number (CN) is the most important characteristic of DF. It is a measure of the ignitability, which, in turn, determines the power, ecological, and economical characteristics of an engine. With increasing CN, the NO_x and CO contents in the exhaust decrease.

The cetane number depends on the group and fraction composition of DF. The cetane number of domestic summer-, winter-, and arctic-grade diesel fuels is 47–51, 45–49, and 38–40, respectively. At the same time, the requirements to the quality of DF, inprosed by the World Fuel Charter become more stringent; CN from 48 for DF of the first group to 55 for DF of the third group [3]. Now, advanced diesel engines are being designed, meant for DT with CN = 58–60 [4].

The goal of this study was to select cetane number improvers for commercial diesel fuels from the Kirishi Refinery and to analyze the effect of these additives on the performance of DF.

EXPERIMENTAL

Samples of diesel fuels (DTZ-0.2 minus 35,[2] DTL-0.2-40, and DTL-0.2-62) and also of paraffins C_{10}–C_{13}, C_{14}–C_{17}, and C_{18}–C_{23} were provided by the Kirishi Refinery.

The paraffin fraction C_{18}–C_{23} was treated to remove arenes by urea dewaxing, recrystallization from acetone, or acid–base purification, followed by carbamide urea. The quality of the resulting product was controlled by n_D^{20} [5] using reference data [6]. The recrystallization proved to be the most efficient treatment technique.

Paraffin fraction C_{18}–C_{23} had after recrystallization the minimal refraction intercept (difference between the refractive index and half of the relative density) typical of paraffins (1.04–1.0461). For arenes, the refraction intercept is much higher (1.0592–1.0627).

The arene content in the test samples of DF was determined using the aniline point technique [7], sulfonation, or directly from ^1H and ^{13}C NMR spectra.

n-Alkanes were determined from the ^1H and ^{13}C NMR data and also by the urea dewaxing method [9]. The cloud and pour points of DF were determined as in [10], with a mixture of acetone and dry ice as a coolant. The ^1H and ^{13}C NMR spectra were recorded on a Bruker AM-500 instrument (500 MHz) with $Si(CH_3)_4$, C_6D_6, and $CDCl_3$ as internal references.

The CN of the initial DF samples and those modified with cetane number improvers was determined on an IDT-69 device. Isopropyl nitrate was prepared in accordance with TU (Technical Specifications) 6-14-944–73 [11]. Physical characteristics of *tert*-butyl hydroperoxide and cumyl hydroperoxide used were consistent with reference data [12].

[1] Fuel from the Kirishi Refinery was studied.

[2] Pour point below –35°C.

1070-4272/03/7608-1351 $25.00 © 2003 MAIK "Nauka/Interperiodica"

Table 1. Cetane numbers of additized diesel fuels

DF	CN improver,* wt %	CN**	DF	CN improver, wt %	CN
DTL-0.2-62	C_{10}–C_{13}, 3	50	DTZ-0.2 minus 35	C_{14}–C_{17}, 5	53
DTL-0.2-40		52	DTZ-0.2 minus 35	IPN, 0.5	54
DTZ-0.2 minus 35		52	DTL-0.2-62	IPN, 2	65
DTL-0.2-62	C_{14}–C_{17}, 3	53	DTL-0.2-40	IPN, 2	59
DTL-0.2-40		52	DTL-0.2-40	C_{18}–C_{23}, 2 + IPN, 1	61
DTZ-0.2 minus 35		48	DTZ-0.2 minus 35	CHPO, 1	60
DTL-0.2-62 (initial)	–	48	DTZ-0.2 minus 35	CHPO, 0.5	56
DTZ-0.2 minus 35 (initial)	–	48	DTL-0.2-40	CHPO, 1	58
			DTL-0.2-62	CHPO, 1	57
DTZ-0.2 minus 35	C_{10}–C_{13}, 5	52	DTZ-0.2 minus 35	BHPO, 0.5	56

* (IPN) Isopropyl nitrate, (CHPO) cumyl hydroperoxide, and (BHPO) butyl hydroperoxide.

** CN was determined by the engine method according to GOST (State Standard) 3122–67.

Table 2. Theoratical cetane numbers estimated by various methods

Method of determination*	DTL-0.2-40	DTL-0.2-62	DTZ-0.2 minus 35
Experimental CN	48	48	45(48)
$CN = [(\nu_{20} + 17.8)1.5879]/\rho_4^{20}$	41.01	42.53	38.84
$CI = 454.74 - 1641.416\rho_4^{15} + 774.74(\rho_4^{15})^{-2} - 0.554t_b + 97.803(\log t)^2$	52.92	53.25	43.8
With a nomogram (GOST 27768–68)	53	53.5	44
$DI = t_{an}\rho_{API}/100$	55.4 (CN = 49)	57.3 (CN = 51.5)	48.4 (CN = 45.7)
$CN = 0.85c_p + 0.1c_n - 0.2c_a$ (from NMR data)	51.8	–	47.2
Group analysis data, %	Alk, 62, ArH, 22, Naphth, 16; CN = 50	Alk, 60, Naphth, 15, ArH, 25; CN = 47.5	Alk, 60, Naphth, 12, ArH, 28; CN = 46
$DI = [(1.8t_{an} + 32)(141.5 - 131.5\rho_4^{15})]/100\rho_4^{15}$	49.2	48.6	49.4

* (DI) Diesel index; (ν_{20}) kinematic viscosity, $m^2\ s^{-1}$; (ρ_4^{15}) relative density of diesel fuel; (c_p, c_n, c_a) content of carbon (wt %) in paraffins, naphthenes, and arenes, respectively.

The effect of the cetane number improvers is shown in Table 1. All the additives used appeared to be quite efficient, yielding a 2 to 17 cetane number benefit for both summer- and winter-grade diesel fuels. This implies that addition of butyl or cumyl hydroperoxide in amount of only 0.3–0.5 wt % is sufficient to raise CN by 5–6 points. It should be pointed out that addition of 3–5 wt % paraffin fractions C_{10}–C_{13}, C_{14}–C_{17}, and even C_{18}–C_{23} appeared to be efficient too.

In the ^{1}H NMR spectra of the DF samples we observed four groups of signals: 6.8–9.2 ppm [hydrogen atoms of aromatic ring (H_a)], 2.0–3.2 ppm [hydrogen atoms of the methine, methylene, and methyl groups in the α position to the aromatic ring (H_α)]; 1.05–2.0 ppm [hydrogen atoms of the methine and methylene groups of alkyl chains and naphthene rings in position more distant than α-position to the rings (H_β)]; and 0.5–1.0 ppm [hydrogen atoms of the methyl groups in position more distant than α and β positions, i.e., at a considerable distance from the aromatic ring (H_γ)].

Typical ^{13}C NMR spectra of diesel fuel show the signals of carbon atoms of the aromatic rings at 110–155 ppm and those of aliphatic and naphthenic structures at 14.1095–32.0658 ppm. The hydrogen atom distribution in the investigated DF samples is given below. Signal intensity (%): DTL-0.2-40: H_a 2.3, H_α 5.64, H_β 57.76, and H_γ 34.3; DTZ-0.2-35: H_a 2.3, H_α 5.7, H_β 60.4, and H_γ 31.6. The carbon atom distribution is as follows. Signal intensity (%): DTL-0.2-40: C_{ar} 23.1, C_{naph} 15.6, and C_{aliph} 62.3; DTZ-0.2-35: C_{ar} 27.6, C_{naph} 14.2, and C_{aliph} 58.2.

In addition to experimental determinations, we estimated the cetane numbers by various theoretical methods (Table 2). The most consistent estimated values were obtained from the NMR data and by using the DI–CN nomogram.

Table 3. Cloud (T_{cl}) and pour (T_p) points of unadditized diesel fuels and those modified with paraffin fractions C_{10}–C_{13}, C_{14}–C_{17}, and C_{18}–C_{23}

DF	Additive, wt %	T_{cl}, °C	T_p, °C	DF	Additive, wt %	T_{cl}, °C	T_p, °C
DTL 0.2-40	–	–8	–14	DTL-0.2-40	C_{18}–C_{23}, 2 + IPN, 1	–6	–31.5
DTL 0.2-62	–	–7	–14	DTZ-0.2 minus 35	C_{14}–C_{17}, 5	–30	–46
DTZ-0.2 minus 35	–	–26	–53	DTZ-0.2 minus 35	C_{10}–C_{13}, 5	–27	–60.2
DTL-0.2-40	C_{10}–C_{13}, 3	–6	–32	DTZ-0.2 minus 35	C_{14}–C_{17}, 3	–29	–51.5
DTL-0.2-40	C_{14}–C_{17}, 3	–5	–30	DTZ-0.2 minus 35	C_{10}–C_{13}, 3	–36	–64

The use of paraffin-containing fractions may deteriorate the cold flow properties of diesel fuel. We measured the cloud and pour points of the DF samples modified with paraffin fractions (Table 3). It was demonstrated that, in these parameters, the investigated summer- and wintergrade diesel fuels with paraffin-containing cetane number improvers meet the existing requirements.

CONCLUSIONS

(1) Paraffin fractions C_{10}–C_{13}, C_{14}–C_{17}, and C_{18}–C_{23} taken in amount of 3–5 wt % demonstrate properties of cetane number improvers. The cloud and pour points of diesel fuels with these additives meet the requirements of GOST 305–82.

(2) Isopropyl nitrate, *tert*-butyl hydroperoxide, and cumyl hydroperoxide used in amount of about 0.5 wt % are efficient cetane number improvers for diesel fuels.

ACKNOWLEDGMENTS

The authors are grateful to O.P. Alekseeva for her help in the study.

REFERENCES

1. Zalishchevskii, G.D., Manufacture of High-Octane Gasoline with Decreased Content of Aromatic Hydrocarbons by Distillation of Reformer Naphthas, *Cand. Sci. Dissertation*, St. Petersburg, 2000.
2. Danilov, A.M., *Primenenie prisadok v toplivakh dlya avtomobilei: Spravochnik* (Use of Additives in Gasoline for Motor Vehicle): A Handbook, Moscow: Khimiya, 2000.
3. Mitusova, T.N., *Neftekhim. Neftepererab.*, 2000, no. 1, pp. 19–21.
4. *Strategicheskie prioritety rossiiskikh neftepererabatyvayushchikh predpriyatii* (Strategic Priorities of Russian Oil Refineries), Somov, V.E., Ed., Moscow: TsNIITEneftekhim, 2002.
5. Pereverzev, A.N., Bogdanov, N.F., and Roshchin, Yu.N., *Proizvodstvo parafinov* (Production of Paraffins), Moscow: Khimiya, 1973.
6. *Khimiya nefti i gaza* (Petroleum and Gas Chemistry), Proskuryakov, V.A., Ed., Leningrad, Khimiya, 1995.
7. Belyanin, V.V. and Erikh, V.V., *Tekhnicheskii analiz nefteproduktov i gaza* (Technical Analysis of Oil Products and Gas), Leningrad: Khimiya, 1975.
8. Bogomolov, A.K. and Khatyntseva, L.I., *Rukovodstvo po analizu neftei* (Manual on Analysis of Oils), Leningrad: Nedra, 1966, pp. 47–50.
9. Rybak, B.M., *Analiz nefti i nefteproduktov* (Analysis of Oil and Oil Products), Moscow: Gostoptekhizdat, 1962, pp. 248–329.
10. Papok, K.K., *Khimmotologiya topliv i smazochnykh masel* (Chemmotology of Fuels and Lubricating Oils), Moscow: Voenizdat, 1987.
11. Englin, B.A., *Primenenie zhidkikh topliv pri nizkikh temperaturakh* (Use of Liquid Fuels at Low Temperatures), Moscow: Khimiya, 1980.
12. Antonovskii, V.L., *Organicheskie perekisnye initsiatory* (Organic Peroxide Initiators), Moscow: Khimiya, 1972, pp. 43–44.

Russian Journal of Applied Chemistry, Vol. 76, No. 8, 2003, pp. 1354–1355. Translated from Zhurnal Prikladnoi Khimii, Vol. 76, No. 8, 2003, pp. 1392–1393.

BRIEF COMMUNICATIONS

Thermal Disproportionation of Hypophosphorous Acid

G. T. Shechkov, I. A. Pevneva, and O. A. Meshkova

Polzunov Altai State Technical University, Barnaul, Russia

Received April 18, 2003

Abstract—Thermal disproportionation of hypophosphorous acid was studied to find the reaction order, the rate constant and activation energy of the process, and also the temperature ranges in which the reaction rate is the highest.

The use of red phosphorus is based on its capability to be oxidized (manufacture of matches, getters, fire-retardants, and components of pyrotechnic formulations) [1–3]. The oxidation yields phosphorous acids (hypophosphorous H_3PO_2, phosphorous H_3PO_3, and phosphoric H_3PO_4) and phosphine PH_3. The formation of these products may result both in retrogradation of properties of phosphorous composites and in shortening of guaranteed shelf lives of articles based on red phosphorus.

However, the kinetics and temperature ranges of transformation of phosphorus acids have not been analyzed in studies devoted to phosphorus oxidation [2–4]. The main goal of the present study was to analyze the fundamental aspects of phosphine formation in disproportionation of hypophosphorous acid of varied concentration and to determine the temperature ranges and kinetic parameters of the process

$$3H_3PO_2 \rightarrow 2H_3PO_3 + PH_3. \quad (1)$$

We studied 50% hypophosphorous acid of reagent grade, TU (Technical Specification) 6-09-1462–76. The acid was diluted with twice-distilled water and concentrated by recrystallization, as described in [5].

The disproportionation was monitored by evolution of PH_3 in the temperature range $(30–160) \pm 1.5$°C in a glass reactor connected to an AGB-67M automated gas burette.

The acid (5 g) was placed in a glass dish mounted on a quartz hook fastened to a ground tap wrench by a fiberglass thread. A sample was rapidly (10 s) introduced into the reactor with a furnace, using the tap wrench.

The sensitivity of the installation was 0.001 to 1 ml, depending on a burette volume. The error in measuring the gas volume was ±5%. A solution of calcium chloride served as a locking liquid.

Analysis for PH_3 was carried out on an LKhM-80 chromatograph by the technique described in [6]. Gas samples (1 ml) were taken from the reactor at intervals of 10–15 min through a hermetic tap made of special rubber. Polysorb-1 served as absorbent. The flow rate of the carrier gas was 24 ml min^{-1}; column temperature, 60°C; measurement error, ±3%. Phosphine for constructing a calibration plot was obtained by hydrolysis of aluminum phosphide and analyzed both chemically and chromatographically.

A thermal analysis of H_3PO_2 was carried out with 200-mg samples on an MOM Q-1500D (Hungary) derivatograph in standard ceramic crucibles at a heating rate of 10 deg min^{-1}.

We revealed low- (30–90°C) and high-temperature (110–200°C) regions of phosphine evolution in disproportionation of H_3PO_2. At low temperatures, the acid reacts with water to give hydrogen, which was detected by mass-spectrometry:

$$H_3PO_2 + H_2O \rightarrow H_3PO_3 + H_2. \quad (2)$$

At high temperatures (>110°C) the disproportionation process (1) occurs at the highest rate at 130–160°C, being complete at 190°C. The process is complicated by gas-phase oxidation of phosphine, beginning at 120°C and ending in combustion of the gas mixture above 160°C.

Kinetic curves of disproportionation are S-shaped. The rate of H_3PO_2 disproportionation grows with the concentration of the acid increasing from 30 to 90%, the disproportionation being of the autocatalytic nature. This feature seems to be associated with

1070-4272/03/7608-1354 $25.00 © 2003 MAIK "Nauka/Interperiodica"

the dependence of the rate of tautomeric regrouping of H_3PO_2 from the inactive form, containing phosphorus(V), to the active form, containing phosphorus(III). The rate constant of the regrouping is extremely low, $k = 10^{-12}$ s^{-1} [4]. Raising the concentration, temperature, and time presumably removes diffusion hindrances for this regrouping.

At 110 and 140°C and process duration of 40–160 min the evolution of phosphine occurs in the kinetic mode and further passes to the diffusion mode. With the temperature increasing to above 140°C, the process passes to the diffusion mode within 40–120 min. The disproportionation reaction in the kinetic mode at high temperatures (110–170°C) is first-order with rate constant $k = 1.96 \times 10^{-5}$ s^{-1} and activation energy of 85 ± 2 kJ mol^{-1}. The transition of the reaction of phosphine evolution from the kinetic to diffusion mode results from the accumulation of the more thermally stable products H_3PO_3 and H_3PO_4, which are formed upon PH_3 oxidation:

$$4PH_3 + 5O_2 \rightarrow 2P_2O_5 + 6H_2, \quad (3)$$

$$P_2O_5 + 3H_2O \rightarrow 2H_3PO_4. \quad (4)$$

A pronounced endothermic effect is observed in the derivatograms at 135°C. It is determined by the equilibrium the endothermic processes of dehydration and disproportionation of H_3PO_2 and also by the exothermic oxidation of the evolving phosphine. The overall activation energy of dehydration, hydration, and disproportionation of H_3PO_2 below 100°C is 44 ± 1 kJ mol^{-1}.

According to the derivatographic data, the activation energy of H_3PO_2 disproportionation in the range 110–140°C is 69.8 ± 2 kJ mol^{-1}, in satisfactory agreement with the activation energy obtained from the kinetic data (85 ± 2 kJ mol^{-1}).

The forming H_3PO_3 disproportionates in the range 190–270°C, with simultaneous oxidation of the evolving PH_3. According to the derivatographic data, the maximum rate of PH_3 oxidation is observed in the range 280–300°C. The corresponding activation energy is 207 ± 10 kJ mol^{-1}.

RERERENCES

1. Van Wazer, I.R., *Phosphorus and Its Compounds*, New York: Interscience, 1958, vol.1.
2. Speranskaya, G.V., Talanov, N.D., and Aziev, L.G., *Zh. Prikl. Khim.*, 1978, vol. 54, no. 8, p. 1705.
3. Korolev, V.V., Talanov, N.D., and Astakhova, G.V., *Izv. Akad. Nauk SSSR, Neorg. Mater.*, 1986, vol. 22, no. 7, pp. 1214–1216.
4. Brodskii, A.A., Blankshtein, V.A., Ershov, V.A., and Talanov, N.D., *Pererabotka fosfora* (Processing of Phosphorus), Leningrad: Khimiya, 1985.
5. Karyakin, Yu.V. and Angelov, N.N., *Chistye khimicheskie veshchestva* (Pure Chemical Substances), Moscow: Khimiya, 1974.
6. Potemkin, L.V. and Musatova, Yu.G., *Gazokhromatograficheskie metody opredeleniya sostava gazovykh vybrosov v fosfornoi promyshlennosti: Uchebnoe posobie dlya rabochikh professii* (Gas-Chromatographic Methods for Determining Composition of Gas Discharges in Phosphorus Industry: Tutorial for Operators), Moscow: NIITEKhKhIM, 1985.

Russian Journal of Applied Chemistry, Vol. 76, No. 8, 2003, pp. 1356–1357. Translated from Zhurnal Prikladnoi Khimii, Vol. 76, No. 8, 2003, pp. 1394–1395.

BRIEF COMMUNICATIONS

Stability of Phosphorus Trihalide Solutions Used in Polarography

L. M. Kisil', I. M. Osadchenko, and A. P. Tomilov

State Research Institute of Organic Chemistry and Technology, Moscow, Russia

Received January 15, 2003

Abstract—The behavior of PCl_3 and PI_3 solutions in acetonitrile containing no more than 0.02 wt % H_2O in storage at room temperature was studied.

Previously [1, 2] we have studied the polarographic behavior of phosphorus trihalide solutions. It was shown that their stability depends on the water content in the solvents.

In this study, we analyze the stability of phosphorus trihalide solutions in acetonitrile, used in polarography.

Since phosphorus trihalides are readily hydrolyzed by water and react with protic organic solvents, their polarographic behavior is studied in aprotic solvents [1–4].

As shown previously, polarograms of phosphorus trihalides at 20–25°C in dimethylformamide and acetonitrile dried by the procedure described in [4] show well defined waves.

The stability of phosphorus trihalides in acetonitrile solutions with composition similar to that used in polarographic studies [1] (no more than 0.02% H_2O) was monitored by UV spectroscopy. The absorption spectra of straight acetonitrile and acetonitrile solutions of PCl_3, PI_3, and HCl (HCl is the main hydrolysis product of PCl_3 in water) are shown in the figure. The PCl_3 spectrum contains two bands peaked at 298 and 365 nm. The PI_3 spectrum contains three bands at 250, 293, and 370 nm. As seen from the figure, no appreciable amount of HCl is formed in the PCl_3 solution, i.e., PCl_3 is not hydrolyzed in acetonitrile solution during the experiment.

The UV spectrum of acetonitrile solution of PCl_3 did not change during its storage for a week. This indicates that PCl_3 is not hydrolyzed noticeably in acetonitrile containing up to 0.02% water, i.e., acetonitrile purified by the procedure described in [4] is suitable as a solvent for polarography. This is confirmed by the fact that the polarogram of PCl_3 in acetonitrile containing no more than 0.02% water does not change after storage of this solution at +3 to +5°C for 7 days. After longer storage, especially at room temperature, the limiting current decreases and a wave appears at more negative potentials. For example, the limiting current of reduction of a 0.23 M PCl_3 solution containing 0.08 M tetraethylammonium perchlorate as a supporting electrolyte decreases from 1.298 to 1.200 μA in 12 days.

When the water content is higher than 0.02%, the half-wave potential of PCl_3 reduction is shifted to the cathodic region:

Water content, %	0.02	0.03	0.06	0.10
$-E_{1/2}$, V	0.915	0.930	0.960	1.920

At water content of 0.06%, a second wave appears at $E_{1/2}$ = –1.93 V (relative to bottom Hg). This is due to reaction of PCl_3 with H_2O present in the solvent.

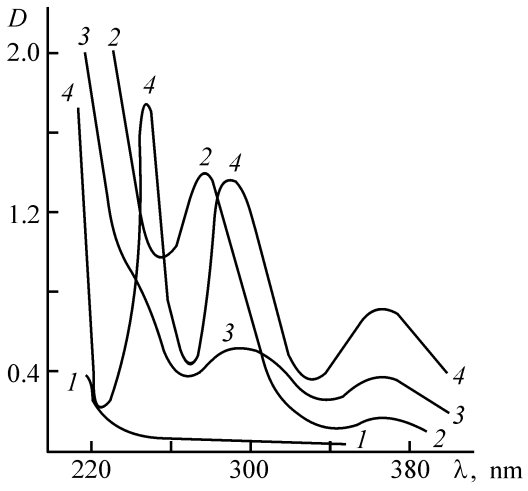

UV spectra of (*1*) straight acetonitrile and acetonitrile solutions of (*2*) HCl, (*3*) PCl_3, and (*4*) PI_3. (*D*) Optical density and (λ) wavelength.

1070-4272/03/7608-1356 $25.00 © 2003 MAIK "Nauka/Interperiodica"

When H_2O is added in concentration exceeding the initial PCl_3 concentration by a factor of 4 (0.38 mM), the first wave becomes weaker, and a wave with $E_{1/2}$ = –1.068 V and another wave at more negative potentials appear. The current of the last wave grows with increasing water content.

Since HCl and H_3PO_3 are the main hydrolysis products of PCl_3, we studied their polarographic behavior in acetonitrile solutions. We found that HCl is reduced in acetonitrile solution of tetraethylammonium perchlorate with $E_{1/2}$ = – 1.06 V (relative to bottom Hg), which agrees with published data [5]. In addition, a wave with $E_{1/2}$ = –0.50 V due to reduction of CH_3CNH^+ cation [6] is observed. The reduction of phosphorus acid under these conditions is also characterized by two waves with $E_{1/2}$ = –1.95 and –2.74 V (relative to saturated calomel electrode) [7]. The total current of both waves is proportional to the H_3PO_3 concentration. Since the current of the waves decreases by a factor of 2 after addition of the maximum amount of water, 50% of PCl_3 is hydrolyzed. Thus, PCl_3 hydrolysis by H_2O in acetonitrile solutions is hindered as compared with the aqueous solution, owing to solvation of PCl_3. This fact is confirmed by IR spectroscopy. The bands in the range 2400–2700 cm^{-1} can be assigned to the $HCl \cdot CH_3CN$ solvate (the band of pure HCl lies at 2480 cm^{-1} [8]).

Since PI_3 is difficulty soluble in acetonitrile, PI_3 was dissolved in benzene at +3°C and the resulting solution was added to an acetonitrile solution of tetraethylammonium perchlorate. Benzene solutions of PI_3 are stable at low temperature in the dark. No visible changes in these solutions were observed after their storage for 10–12 h. In 1–2 days, a lemon yellow PI_3 solution in benzene acquires a Bordeaux shade, probably owing to liberation of iodine. When this solution is kept at 35°C for a long time, it gets turbid, and a yellow precipitate is formed. The half-wave potentials of these solutions are shifted to the negative range by –1.0 to –2.6 V (the polarogam of the initial PI_3 solutions contains two waves with $E_{1/2}$ = –0.04 and –0.42 V [1]).

Thus, solutions of phosphorus trihalides in purified and dried acetonitrile are stable and can be used in polarography.

REFERENCES

1. Kisil', L. M., Osadchenko, I.M., and Tomilov, A.P., *Elektrokhimiya*, 2000, vol. 36, no. 9, pp. 1163–1164.
2. Kisil', L. M., Osadchenko, I.M., and Tomilov, A.P., *Elektrokhimiya*, 2001, vol. 37, no. 9, pp. 1147–1149.
3. Osadchenko, I.M., *Elektrokhimiya fosforsoderzhashchikh soedinenii* (Electrochemistry of Phosphorus-Containing Compounds), Volgograd: Volgograd. Gos. Univ., 2000.
4. Mann, Ch.K. and Barnes, K.K., *Electrochemical Reaction in Nonaqueous Systems*, New York: Marcel Dekker, 1970.
5. O'Donnel, J.F., Ayres, J.T., and Mann, C.K., *Anal. Chem.*, 1965, vol. 37, no. 8, pp. 1161–1163.
6. Kryukova, T.A., Sinyakova, S.I., and Aref'eva, T.V., *Polyarograficheskii analiz* (Polarographic Analysis), Moscow: Goskhimizdat, 1959.
7. Tomilov, A.P., Osadchenko, I.M., and Kisil', L.M., *Elektrokhimiya*, 1975, vol. 11, no. 8, pp. 1213–1214.
8. Janz, G.J. and Danyluk, S.S., *J. Am. Chem. Soc.*, 1959, vol. 81, no. 15, pp. 3850–3854.

Russian Journal of Applied Chemistry, Vol. 76, No. 8, 2003, pp. 1358–1359. Translated from Zhurnal Prikladnoi Khimii, Vol. 76, No. 8, 2003, pp. 1396–1397.

BRIEF COMMUNICATIONS

Calorimetric Study of Specific Heat of Anabasine Nitrate and Glaucine Hydrobromide

B. K. Kasenov, Sh. B. Kasenova, Zh. K. Tukhmetova, S. M. Adekenov, A. Zh. Turmukhambetov, and A. Zh. Abil'daeva

Institute of Phytochemistry, Ministry of Education and Science of the Republic of Kazakhstan, Karaganda, Kazakhstan

Received April 24, 2003

Abstract—The results obtained in studying the isobaric specific heat of alkaloid derivatives, anabasine nitrate and glaucine hydrobromide, in the temperature range from 198 K to the melting point are presented.

Studying the thermochemical and thermodynamic properties of natural compounds and, in particular, alkaloids, is theoretically and practically important for physical chemistry of natural compounds, directed synthesis of biologically active substances with prescribed properties, and determination of new constants to be loaded as input information arrays into fundamental databases and reference books.

Previously, thermodynamic characteristics (enthalpies of dissolution, formation, combustion, and melting; specific heat in the temperature range from 198 K to T_{decomp}) of anabasine alkaloid hydrochloride have been studied [1]. The present communication reports the results obtained in studying the temperature dependence of specific heats of anabasine nitrate and glaucine hydrobromide in the temperature range from 198 K to melting point (T_m).

Analytically pyre anabasine nitrate $C_{10}H_{14}N_2HNO_3$ with melting point of 176–177°C was synthesized by reacting anabasine hydrochloride and silver nitrate (both of analytically pure grade). The compound obtained was identified by IR and NMR spectroscopies.

Glaucine hydrobromide $C_{21}H_{25}NO_4HBr$ of pharmaceutical purity is an antitussive preparation with melting point of 237°C.[1]

The specific heats of the compounds were measured with an IT-S-400 calorimeter. Liquid nitrogen served as cooling agent. The duration of measurements in the whole temperature range, including data processing, did not exceed 2.5 h. The rated maximum error of the instrument was ±10%.

A sample to be studied, placed in a metallic ampule of the measuring cell, was continuously heated by heat flow through a heat flow meter. The time lag of the ampule temperature with respect to the base temperature was measured after each 25°C.

Table 1. Experimental specific heats of anabasine nitrate and glaucine hydrobromide

T, K	$C_p^0 \pm \bar{\delta}$, J g^{-1} K^{-1}	$C_p^0 \pm \mathring{\Delta}$, J mol^{-1} K^{-1}
	Anabasine nitrate	
198	0.7046 ± 0.0180	159 ± 11
223	0.9551 ± 0.0191	215 ± 12
248	1.1540 ± 0.0325	260 ± 20
273	1.2454 ± 0.0282	281 ± 18
298	1.3724 ± 0.0208	309 ± 13
323	1.4729 ± 0.0395	332 ± 25
348	1.6091 ± 0.0317	362 ± 20
373	1.7160 ± 0.0420	387 ± 26
398	1.8228 ± 0.0573	411 ± 36
	Glaucine hydrobromide	
198	0.9929 ± 0.0258	433 ± 31
223	1.0388 ± 0.0282	453 ± 34
248	1.0663 ± 0.0229	465 ± 28
273	1.1236 ± 0.0270	490 ± 33
298	1.1626 ± 0.0344	507 ± 42
323	1.1993 ± 0.0307	523 ± 37
348	0.8003 ± 0.0157	349 ± 19
373	1.0090 ± 0.0247	440 ± 30
398	1.1764 ± 0.0276	513 ± 33
423	1.2796 ± 0.0398	558 ± 48
448	1.3667 ± 0.0405	596 ± 49

[1] Synthesized by Khimfarm Open Joint-Stock Company (Shimkent, Kazakhstan).

1070-4272/03/7608-1358 $25.00 © 2003 MAIK "Nauka/Interperiodica"

Table 2. Coefficients of equations describing the dependence $C_p^0 \sim f(T)$ for the alkaloid derivatives

Compound	a	$b \times 10^3$	$c \times 10^{-5}$	T, K
Anabasine nitrate	152 ± 10	733 ± 49	–(54 ± 4)	198–398
Glaucine hydrobromide	223 ± 16	884 ± 63	13.4 ± 0.9	198–323
	2766 ± 197	–(6945 ± 496)	–	323–348
	2132 ± 152	–(1934 ± 138)	–(1344 ± 96)	348–448

Preliminarily, the measuring instrument was calibrated by determining the heat conductivity K_t of the heat flow meter [2]. For this purpose, five parallel runs with empty ampule, and the same number with a copper sample, were carried out. Similarly, five parallel runs were done at each temperature for each of the compounds under study; the results obtained were averaged and processed by methods of mathematical statistics [3].

At each temperature, the root-mean-square deviation $\bar{\delta}$ was determined for averaged values of specific heat; the random error $\mathring{\Delta}$ was found for molar heat.

The instrument operation was tested by determining the specific heat of α-Al_2O_3: the experimental value $C_p^0(298.15) = 76.0$ J mol^{-1} K^{-1} is in satisfactory agreement with the reference value of 79.0 J mol^{-1} K^{-1} [4].

Table 1 lists experimental values of the specific and molar heat for anabasine nitrate (M = 225.24) and glaucine hydrobromide (M = 436.09). The dependence $C_p^0 \sim f(T)$ is plotted in the figure.

Mathematical processing of the experimental data yielded equations describing the temperature dependences of the specific heat of the compounds $C_p^0 = a + bT + cT^2$, J mol^{-1} K^{-1}, whose coefficients are listed in Table 2.

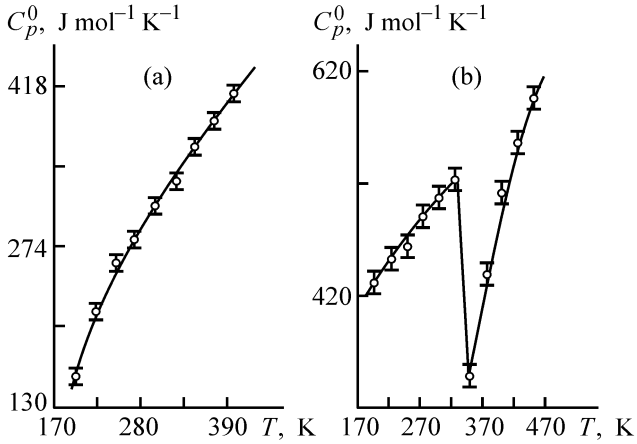

Specific heat C_p^0 of (a) anabasine nitrate and (b) glaucine hydrobromide vs. temperature T.

The error in determining the coefficients in the specific heat equations were found from mean random errors for the whole temperature range.

As seen from Table 1 and the figure, the specific heat of glaucine hydrobromide shows an anomalous peak at 323 K, then falls at 348 K, and then again starts to increase. This is presumably due to a second-order phase transition. In view of this circumstance, three equations describing the dependence $C_p^0 \sim f(T)$ in each portion of the curve (Table 2) were derived for this compound.

The coefficients b and c of the equation describing the dependence $C_p^0 \sim f(T)$ for glaucine hydrobromide in the temperature range 348–448 K have negative sign, which, at first glance, seems paradoxical. With increasing temperature, the contribution from the specific heat component associated with coefficient b grows, and that from the component associated with coefficient c falls. The strong decrease in the component associated with coefficient c leads to an increase in the specific heat, which is confirmed by the good agreement between the experimental and calculated data.

CONCLUSION

The temperature dependences of the specific heat of anabasine nitrate and glaucine hydrobromide were studied in the temperature range from 198 K to the melting (decomposition) point. Equations describing the dependence $C_p^0 \sim f(T)$ were derived from the experimental data obtained for each of the compounds.

REFERENCES

1. Kasenov, B.K., Tukhmetova, Zh.K., Adekenov, S.M., *et al.*, *Zh. Prikl. Khim.*, 2003, vol. 76, no. 1, pp. 31–34.
2. Platunov, E.S., *Teplofizicheskie izmereniya v rezhime* (Thermal Measurements in the Mode), Moscow: Energiya, 1973.
3. Spiridonov, V.P. and Lopatkin, A.A., *Matematicheskaya obrabotka eksperimental'nykh dannykh* (Mathematical Processing of Experimental Data), Moscow: Mos. Gos. Univ., 1970.
4. Robie, R.A., Hewingway, B.S., and Fisher, J.K., *Thermodynamic Properties of Minerals and Related Substances at 298.15 and 1 Bar (10^5 Pascals) Pressure and at Higher Temperatures*. Washington, 1978, p. 456.

Russian Journal of Applied Chemistry, Vol. 76, No. 8, 2003, pp. 1360–1361. Translated from Zhurnal Prikladnoi Khimii, Vol. 76, No. 8, 2003, pp. 1398–1399.

BRIEF COMMUNICATIONS

Thin Near-Surface Layer in a Resist Film

V. I. Trigub, A. V. Plotnov, and A. N. Kiselev

Nizhni Novgorod State Technical University, Nizhni Novgorod, Russia

Received October 16, 2002

Abstract—The structure of the near-surface layer of a polymer film of a resist was studied by atomic-force microscopy.

Lavrishchev *et al*. [1] provided indirect evidence for the presence of a near-surface layer in the (co)polymer film of a resist. They demonstrated that the time required for complete removal of the solvent from the resist film depends on the drying method. We experimentally confirmed the presence of a thin near-surface layer in a resist film [2] and revealed periodic changes in the thickness of copolymer films based on methyl methacrylate and methacrylic acid during their heat treatment at constant temperature, which suggests the presence of a near-surface layer [3]. However, the thickness of the near-surface layer of the (co)polymer films applied as resists in lithography has not been estimated as yet because of the small thickness of resist films (no greater than 1 μm) [4].

A thin near-surface layer in a film of a (co)polymer-based resist must give rise to a barrier effect precluding diffusion of the solvent from the resist film during heat treatment [4, 5]. This effect makes it necessary to revise the conditions of formation of resist films by centrifugation and heat treatment.

The aim of this study was to reveal and analyse the thin near-surface layer in a polymethyl methacrylate (PMMA) film by atomic-force microscopy. A film of the positive electron-sensitive resist was formed on a KDB-4 silicon substrate by centrifugation from a 4.5% diglyme solution of PMMA with molecular weight M = 638400, modified with organohydridedisilane [6]. The viscosity of the electron-sensitive resist was 46.7 cSt, and the rate of its application to the substrate, 850 rpm. After centrifugation, the resist film was dried at 170°C for 30 min in an oven in air. The thickness of the resist after the heat treatment was 1.0 μm. The thin near-surface layer was microprobed on a Topometrix-TMX-2100 atomic-force (AFM) microscope by recording the lateral force acting on the probe during scanning (lateral force measurement, LFM) [7]. The LFM method implies a study of the force of friction between the surface and the probe sliding over it. During scanning, the probe is subject to the friction force from the sample surface

$$F_{\text{fr}} = kN. \quad (1)$$

Here, N is the response force exerted by the sample on the probe, and k, local friction coefficient.

The greater the coefficient h of friction between the probe and the surface section directly contacting the probe, the lighter the section being scanned on the AFM image (i.e., the denser the sample section).

The local friction coefficients k for the probe in Eq. (1) substantially differ from the dry friction coefficients of various materials, as the domain of contact between the probe and the sample is as small as 0.1–1.0 nm.

The near-surface layer of the PMMA resist film was sought by studying the fracture of a silicon substrate with resist applied to its surface. The substrate was fractured at liquid nitrogen temperature by the known procedure [8], which prevented plastic deformation of the resist edge during fraction. However, the facial edges of the sample cannot be studied in an atomic-force microscope because of a force field jump [9]. This undesirable effect can be eliminated by coating the PMMA film with an FP-383 photoresist film [10] by centrifugation at 550 rpm. After centrifugation, the FP-383 resist was heat-treated in an oven at 70°C for 20 min. The resulting FP-383 photoresist film was 7.2 μm thick. The fracture was studied in air in the contact mode. The AFM image of the fracture of the silicon substrate with a double resist coating is shown in the figure. It is seen that the near-surface layer of the PMMA resist along the fracture boundary is 17.2 to 204.7 nm thick. Dark and light domains in

1070-4272/03/7608-1360 $25.00 © 2003 MAIK "Nauka/Interperiodica"

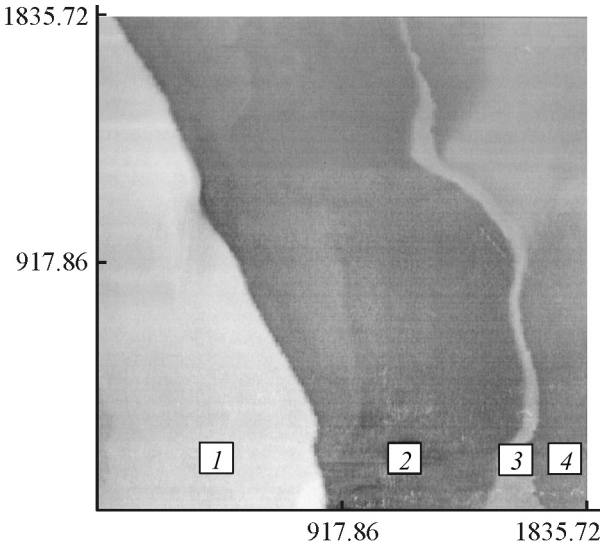

AFM image of the surface fracture (the size is given in nanometers): (*1*) silicon, (*2*) PMMA, (*3*) thin near-surface PMMA layer, and (*4*) FP-383.

the AFM image correspond to less dense and denser materials, respectively. The boundary layer of the PMMA/FP-383 composite has darker color and is situated between domains *3* and *4* (see figure).

CONCLUSIONS

(1) A thin near-surface layer is formed during preparation of a resist film from a polymethyl methacrylate solution in diglyme by centrifugation followed by heat treatment at 170°C.

(2) The density of the near-surface layer exceeds that of the bulk polymer.

(3) The density of the near-surface thin layer of the polymethyl methacrylate film varies from 17.2 to 204.7 nm.

REFERENCES

1. Lavrishchev, V.P., Prokhorov, Yu.I., and Khorina, Z.I., *Elektron. Tekh., Ser. 3: Mikroelektronika*, 1975, issue 1, pp. 86–92.
2. Trigub, V.I., Plotnov, A.V., Bykova, I.N., *et al.*, *Zh. Prikl. Khim.*, 2000, vol. 73, no. 8, pp. 1353–1356.
3. Trigub, V.I., Plotnov, A.V., and Potanina, N.A., *Trudy Sed'moi mezhdunarodnoi nauchno-tekhnicheskoi konferentsii "Aktual'nye problemy tverdotel'noi elektroniki i mikroelektroniki PEM-2000"* (Proc. Seventh Int. Scientific and Technical Conf. "Topical Problems of Solid-State Electronics and Microelectronics" PEM-2000), Taganrog, 2000, part 1, pp. 71–73.
4. Moreau, W.M., *Semiconductor Lithography. Principles, Practices, and Materials*, New York: Plenum, 1988.
5. Trigub, V.I. and Gol'denberg, G.L., *Izv. Vyssh. Uchebn. Zaved., Mater. Elektron. Tekh.*, 1998, no. 4, pp. 41–43.
6. Bulgakova, S.A., Semchikov, Yu.D., Semenov, V.V., *et al.*, *Vysokomol. Soedin., Ser. B*, 1995, vol. 37, no. 4, pp. 706–708.
7. *Fizika tverdogo tela* (Solid State Physics), Khokhlov, A.F., Ed., vol. 1: *Metody polucheniya tverdykh tel i issledovaniya ikh struktury* (Methods of Preparation of Solids and Study of Their Structure), Nizhni Novgorod: Nizhegorod. Gos. Univ., 2000.
8. *Introduction to Integral Optics*, Barnoski, M.K., Ed., New York: Plenum, 1974.
9. Moiseev, Yu.N., Mostepanenko, V.M., Panov, V.I., *et al.*, *Phys. Lett.*, 1988, vol. A132, p. 354.
10. Kurnosov, A.I., *Materialy dlya poluprovodnikovykh priborov i intergral'nykh mikroskhem* (Materials for Semiconductor Devices and Integrated Microcircuits), Moscow: Vysschaya Shkola, 1980.

Russian Journal of Applied Chemistry, Vol. 76, No. 8, 2003, pp. 1362–1364. Translated from Zhurnal Prikladnoi Khimii, Vol. 76, No. 8, 2003, pp. 1400–1401.

In Memory of Professor Ivan Yakovlevich Bashilov (To 50th Anniversary of His Death)

Professor Ivan Yakovlevich Bashilov, a talented scientist and engineer and one of founders of Russia's industry of radioactive and rare metals, passed away on August 20, 1953, in Krasnoyarsk.

I.Ya. Bashilov was born on November 29, 1892, at the town of Kashin in Tver Province, into a large family of an office worker of the uyezd treasury. Allready beginning at the age of 12, Bashilov had to make money for his education himself. Having finished Tver Gymnasium with gold medal in 1911, Bashilov entered the metallurgical department of Emperor Peter the Great Polytechnical Institute in St. Petersburg. The Polytechnical Institute, opened in October 1902, had among its lecturers quite a number of prominent scientists and possessed excellently equipped laboratories, and, therefore, fast acquired a reputation of one of the best technical higher school institutions not only in Russia, but in Europe too. Among those who taught at the metallurgical department were N.S. Kurnakov (1860–1941, academician since 1913), F.Yu. Levinson-Lessing (1861–1939, academician since 1925), V.A. Kistyakovskii (1865–1952, academician since 1929), A.A. Baikov (1870–1946, academician since 1932), and other known scientists.

When still being a student, Bashilov started to work at the Permanent Commission for Study of Russia's Productive Forces (KEPS), which was organized in February 1915, on the initiative of Academician V.I. Vernadskii (1863–1945) and a number of other scientists, at the Academy of Sciences for studying the natural resources of Russia and their industrial use. Bashilov worked under supervision of a prominent geochemist A.E. Fersman (1883–1945, academician since 1919), who was Vernadskii's closest associate.

In 1920–1921, under sever conditions of civil war, Bashilov studied, together with V.G. Khlopin (1890–1950, academician since 1939), the technology for recovery of radium from domestic raw materials (copper-vanadium ores from the Southern Fergana deposit) by recommendation of the Radium board of the Academy of Sciences. When being head of the Pilot radium plant (now in Mendeleevsk, Tatarstan, Russia), Bashilov developed a technology for recovery of all valuable components: radium, uranium, vanadium, and

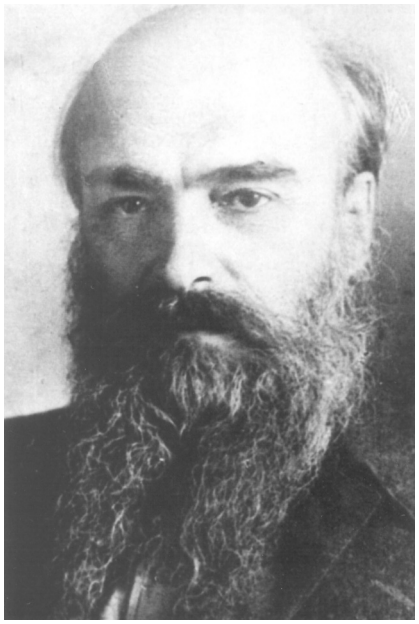

copper, from the starting ore. By December 1, 1921, the first Russia's high-activity radium preparations were obtained [1–5]. In 1922, the Radium Institute was created in Petrograd, and Vernadskii was appointed its first director. The Pilot plant joined the Institute, and Bashilov became a member of its Scientific Council.

In 1925, the facilities for recovery of radioactive metals were amalgamated with those for recovery of other rare metals at one of Moscow plants. Bashilov was appointed manager of the chemical department of the Trust of rare elements in Moscow.

In 1927, Bashilov was sent, as a prominent specialist, to a business trip to Germany and Czechoslovakia for familiarization with activities of chemical plants manufacturing radioactive preparations, rare metals, and their compounds [4, 5]. To the decennial anniversary of the Soviet power, the Radium Institute published Bashilov's monograph *Tekhnologiya radioaktivnykh rud* (Technology of Radioactive Ores, Leningrad, 1927, 96 pp.). Later, other his books were published: *Redkie elementy i ikh ispol'zovanie* (Rare Elements and Their Use, Moscow, 1930, 150 pp.)

1070-4272/03/7608-1362 $25.00 © 2003 MAIK "Nauka/Interperiodica"

and *Vvedenie v tekhnologoyu redkikh elementov* (Introduction to Technology of Rare Elements, Moscow–Leningrad, 1932, 275 pp.). In December 1928, Bashilov became, after many years' break, an external student of the Polytechnical Institute, and, in january of 1929, backed his graduation thesis work "A Study of Processing of Radium-containing Ores," to be qualified as engineer-metallurgist.

In the autumn of 1930, Ivan Yakovlevich was invited by the Scientific Council of the 2nd Moscow State University (later Lomonosov Institute of Fine Chemical Technology) to organize a chair and deliver a course of lectures on chemistry and technology of rare elements [6]. In 1931, Bashilov received an academic degree of a professor. At that same time, he was appointed scientific supervisor of the State Research Institute of Rare Metals (Giredmet, Moscow) and, simultaneously, headed the laboratory of radium at the same institute. In 1937, the degree of a doctor of technical science was conferred on Bashilov.

In the beginning of 1938, the Commission for problems associated with further development of the domestic radium industry was created at the Academy of Sciences of the USSR under Academician Vernadskii's supervision. The commission included, together with Academicians Khlopin and Fersman, also Professor Bashilov. In June 1938, Bashilov, a prominent specialist in the technology of rare and radioactive metals, was nominated a candidate for election into the Academy of Sciences of the USSR. However, on August 21 of the same year, he was arrested by Peoples' Commissariat for Internal Affairs (NKVD) and, on February 14, 1939, sentenced to five years of penal servitude for "counterrevolutionary activities" [5]. Till the beginning of 1943, the scientist served his sentence in Kotlas camps (Arhangelsk Province).

After the end of his term of imprisonment in June 1943, Bashilov was deported, by the order of deputy Peoples' Comissar A.P. Zavenyagin (1901–1957), to Krasnoyarsk, where NKVD was completing the construction of a plant for manufacture and refining of platinum metals. As raw materials served concentrates obtained in processing of sulfide copper-nickel ores from the Norilsk deposit. The scientist was well aware of the complexity of the task, because he had never dealt with platinum-group metals before that. By a twist of fate, Bashilov, chief specialist in the technology of processing of uranium ores, had to work, in the year when the development of the atomic industry was commenced in the country, on refining of platinum-group metals. Being undoubtedly important, this problem was more familiar to quite a number of representatives of the scientific school created in Russia by L.A. Chugaev (1873–1922) and N.S. Kurnakov (1860–1941, academician since 1913).

Owing to his natural capacities and experience, Bashilov fast familiarized himself with a production technology new to him. Already in the beginning of 1945, he was awarded the "Sign of Honor" order, and became, together with others, a laureate of the Stalin (State) Prize (1948) for the development and implementation of new methods for purification of platinum metals.

Soon, the plant started to work using the already well-established technology, and there was no need any more for services of such a high-skilled specialist. He clearly perceived that his knowledge and experience remained uncalled for. His appeals to the government to let him work somewhere to better purpose remained unanswered, he was denied exculpation. Of no avail, either, was his address to the president of the Academy of Sciences of the USSR, despite their long-standing friendship.

Bashilov was much respected by plant workers of any rank, he was highly cultured and attentive and benevolent to those surrounding him.

Ivan Yakovlevich Bashilov died of a heart attack exactly 15 years after his arrest. He was buried in Krasnoyarsk at Pokrovsko-Troitskoe Cemetery. In November 1996, a black-stone monument was erected over his grave, on which an inscription "Now look at my deeds" was carved, together with his bas-relief. Also carved were symbols of chemical elements, to whose manufacture technology Professor Bashilov contributed in different years: uranium, radium, vanadium, ruthenium, rhodium, and iridium.

The charge imposed on Bashilov by a Special Council of NKVD on February 14, 1939, was dismissed by the Supreme Court of the USSR on January 30, 1957.

All those who were lucky to work with Bashilov, or knew him, preserve the dearest memory of this fine man. The most detailed biographic evidence concerning the scientist can be found in a book by V.R. Polishchuk [5], who could see over the personal archive of scientist's daughter, I.I. Bashilova. The book published in connection with the 55th foundation anniversary of the Krasnoyarsk plant of nonferrous metals includes numerous personal reminscences of staff members of the plant about Bashilov.

REFERENCES

1. Glebova, V.I., *O radii i ego promyshlennosti* (Radium and Its Industry), Moscow: Tsentr. UP Vses. Sov. Nar. Khoz. SSSR, 1926.
2. Pogodin, S.A. and Libman, E.P., *Kak dobyli sovetskii radii* (How Soviet Radium Was Obtained), Moscow: Atomizdat, 1977.
3. Morachevskii, A.G., *Zh. Prikl. Khim.*, 1996, vol. 69, no. 11, pp. 1930–1933.
4. Morachevskii, A.G., *Nauch.-tekhn. Vedomosti SPb. Gos. Tekh. Univ.*, 1996, no. 3, pp. 96–99.
5. Polishchuk, V.R., *Repressirovannaya nauka* (Repressed Science), Yaroshevskii, M.G., Ed., Leningrad: Nauka, 1991, vol. 1, pp. 352–366.
6. Bol'shakov, K.A., Zvyagintsev, O.E., and Sazhin, N.P., *Zh. Prikl. Khim.*, 1954, vol. 27, no. 6, pp. 669–670.
7. *I vstal zavod nad Eniseem: Krasnoyarskii zavod tsvetnykh metallov* (And a Plant was Erected over Enysei River: Krasnoyarsk Plant of Nonferrous Metals), Graiver, B.M., Compiler, Krasnoyarsk: Izd.-Poligr. Kompleks "Platina," 1998.

A. G. Morachevskii

Russian Journal of Applied Chemistry, Vol. 76, No. 8, 2003, pp. 1365–1366. Translated from Zhurnal Prikladnoi Khimii, Vol. 76, No. 8, 2003, pp. 1402–1403.

Professor Semen Petrovich Vukolov (To His 140th Birthday Anniversary)

One of the closest pupils and co-workers of D.I. Mendeleev, professor Semen Petrovich Vukolov, who is among the most prominent specialists in explosives and powders, made a major contribution to the improvement of the fighting efficiency of the Russian Navy and to training of engineers-chemists specialized in this field.

S.P. Vukolov was born on September 6 (August 23), 1863, in the Don region at Starocherkasskaya stanitsa (Cossack village). Having received primary education at a local school, he entered Novocherkassk Gymnasium, wherefrom he graduated with gold metal in 1882. When still studying at the gymnasium, he, mostly on his own, mastered German, French, and English languages. In 1882, Vukolov entered, and in 1887 graduated from, the natural department of the physicomathematical faculty at St. Petersburg University. His acquaintance with D.I. Mendeleev (1834–1907) largely determined all the subsequent activities of the young scientist. Having graduated from the university, Vukolov worked for two years in Paris, at the laboratory of professor L.J. Troost (1825–1911), known for his studies in the field of inorganic chemistry. In these years, Vukolov published in Transactions of the Paris Academy of Sciences his first papers: "On Solubility of Gases" and "On Solubility of Carbon Dioxide in Chloroform," and took active part in the preparation of the Brokhaus–Efron Encyclopedia.

In 1890, the Naval Ministry assigned the honored professor Mendeleev to supervise research aimed to develop smokeless powder for naval guns. In August 1891, the scientific-and-technological laboratory was created at the Naval Ministry for solving this problem, and Vukolov occupied the position of junior assistant of the head of the laboratory (in 1906–1918, senior assistant; in 1918–1928, head of laboratory). In one and a half years, smokeless powder for firearms of all the necessary calibers was obtained and tested. The outstanding Mendeleev's contribution to this work was described by Vukolov in detail in an article devoted to the centennial anniversary of Mendeleev's birthday [1]. By 1894, a simple and convenient technological process for industrial manufacture of smokeless powder was developed [2].

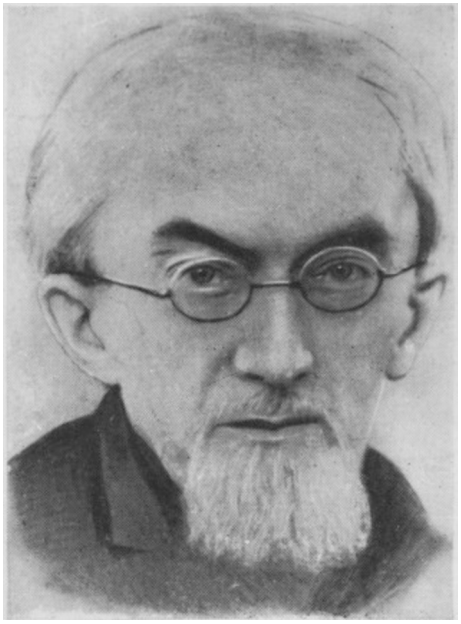

Together with working at the laboratory, Vukolov took part, in the summer of 1899, in a business trip with Mendeleev and other specialists to the Urals for studying the natural and economic conditions of operation of metallurgical plants. As a result of the expedition, quite a number of suggestions on development of metallurgical industry, transport, and economy of the Ural region was made. Mendeleev's memorandum concerning the results of the trip, submitted to the Minister for Finance S.Yu. Vitte (1849–1915), in particular, reads: "The industrial impact of Russia on the entire western Siberia and steppe center of Asia may and must involve the Ural region." The results of the expedition were summarized in a three-volume publication "Ural's Iron Industry in 1899."

By Mendeleev's recommendation, Vukolov took part in the expedition on ice-breaker Ermak (1901), aimed to study magnetic phenomena in the Arctic Ocean. Vukolov went in business trips to England, Germany, France, and the United States to make acquaintance with plants manufacturing explosives and was a participant of international congresses on applied chemistry in London (1909) and New York (1912). By 1911, he had the rank of senior state councilor.

1070-4272/03/7608-1365 $25.00 © 2003 MAIK "Nauka/Interperiodica"

After smokeless powder was put into industrial production, the functions of the Scientific-technological laboratory were extended, largely on Vukolov's initiative, to all kinds of ammunition for the Navy. Technologies for manufacture of trinitrotoluene and tetryl were developed, and these, new by that time, explosives were tested and methods for their use in various kinds of ammunition were studied [3].

In the prewar years (1911–1914), Vukolov and coworkers studied underwater explosions and designed special devices for this purpose. During the war (1914–1918), the efforts of the Laboratory and the associated pilot shops were completely concentrated on the supply of ammunition for the Navy. These works revealed the Vukolov's vigor and talent. In particular, lead azide was used for the first time in Russia in manufacture of caps for various kinds of shells for naval artillery. The scientific and technological results of the activities of the Laboratory were analyzed in [3, 4].

Already the first months of the war revealed the weakness of the military chemical industry of Russia. The available resources of nitric and sulfuric acid were insufficient for satisfying the dramatically increased demand for powders and explosives; benzene, toluene, and other necessary components could not be manufactured in required amount. In February 1915, "Commission for Procurement of Explosives" was organized at the Chief Artillery Department of the Military Ministry. The commission was headed by a professor of the Artillery Academy, lieutenant-general V.N. Ipat'ev (1867–1952, academician since 1916). Vukolov became a member of this commission [5]. He took active part in setting up production of the necessary raw materials at plants of southern Russia, and explosives in Revel (Tallinn), Petrograd, and Kineshma. As is known, a rapid rise in manufacture of explosives and chemical warfare, and other most important chemical industrial products, occurred in Russia already by the end of 1916 [5, 6]. Vukolov's activities during the years of war were honored by a number of state awards, and also by French Legion of Honor.

In 1919–1923, Vukolov was deputy head of the "Special Technical Commission for Inspection of Powders and Explosives" and dealt with problems of accounting and storage of the naval ammunition. From 1919 till 1928, he headed a department at the State Institute of Applied Chemistry, worked in a number of other scientific institutions, and taught at Leningrad University and Naval Academy.

In 1929, about 100 officers of the Russian Navy, allegedly members of a "counterrevolutionary organization at the Naval Department of the Workers'and Peasants' Red Army" were arrested. Vukolov was among them: he was arrested on 27.07.1929 and sentenced on 30.04.1931 to 3 years of imprisonment [7]. However, in January 1932, he was freed and rehabilitated. In 1932–1935, Vukolov worked as senior engineer at the Research Institute of Navy. Simultaneously, in 1932, he created a chair of explosives at the Leningrad Institute of Chemical Technology and headed it till the end of his life. The scientific degree of a doctor of chemical science was conferred on him in 1935, and the rank of a professor, in 1938.

Semen Petrovich Vukolov died on October 10, 1940, in Leningrad. Till the last days of his life he devoted all his energies to pedagogical and research activities. His pupils remember this excellent person who loved his country.

REFERENCES

1. Vukolov, S.P., *Zh. Prikl. Khim.*, 1934, vol. 7, no. 8, pp. 1535–1538.
2. Averbukh, A.Ya., *Trudy In–ta Ist. Estestvozn. Tekh.*, 1962, vol. 39, pp. 222–247.
3. Bagal, L.I., *Zh. Prikl. Khim.*, 1941, vol. 14, no. 4–5, pp. 517–520.
4. Averbukh, A.Ya., The Development of Manufacture of Powders and Explosives in Russia, *Doctoral Dissertation*, Leningrad, 1969.
5. Ipat'ev, V.N., *Rabota khimicheskoi promyshlennosti na oboronu vo vremya voiny* (Defense-related Work of Chemical Industry during the War), Petrograd, 1920.
6. Ipat'ev, V.N., *Khimicheskii komitet pri Glavnom artilleriiskom upravlenii i ego deyatel'nost' dlya razvitiya otechestvennoi khimicheskoi promyshlennosti* (Chemical Committee at Chief Artillery Department and Its Activities Devoted to Development of Domestic Chemical Industry), Petrograd, 1921, part 1.
7. Shoshkov, E.N., *Repressirovannoe Ostekhbyuro* [Repressed Ostekhbyuro (Special Technical Bureau)], St. Petersburg: Nauch.-Inf. Tsentr "Memorial," 1994.

V.S. Shpak and A.G. Morachevskii

Russian Journal of Applied Chemistry, Vol. 76, No. 8, 2003, pp. 1367–1368. Translated from Zhurnal Prikladnoi Khimii, Vol. 76, No. 8, 2003, pp. 1404–1405.

BOOK REVIEWS

Reznik, D.I., Ermakov, G.P., and Shneerson, Ya.M., *Nikel'* (Nickel), 3 vols., Moscow: Nauka i Tekhnika Ltd., 2003, vol. 3, 608 pp.

The final volume of the three-volume monograph (parts VIII–XV, chapters 27–55)[1] contains a vast body of material concerning mainly the nature and processing methods of sulfide copper-nickel ores. Also considered are refining of nickel, recovery of noble and rare metals in processing of nickel and copper-nickel ores, and evidence about world's manufacture and consumption of nickel.

The share of sulfide copper-nickel ores in the total output of nickel ores is 60 – 64%. The main components of the ores are such minerals as pyrrhotine, pentlandite, chalcopyrite, and magnetite. Their various ratios give rise to a wide variety of relative contents of copper and nickel in ores from different deposits. To accessory components are referred cobalt, platinum metals, gold, silver, selenium, and tellurium, which are present in minor amounts. In some deposits, the cost of accessory components, e.g., platinum and palladium, exceeds that of nickel and copper. The authors describe deposits of sulfide copper-nickel ores in the Kola Peninsula and Norilsk region, a deposit discovered in Voronezh province in 1977, and foreign deposits and mines in Canada, Australia, and China (part VIII, ch. 27).

The ninth part of the monograph discusses a wide variety of problems associated with smelting of sulfide copper-nickel raw materials. It considers in detail the blast smelting of a relatively rich lump ore at the Severonikel' combine (beginning in 1938) and Norilsk mining-and-smelting combine (since 1942) and foreign combines, and also autogenous blast smelting of sulfide copper and copper-nickel raw materials (ch. 28). By 1978, the blast smelting was replaced at domestic plants with other processes in order to diminish the discharge of sulfur dioxide into the atmosphere. The authors note that it is possible now to revert to blast smelting by using oxygen-enriched blast and passing to autogenous processes without coke. The same part of the monograph considers reverberatory smelting of sulfide copper-nickel ores and concentrates (chapter 29), electric smelting of copper-nickel raw materials (ch. 30), impoverishment of molten converter slags in electric furnaces (ch. 31), smelting of sulfide concentrates in suspended state (ch. 32), autogenous smelting of copper-nickel ore in a unit with top oxygen blast (ch. 33), smelting in a liquid bath (ch. 34), and other kinds of smelting of sulfide concentrates (ch. 35). The authors emphasize that the development of new smelting processes was due to the necessity to catch and utilize sulfur dioxide, diminish the energy consumption for smelting by using heat released in oxidation of sulfides, and raise the output capacity of smelting units to compensate for the low content of nickel in concentrates.

The tenth part of the monograph contains detailed evidence about conversion of copper-nickel mattes and cooling of converter matte. The aim of conversion (ch. 36) is to remove iron from matte in order to obtain converter matte in which nickel, copper, cobalt, and noble metals are concentrated in the sulfide and, partly, metallic form. In slow cooling of molten converter matte, there occurs separate crystallization of copper and nickel sulfides, which makes it possible to obtain nickel and copper concentrates (ch. 37).

The eleventh part discusses hydrometallurgical techniques for processing of sulfide copper-nickel materials. It describes the following methods: autoclave leaching of rich sulfide concentrates, mattes, and converter mattes in ammonia medium (ch. 38); leaching in sulfuric acid medium (ch. 39); autoclave leaching of intermediate products formed in pyrometallurgical processes (ch. 40); chloride techniques for processing of sulfide nickel concentrates (ch. 41); leaching of sulfide nickel-cobalt concentrates (ch. 42).

The twelfth part of the book is devoted to methods for processing of nickel-pyrrhotine concentrates. These concentrates are obtained by flotation isolation of copper and nickel (pentlandite) concentrates by additional flotation and magnetic separation (ch. 43). Industrial processing of pyrrhotine concentrates is presently done only at single plant in Norilsk. Also

[1] Information about the first two volumes was published previously in Zhurnal Prikladnoi Khimii (2001, vol. 74, no. 4, p. 691 and no. 7, p. 1211). The numbering of parts and chapters is the same through all the three volumes.

1070-4272/03/7608-1367 $25.00 © 2003 MAIK "Nauka/Interperiodica"

described are theoretical foundations of the oxidizing and autoclave leaching of nickel-pyrrhotine concentrates (ch. 44).

The thirteenth part discusses methods for nickel refining: liquid extraction (ch. 45), autoclave technology for manufacture of metallic nickel powders (ch. 46), carbonyl technology for nickel refining (ch. 47),[2] and electrolysis of nickel (ch. 48).[3] Electrolysis is the final procedure in the technological scheme for processing of nickel raw materials, which makes it possible, in addition to obtaining the metal, to solve the problem of recovery of cobalt and platinum group metals into semi-products for further refining. All industrially implemented variants of nickel electrolysis are considered: refining of raw metallic anodes, refining of sulfide anodes, and electric extraction of nickel from sulfuric acid and chloride solutions.

The fourteenth part of the monograph[4] presents information on recovery of platinum group metals, gold, silver, and rare elements in processing of nickel and copper-nickel ores. It describes the following issues: behavior of noble metals in processing of oxidized nickel ores (ch. 49) and sulfide copper-nickel ores (ch. 50); technology for recovery of noble metals and rare chalcogens from electrolyte sludge and other products enriched with these elements (ch. 51).

The final, fifteenth part of the monograph presents statistical data on the scale of manufacture and consumption of nickel. In 2002, the world's output of nickel was 1091 thousand tons, of which Russia produced 236.6 thousand tons, thus occupying the first place with 21.7% of the world's output. The consumption of nickel in Russia was only 31.3 thousand tons (2.7% of the world consumption) (ch. 52). Chapters 53, 54, and 55 present evidence concerning the largest world's plants processing sulfide copper-nickel raw materials and consider the ranges of use of nickel and the trends of prices for nickel, cobalt, and copper at London Metal Exchange in the last 10 years.

Each part of the monograph has its own reference list. The third volume presents a total of 423 references, mainly to publications by domestic authors. The third volume, as also the whole monograph, has clearly pronounced technological orientation. A detailed analysis of production processes at Russian and foreign plants of nickel industry is made. The information value of this capital publication is very high. The authors of the monograph, and I.D. Reznik in the first place, are well aware of the entire history of the development of the domestic nickel industry, which imparts an interesting aspect to the presentation and makes it possible to trace the dynamics of technological changes at the largest plants of the country.

The book gives an exhaustive description of the nickel industry of Russia and other countries. It may be of use for a wide audience of specialists associated with nickel industry and also for graduate students, masters, and postgraduate students specialized in metallurgy of heavy nonferrous metals.

A.G. Morachevskii, I.N. Beloglazov

---

[2] Written by A.S. Mnukhin.

[3] Written by L.V. Volkov.

[4] Written by T.N. Greiver.

Russian Journal of Applied Chemistry, Vol. 76, No. 9, 2003, pp. 1369–1374. Translated from Zhurnal Prikladnoi Khimii, Vol. 76, No. 9, 2003, pp. 1409–1414.

REVIEWS

Reaction Medium and Kinetics of *N*-Vinylsuccinimide Copolymerization

Dedicated to the memory of Prof. Sergei Nikolaevich Ushakov

N. A. Lavrov

St. Petersburg State Technological Institute, St. Petersburg, Russia

Received February 28, 2003

Abstract—Studies in the field of radical copolymerization of *N*-vinylsuccinimide were summarized, and the effect of the reaction medium on the process kinetics was examined. Factors governing the relative activity of the monomers were revealed, and ways to control the reactivity of *N*-vinylsuccinimide in binary copolymerizations were suggested.

September 16, 2003 is the 100th anniversary of Prof. Sergei Nikolaevich Ushakov's birthday. Prof. Ushakov, Corresponding Member of the USSR Academy of Sciences, Honored Scientist of the RSFSR, Honored Inventor of the RSFSR, winner of State Prizes, Doctor of Engineering, contributed much to foundation of the Chair of Chemical Technology of Plastics at the St. Petersburg State Technological Institute (formerly Lensovet Leningrad Technological Institute), Institute of Macromolecular Compounds (Russian Academy of Sciences), and Research Institute of Polymerization Plastics, and also to many other major events in the Soviet science. Ushakov's scientific interests were very diverse. His monographs became reference books for many generations of engineers and researchers, and the results of research work, published in numerous papers, were further developed by his disciples and followers. About 50 years ago, S.N. Ushakov together with A.F. Nikolaev initiated studies in the field of synthesis and application of polymers based on dicarboxylic acid *N*-vinylimides [1–4]. These studies were subsequently continued; their results were published in more than 100 papers, and several tens of inventor's certificates and patents were received. Two doctoral [4, 5] and more than ten candidate's dissertations were defended on this problem at the Chair of Chemical Technology of Plastics, St. Petersburg State Technological Institute.

Among the compounds prepared, polymers derived from *N*-vinylsuccinimide (VSI) aroused the greatest scientific and practical interest; they showed promise for biology and medicine. To expand the assortment of VSI-based polymers, copolymerization of VSI with other monomers was studied. This paper summarizes the results of these studies and analyzes the effect of the reaction medium on the kinetics of synthesis of VSI copolymers, relative activity of the monomers, and compositional uniformity of the copolymers.

The electron-donor substituent in the VSI molecule increases the electron density on the vinyl double bond, which is confirmed by the negative Alfrey–Price parameter e ($e = -0.34$). The increased electron density on the double bond suggests the possibility of preparing VSI polymers by cationic polymerization; however, this method found no application because of the low molecular weight of the products obtained. VSI (co)polymers are mainly prepared by radical (co)polymerization. It should be noted that the conjugation between the lone electron pair of the nitrogen atom and the π electrons of the vinyl group is relatively weak ($Q = 0.13$), which is responsible for fairly low activity of VSI monomer in binary radical copolymerization with other monomers (see table).

The table shows that VSI copolymers are chiefly prepared by copolymerization in the bulk, in organic solvents, and in water. The initiators used are quite traditional: benzoyl peroxide (BP), azobis(isobutyronitrile) (AIBN), and various redox systems.

In binary copolymerizations, VSI is more active than VA and vinyl *n*-butyl ether but less active than styrene and acrylic monomers. Dicarboxylic acid *N*-vinylimides are more active in copolymerizations than many other *N*-vinyl compounds, as noted, e.g., in copolymerization of VSI with *N*-vinylpyrrolidone (VP) and *N*-vinylcarbazole (see table) and of *N*-vinylphthalimide (VPI) with VP: $r_1 = 1.284 \pm 0.04$, $r_2 = 0.35 \pm 0.002$ [22].

It is known that binary radical copolymerization kinetics is affected by various factors. Analysis of the

1070-4272/03/7609-1369$25.00

Constants of VSI (M_1) copolymerization with other monomers under conditions of radical copolymerization

Copolymer M_2	Reaction conditions			r_1	r_2	References
	solvent	initiator	T, °C			
Acrylamide	Water	Ammonium peroxodisulfate–ascorbic acid	20	0.168	1.86	[6]
Acrylonitrile	In the bulk	BP	60	0.16	0.54	[7]
	DMF	AIBN	50	0.10 ± 0.02	0.87 ± 0.05	[8]
n-Butyl acrylate	Dichloroethane	AIBN	60	0.15 ± 0.02	1.55 ± 0.08	[9]
	DMSO	AIBN	60	0.18 ± 0.08	3.68 ± 0.79	[10]
	Acetic anhydride	AIBN	60	0.05 ± 0.02	0.94 ± 0.28	[11]
Vinyl acetate (VA)	In the bulk	BP	60	6.05	0.18	[7]
	″	BP	60	6.10	0.14	[12]
	″	BP	65	5.10	0.175	[13]
	Ethanol	BP	70	5.62	0.17	[14]
	DMSO, molar ratio VSI : DMSO:					
	1 : 3	AIBN	70	2.78	0.04	[15]
	1 : 14	AIBN	70	0.02	0.82	[15]
	Water	Ammonium peroxodisulfate–sodium sulfite	35	1.16 ± 0.20	0.02 ± 0.02	[16]
	″	Manganese tris(acetylacetonate)–acetic acid	25	1,13 ± 0.17	0.30 ± 0.09	[17]
Vinyl *n*-butyl ether	In the bulk	BP	60	15.0	0	[7]
Vinylidene chloride	″	BP	60	0.32	1.44	[12]
N-Vinylcarbazole	Benzene	AIBN	60	1.05	0.3	[18]
N-Vinylpyrrolidone	In the bulk	AIBN	20	1.40	0.37	[19]
	″	AIBN	35	1.36	0.42	[19]
	″	AIBN	45	1.30	0.41	[19]
	Ethanol	AIBN	60	1.50	0.40	[19]
	Dichloroethane	AIBN	60	1.54	0.30	[19]
	Water	AIBN	60	1.05	0.66	[19]
2-Hydroxyethyl	Benzene	AIBN	60	0.09 ± 0.02	7.36 ± 1.66	[20]
methacrylate	DMSO	AIBN	60	0.05 ± 0.05	8.50 ± 0.45	[21]
Dimethyl maleate	Benzene	AIBN	60	1.20	0.04	[18]
Maleic anhydride	″	AIBN	60	0.15	0.03	[18]
Methyl acrylate	In the bulk	BP	60	0.40	1.2	[7]
Methyl methacrylate	″	BP	60	0.064	9.5	[12]
	DMSO	AIBN	70	0.03 ± 0.01	0.12 ± 0.01	[15]
Styrene	In the bulk	BP	60	0.09	7.0	[7]
	″	BP	60	0.07	10.5	[12]
	DMSO, molar ratio VSI : DMSO:					
	1 : 3	AIBN	70	0.06 ± 0.01	3.18 ± 0.01	[15]
	1 : 4	AIBN	70	0	2.88	[15]
	1 : 12	AIBN	70	0.03	7.07	[15]

published data reveals the following factors causing deviations from the classical theory of radical copolymerization and affecting the reactivity of monomers and radicals, the rate constants of elementary reactions, and the overall copolymerization kinetics:

(a) occurrence of a dynamic equilibrium between the forward (polymerization) and reverse (depolymerization) reactions [23–25];

(b) homoassociation of monomers [24] and effect of the solvent polarity on the monomer speciation;

(c) solvation of radicals with solvent molecules, shielding the reaction center [23];

(d) dependence of the rate constants of elementary reactions on the composition of the starting monomeric mixture [24];

(e) selective solvation of macroradicals with monomers [26];

(f) dependence of the copolymerization kinetics and copolymer composition on the initiator concentration [23];

(g) possible interaction of monomers with each other to form a complex [24];

(h) presence of components (solvents, initiators, complexing agents, etc.) forming complexes with monomers [23–25, 27–30];

(i) chain transfer to copolymer macromolecules [24];

(j) effect of penultimate unit, along with the terminal unit, on the copolymerization kinetics [23, 24, 31];

(k) variation of the composition of the forming copolymer with variation of the initiation rate [32];

(l) influence of the heterophase mode of the process on the elementary reactions [23, 24, 33, 34];

(m) influence of the degree of polymerization on the elementary steps of the process [23, 24, 34]; polymerization systems in viscous media can be considered as microheterophase [23];

(n) influence of pH in copolymerization of ionizable monomers [35]; changes in the reaction kinetics under conditions of heterogeneous copolymerization on a solid surface [25, 32];

(o) changes in the reaction kinetics in an emulsion [23, 25];

(p) influence of the solvent composition on the macromolecule conformation [24];

(q) hydrophobic interaction arising in polymer solutions when copolymerization is performed in aqueous-organic media [36];

(r) effect of selective sorption of monomers on the copolymer composition [37].

It should be taken into account that several factors can act simultaneously.

The structural features of VSI and conomomer molecules and the results obtained in experiments on VSI homopolymerization [38] suggest that the VSI copolymerization kinetics will also show deviations from the classical theory. Firstly, VSI and some comonomers, owing to the features of their structure and charge distribution [39], can interact with components of the medium to form intermolecular complexes. In this case, by the reaction medium is understood the whole set of components participating in the process (comonomers, solvents, initiators, etc.). Secondly, the presence of bulky substituents in VSI and comonomer molecules and different polarities of the monomers will result in the fact that addition of monomers to a propagating radical will be influenced by the structure of not only terminal but also penultimate unit of the macrochain. Thirdly, the heterophase mode of the process performed in some solvents, e.g., benzene, may result in that the active center gets immured in the condensed polymer phase. Because of occlusion of macroradicals, the chain termination can occur by the monomolecular mechanism. The access of monomers to the active centers is thus hindered; the diffusion rates of the monomers, especially of those of different polarity, can differ significantly. Therefore, the compositions of the copolymers obtained under conditions of homophase and heterophase copolymerization can differ significantly. The rate of the heterophase copolymerization is usually higher than that of the homophase process. Fourthly, in copolymerization with monomers tending to homoassociation, e.g., with 2-hydroxyethyl methacrylate (HOEMA), the relative activities of the monomers and the compositions of the copolymers can depend on the polarity of the medium. The kinetics of VSI copolymerization can also be influenced by other factors, in particular, by solvation, sorption, macromolecule conformation, etc. Some trends can be expected theoretically; as for experimental data, the following facts have been proved.

N-Vinylsuccinimide can enter into intermolecular interaction with comonomers, e.g., maleic anhydride (MA), and with some solvents: dimethyl sulfoxide (DMSO), dimethylformamide (DMF), and acetic anhydride. Hopff and Becker [18] revealed no complexation of VSI with MA, but in later studies [40, 41] equimolar donor–acceptor complexes of VSI and some other *N*-vinyl monomers (VP, VPI) with MA were detected; this resulted in formation of copolymers of a fixed composition corresponding to the composition of the complex. If the ratio of the starting components was not equimolar, copolymerization yielded an alternating copolymer of the equimolar composition and a homopolymer of the *N*-vinyl monomer, if this monomer was in excess; if MA was in excess, its homopolymer was not formed, and excess MA was recovered unchanged. The compositions of the copolymers prepared in DMF and benzene were similar; this fact was accounted for in [40, 41] by the incapability of the MA–solvent interaction to compete with the donor–acceptor interaction of MA with the

N-vinyl monomer; the possibility of interaction of *N*-vinyl monomers with solvents was not considered in [40, 41]. It was only noted that the solvent affected the copolymerization rate: in benzene, the reaction was faster than in DMF. The causes of this trend were not discussed in [40, 41]; they may be associated with occlusion of the macroradicals, since the process should be heterophase. The difference between the results obtained in [18, 40, 41] may be due to different experimental procedures. In particular, Nikolaev *et al*. [40, 41] first obtained the monomeric complexes and then performed the polymerization. They noted that the donor–acceptor interaction increased in the order MA–VPI < MA–VSI < MA–VP.

The kinetics of copolymerization of VSI with various monomers in solvents was studied in more detail. Complexation of VSI with DMSO was proved by IR spectroscopy [15] and refractometry [42]. The donor–acceptor interaction may involve various groups [39], but interaction of the C=O groups of VSI with the S=O group of DMSO seems to be preferable. Experiments on copolymerization of VSI with *n*-butyl acrylate, VA, HOEMA, methyl methacrylate, and styrene showed that DMSO strongly affects the copolymerization constants (see table).

Interaction of VSI molecules with electron-donor DMSO molecules results in redistribution of the electron density in the monomer molecule and increase in the electron density on the double bond; as a result, the relative activity of VSI decreases compared to polymerization in the bulk or in an inert solvent, dichloroethane. As a result, the copolymerization constants of VSI with VA become closer, and it appears feasible to prepare copolymers with better alternation of the units [43, 44]. The copolymerization constants and the probability of formation of particular microstructures in the copolymer chains depend on the molar ratio of VSI and DMSO (see table). However, in copolymerization of VSI with acrylic monomers, a decrease in the relative activity of VSI results in that the copolymers become less uniform in the composition; therefore, to obtain copolymers with better alternation of the units, the reaction should be performed in an electron-acceptor solvent, e.g., acetic anhydride [45]. Dipole–dipole interaction of monomers with the solvent and solvation effects should be expected in (co)polymerization of VSI in water, but these processes have been studied insufficiently.

Complexation of VSI with a solvent affects the copolymerization constants calculated taking into account both the terminal and penultimate units of the macrochain [46]. Experiments on copolymerization of VSI with HOEMA showed that the penultimate unit only slightly affects the reactivity of the macroradical with the VSI terminal unit, but with the HOEMA terminal unit the effect of the penultimate unit is significant: the VSI penultimate unit decreases, and HOEMA unit enhances the reactivity of such macroradicals toward HOEMA monomers. The occurring processes affect the microstructure of the forming copolymers.

Heterophase copolymerizations in benzene are of applied interest. The processes are fast and allow preparation of copolymers in the form of finely dispesred powders, which simplifies their isolation. Although benzene, like DMSO, is an electron-donor solvent, copolymerization of VSI with HOEMA in benzene yielded copolymers with better alternation of the units than in DMSO. This may be due to a stronger tendency of DMSO to form complexes with VSI, owing to the presence of vacant orbitals on the sulfur atom. Therefore, in DMSO, VSI is less active in copolymerization than in benzene (see table). However, when comparing the copolymerization kinetics of VSI with HOEMA in benzene and DMSO, it should be taken into account that, in nonpolar solvents (dielectric permittivity: benzene 2.28, DMSO 46.45), HOEMA tends to associate, which affects its activity, i.e., the copolymerization of VSI with HOEMA in benzene is complicated by the effect of at least four factors, which are difficult to rank with respect to the extent of their influence.

To complete consideration of experimental data on VSI copolymerization kinetics, one more way to control the relative activity of the monomers should be noted: complexation of the comonomer (rather than VSI) with the components of the medium. This approach was used in experiments on copolymerization of VSI with VA in aqueous solution in the presence of the initiating system manganese tris(acetylacetonate)–acetic acid [17]. It is known that manganese tris(acetylacetonate) forms a complex with VA monomer in the initiation step, which enhances the relative activity of VA. Under these conditions, the copolymerization constants of VSI with VA become closer (see table), which results in formation of the copolymer with better alternation of the units.

Thus, studies commenced on Ushakov's initiative started a comprehensive research on radical copolymerization of VSI. A correlation was elucidated between the structure of the monomers, kinetic parameters of copolymerization, and nature of the reaction medium; factors affecting the VSI reactivity were revealed, and their total effect was analyzed; ways to control the VSI reactivity and prepare VSI copoly-

mers of preset structure and properties, suitable for various applications, were outlined [47].

CONCLUSIONS

(1) The reaction medium strongly affects the relative activity of *N*-vinylsuccinimide in radical copolymerization and the microstructure of the resulting copolymers. The major factors affecting the reaction kinetics are complexation of *N*-vinylsuccinimide or comonomer with components of the medium, homophase or heterophase mode of the process, features of the influence of the penultimate unit on addition of monomers to the propagating radical, and polarity of the medium (affecting the reactivity of monomers that form homoassociates).

(2) Electron-donor solvents enhance the activity of the *N*-vinylsuccinimide radical and decrease the relative activity of the monomer in binary copolymerizations.

(3) Heterophase copolymerization in benzene allows preparation of *N*-vinylsuccinimide copolymers at a higher rate, with isolation of the reaction products as finely dispersed powders.

REFERENCES

1. Nikolaev, A.F. and Ushakov, S.N., *Izv. Akad. Nauk SSSR, Otd. Khim. Nauk*, 1957, no. 10, pp. 1235–1238.
2. Nikolaev, A.F., Ushakov, S.N., and Grinburg, R.B., *Izv. Akad. Nauk SSSR, Otd. Khim. Nauk*, 1959, no. 9, pp. 1631–1635.
3. Nikolaev, A.F., Ushakov, S.N., and Mosh, V., *Izv. Akad. Nauk SSSR, Otd. Khim. Nauk*, 1959, no. 10, pp. 1818–1821.
4. Nikolaev, A.F., Polymers and Copolymers of Vinylamine and Its Derivatives, *Doctoral Dissertation*, Leningrad, 1967.
5. Lavrov, N.A., Structural Features, Reactivity, and Relationships of Polymerization Kinetics of *N*-Vinyl and Acrylic Monomers in Various Media, *Doctoral Dissertation*, St. Petersburg, 2002.
6. Nikolaev, A.F., Bondarenko, V.M., Klubikova, L.E., and Golenishcheva, S.A., *Izuchenie sopolimerizatsii N-vinilsuktsinimida s akrilamidom* (Copolymerization of *N*-Vinylsuccinimide with Acrylamide), Leningrad: Leningr. Tekhnol. Inst. im. Lensoveta, 1975, Available from VINITI, no. 2584–75.
7. Fuzukawa, J., Tsuruta, T., Yamamoto, N., and Fukutani, H., *J. Polym. Sci.*, 1959, vol. 37, no. 131, pp. 215–227.
8. Ulbricht, J. and Tscho Son-Din, *Fazerforsch. Textiltech.*, 1962, vol. 13, no. 10, pp. 433–437.
9. Nikolaev, A.F., Bondarenko, V.M., and Lopukhinskii, L.M., *Sopolimerizatsiya N-vinilsuktsinimida s butilakrilatom* (Copolymerization of *N*-Vinylsuccinimide with Butyl Acrylate), Leningrad: Leningr. Tekhnol. Inst. im. Lensoveta, 1975, Available from VINITI, no. 3271–75.
10. Lavrov, N.A., Sivtsov, E.V., and Nikolaev, A.F., *Zh. Prikl. Khim.*, 1998, vol. 71, no. 12, pp. 2055–2058.
11. Lavrov, N.A., Sivtsov, E.V., and Nikolaev, A.F., *Zh. Prikl. Khim.*, 2000, vol. 73, no. 4, pp. 683–686.
12. Hopff, H. and Schlumbom, P., *Makromol. Chem.*, 1961, vol. 43, no. 3, pp. 173–179.
13. Nikolaev, A.F., Ushakov, S.N., and Mishkileeva, L.S., *Vysokomol. Soedin.*, 1964, vol. 6, no. 2, pp. 287–291.
14. Nikolaev, A.F., Bondarenko, V.M., and Zhukova, N.A., *Zh. Prikl. Khim.*, 1970, vol. 43, no. 6, pp. 1339–1343.
15. Bondarenko, S.G., Nikolaev, A.F., Baranova, S.A., *et al.*, *Vysokomol. Soedin., Ser. A*, 1981, vol. 23, no. 12, pp. 2639–2651.
16. Lavrov, N.A., Nikolaev, A.F., Lepshina, E.M., and Lavrova, T.V., *Zh. Prikl. Khim.*, 1992, vol. 65, no. 9, pp. 2111–2114.
17. Lavrov, N.A., *Zh. Prikl. Khim.*, 1994, vol. 67, no. 9, pp. 1547–1550.
18. Hopff, H. and Becker, G., *Makromol. Chem.*, 1970, vol. 133, pp. 1–12.
19. Nikolaev, A.F., Tereshchenko, G.P., Salivon, I.Ya., *et al.*, *Vysokomol. Soedin., Ser. A*, 1972, vol. 14, no. 11, pp. 2368–2370.
20. Nikolaev, A.F., Bondarenko, V.M., Lavrov, N.A., and Sautin, S.N., *Izv. Vyssh. Uchebn. Zaved., Khim. Khim. Tekhnol.*, 1978, vol. 21, no. 5, pp. 732–735.
21. Lavrov, N.A., Bondarenko, V.M., Nikolaev, A.F., and Sautin, S.N., *Vysokomol Soedin., Ser. B*, 1981, vol. 23, no. 2, pp. 142–144.
22. Gruz, R.I., Shibalovich, V.G., Panarin, E.F., and Ushakov, S.N., *Vysokomol. Soedin., Ser. A*, 1968, vol. 10, no. 9, pp. 2096–2101.
23. Ivanchev, S.S., *Radikal'naya polimerizatsiya* (Radical Polymerization), Leningrad: Khimiya, 1985.
24. Myagchenkov, V.A. and Frenkel', S.Ya., *Kompozitsionnaya neodnorodnost' sopolimerov* (Compositional Nonuniformity of Copolymers), Leningrad: Khimiya, 1988.
25. *Reaktsii v polimernykh sistemakh* (Reactions in Polymer Systems), Ivanchev, S.S., Ed., Leningrad: Khimiya, 1987.
26. Semchikov, Yu.D. and Smirnova, L.A., *Vysokomol. Soedin., Ser. B*, 1999, vol. 41, no. 4, pp. 734–748.
27. Kabanov, S.A., Zubov, V.P., and Semchikov, Yu.D., *Kompleksno-radikal'naya polimerizatsiya* (Radical Complex Polymerization), Moscow: Khimiya, 1987.

28. Spirin, Yu.L., *Reaktsii polimerizatsii* (Polymerization Reactions), Kiev: Naukova Dumka, 1977.
29. Gromov, V.F. and Khomikovskii, P.M., *Usp. Khim.*, 1979, vol. 48, no. 11, pp. 1943–1967.
30. Lavrov, N.A., Sivtsov, E.V., and Nikolaev, A.F., *Reaktsionnaya sreda i kinetika polimerizatsionnykh protsessov* (Reaction Medium and Kinetics of Polymerization Processes), St. Petersburg: Sintez, 2001.
31. *Copolymerization*, Ham, G.E., Ed., New York: Interscience, 1964.
32. Ivanchev, S.S. and Pavlyuchenko, V.N., *Usp. Khim.*, 1994, vol. 63, no. 8, pp. 700–718.
33. Myagchenkov, V.A. and Frenkel', S.Ya., *Usp. Khim.*, 1973, vol. 42, no. 3, pp. 827–853.
34. Gladyshev, G.P. and Popov, V.A., *Radikal'naya polimerizatsiya pri glubokikh stepenyakh prevrashcheniya* (Radical Polymerization at High Conversions), Moscow: Nauka, 1974.
35. Kabanov, V.A. and Topchiev, D.A., *Polimerizatsiya ionizuyushchikhsya monomerov* (Polymerization of Ionizable Monomers), Moscow: Nauka, 1975.
36. Gromov, V.F., Bogachev, Yu.S., Bune, E.V., *et al.*, *Dokl. Akad. Nauk SSSR, Fiz. Khim.*, 1989, vol. 309, no. 4, pp. 871–874.
37. Semchikov, Yu.D., Smirnova, L.A., and Zaitsev, S.D., *Vysokomol. Soedin., Ser. A*, 1995, vol. 37, no. 5, pp. 741–745.
38. Lavrov, N.A., *Plast. Massy*, 2002, no. 7, pp. 10–15.
39. Sivtsov, E.V., Lavrov, N.A., and Nikolaev, A.F., *Plast. Massy*, 2001, no. 10, pp. 26–31.
40. Nikolaev, A.F., Bondarenko, V.M., and Shakalova, N.K., *Vysokomol. Soedin., Ser. B*, 1974, vol. 16, no. 1, pp. 14–16.
41. Nikolaev, A.F., Bondarenko, V.M., and Shakalova, N.K., *Vysokomol. Soedin., Ser. B*, 1973, vol. 15, no. 10, pp. 737–740.
42. Sivtsov, E.V., Lavrov, N.A., and Nikolaev, A.F., *Plast. Massy*, 2001, no. 10, pp. 20–25.
43. Lavrov, N.A., Bondarenko, S.G., Nikolaev, A.F., and Sautin, S.N., *Zh. Prikl. Khim.*, 1984, vol. 57, no. 3, pp. 618–621.
44. Lavrov, N.A., *Plast. Massy*, 2001, no. 12, pp. 28–32.
45. Lavrov, N.A., Sivtsov, E.V., and Nikolaev, A.F., *Plast. Massy*, 2001, no. 10, pp. 43–45.
46. Lavrov, N.A., *Plast. Massy*, 2002, no. 9, pp. 20–26.
47. Lavrov, N.A., Shal'nova, L.I., and Nikolaev, A.F., *Plast. Massy*, 2001, no. 10, pp. 5–9.

Russian Journal of Applied Chemistry, Vol. 76, No. 9, 2003, pp. 1375–1378. Translated from Zhurnal Prikladnoi Khimii, Vol. 76, No. 9, 2003, pp. 1415–1418.

INORGANIC SYNTHESIS AND INDUSTRIAL INORGANIC CHEMISTRY

Nature and Thermal Behavior of Precipitated Calcium–Magnesium Phosphates

V. A. Sinyaev, E. S. Shustikova, L. V. Levchenko, G. A. Tokseitova, and D. Griggs

Bekturov Institute of Chemical Sciences, Ministry of Science and Education of Kazakhstan Republic, Almaty, Kazakhstan

Baylor Stomatological College, Texas University, Scientific Center, Dallas, the United States

Received February 3, 2003

Abstract—A group of crystalline and amorphous calcium–magnesium phosphates were prepared by exchange in solution of sodium orthophosphate and calcium and magnesium chlorides at pH 8–12. The behavior of the phosphates on heating to 1000°C was studied.

Calcium phosphates are components of preparations and materials for modern stomatology and orthopedics [1–4]. Among them, the most widely used compound is hydroxyapatite $Ca_5(PO_4)_3OH$, which is a mineral base of human and animal bone tissues [4–8]. This compound is mainly used in the crystalline form. Its amorphous form, which has not yet been obtained pure, should exhbit considerably higher bioactivity.

Hydroxyapatite is sparingly soluble in water. Therefore, chemical methods of its preparation include exchange reactions in a solution between phosphates and calcium salts [4]. Amorphous phosphates, which can be considered as apatite-related compounds, are precipitated in the presence of substances preventing crystal nucleation and growth. As crystallization inhibitors can serve different substances, e.g., soluble carbonates, fluorides, diphosphates, etc. [4, 9, 10]. Of great interest are magnesium salts, whose behavior in the course of the phosphate precipitation has been considered elsewhere [5, 9–15]. A method has been patented [16], according to which crystallization of the precipitated apatite is prevented by adding soluble magnesium(II) salts in the ratio Mg/Ca = 0.001–1. The presence of Mg^{2+} ions opens new ways to control properties of calcium-containing medical preparations [17]. Moreover, amorphous calcium–magnesium phosphates are interesting precursors for bioceramics.

The goal of this study was to refine the Mg/Ca ratio ensuring formation of amorphous substances from Na_3PO_4 aqueous solutions containing $CaCl_2$ and $MgCl_2$ and to gain insight into the behavior of the precipitated phosphates on heating.

EXPERIMENTAL

We used $CaCl_2$, $MgCl_2$, and sodium hydrophosphate Na_2HPO_4 (analytically pure grade). 5% aqueous solutions containing the required amounts of both chlorides were slowly added dropwise to a solution of Na_2HPO_4 at vigorous stirring. Preliminarily, the Na_2HPO_4 solution was adjusted to pH 12.0 to neutralize acids released upon the hydroxyapatite formation. After most of the substance was precipitated, pH was decreased to 8.0, and then a 5% NaOH solution was added to maintain pH at this level up to the synthesis completion. The precipitates were washed with distilled water (pH 8) to fully remove Cl^- ions, decanted, and filtered through a glass frit. The substances were dried in air at room temperature and studied by IR spectroscopy and X-ray phase and thermal analyses. The IR spectra were recorded on a Specord M80 spectrometer from KBr pellets, and X-ray diffraction patterns were taken on a DRON-3 diffractometer (CuK_α radiation). The thermal analysis of 0.2-g samples heated in platinum crucibles in air at a rate of 10 deg min^{-1} was done with a MOM Q-1500 thermal analyzer (Hungary) using aluminum oxide as reference.

The chemical analysis of the precipitates revealed phosphorus(V), calcium(II), and magnesium(II) in ratios used in the synthesis. According to the X-ray phase analysis (Fig. 1), the substance precipitated with calcium chloride from an Na_3PO_4 solution is crystalline hydroxyapatite [9]. In the diffraction patterns of substances precipitated with calcium chloride in the presence of small amount of $MgCl_2$, the reflections become less intense and more diffuse with growing

1070-4272/03/7609-1375$25.00

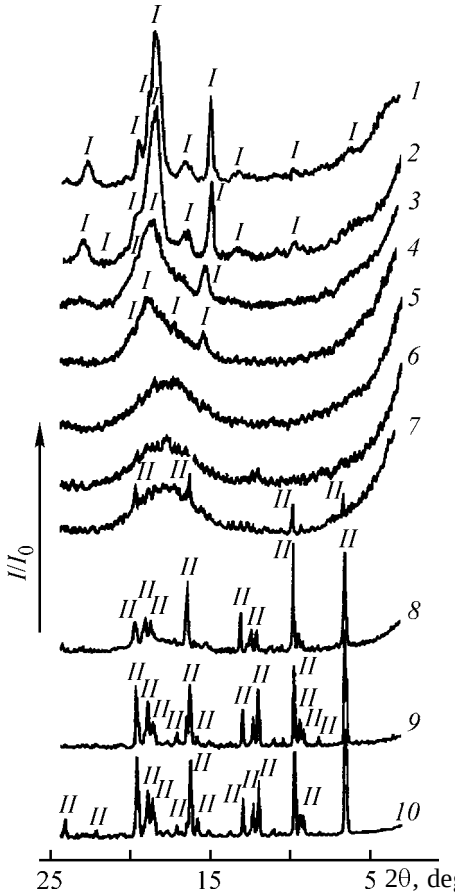

Fig. 1. X-ray diffraction patterns of phosphates precipitated from aqueous solutions containing $CaCl_2$ and $MgCl_2$: (I/I_0) relative reflection intensity and (2θ) diffraction angle; the same for Fig. 4. $MgCl_2/(MgCl_2 + CaCl_2)$ molar ratio: (*1*) 0, (*2*) 0.05, (*3*) 0.10, (*4*) 0.20, (*5*) 0.25, (*6*) 0.35, (*7*) 0.40, (*8*) 0.50, (*9*) 0.80, and (*10*) 1.00. (*I*) $Ca_5(PO_4)_3OH$ and (*II*) $Mg_2OHPO_4 \cdot 3H_2O$.

$MgCl_2/(MgCl_2 + CaCl_2)$ ratio. This means that the less crystalline precipitate is formed. The diffraction patterns of the substances precipitated from solutions at $0.25 \le MgCl_2/(MgCl_2 + CaCl_2) \le 0.35$ suggest that they are amorphous to a maximal extent. The substances formed from solutions with larger amounts of $MgCl_2$ contain the crystalline component $Mg_2OHPO_4 \cdot 3H_2O$, along with the amorphous phase. These data show that formation of crystalline phosphates is inhibited in a narrow range of the $MgCl_2/(MgCl_2 + CaCl_2)$ molar ratios (0.25–0.35), which is considerably narrower than that reported in [16].

One of the reasons why the precipitated calcium–magnesium phosphates are amorphous is that the types of calcium– and magnesium–oxygen polyhedra forming the phosphate structure are different. It is known that the number of oxygen atoms bound to Ca^{2+} ions can reach 12, whereas that for Mg^{2+} ions is commonly four [18]. Owing to such differences, the Ca^{2+} and Mg^{2+} ions present simultaneously in certain ratios in a solution containing PO_4^{3-} ions cannot form surroundings typical of crystalline hydroxyapatite and basic magnesium phosphate. Instead of them, products with the random distribution of cations among PO_4 groups are formed.

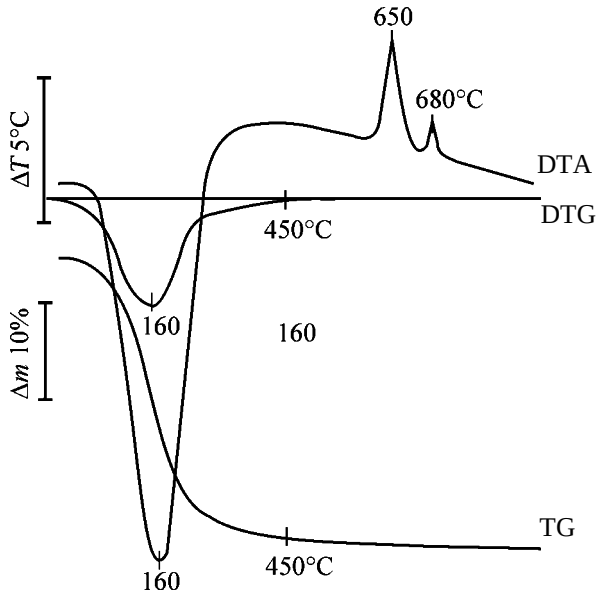

Fig. 2. Thermogram of calcium–magnesium phosphate precipitated at the atomic ratio Mg/(Mg + Ca) = 0.35.

The precipitated calcium–magnesium phosphates dried to constant weight at room temperature are hydrates. Their IR absorption spectra contain strong absorption bands belonging to the O–H stretching vibrations of water molecules. The water of crystallization is lost even on weak heating. Figure 2 shows for the sample whose composition corresponds to the atomic ratio Mg/(Mg + Ca) = 0.35 that the dehydration becomes more active with increasing temperature, with the maximal rate attained at about 160–170°C, and is mainly complete at 400–450°C. The water content in phosphates, as estimated from the thermal analysis data, depends on the sample composition. Figure 3a shows that, with an increase in the magnesium(II) content in the substance, the water content increases to the maximal value, which is reached in the most amorphous products, and then decreases.

Dehydration is an endothermic reaction, and the endothermic peaks in the DTA curves reflect the water content in the substances (Fig. 3b). The endothermic peaks are the strongest for the phosphates with the atomic ratio Mg/(Mg + Ca) $\approx$ 0.35.

The DTA curves of calcium–magnesium phos-

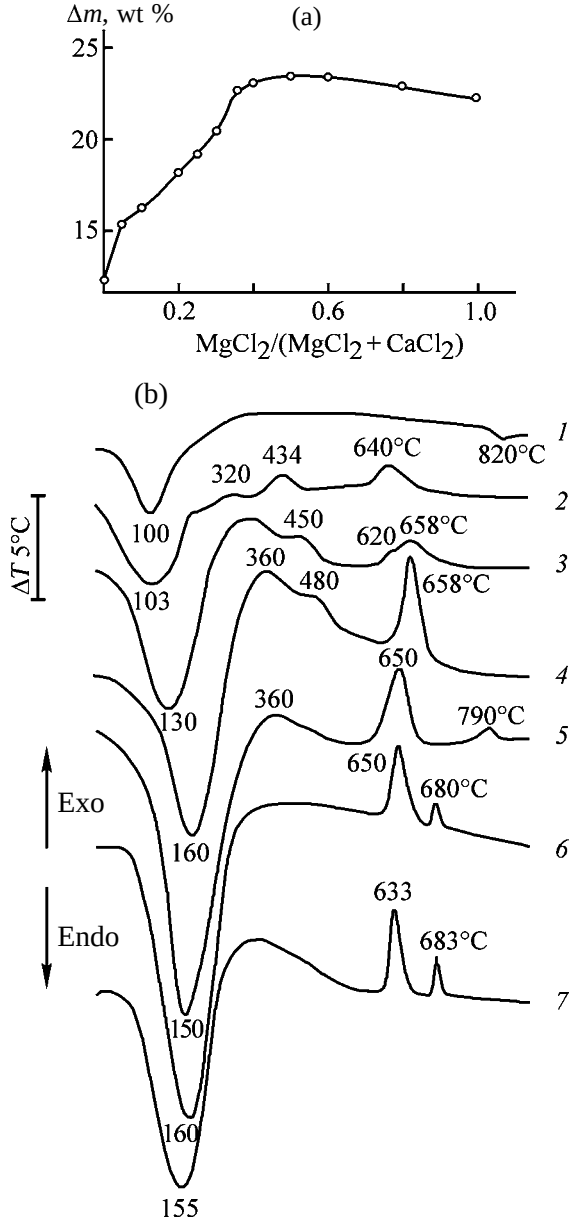

Fig. 3. (a) Weight loss Δm due to dehydration, as determined by thermal analysis, and (b) DTA curves of the precipitated calcium–magnesium phosphates. Mg/(Mg + Ca) atomic ratio: (*1*) 0, (*2*) 0.05, (*3*) 0.10, (*4*) 0.20, (*5*) 0.25, (*6*) 0.35, and (*7*) 0.40.

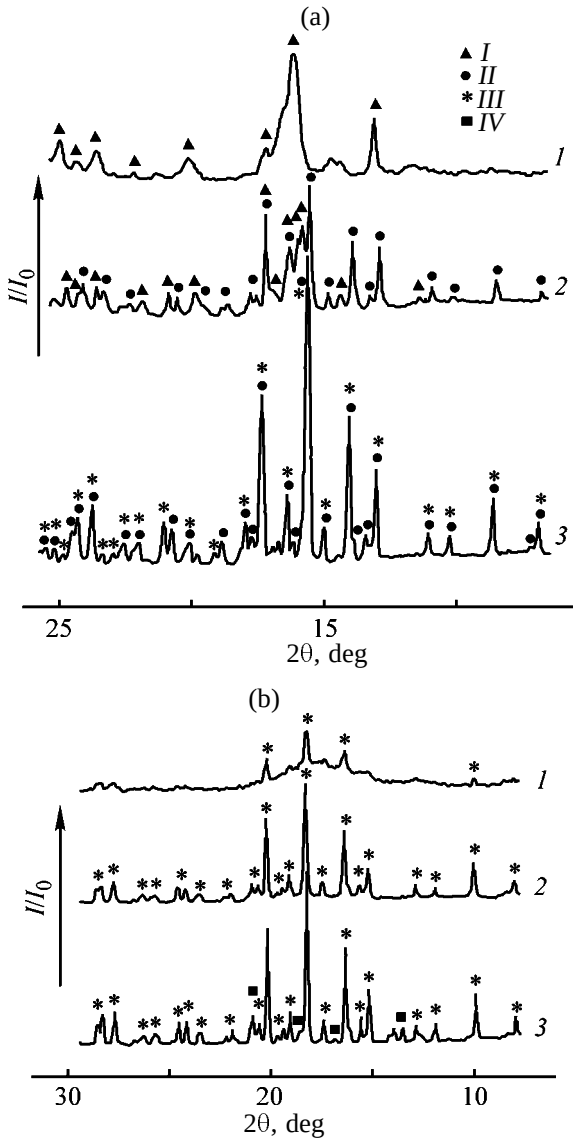

Fig. 4. Diffraction patterns of the thermal dissociation products of phosphates precipitated from solutions containing $CaCl_2$ and $MgCl_2$. $MgCl_2/(MgCl_2 + CaCl_2)$ molar ratio: (a) 0.05 and (b) 0.35. *T*, °C: (a) (*1*) 600, (*2*) 640, and (*3*) 900–1000; (b) (*1*) 580, (*2*) 650, and (*3*) 680–1000. (a) (*I*) $Ca_5(PO_4)_3OH$, (*II*) β-$Ca_3(PO_4)_2$, and (*III*) $Ca_7Mg_2(PO_4)_6$. (b) (*III*) $Ca_7Mg_2(PO_4)_6$ and (*IV*) $Ca_3Mg_3(PO_4)_4$.

phates also contain several exothermic peaks, showing that the thermal transformations are accompanied by heat evolution. An exception is hydroxyapatite, for which only one weak endothermic peak with a minimum at about 820°C is observed. The X-ray phase analysis showed that, at this temperature, apatite partially transforms into β-$Ca_3(PO_4)_2$, and the relative content of this salt somewhat increases with temperature. As known, hydroxyapatite is thermally stable and dissociates only above 1300–1450°C [18–20]. Therefore, the forming β-$Ca_3(PO_4)_2$ can originate from an impurity of a nonstoichiometric compound in the precipitated substance, in which a part of PO_4^{3-} ions is replaced by HPO_4^{2-} ions. Such apatites can dissociate above 700°C to form $Ca_3(PO_4)_2$ [4].

The apatite structure formed with $CaCl_2$ in the presence of a small amount of $MgCl_2$, in particular, at the ratio $MgCl_2/(MgCl_2 + CaCl_2) = 0.05$, remains unchanged up to nearly 600°C. Above this tem-

perature, i.e., when the exothermic transformation at 640°C starts, a part of apatite transforms into $Ca_3(PO_4)_2$ (Figs. 3b, 4a). Interestingly, when a minor amount of Mg^{2+} ions is present in the precipitated phosphate, the temperature of the appearance of β-$Ca_3(PO_4)_2$ decreases from 820 to 640°C, and its content in the heat-treated products increases. Another salt, $Ca_7Mg_2(PO_4)_6$, appears on heating to 900–1000°C.

The structural transformations in amorphous calcium–magnesium phosphates are appreciable at about 580°C, i.e., at temperatures of the onset of the exothermic peaks in the corresponding DTA curves (Figs. 3b, 4b). The crystalline $Ca_7Mg_2(PO_4)_6$ phase appears in the products after the exothermic transformations at about 650°C are complete, and another calcium–magnesium salt, $Ca_3Mg_3(PO_4)_4$, is detected after passing the second exothermic effect (~680°C).

The substances precipitated from solutions at $MgCl_2/(MgCl_2 + CaCl_2) \geq 0.50$ also undergo thermal transformations: the two above-indicated calcium–magnesium phosphates whose relative content depends on the composition are formed above 500°C.

CONCLUSIONS

(1) Crystalline or amorphous substances are precipitated from a sodium orthophosphate solution containing calcium and magnesium chlorides, depending on their relative content.

(2) The crystalline compounds are formed from solutions containing excess of either of two chlorides, whereas amorphous products are formed within the narrow range of molar ratios $MgCl_2/(MgCl_2 + CaCl_2) = 0.25–0.35$.

(3) All the precipitated calcium–magnesium phosphates are hydrates. They lose water of crystallization when heated to 400°C, with the amorphous form preserved, and, depending on composition, they transform into $Ca_5(PO_4)_3OH$, β-$Ca_3(PO_4)_2$, $Ca_7Mg_2 \cdot (PO_4)_6$, and $Ca_3Mg_3(PO_4)_4$ when heated above 500°C.

REFERENCES

1. *Bioceramics of Calcium Phosphate*, De Groot, K., Ed., Boca Raton, Florida: CRC, 1983.
2. LeGeros, R.Z. and LeGeros, J.P., *Encyclopedic Handbook of Biomaterials and Bioengineering*, vol. 2, part A: *Materials*, Wise, D.L., Ed., New York: Marcel Dekker, 1995, pp. 1429–1463.
3. Hench, L.L., *J. Am. Ceram. Soc.*, 1998, vol. 81, no. 7, pp. 1705–1728.
4. *Neorganicheskie fosfatnye materialy* (Inorganic Phosphate Materials), Kanazawa, T., Ed., Kiev: Naukova Dumka, 1998.
5. LeGeros, R.Z., *Prog. Crystal Growth Charact.*, 1981, vol. 4, pp. 1–45.
6. Aoki, H., *Medical Applications of Hydroxyapatite: Bone Mineral, Drug Delivery System, Cancer, HIV, IVH, CAPD, Dental Implant*, Tokyo: St. Louis Ishiyaku Euro America, 1994.
7. *Hydroxyapatite and Related Materials*, Brown, P.W. and Constantz, B., Eds., Boca Raton, Florida: CRC, 1994.
8. Orlovskii, V.P., Komlev, V.S., and Barinov S.M., *Izv. Ross. Akad. Nauk, Neorg. Mater.*, 2002, vol. 38, no. 10, pp. 1159–1172.
9. Harper, R.A., and Posner, A.S., *Mater. Res. Bull.*, 1970, vol. 5, pp. 129–136.
10. Eanes, E.D., and Posner, A.S., *Calc. Tissue Res.*, 1968, no. 2, p. 38.
11. Boskey, A.L., and Posner, A.S., *Mater. Res. Bull.*, 1974, no. 9, p. 907.
12. LeGeros, R.Z., Taheri, M.H., Quirolgico, G.B., and LeGeros J.P., in *Proc. 2nd Int. Congr. on Phosphorus Compounds*, Boston, April 1980, pp. 89–103.
13. LeGeros, R.Z., *Tooth Enamel IV*, Fernhead, R.W. and Suga, S., Eds., Amsterdam: Elsevier, 1984, pp. 32–36.
14. Abbona, F., Lundager Madsen, H.E., and Boistelle, R., *J. Crystal. Growth*, 1986, vol. 74, pp. 581–590.
15. Abbona, F., and Franchini-Angela, M., *J. Crystal Growth*, 1990, vol. 104, pp. 661–671.
16. US Patent 6024985.
17. West, A.R., *Solid State Chemistry and Its Applications*, Chichester: Wiley, 1985.
18. Kutty, T.R.N., *Indian J. Chem.*, 1973, vol. 11, pp. 695–697.
19. Skinner, H.C.W., Kittelberger, J.C., and Beebe, R.A., *J. Phys. Chem.*, 1975, vol. 74, pp. 2017–2020.
20. Ruys, A.J., Brandwood, A., Milthorpe, B.K., *et al.*, *J. Mater. Med.*, 1995, vol. 6, pp. 297–301.

Russian Journal of Applied Chemistry, Vol. 76, No. 9, 2003, pp. 1379–1383. Translated from Zhurnal Prikladnoi Khimii, Vol. 76, No. 9, 2003, pp. 1419–1423.

INORGANIC SYNTHESIS AND INDUSTRIAL INORGANIC CHEMISTRY

Effect of Synthesis Parameters on the Phase Formation in the System $FeSO_4$–H_2O–H^+/OH^-–O_2 ($3.5 \le pH \le 13$)

R. R. Kleshcheva, D. G. Kleshchev, A. V. Tolchev, M. A. Popov, and V. Yu. Pervushin

South-Ural State University, Chelyabinsk, Russia
Chelyabinsk State Pedagogical University, Chelyabinsk, Russia
Research Institute of Pigmental Materials, Limited Liability Company, Chelyabinsk, Russia

Received November 6, 2002; in final form, March 2003

Abstract—Regular trends in the phase formation in the course of oxidation of aqueous $FeSO_4$ solutions and(or) $Fe(OH)_2$ suspensions under steady-state conditions (pH_0 = const, T = const) with atmospheric oxygen were studied within broad ranges of pH, temperature, total concentration $c^0_{Fe(II)}$, and air space velocity.

The oxidation of aqueous solutions of iron(II) salts and(or) suspensions of iron(II) hydroxide with atmospheric oxygen [system $Fe(II)R_n$–H_2O–H^+/OH^-–O_2, where R is Cl^-, NO_3^-, or SO_4^{2-}] underlies industrial processes of synthesizing inorganic pigments, ion-exchange materials, and catalysts based on Fe(III) oxide compounds, including hydrated compounds [1–4]. It was found [2–11] that the phase composition and crystal size of the resulting products depends on both thermodynamic [temperature T and pH of reaction medium, concentration of Fe(II) ions in solution and(or) $Fe(OH)_2$ in suspension, etc.] and kinetic (average oxidation rate $\tilde{V}$) parameters of the synthesis. It was shown [4–6] that, at $\tilde{V} \approx$ const, the phase composition changes in the sequence $\gamma(\delta)$-FeOOH $\rightarrow$ α-FeOOH $\rightarrow$ Fe_3O_4 as the temperature increases, with the average crystal size d in these phases changing in parallel with temperature; at $T \approx$ const, the dependences of the phase composition and crystal size on $\tilde{V}$ are opposite to those mentioned above [6, 11]. The phase composition and crystal size depend on a number of parameters, and there is still no common opinion on what of these parameters is decisive [2, 4–7], which does not allow optimization of the synthesis of products with reproducible properties.

The goal of this work was to refine regular trends in phase formation in the course of oxidation of aqueous $FeSO_4$ solutions and(or) $Fe(OH)_2$ suspensions with atmospheric oxygen (system $FeSO_4$–H_2O–H^+/OH^-–O_2) at quasi-constant temperatures and pH of the reaction medium.

EXPERIMENTAL

The starting reagents were aqueous solutions of $FeSO_4$ (1.7 M, preliminarily reduced with iron powder) and NaOH (6.2 M), both of chemically pure grade.

The oxidation was carried out in a 3 dm^3 reactor equipped with a bubbler with a sprayer for air supply, a stirring device, systems of electrical heating and thermostatic control (± 2°C), a dosing unit for continuous supply of the NaOH solution, and also with systems for continuous monitoring of the redox potential and pH of the medium (pH-340 pH-meter–millivoltmeter). To measure redox potential and pH values, we used, respectively, platinum and hydrogen electrodes coupled with a silver chloride reference electrode. Calculated amounts of an $FeSO_4$ solution and distilled water were charged to the reactor and heated to a specified temperature, and an NaOH solution was fed to adjust the required pH_0 of the reaction medium. After that, we started to feed air into the reactor at a constant rate, and also to feed an NaOH solution to maintain a quasi-constant pH_0 value (± 0.25 units, range $3.5 \le pH_0 \le 8.5$). In some experiments, intermediate samples of suspensions were taken during the oxidation, and the compositions of the liquid and solid phases were determined. The process was completed when the redox potential, which remained constant in the initial stage of the oxidation, started to increase sharply with time τ.

On completion of the oxidation, we determined the residual concentration $c^{\tau_0}_{Fe(II)}$ (τ_0 is the oxidation duration) in the suspension. The total initial concentration of iron(II) $c^0_{Fe(II)}$ in $FeSO_4$ solution and(or) in $Fe(OH)_2$ suspension was varied from 0.25 to 0.8 M (taking into account dilution of the initial $FeSO_4$ solution with NaOH solution); air space velocity V_a, from 125 to 600 $dm^3\ h^{-1}$ per 1 dm^3 of $FeSO_4$ solution

1070-4272/03/7609-1379$25.00

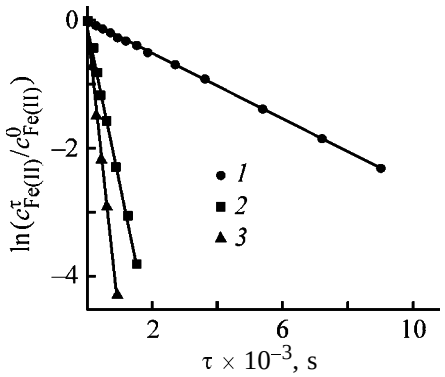

Fig. 1. Oxidation kinetics in the system $FeSO_4$–H_2O–H^+/OH^-–O_2. T = 20°C, $c^0_{Fe(II)}$ = 0.25 M, V_a = 600 dm^3 h^{-1}; the same for Fig. 2. [$c^0_{Fe(II)}$, $c^{\tau}_{Fe(II)}$] Total initial and current Fe(II) concentrations; (τ) time. pH_0: (*1*) 3.5, (*2*) 7.0, and (*3*) 11.0.

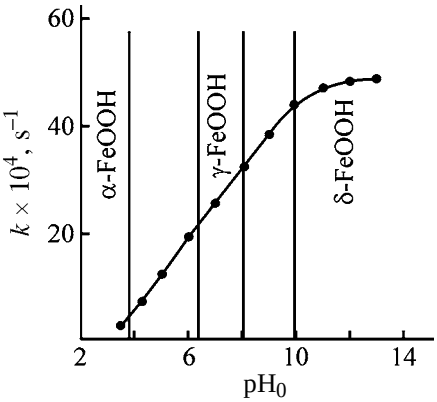

Fig. 2. Rate constant k of the oxidation of $FeSO_4$ solution and(or) $Fe(OH)_2$ suspension and phase composition of the forming precipitate vs. pH_0 of the reaction medium.

and(or) $Fe(OH)_2$ suspension; and temperature and pH_0 of the reaction medium, from 15 to 80°C and from 3.5 to 13, respectively. The resulting samples were separated on a Büchner funnel from the mother solution, washed with water until the absence of sulfate ions in the filtrate, dried to a constant weight at a temperature of about 70°C, and crushed.

The phase composition and crystal size of samples were evaluated by X-ray phase analysis (DRON-3 X-ray diffractometer; filtered FeK_α radiation) and by transmission electron microscopy (UEMV-100K electron microscope), and their chemical composition and $c_{Fe(II)}$ in solution, by volumetric chemical analysis and thermogravimetry (MOM derivatograph, Hungary). The mean crystal size d in the precipitate formed was calculated by a standard technique based on physical broadening of the diffraction peaks $\Delta 2\theta$.

In the first series of experiments, we varied pH_0 of $FeSO_4$ solution and(or) $Fe(OH)_2$ suspension at equal values of the other parameters: $c^0_{Fe(II)} = 0.25 \pm 0.02$ M, $V_a = 600 \pm 50$ dm^3 h^{-1}, and $T = 20 \pm 2$°C. It follows from the experimental data that the dependences of the current concentrations $c^{\tau}_{Fe(II)}$ on time τ can be linearized in the coordinates $\ln[c^{\tau}_{Fe(II)}/c^0_{Fe(II)}]$–$\tau$ (Fig. 1). Therefore, the oxidation is described by the kinetic equation

$$c^{\tau}_{Fe(II)} = c^0_{Fe(II)} \exp(-k\tau), \quad (1)$$

where k is the oxidation rate constant. The values of k were calculated by Eq. (1) from the experimental $c^0_{Fe(II)}$, $c^{\tau_0}_{Fe(II)}$, and τ_0 values.

The dependence of the oxidation rate constant on pH_0 is given in Fig. 2, which shows that, in the range $3.5 \le pH_0 \le 10$, k linearly increases with pH_0 from 2.6×10^{-4} to 4.9×10^{-3} s^{-1}, and as pH_0 increases further to 13.0, the rate constant remains constant within the limits of the experimental error. The results obtained qualitatively agree with the data of [2], indicating that the oxidation rate constant groups as pH of aqueous solutions of Fe(II) salts increases. At the same time, the experimental factor by which k changes when pH of the $FeSO_4$ solution and(or) $Fe(OH)_2$ suspension is changed by unity is considerably (by a factor of approximately 10) smaller than that reported in the monograph [2], which can be caused by different reaction conditions, e.g., different concentrations of Fe(II) ions in solution.

The phase composition and crystal size of the forming precipitate (Fig. 2) also depend on pH_0. In particular, in the ranges $3.5 \le pH_0 \le 4$, $7 \le pH \le 8$, and $10 < pH_0 \le 13$ iron(III) hydroxide–oxides of the α, γ, and δ modifications are formed. Their average crystal size is about 10, 4, and 9 nm, respectively. Samples obtained at $4 < pH_0 < 7$ are two-phase (α- + γ-FeOOH), and, as pH_0 increases, the weight fraction of the γ-FeOOH phase in the precipitates changes in parallel. The phase composition of samples at pH_0 ~9 is not constant: in this pH region, various combinations of iron(III) hydroxide-oxides of α, γ and δ modifications and Fe_3O_4 phases can form.

In the second series of experiments, we varied the temperature and pH_0 of the reaction medium, air space velocity V_a, and total concentration $c^0_{Fe(II)}$. The influence of these parameters on the oxidation rate constant and also on the phase composition and crystal size of the precipitate formed in the system $FeSO_4$–H_2O–H^+/OH^-–O_2 is illustrated by the table. It follows from the table (experiment nos. 1–8) that, at the other parameters fixed, k changes in parallel with temperature, with the relative change of the mean oxi-

Oxidation rate constant k and phase composition and crystal size of the precipitate forming in the system $FeSO_4$–H_2O–H^+/OH^-–O_2

Run no.	pH_0	$c^0_{Fe(II)}$, M	$V(O_2)$, $dm^3\ dm^{-3}\ h^{-1}$	T, °C	$k \times 10^4$, s^{-1}	Phase composition (crystal size, nm) of precipitate
1	3.8	0.30	220	15	1.5	α-FeOOH (10)
2	3.8	0.30	220	30	2.6	α-FeOOH (10) > γ-FeOOH (7)
3	3.8	0.30	220	45	4.1	α-FeOOH (10) ≈ γ-FeOOH (7)
4	4.5	0.25	600	35	6.1	α-FeOOH (8) < γ-FeOOH (5)
5	4.5	0.25	600	55	9.7	α-FeOOH (8) ≈ γ-FeOOH (5)
6	7.5	0.25	440	20	20.1	γ-FeOOH (5)
7	7.5	0.25	440	45	25.6	α-FeOOH (10) > γ-FeOOH (6)
8	7.5	0.25	440	80	33.8	α-FeOOH (15) ≫ Fe_3O_4
9	7.5	0.25	600	20	38.4	α-FeOOH (3.5)
10	7.5	0.25	470	20	30.7	α-FeOOH (8) ≪ γ-FeOOH
11	7.5	0.25	125	20	12.8	α-FeOOH (21) < γ-FeOOH (17)
12	5.0	0.25	600	45	12.8	α-FeOOH (20) ≈ γ-FeOOH (7)
13	5.0	0.80	600	45	7.1	α-FeOOH (20) ≫ γ-FeOOH
14	7.0	0.25	600	40	38.4	α-FeOOH (4)
15	7.0	0.40	600	20	12.8	α-FeOOH (11) ≈ γ-FeOOH (9)
16	7.0	0.50	600	20	5.4	α-FeOOH (17) > γ-FeOOH (14)
17	7.0	0.60	600	20	2.8	α-FeOOH (22)

dation rate η [$\eta = k(T_2)/k(T_1)$, $T_2 > T_1$] decreasing monotonically with an increase in pH_0 3.8 to 7.5.

The temperature dependence of k is apparently responsible for the deviation of the sequences of phase formation in the $FeSO_4$ solution in the range $3.8 < pH_0 < 5.5$ from that found in [4, 5], according to which at a fixed oxidation rate the α-FeOOH phase is formed at higher temperatures than γ-FeOOH. This dependence is broken in run nos. 1–3 (table), which is most likely due to a change in the rate constant of the oxidation of the $FeSO_4$ solution. As pH_0 is increased further, η decreases with temperature growth, and the phase formation sequence takes its usual form: γ- → α-FeOOH → Fe_3O_4 [4, 5], which is illustrated by run nos. 6–8 (table).

An increase in $c^0_{Fe(II)}$ in $FeSO_4$ solutions ($pH_0 < 5.5$) does not exert a significant influence on the average rate of Fe(II) oxidation, but results in an increase in the mean crystal size and in the weight fraction of the high-temperature phase in binary mixtures (table, run nos. 12 and 13).

Vice versa, in the range $5.5 < pH_0 < 8.5$ corresponding to partial precipitation of Fe(II) ions from the solution at $c^0_{Fe(II)} > 0.3$ M, k sharply decreases with increasing $Fe(OH)_2$ content in suspension (table, run nos. 14–17). This is due to a change in the flow characteristics of the suspensions during oxidation. According to [12, 13], in this pH_0 range the phase known in the literature as "green rust II" forms as an intermediate compound. It consists of crystals with a pronounced platelike habit, which results in a sharp increase in the viscosity of suspensions. As a consequence, on the one hand, the solubility and diffusion coefficient of oxygen in the reaction medium decrease, and, on the other, the specific surface area of the gas phase decreases because of the coalescence of air bubbles [14]; this results in decreased oxidation rate constant, increased mean crystal size, and decreased temperature at which the α-FeOOH phase is formed.

Thus, it follows from the table that the phase composition and crystal size of products formed in the system $FeSO_4$–H_2O–H^+/OH^-–O_2 largely depend on the rate of oxidation of the $FeSO_4$ solution and(or) $Fe(OH)_2$ suspension, and the rate constant k, in turn, depends on temperature and pH_0 of the reaction medium, total concentration $c^0_{Fe(II)}$, and air space velocity. In this case, in the entire examined range of variation of the synthesis parameters, the influence of the oxidation rate on the phase composition and particle size of iron(III) oxides is opposite to the influence of temperature. The observed dependence of the phase composition and particle size of the precipitate forming in the system $FeSO_4$–H_2O–H^+/OH^-–O_2 on the oxidation conditions agrees, on the whole, with the published data for similar systems [2, 5, 6, 11]. This suggests that the crystal growth during oxidation of aqueous solutions of iron(II) salts and(or) $Fe(OH)_2$ suspen-

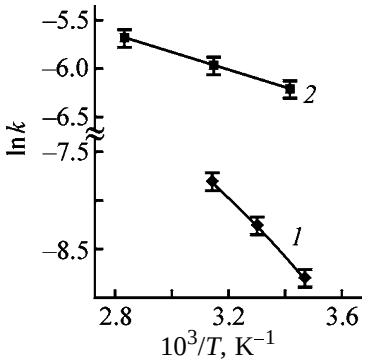

Fig. 3. Temperature dependence of $\ln k$. $c^0_{Fe(II)}$ = 0.25 M. pH_0: (*1*) 3.8 and (*2*) 7.5. Air space velocity, $dm^3\ dm^{-3}\ h^{-1}$: (*1*) 220 and (*2*) 440.

sions, especially at low temperatures, proceeds under conditions of high oversaturation. It results in decreased mean crystal size, increased crystal defectiveness, and formation of phases with disordered crystal structure, e.g., of δ-FeOOH (Fig. 2).

Note that the temperature dependences of the oxidation rate constant, at equal other parameters (table, run nos. 1–3 and 6–8), are satisfactorily linearized in the coordinates $\ln k - 1/T$ (Fig. 3). This points to the activation nature of formation of Fe(III) oxides, accompanied by elementary reactions of the oxidation of iron(II) hydroxoaqua complexes in solution, subsequent hydrolysis of iron(III) hydroxoaqua complexes, and their passing from solution to the condensed state (incorporation of the complexes in the lattice of the forming phases). Figure 3 shows that the apparent activation energy E_a decreases from 25 ± 2 to 7.5 ± 0.7 kJ mol^{-1} as pH_0 increases from 3.8 to 7.5. As pH corresponding to complete hydrolysis of Fe(III) ions in aqueous solutions (~2.4 [1, 2]) is much lower than pH_0 in our experiments, we can assume that the oxidation of iron(II) hydroxoaqua complexes is the limiting stage. In this case, the revealed dependences of k (Fig. 2) and E_a (Fig. 3) on pH_0 can be interpreted from the standpoint of changing degrees of hydrolysis (n values) and relative fractions of various iron(II) hydroxoaqua complexes of the composition $[Fe(OH)_n]^{2-n}_{aq}$ ($0 \le n \le 3$) in solution.

In fact, as shown in [15], Fe(II) ions in aqueous solutions are present as hydroxoaqua complexes with n 0 ($1.5 < pH < 9$), 1 ($4.5 < pH < 12$; the maximum of their weight fraction is reached at pH ~7), 2 ($6.5 < pH < 9.5$; the maximum at pH ~9), and 3 ($pH > 8$). Therefore, at pH_0 3.8, only iron(II) aqua complexes with $n = 0$ are oxidized, and at pH_0 7.5 there are three types of hydroxoaqua complexes with n 0, 1, and 2, with $[Fe(OH)]^+_{aq}$ ($n = 1$) being the major species. Quantum-chemical calculations performed in [16] showed that, as n increases, the energy of the lowest unoccupied $7a_{1g}$-like orbital of iron(II) hydroxoaqua complexes monotonically decreases, and the band gap ΔE_g becomes narrower. Consequently, the reactivity of iron(II) hydroxoaqua complexes increases, which is probably responsible for a decrease in the apparent activation energy of the oxidation.

CONCLUSIONS

(1) The dependences of the oxidation rate constant k and of the phase composition and crystal size of the precipitate formed in the system $FeSO_4$–H_2O–H^+/OH^-–O_2 on the thermodynamic [temperature, pH, total concentration $c^0_{Fe(II)}$] and kinetic (air space velocity) parameters were found for the steady-state oxidation mode (pH_0 = const). The ranges of parameters corresponding to the formation of the Fe_3O_4 and α-, γ-, and δ-FeOOH phases were revealed.

(2) In the range $3.5 < pH_0 \le 7.5$, all other conditions being equal, k changes in parallel with pH_0, whereas the apparent activation energy E_a changes in the opposite direction.

ACKNOWLEDGMENTS

This work was financially supported by the Russian Foundation for Basic Research (project no. P2001urchel 03-03).

REFERENCES

1. Remy, H., *Lehrbuch der anorganischen Chemie*, Leipzig: Akademische, 1961, vol. 2.
2. *Gipergennye okisly zheleza* (Hypergene Iron Oxides), Petrovskaya, N.V., Ed., Moscow: Nauka, 1975.
3. Domingo, C., Rodriguez-Clemente, R., and Bleza, M., *J. Colloid Interface Sci.*, 1994, vol. 165, no. 1, pp. 244–252.
4. Bagautdinova, R.R., Tolchev, A.V., Kleshchev, D.G., and Pervushin, V.Yu., *Zh. Prikl. Khim.*, 1999, vol. 72, no. 10, pp. 1588–1592.
5. Kiyama, M., *Bull. Chem. Soc. Jpn.*, 1974, vol. 47, no. 7, pp. 1646.
6. Krasnobai, N.G., Raspopov, Yu.G., Starikova, T.V., *et al.*, *Zh. Neorg. Khim.*, 1986, vol. 31, no. 9, pp. 2215–2219.
7. Feitknecht, W., *Z. Elektrochem.*, 1959, vol. 63, no. 1, p. 64.

8. Das, R.P. and Anand, S., *Hydrometallurgy*, 1995, vol. 38, no. 2, pp. 161–173.
9. Ishikawa, T., Ishikawa, A., Kandori, K., and Orli, R., *J. Chem. Soc., Faraday Trans.*, 1994, vol. 90, no. 17, pp. 2567–2570.
10. Tolchev, A.V., Bagautdinova, R.R., Kleshchev, D.G., *et al.*, *Lakokras. Mater. Ikh Primen.*, 2001, no. 1, pp. 13–15.
11. Agafonov, G.I., Kleshchev, D.G., Tolchev, A.V., *et al.*, *Lakokras. Mater. Ikh Primen.*, 1999, nos. 7–8, pp. 41–46.
12. Misawa, T., Hashimoto, K., and Shimodaria, S., *Corros. Sci.*, 1974, vol. 4, no. 2, pp. 131–149.
13. Detourney, V., Derie, R., and Chodsi, M., *Z. Anorg. Allg. Chem.*, 1976, vol. 427, nos. 3–4, pp. 265–273.
14. Ur'ev, N.B., *Vysokokontsentrirovannye dispersnye sistemy* (Higly Concentrated Disperse Systems), Moscow: Khimiya, 1980.
15. Intskirveli, L.N., Kolosov, I.V., and Varshal, G.M., *Zh. Neorg. Khim.*, 1975, vol. 20, no. 9, pp. 2388–2391.
16. Bagautdinova, R.R., Kleshchev, D.G., Tolchev, A.V., *et al.*, in *Fiziko-khimicheskie protsessy v neorganicheskikh sistemakh: Sbornik nauchnykh trudov* (Physicochemical Processes in Inorganic Systems: Collection of Scientific Works), Yekaterinburg: Ural. Otd. Ross. Akad. Nauk, 1996, pp. 35–39.

Russian Journal of Applied Chemistry, Vol. 76, No. 9, 2003, pp. 1384–1388. Translated from Zhurnal Prikladnoi Khimii, Vol. 76, No. 9, 2003, pp. 1424–1428.

INORGANIC SYNTHESIS AND INDUSTRIAL INORGANIC CHEMISTRY

Phase Formation in the System FeOOH–$Zn(OH)_2$–H_2O under Hydrothermal Conditions

D. G. Kleshchev, A. V. Tolchev, and V. Yu. Pervushin

South-Ural State University, Chelyabinsk, Russia

Received March 18, 2003

Abstract—Sequence of chemical transformations occurring in the system FeOOH–$Zn(OH)_2$–H_2O in the course of heat treatment at 125–200°C was studied by X-ray phase analysis, electron microscopy, and chemical analysis.

Finely dispersed zinc ferrite (average crystal size from several tens to hundreds of nanometers) with a spinel structure is a promising anticorrosive pigment [1, 2] and a catalyst of chemical reactions of ammonia oxidation, CO_2 and H_2O decomposition, methane synthesis, etc. [3, 4]. Conventional processes for synthesizing ferrites are based on solid-phase reactions of iron oxides, hydroxides, carbonates, and(or) other salts with those of the corresponding metal [4–7], which occur actively in air at a high (above 700°C) temperature. Activation of the mass transfer by calcination of a charge results in agglomeration of particles, occurring in parallel with a chemical reaction and causing polydispersity of the ferrites. Furthermore, ferrites with a spinel-type structure obtained by a ceramic technology can dissolve a significant amount of Fe_2O_3 [5], which results in the formation of a heterogeneous product with irreproducible physicochemical properties.

According to [4, 8], metal(II) ferrites can be obtained by joint hydrolysis of M(II) and Fe(III) ions in aqueous solutions. Chemical transformations of nonequilibrium oxides and hydroxides of *p* and 3*d* metals in solutions are accompanied by active mass exchange between the solid and liquid phases; therefore, we can expect that $ZnFe_2O_4$ will be formed by heat treatment of a mixture of $Zn(OH)_2$ and FeOOH suspensions, in particular, under hydrothermal conditions [9, 10].

The goal of this work was to study regular trends in the phase formation in the system FeOOH–$Zn(OH)_2$–H_2O and to reveal factors affecting the phase composition and crystal size of the resulting product.

EXPERIMENTAL

The starting reagents were aqueous solutions of $FeSO_4$ (chemically pure grade), $ZnSO_4$ (chemically pure grade), and NaOH [GOST (State Standard) 2263–79] of concentrations 1, 6, 2.1, and 6.5 M, respectively. The solutions were preliminarily filtered under pressure to remove mechanical impurities; in addition, the $FeSO_4$ solution was preliminarily reduced with iron powder.

Single-phase (according to X-ray phase analysis and electron microscopy) iron(III) hydroxide-oxides of α (acicular crystals, average size about 0.5 μm, form factor f = 4) and δ (ellipsoidal crystals, average size about 0.1 μm, form factor f = 2) modifications were obtained according to [9] by oxidation of 1 M $FeSO_4$ aqueous solutions (pH 4.5) or $Fe(OH)_2$ suspensions (pH 9.5) with atmospheric oxygen at 25°C. A calculated amount of $ZnSO_4$ solution was added with stirring to FeOOH suspensions at room temperature, then NaOH solution was added, and the reaction mixture was subjected to hydrothermal treatment in autoclaves equipped with stirrers. In laboratory experiments, the hydrothermal treatment was carried out in 0.07 dm^3 autoclaves, whereas enlarged laboratory samples were prepared in 3 dm^3 autoclaves. After the hydrothermal treatment, samples of the resulting product were separated by filtration under pressure from the mother solution, washed to remove water-soluble salts, dried to constant weight at 110°C, and crushed.

The following parameters were varied in the experiments: FeOOH : $Zn(OH)_2$ molar ratio in the initial suspensions, from 1.6 : 1 to 2.4 : 1; pH of suspensions, from 9.0 to 12.0; and temperature T and dura-

1070-4272/03/7609-1384$25.00

Phase composition of samples obtained by hydrothermal treatment of FeOOH and $Zn(OH)_2$ (n = 2) suspensions at various temperatures and durations of the treatment*

FeOOH	T, °C	pH	Phase composition* at indicated τ, h			
			1	2	3	4
δ-	125	9	H ~ Z; $\beta_1 \to \infty$, $\beta_2 \to \infty$	H ~ Z > F; $\beta_1 = 2.3$, $\beta_2 = 1.6$	F > H > Z; $\beta_1 = 0.4$, $\beta_2 = 0.3$	F >> H ~ Z; $\beta_1 = 0.07$, $\beta_2 = 0.05$
	150	9	F > H ~ Z; $\beta_1 = 0.7$, $\beta_2 = 0.45$	F >> H > Z; $\beta_1 = 0.15$, $\beta_2 = 0.10$	F; $\beta_1 = 0$, $\beta_2 = 0$	F; $\beta_1 = 0$, $\beta_2 = 0$
	175	9	F >> H ~ Z; $\beta_1 = 0.09$, $\beta_2 = 0.06$	F; $\beta_1 = 0$, $\beta_2 = 0$	F; $\beta_1 = 0$, $\beta_2 = 0$	F; $\beta_1 = 0$, $\beta_2 = 0$
	150	12	F >> H; $\beta_1 = 0.05$, $\beta_2 = 0$	F >> H; $\beta_1 = 0.04$, $\beta_2 = 0$	F >> H; $\beta_1 = 0.05$, $\beta_2 = 0$	F >> H; $\beta_1 = 0.007$, $\beta_2 = 0$
α-	125	9	H ~ Z; $\beta_1 \to \infty$, $\beta_2 \to \infty$	H ~ Z; $\beta_1 \to \infty$, $\beta_2 \to \infty$	H ~ Z; $\beta_1 \to \infty$, $\beta_2 \to \infty$	H ~ Z; $\beta_1 \to \infty$, $\beta_2 \to \infty$
	150	9	H ~ Z; $\beta_1 \to \infty$, $\beta_2 \to \infty$	H ~ Z; $\beta_1 \to \infty$, $\beta_2 \to \infty$	H ~ Z > F; $\beta_1 = 3.7$, $\beta_2 = 2.5$	F > H ~ Z; $\beta_1 = 0.8$, $\beta_2 = 0.6$
	175	9	F > H ~ Z; $\beta_1 = 0.7$, $\beta_2 = 0.45$	F >> H ~ Z; $\beta_1 = 0.04$, $\beta_2 = 0.03$	F; $\beta_1 = 0$, $\beta_2 = 0$	F; $\beta_1 = 0$, $\beta_2 = 0$
	200	9	F; $\beta_1 = 0$, $\beta_2 \to 0$	F; $\beta_1 = 0$, $\beta_2 \to 0$	F; $\beta_1 = 0$, $\beta_2 \to 0$	F; $\beta_1 = 0$, $\beta_2 \to 0$
	175	12	F >> H; $\beta_1 = 0.07$, $\beta_2 = 0$	F >> H; $\beta_1 = 0.05$, $\beta_2 = 0$	F >> H; $\beta_1 = 0.06$, $\beta_2 = 0$	F >> H; $\beta_1 = 0.08$, $\beta_2 = 0$

* (H) Hematite α-FeO_3, (Z) zincite ZnO, and (F) zinc ferrite $ZnFe_2O_4$; [$\beta_1 = I_{012}(Z)/I_{220}(F)$] the ratio of the integral intensities of the diffraction maxima (012) of hematite and (220) of zinc ferrite; [$\beta_2 = I_{100}(Z)/I_{220}(F)$] ratio of the integral intensities of the diffraction maxima (100) of zincite and (220) of zinc ferrite.

tion τ of hydrothermal treatment, from 125 to 200°C and from 0.5 to 4 h, respectively.

The phase composiiton and crystal size of samples were evaluated by X-ray phase analysis (DRON-3 X-ray diffractometer; filtered FeK_α radiation) and by transmission electron microscopy (UEMV-100K electron microscope). The chemical compositions of solutions and also of intermediate and final products of the synthesis were studied by volumetric chemical analysis. Weight fractions of phases contained in two- and three-phase samples were determined qualitatively from the ratios of integral intensities β_i of nonoverlapping diffraction peaks. The unit cell parameter a of zinc ferrite was determined from reflections with Miller indices (800) and (733) using annealed polycrystalline MgO as an independent reference. The average crystal size d of intermediate and final products was calculated by Selyakov–Scherrer's formula [11] from physical broadening of the diffraction peaks $\Delta 2\theta$. The curve of size distribution of $ZnFe_2O_4$ crystals was plotted on the basis of electron-microscopic data. For this purpose, the average linear size of no less than 200 nonoverlapping crystals was measured in micrographs of the samples. The pigment parameters of samples were determined as described in [12].

The X-ray patterns of samples of the initial suspensions contain only one group of diffraction maxima, which should be assigned to the corresponding modification of iron(III) hydroxide–oxide [13]. Therefore, zinc hydroxide formed by base hydrolysis is in the amorphous state in suspension.

Depending on the parameters of hydrothermal treatment, the X-ray patterns of all the samples after the treatment contain from one to three different sets of reflections, which can be assigned to $ZnFe_2O_4$, α-Fe_2O_3, and ZnO phases [13]. We point out that the formation of iron and zinc oxides upon the hydrothermal treatment agrees with our previous data on the chemical transformations of FeOOH and $Zn(OH)_2$ in solutions [14, 15].

It follows from the experimental data systematized in the table that the kinetics of $ZnFeO_4$ formation depends on three main parameters: heat treatment

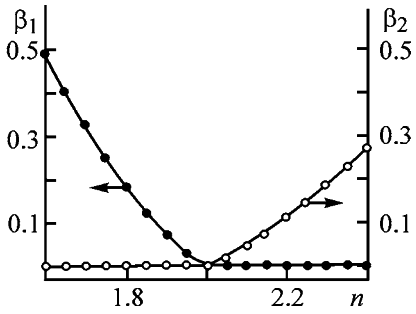

Fig. 1. Ratios of the integral intensities of hematite (012) and zinc ferrite (220) reflections (β_1), and also of zincite (100) and zinc ferrite (220) reflections (β_2) as functions of the molar ratio α-FeOOH/$Zn(OH)_2$ n in the suspension. Hydrothermal treatment conditions: pH 10, T = 200°C, τ = 4 h; the same for Fig. 2.

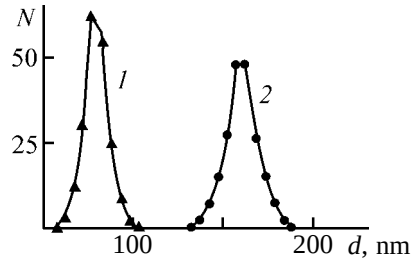

Fig. 2. Size distribution curves for single-phase samples of $ZnFe_2O_4$ synthesized from (1) δ- and (2) α-FeOOH. (N) Number of crystals with size within a $d \pm \Delta d$ range; (d) average size of this fraction of crystals; Δd = 2.5 nm.

temperature, pH of suspension, and phase composition of FeOOH, whereas the phase composition of the samples depends also on the molar ratio FeOOH and $Zn(OH)_2$ in the initial suspension (Fig. 1). In particular, at a fixed phase composition of FeOOH, the rate of $ZnFe_2O_4$ formation monotonically increases with temperature and pH of the suspension, and, when α-FeOOH is used, with the other parameters being the same, the lower temperature boundary of the $ZnFe_2O_4$ formation increases approximately by 25°C as compared to δ-FeOOH. This may be due to the fact that transformations of α-FeOOH, compared to δ-FeOOH, yield larger crystals of α-Fe_2O_3 with a lower reactivity (compared to small crystals) [10].

An increase in the rate of the $ZnFe_2O_4$ formation with increasing pH agrees with the data of [9] that an alkaline medium initiates chemical transformations of nonequilibrium compounds of p and 3d metals. At the same time, when suspensions with pH > 10 are subjected to a hydrothermal treatment, a part of Zn(II) ions remains in solution because of amphoteric nature of zinc compounds [16]. The concentration of Zn(II) monotonically increases with increasing pH, reaching 5–7 g dm^{-3} (in terms of ZnO) at pH 12. This can explain the presence of an α-Fe_2O_3 impurity in $ZnFe_2O_4$ samples prepared by hydrothermal treatment of suspensions with such pH, even in the case of stoichiometric ratio of the components (see table).

To determine the homogeneity region of the forming $ZnFe_2O_4$, we subjected α-FeOOH and $Zn(OH)_2$ suspensions with pH ~ 9 and various molar ratios n to a hydrothermal treatment at 200°C for 4 h. Figure 1 shows that almost single-phase $ZnFe_2O_4$ samples are formed at $n \approx 2$ (some of them contain small amounts of α-Fe_2O_3 or ZnO impurity phase, which results from inaccurate dosage of the components). Samples obtained at $n < 2$ and $n > 2$ are two-phase: $ZnFe_2O_4$ + ZnO and $ZnFe_2O_4$ + α-Fe_2O_3, respectively. In this case, as n deviates from the stoichiometric value, the weight fraction of ZnO or α-Fe_2O_3 phase in the samples increases.

Therefore, the composition of zinc ferrite formed by hydrothermal treatment of aqueous solutions is close to the stoichiometric composition $ZnFe_2O_4$. This conclusion is confirmed by X-ray phase and chemical analyses. These data show that, within the limits of experimental error, single-phase samples of $ZnFe_2O_4$ have the same unit cell parameter a (a = 0.8441 ± 0.0002 nm) and chemical composition (in terms of oxides they contain 33.1 ± 0.5 wt % ZnO and 64.9 ± 0.5 wt % Fe_2O_3). Using the results of the chemical analysis, we have calculated the molar ratio η of zinc and iron(III) oxides in single-phase samples of $ZnFe_2O_4$ (η = 1 : 1), which corresponds to the stoichiometric composition of ferrites.

According to the electron microscopy, $ZnFe_2O_4$ crystals have an isometric shape with clear signs of faces, and their average size d_{av} depends on the above-listed parameters and, to the greatest extent, on the FeOOH crystal size. In particular, for equal conditions of heat treatment (hydrothermal treatment temperature and pH of suspension), d_{av} of $ZnFe_2O_4$ samples obtained from α-FeOOH is approximately twice as high as that of samples synthesized from δ-FeOOH. The increase in the temperature and pH of the suspension results in the growth of the average size of $ZnFe_2O_4$ crystals. Single-phase $ZnFe_2O_4$ samples, as well as other pigments obtained by the hydrothermal procedure [10, 14], are monodisperse, i.e., they are characterized by a narrow size distribution of crystals (Fig. 2), which predetermines their high quality. We found that the main pigmental characteristics of $ZnFe_2O_4$ samples basically depend on d_{av}, and their values monotonically decrease as d_{av} increases. In particular, as d_{av} increases from 75 ($ZnFe_2O_4$ sam-

ple synthesized from δ-FeOOH) to 160 nm (sample obtained from α-FeOOH), the covering power changes from 15 to 9 g m^{-2}, the oil-absorption power, from 35 to 20 g/100 g pigment, and the content of volatile and water-soluble substances, from 0.7 to 0.4 and from 0.5 to 0.2 wt %, respectively.

The table shows that, at relatively low temperatures of hydrothermal treatment, α-Fe_2O_3 and ZnO phases are formed in an earlier stage of the treatment as compared to $ZnFe_2O_4$. Therefore, the formation of the equilibrium phase (zinc ferrite) in the system $FeOOH–Zn(OH)_2–H_2O$ is preceded by the stage of the formation of the α-Fe_2O_3 and ZnO phases, which are metastable in this case, and the whole combination of processes occurring in the system $FeOOH–Zn(OH)_2–H_2O$ can be presented by the scheme

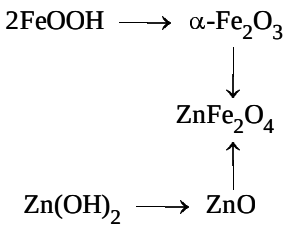

Let us consider possible causes of this phenomenon. According to [9, 10, 14, 15], the transformations of α(δ)-FeOOH and $Zn(OH)_2$ in solutions proceed by the dissolution–precipitation mechanism. This mechanism includes the following elementary stages: (a) dissolution of crystals of a nonequilibrium phase with the formation of hydroxoaqua complexes of the metal ions, which are in equilibrium under specified thermodynamic conditions [17]; (b) reaction between hydroxoaqua complexes yielding nuclei of a new phase and polynuclear crystal-forming complexes, which serve as "building material" for the growing crystals; (c) incorporation of the hydroxoaqua complexes in the surface layer of the nuclei, which is complicated by dehydration, olation, oxolation, and(or) dehydroxylation [9, 15].

The experimental dependences of the formation rate and average size of $ZnFe_2O_4$ crystals on pH of suspension, and also the absence of eligibility in the morphology and size of crystals of the nonequilibrium (α-Fe_2O_3 and ZnO) and forming ($ZnFe_2O_4$) phases (in particular, ZnO crystals are platelike and $ZnFe_2O_4$ crystals are isometric) suggest that the chemical reaction of α-Fe_2O_3 with ZnO in solutions also proceeds by the dissolution–precipitation mechanism.

The dissolution–precipitation mechanism involves a directed mass transfer of a crystal-forming substance from the crystals of a dissolving phase to the nuclei of a forming phase. The nucleation probability and the mass transfer intensity are proportional to the equilibrium concentration c_{CFC} of crystal-forming complexes in solution. Under conditions of low solubility of α(δ)-FeOOH and $Zn(OH)_2$ at relatively low temperatures of the heat treatment, the nuclei of a new phase are formed by the heterogeneous mechanism [18], and the mass transfer proceeds stochastically [19] with equal probabilities of the detachment and incorporation of crystal-forming complexes. In this case, the formation of one or another phase is determined by the probability of formation of the corresponding nuclei.

Oxides, hydroxide–oxides, and hydroxides of *p* and 3*d* metals have similar structural motives. In particular, the crystal lattices of α(γ, δ)-FeOOH and α-Fe_2O_3 phases can be reproduced by oriented incorporation of the same binuclear crystal-forming complex (CFC-1) of the composition $Fe_2(OH)_6 \cdot 4H_2O$ [9, 15]. Therefore, it is most likely that nuclei of α-Fe_2O_3 and ZnO are formed by reactions between hydroxoaqua complexes and(or) crystal-forming complexes of the corresponding metals. The mechanism of the formation of nuclei of $M(II)Fe_2O_4$ phases with a spinel structure, e.g., magnetite, is more complicated. For example, they can be formed by reaction of one crystal-forming complex CFC-1 with two $MFe(OH)_5 \cdot 6H_2O$ complexes (CFC-2) [9]. As a consequence, the probability of the formation of $ZnFe_2O_4$ nuclei at low concentrations c_{CFC} is much less than that of the nuclei of α-Fe_2O_3 and ZnO phases. Therefore, chemical transformations of nonequilibrium FeOOH and $Zn(OH)_2$ in the initial stage of heat treatment proceed toward formation of oxides of the corresponding metals.

The following processes seem to proceed subsequently in systems containing α-Fe_2O_3 and MO. The α-Fe_2O_3 and ZnO phases, which have nonzero solubility, are in equilibrium with the corresponding hydroxoaqua complexes and(or) crystal-forming complexes in solution. As a result of random reactions of the complexes, the nuclei of the equilibrium phase $ZnFe_2O_4$ are formed in this system. Iron(III) and zinc(II) crystal-forming complexes start to get incorporated into the formed nuclei from solution, which results in a decrease in their concentrations to the level lower than c^0_{CFC} and, as a consequence, in the dissolution of α-Fe_2O_3 and ZnO crystals.

The value of c^0_{CFC} changes in parallel with the increase in temperature or pH of the suspension. As c_{CFC} increases, on the one hand, the duration of the latent period of the nucleation stage decreases, and, on the other hand, the intensity of the mass transfer

in the disperse system increases. These trends are manifested as an increase in the rate of $ZnFe_2O_4$ formation and in the average size of its crystals, which agrees with the experimental data.

CONCLUSIONS

(1) Formation of the equilibrium phase ($ZnFe_2O_4$) upon hydrothermal treatment of the system FeOOH–$Zn(OH)_2$–H_2O is preceded by chemical transformations of iron(III) hydroxide–oxides and zinc hydroxide to the corresponding oxides.

(2) The main factors (temperature, pH of suspension, and phase composition of FeOOH) affecting the rate of the $ZnFe_2O_4$ formation and the average size of its crystals have been revealed.

ACKNOWLEDGMENTS

This work was financially supported by the Russian Foundation for Basic Research (project no. P2001-urchel 03-03).

REFERENCES

1. Ermilov, P.I., Indeikin, E.A., and Topmachev, I.A., *Pigmenty i pigmentirovannye lakokrasochnye materialy* (Pigments and Pigmented Paint-and-Varnish Materials), Leningrad: Khimiya, 1974.
2. Dobrovol'skii, I.P., Drobyshev, A.A., Pervushin, V.Yu., and Syutkin, S.A., *Pigmenty i napolniteli iz novykh vidov syr'ya i otkhodov proizvodstva* (Pigments and Filling Materials from New Kinds of Raw and Waste Products), Chelyabinsk: Ploshchad' Evolyutsii, 2001.
3. Zakharchenko, N.I. and Seredenko, V.V., *Visn. Khar'k. Nats. Univ.*, 1999, no. 437, pp. 74–76.
4. Kovalenko, A.Yu., Nugmanov, A.M., and Firsova, L.Yu., *Zh. Neorg. Khim.*, 2002, vol. 47, no. 11, pp. 1787–1792.
5. Letyuk, L.M. and Zhuravlev, G.I., *Khimiya i tekhnologiya ferritov* (Chemistry and Technology of Ferrites), Leningrad: Khimiya, 1983.
6. Tkacova, K., Sehelak, V., Stevulova, N., and Boldyrev, V.V., *J. Solid State Chem.*, 1994, vol. 123, no. 1, pp. 100–108.
7. El-Shobaky Holo, G., *Thermochim. Acta.*, 2000, vol. 343, no. 1–2, pp. 145–150.
8. Hochepied, J.F., Bonville, P., and Pileni, M.P., *J. Phys. Chem. B*, 2000, vol. 104, no. 5, pp. 905–912.
9. Kleshchev, D.G., Sheinkmam, A.I., and Pletnev, R.N., *Vliyanie sredy na fazovye i khimicheskie prevrashcheniya v dispersnykh sistemakh* (Effect of Medium on Phase and Chemical Transformations in Disperse Systems), Sverdlovsk: Ural. Otd. Akad. Nauk SSSR, 1990.
10. Agafonov, G.I., Kleshchev, D.G., Tolchev, A.V., *et al.*, *Lakokras. Mater. Ikh Primen.*, 1999, nos. 7–8, pp. 41–46.
11. Umanskii, Ya.S., Skakov, Yu.A., Ivanov, A.N., and Rastorguev, L.N., *Kristallografiya, rentgenografiya i elektronnaya mikroskopiya* (Crystallography, Roentgenography, and Electron Microscopy), Moscow: Metallurgiya, 1982.
12. Belen'kii, E.F. and Riskin, I.V., *Khimiya i tekhnologiya pigmentov* (Chemistry and Technology of Pigments), Leningrad: Khimiya, 1974.
13. *Powder Diffraction File, Search Manual*, Swarthmore, 1978.
14. Tolchev, A.V., Kleshchev, D.G., Pervushin, V.Yu., and Syutkin, S.A., *Lakokras. Mater. Ikh Primen.*, 2001, nos. 2–3, pp. 16–19.
15. Tolchev, A.V., Bagautdinova, R.R., and Kleshchev, D.G., *Zh. Prikl. Khim.*, 2001, vol. 74, no. 2, pp. 389–394.
16. *Khimicheskaya entsiklopediya* (Chemical Encyclopedia), Moscow: Bol'shaya Ross. Entsiklopediya, 1998, vol. 5.
17. Nazarenko, V.A., Antonovich, V.P., and Nevskaya, E.A., *Gidroliz ionov metallov v razbavlennykh rastvorakh* (Hydrolysis of Metal Ions in Dilute Solutions), Moscow: Atomizdat, 1979.
18. Chernov, A.A., Givargizov, E.I., Bagdasarov, Kh.S., *et al.*, *Obrazovanie kristallov: Sovremennaya kristallografiya* (Formation of Crystals: Modern Crystallography), Moscow: Nauka, 1980, vol. 3.
19. Sheinkman, A.I., in *Fizikokhimiya i tekhnologiya dispersnykh poroshkov* (Physical Chemistry and Technology of Dispersed Powders), Kiev: Inst. Pigm. Mater., Akad. Nauk Ukr. SSR, 1984, pp. 3–7.

Russian Journal of Applied Chemistry, Vol. 76, No. 9, 2003, pp. 1389–1392. Translated from Zhurnal Prikladnoi Khimii, Vol. 76, No. 9, 2003, pp. 1429–1432.

INORGANIC SYNTHESIS AND INDUSTRIAL INORGANIC CHEMISTRY

Effect of Bismuth(III) Complexes $M_3Bi(Nta)_2 \cdot nH_2O$ and $KBi(Edta) \cdot n$Tu on Sea Bacteria, *Ulva Fenestrata* Seaweed, and Macrobiofouling

E. V. Kovaleva, L. A. Zemnukhova, V. M. Nikitin, R. L. Davidovich, and U. V. Kharchenko

Institute of Chemistry, Far East Division, Russian Academy of Sciences, Vladivostok, Russia

Received May 6, 2003

Abstract—The effect of bismuth(III) nitrilotriacetate $M_3Bi(Nta)_2 \cdot nH_2O$ (M = Na, K, Rb, Cs, NH_4, CN_3H_6) and mixed-ligand bismuth(III) complex with ethylenediaminetetraacetate and thiourea $KBi(Edta) \cdot 2tu$ on an association of sea bacteria, seaweed (*Ulva fenestrata*), and biofouling was studied. The minimal concentrations of some of these complexes suppressing bacterial growth were determined.

Metal complexonates are widely used in various fields of science and industry, analytical chemistry, and medicine [1, 2]. Complexonates of Group I and II metals and transition metals were studied most extensively. Data on nontransition metal complexonates are scarce. Previously we prepared anionic bismuth(III) complexes with anions of nitrilotriacetic acid (H_3Nta) and alkali metal, ammonium, and guanidinium cations, $M_3Bi(Nta)_2 \cdot nH_2O$ [3], and mixed-ligand Bi(III) complex with anions of ethylenediaminetetraacetic acid (H_4Edta) and thiourea, $KBi(Edta) \cdot 2tu$ [4]. The crystal structures of $(NH_4)_3Bi(Nta)_2$ [5, 6] and $KBi(Edta) \cdot 2tu$ [7] were determined.

The biological properties of many complexones are understood well. Their molecules do not degrade or transform in a biological medium. These compounds form stable complexes with many metals. They have long been used in toxicology as antidotes [1, 8]. Although some bismuth compounds (nitrates, citrate complexes, basic bismuth gallate, etc.) are used in medicine [2, 9, 10], the biological properties of bismuth(III) are not clearly understood. At the same time, bismuth(III) as well as antimony(III) are thiol poisons, since they selectively react with thiol (–SH) groups of biological molecules, mainly of enzymes, other proteins, and some amino acids [8, 11].

Bismuth(III) chloride and nitrate complexes exhibit bactericidal properties with respect to *Helicobacter pylori* bacteria [12, 13], and $Bi(Nta) \cdot 2H_2O$ and Bi(HEdta), with respect to *Escherichia coli* [14]. No data on bioligical properties of $M_3Bi(Nta)_2 \cdot nH_2O$ (M = Na, Cs, NH_4, and CN_3H_6) and $KBi(Edta) \cdot 2tu$ are reported.

In this work we studied the biological effect of the above bismuth(III) complexes on an association of sea bacteria (sea bacteriocenosis), seaweed (*Ulva fenestrata*), and macrobiofouling.

The bismuth complexes $M_3Bi(Nta)_2 \cdot nH_2O$ (M = Na, K, Rb, Cs, NH_4, and CN_3H_6) and $KBi(Edta) \cdot 2tu$ were prepared by the procedure in [3, 4]. All these complexes are readily soluble water at room temperature.

The biocidal activity of the bismuth complexes in the solid state and in aqueous solution with respect to sea bacteria was estimated by a conventional procedure based on diffusion of a complex in agar containing the test object [15]. The experiments were performed as follows. Fish-peptone agar was poured in a Petri dish. A bacterial suspension isolated form seawater[1] was placed in solidified agar plates. Hollow glass cylinders (0.8 cm in diameter and 1 cm high) were placed upright on the pretreated surface. Either 10^{-3} mol of solid compounds to be studied or 10^{-3}–10^{-4} M solutions of these compounds in distilled water were introduced into the cylinders. The Petri dishes with bacterial inoculation were incubated at 28°C for 48 h. The compound toxicity was estimated from the diameter of the zone of suppressed bacterial growth (ZSBG, cm), around the place of the compound introduction. The stimulating influence of a substance was manifested in more intense bacterial

[1] Rynda Bay, Amur Gulf, Sea of Japan.

1070-4272/03/7609-1389$25.00

Table 1. Estimated activity of the bismuth(III) complexes with respect to sea bacteriocenosis [complex amount 10^{-3} mol, stimulated with $(NH_4)_3Bi(Nta)_2$]

Compound	ZSBG, cm
$Na_3Bi(Nta)_2 \cdot 4H_2O$	2.5
$(CN_3H_6)_3Bi(Nta)_2 \cdot 3H_2O$	1.9
$Cs_3Bi(Nta)_2$	1.7
$KBi(Edta) \cdot 2tu$	1.0
$K_3Bi(Nta)_2$	0.7
$Bi(Nta)_2 \cdot 2H_2O$	0.5

Table 2. Oxygen content in seawater in experiments performed under daylight and in the dark (complex concentration 0.001 g l^{-1})

Compound	O_2 content, g l^{-1}			
	photosynthesis		respiration	
	experiment	reference	experiment	reference
$Na_3Bi(Nta)_2 \cdot 4H_2O$	6.94	6.49	3.38	1.55
$K_3Bi(Nta)_2$	4.25	4.518	2.44	0.071
$Rb_3Bi(Nta)_2$	2.12	4.518	1.568	0.071
$Cs_3Bi(Nta)_2$	2.115	4.518	2.392	0.071
$(NH_4)_3Bi(Nta)_2$	5.175	4.518	2.376	0.071
$(CN_3H_6)_3Bi(Nta)_2 \cdot 3H_2O$	7.4	6.49	0.828	1.55
$KBi(Edta) \cdot 2tu$	4.75	6.49	0.84	1.55

Table 3. Total biomass of fouling*

Compound	$c \times 10^3$, g l^{-2}	m, g l^{-1}	n, %
$Na_3Bi(Nta)_2 \cdot 4H_2O$	1.15	0.008	10
$K_3Bi(Nta)_2$	1.67	0.0095	11.9
$Rb_3Bi(Nta)_2$	1.26	0.0094	11.8
$Cs_3Bi(Nta)_2$	2.72	0.032	40.0
$(NH_4)_3Bi(Nta)_2$	1.26	0.036	45.0
$(CN_3H_6)_3Bi(Nta)_2 \cdot 3H_2O$	1.25	0.0284	35.5
$KBi(Edta) \cdot 2tu$	3.08	0.0213	26.6

* c is the complex content; m, biomass of fouling, and n, ratio of the biomass grown on the examined sample to that on the reference sample.

growth around the cylinder with examined compound as compared to the remaining surface of the agar plate.

The effect of the bismuth(III) complexes on *U. fenestrata* seaweed can be estimated from the oxygen content in the system, which depends on the main metabolic processes, photosynthesis and respiration. The experimental procedure was described in [16]. Thalluses of freshly collected seaweed (5 g) were placed in 1-l aquariums filled with seawater to the top. A 0.01-g portion of a test compound (as determined in preliminary experiments) was added. The reference aquarium was free of the Bi(III) complexes. Some of the aquariums with seaweed were kept at 22–24°C for 24 h under a daylight (photosynthesis), and the others were kept in the dark (respiration). After that, the oxygen content in the seawater was determined by the Winkler procedure [17].

The biofouling was studied in June–October, 2002. To prepare antifouling coatings, the complexes were crushed to fine powders and introduced into a methyl methacrylate solution in amount of up to 50 wt % with respect to dry methyl methacrylate. A suspension of the Bi(III) complexes in a methyl methacrylate solution was applied to one side of Plexiglas plates and dried until it ceased to be sticky. The coated and noncoated plates were fixed in benches which were immersed in sea.[2] The number of each species on the plates was determined visually at intervals of two weeks.

After the completion of the experiment, the biological material was scraped off with a spatula made from an inert material, dried at room temperaure to constant weight, and weighed. The total biomass was determined with respect to the reference sample.

The biological properties of bismuth(III) complexes with Nta^{3-} and $Edta^{4-}$ are presented in Tables 1–3.

$Bi(Nta)_2 \cdot 2H_2O$, $M_3Bi(Nta)_2 \cdot nH_2O$ (M = Na, K, Rb, Cs, NH_4, CN_3H_6), and $KBi(Edta) \cdot 2tu$ are toxic with respect to associates of sea bacteria (Table 1). The precursors of these complexes, $Bi(OH)_3$, H_3Nta, and H_4Edta, have no effect on vital functions of the bacteria. The bactericidal properties of $M_3Bi(Nta)_2 \cdot nH_2O$ differ from those of $KBi(Edta) \cdot 2tu$: ZSBG ranges from 0.5 to 2.5 cm. The most toxic among the examined compounds is $Na_3Bi(Nta)_2 \cdot 4H_2O$.

$(NH_4)_3Bi(Nta)_2$, unlike the other complexes, stimulate bacterial growth: bacterial biomass is accumulated around a cylinder with this complex.

It is difficult to explain why the biological effect or $M_3Bi(Nta)_2 \cdot nH_2O$ is opposite to that of $(NH_4)_3 \cdot Bi(Nta)_2$. This may be due to the structural difference of these complexes {only the $(NH_4)_3Bi(Nta)_2$ structure is known [5, 6]} or to different outer-sphere cations.

[2] Fedorov Bay, Peter the Great Gulf, 2-m depth.

The coordination polyhedron of bismuth(III) in the structure of $(NH_4)_3Bi(Nta)_2$ is a distorted cube (coordination number CN = 8). The Bi–O and Bi–N distances are 2.42×6 and 2.60×2 Å, respectively. Mononuclear complex anions $[Bi(Nta)_2]^{3-}$ and ammonium cations are bonded by hydrogen bonds to form a framework structure.

Among the examined complexes, $KBi(Edta) \cdot 2tu$ is the least toxic with respect to sea bacteriocenosis (Table 1). The coordination number of Bi(III) in the crystal structure of this complex is also 8 [7]. The complex anions $[Bi(Edta)(tu)_2]^-$ are bonded via K^+ cations and with the N–H···O hydrogen bonds into a three-dimensional framework. The bismuth atom forms four Bi–O bonds (2.36–2.48 Å) and two Bi–N bonds (2.46, 2.48 Å) with the Edta anions and two Bi–S bonds (3.09 and 3.22 Å) with the thiourea ligands.

The minimal $M_3Bi(Nta)_2 \cdot nH_2O$ concentration suppressing bacterial growth (MCSBG) in aqueous solutions is 10^{-2} M. In the presence of solutions of these complexes, the diameter of ZSBG varies from 1.4 to 1.6 cm. However, colonies of some bacteria grew even in the ZSBG, which indicated that these bacteria were stable to the Bi(III) complexes. A solution of $KBi(Edta) \cdot 2tu$ is the most toxic; the diameter of ZSBG is 2.5 cm; the MCSBG is 10^{-3} M.

We studied the effect of the bismuth complexes on strains of *p. Psedomonas sp*., *Bacillus sp*., and *Cytophaga sp*. A change in the pigmentation of their colonies, loss of mobility, and induction of sporulation of spore-forming bacteria in the region of substance diffusion indicate morphological and physiological transformations of bacterial cells.

The oxygen content determined in seawater of aquariums with *U. fenestrata* seaweed in the presence and in the absence of the Bi(III) complexes is presented in Table 2.

Some of the examined Bi(III) complexes, as in the case of sea bacteria, inhibit vital functions of seaweed, and the others stimulate their growth.

Analysis of the oxygen content in the aquarium seawater shows that $M_3Bi(Nta)_2 \cdot nH_2O$ (M = Na, NH_4, CN_3H_6) slightly stimulate the photosynthesis. The activity of these complexes as compared to the blank experiment increases in the following order: $NH_4^+ < Na^+ < CN_3H_6$. The complexes $M_3Bi(Nta)_2$ (M = K, Rb, Cs) exhibit algicidal properties. They inhibit photosynthesis, thus decreasing the oxygen content in the aquarium seawater as compared to the dark experiment. The inhibiting effect decreases in the order $K^+ > Rb^+ > Cs^+$. The complex $KBi(Edta) \cdot 2tu$ also inhibits photosynthesis.

The complexes also affect seaweed respiration. $(CN_3H_6)_3Bi(Nta)_2 \cdot 3H_2O$ and $KBi(Edta) \cdot 2tu$ stimulate respiration by a factor of 1/2 as compared to the blank experiment. As a result, the oxygen content in the seawater decreases (Table 2). The other complexes $M_3Bi(Nta)_2 \cdot nH_2O$ (M = Na, K, Rb, Cs, NH_4) almost completely suppress energy metabolism of the plants: in the presence of these complexes, the oxygen content in the seawater strongly increases as compared to that in the blank experiment.

The biocidal properties of $M_3Bi(Nta)_2 \cdot nH_2O$ (M = Na, K, Rb, Cs, NH_4, CN_3H_6), and $KBi(Edta) \cdot 2tu$ with respect to macrobiofouling are presented in Table 3. The study of the dynamics of macrobiofouling on the uncoated plates showed that three types of animals are present in the biomass: *Balanus improvisus*, *Hydrodes ezoensis*, and *Conopeum seurati*. No seaweeds were found in the biofouling.

Analysis of biofouling of plates coated with the Bi(III) complexes revealed the compounds with biocidal properties. All the examined complexes are moderatly toxic or exhibit repellent properties with respect to *Conopeum seurati* cortical pearlwort.

The average biomass grown on the reference plates is 0.08 g cm^{-2}. The biomass grown on the plates correlates with the toxicity of the examined complexes with respect to macrophytes. The most toxic are $M_3Bi(Nta)_2$ complexes (M = Na, K, and Rb) (Table 3).

The ratios of species growing on the plate surface differ. Probably the toxic and repellent properties of the complexes with respect to macrophytes are selective.

CONCLUSIONS

(1) The bismuth(III) complexes exhibit biological activity with respect to sea bacteria and green weeds. The sensitivity of these organisms to the complexes is different.

(2) The biological effect of $(NH_4)_3Bi(Nta)_2$ on sea bacteriocenosis is similar to that on *U. Fenestrata* seaweed. This complex stimulates both bacterial growth and photosynthesis. On the contrary, $KBi(Edta) \cdot 2tu$ inhibits these processes. The biological effect of the other complexes depends on their composition and the biological species.

(3) $Bi(Nta)_2 \cdot 2H_2O$, $M_3Bi(Nta)_2 \cdot nH_2O$ (M = Na, K, Cs, CN_3H_6), and $KBi(Edta) \cdot 2tu$ inhibit growth of

sea bacteria; $M_3Bi(Nta)_2 \cdot nH_2O$ (M = K, Rb, Cs) and KBi(Edta)·2tu inhibit photosynthesis; and $M_3Bi \cdot (Nta)_2 \cdot nH_2O$ (M = Na, K, Rb, Cs, NH_4) inhibit respiration.

(4) $(NH_3)_3Bi(Nta)_2$ stimulates growth of sea bacteria; $M_3Bi(Nta)_2 \cdot nH_2O$ (M = Na, NH_4, CN_3H_6) stimulate photosynthesis; and $(CN_3H_6)_3Bi(Nta)_2 \cdot 3H_2O$ and KBi(Edta)·2tu stimulate respiration.

(5) The Bi(III) complexes are moderately toxic or exhibit repellent properties with respect to organisms growing on Plexiglas plates. The antifouling properties of $M_3Bi(Nta)_2 \cdot nH_2O$ (M = Na, K, Rb) are the most pronounced.

REFERENCES

1. Dyatlova, N.M., Temkina, V.Ya., and Popov, K.I., *Komleksony i komleksonaty metallov* (Complexones and Metal Complexonates), Moscow: Khimiya, 1988.
2. Mashkovskii, M.D. *Lekarstvennye sredstva* (Drugs), Moscow: Meditsina, 1994, part 1.
3. Davidovich, R.L., Loginov, A.A., Medkov, M.A., and Dyatlova, H.M., *Koord. Khim.*, 1989, vol. 15, no. 5, pp. 713–714.
4. Loginov, A.A., Medkov, M.A., Karasev, V.E., and Davidovich, R.L., *Ukr. Khim. Zh.*, 1989, vol. 55, no. 8, pp. 795–799.
5. Suyarov, K.D., Shkol'nikova, L.M., Porai-Koshits, M.A., *et al.*, *Dokl. Akad. Nauk SSSR*, 1990, vol. 311, no. 6, pp. 1397–1400.
6. Malyarik, M.A. and Ilyukhin, A.B., *Koord. Khim.*, 1998, vol. 43, no. 6, pp. 950–960.
7. Davidovich, R.L., Gerasimenko, A.V., and Kovaleva, E.V., *Zh. Neorg. Khim.*, 2001, vol. 46, no. 4, pp. 623–628.
8. Oksengendler, G.I., *Yady i protivoyadiya* (Poisons and Antidotes), Ser.: *Chelovek i okruzhayushchaya sreda* (Human Being and Environment), Leningrad: Nauka, 1982.
9. Kriss, E.E., Volchenkova, I.I., *et al.*, *Koordinatsionnye soedineniya metallov v meditsine* (Metal Complexes in Medicine), Kiev: Naukova Dumka, 1986.
10. RF Patent 2139080.
11. *Vrednye veshchestva v promyshlennosti* (Noxious Substances in Industry), Leningrad: Khimiya, 1997, no. 3, pp. 476–477.
12. Turel, L., Golic, L., Bukovec, P., and Gubina, M., *J. Inorg. Biochem.*, 1998, vol. 71, pp. 53–60.
13. Diemer, R., Keppler, B.K., Dittes, U., *et al.*, *Chem. Ber.*, 1995, vol. 128, pp. 335–342.
14. Summers, S.P., Abboud, K.A., Farrah, S.R., and Palenik, G.J., *Inorg. Chem.*, 1994, vol. 33, no. 1, pp. 88–92.
15. Rodina, A.G., *Metody vodnoi mikrobiologii* (Methods of Aquatic Microbiology), Moscow: Nauka, 1965.
16. Polishchuk, R.A., *Biologicheskie osnovy bor'by s obrastaniem* (Biological Foundations for Fouling Control), Kiev: Naukova Dumka, 1973, pp. 155–193.
17. *Rukovodstvo po metodam khimicheskogo analiza morskikh vod* (Manual on Chemical Analysis of Seawaters), Orodovskii, S.G., Ed., Leningrad: Gidrometeoizdat, 1977.

Russian Journal of Applied Chemistry, Vol. 76, No. 9, 2003, pp. 1393–1395. Translated from Zhurnal Prikladnoi Khimii, Vol. 76, No. 9, 2003, pp. 1433–1435.

INORGANIC SYNTHESIS AND INDUSTRIAL INORGANIC CHEMISTRY

Preparation of High-Purity Silicon Tetrafluoride by Thermal Dissociation of Na_2SiF_6

A. D. Bulanov, D. A. Pryakhin, and V. V. Balabanov

Institute of Chemistry of Ultrapure Substances, Russian Academy of Sciences, Nizhni Novgorod, Russia

Received April 16, 2003

Abstract—The possibility of preparing high-purity silicon tetrafluoride by the thermal dissociation of pure grade Na_2SiF_6 was studied. The impurity composition of the product was studied by IR and atomic emission spectroscopy and by mass spectrometry.

High-purity silicon tetrafluoride SiF_4 is used for preparing fluorine-doped amorphous hydrogenated silicon [1] and ion implantation of silicon and fluorine into gallium arsenide [2]. Because SiF_4 has no intrinsic absorption bands, it is also used as doping additive to decrease the refractive index of quartz glass, which is very important in manufacture of quartz fibers [3]. Also, silicon tetrafluoride is a convenient compound for centrifugal separation of silicon isotopes [4].

The methods for preparing SiF_4 can be subdivided into four groups.

(1) Reaction of elemental silicon with fluorinating agents F^-, SF_6, UF_6, NF_3 [5–10], which is a complex procedure requiring sophisticated equipment.

(2) Fluorination of silicon dioxide [11–15]. This, however, involves problems with hydrolysis of SiF_4 by the reaction by-product, H_2O.

(3) Fluorination of silicon tetrachloride [16–22]. With $SiCl_4$ as the initial compound, it is necessary to treat SiF_4 to remove impurities of mixed fluorochlorosilanes.

(4) Preparation of SiF_4 from hexafluorosilicic acid H_2SiF_6 and hexafluorosilicates of alkali (Li, K, Na) and alkaline-earth (Ba, Ca) metals [23, 24]. It is possible to decompose H_2SiF_6 [25–27] or metal hexafluorosilicates [28–30] with concentrated acids (H_2SO_4 or H_3PO_4). However, silicon tetrafluoride obtained by acid treatment has low purity.

Thermal dissociation of metal hexafluorosilicates is the preferential method [31, 32]. The method is economical and environmentally safe. It was found [33] that SiF_4 obtained by this method from Na_2SiF_6 is relatively pure, because solid sodium fluoride sorbs impurities. The content of the impurities in Na_2SiF_6 and SiF_4 obtained from it is presented in the table [34]. The relative intensity of ions in the mass spectrum of SiF_4 is as follows [34]: SiF_3^+ 96.9, $Si_2OF_6^+$ 3.04, and $SO_2F_3^+$ 0.076.

The dissociation pressure of Na_2SiF_6 within 298–968 K has been determined in [35]. A study [36] of the effect exerted by CO_2, SiO_2, ZrO_2, and HfO_2 on the Na_2SiF_6 thermal dissociation showed that addition of SiO_2 considerably decreases the dissociation rate. The thermal dissociation of K_2SiF_6 in the liquid phase (K_2SiF_6–KCl eutectic) is slower than in the solid

Results of plasma-assisted emission spectroscopic analysis

Element	Content $c \times 10^4$, wt %	
	in Na_2SiF_6	in SiF_4
Li	0.2	0.01
Na	–	1.8
K	8.0	0.3
Mg	6.4	2.3
Ca	18	1.6
B	0.8	<0.01
Al	1.3	1.2
P	5.0	0.08
As	0.2	0.28
V	0.3	<0.01
Cr	8.8	<0.01
Mn	0.4	0.16
Fe	38	0.04
Co	0.7	<0.01
Ni	4.2	<0.01
Cu	0.6	<0.01
Zn	1.0	<0.01
Pb	5.0	0.03
Mo	1.0	<0.01

1070-4272/03/7609-1393$25.00

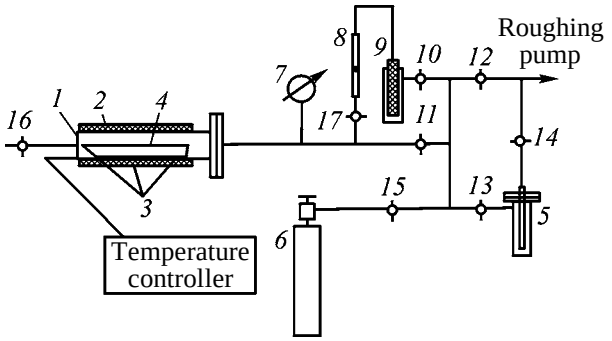

Setup for the silicon tetrafluoride synthesis. For comments, see text.

phase [37]. The influence of the H_2O partial pressure on the K_2SiF_6 thermal dissociation was studied in [38]. It was found that the SiF_4 being formed reacts with H_2O even at a low partial pressure of water vapor to form various gaseous and X-ray amorphous solid fluorosiloxanes.

EXPERIMENTAL

In this study, SiF_4 was prepared by thermal dissociation of pure grade sodium hexafluorosilicate Na_2SiF_6. In this case, the yield of SiF_4 approaches 100%, whereas in the case of the K_2SiF_6 thermal dissociation it is considerably lower owing to K_3SiF_7 formation [39]. Moreover, NaF formed in this reaction can be used for sorption purification of SiH_4 to remove SiF_4 impurity in the course of preparation of silane from silicon tetrafluoride.

The impurity content in pure grade Na_2SiF_6, as determined by laser mass spectrometry, is presented below:

Impurity element	Content, at. %	Impurity element	Content, at. %
B	1×10^{-1}	Cl	1×10^{-3}
C	3×10^{-2}	S	2×10^{-3}
Mg	4×10^{-3}	Ca	3×10^{-2}
Al	4×10^{-4}	Cr	5×10^{-5}
P	2×10^{-2}	Fe	2×10^{-3}

The content of Sc, Ti, V, Mn, Co, Ni, Cu, Zn, Ga, Ge, As, Se, Br, Rb, Sr, Y, Zr, Nb, Mo, Ru, Rh, Pd, Ag, Cd, In, Sn, Sb, Te, I, Cs, Ba, Hf, Ta, W, Re, Os, Ir, Pt, Au, Hg, Tl, Pb, and Bi impurity ions and lanthanides is below the detection limit of this method (1×10^{-4}–2×10^{-5} at. %).

A setup for the silicon tetrafluoride synthesis is shown schematically in the figure. The synthesis was performed in a stainless steel reactor *1* equipped with a resistance heater *2*. The temperature of the heater was adjusted to within ±0.5°C with an R-133 precision temperature controller and a U-013 power amplifier and measured with a Chromel–Alumel thermocouple *3*. A stainless steel boat *4* charged with about 3-kg portion of Na_2SiF_6 was placed into the reactor. The salt was preliminarily dried at 250°C in a vacuum or in a nitrogen flow. Moisture and gases released during preliminary evacuation of Na_2SiF_6 were condensed in a trap *5* cooled with liquid nitrogen.

The thermal dissociation of the salt was performed at 500–620°C in a vacuum. Since the Na_2SiF_6 thermal dissociation is a reversible reaction and the degree of dissociation is pressure-dependent, the forming SiF_4 was fed continuously into a 4-l metallic cylinder *6* cooled with liquid nitrogen.

The pressure in the reactor and the rate of the SiF_4 flow from the reactor into the receiving cylinder were monitored with vacuum gage *7* and rotameter *8*, respectively. To remove suspended particles, SiF_4 was allowed to pass through a Petryanov cloth filter *9*; *10–17* are stopcocks. The SiF_4 yield in the process approached 100%. Up to 1.5 kg of SiF_4 can be obtained on this installation in one process cycle.

The SiF_4 thus obtained was analyzed for the content of molecular impurities by mass spectrometry and IR spectroscopy [40]. Both methods revealed hexafluorodisiloxane as the major impurity. Its content in SiF_4 amounts to several percents, which agrees with the data of [34]. The mass spectrum contained no lines assignable to the BF_3 impurity. The content of metallic impurities in the silicon tetrafluoride obtained, which were concentrated by distilling off the matrix and then analyzed by atomic emission spectroscopy, is presented below:

Impurity	Content, wt %	Impurity	Content, wt %
Al	1×10^{-8}	Mn	3×10^{-10}
Ni	$<2\times10^{-8}$	Ca	7×10^{-8}
Co	$<7\times10^{-8}$	Pb	$<2\times10^{-8}$
Ag	$<3\times10^{-10}$	Sn	$<2\times10^{-8}$
Cd	$<3\times10^{-8}$	Cu	2×10^{-9}
Fe	7×10^{-7}	Ga	$<4\times10^{-9}$
Cr	3×10^{-8}	Sb	$<1\times10^{-7}$
Mg	1×10^{-7}	In	$<1\times10^{-8}$

To perform further isotopic enrichment and use SiF_4 as a doping additive in manufacture of quartz fibers, it was additionally purified by distillation.

CONCLUSION

High-purity SiF_4 was obtained by thermal dissociation of pure grade Na_2SiF_6. IR spectroscopy and mass

spectrometry revealed hexafluorodisiloxane as the major molecular impurity in SiF_4. According to the data of atomic emission spectroscopy, the SiF_4 prepared contains about 10^{-7} wt % metallic impurities.

ACKNOWLEDGMENTS

The study was financially supported by the 6th Expert's Competition of Basic and Applied Scientific Projects of Young Scientists from the Russian Academy of Sciences (grant no. 165).

REFERENCES

1. Nakayama, Y., Wakimura, K., Takahashi, S., *et al.*, *J. Non-Cryst. Solids*, 1985, vols. 77–78, no. 2, pp. 797–800.
2. Tamura, A., Inoue, K., and Onuma, T., *Appl. Phys. Lett.*, 1987, vol. 51, no. 9, pp. 1503–1505.
3. Kuppers, D., Koenings, J., and Wilson, H., *J. Electrochem. Soc.*, 1978, vol. 125, no. 8, pp. 1298–1302.
4. Kvaratskheli, Yu.K., and Sviderskii, M.F., *Konv. Mashinostr.*, 1999, nos. 3–4, pp. 44–48.
5. Nikolaev, N.S., Suvorova, S.N., Gurovich, E.I., *et al.*, *Analiticheskaya khimiya ftora* (Analytical Chemistry of Fluorine), Moscow: Nauka, 1970.
6. Bousguet, J., Carre, J., Claudy, P., *et al.*, *J. Chim. Phys. Phys.-Chim. Biol.*, 1972, vol. 69, no. 6, pp. 1065–1068.
7. Johnson, G.K., *J. Chem. Thermodyn.*, 1986, vol. 18, no. 8, pp. 801–802.
8. Rai-Choudhury, P., *J. Electrochem. Soc.*, 1971, vol. 118, no. 2, pp. 266–269.
9. FRG Patent 3841218.
10. Perrin, J., Meot, J., Siefert, J.-M., *et al.*, *Plasma Chem. Plasma Proc.*, 1990, vol. 10, no. 4, pp. 571–587.
11. Lieser, K.H., and Rosenbaum, I., *Z. Anorg. Allg. Chem.*, 1967, vol. 351, nos. 5–6, pp. 306–308.
12. Green, P.J., and Gard, G.L., *Inorg. Chem.*, 1977, vol. 16, no. 5, pp. 1243–1245.
13. JPN Patent 61-247625.
14. FRG Patent 3841210.
15. US Patent 4382071.
16. Boehm, P.H., *Z. Anorg. Allg. Chem.*, 1969, vol. 365, nos. 3–4, pp. 176–179.
17. Padma, D.K., and Vasudeva Murthy, A.R., *J. Fluorine Chem.*, 1974, vol. 4, no. 2, pp. 241–242.
18. Padma, D.K., Suresh, B.S., and Vasudeva Murthy, A.R., *J. Fluorine Chem.*, 1979, vol. 14, no. 4, pp. 327–329.
19. Legasov, V.A. and Marinin, A.S., *Zh. Neorg. Khim.*, 1972, vol. 17, no. 9, pp. 2408–2410.
20. Ponomarenko, V.A. and Ignatenko, M.A., *Khimiya ftorkremnievykh soedinenii* (Chemistry of Silicone Fluoride Compounds), Moscow: Nauka, 1979.
21. Rakov, E.G., Musorin, V.A., Mel'nichenko, E.I., *et al.*, Abstracts of Papers, *Vsesoyuznaya konferentsiya "Khimiya i tekhnologya redkikh tsvetnykh metallov i solei"* (All-Union Conf. "Chemistry and Technology of Rare Non-Ferrous Matals and Their Salts"), Frunze, 1986, p. 153.
22. Ruff, O., and Albert, K., *Ber.*, 1905, vol. 38, p. 53.
23. FRG Patent 3228177.
24. GDR Patent 89581.
25. Borisov, V.M., and Mel'nikova, S.V., *Zh. Prikl. Khim.*, 1984, vol. 57, no. 3, pp. 705–707.
26. Arkhipova, L.N., Tsybina, M.N., Dvoryazhkina, A.N., *et al.*, *Puti ispol'zovaniya kremneftoristykh produktov proizvodstva mineral'nykh udobrenii* (Ways of Utilization of Silicon Fluoride Products from Manufacture of Mineral Fertilizers), Available from ONIITEKhIM, Moscow, November 13, 1985, no. 1101khn.
27. US Patent 4470959.
28. Zaitsev, V.A., Arkhipova, L.N., Novikov, A.A., *et al.*, *Khim. Prom–st.*, 1974, no. 10, pp. 768–771.
29. Lobas, A.P., and Pishchulin, V.P., Abstracts of Papers, *7-i Vsesoyuznyi simpozium po khimii neorganicheskikh ftoridov* (7th All-Union Symp. on the Chemistry of Inorganic Fluorides), Dushanbe, October 9–11, 1984, p. 210.
30. Pishchulin, V.P., Kretov, A.V., and Ryzhov, I.E., Abstracts of Papers, *8-i Vsesoyuznyi simpozium po khimii neorganicheskikh ftoridov* (8th All-Union Symp. on the Chemistry of Inorganic Fluorides), Polevskoi, August 25–27, 1987, p. 313.
31. FRG Patent 3432678.
32. FRG Patent 3217074.
33. US Patent 4446120.
34. Sanjurjo, A., Nanis, L., Sancier, K., *et al.*, *J. Electrochem. Soc.*, 1981, vol. 128, no. 1, pp. 179–184.
35. Chiotti, P., *J. Less-Common Met.*, 1981, vol. 80, no. 1, pp. 97–104.
36. Chernov, R.V., and Kovzun, I.G., *Ukr. Khim. Zh.*, 1972, vol. 38, no. 4, pp. 318–323.
37. Chernov, R.V. and Dyubova, L.D., Abstracts of Papers, *7-i Vsesoyuznyi simpozium po khimii neorganicheskikh ftoridov* (7th All-Union Symp. on the Chemistry of Inorganic Fluorides), Dushanbe, October 9–11, 1984, p. 343.
38. Stodolski, R., and Kolditz, L., *Z. Chem.*, 1985, vol. 25, no. 5, pp. 190–191.
39. Kolditz, L., Wilde, W., and Bentrup, U., *Z. Chem.*, 1983, vol. 23, no. 7, pp. 246–247.
40. Bulanov, A.D., Balabanov, V.V., Pryakhin, D.A., and Troshin, O.Yu., *Izv. Ross. Akad. Nauk, Neorg. Mater.*, 2002, vol. 38, no. 3, pp. 356–361.

Russian Journal of Applied Chemistry, Vol. 76, No. 9, 2003, pp. 1396–1398. Translated from Zhurnal Prikladnoi Khimii, Vol. 76, No. 9, 2003, pp. 1436–1438.

INORGANIC SYNTHESIS AND INDUSTRIAL INORGANIC CHEMISTRY

Synthesis of Nanolayers of Double Fe(III) and Ni(II) Hydroxide by Ionic Layer Deposition on Quartz and Silicon Surfaces

V. P. Tolstoi and I. V. Samsonova

St. Petersburg State University, St. Petersburg, Russia

Received January 9, 2003

Abstract—Conditions for the synthesis of nanolayers of double Fe(III) and Ni(II) hydroxides by ionic layer deposition on quartz and silicon surfaces were determined. The layers synthesized were studied by X-ray photoelectron spectroscopy, ellipsometry, and UV-Vis and IR Fourier transmission spectroscopy.

It is known that metal hydroxides are effective sorbents and ion exchangers. The method of ionic layer deposition (ILD) opens up new opportunities, as it allows deposition of nanolayers of hydroxides on a surface of an inert support with a preset specific surface area. Conditions for the synthesis of FeOOH by ILD were determined previously [1].

The goal of this work was to study conditions for ILD of nanolayers consisting of hydroxides of two metals. Hydroxides of Fe(III) and Ni(II) were chosen as the objects of the study. We expected that a layer of Fe(III) hydroxide could be obtained by the technique from [1] involving the following successive steps: sorption of Fe^{2+} from a solution of Mohr's salt on the support surface, removal of excess solution by washing with water, oxidation of the sorbed ions with a solution of $H_2O_2(OH^-)$, and removal of excess H_2O_2 solution by washing with water. One such sequence of treatments formed one ILD cycle. Upon multiple repetition of ILD cycles, the thickness of the layer proportionally increased. When synthesizing a layer of double Fe(III) and Ni(II) hydroxide, it is possible to combine oxidation of sorbed Fe(II) ions and sorption of Ni(II) ions and to prepare a layer of the double hydroxide by a minimal number of treatments of the surface with chemicals, using an ammonia solution of an Ni(II) salt. In such solutions, on the one hand, Fe(II) is catalytically oxidized to Fe(III) with oxygen dissolved in water, and, on the other, a layer of Fe(III) hydroxide is formed on the surface and Ni(II) ions are sorbed on this layer [2]. It is also known [3] that the double-charged metal ions sorbed on Fe(III) hydroxide from ammonia solutions are not removed from the surface on washing the sample with water.

EXPERIMENTAL

Melted quartz of KU grade and single-crystalline silicon of the KEF-7.5 grade ([100] orientation), polished to class 14 of surface finish, were used as supports for the synthesis. The quartz supports were washed in acetone and kept at 90–100°C for 10 min in concentrated nitric acid and then washed with water, a KOH solution with pH 9, and again water. The single-crystalline silicon substrates were etched in HF, heated in concentrated HNO_3 for 0.5 h to 90–100°C to form a surface layer of silicon oxide, and

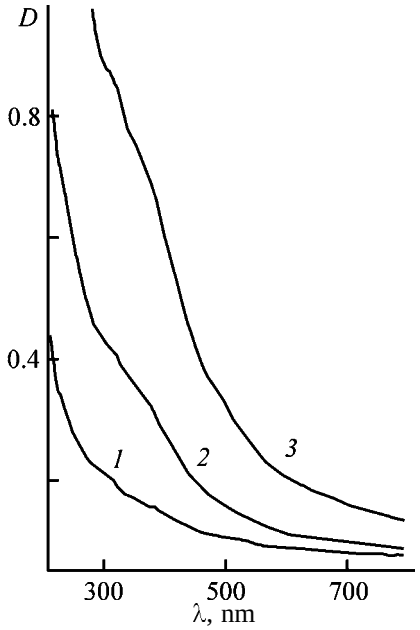

Fig. 1. UV-Vis transmission spectra of nanolayers of Fe(III) and Ni(II) hydroxide synthesized on the surface of melted quartz by (*1*) 10, (*2*) 20, and (*3*) 30 ILD cycles. (*D*) Optical density and (λ) wavelength.

1070-4272/03/7609-1396$25.00

washed with distilled water, a KOH solution with pH 9, and again water.

The reagents for the synthesis were a freshly prepared solution of Mohr's salt $(NH_4)_2[Fe(SO_4)_2]\cdot 6H_2O$ and an ammonia solution of $NiSO_4$ (pH 8.0–8.5) with concentrations of 0.01 M. The ammonia solution was prepared by dissolving a weighed sample of an Ni(II) salt in an 0.1 M solution of $(NH_4)_2SO_4$ with preliminarily added 25% solution of NH_4OH in an amount of 0.15–0.25 ml per 50 ml of the ammonium salt solution [4]. Excess reagents were washed off from the surface with water. The time of treating the supports in reagent solutions and water was 0.5 min.

We used IR Fourier and UV-Vis transmission spectroscopy, X-ray photoelectron spectroscopy, and ellipsometry. The UV-Vis transmission spectra were recorded on a Perkin–Elmer Lambda-9 spectrophotometer at a scan rate of 50 nm min^{-1} and a slit program of 2 nm; the IR Fourier spectra, on a Perkin–Elmer 1760X spectrophotometer (50 scans); and the X-ray photoelectron spectra, on a Perkin–Elmer 5400 spectrometer using MgK_α excitation radiation. The ellipsometric measurements of the thickness of the synthesized layers were carried out on an ellipsometer with a light incidence angle of 45° and λ = 632.8 nm.

As seen from the UV-Vis transmission spectra (Fig. 1), performing 10, 20, and 30 ILD cycles on a quartz plate gives rise to a broad absorption band in the range 200–450 nm with the integral intensity increasing with increasing number of cycles. According to the ellipsometry measurements, one cycle of the treatment of a support results in formation of an approximately 0.7-nm-thick layer on the support surface. According to X-ray photoelectron spectroscopy (Fig. 2), the layer consists of Fe(III), Ni(II), and oxygen atoms, which are characterized by peaks in the spectrum with maxima at 711.9, 855.9, and 531.1 eV, respectively. The positions of the first two peaks allows their assignment to 2*p* electrons of Fe(III) and Ni(II) in the corresponding hydroxides [5]. The concentration ratio Fe(III)/Ni(II) in the layer, determined from the intensities of their peaks, is 1/0.4. Sulfate ions, which could enter into the layer from solutions of the reagents, are absent. The layer also contains H_2O molecules and OH^- groups incorporated into metal hydroxides, which can be identified in the IR Fourier spectrum of the layer (Fig. 3) by the bands of stretching vibrations at 3800–3000 cm^{-1} and of bending vibrations at 1640 and 1560–1392 cm^{-1}, respectively. A broad absorption band in the region of 1000–400 cm^{-1} and a narrow band at 370 cm^{-1} are also seen in the spectrum. According to [6, 7], these spectra can be assigned to amorphous double Fe(III) and Ni(II) hydroxide. In view of all the data obtained in this work, its formula can be presented as $FeNi_{0.4}(OH)_{3.8}\cdot nH_2O$.

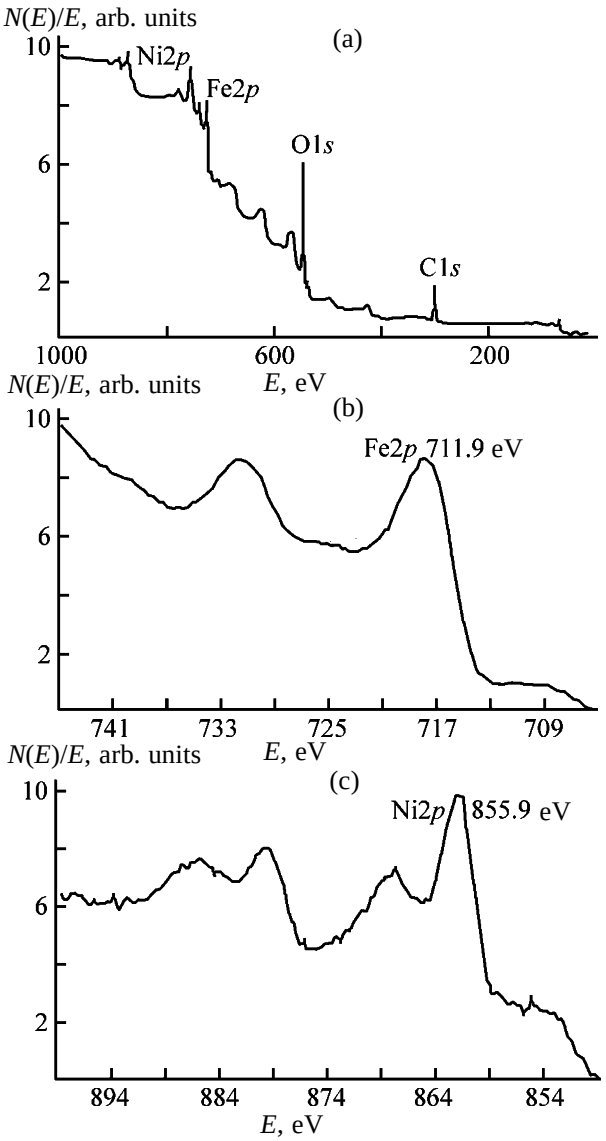

Fig. 2. X-ray photoelectron spectra of a nanolayer of Fe(III) and Ni(II) hydroxide synthesized on the surface of single-crystalline silicon by 20 ILD cycles: [*N*(*E*)/*E*] intensity and (*E*) binding energy. (a) Total spectrum, (b) Fe region, and (c) Ni region.

CONCLUSION

Repeated alternate treatment of a silica surface with a solution of Mohr's salt and an ammonia solution of $NiSO_4$ by the ionic layer deposition technique yields nanolayers of double Fe(III) and Ni(II) hydroxide on

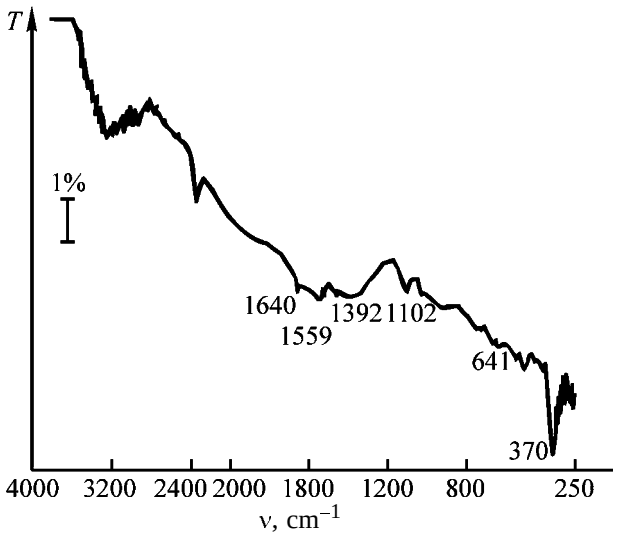

Fig. 3. IR Fourier transmission spectra of a nanolayer of Fe(III) and Ni(II) hydroxide synthesized on the surface of single-crystalline silicon by 20 ILD cycles: (*T*) transmission and (ν) wave number.

the support surface. The concentration ratio Fe/Ni in the layer is 1/0.4, and its thickness can be preset by the number of ionic layer deposition cycles, with one treatment cycle giving an 0.7-nm-thick layer on the surface.

ACKNOWLEDGMENTS

This work was financially supported by the Russian Foundation for Basic Research (project no. 01-03-32427).

REFERENCES

1. Tolstoi, V.P., *Zh. Prikl. Khim.*, 1999, vol. 72, no. 8, pp. 1259–1261.
2. Kanaungo, S.B., *J. Colloid Interface Sci.*, 1994, vol. 162, no. 1, pp. 93–99.
3. Sviridov, V.V. and Branitskii, G.A., *Khimicheskie problemy sozdaniya novykh materialov i tekhnologii* (Chemical Problems of Development of New Materials and Technologies), Sviridov, V.V., Ed., Minsk, 1998, pp. 293–322.
4. Tolstobrov, E.V. and Tolstoi, V.P., *Zh. Obshch. Khim.*, 1999, vol. 69, no. 6, pp. 890–895.
5. Nefedov, V.I., *Rentgenofotoelektronnaya spektroskopiya neorganicheskikh soedinennii* (X-ray Photoelectron Spectroscopy of Inorganic Compounds), Moscow: Khimiya, 1984.
6. Kamnev, A.A., Ristic, M., and Angelov, V., *J. Mol. Struct.*, 1995, vol. 349, pp. 77–80.
7. Plyusnina, I.I., *IK spektry mineralov* (IR Spectra of Minerals), Moscow: Mosk. Gos. Univ., 1977.

Russian Journal of Applied Chemistry, Vol. 76, No. 9, 2003, pp. 1399–1404. Translated from Zhurnal Prikladnoi Khimii, Vol. 76, No. 9, 2003, pp. 1439–1444.

PHYSICOCHEMICAL STUDIES OF SYSTEMS AND PROCESSES

Liquid–Vapor Equilibrium in the Isobutanol–*n*-Butanol–Butyl Butenyl Ether Ternary System, Azeotropy in Butyl Alcohols–Butyl Butenyl Ether–Water Systems, and Separation of Their Components by Distillation

M. N. Rogov, I. I. Sabylin, and A. P. Khvorov

All-Union Research Institute of Pertochemistry, Joint-Stock Company, St. Petersburg, Russia
Salavatnefteorgsintez Joint-Stock Company, Salavat, Bashkortostan, Russia

Received June 2002; in final form, March, 2003

Abstract—Liquid–vapor equilibria and azeotropy in isobutanol–*n*-butanol–butyl butenyl ether ternary system and in isobutanol-butyl butenyl ether and *n*-butanol–butyl butenyl ether binary systems were studied experimentally and calculated, as well as azeotropy in butyl alcohols–butyl butenyl ether–water systems under atmospheric and reduced pressure. Recovery of commercial butyl alcohols by distillation of alcohol–ether fractions was studied.

To decrease losses of commercial products in oxosynthesis of butyl alcohols, recovery of butyl alcohols by distillation of the alcohol–ether fraction should be optimized by mathematical simulation. The simulation requires knowledge of parameters of the liquid–vapor equilibrium and azeotropy in isobutanol–*n*-butanol–butyl butenyl ether ternary system and in binary systems of these compounds.

Oxosynthesis of butyl alcohols yields alcohol–ether fractions as a by-product in amount of 10–15% of the produced butyl alcohols. The content of butyl alcohols in these fractions is 50–70%.

This fraction is used today as a fuel component. Feasibility study shows that recovery of more that 50% of saleable butyl alcohols gives a profit with fast pay-back of investments.

The alcohol–ether fraction contains also saturated C_8 ethers (dibutyl ether, diisobutyl ether, butyl isobutyl ether) and the corresponding C_8 vinyl ethers.

Unsaturated C_8 ethers are formed in the step of C_{12} acetal degradation when butyric aldehydes are hydrogenated to form butyl alcohols. The acetals are present in the raw material to be hydrogenated as by-products of propylene hydroformylation [1].

The liquid–vapor equilibria in butyl alcohol–saturated C_8 ether systems have been extensively studied [2–6]. These processes are simulated well by UNIFAC group procedure [7]. At the same time, no data on the equilibria in butyl alcohol–unsaturated C_8 ether systems are reported. Hence, equilibria in these systems cannot be simulated.

To study the liquid–vapor equilibria in the latter systems, we prepared unsaturated C_8 ether, butyl butenyl ether (BBE).

The synthesis of BBE involves two steps. The first is preparation of C_{12} acetal, dibutyl butyral, from *n*-butyric aldehyde and *n*-butanol purified by distillation.

C_{12} acetal was distilled under reduced pressure and thermolyzed on calcium phosphate catalyst at 200–220°C under atmospheric pressure to form *n*-butanol and BBE.

The unsaturated C_8 ether was isolated by distillation. The boiling point at 760 and 100 mm Hg is 145.4°C and 83.7°C, respectively; density d_4^{20} = 0.773 kg m^{-3}; refractive index n_D^{20} = 1.3974.

No physicochemical properties of this ether are reported in available handbooks. All the other chemicals used in this work were thoroughly purified; their physicochemical parameters were consistent with the published data [8].

The liquid–vapor equilibrium was studied on a circulation unit connected with a manostat. The design of the unit provided minimal consumption of chemicals. The vapor condensed in a receiver was

1070-4272/03/7609-1399$25.00

Table 1. Parameters of liquid–vapor equilibrium in *n*-butanol (1)–BBE (2) and isobutanol (1)–BBE (2)* systems at 760 and 100 mm Hg

n-Butanol–BBE					Isobutanol–BBE				
x_1	y_1	T, °C	Δy_1, mol %	ΔT, °C	x_1	y_1	T, °C	Δy_1, mol %	ΔT, °C
mol %					mol %				
Pressure 760 mm Hg									
5.7	22.2	137.1	–0.8	–0.9	4.2	19.8	138.5	0.9	–0.8
10.8	34.8	134.6	–0.8	1.1	9.7	36.5	134.0	0.7	0.8
20.4	50.1	128.8	–0.3	0.9	18.4	52.0	126.9	–0.9	0.9
32.7	62.2	124.3	0.7	0.8	27.5	64.7	121.5	0.7	0.7
38.4	64.3	123.0	–0.8	0.8	39.8	72.8	116.7	–0.8	0.9
47.9	70.9	121.5	0.8	1.0	45.5	77.7	115.0	0.9	0.9
56.3	72.8	120.2	–1.0	0.8	57.2	82.6	112.4	0.7	0.8
68.0	80.1	119.0	1.6	0.7	69.2	85.0	110.8	–0.8	1.0
79.4	84.7	117.8	1.1	0.2	79.3	89.6	109.7	0.8	0.8
88.3	88.6	116.9	–0.3	–0.5	93.5	94.0	108.9	–0.7	1.0
96.8	95.3	117.6	–0.9	0.1	97.7	98.1	108.1	0.4	0.2
$\lvert\overline{\Delta y}\rvert$ = 0.83 mol %, $\lvert\overline{\Delta T}\rvert$ = 0.71°C					$\lvert\overline{\Delta y}\rvert$ = 0.75 mol %, $\lvert\overline{\Delta T}\rvert$ = 0.80°C				
Pressure 100 mm Hg									
5.0	17.1	79.6	–0.5	–0.6	10.2	35.2	76.7	0.7	0.7
11.4	33.7	75.9	0.9	–0.9	18.7	52.1	72.0	0.8	0.5
22.7	50.6	73.7	0.8	0.9	26.9	62.9	68.9	0.7	0.8
34.8	61.5	70.9	0.7	0.7	40.4	74.4	64.8	0.7	0.7
40.5	63.9	69.6	–0.6	0.3	45.8	77.6	64.0	0.8	1.0
49.8	68.3	68.7	–1.0	0.4	57.6	81.0	61.9	–0.9	0.6
57.2	71.1	67.6	–1.1	–0.2	69.5	84.1	61.3	–0.8	0.9
81.6	80.0	66.4	0.9	–0.9	79.8	86.0	60.8	–0.4	0.7
89.9	83.7	67.9	1.0	0.3	89.1	87.3	60.4	–0.4	0.3
98.7	95.7	69.0	0.2	–0.3	97.9	93.7	60.8	–0.5	0.1
$\lvert\overline{\Delta y}\rvert$ = 0.77 mol %, $\lvert\overline{\Delta T}\rvert$ = 0.55°C					$\lvert\overline{\Delta y}\rvert$ = 0.67 mol %, $\lvert\overline{\Delta T}\rvert$ = 0.63°C				

* x_i and y_i are the content of *i*th component in the liquid and vapor phases, respectively; T is the boiling point of the solution; the same for Table 2.

analyzed by gas chromatography with an accuracy of 0.5 mol %.

The boiling point of the solutions was measured in the course of the experiment with an accuracy of 0.2°C.

The experimental parameters of the liquid–vapor equilibrium in the *n*-butanol (NB)–BBE and isobutanol (IB)–BBE binary systems at 760 and 100 mm Hg are summarized in Table 1, and the parameters for the ternary system at 760 and 100 mm Hg, in Table 2. The differences between the experimental and calculated (NRTL equation [9]) concentrations of the components in the vapor phase and boiling points of the solution components Δy_i and ΔT and the average absolute deviations $\lvert\overline{\Delta y}\rvert$ and $\lvert\overline{\Delta T}\rvert$ are also presented in Tables 1 and 2. The parameters of the liquid–vapor equilibrium in the ternary system were calculated from the NRTL equation parameters, which, in turn, were calculated from the data on the liquid–vapor equilibrium in the binary systems.

As seen from Tables 1 and 2, the calculated parameters agree well with the experimental results.

n-Butanol and BBE form an azeotrope. Under a pressure of 760 mm Hg, the BBE content in the azeotrope is 10.5 mol % (16.9 wt %) and its boiling point is 116.8°C. Under a pressure of 100 mm Hg, the

Table 2. Parameters of liquid–vapor equilibrium in IB (1)–NB (2)–BBE (3) system

x_1	x_2	y_1	y_2	T, °C	Δy_1	Δy_2	ΔT, °C
mol %					mol %		
Pressure 760 mm Hg							
12.5	62.7	16.0	65.4	116.8	1.87	–0.44	–0.4
12.5	75.0	15.2	73.4	116.2	1.71	–1.32	–0.2
24.8	50.2	32.9	49.7	115.9	1.27	–0.02	–1.0
25.3	62.6	33.8	57.8	115.5	–1.08	–0.69	–1.0
37.8	50.2	45.0	44.7	113.8	1.83	–1.12	–0.6
50.0	12.5	68.1	13.3	112.7	1.74	–0.73	–0.4
50.0	24.8	61.8	22.2	112.6	1.80	–0.01	–0.6
62.5	12.7	74.9	10.3	110.9	1.13	0.44	–0.3
62.8	25.3	70.2	20.0	111.2	1.22	–0.12	–0.6
75.1	12.4	81.3	8.7	110.1	0.78	0.59	–0.7
					$\lvert\overline{\Delta y}\rvert$ = 1.08 mol %,		$\lvert\overline{\Delta T}\rvert$ = 0.58°C
Pressure 100 mm Hg							
12.5	62.7	16.7	60.8	67.0	1.68	–0.04	–1.0
12.5	75.0	15.4	65.3	67.9	1.55	0.27	–1.7
24.8	50.2	33.5	46.8	64.9	1.19	–0.79	–0.1
25.3	62.6	30.8	51.4	65.8	1.57	–0.02	–0.7
37.8	50.2	43.6	40.0	64.7	2.24	–1.14	–0.7
50.0	12.5	69.2	11.8	62.8	0.85	–0.06	–0.7
50.0	24.8	62.1	20.2	63.5	1.11	0.09	–1.1
62.5	12.7	72.3	10.9	61.3	2.67	–1.11	0.0
62.8	25.3	67.0	18.6	62.9	1.75	–1.09	–0.9
75.1	12.4	79.4	7.7	61.7	–0.78	0.47	–0.7
					$\lvert\overline{\Delta y}\rvert$ = 1.05 mol %,		$\lvert\overline{\Delta T}\rvert$ = 0.78°C

BBE concentration in the azeotrope is 22.4 mol % (33.3 wt %), and its boiling point is 66.2°C.

No azeotrope was found in the isobutanol–BBE system under atmospheric pressure. However, under reduced pressure (100 mm Hg), the compounds do form an azeotrope [bp 60.2°C, BBE concentration 12.9 mol % (20.4 wt %)].

Calculation by the azeotrope search program showed that ternary azeotropes were formed in the IB–NB–BBE ternary system neither at 760 nor at 100 mm Hg. The study of this system on a high-performance column by the procedure in [10] confirmed this assumption.

In this work we studied phase equilibria in distillation of systems containing saturated butyl alcohols and unsaturated butyl ethers to determine initial parameters for a mathematical model of distillation of commercial butyl alcohols from these systems.

It is known [11] that ternary azeotropes are formed in systems consisting of water, butyl alcohols, and saturated butyl ethers; however, for the similar systems with unsaturated butyl ethers, no data are reported.

In this work we determined the compositions and boiling points of ternary azeotropes in H_2O–IB–BBE and H_2O–NB–BBE systems at a pressure from 100 to 760 mm Hg.

These experiments were performed on a laboratory 50-mm column 150 cm high, packed with $2 \times 3 \times 3$ mm three-edged spirals made from 0.4-mm Nichrome wire.

The column efficiency determined with the IB–NB system [12] was 68–70 TP.

The azeotrope composition was determined by the procedure in [10]. The gaseous distillate was condensed, homogenized with acetone, and analyzed

Table 3. Boiling points T_b and compositions of H_2O–IB–BBE and H_2O–NB–BBE azeotropes at different pressures

P, mm Hg	T_b, °C	Concentration, wt %			BBE : alcohol weight ratio in azeotrope
		H_2O	alcohol	BBE	
		H_2O–IB–BBE			
100	45.9	24.1	20.7	55.2	2.7
200	59.7	25.8	21.9	52.3	2.4
300	68.4	27.2	23.2	49.6	2.1
500	80.6	29.4	25.4	45.2	1.8
760	90.9	31.4	28.5	40.1	1.4
		H_2O–NB–BBE			
100	44.6	27.3	22.8	49.9	2.2
200	58.3	29.4	26.4	44.2	1.7
300	66.9	31.2	27.8	41.0	1.5
500	79.0	33.4	30.0	36.6	1.2
760	89.1	35.7	33.0	31.3	0.95

chromatographically. The results of these experiments are presented in Table 3.

As shown above, the BBE : NB weight ratio strongly increases with decreasing pressure: at 760 and 100 mm Hg it is 0.20 : 1 and 0.50 : 1, respectively. Addition of water to the IB–BBE and NB–BBE systems also increases this ratio (Table 3). Thus, we suggest that butyl alcohol–butyl ether systems can be efficiently separated by distillation under reduced pressure in the presence of water as a separating agent.

Industrial alcohol–ether fractions formed in production of butanols by oxosynthesis have the following composition (wt %): IB 30–50, NB 20–40, saturated buthyl ethers 4–11, unsaturated butyl ethers 5–12, butyl formates 3–7, butyric aldehydes 1–3, and water 1–5.

We studied distillation separation of butanol form an industrial alcohol–ether fraction[1] of the following composition (wt %): IB 39.29, NB 33.34, saturated buthyl ethers 9.87, unsaturated butyl ethers 11.26, butyric aldehydes 2.08, butyl formates 2.74, and water 1.42.

A five-component system containing (wt %) IB 44.2, NB 33.3, dibutyl ether (DBE) 9.8, BBE 11.3, and water 1.4 was used as a model.

To simulate the distillation process, we used parameters of the NRTL equation for the binary system under a pressure of 760 and 100 mm Hg. The parameters calculated by the procedure in [13] are summarized in Table 4.

The saturated vapor pressure of pure components was calculated by the Antoine equation in the following form:

$$\log P = A - \frac{B}{C + T},$$

where P is the saturated vapor pressure (mm Hg), T is the temperature (°C), and A, B, C are the Antoine constants.

The parameters of the Antoine equation for IB, NB, water and DBE taken from [14] were brought to the above form of the equation. The BBE parameters were determined in this work by treatment of the experimental temperature dependence of saturated vapor pressure of BBE (Table 5).

The separation parameters of the model system were computed by the program for calculation of distillation parameters, developed on the basis of the concept in [15, 16].

To recover high-grade NB [GOST (State Standard) 5208–81] and high-grade IB [GOST 9536–79], the content of butyl alcohols and unsaturated compounds in the product should be no less than 99.4 wt % and no more than 0.02 wt %, respectively.

The distillation parameters at which butyl alcohols are separated to the highest extent at the indicated column efficiency and 760 and 100 mm Hg from the alcohol–ether fraction meeting the GOST requirements are presented in Table 6.

As seen from Table 6, under reduced pressure the yield of butyl alcohols is higher at smaller reflux ratios.

On an industrial scale, we suggest to recover butyl alcohols on a 23600-mm column 1000 mm in diameter, equipped with 40 valve single-flow plates.

To check the adequacy of calculation of the quality and the yield of butyl alcohols recovered from the alcohol–ether fraction, we performed a pilot experiment on this column.

The initial alcohol–ether fraction was fed to the 21st plate from the top, and the separating agent (steam) was fed to the 36th plate (in the initial mixture, H_2O : BBE = 1 : 1). The column was sprayed with the organic phase from the florentine with the reflux ratio of 9–10.

[1] Salavatnefteorgsintez Joint-Stock Company.

Table 4. Parameters of NRTL equation

System	760 mm Hg			100 mm Hg		
	τ_{12}	τ_{21}	α_{12}	τ_{12}	τ_{21}	α_{12}
NB–BBE	0.9776	0.1242	0.4	2.1047	–0.1230	0.4
IB–BBE	1.9805	–0.6088	0.3	3.2272	–0.7412	0.3
NB–DBE	1.2734	–0.0729	0.4	1.3068	0.2524	0.4
IB–DBE	3.4845	–1.9043	0.1	0.9872	0.3085	0.4
H_2O–IB	3.5987	0.4653	0.4	3.4984	0.5140	0.4
H_2O–NB	3.5864	0.4951	0.4	3.6000	0.5757	0.4
H_2O–BBE	5.6281	–0.9681	0.1	5.3635	–0.7941	0.1
H_2O–DBE	5.7557	–1.1372	0.1	5.6131	–0.9847	0.1
DBE–BBE	–0.2111	0.2288	0.1	1.3457	–1.0773	0.1

The composition of the fraction obtained by separation from the bottoms was as follows (wt %): H_2O 0.07, IB 50.01, NB 49.88, saturated butyl ethers 0.02, and unsaturated butyl ethers 0.01. Commercial isobutanol and *n*-butanol were recovered by distillation of this fraction on a column with 90 valve plates at a reflux ratio of 12.

Commercial IB was taken off from the seventh plate form the top, and NB, from the bottoms. The quality of the commercial alcohols met the GOST requirements. The yield of IB and NB based on their potential content in the head ether fraction was 75 and 90.3%, respectively.

The yield of high-grade butyl alcohols, calculated on the basis of the developed model, agreed well with the results of the experimental run on the industrial distillation column.

Thus, the experimental and calculated data of this work can be used to design a process for recovery of commercial butyl alcohols from side alcohol–ether fraction at the Salavatnefteorgsintez Joint-Stock Company.

CONCLUSIONS

(1) Liquid–vapor phase equilibria in isobutanol–*n*-butanol–butyl butenyl ether ternary system and in binary systems of these compounds were studied experimentally at 760 amd 100 mm Hg. *n*-Butanol and butyl butenyl ether form an azeotrope at 760 and 100 mm Hg; no azeotropes were found in the isobutanol–butyl butenyl ether system at 760 mm Hg, but at 100 mm Hg this system has an azeotrope. No ternary azeotrope was found in the three-component system. The average absolute error of calculating the equilibrium composition of the ternary system by the NRTL equation from the equilibrium compositions of the binary systems of the components is 1 mol %. The boiling point of the equilibrium ternary system was calculated by this procedure with an absolute error of 0.6–0.8°C. Thus, the calculation results are quite adequate.

Table 5. Parameters of the Antoine equation

Component	*A*	*B*	*C*
IB	7.32707	1248.479	172.850
NB	7.47681	1362.390	178.720
H_2O	7.94915	1657.459	227.020
DBE	6.98250	1431.500	207.000
BBE	6.98250	1431.500	203.600

Table 6. Influence of the efficiency *E*, pressure in the top of the column P_{top}, and reflux ratio (RR) on the theoretical yield *Y* of high-grade butyl alcohols. Pressure drop on a single TP 6 mm Hg; temperature of the reflux in decanter 30°C; weight ratio of the separating agent (H_2O) to sum of butyl alcohols 1 : 1

P_{top}, mm Hg	*E*, TP	Feed plate	Plate for H_2O introduction	RR	*Y*,* %
		TP (from the top)			
760	20	11	17	15.3	47.4
100	20	11	17	10.8	68.9
760	25	13	22	12.2	54.7
100	25	13	22	9.4	84.3
760	35	18	31	9.0	63.7
100	35	18	31	7.2	91.5
760	40	22	37	7.0	68.5
100	40	22	37	5.4	93.1

* Based on the potential content in the alcohol–ether fraction.

(2) As the pressure in the column decreases from 760 to 100 mm Hg, the concentration of butyl butenyl ether in the ternary azeotropes formed in the water–isobutanol–butyl butenyl ether and water–*n*-butanol–butyl butenyl ether systems increases from 31.3 to 49.9 and from 40.1 to 55.2 wt %, respectively.

(3) More than 80 wt % of high-grade butyl alcohols can be isolated from industrial alcohol–ether fractions of the oxosynthesis by azeotropic distillation with water on a column with 25 TP efficiency at a pressure of 100 mm Hg and the reflux ratio of 9–10. The butanol fraction is taken off from the stripping part of the column.

REFERENCES

1. Gankin, V.Yu. and Gurevich, G.S., *Tekhnologiya oksosinteza* (Oxosynthesis Process), Leningrad: Khimiya, 1981.
2. Kogan, V.B., Fridman, V.M., and Kafarov, V.V., *Ravnovesie mezhdu zhidkost'yu i parom* (Liquid–Vapor Equilibrium), Moscow: Nauka, 1996, Book 2.
3. Volkova, L.V., Utkin, O.V., and Katalov, A.I., *Zh. Prikl. Khim.*, 1979, vol. 52, no. 9, pp. 1998–2001.
4. Volkova, L.V., Utkin, O.V., and Katalov, A.I., *Zh. Prikl. Khim*., 1979, vol. 52, no. 10, pp. 2347–2350.
5. Stepanova, E.I., Sabylin, I.I., and Kukharenok, I.S., *Zh. Prikl. Khim*., 1985, vol. 58, no. 4, pp. 937–939.
6. Stepanova, E.I., Sabylin, I.I., and Kukharenok, I.S., *Zh. Prikl. Khim*., 1985, vol. 58, no. 10, pp. 2384–2386.
7. Gmehling, J., Rasmussen, P., and Fredenslung, A., *Ind. Eng. Chem. Process Des. Develop*., 1982, vol. 21, no. 1, pp. 118–120.
8. *Spravochnik khimika* (Chemist's Handbook), Nikol'skii, B.P., Ed., Leningrad: Goskhimizdat, 1963.
9. Renon, H. and Prausnitz, J.M., *Am. Inst. Chem. Eng. J*., 1968, vol. 14, no. 1, pp. 135–144.
10. Kogan, V.B., *Azeotropnaya i ekstraktivnaya rektifikatsiya* (Azeotropic and Extractive Distillation), Leningrad: Khimiya, 1971.
11. Ogorodnikov, S.K., Lesteva, T.M., and Kogan, V.B., *Azeotropnye smesi* (Azeotropic Mixtures), Kogan, V.B., Ed., Leningrad: Khimiya, 1971.
12. Krell, E., *Handbuch der Laboratoriumsdistillation*, Berlin: Wissenschaften, 1958.
13. Bondarenko, Yu.L., Sabylin, I.I., and Kharisov, M.A., *Zh. Prikl. Khim*., 1982, vol. 55, no. 12, pp. 2669–2674.
14. Reid, R.G., Prausnitz, J.M., and Sherwood, T.K., *The Properties of Gases and Liquids*, New York: McGraw-Hill, 1977.
15. Bril', Zh.A., Mozzhukhin, A.S., Petlyuk, F.B., and Serafimov, L.A., *Teor. Osn. Khim. Tekhnol*., 1975, vol. 9, no. 6, pp. 811–821.
16. Bril', Zh.A., Mozzhukhin, A. S., Pershina, L.A., and Serafimov, L.A., *Teor. Osn. Khim. Tekhnol*., 1985, vol. 19, no. 6, pp. 723–728.

Russian Journal of Applied Chemistry, Vol. 76, No. 9, 2003, pp. 1405–1407. Translated from Zhurnal Prikladnoi Khimii, Vol. 76, No. 9, 2003, pp. 1445–1447.

PHYSICOCHEMICAL STUDIES OF SYSTEMS AND PROCESSES

Saturated Vapor Pressure over the Melts of the $NaNO_2$–$NaNO_3$ System

V. I. Glazov, G. P. Dukhanin, and M. Kh. Dkhaibe

Volgograd State Technical University, Volgograd, Russia

Received July 26, 2003

Abstract—The partial pressures of sodium nitrite and sodium nitrate over the system $NaNO_2$–$NaNO_3$ were determined at 798, 823, and 848°C. For sodium nitrate, *A* and *B* coefficients of the Clausius–Clapeyron equation, partial molar heats of vaporization, activities, and activity coefficients were calculated as functions of composition.

Molten nitrites and nitrates of alkali metals and systems based on them are used as high-temperature heat carriers in vulcanization of extruded rubber articles, in heat treatment of metals, and for preparing heat-resistant lubricants [1]. For this reason, study of physicochemical properties of nitrite–nitrate molten salt systems is of both theoretical and applied importance.

In this work, proceeding with studies [2–5] on physicochemical properties of nitrite–nitrate salt melts, we measured the saturated vapor pressure of the system $NaNO_2$–$NaNO_3$ at 798, 823, and 848 K. The experimental procedure and method of determining saturated vapor pressure of individual molten salts have been reported previously [2].

The mass spectrometry data [6, 7] for vapors of alkali metal nitrites and nitrates show that the vapor phase coexisting with nitrite–nitrate melts consists of monomeric molecules. This made it possible to calculate the saturated vapor pressure over pure components and their mixtures from the content of the components in a given volume of the vapor. As previously, the content of the sodium cations in the condensed vapor phase was determined by flame photometry [25], and the concentration of NO_2^- anions, by permanganate titration [8]. The content of $NaNO_2$ and $NaNO_3$ was calculated from these data.

The results of measurements of the vapor pressure over the sodium nitrite and sodium nitrate melts at 798 and 848 K are plotted in Fig. 1. As seen, the concentration dependence of the saturated vapor pressure in the $NaNO_2$–$NaNO_3$ system exhibits negative deviations from Raoult's law, decreasing with increasing temperature. Under isothermal conditions, the vapor

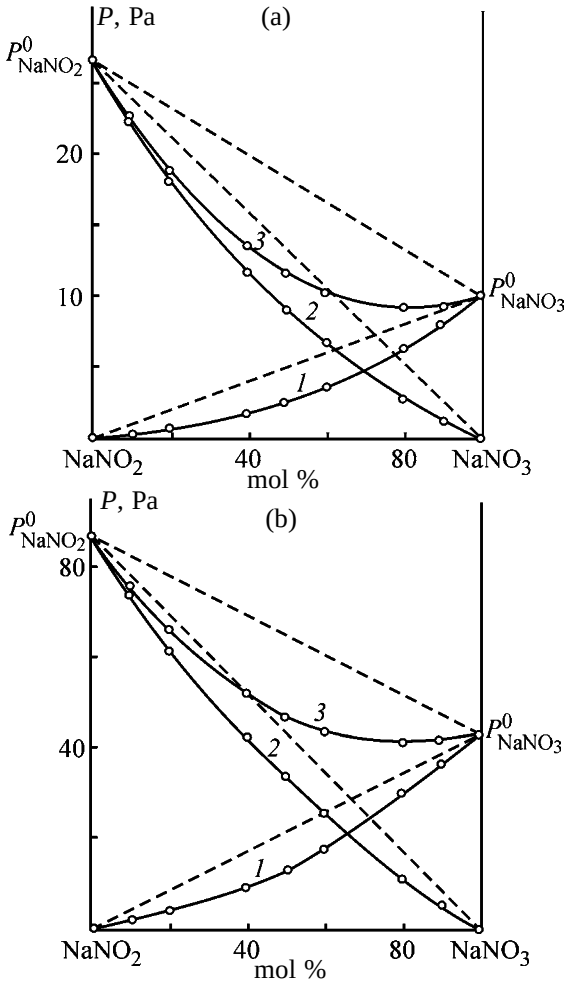

Fig. 1. Vapor pressure *P* over the melts of the system $NaNO_2$–$NaNO_3$ (mol %) at (a) 798 and (b) 848 K. ($P^0_{NaNO_2}$, $P^0_{NaNO_3}$) Vapor pressures over the pure components. (*1*, *2*) Partial pressure of $NaNO_2$ and $NaNO_3$, respectively, and (*3*) total pressure.

1070-4272/03/7609-1405$25.00

Table 1. Saturated vapor pressure P_{NaNO_3}, coefficients A and B of the Clausius–Clapeyron equation, and partial molar heats of vaporization $\Delta H_{vap}^{NaNO_3}$ of sodium nitrate in the system $NaNO_2$–$NaNO_3$

c_{NaNO_3} in melt, mol %	P_{NaNO_3}, Pa, at indicated temperature T, K			Coefficients of equation		$\Delta H_{vap}^{NaNO_3} \times 10^{-3}$, J mol^{-1}
	798	823	848	$A \times 10^{-3}$, K	B	
10	0.29	0.69	1.94	11.159	13.44	213.66
20	0.68	1.82	4.22	10.710	13.37	205.06
40	1.80	4.07	10.33	10.257	13.11	196.39
50	2.50	5.63	14.64	9.568	12.39	183.20
60	3.40	7.92	16.36	9.216	11.02	176.46
80	6.61	14.38	31.00	9.068	10.54	173.63
90	8.21	17.30	36.32	8.635	11.74	165.33
100	10.01	20.84	43.05	8.628	11.81	165.21

Table 2. Activity a and activity coefficient γ of sodium nitrate in the system $NaNO_2$–$NaNO_3$ at various temperatures

T, K	a (numerator) and γ (denominator) at indicated content of $NaNO_3$ in melt, mol %						
	10	20	40	50	60	80	90
798	0.029 / 0.29	0.068 / 0.34	0.18 / 0.44	0.25 / 0.50	0.34 / 0.57	0.66 / 0.83	0.82 / 0.91
823	0.033 / 0.33	0.87 / 0.43	0.19 / 0.48	0.27 / 0.55	0.38 / 0.64	0.69 / 0.86	0.83 / 0.92
848	0.045 / 0.45	0.98 / 0.49	0.24 / 0.60	0.34 / 0.67	0.44 / 0.74	0.72 / 0.9	0.85 / 0.95

pressure over the binary melts monotonically decreases as the content of sodium nitrate in the mixture increases. For component concentrations less than 5 mol %, the saturated vapor pressure as a function of composition is adequately described by Raoult's law. In the region of the equimolar concentrations of the components, the extent of the negative deviations increases.

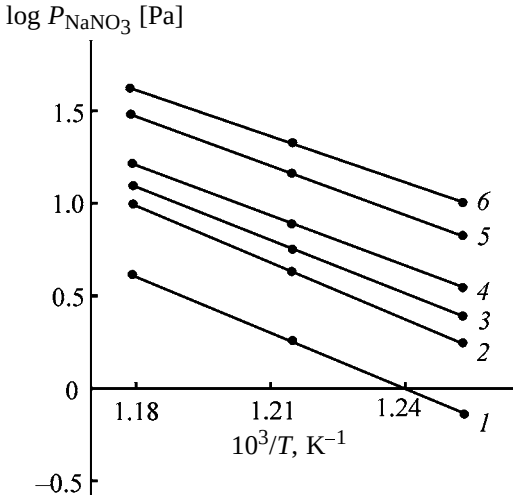

Fig. 2. Vapor pressure of sodium nitrate P_{NaNO_3} in the system $NaNO_2$–$NaNO_3$ vs. temperature T. $NaNO_3$ content in melt, mol %: (*1*) 20, (*2*) 40, (*3*) 50, (*4*) 60, (*5*) 80, and (*6*) 100.

Because the vapor pressures of sodium nitrite and sodium nitrate differ greatly, the total saturated vapor pressure over the system is determined by the $NaNO_3$ partial pressure.

The temperature dependence of the vapor pressure of the components over the melts of various compositions is adequately described by the Clausius–Clapeyron equation $\log P = B - A/T$. The coefficients of the equation are given in Table 1. Figure 2 shows the $\log P = f(1/T)$ plots for different concentrations of sodium nitrate in the melt.

The partial molar heats of vaporization of sodium nitrate from the melts of various compositions were calculated from the slopes of the straight lines

$$\Delta H = 2.3RA,$$

where R is the universal gas constant (8.314 J mol^{-1} K^{-1}).

With decreasing concentration, the heat of vaporization of sodium nitrate increases, i.e., the strength of interaction between the particles increases. The experimental data and results of their processing are presented in Table 1.

The coefficient of the linear correlation of $\log P$ with $1/T$ varies from 0.78 (at low concentrations) to 1.

The experimentally determined saturated vapor pressures over the pure components P_i^0 and their partial pressures P_i in the system were used to calculate the activities ($a_i = P_i/P_i^0$) and the activity coefficients ($\gamma_i = a_i/N_i$) for sodium nitrate in the binary system [9] (N_i is mole fraction of $NaNO_3$ in the melt). The calculation results are presented in Table. 2.

As seen, the activity of sodium nitrate exhibits negative deviations from the mole fraction. Therefore, the calculated activity coefficients are less than unity.

In the system $NaNO_2$–$NaNO_3$, the extent of deviations of the vapor pressure from ideality is larger than in the previously studied system $NaNO_2$–KNO_3 [5]. This may be explained by formation of a continuous series of solid solutions of $NaNO_2$ and $NaNO_3$ and of the chemical compound $NaNO_2 \cdot NaNO_3$ [10, 11].

Studies of N.S. Kurnakov's school [12] have shown that, when a solid ionic compound is melted, a part of ions can form complex species in equilibrium with simple ions. Therefore, the partial pressures of the components in the system decrease, the vapor pressures of the components exhibit considerable deviations from Raoult's law, and, consequently, the activity is not equal to concentration.

CONCLUSIONS

(1) The partial pressures of sodium nitrite and sodium nitrate over the system $NaNO_2$–$NaNO_3$ at 798, 823, and 848 K were determined. For sodium nitrate, the coefficients A and B of the Clausius–Clapeyron equation and the partial molar heats of vaporization were calculated.

(2) The saturated vapor pressure exhibits negative deviations from Raoult's law, indicative of certain interaction of the components in a melt.

(3) The activities and activity coefficients of sodium nitrate were calculated as functions of composition and temperature. The activity of sodium nitrate shows negative deviations from the mole fraction. As a result, the activity coefficient is less than unity.

REFERENCES

1. Chechetkin, A.V., *Vysokotemperaturnye teplonositeli* (High-Temperature Heat Carriers), Moscow: Energiya, 1971.
2. Glazov, V.I., Golod, V.F., and Golovanov, P.S., *Zh. Prikl. Khim.*, 1984, vol. 57, no. 6, pp. 2351–2352.
3. Glazov, V.I., Golovanov, P.S., and Dukhanin, G.P., *Zh. Prikl. Khim.*, 1990, vol. 63, no. 1, pp. 193–195.
4. Glazov, V.I., and Dukhanin, G.P., *Zh. Prikl. Khim.*, 1992, vol. 65, no. 8, pp. 1907–1911.
5. Glazov, V.I., Dukhanin, G.P., and Losev, V.A., *Zh. Prikl. Khim.*, 2002, vol. 75, no. 6, pp. 908–910.
6. Bogarat'yan, N.V., and Nikitin, O.T., *Vestn. Mosk. Gos. Univ.*, 1977, vol. 4, no. 18, pp. 388.
7. Verkhoturov, E.N., Makarov, A. V., and Nikitin, O.T., *Vestn. Mosk. Gos. Univ.*, 1977, vol. 4, no. 18, pp. 392.
8. Williams, W.J., *Handbook on Anion Determination*, London: Butterworth, 1979.
9. Morachevskii, A.G., *Termodinamika zhidkikh splavov* (Thermodynamics of Liquid Alloys), Leningrad: Leningr. Politekh. Inst., 1981.
10. Bergman, A.G., Berul', S.N., and Nikonova, I.N., *Izv. Sekt. Fiz.-Khim. Anal., Inst. Obshch. Neorg. Khim., Akad. Nauk SSSR*, 1953, vol. 23, pp. 183.
11. Protsenko, P.I., and Medvedev, B.S., *Zh. Prikl. Khim.*, 1963, vol. 36, no. 12, pp. 237–240.
12. Lantratov, M.F., and Alabyshev, A.F., *Zh. Prikl. Khim.*, 1953, vol. 26, no. 3, p. 263.

Russian Journal of Applied Chemistry, Vol. 76, No. 9, 2003, pp. 1408–1413. Translated from Zhurnal Prikladnoi Khimii, Vol. 76, No. 9, 2003, pp. 1448–1453.

PHYSICOCHEMICAL STUDIES OF SYSTEMS AND PROCESSES

Influence of Crystallization Conditions in Production of Citric Acid on the Properties of Forming Calcium Sulfate

K. A. Pavlov and B. A. Dmitrevskii

St. Petersburg State Technological Institute, St. Petersburg, Russia

Received July 3, 2003

Abstract—The boundaries of phase equilibria involving calcium sulfate crystal hydrates in a citric acid solution were calculated. The influence exerted by an excess amount of sulfuric acid on the stability of calcium sulfate crystal hydrates in citric acid solutions was considered. The possibility of achieving a hemihydrate mode of citric acid extraction from calcium citrate was studied.

Acid calcium sulfate suspensions are formed in sulfuric acid extraction of citric acid ($C_6H_8O_7$) from calcium citrate $Ca_3(C_6H_5O_7)\cdot 4H_2O$ [1, 2]. The solubility and stability of calcium sulfate ($CaSO_4$) modifications predetermines important parameters of the $C_6H_8O_7$ manufacture process, such as concentration and purity of the product acid, throughput of the stages of suspension filtration and calcium sulfate washing, washing efficiency, conditions of acid evaporation, $CaSO_4$ properties in hydration and dehydration processes, $CaSO_4$ transportability, content of total and crystallization water, and impurity background. All these characteristics are comparatively rarely discussed in the literature.

Citric acid plants mainly employ a semicontinuous extraction process with varying $H_2SO_4 : C_6H_8O_7$ ratio, which predetermines the presence of crystals with different microgranulometric characteristics in citrogypsum. It was found, in particular, that about 60% of the total amount of crystals are isolated parallelogram-shaped crystals 70 μm long and 15 μm wide. Separate finer and coarser gypsum crystals with dimensions of 30×10 and 400×300 μm are found, together with fine crystals of calcium oxalate and shielded crystals of calcium citrate. Such an inhomogeneity of the solid phase is accounted for by the method of $C_6H_8O_7$ extraction from solid $Ca_3(C_6H_5O_7)\cdot 4H_2O$ in a heterogeneous system.

Data on the concentration and temperature boundaries of mutual phase transformations of calcium sulfate crystal hydrates are important for practical use of crystallization processes occurring in sulfuric acid and nitric–sulfuric acid extraction of phosphoric [3] and, apparently, citric acids. Analysis for the content of these compounds in phosphoric and nitric acid solutions was a subject of numerous papers [4, 5]. No published data of this kind could be found for citric acid, and, therefore, these boundaries were determined tentatively by a prognosis graphical-analytical calculation. The points in which calcium sulfate dihydrate ($CaSO_4\cdot 2H_2O$) and hemihydrate ($CaSO_4\cdot 0.5H_2O$) coexist in equilibrium are commonly found by studying their solubility and determining graphically the intersection points of the solubility isotherms of gypsum and calcium sulfate hemihydrate, or by comparing the water vapor pressures over the corresponding solutions with the dissociation pressure of the reversible reaction

$$CaSO_4\cdot 2H_2O(s) \rightleftarrows CaSO_4\cdot 0.5H_2O(s) + 1.5H_2O(vapor). \quad (1)$$

To make a rough prognosis of the conditions (acid concentration, temperature) of phase equilibrium between gypsum and hemihydrate in acid solutions, parameters of dehydration by reaction (1) yielding water vapor were compared with water vapor pressures over solutions of phosphoric [6], nitric, and citric acids.

The dehydration parameters and the equilibrium content of the acid were found on the assumption that dissolved $CaSO_4$ affects only slightly the equilibrium pressure over solution, $P_{H_2O(sol)}$, which is close (equal) to the dehydration pressure $P_{H_2O(dehydr)}$.

To find the acid concentration in a eutonic solution saturated with $CaSO_4\cdot 2H_2O$ and $CaSO_4\cdot 0.5H_2O$, the dependence $P_{H_2O} = f(c_{acid})$ was plotted for each isotherm-polyconcentrate of an acid, and an isobar of P_{H_2O} over gypsum at the same temperature was

1070-4272/03/7609-1408$25.00

drawn to its intersection with the isotherm. Figure 1 exemplifies the construction for 80°C. Table 1 compares the dihydrate–hemihydrate equilibrium conditions for solutions of the three acids, obtained by this method also for other temperatures. The isotherms $P_{H_2O} = f(c_{acid})$ for citric acid emerge from the point corresponding to the water vapor pressure over water and intersect the isobar of water vapor pressure over a solution saturated with citric acid [7]. The isotherms for nitric (HNO_3) and phosphoric (H_3PO_4) acids were plotted using experimental data, and the isotherm for $C_6H_8O_7$ is represented by a prognosis line *3* [6].

It should be noted that the water vapor pressures over solutions of nitric [8, 9] and phosphoric [6] acids are well represented in the literature and the calculated conditions of phase transformation are close to those found experimentally. It is possible that the prognosis data on the content of $C_6H_8O_7$ may be somewhat overestimated. However, these data also indicate that appearance of a more stable phase, $CaSO_4$ hemihydrate, is possible at 80–90°C at citric acid concentrations in the extraction solution exceeding 40%. At 100°C, occurrence of the dihydrate–hemihydrate phase transformation would be expected at a lower concentration of citric acid, which, according to some data [10], stabilizes calcium sulfate hemihydrate.

As already mentioned, the fact that citric acid is a foodstuff results in that it is difficult to use various control agents to affect the crystallization process. Therefore, the main way to control the crystallization process is to vary the temperature and concentration characteristics.

The quality of the forming $CaSO_4$ crystals is the most important characteristic of the crystallization process. The shape and size of calcium sulfate crystals formed in extraction determine the filtering properties of a layer of this material and, consequently, the efficiency of its washing. These parameters of the crystals depend on the temperature and acid concentration, extent and conditions of supersaturation elimination, and relative amounts of Ca^{2+} and SO_4^{2-} ions in solution.

The necessity for controlling the crystallization process predetermines the choice of specific schemes for introduction of raw materials, circulation solutions, and suspensions into the reaction mass, cooling of the reaction mass, and its separation into zones with different temperature and concentration characteristics. For example, with the temperature raised from 30 to 80°C, the length of gypsum crystals increases by a factor of 10–15, and their width, by a factor of 3–5.

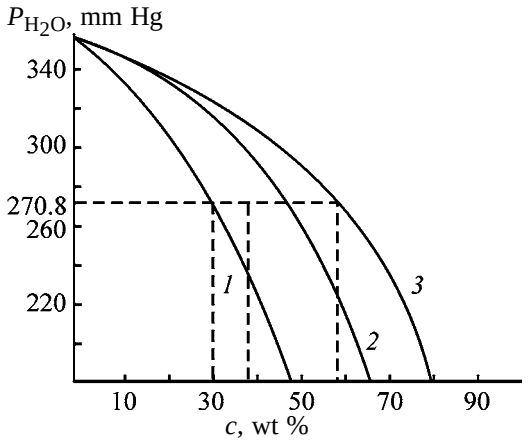

Fig. 1. Graphical illustration of how the acid concentrations are found for the dihydrate–hemihydrate equilibrium at 80°C. (P_{H_2O}) Water vapor pressure and (*c*) acid concentration. System: (*1*) $CaSO_4$–HNO_3–H_2O, (*2*) $CaSO_4$–H_3PO_4–H_2O, and (*3*) $CaSO_4$–$C_6H_8O_7$–H_2O.

Combined dihydrate–hemihydrate extraction techniques, in which calcium sulfate first crystallizes in the form of a metastable phase, $CaSO_4 \cdot 0.5H_2O$, and then transforms into a more stable phase, $CaSO_4 \cdot 2H_2O$, have been implemented, and they showed very good performance in manufacture of H_3PO_4.

As seen from Fig. 1, $CaSO_4$ must crystallize in the form of gypsum in extraction of citric acid under industrial conditions. However, hemihydrate is to be formed on raising the concentration to 55% and temperature to 90°C.

Isotherms–polybars of water vapor over H_2SO_4 solutions exhibit curvilinear behavior (Fig. 2*I* a). Now a polybar will be plotted for the dehydration reaction in the range from 60 to 100°C. The A_{60}–A_{100} line is the locus of points with equal water vapor pressures over gypsum in its conversion into the hemihydrate and over an acid solution. Owing to the relatively low $CaSO_4$ solubility in acid solutions [12], it is assumed that $CaSO_4$ has virtually no effect on the water vapor

Table 1. Parameters of equilibrium dehydration of gypsum into hemihydrate by reaction (1)

T, °C	$P_{H_2O(dehydr)}$, mm Hg [1]	Acid concentration, wt %		
		H_3PO_4	HNO_3	$C_6H_8O_7$
25	9.2	67	47	
60	96.1	56	43	73.5
80	294.7	44	28.5	60.0
90	477.9	33.3	19	–
100	733.4	3.4	2.5	7.0

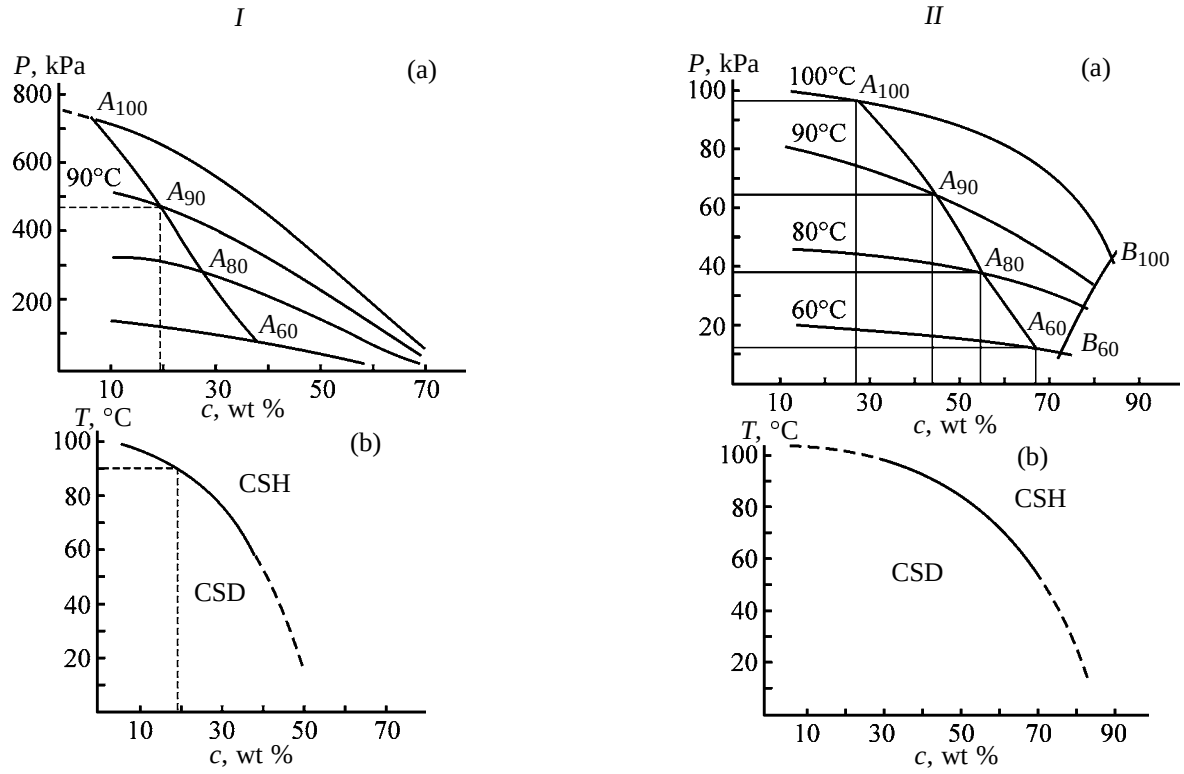

Fig. 2. Equilibrium parameters of gypsum dehydration into hemihydrate for solutions of (*I*) sulfuric and (*II*) citric acids: (*P*) water vapor pressure, (*c*) acid concentration, and (*T*) temperature. (a) Graphical method for determining gypsum dehydration parameters: temperature and acid concentration; (b) recommended line: locus of points corresponding to parameters of the CSD–CSH mutual transformations in acid solutions. CSD, calcium sulfate dihydrate $CaSO_4 \cdot 2H_2O$; CSH, calcium sulfate hemihydrate $CaSO_4 \cdot 0.5H_2O$.

pressure over a solution in water–acid systems. Plotting the A_{60}–A_{100} line on a graph of temperature against H_2SO_4 concentration yields a polythermal diagram of mutual transformations of calcium sulfate crystal hydrates in sulfuric acid (Fig. 2*II* b).

Whereas the concentration dependence of P_{H_2O} over solution has been described in sufficient detail [9], there are only two experimental points in each isotherm for $C_6H_8O_7$ solutions: water and saturated acid solution (Fig. 2*II* a, B_{60}–B_{100} line); the vapor pressure over citric acid solutions is calculated using the similarity theory. The reason for such a choice is the structural similarity of the molecules of both acids, i.e., three stages of dissociation of hydrogen ions, with the first constant K_1 at 25°C equal to 7.6×10^{-3} for phosphoric acid and 7.45×10^{-4} for citric acid [9].

Table 2. Calculated citric acid concentrations $c_{c.a}$ at which the water vapor pressure at 60°C is equal to the indicated water vapor pressure $P_{w.p}$ over phosphoric acid solution with indicated concentration $c_{p.a}$

$P_{w.p}$, kPa	$c_{p.a}$, %	$c_{c.a}$, %
19.62	10	13.2
18.97	20	26.4
17.80	30	39.7
16.04	40	52.6
13.67	50	66.1
12.39	55.6	73.5

Two expressions follow from the similarity theory [13]:

$$c'/c'' = C_c, \quad p'/p'' = C_p, \tag{2}$$

where c' is the $C_6H_8O_7$ concentration; c'', H_3PO_4 concentration; p', water vapor pressure over $C_6H_8O_7$ solution; p'', water vapor pressure over H_3PO_4 solution; C_c and C_p, similarity constants.

Taking the constant C_p to be unity, i.e., equating the water vapor pressures for both the acids, gives for the constant C_p at 60°C a value of 73.5/55.6 = 1.32, where 73.5 stands for the concentration of a saturated solution of $C_6H_8O_7$, and 55.6, for the corresponding concentration of an H_3PO_4 solution, at which the water vapor pressure over solution (12.39 kPa) is

equal to the water vapor pressure over a $C_6H_8O_7$ solution [7].

Using the resulting constant C_c, it is possible to calculate from data on H_3PO_4 [9] the corresponding concentrations for citric acid (Table 2). Thus, the calculated curve of water vapor pressure over a citric acid solution at 60°C is plotted (Fig. 2*II* a). Similar calculations for temperatures of 80, 90, and 100°C yield isotherms–polybars for $C_6H_8O_7$. The A_{60}–A_{100} line is the locus of points corresponding to equal water vapor pressures over gypsum in its conversion into hemihydrate and over a citric acid solution. Plotting the A_{60}–A_{100} line as a graph of temperature against $C_6H_8O_7$ concentration gives a calculated polythermal diagram describing mutual transformations of $CaSO_4$ crystal hydrates in $C_6H_8O_7$ (Fig. 2*II* b).

The prognosis calculations performed, combined with published data on solubility and phase transformations of calcium sulfate crystal hydrates in the systems $CaSO_4$–H_2SO_4–H_2O and $CaSO_4$–$C_6H_8O_7$–H_2O, make it possible to plot a polythermal diagram of mutual phase transformations $CaSO_4 \cdot 2H_2O \rightleftarrows CaSO_4 \cdot 0.5H_2O$ in citric–sulfuric acid solutions (Fig. 3).

Figure 3 shows isotherms connecting the points that correspond to the compositions of the sulfuric and citric acid solutions in which gypsum and calcium sulfate hemihydrate are in equilibrium at a given temperature. The short-dash lines represent isoconcentrates corresponding to mixtures of solutions containing equal amounts of $C_6H_8O_7$ and H_2SO_4. The intersection points of the isotherms and isoconcentrates characterize the composition of solutions in which gypsum and calcium sulfate hemihydrate are simultaneously in metastable equilibrium at a given temperature, i.e., the points at which the water vapor pressure over an acid solution and that of $CaSO_4 \cdot 2H_2O \rightleftarrows CaSO_4 \cdot 0.5H_2O$ dissociation are equal. The line with constant total concentration of $C_6H_8O_7$ + H_2SO_4, equal to 50%, intersects the isotherms of phase transformations at 60 and 80°C. Consequently, to the metastable equilibrium $CaSO_4 \cdot 2H_2O \rightleftarrows CaSO_4 \cdot 0.5H_2O$ at 60°C corresponds a solution containing 32% citric acid and 18% sulfuric acid. Gypsum must be more stable in solutions with a lower content of sulfuric acid, and hemihydrate, in those with higher content of H_2SO_4.

Thus, to obtain at the output of the extraction process a high concentration of citric acid, 50% and more at 80°C, and to ensure crystallization of gypsum, it is necessary to maintain the content of sulfuric acid in solution at a level not exceeding 1%. At H_2SO_4 content higher than 1%, crystallization of calcium sulfate hemihydrate or recrystallization of gypsum into hemihydrate may begin. Similarly, performing the process in the hemihydrate mode requires a ≥5% excess of sulfuric acid in order to prevent the process from passing to the range of joint crystallization of gypsum and hemihydrate, which may lead to formation of poorly filterable fine crystals.

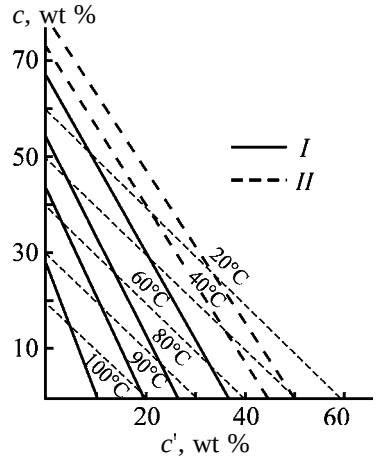

Fig. 3. Polythermal diagram of equilibrium transformations $CaSO_4 \cdot 2H_2O \rightleftarrows CaSO_4 \cdot 0.5H_2O$ in the system $CaSO_4$–H_2SO_4–$C_6H_8O_7$–H_2O: (*c*) citric acid concentration and (*c*') sulfuric acid concentration. (*I*) Isotherms of phase transformations and (*II*) compositions of solutions with constant total concentration.

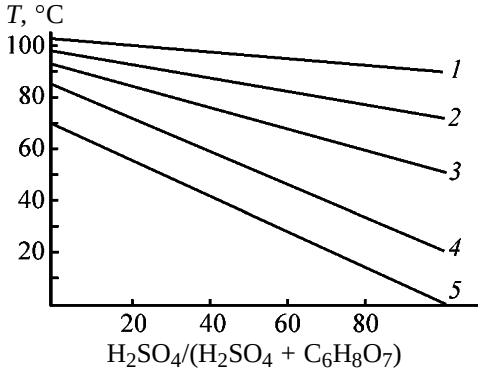

Fig. 4. Concentration ratio and total concentration of sulfuric and citric acids in solutions of the system $CaSO_4$–H_2SO_4–$C_6H_8O_7$–H_2O vs. temperature *T* of equilibrium transformations $CaSO_4 \cdot H_2O \rightleftarrows CaSO_4 \cdot 0.5H_2O$. [$H_2SO_4/(H_2SO_4 + C_6H_8O_7)$] Fraction of sulfuric acid in the total amount of acids. Total concentration of acids (%): (*1*) 20, (*2*) 30, (*3*) 40, (*4*) 50, and (*5*) 60.

The temperatures of phase transformations in solutions of sulfuric and citric acids can be calculated in the same way. As seen in Fig. 4, the temperature of equilibrium phase transformations depends linearly on

Table 3. Calcination of the calcium sulfate samples obtained

$c_{c.a}$, %	Amount of moisture, %, removed at indicated temperature, °C			Total amount of crystal hydrate water, %	Mass fraction	
	20–90	90–160	160–600		gypsum	hemihydrate
30	17.56	19.02	0.92	20.3	88.3	11.7
40	5.08	15.74	1.5	17.1	64.7	35.3
50	8.39	10.8	1.64	12.29	31.22	68.78
Reagent	0.26	19.98	0.89	20.7	93.7	6.3

the ratio of acids in the mixture. With increasing mass fraction of H_2SO_4, the temperature of the phase transition of gypsum into calcium sulfate hemihydrate becomes lower.

The extraction of citric acid from calcium citrate and hydrocitrate was studied, and the possibility of performing dihydrate–hemihydrate extraction was assessed.

A study of extraction from calcium citrate demonstrated that the crystallization of calcium sulfate always begins with the formation of hemihydrate crystals, which disappear by the middle of the process, at citric acid content not exceeding 50%, to give place to gypsum crystals. When the content of citric acid is raised to >50%, the extraction process begins in a similar way and a stable hemihydrate appears by the end of the process, with the amount of the hemihydrate the greater, the higher the content of the acid. In this case, crystals of calcium sulfate hemihydrate precipitate from the mother liquor several hours after its filtration.

Presumably, citric acid present in high concentration decelerates crystallization and recrystallization of calcium sulfate and phase transitions in this material, which results in that the extraction takes much longer time. Such an increase in the process duration may be technologically unacceptable. Attempts to make the extraction process shorter markedly impair the filtration characteristics.

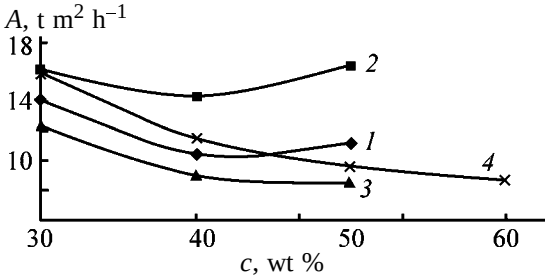

Fig. 5. Effect of a calcium sulfate seed on the throughput *A* of main filtration. (*c*) Content of citric acid. Decomposition of citrate: (*1*) without seed and (*2*) with seed; that of hydrocitrate: (*3*) without seed and (*4*) with seed.

When extraction is performed in the crystallization region of calcium sulfate hemihydrate, the throughput of the main filtration in terms of citric acid increases by a factor of 2, from 1.79 to 3.57 t $(m^2\ h)^{-1}$. Introduction of a seed (mixture of gypsum and hemihydrate, obtained in preceding experiments) improves the quality of hemihydrate crystals and also makes it possible to avoid formation of fine crystals. When the extraction process was carried out in the hemihydrate mode with a seed, the throughput of filtration increased to 4.81 t $(m^2\ h)^{-1}$.

Experiments on calcination of the resulting calcium sulfate samples at different temperatures confirmed that calcium sulfate is mainly present in the form of hemihydrate already at a citric acid content of 50%. For comparison, the results obtained in calcination of reagent-grade gypsum are presented (Table 3).

A study of the extraction of citric acid from calcium hydrocitrate ($CaC_6H_6O_7 \cdot 4H_2O$) under similar conditions demonstrated that mainly gypsum (up to 60%) crystallizes in the existence range of the hemihydrate in the presence of a seed. This may be due to a steeper, compared to the case of $Ca_3(C_6H_5O_7)_2 \cdot 4H_2O$, rise in the content of citric acid in solution in decomposition of $CaC_6H_6O_7 \cdot 4H_2O$; as already mentioned, concentrated citric acid decelerates mutual transformations of the crystal hydrates. Introduction of a seed (mixture of gypsum and an intermediate product, similar to that used in the preceding experiments) improves the crystallization of gypsum and stabilizes this material: no hemihydrate formation is observed. Gypsum exists, in the beginning, as a stable phase and then, with increasing content of $C_6H_8O_7$ in solution, becomes metastable, but is not dehydrated to hemihydrate. Citric acid exerts a stabilizing influence on the solid phase, irrespective of whether or not it is stable under the given conditions. The key factor in this case is what phase existed in the system previously.

Generalization of the data on the throughput of the main filtration reveals two well-pronounced dependences (Fig. 5).

In extraction of citric acid from calcium citrate, an extremum is observed at citric acid content of 40%, with the decrease and increase in throughput around the extremum being due to, respectively, an increase in viscosity and transition to the hemihydrate region of extraction.

In extraction from calcium hydrocitrate, no extremum is observed, since the process does not pass to the hemihydrate mode because of the stabilizing action of citric acid, and calcium sulfate precipitates in the form of gypsum.

On the basis of the experimental data obtained, a procedure for continuous extraction of citric acid from calcium citrate was proposed, together with ways to raise the concentration of the production acid after the extraction stage. It was established that citric acid lowers the rate of phase transformations, which is particularly noticeable at its contents exceeding 40%. In this case, the degree of decomposition of calcium citrate may decrease to 30%, thereby making greater the loss of the target product.

CONCLUSIONS

(1) In extraction of citric acid, calcium sulfate precipitates in conformity with the Ostwald rule first as a metastable crystal hydrate, which is then transformed into a more stable hydrate form; an excess amount of sulfuric acid also shifts the process to the region of joint crystallization of gypsum and the hemihydrate and markedly impairs the quality of the resulting crystals.

(2) Citric acid markedly decelerates hydration and dehydration of calcium sulfate. Gypsum was obtained in 60% citric acid at 90°C and did not undergo dehydration during 90 min of extraction. The lowest throughput of filtration is characteristic of the region with citric acid content ranging from 40 to 50%, i.e., the zone of joint crystallization of gypsum and calcium sulfate hemihydrate, which is confirmed by a prognosis calculation of the metastable equilibrium boundaries.

(3) A method for decomposition of calcium citrate in solution was developed, which makes it possible to carry out the extraction process itself in a homogeneous system. It was established that, at high content of the acid (>50%), calcium sulfate crystallizes predominantly in the form of the hemihydrate $CaSO_4 \cdot 0.5H_2O$.

REFERENCES

1. Smirnov, V.A., *Pishchevye kisloty (limonnaya, molochnaya, vinnaya)* (Foodstuff Acids (Citric, Lactic, Tartaric)), Moscow: Legkaya i Pishchevaya Prom–st., 1983.
2. Savchenko, N.I., Goma, I.G., Novotel'nova, N.Ya., *et al*., *Khlebopekar. Prom–st*., 1974, no. 3, pp. 27–28.
3. Kopylev, B.A., *Tekhnologiya ekstraktsionnoi fosfornoi kisloty* (Technology of Wet-Process Phosphoric Acid), Leningrad: Khimiya, 1981.
4. Pozin, M.E., Kopylev, B.A., and Zinyuk, R.Yu., in *Novye issledovaniya po tekhnologii mineral'nykh udobrenii: Sbornik "Khimiya"* (Advanced Research in Technology of Mineral Fertilizers: Coll. of Works "Chemistry"), 1970, pp. 14–18.
5. *Novye issledovaniya po tekhnologii mineral'nykh udobrenii* (Advanced Research in Technology of Mineral Fertilizers), Sarkits, L.A., Pozin, M.E., Kopylev, B.A., and Zinyuk, R.Yu., Eds., Leningrad: Khimiya, 1970, pp. 23–25.
6. Pozin, M.E. and Zinyuk, R.Yu., *Fiziko-khimicheskie osnovy neorganicheskoi tekhnologii: Uchebnoe posobie dlya vysshikh uchebnykh zavedenii* (Physicochemical Foundations of Inorganic Technology: Textbook for Higher School): St. Petersburg: Khimiya, 1993, 2nd ed., revised.
7. Kruif, C.G. de, Miltenburg, J.C. van, Sprenkels, A.J.J., *et al*., *Thermochim. Acta*, 1982, vol. 58, no. 3, pp. 341–354.
8. *Kompleksnaya azotnokislotnaya pererabotka fosfatnogo syr'ya* (Integrated Nitric Acid Processing of Phosphate Raw Materials), Gol'dinov, A.L., Kopylev, B.A., Abramov, O.B., and Dmitrevskii, B.A., Eds., Leningrad: Khimiya, 1982.
9. *Spravochnik khimika* (Chemist's Handbook), Nikol'skii, B.P., Ed., Moscow: Khimiya, 1985.
10. Singh, N.B. and Pandey, S.P., *Gypsum Lime*, 1990, no. 224, pp. 21–25.
11. Zdanovskii, A.B. and Vlasov, G.A., *Zh. Prikl. Khim*., 1971, vol. 44, no. 1, pp. 15–20.
12. Zinyuk, R.Yu., Pavlov, K.A., Pavlova, T.A., and Kovalenko, L.V., *Zh. Prikl. Khim*., 1997, vol. 70, no. 9, pp. 1570–1572.
13. Bretsznajder, S., *Wlasnosci gazow i cieczy*, Warsaw: Naukowo-Techniczne, 1962.

Russian Journal of Applied Chemistry, Vol. 76, No. 9, 2003, pp. 1414–1417. Translated from Zhurnal Prikladnoi Khimii, Vol. 76, No. 9, 2003, pp. 1454–1457.

SORPTION AND ION-EXCHANGE PROCESSES

Sorption Properties of Natural Aluminosilicates (Clay, Loam, Sandy Loam, Zeolite)

S. A. Evtyukhov and V. G. Berezyuk

Ural State Technical University, Yekaterinburg, Russia

Received May 22, 2002

Abstract—Sorption of Ni^{2+}, Cu^{2+}, Mn^{2+}, Fe^{3+}, and Cr^{3+} from model solutions with natural sorbents (clay, loam, sandy loam, zeolite) was studied. The optimal conditions of sorption were determined. The effect of pH and electrolytes on the sorption efficiency was studied.

A study of sorption properties of natural materials was performed with soil samples (clay, loam, sandy loam, zeolite) collected near Nizhni Tagil and Revda towns (Sverdlovsk oblast) in which the environmental situation is presently very bad. As zeolite sample we took clinoptilolite of the Kholinsk deposit (Buryatia). The compositions of aluminosilicates studied were as follows (SiO_2 and Al_2O_3, wt %): clinoptilolite 65.7 and 11.5; clay 70.1 and 18.2; loam 65.8 and 24.3; and sandy loam 86.8 and 5.6, respectively. Estimation of the sorption power of soils would allow prediction of the danger of groundwater pollution with metals from sewage percolating through soils and monitoring of the features of sorption processes in such technologies as underground and heap leaching [1, 2].

Sorption was studied under static conditions by the method of separate samples. A sorbent sample (m_s, g) was immersed in 100 ml of a model solution with a known metal concentration, and the mixture was agitated with a shaker. The time in which the sorption equilibrium was attained was determined in preliminary experiments. As a rule, the time of contact of the sorbent and solution was no more than 30 min. The required pH was adjusted with 1 N H_2SO_4 or 0.1 N NaOH. The completeness of metal recovery was monitored by the standard methods [3]. Sorption of metal ions was performed with both nonfractionated and fractionated zeolite. The 0.5–1.5-mm fraction proved to be optimal.

To choose metal ions that make the major contribution to the groundwater pollution in the region in question, we collected information on the quantitative and qualitative composition of sewage from industrial plants. The typical pollutants are copper, nickel, manganese, and iron compounds, bichromates, sulfates, and oil products. A study of leaching of clay, loam, and sandy loam in various media showed that the main metal pollutants of the groundwater are Ni^{2+}, Cu^{2+}, Fe^{3+}, and Cr^{3+}. In our experiments, we used $NiSO_4$, $CuSO_4$, $MnSO_4$, $NH_4Fe(SO_4)_2$, $KCr(SO_4)_2$, Na_2SO_4, $Cd(NO_3)_2$, and $Al_2(SO_4)_3$.

The sorption efficiency was estimated by the process time t and degree of metal recovery from the solution S (%):

$$S = (C_{in} - C_{eq}) \times 100/C_{in},$$

where C_{in} and C_{eq} are the initial and equilibrium metal concentration, respectively, mg l^{-1}.

The data were treated by standard methods [4].

The sorption efficiency substantially depends on pH. The effect of pH was studied within the pH range 0.7–8.5. The results are shown in Figs. 1 and 2. In acidic media (pH < 3.0–3.5), the recovery of all the metals studied decreases because of the competitive effect of the acid. At pH > 4.0–4.5, hydrolyzed metal species are formed, which are well sorbed with the sorbent (the recovery with zeolite reaches 98–99.5% and with soils, 65–85%).

Sorption of Ni(II) reaches 98% (pH > 4.0); that of Cu(II), 99.5% (pH > 5.5); and that of Fe(III), 75% (pH ~ 3.0) and more than 90% (pH > 7.5).

Chromium can exist in solution as Cr^{3+} (in acid medium), as hydroxo complexes, or as chromate or bichromate ions [5]; its behavior is rather complex. In neutral and weakly alkaline media, Cr^{3+} is hydrolyzed to chromium(III) hydroxide. The recovery of Cr^{3+} amounts to 96–97% at pH > 2.9.

The recovery of Mn is affected by the features of conversion of manganese compounds into MnO_2

1070-4272/03/7609-1414$25.00

(90% recovery is reached in neutral solutions). The maximum of Cu(II) sorption was 63% on sandy loam, 80–83% on clay and loam, and 87% on zeolite . At larger amounts of the sorbent, the sorption maximum shifts to the acid region. The static capacity of clinoptilolite (g kg^{-1}) was determined to be 1.71 for Ni(II), 1.59 for Cu(II), 0.61 for Cr(III), 1.95 for Fe(III), and 2.31 for Mn(II).

Let us perform the quantitative treatment of the experimental data for Cu(II) assuming that copper sorption with natural sorbents proceeds by the ion-exchange mechanism. Ion exchange in soils was discovered more than 150 years ago. Now, the sorption is considered as the main mechanism of interaction of heavy metals with inorganic components of soils [2]. Heavy metals form with clay minerals both exchangeable and nonexchangeable species.

The ion-exchange equilibria are often described by the equations derived from the law of mass action [6]:

$$\log\varepsilon = A - (Z_1/Z_2)\log a_s, \quad (1)$$

where ε is the distribution coefficient of Cu(II) between the sorbent and solution [i.e., $S/(1 - S)$, where S is the degree of Cu(II) recovery from the solution]; Z_1 and Z_2 are charges of the copper ion and competing cation, respectively; a_s is the activity of the competing cation in the solution; and A is the constant depending on the concentration of electrolyte cations in the solid phase, exchange constant, and activity coefficients of the ion being recovered and the competing ion in the solid phase and solution. This equation is general for all cases of the ion exchange. When the sorption indeed occurs by ion exchange, the $\log\varepsilon$–$\log A_s$ dependence is a straight line with the slope equal to Z_1/Z_2, i.e., to the ratio of the real charges of the exchanging ions.

When the competing ion is hydrogen ion, Eq. (1) transforms into

$$\log\varepsilon = B + Z\text{pH}, \quad (2)$$

where Z is the charge of the cation being recovered and B is the constant similar to constant A for the case of the presence of hydrogen ions as the only competing ions in the system.

The pH dependences of copper sorption, shown in Fig. 2, were treated by Eq. (2), and the Z values obtained are listed in Table 1.

Table 1 shows that the experimental data are described by curves with two linear sections and a bend

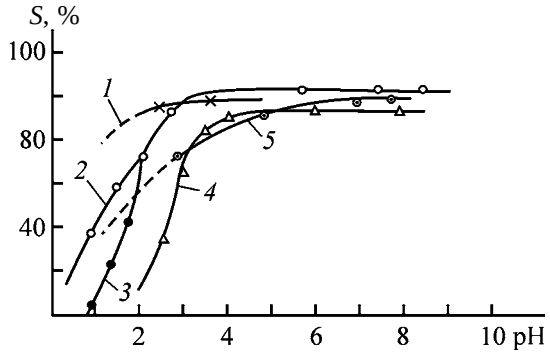

Fig. 1. Degree of metal sorption on clinoptilolite as a function of pH. C_M = 50 mg l^{-1}, m_s = 10 g, t = 30 min. (*S*) Degree of metal sorption from solution; the same for Fig. 2. (*1*) Cr^{3+}, (*2*) Cu^{2+}, (*3*) Ni^{2+}, (*4*) Mn^{2+}, and (*5*) Fe^{3+}.

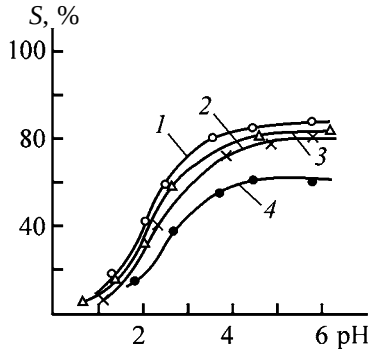

Fig. 2. Degree of Cu^{2+} sorption on natural sorbents as a function of pH. C_{Cu} = 100 mg l^{-1}, m_s = 5 g, t = 30 min. (*1*) Zeolite, (*2*) clay, (*3*) loam, and (*4*) sandy loam.

at pH 2.3–2.5. Within the pH range 0.7–2.3, the Z values are close to 1. In this case, the equivalent exchange of Cu^{2+} with Ca^{2+}, Mg^{2+}, Mn^{2+}, and other cations can occur. When copper exists as single-charged complex ions $CuCl^+$, $CuOH^+$, $CuHCO_3^+$, etc., the equivalent exchange of these ions with H^+ ion is possible.

Within the pH range 2.5–5.5, the $\log\varepsilon$–pH dependence remains linear, but in this case the other proc-

Table 1. Angular coefficients Z of Eq. (2) in sorption of Cu(II)

Sorbent	Z for indicated pH range	
	0.7–2.3	2.5–5.5
Zeolite	0.94	0.34
Clay	0.91	0.28
Loam	0.81	0.39
Sandy loam	0.72	0.25

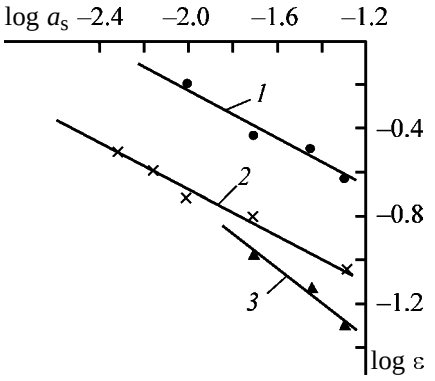

Fig. 3. Coefficients of Cu(II) distribution between clay and solution as a function of activity of competing salt cations in sorption. (ε) Coefficient of Cu(II) distribution between clay and solution and (a_s) activity of competing cations in the solution. (*1*) Na_2SO_4, (*2*) $Cd(NO_3)_2$, and (*3*) $Al_2(SO_4)_3$.

esses are superimposed on the ion-exchange mechanism such as hydrolysis of copper and other metals; the amount of H^+ ions in the system decreases, and copper complex species with the total fractional charge are formed. The contribution of the chemisorption to the interaction of copper cation with natural sorbents also increases.

We also studied the effect of Na_2SO_4, $Cd(NO_3)_2$, and $Al_2(SO_4)_3$ on the sorption Cu(II) at pH 2.25–2.31, when the interaction of Cu^{2+} with the sorbents follows the ion-exchange mechanism. The salt concentration range was 0.005–0.05 M. The experiments showed that the presence of a competing electrolyte in the solution decreases the Cu^{2+} sorption. The experimental data were treated by Eq. (1). The results are shown in Fig. 3 and Table 2. The dependences in Fig. 3 are straight lines, in accordance with assumption on ion-exchange character of interaction of Cu^{2+} with natural sorbents. As seen, suppression of Cu^{2+} sorption with cations increases in the order Na^+ < Cd^{2+} < Al^{3+}. This indicates that the competing effect of the cations added is the stronger, the higher their charge and the smaller their radius.

Table 2. Angular coefficients Z_1/Z_2 of Eq. (1) in sorption of Cu(II)

Sorbent	Salt	Z_1/Z_2
Zeolite	Na_2SO_4	0.53
	$Cd(NO_3)_2$	0.67
	$Al_2(SO_4)_3$	0.42
Clay	Na_2SO_4	0.57
	$Cd(NO_3)_2$	0.45
	$Al_2(SO_4)_3$	0.66
Loam	Na_2SO_4	0.50
	$Cd(NO_3)_2$	0.65
	$Al_2(SO_4)_3$	1.10
Sandy loam	Na_2SO_4	0.44
	$Cd(NO_3)_2$	0.55
	$Al_2(SO_4)_3$	0.75

Figure 2 shows that, in the presence of aluminum sulfate, the exchange between Cu^{2+} and Al^{3+} is approximately equivalent ($Z_1 : Z_2 = 2 : 3$) only for clay. In the other cases, the equivalent exchange was not observed. In accordance with the law of mass action, an increase in salt concentration leads to a decrease in the Cu(II) sorption in the case of ion exchange. When the electrolyte concentration in the solution increases, the ions undergo dehydration to a growing extent and, as a result, the nature of the ions involved in the ion exchange changes. In the process, the exchange "constant" is variable and depends on the degree of hydration (it increases with a decrease in the degree of hydration of ions). Thus, in the case of ion-exchange type of interaction between copper ion and the sorbent, an increase in the ionic strength of the solution, on the one hand, decreases this interaction because of competition and, on the other hand, increases interaction because of the corresponding increase in the exchange constant as a result of the cation dehydration. The real result is the sum of both processes. Such readily interpretable factor as the degree of hydration, which characterizes the deviation of the system with ion exchange from the ideal behavior, is used for a long time to explain the experimental results [7].

Under the experimental conditions (Table 2), the effect of competition of the electrolyte ions prevails over the effect their dehydration; as a result, the dependence

$$\log \varepsilon = f(\log a_s) \quad (Z_1/Z_2 \cong 0.4-0.6).$$

becomes flatter.

A decrease in the degree of hydration of ions with an increase in the electrolyte concentration results in a change in the order of sorbability, which is reflected in the Z_1/Z_2 value (Table 2). As the sorption conditions, e.g., acidity or sorbent mass, are varied, the features of the ion-exchange interaction (i.e., the ratio of charges of exchanging species Z_1/Z_2) change, and under definite conditions Z_1/Z_2 reaches the theoretical value. Thus, equations derived from the law of mass action are valid for ion-exchange sorption of Cu(II) with natural sorbents.

CONCLUSIONS

(1) Optimal conditions of sorption of Ni(II), Cu(II), Mn(II), Fe(III), and Cr(III) on clinoptilolite (95–99% recovery), and Cu(II) compounds on soils (sandy loam, loam, and clay; 77–96% recovery) were found.

(2) The equations derived from the law of mass action well describe the dependence of Cu(II) distribution between the sorbent and solution on the concentration of competing components (acid, salt).

REFERENCES

1. Rybakov, Yu.S., in *Upravlenie vodnykh khozyaistv Rossii* (Management of Water Industry of Russia), Yekaterinburg: Ross. Nauchno-Issled. Inst. Vodnogo Khozyaistva, 1993, pp. 61–63.
2. Korolev, V.A., *Ochistka gruntov ot zagryazneniya* (Decontamination of Soils), Moscow: Nauka, 2001.
3. Lur'e, Yu.Yu., *Analiticheskaya khimiya promyshlennykh stochnykh vod* (Analytical Chemistry of Industrial Sewage), Moscow: Khimiya, 1984.
4. Tikhonov, A.N. and Ufimtsev, M.V., *Statisticheskaya obrabotka rezul'tatov eksperimentov* (Statistical Treatment of Experimental Results), Moscow: Mosk. Gos. Univ., 1988.
5. Glinka, N.L., *Obshchaya khimiya* (General Chemistry), Moscow: Integral, 2002.
6. Berezyuk, V.G. and Evtyukhov, O.V., *Flotatsiya radionuklidov* (Flotation of Radionuclides), Yekaterinburg: Ural. Univ., 1993.
7. *Ionnyi obmen i ego primeneniya* (Ion Exchange and Its Applications), Chmutov, K.V., Ed., Moscow: Akad. Nauk SSSR, 1959.

Russian Journal of Applied Chemistry, Vol. 76, No. 9, 2003, pp. 1418–1422. Translated from Zhurnal Prikladnoi Khimii, Vol. 76, No. 9, 2003, pp. 1458–1462.

SORPTION AND ION-EXCHANGE PROCESSES

Adsorption of $Zn(OAc)_2$ from Aqueous Solutions on the Surface of Activated Carbons Modified with Acetic Acid

Hoang Hyu Bin', H. J. Abanto-Chavez, I. A. Kozhemyakina, Hoang Kim Bong, and O. N. Temkin

Lomonosov Moscow State Academy of Fine Chemical Technology, Moscow, Russia

Received August 4, 2003

Abstract—Adsorption of zinc acetate on the surface of activated carbons modified with acetic acid was studied as a function of the process temperature, initial concentration of the salt, and pH of the initial solution.

Studies of adsorption of zinc acetate from aqueous solutions on the surface of HNO_3-treated activated carbons under conditions of solution circulation with a linear velocity of 12–15 cm s^{-1} through a fluidized bed of the support showed that the adsorption process in the dynamic mode substantially differs from that in the static mode [1, 2]. The dependences of the amount of adsorbed zinc acetate on the process temperature and velocity of solution circulation pass through extrema. The sorption catalysts obtained [2, 3] demonstrated high activity in the synthesis of vinyl acetate [4, 5]. The activity and stability in time of the catalysts prepared in the extreme mode of repeated cyclic changes of the synthesis temperature (175–205–230°C) [4] exceeded the parameters of the commercial catalyst produced by Montecatini Company (MAVC) [4].

The study of other methods of modification of activated carbons (AC) showed that oxidation with hydrogen peroxide and treatment with dilute acetic acid at elevated temperatures give similar results. The technological simplicity of the latter method makes it attractive for commercial production of catalysts of vinyl acetate synthesis.

EXPERIMENTAL

Activated carbon (AGN-2) taken as 1–3-mm particles was dried at 260–280°C and treated with 2–3 wt % acetic acid at the solution to activated carbon volume ratio of 3 : 1. The solution was continuously fed through an AC layer in the reactor for 120 min by a circulation pump at a velocity V = 6–7 cm s^{-1} at 60 ± 5°C. Then, carbon was filtered and heated at 90–95°C for 2 h. The AGN-2 parameters before and after treatment are listed in Table 1.

The catalyst was prepared under conditions of circulation of the zinc acetate solution in alternating directions (from top to bottom and vice versa) and at various solution flow velocities (within the 12–31 cm s^{-1} range). 12 cm^3 of carbon was weighed on an analytical balance and placed in a reactor. The reactor was a glass tube with filters from both sides to restrict displacement of the carbon. Then, the zinc acetate solution was circulated through a mobile carbon bed using circulation pump. The velocity of the solution flow through the reactor was monitored with a rheometer. The variation of the concentration in time was determined by a differential interferometric method. The measurement error was 5%. The best results were obtained at V = 15 cm s^{-1} as in [2, 4]. The catalyst was prepared at 25–85°C.

The specific surface area and the volume and distribution of pores of the supports and catalysts were determined from the adsorption isotherms of vapors of C_6H_6, CH_3COOH (25°C), and liquid nitrogen (78 K) at the initial pressure of 10^{-5}–10^{-6} mm Hg. Adsorption was performed by the method described in [6]. The specific surface area was calculated by the BET

Table 1. Parameters of the pore structure of AGN-2 (AGN-3) activated carbon before and after treatment with acetic acid

Methods of AGN-2 treatment	V_Σ	V_{macro}	V_{meso}	V_{micro}	S_{sp} for C_6H_6, m^2 g^{-1}
	cm^3 g^{-1}				
Initial	0.630	0.275	0.040	0.315	870.5
After treatment with acetic acid	0.638	0.281	0.049	0.308	868.7

1070-4272/03/7609-1418$25.00

method. The differential curves of pore size distribution were calculated from the data of adsorption of CH_3COOH vapor by the Kelvin–Kiselev equation [7].

The catalyst activity was determined in a flow reactor (for details, see [4, 8]) at 175, 205, and 230°C at a constant space velocity of the C_2H_2 + CH_3COOH + N_2 mixture (volume ratio C_2H_2 : CH_3COOH : N_2 = 4 : 1 : 1) of 4.2 h^{-1}.

The comparison of the characteristics of the initial activated carbon AGN-2 and that treated with acetic acid (Table 1, Fig. 1) shows that the pore structure of AC weakly changes after the treatment. The mesopores are somewhat widened, and their volume slightly increases (in Fig. 1, the peak heights and areas increase, and a third peak appears).

The shape of the adsorption kinetics curves at the initial concentration c_0 = 13.5 wt % and temperatures of 25 and 50°C (Fig. 2a, curves *1*, *2*) indicates that the adsorption process is complex, including monomolecular and polymolecular adsorption. An abrupt increase in the concentration of the adsorbed salt, followed by a new plateau, is observed in all the kinetic curves of $Zn(OAc)_2$ adsorption from aqueous solutions at c_0 = 13.5 wt % and 25–50°C after 80–90 min. Interaction of carbon with water is weak [in aqueous solutions of $Zn(OAc)_2$], since carbon is hydrophobic. This fact complicates penetration of the hydrated $Zn(OAc)_2$ molecules from aqueous solution into the carbon interlayer space, the more so as the size of $Zn(OAc)_2$ molecules and particularly of their associates is relatively large for micro- and supermicropores. With time, the surface is gradually coated with a monolayer of zinc acetate associates. After formation of such a layer, the adsorption accelerates (after 80–90 min), and polymolecular adsorption occurs with formation of several layers of the active component as a result of intermolecular interactions. This hypothesis accounts for the most important characteristics of both types of curves of $Zn(OAc)_2$ (Fig. 2) and acetic acid adsorption on activated carbons.

It should be noted that, at a higher zinc acetate concentration (19.6 wt %) and 25–50°C (Fig. 2b, curves *1*, *2*), no inflection was observed. The adsorption reaches a plateau within 60 min, and the plateau lies substantially higher than for the concentration of 13.5 wt %. At higher salt concentrations, the steps of monomolecular and polymolecular adsorption coalesce. At 75°C (Figs. 2a, 2b, curves *3*), maxima appear in the kinetic curves, probably due to the fact that the rapidly sorbed species of zinc acetate (associates, colloidal particles) increase the concentration of the adsorbed salt above the equilibrium concentration. With time, these species again pass into the solution, and the adsorption equilibrium is attained.

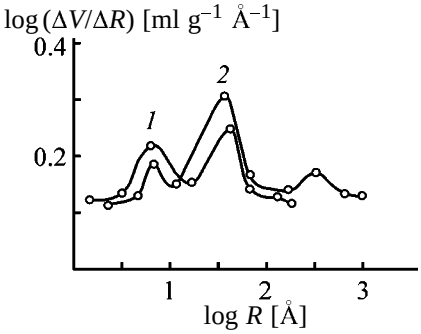

Fig. 1. Differential curves of pore volume distribution in size, $\log(\Delta V/\Delta R)$ vs. $\log R$, for activated carbon AGN-2, plotted from the isotherms of benzene vapor adsorption: (*1*) before treatment and (*2*) after treatment with 10% CH_3COOH.

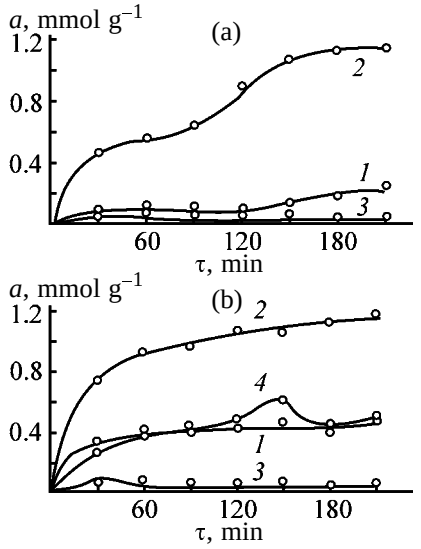

Fig. 2. Variation with time τ of zinc acetate adsorption a from aqueous solutions with CH_3COOH-treated AC at V = 15 cm s^{-1}. T (°C): (*1*) 25, (*2*) 50, and (*3*) 75; (*4*) initial AGN-2. Initial concentration of zinc acetate c_0 (%): (a) 13.5 and (b) 19.6.

The comparison of the kinetic curves of zinc acetate adsorption at 50°C and salt concentration in the solution of 19.6 and 13.5 wt % on activated carbons treated with acetic acid and untreated shows that adsorption in 60 min on treated carbons is substantially (by a factor of 2.5) greater (Fig. 2b, curves *2*, *4*), and the total amount of the adsorbed salt is two times greater (in 2 h at c_0 = 19.6 wt %).

Within the 25–85°C temperature range, the temperature dependence of the amount of the salt adsorbed on carbons treated with acetic acid passes through a pronounced maximum (Fig. 3). The amount of the acetate adsorbed reaches a maximum at 50°C.

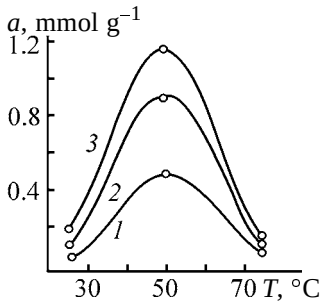

Fig. 3. Adsorption of $Zn(OAc)_2$ a from aqueous solutions on activated carbons treated with acetic acid as a function of temperature of catalyst application T. c_0 = 19.6 wt %, V = 15 cm s^{-1}. τ (min): (*1*) 30, (*2*) 120, and (*3*) 210.

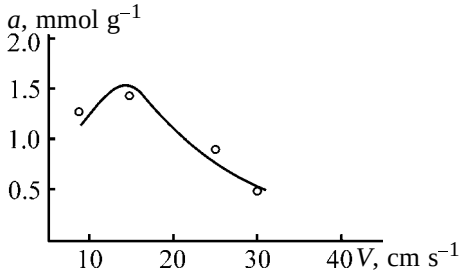

Fig. 4. Limiting adsorption capacity of $Zn(OAc)_2$ a on AGN-2 activated carbon treated with acetic acid as a function of velocity of solution circulation V. T = 50°C, c_0 = 19.6 wt %, pH_{init} 5.6, adsorption time 240 min.

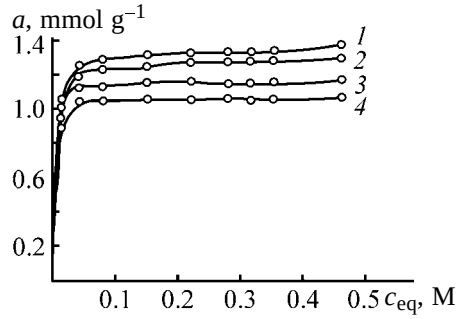

Fig. 5. Isotherms of $Zn(OAc)_2$ adsorption a on AGN-2 activated carbon treated with acetic acid. (c_{eq}) Salt equilibrium concentration. T = 50°C, c_0 = 19.6 wt %, V = 15 cm s^{-1}. pH_{init}: (*1*) 5.6, (*2*) 3.3, (*3*) 8.7, and (*4*) 13.

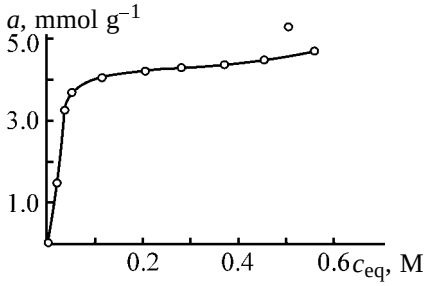

Fig. 6. Isotherm of acetic acid adsorption a on AGN-2 activated carbon at 50°C. (c_{eq}) Acetic acid equilibrium concentration; the same for Fig. 8.

Similar temperature dependences were observed previously for zinc acetate adsorption on the AC surface treated with nitric acid [2, 5] and for mercury chloride adsorption on AC [6, 9]. The dependence of the limiting adsorption capacity for zinc acetate on the velocity of the salt solution circulation also passes through a maximum (Fig. 4), which is attained at the velocity of 15 cm s^{-1}. This velocity was used when studying the temperature (Figs. 1, 3) and pH (Fig. 5) dependences of adsorption. All the isotherms of zinc acetate adsorption within the pH range 2.9–13 correspond to the Langmuir type (Fig. 5). Unexpectedly, the pH dependence of the adsorption capacity passes through a maximum (a_{max} at pH 5.6).

The study of the adsorption of acetic acid at 50°C showed (Fig. 6) that the adsorption capacity for the acid exceeds by a factor 2–3 the maximal capacity for zinc acetate (Fig. 6). Since a substantial part of acetic acid, apparently, exists on the AC surface at the temperature of catalyst drying (90–95°C) in the adsorbed state, the maximum in the pH dependence of the limiting capacity for $Zn(OAc)_2$ can be explained by preferred adsorption of neutral salt species or associates with formation of the surface complexes $H[Zn(OAc)_3]$. Adsorption of such complexes at pH 2.9 (additions of acetic acid) is lower, while increase in the pH above 8 eliminates the adsorbed acid from the AC surface, which also decreases the limiting capacity for zinc acetate. The salt species that are hydrolyzed at pH > 8 are neutralized by the desorbed acetic acid:

$$AcOH_{ads} + [Zn(OAc)(OH)] \rightleftarrows Zn(OAc)_2 + H_2O. \quad (1)$$

Therefore, pH of the solution (in the range of pH > 8) does not change in the course of adsorption. Adsorption of neutral $Zn(OAc)_2$ species at pH < 5 also does not change pH of the solution in time.

Adsorption of the neutral species is not probably single adsorption process. The maximum in the temperature dependence suggests the occurrence of the endothermic processes (decomposition of associates, ion exchange with surface acidic groups) increasing the adsorption capacity within the 25–50°C temperature range. Within this temperature range, the contribution of hydrolysis also increases [formation of Zn(OAc)(OH) and the other species]. Probably, the constancy of pH during adsorption is explained by adsorption of hydrolyzed species at simultaneous binding of acetic acid with the AC surface, i.e., by reaction (1).

Within the 25–75°C temperature range, the temperature dependence of the specific surface area S_{sp}

Table 2. Parameters of catalysts supported on CH_3COOH-treated AGN-2 activated carbon found from adsorption of acetic acid vapor

Catalyst	T, °C	Amount of adsorbed salt,* mmol g^{-1}	Porosity**					S_{sp}, $m^2\ g^{-1}$, for acetic acid	$\nu = \Gamma_{VA}/(l\ h)$ (activity) at 230°C
			W_0^Σ	W_0^1	W_0^2	$B_1 \times 10^6$	$B_2 \times 10^6$		
			$cm^3\ g^{-1}$						
U_0	50	0.078	0.425	0.284	0.141	3.134	6.493	327.5	62.4
U_1	25	0.647	0.154	0.083	0.071	1.460	7.76	66.2	93.6
U_2	50	1.235	0.206	0.110	0.096	2.603	6.65	168.1	163.3
U_3	75	0.135	0.157	0.095	0.062	1.986	8.67	74.37	107.6
U_4	85	0.105	0.105	0.060	0.045	1.043	9.05	52.8	72.8

* Amounts of adsorbed salt at the initial concentration of 19.6 wt% and adsorption time of 4.5 h are presented. U_0 is the catalyst prepared by supporting $Zn(OAc)_2$ aqueous solution on the initial AGN-2 AC.
** Parameters of the Dubinin–Radushkevich equation.

has a maximum at 50°C (Fig. 7); upon adsorption, S_{sp} of AGN-2 decreases from 900 to 168 $m^2\ g^{-1}$.

It should be noted that the pretreatment of the support with acetic acid is the main factor determining the amount of the adsorbed salt and the surface area; the presence of the acid is important specifically in the instant of adsorption. Under optimal temperature conditions of salt application (50°C) and pH 5–6, both the specific surface area of the catalyst and its activity in the vinyl acetate synthesis are maximal (Table 2) and substantially exceed these parameters for the support untreated with the acid. It follows from Table 2 that the total volume of the catalyst pores W^Σ and S_{sp} (Fig. 7) pass through a maximum at 50°C; in spite of a large amount of the salt adsorbed, this indicates more uniform distribution of the salt under these conditions, providing very large specific surface area of the catalyst.

As seen from Fig. 8, at the $Zn(OAc)_2$ equilibrium concentration $c_{eq} < 0.45$ M, all the adsorption isotherms are of the Langmuir type, i.e., the equilibrium adsorption is formation of a monolayer. With increasing c_{eq}, the adsorption passes through a maximum, and the adsorption isotherms acquire a previously unknown shape.

At $c_{eq} < 0.4$ M, the adsorption isotherms are described by the equation

$$a = \frac{a_\infty b_i c_{eq}}{1 + b_i c_{eq}}, \qquad (2)$$

where a_∞ is maximal content of $Zn(OAc)_2$ in the AC unit weight after impregnation (mmol g^{-1}); a, adsorption (mmol g^{-1}); c_{eq}, equilibrium concentration of the salt in the solution (M); and b_i, adsorption constant.

The b_i values are 2.18×10^{-3}, 6.40×10^{-3}, and 1.85×10^{-3} at 25, 50, and 75°C, respectively, having a maximum at 50°C.

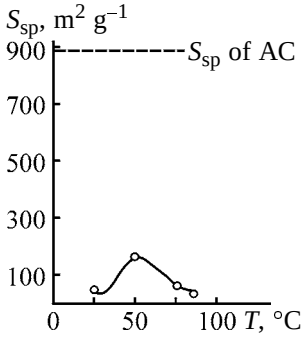

Fig. 7. Specific surface area S_{sp} of the catalyst as a function of the temperature of $Zn(OAc)_2$ application T from aqueous solutions on AGN-2 activated carbon treated with acetic acid.

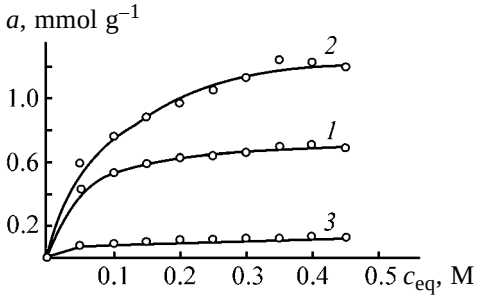

Fig. 8. Isotherm of $Zn(OAc)_2$ adsorption from aqueous solutions on AGN-2 activated carbon treated with acetic acid. Application temperature (°C): (*1*) 25, (*2*) 50, and (*3*) 75.

CONCLUSIONS

1. The study of the adsorption power of CH_3COOH-treated AC with respect to zinc acetate showed that the amount of the adsorbed salt, specific surface area, and catalytic activity in the synthesis of vinyl acetate pass through maxima at the temperature of zinc acetate application of 50°C.

2. The adsorption capacity of CH_3COOH-treated AC at 50°C passes through a maximum at pH 5–6.

3. The adsorption isotherms of zinc acetate on AC treated with acetic acid do not follow the Langmuir law.

REFERENCES

1. Hoang Kim Bong, Fomiteva, T.V., Shestakov, G.K., and Temkin, O.N., *Zh. Prikl. Khim.*, 1997, vol. 70, no. 11, pp. 1782–1786.
2. Hoang Kim Bong, Nyrkova, A.N., Abanto-Chavez, H.J., *et al.*, *Zh. Prikl. Khim.*, 1997, vol. 70, no. 12, pp. 1960–1967.
3. Kheifets, L.I., Neimark, A.V., and Fenelonov, V.B., *Kinet. Katal.*, 1979, vol. 20, no. 3, pp. 760–767.
4. Hoang Kim Bong, Abanto-Chavez, H.J., Shestakov, G.K., *et al.*, *Zh. Prikl. Khim.*, 1998, vol. 71, no. 1, pp. 92–98.
5. Hoang Kim Bong, Temkin, O.N., and Kurlyandskaya, I.I., Abstracts of Papers, *V Int. Conf. "High Technology,"* Yaroslavl, May 19–21, 1998, pp. 95–97.
6. Hoang Kim Bong, Temkin, O.N., and Chobanu, M.M., *Zh. Prikl. Khim.*, 1989, vol. 62, no. 6, pp. 1247–1250.
7. Kiselev, A.V., *Prakticheskie raboty po adsorbtsii i gazovoi khromatografii* (Practical Works on Adsorption and Gas Chromatography), Moscow, 1968.
8. Abanto-Chavez, H.J., *Cand. Sci. (Chem.) Dissertation*, Moscow, 1998.
9. Hoang Kim Bong and Temkin, O.N., *Proc. I Int. Conf. on Activated Carbon*, Berlin, 2000, pp. 532–534.

Russian Journal of Applied Chemistry, Vol. 76, No. 9, 2003, pp. 1423–1426. Translated from Zhurnal Prikladnoi Khimii, Vol. 76, No. 9, 2003, pp. 1463–1466.

SORPTION AND ION-EXCHANGE PROCESSES

Preparation and Characteristics of a Cation Exchanger Based on Oxidized Anthracite

N. V. Sych, N. T. Kartel', and M. F. Kovtun

Institute of Sorption and Endoecological Problems, National Academy of Sciences of Ukraine, Kiev, Ukraine

Received October 28, 2002; in final form, July 2003

Abstract—The features of anthracite oxidation as influenced by temperature and time were determined. Physicochemical and sorption characteristics of the resulting cation exchanger were studied.

Many sorts of natural coals, similar to activated coals, exhibit cation-exchange characteristics, which can be enhanced by oxidative and thermal treatment [1–4]. Oxidation of ordinary activated coals at heating to 400–450°C in air yields so-called oxidized coals [1, 5] having a pronounced capability for selective ion exchange owing to the presence of surface acidic groups substituting metal cations for hydrogen ions. They are also capable to form surface complexes with metal ions and are catalytically active in some reactions. These characteristics can be efficiently used for thorough purification of process solutions, selective recovery and concentration of impurities [6], and production of high-purity substances.

It was of interest to study the possibility of production of cation exchangers based on anthracite, cheap natural coal with inexhaustible resources, high content of carbon, and low ash content.

The goal of this work was to determine the optimum temperature–time conditions of anthracite oxidation and to study physicochemical and sorption characteristics of the resulting cation exchanger.

Experiments were performed with anthracite of the A type,[1] crushed to particles with the size of 0.5–3.0 mm.

Initially anthracite was activated with steam at 850°C to the burn-out of 20, 40, and 60%. The resulting samples were oxidized in humid air at 270, 320, and 370°C to 20–30% burn-out. To estimate the efficiency of oxidation of activated anthracite, the initial (fossil) coal was also subjected to oxidation.

During oxidation, the burn-out was determined at certain time intervals, and the static exchange capacity (SEC) was determined.

In some cases, we measured pH values of oxidized samples and the volume of sorption pores with respect to benzene and methanol [7], studied the sorption activity with respect to iodine and methylene blue (MB), measured the specific surface area S_{sp} with respect to argon, and analyzed oxygen-containing groups by titration with bases of various strength (Boehm method) [8]. According to this method, the total content of oxygen-containing carboxy and phenolic groups was determined from sorption of 0.1 N NaOH solution, the content of weakly and strongly acidic groups, from sorption of 0.1 N Na_2CO_3 solution, and the content of strongly acidic carboxy groups, from sorption of 0.1 N $NaHCO_3$ solution. The content of phenolic and weakly acidic carboxy groups was determined from the corresponding difference in the SEC values.

It is well known [3] that the exchange capacity of a carbon cation exchanger is affected by the chemical nature of the raw material, its porosity, and specific surface area, i.e., by factors governing the accessibility of reaction centers at which ionogenic groups are formed. Coals and, in particular, anthracite are peculiar natural compounds with undeveloped porosity. The specific surface area of fossil anthracite is small (0.7–1.0 $m^2 g^{-1}$); therefore, it is preactivated to develop the porous system and uncover new active centers accessible for atmospheric oxygen. In turn, owing to formation of various acidic groups containing coordination-unsaturated oxygen atoms and bonded to the system of conjugated bonds at the surface of oxidized carbons, the subsequent reactions of carbons with some metal cations involve not only exchange of hydrogen ions for cations but also formation of more or less stable surface complexes in which functional groups of carbons serve as ligands.

[1] Donetsk coal field (Sverdlovsk, Lugansk oblast).

1070-4272/03/7609-1423$25.00

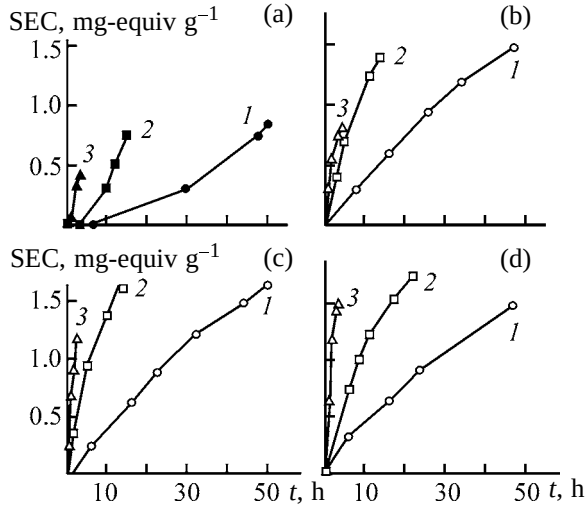

Fig. 1. Kinetic curves of variation of SEC during oxidation of the (a) the initial sample of anthracite and samples preactivated to burn-ou of (b) 20, (c) 40, and (d) 60%. (*t*) Time. Oxidation temperature, °C: (*1*) 270, (*2*) 320, and (*3*) 370.

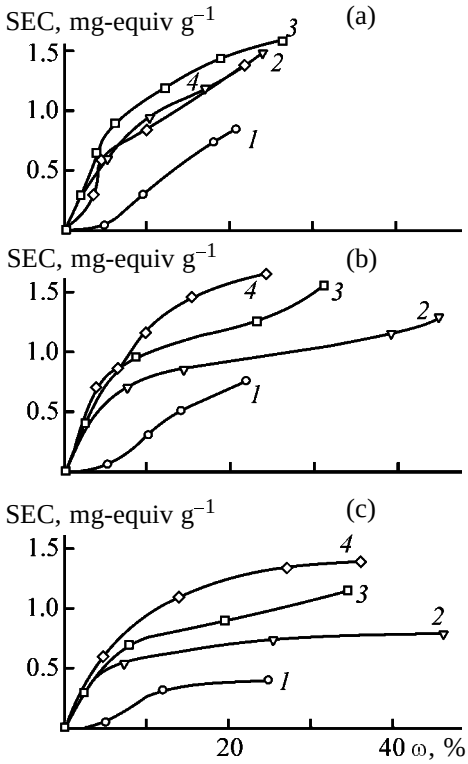

Fig. 2. SEC as a function of burn-out ω in oxidation of the (*1*) initial sample of anthracite and samples preactivated to the burn-out of (*2*) 20, (*3*) 40, and (*4*) 60%. Oxidation temperature, °C: (*1*) 270, (*2*) 320, and (*3*) 370.

A kinetic study of SEC growth with heating is important for understanding the course of anthracite oxidation, in particular, for determining the optimal temperature interval of stability of oxygen-containing groups participating in cation-exchange processes.

The kinetic curves shown in Figs. 1a–1d indicate that the rate of accumulation of functional groups in all the considered cases increases with heating. Thus, the degree of oxidation characterized by SEC equal to 1.0 mg-equiv g^{-1} is attained in several tens hours at 270°C, in 6–8 h at 320°C, and in 2–4 h at 370°C. Preactivation exerts no significant effect on the shape of the kinetic curves: they are linear in the initial portion, with subsequent tendency to saturation. For the initial anthracite, the curves are concave, which is caused by inefficient oxidation in the initial portion of the curve, evidently owing to low development of the surface. For the samples of anthracite preactivated to 20–60% burn-out, the reached values of SEC are close to each other. In oxidation of the initial anthracite, the SEC is considerably lower; in this case, the material expands.

Figures 2a–2c show that formation of protonogenic groups at the surface of anthracites in their oxidation is accompanied by different weight loss (burn-out) depending on the treatment temperature. At 270°C, the samples of preactivated anthracite are characterizad by abrupt increase in SEC, whereas for the initial anthracite accumulation of SEC is decelerated and the reached values of burn-out are considerably lower. At higher oxidation temperature, the difference between the initial and activated samples becomes more pronounced. The higher the burn-out in activation, the higher the reached values of SEC at similar burn-out values.

It is also seen from Fig. 2 that the range 270–320°C is optimal for oxidation of activated anthracite. Apparently, at higher temperatures, burning of carbon is intensified and, correspondingly, the fraction of surface functional groups decreases.

As subjects for sorption studies, we took the samples of activated and oxidized anthracites whose characteristics are listed in the table.

The characteristics of the sorbing materials were estimated by sorption of Cu^{2+}, Pb^{2+}, Cd^{2+}, Zn^{2+}, Cr^{2+}, Co^{2+}, Mn^{2+}, Fe^{3+}, and Ni^{2+} ions from the Ringer solution containing NaCl 9.0, KCl 0.42, $CaCl_2$ 0.24, and $NaHCO_3$ 0.15 g l^{-1} as a salt background. The sorption tests were carried out at pH 4 under static conditions at the ratio solid : liquid = 1 : 100 and contact time of no less than 6 h at continuous stirring. The concentration of ions in the model solution simulating a multicomponent system containing Ca^{2+} ions before and after attainment of the sorption equilibrium was determined by the standard procedure on an S-115M-1 atomic absorption spectrophotometer.

Knowing the filtrate concentration before (c_0) and after (c_s) sorption, the weighed portion of the sorbent m, and the volume of the sample solution V, we evaluated the sorption A and the distribution coefficient K_d of metal ions by the formulas

$$A = (c_0 - c_s)V/m, \qquad K_d = A/c_s \times 100.$$

The sorption isotherms presented in Fig. 3 show that the samples of oxidized anthracite have, as expected, a higher ability to sorb ions of heavy metals than the initial activated analogs.

The sorption efficiency in each case was evaluated by comparison of the K_d values for activated and oxidized samples under standard conditions: c_{eq} = 1 mg l^{-1} and c_{eq} = MPC (maximum permissible concentration) of the studied cations (Fig. 4). According to GOST (State Standard) 2874–82, the MPC values in drinking water are as follows: Cu^{2+} 1.0, Pb^{2+} 0.03, Zn^{2+} 5.0, Cr^{3+} 0.05, Mn^{2+} 0.1, Fe^{3+} 0.3, Co^{2+} 0.1, Ni^{2+} 0.1, and Cd^{2+} 0.001 mg l^{-1}. With respect to the sorbability, the cations can be ranked in the following order: for activated anthracite at c_{eq} = 1 mg l^{-1}, $Fe^{3+} > Cu^{2+} > Pb^{2+} \cong Cd^{2+} > Mn^{2+} > Ni^{2+} > Zn^{2+} > Cr^{3+} > Co^{2+}$; at c_{eq} = MPC, $Fe^{3+} > Cd^{2+} > Cu^{2+} > Pb^{2+} > Mn^{2+} > Ni^{2+} > Co^{2+} > Zn^{2+} > Cr^{3+}$; for oxidized anthracite at c_{eq} = 1 mg l^{-1}, $Cu^{2+} = Pb^{2+} > Fe^{3+} > Cd^{2+} > Mn^{2+} > Ni^{2+} > Co^{2+} > Zn^{2+} > Cr^{3+}$, and at c_{eq} = MPC, $Cd^{2+} > Pb^{2+} > Fe^{3+} = Cu^{2+} > Mn^{2+} > Ni^{2+} > Co^{2+} > Zn^{2+} > Cr^{3+}$.

The diagram of the K_d values (Fig. 4) shows that the maximal sorption selectivity is observed for Cu^{2+}, Pb^{2+}, and Cd^{2+} cations. In this case, the sorption power of oxidized samples increases in sorption of Cu^{2+} by a factor of 3.5, Cd^{2+}, by a factor of 6, and Pb^{2+}, by a factor of 18. For the other cations, K_d increases by a factor of 2–3. This activity series of the ions makes especially promising the use of anthracite cation exchanger for purification of water to remove toxic heavy metals and also for recovery of microimpurities of Zn^{2+}, Cr^{3+}, Co^{2+}, Mn^{2+}, and Ni^{2+} ions in conditioning of process solutions.

CONCLUSION

(1) The efficiency of oxidation of anthracite with humid air and the resulting values of static exchange capacity are governed by temperature conditions of the process and also the degree of preactivation of anthracite. The optimal temperature range to attain

Physicochemical and porosimetric characteristics of carbons used in sorption studies

Characteristic	Anthracite	
	activated	oxidized
Bulk density, g cm^{-3}	0.50	0.42
pH	8.98	3.53
Burn-out,* %	62	68.4
SEC, mg-equiv g^{-1}:		
HCl	0.6	0
NaOH	–	1.5
Content of oxygen-containing groups, mg-equiv g^{-1}:		
strongly acidic carboxy	–	0.8
weakly acidic carboxy	–	0.1
phenolic	–	0.6
W_s, cm^3 g^{-1}:		
with respect to C_6H_6	0.35	0.39
with respect to CH_3OH	0.35	0.39
Sorption of I_2, %	75	61
Sorption of MB, mg g^{-1}	100	112
S_{sp} with respect to argon, m^2 g^{-1}	842	930

* The values of burn-out are given considering activation of the initial raw materials.

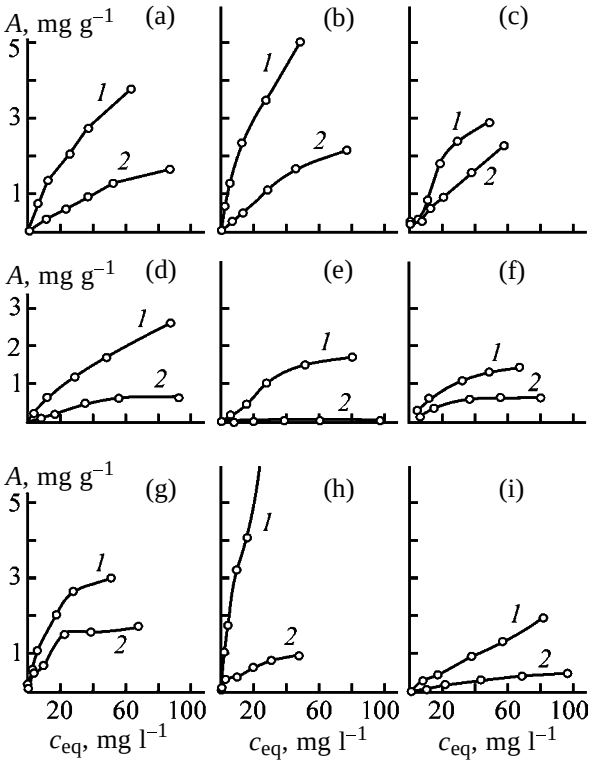

Fig. 3. Isotherms of sorption of metal ions from Ringer solution at pH 4 on (*1*) anthracite samples oxidized at 270°C and (*2*) activated sample. (*A*) Sorption of metal ions and (c_{eq}) equilibrium concentration. (a) Cd^{2+}, (b) Pb^{2+}, (c) Cr^{3+}, (d) Ni^{2+}, (e) Co^{2+}, (f) Mn^{2+}, (g) Fe^{3+}, (h) Cu^{2+}, and (i) Zn^{2+}.

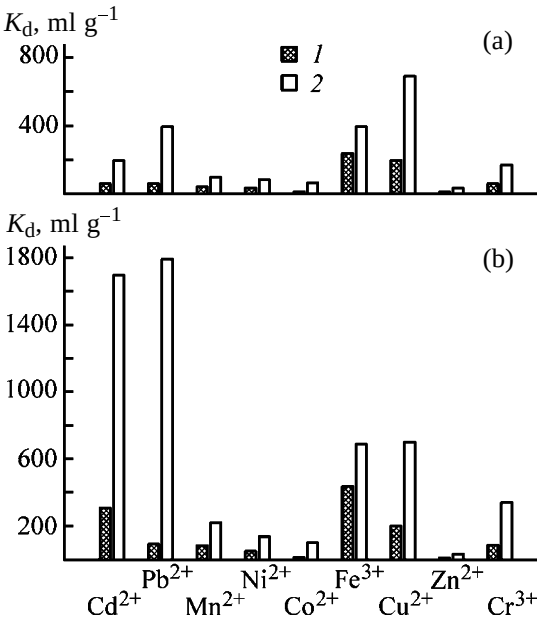

Fig. 4. Diagram of distribution coefficients K_d for the samples of (*1*) activated and (*2*) oxidized at 270°C anthracite at (a) c_{eq} = 1 mg l^{-1} and (b) c_{eq} = MPC.

the maximal static exchange capacity is 270–320°C at 40–60% burn-out of preactivated samples.

(2) Sorption studies showed that oxidation of activated anthracite increases the volume of sorption pores, specific surface area, and, as a consequence, sorption activity with respect to tested substances. In addition, oxidized anthracite is an effective carboxylic cation exchanger with respect to multicharged metal ions.

(3) The series of activity of Cu^{2+}, Pb^{2+}, Cd^{2+}, Zn^{2+}, Cr^{3+}, Co^{2+}, Mn^{2+}, Fe^{3+}, and Ni^{2+} ions in sorption with activated and oxidized anthracite samples under standard conditions (c_{eq} = 1 mg l^{-1} and c_{eq} = MPC) were established. Fairly high selectivity of sorption of Cu^{2+}, Pb^{2+}, and Cd^{2+} ions with oxidized anthracite from multicomponent salt solution was revealed.

REFERENCES

1. Tarkovskaya, I.A., *Okislennyi ugol'* (Oxidized Coal), Kiev: Naukova Dumka, 1981.
2. *Puti pererabotki uglei Ukrainy: Sbornik nauchnykh trudov* (Processing of Ukrainian Coals: Collection of Scientific Works), Kiev: Naukova Dumka, 1988.
3. Butuzova, L.F., in *Adsorbenty na osnove prirodnykh uglei: Sbornik nauchhykh trudov* (Adsorbents Based on Natural Coals: Collection of Scientific Works), Kiev: Naukova Dumka, 1989, pp. 37–49.
4. Butuzova, L.F., Thermochemical Transformations of Oxygen-Containing Groups of Coals, *Doctoral Dissertation*, Donetsk, 1999.
5. Baranov, S.N., Saranchuk, V.I., and Sapunov, V.N., *Khimicheskie produkty iz uglya* (Chemical Products from Coal), Baranov, S.N., Ed., Kiev: Naukova Dumka, 1983.
6. Suranova, Z.P., Grabchuk, O.D., and Tomashevskaya, A.N., *Adsorb. Adsorb.*, 1974, issue 2, pp. 55–57.
7. Kel'tsev, N.K., *Osnovy adsorbtsionnoi tekhniki* (Principles of Adsorption Technique), Moscow: Khimiya, 1984.
8. Boehm, H.P., *Adv. Catal. Relat. Subj.*, 1996, no. 16, pp. 179–274.

Russian Journal of Applied Chemistry, Vol. 76, No. 9, 2003, pp. 1427–1437. Translated from Zhurnal Prikladnoi Khimii, Vol. 76, No. 9, 2003, pp. 1467–1476.

APPLIED ELECTROCHEMISTRY AND CORROSION PROTECTION OF METALS

Topical Problems Associated with Utilization of Lead Battery Scrap

A. G. Morachevskii

St. Petersburg State Polytechnic University, St. Petersburg, Russia

Received July 23, 2003

Abstract—The review summarizes data on the present state of organization of collection and processing of lead battery scrap, the most important variety of lead-bearing secondary raw materials. Hydrometallurgical procedures ensuring recovery and refining of lead with the highest environmental safety are considered in detail. The review is based on publications of 1997–2002.

In the last decade, much attention has been given to collection and processing of lead-bearing secondary raw materials, and in the first place to utilization of spent lead batteries. This problem is becoming increasingly important in economical and environmental regard from year to year [1]. At present, lead batteries are the most widely used secondary chemical power source. These batteries include starter (used for electric start of combustion engines), traction (feeding electric motors of vehicles), and stationary (used in radioelectronic devices and as emergency power sources) batteries. There is no serious alternative to lead batteries in transportation. The rise in manufacture of electromobiles also leads to increasing demand for batteries [2].

According to the International Lead and Zinc Study Group (ILZSG), the main amount of consumed lead is expended for manufacture of lead batteries (%): 72.1 in 1997, 74.2 in 1998, and 74.9 in 1999 [3]. It should be noted for comparison that only 45% of lead was expended for manufacture of lead batteries in 1973 [4]. A considerable amount of lead was spent at that time for production of tetraethyllead (antiknock additive to motor fuel) [5]. Beginning in 1996, tetraethyllead has not been used in any of foreign countries [6].

At present, world's annual output of lead exceeds 6 million tons: 5999 thousand tons in 1998, 6277 thousand tons in 1999, and 6532 thousand tons in 2000 [3]. The monograph [7] gives somewhat smaller figures for the manufacture of refined lead: 5634 thousand tons in 1998 and 5620 thousand tons in 1999. Globally, the fraction of lead produced from secondary raw materials is no less than 55%, being as high as 85–100% in some countries. For reference, not so long ago, in 1986, the manufacture of refined lead from ore exceeded its production from secondary raw materials: the total output was 4009 thousand tons, amount produced from primary raw material was 2179 thousand tons, and that from secondary raw materials, 1830 thousand tons [7]. According to Besser's data [3], 88% of lead manufactured in Russia in 2000 was obtained by processing secondary raw materials (battery scrap, cable sheaths, wastes from battery plants). The main and the most difficultly processed kind of lead-bearing secondary raw materials is battery scrap. The average service life of lead batteries is, depending on the battery purpose and working conditions, 3–5 years, and the extent of recovery of the metal from these batteries is determined by processing technology, occasionally being very high.

Despite that Russia occupies the fourth place in the world as regards its total lead resources (after the United States, Australia, and Kazakhstan), the quality of Russia's deposits is, on the whole, inferior to that in foreign countries [7]. Under present-day conditions, gross investment in the development of the ore base of Russia's lead industry is hardly expectable. Only one third of the exhausted resources of lead is reproduced [8]. In 2001, the manufacture of lead in the form of concentrates was 31.5% of the level of 1990 [7].

Metallurgical plants for ore processing, which remained in the territory of Russia after the geopolitical changes of 1991, Elektrotsink Joint-Stock Company (Vladikavkaz) and Dal'polimetall Joint-Stock Company (Primorskii krai), are equipped with outdated apparatus and do not undergo any reconstruction. Lead is manufactured at the Elektrotsink plant by the

1070-4272/03/7609-1427$25.00

classical scheme of blast smelting, with stock agglomeration done by an imperfect method. The smelting of lead at the Dal'polimetall combine is done with the use of reactive furnace smelting [7].

All over the world, measures are taken for organizing efficient collection of batteries and improving the flowsheet of their utilization. It should be constantly kept in mind that, being economically important, these problems are of profound environmental significance. As regards its impact on living bodies, lead belongs to highly toxic substances, which requires that batteries should be collected to the maximum possible extent [9–14]. In addition to lead, battery scrap contains such toxic substances as antimony and sulfuric acid electrolyte. Spent lead batteries are an important source of environmental pollution with lead in our country [12]. According to expert estimates, dumps, transport yards, and other places all over the territory of Russia contain up to 1 million tons of lead in battery scrap [10], with this figure increasing by 50–60 thousand tons annually. According to other estimates [15], the amount of battery scrap may increase, at the existing state of battery collection and processing, by 150–200 thousand tons every year. Absolutely unacceptable are storage of spent batteries in garages and their removal to dumps, irrespective of the type of wastes to be stored there.

Already in 1998, the developed countries achieved a high level of battery scrap collection (%): UK more than 90, Germany 95, Italy 85, US up to 98, France ~90, Sweden nearly 100, and Japan ~90 [15, 16]. An important role in utilization of lead batteries is played by international and national regulations in this field, effective system for scrap collection and processing, environmental consciousness of citizens, and understanding of the importance of the problem at all levels of the society. In the United States, utilization of batteries is stimulated and supported by the federal administration [17], an infrastructure is created for collection and utilization of batteries, and all battery components find new application. At the same time, there is no system for collection and utilization of spent batteries in Russia, including its central regions, and the efficiency of the existing procedures is poor [18]. Vasin [19] studied the present state of the system for collection of spent batteries in the Moscow region and made an attempt to assess the damage inflicted on the nature by unprocessed batteries.

The Russia's system for processing of nonferrous scrap metals is affected by shortcomings of licensing of this kind of activities [20]. According to the available estimates, up to 70% of the turnover of nonferrous scrap metal and wastes is illegal [21]. One of manifestations of the illegal turnover of scrap and waste are illegal plants. During the years in which Russia has been passing to market economy, small plants appeared which smelt various metals from scrap and waste using low-level technology, without due systems for gas purification and appropriate regulations of storage and disposal of wastes. The products manufactured at plants of this kind have extremely poor quality, but their cost is lower than that at licensed plants with higher-level technology. All these factors largely refer to processing of lead-bearing secondary raw materials.

The lead branch of the nonferrous metallurgy in Russia should be based, in the first place, on utilization of secondary raw materials, have regional structure, and use environmentally safe technologies.

The presently existing flowsheets for processing of lead batteries were analyzed in [15, 22–27]. All the processing plants in the developed countries deal with spent batteries with undischarged electrolyte, in conformity with the existing regulations. The system for collection and transportation of such batteries does not assume any intermediate yards or areas for their opening and crushing. Discharge and utilization of the electrolyte, and other operations, are carried out directly at the plants processing the battery scrap. Unfortunately, the regulations operative in Russia make it possible to receive all kinds of lead batteries "..with discharged electrolyte." Thus, utilization of a toxic electrolyte containing suspended lead oxides and sulfides, which belong to substances of the first degree of hazard, is not subject to any regulations [3].

Two fundamentally different technologies are used in processing of lead battery scrap. The first of these includes preliminary treatment of the battery scrap: crushing and separation of organic components (ebonite, polypropylene, polyethylene, polyvinyl chloride) from lead-containing fractions, oxysulfate and metallic. The last two fractions are processed using various techniques to give the corresponding commercial products.

The second technology consists in smelting of a stock composed of unprocessed batteries with removed electrolyte, fluxes, and fuel. This process yields lead bullion, which should be refined. The organic components burn out, and sulfur passes partly into matte and partly into the gas phase. Chlorine contained in polyvinyl chloride reacts with lead to give lead chloride passing into dust, which requires further processing to recover lead. The process is mainly

carried out in blast furnaces. Irrespective of a technology adopted, plants usually perform the whole set of procedures for scrap processing, from separation of electrolyte and its processing to manufacture of lead, its alloys, and some intermediates. Each of the two technologies has its own advantages and disadvantages. According to a review [15], no more than 10–15% of the world's manufacture of secondary lead from spent batteries was accounted for by smelting of unprocessed lead battery scrap in blast furnaces by 1998.

In view of the existing tendency toward use of chlorine-free separators, the amount of dusts obtained in blast furnaces will decrease. Replacing ebonite with other materials in fabricating battery cases makes lower the total content of sulfur in the battery scrap, diminishes the amount of the forming mattes, and decreases the content of sulfur in the gas phase. Despite these positive tendencies, construction of blast furnaces and gas-purification systems requires gross investment, necessitates processing of the forming intermediate products (dusts and mattes), leads to formation of lead bullion with high content of antimony, and contradicts the present-day conservation trends. In 1997–1998, a German company Warta assembled a blast furnace for processing of lead-bearing secondary raw materials at Kursk battery plant [28]. Unfortunately, it was impossible to find in the literature any data concerning the results obtained with this installation. In the author's opinion, lead battery scrap is a specific kind of secondary raw materials, whose processing must differ significantly in equipment-related and technological regard from that of any type of lead-containing ores. From the standpoint of environment protection and investment in construction of regional plants for utilization of lead batteries, it is hardly advisable to employ technologies that involve smelting of unprocessed battery scrap in blast furnaces. In view of the present-day situation in Russia, there is no reason to create new plants for joint processing of ore and secondary raw materials.

In the case of preliminary cropping of batteries, irrespective of the way in which this is done, the key issue is the method for lead recovery from the oxysulfate fraction. The active pastes from the positive and negative plates of a battery fall into this fraction. On the average, an active paste washed with water contains (wt %) Pb 73.5, Sb 0.3, As up to 0.004, Cu 0.1, Fe 0.05, and SO_4^{2-} 16.7 [14]. The main components of the active paste are $PbSO_4$ and PbO_2, and, to a lesser extent, $PbO \cdot PbSO_4$, Pb_2O_3, and Pb. With account taken of the fact that lead oxides are rather easily reduced to metal by any carbonaceous reducing agent at relatively low temperature (720–740°C), it seems appropriate to convert lead sulfate into lead hydroxide or carbonate by a simple hydrometallurgical procedure (desulfation or desulfurization). In this case, the problem of sulfur utilization is solved completely, with sulfur passing into the aqueous phase in the form of a soluble sulfate. The desulfation process is employed in quite a number of flowsheets at plants in Western countries, its environmental advantages being indubitable. Physicochemical and technological studies of the desulfation process were considered in detail in a review [29]. The best suitable reagents for the desulfation process are aqueous solutions of sodium hydroxide or carbonate [27, 30]. The reaction, which is not subject to any essential kinetic hindrance and is sufficiently fast, is based on much lower solubility products (SP) of lead(II) hydroxide or carbonate, compared to lead sulfate. For example, SP = $10^{-7.8}$ for $PbSO_4$ and varies with temperature only slightly. At the same time, SP for $Pb(OH)_2$ and $PbCO_3$ is, respectively, $10^{-15.3}$ (20°C) and $10^{-13.1}$ (25°C) [29].

Desulfation gives commercial sodium sulfate conforming to quality standards as regards its content of heavy metals [31]. Utilization of sulfur in the form of sodium sulfate has also been recommended by Zaikov and co-authors [32]: in processing of anodic sludges formed in manufacture of copper foil, lead(II) sulfate is converted into carbonate.

An important factor affecting the extent and rate of desulfation is the degree of crushing of the active paste being processed. A factor hindering the desulfation process in repeated use of a mother liquor is accumulation of Na_2SO_4. It was also noted in [11] that the most advanced method for utilization of sulfur is desulfation to give commercial sodium sulfate, gypsum plaster, etc. Mention has been made of the advisability of using potassium carbonate for desulfation of active paste from lead battery scrap [33]. This conclusion is substantiated by the fact that K_2CO_3, being a by-product of alumina manufacture from nepheline raw materials, is produced by the Russian industry in sufficient amounts and the market of potassium sulfate is less saturated than that of sodium sulfate. It was noted in [27] that use of K_2CO_3 can be substantiated not only economically. It is known that no double salt similar to $NaPb_2(CO_3)_2OH$ is formed with potassium carbonate, which facilitates desulfation.

Industrial instrumentation of the desulfation process poses no difficulties. Further processing of the desulfated material consists in thermal decomposition of lead carbonate and concomitant compounds (basic

lead carbonates) and subsequent reduction of lead oxides. Investigations have shown [34] that decomposition of $PbCO_3$ onsets under usual conditions already at 280°C, being complete at 510°C. Reduction of lead(IV) oxide contained in the desulfated paste by solid carbonaceous reducing agents onsets at 380–390°C and is complete at 400–410°C. It should be kept in mind that the saturated vapor pressure of lead at 1000 K is as low as 1.45 Pa (1.09×10^{-2} mm Hg) [35].

An alternative process for recovery of lead from battery scrap, based on dissolution of lead sulfate in aqueous NH_4OH and subsequent recovery of lead by cementation with metal powders, was proposed in [36]. The process was performed in autoclaves at 100°C at a stirring rate of 300 rpm. The effect of various factors on the course of the process was analyzed.

The apparatus for reduction of the desulfated paste and the choice of reducing agents may vary depending on the production scale, investment, and availability of one or another type of equipment. Preliminary briquetting of the starting material with coal powder has no effect on the reduction process. An important conclusion is that lead(II) oxide is reduced with sufficient rate and completeness at a temperature not exceeding 720–740°C.

As already noted, desulfation must be preceded by processing of lead battery scrap in one or another way. According to [15], already by 1998, more than two thirds of waste lead batteries were utilized in the world's practice after preliminary processing. According to the available evidence, the flowsheet with preliminary scrap processing is adopted at the Verkhneivinskii plant of nonferrous metals [37]. Mechanized battery scrap processing is used at the Ryaztsvetmet plant [38].

Let us consider some other flowsheets developed or being developed in Russia with account of the domestic economic capacity. The Gintsvetmet State Research Center of the Russian Federation (Moscow) proposed a technology for processing of battery scrap and other kinds of lead-bearing secondary raw materials with the use of soda-free smelting. The scheme includes mechanized scrap processing, melting of the metallic fraction in a melting kettle, electrothermal smelting of the oxysulfate fraction, refining of lead bullion, and processing of a number of intermediate products, with their subsequent transfer to the corresponding plants (copper matte, arsenic-containing alloy, slag). The main equipment was designed for a plant with output capacity of 15 000 t of lead per year.

A decision has been made, on the basis of an analysis of technologies for cropping battery scrap into fractions, that it is appropriate to accept the offer of an Italian company, Engitec Impianti SpA. The CX-compact installation designed by this company is environmentally safe, has small size, and separates battery scrap into five fractions: metallic, oxysulfate, polypropylene, polyvinyl chloride, and ebonite. The main characteristics of the installation were reported in [23], with references given to publications with detailed description of the CX-compact installation. According to the available data [15], the installation designed in Italy has found wide use in numerous countries.

The central place in the technology proposed by the Gintsvetmet Institute is occupied by matte- and soda-free electric smelting. To smelting are directed, together with the oxysulfate fraction, oxide dross obtained in melting of the metallic fraction in melting kettles and dusts caught in cleaning gases formed in the course of the smelting itself. The theory and technology of the process have been described in a number of reports, beginning in 1988 [38–43]. The authors proceed from the assumption that melts are vigorously agitated in electric smelting by convective flows generated at the electrodes. This creates conditions for reactive smelting; sulfides completely react with oxides and sulfates to give molten lead, rapidly flowing down [40].

The lowering of the temperature of slag melting and, correspondingly, that of the process as a whole is due to the fixed $FeO : SiO_2 : CaO$ ratio and increased content of lead silicates in the slag. No soda is introduced into the stock. Dosing of a reducing agent (coke breeze) controls reduction of sulfates to sulfides, but only in amount necessary for their reaction with oxides to occur. Release of sulfur dioxide into the gas phase shifts the reaction equilibrium and favors complete consumption of the sulfides, which rules out matte formation.

In [39], the experience of utilization of lead-bearing secondary raw materials at the Ryaztsvetmet plant with the use of electric smelting was summarized. The results obtained were compared with the parameters characteristic of other methods for battery scrap processing: smelting in shaft and short-drum-type furnaces. Here, only the results obtained using the Gintsvetmet technology are considered. In this case, the stock contains battery scrap (80–90%), coke (3–4%), and slag-forming materials (5–10%). The smelting products contain 92–94% lead bullion, 3–5% slag, and 4–7% dust. The extent of lead recovery from the raw

materials being processed into lead bullion is as high as 95%. The process temperature is 1100°C [40].

In [40, 42], mention was made of quite a number of advantages of soda-free matte-free electric smelting over battery scrap processing in shaft or short-drum furnaces: the amount of forming waste gases is 3–5 times smaller; also lower is discharge of lead-containing dust into the atmosphere; the technology is virtually waste-free.

A comparative analysis of the feasibility of industrial methods for battery processing was also made in [25, 26]. In the opinion of Koshelev and co-authors [25], certain advantages are observed in the case of melting of unprocessed batteries in a blast furnace; the technology was assessed on the basis of the results obtained at a plant in Germany. Also promising is application of the Vanyukov process to melting of unprocessed battery scrap (melting in a liquid bath). In this case, a continuous operation mode, complete burning of organic components, and high economical and environmental characteristics are achieved. A detailed critical analysis of this standpoint was presented by Besser [26].

Of interest are publications concerned with relatively low-temperature processes of melting of lead-containing materials [44, 45]. One of these [44] suggests processing of the oxysulfate fraction of lead battery scrap by low-temperature soda smelting, with the system Na_2CO_3–NaCl, in which a eutectic mixture exists at 634°C (36.5 mol % NaCl), recommended as salt flux. Sodium sulfate forming in exchange reaction between lead sulfate and soda does not lead to any rise in the melting point of the complex salt system. A carbonaceous reducing agent is introduced after exchange processes in the system are complete, at about 700°C. Thus, the reaction between lead sulfate and sodium carbonate occurs in a salt melt. The possibility of achieving, in principle, a high recovery of lead in the form of metal at minimum amount of noxious substances (sulfur dioxide, chlorine, lead chloride, lead vapor) discharged into the atmosphere was noted in [44].

In [45], melting of lead-containing materials in a lead bath under a layer of sodium hydroxide flux at 550°C was suggested. Experiments were carried out on laboratory scale. A 0.05-kg amount of NaOH is consumed in the bath per 2.5 kg of wastes (lead-rich materials, lead battery scrap). The extent of lead recovery is 98 and 75% in smelting with and without flux, respectively. Spent flux can be used for desulfation of the active paste from lead battery scrap.

An extensive series of recent investigations at the Institute of High-Temperature Electrochemistry, Ural Division, Russian Academy of Sciences, in Yekaterinburg was devoted to physicochemical foundations of processing of lead-containing materials with the use of carbonate melts [46–55]. The method of thermodynamic modeling was widely used in these studies to determine the possibility of occurrence of one or another high-temperature process and to assess tentatively the behavior of impurities. The essence of the technique was described in detail in [56].

A detailed thermodynamic analysis of the possibility of reducing PbO, $PbCl_2$, PbS, and $PbSO_4$ under equilibrium conditions with carbon in carbonate melts of various compositions yielded data on the effect of temperature and other factors on the extent of lead recovery [48, 54]. The monograph [55] mainly discusses two issues: processing of various kinds of lead-containing raw materials, including the active paste of lead batteries, in carbonate melts at temperatures of up to 1000°C and electrochemical processing of oxidized wastes in hydroxide melts. A thermodynamic analysis and laboratory and pilot-plant tests demonstrated that use of molten carbonates ensures nearly 100% reduction of lead compounds, nearly theoretical consumption of a reducing agent, small volume of waste gases, and dramatic decrease in the amount of the forming dust. It should, however, be mentioned that no detailed flowsheet is given in the monograph [55] and other publications of its authors for the case of lead battery scrap. Electrochemical processing of lead oxide with the use of an alkali–carbonate electrolyte can hardly compete with the rapidly occurring pyrometallurgical reduction of lead(II) oxide with any carbonaceous reducing agent at 720–740°C [57, 58]. Use of ionic melts in the technology for processing of lead-bearing secondary raw materials has been described in detail previously [59, 60].

Quite a number of recent investigations have been devoted to physicochemical foundations and technologies of lead refining. In [61, 62], the possibility was demonstrated for lead purification to remove antimony by introducing aluminum into the melt at 700–720°C with subsequent slow cooling of the metal to 340–350°C. Experiments and theoretical calculations produced well-consistent results. Samples taken in the course of cooling contain AlSb intermetallic compound. The content of antimony in lead can be diminished to 0.005 wt %. For deeper purification of lead to remove antimony and some other impurities, it is advisable to use a method based on anodic polarization of a metal being refined in molten sodium hydroxide. In large-scale experiments, 35 kg of a metal

to be refined was charged into the electrolyzer and the yield of refined metal was 99.0–99.5% in terms of charged metal at a process temperature of 340–370°C. The content of antimony can be diminished to 0.001%. Simultaneously, it is possible to remove aluminum, tin, arsenic, and iron, which are not found in lead after anodic polarization, at detection limit of 1×10^{-3}%, irrespective of their initial content [64].

Omel'chuk and co-authors used for selective extraction of tin, bismuth, antimony, and arsenic impurities from lead the method of cathodic refining with molten sodium hydroxide [65]. As is known [59, 60], the method consists in that sodium is deposited on the surface of the refined metal acting as cathode, with the corresponding intermetallic compounds formed. Here, it should be emphasized that deposition of sodium and compound formation constitute a single electrochemical event. Under certain conditions (temperature, current density, etc.), these compounds pass from the cathodic metal into electrolyte. By varying the electrolysis conditions, it is possible to control the order in which the alloy components are extracted. According to the authors' data [65], the method of cathodic refining makes it possible to extract such components as bismuth, antimony, tin, and arsenic virtually completely from lead-based alloys. Highly important for processes of electrochemical refining with the use of ionic melts as electrolyte, and also for other refining techniques involving intermetallic compounds, are their thermodynamic characteristics, and also the thermodynamic properties of the corresponding liquid phases.

The general principles underlying various kinds of intermetallic processes applicable to removal from lead of such impurities as bismuth, antimony, arsenic, and tellurium were considered in [66]. Some investigations have been concerned with thermodynamic properties of liquid alloys and solid phases in the sodium–tellurium system [67], sodium bismuthide (Na_3Bi) [68], liquid alloys in the systems sodium–bismuth and lead–sodium–bismuth [69, 70], and liquid and solid phases in the system sodium–antimony [71]. The pseudobinary system $Pb–Bi_2Mg_3$ was studied using the calorimetric method, integral excess Gibbs energies at 973, 1023, and 1073 K were calculated, and the phase diagram of the system was described [72]. Data on binary systems of edge components were used to calculate in terms of various geometric models the thermodynamic characteristics of liquid alloys in the system lead–magnesium–bismuth [73].

As is known [4, 35], the classical method for bismuth elimination from lead bullion is based on physicochemical interactions in the system Pb–Bi–Ca–Mg–Sb. In [74], alloying processes in the systems Pb–Ca, Bi–Ca, and Pb–Bi–Ca were analyzed and the process of lead purification to remove bismuth at its small content by adding calcium was discussed. Another study [75] considered and compared published data on the phase diagram and thermodynamic properties of the system Ca–Sb and discussed, with account of the results obtained, the equilibrium in the system Ca–Pb–Sb.

A number of investigations have been devoted to analysis of electrochemical processes involving aqueous electrolyte solutions and to study of the nature of solutions of lead compounds in various media, which are of interest for technological practice. In [76], the processes of lead refining and anodic dissolution of Pb–Sn–Sb alloys with an electrolyte based on hydrosilicofluoric acid were discussed. In lead refining, the current efficiency by lead is as high as 99% at current density of 100 A m^{-2} and specific electric power consumption of 30–40 kW h t^{-1}. Nikitin and co-authors proposed a process for lead refining to ultrahigh purity by anodic dissolution in a perchlorate electrolyte with introduction into the anodes of components binding impurities. The theoretical foundations and general principles of this refining technique were considered in detail in [35, 77].

Lebedev [79] studied recovery of lead from anodes in which the total content of antimony, bismuth, and tin may be as high as 12 wt %. The electrolysis is carried out in a sulfamic electrolyte. The metal obtained on the cathode corresponds, as regards its chemical composition, to S1, S2, and S3 brands with the content of the base component of 99.985, 99.95, and 99.90%, respectively.

The solubility of lead sulfate in the quaternary systems $PbSO_4–NaCl–HCl–H_2O$ and $PbSO_4–NaCl–H_2SO_4–H_2O$ has been determined [80]. It was shown that introduction of HCl intensifies chloride leaching of lead. Yurkinskii and co-authors [81, 82] have studied complexation of lead(II) with hydroxide ions under various conditions. In electrolysis of impurity-free alkaline solutions of lead (25 g l^{-1} lead, 100 g l^{-1} alkali, temperature 50°C, current density 100 A m^{-2}), a finely dispersed powder of lead is obtained with a high current efficiency at the cathode, and lead dioxide PbO, at the anode (current efficiency 22.4%) [83].

Analysis of reports published in 1997–2002[1] points to the impelling need, from the economical and en-

[1] Information about patents and inventor's certificates can be found in [1] and is not considered in this review.

vironmental viewpoints, for cardinal improvement of the state of affairs with collection and utilization of lead battery scrap in Russia. At the same time, there is no doubt that processing of lead-bearing secondary raw materials must be the primary source of lead in Russia. There is no reason to expect large-scale manufacture of lead from ore in the near future. The massive import of batteries from abroad and the work of domestic battery plants indicate that there is no danger of any deficiency of lead-bearing secondary raw materials, provided that they are collected properly. Only the already accumulated amount of battery scrap and other kinds of lead-bearing secondary raw materials will be sufficient for satisfying Russia's need for lead for many years to come [84].

Efficient organization of a State-supported system for collection of spent lead batteries in each region of Russia is necessary. Also rather important is improvement of the system for licensing of plants that process battery scrap and other lead-containing materials, irrespective of the scale of production at these plants [20, 85].

As a long ago as 1993, and later [22, 23, 57], we pointed to the advisability of a regional approach to setting up comparatively small-scale plants for processing lead battery scrap and other kinds of lead-bearing secondary raw materials (10–15 thousand tons of lead and lead alloys per year). This conclusion was based on the environmental hazard of these widely occurring technological wastes, which should not be transported to large distances.

A similar position was maintained by Kolotyrkin and Tkachek [86]. In their opinion, lead batteries should be utilized by small plants (100–150 thousand batteries per year, or 2500–3000 t of lead processed annually). Pashchenko [87] noted the necessity for creating a great number of plants for battery scrap processing, each with annual capacity of up to 3.0–3.5 thousand tons of the metal, in regions with gross consumption of batteries and mass flows of secondary raw materials.

It seems rather important to solve two mutually related problems: to choose the optimal capacity of a separate plant for processing of lead-bearing secondary raw materials and to select the flowsheet for processing of battery scrap as the main and most difficultly processed kind of secondary raw materials. With account of the vast territory of Russia, existence of remote regions, transport difficulties, high cost and environmntal unsafety of the transportation of lead battery scrap, the above problems cannot have a unique solution. Specific features of our country do not allow simple copying of the foreign experience, but this experience cannot be disregarded, either.

To supply large consumers of lead, and battery plants in the first place, with a sufficient amount of lead and its alloys and compounds, the unit capacity of a subsidiary plant for processing of not only secondary raw materials, but also the waste formed in manufacture of batteries must correlate with the demand and capacity of the main plant, battery manufacturer. Another approach can be used in estimating the unit capacity of a plant for processing of battery scrap in one or another region, irrespective of whether or not it has lead consumers. In this case, the minimum investment and sufficient environmental safety can be achieved by constructing plants with annual capacity of 10–15 thousand tons of lead or lead–antimony alloy.

Despite the quite acceptable difference in the flowsheets used at plants for processing of lead-bearing secondary raw materials, characterized by different output capacities and specific factors, general approaches can be formulated, which ensure environmental safety and feasibility of production.

In view of the dissimilar chemical natures of lead compounds and different types of impurities in ore and in battery scrap, it seems inappropriate to process these two kinds of raw materials simultaneously in the same apparatus. At the same time, joint processing of battery scrap with wastes formed in manufacture of batteries and other kinds of lead-bearing secondary raw materials is quite acceptable.

In choosing one or another flowsheet or separate operation, account should be taken of the fact that their environmental hazard is associated with the following factors: discharge of lead into the atmosphere, discharge of sulfur compounds, discharge of products formed in burning of the organic fraction (separators, battery cases), amount of wastewater containing heavy metals, amount of unutilizable slag, and content of heavy metals in the slag.

Simultaneously, account should be necessarily taken of the economical factors affecting the choice of technology. To these factors belong expenses for purification of process and ventilation gases to remove noxious substances to below the required level, cost of fuel and electric power, and expenditure for disposal of unutilizable products. The content of lead in waste gases and the total volume of these gases can be diminished dramatically by lowering the temperature of the main reducing process. This can be done if lead oxides, rather than sulfur-containing compounds of

lead (sulfates, sulfides), are reduced. Simultaneously, this leads to a pronounced saving of energy resources. Sulfur contained in the active paste of lead batteries in the form of lead sulfate can be completely utilized in desulfation. Preliminary disassembly of batteries rules out appearance of products formed in burning of organic compounds in waste gases. The problem of possible reuse of polypropylene, ebonite, and polyvinyl chloride after appropriate processing was considered in detail in [88]. According to the authors' data, processed polypropylene can be reused in fabrication of battery cases, and ebonite, in road building; however, the latter technology requires additional ecological-hygienic expertise. Polyvinyl chloride is to be disposed of.

The following sequence of operations seems to be the most appropriate in processing lead battery scrap, irrespective of the production scale:

(i) crushing of battery scrap into the metallic, oxysulfate, and organic fractions;

(ii) desulfation of the oxysulfate fraction;

(iii) reduction of lead oxides with solid reducing agents at relatively low temperatures;

(iv) refining of lead to give metal of highest-quality brands.

In those cases when small plants with annual metal output capacity of 5–7 thousand tons are the matter in question, lead battery scrap can be processed preliminarily in a simplified way, with the use of small-scale mechanization. The possible final products of such plants are lead antimonide obtained in remelting of the metallic fraction in a melting kettle and lead bullion formed in reduction of lead oxides. In the case of insufficient energy resources, mother liquors can be processed to give commercial barium sulfate, rather than be evaporated to give sodium sulfate. Water is recycled in the course of the process.

It should be emphasized the recommendations aimed to diminish the environmental hazards in battery scrap processing are based on the assumption that processing of lead-bearing secondary raw materials differs fundamentally from ore smelting because of the specific features of their chemical composition. It is inadvisable to use in processing of secondary raw materials such procedures as blast smelting, smelting in electrothermal furnaces, or other high-temperature processes.

Of particular interest among foreign plants is that in Freiberg (Germany), specialized in processing of lead battery scrap [89]. The plant was completely modernized in 1997 and processes annually 3.0 million starter batteries, to produce 35 thousand tons of lead and lead alloys, and also 3.5 thousand tons of chemically pure sodium sulfate and 2 thousand tons of polypropylene. Organic substances that cannot be utilized are burned, in conformity with all environmental safety regulations, on a special installation. The extent of lead recovery is 99%, and that of polypropylene exceeds 90%; sulfuric acid and sulfate ions from the battery paste are utilized in the form of sodium sulfate. Lead discharge into the atmosphere is about 7 g per ton of lead, and that into wastewater, less than 1 g per ton of lead. As regards all the process parameters, the plant belongs to the most modern plants for utilization of lead batteries. Its flowsheet envisages battery shredding and separation into fractions and desulfation of the active paste with sodium hydroxide. The grid material is melted in a short-drum furnace to give a lead–antimony alloy. The products obtained upon desulfation are subjected to reductive smelting, also in a short-drum furnace. Lead bullion is directed to refining. The lead–antimony alloy is either refined or serves for preparing necessary formulations. Sodium sulfate crystallizes from solutions used in desulfation; it is then dehydrated and delivered to a storehouse for subsequent selling; the content of lead in this product does not exceed 10 ppm. All steps of battery scrap processing at the plant are controlled from a single center. Further operation of the plant was considered in [90].

The set of the main operations in the flowsheet of the plant is in full agreement with the above recommendations. Owing to the presence of a special installation for burning of ebonite and separators, the amount of plant's wastes is very small. Crushing and separation of battery scrap, desulfation of the active paste, and reduction of lead(II) oxide—all these operations must form the basis of any flowsheet for processing of lead battery scrap. However, reagents for desulfation and refining processes can be varied to give different final products.

ACKNOWLEDGMENTS

The study was supported financially by the Foundation "Basic Research in Chemical Technology" of the Ministry of Education of the Russian Federation (project no. T02-9.4-3298).

REFERENCES

1. Morachevskii, A.G., *Pererabotka vtorichnogo svintsovogo syr'ya: Sovremennoe sostoyanie issledovanii i*

annotirovannyi ukazatel' literatury za 1997–2001 gg. (Processing of Lead-Bearing Secondary Raw Materials: Present-Day State of Investigations into the Problem and Annotated List of References for 1997–2001), St. Petersburg: Sankt-Peterb. Gos. Politekh. Univ., 2003.

2. Gill, T., *Metal Bull. Mon.*, 1997, no. 1, pp. 73, 75–79.
3. Besser, A.D., *Vtor. Resursy*, 2001, nos. 5–6, pp. 53–55.
4. Smirnov, M.P., *Rafinirovanie svintsa i pererabotka poluproduktov* (Refining of Lead and Processing of Intermediate Products), Moscow: Metallurgiya, 1977.
5. Morachevskii, A.G., Shesterkin, I.A., Busse-Machukas, V.B., *et al.*, *Natrii: Svoistva, proizvodstvo, primenenie* (Sodium: Properties, Manufacture, and Use), St. Petersburg: Khimiya, 1992.
6. Magaril, E.R., *Ekologicheskie svoistva motornykh topliv* (Environmental Properties of Motor Fuels), Tyumen: Tyumensk. Neftegaz. Univ., 2000.
7. Ptitsyn, A.M., Dyudin, Yu.K., Svidarovskii, A.N., and Rudnev, B.P., *Otsenka perspektiv razvitiya gorno-metallurgicheskoi bazy ryada metallov v Rossiiskoi Federatsii* (Assessment of Prospects for Development of Mining-and-Smelting Resources of Some Metals in the Russian Federation), Moscow: Ruda i Metally, 2002.
8. Kolpakov, S.V., *Stal'*, 1999, no. 10, pp. 79–80.
9. *Doklad o svintsovom zagryaznenii okruzhayushchei sredy Rossiiskoi Federatsii i ego vliyanii na zdorov'e naseleniya* (Report on Lead Pollution of the Environment in the Russian Federation and Its Impact on People's Health), Moscow: REFIA, 1997.
10. Lisin, V.S. and Yusfin, Yu.S., *Resurso-ekologicheskie problemy XXI veka i metallurgiya* (Resource-Related and Environmental Problems of the XXI Century and Metallurgy), Moscow: Vysshaya Shkola, 1998.
11. Besser, A.D., *Met. Evrazii*, 1997, no. 3, pp. 76–78.
12. Snakin, V.V., *Vestn. Ross. Akad. Nauk*, 1998, vol. 68, no. 3, pp. 214–224.
13. Budnikov, G.K., *Soros. Obraz. Zh.*, 1998, no. 5, pp. 23–29.
14. Morachevskii, A.G., Vaisgant, Z.I., and Korelyakov, A.V., *Zh. Prikl. Khim.*, 2000, vol. 73, no. 7, pp. 1125–1130.
15. Stepanov, B.E., Aksel'rod, A.R., and Dityatovskii, L.I., *Tsvetn. Metall.*, 1998, nos. 8–9, pp. 32–37.
16. Koshelev, V.A., Aksel'rod, A.R., and Rybachuk, N.T., *Tsvetn. Metall.*, 1999, nos. 2–3, pp. 36–40.
17. Larionov, V.G., Skrypnikova, M.N., and Kurkin, P.Yu., *Ekol. Prom–st' Ross.*, 2000, no. 3, pp. 46–47.
18. Izmailov, I.S., *Tsvetn. Met.*, 2001, no. 8, pp. 48–50.
19. Vasin, S.G., *Tsvetn. Metall.*, 2000, nos. 8–9, p. 46.
20. Siryk, V.V., *Tsvetn. Met.*, 2001, no. 6, pp. 21–25.
21. Novichkov, S.V. and Rogachev, S.V., *Tsvetn. Metall.*, 2002, no. 3, pp. 3–5.
22. Morachevskii, A.G., Vaisgant, Z.I., and Demidov, A.I., *Pererabotka vtorichnogo svintsovogo syr'ya* (Processing of Lead-Bearing Secondary Raw Materials), St. Petersburg: Khimiya, 1993.
23. Morachevskii, A.G., *Zh. Prikl. Khim.*, 1997, vol. 70, no. 1, pp. 3–15.
24. Lamm, K.F., *Erzmetall.*, 1998, vol. 51, no. 6, pp. 438–455.
25. Koshelev, V.A., Dityatovskii, L.I., Rybachuk, N.T., and Rodin, A.V., *Tsvetn. Met.*, 2000, no. 4, pp. 69–72.
26. Besser, A.D., *Tsvetn. Met.*, 2000, no. 4, pp. 72–73.
27. Morachevskii, A.G., Vaisgant, Z.I., Bochagina, E.V., and Khabachev, M.N., *Tsvetn. Met.*, 2002, no. 8, pp. 34–37.
28. *Metall* (Österreich), 1998, vol. 52, no. 4, p. 132.
29. Morachevskii, A.G., *Zh. Prikl. Khim.*, 1998, vol. 71, no. 6, pp. 881–890.
30. Morachevskii, A.G., Vaisgant, Z.I., Rusin, A.I., and Khabachev, M.N., *Zh. Prikl. Khim.*, 2001, vol. 74, no. 7, pp. 1075–1077.
31. Morachevskii, A.G., Vaisgant, Z.I., Kal'ko, O.A., *et al.*, *Zh. Prikl. Khim.*, 1997, vol. 70, no. 1, pp. 167–168.
32. Zaikov, Yu.P., Arkhipov P.A., Kryukov, K.V., *et al.*, *Tsvetn. Met.*, 1997, no. 6, pp. 32–33.
33. Smirnov, M.P., Sorokina, V.S., and Gerasimov, R.A., *Tsvetn. Met.*, 1996, no. 9, pp. 13–17.
34. Morachevskii, A.G., Kal'ko, O.A., and Vaisgant, Z.I., *Zh. Prikl. Khim.*, 1995, vol. 68, no. 11, pp. 1899–1900.
35. Kozin, L.F. and Morachevskii, A.G., *Fizikokhimiya i metallurgiya vysokochistogo svintsa* (Physical Chemistry and Metallurgy of High-Purity Lead), Moscow: Metallurgiya, 1991.
36. Schwartz, H.D. and Etsell, T.N., *Hydrometallurgy*, 1997, vol. 47, nos. 2–3, pp. 275–279.
37. Ashikhmin, V.V., Kharitidi, G.P., Starkov, K.E., and Yakovleva, L.M., *Tsvetn. Met.*, 1999, no. 5, pp. 32–34.
38. Larin, V.F., Kim, G.V., Devchich, I.I., *et al.*, *Perspektivnye tekhnologicheskie protsessy i oborudovanie v tsvetnoi metallurgii: Sbornik nauchnykh trudov* (Promising Processes and Equipment of Nonferrous Metallurgy: Coll. of Sci. Works), Ust-Kamenogorsk: VNIItsvetmet, 1988, pp. 12–18.
39. Mantsevich, N.M., Besser, A.D., Gnatovskii, E.S., and Pashchenko, G.G., *Tsvetn. Met.*, 1995, no. 11, pp. 21–25.

40. Besser, A.D., Pashchenko, G.G., Kalnin, E.I., *et al*., *Tsvetn. Met*., 1996, no. 4, pp. 53–55.
41. Tarasov, A.V., *Tsvetn. Met*., 2001, no. 6, pp. 70–75.
42. Tarasov, A.V., Besser, A.D., and Grishin, Yu.G., *Tsvetn. Metall*., 2001, no. 7, pp. 47–48.
43. Besser, A.D., *Tsvetn. Met*., 2001, no. 8, pp. 34–36.
44. Shustrov, A.Yu. and Minenko, Yu.A., *Tsvetn. Met*., 1999, no. 8, pp. 22–25.
45. Margulis, E.V., *Erzmetall*., 2000, vol. 53, no. 2, pp. 85–89.
46. Barbin, N.M., Kazantsev, G.F., Moiseev, G.K., and Vatolin, N.A., Abstracts of Papers, *XI konferentsiya po fizicheskoi khimii i elektrokhimii rasplavlennykh i tverdykh elektrolitov* (XI Conf. on Physical Chemistry and Electrochemistry of Molten and Solid Electrolytes), Yekaterinburg: Ural. Otd. Ross. Akad. Nauk, 1998, vol. 1, pp. 103–104.
47. Moiseev, G.K., Marshuk, L.A., Kazantsev, G.F., *et al*., *Metally*, 1999, no. 3, pp. 27–34.
48. Barbin, N.M., Kazantsev, G.F., Moiseev, G.K., and Vatolin, N.A., in *Ural: Nauka, Ekologiya* (Urals: Science and Ecology), Yekaterinburg: Ural. Otd. Ros. Akad. Nauk, 1999, pp. 288–300.
49. Barbin, N.M., Kazantsev, G.F., Moiseev, G.K., and Vatolin, N.A., *Vestn. Ural'sk. Gos. Tekh. Univ.–Ural'sk. Politekh. Inst*., 2000, no. 1(9), pp. 117–120.
50. Kazantsev, G.F., Moiseev, G.K., Vatolin, N.A., and Barbin, N.M., *Tsvetn. Met*., 2001, no. 8, pp. 44–46.
51. Nekrasov, V.N., Barbin, N.M., Terent'ev, D.I., and Moiseev, G.K., *Rasplavy*, 2001, no. 6, pp. 51–61.
52. Nekrasov, V.N., Barbin, N.M., Terent'ev, D.I., and Moiseev, G.K., Abstracts of Papers, *XII konferentsiya po fizicheskoi khimii i elektrokhimii rasplavlennykh i tverdykh elektrolitov* (XII Conf. on Physical Chemistry and Electrochemistry of Molten and Solid Electrolytes), Nalchik: Kabardino-Balkarsk. Univ., 2001, vol. 1, pp. 203–207.
53. Barbin, N.M., Nekrasov, V.N., Terent'ev, D.I., and Kazantsev, G.F., *Trudy X Rossiiskoi konferentsii "Stroenie i svoistva metallicheskikh i shlakovykh rasplavov"* (Proc. X Russian Conf. "Structure and Properties of Metal and Slag Melts"), Yekaterinburg, 2001, Chelyabinsk: Yuzhno-Ural'sk. Gos. Univ., 2001, vol. 1, pp. 182–189.
54. Moiseev, G.K., Vyatkin, G.P., Barbin, N.M., and Kazantsev, G.F., *Primenenie termodinamicheskogo modelirovaniya dlya izucheniya vzaimodeistvii s uchastiem ionnykh rasplavov* (Use of Thermodynamic Modeling for Study of Interactions Involving Ionic Melts), Chelyabinsk: Yuzhno-Ural'sk. Gos. Univ., 2002.
55. Barbin, N.M., Kazantsev, G.F., and Vatolin, N.A., *Pererabotka vtorichnogo svintsovogo syr'ya v ionnykh solevykh rasplavakh* (Processing of Lead-Bearing Secondary Raw Materials in Ionic Salt Melts), Yekaterinburg: Ural'sk. Otd. Ross. Akad. Nauk, 2002.
56. Moiseev, G.K. and Vyatkin, G.L., *Termodinamicheskoe modelirovanie v neorganicheskikh sistemakh* (Thermodynamic Modeling in Inorganic Systems), Chelyabinsk: Yuzhno-Ural'sk. Gos. Univ., 1999.
57. Morachevskii, A.G., Kal'ko, O.A., and Vaisgant, Z.I., *Zh. Prikl. Khim*., 1995, vol. 68, no. 11, pp. 1899–1903.
58. Vaisgant, Z.I., Morachevskii, A.G., Klebanov, E.B., and Kal'ko, O.A., Abstracts of Papers, *2-i Mezhdunarodnyi simpozium "Problemy kompleksnogo ispol'zovaniya rud"* (2nd Int. Symp. "Problems of Integrated Use of Ores"), St. Petersburg, May 20–24, 1996, pp. 109–110.
59. Morachevskii, A.G., Vaisgant, Z.I., and Demidov, A.I., *Elektrokhimiya svintsa v ionnykh rasplavakh* (Electrochemistry of Lead in Ionic Melts), St. Petersburg: Khimiya, 1994.
60. Morachevskii, A.G., *Zh. Prikl. Khim*., 1999, vol. 72, no. 1, pp. 3–10.
61. Morachevskii, A.G., Vaisgant, Z.I., Khabachev, M.N., and Mal'tsev, V.I., *Zh. Prikl. Khim*., 2000, vol. 73, no. 1, pp. 3–7.
62. Khabachev, M.N., Liquation and Structural Changes in Crystallization of Binary Alloys of Nonferrous Metals under Varied Gravitational Conditions, *Cand. Sci. Dissertation*, St. Petersburg, 2001.
63. Morachevskii, A.G., Vaisgant, Z.I., and Mal'tsev, V.I., *Zh. Prikl. Khim*., 1999, vol. 72, no. 4, pp. 692–693.
64. Morachevskii, A.G., Vaisgant, Z.I., Bochagina, E.V., *et al*., Abstracts of Papers, *Mezhdunarodnaya konferentsiya "Metallurgicheskie tekhnologii i ekologiya"* (Int. Conf. "Metallurgical Technologies and Ecology"), St. Petersburg, June 12–15, 2001, pp. 88–89.
65. Omel'chuk, A.A., Zarubitskii, O.G., Opanasyuk, V.P., *et al*., Abstracts of Papers, *XII Rossiiskaya konferentsiya po fizicheskoi khimii i elektrokhimii rasplavlennykh i tverdykh elektrolitov* (XII Russian Conf. on Physical Chemistry and Electrochemistry of Molten and Solid Electrolytes), Nalchik: Kabardino-Balkarsk. Univ., 2001, vol. 1, pp. 203–207.
66. Morachevskii, A.G., Bochagina, E.V., and Khabachev, M.N., Abstracts of Papers, *X Kol'skii seminar po elektrokhimii redkikh metallov* (X Kola Seminar on Electrochemistry of Rare Metals), Apatity, 2000, p. 60.
67. Morachevskii, A.G., Maiorova, E.A., and Romanchenko, M.N., *Zh. Prikl. Khim*., 1997, vol. 70, no. 8, pp. 1251–1253.
68. Morachevskii, A.G. and Bochagina, E.V., *Zh. Prikl. Khim*., 2000, vol. 73, no. 6, pp. 898–900.

69. Morachevskii, A.G., *Zh. Prikl. Khim.*, 1997, vol. 70, no. 11, pp. 1772–1776.
70. Morachevskii, A.G. and Bochagina, E.V., *Zh. Prikl. Khim.*, 2000, vol. 73, no. 5, pp. 718–723.
71. Morachevskii, A.G. and Bochagina, E.V., *Zh. Prikl. Khim.*, 2000, vol. 73, no. 7, pp. 1084–1086.
72. Zivković, D., Zivković, Z., and Tasić, I., *Thermochim. Acta*, 2000, vol. 362, nos. 1–2, pp. 113–120.
73. Morachevskii, A.G. and Butukhanova, T.V., *Zh. Prikl. Khim.*, 1997, vol. 70, no. 8, pp. 1245–1250.
74. Morachevskii, A.G., Vaisgant, Z.I., and Bochagina, E.V., *Zh. Prikl. Khim.*, 2000, vol. 73, no. 3, pp. 372–377.
75. Morachevskii, A.G. and Bochagina, E.V., *Zh. Prikl. Khim.*, 2002, vol. 75, no. 3, pp. 375–379.
76. Brecka, G., Yein, K., Lange, H.-J., and Paschan, P., *J. Met. (JOM)*, 1997, no. 4, pp. 62–64.
77. Nikitin, A.A., Nefedov, A.N., Zhulanova, A.G., and Shpakova, S.G., *Nov. Nauki Kaz.*, 1997, no. 1, pp. 31–35.
78. Kozin, L.F. and Morachevskii, A.G., *Zh. Prikl. Khim.*, 1990, vol. 63, no. 9, pp. 1913–1926.
79. Lebedev, I.S., *Tsvetn. Met.*, 2001, no. 8, pp. 42–43.
80. Kenzhaliev, B.K., Govyadovskaya, O.Yu., and Kaizhanova, A.K., *Kompl. Ispol'z. Miner. Syr'ya*, 2000, nos. 3–4, pp. 48–53.
81. Yurkinskii, V.P. and Sokolova, N.V., *Zh. Prikl. Khim.*, 1999, vol. 72, no. 10, pp. 1592–1595.
82. Yurkinskii, V.P., Sokolova, N.V., and Popov, V.A., *Zh. Prikl. Khim.*, 2001, vol. 74, no. 3, pp. 419–421.
83. Plekhanov, K.A., Sheveleva, L.D., Zaikov, Yu.P., and Naboichenko, S.S., *Tsvetn. Metall.*, 1998, nos. 11–12, pp. 46–48.
84. Rusin, A.I. and Kol'tsov, M.A., *Elektrokhim. Energet.*, 2002, vol. 2, no. 4, pp. 193–195.
85. Siryk, V.V., *Tsvetn. Metall.*, 2001, no. 7, pp. 24–27.
86. Kolotyrkin, Ya.M. and Tkachek, Z.A., *Ross. Khim. Zh.*, 1993, vol. 37, no. 4, pp. 61–66.
87. Pashchenko, O.A., *Ekol. Priborostr.*, 1991–1992, no. 1, pp. 42–44.
88. Rusakov, N.V. and Doner'yan, L.G., *Tsvetn. Met.*, 2001, no. 8, pp. 46–47.
89. Behrendt, H.-P. and Steil, H.-U., *Erzmetall.*, 1997, vol. 50, no. 6, pp. 398–405.
90. Behrendt, H.-P., *Erzmetall.*, 2001, vol. 54, no. 9, pp. 439–445.

Russian Journal of Applied Chemistry, Vol. 76, No. 9, 2003, pp. 1438–1443. Translated from Zhurnal Prikladnoi Khimii, Vol. 76, No. 9, 2003, pp. 1477–1482.

APPLIED ELECTROCHEMISTRY AND CORROSION PROTECTION OF METALS

Electrolytic Synthesis of Complex Oxide Systems by Cathodic Deposition of Molybdenum Oxide from Aqueous Solutions in the Presence of Nickel(II) and Thiosulfate Ions

V. M. Nagirnyi, R. D. Apostolova, A. S. Baskevich, and E. M. Shembel'

Ukrainian State University of Chemical Engineering, Dnepropetrovsk, Ukraine

Received February 27, 2002; in final form, June 2003

Abstract—Cathodic processes occurring in electrolytic deposition of molybdenum oxide from aqueous solutions of sodium molybdate in the presence of nickel(II) and thiosulfate ions were studied. Conditions for formation of cathodic deposits in the form of complex oxide systems Mo–Ni and Mo_4O_{11}–MoS_2 were determined.

The interest in electrolytic oxide materials is due to their enhanced electrochemical activity and the possibility of creating thin-film ballast-free cathodes for lithium power cells by direct deposition of an oxide material in the form of a compact coating on a metallic support [1–3]. Previously, the possibility of electrolytic synthesis of molybdenum oxide with nonstoichiometric composition in high yield by cathodic deposition from ammonium molybdate solutions has been demonstrated [4]. With account of the modern tendency toward development of high-performance cathode materials for lithium batteries on the basis of complex multicomponent oxide systems, it seemed appropriate to study the possibility of obtaining these materials in quantitative yield by electrolytic deposition of molybdenum oxide in the presence of nickel(II) and thiosulfate ions.

According to the results of preliminary experimental tests, cathodic deposits formed under certain electrolysis conditions from sodium molybdate solutions containing $NiSO_4$ are homogeneous mixtures of molybdenum oxide, nickel (NiO), and a single-phase compound of the type $NiO \cdot Mo_4O_{11}$, $Ni_xM_{4-x}O_{11+y}$. The presence of an electrolytic oxide system Mo–Ni creates certain prerequisites for formation of a sulfide phase (NiS, MoS_2, etc.) in joint deposition at the cathode of molybdenum and nickel oxides in the presence of thiosulfate ions, which may be promoted by the catalytic activity of nickel compounds [5]. This is confirmed by X-ray diffraction patterns of deposits obtained by electrolysis from solutions containing mixtures of the compounds mentioned above. Of interest is a study of cathodic processes and of the preparation conditions and properties of cathodic deposits formed by electrolytic deposition of molybdenum oxide in the presence of nickel(II) and thiosulfate ions.

As base for the study served Na_2MoO_4 solution, which, in contrast to $(NH_4)_2MoO_4$, rules out formation of complexes and molecular ammonia in the course of electrolysis. The solutions were prepared from chemicals of pure and analytically pure grades and distilled water. The electrolysis was performed in a temperature-controlled 0.2 dm^3 cell. As cathode samples served smooth $10 \times 10 \times 0.3$-mm 12Cr18Ni9Ti steel plates with current lead in the form of a thin strip of the same steel. As anodes were used smooth plates of technical-grade VT-1 titanium with $S_c : S_a = 1 : 5$. The materials to be studied were obtained in the form of compact coatings on both sides of the cathode. The experiments were carried out in two-component solutions of Na_2MoO_4 and $NiSO_4$ at their total concentration of 0.12–0.14 M and concentration ratios of 7 : 1 to 1 : 12 (here and hereinafter, molar ratios). The first digits refer to the base component, and the second, to the doping component.

To analyze the influence exerted by the total concentration of the solutions on the nature of the processes under study, experiments at higher concentrations (up to 0.17–0.19 M) were also carried out at a temperature of 85 ± 3°C chosen on the basis of preliminary tests. The efficiency of the cathodic process was evaluated by the conventional current efficiency CE_{conv} (wt %) on the assumption that the whole useful current is expended for formation of molybdenum oxide, whose formula is Mo_4O_{11} according to X-ray structural analysis. In this compound, molybdenum is

1070-4272/03/7609-1438$25.00

pentavalent, and, therefore, Mo_4O_{11} can be regarded as doubled oxide Mo_2O_5 with one coordinated oxygen atom. The latter compound is formed in accordance with the standard equation by a two-electron reaction and, therefore, the electrochemical equivalent can be taken to be

$$[Mo_2O_3]/(2 \times 26.8) = 272/(2 \times 26.8) = 5.07 \text{ g (A h)}^{-1}.$$

Polarization curves j_c–E were measured in a special U-shaped cell on the initial surface of the 12Cr18Ni9Ti steel cathode with the roughness corresponding to ∇ 7–8 at $S_c : S_a = 1 : 5$ ($S_c = 1$ cm^2) and on a film of cathodic deposit, formed preliminarily at j_c = 0.5–50 A cm^{-2}. The nonworking parts of the cathode surface were insulated with an acid-and-alkali-resistant varnish. The potentials were measured relative to a silver chloride reference electrode (E = +0.225 V) with an Shch-4315 digital instrument. The phase composition of the deposits and their approximate quantitative composition were determined by X-ray diffraction analysis on a DRON-2 installation [6].

The dependences of CE_{conv} on the current density j_c in electrolysis of two-component solutions of Na_2MoO_4 and $NiSO_4$ with varied Mo : Ni molar concentration ratios and pH values are shown in Fig. 1. The shape and relative positions of the curves indicate that the ratio of solution component concentrations and the pH value exert a desicive influence on the efficiency and nature of the cathodic processes under study.

At increased pH values (5.5–6.0) and concentration ratios Mo : Ni ≤ 1 in solution, the maximum values of CE_{conv} do not exceed 25%, with the quantitative formation of deposit on the cathode limited to the range j_c = 1.5–5.0 A cm^{-2}, which becomes narrower with increasing relative concentration of nickel(II) ions. In the limiting case (Mo : Ni = 1 : 12), the stability of the electrolysis process is disturbed and mainly hydroxide and metallic nickel start to deposit at the cathode (Fig. 1, curve *2*). The dependence CE_{conv}–j_c for the concentration ratio Mo : Ni = 7 : 1 (Fig. 1, curve *1*) is shifted to higher j_c and has a maximum at j_c > 10 mA cm^{-2}. Deposits of black color with bluish tint, characteristic of molybdenum oxide, are formed on the cathode, which indicates that mainly this compound is contained in the cathodic product. Lowering the solution pH to 3.0–3.5 makes the range of "effective" current densities much wider, with a simultaneous increase in the current efficiency by the cathodic deposit (Fig. 1, curves *1*'–*4*'). The corresponding curves become nearly linear and are arranged in order of increasing CE_{conv} with decreasing relative concentration of nickel ions in solution. The outward appearance of the cathodic deposits changes when passing to higher current densities and molybdate ion contents, and the deposits show tendency toward increasing compactness and susceptibility to brittle failure. In this case, the deposit changes its color from dark gray to bluish black, characteristic of molybdenum oxide deposits.

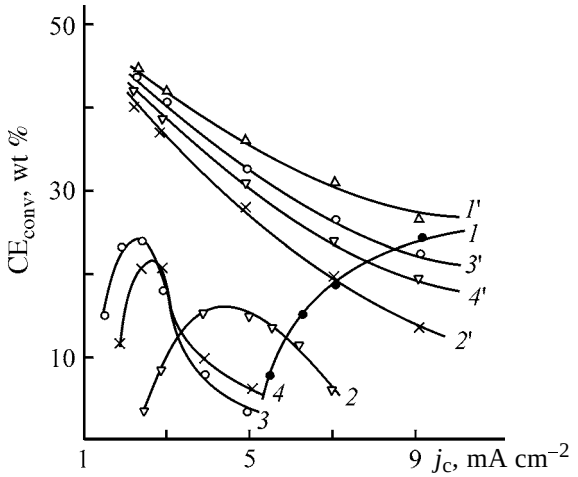

Fig. 1. Conventional current efficiency CE_{conv} vs. current density j_c for cathodic deposits formed in electrolysis of mixed solutions of Na_2MoO_4 and $NiSO_4$. Total concentration 0.12–0.14 M, T = 85°C; the same for Figs. 2 and 4. Mo : Ni concentration ratio: (*1*, *1*') 7 : 1, (*2*, *2*') 1 : 12, (*3*, *3*') 1.5 : 1, and (*4*, *4*') 1 : 1.3. pH: (*1*–*4*) 5.5 and (*1*'–*4*') 3.5.

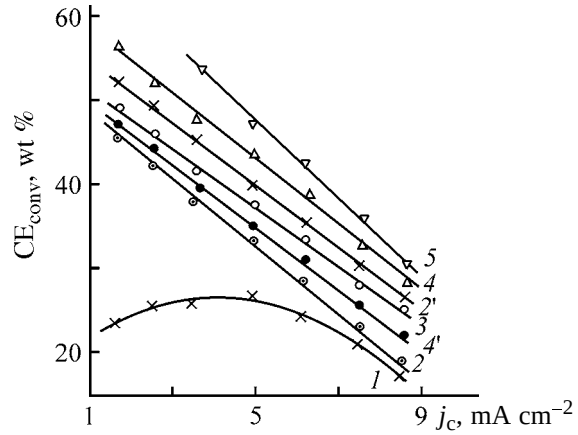

Fig. 2. Conventional current efficiency CE_{conv} vs. current density j_c for cathodic deposits formed in electrolysis of mixed solutions of Na_2MoO_4 and $NiSO_4$ in the presence of 0.01 M $Na_2S_2O_3$. Mo : Ni concentration ratio: (*1*) 1 : 12, (*2*, *2*') 7 : 1, (*3*) 1 : 2.7, (*4*, *4*') 1 : 1.3, and (*5*) 1.5 : 1. pH: (*1*–*5*) 5.5 and (*2*', *4*') 3.5.

Adding $Na_2S_2O_3$ (0.004–0.02 M) to the solutions under study leads to a dramatic increase in the efficiency of the cathodic process in weakly acidic solutions (pH 5.5) at any concentration ratio Mo : Ni (Fig. 2). In this case, nearly all the dependences are

strictly linear in a rather wide range of j_c, irrespective of the solution pH (Fig. 2). The only exception is the dependence for Mo : Ni = 7 : 1 in a solution with pH 5.5, having a maximum at j_c = 3.5 mA cm^{-2}. The corresponding curves are arranged in order of increasing CE_{conv} with decreasing relative concentration of nickel ions in solution at Mo : Ni = 1 : 2.7 to 1.5 : 1. However, at Mo : Ni = 7 : 1, the conventional current efficiency is much lower than that at the inverse ratio of the main components in solution, Mo : Ni = 1 : 12 (Fig. 2, curves *1* and *2*). Lowering the solution pH to 3.5, conversely, makes the tendency toward increase in CE_{conv} at Mo : Ni $\leq$ 1 more pronounced.

Changing the total concentration of the molybdenum and nickel salts from 0.8 to 0.16 M has no pronounced effect on the dependences under consideration or outward appearance of the deposits formed. However, other combinations with higher total content of the main components in solution are, in principle, also possible, including those with thiosulfate ions, for which the properties of the cathodic deposits, characteristic of the conditions under study, are preserved.

In a single-component solution of Na_2MoO_4 (0.1–0.12 M), addition of $Na_2S_2O_3$ at the molar concentration ratio of these compounds of 10 : 1 to 10 : 4 also affects somewhat the value of CE_{conv} and the outward appearance of molybdenum oxide deposits. At the same time, the presence of thiosulfate ions in a nickel sulfate solution (0.005–0.06 M) totally suppresses deposition of nickel hydroxide on the cathode, irrespective of the thiosulfate ion concentration and electrolysis parameters. Possibly, this is the reason why the dependences measured at different Mo : Ni concentration ratios in solution (1 : 12 and 7 : 1) are dissimilar. For example, in the first case, i.e., at high relative concentration of nickel ions in solution, deposition of nickel oxide is nearly completely suppressed and mostly molybdenum oxide and molybdenum sulfide are deposited on the cathode, which leads to an increase in CE_{conv}. In the second case, the codeposition of nickel oxide lowers the rate of formation of the cathodic deposit, which leads simultaneously to equalization of its values at different current densities.

An apparent factor determining the nature of the processes under consideration is the ratio of the amounts of molybdenum and nickel oxides simultaneously deposited at the cathode, and also hydrogen, in the presence of thiosulfate ions and without them. Here, account should be taken of the fact that, when the cathodic deposit is formed, deposition of nickel oxide is preceded by that of nickel hydroxide because of the alkalization of the near-cathode layer:

$$H_2O + e \rightarrow 1/2H_2 + OH^-.$$

In joint deposition and in interaction with the simultaneously deposited molybdenum oxide, nickel hydroxide may lose a water molecule:

$$Ni(OH)_2 + Mo(oxid) \rightarrow NiO + Mo(oxid)\cdot H_2O, \quad (1)$$

$$Mo(oxid)\cdot H_2O + e \rightarrow Mo(oxid) + 1/2H_2 + HO^-. \quad (2)$$

Also possible is simultaneous direct discharge of nickel hydroxide with the loss of a water molecule to give nickel oxide. This can account for the strong influence of the solution pH on the efficiency of the cathodic process, all other electrolysis conditions being the same.

At increased pH values (5.5–6.0) the rate of nickel hydroxide formation at small current densities exceeds that of the joint reaction of molybdenum oxide deposition, and the limiting diffusion current is reached already at relatively low values of j_c (Fig. 1). The deposits formed in this case are inhomogeneous mechanical mixtures of nickel oxide, nickel hydroxide, and molybdenum oxide, and at molybdenum to nickel concentration ratios Mo : Ni < 1 nickel hydroxide and metallic nickel are deposited predominantly (as fine dendrites). Lowering the solution pH decelerates alkalization of the near-cathode layer and thereby changes the ratio of formation rates of nickel hydroxide and molybdenum oxide in such a way that the latter becomes higher and, correspondingly, reactions (1) and (2) proceed at all Mo : Ni concentration ratios. However, hydrogen evolution, whose rate grows with increasing current density, becomes predominant in the overall cathodic process at higher relative concentrations of nickel ions. This correlates with the corresponding decrease in CE_{conv} (Fig. 1, curves *1*'–*4*').

A similar type of the overall cathodic process is also possible in the presence of thiosulfate ions in solutions with pH 5.5–6.0. However, the mechanism of separate and joint reactions is more complex in this case (Fig. 2). This should, presumably, be attributed to the influence exerted by products formed in reduction of thiosulfate ions at the cathode, and sulfur and its compounds in particular. For example, hydrogen sulfide can "acidify" the near-cathode layer, which leads to a decrease in the rate of nickel hydroxide formation, observed in acid solutions (pH 3.0–3.5), and to the corresponding increase in the rate of the reactions occurring in parallel. This is manifested to

a greater extent at molar concentration ratio Mo : Ni ≥ 1 in solution (Fig. 2, curves *2*' and *4*').

The aforesaid is in satisfactory agreement with current–voltage characteristics of the cathodic processes under study, measured at different compositions and pH values of the solutions used (Fig. 3). A common feature of all the j_C–E dependences is the presence of two transition steps connecting three ascending portions (Fig. 3). For each pH value, the lower and upper transition steps are arranged so that the j_C values corresponding to these steps decrease as the relative concentration of nickel ions in solution is made lower. The curves are arranged in the same order with respect to cathode potentials. In this case, a decrease in pH leads to a shift of the corresponding curves (Fig. 3, curves *4* and *5*) relative to their analogs for solutions with increased pH 5.5 (Fig. 3, curves *1* and *3*) to more negative potentials. In the same solution, the process occurs at a stronger cathodic polarization on a surface with preliminarily deposited film of a cathodic deposit (Fig. 3, curves *1* and *1*'); however, the steps in the corresponding curve are smoothed in this case (Fig. 3, curve *1*').

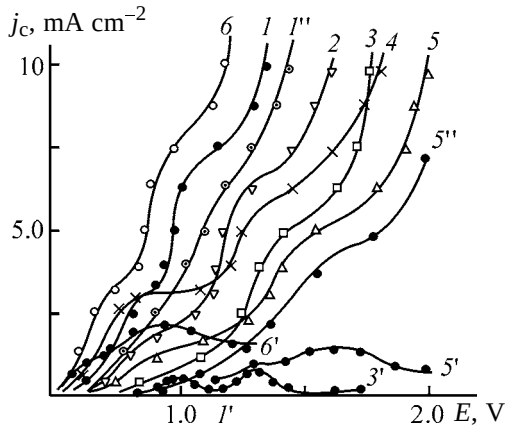

Fig. 3. Cathode potential E vs. current density j_C in electrolysis from mixed solutions of Na_2MoO_4 and $NiSO_4$. pH: (*1*, *1*', *1*'', *2*, *3*, *3*', *6*, *6*') 5.5 and (*4*, *5*, *5*', *5*'') 3.5. Overall cathodic processes, Mo : Ni concentration ratio: (*1*, *5*) 1 : 12; (*1*'') 1 : 12, on a preliminarily formed deposit film; (*2*) 1 : 1.3; (*3*, *4*) 7 : 1; and (*6*) 1 : 12, 0.01 M $Na_2S_2O_3$. Partial processes of cathodic deposit formation, Mo : Ni concentration ratio: (*1*', *5*') *1* : 12; (*3*') 7 : 1; and (*6*') 1 : 12, 0.01 M $Na_2S_2O_3$. Hydrogen evolution, Mo : Ni concentration ratio: (*5*'') 1 : 12.

In the presence of thiosulfate ions at equal Mo : Ni concentration ratios in solution, the curves are shifted to lower cathode potentials so that they remain parallel to the initial lines (without $S_2O_3^{2-}$ ions; Fig. 3, curve *6*), with a simultaneous increase in the current densities corresponding to the transition steps. The partial curves of cathodic deposit formation exhibit a gradual rise to a certain limiting plateau (Fig. 3) with a noticeable step-like transition at lowered intensity of alkalization of the near-cathode layer (Fig. 3, curves *5*' and *6*'). With the cathode potential increasing further, the polarizing current decreases to a certain constant minimum value. The extremum points of the partial curves coincide with the point of transition from the second step in the overall curves to the upper ascending portions. The partial curve of hydrogen evolution lies to the right from the corresponding overall curve, nearly in parallel to this curve, which points to the key role of this process in the kinetics of the overall cathodic process (Fig. 3, curve *5*').

The behavior of the j_C–E dependences under consideration (Fig. 3) indicates that the nature of the cathodic process changes with polarizing current. The step-like dependence of this current on the cathode potential is apparently due to a change in the rate ratio of the individual reactions simultaneously occurring at the cathode. The lower portions of the curves are mainly associated with the formation of nickel hydroxide, accompanied by hydrogen evolution and deposition of molybdenum oxide. In the partial curves (Fig. 3, curves *1*', *3*' and *5*', *6*'), this is manifested by the initial gently sloping and ascending portions. Reaching the limiting current of nickel ion diffusion leads to enhancement of the cathodic polarization and gives rise to the corresponding transition plateaus. The polarizing current corresponding to the extremum points of the lower transition plateaus is closely associated with the relative concentration of nickel ions in solution for each pH value. In solutions with lowered pH value (3.0–3.5), the alkalization of the near-cathode layer is slower, which decelerates nickel hydroxide formation and leads to higher limiting diffusion currents.

The rise in the cathodic polarization after reaching the extremum points of the lower transition step in the curves shifts the cathode potential to negative values, which leads to preferential deposition of molybdenum oxide, whose rate becomes a key factor in the transition region and second ascending portions of the overall curves. To the same factor correspond the steep rise portions and limiting plateaus of the partial curves. In this case, the overall cathodic process becomes more complex because of the simultaneous occurrence of nickel oxide deposition and hydrogen evolution. The limitation of the rate of molybdate ion diffusion toward the cathode surface with increasing polarizing current leads to the subsequent enhancement of the cathodic polarization, with predominance of the rate

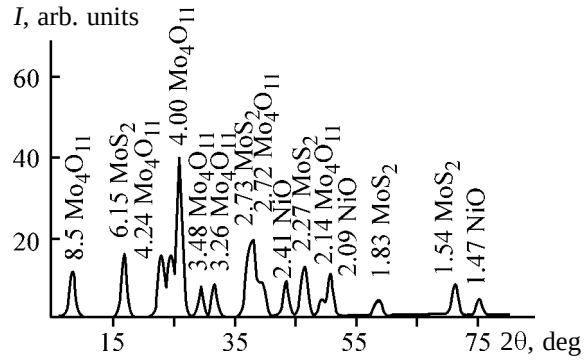

Fig. 4. X-ray diffraction pattern of the cathodic deposit in electrolysis of the solutions under study. Concentration ratio Mo : Ni = 1.5 : 1, pH 5.5, in the presence of 0.01 M $Na_2S_2O_3$. (*I*) Intensity and (2θ) Bragg angle.

of hydrogen evolution, and makes the lower plateaus of the partial curves more pronounced. This circumstance presumably accounts for the fact that the cathodic processes under consideration occur in an acid medium with pH 3.0 (Fig. 3, curves *4*, *5*, *5*') at higher cathodic polarization than in the case of solutions with lower acidity (pH 5.5).

At the same time, all the j_c–E curves in Fig. 3 are shifted with respect to one another to higher cathode potentials with increasing relative concentration of molybdate ions in solution. This is possibly due to strong cathodic polarization of the discharge of MoO_4^{2-} ions and to high hydrogen overvoltage on the surface of the cathodic deposit formed at a sufficient rate in the range corresponding to the second and third portions of the curves. Correspondingly, the transition plateaus between these portions are arranged in order of decreasing current densities corresponding to these plateaus because of the change in the relative rates of hydrogen evolution and molybdenum oxide deposition, with a steady increase in the latter. This is also indicated by a relative increase in the limiting currents of cathodic deposit formation for different pH values (Fig. 3, curves *1*', *3*', *5*') and in the length of the second ascending portions of the overall curves, which lie higher in the above sequence (Fig. 3, curves *1–3* and *4*, *5*).

The shape and relative positions of the overall and partial j_c–E curves for a solution containing $Na_2S_2O_3$ (Fig. 3, curves *6* and *6*') are in agreement with the suggested possible mechanism of influence exerted by thiosulfate ions on the kinetics of the cathodic process, which is manifested in a decrease in the cathodic polarization of the overall process. Together with the possible role played by thiosulfate ions in the "acidification" of the near-cathode layer of the solution owing to formation of hydrogen sulfide in discharge of $S_2O_3^{2-}$ ions and to an increase in the contribution of hydrogen evolution to the overall process, a certain contribution to the mechanism under consideration can be made by simultaneous deposition of sulfur at the cathode. Adsorption of sulfur on the electrode surface presumably makes lower the energy barrier to discharge of molybdate ions, by analogy with a similar phenomenon in electrolytic deposition of metals [7]. This is also confirmed by the relatively high peak in the corresponding partial curve (Fig. 3, curve *6*').

According to the results of an X-ray diffraction analysis, the deposits under study are multiphase systems with clearly pronounced phases of molybdenum oxide Mo_4O_{11}, nickel oxide NiO, and molybdenum sulfide (Fig. 4). The oxide phase of molybdenum, which is virtually independent of the solution composition and electrolysis parameters, predominates (88–95 wt %). The content of nickel oxide NiO and molybdenum sulfide MoS_2 in the deposits may vary within 0.5–3 and 1–9 wt %, respectively, with the greater values corresponding to higher content of the components in solution.

The structure and bonding in the systems under study cannot be described unambiguously on the basis of the available experimental data. However, with account taken of the inevitable interaction, on the molecular level, of the phases codeposited at the cathode in the course of electrolysis, it may be assumed that the materials obtained are homogeneous mixtures with a tendency toward ordered chemically interrelated structure. To obtain deposits with the optimal, under the experimental conditions, content of the doping phases, MoS_2 and NiO, the concentration ratio of the molybdenum and nickel salts in solution (total concentration 0.08–0.14 M) must fall within the range from 2 : 1 to 1 : 3 at $Na_2S_2O_3$ concentration equal to the lower concentration of the main component.

CONCLUSION

A study of the efficiency and current–voltage characteristics of the cathodic processes, and also of the phase composition of the cathodic deposits formed in electrolysis of mixed solutions of sodium molybdate and nickel sulfate (total concentration 0.08–0.14 M) in the presence of sodium thiosulfate (0.01–0.012 M) in relation to their composition and electrolysis conditions, revealed the possibility of obtaining in quantitative yield materials in the form of multiphase systems composed of a homogeneous mixture of nickel and

molybdenum oxides and sulfides. Stable electrolysis conditions are achieved at $85 \pm 3°C$, j_c = 3.5–7.5 mA cm^{-2}, pH 5.0–6.0, molar ratio of the components in the range from 2 : 1 to 1 : 3, and thiosulfate concentration of 0.01–0.012 M.

REFERENCES

1. Shembel', E.M., Apostolova, R.D., and Nagirnyi, V.M., *Elektrokhimiya*, 2000, vol. 36, no. 1, pp. 41–48.
2. Shembel', E.M., Nagirnyi, V.M., Apostolova, R.D., and Chaikovskaya, V.M., *Zh. Prikl. Khim.*, 2000, vol. 73, no. 3, pp. 409–412.
3. Shembel, E.M., Apostolova, R.D., Nagirny, V.M., *et al.*, *The 197th Meeting of the Electrochemical Society*, Toronto, May 14–18, 2000, p. 105.
4. Shembel', E.M., Nagirnyi, V.M., Apostolova, R.D., and Chaikovskaya, V.M., *Zh. Prikl. Khim.*, 2000, vol. 73, no. 3, pp. 409–412.
5. *Kratkaya khimicheskaya entsiklopediya* (Concise Chemical Encyclopedia), Moscow: Sovetskaya Entsiklopediya, 1964, vol. 3, pp. 470–471.
6. Mirkin, A.I., *Spravochnik po rentgenostrukturnomu analizu polikristallov* (Handbook of X-ray Diffraction Analysis of Polycrystals), Moscow: Gos. Izd. Fiz.-Mat. Lit., 1961.
7. Sadakov, G.A., *Gal'vanoplastika* (Electroplating), Moscow: Mashinostroenie, 1987.

Russian Journal of Applied Chemistry, Vol. 76, No. 9, 2003, pp. 1444–1450. Translated from Zhurnal Prikladnoi Khimii, Vol. 76, No. 9, 2003, pp. 1483–1489.

APPLIED ELECTROCHEMISTRY AND CORROSION PROTECTION OF METALS

Modifying Additives to Electrolytes for Anodic Treatment of Alloys in Development of Resource-Saving Technologies

E. A. Fedorova

Nizhni Novgorod State Technical University, Nizhni Novgorod, Russia

Received November 6, 2002; in final form, April 2003

Abstract—The effect of modifying additives on the processes of anodic treatment of alloys was studied and the role of adsorption effects in development of resource-saving technologies for metal working was established.

A topical problem of modern technologies for anodic treatment of metal articles consists in imparting certain functional properties to their surfaces at high output capacity and good environmental safety. The vast practical experience accumulated in this field mainly refers to treatment of surfaces of technically "pure" metals and high-alloy steels [1–3]. Solutions for electrochemical polishing (ECP), most widely used for this purpose, still include highly toxic phosphoric–sulfuric–chromic acid electrolytes. There is virtually no effective environmentally acceptable substitute for these solutions [2].

It has been established previously that the quality of anodic treatment of alloys in the conventional electrolytes becomes poorer with decreasing degree of steel alloying in the order 12Cr18Ni10Ti > 95Cr18 > 40Cr13 > 12Cr13 > 08kp [4] and with increasing degree of alloying of aluminum and titanium alloys in, respectively, the series AMg < AMts < D16 [5] and VT6 < VT8 < VT16 [6]. Introduction of modifying adamantane additives into the phosphoric–sulfuric acid solution for ECP, or their combination with glycerol or alkali metal cations in a phosphoric acid electrolyte, makes faster the smoothening of the microroughness of the alloy surface [4–6].

When selecting additives, two quantities are taken into account [3]: surface tension of the electrolyte with additive and the anodic polarization of a process, which, however, cannot serve as the only criteria in development of resource-saving technologies.

Here we analyze the influence exerted by additives introduced into modified electrolytes for ECP on the processes and results of anodic treatment of alloys in order to predict the electrolyte compositions and develop resource-saving technologies.

EXPERIMENTAL

Anodic treatment of alloys with varied degree of alloying was performed with electrolytes of different compositions (M): phosphoric acid (PA) 11 H_3PO_4; phosphoric–sulfuric acid (PSA) 10 H_3PO_4, 3.7 H_2SO_4; phosphoric–sulfuric acid glycerol (PSAG) 14 H_3PO_4, 0.5 H_2SO_4, 1.2 $C_3H_8O_3$ at 303–333 K for steels and aluminum alloys; hydrofluoric–sulfuric acid (HFSA) 11.5 H_2SO_4, 5.5 HF; and hydrofluoric–sulfuric acid glycerol (HFSAG) 11.5 H_2SO_4, 5.5 HF, 2.0 $C_3H_8O_3$ at 293 K for titanium alloys. Data on the elemental composition of the surface of steel and aluminum and titanium alloys, according to the results of electron-probe microanalysis, are listed in Tables 1–3.

As modifying additives were studied organic compounds with varied steric structure and different functional groups: linear [triethanolamine $N(C_2H_4OH)_3$] and heterocyclic (hexamethylenetetramine $C_6H_{12}N_4$) amines; alicyclic hydrocarbons of the adamantane series with the general formula $C_{10}H_{16-n}R_n$, where R is H (Ad, adamantane), OH (hydroxyadamantane),

Table 1. Elemental composition of steel surface

Steel	Composition of ECP solution	Content, wt %				
		Al	Si	Cr	Ni	Ti
12Cr18Ni10Ti	–	0.6	1.0	18.0	9.7	0.7
	PSA	0.4	0.9	18.2	9.8	0.8
30Cr13	–	0.9	2.0	13.2	<0.2	<0.2
	PSA	<0.2	0.7	13.2	<0.2	<0.2
95Cr18	–	0.7	2.0	17.8	<0.2	<0.2
	PSA	<0.2	0.7	18.2	<0.2	<0.2

1070-4272/03/7609-1444$25.00

Table 2. Elemental composition of aluminum alloy surface

Al alloy	Content, wt %				
	Mg	Mn	Ni	Cu	Fe
A6N	<0.2*	<0.2	0.61	<0.2	<0.2
	<0.2	<0.2	0.63	<0.2	<0.2
AMg	0.97	<0.2	<0.2	<0.2	0.37
	0.89	<0.2	<0.2	<0.2	0.26
AMts	0.89	1.03	<0.2	<0.2	0.38
	0.50	<0.2	<0.2	<0.2	0.38
D16	1.47	0.52	<0.2	3.69	0.35
	1.00	<0.2	<0.2	<0.2	0.26

* Numerator, data for the initial sample; denominator, for a sample subjected to anodic treatment in PSA electrolyte, J_a = 12 A dm^{-2}, T = 333 K, τ = 5 min.

Br (bromoadamantane), $NHCOCH_3$ (acetylaminoadamantane), and C_2H_4–$NH_2 \cdot HCl$ (Re, remantadine), and also their combinations with glycerol (Gl) or alkali metal cations.

Adsorption effects at the electrolyte–alloy interface in the initial and anodically polarized states were studied with a number of independent methods by measuring the contact angle for a drop of electrolyte [7], surface hardness by Rebinder [8], contact potential [5], and potential decay (with the differential pseudocapacitance determined) [9], and also using the potentiostatic and potentiodynamic methods at potential sweep rates of 0.01–0.02 V s^{-1} with correction for the ohmic voltage drop in a film [10].

The anodic polarization of the electrodes was done with P5848, ON-405, and PI-50-1 potentiostats, LKD-4 recorder, three-electrode glass (for steels and aluminum alloys) or fluoroplastic (for titanium alloys) cell, and saturated silver chloride reference electrode. The potentials are given relative to standard hydrogen electrode.

The elemental composition of the surface of the initial and polished samples was determined with a Philips SEM-515 scanning electron microscope (the Netherlands) with an EDAX-9900 energy-dispersive detector (the United States).

Changes in the functional properties of the alloy surface after anodic treatment were evaluated by substructure parameters: microscopic deformation ε and density of dislocations inside subgrains (ρ_e, cm^{-2}) and at their boundaries (ρ_L, cm^{-2}), determined on a DRON-3M diffractometer in CuK_α radiation by the approximation method, and also by surface roughness R_a (μm) and relative smoothening Y (%) [11].

X-ray diffraction analysis of the substructure parameters of the initial surface of the alloys demonstrated that raising the degree of alloying of aluminum and titanium alloys leads to an increase in the microscopic deformation level and density of dislocations, which are chaotically distributed and form subgrain boundaries. Each structural component of the alloys dissolved in the conventional electrolytes in a certain range of potentials at its own rate on applying anodic polarization, which was reflected in a change in the elemental composition of the alloy surface after anodic treatment (Table 1).

Partial replacement of water in PSA and HFSA ECP solutions with glycerol made less pronounced the selective etching of the alloying components of the alloys. In glycerol-containing electrolytes, the rates of anodic dissolution of aluminum alloys (evaluated by the etched layer thickness δ, μm) decreased, and the relative smoothening Y (%) of the article surfaces did

Table 3. Elemental composition of titanium alloy surface

Ti alloy	Alloying components, wt %			Impurities, no more than, wt %		
	Al	Mo	V	Zr	Fe	Si
VT1-0	–	–	–	–	0.2	0.08
	–	–	–	–	–	–
VT6	6.26*	–	3.9	0.2	0.2	0.15
	6.6–7.0	–	4.0–4.2	0.2	0.2	0.15
VT8	6.3–6.6	2.8–3.2	–	0.24	0.22	0.66
	6.6–8.0	3.4–4.0	–	0.2	0.26	0.4
VT16	3.4–3.5	5.0–5.1	3.9–4.0	0.2	0.25	0.2
	3.0–3.3	5.2–5.4	3.8–4.2	0.2	0.3	0.2

* Numerator, data for the initial sample; denominator, for a sample subjected to anodic treatment in HFSA electrolyte, J_a = 30 A dm^{-2}, T = 290 K, τ = 5 min.

Table 4. Effect of modifying additives to PSA electrolyte on the rate δ of anodic dissolution and relative smoothening *Y* of alloy surface

Modifier, M	Brand of aluminum alloy									
	AD1		A6N		AMg		AMts		D16	
	δ, μm	*Y*, %	δ, μm	*Y*, %	δ, μm	*Y*, %	δ, μm	*Y*, %	δ, μm	*Y*, %
–	4.46	42.8	4.60	41.4	4.68	36.8	5.05	37.2	5.35	34.7
$C_3H_8O_3$, 1.2	2.50	49.6	2.55	47.6	2.76	48.2	2.90	46.3	3.01	42.0
$C_3H_8O_3$, 1.2 + additive, 0.02:	3.47	53.0	3.68	51.8	3.84	50.8	2.97	48.5	3.97	46.4
Ad	2.49	69.8	2.53	69.2	2.62	67.6	2.81	64.8	2.96	64.5
AdP	3.10	70.4	3.15	68.5	3.26	65.6	3.38	67.7	3.41	60.8
Re	2.77	73.2	2.78	72.7	3.09	70.1	3.22	69.0	3.25	65.7

Table 5. Roughness R_a and microscopic deformation ε of alloy surface in ECP electrolytes. Initial roughness of alloy surface 0.63 μm, time of anodic treatment τ = 5 min

Alloy brand	R_a, μm	ε	Additive, M					
			$C_3H_8O_3$, 1.2–2.0		$C_3H_8O_3$, 1.2–2.0 + Ad, 0.7×10^{-2}		$C_3H_8O_3$, 1.2–2.0 + Re, 2.9×10^{-2}	
			R_a, μm	ε	R_a, μm	ε	R_a, μm	ε
Mg*	0.735	2×10^{-4}	0.380	3×10^{-5}	0.238	0	0.220	0
AMts*	0.726	2×10^{-4}	0.391	5×10^{-5}	0.289	0	0.224	0
D16*	0.730	3×10^{-4}	0.423	8×10^{-5}	0.342	0	0.250	0
VT-0**	0.825	1×10^{-4}	0.320	2×10^{-5}	0.238	0	0.256	0
VT6**	0.830	2×10^{-4}	0.342	3×10^{-5}	0.302	0	0.242	0
VT16**	0.825	1×10^{-3}	0.376	2×10^{-4}	0.342	3×10^{-5}	0.302	0

* Electrolyte composition, M: 14 H_3PO_4, 0.5 H_2SO_4; j_a = 12 A dm^{-2}; T = 333 K.
** Electrolyte composition, M: 11.5 H_2SO_4, 5.5 HF; j_a = 30 A dm^{-2}, T = 293 K.

not exceed 50% (Table 4). Also, a dependence of δ on the chemical composition of the surface layer of the alloys was clearly observed (Tables 1–4): with increasing degree of alloying, the rates of anodic dissolution became higher and the quality of the anodic treatment of article surfaces was impaired (Table 4).

The required functional properties of the alloy surfaces were achieved, with the microscopic deformation of the alloy surfaces eliminated (Table 5) and relative smoothening increased to 65–70%, only upon introduction into the electrolytes of modifying additives of the adamantane series, or when the solution contained simultaneously alkali metal cations and adamantane additives, or glycerol and adamantane additives.

The run of the isotherms of the surface tension σ_s (N m^{-1}) of the electrolytes with additives demonstrates that the chosen modifying additives of the adamantane series act as surfactants at the interface between the polishing electrolyte and vapor (Fig. 1, curve *1*). After anodic treatment, adamantane preserves its surface-active properties (Fig. 1, curve *2*). The observed slight increase in the surface tension of the electrolyte points a decrease in the surfactant concentration at the electrolyte–vapor interface, probably, because of the adsorption of the additives onto the electrode surface.

The behavior of the modifying additives in polishing electrolytes on the initial surface of the alloys is reflected in kinetic dependences of electrolyte drop spreading over the surface of 12Cr18Ni10Ti steel (Fig. 2). These curves exhibit two clearly pronounced "plateaus" characterized by quasi-equilibrium contact angles θ_0 and θ (Fig. 2), which made it possible to evaluate the surface energy of viscous spreading, ΔG^S and the spreading factor *S* (Table 6).

Comparison of the Gibbs energies of spreading of supporting electrolytes (ΔG^S = 14 mJ m^{-2}) and those with modifying additives (ΔG^S = 4–6 mJ m^{-2}) indicates that the additives introduced exert hindering action. This is also confirmed by the values of the spreading factor (Table 6).

The relationship between the surface tension and the surface concentration Γ in adsorption at low concentrations of additives is described by the Gibbs adsorption isotherm looking as follows in the integral form:

$$-\int_{\sigma_0}^{\sigma} d\sigma = RT\, d\ln c, \quad (1)$$

where σ_0 is the surface tension at the electrolyte–vapor interface, and σ is the interfacial tension at the electrolyte–alloy interface; for adsorption of an additive on the solid surface, $\sigma_0 \equiv \sigma_{a-v}$ and $\sigma \equiv \sigma_{a-a.l.}$, where σ_{a-v} and $\sigma_{a-a.l.}$ are the surface tensions at the interfaces between the alloy and the vapor and between the alloy and the adsorption layer, respectively; c is the concentration of the additive (M).

Using a combination of Young equations

$$\cos\theta_0 = (\sigma_{a-v} - \sigma_{e-a})/\sigma_{e-v} \quad (2)$$

(σ_{e-a} and σ_{e-v} are the surface tensions at the electrolyte–alloy and electrolyte–vapor interfaces, respectively), on the assumption that

$$\sigma_{a-v} = \text{const}, \quad d\sigma_{a-v}/dC = 0, \quad (3)$$

and taking into account Eq. (1), one can obtain a formula for calculating the surface concentration:

$$\Gamma_{a-a.l.} = \frac{d(\cos\theta)\sigma_{e-v}}{dc}\frac{c}{RT}. \quad (4)$$

Graphical differentiation of the curve describing the dependence $\sigma_{e-v}\cos\theta = f(\ln c)$ was used to calculate the maximum surface concentration of adamantane, $\Gamma_{max} = 5.0\times10^{-11}$ mol cm^{-2}, and remantadine, $\Gamma_{max} = 9.0\times10^{-11}$ mol cm^{-2}. This indicates that the adsorption occurs by the chemisorption mechanism to give associates of etching products of the alloy components [Fe(III), Fe(II), Cr(III), Cr(VI), Ni(II), Ti(IV), Al(III), and Mg(II)] with adamantane and remantadine. As a result, adsorbed molecules of the additives and their associates with metal ions are accumulated, in addition to metal phosphates and sulfates, in the viscous near-surface layer.

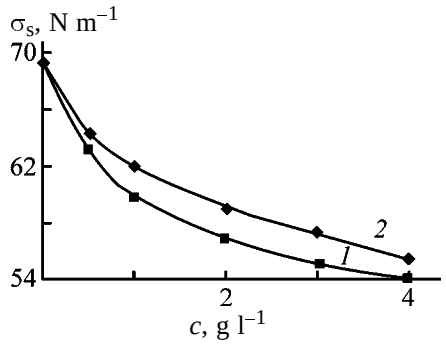

Fig. 1. Isotherms of surface tension σ_s of adamantane-containing PSA solution (*1*) before and (*2*) after adsorption on the surface of 12Cr18Ni10Ti steel. (*c*) Adamantane concentration. Solution (M): H_3PO_4 10 and H_2SO_4 3.7; the same for Figs. 2 and 5.

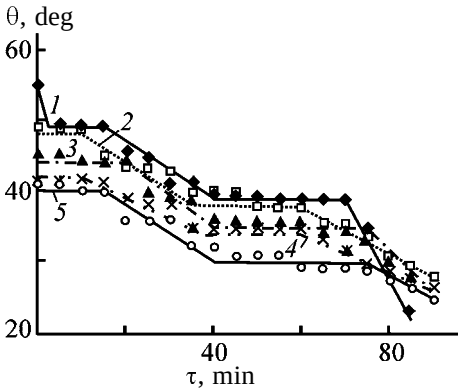

Fig. 2. Kinetic curves of spreading of a PSA solution drop over the surface of 12Cr18Ni10Ti steel. (θ) Spreading angle and (τ) spreading time. (*1*) Additive-free solution; adamantane additive (g l^{-1}): (*2*) 1.0, (*3*) 2.0, (*4*) 3.0, and (*5*) 4.0.

The dependences of the Rebinder surface hardness on the potential, identified with the electrocapillary curves of the work of surface formation [8] for anodically polarized D16 aluminum (Fig. 3) and VT16 titanium alloys (Fig. 4), are characterized, similarly to those measured on a 12Cr18Ni10Ti steel anode [8], by several clearly pronounced maxima E_{max} of hardness.

Table 6. Parameters of spreading of PSA electrolyte drop on steel surface in the presence of organic additives

Additive, 3 g l^{-1}	θ_0, deg/cosθ_0	θ, deg	$-\Delta G^S$, mJ m^{-2}	S, mJ m^{-2}
–	55/0.574	38	14	–29
Adamantane	42/0.743	34	5	–14
Hydroxyadamantane	41/0.755	32	5	–13
Remantadine	45/0.707	36	6	–14
Hexamethylene-tetraamine	48/0.669	39	6	–20

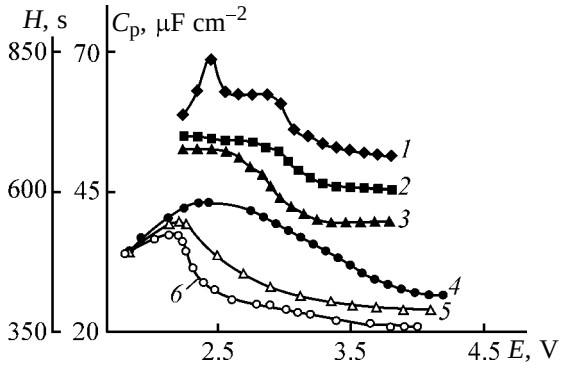

Fig. 3. (*1–3*) Work of surface formation, evaluated by the electrocapillary method, and (*4–6*) differential pseudocapacitance C_p vs. anode potential E of a D16 aluminum electrode at 293 K. 11.0 M H_3PO_4 solution with additive (M): (*1, 4*) K_2SO_4 0.17, (*2, 5*) $C_{10}H_{16}$ 7.3×10^{-3}, and (*3, 6*) K_2SO_4 0.17 and $C_{10}H_{16}$ 7.3×10^{-3}.

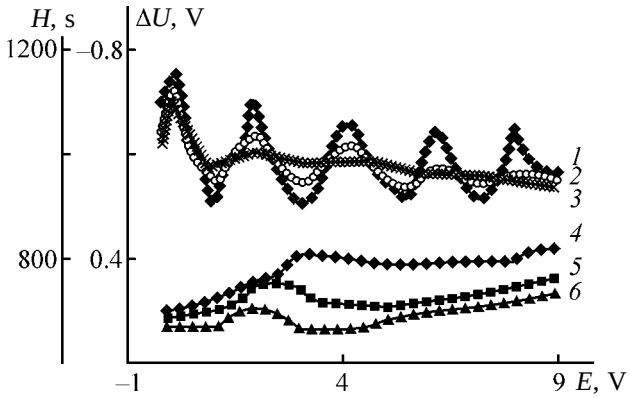

Fig. 4. (*1–3*) Work of surface formation H and (*4–6*) contact potential difference ΔU vs. anode potential of titanium (VT16) electrode at 293 K. Solution (M): (*1, 4*) H_2SO_4 11.5, HF 5.5, KF 0.52, and $C_3H_8O_3$, 2.0; (*2, 5*) the same + $C_6H_{12}N_4$ 0.02; (*3, 6*) the same as (*1, 4*) + $C_{10}H_{15}$–C_2H_4–$NH_2\cdot HCl$ 0.02.

Introduction of adamantane $C_{10}H_{16}$, hexamethylenetetramine $C_6H_{12}N_4$, remantadine $C_{10}H_{15}$–C_2H_4–$NH_2\cdot HCl$, and K_2SO_4 into the supporting electrolytes leads to a dramatic decrease in the work of anode surface formation near the maxima and to a slight increase in the hardness at its minima (Figs. 3, 4). This effect was particularly pronounced in solutions with additives belonging to the adamantane series or in the case of simultaneous presence of $C_{10}H_{16}$ and K_2SO_4 in solution.

The observed change in the contact potential difference ΔU (V) with increasing positive potential at the anodically oxidized alloys and growing oxidation time (Fig. 4), which reflects an increase in the electron work function λ_i [5], indicates that charged anodic films with excess negative charge are formed on the surface of anodically polarized alloys. After opening the circuit in air, these charges recombine, i.e., leak to the metal base. The presence of an excess negative charge in oxide films in anodic polarization of the titanium electrode correlates with the existence of several electrocapillary curves of the work of surface formation (Fig. 4).

Addition of adamantane, and especially introduction of a combination of K_2SO_4 and $C_{10}H_{16}$ additives into the supporting electrolyte, make the adsorption pseudocapacitance of the D16 alloy lower (Fig. 3).

The fact that modifying additives make lower the work of surface formation at peaks of the electrocapillary curves (Figs. 3, 4), the electron work function (Fig. 4), and the adsorption pseudocapacitance (Fig. 3) is a direct confirmation of adsorption of these additives on the surface of anodically polarized alloys in a wide range of potentials, including the potentials of electropolishing, under conditions of competitive adsorption of anions and radical anions (e.g., HSO_4'), radical hydrogen peroxide species HO_2', PO_4''', etc.

The chemisorption of adamantane molecules on the surface of an alloy being polished is also confirmed by results of mass-spectrometric analysis of an extracted solution obtained upon cathodic reduction of an oxide layer formed on the surface of the 12Cr18Ni10Ti steel in an electrolyte with addition of adamantane. Species characterized by m/z = 135 were found in the solution being analyzed, which corresponds to the presence of a highly stable adamantyl cation $C_{10}H_{15}^+$ in the solution. Thus, adamantane molecules may be incorporated into the surface anodic oxide layer (AOL) and affect its properties.

The electron work function of an anodically polarized VT16 alloy became lower in the presence of hexamethylenetetramine and, especially, remantadine in a glycerol-containing solution (Fig. 4). It may be assumed that species of modifying additives, e.g., remantadine, are chemisorbed on the surface of the titanium alloy and thereby give rise to impurity states with positive effective charge in the band gap of *n*-type titanium oxide TiO_2 [12], which leads to an increase in the free electron concentration in the oxide.

The facilitation of transport processes in the AOL may lead to an increase in the rate of metal ionization, compared to a glycerol-containing electrolyte without surfactant, which was confirmed experimentally for the example of aluminum alloys (Table 4). Automated correction for the ohmic voltage drop across the film made it possible to evaluate the resistance of the AOL on the D16 alloy to decrease from 440–480 to 237–

Table 7. Current efficiency CE^{all} for reactions of anodic dissolution of alloys and fraction of current Q_{O_2} consumed for O_2 evolution at different current densities j_a on 12Cr18Ni10Ti steel

j_a, A dm^{-2}	Electrolyte*					
	no. 1		no. 2		no. 3	
	CE^{all}, %	Q_{O_2}, %	CE^{all}, %	Q_{O_2}, %	CE^{all}, %	Q_{O_2}, %
20	73.8	20.9	63.8	26.9	60.0	27.8
30	63.6	38.2	53.6	38.2	51.6	32.3
40	56.8	37.3	46.8	47.3	44.5	38.2
50	52.5	43.3	42.5	52.3	41.9	43.0
60	50.2	44.2	40.2	54.2	39.3	45.4

* Electrolyte composition (M): no. 1: 11 H_3PO_4 and 0.5 H_2SO_4; no. 2: 11 H_3PO_4 and 0.17 K_2SO_4; no. 3: 10 H_3PO_4, 0.17 K_2SO_4, and 7.35×10^{-3} $C_{10}H_{16}$.

250 Ω cm^{-2} in the presence of 0.02 M of remantadine in a PSAG solution.

In a PSA electrolyte, the rates of anodic dissolution of the aluminum alloys decreased upon introduction of adamantane additives.

The ohmic resistance of AOL formed on 12Cr-18Ni10Ti steel in aqueous PA and PSA electrolytes with modifying additives increased, especially in the transpassive region, in the case when a film of reaction products was already formed on the anode surface. The film resistance related to unit surface area of a steel being treated increased from 15 to 25 and 29 Ω cm^{-2}, respectively, in the presence of adamantane and bromoadamantane in the PSA electrolyte and to 28 Ω cm^{-2} upon joint introduction of K_2SO_4 and adamantane additives into an aqueous PA polishing solution.

The observed hindrance of the anodic dissolution of the alloys by $C_{10}H_{16}$ (Table 4) and K_2SO_4 + $C_{10}H_{16}$ (Table 7) additives in aqueous PA and PSA ECP electrolytes will extend the working life of alloy–electrolyte process media in the case of chemical and electrochemical stability of the additives in the solutions.

A quantitative analysis by ascending chromatography for adamantane in a PSA electrolyte used for anodic treatment of steels and for remantadine in PSAG electrolyte used for aluminum alloys demonstrated that the content of the additives in the solutions remained virtually unchanged after passing 250 and 120 A h l^{-1} of electricity, respectively.

Measurements of the surface tension of polishing solutions with the surfactant additives under study demonstrated that reaching the original value of σ_s corresponds for adamantane additives to passing 260–320 A h l^{-1} of electricity, this value being lower for other types of additives (Fig. 5). This indicates a higher electrochemical stability of compounds of the adamantane series.

The established pattern of the anodic behavior and state of the surface of the alloys under study in the presence of modifying additives to electrolytes for anodic treatment revealed the following basic directions of research for developing resource-saving technologies: (1) extending the working life of process media constituted by an alloy being treated and an electrolyte; (2) lowering the energy expenditure for anodic treatment; (3) decelerating accumulation of metal ions in electrolytes; (4) improving the quality of surface treatment of alloys with heterogeneous composition by introducing modifying additives possessing such basic properties as inhibition of metal ionization, faster formation of a viscous near-electrode layer via interaction of additive molecules with prod-

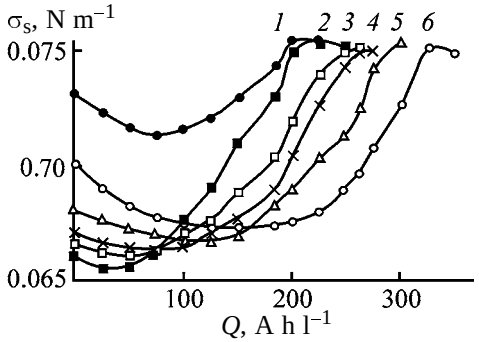

Fig. 5. Surface tension σ_s of PSA electrolyte in the course of its exhaustion. (Q) Quantity of electricity passed. Additive: (1.0 g l^{-1}): (*1*) $C_6H_{12}N_4$, (*2*) $N(C_2H_4OH)_3$, (*3*) $C_{10}H_{15}NHCOCH_3$, (*4*) $C_{10}H_{15}Br$, (5) $C_{10}H_{15}OH$, and (*6*) $C_{10}H_{16}$.

ucts of chemical and anodic dissolution of alloys, and improvement of the quality of the anodic oxide film via adsorption of additive molecules on the alloy surface at high positive potentials.

The rates of accumulation of metal ions in solutions were also lowered (1) by modifying the electrolyte compositions by replacing the solvent in aqueous solutions with a more viscous component (e.g., glycerol) decelerating the selective etching of microscopic areas on the article surface, (2) by excluding sulfuric acid from the PSA electrolyte in order to deposit poorly soluble phosphates of the metals contained in the alloys in the course of electrolysis, and (3) by binding the soluble components of the alloys into complexes stable in electrolytes for anodic treatment.

Development of resource-saving technologies should also involve studies concerning regeneration of spent ECP electrolytes and purification of washing and waste water to recover valuable components.

Adamantane and its derivatives proved to be versatile additives for virtually any brand of the alloys studied; they have high efficiency already at a low content in solution (0.2–2.0 g l^{-1}), low expenditure [$3-4\times10^{-3}$ g $(A\ h)^{-1}$], and chemical and electrochemical stability in anodic treatment, ensuring low energy expenditure in this process (0.8–4.0 A h l^{-1}) and long working life of alloy–electrolyte process media.

The highest working capacity of up to 400–420 A h l^{-1}, exceeding that of the presently employed electrolytes by a factor of 2, is observed for a PA solution with modifying additives of an alkali metal sulfate and adamantane compounds for anodic treatment of steels and Al alloys. This electrolyte is characterized by long working life of the solution because of the lowered current efficiency in anodic dissolution of alloys and simplicity of regeneration, shorter duration and lower energy intensity of the process, less expensive solution components, and lower expenditure for neutralization of spent solutions.

CONCLUSIONS

(1) The concept for choice of modifying additives of organic substances to electrolytes for polishing of alloys with varied degree of alloying on the basis of the whole set of their physicochemical properties was formulated.

(2) The effect of adsorption on the macro- (changes in the structure of the viscous near-electrode layer by the additives) and microscopic levels (changes in the properties of the surface anodic oxide films) in anodic treatment of alloys in electrolytes with modifying additives was established.

(3) It was shown that adamantane and remantadine additives to alloy polishing electrolytes lead to formation of impurity states with positive effective charge in the band gap of semiconducting oxide films. This facilitates or hinders (depending on the conduction type of the film) migration of ions across the film and improves the quality of treatment by smoothing the microroughness and eliminating microscopic deformations of the surface of metal articles.

REFERENCES

1. Grilikhes, S.Ya., *Elektrokhimicheskoe i khimicheskoe polirovanie: Teoriya i praktika: Vliyanie na svoistva metallov* (Electrochemical and Chemical Polishing: Theory and Practice: Effect on Metal Properties), Leningrad: Mashinostroenie, 1987.
2. Vinogradov, S.S., *Ekologicheski bezopasnoe gal'vanicheskoe proizvodstvo* (Environmentally Safe Electroplating), Moscow: Globus, 1998.
3. Shtan'ko, V.M. and Karyazin, P.P., *Elektrokhimicheskoe polirovanie metallov* (Electrochemical Polishing of Metals), Moscow: Metallurgiya, 1979.
4. Fedorova, E.A., *Zh. Prikl. Khim.*, 2001, vol. 74, no. 4, pp. 598–602.
5. Fedorova, E.A., *Fiz. Khim. Obrab. Mater.*, 2001, no. 2, pp. 36–40.
6. Fedorova, E.A., *Zh. Prikl. Khim.*, 2001, vol. 74, no. 11, pp. 1775–1779.
7. Adamson, A.W., *Physical Chemistry of Surfaces*, New York: Wiley, 1976.
8. Fedorova, E.A., Naumov, V.I., and Shul'pina, I.G., *Elektrokhimiya*, 1993, vol. 29, no. 5, pp. 585–591.
9. Mirkind, L.A., Fioshin, M.Ya., and Dubinin, A.G., *Elektrokhimiya*, 1972, vol. 8, no. 5, pp. 794–795.
10. Fedorova, E.A., Mitrofanov, E.V., and Flerov, V.N., *Izv. Vyssh. Uchebn. Zaved., Khim. Khim. Tekhnol.*, 1986, vol. 29, no. 5, pp. 27–29.
11. Fedorova, E.A., Suchkov, A.I., Tsareva, I.N., and Flerov, V.N., *Fiz. Khim. Obrab. Mater.*, 2000, no. 1, pp. 63–67.
12. Fedorova, E.A., *Gal'vanotekh. Obrab. Poverkhn.*, 2001, vol. 9, no. 1, pp. 41–46.
13. Bakaev, V.V., Fedorova, E.A., and Flerov, V.N., *Zh. Prikl. Khim.*, 2001, vol. 74, no. 11, pp. 1899–1901.

Russian Journal of Applied Chemistry, Vol. 76, No. 9, 2003, pp. 1451–1454. Translated from Zhurnal Prikladnoi Khimii, Vol. 76, No. 9, 2003, pp. 1490–1493.

APPLIED ELECTROCHEMISTRY AND CORROSION PROTECTION OF METALS

Kinetics of Reaction of Nickel(II) Hydroxide with Sulfuric Acid

A. I. Demidov and M. S. Kokhatskaya

St. Petersburg State Polytechnic University, St. Petersburg, Russia

Received July 17, 2003

Abstract—Changes in the concentrations of nickel(II) sulfate and sulfuric acid in the course of the dissolution of nickel(II) hydroxide powder in sulfuric acid of various concentrations at 25, 50, and 75°C were evaluated from variation of the electrolyte resistance. The rate constant and activation energies of the dissolution were calculated.

Leaching with ammonia or an acid is widely used in reprocessing of solid nickel-containing waste [1–4]. Owing to the high solubility of nickel sulfate, the acid leaching of nickel hydroxide from spent nickel–iron batteries is more efficient than ammonia leaching. The acid leaching involves transformation of nickel compounds into sulfate form and treatment to remove impurities; in the process, nickel sulfate is not separated from a solution [4].

The goal of this work was to develop a method of studying the reaction of $Ni(OH)_2$ in solutions with H_2SO_4 and to choose a canonic equation which would describe adequately the experimental data. For this purpose, the nickel(II) hydroxide powder was dissolved in sulfuric acid solutions of different concentrations (0.1–0.5 N) at 25, 50, and 75°C. We used in the study the following chemicals: $Ni(OH)_2$ intended for manufacture of alkaline batteries containing no less than 58.5–59.0% Ni in terms of dry substance and chemically pure grade H_2SO_4. The study was performed in a temperature-controlled conductometric cell at vigorous agitation of the solution with a magnetic stirrer. The solution volume was 100 ml, and the weighed portion was varied from 0.5 to 2.5 g. No less than seven replicate tests were performed.

Let us consider the reaction of $Ni(OH)_2$ with H_2SO_4:

$$Ni(OH)_2 + H_2SO_4 \rightarrow NiSO_4 + 2H_2O. \qquad (1)$$

In the course of the nickel hydroxide dissolution in sulfuric acid, very mobile hydrogen ions are replaced for less mobile nickel ions. As a result, in the course of the process the electrical conductivity of the solution changes. In view of this fact, the total specific electrical conductivity of a solution χ_Σ can be calculated by the equation

$$\chi_\Sigma = \chi_{H_2SO_4}(1 - x) + \chi_{NiSO_4}x, \qquad (2)$$

where x is the fraction of $NiSO_4$ at the total amount of the reactants accepted as unity; $\chi_{H_2SO_4}$ and χ_{NiSO_4} are the specific electrical conductivities of H_2SO_4 and $NiSO_4$, respectively [5].

To determine the nickel sulfate and sulfuric acid concentrations in a solution, the solution resistance in the course of the dissolution was measured over a period of 30 min with a step of 30 s using an E7-15 immitance meter. A change in the resistance upon dissolution of nickel hydroxide in sulfuric acid at 50°C is presented in Fig. 1. Then, the resistance was recalculated to the specific electrical conductivity:

$$\chi_\Sigma = K/R_t,$$

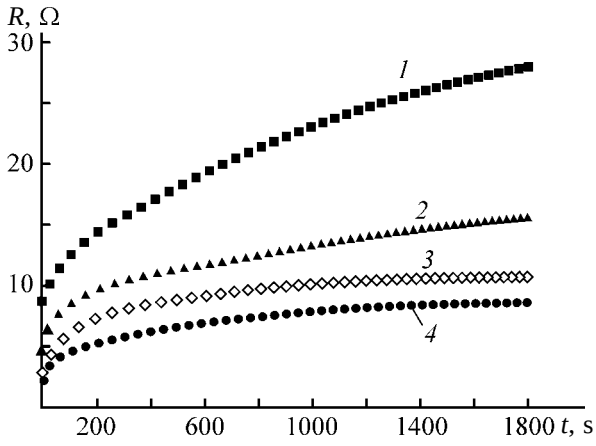

Fig. 1. Variation of the resistance R with time t in the course of nickel hydroxide dissolution in sulfuric acid solutions of different concentrations at 50°C. Concentration, g-equiv l^{-1}: (*1*) 0.1, (*2*) 0.2, (*3*) 0.4, and (*4*) 0.5; the same for Fig. 2.

1070-4272/03/7609-1451$25.00

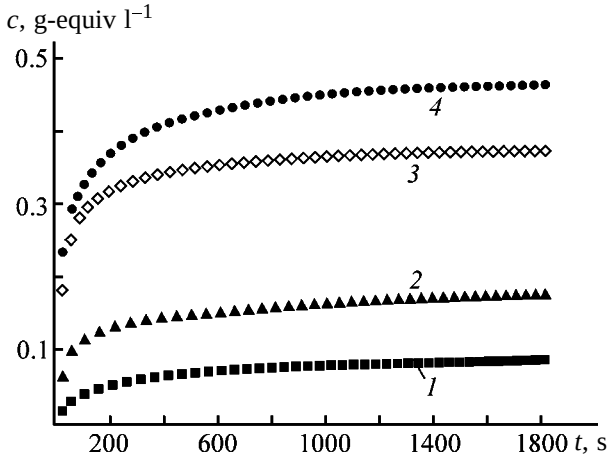

Fig. 2. Variation of the nickel sulfate concentration c with time t in the course of nickel hydroxide dissolution in sulfuric acid solutions of different concentrations at 50°C.

where K is the cell constant (0.260 – 0.277 cm^{-1}), and R_t is the solution resistance at time t.

The nickel sulfate concentration was determined from the χ_Σ value, found experimentally and calculated by Eq. (2). Variation of the nickel sulfate concentration with time at 50°C is shown in Fig. 2.

Table 1. Comparison of the results of conductometric and spectrophotometric determinations of the nickel sulfate concentration c_{NiSO_4}

$c_{H_2SO_4}$, g-equiv l^{-1}	c_{NiSO_4}, g-equiv l^{-1}, at indicated temperature, °C		
	25	50	75
Conductometric method			
0.1	0.0647 ± 0.005	0.0916 ± 0.003	0.0969 ± 0.002
0.2	0.1214 ± 0.006	0.1802 ± 0.006	0.1910 ± 0.004
0.4	0.2559 ± 0.009	0.3750 ± 0.002	0.3839 ± 0.001
0.5	0.3912 ± 0.008	0.4661 ± 0.006	0.4834 ± 0.002
Spectrophotometric method			
0.1	0.0640 ± 0.005	0.0906 ± 0.004	0.0969 ± 0.002
0.2	0.1209 ± 0.006	0.1786 ± 0.006	0.1912 ± 0.005
0.4	0.2259 ± 0.009	0.3749 ± 0.003	0.3838 ± 0.002
0.5	0.3907 ± 0.009	0.4672 ± 0.006	0.4863 ± 0.002

Table 2. Degree of nickel recovery α upon dissolution of $Ni(OH)_2$ in H_2SO_4 solutions

Solution no.	$c_{H_2SO_4}$, g-equiv l^{-1}	α, %, at indicated temperature, °C		
		25	50	75
1	0.1	65	92	97
2	0.2	61	89	96
3	0.4	64	94	96
4	0.5	78	93	97

The results obtained were compared with the data of the spectrophotometric analysis. The results of conductometric and spectrophotometric determinations of the nickel sulfate concentration at the end of the experiment are given in Table 1. As seen, the values of the nickel sulfate concentration calculated conductometrically agree well with the spectrophotometric data. This allows the conductometric method to be used for determining the nickel concentration in solution at any time.

The obtained values of the running and initial concentrations of sulfuric acid were used to calculate the degree of nickel dissolution at any time:

$$\alpha = (c_0 - c)/c_0,$$

where α is the degree of nickel dissolution; c_0 and c are the initial and running concentrations of sulfuric acid, respectively.

The calculated degrees of nickel dissolution by the end of the experiment are given in Table 2.

The experimental data were processed by different kinetic equations [7–9]. However, the experimental plots could be linearized only using an equation of the Erofeev–Kolmogorov type:

$$\alpha = 1 - \exp(-kt^n),$$

where α is the degree of dissolution; k, rate constant; t, time; and n, exponent taking into account the reaction order and a change in the surface area in the course of dissolution of the nickel hydroxide powder.

Writing Eq. (1) in the ionic form

$$1/2Ni(OH)_2 + H^+ \rightarrow 1/2Ni^{2+} + H_2O, \qquad (3)$$

we obtain:

$$-\frac{dc_{H^+}}{dt} = k' c_{H^+}, \qquad \frac{dc_{H^+}}{c_{H^+}} = k' dt, \qquad (4)$$

where k' is the parameter dependent on the area of the $_{solid}$ substance surface.

Let us integrate Eq. (4):

$$\ln c_{H^+} = -k't + \text{const}.$$

At the beginning of the process (at $t = 0$),

$$\text{const} = \ln c_0,$$

where c_0 is the initial concentration of hydrogen ions in a solution.

Then

$$\ln(c_{H^+}/c_0) = -k't,$$

$$1 - c_{H^+}/c_0 = 1 - \exp(-k't),$$

$$1 - c_{H^+}/c_0 = \alpha.$$

Consequently,

$$\alpha = 1 - \exp(-k't). \quad (5)$$

A change in the area of the solid particle surface in the course of the reaction can be described by the equation

$$S = \text{const}\, t^m, \quad m < 0,$$

then

$$k' = kt^m.$$

Substitution of k' into Eq. (5) yields the Erofeev–Kholmogorov type equation:

$$\alpha = 1 - \exp(-kt^{m+1}).$$

Taking $n = m + 1$, we obtain

$$\alpha = 1 - \exp(-kt^n). \quad (6)$$

The experimental data show that $0.135 < n < 0.916$ for the concentration and temperature intervals studied.

Applicability of Eq. (6) was verified by the linearity of the dependence $\ln[-\ln(1-\alpha)] = f(\ln t)$ obtained by taking two times the logarithm of the initial equation [9]. The $\ln[-\ln(1-\alpha)] = f(\ln t)$ dependences are plotted in Fig. 3. The rate constant k is calculated from the equation

$$\ln k = \ln[-\ln(1-\alpha)] - n(\ln t).$$

Linearization of the experimental graphs (3) shows that Eq. (6) adequately describes the kinetics of dissolution of the nickel hydroxide powder in sulfuric acid.

Then, the straight lines obtained were approximated by the direct least-squares method. As a result, $\ln k$ was determined. The rate constant was found, and the activation energy of the reaction was calculated after taking antilogarithm. The activation energy was

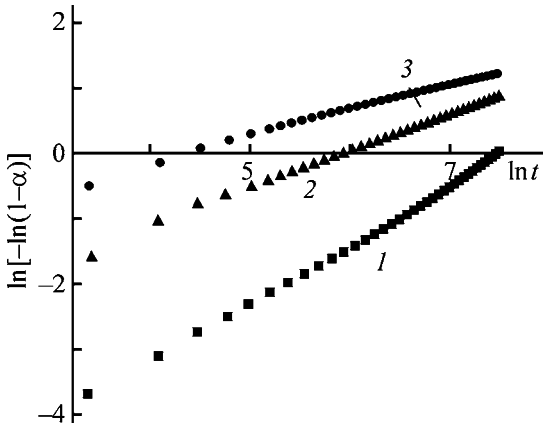

Fig. 3. The $\ln[-\ln(1-\alpha)]$–$\ln t$ dependence for nickel hydroxide dissolution in 0.1 N sulfuric acid at various temperatures. Temperature, °C: (*1*) 25, (*2*) 50, and (*3*) 75.

calculated by the formula

$$\Delta E = \frac{RT_1T_2\ln(k_2/k_1)}{T_2 - T_1},$$

where R is the universal gas constant (8.314 J mol^{-1} × K^{-1}); k_1 and k_2 are the rate constants at temperatures T_1 = 298.15 and T_2 = 348.15 K, respectively.

The final results of the calculation are presented in Table 3.

Table 3. Rate constant k and activation energy ΔE of the process

$c_{H_2SO_4}$, g-equiv l^{-1}	k, s^{-1}, at indicated temperature, °C			ΔE, kJ mol^{-1}
	25	50	75	
0.1	0.00101	0.03196	0.16740	88
0.2	0.00171	0.13921	0.33367	91
0.4	0.00895	0.29561	1.21531	85
0.5	0.00977	0.21541	0.77260	75

The values of the activation energy show that the dissolution of nickel hydroxide powder in 0.1–0.5 N sulfuric acid in the temperature range 25–75°C is kinetically controlled.

CONCLUSIONS

(1) The nickel sulfate and sulfuric acid concentrations at each time were determined from the results of measurement of the solution resistance in the course of dissolution. The values of the nickel sulfate concentration at the end of the experiment agree well with the data of the spectrophotomertic analysis.

(2) The obtained dependences are described by the Erofeev–Kholmogorov type equation. Within 25–75°C, the dissolution of nickel(II) hydroxide powder in 0.1–0.5 N sulfuric acid is kinetically controlled.

REFERENCES

1. Demidov, A.I. and Krasovitskaya, O.A., *Nauchno-Tekh. Vestn. Sankt-Peterb. Gos. Tekh. Univ.*, 2001, no. 1, pp. 112–123.
2. Demidov, A.I., and Krasovitskaya, O.A., *Zh. Prikl. Khim.*, 2000, vol. 73, no. 10, pp. 1656–1660.
3. RF Patent 2178933.
4. Kupryakov, Yu.P., *Proivodstvo tyazhelylh i tsvetnykh metallov iz loma i otkhodov* (Production of Heavy Metals from Scrap and Waste), Kharkov: Osnova, 1992.
5. *Spravochnik fizicheskikh, khimicheskikh i tekhnologicheskikh velichin* (Reference Book on Physical, Chemical, and Technological Quantities), Martens, L.K., Ed., Moscow: Sov. Entsiklopediya, 1930, vol. 4.
6. Vasil'ev, V.P., *Praktikum po analiticheskoi khimii: Uchebnoe posobie dlya vuzov* (Practical Course of Analytical Chemistry: Textbook for Higher Schools), Moscow: Khimiya, 2000.
7. Beloglazov, I.N., Morachevskii, A.G., and Zhmarin, E.E., *Kineticheskie zakonomernosti protsessov rastvoreniya i vyshchelachivaniya* (Kinetic Features of Dissolution and Leaching), Moscow: Ruda i Metally, 2000.
8. Vol'dman, G.M., and Zelikman, A.N., *Teoriya gidrometallurgicheskikh protsessov: Uchebnik dlya vuzov* (Theory of Hydrometallurgical Processes: A Textbook for Higher Schools), Moscow: Metallurgiya, 1993.
9. Naboichenko, S.S., and Lobanov, V.G., *Praktikum po gidrometallurgii: Uchebnoe posobie dlya vuzov* (Practical Course of Hydrometallurgy: Textbook for Higher Schools), Moscow: Metallurgiya, 1992.

Russian Journal of Applied Chemistry, Vol. 76, No. 9, 2003, pp. 1455–1460. Translated from Zhurnal Prikladnoi Khimii, Vol. 76, No. 9, 2003, pp. 1494–1499.

CATALYSIS

Deactivation of Iron–Gallium Oxide Catalyst for Ammonia Oxidation

N. I. Zakharchenko

Zhukovsky National Aerospace University, Kharkov, Ukraine

Received January 29, 2003

Abstract—An iron–gallium oxide catalyst (97.0 wt % Fe_2O_3, 3.0 wt % Ga_2O_3) was studied in high-temperature oxidation of ammonia. Reasons for the deactivation of the catalyst at elevated temperature were analyzed.

Catalytic oxidation of ammonia to nitrogen(II) oxide is the basis of the industrial method for manufacture of nitric acid [1]. In view of the high cost, shortage, and unrecoverable loss of commercial catalysts in industrial processes (platinum, rhodium, and palladium alloys), a search for effective nonplatinum catalysts is a topical problem. Iron(III) oxide is a promising base for catalysts of this kind; it is used industrially as a component of the second stage of a combined system for ammonia oxidation [1]. Commonly, high activity and selectivity with respect to nitrogen(II) oxide are preserved and the thermal and chemical stability of iron(III) oxide is improved using various modifying additives and, in particular, metal oxides [1–8].

Gallium(III) oxide (Ga_2O_3) is used as a modifying additive for iron-containing catalysts with varied content of modifying agent [1, 7, 8], but these catalysts are deactivated at elevated temperatures, with their selectivity with respect to nitrogen(II) oxide decreasing [1, 7]. Reasons for the deactivation of iron–gallium oxide catalysts are virtually unknown [1, 7]. The present study is concerned with deactivation of a highly selective iron–gallium catalyst (97.0 wt % Fe_2O_3, 3.0 wt % Ga_2O_3) in high-temperature oxidation of ammonia.

The catalyst was prepared by thermal decomposition in air of a mixture of hydrated iron nitrate [$Fe(NO_3)_3 \cdot 9H_2O$] and gallium nitrate [$Ga(NO_3)_3 \cdot 9H_2O$] of chemically pure grade, taken in calculated amounts, using a procedure described in [9]. The temperature of finishing thermal treatment of the catalyst grains was 1143 K.

An X-ray phase analysis was made on a Siemens D-500 powder diffractometer (CuK_α radiation, graphite monochromator) in the path of the diffracted beam. The phases manifested in the diffraction patterns were identified using a JCPDS file shipped with the diffractometer.

IR absorption spectra were measured on a Perkin–Elmer 577 spectrophotometer at 200–2000 cm^{-1} using KBr technique. The selectivity of the catalysts with respect to NO (S_{NO}) was determined on a flow-through installation with a quartz reactor 2×10^{-2} m in diameter, using the procedure described in [1]. The height of the bed of catalyst grains of size $(2 \times 3) \times 10^{-3}$ m was $(4–12) \times 10^{-2}$ m; content of ammonia in the ammonia–air mixture (AAM), ~10.0 vol %; time of contact, 6.89×10^{-2} s (normal conditions, n.c.), the optimal value according to previously obtained data; pressure, 0.101 MPa. The testing temperature was close to the optimal value for a single-component iron oxide catalyst (1103 K): in separate tests, it was varied within the range 1103–1173 K. The composition of the products of ammonia oxidation on the catalysts was determined using the known technique [10], by analyzing the gas mixture for the content of NH_3, O_2, N_2, NO, and N_2O before and after the catalysts. The sensitivity limit of this analytical procedure was (vol %) 3.0×10^{-3} for NH_3, 3.5×10^{-3} for NO, and 5.0×10^{-3} for O_2, N_2, and N_2O.

The specific surface area of the catalysts was measured by the method of low-temperature adsorption of nitrogen and calculated by the BET equation, using a standard procedure [11].

The binding energies of the surface oxygen to the catalysts were found from the temperature dependence of the equilibrium oxygen pressure over the surface of the compounds, using the procedure described in [12].

The basic characteristics of the iron–gallium catalyst are listed in Table 1.

According to the results of an X-ray diffraction analysis, the unused catalyst is a solid solution of

1070-4272/03/7609-1455$25.00

Table 1. Basic parameters of a catalyst for ammonia oxidation containing (wt %) 97.0 Fe_2O_3 and 3.0 Ga_2O_3

Run no.	Parameter (designation)	Numerical value
1	Maximum selectivity with respect to NO (S_{NO}) at optimal temperature, %	95.5
2	Optimal temperature T, K	1103
3	Specific surface area S, $m^2\ g^{-1}$	9.0
4	Limiting ammonia load X, $m^3\ h^{-1}\ m^{-2}$	9.92×10^3
5	Breakthrough of ammonia under critical process conditions, Y, rel. %	0.04
6	Optimal time of contact, τ_{opt}, at linear flow velocity of reagents of 0.19 m s^{-1} and T = 1103 K, s	6.89×10^{-2} (n.c.) or 2.25×10^{-2} (work. cond.)
7	Optimal linear flow velocity of AAM, w, at $\tau = 6.89 \times 10^{-2}$ and T = 1103 K, m s^{-1}	0.19 (n.c.) or 0.77 (work. cond.)
8	Ignition temperature, T_{ign}, K	531

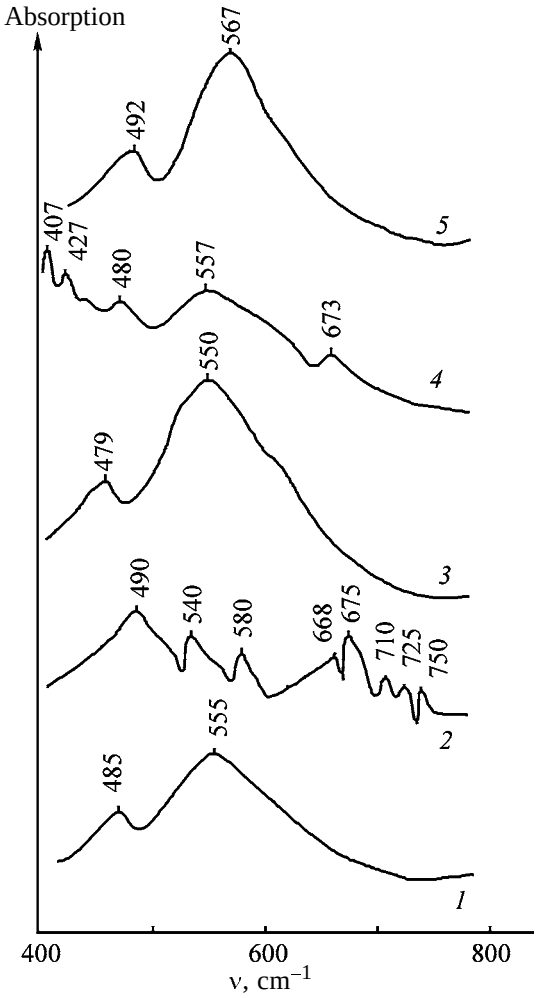

Fig. 1. IR absorption spectra of (*1*) α-Fe_2O_3, (*2*) β-Ga_2O_3, (*3*) unused iron–gallium catalyst, (*4*) surface (ferromagnetic) layer of iron–gallium catalyst upon operation, and (*5*) iron–gallium catalyst (nonmagnetic fractions) upon operation. (ν) Wave number.

gallium(III) oxide in hematite (α-Fe_2O_3), with the structure of the α-Al_2O_3 (corundum) type, i.e., $(Fe_xGa_{1-x})_2O_3$. The X-ray diffraction patterns of the fresh catalyst are characterized by main lines with interplanar spacings of 0.3682, 0.2693, 0.2511, 0.2214, 0.1846, 0.1695, 0.1484, and 0.1454 nm. These values are typical of the rhombohedral structure of α-Fe_2O_3 [3], but are shifted to greater reflection angles, which corresponds to a decrease in the lattice constant a of iron oxide from 0.5434 to 0.5423 nm. No gallium oxide lines were found in the catalyst, which points to the formation of a solid solution of gallium(III) oxide in hematite. IR spectra of unused catalyst contain absorption bands at 479 and 550 cm^{-1}. These values are typical of iron(III) oxide (485, 555 cm^{-1}) (Fig. 1), but are shifted to lower frequencies, which is accounted for by replacement, in solid formation, of a part of Fe^{3+} ions in the structure of hematite by havier Ga^{3+} ions. No β-Ga_2O_3 bands were found in the IR spectra of the catalyst, probably because of the fact that the absorption bands characteristic of gallium(III) oxide are close to those of hematite (Fig. 1), but the content of gallium oxide is insufficient for clear manifestation of the absorption bands of Ga_2O_3.

Studies of how the catalyst selectivity depends on the working time (Fig. 2) indicate that the iron–gallium catalyst exhibits higher stability than α-Fe_2O_3. The catalyst selectivity at 1103 and 1173 K decreased by 1.7 and 4.5%, respectively, after 90 h of operation. At the same time, the selectivity of iron(III) oxide decreased under the same conditions by 2.3 and 6.4%, respectively (Fig. 2). Raising the process temperature leads to stronger deactivation of both iron–gallium and iron oxide catalysts (Fig. 2). X-ray diffraction patterns of the surface layers of an iron–gallium catalyst that

Table 2. Binding energy of the surface oxygen of catalysts, q_S, and their selectivity with respect to nitrogen(II) oxide, S_{NO}

Run no.	Catalyst	Working time of catalyst, h	q_S,* kJ mol^{-1} O_2	S_{NO}, %, at 1173 K
1	Iron–gallium (Fe_2O_3 97.0 wt %, Ga_2O_3 3.0 wt %)	3	134.3	93.0
2	Iron–gallium	90	148.2	88.5
3	α-Fe_2O_3	3	144.6	91.2
4	β-Ga_2O_3	3	231.5	1.9
5	Fe_3O_4	3	226.5	4.1

* q_S in the oxidized state of the catalyst surface.

worked at 1173 K contain lines of a rhombohedral solid solution of gallium(III) oxide in hematite, together with weak lines with interplanar spacings of 0.4850, 0.2970, 0.2430, 0.2102, 0.1713, 0.1615, and 0.1487 nm, typical of magnetite (Fe_3O_4) [3]. In this case, magnetite and the iron–gallium catalyst do not form solid solutions, being present as a mixture of separate phases.

The formation of magnetite is confirmed by IR data. The IR spectra of the surface layers of a catalyst after operation (magnetic fractions) contain absorption bands at 407, 427, 481, 558, and 673 cm^{-1} (Fig. 1), characteristic of magnetite [13]. According to [9, 14], magnetite suppresses the catalyst selectivity, being a low-active phase: the selectivity of magnetite is 7.0% at 1073 K.

Only two nitrogen compounds were found in the products formed in ammonia oxidation on the catalyst under study: N_2 and NO; no breakthrough of ammonia was detected. Thus, the overall conversion of the starting substance is 100.0%.

High-temperature catalytic oxidation of ammonia proceeds by two concurrent pathways [1, 15]:

$$4NH_3 + 5O_2 = 4NO + 6H_2O, \quad (1)$$

$$4NH_3 + 3O_2 = 2N_2 + 6H_2O. \quad (2)$$

The redox mechanism of the reactions [15] predetermines the relationship between the selectivity and the binding strength of chemisorbed oxygen to the catalyst surface [12, 15]. As measure of strength of oxygen binding to the catalyst can serve the heat of chemisorption [12, 15]. For catalysts of certain nature and, in particular, metal oxides, there exists the optimal energy of oxygen binding to the catalyst surface, at which the selectivity with respect to nitrogen(II) oxide is the highest [12, 15, 16]. Deviation from the optimal oxygen binding energies leads to lower catalyst selectivity with respect to NO, and to higher selectivity with respect to N_2.

The experimental binding energies of surface oxygen of the iron–gallium catalyst and its constituents are listed in Table 2.

The energies of oxygen binding to the surface of the forming magnetite and of the catalyst after its operation surpass the corresponding characteristics of the iron–gallium catalyst before operation.

In the formation of a product of deeper oxidation of ammonia, i.e., nitrogen(II) oxide, a greater number of oxygen–catalyst bonds is ruptured than that in the formation of molecular nitrogen. This means that the selectivity of the catalyst with respect to NO must decrease with increasing binding energy of adsorbed oxygen, which is, indeed, observed for magnetite and used catalyst, in which Fe_3O_4 was found.

Gallium(III) oxide is characterized, as a constituent of the iron–gallium catalyst, by high binding energy of oxygen to the surface (231.5 kJ mol^{-1} O_2), which is comparable with a similar characteristic for magnetite (226.5 kJ mol^{-1} O_2): the selectivities of these two phases with respect to NO are close (1.9 and 4.1%, respectively) and rather low.

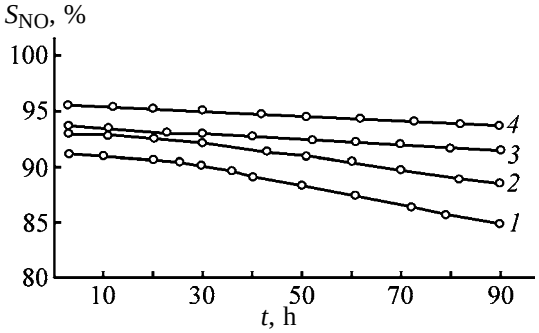

Fig. 2. Catalyst selectivity with respect to nitrogen(II) oxide, S_{NO}, vs. working time t: (*1*) α-Fe_2O_3, 1173 K; (*2*) Fe_2O_3–Ga_2O_3 (3.0 wt % Ga_2O_3), 1173 K; (*3*) α-Fe_2O_3, 1103 K; and (*4*) Fe_2O_3–Ga_2O_3 (3.0 wt % Ga_2O_3), 1103 K.

Table 3. Changes in chemical composition and mass of catalysts for ammonia oxidation in their operation at 1173 K

Run no.	Catalyst	Chemical composition, wt %			Content of Ga_2O_3 in $(Fe_xGa_{1-x})_2O_3$ solid solution, wt %	Mass loss by catalyst, %
		Fe_2O_3	Ga_2O_3	Fe_3O_4		
1	Unused iron–gallium	97.00	3.00	–	3.00	–
2	Iron–gallium after 90 h of operation	94.52	2.56	2.92	2.64	0.5
3	Unused β-Ga_2O_3	–	100.00	–	–	–
4	β-Ga_2O_3 after 20 h of operation	–	100.00	–	–	7.1

The product of phase transformations of the catalyst (magnetite) may be formed both in the redox reaction of ammonia oxidation [1–3, 5, 6, 15, 17] and in direct interaction of the parts of the catalyst surface that are characterized by low catalyst–oxygen binding energies with a strong reducing agent in the reaction medium, in accordance with the equation

$$9(Fe_xGa_{1-x})_2O_3 + 2xNH_3 = 6xFe_3O_4 + 9(1 - x)Ga_2O_3 + xN_2 + 3xH_2O. \quad (3)$$

The deficiency of Fe^{3+} ions in the surface layers of the catalyst (magnetite formation) leads to a local increase in the content of gallium(III) oxide in a hematite-based solid solution and a decrease in the selectivity of the catalyst with respect to NO (Table 2). According to X-ray phase analysis, no gallium(III) oxide was found as a separate phase, i.e., there was no decomposition of the solid solution. Gallium(III) oxide, as a component of a solid solution, may undergo, under the action of a strong reducing agent (ammonia) at high temperature (1073–1173 K), phase transformations in accordance with the reaction equation

$$3Ga_2O_3 + 4NH_3 = 3Ga_2O + 2N_2 + 6H_2O. \quad (4)$$

The transformation product, Ga_2O, readily sublimes at 1073–1173 [18] and thereby enters the gas flow of reagents. With account of the transformations of gallium(III) oxide, the equation describing reaction (3) can be written as follows:

$$9(Fe_xGa_{1-x})_2O_3 + 2(6 - 5x)NH_3 = 6xFe_3O_4 + 9(1 - x)Ga_2O + (6 - 5x)N_2 + 3(6 - 5x)H_2O, \quad (5)$$

where $0 \le x \le 1$.

The thermodynamic probability of reduction by ammonia of iron(III) oxide [19] as a component of the $(Fe_xGa_{1-x})_2O_3$ solid solution by the equation

$$9Fe_2O_3 + 2NH_3 = 6Fe_3O_4 + N_2 + 3H_2O \quad (6)$$

is higher than that of gallium(III) oxide reduction [18] and grows with increasing temperature. After 90 h of operation of an iron–gallium catalyst at 1173 K, magnetite was found in amount of 2.92 wt % (Table 3). For the iron oxide catalyst, the content of Fe_3O_4 in the surface layers was 4.80 wt % under the same testing conditions [9]. The intensity of phase transformations of the catalyst, $(Fe_xGa_{1-x})_2O_3$ solid solution, to give magnetite is somewhat lower than that of individual iron(III) oxide.

Processes (4) and (5) may lead to mass loss by catalyst because of Ga_2O sublimation. Indeed, its mass decreased by 0.5% after 90 h of catalyst operation at 1173 K. Hematite, magnetite, and gallium(III) oxide are nonvolatile thermally stable compounds in air at the testing temperatures [20]. To confirm the transformation of gallium(III) oxide, a component of the iron–gallium catalyst, in the course of high-temperature oxidation of ammonia, a mixture of substances after the catalyst was passed through columns cooled by a mixture of solid carbon dioxide and acetone (temperature of cooling mixture 213–203 K). The dramatic decrease in the temperature of the reaction products made it possible to minimize the interaction in the gas phase between gallium(I) oxide and oxidizing agents contained in the reaction mixture, nitrogen(II) oxide and oxygen, by the equations [18]

$$Ga_2O + 2NO = Ga_2O_3 + N_2, \quad (7)$$

$$Ga_2O + O_2 = Ga_2O_3. \quad (8)$$

In particular, process (7) may lead to nitrogen defixation, as in the side reaction of ammonia oxidation at short time of contact, in accordance with the equation

$$4NH_3 + 6NO = 5N_2 + 6H_2O, \quad (9)$$

i.e., to a decrease in the catalyst selectivity with respect to NO. Under the experimental conditions, Ga_2O vapor condensed on column walls, and water was frozen to ice (other substances contained in the

reaction mixture were carried away by the gas flow). After shutting down the reactor, the columns were purged with inert gas (Ar) and heated to T = 473 K to remove water. A film was found on the column walls. The substance of this film was identified by X-ray diffraction analysis as gallium(I) oxide. The IR spectra of this compound contain absorption bands at 472 and 809 cm^{-1}, characteristic of Ga_2O [21].

A low content of gallium(III) oxide in the solid solution leads to relatively small loss of mass by the iron–gallium catalyst at 1173 K. Chemical analyses performed using the procedure described in [22] demonstrated that the content of Ga_2O_3 in the $(Fe_xGa_{1-x})_2O_3$ solid solution decreased in the course of catalyst operation from 3.00 to 2.64 wt % (Table 3).

In tests of individual gallium oxide (β-Ga_2O_3) as a catalyst for ammonia oxidation, a pronounced decrease in its mass, by 7.1% after 20 h of operation at 1173 K, was observed (Table 3). X-ray phase and IR spectral analyses demonstrated that, under the action of the reaction medium, β-Ga_2O_3 undergoes, similarly to the iron–gallium catalyst, phase and chemical transformations to give volatile gallium(I) oxide. Thermal treatment of β-Ga_2O_3 at the same temperature in air did not lead to any decrease in the oxide mass, i.e., the catalyst is nonvolatile and thermally stable under these conditions. Consequently, the mass deficiency of the β-Ga_2O_3 catalyst under the conditions of high-temperature oxidation of ammonia is associated with the influence of the redox reaction medium, redox mechanism of the reaction [1–3, 5, 6, 15, 17], and processes (4) and (5).

The thermodynamic probability of oxidation of the forming low-active compound Fe_3O_4 by oxygen from AAM by the equation

$$4Fe_3O_4 + O_2 = 6Fe_2O_3 \quad (10)$$

is lower than that of processes (3) and (6) and decreases with increasing reaction temperature [19, 23]. It becomes possible that Fe_3O_4 is accumulated in the surface layers of the catalyst at elevated temperature. Being a volatile product of phase transformations of the catalyst, gallium(I) oxide sublimes from its surface, which makes lower the content of Ga_2O_3 in the iron–gallium catalyst (Table 3). High-temperature redox processes in which new phases (Fe_3O_4, Ga_2O) are formed and the catalyst surface is regenerated are unbalanced and result in accumulation of the low-selectivity compound (magnetite) and changes in the composition of the $(Fe_xGa_{1-x})_2O_3$ solid solution. With increasing temperature, the unbalance of the phase transformations of the catalyst becomes more pronounced.

Table 4. Changes in structural and catalytic properties of iron–gallium catalyst (3.0 wt % Ga_2O_3) in the course of its operation at 1173 K*

t, h	S_{NO}, %	s, $m^2\ g^{-1}$	n, nm	$X \times 10^{-3}$, $m^3\ h^{-1}\ m^{-2}$
3	93.0	8.7	120	9.58
11	92.8	7.4	134	8.15
20	92.5	6.1	150	6.72
30	92.1	4.8	170	5.29
43	91.3	3.7	200	4.08
51	90.9	3.1	220	3.42
60	90.3	2.7	237	2.97
70	89.7	2.3	253	2.53
82	89.0	1.9	270	2.09
90	88.5	1.7	280	1.87

* t is the time of operation, and n, the rms particle size.

In addition, the catalyst undergoes, under the action of elevated temperature, recrystallization with a decrease in the specific surface area (Table 4) from 8.7 to 1.7 $m^2\ g^{-1}$ (90 h of operation at 1173 K) and, consequently, in the number of active centers on the surface [1]. The size of catalyst particles grows from 120 to 280 nm.

A study of an iron–gallium catalyst subjected to thermal treatment in air at 1173 K (90 h) demonstrated that the specific surface area of the catalyst decreases by 7.5 $m^2\ g^{-1}$, i.e., within the same limits as in the case of a catalyst operating in an ammonia–air medium (Table 4), but the selectivity of this catalyst decreases by only 0.6%. No phase transformations were observed in the catalyst treated in air. The energy of oxygen binding to the surface of a catalyst treated in air increases only slightly (from 134.3 to 136.0 kJ mol^{-1} O_2), which leads to an insignificant decrease in its selectivity. In the IR spectra of the deactivated catalyst (Fig. 1), the absorption bands at 492 and 567 cm^{-1}, characteristic of "metal–oxygen" vibrations, are shifted to higher frequencies, compared to the similar absorption bands (479 and 550 cm^{-1}) of unused catalyst. Changes of this kind are also observed for a catalyst subjected to thermal treatment in air. Such a shift of absorption bands is accounted for by a decrease in the metal–oxygen bond length (an increase in the force constant of the bond), which is observed in recrystallization of solids [24], and leads to an increase in the energy of binding of adsorbed oxygen to the catalyst surface. The reaction occurs under conditions that are far from being critical, i.e.,

is limited by diffusion of ammonia toward the outer surface of the catalyst. Therefore, the specific surface area has no significant influence on the selectivity of the iron–gallium catalyst with respect to nitrogen(II) oxide [1–3, 5, 6, 17], i.e., the decrease in selectivity at 1173 K is mainly due to phase and chemical transformations of the catalyst. Under critical conditions of the reaction (catalyst "decay"), recrystallization processes and decrease in the specific surface area of the catalyst diminish its limiting load, i.e., activity, from 9.58×10^3 to 1.87×10^3 m^3 NH_3 $(h\,m^2)^{-1}$ (90 h of operation).

CONCLUSIONS

(1) A study of factors responsible for deactivation of an iron–gallium oxide catalyst (97.0 wt % Fe_2O_3, 3.0 wt % Ga_2O_3) in high-temperature oxidation of ammonia demonstrated that the catalyst undergoes phase and chemical transformations leading to formation of low-selective magnetite and volatile gallium(I) oxide. The deactivation process is accompanied by structural changes: recrystallization and decrease in the specific surface area of the system.

(2) Data on the deactivation of the catalyst can be used in developing theoretical and practical foundations for design of high-performance catalysts for ammonia oxidation.

REFERENCES

1. Karavaev, M.M., Zasorin, A.P., and Kleshchev, N.F., *Kataliticheskoe okislenie ammiaka* (Catalytic Oxidation of Ammonia), Moscow: Khimiya, 1983.
2. Zakharchenko, N.I. and Seredenko, V.V., *Zh. Prikl. Khim.*, 1999, vol. 72, no. 11, pp. 1921–1923.
3. Zakharchenko, N.I., *Zh. Fiz. Khim.*, 2002, vol. 76, no. 7, pp. 1213–1220.
4. Ukrainian Patent 35424A.
5. Zakharchenko, N.I., *Zh. Prikl. Khim.*, 2001, vol. 74, no. 2, pp. 226–231.
6. Zakharchenko, N.I., *Kinet. Katal.*, 2001, vol. 42, no. 5, pp. 747–753.
7. Zasorin, A.P., Zakharchenko, N.I., and Karavaev, M.M., in *Azotnaya promyshlennost'* (Nitrogen Industry), Moscow: NIITEKhIM, 1980, issue 6, pp. 15–18.
8. Podurovskaya, O.N., *Katalizatory dlya okisleniya ammiaka (Bibliografiya patentov, zayavok i avtorskikh svidetel'stv)* (Catalysts for Ammonia Oxidation (Bibliography of Patents, Patent Applications, and Inventor's Certificates)), Moscow: NIITEKhIM, 1972.
9. Zasorin, A.P., Zakharchenko, N.I., and Karavaev, M.M., *Izv. Vyssh. Uchebn. Zaved, Khim. Khim. Tekhnol.*, 1980, vol. 23, no. 10, pp. 1274–1276.
10. Alkhazov, T. G., Gasan-zade, G.Z., Osmanov, M.O., and Sultanov, M.Yu., *Kinet. Katal.*, 1975, vol. 16, no. 6, pp. 1230–1234.
11. Buyanova, N.E., Karnaukhov, A.P., and Alabuzhev, Yu.A., *Opredelenie udel'noi poverkhnosti katalizatorov* (Determination of Specific Surface Area of Catalysts), Moscow: Khimiya, 1973.
12. Boreskov, G.K., *Geterogennyi kataliz* (Heterogeneous Catalysis), Moscow: Nauka, 1986.
13. Bogdanovich, N.P., Vorob'ev, Yu.P., Men', A.N., *et al., Opt. Spektrosk.*, 1970, vol. 29, no. 6, pp. 1151–1153.
14. Zakharchenko, N.I., *Izv. Vyssh. Uchebn. Zaved., Khim. Khim. Tekhnol.*, 2001, vol. 44, no. 2, pp. 126–129.
15. Golodets, G.I., *Geterogenno-kataliticheskie reaktsii s uchastiem molekulyarnogo kisloroda* (Heterogeneous-Catalytic Reactions Involving Molecular Oxygen), Kiev: Naukova Dumka, 1977.
16. Il'chenko, N.I., Pyatnitskii, Yu.I., and Pavlenko, N.V., *Teor. Eksp. Khim.*, 1998, vol. 34, no. 5, pp. 265–281.
17. Zakharchenko, N.I., *Funct. Mater.*, 2002, vol. 9, no. 2, pp. 255–263.
18. Ivanova, R.V., *Khimiya i tekhnologiya galliya* (Chemistry and Technology of Gallium), Moscow: Metallurgiya, 1973.
19. Zakharchenko, N.I. and Protiven', I.N., *Termodinamicheskii analiz kataliticheskikh sistem MeO–Fe_2O_3, gde Me – Ve, Mg, Ca, v usloviyakh vozdeistviya reaktsionnoi sredy* (Thermodynamic Analysis of Catalytic Systems MeO–Fe_2O_3 (Me = Be, Mg, Ca) under Conditions of Effect of the Reaction Medium), Available from NIITEKhIM, Cherkassy, June 17, 1993, no. 128–93-khp.
20. Kazenas, E.K. and Chizhikov, D.M., *Davlenie i sostav para nad okislami khimicheskikh elementov* (Pressure and Composition of Vapor over Oxides of Chemical Elements), Moscow: Nauka, 1976.
21. Hincheliffe, A.J. and Ogden, J.S., *J. Phys. Chem.*, 1973, vol. 77, no. 10, pp. 2537–2543.
22. Kryachkova, T.N. and Gordeeva, M.N., *Voprosy analiticheskoi khimii mineral'nykh veshchestv* (Analytical Chemistry of Mineral Substances), Leningrad: Leningr. Gos. Univ., 1966, pp. 175–187.
23. Tret'yakov, Yu.D., *Tverdofaznye reaktsii* (Solid-Phase Reactions), Moscow: Khimiya, 1978.
24. Davydov, A.A., *IK-spektroskopiya v khimii poverkhnosti okislov* (IR Spectroscopy in Surface Chemistry of Oxides), Novosibirsk: Nauka, 1984.

Russian Journal of Applied Chemistry, Vol. 76, No. 9, 2003, pp. 1461–1465. Translated from Zhurnal Prikladnoi Khimii, Vol. 76, No. 9, 2003, pp. 1500–1504.

CATALYSIS

Conjugate Conversion of Methanol and Lower Alkanes C_3–C_4 on Zeolite-Containing Catalysts

L. M. Koval', S. S. Safronova, E. B. Chernov, V. V. Bolotov, and N. V. Zhukova

Tomsk State University, Tomsk, Russia

Received December 17, 2002; in final form, May 2003

Abstract—Simultaneous conversion of methanol and lower alkanes C_3–C_4 on high-silica zeolites of ZSM-5 type of various compositions (SiO_2/Al_2O_3 30, 50, 90) was studied. The catalytic activity of zeolite catalysts and their physicochemical properties (acidity, sorption capacity, and pore structure) were evaluated.

Efficient utilization of cheap hydrocarbon resources such as natural and casing-head gas, gas condensate, and light paraffins in production of gasoline, lower olefins, arenes, and other valuable products is still urgent. Simultaneous conversion of methanol and lower alkanes C_3–C_4 into olefins and arenes is a new promising approach. Implementation of this process predominantly depends on the development of new heat-resistant catalysts [ZSM-5 high-silica zeolites (HSZ)] catalyzing conversion both of hydrocarbons into arenes and of methanol into alkenes.

This work was aimed to study the conjugate conversion of methanol and lower alkanes on high-silica zeolite catalysts of various compositions as influenced by the process parameters (temperature and space velocity) and to evaluate the relationship between the catalytic, acid, and sorption properties of these zeolites.

EXPERIMENTAL

High-silica zeolites were prepared by hydrothermal synthesis from aluminosilica gels in the presence of hexamethylenediamine upon heating at 448 K for 4–6 days; then the zeolites were decationized with 25% aqueous NH_4Cl at 363 K for 2 h, dried, and calcined in air at 823 K for 8 h. The acid properties of the zeolite-containing catalysts were determined by temperature-programmed desorption (TPD) of ammonia according to the procedure given in [1]. The sorption and structural properties of the resulting zeolites were studied on a vacuum unit equipped with a McBain quartz balance. The sorbates were benzene and methanol; the pore size distribution was calculated from the desorption isotherms of benzene.

The conjugate conversion of methanol and lower alkenes (wide-cut fraction) into hydrocarbons on the zeolite-containing catalysts was performed at 673–873 K and atmospheric pressure on a flow-type unit with a fixed catalyst bed (4 cm^3) at space velocities of methanol and lower alkanes of 1 and 240 h^{-1}, respectively. The gaseous and liquid reaction products were analyzed by chromatography at programmed heating from 323 to 493 K. The yield of the conversion products of methanol and propane–butane mixture and the number of the acid centers in the catalysts were determined by this method with an accuracy of ±2.5%.

We studied the conjugate conversion of methanol and lower alkanes on HSZ (SiO_2/Al_2O_3 30) as influenced by temperature and space velocity of the raw materials. Table 1 shows the data on the composition of hydrocarbon fraction obtained by methanol conversion on H-ZSM-5 at 644 K and 1 h^{-1} space velocity of methanol [2], by conversion of lower alkanes on H-ZSM-5 at 873 K and space velocity of propane–butane mixture of 100 h^{-1} [3], and by simultaneous conversion of methanol with lower alkanes on the H-ZSM-5 type zeolite in the 673–823 K range and alkanes : methanol space velocity ratio of 240 : 1.

The choice of the temperature range was governed by the fact that the lower temperature limit corresponds to the efficient conversion of methanol and the upper limit, to activation of lower alkanes [4]. The experimental data show that the conjugate conversion yields the same set of the reaction products as the individual processes, and the yield of the products is intermediate. The conjugate conversion at 823 K yields significant amounts of olefins (about 30 wt %) and at 623 K, large amounts of *i*-butane (25.4 wt %), alkylbenzenes (about 40 wt %), and low amount of naphthalenes (1.9 wt %). With increasing temperature, conversion of lower alkanes increases. As the conversion of the propane–butane mixture increases from 38 to 65%, the yields of hydrogen, methane (from 3 to

1070-4272/03/7609-1461$25.00

Table 1. Conversion products of hydrocarbons on H-HSZ-30 catalyst

Hydrocarbon	*T*, K	α, %		Conversion products, wt %						
		methanol	alkanes	hydrogen	methane	ethane	ethene	propane	propene	*i*-butane
Methanol	644	100	–	–	1.0	0.6	0.5	16.2	1.0	18.7
Methanol + alkanes C_3–C_4	673	100	38	1.2	3.3	6.4	3.1	–	3.0	25.4
	723	″	38	2.5	11.8	10.2	5.0	–	6.0	15.6
	773	″	54	2.4	20.4	16.7	7.8	–	8.5	6.3
	823	″	65	4.5	31.2	13.9	12.0	–	13.5	4.6
Alkanes	823	–	95	3.1	36.1	19.9	8.6	–	4.3	–

Hydrocarbon	*T*, K	Conversion products, wt %						
		n-butane	butenes	benzene	toluene	xylenes	arenes C_{9+}	naphthalenes
Methanol	644	5.6	0.5	1.7	10.5	17.2	11.6	0.2
Methanol + alkanes C_3–C_4	673	–	4.5	2.4	13.5	23.7	9.0	1.9
	723	–	4.6	3.8	14.7	13.2	6.5	1.7
	773	–	2.4	1.6	6.3	12.7	2.6	1.0
	823	–	3.7	1.3	5.3	4.6	1.9	1.1
Alkanes	823	–	–	8.5	10.1	3.9	1.8	4.2

31 wt %), ethane, ethylene, and propylene (from 3 to 12–14 wt %) grow significantly, whereas the selectivity with respect to aromatic hydrocarbons decreases from 47 to 12 wt %.

Thus, at high temperatures lower alkanes are activated and their cracking accelerates. High temperature accelerates the removal of the reaction products from the surface, increasing the fraction of lower gaseous hydrocarbons which have no time to participate in subsequent oligomerization, cyclization, etc.; as a result, the yield of arenes decreases.

The yields of the conversion products as influenced by the ratio of the space velocities of methanol and lower alkanes at 773, 823, and 873 K are listed in Table 2. The space velocity of the propane–butane mixture was constant (240 h^{-1}), and the space velocity of methanol was 0.4, 0.9, and 1.7 h^{-1}. The increase in the space velocity of methanol to 1.7 h^{-1} does not noticeably affect the overall conversion of the propane–butane mixture, and its change does not exceed ±5%. However, methanol clearly affects the distribution of the products of conjugate conversion.

Methanol increases the selectivity with respect to alkenes C_2–C_4, and at 773 K their fraction increases from 3.3 in the absence of methanol to 15.6 wt % (methanol space velocity 0.4 h^{-1}). Although at different temperatures the effect of methanol on the degree of conversion and selectivity is different, some trends can be revealed.

With increasing space velocity of the methanol supply from 0.4 to 1.7 h^{-1}, the selectivity with respect to alkenes C_2–C_4 increases from 15.6 to 21.3 wt % at 773 K, from 17.5 to 35 wt % at 823 K, and to a still greater extent at 883 K. The selectivity with respect to aromatic hydrocarbons C_6–C_{10} increases also, the selectivity with respect to arenes varies within the 15.6–27.7 wt % range at 773 K, and with increasing temperature their yield decreases. At the same time, the increase in the methanol content increases the selectivity with respect to arenes and alkenes and decreases the yield of lower alkanes C_1–C_2, on the average, from 60 to 30 wt % in the entire temperature range studied.

The dependence of the selectivity with respect to aromatic hydrocarbons C_6–C_{10}, alkenes C_2–C_4, and alkanes C_1–C_2 on the silica ratio (*M*), i.e., the silica–alumina ratio in the zeolite, is shown in Table 3. At 773 K, with increasing silica ratio, the selectivity with respect to alkenes C_2–C_3 increases from 13.3 to 22.4 wt % and the selectivity with respect to aromatic hydrocarbons remains almost constant and varies within 23–25 wt % range. The conversion of the initial alkanes C_3–C_4 at 773 K with increasing content of alumina in the zeolite increases from 66 to 73 wt %. At 823 and 873 K, with decreasing alumina content (silica ratio 30 and 90), the selectivity with respect to alkenes C_2–C_3 decreases from 34.12 to 17.1 wt %. The content of aromatic hydrocarbons increases from 13.54 to 24.90 wt % with increasing silica ratio

Table 2. Products of conjugate conversion of methanol and alkanes C_3–C_4 at H-HSZ-30 catalyst as influenced by space velocity of methanol *V*; space velocity of propane–butane mixture 240 h^{-1}

T, K	*V*, h^{-1}	α, %	Conversion products, wt %							
			hydrogen	methane	ethane	ethene	propene	*i*-butane	benzene	toluene
773	0	87	6.8	42.4	22.0	1.7	1.6	0.8	5.2	6.7
	0.4	63	2.0	35.2	24.4	8.6	7.0	5.4	2.4	5.6
	0.9	73	8.5	31.2	17.7	7.3	6.0	4.9	3.8	10.0
	1.7	71	6.4	22.8	12.2	11.3	10.0	8.3	2.9	8.5
823	0	88	7.3	36.5	18.0	4.8	2.6	1.5	6.3	8.0
	0.4	93	2.8	42.0	20.6	10.9	6.6	1.5	2.6	5.3
	0.9	78	10.6	29.0	12.4	18.6	12.8	3.1	1.6	4.1
	1.7	85	11.9	22.1	4.5	20.3	14.6	3.7	1.8	6.4
873	0	93	10.0	48.4	8.8	9.8	2.8	–	5.5	5.6
	0.4	87	2.7	34.8	14.7	22.0	10.2	1.1	2.8	5.3
	0.9	85	18.6	27.2	6.6	21.4	12.7	1.8	1.5	3.8
	1.7	89	23.5	26.8	3.3	19.6	10.8	0.9	1.0	4.0

T, K	*V*, h^{-1}	Conversion products, wt %					
		xylenes	arenes C_{9+}	naphthalenes	Σ alkanes C_1–C_2	Σ alkenes C_2–C_4	Σ arenes C_6–C_{10}
773	0	4.2	1.5	7.2	65.2	3.3	17.6
	0.4	5.6	2.0	1.6	65.0	15.6	15.6
	0.9	3.5	4.8	2.0	53.8	13.3	22.3
	1.7	11.1	5.2	1.2	43.3	21.3	27.7
823	0	5.6	1.5	4.9	56.0	7.4	21.4
	0.4	4.6	1.7	1.2	64.1	17.5	14.2
	0.9	5.1	2.0	0.6	44.5	31.4	12.8
	1.7	10.2	3.7	0.5	30.3	34.9	22.1
873	0	3.0	1.0	5.0	57.0	12.6	15.1
	0.4	4.2	1.4	0.8	50.6	32.2	13.7
	0.9	4.5	1.5	0.5	35.6	44.1	11.3
	1.7	7.4	2.3	0.5	31.0	30.4	14.7

from 30 to 50 and remains approximately the same (23.3 wt %) for the sample with M = 90. The conversion of the starting lower alkanes strongly increases with increasing temperature above 773 K, but its dependence on the silica ratio is ambiguous; at 823 K the conversion increases from 77 to 90 wt % with increasing silica ratio, but at 873 K this increase is insignificant, from 85 to 89 wt %.

The catalytic activity of the zeolites in question in conversion of methanol and lower alkanes C_3–C_4 is due to the presence of acid centers on their surface. Thus, it was of particular interest to reveal a correlation between their acid properties and catalytic parameters. There are no generally accepted views on how the acidity of the zeolite surface centers correlates with the silica ratio. It was shown that, with increasing SiO_2/Al_2O_3 ratio in the zeolite framework, the strength of the acid centers increases [3, 5, 6], remains unchanged [7], and decreases [8]; i.e., there is no direct correlation of the concentration and strength of the acid centers with the HSZ silica ratio. This suggests that we can only determine the optimal silica ratio ensuring the highest catalytic activity of the sample in the process studied.

The concentration of the acid centers in HSZ and their strength were determined by temperature-programmed desorption of ammonia (Table 4). The TPD spectra show the presence of two acid centers; the low-temperature form is assigned [9, 10] to the weak acid, predominantly Lewis, centers, and the high-temperature maximum belongs to the strong acid centers (predominantly Brønsted proton centers). The amount of desorbed ammonia in the temperature range studied, which is determined by the number of the acid centers of both types, and the positions of the maxima in the ammonia TPD spectra, indirectly characterizing the strength of the acid centers occurring on the HSZ surface, are given in Table 5.

Table 3. Products of conjugate conversion of methanol and alkanes C_3–C_4 at HSZ catalyst as influenced by silica ratio; space velocity ratio of propane–butane mixture and methanol 240 : 1

T, K	*M*	α, %	Conversion products, wt %							
			hydrogen	methane	ethane	ethene	propene	*i*-butane	benzene	toluene
773	30	73	8.6	31.3	17.7	7.3	6.0	4.9	3.8	10.0
	50	67	4.8	25.0	24.5	8.1	5.3	5.6	3.7	8.6
	90	66	4.2	23.1	16.2	12.3	10.1	7.0	3.0	8.2
823	30	77	10.6	29.0	12.4	18.6	12.8	3.1	1.6	4.1
	50	76	6.6	25.8	11.6	16.8	11.0	3.2	2.8	7.5
	90	90	18.1	28.3	11.1	11.6	5.6	1.2	2.8	7.6
873	30	85	18.6	27.2	6.6	21.5	12.7	1.8	1.4	3.8
	50	84	14.5	30.8	12.3	17.2	9.7	1.3	1.9	4.4
	90	89	29.0	30.0	3.9	16.3	7.2	1.7	4.4	4.0

T, K	*M*	Conversion products, wt %					
		xylenes	arenes C_{9+}	naphthalenes	Σ alkanes C_1–C_2	Σ alkenes C_2–C_4	Σ arenes C_6–C_{10}
773	30	3.5	4.8	2.0	53.9	13.3	22.2
	50	9.1	4.0	1.5	55.0	13.4	25.3
	90	10.1	3.2	1.1	46.2	22.4	24.5
823	30	5.1	2.1	0.6	44.4	31.4	13.5
	50	10.1	3.6	0.9	40.6	27.8	24.0
	90	9.7	3.2	0.0	40.7	17.1	23.3
873	30	4.5	1.5	0.5	35.6	34.1	11.1
	50	5.7	1.7	0.6	44.5	26.9	13.6
	90	1.3	1.7	0.5	34.0	23.5	13.15

Table 4. Structural parameters of HSZs

Catalyst	Limiting sorption capacity	Volume of intermediate pores	Volume of micropores	Coefficient in the Dubinin–Radushkevich equation		Diameter of mesopores, nm, in maximum		
	$cm^3\ g^{-1}$			$B_1 \times 10^8$	$B_2 \times 10^8$	1	2	3
H-HSZ-30	0.09	0.03	0.06	0.31	3.34	20	35	75
H-HSZ-50	0.09	0.03	0.06	0.32	2.87	17	35	–
H-HSZ-90	0.08	0.03	0.05	0.30	1.97	13	32	80

As seen from Table 5, with increasing silica ratio from 30 to 90 the total concentration of the acid centers decreases from 1.17 to 0.48 mmol l^{-1}, which is due to a decrease in the content of alumina in the zeolite framework. In accordance with low-temperature shifts of the desorption peaks, the strength of the acid centers of both types decreases with increasing silica ratio. The HSZ sample with *M* = 30 is characterized by the highest concentration of the acid centers on its surface with predominance of low-temperature acid centers (type I : type II = 1 : 0.75). For this zeolite sample, the alkene : arene ratio is 3 : 1 at 823–873 K. For the samples with *M* 50 and 90, the concentration ratio of the acid centers of both types is similar (type I : type II = 0.75 : 1). Moreover, the strength of the acid centers of both types in these samples is also similar, which causes their nearly equal catalytic activity with respect to aromatic hydrocarbons in the entire temperature range (773–873 K) and difference in the selectivity with respect to alkenes from the

Table 5. Acid properties of HSZs

Catalyst	T_{max}, K		Content of acid centers, mmol g^{-1}	
	1	2	1	2
H-HSZ-30	476	765	0.67	0.50
H-HSZ-50	467	722	0.28	0.38
H-HSZ-90	471	712	0.20	0.28

sample with a lower silica ratio (*M* 30) and a higher content of stronger acid centers of type I, providing dehydrogenation of the starting alkanes and oligomerization of alkenes.

Thus, the activity of the zeolite catalysts and their selectivity with respect to aromatic and olefin hydrocarbons in the course of conjugate conversion of methanol and lower alkanes C_3–C_4 predominantly depends not on the total content of the acid centers, but on the concentration of the strong acid centers on the catalyst surface, which activate the alkane molecules and promote dehydrogenation and subsequent aromatization of hydrocarbons.

As seen from the data on the pore structure (Table 4), the sorption capacity for benzene of all the zeolites in question is similar and comprises 0.08–0.09 $cm^3\ g^{-1}$, and the greatest contribution to the total pore volume is made by micropores (0.04–0.06 $cm^3\ g^{-1}$). The greatest volume of micropores was found in zeolite with *M* 30 and 50 (0.06 $cm^3\ g^{-1}$). According to the theory of the volume filling of micropores (TVFM), the zeolite samples studied contain two types of micropores with different size, corresponding to the parameters B_1 and B_2 in the TVFM equation indirectly characterizing the micropore size. The parameter B_1 for zeolites with various silica ratios varies insignificantly in the $(0.30-0.32)\times10^{-8}$ range. The parameter B_2 with increasing silica ratio from 30 to 90 decreases from 3.34×10^{-8} to 1.97×10^{-8}, i.e., with increasing silica ratio the size of the zeolite micropores decreases. Similar trend in the decrease of the zeolite pore size was found in [11]. Analysis of the structural parameters of zeolites and their acid properties showed that the micropore size (characterized by B_2) varies in parallel with the total concentration of the acid centers.

The data on the methanol sorption on the zeolites with various silica ratios showed that H-HSZ-30 zeolite with the greater total volume and size of micropores has greater sorption capacity for methanol. The isotherms of the methanol sorption calculated from the Dubinin–Astakhov equation with two exponents [12] suggest that the zeolite contains two type of micropores with different characteristic energies. This confirms our above conclusions on the pore structure, made from the data on the benzene sorption. The increase in the characteristic energy with increasing silica ratio indicates that the micropore size decreases.

Thus, study of the catalytic activity of zeolites with various silica ratios in the course of conjugate conversion of methanol and lower alkanes C_3–C_4 and analysis of their sorption, structural, and acid properties showed that the sample (*M* 30) exhibiting a high selectivity in alkene formation is characterized by the higher content and greater strength of the acid centers and exhibits high sorption capacity for methanol, probably due to the larger micropore size.

CONCLUSION

(1) The yield of alkenes in conjugate conversion of methanol and lower alkanes C_3–C_4 increases with the temperature and space velocity of the methanol supply.

(2) The highest catalytic activity is shown by the zeolite sample with the silica ratio of 30, which is characterized by the maximal concentration and strength of the acid centers and by coarser micropores.

(3) The zeolite samples with smaller pores and lower concentration and strength of the acid centers (silica ratio 50 and 90) can be used in synthesis of alkylaromatic hydrocarbons at low temperature.

REFERENCES

1. Vosmerikov, A.V. and Erofeev, V.I., *Zh. Fiz. Khim.*, 1995, vol. 69, no. 5, pp. 787–790.
2. Liderman, D., Jacobs, S., and Voltz, S., *Ind. Eng. Chem. Process Des. Develop.*, 1978, vol. 17, no. 3, pp. 340–346.
3. Gaivoronskaya, Yu.I., *Cand. Sci. Dissertation*, Tomsk, 2000.
4. Novak, S., Hünschel, H., Lunch, N., *et al.*, *Neftekhim.*, 1987, vol. 27, no. 6, pp. 736–749.
5. Minachev, Kh.M. and Dergachev, A.A., *Usp. Khim.*, 1990, vol. 59, no. 9, pp. 1522–1554.
6. Kazanskii, V.B., *Kinet. Katal.*, 1982, vol. 23, no. 6, pp. 1334–1348.
7. Parillo, D.J., Lee, C., and Gorte, R.J., *Appl. Catal.*, 1994, vol. 110, no. 1, pp. 67–74.
8. Korobitsyna, L.L., *Cand. Sci. Dissertation*, Tomsk, 1998.
9. Koval', L.M. and Gaivoronskaya, Yu.I., *Izv. Vyssh. Uchebn. Zaved., Khim. Khim. Technol.*, 1999, vol. 42, no. 6, pp. 121–126.
10. Erofeev, V.I., Trofimova, A.S., Koval', L.M., and Ryabov, Yu.V., *Zh. Prikl. Khim.*, 2000, vol. 73, no. 12, pp. 1969–1974.
11. Dutta, P.K., *J. Phys. Chem.*, 1988, vol. 92, no. 2, pp. 354–357.
12. Rodionov, A.I., Klushin, V.N., and Torocheshnikov, N.S., *Tekhnika zashchity okruzhayushchei sredy* (Technique of Environmental Protection), Moscow: Khimiya, 1989.

Russian Journal of Applied Chemistry, Vol. 76, No. 9, 2003, pp. 1466–1471. Translated from Zhurnal Prikladnoi Khimii, Vol. 76, No. 9, 2003, pp. 1505–1510.

ENVIRONMENTAL PROBLEMS OF CHEMISTRY AND TECHNOLOGY

Water Purification with Titanium Compounds To Remove Fluoride Ions

E. P. Lokshin and M. L. Belikov

Tananaev Institute of Chemistry and Technology of Rare Elements and Mineral Raw Materials, Kola Scientific Center, Russian Academy of Sciences, Apatity, Murmansk oblast, Russia

Received April 18, 2003

Abstract—Sorption of fluoride ions from water by titanium compounds was studied. The possibility of deep purification of fluorine-containing wastewater with water-soluble oxotitanium(IV) sulfates was analyzed and the optimal conditions of this process were determined.

Millions of cubic meters of wastewater are formed at a number of mining plants at the Kola Peninsula because of the presence of villiaumite in the ore. These effluents are characterized by increased concentration (up to 10 mg l^{-1}) of fluoride ions. Part of wastewater finds its way to fish farming ponds without being purified. Liquid effluents with increased content of fluoride ions are also present in some other regions of Russia. According to the existing regulations, the concentration of fluoride ions must not exceed 1.4 mg l^{-1} in drinking water reservoirs and 0.75 mg l^{-1} in fishery ponds.

Fluoride ions can be recovered by precipitation, sorption, and electrochemical methods.

It has been recommended to purify solutions from hydrometallurgical processing of tungsten raw materials using the lime method, although purification to the MPC (maximum permissible concentration) was not achieved [1]. At an F^- concentration in weakly mineralized water of 12 mg l^{-1}, introduction of 8 g l^{-1} of CaO and subsequent carbonation for 90 min diminished the concentration of fluoride ions to 1.25 mg l^{-1}, and introduction of 10 g l^{-1} of CaO, to 0.37 mg l^{-1} [2]. A high purification efficiency was achieved by addition of a considerable excess of compounds promoting "salting-out" of the forming fluorite and their subsequent sorption with de-ashed pyrocarbon [3] or zeolites [4].

The use of aluminum sulfate (in amount corresponding to 0.95 g l^{-1} in terms of alumina) at pH 6–7 and settling time not exceeding 0.5 h made it possible to diminish $[F^-]$ from 9.3 to 1.5 mg l^{-1} [5]. The efficiency of removal of fluoride ions increases in the presence of soluble salts of calcium [6]. Sodium and calcium aluminates sorb fluoride ions, with the orthoform being the most effective among calcium aluminates [7, 8]. The use of aluminosilicate materials for precipitation of fluoride ions failed to offer any additional advantages [9, 10].

The disadvantages of the techniques mentioned above are as follows.

Sorbents saturated with fluoride ions cannot be regenerated and reused, and their disposal may lead to migration of fluoride ions into the environment.

Additional water purification to remove aluminum(III) is necessary if water is to be discharged into drinking water or fishery reservoirs; according to GOST (State Standard) 2874–82, the maximum permissible concentration of aluminum ions in drinking water is 0.5 mg l^{-1}.

The fluoride ion can be precipitated in the form of fluoroapatite by introducing soluble compounds of calcium and the phosphate ion into a solution with pH 6–11.5 [1]. However, purification by this method takes a long time (the concentration of fluoride ions in a 100-ml portion of solution decreased from 10 to 1.2–1.8 mg l^{-1} in 5 h, and to 0.1–0.6 mg l^{-1} in 35 h). In addition, although it has been reported that deep purification is achieved at the stoichiometric consumption of reagents [11], it has been shown that this method leads to secondary contamination of water with foreign ions because of the high consumption of chemicals.

It has been suggested to use a sorption–precipitation method for purification of wastewater to remove fluoride ions by its treatment with lime milk to pH 8–

1070-4272/03/7609-1466$25.00

11 and subsequent introduction of adsorbents, water-soluble titanium fluorides (potassium, sodium, and lithium hexafluorotitanates) [12]. A report of the high efficiency of this technique (residual concentration of fluoride ions of 0.3 mg l^{-1} at initial concentration of 3–5 g l^{-1}) seems to be doubtful because of the unclear mechanism of F^- sorption by hexafluorotitanates of alkali metals, which are readily hydrolyzable in alkaline media, with the release of fluoride ions.

The residual concentration of fluoride ions in the case of their sorption from wastewater by $CaSO_4$ synthesized in the presence of sulfocarbon in a solution being purified was 5 mg l^{-1} and more [13].

Purification of water with rare-earth metals as precipitants or adsorbents [14] fails to ensure sufficiently complete removal of fluoride ions, since the solubility of rare-earth metal fluorides is not low enough [15] and, moreover, strongly depends on the pH value and ionic composition of the solution.

The use of anion-exchange resins of various brands in the OH^- form in an equivalent mixture with KU-2 cation-exchange resin in the H^+ form made it possible to recover sodium fluoride from neutral and weakly alkaline solutions containing 5.6–8.0 g l^{-1} of fluoride ions to an extent of 98–99.5% (28–40 mg l^{-1}); however, the residual concentration of F^- remained high [16].

A chelate ion-exchange resin modified with cerium can be used for removal of fluoride ions from solutions [17]. A common disadvantage of ion-exchange techniques is the necessity for thorough preliminary removal of suspended particles from solutions and difficulties encountered in processing large amounts of solutions.

Use of electrochemical methods [18] gives no way of processing large amounts of wastewater and involves gross energy expenditure.

Thus, the known techniques show various disadvantages and, therefore, cannot be used for industrial purification of wastewater discharged into drinking water reservoirs. Moreover, these techniques, as a rule, do not involve processing of solid products saturated with fluorides ions. These products, in turn, act, when stored, as a source of environment contamination with fluorine.

The aim of this study was to develop a method not only involving deep purification of wastewater to remove F^-, but also enabling utilization of fluoride ions and regeneration of the sorbent.

EXPERIMENTAL

Sorption of fluoride ions with hydrated oxotitanium(IV) hydroxide was performed from NaF solutions with fluoride ion concentration of 1.0 g l^{-1}, in which the initial pH_{in} value was adjusted to 4, 5, and 6 with hydrochloric acid.

Hydrated oxotitanium(IV) hydroxide was obtained by dissolving a weighed portion of $TiOSO_4 \cdot 2H_2O$ [TU (Technical Specification) 6-09-01-279–85] in water and separating the precipitate formed in hydrolysis from the liquid phase by centrifugation. Then the precipitate was washed with water until washing water containing no SO_4^{2-} ions was obtained.

The obtained hydrated oxotitanium(IV) hydroxide was used to sorb F^- from 30 ml of NaF solution under continuous agitation with a magnetic stirrer. In the process, the concentration of fluoride ions and the pH value were monitored with ion-selective electrodes and I-160 pH meters. After the equilibrium was attained (in 40–60 min), the solution was separated by centrifugation from the precipitate and a fresh portion of an NaF solution with the same initial pH was added to the precipitate. In each stage, the solution to sorbent mass ratio α was 50. The procedure was repeated until the sorption activity of the precipitate started to decrease steeply. The atomic ratio of the total amount of sorbed F^- and TiO_2 was calculated. The value of K_d was found from the equation

$$K_d = \frac{\alpha_{F^-} \alpha_1}{100 - \alpha_{F^-}}, \quad (1)$$

where α_{F^-} is the fraction of sorbed F^- relative to the total amount brought in contact with the adsorbent (%), and α_1 is the mass ratio of the total amount of solution brought in contact with the sorbent and of the sorbent itself.

The experimental results obtained are listed in Table 1.

Fluoride ions are sorbed by oxotitanium(IV) hydroxide from aqueous solutions by the reaction

$$TiO_{1+x}(OH)_{2-2x} + yF^- = TiO_{1+x}(OH)_{2-2x-y}F_y + yOH^-. \quad (2)$$

Reaction (2) proceeds to such a full extent that it is used for quantitative determination of OH^- groups bound to titanium [19]. It has been established [19] that the efficiency of sorption of fluoride ions depends on how hydrated titanium dioxide is prepared and on

Table 1. Sorption of fluoride ions by hydrated oxotitanium(IV) hydroxide

Run no.	Parameter	Degree of sorption			
		1	2	3	4
1	Final concentration of F^-, g l^{-1}	0.013	0.25	0.38	0.6
	pH_{in}	4	4	4	4
	pH_{fin}	3.5	4.8	4.7	5
	K_d, cm^3 g^{-1}	3800	700	1034	1133
	β	0.22	0.39	0.53	0.62
2	Final concentration of F^-, g l^{-1}	0.035	0.5	0.9	–
	pH_{in}	5	5	5	–
	pH_{fin}	4.9	6.05	6.05	–
	K_d, cm^3 g^{-1}	1380	300	350	–
	β	0.24	0.365	0.39	–
3	Final concentration of F^-, g l^{-1}	0.01	0.33	0.8	–
	pH_{in}	6	6	6	–
	pH_{fin}	4.3	5.46	6	–
	K_d, cm^3 g^{-1}	4950	506	412	–
	β	0.22	0.37	0.42	

the anionic and cationic composition of the solution from which F^- sorption is carried out. As a result of olation and oxolation processes, oxotitanium(IV) hydroxide may have, depending on synthesis conditions, different numbers of hydroxo groups per titanium atom. Although it has been reported that $Ti(OH)_4$ can be obtained [20], this is not the case because of the high rates of olation and oxolation. Neutralization of $TiCl_4$ with ammonia or ammonium carbonate at room temperature gives $TiO(OH)_2$ [21]. However, this form is also unstable, and oxotitanium hydroxide, $TiO_{1+x}(OH)_{2-2x}$, species with $x < 1$ are gradually formed. By boiling of $TiCl_4$–HCl–H_2O and $TiOSO_4$–H_2SO_4–H_2O mixtures, air-dry products of the composition $TiO_{2-x}(OH)_{2x}$, with $x = 0.04 \pm 0.05$ and 0.05 ± 0.01, respectively, have been obtained, and neutralization of $TiCl_4$ with potassium hydroxide at room temperature yields a product with $x = 0.225 \pm 0.05$ [22]. In the last case, part of OH^- groups was probably converted into OK^- groups as a result of sorption of potassium cation.

Table 1 shows that hydrated oxotitanium(IV) hydroxide effectively sorbs fluoride ions from aqueous solutions. In accordance with reaction (2), sorption must be accompanied by an increase in the solution pH; however, the final pH_{fin} of a solution decreased in first stages of its use in sorption. This can be attributed to the fact that precipitates formed in hydrolysis of oxotitanium(IV) sulfate [23] contain a considerable amount (up to 8 wt %) of sulfate groups.

Therefore, the sorption of fluoride ions may be accompanied, together with reaction (2), by liberation of H^+ and, as a consequence, by a decrease in pH. The fact that a decrease in pH was observed in the first stages of sorption indicates that liberation of sulfuric acid occurs more easily than reaction (2). In later sorption stages, pH either stabilizes (run no. 1) or grows.

If it is assumed [24] that residual sulfate groups in hydrated oxotitanium(IV) hydroxide are present in the form of the acid $HOTiO–OSO_2OH$, then sorption of fluoride ions can be represented, in addition to reaction (2), by the reactions

$$HOTiO–OSO_2OH \rightarrow HOTiO–OSO_2O^- + H^+, \quad (3)$$

$$NaF \rightarrow Na^+ + F^-, \quad (4)$$

$$HOTiO–OSO_2O^- + F^- \rightarrow (HO)TiOF + SO_4^{2-}. \quad (5)$$

Reactions (3)–(5) must result in that the concentration of hydrogen ions in solution grows and sulfate ions pass into solution. After the acid $HOTiO–OSO_2OH$ is exhausted, sorption of fluoride ions proceeds by reaction (2) leading to the observed increase in pH.

Table 1 shows that K_d first decreases somewhat and then grows with increasing solution pH_{in}. With pH_{in} varying within the range 4–6, β changes only slightly in the first stages of sorption, but then it decreases by a factor of approximately 1.5 with the pH_{in}

increasing from 4 to 5–6, which points to a dramatic decrease in the number of sorption-active groups.

After regeneration of a sorbent "saturated" with fluorine by treating the sorbent with a 0.107 N sodium hydroxide solution and then washing it thoroughly with water, the sorption activity of the sorbent decreased dramatically: Under the experimental conditions, the residual concentration of F^- was 0.65 g l^{-1}, instead of 0.01–0.035 g l^{-1} in the case of a fresh sorbent. The possible reasons for such a behavior are as follows: conversion of OH^- groups into ONa^- groups and their inability to exchange for fluoride ions, intensification of olation–oxolation reactions in the alkaline medium, and disappearance of sulfate groups from the solvent.

Thus, even though freshly prepared hydrated oxotitanium(IV) hydroxide sorbs F^- rather effectively, its recycling after regeneration with alkaline solutions is inefficient.

The experimental data obtained suggest that $TiOSO_4 \cdot H_2O$, which is readily obtained in processing titanium-containing mineral raw materials, can be used directly for sorption of fluoride ions from aqueous solutions.

In studying sorption of fluoride ions by oxotitanium(IV) sulfate, account was taken of the fact that wastewater from a number of mining plants of the Kola industrial region commonly shows alkaline reaction because of the presence of NaF. Although sulfate ions will find their way into water instead of fluoride ions, their maximum permissible concentration in the aqueous phase (MPA) is relatively high (500 mg l^{-1}); however, the expenditure of oxititanium(IV) sulfate should be kept within the limits allowing discharge of purified water into water reservoirs.

In the experiments, a certain amount of $TiOSO_4 \cdot 2H_2O$ was introduced into solutions with prescribed concentration of F^-. The resulting mixture was agitated, with the pH value monitored continuously. Hydrolysis of titanyl(IV) sulfate occurred in the solution, and the forming precipitate sorbed fluoride ions. The concentration of F^- was also monitored continuously, if the pH value of the mixture allowed this. In those experiments in which the equilibrium pH value did not correspond to a value that enabled F^- concentration measurements, the solid phase was separated before determining the concentration, and the pH of the filtrate was adjusted to 4.1–4.3 with a sodium hydroxide solution. In performing the sorption at constant pH, this constant prescribed value was maintained, when necessary, by adding dropwise a concentrated (250 g l^{-1}) NaOH solution. After F^- sorption terminated, the precipitate formed was separated, and the residual content of titanium(IV) in the purified solution was determined spectrophotometrically using a titanium(IV) peroxo complex.

Table 2. Sorption from solutions containing 10 mg l^{-1} of F^- (pH_{in} 6.70) with pH maintained at 4–4.5

Parameter	$TiOSO_4 \cdot 2H_2O$ expenditure, mg l^{-1}		
	100	400	800
Final concentration of F^-, mg l^{-1}	7	2*	0.6*
pH_{fin}	4.00	4.02	4.5
β	0.310	0.206	0.127
K_d, cm^3 g^{-1}	4290	10 000	24 620

* pH value was maintained constant during sorption by introducing NaOH.

A study of the influence exerted on the sorption efficiency by expenditure of solvent at pH maintained at 4–4.5 (the strongest sorption was observed at this pH value) demonstrated that deep purification of wastewater to remove F^- can be achieved with oxotitanium(IV) sulfate (Table 2). In this case, titanium completely passes from the solution being purified into the precipitate. Deeper purification can be achieved at higher expenditure of oxotitanium sulfate (smaller β).

At higher concentrations of F^- in the initial solution, greater expenditure of the sorbent may be required. Table 3 shows that, with increasing amount of introduced $TiOSO_4 \cdot 2H_2O$, pH_{fin} and efficiency of F^- sorption decrease and there occurs secondary contamination with titanium(IV) of the solution being purified. This contamination becomes more pronounced with decreasing pH.

With the pH_{fin} increasing from 4.5 to 5 at a constant $TiOSO_4 \cdot 2H_2O$ expenditure (200 mg l^{-1}), β decreases more steeply (Table 4) than in the case when hydrated oxotitanium(IV) hydroxide is used for sorption (Table 1).

The optimal pH_{fin} value of sludge is 4–4.5, since, in this case, the values of β and K_d are sufficiently high and the introduced titanium is completely precipitated from the solution.

The purification efficiency is virtually independent of whether the sorbent is added in several portions (Table 5) or in one portion (Table 2, 800 mg l^{-1}). However, the 5-fold drop in β at decreasing initial

Table 3. Sorption from solutions containing 2–10 mg l^{-1} of F^- without adjustment of pH

Parameter	$TiOSO_4 \cdot 2H_2O$ expenditure, mg l^{-1}					
	165	200	400	600	1000	2000
Initial concentration of F^-, mg l^{-1}	2	2	10	10	10	10
Final concentration of F^-, mg l^{-1}	1.0	0.5	2.9	2.7	2.0	2.0
pH_{in}	6.30	6.30	6.7	6.7	6.7	6.7
pH_{fin}	4.40	4.30	2.70	2.60	2.30	1.50
$TiOSO_4 \cdot 2H_2O$ in solution, mg l^{-1}	–	–	32.3	68.6	117.6	220.5
β	0.062	0.077	0.20	0.12	0.094	0.046
K_d, $cm^3\ g^{-1}$	6060	15 000	6660	4245	4536	2248

Table 4. Effect of pH on efficiency of F^- sorption. Initial concentration of F^- 10 mg l^{-1}, pH_{in} 6.70

Parameter	pH_{fin}					
	3.5	4.2	4.5	5.0	6.6	7.0
Final concentration of F^-, mg l^{-1}	4.7	5.0	5.5	8.0	8.0	8.0
$TiOSO_4 \cdot 2H_2O$ in solution, mg l^{-1}	≤1	–	–	–	–	–
β	0.272	0.257	0.231	0.102	0.102	0.102
K_d, $cm^3\ g^{-1}$	5638	5000	4090	1250	1250	1250

Table 5. Sorption from solutions containing 10 mg l^{-1} of F^- (pH_{in} 6.70) with $TiOSO_4 \cdot 2H_2O$ introduced into solution in portions, with the precipitates separated and pH ≥ 4 maintained in each stage

Parameter	Stage						
	1	2	3	4	5	6	7
Final concentration of F^-, mg l^{-1}	7.0	3.4	2.8	1.8	1.45	1.1	0.5
pH_{in}	6.7	4.0	4.15	4.18	4.06	4.20	4.15
$TiOSO_4 \cdot 2H_2O$ introduced, mg l^{-1}:							
in a stage	100	200	100	100	100	100	100
total	100	300	400	500	600	700	800
β:							
in a stage	0.310	0.185	0.063	0.102	0.036	0.036	0.062
total	0.310	0.227	0.186	0.169	0.147	0.136	0.128
K_d, $cm^3\ g^{-1}$:							
in a stage	4290	5280	2175	5520	1332	6220	12 015
total	4290	6461	6445	9102	9830	12 000	23 750

concentration of fluorine in solution (Table 5, stages 1 and 7) indicates that sorbent portions brought in contact with a solution with low F^- concentration are not saturated with the fluoride. The total expenditure of the sorbent can be lowered if the process is carried out in a step-like counterflow mode, with a solution richer in fluoride ions purified using the sorbent already brought in contact with an F^--depleted solution.

At $TiOSO_4 \cdot 2H_2O$ expenditure of 800 mg l^{-1}, which is sufficient for deep purification of wastewater containing 10 mg l^{-1} of F^-, only 423 mg l^{-1} of SO_4^{2-} ions is introduced into water at the permissible concentration of 500 mg l^{-1}. Using $TiOSO_4 \cdot H_2O$ instead of $TiOSO_4 \cdot 2H_2O$ has no effect on the process of wastewater purification.

To conclude, it should be noted that 94.2–97.5% of fluoride ions are distilled off from titanium-containing sulfuric acid solutions already at 100°C [25]. This

enables treatment of the isolated solid product with sulfuric acid to give HF gas, which can be used for manufacture of various fluorine-containing compounds, and water-soluble titanium sulfates, suitable for reuse in wastewater purification.

CONCLUSIONS

(1) Wastewater can be efficiently purified to remove fluoride ions with titanium(IV) compounds and, in particular, with hydrated oxotitanium sulfates. The lowest F^- concentration achieved in this case, 0.5–0.6 mg l^{-1}, is lower than that required by regulations for fishery ponds. The optimal conditions of the purification process were determined.

(2) In the optimal modes of the purification process, wastewater is not contaminated secondarily with titanium compounds and the concentration of the introduced sulfate ions in purified water does not exceed the permissible level.

(3) Processing of the resulting solid product containing titanium and fluorine, with sorbent regeneration and manufacture of usable fluorine compounds, will enable purification of fluorine-containing wastewater without any necessity for disposal of sorbents saturated with fluoride ions.

REFERENCES

1. Palant, A.A., Tagirov, R.K., and Tovtin, A.V., *Tsvetn. Met.*, 1999, no. 10, pp. 47–49.
2. Morozova, V.A. and Kirillova, G.I., *Tsvetn. Met.*, 1992, no. 10, pp. 34–35.
3. USSR Inventor's Certificate no. 1122614.
4. USSR Inventor's Certificate no. 1696398.
5. Komandenko, V.M. and Leikhner, A.B., *Tsvetn. Metall.*, 1988, no. 4, pp. 43–45.
6. Nair, Sh., Jallan, G., and Pandey, G.S., *Fluoride*, 1990, vol. 23, no. 1, pp. 35–42.
7. Hongue, H. and Hideaki, S., *ISIJ Int.*, 2001, vol. 41, no. 5, pp. 506–512.
8. US Patent 5910251.
9. Komandenko, V.M., in *Organizatsiya sistem oborotnogo vodosnabzheniya i ekspluatatsiya vodokhranilishch na predpriyatiyakh tsvetnoi metallurgii* (Development of Systems for Recycled Water Supply and Exploitation of Water Reservoirs at Plants of Nonferrous Metallurgy), Alma-Ata: Kazmekhanobr, 1988, pp. 77–81.
10. Ignatkina, V.A., Rebrova, T.I., and Gritsaenko, A.V., *Tsvetn. Metall.*, 1990, no. 8, pp. 64–65.
11. US Patent 4226710.
12. USSR Inventor's Certificate no. 1682321.
13. USSR Inventor's Certificate no. 1291548.
14. Tokunaga, Sh., Hakuta, T., and Wasay, S., *J. Nat. Inst. Mater. Chem. Res.*, 1999, vol. 7, no. 6, pp. 292–334.
15. Menon, M.P. and James, J., *J. Chem. Soc., Faraday Trans.*, 1989, vol. 85, no. 9, pp. 2683–2694.
16. Starostin, V.V. and Krainova, L.P., in *Kompleksnaya pererabotka mineral'nogo syr'ya piro- i gidrometallurgicheskimi sposobami* (Integrated Processing of Mineral Raw Materials by Methods of Pyro- and Hydrometallurgy), Moscow: VIMS, 1982, pp. 18–25.
17. Haron, M.J., Yunus, W.M.Z., and Wan, J., *J. Environ. Health A*, 2001, vol. 36, no. 5, pp. 727–734.
18. Komandenko, V.M., in *Razrabotka i vnedrenie besstochnykh sistem vodopol'zovaniya i ekspluatatsii khvostokhranilishch* (Development and Implementation of Zero-Drain Systems for Water Management and Exploitation of Tailing Ponds), Alma-Ata: Kazmekhanobr, 1984, pp. 84–88.
19. Belinskaya, F.A. and Makarova, E.D., in *Ionnyi obmen i ionometriya* (Ion Exchange and Ionometry), Leningrad: Leningr. Gos. Univ., 1976, issue 1, pp. 40–43.
20. Filina, L.P. and Belinskaya, F.A., in *Ionnyi obmen i ionometriya* (Ion Exchange and Ionometry), Leningrad: Leningr. Gos. Univ., 1990, issue 7, pp. 15–34.
21. Limar', T.F., Savos'kina, A.I., Andreeva, V.I., and Mank, V.V., *Zh. Neorg. Khim.*, 1969, vol. 14, no. 9, pp. 2307–2312.
22. Dolmatov, Yu.D. and Rogachevskaya, G.L., *Zh. Prikl. Khim.*, 1973, vol. 46, no. 5, pp. 964–967.
23. Khazin, L.G., *Dvuokis' titana* (Titanium Dioxide), Leningrad: Khimiya, 1970.
24. Goroshchenko, Ya.G., *Khimiya titana* (Chemistry of Titanium), Kiev: Naukova Dumka, 1970.
25. Petrov, V.B., Muzhdabaeva, M.A., and Prokof'eva, T.A., in *Fiziko-khimicheskie i tekhnologicheskie issledovaniya pererabotki mineral'nogo syr'ya* (Physicochemical and Technological Studies of Processing of Mineral Raw Materials), Apatity: Kol'sk. Nauchn. Tsentr Ross. Akad. Nauk, 1989, pp. 84–87.

Russian Journal of Applied Chemistry, Vol. 76, No. 9, 2003, pp. 1472–1475. Translated from Zhurnal Prikladnoi Khimii, Vol. 76, No. 9, 2003, pp. 1511–1514.

ENVIRONMENTAL PROBLEMS OF CHEMISTRY AND TECHNOLOGY

Ozonation of Fulvic Acids of Natural Waters in Aqueous Solutions

G. V. Slavinskaya and V. F. Selemenev

Voronezh State University, Voronezh, Russia

Received March 26, 2003

Abstract—Ozonation of fulvic acids of natural waters in aqueous solutions was studied.

It is known that water chlorination gives rise to its contamination with carcinogenic organic impurities [1]. Therefore, ozone is widely used today as oxidant instead of chlorine in water treatment. Ozonation is used for treating drinking and ultrapure water, for breakdown of organic impurities in wastewater, etc. [2–6]. Ozonation of natural waters is actively studied to elucidate the possibility of water decontamination from ozonation products by various techniques, including coagulation and sorption.

Taking into account that fulvic acids (FAs) are, as a rule, the main organic impurity present in natural waters, we studied in this work their ozonation in aqueous solutions.

EXPERIMENTAL

Fulvic acids were isolated from Neva water by the technique reported in [8]. The ozonation of fulvic acid solutions was carried out in a glass column of bubble type 70 mm in diameter at pH 7.1 typical of Neva water. The experiments on water treatment by coagulation with iron sulfate combined with liming were carried on the same column at pH 9. The air–ozone flow containing 6.8–10.0 mg dm^{-3} ozone was generated by an ozonizer with the performance of 2 g O_3 min^{-1} at the air flow rate of about 1 dm^3 min^{-1}. The difference between the ozone concentration in the aqueous solution before and after its reaction with FAs was determined by the method reported in [9].

As seen from Fig. 1, on ozonation of neutral FA solutions, the color index measured at 350 nm (an SF-46 spectrophotometer) decreases to a lesser extent than on ozonation of weakly alkaline FA solutions.

The color of fulvic acids is due to the fact that these molecules contain a polycyclic aromatic core and peripheral chains, with a common system of conjugated double bonds giving a continuous absorption band in the range 200–350 nm [10]. On oxidation with ozone, this chromophoric molecular system is broken down.

The FA degradation is manifested in the electronic absorption spectra (Fig. 2) as a decrease in the optical

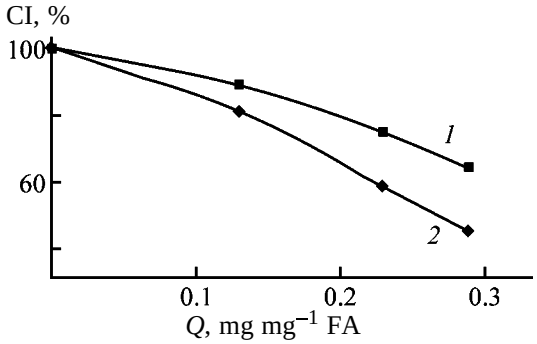

Fig. 1. Residual color index CI as a function of the ozone amount Q that reacted with FAs at pH (*1*) 7 and (*2*) 9.0.

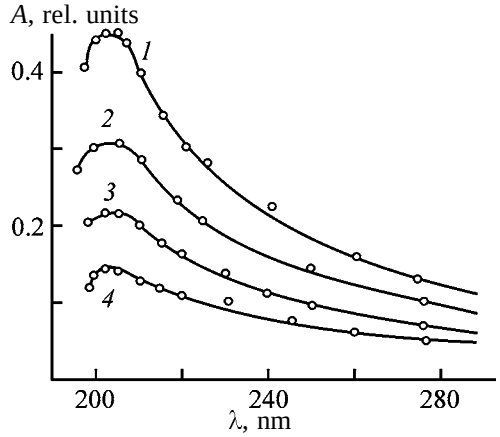

Fig. 2. Electronic absorption spectra of FAs (*1*) before and (*2*) after ozonation. Q (mg mg^{-1} FA): (*1*) 0, (*2*) 0.13, (*3*) 0.23, and (*4*) 0.29. (*A*) Optical density and (λ) is wavelength.

1070-4272/03/7609-1472$25.00

density at invariable shape of the spectra. These spectra show that, on ozonation, only a certain fraction of FA molecules degrade.

The effect of ozonation on the molecular-weight distribution of FAs was studied by gel chromatography on a column 10 mm in diameter packed with Molselect G-50 gel (gel bed height 300 mm, sample volume 0.1 ml). Water was used as eluent. The gel chromatograms of the initial FAs and those after ozonation have two elution bands (Fig. 3). The first elution band (*I*) belongs to the high-molecular-weight fraction of FAs (HMWF). This fraction, due to its steric features, cannot penetrate into gel and, therefore, is eluted first. The second elution band belongs to low-molecular-weight fraction of FAs (LMWF). Figure 3 shows that, after ozonation, the relative content of HMWF (band *I* in gel chromatograms *1*' and *2*') decreases and, correspondingly, the LMWF content (band *II*) increases. These gel chromatograms also show that, with increasing pH from 7.1 to 9.0, the degree of HMWF degradation increases from 20 to 60%. We found that the initial molecular weight of HMWF (8900) does not noticeably change after ozonation. At the same time, the LMWF molecular weight decreases from the initial value of 6400 to 5300 and 4000 after ozonation in neutral and alkaline media, respectively. The decrease in the molecular weight of organic compounds to values <5000 on ozonation was noted in [12].

To elucidate how ozonation affects the FA structure, the IR spectra of both HMWF and LMWF were recorded on a Specord UV Vis-235 spectrophotometer (KBr pellets) before and after ozonation. These studies showed that, after ozonation, the bands of the C–H stretching vibrations at 2950 and 2880 cm^{-1} disappear. Taking into account that the intensity of the absorption band of the bending vibrations of the methyl groups of FAs at 1460 cm^{-1} also decreases after ozonation [13, 14], we can suggest that the disappearance of the above-noted C–H stretching bands after ozonation is caused by degradation of the methyl groups.

Another effect of FA ozonation is transformation of a sharp absorption band of skeletal C–C vibrations of the benzene rings at 1510 cm^{-1} into a weak absorption peak. This fact shows that, on ozonation, some fraction of the aromatic rings is broken down. The strengthening of the absorption bands at 1720 and 1400 cm^{-1} shows that ozonation results in an increase in the content of carbonyl groups.

It should be noted that, after ozonation, LMWF contains not only products of FA reaction with ozone

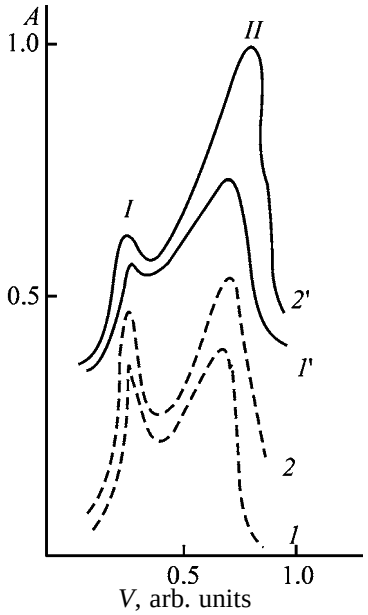

Fig. 3. Gel chromatogram of FA (*1*, *2*) before and (*1*', *2*') after ozonation at (*1*, *1*') pH 7.1 and (*2*, *2*') pH 9.0. (*A*) Optical density of eluate and (*V*) eluate volume.

but also low-molecular-weight species formed by HMWF degradation. Therefore, the IR spectra reflect the total amount of low-molecular-weight fractions of both origins. The amount of the COOH groups increases owing to oxidation of the terminal methyl groups of FA molecules, which is manifested in disappearance of the absorption bands at 2950 and 2880 cm^{-1}.

The possibility of oxidation of the peripheral hydrocarbon groups of FAs into carboxy groups was analyzed by Orlov [10]. In our case, the IR spectrum of the initial FAs contains no absorption band at 3030 cm^{-1} typical of benzene rings with more than four substituents, but contains the bands of C–C vibrations at 1620, 1500 and 1450 cm^{-1} characteristic of less substituted benzene rings. The substituents can be oxidized with ozone to form benzenepolycarboxylic acids.

We also determined the elemental composition, weight content, and permanganate oxidizability (PO) of the ozonation products. To compare the weight content of FAs in the initial solution and that after ozonation, we used the completely dimeneralized FAs. The effect of ozonation of FA solution on the amount of their dry residue (after drying of FA solution under an Infratherm lamp at 34–36°C) is demonstrated in Table 1.

These results show that, after ozonation of FA solution, the weight content of FAs decreases insig-

Table 1. Elemental composition of FAs of Neva water before and after ozonation*

O_3 reacted, mg O_3 mg^{-1} FA	Content, %				C_{FA}	Decrease in C_{FA}	PO, mg O_2 dm^{-3}
	C	H	N	O	g kg^{-1} of solution		
0	46.7	5.0	1.2	47.1	2.168	–	500
0.23	40.4	6.4	1.5	51.7	1.984	0.184	310
0.29	38.1	9.3	2.5	50.1	2.010	0.158	–

* Determination accuracy: C ±0.2, H ±0.05, N ±0.04, O ±0.03; FA ±0.0005; and PO ±10.

nificantly. However, under the same conditions, the elemental composition of FAs substantially changes. It was found that, on ozonation, the carbon content in FAs decreases, whereas the content of H, N, and O increases. We believe that enrichment of FAs in nitrogen is caused by formation of nitrogen oxides in the ozonizer from atmospheric nitrogen. The relatively small loss of carbon suggests that carbon is oxidized not only to CO_2, but also to various oxygen-containing hydrocarbon groups (not only carboxy, but also keto, aldehyde, ether, and alcoholic groups). The permanganate oxidizability shows that ozonation decreases the content of readily oxidizable fractions by 40%.

The content of the carboxy groups in FAs before and after ozonation was determined by potentiometric titration from a single sample. Based on the titration curves, we calculated both the ionization constants of the COOH groups of FAs by the Henderson–Hasselbach equation and the equivalent weights of fulvic acids before and after ozonation (Table 2).

Table 2 shows that the COOH group content in FAs increases after ozonation by 50%. Ozonation increases both the dissociation constant of the carboxy groups (K_a) and the electrical conductivity χ. At the same time, the equivalent weight of FAs decreases owing to degradation.

To elucidate what products are formed upon ozonation of FAs, the ozonized FAs solutions were fractionated by high-performance liquid chromatography (HPLC). Fractionation was performed on an Milikhrom multicolumn chromatograph equipped with a spectrophotometric detector sensitive in the range 190–260 cm^{-1} and a 2 × 62-mm column packed with Silosorb-600 sorbent with particle size of 5×10^3 nm. Amino acids contained in the fulvic acids were determined by the method described in [15]. A fulvic acid solution (5–10 μl) was introduced into the chromatographic column and eluted with a water–acetonitrile (40 : 60)–0.35 NH_4OH mixture until the optical density A in the measuring and reference cells became equal.

Table 2. Effect of ozonation on FA properties

O_3 reacted, mg O_3 mg^{-1} FA	C_{CO_2H}, mg-equiv g^{-1}	FA equivalent weight	pK_a*	$\chi \times 10^{-4}$, Ω^{-1} cm^{-1}
0	4.15	242	4.2	3.87
0.13	6.46	148	3.7	7.17
0.23	6.62	138	3.5	7.82
0.29	6.68	153	3.6	9.90

* Determination accuracy ±0.05.

Under these conditions, a chromatogram contains four elution bands, the first of which refers to amino acids. In the chromatograms of ozonized FAs, the height of all the elution bands decreases irrespective of pH, and this decrease was the more pronounced, the greater amount of ozone reacted with FAs. This chromatographic analysis showed that FA ozonation results in their degradation. However, we found no new elution bands in the chromatograms, i.e. the chomatographic method used is incapable of detecting the products of FA degradation.

CONCLUSIONS

(1) On reaction with ozone, both the high- and low-molecular-weight fractions of fulvic acids are broken down. The products of fulvic acid ozonation have lower degree of aromaticity and lower molecular weight. At the same time, the content of carboxy groups in them increases. This factor can favor sorption of the products of fulvic acids degradation on anion exchangers by the anion-exchange mechanism.

(2) In ozonation of fulvic acids, the degree of their degradation increases in going from neutral (pH 7.1) to alkaline (pH 9) solutions. After ozonation, the weight content of fulvic acids decreases by 7–8% in neutral (pH 7.1) and by 17–18% in alkaline (pH 9.0) solutions.

REFERENCES

1. Slavinskaya, G.V., *Khim. Tekhnol. Vody*, 1991, vol. 13, no. 11, pp. 1013–1022.
2. Shevchenko, M.A., Marchenko, P.V., Taran, P.N., and Lizunov, V.V., *Okisliteli v tekhnologii vodopodgotovki* (Oxidants in Water Treatment Technology), Kiev: Naukova Dumka, 1979.
3. Apel'tsin, E.I., Alekseeva, L.P., and Cherskaya, N.O., *Vodosnabzh. Sanit. Tekh*., 1992, no. 4, pp. 9–11.
4. Moniwa Takeo, *J. Jpn. Water Works Assoc*., 1995, vol. 64, no. 10, pp. 26–30.
5. Stopka, K., *Eng. Dig.* (Toronto), 1988, vol. 31, no. 20, pp. 22–23.
6. Grant, D., *Water Waste Treat.* (UK), 1996, vol. 39, no. 3, pp. 7–9.
7. Shevchenko, M.A., *Organicheskie veshchestva v prirodnoi vode i metody ikh udaleniya* (Organic Compounds in Natural Water and Methods for Their Removal), Kiev: Naukova Dumka, 1966.
8. Slavinskaya, G.V. and Selemenev, V.F., *Ful'vokisloty prirodnykh vod* (Fulvic Acids of Natural Waters), Voronezh: Voronezh. Gos. Univ., 2001.
9. Lur'e, Yu.Yu., *Unifitsirovannye metody analiza vod* (Standard Methods for Water Analysis), Moscow: Khimiya, 1971.
10. Orlov, D.S., *Gumusovye kisloty pochv* (Humus Acids of Soils), Moscow: Mosk. Gos. Univ., 1974.
11. Aivazov, B.V., *Vvedenie v khromatografiyu* (Introduction to Chromatography), Moscow: Vysshaya Shkola, 1983.
12. Garret, M. and Cavelier, C., *Water Res*., 1986, vol. 20, no. 12, pp. 1477–1488.
13. Bellamy, L.J., *The Infra-Red Spectra of Complex Molecules*, London: Methuen, 1954.
14. Orlov, D.S. and Osipova, N.N., *Infrakrasnye spektry pochv i pochvennykh komponentov* (Infrared Spectra of Soils and Soil Components), Moscow: Mosk. Gos. Univ., 1988.
15. Styskin, E.P., Itsikson, L.B., and Braude, E.V., *Praktika vysokoeffektivnoi zhidkostnoi khromatografii* (Practice of High-Performance Liquid Chromatography), Moscow: Khimiya, 1986.

Russian Journal of Applied Chemistry, Vol. 76, No. 9, 2003, pp. 1476–1478. Translated from Zhurnal Prikladnoi Khimii, Vol. 76, No. 9, 2003, pp. 1515–1517.

ENVIRONMENTAL PROBLEMS OF CHEMISTRY AND TECHNOLOGY

Regeneration of Exhausted Chrome Tanning Solutions from Leather Production as a Method Preventing Environmental Pollution with Chromium

V. P. Panov, E. M. Gyul'khandan'yan, and A. S. Pakshver

St. Petersburg State University of Technology and Design, St. Petersburg, Russia

Received February 5, 2003

Abstract—Photochemical degradation of organic impurities in exhausted chrome tanning solutions is studied. A method for regeneration of these solutions is proposed, allowing reduction of chromium loss with wastewater.

Leather production in the volume of water consumption and, correspondingly, in the volume of water supply ranks first among the branches of light industry. Since tanneries are arranged mostly near water basins used as sources of drinking and industrial water, the problem of preventing pollution of these basins with leather production discharges is very topical.

After tanning of hide (skin after removal of the hair side), 22 to 35% of the chrome tanning agent remains in exhausted tanning solutions, which corresponds to a residual chromium concentration of 3–8 g l^{-1} (recalculated to Cr_2O_3). According to published data, more than 25 000 t of Cr(III) is discharged to the environment with leather production wastes all over the world, whereas the discharge from metallurgical works is about 1500 t [1–4].

One of the promising ways to reduce the discharge of chrome tanning agents and, correspondingly, the Cr(III) consumption is recycling of chrome tanning solutions. Recovery of chromium(III) from exhausted tanning solutions by precipitation requires large amounts of alkaline reagents and sulfuric acid for dissolution. The resulting Cr(III) hydroxide sludge is poorly settled and filtered, being contaminated with residual proteins.

Presently growing efforts are devoted to developing methods of waste treatment without phase transfer, for example, ultrafiltration on various membranes allowing separation of solutes, fats, and protein residues [5]. However, to provide reasonable service life for the membranes, the solutions should be pretreated to thoroughly remove suspended materials prior to ultrafiltration. Wide application of the method is also limited by high cost and batch process mode.

The problem of recycling of tanning solutions may be solved only after solving the problem of removal of organic impurities from them, for example, by degradation. Recent studies demonstrate high efficiency of liquid-phase oxidation of organic impurities under the combined effect of active oxygen, hydroxy radicals formed in UV treatment of the solutions after addition of hydrogen peroxide, and ozone. In this case, degradation of organic acids, particularly, amino acids proceeds more rapidly by two orders of magnitude than with the use of an oxidant only [6, 7].

There is no information in the literature on the effect of UV irradiation on Cr(III) complexes with amino acids. It may be expected that photolysis will break down such complexes, providing mineralization of the amino acids. As a result, the chrome tanning agent will be regenerated.

In this work we studied photochemical degradation of organic impurities with simulated and actual exhausted tanning solutions. The process was monitored by the chemical oxygen demand (COD) using the standard procedure. The amino acid concentration was determined by paper partition chromatography using water–acetone–*n*-propanol–acetic acid (1 : 2 : 1.5 : 0.2) as a mobile phase and polarography. Experiments on determination of COD of solutions containing such amino acids as glycine, β-alanine, *DL*-proline, and arginine showed that, under the COD determination conditions (boiling in 18 N sulfuric acid for 2 h), the degree of mineralization of organic impurities ranges

1070-4272/03/7609-1476$25.00

from 86 to 94%, which was then taken into account in interpretation of the results.

In the experiments we used a photoreactor with UV irradiation from the top (monochromatic radiation at λ = 254 nm, dose rate 30 W l^{-1}, irradiation time 120 min) and supply of hydrogen peroxide.

In the simulated solutions, the concentrations of glycine and β-alanine (recalculated to COD) were 670 mg O_2 l^{-1} each. After addition of the tanning agent to a Cr_2O_3 concentration of 4 g l^{-1}, COD increased to 2440 mg O_2 l^{-1} as a result of the presence of organic impurities in it. The experiments showed that photolysis of amino acids in aqueous solutions proceeds slowly, but considerably accelerates in the presence of the chrome tanning agent (Fig. 1). Evidently, in acid solutions, Cr(III) compounds behave as catalysts [8]. The results obtained demonstrate a possibility of a sufficiently exhaustive photochemical degradation of organic impurities.

Even stronger acceleration of the UV degradation of organic impurities is realized in the presence of H_2O_2. After addition of H_2O_2, COD, determined by the standard procedure, increased, since H_2O_2 acts as a reducing agent with respect to $K_2Cr_2O_7$ (potassium bichromate is the commonly used oxidant in COD determinations). The stoichiometric amount of hydrogen peroxide (relative to the initial COD of the solution) was estimated as

$$M_{H_2O_2} = COD_0 M_{exp(H_2O_2)}/M_{exp(O_2)}.$$

After addition of H_2O_2 in amount of 50, 100, and 150% relative to the stoichiometric amount into the solution with COD_0 = 4200 mg O_2 l^{-1}, COD increased to 6000, 8050, and 10 000 mg O_2 l^{-1}, respectively. Similar trends were also observed in the corresponding aqueous H_2O_2 solutions. Without UV treatment, COD of the chrome tanning solutions remained practically unchanged in 60–120 min at 20–25°C. After addition of H_2O_2 (60–130% against the stoichiometry) to the initial tanning solution (Cr_2O_3 concentration 3.5 g l^{-1}, COD 1370 mg O_2 l^{-1}), UV treatment resulted in decreasing COD (Table 1).

The most significant change in COD was observed in the first 60 min of UV treatment. In this time, the degree of degradation of organic impurities approaches 55–70% (75–85% in 2 h). The residual content of organic impurities is quite acceptable for reuse of exhausted tanning solutions. It appeared inexpedient to increase the amount of H_2O_2 above 100%, since, with increasing amount, the residual COD does not noticeably decrease.

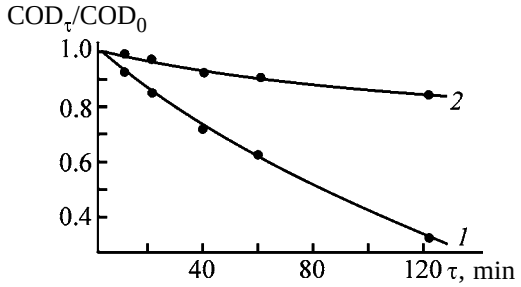

Fig. 1. Relative decrease in the COD (COD_τ/COD_0) in the course of photochemical treatment (*1*) with and (*2*) without chrome tanning agent. (τ) Irradiation time.

UV treatment of 2.6×10^{-2} M glycine solutions with introduction of H_2O_2 (100% against the stoichiometry of glycine mineralization to CO_2, H_2O, and NH_3) provides a 60–65% decrease in COD in 10–20 min. After introduction of Cr(III) (4 g l^{-1} recalculated to Cr_2O_3) into the solutions, COD decreased by 80–85%.

To estimate the efficiency of the photochemical degradation of organic impurities in exhausted chrome tanning solutions, we carried out experiments with actual industrial waste formed after tanning of pig hide. The initial Cr(III) concentration was 3.9 g l^{-1} (recalculated to Cr_2O_3), pH 3.7, and COD, 3700 mg O_2 l^{-1}. The experiments were performed at 293 K with addition of H_2O_2 (Table 2).

The results reveal complex interactions between components of the system. In the initial period of UV treatment, the radiation energy goes to degradation of organic impurities (photolysis in the absence of H_2O_2) or, in the presence of H_2O_2, to its photolysis. UV radiation may break down Cr(III) complexes with amino acids with formation of some intermediates, but without considerable change in COD. Actual solutions contain saturated organic compounds, whose degradation is hindered. After the initial (in the first 30–40 min) degradation of complex structures in the

Table 1. Degradation of organic impurities in model solutions in the course of UV treatment

τ, min	COD, mg O_2 l^{-1}, at indicated amount of H_2O_2 added, % of stoichiometry		
	60	100	130
0	2250	2720	3190
30	1480	1600	1800
60	1010	810	970
90	730	430	610
120	610	310	520

Table 2. Degradation of organic impurities in exhausted chrome tanning solutions in the course of UV treatment

τ, min	COD, mg O_2 l^{-1}, at indicated amount of H_2O_2 added, % of stoichiometry		
	0	50	100
0	3700	5550	7400
10	2820	5240	5730
20	2510	5100	5200
40	2330	5020	4960
60	2220	4410	4100
90	2100	2820	1620
120	1850	1760	930

presence of H_2O_2, COD considerably decreases, as in simple photolysis.

The rate of the photochemical degradation of organic impurities depends on their nature, as demonstrated by the experiments on UV treatment of actual exhausted solutions after tanning of goatskin. The initial Cr(III) concentration was 4 g l^{-1} (recalculated to Cr_2O_3); COD, 1780 mg O_2 l^{-1}; radiation dose rate, 15 W l^{-1}. At an H_2O_2 dose of 25–70% against the stoichiometry, even in 30–60 min, the degree of degradation approached 50–70% (Fig. 2). Since for recycled solution there is no need in full mineralization of organic impurities, it is enough to perform the UV treatment for 60–90 min.

Under industrial conditions (70-l tanning drum), we performed experiments on tanning of goatskin with fresh and recycled tanning solutions, all other conditions being equal. Prior to the experiments, the exhausted solutions after UV treatment were conditioned with the fresh tanner. Six batches of hide were tanned. The quality of all the resulting leathers was practically the same. The shrinkage temperature of leather ranged from 108.2 to 110 and from 107.8 to 109°C with the use of the fresh and regenerated tanning solutions, respectively. The shrinkage test results met the technical regulations.

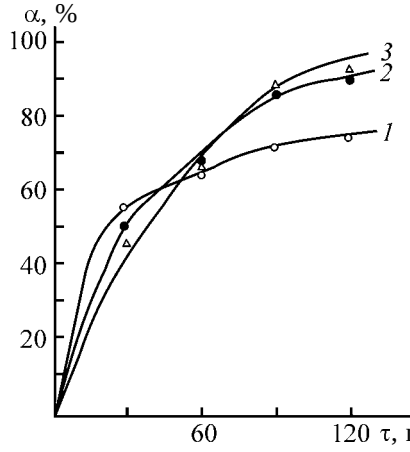

Fig. 2. Total degree of degradation of organic impurities and hydrogen peroxide α as a function of the UV treatment time τ. Amount of H_2O_2 added (% of stoichiometry): (*1*) 25, (*2*) 50, and (*3*) 75.

The results obtained provided a basis for developing a new method of regeneration of exhausted chrome tanning solutions from leather production [9]. In this method, the volume of the chrome tanning agent discharged or delivered to alkaline treatment stage can be reduced by a factor of 4–6.

CONCLUSIONS

(1) Exhausted chrome tanning solutions can be regenerated by UV treatment at a wavelength of 254 nm.

(2) Introduction of hydrogen peroxide in the solution considerably intensifies degradation of organic impurities (in actual systems, 60–90-min irradiation provides 50–75% degradation). Chromium(III) compounds were proved to accelerate degradation of organic impurities.

(3) The quality of leather produced with regenerated tanning solutions was demonstrated to be virtually the same as with a fresh tanning solution. The proposed regeneration method allows reduction in the chromium loss with wastewater by a factor of 4–6.

REFERENCES

1. Stern, O and Zelinski, M., *Bor. Cipotech.*, 1993, vol. 43, no. 8, pp. 314–343.
2. Covington, F. and Arnold, G., *Leder*, 1987, vol. 82, no. 5, pp. 105–106.
3. Trabel, H., *Leather Manuf.*, 1987, vol. 105, no. 8, pp. 6–11.
4. Laskov, Yu.M., Fedorovskaya, T.G., and Zhmakov, G.N., *Ochistka stochnykh vod predpriyatii kozhevennoi i mekhovoi promyshlennosti* (Wastewater Treatment in Leather and Fur Industries), Moscow: Leg. Pishch. Prom–st., 1984.
5. Eder, W., *Pelzwirtschaft*, 1992, no. 7, pp. 34–40.
6. Paul, D. and Conterl, W.J., *Environ. Sci. Health*, 1980, vol. 25, no. 8, pp. 353–385.
7. Kochony, J. and Bolton, J., *J. Phys. Chem.*, 1991, vol. 95, no. 13, pp. 5116–5120.
8. Hustert, K. and Zepp, R.G., *Chemosphere, Ser. B*, 1992, vol. 24, no. 3, pp. 1055–1060.
9. RF Patent 2129992.

Russian Journal of Applied Chemistry, Vol. 76, No. 9, 2003, pp. 1479–1482. Translated from Zhurnal Prikladnoi Khimii, Vol. 76, No. 9, 2003, pp. 1518–1521.

PROCESSES AND EQUIPMENT OF CHEMICAL INDUSTRY

Effect of Contamination and Cleaning of a Microfiltration Membrane in Filtration of an Aqueous Extract of Dog-Rose

B. T. Sagdullaev, E. V. Safonova, and M. A. Khodzhaeva

Yunusov Institute of Chemistry of Vegetable Compounds, Academy of Sciences of the Republic of Uzbekistan, Tashkent, Uzbekistan

Received February 26, 2003

Abstract—The main factors responsible for decrease in the filtration flux (membrane throughput) in removal of pectin substances from an aqueous extract from dog-rose fruits and reasons for membrane contamination were studied. The method for membrane cleaning with distilled water and additional cleaning agents, aqueous solutions of NaOH and HNO_3, was optimized.

Microfiltration is one of baromembrane methods for solution separation, which is used to remove microparticles, bacteria, grease drops, yeast cells, and colloids from suspensions. This method is based on the sieve mechanism, i.e., the filtering membrane can catch from solutions particles and large dissolved molecules. This yields two products, retentate and permeate. The retentate is a suspension that cannot pass across the membrane, and, therefore, the retentate concentration grows in the course of the filtration process. The permeate is a solution that has passed across the membrane and contains no large molecules [1, 2].

According to the IUPAC classification (1985), microfiltration membranes have pores more than 50 nm in size [3].

Microfiltration is a promising and attractive method for concentration of macromolecules, desalination (mainly for removal of low-molecular-weight compounds from macromolecular solutions), fractionation of macromolecules, and clarification, pasteurization, and sterilization of juices, wines, beer, and dairy products, and also in manufacture of biologically active substances [4–6].

The main advantage of this method is its high throughput. However, the throughput (filtration flux) decreases in the course of filtration, which is mainly due to membrane contamination and concentration polarization [7]. Commonly, the filtration flux decreases upon contamination, but occasionally the membrane selectivity is also altered. These changes are observed during the entire process and even may make necessary membrane replacement [8].

The effect of factors responsible for membrane contamination has been poorly studied. In principle, all the components (with exception of the solvent) involved in filtration can contaminate the membrane. Physicochemical properties of individual components, membrane, and the bulk of the flow being filtered determine the nature and amount of contamination. Not infrequently, substances dominating in the contamination are present in trace amounts and their concentration has virtually no effect on the main components involved in the separation process. For example, the flux decreases in most of aqueous solutions through deposition of particles or microorganisms present in these solutions [9].

Certain difficulties are encountered in identifying the component making the main contribution to contamination and in determining the extent of this contribution.

Many researchers explain the fast decrease in the permeate flux by the occurrence of concentration polarization, which leads to formation of a gel layer [10, 11]. The simultaneous decrease in the flux is attributed to membrane contamination. However, the contamination may occur very rapidly, since the time necessary for adsorption of macromolecules on the membrane surface may be as short as several seconds. It should be noted that the factors responsible for the decrease in the membrane throughput include slow increase in the solution viscosity because of particle retention (in solution concentration), concentration polarization, and slow physicochemical changes in the structure of the membrane or substances [11].

The cleaning of membrane is one of the most im-

1070-4272/03/7609-1479$25.00

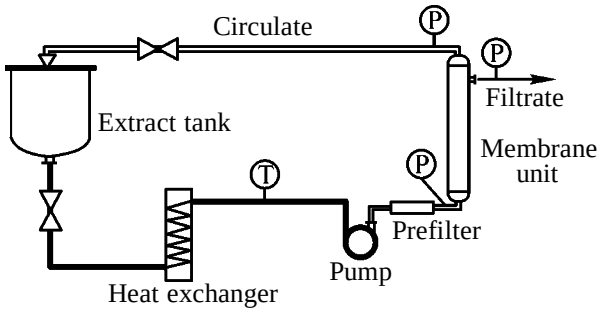

Fig. 1. Schematic of the microfiltration process.

portant processes for preservation of its properties (permeability and selectivity). Theoretically, the process of membrane cleaning must be effective, simple, and executable without disassembly of the membrane unit. In doing so, the membrane and filtering installation should not be damaged and the cleaning procedure must conform to all sanitary and hygienic regulations.

The present communication reports the results obtained in studying the effect of the main factors (transmembrane pressure and temperature) on the membrane contamination in removal of pectin substances from an aqueous extract from fruits of *Rosa canina L.* dog-rose and evaluates the efficiency of various cleaning agents.

EXPERIMENTAL

The experiments were carried out on an Alpma microfiltration installation (Germany) with two membrane units, each comprising nine cylindrical ceramic membranes (Fig. 1). The total effective filtration area was 2.2 m^2. Monolithic ceramic Kerasep membranes (France) had rated pore size of 0.2 μm. The overall diameter of the membrane with 19 channels (channel diameter 2.5 mm) was 20 mm. This membrane is thermally and chemically stable in contact with chemical cleaning agents at 20–85°C and pH 1–14, and also in sterilization with steam at 121°C (for 40 min).

The filtration flux across the membrane was ($l\ h^{-1}\ m^{-2}\ bar^{-1}$) 3600 for distilled water, 2000 for spring water, 500–1500 for contaminated water, and 80–250 for fruit juices. The effect of pressure on the flow rate of a fluid being filtered was studied under transmembrane pressure of 100–300 kPa, and the influence of solution temperature on the filtration process, at 25–50°C and constant pressure (200 kPa).

The experiments were carried out with an aqueous extract produced from dog-rose fruits used in manufacture of the Kholosas preparation. The total amount of extractive substances in the extract was 1.5 wt %, and the content of pectin substances, 0.047 wt %. The extract also contained a number of other compounds: flavonoids, several organic acids (citric, malic, ascorbic), pigments, mineral substances, etc.

The specific throughput of a filter is determined by the flux J [amount of substance (solution volume) that passes across a unit surface area in unit time, $m^3\ m^{-2}\ s^{-1}$].

The flux can be found as the ratio of the increasing volume of permeate, ΔV, collected in unit time Δt, to the area of the effective membrane surface, or mass-transfer area, S:

$$J = \frac{\Delta V/\Delta t}{S}. \quad (1)$$

The flux of pure solvent, J_w, passing across a clean (new) membrane can be expressed as

$$J_w = \frac{\Delta P}{\mu_p R_m}, \quad (2)$$

where ΔP is the transmembrane pressure (Pa); μ_p, permeate viscosity (Pa s); and R_m, membrane resistance to a flow of pure solvent (m^{-1}).

As already mentioned, the effect of contamination and concentration polarization is commonly regarded as an additional membrane resistance R_f, resulting from adsorption of particles on the surface of the membrane and within its pores [12].

Equation (2) can be used to account for the contamination effect by including the additional resistance R_f to the flow passing across the contaminating layer (Darcy law):

$$J_w = \frac{\Delta P}{\mu_p(R_m + R_f)}. \quad (3)$$

The value of R_f varies with pressure, solution concentration, and rate of solution circulation at low pressures; however, at its high values, pressure has no significant effect on the process [13].

At constant ΔP, μ_p, and R_m, the resistance R_f becomes a function of time.

Membrane cleaning is the most important procedure in all membrane processes. All membranes, including liquid membranes, are contaminated in operation, and, as a consequence, their throughput decreases to below the acceptable level. As a result, the substances contaminating the membrane must be removed from the surface and pores of the membrane by special cleaning techniques. The cleaning is done

to remove not only contaminating deposits, but also microorganisms to conform to hygienic regulations.

Frequently, additional maintenance of the membrane (chemical pretreatment) makes higher the permeate flux [14]. In this study, the microfiltration membrane was preliminarily treated by circulation of a 0.005 M solution of NaOH. This was done at a temperature of 50°C and transmembrane pressure of 0.5 bar for 0.5 h.

Immediately after the treatment of the membrane, experiments aimed to determine the flux J_w for pure solvent (water) were carried out. This value was used in calculating the maximum throughput and cleanness of the membrane.

Further, the membrane unit was subjected to contamination with an aqueous extract of dog-rose fruits, which was circulated for 30 min with continuous filtration. The decrease in the membrane throughput and appearance of a considerable amount of deposits on it were monitored by measuring the permeate flux J_p.

Additional chemical cleaning was performed after rinsing the system with distilled water for 15 min (without circulation) and 0.5% solution of NaOH for 40 min with full circulation (of permeate and retentate), at controlled temperature. The permeate flux in the course of cleaning was measured, and rinsing was done, using a volumetric cylinder and a stopwatch.

In parallel, experiments on membrane cleaning with 0.5% HNO_3 for 40 min and preliminary washing with distilled water for 15 min were carried out. The efficiency of the cleaning process was evaluated as the ratio of the flux J_c during cleaning to flux J_w of pure solvent determined on a clean (new) membrane (before its being contaminated).

The restoration of the initial flux J_r (%) was evaluated by the formula

$$J_r = (J_c/J_w) \times 100. \quad (4)$$

The extent of membrane contamination affects the permeate flux, which markedly decreases with increasing contamination. The flux is frequently high at the beginning of the filtration process and markedly decreases in the course of time [11]. In the present study, the contamination model is analyzed at different pressures and temperatures.

Figure 2a shows how the transmembrane pressure affects the flux decay. The data obtained indicate that the flux grows with the transmembrane pressure increasing from 100 to 300 kPa. However, after 15 min this difference becomes insignificant, and then, with the membrane becoming contaminated, changes in

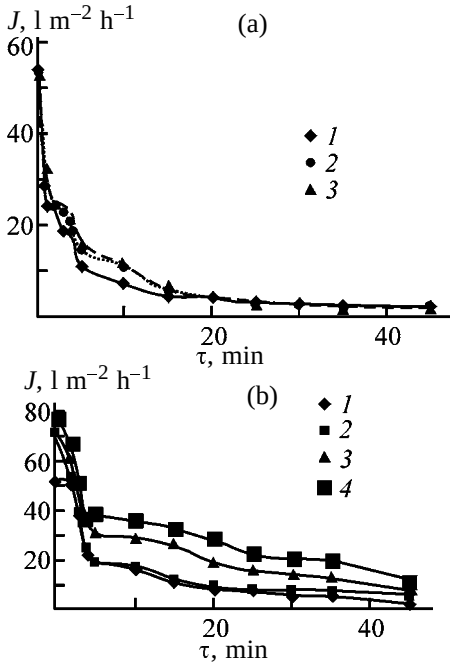

Fig. 2. Permeate flux J vs. time τ. (a) Transmembrane pressure (kPa): (*1*) 100, (*2*) 200, and (*3*) 300. (b) Permeate temperature (°C): (*1*) 25, (*2*) 35, (*3*) 40, and (*4*) 50 (transmembrane pressure 200 kPa).

pressure do not lead to the expected change in the flux. This phenomenon can be only accounted for by the individual properties of the membrane (morphology, chemical nature of its material) and the fluid being filtered.

Also, the effect of temperature on the flux was studied. The experiments were performed at different temperatures (from room temperature to 50°C) and constant transmembrane pressure of 200 kPa.

Figure 2b shows that the flux grows with increasing temperature, which can be accounted for by the effect of temperature on the solution viscosity and mass-transfer coefficient, with the resulting improvement of the transfer of high-molecular-weight components of the extract from the membrane surface into the common flow.

To determine the effective temperature in membrane cleaning, experiments were done at 25 to 65°C by washing with distilled water at low transmembrane pressure (50 kPa).

The optimal temperature for membrane cleaning was found to be 55°C, as shown in Fig. 3. Raising the temperature further leads to poor flux restoration. This is accounted for by better separation into constituents and/or dissolution of deposits on the membrane surface at higher temperatures. This gives rise to free fine particles, which can be more firmly fixed within the

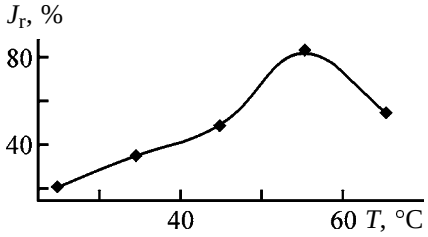

Fig. 3. Effect of temperature on the cleaning process: extent of restoration of the initial flux J_r.

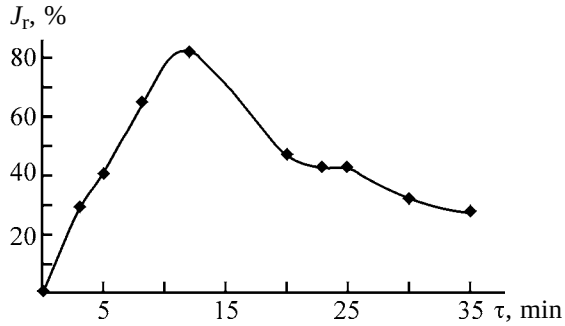

Fig. 4. Extent of restoration of the initial flux J_r vs. time τ of membrane cleaning.

pores of the membrane than coarser particles [15].

Figure 4 shows a typical curve of restoration of the flux of distilled water at 55°C The curve reaches a maximum (82%) in 12 min and then gradually descends. The appearance of the peak in the flux restoration curve can, probably, be accounted for by the mechanism described in [13]. After the cleaning procedure, coarse settled particles can be removed, and, therefore, a tendency toward increase in the flux is observed originally. However, at the same time, some fine particles formed upon dissolution of a part of large molecules may find their way into narrow pores and be adsorbed there.

It is also possible that, in rinsing a membrane with water, fine particles situated between coarse particles (or attached to them) are shifted deeper inside the pores. It should be added to the aforesaid that the peak width may be affected by hydration of particles within pores, which also leads to poorer restoration of the initial flux.

Additional cleaning of the membrane after its washing with distilled water demonstrated that the following values are achieved after 10 min: $J_r(\text{NaOH}) = 98.2\%$, $J_r(\text{HNO}_3) = 92.3\%$.

CONCLUSIONS

(1) The results obtained in studying the permeate flux in microfiltration of an aqueous extract of dog-rose fruits show that the membrane contamination is affected by the process pressure and temperature.

(2) The highest flux of the fluid being filtered is observed in the initial stage of filtration, and then the flux decreases.

(3) The main factor in membrane contamination is clogging of its pores.

(4) A contaminated membrane can be washed with distilled water, with 82% of its initial throughput restored in 12 min. Additional application of chemical cleaning agents for 10 min gives 98.2% for NaOH and 92.3% for HNO_3.

REFERENCES

1. Dytnerskii, Yu.I., *Baromembrannye protsessy: Teoriya i raschet* (Baromembrane Processes: Theory and Calculation), Moscow: Khimiya, 1986.
2. Huisman, I., in *Crossflow Microfiltration of Particle Suspensions: The Influence of Hydrodynamics and Physico-Chemical Interactions*, Lund (Sweden): Lund Univ., 1998, p. 110.
3. Howell, J., Sanchez, V., and Field, R.W., *Membranes in Bioprocessing: Theory and Applications*, London: Blackie Academic & Professional, 1993, p. 241.
4. Soifer, R.D., *Zh. Vses. Khim. O–va. im. D.I. Mendeleeva*, 1987, vol. 32, no. 6, pp. 661–669.
5. Karbachsch, M. and Perl, H., *Zh. Vses. Khim. O–va. im. D.I. Mendeleeva*, 1987, vol. 32, no. 6, pp. 669–673.
6. Kozlov, M.P. and Dubyaga, V.P., *Plast. Massy*, 1982, no. 9, pp. 49–51.
7. Ghosh, R., *J. Membrane Sci.*, 2002, vol. 195, no. 1, pp. 115–123.
8. Tragardh, G., in *Food Processing Recent Developments*, New York: Elsevier Science, 1995, p. 233.
9. Zeman, L.J. and Zydney, A.L., in *Microfiltration and Ultrafiltration Principles and Applications*, New York: Dekker, 1996, p. 256.
10. Altmann, J. and Ripperger, S., *J. Membrane Sci.*, 1997, vol. 124, no. 1, pp. 119–128.
11. Marshall, A.D., Munro, P.A., and Tragardh, G., *J. Membrane Sci.*, 1997, vol. 130, nos. 1–2, pp. 23–30.
12. Gan, Q., Howell, J.A., Field, R.W., *et al.*, *J. Membrane Sci.*, 1999, vol. 155, no. 2, pp. 277–289.
13. Makardij, A., Chen, X.D., and Farid, M.M., *Food Bioprod. Process.*, 1999, vol. 77, no. C2, pp. 107–113.
14. Bird, M.R., in *Cleaning and Disinfection in the Dairy and Food Processing Industries: Notes of Continued Education*, Auckland Univ., School of Engineering in Association with ICI Chemical Cleaning, 1997, p. 123.
15. Hatziantoniou, D. and Howell, J., *12th Annual Meet. of North American Membrane Society (NAMS)*, Lextington, KY (the United States), 2001, p. 63.

Russian Journal of Applied Chemistry, Vol. 76, No. 9, 2003, pp. 1483–1488. Translated from Zhurnal Prikladnoi Khimii, Vol. 76, No. 9, 2003, pp. 1522–1527.

ORGANIC SYNTHESIS AND INDUSTRIAL ORGANIC CHEMISTRY

Comparative Assessment of the Solvating Powers of Solvents of Different Nature with Respect to Condensed Aromatic Hydrocarbons

S. M. Leshchev and A. V. Sin'kevich

Belarussian State University, Minsk, Belarus

Received January 8, 2003

Abstract—The solubilities of anthracene, tetracene, 1,2-benzanthracene, chrysene, pyrene, perylene, α,α'-dinaphtyl, rubrene, and decacyclene in solvents of different nature and polarity (hydrocarbons and halogenated hydrocarbons, alcohols, ketones, ethers, and esters) were determined at 20 ±1 °C. The distribution of benzene and naphthalene in the organic solvent–water system was studied. The Gibbs energy of transfer of aromatic hydrocarbons from *n*-octane to organic solvents was calculated.

Condensed aromatic hydrocarbons (CAHs) and their derivatives, whose molecules contain fused benzene rings, are present as complex mixtures in oil, coal tar, and pyrolysis products of organic compounds. On the one hand, CAHs are valuable raw materials for chemical industry and on the other, highly toxic and hazardous environmental pollutants. Aromatic hydrocarbons are separated and isolated from various objects by liquid extraction and crystallization using selective solvents [1, 2].

By now, for CAHs, whose molecules contain up to four benzene rings, the relationships in extraction from hydrocarbon solutions with strongly polar organic solvents are fairly well understood [3]. However, there are virtually no published systematized data on the solubility of CAHs in weakly and moderately polar solvents miscible with liquid aliphatic hydrocarbons. Many of these solvents have low boiling points and are easily recovered, which makes them suitable for wide application in chemical and petrochemical industries. A systematic study of the relationships in solvation of CAHs with these solvents will enable, in turn, development of efficient methods of their separation, isolation, and concentration from various objects (soils, resins, asphaltenes, etc.).

Therefore, this study was aimed at deriving systematized information about the solvency and solvating power of weakly and moderately polar solvents with respect to CAHs and about their dependence on the nature and structure of the solvent molecules.

EXPERIMENTAL

We used the following CAHs: anthracene, tetracene, 1,2-benzanthracene, chrysene, pyrene, perylene, α,α'-dinaphtyl, 5,6,11,12-tetraphenylnaphthacene (rubrene), and decacyclene purified be recrystallization. The structural formulas of decacyclene and rubrene are given below:

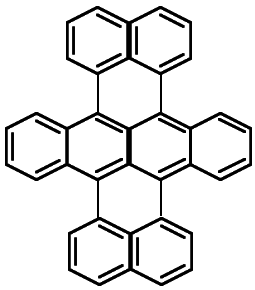

Rubrene

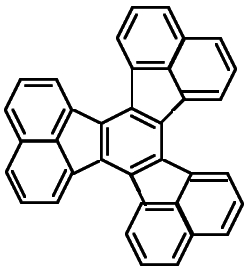

Decacyclene

As organic solvents we used pure grade *n*-octane purified by sulfuric acid extraction, as well as 2,2,5-trimethylpentane (isooctane), cyclohexane, cyclohexene, benzene, α-methylnaphthalene, chlorobenzene, carbon tetrachloride CCl_4, methylene chloride CH_2Cl_2, chloroform $CHCl_3$, 1,1- and 2,2-tetrachloroethane, methyl iodide, methylene iodide, diethyl ether (DEE), dibutyl ether (DBE), ethyl acetate, amyl acetate, acetone, methanol, propanol, and isopropanol (pure grade).

The solubilities of CAHs were determined by different procedures. In the case of liquids transparent at wavelengths corresponding to absorption of aromatic

1070-4272/03/7609-1483$25.00

Table 1. Distribution constants of naphthalene in the organic solvent–water systems and CAH solubility in solvents of different nature and polarity

Solvent	*P*		*S*, M						
	benzene	naphthalene	anthracene	tetracene	1,2-benzanthracene	chrysene	α,α'-dinaphthyl	perylene	pyrene
Octane	200	3100	9.2×10^{-3}	9.1×10^{-4}	1.8×10^{-2}	1.6×10^{-3}	2.6×10^{-2}	7.5×10^{-4}	8.3×10^{-2}
Isooctane	–	2200	–	–	1.3×10^{-2}	–	–	5.4×10^{-4}	5.1×10^{-2}
Cyclohexane	360	5600	1.7×10^{-2}	1.6×10^{-3}	3.2×10^{-2}	–	4.3×10^{-2}	1.5×10^{-3}	–
Cyclohexene	430	8100	3.2×10^{-2}	4.0×10^{-3}	1.1×10^{-1}	–	8.9×10^{-2}	2.8×10^{-3}	2.1×10^{-1}
Benzene	632	14 500	6.6×10^{-2}	9.6×10^{-3}	1.9×10^{-2}	1.7×10^{-2}	2.7×10^{-1}	9.3×10^{-3}	5.5×10^{-1}
α-Methylnaphthalene	–	–	8.6×10^{-2}	1.3×10^{-3}	–	–	–	–	–
CH_2Cl_2	710	19 000	1.0×10^{-1}	1.7×10^{-2}	–	3.7×10^{-2}	–	1.6×10^{-2}	1.05
$CHCl_3$	750	16 300	8.8×10^{-2}	1.8×10^{-2}	6.1×10^{-1}	5.4×10^{-2}	4.7×10^{-1}	1.4×10^{-2}	9.8×10^{-1}
CCl_4	450	8800	3.5×10^{-2}	5.1×10^{-3}	1.3×10^{-1}	9.7×10^{-3}	1.7×10^{-1}	4.7×10^{-3}	–
$CHCl_2$–$CHCl_2$	–	–	1.7×10^{-1}	–	–	–	–	3.1×10^{-2}	–
Chlorobenzene	–	–	8.0×10^{-2}	–	–	–	–	–	
CH_3I	–	–	1.5×10^{-1}	–	–	–	–	–	1.32
CH_2I_2	–	–	4.0×10^{-2}	–	–	–	–	–	–
DEE	–	–	2.9×10^{-2}	–	–	–	–	–	2.5×10^{-1}
DBE	–	–	1.8×10^{-2}	–	–	–	–	2.4×10^{-3}	1.2×10^{-1}
Ethyl acetate	–	–	4.0×10^{-2}	–	–	–	–	–	–
Amyl acetate	520	10 500	4.5×10^{-2}	6.2×10^{-3}	2.2×10^{-1}	–	–	–	–
Acetone	–	–	4.6×10^{-2}	6.8×10^{-3}	–	–	6.4×10^{-2}	–	3.8×10^{-1}
Methanol	–	–	5.1×10^{-3}	–	–	–	–	–	2.8×10^{-2}
Propanol	–	–	8.1×10^{-3}	–	–	–	–	–	5.0×10^{-2}
Isopropanol	–	–	5.0×10^{-3}	–	–	–	–	–	2.9×10^{-2}

substances, we used UV spectrophotometry, and in the case of volatile UV-absorbing liquids (benzene and acetone), gravimetry. We prepared saturated solutions of aromatic substances in the solvents studied. Next, into a preliminarily weighed clean dry weighing bottle, the required volume of saturated solution of the aromatic compound was introduced, whereupon the solvent was evaporated and the weighing bottle with the substance was weighed. For high-boiling UV-absorbing liquids (α-methylnaphthalene, chlorobenzene), we measured the volume of the liquid required for complete dissolution of the precisely weighed portion of a solid aromatic hydrocarbon.

All the experiments were run at 20 ± 1°C. Based on the data obtained, we calculated the Gibbs energies of transfer (hereinafter, energies of transfer) of hydrocarbons from *n*-octane to the solvents under study:

$$\Delta G_t^0 = -2.3RT\log\frac{S}{S_{oct}}, \quad (1)$$

where S and S_{oct} are the solubilities, mol l^{-1}, of an aromatic hydrocarbon in organic solvent and in *n*-octane, respectively.

The energies of transfer of benzene, which is unlimitedly soluble in the solvents under study, and naphthalene, whose solubility exceeded 1 mol l^{-1}, were calculated by the equation

$$\Delta G_t^0 = -2.3RT\log\frac{P}{P_{oct}}, \quad (2)$$

where P and P_{oct} are the distribution constants of naphthalene in the organic solvent–water and *n*-octane–water extraction systems, respectively.

We described in detail the procedures for studying the benzene and naphthalene distribution in [3, 4]. The parameters S and P were estimated accurately to within 10%, and ΔG_t^0, to within 0.42–0.83 kJ mol^{-1}.

Tables 1 and 2 list the parameters P and S for CAHs and their corresponding energies of transfer from *n*-octane to solvents of different nature and polarity, miscible with it. The ΔG_t^0 parameter is, evidently, a measure of the solvating power of a solvent with respect to CAH.

Table 2 suggests that the majority of the solvents have negative energies of transfer. The energies of

Table 2. Energies of CAH transfer from *n*-octane to organic solvents miscible with *n*-octane

Solvent	I_{CH_2}* [5]	ΔG_t^0, kJ mol^{-1}								
		benzene	naphthalene	anthracene	tetracene	1,2-benzanthracene	chrysene	α,α'-dinaphthyl	perylene	pyrene
Isooctane	0.007	0.79	0.83	–	–	0.79	–	–	0.79	1.17
Cyclohexane	–0.012	–1.42	–1.46	–1.54	–1.38	–1.38	–	–1.21	–1.67	–0.88
Cyclohexene	–0.006	–1.88	–2.33	–3.00	–3.58	–4.46	–	–	–3.17	–2.25
Benzene	0.00	–2.79	–3.75	–4.79	–5.71	–5.79	–5.71	–5.67	–6.13	–4.58
α-Methylnaphthalene	0.018	–	–	–5.42	–0.88	–	–	–	–	–
CH_2Cl_2	0.015	–3.08	–4.42	–5.79	–7.08	–	–7.58	–	–7.42	–6.17
$CHCl_3$	–0.005	–3.21	–4.04	–5.46	–7.17	–8.54	–8.50	–7.00	–7.29	–6.00
CCl_4	–0.015	–1.96	–2.54	–3.21	–4.17	–4.67	–4.42	–4.54	–4.46	–
$CHCl_2$–$CHCl_2$	–	–	–	–7.08	–	–	–	–	–9.04	–
Chlorobenzene	0.000	–	–	–5.25	–	–	–	–	–	–
CH_3I	0.003	–	–	–6.79	–	–	–	–	–	–
CH_2I_2	0.14	–	–	–3.58	–	–	–	–	–	–
DEE	0.008	–	–	–2.79	–	–	–	–	–	–2.67
DBE	0.012	–0.63	0.25	–1.63	–	–2.17	–	–	–2.79	–
Ethyl acetate	0.058	–	–	–3.58	–	–	–	–3.00	–	–
Amyl acetate	0.030	–2.33	–2.96	–3.83	–4.67	–6.08	–	–	–	–
Acetone	0.083	–	–	–3.92	–4.88	–	–	–2.17	–	–3.71
Methanol	0.11	–	–	1.42	–	–	–	–	–	2.63
Propanol	0.068	–	–	0.29	–	–	–	–	–	1.21
Isopropanol	0.074	–	–	1.46	––	–	–	–	–	2.54

* I_{CH_2} is the methylene group increment.

transfer are positive only for isooctane (minor) and alcohols (relatively high). The energy of transfer from isooctane to octane is weakly dependent on the hydrocarbon structure, being 0.79 kJ mol^{-1} on the average.

The influence of the structure of aliphatic hydrocarbons on the intensity of the dispersion interactions of CAHs with hydrocarbons is distinct along the isooctane–octane–cyclohexane series. For example, a minor positive value of the ΔG_t^0 parameter characterizing transfer of the aromatic hydrocarbon from octane to isooctane suggests that branching of the molecule of aliphatic hydrocarbon decreases its solvating power. This is due to the so-called "voids" in the structure of the branched hydrocarbon. Cyclization of linear paraffin molecules (cyclohexane), on the contrary, affords a denser packing of the solvent molecules. This effect is particularly prominent in the case of molecules with a larger number of carbon atoms (rubrene, decacyclene). On the whole, the ΔG_t^0 parameter in the naphthalene–anthracene–1,2-benzanthracene series is weakly influenced by the hydrocarbon structure.

Solvents whose molecules contain polar segments or π bonds are typically characterized by large negative ΔG_t^0 parameters. Solvation by these solvents can proceed either via π complex formation or solvation of the protons in the aromatic rings. For example, upon introducing a multiple bond into the solvent molecule (series cyclohexane–cyclohexene–benzene), the solvation power of the solvent sharply increases. This is probably due to polarizability of the π systems and existence of instant dipoles in the molecules of aromatic hydrocarbons, which intensifies the dispersion interactions. The importance of π electrons in CAH solvation is indirectly supported by a sharp increase in the boiling and melting points of condensed hydrocarbons with increasing number of fused benzene rings. Hence, benzene with its polarizable π system is inferior (just insignificantly) in the solvating power only to chloroform and methylene chloride, despite its significantly lower polarity. Naturally, α-methylnaphthalene is a more active solvating agent for CAH than benzene (Table 2).

In unassociated solvents (chloroform, methylene chloride) characterized by a high density of the negative charge on the chlorine atoms and by strongly polarized bonds, evidently, there exist electrostatic

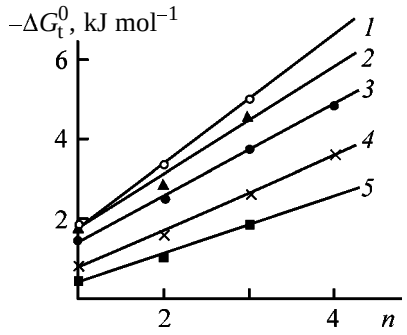

Variation of the energy of transfer ΔG_t^0 with the number of fused rings n in CAHs: (*1*) CH_2Cl_2, (*2*) $CHCl_3$, (*3*) benzene, (*4*) amyl acetate, and (*5*) CCl_4.

interaction forces between the solvent molecule dipoles and instant dipoles of the solute. The relative strength of such forces depends on the polarity and polarizability of the molecules. As a result, these solvents exhibit more negative energies of transfer than other weakly polar solvents. Shielding of the electron-accepting center and replacement of all the protons by chlorine atoms (CCl_4) is accompanied by a significant decrease in the solvating power of the solvent. At the same time, the chlorine atoms of halogenated hydrocarbons, evidently, make a significant contribution to the total energy of CAH solvation. Interestingly, this contribution sharply increases with increasing polarizability of the halogen-containing group (CH_3I). The factors responsible for a decrease in the solvating power on changing from CH_3I to CH_2I_2 will be discussed below.

The solvent polarity exerts an ambiguous effect on the energy of transfer. The dissolving power of a solvent with respect to CAH usually tends to decrease with increasing polarity of the solvent (alcohols and esters), and in the case of ethers it markedly increases. High polarity of organic solvent typically strengthens its three-dimensional structure [5], promoting "expulsion" of weakly polar CAH molecules.

As a measure of this "expulsion" we can take the increment of the methylene group I_{CH_2} into the logarithm of the distribution constant between the hydrocarbon and solvent. In the case of the solvents studied (except for alcohols, methylene iodide, ethyl acetate, and acetone), the increment of the methylene group is fairly small and does not exert the deciding influence on the pattern of variation of G_t^0 with the number of the aromatic rings in the hydrocarbon molecules. Interestingly, a significant difference in ΔG_t^0 for methyl iodide and methylene iodide is due specifically to the difference in the I_{CH_2} parameters, and methylene iodide is immiscible with aliphatic hydrocarbons, unlike methyl iodide. As to alcohols, significantly positive ΔG_t^0 values are due to both fairly high I_{CH_2} values and strong self-association of alcohols, which sharply weakens their solvating power.

Table 3. Coefficients in correlation equation (3)

Solvent	*a*	*b*
	kJ mol^{-1}	
Benzene	–2.79	–0.96
CCl_4	–2.04	–0.58
$CHCl_3$	–3.29	–1.13
CH_2Cl_2	–3.08	–1.33
Amyl acetate	–2.38	–0.75

The solvating and dissolving powers of a solvent with respect to such CAHs as naphthalene, anthracene, and tetracene (chrysene) can be estimated using the plots of the energy of transfer of aromatic hydrocarbons vs. the number of fused aromatic rings (see figure). This plot is linear for all the solvents studied by us. The figure shows that the solvating and dissolving powers of a solvent are the greater, the greater the section cut at the ordinate axis and the greater the slope. The ΔG_t^0 parameters can also be described by the equation

$$\Delta G_n^0 = a + bn, \quad (3)$$

where a is the energy of benzene transfer from *n*-octane to a solvent, kJ mol^{-1}; b, increment into the transfer energy upon adding to the benzene molecule each new aromatic ring; and n, number of fused aromatic rings.

Table 3 lists the coefficients from Eq. (3). It is seen that, among the most extensively studied solvents, the greatest solvating powers with respect to CAHs are exhibited by chloroform, methylene chloride, and benzene. For less extensively studied solvents, the anthracene transfer energy can serve as a measure of the solvating power. The linearity of the ΔG_t^0–n dependence, evidently, allows calculation of the energies of transfer from *n*-octane to a solvent for other condensed aromatic hydrocarbons using the ΔG_t^0 parameters for anthracene and benzene.

By contrast to polar solvents, the ΔG_t^0 parameters of CAHs for the majority of weakly polar organic solvents miscible with *n*-octane are independent, within the experimental error, of the type of connection of aromatic rings in these substances (tetracene–

Table 4. Energies of transfer of decacyclene and rubrene from *n*-octane to weakly polar organic solvents

Solvent	Decacyclene			Rubrene		
	S, M	ΔG_t^0, kJ mol^{-1}		*S*, M	ΔG_t^0, kJ mol^{-1}	
		experiment	calculation*		experiment	calculation*
Octane	3.4×10^{-6}	–	–	2.3×10^{-4}	–	–
Cyclohexane	3.65×10^{-5}	–5.75	–5.83	2.2×10^{-3}	–5.50	–6.75
Cyclohexene	8.80×10^{-5}	–7.92	–8.21	7.4×10^{-3}	–8.42	–10.8
Benzene	2.83×10^{-4}	–10.7	–14.0	3.9×10^{-2}	–12.5	–16.9
CH_2Cl_2	8.15×10^{-4}	–13.3	–15.6	–	–	–
$CHCl_3$	7.36×10^{-4}	–13.0	–15.4	9.3×10^{-2}	–14.6	–16.8
CCl_4	2.22×10^{-4}	–10.1	–10.2	2.3×10^{-2}	–11.2	–11.5
Amyl acetate	2.24×10^{-4}	–10.2	–9.88	–	–	–

* Using the additivity method, by Eqs. (4) and (5).

1,2-benzanthracene–chrysene), as well as of the degree of connectivity of the naphthyl substituents in molecules (α,α'-dinaphthyl, perylene). At the same time, in the case of solvents having the greatest solvating power with respect to CAHs (Table 2), as well as in the case of extraction of CAHs with strongly polar solvents, their solvating power markedly increases on going from linear to angular connection of rings in CAH molecules [3].

To elucidate the suitability of the method of increments for predicting the ΔG_t^0 parameters of complex aromatic hydrocarbons, we studied CAHs with complex structures, rubrene and decacyclene. Based on their solubilities, we calculated the energies of transfer of decacyclene and rubrene from *n*-octane to the solvents studied using the following equations:

$$\Delta G_t^0(\text{decacyclene}) = 3\Delta G_t^0(\text{naphthalene}) + \Delta G_t^0(\text{benzene}) - 6\times2.3RTI_{CH_2}, \quad (4)$$

$$\Delta G_t^0(\text{rubrene}) = \Delta G_t^0(\text{tetracene}) + 4\Delta G_t^0(\text{benzene}) - 4\times2.3RTI_{CH_2}, \quad (5)$$

where ΔG_t^0(decacyclene), ΔG_t^0(naphthalene), ΔG_t^0(benzene), ΔG_t^0(rubrene), and ΔG_t^0(tetracene) are the energies of transfer of the corresponding substance from *n*-octane to weakly polar organic solvent; the latter term characterizes the contribution from the hydrogen atoms to the energy of transfer [6].

Let us compare the experimental and calculated data. Table 4 shows that, for the solvents exhibiting the greatest solvating powers with respect to CAHs ($CHCl_3$, CH_2Cl_2, and benzene), the experimental values noticeably exceed the calculated ΔG_t^0 values.

This is probably due to the mutual influence of the groups constituting the molecules of substituted CAHs. This, in turn, weakens the solvation of decacyclene and rubrene by the CAHs with the greatest solvating powers.

At the same time, transfer of decacyclene and rubrene from *n*-octane to weakly polar solvents exhibiting nonspecific solvation powers with respect to CAHs (amyl acetate, CCl_4, cyclohexane, cyclohexene) can be adequately described using the additivity principle. Probably, specifically a relatively small affinity of these solvents for aromatic hydrocarbons, including decacyclene, prevents them from adequately responding to the change in the conjugation energy of π electrons in a substance molecule.

CONCLUSIONS

(1) Condensed aromatic hydrocarbons with simple structures exhibit virtually linear dependence of ΔG_t^0 on the number of aromatic rings in hydrocarbons. This suggests an independent, to a first approximation, solvation of individual rings. Thus, the additivity principle can be applied to predicting the solubilities of these hydrocarbons and their derivatives in weakly polar solvents.

(2) For solvents that have strong solvating power with respect to condensed aromatic hydrocarbons, the additivity principle is of a limited use. In this case, the calculational formulas should, evidently, be added with special correction terms to take into account the mutual influence of the groups in the molecules of the substances studied.

REFERENCES

1. Sulimov, A.S., *Proizvodstvo aromaticheskikh uglevodorodov iz neftyanogo syr'ya* (Production of Aromatic Hydrocarbons from Oil Raw Materials), Moscow: Khimiya, 1975.
2. Bittrich, G.I., Gaile, A.A., Lempe, D., *et al*., *Razdelenie uglevodorodov s ispol'zovaniem selektivnykh rastvoritelei* (Separation of Hydrocarbons Using Selective Solvents), Leningrad: Khimiya, 1987.
3. Leshchev, S.M. and Sinitsyna, A.V., *Neftekhimiya*, 1997, vol. 37, no. 6, pp. 552–556.
4. Leshchev, S.M. and Sinitsyna, A.V., *Neftekhimiya*, 1997, vol. 37, no. 1, pp. 56–61.
5. Leshchev, S.M., Novik, N.P., Onishchuk, V.I., and Sin'kevich, A.V., *Zh. Fiz. Khim*., 2001, vol. 75, no. 10, pp. 1800–1805.
6. Leshchev, S.M. and Novik, N.P., *Zh. Strukt. Khim*., 1999, vol. 40, no. 3, pp. 514–519.

Russian Journal of Applied Chemistry, Vol. 76, No. 9, 2003, pp. 1489–1493. Translated from Zhurnal Prikladnoi Khimii, Vol. 76, No. 9, 2003, pp. 1528–1532.

ORGANIC SYNTHESIS AND INDUSTRIAL ORGANIC CHEMISTRY

Effect of Humic Acids on the State of Disperse, Acid, and Vat Dyes in Aqueous Solutions

Yu. S. Vashurina, A. S. Pogorelova, and Yu. A. Kalinnikov

Institute of Chemistry of Solutions, Russian Academy of Sciences, Ivanovo, Russia

Received May 22, 2003

Abstract—Effect of humic acids (biopolymeric compounds of anionic type recovered from peat) on the state of disperse, acid, and vat dyes in aqueous solutions was studied; vat dye was studied in the form of water-soluble sodium salt of leuco acid.

The adsorption and diffusion processes occurring in aqueous solutions of organic dyes [1] in the course of textile dyeing can be controlled by addition of various synthetic textile-processing chemicals, which are environmentally hazardous and fairly expensive [2]. Hence, search for new readily available and environmentally safe compounds to improve the dyeing process is urgent.

As such compounds, we studied humic acids, biopolymeric compounds of irregular structure, which contain various functional groups [3] and can react with both hydrophilic [4–6] and hydrophobic [7–11] organic compounds. Humic acids are human safe and are already used as broad-spectrum medical products [12, 13]. The effect exerted by a humic sample recovered from peat of deep degradation [14] on the state of three organic dyes of different classes was studied by spectroscopy.

EXPERIMENRAL

In our work we used the following dyes: Disperse Red 2S (1-hydroxy-4-amino anthraquinone), Acid Green Anthraquinone N2S (sulfonated 1,4-dibutylphenylaminoanthraquinone), and Vat Goldish-Yellow KKh (brominated dibenzopyrenoquinone). The dyes were preliminarily treated to spectral purity by known procedures [15–17]. The humic preparation was used as an aqueous solution with pH 8.4; under these conditions, humic acids behave as anionic polyelectrolytes [18, 19], whose total charge is determined by complete dissociation of carboxy groups and partial dissociation of phenolic hydroxy groups. The content of carboxy and hydroxy groups in peat humic acids is 2.50–3.65 and 3.3–4.2 mg-equiv g^{-1}, respectively [3, 20–22]. The measurements were carried out at 20°C.

Since humic acids can affect dyes in both truly dissolved (I) and associated (II) form, we studied the disperse and acid dyes at two concentrations of humic acid. At the first, relatively low concentration c_I, the dyes occur in solution in the monomeric form; at this concentration, the Lambert–Bouguer–Beer law is obeyed. At the second, relatively high concentration c_{II}, significant deviations from the above law are observed, which suggests association of dyes. The vat dye, which was dissolved using large amounts of electrolytes [$NaHSO_3$ (reducing agent) and NaOH], occurs in the above solutions in the associated form.

The experimental dependences of the position of the long-wave absorption maximum in the spectrum of Disperse Red 2S on the concentration of humic acid c_{HA} in solution for both forms I and II are shown in Fig. 1a.

As seen, associates of 1-hydroxy-4-aminoanthraquinone, appearing in water in the absence of any additives with increasing its concentration by a factor of 35, slightly shift λ_{max} to longer waves by 1–2 nm. This effect of the dye association is well known and is predicted by physicomathematical simulation. It is known that the main shift of the absorption peak occurs upon formation of dimers, and it remains virtually constant with subsequent coarsening of the associates [23].

On adding humic acids into a disperse dye solution, the bathochromic shift of λ_{max} reaches 5–9 nm, which suggests interaction between the dye and additive. Moreover, the difference in λ_{max} of the monomeric I and associated II forms of the disperse dye in the presence of the biopolymeric compound shows that both forms of the dye-nonelectrolyte can interact with humic acids.

1070-4272/03/7609-1489$25.00

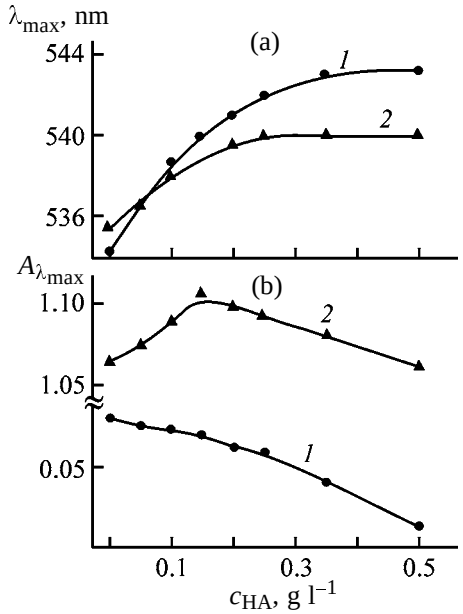

Fig. 1. (a) Position of the long-wave absorption band and (b) intensity of absorption of the aqueous solution of Disperse Red 2S dye as influenced by concentration of humic acids c_{HA}. (λ_{max}) Wavelength of the absorption maximum of the dye and ($A_{\lambda_{max}}$) Optical density of solutions at the wavelength of absorption maximum of the dye; the same for Fig. 2. Dye form: (*1*) monomeric and (*2*) associated.

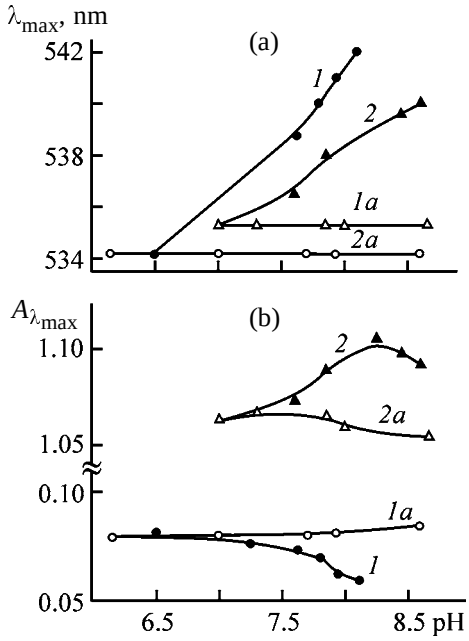

Fig. 2. (a) Position of the long-wave absorption maximum and (b) intensity of absorption of the aqueous solution of Disperse Red 2S dye as influenced by solution pH with addition of (*1*, *2*) humic acids and (*1a*, *2a*) sodium hydroxide. Dye form: (*1*, *1a*) monomeric and (*2*, *2a*) associated; the same for Fig. 3.

Hence, the decrease in the absorption intensity at low concentration of 1-hydroxy-4-aminoanthraquinone in aqueous solution (Fig. 1b, curve *1*) can be due to the dye–humic polymer heteroassociation, rather than to agglomeration of the monomers (homoassociation).

When the disperse dye in solution is initially associated, the resulting dependence (Fig. 1, curve *2*) reflects the sum of two simultaneously occurring processes differently affecting the parameter in question.

Wavelengths of the absorption peaks in the spectra of aqueous solutions of Acid Green Anthraquinone N2S dye

c_{HA}, g l^{-1}	T, °C	λ_{max}, nm, at indicated dye concentration, M	
		~5×10^{-5} (I)	~5×10^{-4} (II)
–	20	λ_{max_1} = 644.9, λ_{max_2} = 689.3	λ_{max_1} = 646.5, λ_{max_2} = 695.1
0.05–0.25	20	λ_{max_1} = 644.9 λ_{max_2} = 689.3,	λ_{max_1} = 646.5, λ_{max_2} = 695.1
–	70	λ_{max_1} = 644.9, λ_{max_2} = 689.3	λ_{max_1} = 644.9, λ_{max_2} = 691.2
0.05–0.25	70	–	–

The first of them is the interaction of the monomers of Disperse Red 2S dye with humic acids, which decreases the light absorption, and the second is related to breakdown of these associates, which, on the contrary, increases the extinction coefficients. These effects prevail in the ascending and descending sections of the experimental dependences, respectively.

As seen from Fig. 2, changes in the state of the disperse dye in aqueous solutions on adding weakly alkaline sample of humic acids are not due to increasing solution pH, because at similar alkalization of solution with sodium hydroxide (Fig. 2, curves *1a* and *2a*) no shift of λ_{max} and no significant changes in the adsorption of the dye solution are observed.

The effect of humic acids on the Acid Green Anthraquinone N2S dye (anionic-type dye-electrolyte) is illustrated in the table and in Figs. 3a and 3b. Addition of humic acids into the aqueous solutions of the anionic dye does not affect λ_{max} (see table). At the same time, association of the Acid Green Anthraquinone N2S dye in fairly concentrated solutions (c_{II}) causes the bathochromic shift of λ_{max}, reaching 6 nm.

These experimental results (table, Fig. 3a) suggest that there are no direct interactions of the acid anthra-

quinone dye with humic acids in neutral and weakly alkaline aqueous solutions in question, although anthraquinone derivatives tend to interact in aqueous solutions. The examples of such interaction are homoassociation of Disperse Red 2S and Acid Green Anthraquinone N2S and heteroassociation of Disperse Red 2S with humic acids. The lack of interaction of Acid Green Anthraquinone N2S with humic acids is obviously due to mutual repulsion of the anionic dye and anionic polyelectrolyte.

Humic acids, when added even in small amounts (0.025–0.075 g l^{-1}) into an aqueous solution of the associated acid dye, promote to some extent breakdown of the associates, which is confirmed by increasing absorption density of the dye solution. However, in contrast to the disperse dye, this phenomenon is most likely due to the fact that the polyelectrolyte breaks down the water structure, stabilizing the dye in the monomeric form [2].

The second rise in the dependence of the absorption density at the concentration of humic acids of 0.22–0.25 g l^{-1} is obviously due to the phenomenon actively discussed in papers concerning solubilization of hydrophobic organic compounds with humic acids [8, 10]. It is interpreted as micellization of an organic compound with a humic polymer, which undergoes conformational transformation at certain concentration in solution [24, 25] and becomes able to form micelles with possible incorporation of a foreign component into the micelle core.

As seen from Fig. 3b, the effect of humic acids is not associated with an increase in the solution pH on adding biopolymeric additives.

The leuco forms of the vat dye, which are unstable because of the possibility of the reverse oxidation and association, were studied spectrophotometrically by a specially designed procedure providing high reproducibility of the spectra. In this procedure we took into account changes in the state of the vat dye in humic acid free solutions in the course of the experiment. For this purpose, we alternately measured the absorption density of the blank solutions and dye solutions containing various amounts of humic acids; simultaneously we fixed the time τ of each measurement and then plotted the baseline *1* and experimental curves *2*, respectively (Fig. 4a). The desired dependence of the absorption density of the dye solution ΔA on the concentration of humic acids was determined by subtraction of $A_{\lambda_{max}}$ of the blank solutions from $A_{\lambda_{max}}$ of the polymer-containing liquid systems in

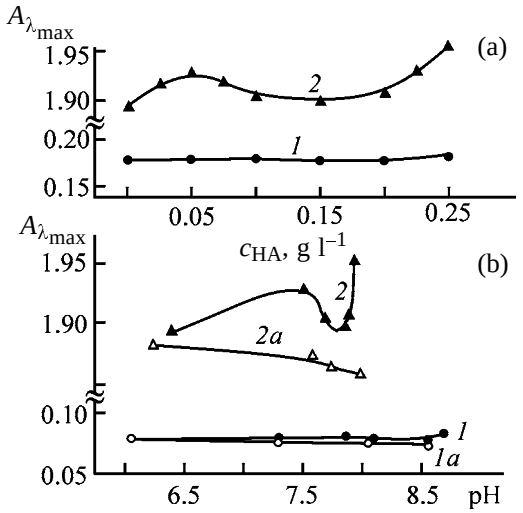

Fig. 3. Optical density of aqueous solutions of Acid Green Anthraquinone N2S dye as a function of concentration of (*1, 2*) humic acids and (*1a, 2a*) sodium hydroxide. ($A_{\lambda_{max}}$) Optical density of solutions at the wavelength of the dye absorption maximum and (c_{HA}) concentration of humic acid in aqueous solution (M).

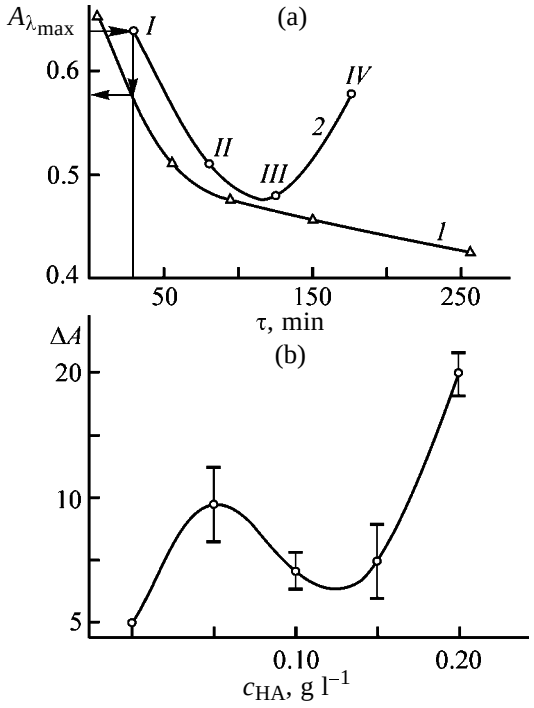

Fig. 4. (a) Experimental data on the absorption density of Vat Goldish-Yellow KKh dye and (b) their treatment to reveal the influence of the concentration of humic acids c_{HA} in aqueous solution. ($A_{\lambda_{max}}$) Optical density of solutions at the wavelength of the dye absorption maximum, (τ) time, and (ΔA) change in the absorption density. (a) c_{HA}, g l^{-1}: (*I*) 0.05, (*II*) 0.10, (*III*) 0.15, and (*IV*) 0.20.

the points corresponding to the moments of recording the absorption density in solutions containing humic acids (Fig. 4b).

As seen from Fig. 4b, the shape of the curve corresponding to the reduced vat dye is similar to the curve shown in Fig. 3a, characterizing the state of associated acid dye in solution, which suggests general similarity of the processes induced by humic acid additions in the aqueous solutions of the dyes in question. At the same time, changes in the absorption density of the vat dye solution are more pronounced. Obviously, the more hydrophobic the dye, the greater the role of structural factors in its hydration, and the deeper the breakdown of the dye associates in the presence of structure-breaking agents. The more hydrophobic the compound, the stronger its micellization with humic acids [7, 8].

Thus, we found that humic acids being added into aqueous solutions of synthetic textile dyes of various types promote various interactions, whose mechanism primarily depends on the molecular structure of the dyes and content of the additives. The latter factor can be used to control the state of the dye and thus to modify its characteristics. Thus, humic acids show promise for development of new formulations for textile dyeing.

CONCLUSIONS

(1) Disperse Red 2S dye (1-hydroxy-4-aminoanthraquinone) interacts with humic acids in aqueous solutions in both monomeric and associated forms.

(2) Humic acids being added into a solution of Acid Green Anthraquinone N2S dye (sulfonated 1,4-dibutylphenylaminoanthraquinone) break the dye associates, which is due to the breakdown of the water structure and possible incorporation of the dye molecules into the core of a micelle formed by the natural polymer.

(3) Changes in the spectral properties of the acid dye and reduced vat dye in the presence of humic acids are similar. The more pronounced spectral changes in the case of the vat dye are probably due to its high hydrophobicity and significant contribution of structural effects to its hydration.

REFERENCES

1. Mel'nikov, B.N., Moryganov, A.P., and Kalinnikov, Yu.A., *Teoriya i praktika vysokoskorostnoi fiksatsii krasitelei na tekstil'nykh materialakh* (Theory and Practice of High-Speed Fixation of Dyes on Textile Materials), Moscow: Legprombytizdat, 1987.
2. Coates, E., *J. Soc. Dyers Colour.*, 1969, vol. 85, no. 8, pp. 355–368.
3. Orlov, D.S., *Gumusovye kisloty pochv i obshchaya teoriya gumifikatsii* (Soil Humus Acids and General Theory of Humus Formation), Moscow: Mosk. Gos. Univ., 1990.
4. Graber, E.R. and Borisover, M.D., *Environ. Sci. Technol.*, 1998, vol. 32, pp. 258–263.
5. Ohga, K., Tsuruhara, T., Egashira, N., and Kuroi, T., *Anal. Sci.*, 1990, vol. 6, pp. 837–842.
6. Landgraf, M.D., Silva, S.C. da, and O'Rezende, M.O. de, *Anal. Chim. Acta*, 1998, vol. 368, pp. 155–164.
7. Xing, B., *Environ. Pollut.*, 2001, vol. 111, pp. 303–309.
8. Kress, B.M. and Ziechmann, W., *Chem. Erde*, 1977, vol. 36, pp. 209–219.
9. Hayes, T.M., Hayes, M.H.B., Skjemstad, J.O., *et al.*, *Humic Substances and Organic Matter in Soil and Water Environments: Characterization, Transformation, and Interactions*, St. Paul: Univ. of Minnesota, 1996.
10. Engeberston, R.R. and Wandruszka, R., *Environ. Sci. Technol.*, 1999, vol. 33, pp. 4288–4303.
11. Shinozuka, N., Lee, C., and Hayano, S., *Sci. Total Environ.*, 1987, vol. 62, pp. 311–314.
12. FRG Patent Appl. 38 269 635.
13. Lishtvan, I.I., Dolidovich, E.F., and Sheremet, L.S., Abstracts of Papers, *Sozdanie vysokoeffektivnykh protsessov pererabotki i ispol'zovaniya tverdykh goryuchikh iskopaemykh, poluchenie al'ternativnykh topliv i neftekhimicheskikh produktov iz uglya: Vsesoyuznaya nauchno-prakticheskaya konferentsiya* (Development of Highly Efficient Processes for Treatment and Utilization of of Solid Combustible Minerals, Production of Alternative Fuels and Petrochemical Products from Coal: All-Union Scientific and Practical Conf.), Donetsk, 1989, pp. 106–107.
14. Ponomareva, V.V. and Plotnikova, T.A., *Gumus i pochvoobrazovanie* (Humus and Soil Formation), Leningrad: Nauka, 1980.
15. Kalinnikov, Yu.A., State of Disperse Dyes in Mixed Solvents, *Cand. Sci. Dissertation*, Ivanovo, 1978.
16. Vashurina, I.Yu., Association of Active Dyes and Development of an Efficient Process for Dyeing and Anticrease Finishing of Cotton Fabrics, *Cand. Sci. Dissertation*, Ivanovo, 1988.
17. Nikol'skaya, S.A., Development of Combined Processes for Mercerization and Dyeing of Cotton Fabrics

with Vat Dyes, *Cand. Sci. Dissertation*, Ivanovo, 1989.

18. Safarova, S.A. and Umarova, Kh.A., *Tr. Samarkand. Univ.*, 1978, no. 369, pp. 54–59.
19. Marinsky, J.A. and Ephraim, J., *Environ. Sci. Technol.*, 1986, vol. 20, no. 4, pp. 249–354.
20. Stevenson, F.J., *Humic Chemistry: Genesis, Composition, Reaction*, New York: Wiley, 1982, vol. 1.
21. Brunelot, G., Adrian, P., Rouiller, J., *et al.*, *Chemosphere*, 1989, vol. 19, no. 89, pp. 1413–1419.
22. Arp, P.A., *Can. J. Chem.*, 1983, vol. 61, no. 7, pp. 1671–1682.
23. Cantor, Ch.R. and Schimmel, P.R., *Biophysical Chemistry*, part 2: *Techniques for the Study of Biological Structure and Function*, San Francisco: Freeman, 1980.
24. Conte, P. and Piccolo, A., *Environ. Sci. Technol.*, 1999, vol. 3, pp. 1682–1690.
25. Zhorobekova, Sh.Zh. and Mal'tseva, G.M., *Khim. Tverd. Topl.*, 1987, no. 3, p. 34–37.

Russian Journal of Applied Chemistry, Vol. 76, No. 9, 2003, pp. 1494–1496. Translated from Zhurnal Prikladnoi Khimii, Vol. 76, No. 9, 2003, pp. 1533–1535.

ORGANIC SYNTHESIS AND INDUSTRIAL ORGANIC CHEMISTRY

Inhibiting Effect of Sulfur-Containing Alkylphenols on Oxidation of Vaseline Oil

E. I. Terakh, P. I. Pinko, O. V. Zaitseva, and A. E. Prosenko

Research Institute of Chemistry of Antioxidants, Novosibirsk State Pedagogical University, Novosibirsk, Russia

Received March 3, 2003

Abstract—A comparative study was made of antioxidative properties of sulfur-containing 2,6-di-*tert*-butylphenol derivatives in a model reaction of autooxidation of Vaseline oil.

Sulfur-containing derivatives of sterically hindered phenols occupy a prominent place among antioxidants used today to prevent oxidative degradation of various organic materials (polymers, fuels, lubricating oils, plastics, fibers) [1, 2]. The high antioxidant activity (AOA) of such compounds is due to the presence of two active fragments: phenolic and sulfur-containing, which show a synergistic effect [3, 4]. The relationship between the structure and antioxidative performance of sulfur-containing phenolic antioxidants (SPAOs) is complex, because the inhibiting properties of these compounds are governed by the structure of phenolic and sulfur-containing fragments, their number and mutual arrangement, and also by the properties of the substrate and oxidation conditions [5]. At the same time, elucidation of this relatioship is very important for theory and practice, as it would allow directed synthesis of more effective antioxidants.

In this work we studied the antioxidative activity of sulfur-containing alkylphenols **I**–**XVII** in a model reaction of autooxidation of Vaseline oil (see table) and analyzed the structure–activity relationship for these inhibitors. The inhibiting effect exerted by sulfur-containing alkylphenols on oxidation of Vaseline oil was evaluated by the induction period τ. As reference antioxidants we used Ionol, Probucol, TB-3, and SO-3.

We found that all the sulfur-containing alkylphenols **I**–**XVII** exhibit pronounced antioxidative activity, increasing the induction period of Vaseline oil oxidation by a factor of 5–30. A certain correlation is revealed between the structure of the antioxidant molecule (length of the alkyl chain separating the phenolic and sulfur-containing fragments; structure of substituent at the S atom; number of sulfide and phenolic fragments) and its inhibiting effect.

In the series of unsymmetrical sulfides **I**–**III** with different length of the *p*-alkyl chain, AOA grows with increasing number of methylene units separating the phenolic and sulfide fragments. This may be associated with changes in the antiradical activity [6].

The antioxidative activity of unsymmetrical sulfides **II** and **IV**–**IX** varies depending on the length and extent of branching of the aliphatic substituent at

Induction periods τ of Vaseline oil oxidation inhibited with antioxidants. Antioxidant concentration c_a = 2 μmol g^{-1}, 180°C

Antioxidant	τ, min
$R(CH_2)_2SBu$ (**I**)	123 ± 7
$R(CH_2)_3SBu$ (**II**)	140 ± 7
$R(CH_2)_4SBu$ (**III**)	170 ± 10
$R(CH_2)_3SMe$ (**IV**)	42 ± 3
$R(CH_2)_3SEt$ (**V**)	155 ± 2
$R(CH_2)_3SPr$ (**VI**)	150 ± 2
$R(CH_2)_3SC_{18}H_{37}$ (**VII**)	105 ± 6
$R(CH_2)_3SBu$-*s* (**VIII**)	113 ± 3
$R(CH_2)_3SBu$-*t* (**IX**)	137 ± 4
$R(CH_2)_3SPh$ (**X**)	29 ± 3
$R(CH_2)_3SCH_2Ph$ (**XI**)	37 ± 2
$R(CH_2)_3SH$ (**XII**)	23 ± 2
$R(CH_2)_3SS(CH_2)_3R$ (**XIII**)	96 ± 8
$[R(CH_2)_3S]_3P$ (**XIV**)	118 ± 6
$R(CH_2)_3S(O)Et$ (**XV**)	73 ± 5
$R(CH_2)_3S(O)S(CH_2)_3R$ (**XVI**)	44 ± 3
$R(CH_2)_3S(O)(CH_2)_3R$ (**XVII**)	46 ± 3
RCH_3 (Ionol)	34 ± 2
$RSC(CH_3)_2SR$ (Probucol)	72 ± 5
RCH_2SCH_2R (TB-3)	18 ± 3
$R(CH_2)_3S(CH_2)_3R$ (CO-3)	67 ± 5
Control	5 ± 2

* R = 2,5-di-*tert*-butyl-4-hydroxyphenyl.

1070-4272/03/7609-1494$25.00

the sulfur atom. In going from *S*-methyl-substituted sulfide **IV** to *S*-ethyl derivative **V**, the antioxidative activity becomes appreciably stronger, in accordance with the increased electron density on the sulfur atom. However, with the length of the *S*-alkyl substituent increasing further in the series **VI**–**II**–**VII**, the inhibiting effecr becomes weaker. The lower AOA of sulfide **VII** is probably due to steric hindrance produced by the bulky octadecyl group. This group prevents access of hydroperoxides to the sulfur atom and thus decreases its antiperoxide activity.

The differences in the AOA of isomeric sulfides **II**, **VIII**, and **IX** may be due to resultant effect of two factors: different electron-donor powers of isomeric butyl radicals and susceptibility of the S–C bond to free-radical cleavage. On the one hand, in going from primary to secondary and then tertiary butyl radicals, the inductive effect increases, and the reactivity of the sulfide fragment toward a hydroperoxide should increase in parallel in the order **II**–**VIII**–**IX**. On the other hand, in the same series of sulfides, the S–C bond energy decreases, and this bond becomes more susceptible to thermal cleavage. As a result, sulfides **II** and **IX** exhibit similar AOA with respect to Vaseline oil.

Replacement of the aliphatic substituent at the sulfur atom in alkyl arylalkyl sulfides by phenyl or benzyl group (compounds **X** and **XI**, respectively) causes a decrease in AOA. Compounds **X** and **XI** inhibit oxidation by a factor of 1.6–2.0 more efficiently than TB-3 but by a factor of 2.0–2.5 less efficiently than Probucol and by a factor of 3.6–5.0 less efficiently than sulfides **II** and **V**–**IX**. The low inhibiting activity of **X** and Probucol, compared to **II** and **V**–**IX**, is probably due to the conjugation of the sulfur lone electron pair with the aromatic ring, weakening the antiperoxide activity of the sulfide group. In the case of sulfide **XI** and TB-3, the low AOA may be due to thermal decomposition of the primary products of their oxidation [7].

Thiol **XII**, as compared to the other sulfur-containing alkylphenols, showed poor AOA with respect to Vaseline oil, which may be due to thermal oxidative cleavage of the S–H bond and generation of thiyl radicals, which can participate in chain propagation [8, 9], lowering the inhibiting performance of **XII**:

$$RH + R'S^{\cdot} \rightarrow R'SH + R^{\cdot}.$$

Comparison of the antioxidative properties of sulfur-containing alkylphenols differing in the relative content of sulfur in the molecule showed that compounds **V**, **XIII**, and **XIV** with equal numbers of phenolic and sulfide fragments inhibit oxidation of Vaseline oil more efficiently than does SO-3 inhibitor containing two phenolic groups per sulfur atom. These differences are apparently due to the fact that, at equal concentration of phenolic groups, SO-3 deactivates a smaller number of hydroperoxide molecules than its analogs **V**, **XIII**, and **XIV** [3].

The significant contribution of the antiperoxide activity of the sulfur-containing fragment to the total inhibiting activity of sulfur-containing alkylphenols is confirmed by the fact that compounds **V**, **XIII**, and SO-3 surpass in AOA their analogs **XV**–**XVII** with partially oxidized sulfur-containing fragments.

Among the sulfur-containing alkylphenols studied, compounds **I**–**III**, **V**–**IX**, **XIII**, and **XIV** proved to be the most effective inhibitors of Vaseline oil oxidation; they surpass in the antioxidative power the multifunctional antioxidant Ionol and commercial SPAOs: Probucol, TB-3, and SO-3.

EXPERIMENTAL

Vaseline oil was purchased from Tatkhimfarmpreparaty (Kazan). Oxidation was monitored by the oxygen uptake, which was measured at 180°C and 1 atm with a gasometric unit similar to that described in [10]. The total volume of the sample being oxidized was 5 ml, and the concentration of antioxidants, 2 μmol g^{-1} oil. The kinetic curves were plotted, from which the induction period was determined as the interception point of secants to the curve portions corresponding to the initial and final rates of Vaseline oil oxidation. Four or five replicate runs were performed with each antioxidant; the figures in the table are average values with the rms deviation.

2,6-Di-*tert*-butyl-4-methylphenol (Ionol) was purchased from Acros Organics, and 2,2-bis(3,5-di-*tert*-butyl-4-hydroxyphenylthio)propane (Probucol), from Sigma. SPAOs {bis(3,5-di-*tert*-butyl-4-hydroxybenzyl) sulfide (TB-3); bis[3-(3,5-di-*tert*-butyl-4-hydroxyphenyl)propyl] sulfide (SO-3); alkyl[ω-(3,5-di-*tert*-butyl-4-hydroxyphenyl)alkyl] sulfides **I**–**XI**; 3-(3,5-di-*tert*-butyl-4-hydroxyphenyl)-1-propanethiol **XII**; bis-[3-(3,5-di-*tert*-butyl-4-hydroxyphenyl)propyl] disulfide **XIII**; tris[3-(3,5-di-*tert*-butyl-4-hydroxyphenyl)-propyl] phosphorotrithioite **XIV**; ethyl [3-(3,5-di-*tert*-butyl-4-hydroxyphenyl)propyl] sulfoxide **XV**; *S*-[3-(3,5-di-*tert*-butyl-4-hydroxyphenyl)propyl] 3-(3,5-di-*tert*-butyl-4-hydroxyphenyl)propanethiosulfinate **XVI**; bis[3-(3,5-di-*tert*-butyl-4-hydroxyphenyl)propyl] sulfoxide **XVII**} were prepared by previously developed

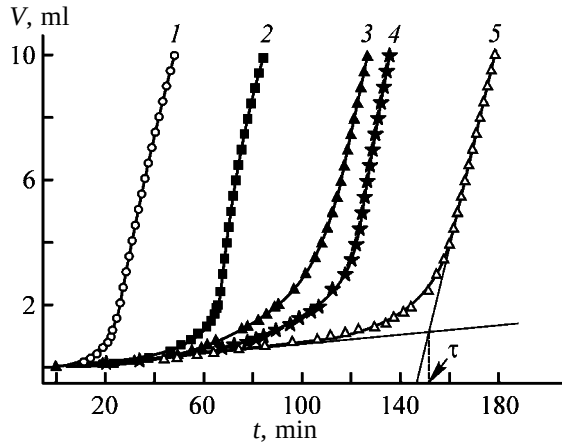

Kinetic curves of Vaseline oil oxidation in the presence of (*1*) thiol **XII**, (*2*) SO-3, (*3*) disulfide **XIII**, (*4*) thiophosphite **XIV**, and (*5*) sulfide **V**. (*V*) Volume of oxygen taken up and (*t*) time.

procedures [1, 3, 11–15]. The main substance content in the samples was 97–99%.

CONCLUSION

The antioxidative activity of sulfur-containing 2,6-di-*tert*-butylphenol derivatives depends on the structure of the sulfur-containing fragment and on the number and mutual arrangement of the sulfur-containing and phenolic fragments in their molecules; in some cases, it considerably surpasses the activity of the known commercial oxidation inhibitors.

REFERENCES

1. Gorbunov, V.N., Maslov, N.N., and Gurvich, Ya.A., *Khimiya i tekhnologiya stabilizatorov polimernykh materialov* (Chemistry and Technology of Stabilizers of Polymeric Materials), Moscow: Khimiya, 1981.
2. *2,6-Di-tret-butilfenol v organicheskom sinteze stabilizatorov dlya polimerov: Obzornaya informatsiya* (2,6-Di-*tert*-butylphenol in Organic Synthesis of Polymer Stabilizers: Review), ser.: *Khimikaty dlya polimernykh materialov* (Chemicals for Polymeric Materials), Moscow: NIITEKhIM, 1987.
3. Pinko, P.I., Terakh, E.I., Gorokh, E.A., *et al.*, *Zh. Prikl. Khim.*, 2002, vol. 75, no. 10, pp. 1694–1698.
4. Terakh, E.I., Prosenko, A.E., Nikulina, V.V., and Zaitseva, O.V., *Zh. Prikl. Khim.*, 2003, vol. 76, no. 2, pp. 261–265.
5. Prosenko, A.E., Terakh, E.I., Gorokh, E.A., *et al.*, *Zh. Prikl. Khim.*, 2003, vol. 76, no. 2, pp. 256–260.
6. Prosenko, A.E., Kandalintseva, N.V., and Tolstikov, G.A., *Kinet. Katal.*, 2002, vol. 43, no. 1, pp. 34–38.
7. Scott, G. and Suharto, R., *Eur. Polym. J.*, 1984, vol. 20, no. 2, pp. 139–147.
8. *Comprehensive Organic Chemistry. The Synthesis and Reactions of Organic Compounds*, Barton, D. and Ollis, W.D., Eds., vol. 2: *Phosphorus Compounds*, Sutherland, I.O., Ed.; vol. 3: *Sulphur Compounds*, Jones, D.N., Ed., Oxford: Pergamon, 1979.
9. Kadochnikova, G.D., Perevozkina, M.G., Ushkalova, V.N., and Moskvichev, Yu.A., in *Svobodnoradikal'noe okislenie lipidov v eksperimente i klinike* (Free-Radical Oxidation of Lipids in Experiment and Clinics), Tyumen: Tyumen. Gos. Univ., 1997, part 2, pp. 113–119.
10. Tsepalov, V.F., *Issledovanie sinteticheskikh i prirodnykh antioksidantov in vivo i in vitro* (*In vivo* and *in vitro* Studies of Synthetic and Natural Antioxidants), Moscow: Nauka, 1992, pp. 16–26.
11. Prosenko, A.E., Terakh, E.I., Kandalintseva, N.V., *et al.*, *Zh. Prikl. Khim.*, 2001, vol. 74, no. 11, pp. 1839–1843.
12. RF Patent 1 370 952.
13. RF Patent 1 642 708.
14. USSR Inventor's Certificate no. 1 340 123.
15. Skorobogatov, A.A. and Prosenko, A.E., in *Sbornik nauchnykh rabot studentov i molodykh uchenykh* (Coll. of Scientific Works of Students and Young Scientists), Novosibirsk: GTsRO, 2002, issue 4, pp. 120–126.

Russian Journal of Applied Chemistry, Vol. 76, No. 9, 2003, pp. 1497–1501. Translated from Zhurnal Prikladnoi Khimii, Vol. 76, No. 9, 2003, pp. 1536–1540.

MACROMOLECULAR CHEMISTRY AND POLYMERIC MATERIALS

Nanostructured Carbon Coatings on Polyethylene Films

A. P. Alekhin, A. G. Kirilenko, R. V. Lapshin, R. I. Romanov, and A. A. Sigarev

Lukin Research Institute of Physical Problems, Federal State Unitary Enterprise, Moscow, Russia

Received May 26, 2003

Abstract—The properties of medical low-density polyethylene films with carbon coatings improving the biological compatibility of the polymer were studied by electron and scanning atomic-force microscopy, as well as by IR, Raman, visible, and UV spectroscopy.

A promising line in development of hemocompatible materials is modification of the polymer surface by deposition of coatings having the desired biochemical properties [1]. Understanding of the formation mechanism of hemocompatible surfaces requires studying the properties of the modifying coating.

Among the materials suitable for modification of medical polymers, in particular, low-density polyethylene (LDPE), is carbon [2] with its unique properties, above all, the occurrence in various chemical modifications: sp^3 (diamond), sp^2 (diamond-like), and *sp* (carbyne). Carbon is expected to be well compatible biologically with blood plasma proteins and living cells of the human body, because these cells consist, primarily, of organic, i.e., carbon-containing compounds. Lastly, it is possible to build on the surface of a polymer support the required cluster formations from carbon (nanostructured carbon), matching in the thermodynamic and geometric parameters a certain type of molecules of blood plasma proteins. This makes possible formation of a high-quality polymer–blood interface when using carbon as the modifying coating.

In this work, we studied LDPE-supported nanostructured carbon by physical methods.

EXPERIMENTAL

As the model material for the support we used a 50-μm-thick film of LDPE [GOST (State Standard) 10354–82]. Rectangular 25×20-mm pieces of the LDPE film were cut out in a such way that their longer sides made the same angle with the axis of film extension during its preparation.

Carbon coatings were deposited onto the polymer films in a working chamber of a UVNIPA-1 vacuum setup (manufactured by the Kvarts Kaliningrad Machine-Building Plant) by pulse plasma-arc spraying of a graphite target at the residual gas pressure of ca. 7.5×10^{-4} torr. The LDPE sample was fixed in a holder at a distance of 35 cm from the carbon target surface; the working surface of the polymer was perpendicular to the direction of propagation of the carbon ion flow.

The ignition electrodes in the UVNIPA-1 setup were used for initiating a ~0.01-s pulse electric-arc discharge on the surface of a cold in the bulk graphite cathode. The discharge produced carbon plasma whose ions were then accelerated in an electric field with a potential difference of 450 V and condensed on the working surface of the support. The sample surface was modified at various frequencies f of the pulses generated by the carbon plasma generator (0.1, 0.3, and 1 Hz).

The pulsed condensation of the carbon coating (with the pause being more than 10 times longer than the plasma discharge period) improves the heat removal from the carbon coating condensation zone. This makes less probable melting of the structural elements of the polymer matrix and favors stabilization of the surface modification process. The setup used by us provided the carbon film deposition rate of ~0.15 nm per pulse. We estimated the rate constant of the coating thickness growth by X-ray photoelectron spectroscopy using the procedure from [3]. For comparing the modified and initial LDPE film surfaces, a segment of the sample was shielded from the ion beam. The thickness of the deposited carbon films was 1.5–15 nm on the average, which corresponds to N = 10–100 pulses of the coating deposition.

The LDPE film surface morphology was examined by scanning probe atomic-force microscopy (AFM)

1070-4272/03/7609-1497$25.00

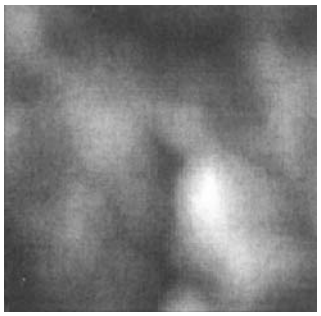

Fig. 1. Unmodified (with carbon) LDPE surface with a characteristic developed random structure.

using a Solver P4 NT-MDT microscope. We used a cantilever (Lukin Research Institute of Physical Problems, Federal State Unitary Enterprise) with the elasticity coefficient of 20 N m^{-1}, resonance frequency of ~132 kHz, and needle tip radius less than 10 nm. The measurements were run in the tapping mode in air at room temperature. The limiting resolution of the microscope was estimated from the minimal discernible film surface elements at 20–30 nm. The maximal scanning field was 6×6 μm in size.

The morphology of the surface of the modified films was preliminarily studied by raster electron microscopy (REM). We used an Camscan 4, Cambridge, microscope with a typical magnification of $\times 3500$–5400 corresponding to the examined fields with a size of tens of micrometers. Based on analysis of the features of REM relief image typical for this scale, we made express estimates of the performance of the process equipment when optimizing the parameters of the pulse process of carbon deposition.

Certain structural features of the LDPE films were analyzed by optical spectroscopy (IR, visible, and UV). We measured the transmission spectra of the samples under normal incidence of the light onto the surface. Polarization IR spectra at 500–4000 cm^{-1} were measured on a Michelson 100 (Bomem) IR Fourier spectrometer equipped with a cooled HgCdTe detector and a lattice polarizer on a KRS-5 plate (SPECAC). The UV and visible spectra of the samples at 200–900 nm were recorded with a U3000 Hitachi spectrophotometer.

The electronic structure of the carbon coatings was studied by Raman spectroscopy at 100–1800 cm^{-1}. These spectra were measured using a depolarized radiation from an argon laser at 488 nm (5 mW power) by the procedure from [4]. The focus spot was 50 μm in size. The Raman spectra obtained were typical for solid diamond-like films [4, 5].

We preliminarily compared the morphologies of the modified surfaces of LDPE samples by scanning electron microscopy [frequency of generation of the discharge pulses in plasma f = 1 Hz; number of pulses 10 and 50; carbon film thickness (one pulse corresponds to ~0.15 nm) 1.5 and 7.5 nm (samples I and II, respectively)]. The morphology of the samples proved to be globular-fibrillar for sample I and fibrillar for sample II; the fibrils were predominantly oriented along the image diagonal.

The procedure developed by us allows reliable reproduction of the morphology of the modified polymer surface. On the sample I surface, there were globular-fibrillar structures 0.5 to 2.0 μm in size, and on the sample II surface, fibrillar structures 3–4 μm in size. Presumably, the structures with a typical size close to that of thrombocyte will strongly influence the adhesion of thrombocytes.

The sample surface morphology was examined in more detail by AFM. The samples were divided into three groups comprising samples whose modified layer was formed at f of 0.1, 0.3, and 1.0 Hz. From each group we took samples with coatings obtained at different numbers of pulses N, 10, 50, and 100, corresponding to the coating thicknesses of 1.5, 7.5, and 15 nm, respectively.

For coatings with these thicknesses, the carbon layer is not continuous; it consists of clusters (islands) tens and hundreds of nanometers in size. The size of the carbon-free areas in the sample depends on the number of the carbon deposition pulses N and the frequency of their generation f. To ensure high-precision and linear measurements, we developed a method of active scanning and positioning. This implies the use of specific structures on the surface under study (in our case, carbon clusters) as the reference points in movings. This eliminates the effect of the thermal drift, nonlinearity, and nonorthogonality of the piezoscanner on the results of examining the nanostructures.

The image of the initial LDPE surface demonstrates a characteristic developed random structure (Fig. 1).

The image of the carbon-modified polyethylene surface obtained with the carbon plasma generator operating at f = 0.1 Hz reveals the presence of elongated carbon clusters, 70–200 nm in size on the average. It should be noted that, at N = 10, the length and width of a surface element are in a ratio of approximately 1 : 3; the distance separating the clusters is approximately equal to the size of the clusters, and at N = 50 this distance decreases to 20–100 nm.

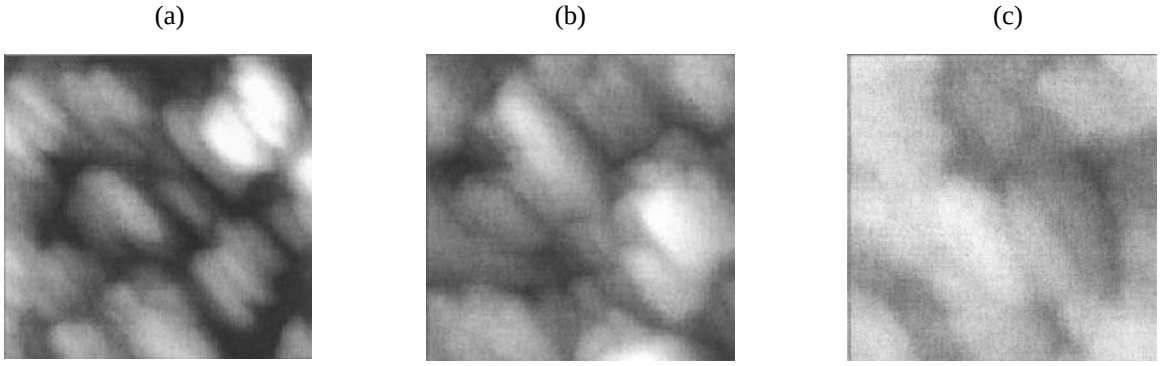

Fig. 2. Carbon-modified LDPE surface; the frequency of pulse generation by the carbon plasma generator 1 Hz. Number of pulses *N*: (a) 10, (b) 50, and (c) 100. Coating thickness, nm: (a) 1.5, (b) 7.5, and (c) 15.0.

The scans of the carbon-modified polyethylene surface obtained at f = 0.3 Hz reveal oval clusters 70–150 nm in size. The cluster length-to-width ratio is close to 2. The degree of filling of the polyethylene surface with the clusters increases relative to the case of f = 0.1, and the distance separating the clusters decreases to 10–70 nm.

The carbon coatings formed at f = 1 Hz exhibit a nanostructure with disk-like clusters 120–150 nm in size; the distance separating the clusters decreases to 5–20 nm.

Figure 2 presents the most typical images for different numbers of pulses.

The optical spectroscopic studies showed that the initial and modified polymer films obtained with 10, 50, and 100 pulses have different spectra within 200–900 nm. The transmission is inversely proportional to the number of the carbon deposition pulses or the thickness of the film formed. The transmission band edge is located at $\lambda \sim 200$ nm, which is due to strong light absorption by the polymer at $\lambda \leq 200$ nm.

Figure 3 shows the relative transmission T/T_0 spectra of the modified polymers (T_0 is the transmission of the initial samples of this polymer). It is seen that, with the growth of the carbon coating, the transmission tends to substantially decrease, especially in the UV range. Possible reasons for the characteristic decrease in transmission of the samples are light absorption and scattering on the carbon clusters. Analysis of the characteristic decrease in the relative transmission T/T_0 allowed estimation of the size of the carbon clusters. For example, the carbon clusters of the modified sample obtained at 100 pulses can be 100–200 nm in size. The sizes of the carbon clusters estimated from the spectral and AFM data agree well.

It should be noted that the samples modified at different pulse generation frequencies (0.1, 0.3, and 1.0 Hz) show similar trends in variation of the relative transmission T/T_0 spectra in the UV and visible ranges with the number of pulses.

In the middle IR range, we revealed a number of the most intense characteristic absorption bands of the CH_2 groups in the spectra of LDPE. The IR spectra of the modified polymer films are very close to that of the initial polymer film. The observed modulation of the baseline in the transmission spectrum is due to interference of the IR radiation in the polymer film, which complicates analysis of weak absorption bands in the differential spectra.

Studies of the optical properties of carbon films showed that the band gap for them can be estimated by the procedure from [6] at 2.1 eV; the extinction coefficient ε is determined as

$$æ = \alpha\lambda/4\pi,$$

where α = 0.06 is the absorption coefficient at λ = 550 nm.

These parameters also correspond to diamond-like films [7].

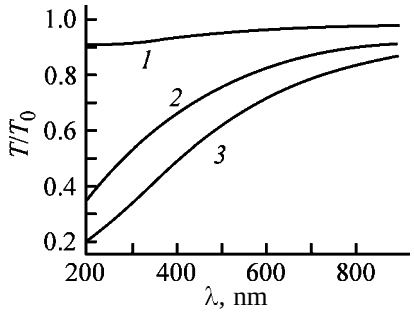

Fig. 3. Relative transmission T/T_0 of the LDPE films with carbon coatings of different thicknesses. (λ) Wavelength. Coating thickness, nm: (*1*) 1.5, (*2*) 7.5, and (*3*) 15.0.

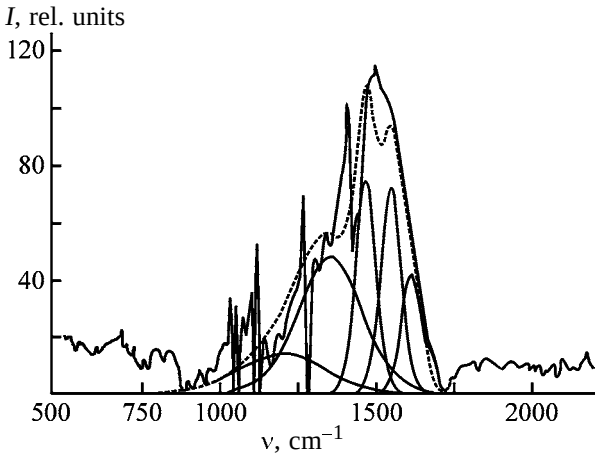

Fig. 4. Raman spectra of the carbon layers obtained by arc pulse-plasma spraying of graphite. N = 50, f = 1.0 Hz. (I) Intensity and (ν) wave number.

Comparison of the spectra of polyethylene before and after sputtering shows that the line positions and their relative intensities do not change significantly. There is only general decline in intensity, probably due to shielding of polyethylene by the carbon layer. It can be supposed that the surface processes associated with the film deposition produce no changes in the bulk of the polyethylene support.

To gain additional information about the structure of the modifying carbon coatings, we carried out mathematical analysis of their Raman spectra. Figure 4 presents the Raman spectrum of the modifying carbon coatings for N = 50 and f = 1 Hz (for other N and f, the spectra are similar). This analysis consisted in resolution of the experimental spectrum into three model subspectra determined as mixed Lorenzian–Gaussians by the relationship

$$F(x) = \text{peak height}/[1 + M(x - x_0)^2/\beta^2]$$

$$\times \exp(1 - M)\ln 2(x - x_0)^2/\beta^2,$$

where x_0 is the peak center position and β, a parameter equal approximately to the half of the full width at half maximum (FWHM).

Such spectra (Fig. 4) are characterized by two wave numbers: 1355 (D line) and 1580 cm^{-1} (G line) responsible for sp^3 diamond (1322 cm^{-1}) and sp^2 graphite (1580 cm^{-1}) electronic structures, respectively. For certain samples, we sometimes observed another peak with a wave number of 1200 cm^{-1} characterizing the disordering of the sp^3 electronic structure.

The characteristics of the Raman spectra of the samples after resolution are listed in the table.

These data were calculated from the parameter β by the iteration method. The parameter M determines the degree of mixing and is equal to 1 for pure Lorenzian and to 0 for pure Gaussian peaks. We varied such parameters of the model subspectra as intensity, Lorenzain-to-Gaussian ratio, and peak width with the aim to achieve the best agreement between the superposition of the model subspectra and the experimental spectrum. As the criterion of fitting quality we took the χ^2 parameter.

The Raman shift of one of the most intense lines is 1550 cm^{-1}. This suggests predominant graphite modification of the carbon layers under study with the sp^2 hybrid bond. This peak is also significantly shifted relative to the typical position of the G line (1580 cm^{-1}). This shift is due to the presence in the carbon layers of sp^3 bonds, along with sp^2 bonds, as well as to angular disorientation for sp^2 bonds [5, 6]. This disorientation is also confirmed by the presence in the resolved spectrum of a broadened peak at 1200 cm^{-1} [7].

The spectra of all the samples studied contained another broadened peak near 1350 cm^{-1}. It is also shifted to larger wave numbers from the typical position of the D peak (1332 cm^{-1}). This peak suggests the presence in the obtained layers of carbon with the sp^3 hybrid bond [7].

The presence in the resolved spectra of peaks at 1450 cm^{-1} confirms oxygen bonding with the deposited carbon.

The peak at 1615 cm^{-1} suggests the presence of C–H chemical bonds in the layers.

Analysis of the parameters of the Raman spectra such as the Raman shift and the height and width of the model subspectra using the data from [7] allows the following conclusions about the electronic structure of the layers formed on the polymer supports. These layers contain carbon with both sp^2 and sp^3 hy-

Characteristics of the Raman spectra after resolution (N = 50, f = 1.0 Hz)

Raman shift of the peak, cm^{-1}	Intensity, rel. units	FWHM, cm^{-1}
1200	15	300
1350	45	250
1450	75	100
1550	70	100
1650	40	75

bridizations. According to the general thermodynamic principles, the sp^2 states are integrated into small clusters. Among these, the most probable energetically are clusters in the form of six-membered rings, either single or fused. The average size of the clusters, most probably, does not exceed 2–3 nm. The sp^2 hybrid bonds inside the clusters exhibit disorientation in angles, and the rings have the shape of irregular hexagons. The clusters are linked by sp^3 hybrid bonds and randomly oriented with respect to one another.

This pattern corresponds to the cluster model of amorphous carbon substantiated in [8, 9].

CONCLUSIONS

(1) The optimal conditions for formation of a cluster structure on the polymer surface are the pulse generation frequency of 1–2 Hz and the deposition rate of the carbon-containing films of 0.1–0.2 nm s^{-1}.

(2) The following conditions can be recommended for deposition of a modifying coating onto medical polymers: process temperature no higher than 60°C; pulse generation frequency 1–2 Hz; pulse number 30–50; and thickness of the layer deposited during one pulse 0.15 nm.

ACKNOWLEDGMENTS

This work was financially supported by the Russian Foundation for Basic Research, project no. 02-03-32615.

REFERENCES

1. *Biosovmestimost'* (Biocompatibility), Sevast'yanov, V.I., Ed., Moscow, 1999.
2. Chu, P.K., Tang, B.Y., Wang, L.P., and Huang, N., *Rev. Sci. Instr.*, 2001, vol. 72, no. 3B, p. 1660–1665.
3. Alekhin, A., Fominskii, V., Markeev, A., *et al.*, *Appl. Surface Sci.*, 1994, vol. 78, pp. 437–442.
4. Alekhin, A.P., Vrublevskii, A.I., Markeev, A.M., *et al.*, *Poverkhn. Nauka*, 1996, no. 10, pp. 47–52.
5. Yoshitake, T., Nishiyama, T., and Nagayama, K., *Jpn. J. Appl. Phys.*, 2001, vol. 40, pp. L573–L575.
6. Tamba, M., Kawamura, K., Okazaki, K., and Amemiya, H., *Jpn. J. Appl. Phys.*, 2001, vol. 40, pp. 1064–1066.
7. Feldman, L.C. and Mayer, J.W., *Fundamentals of Surface and Thin Film Analysis*, New York: North-Holland, 1986.
8. Dillon, R.O., *Phys. Rev. B*, 1984, vol. 30, pp. 870–873.
9. Robertson, J., *Diam. Relat. Mater.*, 1995, vol. 4, pp. 297–302.

Russian Journal of Applied Chemistry, Vol. 76, No. 9, 2003, pp. 1502–1508. Translated from Zhurnal Prikladnoi Khimii, Vol. 76, No. 9, 2003, pp. 1541–1547.

MACROMOLECULAR CHEMISTRY AND POLYMERIC MATERIALS

Curing of Oligomers with Thermoreactive Norbornene, Chalcone, and Maleimide Groups

A. V. Sidorovich, O. E. Prasolova, V. K. Lavrent'ev, G. I. Nosova, N. A. Solovskaya, and V. V. Kudryavtsev

Institute of Macromolecular Compounds, Russian Academy of Sciences, St. Petersburg, Russia

Received June 10, 2003

Abstract—Curing of powdered chalcone-containing oligoimides with terminal maleimide or norbornenedicarboxylic acid imide groups was studied by differential scanning calorimetry. The calorimetric characteristics of curing were discussed in relation to the chemical structure and conformational isomerism of the oligomers.

One of urgent problems in preparation of polymeric composites is development of high-heat-resistance reinforced plastics based on polyimides and related compounds, with the characteristics meeting the requirements of modern engineering. In this connection, it becomes necessary to elucidate relationships between curing conditions and structure of oligomers containing various thermoreactive groups, with the aim to find oligomers suitable as binders in high-heat-resistance composites.

In this work, we studied how the phase and aggregation state of a series of monomers and oligomers containing norbornenedicarboxylic acid imide, maleimide, and chalcone functional groups varies in the course of thermal cross-linking.

EXPERIMENTAL

The chemical structures of oligomers **1**–**6** and the corresponding monomers **1'**–**6'** are given below:

Series I

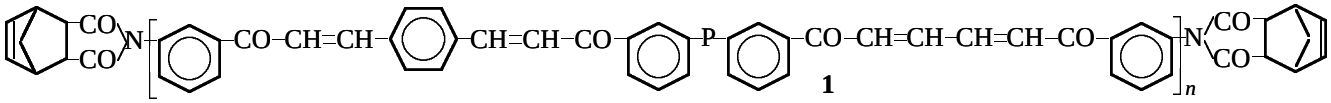

1

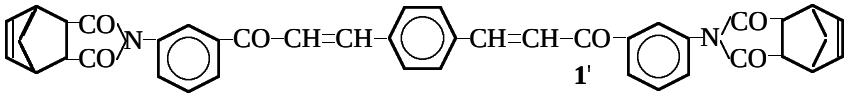

1'

Series II

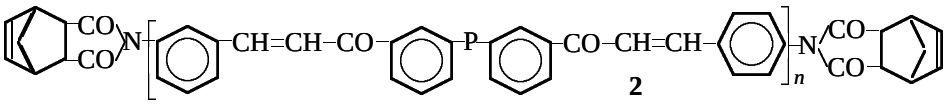

2

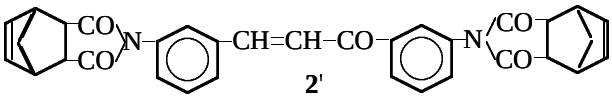

2'

Series III

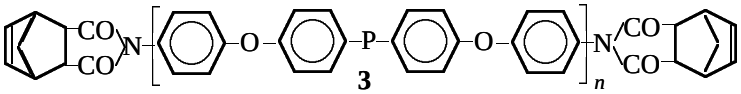

3

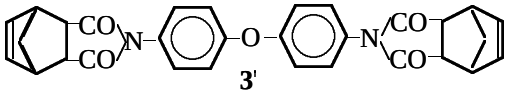

3'

1070-4272/03/7609-1502$25.00

Series IV

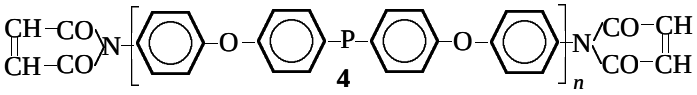

4

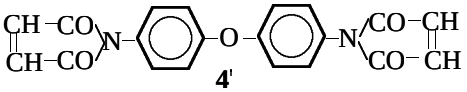

4'

Series V

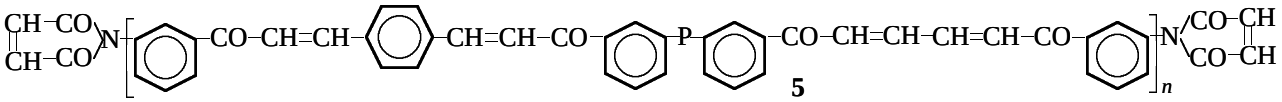

5

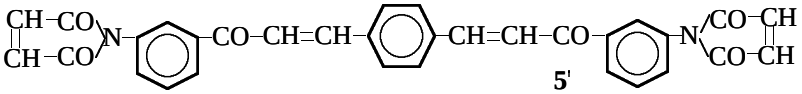

5'

Series VI

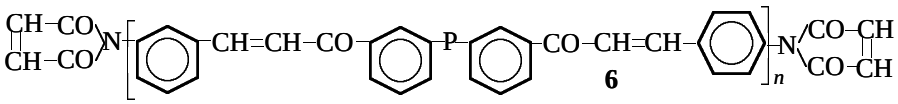

6

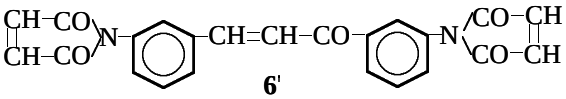

6'

where P = 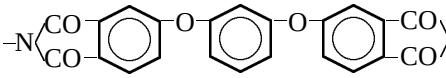 .

Monomers **1'**–**6'** were prepared by acylation of chalcone-containing diamines **C1** and **C2** with 4,4'-diaminodiphenyl ether (DADPE), maleic anhydride, or 5-norbornene-2,3-dicarboxylic anhydride, respectively:

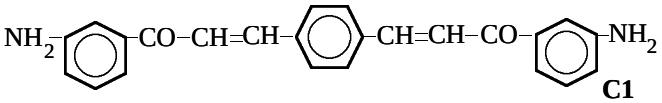

C1

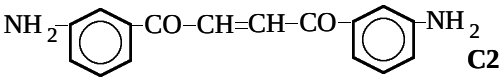

C2

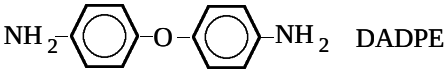

DADPE

Oligomers **1**–**3** and monomers **1'**–**3'** have the terminal norbornenedicarboxylic acid imide group (**a**), and oligomers **4**–**6** and **4'**–**6'**, maleimide group (**b**):

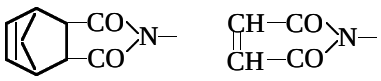

a **b**

Oligomers **1**–**6** were prepared from 1,4-bis[3-oxo-3-(3'-aminophenyl)-1-propenyl]benzene [1] (bischalcone **C1**), 1,4-bis(3'-aminophenyl)-2-butene-1,4-dione [2] (chalcone **C2**), DADPE, and 1,3-bis(3',4'-dicarboxyphenoxy)benzene dianhydride (DA-P) by the following scheme:

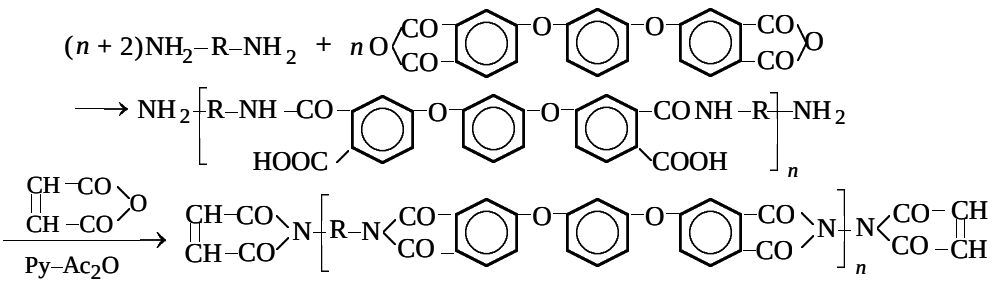

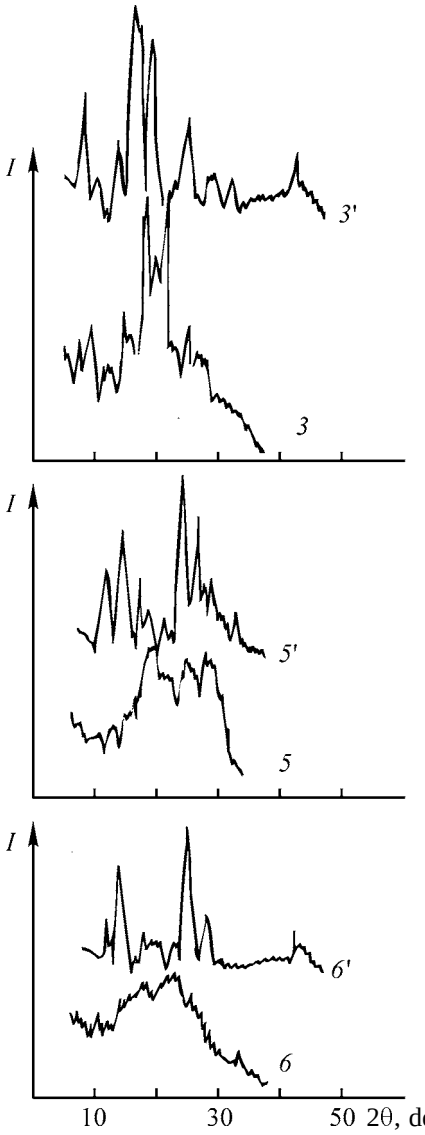

Fig. 1. Diffraction patterns of the monomers and oligomers of series III, V, and VI: (*I*) intensity and (2θ) Bragg angle. Curve numbers are monomer and oligomer numbers; the same for Figs. 2 and 3.

where R =

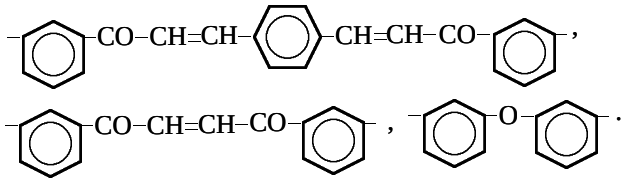

Dianhydride DA-P was added to a solution of appropriate diamine in dimethylformamide (DMF) at 20°C. The solution was stirred for 3 h, after which maleic or 5-norbornene-2,3-dicarboxylic anhydride was added. The oligomer concentration was 30 wt %. After 2 h, the imidizing mixture of acetic anhydride and pyridine (2 : 1 by volume) was added in a fivefold molar excess relative to the reactive units, and the solution was left overnight. Then the solution was stirred for an additional 2 h at 60–70°C, and the polymer was precipitated with methanol. The powders were vacuum-dried at 50°C. Monomers **1**'–**6**' were prepared similarly but without DA-P.

Compounds **1**–**6** and **1**'–**6**' were characterized by IR and electronic spectra. According to the IR spectra, the degree of imidization was 95–97%. The electronic spectra of **1**, **1**', **5**, and **5**' exhibited absorption with λ_{max} = 360 nm, characteristic of bischalcone **C1**, and those of **2**, **2**', **6**, and **6**', absorption with λ_{max} = 308 nm, characteristic of chalcone **C2**.

Curing of monomers and oligomers was monitored by calorimetric, X-ray diffraction, and thermomechanical methods. Calorimetric measurements were performed in the range 30–400°C with a DSM-2M calorimeter at a scanning rate of 16 deg min^{-1} and theshold sensitivity of 0.04 MW [3].

X-ray diffraction data were obtained with a DRON-2 diffractometer using Ni-filtered CuK_α radiation. Thermomechanooptical measurements were performed with a Boetius heating stage; the softening range was evaluated visually from changes in the powder particle shape and in the response on pressing.

In the initial state, powders of monomers **1**'–**6**' were highly crystalline substances; the phase state of oligomers **1**–**6** depended on their chemical structure: oligomers **2** and **4** were crystalline; **5** and **1**, mesomorphic; and the others, amorphous. Figure 1 shows the X-ray diffraction patterns of monomers **3**', **5**', and **6**' and of crystalline (**3**), mesomorphic (**5**), and amorphous (**6**) polymers.

The thermograms of oligomers and monomers of series I–VI are compared in Fig. 2. The monomers exhibit thermal effects in two ranges, with different signs of the effects: endothermic (melting of crystals) and exothermic (curing due to cross-linking of thermoreactive groups). The oligomers exhibit thermal effects in three ranges. The effects manifested at low and moderate temperatures are endothermic, and the high-temperature effects are exothermic. The low-temperature range, 50–150°C, is similar for all the oligomers; it corresponds to removal of residual solvents used in the synthesis of the oligomers. As it has no relation to the structure of the oligomers, it is not discussed further. The medium- and high-temperature ranges are different for different oligomers. The DSC curves of some oligomers, recorded on heating to 400°C , do not return to zero (baseline), suggesting

Temperature ranges of endo- and exothermic effects, ΔT_{endo} and ΔT_{exo}, of monomers and oligomers; softening ranges, ΔT_s, of oligomers

Monomers			Oligomers			
no.	ΔT_{endo}, °C	ΔT_{exo}, °C	no.	ΔT_{endo}, °C	ΔT_{exo}, °C	ΔT_s,* °C
1'	220–260	230–340	**1**	150–240	230–390	200–265
2'	240–280	250–380	**2**	130–240	250–390	190–250
3'	240–330	310–380	**3**	190–270	280–380	220–270
4'	150–200	230–360	**4**	160–250	230–390	–
5'	250–280	280–350	**5**	140–230	230–400	230 with partial fusion, onset of cross-linking
6'	140–220	215–310	**6**	130–220	215–370	100–210

* Determined by a thermomechanooptical method.

incompleteness of double bond opening or instability of the process. Repeated scanning to a higher temperature (450°C) revealed no exothermic effects. Hence, curing that occurred in these monomers in the course of the first scanning to 400°C went to completion, and a new equilibrium state was formed.

The temperature ranges of the endothermic (ΔT_{endo}) and exothermic (ΔT_{exo}) effects exhibited by the monomers and oligomers, and also the softening ranges (ΔT_s) evaluated by a thermomechanooptical method are listed in the table. The lower boundary of the softening range corresponds to the onset of fusion of powder particles, followed by spreading and passing to the hyperelastic state at the upper boundary of this range.

Oligomer **5**, in contrast to the other oligomers, showed no softening range; caking and darkening of the powder started without fusion.

Comparison of the ranges ΔT_{endo} for monomers **1'**–**6'** and oligomers **1**–**6** shows that, in going from monomers to the corresponding oligomers, ΔT_{endo} shifts to lower temperatures in the case of **1**–**3** and **5**, remains virtually the same in the case of **6**, and shifts to higher temperatures in the case of **4**. Comparison of the temperature ranges in which the monomers exhibit endothermic effects (melting) with the softening ranges of the oligomers shows that softening of the oligomers occurs at lower temperatures than melting of the monomers. For example, softening of **3** is complete at 270°C, and melting of **3'**, at 330°C. These differences in the ranges of the endo- and exothermic effects are due to the influence of structural conformational isomerism: Oligomers have a larger number of rotational isomers than the corresponding monomers. In the case of oligomers, the softening range depends on both the chemical structure and the rotational isomerism (number of rotational isomers). Crystallization of oligomers **3** and **4** is due to greater, compared to the other oligomers, conformational freedom because of the presence of the DADPE fragment containing no thermoreactive double bonds, and mesomorphic structure of **1** and **5** is due to specific conformational features of the **C1** fragment, compared to **C2** in amor-

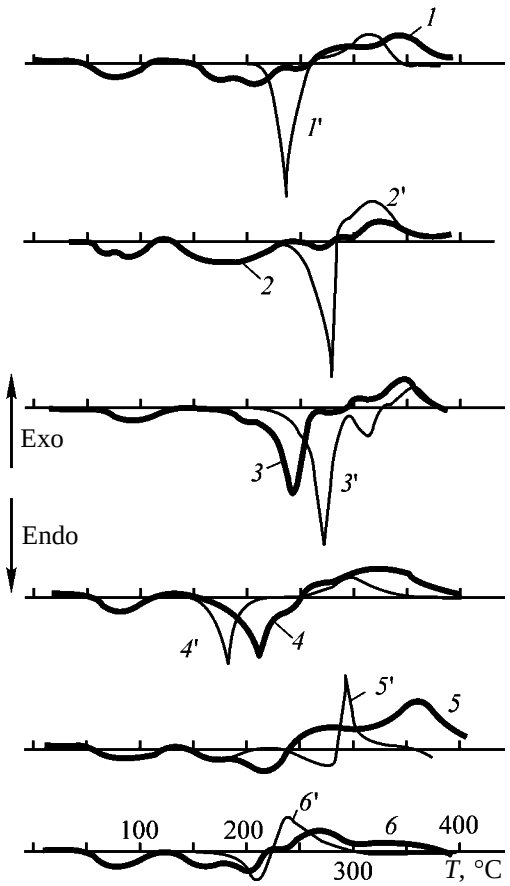

Fig. 2. Thermograms of monomers and oligomers of series I–VI. (*T*) Temperature; the same for Fig. 3.

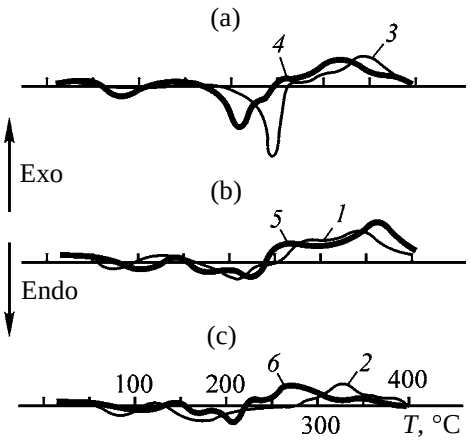

Fig. 3. Thermograms of oligomers (a) **3** and **4**, (b) **1** and **5**, and (c) **2** and **6**.

phous oligomers **2** and **6**. The maximum of the melting peak in the DSC curve of oligomer **3** (Fig. 2) is lower, compared to the corresponding monomer **3**', by 40°C, whereas in the case of **4** it is 25°C higher.

Crystalline oligomer **3** has the lattice similar to that of the monomer, as suggested by coincidence of several reflections, but more defective, as indicated by lower intensity of reflections. The lattice of **4** differs from that of **4**'.

Figure 3 shows the thermograms of the oligomers grouped with respect to the phase state: crystalline (**3**, **4**, Fig. 3a), mesomorphic (**1**, **5**, Fig. 3b), and amorphous (**2**, **6**, Fig. 3c). It is clearly seen that the energy characteristics of the curing transitions correlate with the phase state. The heats of endothermic transitions regularly decrease in going from crystalline (**3**, **4**; 42 kJ kg^{-1}) to mesomorphic (**1**, **5**; 26 kJ kg^{-1}) and amorphous (**2**, **6**; 21 kJ kg^{-1}) oligomers. The respective heats of exothermic transitions are 78, 161, and 51 kJ kg^{-1}. The considerably larger heat of the exothermic transition (curing) in the case of **1** and **5**, with the transition extending to 400°C, is due to the more pronounced conformational isomerism, compared to **2** and **6**.

Within each pair in Fig. 3, the oligomers differ only in the structure of the terminal group. Comparison of the thermograms of **3** and **4**, **1** and **5**, or **2** and **6** reveals the effect of the terminal group on curing. In the case of oligomers **3** and **4** containing the diphenyl oxide unit and no chalcone units, replacement of the terminal norbornenedicarboxylic acid imide group (Fig. 3a, curve *3*) by maleimide group (Fig. 3a, curve *4*) shifts the melting range, curing range, and maximum of the exothermic effect to lower temperatures by 50, 25, and 30°C, respectively.

In the compound with the bischalcone (**C1**) fragment, replacement of the norbornenedicarboxylic acid imide group (Fig. 3b, curve *1*) by the maleimide group (Fig. 3b, curve *5*) affects the melting range of the mesophase insignificantly, but considerably extends the curing range: Curing is not complete even at 400°C, whereas in the case of **1** (Fig. 3b, curve *1*) it is virtually complete at 400°C. In oligomers with the chalcone (**C2**) fragment, the norbornenedicarboxylic acid imide group (Fig. 3c, curve *2*), compared to the maleimide group (Fig. 3c, curve *6*), does not alter the range of transition from the amorphous to softened state but noticeably (by 50–60°C) shifts the exothermic effect to higher temperatures. Compound **6** with the maleimide group (Fig. 3c, curve *6*) exhibits the narrowest curing range and the lowest temperature in the maximum of the exothermic effect, 270°C.

The thermograms in Fig. 3 show that the temperature ranges of the exothermic effects of the oligomers with the norbornenedicarboxylic acid imide terminal groups (curves *1–3*) differ to a lesser extent compared to the oligomers with the maleimide terminal groups (curves *4–6*). For example, in the case of **4** the exothermic effect is complete at 400°C; in the case of **5**, it is not complete at this temperature; and in the case of **6**, it is complete even at 370°C, which is more favorable for using the oligomer as a binder. Therefore, we chose **6** for further experiments aimed to determine the activation energy of curing. For this purpose, we heated samples of **6** to 523, 533, 543, and 573 K at a rate of 32 deg min^{-1} and obtained the isotherms of heat release capacity Qt. The isotherms plotted in the coordinates Qt–t (Fig. 4a) and $\ln(Qt)$–t (Fig. 4b) show that curing at 523, 533, 543, and 573 K is a first-order reaction; its rate constant is $k = -\mathrm{d}[\ln(Qt)]/\mathrm{d}t$. Fig. 4c shows a plot of $\ln k$ vs. reciprocal temperature $1/T$. From this plot, we determined the activation energy $E_a = 8.314\,\mathrm{d}(\ln k)/\mathrm{d}(1/T) = 79$ kJ mol^{-1}. For cross-linking of bisbornenimide, Liu *et al.* report a somewhat higher value, 94 kJ mol^{-1}. This fact is consistent with our DSC data that oligomers **1** and **3** with the norbornenedicarboxylic acid imide terminal groups exhibit higher temperatures of the onset and end of the exothermic effect and higher heat of curing, compared to **6**.

We found that the course of cross-linking is influenced by preliminary pressing of oligomer powders: The exothermic effect starts at lower temperatures. We performed experiments with samples of oligomer powders compacted before curing at a pressure of 50 atm in a mold with a punch diameter of 10 mm. Upon pressing, the initially weakly colored powders

became yellow, dark yellow, and brown, and in some places even dark brown. The temperature of the onset of the exothermic effect decreased after pressing by the following values ΔT_{exo}:

Oligomer	ΔT_{exo}, °C
4	8
1	12
2	17
3	17
5	22
6	36

It is seen that, for **6**, ΔT_{exo} is as large as 36°C, whereas for **4** it only slightly exceeds the measurement error.

The dependence of ΔT_{exo} on the oligomer structure can also be explained by the influence of the concentration of thermoreactive bonds and by conformational features. As in the case of nonpressed powders, the conditions for cross-linking are optimal in **6**.

It should be noted that the influence of pressure on chemical processes was examined in numerous studies. Analysis of their results allows us to interpret the decrease in the temperature of the exothermic effect upon pressing as follows. It is well known that polymerization of many unsaturated organic compounds (olefins, dienes, organosilicon compounds, etc.) accelerates at high pressures. Many monomers that do not polymerize at atmospheric pressure (in particular, tri- and tetrasubstituted ethylenes, aliphatic aldehydes) polymerize at high pressure [5]. Application of a high pressure accelerates polymerization both in liquids and in powders. Furthermore, polymers prepared in the liquid phase at high pressures usually have higher molecular weight [6–8]. The pressure in the course of plastic deformation plays an initiating role in solid-phase polymerization of powders of acrylamide [9] and various heteroarylenes [10]. Solid-phase reactions are accelerate at high pressures also without plastic flow. For example, application of a high pressure considerably accelerated synthesis of the double salt syngenite–schoenite, which allowed its preparation at room temperature [11]. Acceleration of solid-phase reactions at high pressure is due to increase in the number of contacts between particles in the powder. The same factor is apparently responsible for a change in the powder color upon pressing and for a decrease in the curing temperature. In our case, the pressure was insufficient to initiate the reaction, but it decreased the reaction onset temperature.

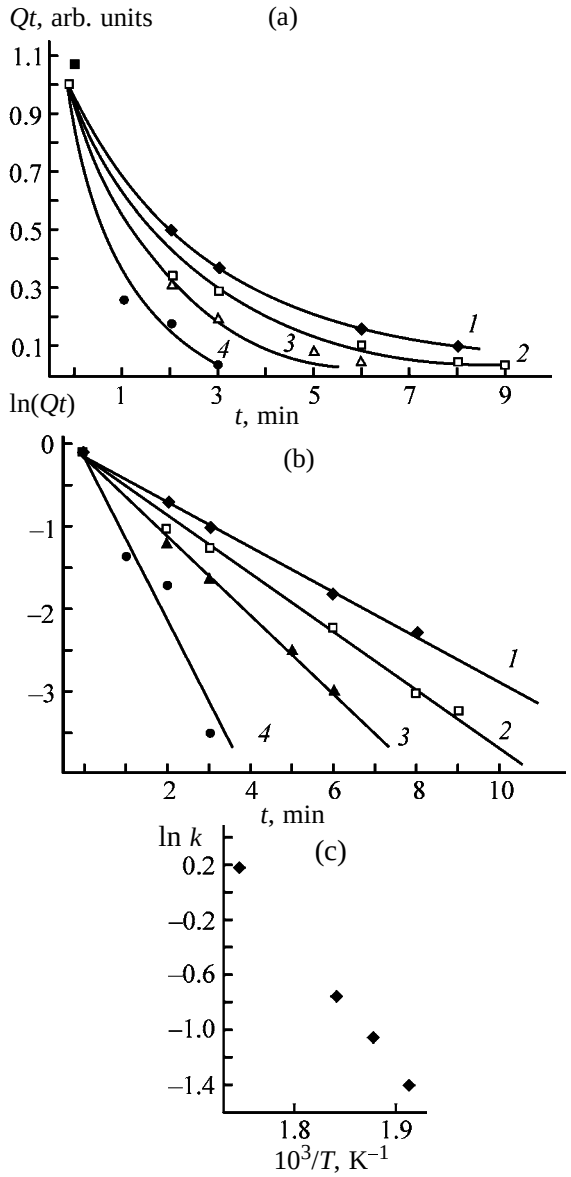

Fig. 4. Thermal and kinetic characteristics of curing of **6**: (a, b) isotherms of the heat release capacity *Qt*, plotted in the coordinates *Qt*–time *t* and ln(*Qt*)–*t*; (c) temperature dependence of the reaction rate constant *k* in the Arrhenius coordinates. *T*, K: (*1*) 523, (*2*) 533, (*3*) 543, and (*4*) 573.

CONCLUSIONS

(1) Curing of oligomers containing thermoreactive chalcone fragments with norbornenedicarboxylic acid imide and maleimide terminal units was studied. The formula of the oligomer exhibiting the best curing characteristics and showing promise as a binder was suggested, and the activation energy of curing of this oligomer was determined.

(2) Preliminary pressing of oligomers decreases the temperature of the exothermic effect of curing.

REFERENCES

1. JPN Patent 62–12 749.
2. JPN Patent 60 – 6729.
3. Sidorovich, A.V. and Kotel'nikov, G.V., *Vysokomol. Soedin., Ser. A*, 1983, vol. 25, no. 12, pp. 2623–2625.
4. Liu, Y., Sum, X.D., Xie, X.Q., and Scola, D.A., *J. Polym. Sci., Part A: Polym. Chem.*, 1998, vol. 36, pp. 2653–2665.
5. Gonikberg, M.G., *Khimicheskoe ravnovesie i skorosti reaktsii pri vysokikh davleniyakh* (Chemical Equilibrium and Rates of High-Pressure Reactions), Moscow: Akad. Nauk SSSR, 1960.
6. Kobeko, P.P., Kuvshinskii, E.V., and Semenova, A.S., *Zh. Fiz. Khim.*, 1950, vol. 24, no. 3, pp. 345–353.
7. Kobeko, P.P., Kuvshinskii, E.V., and Semenova, A.S., *Zh. Fiz. Khim.*, 1950, vol. 24, no. 4, pp. 415–424.
8. Melekhina, E.V. and Kuvshinskii, E.V., *Zh. Fiz. Khim.*, 1958, vol. 32, no. 5, pp. 1016–1027.
9. Zhorin, V.A., Zelenetskii, A.N., Matukhina, E.V. and Razumovskaya, I.S., *Vysokomol. Soedin., Ser. B*, 2002, vol. 44, no. 10, pp. 1843–1847.
10. Zhorin, V.A., Chesnokova, A.E., Berestneva, G.L., *et al.*, *Vysokomol. Soedin., Ser. B*, 1984, vol. 26, no. 2, pp. 140–142.
11. Lepeshkov, N.I., Savitskii, E.M., and Fradkina, Kh.B., *Izv. Sekt. Fiz.-Khim. Anal., Inst. Obshch. Neorg. Khim., Akad. Nauk SSSR*, 1954, vol. 25, pp. 144–150.

Russian Journal of Applied Chemistry, Vol. 76, No. 9, 2003, pp. 1509–1513. Translated from Zhurnal Prikladnoi Khimii, Vol. 76, No. 9, 2003, pp. 1548–1552.

MACROMOLECULAR CHEMISTRY AND POLYMERIC MATERIALS

Comparative Study of Solutions and Gels of Sodium Carboxymethyl Cellulose Produced from Cotton and Wood Cellulose

V. V. Medvedeva, N. V. Volkova, Yu. D. Semchikov, and A. V. Tikhomirov

Research Institute of Chemistry, Lobachevsky Nizhni Novgorod State University, Nizhni Novgorod, Russia
Oktyabr' Plant, Joint-Stock Company, Nizhni Novgorod, Russia

Received April 24, 2003

Abstract—Viscosity and gelation characteristics of aqueous solutions of sodium carboxymethyl cellulose produced from cotton and wood cellulose were studied.

Sodium salt of carboxymethyl cellulose (Na-CMC) is a cellulose ether (CE) produced on a large scale. This is due to its valuable characteristics and relatively easy production. It finds wide applications in petroleum, textile, food, and pharmaceutical industries as stabilizing agent, thickener, adhesive, and film-forming substance [1–3]. Dilute aqueous solutions of Na-CMC are efficiently structured by multivalent metal ions with formation of coordinatively cross-linked gels. These gels are widely used in gas-and-oil industry as viscoelastic systems in secondary treatment of oil wells and hydraulic fracturing of strata [4, 5]. All these characteristics of Na-CMC are governed by the degree of polymerization, degree of substitution, molecular-weight distribution, and uniformity of distribution of carboxy groups along the chain [3, 6]. In turn, these characteristics depend on the procedure of Na-CMC production and also on the raw materials used in production (such data are scarce).

The aim of this work was to study viscosity and gelation characteristics of aqueous solutions of Na-CMC produced from cotton cellulose in comparison with the characteristics of Na-CMC produced from wood cellulose (sulfite cooking).

EXPERIMENTAL

In the study we used three samples of Na-CMC produced from cotton cellulose (sample nos. 1–3) and two samples of Na-CMC of the 85/600 (sample no. 4) and 85/800 (sample no. 5) types produced from wood cellulose. The characteristics of the samples are listed in Table 1.

All the experiments were carried out at $22 \pm 2°C$. Viscosity characteristics of aqueous solutions of Na-CMC were studied on a Hoeppler ball viscometer.

To prepare gel-forming compositions, we used a solution of the polymer (2.0 wt %) in double-distilled water and solutions of chrome–potassium alum $KCr(SO_4)_2 \cdot 12H_2O$ (1.0–5.0 wt %), serving as a cross-linking agent. The initial pH 12.3 was adjusted with 0.2 wt % KOH. The concentration limits of gelation and the onset of syneresis were determined visually [7, 8]. The minimal concentrations of the polymer and cross-linking agent were determined from the loss of the solution fluidity under gravity in turning-over of the ampule in which the cross-linking occurred after combining the solutions of the polymer and chromium salt. The onset of syneresis was determined from the appearance of water drops at the gel–air boundary. The amount of water separated from the gel in syneresis was evaluated by weighing. The modulus of elasticity G of coordinatively cross-linked Na-CMC gels was determined by penetration using spherical indentors with various radii depending on the gel elasticity [9, 10]. The experiment was carried out at the values of imposed force initiating no creep of the system. According to the Herz theory [9], with the use of a spherical indentor the elasticity modulus of a gel is given by the relation

$$G = \frac{3F}{16h^{3/2}R^{1/2}},$$

where F is the force applied to the spherical indentor, R is its radius, and h is the depth of immersion into the gel.

1070-4272/03/7609-1509$25.00

Table 1. Characteristics of Na-CMC sample

Sample no.	Degree of polymerization	Degree of substitution, %	Content of the main substance, %	Viscosity of 2 wt % solutions, mPa s
1	580	74	60.6	350
2	540	49	71.6	202
3	780	66	59.0	790
4	588	81	49.2	280
5	800	81	49.6	580

To determine the concentration range of existence of gels in the system Na-CMC–Cr(III) salt, we obtained isothermal phase diagrams in the coordinates polymer concentration–concentration of cross-linking agent for three samples of Na-CMC synthesized from cotton cellulose (Fig. 1). Curves *1–3* correspond to solution–gel transitions for each system, and curves *1*'–*3*', to transitions from the gel to the system with phase separation, which corresponds to separation of water from the gel at the instant of its formation. Figure 1 shows that there is a critical concentration of polymer c_{cr} below which gelation does not proceed irrespective of the concentration of the Cr(III) salt. The c_{cr} value is an important characteristic of the system, since it governs the economical efficiency of using these systems in practice (in secondary treatment of oil wells, hundreds of cubic meters of the polymer solution are pumped into oil wells).

Figure 1 shows that c_{cr} in this system increases not only with decreasing molecular weight of the polymer

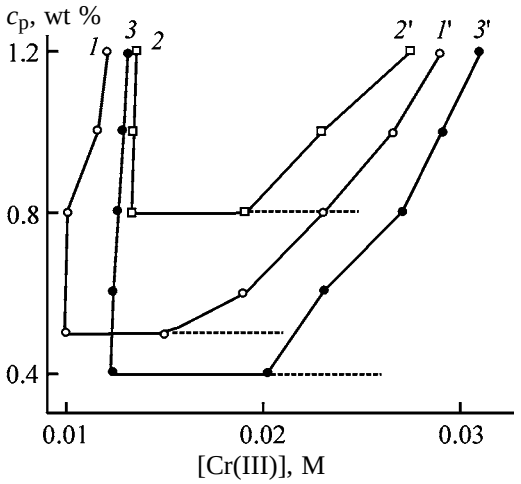

Fig. 1. Isothermal phase diagrams in the coordinates polymer concentration c_p–concentration of Cr(III) salt [Cr(III)] for Na-CMC sample nos. (*1*, *1*') 1, (*2*, *2*') 2, and (*3*, *3*') 3. (*1–3*) Transition solution–gel and (*1*'–*3*') phase separation of the system (instantaneous syneresis).

[10] but also with decreasing degree of substitution of Na-CMC at approximately the same degrees of polymerization. This fact can be explained in terms of the existing concept of the behavior of polyelectrolyte macromolecules in solution. With increasing degree of carboxymethylation of cellulose macromolecule, its total charge increases. This results in significant increase in the polymer rigidity and elongation of the polymer chain [11], which makes lower the polymer concentration in the solution required for gelation. On the whole, these data confirm the previous conclusion that the critical concentration of the polymer in the reaction with polyvalent metal ions is governed by the conformation of polymer macromolecules in the solution [12].

It should be also noted that, with increasing degree of substitution of Na-CMC, the critical concentration of the cross-linking agent [Cr(III) salt] required for the gelation decreases.

Long-term visual monitoring of the resulting gels revealed gradual syneresis, i.e., with time the solvent separates from the gel. The syneresis intensity is governed by the system composition. The rate of syneresis development and the volume of separated water are maximal for systems whose compositions correspond to the right part of the phase diagram (transition from the gel to the system with phase separation).

The stability of gels is characterized by dashed lines in the isothermal phase diagrams, corresponding to the same times of syneresis onset, i.e., time intervals from the onset of coordination cross-linking to visual observation of syneresis in the resulting gel. The results for Na-CMC sample nos. 1 and 2 are shown in Figs. 2a and 2b, respectively. Analysis of these data allows a conclusion that syneresis begins earlier for Na-CMC gels with the minimum degree of substitution (49%) than for the gel samples whose degree of substitution is more than 60%. For example, the stability of gels based on sample no. 2 does not

exceed 3 months, while for the most part of systems syneresis proceeds within a week (Fig. 2b).

Thus, our results show that the degree of carboxymethylation of Na-CMC is the important characteristic governing the gelation power of the system Na-CMC–Cr(III) salt. The decrease in the degree of substitution to 50% results in an increase in the minimal concentration of the polymer required for gelation, narrowing of the concentration range of the gel existence, and deterioration of the characteristics of the resulting gels (decrease in their stability in time and increase in the amount of released water).

The main part of this work was devoted to comparative analysis of viscosity and gelation characteristics of aqueous solutions of Na-CMC synthesized on the basis of wood (sulfite; sample nos. 4 and 5) and cotton cellulose (sample nos. 1–3). In the first stage, we studied the stability of aqueous solutions of various Na-CMC samples in storage. These studies are necessary for forecasting the efficiency of using one or another sample of Na-CMC in practice, e.g., in gas-and-oil industry as mud stabilizers and viscoelastic systems (gels) in secondary treatment of oil wells. The variation of viscosity characteristics of the solutions of three Na-CMC samples (2.0 wt %) in time in the relative coordinates is presented in Fig. 3.

Figure 3 shows that solution of sample no. 1 produced from cotton cellulose (degree of substitution 74%) is more stable in time: in 3 months, its viscosity decreases by a factor of only 2 (curve *1*), and the viscosity of solution of sample no. 4 (2 wt %), produced from wood cellulose, increases by more than an order of magnitude (curve *3*). This is apparently caused by the fact that commercial Na-CMC is extremely heterogeneous in the degree of cellulose carboxymethylation. The presence of weakly alkylated crystalline regions causes aggregation and association of Na-CMC macromolecules in the solution. Since the degree of crystallinity of cotton cellulose is higher than that of wood cellulose, Na-CMC produced from cotton cellulose contains greater number of crystalline regions preserving the structure of the initial cellulose. Therefore, apparently, moderately concentrated solutions of this cellulose are structured in a greater extent (Table 1) and retain the initial characteristics for a longer time.

It should be noted that this effect disappears with decreasing degree of substitution of Na-CMC. The viscosity of its 2 wt % solution decreases (Table 1) and its stability gets worse (Fig. 3, curve *3*). This fact can be explained by a decrease in the polymer solubility with increasing number of carboxymethyl groups

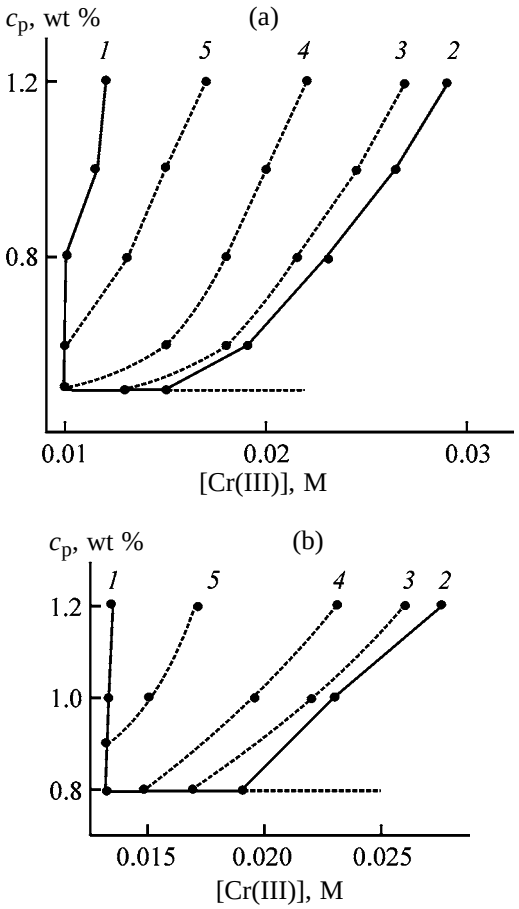

Fig. 2. Isothermal phase diagrams in the coordinates polymer concentration c_p–concentration of chromium salt [Cr(III)] for Na-CMC sample nos. (a) 1 and (b) 2. (*1*) Solution–gel transition. Time of the onset of syneresis (days): (a) (*2*) 0, (*3*) 1, (*4*) 70, and (*5*) 120; (b) (*2*) 0, (*3*) 1, (*4*) 6, and (*5*) 60.

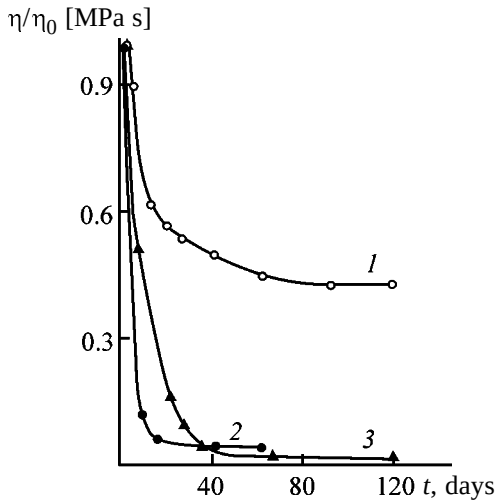

Fig. 3. Variation of viscosity η in time t relative to the initial value η_0 for Na-CMC sample nos. (*1*) 1, (*2*) 2, and (*3*) 4, produced from cotton and wood cellulose.

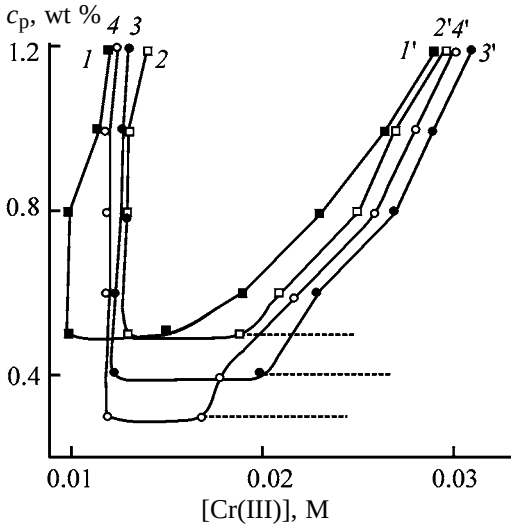

Fig. 4. Isothermal phase diagrams in the coordinates polymer concentration c_p–concentration of chromium salt [Cr(III)] for sample nos. (*1*, *1*') 1, (*2*, *2*') 3, (*3*, *3*') 4, and (*4*, *4*') 5 of Na-CMC produced from cotton and wood cellulose. (*1*–*4*) Solution–gel transition and (*1*'–*4*') phase separation of the system (instantaneous syneresis).

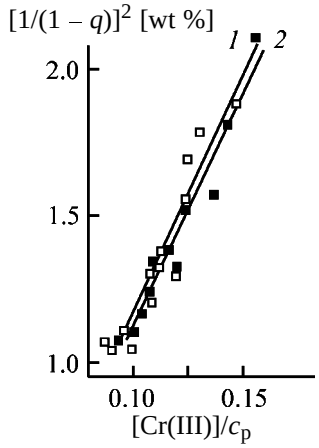

Fig. 5. The limiting relative amount of water q released in syneresis of gels as a function of weight ratio of components in the system $[Cr(III)]/c_p$ in the coordinates of relation (2) for samples nos. (*1*) 1 and (*2*) 4 of Na-CMC produced from cotton and wood cellulose.

in the chain (low-substituted cellulose ethers dissolve only in dilute alkali solutions).

Furthermore, we carried out a comparative analysis of the gel-forming power exhibited by solutions of Na-CMC of various origins in the presence of the Cr(III) salt, and also of the characteristics of the resulting gels (elasticity, stability in time, and syneresis intensity).

The concentrations corresponding to the transitions solution–gel and gel–phase separation for cotton and wood Na-CMC samples with the same molecular weights are close (Fig. 4). The critical concentrations of the polymers are also the same when the degree of substitution of cotton cellulose is more than 70% and increase from 0.3 to 0.4 wt % when the degree of substitution of Na-CMC produced from cotton cellulose is less than 70% (the degree of substitution of wood Na-CMC in both cases is higher, 81%). In this case, gelation of a solution of Na-CMC synthesized from cotton cellulose, with a degree of substitution more than 70%, requires a lower concentration of the cross-linking agent, which is important from both economical and environmental standpoints. This means that smaller amounts of the chromium ions fall into the interior of the Earth.

The stability of the resulting gels in time is approximately the same for cotton and wood Na-CMC at similar degrees of substitution [10]. A decrease in the degree of substitution abruptly deteriorates the stability of gels.

Figure 5 shows the syneresis results for the samples of cotton and wood Na-CMC with a close molecular weight, plotted in the coordinates of the relationship proposed previously [13]. This relationship was obtained considering a decrease in the size of the subchains (distances between cross-linking points) in the coordination cross-linking reaction. In this case, the number of subchains and the density of units in these subchains increase. Then, variation of the gel volume in syneresis V_0/V is given by

$$V_0/V = \nu^{1/2}, \quad (1)$$

where ν is the number of cross-links.

When

$$\nu \sim \frac{[Cr(III)]}{[Na\text{-}CMC]},$$

$$V_0/V \sim 1/(1-q)$$

(q is the relative amount of water released in syneresis), we obtain

$$[1/(1-q)]^2 = k\frac{[Cr(III)]}{[Na\text{-}CMC]} + \text{const}. \quad (2)$$

Figure 5 shows that the volumes of water released in syneresis of gels of cotton and wood cellulose are close (curves in Fig. 5 virtually coincide).

A study of the physicomechanical characteristics of gels is also important for their practical use, in particular, for predicting their behavior under various

Table 2. Modulus of elasticity *G* of 1.2% gels of Na-CMC

[Cr(III)], M	Sample no.	*G*, Pa
0.020	1	800
	2	175
	3	650
	4	600
	5	400
0.024	1	1400
	2	360
	3	1200
	4	1200
	5	1000

conditions. The modulus of elasticity is the main rheological characteristic of gels, since, by definition, gels are systems with lost fluidity.

The moduli of elasticity *G* of two gels based on various Na-CMC samples are listed in Table 2. The *G* value for the gels based on cotton Na-CMC is somewhat higher provided that the degree of substitution is more than 60%.

CONCLUSIONS

(1) Viscosity and gelation characteristics of aqueous solutions of sodium salt of carboxymetyl cellulose produced from cotton cellulose are governed by both molecular weight of the polymer and degree of carboxymethylation. A decrease in the degree of substitution to less than 50% results in an increase in the critical concentrations of the polymer and cross-linking agent required for gelation and in deterioration of the characteristics of the resulting gels.

(2) The viscosity of moderately concentrated solutions of cotton Na-carboxymethyl cellulose is higher and its values are more stable in time, as compared to wood Na-carboxymethyl cellulose.

(3) The gelation power, stability in time, and intensity of syneresis of coordinatively cross-linked gels of cotton and wood Na-carboxymethyl cellulose are similar. However, for formation of gel from solutions of cotton Na-carboxymethyl cellulose with the degree of substitution more than 70%, lower concentrations of the cross-linking agent are required.

(4) At close degrees of substitution, the elastic characteristics of the gels based on cotton Na-carboxymethyl cellulose are higher compared to the sample produced from wood cellulose.

REFERENCES

1. Bytenskii, V.Ya. and Kuznetsov, E.P., *Proizvodstvo efirov tsellyulozy* (Production of Cellulose Ethers and Esters), Leningrad: Khimiya, 1974.
2. Petropavlovskii, G.A., *Gidrofil'nye chastichno zameshchennye efiry tsellyulozy i ikh modifikatsiya putem khimicheskogo sshivaniya* (Hydrophilic Partially Substituted Cellulose Ethers and Esters and Their Modification by Chemical Cross-Linking), Leningrad: Nauka, 1988.
3. *Cellulose and Cellulose Derivatives*, Bikales, N. and Segal, L., Eds., New York: Wiley, 1971, part 4.
4. Shvetsov, I., Bakaev, G., Kabo, V., *et al.*, *Neft. Khoz.*, 1994, no. 4, pp. 37–44.
5. Ely, J.W., Schubarth, S.K., Wolters, B.C., and Kromer, J.C., *Oil Gas J.*, 1992, vol. 90, no. 23, pp. 66–70.
6. Doronina, I.K. and Aver'yanova, V.M., *Vysokomol. Soedin., Ser. B*, 1980, vol. 22, no. 12, pp. 886–890.
7. Allain, C. and Salome, L., *Biological and Synthetic Polymer Networks*, Kramer, O., Ed., Amsterdam: Elsevier, 1988, pp. 291–303.
8. Medvedeva, V.V., Myasnikova, L.I., Semchikov, Yu.D., and Rogovina, L.Z., *Vysokomol. Soedin., Ser. B*, 1995, vol. 37, no. 6, pp. 1040–1042.
9. Nielsen, L.E., *Mechanical Properties of Polymers and Composites*, New York: Marcel Dekker, 1974.
10. Medvedeva, V.V., Myasnikova, L.I., Semchikov, Yu.D., and Rogovina, L.Z., *Vysokomol. Soedin., Ser. B*, 1998, vol. 40, no. 6, pp. 492–497.
11. Grosberg, A.Yu. and Khokhlov, A.R., *Statisticheskaya fizika makromolekul* (Statistical Physics of Macromolecules), Moscow: Nauka, 1989.
12. Medvedeva, V.V. and Semchikov, Yu.D., *Vysokomol. Soedin., Ser. B*, 2001, vol. 43, no. 6, pp. 1074–1078.
13. Medvedeva, V.V., Myasnikova, L.I., and Semchikov, Yu.D., *Vysokomol. Soedin., Ser. A*, 2000, vol. 42, no. 5, pp. 840–848.

Russian Journal of Applied Chemistry, Vol. 76, No. 9, 2003, pp. 1514–1518. Translated from Zhurnal Prikladnoi Khimii, Vol. 76, No. 9, 2003, pp. 1553–1557.

MACROMOLECULAR CHEMISTRY AND POLYMERIC MATERIALS

Physicochemical Modification of Cellulose Acetate for Manufacturing Films, Membranes, and Biofilters

A. B. Shipovskaya, N. V. Evseeva, and G. N. Timofeeva

Chernyshevsky State University, Saratov, Russia
Research Institute of Chemistry, Chernyshevsky State University, Saratov, Russia
Institute of Biochemistry and Physiology of Plants and Microorganisms, Russian Academy of Sciences, Saratov, Russia

Received January 20, 2003

Abstract—Modification of cellulose acetate with vapor of a mixture of water and a solvent in which cellulose derivatives form a lyotropic liquid-crystal phase, aimed at preparation of films, membranes, and biofilters, is studied. The resulting materials are capable of removing excess blood cholesterol with no concomitant decrease in the blood protein and electrolyte levels.

It is known that cellulose acetates provide a basis for production of a wide spectrum of film materials of various purposes from reverse osmosis to microfiltration [1]. The effect of such separating systems is based mostly on the pore size, and, in some cases, on the Donnan exclusion of counterions by fixed charges of the membrane.

Cellulose acetate films, membranes, and biofilters are used in mass-transfer apparatuses for treating blood or serum to remove metabolites and xenobiotics [2]. Plasma exchange therapy (plasmopheresis) is used to remove lipids, coarsely dispersed proteins, and toxins from blood. Membrane plasma filters mostly do not have a sufficient selectivity (in separating excess cholesterol from blood, vitally important protein substances and electrolytes are also retained) [3]. In some cases, in filtration of plasma, proteins coagulate, blocking the membrane pores, decreasing its performance, and even making it fully unusable [4, 5].

Therefore, it is a quite topical problem to develop filtering materials capable of retaining cholesterol, but not other vitally important blood components. This problem was tackled to be solved in various manners [6–8].

In this work we studied physicochemical modification of cellulose acetates with vapor of a mixture of water and a solvent in which cellulose derivatives form a lyotropic liquid-crystal phase. The method allows preparation of films, membranes, and biofilters capable of retaining excess cholesterol with no concomitant decrease in the blood protein and mineral salt level [9].

EXPERIMENTAL

In experiments we used powdered air-dry cellulose diacetate (CDA) of the wood or cotton origin. The content of bound acetic acid in the samples was 54.5–55.3%; viscosity-average molecular weight of wood and cotton CDA, 8.2×10^4 and 7.0×10^4, respectively; and their bulk density, 1.3–1.32 g cm^{-3}.

Modification of CDA was carried out under ambient conditions in a closed vessel partly filled with an aqueous–organic mixture. As a sorbate we used binary mixtures of distilled water and DMSO or dimethylacetamide (DMAA) (both of analytically pure grade). The water to organic solvent volume ratio varied from 90 : 10 to 99 : 1. An 0.5-mm sieve filled with powdered CDA was arranged at a distance of 5 cm over the surface of the liquid phase, and the polymer was exposed to solvent vapor. The amount of absorbed vapor was determined gravimetrically with a WT torsion balance to within 0.0002 g. The degree of vapor sorption was varied from 0 to 10 wt %. As the polymer was saturated with the sorbate vapor, it was sampled for film forming.

In the work we studied reference and modified CDA samples and also membranes prepared from them. As a solvent for the polymer we used the conventional process solvent, a mixture of acetone with water (95 : 5; analytically pure grade). The CDA concentration in the film-forming solutions was 3 and 5% for wood and cotton CDA, respectively. The membranes were formed under ambient conditions by solution casting onto finished glass plates using a

1070-4272/03/7609-1514$25.00

round glass draw plate, followed by solvent removal. The support plates were degreased with ethanol and acetone prior to use. The solvent removal was monitored by the sample weight. All the resulting membranes were milk-white in color. Their thickness was 90–110 μm.

The filtering properties of membranes were studied on a laboratory system with a separating cell of the plate-and-frame type. Cholesterol, total protein, and electrolytes in blood plasma before (penetrate) and after membrane filtration (permeate) were determined on a Humolize-2000 programmable photometer according to standard procedures.

Electrophoresis of proteins in a polyacrylamide gel was carried out by the Laemmli method on a vertical electrophoresis apparatus (plate size 12 × 12 cm, gel layer 0.1 cm). Plasma proteins were preliminarily separated into subunits. To a plasma sample, an equal volume of a buffer solution was added [0.125 M Tris-HCl (pH 6.8), 4% sodium dodecyl sulfate, 20% glycerol, and 5% β-mercaptoethanol]. The fix and finished gels contained 12.5 and 5% acrylamide, respectively. Electrophoresis was performed at a constant current strength (20 mA). When proteins approached the fix gel boundary, the current was increased to 30 mA. After completion of the process, the gel was stained with 0.25% Coomassie Blue R-250 in a mixture of 50% ethanol and 12% acetic acid, and then the polymer matrix was destained in an aqueous solution containing 50% ethanol and 12% acetic acid. As MW markers we used ovotransferrin (MW 78×10^3), albumin (66.3×10^3), ovalbumin (42.7×10^3), carbonic anhydrase (30×10^3), myoglobin (17×10^3), and cytochrome C (12.3×10^3).

The optical rotation of the reference and modified CDA samples (0.5 g dl^{-1}) was measured on an SM-2 rotary polarimeter (λ_{Na} = 589 nm) [11] to within 0.04°. A DNAS18-04.2 lamp was used as a light source. The optical activity expressed in [α] units (specific optical rotation) was determined to be +30° and +12° for wood and cotton CDA, respectively.

To obtain biofilters of a definite 3D structure, the initial polymer was modified with vapor of an aqueous-organic mixture (water–DMSO or water–DMAA at a component volume ratio from 90 : 10 to 99 : 1).

Selection of DMSO and DMAA was caused by the fact that they are classified with aprotic dipolar solvents [12] in which cellulose derivatives form lyotropic LC solutions [13]. Furthermore, it was demonstrated previously [14, 15] that DMSO and DMAA and their mixtures with water, being in the vaporous state, have

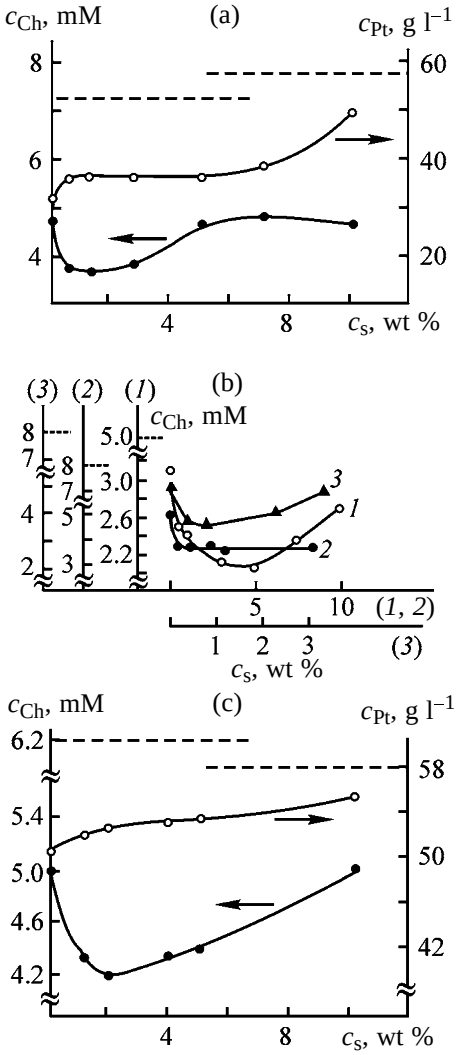

Fig. 1. Cholesterol (c_{Ch}) and protein concentrations (c_{Pt}) in the permeate after filtration of blood plasma through reference and modified CDA membranes. (c_s) Degree of absorption of the sorbate vapor on the polymer. (a) H_2O : DMSO = 90 : 10; (b): (*1*) H_2O : DMAA = 95 : 5, (*2*) H_2O : DMSO = 95 : 5, and (*3*) H_2O : DMSO = 98 : 2; and (c) H_2O : DMSO = 99 : 1. The cholesterol and protein concentrations in the initial plasma are shown by the horizontal dashed lines.

a significant effect on the structure formation in cellulose acetates, opening the door for preparation of a broad spectrum of polymeric materials of various purposes [16, 17]. It should be pointed out that the effect of solvent vapor on the structure of cellulose acetate is much stronger and more specific as compared to addition of equal amounts of the same liquids to the polymer solution [14, 15]. Note also that aqueous DMSO is widely used as a medicine (Pharmacopoeia Article "Dimexidum" 75-244-9). Figure 1 shows the results on filtration of blood plasma through membranes fabricated from modified CDA. The cholesterol (c_{Ch}) and

Table 1. Results of blood plasma filtration through modified CDA membranes*

Active medium	α, %	c_s^{min}, wt %
H_2O : DMSO:		
90 : 10	20–25	No more than 3.0
95 : 5	26–30	No more than 3.0
98 : 2	26–28	No more than 2.0
99 : 1	14–16	No more than 0.3
H_2O : DMAA = 95 : 5	30–33	No more than 5.0

* (α) Maximal effect of retention of cholesterol (against the reference membrane) and (c_s^{min}) minimal value corresponding to the maximal retention effect with respect to cholesterol.

Table 2. Results of blood plasma filtration through reference and modified CDA membranes

Active medium	Absorption of sorbate, %	Concentrations of electrolytes after filtration, mM		
		c_{Na}	c_K	c_{Ca}
–	–	121.1	2.59	0.71
H_2O : DMSO = 90 : 10	0.2	131.6	2.72	0.73
	1.0	131.9	2.73	0.74
	2.5	131.2	2.72	0.74
	5.0	130.9	2.74	0.75
	10.0	120.4	2.52	0.71

protein (c_{Pt}) concentrations in the permeate after filtration through the reference (commercial) CDA membrane are given on the ordinate axis. Figures 1a and 1b (curves *1*) show data obtained with wood CDA, and Figs. 1b (curves *2, 3*) and 1c, with cotton CDA.

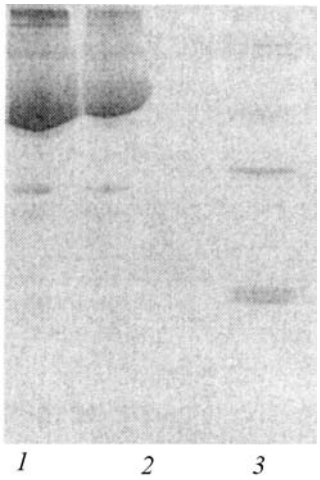

Fig. 2. Electrophoresis in polyacrylamide gel: (*1, 2*) protein fractions in the penetrate and permeate, respectively, and (*3*) markers.

As seen, the membranes fabricated from modified CDA (of both wood and cotton origin) demonstrate higher retaining capacity for cholesterol and lower retaining capacity for protein and electrolytes, as compared to the initial CDA membranes (Fig. 1). The degree of retention of cholesterol on the CDA membranes modified with H_2O–DMSO (90 : 10, 95 : 5, and 98 : 2) vapor is higher by 20–30% as compared to the reference membrane (Table 1). For the membranes modified with H_2O–DMAA (95 : 5) vapor, the effect is 30–33%, and with H_2O–DMSO (99 : 1), 14–16%. Data on the concentrations of electrolytes in the permeate (Table 2) show that c_{Na}, c_K, and c_{Ca} in blood plasma after filtration through modified CDA membranes are higher than those after filtration through the reference membrane. It is of primary importance that the modified membranes do not retain proteins (Figs. 1a, 1b). As an example, Fig. 2 shows data on electrophoresis of the initial plasma and plasma after filtration through a membrane from cotton CDA that sorbed 2.5 wt % of H_2O–DMSO (90 : 10) vapor. As seen, fractions 2 and 3 are practically identical in the protein composition.

For all the systems CDA–aqueous-organic vapor, the sorption of the sorbate vapor is very low, being no more than 5 wt % (Fig. 1, Table 1). Therefore, the content of an individual solvent (DMSO or DMAA) in any of the products formed is below 10^{-4} wt %. Nevertheless, even such a small absorption of the vapor by the polymer provides (if the modified structure of CDA is preserved in a membrane), on the one hand, selective separation of optically active components of blood plasma and, on the other hand, efficient retention of one of them (cholesterol) with no decrease in the content of another (protein) and also of electrolytes.

Cellulose acetates are classified with optically active polysaccharides. Shipovskaya and Timofeeva have demonstrated [14, 15] that solvents forming lyotropic mesophases with cellulose and its derivatives, being in the vaporous state, have a strong effect on the optical activity of cellulose esters. It was shown that modification of CDA with an aqueous-organic vapor in which one component is a mesogenic solvent initiates a change in the structure of the cellulose ester at the stereoisomeric level.

Figure 3 shows the dependence of the specific optical rotation [α] of the CDA solutions on the degree of modification of the polymer with the sorbate vapor. The reference samples of CDA in aqueous acetone are characterized by positive [α]: +30° and +12° for wood and cotton CDA, respectively. For the samples modi-

fied with vapor of a mixture of water and a specific solvent, we observed not only a change in the absolute value of the specific optical rotation, but also the inversion of the sign of [α].

Absorption of a small amount (up to 1–2 wt %) of the sorbate vapor on the wood CDA is accompanied by a considerable change in the optical activity, with [α] passing from the positive to the negative range (Fig. 3). Increasing degree of sorption of the sorbate vapor to 4–5 wt % results in further increase in negative [α]. At last, absorption of more than 5 wt % of H_2O–DMSO (90 : 10) vapor no longer changes the value and sign of [α] (plateau in curve *1*). Absorption of a large amount of H_2O–DMAA (90 : 10) decreases induced negative [α] (curve *2*). For cotton CDA, a significant change in the value and sign of [α] is observed after absorption of about 0.1 wt % of the sorbate vapor, and the [α]–c_s curve flattens out after absorption of 0.5 wt % of the vapor (curve *3*).

The results obtained (Figs. 1, 3 and Tables 1, 2) show a correlation between the filtering properties of the modified CDA membranes and the optical activity of the polymer. The membranes capable of selectively separating such optically active compounds as cholesterol and steroids (proteins) were obtained on the basis of CDA with a modified 3D structure characterized by a negative induced [α]. The correlation between the polymer structure and its optical activity follows a dose–effect regular trend, the most significant effect being observed at small amounts of the absorbed sorbate vapor.

It is worth noting that, in filtration of blood plasma through a modified CDA membrane, we observed a decrease in the concentration of the toxic metabolite, bilirubin, in the permeate and its selective separation from the protein fraction [18].

The authors are grateful to B.M. Zelikson for the interest in the work and valuable discussions of the membrane filtration data.

CONCLUSIONS

(1) Treatment of cellulose acetate with vapor of a mixture of water and a solvent in which cellulose derivatives form a lyotropic liquid-crystal phase provides physicochemical modification not only at the supramolecular level, but also at a delicate conformational level involving the stereochemical structure of the polysaccharide.

(2) The modification is a controllable process, as following a dose–effect regular trend. It can be interrupted at any stage of formation of the 3D structure of the polymer.

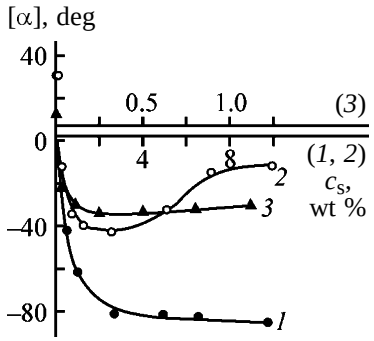

Fig. 3. Specific optical rotation [α] in CDA solutions as a function of the degree of sorption c_s of the sorbate vapor on the polymer. Sorbate: (*1*) H_2O–DMSO (90 : 10), (*2*) H_2O–DMAA (90 : 10), and (*3*) H_2O–DMSO (95 : 5). λ = 589 nm; T = 20°C.

(3) Films, filters, and membranes prepared from modified cellulose diacetate demonstrate an exceptional capability for retention of excess cholesterol with no concomitant decrease in the blood protein and mineral salt level.

(4) The membranes meet the requirements on the selectivity of removal of cholesterol from plasma and also on the predictability. To all appearance, they should be quite biocompatible (in using the modified cellulose diacetate films for filtration of plasma, the contact of the polymer surface with blood cells is excluded).

ACKNOWLEDGMENTS

The work was financially supported by the Russian Foundation for Basic Research (project no. 00-03-33058a).

REFERENCES

1. Kesting, R.E., *Synthetic Polymeric Membranes*, New York: Wiley, 1991.
2. Perepechkin, L.P. and Perepechkina, N.P., *Khim. Volokna*, 1999, no. 6, pp. 3–11.
3. USSR Inventor's Certificate no. 1722504.
4. Chenoweth, D.E., *Artif. Organs*, 1984, no. 8, pp. 281–287.
5. Hamilton, R.J. and Adkinson, N.F., *Artif. Organs*, 1984, no. 8, pp. 311–317.
6. Diederich, F. and Peterson, B., *Angew. Chem., Int. Ed.*, 1994, vol. 33, pp. 1621–1624.
7. FR Patent 2346016.
8. US Patent 5366724.
9. RF Patent 2174130.

10. Laemmli, U.K., *Nature*, 1970, vol. 277, pp. 680–685.
11. Kettering, Ch.F., *Newer Methods of Polymer Characterization*, New York: Wiley, 1964.
12. Reichardt, Ch., *Solvents and Solvent Effects in Organic Chemistry*, Weinheim: VCH, 1988.
13. Kulichikhin, V.G. and Golova, L.K., *Khim. Drev.*, 1985, no. 3, pp. 9–27.
14. Shipovskaya, A.B. and Timofeeva, G.N., *Vysokomol. Soedin., Ser. A*, 2001, vol. 43, no. 7, pp. 1237–1244.
15. Shipovskaya, A.B. and Timofeeva, G.N., *Vysokomol. Soedin., Ser. A*, 2003, vol. 45, no. 1, pp. 101–105.
16. Shipovskaya, A.B., Timofeeva, G.N., and Borisova, S.V., Abstracts of Papers, *Vserossiiskaya onferentsiya "Membrany-2001"* (Russian Conf. "Membranes-2001"), Moscow, 2001, p. 208.
17. Shipovskaya, A.B., Timofeeva, G.N., and Osipova, O.V., in *Struktura i dinamika molekulyarnykh system: Sbornik statei* (Structure and Dynamics of Molecular Systems: Collection of Papers), Ioshkar-Ola: Mariisk. Gos. Tekh. Univ., 2001, issue 8, vol. 2, pp. 151–155.
18. Shipovskaya, A.B., Starovoitova, N.V., and Timofeeva, G.N., Abstracts of Papers, *Tret'ya Vserossiiskaya konferentsiya molodykh uchenykh "Sovremennye problemy teoreticheskoi i eksperimental'noi khimii"* (Third Russian Young Researchers' Conf. "Modern Problems of Theoretical and Experimental Chemistry"), Saratov, 2001, p. 210.

Russian Journal of Applied Chemistry, Vol. 76, No. 9, 2003, pp. 1519–1523. Translated from Zhurnal Prikladnoi Khimii, Vol. 76, No. 9, 2003, pp. 1558–1562.

MACROMOLECULAR CHEMISTRY AND POLYMERIC MATERIALS

Color Stabilization of Polymers with Formulations Containing Di(hydroxyphenyl)methane Stabilizers

S. V. Bukharov, L. K. Fazlieva, G. N. Nugumanova, E. N. Cherezova, and N. A. Mukmeneva

Kazan State Technological University, Kazan, Tatarstan, Russia

Received February 21, 2003; in final form, June 2003

Abstract—The possibility was examined of developing noncoloring stabilizing formulations based on di(hydroxyphenyl)methane stabilizers with addition of agents that decompose hydroperoxides without generation of radicals and thus inhibit formation of α-hydroxyphenylmethylenequinones, or of components that ensure transformations of these quinones into colorless products.

Preservation of the initial color (color stabilization) of polymeric products and articles is an important aspect of polymer stabilization. Variation of the polymer color due to aging is inadmissible for many items made from polyolefins, polyvinyl chloride, and colorless and colored rubbers. The mechanism responsible for changes in the polymer color are diverse [1] and can be subdivided into three main groups: (1) formation of chromophoric systems in the initial polymer, initiated by abnormal fragments (weak points) or polyvalent metal impurities; (2) degradation of macromolecules; and (3) oxidative transformations of additives, in particular, of stabilizers.

In chemically resistant polymers, color primarily originates from oxidation of phenolic stabilizers to give chromophoric products. The tendency to form such products depends on the stabilizer structure [2]. There are indications in the literature that the methylene bridge in di(hydroxyphenyl)methane stabilizers is responsible for coloration [3, 4], as their oxidative transformations yield colored methylenequinones [5]. For example, hydrogalvinoxyl **I**, oxidation product of bis(3,5-di-*tert*-butyl-4-hydroxyphenyl)methane **II**, has a long-wave absorption maximum at 398 nm, responsible for its yellow color:

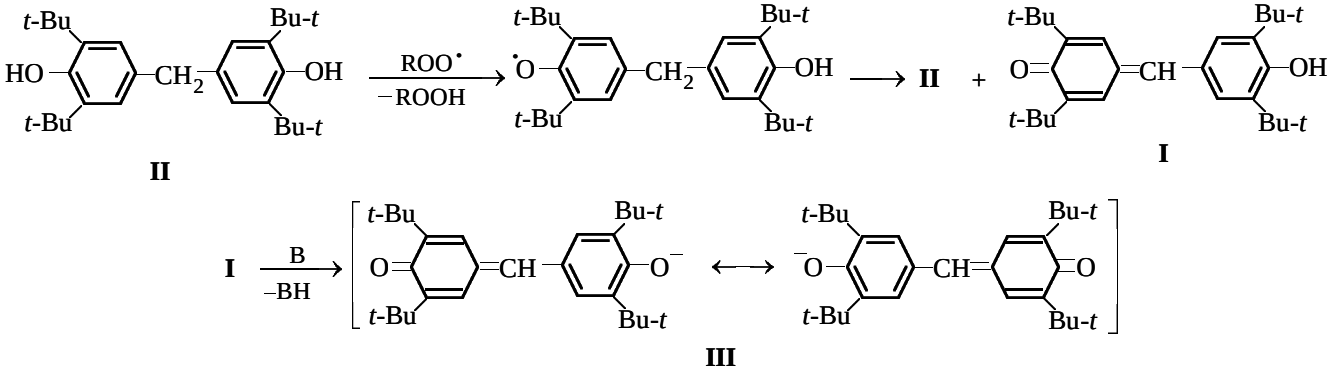

Methylenequinones in which substituents at the α-C atom are weaker electron donors than 4-hydroxy-3,5-di-*tert*-butylphenyl absorb in the UV range only [6]; therefore, such antioxidants as 2,4,6-tris(3',5'-di-*tert*-butyl-4'-hydroxybenzyl)mesitylene (Ionox-330) and pentaerythritol tetrakis[β-(3,5-di-*tert*-butyl-4-hydroxyphenyl)propionate] (Irganox 1010) do not cause the polymer coloration.

Furthermore, in some cases di(hydroxyphenyl)-methane stabilizers can cause deeper (violet) coloration of polymers [7, 8] owing to ready formation of

1070-4272/03/7609-1519$25.00

mesomeric anions of type **III** from α-hydroxyphenyl-substituted methylenequinones under the action of basic components present in polymeric formulations or on surface contact with bases [9].

Thus, to develop noncoloring stabilizing formulations based on di(hydroxyphenyl)methane stabilizers, it is necessary to prevent accumulation of α-hydroxyphenylmethylenequinoid products, so as to avoid yellow coloration produced by these products themselves and to exclude formation of intensely colored mesomeric anions.

In this work, our examined the possibility of solving the problem by converting α-hydroxyphenylmethylenequinones into colorless products. It is known that sterically hindered methylenequinones are highly reactive toward nucleophilic agents [10] and readily form colorless addition products. It seemed appropriate to test for this purpose various commercially available alcohols, amines, mercaptans, or phosphites. In particular, it is well known that addition of phosphites eliminates coloration of polymers owing to conversion of colored quinoid compounds into colorless benzoid derivatives [11].

However, experiments with hydrogalvinoxyl **I** as a model α-hydroxyphenyl-substituted methylenequinone showed that prolonged contact at 20°C or refluxing of its solutions with mono- and diethanolamines, diphenylguanidine, diethylhydroxylamine, tri(2,4,6-di-*tert*-butylphenyl) phosphite, and dimethyl hydrogen phosphite did not result in decolorization. Upon dissolution of **I** in ethanol, a certain amount of the addition product did form, as indicated by thin-layer chromatography, but longer contact, refluxing, and addition of an acid did not result in exhaustion of **I**.

Individual adducts with morpholine (**IV**) and water (**V**) were obtained by reactions of **I** with excess aqueous ammonia and morpholine, respectively.

Products **IV** and **V** are stable in the crystalline form, but more or less rapidly decompose in chloroform, benzene, alcohol, acetone, and DMSO with regeneration of **I**. Decomposition occurs more actively in polar solvents and on adding an acid.

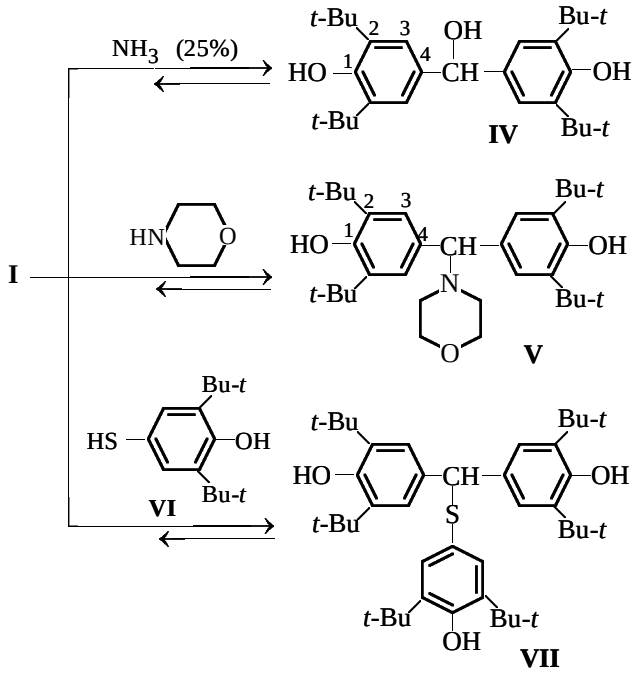

Komissarov *et al.* reported that substituted di(hydroxyphenyl)methane derivatives in which one of the hydroxy groups is in *o*-position relative to methine carbon atom reversibly dissociate in polar solvents [12, 13]. They believe that dissociation is due to concerted proton transfer involving a solvent molecule:

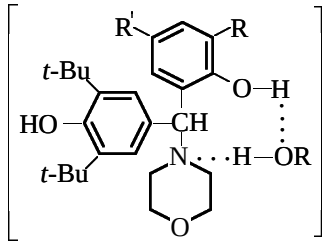

Our data show that the presence of protic solvents and *o*-position of one of hydroxy groups are not necessary conditions for such dissociation. Apparently, the driving force of the process is the high stability of the intermediate di(hydroxyphenyl)methyl carbocation **A**, promoting dissociation even in solvents uncapable of specific solvation:

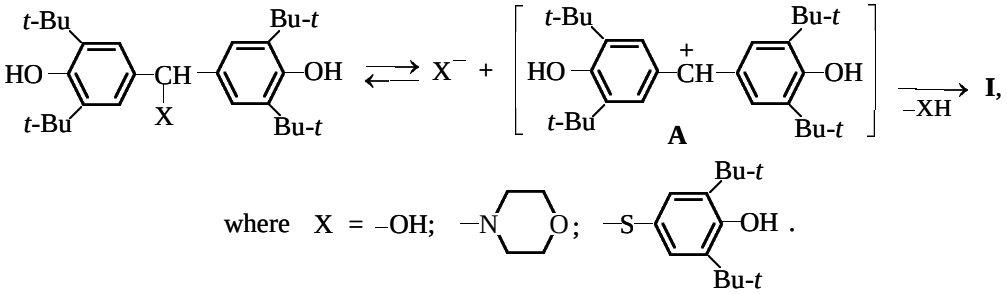

Table 1. Color stability of HDPE in the presence of stabilizers

Stabilizer	*c*, wt %	Color, points	
		after extrusion	after thermal aging (175°C, 8 h)
Irganox 1010	0.1	1	1
VIII	0.1	2–3	5
VIII + **VI**	0.05 ± 0.05	1	3

Table 2. Color stability and heat resistance of BR in the presence of stabilizers (170°C)

Stabilizer	*c*, wt %	Induction period of oxidation τ, min	Color (points) after oxidation for indicated time, h					
			initial	1	2	3	4	5
None	–	30	1	1	2	2–3	3–4	3–4
IX	0.2	120	1	1	1–2	2	2–3	2–3
X	0.2	325	1	5	5–6	6	7	8
IX + **X**	0.1 ± 0.1	185	1	2	3	3–4	4	4
	0.067 ± 0.133	220	1	2	2–3	3	4	4

Adduct **VII** of **I** with 2,6-di-*tert*-butyl-4-mercaptophenol **VI** can be obtained even at equimolar ratio of the reactants. Adduct **VII** also partially dissociates in solutions to **I** and **VI**; however, in the solid phase, compound **VII** it is stable up to the melting point (192°C). This fact allows the use of mercaptophenol **VI** as a component of di(hydroxyphenyl)methane-based stabilizing formulations that do not impart color to polymers. The α-hydroxyphenylmethylenequinoid compounds formed by inhibited oxidation of the stabilizers can react with **VI** to give colorless products stable in the course of processing of the polymer melt and service of polymer items. For example, extrusion at 190°C of high-density polyethylene (HDPE) containing a di(hydroxyphenyl)methane stabilizer, 2,4,6-tris(3',5'-di-*tert*-butyl-4'-hydroxybenzyl)resorcinol **VIII**, is accompanied by coloration of the polymer. At the same time, with the stabilizing formulation consisting of **VIII** and **VI**, the initial color of the polymer can be preserved in the course of extrusion (Table 1).

Apparently, the intensity of accumulation of colored α-hydroxyphenylmethylenequinone can be substantially reduced by introducing compounds that decompose hydroperoxides without generation of free radicals. Such compounds, e.g., phosphorous acid esters, suppress degenerate branching of oxidation chains and hence inhibit consumption of phenolic stabilizers and formation of methylenequinones [14].

We examined the influence exerted by an aromatic phosphite, tris(2,4-di-*tert*-butylphenyl) phosphite **IX**, on the color stability and heat resistance of polymeric formulations based on butyl rubber (BR) and ethylene–propylene rubber (SKEPT), containing di(2-hydroxy-3-*tert*-butyl-5-methylphenyl)methane **X**, and of HDPE stabilized with 2,4,6-tris(3',5'-di-*tert*-butyl-4'-hydroxybenzyl)resorcinol **VIII**:

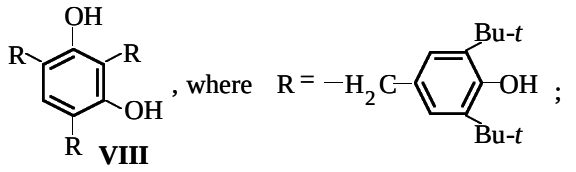

VIII

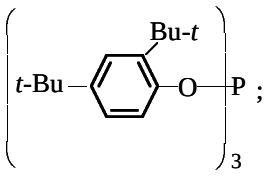

IX

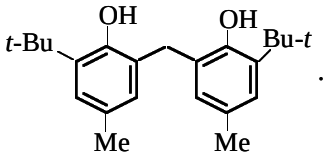

X

Long-term tests of BR (exposure to air for 6 months at room temperature) showed that the samples containing phosphite **IX** did not change color, whereas the polymer stabilized only with **X** became light brown. The parameters of the color stability and heat resistance of BR in the course of oxidation at 170°C are listed in Table 2, showing an additive thermostabilizing effect of the mixed formulations and a significant color-stabilizing effect of phosphite **IX**. Similar trends are observed with the phenol **X**–phosphite **IX** formulation used for stabilization of SKEPT rubber (Table 3).

Table 3. Color stability and heat resistance of SKEPT rubber in the presence of stabilizers (150°C)

Stabilizer	*c*, wt %	Induction period of oxidation τ, min	Color (points) after oxidation for indicated time, h			
			initial	1	2	3
None	–	15	1	–	–	–
IX	0.2	100	2	2	2	3
X	0.2	225	2	4	5	7
IX + **X**	0.1 + 0.1	185	2	2	2	3

Table 4. Color stability and heat resistance of HDPE in the presence of stabilizers (195°C)

Stabilizer	*c*, wt %	Induction period of oxidation τ, min	Color (points) after oxidation for indicated time, h			
			initial	1	2	3
None	–	15	1	1	1	2
Irganox 1010	0.1	115	1	1	1–2	2
VIII	0.1	165	2	2	3	3
VIII	0.2	390	2	2	3	3
IX	0.2	15	1	1	1	1–2
IX + VIII	0.067 + 0.133	215	1	2	2	3
	0.1 + 0.1	195	1	2	2	2

A combination of phenol **VIII** with phosphite **IX** in HDPE exhibits a small synergistic thermostabilizing effect and also enhances the color resistance of this polymer (Table 4). This formulation is not inferior or in performance to Irganox 1010.

Thus, addition of hydrolysis-resistant aromatic phosphite **IX** enhances the color stability of polymers stabilized with di(hydroxyphenyl)methane stabilizers. The color-stabilizing effect of phosphite **IX**, taking into account its inertness toward model α-hydroxyphenylmethylenequinone **I**, should be attributed to the capability of **IX** to suppress degenerate branching of oxidation chain by decomposing hydroperoxides without radical generation.

EXPERIMENTAL

In our study we used nonstabilized samples of commercial gas-phase HDPE (brand 289) and of BR-1675 rubber. SKEPT-40 ethylene–propylene rubber was treated with a 3 : 7 toluene–ethanol mixture for 9 h in a Soxhlet apparatus to extract additives. The stabilizers were added with stirring into 10% pentane solutions of the rubbers. After stirring for 40–60 min (to complete dissolution of the additive), the solvent was evaporated in a vacuum oven. Into HDPE, stabilizers were introduced with rollers (160±5°C, 5± 1 min) or from solutions, by thorough mixing with a polyethylene powder in a porcelain cup at room temperature to complete evaporation of the solvent, followed by drying in a vacuum oven to constant weight.

Extrusion of HDPE was performed with an IIRT capillary viscometer (capillary diameter 2.095± 0.005 mm) at 190±0.5°C and a load of 5 kgf, after keeping for 5 min in the heated device.

Thermal oxidation of polymeric compounds was performed on a manometric unit in oxygen at 150–195°C, P_{O_2} = 250 mm Hg. The sample weight was ~100 mg. The dependences $\Delta P_{O_2} = f(\tau_0)$ were plotted, and the induction periods of oxidation were determined from the slopes. The color of polymer samples was evaluated using a 10-point scale (1, white; 10, black) after thermal oxidation in air at 150–195°C.

The ^{1}H and ^{13}C NMR spectra were recorded on a Varian Gemini 200 spectrometer (working frequency 200 and 50 MHz for ^{1}H and ^{13}C, respectively) relative to residual protons of deuterated solvents.

Di(3,5-di-*tert*-butyl-4-hydroxyphenyl)hydroxymethane IV. To a solution of 1 g of hydrogalvinoxyl **I** in 50 ml of acetone, we added 30 ml of 25% aqueous ammonia and left overnight. The white precipitate was filtered off, washed with water, and dried. Yield 0.73 g (70%), mp 222–225°C (with decomposition).

^{1}H NMR spectrum ($CDCl_3$), δ, ppm: 1.42 s (36H, CMe_3), 2.03 s (1H, OH), 4.41 s (1H, CH), 5.02 s (2H, OH), 7.13 s (4H, ArH). ^{13}C NMR spectrum ($CDCl_3$), δ_C, ppm: 30.5 (C*Me*$_3$), 34.5 (*C*Me$_3$), 64.1 (CH), 124.7 (C^3), 135.1 (C^4), 135.3 (C^2), 152.5 (C^1).

Found, %: C 78.85; H 10.36.
$C_{29}H_{44}O_3$.
Calculated, %: C 79.04; H 10.06.

***N*-[Di(3,5-di-*tert*-butyl-4-hydroxyphenyl)]methylmorpholine V.** A 0.15-g portions of **I** was dissolved in 1 ml of acetone, and 10 ml of morpholine was added. The solution first turned red and then quickly became colorless. After that, 70 ml of water was added, and the white precipitate was filtered off, washed with water, and dried. The product gets slightly yellow in the course of isolation. Yield 0.162 g (89.5%), mp 150–162°C (with decomposition). ^{1}H NMR spectrum ($CDCl_3$), δ, ppm: 1.42 s (36H, CMe_3), 2.29 t (4H, CH_2N, J^3 4.6 Hz), 3.68 t (4H, CH_2O, J^3 4.6 Hz), 3.97 s (1H, CH), 5.04 s (2H, OH), 7.22 s (4H, ArH). ^{13}C NMR spectrum ($CDCl_3$), δ_C, ppm: 30.5 (C*Me*$_3$), 34.4 (*C*Me$_3$), 53.4 (CH_2N), 67.5 (CH), 77.6 (CH_2O), 125.0 (C^3), 134.4 (C^4), 136.1 (C^2), 151.3 (C^1).

Found, %: C 78.15; H 10.36; N 2.30.
$C_{33}H_{51}O_3N$.
Calculated, %: C 77.75; H 10.08; N 2.75.

(3,5-Di-*tert*-butyl-4-hydroxyphenylthio)bis(3′,5′-di-*tert*-butyl-4′-hydroxyphenyl)methane VII. A 1-g portion of **I** and 0.56 g of mercaptophenol **VI** were dissolved in 5 ml of acetone. A white precipitate started to form immediately. The mixture was stirred for 0.5 h. The precipitate was filtered off, washed with acetone, and dried. Yield 1.4 g (90%), mp 190–192°C. ^{1}H NMR spectrum ($CDCl_3$), δ, ppm: 1.30 s (18H, CMe_3), 1.41 s (36H, CMe_3), 5.04 s (2H, OH), 5.05 s (1H, OH), 5.19 s (1H, CH), 6.98 s (2H, ArH), 7.21 s (4H, ArH).

Found, %: C 78.51; H 9.82; S 4.61.
$C_{43}H_{64}O_3S$.
Calculated, %: C 78.13; H 9.76; S 4.85.

CONCLUSIONS

(1) Mercaptophenol **VI** forms colorless adducts with α-hydroxyphenylmethylenequinoid compounds and thus shows promised as a component of noncoloring stabilizing formulations based on di(hydroxyphenyl)methane stabilizers.

(2) Addition of aromatic phosphite **IX** as an agent decomposing hydroperoxides without radical generation and inhibiting formation of α-hydroxyphenylmethylenequinones enhances the color stability of polymers stabilized with di(hydroxyphenyl)methane stabilizers.

REFERENCES

1. Mukmeneva, N.A., *Doctoral Dissertation*, Kazan, 1981.
2. Gurvich, Ya.A., Zolotarevskaya, L.K., and Kumok, S.T., *Fenol'nye stabilizatory: Tematicheskii obzor* (Phenolic Stabilizers: A Topical Review), Moscow: TsNIITEneftekhim, 1978.
3. Gurvich, A.Ya. and Kumok, S.T., *Fenol'nye stabilizatory. Sostoyanie i perspektivy: Tematicheskii obzor* (Phenolic Stabilizers. State of the Art and Prospects: A Topical Review), Moscow: TsNIITEneftekhim, 1990.
4. Botez, C., *Ind. Usoara*, 1974, vol. 21, no. 12, pp. 622–624.
5. Volod'kin, A.A., Ostapets-Sveshnikova, G.D., and Ershov, V.V., in *Sintez i issledovanie effektivnosti khimikatov dlya polimernykh materialov* (Synthesis and Study of Performance of Chemicals for Polymeric Materials), Tambov: NII Khimpolimer, 1970, issue 4, pp. 78–81.
6. Ershov, V.V., Nikiforov, G.A., and Volod'kin, A.A., *Prostranstvenno-zatrudnennye fenoly* (Sterically Hindered Phenols), Moscow: Khimiya, 1972.
7. Afanas'ev, S.V., Lazareva, E.P., and Zhdanova, A.N., *Vestn. Mosk. Univ., Ser. 2: Khim.*, 1989, vol. 30, no. 4, pp. 406–408.
8. Afanas'ev, S.V., *Kauchuk Rezina*, 1994, no. 4, pp. 20–22.
9. Bukharov, S.V., Pod'yachev, S.N., Syakaev, V.V., and Zgadzai, O.E., *Zh. Obshch. Khim.*, 1998, vol. 68, no. 3, pp. 461–466.
10. Volod'kin, A.A. and Ershov, V.V., *Usp. Khim.*, 1988, vol. 57, no. 4, pp. 595–624.
11. Kirpichnikov, P.A., Mukmeneva, N.A., and Pobedimskii, D.G., *Usp. Khim.*, 1983, vol. 52, no. 11, pp. 1831–1851.
12. Komissarov, V.N., Abstracts of Papers, *Vsesoyuznaya konferentsiya po khimii khinonov i khinoidnykh soedinenii* (All-Union Conf. on Chemistry of Quinones and Quinoid Compounds), Novosibirsk, 1991, pp. 15–16.
13. Komissarov, V.N., Kharlanov, V.A., Ukhin, L.Yu., *et al.*, *Zh. Org. Khim.*, 1992, vol. 28, no. 3, pp. 513–517.
14. Emanuel', N.M. and Buchachenko, A.L., *Khimicheskaya fizika stareniya i stabilizatsii polimerov* (Chemical Physics of Aging and Stabilization of Polymers), Moscow: Nauka, 1988.

Russian Journal of Applied Chemistry, Vol. 76, No. 9, 2003, pp. 1524–1526. Translated from Zhurnal Prikladnoi Khimii, Vol. 76, No. 9, 2003, pp. 1563–1565.

BRIEF COMMUNICATIONS

Electrodeposition of Nickel–Tungsten Alloy from Acetate Electrolyte

I. G. Kapralova, Yu. P. Perelygin, and T. K. Semchenko

Penza State University, Penza, Russia

Received April 28, 2003

Abstract—Deposition of coatings of nickel–tungsten alloys from acetate electrolyte was studied. The dependences of the relative content of components in the alloy on the electrolysis conditions were elucidated.

Electrolytic nickel–tungsten alloys are characterized by high wear resistance, elevated microrigidity, and corrosion resistance in a wide temperature range [1].

Electrolytic deposition of nickel–tungsten alloys is performed at elevated temperatures at high current densities over a wide range of pH from solutions containing tartrate, diphosphate, citrate, sulfamate, and sulfosalicylate ions in the absence and in the presence of ammonium ions, and borate ions in combination with hydrogen peroxide [2]. The rate of alloy deposition and the content of tungsten in the alloys can be increased by using current pulses [3].

It is of a certain scientific and applied interest to study the possibility of electroplating of nickel–tungsten alloys from acetate solution, since the acetate nickel–plating electrolyte has been studied fairly comprehensively and has some advantages over other known nickel–plating electrolytes.

We studied the deposition of nickel–tungsten alloy in a 200-ml rectangular cell using insoluble graphite or platinum anodes. The electrolyte had the following composition (g l^{-1}): nickel acetate (in terms of the metal) 50, sodium tungstate (in terms of the metal) 10, sodium acetate 100, and saccharin 1. The deposition was carried out at 20°C, current density of 10 A dm^{-2}, and pH 4.

The nickel content in alloys was determined by EDTA titration. The tungsten content was determined photocolorimetrically with potassium thiocyanate [7]. The internal stresses in coatings were evaluated by the method of flexible cathode [8], and the wear resistance, by the procedure described in [9]. The results were treated by the least-squares method using relationships given in [10] and the software from [11]. The correlation coefficient of the equations given below is 0.98–0.99.

An increase in the tungsten(VI) concentration in the electrolyte results in cracking of coating, increase in its luster, decrease in the current efficiency (CE) by the alloy, and increase in the tungsten content in the coating (see table). The correlation between the component ratio in the alloy and the ratio of the ion concentrations in the electrolyte is described by the Akhumov–Rozen equation [12]

$$\log[\mathrm{Ni}]/[\mathrm{W}] = 0.55 + 0.707\log[\mathrm{Ni}^{2+}]/[\mathrm{W}^{6+}].$$

Introduction of saccharin into the electrolyte (1 g l^{-1}) decreases the internal stresses in the alloy coating from 250 to 170 MPa, and addition of 1,4-butynediol (5 ml l^{-1}) further decreases the internal stresses to 18.6 MPa, with the coatings becoming semilustrous. The coating composition and current efficiency are affected by these additives insignificantly.

The influence of the cathodic current density, temperature, and pH of solution were studied using an electrolyte containing 10 g l^{-1} of tungsten.

An increase in the current density from 7.5 to 12.5 A dm^{-2} results in a decrease in the tungsten content in the alloy from 12 to 7% (Fig. 1a, curve *1*), with the current efficiency increasing from 26 to 50% (Fig. 1b, curve *1*). The dependence of the ratio between the component contents in the alloy on the cathodic current density i_c (A dm^{-2}) is described by the equation [10]

$$\log[\mathrm{Ni}]/[\mathrm{W}] = -0.15 + 1.15\log i_c.$$

As the temperature increases from 10 to 40°C, the content of the highmelting component in the alloy decreases from 20 to 4.5% (Fig. 1a, curve *2*), with the cathodic current efficiency increasing from 6.5 to 45% (Fig. 1b, curve *2*). The dependence of the component ratio in the alloy on temperature T (K) is described

1070-4272/03/7609-1524$25.00

Influence of tungsten(VI) content in the electrolyte on the coating morphology and deposition parameters

Component content				CE by alloy, %	Appearance of coating
in electrolyte, g l^{-1}		in alloy, %			
Ni(II)	W(VI)	Ni(II)	W(VI)		
50	5	95	5	32	Dull
50	10	91	9	30	Semilustrous
50	15	89	11	27	Semilustrous
50	20	88	12	22	Semilustrous

by the equation [10]

$$\log[\mathrm{Ni}]/[\mathrm{W}] = 8.2 - 2132/T.$$

The change in pH of the solution from 3 to 5 results in an increase in the current efficiency from 21 to 42% (Fig. 1b, curve *3*) and in a decrease in the tungsten content from 20 to 5% (Fig. 1a, curve *3*).

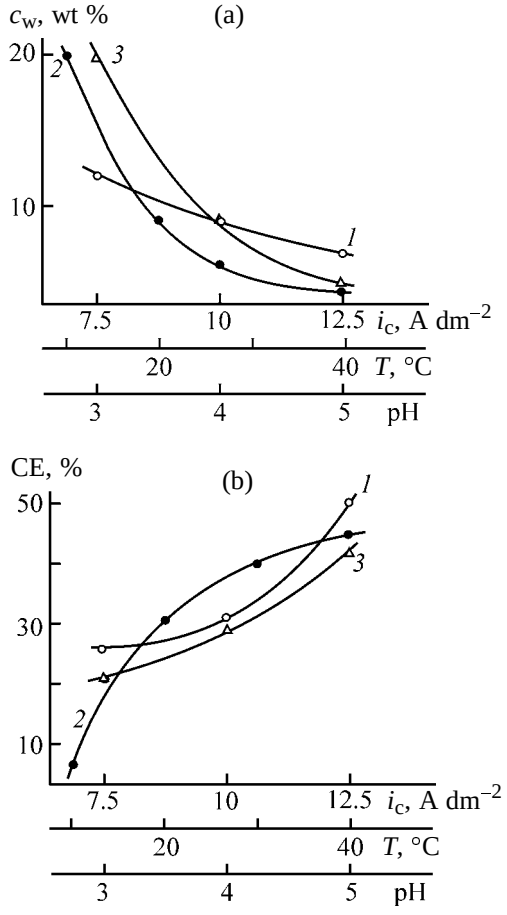

Fig. 1. Plots of (a) tungsten content c_W in the alloy and (b) current efficiency by the alloy vs. (*1*) current density i_c, (*2*) pH, and (*3*) temperature T.

The dependence of the component ratio on pH in the range under study is described by the equation [10]

$$\log[\mathrm{Ni}]/[\mathrm{W}] = -0.4 + 0.4\mathrm{pH}.$$

The alloy is not deposited to an appreciable extent from the electrolyte with pH less than 2, and a precipitate is gradually formed in this electrolyte.

An increase in the sodium acetate concentration from 100 to 150 g l^{-1} does not affect the alloy composition, but results in an increase in the current efficiency from 30 to 40%.

Thus, to obtain semilustrous coatings containing from 5 to 20% tungsten, we can recommend the electrolyte of the following composition (g l^{-1}): nickel acetate (in terms of the metal) 50, sodium tungstate (in terms of the metal) 5–20, sodium acetate 100–150; pH 3–5. The coating is deposited at 20–40°C and cathodic current density of 10–12.5 A dm^{-2} using insoluble platinum anodes. The current efficiency by the alloy under these conditions is 30–50%.

The wear resistance of the plated alloy containing 9% W exceeds the resistance of pure nickel by a factor of 10.

REFERENCES

1. Vas'ko, A.T., *Elektrokhimiya molibdena i vol'frama* (Electrochemistry of Molybdenum and Tungsten), Kiev: Naukova Dumka, 1977.
2. Purovskaya, O.G., Stepanova, L.I., and Ivashkevich, L.S., *Gal'vanotekh. Obrab. Poverkhn.*, 1977, vol. 5, no. 1, p. 25.
3. Gryaznova, T.I., Kotov, V.L., and Krivitskaya, A.K., in *Teoriya i praktika elektroosazhdeniya metallov i splavov: Materialy seminara* (Theory and Practice of Electrodeposition of Metals and Alloys: Proc. Workshop), Penza: Dom Nauchno-Tekh. Propagandy, 1983.

4. Kudryavtsev, N.T., Loseva, E.I., Tsupak, T.E., and Mel'nikov, V.V., *Izv. Akad. Nauk Latv. SSR, Ser. Khim.*, 1980, no. 3, pp. 301–303.
5. Bek, R.Yu., Tsupak, T.E., Borodikhina, L.I., and Nguen Zui Shi, *Elektrokhimiya*, 1983, vol. 19, no. 9, p. 1149.
6. Tsupak, T.E., Andreev, I.N., Valeev, I.N., and Nguen Zui Shi, *Zh. Prikl. Khim.*, 1985, vol. 58, no. 2, pp. 392–394.
7. Vyacheslavov, P.M., *Novye elektrokhimicheskie pokrytiya* (New Electroplated Coatings), Leningrad: Lenizdat, 1972.
8. Popereka, M.Ya., *Vnutrennie napryazheniya elektricheski osazhdaemykh metallov* (Internal Stresses in Electroplated Metals), Novosibirsk: Nauka, 1966.
9. Vinogradov, S.N. and Shumilina, N.I., *Zashch. Met.*, 1976, vol. 12, no. 4, pp. 482–484.
10. Perelygin, Yu.P., *Elektrokhimiya: Raspredelenie toka na elektrode pri odnovremennom protekanii neskol'kikh reaktsii* (Electrochemistry: Current Distribution over an Electrode with Several Reactions Occurring Simultaneously), Penza: Penz. Tekh. Univ., 1997.
11. D'yakonov, V.P., *Spravochnik po algoritmam i programmam na yazyke Beisik dlya personal'nykh EVM* (Handbook of Algorithms and Programs in BASIC for Personal Computers), Moscow: Nauka, 1987.
12. Akhumov, E.I. and Rozen, B.Ya., *Dokl. Akad. Nauk SSSR*, 1956, vol. 109, no. 6, pp. 1149–1151.

Russian Journal of Applied Chemistry, Vol. 76, No. 9, 2003, pp. 1527–1529. Translated from Zhurnal Prikladnoi Khimii, Vol. 76, No. 9, 2003, pp. 1566–1568.

BRIEF COMMUNICATIONS

Identification of Ethylenediamine-*N*,*N*'-bis(isopropylphosphonic) Acid by X-ray Diffraction

E. G. Afonin and G. G. Aleksandrov

Laboratory of Chemical Engineering, State Enterprise, Kaluga, Russia
Kurnakov Institute of General and Inorganic Chemistry, Russian Academy of Sciences, Moscow, Russia

Received May 6, 2003

Abstract—A powder X-ray diffraction study of a polycrystalline sample of ethylenediamine-*N*,*N*'-bis(isopropylphosphonic) acid dihydrate (Phosphicine drug) isolated from aqueous solution showed that the product is single-phase. The diffraction pattern allows identification and detection of Phosphicine in mixtures with other substances. The thermal transformations of the compound were studied by differential thermal and thermal gravimetric analyses.

Ethylenediamine-*N*,*N*'-bis(isopropylphosphonic) acid, $H_2O_3P–C(CH_3)_2–NH–CH_2CH_2–NH–C(CH_3)_2–PO_3H_2$ (H_4L, Phosphicine) has very low toxicity and is used in medicine as antidote against toxic and radioactive metals [1, 2]. H_4L forms in aqueous solutions stable complexes with bi- and trivalent metal cations, showing selectivity with respect to Cu^{2+} ions [2–4]. The solid complexes $KLnL \cdot nH_2O$ [5] and $CuH_2L \cdot 2H_2O$ [6] were prepared; the structure of the copper complex was determined by single crystal X-ray diffraction [6].

In this work, we examined the possibility of identifying ethylenediamine-*N*,*N*'-bis(isopropylphosphonic) acid by powder X-ray diffraction.

EXPERIMENTAL

The powder X-ray diffraction patterns were taken on a DRON-3M diffractometer (Ni-filtered CuK_α radiation, 2θ 2°–60°). Thermal analysis was performed with an OD-103 derivatograph (quartz crucible, sample weight 100 mg) in air in the range 20–500°C at a heating rate of 2.5 deg min^{-1}. The temperature of the onset of H_4L decomposition was determined by the procedure described in [7].

$H_4L \cdot 2H_2O$ [TU (Technical Specification) 6-09-14-1806–75] was of pure grade. The substance was additionally purified by double precipitation from an alkaline solution with a mineral acid. For this purpose, $H_4L \cdot 2H_2O$ was dissolved in 10% NaOH, which was added dropwise, acidified with 1 M HCl to pH 2, and left overnight. After that, the crystalline precipitate was filtered off with a glass frit at reduced pressure, washed with water to negative reaction of wash waters for Cl^- and then with ethanol, and dried at room temperature to constant weight.

Found, %: C 27.8, H 7.4, N 8.0, P 18.2.
$C_8H_{26}N_2O_8P_2$.
Calculated, %: C 28.24, H 7.70, N 8.23, P 18.21.

Ethylenediamine-*N*,*N*'-bis(isopropylphosphonic) acid crystallizes from aqueous solutions at room temperature in the form of $H_4L \cdot 2H_2O$. Its experimental powder X-ray diffraction pattern coincides with that calculated from the single crystal X-ray diffraction data for this compound [8, 9] (see table), which indicates, in combination with the analytical data, that the polycrystalline sample is single-phase. The X-ray diffraction pattern contains no foreign reflections with the intensity $I \geq 0.5\%$.

$H_4L \cdot 2H_2O$ is poorly soluble in water, DMSO, DMF, acetic acid, ethanol, isopropanol, glycerol, acetone, chloroform, and benzene. It passes into solution under the action of 1 M solutions of ammonia, alkalis, sodium carbonate, sodium hydrogen carbonate, and mineral acids.

Thermal analysis shows that $H_4L \cdot 2H_2O$ starts to lose water of crystallization at 70°C. The first water molecule is eliminated fast at a relatively low temperature. Further dehydration (DTA_{min} 130°C) is slow; in particular, at 160°C in 1 h $H_4L \cdot 2H_2O$ loses 1.45 water molecules, and the constant weight loss value of 10.2% corresponding to the loss of 1.9 H_2O molecules is attained only after heating for no less than

1070-4272/03/7609-1527$25.00

Powder X-ray diffraction pattern of ethylenediamine-*N*,*N*'-bis(isopropylphosphonic) acid dihydrate*

hkl	Found		Calculated		*hkl*	Found		Calculated	
	d, Å	*I*, %	*d*, Å	*I*, %		*d*, Å	*I*, %	*d*, Å	*I*, %
100	9.17	100	9.176	99	042			2.246	1.5
020	6.42	14	6.419	85	$\bar{1}60$	2.239	3	2.238	16
$\bar{1}20$	6.22	0.8	6.211	4	$\bar{4}11$			2.231	3
011	5.65	8	5.648	52	$\bar{3}22$			2.227	1.9
$\bar{1}11$	5.13	9	5.123	57	$\bar{2}60$	2.209	1.0	2.211	5
200	4.589	36	4.588	24	$\bar{4}40$			2.207	1.5
111	4.557	18	4.549	100	$\bar{3}51$			2.197	4
$\bar{2}20$	4.417	2	4.414	10	302	2.195	0.9	2.193	1.92
$\bar{2}11$	3.821	5	3.817	20	$\bar{4}31$			2.190	4
$\bar{1}31$	3.624	3	3.617	18	331	2.069	0.6	2.073	2
031	3.542	1.4	3.538	7	013			2.069	3
$\bar{1}40$	3.358	13	3.361	39	411	2.030	0.2	2.034	4
211			3.351	41	$\bar{3}42$			2.026	1.6
220	3.297	1.0	3.293	3	113			1.998	2
$\bar{2}31$	3.216	0.8	3.215	4	160	1.957	0.2	1.957	3
040			3.209	1.1	322			1.950	4
$\bar{3}20$	3.149	4	3.154	7	$\bar{5}20$	1.925	1.6	1.924	6
002			3.145	15	$\bar{2}13$			1.922	1.9
131	3.058	4	3.056	1.7	$\bar{4}22$	1.907	1.0	1.909	1.5
102	2.969	0.3	2.975	3	251			1.905	1.4
$\bar{3}11$	2.856	1.6	2.852	8	$\bar{1}33$	1.881	0.3	1.894	1.6
022	2.826	1.0	2.824	12	033			1.883	1.6
$\bar{1}22$	2.785	3	2.086	5	213	1.854	0.4	1.853	4
140			2.780	18	$\bar{1}71$			1.830	4
$\bar{3}31$	2.665	0.8	2.665	14	$\bar{5}31$	1.831	0.5	1825	1.5
$\bar{3}40$	2.640	0.6	2.648	2	$\bar{1}62$			1.823	1.1
122	2.604	0.2	2.604	3	$\bar{4}42$	1.803	0.2	1.806	1.1
202			2.594	1.3	071	1.764	0.4	1.761	1.8
$\bar{2}22$	2.557	0.6	2.561	1.5	$\bar{3}13$			1.754	1.6
311			2.552	1.3	431	1.738	0.2	1.737	1.4
231	2.519	0.8	2.515	8	$\bar{3}62$			1.729	2
$\bar{1}51$	2.475	0.5	2.475	6	$\bar{3}33$	1.707	0.1	1.708	2
$\bar{2}51$	2.402	0.3	2.402	2	$\bar{5}51$			1.700	1.1
051	2.378	0.6	2.377	6	162	1.663	0.3	1.662	1.3
$\bar{1}42$			2.297	1.1	$\bar{5}22$	1.641	0.3	1.641	1.7
222	2.274	1.0	2.274	8	$\bar{3}53$	1.560	0.2	1.563	1.3
					$\bar{4}80$	1.554	0.3	1.553	1.1

* (*d*) Interplanar spacings corresponding to the reflections with the relative intensities $I \geq 1\%$.

5–6 h. Thermal decomposition of H_4L becomes noticeable rate even at 180°C (DTA_{min} 190, 205°C). Further heating is accompanied by a major weight loss due to release of gaseous pyrolysis products (DTA_{min} 340°C), with cleavage of the C–P bonds in the H_4L molecule. Medved' and Rudomino [10] reported for the compound the melting point of 235–236°C, but we revealed no endothermic effect in the DTA curve in this temperature region.

CONCLUSIONS

(1) Thermal analysis of ethylenediamine-*N*,*N*'-bis-(isopropylphosphonic) acid dihydrate showed that the compound has no well-defined dehydration, melting, and decomposition points suitable for identification.

(2) Powder X-ray diffraction allows reliable check of the phase purity of the compound and identification

of this compound in mixtures with other substances, in particular, in ready drug forms.

ACKNOWLEDGMENTS

The study was financially supported in part by ICDD.

REFERENCES

1. Arkhipova, O.G., Yur'eva, E.I., and Dyatlova, N.M., *Zh. Vses. Khim. O–va. im. D.I. Mendeleeva*, 1984, vol. 29, no. 3, pp. 316–320.
2. Dyatlova, N.M., Temkina, T.Ya., and Popov, K.I., *Kompleksony i kompleksonaty metallov* (Complexones and Metal Complexonates), Moscow: Khimiya, 1988.
3. Dyatlova, N.M., Temkina, V.Ya., and Kolpakova, I.D., *Kompleksony* (Complexones), Moscow: Khimiya, 1970.
4. Dyatlova, N.M., *Zh. Vses. Khim. O–va. im. D.I. Mendeleeva*, 1984, vol. 29, no. 3, pp. 247–260.
5. Khramov, V.P., *Kompleksonaty RZE* (REE Complexonates), Saratov: Saratov. Univ., 1974.
6. Shkol'nikova, L.M., Poznyak, A.L., Bel'skii, V.K., *et al.*, *Koord. Khim.*, 1986, vol. 12, no. 7, pp. 981–990.
7. Afonin, E.G., *Zh. Obshch. Khim.*, 2001, vol. 71, no. 1, pp. 83–86.
8. Polyanchuk, G.V., *Cand. Sci. Dissertation*, Moscow, 1986.
9. Shkol'nikova, L.M., Polyanchuk, G.V., Zavodnik, V.E., *et al.*, *Zh. Strukt. Khim.*, 1987, vol. 28, pp. 124–137.
10. Medved', T.Ya. and Rudomino, M.V., *Metody Poluch. Khim. Reakt. Prep.*, 1969, no. 18, pp. 224–227.

Russian Journal of Applied Chemistry, Vol. 76, No. 9, 2003, p. 1530. Translated from Zhurnal Prikladnoi Khimii, Vol. 76, No. 9, 2003, pp. 1569.

BRIEF COMMUNICATIONS

Synthesis of Monochloroacetic Acid from Ethylene Chlorohydrin

N. V. Svetlakov, V. G. Nikitin, and E. A. Nikolaeva

Kazan State Technological University, Kazan, Tatarstan, Russia

Received May 22, 2003

Abstract—The possibility of preparing monochloroacetic acid by oxidation of ethylene chlorohydrin with nitric acid was examined.

Monochloroacetic acid (MCAA) is widely used in production of polymers, pesticides, pharmaceuticals, etc. The main industrial and laboratory procedures for MCAA synthesis, and also its properties and application fields are described in [1]. The main industrial process for MCAA synthesis, chlorination of acetic acid, has a number of drawbacks; in particular, di- and trichloroacetic acids are formed as by-products, and their separation involves certain problems.

MCAA can be prepared by oxidation of ethylene chlorohydrin (ECH) with CrO_3 [2], but this procedure is of little promise for industrial use because of toxicity and high cost of the oxidant.

In this work, we prepared MCAA by oxidation of ECH with nitric acid, a readily available and relatively cheap oxidant used in industry for preparing carboxylic acids (e.g., oxalic, adipic) [3]. Oxidation of ECH was performed with 60–80% HNO_3; ECH was added at 20–25°C. The reaction was accompanied by slight warming-up and release of nitrogen oxides coloring the reaction mixture. After that, the temperature increased to 60–70°C, with vigorous evolution of nitrogen oxides.

ECH is oxidized with nitric acid to MCAA more difficultly compared to unsubstituted alcohols [3]. Presumably, oxidation of ECH with concentrated HNO_3 involves intermediate formation of ECH nitrates and nitrites [4, 5], which are relatively stable in an electrophilic medium. When kept in an acid solution, these ECH esters decompose to MCAA.

EXPERIMENTAL

The IR spectrum of MCAA in Vaseline oil was recorded on a UR-20 spectometer. The ^1H NMR spectrum of MCAA was taken in acetone-d_6 on a Tesla-497 spectrometer (working frequency 100 MHz) at room temperature against internal HMDS.

ECH was of pure grade; technical-grade 97% HNO_3 was diluted to the required concentration with distilled water.

To prepare monochloroacetic acid, ECH (17 g, 0.2 mol) was added with stirring at 20–25°C to 80% HNO_3 (63 g as calculated on 100% HNO_3, 1 mol). In the process, the temperature rose by 2–3°C, and nitrogen oxides (which were not analyzed) were released. After stirring for 0.5 h, the mixture became colorless owing to removal of nitrogen oxides. Then the stirring was stopped, and the temperature of the reaction mixture was controlled, so as to prevent self-heating above 60–70°C. After reaction completion, the mixture was stirred at 20°C to remove nitrogen oxides; unchanged HNO_3 and H_2O were distilled off in a water-jet-pump vacuum. The bottom residue was transferred into a beaker, in which it crystallized within 20–30 min. The crystalline precipitate was filtered off and dried in air; yield of MCAA 16.5 g (85%), mp 62°C [from chloroform; published data [1]: mp 63°C (α-modification)]. IR spectrum, ν, cm^{-1}: 1716, 2100–3250 (COOH). ^1H NMR spectrum, δ, ppm: 4.0 s (2H, CH_2Cl), 10.0 s (1H, COOH).

REFERENCES

1. Zanaveskin, L.N., Aver'yanov, V.A., Kunitsyn, D.G., and Bulanov, V.N., *Khim. Prom–st.*, 2001, no. 5, pp. 28–45.
2. *Dictionary of Organic Compounds*, Heilborn, I. and Banbury, H.M., Eds., London: Eyre and Spottiswoode, 1946, vol. 2. Translated under the title *Slovar' organicheskikh soedinenii*, Moscow: Inostrannaya Literatura, 1949, vol. 2, p. 29.
3. Freidlin, G.N., *Alifaticheskie dikarbonovye kisloty* (Aliphatic Dicarboxylic Acids), Moscow: Khimiya, 1978.
4. Orlova, E.Yu., *Khimiya i tekhnologiya brizantnykh vzryvchatykh veshchestv* (Chemistry and Technology of High Explosives), Moscow: Oborongiz, 1960, pp. 301–355.
5. *Comprehensive Organic Chemistry. The Synthesis and Reactions of Organic Compounds*, Barton, D. and Ollis, W.D., Eds., vol. 2: *Nitrogen Compounds*, Oxford: Pergamon, 1979.

1070-4272/03/7609-1530$25.00

Russian Journal of Applied Chemistry, Vol. 76, No. 9, 2003, pp. 1531–1533. Translated from Zhurnal Prikladnoi Khimii, Vol. 76, No. 9, 2003, pp. 1570–1572.

HISTORY OF CHEMISTRY AND CHEMICAL TECHNOLOGY

Professor Yakov Ivanovich Gerasimov

(to Centennial Anniversary of His Birthday)

Corresponding member of the Academy of Sciences of the USSR Yakov Ivanovich Gerasimov, a scientist, pedagogue, and research organizer, made an outstanding contribution to the development of physical chemistry and its most important branch, chemical thermodynamics, in our country. All his main scientific and pedagogical activities had been associated with the Moscow State University for more than 60 years.

Ya.I. Gerasimov was born on September 23, 1903, in Valdai, Novgorod province, into a doctor's family. Despite the early death of their father, the children were excellently educated and bred thanks to the efforts of their mother. Beginning in his childhood, the scientist-to-be was quite at home in English, French, and German, was familiar with history and literature, and practiced music. In 1920, he finished a secondary school in Rybinsk, Yaroslavl province, and in the same year entered the chemical division of the Physicomathematical Faculty of the Moscow University. Among the teachers with whom his was the closest were I.A. Kablukov (1857–1942) and A.V. Rakovskii (1879–1941). Kablukov was one of the first physical chemists and a contemporary of D.I. Mendeleev (1834–1907). He worked at A.M. Butlerov's (1828–1886) laboratory in St. Petersburg and W. Ostwald's (1853–1932) laboratory in Leipzig, was on friendly terms with S. Arrhenius (1859–1927) and well acquainted with van't Hoff (1852–1911), and made a major contribution to the development of the theory of solutions, thermochemistry, and other fields of physical chemistry and chemical engineering. He became an honorary member of the Academy of Sciences of the USSR in 1932. Particularly strong influence was exerted on the formation of Gerasimov's scientific view of the world by Rakovskii, whose main studies were concerned with problems of chemical thermodynamics and with heterogeneous equilibria. Rakovskii was the author of one of the best domestic textbooks of physical chemistry (1938) and became a corresponding member of the Academy of Sciences of the USSR in 1933.

Gerasimov graduated from the University in 1925; however, already beginning in 1923 he worked as laboratory assistant with Kablukov and performed

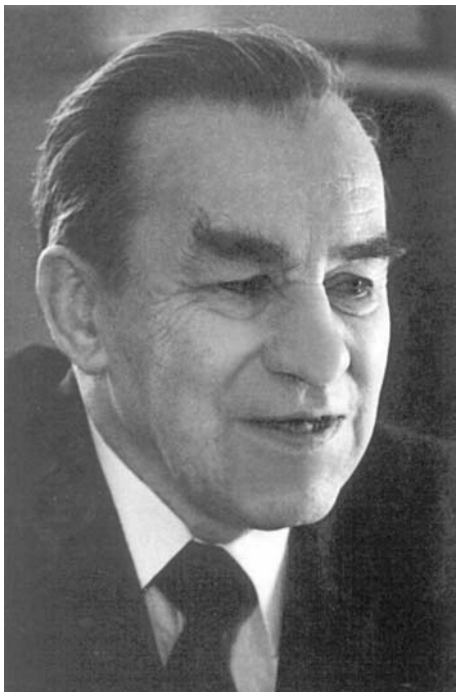

demonstrational experiments during his lectures. Later, Gerasimov made a scientific career from postgraduate student to professor (1942) and head of the chair of physical chemistry at the Moscow University (1952). He became candidate of chemistry in 1935 and doctor of chemistry in 1940. In October 1953, he was elected a corresponding member of the Academy of Sciences of the USSR (Division of Chemical Sciences, Physical Chemistry). In addition to working at the University, Gerasimov took an active part in research conducted at the Institute of Nonferrous Metals (Gintsvetmet), headed the Chemical Editorial Office at the State Publishing House for Foreign Literature, and delivered lectures at a number of higher school institutions in Moscow.

Gerasimov's scientific activities, commenced in 1925, were devoted to a wide variety of thermodynamic problems largely associated with the needs of the industrial practice. His studies of 1927–1934, concerned with equilibria in water–salt systems, were performed at laboratories of Moscow University and the Institute of Pure Chemical Reagents, where Rakovskii

1070-4272/03/7609-1531$25.00

worked. The first Gerasimov's publication was titled "On Synthesis of Chemically Pure Ammonium Bichromate" [*Trudy Instituta Chistykh Khimisheskikh Reaktivov* (Transactions of the Institute of Pure Chemical Reagents), 1927]. Rakovskii always demanded that the research techniques and results obtained should be highly reliable. This feature also became characteristic of his disciples [1].

Already in the early 1930s, Gerasimov commenced investigations in the field of thermodynamics of metallurgical systems and processes. Together with his co-workers, he studied heterogeneous equilibria involving sulfides and other compounds of zinc, lead, copper, nickel, and cobalt with hydrogen and carbon monoxide in order to obtain data on the thermodynamic characteristics of the corresponding processes. A number of original investigation techniques were developed. The results obtained in the series of metallurgical studies were summarized in Gerasimov's doctoral dissertation.

In 1932–1934, Gerasimov and A.N. Krestovnikov published a three-volume textbook *Khimicheskaya termodinamika v tsvetnoi metallurgii* (Chemical Thermodynamics in Nonferrous Metallurgy) presenting a vast body of reference data on thermodynamic properties of a large group of nonferrous metals and their most important compounds. Later (1960–1973), this book was much expanded (to seven volumes). The authors collected, treated, and critically assessed published evidence concerning the thermodynamic properties of hundreds of compounds that are of interest to chemists and metallurgists.

Of particular interest are reviews of topical publications, written by Gerasimov in different years: "Chemical Thermodynamics and Molecular Spectra" (*Usp. Khim.*, 1933, no. 4), "On Thermodynamics of Metal–Slag Equilibria" (*Stal'*, 1947, no. 1), "Activity of Metallic Oxides in Melts with Silica and Calcium Oxide" (*Stal'*, 1947, no. 5), and "Thermodynamic Properties of Solid and Liquid Metallic Melts and Their Relationship with Phase Diagrams" (*Zh. Fiz. Khim.*, 1967). All the reviews are characterized by rigorous and simple manner of presentation. Gerasimov was among those who initiated the introduction of statistical methods for calculation of thermodynamic quantities in our country.

Beginning in 1943, Gerasimov headed the laboratory of chemical thermodynamics at the chair of physical chemistry, Moscow State University. The main task of the laboratory during the postwar years was to search for heat-resistant materials and coatings, required by new technologies. In this context, wide-scale investigations of the thermodynamic properties of ferrites, tungstates, and molybdates were carried out. In the early 1950s, the emf method started to be used at the laboratory for studying the thermodynamic characteristics of liquid and solid metal alloys and, later, oxides and salts of rare metals. Solid electrolytes with anionic conduction (oxygen- and fluorine-ionic) found wide use together with molten and solid electrolytes with cationic conduction. The saturated vapor pressure was measured, and its molecular composition was studied, using versions of the Knudsen method. Rather advanced and diverse investigation techniques made it possible to expand substantially the variety of objects that could be studied. New data were obtained on the thermodynamic properties of quite a number of alkali metal containing alloys, chalcogenides, and alloys and compounds of rare-earth metals. The general goal of these studies was to create thermodynamic foundations of materials science. Calculation methods of chemical thermodynamics, combined with the known thermodynamic functions of substances, make it possible to prodict properties of a material synthesized from these substances. During the entire period of his scientific activities, Gerasimov always strove to introduce thermodynamic data into practice. This standpoint of the scientist was clearly reflected in his publications "Thermodynamics of Solutions at High Temperature and Its Use in Theoretical Metallurgy" (*Usp. Khim.*, 1945, no. 4) and "Chemical Thermodynamics and Some Promising Fields of Its Application" (in co-authorship with G.F. Voronin, *Vestn. Akad. Nauk SSSR*, 1970, no. 3). Gerasimov also wrote "Review of Research at the Laboratory of Chemical Thermodynamics, Chemical Faculty, Moscow State University" [2], in which particular attention was given to studies in the field of thermodynamics of intermetallic compounds and metal oxides, carried out at the laboratory in 1953. Studies of the preceding period of time were also briefly reviewed.

In 1981, Gerasimov was among those who were awarded a State Prize of the USSR for investigations in the field of thermodynamics.

During the entire period of his many-year pedagogical activities, Gerasimov paid much attention to improving the methods for teaching of physical chemistry at higher-school institutions of our country. He headed a group of authors, edited the whole manuscript, and wrote himself the chapters devoted to foundations of thermodynamics, thermodynamics of solutions, chemical equilibrium, and electrochemistry in creating a fundamental textbook *Kurs fizicheskoi khimii* (Course of Physical Chemistry) (two volumes, for chemical faculties of universities) published in two

editions (1963 and 1973) and translated into English, Spanish, Arabic, and Azerbaijani. Gerasimov paid much attention to methodological problems associated with teaching of physical chemistry. Of much interest are his papers "On the Object and Scope of Physical Chemistry" [3] and "On Some Fundamental Concepts of Thermodynamics" [4]. During many years, Gerasimov delivered a course of lectures in physical chemistry and special courses "Thermodynamics of Solutions" and "Selected Chapters of Thermodynamics." Together with V.A. Geiderikh, he wrote a book *Termodinamika rastvorov* (Thermodynamics of Solutions) (1980). Gerasimov translated into Russian or edited translations of numerous foreign publications. In particular, he was the scientific editor of translations of a two-volume course of physical chemistry by Moelwyn-Hughes (1962) and a monograph by A. Munster (1971).

A number of Gerasimov's papers were concerned with history of chemistry. These papers analyzed investigations of the solubility of carbon dioxide in salt solutions (1952) carried out by I.M. Sechenov (1829–1905), mutual solubility of liquids (1950) carried out by V.F. Alekseev (1852–1919), and adsorption and thermodynamics of irreversible processes (together with A.V. Kiselev, 1949) performed by Rakovskii.

During nearly 30 years, Gerasimov headed the largest chair of physical chemistry, which included 11 laboratories with more than 400 staff members. The scientist and pedagogue, he possessed exceptional personal qualities, being a good-wishing man adhering to his principles, with extensive life experience, and was greatly respected both in our country and abroad. Gerasimov conducted extensive scientific-organizational work. During many years, he headed the Scientific Council for chemical thermodynamics and thermochemistry of the Academy of Sciences of the USSR. For more than 25 years, till the end of his life, he was Editor-in-Chief of *Zhurnal Fizicheskoi Khimii* (Soviet, now Russian Journal of Physical Chemistry) published by the Academy of Sciences and a member of the editorial board of the international journal devoted to chemical thermodynamics (*Journal of Chemical Thermodynamics*). During 10 years he was a member of a committee of IUPAC. He knew personally, and maintained scientific contacts with most of the leading world's specialists in chemical thermodynamics.

For his services in the training of highly skilled scientists and pedagogues and in the development of the domestic science Gerasimov was honored with a number of State awards.

Yakov Ivanovich Gerasimov passed away on March 17, 1983 at the age of 79. The domestic chemical science suffered a grievous loss. In 1988, the Nauka publishing house published posthumously selected works of the scientist [5], prepared by staff members of the laboratory of chemical thermodynamics, Chemical Faculty, Moscow State University. The foreword of the collection of works mentioned that the main merit of Gerasimov and his school consists in that they developed experimental techniques for thermodynamic investigations and obtained, using these techniques, a large body of data on properties of various substances and materials of interest to science and technology.

All those who knew Yakov Ivanovich Gerasimov, a prominent scientist and excellent person, deeply respected and sincerely liked him.

REFERENCES

1. *Adam Vladislavovich Rakovskii*, Gerasimov, Ya.I., Ed., Moscow: Mosk. Otd. Vses. Khim. O–va. im. D.I. Mendeleeva, 1949.
2. Gerasimov, Ya.I., in *Sovremennye problemy fizicheskoi khimii* (Modern Problems of Physical Chemistry), Moscow: Mosk. Gos. Univ., 1972, pp. 3–33.
3. Gerasimov, Ya.I., *Vestn. Mosk. Gos. Univ., Ser. Matem., Mekh., Astronom., Fiz., Khim.*, 1956, no. 2, pp. 133–142.
4. Gerasimov, Ya.I., *Vestn. Mosk. Gos. Univ., Ser. Matem., Mekh., Astronom., Fiz., Khim.*, 1958, no. 1, pp. 177–181.
5. Gerasimov, Ya.I., *Izbrannye trudy: Obshchie voprosy fizicheskoi khimii i termodinamiki. Termodinamicheskie osnovy materialovedeniya* (Selected Works: General Problems of Physical Chemistry and Thermodynamics, Thermodynamic Foundations of Materials Science), Moscow: Nauka, 1988.

A. G. Morachevskii and G. F. Voronin

Russian Journal of Applied Chemistry, Vol. 76, No. 9, 2003, pp. 1534–1535. Translated from Zhurnal Prikladnoi Khimii, Vol. 76, No. 9, 2003, p. 1573–1574.

OBITUARIES

Professor Aleksandr Leonovich Rotinyan (1913–1991)

Aleksandr Leonovich Rotinyan, a remarkable person and prominent scientist who tirelessly paved new ways in electrochemical science and technology, a talented pedagogue who supplied Russia's electrochemical school with highly skilled specialists, would be 90. During many years he had been a member of the Editorial Board of *Zhurnal Prikladnoi Khimiii* (Soviet, now Russian Journal of Applied Chemistry) and took an active part in its work.

Aleksandr Leonovich Rotinyan was born on August 13, 1913, in St. Petersburg. His father, Leon Aleksandrovich Rotinyan (1879–1964), was a lecturer at the chair of physical chemistry and theoretical electrochemistry at the St. Petersburg Polytechnic Institute. Later, Professor L.A. Rotinyan, a known physical chemist, delivered lectures at a number of higher-school institutions of Russia.

In 1935, A.L. Rotinyan graduated from the Chemical Faculty of the Yerevan Polytechnic Institute, and in 1938, finished his postgraduate education at the Leningrad Polytechnic Institute. A.L. Rotinyan's scientific and pedagogical activities, which he commenced as docent at the Novocherkassk Polytechnic Institute, were interrupted by the beginning of the war. From June 1941 till September 1945 he served in Soviet Army and participated in action at the Leningrad Front. His war merits are honored with Government awards.

During the period from 1945 till 1960, A.L. Rotinyan's activities were associated with the Gipronikel' research and design institute, where he made a career from senior researcher to deputy director for research work. There, extensive research and technological work were carried out under his direct supervision, with his most active personal involvement, in the fields of hydrometallurgy of nickel, kinetics of calcination processes, leaching, cementation, hydrolysis, hydration, and formation of difficultly soluble hydrates and basic salts that are in equilibrium with the solid phase.

The set of these investigations served as a basis for the development of an industrial process for manufacture of high-purity nickel suitable for preparing heat-resistant nickel-based alloys. Aleksandr Leonovich

was awarded, together with specialists from the Gipronikel' institute and Severonikel' combine, a 1949 State Prize of the USSR in science and technology. High-purity domestic nickel is manufactured up to now at two largest combines of the country by the technology suggested and introduced by Rotinyan and co-workers at the Severonikel' combine in 1947–1948.

The fundamental studies in the theory of joint discharge of ions in electrolytic deposition of metals, published by A.L. Rotinyan and V.L. Kheifets in 1952–1953, found use in various fields of chemical technology and led to further development of the theory. Highly important were studies, carried out in the same years, in the field of dissolution kinetics of solids with complex composition, and also development and introduction of a new intensified method for synthesis of nickel carbonyl. In 1952, A.L. Rotinyan became doctor of engineering.

Further scientific and pedagogical activities of Aleksandr Leonovich were associated with the Lensovet Technological Institute in Leningrad; he became a professor in 1960 and headed the chair of technology of electrochemical industries in 1969.

1070-4272/03/7609-1534$25.00 © 2003 MAIK "Nauka/Interperiodica"

The investigations carried out by A.L. Rotinyan and his disciples during 30 years were related to the most important directions of modern theoretical and applied electrochemistry. A major contribution to theory and practice was made by studies concerned with the mechanism and fundamental kinetic aspects of metal electrodeposition processes, considered with account of the acidity of the near-electrode layer, process stages, and ionic equilibria in solution. Investigations concerned with joint discharge of zinc and hydrogen ions at a zinc electrode, redox potentials of cobalt ions, and kinetics of electrodeposition of nickel–cobalt, iron–cobalt, and iron–nickel alloys were carried out at the institute. The method of a microscopic glass electrode, suggested by A.L. Rotinyan for measuring the acidity of the near-electrode layer, found use at numerous domestic and foreign laboratories.

Mention should be made of a series of investigations by A.L. Rotinyan and co-workers in the field of chemical power cells. These studies were aimed both to improve the already existing electric power sources and to develop new systems with the use of organic solvents. Aleksandr Leonovich supervised studies of main physicochemical properties of inorganic salts in aprotic organic solutions, equilibria in halide solutions of zinc and cadmium in dimethylacetamide and dimethylformamide, kinetics and mechanism of electrochemical reactions of lithium charging–discharge in ethers, and reduction of metal oxides and chalcogenides in organic solvents.

The concepts of the course of electrode reactions, suggested by A.L. Rotinyan, which are extensively used by researchers to solve widely varying problems of applied electrochemistry, served as a basis for the development of new directions in electrochemical technology.

A.L. Rotinyan was a talented pedagogue who trained a great number of engineers and candidates of science, working successfully in the industry and at higher-school institutions in our country and abroad. He was the author of more than 300 scientific papers, books, and inventions. A.L. Rotinyan took an active part in writing the textbook *Prikladnaya elektrokhimiya* (Applied Electrochemistry), which ran through three editions, and monographs *Teoreticheskaya elektrokhimiya* (Theoretical Electrochemistry), *Optimizatsiya proizvodstva khlora* (Optimization of Chlorine Manufacture), and *Osnovy metallurgii* (Foundations of Metallurgy).

Rather diverse and fruitful were A.L. Rotinyan's scientific-organizational activities. As a prominent specialist in applied electrochemistry he headed the Electrochemical Technology Section of the Scientific Council for Electrochemistry at the Academy of Sciences of the USSR, was a member of the Editorial Board of *Elektrokhimiya* (Electrochemistry) journal, supervised the permanent seminar on electrochemistry of the *Znanie* (Knowledge) society, and was Chairman of the Specialized Council for conferring scientific degrees at the Technological Institute.

Aleksandr Leonovich Rotinyan was a scientist with encyclopedic knowledge and a broad-minded person of high culture. His surprising intuition helped him to distinguish promising directions of research, which were invariably supported by him.

Any person who was acquainted with A.L. Rotinyan was subject to the charm of his vivid personality. Colleagues and disciples remember Aleksandr Leonovich as an exceedingly well-wishing person always ready to give help to those who addressed him and to support them.

A.L. Rotinyan died on March 30, 1991, at the age of 77. Aleksandr Leonovich belongs to those who will be always remembered by grateful disciples and colleagues.

K. I. Tikhonov, A. G. Morachevskii,
L. V. Volkov, and Z. P. Arkhangel'skaya

Russian Journal of Applied Chemistry, Vol. 76, No. 9, 2003, pp. 1536–1537. Translated from Zhurnal Prikladnoi Khimii, Vol. 76, No. 9, 2003, pp. 1575–1576.

INFORMATION

XI International Conference on Chemistry of Organic and Organoelement Peroxides

The 11th International Conference on Chemistry of Organic and Organoelement Peroxides was held from June 24 to 26, 2003 in Moscow. The conference was organized on the basis of the Semenov Institute of Chemical Physics, Russian Academy of Sciences (ICP RAS), Moscow and Emanuel Institute of Biochemical Physics, Russian Academy of Sciences (IBCP RAS), Moscow.

The Conference organizers were the Russian Academy of Sciences, ICP RAS, IBCP RAS, Russian Foundation for Basic Research (RFBR), and Lobachevsky State University (Nizhni Novgorod).

The conference participants were more than 450 scientists representing 52 research centers from Russia and CIS countries. The Conference was held in the form of a series of minisymposia on 5 dedicated topics. In the opening ceremony, V.L. Antonovskii, E.T. Denisov, and A.A. Berlin outlined the topicality of the problems concerning synthesis, properties, and applications of peroxides from the theoretical and applied standpoints. Peroxides were said to represent an important class of chemical compounds taking a great part in chemistry, biology, and medicine.

The motto of the Conference was "Chemistry of Peroxides on the Way to the Third Millenium," and the major attention was paid to results obtained in this area in the last four years. The problems considered at the conference included questions of theoretical chemistry (homolysis models, spin chemistry, catalysis, redox reactions, rearrangement, structure–reactivity relationship, transformation of the chemical energy to the light energy, chain reactions), polymer chemistry and technology (initiation of radical polymerization, cross-linking, functionalization), chemical industry (foundry, fuel additives, bleaching of fabrics and other materials, adhesive and varnish components, combustion, film coating); biology (normal and pathological processes; lipid oxidation; synthesis of steroids, prostaglandins, etc.; chemiluminescence of organisms), ecology (atmospheric processes, autooxidation, biochemical oxidation in water and soil), and synthesis (radical reactions, synthesis of alcohols and ketones, epoxidation).

The first session of the Conference was devoted to the problems of synthesis and reactivity of peroxides. The session included 20 oral and 26 poster presentations. Particular emphasis was made on such questions as interaction of peroxides with various organic and inorganic compounds, synthesis and reactivity of peroxides, determination of the rate constants of reactions of peroxy radicals with organic and inorganic compounds, photooxygenolysis, kinetics and mechanisms of oxidation of various chemical groups by peroxides, calculation of bond (dissociation) energy of various peroxides, and quantum chemical study of the structure and conformations of peroxides.

The second session covered the problems of physical and analytical chemistry of peroxides. The session included 8 oral and 17 poster presentations devoted to the kinetic features of decomposition of peroxides, calculation of the activation volume of thermal transformation of peroxides, effect of surfactants on decomposition of peroxides, new supramolecular model for the mechanism of peroxide decomposition, theoretical estimation of the formation enthalpies and dissociation energies of –O–O– bonds, quantum chemical calculation of the kinetic parameters of decomposition of organic and inorganic peroxides, and catalyzed and inhibited decomposition of peroxides.

The topic of the third session (28 oral and 31 poster presentations) was the study of peroxides as intermediate products of oxidation in chemical and biological processes. In this session, a particular attention was paid to oxidation of lipids with microbial lipoxygenase, the chain mechanism of decomposition of peroxides, effect of nanostructures in hydrocarbons on the oxidation mechanism, effects of antioxidants and peroxides on the plant cell growth as influenced by the physicochemical parameters of elementary reactions, development of supramolecular catalysts, and characterization of oxidation products.

The fourth session "Peroxides in Organic Synthesis, Polymer Processing, and Other Processes" included 6 oral and 28 poster presentations covering such problems as determination of explosive characteristics of organic peroxides, modification of polymeric surfaces with peroxides, synthesis of new initiators of radical telomerization, development of new

1070-4272/03/7609-1536$25.00

principles of homolytic phosphorylation, the use of peroxides in manufacture of mold cores and casting molds, the use of oligomeric peroxides for preparation of petroleum polymer epoxy resins, and application of functionalized peroxides as reagents for synthesis of peroxy monomers, surface-active initiators, and reactive surface modifiers.

Finally, the fifth session (13 oral and 12 poster presentations) covered the problems of ecology and the use of hydrogen peroxide for sterilization. The participants reported on new chemical disinfectant based on environmentally friendly hydrogen peroxide, new metal–containing catalysts based on hydrogen peroxide, reactions of hydrogen peroxide with metal porphyrins, photocatalyzed synthesis of organic compounds, general questions of applications of hydrogen peroxides in the environmental chemistry, etc.

The Conference showed that peroxides, as chemical compounds, continue to attract close attention of chemical researchers and practical persons, the biochemical, biological, and even medical aspects of peroxide research being of steadily growing interest.

The next 12th Conference will be held in 2006. The abstracts of the 11th Conference are available from the library of the Institute of Chemical Physics, RAS, and the proceedings will be published in 2004 in the United States (Nova Science Publishers, New York).

G. E. Zaikov, L. L. Madyuskina, and L. A. Zimina

Russian Journal of Applied Chemistry, Vol. 76, No. 9, 2003, pp. 1538–1539. Translated from Zhurnal Prikladnoi Khimii, Vol. 76, No. 9, 2003, pp. 1577–1578.

INFORMATION

14th Annual BCC Conference on Flame Retardancy "New Technological Achievements and Developments in the Field of Flame Retardancy of Polymer Materials" (FR Materials, Applications, Scientific and Technological Achievements, Market for FR Products)

The 14th Annual Conference on Flame Retardancy of Polymer Materials was held from June 2 to 4, 2003 in Stamford, Connecticut (the United States). The Conference was organized by the Business Communications Co (BCC).

The Conference covered the following topics:

(1) review of the current state of science and technology in FR;

(2) review of the applications and markets for FR products;

(3) recent developments in local and global standardization and in testing technology;

(4) problems of toxicity and environmental issues;

(5) halogen-based and non-halogen-based flame-retardant chemicals, synergism, intumescence, FR mechanisms, modeling, flame parameters, and inherently FR polymers.

(6) review of developments on fire control, containment, and FR enablement.

The 2003 highlights were as follows: nanomaterials, flame-retarding steel components, new fabric and vehicle FR developments, and news from Europe. The conference participants were about 100 scientists from the Unites States, Canada, Russia, the United Kingdom, Israel, France, Belgium, Germany, Italy, and Poland. Professor Menachem Lewin, who is the Program Chairman of this annual conference for already 14 years, in his opening remarks outlined that polymer combustion studies demonstrate a need in developing both theoretical and applied approaches in their close interlink. The reports presented at the Conference were discussed in five sessions. The first session "Review and Mechanism of Flame Retardancy" included six oral presentations. T.R. Hull (the United Kingdom) in his lecture reported on combustion studies in a purser furnace; T. Kashiwagi (the Unites States), on flame retardant mechanism of polymer clay nanocomposites; J.E.J. Staggs (the United Kingdom), on simulation of thermal degradation of linear polymers; and M. Nyden (NIST), on a unified reaction rate theory for large molecules in condensed phases.

Two other reports presented at this session were devoted to new developments in FR polyurethanes [S. Levchik (the Unites States)] and environmental aspects in polymer FR [G.E. Zaikov and S.M. Lomakin (Russia)].

The second session "Halogen- and Non-Halogen-Based FR Systems" included eight oral and one poster presentations. A.R. Horrocks (the United Kingdom) reported on the capacity of heavy metal ions to enhance the flame-retardant activity of ammonium polyphosphate; Dr. Shiow-Ching Lin (the Unites States), on fire resistance of fluoropolymers; and I. Finberg (Israel) and T. Geran (the United States), on development of fire-retarded plastics with reduced content or no presence of antimony trioxide.

The next four reports were devoted to applications of silicone-phosphonates [S. Gallagher (the United States)], enhanced performance of phosphate- and sulfonate-based intumescent agents [P.S. Rhodes (the United States)], improvement of the fire behavior of PVA-using binary and ternary mineral compositions [J.M. Lopez-Cuesta (France)], and use of iron compounds in non-halogen FR systems [E.D. Weil (the United States)]. Finally, K.K. Shen (the United States) reported on firebrake zinc borates as fire retardants in halogen-free polyolefins.

The poster presentation made by J. Hicks, P.J. Davies, A. Alderson, and A.R. Horrocks (the United States) provided information on the burning behavior of polyacrylonitrile fiber-forming polymers in the presence of phosphorus-containing FRs. The third session "Flame Retardancy of Nanocomposites" included six oral presentations. In the first one, S. Bourbigot and J.W. Gilman (NIST), C.A. Wilkie, and A.B. Morgan (both the United States) examined the problems of processing, characterization, thermal stability, and

1070-4272/03/7609-1538$25.00

flammability of polystyrene clay nanocomposites. The talk was followed by a fruitful discussion. Then S. Padbury (the United Kingdom) reported on the effect of P-containing flame retardant and nanoclays on behavior of polyamides 6 and 6.6. The next four talks were devoted to progress on nanostructurated flame retardants [G. Beyer (Belgium)], recent advances in fire retardancy based on nanocomposites [C.A. Wilkie (the United States)], fire performance of polystyrene/silica nanocomposites prepared by extrusion [G.L. Nelson (the United States)], and regulatory activity governing brominated flame retardants in Europe and the United States [T. Hull (the United Kingdom)]. The fourth session "Consumer Focus—Industrial Applications" included eight oral presentations. The first four talks were devoted to the thermal and fire behavior of polypropylene/flax biocomposites [B. Schartel (Germany)], the use of red phosphorus for flame proofing of polyolefins [N. Gatti (Italy)], ignitability of wood treated with different FRs [R. Kozlowski (Poland)], and cotton batting barriers for soft furnishings [S. Wolf, P.J. Wakelyn (the United States)]. In the next four reports, the authors discussed thermal stability and FR of rigid PU foams [K. Pielichowski (Poland)], new developments in durable flame retardant finishing of cotton textiles [C.Q. Yang (the United States)], halogen content analysis of fire redardants [R. Fehrenbach (the United States)], and new FR materials for military applications [U. Sorathia (the United States)].

The final fifth session "Testing Standards and Toxicity" included seven oral presentations. The first one entitled "How to Get Your Product CE-Labeled? First Experiences with Euroclasses" was presented by P.Vandervelde (Belgium). J.S. Stimitz (the United States) talked about properties of plastic materials for use in 42 volt automotive applications, and M.M. Hirschler (the United States), about fire hazard assessment of personal computers in a home and in a small office. The next four reports in this session were devoted to studies on the combustion behavior of polystyrene systems flame retarded with phosphorus [D. Price (the United States)], comparison of fire properties of automotive materials [M.L. Janssens (the United States)], the correlation of heat release calorimetry measurements [R. Filipczak (the United States)], and potential effects of combustion products of brominated fire-retardant chemicals on egress time in home fire scenarios [T.A. Thomas (the United States)].

The 14th Conference on Flame Retardancy of Polymer Materials showed that the problems considered are of great importance for science and technology. The next 15th Conference will be held in Stamford, Connecticut (the United States) in 2004.

G. E. Zaikov, M. I. Artsis, and L. L. Madyuskina

Russian Journal of Applied Chemistry, Vol. 76, No. 9, 2003, p. 1540. Translated from Zhurnal Prikladnoi Khimii, Vol. 76, No. 9, 2003, p. 1579.

BOOK REVIEWS

Motov, D.L., *Fizikokhimiya i sul'fatnaya tekhnologiya titano-redkometall'nogo syr'ya* (Physical Chemistry and Sulfate Technology of Titanium–Rare-Metal Raw Materials)

Apatity: Kol'skii Nauchnyi Tsentr Ross. Akad. Nauk, 2002, part 1, 189 pp.; part 2, 163 pp.

In the Kola Peninsula, there are unique deposits of titanium–rare-metal raw materials. Of particular importance among titanium-containing minerals are perovskite, sphene, and titanomagnetite, and also loparite, which is a complex titanium–rare-metal raw material. Of chief interest among zirconium minerals are eudialyte and baddeleyite. For all of the titanium-containing ores found in the Kola Peninsula there are rather efficient dressing schemes yielding various concentrates of required composition.

The main industrial products produced by one or another scheme for processing of complex titanium or zirconium raw materials are titanium dioxide for various purposes, titanium tetrachloride, technical-grade niobium pentoxide with admixtures of titanium and tantalum, niobium and titanium pentoxides for manufacture of the metals, concentrates of rare-earth elements, and zirconium dioxide as refractory material.

The choice of a technique for processing of titanium–niobium raw materials is largely determined by the kind of titanium products to be manufactured. D.L. Motov's monograph, devoted to physicochemical foundations and technology of sulfuric acid processing of titanium–rare-metal raw materials, comprises two parts. The first part covers the physicochemical foundations of sulfuric acid technology for recovery of titanium, zirconium, and hafnium compounds from titanium–rare-metal raw materials and also the results of development of flowsheets for integrated sulfuric acid processing of loparite, sphene, and titanomagnetite. The second part discusses sulfuric acid processing of other kinds of raw materials: of titanate (perovskite), titanosilicate (leucoxene), and zirconium (eudialyte, baddeleyite) types.

Using methods of physicochemical analysis, the author obtained a vast body of reference-type data on solubility in the systems MeO_2–SO_3–H_2O (Me = Ti, Zr, Hf) at temperatures ranging from 20 to 300°C, and also on more complex equilibria. Sulfate and sulfatometallate compounds isolated in studying the systems are characterized using chemical, crystal-optical, X-ray phase, and thermogravimetric analyses.

The process characteristics of breakdown of loparite, perovskite, and sphene concentrates with sulfuric acid or its mixture with ammonium sulfate are described. In processing of loparite, titanium can be separated from niobium and tantalum. The first part of the monograph also presents results obtained in studying and optimizing sulfuric acid processing of sphene, which is one of the most important minerals of the Khibins. In addition to being a component of apatite–nepheline ores, sphene forms in the Kola Peninsula separate ore deposits. Processing of sphene can give various pigments.

The second part of the monograph considers methods of integrated processing of titanate and titanosilicate raw materials to obtain titanium dioxide pigment. Zirconium (hafnium) compounds can be recovered from eudialyte of complex composition, whose ores are mainly found in the Lovosero massif, and from baddeleyite, natural zirconium dioxide, which is an admixture mineral in one of iron-ore deposits in the Kola Peninsula. The final section of the second part contains evidence concerning certain fields of application of titanium and zirconium compounds.

Motov's monograph, published in an edition of only 100 copies, is packed with experimental material and flowsheets. The book is intended for a relatively small audience of readers specialized in processing of the above-mentioned kinds of raw materials or in use of the products obtained.

A. G. Morachevskii

1070-4272/03/7609-1540$25.00 © 2003 MAIK "Nauka/Interperiodica"

Russian Journal of Applied Chemistry, Vol. 76, No. 9, 2003, pp. 1541–1542. Translated from Zhurnal Prikladnoi Khimii, Vol. 76, No. 9, 2003, pp. 1580–1581.

BOOK REVIEWS

Habashi, F., *From Alchemy to Atomic Bombs: History of Chemistry, Metallurgy, and Civilization*

Quèbec City (Canada): Laval University, 2002, 357 pp.

The book written by F. Habashi, a know Canadian scientist working in the field of nonferrous metallurgy, considers in a sufficiently popular form a wide variety of problems associated with the development of chemistry, physics, and metallurgy from the ancient times till the present days. Particular value and attractiveness is imparted to the book by the richest illustrative material, photographs of scientists, various events, commemorable places, process schemes, etc. (the book contains 223 illustrations, 30 of these colored). All the photographs and drawings are of extremely high quality. Separate sections of the book had been published, mainly in not readily available Canadian journals.

The book comprises 11 small chapters and has author and bibliographic indexes. Chapter 1 (Mythology, pp. 1–22) presents evidence of historical-mythological nature and pays much attention to the origin of the names of metals, associated with various mythological characters (from cobalt, 1735, to promethium, 1945; a total of 15 metals). Chapter 2 (The Four Elements, pp. 23–46) describes the concepts of Empedocles (ca. 490–430 BC), an ancient Greek philosopher who recognized four elements: fire, air, water, and soil, naming them "roots of all." Also considered are the viewpoints of other philosophers: Aristotle (384–322 BC), Galen (130–201), Agricola (1494–1555), and the philosophy of Zoroaster prophet. Chapter 3 (Alchemy, pp. 47–100) is devoted to the origin and development of alchemy. Chapter 4 (The Alchemists, pp. 102–154) presents brief biographic evidence concerning a large number of scientists who were, to varied extent, on the standpoint of alchemy both in Arab countries and, later, in West Europe. To these belong Ibn Sina (Avicenna) (980–1036), T. Paracelsus (1493–1541), van Helmont (1577–1644), R. Boyle (1627–1691), G.E. Stahl (1660–1734), and other scientists.

Chapter 5 (Reform in Chemistry, Mineralogy and Metallurgy, pp. 155–182) includes materials characterizing the reform in natural sciences in the XVIII and XIX centuries. Special attention is given to the works of A. Lavoisier (1743–1794), who was the first to cast doubt on the theory of phlogiston. Together with a number of other scientists, Lavoisier developed principles of a new chemical nomenclature, published his "Elementary Course of Chemistry," and made a number of major discoveries. The chapter recognizes the merits of J. Dalton (1766–1844), reforming activities of J.J. Berzelius (1779–1848), and works of F.A. Kekulé (1829–1896), S. Cannizzaro (1826–1910), and quite a number of other outstanding scientists of the XIX century.

Chapter 6 (Discovery of Electricity, pp. 183–210) is devoted to the investigations which led to the discovery of electricity 200 years ago. L. Galvani (1737–1798), A. Volta (1745–1827), M. Faraday (1791–1867), S. Arrhenius (1859–1927) are mentioned among others. H. Davy (1778–1829), R. Bunsen (1811–1899), and H.E. Saint-Claire Deville (1818–1881) are named fathers of electrometallurgy. Chapter 7 (Classification of the Elements, pp. 211–234) discusses studies concerned with the classification of elements. Mention is made of the discovery of the Periodic law by D.I. Mendeleev (1834–1907) and later studies in this field. Chapter 8 (The Modern Physics: Discovery of X-rays, pp. 235–272) is devoted to the advances in physics, beginning with the end of the XIX century. The attention is focused on the discovery by W.K. Röntgen (1845–1923). Chapter 9 (Radioactivity: Chemistry and Physics United, pp. 257–272) describes the development of investigations into radioactivity from H. Becquerel (1852–1908) to G. Seaborg (1912–1999). Chapter 10 (Uranium Fission, pp. 273–294) briefly describes the history of discovery of uranium fission. The author, in particular, gives a list of outstanding scientists who emigrated from Germany, Austria, Italy, and Denmark in 1933–1943. These include 20 Nobel Prize Laureates in physics or chemistry. Chapter 11 (Atomic Bombs, pp. 295–338) is devoted to the history of development of nuclear warfare in the United States.

Habashi's book is of indubitable interest, it is well written and could possibly be a useful textbook in

1070-4272/03/7609-1541$25.00 © 2003 MAIK "Nauka/Interperiodica"

studying the history of science. Unfortunately, the contribution of Russian scientists to the development of the world civilization is reflected to an apparently insufficient extent. Only Mendeleev's discovery of the Periodic law is described in comparatively full detail. Also mentioned are investigations by V.N. Ipat'ev (1867–1952), who developed, in about 1900, the principles of the process of metal recovery from aqueous solutions with hydrogen at high temperature and pressure. Mention is also made of the explanation by N.N. Semenov (1896–1986) in 1928 of the oxidation of phosphorus vapor by water vapor in terms of the concept of branched chain reactions, for which he was later (in 1956) awarded a Nobel Prize, together with C. Hinshelwood (1897–1967). There are no other mentions of the investigations by Russian scientists. At the same time, judging from the topics covered by the book and its structure, it would seem quite appropriate to describe rather diverse investigations by M.V. Lomonosov and the discovery of electroplating by B.S. Jacobi (1838) and to mention studies of reduction of metal oxides by N.N. Beketov, A.S. Popov's investigations concerned with practical application of electromagnetic waves, and V.E. Grum-Grzhimailo's hydraulic theory of flame motion.

A. G. Morachevskii and I. N. Beloglazov

Russian Journal of Applied Chemistry, Vol. 76, No. 10, 2003, pp. 1543–1558. Translated from Zhurnal Prikladnoi Khimii, Vol. 76, No. 10, 2003, pp. 1585–1600.

REVIEWS

Quantum-Chemical Analysis of Electronic Excitation and Reactivity of Olefins and Dienes

K. K. Kalnin'sh and S. G. Semenov

Institute of Macromolecular Compounds, Russian Academy of Sciences, St. Petersburg, Russia
St. Petersburg State University, St. Petersburg, Russia

Received June 20, 2003

Abstract—Results obtained in studying the structure of olefin and diene molecules, and complexes of these, in the ground and lower excited states by RHF, ROHF, GVB/DN, and 6-31G* quantum-chemical methods are presented. Attention is paid to the identity of the main structural and electronic parameters of triplet T_1 and singlet S_1 states forming a reactive fourfold spin-degenerate diradical equilibrium excited state $(S \cdot T)_1$ having the lowest energy. A new mechanism of cyclodimerization of ethylene and tetrafluoroethylene and anionic polymerization of dienes, involving the $(S \cdot T)_1$ states, is suggested.

INTRODUCTION

The rapid development of computers and their accessibility to a great number of chemists enable the introduction of mathematical modeling techniques into chemical practice and technology. In this context, the problem of adequate quantum-chemical description of elementary processes determining the course of chemical reactions and properties of their products is topical. A key issue in the theory of chemical reactions is elucidation of the mechanism of formation/rupture of a chemical bond. The necessity for using new theoretical approaches in combination with a quantummechanical calculation becomes apparent.

The concepts of intermediate species of diradical nature are increasingly frequently invoked in analyzing the mechanism of thermal and photochemical reactions [1, 2]. In particular, it is believed [1] that the reaction of formation/cleavage of a four-membered ring in the cyclobutane molecule

$$\boxed{\text{H}} \rightleftarrows H_2C{=}CH_2 + H_2C{=}CH_2 \qquad (1)$$

passes through two intermediate states, each involving diradical species. Here, two permanent components of the conventional scheme of a chemical reaction are represented. These are the intermediate state characterizing the active stage of the reaction and intermediate products formed in the reaction.

According to the results of a quantum-chemical calculation [1], the energy of the diradical state in reaction (1) is 4 kcal mol^{-1} lower than the experimental activation energy of cyclobutane decomposition (62.5 kcal mol^{-1}). At the same time, the calculations carried out in [4] demonstrate that the diradical state has much lower energy: it lies 20 kcal mol^{-1} lower than the top of the activation barrier for cyclobutane decomposition (see below).

Analysis of published evidence shows clearly the ambiguity of definition of the notion of "diradical." Some researchers, following the classical theory of chemical structure, understand by radicals and diradicals chemical compounds with subvalent (valence-deficient) atoms [5, 6]. In this sense, free radicals are tetramethylene $^{\cdot}CH_2CH_2CH_2CH_2^{\cdot}$ (including two trivalent terminal carbon atoms) [1], carbenes $:CH_2$, $:CF_2$ and carbon oxide $:CO$, which contain bivalent carbon atoms, but not the O_2 molecule whose oxygen atoms have normal valence.

Others regard as radicals and diradicals paramagnetic species whose spin multiplicities are other than unity. The authors of [7] make the notion of diradicals narrower by attributing to them those bifunctional systems in which two radical centers have independent properties. A similar definition of this notion assumes a small singlet–triplet splitting and/or quasi-degeneracy of singly occupied electron levels [8]. This is the case for tetramethylene, excited states of the n-π^* type, and charge-transfer complexes. However, carbenes do not satisfy this requirement and cannot be considered diradicals in this sense. In this context, it becomes necessary to reconsider the properties and

1070-4272/03/7610-1543 $25.00 © 2003 MAIK "Nauka/Interperiodica"

structure of diradical species with high chemical activity.

In the general case, one has to consider the diradical nature of molecules (case of locally excited states) and complexes of molecules (case of excited excimer or exciplex states). These cases differ in the localization of radical centers: within a single molecule (local excitation) or within several, commonly two, molecules (excimers or exciplexes). The diradical states of photoexcited species (molecules or complexes of these) are well known and will not be specially discussed here (see, e.g., [9]). As for the thermal electronic excitation, the forming excited species have been poorly studied experimentally and not at all theoretically. Mention should be made here of only few studies [4, 10, 11] carried out by the authors of the present review.

When considering the quasi-degeneracy of the triplet and singlet states of ethylene, Salem [8] understands by the latter the ground state S_0 with changed (orthogonal) configuration. However, this means that, according to the commonly accepted concept, not only reactants and products, but also all intermediates formed in the chemical process must belong to the potential surface of this state. The properties of these species, e.g., absorption spectra, must correspond to the ground electronic state. However, experimental data cast doubt on this common viewpoint. In particular, studies of perfluoro-olefins [12–15] revealed absorption by intermediates in the visible spectral range, whereas the starting perfluoro-olefins absorb in the state S_0 in the vacuum ultraviolet range.

This review presents experimental and calculated data on the reactivity of olefins and dienes and gives their theoretical interpretation in terms of the concept of thermal electronic excitation in an elementary chemical process [16]. Two types of chemically active species, which are thermally generated in the dark and possess diradical properties, are considered. To the first type belong excited olefin molecules (ethylene and its derivatives), in which closely spaced (~1.5 Å) radical centers are localized on carbon atoms of a degraded double bond. The second type comprises electronically excited complexes: excimers between identical molecules (of, e.g., olefins) or exciplexes between different molecules (e.g., butadiene molecule and the corresponding anion). In species of the second type, free valences are distributed among atoms of the interacting molecules and valence-deficient atoms are spaced by several angstroms. The common feature of all the species is that they are in an electronically excited state of local or intermolecular nature.

THEORY AND CALCULATION PROCEDURES

Bond indices and free valence indices of atoms. Chemical bonds between atoms are characterized by equilibrium internuclear spacings and indices [17, 18]

$$I_{AB} = \sum_{a\in A}\sum_{b\in B}(PS)_{ab}(PS)_{ba}, \quad (2)$$

where a and b are the numbers of orbitals belonging to atoms A and B.

The matrix P in formula (2) is constituted by expansion coefficients of the electron density $\rho(r)$ [19] in partial products of atomic orbitals (AO) $\chi_a(r)$ $\chi_b^*(r)$:

$$\rho(r) = \sum_A\sum_B\sum_{a\in A}\sum_{b\in B}\chi_a(r)P_{ab}\chi_b^*(r) = \chi(r)P\chi^+(r), \quad (3)$$

$S = \int \chi^+(r)\chi(r)d^3r$ is a metric matrix, and $\chi(r)$ is a row of basis AO.

The diagonal elements of the matrix product PS are identified with electron occupancies of AO [20, 21]:

$$n_a = (PS)_{aa}. \quad (4)$$

Comparison of the sum of bond indices with the valence index

$$V_A = \sum_{a\in A}(2n_a - n_a^2) - \sum_{a\neq a'\in A}(PS)_{aa'}(PS)_{a'a} \quad (5)$$

suggested in a monograph [22] makes it possible to define the free valence of each atom as the difference [23]

$$F_A = V_A - \sum_{B(\neq A)} I_{AB}. \quad (6)$$

The total valence of a molecule or radical is defined as a sum of atomic valences, minus a doubled sum of indices of intraradical chemical bonds [24]

$$V_{mol} = \sum_{a\in mol}(2n_a - n_a^2) - \sum_{a\neq a'\in mol}(PS)_{aa'}(PS)_{a'a}$$
$$= \sum_A(V_A - \sum_{B(\neq A)} I_{AB}) = \sum_A F_A = F_{mol}, \quad (7)$$

where a and a' are the numbers of all the basis AO χ.

According to formula (7), the free valences F_A are additive quantities characterizing the distribution of the total valence of a chemical compound (free radical, diradical, excited molecule) among the constituent atoms A.

Occupancies of molecular orbitals (MO) and the valence of a molecule. In the RHF approximation, the ground N-electron state S_0 of a molecule is characterized by a set of molecular orbitals with integer occupancies $n_i = 2$ ($i = 1, 2, 3, N/2$), which is named electronic configuration. In this case, the free

valence of the molecule as a whole and the free valence of each atom are zero: $V_{mol} = F_{mol} = 0$ and $F_A = 0$. The ROHF approximation is the simplest method for describing the triplet state T_1, in which the single-determinant wave function Ψ is the eigenfunction of the operator of squared N-electron spin. In this case, the electronic configuration of a molecule includes, together with doubly occupied orbitals ($n_i = 2$ for $i = 1, 2, \ldots, N/2 - 1$), also two singly occupied orbitals ($n_i = 1$ for $N/2$, $N/2 + 1$), and the total valence satisfies the relation $V_{mol} = F_{mol} = 2$. In the ROHF approximation, the free atomic valences F_A [23] coincide with spin occupancies of atoms, n_A^s [25]. In the GVB approximation for an excited singlet state S_1 described by two-determinant wave function, the free valence is expressed in terms of a pair of occupancies $n_{N/2} + n_{N/2+1}$ of active natural MO:

$$V_{mol} = F_{mol} = 2n_{N/2} - n_{N/2}^2 + 2n_{N/2+1} - n_{N/2+1}^2 = 2n_{N/2}n_{N/2+1}. \quad (8)$$

The atomic components F_A of the total valence (7) can be used to evaluate the relative reactivities of the atoms and reveal reaction centers in excited molecules, free radicals, and diradicals.

It is noteworthy that the above-mentioned indices of chemical bonds and free valence indices differ from the indices in the output file of GAMESS software (version 6.2) [26]. The point is that, immediately after publication of [23] in 1984, its author redefined, following the concept of [27–29], the chemical bond index by including into it an additional term [30] given by

$$I'_{AB} = I_{AB} + \sum_{a\in A}\sum_{b\in B}(QS)_{ab}(QS)_{ba}. \quad (9)$$

Here, matrix Q is constituted by expansion coefficients of the spin density $\rho^s(r)$ [19] in pair products of atomic orbitals $\chi_a(r)\chi_b^*(r)$:

$$\rho^s(r) = \sum_A\sum_B\sum_{a\in A}\sum_{b\in B}\chi_a(r)Q_{ab}\chi_b^*(r) = \chi(r)Q\chi^+(r), \quad (10)$$

with the spin density normalized in accordance with the equality

$$\int \rho^s(r)\,d^3r = \sum_A\sum_{a\in A}(QS)_{aa} = 2M_S, \quad (11)$$

and the diagonal elements of the matrix product QS yielding the above-mentioned spin occupancies $n_A^s = (QS)_{aa}$ and $n_A^s = \sum_{a\in A} n_n^a$.

It is this variant of the theory that is implemented in the GAMESS software; however, the free valence indices by Mayer, found from formula (6) with modified indices I'_{AB}, yield in the aggregate a value different from the free valence of the whole molecule (free radical). In this context, the original variant of the theory [18, 22, 23] seems to be preferable and was used to analyze the reactivities of organic electronically excited molecules in [4].

Basis orbitals and optimization procedures. The molecular orbitals were represented in 6-31G* or DH (Dunning & Hay [31]) basis sets. The configuration of the triplet states T_1 is obtained via energy minimization in the ROHF approximation without symmetry-related limitations. For singlet excited states S_1, it is advisable to use the GVB method in the modes of energy minimization (with fixed occupancies of the active natural MO $n_{N/2} = n_{N/2+1} = 1$) or saddle point search (with these occupancies varied at $n_{N/2} + n_{N/2+1} = 2$). It seems natural to take as the starting nuclear configuration that of the corresponding triplet state T_1. As demonstrated below, the structural parameters of these two states are, indeed, very close.

LOCALLY EXCITED DIRADICAL STATES OF OLEFINS

In the gas phase, tetrafluoroethylene (TFE) C_2F_4 (**I**-F), hexafluoropropylene C_3F_6 (**II**-F), *trans*-perfluorobutene-2 2-C_4F_8 (**III**-F), perfluorobutene-1 1-C_4F_8 (**IV**-F), and and a number of other floroderivatives show much higher thermal stability, compared with ethylene and its derivatives. On heating perfluoroolefins to "prepyrolysis" temperatures of 700–1500 K, Buravskii and Kolbanovskii [13] confirmed for the first time the existence of previously unknown species (intermediates) with diradical properties. They also established the monomolecular type of the reaction in which intermediates are formed [13]. This fact indicates that the intermediates are identical in their empirical formula to the starting compounds and, consequently, can be designated as $C_2F_4^*$, $C_3F_6^*$, 1-$C_4F_8^*$, and 2-$C_4F_8^*$.

The method of kinetic spectroscopy revealed two absorption bands of intermediates in the UV and visible ranges (nm): $C_2F_4^*$ 236.5 and 500; $C_3F_6^*$ 240 and 477.5; 1-$C_4F_8^*$ 242.5 and 460, which do not coincide with the characteristic absorption bands of the starting compounds: C_2F_4 188 and C_3F_6 185. Special-purpose experiments, in which the same intermediates were generated from different starting compounds, revealed their direct involvement in the formation of new chemical compounds. For example, the intermediate of tetrafluoroethylene, $C_2F_4^*$, decomposes into two

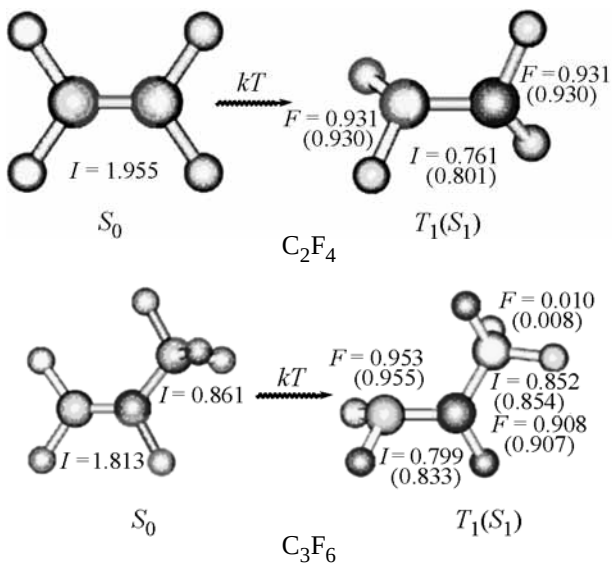

Fig. 1. Structure of C_2F_4 and C_3F_6 molecules in the ground singlet (S_0) and excited triplet (T_1) states; I are bond indices, and F, free valence indices of carbon atoms (ROHF/DH); values of the same parameters for a singlet excited state S_1 (GVB/DH) are given in parentheses.

tetrafluoromethylenes, which add to $C_2F_4^*$ to form hexafluoriopropylene [12]:

$$C_2F_4 \rightarrow C_2F_4^* \overset{kT}{\rightleftarrows} :CF_2 + CF_2, \qquad (12)$$

$$C_2F_4^{\cdot} + :CF_2 \rightleftarrows C_3F_6^* \rightleftarrows C_3F_6. \qquad (13)$$

The authors of [15] believe that the intermediates $C_2F_4^*$, $C_3F_6^*$, 1-$C_4F_8^*$, and 2-$C_4F_8^*$ are previously unknown, low-lying excited singlet states of the respective perfluoro-olefins, which are formed in the monomolecular reaction on heating these latter in the gas phase. However, quantum-chemical calculations in terms of the method of the intermediate state [32], available in the literature, give no way of making any conclusion about the structure of intermediates.

The new concept of the nature of intermediates of perfluoro-olefins as electronically excited molecules in a triplet state was described in [33]. This viewpoint follows from the general concept of thermal electronic excitation in chemical reactions [16]. The role of triplet excited molecules and complexes in polymerization–depolymerization reactions was considered in [10, 34, 35]. In elucidating the mechanism of chemical reactions involving triplet molecules, a question necessarily arises as to how the triplet T_1 states are transformed in the course of a chemical process into a singlet ground state S_0 of the stable reaction product. This question cannot be answered without taking into account the singlet excited states S_1. In this context, the procedure for quantum-chemical calculation of singlet states S_1 was reconsidered in [4].

The energy of triplet states, $E(T_1)$, is, as a rule, lower than the energy of singlet states, $E(S_1)$ [7]. The difference of the energies, $E(S_1) - E(T_1)$, which is named singlet–triplet splitting, is high for π–π^* (up to 80 kcal mol^{-1}), but low for n-π^* states and charge-transfer states (5–10 kcal mol^{-1}). For ethylene C_2H_4, the value of $E(T_1)$ is 82.1 (experimental value [7]) or 81.8 kcal mol^{-1} (ROHF/6-31G** calculation for the vertical transition $T_1 \leftarrow S_0$), and the experimental singlet–triplet splitting is 69.2 kcal mol^{-1} [7].

The energy of the nonequilibrium singlet excited states S_1 of olefins in the case of a vertical transition can be found from absorption spectra, but the energies of excited states for equilibrium, relaxed states S_1 are mostly determined from quantum-chemical calculations. Excited olefin molecules are characterized by rotation about the unsaturated bond C=C

$$R^1HC{=}CHR^2 \xrightarrow{h\nu,\ kT} R^1HC^{\cdot}{-}C^{\cdot}HR^2 \qquad (14)$$

to give diradical structures, which either relax $C^{\cdot}-C^{\cdot}$ nonradiatively into the ground singlet state S_0, or are involved in chemical reactions as diradical species. It is the conformational instability of planar olefin structures in the excited state that gives rise to an effective channel of nonradiative energy dissipation.

Structure of triplet states of olefins and perfluoro-olefins. It is known that the triplet, so-called phantom states of ethylene and its derivatives, e.g., stilbene [36, 37], have a perpendicular configuration. Via these states occurs *cis–trans*-isomerization, i.e., rotation about the C=C bond by 180°. Triplet states of ethylene and other olefins have diradical nature, irrespective of whether they have perpendicular (in relaxed state) or planar (in the case of a vertical transition) configuration. The decrease in the index of the C=C bond in a triplet excitation has electronic origin and is not related directly to a transition of a molecule to the perpendicular configuration. For example, the index of the C=C bond of ethylene, I = 1.91, decreases to I = 0.79 in the vertical transition $T_1 \leftarrow S_0$ without any change in the planar structure. As a result of relaxation of the T_1 state, its energy decreases, the chemical bond energy grows, and the bond index increases to I = 0.92. In this regard, the excited state of ethylene differs fundamentally from the ground state, for which the molecular energy increases, the chemical bond becomes weaker, and the C=C bond index decreases when the planar structure is distorted.

Table 1. Geometric parameters of molecules and diradicals C_2X_4 (**I**-X) and C_3X_6 (**II**-X) in equilibrium configurations in the states S_0, S_1, and T_1, calculated by RHF/DH, GVB/DH, and ROHF/DH methods

Molecule	Parameter	X = F			X = H		
		S_0 RHF	S_1 GVB	T_1 ROHF	S_0 RHF	S_1 GVB	T_1 ROHF
I-X	Bond length, Å:						
	C=C	1.307 (1.311)*	1.489	1.492	1.316 (1.339)	1.469	1.465
	C–X'	1.341 (1.319)	1.352	1.351	1.076 (1.086)	1.076	1.076
	C–X"	1.341 (1.319)	1.355	1.356			
	Angle, deg:						
	X'CX"	112.6	111.2	110.8	116.5	117.5	117.2
	X'CC	123.7 (123.7)	114.6	114.5	121.7 (121.2)	121.3	121.3
	X"CC	123.7 (123.7)	116.2	116.4			
	X'CCX'	180.0	146.5	153.7			
	X"CCX"	0.0	50.1	56.5	0.0	89.0	80.5
						89.5	87.8
						90.5	91.8
						91.0	99.9
II-X	Bond length, Å:						
	C=C	1.314	1.483	1.482	1.318	1.474	1.470
	C^1–X'	1.333	1.352	1.352	1.077	1.077	1.078
	C^1–X"	1.333	1.356	1.357	1.076	1.076	1.076
	C^2–X	1.364	1.360	1.361	1.080	1.079	1.080
	C^2–C^3	1.497	1.503	1.504	1.502	1.503	1.504
	Angle, deg:						
	X'C^1X"	111.4	111.1	110.5	116.7	117.3	117.2
	XC^2C^3	112.3	113.6	113.4	115.9	117.8	117.3
	X'C^1C^2	125.7	115.0	115.1			
	X"C^1C^2	122.9	116.0	116.2			
	X'C^1C^2X	180.0	74.7	71.7	180.0	82.4	101.7
	X"C^1C^2X	0.0	57.2	59.7	0.0	102.1	79.1

* Experimental data of [38–40] given in parentheses.

The molecules of perfluoro-olefins C_2F_4, C_3F_6 (Fig. 1, Table 1), 1-C_4F_8, and 2-C_4F_8 (Fig. 2, Table 1) have planar structure in the ground singlet state, except in the 1-C_4F_8 molecule, in which the CF_3 group lies outside the plane of the central fragment $\rangle C{=}C\langle$. In the triplet state T_1, these molecules undergo rotation about the $^{\bullet}C-C^{\bullet}$ bond and take a nearly perpendicular configuration. In this case, fluoro-olefins are characterized by a significant decrease in the F–C–C angle at radical $C^{\bullet}$ centers from 123°–125° (S_0) to 114°–116° (T_1), whereas for unsubstituted olefins, the decrease in the H–C–C angle upon transition to the triplet state is small, from 121°–121.9° (S_0) to 121.1°–121.4° (T_1).

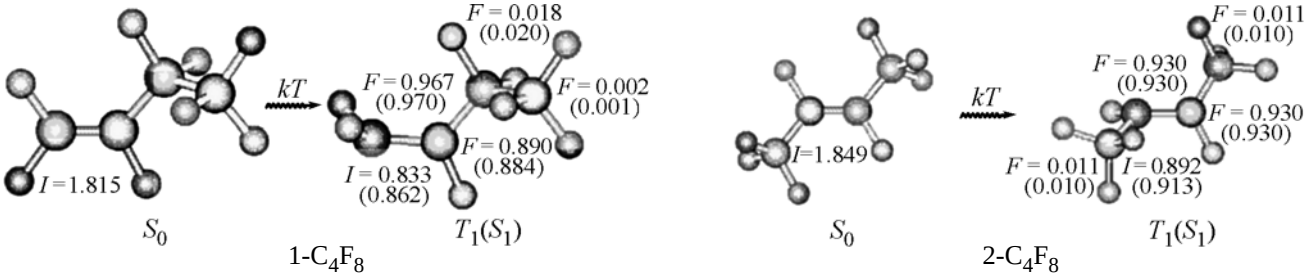

Fig. 2. Structure of 1-C_4F_8 and 2-C_4F_8 molecules in the ground singlet (S_0) and excited triplet (T_1) states; F are free valence indices of carbon atoms (ROHF/DH); values of the same parameter for a singlet excited state S_1 (GVB/DH) are given in parentheses.

Table 2. Valences V_{mol}, occupancies of active natural molecular orbitals n_1 and n_2, and energies ΔE_{tot} of singlet (S_1) and triplet (T_1) electronic states of molecules C_2F_4 (**I**-F), C_3F_6 (**II**-F), 2-C_4F_8 (**III**-F), C_2H_4 (**I**), C_3H_6 (**II**), and 2-C_4H_8 (**III**) relative to ground states S_0

Molecule	State	Method//Configuration	DH				6-31G*			
			V_{mol}	n_1	n_2	ΔE_{tot}, kcal mol^{-1}	V_{mol}	n_1	n_2	ΔE_{tot}, kcal mol^{-1}
I-F	S_0	RHF//S_0	0.000	2.000	0.000	0.0	0.000	2.000	0.000	0.0
	T_1	ROHF//T_1	2.00	1.000	1.000	23.1	2.000	1.000	1.000	28.0
	S_1	GVB/T_1	1.974	1.113	0.887	26.4	1.942	1.170	0.830	31.5
	S_1	GVB//S_1	2.000	1.001	0.999	26.8	2.000	0.999	1.001	32.3
II-F	S_0	RHF//S_0	0.000	2.000	0.000	0.0	0.000	2.000	0.000	0.0
	T_1	ROHF//T_1	2.000	1.000	1.000	29.6	2.000	1.000	1.000	35.8
	S_1	GVB//T_1	2.000	1.002	0.998	32.8	1.998	1.035	0.965	39.6
	S_1	GVB//S_1	2.000	0.998	1.002	32.8	2.000	0.993	1.007	39.5
III-F	S_0	RHF//S_1	0.000	2.000	0.000	0.0	0.000	2.000	0.000	0.0
	T_1	ROFH//T_1	2.000	1.000	1.000	30.7	2.000	1.000	1.000	37.1
	S_1	GVB//T_1	1.996	1.046	0.954	33.2	1.987	0.919	1.081	40.1
	S_1	GVB//S_1	2.000	1.003	0.997	33.2	2.000	0.996	1.004	40.3
I	S_0	RHF//S_0	0.000	2.000	0.000	0.0	0.000	2.000	0.000	0.0
	T_1	ROHF//T_1	2.000	1.000	1.000	42.9	2.000	1.000	1.000	46.1
	S_1	GVB//T_1	2.000	0.998	1.002	44.1	2.000	1.005	0.995	52.2
	S_1	GVB//S_1	2.000	1.000	1.000	44.0	2.000	0.999	1.001	47.6
II	S_0	RHF//S_0	0.000	2.000	0.000	0.0	0.000	2.000	0.000	0.0
	T_1	ROHF//T_1	2.000	1.000	1.000	44.3	2.000	1.000	1.000	47.0
	S_1	GVB//T_1	2.000	1.000*	1.000*	45.4	1.998	1.028	0.972	48.6
	S_1	GVB//S_1	2.000	0.999	1.001	45.4	2.000	1.000	1.000	48.5
III	S_0	RHF//S_0	0.000	2.000	0.000	0.0	2.000	2.000	0.000	0.0
	T_1	ROFH//T_1	2.000	1.000	1.000	44.9	1.000	1.000	1.000	47.7
	S_1	GVB//T_1	1.762	1.345	0.655	43.3	1.999	1.018	0.982	49.1
	S_1	GVB//S_1	2.000	1.002	0.998	46.0	2.000	1.001	0.999	49.1

* Occupancies n_1 and n_2 fixed in the course configuration optimization.

The experimental data available for the ground state of the molecules [38–40] are in satisfactory agreement with the values calculated by the RHF/DH or RHF/6-31G* method (Table 1). Previously, the structure of unexcited molecules of ethylene and its fluoroderivatives has been studied in detail by *ab initio* methods, including the MP2 technique [41].

In the triplet state, the free valence indices F_A (Figs. 1 and 2), which are equal to spin occupancies, are located at carbon atoms of a degraded double CC bond, with the distribution of F_A weakly dependent on the type of a substituent at this bond (F or C). In the triplet state, olefin molecules become diradicals, with all the ensuing consequences in spectral and chemical regard.

Structure of singlet excited states S_1. In calculating a singlet excited state S_1, there arises the problem of a variational collapse, which can be eliminated by using the GVB method with fixed occupancies of active natural MO at $n_1 = n_2 = 1$ or with variation of these occupancies at $n_1 + n_2 = 2$. Both the approaches give identical results for geometric parameters, energies, and occupancies. The geometric characteristics of olefin molecules in the S_1 state (Table 1), calculated under these assumptions, are close to the corresponding parameters of the molecules in the triplet states. This gives reason to maintain that the 3*D* structure of olefin molecules in the lower excited states T_1 and S_1 is the same. It should be noted that optimization at $n_1 = n_2 = 1$ reveals a minimum on the potential surfaces for T_1 and S_1 (absence of imaginary frequencies in the vibrational spectrum), whereas occupancy variation at $n_1 + n_2 = 2$ localizes the saddle point on the S_1 surface at the same energy (presence of a single imaginary frequency in the spectrum).

A quantum-chemical calculation yielded unexpectedly close energies of the singlet and triplet states (Table 2); the triplets lie below singlets (by

Table 3. Quantum-chemical total energies E_{tot}, squared total spins $<S^2>$, and enthalpies ΔH of lower excited states of perfluoro-olefins (UHF/DH) with account of the energy Δ_{vib0} of zero vibrations and thermochemical corrections for temperatures 0–700 K

Molecule	ΔE_{tot}, kcal mol^{-1}	$<S^2>$	Δ_{vib0}	ΔH_{calc} (kcal mol^{-1}) at indicated temperature T, K						ΔH_{exp}, kcal mol^{-1} [9]
				0	298.15	400	500	600	700	
I-F	20.7	2.011	–1.4	19.3	19.6	19.7	19.7	19.8	19.8	18
II-F	26.9	2.013	–1.7	25.2	25.5	25.7	25.7	25.8	25.9	18
III-F	27.8	2.014	–1.8	26.0	26.3	26.4	26.5	26.6	26.7	18
IV-F	27.7	2.015	–0.4	27.3	27.2	27.7	27.3	27.3	27.3	18

1–3 kcal mol^{-1}), in agreement with the general experimental pattern. The uncommon nature of this result is emphasized by the fact that the singlet–triplet splitting $E(S_1)$–$E(T_1)$ for vertical transitions in olefins, e.g., ethylene, is gigantic (3 eV). The dramatic, nearly 30-fold decrease in the $E(S_1)$–$E(T_1)$ splitting on passing to the equilibrium excited state S_1 is, apparently, a consequence of the elimination of the exchange interaction between π-electrons as a result of a structural transformation of the ethylene molecule from planar to perpendicular configuration.

The values of n_1 and n_2 in the optimal configuration are 1.000 for all the eight olefin molecules studied, **I**–**IV** and **I**-F–**IV**-F (Table 2 lists data for 6 molecules). The valences V_{mol} of the molecules in the singlet (S_1) and triplet (T_1) states take the maximum possible, for a two-determinant wave function, value of 2.000. The exception is provided by those S_1 states which were calculated by the GVB//T_1 method for an equilibrium triplet configuration. However, V_1, n_1, and n_2 are close to their optimal values in these cases, too, which confirms that the molecular structures in the S_1 and T_1 states are identical.

Energies of equilibrium excited states of olefins and perfluoro-olefins. A specific feature of perfluoro-olefins (Table 2) is that the excitation energies are low and lie within the thermally accessible range (~1 eV). Another important point is that the energies of singlet (S_1) and triplet (T_1) states coincide, i.e., there exist fourfold degenerate states of olefins, $(S \cdot T)_1$, of diradical nature. Also, as substituents are introduced at the double bond of perfluoro-olefins, a certain increase in the energy of the S_1 and T_1 states is observed. The corresponding levels for unfluorinated olefins (Table 2) lie at approximately twice higher energies, being virtually independent of the type of a substituent at the double bond.

In Table 3, the calculated electronic excitation energies of the molecules are corrected for the energies of zero vibrations and thermochemical contributions (vibrational, rotational, etc.), which become noticeable at elevated temperatures. The resulting enthalpies of excitation can be directly compared with experimental enthalpies of formation of intermediates (excited species) [15]. The best agreement between experiment and calculation is observed for the simplest representative of perfluoro-olefins, TFE (Table 3): 18 and 19.8 kcal mol^{-1} at 700 K. Replacing the fluorine atoms in the TFE molecules with perfluoroalkyl substituents leads to a noticeable increase in the calculated enthalpy of excitation; however, no dependence of the experimental enthalpy of formation of intermediates on the type of substituent was observed in [15].

THERMOEXCIMERS IN CYCLODIMERIZATION OF ETHYLENE AND PERFLUOROETHYLENE

An important consequence of the concept [16] of electronic excitation as a necessary stage of a chemical reaction is the conclusion that the reaction structure (intermediate in terms of [15]), which precedes the formation/rupture of a chemical bond, has radical (diradical) nature. For the reaction of TFE cyclodimerization

$$C_2F_4 + C_2F_4 \overset{kT}{\rightleftarrows} C_2F_4^* + C_2F_4 \rightleftarrows C^{\bullet}F_2{-}C^{\bullet}F_2...CF_2{=}CF_2 \overset{kT}{\rightleftarrows} C^{\bullet}F_2{-}CF_2{-}CF_2{-}C^{\bullet}F_2 \overset{kT}{\rightleftarrows} \boxed{F} \quad (15)$$

this means that the formation of stable perfluorocyclobutane F is preceded by a number of radical stages, with the direct processes of binding of two unexcited molecules

$$C_2F_4 + C_2F_4 \rightleftarrows \boxed{F} \quad (16)$$

not occurring at all. In single-stage reactions of the type (16), radical stages are concealed and cannot be revealed experimentally because of their short lifetime.

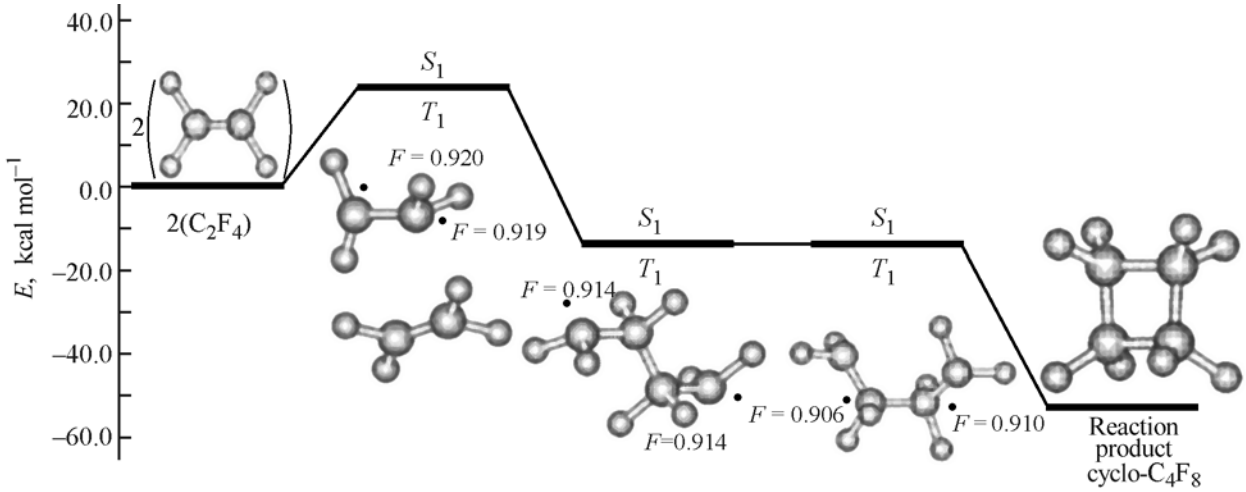

Fig. 3. Energy diagram of the reaction of C_2F_4 cyclodimerization (RHF, ROHF, GVB/DH); *F* are free valence indices of terminal carbon atoms. (*E*) Energy; the same for Figs. 4, 7, and 8.

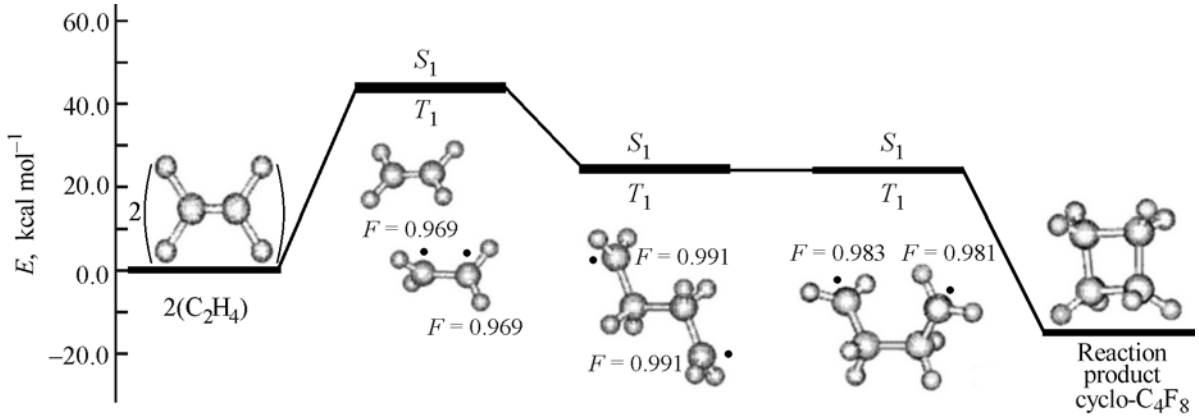

Fig. 4. Energy diagram of the reaction of C_2H_4 cyclodimerization (RHF, ROHF, GVB/DH); *F* are free valence indices of terminal carbon atoms.

In view of the concepts of diradical nature of the $(S \cdot T)_1$ states and new experimental data [12, 14, 15], the mechanism of TFE cyclodimerization was reconsidered in [4, 33, 42]. Direct experimental confirmation of the radical nature of the reaction of TFE cyclodimerization [14, 15] is of great importance for understanding of the mechanism of this and many other reactions.

Thermal cyclodimerization of TFE is similar to the corresponding photochemical reaction of anthracene (A) dimerization, which proceeds via the excimer state AA^* [43]. In either case, a complex, named excimer, is formed between the excited and unexcited molecules. In TFE dimerization (Fig. 3), the potential barrier of the reaction is determined by the enthalpy of formation of the complex (thermoexcimer) TFE TFE^*, which can be calculated as triplet energy. A collision of TFE^* and TFE molecules (quenching of TFE^*) leads to formation of intermediate perfluorotetramethylene C_4F_8.

The diradical C_4F_8 was first recorded as a stable species, presumably in *trans*-configuration, by its absorption spectrum (230 nm) in the millisecond time range [14]. The lifetime of its hydrogen analogue C_4H_8 is much shorter, being equal, depending on the pumping energy, to 300–800 fs [1], but in the case in question, the diradical C_4H_8 has *cis*-configuration. The diradicals C_4F_8 (C_4H_8) are relaxed electronically excited singlet (S_1) and triplet (T_1) states of the final product of the reaction, cyclobutane. The theoretical activation energies E_a of the cleavage of a four-membered ring

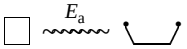

are the same for cyclo-C_4F_8 and cyclo-C_4H_8 (39 kcal mol^{-1}) (Figs. 3 and 4). The difference in the optimized geometric parameters of singlet and triplet diradicals is negligibly small; for example, the lengths of the central bond C–C in the *cis*-C_4F_8 di-

radical coincide for the S_1 and T_1 states, being equal to 1.547 Å. The energies of these states are also rather close (with the difference not exceeding 0.1 kcal mol^{-1}). The radical centers in the molecules of tetramethylenes are localized at terminal carbon atoms and are characterized by free valences close to unity. The total valence of the diradicals in the ROHF approximation is exactly 2 for the triplet state and varies within 1.890–1.990 for the equilibrium singlet state (GVB/DH method).

If the activation energy $E_a(\rightarrow)$ of forward cyclization is taken to be equal to the triplet energy of TFE, 20.7 kcal mol^{-1} (Table 3), and the enthalpy ΔH, to be 52.7 kcal mol^{-1} (experimental value 53.1 kcal mol^{-1} [44]), then the calculated activation energy of the reverse reaction $E_a(\leftarrow) = 20.7 + 52.7 = 73.4$ kcal mol^{-1}. The experimental activation energy of reaction (16) of perfluorocyclobutane decomposition into two TFE molecules (79.2 ± 1 kcal mol^{-1} [12]) exceeds somewhat the calculated value obtained by the authors of this review. At the same time, [12] presents data of other authors, according to which $E_a^{exp}(\leftarrow)$ vary within 74.4–75.6 kcal mol^{-1}.

It is assumed that the reaction proceeds in accordance with Eq. (15): upon encounter of TFE and TFE* molecules, the excited complex $^{1,3}(C^{\bullet}F_2–C^{\bullet}F_2...CF_2=CF_2$ transforms into the diradical $C^{\bullet}F_2–CF_2–CF_2–C^{\bullet}F_2$ with electronic structure $(S \cdot T)_1$. *trans*-1,4-Diradical has nonplanar structure ($\angle$CCCC = 163.9°) with terminal radical centers on which a free valence $F = 0.914$ is concentrated. The $C^{\bullet}F_2–CF_2$ and $CF_2–CF_2$ bond lengths are, respectively, 1.523 and 1.552 Å. 1.4-Diradical readily assumes the *cis*-configuration, then undergoes internal conversion $S_0 \leftarrow\sim\sim S_1$, and, on the way to the ground singlet state S_0, is stabilized in the form of the reaction product, perfluorocyclo-butane. The C–C bond length in a symmetric (D_{2d}) nonplanar molecule of cyclo-C_4F_8 is the same as that in the molecule of cyclo-C_4H_8 (1.559 Å).

It may be assumed that the reversible reaction (1) of ethylene cyclodimerization can be described in a similar way. In this case, all the levels in the energy diagram (Fig. 4) lie much higher than the corresponding levels for the reaction of TFE dimerization (Fig. 3). For example, the heats of formation of cyclobutane and perfluorocyclobutane are 15.2 and 53.0 kcal mol^{-1}, respectively. In the case of ethylene, the heats of formation of 1,4-biradicals are positive, being negative for TFE, and, therefore, 1,4-perfluorodiradicals must be much more stable than their

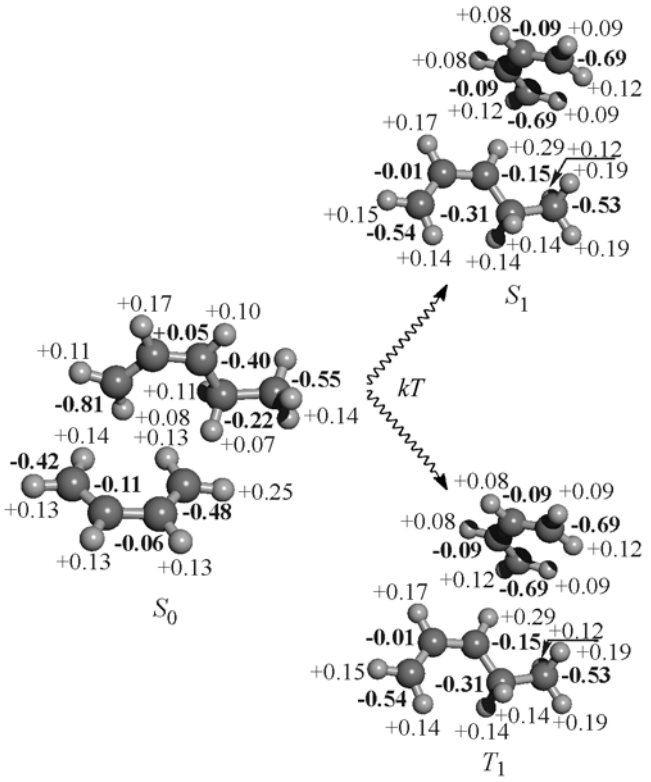

Fig. 5. Distribution of charge among atoms in a complex of *cis*-2-penten-1-yl anion with *cis*-butadiene in singlet ground (S_0, RHF/DH), singlet excited (S_1, GVB/DH), and triplet excited (T_1, ROHF/DH) states.

hydrogen analogues. The calculated activation energy of the reaction of cyclobutane decomposition into two ethylene molecules (59.1 kcal mol^{-1}) is in satisfactory agreement with the experimental value of 62.5 kcal mol^{-1} [3].

Thus, a new mechanism of the reaction of ethylene and TFE dimerization, including thermal electronic excitation of a complex of molecules of the excimer type, was suggested in [4, 33, 42]. Alternative analysis of the reaction [1, 15] in terms of the transition state method fails to provide an adequate quantitative description and to account for the properties of experimentally observed electronically excited olefin intermediates.

ELECTRONICALLY EXCITED COMPLEXES (THERMOEXCIPLEXES) OF BUTADIENE

The above radical mechanism of ethylene dimerization can be extended to the case of polymerization, whose elementary stage includes local triplet excitation of the ethylene molecules within the reaction complex constituted by a free radical and ethylene

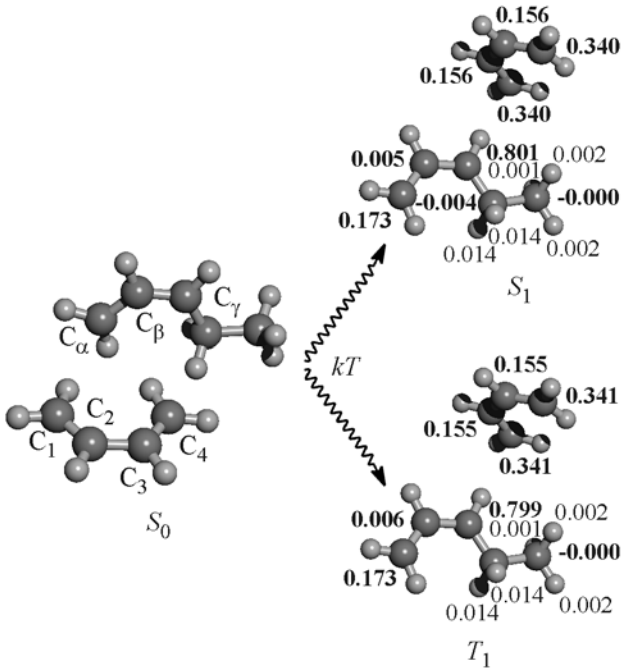

Fig. 6. Distribution of free valence indexes among atoms in a complex of *cis*-2-penten-1-yl anion with *cis*-butadiene in singlet, S_1 (GVB/DH), and triplet, T_1 (ROHF/DH), excited states and structure of the complex in the singlet ground state S_0 (RHF/DH).

molecule. The general pattern of the process was discussed in [45], but rigorous nonempirical calculation of complexes of uncharged radical species by the existing methods fails to produce satisfactory results. More adequate results are obtained for anionic polymerization of dienes (butadiene, isoprene) [11, 35, 46–51], which have been extensively studied by spectral and quantum-chemical methods previously [52–62]. Because of this circumstance, an example of a theoretical analysis of reaction complexes of butadiene with the corresponding anionic and lithium species in terms of the concept of thermal electronic excitation is given below.

Quasi-degenerate singlet (S_1) and triplet (T_1) states of reaction complexes. Modeling of elementary stages of anionic polymerization of butadiene is possible for a particular case of complexes formed by butadiene CH_2=CH–CH=CH_2 with 2-penten-1-yl anion CH_3–CH_2–CH=CH_2^- (V-an). Figure 5 illustrates a complete transfer of an electron (Δq = 0.98) between reactant molecules upon excitation of the complex into a singlet (S_1) or triplet (T_1) state. It is important that both the excited states are characterized by identical charge distributions among atoms of the 2-pentene-1-yl radical and the anion-radical of butadiene.

Another important issue is the virtually absolute identity of the free valence indices F_A for the triplet (T_1) and singlet (S_1) excited states (Fig. 6). The values of F_A coincide with spin occupancies calculated for the triplet state as a sum of atomic contributions to boundary orbitals. In a similar way are found free valence indices for the excited singlet state S_1. Also close are the geometric parameters of the complex 2-penten-1-yl anion...butadiene (Table 4) in the states T_1 and S_1, with the optimized structure of the complexes corresponding to a minimum on the potential-energy surface, which is confirmed by absence of imaginary frequencies in the vibrational spectrum.

Finally, mention should be made of the singlet-triplet splitting, which is negligibly small (0.17 kcal mol^{-1}).

Table 4. Optimized (RHF, ROHF, GVB/DH) configurations of molecules and complexes with *cis*-butadiene in singlet (S_0 and S_1) and triplet (T_1) states

Molecule or complex	C_α–C_β	C_β–C_γ	$\angle C_\alpha C_\beta C_\gamma$, deg	C_α–Mt	C_β–Mt	C_γ–Mt	C_1–Mt	C_2–Mt	C_α–C_1	C_α–C_4	C_γ–C_2	C_γ–C_4
	Å			Å								
cis-2-Penten-1-yl anion:	1.42	1.41	130.1									
S_0	1.40	1.39	130.4						4.03	4.10	3.80	5.40
T_1	1.35	1.44	126.6						6.40	6.40	4.20	4.20
S_1	1.35	1.44	126.6						6.42	6.42	4.22	4.22
cis-2-Penten-1-yl-lithium:	1.42	1.39	125.9	2.14	2.11	2.18						
S_0	1.42	1.39	126.5	2.16	2.11	2.24	2.72	2.52	4.20	4.36	4.77	4.70
T_1	1.35	1.45	126.0	2.52	2.68	3.36	2.30	2.20	4.55	4.40	5.30	4.94
S_1	1.35	1.45	126.0	2.52	2.75	3.46	2.30	2.20	4.39	4.54	5.05	5.44

Table 5. Microscopic structure of polybutadiene in relation to nature of active center and solvent (initial AC concentration n_0, initial bd concentration ~2 M)

AC	Solvent	Electron donor D	[D]/[Li]	T, °C	$n_0 \times 10^3$, M	Content of indicated units, %			Reference
						1,4-*cis*-	1,4-*trans*-	1,2-	
BuLi	Heptane			35	0.5	42	49	9	[35]
BuLi	Hexane	THF	10				Σ = 30	70	[63]
BuLi	THF			20	5		12	88	[35]
DSTMS	THF			–78	2		8	92	[35]
OLC	CH			20	0.01	28	68	4	[54]**
OLC	Hexane			20	3	62	30	8	[54]**
OLC	Heptane			20	12.4	44	46	10	[54]**
BuLi*	HCS	Diglyme	0.8	30		22		78	[54]***
BuLi	HCS	TMED	2.0	20		10	10	80	[54]***
BuLi	HCS	2,3-DMB	0.5	20		10	10	80	[54]***

* BuLi, *n*-butyllithium; THF, tetrahydrofuran; 2,3-DMB, 2,3-dimethoxybutane; CH, cyclohexanone; OLC, organolithium compounds; HCS, hydrocarbon solvent; DSTMS, disodiumtetramer of α-methylstyrene; TMED, tetramethylethylenediamine.

** Data from Table 1.12.

*** Data from Table 1.19.

The close energies of the S_1 and T_1 states, combined with the above-mentioned coincidence of charges, free valence indices, and geometric parameters, suggest the existence of a fourfold degenerate diradical state of the complex, $(S \cdot T)_1$, with low energy, which is directly involved in the events of rupture and formation of a chemical bond.

Structure of complexes formed by free anions and butadiene. Now a system constituted by a V-an anion in *cis*-conformation and *cis*-butadiene (bd) will be considered in more detail. In a real polymerizing system containing "living" (polybutadien)yl-lithium and butadiene, anions are formed in noticeable amounts in polar electron-donor solvents (D), e.g., THF, as a result of dissociation of ion pairs:

$$\sim\sim\sim C^- Mt^+ \overset{D}{\rightleftarrows} \sim\sim\sim C^- Mt^+ \cdot D. \qquad (17)$$

The difference between the energies of *cis*- and *trans*-isomers of butadiene is 3.34 kcal mol^{-1} (RHF/DH), and, consequently, the fraction of *cis*-isomer in solution is insignificant (<1%). However, *cis*-butadiene forms more stable complexes, compared with the *trans*-form, and is more active in polymerization. Therefore, the review only presents data for *cis*-butadiene and the role played in polymerization by *trans*-butadiene is considered in [35]. An RHF/DH calculation shows that the free *cis*-2-penten-1-yl anion has π-allyl structure with approximately equal C_α–C_β and C_β–C_γ bond lengths (Table 4). However, the charges on atoms C_α and C_γ are different, being equal to, respectively, –0.81 and –0.42. In the optimized structure of the complex (Fig. 5), the molecular planes are mutually perpendicular, which points to a predominating role of interaction between local centers, whereas the overlapping of boundary orbitals, which requires a planar orientation of the 2-penten-1-yl anion and butadiene, is less important.

The transition of the V-an anion from the free state into a complex with butadiene has no essential influence on its geometric parameters (Table 4) or on charges (q_α = –0.81, q_γ = –0.41). It would be expected, on the basis of the prevailing concept of charge control, that butadiene should mainly add to the C_α atom to give 1,4-unit in the polymer chain. This assumption is not, however, confirmed by experiment, which demonstrates the predominant formation of 1,2-units in the electron-donor THF solvent (Table 5). Figure 7 shows the energy levels found for the gas phase and solution in inert *n*-heptane. It can be seen that the heats of formation of the *cis*-V-an...*cis*-bd complex in the S_0 states are significantly different for these two cases: 4.8 and 1.0 kcal mol^{-1}, respectively. Consequently, complexes with 2-penten-1-yl and, presumably, other anions are unstable in an inert solution.

In the electronically excited state of the complex (S_1 or T_1), there occurs complete transfer of an elec-

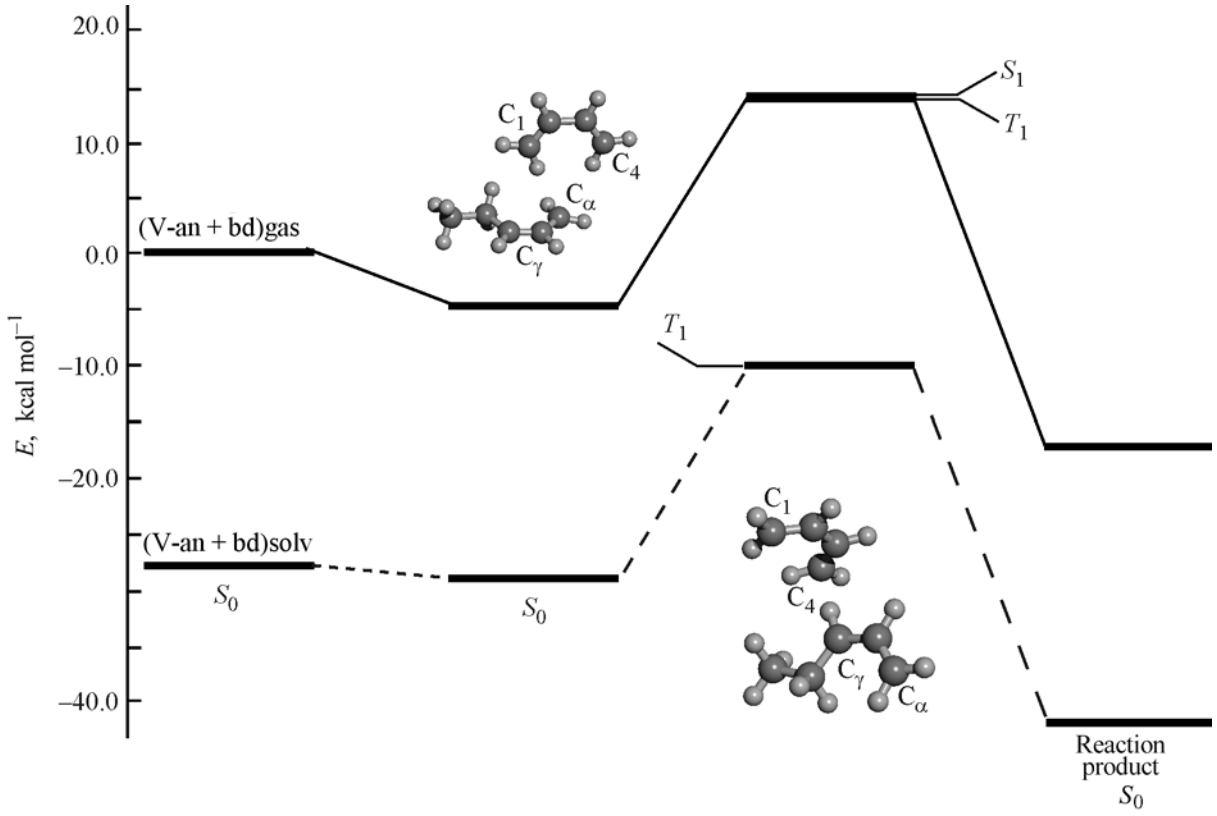

Fig. 7. Energy diagram of the reaction of *cis*-penten-1-yl anion with *cis*-butadiene (solvent taken into account in the RSM approximation; RHF, ROHF, and GVB/DH methods). *Solid lines*, gas phase; *dashed lines*, solution in *n*-pentane; energy levels of the starting reagents V-an+bd, reaction product, and complex in the ground (S_0) and excited (S_1 and T_1) states are shown.

tron from the anion to the butadiene molecule to give a free chain radical and anion-radical of the monomer, which can be judged from the distribution of charge density and free valence indices (Figs. 5 and 6). The highest chemical activity for the complex shown in Fig. 6 is exhibited by the C_γ atom of the 2-penten-1-yl radical (F_A = 0.80) and atoms C_1 and C_4 of the anion radical of butadiene (F_A = 0.34). It is these carbon atoms that are the most closely spaced in the reagent molecules (R = 4.20 Å) and, in principle, can form a chemical bond through spin coupling, which must give rise to 1,2-units in polybutadiene. This theoretical prediction is in full agreement with experimental data (Table 6) [35, 52, 54, 62, 64].

Table 6. Charges q on C_α and C_γ carbon atoms in *cis*- and *trans*-2-penten-1-yl anion, calculated by semiempirical and *ab initio* methods (RHF, definition of q by Mulliken)

Calculation method	*cis*-		*trans*-	
	$-q(C_\alpha)$	$-q(C_\gamma)$	$-q(C_\alpha)$	$-q(C_\gamma)$
CNDO	0.290	0.311	0.289	0.317
INDO	0.267	0.321	0.267	0.327
MNDO	0.444	0.539	0.445	0.545
AM1	0.594	0.582	0.595	0.589
PM3	0.644	0.654	0.644	0.665
RHF/STO-6G	0.336	0.261	0.336	0.263
RHF/DH	0.808	0.419	0.805	0.430
RHF/6-31G*	0.625	0.404	0.615	0.402
RHF/6-31G**	0.517	0.356	0.506	0.358
RHF/6-311G**	0.504	0.407	0.483	0.402

The activation energy of the electron-transfer reaction, which determines the potential barrier for the overall reaction of addition of a butadiene molecule to V-an, can be calculated as the energy of the diradical state $(S \cdot T)_1$ relative to the level of free reagents. For the system shown in Fig. 7, this value is 14.2 kcal mol^{-1} in the gas phase and 17.9 kcal mol^{-1} in an inert medium of heptane.

Structure of complexes formed by 2-penten-1-yl-lithium with butadiene. A polymer mostly composed of 1,4-*cis*(*trans*)-units is formed in polymeriza-

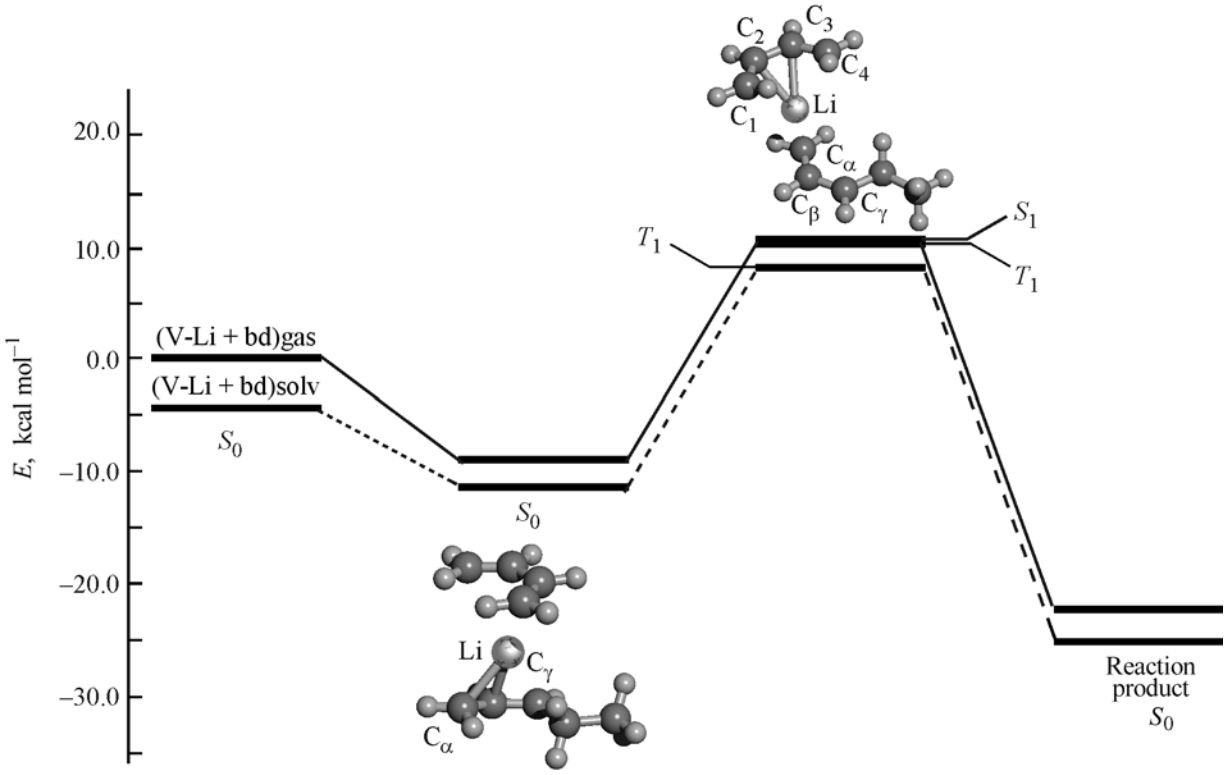

Fig. 8. Energy diagram of the reaction of *cis*-penten-1-yl-lithium with *cis*-butadiene (solvent taken into account in the RSM approximation; RHF, ROHF, and GVB/DH methods). *Solid lines*, gas phase; *dashed lines*, solution in *n*-pentane; energy levels of the starting reagents V-Li+bd, reaction product, and complex in the ground (S_0) and excited (S_1 and T_1) states are shown.

tion of butadiene in hydrocarbon solvents (hexane, heptane) in the absence of free anions (Table 5). It is commonly believed that chain grows under these conditions on monomeric and associated forms of the organolithium compound, and the 1.4-structure is fixed in the terminal unit of the active center as a result of incorporation of bd at the C_α–Mt bond [52–62]. Calculation of a model complex by the RHF/DH method yields a nearly α-alkyl structure (Fig. 8, Table 4), and the distribution of atomic charges differs only slightly from that in the V-an...butadiene complex considered above: q_α = –0.73, q_γ = –0.38.

The complex of *cis*-2-penten-1-yl-lithium with *cis*-butadiene has in the ground state such a structure (Fig. 8, Table 4) that the monomer molecule is oriented toward the Li atom, with inequality of charges on C_α and C_γ atoms preserved (–0.73 and –0.35, respectively). In the triplet excited state of the complex, charge transfer to the butadiene molecule (Δq = –0.52) is accompanied by a shift of the Li^+ cation, which is situated at equal distances from the terminal carbon atoms (2.30 Å), but closer to the central atoms (2.20 Å) of the anion-radical of butadiene. The resulting process is that the Li atom is transferred and two radical species are formed: 2-penten-1-yl radical and a radical of butadiene-lithium. The chemical bond is formed in the singlet state in the course of relaxation of the diradical state of the complex: $(S \cdot T)_1 \rightsquigarrow S_0$

In accordance with the free valence indices, the terminal atoms C_1 and C_4 of *cis*-butadiene-lithium ($F_1 = F_4 = 0.34$), which are closer to the carbon atom C_α (F_α = 0.17), at 4.40 and 4.55 Å, than to C_γ (F_γ = 0.80), 4.94 and 5.30 Å, in the triplet state of the complex. These data predict, in agreement with experiment (Table 5), preferable formation of a chemical bond between the α-carbon atom of the chain radical and one of the atoms C_1 or C_4 of butadiene, to give 1,4-units in the chain of polybutadiene.

As a theoretical parameter characterizing the reactivity of the system 2-penten-1-yl-lithium...butadiene can be taken the calculated energy of the excited level $(S \cdot T)_1$, which is 10.4 kcal mol^{-1} for the gas phase and 12.6 kcal mol^{-1} for a solution in heptane (Fig. 8). In contrast to the case of the anionic complex, the enthalpy of formation of this complex in

the ground state changes, on passing from the gas phase to a heptane solution, only slightly, from 9.1 to 7.0 kcal mol^{-1}. Comparison of the given system with the V-an...butadiene complex shows a higher chemical activity of the lithium forms, compared with the anionic ones. This theoretical conclusion is in an apparent contradiction with the widely accepted opinion that the chemical activity of anions is at the maximum possible level.

On principles of charge and spin control over polymerization reaction. Data on atomic charges are commonly obtained from quantum-chemical calculations. However, it is known that calculated charges are rather sensitive to a calculation procedure, and in the case of nonempirical methods, to a basis. In numerous theoretical studies in the field of anionic polymerization, carried out in the 1970s–1990s [53, 57, 59, 65], calculations were mostly performed using semiempirical methods, which yield charge distribution for free anions, $|q(C_\gamma)| \geq |q(C_\alpha)|$, satisfying the charge control principle. Indeed, vinyl $-CH=CH_2$ and $-C(CH_3)=CH_2$ units are generated in the polymer chain in polymerization of butadiene and isoprene in electron-donor solvents, in which formation of free anions is observed, through addition of the monomer to the C_γ atom carrying the highest amount of negative charge (Table 6).

At present, *ab initio* methods, which provide a more adequate description of the geometric configuration and electronic characteristics of molecules, compared with semiempirical methods, are widely used. However, the *ab initio* techniques yield exactly the opposite charge distribution (Table 6): $|q(C_\alpha)| > |q(C_\gamma)|$, and, consequently, calculations of this kind are in contradiction with the principle of charge control in the formation of the microscopic structure of polydienes. This contradiction can be accounted for in two ways: (1) *ab initio* methods are not quite correct in evaluation of charges on atoms, and (2) the very principle of charge control is inadequate.

In terms of the approach used in [11, 35, 48–51], there is no need to invoke the charge control principle. The properties of reaction complexes in the electronically excited state are controlled by the distribution of free valence indices, rather than by that of atomic charges, and these distributions are not in agreement with each other. Moreover, the probability of formation of a chemical bond depends on the configuration of the excited complex, i.e., on the proximity of the potentially active centers of interaction.

CONCLUSION

The known processes, such as dimerization of ethylene or anionic polymerization of butadiene, can be explained in a novel way, and in agreement with experimental data, in terms of the concept of thermal electronic excitation in an elementary chemical process. This is done by considering a real physical process, electronic excitation of a molecule or a reaction complex to low-lying states S_1 or T_1 of radical or diradical nature. It is assumed that the events of rupture/formation of a chemical bond occur at the atom with sufficiently large free valence index, rather than at the atom with the greatest negative charge.

REFERENCES

1. Pedersen, S., Herek, J.L., and Zewail, A.H., *Science*, 1994, vol. 266, pp. 1359–1364.
2. *Diradicals*, Borden, W.T., Ed., New York: Wiley, 1982.
3. Benson, S.W., *Thermochemical Kinetics*, New York: Wiley, 1976, 2nd ed.
4. Kalnin'sh, K.K., Semenov, S.G., and Panarin, E.F., *Dokl. Ross. Akad. Nauk*, 2003, vol. 390, no. 3, pp. 350–354.
5. Jug, K., *J. Comp. Chem.*, 1984, vol. 5, no. 6, pp. 555–561.
6. Jug, K., *Tetrahedron Lett.*, 1985, vol. 26, no. 11, pp. 1437–1440.
7. Barltrop, J.A. and Coyle, J.D., *Excited States in Organic Chemistry*, London: Wiley, 1975.
8. Salem, L. and Rowland, C., *Angew. Chem., Int. Ed. Engl.*, 1972, vol. 11, pp. 92–100.
9. *The Exciplex*, Gordon, M. and Ware, W.R., Eds., New York: Academic, 1975.
10. Kalnin'sh, K.K., *Phys. Chem. Chem. Phys.*, 2001, vol. 3, no. 2, pp. 4542–4546.
11. Kalninsh, K.K. and Podolsky, A.F., *Int. J. Quantum Chem.*, 2002, vol. 88, no. 5, pp. 624–633.
12. Buravtsev, N.N., Grigor'ev, A.S., and Kolbanovskii, Yu.A., *Kinet. Kataliz*, 1985, vol. 26, no. 1, pp. 7–14.
13. Buravtsev, N.N., Kolbanovskii, Yu.A., and Ovsyannikov, A.A., *Izv. Ross. Akad. Nauk, Ser. Khim.*, 1995, no. 10, pp. 2048–2050.
14. Buravtsev, N.N. and Kolbanovskii, Yu.A., *J. Fluorine Chem.*, 1999, vol. 96, pp. 35–42.
15. Buravtsev, N.N., Kolbanovskii, Yu.A., and Ovsyannikov, A.A., *Zh. Prikl. Khim.*, 2002, vol. 75, no. 4, pp. 612–619.
16. Kalnin'sh, K.K., *Elektronnoe vozbuzhdenie v khimii*

(Electronic Excitation in Chemistry), St. Petersburg: SPb. Gos. Univ. Technol. Dizaina, 1998.

17. Giambiagi, M., Giambiagi, M., Grempel, D.R., and Heymann, C.D., *J. Chim. Phys.*, 1975, vol. 72, no. 1, pp. 15–22.
18. Giambiagi, M.S. de, Giambiagi, M., and Jorge, F.E., *Z. Naturforsch.*, 1984, vol. 39a, pp. 1259–1273.
19. McWeeny, R., *Rev. mod. Phys.*, 1960, vol. 32, no. 2, pp. 335–369.
20. McWeeny, R., *J. Chem. Phys.*, 1951, vol. 19, pp. 1614–1615.
21. Mulliken, R.S., *J. Chem. Phys.*, 1955, vol. 23, pp. 1833–1840.
22. Dmitriev, I.S. and Semenov, S.G., *Kvantovaya khimiya – ee proshloe i nastoyashchee. Razvitie elektronnykh predstavlenii o prirode khimicheskoi svyazi* (Quantum Chemistry: Its Past and Future, Development of Electronic Concepts of the Nature of Chemical Bond), Moscow: Atomizdat, 1980.
23. Mayer, I., *Int. J. Quantum Chem.*, 1984, vol. 26, pp. 151–154.
24. Tulub, A.V. and Semenov, S.G., *Valentnost' (Sovremennye aspekty staroi problemy)* [Valence (Modern Aspects of the Old Problem)], Leningrad: Znanie, 1989.
25. Weeny, R.Mc. and Sutcliffe, B.T., *Methods of Molecular Quantum Mechanics*, London: Academic, 1969.
26. Schmidt, M.W., Baldridge, K.K., and Boatz, J.A., *et al., J. Comput. Chem.*, 1993, vol. 14, no. 11, pp. 1347–1363.
27. Borisova, N.P. and Semenov, S.G., *Vestn. Len. Gos. Univ.*, 1973, no. 16, pp. 119–124.
28. Borisova, N.P. and Semenov, S.G., *Vestn. Len. Gos. Univ.*, 1976, no. 16, pp. 98–103.
29. Semenov, S.G., *Valence Theory in Progress*, Moscow: Mir, 1980, pp. 150–169.
30. Mayer, I., *Chem. Phys. Lett.*, 1984, vol. 117, no. 4, pp. 396–396.
31. Dunning, T.H. and Hay, P.J., *Methods of Electronic Structure Theory*, Shaefer, H.F., Ed., New York: Plenum, 1977, vol. 3, pp. 1–27.
32. Trinquier, G. and Barthela, J.C., *J. Am. Chem, Soc.*, 1990, vol. 112, no. 25, pp. 9121–9130.
33. Kalnin'sh, K.K. and Panarin, E.F., *Dokl. Ross. Akad. Nauk*, 2002, vol. 384, no. 3, pp. 350–354.
34. Kalnin'sh, K.K., *Zh. Fiz. Khim.*, 2000, vol. 74, no. 1, pp. 117–124.
35. Kalnin'sh, K.K. and Podol'skii, A.F., *Zh. Strukt. Khim.*, 2001, vol. 42, no. 6, pp. 1071–1084.
36. Gorner, H. and Schulte-Frohlinde, D., *J. Phys. Chem.*, 1978, vol. 85, no. 25, pp. 2653–2659.
37. Caldwell, R.A. and Schwerzel, R.E., *J. Am. Chem. Soc.*, 1972, vol. 94, no. 3, pp. 1035–1037.
38. Carlos, J.L., Karl, R.R., and Bauer, S.L., *J. Chem. Soc., Faraday. Trans. 2*, 1974, vol. 70, pp. 177–187.
39. Hormony, M.D., Laurie, V.W., Kuezkowski, R.L., *et al.*, *J. Phys. Chem. Ref. Data*, 1979, vol. 8, pp. 619–627.
40. Laurie, V.W. and Pence, D.T., *J. Chem. Phys.*, 1963, vol. 38, pp. 2693–2697.
41. Borisov, Yu.A., *Zh. Strukt. Khim.*, 2002, vol. 43, no. 5, pp. 794–802.
42. Kalnin'sh, K.K., *Zh. Prikl. Khim.*, 2002, vol. 75, no. 4, pp. 603–611.
43. Ferguson, F., Castellan, A., Deskergue, J.-P., and Bonas-Laurent, H., *Chem. Phys. Lett.*, 1981, vol. 78, no. 3, pp. 446–450.
44. Atkinson, B. and Trenwith, A.B., *J. Chem. Soc.*, 1953, pp. 2082–2087.
45. Kalnin'sh, K.K. and Panarin, E.F., *Dokl. Ross. Akad. Nauk*, 1993, vol. 333, no. 1, pp. 37–39.
46. Kalnin'sh, K.K., Podol'skii, A.F., Kutsenko, A.D., and Semenov, S.G., *Vysokomol. Soedin., Ser. A*, 1990, vol. 32, no. 2, pp. 316–321.
47. Kalnin'sh, K.K. and Podol'skii, A.F., *Vysokomol. Soedin., Ser. A*, 1991, vol. 33, no. 10, pp. 2215–2224.
48. Kalnin'sh, K.K. and Podol'skii, A.F., *Vysokomol. Soedin.*, 2000, vol. 42, no. 5, pp. 751–758.
49. Kalnin'sh, K.K. and Podol'skii, A.F., *Zh. Strukt. Khim.*, 2000, vol. 41, no. 4, pp. 701–708.
50. Kalnin'sh, K.K. and Podol'skii, A.F., *Zh. Strukt. Khim.*, 2003, vol. 44, no. 4, pp. 602–615.
51. Kalnin'sh, K.K. and Panarin, E.F., *Dokl. Ross. Akad. Nauk*, 2001, vol. 377, no. 6, pp. 786–791.
52. Dolgoplosk, B.A. and Tinyakova, E.I., *Metalloorganicheskii kataliz v protsessakh polimerizatsii* (Organometallic Catalysis in Polymerization), Moscow: Nauka, 1985.
53. Erusalimskii, G.B. and Lyubetskii, S.G., *Protsessy ionnoi polimerizatsii* (Ionic Polymerization Processes), Leningrad: Khimiya, 1974.
54. Monakov, Yu.B. and Tolstikov, G.A., *Kataliticheskaya polimerizatsiya 1,3-dienov* (Catalytic Polymerization of 1,3-Dienes), Moscow: Nauka, 1990.
55. Ofstead Eilert, *Int. Symp. Ionic Polymerization*, Paris, 1997, pp. 164–167.
56. Erussalimsky, G.B. and Kormer, V.A., *Eur. Polym. J.*, 1980, vol. 16, pp. 463–467.

57. Erusalimskii, G.B., Dolinskaya, E.R., Rozinova, O.A., and Kormer, V.A., *Zh. Vses. Khim. O–va im. D.I. Mendeleeva*, 1991, vol. 36, no. 1, pp. 99–105.
58. Sabirov, Z.M., Monakov, Yu.B., Ponomarev, O.A., *et al.*, *Zh. Fiz. Khim.*, 1985, vol. 59, no. 5, pp. 1136–1142.
59. Bondarenko, G.N. and Dolgoplosk, B.A., *Vysokomol. Soedin., Ser. A*, 1996, vol. 38, no. 3, pp. 464–468.
60. Szwarc, M. and Van Beylen, M., *Ionic Polymerization and Living Polymers*, New York: Chapman and Hall, 1993.
61. Lubnin, A.V., Osetrova, L.V., and Podkorytov, I.S., Zh. Obshch. Khim., 1989, vol. 59, no. 5, pp. 1159–1168.
62. Erusalimskii, B.L., Davidyan, A.A., Nikolaev, N.I., *et al.*, *Vysokomol. Soedin., Ser. A*, 1983, vol. 25, no. 10, pp. 2121–2125.
63. Gantmakher, A.R., *Vysokomol. Soedin., Ser. A*, 1971, vol. 13, no. 6, pp. 1263–1277.
64. Arest-Yakubovich, A.A., Kristal'nyi, E.V., and Zhuravleva, I.L., *Vysokomol. Soedin., Ser. B*, 1994, vol. 36, no. 9, pp. 1553–1555.
65. Bondarenko, G.N., Sverchinskaya, S.B., Misurkin, I.A., *et al.*, *Dokl. Akad. Nauk SSSR*, 1983, vol. 272, no. 1, pp. 130–135.

Russian Journal of Applied Chemistry, Vol. 76, No. 10, 2003, pp. 1559–1563. Translated from Zhurnal Prikladnoi Khimii, Vol. 76, No. 10, 2003, pp. 1601–1605.

INORGANIC SYNTHESIS AND INDUSTRIAL INORGANIC CHEMISTRY

Sulfuric Acid Technology for Processing of Eudialyte Concentrate

V. N. Lebedev

Tananaev Institute of Chemistry and Technology of Rare Elements and Mineral Raw Materials, Kola Scientific Center, Russian Academy of Sciences, Apatity, Russia

Received April 18, 2003

Abstract—Sulfuric acid decomposition of eudialyte was studied, and a technological process including two-stage treatment with sulfuric acid, separation and washing of an insoluble residue, successive hydrolytic precipitation of zirconium and iron-manganese concentrates from solution, and recovery of rare-earth elements from the insoluble residue by leaching, was considered. It was found that zirconium(IV) is recovered from a complex carbonate precipitate in the form of a basic sulfate.

Eudialyte from the Lovozero deposit finds no use because of the low content of rare metals [content in the concentrate (wt %): 10–12 ZrO_2, 2–2.5 Ln_2O_3, 0.7–0.9 Nb_2O_5] and the lack of any efficient technology for obtaining high-quality zirconium products, even though the amount of zirconium and rare-earth elements (REE) contained in this deposit is hundreds of times that in the rest of the world [1, 2]. Technological variants including decomposition with sulfuric, hydrochloric, or nitric acids, in which all the components of the eudialyte concentrate (EC) were used and utilized, have been suggested, but it was reported that only processing of about 1 million tons of EC can be costeffective [3].

The key issue of the technology is the integrated use of the concentrate components and the maximum recovery of zirconium(IV) at the minimum consumption of the acid, since the neutralizing components, ammonia and soda, are much more expensive than, e.g., sulfuric acid. In the acid technologies for processing of rare-earth raw materials, the whole amount of acid used for decomposition is to be neutralized to recover the components and utilize wastes.

As a rule, the degree of EC decomposition with acids is not too high, 65–80 wt % [4–6]. The best performance is ensured by use of H_2SO_4, but sufficiently high recovery can be only achieved at a 8–10-fold excess of acid [7–9] or by introduction of 6 mol of the fluoride ion per 1 mol of zirconium(IV) at a threefold excess of sulfuric acid [10]. Sufficiently high recovery at small excess is achieved by using the method described in [11]. Presumably, this occurs because of the additional concentrate decomposition in drying, since the concentration of the acid increases upon water evaporation, and this creates conditions for more complete decomposition at elevated temperature. However, this method is hardly acceptable because of the necessity for drying of a large amount of a gel-like sulfation product.

Use of sulfuric acid has a number of advantages. These are the following: low cost, volatility, and corrosion activity of the acid; separation of some ballast components together with the insoluble residue; higher, compared with that achieved with other acids, degree of decomposition. It has been suggested to recover zirconium(IV) from solution by neutralization [12], extraction [10], and precipitation of zirconium(IV) phosphate [8, 9]. In the case of phosphate precipitation, the amount of impurities captured into the precipitate is large, and processing of zirconium(IV) phosphate into required products is difficult. In the author's opinion, no selective recovery of zirconium has been achieved in studies concerned with extractive processing of solutions. Presumably, the only remaining acceptable technique is precipitation by solution neutralization.

The amount of niobium(V) passing into solution in decomposition with 30–50% sulfuric acid is 40–50%. To achieve a more complete recovery, it has been suggested to introduce hydrogen peroxide in the course of decomposition and leaching [13] or to decompose eudialyte at 180–230°C with 50% acid [14]. True,

1070-4272/03/7610-1559 $25.00 © 2003 MAIK "Nauka/Interperiodica"

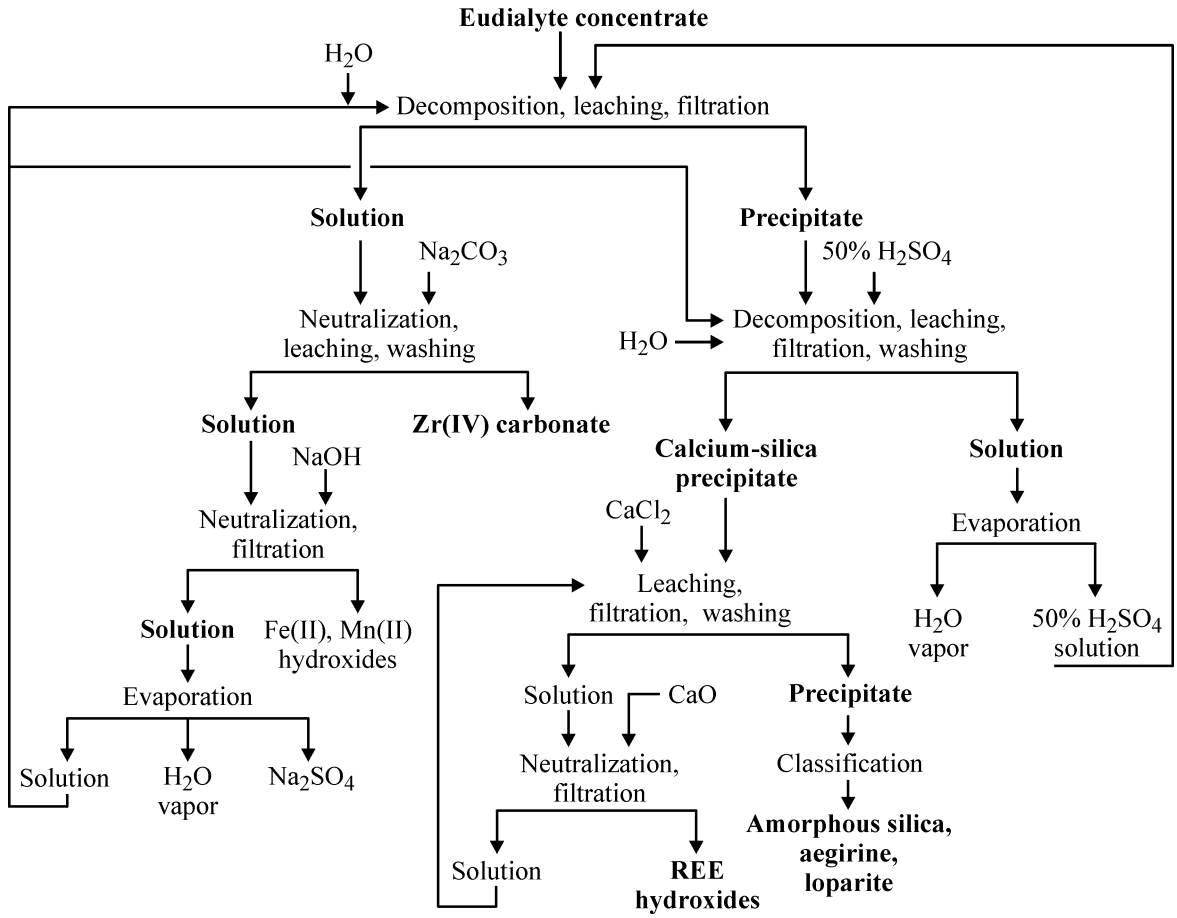

the above conditions more refer to decomposition of loparite contained in EC as impurity. Taking into account the necessary deficit of acid in the technology, high recovery of niobium(V) can be hardly expected.

The amount of rare-earth elements, which constitute a second in importance component of eudialyte, passing into a calcium-silica precipitate in sulfuric acid decomposition is 75–90% [11]; at high dilution the amount of yttrium passing into solution may be 50% [10].

The present communication is concerned with the main procedures used in the integrated sulfuric acid technology of eudialyte [15]. These are the following: sulfuric acid decomposition, formation of a precipitate of zirconium(IV), titanium(IV), niobium(V), iron(III), and aluminum (III) carbonates; formation of an iron-manganese precipitate by neutralization with an alkali; recovery of sodium sulfate by evaporation (see scheme). The recovery of REE from the calcium-silica precipitate by leaching with a calcium nitrate or chloride solution has been studied earlier [16].

EXPERIMENTAL

The EC used in the experiments had the following composition (wt %): ZrO_2 10.5, SiO_2 51.4, Fe_2O_3 4.4, Al_2O_3 4.7, TiO_2 1.1, Ln_2O_3 2.4, MnO 2.0, CaO 5.7, Na_2O 12.4, Nb_2O_5 0.6. In the total REE (wt %, oxides): La 12, Ce 31, Pr 3.9, Nd 14.5, Sm 3.1, Eu 0.79, Gd 2.9, Tb 0.66, Dy 3.68, Ho 1.32, Er 2.32, Tu 0.53, Yb 1.9, Lu 0.43, Y 18.7. An interesting feature of this batch of EC was the high, up to 2.5 wt %, content of loparite, with this content being as high as 40 wt % in coarse fractions.

The eudialyte concentrate was decomposed in a fluoroplastic vessel with a stirrer in a thermostated water bath. The sludge obtained after decomposition and leaching was filtered in a vacuum across a Lavsan filter. The composition of the precipitates obtained was analyzed by X-ray fluorescence method, and that of solution, by atomic-absorption spectroscopy.

It has been suggested, to prevent passing of silicon into solution, to dehydrate the sulfate mass in EC decomposition with sulfuric acid [11, 14] or to per-

Table 1. EC decomposition with sulfuric acid*

Run no.	H_2SO_4, % relative to stoichiometry	Solution				Precipitate			
		V, ml	concentration of oxides, g l^{-1}			W, $m^3\ m^{-2}\ h^{-1}$	m, g	ZrO_2, wt %	α, %
			Zr	Ln	Si				
1	100	350	16.5	0.53	5.5	0.06	83	4.6	64
2	110	400	17.2	0.64	2.3	0.2	84	3.8	70
3	110	400	19.6	0.77	1.2	0.3	78	2.6	80.1
4	150	450	18.4	0.93	0.48	0.6	72	2.4	83.8
5	200	400	22.0	0.87	0.17	2.0	78	2.1	82.4
6	100**	420	22.8	0.89	1.3	0.35	80	1.9	85.7
7	150**	450	23.6	0.96	0.4	0.9	75	1.6	88.6
8	200**	350	25.5	–	–	0.75	78	1.6	88.6
9	100***	350	26.9	–	–	0.8	76	1.2	90.0

* W, filtration rate; α, ZrO_2 recovery.

** Introduction of up to 2 mol F^- per mol of Zr.

*** Decomposition [11].

form decomposition at elevated temperature in an excess amount of acid, with slow charging of the concentrate [5, 6]. A method for decomposition with concentrated acid, with gradual dilution of the resulting sludge, has been suggested [12]. The results of the experiments on decomposition are listed in Table 1.

As follows from the data obtained, the degree of ZrO_2 decomposition is low and increases with the consumption of the acid. A virtually unfilterable sludge is formed at stoichiometric consumption of the acid. The rate of filtration is directly related to the acidity of the system and, as a result, to the content of silicic acid in solution. The concentration of SiO_2 in solution changes from 5.5 g l^{-1} at acid consumption of 100% relative to stoichiometry to 0.15 g l^{-1} at 200%. Even though the introduction of the fluoride ion within the limits studied, improves the process characteristics, it fails to ensure complete decomposition of the concentrate, with better effect achieved on raising the expenditure of the acid. It has been shown previously [17] that eudialyte is nonuniform in composition and more severe conditions are necessary for decomposition of the remaining 20–30% of the concentrate, compared with those for the primary concentrate. Therefore, a 10-fold excess, or threefold in the presence of fluoride ions, of the acid is necessary for complete decomposition.

The excess amount of the acid in the production solution could be neutralized with EC, with the two-stage decomposition thus used. In treatment with eudialyte, up to 0.4–0.6 N is neutralized; however, silicic acid passes into solution under these conditions. A two-stage decomposition with precipitation of silica was achieved with decomposition under spontaneous drying of the precipitate in the first stage and an excess of acid, sufficient for precipitation of silica, in the second. The decomposition was carried out in both stages with approximately 50% acid at overall consumption of 105% relative to stoichiometry. After secondary decomposition and leaching, the solution was filtered, evaporated to 50%, and used to decompose a fresh portion of the concentrate. The reaction proceeded vigorously to give a dry mass. In leaching of this mass, the concentration of silicic acid in solution was 0.03–0.05 g l^{-1} of SiO_2. After three cycles of decomposition (100-g portion of eudialyte in each cycle), the production solution (370 ml) contained 36.1 g l^{-1} of ZrO_2 at acidity of 0.9 N. The solution obtained after secondary decomposition of the precipitate formed in the first stage (370 ml) contained 13.8 g l^{-1} of ZrO_2 at acidity of 5.1 N, and the washing solution (140 ml), 6.3 g l^{-1} at 2.9 N. A 84.5-g portion of insoluble residue contained 1.5% ZrO_2, which corresponds to recovery of 88%. The results obtained in recovery by two-stage treatment are close to those for the technique described in [11]; however, it seems that solution evaporation is simpler technologically and less energy-consuming than drying of the whole amount of the sulfate mass.

Two-stage decomposition at minimum consumption of acid ensures a sufficiently high recovery, but REE can pass into solution in acid treatment of a sec-

Table 2. Solubility of lanthanide sulfates in sulfuric acid solution

H_2SO_4, M	Ln(III) concentration in solution, $M \times 10^{-2}$, in the presence of indicated amount of Na_2SO_4, g l^{-1}				
	0	25	50	75	100
0	0.36	n.f.*	n.f.	n.f.	n.f.
0.2	3.7	2.5	1.9	1.5	1.1
0.5	3.9	3.5	3.2	3.1	2.7
2	4.4	1.06	0.46	0.4	0.3
5	2.4	n.f.	n.f.	n.f.	n.f.

* n.f., not found.

Table 3. Elemental composition of dry carbonate residue

Run no. (see Table 1)	Content of oxides, wt %						
	Zr	Si	Fe	Mn	Ti	Nb	Al
2	71.3	3.7	5.3	0.8	1.7	1.3	17.2
3	73.5	0.8	5.7	0.7	1.9	2.0	14.3
5	68.8	0.5	5.6	1.1	2.1	2.0	21.7
7	68.5	1.5	5.2	0.7	2.3	1.4	22.9
7*	86.9	0.65	2.5	0.78	2.7	2.0	1.0
10**	71.4	1.5	6.5	1.0	2.1	2.7	13.4

* Precipitate formed in run no. 7 treated with 1% HCl.

** Precipitate from solution obtained upon two-stage decomposition.

ondary precipitate. To retain REE in the precipitate, it is necessary to create a sodium sulfate salt background in the acid solution, which can be easily done by diluting the acid with mother liquors obtained by evaporation of sodium sulfate solutions. The necessary sodium sulfate concentrations are substantiated in Table 2. It can be seen that presence of minor amounts of sodium sulfate in acid solutions is sufficient for REE precipitation, and washing with weakly acidic solutions (0.2–0.5 N) is to be restricted.

It was recommended in [11] to recover zirconium(IV) from solution by precipitation with ammonia after separation of iron aluminum ammonium alum by freezing, with preliminary oxidation of iron. Precipitation with soda was carried out without separation of alum, since utilization of sodium sulfate is more feasible, whereas separation of alum is expensive and poorly efficient. The precipitation was done from solutions obtained in the runs mentioned in Table 1. Dry soda was introduced until a precipitate appeared, and then the pH value was adjusted with a 10% Na_2SO_4 solution to 4.8–5.0. The precipitates formed were washed by single repulpation at s : l = 1 : 2 and dried. The yield of dry residue was 12.5–16 g per 100 g of EC. The composition of the precipitates is listed in Table 3.

Treatment with a solution of weak acid can be used to raise the content of zirconium in the precipitate via removal of aluminum, and part of iron and silicon, by washing. However, iron and manganese contained in the precipitate are partly oxidized in the course of precipitation, and removal of their oxidized forms by washing is impossible. Humid precipitate is easily dissolved in acids, and, therefore, zirconium can be recovered selectively by any conventional technique. For example, after dissolving the precipitate in hydrochloric acid, separating the insoluble residue, and heating the solution to boiling at acidity of 20 g l^{-1}, zirconium precipitates as a basic sulfate with the following composition (after calcination, wt %): ZrO_2 92.7, TiO_2 3.7, Nb_2O_5 2.6, Fe_2O_3 0.1, MnO_2 0.05. The extraction of zirconium into the precipitate was 93.5%. Presumably, repulpation ensured the necessary ratio between zirconium and the sulfate ion. The main difficulty in precipitate processing is the presence of silicic acid hindering the filtration.

The order in which the evaporation and neutralization procedures are performed must determine the requirements to the quality of sodium sulfate. For glass manufacturing purposes, sodium sulfate is to be isolated after separation of iron and manganese, even though the content of iron(II) did not exceed 0.01 wt % in direct evaporation after washing precipitated sodium sulfate with cold water. If sodium silicate solution is to be obtained, the requirements should be less stringent. The fraction of recycled sodium sulfate may be as high as 100%, and this does not diminish the solubility of the main components. The amount of sodium sulfate extracted from the system can be easily controlled because of its high temperature gradient of solubility, from 4 wt % at 0°C to 33 wt % at 33°C.

After separation of the zirconium product, the solution was neutralized to pH 9.5, and the precipitate was filtered off and washed with water on the filter. The amount of dry precipitate was 2.3–4.1 g, and the content of MnO_2, 40–50 wt % at a yield of 55–70%.

CONCLUSIONS

(1) A study of sulfuric acid decomposition of the eudialyte concentrate led to a conclusion that a two-

stage process, ensuring a 88% recovery of zirconium(IV) at minimum consumption of the acid, is necessary.

(2) A method for two-stage decomposition was developed, which ensures that silicic acid passes into the precipitate because of a spontaneous dehydration in the first stage and high acidity in the second.

(3) A scheme of integrated sulfuric acid processing of eudialyte was suggested and the main technological procedures involved were verified in large-scale laboratory experiments.

REFERENCES

1. Bykhovskii, L.Z., Zubkov, L.B., and Osokin, E.D., *Tsirkonii Rossii: sostoyanie, perspektivy osvoeniya i razvitiya mineral'no-syr'evoi bazy* (Russia's Zirconium: State of Affairs and Prospects for Development of Mineral Resources), Moscow: Vseross. Inst. Miner. Syr'ya, 1998.
2. Musatov, I.A., *Khimicheskaya pererabotka loparitovogo kontsentrata* (Chemical Processing of Loparite Concentration), Apatity: Kol'sk. Nauchn. Ts. Ross. Akad. Nauk, 1992, pp. 3–5.
3. Chistov, L.B., Okhrimenko, V.E., Yufryakov, V.A., and Butova, M.N., Abstracts of Papers, *Mezhdunarodnyi simpozium "Strategiya ispol'zovaniya i razvitiya mineral'no-syr'evoi bazy redkikh metallov Rossii v XXI veke"* (Int. Symp. "Strategy of Use and Development of Russia's Mineral Resources of Rare Metals in the XXI Century"), Moscow: Vseross. Inst. Miner. Syr'ya, 1998, pp. 366–367.
4. Chekmarev, A.M., Chizhevskaya, S.V., Ponomarev, N.L., *et al., Khimiya i tekhnologiya redkikh metallov: Sbornik nauchnykh trudov MKhTI im. D.I. Mendeleeva* (Chemistry and Technology of Rare Metals: Coll. of Sci. Works of Mendeleev Institute of Chemical Technology, Moscow), Moscow, 1986, issue 143, pp. 3–7.
5. Kislykh, V.V., Zakharov, V.I., Motov, D.L., *et al., Khimicheskaya tekhnologiya kompleksnoi pererabotki redkometall'nogo syr'ya* (Chemical Technology for Integrated Processing of Rare-Earth Mineral Raw Materials), Apatity: Kol'sk. Nauchn. Ts. Ross. Akad. Nauk, 1988, pp. 3–5.
6. Zakharov, V.I., Kislykh, V.V., Masloboev, V.A., *et al., Khimicheskaya tekhnologiya redkikh elementov i mineral'nogo syr'ya* (Chemical Technology for Integrated Processing of Rare-Earth Mineral Raw Materials), Apatity: Kol'sk. Nauchn. Ts. Ross. Akad. Nauk, 1986, pp. 5–7.
7. Zakharov, V.I., Masloboev, V.A., Ponomarev, N.L., *et al., Khimicheskaya tekhnologiya redkikh elementov i mineral'nogo syr'ya* (Chemical Technology for Integrated Processing of Rare-Earth Mineral Raw Materials), Apatity: Kol'sk. Nauchn. Ts. Ross. Akad. Nauk, 1986, pp. 8–12.
8. Bashilov, I.Ya., *Khibinskie apatity* (Apatites from Khibiny), Leningrad: Ob''ed. Nauch. Tekh. Izd., 1935, no. 8, pp. 102–113.
9. Tishchenko, V.E. and Sidorkina, A.P., *Zh. Prikl. Khim.*, 1935, vol. 8, no. 7, pp. 1117–1125.
10. Dibrov, I.A., Chirkst, D.E., and Litvinova, T.E., *Tsvet. Met.*, 2002, no. 12, pp. 38–43.
11. Motov, D.L. and Leshtaeva, T.G., *Khimicheskaya tekhnologiya redkometall'nogo syr'ya* (Chemical Technology of Rare-Earth Raw Materials), Moscow: Nauka, 1966, pp. 5–16.
12. Motov, D.L. and Leshtaeva, T.G., *Khimicheskaya tekhnologiya redkometall'nogo syr'ya* (Chemical Technology of Rare-Earth Raw Materials), Moscow: Nauka, 1966, pp. 16–26.
13. Tyurkina, L.P. and Motov, D.L., *Khimicheskaya tekhnologiya redkikh elementov i mineral'nogo syr'ya* (Chemical Technology of Rare Earths and Mineral Raw Materials), Apatity: Kol'sk. Nauchn. Ts. Ross. Akad. Nauk, 1986, pp. 12–15.
14. Kolenkova, M.A., Yashnikova, O.M., Ermakova, E.V., and Shafeeva, N.Kh., *Izv. Vyssh. Uchebn. Zaved., Tsvet. Metall.*, 1984, no. 4, pp. 121–123.
15. RF Patent 2 183 225.
16. Lebedev, V.N. and Rudenko, A.V., *Khim. Tekhnol.*, 2002, no. 12, pp. 27–30.
17. Lebedev, V.N., Shchur, T.E., Maiorov, D.V., *et al., Zh. Prikl. Khim.*, 2003, vol. 76, no. 8, pp.1233–1237.

Russian Journal of Applied Chemistry, Vol. 76, No. 10, 2003, pp. 1564–1567. Translated from Zhurnal Prikladnoi Khimii, Vol. 76, No. 10, 2003, pp. 1606–1608.

INORGANIC SYNTHESIS AND INDUSTRIAL INORGANIC CHEMISTRY

A Study of Evaporation of Complex Oxide Systems Based on Chromium(III) Oxide

V. A. Popov, S. I. Lopatin, L. Sh. Tsemekhman, L. A. Pavlinova, S. P. Kormilitsyn, and V. V. Barsegyan

Institut Gipronikel' Joint-Stock Company, St. Petersburg, Russia
Noril'skii Nikel', Russian Joint-Stock Company, Moscow, Russia

Received November 25, 2002; in final form, July 2003

Abstract—Evaporation of chromium ore and concentrates was studied using high-temperature differential mass-spectrometry. The data obtained, concerning the component vapor pressures in evaporation of complex oxide systems in the range 1700–2100 K, can be used to calculate the evaporation loss in melting and to assess the possibility of utilization of the sublimates formed.

Melting of a chromite raw material (CRM) [1] involves processes that occur at high-temperatures (2000–2100 K) and are poorly understood as regards the composition of the vapor phase in equilibrium with a melt. It is of indubitable scientific interest to study the evaporation of such a complex oxide system as molten ore or concentrate.

Experimental data on the composition and vapor pressure over the individual oxides of chemical elements present in the systems studied are summarized and classified in a monograph [2].

Chromium oxide Cr_2O_3 evaporates congruently [3], in accordance with the reactions:

$$Cr_2O_{3(solid)} = 2Cr_{(gas)} + 3O_{(gas)}, \quad (1)$$

$$Cr_2O_{3(solid)} = 2CrO_{(gas)} + O_{(gas)}, \quad (2)$$

$$Cr_2O_{3(solid)} = CrO_{2(gas)} + CrO_{(gas)}. \quad (3)$$

The ratio of partial pressures of Cr, CrO, and CrO_2 within the temperature range 1850–2010 K is 100 : 6 : 3.

Iron forms with oxygen three oxides: Fe_2O_3, Fe_3O_4, and FeO. When heated to 1200–1500, Fe_2O_3 and Fe_3O_4 dissociate, with molecular oxygen passing into a vapor and FeO accumulating in condensed phase. Wustite evaporates congruently at 1700–1850 K with dissociation into atomic iron and oxygen [4]:

$$FeO_{(solid)} = Fe_{(gas)} + 1/2O_{2(gas)}. \quad (4)$$

The partial pressure of FeO does not exceed 3% of the total pressure.

Silicon oxide SiO_2 evaporates congruently in the temperature range 1800–2000 K with dissociation into gaseous silicon monoxide and oxygen [2]:

$$SiO_{2(solid)} = SiO_{(gas)} + 1/2O_{2(gas)}. \quad (5)$$

When heated, magnesium and aluminum oxides dissociate virtually completely into gaseous oxygen and atomic metal vapor [2]:

$$MgO_{(solid)} = Mg_{(gas)} + 1/2O_{2(gas)}, \quad (6)$$

$$Al_2O_{3(solid)} = 2Al_{(gas)} + 3/2O_{2(gas)}. \quad (7)$$

In addition, the oxides AlO, Al_2O, and Al_2O_2 are present in minor amounts (2–3%) in a vapor over aluminum oxide.

The evaporation of CRM was studied using high-temperature differential mass-spectrometry, which is one of the most informative methods for physicochemical analysis of multicomponent systems. The method enables direct qualitative and quantitative determination of the vapor composition in a wide range of temperatures and compositions of the condensed phase.

The study was carried out on an MS-1301 mass-spectrometer. A sample was evaporated from a Knudsen cell heated by electron bombardment. The temperature was measured to within ±5°C with an EOP-66 optical pyrometer. The instrument was preliminarily

1070-4272/03/7610-1564 $25.00 © 2003 MAIK "Nauka/Interperiodica"

calibrated against vapor pressure of gold [5]. The ionizing energy was 25 eV, which made it possible to partially suppress dissociative ionization and to simplify interpretation of mass-spectra. The partial vapor pressures of the components were determined by comparing ion currents, with gold as reference. The vapor pressure of gold, p_{Au} (Pa), was calculated by the formula [5]:

$$\log p_{Au} = -18\,013/T + 10.8772. \quad (8)$$

The experimental procedure employed was described in detail in [6].

The composition of the samples studied is listed in Table 1.

Sample no. 1 was evaporated at 1700–2100 K from a tungsten Khudsen cell. Fe^+, Cr^+, CrO^+, CrO_2^+, SiO^+, Mg^+, Al^+, Al_2O^+, AlO^+, $Al_2O_2^+$, WO_2^+, and WO_3^+ ions were observed in the mass-spectrum in the course of evaporation. The vapor mass-spectra and the dependences of ion current on the time and temperature of sublimation, and also the fact that the energies at which the ions appeared, which are equal to the ionization energies of the corresponding molecules [7], showed that the vapor over a sample studied contains the following molecules: Fe, Cr, CrO, CrO_2, SiO, Mg, Al, Al_2O, AlO, Al_2O_2, WO_2, and WO_3 in different temperature intervals. The CrO and CrO_2 pressures constitute 3–5% of the chromium pressure and depend on temperature and oxygen pressure. Tungsten oxides are formed in the interaction of the chamber wall material with a sample. Molecular and atomic oxygen is also present in the vapor, but direct measurements of partial oxygen pressures are impossible because of the high-intensity background at *m*/*e* 16 and 32 and the fact that O_2 and O are not condensed on cool parts of the mass-spectrometer. At the same time, these pressures can be estimated using reference data [8] on the equilibrium constants of the reactions:

$$WO_{3(gas)} = WO_{2(gas)} + O_{(gas)}, \quad (9)$$

$$WO_{3(gas)} = WO_{2(gas)} + 1/2O_{2(gas)}. \quad (10)$$

Figure 1a shows how the partial pressures of the components over the chromium concentrate vary with time and temperature. The atomic iron and oxygen are major vapor components within 1700–1850 K. The iron vapor pressure at 1700 K is 0.2 Pa and remains virtually unchanged for a long time. The iron vapor pressure increases by an order of magnitude with temperature raised to 1850 K, and, in the course of an isothermal exposure, decreases as the condensed phase becomes depleted of iron oxide. Atomic chromium and SiO, whose partial pressures increase somewhat, appear in the vapor at this temperature, and a minor amount of atomic magnesium, at the end of the isothermal exposure. With the temperature raised to 2000K, the Fe, Cr, Mg, and SiO pressures increase, and, in addition, atomic aluminum appears in the vapor. In the course of the isothermal exposure, the partial pressure of atomic iron decreases rapidly, and that of chromium, magnesium, and silicon monoxide, first increases and then starts to decrease gradually. In the process, the aluminum vapor pressure remains constant (0.03–0.04 Pa). With the temperature raised to 2100K, the Cr, Mg, and SiO pressures first increase and then decrease to the background level, with first magnesium totally removed

Table 1. Initial composition of samples studied

Sample no.	Content, mol %					
	FeO	Cr_2O_3	MgO	SiO_2	CaO	Al_2O_3
1 (concentrate)	16.5	31.0	36.2	6.3	–	10.0
2 (ore)	8.7	12.2	37.7	32.4	2.5	6.4
3 (concentrate)	11.0	21.1	42.3	16.4	1.1	8.1
4 (concentrate)	12.6	29.0	37.5	8.9	0.8	11.2

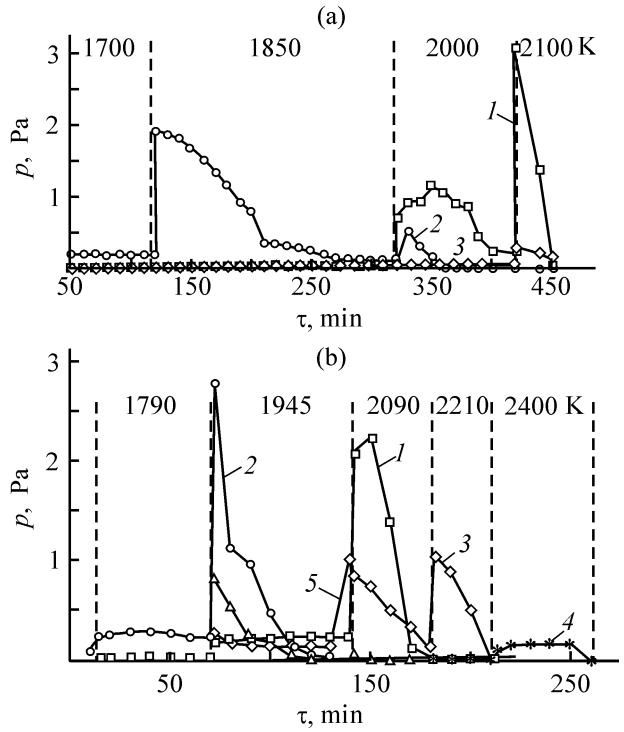

Fig. 1. Partial pressures of the main vapor components *p* over samples (a) no. 1 and (b) no. 3 vs. experiment duration τ and temperature. (*1*) Cr, (*2*) Fe, (*3*) Mg, (*4*) SiO, and (*5*) Al.

Table 2. Activities of Cr_2O_3 at various compositions of condensed phase (sample no. 1)

T, K	$a_{Cr_2O_3}$	$\gamma_{Cr_2O_3}$	Content, mol %				
			FeO	Cr_2O_3	MgO	SiO_2	Al_2O_3
1850	0.031	0.09	11.1	32.8	38.8	6.7	10.7
1850	0.038	0.11	7.6	34.1	40.3	6.9	11.1
1850	0.11	0.29	5.9	37.3	44.6	–	12.3
2000	0.35	0.91	2.3	38.4	46.2	–	13.1

from the sample, and then chromium and silicon monoxide. Atomic aluminum is the last component to evaporate from residues of chromium concentrate at 2200–2300 K. In this temperature range, no ion signals corresponding to atomic iron, magnesium, chromium, and SiO were recorded.

The method of differential mass-spectrometry was used to determine the activity of chromium(III) oxide in the condensed phase. Pure Cr_2O_3 served as reference. Transition from the working chamber to the reference chamber and back took 20–30 s, which enabled sufficiently fast measurement of ion current intensities and determination of the partial pressures of components over a sample and reference. The Cr_2O_3 activity was calculated by the formula:

$$a_{Cr_2O_3} = \frac{p^2(Cr)\,p^3(O)}{p_0^2(Cr)\,p_0^3(O)}, \qquad (11)$$

where p and p_0 are the partial vapor pressures of the components over the sample and reference, respectively.

The partial pressures of atomic oxygen were replaced, according to Eq. (9), with the $p(WO_3)/p(WO_2)$ ratio. Then

$$a_{Cr_2O_3} = \frac{p^2(Cr)\,p^3(WO_3)\,p_0^3(WO_2)}{p_0^2(Cr)\,p_0^3(WO_3)\,p_0^3(WO_2)}, \qquad (12)$$

The activities, activity coefficients, and the corresponding concentrations of the components, calculated from the evaporation curves, are listed in Table 2.

Sample nos. 2–4 were evaporated from a double molybdenum chamber, with gold used as reference. The Cr_2O_3 activity for these samples of initial composition (3.5×10^{-4}, 5.5×10^{-4}, and 7.5×10^{-4}, respectively) was determined as it was done for sample no. 1 with account of the change of the chamber material (Mo instead of W). The activity coefficients are 2.9×10^{-3}, 2.6×10^{-3}, and 2.6×10^{-3}, respectively.

Figure 1b demonstrates the dependence of the partial vapor pressures of the components over sample no. 3 on the evaporation time and temperature. Atomic iron and oxygen are major vapor components at 1700–1800 K. The vapor pressure of iron is as high as 0.25 Pa at 1800 K and remains virtually unchanged for a long time. With the temperature raised to 1950 K, the iron vapor pressure increases by approximately an order of magnitude, and Cr, SiO, and Mg appear in the vapor phase. In the course of isothermal exposure, the partial pressures of Fe and SiO decrease to virtually the background value, the Mg vapor pressure decreases somewhat, and the Cr vapor pressure increases slightly. After the temperature is raised to 2080 K, the vapor pressures of Cr and Mg increase and then decrease in the course of isothermal exposure. On further heating to 2200 K, the vapor pressure of chromium remains at the minimum level, whereas that of magnesium increases and then decreases to a background value in the course of exposure. The last component evaporating from residues of chromium concentrate at 2200–2400 K is atomic aluminum. The evaporation of sample no. 2 and 4 occurred similarly.

In the system studied, negative deviation from ideal behavior was observed, proportional to the content of iron oxide in the condensed phase.

CONCLUSIONS

(1) It was established that, first, iron and then chromium, silicon, magnesium, and aluminum, evaporate from the chromite raw material under heating. The vapor pressure of these components at 1700–2100 K was determined.

(2) The activity of chromium(III) oxide in the condensed phase was calculated. It was shown that the system shows negative deviation from ideality, proportional to the content of iron(II) oxide in the condensed phase.

REFERENCES

1. Kormilitsyn, S.P., Voikhanskaya, N.L., Miroevskii, G.P., *et al.*, *Tsvet. Met.*, 2001, no. 2, pp. 96–100.
2. Kazenas, E.K. and Tsvetkov, Yu. V., *Isparenie oksidov* (Evaporation of Oxides), Moscow: Nauka, 1997.
3. Milushin, M.I., and Nazarenko, I.I., Abstracts of Papers, *XI Vsesoyuznaya konferentsiya po kalorimetrii i khimicheskoi termodinamike* (XI All-Union Conf. on Calorimetry and Chemical Thermodynamics), Novosibirsk, 1986, part I, pp. 120–121.
4. Kazenas, E.K. and Tagirov, V.K., *Metally*, 1995, no. 2, pp. 31–37.
5. Paule, R.C. and Mandel, J., *Pure Appl. Chem.*, 1972, vol. 31, no. 3, pp. 371–394.
6. Semenov, G.A., Belov, A.N., Baidin, V.N., *et al.*, *Izv. Akad. Nauk Lit. SSR*, vol. 6, ser. B, pp. 515–518.
7. *Energiya razryva khimicheskikh svyazei: Potentsialy ionizatsii i srodstvo k elektronu. Spravochnik* (The Energy of Rupture of Chemical Bonds: Ionization Potentials and Electron Affinity: Reference Book), Kondrat'ev, V.N., Ed., Moscow: Nauka, 1974.
8. *Termodinamicheskie svoistva individual'nykh veshchestv. Spravochnik* (Thermodynamic Properties of Individual Substances: Reference Book), Glushko, V.P., Ed., Moscow: Akad. Nauk SSSR, vols. 1–4, pp. 1978–1984.

Russian Journal of Applied Chemistry, Vol. 76, No. 10, 2003, pp. 1568–1571. Translated from Zhurnal Prikladnoi Khimii, Vol. 76, No. 10, 2003, pp. 1609–1613.

INORGANIC SYNTHESIS AND INDUSTRIAL INORGANIC CHEMISTRY

Effect of Seed on Supersaturation and Scale Growth in Flow-through Crystallizers and Evaporating Apparatus

O. D. Linnikov

Institute of Solid State Chemistry, Ural Division, Russian Academy of Sciences, Yekaterinburg, Russia

Received March 28, 2003

Abstract—The problem of choosing the most effective concentration of seed crystals for controlling the supersaturation and scale growth rate in flow-through crystallizers and evaporating apparatus is considered theoretically. Equations describing these processes are derived and compared with published experimental data.

Seed crystals are widely used in crystallization and evaporating processes. The size of crystals obtained in crystallization can be controlled by changing the seed concentration. Addition of seed crystals to an industrial or natural mineralized water being evaporated makes it possible to diminish scale formation [1]. For example, the method for preventing scale formation by using seed crystals has been employed during many years for thermal desalination of Caspian Sea water [1, 2]. There is evidence of successful application of a seed to diminish formation of calcium sulfate scale [3–5]. The method of seed crystals can also be used to prevent formation of calcium carbonate scale in geothermal power engineering [6]. In spite of such a wide application of seeds, their most effective concentration in various processes is selected empirically in many instances. In this study, the problem is analyzed theoretically.

The rate of scale growth is known to decrease in the presence of seed crystals. Seed crystals remove scale-forming salts from solutions. Consequently, solution supersaturation also decreases in the presence of seed crystals. Let us consider how introduction of a seed affects the solution supersaturation.

In the simplest case, for a solution volume v in an apparatus and total surface area of seed crystals equal to S, the average growth rate of crystals V is independent of time and supersaturation and the following mass M of a scale-forming salt will be removed during time τ_0 from the solution:

$$M = SV\rho_T\tau_0. \quad (1)$$

Here ρ_T is the density of the scale-forming salt (kg m^{-3}) and τ_0 is the residence time of the solution in the apparatus (s).

The concentration of the solution is given by

$$c = \frac{c_i v - M}{v} = \frac{c_i v - SV\rho_T\tau_0}{v} = c_i - \frac{SV\rho_T\tau_0}{v}, \quad (2)$$

where c_i and c are the initial and running salt concentrations in the solution (kg m^{-3}).

The concentration of the scale-forming salt in solution is seen to be a linear function of the total surface area of seed crystals, S, and the residence time of the solution in apparatus, τ_0.

However, in the general case, the growth rate of seed crystals depends on the concentration of a scale-forming salt in solution (solution supersaturation). The growth rates of seed crystals, V, and scale, V_R, are described by the equations:

$$V = k(c - c_0)^n, \quad (3)$$

$$V_R = k_R(c - c_0)^m. \quad (4)$$

Here k and k_R are average growth rate coefficients of seed crystals and scale, respectively; V and V_R, the average growth rates of seed crystals and scale (m s^{-1}); c_0, the solubility of the scale-forming salt in solution (kg m^{-3}); n and m, the growth rate orders.

Commonly, n = 1–2 and m = 1–2. Therefore, four combinations of n and m can be considered: 1) $n = m = 1$; 2) $n = 1$, $m = 2$; 3) $n = m = 2$ and 4) $n = 2$, $m = 1$.

(1) $n = m = 1$. In this case, the following mass dM of the scale-forming salt will be removed from the solution during a time dτ:

$$dM = SV\rho_T d\tau. \quad (5)$$

1070-4272/03/7610-1568 $25.00 © 2003 MAIK "Nauka/Interperiodica"

Taking into account the equality $dM = -vdc$ and substituting Eq. (3) into expression (5), we obtain:

$$-\frac{dc}{d\tau} = \frac{S\rho_T}{v}k(c - c_0) = \frac{S}{v}K(c - c_0). \quad (6)$$

Here $K = k\rho_T$ is the growth rate coefficient of seed crystals ($m\ s^{-1}$).

After integration, we have:

$$\ln\frac{c - c_0}{c_i - c_0} = -\frac{S}{v}K\tau_0. \quad (7)$$

From Eq. (7) follows formula (8) relating the solution supersaturation to the total surface area of seed crystals and to the residence time of the solution in an apparatus:

$$\Delta c = c - c_0 = (c_i - c_0)\exp\left(-\frac{S}{v}K\tau_0\right) = \Delta c_i\exp\left(-\frac{S}{v}K\tau_0\right). \quad (8)$$

Here $\Delta c = c - c_0$ is the solution supersaturation ($kg\ m^{-3}$) and $\Delta c_i = c_i - c_0$ is the initial supersaturation (of a solution free of seed crystals) ($kg\ m^{-3}$).

Substitution of (8) in expression (4) gives the equation for the rate of scale growth ($m = 1$):

$$V_R = k_R\Delta c = k_R\Delta c_i\exp\left(-\frac{S}{v}K\tau_0\right). \quad (9)$$

(2) $n = 1$, $m = 2$. In this case, the dependence of the solution supersaturation on the total surface area of seed crystals and on the duration of solution residence in the apparatus remains unchanged and is described by formula (8). Therefore, substitution of (8) into Eq. (4) yields

$$V_R = k_R\Delta c_i^2\exp\left(-\frac{S}{v}K\tau_0\right). \quad (10)$$

It can be seen that, on the whole, the dependence of the rate of scale growth on the residence time of the solution in an apparatus and on the total surface area of seed crystals remains nearly the same.

(3) $n = m = 2$. At $n = 2$, Eq. (3) takes, after integration and transformations, the form

$$\Delta c = \frac{\Delta c_i}{1 + K\Delta c_i\frac{S}{v}\tau_0}. \quad (11)$$

It is noteworthy that the growth rate coefficient of seed crystals, K, in Eq. (11) has the dimensionality $m^4\ s^{-1}\ kg^{-1}$.

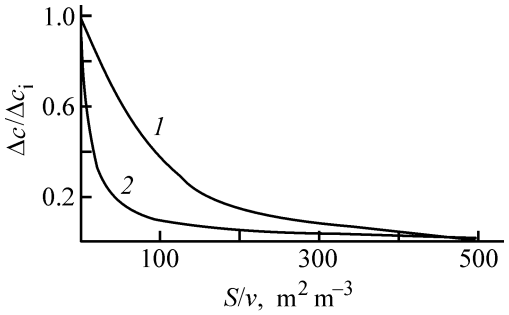

Fig. 1. Dependence of $\Delta c/\Delta c_i$ ratio on specific surface area S/v of seed crystals in solution (theoretical curves). $\tau_0 = 100$ s. (*1*) $n = 1$, $K = 1 \times 10^{-4}$ m s^{-1}; (*2*) $n = 2$, $K = 1 \times 10^{-4}$ $m^4\ s^{-1}\ kg^{-1}$, $\Delta c_i = 10$ kg m^{-3}.

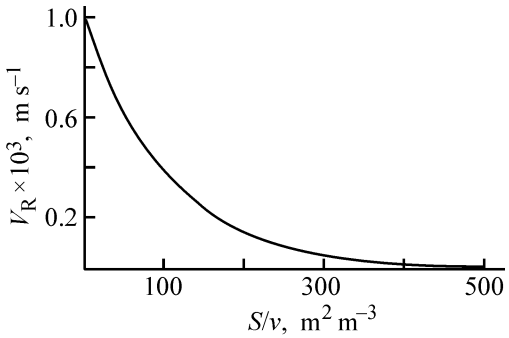

Fig. 2. Influence of specific surface area S/v of seed crystals in solution on scale growth rate V_R [theoretical curve according to Eq. (9)] $K = 1 \times 10^{-4}$ m s^{-1}, $k_R = 1 \times 10^{-4}$ $m^4\ s^{-1}\ kg^{-1}$, $n = m = 1$, $\Delta c_i = 10$ kg m^{-3}, $\tau_0 = 100$ s.

Substitution of (11) in expression (4) gives ($m = 2$)

$$V_R = \frac{k_R\Delta c_i^2}{\left(1 + K\Delta c_i\frac{S}{v}\tau_0\right)^2}. \quad (12)$$

(4) $n = 2$, $m = 1$. If $n = 2$, the solution supersaturation is described by Eq. (11). Therefore, the expression for the scale growth rate has the form

$$V_R = \frac{k_R\Delta c_i}{1 + K\Delta c_i\frac{S}{v}\tau_0}. \quad (13)$$

Theoretical curves describing the dependence of the $\Delta c/\Delta c_i$ ratio on the specific surface area of seed crystals in solution, S/v, in accordance with Eqs. (8) and (11), are shown in Fig. 1. It is seen that, if $K = 1 \times 10^{-4}$ m s^{-1} for $n = 1$ or $K = 1 \times 10^{-4}$ $m^4\ s^{-1}\ kg^{-1}$ for $n = 2$ (typical values), then the solution supersaturation decreases dramatically with the specific surface area of seed crystals increasing from 0 to 100–200 $m^2\ m^{-3}$. Further increase in the specific surface area of seed crystals to above 100–200 $m^2\ m^{-3}$ does not lead to any significant additional decrease in the ratio $\Delta c/\Delta c_i$. A similar dependence takes place for the scale growth rate (Fig. 2).

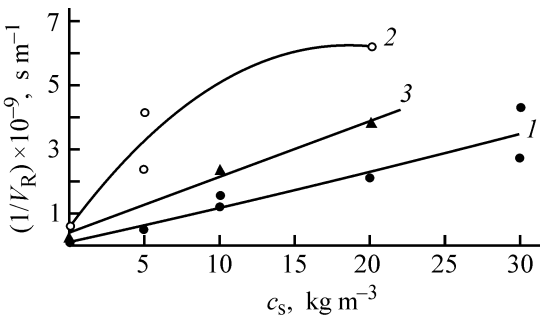

Fig. 3. Experimental data of [4], plotted in the coordinates of Eq. (16). T = 70°C. Δc_i (kg m^{-3}): (*1*) 1.50, (*2*) 0.68, (*3*) 1.09. *Points*, experimental data; *lines*, theoretical curves [calculation by Eq. (16)].

It is of interest to compare the obtained theoretical dependences with published data [4–6]. Formation of scale in the form of calcium sulfate (sulfate scale) was studied by Kaldaeva [4]. The effect of calcium sulfate seed crystals on the scale growth was studied. It was found that the growth rates of seed and scale crystals are described by Eqs. (3) and (4) for $n = m = 2$. The plot constructed on the basis of the data obtained in [4] in Fig. 3 is similar to the curve in Fig. 2 of the present study. The experimental data from Fig. 3 of [4] are listed in Table 1.

Table 1. Experimental data on the rate of sulfate scale growth for various concentrations of seed crystals, c_s, and solution temperatures (from Fig. 3 of [4])

T, °C	Δc_i, kg m^{-3}	c_s, kg m^{-3}	$V_R \times 10^9$, m s^{-1}
50	0.95	0	2.40
		5	0.45
		5	0.37
		10	0.38
		10	0.32
70	0.68	0	1.68
		5	0.42
		5	0.24
		20	0.16
	1.09	0	3.35
		10	0.42
		20	0.26
	1.50	0	6.72
		5	2.40
		5	2.28
		10	0.84
		10	0.65
		20	0.47
		30	0.36
		30	0.23

To compare Kaldaeva's experimental data [4] with Eq. (12), we transform this equation to

$$\frac{1}{V_R} = \frac{\left(1 + K\Delta c_i \frac{S}{\nu}\tau_0\right)^2}{k_R \Delta c_i^2} = \frac{1}{k_R \Delta c_i^2} + \frac{2K\tau_0}{k_R \Delta c_i}\left(\frac{S}{\nu}\right) + \frac{(K\tau_0)^2}{k_R}\left(\frac{S}{\nu}\right)^2. \quad (14)$$

Assuming that seed crystals have a near-spherical shape and taking into account that

$$\frac{S}{\nu} = \frac{S_{cr}}{m_{cr}} c_s = \frac{\pi d_{cr}^2}{\frac{1}{6}\pi d_{cr}^3 \rho_T} c_s = \frac{6}{d_{cr}\rho_T} c_s, \quad (15)$$

where c_s is the concentration of seed crystals in solution (kg m^{-3}); d_{cr}, the average diameter of seed crystals (m); $S_{cr} = \pi d_{cr}^2$, the average surface area of a single seed crystal (m^2); $m_{cr} = 1/6(\pi d_{cr}^3 \rho_T)$, the average mass of a single seed crystal (kg), we finally obtain

$$\frac{1}{V_R} = \frac{1}{k_R \Delta c_i^2} = \frac{12K\tau_0}{k_R \Delta c_i d_{cr}\rho_T} c_s + \frac{36(K\tau_0)^2}{k_R (d_{cr}\rho_T)^2} c_s^2. \quad (16)$$

Equation (16) is a parabolic regression. Typical dependencies obtained by processing the experimental data of Table 1 are shown in Fig. 3 in the coordinates of this equation. It is seen that Kaldaeva's experimental data [4] are satisfactorily approximated by Eq. (16).

Data obtained with calcium carbonate seed crystals used to prevent scale formation in geothermal power engineering have been reported by Akhmetov [6]. The effect of seed crystals on the concentration of Ca^{2+} ions in a solution passed through an apparatus was studied. The experimental results of [6] are listed in Tables 2 and 3. The data in the last column of Table 2 suggest that the $CaCO_3$ solubility in the solution under study was about 50 mg l^{-1}.

To analyze Akhmetov's experimental data [6], we transform Eqs. (8) and (11). After substituting formula (15), we obtain

$$\Delta c = \Delta c_i \exp\left(-\frac{S}{\nu}K\tau_0\right) = \Delta c_i \exp\left(-\frac{6}{d_{cr}\rho_T}K\tau_0 c_s\right), \quad (17)$$

$$\Delta c = \frac{\Delta c_i}{1 + K\Delta c_i \frac{S}{\nu}\tau_0} = \frac{\Delta c_i}{1 + \frac{6K\Delta c_i}{d_{cr}\rho_T}\tau_0 c_s}. \quad (18)$$

A verification of Eqs. (17) and (18) demonstrated that the data of [6] are best described by expression

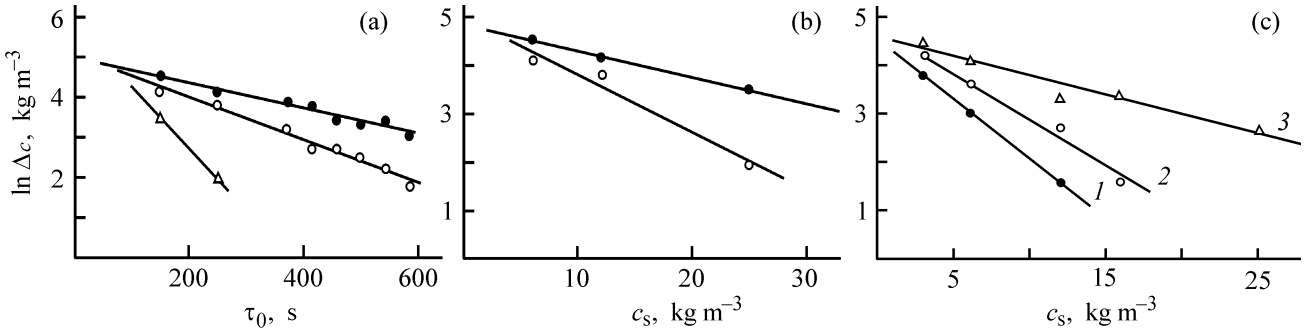

Fig. 4. Experimental data of [6] in the coordinates of modified Eq. (17). (a) c_s (kg m^{-3}): (*1*) 6, (*2*) 12, and (*3*) 25. (b) τ_0 (s): (*1*) 149 and (*2*) 249. (c) $d_{cr} \times 10^6$ (m): (*1*) 56, (*2*) 82, and (*3*) 150.

(17). Akhmetov's experimental data [6] (Tables 2 and 3 of the present study) are shown in Figs. 4a–4c in the coordinates of modified Eq. (17) (after taking logarithms). It is seen that all the experimental data well fall on straight lines. This confirms the applicability of expression (17) and indicates that the equation describing the seed crystal growth is first-order [formula (8)]. The data in Fig. 4c can be used to estimate the growth rate coefficient of seed crystals, *K*, under the experimental conditions of [6], by using formula (17). For example, calculation gives $K = 7.75 \times 10^{-6}$ m s^{-1} for $d_{cr} = 56 \times 10^{-6}$ m, $K = 8.94 \times 10^{-6}$ m s^{-1} for $d_{cr} = 82 \times 10^{-6}$ m, and $K = 6.64 \times 10^{-6}$ m s^{-1} for $d_{cr} = 150 \times 10^{-6}$ m. Hence the average *K* is 7.69×10^{-6} m s^{-1}.

Table 2. Concentration of Ca^{2+} ions, *c*, in solution as a function of its residence time in an apparatus (Fig. 2 of [6]), $T = 98°C$

τ_0, s	$c \times 10^{-3}$ (kg m^{-3}) at c_s, kg m^{-3}		
	6	12	25
149	143	113	83
249	111	95	57
371	99	75	50
414	93	65	51
457	80	65	50
500	78	62	56
543	81	59	54
586	71	56	48

Table 3. Influence of average diameter of seed crystals on the concentration *c* of Ca^{2+} ions in solution (Fig. 3 of [6]), $\tau_0 = 586$ s, $T = 98°C$

c_s, kg m^{-3}	$c \times 10^{-3}$ (kg m^{-3}) at $d_{cr} \times 10^6$, m		
	56	82	150
3	96	118	140
6	70	87	111
12	55	65	79
16	51	55	80
25	52	58	65

Unfortunately, verification of other equations of the present study seems to be impossible because of the lack of required published experimental data. Nevertheless, the results obtained can be used for carrying out approximate calculations in designing industrial apparatus and for choosing the optimal concentrations of seed crystals to prevent scale formation, and also for controlling the mass-crystallization processes.

To conclude, it should be noted that Eqs. (1)–(13) were derived on the assumption that the total surface area of seed crystals much exceeds the scale surface area. Therefore, the mass of scale-forming salt deposited on the scale surface could be neglected.

REFERENCES

1. Apel'tsin, I. Z. and Klyachko, V.A., *Opresnenie vody* (Water Desalination), Moscow: Gosstroiizdat, 1968.
2. Chernozubov, V.B., Zaostrovskii, F.G., Novikov, E.P., and Tkach, V.I., *Opresnenie solenykh vod* (Desalination of Salt Water), Moscow: TsBNTI, 1966, pp. 14–17.
3. Gainey, R.J., Thorp, C.A., and Cadwallader, E.A., *Ind. Eng. Chem.*, 1963, vol. 55, no. 3, pp. 39–43.
4. Kaldaeva, I.L., Formation and Methods for Its Restriction in Evaporating Apparatus, *Cand. Sci. (Chem.) Dissertation*, Moscow, 1993.
5. Rautenbach, R. and Widua, J., *Proc. World Congress on Desalination and Water Sciences*, Abu Dhabi, 1995, vol. 3, pp. 559–576.
6. Akhmetov, G.Ya., *Metod zatravochnykh kristallov v geotermal'noi energetike* (Method of Seed Crystals in Geothermal Power Engineering), Available from INFOREHNERGO, 1986, Moscow, no. 11501203133D.

Russian Journal of Applied Chemistry, Vol. 76, No. 10, 2003, pp. 1572–1576. Translated from Zhurnal Prikladnoi Khimii, Vol. 76, No. 10, 2003, pp. 1614–1618.

INORGANIC SYNTHESIS AND INDUSTRIAL INORGANIC CHEMISTRY

Phase Relations and Electrical Properties of Phases in Systems Na_2MoO_4–$AMoO_4$–$R_2(MoO_4)_3$ (A = Mg, Mn, Co, Ni; R = Cr, Fe)

I. Yu. Kotova and N. M. Kozhevnikova

Baikal Institute of Nature Management, Siberian Division, Russian Academy of Sciences, Ulan-Ude, Buryatia, Russia

Received March 28, 2003

Abstract—The subsolidus region of ternary salt systems Na_2MoO_4–$AMoO_4$–$R_2(MoO_4)_3$ was studied. It was established that phases $Na_{1-x}A_{1-x}R_{1+x}(MoO_4)_3$, $0 \le x \le 0.2$–0.3 of variable composition with rhombohedral lattice ($R\bar{3}c$) and ternary molybdates $NaA_3R(MoO_4)_5$ of triclinic crystal system ($P\bar{1}$) are formed in the system. The electrical characteristics of ternary molybdates and the effect of the cation nature on the homogeneity region of the phases and type of conduction were studied.

The interest in oxygen-containing compounds of molybdenum is caused by their wide application in both new and traditional fields of science and engineering. Matrixes for fixation of long-lived isotopes, phosphors, laser materials, ferroelectrics, piezoelectrics, catalysts for organic synthesis, superionics, high-temperature binders and other materials have been obtained on the basis of composite oxides with various cations and a tetrahedral anion [1–3]. In this context, a physicochemical analysis of systems of this kind, synthesis of new compounds, and a study of their structure and properties, including electrical properties, are being carried out.

It is necessary to note that the rhombohedral phases are of particular interest because they exhibit a crystal-chemical similarity with compounds of the NASICON type, which are characterized by superionic properties [3–9], and the possibility of iso- and heterovalent substitutions in the rhombohedral skeleton enables smooth variation of properties of materials based on them.

The aim of this study was to analyze phase relations in the systems Na_2MoO_4–$AMoO_4$–$R_2(MoO_4)_3$, (A = Mg, Mn, Co, Ni; R = Cr, Fe) and the type of conduction in ternary molybdates.

EXPERIMENTAL

Starting components for a study of the systems were molybdates of double-charged metals, sodium, iron(III), and chromium(III), synthesized by the solid-phase technique, specifically, by sintering the oxide of a corresponding metal, Na_2CO_3, $Fe(NO_3)_3 \cdot 9H_2O$, and molybdenum trioxide, taken in stoichiometric ratio. The compounds $NaR(MoO_4)_2$ (R = Cr, Fe) were synthesized at 550–650°C in the course of 100–150 h. All the starting compounds were preliminarily calcined, for their full dehydration, at temperatures 100–200°C lower than their melting points. The annealing was carried out in the range 550–750°C. The duration of calcination at each temperature was 100–200 h. Nonequilibrium samples were annealed additionally. To determine the homogeneity regions, ternary molybdates were obtained from preliminarily synthesized neutral molybdates. The value of x was varied from 0 to 1.00 in steps of 0.1. The annealing was done in the range 550–750°C, with intermediate grinding after every 20–30 h. The duration of calcination at each temperature was 150–250 h.

The phase composition was monitored, as equilibrium was attained, by means of X-ray diffraction analysis with a DRON-2.0 diffractometer and a chamber-monochromator of the Guignet–de-Wolf type (Cu_{K_α} radiation, Ge as internal standard). A differential thermal analysis was carried out on an MOM OD-103 derivatograph (rate of temperature rise 10 deg min^{-1}, sample weight 0.3–0.4 g).

Electrical measurements in the range 200–600°C were carried out in the heating–cooling mode, using 0.15–0.2-cm-thick dense ceramic discs sintered at

1070-4272/03/7610-1572 $25.00 © 2003 MAIK "Nauka/Interperiodica"

Table 1. Crystallographic and thermal characteristics of $Na_{1-x}Mg_{1-x}R_{1+x}(MoO_4)_3$

Compound	*a*, Å	*c*, Å	*V*/*Z*, Å^3	*c*/*a*	mp, °C
$NaMgCr(MoO_4)_3$	9.353(2)	23.102(3)	291.7	2.470	865
$Na_{0.7}Mg_{0.7}Cr_{1.3}(MoO_4)_3$	9.361(3)	23.182(7)	293.2	2.476	860
$NaMgFe(MoO_4)_3$	9.375(4)	23.226(5)	294.6	2.477	790
$Na_{0.7}Mg_{0.7}Fe_{1.3}(MoO_4)_3$	9.391(2)	23.292(3)	296.5	2.498	790

600–700°C, with platinum electrodes deposited onto their surface. An E8-4 bridge was used for ac measurements at a frequency of 10 kHz, with an R5025 capacitance box (accuracy ±5%) which extended the measurement range of the dielectric loss tangent. A voltage of 60 mV was used in dc measurements. The electronic and ionic transfer numbers were determined by Vest and Tallan's method [10].

The systems Na_2MoO_4–$AMoO_4$ (A = Mg, Mn, Co, Ni) and Na_2MoO_4–$R_2(MoO_4)_3$ (R = Cr, Fe) were studied in [11–15], and, therefore, were not analyzed additionally here.

To study interactions in the system Na_2MoO_4–$MgMoO_4$–$R_2(MoO_4)_3$, mixtures of neutral and binary molybdates were prepared in a specified stoichiometric ratio, including the compositions corresponding to intersection points for all the sections existing in the system. The samples were annealing in the range 300–700°C. An analysis of the data obtained in studying the phase composition of the compounds lying at the intersection points and at the points located in the plane of the triangle Na_2MoO_4–$MgMoO_4$–$R_2(MoO_4)_3$ demonstrated that the phase relations in the subsolidus region for the iron-containing systems at 600°C and for the chromium-containing systems 650°C are characterized by the following quasibinary sections: $MgMoO_4$–$NaMg_3R(MoO_4)_5$; $Na_{2-2x}Mg_{2+x}(MoO_4)_3$, $0.4 \le x \le 0.5$–$NaMg_3R(MoO_4)_5$; $NaMg_3R(MoO_4)_5$–$R_2(MoO_4)_3$; $NaMg_3R(MoO_4)_5$–$Na_{1-x}Mg_{1-x}R_{1+x}(MoO_4)_3$, $0 \le x \le 0.3$; $Na_{2-2x}Mg_{2+x}(MoO_4)_3$–$Na_{1-x}Mg_{1-x}R_{1+x}(MoO_4)_3$; $Na_{2+2x}Mg_{1-x}(MoO_4)_2$, $0 \le x \le 0.2$–$Na_{1-x}Mg_{1-x}R_{1+x}(MoO_4)_3$; Na_2MoO_4–$Na_{1-x}Mg_{1-x}R_{1+x}(MoO_4)_3$; $NaR(MoO_4)_2$–$Na_{1-x}Mg_{1-x}R_{1+x}(MoO_4)_3$; $Na_{1-x}Mg_{1-x}R_{1+x}(MoO_4)_3$–$R_2(MoO_4)_3$ (Fig. 1).

According to the results of X-ray phase analysis, the ternary compounds $NaMg_3R(MoO_4)_5$ and $NaMgR(MoO_4)_3$ show no noticeable homogeneity region along the section $NaR(MoO_4)_3$–$MgMoO_4$ (R = Cr, Fe), whereas the homogeneity region in the plane of the triangle along the section $NaMgR(MoO_4)_3$–$R_2(MoO_4)_3$ is 9.8 mol % wide.

Along the section $NaMgR(MoO_4)_3$–$R_2(MoO_4)_3$, phases of variable composition, $Na_{1-x}Mg_{1-x}R_{1+x}(MoO_4)_3$, $0 \le x \le 0.3$, are formed. They are solid solutions of subtraction, based on the ternary molybdate $NaMgR(MoO_4)_3$. According to the X-ray data (positions of reflections and their relative intensities in X-ray diffraction patterns), these solid solutions are isostructural to the ternary sodium–zinc–scandium molybdate [16] having a rhombohedral lattice (space group $R\bar{3}c$, $Z = 6$) (Table 1).

Taking into account that the starting compounds have the same formulas and structures, it would be expected that the phase relations in the systems containing manganese, cobalt, and nickel molybdates must be similar to those in the system under study: Na_2MoO_4–$MgMoO_4$–$R_2(MoO_4)_3$ (R = Cr, Fe). Therefore, the study of phase formation in these ternary systems was restricted to an analysis of samples whose composition corresponded to the intersection point of the lines $AMoO_4$–$NaR(MoO_4)_2$ and $Na_{2-2x}A_{2+x}(MoO_4)_3$, $0.4 \le x \le 0.5$–$R_2(MoO_4)_3$; $AMoO_4$–$NaR(MoO_4)_2$; $Na_{2+2x}Mg_{1-x}(MoO_4)_2$, $0 \le x \le 0.2$–$R_2(MoO_4)_3$.

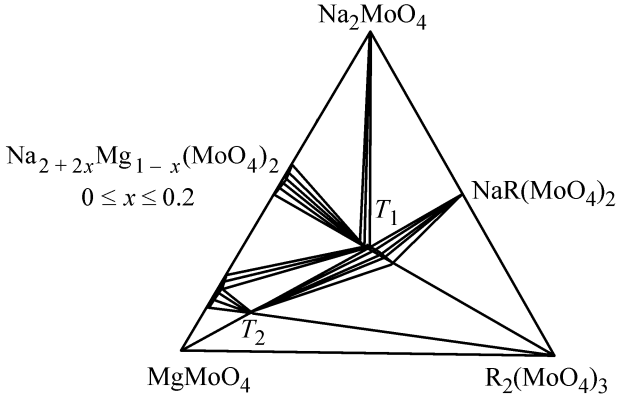

Fig. 1. Phase relations in the systems Na_2MoO_4–$MgMoO_4$–$R_2(MoO_4)_3$ (R = Cr, Fe). (T_1) $Na_{1-x}Mg_{1-x}R_{1+x}(MoO_4)_3$ and (T_2) $NaMg_3R(MoO_4)_5$.

Table 2. Crystallographic and thermal characteristics of $NaA_3R(MoO_4)_5$

Compound	*a*	*b*	*c*	α	β	γ	*V*/*Z*, Å^3	ρ_{calc}, g cm^{-3}	ρ_{calc}, g cm^{-3}	mp, °C
	Å			deg						
$NaNi_3Cr(MoO_4)_5$	6.936(2)	17.571(4)	6.845(2)	87.99(2)	101.47(3)	92.25(2)	408.4			880
$NaMg_3Cr(MoO_4)_5$	6.948(3)	17.575(6)	6.862(2)	88.03(1)	101.39(2)	92.16(2)	410.3			950
$NaCo_3Cr(MoO_4)_5$	6.964(2)	17.579(3)	6.879(1)	88.02(1)	101.36(3)	92.12(3)	412.4	4.232	4.21	840
$NaMn_3Fe(MoO_4)_5$	6.965(2)	17.585(4)	6.884(2)	88.00(2)	101.35(1)	92.14(2)	412.9			860
$NaNi_3Fe(MoO_4)_5$	6.938(2)	17.573(5)	6.851(1)	87.94(2)	101.46(3)	92.29(2)	408.8			820
$NaMg_3Fe(MoO_4)_5$	6.951(1)	17.582(4)	6.845(2)	87.91(2)	101.43(2)	92.23(1)	410.9	3.844	3.82	890
$NaCo_3Fe(MoO_4)_5$	6.966(1)	17.581(4)	6.883(2)	87.94(2)	101.34(3)	92.19(2)	412.8			870
$NaMn_3Fe(MoO_4)_5$	6.964(3)	17.583(5)	6.892(2)	87.92(2)	101.25(2)	92.12(2)	413.4			850

It was found that at 650–700°C the compounds $NaAR(MoO_4)_3$ (A = Mn, Co, Ni; R – Cr, Fe) are formed, together with phases of variable composition on their base, with various homogeneity regions in the series of both double- and triple-charged elements. In spite of the fact that all molybdates of doublecharged elements A (Mg, Mn, Co, and Ni) have the same symmetry (structural type of α-$MnMoO_4$), the homogeneity region depends on the nature of an element. When small double-charged ions (Ni^{2+}) and highly polarizing cations (Co^{2+}) are introduced into the skeleton, the region of existence of rhombohedral phases is narrowed down to $x = 0.2$. The phases with A = Mg have the widest region of existence, $0 \le x \le 0.3$. It is necessary to note that the individual manganese-, cobalt-, and nickel-containing phases at $x = 0-0.1$ could not be isolated by varying the temperature and annealing time. Alongside with the phases $Na_{1-x}A_{1-x}R_{1+x}(MoO_4)_3$, the binary molybdate $NaR(MoO_4)_2$ is present in the annealed samples. This structural type (skeleton) is the most favorable for magnesium compounds.

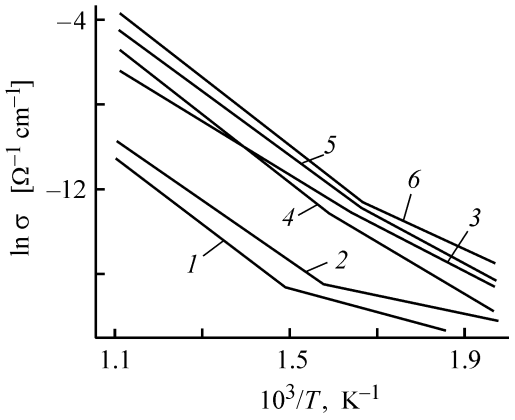

Fig. 2. Dependence of electrical conductivity σ on temperature *T*. (*1*) $NaMg_3Cr(MoO_4)_5$, (*2*) $NaMg_3Fe(MoO_4)_5$, (*3*) $NaMgCr(MoO_4)_3$, (*4*) $Na_{0.7}Mg_{0.7}Cr_{1.3}(MoO_4)_3$, (*5*) $NaMgFe(MoO_4)_3$, and (*6*) $Na_{0.7}Mg_{0.7}Fe_{1.3}(MoO_4)_3$.

It was found in [17] that the widest homogeneity regions are observed in aluminum molybdates, in which manganese and magnesium are double-charged elements and $x = 0.5$. Introduction of such ions as Cr and Fe, which are larger than Al, into the rhombohedral skeleton makes the homogeneity region narrower: $x = 0.3$.

According to the results of X-ray phase analysis, the formation of ternary compounds in $3Co(Ni)MoO_4$–$NaR(MoO_4)_2$ (R = Cr, Fe) mixtures begins at 600–650°C, and in $3Mg(Mn)MoO_4$–$NaR(MoO_4)_2$ (R = Cr, Fe), at 550–600°C. The ternary molybdates of 3 : 1 composition were obtained as single-phase products at 650–700°C and calcination time of 150–200 h.

The compounds $NaA_3R(MoO_4)_5$ were synthesized from neutral molybdates at 1 : 6 : 1 ratio of the starting components, 700–750°C, and calcination time of 200–300 h. Ternary molybdates are formed in synthesis from neutral molybdates in a number of successive stages. Binary molybdates $NaR(MoO_4)_2$ and $AMoO_4$ were revealed as intermediate products. The results obtained suggest that, when a ternary molybdate is synthesized by the reaction of $AMoO_4$ with a binary molybdate of single- and three-charged elements, the equilibrium is attained faster, and at a lower temperature, as compared with reaction mixtures of Na_2MoO_4, $AMoO_4$, and $R_2(MoO_4)_3$.

An X-ray study of the synthesized compounds $NaA_3R(MoO_4)_5$ (A = Mg, Mn, Co, Ni; R = Cr, Fe) demonstrated that they are isostructural to each other and crystallize in the triclinic crystal system ($P\bar{1}$, $Z = 2$), which places them in a new structural family [18] (Table 2).

Table 3. Electrical characteristics of $NaA_3R(MoO_4)_5$

Compound	300°C		600°C		*E*, eV
	σ, Ω^{-1} cm^{-1}	t_e	σ, Ω^{-1} cm^{-1}	t_e	
$NaMg_3Fe(MoO_4)_5$	1.82×10^{-8}	0.28	1.20×10^{-5}	0.62	6.07
$NaMn_3Fe(MoO_4)_5$	1.39×10^{-8}	0.25	1.40×10^{-5}	0.64	5.97
$NaMg_3Cr(MoO_4)_5$	1.13×10^{-8}	0.35	1.10×10^{-5}	0.67	6.18

Table 4. Electrical characteristics of phases of variable composition, $Na_{1-x}A_{1-x}R_{1+x}(MoO_4)_3$, $0 \le x \le 0.3$, R = Cr, Fe

Compound	300°C		600°C		*E*, eV
	σ, Ω^{-1} cm^{-1}	t_e	σ, Ω^{-1} cm^{-1}	t_e	
$NaMgCr(MoO_4)_3$	6.25×10^{-8}	0.75	2.15×10^{-3}	0.72	2.43
$Na_{0.7}Mg_{0.7}Cr_{1.3}(MoO_4)_3$	1.62×10^{-8}	0.80	1.01×10^{-2}	0.79	2.33
$NaMgFe(MoO_4)_3$	9.09×10^{-8}	0.78	8.26×10^{-3}	0.75	2.26
$Na_{0.7}Mg_{0.7}Fe_{1.3}(MoO_4)_3$	1.06×10^{-7}	0.80	1.47×10^{-2}	0.81	2.17

It was found that the total conductivity of ternary molybdates $NaA_3R(MoO_4)_5$ varies within the limits 10^{-8}–10^{-5} Ω^{-1} cm^{-1} as temperature increases from 200 to 600°C. There is only a single bend in the $\ln\sigma$–$1/T$ curves (Fig. 2), which is associated with transition from impurity conduction to that of the intrinsic type. On the basis of temperature dependences of the electrical conductivity and transfer numbers, a conclusion was made that the ternary molybdates exhibit mixed ionic-electronic conduction, with the ionic component predominant up to 360°C (t_e = 0.25–0.35) and the electronic component much exceeding it in the range 360–600°C (t_e = 0.62–0.67). The activation energies *E* of the electronic conductivity of the compounds are shown in Table 3. With increasing radii of double- and triple- charged cations, the conductivity becomes higher.

In all the cases, the dielectric constant and the dielectric loss tangent grow exponentially without anomalies with increasing temperature.

With increasing temperature, the total conductivity of rhombohedral phases $Na_{1-x}A_{1-x}R_{1+x}(MoO_4)_3$ varies within the limits 10^{-8}–10^{-2} Ω^{-1} cm^{-1}.

The predominantly ionic conduction (t_i = 0.72–0.81) is characteristic of the compounds obtained. It was found that the conductivity grows in the series of solid solutions with *x* increasing from 0 to 0.3 and with increasing radius of triple-charged cation (Fig. 2 and Table 4), which is associated with the structural features of NASICON-like phases, whose structure is a three-dimensional porous skeleton composed of apex-connected MoO_4 tetrahedra and MO_6 octahedra of double- and triple-charged cations. The Na^+ cations are situated within the spacious voids of the skeleton, which are combined into a system of communicating channels [16]. Hetero-charge substitution $Na^+ + M^{2+} = M^{3+} + \square$ in the series of solid solutions results in the formation of additional vacancies in the sodium sublattice, which affects the mobility of sodium cations, i.e., the possibility of their freer motion in the voids along the conduction channels. With *x* increasing from 0 to 0.3, the electrical conductivity grows from 8.26×10^{-3} to 1.47×10^{-2} for iron-containing phases and from 2.15×10^{-3} to 0.01×10^{-2} Ω^{-1} cm^{-1} for chromium-containing phases. It was found that the large sizes of both the octahedra and the tetrahedra lead to high ionic conductivity [3]. At 600°C, the electrical conductivity of $NaMgCr(MoO_4)_3$ ($r_{Cr^{3+}}$ = 0.62 Å) and $NaMgFe(MoO_4)_3$ ($r_{Fe^{3+}}$ = 0.65 Å) is 2.15×10^{-3} and 8.26×10^{-3} Ω^{-1} cm^{-1}, respectively.

The dielectric constant ε and the dielectric loss tangent tanδ depend on temperature exponentially for $Na_{1-x}A_{1-x}R_{1+x}(MoO_4)_3$. The absence of extrema in the curves for the dielectric constant and dielectric loss tangent indicates the absence of phase transitions and ferroelectric properties in NASICON-like ternary molybdates.

Comparison of the results obtained in this study with the data of [19] shows that the highest conductivity among sodium and potassium ternary molybdates $MAR(MoO_4)_3$ and phases of variable composition on their base, $M_{1-x}A_{1-x}R_{1+x}(MoO_4)_3$, $0 \le x \le 0.6$–0.2

(A = Ni, Mg, Co, Mn; R = Al, In, Sc, Yb, Lu) is observed for sodium-containing rhombohedral phases, which makes them promising materials for solid electrolytes.

CONCLUSIONS

(1) A study of phase relations in the subsolidus region of the systems Na_2MoO_4–$AMoO_4$–$R_2(MoO_4)_3$ (A = Mg, Mn, Co, Ni; R = Cr, Fe) demonstrated that ternary molybdates $NaA_3R(MoO_4)_5$ and $NaAR(MoO_4)_3$ and phases of variable composition on their base with different homogeneity regions are formed.

(2) The electrical characteristics of $NaA_3R(MoO_4)_5$ and $Na_{1-x}A_{1-x}R_{1+x}(MoO_4)_3$ were studied. It was found that $NaA_3R(MoO_4)_5$ have low conductivity (10^{-8}–10^{-5} Ω^{-1} cm^{-1}) with predominant electronic component. The rhombohedral phases of variable composition have predominantly ionic conduction. The conductivity in the homogeneity region grows steadily with increasing concentration of vacancies in the sodium sublattice and also with increasing size of the triple-charged cation (Cr → Fe).

REFERENCES

1. Trunov, V.K., Efremov, V.A., and Velikodnyi, Yu.A., *Kristallokhimiya i svoistva dvoinykh molibdatov* (Crystal Chemistry and Properties of Binary Molybdates), Leningrad: Nauka, 1986.
2. Dzhurinskii, B.F., Zorina, L.N., Lysanova, G.V., *et al.*, *Izv. Akad. Nauk SSSR, Neorg. Mater.*, 1980, vol. 16, no. 1, pp. 110–113.
3. Stefanovich, S.Yu., Ivanova, L.A., and Astaf'ev, A.V., *Ionnaya i superionnaya provodimost' v segnetoelektrikakh. Khimicheaskaya promyshlennost'. Nauchno-tekhnicheskie prognozy v oblasti fiziko-khimicheskikh issledovanii* (Ionic and Superionic Conduction in Ferroelectrics. Chemical Industry. Scientific and Technical Forecasts in the Field of Physicochemical Research), Moscow: Khimiya, 1989.
4. Bukun, N.G., Domashnev, I.A., Moskvina, E.I., and Ukshe, E.A., *Neorg. Mater.*, 1988, vol. 24, no. 3, pp. 443–447.
5. Kalinin, V.B. and Stefanovich, S.Yu., *Neorg. Mater.*, 1982, vol. 18, no. 9, pp. 1567–1571.
6. Goodenough, J.B., Hong, H. Y–P., and Kafalas, J.A., *Mater. Res. Bull.*, 1979, vol. 11, no. 2, pp. 203–219.
7. Nogai, A., Kalinin, V.B., Stefanovich, S.Yu., and Gagulin, V.V., *Zh. Neorg. Khim.*, 1988, vol. 33, no. 3, pp. 747–751.
8. Ivanov-Shits, A.K., Bykov, A.B., and Verin, I.A., *Kristallografiya*, 1996, vol. 41, no. 6, pp. 1060–1062.
9. Golubev, A.M., Kalinin, V.B. and Maksimov, B.A., *Kristallografiya*, 1999, vol. 44, no. 6, pp. 1014–1016.
10. Vest, R.V. and Tallan, N.H., *J. Appl. Phys.*, 1965, vol. 36, no. 2, pp. 543–547.
11. Efremov, V.A., Zhukovskii, V.M., and Petrosyan, Yu.T., *Zh. Neorg. Khim.*, 1976, vol. 21, no. 1, pp. 209–213.
12. Klevtsova, R.F., Kim, V.G., Klevtsov, P.V., *Kristallografiya*, 1980, vol. 25, no. 1, pp. 209–213.
13. Efremov, V.A., Petrosyan, Yu.T., and Zhukovskii, V.M., *Zh. Neorg. Khim.*, 1977, vol. 22, no. 1, pp. 175–179.
14. Solodovnikov, S.F., Solodovnikova, Z.A., Klevtsov, P.V., and Zoltova, E.S., *Zh. Neorg. Khim.*, 1995, vol. 40, no. 2, pp. 305–311.
15. Klevtsov, P.V., Kozeeva, L.P., and Klevtsova, R.F., *Zh. Neorg. Khim.*, 1975, vol. 20, no. 11, pp. 2999–3002.
16. Lazoryak, B.I. and Efremov, V.A., *Zh. Neorg. Khim.*, 1987, vol. 32, no. 3, pp. 652–656.
17. Kozhevnikova, N.M., Mokhosoev, M.V., Alekseev, F.P., *et al.*, *Zh. Neorg. Khim.*, 1989, vol. 34, no. 7, pp. 1837–1839.
18. Klevtsova, R.F., Vasil'ev, A.D., Kozhevnikova, N.M., *et al.*, *Zh. Strukt. Khim.*, 1993, vol. 34, no. 5, pp. 147–151.
19. Murzakhanova, I.I., Kozhevnikova, N.M., and Mokhosoev, M.V., *Zh. Neorg. Khim.*, 1991, vol. 36, no. 11, pp. 2769–2771.

Russian Journal of Applied Chemistry, Vol. 76, No. 10, 2003, pp. 1577–1582. Translated from Zhurnal Prikladnoi Khimii, Vol. 76, No. 10, 2003, pp. 1619–1624.

SORPTION AND ION-EXCHANGE PROCESSES

Adsorption Properties of Natural Carbonaceous Adsorbents and Thermally Expanded Graphite

Yu. I. Tarasevich, S. V. Bondarenko, V. V. Brutko, A. I. Zhukova, G. N. Malysh, and I. G. Polyakova

Dumansky Institute of Colloid Chemistry and Chemistry of Water, National Academy of Sciences of the Ukraine, Kiev, Ukraine

Received May 13, 2002; in final form, March 2003

Abstract—Structural and sorption characteristics of natural carbonaceous sorbents and thermally expanded graphite were examined. Acid–base sites on the sorbent surface were characterized qualitatively and quantitatively. The performance of the materials in wastewater treatment to remove anionic surfactants was studied.

Search for, and characterization and practical application of efficient and sufficiently cheap natural sorbents for treatment of natural and waste water is a topical problem [1, 2]. For this purpose, natural and synthetic carbonaceous sorbents are widely used [3, 4]. The use of carbonaceous adsorbents from domestic deposits or those modified by domestically developed processes appears to be the most expedient from the cost-effectiveness standpoint. Therefore, we started studies of natural porous coal, natural graphite, and thermally expanded (foamed) graphite (TEG) for water treatment.

Natural porous coal is a young coal, precursor of brown coal, whose deposits are found in the Donets Basin (Ukraine). Natural graphite was taken from the Zaval'e deposit (Kirovograd oblast, Ukraine).

TEG samples were prepared using the procedure described in [5]. Chemically enriched natural graphite of GAK-2 brand {GOST (State Standard) 0273–78 [6]} was treated with a mixture of concentrated sulfuric acid and 30% hydrogen peroxide for 30 min. Hydrolysis of the intercalate (graphite bisulfate) yields oxidized graphite, which is subjected to thermal treatment in a gas furnace at 627°C. Finally, TEG is treated in a roasting apparatus at 427° under nitrogen for 30 s to remove residual sulfur compounds.

As the first stage of the study, we analyzed the structural and sorption characteristics of the above-indicated materials, including the nature and amount of functional groups on their surface and adsorption capacity for some anionic surfactants.

EXPERIMENTAL

Low-temperature (77 K) static adsorption of nitrogen on the test sorbents was carried out on an ASAP 2000 M instrument (Micromeritics, the United States). The sample pretreatment temperature was 393 K. From the isotherms obtained using the ASAP software, we determined the BET specific surface areas S_{N_2}, total pore volume V_Σ, volume of micropores W_0, and pore size distribution.

To gain better insight into the structure of the carbonaceous materials and to estimate the hydrophilicity of their surface, we measured the adsorption–desorption isotherms of *n*-hexane and water vapor, using a vacuum adsorption system with a McBain–Bakr quartz spring balance at 298 K (temperature of preliminary vacuum treatment of samples, 393 K). Using the BET equation, we determined from the adsorption isotherms the nominal monolayer capacity and the effective specific surface area of the sorbents. From the hexane desorption isotherms obtained at relative pressures P/P_s = 0.3–0.9, we estimated the pore size distribution of the samples by the Kelvin–Thomson equation.

Acidic and basic reactive groups on the sorbent surface were determined by conductometric back titration [7]. Weighed portions (0.5 and 0.1 g) of the sorbents were placed in 20 ml of CO_2-free distilled water and allowed to stand for 24 h at 293 K in flasks with ground-glass stoppers, with intermittent stirring. Then 1 ml of 0.1 M KOH or HCl was added, and

1070-4272/03/7610-1577 $25.00 © 2003 MAIK "Nauka/Interperiodica"

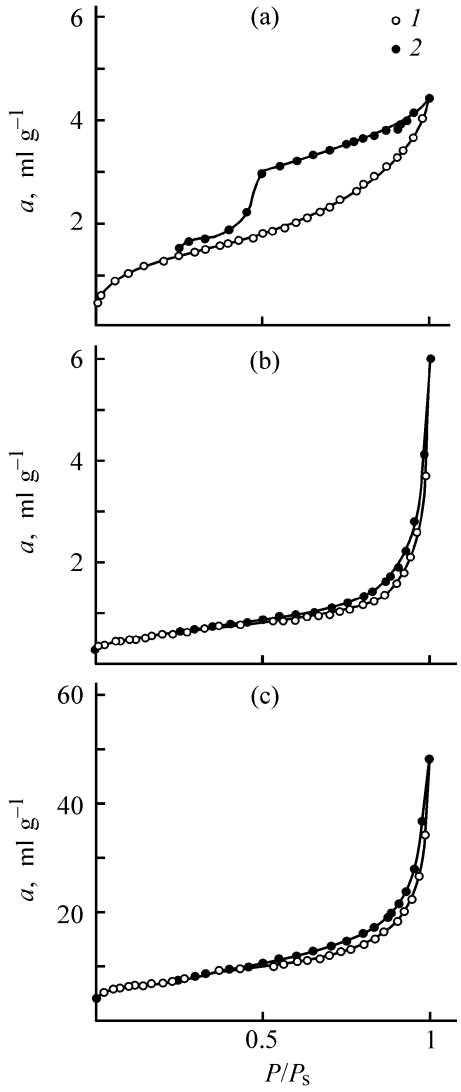

Fig. 1. Isotherms of (*1*) sorption and (*2*) desorption of nitrogen at 77 K: (a) natural coal, (b) natural graphite, and (c) TEG. (*a*) Adsorption and (P/P_s) relative pressure; the same for Figs. 2 and 3.

the suspensions were titrated with 0.1 M HCl or KOH, respectively. The volumes of the standard solutions were measured with a standardized 1-ml burette equipped with a special microdoser. The electrical conductivity of the suspensions was measured with a P5021 ac bridge in a temperature-controlled conductivity cell with flat Pt electrodes and a magnetic stirrer. Contact with the atmosphere was enabled through an absorption tube filled with soda lime. From the conductometric titration curves, the amount of acidic and basic centers (μg-equiv g^{-1}) was estimated as

$$n_{H^+(OH^-)} = \frac{c_{HCl(KOH)}V_1 - c_{KOH(HCl)}V_2}{m} \times 10^3,$$

where $c_{HCl(KOH)}$ is the acid or alkali concentration (M); V_1, the volume (ml) of the acid or alkali added to the suspension; V_2, the volume (ml) of the titrant consumed for titration of free acid or alkali; m, the sorbent weight (g).

The amount of active centers was determined to within 5%.

The nature and strength of the active sites on the sorbent surface were determined by potentiometric titration over the pH range 2.3–10.8, using the single-portion method [8]. The portions were 0.5 g for natural coal and graphite samples and 0.1 g for TEG samples. The total solution volume was 40 ml in each case. As supporting electrolyte served 1 M KCl. All solutions were prepared in CO_2-free distilled water. The contact time of the sorbents with 0.1 M KOH or 0.1 M HCl in 1 M KCl was 24 h at 273 K. For natural coal in KOH, the contact time was 15 min because of the instability of sorbents and ion exchangers based on natural coal in alkaline solutions [9]. The pH in the systems was measured on an EV-74 universal ion meter with ESL-05G working glass electrode and EVL-1MZ immersible saturated Ag/AgCl reference electrode. The glass electrode was calibrated once a week against three standard buffer solutions. The measurements were conducted at 273 K in a hermetically sealed temperature-controlled cell equipped with a magnetic stirrer. Contact with the atmosphere was enabled through an absorption tube packed with soda lime. The potentiometric titration curves were plotted in the coordinates pH–V, where V is the volume (ml) of the acid or alkali added to the system. From the titration curves, we estimated at fixed pHs (9.0 and 9.8) the exchange capacity of the sorbents E (μg-equiv g^{-1}) to within 5%.

We examined the performance of the adsorbents under study in recovery of anionic surfactants. As a typical anionic surfactant we selected Sulfonol [sodium dodecylbenzenesulfonate $C_{12}H_{25}C_6H_4SO_3Na$; MW 348, CMC 420 mg l^{-1} (1.2×10^{-3} M)]. To obtain Sulfonol adsorption isotherms on the carbonaceous sorbents, we prepared 8–10 aqueous Sulfonol solutions with concentrations of 2.5–100 mg l^{-1} (7.1×10^{-6}–2.6×10^{-4} M). Weighed portions of dry sorbents were placed in these solutions and equilibrated for 5 days. Then the solid phase was separated by centrifugation at 6000 rpm, and the equilibrium Sulfonol concentrations were determined spectrophotometrically at λ = 227 nm ($\varepsilon = 44 \times 10^3$ cm^{-1}) on a Specord UV-VIS instrument.

The low-temperature nitrogen adsorption isotherms of the sorbents studied are presented in Fig. 1. It fol-

Table 1. Specific surface area S, total pore volume V_Σ, micropore volume W_0, nominal monolayer capacity a_m, and effective pore radius r_{ef} of carbonaceous adsorbents

Sorbents	S, $m^2\ g^{-1}$			V_Σ	W_0	a_m, mmol g^{-1}		r_{ef}, nm	
	N_2	n-C_6H_{14}	H_2O	ml g^{-1}		n-C_6H_{14}	H_2O	N_2	n-C_6H_{14}
Natural coal	4.7	3.0	127	0.007	0.0003	0.10	1.960	1.8; 2.0	1.8–3.0
Natural graphite	2.0	3.0	4.0	0.010	0.0004	0.01	0.084	1.2; 2.0; 24.5	–
TEG	24.1	15.0	5.2	0.080	0.0052	0.05	0.096	1.3; 2.0; 22.5	1.0–2.3

lows from the type of the isotherms that all the sorbents have a nonuniform porous structure. In particular, the sharp rise at $P/P_s < 0.05$ suggests the presence of micropores in the structure of carbonaceous materials. However, the observed volume W_0 of micropores is rather small (Table 1), suggesting that they do not contribute significantly to the adsorption capacity of the sorbents. At relative pressures P/P_s of 0.20 to 0.98, a capillary–condensation hysteresis loop is observed, caused by the presence of mesopores in the sorbent structure. Indeed, the pore size distribution curves demonstrate domination of mesopores with effective radii of about 1.2, 2.0, and 22.5–25 nm. The platelike shape of particles of carbonaceous materials suggests a slotlike shape of the mesopores, which is also supported by the shape of the hysteresis loop of type *B* [10].

The adsorption–desorption isotherms of *n*-hexane and water on the carbonaceous adsorbents studied are similar to the corresponding isotherms obtained for nitrogen. Initially ($P/P_s < 0.1$) all the isotherms are convex toward the ordinate. Then, in the isotherms of the initial and thermally expanded graphite, a hysteresis loop is observed, which closes at $P/P_s \sim 0.02$. For natural coal, the hysteresis loop in the isotherms of adsorption of hexane and water is considerably broader than for the other sorbents, extending to $P/P_s = 0$. This is associated with swelling of the sorbent texture (submicroscopic structure). The ability of some sorts of bituminous coals and hard and soft brown coals to swell was reported in [9]. For the same reason, Lishtvan *et al.* [11] observed the adsorption isotherms of water and hydrocarbon vapor on brown coals and peat with an anomalous hysteresis loop.

We have demonstrated previously [12] that the presence of a considerable amount of hydrophilic centers on the surface of coal stacks is an important factor responsible for significant adsorption of water. The results showed that the limiting adsorption of water on mesoporous coal exceeds that of hexane by about a factor of 3, suggesting considerable amount of hydrophilic centers on the sorbent surface.

The reverse was observed with the initial and thermally expanded graphite: the amount of adsorbed hexane is much higher than that of water (Figs. 2, 3), which is a clear indication of highly hydrophobic surface of both the graphite samples.

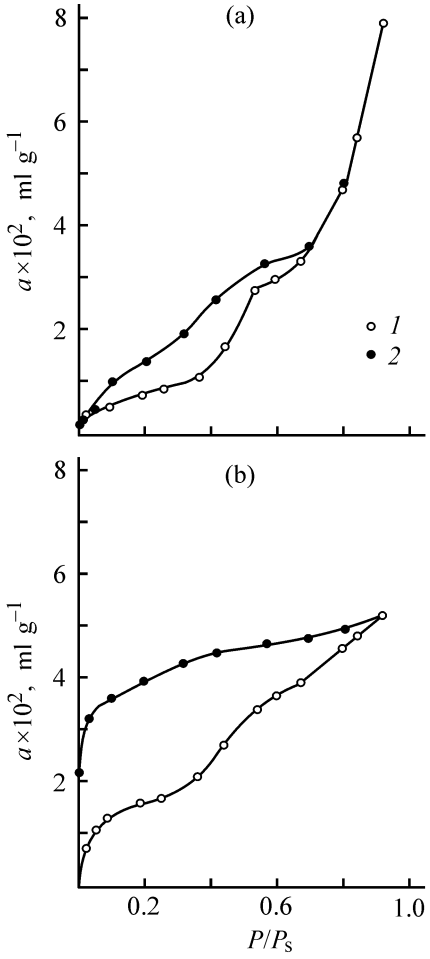

Fig. 2. (*1*) Adsorption and (*2*) desorption isotherms of hexane vapor at 298 K: (a) TEG and (b) natural coal; the same for Fig. 3.

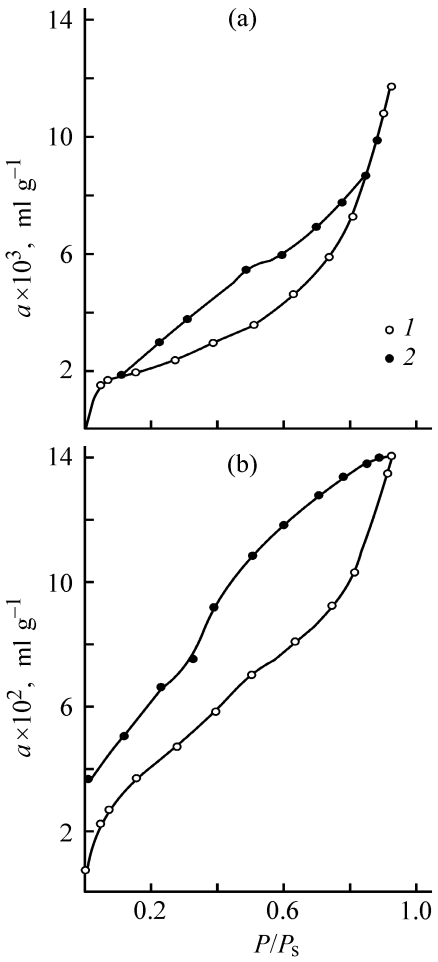

Fig. 3. (*1*) Adsorption and (*2*) desorption isotherms of water vapor at 298 K.

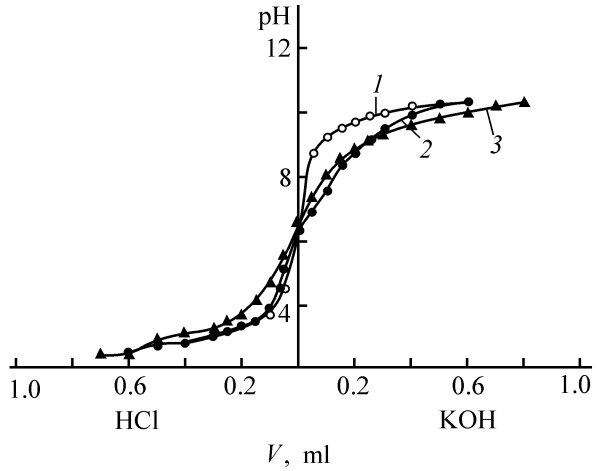

Fig. 4. Potentiometric titration curves. (*V*) Titrant volume. (*1*) Blank experiment, (*2*) TEG, and (*3*) natural graphite.

It follows from the potentiometric titration curves (Fig. 4) that all the carbonaceous adsorbents studied are weakly acidic polyfunctional cation exchangers: the titration curves demonstrate nearly the same smooth slopes over a wide pH range and also weakly pronounced inflections.

In the acidic range, the titration curve of the initial graphite runs slightly above the titration curves obtained in the blank experiment and with TEG. In the range from pH 3.5–3.7 to 9.0–9.5, pH increases more sharply, which is probably due to gradual (as pH increases) involvement in dissociation of surface carboxy and phenolic hydroxy groups [9, 13, 14]. From comparison of the titration curves of the adsorbents with the result of the blank experiment [15], we estimated their total exchange capacity E (μg-equiv g^{-1}): TEG 160–170 (pH 9.0) and initial graphite 60 (pH 9.5). These results are well consistent with the conductometric data discussed below.

It should be noted that data on conductometric titration of the initial graphite revealed the presence of some basic functional groups that are neutralized with 0.1 HCl. It may be suggested that these are the surface OH groups, which is supported by the conductometric titration data on the concentrations of acidic (c_{H^+}) and basic (c_{OH^-}) centers in the sorbents studied. Natural coal contains acidic centers only (c_{H^+} = 140 μg-equiv g^{-1}); the initial graphite, both acidic (c_{H^+} = 60 μg-equiv g^{-1}) and basic centers (c_{OH^-} = 20 μg-equiv g^{-1}); and TEG, acidic centers only (c_{H^+} = 160 μg-equiv g^{-1}). As seen, only the initial graphite contains basic centers. Most likely, it is this fact that is responsible for the above-mentioned higher run of the acidic branch in the potentiometric titration curve of the initial graphite relative to the curve obtained in the blank experiment.

Water molecules, as known [16], interact with acids and bases and, therefore, the adsorption method gives the total amount of active centers.

Estimation of the concentration of active centers on the sorbent surface from the specific surface area determined from the hexane adsorption (Table 1) gives 2.8×10^{19}, 1.6×10^{19}, and 0.64×10^{19} m^{-2} for natural coal, initial graphite, and TEG, respectively. As expected, the amount of active centers is the highest in mesoporous coal, exceeding that in graphitized thermal black [17].

The number of water molecules bound to an active center was estimated from the nominal monolayer capacity, determined by the BET equation (Table 1), to be 14, 1.05, and 0.6 for the coal, initial graphite, and TEG, respectively. Evidently, the high concentration of active centers in the mesoporous carbon enables association of water molecules on its surface

Table 2. Limiting adsorption, a_{max}, and degree of Sulfonol recovery, α, from aqueous solutions with different concentrations c_0

Sorbent	a_{max}, mg g^{-1}	α, %, at indicated c_0, mg l^{-1}	
		20	70
Natural coal	5.8	43	34
Natural graphite	3.1	35	21
TEG	31.0	99	84

even at low P/P_s. The cluster mechanism of water adsorption on hydrophilic centers of carbonaceous sorbents is supported by data reported in [18].

The concentration of active sites strongly influences the adsorption of water, mainly at low coverage of the sorbent surface [19]. It should be borne in mind, however, that formation of clusters of water molecules near active hydrophilic centers favors swelling of the porous carbon texture under water vapor and, as a result, influences the adsorption of water at higher coverage.

It follows from the shape of the sorption–desorption isotherm of hexane on mesoporous coal (inflection in the adsorption branch at $P/P_s \approx 0.5$) and also from the residual amount of hexane after a short-time vacuum treatment of a sample (~2×10^{-2} ml g^{-1}) that this material swells under hexane vapor too, as a capillary-condensation film of the hydrocarbon is formed in its pore space. From the inflection point in the sorption branch, we estimated the minimum halfwidth of slotlike mesopores. We obtained 2.5 and 2.9 nm for natural coal and TEG, respectively, which is comparable with the values obtained by the Kelvin–Thomson equation (Table 1).

The isotherms of Sulfonol adsorption on the sorbents studied are shown in Fig. 5. All the isotherms demonstrate a clearly pronounced convexity toward the ordinate at low coverage.

Compared with the initial graphite and porous coal, the adsorption on TEG is higher by an order of magnitude (28.0 against 2.5–3.0 mg g^{-1} at c_S = 40 mg l^{-1}). In this case, adsorption is mainly controlled by the dispersion interaction of the alkyl chain of Sulfonol with the carbon surface.

From the results of the adsorption experiments, we estimated the degree of Sulfonol recovery at two Sulfonol concentrations (Table 2). The results obtained show that the degree of Sulfonol recovery decreases in the order TEG > natural coal > initial graphite.

It should be noted out that TEG ensures virtually total recovery of Sulfonol at its concentration in water of up to 20 mg l^{-1}. At c_S = 70 mg l^{-1}, the degree of recovery is 84% (Sulfonol MPC in discharged water is 0.5 mg l^{-1}).

CONCLUSIONS

(1) Natural carbonaceous sorbents have a nonuniform porous structure with predominance of slotlike mesopores. The size of the slotlike mesopores was determined.

(2) The sorbents studied are weakly acidic polyfunctional cation exchangers.

(3) The concentration of active hydrophilic sites on the surface of natural carbonaceous sorbents is estimated, and it is shown that adsorption of the water molecules on the natural coal surface proceeds by the cluster formation mechanism. Natural coal is capable of swelling in water and *n*-hexane vapors.

(4) Thermally expanded graphite shows promise as a sorbent for recovery of anionic surfactants from wastewaters.

ACKNOWLEDGMENTS

The study was supported financially by the INTAS program (project no. 00-505).

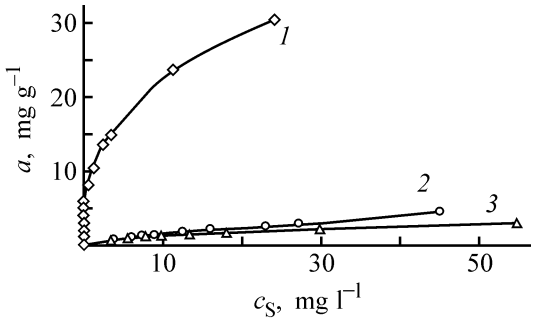

Fig. 5. Isotherms of sulfonol adsorption on carbonaceous sorbents at 293 K: (*1*) TEG, (*2*) natural coal, and (*3*) natural graphite. (a) Adsorption and (c_S) Sulfonol concentration in solution.

REFERENCES

1. Tarasevich, Yu.I., *Prirodnye sorbenty v protsessakh ochistki vody* (Natural Sorbents in Water Treatment Processes), Kiev: Naukova Dumka, 1981.
2. *Adsorption from Solution at the Solid/Liquid Interface*, Parfitt, G.D. and Rochester, C.H., Eds., London: Academic, 1983.
3. Kienle, H. and Bader, E., *Aktivkohle und ihre industrielle Anwendung*, Stuttgart: Enke, 1980.
4. Koganovskii, A.M., Klimenko, N.A., Levchenko, T.M., and Roda, I.G., *Adsorbtsiya organicheskikh veshchestv iz vody* (Adsorption of Organic Compounds from Water), Leningrad: Khimiya, 1990.
5. Ukrainian Patent no. 38 655.
6. Zayats, M.M., *Khim. Prom–st. Ukr.*, 1994, no. 4, pp. 9–17.
7. Vasil'ev, N.G., Golovko, L.V., and Ovcharenko, F.D., *Kolloidn. Zh.*, 1976, vol. 38, no. 5, pp. 842–846.
8. Kunin, R. and Myers, J., *Ion-Exchange Resins*, New York: Wiley, 1950.
9. Helfferich, F.G., *Ion Exchange*, New York: McGraw–Hill, 1962.
10. Gregg, S.J. and Sing, K.S.W., *Adsorption, Surface Area, and Porosity*, London: Academic, 1982.
11. Lishtvan, I.I., Kruglitskii, N.N., and Tretinnik, V.Yu., *Fiziko-khimicheskaya mekhanika guminovykh veshchestv* (Physicochemical Mechanics of Humic Substances), Minsk: Nauka i Tekhnika, 1976.
12. Tarasevich, Yu.I. and Rak, V.S., *Kolloidn. Zh.*, 1998, vol. 60, no. 1, pp. 84–88.
13. Griessbach, R., *Austauschadsorption in Theorie und Praxis, Allgemeiner Teil*, Berlin: Akademie, 1957.
14. Strazhesko, D.N. and Tarkovskaya, I.A., *Adsorb. Adsorb.* (Kiev), 1972, no. 1, pp. 7–17.
15. *Ionity v khimicheskoi tekhnologii* (Ion Exchangers in Chemical Technology), Nikol'skii, B.P. and Romankov, P.G., Eds., Leningrad: Khimiya, 1982.
16. Bell, R.P., *The Proton in Chemistry*, London: Chapman and Hall, 1973.
17. Vartapetyan, R.Sh. and Voloshchuk, A.M., *Usp. Khim.*, 1995, vol. 64, no. 11, pp. 1055–1072.
18. Brennan, J.K., Bandosz, T.J., Thomson, K.T., and Gubbins, K.E., *Colloids Surf., Ser. A*, 2001, vols. 187–188, pp. 539–568.
19. Vartapetyan, R.Sh., Voloshchuk, A.M., Dubinin, M.M., and Moskovskaya, T.A., *Izv. Akad. Nauk SSSR, Ser. Khim.*, 1988, no. 9, pp. 1961–1966.

Russian Journal of Applied Chemistry, Vol. 76, No. 10, 2003, pp. 1583–1588. Translated from Zhurnal Prikladnoi Khimii, Vol. 76, No. 10, 2003, pp. 1625–1630.

APPLIED ELECTROCHEMISTRY AND CORROSION PROTECTION OF METALS

Electrochemically Deposited Zinc–Nickel Alloys

T. V. Gaevskaya, T. V. Byk, and L. S. Tsybul'skaya

Research Institute of Physicochemical Problems, Belarussian State University, Minsk, Belarus

Received May 6, 2003

Abstract—The mechanism of formation of a zinc–nickel alloy under the conditions of normal and anomalous electrochemical codeposition (accompanied by enrichment of the deposit with nickel or zinc) were studied. The manner in which the composition, structure, and properties of the zinc–nickel alloy vary with the electrolyte composition (nature of ligands and molar ratio of codeposited metals) and deposition conditions (potential and current density) was determined.

The increasing requirements to the functional properties of zinc coatings created a need for development of processes for electrodeposition of zinc alloys [1–4]. One of promising ways to improve the corrosion resistance of zinc coatings is their alloying with nickel, which makes it possible to decrease the thickness of a coating at its same protecting capacity, raise its thermal resistance, and, in some cases, avoid use of toxic cadmium. To solve numerous topical problems concerning the deposition of functional coatings, it is necessary to study the specific features of formation, structure, and properties of electrochemically deposited zinc–nickel coatings.

Despite the great number of studies concerned with this problem, a number of issues are controversial and insufficiently studied. For example, it is not understood completely, in which cases there occurs anomalous codeposition of Zn and Ni, which consists in predominant deposition of the more electronegative metal (Zn) into the alloy [5–13]. The available published evidence and experimental data on the composition of zinc–nickel-plating electrolytes give no way of elucidating properly the ways to control the chemical and phase composition, microstructure, and properties of the alloy by varying the electrolyte composition and deposition conditions. Data on the conditions under which phases of nonequilibrium composition are formed and on structural and phase transformations occurring upon heat treatment of electrolytic zinc–nickel coatings cannot be found in the literature, either.

The aim of this study was to analyze the electrochemical deposition of Zn and Ni from both simple and complex electrolytes, establish the effect of solution composition on the deposition rate, determine the chemical and phase composition of a zinc–nickel alloy, and reveal the relationship between the structure and properties of zinc–nickel coatings.

EXPERIMENTAL

A zinc–nickel alloy was deposited onto a copper or stainless steel support at 20°C from weakly acid chloride solution (I) of composition (M): $ZnCl_2$ 0.09–0.36, $NiCl_2$ 0.09–0.36, and NH_4Cl 3.0, at pH 4.5 ± 0.2, and from electrolyte (II) containing (M): ZnO 0.05–0.15, $NiCl_2$ 0.05–0.20, NH_4Cl 3.0, and $Na_4P_2O_7$ 0.3, at pH 6.5 ± 0.2. The Zn(II) and Ni(II) concentrations in electrolyte (I) were varied within 0.09–0.36 M at constant total concentration of the metal ions (0.45 M) and Zn(II)/Ni(II) ratio of 0.25 to 4.0. The Zn(II) and Ni(II) concentrations in electrolyte (II) were varied from 0.05 to 0.15 M, with their total concentration in the solution of 0.2 M and Zn(II)/Ni(II) ratio in the range from 0.3 to 3.0. The current density was varied within the range from 0.05 to 4.0 A dm^{-2}. The content of Zn and Ni in an alloy was determined by atomic-emission spectroscopy on a SPECTRO FLAME MODULA multiple-element emission spectrometer. The analysis error did not exceed 1%.

The rate of electrochemical deposition of the zinc–nickel alloy was estimated gravimetrically. The polarization dependences of the steady-state cathode current on the electrode potential, used in studying the deposition of a zinc–nickel coating, were measured with a P-5827M potentiostat. As working electrode was used 1-cm^2 copper plate degreased and etched in a dilute (1 : 1) HCl solution; a silver chlo-

1070-4272/03/7610-1583 $25.00 © 2003 MAIK "Nauka/Interperiodica"

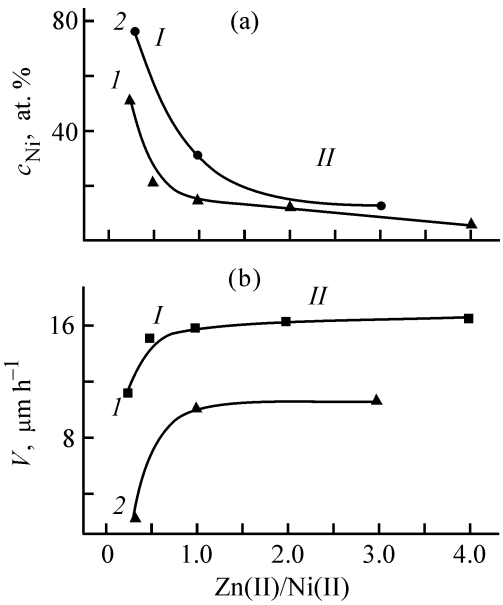

Fig. 1. (a) Nickel content c_{Ni} in the alloy and (b) deposition rate V vs. Zn(II)/Ni(II) molar ratio for various electrolytes. Electrolyte: (*1*) (I) and (*2*) (II).

ride electrode served as reference, and platinum electrode, as auxiliary electrode.

The microstructure of the films was studied by X-ray diffraction analysis (DRON-3 diffractometer, Cu_{K_α}-radiation). X-ray diffraction patterns were measured at a scanning rate of 1 deg min^{-1} at angles $2\theta = 10°–85°$. The crystal lattice parameters and sizes of coherent domains were determined by the method of Cauchy's approximating function. The structural and phase transformations were studied on zinc–nickel films heated for 1 h in a vacuum at temperatures of 200 to 800°C at a step of 200°C.

The corrosion resistance of the zinc–nickel coatings (thickness 6.5 ± 0.5 μm) was determined by measuring the polarization curves of anodic dissolution of a coating and cathodic evolution of hydrogen. The polarization curves were obtained with a PI-50-1.1 potentiostat in the potentiodynamic mode at potential sweep rate of 2 mV s^{-1}, with fresh portions of a 3% NaCl solution (50 ml) and a new working electrode used. The potentials are given relative to a saturated silver chloride reference electrode. The auxiliary electrode was made of platinum; as working electrode served a steel plate onto which zinc–nickel alloy of varied chemical composition was electrodeposited. The measurements were done at 20 ± 1°C with natural aeration (without stirring the solution). The results were represented as E–log i plots. The linear portions of the cathodic and anodic curves were extrapolated to the stationary potentialof the metal to determine the corrosion current density i_{cor} (μA cm^{-2}) and the dissolution potential E_d (V).

The dependences of the nickel content c_{Ni} in the alloy and the deposition rate V on the Zn(II)/Ni(II) ratio are shown in Figs. 1a and 1b for the electrolytes studied. The curves consist of two portions: (*I*) Zn(II)/Ni(II) = 0.25–1.0 and (*II*) Zn(II)/Ni(II) = 1.0–4.0. Each of these is characterized by a certain type of variation of the nickel content and deposition rate. For electrolyte (I), the Ni content in the forming alloy decreases from 51.6 to 14.0 at.% and the deposition rate increases from 11.2 to 15.9 μm h^{-1}, as the Zn(II)/Ni(II) ratio grows from 0.25 to 1.0 (portion *I*). With the Zn(II)/Ni(II) ratio increasing from 1.0 to 4.0, the deposition rate remains virtually unchanged, whereas the amount of codeposited nickel decreases from 14.0 to 5.0 at.% (portion *II*). It was established that, for electrolyte (I), the ratio c_{Ni}/c_{Zn} of metal concentrations in the alloy is considerably lower than the Ni(II)/Zn(II)ratio in solution. This indicates that the codeposition of Zn and Ni from the solution studied has anomalous character.

For electrolyte (II), the deposition rate increases from 2.2 to 10.0 μm h^{-1} and the Ni content in the coatings decreases from 76.4 to 30.2 at.% with the Zn(II)/Ni(II) ratio growing from 0.3 to 1.0 (Fig. 1, portion *I*). As in the case of electrolyte (I), an increase in the Zn(II)/Ni(II) ratio to 3.0 has no effect on the deposition rate of the alloys, but, at the same time, leads to further decrease (to 12.0 at.%) in the amount of codeposited nickel in them (Fig. 1, portion *II*). It should be noted that, at comparatively low Zn concentration in the solution, when the Ni content in the alloy becomes as high as 76.4 at.%, the zinc–nickel alloy is deposited at a very low rate (2.2 μm h^{-1}). Probably, despite that the hydrogen overvoltage on the alloy of the given composition is nearly the same as that on pure nickel, the potential of its deposition is close to the deposition potential of pure Zn. As a result, the cathodic deposition of such an alloy is accompanied by more intense hydrogen evolution, compared with that observed in a pure solution of nickel salt, and it is this circumstance that leads to a decrease in the deposition rate of the alloy.

To compare the processes in which zinc–nickel alloys are formed from solutions (I) [at molar ratio Zn(II)/Ni(II) = 0.5] and (II) [at molar ratio Zn(II)/Ni(II) = 3.0], a potentiostatic study was carried out in the potential range from 0 to –1.4 V. The chosen Zn(II)/Ni(II) ratio ensured deposition of alloys of the same chemical composition (~20 at.% Ni) under the conventional electroplating conditions (at i_c = 1 A dm^{-2}).

The potentiostatic cathodic polarization curves in Fig. 2 show that the cathodic current density in deposition of a zinc–nickel alloy from solution (I) starts to grow even at –0.75 V (curve *1*), whereas in the case of solution (II), it starts to increase at a more negative potential equal to –0.95 V (curve *2*). It should be noted that, in the case of solution (I), the polarization curve (Fig. 2, curve *1*) shows an inflection in the potential range –1.0…–1.1 V, which, in all probability, is due to a relatively low efficiency of nickel(II) reduction from the given electrolyte. The reduction of zinc(II), which fills the working surface, hinders nickel reduction.

The study of the effect of deposition potential on the chemical composition of zinc–nickel coatings formed demonstrated that the shift of the potential to the cathodic region, from –0.75 to –1.3 V, leads to a decrease in the Ni content from 75.3 to 14.6 at.% in the coatings obtained from solution (I) (Fig. 3, curve *1*). The deposition of zinc–nickel coatings from solution (II) at –0.75 V was not performed, since, according to the potentiostatic curves obtained, the current density is virtually zero under these conditions, and no zinc–nickel alloy is formed. Therefore, for the initial deposition potential from a given solution was taken the potential corresponding to the onset of formation of a zinc–nickel alloy ($E = -0.95$V). With potential varied from –0.95 to –1.3 V, the Ni content in the coatings obtained from solution (II) decreased from 89.2 to 21.2 at.% (Fig. 3, curve *2*). The dashed lines *1*' [for solution (I)] and *2*' [for solution (II)] in Fig. 3 divide the alloy deposition process into two regions of normal and anomalous codeposition. These lines indicate that normal deposition (predominantly Ni is deposited into the alloy) in the case of solution (II) (virtually the entire curve *2* lies above dashed line *2*'), and anomalous deposition (predominantly zinc is included in the alloy), in the case of solution (I) (virtually the entire curve *1* lies below dashed line *1*').

The influence of the current density on the chemical composition of zinc–nickel coatings deposited from the above two electrolytes was studied at Zn(II)/Ni(II) = 0.5 for electrolyte (I) and Zn(II)/Ni(II) = 3.0 for electrolyte (II). Figure 3b shows that raising the current density from 0.05 to 0.25 A dm^{-2} leads to a dramatic decrease in the Ni content in the coatings; with the current density raised further, to 4.0 A dm^{-2}, a slight increase, from 17.7 to 22.3 at.%, in the nickel content was observed in the case of solution (II) (Fig. 3b, curve *2*) and a more considerable increase, from 14.2 to 28.0 at.%, in the case of solution (I) (Fig. 3b, curve *1*).

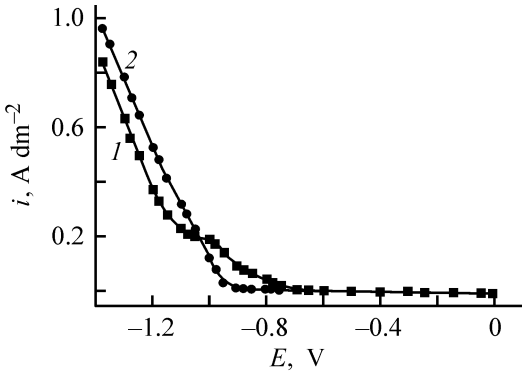

Fig. 2. Potentiostatic cathodic polarization curves for deposition of zinc–nickel alloy from (*1*) solution (I) and (*2*) solution (II). (*i*) Current density and (*E*) deposition potential. Zn(II)/Ni(II) molar ratio: (*1*) 0.5 and (*2*) 3.0; the same for Figs. 3, 4.

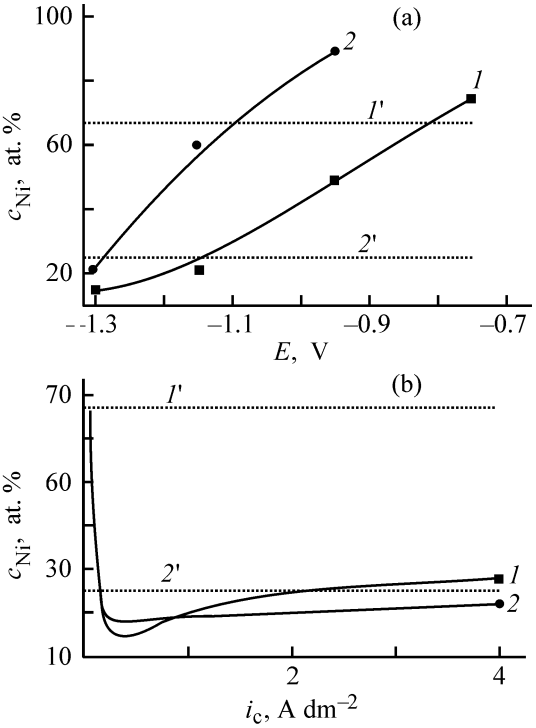

Fig. 3. Nickel content c_{Ni} in the alloy vs. (a) deposition potential E and (b) current density i_c for (*1*) solution (I) and (*2*) solution (II). The lines separating the regions of normal and anomalous deposition of the zinc–nickel alloy: (*1*') for solution (I) and (*2*') for solution (II).

Zinc-enriched coatings (with Ni content lower than that in solution) can be obtained from solution (I) over virtually the entire range of current densities studied. At the same time, alloys with content of Ni close to that in solution (region of normal deposition above dashed line *2*') and those with Ni content lower than that in solution (region of anomalous

Table 1. Structure of Zn–Ni films deposited from electrolytes (I) and (II)

Coating	c_{Ni}, at.%	Phase composition	Coherent domain, nm	Lattice parameter, nm
		Electrolyte (I)		
Ni	100	Ni (crystalline)	30	a = 0.35238 [15]
Zn	0	Zn (crystalline)	150	$a = b$ = 0.26648, c = 0.49456 [15]
Zn–Ni	2	"	120	$a = b$ = 0.26648, c = 0.49450
	5.0	Zn (crystalline)	100	–
		Ni_5Zn_{21} (γ-phase)	25	
	14.0	Ni_5Zn_{21} (γ-phase)	20	–
		Zn (crystalline)	30	
	20.7	Ni_5Zn_{21} (γ-phase)	25	–
		Ni (crystalline)	25	
	51.6	Solid solution of Ni in Ni_5Zn_{21}	20	–
		Ni (crystalline)	20	
		Electrolyte (II)		
Ni	100	Ni (crystalline)	25	a = 0.35238 [15]
Zn	0	Zn (crystalline)	100	$a = b$ = 0.26648, c = 0.49456 [15]
Zn–Ni	12.0	Ni_3Zn_{22} (δ-phase)	68	–
	19.0	Ni_5Zn_{21} (γ-phase)	30	a = 0.89168 [16]
	21.2	Solid solution of Ni in Ni_5Zn_{21}	40	a = 0.8915
	33.4	"	40	a = 0.8908
	68.0	Solid solution of Zn in Ni (α-phase)	5	a = 0.3576
	76.4	"	5	a = 0.3589

deposition below *2'* line) are deposited from solution (II).

It is not well understood, especially for solution (I), why the Ni content grows with current density increasing from 0.25 to 4.0 A dm^{-2} (Fig. 3b). The possible reason is the higher surface activity of zinc ions, compared with nickel ions [7]. This results in a predominant discharge of zinc ions at the cathode at low current densities (0.25 A dm^{-2}), to which corresponds a dramatic decrease in the Ni content in the alloys. As the rate of zinc ion reduction increases, the concentrations of ions in the dense part of the double layer are redistributed: the concentration of zinc ions decreases owing to diffusion hindrance, whereas that of nickel ions increases. As a result, with current density increasing to 4.0 A dm^{-2}, the alloy is enriched with nickel.

Thus, the anomalous deposition of the Zn–Ni alloys, accompanied by their enrichment with zinc, occurs under steady-state conditions of electrochemical deposition (i_c = 1.0 A dm^{-2}) in the case of solution (I), irrespective of the concentrations of ions of metals being codeposited. At the same time, in the case of solution (II), it occurs solely at Zn(II)/Ni(II) ≥ 1. Irrespective of the composition of zinc- and nickel-plating solutions, the mechanism of codeposition of Zn and Ni can be changed from anomalous to normal by varying the deposition conditions (potential or current density). For example, under certain conditions [at Zn(II)/Ni(II) = 0.3 in solution and i_c = 1.0 A dm^{-2}; or at Zn(II)/Ni(II) = 3.0 and E = –0.95… –1.3 V or i_c = 0.05–0.15 A dm^{-2}], the codeposition of Zn and Ni from solution (II) occurs by the normal mechanism. Presumably, the codeposition from the above electrolyte is favored by the lower difference between the redox potentials of zinc(II) and nickel(II) [14].

An X-ray diffraction study demonstrated that the composition of an electroplating solution strongly affects the structure of zinc–nickel films. The Zn–Ni alloys obtained from solution (I) with low Ni content (up to 2 at.%) are isostructural to crystalline Zn, with the crystal lattice parameter in agreement with the published value. The alloys containing 5.0 to 14.0 at.% Ni consist of two phases: crystalline Zn and Ni_5Zn_{21} intermetallic compound (γ-phase), with the fraction of crystalline Zn decreasing and that of the γ-phase increasing when the content of Ni becomes higher. With the nickel content in the films growing from 20.7 to 51.6 at.%, the phase of crystalline Ni appears, along with the above intermetallic compound, and the fraction of the γ-phase decreases, whereas the fraction of crystalline Ni increases (Table 1).

The zinc–nickel alloys deposited from solution (II) containing 12.0 to 76.4 at.% Ni have homogeneous structure (Table 1). In contrast to the case of solution (I), neither crystalline Zn, nor the γ-phase appear in the alloy containing 12.0 at.% Ni, with only a single δ-phase formed, Ni_3Zn_{22} intermetallic compound with composition corresponding to a Ni content in the alloy equal to 12.0 at.%.

An increase in the content of Ni in the films to 19 at.% leads to formation of the Ni_5Zn_{21} intermetallic compound with crystal lattice parameter corresponding to the published value. At Ni content in the films of up to 33.4 at.% Ni, a solid solution of Ni in Ni_5Zn_{21} is formed, and at higher Ni content (68.0 and 76.4 at.%), an equilibrium solid solution of Zn in Ni (α-phase). An X-ray phase analysis demonstrated that, with increasing Ni content in the films, the grain size decreases from hundreds of nanometers (100–150 nm for Zn) to several nanometers (2–5 nm for zinc–nickel alloy containing 76.4–89.2 at.% Ni).

The data on how the composition of films changes in the course of their growth from solutions (I) and (II) demonstrated that the composition of a zinc–nickel film is inhomogeneous across its thickness (Fig. 4). The content of Ni decreases with the thickness of a deposited film increasing to 1 μm, with the composition remaining comparatively unchanged at thicknesses exceeding 1 μm. This is probably due to the fact that, in the initial stage, mostly Ni is deposited as a more inert metal. Then, the forming Ni monolayer can capture zinc adatoms, which results in prephase deposition of Zn and its subsequent predominant deposition into the alloy [8–13]. It was shown that the change in the Ni content observed in the course of film growth, is accompanied by a change in the phase composition of the films. For example, the films less than 0.3 μm thick consist of an X-ray-amorphous solid solution of Zn in Ni and a minor amount of finely crystalline Zn.

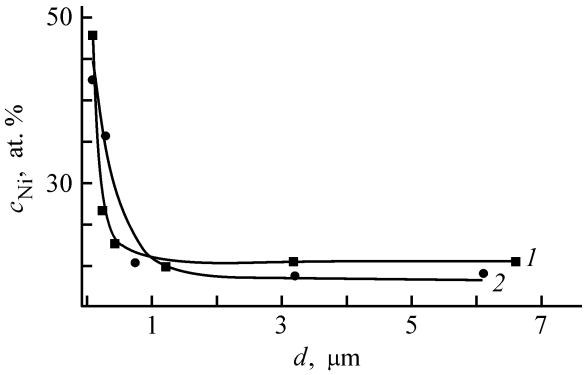

Fig. 4. Nickel content c_{Ni} in the alloy vs. coating thickness d for (*1*) solution (I) and (*2*) solution (II).

It was found that, at low current densities (i_c = 0.05 A dm^{-2}) and low polarization potentials (E = –0.75…–1.15 V), X-ray-amorphous or poorly crystallized solid solutions of Zn in Ni are formed. Presumably, this is due to the nonequilibrium conditions of alloy electrocrystallization. Probably, the hydrogen evolution, accelerated at higher content of Ni in the alloy, also plays a certain role. A combination of the processes of growth of the metallic phase and its hydrogenation impede the normal growth of crystallites.

A study of the structural and phase transformations in the zinc–nickel films of varied composition, heat-treated in a vacuum, demonstrated the complexity of the occurring processes. On heating the initial samples of Zn–Ni films at 200–800°C in a vacuum, there appear phases not revealed at room temperature: $NiZn_3$ intermetallic compound and a solid solution of Ni in Zn. On being heated at 400–800°C, the alloys are enriched with Ni, which is probably due to the formation of the initial zinc–nickel films under nonequilibrium conditions. As a result, evaporation of Zn from intermetallic compounds of various compositions (Ni_5Zn_{21}, NiZn, and Ni_3Zn_{22}) with the subsequent formation and dissociation of nonstoichio-

Table 2. Effect of the chemical and phase composition of Zn–Ni coatings on their corrosion resistance

Solution	c_{Ni}, at.%	Phase composition	E_p, V	i_{cor}, μA cm^{-2}
(I)	–	Zn (crystalline)	–1.00…–1.02	12.0
	5.0–14.0	Zn (crystalline) Ni_5Zn_{21} (γ-phase)	–0.98…0.96	5.0–5.5
	20.7–51.6	Ni (crystalline) Ni_5Zn_{21} (γ-phase)	0.88…–0.85	2.0–2.5
(II)	12.0	Ni_3Zn_{22} (γ-phase)	–0.70	0.8–1.0
	19.0	Ni_5Zn_{21} (δ-phase)	–0.70	0.1–0.2
	33.4	Solid solution of Ni in Ni_5Zn_{21}	–0.68	0.3–0.4
	68.0–76.4	Solid solution of Zn in Ni (α-phase)	–0.65…–0.63	0.2–0.3

metric compounds, and also that from solid solutions, occur at lower temperatures, compared with those indicated by the phase diagram of a zinc–nickel metallurgical alloy [15].

An electrochemical study demonstrated that, with increasing Ni content in the alloy, the potentials of the onset of dissolution of zinc–nickel coatings in a 3% NaCl solution are shifted toward anodic potentials, and the corrosion currents, as a rule, decrease (Table 2).

It was established that the corrosion-electrochemical behavior of zinc–nickel film coatings depends not only on the chemical, but also on the phase composition. The lowest corrosion currents (0.1–0.2 μA cm^{-2}) are characteristic of single-phase films [compositions with a single intermetallic compound Ni_5Zn_{21} (γ-phase) or Ni_3Zn_{22} (δ-phase), a solid solution of zinc in nickel (α-phase), or a solid solution of nickel in Ni_5Zn_{21}]. The heterogeneous phase composition of a coating (crystalline Zn or Ni present along with the γ-phase) leads to a decrease in its corrosion resistance (Table 2).

CONCLUSIONS

(1) The conditions for occurrence of normal or anomalous codeposition accompanied by enrichment of the deposit with, respectively, nickel or zinc were determined from the results obtained in a study of the influence exerted by the solution composition (nature of ligands and molar ratio of codeposited metals) and deposition conditions (potential and current density) on the chemical composition and deposition rate of Zn–Ni films. This opens up opportunities for varying widely the Ni content in the coatings (from less than 2 to 90 at.%).

(2) The influence exerted by the composition of a solution for electrodeposition of zinc–nickel films on their microstructure and phase composition were studied [formation of films with homogeneous phase composition (Ni_5Zn_{21} and Ni_3Zn_{22} intermetallic compounds and solid solutions of Zn in Ni and Ni in Ni_5Zn_{21}) from electrolyte (II) under varied deposition conditions and formation of two-phase films (Ni_5Zn_{21} in a mixture with crystalline Zn or Ni) from electrolyte (I)]. The conditions for formation of nonequilibrium X-ray-amorphous solid solutions of Zn in Ni at low current densities (i_c = 0.05 A dm^{-2}), low polarization potentials (E = –0.75…–1.15 V), or small film thicknesses (less than 0.3 μm) were determined.

(3) It was shown that zinc–nickel alloy coatings of homogeneous composition (Ni_5Zn_{21} intermetallic compound, solid solutions of Zn in Ni and Ni in Ni_5Zn_{21}) exhibit enhanced corrosion resistance.

REFERENCES

1. Tsybul'skaya, L.S., Gaevskaya, T.V., Byk, T.V., and Klavsut', G.N., *Zh. Prikl. Khim.*, 2001, vol. 74, no. 10, pp. 1628–1632.
2. Lee, H.Y. and Kim, S.G., *Surface Coat. Technol.*, 2000, vol. 135, pp. 69–74.
3. Park, H., and Szpunar, J.A., *Corrosion Sci.*, vol. 40, nos. 4–5, pp. 525–545.
4. Vagramyan, T.A., Kharlamov, V.I., and Kudryavtsev, V.N., *Zashch. Met.*, 1996, vol. 32, no. 4, pp. 389–395.
5. Hall, D E., *Plat. Surface Finish.*, 1983, vol. 70, no. 11, pp. 47–59.
6. Grigoryan, N.S., Kudryavtsev, V.N., Zhdan, P.A., *et al., Zashch. Met.*, 1989, vol. 25, no. 2, pp. 288–290.
7. Yur'ev, B.P. and Volkov, L.V., *Zh. Prikl. Khim.*, 1965, vol. 38, nos. 1–2, pp. 66–72.
8. Nicol, M.J. and Philip, H.I., *J. Electroanal. Chem.*, 1976, vol. 70, p. 233.
9. Karbasov, B.G. and Isaev, N.N., *Elektrokhimiya*, 1986, vol. 22, no. 3, pp. 427–429.
10. Roev, V.G. and Gudin, N.V, *Elektrokhimiya*, 1996, vol. 32, no. 3, pp. 356–361.
11. Fratesi, R. and Roventi, G., *J. Appl. Electrochem.*, 1992, vol. 22, pp. 657–662.
12. Ohtsuka, T. and Komori, A., *Electrochim. Acta*, 1998, vol. 43, pp. 3269–3276.
13. Elkhatabi, F., Bendalla, M., Sarret, M., and Muller, C., *Electrochim. Acta*, 1999, vol. 44, pp. 1645–1653.
14. Byk, T.V., Tsybul'skaya, L.S., and Gaevskaya, T.V., *Izv. Nats. Akad. Nauk Belarusi. Ser. Khim. Nauk*, 2002, no. 1, pp. 54–58.
15. Mirkin, L.I., in *Spravochnik po rentgenostrukturnomu analizu polikristallov* (Handbook of X-Ray Structural Analysis of Polycrystals), Umanskii, Ya.S., Ed., Moscow: Fizmatgiz, 1961.
16. Hansen, M. and Anderko, K., *Constitution of Binary Alloys*, New York: McGraw–Hill, 1958.

Russian Journal of Applied Chemistry, Vol. 76, No. 10, 2003, pp. 1589–1592. Translated from Zhurnal Prikladnoi Khimii, Vol. 76, No. 10, 2003, pp. 1631–1634.

APPLIED ELECTROCHEMISTRY AND CORROSION PROTECTION OF METALS

Electrochemical Synthesis of Black Cobalt

N. D. Ivanova, E. I. Boldyrev, S. V. Ivanov, and I. S. Makeeva

Vernadskii Institute of General and Inorganic Chemistry, National Academy of Sciences of the Ukraine, Kiev, Ukraine
National Aviation University, Kiev, Ukraine

Received March 4, 2003

Abstract—The possibility of depositing black cobalt coatings from fluoride-containing electrolytes based on cobalt sulfate was studied.

Black cobalt coatings, which are not general-purpose coatings [1], are, nevertheless, in sufficient demand by various industries.

Black cobalt has light absorption coefficient of 92–96%, and, therefore, it is occasionally used instead of black chromium coatings [2]. Owing to their high corrosion resistance, cobalt oxide compounds are used as protecting decorative coatings for iron [3]. In recent years, such compounds have received rather wide acceptance as components of a nickel-based cathode material [4–6] in chemical power sources and also in solar cells [7]. In additiion, they are also used as an effective and selective catalyst for a number of reactions [8].

Cobalt oxide compounds are conventionally obtained by the thermal method [9] and also by electrochemical deposition from electrolytes based on cobalt sulfate, acetate, chloride, or nitrate [10]. At the same time, with electrolytes containing fluoride ions as ligands, the technology for obtaining oxide compounds of a number of transition metals can be substantially simplified through use, under these conditions, of a bifunctional electrochemical system electrode | film | electrolyte [11], whose central phase contains low- or high-charged forms of a metal in question. At the electrolyte | film interface, the film itself is formed through electrolytic reduction of ions of the discharging metal (or electrolytic oxidation of the metal) to an intermediate oxidation state and dissolution of the film in the electrolyte. At the electrode | film interface, the film substance is consumed for its further reduction to metal or oxidation to the highest oxidation state. As a result of these simultaneous processes, the film is permanently in the state of dynamic equilibrium. As a rule, such oxide compounds have reproducible composition; depending on the process conditions, they can be obtained either as compact film coatings, usually black, or as powders [12].

The aim of this study was to synthesize electrochemically cobalt compounds of oxide nature, to identify their composition, and to analyze their properties.

EXPERIMENTAL

Deposits of black cobalt were obtained on cathodes made of 1Kh18N10T steel, in a 250-ml polyethylene cell. The deposition rate ($g\ A^{-1}\ h^{-1}$) was determined from an increase in the precipitate weight during electrolysis. In the experiments, solutions containing chemically pure $CoSO_4$ and $(NH_4)_2SO_4$, and also various concentrations of special-purity hydrofluoric acid, were used. A solution containing 1.0 M of chemically pure Na_2SO_4 served as supporting electrolyte.

The deposits were obtained as powders and as thin films adhering to a support. In the first case, the deposit was separated from the cathode (scraped off), thoroughly washed with distilled water to remove trace amounts of the electrolyte, and dried to constant weight over phosphorus(V) oxide in a desiccator under inert atmosphere. The dried deposit consisted of a stable compound, which did not change its composition upon further storage in air. In the second case, 7–10-μm-thick compact films were obtained, which ruled out any contact of the supporting electrolyte with the cathode material, since the coating was nonporous. The electrodes covered by black cobalt films were washed with distilled water and then dried in air to constant weight.

The composition of the electrochemically synthesized cobalt oxide compounds was subjected to chem-

1070-4272/03/7610-1589 $25.00 © 2003 MAIK "Nauka/Interperiodica"

Composition of black cobalt at various ligand concentrations in the electrolyte

Concentration of F^- ions, g l^{-1}	Content, wt %				
	Co_{tot}	Co_{met}	$O_{2\,tot}$*	OH-groups**	H_2O**
0.05	80.0	47.0	21.0	5.0	7.0
0.1	81.0	50.0	20.0	4.0	6.5
0.2	82.0	52.0	19.0	3.0	6.5
0.4	83.0	54.0	17.0	2.5	6.0
0.6	83.5	55.0	16.0	2.0	5.8

* $O_{2\,tot}$ is the total content of O_2, determined from NAA data.
** According to DTG data.

ical phase analysis, which made it possible to determine the total amount of cobalt and its content in the form of metal [13].

A thermogravimetric analysis was carried out on an Orion derivatograph, with samples heated in air to 1000°C at a rate of 5 deg min^{-1}.

The total content of oxygen (including that contained in H_2O molecules and OH^- groups) was determined by neutron activation analysis (NAA) [14]. The relative error of the method was 1.5%.

The porosity of the coatings was found by placing a filter paper impregnated with a mixture of $K_3Fe(CN)_6$, KCl, and NH_4Cl on their surface (in this case, a black cobalt coating was deposited on St.3 steel).

The microhardness of black cobalt coatings was determined on a PMT-3 hardness gage with indenter load of 20 g.

Chronovoltammograms were recorded using a PI-50-1 pulsed potentiostat and a PDA1-004 laboratory compensation X–Y recorder at a potential sweep rate of 0.002–0.1 V s^{-1}, with compensation of the I-R error. In the experiments, a three-electrode glass cell

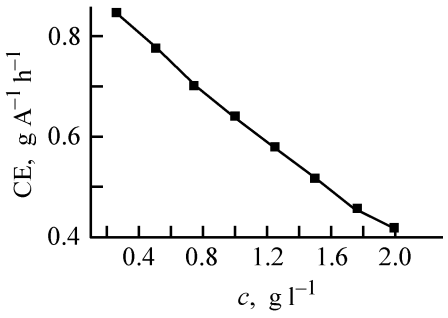

Fig. 1. Current efficiency (CE) by the composite product vs. concentration c of hydrofluoric acid in the electrolyte.

was used, in which a platinum plate of area 4 cm^2 served as auxiliary electrode. A plate of stainless steel, with area of 0.5 cm^2, pressed-in in Teflon was used as working electrode. The current density was related to the geometric surface area of the electrode. Before a measurement, the working electrode was scraped with fine emery paper, polished with filter paper, degreased with Vienna lime, and activated in diluted HCl, which ensured good reproducibility of the results obtained. A saturated calomel electrode served as reference. The potentials are given relative to a standard hydrogen electrode. All the experiments were carried out at 20 ± 0.1°C.

The optimal composition of the electrolyte and optimal conditions of electrolysis were determined in preliminary experiments. Electrolyte composition (g l^{-1}): $CoSO_4 \cdot 7H_2O$ (in terms of the metal) 10, $(NH_4)_2SO_4$ 25, and HF (40%) 1.0. The cathode current density was 40–60 A dm^2, the electrolyte temperature was 18–25°C. The duration of electrolysis was determined by the necessity for obtaining either a powder or a compact film.

Raising the current density and electrolysis duration favors deposition of a powder-like deposit. At a current density of 40–60 A dm^2, 7–10-μm-thick compact films are electrodeposited within 5 minutes. This electrolyte and these electrolysis conditions were selected as basic experimental conditions.

The dependence of the current efficiency by the composite deposit containing cobalt oxide compounds on the concentration of hydrofluoric acid is shown in Fig. 1. The amount of black cobalt, i.e., the current efficiency by the product decreases almost linearly with increasing concentration of fluoride ions in the electrolyte.

The composition of the compound is mainly determined by the concentration of fluoride ions. Raising their concentration in the electrolyte results in an increase in the content of both the total cobalt, Co_{tot}, and metallic cobalt, Co_{met}, and, correspondingly, in a decrease in the content of the oxide phase (see table). It follows from these data that the composition of the compound obtained can be rather easily controlled by varying the concentration of fluoride ions, which changes the amount of oxygen in the product and thus determines the degree of deviation from its stoichiometric composition.

The resulting films are black, being comparable with black chromium coatings in their light absorption. At the same time, the microhardness of black cobalt films varies within 250–300 MPa, which is

much lower than that of black chromium films. It is necessary to point out that, even at small coating thickness not exceeding 4–6 μm, no pores are found in the coating, i.e., the films are rather dense.

The chronovoltammogram characterizing the electrolytic reduction of cobalt(II) ions, accompanied by deposition of its oxide compounds, is shown in Fig. 2. Raising the concentration of fluoride ions at constant concentration of cobalt(II) ions and fixed solution pH leads to a shift of the chronovoltammograms in the negative direction along the potential axis. In this case, the limiting current at potentials of 1.25 to 0.5 V also decreases. A similar phenomenon has been observed in formation of complexes, whose dissociation is strongly hindered kinetically [15, 16], and also in partly complexed systems, which arise when minor amounts of ligands forming complexes with metal ions are added to a system [17].

As noted above, in this case, the content of metallic cobalt in the deposits increases, and the amount of the oxide phase decreases (see table); the color of the deposit changes to dark gray. Black cobalt is deposited in the range of electropositive potentials.

Raising the potential sweep rate leads to an increase in the limiting currents of electrolytic reduction of cobalt(II) ions in the solution of optimal composition. The dependence of I on $V^{1/2}$ is approximated by straight lines (Fig. 3), which points to the diffusion kinetics of the process characterized by this part of the polarization curve. At constant rate of polarization variation, $|dE/d\tau|$, the limiting current in the chronovoltammogram is proportional to the initial concentration of cobalt(II) ions in the electrolyte, which is attributable to direct discharge of the reacting species under diffusion limitation without any preliminary chemical stages.

The contribution of diffusion and migration to the total mass transfer of electrically active species was estimated by measuring the polarization of an electrode in solutions containing or not containing a supporting electrolyte. When the supporting electrolyte was added to the solution, the limiting currents in the electrolytes with various concentrations of fluoride ions decreased to virtually the same value (Fig. 2). This suggests that a substantial contribution to the mass transfer in electrolytic reduction of cobalt(II) ions is made by the migration component, whose presence predetermines the comparatively high limiting current densities in the electrolyte in electrolytic reduction of cobalt(II) ions from the fluoride-containing electrolyte.

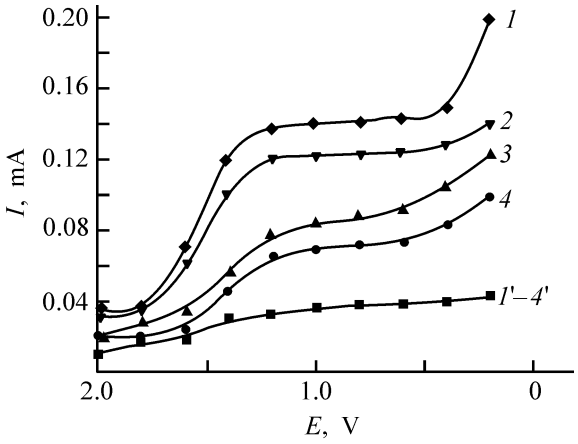

Fig. 2. Chronovoltammograms of electrolytic reduction of Co(II) ions at potential sweep rate of 5 mV s^{-1}. (I) current and (E) potential. Concentration of hydrofluoric acid in the electrolyte (g l^{-1}): (*1*) 0.05, (*2*) 0.1, (*3*) 0.2, (*4*) 0.4, (*1'–4'*) the same in the presence of a supporting electrolyte.

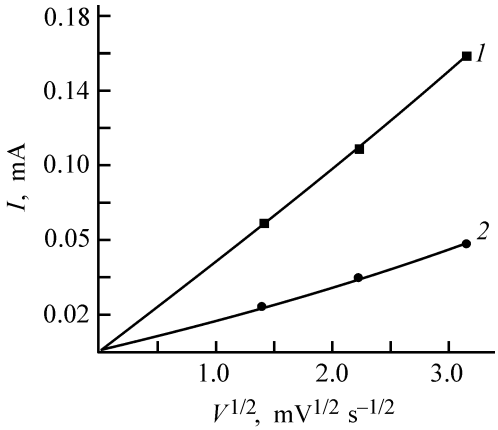

Fig. 3. Limiting current I in the chronovoltammogram of the solutions containing 0.05 g l^{-1} of hydrofluoric acid (*1*) in the absence and (*2*) in the presence of a supporting electrolyte vs. the potential sweep rate $V^{1/2}$.

CONCLUSIONS

(1) Conditions for obtaining black cobalt (composed of cobalt oxide compounds) in the form of compact films or powder were developed.

(2) It was established that the current efficiency and the composition of black cobalt are determined by the concentration of fluoride ions in an electrolyte.

(3) It was found that the electrodeposition of black cobalt occurs at positive potentials and is controlled by diffusion and migration processes.

REFERENCES

1. Ivanova, N.D., Ivanov, S.V., and Boldyrev, E.I., *Galvanotekhnika: Ftorsoderzhashchie electrolity i rastvory: Spravochnik* (Electroplating: Fluorine-containing Electrolytes and Solutions: Handbook), Kiev: Naukova Dumka, 1993.
2. Ivshin, Ya.V., Abstracts of papers, *IX Vsesoyuznaya nauchno-tekhn. konferentsiya po elektrokhimii i tekhnologii "Galvanotekhnika-87"* ("Galvanotechnique-87" IX All-Union Conf. on Electrochemistry and Technology), Kazan, 1987, pp. 222–223.
3. US Patent 3639177.
4. Rakityanskaya, O.F. and Stupinichenko, R.N., *Ukr. Khim. Zh.*, 1999, vol. 65, nos. 7–8, pp. 40–45.
5. Chang, Z., Lhao, Y., and Yunchang, D., *J. Power Sources*, 1999, vol. 77, pp. 69–73.
6. Pralong, V. and Delahaye-Vidal, A., *J. Electrochem. Soc.*, 2000, vol. 147, no. 4, pp. 1306–1313.
7. Nagrani, N. and Rajendran, S., *Sol. Energy Mater.*, 1991, vol. 22, no. 4, pp. 293–302.
8. Vodyankin, A.Yu., Kurina, L.N., and Shilyaeva, L.P., *Zh. Prikl. Khim.*, 1999, vol. 72, no. 6, pp. 1028–1029.
9. Boggio, R., Caruguti, A., and Trasatti, S., *J. Appl. Electrochem.*, 1987, vol. 17, no. 4, pp. 828–840.
10. Sidorov, Yu.V., Sharifzyanova, O.N., and Ivshin, Ya.V., Abstracts of Papers, *Vserossiiskaya studencheskaya nauchnaya konferentsiya* (All-Russia Student Sci. Conf.), Kazan, 1988, p. 56.
11. Ivanova, N.D. and Ivanov, S.V., *Usp. Khim.*, 1993, vol. 62, no. 10, pp. 907–918.
12. Ivanova, N.D. and Ivanov, S.V., *Functional Materials*, 2000, vol. 7, no. 1, pp. 5–26.
13. Pyatnitskii, I.V., *Analiticheskaya khimiya kobal'ta* (Analytical Chemistry of Cobalt), Moscow: Nauka, 1965.
14. Beckurts, K.H. and Wirtz, K., *Neutron Physics*, Berlin: Springer, 1964.
    Ivanov, S.V. and Filatov, K.V., *Zh. Prikl. Khim.*, 1996, vol. 69, no. 11, pp. 1857–1861.
15. Ivanov, S.V. and Filatov, K.V. *Zh. Prikl. Khim.*, 1996, vol. 69, no. 11, pp. 1857–1861.
16. Ivanov, S.V. and Trotsyuk, I.V., *Zashch. Met.*, 1999, vol. 35, no. 3, pp. 265–272.
17. Survila A.A., *Elektrodnye protsessy v sistemakh labil'nykh kompleksov metallov* (Electrode Processes in the Systems of Labile Metal Complexes), Vilnius: Mosklas, 1989.

Russian Journal of Applied Chemistry, Vol. 76, No. 10, 2003, pp. 1593–1596. Translated from Zhurnal Prikladnoi Khimii, Vol. 76, No. 10, 2003, pp. 1635–1638.

APPLIED ELECTROCHEMISTRY AND CORROSION PROTECTION OF METALS

Electrolytic Recovery of Cadmium from Cyanide Washing Solutions on Filtering Carbon-Graphite Electrodes

V. K. Varentsov

Institute of Solid-State Chemistry and Mechanochemistry, Siberian Division, Russian Academy of Sciences, Novosibirsk, Russia

Received April 17, 2003

Abstract—Electrorecovery of cadmium(II) on filtering carbon-graphite electrodes from washing cyanide solutions formed in cadmium-plating of articles in a cyanide electrolyte was studied. The effect of the dilution factor of the supporting electrolyte on the run of cathodic polarization curves, pH value, and solution resistivity was analyzed. The influence exerted by the efficiency of cadmium(II) recovery on the carbon-graphite electrodes was studied in relation to current density, solution flow rate, cadmium(II) concentration in solution, dilution factor of the supporting electrolyte, and material of the carbon-graphite electrode. The possibility of dissolution of cadmium deposited onto a filtering carbon-graphite electrode via anodic dissolution or because of the operation of a short-circuited electrochemical system constituted by the carbon-graphite electrode, cadmium, and cyanide solution was considered.

Cadmium coatings are used in various industries (machine-building, electronic, radio, etc.). Despite the attempts to replace these coatings, they remain irreplaceable in some cases because of their special properties [1]. The necessity for substituting cadmium-plating electrolytes is due to the high toxicity of cadmium compounds. The best performance, especially in deposition of coatings on articles of complex configuration, is exhibited by cyanide cadmiumplating electrolytes. The fact that complex Cd(II) compounds are rather stable leads to difficulties in selecting methods for detoxication of washing solutions, wastewater, and spent electrolytes. In most cases, the methods used in industry and recommended for implementation fail to ensure high degree of solution purification and recycling of recovered cadmium [2, 3]. It should be noted that cadmium is a rare metal and its cost is rather high. Therefore, it is necessary to develop, together with methods for detoxication of cadmium-containing solutions, also techniques ensuring recycling of cadmium. Of indubitable interest in this context are electrochemical methods and, in particular, electrolysis with filtering carbon-graphite electrodes, which make it possible to detoxicate solutions and obtain compact pure metal reusable in fabrication of soluble anodes for electroplating baths or in electrolyte preparation [4, 5]. The present communication reports on a study of electrorecovery of Cd(II) from cyanide solutions that model washing water in relation to solution composition, electrolysis conditions, and type of a carbon filtering cathode.

EXPERIMENTAL

An industrial cadmium-plating electrolyte of composition ($g\ l^{-1}$): CdO 50, NaCN 90, Na_2SO_4 30, NaOH 5, $NiSO_4$ 1, dextrin 1, was chosen for study. The supporting electrolyte contained all the above components except cadmium. To obtain a necessary concentration of Cd(II), the supporting electrolyte was diluted by a factor of *n* and a certain amount of the industrial cadmium-plating electrolyte of the above composition was added. The electrolytic cell employed and the installation for electrochemical studies with filtering carbon-graphite electrodes (FCE) were described in [5]. The cathode was made of an NTM-100 material, its overall surface area was 30 cm^2; as anode served a grid made of platinum-plated titanium, as anolyte was used a 2% solution of Na_2SO_4. The electrode spaces were separated by an ion-exchange membrane of the MK-40 type.

The electrical conductivity of solutions was measured with a VM-503 ac bridge, and the pH value, with an OR-265/1 pH-meter. Polarization curves were measured on a cadmium microelectrode 1 mm in diameter with surface freshened in the electrolyte so-

1070-4272/03/7610-1593 $25.00 © 2003 MAIK "Nauka/Interperiodica"

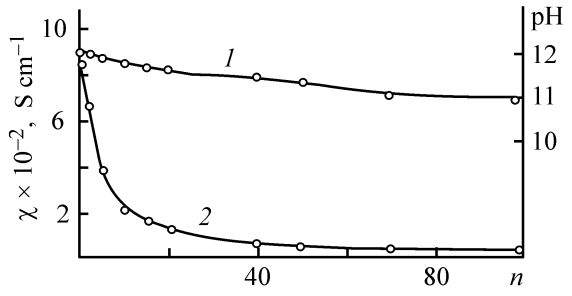

Fig. 1. Effect of the dilution factor n of the supporting electrolyte on (*1*) pH value, and (*2*) electrical resistivity χ of solution. Initial Cd(II) concentration in solution 100 mg l^{-1}; the same for Fig. 2.

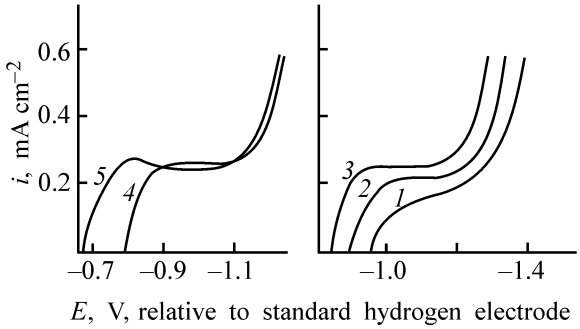

Fig. 2. Effect of the dilution factor n of the supporting electrolyte on the polarization characteristic of the process of cadmium(II) reduction. (*i*) Current density and (*E*) electrode potential. Supporting electrolyte dilution factor (times): (*1*) 2, (*2*) 5, (*3*) 10, (*4*) 20, and (*5*) 100.

lution, using the procedure and setup described in [6] and an RA-2 polarograph, with potential sweep rate of 120 mV min^{-1}.

The efficiency of Cd(II) electrorecovery was evaluated by the following parameters: degree of recovery $\alpha = (c_0 - c_\tau)/c_0$ and current efficiency by cadmium

$$CE = [(c_0 - c_\tau)V \times 26.8]/(I\tau M_{eq}),$$

where c_0 and c_τ are the initial and final concentrations of cadmium in solution (g l^{-1}); V, the solution volume; I, the current at which electrolysis is carried out (A); τ, the experiment duration (h); 26.8 A h mol^{-1}, the Faraday constant; M_{eq}, the molar mass of the metal equivalent.

The influence exerted by the solution composition and the solution flow rate on the electrolytic recovery of Cd(II) was studied in the direct-flow mode. The solution from which Cd(II) was recovered was passed a single time through a cell with a carbon-graphite cathode and sampled at the outlet of this cell. The samples were analyzed for the content of Cd(II) by the atomic-absorption method.

In accordance with the previously suggested approach, which was used in the development of methods for recovery of metals from washing solutions formed in electrodeposition processes [4], polarization studies were carried out and the effect of dilution of the supporting cadmium-plating electrolyte on its electrical conductivity and pH value was studied, in order to assess the feasibility of Cd(II) electrorecovery. Investigations of this kind were necessitated by the fact that articles are washed in a non-flow-through bath. This leads to gradual accumulation of metal ions and components of the supporting electrolyte in the washing solution. If a working electrolyzer is connected to the washing bath, there will occur permanent recovery of Cd(II) introduced with the articles, with the result that components of the cadmium-plating electrolyte accumulate in the washing bath.

It is known that the efficiency of electrorecovery of metals on FCE is determined not only by the current mode, but also by the ratio of electrical conductivities of the electrolyte (χ) and the carbon filtering electrode (χ_{FCE}), by potentials of metal deposition and hydrogen evolution, and by the length of the plateau of the limiting diffusion current of metal deposition.

It can be seen from Fig. 1 that, with the supporting electrolyte diluted, the electrical resistivity of the solution decreases and the pH value varies within unit range (from 12 to 11 upon 100-fold dilution of the supporting electrolyte). The polarization curves in Fig. 2 demonstrate that, with the solution diluted, the stationary zero-current potential shifts in the positive direction and the plateau of the limiting current of Cd(II) electrodeposition becomes longer. Analysis of the data in Figs. 1 and 2 indicates that cadmium(II) can be electrolytically recovered from washing solutions formed in cadmium-plating of articles in a cyanide electrolyte.

The dependences of the degree of recovery and current efficiency by cadmium on the dilution factor of the supporting electrolyte at constant initial concentration of cadmium(II), shown in Fig. 3, indicate that the solution composition strongly affects the efficiency of cadmium electrodeposition. The best process parameters are obtained at supporting electrolyte dilutions by a factor of 5 to 15. Making this parameter greater or smaller leads to a decrease in the degree of Cd(II) recovery and current efficiency by Cd(II). With the dilution factor changing from 22 to 100 the process parameters decrease only slightly.

The plot describing the dependence of the degree of Cd(II) recovery on current density (Fig. 3b) shows that Cd(II) recovery grows with the current density increasing to 500–1000 A m^{-2}. With the current den-

sity increasing further (to 5000 A m^{-2}), the degree of Cd(II) recovery not only fails to increase, but even decreases somewhat, whereas the current efficiency falls dramatically. For example, the current efficiency is approximately 36% at 1000 A m^{-2}, and only about 4% at 5000 A m^{-2}. Under these conditions, the main amount of electricity is apparently consumed for hydrogen evolution. Therefore, it is appropriate to perform electrolytic recovery of Cd(II) at current densities not exceeding 1000 A m^{-2}.

Figure 3c shows the results characterizing the effect of Cd(II) accumulation in the washing solution on the parameters of the process of Cd(II) electrorecovery. It is of interest that the degree of Cd(II) recovery is the highest under the chosen process conditions at Cd(II) concentrations of about 100 mg l^{-1}. Apparently, the fraction of current consumed for concurrent processes, the main of which is reduction of hydrogen ions, is higher at lower initial concentrations of Cd(II), which is confirmed by a decrease in the current efficiency by cadmium. At Cd(II) concentrations exceeding 100 mg l^{-1}, the decrease in the degree of cadmium(II) recovery is presumably due to a shift of the place at which cadmium is deposited on the FCE to the front side of the electrode. As a result, the fraction of the electrode surface onto which cadmium is deposited decreases.

The parameters of Cd(II) electrorecovery largely depend on the rate at which the solution flows through the electrode (Fig. 3d). Making the solution flow rate lower, which is equivalent to longer residence time of the solution within the electrode, leads to a significant increase in the degree of Cd(II) recovery. For example, the degree of Cd(II) recovery is as high as 95% at a solution flow rate of 0.01 ml s^{-1} and a single pass of the solution through the electrode volume. With the solution flow rate increasing to 0.4 ml s^{-1}, the degree of recovery falls to 5%.

The possibility of using various nonwoven fibrous carbon materials (FCM) for recovery of Cd(II) was studied. The results obtained are listed in the table, whence follows that all the materials considered can be used in electrorecovery of Cd(II) from cyanide solutions. Preferable materials are Mtilon and VVP-66-95 wad. The characteristics of the materials represented in the table were described in [5].

The maximum amount of cadmium, which can be precipitated without impairing the output capacity of the process was 10–15 kg kg^{-1} of the material. In order to assess the possibility of recycling of the recovered cadmium (to be used as the material of a soluble anode in a cadmium-plating bath) and FCM regeneration, cadmium deposited onto FCE was dissolved in a cyanide electrolyte. The dissolution was done at anode current density of 0.5 A m^{-2}, with cadmium dissolved without any difficulties.

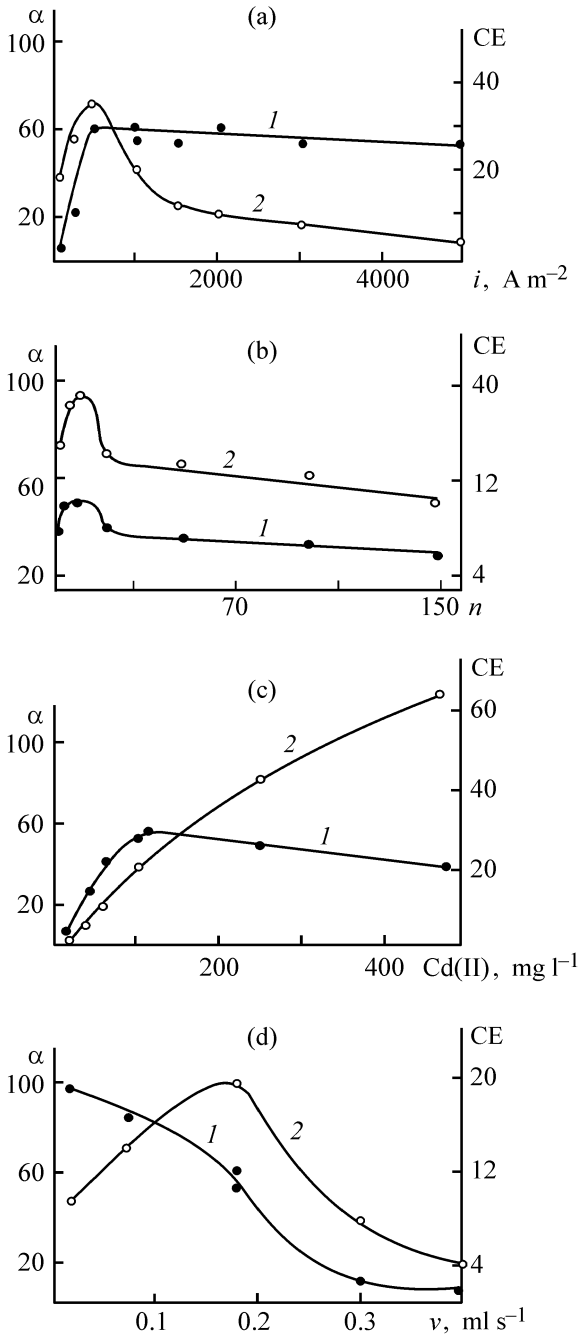

Fig. 3. (*1*) Degree of recovery, α, and (*2*) current efficiency CE by cadmium vs. (a) current density *i*, (b) dilution factor *n* of the supporting electrolyte, (c) initial Cd(II) concentration in solution, and (d) solution flow rate v. Initial Cd(II) concentration in solution 100 mg l^{-1}, cathode current density 500 A m^{-2}, solution flow rate 0.2 ml s^{-1}.

In addition, it was established that effective dissolution of cadmium in flowing electrolyte is pos-

Effect of the material of the carbon cathode on the Cd(II) recovery from cyanide solution (initial Cd(II) concentration 100 mg l^{-1}, current density 1000 A m^{-2}, solution flow rate 0.2 ml s^{-1})

FCM	α, %	CE, %	Output capacity, m^3 kg^{-1} FCM/day
NTM-200	52	5.5	42.4
NTM-100	69	8.1	53.4
Mtilon	89	11.2	66.2
VVP-66-95	74	8.3	57.4
KNM	68	7.8	63.3

sible without applying any external voltage because of the operation of a short-circuited electrochemical system constituted by cadmium, electrolyte solution, and FCM. The possibility of cadmium dissolution through operation of this short-circuited system is ensured by the substantial difference in standard potential between the cadmium and carbon-graphite electrodes, which varies within the range 0.8–1.1 V (depending on the electrolyte composition).

In both cases, cadmium deposited on an FCM dissolves both in the cadmium-plating electrolyte and in the supporting electrolyte containing no Cd(II), to give a cadmium-plating electrolyte. In all cases, the carbon electrode can be reused without impairing the characteristics of the Cd(II) electrorecovery process.

In order to verify the results obtained, an experiment modeling the electrorecovery of Cd(II) in the case of an automated cadmium-plating line was carried out. The operation parameters of the automated line, washing procedure, and the main galvanic process were taken from industry. Into a solution circulated between the electrolyzer and the tank at a rate of 0.2 ml s^{-1} were introduced, at regular intervals of time (20 min), portions of the cadmium-plating electrolyte of composition mentioned above. The electrorecovery of Cd(II) was carried out at current densities in the range 500–1000 A m^{-2}, the rise in the Cd(II) concentration in solution, modeling a single washing of articles, was varied from 42 to 115 mg l^{-1}. The suggested process modes ensure that the concentration of Cd(II) in solutions in the catching bath is maintained constant at 20–40 mg l^{-1}. This indicates that the whole amount of Cd(II) introduced with articles into the washing bath is recovered between successive article washings.

On the basis of the results obtained, tests were performed at a machine-building plant. The electrolytic recovery of Cd(II) was done from the solution of a catching bath. The suggested modes ensured a more than 99% recovery of Cd(II), which makes it possible to recommend the process of electrolytic recovery of Cd(II) from washing cyanide solutions onto filtering carbon electrodes for industrial use.

CONCLUSIONS

(1) A study of the effect of dilution of the supporting cadmium-plating cyanide electrolyte on the cathodic polarization curve, pH value, and electrical resistivity of the solution led to a conclusion that effective recovery of Cd(II) from washing solutions formed in cadmium-plating of articles in a cyanide electrolyte is possible.

(2) It was shown that the efficiency of Cd(II) electrorecovery, characterized by the degree of Cd(II) recovery and current efficiency, from solutions modeling washing cyanide solutions depends on current density, solution flow rate, dilution factor of the supporting electrolyte, initial concentration of cadmium(II) in solution, and the type of a FCM used.

(3) By varying the parameters mentioned above, a high degree of Cd(II) recovery can be achieved; the amount of cadmium deposited onto a carbon-graphite electrode without impairing the efficiency of its recovery is 10–15 g g^{-1} of fibrous carbon material.

(4) Dissolution of cadmium deposited onto a filtering carbon-graphite electrode, caused by anodic polarization and by operation of a short-circuited electrochemical system in the cadmium-plating or supporting electrolyte, enables recycling of cadmium and multiple use of the fibrous carbon material.

REFERENCES

1. Kudryavtsev, N.T., *Elektroliticheskie pokrytiya metallami* (Electroplated Coatings with Metals), Moscow: Khimiya, 1979.
2. Smirnov, D.N. and Genkin, V.E., *Ochistka stochnykh vod v protsessakh obrabotki metallov* (Purification of Wastewater in Metal Processing), Moscow: Metallurgiya, 1980.
3. Zapol'skii, A.K. and Obraztsov, V.V., *Kompleksnaya pererabotka stochnykh vod gal'vanicheskogo proizvodstva* (Integrated Processing of Wastewater Formed at Galvanic Shops), Kiev: Tekhnika, 1989.
4. Varentsov, V.K., *Izv. Sib. Otd. Akad. Nauk, SSSR, Ser. Khim. Nauk*, 1988, no. 1, pp. 124–138.
5. Varentsov, V.K., *Intensifikatsiya elektrokhimicheskikh protsessov* (Intensification of Electrochemical Processes), Tomilov, A.P., Ed., Moscow: Nauka, 1988, pp. 94–118.
6. Kletenik, Yu.B., Bek, R.Yu., Polyakin, L.Yu., and Zamyatin, A.P., *Izv. Sib. Otd. Akad. Nauk, SSSR, Ser. Khim Nauk*, 1985, issue 1, no. 2, pp. 93–97.

Russian Journal of Applied Chemistry, Vol. 76, No. 10, 2003, pp. 1597–1599. Translated from Zhurnal Prikladnoi Khimii, Vol. 76, No. 10, 2003, pp. 1639–1641.

APPLIED ELECTROCHEMISTRY AND CORROSION PROTECTION OF METALS

Modification with Manganese of Anodic Layers Containing Tungsten Oxides

I. V. Lukiyanchuk, V. S. Rudnev, E. S. Panin, T. A. Kaidalova, and P. S. Gordienko

Institute of Chemistry, Far-Eastern Division, Russian Academy of Sciences, Vladivostok, Russia

Received April 14, 2003

Abstract—The influence exerted by addition of manganese(II) acetate or potassium permanganate to an electrolyte with $Na_2H[PW_{12}O_{40}]$ on the content of manganese in tungsten-containing anodic-spark layers on aluminum alloy was studied.

The method of anodic-spark deposition makes it possible to form on the surface of rectifying metals a coating based on the components of a metal (alloy) being treated and of the electrolyte. One of ways to obtain anodic-spark layers of complex composition is to use electrolytes with complex anions, e.g., isopolyoxoanions (IPA) and heteropolyoxoanions (HPA) or to create conditions for their formation in solution [1–3].

It is known [4–6] that polyoxoanions can react both with a metal being anodized, so that it passes into solution, and with cations and anions of the electrolyte. Incorporated into negatively charged complexes, all the components mentioned can be delivered to the anode surface. High-temperature interactions of the components of the anodic film and electrolyte, including thermolysis of compounds at the anode, are possible in the vicinity of spark and microarc discharges. The coatings contain conversion products insoluble in a given electrolyte: salts, oxides, or glasses on their base.

In [7], formation of coatings on an AMtsM alloy in an electrolyte with $Na_2H[PW_{12}O_{40}]$[1] was studied, and anodic layers containing crystalline $WO_{2.9}$ were obtained.

The aim of the present study was to analyze specific features of manganese incorporation into coatings formed in the $Na_2H[PW_{12}O_{40}]$ electrolyte and to determine how presence of manganese in the cation or anion of a salt being added affects the coating composition.

[1] In [7], the salt composition was erroneously indicated as $N_2H[PW_{12}O_{42}]$.

Anodic layers on samples of AMtsM aluminum alloy (97% Al, 1–1.6% Mn) were formed galvanostatically at a current density of 1–10 A dm^{-2} in the course of 10 min. Sample preparation, electrochemical cell design, systems for cooling and stirring the electrolyte, thyristor unipolar power source, and methods for determining the phase and elemental composition have been described previously [7, 8]. The electrolytes were prepared from distilled water and the reagents $Na_2H[PW_{12}O_{40}] \cdot 9H_2O$ (chemically pure), $Mn(CH_3COO)_2 \cdot 4H_2O$ (analytically pure), and $KMnO_4$ of pure grade. All the electrolytes were prepared by pouring solutions together at room temperature. The base electrolyte no. 1 contained 83×10^{-3} M of $Na_2H[PW_{12}O_{40}]$, which corresponds to overall concentration of tungsten in solution equal to 0.1 M. Into electrolyte nos. 2 and 3, 8.3×10^{-3} M of, respectively, $Mn(CH_3COO)_2$ and $KMnO_4$ were introduced.

The parameters of the electrolytes (pH value and resistivity æ) before and after their use for anodic-spark treatment of aluminum alloy, and also the phase and elemental composition of the coatings formed, are listed in the table. It should be noted that, according to microprobe analysis, a chemically polished sample prepared for anodic-spark treatment contains (wt %): 98 Al and 1.22 Mn, and the X-ray diffraction pattern of the sample contains, in addition to aluminum peaks, low-intensity peaks of $Al(OH)_3$.

Introduction of manganese compounds changes the color of the initial electrolytes (no. 1 colorless, no. 2 yellow, no. 3 red-violet) but does not affect significantly the pH of the electrolytes. At the same time, permanganate ions (electrolyte no. 3) are unstable in an acid medium. When the electrolyte is allowed to

1070-4272/03/7610-1597 $25.00 © 2003 MAIK "Nauka/Interperiodica"

Effect of addition of manganese salts on parameters of electrolytes and on elemental and phase composition of coatings based on AMtsM aluminum alloy Phase composition of $WO_{2.9}$ coating

Electrolyte no.	pH	æ, S cm^{-1}	*i*, A dm^{-2}	Characteristics of anodic layers						
				color	Average content,* wt %					
					Al	W	P	Mn	Na	K
1	2.0**/1.8	4.5**/4.8	1–10	Black	6.7	46.8	0.64	0.18	0.18	–
			3–10	Green	0.11	56.9	0.26	0.04	0.12	–
2	1.9/2.0	5.4/4.3	1–10	Beige	0.34	54.3	0.39	1.35	0.03	
3	1.8/2.1	4.7/3.4	1–10	″	0.15	53.5	0.33	1.30	0.06	0.07

* Content of elements in coatings determined by electron-beam X-ray fluorescence microanalysis.

** Numerator, pH value and æ for the initial electrolyte; denominator, the same after anodizing.

stand, a bulky white precipitate, turning brown in air, is formed. After an anodic-spark treatment of the AMtsM alloy, X-ray phase analysis of the precipitate formed in electrolyte no. 3 shows the presence of β-$Na_{0.7}MnO_2$, $Na_2W_4O_{13}$, and $WO_{2.9}$.

As follows from the table, introduction of manganese compounds in a cationic or anionic form has no effect on the phase composition of coatings formed on the AMtsM alloy. In both cases, the X-ray diffraction pattern shows peaks corresponding to the $WO_{2.9}$ phase. At the same time, a change is observed in the outward appearance and color of the coatings, the latter being the same in electrolyte nos. 2 and 3 (see figure). In electrolyte no. 1, mat black layers are formed, with green point-like areas chaotically scattered over them. At the same time, in electrolyte nos. 2 and 3, beige coatings are formed on the surface of a shining and transparentprimary (prespark) anodic oxide film. In all probability, the change of coloration from green to beige is due to incorporation of manganese into the tungsten oxide lattice. Green and beige areas are formed in all the three electrolytes by the island mechanism, similarly to the case of anodic-spark deposition of coatings in a vanadate-phosphate electrolyte [1, 9]. First, nuclei of the new phase appear, and then they gradually expand to fill the increasing fraction of the surface area. In the process, the sparking is concentrated on the periphery of a growing area of the new phase.

The elemental composition of green and beige coatings is independent of the current density. The difference of beige coatings from green ones consists in an increase in the content of manganese to 0.8–1.7 wt % (table lists average values for coatings obtained in

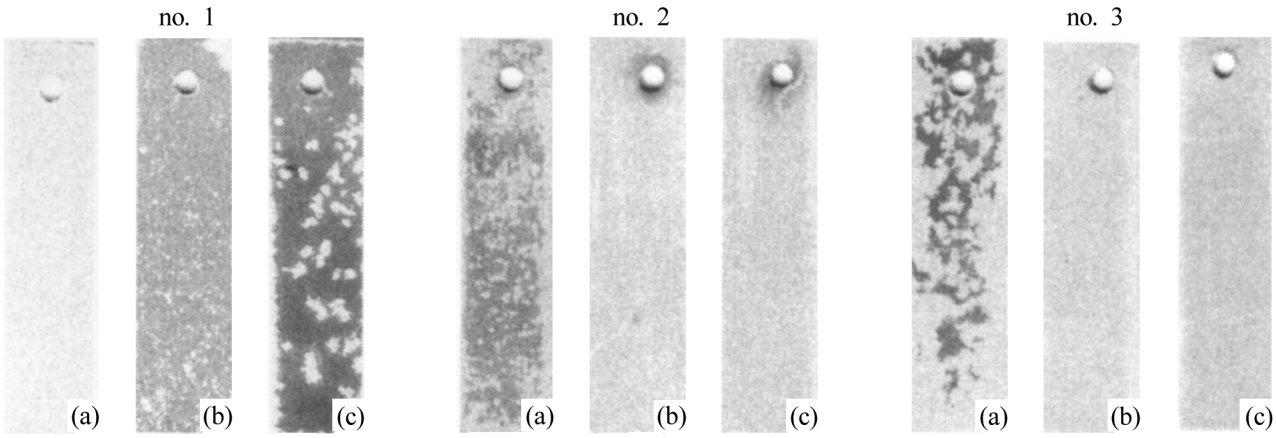

Outward appearance of coatings formed on aluminum alloy in electrolyte nos. 1–3. Current density (A dm^{-2}): (a) 1, (b) 2, (c) 10.

the current density range under study). The fact that introduction of manganese compounds into the base electrolyte leads to an increase in the concentration of the transition metal in anodic-spark layers indicates that the metal is incorporated into the coatings from the electrolyte, rather than from the substrate.

The incorporation of manganese is presumably due to thermolysis of compound manganese-containing HPA or colloid particles at the electric breakdown channels. The latter is possible for the $KMnO_4$-containing electrolyte, in which a precipitate is formed.

The approach considered can also be presumably applied to modification of tungsten-containing coatings with other transition metals, which is promising for obtaining functional coatings, e.g., catalytically active structures, on the support surface.

CONCLUSIONS

(1) Anodic films formed on an AMtsM aluminum alloy in an electrolyte with $Na_2H[PW_{12}O_{40}]$ (8.3×10^{-3} M) contain crystalline $WO_{2.9}$. Addition of 8.3×10^{-3} M of $Mn(CH_3COO)_2$ or $KMnO_4$ to the electrolyte has no effect on the phase composition, but leads to incorporation of up to 1.7 wt % Mn into the coatings and to a change in the coating coloration from green to beige. The latter points to the presence of manganese in the tungsten oxide lattice.

(2) The layer containing tungsten oxides, both with and without manganese inclusions, is formed on the anode surface by the island mechanism: areas of new phase appear on the film surface, expand, and merge to give a new layer.

ACKNOWLEDGMENTS

The study was supported by Far-Eastern Division of the Russian Academy of Sciences, grant no. 03-1-0-04-011.

REFERENCES

1. Rudnev, V.S., Gordienko, P.S., Kon'shin, V.V., *et al.*, *Electrokhimiya*, 1996, vol. 32, no. 10, pp. 1242–1246.
2. Lukiyanchuk, I.V., Rudnev, V.S., Tyrina, L.M., *et al.*, *Zh. Prikl. Khim.*, 2002, vol. 75, no. 12, pp. 2009–2015.
3. USSR Inventor's Certificate, no. 964026.
4. Carrier, X., Lambert, J.F., and Che, M., *J. Am. Chem. Soc.*, 1997, vol. 119, pp. 10137–10146.
5. Maksimovskaya, R.I., Fedotov, M.A., and Maksimov, G.M., *Zh. Neorg. Khim.*, 1985, vol. 30, no. 4, pp. 918–924.
6. Pop, M.S., *Geteropoli- i izopolioksometallaty* (Heteropoly- and Isopolyoxometallates), Novosibirsk: Nauka, 1990.
7. Rudnev, V.S., Lukiyanchuk, I.V., Kon'shin, V.V., and Gordienko, P.S., *Zh. Prikl. Khim.*, 2002, vol. 75, no. 7, pp. 1099–1103.
8. Lukiyanchuk, I.V., Rudnev, V.S., Kaidalova, T.A., *et al.*, *Zh. Prikl. Khim.*, 2000, vol. 73, no. 6, pp. 926–929.
9. Lukiyanchuk, I.V., Chetyrbotskii, A.N., and Rudnev, V.S., *Sbornik nauchnykh trudov Vserossiiskogo simpoziuma "Khimiya: fundamental'nye i prikladnye isledovaniya, obrazovanie (KhIFPI-02)", 24–27 iyunya 2002 g.* (Proc. All-Russia Symp. "Chemistry: Basic and Applied Research, Education (KhIFPI-02)," June 24–27, 2002), Khabarovsk: Dal'nauka, 2002, vol. 1, pp. 135–137.

Russian Journal of Applied Chemistry, Vol. 76, No. 10, 2003, pp. 1600–1605. Translated from Zhurnal Prikladnoi Khimii, Vol. 76, No. 10, 2003, pp. 1642–1647.

APPLIED ELECTROCHEMISTRY AND CORROSION PROTECTION OF METALS

A Study of Composition and Structure of Aluminozirconium Hydroxides Obtained by Coprecipitation in Membrane Electrolyzer

R. G. Romanova, A. A. Lamberov, and E. V. Petrova

Kazan State Technological University, Kazan, Tatarstan, Russia

Received March 25, 2003

Abstract—Fundamental aspects of formation of aluminum and zirconium hydroxides in their coprecipitation under the action of products of electrode reactions in a membrane electrolyzer were studied. The influence exerted by precipitation conditions (temperature and pH value) on the phase composition and porous structure of coprecipitated systems was analyzed.

Coprecipitated aluminozirconium hydroxides (AZH) and oxides are used as supports for high-efficiency catalysts for important catalytic processes, such as isomerization, reforming, etc. The use of zirconium dioxide is due to its ability to create stable systems with developed surface.

Previously, the structure and acid-base properties of aluminum hydroxides and oxides synthesized in a membrane electrolyzer have been studied. It has been found that aluminum hydroxides precipitated in the anode chamber of the electrolyzer differ significantly from those obtained by the conventional technologies both in phase composition and porous structure and in distribution of acid-base centers over their surface [1–4].

The formation of a heterogeneous phase in precipitation of poorly soluble compounds is a complex process including stages of salt hydrolysis to give low-molecular forms of hydroxo complexes, their polycondensation, and subsequent precipitation of a hydroxide, first as primary particles and then as disordered aggregates and the crystalline phase [5].

The processes of formation of binary hydroxides in coprecipitation are more complex and may lead to crystallization in two directions: to give individual phases or heteronuclear spinel structures. In the case of precipitation in an electrochemical cell, the formation of the hydroxide structure is complicated by the effect of electric field on dispersed systems, which leads to quite a number of nonequilibrium electric surface phenomena changing fundamentally the characteristics of the heterogeneous phase. Polynuclear particles formed under real conditions determine the structure and surface characteristics of the resulting systems based on poorly soluble hydroxides. In this context, it seemed a topical task to study the fundamental aspects of formation of binary systems in their precipitation in a membrane electrolyzer.

The aim of this study was to analyze the influence exerted by conditions of coprecipitation by products formed in electrode reactions on the composition and structure of aluminozirconium hydroxides.

EXPERIMENTAL

The precipitation was performed in the anode chamber of a membrane electrolyzer [1] by continuous introduction of sodium aluminate into a $ZrO(NO_3)_2$ solution. Platinum served as anode, and Kh18N9T steel, as cathode. The anode and cathode spaces were separated by an MK-40 cation-selective membrane. The precipitation was done at pH ranging from 6 to 10 at temperatures of 303–343 K. The suspension obtained upon precipitation was subjected to electrochemical purification to remove sodium ions and aged in mother liquor for 48 h. The $ZrO_2 : Al_2O_3$ molar ratio in the hydroxides synthesized varied from 1 : 0.73 to 1 : 1.85.

The content of sodium and aluminum ions was determined by flame photometry and complexometry. Analysis for zirconium(IV) was carried out by X-ray fluorescence method on a VRA-20 instrument. A sam-

1070-4272/03/7610-1600 $25.00 © 2003 MAIK "Nauka/Interperiodica"

Table 1. Preparation conditions and characteristics of AZH synthesized

Sample no.	Precipitation conditions					Bulk density, g cm^{-3}	M^*	M^{**}	Calcination loss, %
	T, K	pH/pH$_{fin}$	τ, min				g		
			precipitation	finishing treatment	Σ				
1	303	6/4.5	140	10	155	0.954	27.2	16.3	40.15
2	303	6/4.5	395	5	400	0.806	55.3	34.0	38.53
3	303	8/4.5	390	25	415	0.843	52.7	33.0	37.44
4	303	9/4.0	380	35	415	0.807	60.5	36.4	39.79
5	303	10/4.5	230	20	250	0.756	41.4	27.7	33.05
6	323	6/4.5	270	30	300	0.789	43.2	29.3	32.21
7	323	8/3.0	115	25	140	0.972	43.5	29.7	31.81
8	323	9/4.5	175	15	190	0.737	43.2	29.8	31.13
9	323	10/4.5	220	35	255	0.788	42.8	28.8	32.69
10	343	6/4.5	290	7	297	0.964	36.5	26.0	28.72
11	343	8/4.0	125	30	155	0.774	32.0	21.5	32.70
12	343	9/4.5	300	20	320	1.112	36.0	24.1	33.19
13	343	10/4.5	160	60	220	0.929	37.2	25.4	31.85

* Precipitate mass after drying at 403 K. ** Precipitate mass after calcination at 1123 K.

ple was preliminarily mixed with an inert substrate in 1 : 15 ratio and pelletized. As inert substrate served boric acid of chemically pure grade. Reference samples with known content of zirconium(IV) were prepared in a similar way using zirconium dioxide of special-purity grade. The content of water in the samples was found from calcination loss at 1123 K.

The crystal structures were studied on a DRON-3M diffractometer with Fe$_{K_\alpha}$ radiation and graphite monochromator in the secondary beam. As reference were used structures represented in the Inorganic Crystal Structure Database (ICSD for WWW).

The pore structure was determined by the method of low-temperature adsorption of nitrogen. The adsorption measurements for determining the specific surface area, pore volume, and pore diameter distribution were carried out on Micrometrics ASAP-2400 instrument. For analysis, a 0.8–1.0-g portion of a preliminarily powdered catalyst was taken and placed in the ampule of the analyzer. The sample was heated to 523 K and kept under vacuum with residual pressure of 0.1 mm Hg for 4 h, the ampule was filled with helium and weighed, and adsorption–desorption of nitrogen was carried out. The adsorption–desorption isotherms were measured at 77 K, with degassing to residual pressure of 0.03 mm Hg. In calculations, the density of nitrogen in normal liquid state was taken to be 0.808 g cm^{-3}, and the molecular cross section for nitrogen, 0.1620 nm^2. The measurement accuracy of pore volume and pore size distribution was ±13%, and that of specific surface area, ±3%.

Thermochemical studies were carried out with a Perkin–Elmer TGS-2 thermogravimetric analyzer and SETARAM DCK 111 differential scanning calorimeter.

As can be seen from Table 1, the rate of precipitation of aluminozirconium hydroxides at 303 K with electrochemically generated protons depends on the acidity of the medium only slightly in the pH range 6–9. In a more alkaline medium (pH 10), an excess content of hydroxide ions accelerates the hydrolysis process, with the result that precipitation is faster by a factor of 1.8.

Raising the temperature also makes the precipitation rate higher because of the increasing mobility of reacting particles. However, this leads to a strong effect of the pH value on the rate of AZH precipitation, which manifests itself in the appearance of a maximum at pH 8. The anomalously high precipitation rate under these conditions is probably due to formation of particles of a heterogeneous phase, which have uncharged surface (point of zero charge, p.z.c.), with the result that fast coagulation of the precipitate occurs.

As shown in [6], the point of zero charge strongly depends on the anionic composition of a solution and lies at pH 8.8–9.3 for zirconogels obtained from $ZrO(NO_3)_2$. The true state of the neutrality of heterogeneous particles is determined by the distribution of hydroxonium and hydroxy ions between the charged gel surface and electrolyte solution. In the presence of a directed electric field, a certain contribution is

Table 2. Composition of AZH synthesized

Sample no.	Composition, mol $g^{-1} \times 10^3$				$ZrO_2 : Al_2O_3 : H_2O$	$MO_p : H_2O$
	ZrO_2	Al_2O_3	Na_2O	H_2O		
1	2.97	2.18	0.18	22.3	1 : 0.73 : 7.51	1 : 4.18
2	2.18	3.33	0.11	21.4	1 : 1.53 : 9.81	1 : 3.81
3	2.45	2.88	0.50	20.8	1 : 1.18 : 8.49	1 : 3.57
4	2.14	3.28	0.07	22.1	1 : 1.53 : 10.3	1 : 4.03
5	2.29	3.62	0.29	18.4	1 : 1.58 : 8.03	1 : 2.97
6	2.12	3.93	0.26	17.9	1 : 1.85 : 8.44	1 : 2.84
7	2.63	3.45	0.09	17.7	1 : 1.31 : 6.73	1 : 2.87
8	2.31	3.72	0.40	19.2	1 : 1.61 : 8.31	1 : 2.99
9	2.37	3.59	0.25	18.2	1 : 1.52 : 7.68	1 : 2.93
10	2.70	3.53	0.34	16.0	1 : 1.31 : 5.93	1 : 2.44
11	2.47	3.58	0.05	18.2	1 : 1.45 : 7.37	1 : 2.98
12	2.58	3.24	0.33	18.4	1 : 1.26 : 7.13	1 : 2.99
13	2.50	3.52	0.24	17.7	1 : 1.41 : 7.08	1 : 2.83

also made by particle orientation along the external field vector and by polarization coagulation, which, in the end, determine the real $pH_{p.z.c.}$ and, correspondingly, the rate of formation of the heterogeneous phase. A lower $pH_{p.z.c.}$ is observed for gels susceptible to polymerization [6], and, therefore, it may be stated that electrical-surface phenomena occurring in electrochemical precipitation favor formation of polymer particles.

It can be seen from Table 2 that the composition of hydroxides obtained in the anode chamber of the membrane electrolyzer also depends on precipitation conditions. The loss upon calcination of the hydroxides at 1123 K is 28–40%, which corresponds to 2.44–4.18 mol of water per 1 mol of metal oxide. It should be noted that the ratio $M_xO_y : H_2O = 1 : \sim 4$ is only observed at 303 K in the pH range 6–9. With increasing precipitation temperature, this ratio tends to 1 : 3.

It is significant that the content of water in the samples synthesized grows with increasing mole fraction of zirconium dioxide. For example, with the $ZrO_2 : Al_2O_3$ changing from 1 : 1.53 to 1 : 0.73, the amount of water per 1 mol of oxide increases from 3.81 to 4.18 mol. Virtually in the whole range of temperatures studied, the dependence of the molar content of water in AZH on the precipitation pH shows extremal behavior with a weak maximum at pH 8–9.

It should be noted that the precipitation temperature affects the AZH composition. For example, for the hydroxides obtained at pH 6, the content of water in their composition decreases rather substantially, from 3.81 to 2.44 mol, with the precipitation temperature increasing from 303 to 343 K. At the same time, performing the precipitation process at pH 8–9 leads to a pronounced decrease in the amount of water only with temperature increasing from 303 to 323 K, with further rise in temperature virtually not affecting the AZH composition. For the hydroxides obtained at pH 10, the mole fraction of water in their composition decreases somewhat with increasing precipitation temperature.

Analysis of published data [6–8] shows that the amount of water molecules in zirconogels obtained in precipitation with chemical reagents mainly depends on the precipitation pH, being equal to 0.7–1.8 mol per molecule of zirconium dioxide. The authors of [8] synthesized aluminozirconium hydroxides of composition $(ZrO_2 + Al_2O_3) : H_2O = 1 : 1.6$, which are similar to the samples used in the present study, by treating oxo zirconium and aluminum nitrate solutions with a 3 N ammonia solution. The content of water in individual aluminum hydroxides prepared in electrochemical precipitation [2] varied with temperature and precipitation pH in the range 1.29–1.6 mol mol^{-1} Al_2O_3. The experimental results obtained (Table 2) show that binary aluminozirconium hydroxides synthesized under the action of electrochemically generated protons are distinguished by higher content of water, compared with individual and complex hydroxides obtained in chemical precipitation.

Thermogravimetry and differential scanning calorimetry (DSC) were used to study thermal decomposition of the samples synthesized. It can be seen from

the derivatograms obtained (Fig. 1) that the mass loss by AZH samples occurs stepwise in two or three stages and is accompanied by endothermic effects at 400, 590–600, and 700 K. Thermal decomposition below 400 K results in removal of water from the xerogel of zirconium hydroxide, and that at 553–603 K, probably, leads to decomposition of aluminum hydroxide of bayerite modification, with release of structural water. Intermicellar moisture is first removed from broad pores, and then from fine pores within secondary crystals. At 688–700 K, finely crystalline pseudoboehmite decomposes. The DSC curves obtained for AZH samples are mainly characterized by two peaks (Fig. 2). The peak at temperatures of the first endothermic effect has complex broadened structure, and the peak in the range of temperatures of the second endothermic effect shows a clearly pronounced narrow dip. For some of the samples, a third low-intensity broadened endothermic peak is observed. The thermogravimetric and DSC data obtained were used to calculate the corresponding heat effects to be 45–107 kJ mol^{-1}.

The electrical-surface phenomena occurring in the process of formation of a heterogeneous phase in an electric field determine the structure and composition of the resulting systems and, in particular, the content of counter ions, whose role is played by sodium ions in coprecipitation of AZH. As shown previously [4], immediately after precipitation the residual content of Na_2O in electrochemically synthesized individual aluminum hydroxides grows with increasing pH and precipitation temperature, being equal to 0.66–5.5%. One of advantages of the electrochemical method for synthesis of hydroxides is the possibility of purification of the systems obtained to eliminate simultaneously the undesirable impurity ions, which are removed, already in the process of synthesis, from the precipitation chamber into the opposite chamber of the membrane electrolyzer through electromigration. To purify the hydroxides completely, it is suggested to subject the suspension to an additional "finishing" treatment consisting in that the electrolysis process is continued after the precipitation is complete. As the criterion of completeness of the purification process serves a decrease in the current density to a constant value, with the pH value in the anode chamber becoming 4–4.5. It has been shown previously that carrying out a finishing treatment of aluminum hydroxides makes the content of Na_2O as low as 0.01–0.08 wt %.

It can be seen from Table 2 that the residual content of sodium ions in precipitation of binary aluminozirconium hydroxides depends on electrolysis con-

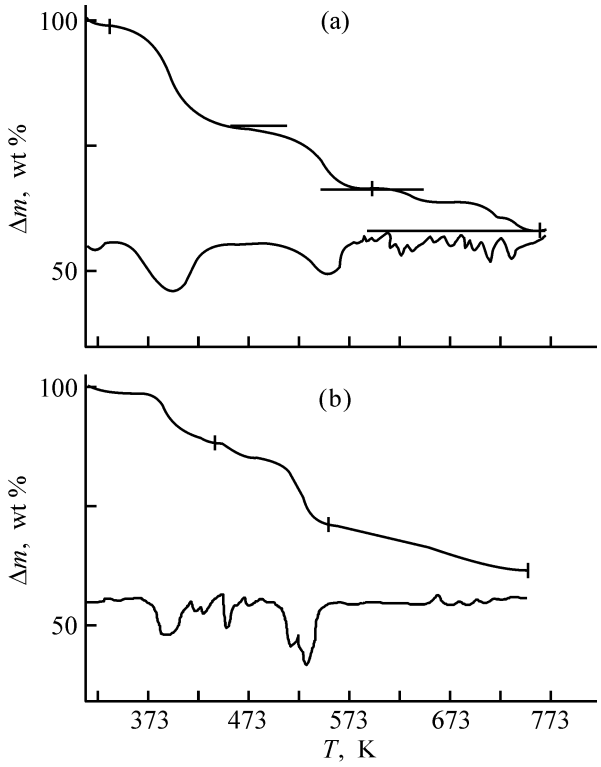

Fig. 1. Derivatograms of AZH samples. (Δm) Change in mass and (T) temperature. Sample: (a) no. 2 and (b) no. 3; the same for Fig. 2.

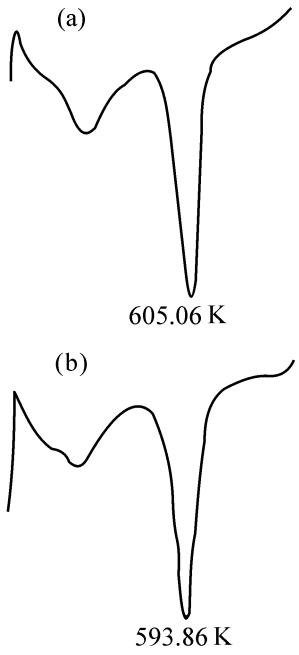

Fig. 2. DSC curves for AZH samples. T_{sc} = 293.2–773.2 K, sensitivity 1 mV, heating rate 20 deg min^{-1}, recorder chart motion velocity 5 mm min^{-1}.

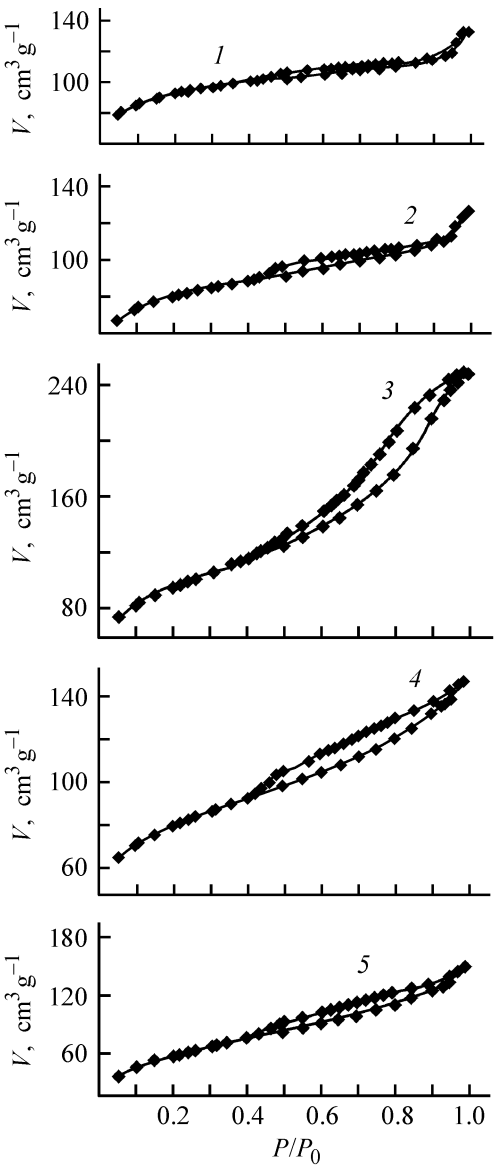

Fig. 3. Adsorption isotherms of sample nos. (*1*) 4, (*2*) 8, (*3*) 10, (*4*) 12, and (*5*) 130. (*V*) Micropore volume and (P/P_0) relative pressure.

ditions and varies within the range 0.34–3.12 wt %. However, in contrast to the case of individual aluminum hydroxides, the content of Na_2O in AZH samples changes stepwise with increasing temperature and pH value. Similar dependences are observed for samples synthesized at 323 and 343 K: the hydroxides obtained at pH 8 contain the minimum amount (0.56 and 0.34 wt %), and those synthesized at pH 9, the maximum (2.51 and 2.04 wt %) amounts of Na_2O. These dependences are in conformity with the concept of the point of zero charge of the surface, which favors formation of a heterogeneous phase with minimum sorption capacity for ions (Na^+ in the case in question). A reverse dependence is observed at 303 K: AZH synthesized at pH 8 contain the maximum amount, and those obtained at pH 9, the minimum amount of Na_2O. Probably, the point of zero charge of AZH-based systems is shifted to pH 9 at not-too-high temperatures.

It should be noted that, depending on temperature, the content of sodium impurity ions in precipitates obtained at one and the same pH value varies differently. For example, the content of sodium ions grows with increasing precipitation temperature at pH 6, and, by contrast, decreases steeply with temperature increasing from 303 to 323 K at pH 8. For AZH obtained at pH 10, the precipitation temperature affects the content of sodium ions only slightly, whereas for samples synthesized at pH 9, the temperature dependence of this content shows a maximum at 323 K. Comparison of the experimental data obtained with the results of previous studies [1–4] shows that the pattern of mass transfer of sodium ions into the cathode chamber from a suspension of binary hydroxides is more complex than that in the case of similar suspensions of individual hydroxides.

A study of the samples by the method of low-temperature nitrogen adsorption demonstrated that the AZH synthesized are characterized by microporous structure with pore diameter of about 10 Å and mesopores with a maximum in the pore volume distribution over pore radii at 38 Å. At room temperature, the pore structure of the precipitate is mainly represented by micropores, which is indicated by isotherms of nitrogen adsorption, characterized by high adsorption at low relative pressures and nearly horizontal plateau up to $P/P_0 = 0.9$ (Fig. 3).

The micropore volumes calculated using the Dubinin–Radushkevich method for samples obtained under varied conditions were 0.15 to 0.12 $cm^3\ g^{-1}$. Raising the precipitation temperature leads to a certain decrease in the fraction of micropores (by approximately 15%) and to a simultaneous increase in the mesopore volume by nearly a factor of 2. The change in the pore structure results in a significant transformation of the adsorption isotherm: the slope of the curve at $P/P_0 = 0.2–0.9$ increases and the hysteresis loop becomes much wider.

It should be noted that the most developed porous structure is formed in precipitation at low pH values, with the samples obtained containing a great number of both meso- and micropores. In this case, broad bands appear in the curve of pore volume distribution over effective diameters in the form of bends at 50 and 78 Å, which points to the formation of larger-diameter pores of varied nature. These samples have the greatest specific surface area calculated by the BET

method. For example, S_{sp} is 317 $m^2 g^{-1}$ for a sample synthesized at pH 6 and temperature of 343 K, whereas for AZH obtained at pH 9–10 and 343–363 K, the specific surface area is in the range 250–277 $m^2 g^{-1}$, with the pore volume varying within 0.2–0.4 $cm^3 g^{-1}$.

The X-ray diffraction patterns of the hydroxides obtained show reflections corresponding to aluminum hydroxides of the bayerite and pseudoboehmite modifications. After calcination of the samples at 873 K, the γ-Al_2O_3 phase is revealed by X-ray diffraction analysis, the ZrO_2 phase being X-ray-amorphous under these conditions. Studies of the thermal decomposition of the systems obtained also confirm this phase composition. Comparison of the structural parameters of the AZH synthesized with those of individual hydroxides obtained under similar conditions indicates that the processes in which the structure of individual and coprecipitated hydroxides is formed are different.

CONCLUSION

The experimental study demonstrated that the conditions of precipitation in synthesis of aluminum and zirconium hydroxides with electrochemically generated reagents make it possible to vary widely both the composition and the porous structure of the systems obtained, which opens up new opportunities for development of supports and catalysts with prescribed structural characteristics.

ACKNOWLEDGMENTS

The study was supported financially by the Russian Foundation for Basic Research (project no. 01-03-32857) and Scientific Program "Universities of Russia" (project no. UR.05.01.022).

REFERENCES

1. Lamberov, A.A., Romanova, R.G., and Liakumovich, A.G., *Kinet. Kataliz*, 1999, vol. 40, no. 3, pp. 472–479.
2. Lamberov, A.A., Romanova, R.G., and Liakumovich, A.G., *Zh. Prikl. Khim.*, 1999, vol. 72, no. 8, pp. 1310–1314.
3. Lamberov, A.A., Romanova, R.G., and Liakumovich, A.G., *Zh. Prikl. Khim.*, 1999, vol. 72, no. 5, pp. 772–779.
4. Lamberov, A.A., Kalinina, I.V., Egorova, S.R., *et al.*, *Zh. Prikl. Khim.*, 1998, vol. 71, no. 9, pp. 1461–1466.
5. Krivoruchko, O.P., *Nauchnye osnovy prigotovleniya katalizatorov: Sbornik nauchnykh trudov* (Scientific Foundations of Catalyst Preparation: Coll. of Sci. Works), Novosibirsk, 1990, pp. 137–155.
6. Pechenyuk, S.I. and Kalinkina, E.V., *Izv. Akad. Nauk, Ser. Khim.*, 1996, no. 11, pp. 2653–2657.
7. Ivanova, A.S., Dzis'ko, V.A., and Moroz, E.M., *Kinet. Kataliz*, 1989, vol. 30, no. 5, pp. 1167–1173.
8. Chertov, V.M. and Makovskaya, T.F., *Kolloid. Zh.*, 1984, vol. 46, no. 1, pp. 85–90.

Russian Journal of Applied Chemistry, Vol. 76, No. 10, 2003, pp. 1606–1610. Translated from Zhurnal Prikladnoi Khimii, Vol. 76, No. 10, 2003, pp. 1648–1652.

APPLIED ELECTROCHEMISTRY AND CORROSION PROTECTION OF METALS

Influence of Zinc Intercalation on Processes in Nickel Oxide Electrode and on Service Life of Nickel–Zinc Battery

Z. P. Arkhangel'skaya, T. B. Kas'yan, and M. M. Loginova

Akkumulyatornaya Kompaniya Rigel', Open Joint-Stock Company, St. Petersburg, Russia

Received May 28, 2003

Abstract—The dependence of capacity and service life of a nickel–zinc battery on the mechanism of zinc transfer and the rate of zinc intercalation into nickel oxide electrodes differing in the conductivities of the active paste and porous structures was studied.

The problem of raising the service life of nickel–zinc (NZ) batteries, which permanently attracts attention, is mostly solved by using various methods for making lower the solubility of zinc at the negative electrode. It is a common practice to use for this purpose electrolytes with as low KOH concentration as possible and F^- and CO_3^{2-} ions added to the electrolyte and $Ca(OH)_2$, $Sr(OH)_2$, and other additives to the active paste of the zinc electrode. These additives form with zinc oxide, complex compounds sparingly soluble in alkaline solutions [1–3]. This makes it possible to slow down the processes leading to intraelectrode transfer of zinc in the negative electrode and to "loss of its shape," a factor limiting the service life of NZ batteries.

It can be seen from [1–5] that, presently, the service life of NZ batteries is 300–400 cycles, and the Evercell company achieved a service life of 600 cycles [3].

So far, all attempts to raise further the service life of NZ batteries have failed, which is still attributed to the necessity for improving the negative electrode. At the same time, it was determined in [6] that the decrease in the capacity of NZ batteries after 300–400 cycles is due to impaired working capacity of the nickel oxide electrode (NOE) on a metal-ceramic (MC) support. The authors failed to reveal the reason for its degradation, since the assumption that the structure of the active paste degrades was not confirmed.

A decrease in the capacity of a NZ battery, associated with deteriorated chargeability of an NOE on an MC support after 250 cycles, was also noted in [7]. The observed dramatic rise in the potential in anodic polarization and increase in oxygen evolution were accounted for by nonuniform distribution of current over the NOE surface, which results in an unbalance in the degree of charging of different areas on the surface of the positive and negative electrodes, and, as consequence, in the loss of shape by the zinc electrode and in its local passivation.

Data indicating that processes occurring on NOE can strongly affect the working capacity of the zinc electrode and limit the service life of an NZ battery have been obtained recently using a compacted NOE made of spherical nickel hydroxide containing cobalt hydroxide as additive on a foamed-nickel (FN) support [8]. In a battery with NOE on an FN support, the intraelectrode mass transfer in the zinc electrode is strongly decelerated, and its shape is retained after up to 200–250 cycles. This is accounted for by the increased conductivity of active paste [spherical $Ni(OH)_2$], which affects the uniformity of the current distribution both within the active paste and over the surface of the zinc electrode.

It was also revealed that accumulation of zinc in an FN-supported NOE as a result of interelectrode mass transfer, occurs in the course of direct incorporation of zinc into the structure of $Ni(OH)_2$, with the stages of its deposition within pores in the form of $Zn(OH)_2$ or ZnO bypassed.

The results obtained suggest that incorporation of zinc also occurs in an MC-supported NOE, but is not manifested clearly, being preceded by deposition of ZnO within the porous space of the electrode.

1070-4272/03/7610-1606 $25.00 © 2003 MAIK "Nauka/Interperiodica"

EXPERIMENTAL

This study considers processes associated with zinc incorporation and their influence on the efficiency of NOE and the service life of an NZ battery for the case of NTs-25 batteries with positive electrodes on FN and MC supports. The batteries differed only in the positive electrodes. All other elements and the design were the same.

It is of interest to study simultaneously the intercalation processes on two types of electrodes in view of the fundamental difference in their structural parameters and active paste conductivities. The electrode with an MC support contains the active paste in the form of a $Ni(OH)_2$ layer covering the surface of deep pores of the support. At low active paste conductivity, the anodic and cathodic processes on the electrode occur in the inner-diffusion mode and are accompanied by a considerable change in the concentration of hydroxide ions and by decomposition of hydroxo zincate ions present in the electrolyte.

By contrast, the active paste of NOE on an FN support is composed of densely compacted $Ni(OH)_2$ particles with radius of 10 to 30 μm. The closed pores have the same size. Therefore, their contribution to current transport in the electrolyte is insignificant.

The active paste of NOE on an FN support contains cobalt hydroxide as an additive (5–6%), which is transformed in the course of battery forming into the compound $Ni_{1-x}Co_xOOH$ exhibiting electronic conduction [9]. Owing to these features, the electrochemical processes in the electrode mainly occur on its outer surface, with the current flowing within the electrode, predominantly in the solid phase. Also, Zn is introduced in amount of 2–4%, i.e., an amount not affecting adversely the working capacity of the electrode [10], into spherical Ni(OH) to preclude formation of the γ-phase.

The basic parameters of the batteries studied are listed in Table 1.

In all the batteries, the same sets of separators and the same amounts of the electrolyte containing (M): 7 KOH + 1 LiOH, were used. This made it possible to determine the characteristics of interest under the comparable conditions.

The batteries with MC-supported NOE were formed in two cycles, with a charging capacity C equal to $1.0\,C_{theor}$ imparted in each cycle. The batteries with NOE on an FN support were also formed in two cycles, with capacities $1.0\,C_{theor}$ and $1.4\,C_{theor}$ imparted in the first and second cycle, respectively. The cycling was done in the following mode: a two-or-three stage charging with decreasing current to a voltage not exceeding 1.98 V in each stage, and discharge with a 5 A current to a voltage of 1.2 V.

Table 1. Basic parameters of NTs-25 batteries with NOE of different types (thickness 0.9–1.0 mm, electrolyte volume 105 ml)

NOE support	Theoretical capacity of NOE (+) for $Ni^{2+} \rightleftarrows Ni^{3+}$ transition, A h	Theoretical capacity ratio of electrodes (–)/(+) in battery
FN	50	2.0/1
MC	33	3/1

In the course of cycling, the charging and discharge capacities, KOH and $Zn(OH)_4^{2-}$ concentrations in the electrolyte, content of zinc in the active paste of both types of electrodes, and cobalt content in the NOE on an FN support were monitored.

In some tests, the solubility of zinc present in the NOE was determined. This made it possible to determine the amount of zinc incorporated, since, according to the data of [11], the solubility of zinc incorporated into the NOE structure in KOH solutions is two orders of magnitude lower than that of ZnO. For dissolution, a 5 M KOH solution was used, with concentration close to that established in the electrolyte of the battery. The electrolyte volume exceeded by about a factor of 10 that necessary for zinc dissolution. The dissolution time was, in accordance with the data of [11], 7 days.

In battery cycling, the primary attention was given to elucidating the dynamics of zinc incorporation into the active paste of the electrodes studied. Because approximately the same charging capacities were imparted to both types of batteries in cycling, the accumulation was estimated in grams per cycle (Fig. 1) and then recalculated to percentage content in the active paste of the NOE studied.

It was established that the accumulation of zinc in the $Ni(OH)_2$ electrode on an FN support occurs at a rather high rate in the initial cycles, is decelerated by approximately a factor of 2 after 60–70 cycles, and then continues at a constant rate (Fig. 1). By the 200th cycle, 18 g of zinc was accumulated in the positive electrodes of the battery, and then the process virtually terminated. Analyses showed that the main part of the accumulated zinc (85–87%) is not dissolved

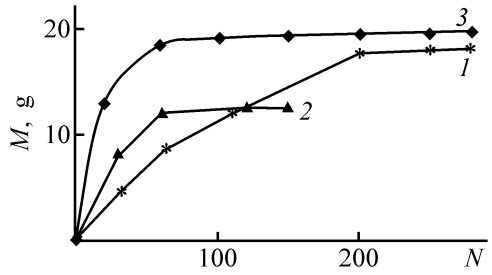

Fig. 1. Variation of the amount M of zinc in NOE on (*1*) NF and (*2*, *3*) MC support in the course of cycling of NTs-25 batteries. (N) Number of cycles; the same for Figs. 2–4. (*1*, *2*) amount of intercalated zinc, and (*3*) total amount of zinc intercalated and accumulated in the form of ZnO.

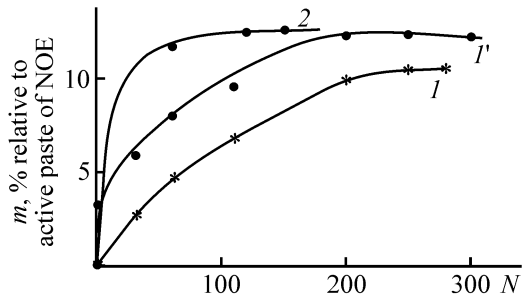

Fig. 2. Variation of the content m of zinc intercalated into NOE on (*1*, *1*') FN and (*2*) MC support in cycling of NTs-25 batteries. (*1*') Total amount of zinc, including that in the starting material (3.2%).

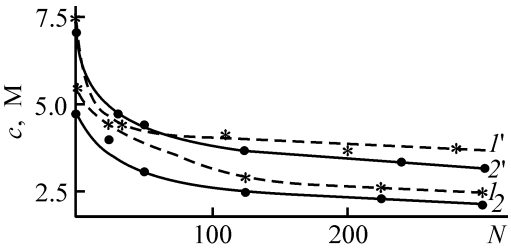

Fig. 3. Variation of the KOH concentration in the electrolyte in cycling of NTs-25 batteries with NOE on (*1*, *1*') FN and (*2*, *2*') MC support. (*1*, *2*) Charged battery; (*1*', *2*') discharged battery; the same for Fig. 4.

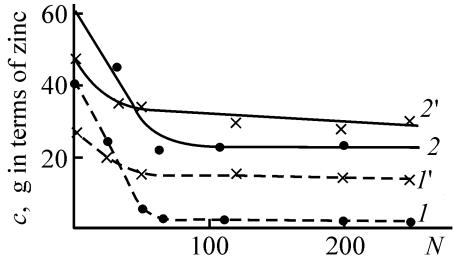

Fig. 4. Variation of the zincate ion concentration c in the electrolyte of NTs-25 batteries with NOE on (*1*, *1*') FN and (*2*, *2*') MC support.

in KOH, i.e., the accumulated zinc is incorporated into $Ni(OH)_2$.

The incorporation of zinc into the structure of $Ni(OH)_2$ in MC electrodes is accompanied by deposition of ZnO within the electrode pores in charging. In the course of discharges, when the concentration of hydroxide ions in the pores increases dramatically, zinc partly dissolves again [12]. In the process, part of zinc from the zincate complex formed is incorporated into the structure of $Ni(OH)_2$ (Fig. 1, curve *2*), and another part returns into the electrolyte. Since the forming zincate ions are present directly in the reaction zone, the incorporation of zinc into $Ni(OH)_2$ occurs at a higher rate than that into the FN-supported electrode, being complete after 60–70 cycles, i.e., simultaneously with the termination of ZnO deposition. At more intense incorporation of zinc into the NOE on an MC support, the amount of zinc accumulated, in the end, in this electrode is smaller than that in the NOE on an FN support. The total amount of zinc incorporated into the MC-supported electrode and accumulated in its pores in the form of ZnO is represented by curve *3* in Fig. 1.

In both the electrodes, the intercalation slows down as 10–12% zinc is accumulated (Fig. 2), i.e., an amount which can be incorporated into β-$Ni(OH)_2$ before the onset of its destruction through transformation into the α-form [10]. The variation of the zinc content (%) in the FN-supported NOE is represented by curves *1* and *1*' in Fig. 2. Curve *1* shows the content of zinc accumulated in the electrodes of the battery in the course of cycling, and curve *1*', the total amount of zinc, including that contained initially in the initial paste (3.2%). With this correction, the maximum percentage content of zinc in both types of electrodes is virtually the same.

The difference in the dynamics of zinc incorporation into the active paste of the electrodes considered does not affect the manner in which the KOH concentration in the electrolyte varies (Fig. 3). A considerable initial decrease in the concentration of OH^- ions is mainly due to transfer of carbonate ions from the electrodes into the electrolyte [13]. After this process is complete, the concentration of KOH in charged and discharged batteries stabilizes at about the same level. It is noteworthy that the decrease in the KOH concentration to the steady-state value occurs in parallel with a decrease in the rate of zinc incorporation into the FN-supported NOE.

However, the specific features of processes occurring in the FN-supported NOE studied are clearly manifested in the variation of the concentration of zincate ions (Fig. 4). After a battery is formed, the

Table 2. Variation of the amount of zinc intercalated into an NOE on FN and MC supports in cycling and its influence on the service life of NZ battery

NOE support	Cycles	c_{KOH}, M	Amount of intercalated zinc		Amount of zinc deposited in a cycle, g	Number of cycles	
			g	% relative to active paste of NOE		before the start of a decrease in capacity from C_{nom}	at a capacity decreased to $0.6C_{nom}$
FN	1	7.0	–	–	–	200	300–400
	Up to 60	4.2	8.6	5	0.14		
	60–200	3.9	18	10.6	0.06		
	200–300	3.7	18	10.8	~0		
MC	1	7.0	–	–	–	60–100	150–300
	Up to 60	4.0	12.6	12.0	0.21		
	60–200	3.7	12.6	12.1	~0		

zinc(II) concentration in the electrolyte of the charged battery is 40 g l^{-1}. Further cycling of the battery to 60th cycle is accompanied by a decrease in the concentration to a virtually zero value (2–3 g l^{-1}) at a rate of 0.6 g per cycle, with 0.14 g of Zn incorporated. After 200 cycles, 18 g of Zn is incorporated into the FN-supported NOE, i.e., approximately 0.09 g Zn per cycle, which corresponds to an average loss of zinc(II) of 0.9 g l^{-1} from the electrolyte (the electrolyte volume in the battery is 0.1 l, Table 2).

The deficit is compensated for by the diffusion flow from the zinc electrode into the NOE. With increasing number of cycles, the diffusion flux becomes greater owing to an increase in difference between the zincate ion concentrations in the zone of zinc electrode and in the zone of NOE. As a result, the average concentration of zinc in the electrolyte decreases.

After 60 cycles, when the Zn(II) concentration in the electrolyte of a charged battery decreases to the minimum value, a quasi-equilibrium state is attained at a constant diffusion flux. With the difference in the zincate ion concentrations in the zones of the negative and positive electrodes increased to the maximal value, the loss of zincate ions (in electrolyte volume), which disturbs equilibrium in the system operating in the reversible mode, is compensated for by the zinc electrode. In the process, the intercalation of zinc proceeds at a constant rate (about 0.06 g per cycle) during a long period (200 cycles) till termination of the process (Table 2).

The concentration of zincate ions in batteries with positive MC electrodes is higher than that in batteries with FN electrodes. Being controlled in the absence of diffusion by the very event of electrochemical intercalation, the concentration decreases in the initial cycles because of the deposition of zinc oxide within NOE in charging and only its partial return into the electrolyte in discharge (Fig. 4). For the same reason, the steady-state concentration in further cycling is higher than that in a battery with an NOE on an FN support. Part of zinc from $Zn(OH)_4^{2-}$ ions formed in pores of MC electrodes is incorporated into the NOE structure at a rate exceeding that of incorporation into an NOE on an FN support by, on the average, a factor of 2 (Table 2).

The correlation between the beginning of decrease in the charging capacity of an NZ battery and incorporation of 10–12% Zn into an NOE on an FN support is illustrated by Fig. 5. As noted in [8], this hinders the anode process at NOE and leads to a decrease in the charging capacity to the minimum value of $0.6C_{ther}$ in approximately 100 cycles [8].

In estimating the service life of the NZ battery under consideration, having an FN-supported NOE, account is taken of the possibility of making it longer (by about 50–100 cycles) by using an electrolyte

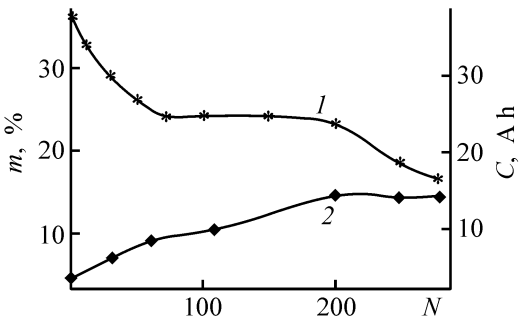

Fig. 5. Variation of (*1*) charge capacity *C* of NTs-25 battery and (*2*) the zinc amount in NOE with FN support in cycling. (*m*) Content of zinc in the active paste of NOE, including that in the initial $Ni(OH)_2$, and (*N*) number of cycles.

with lower initial KOH concentration (Table 2). It is also appropriate to use spherical $Ni(OH)_2$ containing the minimum amount of zinc, which can also prolong the service life by 50–100 cycles.

Thus, the service life of the battery under study, with an NOE on an FN support, may be as long as 400–500 cycles, provided that the influence of other known negative factors (such as growth of zinc dendrites and disintegration of separators) is suppressed by the known methods.

CONCLUSIONS

(1) The service life of a nickel–zinc battery is limited by a decrease in its capacity, associated with incorporation of zinc into the $Ni(OH)_2$ structure in amounts hindering the electrochemical processes in the battery. The number of cycles ensured by a battery without any decrease in capacity and the total service life depend on the conditions of transfer of zincate ions into the intercalation zone.

(2) In batteries with a nickel oxide electrode on a metal-ceramic support, the incorporation of zinc is facilitates by deposition of ZnO within the pores of the electrode operating in the inner diffusion mode and considerable changes in the KOH concentration in the pores. Therefore, the incorporation occurs at the maximum rate, which is limited solely by the electrochemical process itself.

(3) In batteries with a nickel oxide electrode on a foamed-nickel support, operating in the outer-diffusion mode, the rate of zinc incorporation is twice lower, since it is limited by transport of zincate ions into the reaction zone.

(4) With a nickel oxide electrode on a foamed-nickel support used instead of a metal-ceramic electrode, the service life of a nickel zinc battery can be prolonged from 150–300 cycles to 400–500 cycles, with stable capacity ensured during 300 cycles.

REFERENCES

1. Adler, T.C., McLarnon, F.R., and Cairns, E.J., *J. Electrochem. Soc.*, 1993, vol. 140, no. 2, pp. 289–294.
2. Alekseeva, M.A., Arkhangel'skaya, Z.P., Ivanova, R.P., *et al.*, *Zh. Prikl. Khim.*, 1999, vol. 72, no. 3, pp. 425–430.
3. Sharma, A.P., *J. Electrochem. Soc.*, 1986, vol. 133, no. 11, pp. 2215–2219.
4. Alekseeva, M.A., Arkhangel'skaya, Z.P., Ivanova, R.P., *et al.*, *Zh. Prikl. Khim.*, 1997, vol. 70, no. 12, pp. 1975–1980.
5. Jindra, J., *J. Power Sources*, 2000, vol. 88, pp. 202–205.
6. Pliverlich, R.F., McLarnon, F.R., and Cairns, E.J., *J. Appl. Electrochem.*, 1995, vol. 25, no. 5, pp. 433–440.
7. Alekseeva, M.A., Arkhangel'skaya, Z.P., Ivanova, R.P., *et al.*, *Zh. Prikl. Khim.*, 1998, vol. 71, no. 6, pp. 940–946.
8. Arkhangel'skaya, Z.P., Kas'yan, T.B., Loginova, M.M., and Raikhel'son, L.B., *Zh. Prikl. Khim.*, 2003, vol. 76, no. 6, pp. 935–959.
9. Pralong, V., Delahaye-Vidal, A., Beaudoin, B.J., *et al.*, *J. Electrochem. Soc.*, 2000, vol. 147, no. 4, pp. 1306–1313.
10. Ezhov, B.B., Egorova, S.A., and Golinova, I.M., *Zh. Prikl. Khim.*, 1992, vol. 65, no. 1, pp. 11–15.
11. Ezhov, B.B. and Kamnev, A.A., *Zh. Prikl. Khim.*, 1992, vol. 65, no. 3, pp. 544–550.
12. Arkhangel'skaya, Z.P., Ivanova, R.P., Kas'yan, T.B., and Raikhel'son, L.B., *Zh. Prikl. Khim.*, 2001, vol. 74, no. 4, pp. 589–592.
13. Arkhangel'skaya, Z.P., Ivanova, R.P., Kas'yan, T.B., and Raikhel'son, L.B., *Zh. Prikl. Khim.*, 2001, vol. 74, no. 9, pp. 1438–1442.

Russian Journal of Applied Chemistry, Vol. 76, No. 10, 2003, pp. 1611–1614. Translated from Zhurnal Prikladnoi Khimii, Vol. 76, No. 10, 2003, pp. 1653–1657.

APPLIED ELECTROCHEMISTRY AND CORROSION PROTECTION OF METALS

Lithium Salts of *N*,*N*'-Disubstituted Pentanesulfinamidines as Promising Additives for Lithium Power Sources

I. V. Koval', E. M. Shembel', O. V. Chervakov, T. G. Oleinik, and N. I. Globa

Ukrainian State Chemical Engineering University, Dnepropetrovsk, Ukraine
Enerl Inc., Florida, The Unites States

Received May 6, 2003

Abstract—A procedure for preparing new lithium salts with large organic anions, which can be used as additives to nonaqueous electrolytes of high-capacity chemical power sources, was developed. The electrochemical properties of the salts were studied.

Solutions of inorganic lithium salts in pure aprotic solvents or their mixtures are widely used as electrolytes in lithium power sources intended for different purposes.

Recently researchers' efforts have been focused on development of procedures for preparing new, cheap, nontoxic, moisture- and heat-resistant, and chemically and electrochemically stable salts readily soluble in aprotic solvents [1]. This is due to necessity for improvement of the performance of primary and, especially, secondary lithium-metal and lithium-ionic batteries.

The physicochemical properties of lithium organic salts depend on their chemical structure: the nature of the atom to which lithium is bonded and the type of this bond [2]; the nature and size of the anion; the degree of delocalization of the negative charge, which affects the stability of the salt anion [1].

The anion affects the properties of a nonaqueous electrolyte and of lithium power sources for the following reasons. In aprotic solvents, anions are solvated by dipole–dipole interactions which depend on mutual polarization of the anion and the solvent molecules. As the size of the organic anion increases, the polarization becomes stronger, thus enhancing the interaction between the anion and the solvent molecule [3].

Among the known lithium organic salts, lithium salt of bis(trifluoromethanesulfonyl)imide $LiN(SO_2CF_3)_2$ is the most promising as electrolyte for lithium power sources [4–15]. Liquid solutions of this salt have high electrical conductivity and are electrochemically stable up to 4.8 V (relative to lithium reference electrode) [2].

The lithium salt of bis(trifluoromethanesulfonyl)-imide and its structural analogues $LiN(SO_2CF_2CF_3)_2$, $LiN(SO_2C_4F_9)_2$, $LiN[(CF_3SO_2)(C_4F_9SO_2)]$ are also used for preparing polymeric electrolytes. The anion size in these lithium organic salts can strongly affect the structural and electrochemical properties of polymeric electrolytes derived from these salts [4].

Lithium salt of bis(trifluoromethanesulfonyl)imide $LiN(SO_2CF_3)_2$ was prepared from bis(trifluoromethanesulfonyl)imide, which is a relatively strong NH acid forming a stable N-anion owing to the presence of two electron-acceptor trifluoromethanesulfonyl groups. Bis(trifluoromethanesulfonyl)imide is not readily available, since substitution of chlorine atoms in the trichloromethyl groups with fluorine [16] requires special equipment and conditions that are difficult to provide in a common chemical laboratory. Alternative components of polymeric electrolytes are lithium salts of aromatic bis(sulfonyl)imides and, in particular, bis(*p*-nitrobenzenesulfonyl)imide $(p\text{-}NO_2C_6H_4SO_2)_2NH$, which is also a relatively strong acid, pK_a 3.2 (aqueous solution) [17].

The structure and acid properties of *N*,*N*'- bisarenesulfonyl substituted imides of iminosulfinic acids are similar to those of aromatic bis(sulfonyl)imides [18]. These compounds inhibit thermooxidative degradation of polymers [19], which is important for electrolytes derived from halogen-containing polymers (polyvinyl chloride, polyvinylidene chloride, polyvinylidene fluoride, etc.).

1070-4272/03/7610-1611 $25.00 © 2003 MAIK "Nauka/Interperiodica"

In this study, we prepared lithium salts of *N,N'*-bis-(benzenesulfonyl)pentanesulfinamidine and *N,N'*-bis-(*p*-toluenesulfonyl)pentanesulfinamidine and analyzed these salts as additives to liquid and polymeric electrolytes of lithium power sources.

EXPERIMENTAL

N,N'-Bis(benzenesulfonyl)pentanesulfinamidine and its lithium salt were prepared by the following procedures.

***N,N'*-Bis(benzenesulfonyl)pentanesulfinamidine (Ia).** To a solution of dipentyldisulfide (0.001 mol) in acetone (10 ml), sodium salt of *N*-chlorobenzenesulfonamide (0.0042 mol) was added. The mixture was shaken for 30 min, allowed to stand for 12–15 h to negative reaction for available chlorine, and filtered. The solvent was evaporated, and the residue was treated with 10% $NaHCO_3$ (20 ml) and filtered. Compound **Ia** (0.18 g, 43.9%) was isolated from acidified filtrate. The product was identified by melting point (mixing with an authentic sample) and by IR spectroscopy.

Compound **Ib** was prepared similarly in 45.4% yield.

Lithium salt of *N,N'*-bis(benzenesulfonyl)pentanesulfinamidine (IIa). To a solution of **Ia** (0.001 mol) in acetone (10 ml), equimolar amount of LiOH dissolved in a minimal volume of methanol or water was added. The reaction mixture was shaken for several minutes and filtered. The solvent was removed in air. The residue was dried to constant weight in a desiccator over $CaCl_2$. Compound **IIa** was obtained in the form of a colorless powder decomposing at 88–90°C.

Found (%): N 6.34

$C_{17}H_{21}N_2O_4S_3Li$.

Calculated (%): N 6.66.

Salt **IIb** was prepared similarly in quantitative yield in the form of a colorless powder decomposing at 147–150°C.

Found (%): N 6.12

$C_{19}H_{25}N_2O_4S_3Li$.

Calculated (%): N 6.25.

The IR spectra (KBr pellets) were recorded on a UR-20 spectrophotometer.

The dissociation constant pK_a of **IIa** in a 1% methanol solution was determined by potentiometric titration at 24 ± 2°C on a pH-121 millivoltmeter with an automated titration unit. Glass ESP/41-G-04 electrode served as working electrode, and a silver chloride electrode, as reference electrode. A 0.1 M solution of **Ia** was titrated with 0.1 M KOH.

The electrical conductivity of these salts in nonaqueous electrolytes was measured and the range of electrochemical stability of these solutions was determined. The behavior of the modified electrolytes in model secondary lithium power sources Li–MnO_2 and Li–V_6O_{13} was studied.

The electrical conductivity of solution of the lithium salts in aprotic organic solvents was measured by impedance spectroscopy in a temperature-controlled glass electrochemical cell with parallel platinum electrodes. The measurements were performed at a working frequency of 80 kHz and temperature of 24 ± 2°C. The electrolyte conductivity χ (S cm^{-1}) was calculated by the equation

$$\chi = KG,$$

where G is the conductance of the electrolyte in the cell (S), and K is the cell constant determined using 0.01 M aqueous solution of KCl (cm^{-1}).

The range of electrochemical stability of the lithium salts was determined by cyclic voltammetry under potentiodynamic conditions. The experiment was performed under an argon atmosphere in a three-electrode Teflon cell of disc design, containing working, reference, and auxiliary electrodes. The reference and auxiliary electrodes were made of metallic lithium. A platinum plate with surface area of 8.0×10^{-3} cm^2 was used as working electrode. The electrode potential was set with a PI-50-1.1 potentiostat and a PR-8 programmer. The sweep rate was 20 mV s^{-1}. The cyclovoltammograms were recorded on a PDA-1 *XY*-recorder in the potential range from 1.1 to 4.6 V.

Polymeric electrolytes (PEs) were prepared on glass supports from THF solutions containing a polymer, lithium salt, and additive (synthesized lithium salt with organic cation). The PE films were dried for 24 h at room temperature and for 48 h in a vacuum at 45°C.

Charging–discharge cycling of the model lithium power sources with polymeric electrolytes containing the synthesized lithium organic salts was performed in the geometry of 2325 disc battery. The electrode structure was obtained by layer-by-layer application of the polymeric electrolyte between lithium anode and cathode. The thickness of the polymeric electrolyte and the lithium anode was 0.03 and 0.8 mm, respec-

tively. The cathode was prepared from a mixture of chemically synthesized MnO_2 or V_6O_{13} (80 wt %), carbon (5 wt %), graphite (5 wt %), and F-4D fluoroplastic binder (10 wt %).

N,*N*'-Bis(benzenesulfonyl)pentanesulfinamidines were obtained using the known modified procedure [20]. Dipentyl disulfide was oxidatively iminated with sodium *N*-chloroarenesulfonamide in acetone by the reaction

$$(C_5H_{11}S)_2 + 4ArSO_2NNaCl \xrightarrow[-4NaCl]{} C_5H_{11}-S(=NSO_2-Ar)-NHSO_2-Ar$$

Ia, **Ib**

Compounds **Ia** and **Ib** were indetified by melting points (mixing with known samples), by determining the neutralization equivalent, and by IR spectroscopy. These compounds are relatively strong NH acids (pK_a of **Ia** is 2.91), which can be titrated with an alkali in alcoholic solution in the presence of Methyl Red as indicator. The equivalent weight determined by titration agrees with the calculated data. The IR spectra of Ia and Ib contain the bands of stretching vibrations of the SO_2 (1160–1158 and 1310–1335 cm^{-1}) S=N (753–765 cm^{-1}), CH_3 (2925–2950 cm^{-1}), CH_2 (2841–2850 cm^{-1}), and CH (ar.) (1485–1533 cm^{-1}) groups. Two strong bands in the range 3250–3360 cm^{-1} are assigned to N–H stretching vibrations. This type of absorption by the N–H bonds is due to prototropic tautomerism in the N–S–N triad, which has been found previously in *N*,*N*'-bis(arenesulfonyl)sulfinamidines [18].

The lithium salts were prepared by neutralization of appropriate pentanesulfinamidines with equimolar amounts of LiOH in acetone–methanol–water mixture [21]:

$$\textbf{Ia}, \textbf{Ib} + LiOH \xrightarrow[-H_2O]{} \left[C_5H_{11}-S(=NSO_2-Ar)-NSO_2-Ar\right]^- Li^+$$

IIa, **IIb**

where Ar = Ph (**a**), *p*-MeC_6H_4 (**b**).

The solvents were evaporated in air, and the residue was dried in a desiccator over $CaCl_2$. **IIa** and **IIb** were obtained in the form of colorless hygroscopic powders or oily substances decomposing in a wide temperature range.

The composition and structure of salts **IIa** and **IIb** was confirmed by elemental analysis and IR spectroscopy. The IR spectra of these compounds contain the bands of stretching vibrations of the SO_2 (1160–1165 and 1310–1330 cm^{-1}) and S=N (1030–1040 cm^{-1}) groups and bands of other groups. The NH bands are absent.

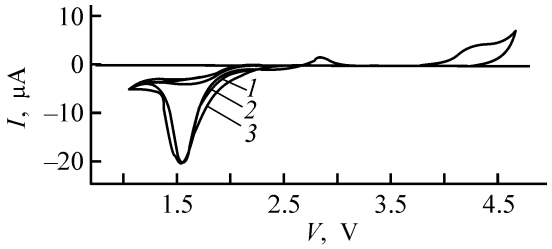

Fig. 1. Cyclic voltammogram of 0.5 M solution of lithium salt **IIa** in PC. Sweep rate 20 mV s^{-1} (*I*) Current and (*V*) voltage.

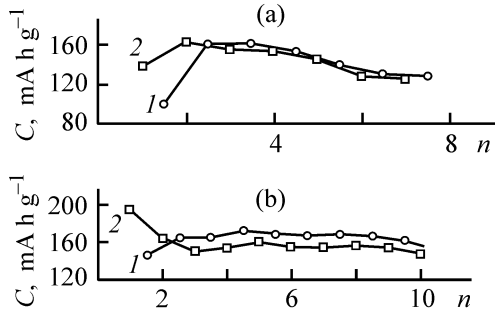

Fig. 2. Specific capacity *C* of Li/PE/MnO_2 system in a 2325 battery vs. the number of charging–discharge cycles. PE composition: (a) c-PVC : PC : $LiCF_3SO_3$ = 19.2 : 75.1 : 5.7 and (b) c-PVC : PC : $LiCF_3SO_3$: **IIa** = 18.1 : 72.5 : 3.1 : 6.3. (*n*) Cycle no. $I_{charge} = I_{discharge}$ = 100 μA.

Salts **IIa** and **IIb** are readily soluble in aprotic solvents.

The conductivity of a 0.24 M solution of **IIa** in dimethylformamide and 0.5 M solution of **IIb** in propylene carbonate (PC) is 6.0×10^{-3} and 5.2×10^{-4} S cm^{-1}, respectively.

Cyclic voltammograms of a 0.5 M solution of **IIa** in PC, recorded on a platinum electrode under potentiodynamic conditions, are shown in Fig. 1. As seen from Fig. 1, this compound is stable under conditions of repeated potential sweeping in the range 1.1–4.6 V.

Since this additive is electrochemically stable in a wide potential range, it can be used in lithium power sources with different discharge voltages: 3.8 (lithium–ionic systems), 2.8 (lithium–metal secondary systems with oxide cathode), and 1.8 V (lithium–metallic systems with sulfide cathode).

We used salt **IIa** as a modifying additive to PE based on chlorinated polyvinyl chloride (c-PVC) or vinylidene fluoride–hexafluoropropylene copolymer.

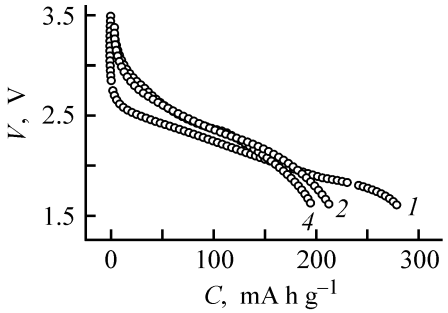

Fig. 3. Discharge curve of the Li/PE/V_6O_{13} system. Polymeric electrolyte based on microporous vinylidene fluoride–hexafluoropropylene copolymer modified with lithium salt **IIa**. I_{charge} = 120, $I_{discharge}$ = 290 μA. (*V*) Voltage, and (*C*) specific capacity. *Digits at the curves* correspond to the cycle numbers.

Power sources with plasticized and microporous PEs modified with lithium salt of *N,N'*-bis(benzenesulfonyl)pentanesulfinamidine **IIa** have good charging–discharge parameters and are stable under conditions of repeated cycling of the Li–MnO_2 (Figs. 2a, 2b) and Li–V_6O_{13} (Fig. 3) systems. It should be noted that addition of **IIa** makes longer the shelf life of the Li-V_6O_{13} system. The discharge curves of a model lithium power source with a V_6O_{13} cathode, stored for 1 month, are shown in Fig. 3.

CONCLUSIONS

(1) Lithium salts of *N,N'*-bis(benzenesulfonyl)pentanesulfinamidine and *N,N'*-bis(*p*-tolyenesulfonyl) pentanesulfinamidine were synthesized.

(2) The electrical conductivity of nonaqueous solutions of these salts is relatively high even at low salt concentration . The conductivity of a 0.24 M solution of **IIa** in dimethylformamide and 0.5 M solution of **IIb** in propylene carbonate is 6.0×10^{-3} and 5.2×10^{-4} S cm^{-1}, respectively.

(3) Solutions of the lithium salts in propylene carbonate are electrochemically stable at potentials of 1.1 to 4.6 V relative to lithium reference electrode.

(4) The lithium salt of *N,N'*-disubstitued pentanesulfinamidine can be used as additive to polymeric electrolytes to stabilize the discharge properties and decrease the self-discharge of lithium power sources.

ACKNOWLEDGMENTS

The authors are grateful to O.V. Kolomoets and I.M. Maksyuta for studying the conductivity and electrochemical stability of the electrolytes.

REFERENCES

1. Barthel, J., Buestrich, R., Gores, H.J., *et al.*, *J. Electrochem. Soc.*, 1997, vol. 144, no. 11, pp. 3866–3870.
2. Kita, F. Sakata, H., Kawakami, A., *et al.*, Abstracts of Papers, *1999 Joint Int. Meet.*, Honolulu, Hawaii, October 17–22, 1999, abstract no. 341.
3. Parker, A.J., *Usp. Khim.*, 1963, vol. 32, no. 10, pp. 1270–1295.
4. Passerini, S., Appetecchi, G.B., Villano, P., *et al.*, Abstrcats of Papers, *2001 Joint Int. Meet.*, San Francisco (USA), September 2–7, 2001, abstract no. 94.
5. Saito, Y., Capiglia, C., Yamamoto, H., and Mastarelli, P., *J. Electrochem. Soc.*, 2000, vol. 145, no. 5, pp. 1645–1650.
6. Krause, L.I., Lamanna, W., Summerfield, J., *et al.*, *J. Power Sources*, 1997, vol. 68, pp. 320–324.
7. Abraham, K.M. and Jiang, Z., *J. Electrochem. Soc.*, 1997, vol. 144, no. 6, pp. L136–L138.
8. Xia, Y., Tatsumi, K., Fujieda, T., *et al.*, *J. Electrochem. Soc.*, 2000, vol. 147, no. 6, pp. 2050–2056.
9. Yamada, O., Ishikawa, M., and Morita, M., *Electrochim. Acta*, 2000, vol. 45, pp. 2197–2201.
10. Aihara, Y., Hayamizu, K., Sugimoto, K., *et al.*, *J. Power Sources*, 2001, vols. 97–98, pp. 628–631.
11. Itoh, T., Hirata, N., Wen, Z., *et al.*, *J. Power Sources*, 2001, vols. 97–98, pp. 637–640.
12. Li, Q., Takeda, Y., Imanish, N., *et al.*, *J. Power Sources*, 2001, vols. 97–98, pp. 795–797.
13. Matsuda, Y. and Takenutsu, T., Abstract of Papers, *10 Int. Meet. on Lithium Batteries*, Como (Italy), May 28–June 2, 2000, abstract no. 288.
14. Lee, W.C., Joachin, H.J., and Prakash, J., Abstracts of Papers, *198th Meet. of the Electrochemical Society*, Phoenix (USA), October 22–27, 2000, abstract no. 143.
15. Ogumi, Z., Ohkubo, T., Abe, T., *et al.*, Abstracts of Papers, *198th Meeting of the Electrochemical Society*, Phoenix (USA), October 22–27, 2000, abstract no. 159.
16. Koval', I.V., *Usp. Khim.*, 1991, vol. 60, no. 8, pp. 1645–1679.
17. Reibel, L. Bayound, S., Baudri, P., and Majastre, H., *Electrochim. Acta*, 1998, vol. 43, nos. 10–11, pp. 1171–1176
18. Koval', I.V., *Sulfur Rep.*, 1993, vol. 14, pp. 149–221.
19. Koval', I.V., Oleinik, T.G., Basanets, K.S., *et al.*, Abstracts of Papers, *Nauchno-teknicheskaya konferentsiya "Perspektivy razvitiya promyshlennosti plastmass v Ukraine"* (Scientific and Technical Conf. "Prospects of Development of Plastic Production Industry in Ukraine"), Lviv, September 12–17, 1995, p. 63.
20. Koval', I.V., Tarasenko, A.I., and Kremlev, M.M., *Zh. Org. Khim.*, 1986, vol. 22, no. 2, pp. 410–415.
21. US Patent Appl. 10/122,788.

Russian Journal of Applied Chemistry, Vol. 76, No. 10, 2003, pp. 1615–1619. Translated from Zhurnal Prikladnoi Khimii, Vol. 76, No. 10, 2003, pp. 1658–1662.

CATALYSIS

Direct Single-Stage Conversion of Synthesis Gas to Dimethoxymethane: Influence of the Sequence of Metal Introduction into Cu, Pd-Zeolite Catalysts on the Degree of Cu and Pd Reduction and Catalyst Acidity

N. V. Vlasenko and Yu. N. Kochkin

Pisarzhevskii Institute of Physical Chemistry, National Academy of Sciences of the Ukraine, Kiev, Ukraine

Received March 25, 2003

Abstract—The influence of the sequence of Cu and Pd introduction into zeolite matrice when preparing Cu, Pd-zeolite catalysts on their acidity and degree of metal reduction was studied. The mutual influence of Cu and Pd on their reducibility was analyzed. The selectivity of Cu, Pd-zeolite catalysts in conversion of synthesis gas to different products was elucidated.

Dimethoxymethane (DMM) is a promising additive to diesel oil [1]. It is known [2] that this compound can be prepared in high yield by condensation of methanol with formaldehyde at 150-180°C and a pressure of 1 MPa. Another promising route to this product is the single-stage conversion of synthesis gas. Thermodynamic calculations showed that this route is feasible under fairly mild conditions (180–220°C, pressure above 0.5 MPa). In this process, Pd, Cu-containing zeolites can be used as catalysts. Under these conditions, DMM can be prepared in a single stage combining three reactions: hydrogenation of synthesis gas to methanol, dehydrogenation of methanol to formaldehyde, and DMM formation by condensation of methanol with formaldehyde.

It is known [4, 5] that, in preparing supported catalysts, the most uniform distribution of metals on the support surface is achieved with ion-exchange supports by ion-exchange sorption of metals, e.g., from aqueous solution of their ammine complexes [4, 5]. To obtain catalytically active surface, a metal-containing precursor is calcined and then reduced with hydrogen [6, 7]. In this treatment, the support surface is dehydroxylated and deammonated, and the reduced metals can be oxidized by reaction with the support.

A catalyst prepared by this technique is a polyfunctional system containing catalytically active metallic and free acid sites. Owing to the mutual influence of these sites, the metal atoms can modify the acid sites and, in turn, the acid sites can affect the valence state of the metal [4]. For reduced catalysts containing several metals, their chemical composition is controlled not only by interaction of the metals with the support surface, but also by interactions between different metals. Thus, the features of physicochemical processes occurring during catalyst preparation are responsible for the state of the catalyst surface, and, ultimately, for the activity of the catalytic sites. The mutual influence of copper and palladium has been mainly studied for catalysts prepared by simultaneous application of these metals on a support surface [8, 9]. In these studies, due attention was not given to the influence of the sequence of the metal application. However, it is known that this factor can affect substantially the catalyst properties [10].

In this study, we analyzed how the sequence of introduction of Cu and Pd in a zeolite catalyst designed for single-stage conversion of synthesis gas to dimethoxymethane affects both the catalyst acidity and the degree of reduction of the metals.

EXPERIMENTAL

When preparing Cu, Pd-zeolite catalysts, we used Ps(60) and Ps(200) Pentasil zeolites as supports. The Ps(60) and Ps(200) zeolites have the $SiO_2 : Al_2O_3$ ratio of 60 an 200 and the cation-exchange capacity (CEC) of 0.20 and 0.57 mg-equiv g^{-1}, respectively.

1070-4272/03/7610-1615 $25.00 © 2003 MAIK "Nauka/Interperiodica"

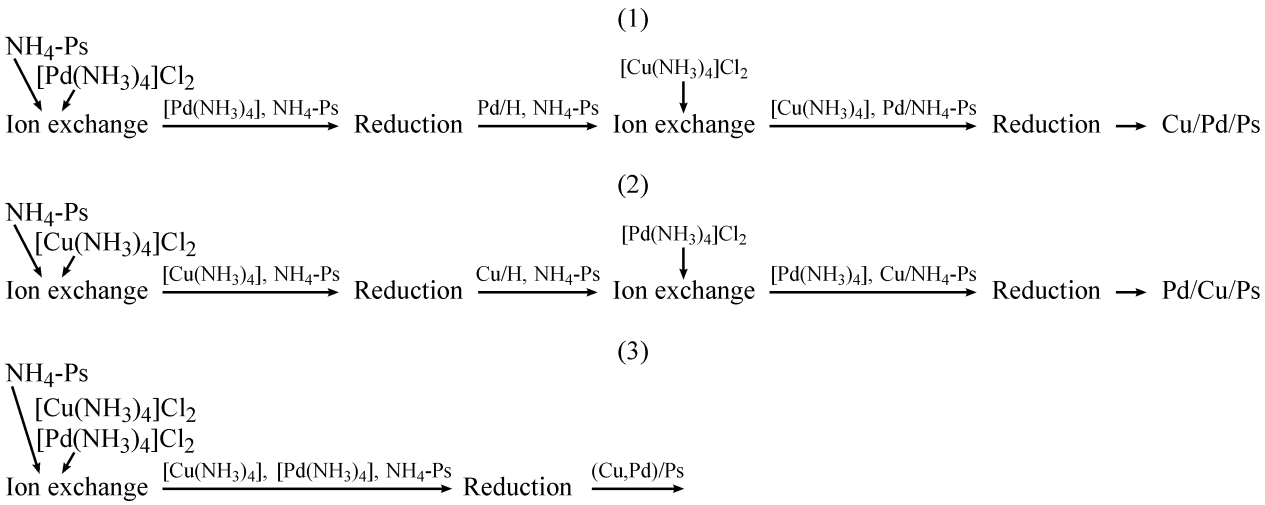

Fig. 1. Scheme of preparing Cu, Pd-containing Pentasils.

These Pentasils were converted to the NH_4 form and then modified with Pd and Cu by ion exchange with aqueous $Pd(NH_3)_4Cl_2$ and $Cu(NH_3)_4Cl_2$. This procedure was carried out in the course of 3 days, which was followed by washing the metal-containing Pentasil to remove Cl^- and drying at 100–110°C for 6 h. The resulting catalyst precursor was reduced with hydrogen at its flow rate of 50 ml min^{-1} and temperature of 300°C for 5 h.

Figure 1 shows the sequence of procedures in preparing Cu, Pd-containing Pentasils. The catalyst designations used in this study reflect the sequence of procedures used in their preparation. For example, the designation Pd/Cu/Ps(200) means that the sequence of procedures was as follows: copper introduction, copper reduction, palladium introduction, and palladium reduction. The designation (Pd,Cu)/Ps(200) means that both metals were introduced simultaneously and then the Pd, Cu-containing Pentasil was reduced with hydrogen. Along with bimetallic catalysts, we also prepared those containing copper or palladium only.

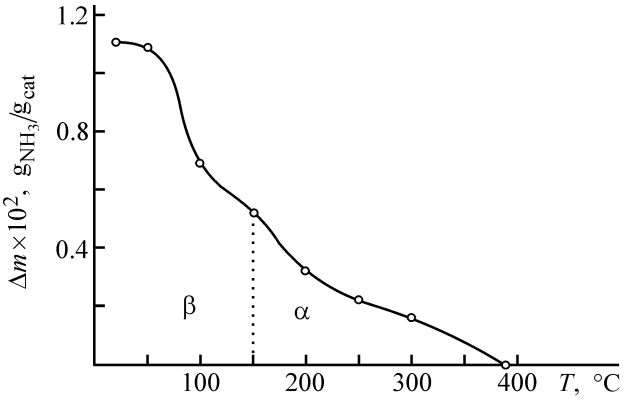

Fig. 2. Amount Δm of ammonia sorbed on a sample of the starting Pentasil Ps(200) vs. temperature T. Ranges corresponding to acid centers: (β) low-temperature and (α) high-temperature.

All the catalyst samples were prepared separately. Because the procedure used does not ensure an absolutely reproducible metal content, the catalyst samples were characterized by the degree of metal reduction [percentage of reduced metal relative to its total content in the catalyst).

The acidity of the metal-containing catalysts based on Pentasil was determined by ammonia sorption Δm (g_{NH_3}/g_{cat}) at different temperatures [11]. The content of acid centers in the catalysts was calculated assuming that one acid center sorbs one ammonia molecule [12].

The metal content in the catalysts was determined by the standard technique [13, 14]. The content of oxidized and reduced forms of metals was determined by difference in their leaching with aqueous inorganic acids. In order to elucidate where the metals are localized in the zeolite matrice, we studied how introduction of the metal into the zeolite affects the distribution of the acid sites. To determine the total content of the acid ion-exchange sites in the zeolite, the initial Pentasil sample in the NH_4^+ form was converted to its acid form by heating at 500°C for 3 h. In these experiments we used Pentasil Ps(200).

Our data on the total concentration of acid centers and the concentration of low(β)- and high-temperature (α) centers are listed in Table 1. The temperature ranges corresponding to these acid centers and the concentrations of low (β)- and (α) high-temperature centers were determined from the curves of NH_3 thermal desorption from H-Pentasil (Fig. 2). These curves

Table 1. Acid characteristics of metal-containing zeolite catalysts based on Pentasil Ps(200)

Sample	Acid center concentration, $n \times 10^{-20}$			T_d,* °C
	c_Σ (>50°C)	c_β (50–150°C)	c_α (>150°C)	
H-Ps(200):				
initial	3.8	2.0	1.8	390
reduced	3.8	2.3	1.5	410
Pd/Ps(200)	3.9	2.6	1.3	285
Cu/Ps(200)	3.3	2.3	1.0	262
Cu/Pd/Ps(200)	3.2	2.1	1.1	190
Pd/Cu/Ps(200)	3.5	2.7	0.8	220
(Pd,Cu)/Ps(200)	3.4	3.0	0.4	200

* (T_d) Temperature of complete desorption of ammonia.

Table 2. Content and degree of reduction (α) of Pd and Cu in Pd, Cu-Pentasils

Sample	Pd content, %			Cu content, %			α, %	
	Pd^{n+}	Pd^0	Pd_Σ	Cu^{n+}	Cu^0	Cu_Σ	Pd	Cu
Pd/Ps(200)	0.70	0.80	1.50	–	–	–	53.33	–
Cu/Ps(200)	–	–	–	0.30	0.02	0.32	–	6.25
Cu/Pd/Ps(200)	0.32	0.17	0.49	0.38	0.08	0.46	34.69	17.39
Pd/Cu/Ps(200)	0.39	0.24	0.63	0.36	0.06	0.42	38.10	14.29
(Pd,Cu)/Ps(200)	0.55	0.22	0.77	0.70	0.09	0.79	28.57	11.39
Pd/Ps(60)	0.30	0.70	1.00	–	–	–	70.00	–
Cu/Ps(60)	–	–	–	0.52	0.03	0.55	–	5.45
Cu/Pd/Ps(60)	0.58	0.43	1.01	0.94	0.12	1.06	42.57	11.32
Pd/Cu/Ps(60)	0.66	0.88	1.54	0.47	0.25	0.72	57.14	34.72
(Pd,Cu)/Ps(60)	0.18	0.44	0.62	0.33	0.07	0.40	70.97	17.50

have two separate temperature ranges 50–150 and >150°C corresponding to desorption of ammonia from two different types of acid centers.

Table 1 shows that introduction of metals into a Pentasil, as a rule, decreases the total content of high-temperature acid centers α. This data are consistent with the known fact [15] that, in cation exchange, cations are primarily sorbed on the strongest acid centers. In our experiments, the prevailing sorption of metals on strong acid centers is indicated by the fact that the complete desorption of ammonia from metal-containing zeolites (especially bimetallic catalysts) occurs at lower temperature than desorption from the starting H-Pentasil (Table 1).

We found that the content of the β-centers in the metal-containing Pentasils exceeds that in the starting H-Pentasil. We suggest that, in the course of ion exchange, the sorption of a metal on the α-centers gives rise to new β-centers. This process is similar to the known phenomenon of partial conversion of α centers into β centers in thermal treatment of the starting Pentasil in a hydrogen atmosphere (Table 1). The relative increase in the content of the β-centers on thermal treatment is, however, less pronounced than that upon introduction of metals.

The amount of reduced (M^0) and oxidized (M^{n+}) metals present in the reduced metal-containing catalysts based on Ps(60) and Ps(200) was determined by chemical analysis. This analysis showed that, in all the cases, the degree of reduction of palladium exceeds that of copper (Table 2), and the degree of reduction of both metals grows with increasing aluminosilicate ratio of the catalyst. This trend is more pronounced for palladium than for copper.

We found that the degree of metal reduction in the catalysts decreases in the following order. For Pd: Pd > Pd/Cu > Cu/Pd > (Pd,Cu) [Ps(200)], (Pd,Cu) ≈ Pd > Pd/Cu > Cu/Pd [Ps(60)], and for Cu: Cu/Pd > Pd/Cu > (Pd,Cu) > Cu [Ps(200)]; Pd/Cu > (Pd,Cu) > Cu/Pd > Cu [Ps(60)].

These series for both Pd and Cu are generally similar, except for the position of the (Pd,Cu) cat-

alyst for the Pd series and that of the Cu/Pd catalyst for the Cu series. We found that the Cu content in the (Pd,Cu) supported by Ps(200) and in the Cu/Pd catalyst supported by Ps(60) is 112 and 115%, respectively, of the IEC of the corresponding zeolites. We believe that, under these conditions, zeolite is completely coated with copper, which hinders the palladium reduction. These processes affect the ranking of (Pd,Cu)/Ps(200) and Cu/PdPs(60) catalysts. If the catalysts with superequivalent copper content are disregarded, the metal reducibility must decrease (irrespective of the Pentasil type) in the following order. For Pd: (Pd/Cu) ≈ Pd > Pd/Cu > Cu/Pd and for Cu: Cu/Pd > Pd/Cu > (Pd,Cu) > Cu.

These revised sequences reflect the mutual influence of palladium and copper on their reducibility in preparing the bimetallic catalysts. It should be noted that, in preparing catalysts containing only palladium (Pd/Ps) or copper (Cu/Ps), palladium is completely reduced whereas copper is reduced to the minimun extent. For bimetallic catalysts, copper binds palladium and palladium promotes the copper reduction owing to the mutual influence of the metals.

We believe that the mutual influence of palladium and copper is associated with the difference in their interaction with hydrogen. It is known that palladium dissolves hydrogen by the mechanism of its atomization and irreversible chemisorption of hydrogen atoms. It is possible that activated hydrogen reduces copper to metal in Pd, Cu catalysts. In contrast to palladium, metallic copper sorbs hydrogen reversibly. It is known [16] that introduction of copper into a Pd-containing catalyst decreases its sorption power for hydrogen, which, in turn, makes lower the degree of palladium reduction. The data reported in [7] show that oxidized forms of palladium and copper are stabilized by the formation of a bimetallic compound in which bulkier palladium atoms are incorporated into the copper crystal lattice.

Our preliminary studies on catalytic features of Pd, Cu-zeolite catalysts showed that all the catalytic systems under consideration actively catalyze conversion of synthesis gas to methanol, dimethyl ether, dimethoxymethane, and methyl formate under fairly mild conditions (120–225°C, 1 MPa). The ratio between different products is strongly dependent on the catalyst type.

In conversion of synthesis gas, the primary product is methanol [3]. We found that, with the use of catalysts with high degree of palladium reduction [Pd/Cu/Ps(200), Pd/Cu/Ps(60)], this process stops after CO conversion to methanol, i.e., these catalysts are selective for methanol synthesis (up to 90%).

At low temperatures (<160–180°C), methanol is mainly converted to dimethyl ether. The selectivity of the catalysts for this product increases with decreasing degree of copper reduction, suggesting that, in this case, oxidized copper is the catalytic species.

Dimethoxymethane is formed at 180°C and higher temperatures along with methyl formate as a by-product. The selectivity of catalysts for DMM synthesis increases in the order Cu/Pd/Ps(60) < Pd/Cu/Ps(60) < Pd/Cu/Ps(200), (Pd,Cu)Ps(200). The selectivity of Pd/Cu/Ps(200) and (Pd/Cu)/Ps(200) catalysts is 12%. The Cu/Pd/Ps(200) and (Pd,Cu)Ps(60) catalysts are inert in DMM synthesis. Our experiments showed that Pentasil (Ps200) modified with Pd and Cu by their successive (first Cu, then Pd) or simultaneous introduction into the zeolite matrice is the most promising catalyst for single-stage production of DMM from synthesis gas.

CONCLUSIONS

(1) When preparing Pd, Cu-containing zeolite catalysts, their chemical composition, acidity, and catalytic activity are mainly controlled by the sequence of introducing the metals into the zeolite matrice.

(2) Introduction of Pd and Cu into the zeolite matrice makes the concentration of strong acid centers lower and that of concentration of weak acid centers higher. Simultaneous introduction of Pd and Cu decreases the content of strong acid centers to the greatest extent, as also does introduction of Cu before Pd or introduction of Cu only.

(3) The valence state of Pd and Cu in Pd, Cu zeolite catalysts is controlled by the mutual influence of these metals; palladium is mainly converted to metal, whereas Cu is predominantly preserved in the oxidized form. For bimetallic catalysts, copper hinders palladium reduction, whereas palladium promotes copper reduction.

ACKNOWLEDGMENTS

The authors are grateful to E.E. Knyazeva for the submitted Pentasil samples.

REFERENCES

1. Vertin, K.D., Ohi, J.M., Naegeli, D.W., *et al.*, in *Int. Spring Fuels & Lubricants Meet. & Exposition*, Dearborn, Michigan (USA), May 3–6, 1999, pp. 1–15.

2. Pavlenko, N.V., Kochkin, Yu.N., Vlasenko, N.V., *et al.*, *Teor. Exp. Khim.*, 2000, vol. 36, no. 2, pp. 111–115.
3. Vlasenko, N.V., Kochkin, Yu.N., and Pavlenko, N.V., *Ukr. Khim. Zh.*, 2002, vol. 68, no. 9, pp. 21–26.
4. Canizares, P., de Lucas, A., Dorado, F., *et al.*, *Appl. Catal. A, Gen.*, 1988, vol. 169, no. 1, pp. 137–150.
5. Drozdova, L., Novakova, J., Schulz-Ekloff, G., and Jaeger, N.I., *Micropor. and Mesopor. Mater.*, 1999, vol. 28, no. 3, pp. 395–403.
6. Gates, B.C., *Chem. Rev.*, 1995, vol. 95, pp. 511–522.
7. Pinno, F., *Catal. Today*, 1998, vol. 41, pp. 129–137.
8. Edelmann, A., Schieber, W., Vinek, H., and Jentys, A., *Catal. Lett.*, 2000, vol. 69, nos. 1–2, pp. 11–16.
9. Nosova, L.V., Zavoiskii, V.I., Kalinkin, A.V., *et al.*, *Kinet. Katal.*, 1995, vol. 36, no. 3, pp. 362–369.
10. Batista, J., Pintar, A., and Ceh, M., *Catal. Lett.*, 1997, vol. 43, nos. 1–2, pp. 79–84.
11. Tanabe, K., *Tverdye kisloty i osnovaniya* (Solid Acids and Bases), Moscow: Mir, 1973.
12. Kapustin, G.I., Kustov, l.M., and Glonti, G.O., *Kinet. Katal.*, 1984, vol. 25, no. 5, pp. 1129–1134.
13. *GOST* (State Standard) *4388–72: Drinking Water*.
14. Ginzburg, S.I. and Gladyshevskaya, K.A., *Rukovodstvo po khimicheskomu analizu platinovykh metallov i zolota* (Manual on Chemical Analysis of Platinum Metals and Gold), Moscow: Nauka, 1965.
15. Topchieva, K.V., *Primenenie tseolitov v katalize* (Application of Zeolites in Catalysis), Boreskov, G.K. and Minachev, Kh.M., Eds., Novosibirsk: Nauka, 1977, pp. 21–41.
16. Galy, L. and Vannice, M.A., *Appl. Catal. A, Gen.*, 1991, vol. 69, no. 2, pp. 291–304.

Russian Journal of Applied Chemistry, Vol. 76, No. 10, 2003, pp. 1620–1625. Translated from Zhurnal Prikladnoi Khimii, Vol. 76, No. 10, 2003, pp. 1663–1668.

MACROMOLECULAR CHEMISTRY AND POLYMERIC MATERIALS

Complexation in Water-Soluble Systems Poly-*N*-vinylpyrrolidone–Fullerene C_{60}

O. V. Ratnikova, E. Yu. Melenevskaya, M. V. Mokeev, and V. N. Zgonnik

Institute of Macromolecular Compounds, Russian Academy of Sciences, St. Petersburg, Russia

Received July 8, 2003

Abstract—Complexes of fullerene C_{60} with poly-*N*-vinylpyrrolidone were prepared by various procedures in the presence of additional agents in solution (systems C_{60}–poly-*N*-vinylpyrrolidone and ternary system C_{60}–tetraphenylporphyrin–poly-*N*-vinylpyrrolidone) and in the solid phase (C_{60}–polyvinylpyrrolidone and C_{60}–KBr–poly-*N*-vinylpyrrolidone). Formation of a donor–acceptor bond in the system C_{60}–poly-*N*-vinylpyrrolidone was studied by ^{13}C NMR. The conditions under which the ternary complex C_{60}–tetraphenylporphyrin–poly-*N*-vinylpyrrolidone with fullerene content varied from 1 to 5 wt % can be obtained were found.

One of research lines in chemistry of fullerenes is preparation of their water-soluble derivatives. This problem has attracted deep interest after discovery of the biological activity of C_{60} [1, 2]. However, these studies are complicated by the fact that fullerene is virtually insoluble in water.

Various methods for C_{60} conversion into the water-soluble state, including covalent addition of hydrophilic groups to its molecule, have been suggested [3, 4]. It was found that, for efficient use of fullerene, it is necessary to obtain its water-soluble derivatives in which C_{60} occurs in the form of a monomer and distortion of its structure is at a minimum. In fullerene derivatives with covalent bonding, the structural distortion is too strong.

In this context, it is of interest to prepare such water-soluble derivatives of C_{60} in which fullerene is retained by nonvalent interactions. One way to produce water-soluble systems is complexation of C_{60} with poly-*N*-vinylpyrrolidone (PVP).

The interactions in this system are poorly understood, and the content of fullerene in complexes with PVP can be only varied in a narrow range (up to 1%).

The goal of this study was to prepare PVP-based water-soluble fullerene-containing systems with varied content of fullerene, optimize conditions for preparing systems with various fullerene concentrations, and examine the influence of the state of the polymer and fullerene on the complex composition.

EXPERIMENTAL

We used fullerene C_{60} produced by the Fullerene Technologies (Russia) with 99.5% content of the main substance, *meso*-tetraphenylporphyrin produced by Sigma (USA) with 99.5% purity, and commercial PVP with molecular weights of 8000 and 12 000, containing no high-molecular-weight fractions.

Complexes C_{60}–PVP were synthesized from a solution by the procedure described in [6] and also by a solid-phase reaction involving dispersion of powdered C_{60} and PVP in a vacuum (10^{-6} mm Hg). For solid-phase experiments, PVP was initially dried in a vacuum at 140°C, and then fullerene was added under the conditions of a vacuum system. In some runs, KBr was also added simultaneously with C_{60}. To recover the water-soluble fraction, the product was dissolved in water and a filtered solution was dried lyophilically. Ternary water-soluble complexes C_{60}–tetraphenylporhyrin (TPP)–PVP were also prepared by a two-stage procedure [7].

The content of fullerene and porphyrin in the water-soluble product was determined from the electronic spectra of sample solutions in chloroform, using the extinction coefficients of the absorption bands of fullerene (λ = 258 nm) and porphyrin (λ = 419 nm).

The electronic spectra of the sample solutions were recorded on a Specord M40 spectrophotometer. The ^{13}C NMR spectra of aqueous solutions of complexes

1070-4272/03/7610-1620 $25.00 © 2003 MAIK "Nauka/Interperiodica"

were recorded on a Bruker-500 spectrometer at room temperature, and spectra of solid samples, on a Bruker CXP-100 spectrometer operating at 25.18 MHz (rotation rate of the samples, 3–4 KHz). Chemical shifts were related to tetramethylsilane. Solutions of complexes in D_2O were preliminarily kept at 80°C for 1 h.

Homogeneous mixing of hydrophobic C_{60} molecules with a hydrophilic polymer and preparation of complexes with high content of C_{60} involve considerable difficulties caused by the absence of a common solvent for the components. In particular, this process is complicated by fullerene aggregation both in individual solvents and in a solvent-precipitant mixture [8, 9], which apparently takes place in synthesis of complexes (the complexes are synthesized by the procedure described in [6], by combining equal volumes of solutions of C_{60} in benzene and PVP in chloroform, the latter solvent being a bad solvent for fullerene).

With the aim to improve the quality of C_{60} retained by the polymer in water, we used various procedures for preparation of complexes. To decrease the degree of fullerene aggregation in the initial solution, we prepared complexes from a solution of the initial components both in an individual solvent (benzene) and in its mixture with the minimum amount of a precipitant (chloroform) (Table 1). The resulting product contains greater amount of C_{60} (1.7%) than the product prepared by the traditional procedure (less than 1%), but is significantly less soluble in water than the initial polymer. It is apparent that true solutions of PVP in benzene are not formed. Hence, fullerene reacts with the aggregated polymer to give a stable complex of several PVP macromolecules with fullerene.

It was found that the efficiency of the reaction of fullerene with the polymer in solution increases when interpolymer complexes are formed [10]. Apparently, in this case, association of PVP in benzene in the absence of fullerene association is favorable for the reaction with C_{60}, but intermolecular complexes do not form true solutions in water.

Another procedure decreasing the fraction of aggregated fullerene in solution is synthesis of complexes in the presence of a third agent, TPP, which also forms water-soluble complexes with PVP. It has been shown previously that this procedure allows preparation of water-soluble complexes with higher fullerene content than that in the binary system C_{60}–PVP [11]. In the first stage of synthesis, binary complex C_{60}–TPP is prepared by the procedure involving evaporation of benzene from a mixture of fullerene and porphyrin solutions and thermal treatment of the resulting solid residue [7]. In cocrystallization from organic solvents, fullerene and porphyrin form chain structures or complexes in which fullerene molecules are separated by porphyrin rings [12, 13]. The assumption that this C_{60}–TPP complex shows a weaker tendency to aggregate in solution than the initial fullerene is confirmed by comparative studies by the neutron scattering method [7]. Fundamental distinctions in the scattering patterns of C_{60} solutions and solutions of C_{60}–TPP complexes, suggesting the absence of coarse aggregates in the latter case, were found. At the same time, mixing of the TPP and C_{60} solutions did not result in a decrease in the fullerene aggregation [7].

Table 1. Composition of C_{60}–PVP complexes prepared under various conditions

Complex no.*	Reaction conditions	Solvent	C_{60} content in the water-soluble fraction, %
1	In solution	Toluene : chloroform = 1 : 1	0.8
2	″	Benzene : chloroform = 1 : 1	0.7
3	″	Benzene : chloroform = 2 : 1	0.7
4	″	Benzene	1.7
5	In solid phase	–	2.1
6	″	–	2.3

* Initial substance: complex nos. 1–5, C_{60} and PVP; complex no. 6, C_{60}, PVP, and KBr.

When three components, C_{60}, TPP, and PVP, are combined simultaneously, there is no increase in the C_{60} content in the composition of the ternary complex. As seen from Table 2, the polymer predominantly binds porphyrin, which is less hydrophobic than C_{60}. Based on these data, we prepared ternary water-soluble complexes C_{60}–TPP–PVP by a procedure involving two stages: preliminary complexation of C_{60} with TPP and further mixing of the resulting product with the polymer.

The conditions of synthesis of the C_{60}–TPP complex, in particular, thermal treatment in a vacuum, were optimized. NMR data suggest for solid samples that the intensity and duration of thermal treatment of the complex affect the extent to which the electron density is shifted from TPP to fullerene. This is seen from the chemical shifts of the corresponding nuclei in the NMR spectra (Table 3). A higher heating temperature promotes efficient reaction of the components. At the same time, it was found that, above 200°C,

Table 2. Synthesis of fullerene complexes with PVP and TPP

Complex no.	Synthesis conditions	Solvent	Composition of water-soluble product, wt%	
			C_{60}	TPP
1	Simultaneous mixing of components	Benzene : chloroform = 2 : 1	0.7	2.1
2	Use of preliminarily prepared C_{60}–TPP complex	Benzene	1.3	0.7
3	The same	Benzene : chloroform = 2 : 1	3.2	1.7
4	〃	〃	3.7	1.7
5	Under the conditions for complex no. 2 at 100°C	〃	5.7	2.1
6	The same, at 200°C	〃	6.4	2.2

Table 3. ^{13}C NMR chemical shifts for the complexes C_{60}–TPP (solution in CS_2–tetrahydrofuran–d_8) and C_{60}–TPP–PVP (in solid phase)

Sample	Chemical shift δ, ppm				
	C_{60}	TPP		PVP	
				C=O	H_2C–N
Initial substance	143.35	142.69	135.09	175.47	43.24
C_{60}–TPP complex synthesized at 100°C (**I**)	143.21	142.51	134.89	–	–
C_{60}–TPP complex synthesized at 200°C (**II**)	143.02	142.52	134.84	–	–
PVP–C_{60}–TPP synthesized from complex:					
I	142.00	144.64	–	174.31	40.91
II	140.23	148.75	–	173.14	40.91

C_{60} reacts with TPP, presumably via the N–H groups of the porphyrin ring. This is suggested by changes in the electronic spectrum of the solution of the complex in benzene: a decrease in the intensities of the characteristic bands of fullerene and porphyrin and appearance of a new absorption band peaked at 360 nm. Thus, we found that the optimum temperature of thermal treatment of the solid C_{60}–TPP complex prepared in the first stage is 200°C.

As seen from Table 2, we synthesized from the C_{60}–TPP complex prepared at the optimal temperature water-soluble systems with significant amount of C_{60}. It is possible that the state of components in the ternary water-soluble complex C_{60}–TPP–PVP is governed by the composition and structure of binary systems C_{60}–TPP. This conclusion is in good agreement with the results of NMR studies of ternary systems in solids state. In the spectra of the water-soluble system C_{60}–TPP–PVP, the C_{60} signal is shifted upfield, and the signal assigned to the porphyrin ring, downfield, i.e., the electron density in the complexes is redistributed due to the interaction of the components. In the NMR spectra of the ternary system based on the C_{60}–TPP complex (heating temperature 200°C), the shift of the signals is more pronounced (Table 3).

It should be noted that, in this case (in the absence of solvent, water), the signals of carbon atoms of PVP, both carbonyl and methylene, adjacent to the nitrogen atom in the ring, are also shifted upfield.

The presence of a significant amount of water, both sorbed and chemically bound [14], in the initial polymer inhibits the reaction of C_{60} with PVP. As shown previously [14], a water molecule in the complex with PVP acts as an acceptor of the electron density from the carbonyl groups of polymer. Thus, water can compete with fullerene in complexation. This is also suggested by comparative solid-state

NMR studies of the initial (moist) PVP, PVP dehydrated by thermal treatment, and PVP–C_{60} system prepared from thermally treated PVP (Table 4). The presence of both water and C_{60} molecules in the system results in a similar effect: downfield shift of the ^{13}C NMR signal of carbonyl group, i.e., shift of the electron density, resulting in deshielding of the carbon atom. Considering that water molecules interact with virtually each carbonyl oxygen and the fraction of PVP units interacting with C_{60} is no more than 5% of the total number of units, it is conceivable that the acceptor power of fullerene is significantly higher. Nevertheless, removal of adsorbed water must favor interaction of C_{60} with PVP.

With the aim to eliminate the influence of water contained in the polymer on the interaction of C_{60} with PVP, compounds C_{60}–PVP were prepared in the solid phase. The reaction in the absence of solvent excludes formation of C_{60} solvates, i.e., competition of solvent and PVP for the interaction with C_{60}.

As a result of thermal treatment of the polymer in a vacuum (at 140°C), not only adsorbed water, but also a significant part of chemically bonded water molecules are removed [14]. In this case, the electron-donor power of carbonyl groups increases, which is confirmed by the NMR studies: upfield shift of the carbonyl carbon signal upon thermal treatment (Table 3).

As the third component, we added KBr. It was shown that the presence of a salt facilitates dispersion of coarse fullerene crystallites [15]. We studied the influence of KBr on dispersion and found that the presence of KBr accelerates the complexation. In this case, higher concentrations of fullerene are attained in aqueous solutions than in binary systems C_{60}–PVP prepared by a similar procedure (Table 1). In the solid-state NMR spectra of C_{60}–PVP and C_{60}–KBr–PVP systems, we revealed no changes suggesting formation of donor–acceptor bonds between fullerene and the polymer. Presumably, fullerene is not dispersed to molecular species during mechanical treatment and is retained in aqueous solution only by hydrophobic interaction between the C_{60}–KBr compound formed and PVP. It is possible that the contact of C_{60} with KBr prevents formation of donor–acceptor complexes in the system C_{60}–KBr–PVP.

It was of importance to compare the behavior of solid-phase compounds and complexes prepared in organic solvents. Comparative studies of aqueous solutions of these samples were carried out by light scattering and neutron scattering methods. It was found that the characteristics of the aggregation observed (size and concentration of structured particles found in concentrated solutions by neutron scattering and their behavior upon dilution, studied by light scattering in more dilute solutions) does not depend on the sample preparation procedure and is governed only by the fullerene content in these samples [15, 16]. Thus, the proposed procedure for preparing C_{60}–PVP compounds in the solid phase offers advantages over the synthesis in solutions, since it allows preparation of systems similar in their behavior in aqueous solutions to complexes with higher content of C_{60} less strongly bound to the polymer.

Table 4. ^{13}C NMR chemical shifts (in solid) in the spectra of PVP and systems PVP–H_2O and C_{60}–PVP

Sample	Chemical shifts δ, ppm		
	C_{60}	C=O	H_2C–N
		PVP	
Initial PVP (contains H_2O)	–	175.47	43.24
Dehydrated PVP	–	172.85	42.09
PVP–C_{60}	142.87	174.90	42.38

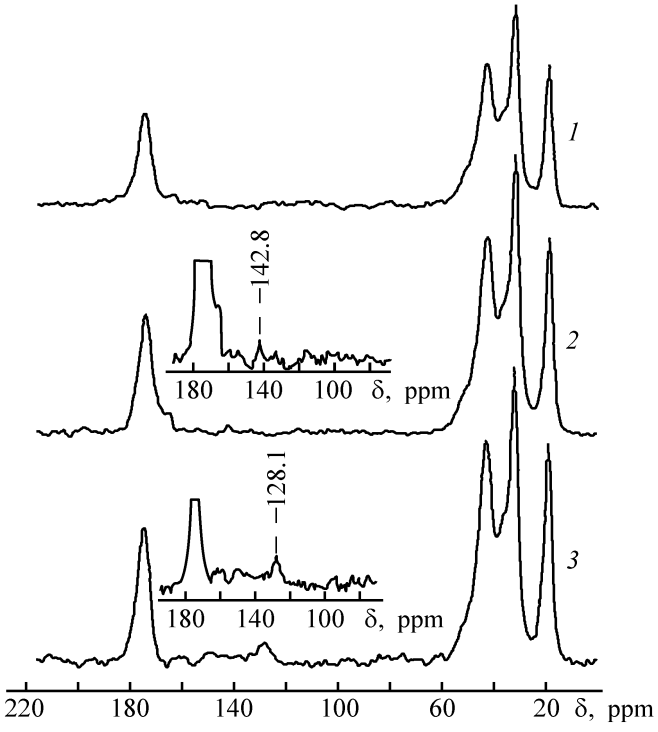

^{13}C NMR spectra of solid samples. (δ) Chemical shift. (*1*) Initial PVP; C_{60}–PVP complex: (*2*) after lyophilic drying and (*3*) prepared from organic solvents, before lyophilic drying.

Table 5. ^{13}C NMR chemical shifts of C_{60}–PVP complexes in D_2O solutions

Sample	Chemical shift δ, ppm, of PVP carbon atoms						New signals	
	C=O	C_4	C_3	C_5	C_1	C_2		
Initial PVP	180.30	48.35	45.06	36.31	33.70	20.18	–	–
C_{60}–PVP:								
before heating	180.40	48.35	44.90	36.31	33.91	20.18	32.59	22.57
after heating*	184.00	47.28	44.89	36.31	33.87	20.14	32.57	23.00

* Aqueous solutions of the samples were heated for 1 h at 80°C.

We studied complexation in the systems C_{60}–PVP prepared from organic solvents, by NMR in the solid state and in solution.

In the system C_{60}–PVP, an ESR signal was recorded [17]. This signal was assigned to electron transfer from the carbonyl group of PVP to the C_{60} molecule to give a fullerene radical anion. This signal appeared in the spectrum of the solid product after thorough removal of solvents in a vacuum upon prolonged heating.

Solid-state NMR spectra of the system C_{60}–PVP prepared similarly after removal of organic solvents show that fullerene occurs in the form of a solvate with toluene (see figure). This is suggested by the signal of toluene bound to C_{60} (δ 128 ppm). At the same time, the C_{60} signal is broadened and split into several peaks, which is caused by hindered rotation of the fullerene molecule. During lyophilic drying of C_{60}–PVP, toluene is completely removed and the signal of C_{60} is shifted upfield (by approximately 0.5 ppm), which suggests a shift of the electron density from the carbonyl group of the polymer to the C_{60} molecule in complexation.

Data of NMR in solid state, obtained for C_{60}–TPP–PVP complexes (Table 3), also suggest that carbonyl groups of the polymer are involved in interactions in the ternary system and the interaction of the polymer with fullerene is of donor–acceptor nature, as discussed above.

In the NMR spectra of the complexes in D_2O solutions, we found new signals of the polymer, assigned to the carbonyl carbon atom and C_2 and C_5 atoms (Table 5) according to their integral intensities:

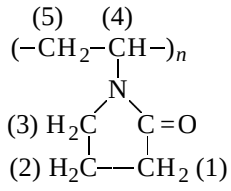

The latter signals appear in the spectrum immediately after the dissolution of the sample. The new signal of the carbonyl carbon atom appears in the spectrum after heating of the solution. These data suggest that, in the solution of the ternary complex, fullerene initially interacts with the hydrophobic part of the polymer molecule. After heating, carbonyl groups additionally interact with the carbon atoms of PVP carbon chain and C_{60} molecule to give a donor–acceptor complex. This specific character of formation of donor–acceptor bonds is apparently observed in the porphyrin-free system, too.

The new signal in the ^{13}C NMR spectrum of PVP in the complex, assigned to the C_5 atom, is shifted upfield relative to the initial signal. This position of the signal can be also accounted for by displacement of water molecules because of the appearance of hydrophobic fullerene–PVP bonds. Similar upfield shifts were observed for ternary complexes with TPP (Table 3) by the solid state NMR spectroscopy.

The results obtained suggest that in dissolution of fullerene-containing PVP in water, bonds between components are finally formed. In this case, substitution of a large C_{60} molecule with more pronounced acceptor power for water molecules results in a redistribution of the electron density in the PVP unit. Although PVP, as a whole, is an electron donor with respect to fullerene, C_2 and C_5 carbon atoms increase somewhat the electron density in complexation with fullerenes.

Thus, after passing into aqueous solution, additional bonds between polymer chains and fullerene molecules, both donor–acceptor and hydrophobic, are formed, which favors retention of C_{60} in water. In this case, only small fraction of fullerene molecules form donor–acceptor bonds with the polymer.

CONCLUSIONS

(1) Water-soluble formulations C_{60}–poly-*N*-vinylpyrrolidone and C_{60}–KBr–poly-*N*-vinylpyrrolidone were prepared by solid-phase reaction in a vacuum. Synthesis of the product in the presence of KBr results in increased content of C_{60} in its composition as compared with the binary system C_{60}–poly-*N*-vinylpyrrolidone. In this case, C_{60} is less firmly bound to the polymer. Removal of the hydrate shell of poly-*N*-vinylpyrrolidone upon thermal treatment promotes interaction of the components in the complex.

(2) Water-soluble complexes C_{60}–poly-*N*-vinylpyrrolidone were prepared in solution in the presence of tetraphenylporphyrin, an agent promoting molecular dispersion of C_{60} in the course of complexation. The optimal conditions of preparation of ternary complexes with high content of fullerene were found.

ACKNOWLEDGMENTS

This work was supported financially by the State Scientific and Engineering Program "Topical Lines of Research in Solid-State Physics," line "Fullerenes and Atomic Clusters," and by the Russian Foundation for Basic Research (project no. 03-03-32633).

REFERENCES

1. Friedman, S.H., DeCamp, D.L., Sijbesma, R.P., *et al.*, *J. Am. Chem. Soc.*, 1993, vol. 115, no. 15, pp. 6506–6509.
2. Da Ros, T. and Prato, M., *Chem. Commun.*, 1999, pp. 663–669.
3. *Fullerenes: Chemistry, Physics, and Technology*, Kadish, K.M. and Ruoff, R.S., Eds., New York, 2000.
4. Chiang, L.Y., Wang, L.-T., Swirczewski, J.W., *et al.*, *J. Org. Chem.*, 1994, vol. 59, pp. 3960–3968.
5. Guldi, D.M. and Prato, M., *Acc. Chem. Res.*, 2000, vol. 33, pp. 695–703.
6. Yamakoshi, Y.N., Yamagami, T., and Fukuhara, K., *J. Chem. Soc., Chem. Comm.*, 1994, pp. 517–518.
7. Melenevskaya, E.Yu., Ratnikova, O.V., Evlampieva, N.P., *et al.*, *Vysokomol. Soedin., Ser. A*, 2003, vol. 45, no. 7 (in press).
8. Torok, Gy., Lebedev, V.T., and Cser, L., *Fiz. Tverd. Tela*, 2002, vol. 44, pp. 546–547.
9. Rudalevige, T., Francis, A.H., and Zand, R., *J. Phys. Chem., Ser. A*, 1998, vol. 102, pp. 9797–9802.
10. Anufrieva, E.V., Krakovyak, M.G., Anan'eva, T.D., *et al.*, *Fiz. Tverd. Tela*, 2002, vol. 44, pp. 443–444.
11. Vinogradova, L.V., Melenevskaya, E.Yu., Khachaturov, A.S., *et al.*, *Vysokomol. Soedin., Ser. A*, vol. 40, no. 11, pp. 1854–1862.
12. Boyd, P.D.W., Hodgson, M.S., Rickard, C.E.F., *et al.*, *J. Am. Chem. Soc.*, 1999, vol 121, no. 45, pp. 10487–10495.
13. Ishii, T., Kanehama, R., Aizawa, N., *et al.*, *J. Chem. Soc., Dalton Trans.*, 2001, no. 20, pp. 2795–2801.
14. Lebedeva, T.L., Fel'dshtein, M.M., Kuptsov, S.A., and Plate, N.A., *Vysokomol. Soedin., Ser. A*, 2000, vol. 42, no. 9, pp. 1504–1523.
15. Tarasova, E.V., Ratnikova, O.V., Melenevskaya, E.Yu., *et al.*, Abstracts of Papers, *4th Int. Symp. "Molecular Order and Mobility in Polymer Systems,"* St. Petersburg, June 3–7, 2002, p. 164.
16. Lebedev, V.T., Torok, Gy., Cser, L., *et al.*, Abstract of Papers, *4th Int. Symp. "Molecular Order and Mobility in Polymer Systems,"* St. Petersburg, June 3–7, 2002, p. 162.
17. Chen, Y.-H., Khairullin, I.I., Suen, M.-P., and Hwang, L.-P., *Fullerene Sci. Technol.*, 1999, vol. 7, no. 5, pp. 807–824.

Russian Journal of Applied Chemistry, Vol. 76, No. 10, 2003, pp. 1626–1630. Translated from Zhurnal Prikladnoi Khimii, Vol. 76, No. 10, 2003, pp. 1669–1674.

MACROMOLECULAR CHEMISTRY AND POLYMERIC MATERIALS

Electrochemical Synthesis of Thin Films of Polymers Derived from [NiSalen] and [NiSalphen]

G. A. Shagisultanova and L. P. Ardasheva

Herzen State Educational University, St. Petersburg, Russia

Received April 8, 2003

Abstract—Electrochemical synthesis of conducting polymeric Ni(II) complexes with *N,N'*-bis(salicylidene)-ethylenediamine and *N,N'*-bis(salicylidene)-*o*-phenylenediamine was studied. The kinetic of this process was examined. The possibility of preparing the polymeric films with a definite thickness ranging from 0.01 to 2 μm was assessed.

It is known that electrochemical oxidative polymerization of Ni(II) complexes with *N,N'*-bis(salicylidene)ethylenediamine (Salen) and *N,N'*-bis(salicylidene)-*o*-phenylenediamine (Salphen) and their derivatives in weakly or moderately electron-donor solvents gives thin conducting films [1–8].

Electrochemical synthesis of polymeric transition-metal complexes with structurally different macrocyclic ligands, including those of the Salen type, has been the subject of numerous recent studies [2, 9–15]. The resulting polymers with controllable thickness have high redox conductivity; their reduced and (or) partially oxidized forms exhibit photoelectric activity [9–15].

Thus, a wide variety of conducting polymeric Cu(II), Pt(II), Co(II), Pd(II), and Ni(II) complexes insoluble in water and organic solvents have been grown on solid supports and studied. The parameters of the electrochemical synthesis and the kinetics of polymer formation have been analysed. The charge diffusion coefficient D_{ct} in the polymer bulk, which characterizes the rate of charge transfer in the polymer in a solution of a supporting electrolyte, has been calculated [2, 9–12]. The suggested mechanism of polymer formation is based on existence of a single resonance structure of the initial monomers and transformation of this structure into another structure with redistribution of the electron density in the macrocycle [16].

Although orangometallic polymers have been studied extensively, optimization of their synthesis and analysis of their structure, stability, and properties remain a topical task.

In this study, we analyzed in detail the electrochemical (potentiostatic conditions) synthesis of polymers derived from [NiSalen] and [NiSalphen] and determined the kinetic parameters of this process.

EXPERIMENTAL

The complexes [NiSalen] and [NiSalphen] were synthesized by the procedure in [17]

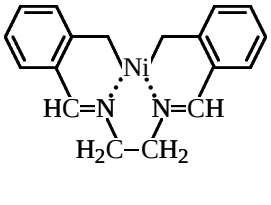

[NiSalen]

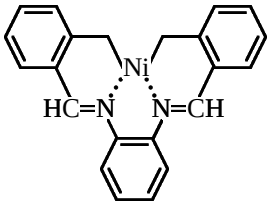

[NiSalphen]

Electrochemical measurements were performed on a PI-50-1 pulsed potentiostat in the potentiostatic and potentiodynamic modes with linear potential sweep at a rate of 0.01 to 0.5 V s^{-1}, using a PR-8 programmer. We used an three-electrode electrochemical cell with separated compartments. Platinum wire (99.99% Pt) with surface area of 0.25 cm^2, sealed in glass, served as working electrode; a platinum gauze was an auxiliary electrode. All potentials were measured relative to a silver chloride electrode filled with a saturated NaCl solution.

The monomer concentration in the working solution was 1 mM. The supporting electrolyte was 0.1 M solution of tetraethylammonium perchlorate (Et_4NClO_4) in acetonitrile (CH_3CN) dried by the procedure de-

1070-4272/03/7610-1626 $25.00 © 2003 MAIK "Nauka/Interperiodica"

scribed in [18]. The solution was deaerated with high-purity argon.

The film thickness was calculated by the procedure described in [19].

The cyclic voltammogram measured by single potential sweep in an acetonitrile solution of [NiSalen] is shown in Fig. 1. Comparison of the peak current with those measured in propylene carbonate $C_3H_6CO_3$ in a single potential sweep cycle [2, 9] confirmed that the deposition rate of the polymer in CH_3CN is higher than that in $C_3H_6CO_3$. Probably, diffusion of the monomer to the near-electrode space in more viscous $C_3H_6CO_3$ is slower.

As a rule, the intensity of anodic and cathodic peaks grows with increasing the number of potential sweep cycles in solutions of nickel(II) complexes. The cathodic peak current in acetonitrile solution of [NiSalen] increases during five cycles of potential sweep from 0.0 to 1.6 V at a rate of 0.001 V s^{-1} and then decreases rapidly [7]. However, this phenomenon cannot be interpreted unambiguously. Vilas-Boas *et al.* [7] suggest that the decrease in the peak current in the course of polymerization may be due both to "superoxidation" caused by irreversible oxidation of the ligand at high potentials and to lowering of the complex concentration near the working electrode.

Stable multilayer poly[NiSalen] films with thickness ranging from 0.01 to 2 μm can be prepared by potential sweep from 0.0 to +1.2 V at a rate of 0.05 V s^{-1}.

As in our previous study [2], a dark yellow film insoluble in water and organic solvents is deposited on the electrode surface, which confirms the formation of stable solid oxidation products of [NiSalen] in the course of continuous potential sweep. A yellow-brown conducting film of poly[NiSalphen] was prepared similarly.

Polymeric [NiSalen] and [NiSalphen] were deposited in the potentiostatic and potentiodynamic modes. Potentiodynamic synthesis was performed by cyclic sweeping of the potential of the working electrode in a solution of the initial monomer in a certain range for each complex: 0.0–1.2 V for [NiSalen] and 0.0–1.3 V for [NiSalphen]. The potentiostatic synthesis is performed at a constant accumulation potential determined experimentally. The accumulation potential, at which the deposition rate of the electrochemically active polymer is the highest was considered to be the optimal. The potentionstatic accumulation mode has an advantage over, the potentiodynamic procedure in that it allows rapid deposition of thick films. In this study, [NiSalen] and [NiSalphen] were polymerized

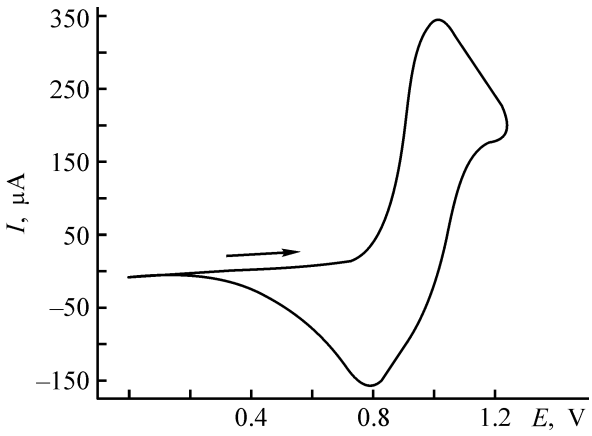

Fig. 1. Cyclic voltammogram of anodic polymerization of [NiSaen] in 0.1 M Et_4NClO_4 in CH_3CN (first cycle). $c_{complex} = 1 \times 10^{-3}$ M, $V_s = 0.05$ V s^{-1}. (*I*) Current and (*E*) potential; the same for Fig. 2.

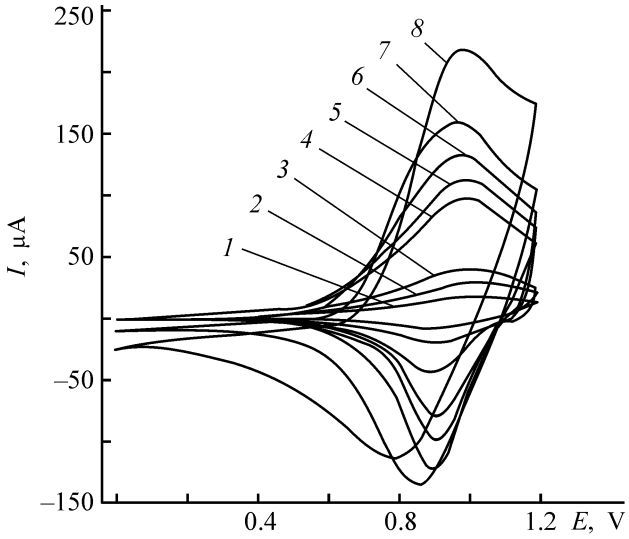

Fig. 2. Cyclic voltammograms illustrating solid-phase redox processes in poly[NiSalen] films deposited in (*1*) 0.5, (*2*) 1.0, (*3*) 2.0, (*4*) 5.0, (*5*) 7.0, (*6*) 10.0, (*7*) 17.0, and (*8*) 43.0 min in the potentiostatic mode at $E_a = 1.1$ V. CH_3CN, Et_4NClO_4, $V_s = 0.01$ V s^{-1}; the same for Figs. 3 and 4.

mainly in the potentiostatic mode at a potential of 1.1 ± 0.05 V.

The electrodes coated with [NiSalen] and [NiSalphen] were immersed in a solution of the supporting electrolyte, and their potential was swept in the ranges 0.0–1.2 and 0.0–1.3 V, respectively. The cathodic and anodic waves in the cyclic voltammograms characterize electron transfer in the bulk of the polymer. Cyclic voltammograms recorded at the potential sweeping of the electrode coated with poly [NiSalen] films of varied thickness (sweep rate 0.01 V s^{-1}) in a solution of pure supporting electrolyte are shown in Fig. 2.

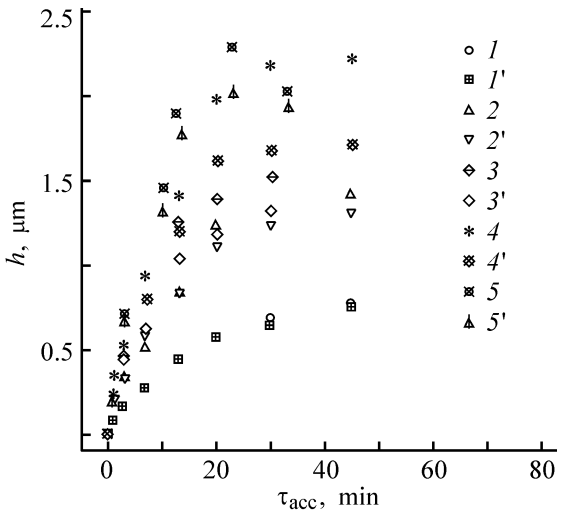

Fig. 3. Thickness h of poly[NiSalen] films deposited from solutions with monomer concentration of (*1*, *1*') 0.5, (*2*, *2*') 0.75, (*3*, *3*') 1.0, (*4*, *4*') 1.5, and (*5*, *5*') 2 mM vs. the accumulation time τ_{acc}. The film thickness was calculated from the quantity of electricity spent for (*1*–*5*) oxidation and (*1*'–*5*') reduction of the polymer.

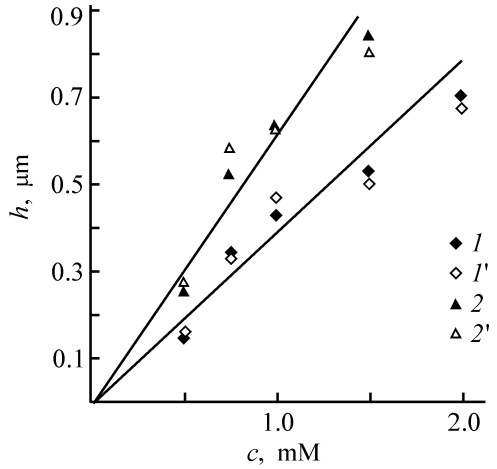

Fig. 4. Thickness h of poly[NiSalen] films grown for (*1*, *1*') 3 and (*2*, *2*') 7 min vs. the monomer concentration in the solution c. The film thickness was calculated from the quantity of electricity spent for (*1*, *2*) oxidation and (*1*', *2*') reduction of the polymer.

It can be seen that the anodic peak at $E_a \approx 0.6$ V appears and is shifted to positive potentials with an increasing deposition time and, hence, the film thickness. The shift of the first oxidation potential at $E_a \approx 0.6$ V (sweep rate 0.01 V s^{-1}) is the most pronounced at the thickness of poly[NiSalen] film larger than 0.7-μm. This peak disappears upon further growth of the film. In this case, the cyclic voltammogram contains a single wave at $E_a \approx 0.95$ V (Fig. 2). We suggest that the characteristics of redox processes in thick polymer layers differ from those for thin films. Thus, the shift and the subsequent disappearance of the first anodic peak at $E_a \approx 0.6$ V in cyclic voltammograms can be regarded as a quantitative characteristic of the transition from thin to thick polymeric films, which differ in structure and physicochemical properties.

There exist two forms of the polymeric substance: yellow-brown oxidized, which turns dark brown with increasing thickness of a polymeric film, and yellow reduced. These forms determine the electrochromic properties of a polymer. The oxidized form is deposited in the potentiostatic mode (0.5–60 min, E = 1.05 V) and can be rapidly converted to the reduced form by potentiostatic reduction at E = 0.0 V in a solution of pure supporting electrolyte. The reduction time τ_{red} is equal to the time of oxidative polymerization. The oxidized form is spontaneously reduced in a solution of the supporting electrolyte within 30–120 min (depending on the film thickness) after the applied voltage is switched off. The thicker the film, the slower its spontaneous reduction. It should be noted that the cathodic potential never reaches 0.0 V in the course of spontaneous reduction of the polymer. Our experimental results show that the limiting, so-called equilibrium potential of spontaneous reduction is equal to the potential at which the anodic wave in the cyclic voltammograms starts to grow, i.e., at which the electrostimulated oxidation of the reduced form starts. Along with spontaneous reduction, spontaneous oxidation of the polymer was observed. The polymer reduced under potentiostatic conditions at E = 0.0 V is oxidized in a pure supporting electrolyte after the applied voltage is switched off. The potential of the electrode coated with the polymeric film increases to a value equal to the potential recorded by the end of the spontaneous reduction. Thus, the so-called intermediate redox form is formed both by spontaneous reduction and by spontaneous oxidation of the polymer. The potential of this form depends on the film thickens and the nature of a supporting electrolyte.

Our experimental results show that polymer thickness h is one of the most important parameters determining the rate of charge transfer in the polymer.

To calculate the thickness h of a polymeric film, we recorded cyclic voltammograms at slow potential sweep (0.01 V s^{-1}). Under these conditions, the film is deposited by the adsorption mechanism ensuring reduction or oxidation of all molecular fragments of the polymeric chain. The dependence of h of poly[NiSalen] on the time of accumulation in the potentiostatic mode at different concentrations of the complex in solution is shown in Fig. 3. On the whole, the polymer formation accelerates with increasing

monomer concentration in solution. In the initial deposition steps (up to 7 min), the dependence of h on the monomer concentration at constant accumulation time is linear (Fig. 4). Upon further electrode polarization in a solution of the nickel complex (for more than 15–20 min), polymerization decelerates and the curve flattens out. When the films are deposited from highly concentrated solutions, h passes through a maximum and then decreases. At low monomer concentration, the curve flattens out owing to a decrease in the monomer concentration near the electrode. The influence of the concentration on the rate of polymer growth is the most pronounced in going from 0.5 to 0.75 mM monomer solutions. At higher monomer concentration (up to 2 mM), the dependence of the thickness of polymeric film on the monomer concentration becomes less steep, being, on the whole, nonlinear (Fig. 4).

It should be noted that the dependence of the thickness of polymeric film grown from a solution with monomer concentration of 2.0 mM on the accumulation time passes through a maximum. Since the curves measured in the first deposition steps are similar for all monomer concentrations, we suggest that, in 20 min, the polymerization is decelerated and the curve flattens out. However, it can be seen from Fig. 3 that at the monomer concentration of 2 mM the curve has ascending and descending portions, which reflects the decrease in the electrical conductivity of the polymer. At high monomer concentration in the working solution, the polymerization accelerates and a film with a high content of structural defects grows [20], which makes lower the redox conductivity of the polymer.

We calculated the polymer thickness from the area under the cathodic (h_c) and anodic (h_a) portions of the cyclic voltammograms (Fig. 3). As seen from Fig. 3, the thicknesses of poly[NiSalen] films calculated from the areas under the cathodic and anodic portions become different when the thickness reaches 0.7 μm. The thicknesses of these films, calculated from the anodic portion are higher than those calculated from the cathodic portion. Thus, the calculated thickness of the oxidized conducting polymeric film grown at any monomer concentration is slightly larger than that of the reduced film. The higher the monomer concentration in the working solution, the greater the difference between the currents of anodic and cathodic portions of the cyclic voltammograms and hence, the greater is the difference between h_a and h_c. The decreased activity of the polymer films in reduction is due to the presence of residual oxidized fragments in the polymer, which are electron traps or have a "frozen" charge [21, 22].

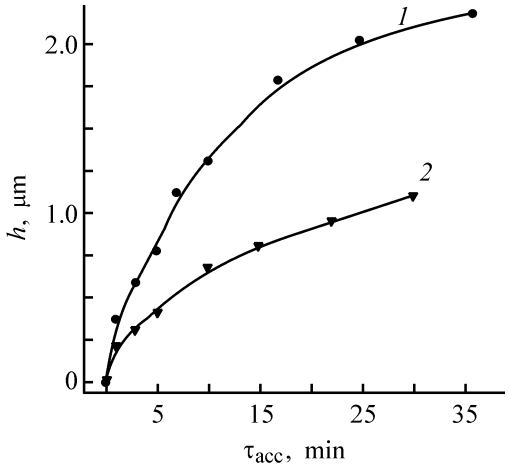

Fig. 5. Thickness h of (*1*) poly[NiSalen] and (*2*) poly[NiSalphen] vs. the accumulation time τ_{acc}. CH_3CN, Et_4NClO_4, E_a = 1.1 V, continuous growth.

The dependences of the thickness of poly[NiSalen] and poly[NiSalphen] films on the time of accumulation on the electrode at the optimal potentials are shown in Fig. 5 (curves *1*, *2*). It can be seen that the poly[NiSalen] film is thicker than the poly[NiSalphen] film grown under the same conditions. Probably, polymerization of [NiSalphen] on the electrode surface is sterically hindered owing to the presence of the third phenyl ring in the ligand.

We examined the possibility of stepwise growth of polymer films. An electrode coated with the polymer for a definite time was immersed in a pure supporting electrolyte and a cyclic voltammogram was recorded. Then the electrode was placed in the monomer solution and the polymerization runs (up to 15 steps dependening on the experimental conditions) were continued. We found that a polymeric film can be grown stepwise. The thickness of the thus obtained polymeric film was close to that of the film grown in a single step during the same time.

CONCLUSIONS

(1) Electrochemical synthesis of polymeric nickel(II) complexes in the potnetiostatic mode was studied. The best accumulation potential providing fastest growth of the electroactive layer is 1.1 ±0.5 V.

(2) The redox conductivity of the polymer may decrease with increasing monomer concentration in the working solution.

(3) The polymeric film can be grown by both continuous and stepwise deposition, which is of practical importance.

ACKNOWLEDGMENTS

This work was supported financially by the Russian Foundation for Basic Research (project no. 01-03-33155), Ministry of Education of Russian Federation (grant E00.-5.0-210), and Committee for Science and Higher School of St. Petersburg (grant of St. Petersburg in the field of science and engineering for the year 2002, contract no. 207).

REFERENCES

1. Goldsby, K.A., *J. Coord. Chem.*, 1988, vol. 19, no. 3, pp. 83–90.
2. Shagisultanova, G.A., *Teor. Eksp. Khim.*, 1991, vol. 27, no. 3, pp. 330–338.
3. Bedioui, F., Labbe, E., Gutierrez-Granados, S., and Devynck, J., *J. Electroanal. Chem. Interfacial Electrochem.*, 1991, vol. 301, nos. 1–2, pp. 267–274.
4. Audebert, P., Captdevielle, P., and Maumy, M., *Synth. Met.*, 1991, vols. 41–43, pp. 3049–3052.
5. Dahm, C.E. and Peters, D.G., *Anal. Chem.*, 1994, vol. 66, no. 19, pp. 3117–3123.
6. Dahm, C.E., Peters, D.G., and Simonet, J., *J. Electroanal. Chem.*, 1996, vol. 410, no. 2, pp. 163–171.
7. Vilas-Boas, M., Freire, C., de Castro B., *et al.*, *Inogr. Chem.*, 1997, vol. 36, no. 22, pp. 4919–4929.
8. Vilas-Boas, M., Freire, C., de Castro B., *et al.*, *Chem. Eur. J.*, 2001, vol. 7, no. 1, pp. 139–150.
9. Popeko, I.E., Synthesis and Properties of polymeric Partially Oxidized Nickel, Palladium, and Platinum Complexes with Schiff Bases, *Cand. Sci. Dissertation*, Leningrad, 1993.
10. Shagisultanova, G.A., Borisov, A.N., and Orlova, I.A., *J. Photochem. Photobiol. A. Chem.*, 1997, vol. 103, no. 3, pp. 249–255.
11. Orlova, I.A., Synthesis and Properies of New Photo- and Electroactive Polymeric Transition Metal Complexes with Schiff Bases, *Cand. Sci. Dissertation*, Moscow, 1997.
12. Shagisultanova, G.A., Orlova, I.A., Ardasheva, L.P., and Popova, E.O., *J. Macromol. Phys.*, 1998, vol. 136, pp. 91–95.
13. Ardasheva, L.P., Luminescence Spectral and Electrochemical Properties of Platinum(II) and Palladium(II) Complexes with Schiff Bases, *Cand. Sci. Dissertation*, Moscow, 1999.
14. Shagisultanova, G.A. and Ardasheva, L.P., *Zh. Neorg. Khim.*, 2001, vol. 46, no. 3, pp. 411–419.
15. Ardasheva, L.P. and Shagisultanova, G.A., *Zh. Prikl. Khim.*, 2001, vol. 74, no. 2, pp. 311–319.
16. Shagisultanova, G.A. and Kuznetsova, N.N., *Koord. Khim.*, 2003, vol. 29, no. 9, pp. 1–8.
17. Holm, R.H., Everett, G.W., and Chakravorty, A., *Prog. Inorg. Chem.*, 1966, vol. 7, pp. 183–186.
18. Gordon, A.J. and Ford, R.A., *The Chemist's Companion, A Handbook of Practical Data, Techniques, and References*, New York: Wiley, 1972.
19. Khannanov, N.K., Yatsun, T.F., Shafirovich., B.Ya., and Strelets, V.V., *Izv. Akad. Nauk SSSR, Ser. Khim.*, 1983, no. 6, pp. 1282–1289.
20. Roncali, J., Lemaire, M., Garreau, R., and Garnier, F., *Synth., Met.*, 1987, vol. 18, nos. 1/3, pp. 189–184.
21. Alpatova, N.M., Semenikhin, O.A., Ovsyannikova, E.V., *et al.*, *Elektrokhimiya*, 2000, vol. 36, no. 9, pp. 1045–1052.
22. Vorotyntsev, M.A. and Badiali, J.P., *Electrochim. Acta*, 1994, vol. 39, no. 2, pp. 289–306.

Russian Journal of Applied Chemistry, Vol. 76, No. 10, 2003, pp. 1631–1636. Translated from Zhurnal Prikladnoi Khimii, Vol. 76, No. 10, 2003, pp. 1675–1681.

MACROMOLECULAR CHEMISTRY AND POLYMERIC MATERIALS

Electro- and Photoelectroactivity of Thin-Layer Polymers Based on [NiSalen] and [NiSalphen] Complexes

G. A. Shagisultanova, L. P. Ardasheva, and I. A. Orlova

Herzen Russian State Educational University, St. Petersburg, Russia

Received April 8, 2003

Abstract—New experimental data on physicochemical properties of polymeric nickel(II) complexes with *N*,*N*'-bis(salicylidene)ethylenediamine and *N*,*N*'-bis(salicylidene)-*o*-phenylenediamine (including redox conductivity, photoactivity in a solution of a supporting electrolyte, and electrochemical stability) were obtained. The rate of charge transport in the polymeric matrix was studied as a function of the polymer film thickness.

Electrochemical synthesis and study of thin-layer metal-containing polymers attracts much researchers' attention [1]. The electrochemical synthesis allows preparation of conducting polymers on solid supports as solid and uniform films with controllable thickness. Transition metal complexes with macrocyclic ligands of various compositions and structures, which are structural units in the synthesis of these polymers, determine the variety of their properties [1–10], e.g., redox conductivity, photosensitivity, sensor and catalytic properties.

It has been found previously [6, 11] that, when immersed in a solution of a supporting electrolyte, polymers based on transition metal complexes with ligands of the *N*,*N*'-bis(salicylidene)ethylenediamine (Salen) type in the reduced and (or) partially oxidized state are photoelectroactive and can exhibit a positive photovoltaic effect [6, 11]. The maximum positive change in the potential of the electrode with the polymer layer applied by electrochemical synthesis was first found for poly[PdSalen] and amounted to 450 mV [12]. The photoelectroactivity is the major property required of polymers to be used in accumulation and conversion of the energy of light.

Thus, these polymers are promising materials in production of sensors, electro- and photocatalysts, and solid-phase galvanic cells.

In the preceding publication [13], we considered the optimal conditions of the synthesis and the kinetic aspects of formation of polymers based on Ni(II) complexes with *N*,*N*'-bis(salicylidene)ethylenediamine (Salen) and *N*,*N*'-bis(salicylidene)-*o*-phenylenediamine (Salphen). In this study, we analyzed the electro- and photoinduced charge transfer in poly[NiSalen] and poly[NiSalphen] and the electrochemical stability of these polymers.

EXPERIMENTAL

The method of the electrochemical measurements was described in [14].

The photoelectric measurements were performed on a device including an irradiation source (DRSh-1000 lamp), a potentiometric recorder, and a photoelectrochemical cell. A cell with parallel-plate windows was the working part of a two-electrode Pyrex glass cell. The samples were irradiated with focused polychromatic light; the IR light was cut off by two water filters. A silver chloride electrode filled with a saturated NaCl solution was used as reference. A platinum (99.99% Pt) wire with surface area of 0.25 cm^2 sealed in the glass served as indicator electrode. The electrode was coated with a layer of the polymer studied, which was deposited in the course of the electrochemical synthesis. A 0.1 M solution of tetraethylammonium perchlorate Et_4NClO_4 in acetonitrile CH_3CN was used as a supporting electrolyte.

The capability for reversible electroinduced charge transfer is one of the major properties of Ni(II) polymers studied and the related polymeric compounds.

Among conducting polymers, two main groups are distinguished. To the first group belong polymers with electrons delocalized over very extended polyconjugated systems. These are mainly organic polymers containing no metal [9, 15–17]. The second

1070-4272/03/7610-1631 $25.00 © 2003 MAIK "Nauka/Interperiodica"

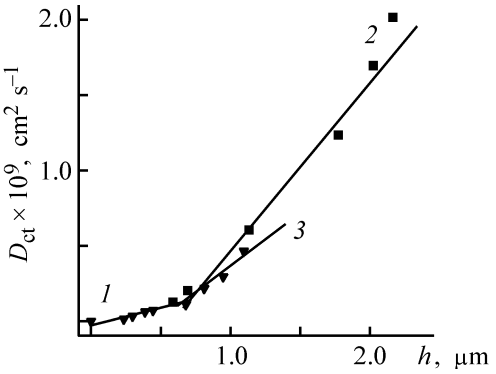

Fig. 1. Charge diffusion coerfficient D_{ct} vs. the thickness h of (*1, 2*) poly[NiSalen] and (*1, 3*) poly[NiSalphen] films. CH_3CN, Et_4NClO_4, E_{acc} = 1.1 V.

group includes so-called redox polymers, in which the electronic conductivity is due to electron hopping between low-mobility redox centers incorporated into a polymeric matrix with low electronic conductivity [1, 18, 19]. Two types of redox polymers are distinguished. The first of them are redox polymers, which can be prepared by electrochemical oxidation or reduction of individual coordination compounds of transition metals with organic ligands [1, 3]. The second type includes the so-called composites consisting of an organic polymeric matrix with metal ions (mainly of variable valence) and separate molecules of metal complexes incorporated into its internal voids by various procedures.

It is known that the conductivity of organic polyconjugated polymers is several orders of magnitude higher than that of the redox polymers and is essentially independent of the polymer chain length, but is determined by conformation and morphology of macromolecules, i.e., by the supramolecular structure of a substance [15].

As a quantitative characteristic of the rate of charge transfer in the polymer phase bulk, we used the charge diffusion coefficient D_{ct} (cm^2 s^{-1}) calculated by Randles-Shevchik equation

$$I_p = (2.69 \times 10^5) n^{3/2} S (D_{ct})^{1/2} V_p^{1/2} c_0,$$

where I_p is the peak current (A); n, number of electrons transferred in an elementary event; S, electrode surface area (cm^2); V_p, potential sweep rate (V s^{-1}); c_0, concentration of the electrochemically active species in the polymer film (mol cm^{-3}) [20].

Depending on the nature of the limiting stage, the D_{ct} values characterize the electron self-exchange between the heterocharged fragments or diffusion of the supporting electrolyte ions in the polymer phase. It is known [20] that D_{ct} varies within the range 10^{-13}–10^{-8} cm^2 s^{-1} when the rate-determining stage is the rate of the diffusion of the supporting electrolyte ions and is higher than 10^{-7} cm^2 s^{-1} when the rate of charge transfer in the polymer phase is limited by the rate of the electron exchange between the heterocharged fragments in the polymer chain.

We calculated the D_{ct} values from cyclovoltammograms (CVAs) recorded at high potential sweep rates (≥0.1 V s^{-1}) under the conditions of incomplete oxidation or reduction of the polymer film. In this case, the redox reactions in the polymer phase proceed in the semi-infinite diffusion mode, when the dependence of currents of voltammogram peaks on $V_p^{1/2}$ is linear.

Vilas-Boas *et al*. [21] calculated, using several independent methods, the diffusion coefficient in the polymer based on the Ni(II) complex with *N,N'*-bis-(salicylidene)butane-2,3-diamine (Salt-Me) prepared by potentiodynamic synthesis and found that D_{ct} grows with increasing polymer film thickness, especially for thin films. The maximum thickness of films of poly[NiSalt-Me] films deposited on the electrode in [21] was attained after 50 potential sweep cycles and was calculated to be 0.6 μm. In our experiments, a similar thickness of poly[NiSalen] and poly[NiSalphen] was attained within 3–7 min in the potentiostatic mode (E_{acc} = 1.1 V, initial concentration of the metal complex in the solution 1 mM).

We found that, for poly[NiSalen] and poly[NiSalphen], D_{ct} is limited by the rate of motion of counterions in the polymer bulk and grows with increasing thickness of the conducting layer (Fig. 1). For a 1.5–2.0 μm thick poly[NiSalen] film, D_{ct} was relatively high for complexes with ligands of this type: 10^{-9} cm^2 s^{-1}.

The D_{ct} values corresponding to various thicknesses of the polymeric conducting substance, calculated both for highest peak of the anodic current in CVAs at E_a ~ 0.95 and 1.05 V and for the corresponding cathodic current at E_c ~ 0.85 and 0.92 V for poly-[NiSalen] and poly[NiSalphen], respectively, are listed in Table 1.

As seen, the D_{ct} values characterizing the rates of diffusion of counterions in polymer oxidation are lower than the D_{ct} values characterizing reduction. For thin poly[NiSalphen] films, this difference reaches 100% and decreases with increasing film thickness. The above difference for oxidation and reduction may be due to the fact that the polymers in the reduced

Table 1. Charge diffusion coefficients D_{ct} calculated for anodic and cathodic peaks at various thicknesses of the polymer film h

Poly[NiSalen]			Poly[NiSalphen]		
h, μm	D_{ct} ($cm^2\ s^{-1}$) of indicated peak		h, μm	D_{ct} ($cm^2\ s^{-1}$) of indicated peak	
	anodic	cathodic		anodic	cathodic
0.37	4.4×10^{-11}	6.6×10^{-11}	0.22	1.4×10^{-11}	2.8×10^{-11}
0.59	1.2×10^{-10}	2.0×10^{-10}	0.31	3.9×10^{-11}	7.2×10^{-11}
0.69	2.1×10^{-10}	2.8×10^{-10}	0.42	6.7×10^{-11}	1.2×10^{-10}
1.14	6.0×10^{-10}	6.5×10^{-10}	0.67	1.3×10^{-10}	2.4×10^{-10}
1.78	1.2×10^{-9}	1.3×10^{-9}	0.80	2.1×10^{-10}	2.6×10^{-10}
2.02	1.7×10^{-9}	1.7×10^{-9}	0.95	3.0×10^{-10}	3.6×10^{-10}
2.17	2.0×10^{-9}	1.8×10^{-9}	1.10	4.6×10^{-10}	5.7×10^{-10}

state have a more compact structure. Direct measurements of the polymer film thickness showed that the oxidized polymer film is 60% thicker than the reduced polymer film [22]. The IR and XPES data indicate that ions of the supporting electrolyte and solvent molecules are virtually absent in the bulk of the polymer in the reduced state [23].

Thus, a decrease in the rate of penetration of ions and solvent molecules into the polymer in the reduced state in the course of its oxidation may be associated with a decrease in the volume of the free space in the bulk of the reduced form of the polymer in comparison with the oxidized form because of the denser molecular packing. At the same time, the oxidized form contains inner free space sufficient for exit of molecules of the supporting electrolyte. As a result, D_{ct} increases for the reduction process. The obtained experimental data on the effect of the polymer film thickness on D_{ct} are in agreement with data of [21].

As seen from Table 1, the D_{ct} values for poly[NiSaphlen] are somewhat lower than those for poly[NiSalen] at the same thickness. The difference between the D_{ct} values for these polymers is greater in the case of anodic processes, as compared with cathodic processes. Presumably, owing to existence of an additional phenyl ring, poly[NiSalphen] has a smaller volume of the free space than poly[NiSalen].

However, with increasing thickness of the conducting polymeric film to h = 2.0 μm (poly[NiSalen]) the D_{ct} values calculated from the anodic and cathodic branches of CVAs become close. Nevertheless, the subsequent increase in the time of the positive polarization of the electrode gives another dependence. Namely, for poly[NiSalen] (h = 2.17 μm), anodic D_{ct} exceeds cathodic D_{ct}. With increasing thickness, less compact films are probably formed, the volume of the free space in the layers adjacent to the electrolyte–polymer phase boundary grows, and ions of the supporting electrolyte and solvent molecules penetrate into the film bulk with weaker hindrance than that in thinner films of the polymer. However, in this case, exit of counterions from deeper near-electrode layers of the polymeric phase is complicated because of structural heterogeneities accumulating with film growth.

For poly[NiSalphen], the pattern of variation of D_{ct} for anodic and cathodic processes with increasing film thickness is similar. However, we can assume that, even in poly[NiSalphen] with relatively large h (~1 μm), the volume of the free space is smaller than that in the similar poly[NiSalen], since the D_{ct} values remain unequal, similar to those in the thin-layer samples.

It should be noted that the rise in the redox conductivity of the polymeric supramolecules with increasing film thickness is untypical of the known conducting materials, although we have also noted in previous studies that the redox activity of polymers based on transition metal complexes with Salen type ligands grows with increasing thickness of the conducting polymer [11–14, 24, 25]. The effect of the redox activity growth with increasing thickness of polymeric copper aminophthalocyanines was noted in [16]. Alpatova *et al*. [16] suggest that, with increasing thickness of the polymer film, the system of conjugated π bonds develops, and, as a result, hopping mechanism of the electron transport typical of redox polymers transforms into the polaronic mechanism characteristic of polymers with conjugated bonds.

The absence of conductivity in solvents with high donor power is a characteristic feature of the metal-free conducting organic polymers with developed π system (e.g., in dimethyl sulfoxide and dimethylformamide with potential sweep within the range of pos-

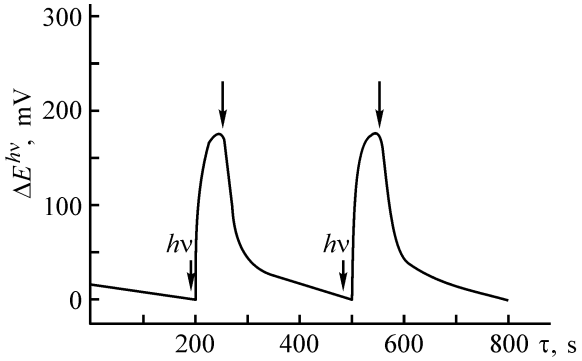

Fig. 2. Typical curve of variation of the potential $\Delta E^{h\nu}$ of the electrode with applied poly[NiSalphen] layer under the action of polychromatic light. h_{film} = 0.29 μm, CH_3CN, Et_4NClO_4; source of light, DRSh-1000 lamp. (τ) time.

itive values). It has been found [26–28] that solid-phase redox reactions are also untypical of polymers based on metal complexes with Salen type ligands, immobilized on an electrode immersed in a solvent with high donor power.

In Fig. 1, we can distinguish three linear sections with different slopes. The first (straight line *1*) with small slope is independent of the ligand structure and reflects the dependence of D_{ct} on h in the initial stages of film thickness growth, i.e., for relatively thin layers of poly[NiSalen and poly[NiSalphen]. Straight line *2* reflects further increase in D_{ct} with h for poly[NiSalen], and straight line *3* for poly[NiSalphen]; the more pronounced growth of D_{ct} with increasing thickness of the electroactive layer and, hence, the greater slope is observed for poly[NiSalen]. It should be noted that the boundary thickness of polymer films at which the slope of the curve changes lies at about of 0.7 μm.

Thus, the observed rise in the rate of charge diffusion in the polymer phase with increasing film thickness is probably caused by the change in its morphology and in the number of physicochemical characteristics, including the porosity of the polymeric substance [15].

When discussing the influence of the polymer film thickness on the character of the electroinduced charge transfer, we should take into consideration that the simultaneous increase in the thickness of the conducting layer and in the potential rate results in electrochemical overvoltage associated with deceleration of the redox reactions in the solid phase. As known, this phenomenon is characterized by an increase in the difference of the potentials corresponding to the anodic and cathodic processes and, as a result, is reflected in CVAs in that the anodic and cathodic peaks are shifted and move away from each other. For poly[NiSalen], the shift of the potential of the cathodic peak is greater than that for the anodic peak: from E_c ~ +0.92 V (accumulation time τ_a = 0.5 min) to E_c ~ +0.85 V (τ_a = 17 min) at sweep rate of 0.01 V s^{-1}. Similar changes in CVAs and shifts of the anodic and cathodic peaks with increasing thickness have been described previously for related polymeric systems [24, 25]. Probably, the overvoltage is caused by a decrease in the rate of penetration and exit of the supporting electrolyte ions in the course of oxidation and reduction of thick polymer films when relatively high potential sweep rates are used. It is assumed that thick polymeric films contain large amounts of structural defects, microheterogeneities, and cross-links. In turn, this causes slower motion of counterions in the free volume of the polymer.

Thus, the D_{ct} values and differences of the potentials of the anodic and cathodic processes are the basis for a quantitative correlation between the thickness of the polymer film formed on the electrode surface and the degree of reversibility of the solid-phase redox reactions.

It was established for the first time that, in the supporting electrolyte solution under continuous irradiation with polychromatic light, the change in the potential $\Delta E^{h\nu}$ (mV) of the electrode coated with a polymeric film of poly[NiSalen] or [NiSalphen] is positive and reaches several tens of millivolts.

The maximum value of $\Delta E^{h\nu}$ amounted to 250 and 190 mV for [NiSalen] and [NiSalphen], respectively. A typical curve of the potential change, recorded when an electrode coated with electrochemically immobilized poly[NiSalphen] is irradiated with polychromatic light, is shown in Fig 2.

The photovoltaic effect was found only for the polymer in the reduced or partially oxidized state. Thus, only chain fragments that exist in the ground electronic state and are characterized by the maximum aromaticity of phenyl rings can be photodetectors [23]. Previously, Orlova [12] has assumed that photoexcitation of the reduced form of the polymer is accompanied by charge transport and accumulation of oxidized fragments, similar to those proceeding under the action of the electric potential. Hence, the presence of charge-compensating ions in the polymer phase is the necessary condition for maintaining the macroneutrality of the polymer under photoexcitation.

Multiple alternation for each polymer of photoexcitation and dark phase, resulting in that the potential of the electrode in the supporting electrolyte spontaneously returns to its initial value, showed that the max-

Table 2. Potential $\Delta E^{h\nu}$ of the electrode with polymeric layer under the action of polychromatic light at various thicknesses h of the film (CH_3CN, Et_4NClO_4)

Poly[NiSalen]			Poly[NiSalphen]		
h, μm	$\Delta E^{h\nu}$, mV		h, μm	$\Delta E^{h\nu}$, mV	
	maximum	average		maximum	average
0.10	75	60 ± 5	0.09	85	75 ± 5
0.20	170	115 ± 10	0.14	160	130 ± 10
0.26	250	170 ± 20	0.29	190	165 ± 10
0.36	135	110 ± 10	0.43	170	140 ± 10

Table 3. Electrochemical stability of poly[NiSalen] depending of the external factors

Experimental conditions	τ_H = 5 min			τ_H = 15 min		
	h_{in}	h_{fin}	loss, %	h_{in}	h_{fin}	loss, %
	μm			μm		
Continuous potential sweep, in the range from 0.0 to +1.2 V (τ_{sc} = 30 min, V_p = 0.05 V s^{-1})	0.49	0.3	40	0.85	0.48	45
Exposure to a solution of the supporting electrolyte, min:						
30	0.37	0.35	5	0.93	0.61	35
60	0.37	0.31	15	0.93	0.49	45
Exposure of the oxidized form to air, min:						
30	0.41	0.27	30	1.13	0.64	45
60	0.41	0.19	50	1.13	0.3	75
Exposure of the reduced form to air, min:						
30	0.45	0.45	0	0.75	0.75	0
60	0.45	0.45	0	0.75	0.75	0

imum value of $\Delta E^{h\nu}$ is reached in the first irradiation run. Later on, $\Delta E^{h\nu}$ decreases, and after 5–7 irradiation runs it becomes constant (Table 2).

We experimentally found that $\Delta E^{h\nu}$ passes through a maximum with increasing thickness of the polymer film (Table 2) and is independent of the oxygen presence in the supporting electrolyte solution.

It was also found that the polymeric films are photostable and keep the initial thickness of the conducting substance after irradiation is terminated.

The stability (including electrochemical stability, whose criterion is the ability of a polymeric system to keep the redox conductivity under the action of external factors) is the major property making organometallic polymers promising as novel materials.

The results obtained in studying the polymer stability, estimated as preservation of the thickness of the electroactive substance after continuous potential sweep, prolonged exposure to the supporting electrolyte solution, and action of air, are listed in Table 3.

It can be seen that the most rapid and substantial decrease in the thickness of the conducting polymer films is caused by continuous potential sweep. When the potential of an electrode coated with polymeric film in the pure supporting electrolyte is varied relatively slowly within the 0.05–0.01 V s^{-1} range, the electrochemical degradation accelerates and the redox conductivity of the polymeric substance decreases, especially for thick films. In addition, the degrading action of the solvent should be noted. This conclusion follows from the decrease in the conductivity of the polymer after prolonged exposure to a solution of pure supporting electrolyte.

In air, the reduced form of the polymer is substantially more stable as compared with the oxidized form. The latter may contain chain fragments with unpaired electrons. Their high chemical activity may favor reactions with air components, which, in turn, may result in irreversible structural distortions in the system of the conjugated bonds responsible for conducting properties of the polymeric substance.

CONCLUSIONS

(1) The rate of charge transfer in poly[NiSalen] and poly[NiSalphen] is determined by the mobility of the supporting electrolyte ions and grows with increasing thickness of the polymer film. In contrast to thin films, the D_{ct} value for thick films of the electroactive substance ($h > 0.7$ μm) depends on the ligand structure.

(2) Poly[NiSalen] and poly[NiSalphen] immobilized on an electrode immersed in an electrolyte solution are capable of photoinduced charge transfer. The photovoltaic effect depends on the irradiation intensity and film thickness and is independent of the presence of oxygen in the supporting electrolyte solution. The maximum values of $\Delta E^{h\nu}$ for poly[NiSalen] and poly[NiSalphen] are 250 and 190 mV, respectively.

(3) The reduced forms of the polymers are substantially more stable in air as compared with oxidized forms.

ACKNOWLEDGMENTS

The study was supported financially by the Russian Foundation for Basic Research (project no. 01-03-33155), Ministry of Education of the Russian Federation (project no. E00.-5.0-210), and Committee for Science and Higher School of St. Petersburg (project of St. Petersburg in the Field of Scientific and Technical Activities, 2002, contract no. 207).

REFERENCES

1. Abruna, H.D., *Coord. Chem. Rev.*, 1988, vol. 86, no. 1, pp. 135–189.
2. Goldsby, K.A., *J. Coord. Chem.*, 1988, vol. 19, no. 3, pp. 83–90.
3. Shagisultanova, G.A., *Teor. Eksp. Khim.*, 1991, vol. 27, no. 3, pp. 330–338.
4. Dahm, C.E. and Peters, D.G., *Anal. Chem.*, 1994, vol. 66, no. 19, pp. 3117–3123.
5. Vilas-Boas, M., Freire, C., de Castro, B, *et al.*, *Inorg. Chem.*, 1997, vol. 36, no. 22, pp. 4919–4929.
6. Shagisultanova, G.A., Borisov, A.N., and Orlova, I.A., *J. Photochem. Photobiol. A: Chem.*, 1997, vol. 103, no. 3, pp. 249–255.
7. Reddinger, J.L. and Reynolds, J.R., *Chem. Mater.*, 1998, vol. 10, no. 1, pp. 3–5.
8. Gobi, K.V., Tokuda, K., and Ohsaka, T., *Electrochim. Acta*, 1998, vol. 43, no. 9, pp. 1013–1022.
9. Alpatova, L.M., Semenikhin, O.A., Ovsyannikova, E.V., *et al.*, *Elektrokhimiya*, 2000, vol. 36, no. 9, pp. 1045–1052.
10. Kingsborough, R.P. and Swager, T.M., *Angew. Chem. Int.* Ed., 2000, vol. 39, no. 16, pp. 2897–2900.
11. Shagisultanova, G., Orlova, I., Ardasheva, L., and Popova, E., *J. Macromol. Phys. Macromol. Symp.*, 1998, vol. 136, pp. 91–97.
12. Orlova, I.A., Synthesis and Properties of Novel Photo- and Electroactive Polymers Based on Transition Metal Complexes with Shciff Bases, *Cand. Sci. Dissertation*, Moscow, 1997.
13. Shagisultanova, G.A. and Ardasheva, L.P., *Zh. Prikl. Khim.*, 2003, vol. 76, no. 10, pp. 1669–1674.
14. Shagisultanova, G.A. and Ardasheva, L.P., *Zh. Neorg. Khim.*, 2001, vol. 46, no. 3, pp. 411–419
15. Vorotyntsev, M.A. and Levi, M.D., *Itogi Nauki, Ser.: Elektrokhimiya*, 1991, vol. 34, pp. 154–220.
16. Alpatova, N.M., Ovsyannikova, E.V., Semenikhin, O.A., *et al.*, *Elektrokhimiya*, 2000, vol. 36, no. 2, pp. 173–179.
17. Simon, J. and Andre, J.-J., *Molecular Semiconductors, Photochemical Properties and Solar Cells*, Berlin: Springer, 1985.
18. White, B.A. and Murray, R.W., *J. Am. Chem. Soc.*, 1987, vol. 109, no. 9, pp. 2576–2581.
19. Hurrel, H.C. and Abruna, H.D., *Inorg. Chem.*, 1990, vol. 29, no. 4, pp. 736–741.
20. Khannanov, N.K., Yatsun, T.F., Shafirovich, V.Ya., and Strelets, V.V., *Izv. Akad. Nauk SSSR, Ser. Khim.*, 1983, no. 6, pp. 1282–1289.
21. Vilas-Boas, M., Freire, C., de Castro, B., and Hillman, A.R., *J. Phys. Chem. B*, 1998, vol. 102, no. 43, pp. 8533–8540.
22. Hamnett, A., Abel, J., Eameaim, J., *et al.*, *J. Phys. Chem. Chem. Phys.*, 1999, vol. 1, no. 22, pp. 5147–5156.
23. Shagisultanova, G.A. and Kuznetsova, N.N., *Koord. Khim.*, 2003, vol. 29, no. 9, pp. 1–8.
24. Ardasheva, L.P., Spectral-Luminescent, Photochemical, and Electrochemical Properties of Platinum(II) and Palladium(II) Complex Compounds with Schiff Bases, *Cand. Sci. Dissertation*, Moscow, 1999.
25. Ardasheva, L.P. and Shagisultanova, G.A., *Zh. Prikl. Khim.*, 2001, vol. 24, no. 2, pp. 311–319.
26. Kaufman, F.B. and Engler, E.H., *J. Am. Chem. Soc.*, 1979, vol. 101, no. 3, pp. 547–549.
27. Kapturkiewicz, A. and Behr, B., *Inorg. Chim. Acta*, 1983, vol. 69, pp. 247–251.
28. Azevedo, F., Carrondo, M.A.A.F.C.T., Castro, B., *et al.*, *Inorg. Chim. Acta*, 1994, vol. 219, no. 1, pp. 43–54.

Russian Journal of Applied Chemistry, Vol. 76, No. 10, 2003, pp. 1637–1642. Translated from Zhurnal Prikladnoi Khimii, Vol. 76, No. 10, 2003, pp. 1682–1687.

MACROMOLECULAR CHEMISTRY AND POLYMERIC MATERIALS

Dipole Structure and Electrooptical Properties of Poly-*N*-vinylpyrrolydone in Nonaqueous Solvents

N. P. Evlampieva, T. A. Dmitrieva, and E. I. Ryumtsev

Research Institute of Physics, St. Petersburg State University, St. Petersburg, Russia

Received May 12, 2003

Abstract—Electrooptical Kerr effect and dielectric polarization were studied for poly-*N*-vinylpyrrolidone solutions in chloroform and in mixed chloroform–CCl_4 solvent. The results were compared with those for an analogue of the monomeric unit of poly-*N*-vinylpyrrolidone, low-molecular-weight compound *N*-methylpyrrolidone.

Poly-*N*-vinylpyrrolidone (PVP) is one of the major synthetic polymers used in medicine and pharmacology; it exhibits extremely valuable properties. PVP is biologically inert, fairly stable thermally and chemically, nontoxic for living bodies, and capable of complexing with diverse compounds in aqueous media. This made PVP suitable for extensive use in production of drugs, medical preparations, and cosmetics [1].

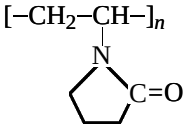

PVP

Studies of the properties of biologically active molecular complexes of PVP with fullerene C_{60} [2] and PVP derivatives with covalently bound C_{60} [3] revealed a very strong dependence of the electrooptical properties of these compounds on their composition and type of bonding between fullerene and PVP. However, there are no published data on specific features of the electrooptical behavior of PVP in solutions. Therefore, we studied the Kerr effect of PVP in nonaqueous media. The solvents were chosen so as to eliminate the influence of aggregation phenomena and enable correlation of the molecular structure of PVP, which has been extensively studied by various methods [1], with the electrooptical properties of PVP and its derivatives.

In this study, we analyzed by the methods of electrooptical Kerr effect and dielectric polarization two PVP samples with different molecular weights (MWs) (Table 1) in chloroform and mixed 1 : 1 (by volume) chloroform–carbon tetrachloride (CCl_4) solvent. The PVP-1, 2 samples were synthesized at the Institute of Macromolecular Compounds, Russian Academy of Sciences. The analogue of the monomeric unit of PVP, *N*-methylpyrrolidone (MP) produced by Sigma S0760, was studied by the Kerr effect method in chloroform

Table 1. Specific electrooptical Kerr constants K, specific dielectric polarizations μ_2/M for MP and PVP-1, 2 in organic solvents, and optical polarizability anisotropy Δb for the PVP monomeric unit

Sample	M	$K \times 10^{10}$, $cm^5\ g^{-1}(300\ V)^{-2}$ in chloroform	$K \times 10^{10}$, $cm^5\ g^{-1}(300\ V)^{-2}$ in chloroform–CCl_4	$(\mu_2/M) \times 10^{36}$, $D\ g^{-1}$ in chloroform–CCl_4	$\Delta b \times 10^{25}$,* cm^3
MP	99.1	+1.75	–	0.167	–
PVP-1	10000	–0.80	–0.2	0.022	–10
PVP-2	38000	–0.82	–0.2	0.025	–10

* Determined in [4] by the birefringence method for the homologous series of samples and fractions of PVP in benzyl alcohol solutions.

1070-4272/03/7610-1637 $25.00 © 2003 MAIK "Nauka/Interperiodica"

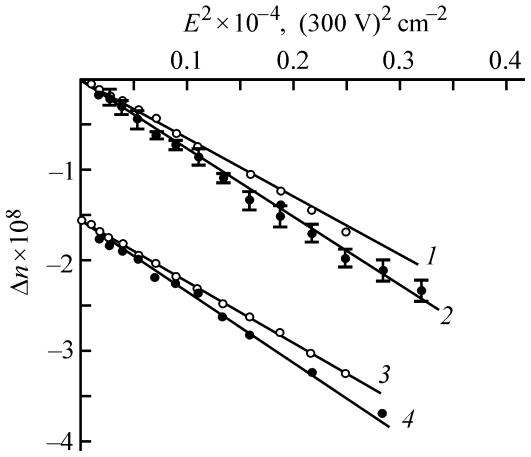

Fig. 1. Variation of the birefringence Δn with the squared electric field intensity, E^2, for PVP-1 sample in mixed chloroform–CCl_4 solvent at solution concentration, g cm^{-3}, of (*2*) 6.14×10^{-2} and (*4*) 3.85×10^{-2}. Straight lines (*1*) and (*3*) correspond to the solvent. Straight lines (*3*) and (*4*) are shifted along the ordinate axis by 1.5×10^{-8}.

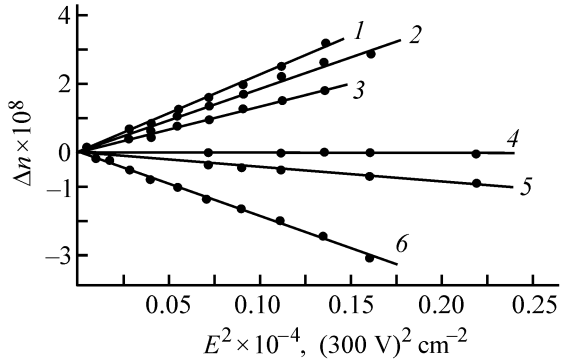

Fig. 2. Variation of the birefringence Δn of MP with the squared electric field intensity E^2 in chloroform at concentration, g cm^{-3}, of (*1*) 30.5×10^{-2}, (*2*) 18.3×10^{-2}, (*3*) 17.3×10^{-2}, (*4*) 9.8×10^{-2}, (*5*) 4.6×10^{-2}, and (*6*) 0.00.

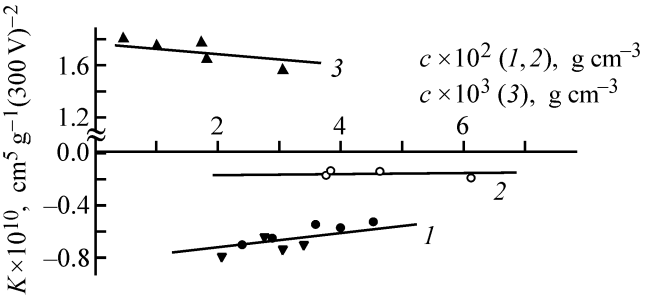

Fig. 3. Concentration dependences of the specific Kerr constant K for (*1*) PVP-1,2 samples in chloroform, (*2*) PVP-1 sample in the mixed chloroform–CCl_4 solvent, and (*3*) MP in chloroform.

only. The solvents used had the following characteristics: refractive index $n_0 = 1.4456 \pm 0.0005$, dielectric constant $\varepsilon_0 = 4.813 \pm 0.001$, and density $\rho_0 = 1.4891 \pm 0.0008$ g cm^{-3} for chloroform and $n_0 = 1.4536 \pm 0.0004$, $\varepsilon_0 = 3.364 \pm 0.003$, and $\rho_0 = 1.5358 \pm 0.0008$ g cm^{-3} for the chloroform–CCl_4 mixture. The characteristics of the solvents were determined at 21°C by the standard methods; the Kerr effect and the dielectric constant in polymer solutions were measured at 21°C as well.

The birefringence of solutions subjected to pulse electric field [(Kerr effect), hereinafter, bire-fringence in electric field, BE] was measured by the compensation method [5] at rectangular pulse duration of 1 ms. The parameters of the setup and the measurement cell corresponded to those described in [6]. The equilibrium (i.e., independent of the frequency and duration of electric pulses) electrooptical properties of the samples were characterized by the specific Kerr constant K

$$K = \lim_{\substack{c \to 0 \\ E \to 0}} (\Delta n - \Delta n_0)/E^2 c. \qquad (1)$$

Here, $(\Delta n - \Delta n_0)$ is the difference between the birefringences of the solution of concentration c and of the solvent, and E, the electric field intensity in the measurement cell.

In the solvents used, PVP exhibited a minor negative intrinsic (minus the contribution from the solvent) electrooptical effect proportional to the squared electric field intensity, in accordance with the Kerr law for molecular-dispersed media. Figure 1 shows the plots of the optical birefringence Δn against the squared electric field intensity, E^2, for PVP-1 sample. It is seen that the difference in Δn between the solution and solvent is small, though exceeding the measurement error. Figure 2 shows the same dependences for MP solutions in chloroform. Since the electrooptical Kerr effect is positive for MP and negative for chloroform, the sign of the electrooptical effect of the solution changed with the MP concentration in chloroform (Fig. 2).

The specific Kerr constant of the samples was determined, in accordance with Eq.(1), from the $K = f(c)$ plot (Fig. 3). Here, each K value is the slope of the $\Delta n = f(E^2)$ plot estimated at a certain concentration of the solution. Thus, for PVP-1 sample we obtained the Kerr constants $K = -(0.80 \pm 0.07) \times 10^{-10}$ g^{-1} cm^5 (300 V)$^{-2}$ in chloroform and $K = -(0.20 \pm 0.05) \times 10^{-10}$ g^{-1} cm^5 (300 V)$^{-2}$ in the mixed solvent. These constants were identical, within the experimental error, to those of the second sample,

PVP-2, which is typical of polymers in the Gaussian region of properties [5]. The fourfold difference between the specific Kerr constants in chloroform and the mixed solvent is due to the difference in the internal field factors for these solvents, which depend on the dielectric constant and refractive index of the medium subjected to electric field [5]. The results of the electrooptical measurements are summarized in Table 1.

The dielectric constant ε of the PVP solutions in the mixed solvent was measured in a cylindrical titanium capacitor with intrinsic capacitance of 92.62 pF at 700 kHz. We used an E12-1 instrument for capacitance measurements. The mixed solvent for dielectric measurements was formulated specially for decreasing the ε_0 parameter. The refractive indices of the solutions n were determined on an IRF-23 refractometer. The resulting increments of the dielectric constant $(\varepsilon - \varepsilon_0)/c$ and of the squared refractive index $(n^2 - n_0^2)/c$ for the solutions were used for calculating the specific dielectric polarization μ^2/M of the samples [7]:

$$(\mu^2/M) = 27kT[(\varepsilon - \varepsilon_0)/c - (n^2 - n_0^2)/c]/[4\pi N_A(\varepsilon_0^2 + 2)^2]. \quad (2)$$

Here, μ is the dipole moment; M, molecular weight; k, Boltzmann constant; T, absolute temperature; and N_A, Avogadro number.

Poly-*N*-vinylpyrrollidone belongs to carbon-chain polymers whose polar properties are determined by the pendant radical (for PVP, by polar pyrrolidone ring) with the dipole moment not rigidly bound to the backbone. A similar dipole structure is characteristic of comb-shaped mesomorphic polyacrylates [8].

With poly(alkylphenoxycarbonylphenyl methacrylates) (PAPCPM) as examples, Tsvetkov *et al.* [9] showed, for the first time, that, for interpreting the dielectric and electrooptical properties of polymers with polar –C=O group situated in close proximity of the backbone, it is necessary to distinguish the contributions from the dipole moment components of the pendant groups that are parallel and perpendicular to the chain propagation direction. The perpendicular components for PAPCPM (Fig. 4) are not ordered along the backbone (Fig. 4, vector **h**) and do not contribute to the total dipole moment of the macromolecule.

A specific feature of polymers containing polar pendant substituents is the difference (occasionally not only in magnitude but also in sign) between the electrooptical properties of the low-molecular-weight

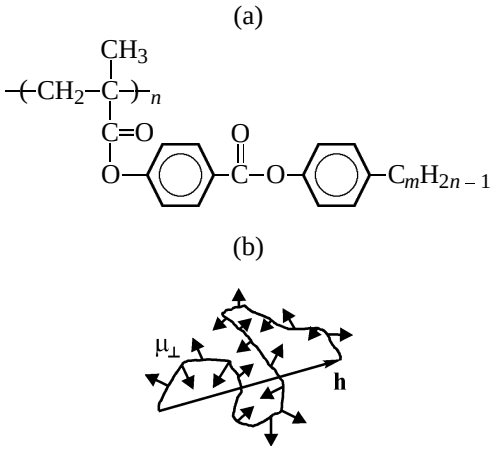

Fig. 4. (a) Chemical and (b) dipole structures of PAPCPM molecules.

structural analogue of the pendant substituent and the polymer proper, measured in the same solvents [5, 8]. This is mainly due to long-range interaction of pendant groups in the polymer chain, manifested in their mutual orientation. Strongly interacting polar and optically anisotropic groups in the pendant chain of the PAPCPM molecule are responsible for intramolecular ordering. As a result, the optical anisotropy of polarizability of the PAPCPM monomeric unit in the direction perpendicular to the chain propagation direction exceeds that in the chain propagation direction. This is responsible, in turn, for a negative dynamooptical Maxwell effect (or flow birefringence) in PAPCPM solutions [9], which is, essentially, birefringence in solutions under shear forces of the flow. The sign of the flow birefringence of a polymer in solution is directly related to that of the anisotropy of the optical polarizability of the repeating unit in the chain [10].

Many of comb-shaped polymers characterized by enhanced equilibrium (Kuhn segment length $A \sim 100 \times 10^{-8}$ cm and over) and kinetic rigidity owing to orientation interaction of the pendant groups exhibit in the Gaussian MW range the Maxwell and electrooptical Kerr effects with identical signs [6, 8]. This is a common property of Gaussian chains for which, on the average, the three main directions in the polymer coil, namely, the directions of the greatest geometric extension and of the orientation-axis and orientation-polar ordering typically coincide. This suggests that such properties of polymers as polarizability anisotropy and the total dipole moment should be analyzed in axes related to the chain propagation direction or, in accordance with the Gaussain statistics of polymer chains, to the direction of the vector **h** connecting the ends of the macromolecule (Fig. 4) [11].

Table 2. Eigenvalues of the optical polarizability tensor, a_i, (i = 1, 2, 3) calculated by PM3 quantum-chemical method and dipole moment projections μ_i onto the main optical axes of MP molecule

Value of i	$a_i \times 10^{25}$, cm^3	μ_i,* D
1	84.5	2.33
2	70.5	1.84
3	45.9	–1.44

* $\mu = (\mu_1^2 + \mu_2^2 + \mu_3^2)^{1/2}$ = 3.3 D is the total dipole moment of the MP molecule.

The behavior of PVP, observed in studies of the birefringence of its solutions in a flow and in electric field suggests that the properties of PVP and PAPCPM are identical, although these polymers substantially differ in the structure of their pendant substituents and PVP by no means belongs to polymers with enhanced chain rigidity. The equilibrium rigidity of PVP was estimated hydrodynamically [12] from the Kuhn segment length of $(21 \pm 1) \times 10^{-8}$ cm. This means that correlation in the PVP chain can extend over approximately seven monomeric units. The birefringence in electric field, measured for PVP solutions in chloroform and mixed chloroform–CCl_4 solvent, has negative sign. The polarizability anisotropy of the monomeric unit of PVP, as estimated by the birefringence method (Table 1), is also negative. Also, similarly to PAPCPM [9], the electrooptical specific Kerr constants for PVP and its monomeric unit analogue, MP, differ in magnitude and sign (Table 1). Our experimental data allow a more detailed analysis of the correlation between the dipole structure of PVP and its electrooptical and dielectric properties. Let us consider an analogue of the PVP monomer unit, low-molecular-weight MP.

Measurements of the electrooptical Kerr effect for MP solutions in chloroform showed that MP has a positive specific Kerr constant of $+(1.75 \pm 0.09) \times 10^{-10}$ g^{-1} cm^5 (300 V)$^{-2}$. Theoretically, the specific Kerr constant of a low-molecular-weight substance is related to the anisotropy of optical polarizability, Δa, and the magnitude and direction of the constant dipole moment μ of its molecules by

$$K = \frac{2\pi N_A (n_0 + 2)^2 (\varepsilon_0 + 2)^2}{1215 kT n_0 M} \Delta a \left[2\Delta a + \frac{\mu^2}{kT} \left(3\cos^2 \beta - 1 \right) \right]. \quad (3)$$

Here, β is the angle between the greatest polarizability axis of the molecule and the μ direction.

Based on the experimental value of K and value of Δa and μ, it is possible to estimate the angle β and, thus, to gain insight into the dipole geometry of MP. The MP molecule is relatively small, and we calculated its optical polarizability tensor and dipole moment by the PM3 semi-empirical quantum-chemical method [13], using the HyperChem software [14]. The results are summarized in Table 2.

Using the eigenvalues of the polarizabilty tensor, a_1, a_2, a_3, we calculated the anisotropy of optical polarizability of MP, $\Delta a = [(a_1 - a_2)^2 + (a_2 - a_3)^2 + (a_3 - a_1)^2]/2 = 33.9 \times 10^{-10}$ cm^3. Also, the calculations showed that MP has large constant dipole moment μ = 3.3 D. Next, we calculated by formula (3) the angle β between the directions of the greatest optical polarizability of the MP molecule and of its constant dipole moment. The resulting β = 45.7°, estimated from electrooptical measurements, agrees well with the quantum-chemical data:

$$\beta = \arccos(|\mu_1|/\mu) = 45.1°.$$

The dipole geometry of the MP molecule is characterized by the main directions shown in Fig. 5. The constant dipole moment is directed along the –C=O bond of the pyrrolidone ring; a_1 is directed along the axis of the greatest optical polarizability of the MP molecule, as predicted by the theoretical calculation. Such a dipole geometry of MP is responsible for the fact that, in the PVP chain, the dipole moment of each pyrrolidone ring in the polymer structure is directed at a large angle to the backbone direction.

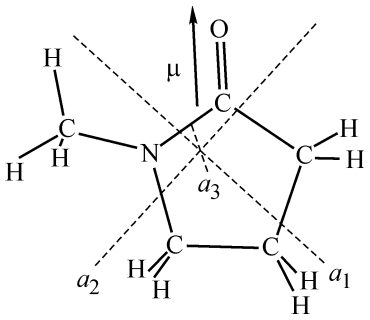

Fig. 5. Directions of the main axes of optical polarizability and constant dipole moment in the MP molecule.

The angle θ between the direction of the constant dipole moment of the pyrrolidone ring and the PVP backbone direction can be estimated using the theoretical expression for the Kerr constant K_∞ of the polymers in the Gaussian range of properties, where it is independent of the molecular weight [8]:

$$K_\infty = 2B\Delta b(\mu_1^2 \cos^2 \theta / M_1) s^2. \quad (4)$$

Here, $B = \pi N_A(n_0^2 + 2)^2(\varepsilon_0 + 2)^2/(1215 n_0 k^2 T^2)$ is the optical coefficient; Δb, the optical anisortopy of the monomer unit; μ_1 and M_1, the dipole moment and molecular weight of the monomer unit of the polymer, respectively; and s, the number of monomer units in the statistical Kuhn segment of the polymer.

Using the experimental values $K_\infty = -0.8 \times 10^{-10}$ g^{-1} cm^5 (300 V)$^{-2}$ for PVP-1 in chloroform, $\Delta b = -10 \times 10^{-25}$ cm^3 [4], $s = 7$ [12], and the μ_1^2/M_1 value corresponding to the experimental value for the MP analog of the PVP monomer unit (Table 1), we can estimate θ at 84.4°.

A similar calculation based on the data for the equilibrium Kerr effect for PVP-1 in the mixed solvent yielded $\theta = 86.4°$.

A close value was obtained using the experimental specific dielectric polarizations μ^2/M of the PVP-1 and PVP-2 samples in the mixed solvent, listed in Table 1. As known [11], the total dipole moment μ of the polymer molecule modeled by a Gaussian chain varies with the number of the monomer units in the statistical Kuhn segment, s, in the region of large MWs as

$$\mu^2/M = (\mu_1^2 \cos^2\theta/M_1)s. \quad (5)$$

Here, $\mu_1\cos\theta$ is the component of the constant dipole moment of the monomer unit of the polymer in the backbone direction.

By substituting into formula (5) the experimental value of μ^2/M for PVP-2 in the mixed solvent, the value $\mu^2/M_1 = 0.167 \times 10^{-36}$ D^2 g^{-1} corresponding to the monomer, and $s = 7$, we obtain $\theta = 82°$.

Thus, the electrooptical properties and dielectric polarization of the PVP solutions suggest that the constant dipole moment of the pyrrolidone ring is virtually perpendicular to the backbone. This, evidently, results from steric hindrance to orientation of bulky and strongly polar rings linked by weakly polar flexible vinyl chain. Large constant dipole moments of the pyrrolidone rings are perpendicular to the backbone and virtually cancel out in the bulk of the PVP polymer coil in the equilibrium state. This decreases the specific dielectric polarizations of PVP in solutions by almost an order of magnitude relative to low-molecular-weight MP and is responsible for small and negative electrooptical effect in solutions of this polar polymer. This is illustrated by Fig. 6 demonstrating the structure of the PVP hexamer, optimized by the PM3 quantum-chemical semiempirical method. The arrows show the directions of the dipole moments of the pyrrolidone rings. It is seen that the dipoles

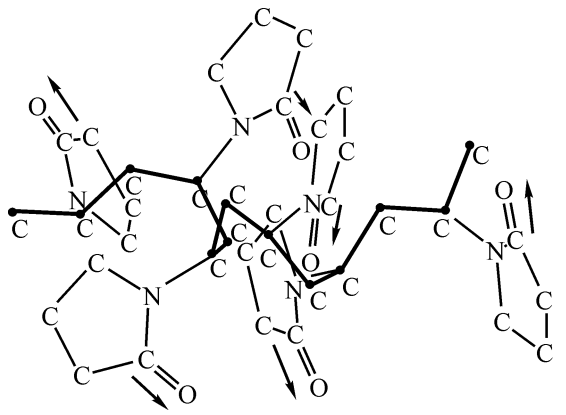

Fig. 6. Structure of the PVP hexamer, optimized by PM3 quantum chemical method. The PVP backbone is shown by a thick line; the hydrogen atoms are not indicated; *arrows* show the directions of the constant dipole moments of the pyrrolidone rings.

are not ordered along the PVP chain propagation direction; they are oriented in the neighboring monomeric units toward one another and are predominantly orthogonal to the vinyl chain.

CONCLUSIONS

(1) Dipole moments of polar pyrrolidone rings in the polymer molecule are oriented, on the average, at large angles of ~82°–87°, i.e., are virtually perpendicular, to the backbone.

(2) The orientation of the pyrrolidone rings is weakly correlated with the chain propagation direction, and their dipole moments virtually cancel out in the PVP bulk and do not contribute to the total dipole moment of the macromolecule.

(3) The above-mentioned specific features of the dipole structure are responsible for the fact that PVP, in which each monomeric unit has a significant dipole moment of ~3.3 D, exhibits a weak electrooptical Kerr effect which differs in sign and magnitude from that in its monomeric unit analogue, MP. PVP is also characterized by a small, relative to MP, specific dielectric polarization in solutions.

The results of this study are suitable for further analysis of the electrooptical and dielectric properties of PVP, in particular, fullerene-containing derivatives [2, 3].

ACKNOWLEDGMENTS

The authors are grateful to O.V. Nazarova (Institute of Macromolecular Compounds, Russian Academy of Sciences) for synthesis of the PVP samples.

REFERENCES

1. Kirsh, Yu. E., *Poli-N-vinilpirrolidon i drugie poli-N-vinilamidy: Sintez i fiziko-khimicheskie svoistva* (Poly-*N*-Vinylpirrolidone and Other Poly-*N*-Vinylamides: Synthesis and Physicochemical Properties), Moscow: Nauka, 1998.
2. Evlampieva, N.P., Lavrenko, P.N., Melenevskaya E.Yu., *et al.*, *Fiz. Tverd. Tela*, 2002, vol. 44, issue 3, pp. 537–540.
3. Ryumtsev, E.I., Evlampieva, N.P., Nazarova, O.V., *et al.*, *Dokl. Ross. Akad. Nauk*, 2003 (in press).
4. Frisman, E.V. and Sibileva, M.A., *Vysokomol. Soedin.*, 1961, vol. 3, no. 7, pp. 1284–1287.
5. Tsvetkov, V.N., *Zhestkotsepnye polimernye molekuly* (Rigid-Chain Polymer Molecules), Leningrad: Nauka, 1986.
6. Evlampieva, N.P., Yakimanskii, A.V., Pavlov, G.M., *et al.*, *Zh. Prikl. Khim.*, 2002, vol. 75, no. 10, pp. 1699–1706.
7. Minkin, V.I., Osipov, O,A., and Zhdanov, Yu.A., *Dipol'nye momenty v organicheskoi khimii* (Dipole Moments in Organic Chemistry), Leningrad: Khimiya, 1968.
8. *Zhidkokristallicheskii poryadok v polimerakh* (Liquid Crystalline Order in Polymers), Blyumshtein, A., Ed. Moscow: Mir, 1981, issue 2.
9. Tsvetkov, V.N., Rjumtsev, E.I., Shtennikov, I.N., *et al.*, *Eur. Polym. J.*, 1973, vol. 9, pp. 481–492.
10. Tsvetkov, V.N., Eskin, V.E., and Frenkel, S.Ya., *Struktura makromolekul v rastvorakh* (Structure of Macromolecules in Solutions), Moscow: Nauka, 1965.
11. Flory, P.J., *Statistical Mechanics of Chain Molecules*, New York: Interscience, 1969.
12. Pavlov, G.M., Panarin, E.F., Korneeva, E.V., *et al.*, *Vysokomol. Soedin., Ser. A*, 1990, vol. 32, no. 6, pp. 1190–1196.
13. Stewart, J.J.P., *J. Comput. Chem.*, 1989, vol. 10, pp. 209–220.
14. Stewart, J.J.P., Orbital Program, *J. Computer-Aided Mol. Des.*, 1990, no. 4, pp. 1–105.

Russian Journal of Applied Chemistry, Vol. 76, No. 10, 2003, pp. 1643–1646. Translated from Zhurnal Prikladnoi Khimii, Vol. 76, No. 10, 2003, pp. 1688–1691.

MACROMOLECULAR CHEMISTRY AND POLYMERIC MATERIALS

Lightfastness of IR Light Filters on Polymer Base

N. B. Sokolova, L. P. Kovzhina, N. M. Dmitrieva, and O. V. Chernyat'eva

St. Petersburg State Technological Institute, St. Petersburg, Russia

Received June 10, 2003

Abstract—The photostabilizing properties of nickel and platinum ethylenedithiolate complexes used as IR absorbents in polymeric film light filters containing heterocyclic azo dyes were studied.

The majority of modern optical filters, along with having the main spectral characteristic in the visible range, also exhibit IR absorption bands suppressing the "parasitic" transmission of the filter in the IR range. Addition to dye formulations of IR-absorbing substances may affect the properties of dyes and, in particular, their lightfastness.

Among various classes of IR-absorbing substances, nickel and platinum ethylenedithiolate complexes form a particular group [1]; their solutions have no pronounced absorption bands in the visible range. Thus, these complexes do not affect noticeably the main spectral characteristics of the filters. One more advantage of transition metal ethylenedithiolate complexes is their capability for photostabilization of some polymeric compounds [2].

In this study, we prepared five ethylenedithiolate complexes **I**–**V** (Table 1) and examined their effect on yellow-orange filter dyes **VI**–**IX** of the thiophene and furan series (Table 2). These dyes are frequently used in cutoff and band-pass polymeric light filters on the cellulose acetobutyrate base. This polymer is the most convenient as the film-forming component, thanks to its high transparency, absence of shrinkage, moisture resistance, etc. [3].

Table 1. Filter IR absorbents 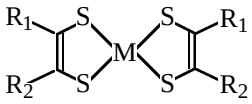

Dye	Name	R_1	R_2	M	λ_{max}, nm
I	Bis(1,2-dimethylethylenedithiolato)platinum	CH_3	CH_3	Pt	740
II	Bis(1,2-dimethylethylenedithiolato)nickel	CH_3	CH_3	Ni	770
III	Bis(1,2-diphenylethylenedithiolato)nickel	C_6H_5	C_6H_5	Ni	850
IV	Bis[1,2-di(3',4'-dimethoxy)phenylethylenedithiolato]nickel	3,4-$(OCH_3)_2C_6H_5$	3,4-$(OCH_3)_2C_6H_5$	Ni	950
V	Bis[1-(4'-dimethylamino)phenyl-2-phenylethylenedithiolato]nickel	*p*-$N(CH_3)_2C_6H_5$	C_6H_5	Ni	1070

Table 2. Filter yellow-orange azo dyes of the thiphene and furan series 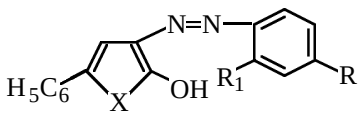

Dye	Name	X	R_1	R	λ_{max}, nm
VI	2-Phenyl-4-(2'-carboxy)phenylazo-5-hydroxyfuran	O	COOH	H	440
VII	2-Phenyl-4-(2',4'-dimethyl)phenylazo-5-hydroxyfuran	O	CH_3	CH_3	440
VIII	2-Phenyl-4-(2'-carboxy)phenylazo-5-hydroxythiophene	S	COOH	H	470
IX	2-Phenyl-4-(2',4'-dimethyl)phenylazo-5-hydroxythiophene	S	CH_3	CH_3	480

1070-4272/03/7610-1643 $25.00 © 2003 MAIK "Nauka/Interperiodica"

Table 3. Degree of photochemical degradation of monoazo dyes **VI**–**IX** of the furan and thiophene series in films in the absence and in the presence of ethylenedithiolate complexes **I**–**V** (irradiation time 1 h)

Dye		PD, %	ΔPD, %
	VI	11.96	
	VII	56.68	
	VIII	6.40	
	IX	48.52	
VI +	**I**	5.95	+6.01
	II	3.64	+8.32
	III	7.02	+4.94
	IV	3.46	+8.47
	V	4.94	+7.02
VII +	**I**	14.76	+41.92
	II	11.07	+45.61
	III	7.69	+48.89
	IV	8.17	+48.51
	V	6.75	+49.93
VIII +	**I**	3.38	+3.02
	II	2.78	+3.62
	III	1.92	+4.48
	IV	1.44	+4.96
	V	0.67	+5.73
IX +	**I**	12.64	+35.88
	II	15.26	+33.26
	III	9.11	+39.41
	IV	5.52	+43.00
	V	5.54	+42.98

The lightfastness of azo dyes **VI**–**IX** in the acetobutyrate matrix has been studied previously both with individual dyes [4, 5] and with various dye mixtures [6]; the necessity for photostabilization of the filter dyes was revealed.

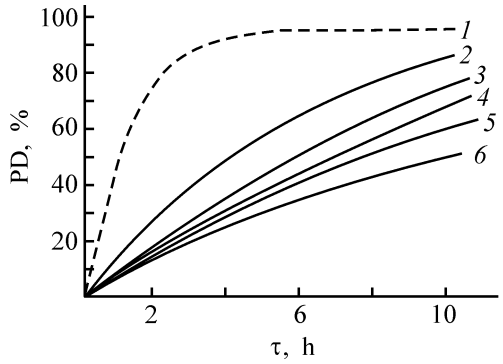

Fading curves of dye **VII** in an acetobutyrate film. (PD) Degree of photochemical degradation and (τ) time. Second component: (*1*) none, (*2*) **I**, (*3*) **II**, (*4*) **IV**, (*5*) **III**, and (*6*) **V**.

Photochemical degradation of ethylenedithiolate complexes in cellulose acetobutyrate and the photostabilizing properties of these complexes have not been studied previously.

We prepared nine film samples with individual dyes and 20 film samples with binary mixtures of an azo dye with an IR absorbent.

The photochemical degradation of dyed films was studied under conditions of accelerated photochemical aging. Samples were irradiated with a xenon lamp whose emission spectrum is similar to that of the Sun.

The rate of dye degradation in the polymeric matrix was determined from the degrees of its photochemical degradation (PD, %), measured at regular intervals (15, 30, 45 min; 1, 2, 3, ..., 10 h):

$$\mathrm{PD} = \frac{D_0 - D_i}{D_0} \times 100.$$

Here D_0 and D_i are the optical densities of the dye at the chosen wavelength, determined before irradiation and after irradiation for a definite period, respectively.

To eliminate the possible contribution from photochemical degradation of the polymer base, the electronic absorption spectra of films were measured relative to a colorless acetobutyrate film irradiated under the same conditions. The analytical wavelengths corresponded to the absorption peaks of the dyes (Tables 1, 2).

In the range of maximal absorption of IR dyes **I**–**V**, heterocyclic azo dyes have no absorption; therefore, calculation of the degree of photochemical degradation of **I**–**V** involved no problems. In the range 440–480 nm, in which the azo dyes in hand have absorption peaks, the measured optical density is the sum of the optical densities of the azo dyes and dithiolate complexes, which also exhibit certain short-wavelength absorption; the optical density of **I**–**V** in this range should be taken into account in the calculations. It was evaluated from data on photochemical degradation of individual nickel and platinum ethylenedithiolate complexes in an acetobutyrate film irradiated under the same conditions as those for the binary formulations. The results are listed in Tables 3 and 4.

Using the data in Tables 3 and 4, we plotted the fading curves for each dye in the absence and in the presence of a second component; the curves for azo dye **VIII** are shown as example in the figure.

To discuss the results, it is appropriate to use data on photochemical degradation in 1 h, because longer irradiation may cause accumulation of degradation prod-

ucts in amounts in which they affect the optical density in the short-wavelength part of the visible spectrum.

The degrees of photochemical degradation of the dye in the film in the absence (PD_{ind}) and in the presence (PD_m) of the second component were compared, and their difference ΔPD was calculated:

$$\Delta PD = PD_{ind} - PD_m.$$

ΔPD is positive when the dye lightfastness is enhanced in the presence of the second component and negative in the opposite case (Tables 3, 4).

These results show that, in cellulose acetobutyrate, as in the previously described polymers, ethylenedithiolate complexes **I**–**V** exhibit photostabilizing properties, strongly diminishing the photochemical degradation of heterocyclic azo dyes (Table 3). This effect is especially pronounced with the least lightfast dyes, xylidine derivatives of furan (**VII**) and thiophene (**IX**). These dyes, when used in combination with ethylenedithiolates, exhibit lightfastness comparable with that in the best representatives of this class, anthranilic acid derivatives **VI** and **VIII** stabilized with an intramolecular hydrogen bond. The lightfastness of **VI** and **VIII** is also enhanced appreciably in the presence of ethylenedithiolates (Table 3). The lightfastness of **I**–**V** is not affected noticeably by the presence of azo dyes (Table 4).

The photostabilizing effect of nickel and platinum ethylenedithiolate complexes is presumably due to several factors: possible coordination of the azo dye with the complex, aggregation of azo dyes under the influence of the complexes, and ability of the complexes to quench singlet oxygen [7].

EXPERIMENTAL

The procedure for laboratory preparation of polymeric film light filters was described in detail in [8].

The electronic absorption spectra were measured on an SF-16 spectrophotometer. The solvent for the dyes and polymer was a chloroform–ethanol mixture (85 : 15 by weight).

Films were irradiated on a Standard Xenon Long-Life Fade Meter XFL-1 installation for accelerated photochemical aging. The first four irradiation runs continued for 15 min, and the subsequent runs, for 1 h each, until the total irradiation time reached 10 h. After the irradiation was complete, the films were stored in the dark at room temperature for no less than 24 h, after which the electronic absorption spectrum of the film was recorded, and the degree of photochemical degradation of each component, calculated.

Table 4. Degree of photochemical degradation of ethylenedithiolate complexes **I**–**V** in films in the absence and in the presence of azo dyes **VI**–**IX** (irradiation time 1 h)

Dye		PD, %	ΔPD, %
	I	3.50	
	II	7.53	
	III	1.72	
	IV	3.30	
	V	1.06	
I +	**VI**	1.63	+1.87
	VII	5.37	–1.87
	VIII	2.67	+0.83
	IX	2.25	+1.25
II +	**VI**	2.89	+4.64
	VII	7.03	+0.50
	VIII	2.89	+4.64
	IX	3.82	+3.71
III +	**VI**	4.28	–2.56
	VII	1.84	–0.12
	VIII	0.59	+1.13
	IX	1.49	+0.23
IV +	**VI**	1.16	+2.14
	VII	2.87	+0.43
	VIII	0.98	+2.32
	IX	0.78	+2.52
V +	**VI**	1.17	–0.11
	VII	2.26	–1.20
	VIII	0.34	+0.72
	IX	0.96	+0.10

The dyes were prepared by published procedures [9, 10].

CONCLUSION

Nickel and platinum ethylenedithiolate complexes are effective IR absorbents in polymeric film light filters; they also exert a photostabilizing effect on heterocyclic azo dyes in the polymeric matrix.

ACKNOWLEDGMENTS

The study was supported financially by the International Scientific and Technical Program "Scientific Research of Higher School in Priority Directions of Science and Engineering" (project no. P-265).

REFERENCES

1. El'tsov, A.V., Sokolova, N.B., Shul'gina, E.S., and Dmitrieva, N.M., *Zh. Prikl. Khim.*, 1993, vol. 66, no. 7, pp. 1561–1573.
2. JPN Patent Appl. 62-267360.
3. Shul'gina, E.S., Veller, E.A., El'tsov, A.V., *et al.*, in *Mezhvuzovskii sbornik "Khimiya, tekhnologiya i primenenie plastmass"* (Intercollegiate Coll. "Chemistry, Technology, and Applications of Plastics"), Leningrad: Leningr. Tekhnol. Inst. im. Lensoveta, 1981, pp. 74–77.
4. Kovzhina, L.P., Sokolova, N.B., Dmitrieva, N.M., and Pesenko, E.V., *Zh. Prikl. Khim.*, 1996, vol. 69, no. 3, pp. 477–482.
5. Kovzhina, L.P., Sokolova, N.B., and Dmitrieva, N.M., *Zh. Prikl. Khim.*, 1998, vol. 71, no. 3, pp. 453–458.
6. Kovzhina, L.P., Sokolova, N.B., Dmitrieva, N.M., and Popova, T.N., *Zh. Prikl. Khim.*, 1998, vol. 71, no. 12, pp. 2024–2028.
7. Kuramoto, N. and Asao, K., *Dyers Pigm.*, 1990, vol. 12, no. 1, pp. 66–77.
8. Kovzhina, L.P., Sokolova, N.B., Dmitrieva, N.M., and Vins, T.Yu., *Zh. Prikl. Khim.*, 1999, vol. 72, no. 9, pp. 1507–1509.
9. Khattab, S.A., Shawali, S.A., and Farad, A.M., *J. Chem. Eng. Data*, 1977, vol. 22, no. 1, pp. 104–110.
10. Schrawzer, J.N. and Mayweg, V.P., *J. Am. Chem. Soc.*, 1965, vol. 87, no. 6, pp. 1483–1489.

Russian Journal of Applied Chemistry, Vol. 76, No. 10, 2003, pp. 1647–1650. Translated from Zhurnal Prikladnoi Khimii, Vol. 76, No. 10, 2003, pp. 1692–1695.

MACROMOLECULAR CHEMISTRY AND POLYMERIC MATERIALS

N-Methacryloylaminodeoxyglucose Copolymers Containing Unsaturated Acid and Activated Ester Units

O. V. Nazarova, N. G. Fomina, E. V. Afanas'eva, and E. F. Panarin

Institute of Macromolecular Compounds, Russian Academy of Sciences, St. Petersburg, Russia

Received June 24, 2003

Abstract—Copolymers of *N*-methacryloylaminodeoxyglucose with acrylic and methacrylic acids were prepared by radical copolymerization. The reactions of these copolymers with *p*-nitrophenol, *N*-hydroxysuccinimide, and *N*-hydroxyphthalimide in the presence of *N*,*N*'-dicyclohexylcarbodiimide were studied.

Owing to their high reactivity, polymeric activated esters show much promise for syntheses of graft and block copolymers, preparation of cross-linked polymeric structures, and modification of various biologically active substances (BASs) [1]. Much researchers' attention is attracted now by new polymeric carriers for BASs, polyvinyl saccharides and, in particular, by polymers of *N*-methacryloylaminodeoxyglucose (MAG) [2–9].

Polyvinyl saccharides are biologically active; in particular, they exhibit immunomodulating properties [7, 8]. Furthermore, *in vivo* experiments showed that, when administered to a living body, the polymers containing carbohydrate fragments as target-recognizing vectors, are selectively localized in definite organs, i.e., these units ensure directed transport of polymeric systems [10] and enhance their bioadhesion [11]. To make polyvinyl saccharides suitable as polymeric carriers, it is necessary to introduce into them highly reactive functional groups reacting with BASs under mild conditions.

The goal of this study was to develop procedures for introducing activated ester units into polyvinyl saccharides.

We tested two procedures for introducing reactive ester units into poly-MAG: (1) radical copolymerization of MAG with activated esters of unsaturated acids and (2) introduction of activated ester groups into polymers by polymer-analogous transformations.

EXPERIMENTAL

N-Methacryloylaminodeoxyglucose was prepared as described in [2]. Activated *p*-nitrophenyl (NPE) and *N*-hydroxysuccinimide (HSIE) esters of unsaturated acids (acrylic, AA; methacrylic, MAA) were prepared as described in [12, 13]. Copolymerization of MAG with unsaturated acids was performed at 60°C for 24 h, and copolymerization with activated esters, at 50°C for 1–2 h in dimethylformamide (DMF) in the presence of a radical polymerization initiator, azobis(isobutyronitrile) (AIBN). The polymers were precipitated by pouring their solutions into diethyl ether.

Reactions of MAG–unsaturated acid copolymers with hydroxy compounds (*p*-nitrophenol, NP; *N*-hydroxysuccinimide, HSI; *N*-hydroxyphthalimide, HPI) were performed in DMF in the presence of *N*,*N*'-dicyclohexylcarbodiimide (DCC) [12]. After a reaction was complete, the dicyclohexylurea precipitate was filtered off, and the polymer was isolated with diethyl ether.

The content of carboxy groups in MAG–acid copolymers was determined by potentiometric titration with 0.1 N NaOH. The content of activated ester (*N*-hydroxyphthalimide ester, HPIE; HSIE; NPE) units in the copolymers was estimated spectrophotometrically (SF-46 spectrophotometer) from the absorption of, respectively, AA HPIE units (λ_{max} = 295 nm, ε = 2100 l mol^{-1} cm^{-1}) [13], HSI anion released in aminolysis of the copolymers with 0.1 N NH_4OH (λ_{max} = 260 nm, ε = 8600 l mol^{-1} cm^{-1}) [13], and bound NP (λ_{max} = 274 nm, ε = 9500 l mol^{-1} cm^{-1}) [14]. The intrinsic viscosities of copolymers were determined with an Ubbelohde viscometer in 0.1 M Na_2SO_4 at 25°C. The molecular weight of the MAG–AA copolymer (8.0 mol % acid units) was calculated using the same parameters of the Mark–Kuhn–Houwink equation as for poly-MAG [4]:

$$[\eta] = 8.29 \times 10^{-4} M^{0.49}.$$

1070-4272/03/7610-1647 $25.00 © 2003 MAIK "Nauka/Interperiodica"

Table 1. Copolymerization of MAG (M_1) with unsaturated acids (M_2): [M_1 + M_2] = 10 wt %, [AIBN] = 3% based on [M_1 + M_2], DMF, 60°C, 24 h

Copolymer no.	Monomeric mixture		Copolymer		
	M_2	[M_2], mol %	[M_2], mol %	$[\eta]^*$, dl g^{-1}	M_η
1	AA	10	8.0	0.08	22000
2	AA	30	23.5	0.08	Not determined
3	AA	40	41.0	0.07	
4	MAA	36	27.4	0.07	″

Aminolysis of a MAG copolymer containing NPE units was monitored spectrophotometrically. A solution of the copolymer in DMF was placed in a temperature-controlled (25°C) cell (d = 0.2 cm), and a solution of an amine in DMF was added. The concentration of NPE units was 0.6×10^{-3} M, and the molar ratio [amine] : [ester units] = 150 : 1. The reaction course was monitored by a decrease with time of the optical density at the wavelength corresponding to the absorption peak of bound NP [14]. The time from mixing the reactants to starting the measurements did not exceed 10–15 s.

We failed to prepare the desired copolymers by radical copolymerization of MAG with NPE or HSIE of acrylic and methacrylic acids in the presence of AIBN. In all the cases, the polymer obtained contained no activated ester units. The MAG molecules contain hydroxy groups, in particular, a primary OH group. It is known that hydroxy compounds react with activated esters, with the reaction rate growing with temperature [15, 16]. Apparently, MAG reacts with activated esters at 50°C (conditions of radical polymerization in the presence of AIBN).

Therefore, we tested another procedure for introducing reactive groups: polymer-analogous transformations. For this purpose, we first prepared by radical copolymerization the copolymers of MAG with unsaturated acids, AA and MAA. Then these copolymers were treated with an appropriate hydroxy compound in the presence of a dehydrating agent, DCC, to obtain MAG copolymers containing activated ester (NPE, HSIE, HPIE) units:

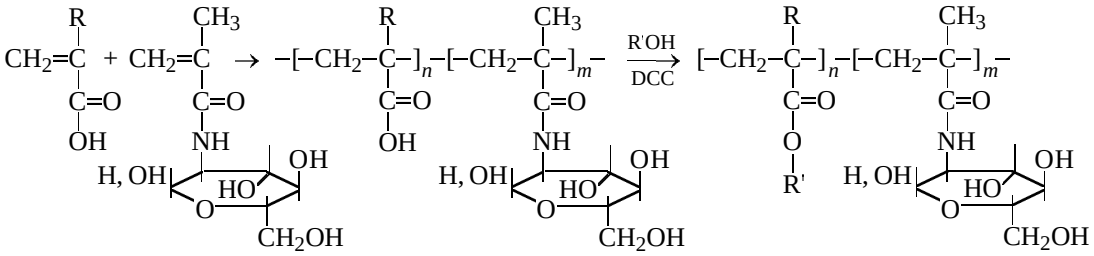

where R = H, CH_3; R' = $-C_6H_4-NO_2$; 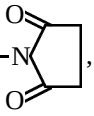 , 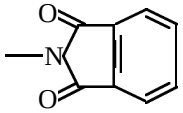 .

Since one of the main requirements to polymeric carriers for BASs is relatively low molecular weight [17], MAG–acid copolymers were prepared at low concentrations of the monomers (10 wt %) and high concentration of the initiator (3 wt % based on the sum of the monomers). The carboxyl-containing copolymers were prepared in 93–95% yield; their characteristics are listed in Table 1. As seen from the above data, the intrinsic viscosities of the copolymers are relatively low: 0.07–0.08 dl g^{-1}. The MAG–AA copolymer containing 8 mol % acid units has M_η = 22000, which meets the requirements to polymeric carriers for BASs (Table 1, polymer no. 1).

Data on reactions of MAG–acid copolymers with hydroxy compounds are listed in Table 2. In all the cases, the copolymers prepared contained activated ester units. However, the degree of esterification of carboxy groups depended on the structure of the starting copolymer. For example, the conversion of MAG–MAA copolymer (27.7 mol % acid units) in the reaction with NP (acid : NP : DCC ratio 1 : 1.2 : 1.2) is as low as 5%, whereas the conversion of the MAG–AA copolymer of similar composition (26.7 mol % acid units) under the same conditions reaches 44%. The amount of ester groups introduced into the copolymer also depends on the reactant ratio. For example, at

Table 2. Reactions of MAG–acid copolymers with hydroxy compounds (HCs)

Co-polymer no.	Starting copolymer			Reaction conditions		Reaction product		
	acid	[COOH], mol %	[η], dl g^{-1}	HC	[COOH] : [HC] : [DCC], mol %	[–O–R'], mol %	α, %	[η]*, dl g^{-1}
5	AA	23.5	0.08	NP	1 : 1.2 : 1.2	10.3	43.8	0.08
6	AA	23.5	0.08	NP	1 : 2 : 2	16.6	70.8	0.07
7	AA	23.5	0.08	NP	1 : 3.5 : 3.5	19.2	71.9	Not determined
8	AA	23.5	0.08	HPI	1 : 1 : 1	13.7	58.4	0.07
9	AA	23.5	0.08	HSI	1 : 2 : 2	14.5	62.0	0.07
10	MAA	27.7	0.07	HSI	1 : 1.2 : 1.2	1.2	4.3	Not determined
11	MAA	27.7	0.07	HSI	1 : 2 : 2	3.4	12.5	″
12	MAA	27.7	0.07	HSI	1 : 3.5 : 3.5	3.6	13.2	″

the acid : NP : DCC ratio of 1 : 2 : 2, the conversions α of the MAA and AA copolymers are 15 and 72%, respectively. However, the conversion did not increase further at larger relative amounts of NP and DCC. A similar influence of the structure of acid units and reactant ratio has been observed previously in reactions of NP with copolymers of *N*-vinylpyrrolidone (VP) with unsaturated acids [12].

Reactions of MAG–AA copolymers with HSI and HPI also proceed to high (up to 60%) conversions (Table 2). The resulting copolymers, containing activated ester units, react with amines. For example, copolymer no. 6 (MAG : AA : AA NPE = 76.5 : 6.9 : 16.6 mol %) reacts with *n*-butylamine by the scheme

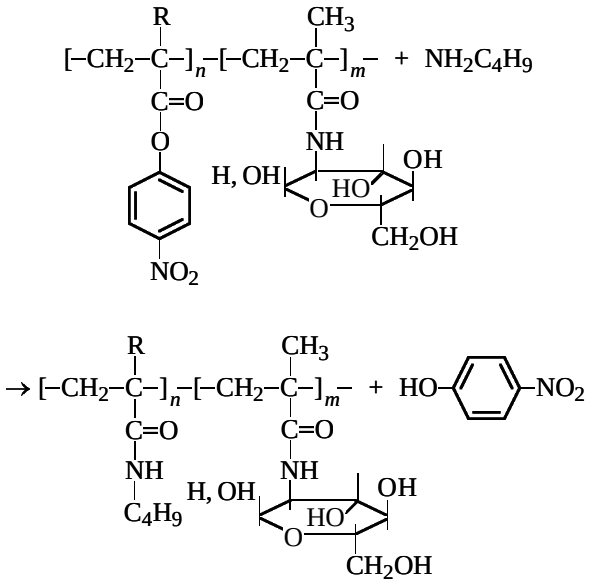

with the release of free NP (λ_{max} = 320 nm), which is accompanied by a decrease in the absorption of bound NP (λ_{max} = 274 nm) [14] (see figure). The times of 20% and 50% conversion of the reactive ester groups in the reaction with the amine are 3 and 24 min, respectively, and the maximum attainable conversion is 92%. In the absence of *n*-butylamine, the intensity of the absorption band with λ_{max} = 274 nm did not change noticeably in the course of several days (see figure).

Interchain interaction of the copolymers synthesized with VP copolymers containing primary amino groups in pendant chains, e.g., with copolymers of VP and vinylamine or allylamine at 5–10 wt % concentration of the sum of the polymers, yields a gel owing to the reaction of amino and activated ester groups, as in the case of VP copolymers containing activated ester units [18].

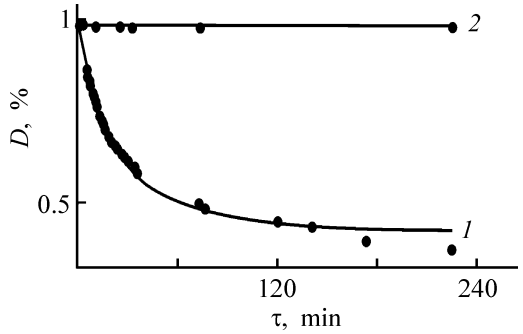

Optical density *D* (λ_{max} = 274 nm) of a solution of copolymer no. 6 in DMF vs. time τ (*1*) in the presence and (*2*) in the absence of *n*-butylamine. Concentrations, M: NPE units 0.6×10^{-3} and *n*-butylamine 0.09.

CONCLUSION

Polymer-analogous transformations allow introduction into poly-*N*-methacryloylaminodeoxyglucose of activated ester groups reactive toward amine-containing compounds, which makes these polymers promising as polymeric carriers for biologically active substances.

ACKNOWLEDGMENTS

The study was supported financially by the Russian Foundation for Basic Research (project nos. 02-03-33110a and NSh-1823.2003.3).

REFERENCES

1. Nazarova, O.V. and Panarin, E.F., *Zh. Prikl. Khim.*, 1999, vol. 72, no. 4, pp. 529–541.
2. Klein, J. and Herzog, D., *Makromol. Chem.*, 1987, vol. 188, no. 6, pp. 1217–1232.
3. Jhurry, D., Deffieux, A., and Fontanille, M., *Makromol. Chem.*, 1992, vol. 193, no. 12, pp. 2997–3007.
4. Pavlov, G.M., Korneeva, E.V., Mikhailova, N.A., *et al.*, *Vysokomol. Soedin., Ser. A*, 1993, vol. 35, no. 10, pp. 1647–1650.
5. Ivanova, N.P., Panarin, E.F., and Denisov, V.M., *Zh. Prikl. Khim.*, 1998, vol. 71, no. 1, pp. 114–118.
6. Panarin, E.F., Ershov, A.Yu., Ivanova, N.P., and Efremova, O.N., *Zh. Prikl. Khim.*, 1999, vol. 72, no. 11, pp. 1872–1875.
7. Panarin, E.F., Ivanova, N.P., Belokhvostova, A.T., and Potapenkova, L.S., *Immunologiya*, 1999, no. 2, pp. 26–28.
8. Panarin, E.F., Ivanova, N.P., Belokhvostova, A.T., and Potapenkova, L.S., *Khim.-Farm. Zh.*, 2002, vol. 36, no. 4, pp. 19–22.
9. Shantha, K.L. and Harding, D.R.K., Eur. Polym. J., 2003, vol. 39, no. 1, pp. 63–68.
10. Pimm, M.V., Perkins, A.C., Duncan, R., and Ulbrich, K., *J. Drug Target.*, 1991, vol. 1, no. 1, pp. 125–131.
11. Rathi, R.S., Kopeckova, P., Rihova, B., and Kopecek, J., *J. Polym. Sci., Part A: Polym. Chem.*, 1991, vol. 29, no. 13, pp. 1895–1902.
12. Nazarova, O.V., Copolymers of Hydrophilic Monomers and Activated Esters of Unsaturated Carboxylic Acids as Carriers for Biologically Active Substances, *Cand. Sci. Dissertation*, Leningrad, 1990.
13. Nazarova, O.V., Solovskij, M.V., Panarin, E.F., *et al.*, *Eur. Polym. J.*, 1992, vol. 28, no. 1, pp. 97–100.
14. Rejmanova, P., Labsky, J., and Kopecek, J., *Makromol. Chem.*, 1977, vol. 178, no. 8, pp. 2159–2168.
15. Batz, H.G., Franzman, G., and Ringsdorf, H., *Makromol. Chem.*, 1973, vol. 172, pp. 27–47.
16. Mahmoud, A.A., Shaaban, A.F., Khalil, A.A., and Messiha, N.N., *Angew. Makromol. Chem.*, 1977, vol. 178, no. 8, pp. 2159–2168.
17. Plate, N.A. and Vasil'ev, A.E., *Fiziologicheski aktivnye polimery* (Physiologically Active Polymers), Moscow: Khimiya, 1986.
18. Nazarova, O.V., Afanas'eva, E.V., Panarin, E.F., and Gorbunova, O.P., *Vysokomol. Soedin.*, 1997, vol. 39, no. 5, pp. 862–867.

Russian Journal of Applied Chemistry, Vol. 76, No. 10, 2003, pp. 1651–1654. Translated from Zhurnal Prikladnoi Khimii, Vol. 76, No. 10, 2003, pp. 1696–1700.

MACROMOLECULAR CHEMISTRY AND POLYMERIC MATERIALS

Electret Effect in Compounds of Polystyrene with Aerosil

M. F. Galikhanov, D. A. Eremeev, and R. Ya. Deberdeev

Kazan State Technological Institute, Kazan, Tatarstan, Russia

Received June 9, 2003

Abstract—Coronoelectrets based on polystyrene and composites of polystyrene with Aerosil were studied.

The electret state is characteristic of virtually all insulators [1]. In recent years, the field of application of electrets, i.e., insulators producing strong electrostatic field in the surrounding space, has expanded rapidly. Their applications range from home facilities to special-purpose equipment; they include acoustic converters, dosimeters, gas filters, systems for electron focusing, elements of friction units, gaskets, systems for corrosion protection, etc. [1–3]. New fields of application of electrets have appeared recently in medicine and biotechnology [4].

For the most part, electrets with stable external electric field are produced from nonpolar polymers in which the presence of deep levels trapping charge carriers plays an important role. Impurity ions, interfaces between crystalline and amorphous phases, and free volume of the polymer serve as energy traps. However, highly stable electrets with good service characteristics can be produced only from a limited set of materials. Straight polymers as main material for electrets do not have the mechanical, thermal, and other characteristics required for their practical use.

To produce electret materials with prescribed characteristics, it is appropriate to use formulations composed of a polymeric binder and various fillers. However, the general pattern of variation of electret characteristics of polymers upon filling was not determined. As a result, progress in practical development of polymer composite electrets is ahead of their theoretical analysis. In this context, it is of interest to study the features of polarization of various composites.

EXPERIMENTAL

We used polystyrene (PS) of the PSM 115 grade [GOST (State Standard) 20282–86] with density of 1.06 g cm^{-1}, viscosity-average molecular weight of 3×10^5, and electrical resistivity of 2×10^{14} Ω m and Aerosil of the A175 grade (GOST 14922–77) with diameter of the initial aggregates of 14 nm and specific adsorption surface area of 175 ± 20 m^2 g^{-1}.

The polymer and filler were blended on laboratory microrolls at 175 ± 5°C for 3 min. Plates 1.1–1.2 mm thick were manufactured by pressing at 170 ± 5°C for 5 min (GOST 12019–66). Polymer plates were polarized in the field of a corona discharge with the use of an electrode containing 196 sharp needles uniformly arranged on a 7×7 cm^2 area. The distance between the plates and electrode was 20 mm; polarization voltage, 35 kV; polarization duration, 60 s. Before polarization, the plates were kept in a thermostat at 90°C for 10 min.

The surface potential of the electrets, V_e, was measured every 24 h for 150 days by the vibration electrode method (noncontact induction method) according to GOST 25209–82 (measuring error 0.15%). The time interval from polarization of the plate to the first measurement of its surface potential was 1 h. The electrets were stored in nonshorted state in paper pacages. The surface charge density σ_{ef} was calculated by the formula

$$\sigma_{ef} = U_c \varepsilon \varepsilon_0 / \delta,$$

where U_c is the compensation voltage; ε, the relative permittivity of the composite; ε_0, the permittivity of free space, equal to 8.854×10^{-12} F m^{-1}; δ, the electret thickness [2].

The error in σ_{ef} calculation was 0.18%.

Thermally stimulated depolarization currents were measured after 150 days of storage under linear heating at a constant rate of 5 deg min^{-1}, using an electronic recorder of small currents with special measuring cell with blocking aluminum electrodes and Teflon gasket [3]. The thermally stimulated depolarization (TSD) spectrum was recorded and visualized on a PC using NVL 03 Driver software.

1070-4272/03/7610-1651 $25.00 © 2003 MAIK "Nauka/Interperiodica"

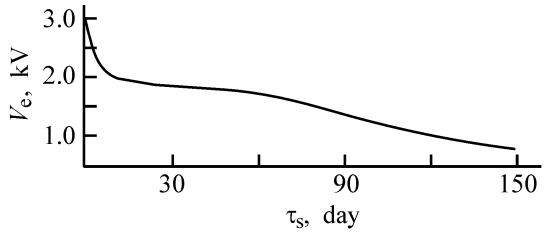

Fig. 1. Surface potential of the polystyrene-based coronoelectret, V_e, vs. storage time τ_s.

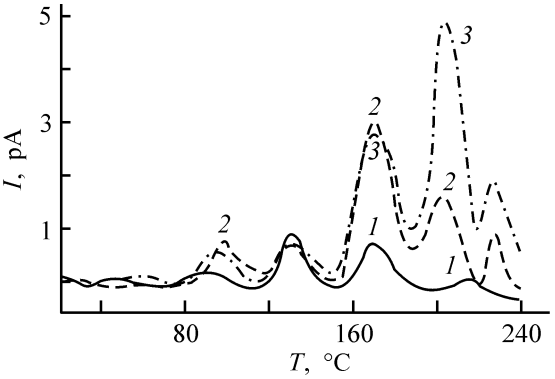

Fig. 2. Currents of thermally stimulated depolarization of coronoelectrets, *I*, based on (*1*) straight polystyrene and composites of polystyrene with (*2*) 6 and (*3*) 10 vol % of Aerosil.

The activation energy of charge relaxation, W_a (trap depth), was evaluated from the initial slope of the TSD current peak (Garlick–Gibson method) [1].

In corona polarization, when one of the polarizing electrodes is ionized air plasma, charge carriers are adsorbed on the surface of the insulator. In this case, ions either transfer their charge to the insulator and return to air or penetrate into the surface area of the insulator, where they are captured by energy traps.

Impurity ions, interface, free volume of polymer, defects of monomeric units, irregularities in the chains, and crystallite imperfections often serve as traps. Chemically active impurities, specific surface defects caused by oxidation processes, adsorbed molecules, and differences in the short-range order of molecules at the surface and in the bulk can serve as surface traps for low-energy charge carriers (shallow traps). The stability of a coronoelectret is mainly governed by the type of energy traps into which most of the injected charge carries fall (deep or shallow).

Polystyrene coronoelectrets have fairly high and stable values of the surface potential V_e (Fig. 1) and effective surface charge density σ_{ef}. It is precisely this fact that account for the researchers' interest in these materials [5–7].

A study of TSD spectra of the polystyrene coronoelectret, performed after 150 days of storage, revealed the presence of two levels capturing injected charge carriers (Fig. 2). The primary level with activation energy of charge relaxation, $W_a = 1.15 \pm 0.05$ eV, is eliminated at 125–130°C. It is likely that, at this temperature, the segmental mobility of polystyrene macromolecules becomes sufficient for liberation of injected charge carriers from structural energy traps. Indeed, at 106–110°C, polystyrene passes from glassy to hyperelastic state. Above this temperature, bulky pendant groups can fairly easily rotate, overcoming the intramolecular and intermolecular interactions. The difference between the temperatures of destruction of energy traps of this type and the glass transition point may be due to high rate of temperature variation in measurement of thermally stimulated depolarization currents, not comparable with the relaxation rate of macromolecular chains and their segments.

The secondary level capturing charge carriers, with trap depth of 1.05 ± 0.05 eV, eliminated at 160–165°C. This temperature is close to the flow point of polystyrene, above which interchain interactions in the polymer are virtually absent (Fig. 2).

Composite materials have features affecting formation and relaxation of electret charge. For example, in filling of polymers as one of the possible ways to produce electret composite materials, new structural elements that can serve as traps of charge carriers arise. These are interfaces, at which accumulation of charge carriers is caused by the difference in conductivity between the phases (Maxwell–Wagner effect), loosened adsorption layer of the polymer, and overstrained segments of macromolecules.

It is well known that radicals formed in degradation of macromolecules can act as deep traps [3]. In blending of polymers with fillers, high shear stresses arise on the rolls, which inevitably results in mechanochemical processes in the polymer. In this case, macromolecules are cleaved to form radicals.

This must result in enhancement of electret characteristics of polymeric coronoelectrets. However, a study of composites of polymers with dispersed fillers revealed that the composition of a composite exerts a complicated influence on its characteristics [3, 8–12]. Both improvement and degradation of the electret characteristics of polymer composites with increasing content of fillers were observed.

The aforesaid makes interesting a study of polymer composite coronoelectrets based on polystyrene

and dispersed fillers. Previously, electrets based on various polymers with different modifications of silicon dioxide have been studied: polymethyl methacrylate with block silica gel [10, 11], polyamide PA-6 with fiber glass [12], and polyvinyl butyral with fiber glass fabric [3]. Therefore, powdered Aerosil with general chemical formula SiO_2 was chosen as filler.

The studies showed that the presence of a filler significantly affects the electret effect in polystyrene: with increasing content of Aerosil in the composite, the surface potential and effective surface charge density measured after 150 days of storage initially increase and then decrease (Fig. 3). For all the composites studied, the surface charge is stable after 150 days of storage; therefore, a comparison of their electret characteristics at this instant of time is quite correct. A similar dependence of charge density of thermally stimulated depolarization of metal-containing polymeric electrets on the content of fiber glass fabric in polyvinyl butyral has been observed previously [3].

The increase in V_e and σ_{ef} of polystyrene upon filling with Aerosil can be accounted for by appearance in the material of new energy traps for injected charge carriers with wide energy range. A study of the TSD spectra of filled electret compounds (Fig. 2) showed the presence of new traps for injected charge carriers, which disappeared at 200–205 and 220–230°C. Most likely, these traps are due to appearance of the polymer–filler interface, since in filling the main part of new traps appear at this interface. This is also caused by the Maxwell–Wagner effect, presence of various polar groups at the silicon dioxide surface, and appearance of loosened adsorption layer at the filler surface. The observed enhancement of electret characteristics was accounted for in [3] by formation of more perfect supramolecular structures, which has a positive effect on the formation of the electret charge. This phenomenon can take place in the composites considered. The activation energies of charge relaxation from new trap levels were 1.35 ± 0.05 and 1.20 ± 0.05 eV for the electret from the polystyrene composite with 6 vol % of Aerosil.

It was found that the intensity and position of peaks of TSD currents, characteristic of neat polystyrene, vary with filling (Fig. 2). This is most likely due to the presence of adsorption layer of polymer at the filler surface with low lability; as a result, the mobility of various kinetic units of the polymer decreases and the relaxation times of its macromolecules increase. For the composite of polystyrene with 6 vol % Aerosil, W_a is 1.10 ± 0.05 and 1.95 ± 0.05 eV for primary and secondary traps for charge carriers, respectively.

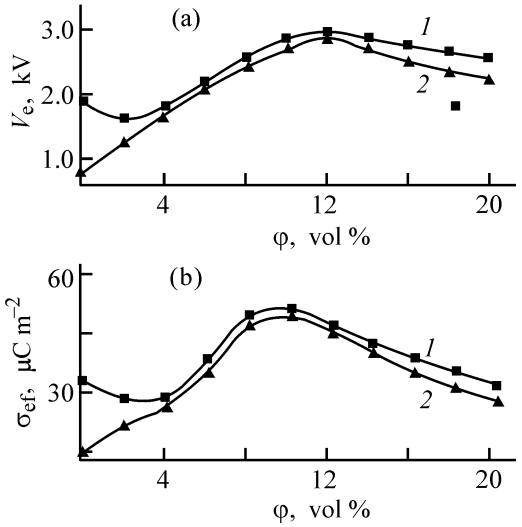

Fig. 3. (a) Surface potential V_e and (b) surface charge density σ_{ef} of coronoelectrets based on polystyrene and Aerosil vs. A175 filler content φ after (*1*) 30 and (*2*) 150 days of storage.

Raising the filler content results in an increase in the interface area and, hence, in the number of traps, which must improve the electret characteristics. Actually, for a coronoelectret based on polystyrene with 10 vol % of Aerosil W_a is 3.15 ± 0.05 and 1.75 ± 0.05 eV for tertiary and quaternary traps for charge carriers, respectively (Fig. 2).

However, with the filler content increasing further, the V_e and σ_{ef} values decrease (Fig. 3), which is unexpected. A decrease in charge with increasing filler content can be accounted for by a decrease in the amount of polarizable polymeric material: substitution of nonpolarizable filler for electretized polystyrene must inevitably affect the characteristics of coronoelectrets, which is actually observed for the dependences of V_e and σ_{ef} on the filler content (Fig. 3). In addition, even for the polystyrene composites with 10 vol % filler, the W_a values for primary and secondary trap levels for charge carriers (1.05 ± 0.05 and 1.80 ± 0.05 eV, respectively) are lower than the corresponding values for the composites with 6 vol % Aerosil. At a still higher Aerosil content, the intensities of these peaks decrease further. This can be accounted for as follows.

An increase in the total number of traps also makes greater the number of shallow traps. During polarization, shallow surface traps are saturated with injected charge carries first. An increased content of injected charge carriers in the surface layer makes higher its conductivity, which leads to high relaxation rate of the coronoelectret charge. This impairs

Variation of the surface potential of polystyrene-based composite of coronoelectrets in thermal treatment

A175, vol %	Before thermal treatment		*T*, °C	After thermal treatment for indicated period, h					
				1		168		336	
	V_e, kV	σ_{ef}, μC m^{-2}		V_e, kV	σ_{ef}, μC m^{-2}	V_e, kV	σ_{ef}, μC m^{-2}	V_e, kV	σ_{ef}, μC m^{-2}
6	2.05	35.6	150	2.00	34.7	1.55	26.9	1.45	25.2
	2.05	35.6	170	2.05	35.6	1.20	20.8	1.15	20.0
	2.05	35.6	190	1.45	25.2	0.75	13.0	0.7	12.2
10	2.70	49.8	150	2.70	49.8	2.20	40.6	2.05	37.8
	2.70	49.8	170	2.65	48.9	2.00	36.9	1.90	35.0
	2.70	49.8	190	1.90	35.0	1.00	18.4	0.95	17.5

the electret characteristics of polystyrene composites after reaching a certain extent of filling.

Filling of polystyrene with Aerosil particles changes the characteristics of supramolecular structure formation (size, shape, and type of size distribution) and packing density, which may also lead to changes in its electret characteristics (Fig. 3).

Our results suggest that even processing of composite coronoelectrets by traditional procedures involving reprocessing of plastics at a temperature less than 190°C can yield products with electret properties, since some traps for injected charge carriers disappear above this temperature (with account of the high relaxation rates of macromolecules).

To verify this assumption, electret plates based on polystyrene compounds were kept in thermostat at 150°C, 170°C, and 190°C. Changes in the surface potentials in thermal treatment are listed in the table.

It is seen that charge relaxation is not complete, which confirms our assumption.

CONCLUSIONS

(1) In electrets based on polystyrene, two trapping levels injected charge carriers, responsible for the high and stable electret properties of the composites, were found.

(2) Addition of silicon dioxide gives rise to new trapping levels at the polymer–filler interface and changes the energy depth of the existing levels, which increases the surface potential and the effective surface charge density of polystyrene electrets. Raising the filler content above 10–12 vol % leads to deterioration of the electret characteristics of composites owing to a decrease in the amount of polarized polymeric material and increased conductivity of the surface layer, which makes faster the relaxation rate of coronoelectret charge. Electrets with prescribed characteristics can be prepared by varying the component ratio.

(3) The prepared sheet and film coronoelectrets based on composites of polystyrene with Aerosil can be processed into other articles without loss of their electret properties.

REFERENCES

1. *Electrets*, Sessler, G.M., Ed., Berlin: Springer, 1980.
2. Lushcheikin, G.A., *Polimernye elektrety* (Polymeric Electrets), Moscow: Khimiya, 1984.
3. Pinchuk, L.S. and Gol'dade, V.A., *Elektretnye materialy v mashinostroenii* (Electret Materials in Mechanical Engineering), Gomel: Infotribo, 1998.
4. Makarevich, A.V., Pinchuk, L.S., and Gol'dade, V.A., *Elektricheskie polya i elektroaktivnye materialy v biotekhnologii i meditsine* (Electric Fields and Electrically Active Materials in Biotechnology and Medicine), Gomel: IMMS NANB, 1998.
5. Tripathi, A.K. and Pillai, P.K.-C., *Proc. 5th Int. Symp. on Electrets*, Heidelberg, 1984, pp. 138–141.
6. Singh, R. and Datt, S.C., *Proc. 5th Int. Symp. on Electrets*, Heidelberg, 1984, pp. 191–194.
7. US Patent 5 610 455.
8. Vertyachikh, I.M., Pinchuk, L.S., and Tsvetkova, E.A., *Vysokomol. Soedin., Ser. B*, 1987, vol. 29, no. 6, pp. 460–463.
9. Galikhanov, I.M., Eremeev, D.A., and Deberdeeva, R.Ya., *Plast. Massy*, 2002, no. 10, pp. 26–28.
10. Kalogeras, I.M., Pallikari-Viras, F., and Vasslikou-Dova, A., *Proc. 9th Int. Symp. on Electrets*, Shanghai (China), 1996, pp. 499–502.
11. Kalogeras, I.M., Vasslikou-Dova, A., and Neagu, E.R., *Proc. 9th Int. Symp. on Electrets*, Delphi (Greece), 1999, pp. 545–548.
12. Sviridenok, A.I., Kovalevskaya, T.I., Kravtsov, A.G., and Bernatskaya, Zh.I., *Dokl. Akad. Nauk Bel.*, 2000, vol. 44, no. 5, pp. 119–122.

Russian Journal of Applied Chemistry, Vol. 76, No. 10, 2003, pp. 1655–1658. Translated from Zhurnal Prikladnoi Khimii, Vol. 76, No. 10, 2003, pp. 1701–1704.

MACROMOLECULAR CHEMISTRY AND POLYMERIC MATERIALS

2-Phenyl-5-(4-Biphenylyl)-1,3,4-Oxadiazole and 2-(4'-*tert*-Butylphenyl-5)-(4''biphenylyl)-1,3,4-Oxadiazole in a Polymethyl Methacrylate Based Plastic Scintillator

V. N. Salimgareeva, R. M. Polevoi, V. A. Ponomareva, N. S. Sannikova, S. V. Kolesov, and G. V. Leplyanin

Institute of Organic Chemistry, Ufa Scientific Center, Russian Academy of Sciences, Ufa, Bashkortostan, Russia

Received May 6, 2003

Abstract—The fluorescence intensity was studied for the scintillation formulation including 1,1,3-trimethyl-3-phenylindan and 2-phenyl-5-(4-biphenylyl)-1,3,4-oxadiazole, 2-(4'-*tert*-butylphenyl-5-(4''-biphenylyl)-1,3,4-oxadiazole, and 1,4-di(5-phenyl-2-oxazolyl)benzene. The scintillation efficiency was determined for the polymethyl methacrylate based plastic scintillator containing the above-listed compounds as luminescent additives.

2,5-Diaryl derivatives of 1,3,4-oxadiazoles are known to exhibit luminescent properties [1]. The high-intensity fluorescence and the short lifetime of the excited state of these compounds made them suitable for scintillation devices.

One of oxadiazole derivatives, 2-phenyl-5-(4-biphenylyl)-1,3,4-oxadiazole (PBD), is used as scintillation activator or luminescent additive enhancing the light pulse from plastic scintillators (PSs) based on polystyrene [2], polyvinylxylene [3], and polyvinyltoluene [4]. 2-Phenyl-5-(4-biphenylyl)-1,3,4-oxadiazole and another oxadizaole derivative, 2-(4'-*tert*-butylphenyl-5-(4''-biphenylyl)-1,3,4-oxadiazole (B-PBD), have been suggested as luminescence activators for PSs based on polymethyl methacrylate (PMMA) [5–7].

PBD and B-PBD are among the best scintillation activators. They can effectively replace *p*-terphenyl (PPP) used in liquid and plastic scintillators. PPP is superior to PBD and B-PBD in the luminescent properties (fluorescence lifetime of PPP is 0.95 s, against 1.0 s of PBD, and the quantum yield of luminescence of PPP, 0.93, against 0.83 for PBD [8]), but exerts a weaker influence on the scintillation properties of formulations. For example, the xylene solution of PBD has a light output of 59% relative to that of anthracene crystals, and the light output of a PPP solution in xylene is 48% [1]. When PBD replaces PPP in the PS based on polyvinylxylene, also containing 1,4-di(5-phenyl-2-oxazolyl)benzene (POPOP), the light output increases from 130–135 to 140–145% relative to polystyrene-based PS [3].

In this study, we attempted to use PBD B-PBD as luminescent additives to replace PPP acting as luminescence activator in the previously suggested [9] PMMA-based scintillator, also containing 1,1,3-trimethyl-3-phenylindan (TMPI) and POPOP as additives. The choice of PBD and B-PBD as luminescence activators was also governed by the fact that, similarly to PPP, they absorb light in the region of TMPI luminescence [10]. Moreover, PBD and B-PBD are more soluble than PPP in conventional scintillation solvents: Saturated toluene solution of PPP at 25°C contains 8 g l^{-1} of the luminescent additive, and that of PBD, 20 g l^{-1} [1]. PPP [11] and PBD (B-PBD) in methyl methacrylate (MMM) and PMMA proved to have the same solubilities. A better, compared with PPP, solubility of these additives must improve the scintillation characteristics of the formulations, since an increase in the concentrations of each additive tends to decrease the light flash amplitude [4].

EXPERIMENTAL

The experimental procedure was described in [1]. The scintillation characteristics of a PS are determined by the spectral-luminescent properties of all its constituent luminescent additives. 1,1,3-Trimethyl-3-phenylindan exhibits absorption and luminescence at 210–290 and 270–310 nm, respectively (Fig. 1). The absorption of PBD and B-PBD at 230–350 nm completely overlaps the luminescence of TMPI, and the medium (PMMA with TMPI additive) is transparent

1070-4272/03/7610-1655 $25.00 © 2003 MAIK "Nauka/Interperiodica"

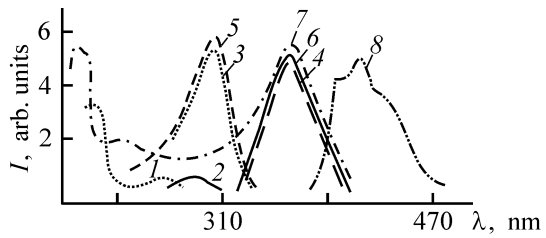

Fig. 1. (*1*, *3*, *5*, *7*) Absorption and (*2*, *4*, *6*, *8*) luminescence spectra of (*1*, *2*) TMPI, (*3*, *4*) PBD, (*5*, *6*) B-PBD, and (*7*, *8*) POPOP. Heptane solution, concentration 2×10^{-2} M. (*I*) Intensity and (λ) wavelength.

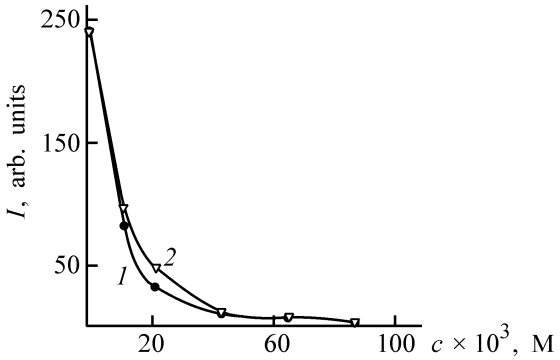

Fig. 2. Luminescence intensity *I* of TMPI at λ = 288 nm vs. concentration *c* of (*1*) PBD and (*2*) B-PBD. Excitation light wavelength λ_{exc} = 250 nm.

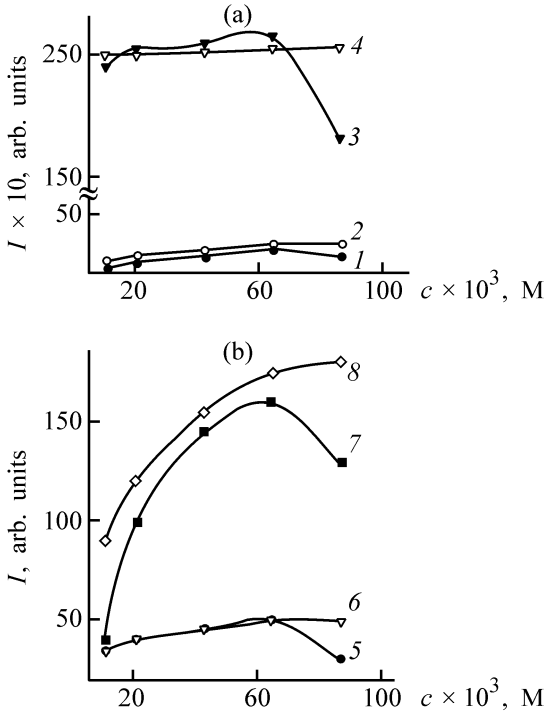

Fig. 3. Luminescence intensity *I* vs. concentration *c* in polymethyl methacrylate of (*1*, *3*, *5*, *7*) PBD and (*2*, *4*, *6*, *8*) B-PBD. (a) PBD and B-PBD at λ = 366 nm and (b) POPOP at λ = 418 nm. Excitation light wavelength λ_{exc}, nm: (*1*, *2*, *5*, *6*) 303 and (*3*, *4*, *7*, *8*) 250.

in this range. As known [1], electron-donating substituents in the *para* position of the phenyl radicals cause a bathochromic effect. This also follows from a comparison of the absorption and fluorescence spectra of PBD and B-PBD (Fig. 1). Moreover, the luminescence intensity tends to increase somewhat in going from PBD to B-PBD.

The complete overlapping of the absorption bands of PBD (B-PBD) with the luminescence bands of TMPI, as well as the high quantum yield (0.27) and short lifetime of fluorescence (8 ns) of the donor, TMPI, favors transfer of the absorbed energy, thereby converting the transferred energy to the electronic excitation energy of the molecules of the acceptor [PBD (B-PBD)]. This is also favored by higher extinction coefficients for PBD (B-PBD) absorption bands, compared with TMPI (4.5×10^4, 4.4×10^4 [1], and 1.69×10^3 l mol^{-1} cm^{-1} [10], respectively). The energy is transferred from TMPI to PBD (B-PBD) virtually without losses at a high rate, as evidenced by a decrease in the TMPI fluorescence intensity almost to zero with the PBD (B-PBD) concentration increasing to 6.5×10^{-2} M and over (Fig. 2). Based on the data from [12], we estimated the rate constants of energy transfer by the dipole-dipole mechanism (such as, e.g., singlet-singlet energy transfer between the organic molecules) at 1.27×10^{10} (1.35×10^{10}) and 6.78×10^9 l mol^{-1} s^{-1} for TMPI–PBD (B-PBD) and TMPI–PPP systems, respectively. The higher rate of energy transfer from TMPI to B-PBD and from B-PBD to POPOP, compared with that from TMPI to PBD and from PBD to POPOP, evidently intensifies the fluorescence of POPOP in the TMPI–B-PBD–POPOP system, compared with the TMPI–PBD–POPOP system irradiated at λ = 250 nm (Fig. 3).

Under excitation at λ_{exc} = 303 nm (without TMPI absorption), the fluorescence intensity of PBD dissolved in PMMA grows only slightly with increasing PBD concentration (Fig. 3a) and reaches a maximum at 1.5 wt % (6.5×10^{-2} M). Further increase in the PBD concentration decreases the luminescence intensity, i.e., there occurs concentration quenching. In the case of POPOP (Fig. 3a, curve *5*), the luminescence intensity varies with the PBD concentration in this system in a similar way. A decrease in the POPOP fluorescence intensity at PBD concentrations above 1.5% is also due to concentration quenching of the activator. Evidently, the rate of energy transfer from PBD to POPOP is comparable with, or lower than the self-quenching rate of PBD.

When a sample containing TMPI and PBD is excited at λ_{exc} = 250 nm, the PBD fluorescence intensity

increases sharply (Fig. 3a, curve *3*) and varies with increasing concentration of the luminescent additive similarly to the case of λ_{exc} = 303 nm (Fig. 3a, curve *1*). The luminescence intensity of POPOP also changes significantly (Fig. 3b, curve *7*). Unlike the case of λ_{exc} = 303 nm, light is absorbed at λ_{exc} = 250 nm by both PBD and TMPI. Therefore, in the region of the POPOP absorption, the total emission energy of PBD is due to absorption of the primary excitation energy and its acceptance from the donor, TMPI. The energy absorbed by POPOP is converted into fluorescence with higher intensity than in the case of λ_{exc} = 303 nm.

Upon introduction of a butyl group into the PBD molecule, not only the absorption and luminescence maxima shift and light emission by this compound is enhanced, but also the patterns of variation of the PBD and POPOP fluorescence intensities with the B-PBD concentration change. These dependences, unlike the case of PBD, are described by curves leveling off under excitation at λ_{exc} = 250 and λ = 303 nm (Fig. 3, curves *2*, *4*, *6*, *8*). Evidently, the transfer of the photoexcitation energy from TMPI to B-PBD and from B-PBD to POPOP is more probable than that in the case of PBD.

Transfer of the excitation energy from the secondary solvent, TMPI, to the activator, PBD (B-PBD), at a high rate and virtually without losses favors high scintillation efficiency of the polymer formulation, also containing POPOP acting as spectrum shifter. The light output of this scintillator at the optimal content of PBD and B-PBD of 1.5 wt % (6.5×10^{-2} M) is 143–145%, and in the case of a PS with the optimal PPP content (0.4%, or 1.7×10^{-2} M) and identical content of TMPI (35%, or 1.48 M) and POPOP (0.02%, or 2.75×10^{-4} M) it does not exceed 130% relative to the PS consisting of PMMA, naphthalene (15%), 2,5-diphenyloxazole (0.3%), and POPOP (0.06%) [11].

The plot of the scintillation efficiency η against the concentrations of the activators for the PMMA-based PS containing TMPI, POPOP, and PBD (B-PBD) has a maximum: η grows with the PBD (B-PBD) content increasing to 1.5 wt % (6.5×10^{-2} M), whereupon the light output decreases with increasing concentration (Fig. 4). As seen from Fig. 4, the scintillation efficiency of PS and the fluorescence intensity of the PBD activator exhibit similar trends upon variation of the PBD concentration and identical positions of the peaks and inflection points in the corresponding curves. Evidently, the luminescent properties of the additive determine its scintillation properties, and energy transfer from excited TMPI molecules to PBD

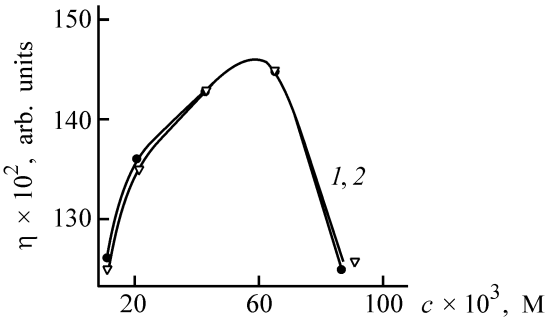

Fig. 4. Variation of the scintillation efficiency η, with the concentration *c*, of (*1*) PBD and (*2*) B-PBD.

molecules and from PBD to POPOP molecules follows the same mechanism in the cases of photo- and γ-excitation. The mechanism of energy transfer to B-PBD at B-PBD concentrations above 6.5×10^{-2} M (1.5 wt %) evidently depends on the nature of the excitation sources, as indicated by the difference in the run of the curves in this concentration range.

Plastic scintillators based on PMMA are typically prepared by free-radical polymerization of methyl methacrylate in which organic luminophores are soluble. The participation of luminophores in chain propagation and copolymerization reactions is responsible for changes in their structures, affecting the spectral characteristics and resulting in the loss of the luminescent activity. We have shown [13] that TMPI, PBD (B-PBD), and POPOP used in the scintillator of interest do not react with the propagating macroradicals: They do not inhibit the process and do not act as chain-transfer agents. These additives are present in the resulting polymer as solutes in a solid solution, and their favorable combination is responsible not only for preservation but also for sensitization of their fluorescence and scintillation.

CONCLUSIONS

(1) The photoexcitation energy is transferred from 1,1,3-trimethyl-3-phenylindan to 2-phenyl-5-(4-biphenylyl)-1,3,4-oxadiazole or 2-(4'-*tert*-butylphenyl)-5-(4''-biphenylyl)-1,3,4-oxadiazole, without losses at high rate.

(2) Polymethyl metahcrylate based plastic scintillators comprising 1,1,3-trimethyl-3-phenylindan, 2-phenyl-5-(4-biphenylyl)-1,3,4-oxadiazole or 2-(4'-*tert*-butylphenyl)-5-(4''-biphenylyl)-1,3,4-oxadiazole, and 1,4-di(5-phenyl-2-oxazolyl)benzene as luminescent additives exhibit a light output exceeding by a factor of 1.1 that of the formulation containing *p*-terphenyl in place of 1,3,4-oxadiazole derivatives.

REFERENCES

1. Krasovitskii, B.M. and Bolotin, B.M., *Organicheskie lyuminofory* (Organic Luminophores), Moscow: Khimiya, 1984.
2. Nagornaya, L.L., Bezuglyi, V.D., and Grekov, A.P., *Opt. Spektrosk.*, 1961, vol. 10, no. 4, pp. 555–556.
3. Gunder, O.A., Koval', L.P., Grigor'eva, V.I., *et al.*, in *Monokristally, stsintillyatory i organicheskie lyuminofory* (Single Crystals, Scintillators, and Organic Lumonophores), Kharkov: Monokristallreaktiv, 1972, issue 6, part 1, pp. 79–82.
4. Malinovskaya, S.A., Snagoshchenko, L.P., Vetrenko, L.P., *et al.*, in *Monokristally, stsintillyatory i organicheskie lyuminofory* (Single Crystals, Scintillators, and Organic Lumonophores), Kharkov: Monokristallreaktiv, 1972, issue 6, part 1, pp. 122–126.
5. FRG Patent 2614519.
6. Klawonn, F., Kleinknecht, K., and Pollmann, D., *Nucl. Instr. Meth. Phys. Res.*, 1982, vol. 195, no. 3, pp. 483–489.
7. Jiang, Y., Yuan, H., Liang, W., and Li, H., *He Dianzixue Yu Tance Jishi*, 1991, vol. 11, no. 1, pp. 62–64.
8. Berlman, J.B., *Handbook of Fluorescence Spectra of Aromatic Molecules*, New York: Academic, 1971.
9. USSR Inventor's Certificate, no. 1123291.
10. Salimgareea, V.N., Ostakhov, S.S., Ponomareva, V.A., *et al.*, *Zh. Prikl. Khim.*, 2003, vol. 76, no. 8, pp. 837–838.
11. Salimgareeva. V.N., Polevoi, R.M., Kolesov, S.V., *et al.*, *Zh. Prikl. Khim.* (in press).
12. Ermolaev, V.L., Sveshnikov, E.B., and Shakhverdov, T.A., *Usp. Khim.*, 1975, vol. 44, no. 1, pp. 49–74.
13. Salimgareeva, V.N., Sannikova, N.S., and Leplyanin, G.V., *Bashk. Khim. Zh.*, 1997, vol. 4, no. 1, pp. 32–36.

Russian Journal of Applied Chemistry, Vol. 76, No. 10, 2003, pp. 1659–1661. Translated from Zhurnal Prikladnoi Khimii, Vol. 76, No. 10, 2003, pp. 1705–1707.

MACROMOLECULAR CHEMISTRY AND POLYMERIC MATERIALS

Rheological and Electrical Properties of an Oligomeric Formulation as Influenced by Fractional Composition of Conducting Filler

V. A. Val'tsifer and N. A. Gubina

Institute of Technical Chemistry, Ural Division, Russian Academy of Sciences, Perm, Russia

Received April 18, 2003

Abstract—The effect of bifractional composition of conducting filler on the electrical and rheological properties of oligomeric compound was studied.

Conducting polymeric materials are frequently prepared by addition of conducting dispersed components [1, 2]. When a conducting component is added in amount exceeding certain fraction, a three-dimensional network of contacting particles is formed, and this structure determines the conductivity of the polymeric compound. Usually, polymeric compounds become conducting at a volume fraction of coarse filler of 23–25 vol % [3].

It is known that finely dispersed components, e.g. carbon black, tend to structurize in an oligomeric medium [4, 5] and form continuous structures extending over the entire system, making it conducting [6]. Formation of such structures obviously affects the rheological properties of the polymer, because they increase the energy of dissipation in a flowing system, i.e., the viscosity of the system grows. The volume content of the carbon black at which an oligomeric compound becomes conducting does not exceed 1 vol %.

To develop conducting polymers using conducting dispersed components, it is necessary to understand the patterns of formation of continuous networks from disperse particles in an oligomeric binder. In this study, we analyzed the rheological and electrical properties of oligomeric suspensions as influenced by an electrically conducting filler.

The structuring of carbon black consisting of coarse and fine fractions in the oligomeric dispersion medium was studied on a special rheological-conductometric device [5] equipped with a rheoviscometer of the Rheotest-2.1 type and a digital unit for data processing, interfaced to PC.

The experiments were performed using nongranulated carbon black (specific surface area 100 $m^2 g^{-1}$) and graphite (particle size 50–80 μm), with butadiene-isoprene oligomer (*M* 5000) as a dispersion phase. The formulations studied were prepared in a vacuum mixer (250 rpm, 1000 Pa) in the course of 30 min at a temperature of 60°C in the water jacket of the stirrer. The mixture was placed in the measuring cell of the rheological-conductometric device, and the cell was thermostated for 1 h. Then, the initial parameters of the device were set, the inner structure of the formulation in the measuring cell was destroyed at a shear rate of about 2×10^2 s^{-1}, and the processes occurring in the compound were studied.

The increase in the conductivity of the formulations indicated that the carbon black particles are involved in structuring and form three-dimensional (3D) conducting agglomerates extending over the entire volume of the measuring cell. As seen from microscopic data, the current passing through the formulation containing continuous networks of carbon black particles is proportional to the number of particle macrochains in the system.

Finely disporsed particles can form continuous networks extending over the entire system and affecting the macroproperties of the oligomeric compound, especially its rheological properties; primarily, the dissipation energy of the compound flow (or its viscosity) must increase. In the case of a conducting filler (e.g., carbon black), formation of 3D continuous networks would strongly affect the formulation properties, making the material conducting. Obviously,

1070-4272/03/7610-1659 $25.00

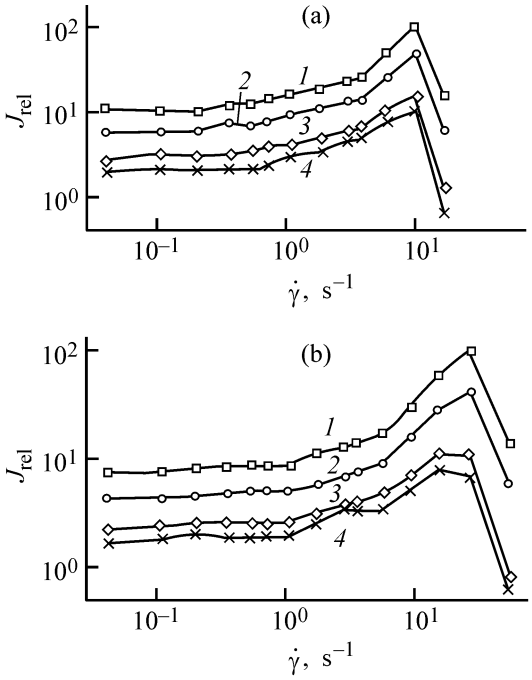

Fig. 1. Relative electrical conductivity J_{rel} of formulation containing carbon black (3 wt %) vs. shear rate $\dot{\gamma}$ at (a) 60 and (b) 80°C. Graphite content, wt %: (*1*) 20, (*2*) 10, (*3*) 5, and (*4*) 2.5.

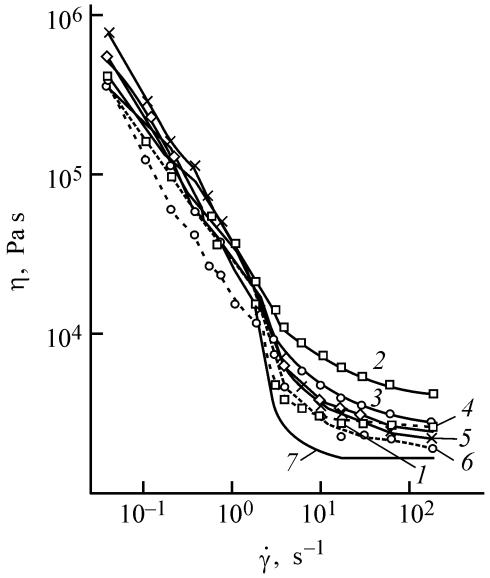

Fig. 2. Viscosity η of oligomer formulation at 60°C vs. the shear rate $\dot{\gamma}$. Graphite content, wt %: (*1*) 22, (*2*) 20, (*3*) 10, (*4*) 5, (*5*) 2.5, and (*6*) 0. Carbon black content, wt %: (*1*, *7*) 0 and (*2–6*) 3.

the length of the continuous chains must be comparable with the distance between the electrodes. Thus, the conductivity of filled polymers is a more sensitive criterion of formation of continuous 3D networks than the viscosity. A sharp increase in the system viscosity may be also due to structuring of particles without formation of networks of a size comparable with the interelectrode distance.

Thus, preparation of conducting formulations based on finely dispersed fillers requires structuring of particles into chains, whose size exceeds the particle size by many orders of the magnitude, with the number of particles in a chain exceeding thousands and tens of thousands. However, such complex systems can be easily broken. A question arises as to how the formulation properties will change upon addition of coarse conducting particles. We assume that these coarse particles can act as centers of carbon black structuring; in this case, the length of continuous carbon black chains required to form a conducting system would significantly decrease.

The dependences of the relative electrical current (i.e., the ratio of the conductivities of formulations containing a mixture of carbon black and graphite and carbon black only, other conditions being equal) are shown in Fig. 1a. We found no conductivity in the mixture containing up to 22 wt % graphite, whereas the oligomer containing 3 wt % of carbon black is a conductor (Fig. 1a). However, the conductivity of the system increases sharply upon addition of graphite to an oligomer containing carbon black (3 wt %). At increased shear rate, the internal structure of the formulation is broken and its conductivity decreases. Similar dependences obtained at higher temperature are shown in Fig. 1b. As seen, the effect of graphite becomes stronger with increasing shear rate; the maximal effect at 60°C corresponds to a shear rate of 10 s^{-1}, and that at 80°C, to 20 s^{-1}.

The influence of the filler content on the oligomer structuring is shown in Fig. 2. As seen, the viscosities of formulations containing carbon black only (curve *6*) and graphite only (curve *1*) are the lowest. The higher viscosity of the pure oligomer in comparison with the formulations containing both graphite (22 wt %) and carbon black (3 wt %) at small sheare rates is probably due to the structuring of the oligomer and the effect of the dispersed components on the resulting structures.

CONCLUSION

Coarsely dispersed filler added to an oligomeric formulation intensifies the structuring of the finely dispersed filler. Graphite when added to butadiene-isoprene oligomer simultaneously with carbon black

substantially enhances the conductivity of the system and increases its viscosity.

REFERENCES

1. Berlin, A.A., Vol'fson, S.A., Oshmyan, V.G., and Enikolopov, N.S., *Printsipy sozdaniya kompozitsionnykh materialov* (Design Philosophy of Composite Materials), Moscow: Khimiya, 1990.
2. Gul', V.E. and Shenfil', L.Z., *Elektroprovodyashchie polimernye kompozitsii* (Conducting Polymeric Compounds), Moscow: Khimiya, 1984.
3. Val'tsifer, V.A. and Gubina, N.A., *Plast. Massy*, 1999, no. 5, pp. 30–31.
4. Shendrik, E.N., Val'tsifer, V.A., and Klyachkin, Yu.S., *Structura i svoistva kompozitov na osnove dispersnykh sistem* (Structure and Properties of Composites Based on Disperse Systems), Sverdlovsk; Ural. Otd. Ross. Akad. Nauk, 1991, pp. 74–80.
5. Val'tsifer, V.A. and Pogorelov, B.A., *Kolloidn. Zh.*, 1995, vol. 57, no. 6, pp. 909–911.
6. Kozlov, G.V., Val'tsifer, V.A. and Pogorelov, B.A., *Kolloidn. Zh.*, 1992, vol. 54, no. 3, pp. 73–75.

Russian Journal of Applied Chemistry, Vol. 76, No. 10, 2003, pp. 1662–1668. Translated from Zhurnal Prikladnoi Khimii, Vol. 76, No. 10, 2003, pp. 1708–1714.

MACROMOLECULAR CHEMISTRY AND POLYMERIC MATERIALS

Synthesis and Thermal Transformations of Bis[4-(1-hydroxyethyl)phenyl] Ether Dimethacrylate

B. A. Zaitsev, G. I. Khramova, and T. S. Tsygankova

Institute of Macromolecular Compounds, Russian Academy of Sciences, St. Petersburg, Russia

Received January 30, 2003

Abstract—Thermal curing of bis[4-(1-hydroxyethyl)phenyl] ether dimethacrylate was studied.

Processing of thermoreactive resins into heat-resistant polymeric materials involves a serious problem: For curing to be efficient, the curing temperature T_c should be maintained higher than the glass transition point T_g of the system being cured. In the highly viscous medium of a thickly cross-linked polymeric matrix at a temperature below T_g, curing drastically decelerates, because transport of reactants to the reaction zone becomes severely hindered. Participation of adjacent functional groups in polymer-analogous transformations might eliminate this problem [1–3].

Being a polyfunctional monomer, bis[4-(1-hydroxyethyl)phenyl] ether dimethacrylate (DM) may be of considerable interest in this respect. It is a component of Rolivsans, novel heat-resistant thermoreactive resins used in modern engineering [4–6]. Owing to the presence of unsaturated methacrylate groups, it is involved in common three-dimensional (3D) polymerization, forming network polymers similar to the well-known diol methacrylates [7–9]. However, a specific feature of DM is the presence of latent ("sleeping") fragments $-C_6H_4-CH(CH_3)-O-CO-$, allowing high-temperature rearrangement of the initial polymeric network of DM in the course of further curing at elevated temperatures. In this study, we analyzed the mechanism of thermal transformations of DM and the structure and properties of the cured products.

Bis[4-(1-hydroxyethyl)phenyl] ether dimethacrylate is formed in synthesis of Rolivsan MV-1, which is a monomer–oligomer compound prepared chemically, i.e., by transformations of a secondary aromatic diol, bis[4-(1-hydroxyethyl)phenyl] ether (BOPE), in the presence of methacrylic acid (MAA), catalyzed with strong mineral acids [10–14]. Pure DM was prepared for the first time by acylation of BOPE with methacryloyl chloride (MAC) [12, 13]. According to ozonolysis data, the content of double bonds in DM is 0.504 mol per 100 g; ester number, 272 mg KOH per gram; n_D^{20}, 1.5410; gelation time at 150°C, 2 min.

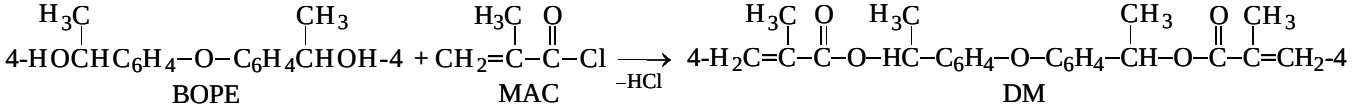

Thermal transformations of DM were studied by IR spectroscopy, differential scanning calorimetry (DSC), and elemental, thermogravimetric, and thermomechanical analyses. The IR study of DM was perfoirmed in the temperature range 140–370°C (isothermal heating at 140°C and dynamic heating of a thin film between KBr and NaCl plates at an average rate of 1.4 deg h^{-1}.

The IR spectrum of DM (Fig. 1a, curve *1*) contains absorption bands of unsaturated and aromatic groups at 3070–3060, 3030, 2975, 1630, 1600, 1500, 940, 870, and 830 cm^{-1}, of methyl and methylene groups at 2975, 2930, and 2870 cm^{-1}, and of methine groups at 2900 cm^{-1}; it also contains strong absorption bands of methacrylate ester and diphenyl ether groups at 1715 and 1240 cm^{-1}; bands at 1170, 1060, and

1070-4272/03/7610-1662 $25.00 © 2003 MAIK "Nauka/Interperiodica"

1010 cm^{-1} originate from stretching vibrations of the C–O bond in ester and ether groups.

The mechanism of thermal transformations of another monomer, 4-vinylphenyl-4-(1-methacryloyloxyethyl)phenyl ether (MV), which is also a component of Rolivsan MV-1 [12, 13, 15], has been studied previously [12, 13, 15]. DM can be expected to behave similarly (with corrections for differences in the structure and reactivity), and the following scheme of cleavage (or activation) of latent ester groups with formation of MAA, MV, and bis(4-vinylphenyl) ether (DV) can be suggested:

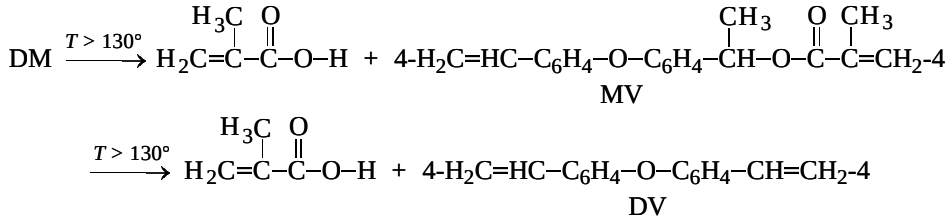

It should be noted that, in contrast to MV, even short (1–2 h) heating of DM at 140°C causes substantial changes in the IR spectrum (Fig. 1a, curve *2*), which are due not only to the onset of the expected 3D radical polymerization (the gelation time of DM at 140°C is as short as several minutes) but also to the cleavage of the ester groups, according to the above scheme. Dimethacrylate and bridging units of the initial network polymer, formed by it, are unstable at this temperature and start to noticeably decompose to give MAA and MV, which, in turn, decomposes to DV, MAA, and/or their units. This process gives rise in the IR spectrum of DM to a new band of out-of-plane bending vibrations of the H–C=C fragment of the 4-CH_2=CH–C_6H_4–O–C_6H_4– group at ~902 cm^{-1} [15–18]. The C=C stretching vibration band at 1630 cm^{-1} simultaneously grows in intensity. Therefore, it is not surprising that, in the initial period (1–2 h) of DM heating, the bands at 902 and 1630 cm^{-1} noticeably grow in intensity (Fig. 1a, curve *2*), compared to the starting monomer. However, further heating causes the intiensities of these bands to decrease owing to participation of the methacrylate and styrene groups in (co)polymerization (Fig. 1a, curves *3*–*5*). Therefore, upon prolonged heating of the sample at 140°C and higher temperatures, these bands gradually decrease in intensity, as also does the band at 940 cm^{-1} belonging to out-of-plane bending vibrations of the H–C= fragment of the methacrylate group (Fig. 1a, curves *1*, *2*). Thus, at high temperatures, unsaturated products formed from DM by cleavage of methacrylate groups (see above) are involved in thermal copolymerization of the system, which becomes multicomponent.

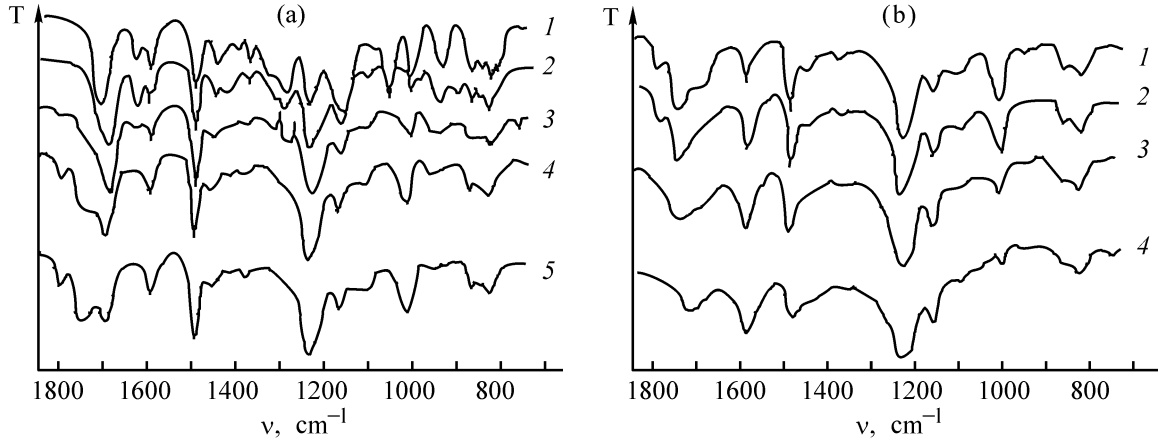

Fig. 1. IR spectra of DM and products of its thermal transformations. Heating rate 1.4 deg h^{-1}. (a) (*1*) Initial DM; heating range 140–190°C; final temperature, °C: (*2*) 142, (*3*) 160, (*4*) 180, and (*5*) 190. (b) Heating range 200–350°C; final temperature, °C: (*1*) 200, (*2*) 260, (*3*) 290, and (*4*) 350. (ν) Wave number and (T) transmission.

Table 1. Conversion of unsaturated and ester groups in the course of dynamic (~1.4 deg h^{-1}) heating of DM, according to IR data*

T, °C	D	c/c_0	D	D	D	c/c_0	D	c/c_0
	at indicated ν, cm^{-1}							
	1630		1240	1060	940		902	
130	0.24	0	0.84	0.60	0.28	0	0.00	0
140	0.20	0.83	0.77	0.05	0.18	0.64	0.11	0.61
150	0.15	0.62	0.83	0.01	0.15	0.54	0.09	0.50
160	0.09	0.38	0.82	–	0.11	0.39	0.05	0.28
170	0.06	0.25	0.85	–	0.06	0.21	0.02	0.11
180	0.04	0.17	0.80	–	0.02	0.07	0.01	0.06

* (D) Optical density; (ν) wave number, cm^{-1}; (c, c_0) running and initial concentrations of functional groups in DM, M. It is assumed that the ratio of the optical densities D/D_0 (D_0, before heating; D, after heating) of DM is proportional to the conversion c/c_0 of the corresponding unsaturated group.

Table 2. Variation of the intensity of some absorption bands in the IR spectra of DM in the course of dynamic (~1.4 deg h^{-1}) heating*

T, °C	D (1803 cm^{-1}), C=O	c_{anhydr}, %	D (1600 cm^{-1}), Ar	D (1500 cm^{-1}), Ar	D (1240 cm^{-1}), O–C in Ar	D (830 cm^{-1}), H–C= in Ar
140/3 h**	0.02	2.0	0.20	0.42	0.77	0.21
140/6 h**	0.03	3.3	0.20	0.44	0.77	0.21
150	0.04	4.4	0.20	0.62	0.87	0.20
160	0.05	5.6	0.19	0.63	0.86	0.20
170	0.07	7.8	0.19	0.50	0.82	0.19
180	0.13	14.4	0.19	0.55	0.80	0.16
190	0.14	15.6	0.20	0.43	0.73	0.16
200	0.15	16.7	0.20	0.42	0.74	0.15
210	0.16	17.8	0.21	0.40	0.78	0.15
220	0.18	20.0	0.22	0.42	0.76	0.16
230	0.17	18.9	0.21	0.37	0.68	0.15
240	0.18	20.0	0.24	0.43	0.76	0.15
250	0.16	17.8	0.24	0.42	0.71	0.14
260	0.14	15.6	0.28	0.41	0.73	0.14
270	0.14	15.6	0.30	0.40	0.77	0.14
280	0.10	11.1	0.31	0.36	0.70	0.14
290	0.08	8.9	0.31	0.30	0.67	0.13
300	0.05	5.6	0.31	0.28	0.61	0.13
310	0.04	4.4	0.33	0.27	0.59	0.12
320	0.04	4.4	0.35	0.26	0.61	0.13
330	0.03	3.3	0.30	0.29	0.64	0.12
340	0.03	3.3	0.34	0.21	0.56	0.10
350	0.01	1.1	0.28	0.17	0.46	0.09
370	0.00	0.0	0.25	0.19	0.38	0.11

* (D) Optical density; 1803 cm^{-1} is the C=O vibration frequency of methacrylic anhydride; Ar = 4-C_6H_4–O–C_6H_4-4; (c_{anhydr}) content of anhydride groups.

** Isothermal heating at 140°C.

Comparison of the IR spectra of DM, MV, and DV monomers (Tables 1, 2) with those of DM thermal transformation products, measured under similar conditions, shows how the degree of DM unsaturation varies in the course of slow dynamic heating in the range 130–180°C. For this purpose, we first determined the experimental intensities of the absorption bands (at 900, 940, and 1630 cm^{-1}) of DM, MV, and

DV monomers used as reference; the IR spectra were recorded under similar conditions.

Let us denote as *A* and *B* the contributions from methacrylate and styrene (4-CH_2=CH–C_5H_4–) groups to the total intensity of an absorption band of the monomer and assume these contributions to be additive. Then the spectrum of DM corresponds to 2*A*; that of MV, to *A* + *B*; and that of DV, to 2*B*. From the spectra of these three monomers, we can estimate that contribution *A* to the bands at 1630, 940, and 900 cm^{-1} is 0.12–0.13, 0.14–0.18, and 0.00, and contribution *B* to the same bands, 0.10–0.11, 0.00, and 0.14–0.18, respectively.

From these data, we can determine how the conversion c/c_0 of the CH_2=CH and CH_2=C(CH_3) groups varies in the course of DM heating. Table 1 shows that, in the range 160–180°C, the concentration of unsaturated groups of the styrene and methacrylate types in the system abruptly decreases owing to their involvement in the radical copolymerization of the system components. It should be noted that the kinetic data obtained in the isothermal (Fig. 2) and dynamic modes of DM heating are well consistent.

As for other major IR manifestations of the cleavage of ester groups in DM, Fig. 1 shows that, on heating, the methacrylate C=O absorption band at 1715 cm^{-1} gets broadened and shifted toward lower frequencies (1700–1685 cm^{-1}) corresponding to absorption of the carboxy group in MAA [15, 18]. Finally, the intensity of the methacrylate C–O stretching band at 1060 cm^{-1} abruptly decreases already at the very beginning of DM heating at 140°C. Simultaneously, the methacrylate H–C= bending band at 940 cm^{-1} gets considerably broadened and shifted owing to superposition of the carboxyl O–H bending band of MAA and/or its unit at 935 ± 15 cm^{-1}; also, broad OH stretching bands of carboxy group appear at 3570–3500 and 2700–2500 cm^{-1}, and a band of the C–O bond in carboxy group appears at 1420 cm^{-1} [19].

It could be expected that cleavage of DM according to the above scheme would be accompanied by a decrease in the content of CH_3 and CH_{tert} groups. Indeed, the intensities of the stretching vibration bands of the methyl (2980, 2930, 2870 cm^{-1}) and methylene (2890 cm^{-1}) C–H bonds and of the C–H bending vibrations (1370 cm^{-1}) appreciably decrease in the course of DM heating. A similar pattern has been observed previously in thermal transformations of other methacrylates of secondary aromatic alcohols [12, 13, 15, 18], e.g., MV [15]. In particular, it was shown that MV units in the network (co)polymer prepared by thermal polymerization of MV are also cleaved to give DV units.

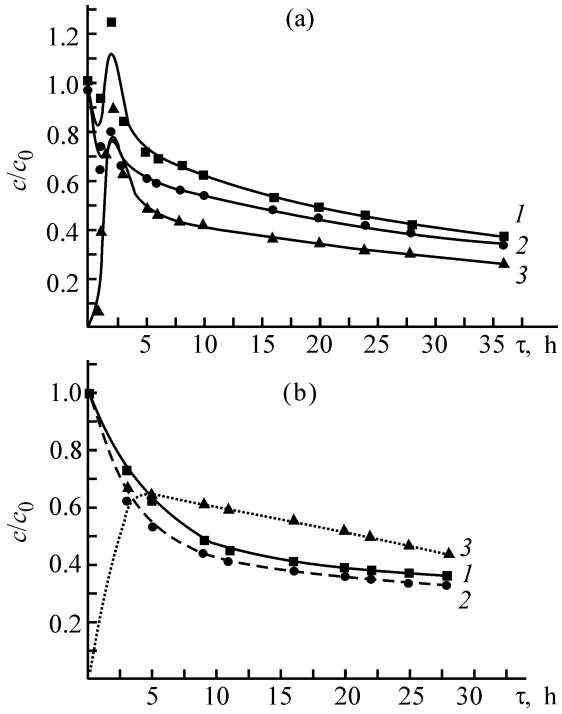

Fig. 2. Kinetics of transformations of unsaturated groups in the course of isothermal heating of DM (140°C) between (a) KBr and (b) NaCl plates. (c, c_0) Initial and running concentrations of functional groups, M. ν, cm^{-1}: (*1*) 1630 [CH_2=CH and CH_2=C(CH_3)], (*2*) 940 [CH_2=C(CH_3)], and (*3*) 902 (CH_2=CH). The c/c_0 ratios were calculated from changes in the intensities of the indicated absorption bands in the IR spectra of transformation products of DM and model monomers (MV, DV).

As the temperature is raised further to 180–200°C and more, one more parallel reaction starts to make a major contribution to the thermal transformations: formation of methacrylic anhydride (MA) units from MAA units in the network polymer, which yields substituted glutaric anhydride units. In the IR spectra of DM recorded in the course of curing, the carbonyl absorption bands at 1803 and 1755 cm^{-1}, characteristic of the anhydride group, steadily grow in intensity (Fig. 1a, curves *4*, *5*; Fig. 1b, curves *1*, *2*; Fig. 3; Table 2). To compare, glutaric anhydride shows carbonyl absorption at 1802 and 1761 cm^{-1} [19]. Naturally, as anhydride units are formed, the absorption band of carboxyl C=O group at 1690 cm^{-1} decreases in intensity.

Heating to 250–300°C causes give rise to broad bands at 1660–1680 cm^{-1} in the IR spectra of DM curing products (Fig. 1b); these bands originate from stretching vibrations of ketone carbonyl group [19].

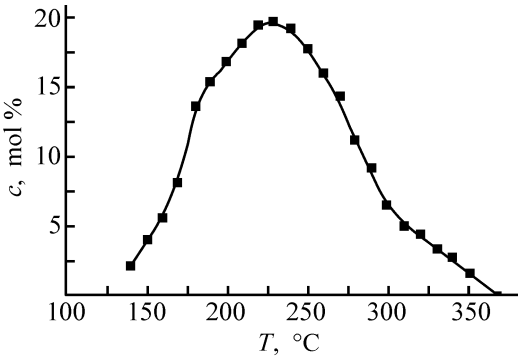

Fig. 3. Kinetics of formation of methacrylic anhydride units in the course of DM heating in the temperature range 140–370°C at average rate of ~1.4 deg min^{-1} between KBr plates: (*c*) concentration of anhydride groups and (*T*) temperature.

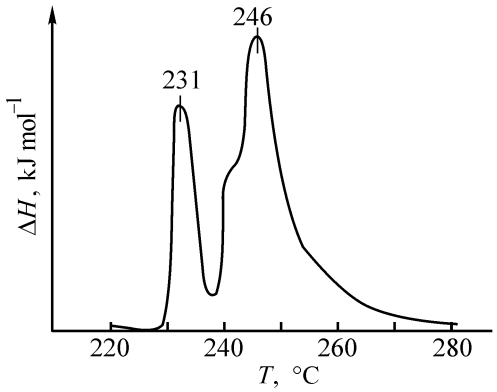

Fig. 4. Thermogram of DM curing (DSC, scanning rate 4 deg min^{-1}). (*T*) Temperature and (ΔH) thermal effect.

As shown previously in comprehensive studies of related compounds and systems by various methods [12, 13, 15, 18], these changes in the IR spectra are due to fast solid-phase Friedel–Crafts acylation of diphenyl ether groups with adjacent MA units, yielding thermally stable methylenetetralone units in the network copolymer. Figure 3 shows that the consumption of anhydride groups in polymer-analogous acylation reactions results in a fairly sharp decrease in their content in the network copolymer in the final stage of DM curing (in the temperature range 250–300°C).

The IR spectra of products of DM curing in the range 300–370°C allow evaluation of the resistance of units and some groups of the resulting network copolymer to thermal oxidative degradation in air. Figures 1b (curve *4*) and 3 show that the least thermally stable fragments of the copolymer are MA units; they degrade in the course of slow heating of the sample from 300 to 370°C. The intensities of the absorption bands of aromatic and diphenyl ether groups also gradually decrease in the course of prolonged heating, but remain relatively high even after heating to 370°C (Table 2). An exception is an appreciable growth of the band at 1600 cm^{-1}, belonging to the C=C bond in Ar and sensitive to conjugation [19]; apparently, high-temperature degradation results in the formation of polyconjugated (polycyclic) structures.

High-temperature curing of DM and related compounds [15, 18], causing cardinal structural changes as indicated by IR spectroscopy, was also studied by DSC. The observed pattern of thermal effects is consistent with the above-considered mechanism of thermal transformations of DM following from IR data, taking into account a significant difference in the heating rates (IR, 1.4 deg h^{-1}; DSC, 4 deg min^{-1}). At high heating rates, structural changes are usually manifested much more sharply than under conditions of isothermal heat treatment or slow heating.

Figure 4 shows that the exothermic peak observed at 231°C (first step of thermal transformations of DM) is apparently due to prevailing 3D (co)polymerization of methacrylate and styrene monomers. Such processes are accompanied by substantial heat release [20]. In the range 234–238°C, the heat release abruptly weakens, which may be due to prevalent contribution of concomitant endothermic cleavage of ester groups. Finally, the exothermic peaks observed at 240 and 246°C may be due to the major contribution from copolymerization of unsaturated compounds formed by DM cleavage (as shown above) and from polycyclization (formation of anhydride units from MAA units) in the final stage of DM curing (post-curing). The total thermal effect of DM transformations is about 69 kJ mol^{-1}, whereas the heat of polymerization of DV (which contains no cleavable ester groups), determined under the same conditions (kJ mol^{-1}), is considerably higher: 97 [21] or 114 [16]. Thus, the difference in the total heats of curing of DM and DV is mainly due to the fact that curing of DV involves only exothermic reactions of 3D polymerization, whereas curing of DM is accompanied, along with polymerization, by endothermic cleavage of ester groups.

The structural transformations of DM can be generally regarded as high-temperature dehydration, with water removal from the glassy polymeric matrix by molecular diffusion. Presumably, total cleavage of 1 mol of DM or its polymer (polyDM) by the above-given scheme is accompanied by release of 2 mol of MAA (or polyMAA); its transformation into the anhydride, in turn, results in release of 1 mol of H_2O:

$$\underset{\text{PolyDM}}{(C_{24}H_{26}O)_n} \xrightarrow[-H_2O]{160\text{–}230^\circ C} \underset{\text{DV–MA copolymer}}{-(C_{16}H_{14}O)_{n-m}-(C_8H_{10}O_3)_m-},$$

where $n = 1$, $m = 0.5$.

In this case, the molar ratio of DV and MA units in the copolymer will be 1 : 1. Then, if we assume that the high-temperature Friedel–Crafts acylation of diphenyl ether groups with adjacent anhydride groups in polymer chains to give methylenetetralone and MAA units goes to completion, then the composition of the acylated copolymer can be determined from the following scheme:

$$\underset{\text{DV–MA copolymer}}{-(C_{16}H_{14}O)_{0.5}-(C_8H_{10}O_3)_{0.5}-} \xrightarrow[-0.25H_2O]{\text{Acylation with MA}} \underset{\text{Acylated DV–MA copolymer}}{-(C_{20}H_{18}O_2)_{0.5}-(C_8H_{10}O_3)_{0.25}-}$$

Elemental analysis shows that, upon heating of DM samples to 300°C, the carbon content grows from 73.2 to 77.7%. The latter value is intermediate between the values calculated for the copolymer compositions before (76.6% C) and after (78.5% C) acylation. Calculation shows that, in the course of formation of these copolymers, transformation of carboxy groups into anhydride groups (followed in the latter case by acylation) should result in the release of 9.6 and 12.1% H_2O, respectively. However, the total amount of volatiles released in the course of dynamic (1.4 deg h^{-1}) heating of DM from 20 to 300°C does not exceed 7.7%. The fact that the amount of released water is lower than expected may be due to partial degradation (decarboxylation) of MAA and anhydride units upon prolonged heating of the samples (for more than 70 h) in the range 200–300°C. Previous mass-spectrometric studies have shown [12, 18] that, at temperatures exceeding 200°C, thermal degradation (mainyl decarboxylation) of methacrylic acid units makes a small but appreciable contribution.

Based on the above data, the polymeric structure finally formed in the course of DM curing at 250–300°C can be represented as follows:

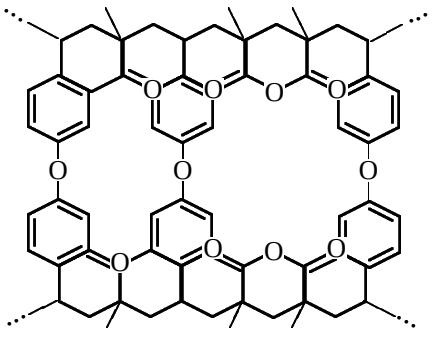

Fast solid-phase reactions in thickly cross-linked polymeric matrices have been studied previously as applied to curing of Rolivsans [5, 6, 21], model systems [12, 13, 18], and related compounds [15, 21]. As noted above, the fact that the reactions occur in thickly cross-linked polymeric matrices at temperatures much lower than the softening point (~403°C), when the transport of reactants to the reaction zone is usually hindered, is an advantage of such systems. However, in the systems under consideration, the vibrational and rotational motion of adjacent groups is sufficiently free for the reactions to be fast [12].

The above-discussed mechanism of DM curing explains why it is possible to prepare heat-resistant polymers and plastics from this thermally unstable monomer. According to dynamic (4.5 deg min^{-1}) thermogravimetric analysis in air, the temperatures of 5 and 10% weight loss by thermally rearranged polyDM are 340 and 390°C, respectively, and the breaking bending stress of fiber glasses based on polyDM is 330 (20°C), 220 (300°C), and 50 MPa (320°C).

EXPERIMENTAL

DM was prepared according to [12, 13]; a colorless glycerol-like liquid, yield 45–50%, n_D^{20} 1.541. Found, %: C 73.20, H 6.6. Ester number (mg KOH per gram product): found 272.0; calculated 274.8.

Bis(4-vinylphenyl) ether (DV) and 4-vinylphenyl 4-(1-methacryloyloxyethyl)phenyl ether (MV) were prepared as described in [12–14].

The IR spectra were measured on a Specord 75-IR spectrometer in a thin film. Calorimetric measurements were performed with a Perkin–Elmer DSC-1B differential scanning microcalorimeter, as described in [20]. Exclusion liquid chromatography (ELC) was carried out on a GPC-Waters chromatograph at 20°C using columns packed with Ultrastyragel 500 Å and $CHCl_3$ or toluene as eluent. Dynamic thermogravimetric analysis of samples was performed on a Paulik–Paulik–Erdey MOM C derivatograph (Hungary) at a heating rate of 4.5 deg min^{-1}. The softening point was determined with a Vicat device (Institute of Macromolecular Compounds, Russian Academy of Sciences; indenter load 1 kg, indenter cross section 1 mm^2).

Fiber glasses were prepared by hot pressing of prepregs on T-10-80 fiber glass fabric at a pressure of ~1 kg cm^{-2}, with heating from 20 to 300°C at a rate of 1.4 deg min^{-1}.

CONCLUSIONS

(1) Thermal transformations of DM yield heat-resistant thermoreactive polymers; common 3D radical polymerization of DM, giving the initial thermally unstable network polymer, is accompanied by thermally initiated solid-phase consecutive-parallel reactions between adjacent groups in chains of the polymer network.

(2) Thermal transformations of DM involve a set of consecutive-parallel reactions of 3D polymerization, cleavage of ester groups of the monomeric unit in the network polymer, formation of anhydride from adjacent MAA units, acylation of diphenyl ether groups with adjacent anhydride groups, decarboxylation of MAA, and degradation of methacrylic anhydride units.

REFERENCES

1. *Chemical Reactions of Polymers*, Fettes, E.M., Ed., New York: Interscience, 1964. Translated under the title *Khimicheskie reaktsii polimerov*, Moscow: Mir, 1967, vol. 1, pp. 41–44.
2. Zaitsev, B.A., Abstracts of Papers, *XVI Mendeleevskii s"ezd po obshchei i prikladnoi khimii* (XVI Mendeleev Congr. on General and Applied Chemistry), Moscow, 1998, no. 2, pp. 304–305.
3. Zaitsev, B.A., Abstracts of Papers, *VIII Mezhdunarodnaya konferentsiya po khimii i fizikokhimii oligomerov "Oligomery-2002"* (VIII Int. Conf. on Chemistry and Physical Chemistry of Oligomers "Oligomers-2002"), Chernogolovka, September 9–14, 2002, p. 193.
4. Zaitsev, B.A., Khramova, G.I., Dantsig, L.L., *et al.*, *Plast. Massy*, 1981, no. 9, pp. 12–13.
5. Zaitsev, B.A., Khramova, G.I., Tsygankova, T.S., *et al.*, *Mekh. Kompozitn. Mater.*, 1982, no. 5, pp. 775–778.
6. Zaitsev, B.A., *Sintez, struktura i svoistva polimerov* (Synthesis, Structure, and Properties of Polymers), Leningrad: Nauka, 1989, pp. 66–77.
7. Berlin, A.A., Kefeli, T.Ya., and Korolev, G.V., *Poliefirakrilaty* (Polyether Acrylates), Moscow: Nauka, 1967.
8. Berlin, A.A., Korolev, G.V., Kefeli, T.Ya., and Sivergin, Yu.M., *Akrilovye oligomery i materialy na ikh osnove* (Acrylic Oligomers and Materials Based on Them), Moscow: Khimiya, 1983.
9. Korolev, G.V., Mogilevich, M.M., and Golikov, I.V., *Setchatye poliakrilaty* (Network Polyacrylates), Moscow: Khimiya, 1995.
10. Zaitsev, B.A., Khramova, G.I., and Dantsig, L.L., *Vysokomol. Soedin., Ser. A*, 1982, vol. 24, no. 12, pp. 2467–2474.
11. Zaitsev, B.A., Dantsig, L.L., and Khramova, G.I., *Zh. Org. Khim.*, 1983, vol. 19, no. 11, pp. 2340–2349.
12. Zaitsev, B.A., Regular Trends in Formation, Structure, and Properties of Heat-Resistant Network Polyarylenes, *Doctoral Dissertation*, Leningrad, 1983.
13. Khramova, G.I., Regular Trends in Formation and Cross-Linking of Secondary Aromatic Diol Methacrylates and Monomer–Oligomer Systems Based on Them, *Cand. Sci. Dissertation*, Leningrad, 1985.
14. Zaitsev, B.A., Khramova, G.I., Tsygankova, T.S., *et al.*, Abstracts of Papers, *VIII Mezhdunarodnaya konferentsiya po khimii i fizikokhimii oligomerov "Oligomery-2002"* (VIII Int. Conf. on Chemistry and Physical Chemistry of Oligomers "Oligomers-2002"), Chernogolovka, September 9–14, 2002, p. 252.
15. Zaitsev, B.A., Khramova, G.I., Tsygankova, T.S., *et al.*, *Acta Polym.*, 1985, vol. 36, no. 10, pp. 521–526.
16. Zaitsev, B.A., Lukasov, S.V., Kiseleva, R.F., *et al.*, *Acta Polym.*, 1985, vol. 36, no. 10, pp. 527–530.
17. Zaitsev, B.A., Kiseleva, R.F., and Gusarova, I.O., *J. Polym. Sci. A*, 1996, vol. 34, no. 7, pp. 1165–1181.
18. Zaitsev, B.A., Tsygankova, T.S., and Khramova, G.I., *Vysokomol. Soedin., Ser. B*, 1982, vol. 24, no. 7, pp. 507–511.
19. Bellamy, L.J., *The Infra-Red Spectra of Complex Molecules*, New York: Wiley, 1957.
20. Bresler, S.E. and Erusalimskii, B.A., *Fizika i khimiya makromolekul* (Physics and Chemistry of Macromolecules), Moscow: Nauka, 1965, pp. 214–215.
21. Lukasov, S.V., Zaitsev, B.A., Tsygankova, T.S., *et al.*, *Plast. Massy*, 1985, no. 2, pp. 56–58.

Russian Journal of Applied Chemistry, Vol. 76, No. 10, 2003, pp. 1669–1673. Translated from Zhurnal Prikladnoi Khimii, Vol. 76, No. 10, 2003, pp. 1715–1719.

MACROMOLECULAR CHEMISTRY AND POLYMERIC MATERIALS

Potassium Iodide in Coloring of Polyvinyl Alcohol Film in Oxidizing Solution

N. G. Ariko and V. E. Agabekov

Institute of Chemistry of Novel Materials, Belarussian National Academy of Sciences, Minsk, Belarus

Received April 2, 2002

Abstract—Conversion of potassium iodide in polyvinyl alcohol film by its treatment in the $(NH_4)_2S_2O_8$–$CuSO_4$–KI–KCl–H_2SO_4–H_2O oxidizing solution, leading to coloring of the film with molecular iodine, was studied. The conversion mechanism was analyzed as influenced by each component of the oxidizing solution.

Iodine-colored uniaxially oriented polyvinyl alcohol (PVA) films are used in transmission, reflection, and semitransmission polarizers widely employed in production of liquid-crystal displays.

PVA films are most often colored with iodine sorbed from aqueous solution of I_2 and KI [1]. Previously [2], a new procedure has been developed in which a PVA film containing KI is colored using an $(NH_4)_2S_2O_8$–$CuSO_4$–KI–KCl–H_2SO_4–H_2O oxidizing solution. It was found that this solution is most effective if it contains simultaneously $(NH_4)_2S_2O_8$, $CuSO_4$, and KI, whereas in the absence of $CuSO_4$ or KI, the coloring efficiency drastically decreases [3].

In this study, we analyzed the coloring of a KI-containing PVA film in the course of its treatment in the oxidizing solution and the role of the solution components in the oxidation reactions proceeding in the film and solution, because published data on this matter are lacking.

EXPERIMENTAL

The polyvinyl alcohol films were cast on glass supports using a greasing-type draw plate and 11% aqueous solution of V-1N polyvinyl alcohol containing ethanol, glycerol, KI, and boric acid (5, 2.5, 0.04, and 0.1 wt %, respectively) and then dried at 24–26°C to residual moisture content of 6–7%.

To prepare a film polarizer, a dried film fixed in special clamps was placed in an aqueous oxidizing solution heated to 32 ± 2°C and containing (wt %) 0.1 $(NH_4)_2S_2O_8$, 0.1 $CuSO_4$, 0.01 KI, 17–20 KCl, and 0.1 H_2SO_4. The resulting yellow-colored film was washed with a 1% solution of boric acid H_3BO_3 at 24 ± 2°C and treated with a saturated H_3BO_3 solution heated to 42 ± 2°C. As a result, the film became blue owing to the formation of the "blue" dichroic complexes PVA–$(I_2)_n$ [4, 5]. The reaction of boric acid with polyvinyl alcohol yields boric acid esters [6], which link the polymeric chains and fix iodine in the film. Then, the film was placed in an aqueous fixing solution containing KI, CdI_2, H_3BO_3, $ZnCl_2$, and HCl (0.01, 0.1, 0.4, 15, 0.1 wt %, respectively) and washed in distilled water warmed to 24 ± 2°C. Treatment in the fixing solution made the film coloring more uniform.

To obtain an efficiently polarizing PVA film, it should be uniaxially stretched by a factor of at least 3.5–4. The wet film was fixed in a device with a lowering bar, stretched by a factor of 4, and dried in an oven for 1 h at 60 ± 5°C.

All the required solutions were prepared using pure grade reagents, ultrapure 11-5 grade concentrated H_2SO_4, and distilled water; the iodine solution was prepared from a reference formulation.

The absorption spectra of iodine-containing solutions were recorded immediately after their preparation, on a Specord UV-VIS spectrophotometer. To study the reaction kinetics of KI and $(NH_4)_2S_2O_8$, the optical density of the reaction mixture was recorded in the course of the experiment on a KFK-3 photometer. The concentrations of I_3^- and I_2 were calculated from the optical densities at 350 and 460 nm, respectively, using the extinction coefficients for I_3^- (ε_{350} = 26400 and ε_{460} = 975) and I_2 (ε_{350} = 18 and ε_{460} = 746) [7]. The measurements were performed at 20°C.

1070-4272/03/7610-1669 $25.00

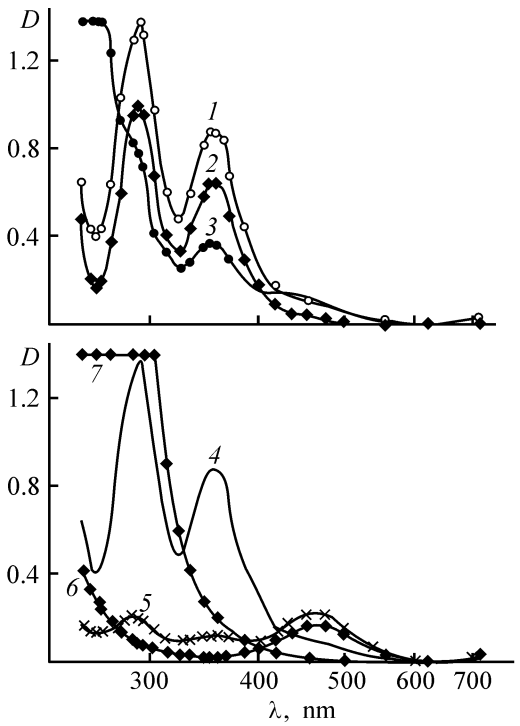

Fig. 1. Absorption spectra of iodine solutions containing (*1*) no additives and those with addition of (*2*) KI, (*3*) KCl, (*4*) $CuSO_4$, (*5*) $(NH_4)_2S_2O_8$, and (*6*) $(NH_4)_2S_2O_8$ + $CuSO_4$, and (*7*) oxidizing solution. (*D*) Optical density and (λ) wavelength. Concentration $c \times 10^4$, M: I_2 (*2*) 1.0, (*1, 3*) 1.5, and (*4–6*) 2.5; KI (*2*) 0.12; KCl (*3*) 0.13; $CuSO_4$ (*4, 6*) 8.0; and $(NH_4)_2S_2O_8$ (*5, 6*) 8.8.

The yellow coloring of the colorless PVA film upon its contact with the oxidizing solution suggests that molecular iodine is formed in its bulk. It was found that the rate and intensity of the film coloring strongly decrease in the absence of $CuSO_4$ and KI in the oxidizing solutions, whereas the greatest effect is observed when $(NH_4)_2S_2O_8$, $CuSO_4$, and KI are present simultaneously [3].

It is known that peroxydisulfate anions oxidize iodide ions by the following overall reaction [8]

$$S_2O_8^{2-} + 2I^- \rightarrow 2SO_4^{2-} + J_2. \quad (1)$$

Since the oxidizing solution contains excess peroxydisulfate anions relative to I^-, I^- must be completely converted into molecular iodine. Actually, in the course of preparation, the solution becomes brown owing to the formation of molecular iodine, but then this color disappears.

The absorption spectra of the oxidizing solution and those of iodine solutions in the absence of additives and in the presence of components of the oxidizing solution are shown in Fig. 1. The spectra of aqueous iodine solutions (Fig. 1, spectra *1–6*) exhibit three bands at 286–287 nm (I), 350–352 nm (II), and 460 nm (III), and no absorption bands are observed in the spectrum of the oxidizing solution at $\lambda > 400$ nm (Fig. 1, spectrum *7*).

According to [4, 7], absorption bands I and II belong to the anion I_3^-, and III, to molecular iodine I_2. The intensity ratio of the absorption bands in spectra 1–4 (Fig. 1) indicates that iodine occurs in these systems predominantly as complex anion I_3^-, which is formed by the reaction between I_2 and I^- present in the reference formulation:

$$I^- + I_2 \rightleftarrows I_3^-. \quad (2)$$

On introducing additional KI (Fig. 1, spectrum *2*), iodine is completely converted into I_3^-, which is confirmed by an increase in the intensity of bands I and II and by disappearance of band III. When KCl is added (Fig. 1, spectrum *3*), the absorption in the short-wavelength range becomes so intense that band I is observed as a shoulder. Copper sulfate (Fig. 1, spectrum *4*) does not affect noticeably the intensity of the absorption bands of I^- and I_3^- as compared with spectrum *1* (Fig. 1). In the presence of $(NH_4)_2S_2O_8$ oxidant (Fig. 1, spectrum *5*), absorption bands I and II gradually decrease in intensity and finally completely disappear in the course of measurements, whereas the intensity of band III increases indicating that I_3^- is converted into molecular iodine I_2. Copper sulfate strongly accelerates this process, and only the band at 460 nm typical of I_2 is observed from the very beginning (Fig. 1, spectrum *6*).

These spectral data confirm that reaction (1) proceeds in the oxidizing solution, but the oxidation of I^- is not terminated at the stage of formation of molecular iodine, because the corresponding band III is absent in the spectrum of this solution (Fig. 1, curve *7*).

To elucidate the pathways of iodine conversion in the oxidizing solution, we studied the kinetics of the reaction between KI and $(NH_4)_2S_2O_8$, catalyzed with $CuSO_4$. The concentrations of the oxidant and catalyst in this set of tests corresponded to their content in the oxidizing solution, and the concentration of potassium iodide was varied within 0.004–0.020 wt % or $(0.5–2.5) \times 10^{-3}$ M.

Immediately after mixing of the solutions [$(NH_4)_2S_2O_8$ was added to a mixture of KI and $CuSO_4$ directly in the cell of a KFK-3 photometer], a strong band at 353 nm and a broad band at 460 nm appeared in the absorption spectra; these bands belong

to complex I_3^- and molecular iodine I_2. As seen from Fig. 2, variations in the optical density D_{350} with time correspond to the changes in the content of I_3^- in solution. The peaks in the curves describing the D_{350}–t kinetic dependences indicate that the complex anion is the reaction intermediate.

The effect of the initial concentration of KI on the concentration of I_3^- formed in the initial stage of the reaction $[I_3^-]_{1\,min}$ is shown in Fig. 3; this value was calculated from D_{353} recorded 1 min after mixing of the solutions. As a matter of fact, $[I_3^-]_{1\,min}$ is the rate of oxidation of the initial iodide ions, because at this instant of time $[I^-] >> [I_3^-]$ and the rate of consumption of the complex anions is insignificant. Since the $[I_3^-]_{1\,min}$–$[KI]_0$ dependence is linear, this is a first-order reaction. The same reaction order is observed for oxidation of iodide ions with peroxydisulfate anions without catalyst [9]. This fact can be accounted for by occurrence of the reaction yielding atomic iodine:

$$\left.\begin{aligned} &I^- + S_2O_8^{2-} \rightarrow [S_2O_8^{3-}] \rightarrow I + S_2O_8^{3-},\\ &S_2O_8^{3-} \rightarrow SO_4^{2-} + SO_4^- \quad \text{or}\\ &I^- + S_2O_8^{3-} \rightarrow 2SO_4^{2-} + I. \end{aligned}\right\} \qquad (3)$$

Apparently, in the presence of a catalyst (copper compounds), the mechanism remains similar. The rate constant of the first-order reaction, $k_1 \sim 0.7 \times 10^{-3}$ s^{-1}, was calculated from the data in Fig. 3.

When the maximal concentration of triiodide anions $[I_3^-]_{max}$ is attained in the course of reaction, the major fraction of the initial iodide ions is already oxidized and, thus, the concentration of I_3^- becomes comparable with the concentration of the remaining I^- anions. The color of the reaction mixture turns from yellow to orange. At this stage, the rates of oxidation of I_3^- and I^- are comparable. The $[I_3^-]_{max}$–$[KI]_0$ dependence (Fig. 3) suggests that formation of I_3^- proceeds with two KI molecules involved [reactions (2) and (3)].

In the final stage of oxidation of potassium iodide [after passing the peak in the kinetic curves (Fig. 2)] at $[I^-] << [I_3^-]$, the formation of the complex triiodide anions stops and only their oxidation proceeds. Since formation of I_3^- does not affect noticeably the oxidation potential of the I_2/I^- couple [10], we suggest that the oxidation of I_3^- proceeds similarly to that of I^-:

$$\left.\begin{aligned} &I_3^- + S_2O_8^{2-} \xrightarrow{k_2} I_2 + I + S_2O_8^{3-},\\ &S_2O_8^{3-} \rightarrow SO_4^{2-} + SO_4^- \quad \text{or}\\ &I_3^- + S_2O_8^{3-} \rightarrow 2SO_4^{2-} + I_2 + I. \end{aligned}\right\} \qquad (4)$$

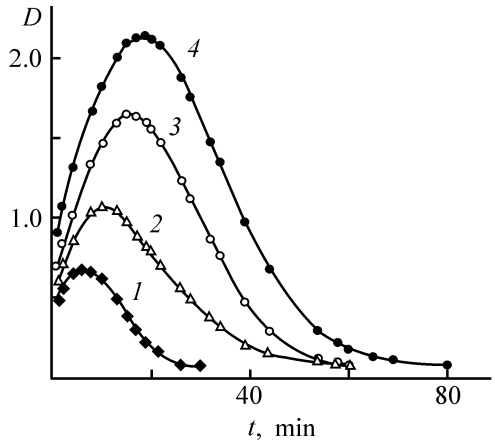

Fig. 2. Optical density D_{350} of the reaction mixture of KI and $(NH_4)_2S_2O_8$ vs. time; concentration of $(NH_4)_2S_2O_8$ 8.8×10^{-3} M. Concentration of KI $c \times 10^3$, M: (*1*) 0.8, (*2*) 1.2, (*3*) 1.4, and (*4*) 1.6.

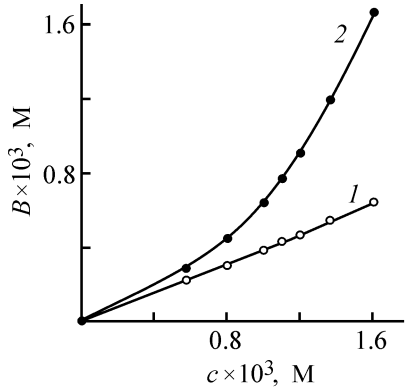

Fig. 3. Concentration of I_3^- B vs. the initial concentration c of KI in the reaction mixture. (*1*) $[I_3^-]_{1min}$ and (*2*) $[I_3^-]_{max}$.

The experimental points of the descending sections of the kinetic curves (Fig. 2) in the $\log[I_3^-]_t$–t coordinates are well fitted with straight lines, which indicates first-order oxidation of I_3^- and is consistent with the mechanism (4). The rate constant of the first-order reaction, $k_2 \approx 1.5 \times 10^{-3}$ s^{-1}, was calculated from the slopes of the $\log[I_3^-]_t$–t dependences. The constant k_1 is two times smaller than k_2, i.e., the complex anion is oxidized more readily than the initial iodide anion. Moreover, k_1 and k_2 are independent of the concentration of ammonium peroxydisulfate; at large oxidant excess, I^- and I_3^- are oxidized in solution in pseudo-first-order reactions.

The total amount of iodine formed by the instant of complete conversion of iodide and triiodide ions corresponds to the stoichiometry of the overall reaction (1) (Fig. 4).

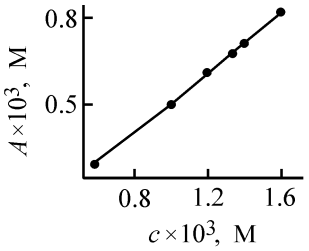

Fig. 4. Content of I_2 A vs. the initial concentration c of KI.

The acceleration effect of copper(II) on the oxidation of iodide ions by peroxydisulfate anions was studied in [10]. It was believed that copper(II) ions catalyze the oxidation, and the linear dependence of the reaction rate on the Cu^{2+} concentration was attributed to formation of the copper(II) iodide complex, which then reacts with peroxydisulfate anions:

$$\left.\begin{aligned} &Cu^{2+} + I^- \rightleftarrows CuI^+, \\ &CuI^+ + S_2O_8^{2-} \rightleftarrows [ICuS_2O_8^-], \\ &ICuS_2O_8^- \rightarrow Cu^{2+} + 2SO_4^{2-} + I^-, \\ &I^+ + I^- \rightarrow I_2. \end{aligned}\right\} \quad (5)$$

However, a study of this reaction in solutions similar to the oxidizing solution [3] showed that $S_2O_8^{2-}$ is a stronger oxidant than copper(II) ions (see table).

With $(NH_4)_2S_2O_8$ and $CuSO_4$ present simultaneously, the reaction was sharply accelerated and completed in 1–2 min. Thus, ammonium peroxydisulfate can be regarded as oxidant, and copper sulfate, as reaction catalyst. However, it was found [3] that for rapid and complete oxidation of iodide ions, Cu^{2+} should be taken not in a catalytic amount but in amount comparable with that of $S_2O_8^{2-}$ (optimal ratio 1 : 1).

It is known that the effect of silver(I), copper(II), and mercury(II) salts in redox processes is often related to counterpolarization of the oxidant molecules through partial formation of undissociated molecules of these strongly polarizing cations or complex ions with these metal cations (as central atoms) [11, 12]. The oxidative power of the undissociated molecules is the greatest. Thus, acceleration of the oxidative conversion of potassium iodide in the coloring solution is probably due to the counterpolarization of peroxydisulfate anions. Reactions (2) in the presence of $CuSO_4$ can be represented as:

$$\left.\begin{aligned} &Cu^{2+} + S_2O_8^{2-} \rightleftarrows CuS_2O_8, \\ &I^- + CuS_2O_8 \rightleftarrows [CuS_2O_8I^-], \\ &CuS_2O_8^- \rightarrow Cu^{2+} + SO_4^{2-} + SO_4^- \text{ or} \\ &CuS_2O_8^- + I^- \rightarrow Cu^{2+} + 2SO_4^{2-} + I. \end{aligned}\right\} \quad (6)$$

It is known that hydrogen ions exhibit no specific catalytic effect in a reaction between peroxydisulfate and iodide ions [8]. Actually, addition of sulfuric acid to a solution containing KI, $(NH_4)_2S_8$, and $CuSO_4$ does not accelerate the oxidation of potassium iodide.

The oxidation of potassium iodide in the presence of $(NH_4)_2S_2O_8$ and $CuSO_4$ does not stop upon formation of molecular iodine. As the reaction is continued, the intensity of the band at 460 nm gradually decreases and the orange color of the solution disappears, to the point of complete decoloration. Thus, the molecular iodine formed is oxidized by excess oxidant to the iodate ions [13]. When a reducing agent (e.g., sodium thiosulfate) is added to the decolorized solution, iodine is recovered by the reaction of IO_3^- with the reducing agent [14]. Oxidation of iodine was also found in studies of I_2 precipitation in the reaction of KI with $(NH_4)_2S_2O_8$ [12].

Thus, the oxidizing solution used for coloring of the PVA films contains, along with peroxydisulfate anions, also iodate ions, which are the products of oxidation of iodide ions. On treatment of a KI-containing PVA film with this solution, IO_3^-, being smaller than $S_2O_8^{2-}$, penetrates into the polymer and oxidizes KI. By controlling the contact time, the reaction can be terminated when the iodide ions required for the film coloring are formed in the largest amounts. The involvement of the iodate ions in the oxidation shows why sulfuric acid should be added to the coloring solution, because IO_3^- ions are more reactive in acidic solutions [8]:

$$IO_3^- + 6H^+ + 5I^- \rightarrow 3I_2 + 3H_2O. \quad (7)$$

The oxidation of potassium iodide in the film by reaction (7) provides accumulation of additional iodine in its bulk [10].

Our experimental data revealed the role of $(NH_4)_2S_2O_8$, $CuSO_4$, KI, and H_2SO_4 in the oxidizing

Oxidation of iodide ions in solution containing KCl and H_2SO_4 (17 and 0.1 wt %, respectively) (reaction time 15 min, 20 ± 0.5°C)

Component	Concentration $c \times 10^3$, M				
$(NH_4)_2S_2O_8$	8.8	8.8	–	–	–
$CuSO_4$	–	–	8.0	8.0	8.0
KI	1.2	3.0	1.2	3.0	6.0
$[I_2]_{exp}$	0.60	1.70	0.10	0.10	0.15
$[I_2]_{cal}$	0.60	1.50	0.30	0.75	1.50

solution used for coloring of PVA films with iodine. Potassium chloride is added to the solution to prevent dissolution of the films being treated and to suppress their decoloration [15]. The concentration ranges of the components in the coloring solution provide optimal accumulation of iodine in the film and, after subsequent treatment in H_3BO_3 solutions and fixing, allow preparation of polarizers with the required transmission in the 400–700 nm range and high polarizing power. At the component concentrations smaller or greater than the optimum, either increased film transmission with decreased polarizing power, or increased polarizing power with decreased transmission are observed [2].

We found that the time t of contact of the PVA film with the oxidizing solution strongly affects its coloring. Upon prolonged contact, the film is partially decolorized, affecting the optical properties of the polarizer. The dependence of the optical density of the polarizer film in the 480–800 nm range, i.e., in the absorption range typical of dichroic complexes PVA–$(I_2)_n$ [16, 17], on the contact time t is shown in Fig. 5. As seen, all the curves pass through a maximum. The decrease in the content of these complexes with time is associated with a decrease in the amount of I_2 in the film bulk due to its oxidative conversion, proceeding predominantly in the surface layer of the film. To remove excess oxidants, the film is treated in a fixing solution containing potassium and cadmium iodides and subsequently washed with distilled water.

The optimal time of treatment of the PVA film containing 0.04 wt % of KI in the oxidizing solution of given composition is 30–60 s.

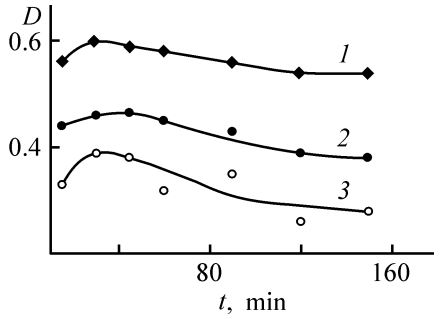

Fig. 5. Optical density D of the polarizer film as influenced by the time t of contact of the film with the oxidizing solution; film thickness 70–75 μm. Wavelength, nm: (*1*) 620, (*2*) 480, and (*3*) 800.

CONCLUSIONS

(1) Iodide ions are oxidized by ammonium peroxydisulfate to iodate ions with intermediate formation of triiodide ions and molecular iodine in the oxidizing solution containing $(NH_4)_2S_2O_8$, $CuSO_4$, KI, KCl, and H_2SO_4.

(2) During oxidative treatment of a polyvinyl alcohol film, potassium iodide occurring in the film bulk is first oxidized by iodate ions diffusing from the solution. As a result, the iodate ions provide accumulation of additional molecular iodine required to form dichroic complexes in the polymer.

(3) The coloration efficiency of the polyvinyl alcohol film is determined by the maximal accumulation of molecular iodine in its bulk and depends on the concentrations of $(NH_4)_2S_2O_8$, $CuSO_4$, and KI in the oxidizing solution and on the time of contact of the film with this solution.

REFERENCES

1. Shurkliff, W.A., *Polarized Light. Production and Use*, Cambridge, Mass.: Harvard Univ., 1962.
2. Belarussian Patent 1706.
3. Kosmacheva, T.G., Ariko, N.G., Agabekov, V.E., and Verbitskii, V.V., *Vestsi Nats. Akad. Navuk Bel., Ser. Khim. Navuk*, 1998, no. 3, pp. 107–112.
4. Zwik, M.M., *J. Appl. Polym. Sci.*, 1965, vol. 9, no. 10, pp. 2394–2424.
5. Hayashi, S., Tanabe, Y., and Hojo, N., *Makromol. Chem.*, 1977, vol. 178, no. 10, pp. 1679–1687.
6. Deuel, H. and Neukom, H., *Makromol. Chem.*, 1949, vol. 3, no. 1, pp. 137–141.
7. Awtrey, A.D. and Connick, R.E., *J. Am. Chem. Soc.*, 1951, vol. 73, no. 7, pp. 1842–1843.
8. Kolthoff, I.M., Belcher, R, Stenger, V. A., and Matsuyama, G., *Volumetric Analysis*, vol. III, *Titration Methods: Oxidation-reduction Reactions*, New York: Interscience, 1957.
9. Taube, H., *J. Am. Chem. Soc.*, 1942, vol. 64, no. 1, pp. 161–164.
10. Latimer, W. M., *The Oxidation States of The Elements and Their Potentials In Aqueous Solutions*, 2nd ed., New York: Prentice–Hall, 1952.
11. Lyubimova, V.A., *Izv. Vyssh. Uchebn. Zaved., Khim. Khim. Tekhnol.*, 1963, no. 1, pp. 49–52.
12. Gadzhiev, R.G., Mukhametshina, Z.B., and Chekmarev, A.M., *Zh. Neorg. Khim.*, 1991, vol. 36, no. 5, pp. 1174–1178.
13. Nekrasov, B.V., *Kurs obshchei khimii* (Course of General Chemistry), Moscow: Goskhimizdat, 1981, pp. 421–434.
14. Charlot, G., *Les Methods de la Chemie Analytique, Analyse quantitative Minerale*, Quatrieme Edition, Paris: Masson, 1961.
15. US Patent 2 255 940.
16. Takamiya, H., Matsuyama, T., Tanigami, T., *et al., Rep. Prog. Polym. Phys. Jpn*, 1990, vol. 33, pp. 225–228.
17. Djojosubroto, H. and Tanizaki, Y., *Bull. Chem. Soc. Jpn.*, 1970, vol. 43, no. 10, pp. 3025–3028.

Russian Journal of Applied Chemistry, Vol. 76, No. 10, 2003, pp. 1674–1678. Translated from Zhurnal Prikladnoi Khimii, Vol. 76, No. 10, 2003, pp. 1720–1724.

MACROMOLECULAR CHEMISTRY AND POLYMERIC MATERIALS

Properties of Aqueous Solutions of Mixtures of Methyl Cellulose and Hydroxypropyl Cellulose

L. I. Kutsenko, E. B. Karetnikova, A. M. Bochek, and L. M. Kalyuzhnaya

Institute of Macromolecular Compounds, Russian Academy of Sciences, St. Petersburg, Russia

Received June 24, 2003

Abstract—Rheological properties of dilute and moderately concentrated aqueous solutions of mixtures of methyl cellulose and hydroxypropyl cellulose and gelation in these solutions were studied. Using the solvent vapor sorption, the compatibility of the polymer pair was examined and the composition range in which the thermodynamic compatibility is realized was determined.

Characteristics of methyl cellulose (MC) solutions and films and fibers manufactured on their basis can be altered by chemical modification of the polymer. Previously it has been demonstrated that introduction of polar (cyanoethyl) and nonpolar (propyl) groups into MC macromolecules modifies the thermodynamic affinity of the polymer for water and the rheological characteristics of solutions of mixed cellulose ethers [gelation point (T_g) and cloud point (T_c) decrease] [1, 2]. Introduction of substituents containing hydroxy groups (e.g. hydroxypropyl) enhances the emulsifying capacity of the solutions and their resistance to salts and also raises the gelation point [3]. It is of scientific and practical interest to modify MC through combination with another cellulose ether, hydroxypropyl cellulose (HPC), in a common solvent, water.

Therefore, we analyzed in this study the viscous characteristics of aqueous solutions of MC–HPC mixtures, as influenced by the mixture composition and temperature, and also the gelation conditions and thermodynamic compatibility of these two polymers.

EXPERIMENTAL

In experiments, we used MC with a degree of substitution (DS) of 1.7 and degree of polymerization (DP) of 900 and HPC with molar substitution (MS) of 3 and DP 800. Mixed solutions of MC and HPC were prepared from equally concentrated stock solutions taken in various mass proportions. Distilled water was used as a solvent. The viscous characteristics of dilute solutions were measured at 20°C with an Ubbelohde viscometer. Rheological properties of concentrated solutions were studied with a Rheotest-2.1 rotation viscometer under shear stress of 3–600 Pa. The gelation point T_g was determined with a Hoeppler viscometer. The compatibility of MC and HPC was determined by the method of solvent vapor sorption on films of various compositions, formed from 2% aqueous solutions.

Viscometry is often used to characterize the interaction between two different polymers in a common solvent [4–6]. This method records the deviation of the viscosity of dilute polymer solutions from the theoretical values estimated from the weight-average viscosities of two individual polymers. The deviation can be regarded as a measure of intermolecular interactions between different polymers. In this study, to characterize intermolecular interactions between MC and HPC in aqueous solutions, we determined the intrinsic viscosity $[\eta]$ of the initial components and their mixtures. The theoretical intrinsic viscosity $[\eta]_{th}$ was estimated as

$$[\eta]_{th} = [\eta]_1 c_1/c + [\eta]_2 c_2/c, \quad (1)$$

where c is the total polymer concentration ($c = c_1 + c_2$), and c_1 and c_2, the concentrations of the first and second components.

The experimental and theoretical composition dependences of $[\eta]$ are shown in Fig. 1. The experimental curve *1* demonstrates positive deviations from ideality over the entire composition range, which is an indication of intermolecular interactions between the polymers in solutions. This can be attributed to the formation of some structures whose hydrodynamic volume is higher than the weight-average hydrodynamic volume of two individual components. The maximum deviation of $[\eta]_{exp}$ from the theoretical value is observed for the mixture with 50% HPC.

1070-4272/03/7610-1674 $25.00 © 2003 MAIK "Nauka/Interperiodica"

It is known that the behavior of polymer mixtures is governed by the degree of compatibility of the components. For a series of synthetic nonionic polymers, we evaluated the thermodynamic compatibility of the components in solutions on the basis of intrinsic viscosity measurements. According to the criterion suggested in [7], we used as the measure of compatibility $\Delta i/\Delta\eta_i$.

$$\Delta i/\Delta\eta_i = ([\eta]_{exp} - [\eta]_{th})/([\eta]_2 - [\eta]_1), \qquad (2)$$

where Δi is the difference between the experimental and theoretical [η] of the mixture, and $\Delta\eta_i$, the difference between [η] of the first and second components of the mixture.

For compatible polymers, this parameter is 0.1 or close to this value irrespective of the sign. Figure 1 (curve *3*) shows the dependence of $\Delta i/\Delta\eta_i$ on the composition of the MC–HPC mixture. As seen, the maximum $\Delta i/\Delta\eta_i$ is observed in a mixture containing 50% HPC, i.e., the system is incompatible in this composition range. For other compositions, the parameter $\Delta i/\Delta\eta_i$ is close to 0.1, suggesting that MC and HPC are compatible.

To examine the compatibility of MC and HPC and characterize the polymer–polymer and polymer–water interactions, we also used the solvent vapor sorption method [8]. Films prepared from the individual polymers and their mixtures were dried in a vacuum, placed in closed vessels with water, and allowed to stand under a saturated water vapor at 20°C until equilibration. Then the films were weighed, and the degree of swelling was estimated as

$$Q = (P_{swell} - P_{dry})/P_{dry}, \qquad (3)$$

where P_{dry} and P_{swell} are the weights of the dry and swollen film, respectively.

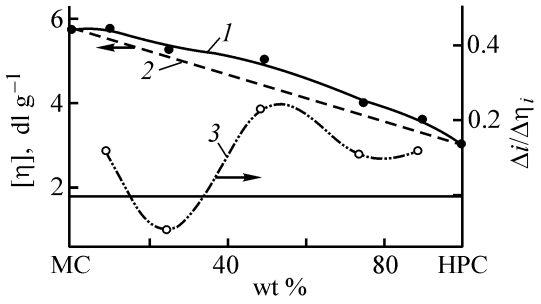

Fig. 1. (*1*) Experimental $[\eta]_{exp}$ and (*2*) theoretical $[\eta]_{th}$ intrinsic viscosities, and (*3*) $\Delta i/\Delta\eta_i$ vs. the solution composition.

Data on the sorption of water vapor on MC, HPC, and their mixtures are summarized in the table below. From the degree of swelling of the films, we estimated parameters of the polymer–solvent interaction χ_1 for MC, HPC, and their mixtures, using the Flory–Huggins equation [9].

$$\ln a_1 = \ln(p_1/p_1^0) = \ln(1 - \varphi_2) + \varphi_2 + \chi_1\varphi_2^2, \qquad (4)$$

where a_1 is the solvent activity, and p_1/p_1^0, the relative pressure of the solvent vapor.

The experiments were carried out at the saturated pressure of the solvent vapor, i.e., $a_1 = p_1/p_1^0 = 1$ and $\ln a_1 = 0$. The volume fraction of the polymer was calculated by

$$\varphi_2 = 1/[1 + (d_2/d_1)Q], \qquad (5)$$

where d_1 and d_2 are the solvent and polymer densities, respectively, and Q, the amount of the adsorbed solvent (g g^{-1}).

The sample density was determined by hydrostatic weighing in heptane. The polymer–polymer interac-

Amount of adsorbed water Q, volume fractions of the solvent φ_1 and polymer φ_2, parameters of the interactions polymer–solvent χ_1 and polymer–polymer χ_{23}, and size of the solvent associates $c_1g_1 + 1$ and their amount N_c

Content, wt %		Q, g g^{-1}	φ_1	φ_2	χ_1	χ_{23}	$c_1g_1 + 1$	N_c
MC	HPC							
100	0	0.896	0.540	0.460	0.74	–	4.9	18.1
90	10	0.880	0.536	0.464	0.74	–0.13	4.8	18.3
75	25	1.153	0.603	0.397	0.68	0.14	5.7	20.2
50	50	4.420	0.855	0.145	0.55	0.52	17.8	24.8
25	75	1.057	0.585	0.415	0.70	–0.24	5.5	19.2
10	90	1.362	0.646	0.354	0.65	–0.17	6.4	21.3
0	100	1.724	0.698	0.302	0.63	–	7.9	21.7

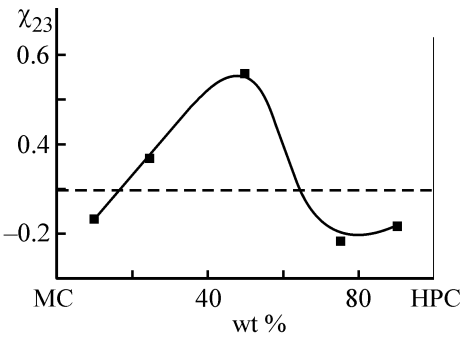

Fig. 2. Polymer–polymer interaction parameter χ_{23} vs. the solution composition.

tion parameter was estimated from the sorption data by the Patterson equation (6) [10].

$$\chi_{23} = (\chi_{12}\varphi_a + \chi_{13}\varphi_b - \chi_{1(23)})/\varphi_a\varphi_b, \quad (6)$$

where χ_{12}, χ_{13}, and $\chi_{1(23)}$ are the Flory–Huggins interaction parameters of, respectively, the individual MC and HPC and their mixtures with water; φ_a and φ_b are the volume fractions of the polymers in a mixture.

Scott has demonstrated [11] that $\chi_{23} < 0$ for compatible polymer mixtures. Therefore, any positive value of χ_{23} suggests that the polymers are incompatible. The table shows that the mixtures containing 25–50% HPC are incompatible ($\chi_{23} > 0$). For the mixtures with 10 and >75% HPC, $\chi_{23} < 0$, i.e., the systems are compatible.

It should be pointed out that data on the compatibility of NC and HPC, obtained in the solvent vapor sorption experiments, are consistent with the viscometric data obtained for dilute solutions and also with the theoretical results yielded by Eq. (2) (Fig. 1, curve *3*). As a graphic demonstration, Figure 2 shows the composition dependence of χ_{23}. As seen, both methods give nearly coincident composition ranges in which MC and HPC are compatible. Here, one should keep in mind that data on compatibility of polymers, obtained in studying properties of dilute solutions of polymer mixtures, are not always confirmed by the solvent vapor sorption method.

In the bulk of a polymer, adsorbed solvent molecules can form associates if the cohesion forces between the sorbate molecules are stronger than those between the sorbate and the polymer [12]. The average size of the associates, i.e., the number of molecules in the associate can be estimated by the Zimm–Lundberg equation (7) [12].

$$c_1 g_{11} + 1 = (1 - \varphi_1)(\partial \ln \varphi_1 / \partial \ln a_1)_{p,T}, \quad (7)$$

where g_{11} is the cluster formation integral; and c_1, φ_1, and a_1, the molar concentration, volume fraction, and activity of the solvent, respectively.

Combining the Flory–Huggins and Zimm–Lundberg equations, Starkweather has derived the following relationship for the size of associates [13]:

$$c_1 g_{11} + 1 = 1/(1 - 2\chi_1\varphi_1), \quad (8)$$

where χ_1 is the polymer–solvent interaction parameter in the Flory–Huggins equation.

The number of associates in the polymer matrix was calculated by

$$N_c = W/(c_1 g_{11} + 1), \quad (9)$$

where W is the amount of adsorbed solvent (g per 100 g dry polymer).

As seen from the table, the amount of associates and their size are larger in a mixture containing 50% HPC.

It may be suggested that the size of solvent associates and their amount are influenced by the properties and thermodynamic compatibility of macromolecules of the polymeric components constituting the mixture, as well as the morphology of the films formed. Like cellulose itself, MC and HPC are partially crystallizable polymers. With increasing fraction of amorphous zones in the polymers and their mixtures, i.e., with decreasing degree of ordering, the volume of the polymer matrix in which associates can be formed will increase. With incompatible polymers, a porous matrix appcars in film formation. This matrix has larger specific surface area and higher porosity as compared with the films prepared from the individual polymers. As the specific surface area and porosity of the films increase, the volume in which solvent associates can be formed increases too, which is supported by experimental data. Thus, the films containing 50% HPC are cloudy in their outward appearance, unlike the films of other compositions.

To gain better insight into the intermolecular interactions between macromolecules of different kinds in moderately dilute solutions, we studied the rheological characteristics of 2% MC–HPC mixtures at various temperatures.

Figure 3 shows the flow curves of the solutions studied. As seen, these solutions demonstrate an incompletely Newtonian flow behavior. At shear stresses of up to log $\tau \sim 1.8$–2.0 (τ, 10^{-1} Pa), nearly New-

tonian flow is observed, and at higher shear streses, a structural viscosity branch. With increasing HPC fraction, the viscosity of mixed solutions decreases. With the solutions heated to 50°C, the shape of the log η–*T* curves changes (Fig. 4). Above 40°C, a physical thermally reversible gel is formed, which, in turn, leads to an increase in viscosity. In a solution containing 25% HPC, we also observed gel formation accompanied by increasing viscosity. In the HPC solution (Fig. 4, curve *5*), gel formation does not occur with increasing temperature, but the solution gets turbid, suggesting phase separation (precipitation of HPC from the solution). This makes lower the polymer concentration in solution, which results in a sharper decrease in the viscosity above 40°C.

From the temperature dependences of the viscosity, we estimated the enthalpy of activation of viscous flow of the solutions E_a (at temperatures at which no gel formation is observed, i.e., at 20–40°C). From the flow curves we estimated the degree of structurization in the solutions, defined as the ratio $[(\eta_0 - \eta_1/\eta_0] \times 100$ (%), where η_0 and η_1 are the solution viscosities at $\log \tau = 1.7$ and 3.0, respectively.

Figure 5 shows the composition dependences of the viscosity, activation enthalpy of viscous flow, and degree of structurization in MC–HPC mixtures. The viscosity of the mixed solutions and degree of their structurization (curves *1* and *3*) are higher than the additive values, which can be attributed to the formation of new mixed structural elements in solutions by virtue of intermolecular interaction between like and unlike macromolecules and also to the formation of a new 3*D* system of hydrogen bonds in the solutions. The composition dependence of E_a is more complex (Fig. 5, curve *2*). Positive deviations of E_a are observed at an HPC content below 50%, and negative deviations, above 50%. The positive and negative deviations of E_a suggest the formation of different associates, depending on the nature and concentration of a predominant polymer. The evolution of the viscosity, solutions structurization, and E_a can be attributed to changes in the thermodynamic affinity of a polymer for a solvent after addition of another polymer, and also to interaction between unlike macromolecules and phase separation in the solutions, caused by the incompatibility of the polymer pair [9].

Sarkar has demonstrated [3] that introduction of hydroxypropyl groups into glucoside units of MC raises the gelation point in aqueous solutions of the mixed ether, methyl hydroxypropyl cellulose, as compared with straight MC. It may be suggested that

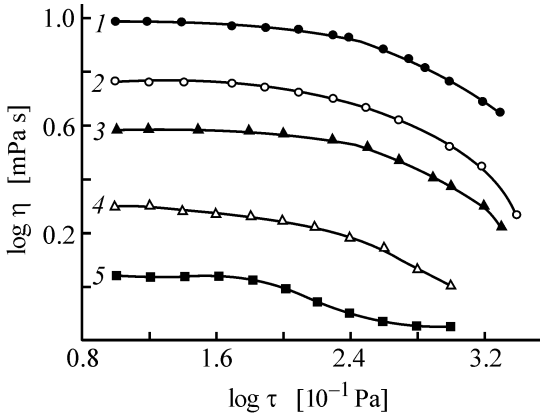

Fig. 3. Flow curves of 2% solutions at 20°C: (*1*) MC, (*2*–*4*) MC–HPC, and (*5*) HPC. (η) Viscosity and (τ) shear stress. HPC content (wt %): (*2*) 25, (*3*) 50, and (*4*) 75; the same for Fig. 4.

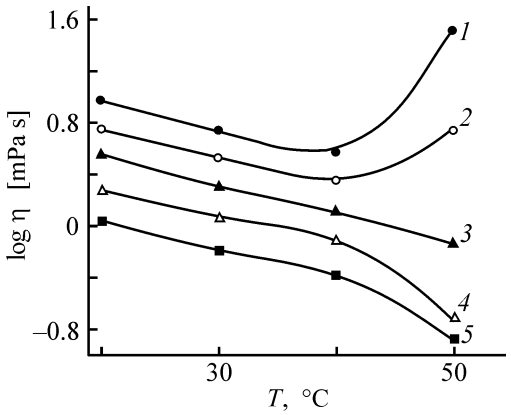

Fig. 4. Viscosity η vs. temperature *T* in solutions of (*1*) MC, (*2*–*4*) MC–HPC, and (*5*) HPC.

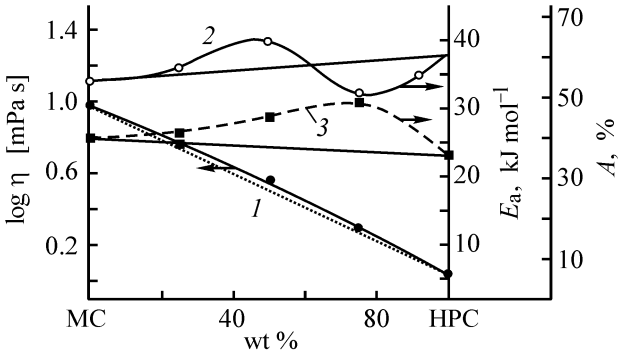

Fig. 5. (*1*) Viscosity η, (*2*) E_a, and (*3*) degree of structurization, *A*, vs. the solution composition.

the gelation point in mixed MC–HPC solutions differs from that in MC solutions, too.

The gelation (T_g) and cloud (T_{cl}) points were determined from changes in the viscosity with a Hoeppler viscometer and also photocolorimetrically with

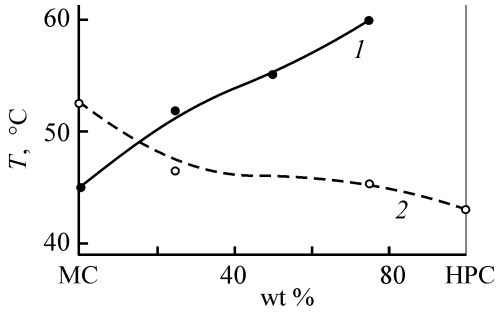

Fig. 6. (*1*) Gelation and (*2*) cloud points vs. the solution composition.

a KFK-2 laboratory concentration photocolorimeter in a temperature-controlled cell at a wavelength of 670 nm [1, 2]. The results obtained are shown in Fig. 6.

With growing HPC fraction, T_g increases and T_{cl} decreases. When heated, HPC does not form a gel [14]. Therefore, the increase in T_g is probably due to the interaction between unlike polymers in a common solvent through hydrogen bonding. As a result, the hydrophobic interaction between the trisubstituted MC units weakens, and the thermal resistance of the MC macromolecules increases. The decrease in T_{cl} is associated with increasing weight fraction of HPC which is separated from the solution on heating [14], thus increasing the solution turbidity.

CONCLUSIONS

(1) Rheological properties of dilute and moderately concentrated aqueous solutions of methyl cellulose, hydroxypropyl cellulose, and their mixtures were studied.

(2) In mixed polymer solutions, positive deviations of the solution viscosity from the theoretical values were observed, suggesting the formation of new mixed structural elements in solutions as a result of intermolecular interactions between like and unlike macromolecules and also the formation of a new 3*D* system of hydrogen bonds.

(3) The solubility of methyl cellulose and hydroxypropyl cellulose was studied by the solvent vapor sorption method at various compositions. It was found that The polymers are thermodynamically compatible in mixtures containing 10 and >75 wt % hydroxypropyl cellulose. In mixtures containing 25 to 75 wt % hydroxypropyl cellulose, the polymers are incompatible. In the polymer mixtures, adsorbed molecules of the solvent form associates, whose amount and size are the largest in an incompatible mixture containing 50% hydroxypropyl cellulose.

(4) With increasing fraction of hydroxypropyl cellulose, the gelation point increases and the cloud point decreases.

REFERENCES

1. Bochek, A.M., Nud'ga, L.A., Petrova, V.A., and Petropavlovskii, G.A., *Zh. Prikl. Khim.*, 2000, vol. 73, no. 2, pp. 304–308.
2. Bochek, A.M., Petropavlovskii, G.A., Kutsenko, L.I., and Karetnikova, E.B., *Zh. Prikl. Khim.*, 2000, vol. 73, no. 1, pp. 152–155.
3. Sarkar, N., *J. Appl. Polym. Sci.*, 1979, vol. 24, no. 4, pp. 1073–1087.
4. Williamson, G.R. and Wright, B., *J. Polym. Sci., Part A*, 1965, vol. 3, pp. 3885–3891.
5. Staikos, G.B., *Macromol. Chem.*, 1991, vol. 192, pp. 2649–2657.
6. Budtova, T.V., Bel'nikevich, N.G., Belyaev, V.M., *et al.*, *Vysokomol. Soedin., Ser. B*, 1991, vol. 33, no. 7, pp. 520–524.
7. Feldman, D. and Russu, M., *Eur. Polym. J.*, 1970, vol. 6, pp. 627–638.
8. *Eksperimental'nye metody v adsorbtsii i molekulyarnoi khromatografii* (Experimental Methods in Adsorption and Molecular Chromatography), Kiselev, A.V. and Dantsig, V.P., Eds., Moscow: Mosk. Gos. Univ., 1973.
9. Tager, A.A., *Fizikokhimiya polimerov* (Physical Chemistry of Polymers), Moscow: Khimiya, 1968.
10. Su, C.S. and Patterson, D., *Macromolecules*, 1974, vol. 10, pp. 708–712.
11. Scott, R.L., *J. Polym. Sci.*, 1952, vol. 9, pp. 423–432.
12. Zimm, B.N. and Lundberg, I.L., *Phys. Chem.*, 1953, vol. 60, pp. 425–428.
13. Howard, W. and Starkweather, Ir., in *Structure–Solubility Relationships in Polymers*, New York: Academic, 1977, pp. 21–31.
14. Bytenskii, V.Ya. and Kuznetsova, E.P., *Proizvodstvo efirov tsellyulozy* (Manufacture of Cellulose Ethers and Esters), Leningrad: Khimiya, 1974.

Russian Journal of Applied Chemistry, Vol. 76, No. 10, 2003, pp. 1679–1682. Translated from Zhurnal Prikladnoi Khimii, Vol. 76, No. 10, 2003, pp. 1725–1728.

MACROMOLECULAR CHEMISTRY AND POLYMERIC MATERIALS

Fabrication of Microcrystalline and Powdered Cellulose from Short Flax Fiber and Flax Straw

A. M. Bochek, I. L. Shevchuk, and V. N. Lavrent'ev

Institute of Macromolecular Compounds, Russian Academy of Sciences, St. Petersburg, Russia

Received June 24, 2003

Abstract—Conditions of manufacture of microcrystalline cellulose from variously treated short flax fibers and of powdered cellulose from flax straw were examined. The effect of fats, waxes, and pectins contained in the fibers on the kinetics of hydrolysis of the polysaccharide was studied.

Production of flax-fiber-based textile materials grows steadily. Among the problems arising in flax fiber processing in textile industry is utilization of wastes [flax stalks (boon) and short fibers] after separation of long fibers for manufacture of yarn.

Food, cosmetic, and fragrance industries widely use microcrystalline cellulose (MCC) manufactured from cotton linter or treated wood cellulose [1–3]. It is of scientific and practical interest to use short flax fibers and stalks for manufacture of microcrystalline and powdered cellulose, and also as a raw material instead of cotton linter in production of cellulose ethers and esters.

Therefore, we analyzed in this study conditions of manufacture of powdered and microcrystalline cellulose from variously treated short flax fiber and also from flax stalks. For comparison, the kinetics of hydrolysis of cotton linter was also studied.

EXPERIMENTAL

As starting materials we used short flax fiber and flax straw (from the Nevel Plant), and also cotton linter. The degree of polymerization (DP) of cellulose in the initial flax and cotton fibers was 2850 and 1600, respectively. The DP was determined viscometrically in cellulose solutions in Cadoxene.

The samples of flax fiber and straw were characterized by their chemical composition (see table). The cellulose content was determined by the Kurschner–Hoffner method [4]; lignin, by Komarov's method [4]; fats and moisture and ash contents, according to the procedures described in [4, 5]; pectins, by the calcium pectate method [5]; and nitrogen, by the Kjeldahl method, using the procedure described in [5].

Flax and cotton fibers were hydrolyzed under similar conditions. To optimize the process, flax straw was preliminarily chopped in an MN-250 knife mill and graded with a metallic sieving stack. For hydrolysis, we used the 0.1–1.0 mm fraction.

For manufacture of MCC, mineral acids (HCl, H_2SO_4, and HNO_3) are commonly used [2, 3]. In this study, the fibers were hydrolyzed in 2.5 M HCl at 105°C with mechanical stirring. In the course of hydrolysis, samples of the hydrolyzate were taken, washed with distilled water to pH 7.0, wetted with ethanol, and dried at 105°C to constant weight. The thus prepared samples were then ball-milled for 0.5 h and graded with a sieving stack. The DP was determined from the viscosity of solutions in Cadoxene. Treat-

Chemical composition of flax fibers and stalks

Component	Content, wt %	
	flax straw (flax stalks)	short fibers
Ash	2.1	1.3
Fats and waxes	2.0	1.2
Lignin	31.6	4.8
Nitrogen	Not determined	0.3
Cellulose	47.2	72.1
Pectins	2.5	1.2
Other hemicelluloses	7.8	13.9
Moisture content	6.4	5.2

1070-4272/03/7610-1679 $25.00 © 2003 MAIK "Nauka/Interperiodica"

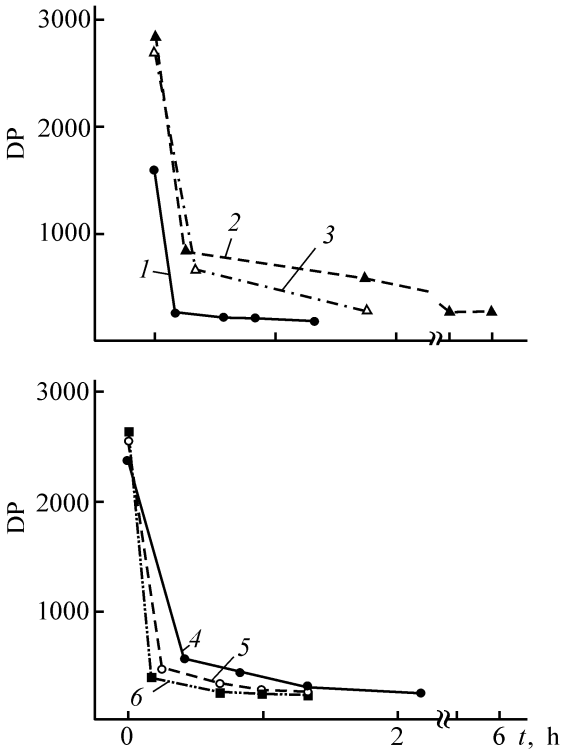

Fig. 1. Evolution of DP in the course of hydrolysis. (*t*) Time. (*1*) Cotton cellulose and (*2–6*) flax fiber: (*2*) no treatment, (*3*) after removal of fats, (*4*) after removal of fats and treatment with hot water, (*5*) after removal of fats and pectins, and (*6*) after bleaching.

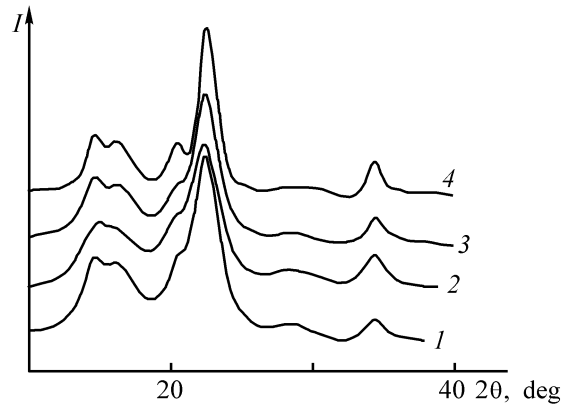

Fig. 2. X-ray diffraction pattern of MCC samples obtained from (*1*) untreated flax fiber, (*2*) that after removal of fats, (*3*) bleached flax fibers, and (*4*) cotton linter. (*I*) Intensity and (2θ) Bragg angle.

ment of flax fiber to remove fats, waxes, and pectins was carried out using the procedure described in [5]. Fats and waxes were removed by treatment with an alcohol–benzene mixture in a Soxhlet apparatus. Pectins were removed by treating the defatted fibers with aqueous solutions of HCl and ammonium citrate [6].

A part of the initial flax fiber and stalks was bleached. Samples (9–10 g) were placed in a bleach liquor (500 ml) and heated at 100°C for 3 h (nitrogen bubbling) with mechanical stirring. The composition of the bleach liquor was as follows: 10 g of NaOH and 6.5 g of $Na_2S_2O_3$ in 500 ml of distilled water. The samples after bleaching were washed with distilled water to pH 7.0.

The crystallinity index was determined in pelletized samples by X-ray diffraction analysis [7] on a DRON-2 diffractometer (Cu_{K_α} radiation, Ni filter).

Figure 1 shows the kinetics of hydrolysis of the samples. In the initial samples, the DP in flax cellulose is higher than that in cotton cellulose, which is consistent with published data [5, 8]. In cotton linter, the "limiting" DP of cellulose after hydrolysis was 180, while the DP of cellulose in flax fiber decreased to 230–240. The differences in DP of cellulose in hydrolyzed samples can be attributed to spesific features of the fine structure of flax and cotton fibers and also to different sizes of crystallites of the natural polymer in the fibers.

In contrast to cotton, flax fibers contain more fats, waxes, pectins, and hemicelluloses [5, 8], which affects the hydrolysis rate. Fats and waxes prevent wetting of the fibers with aqueous HCl and also its diffusion into the fibers, affecting the time in which the limiting DP is reached. Removal of fats, waxes, and pectins increases the rate of hydrolysis of flax cellulose. As seen, treatment of flax fiber to remove the indicated components results in that the time of establishment of the limiting DP approaches that typical of cotton cellulose. It should be pointed out that any treatment of flax fiber to remove fats, pectins, and other associated compounds decreases the molecular weight of cellulose. Figure 1 shows that, in untreated fibers, the DP of cellulose is 2850. As fats and pectins were removed, the DP decreased to 2550 (curves *4–6*). After bleaching, the DP of cellulose decreased to 2650.

Figure 2 demonstrates X-ray diffraction patterns of MCC samples obtained from variously treated fibers. The crystallinity index of cotton MCC was determined to be 0.67. In MCC samples prepared from flax fiber, the crystallinity index increased as the accompanying comitant compounds were removed (from 0.64 for untreated fiber to 0.67 for bleached fiber).

The cross-sectional size L_{eff} of cellulose crystallites in flax and cotton fibers was estimated by the Debye–Scherrer method.

$$L_{\text{eff}} = 0.9\lambda/\beta\cos\theta, \quad (1)$$

where $\beta = \sqrt{\beta_o^2 - \beta_i^2}$; λ is the wavelength of Cu_{K_α} radiation (0.154 nm); θ, the diffraction angle from the 002 plane (11.25°); β, the corrected halfwidth of the reflections (002); and β_o and β_i, the observable halfwidth and instrumental broadening of the line, respectively.

In cotton MCC, L_{eff} was estimated to be 3.8 nm, which is well consistent with published data [3, 7]. In flax MCC, L_{eff} appeared to be higher (4.5–5.2 nm). These values well correlate with the above-mentioned higher DP of flax cellulose. The differences in hydrolysis kinetics between flax and cotton celluloses, and also the observed higher limiting DP of flax cellulose are caused both by the presence of accompanying compounds in flax fibers and by larger cross-sectional size of cellulose crystallites.

The crystallite size distribution in the MCC samples is shown in Fig. 3. MCC prepared from cotton linter contains no particles larger than 500 μm. In all the MCC samples, the major fraction of particles has the size ranging from 100 to 200 μm. In MCC obtained from flax fiber, we also found particles of 500 μm and more in size, which can be attributed to the presence of residues of stalks (boon) in short flax fibers. These residues have a different chemical composition and a higher resistance to hydrolysis. Furthermore, the presence of waxes and pectins in the samples has a negative effect on the disintegration rate of the dried material in the course of ball-milling before fractionation.

Conversion of the flax stalks fraction into the powdered form in treatment with HCl takes a longer time (>10 h) as compared with hydrolysis of flax fiber under the same conditions. The hydrolysis of flax stalks is decelerated at high content of lignin (see table). Therefore, we did not study the kinetics of hydrolysis of flax stalks. Based on data presented in Fig. 1, the initial flax straw fiber was treated with 2.5 M HCl for 6 h (time of establishment of the limiting DP for untreated flax fiber), and flax straw fiber after bleaching, for 2 h. Figure 4 shows the particle size distribution in the initial flax straw fiber and in that after hydrolysis. As seen, the curves differ only slightly from each other. The only observed trend is a decrease in the fraction smaller than 700 μm in size. However, the fraction >200 μm did not increase, i.e., powdered cellulose can be obtained under the experimental conditions of hydrolysis of flax straw fibers.

To conclude, MCC can be manufactured from short flax fiber, and powdered cellulose, from chopped flax straw. The cellulose samples thus obtained find use in various areas instead of MCC from cotton and wood cellulose.

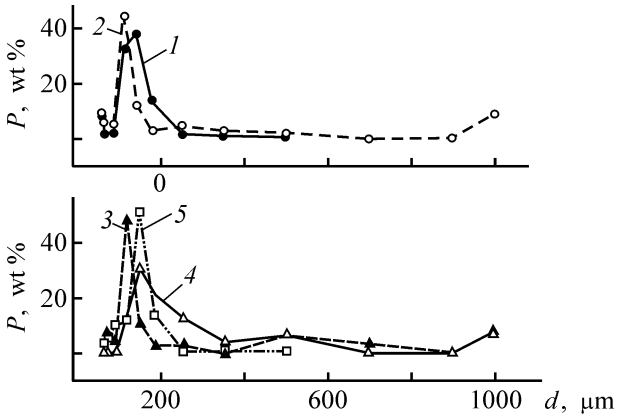

Fig. 3. Crystallite size distribution in MCC. (*P*) Fraction and (*d*) effective size; the same for Fig. 4. (*1*) Cotton fibers and (*2–5*) flax fiber: (*2*) untreated, (*3*) that after removal of fats and treatment with hot water, (*4*) after removal of fats and pectins, and (*5*) after bleaching.

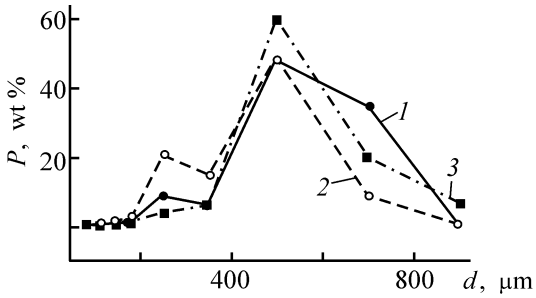

Fig. 4. Particle size distribution in flax straw fiber: (*1*) beaten initial fiber, (*2*) after hydrolysis (untreated), and (*3*) after hydrolysis (bleached).

CONCLUSIONS

(1) Conditions of manufacture of microcrystalline cellulose from short flax fiber of various cleaning grades and of powdered cellulose from flax straw are studied.

(2) The kinetics of flax cellulose hydrolysis is influenced by fats, pectins, and lignins contained in the fibers. Removal of fats, waxes, and pectins increases the hydrolysis rate.

(3) The effective cross size of the crystallites in flax fiber is larger than that in cotton fiber.

REFERENCES

1. Battista, O.A., in *Cellulose and cellulose derivatives*, Bikales, N.M. and Segal, L., Eds., New York: Wiley, 1971. Translated under the title *Tselluloza i ee proizvodnye*, Moscow: Mir, 1974, pp. 412–423.
2. Petropavlovskii, G.A., *Gidrofil'nye chastichno zame-*

shchennye efiry tsellyulozy i ikh modifikatsiya putem khimicheskogo sshivaniya (Hydrophilic, Partially Substituted Cellulose Ethers and Esters and Their Modification by Chemical Cross-Linking), Leningrad: Nauka, 1988.

3. Kotel'nikova, N.E., Petropavlovskii, and Khou Yunfa, in *Khimiya i delignifikatsiya tsellyulozy* (Chemistry and Delignification of Cellulose), Zakis, G.F., Ed., Riga: Zinatne, 1991, pp. 79–88.
4. *Prakticheskie raboty po khimii drevesiny* (Practical Works on Wood Chemistry), Nikitin, V.M., Ed., Moscow: Lesnaya Prom–st., 1965.
5. *Spravochnik khimicheskoi tekhnologii obrabotki l'nyanykh tkanei* (Handbook of Chemical Finishing of Linen Fabric), Fridlyand, G.I., Ed., Moscow: Legkaya Industriya, 1973.
6. Bochek, A.M., Zabivalova, N.M., Shamolina, I.I., *et al.*, *Zh. Prikl. Khim.*, 2002, vol. 75, no. 9, pp. 1549–1554.
7. Ioelovich, M.Ya. and Veveris, G.P., *Khim. Drev.*, 1987, no. 5, pp. 72–80.
8. *Pryadenie l'na i khimicheskikh volokon: Spravochnik* (Flax and Chemical Fiber Spinning: A Handbook), Karyakin, L.B. and Ginzburg, L.N., Eds., Moscow: Legprombytizdat, 1991.

Russian Journal of Applied Chemistry, Vol. 76, No. 10, 2003, pp. 1683–1685. Translated from Zhurnal Prikladnoi Khimii, Vol. 76, No. 10, 2003, pp. 1729–1731.

CHEMISTRY OF FOSSIL FUEL

Molecular Composition of Sulfur-Containing Waste from Desulfurization of Tengiz Crude Oil

V. A. Solomin, G. K. Bishimbaeva, V. V. Lyapunov, S. O. Zhumabekova, U. Zh. Dzhusipbekov, Sh. M. Umbetova, and E. A. Dzhakhmetov

Bekturov Institute of Chemical Sciences, Ministry of Education and Science of the Republic of Kazakhstan, Almaty, Kazakhstan

Received April 10, 2003

Abstract—The molecular composition of sulfur-containing waste from desulfurization of Tengiz (Kazakhstan) crude oil was studied by gas chromatography–mass spectrometry.

The presence of mercaptants and other aggressive sulfur-containing compounds in most of hydrocarbon raw materials from West Kazakhstan deposits gives rise to specific problems in extraction, transportation, storage, and processing, making urgent desulfurization of oils and petroleum products.

The Tengiz deposit is one of the largest oil and gas deposits in Kazakhstan. Tengiz crude oil is a high-quality light product; it, however, contains much sulfur compounds: 20–30 vol % H_2S, 0.45–1.15 wt % total sulfur, 0.001–0.009 wt % mercaptans, and 0.001–0.2 wt % sulfides and disulfides [1].

Among the existing methods for oil desulfurization, hydrorefining is the most widely used in industry. The process involves cleavage of organosulfur compounds in a medium of a hydrogen-containing gas in the presnece of catalysts, to obtain H_2S and H_2O. The major fraction of H_2S is then trapped and converted into elemental sulfur by the Claus process (oxidation on titanium oxide catalysts) or removed by base treatment.

Treatment of oil and gas to remove sulfur compounds results in formation of large amounts of a sulfur-containing waste, which inevitably leads to an environmental impact. Therefore, a study the molecular composition of the organic component of this waste is topical. Such data are also necessary for efficient utilization of processing products of high-sulfur oils.

EXPERIMENTAL

To determne the molecular composition of the organic component of the sulfur-containing waste from oil desulfurization, a 50-g sample was extracted 10 times with 800 ml of distilled water in a Soxhlet apparatus. The resulting solution (500 ml) was extracted in a separatory funnel with three 20-ml portions of ultrapure grade methylene chloride. The extract was concentrated and analyzed on a Hewlett–Packard 5890/5972 gas chromatograph–mass spectrometer. An SPB-5 (Supelco) capillary column (30 m × 0.25 mm i.d., coating thickness 0.25 μm) was used. The carrier gas was helium (linear velocity 43 cm s^{-1}). The injector and interface temperatures were 280°C. The temperature schedule of the column was as follows: 30°C, 4 min; heating to 180°C at a rate of 10 deg min^{-1}; heating to 280°C at a rate of 15 deg min^{-1}; 280°C, 5 min. The mass-spectrometric detector was used in the scan mode.

The total content of hydrocarbons in the sulfur sample was determined by extraction with carbon tetrachloride, followed by measurement of the absorption at 2940 cm^{-1} (Specord M-80 IR spectrometer, Carl Zeiss, Jena).

According to the chemical classification [2], Tengiz crude oil belongs to the mercaptan type and contains relatively low-boiling and reactive sulfur compounds (H_2S, mercaptans, disulfides). It also contains [1] derivatives of oxidized sulfur (sulfoxides, sulfones); their total content is 13.3 wt % relative to total sulfur.

In this study, we identified by gas chromatography–mass spectrometry the major components and organic impurities of the sulfur-containing waste from oil desulfurization. The chromatogram of the hexane ex-

1070-4272/03/7610-1683 $25.00 © 2003 MAIK "Nauka/Interperiodica"

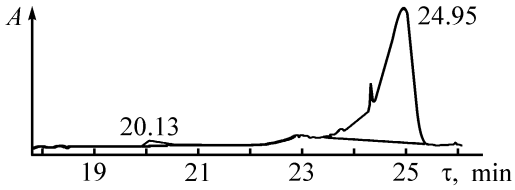

Fig. 1. Chromatogram of a hexane extract from the sulfur-containing waste from oil desulfurization. (τ) Retention time; the same for Fig. 3.

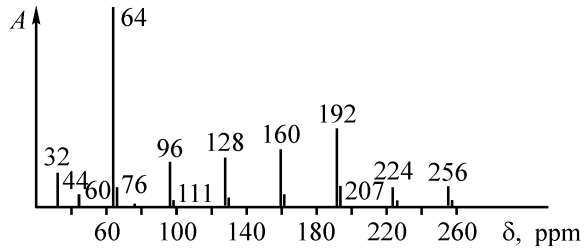

Fig. 2. Mass spectrum corresponding to the S_8 peak in the chromatogram.

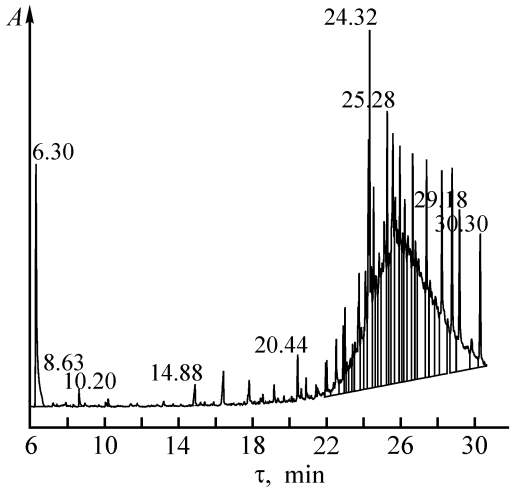

Fig. 3. Chromatogram of the organic fraction of the extract from the sulfur-containing waste.

tract of this product in hexane (Fig. 1) corresponded to the chromatogram of elemental sulfur. A relatively weak peak at τ = 20.13 min was assigned to S_6, and a strong peak at 25.95 min, to S_8. The shape of the latter peak, with broadened wing on the side of short retention times, may be due to partial transformation of this sulfur modification to a lower-molecular-weight form under the conditions of gas-chromatographic analysis. The mass spectrum (Fig. 2) is typical of sulfur; the difference between the main peaks is 32 amu, which corresponds to the atomic weight of S.

The total content of petroleum hydrocarbons in the final sulfur-containing waste was estimated by IR spectroscopy to be 23 mg kg^{-1}. In this study, we analyzed the molecular composition of hydrocarbons present in the sulfur-containing waste. We assumed that the major components of the hydrocarbon fraction must be crude oil components that remained unchanged upon desulfurization: paraffins, cycloparaffins, etc. Also of considerable interest were organic products that could be formed under the processing conditions by oxidation, dehydration, etc. Such or-

Molecular composition of the organic fraction of the extract of Tengiz sulfur

Retention time, min	Compound	Content, rel. %	Retention time, min	Compound	Content, rel. %
14.88	Octanoic acid	0.42	25.27	Heneicosane	4.21
16.41	Nonanoic acid	0.64	25.40	11-Docosene	3.50
17.81	Decanoic acid	0.50	25.71	Octadecanoic acid	3.66
19.70	Pentadecane	0.08	25.96	Docosane	5.62
20.43	Dodecanoic acid	0.64	26.22	2,6,10,15-Tetramethylnonadecane	5.25
22.02	2,6,10,14-Tetramethylpentadecane	0.80			
22.52	Tetradecanoic acid	1.43	26.40	2-Methyldocosane	2.12
22.90	Octadecane	1.19	26.66	Tricosane	5.57
23.42	3-Nonadecene	1.06	26.80	2-Methyltricosane	1.17
23.75	Nonadecane	3.95	26.97	3-Methyltricosane	1.91
23.87	2,6,11-Trimethylheptadecane	2.31	27.41	Tetracosane	5.09
24.11	9-Hexadecenoic acid	3.52	27.59	2,6,11-Trimethylheneicosane	5.67
24.54	Eicosane	3.90	28.23	Pentacosane	7.18
24.68	7-Cyclohexylpentadecane	3.26	29.19	Hexacosane	5.96
24.85	3-Methyleicosane	3.45	29.84	3-Methylhexacosane	1.62
25.12	10-Methyleicosane	3.58	30.30	Octacosane	2.23

ganic compounds may be water-soluble (so-called translocation forms of hydrocarbons) and, therefore, environmentally hazardous [3].

To determine the molecular composition of oxidized (hydrophilic) petroleum products, we used in this study a special extraction procedure. The sulfur-containing waste was repeatedly extracted in a Soxhlet apparatus with water, and the resulting aqueous phase was extracted with methylene chloride. The results of chromatographic analysis of the extract thus obtained are given in the table and in Fig. 3.

As seen from the table, we identified in the sulfur-containing waste from desulfurization of high-sulfur crude oil more than 30 organic compounds, among which the major components were paraffins, saturated and unsaturated C_8–C_{19} carboxylic acids, and alicyclic compounds containing linear alkyl substituents.

A significant fraction of the organic compounds detected in the sulfur-containing waste are the initial oil components adsorbed in unchanged form on the product surface in the course of crude oil desulfurization.

At the same time, aliphatic carboxylic acids present in the sulfur-containing waste (see table) may originate from oxidation of crude oil hydrocarbons in the Claus process in the stage of H_2S oxidation, and also from transformations of the product in the course of irs prolonged storage in air under the action of atmospheric oxygen and moisture.

CONCLUSIONS

(1) The final sulfur-containing waste from desulfurization of Tengiz high-sulfur crude oil and gas contains impurities of aliphatic and cyclic organic compounds.

(2) A study by gas chromatography–mass spectrometry revealed that the hydrocarbon fraction of the product contains aliphatic carboxylic acids.

REFERENCES

1. Nadirov, N.K., Bakirova, S.F., and Buyanova, N.S., *Neft' Gaz Kaz.*, 1997, no. 2, pp. 54–57.
2. Solomin, V.A., Lyapunov, V.V., Zhumabekova, S.O., *et al., Izv. Min. Obraz. Nauki Resp. Kaz., Nats. Akad. Nauk Resp. Kaz., Ser. Khim.*, 2002, no. 4, pp. 81–90.
3. Solomin, V.A., Lyapunov, V.V., Zhumabekova, S.O., *et al.*, in *Mezhdunarodnyi simpozium, posvyashchennyi 100-letiyu A.B. Bekturova: Izbrannye trudy* (Int. Symp. Dedicated to Centennial of A.B. Bekturov: Selected Papers), Almaty, 2001, pp. 520–526.

Russian Journal of Applied Chemistry, Vol. 76, No. 10, 2003, pp. 1686–1691. Translated from Zhurnal Prikladnoi Khimii, Vol. 76, No. 10, 2003, pp. 1732–1737.

CHEMISTRY OF FOSSIL FUEL

Genetic Relationship of Anthraquinones and Allied Derivatives from Brown Coal Organic Matter with the Starting Biological Material

V. V. Platonov, A. Yu. Shvykin, E. A. Sharabanova, and V. A. Proskuryakov

Leo Tolstoy State Pedagogical University, Tula, Russia
St. Petersburg State Technological Institute, St. Petersburg, Russia

Received January 18, 2003; in final form, August 2003

Abstract—The possible genetic relationship of anthraquinone and allied derivatives from brown coal organic matter with the starting biological material was studied.

Substituted anthaquinones, their derivatives, compounds of the anthrone and anthracene series, and also benzo- and naphthoquinones were identified by a set of physicochemical methods in extracts and semicoking tars of brown coals, with coals from the Berezovo deposit of the Kansk–Achinsk fields as example [1–10].

It is known that anthraquinone derivatives constitute the most abundant group of natural quinones, and, by now, hundreds of such compounds have been isolated, mainly from monocotyledonous and dicotyledonous flowering plants, lower fungi, and some lichens; these compounds have also been found in some insects and marine invertebrates of the Echinodermata class (sea lilies, Crinoidea) [11–20].

Virtually all natural anthraquinones contain hydroxy and methoxy groups in various positions and, frequently, methyl, propyl, isoprenyl, hydroxymethyl, aldehyde, and carboxy groups in the β-position. In plants, anthraquinones are often bound to sugars, as O- and C-glycosides [10, 11].

Comparison of the anthraquinones and related compounds that have been identified in the examined coal products with native anthraquinones shows that none of the structures identified in coals directly corresponds to native structures. Only one coal compound, dihydroxymethoxypropenylanthraquinone, can be related to nalgiovensin **I** [10, 11, 19] as dehydration product; dehydration could have occured in the course of coal formation or thermochemical transformations of the organic matter of coal (OMC) during semicoking:

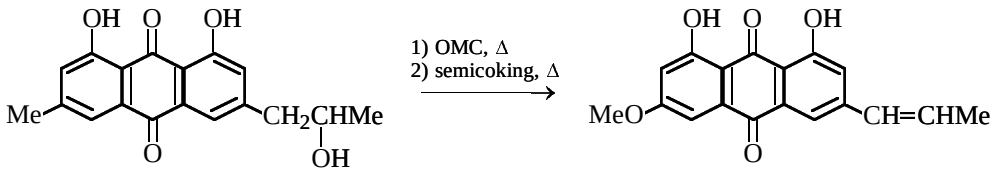

I

The other anthraquinones and related compounds contain substituents that are, as a rule, untypical of natural anthraquinones. Therefore, several possible pathways of biogeo- and thermochemical transformations of natural anthraquinone structures and several possible routes of formation of anthraquinone fragments in OMC from other native precursors in the course of coal formation and semicoking were suggested.

In the course of peat and, subsequently, coal formation, glycoside moieties of natural O- and C-anthraglycosides can partially degrade, with preservation of the anthraquinone core and its subsequent incorporation into the forming geopolymers. The same concerns anthraquinones with hydroxymethyl, hydroxypropyl, aldehyde, and isoprenyl substituents. In the course of subsequent semicoking, these fragments are elimi-

1070-4272/03/7610-1686 $25.00 © 2003 MAIK "Nauka/Interperiodica"

nated, probably with rearrangement and isomerization of substituents, to finally form structures detected in semicoking tars. This transformation pathway is apparently responsible for the appearance of vinyl and ethyl substituents in the identified anthraquinones. (+)-Carminic acid **II** [11] or related compounds could have been the starting biogenic natural anthraglycosides. Partial degradation of the glucopyranose ring in **II**, followed by decarboxylation and dehydroxylation of degradation product **III** to give **IV**, can occur in the initial step of peat genesis with participation of fungi and bacteria [13]. Subsequent transformations of the organic matter under reductive conditions in later stages of peat and coal formation may involve hydrogenation of vinyl groups to ethyl groups, to give compounds like **V**:

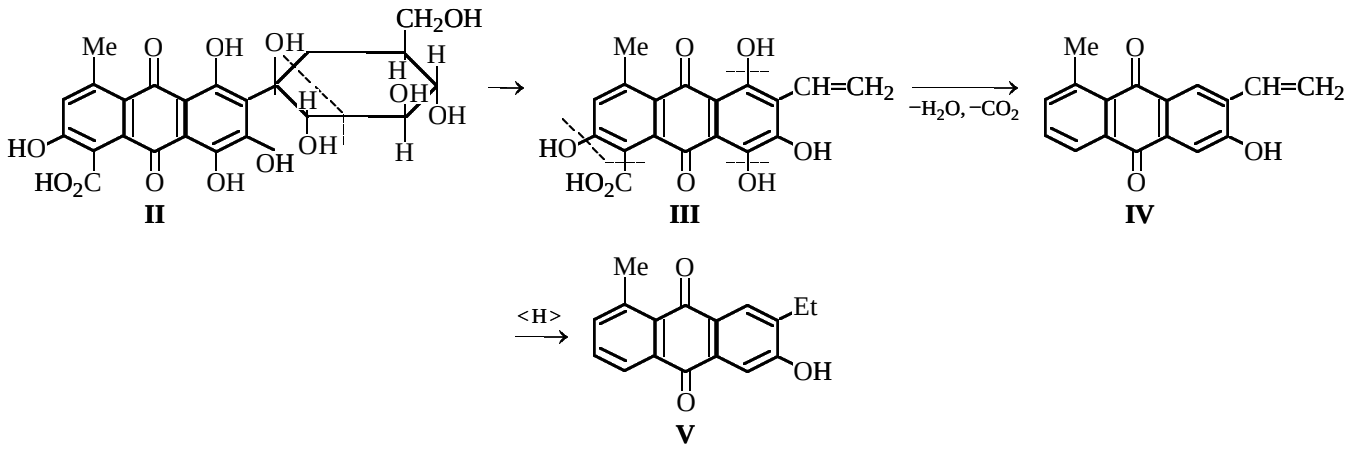

II **III** **IV** **V**

A few representatives of natural anthraquinones, e.g., sopheranin **VI** [21] and nataloin **VII** [11], contain vinyl and 2-hydroxyethyl substituents:

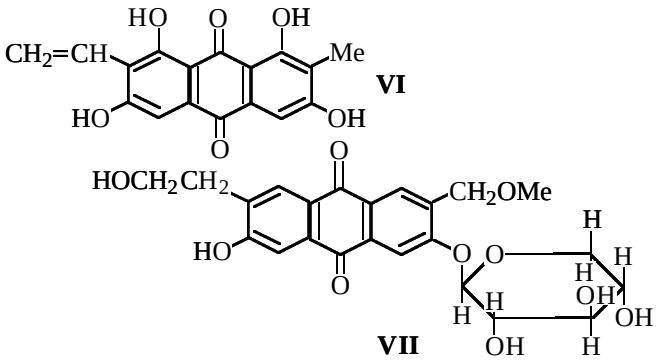

VI **VII**

Biogeochemical transformations of **VI** and **VII** could be similar to those shown in the scheme.

We believe that one of the main probable pathways yielding anthraquinone fragments in the course of coal formation and semicoking is the Diels–Alder reaction of natural naphtho- and benzoquinone derivatives with acyclic and monocyclic terpenes and terpenoids. It is known [19] that such reactions give 1,4,4*a*,9*a*-tetrahydroanthraquinone derivatives in high yields; these compounds are then virtually quantitatively oxidized by atmospheric oxygen to give the corresponding anthraquinones:

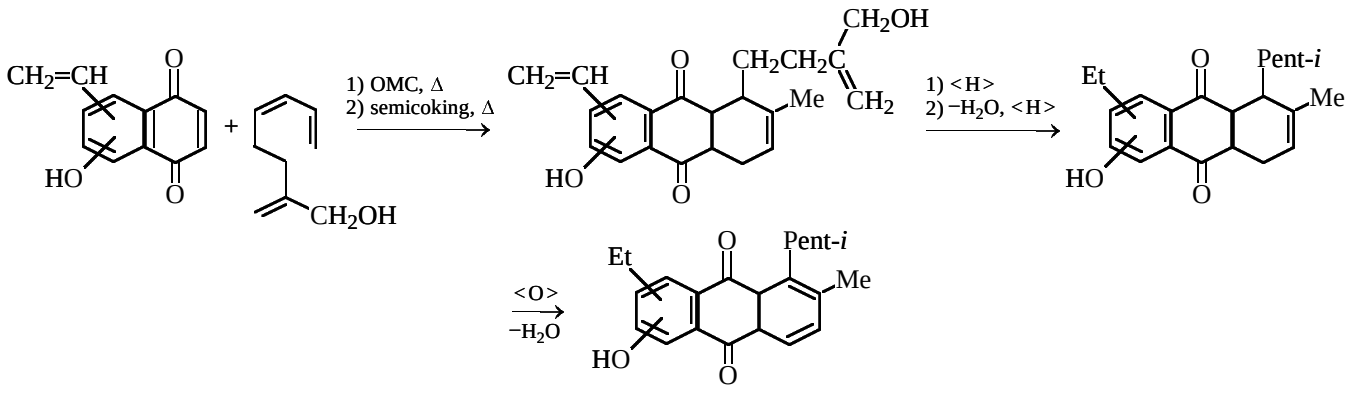

Processes of this kind may involve not only natural naphthoquinones, but also benzoquinone derivatives, and the reactions themselves may occur in the early (peat genesis) step of coal formation in the presence of atmospheric oxygen, which is necessary for oxidation of the primary products of diene synthesis, 1,4,4*a*,9*a*-tetrahydroanthraquinone derivatives, to anthraquinones.

The arising structures were subsequently either accumulated in pores of the forming macromolecular matrix of coal as a mobile phase or incorporated into the forming geopolymer via donor–acceptor, hydrogen, or ester bonds; these structures could have also undergone dehydration and hydrogenation under reductive conditions in the later steps of sedimentogenesis and diagenesis in the absence of atmospheric oxygen, which finally resulted in the transformation of hydroxyisopentadienyl and vinyl groups into isopentyl and ethyl groups.

The possibility of this pathway of anthraquinone formation in coals is supported by identification in the semicoking tars under consideration of a series of benzo- and naphthoquinone derivatives which can act as dienophiles in this process, such as juglone, fumigatin, spinulosin, 2,6-dimethoxybenzoquinone, and structures related to plumbagin, alkannin, shikonin, shikalkin, and javanicin [11, 13–16]. Among naphthoquinones, these reactions could have involved phylloquinone and menaquinone structures widely abundant in plants, and, among benzoquinones, ubiquinone and plastoquinone derivatives participating in respiration and hydrogen transfer in the course of oxidative phosphorylation [11, 13–16]. The coal products studied are also characterized by high content and diversity of native and transformed (bio- geo- and thermochemically) acyclic and monocyclic terpenes and terpenoids playing in these reactions the role of dienes and originating mainly from coniferous plants [23], which made a predominant contribution to coal-forming phytocenosis of coal [23, 24].

The above-mentioned phyllo- and menaquinone structures, belonging to the naphthoquinone series and widely abundant in plants, can also undergo cyclization under the conditions of coal formation and semicoking, to give anthraquinone structures containing isopentyl and methyl groups, as shown for cyclization of menaquinone-2 (**IX**) as example:

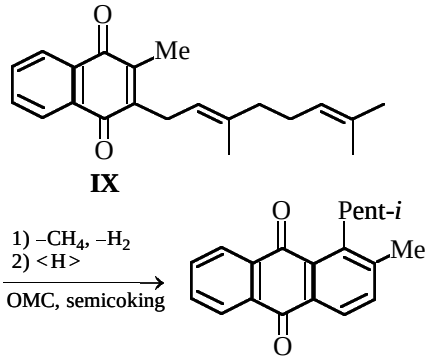

IX

Similarly, structures of ubi- and plastoquinones, belonging to the benzoquinone series, can transform into the corresponding naphthoquinones, which subsequently react with terpenoids (diene synthesis) to give anthraquinone fragments of OMC. The intermediate naphthoquinone structures can also originate from numerous substituted naphthalenes, tetralins, tetralinols, tetralindiols, and naphthols (genetically related to mono- and bicyclic sesquiterpenoids of coniferous plants), which have also been identified in various fractions of the semicoking tars studied [3–10]. Being prone to dehydrogenation, dehydration, and oxidation, these structures can be oxidized under coal weathering conditions into the corresponding naphthoquinones, which subsequently transform into anthraquinone derivatives.

Presumably, anthraquinone fragments of OMC may have also been formed by condensation of substituted benzoic acids with intermediate formation of 2-benzoylbenzoic acids [19]. These reactions occur in the presence of Lewis acids and, under the conditions of coal formation, can be catalyzed by aluminosilicates and organomineral complexes contained in the mineral matter of coal. This synthesis pathway is probable for polymethyl-, methylamino-, and pyrrolidinoanthraquinones:

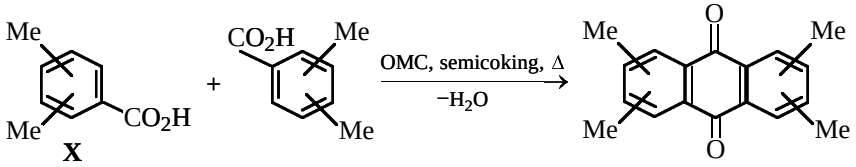

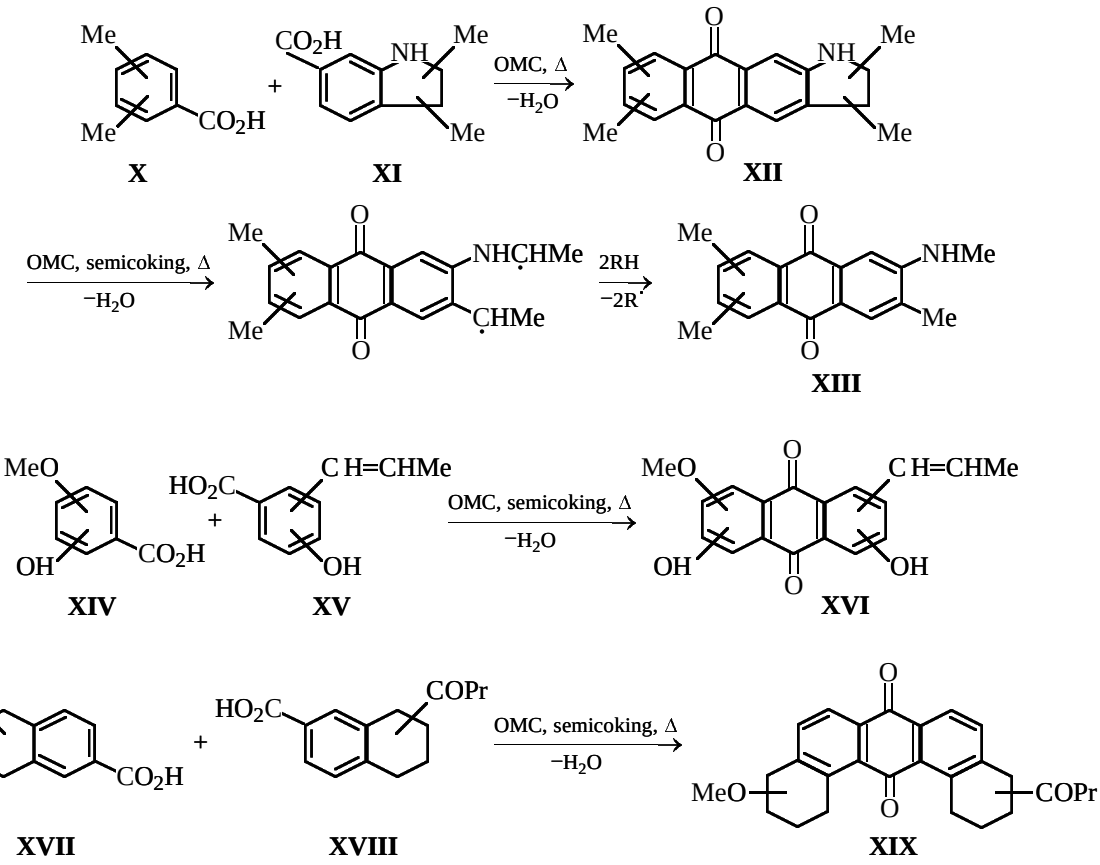

Dimethylbenzoic acid **X** may be produced by microbial oxidation of OMC in the weathering step. Dimethylindolinecarboxylic acid **XI** may have originated from biogeochemical transformations of native indole compounds, e.g., indole alkaloids. A large number of indole, indoline, and genetically related structures have been identified in various close-cut fractions of organic bases, phenols, and asphaltenes of the semicoking tar studied [3, 6, 9, 25, 26]. In the course of further semicoking, anthraquinones with the pyrrolidine ring of type **XII** can transform into anthraquinones like **XIII** by radical cleavage of the pyrrolidine ring. In turn, vanillic (**XIV**) and propenylhydroxybenzoic (**XV**) acids, which are probable precursors of structure **XVI**, are, most probably, genetically related to lignin of the initial plants involved in primary sedimentation. Tetralincarboxylic acids **XVII** and **XVIII**, probable precursors of anthraquinone **XIX**, are apparently products of biogeochemical transformations of sesquiterpenoids of coniferous plants.

Both benzoic acid itself and its substituted derivatives (*p*-hydroxybenzoic, salicylic, vanillic, syringic, β-resorcylic, protocatechuic, veratric acids, etc.) have been identified in aqueous extracts of coals [1, 3]. These acids widely occur in plants in free form and as esters. Esters of vanillic and syringic acids are components of wood lignin. Orsellic, lecanoric, and evernic acids are the most important substituted benzoic acids of lichens [13–16].

Anthraquinone fragments of OMC could have also been formed by reactions of leuco compounds (anthrahydroquinones) with aldehydes, with intermediate formation of hydroxyalkyl derivatives, which are subsequently reduced to alkylanthrahydroquinones. The latter products are then oxidized by atmospheric oxygen (e.g., in the course of coal weathering) to the corresponding alkylanthraquinones. This transformation route is known in synthetic chemistry of anthraquinone as the Marschalk reaction [19]. This reaction readily occurs with hydroxyanthrahydroquinones which, in turn, can be formed, along with the required aldehydes, from the initial natural hydroxyanthraquinones and carboxylic acids under reductive anaerobic conditions in the steps of late peat genesis and early diagenesis. 1-Hydroxy- (**XX**) and 1,8-dihydroxyanthraquinone (**XXI**) can also enter into the Marschalk reaction [11, 27] to give the corresponding coal anthraquinones:

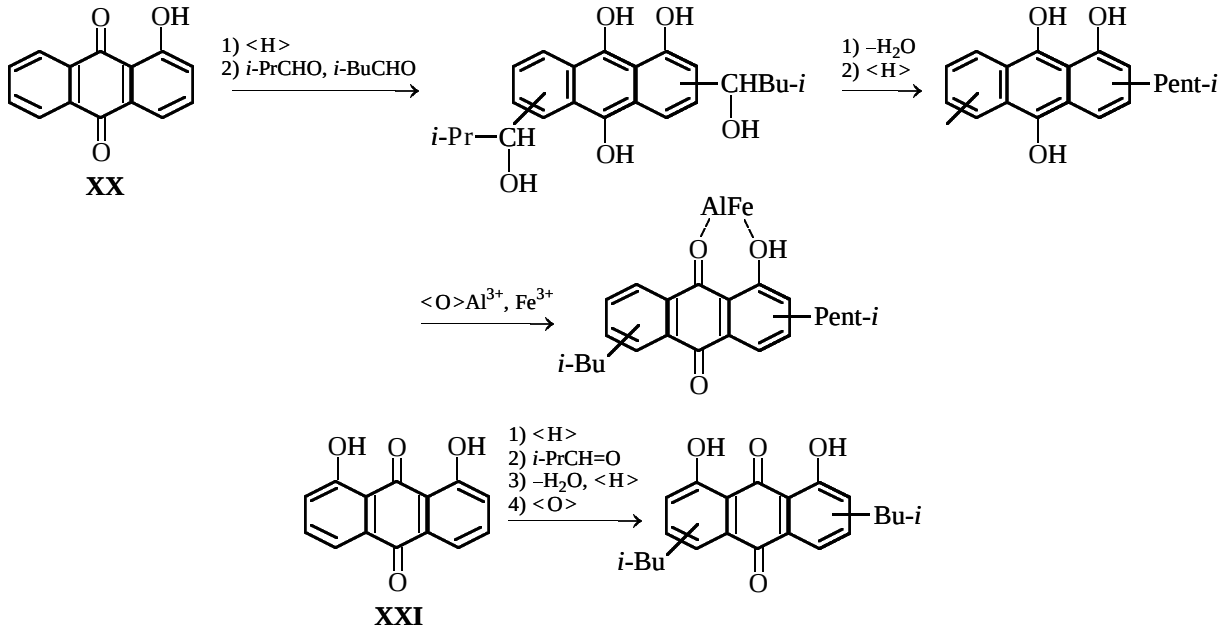

XX

XXI

Anthrone and anthracene derivatives are apparently formed by reduction of anthraquinone precursors in anaerobic reductive steps of peat and coal formation:

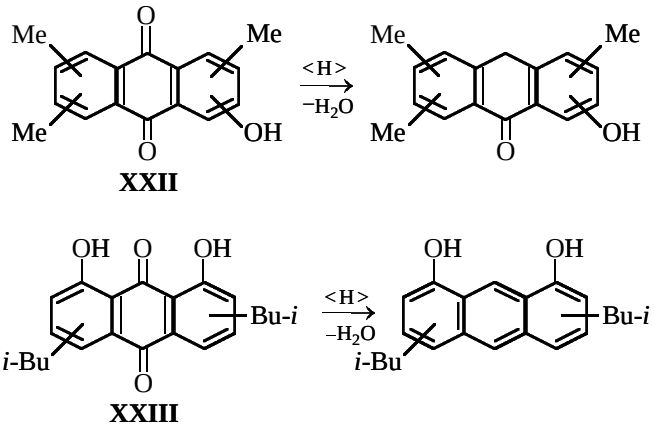

XXII

XXIII

Anthraquinones **XXII** and **XXIII**, in turn, could have been formed by the above-considered reactions: condensation of benzoic acids and Marschalk reaction, respectively. Other hexahydro- and octahydroanthrone derivatives may, presumably, be products of condensation of sesquiterpenoids of coniferous plants or of the Diels–Alder reaction of benzo- and naphthoquinone derivatives with diene-containing OMC fragments, followed by reduction.

Thus, the most probable initial bioproducers of the identified coal anthraquinone structures and their possible precursors are Mesozoic evolutionary precursors of flowering plants, insects, and lower fungi, which were involved in primary degradation of the initial biomaterial in the primary peat-genesis step of coal formation, and also lichens and coniferous plants. These conclusions are confirmed by the results of earlier geochemical studies of products obtained from Kansk–Achinsk coals (composition of terpenoids, azulenes, adamantanes, and pyrone derivatives: flavonoids, coumarins, chromones, isocoumarins) and by data obtained in geological and paleontological reconstruction of primary sedimentation and subsequent transformation of the initial organic matter [23, 24, 28]. According to these data, coal formation occurred under terrigenous conditions. The main bioproducers were Mesozoic coniferous plants, with active participation of lower fungi and aerobic bacteria in primary degradation of the starting organic matter in the initial step of peat formation.

CONCLUSIONS

(1) The probable initial bioproducers of anthraquinone structures detected in lignite extracts and semicoking tars are Mesozoic evolutionary precursors of flowering plants, insects, fungi, aerobic bacteria, lichens, and coniferous plants.

(2) Possible pathways of formation of anthraquinone structures in the steps of peat and coal formation, and also in low-temperature degradation of the organic matter of coal were suggested.

REFERENCES

1. Platonov, V.V., Klyavina, O.A., and Kamneva, A.I., *Goryuch. Slantsy*, 1988, vol. 5, no. 3, pp. 297–313.

2. Platonov, V.V., Klyavina, O.A., and Okushko, V.D., *Khim. Tverd. Topl.*, 1990, no. 4, pp. 74–83.
3. Platonov, V.V., Chemical Structure of the Organic Matter of Brown Coals, Their Reactivity, and Ways of Utilization of Thermal Degradation Products, *Doctoral Dissertation*, St. Petersburg, 1993.
4. Klyavina, O.A., Chemical Structure and Transformations of Neutral Oxygen-Containing Compounds from Brown Coals, *Cand. Sci. Dissertation*, Tula, 1994.
5. Platonov, V.V., Klyavina, O.A., Ivleva, L.N., *et al.*, *Khim. Tverd. Topl.*, 1989, no. 3, pp. 37–44.
6. Platonov, V.V., Ivleva, L.N., Klyavina, O.A., *et al.*, *Khim. Tverd. Topl.*, 1989, no. 4, pp. 116–121.
7. Platonov, V.V., Klyavina, O.A., Ivleva, L.N., *Goryuch. Slantsy*, 1988, vol. 5, no. 1, pp. 69–72.
8. Platonov, V.V., Klyavina, O.A., Ivleva, L.N., *et al.*, *Khim. Tverd. Topl.*, 1987, no. 2, pp. 38–46.
9. Platonov, V.V., Klyavina, O.A., Vol'-Epshtein, A.B., *et al., Khim. Tverd. Topl.*, 1989, no. 5, pp. 29–34.
10. Platonov, V.V., Klyavina, O.A., Kasimtseva, T.V., *et al., Khim. Tverd. Topl.*, 1988, no. 2, pp. 43–48.
11. Thomson, R.H., *Naturally Occurring Quinones*, London: Academic, 1971.
12. Muzychkina, R.A., *Prirodnye antrakhinony. Biologicheskie svoistva i fiziko-khimicheskie kharakteristiki* (Natural Anthraquinones. Biological Properties and Physicochemical Chartacteristics), Moscow: Fazis, 1998.
13. Goodwin, T.W. and Mercer, E.I., *Introduction to Plant Biochemistry*, Oxford: Pergamon, 1983, 2nd ed.
14. *Biochemistry of Phenol Compounds*, Harborne, J., Ed., London: Academic, 1964.
15. Zaprometov, M.N., *Osnovy biokhimii fenol'nykh soedinenii* (Fundamentals of Biochemistry of Phenol Compounds), Moscow: Vysshaya Shkola, 1974.
16. Blazej, A., *Rastlinne fenolove zluceniny*, Bratislava: Alfa, t. Pravda, 1973.
17. Vetchinkin, A.R., *Estestvennye organicheskie krasyashchie veshchestva* (Natural Organic Dyes), Saratov: Privolzhskoe knizhnoe, 1966.
18. Mayer, F., *Chemie der Organischen Farbstoffe*, Bd. 2, *Naturliche Organische Farbstoffe*, Berlin, 1935.
19. Gorelik, M.V., *Khimiya antrakhinonov i ikh proizvodnykh* (Chemistry of Anthraquinones and Their Derivatives), Moscow: Khimiya, 1983.
20. Fain, V.Ya., *9,10-Antrakhinony i ikh primenenie* (9,10-Anthraquinones and Their Applications), Moscow: Tsentr Fotokhimii, Ross. Akad. Nauk, 1999.
21. Malhotra, S. and Misra, K., *Planta Med.*, 1982, vol. 46, no. 4, pp. 247–249.
22. Mayo, P. de, *Mono- and Sesquiterpenoids*, New York: Interscience, 1959.
23. Shvykin, A.Yu., Genetic Relationship of Terpenoids and Structurally Allied Compounds of Organic Matter of Brown Coals with the Initial Biological Material, *Cand. Sci. Dissertation*, St. Petersburg, 1998.
24. *Geologiya mestorozhdenii uglya i goryuchikh slantsev SSSR* (Geology of Coal and Oil Shale Deposits in the Soviet Union), Skrobov, S.A., Ed., Moscow: Nedra, 1964, vol. 8.
25. Platonov, V.V., Klyavina, O.A., and Tabolenko, N.V., *Khim. Tverd. Topl.*, 1987, no. 4, pp. 27–32.
26. Platonov, V.V., Tabolenko, N.V., and Klyavina, O.A., *Khim. Tverd. Topl.*, 1987, no. 5, pp. 56–61.
27. Fourmier, G., Berch, C.A., and Paris, R.R., *Phytochemistry*, 1975, vol. 14, no. 9, p. 2099.
28. Podshibyakin, S.I., Genetic Relationship of Compounds of the Pyrone Series from the Organic Matter of the Kansk–Achinsk Brown Coal with the Initial Biological Material, *Cand. Sci. Dissertation*, St. Petersburg, 2000.

Russian Journal of Applied Chemistry, Vol. 76, No. 10, 2003, pp. 1692–1693. Translated from Zhurnal Prikladnoi Khimii, Vol. 76, No. 10, 2003, pp. 1738–1739.

BRIEF COMMUNICATIONS

Hydrochloric Acid Technology of Loparite

G. S. Skiba, N. B. Voskoboinikov, A. V. Solov'ev, V. I. Zakharov, V. T. Kalinnikov, V. N. Korovin, L. A. Nosova, and V. V. Komol'tsev

Tananaev Institute of Chemistry and Technology of Rare Elements and Mineral Raw Materials, Kola Scientific Center, Russian Academy of Sciences, Apatity, Russia

Received December 6, 2002; in final form, April 2003

Abstract—A hydrochloric acid technology for loparite processing on enlarged laboratory scale was developed. Extractive recovery of a sum of titanium(IV), niobium(V), and tantalum(V) was carried out in the continuous mode.

The domestic mineral resources of niobium, tantalum, and rare-earth elements (REE) occupy the leading position in the world in quantity, but are inferior to foreign resources in ore quality, mining conditions, and geographical-economical position. Now, Russia has the only surveyed and developed deposit of complex raw materials for manufacture of tantalum, niobium, rare-earth elements of the cerium group, and titanium: this is the Lovozero deposit of loparite.

Commercial tantalum and niobium, technical-grade titanium product, and a concentrate of REE chlorides are obtained together with radioactive elements contained in the loparite concentrate.

Loparite is a complex raw material with small amount of ballast elements (sodium and calcium), less than 10% in aggregate. Developing an efficient technology for processing of loparite will ensure a high profitability of the production process.

The chlorine technology requires chlorine gas. The sulfuric and nitric acid technologies failed to produce good results under industrial conditions [1]. The hydrofluoride technology, which is only in the laboratory stage of development, employs hydrofluoric acid, the most expensive and ecologically hazardous reagent.

In this context, it is the authors' opinion that the hydrochloric technology for loparite processing is rather promising.

Investigations in this direction were carried out in the 1960s–1970s, but failed to advance beyond the stage of laboratory development.

At present, the possibility of practical implementation of the hydrochloric acid technology of loparite is stronger. For example, attention was called in [3] to the fact that the number of investigations employing a hydrochloric medium is substantial [4]. Previously, its use in hydrometallurgical practice was hindered by the lack of necessary materials for apparatus. The appearance of new acid-resistant materials, plastics, special alloys, graphite with special impregnators, acid-resistant rubbers, and ceramics enabled use of hydrochloric acid in those cases when this is economically efficient.

The investigation performed demonstrated that treatment of the loparite concentrate with a 37% solution of hydrochloric acid at 95°C, breakdown time of 6 h, l : s = 3–5, and concentrate grain size of +0.08…+0.05 leads to >98% recovery for components soluble in HCl. The residue contains, in amount of 3–4% relative to the mass of the starting concentrate, ballast materials insoluble in hydrochloric acid: aegirine, quartz, and feldspar. The production solutions contain, depending on breakdown conditions, the following components (g l^{-1}): TiO_2 70–150, Nb_2O_5 7–35, Ta_2O_5 0.8–3.0, ΣREE 35–130. In addition, the solution contains chlorides of calcium, strontium, sodium, potassium, iron, and radioactive elements.

Extractive recovery of titanium(IV), niobium(V), and tantalum(V) with the use of octanol was developed and tested under laboratory and enlarged laboratory conditions, with these metals separated from all the accompanying impurities. The results obtained in enlarged-scale extraction experiments carried out on a box-type mixing extraction cascade, are listed

1070-4272/03/7610-1692 $25.00 © 2003 MAIK "Nauka/Interperiodica"

Distribution of titanium(IV), niobium(V), and tantalum(V) in extraction with 50% octanol (diluent, kerosene)*

Stage no.	TiO_2	Nb_2O_5	Ta_2O_5	ρ	c_s	TiO_2	Nb_2O_5	Ta_2O_5	ρ	c_s	o : w
1	45.26	9.45	0.067	0.979	56.23	47.0	2.575	0.244	1.236	91.06	1.05
2	32.38	9.9	0.112	0.978	46.72	35.0	2.003	0.244	1.219	75.48	0.89
3	25.38	9.51	0.12	0.951	39.78	29.0	2.003	0.281	1.225	68.19	0.6
4	18.41	7.28	0.22	0.937	30.74	22.0	0.772	0.305	1.186	62.94	1.32
5	11.28	3.53	0.27	0.901	17.74	4.18	0.501	0.513	1.189	67.01	2.21
6	8.0	2.43	0.20	0.918	15.91	3.95	0.286	0.391	1.196	64.45	1.03
7	7.34	2.12	0.32	0.919	13.16	3.43	0.186	0.268	1.195	63.54	0.71
8	5.22	0.99	0.29	0.918	9.89	2.93	0.172	0.317	1.154	63.96	0.76
9	1.84	0.33	0.36	0.893	5.02	1.63	0.041	0.146	1.178	41.84	0.82
10				0.910	3.42	1.26	0.020	0.096	1.180	55.76	1.15
11				0.910	2.49	0.60	0.006	0.018	1.177	47.0	0.74
12				0.910	1.86	0.51	<0.001	0.0037	1.178	48.38	0.84
13				0.912	1.40	0.475	<0.001	0.002	1.174	62.25	0.71
14				0.911	1.48	0.475	<0.001	0.002	1.178	48.95	0.68

* Starting solution: ρ 1.267 g cm^{-3}, c_s 101.9 g l^{-1}, TiO_2 78 g l^{-1}, Nb_2O_5 12.16 g l^{-1}, Ta_2O_5 0.78 g l^{-1}, ΣREE 40 g l^{-1}, ThO_2 0.76 g l^{-1}, U 0.02 g l^{-1}. Extracting agent: ρ 0.924 g cm^{-3}, μ 15.85 cP. Extract: ρ 0.980 g cm^{-3}, c_s 68 g l^{-1}, HCl 3.25 M, TiO_2 76.26 g l^{-1}, Nb_2O_5 12.05 g l^{-1}, Ta_2O_5 0.067 g l^{-1}, μ 40.69 cP, ThO_2 not found, U not found. Raffinate: ρ 1.202 g cm^{-3}, TiO_2 0.475 g l^{-1}, Nb_2O_5 <0.001 g l^{-1}, Ta_2O_5 0.002 g l^{-1}, ΣREE 38 g l^{-1}, ThO_2 0.621 g l^{-1}, U 0.036 g l^{-1}.

in the table. Re-extraction was performed with water, the rate of stratification was 1.5 m h^{-1} in both cases. This value ensured a stable course of the process, and recycled extracting agent contained no impurities. The loss of niobium(V) and tantalum(V) with the raffinate was 0.008 and 0.24%, respectively. The content of ΣREE in the extract was less than 0.5 g l^{-1}. No radioactive elements were found in the re-extract.

The possibility of extractive recovery of thorium(V) from solutions after isolation of titanium(IV), niobium(V), and tantalum(V) was established; the degree of thorium(V) extraction into the organic phase in a single stage was 86%. The regeneration conditions of hydrochloric acid by extraction with octanol were determined; the acid can be partly returned by the known techniques from sodium and iron chlorides produced in the technology. The "cold chlorination" process described in [5] was tested in separation of titanium(IV) and niobium(V). The process consists in obtaining $TiCl_4$ (the most promising product for obtaining high-quality TiO_2) via the compound K_2TiCl_6. This compound is precipitated from a titanium sulfate solution saturated with KCl and HCl at 0°C. Since K_2TiCl_6 is unstable, precipitation of a more stable and less soluble compound, Cs_2TiCl_6, was also studied. The possibility of 90% extraction of titanium(IV) into precipitate was established; in this case, the loss (recoverable) of niobium(V) with the precipitate did not exceed 4%, since niobium(V) forms no double compound. Further processing of the double salt is performed by heating and evaporation of $TiCl_4$. The residue containing niobium(V) and alkali metal chlorides is recycled into the stage of precipitation of the double salt.

CONCLUSIONS

(1) The loparite concentrate is virtually completely decomposed with 37% hydrochloric acid at a temperature of 95°C at l : s = 4 : 1 in the course of 6 h.

(2) Recovery of titanium(IV), niobium(V), and tantalum(V) into the organic phase, with their separation from other elements remaining in the raffinate, was carried out on an enlarged-laboratory scale on an extraction cascade.

(3) Separation of titanium(IV) and niobium(V) contained in re-extracts is performed via precipitation of poorly soluble Cs_2TiCl_6. $TiCl_4$, which is used in manufacture of a pigment, is obtained from this compound by evaporation.

REFERENCES

1. Plotnikov, V.P. and Antonov, V.I., *Khimicheskaya tekhnologiya loparitovogo kontsentrata* (Chemical Technology of Loparite Concentrate), Apatity: Kol'sk. Nauchn. Ts. Ross. Akad. Nauk, 1992, pp. 5–14.
2. Murach, N.N., Povedskaya, L.G., and Kulifeev, V.K., *Trudy In–ta Tsvet. Met., im. M.I. Kalinina*, Moscow, 1963, no. 35, pp. 171–174.
3. Chekmarev, A.M. and Yurtov, E.V., *Khim. Tekhnol.*, 2000, no. 1, pp. 41–44.
4. RF Patent 2 149 908.
5. Khazin, L.G., *Dvuokis' titana* (Titanium Dioxide), Leningrad: Khimiya, 1970.

Russian Journal of Applied Chemistry, Vol. 76, No. 10, 2003, pp. 1694–1695. Translated from Zhurnal Prikladnoi Khimii, Vol. 76, No. 10, 2003, pp. 1740–1741.

BRIEF COMMUNICATIONS

Chemical Properties of the K_2O–Al_2O_3–SiO_2–P_2O_5 System Activated with Mn(II) Oxide

I. M. Batyaev, S. M. Begel'dieva, E. B. Kleshchinov, and S. M. Shilov

Herzen State Pedagogical University, St. Petersburg, Russia

Received February 26, 2002; in final form, June 2003

Abstract—Synthesis and some chemical properties of the Al_2O–SiO_2–P_2O_5 system activated with MnO were studied.

Presently, the interest in laser glasses remains intense. Long-term studies have shown that phosphate glasses are advantageous as regards their technological effectiveness and preservation of their working properties upon introduction of considerable amounts of an activator.

This study is concerned with the chemical properties of the K_2O–Al_2O_3–SiO_2–P_2O_5 system activated with MnO. The K_2O–Al_2O_3–SiO_2–P_2O_5 system, which contains oxides of elements belonging to different groups of the periodic system, can be used as effective glass matrix for preparing luminescent and laser materials [1–3].

The matrix was prepared by fusing potassium metaphosphates and aluminum orthophosphate with silicon oxide (of optical-glass-making grade) in a high-temperature furnace for 8 h. The matrix obtained was powdered, and then the activator was introduced in the form of MnO_2 which was reduced with ammonium tartrate to Mn^{2+} at 1200–1250°C in the course of synthesis. To preclude oxidation of Mn(II) to Mn(IV), the reduction was performed in a CO_2 atmosphere.

The activated glass was poured into a metallic ingot mold and annealed at 300°C for 4 h. The sample obtained had no visually observed coloration (MnO_2 concentration 1.8 mol %, optical density D = 0.45 at λ = 410 nm, ρ = 2.67 g cm^{-3}). The glass obtained has the composition $18K_2O$–$11Al_2O_3$–$10SiO_2$–$61P_2O_5$: MnO_2(1.8 mol %).

The electronic absorption spectrum of the potassium–alumino–silica–phosphate glass (PASPhG)–Mn^{2+} is shown in Fig. 1. The highest-intensity absorption band is peaked around 410 nm and corresponds to the $^6A_1 \rightarrow {}^4A_1$ transition, which is virtually independent of the crystal field strength. At the long-wavelength wing of this band, a weakly resolved band associated with the $^6A_1 \rightarrow {}^4T_1$ transition is observed at 540 nm.

The luminescence spectrum of (PASPhG)–Mn^{2+} (Fig. 2) has the form of a broad asymmetric band peaked at around 630 nm, with half-width of 100 nm (2600 cm^{-1}). According to the existing concepts, this type of Mn^{2+} luminescence corresponds to an octahedral configuration. The luminescence decay time is 2 ms.

The spectral, luminescence, and kinetic characteristics remain at a practically acceptable level. The developed laser matrix opens up wide opportunities for use of MnO_2 as sensitizer of REE ions in the PASPhG.

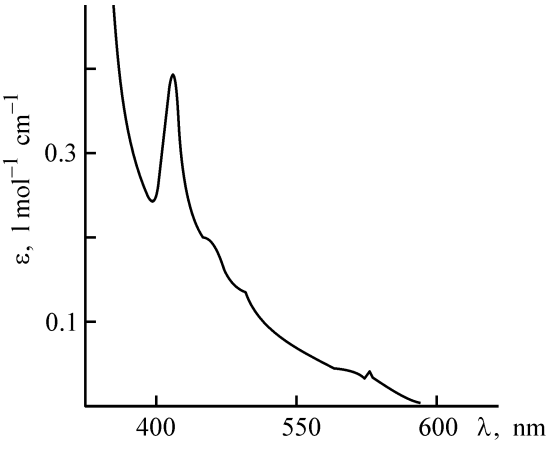

Fig. 1. Electronic absorption spectrum of Mn^{2+} in PASPhG. (ε) Molar extinction coefficient and (λ) wavelength.

1070-4272/03/7610-1694 $25.00 © 2003 MAIK "Nauka/Interperiodica"

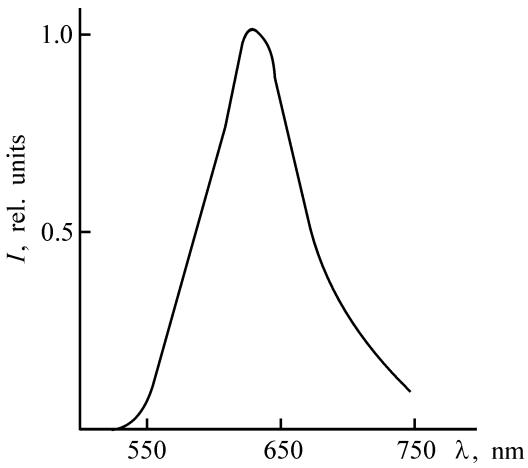

Fig. 2. Luminescence spectrum of Mn^{2+} in PASPhG. (I) Intensity and (λ) wavelength.

It has been considered for years that only REE ions (Nd^{3+}, Er^{3+}, Yb^{3+}, Ho^{3+}, etc.) can play the role of lasing ions in glassy matrices. This conclusion has been supported by a number of unsuccessful attempts to create a laser material based on a glass activated with 3*d*-element ions and, in particular, with Cr(III) ions. However, the results obtained in [4–15] made it possible to develop and manufacture a laser material based on a Ti(III)-activated glass of composition $Al(PO_3)_3$–Ti^{3+}. The given composition of the matrix appeared to have the best physicochemical properties and, in particular, the highest resistance to high-intensity laser light, which is an important characteristic of a glassy laser material.

The glass samples synthesized were irradiated with gigantic laser pulses (λ = 532 nm, incident power density of up to 100 MW cm^{-2}, pulse width 3.3×10^{-8} s), i.e., with energy of 3 J cm^{-2} at its uniform distribution over the irradiated area. The degree of resistance to light was determined from a possible decrease in the luminescence signal from a target (5 mm in diameter) subjected to a sequence of laser light pulses. It was found that, after several tens of pulses, the luminescence intensity remained unchanged. Consequently, the luminescent centers did not undergo any pronounced destruction, and no centers capable of absorbing or attenuating both the exciting and the emitted light appeared in the material. The sample in the form of a disc of diameter d = 5 mm and thickness l = 3 mm was irradiated with a gigantic pulse at the wavelength of the second harmonic of a neodymium laser, with the pumping intensity varied widely, up to the maximal value of 75 MW cm^{-2}. A single-pass lasing was obtained with this glass.

The results obtained have aroused interest in a systematic study of spectral and luminescence properties of other 3*d*-ions in glassy matrices and in analysis of the previously studied systems from the standpoint of their possible application as active media and sensitizers for lasers.

REFERENCES

1. *Spravochnik po lazeram* (Reference Book on Lasers)], Prokhorov, A.M., Ed., Moscow: Sov. Radio, 1978, vol. 1.
2. *Lazernye fosfatnye stekla* (Phosphate Glasses for Lasers), Zhabotinskii, M.E., Ed., Moscow: Nauka, 1980.
3. Anikeev, Yu.G., Zhabotinskii, M.E., and Kravchenko, V.B., *Lazery na neorganicheskikh zhidkostyakh* (Lasers Operating on Inorganic Liquids), Moscow: Nauka, 1986.
4. Kuchma, I.G., Fedorov, Yu.K., and Fromzel', V.A., *Opt. Spektrosk.*, 1986, vol. 61, no. 1, pp. 95–100.
5. Gapontsev, V.P., Gromov, A.K., Isineev, A.A., *et al.*, *Proc. of the Int. Conf. on Lasers 82*, USA, 1982, p. 310.
6. Mak, A.A., Soms, L.N., Fromzel', V.A., *et al.*, *Lasery na neodimovom stekle* (Neodymium-Glass lasers), Moscow: Nauka, 1990.
7. Batyaev, I.M. and Kleshchinov, E.B., *Pis'ma Zh. Tekh. Fiz.*, 1996, vol. 22, no. 12, pp. 34–38.
8. Batyaev, I.M. and Sukhanov, S.B., *Opt. Spektrosk.*, 1992, vol. 72, no. 6, pp. 1367–1370.
9. Batyaev, I.M. and Golodova, I.V., *Opt. Spektrosk.*, 1994, vol. 77, no. 1, pp. 81–83.
10. Batyaev, I.M. and Kleshchinov, E.B., *Pis'ma Zh. Tekh. Fiz.*, 1997, vol. 23, no. 21, pp. 7–11.
11. Batyaev, I.M. and Kleshchinov, E.B., *Zh. Obshch. Khim.*, 1997, vol. 67, no. 7, pp. 1207.
12. Kleshchinov, E.B., Nonradiative Energy Transfer and Titanium(III)-Sensitized Luminescence of Some Triply Charged Rare-Earth Elements in the K_2O–Al_2O_3–SiO_2–P_2O_5 Glass, *Cand. Sci. Dissertation*, St. Petersburg, 1997.
13. Batyaev, I.M. and Sukhanov, S.B., *Pis'ma Zh. Tekh. Fiz.*, 1994, vol. 20, no. 10, pp. 38–42.
14. Batyaev, I.M. and Kleshchinov, E.B., *Opt. Spektrosk.*, 1995, vol. 78, no. 3, pp. 468–470.
15. Aristov, A.V., Kozlovskii, D.A., Batyaev, I.M., and Kobezhikov, Yu.G., *Opt. Zh.*, 2000, vol. 67, no. 3, pp. 8–15.

Russian Journal of Applied Chemistry, Vol. 76, No. 10, 2003, pp. 1696–1698. Translated from Zhurnal Prikladnoi Khimii, Vol. 76, No. 10, 2003, pp. 1742–1744.

BRIEF COMMUNICATIONS

Phase Equilibria in the System $CuO–Fe_2O_3–Sb_2O_4–O_2$

B. G. Golovkin and G. V. Bazuev

Institute of Solid-State Chemistry, Ural Division, Russian Academy of Sciences, Yekaterinburg, Russia

Received December 17, 2002

Abstract—Results of X-ray phase analysis were used to construct the phase diagram of the system CuO–Fe_2O_3–Sb_2O_4–O_2 at 1000°C in air. Two $Cu_{2x}Fe_{4-3x}Sb_xO_6$ solid solutions ($0 \le x \le 0.154$ and $0.923 \le x \le 1$) of, respectively, hematite and bixbyite structure were identified.

A study of phase formation in the sistem Fe_2O_3–Sb_2O_4–CuO is of interest in the context of a search for catalysts for propylene [1] and butylene [2] oxidation and use of these materials in storage devices and microwave matching elements [3, 4].

In the system CuO–Fe_2O_3 in air, below 1040°C, there exists a cubic modification of copper(II) ferrite $CuFe_2O_4$ (a = 8.39 Å) transformed into a tetragonal modification (a = 8.23 Å and c = 8.70 Å) at 380°C. Above 1040°C, $CuFe_2O_4$ transforms into copper(I) ferrite $CuFe_5O_8$ with loss of oxygen. Both the ferrites and Fe_3O_4 form a continuous series of solid solutions of general formula $Cu_xFe_{3-x}O_4$ ($0 \le x \le 1$) [3–6].

In each of the systems Fe_2O_3–Sb_2O_5 and CuO–Sb_2O_5 in air, only a single compound is formed, $FeSbO_4$ with rutile structure [7] (stable up to 1270°C [8]) and $CuSb_2O_6$ with trirutile structure [7, 9]. The latter compound starts to decompose at about 1020°C to give $Cu_8Sb_2O_9$ [10].

The results obtained in studying the system Sb_2O_3–Sb_2O_5 are reviewed in [7, 11–14]. Antimony oxide Sb_2O_3 exists in two polymorphic modifications: low-temperature rhombic and high-temperature cubic, with phase transition temperature of about 500°C in inert atmosphere [11]. In air, Sb_2O_3 is oxidized at this temperature to α-Sb_2O_4, which transforms into β-Sb_2O_4 above $T \sim 1000$°C [7, 11, 12]. After calcination of hydrated antimony(V) oxide at 300°C in air, Sb_6O_{13} is first formed, which is reduced to α-Sb_2O_4 at 800°C [11] and remains stable up to about 1000°C, and then transforms into β-Sb_2O_4. At $T \sim 1200$°C, the last compound starts to dissociate to give Sb_2O_3 [11]. Anhydrous Sb_2O_5, existing in two polymorphic modifications, can be obtained solely under elevated pressure in oxygen [14].

Among ternary compounds of the given system, the previously obtained cubic complex oxide Cu_2FeSbO_6 of bixbyite structure (a = 9.5622 Å) [15, 16] is known (so-called structural type *C* typical of a number of rare-earth oxides, such as α-Mn_2O_3, etc.).

EXPERIMENTAL

As starting reagents for synthesis of samples were used analytically pure oxides CuO, Sb_2O_3, and Fe_2O_3. The samples were synthesized by the conventional ceramic technology first at 660°C (20 h) and then at 1000°C (100 h). The reaction course was monitored by means of X-ray phase analysis (XPA, DRON-2 diffractometer, Cu_{K_α} radiation). The XPA sensitivity with respect to the phases formed in the annealing products was, on the average, 0.5–1.0 wt %.

The results obtained in analysis of the annealing products are presented in the form of a phase diagram (see Fig. 1). In accordance with the published data mentioned above, antimony enters in the course of synthesis into the composition of the complex oxides $FeSbO_4$, $CuSb_2O_6$, and Cu_2FeSbO_6 in the oxidation state +5, although the oxide $Sb^{3+}Sb^{5+}O_4$ is a stable simple antimony oxide in air below 1200°C [14]. For this reason, the $CuSb_2O_6$–$FeSbO_4$–Sb_2O_4 compositions are plotted in the diagram using a nonuniform scale method [17]. In the system, two ternary phases of the general formula $Cu_{2x}Fe_{4-3x}Sb_xO_6$ were identified: the first with a homogeneity region $0 \le x \le 0.154$ (solid solution based on hematite Fe_2O_3) and the second, with Cu_2FeSbO_6 bixbyite structure, for which $0.923 \le x \le 1$. The edge compositions of the first phase are hematite Fe_2O_3 [x = 0, hexagonal crystal system, corundum structure, a = 5.032(2), c = 13.738(5) Å] and $Fe_{3.538}Cu_{0.308}Sb_{0.154}O_6$ [x = 0.154;

1070-4272/03/7610-1696 $25.00 © 2003 MAIK "Nauka/Interperiodica"

a = 5.051(2), c = 13.778(5) Å]. The edge compositions of the second phase are dark brown Cu_2FeSbO_6 (x = 1) and $Cu_{1.846}Fe_{1.231}Sb_{0.923}O_6$ [x = 0.923, a = 9.5515(7) Å]. Because the figurative points for the given solid solutions lie on the straight line connecting Cu_2FeSbO_6 and Fe_2O_3, they can be regarded as solid solutions of Cu_2FeSbO_6 in Fe_2O_3 and, *vice versa*, of Fe_2O_3 in Cu_2FeSbO_6. This suggests that antimony is present in the given solutions in the oxidation state +5.

Reducing the indices of the edge compositions of the solid solutions obtained to integers gives hematite-like $Fe_{23}Cu_2SbO_{39}$ and bixbyite-like $Cu_{12}Fe_8Sb_6O_{39}$. To elucidate the substitution scheme, they are represented as nA_2BCO_6, where A is a complex cation, and B and C are complex anions. This gives $(Fe_{11}Cu_2)_2 \times [(Fe_{13})(Fe_{11}Sb_2)]O_{78}$ and $(Cu_{12}Fe)_2[(Fe_{13})(FeSb_{12})]O_{78}$, respectively, at n = 13.

As seen from these formulas, the substitution takes place in the sublattices A and C, with the homogeneity region twice larger for hematite solid solutions.

As is known [18, 19], one of Fe_2O_3 modifications is bixbyite (a = 9.393 Å) ([18, 19]). This suggests that a continuous series of $Cu_{2x}Fe_{4-3x}Sb_xO_6$ solid solution of bixbyite structure ($0 \le x \le 1$) can be formed under appropriate conditions. At the same time, hematite has a more densely packed structure, compared with bixbyite (this conclusion follows from a comparison of unit cell volumes of the Fe_2O_3 modifications being analyzed, reduced to the same formula unit). This suggests that the range of existence of hematite solid solutions can be extended under appropriate synthesis conditions.

When heated to about 1100°C, the bixbyite solid solutions obtained dissociate to give $FeSbO_4$, Fe_2O_3, and $Cu_8Sb_2O_9$ by the reaction:

$$4Cu_2FeSbO_6 \cdot mFe_2O_3 \xrightarrow{1100°C} Cu_8Sb_2O_9 + 2FeSbO_4 + (m + 1)Fe_2O_3 + 2O_2\uparrow.$$

Thermal treatment of Cu_2FeSbO_6 at 950°C under a pressure of 60 kbar did not result in any structural transformations [20]. With pressure raised to 90 kbar at the same temperature, dissociation into CuO and $FeSbO_4$ occurred.

The $Cu_9Sb_4O_{19}$ phase was synthesized at 1000°C under oxygen pressure of 10 bar in [12]. To obtain this phase, compositions of the partial system $CuO–CuSb_2O_6$ indicated in Fig. 1 were tested. For this purpose, they were subjected to additional annealing in oxygen at 950°C for 20 h under normal pressure.

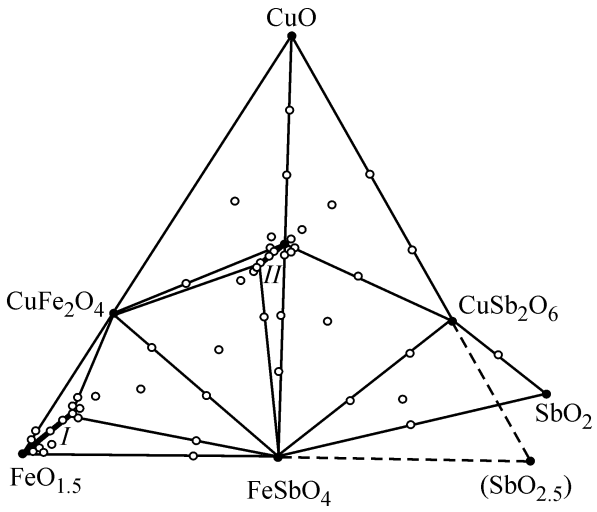

Phase diagram of the system $CuO–Fe_2O_3–Sb_2O_4–O_2$ at 1000°C in air. (*I*) $Cu_{2x}Fe_{4-3x}Sb_xO_6$, $0 \le x \le 0.154$ and (*II*) $Cu_{2x}Fe_{4-3x}Sb_xO_6$, $0.923 \le x \le 1$. *Small circles* stand for the figurative points of annealed compositions.

The reaction products consisted, however, solely of a mixture of CuO and $CuSb_2O_6$.

CONCLUSION

The phase diagram of the system $CuO–Fe_2O_3–Sb_2O_4–O_2$ at 1000°C in air was constructed. In the region of the $CuO–Fe_2O_3–FeSbO_4–CuSb_2O_6$ compositions, two $Cu_{2x}Fe_{4-3x}Sb_xO_6$ solid solutions were identified: with structure of hematite (homogeneity region $0 \le x \le 0.154$) and bixbyite (homogeneity region $0.923 \le x \le 1$), in which antimony is present in the oxidation state +5. Iron(III) and copper(II) antimonates are in equilibrium with each other and with Sb_2O_4.

REFERENCES

1. Hutchings, G.J., Bowker, M., Crossley, A., *et al.*, *Catal. Today*, 1991, vol. 10, no. 3, pp. 413–418.
2. Boreskov, G.K., Ven'yaminov, S.A., and Shchukin, V.V., *Dokl. Akad Nauk SSSR*, 1970, vol. 192, no. 4, p. 831.
3. Zinovik, M.A., and Davidovich, A.G., *Zh. Neorg. Khim.*, 1981, vol. 26, no. 6, p. 1586.
4. Sapozhnikova, E.Ya., Davidovich, A.G., Roizenblat, E.M., *et al.*, *Zh. Neorg. Khim.*, 1981, vol. 26, no. 7, p. 1751.
5. Zinovik, M.A., *Zh. Neorg. Khim.*, 1988, vol. 33, no. 10, p. 2689.
6. Shchepetkin, A.A., *Fiziko-khimicheskii analiz oksidov na osnove metallov peremennoi valentnosti* (Physico-

chemical Analysis of Oxides of Variable Valence Metals), Moscow: Nauka, 1987.

7. *Diagrammy sostoyaniya system tugoplavkikh oksidov* (Phase Diagrams of Systems Based on Refractory Oxides), Galakhov, F.Ya., Ed., Leningrad: Nauka 1986, issue 5, part 2.
8. Walczak, J., Filpek, E., and Bosacka, M., *Solid State Ionics*, 1997, vols. 101–103, p. 1363.
9. Nakua, A., Yun, H., Reimers, J.N., *et al.*, *J. Solid State Chem.*, 1991, vol. 91, no. 1, p. 105.
10. Shimada, S., and Mackenzie, K.J.D., *Thermochim. Acta*, 1982, vol. 56, p. 73.
11. Zenkovets, G.A., Olen'kova, I.P., and Tarasova, D.V., *Izv. Sib. Otd. Akad. Nauk SSSR, Ser. Khim. Nauk*, 1986, vol. 11, no. 4, p. 53.
12. Varfolomeev, M.B., Shostak, I.S., Sotnikova, M.N., *et al.*, *Izv. Akad Nauk SSSR, Ser. Neorg. Mater.*, 1975, vol. 11, no. 5, p. 962.
13. Pletnev, R.N., Ivakin, A.A., Kleshchev, D.G., *et al.*, *Gidratirovannye oksidy elementov IV and V grupp* (Hydrated Oxides of Group-IV and -V Elements), Moscow: Nauka, 1986.
14. Rumpel, Y., Berndt, W., Adam, K., *et al.*, *Z. Naturforsch.*, 1978, vol. 33, no. 1, p. 39.
15. Bazuev, G.V., and Golovkin, B.G., *Dokl. Ross. Akad. Nauk*, 1993, vol. 330, no. 1, p. 57.
16. Bazuev, G.V., Colovkin, B.G., Zubkov, V.G,. *et al.*, *J. Solid State Chem.*, 1994, vol. 113, no. 1, p. 132.
17. Colovkin, B.G., *Dokl. Akad. Nauk SSSR*, 1992, vol. 322, no. 3, p. 549.
18. Ben-Dor, L., Fischbein, E., Felner, S., *et al.*, *J. Electrochem. Soc.*, 1977, vol. 124, no. 3, p. 451.
19. Geller, S., *Acta Cryst., Ser. B.*, 1971, vol. 27, no. 4, p. 821.
20. Bazuev, G.V., Colovkin, B.G., Kadyrova, N.I., *et al.*, *Dokl. Ross. Akad. Nauk*, 1997, vol. 353, no. 5, p. 622.

Russian Journal of Applied Chemistry, Vol. 76, No. 10, 2003, pp. 1699–1701. Translated from Zhurnal Prikladnoi Khimii, Vol. 76, No. 10, 2003, pp. 1745–1747.

BRIEF COMMUNICATIONS

Effect of Conditions of Electric-Spark Dispersion of Zinc on the Quality of the Product Obtained

R. K. Bairamov

Olimpiya Ltd., Novomoskovsk, Tula oblast, Russia

Novomoskovsk Institute, Mendeleev Russian University of Chemical Technology, Novomoskovsk, Tula oblast, Russia

Received November 21, 2002; in final form, June 2003

Abstract—Influence exerted by additives introduced into the working solution, and by iron or copper formed in electric-spark dispersion of these metals and zinc, on the quality of the products obtained in electric erosion was studied.

As noted previously [1], the attention given to the behavior of dispersed metal particles after their removal from the spark discharge zone is insufficient. This is due to the fact that the literature covers incompletely the application of the method of electric-spark dispersion of metals for obtaining highly dispersed materials, even though the working principle of the method has long been known and is employed successfully in metal working and, in particular, in electric-erosion processing of metal articles to obtain complex profiles and apertures [2, 3].

The present study is concerned with the influence exerted by additives introduced into the working solution, and by iron or copper formed in electric-spark dispersion of these metals and zinc, on the quality of the products obtained in the process.

The product quality was checked by determining its absorption capacity in gas purification to remove hydrogen sulfide. The electric-spark dispersion of metal was carried out on an installation, and using a procedure, described in [1]. The reactor was for the most part filled with zinc granules and had zinc electrodes fixed at its edges. As working solution served distilled water with various additives. Pulsed current (pulse repetition frequency 700 Hz) was passed through the reactor [4]. The product obtained in electric erosion of zinc was filtered off and dried at a temperature of 100°C.

Further, the dried product was compacted and then ground. To determining the absorbing capacity of the samples studied, the 0.25–0.50-mm fractions were taken. The sulfur absorption capacity of a sample, Q (wt %), is the amount of sulfur absorbed by unit mass of the sample in gas purification to remove H_2S, which is defined as the ratio of the sample masses (g) before and after an experiment, multiplied by 100. The sulfur absorption capacity was determined by passing a gas mixture containing hydrogen and 1.3–1.4 vol % hydrogen sulfide (which is 18–18.5 g m^{-3} in terms of elementary sulfur) through a sample bed at a rate of 5000 h^{-1}. The temperature of the sample bed was maintained at 400°C, and the gas mixture was passed to complete saturation with sulfur, i.e., until the concentrations of H_2S in the gas mixture before and after the sample became equal.

Figure 1 shows the results obtained in studying the influence exerted by the working solution components used in electric erosion on the value of Q for

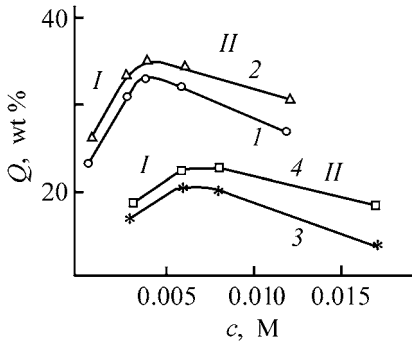

Fig. 1. Sulfur absorption capacity Q of samples prepared from products formed in electric erosion of zinc vs. concentration c of additives present in the working solution. Sludge treatment temperature 25°C, treatment duration 4 h. Additive: (*1, 2*) citric acid and (*3, 4*) tartaric acid. (*1, 3*) Sample drying temperature 100°C; (*2, 4*) temperature and time of sample calcination 450°C and 5 h.

1070-4272/03/7610-1699 $25.00 © 2003 MAIK "Nauka/Interperiodica"

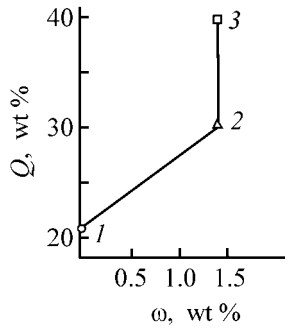

Fig. 2. Sulfur absorption capacity Q of samples prepared from products formed in electric erosion of (point *1*) zinc, and zinc with addition of (point *2*) iron and (point *3*) copper to the working solution. Working solution 0.012 M oxalic acid, sludge treatment temperature 25°C, treatment duration 4 h. Amount of admixture in a sample, ω (wt %): (*1*) 0 and (*2*, *3*) 1.4.

samples prepared from products formed in electric-spark dispersion of zinc. In electric-spark dispersion of a metal, the additives introduced into the working solution are thermally decomposed in the spark discharge zone [5]. As a result, atomic oxygen, carbon and carbon-containing residues are formed (the additives present in the working solution also undergo thermal decomposition in the course of electric erosion of zinc). The atomic oxygen thus formed is involved in the formation of an oxide film on the surface of dispersed zinc [5]. It can be seen from Fig. 1 that, with increasing concentration of the additives, the sulfur absorption capacity of samples prepared from erosion products first grows and then, having reached its limiting value (portion *I*, curves *1* and *3*), starts to decrease (portion *II*). The rise in sulfur absorption capacity in portion *I* of the Q–c curve is apparently due to reduction of the oxide film on the surface of dispersed Zn particles by hydrogen from the gas mixture to be purified to remove hydrogen sulfide. Further, dispersed Zn, freed of the oxide film, reacts with H_2S to give zinc sulfide. The certain decrease in the sulfur absorption capacity of the samples (portion *II*) is possibly due to an increase in the content of compounds formed in interaction of dispersed Zn particles with other products of thermal decomposition of the additives, which are not involved in the process of gas purification to remove H_2S.

For comparison, Fig. 1 shows the sulfur absorption capacity of samples prepared from products obtained in electric erosion of zinc in a working solution containing the additives considered (curves *2* and *4*) and precalcined at 450°C. It can be seen that the manner in which the sulfur absorption capacity varies is the same as that for dried samples, with only the sulfur absorption capacities being somewhat higher. This is probably due to oxidation, during sample calcination, of a part of compounds formed in interaction of dispersed metal with other products of thermal decomposition of the additives, to give active zinc oxide. This oxide further reacts with H_2S to give ZnS [6]. Thus, analysis of the data obtained suggests that the nature of additives introduced into the working solution strongly affects the quality of products formed in electric erosion of zinc.

Interesting results were obtained in electric-spark dispersion of zinc together with iron or copper. For this purpose, minor amounts of iron or copper granules were introduced into a reactor packed with zinc granules in such a way that approximately 1.4 wt % iron or copper was dispersed together with zinc in electric erosion. A solution of oxalic acid was used as the working solution. Figure 2 shows data on sulfur absorption capacity of samples prepared from products of electric erosion of Zn (point *1*), Zn with Fe (point *2*), and Zn with Cu (point *3*). It can be seen that presence of a minor amount of Fe or Cu in the erosion product leads to a substantial increase in the sulfur absorption capacity of the samples. Thus, the quality of the product obtained markedly changes under these conditions of the electric erosion process.

It is known that one and the same compound formed from different substances exhibits varied catalytic properties. For instance, ZnO obtained by heating various zinc-containing compounds, e.g., $ZnCO_3$ and $Zn(OH)_2$, shows different sulfur absorption capacities (32.0 and 21.9 wt %), all other conditions being the same. Such a difference between the sulfur absorption capacities of the samples is commonly attributed to varied perfection of the crystal lattice of zinc oxide [7]. For example, in heating of $ZnCO_3$, its crystal lattice is already disintegrated, whereas that of the reaction product, ZnO, is not complete yet.

The increased sulfur absorption capacities of the samples prepared from erosion products containing Zn and Fe or Zn and Cu (with the amount of the two second components equal to 1.4 wt %), observed in Fig. 2, are possibly due to incorporation of a part of Fe or Cu into the crystal lattice of Zn to form defects whose amount depends on the nature of a metal being introduced. These defects may further behave as active centers in gas purification to remove H_2S, which, in the end, leads to an increase in sulfur absorption capacity.

CONCLUSION

The quality of products obtained in electric erosion is strongly affected by additives introduced into the

working solution, and also by iron or copper formed in their joint electric-spark dispersion with zinc. It is suggested that the increased sulfur absorption capacities of samples prepared from zinc erosion products containing minor amounts of iron or copper are due to incorporation of these metals into the crystal lattice of zinc to form defects that behave as active centers in gas purification.

REFERENCES

1. Bairamov, R.K., Vedernikova, N.R., and Ermakov, A.I., *Zh. Prikl. Khim.*, 2001, vol. 74, no. 10, pp. 1703–1705.
2. *Elektrotekhnologicheskie promyshlennye ustanovki* (Electric Technological Industrial Installations), Svenchanskii, A.D., Ed., Moscow: Energoizdat, 1982.
3. Popilov, L.Ya., *Osnovy elektrotekhnologii i novye ee raznovidnosti* (Fundamentals of Electric Technology and Its New Varieties), Leningrad: Mashinostroenie, 1971.
4. Bairamov, R.K., *Zh. Prikl. Khim.*, 2003, vol. 76, no. 5, pp. 771–773.
5. Bairamov, R.K., Ermakov, A.I., and Vedernikova, N.R., *Zh. Prikl. Khim.*, 2001, vol. 74, no. 10, pp. 1708–1710.
6. *Ochistka tekhnologicheskikh gazov* (Purification of Technological Gases), Semenova, T.A. and Leites, I.L., Eds., Moscow: Khimiya, 1977.
7. Remy, H., *Lehrbuch der anorganischen Chemie*, Leipzig: Akademische, Geest and Portig K.-G., 1961, Bd. 2.

Russian Journal of Applied Chemistry, Vol. 76, No. 10, 2003, pp. 1702–1704. Translated from Zhurnal Prikladnoi Khimii, Vol. 76, No. 10, 2003, pp. 1748–1750.

BRIEF COMMUNICATIONS

Desulfation of Active Paste from Lead Battery Scrap with Potassium Carbonate

A. G. Morachevskii, E. V. Bochagina, and M. N. Khabachev

St. Petersburg State Polytechnical University, St. Petersburg, Russia

Received August 13, 2003

Abstract—The results obtained in studying the desulfation of the active paste from lead battery scrap with the use of an aqueous solution of potassium carbonate are discussed.

It has been repeatedly noted previously that the most ecologically efficient way to utilize sulfur in processing of the sulfate-oxide fraction of lead battery scrap is desulfation (desulfurization) with carbonates or hydroxides of alkali metals or ammonium [1–7]. The desulfation processes are based on much lower solubility products (SP) of lead(II) hydroxide or carbonate, compared with lead(II) sulfate. For example, SP of $PbSO_4$ is $10^{-7.8}$ at 25°C varies with increasing temperature only slightly [8]. At the same time, the SP values for $Pb(OH)_2$ and $PbCO_3$ are, respectively, $10^{-15.3}$ (20°C) and $10^{-13.1}$ (25°C). Physicochemical and technological studies of the process of desulfation of lead-containing materials were considered in detail in a review [9]. Desulfation with sodium carbonate solutions has been studied extensively [10–14], whereas use of potassium carbonate for this purpose is understood to lesser extent. Smirnov and co-authors noted [5] that, being a by-product in processing of nepheline raw materials, potassium carbonate is manufactured in sufficient amounts (0.31 ton of potash is produced at the Achinsk combine per 1 ton of Al_2O_3). In addition, the reaction with lead sulfate

$$PbSO_4 + K_2CO_3 = PbCO_3 + K_2SO_4 \qquad (1)$$

yields potassium sulfate, which is in high demand, compared with sodium sulfate. In [5], some parameters of the process of desulfation with K_2CO_3 were reported: process temperature 50°C, solid-to-liquid ratio (s : l) 1 : 5, process duration 2 h, degree of sulfur recovery 95%.

The same communication reported the results obtained in laboratory experiments on desulfation of the active paste from positive and negative plates of a lead battery with K_2CO_3 solutions. According to analytical data (weighing method), the starting active paste from various battery plates contained, after being washed with water and dried, 45 wt % $PbSO_4$ (14.3% SO_4^{2-}). According to X-ray phase analysis, the main components of the active paste are $PbSO_4$ (anglesite) and lead oxide PbO_2 (plattnerite, tetragonal modification), present in comparable amounts (Fig. 1a). Also, a very small amount of the orthorhombic modification (α-PbO_2), and trace amounts of PbO (tetragonal modification) and metallic lead, may be present. A mineralogical characterization of the active paste was made in [15]. It was also noted that the main components are $PbSO_4$ and PbO_2 in the tetragonal and rhombic forms.

According to the results of a sieving analysis, the starting material had average and maximum grain size of 0.17 and 0.40 mm, respectively. The amount of active paste used in each experiment was 30 g, the excess of potassium carbonate over the value required by the reaction equation was 20%, the s : l ratio was varied from 1 : 4 to 1 : 5. The experiments were carried out at a temperature of 50°C under continuous vigorous stirring. After an experiment was complete, the filtered-off mass was washed, dried at 150°C for 2 h, and the filtrate was analyzed for the content of the sulfate ion by the weighing method. A set of experiments demonstrated that, after 45 min, the degree of recovery of the sulfate ion from the active paste is, on the average, as high as 99.5%. It should be noted here that the mass of the initial weighed portion decreases, on the average, by 2 g (by 6.7%), which is somewhat higher than the value expected under assumption that only reaction (1) occurs. Together with the formation of cerussite $PbCO_3$,

1070-4272/03/7610-1702 $25.00 © 2003 MAIK "Nauka/Interperiodica"

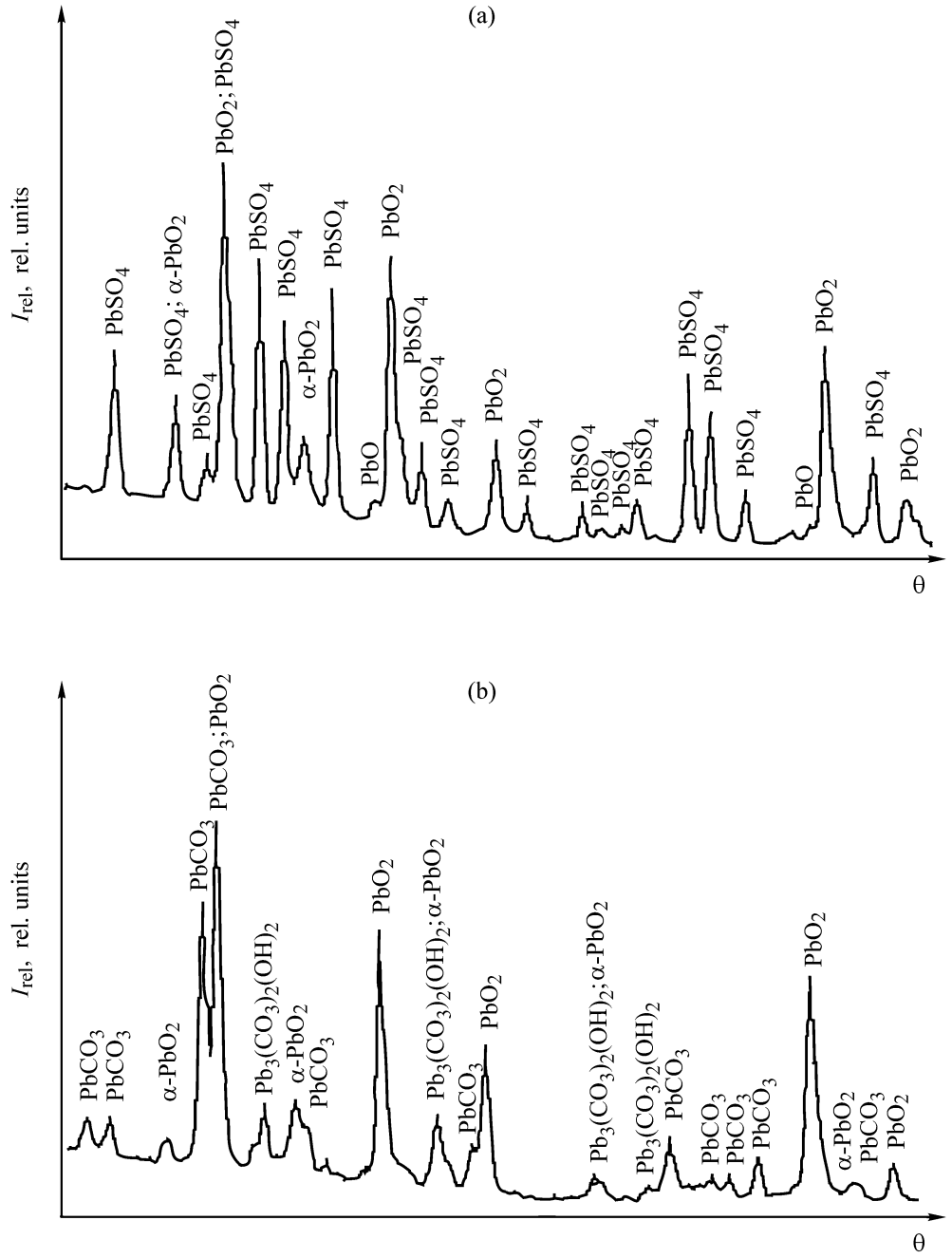

Fig. 1. X-ray diffraction patterns of (a) starting active paste and (b) that after desulfation. (I_{rel}) Relative intensity of diffraction lines and (θ) Bragg angle. The diffraction lines are assigned to the phases revealed; the content of a phase is proportional to the relative intensity of a line.

a minor amount of hydrocerussite $Pb_3(CO_3)_2(OH)_2$ is formed by the reaction [9, 16]:

$$3PbSO_4 + 4K_2CO_3 + 2H_2O = Pb_3(CO_3)_2(OH)_2 + 3K_2SO_4 + 2KHCO_3.$$

An X-ray diffraction analysis confirmed the presence of hydrocerussite in the desulfation products, in relatively small amounts, compared with those of cerussite and plattnerite. It should be noted that, in contrast to desulfation with soda, no double salt similar to the compound $NaPb_2(CO_3)_2OH$ is formed in desulfation with potash. This confirms the results obtained in [16] and in earlier investigations in this field.

In several sets of experiments, the paste being desulfated was sampled 15, 30, and 45 min after the be-

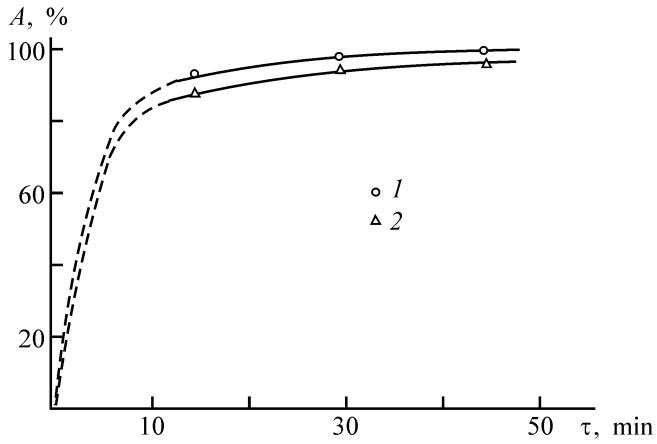

Fig. 2. Degree *A* of recovery of sulfate ions from the active paste vs. time τ. s : l: (*1*) 1 : 4 and (*2*) 1 : 5.

ginning of the process and the content of SO_4^{2-} ions in the samples was determined. As can be seen from Fig. 2, the main part of SO_4^{2-} ions pass into solution at least during the first 10 min of the process. The s : l ratio (1 : 4 or 1 : 5) has virtually no effect on the course of desulfation, with the curves coinciding to within the experimental error.

CONCLUSION

The process of desulfation of the active paste from lead battery scrap in an aqueous solution of K_2CO_3 at 50°C is fast, with the desulfation degree as high as 99.5%. The main components of the desulfated paste are cerussite $PbCO_3$ and plattnerite PbO_2. Also, a minor amount of hydrocerussite $Pb_3(CO_3)_2(OH)_2$ is present.

ACKNOWLEDGMENTS

The study was supported financially by the Foundation "Basic Research in Chemical Technology," Ministry of Education of the Russian Federation, grant no. TO2–9.4–3298.

REFERENCES

1. Morachevskii, A.G., Vaisgant, Z.I., and Korelyakov, A.V., *Zh. Prikl. Khim.*, 2000, vol. 73, no. 7, pp. 1125–1130.
2. Morachevskii, A.G., Vaisgant, Z.I., Bochagina, E.V., and Khabachev, M.N., *Tsvet. Met.*, 2002, no. 8, pp. 34–37.
3. Morachevskii, A.G., *Pererabotka vtorichnogo svintsovogo syr'ya: Sovremennoe sostoyanie issledovanii i annotirovannyi ukazatel' literatury za 1997–2001 gg.* (Processing of Secondary Lead Raw Materials: Present State of Investigations and Annotated Bibliographic List for 1997–2001), St. Petersburg: SPb Gos. Tech. Univ., 2003.
4. Morachevskii, A.G., *Zh. Prikl. Khim.*, 2003, vol. 76, no. 9, pp. 1467–1476.
5. Smirnov, M.P., Sorokina, V.S., and Gerasimov, R.A., *Tsvet. Met.*, 1996, no. 9, pp. 13–17.
6. Besser, A.D., *Met. Evrazii*, 1997, no. 3, pp. 76–78.
7. Behrendt, H.-P. and Steil, H.U., *Erzmetall*, 1997, vol. 50, no. 6, pp. 398–405.
8. Kumok, V.N., Kuleshova, O.M., and Karabin, L.A., *Proizvedeniya rastvorimosti* (Solubility Products), Novosibirsk: Nauka, 1983.
9. Morachevskii, A.G., *Zh. Prikl. Khim.*, 1998, vol. 71, no. 6, pp. 881–890.
10. Arai, K. and Toguri, J.M., *Hydrometallurgy*, 1984, vol. 12, pp. 49–59.
11. Gong, Y., Dutrizac, J.E., and Chen, T.T., *Hydrometallurgy*, 1992, vol. 28, pp. 399–421.
12. Gong, Y., Dutrizac, J.E., and Chen, T.T., *Hydrometallurgy*, 1992, vol. 31, pp. 175–199.
13. Lyakov, N., Tsaneva, M., Kharlampiev, G., and Girdzhev, N., *Godishnik na visshiya khimikotekhnologicheski in-t Sofiya* (Yearbook of Higher Institute of Chemical Technology in Sofia, book 3, 1992–1993, vol. 31, pp. 36–45.
14. Morachevskii, A.G., Vaisgant, Z.I., Rusin, A.I., and Khabachev, M.N., *Zh. Prikl. Khim.*, 2001, vol. 74, no. 7, pp. 1075–1077.
15. Chen, T.T. and Dutrizac, J.E., *Hydrometallurgy*, 1996, vol. 40, pp. 223–245.
16. Bulakhova, V.I. and Ben'yash, E.Ya., *Sbornik nauchnykh trudov VNIItsvetmet* (Coll. of Sci. Works of VNIItsvetmet), Ust'-Kamenogorsk, 1970, no. 21, pp. 77–79.

Russian Journal of Applied Chemistry, Vol. 76, No. 10, 2003, pp. 1705–1709. Translated from Zhurnal Prikladnoi Khimii, Vol. 76, No. 10, 2003, pp. 1751–1755.

Wilhelm Ostwald (To 150th Anniversary of His Birthday)

The 1909 Nobel Prize Laureate in chemistry, W. Ostwald is widely known as one of founders of physical chemistry, a scientist and pedagogue, philosopher, and historian of science. He made an outstanding contribution to the development of the theory of electrolyte solutions and the theory of kinetics and catalysis. Together with J. Van't Hoff (1852–1911, 1901 Nobel Prize in chemistry), he founded the first specialized journal of physical chemistry and created a prominent international school of physical chemists. Numerous W. Ostwald's work have been translated into Russian. In 1896, W. Ostwald became a foreign corresponding member of the St. Petersburg Academy of Sciences.

Friedrich Wilhelm Ostwald was born on September 2, 1853, in Russia, in Riga, an administrative and cultural center of the former Liefland Province, into a family of Baltic Germans. His father, Gottfried Ostwald, was owner of a small barrel shop and a skillful barrel maker himself. Already when studying at Riga Realgymnasium, W. Ostwald became devoted to chemistry and, having finished his secondary education in 1872, entered the physicomathematical faculty of the University of Dorpat (now Tartu). At those years, Dorpat was a town of Liefland Province that was second in economic and cultural importance only to Riga. The studies at the university were in German (till 1889; later, in Russian). Chemistry was taught at the University of Dorpat at a sufficiently high level. The chair of chemistry was headed by professor Carl Schmidt (1822–1894), a corresponding member of the St. Petersburg Academy of Sciences since 1873. His main studies were devoted to analytical, physiological, and agricultural chemistry. As assistant at Schmidt's laboratory worked Johan Lemberg (1842–1902), also an erudite pedagogue and scientist, one of those who founded in Russia a field of science named "chemical geology." The formation of W. Ostwald's scientific view of the world was strongly affected by professor of physics A. von Oettingen (1836–1920).

In April 1875, W. Ostwald graduated from the university with a degree of a candidate of chemistry and, beginning in July of the same year, started to work as assistant at the physics laboratory of the university. Simultaneously, the young scientist commenced his

W. Ostwald, 1887.

experimental investigations. As object of study served acids and salts, whose interaction was analyzed in terms of chemical affinity. W. Ostwald chose as an experimental technique measurements of volume in the reaction of neutralization; later, he also studied other physical properties (refractive index, viscosity, electrical conductivity). In the autumn of 1877, W. Ostwald, having passed necessary examinations, presented dissertation "Volume-Chemical Study of Affinity" for the degree of master of chemistry, and already in December 1878, the degree of doctor of chemistry was conferred on him after he presented his doctoral dissertation "Volume-Chemical and Optical-Chemical Studies."

Beginning in March 1880, W. Ostwald started to work as privat-docent at C. Schmidt's chemical laboratory, but only for a short time: already in December 1881, at the age of 28, he was appointed professor of chemistry at Riga Polytechnic Institute (Polytechnicum) and started lecturing there in January 1882. Riga Polytechnicum, founded in 1862, was the oldest polytechnic educational institution of Russia. The teaching was in German, despite that students of various nationalities studied at the institute. In January 1883, W. Ostwald toured for the first time cities of

1070-4272/03/7610-1705 $25.00 © 2003 MAIK "Nauka/Interperiodica"

Germany and Switzerland and made acquaintance with the best research laboratories and leading chemists and physicists in these countries. In particular, he visited for the first time Leipzig, which was a prominent book-publishing center of that time. With account of his impressions of the trip, a new, well-equipped chemical laboratory was organized at Riga Polytechnicum in 1885. Together with being engaged in pedagogical and organizational activities, W. Ostwald paid much attention to experimental studies. In the beginning of June 1884, he received a paper by young Swedish scientist Svante Arrhenius (1859–1927, 1903 Nobel Prize in chemistry, foreign corresponding member of the St. Petersburg Academy of Sciences since 1903, honorary member of the Academy of Sciences of the USSR since 1926) "A Study of Electrical Conductivity of Electrolytes" (dissertation for the degree of doctor of philosophy). The dissertation was presented on May 26, 1884, at the University of Upsala (Sweden); however, Swedish scientists remained skeptical about Arrhenius's ideas of electrolytic dissociation. At the same time, W. Ostwald immediately understood that Arrhenius's study involved novel approaches, which can strongly affect further development of the theory of solutions and electrochemistry. Already in August 1884, W. Ostwald went to Sweden to make personal acquaintance with Arrhenius [1]. Ostwald's arrival and his support were exceedingly important for Arrhenius and his theory, and this became the beginning of close friendship between the two scientists.

In 1885, W. Ostwald carried out intensive experimental research at his laboratory. In a letter to Arrhenius (1886), he wrote: "...determined the electrical conductivity of 120 acids and performed about 2000 experiments..." [2]. During his residence in Riga (1882–1886), W. Ostwald published more than 30 experimental papers. In the spring and summer of 1886, Arrhenius worked during about six months at W. Ostwald's laboratory. Using a viscometer designed by W. Ostwald, he studied, in particular, the viscosity of dilute aqueous solutions.

In Riga, W. Ostwald completed his fundamental two-volume textbook of general chemistry, which paid much attention to advances in physical chemistry, and work on which was commenced already in Derpt. Both volumes were published in Leipzig [*Lehrbuch der allgemeinen Chemie* (Textbook of General Chemistry), 1885, vol. 1; 1887, vol. 2]. Having completed the textbook, W. Ostwald started to make preparations for publication of a new international physicochemical journal [*Zeitschrift für physikalische Chemie* (Journal of Physical Chemistry)]. W. Ostwald's initiative was supported by prominent scientists from many European countries, including D.I. Mendeleev (1834–1907) and N.A. Menshutkin (1842–1907). Already in June 1887, the first issue of the journal was published in Leipzig; W. Ostwald and J. Van't Hoff, a professor of Amsterdam University, became its editors.

As Stradins noted in his publications devoted to the Riga period of W. Ostwald's activities [3, 4], the scientific achievements of the young professor from Riga, publication of a textbook and journal by him, and his foreign trips got him international fame. In the spring of 1887, W. Ostwald was invited to fill a vacancy of a professor of physical chemistry at Leipzig University, the oldest in Germany (founded in 1409). In the autumn of 1887, W. Ostwald's commenced his pedagogical and scientific activities in Leipzig, where he managed to organize a physicochemical laboratory, which soon became a kind of center of new directions in physical chemistry: Arrhenius's theory of electrolytic dissociation, Van't Hoff's osmotic theory, and theory of catalysis. In 1888, W. Nernst (1864–1941, 1920 Nobel Prize in chemistry) was invited to work at the laboratory as assistant and started studies of the electromotive force of galvanic cells. The closest W. Ostwald's associates also included E. Beckmann (1853–1923), who suggested the design of a high-precision thermometer for determining the molecular weight of solutes by cryoscopy and ebullioscopy, and G. Bredig (1868–1944) specializing in catalysis. Long time was spent at W. Ostwald's laboratory by S. Arrhenius and P. Walden (1863–1957, academician of the St. Petersburg Academy of Sciences since 1910), who was a professor of Riga Polytechnicum and W. Ostwald's pupil.

Despite that W. Ostwald moved to Leipzig, his scientific relations with Riga were not terminated, and a number of W. Ostwald's pupils and colleagues continued earlier commenced investigations. In 1903, W. Ostwald was elected honorary member of the Riga Polytechnic Institute, first translations of his books into Russian were published in Riga. W. Ostwald's relatives also lived in Riga [3]. Particularly close were W. Ostwald's personal and scientific relationships with Walden, who wrote first W. Ostwald's biography in 1903.

W. Ostwald's laboratory in Leipzig was visited by young scientists from many European countries, USA, and Japan. The first among Russian scientists, not counting Walden, was V.A. Kistyakovskii (1865–1952, academician of the Academy of Sciences of the USSR since 1929), who graduated, with a degree of candidate, from the physicomathematical faculty

of St. Petersburg University in January 1889 and decided, on his own initiative, to continue education at W. Ostwald's laboratory in 1889–1890. Kistyakovskii was well acquainted with modern concepts of the theory of solutions, since the Planck–Arrhenius hypothesis was the subject of his graduation thesis. This was one of the first publications in Russia, in which the concepts of Arrhenius, Van't Hoff, W. Ostwald, and M. Planck (1858–1947, 1918 Nobel Prize in physics) were subjected to detailed critical analysis. In Leipzig, Kistyakovskii studied, under the supervision of W. Ostwald and Arrhenius, the electrical conductivity of aqueous solutions of a number of double salts in order to determine the composition of ions formed in dissolution of these salts. The notion of double and complex salts was introduced by W. Ostwald in 1889; in the Russian chemical literature, this notion appeared after Kistyakovskii's publication [5, 6].

In the summer of 1889, privat-docent I.A. Kablukov (1857–1942, honorary academician of the Academy of Sciences of the USSR since 1932) arrived in Leipzig, on a business trip from Moscow University [7]. He studied the electrical conductivity of hydrogen chloride solutions in various solvents. At that same time, A.V. Speranskii (1865–1919), who graduated from Moscow University in 1888 (later, professor of Kiev University), continued his education at W. Ostwald's laboratory. In different years, the following representatives of Russia worked in Leipzig: V.F. Timofeev (1858–1923), D.P. Turababa (1863–1933), A.V. Sapozhnikov (1868–1935), N.A. Shilov (1872–1930), L.V. Pisarzhevskii (1874–1938, academician of the Academy of Sciences of the USSR since 1930), and A.V. Rakovskii (1879–1941, corresponding member of the Academy of Sciences of the USSR since 1933). Young talented scientists from different countries made especially high the level of studies at the physicochemical laboratory of Leipzig University. To Kistyakovskii belongs the well-known phrase: "It is a common opinion that W. Ostwald created a prominent school of physical chemists, but, vice versa, it may be said that this prominent school created W. Ostwald" [8].

During the period from 1887 till 1906, the international school of physical chemists, headed by W. Ostwald, gave to the world science about 70 scientists, who became professors and heads of laboratories and chairs in different countries [2, 3].

Kistyakovskii in St. Petersburg and Kablukov in Russia, active supporters of new concepts of the nature of solutions, had to deal with strong opponents of the theory of electrolytic dissociation. These included leading Russian chemists of that time: Mendeleev, D.P. Konovalov (1856–1929, academician of the Academy of Sciences of the USSR since 1923), M.D. L'vov (1848–1899), N.N. Beketov (1827–1911, academician of the St. Petersburg Academy of Sciences since 1886), F.M. Flavitskii (1848–1917, professor of Kazan University, corresponding member of the St. Petersburg Academy of Sciences since 1907), and others. More tolerant and unbiased toward Arrhenius's hypothesis was Menshutkin, a professor of St. Petersburg University. Kistyakovskii and, later, Kablukov considered it their task to bring together the two different standpoints concerning the nature of solutions, based on the concept of hydration of ions and their interaction with the solvent.

In 1888, W. Ostwald established an important relationship between the degree of dissociation of an electrolyte and its concentration (Ostwald's dilution law). In 1888–1889, the scientist continued investigations of the electrical conductivity of organic acids to determine the dependence of their constant of electrolytic dissociation on the composition and structure of an acid and established important relationships between the structure and reactivity of organic molecules and studied dissociation of dibasic acids. In 1890–1892, W. Ostwald paid much attention to dyed solutions and their absorption spectra and developed a theory of acid-base indicators. Based on this and other investigations in the field of analytical chemistry, he wrote a manual *Scientific Foundations of Analytical Chemistry* (1894).

In 1889, W. Ostwald founded a series of publications, *Klassiker der exakten Wissenschaften* (Classics of Exact Science), which became widely known, and, later, *Ostwalds Klassiker der exakten Wissenschaften*, which promoted and popularized works of world's most prominent scientists. In 1893, one of W. Ostwald's teachers, professor Oettingen, finished his pedagogical and scientific activities at Dorpat University and moved, by W. Ostwald's invitation, to Leipzig to engage himself in preparation and publication of current issues of the series *Klassiker der exakten Wissenschaften*. In 1966, the 250th issue was published, devoted to W. Ostwald's works in the field of chemical affinity. In 1988, a special monograph was published in tribute of the centennial foundation anniversary of the series [9].

W. Ostwald was among those who initiated foundation of specialized research institutes to solve the most topical problems of chemistry. This idea was embodied in Germany: in 1896, the Institute of Physical Chemistry and Electrochemistry was orga-

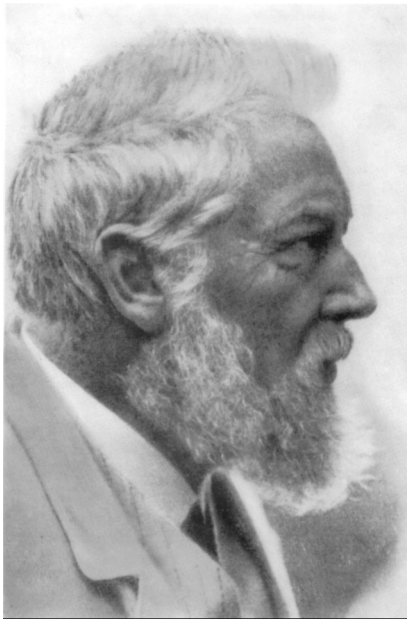

W. Ostwald, 1927.

nized in Gottingen for Nernst, who headed the chair of physical chemistry at Gottingen University at that time. In the end of 1897, the Institute of Physical Chemistry was organized in Leipzig for W. Ostwald. The main directions of research at the institute were kinetics and catalysis. W. Ostwald commenced investigations in these fields of physical chemistry already when living in Riga. In 1890, he published an important paper "Autocatalysis," which initiated wide-scale investigations in the field of catalysis. In 1895, there appeared another paper of fundamental importance: "On the Nature of Catalytic Processes." Among the closest W. Ostwald's associates, the already mentioned Bredig studied heterogeneous catalysis. Later (in 1900–1906), extensive studies of the kinetics of homogeneous reactions were carried by M. Bodenstein (1871–1942). Shilov studied the kinetics of conjugated reactions. Results of numerous investigations were summarized by W. Ostwald in a monograph *Über Kataluse* (On Catalysis, Leipzig, 1902; Russian translation in 1903). W. Ostwald's investigations in the field of catalysis were analyzed in detail in a monograph by N.I. Rodnyi and Yu.I. Solov'ev [2].

In August 1906, W. Ostwald finished teaching at Leipzig University. The exceedingly intensive work for 20 years resulted in fatigue and strain. By that time, W. Ostwald was comfortably off and had the rank of privy councilor. Together with the numerous members of his family (three sons and two daughters) he settled at his Energetik country-house at a small town of Grossbothen approximately 30 km southwest of Leipzig.

Shortly before resigning, in the spring of 1904, W. Ostwald delivered a Faraday lecture "Compounds and Elements" at Royal Institute in London. In 1906, in the framework of the first program of exchange of scientists between Germany and the United States, W. Ostwald delivered lectures at a number of universities in USA during a year.

In 1909, as already mentioned, W. Ostwald won Nobel Prize in chemistry "... in recognition of his work on catalysis and for his investigations into the fundamental principles governing chemical equilibria and rates of reaction" [10]. The presentation of the scientist by Swedish Royal Academy of Sciences emphasized the importance of W. Ostwald's discoveries not only for the development of theory, but also for practical use, e.g., for manufacture of sulfuric acid or synthesis of indigo-based dyes. Among the scientists who nominated W. Ostwald for the Nobel Prize was Kablukov.

Having freed himself from his duties as a professor of Leipzig University and head of the Physicochemical Institute, to become a "freelance professor," W. Ostwald could deal with the issues he had always been interested in. One of these was the development of science and the role played in this process by scientific creative work of separate scientists. In 1909, W. Ostwald published a book *Grosse Männer* (Great Men, Leipzig, 1909; Russian translation in 1910), which analyzed the career of six scientists: three chemists (H. Davy, J. Liebig, Ch. Jerard) and three physicists (M. Faraday, R. Mayer, and H. Helmholtz). W. Ostwald's ideas concerning the problems associated with chemical education, influence of age on scientific activities, formation of scientific schools, and quite a number of other issues of research organization have remained topical up to now. During his entire scientific career, W. Ostwald expressed keen interest in the history of science. He studied in most detail the evolution of electrochemistry and described it in a monograph *Elektrochemie: Ihre Geschichte und Lehre* (Electrochemistry: History and Theory, 1895). Later, in 1910, W. Ostwald described the history of electrochemistry in a more popular form; in 1911, this book was translated into Russian.

W. Ostwald proceeded from the assumption that elucidating the laws governing the development of science yields a key to understanding of the present-day situation in science and must ensure deeper understanding of general aspects of the development of society [2].

Already in the late 1890s, W. Ostwald's attention was attracted by philosophical problems of natural science; the scientist's standpoint was described in

his book *Vorlesungen über Naturphilosophie* (Lectures on Natural Philosophy, 1902; Russian translation in 1903) and later publications [2]. W. Ostwald's concept of energy as fundamental principle of the physical world and scientist's skepticism toward the atomic-molecular theory have been repeatedly subjected to justified criticism [11].

W. Ostwald's scientific and organizational activities were extensive and diverse, and his creative heritage is vast. The scientist's career has been the subject of numerous publications, including a detailed autobiography (1926–1927) and recollections of his son, Walter Ostwald (1953). Sufficiently detailed evidence of biographic nature can be found in known reference books [12–14].

Wilhelm Ostwald died on April 4, 1932, at the age of 79. He became part of the history of science as one of the most outstanding natural scientists of his time.

REFERENCES

1. Solov'ev, Yu.I. and Figurovskii, N.A., *Svante Arrenius* (Svante Arrhenius), Moscow: Akad. Nauk SSSR, 1959.
2. Rodnyi, N.I. and Solov'ev, Yu.I., *Vil'gel'm Ostval'd* (Wilhelm Ostwald), Moscow: Nauka, 1969.
3. Stradins, J., *Izv. Akad. Nauk, LatvSSR*, 1979, no. 7, pp. 33–44.
4. Stradins, J., *Latvijas Kimijas Zurn.*, 2002, no. 1, pp. 10–19.
5. Figurovskii, N.A. and Roman'kov, Yu.I., *Vladimir Aleksandrovich Kistyakovskii*, Moscow: Nauka, 1967.
6. Solov'ev, Yu.I., *Iz istorii estestvoznaniya i tekhniki Pribaltiki* (Excerpts from the History of Natural Science and Technology in Baltic Countries), Riga: Zinatne, 1968, pp. 147–156.
7. Solov'ev, Yu.I., Kablukova, M.I., and Kolesnikov, E.V., *Ivan Alekseevich Kablukov*, Moscow: Akad. Nauk SSSR, 1957.
8. Kistyakovskii, V.A., *Izv. Akad. Nauk, SSSR. Ser. VII, Matem. Estestv. Nauk*, 1934, no. 4, pp. 431–442.
9. Dunsch, L. and Müller, H., *Ein Fundament zum Gebäude der Wissenschaften*, Leipzig: Akademische, 1988.
10. *Nobel Prize Winners*, Wasson, T., Ed., New York: H.W. Wilson Co., 1987.
11. Solov'ev, Yu.I., *Vopr. Filos.*, 1963, no. 6, pp. 87–96.
12. Musabekov, Yu.S. and Chernyak, A.Ya., *Vydayushchiesya khimiki mira* (World's Outstanding Chemists), Moscow: Kniga, 1971.
13. Tuchs, G., Heinig, K., Kertscher, G. *et al.*, *Biographien bedeutender Chemiker*, Berlin: Volk und Wissen Volkseigener, 1977.
14. *Dictionary of Scientific Biography*, Ch. Gillespie, Ed., vol. 15, Supplement 1, New York: Charles Scribner's Sons, 1981, pp. 455–469.

A. G. Morachevskii

Russian Journal of Applied Chemistry, Vol. 76, No. 11, 2003, pp. 1711–1719. Translated from Zhurnal Prikladnoi Khimii, Vol. 76, No. 11, 2003, pp. 1761–1770.

REVIEWS

Effect of Hydrogen Bonding on Cellulose Solubility in Aqueous and Nonaqueous Solvents

A. M. Bochek

Institute of Macromolecular Compounds, Russian Academy of Sciences, St. Petersburg, Russia

Received June 18, 2003

Abstract—Interrelation between the hydrogen bonding energy in cellulose and its solubility in aqueous and nonaqueous solvents is examined. Factors controlling the solubility and selection criteria for nonaqueous solvents for cellulose are analyzed.

Among polymers widely used in various areas of human activities, cellulose, as a steadily renewable native polymer, and its derivatives are of great importance. In this connection, development of green technologies for cellulose processing is a topical problem. Native cellulose fibers are used essentially in textile and pulp and paper industries. It is important also that cellulose and its derivatives as films, fibers, and granules are manufactured generally through polymer solutions [1, 2].

Fabrication of rayon through the xanthate, which was a common process until the mid1980s, includes the use of toxic carbon disulfide [3–6]. In the last two decades, in Russia and other countries, new solvent systems for cellulose were intensively studied as alternatives to the viscose process. Among these systems were nonaqueous (tertiary amine *N*-oxides, aprotic solvents with addition of LiCl, DMF with N_2O_4, trifluoroacetic acid, etc.) and aqueous solvents like aqueous $ZnCl_2$, NaOH, and H_3PO_4 [7–13]. Most of these solvents have not found practical use because of such reasons as toxicity and environmental hazard, limited solvency, problems arising in developing closed processes, and high power consumption in solvent regeneration.

Criteria for predicting the solvency with respect to cellulose are searched for many years. Knowledge of only the thermodynamics of the polymer–solvent interaction does not allow theoretical prediction of the solubility of cellulose in one or another solvent. The solubility of cellulose is influenced by such factors as the fiber morphology, molecular weight, degree of structurization, i.e., origin of the polymer, and also by hydrogen bonding in its structure. All these factors affect characteristics of cellulose solutions and, indirectly, the performance of the resulting fibers and films.

Therefore, it appeared advisable to summarize and correlate information on hydrogen bonding in cellulose and other factors controlling its solubility in aqueous and nonaqueous solvents, and also on the selection criteria for solvents for cellulose.

1. SOLUBILITY PARAMETER δ OF CELLULOSE AND HYDROGEN BONDING IN THE NATIVE POLYMER

The presence of one primary (C^6) and two secondary (C^2, C^3) hydroxy groups in an anhydroglucose unit of cellulose predetermines the occurrence of a system of inter- and intrachain hydrogen bonds in the native polymer. This strongly limits the range of one-component solvents suitable for practical use.

The first systematic studies of hydrogen bonding in ordered regions of the cellulose structure were reported in [14–18]. The conformations of cellulose macromolecules and hydrogen bonding in them were actively studied by Zhbankov and coworkers [19, 20]. In these works, IR absorption spectra of cellulose in the OH stretching region (3000–3700 cm^{-1}) were analyzed to elucidate the arrangement of intra- and interchain hydrogen bonds. Since introduction of instruments of new generation (FTIR spectrometers), these works have been brought up to a higher standard [21–25].

Basing on the Sarko and Blackwell's elementary unit models [26–28], Zbankov and Kozlov [20] theoretically analyzed hydrogen bonding in highly ordered regions of the cellulose structure with parallel arrangement of the cellulose chains. They considered the most stable conformations of the native cellulose chains. The results are given in Fig. 1 and Table 1.

The theoretical estimates confirmed the occurrence of two intra- and one interchain hydrogen bonds in

1070-4272/03/7611-1711$25.00

Table 1. Characteristics of hydrogen bonds in native cellulose (C1) [20]

Type of bonding	O···H distance, Å	E_h, kJ mol^{-1}
Intrachain	1.81	13.2 [26]
$O^{3'}$–H···O^5	1.86	11.5 [28]
O^2–H···$O^{6'}$	1.74	14.9
	1.91	10.0
Interchain	1.96	8.6
$O^{6'}$–H···$O^{3''}$	1.82	12.8

the elementary unit of native cellulose. Table 1 shows that the hydrogen bonding energy in cellulose ranges from 8.5 to 15.0 kJ mol^{-1}. Dissolution of cellulose requires breaking of at least all the interchain hydrogen bonds. There are a number of solvents capable of forming hydrogen bonds with the energies E_h above 13.0 kJ mol^{-1}. These are alcohols, aldehydes, amines, some aprotic solvents, etc. [29]. Water forms hydrogen bonds with E_h = 18.0–21.0 kJ mol^{-1} [29]. However, cellulose does not dissolve in water and the above-indicated solvents under any conditions, suggesting the realization of hydrogen bonds in cellulose with an energy above 21.0 kJ mol^{-1}. Naimark *et al*. [30] studied the interaction of cellulose with plasticizing aprotic and proton-donor solvents and suggested that amines can form hydrogen bonds with the OH groups of cellulose with E_h >21.0 kJ mol^{-1}.

One of the parameters characterizing intermolecular interactions in polymers is the solubility parameter δ introduced by Hildebrand in his regular solution theory [31]. Knowledge of this parameter allows prediction of the cohesion energy of a polymer E_{coh} and also of the nature of intermolecular interactions in the polymer, which may be helpful in directed search for good solvents.

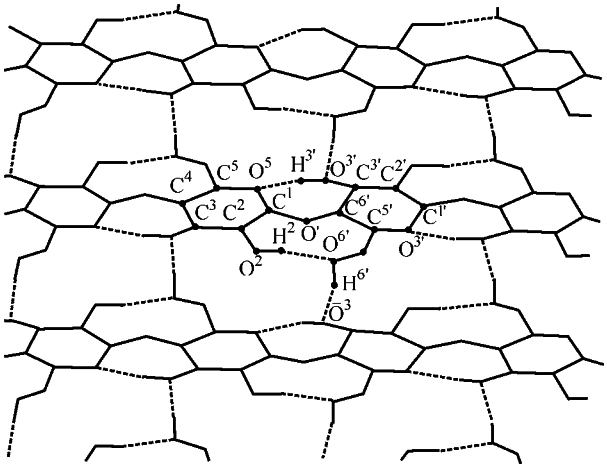

Fig. 1. Intra- and interchain hydrogen bonding in ordered regions of the structure of native cellulose [20].

From the equilibrium swelling, Thode and Guide [32] have determined δ = 28.6 (J cm^{-3})$^{0.5}$ for cellulose. In studying the plasticizing properties of solvents, Naimark *et al*. [30] obtained δ = 52.8 (J cm^{-3})$^{0.5}$, which was assigned to amorphous cellulose. The theoretical estimates obtained for some physical and physicochemical characteristics of cellulose and other polysaccharides revealed that the energy of intermolecular interaction in cellulose amounts to 207.0 kJ mol^{-1}, which corresponds to δ = 29.2 (J cm^{-3})$^{0.5}$ [33]. The cohesion energy of cellulose was reported to be 1296.0 kJ mol^{-1} [34]. Berger and Keck [35] obtained δ = 53.4 (J cm^{-3})$^{0.5}$ for cellulose in crystallites. Swelling of films of hydrated cellulose in aprotic and proton-donor solvents was studied in [36, 37]. In these works we demonstrated that knowledge of the dependences of the degree of swelling on δ of a solvent does not allow estimation of δ of cellulose.

Hansen suggested to consider the cohesion energy of solvents and polymers as a sum of three terms [38, 39]:

$$\delta = \left(\frac{E_{coh}}{V}\right)^{0.5} = \left(\frac{E_d + E_p + E_h}{V}\right)^{0.5} = (\delta_d^2 + \delta_p^2 + \delta_h^2)^{0.5}. \quad (1)$$

where E_d, E_p, and E_h are the contributions of the dispersion and dipole–dipole interactions and hydrogen bonding, respectively, to the cohesion energy; and *V*, volume.

To characterize the parameters of intermolecular interactions, primarily of hydrogen bonding, in cellulose, we proposed a new procedure for determination of the solubility parameter of cellulose and estimated for the first time the partial contributions of the dispersion (δ_d) and dipole–dipole (δ_p) interactions and hydrogen bonding (δ_h) to δ [36]. The procedure involves determination of δ of cellulose acetates with various degrees of substitution (DS) from their solubility diagrams in mixed solvents reported by Malm *et al*. [40]. The δ vs. DS plots appeared to be linear (Fig. 2). By extrapolation of these dependences to zero DS, δ, δ_d, δ_p, and δ_h were determined to be 55.7, 11.7, 35.9, and 42.2 (J cm^{-3})$^{0.5}$, respectively. The δ value thus obtained exceeds considerably that of water and other common solvents. High values of δ, δ_p, and δ_h of cellulose are caused by the features of its chemical structure, specifically, by the system of intra- and

interchain hydrogen bonds contributing significantly to E_{coh} of the polymer.

The theoretical δ as well as δ_d, δ_p, and δ_h appeared to be considerably lower than those obtained experimentally [36, 37, 41]. Discrepancies in δ of cellulose estimated by various methods are probably due to the fact that the contributions of dipole–dipole interactions and hydrogen bonding to the cohesion energy were taken into account to a different extent in each method.

From the experimental δ_h we estimated the hydrogen bonding energy to be E_h = 25.0 kJ mol^{-1} [36, 37], which is about twice that published in the literature for interchain hydrogen bonds in cellulose (Table 1). The value E_h = 25 kJ mol^{-1} is well consistent with that estimated from the shift of the OH absorption bands in IR spectra of cellulose of various origins. Sugiyama *et al*. [42] reported the frequencies of 3240 and 3270 cm^{-1} for the H-bonded OH groups in polymorphs I_α and I_β of cellulose, respectively. From these frequencies, one may estimate the corresponding E_h values using the Sokolov's equation [29]. The result is 26.1 and 23.8 kJ mol^{-1} for the bands at 3240 and 3270 cm^{-1}, respectively, which is in good agreement with E_h estimated from δ_h.

Finally, it is the high E_h typical of hydrogen bonding in cellulose (up to 25 kJ mol^{-1}) that restricts the range of solvents suitable for cellulose.

2. TERTIARY AMINE *N*-OXIDES

Many efforts were made to establish a correlation between the structure of amine oxides and their solvency with respect to cellulose. As early as in 1939, Graenacher and Sallmann have demonstrated that aliphatic and cyclic amine oxides dissolve cellulose at elevated temperature to form 7–9% solutions [43]. They have also formulated the selection criteria: oxides of tertiary amines should contain no more than 14 carbon atoms and be free from aromatic radicals. At that time, amine oxides found no practical application because of relatively low attainable cellulose concentrations. In 1969, Johnson reported on dissolution of cellulose in heterocyclic amine oxides like *N*-methylmorpholine *N*-oxide (NMMO) [44, 45]. He suggested that amine oxides are capable of breaking hydrogen bonds between the OH groups of cellulose chains even in crystalline regions of the cellulose structure by virtue of formation of stronger hydrogen bonds between the OH groups of the polymer and the oxygen atom of an oxide: Cell–O–H···O$^-$←N$^+$R$_3$.

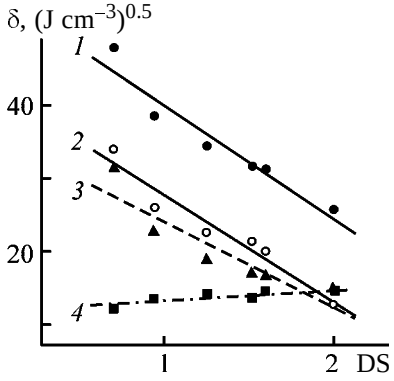

Fig. 2. (*1*) δ, (*2*) δ_h, (*3*) δ_p, and (*4*) δ_d of cellulose acetates as functions of DS [37].

In 1979–1980, Franks and Varga studied the solvency of a broad range of amine oxides of various structures (32 amine oxides) [46, 47]. They have demonstrated that the solvency of amine oxides depends on the water content of the solution and offered certain physical and chemical or, rather, structural criteria for evaluation of amine oxides as solvents for cellulose [48]: (1) *N*-Oxide should be a tertiary amine derivative; (2) preferably, a tertiary amine *N*-oxide having a cyclic molecular structure should be taken, except for triethylamine *N*-oxide (TEAO) and *N*,*N*-dimethylethanolamine *N*-oxide (DMEAO); (3) the size of the ring should be no larger than the size of the glucopyranose unit (5.15 Å); (4) amine oxide should have high dipole moment (at least 4.5 D) to be capable of breaking the hydrogen bonds between the OH groups of cellulose; and (5) solvent should contain water within a specified critical range, to dissolve cellulose at a given temperature.

Franks and Varga offered a so-called polar-steric dissolution mechanism, with special emphasis on the structure of substituents at the nitrogen atom. With the above criteria being met, the hydrophobic part of the amine oxide molecule solvates the glucopyranose unit, shielding it from the nearest neighboring units and promoting dissolution of cellulose.

However, the above-given selection criteria cannot explain different behavior of specific amine oxides with respect to cellulose. For example, NMMO dissolves cellulose, but *N*-ethylmorpholine *N*-oxide (NEMO) does not; TEAO dissolves cellulose, but trimethylamine *N*-oxide (TMAO) does not, even though having a high dipole moment (5.02 D).

Other authors [49, 50] proposed to add two more criteria to those considered above, namely, the basicity of amine oxides (pK_a ~ 5.0) and the steric factor at the nitrogen atom. Shielding of the oxygen of the

Table 2. Interaction energies of amine oxides with water (E_h) and in dimers (E_{dim}) [57]

Amine *N*-oxide	μ, D	E_h	E_{dim}	Solvency*
		kJ mol^{-1}		
TMAO	5.14	28.9	43.9	–
TEAO	4.52	25.9	40.5	+
MO	4.05	18.4		–
NMMO	4.25	25.5	26.4	+
NEMO	4.12	22.5	26.4	–

*(–) Does not dissolve and (+) dissolves.

N→O group by a substituent at the same nitrogen atom may result in the total loss of the solvency even in oxides of high polarity and basicity. Consideration of the steric factor allows understanding of the facts that NMMO dissolves cellulose, but NEMO does not. The methyl substituent is not bulky enough to shield the oxygen atom, permitting strong hydrogen bonding with the OH groups of cellulose. On the contrary, the ethyl substituent strongly shields the oxygen atom of the N→O group, hindering hydrogen bonding. Unfortunately, inclusion of the steric factor into consideration is insufficient to explain the inverse pattern observed for aliphatic amine oxides (TEAO dissolves cellulose, but TMAO does not).

Philipp and coworkers [11, 51] proposed another dissolution mechanism involving formation of a donor–acceptor transition complex. However, inclusion of such a stage into consideration allows explanation of the fact of cellulose solubility, but not its quantitative theoretical prediction.

Analyzing cellulose solubility in the framework of the donor–acceptor interaction, Tsvetkov [52] suggested that cellulose could dissolve only in solvents of high electron-donor power ($DN_{SbCl_5} > 40$). The donor number of NMMO was estimated to be just about 40 [50]. It should be pointed out that the donor number is a measure of the total interaction energy of a given solvent with $SbCl_5$, but it does not always provide information on the specific interaction of the solvent with a fixed functional group of the polymer. For example, DN_{SbCl_5} of diamines, ethylenediamine and tetramethylethylenediamine, were estimated to be 50 and 55, respectively. However, they do not dissolve cellulose [53]. Note also that *DN* of solvents can depend on the determination procedure [54].

Tsygankova *et al*. [55] have performed MNDO quantum chemical calculations of some electronic structure parameters (dipole moment, ionization potential, and electron density distribution) for a series of tertiary amine oxides both not dissolving (TMAO) and dissolving cellulose (TEAO, NMMO, and NMMO monohydrate). The authors found no significant differences in the above-indicated parameters of the electronic structure which could explain the lack of the solvency in the amine oxides that are very similar in their electronic structure to those dissolving cellulose.

Yakimanskii *et al*. [56] applied the same calculation procedure to broader ranges of amine oxides and their monohydrates and calculated a larger set of electronic characteristics. They studied the electronic structure of TMAO, TEAO, morpholine *N*-oxide (MO), NMMO, NEMO, DMEAO, and their monohydrates and also the cellulose solubility in them. The electronic structure analysis included such characteristics as the HOMO and LUMO energies, dipole moment and its derivatives, charge distribution, and $2p_x$, $2p_y$, and $2p_z$ populations. As in [55], results revealed that none of the parameters taken alone could be used as a criterion for predicting the cellulose solvency of amine oxides. It may be suggested that it is governed by some set of electronic structure parameters, each being responsible for certain contribution to the total solvent–polymer interaction energy.

The affinity of amine oxides for water can be used to elucidate their affinity for the OH groups of cellulose. Yakimanskii *et al*. [56] have estimated the energy of hydrogen bonding E_h between water and amine oxides. For completeness sake, Bochek *et al*. [57] have also estimated the cohesion energies of solvents in dimers E_{dim}. In the anhydrous state, NMMO molecules are arranged so that the dipolar N→O bonds in the adjacent molecules are antiparallel [58].

Table 2 shows that only combined analysis of the energies of hydrogen bonding of amine oxides with the OH groups (E_h), on the one hand, and the cohesion energies of amine oxides in dimers E_{dim}, on the other hand, opens the door for formulation of the selection criteria for solvents for cellulose. As shown above, cellulose is soluble in amine oxides capable of forming high-energy (>25.0 kJ mol^{-1}) hydrogen bonds with the OH groups. The value of 25 kJ mol^{-1} corresponding to the maximal hydrogen bonding energy in cellulose bounds the range of one-component solvents for cellulose. It is seen also that the ability of amine oxides to form hydrogen bonds with E_h >25 kJ mol^{-1} is a necessary but not sufficient condition to ensure cellulose solubility. It is also necessary that E_{dim} of solvents be lower than, or at least close to the indicated critical value. The enthalpy of

cellulose interaction with NMMO monohydrate was found to be ΔH_{int} = 24.6 [52, 59] and 24.1 kJ mol^{-1} [60]. The validity of these estimates is supported by the closeness of E_h and ΔH_{int} in the case of NMMO monohydrate.

As seen, E_h and E_{dim} are close to each other only in NMMO. In aliphatic TMAO and TEAO, E_{dim} is considerably higher. Cellulose dissolves in amine oxides upon heating. Although hydrogen bonding between an amine oxide and the OH groups of cellulose is an exothermic reaction, elevation of the temperature is needed to overcome the self-association and crystallization in the solvent [61]. The E_{dim} in amine oxides can be lowered also by adding certain critical amount of water, which results in reduction of the melting point of NMMO monohydrate (TEAO monohydrate is a liquid at room temperatures). It could be concluded from Table 2 that TMAO, having the highest E_h (28.9 kJ mol^{-1}) among the solvents studied, should demonstrate the highest cellulose solvency. However, this solvent has also the highest E_{dim}, and neither elevation of the temperature nor addition of water allows reduction of E_h to the desired value. It is not unlikely that some additional conditions are necessary for TMAO to provide decrease in E_{dim}.

3. AMIDE/LiCl NONAQUEOUS SOLVENT SYSTEMS

Like tertiary amine *N*-oxides, some nonaqueous solvent systems containing an aprotic solvent and LiCl can directly dissolve underivatized cellulose. The interest in such systems is initiated by the possibility of dissolution of synthetic and natural polymers other than cellulose, to obtain highly concentrated solutions convenient for formation of fibers and films.

Initially, the system dimethylacetamide (DMAA)–LiCl was employed for dissolution of proteins [62], amides [63], and chitin [64, 65]. Then, McCormic *et al*. [66] have demonstrated that DMAA–LiCl can dissolve cellulose with formation of concentrated solutions containing mesomorphic phases. Among a great number of nonaqueous salt-containing systems, only certain amides with addition of LiCl dissolve cellulose. These are DMAA, methylpyrrolidone, and hexamethylphosphoric triamide [17, 62, 67, 68]. Recent studies [69, 70] revealed that cellulose is soluble also in a series of other LiCl-containing nonaqueous systems.

Tsygankova *et al*. [71] performed quantum chemical study of the DMAA–LiCl system, including the electronic structure and geometry of the $(DMAA)_n \cdot LiCl$ complexes. They found that, at n = 3, a high negative charge is localized on the Cl^- ion of the molecular complex formed, increasing the tendency to hydrogen bonding with organic hydroxy compounds via the chloride ion.

By now, researchers offered seven mechanisms for dissolution of cellulose in the DMAA–LiCl system [10, 13, 64, 66, 69, 72]. Several authors [62, 66, 72] believe that cellulose interacts with the DMAA–LiCl complexes in which LiCl occurs in the ionic form. The thought of other authors [64, 67, 69] is that lithium chloride is in the molecular form. Yakimanskii *et al*. [73] analyzed the electronic structure of DMAA and DMF complexes with both ionic and molecular LiCl using MNDO calculations. The system DMF–LiCl, which does not dissolve cellulose under the same conditions, was selected as a reference.

Analysis of the electronic structure parameters (charge distribution, bonding energy, and dipole moments) of the complexes with LiCl in the molecular form revealed no significant differences between the corresponding parameters of the two systems, which could account for the lack of solubility in the DMF–LiCl system.

For the complexes with ionic LiCl, dissociation of LiCl in the amides should be taken into account [Eqs. (2) and (3)]. Assuming that the complexes interact with cellulose via Cl^- ion, the difference in the cellulose solvency of the systems should be attributed to the different dissociation energies (E_d).

$$DMAA \cdots LiCl \rightleftarrows [DMAA \cdots Li]^+ + Cl^-, \quad (2)$$

$$DMF \cdots LiCl \rightleftarrows [DMF \cdots Li]^+ + Cl^-. \quad (3)$$

MNDO calculations with full optimization of the geometry of the ionic complexes $[DMAA \cdots Li]^+Cl^-$ and $[DMF \cdots Li]^+Cl^-$ were performed. The E_d for reaction (2) appeared to be lower by 23.0 kJ mol^{-1} as compared to (3), i.e., LiCl more readily dissociates in DMAA. Comparison of the estimated bonding energies between water molecules and the resulting cations $[DMAA \cdots Li]^+$ and $[DMF \cdots Li]^+$ showed that they are similar, being 110.0 and 113.3 kJ mol^{-1}, respectively.

At the same LiCl concentrations in the amide solutions, the amount of reactive cations $[amide \cdots Li]^+$ will be considerably higher in DMAA, which, evidently, is responsible for the ability of the DMAA–LiCl system to dissolve cellulose [69]. This analysis

is supported by the results reported in [74], demonstrating that cellulose dissolves in both the DMAA–LiCl and DMF–LiCl systems. However, in the case of the latter system, dissolution requires activation of cellulose with liquid ammonia.

The established correlation between the cellulose solvency of the nonaqueous amide–LiCl systems and the degree of dissociation of LiCl in them confirms the concept that dissolution of cellulose proceeds through interaction with the complex amide···LiCl in which the salt occurs in the ionic form.

4. EFFECT OF PHYSICOCHEMICAL MODIFICATION ON HYDROGEN BONDING IN CELLULOSE

Solubility of cellulose in technology-relevant solvents can be realized through a decrease in its cohesion energy by virtue of weakening of the hydrogen bonding. Dissolution of cellulose in the cuprammonium solvent followed by precipitation changes the crystallinity index of the polymer [75]. Regenerated cellulose with a low crystallinity index is soluble in aqueous NaOH. The solubility considerably decreases with increasing molecular weight. Any cellulose polymorph can be fully dissolved in 5% NaOH, as demonstrated with 2% cellulose solutions [76].

The effect of modification of the system of hydrogen bonds in cellulose by steam explosion on its solubility in 9% alkali was studied in [77–80]. In these works, cellulose of various origins and polymorphs (CI, CII, and CIII) with different MWs and crystallinity indices was studied. Treatment by steam explosion produces degradation of cellulose macromolecules and partial break of intra- and interchain hydrogen bonds. The solubility of cellulose in aqueous alkali increases as MW decreases and hydrogen bonds (primarily intrachain bonds $O^5\cdots HO^{3'}$ and $O\text{–}H^2\cdots O^{6'}\text{–}H$) break. From cellulose thus treated, 4–5% solutions can be obtained, suitable for fiber formation [81].

However, this process for rayon production has not found wide use. In our opinion, the major drawbacks are low degree of polymerization ($DP < 400$) and low concentration of the resulting cellulose solutions (4–5%).

The hydrazine process for preparation of cellulose solutions [12] may also be classified with the processes based on partial breaking of hydrogen bonds in the polymer through physical impact. It is known that a series of amines, among them hydrazine, at atmospheric pressure form high-molecular-weight inclusion compounds with cellulose [82]. True solutions of cellulose can be obtained by heating the polymer in hydrazine at 100–200°C and a pressure of up to 0.7 MPa (7.0 atm). Evidently, elevated pressure modifies both the system of hydrogen bonds in cellulose and physicochemical properties of the solvent.

5. CHEMICAL MODIFICATION OF CELLULOSE

Introduction of new functional groups into cellulose macromolecules modifies the initial system of hydrogen bonds, distorts the regular arrangement of cellulose chains, and changes the supramolecular structure of the polymer toward a decrease in the macrochain ordering.

It is known [83] that a series of cellulose derivatives, viz., methyl cellulose, ethyl hydroxyethyl cellulose, hydroxyethyl cellulose, hydroxypropyl cellulose, hydroxypropyl methyl cellulose, methyl ethyl cellulose, and carboxymethyl cellulose sodium salt dissolve in water, the convenient solvent from the technological standpoint. The indicated cellulose derivatives are widely used as gelling agents, thickeners, stabilizers, and emulsifiers in food industry [1].

Introduction of the acetate groups within a rather narrow DS range from 0.4 to 1.0 makes cellulose water-soluble [84–86]. A necessary condition of solubility of cellulose acetate (CA) in water is a regular distribution of the substituents along the macrochains and in the anhydroglucose units [40, 86, 87]. Therefore, it appears advisable to analyze factors influencing the solubility of cellulose derivatives with an example of CA.

In [88] we reported the results of a comparative study of interaction of cellulose and CA of various DS with water, ethanol, and chloroform, aimed at elucidation of the effect of modification of the system of hydrogen bonds, produced in cellulose by introduction of the acetate groups, on the thermodynamic affinity of the polymers for water.

Introduction of the acetate groups into cellulose increases the difference in the surface energy γ of the polymer and a solvent, i.e., promotes hydrophobization of the polymer, thus making worse the wettability of the polymer with water and hindering the diffusion of the solvent to the polymer matrix. With further increasing DS, the difference in γ between the polymer and a solvent becomes so large that cellulose triacetate does not longer dissolve in water. It is the increase in the hydrophobicity of the polymer that determines

the DS upper limit in water-soluble cellulose acetates of 1.0.

In [88] we demonstrated that the solubility of CA in water is realized within the DS range in which δ of the polymer is equal to or lower than δ of a solvent. In this range, the polymer–solvent interaction parameter χ_1 is minimal. To obtain water-soluble CA, it is necessary to decrease the contribution of hydrogen bonding to the cohesion energy, which was dominant in the initial cellulose. Introduction of small amounts of the acetate groups (on the condition of their regular distribution in the macromolecular chains and glucose units) significantly modifies the system of hydrogen bonds typical of the initial cellulose toward a decrease in the amount and energy of these bonds, which predetermines the phenomenon of solubility in water. Further increase in the content of acetate groups is accompanied by increasing difference in the surface tension between the polymer and the solvent (hydrophobization of the polymer), resulting in the loss of solubility. Cellulose propionates obtained by a similar process are insoluble in water because of a stronger increase in their hydrophobicity [1]. Therefore, the solubility of CA in water is a result of modification of the initial system of hydrogen bonds toward a decrease in their energy and amount (supramolecular level) and also of a change in the hydrophilic–hydrophobic balance of the macromolecules (molecular level) [88].

Processes of cellulose dissolution through chemical modification include those with mineral or organic acids as solvents. In acid solutions, derivatization of cellulose occurs with formation of soluble products. Among the acid solvents are nonaqueous systems with formic acid (cellulose formate is formed as a soluble product), trifluoroacetic acid (cellulose trifluoroacetate), DMF–N_2O_4, DMF–SO_3, dimethyl sulfoxide–paraformaldehyde, and also concentrated mineral acids [7, 8].

CONCLUSION

Analysis of the literature shows that the presence of hydrogen bonds with an energy of up to 25.0 kJ mol^{-1} in cellulose strongly confines the range of solvents for this polymer. Therefore, it is rational to search for new solvent systems for cellulose in at least two directions. The first one is search for solvents capable of forming hydrogen bonds with an energy above 25 kJ mol^{-1}, taking into account that strongly polar solvents tend to association, as was demonstrated with an example of tertiary amine *N*-oxides. In nonaqueous mixed solvent systems (amide + LiCl), the solubility of cellulose is controlled by the amount of reactive cations formed and also by the polymer preactivation conditions.

Another line is to decrease the energy of hydrogen bonds in cellulose by physicochemical or chemical modification.

REFERENCES

1. Petropavlovskii, G.A., *Gidrofil'nye chastichno zameshchennye efiry tsellyulozy i ikh modifikatsiya putem khimicheskogo sshivaniya* (Hydrophilic Partially Substituted Cellulose Ethers and Esters and Their Modification by Chemical Cross-Linking), Leningrad: Nauka, 1988.
2. Papkov, S.P., *Polimernye voloknistye materialy* (Polymeric Fibrous Materials), Moscow: Khimiya, 1986.
3. Papkov, S.P. and Kulichikhin, V.G., *Khim. Volokna*, 1981, no. 2, pp. 29–33.
4. Serkov, A.G., *Viskoznye volokna* (Viscose Fibers), Moscow: Khimiya, 1981.
5. Papkov, S.P., *Khim. Volokna*, 1991, no. 2, pp. 30–32.
6. Papkov, S.P., *Khim. Volokna*, 1993, no. 2, pp. 43–46.
7. Hudson, S.M. and Cuculo, J.A., *J. Macromol. Sci., Ser. C: Rev. Macromol. Chem.*, 1980, vol. 187, no. 1, pp. 1–82.
8. Mancier, D. and Vincendon, M., *Bull. Soc. Chim. Fr.*, 1981, vol. 2, nos. 7–8, pp. 319–327.
9. Turbac, A.F., Hammer, R.B., Davies, R.E., *et al.*, *Chem. Technol.*, 1980, vol. 10, pp. 51–57.
10. Philipp, B., *Polym. News*, 1990, vol. 15, no. 6, pp. 170–175.
11. Philipp, B., *J. Macromol. Sci., Ser. A: Pure Appl. Chem.*, 1993, vol. 30, nos. 9–10, pp. 703–714.
12. Grinshpan, D.D., *Nevodnye rastvoriteli tsellyulozy* (Nonaqueous Solvents for Cellulose), Minsk: Bel. Gos. Univ., 1991.
13. Gagnaire, D., Saint-German, J., and Vincendon, M., *J. Appl. Polym. Sci., Appl. Polym. Symp.*, 1983, vol. 37, pp. 261–275.
14. Marriman, H.J. and Mann, J., *J. Appl. Chem.*, 1954, vol. 4, pp. 204–211.
15. Marriman, H.J. and Mann, J., *J. Polym. Sci.*, 1956, vol. 21, pp. 301–311.
16. O'Connor, R.T., DuPre, E.F., and McCall, E.R., *Text. Res. J.*, 1958, vol. 28, pp. 382–392.
17. Tsubui, M., *J. Polym. Sci.*, 1957, vol. 25, pp. 159–171.
18. Liang, C.Y. and Marchessault, R.T., *J. Polym. Sci.*, 1959, vol. 37, pp. 385–395.

19. Zhbankov, R.G., *Infrakrasnye spektry tsellyulozy i ee proizvodnykh* (Infrared Spectra of Cellulose and Its Derivatives), Minsk: Nauka i Tekhnika, 1964.
20. Zhbankov, R.G. and Kozlov, P.V., *Fizika tsellyulozy i ee proizvodnykh* (Physics of Cellulose and Its Derivatives), Minsk: Nauka i Tekhnika, 1983.
21. Michell, A., *Carbohydr. Res*., 1990, vol. 197, pp. 53–60.
22. Fengel, D., *Holzforschung*, 1992, vol. 46, no. 4, pp. 283–288.
23. Kondo, T., *Cellulose*, 1997, vol. 4, no. 4, pp. 281–292.
24. Hinterstoisser, B. and Salmen, L., *Cellulose*, 1999, vol. 6, no. 3, pp. 251–263.
25. Michell, A.L. and Higgins, H.G., *Cellulose*, 1999, vol. 6, no. 1, pp. 89–91.
26. Sarko, A. and Muggli, R., *Macromolecules*, 1974, vol. 7, no. 4, pp. 486–494.
27. Sarko, A., Southwick, T., and Haysay, J., *Macromolecules*, 1976, vol. 9, no. 5, pp. 857–863.
28. Gardner, K.H. and Blackwell, J., *Biopolymers*, 1974, vol. 13, pp. 1975–2001.
29. Karyakin, A.V. and Kriventsova, G.A., *Sostoyanie vody v organicheskikh i neorganicheskikh soedineniyakh* (State of Water in Organic and Inorganic Compounds), Moscow: Nauka, 1973.
30. Naimark, N.I., Kosobutskaya, A.A., and Tarakanov, O.G., *Zh. Prikl. Khim.*, 1984, vol. 57, no. 7, pp. 1588–1591.
31. Hildebrand, J. and Scott, R., *The Solubility of Nonelectrolytes*, New York: Reinhold, 1949.
32. Thode, E.F. and Guide, R.G., *TAPPI J*., 1959, vol. 42, no. 1, pp. 35–39.
33. Askadskii, A.A., Bolobova, A.V., Kondrashchenko, V.I., *et al*., *Vysokomol. Soedin., Ser. A*, 2000, vol. 42, no. 3, pp. 517–529.
34. Salmen, N.L. and Back, E.L., *TAPPI J*., 1977, vol. 60, no. 12, pp. 137–140.
35. Berger, W. and Keck, M., *Cellulose Sources and Exploitation: Industrial Utilization, Biotechnology, and Physicochemical Properties*, Kennedy, J.F., Phillips, G.O., and Williams, P.O., Eds., London: Ellis Horwood, 1990, pp. 69–78.
36. Bochek, A.M. and Petropavlovsky, G.A., *Cellulose Chem. Technol*., 1993, vol. 27, no. 6, pp. 587–596.
37. Bochek, A.M., Solutions of Cellulose and Its Derivatives in Nonaqueous Solvents and Films on Their Basis, *Doctoral Dissertation*, St. Petersburg, 2002.
38. Hansen, Ch.M., *J. Paint Technol*., 1967, vol. 39, no. 505, pp. 104–117.
39. Hansen, Ch.M. and Skaarup, K., *J. Paint Technol*., vol. 39, no. 511, pp. 511–514.
40. Malm, C.J., Barkey, K.T., Salo, M., *et al*., *Ind. Eng. Chem*., 1957, vol. 49, no. 1, pp. 79–83.
41. Myagkova, N.V., Effect of the Degree of Substitution on the Hydrodynamic and Thermodynamic Properties of Cellulose Acetate Solutions, *Cand. Sci. Dissertation*, Tashkent, 1988.
42. Sugiyama, J., Persson, J., and Chanzy, H., *Macromolecules*, 1991, vol. 24, no. 9, pp. 2461–2466.
43. US Patent 2179181.
44. UK Patent 1144048.
45. US Patent 3447939.
46. FR Patent 2423559.
47. US Patent 4196282.
48. Armstrong, R.H., Varga, J.K., and McCorsley, C.C., *TAPPI Conf. Papers, 5th Int. Conf. on Dissolving Pulp*, Wien, 1980, pp. 100–104.
49. Golova, L.K., Kulichikhin, V.G., and Papkov, S.P., *Vysokomol. Soedin., Ser. A*, 1986, vol. 28, no. 9, pp. 1795–1809.
50. Kulichikhin, V.G., Golova, L.K., Kruchinin, N.P., *et al*., *Preprints of IV Int. Symp. on Chemical Fibers*, Kalinin (Russia), 1986, vol. 2, pp. 200–205.
51. Philipp, B., Schleicher, H., and Wagenknecht, W., *Cellulose Chem. Technol*., 1975, vol. 9, pp. 265–282.
52. Tsvetkov, V.G., in *Termodinamika organicheskikh soedinenii: Mezhvuzovskii sbornik* (Thermodynamics of Organic Compound: Intercollegiate Collection), Gor'kii, 1986, pp. 85–93.
53. Rodnikova, M.N., Tsvetkov, V.G., and Dudnikova, K.T., Abstracts of Papers, *IV Vsesoyuznaya konferentsiya po termodinamike organicheskikh soedinenii* (IV All-Union Conf. on Thermodynamics of Organic Compounds), Kuibyshev, 1985, p. 202.
54. Abakshin, V.A., Eliseeva, O.V., Krasnoperova, A.P., *et al*., *Dokl. Akad. Nauk SSSR*, 1991, vol. 317, no. 5, pp. 1140–1143.
55. Tsygankova, N.G., Bubel', O.N., Grinshpan, D.D., *et al*., *Vestsi Akad. Navuk Bel. SSR, Ser. Khim. Navuk*, 1988, no. 5, pp. 35–37.
56. Yakimanskii, A.V., Bochek, A.M., Zubkov, V.A., *et al*., *Zh. Prikl. Khim*., 1991, vol. 64, no. 3, pp. 622–626.
57. Bochek, A.M., Petropavlovsky, G.A., and Yakimansky, A.V., *Cellulose and Cellulose Derivatives: Physico-Chemical Aspects and Industrial Applications*, Kennedy, J.F., Phillips, G.O., Williams, P.O., and Piculell, L., Eds., Cambridge: Woodhead, 1995, pp. 131–137.
58. Maia, E.R., Peguy, A., and Perez, S., *Acta Crystallogr*., 1981, vol. 37, pp. 1858–1862.
59. Ivanov, A.V., Shmakov, V.A., Tsvetkov, V.G., *et al*., *Izv. Vyssh. Uchebn. Zaved., Khim. Khim. Tekhnol*., 1992, vol. 35, no. 2, pp. 58–62.

60. Novoselov, N.P., Sashina, E.S., Khanin, V.A., *et al*., *Zh. Prikl. Khim*., 1999, vol. 72, no. 3, pp. 500–504.
61. Novoselov, N.P., Sashina, E.S., Tager, E., *et al*., *Zh. Prikl. Khim*., 1999, vol. 72, no. 7, pp. 1192–1194.
62. Dawsey, T.R. and McCormick, C.L., *J. Macromol. Sci. Rev., Ser. C: Macromol. Chem. Phys*., 1990, vol. 30, nos. 3–4, pp. 405–440.
63. Panar, M. and Bester, L.E., *Macromolecules*, 1977, vol. 10, no. 6, pp. 1401–1406.
64. Vincendon, M., *Makromol. Chem*., 1985, vol. 186, pp. 1787–1795.
65. Terbojevich, M., Carraro, C., and Cosani, A., *Carbohydr. Res*., 1988, vol. 180, no. 1, pp. 73–86.
66. McCormick, C.L., Callais, P.A., and Hutchinson, B.H., *Macromolecules*, 1985, vol. 18, no. 12, pp. 2394–2401.
67. Nels, I., Wagenknecht, W., Philipp, B., and Stschebina, D., *Prog. Polym. Sci*., 1994, vol. 19, pp. 29–78.
68. Pratsenko, V.E., Bil'dyukevich, A.V., Kaputskii, F.H., *et al*., *Khim. Volokna*, 1989, no. 2, pp. 10–11.
69. Herlinger, H. and Hirt, P., *Chemiefas. Textilind*., 1987, vols. 37/38, pp. 778–792.
70. Takaragi, A., Minoda, M., Miyamoto, T., *et al*., *Cellulose*, 1999, vol. 6, no. 2, pp. 93–102.
71. Tsygankova, N.G., Grinshpan, D.D., and Koren, A.O., *Cellulose Chem. Technol*., 1996, vol. 30, nos. 5–6, pp. 353–357.
72. El-Kafrawy, A., *J. Appl. Polym. Sci*., 1982, vol. 27, no. 7, pp. 2435–2443.
73. Yakimanskii, A.V., Bochek, A.M., Zubkov, V.A., *et al*., *Zh. Prikl. Khim*., 1993, vol. 66, no. 12, pp. 2829–2832.
74. Morgenstern, B. and Berger, W., *Acta Polym*., 1993, vol. 44, no. 2, pp. 100–102.
75. Kamide, K., Okajima, K., Matsui, T., *et al*., *Polym. J*., 1984, vol. 16, no. 12, pp. 857–866.
76. Isogai, A. and Atalla, R.H., *Cellulose*, 1998, vol. 5, pp. 309–319.
77. Yamashiki, T., Matsui, T., Saitoh, M., *et al*., *Brit. Polym. J*., 1990, vol. 22, no. 1, pp. 73–83.
78. Yamashiki, T., Matsui, T., Saitoh, M., *et al*., *Brit. Polym. J*., 1990, vol. 22, no. 2, pp. 121–128.
79. Yamashiki, T., Matsui, T., Saitoh, M., *et al*., *Brit. Polym. J*., 1990, vol. 22, no. 3, pp. 201–212.
80. Kamide, K., Okajima, K., and Kowsaka, K., *Polym. J*., 1992, vol. 24, no. 1, pp. 71–86.
81. Yamashiki, T., Matsui, T., Kowsaka, K., *et al*., *J. Appl. Polym. Sci*., 1992, vol. 44, no. 4, pp. 691–698.
82. Goikhman, A.Sh. and Solomko, V.P., *Vysokomolekulyarnye soedineniya vklyucheniya* (Macromolecular Inclusion Compounds), Kiev: Naukova Dumka, 1982.
83. Hofman, A.S., *Polymer Gels, Fundamentals and Biomedical Applications*, Rossi, D. de, Kajivara, K., Osada, Y., and Yamaushi, A., Eds. *(Proc. Int. Symp. on Polymer Gels, Tsukuda-shi (Japan), September 18–21, 1989)*, New York: Plenum, 1991, pp. 289–298.
84. Rakhmanberdyev, G., Petropavlovskii, G.A., and Usmanov, Kh.U., *Cellulose Chem. Technol*., 1978, vol. 12, no. 2, pp. 153–176.
85. Miyamoto, T., Sato, Y., Shibata, T., *et al*., *J. Polym. Sci., Polym. Chem. Ed*., 1985, vol. 23, no. 5, pp. 1373–1381.
86. Kamide, K., Okajima, K., and Kowsaka, K., *Polym. J*., 1987, vol. 19, no. 12, pp. 1404–1412.
87. Rakhmanberdyev, G., Water-Soluble Acetyl Cellulose, *Cand. Sci. Dissertation*, Leningrad, 1968.
88. Bochek, A.M. and Kalyuzhnaya, L.M., *Zh. Prikl. Khim*., 2002, vol. 75, no. 6, pp. 1007–1011.

Russian Journal of Applied Chemistry, Vol. 76, No. 11, 2003, pp. 1720–1723. Translated from Zhurnal Prikladnoi Khimii, Vol. 76, No. 11, 2003, pp. 1771–1774.

INORGANIC SYNTHESIS AND INDUSTRIAL INORGANIC CHEMISTRY

Processing of Precipitates of Hydrated Tantalum(V), Niobium(V), and Titanium(IV) Oxides in Loparite Technology

V. G. Maiorov, A. I. Nikolaev, and V. K. Kopkov

Tananaev Institute of Chemistry and Technology of Rare Elements and Mineral Raw Materials, Kola Scientific Center, Russian Academy of Sciences, Apatity, Murmansk oblast, Russia

Received June 6, 2003

Abstract—Conditions were studied for the dissolution in HF of hydrated tantalum(V), niobium(V), and titanium(IV) oxides, which are formed by acid decomposition of loparite, and also for the selective extraction of Ta(V) with octanol from the resulting fluotitanic solutions.

One of the largest sources of titanum–rare metal raw materials in Russia, Lovozero deposit of loparite ores, is located on the Kola peninsula. As compared to conventional raw materials used abroad (pyrochlore, tantalite, columbite, etc.), rare-earth titanoniobate loparite is a lean rare-metal raw material, but at the same time it contains several valuable components: tantalum(V), niobium(V), titanium(IV), and rare earths(III). After dressing, the loparite concentrate contains (wt %) Ta_2O_5 0.60–0.65, Nb_2O_5 7–8, TiO_2 38–40, and Ln_2O_3 30–32 [1].

Growth of the production of loparite concentrate not only makes it possible to meet the demands of the existing and future applications of rare and rare-earth elements, but also allows the export of these elements. Because of the complex composition of loparite, problems arise with the separation of its useful components and their recovery as commercial products. An efficient direction in loparite processing is its acid decomposition with HNO_3 or HCl [2, 3]; in the process, rare earths(III), strontium(II), calcium(II), and other components pass into solution, whereas tantalum(V), niobium(V), and titanium(IV) are concentrated in the precipitated hydrate cake (HC) as hydrated oxides. The hydrate cake is dissolved in hydrofluoric acid with the subsequent extractive separation of tantalum(V), niobium(V), and titanium(IV) [4–7]. Hydrofluoric acid can be practically completely regenerated by pyrohydrolysis with simultaneous formation of metal oxides; the regenerated HF is recycled to the HC dissolution [2].

This work was mainly focused on HC dissolution in hydrofluoric acid with the aim to minimize HF consumption and to obtain solutions with high contents of target components, and also on the search for conditions of tantalum(V) selective extraction from the acid fluoride solution. The composition of the examined HC samples after nitric acid (HNO_3) and hydrochloric acid (HCl) breakdown is given in Table 1. Hydrate cakes were obtained in the trials of the corresponding processes [3, 8]. The presence of rare earths(III) in HC(HNO_3) results from the presence of non-decomposed loparite.

A 50-g sample was placed in a beaker equipped with a stirrer and a lid (all fluoroplastic) and filled with an HF solution (400 g l^{-1}) preheated to a specified temperature. The amount of HF corresponding to the reaction stoichiometry was calculated assuming formation of $HTaF_6$, $HNbF_6$, H_2TiOF_4, H_2SiF_6, and LnF_3 (according to [4, 9], these compounds dominate in the system under study). The dissolution was carried out in a thermostat at 20 ± 1 or 50 ± 1°C for 6 h. After filtration, the precipitate was washed with water by repulping at s : l ≈ 1 : 5, filtered off, and dried at approximately 100°C. The procedures for extraction of Ta(V) and Nb(V) from fluoride solutions and for analytical control are given in [4].

Figures 1 and 2 show that decomposition of HC(HNO_3) involves a greater amount of HF than the

Table 1. Composition of HC after loparite acid decomposition

Cake	Content, wt %				
	Ta_2O_5	Nb_2O_5	TiO_2	Ln_2O_3	SiO_2
HC(HNO_3)	0.77	10.2	51.6	5.8	2.2
HC(HCl)	0.50	8.4	63.6	–	–

1070-4272/03/7611-1720$25.00

dissolution of HC(HCl). This is apparently due to the presence of a loparite impurity in HC(HNO_3) and, as a consequence, to the formation of a precipitate of fluorides of rare-earth elements, which hampers the dissolution of hydrated oxides of rare metals in HF. Unchanged loparite can be fairly easily separated by hydroclassification [2], which will allow the consumption of HF for the decomposition of HC(HNO_3) to be reduced.

In dissolution of the two kinds of HC at HF deficiency, titanium(IV) behaves differently. According to X-ray phase analysis, HC contains an impurity TiO_2-rutile phase, and its content in HC(HCl) is higher than in HC(HNO_3). As rutile relatively difficultly dissolves in HF, the passing of the elements into the liquid phase in the course of HC(HNO_3) decomposition decreases in the order Ti(IV) > Ta(V) ≥ Nb(V), and for HC(HCl), in the order Ta(V) > Nb(V) ≥ Ti(IV).

It is interesting that, at 20°C, rare elements are recovered into solution from HC(HCl) at a low HF consumption better than at 50°C. Presumably, under the conditions of HF deficiency and of heating, Ta(V), Nb(V), and Ti(IV) fluorides are hydrolyzed to give poorly soluble oxofluorides. When the HF amount exceeds that required by the stoichiometry, which ensures sufficiently high content of free HF in the solution, the recovery of the elements into the liquid phase at 50°C is higher than at 20°C.

The behavior of Ta(V), Nb(V), and Ti(IV) during the dissolution of HC should be studied additionally. However, it should be noted that the above-mentioned features of the distribution of rare elements between the solid and liquid phases are observed only under conditions of HF deficiency. With large amounts of HF, ensuring virtually complete recovery of the target components into the liquid phase, which is of the greatest interest for technology, the difference in the distribution of Ta(V), Nb(V), and Ti(IV) is leveled out, and their behavior becomes similar.

Thus, we recommend to dissolve HC(HNO_3) and HC(HCl) at approximately 50°C, with the amount of HF being 130 and 115% of the stoichiometric amount, respectively. The solutions obtained under these conditions (with 400 g l^{-1} HF) contain (g l^{-1}) TiO_2 200–250, HF 320–340, and HF_{free} 50–75; hereinafter HF_{free} is the calculated content of HF in excess of that required for the formation of $HTaF_6$, $HNbF_6$, H_2TiOF_4, and H_2SiF_6. Tantalum(V) and niobium(V) can be most efficiently recovered from the fluotitanic solutions by extraction. In this case there is no need to add sulfuric or another inorganic acid into the system to improve the extraction and separation of tantalum(V) and niobium(V) [9], as the necessary acidity is provided by the formation of tetrafluorooxotitanic acid H_2TiOF_4 in the system [4–7].

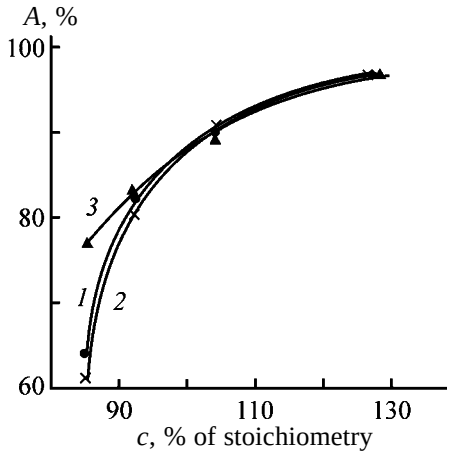

Fig. 1. Influence of HF amount taken *c* on the recovery *A* of (*1*) Ta(V), (*2*) Nb(V), and (*3*) Ti(IV) into the liquid phase from HC(HNO_3) at 50°C.

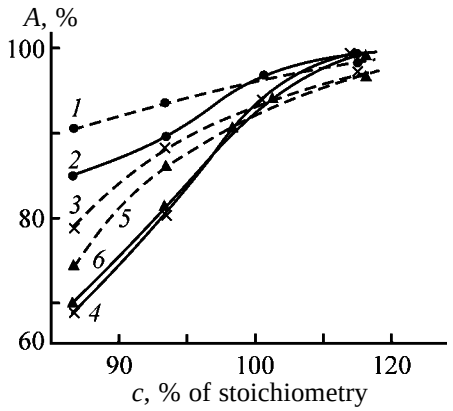

Fig. 2. Influence of HF amount taken *c* on the recovery *A* of (*1, 2*) Ta(V), (*3, 4*) Nb(V), and (*5, 6*) Ti(IV) from HC(HCl) at (*1, 3, 5*) 20 and (*2, 4, 6*) 50°C.

To recover pure tantalum(V) and niobium(V) compounds from fluotitanic solutions, we previously suggested flowsheets based on successive extraction of Ta(V) and Nb(V) with tributyl phosphate (TBP) [4, 5] or on the extraction of the sum of Ta(V) and Nb(V) with 1-octanol (OCL) followed by separation of the target components in the back-extraction stage [6, 7]. The use of OCL as an extractant is preferential, because it is more stable in an acidic medium than TBP [10].

The drawback of the flowsheet involving OCL [6, 7] is the joint extraction of Ta(V) and Nb(V). At the same time, the scheme of successive extraction of Ta(V) and Nb(V) [9] is more convenient both for controlling the process and for ensuring reproducibly high quality of the product. This flowsheet is also

Table 2. Successive extraction of tantalum(V) and niobium(V) by OCL from fluotitanic solutions

Experiment no.	Content in initial solution, g l^{-1}				$V_{org} : V_{aq}$	Recovery, %		
	HF_{free}	Ta_2O_5	Nb_2O_5	TiO_2		Ta(V)	Nb(V)	Ti(V)
1	~75	7.2	106	505	0.3 : 1	92.0	80.0	3.4
2	~75	7.2	106	505	0.5 : 1	97.3	90.7	5.7
3	~75	7.2	106	505	0.7 : 1	98.7	94.4	–
4	~38	7.2	53	252	0.04 : 1	73.1	0.8	–
5	~38	7.2	53	252	0.07 : 1	79.6	4.8	0.17
6	~38	3.6	53	252	0.10 : 1	89.0	8.1	0.21
7	~38	7.2	53	252	0.17 : 1	94.0	16.4	–
8	100	–	20	200	1.8 : 1	–	73.0	9.0
9	120	–	20	200	2 : 1	–	83.5	7.1
10	180	–	20	200	1 : 1	–	81.8	3.0
11	164	–	86	301	0.5 : 1	–	73.2	–
12	164	–	86	301	0.6 : 1	–	78.8	–
13	175	–	62	328	0.5 : 1	–	84.0	3.2

characterized by smaller flows of the extractant and, correspondingly, by better economical parameters (Table 2).

After HC decomposition with hydrofluoric acid, the solutions were evaporated to the TiO_2 content of about 500 g l^{-1} to reduce flows in the extraction processing stage and to distill off excess HF which can be used for HC dissolution. However, the joint extraction of Ta(V) and Nb(V) from the evaporated solutions still takes place (Table 2, run nos. 1–3), apparently, owing to high content of both HF_{free} and H_2TiOF_4. To reduce the concentration of HF_{free} and to improve the separation of Ta(V) and Nb(V) [9], we used the simplest way of the process control [11], dilution. The twofold dilution resulted in successful selective extraction of Ta(V) (Table 2, run nos. 4–7). Under the best conditions ($V_{org} : V_{aq}$ = 0.1 : 1), 89% of Ta(V) is extracted in a single stage at insignificant recovery of Nb(V) and especially Ti(IV) (about 8 and 0.2%, respectively). With a continuous counterflow process, it is possible to extract Ta(V) virtually completely in 4–5 equilibrium steps and to obtain an extract containing 30–40 g l^{-1} Ta_2O_5.

The addition of HF to the solution from which Ta(V) was removed allows also efficient recovery of Nb(V) at a low Ti(IV) coextraction (Table 2, run nos. 9, 10, 12, and 13). Table 2 shows that an increase in the HF concentration reduces the passing of Ti(IV) into the organic phase, apparently owing to an increase in the relative content of the poorly extracted dibasic acid H_2TiF_6 [6] among fluotitanic acids. However, the drawback of the suggested process for Nb(V) extraction is the necessity of introducing large amounts of HF into the system, which makes worse the economical parameters of the process owing to the additional consumption of the expensive chemical and to an increase in flows of organic and aqueous solutions in the system. A better choice is the repeated evaporation of the solution after Ta(V) recovery to the TiO_2 content of about 500 g l^{-1} and the extraction of Nb(V) at a relatively low ratio $V_{org} : V_{aq}$ = 0.5 : 1 (Table 2, run no. 2) to obtain the extract containing up to 200 g l^{-1} Nb_2O_5. This approach allows realization of a compact process providing a high content of target components in extracts, considerably decreased consumption of chemicals (including the consumption during washing of organic phases), and reduced size of the equipment.

Thus, the data obtained allow us to offer the following principal scheme involving OCL extraction for the processing of solutions from HC decomposition: evaporation of the solution to the TiO_2 content of about 500 g l^{-1}, followed by dilution by a factor of 1.5–2; extraction of Ta(V) at $V_{org} : V_{aq} \approx 0.1 : 1$, evaporation of the aqueous solution to the TiO_2 content of 500 g l^{-1}; extraction of Nb(V) at $V_{org} : V_{aq} \approx 0.5 : 1$; and then pyrohydrolysis of the fluotitanic raffinate to obtain commercial TiO_2 and regenerate HF [2].

Impurities can be efficiently removed from Ta(V) and Nb(V) extracts by washing with fluoride solutions of these elements, aqueous solutions of HF and(or) H_2SO_4, or water, and the purified target components can be back-extracted with water [6, 7, 12, 13].

The conditions of HC dissolution and of Ta(V) and Nb(V) extraction found in this work are also suitable after slight modification for the acid (HNO_3 or HCl) decomposition of another rare-earth titanoniobate, perovskite, a high-grade deposit of which is also located on the Kola peninsula [14].

CONCLUSIONS

(1) The precipitate of hydrated Ta(V), Nb(V), and Ti(V) oxides formed by nitric or hydrochloric acid decomposition of loparite should be dissolved in HF taken in amount of 130 and 115%, respectively, relative to the amount corresponding to the stoichiometry of the formation of fluoride complexes of these elements.

(2) Conditions were found for the successive extraction of Ta(V) and Nb(V) with octanol from fluotitanic solutions to obtain extracts containing 30–40 g l^{-1} Ta_2O_5 and up to 200 g l^{-1} Nb_2O_5.

ACKNOWLEDGMENTS

This work was financially supported by the Russian Foundation for Basic Research (project no. 03-03-96148).

REFERENCES

1. Kudrin, V.S., Rozhanets, A.V., Chistov, L.B., *et al.*, *Tantal Rossii: sostoyanie, perspektivy osvoeniya i razvitiya mineral'no-syr'evoi bazy "Mineral'noe syr'e". Ser. geologo-ekonomicheskaya* (Tantalum of Russia: State and Prospects for Management and Development of the Mineral Raw Material Base "Mineral Raw Materials." Geology-Economical Ser.), Moscow: Russian Institute of Mineral Raw Materials, 1999, no. 4.
2. Sklokin, L.I., Zots, N.V., Shestakov, S.V., *et al.*, *Tsvetn. Met.*, 2000, no. 10, pp. 48–53.
3. Zots, N.V., Kasikova, N.I., Kasikov, A.G., *et al.*, in *Trudy Rossiisko-indiiskogo simpoziuma "Metallurgiya tsvetnykh i redkikh metallov"* (Proc. Russian-Indian Symp. "Metallurgy of Non-Ferrous and Rare Metals"), Moscow, 2002, pp. 10–16.
4. Maiorov, V.G., Nikolaev, A.I., and Kopkov, V.K., *Zh. Prikl. Khim.*, 1999, vol. 72, no. 6, pp. 929–932.
5. Mayorov, V.G. and Nikolaev, A.I., *Hydrometallurgy*, 1996, vol. 41, pp. 71–78.
6. Maiorov, V.G., Nikolaev, A.I., Sklokin, L.I., *et al.*, *Zh. Prikl. Khim.*, 2001, vol. 74, no. 6, pp. 920–923.
7. Mayorov, V.G. and Nikolaev, A.I., *Hydrometallurgy*, 2002, vol. 66, pp. 77–83.
8. Zots, N.V., Shestakov, S.V., and Yurova, L.I., in *Trudy IV nauchnoi konferentsii "Razvitie redkometal'noi promyshlennosti v Rossii na baze loparita"* (Proc. IV Scientific Conf. "Development of Rare-Metal Industry in Russia on the Basis of Loparite"), St. Petersburg, 2001, pp. 104–106.
9. Babkin, A.G., Maiorov, V.G., and Nikolaev, A.I., *Ekstraktsiya niobiya i tantala i drugikh elementov iz ftoridnykh rastvorov* (Extractions of Niobium, Tantalum, and Other Elements from Fluoride Solutions), Leningrad: Nauka, 1988.
10. Maiorov, V.G., Baklanova, I.V., Nikolaev, A.I., and Safonova, L.A., *Zh. Prikl. Khim.*, 2000, vol. 73, no. 10, pp. 1636–1640.
11. Nikolaev, A.I., Maiorov, V.G., and Baklanova, I.V., *Zh. Prikl. Khim.*, 2002, vol. 75, no. 11, pp. 1784–1788.
12. Maiorov, V.G., Nikolaev, A.I., and Kopkov, V.K., *Zh. Prikl. Khim.*, 2001, vol. 74, no. 3, pp. 357–360.
13. Maiorov, V.G., Nikolaev, A.I., and Kopkov, V.K., *Zh. Prikl. Khim.*, 2002, vol. 75, no. 9, pp. 1422–1426.
14. Nikolaev, A.I. and Maiorov, V.G., *Pererabotka netraditsionnogo titanovogo syr'ya Kol'skogo poluostrova* (Processing of Nonconventional Titanium Raw Materials of the Kola Peninsula), Apatity: Kol'sk. Nauchn. Tsentr Ross. Akad. Nauk, 1991.

Russian Journal of Applied Chemistry, Vol. 76, No. 11, 2003, pp. 1724–1727. Translated from Zhurnal Prikladnoi Khimii, Vol. 76, No. 11, 2003, pp. 1775–1778.

INORGANIC SYNTHESIS AND INDUSTRIAL INORGANIC CHEMISTRY

Influence of Conditions of Zinc Selenide Oxidation with Atmospheric Oxygen on the Composition of Volatile Products

E. L. Tikhonova, P. E. Gaivoronskii, Yu. E. Elliev, E. M. Gavrischuk, S. M. Mazavin, and E. V. Yashina

Lobachevsky State University, Nizhni Novgorod, Russia
Institute of Chemistry of High-Purity Substances, Russian Academy of Sciences, Nizhni Novgorod, Russia

Received June 11, 2003

Abstract—The qualitative and quantitative composition of volatile products of zinc selenide oxidation with atmospheric oxygen was determined. The influence of the process conditions on quantitative composition of the volatile products was studied.

Oxidative roasting of ZnSe is one of ways of processing waste from its production. The advantages of this method are that it does not require sophisticated equipment and large amounts of expensive chemicals. However, published data on the oxidation of powders [1–3], polished plates [3, 4], and single crystals [5, 6] of ZnSe are ambiguous [7]. In particular, the composition of volatile products of ZnSe oxidation with oxygen is still unclear.

In this connection, our goal was to determine the quantitative composition of the volatile products of ZnSe oxidation with atmospheric oxygen and also to study how the process conditions affect their ratio. The objects of the study were wastes of ZnSe plates and spent polishing powders of various grain-size distributions from manufacture of optical components for IR engineering from polycrystalline zinc selenide.

EXPERIMENTAL

The oxidation of small (10–30 g) amounts of ZnSe without forced air circulation (installation I) was described in detail in [7].

We developed and manufactured installation II for the oxidation of large (0.5–1.5 kg) amounts of zinc selenide. It includes an inclined tubular quartz reactor of length l = 400 mm and diameter d = 50 mm and three receivers connected by ground-quartz joints. The design of the first receiver allows unloading of the formed product during operation of the installation. Owing to the inclined arrangement of the reactor and receivers, a nonforced steady-state air flow arises when the reactor is heated with a tubular resistance furnace.

Later we developed and manufactured installation III for the oxidation of 400–500 g of zinc selenide in a forced air flow (Fig. 1). The installation includes a quartz reactor (l = 1150, d = 16 mm) and two receivers. The first of them consists of a narrow part (l = 305, d = 20 mm) and a wide part (l = 370, d = 40 mm). The receiver is tightly connected to the reactor by the narrow part, and the wide part serves for collecting volatile products. The second receiver, which has the size of the wide part of the first receiver, is connected to it by ground-quartz joints. The reactor is heated with a tubular resistance furnace. The controllable air flow is created with a compressor; a special unit is arranged at the outlet to keep the flow constant. The flow rate at the reactor outlet was measured at regular intervals with a rotameter. The completeness of the condensation of volatile products was checked at the outlet of the second receiver using a qualitative test for Se(IV) with thiourea according to the technique suggested in [8].

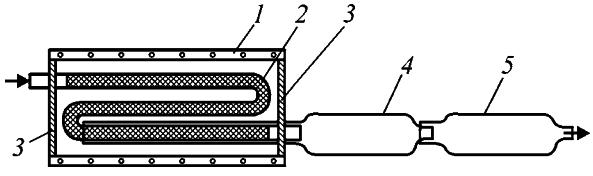

Fig. 1. Installation for the oxidation of zinc selenide in a forced air flow: (*1*) tubular resistance furnace, (*2*) reactor with a substance sample, (*3*) asbestos gasket, and (*4*, *5*) receivers for volatile products.

1070-4272/03/7611-1724$25.00 © 2003 MAIK "Nauka/Interperiodica"

In all experiments, the grain-size distribution of powders was determined by mesh analysis. The temperature was measured accurate to 3% using a preliminarily calibrated chromel–alumel thermocouple. The degree of ZnSe conversion was determined by a gravimetric procedure: a preliminarily weighted reactor with a weighed sample of the substance was taken from the furnace, cooled, and weighed. To analyze volatile oxidation products, the receivers were detached at regular intervals, weighed, and volatile oxidation products were withdrawn.

Volatile oxidation products were qualitatively analyzed by chemical methods. For this purpose, the products were dissolved in distilled water, and the undissolved residue was filtered off. The filtrate was treated with sodium sulfite in a hydrochloric acid medium, hydrogen sulfide, thiourea, and hydrochloric acid solution of tin(II) chloride according to the procedure suggested in [9]. In the case of the first three reagents, a red precipitate of elemental selenium was formed, which suggests the presence of SeO_3^{2-} and SeO_4^{2-} ions in solution. To determine them separately, we used tin(II) chloride, which reacts in solution only with SeO_3^{2-} ions to form a precipitate of elemental selenium at temperatures below 20°C, whereas SeO_4^{2-} ions are reduced to selenium with tin(II) chloride only on boiling the solution. The precipitate after filtration was boiled with a 1.5 M Na_2SO_3 solution, which is, according to [10], a selective solvent for selenium. The treatment of the resulting product (Na_2SeSO_3) with concentrated sulfuric acid yields a red precipitate of elemental selenium. We also used a reaction of the precipitate with cold H_2SO_{4conc}. It reacts with selenium to give a green solution ($SeSO_3$), which also forms a red precipitate of elemental selenium on dilution [11].

To determine the quantitative composition of volatile reaction products, we used a technique developed and described in detail in [12]. It involves dissolution of the weighed product in distilled water, filtration of the precipitate, and its drying and weighing.

The oxidation of zinc selenide in a nonforced air flow was carried out on installation II at 600°C, which was found to be optimal for ZnSe oxidation [7]. The weight of the ZnSe sample was 600 g, and the particle size, 0.6–2.5 mm. The qualitative analysis of volatile products by the above-described technique showed that the precipitate was elemental selenium and the filtrate, solution of H_2SeO_3 formed upon dissolution of the liberated SeO_2 in water. Therefore, the volatile product of ZnSe oxidation with atmospheric oxygen is a mixture of elemental selenium and its dioxide;

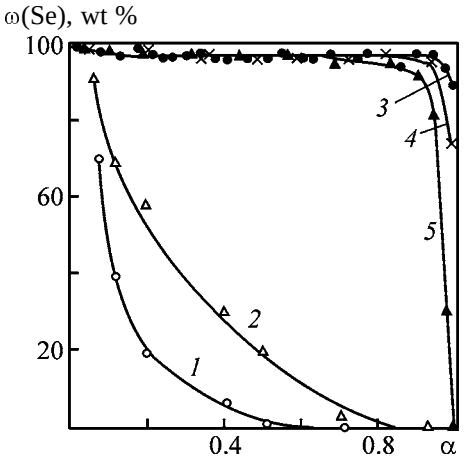

Fig. 2. Content of selenium ω(Se) in volatile products of zinc selenide oxidation with atmospheric oxygen. (α) Degree of ZnSe conversion. Oxidation on installation II in (*1*) nonforced and (*2*) forced air flow; oxidation on installation III at a flow rate (ml min^{-1}) of (*3*) 9.5, (*4*) 40, and (*5*) 110.

their ratio varies in the course of the process (Fig. 2, curve *1*). It was found previously that ZnO is a nonvolatile oxidation product [7]. Thus, we suggest the following equation for the oxidation of zinc selenide:

$$ZnSe + (1/2 + y)O_2 \rightarrow ZnO + xSe + ySeO_2.$$

where the coefficients x and y change during the process ($x + y = 1$).

As seen from Fig. 2, the content of elemental selenium in the products is high, especially in the beginning of the process. It contradicts the previous thermodynamic calculations [7], according to which SeO_2 is the main volatile product of the reaction between ZnSe and atmospheric oxygen. Furthermore, when air is passed through the reactor fully packed with the charge, the content of elemental selenium in the products is even higher (Fig. 2, curve *2*).

To account for this inconsistency, we assumed that, when SeO_2, which is a highly active oxidant, passes through a bed of unchanged ZnSe, the following reaction between these compounds is possible:

$$2ZnSe + SeO_2 \rightarrow 2ZnO + 3Se.$$

We performed a thermodynamic calculation of the system ZnSe–SeO_2 in the temperature range 500–1500 K, which confirmed the possibility of this process. The calculated equilibrium concentrations of the components (mole per total number of moles of the starting compounds) are shown in Fig. 3. It is seen from Fig. 3 that Se_2 is the major volatile product of

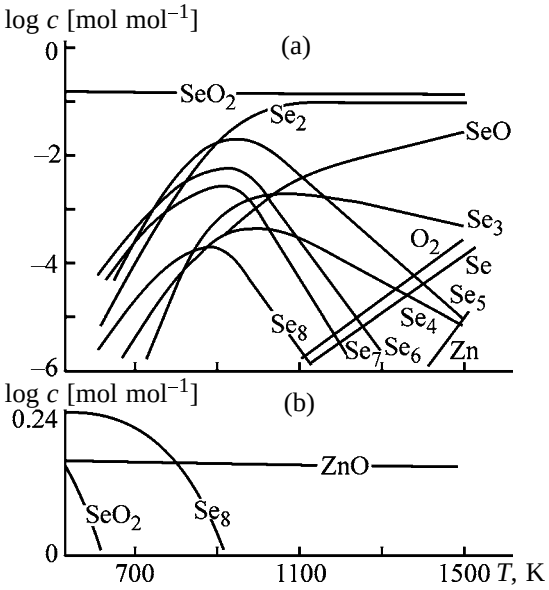

Fig. 3. Temperature dependence of the equilibrium composition of the system ZnSe–SeO_2. (*c*) Equilibrium concentration of a component. Phase: (a) gas and (b) solid.

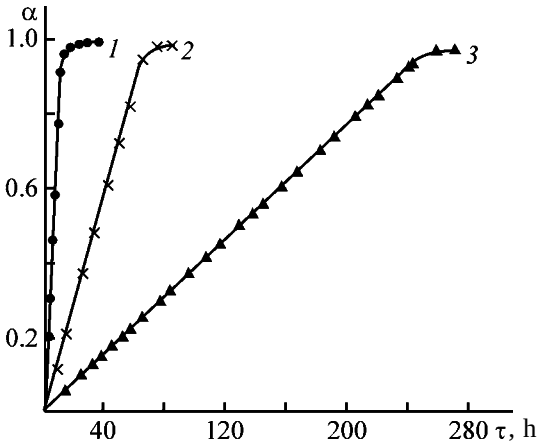

Fig. 4. Kinetic curves of ZnSe oxidation in a forced air flow: (α) degree of zinc selenide conversion and (τ) time; the same for Fig. 5. Flow rate, ml min^{-1}: (*1*) 110, (*2*) 40, and (*3*) 9.5.

the reaction. Its content in the gas phase increases in the range 600–1000 K and does not noticeably change at higher temperatures. The content of condensed selenium is maximal in the range 500–700 K and decreases to zero at 900 K. Therefore, under the conditions ensuring complete reduction of the liberated SeO_2 with ZnSe, with no excess O_2 in the flow, we can expect that the resulting volatile product will consist exclusively of elemental selenium. To check this assumption, we performed experiments on installation III.

The experiments on the oxidation of ZnSe in a forced air flow were carried out at 600°C with particles of the size 2.5–4.5 mm in the range of the air flow rate 9.5–110 ml min^{-1}. When the air flow is passed through the reactor, the oxidation initially occurs in the narrow zone in the beginning of the reactor, which can be visually monitored as a change in the color of the charge from lemon yellow (ZnSe color) to white (ZnO color). In this case, the volatile products pass through a bed of ZnSe not exposed to oxidation and react with it. In time, the length of the white zone increases (and the length of the bed of unchanged ZnSe, correspondingly, decreases), and by the end of the process the whole charge becomes a white powder. The corresponding curves of the zinc selenide conversion vs. time are flattening out straight lines (Fig. 4).

Figure 4 shows that, as the air flow rate increases, the time of complete oxidation substantially decreases, being 260, 66, and 11 h at the flow rates of 9.5, 40, and 110 ml min^{-1}, respectively. We failed to reach complete condensation of SeO_2 for flows with rates higher than 110 ml min^{-1}, at practically complete condensation of elemental selenium. In this case, we can only suggest that the SeO_2 content in the oxidation products is noticeable and also that, starting from 90–95% conversion, the product consists exclusively of SeO_2. At the flow rates of 9.5, 40, and 110 ml min^{-1}, as seen from Fig. 2, curves *3*–*5*, the content of elemental selenium is virtually the same (95–99 wt %). The difference appears only in the final parts of the curves. In this case, an increase in the flow velocity results in incomplete reducton of SeO_2, because the small segment of remaining ZnSe is passed by the flow faster. Furthermore, when the flow rate exceeds 40 ml min^{-1}, excess O_2 starts to exert an effect, namely, starts to oxidize the forming selenium, which results in an increase in the SeO_2 content in the products.

The oxidation conditions can be changed so as to obtain SeO_2 free from elemental selenium. For this purpose, forming elemental selenium should be oxidized. We suggested two oxidation modes: oxidation of the products with atmospheric oxygen at the reactor outlet and introduction of additional oxidizing agents into the air flow. We used HNO_{3conc} as the additional oxidizing agent, placing boats with it into the reactor in front of boats with the ZnSe powder. In these cases, the volatile product was pure SeO_2 containing no elemental selenium. The content of impurities in the resulting product was determined by direct atomic emission spectroscopy. The content of impurities in SeO_2 obtained by "afteroxidation" at the reactor outlet (sample 1) and in the presence of HNO_3 vapor in the flow (sample 2) is given in the table.

Content of impurities in selenium dioxide samples

Sample no.	Impurity content, wt %					
	Mg	Fe	Si	Al	Cu	Zn
1	3×10^{-5}	2×10^{-4}	2×10^{-3}	$<1\times10^{-4}$	3×10^{-5}	$<3\times10^{-4}$
2	3×10^{-5}	2×10^{-4}	3×10^{-4}	2×10^{-5}	1×10^{-5}	3×10^{-3}

Furthermore, we found that HNO_3 vapor accelerates ZnSe oxidation with atmospheric oxygen. The corresponding kinetic curves are shown in Fig. 5.

Figure 5 shows that the time of complete oxidation of ZnSe particles of size 0.6–1.5 mm at 560°C is 180 min in the absence of HNO_3 vapor and 130 min in its presence. In the case of $3.5 \times 2.7 \times 0.4$-mm plates, the time of complete oxidation is 420 and 330 min in the absence and in the presence of the acid vapor, respectively.

CONCLUSIONS

(1) The volatile products of zinc selenide oxidation with atmospheric oxygen are selenium and selenium dioxide, their ratio changing in the course of the process.

(2) Unchanged zinc selenide can react with selenium dioxide to form selenium.

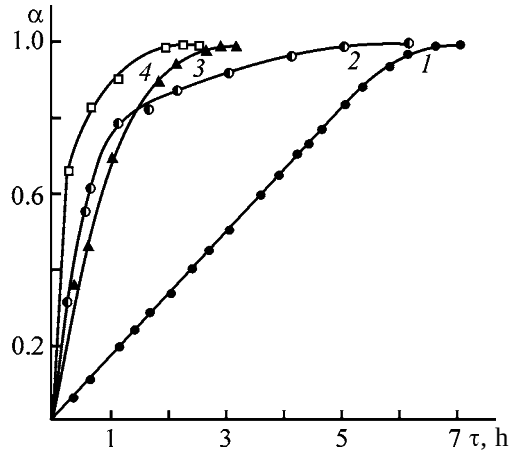

Fig. 5. Kinetic curves of the oxidation of ZnSe powders and plates in a nonforced air flow in the absence and presence of nitric acid vapor. (*1*, *2*) Plates and (*3*, *4*) powders; (*1*, *3*) without HNO_3 and (*2*, *4*) with HNO_3.

(3) Introduction of nitric acid vapor in the flow accelerates ZnSe oxidation and results in the formation of selenium dioxide free from elemental selenium.

REFERENCES

1. Korneeva, I.V. and Novoselova, A.V., *Zh. Neorg. Khim.*, 1960, vol. 5, no. 10, pp. 2265–2268.
2. Pinaev, G.F., Murashkevich, A.N., and Goryaev, V.M., *Izv. Akad. Nauk SSSR, Neorg. Mater.*, 1976, vol. 12, no. 7, pp. 1301–1304.
3. Stepanova, N.D., Kalinkin, I.P., and Sokolov, V.A., *Izv. Akad. Nauk SSSR, Neorg. Mater.*, 1975, vol. 11, no. 6, pp. 1030–1034.
4. Shpil'kin, A.D., Magomedov, Z.A., and Semiletov, S.A., *Izv. Akad. Nauk SSSR, Neorg. Mater.*, 1981, vol. 17, no. 6, pp. 1004–1007.
5. Kulakov, M.P. and Fadeev, A.V., *Izv. Akad. Nauk SSSR, Neorg. Mater.*, 1983, vol. 19, no. 3, pp. 347–351.
6. Gunchenko, N.N., Dronova, G.N., Maksimova, I.A., *et al.*, *Izv. Akad. Nauk SSSR, Neorg. Mater.*, 1988, vol. 24, no. 1, pp. 36–40.
7. Khlopochkina, E.L., Gaivoronskii, P.E., Gavrischuk, E.M., *et al.*, *Zh. Prikl. Khim.*, 2001, vol. 74, no. 7, pp. 1051–1053.
8. Nazarenko, I.I. and Ermakov A.N., *Analiticheskaya khimiya selena i tellura* (Analytical Chemistry of Selenium and Tellurium), Moscow: Nauka, 1971.
9. Buketov, E.A., Moiseevich, O.Yu., and Ugorets, M.Z., *Zavod. Lab.*, 1964, no. 7, pp. 787–788.
10. Filippova, N.A., Martynova, L.A., Savina, E.V., and Kulichikhina, R.D., *Zavod. Lab.*, 1960, vol. 26, no. 4, pp. 401–410.
11. Kudryavtsev, A.A., *Khimiya i tekhnologiya selena i tellura* (Chemistry and Technology of Selenium and Tellurium), Moscow: Metallurgiya, 1968.
12. Gaivoronskii, P.E., Khlopochkina E.L., Elliev, Yu.E., *et al.*, *Vestn. Nizhegorod. Gos. Univ., Khim.*, 1998, no. 1, pp. 8–11.

Russian Journal of Applied Chemistry, Vol. 76, No. 11, 2003, pp. 1728–1733. Translated from Zhurnal Prikladnoi Khimii, Vol. 76, No. 11, 2003, pp. 1779–1784.

PHYSICOCHEMICAL STUDIES OF SYSTEMS AND PROCESSES

Thermodynamic Properties of Liquid Alloys of the System Iron–Nickel–Cobalt

A. G. Morachevskii, L. Sh. Tsemekhman, L. B. Tsymbulov, and N. A. Fedorova

St. Petersburg State Polytechnic University, St. Petersburg, Russia
Gipronikel' Institute, Joint-Stock Company, St. Petersburg, Russia

Received September 9, 2003

Abstract—The integral molar excess Gibbs energy and the enthalpy of mixing of liquid alloys of the ternary system iron–nickel–cobalt at 1600°C were calculated by various methods from data on the boundary binary systems. The data for the boundary binary systems are analyzed in detail.

Calculated thermodynamic properties of liquid alloys of the ternary system Cu–Ni–Fe have been reported previously [1, 2]. Proceeding with studies of liquid metal systems, which are important for thermodynamic analysis of pyrometallurgical processes occurring in nickel production, we calculated in this work the integral molar Gibbs energy and the enthalpy of mixing of liquid alloys of the system Fe–Ni–Co at 1600°C, using different geometric models and analytical approach. The available data on thermodynamic properties of this system are limited. Velišek *et al.* [3] measured the saturated vapor pressure to determine the component activities only at 1227°C, i.e., for alloys in the solid state. In [4], a Knudsen cell and a mass spectrometer were used to determine the activity of each of the components of the ternary system within 1200–1650°C, but the system was studied solely along the section with the component ratio $x_{Fe} : x_{Ni} = 9 : 1$ (where x_i is the mole fraction of component in the alloy). The melt–vapor equilibrium for eight compositions of the ternary system Fe–Ni–Co at 1600°C was studied in [5]. The condensate composition was determined by chemical methods. The obtained data and data for binary systems, subjected to a systematic treatment, were used to obtain the equations reflecting the dependence of the vapor phase composition on the composition of the liquid phase and to calculate the coefficients of the component activity. To our knowledge, there are no other thermodynamic studies of liquid alloys of the system Fe–Ni–Co.

Analysis of the phase diagram of the Fe–Ni–Co system [6] shows that the liquid alloys will exhibit very moderate deviations from ideality. Then, it is necessary to scrutinize the data for the boundary binary systems used in calculation of the thermodynamic characteristics of the ternary system by any model. The thermodynamic properties of liquid alloys of the Fe–Ni system were repeatedly studied; the results are summarized in [1, 7–9]. Although the deviations (negative) from ideality exhibited by the Fe–Ni binary system are moderate, they markedly exceed the deviations in the other boundary systems, Fe–Co and Ni–Co, and are essentially responsible for the deviations in the Fe–Ni–Co ternary system as a whole. The comprehensive information for estimating ΔG^{ex} at 1600°C in the Fe–Ni system is presented in [10–12]. In all the three studies, the Knudsen effusion method combined with mass spectrometry was used. The results of these works agree fairly well with each other (Fig. 1). The ΔG^{ex} values (Table 1) used for calculation were chosen taking into account the recommendations from [7, 9]. The enthalpy of mixing of the Fe–Ni system was estimated using data of [10] and results [13, 14] of calorimetric measurements (Fig. 2). The calculated ΔH values were chosen based on the recommendations from [7].

The thermodynamic properties of liquid alloys of the system Fe–Co have been also repeatedly studied. Early studies are summarized in a monograph [7] and a review [15]. Analysis of the whole set of the data and evaluation of the experimental methods and other investigations suggest that the most reliable ΔG^{ex} values were obtained for the Fe–Co system at 1600°C in [16, 17]. At the same time, for estimating ΔH, we will use the data from [14, 18]. As seen from Table 1, the ΔG^{ex} and ΔH values for the Fe–Co system are of different sign, which is admissible when these thermodynamic functions are low in absolute values and the excess entropy of mixing is negative.

1070-4272/03/7611-1728$25.00

Table 1. Integral molar thermodynamic characteristics of the boundary binary systems at 1600°C

Fe–Ni			Fe–Co			Ni–Co		
x_{Ni}	ΔG^{ex}	ΔH	x_{Co}	ΔG^{ex}	ΔH	x_{Co}	ΔG^{ex}	ΔH
	kJ mol^{-1}			kJ mol^{-1}			kJ mol^{-1}	
0.10	–0.66	–0.95	0.10	0.14	–0.35	0.10	–0.22	0.17
0.20	–1.25	–1.76	0.20	0.40	–0.74	0.20	–0.40	0.30
0.30	–1.80	–2.62	0.30	0.73	–1.10	0.30	–0.52	0.38
0.40	–2.33	–3.53	0.40	1.09	–1.38	0.40	–0.60	0.42
0.50	–2.76	–4.29	0.50	1.35	–1.53	0.50	–0.63	0.42
0.60	–3.02	–4.66	0.60	1.42	–1.54	0.60	–0.61	0.39
0.70	–2.93	–4.41	0.70	1.32	–1.38	0.70	–0.53	0.33
0.80	–2.40	–3.44	0.80	1.06	–1.05	0.80	–0.41	0.24
0.90	–1.41	–1.84	0.90	0.66	–0.59	0.90	–0.23	0.13

The thermodynamic properties of liquid alloys of the system Ni–Co are summarized in [19]. The data obtained by Tomiska *et al*. [20] using the Knudsen effusion method combined with mass spectrometry seem to be the most reliable. According to these data, in the Ni–Co system in the liquid state the activity isotherms of both components exhibit slight deviations from ideality; the Gibbs energy is negative over the entire composition range, passing through a minimum of –0.550 kJ mol^{-1} at x_{Co} = 0.528. The enthalpy of mixing is positive, with the maximal value of 0.425 kJ mol^{-1} at x_{Co} = 0.460 [20]. The ΔH values from [20] are in satisfactory agreement with the Predel and Mohs's calorimetric results [21]. At the same time, in a review [19], with due regard for [22], somewhat lower values were recommended for the enthalpy of mixing: ΔH of about 0.330 kJ mol^{-1} near the equiatomic composition. In calculation of ΔH for the ternary system, we used the data of [20] (Table 1).

In the past two decades, major attention has been paid to application of various calculation procedures to estimation of the thermodynamic properties of ternary and more complex liquid metal systems from data on boundary binary systems [18, 23–27]. Geometric models in which the integral molar properties of a ternary system are calculated using the surface of a relatively simple geometric form have found the widest application. The models can be subdivided into two groups: symmetric and asymmetric. In the first case, nonequivalent participation of the boundary binary systems is laid into the algorithm for calculating the integral property; the calculation result is, to a certain extent, dependent on the component arrangement chosen for the ternary system. In the second case, the component arrangement does not affect the

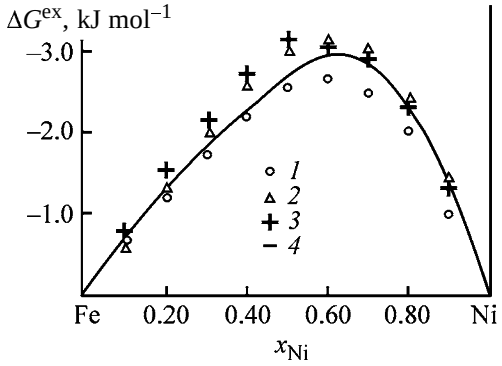

Fig. 1. Integral molar excess Gibbs energy ΔG^{ex} of liquid alloys of the Fe–Ni system vs. composition (x_{Ni}) at 1600°C. Points calculated from data: (*1*) [10], (*2*) [11], and (*3*) [12]; (*4*) values accepted for calculation.

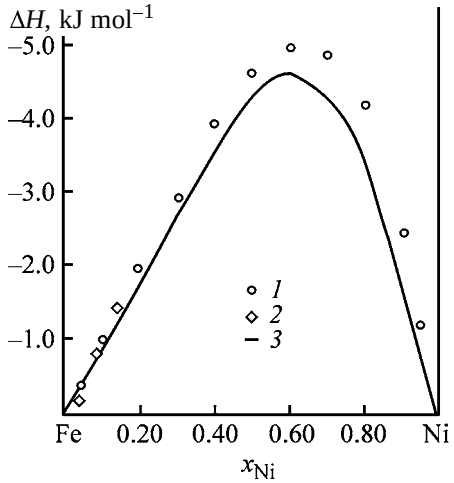

Fig. 2. Integral molar enthalpy of mixing ΔH of liquid alloys of the Fe–Ni system vs. composition (x_{Ni}). Points calculated from data: (*1*) [10] and (*2*) [13]; (*3*) values accepted for calculation.

Table 2. Results of calculation of ΔG^{ex} and ΔH in the Fe–Ni–Co ternary system at 1600°C

x_{Fe}	$x_{Ni} : x_{Co} = 3 : 1$		$x_{Ni} : x_{Co} = 1 : 1$		$x_{Ni} : x_{Co} = 1 : 3$	
	ΔG^{ex}	ΔH	ΔG^{ex}	ΔH	ΔG^{ex}	ΔH
	kJ mol^{-1}					
0.00	–0.47	0.34	–0.63	0.42	–0.47	0.28
0.10	–1.25 ± 0.04	–1.28 ± 0.03	–0.85 ± 0.06	–0.86 ± 0.05	–0.22 ± 0.03	–0.64 ± 0.04
0.20	–1.68 ± 0.13	–2.56 ± 0.05	–0.95 ± 0.06	–1.84 ± 0.10	–0.01 ± 0.05	–1.32 ± 0.07
0.30	–1.86 ± 0.08	–3.30 ± 0.09	–0.90 ± 0.06	–2.40 ± 0.15	0.20 ± 0.03	–1.75 ± 0.12
0.40	–2.03 ± 0.04	–3.49 ± 0.13	–0.92 ± 0.05	–2.57 ± 0.19	0.25 ± 0.06	–1.93 ± 0.14
0.50	–1.82 ± 0.02	–3.24 ± 0.18	–0.80 ± 0.06	–2.44 ± 0.18	0.25 ± 0.03	–1.90 ± 0.13
0.60	–1.55 ± 0.01	–2.72 ± 0.11	–0.71 ± 0.03	–2.12 ± 0.14	0.17 ± 0.01	–1.69 ± 0.09
0.70	–1.22 ± 0.01	–2.08 ± 0.06	–0.61 ± 0.01	–1.68 ± 0.07	0.06 ± 0.01	–1.36 ± 0.05
0.80	–0.86 ± 0.01	–1.45 ± 0.02	–0.44 ± 0.01	–1.18 ± 0.03	–0.02 ± 0.01	–0.95 ± 0.02
0.90	–0.44 ± 0.01	–0.79 ± 0.01	–0.23 ± 0.01	–0.64 ± 0.01	–0.04 ± 0.01	–0.49 ± 0.01

final result. Schematic geometric models are presented in Fig. 3. Schemes *I–III* illustrate the asymmetric methods of calculating the integral property. The arrangement of components commonly corresponds to the minimal deviation from the ideality exhibited by system *1–3* in calculation along the secants with the constant $x_1 : x_3$ ratio. The most widely used calculation procedure is scheme *I* (Toop method). Koehler, Muggiani, and Colinet models (*II*, *III*, and *IV*, respectively) are symmetrical with respect to the indices numbering the system components. Point *O* (Fig. 3) designates the composition of the ternary alloy for which an integral thermodynamic property is calculated. Points *A*, *B*, and *C* indicate the compositions of binary boundary systems whose integral values are used in calculations. Model *V* allows two calculation procedures using the integral values in points *A*, *B*, and *C* or in points *A*', *B*', and *C*'. As a rule, two calculation procedures are used in parallel, with the results averaged. The corresponding algorithms are given in [2, 26, 27] and are not repeated here. The calculations using all models were performed along the secants of the concentration triangle with the constant $x_{Ni} : x_{Co}$ ratio (3 : 1, 1 : 1, and 1 : 3). The calculations using all the six models yield reasonably consistent results. The average ΔG^{ex} and ΔH values for the system Fe–Ni–Co are given in Table 2, along with the average deviation. As in [2], none of the methods can be considered as inadequate. The lines of the equal ΔG^{ex} and ΔH values are shown in Figs. 4a and 4b. All the models are based on the concept that the boundary binary systems produce independent effect on the integral thermodynamic characteristic of the ternary system.

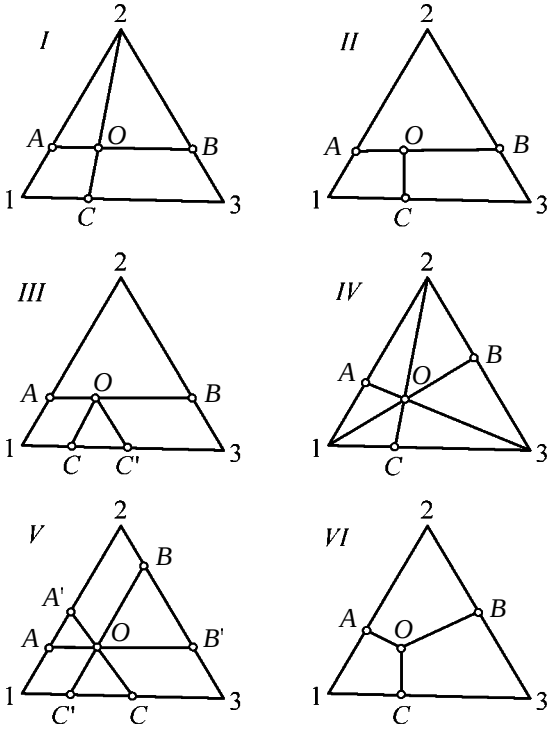

Fig. 3. Schemes of typical geometric models for calculating integral molar properties of ternary systems.

As shown previously [1, 2, 23], the dependence of ΔG^{ex} and ΔH on the composition of binary systems can be presented by the Redlich–Kister polynomials:

$$\Delta G^{ex} = x_1 x_2 [b + c(2x_1 - 1) + d(2x_1 - 1)^2,$$

$$\Delta H = x_1 x_2 [b' + c'(2x_1 - 1) + d'(2x_1 - 1)^2].$$

In the given case, x_1 and x_2 characterize the composition of the corresponding binary systems. Num-

bering and arrangement of the ternary system components, accepted by us, suggests the following designation for the binary systems: Co–Fe (1–2), Fe–Ni (2–3), and Ni–Co (3–1). Processing of experimental data from Table 1 yields the following values of the polynomial coefficients (ΔG^{ex} and ΔH, kJ mol^{-1}):

System	b	c	d
Co–Fe	5.2801	3.5035	–1.7652
Fe–Ni	–11.1043	6.1540	–0.7691
Ni–Co	–2.5158	0.0500	0.0122

System	b'	c'	d'
Co–Fe	–6.1419	–1.6528	1.5121
Fe–Ni	–17.1611	9.0480	2.5736
Ni–Co	1.6717	0.2934	–0.0074

The equations with the above coefficients describe the experimental data with a high accuracy. In this case, there is no need to describe the concentration dependences of thermodynamic functions by polynomials of the third or higher degrees.

Use of polynomials allows calculation of the limiting partial molar thermodynamic functions and the coefficients of component activity. As known [2, 23],

$$\left(\frac{\Delta G^{ex}}{x_1x_2}\right)_{x_1\to 0} = (\Delta G_1^{ex})^{\infty},$$

$$\left(\frac{\Delta G^{ex}}{x_1x_2}\right)_{x_2\to 0} = (\Delta G_2^{ex})^{\infty}.$$

Based on these expressions, without graphical plotting, we obtained the following limiting thermodynamic characteristics for the binary systems at 1600°C:

	$(\Delta G^{ex})^{\infty}$, kJ mol^{-1}	$\ln\gamma^{\infty}$	γ^{∞}
	Cobalt–iron system		
Co	–0.0114	-7.32×10^{-4}	0.999
Fe	7.018	0.451	1.569
	Iron–nickel system		
Fe	–18.027	–1.158	0.314
Ni	–5.719	–0.367	0.693
	Nickel–cobalt system		
Ni	–2.554	–0.164	0.849
Co	–2.454	–0.158	0.854

As a whole, the calculation results reasonably agree with the experimental data [7, 10, 16].

The change in the excess Gibbs energy of the ternary system can be presented as a sum of the independent contributions [1, 23]:

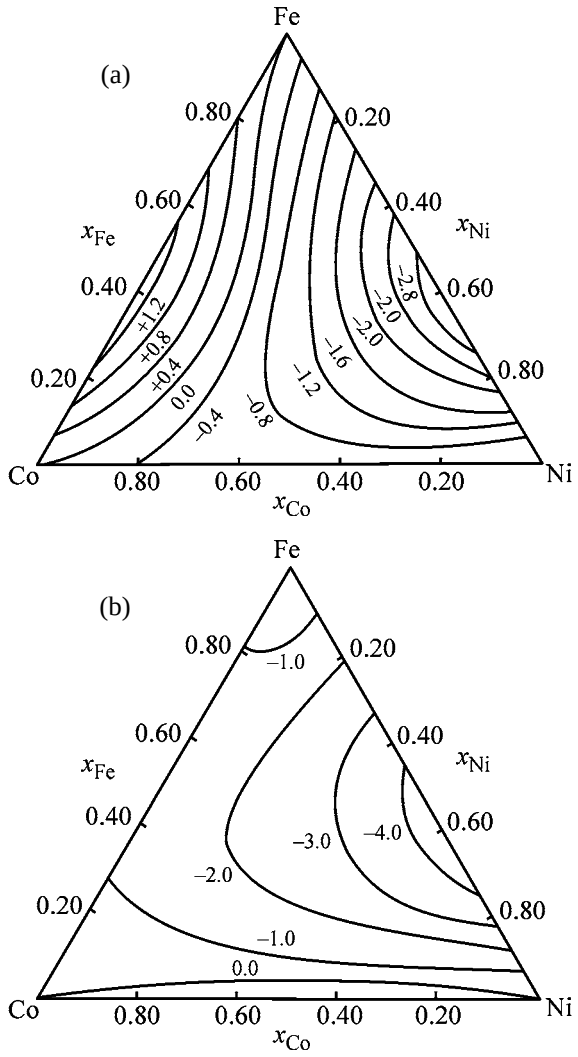

Fig. 4. Lines of the equal values of (a) integral molar excess Gibbs energy ΔG^{ex} and (b) enthalpy of mixing ΔH in alloys of the ternary system Fe–Ni–Co at 1600°C.

$$\Delta G^{ex} = \Delta G_{12}^{ex} + \Delta G_{23}^{ex} + \Delta G_{31}^{ex} + \Delta G_{123}^{ex}.$$

The first three terms can be estimated from the coefficients of the above polynomials. To estimate the ΔG_{123}^{ex} contribution, it is necessary to have data on the ternary system. At the same time, experience shows that there is no need to take into account ternary interactions. The final equation for calculating ΔG^{ex} has the form

$$\Delta G^{ex} = x_1x_2[b_{12} + c_{12}(x_1 - x_2) + d_{12}(x_1 - x_2)^2] + x_2x_3[b_{23} + c_{23}(x_2 - x_3) + d_{23}(x_2 - x_3)^2] + x_3x_1[b_{31} + c_{31}(x_3 - x_1) + d_{31}(x_3 - x_1)^2].$$

Table 3. Results of polynomial calculation of ΔG^{ex} and ΔH in the Fe–Ni–Co ternary system at 1600°C

x_{Fe}	$x_{Ni} : x_{Co} = 3 : 1$		$x_{Ni} : x_{Co} = 1 : 1$		$x_{Ni} : x_{Co} = 1 : 3$	
	ΔG^{ex}	ΔH	ΔG^{ex}	ΔH	ΔG^{ex}	ΔH
	kJ mol^{-1}					
0.20	–1.73	–2.48	–0.92	–1.75	0.02	–1.29
0.40	–1.97	–3.39	–0.90	–2.51	0.23	–1.90
0.60	–1.57	–2.80	–0.72	–2.14	0.16	–1.66
0.80	–0.84	–1.37	–0.44	–1.09	–0.02	–0.88

The terms x_1, x_2, and x_3 in this equation characterize the composition of the ternary alloy. The expression for calculating ΔH in the Fe–Ni–Co ternary system is similar, with the coefficients b', c', and d'. The results of polynomial calculation of ΔG^{ex} and ΔH are presented in Table 3.

The results of calculation by geometric models and using polynomials that reflect the contribution of binary systems are in reasonable agreement. This indirectly confirms that the values of the corresponding thermodynamic functions accepted by us for the boundary binary systems adequately reflect the real form of the surface of the thermodynamic functions of the ternary system.

CONCLUSIONS

(1) Liquid alloys of the iron–nickel–cobalt system exhibit moderate alternating deviations from ideality: at compositions adjacent to the Fe–Ni side, the integral molar excess Gibbs energy is negative, whereas at compositions adjacent to the Fe–Co side it is positive.

(2) All the six geometric models used for calculating the integral molar thermodynamic properties of the Fe–Ni–Co ternary system from data on boundary binary systems, as well as the method using the polynomials for the binary systems, yield similar results.

REFERENCES

1. Morachevskii, A.G., Fedorova, N.A., Tsymbulov, L.B., and Tsemekhman, L.Sh., *Zh. Prikl. Khim.*, 2002, vol. 75, no. 11, pp. 1801–1805.
2. Morachevskii, A.G., Ryabko, A.G., and Tsemekhman, L.Sh., *Termodinamika zhidkikh splavov sistemy nikel'–med'–zhelezo* (Thermodynamics of Liquid Alloys of the System Nickel–Copper–Iron), St. Petersburg: Sankt-Peterb. Gos. Tekh. Univ., 2002.
3. Velišek, J., Vreštal, J., and Stránsky, K., *Kovové Mater.*, 1976, vol. 14, no. 2, pp. 121–136.
4. Fraser, D.G., and Rammensee, W., *Geochim. Cosmochim. Acta*, 1982, vol. 46, pp. 549–556.
5. Tsemekhman, L.Sh., Alekseeva, N.N., and Parshukova, L.N., *Metally*, 2000, no. 1, pp. 25–29.
6. Bannykh, O.A., Budberg, P.B., Alisova, S.P., *et al.*, *Diagrammy sostoyaniya dvoinykh ili mnogokomponentnykh sistem na osnove zheleza* (Phase Diagrams of Iron-Based Binary or Multicomponent Systems), Moscow: Metallurgiya, 1986.
7. Batalin, G.I., *Termodinamika zhidkikh splavov na osnove zheleza* (Thermodynamics of Liquid Iron Alloys), Kiev: Vishcha Shkola, 1982.
8. Velišek, J., *Kovové Mater.*, 1982, vol. 20, no. 3, pp. 48–53.
9. Lee, B.J., *CALPHAD*, 1993, vol. 17, no. 3, pp. 251–268.
10. Kubaschewski, O., Geiger, K.-H., and Hack, K., *Z. Metallkunde*, 1977, vol. 68, no. 5, pp. 337–341.
11. Conard, B.R., McAneney, T.B., and Sridhar, R., *Met. Trans. B*, 1978, vol. 98, September, pp. 463–468.
12. Rammensee, W., and Fraser, D.G., *Ber. Bunsenges. Phys. Chem.*, 1981, vol. 85, pp. 588–592.
13. Wang, H., Luck, R., and Predel, B., *J. Phase Equil.*, 1993, vol. 14, no. 1, pp. 48–53.
14. Batalin, G.I., Minenko, N.N., and Sudavtseva, V.S., *Metally*, 1974, no. 5, pp. 99–103.
15. Fernandez Guillermet, A., *High Temp.–High Press.*, 1987, vol. 19, no. 5, pp. 477–499.
16. Belton, G.R., and Fruehan, R.J., *J. Phys. Chem.*, 1967, vol. 71, no. 5, pp. 1403–1409.
17. Tomiska, J., and Neckel, A., *Z. Metallkunde*, 1986, vol. 77, no. 10, pp. 649–653.
18. Wang, H., Luck, R., and Predel, B., *J. Non-Cryst. Solids*, 1993, vol. 156–158, pp. 388–392.
19. Fernandez Guillermet, A., *Z. Metallkunde*, 1987, vol. 78, no. 9, pp. 639–647.

20. Tomiska, J., Nowotny, H., Erdelyi, L., and Neckel, A., *Ber. Bunsenges. Phys. Chem*., 1979, vol. 83, pp. 1035–1042.
21. Predel, B., and Mohs, R., *Arch. Eisenhuttenwes*., 1970, vol. 41, no. 1, pp. 61–66.
22. Iguchi, Y., Tozaki, Y., Kakizaki, M., *et al*., *Iron Steel Inst. Jpn*., 1977, vol. 63, pp. 953–961.
23. Morachevskii, A.G., *Termodinamika rasplavlennykh metallicheskikh i solevykh sistem* (Thermodynamics of Molten Metal and Salt Systems), Moscow: Metallurgiya, 1987.
24. Morachevskii, A.G., and Sladkov, I.B., *Termodinamicheskie raschety v metallurgii. Spravochnik* (Thermodynamic Calculations in Metallurgy. Reference Book), Moscow: Metallurgiya, 1993.
25. Chou, K.-Ch. and Chang, Y.A., *Ber. Bunsenges. Phys. Chem*., 1989, vol. 93, pp. 735–741.
26. Luck, R., Wang, H., and Predel, B., *Z. Metallkunde*, 1991, vol. 82, no. 10, pp. 805–809.
27. Morachevskii, A.G., and Butukhanova, T.V., *Zh. Prikl. Khim*., 1997, vol. 70, no. 8, pp. 1245–1250.

Russian Journal of Applied Chemistry, Vol. 76, No. 11, 2003, pp. 1734–1736. Translated from Zhurnal Prikladnoi Khimii, Vol. 76, No. 11, 2003, pp. 1785–1787.

PHYSICOCHEMICAL STUDIES OF SYSTEMS AND PROCESSES

Thermodynamic Calculation of Solubility of Crystalline Halides and Sulfides in Water and Acid Solutions

S. E. Shkol'nikov

Kirov State Academy of Forestry Engineering, St. Petersburg, Russia

Received February 19, 2003

Abstract—The influence of the pH of nonoxidizing acid solutions on the solubility of a number of crystalline halides and sulfides was calculated thermodynamically.

The rate of dissolution of chalcogenide materials intended for membranes of ion-selective electrodes (ISE) in various model solutions has been studied previously [1, 2]. At the same time, it is no less important to know the thermodynamic characteristic of solubility of sensor materials, which is determined by the molar concentration of the saturated solution in aqueous–organic media. The solubility is a function of temperature, structural and chemical features of a membrane, and characteristics of the liquid medium being analyzed: ionic and molecular composition, pH, and true redox potential [2].

In this study, the thermodynamic method was used to calculate the solubility under the standard conditions for a number of binary inorganic compounds in pure water at pH 7 (s^0, g l^{-1}) and in aqueous solutions of nonoxidizing acids at pH 5, 3, and 1 (for example, in HCl or HBr solutions) in the absence of similar ions and without appreciable complexation. The objects of calculation were crystalline halides of silver and thallium(I), fluorides of lanthanum and other Group II–III elements, and sulfides of silver, cadmium, lead(II), copper(II), and mercury(II), which are used [3] or show promise [1, 2] for preparation of ISE membranes.

In aqueous solution saturated with respect to a difficultly soluble electrolyte M_mA_n, a heterogeneous chemical equilibrium is attained:

$$M_mA_n(cr) \rightleftarrows mM^{n+}(s) + nA^{m-}(s), \quad (1)$$

whose thermodynamic constant

$$K_s^0 = US^T + a_M^m a_A^n = (ms^0)^m (ns^0)^n \quad (2)$$

can be used to calculate the molar solubility of a compound in pure water (s^0, M) at a less than 10^{-4} M ionic strength of a solution [4] by the formula

$$s^0 = (K_s^0/m^m n^n)^{1/(m+n)} \quad (3)$$

or Ms^0 (g l^{-1}), where M is the molar weight of a compound M_mA_n.

The K_s^0 constant was calculated using the thermodynamic relation

$$\ln K_s^0 = -\frac{\Delta G_{s,298}^0}{R \times 298} = -0.404 \Delta G_{s,298}^0, \quad (4)$$

where the standard change in the Gibbs energy $\Delta G_{s,298}^0$ for the dissolution process (1) was calculated by the equation

$$\Delta G_s^0 = m\Delta G_{f,M^{n+}}^0 + n\Delta G_{f,A^{m-}}^0 + m\Delta G_{f,M_mA_n}^0. \quad (5)$$

The ΔG_f^0 values of the ion formation in aqueous solution were taken from [5], and the ΔG_f^0 values of formation of a compound M_mA_n (cr, g) in crystalline or glassy state at 298 K were taken from a reference book [6] or calculated by known methods.

In calculation of the solubility of the M_mA_n crystals in nonoxidizing acid media by the equation

$$s^{m+n} = \frac{K_s^0}{m^m n^n f_M^m f_A^n x_A^n}, \quad (6)$$

account was made for the molar activity coefficients of M^{n+} and A^{m-} ions and the mole fraction x_A of A^{m-} free anions not bound into weak acid species (HF, HS^-, and H_2S) [4, 5].

For a heterogeneous equilibrium in a nonoxidizing

1070-4272/03/7611-1734$25.00

Results of thermodynamic calculation of the dissolution parameters of crystalline materials in H_2O and in nonoxidizing acid medium under the standard conditions

Composition	P_i, %	$\Delta G^0_{s,298}$, kJ mol^{-1}	pK^0_s		s^0, g l^{-1}, in H_2O	s, g l^{-1}, at indicated pH	
			calculated	[4]		3	1
AgCl	30	55.6	9.74	9.74	0.0019	0.002	0.002
AgBr	22	68.6	12.04	12.27	1.4×10^{-4}	1.5×10^{-4}	1.8×10^{-4}
AgI	15	91.6	16.06	16.08	2.1×10^{-6}	2.2×10^{-6}	2.9×10^{-6}
TlCl	43	20.6	3.62	3.77	3.11	3.23	4.26
TlBr	34	28.7	5.03	5.41	0.57	0.59	0.78
TlI	26	41.9	7.35	7.24	0.079	0.082	0.085
β-BeF_2	80	34.3	6.02	–	0.282	0.564	12.4
BeF_2(glass)	80	31.4	5.50	–	0.424	0.848	18.7
α-BeF_2	80	9.4	1.66	–	0.94	1.88	41.4
γ-BeF_2	80	1.3	0.23	–	2.77	5.54	122
MgF_2	85	48.3	8.40	8.19	0.075	0.149	3.28
CaF_2	88	59.9	10.49	10.40	0.017	0.034	0.74
SrF_2	89	49.3	8.64	8.60	0.107	0.215	4.81
InF_3	76	52.0	9.10	(ds)	0.40	0.88	33.4
ScF_3	83	59.0	10.36	(is)	0.11	0.25	9.7
YF_3	85	156	27.40	(is)	9×10^{-6}	2×10^{-5}	8×10^{-4}
LaF_3	87	105	18.40	(is)	0.002	0.005	0.183
Ag_2S	12	284	49.82	49.70	4×10^{-15}	2×10^{-10}	5×10^{-9}
HgS	8	305	53.40	52.40	3×10^{-24}	1×10^{-17}	2×10^{-15}
CuS	12	204	35.80	35.20	2×10^{-16}	2×10^{-9}	4×10^{-7}
CdS	22	152	26.75	27.80	2×10^{-12}	1×10^{-5}	0.003
PbS	12	155	27.18	26.60	1×10^{-11}	8×10^{-5}	0.017

Note: (ds) Difficultly soluble and (is) virtually insoluble [8].

acid

$$MF_n(cr, g) + nH^+(s) \rightleftarrows M^{n+}(s) + nHF(s),$$

whose thermodynamic constant is $K_a = K^0_{s,MF_n}/K^n_{HF}$, the acid resistance of crystalline and glassy fluorides was calculated by formula (6) using the relationship

$$x_{F^-} = \frac{K_{HF}}{[H^+] + K_{HF}}, \quad (7)$$

whereas at pH ≤ 3, when $[H^+] > K_{HF}$, it can be calculated by the approximate formula

$$s^{n+1} = \frac{K^0_s[H^+]^n}{n^n f_M f_F^n K^n_{HF}}. \quad (8)$$

For a heterogeneous chemical equilibrium in a nonoxidizing medium,

$$M_mS_n(cr, g) + 2nH^+(s) \rightleftarrows mM^{(2n/m)+}(s) + nH_2S(s),$$

the acid resistance of the M_mS_n crystals and glasses can be calculated, taking into account that $x_{S^{2-}} \approx K_{H_2S}[H^+]^2$ at pH ≤5 and $K_{H_2S} = 2.5\times10^{-20}$ [4], by the generalized equation

$$s^{m+n} = \frac{K^0_s[H^+]^{2n}}{m^m n^n f_M^m f_S^n K^n_{H_2S}}. \quad (9)$$

The calculation results are presented in the table, where $pK^0_s = -\log K^0_s$ and P_i is the degree of ionicity (%) of the M–A chemical bond in a compound M_mA_n, determined from the difference in the electronegativites of A and M elements using the Pauling curve [7]. Table 1 shows that, for a majority of difficultly soluble compounds, the pK^0_s values calculated by Eq. (4) reasonably agree with the data from a reference book [4] (the average deviation $\Delta pK^0_s = \pm0.19$). Exceptions are cadmium and mercury(II) sulfides, for which the ΔG^0_s and K^0_s values must be refined. With increasing ionicity of silver and thallium(I) halides in the series I → Br → Cl → F, their solubility in water s^0 increases (see table). The least soluble in water are HgS, CuS, and Ag_2S crystals, in which the M–S

bonds are mainly covalent. The AgF, TlF, and BeF_2 ionic crystals have the highest solubility in water (P_i = 70–85%), with the BeF_2 solubility, like GeO_2 solubility (α, β) [8], considerably depending on the crystal structure (α-, β-, and γ-modifications). The solubility of the BeF_2 glass ($BeF_{4/2}$ structural unit) is somewhat higher than that of a stable β-BeF_2 crystal of the α-quartz hexagonal structure, but lower than that of the other BeF_2 modifications (see table).

Due to the salt effect, the solubility of silver and thallium(I) halides in nonoxidizing acid solutions increases only slightly (1.3-fold as pH is decreased from 7 to 1). As pH is decreased from 7 to 3 and from 7 to 1, the solubility increases by factors of about 2 and 44, respectively, for the fluorides MF_2 and by factors of 2.3 and 86, respectively, for MF_3. This is largely due to binding of fluoride ions into molecules of a weak acid, HF. The solubility of sulfides MS (M is Pb, Cd, Cu, or Hg) increases more appreciably, namely, by a factor of $\sim 10^7$ as pH is decreased from 7 to 3 and further by a factor of 230 as pH is decreased from 3 to 1. Therefore, PbS, LaF_3, ScF_3, CaF_2, and TlI crystals are unsuitable as ISE membranes in strongly acidic solutions. The Ag_2S, HgS, CuS, AgI, AgBr, and YF_3 crystalline membranes can be used at pH 1 (their solubility is less than 0.2 mg l^{-1}).

CONCLUSIONS

(1) The solubility of crystalline silver and thallium(I) halides increases as the degree of their ionicity grows in the series I $\rightarrow$ Br $\rightarrow$ Cl $\rightarrow$ F.

(2) As pH is decreased from 7 to 1, the solubility of silver and thallium(I) halides grows only slightly (by a factor of 1.3); that of fluorides MF_2 and MF_3, considerably (by a factor of 40–90), and that of sulfides MS (M is Pb, Cd, Cu, or Hg), to the greatest extent (by a factor of $\sim 10^9$).

REFERENCES

1. Shkol'nikov, E.V., Kocheregin, S.B., and Shkol'nikova, A.M., *Zh. Prikl. Khim.*, 1997, vol. 70, no. 12, pp. 1983–1986.
2. Shkol'nikov, E.V., *Fiz. Khim. Stekla*, 2000, vol. 26, no. 6, pp. 861–869.
3. *Handbook of Electrode Technology*, Cambridge (the United States): Orion Research, 1982.
4. Lur'e, Yu.Yu., *Spravochnik po analiticheskoi khimii* (Handbook on Analytical Chemistry), Moscow: Khimiya, 1979.
5. Vasil'ev, V.P., *Termodinamicheskie svoistva rastvorov elektrolitov: Uchebnoe posobie* (Thermodynamic Properties of Electrolyte Solutions: Textbook), Moscow: Vysshaya Shkola, 1982.
6. *Termodinamicheskie svoistva individual'nykh veshchestv* (Thermodynamic Properties of Individual Substances), Glushko, V.P., Ed., Moscow: Nauka, 1979–1981, vols. 1–4.
7. Ormont, B.F., *Vvedenie v fizicheskuyu khimiyu i kristallokhimiyu poluprovodnikov: Uchebnoe posobie dlya vysshikh uchebnykh zavedenii* (Introduction to Physical Chemistry and Crystal Chemistry of Semiconductors. Textbook for Higher Schools), Moscow: Vysshaya Shkola, 1973.
8. Efimov, A.I., Belorukova, L.P., Vasil'kova, I.V., and Chechev, V.P., *Svoistva neorganicheskikh soedinenii: Spravochnik* (Properties of Inorganic Compounds: Handbook), Leningrad: Khimiya, 1983.

Russian Journal of Applied Chemistry, Vol. 76, No. 11, 2003, pp. 1737–1743. Translated from Zhurnal Prikladnoi Khimii, Vol. 76, No. 11, 2003, pp. 1788–1793.

APPLIED ELECTROCHEMISTRY AND CORROSION PROTECTION OF METALS

Dissolution of Palladium Deposited onto a Fibrous Carbon Cathode in Nitric Acid Solution through Operation of a Short-Circuited Electrochemical System

V. I. Varentsova and V. K. Varentsov

Institute of Solid-State Chemistry and Mechanochemistry, Siberian Division, Russian Academy of Sciences, Novosibirsk, Russia

Received April 17, 2003

Abstract—Dissolution in 3.5 M NHO_3 of palladium deposited onto a fibrous carbon electrode from hydrochloric and nitric acid solutions was studied. The factors influencing the dissolution of palladium in contact with the electrode were revealed using a model of short-circuited electrochemical system.

Dilute palladium solutions widely occur in various industries, e.g., in hydrometallurgy, in electrolytic metallurgy, and in processing of spent catalysts and nuclear fuel. Various procedures have been suggested for recovery of palladium from the forming (mainly nitric and hydrochloric acid) solutions [1, 2]. One of effective techniques is electrolysis with filtering three-dimensional electrodes and, in particular, with electrodes made of fibrous carbon materials (FCMs), which have been used previously in recovery of noble metals in hydrometallurgy and electrolytic metallurgy and in processing of spent catalysts [3–5]. In the course of electrolysis, the metals are concentrated within a fibrous carbon electrode (FCE), with 15–30 kg of metal deposited per 1 kg of FCM. Platinum-group metals are deposited from hydrochloric and nitric acid solutions with high degrees of recovery [4, 5]. However, it has been established, in the case of electrodeposition from nitric acid solutions, that palladium deposited onto an FCE dissolves after the external voltage is switched off, whereas in deposition of palladium from hydrochloric acid solutions, no dissolution is observed. A similar phenomenon of zinc dissolution in recovery of the metal from alkaline electrolytes has been reported previously [6]. It was established that zinc deposited onto an FCE dissolves in the alkaline electrolyte through operation of a short-circuited electrochemical system (SES) Zn–FCE–electrolyte.

The possibility that deposited palladium can dissolve in a nitric acid solution through operation of SES is based on the difference of standard electrode potentials of palladium and FCM. When in contact with FCM in a nitric acid solution, palladium can form an SES in which the metal undergoes anodic dissolution. Taking into account the ability of palladium to form complexes with nitrate and nitrite ions, which are always present in an HNO_3 solution [9], it may be suggested that anodic dissolution of palladium will be accompanied by formation of the corresponding complex compounds. Based on the stability constants of nitrate ($K = 1.2 \pm 0.4$ [10]) and nitrite ($K = 1.4 \times 10^{15}$ [11]) palladium(II) complexes, the anodic dissolution of palladium can be represented as

$$Pd + 4NO_2^- = Pd(NO_2)_4^{2-} + 2e, \qquad E^0 = 0.54 \text{ V}. \quad (1)$$

Cathodic reduction of nitric acid to nitrous acid and nitrogen oxides ($E_0 + 0.94$ and $+0.96$ V, respectively) and of dissolved oxygen ($E^0 = +1.229$ V) are possible on the FCM surface. Vetter [9], who studied in detail the kinetics of cathodic reduction of HNO_3 on an inert electrode, demonstrated that the final product of its reduction is nitrous acid, with the formation of nitrogen oxides N_2O_4 and NO_2 considered as intermediate stages.

The dissolution of palladium in SES may lead to the loss of the metal in its electrolytic recovery from nitric acid solutions. At the same time, this process can be used to separate and concentrate palladium in dissolution of metals deposited from the solutions mentioned above.

The aim of this study was to analyze how palladium deposited onto FCE from hydrochloric and nitric acid solutions dissolves through operation of the SES Pd–FCE–3.5 M HNO_3.

1070-4272/03/7611-1737$25.00

EXPERIMENTAL

Palladium was electrodeposited onto an FCE from model and real nitric and hydrochloric acid solutions, using the procedure, technique, and cell described in [3, 12], with solution circulated through the FCE volume at a rate of 18 ml min^{-1} and the electrode zones separated by an MK-40 ion-exchange membrane. The cathode was polarized with a B-5-49 power source. As FCE served carbonized fibrous carbon material NT-1 containing about 85 wt % graphite [3]. A perforated titanium plate was used as current lead to the FCE; platinum grid, as anode; and 2% Na_2SO_4 solution, as anolyte. The efficiency of palladium electrodeposition was evaluated by the degree of recovery $\alpha = (c_0 - c_\tau)/c_0$ and by the current efficiency

$$CE = (c_0 - c_\tau)V \times 26.8/(I\tau M_{eq}),$$

where c_0 and c_τ are the initial and final palladium(II) concentrations in solution (g l^{-1}); V, solution volume (l); I, current at which electrolysis is carried out (A); τ, experiment duration (h); 26.8 A h mol^{-1}, Faraday constant; and M_{eq}, molar mass of the metal equivalent.

Palladium electrodeposited onto the FCE was dissolved in the cell mentioned above, with a nitric acid solution pumped through the FCE volume at a prescribed rate m_v, or in a glass cell in a nonflowing 3.5 M solution of nitric acid. The amount of dissolved palladium was determined from the loss of mass by the FCE with palladium and by the atomic-absorption method from changes in the palladium(II) concentration in solution. The dissolution rate W_{Pd} of palladium deposited onto the FCE was calculated per the overall area of FCE with thickness of about 3 mm.

The content of nitrous acid was determined by permanganatometric titration by the Lunge method [13].

The dissolution of palladium deposited onto the FCE was analyzed qualitatively using the known method for modeling of a microvoltaic cell with a macrovoltaic cell [14]. The electrodes of the latter, FCM, palladium plate, or a palladium plate with palladium deposited onto it from a hydrochloric or nitric acid solution, were placed in an HNO_3 solution. The use of this method for studying the electrochemical process in the system in question is due to the macrokinetic nature of processes characterizing the FCM operation.

Since the reproducibility of the results obtained depends on the method used for pretreatment of the palladium plate surface, the surface was treated under fixed conditions: a plate was subjected to mechanical grinding, polishing on felt, and successive washing with an Na_2CO_3 solution, alcohol, and distilled water. Palladium was electrodeposited onto a palladium plate from a nitric acid solution containing 0.3 g l^{-1} Pd(II) and 3.5 M HNO_3 and from a hydrochloric acid solution containing 2 M HCl and 2.5 (solution no. 1) or 0.3 g l^{-1} Pd(II) (solution no. 3) in a nonflowing electrolyte at current density of 100 A m^{-2} in the course of 25–50 min. After electrolysis, the plate was washed with distilled water and dried in air. The amount of deposited palladium was 0.5–2.5 mg cm^{-2}.

The electrode potentials were measured relative to a saturated silver chloride electrode with an OP-265/1 pH-meter and recalculated to the hydrogen scale. The results of no less than 4–5 measurements were averaged; the mean deviation was ±20 mV in measuring the electrode potential of the palladium plate, ±40 mV for the palladium-plated plate, and ±5 mV for FCM.

A study of palladium electrodeposition onto FCM from real and model nitric and hydrochloric acid solutions demonstrated that palladium is recovered to high extent from solutions of both types (Fig. 1). The current efficiency by palladium, calculated for 90% recovery, is 5–25%; it grows with increasing concentration of palladium(II) and decreasing concentration of acid in solution and falls with increasing current density and degree of palladium recovery. The low current efficiency by palladium is due to the concurrent reduction of hydrogen ions and nitric acid.

In electrolytic recovery of palladium from real solutions, platinum metals, such as rhodium and ruthenium, are deposited together with palladium.

A study of how palladium deposited onto FCE from model solutions dissolves in 3.5 M HNO_3 revealed that the rate of dissolution of palladium electrodeposited from nitric acid is 4–6 times that in the case of palladium electrodeposition onto FCM from a hydrochloric acid solution.

Table 2 lists the results obtained in measuring the corrosion potential E_{cor} of FCE with palladium deposited onto it from nitric acid (I) and hydrochloric acid (II) solutions in the course of palladium dissolution in 3.5 M HNO_3. Table 2 shows that, in dissolution of palladium deposited from a nitric acid solution, E_{cor} grows fast with increasing time of contact with a 3.5 M HNO_3 solution. When E_{cor} reaches a value of 0.88 V, palladium starts to dissolve, as determined visually from the appearance of yellow coloration in the near-boundary layer. It was found in different

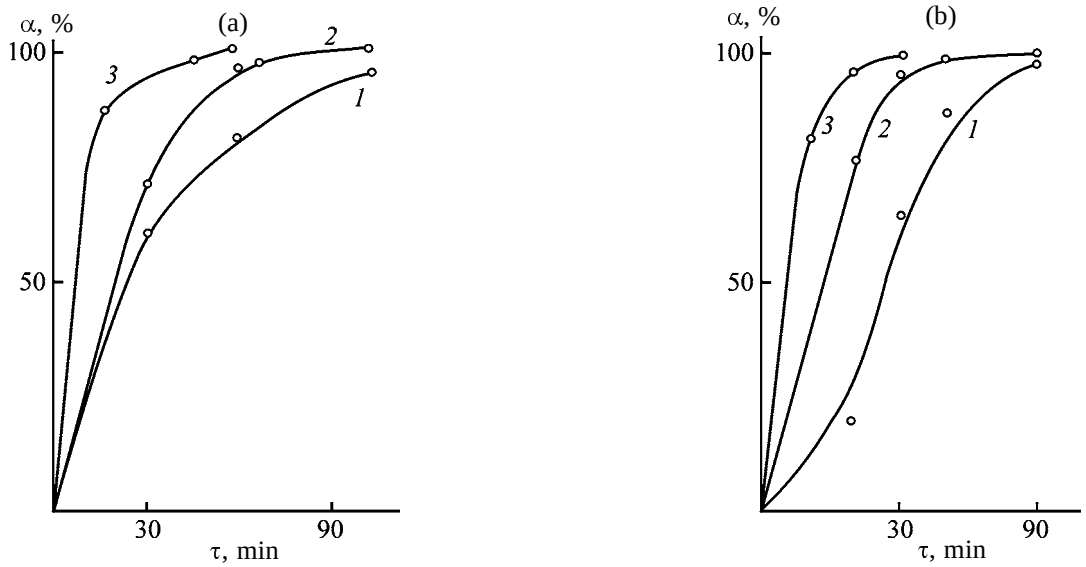

Fig. 1. Degree of electrolytic recovery α of palladium from (a) hydrochloric and (b) nitric acid solutions vs. electrolysis duration τ. (a) Overall cathode area, cm^2: (*1*) 30 and (*2*, *3*) 2. Concentration of components in spent solution from gold refining ($g\ l^{-1}$; in terms of metal): (*1*) Au 6.2, Pt 1.1, Pd 2.2, Cu 0.5, and HCl 50; (*2*, *3*) Au 3.9, Cu 0.15, Fe 1.0, Ni 0.01, Pd 0.07, Pt 0.05, Rh 0.01, Zn 0.03, and HCl 50. Current density, $A\ m^{-2}$: (*1*) 800, (*2*) 600, and (*3*) 1000. (b) Overall cathode area 2 cm^2. Model solution, $g\ l^{-1}$: Pd(II) 0.17 and HNO_3 220. Current density, $A\ m^{-2}$: (*1*) 250, (*2*) 500, and (*3*) 1000.

experiments that palladium starts to dissolve after 5–10 min of contact with the HNO_3 solution. In the case when FCM with palladium deposited from a hydrochloric acid solution is brought in contact with an HNO_3 solution, E_{cor} = 0.88 V is reached, and palladium starts to dissolve, only after keeping in the solution for 1 h, i.e., in this case, the period of time preceding palladium dissolution is much longer (40–60 min).

Figure 2 shows the stationary potentials of palladium and palladium-plated plates, $E_{st.Pd}$, as a function of the time during which the electrodes were kept in a 3.5 M HNO_3 solution. It can be seen that $E_{st.Pd}$ reaches a value of 0.94 V after the plate is kept in the HNO_3 solution for 20–30 min (curve *1*). It should be noted that $E_{st.Pd}$ grows gradually with increasing time of keeping in the HNO_3 solution. After 1.5 h, the stationary potential becomes 1.01 V, the plate surface is covered with a black palladium oxide layer, and the concentration of palladium in solution is 2.5 $mg\ l^{-1}$. The concentration of nitrous acid increases from 0.0006 (initial 3.5 M HNO_3 solution) to 0.0014 M (after 1.5 h of operation of the voltaic cell).

According to published data, $E_{st.Pd}$ is of corrosion nature in nitric acid solutions [8]. Taking into account the appearance of palladium(II) ions in solution, the rise in the concentration of nitrous acid in solution, and the values of the stability constants of nitrate and nitrite complexes of palladium(II), it may be assumed that palladium is oxidized in anodic regions to give palladium(II) nitrite complexes [reaction (1)] and surface oxides:

$$Pd + H_2O = PdO + 2H^+ + 2e, \qquad E^0 = 0.858\ V. \quad (2)$$

In the cathodic regions, nitric acid is reduced. The stationary potential of palladium-plated electrodes is more negative than the value characteristic of the palladium plate and depends on the nature of the solution from which palladium was deposited and on the palladium concentration in solution (Fig. 2, curves *2*–*4*).

Table 1. Dissolution rate W_{Pd} of palladium in the system Pd–FCM–3.5 M HNO_3. Solution volume 50 ml; amount of palladium deposited onto FCE at current density i = 1000 $A\ m^{-2}$ in 20 min equal, on the average, to 60% of the FCM mass

Dissolution conditions		W_{Pd}, $mg\ cm^{-2}\ h^{-1}$	Electrolyte
m_v, $ml\ cm^{-2}\ s^{-1}$	τ, min		
0	30	23.1	0.3 $g\ l^{-1}$ Pd, 3.5 M HNO_3
0.3	15	30.4	0.3 $g\ l^{-1}$ Pd, 3.5 M HNO_3
0	70	6	0.3 $g\ l^{-1}$ Pd, 2 M HCl
0.3	50	5	0.3 $g\ l^{-1}$ Pd, 2 M HCl

Table 2. Variation of the corrosion potential E_{cor} in SES Pd–NT-1–3.5 M HNO_3 with time of keeping the FCE in a solution

τ, min	E_{cor}, V		τ, min	E_{cor}, V	
	I	II		I	II
1	0.74	0.68	20	1.03	0.72
2	0.75	0.68	30	1.04	0.73
4	0.76	0.69	45	–	0.75
5	0.76	0.70	55	–	0.76
6	0.88	0.70	60	–	0.88
10	0.96	0.71	75	–	0.97
15	1.04	0.71	90	–	1.03

In the case when palladium was deposited onto the plate from a hydrochloric solution no. 2 (Fig. 1, curve *4*), no palladium was found in solution after keeping such an electrode in 3.5 M HNO_3. $E_{st.Pd}$ is more negative by about 0.8 V than the potential characteristic of the palladium plate. According to published data [15], the more negative stationary potential of palladium-plated palladium, compared to that of the palladium plate, is due to the presence of sorbed hydrogen in the cathodic deposit. The ability of metallic palladium to absorb large amounts of hydrogen gas (up to 50–70 $cm^3\ g^{-1}$ palladium) has long been known [15–17]. The issues associated with absorption and adsorption of hydrogen by palladium in the course of electrolysis (compact metal or that electrolytically deposited on various substrates: platinum, palladium, or carbon, including carbon fabrics) and with the properties of the resulting deposits were considered in [15, 17]. It was established that the amount of sorbed hydrogen is larger for electrodeposited palladium, compared to the palladium plate, and it grows with increasing dispersity of the deposit obtained, with the deposition potential shifted to the electronegative side. Depending on the electrodeposition potential, the atomic ratio H/Pd is 0.62–0.68 and may become as high as 1.1 [15, 17].

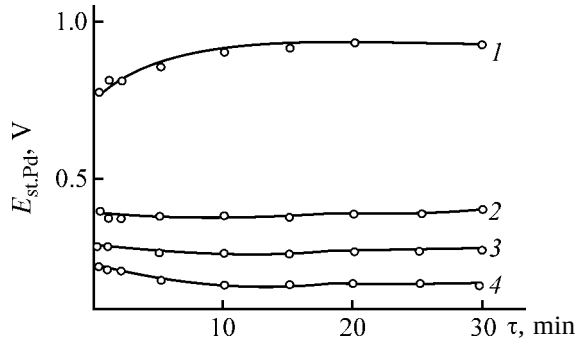

Fig. 2. Stationary electrode potential of palladium, $E_{st.Pd}$ (vs. standard hydrogen electrode), vs. time τ of keeping in 3.5 M HNO_3 solution. (*1*) Plate; (*2–4*) plate palladium-plated in (*3*) nitric acid solution and hydrochloric acid solution nos. (*2*) 1 and (*4*) 2.

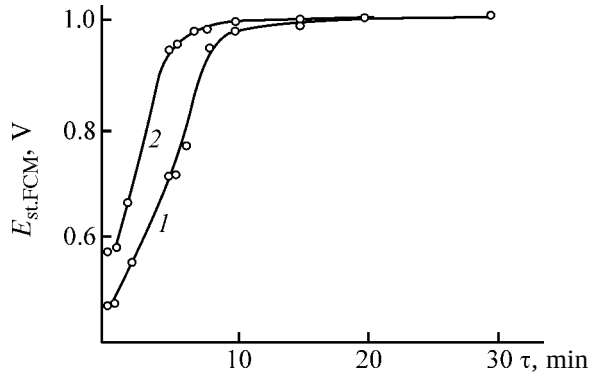

Fig. 3. Stationary electrode potential, $E_{st.FCM}$ (vs. standard hydrogen electrode), vs. time τ of keeping in a 3.5 M HNO_3 solution before (*2*) and (*1*) after cathodic treatment.

Figure 3 shows the results obtained in measuring the stationary electrode potentials of FCM, $E_{st.FCM}$. The steady-state value of the stationary potential of the initial NT-1 sample is 1.06 V. Samples subjected to cathodic treatment are characterized by longer time in which a steady-state value of $E_{st.FCM}$ is attained. Raising the time during which samples are kept in an HNO_3 solution to 2 h leads to an increase in $E_{st.FCM}$. According to published data [18, 19], the value of $E_{st.FCM}$ in nitric acid solutions is determined by the reduction of nitric acid and products of its reduction and disproportionation, and also by FCM corrosion to give surface oxides. The occurrence of oxidation processes is indicated by the shift of $E_{st.FCM}$ in the positive direction with increasing duration of contact with a nitric acid solution and also by the data of [20], according to which the mass of FCM increases and its conductivity decreases dramatically when the material is brought in contact with the same solution.

Table 3 lists the parameters characterizing the operation of a voltaic cell constituted by palladium plates and FCM: corrosion potential E_{cor}, corrosion current I_{cor}, and degrees of anodic (C_a), cathodic (C_c), and ohmic (C_{ohm}) control, calculated using the known equations [21]. The calculations were performed using E_{st} values after 30 min of keeping in a nitric acid solution (Fig. 2). Palladium was electrodeposited onto the plate from the following solutions: 2.5 $g\ l^{-1}$ Pd(II) and 2 M HCl (run no. 2), 0.3 $g\ l^{-1}$ Pd(II) and 2 M HCl (run no. 3), and 0.3 $g\ l^{-1}$ Pd(II) and 3.5 M HNO_3 (run no. 4).

Table 3. Effect of the state of palladium on parameters characterizing the operation of the voltaic cell Pd–NT-1–3.5 M HNO_3

Run no.	τ, min	$E_{cor.Pd}$, V	C_a, %	$E_{cor.NT-1}$, V	C_c, %	C_{ohm}, %	I_{cor}, μA
			Pd plate				
1	10	1.04	83.4	1.05	8.3	8.3	15
	30	1.05	91.7	1.06	0	8.3	13
	60	1.05	91.7	1.06	0	8.3	10
			Palladium-plated Pd				
2	10	0.91	77.3	0.99	10.6	12.1	180
	30	0.95	83.3	1.03	4.6	12.1	90
	60	0.96	84.9	1.04	3.0	12.1	60
3	10	0.19	0.6	0.62	50.3	49.1	2500
	15	0.23	5.1	0.64	48.1	46.9	2300
	30	0.31	14.3	0.71	40.0	45.7	1300
	60	0.59	46.3	0.89	19.4	34.3	350
4	10	0.62	42.1	0.77	38.2	19.7	1000
	15	0.67	48.7	0.79	35.5	15.8	900
	30	0.79	64.5	0.89	22.4	13.1	340
	60	0.89	77.6	0.96	13.2	9.2	120

Table 1 shows that the corrosion potential of the palladium plate is 0.1 V more positive than its stationary value, and the degree of anodic control is about 92%. In the case when the plate is palladium-plated from a hydrochloric acid solution containing 2.5 g l^{-1} Pd(II), the electrical resistance in the system increases somewhat. The corrosion current increases sixfold (run no. 2); during 30 min of operation of such a voltaic cell, the concentration of palladium(I) in a solution of volume 50 ml becomes as high as 5.7 mg l^{-1}. Preliminary cathodic treatment of NT-1 has no significant effect on the operation of the voltaic cell.

If palladium was electrolytically deposited onto the plate from hydrochloric acid solution no. 2 with a low content of Pd(II) (run no. 3), then the voltaic cell initially (during the dirst 30 min) operates under cathodic control and no palladium(II) is detected in the solution. Also, the ohmic loss in the system increases substantially. These results suggest occurrence on the anode of a reaction that is not associated with palladium dissolution, does not control the operation of the voltaic cell, and makes the electrical resistance in the system much higher. This is, presumably, due to an increase in the resistance of electrolytically deposited palladium because of the hydrogen sorption and formation by palladium of compounds with hydrogen. The current characterizing the operation of this voltaic cell is the highest among the voltaic systems considered. After 60 min of operation of the voltaic cell, the electrical resistance in the system decreases considerably, the polarization of the palladium electrode becomes stronger, and ions of dissolved palladium appear in the system. All this suggests that the anodic reaction occurring during the first 30 min of operation of the voltaic cell is electrooxidation of hydrogen sorbed by the palladium deposit. The possibility of occurrence of such processes is known [17].

If palladium is electrodeposited onto the plate from a solution containing 0.3 g l^{-1} Pd(II) and 3.5 M HNO_3 (run no. 4), then an increase in the degree of cathodic control to 35–38% is only observed in the first 15 min, and the ohmic loss grows during this period of time to 16–20%, i.e., the contribution from electrooxidation of sorbed hydrogen is much lower.

It follows from the results obtained that the operation of the voltaic cell strongly depends on the type of the palladium electrode (plate or palladium-plated plate). Of importance in the latter case are the nature of the solution and the initial content of palladium(II) in the electrolyte from which palladium was deposited. These two factors determine the relative amounts of current consumed for deposition of palladium, hydrogen evolution, and reduction of HNO_3. Apparent-

ly, at the same current mode of the electrolysis process, the quantity of electricity consumed for hydrogen evolution from an electrolyte containing 0.3 g l^{-1} Pd(II) exceeds that for an electrolyte with 2.4 g l^{-1} palladium(II). In contrast to hydrochloric acid solutions, reduction of nitric acid is possible, together with reduction of palladium(II) and hydrogen ions, in electrodeposition of palladium from a nitric acid solution. In this case, the fraction of current consumed for reduction of hydrogen ions must be smaller. It follows from the values of standard potentials that mainly reactions of reduction of palladium and nitric acid occur at the cathode in a nitric acid solution, and reduction of palladium and hydrogen ions, in a hydrochloric acid solution. Therefore, the fraction of hydrogen sorbed by palladium(II) in the former case is smaller than that in the latter.

Thus, the reason for the strong difference between the rates of dissolution in nitric acid of palladium deposited from nitric and hydrochloric acid solutions is that the cathodic deposit contains sorbed hydrogen whose oxidation precedes the dissolution of palladium. If only the time of dissolution of palladium is taken into account in calculating the rate of dissolution of palladium deposited onto FCE from a hydrochloric acid solution, then the results obtained in dissolution of palladium deposited from nitric and hydrochloric acid solutions are comparable.

The dissolution of palladium deposited onto FCE from nitric acid solutions, caused by SES operation, makes it possible to quantitatively separate palladium from codeposited platinum metals. For example, electrodeposition of palladium from a model nitric acid solution containing (g l^{-1}) Pd(II) 0.110, Rh(III) 0.095, Ru(II) 0.077, and HNO_3 189 onto an NT-1 FCM gave a cathodic deposit with Pd : Rh : Ru mass ratio of 50.5 : 32.1 : 17.4. Dissolution of this deposit in 3.5 M HNO_3 without applying external voltage yielded a solution with the Pd : Rh : Ru mass ratio of 95.1 : 1.1 : 3.0 and palladium(II) concentration of 500 mg l^{-1}. In subsequent electrolytic recovery of palladium from this solution into an FCM cathode, a cathodic deposit with more than 99% palladium was obtained.

CONCLUSIONS

(1) It was shown that electrodeposition of palladium from nitric and hydrochloric acid solutions onto electrodes made of a fibrous carbon material occurs with high degree of recovery (>98%). The current efficiency by palladium is 5–25%, depending on concentrations of palladium(II) and hydrochloric acid in a solution and on current density. The low current efficiency is due to cuncurrent reduction of hydrogen ions and nitric acid.

(2) It was established that palladium deposited onto a fibrous carbon electrode dissolves in a 3.5 M HNO_3 solution with applying any external voltage through operation of a short-circuited electrochemical system constituted by Pd, fibrous carbon material, and 3.5 M HNO_3. The dissolution rate depends on the nature and composition of the solution from which palladium is deposited. The cathodic deposit obtained in electrodeposition from a nitric acid solution dissolves 4–5 times faster than that obtained from a hydrochloric acid solution.

(3) It was demonstrated, using a model short-circuited electrochemical system, that the reason for the strong difference between the rates of dissolution in nitric acid of palladium deposited from nitric and hydrochloric acid solutions is the presence in the cathodic deposit of sorbed hydrogen whose oxidation precedes the dissolution of palladium. The contribution from this process is much lower for cathodic deposits obtained in electrodeposition from nitric acid solutions.

(4) It was concluded that dissolution in a nitric acid solution of palladium on a fibrous carbon electrode through operation of a short-circuited electrochemical system can be used to enrich a solution with palladium and to separate the metal from the concomitant platinum metals.

REFERENCES

1. Plaksin, I.N., *Metallurgiya blagorodnykh metallov* (Metallurgy of Noble Metals), Moscow: Metallurgizdat, 1958.
2. Jaeger, G., *Affinazh blagorodnykh metallov elektrolizom* (Refining of Noble Metals by Electrolysis), Moscow: Tsvetmetizdat, 1932.
3. Varentsov, V.K., *Intensifikatsiya elektrokhimicheskikh protsessov* (Intensification of Electrochemical Processes), Tomilov, A.P., Ed., Moscow: Nauka, 1988, pp. 94–118.
4. Varentsova, V.I. and Varentsov, V.K., *Tsvetn. Met.*, 1997, no. 1, pp. 46–48.
5. Varentsov, V.K., Varentsova, V.I., Kablukov, V.I., *et al.*, *Tsvetn. Met.*, 1997, no. 7, pp. 34–37.
6. Dobos, D., *Electrochemical Data*, Budapest: Akademiai Kiado, 1978.
7. Varentsov, V.K. and Varentsova, V.I., *Zh. Prikl. Khim.*, 1997, vol. 70, no. 1, pp. 83–86.

8. Korovin, N.V., *Korrozionnye i elektrokhimicheskie svoistva palladiya* (Corrosive and Electrochemical Properties of Palladium), Moscow: Metallurgiya, 1976.
9. Vetter, K.J., *Elektrochemische Kinetik*, Berlin: Springer, 1961.
10. Jorgensen, C.K. and Parthasarathy, V., *Acta Chem. Scand.*, 1978, vol. A32, pp. 957–962.
11. Vishomirskis, R.M., A Study of the Kinetics of Electrodeposition of Metals from Complex Electrolytes, *Doctoral Dissertation*, Vilnius, 1966.
12. Varentsov, V.K. and Varentsova, V.I., *Zh. Prikl. Khim.*, 1999, vol. 72, no. 4, pp. 605–609.
13. Kreshkov, A.P., *Osnovy analiticheskoi khimii* (Fundamentals of Analytical Chemistry), Moscow: Khimiya, 1965.
14. Akimov, S.G., *Teoriya i metody issledovaniya korrozii metallov* (Theory and Methods for Study of Metal Corrosion), Moscow: Akad. Nauk SSSR, 1945.
15. Fedorova, A.M. and Frumkin, A.N., *Zh. Fiz. Khim.*, 1953, no. 2, pp. 247–260.
16. *Hydrogen in Metals*, Alefeld, G. and Völkl, J., Eds., Berlin: Springer, 1978.
17. Podlovchenko, B.I., Petukhova, R.P., Kolyadko, E.A., and Lifshits, A.D., *Elektrokhimiya*, 1976, vol. 12, no. 5, pp. 813–816.
18. Tarasevich, M.R., *Elektrokhimiya uglerodnykh materialov* (Electrochemistry of Carbon Materials), Moscow: Nauka, 1984.
19. Yakovlev, A.V., Finaenov, A.I., and Nikitina, L.E., *Zh. Prikl. Khim.*, 1999, vol. 72, no. 4, pp. 589–593.
20. Varentsov, V.K., Varentsova, V.I., and Renard, E.V., *Zh. Prikl. Khim.*, 2002, vol. 75, no. 1, pp. 60–62.
21. Levin, A.I., *Teoreticheskie osnovy elektrokhimii* (Theoretical Foundations of Electrochmistry), Moscow: Metallurgiya, 1972.

Russian Journal of Applied Chemistry, Vol. 76, No. 11, 2003, pp. 1744–1746. Translated from Zhurnal Prikladnoi Khimii, Vol. 76, No. 11, 2003, pp. 1794–1796.

APPLIED ELECTROCHEMISTRY AND CORROSION PROTECTION OF METALS

Electrochemical Oxidation of Tantalum in $LiNO_3$–$NaNO_3$–KNO_3 Melt

V. P. Yurkinskii, E. G. Firsova, and E. V. Afonicheva

St. Petersburg State Polytechnic University, St. Petersburg, Russia

Received July 1, 2003

Abstract—Growth kinetics of anodic oxide films on tantalum in a molten eutectic mixture of lithium, sodium, and potassium nitrates was studied and the influence exerted by introduction of hydroxide and chromate ions into the nitrate mixture was considered. The basic kinetic parameters of anodic oxidation of tantalum under galvanostatic conditions were determined.

Oxidation of tantalum is widely used in various fields of technology. Use of molten salts and, in particular, nitrates makes it possible to intensify anodic oxidation of Ta and to obtain oxide coatings with better service characteristics, compared with the coatings formed in aqueous electrolytes [1, 2]. It has been established that the presence of oxygen-containing ions in a melt strongly affects the kinetics of formation of oxide films on rectifying metals and their electrical properties [3, 4].

In continuation of previous investigations [2, 5], we studied the growth kinetics of anodic oxide layers on tantalum in a molten eutectic mixture of lithium (37.5 mol %), sodium (18 mol %), and potassium nitrates and the influence exerted by introduction of hydroxide and chromate ions into the nitrate melt.

EXPERIMENTAL

The study was carried out in the temperature range 413–503 K in a nitrogen atmosphere. The design of the electrochemical cell and methods used for pretreatment of nitrate salts and the electrode material have been described previously [3, 5].

Hydroxide and chromate ions were introduced into the melt in the form of KOH and Na_2CrO_4 of chemically pure grade. Na_2CrO_4 was preliminarily remelted and KOH was dehydrated by prolonged vacuum treatment in the course of heating (1.5–2.0 h) from room temperature to 800 K, with subsequent keeping at this temperature for about 3–4 h. The content of potassium hydroxide in the nitrate melt was 2 wt %; sodium chromate was introduced into the melt to saturation.

Tantalum was oxidized in the galvanostatic mode at current densities of 2.5–15 A m^{-2}. The procedure for galvanostatic measurements was described in [2, 5].

The thickness of the oxide film was determined by the capacitance technique [3, 6].

The dependences of the potential of the tantalum anode on the oxidation time for all the melts under study at different temperatures and current densities were linear. Figure 1 shows as an example the *E–i* curves obtained in the $LiNO_3$–$NaNO_3$–KNO_3–Na_2CrO_4 melt.

As is known [6], the linear run of the *E–i* curves is observed in oxidation of rectifying metals at high field strengths in the oxide film. In this case, the anodic process is limited by mass transfer of ions across the oxide layer formed on the surface of tantalum. The growth of oxide layers under conditions of high field strength in the oxide film is characterized by the de-

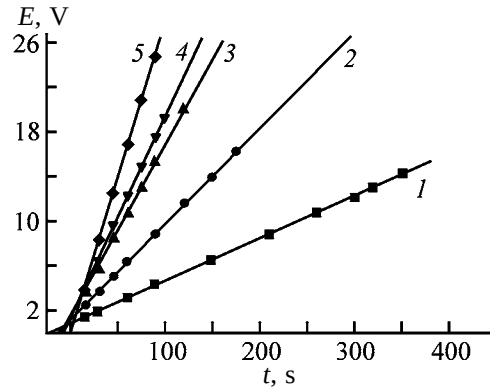

Fig. 1. Chronopotentiometric dependence obtained on tantalum at 428 K in the $LiNO_3$–$NaNO_3$–KNO_3–Na_2CrO_4 melt. (*E*) Potential and (*t*) time. Current density, A m^{-2}: (*1*) 2.11, (*2*) 4.44, (*3*) 7.37, (*4*) 8.70, and (*5*) 11.81.

1070-4272/03/7611-1744$25.00

Parameters of anodic oxidation of tantalum in the $LiNO_3$–KNO_3–$NaNO_3$ melt with additives, calculated using Eqs. (1)–(4) on the basis of experimental data. $W = 1.3 \pm 0.2$ eV, $a = 0.34 \pm 0.04$ nm, $\ln j_0$ (j_0, A m^{-2}) $= 26.5 \pm 4.5$

Additive	T, K	η, %	$-n$	m	C	$-D$	$d\delta/dt$, m s^{-1}
No additive	413	100 ± 7	0.50	0.85	2.0691	0.0036	1.78×10^{-10}
	428	96 ± 4	0.90	1.07			
	453	90 ± 7	0.82	1.11			
	478	85 ± 4	0.97	1.21			
	503	81 ± 5	–	–			
Na_2CrO_4 (sat.)	413	100 ± 6	3.64	0.99	0.0835	0.0001	5.82×10^{-11}
	428	98 ± 3	4.08	1.12			
	453	95 ± 5	4.09	1.14			
	478	85 ± 4	4.17	1.08			
	503	75±2	4.26	1.17			
KOH (2 wt %)	413	75 ± 4	3.71	1.10	0.1321	0.0002	8.12×10^{-11}
	428	69 ± 6	3.65	1.00			
	453	62 ± 5	3.76	1.22			
	478	55 ± 7	–	–			
	503	47 ± 3	4.79	1.66			

pendence of the ion current on the field strength, which is described by the Günther–Schulze equation [6]

$$j\eta = j_0 \exp(-W/kT) \exp(qaE_f/kT), \quad (1)$$

where j is the current density (A m^{-2}); η, current efficiency determining the fraction of the ion current j_i ($j_i = \eta j$) in the oxide; E_f, field strength (V m^{-1}); W, activation energy (eV); a, activation distance (nm); q, charge of an ion moving in the oxide (C); and j_0, constant determined by the nature of a metal (A m^{-2}).

The linear run of the dependence $\ln(j\eta)$–E_f confirms the applicability of Eq. (1) to the process under study. Figure 2 exemplifies such a dependence for the nitrate melt $LiNO_3$–$NaNO_3$–KNO_3 at several temperatures. All the dependences show similar types of behavior for all the temperatures in the range under study.

The values of η, W, a, and j_0 were found using Eq. (1) from experimental data. It was taken in the calculations that metal ions move across the oxide film. As established in [2, 5], mainly the higher oxide Ta_2O_5 is formed on the surface of tantalum being oxidized in a nitrate melt. Therefore, the density ρ (g cm^{-3}) and the dielectric constant ε of the oxide layer were taken to be, respectively, 7.93 and 27.6 [6]. The calculation results are listed in the table.

It can be seen that the current efficiency of tantalum oxidation decreases steadily in the temperature range under study. With account of Eq. (1), this indicates that the current flowing across the oxide film in electrochemical oxidation of tantalum in a nitrate melt is a sum of the ionic ($j\eta$) and electronic currents, with the share of the latter growing with temperature.

The slope of the E–t dependence (Fig. 1), which characterizes the rate of anodic oxidation of tantalum, is described by the equation

$$dE/dt = E_f d\delta/dt, \quad (2)$$

where $d\delta/dt$ is the oxidation rate (m s^{-1}); dE/dt, variation rate of the anode potential (V s^{-1}); and E_f, electric field strength in the oxide (V m^{-1}).

In this case, the variation rate of the anode potential grows with increasing density of the polarizing current and is a linear function of temperature [6].

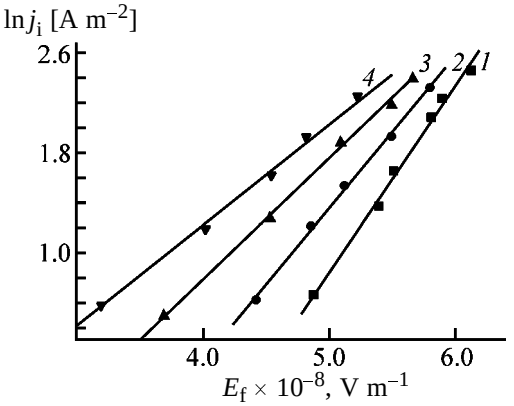

Fig. 2. $\ln j_i$ vs. electric field strength E_f in the oxide film, obtained for the $LiNO_3$–$NaNO_3$–KNO_3 melt. T, K: (*1*) 413, (*2*) 428, (*3*) 453, and (*4*) 478.

It was established that, at constant temperature, the dependence of the variation rate of the anode potential on the ionic current density is described by the equation

$$\ln(dE/dt) = n + m\ln(j\eta), \quad (3)$$

and the temperature dependence of the variation rate of the potential at current density of 1 A m^{-2}, by the empirical equation

$$(dE/dt) = c + DT. \quad (4)$$

The rates of tantalum anodizing and the coefficients of Eqs. (3) and (4) are listed in the table.

As seen from the table, the melt composition strongly affects the kinetic characteristics of tantalum anodizing. For example, the presence of hydroxide and chromate ions in a nitrate melt leads to a decrease in the current efficiency and oxidation rate of tantalum. On introduction of OH^- and CrO_4^{2-} ions into the melt, simultaneously with electrochemical oxidation of nitrate ions [7]

$$NO_3^- = NO_2 + 1/2O_2 + e, \quad (5)$$

one of the following reactions occurs [8, 9]:

$$2OH^- = H_2O + 1/2O_2 + 2e, \quad (6)$$

$$2CrO_4^{2-} = Cr_2O_7^{2-} + 1/2O_2 + 2e. \quad (7)$$

The simultaneous occurrence of reactions (5), (6) or (5), (7) should intensify tantalum oxidation. However, this is not the case. Possibly, this is due to incorporation of the anions mentioned above into the oxide film and to degradation of its dielectric properties. Apparently, addition of hydroxide ions also makes higher the corrosiveness of the melt toward Ta_2O_5. As a result, the current efficiency η and the oxidation rate $d\delta/dt$ decrease. According to [8], the activation energy W of electrochemical oxidation of tantalum in an orthophosphoric acid solution is 2.17 eV, and that in the nitrate melt $NaNO_3$–KNO_3, 1.56 eV [2]. In this study, a value of 1.3 ± 0.2 eV was obtained for the $LiNO_3$–$NaNO_3$–KNO_3 melt, in reasonable agreement with the data of [2]. Also in good agreement are the values of a and j_0 (see table), found for both the nitrate melts [2].

CONCLUSIONS

(1) Oxide layers grow on tantalum in the nitrate melts studied in accordance with the Günther–Schulze equation. The kinetic parameters of the process were determined.

(2) The current efficiency of tantalum oxidation decreases with increasing temperature.

(3) The melt composition affects the kinetic characteristics of tantalum anodizing. The presence of hydroxide and chromate ions leads to a decrease in the current efficiency and oxidation rate of tantalum.

REFERENCES

1. Inman, D. and Lavering, D.G., in *Comprehensive Treatise on Electrochemistry*, 1983, vol. 7, pp. 93–640.
2. Yurkinskii, V.P., *Rasplavy*, 1988, no. 4, pp. 74–82.
3. Yurkinskii, V.P., Vorob'eva, N.B., Morachevskii, A.G., *et al.*, *Zh. Prikl. Khim.*, 1979, vol. 52, no. 2, pp. 241–245.
4. Yurkinskii, V.P., Firsova, E.G., and Morachevskii, A.G., *Elektrokhimiya*, 1984, vol. 20, no. 7, pp. 980–982.
5. Yurkinskii, V.P., Makhalova, M.Yu., Firsova, E.G., and Morachevskii, A.G., *Zh. Prikl. Khim.*, 1988, vol. 61, no. 1, pp. 54–60.
6. Joung, L., *Anodic Oxide Films*, London: Academic, 1961.
7. Swofford, H.S. and Laitinen, H.A., *J. Electrochem. Soc.*, 1963, vol. 110, pp. 814–820.
8. Zakgeim, L.N., *Elektrokhimicheskie kondensatory* (Electrochemical Capacitors), Moscow: Gosenergoizdat, 1963.

Russian Journal of Applied Chemistry, Vol. 76, No. 11, 2003, pp. 1747–1751. Translated from Zhurnal Prikladnoi Khimii, Vol. 76, No. 11, 2003, pp. 1797–1801.

APPLIED ELECTROCHEMISTRY AND CORROSION PROTECTION OF METALS

Regeneration of Iron(III) Chloride Etching Solutions Containing Organic Additives

A. G. Belobaba, A. I. Maslii, and O. N. Shevtsova

Institute of Solid-State Chemistry and Mechanochemistry, Siberian Division, Russian Academy of Sciences, Novosibirsk, Russia

Received April 14, 2003

Abstract—The behavior of inorganic macrocomponents (Fe^{3+}, Fe^{2+}, Cu^{2+}, and Cl^{-}) and organic additives (judged from the relative concentration of total carbon) in regeneration and reuse of spent etching solutions used in fabrication of copper type-plates was studied. The conditions of electrochemical and sorption stages of the regeneration process were discussed.

Chemical etching with $FeCl_3$-based solutions is used in printing industry to obtain relief images on copper type-plates [1]. As a rule, the starting etching solution contains approximately (g l^{-1}): Fe^{3+} 90, Fe^{2+} 20, and Cu^{2+} 10. In etching a type-plate, the concentration of the oxidizing agent (Fe^{3+}) decreases and etching products (Fe^{2+} and Cu^{2+}) are accumulated. This leads to a decrease in the rate of etching and deterioration of its quality and necessitates replacement of the etching solution with its fresh portions. Since the cost of preparation of a fresh etching solution and that of utilization of spent etchant are rather high, the most natural solution of this technological and, simultaneously, environmental problem consists in regeneration and reuse of etching solutions.

The clear-cut distinction of the etching solution used in printing industry from a similar solution employed in manufacture of printed-circuit boards consists in that it contains organic additives introduced to ensure the required quality of etching. The behavior of these additives in the etching process and in regeneration of these solutions has not been studied so far. Therefore, two problems are to solved in developing the process and apparatus for regeneration of etching solutions of this kind. It is necessary to ensure the optimal mode of regeneration of inorganic components and also to study the behavior of organic additives in recycling of the etching solutions and determine the conditions under which the solutions can be purified to remove organic substances. Tackling with these problems was the aim of this study.

EXPERIMENTAL

A spent etching solution contains, in addition to $FeCl_3$, also $FeCl_2$ and $CuCl_2$. An ideal technique for regeneration of solutions of this kind is the membrane electrolysis [2, 3], since this method makes it possible to reverse, at the expense of electric power, the chemical reactions occurring in etching and thus to restore the composition of the solution without introducing into it any additional chemicals (oxidizing and reducing agents). The solution is regenerated in two stages in an electrolyzer with an anion-exchange membrane. In the first stage, the etching solution is subjected to cathodic treatment, with the result that Fe^{3+} is reduced to Fe^{2+}, and Cu^{2+}, to metallic copper:

$$FeCl_3 + e = FeCl_2 + Cl^-, \quad (1)$$

$$CuCl_2 + 2e = Cu + 2Cl^-. \quad (2)$$

The treated catholyte contains the required amount of Cu^{2+}, but the ratio of Fe^{3+} to Fe^{2+} ion concentrations is far from being normal. Therefore, anodic treatment of the solution, carried out in the second stage of regeneration, is necessary. In the process, oxidation of Fe^{2+} to Fe^{3+} and transfer of Cl^- across the membrane from the cathode chamber into the anode one leads to formation of an $FeCl_3$ solution:

$$FeCl_2 - e + Cl^- = FeCl_3. \quad (3)$$

In the course of anodic treatment, the concentration of Fe^{2+} in the anolyte decreases and that of Fe^{3+} increases. As a result, the concentrations of all the

1070-4272/03/7611-1747$25.00

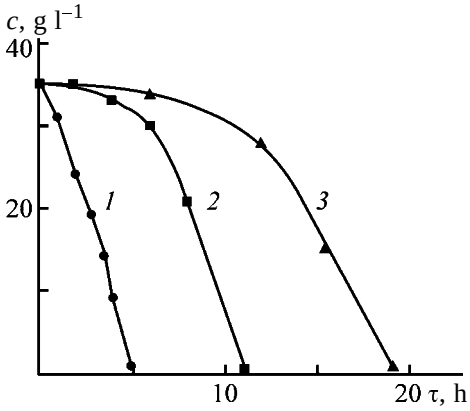

Fig. 1. Variation of the concentration c of copper(II) ions in the catholyte in the course of electrochemical regeneration at different current densities. (τ) Time. Current density (A dm^{-2}): (*1*) 1.5, (*2*) 3, and (*3*) 6.

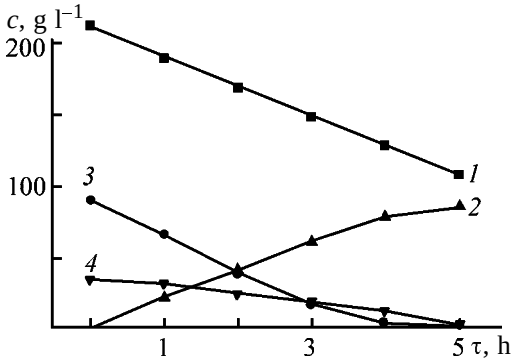

Fig. 2. Variation of the concentration *c* of catholyte macrocomponents with time τ of electrolysis. Current density i = 6 A dm^{-2}; the same for Fig. 3. Macrocomponent: (*1*) Cl^-, (*2*) Fe^{2+}, (*3*) Fe^{3+}, and (*4*) Cu^{2+}.

macrocomponents become close to those in the starting etching solution at a certain instant of time, and the solution being regenerated can be reused in etching.

A model etching solution, for which the cathodic regeneration mode was chosen, contained $FeCl_3$ and $CuCl_2$, with Fe^{3+} and Cu^{2+} concentrations of 95 and 35 g l^{-1}, respectively. An $FeCl_2$ solution (110 g l^{-1} in terms of Fe^{2+}) served as anolyte. The solutions were prepared from pure-grade chemicals and distilled water. The experiments wee performed in a membrane electrolyzer in the galvanostatic mode at current densities i of 1.5–6 A dm^{-2}. The electrode spaces were separated by an MA-40 anion-exchange membrane. The cathode was made of titanium, and the anode, of graphite. The working areas of the electrodes and the membrane were 0.36 dm^2. The solution volume in each of the chambers was 250 ml. During electrolysis, the catholyte and anolyte in the non-flow-through chambers were agitated with compressed air from a microcompressor.

In the course of regeneration, the concentrations of macrocomponents in the catholyte and anolyte, current strength, cathode and anode potentials (relative to a saturated calomel electrode), pH value, and temperature and volume of the solution were monitored. The concentrations of Fe^{3+}, Fe^{2+}, and Cl^- were determined by titration [4], and the total Cu, by the atomic-absorption method. Direct cathodic voltammetry on a renewable graphite electrode [5] was employed for proximate analysis of the solutions for these components. The concentration of organic substances in the solutions was found from the total organic carbon by the method developed in [6].

The optimal working parameters of electrolysis are to be found experimentally for any particular type of etching solution, depending on its composition. The choice is due to the necessity for satisfying simultaneously several conditions ensuring the maximum rate of copper recovery, preventing electrolyte overheating, and precluding occurrence of side electrode processes.

Figure 1 shows how the concentration of copper(II) ions in the catholyte varies in the course of electrolysis at different current densities. It can be seen that, depending on the current density, two different ways of development of the cathodic process are observed: successive and parallel reduction of Fe^{3+} and Cu^{2+}. At low current densities, these ions are reduced successively: first, mainly Fe^{3+} ions are reduced, with virtually no metallic copper recovered, and only after the concentrations of Fe^{3+} and Cu^{2+} become close, the rate of copper recovery increases. With increasing current density, the initial delay in the beginning of copper deposition shortens dramatically and virtually vanishes at i = 6 A dm^{-2}. Naturally, the reduction of Fe^{3+} leads to an increase in the concentration of Fe^{2+} (Fig. 2). Simultaneously, the concentration of Cl^- ions decreases because of their migration into the anode chamber, i.e., the process of electrochemical regeneration is described virtually quantitatively by a set of equations (1)–(3). A minor deviation from this scheme consists in the appearance of a small amount of copper ions in the anolyte (up to 1.5 g l^{-1}) in the final stage of electrolysis. This is presumably due to formation in the catholyte of negatively charged complexes of copper(I) ($CuCl_2^-$ and $CuCl_3^{2-}$) in the first stage of copper(II) discharge and to their migration across the anion-exchange membrane into the anode chamber.

Further intensification of copper recovery by raising the current density is limited, on the one hand, by

solution heating and, on the other, by side reactions of H_2 evolution at the cathode and Cl_2 evolution at the anode. The solution heating is limited by the thermal stability of the ion-exchange membrane (about 50°C). Evolution of chlorine at the anode is unacceptable environmentally, and evolution of hydrogen at the cathode is accompanied by an undesirable increase in pH in the near-cathode layer and by formation of iron and copper hydroxides. For example, during cathodic treatment at current density of 6 A dm^{-2}, the pH of the catholyte grows from 0.2 to 1–1.7, i.e., to values at which $Fe(OH)_3$ may start to form, and the solution temperature increases to 40°C (Fig. 3), approaching the maximum permissible value. In this context, raising the current density further is hardly advisable.

A pilot batch of real spent solutions was regenerated under the chosen conditions on an electromembrane installation comprising an electrolyzer, a dc power source (12 V, 50 A), a microcompressor for air bubbling in order to agitate the catholyte and anolyte, and an electronic thermometer. The cathode and anode were made of titanium and graphite, respectively. The working area of each of the electrodes was 4 dm^2, and the membrane area, 6.6 dm^2; the volumes of the catholyte and anolyte were 20 l each.

Figure 4 shows anodic and cathodic current–voltage characteristics of a real etching solution at characteristic points of its regeneration: (1) starting spent solution and the same solution after (2) cathodic and (3) anodic treatments. The voltammograms enable prompt monitoring of the regeneration process and make it possible to evaluate the concentrations of macrocomponents in the catholyte and anolyte in order to terminate at due time the solution treatment. As regards the quantitative interpretation of the curves, it should be noted that the cathodic peak at φ = 400 mV is related to reduction of Fe^{3+} to Fe^{2+}. The potential of Cu^{2+} reduction to Cu^+ lies in the same range of potentials [7], so that the peaks of Fe^{3+} and Cu^{2+} reduction virtually coincide. The second peak in the cathodic part of the voltammogram (φ = –350 mV) is associated with reduction of Cu^+ to metallic copper. In the anodic part of the voltammogram, there is a single peak at φ = 750 mV, which corresponds to oxidation of Fe^{2+} to Fe^{3+}. The voltammograms also show the potentials of side electrode reactions: evolution of Cl_2 at the anode is possible at φ ≈ 1.5–1.6 V, and that of hydrogen at the cathode, at about –(0.6–0.7) V. Comparison of the current–voltage curves in Fig. 4 shows that electrochemical regeneration ensures that the excess concentration of copper(II) is removed

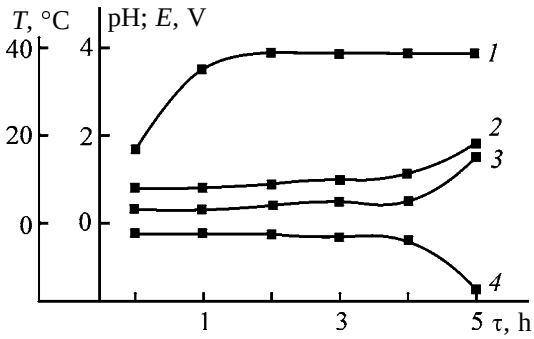

Fig. 3. (*1*) Solution temperature *T*, potentials *E* of (*2*) anode and (*4*) cathode, and (*3*) pH of the catholyte vs. electrolysis time τ in regeneration of a model solution.

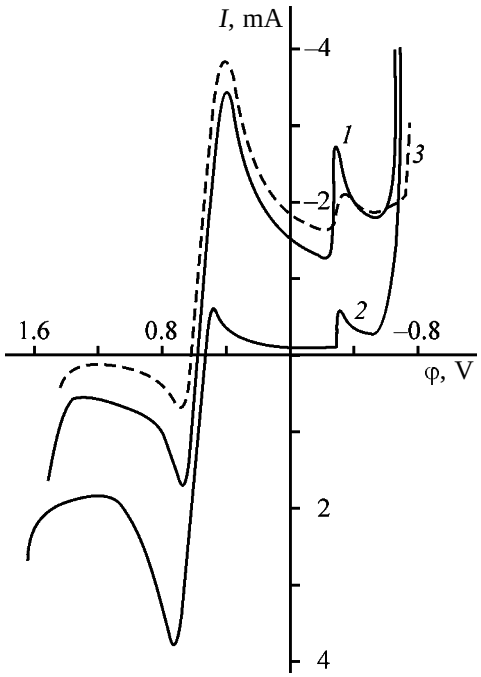

Fig. 4. Anodic and cathodic current–voltage characteristics of (*1*) spent etching solution and that being subjected to regeneration after stages of (*2*) cathodic and (*3*) anodic treatments. Measurement conditions: graphite electrode with mechanically renewed surface (S = 0.03 cm^2), potential sweep rate 20 mV s^{-1}, and temperature 25°C; the same for Fig. 5. (*I*) Current and (φ) potential (vs. saturated calomel electrode); the same for Fig. 5.

from a solution and the necessary Fe^{3+}/Fe^{2+} ratio is restored.

Prolonged studies of the electrochemical regeneration demonstrated that, if the recommended current density of 6 A dm^{-2} is used, the main electrolysis parameters in processing of real etching solutions in the electromembrane setup (cathode and anode potentials, voltage drop across the membrane, and solution temperature) are close to their limiting values but do

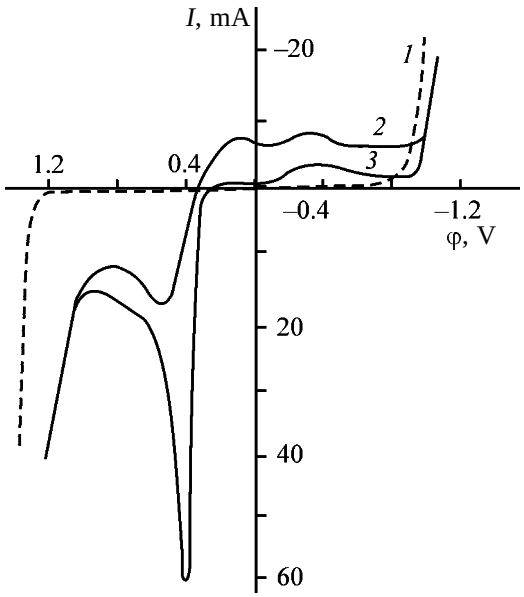

Fig. 5. Cathodic and anodic polarization curves of (*1*) supporting electrolyte (2 M NaCl + 0.15 M HCl) and solutions with addition (1 g l^{-1}) of (*2*) stabilizer and (*3*) calibrator.

not exceed them, which indicates that the regeneration mode is nearly optimal. The setup has been working in this mode for already more than three years. During this period of time, more than 10 000 l of the etching solution has been regenerated. The average processing rate of the etching solution was 12 l day^{-1}, and the energy expenditure, 0.27 kW h l^{-1}, with copper deposited at the cathode in the form of a powder and periodically removed from the titanium cathode when replacing the regenerated solution.

The prolonged experience of electrochemical regeneration of spent etching solutions in manufacture of copper type-plates demonstrated the efficiency of membrane electrolysis, which makes it possible not only to restore the etching ability of the solution, but to recover copper from it. However, it was established that the quality of the type-plates became poorer after 4–5 etching cycles, although all the macroscopic parameters of the regenerated solutions were normal.

The most probable reason for the impaired quality of etching is accumulation of organic additives or products of their degradation in the solution. The organic substances contained in a mixture of two brand-name additives, calibrator and stabilizer, are added to the solution to ensure high quality and fast etching rate.

The behavior of additives in the course of regeneration can be prognosticated qualitatively if their electrochemical activity, i.e., the ability to be oxidized or reduced at electrodes, and also their chemical stability are known. Figure 5 shows voltammograms of the supporting electrolyte, and also of the calibrator and stabilizer. It can be seen that both the organic additives are electrochemically active, i.e., exhibit peaks of both reduction and oxidation in the working range of potentials. Since it is known that one of the additives contains thiourea and formamidine disulfide (FADS), it should be mentioned that these substances are chemically unstable. For example, FADS decomposes in the course of time into thiourea, cyanamide, and sulfur [8]. Thiourea, in turn, may decompose in acid solutions to give H_2S [9]. Thus, it follows from the results presented that the organic additives used in etching are active electrochemically and unstable chemically. Therefore, they may decompose, with decomposition products accumulated both in the etching stage and in any of the two stages in electrochemical regeneration of solutions.

Quantitative monitoring of organic additives in etching solutions is strongly complicated by specific features of the etchant, highly intense coloration and high concentration of macrocomponents. Such a composition of the supporting solution made impossible use for this purpose of UV spectroscopy [8], voltammetry[1], and various chemical methods based on oxidation of organic substances (chemical consumption of oxygen, permanganate oxidizability, etc.) [10]. The only method applicable to determination of the total organic carbon is that [6] according to which organic substances contained in a solution are found from the amount of CO_2 evolved in mineralization of the etching solution in the presence of H_2O_2 and under its irradiation with UV light in a closed quartz reactor.

The changes in the concentration of the total organic carbon (g l^{-1}) in electrochemical regeneration of samples of etching solutions with low (sample 1) and high (sample 2) concentration of organic substances are presented below:

Treatment stage	Sample no. 1	Sample no. 2
Starting solution	0.25	0.95
Cathodic treatment	0.20	0.75
Anodic treatment	0.15	0.65

It can be seen that the content of organic substances decreases in both cathodic and anodic treatment of a solution. The relative degree of removal of organic additives is the higher, the lower their initial content

[1] Characteristic peaks of organic additives (Fig. 5) lie within the same range of potentials as the peaks of the macrocomponents (Fig. 4), but their intensity is much lower than that of the latter (by approximately two orders of magnitude).

Residual concentration of total organic carbon, c_{res}, in sorption purification of two samples of etching solutions with various specific charges q of Sibunit sorbent. Solution agitation by air, contact time 3 h

Sample	c_{res}, g l^{-1}, at indicated q, g l^{-1}					
	0	10	30	50	60	100
1	0.25	0.18	–	0.05	–	0.05
2	0.95	0.80	0.65	–	0.55	0.50

(70% for the lower curve and 30% for the upper one). The decrease in the recovery of organic impurities with their increasing concentration in the starting solution may be due to gradual accumulation of products formed in their conversion, which are more stable against electrochemical treatment. Anyway, it may be concluded on the basis of the aforesaid that accumulation of organic substances in high concentrations is inadvisable and it is necessary to regularly purify etching solutions to remove organic impurities.

The most appropriate technique to be used for this purpose is sorption by activated carbon, and one of the most promising sorbents is a new carbon material Sibunit [11]. This sorbent is distinguished by high mechanical, chemical, and thermal stability (1000–1500°C) and is simple in regeneration. The efficiency of sorption purification was confirmed on solutions with the maximum and minimum content of organic impurities.

The table illustrates the influence exerted by the sorbent charge on the removal of organic substances. It can be seen that the first portions of the sorbent show the most effective performance, especially in solutions with relatively low concentration of organic impurities. At Sibunit expenditure exceeding 50 g l^{-1}, the sorption slows down, and, therefore, the recommended specific expenditure of the sorbent for purification of etching solutions to remove organic substances is about 50–60 g l^{-1}.

Enlarged-scale tests of joint electrochemical and sorption regeneration of industrial $FeCl_3$-based etching solutions with organic additives gave good results as regards both the rate and quality of etching with regenerated solutions, close to those for fresh etchants.

CONCLUSIONS

(1) A study of the behavior of inorganic macrocomponents (Fe^{3+}, Fe^{2+}, Cu^{2+}, and Cl^-) and organic additives of spent etching solutions in their electrochemical regeneration and recycling of regenerated solutions demonstrated that successive cathodic and anodic treatments of etching solutions restore the concentrations of the macrocomponents to the required level and remove up to 30% of organic impurities.

(2) An integrated method for regeneration of etching solutions was developed. This method combines electrochemical and sorption stages and allows reuse of a regenerated solution, which ensures the required rate and quality of etching.

ACKNOWLEDGMENTS

The authors are grateful to T.G. Kuznetsova for analysis of solution samples for the content of total organic carbon.

REFERENCES

1. Geodakon, I.A., *Proizvodstvo klishe* (Manufacture of Type-Plates), Moscow: Kniga, 1972.
2. US Patent 3394060.
3. Anishchenko, I.A., Aleksandrova, Z.F., Fedorova, N.N., and Shatalov, A.Ya., *Teoriya i praktika sorbtsionnykh protsessov* (Theory and Practice of Sorption Processes), Voronezh: Voronezh. Univ., 1985, no. 17, pp. 119–121.
4. Charlot, G., *Les methods de la chimie analytique. Analyse quantitative minerale*, Paris: Masson, 1961, 4th ed.
5. Kletennik, Yu.B., Polyakin, L.Yu., Tarasova, V.A., *et al.*, *Izv. Sib. Otd. Akad. Nauk SSSR, Ser. Khim. Nauk*, 1985, issue 6, pp. 63–65.
6. Kusnetsova, T.G. and Savinov, E.N., *J. Adv. Oxid. Technol.*, 1999, vol. 4, no. 2, pp. 218–221.
7. Balagurova, T.A., Kucherenko, V.I., and Flerov V.N., *Zh. Prikl. Khim.*, 1973, vol. 46, no. 2, pp. 324–328.
8. Maslii, A.I. and Lupenko, G.K., *Izv. Sib. Otd. Akad. Nauk SSSR, Ser. Khim. Nauk*, 1974, no. 12, issue 5, pp. 12–15.
9. Damaskin, B.B., Petrii, O.A., and Batrakov, V.V., *Adsorbtsiya organicheskikh soedinenii na elektrodakh* (Adsorption of Organic Compounds on Electrodes), Moscow: Nauka, 1968.
10. Lur'e, Yu.Yu., *Analiticheskaya khimiya promyshlennykh stochnykh vod* (Analytical Chemistry of Industrial Wastewater), Moscow: Khimiya, 1984.
11. Plaksin, G.V., *Khim. Inter. Ustoich. Razv.*, 2001, vol. 9, no. 5, pp. 609–620.

Russian Journal of Applied Chemistry, Vol. 76, No. 11, 2003, pp. 1752–1758. Translated from Zhurnal Prikladnoi Khimii, Vol. 76, No. 11, 2003, pp. 1802–1808.

APPLIED ELECTROCHEMISTRY AND CORROSION PROTECTION OF METALS

Effect of Certain Organic and Inorganic Salts on Dissolution of Zinc

V. V. Ekilik, E. A. Tugolukova, and A. G. Berezhnaya

Rostov State University, Rostov-on-Don, Russia

Received August 8, 2002; in final form, June 2003

Abstract—Dissolution of zinc in a borate buffer solution with addition of substituted pyridinium perchlorates and some inorganic salts was studied. The performance of additives in the active and passive states and in the case of local depassivation of zinc was compared using various methods, including correlation analysis.

Data on additives used in anodic dissolution of zinc in borate buffer solutions are limited to aromatic amino acids and their salts [1], and also to certain inorganic compounds [2], which inhibit or promote the process.

The aim of this study was to elucidate the mechanism and character of zinc dissolution, reveal the influence of substituents in pyridinium cations, and compare the effects of organic and inorganic salts.

EXPERIMENTAL

Dissolution of zinc (99.9% Zn) was studied by measuring polarization curves with stepwise (with intervals of 30 s) increasing potential E, anodic chronoammograms at constant E, and cyclic chronovoltammograms in a borate buffer solution (pH 7.4) bubbled with purified argon. The electrode, having the form of a plate with working surface area of 1 cm^2, was conditioned with emery paper with decreasing grain size (2–0) and degreased with purified ethanol. The measurements were performed in a three-electrode cell with separated catholyte and anolyte at 25°C. Saturated silver chloride electrode was used as reference, relative to which all E values are given.

As additives were used $KClO_4$, $LiClO_4$, KCl, KBr (all salts of chemically pure grade) and pyridinium perchlorates

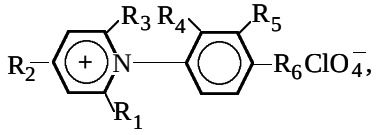

where $R_1 = R_2 = R_3 = CH_3$, $R_5 = R_6 = H$, $R_4 = NH_2$ (no. 1); $R_1 = R_2 = R_3 = CH_3$, $R_4 = R_6 = H$, $R_5 = NH_2$ (no. 2); $R_1 = R_2 = R_3 = CH_3$, $R_5 = R_6 = H$, $R_4 = Br$ (no. 3); $R_1 = R_2 = R_3 = C_6H_5$, $R_4 = R_6 = H$, $R_5 = NH_2$ (no. 4); $R_1 = R_2 = R_3 = C_6H_5$, $R_4 = R_5 = H$, $R_6 = NH_2$ (no. 5); $R_1 = R_2 = R_3 = C_6H_5$, $R_5 = R_6 = H$, $R_4 = Br$ (no. 6); $R_1 = R_3 =$ 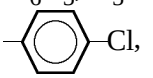 , $R_2 = C_6H_5$, $R_4 = R_5 = R_6 = H$ (no. 7).

The effect of the additives on the dissolution process was evaluated by the coefficient $K = i/i_1$, where i and i_1 are the process rates in, respectively, straight solution and that with an additive.

Before analyzing the influence exerted by the additives, it is appropriate to consider in brief the kinetics and mechanism of anodic dissolution of zinc.

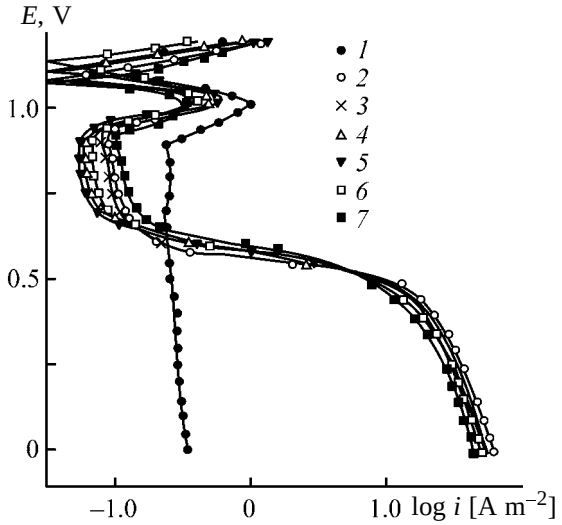

Fig. 1. Polarization curves measured in (*1*) straight solution and (*2–7*) solutions with a mixture of additive no. 2 and $KClO_4$. Mixture concentration 1 mM. (*E*) Potential and (*i*) current density. Concentration $c \times 10^4$ of additive no. 2, M: (*2*) 0, (*3*) 1.0, (*4*) 2.0, (*5*) 5.0, (*6*) 7.0, and (*7*) 10.0.

1070-4272/03/7611-1752$25.00

In accordance with the data of [1], zinc is anodically passivated (Fig. 1) and is not subject to local passivation in the absence of additives.

The nature of the hindered stage was judged from results of potentiostatic and chronovoltammetric measurements. According to the theory of cyclic voltammetry [3], the criterion of a reversible diffusion-controlled process is the presence of linear dependences of the current densities of the anodic and cathodic peaks on the square root of the variation rate of E. Another necessary condition is that the difference of the peak potentials must not exceed $58/n$ mV, where n is the number of electrons. As can be seen from Fig. 2, only the first condition is satisfied. Consequently, the process occurs in the equilibrium mode, but is irreversible. Since E_{ap} and i_{ap} are the critical E_p and i_p of passivation, the data in Fig. 2 illustrate the role of diffusion in the transition of the metal to the passive state. The decrease in the diffusion limitations on the process with increasing potential sweep rate V causes a pronounced rise in E_{ap} and i_{ap}, i.e., hinders passivation. The important role of mass-transfer in the solid phase in formation and reduction of the oxide in passivation and activation of a copper electrode under conditions of reversible dissolution was mentioned in [4]. Presumably, the anodic peak does not correspond under the conditions considered to only equilibrium formation of zinc oxide, since metal dissolution occurs in parallel with film formation.

It should also be noted that, in the absence of an active–passive transition, no anodic peak is observed in the cyclic voltammogram, in contrast to the cathodic peak. This was demonstrated for the NiZn alloy with 20 wt % Ni, which is passive even at the potential of free corrosion, although the dependence of the current density of total passivation, i_{tp}, on $V^{1/2}$ is similar to that shown in Fig. 2.

The anodic chronoammograms in Fig. 2 describe dissolution of zinc in the active and passive states. In a straight solution, the time dependence of the rate of active dissolution is characterized by three regions: at $\tau < 50$ s, the straight lines i–$\tau^{1/2}$ (Fig. 3c) indicate, with account taken of the diffusion-kinetic mode of the process [5, 6], that the rates of the charge-transfer (i_e) and nonstationary-diffusion (i_{nd}) stages are comparable [7]; at 50 s $< \tau <$ 3 min, the straight lines i–$\tau^{-1/2}$, extrapolated to the origin of coordinates (Fig. 3b), indicate that nonstationary diffusion is the rate-limiting stage [7]; at $\tau > 5$ min, when $i \neq f$ (Fig. 3b), the process is controlled by stationary liquid-phase diffusion at a rate i_{sd}.

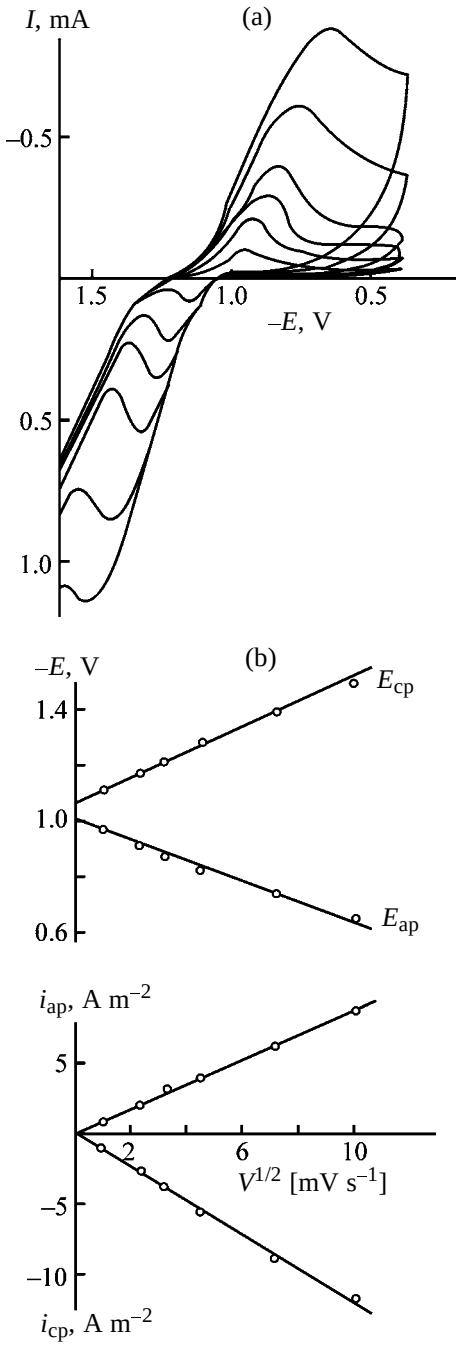

Fig. 2. (a) Chronoammograms measured in straight solution and (b) dependences of the potentials E_{cp} and E_{ap} and current densities i_{cp} and i_{ap} corresponding to cathodic and anodic peaks in the chronovoltammograms on the potential sweep rate V. Potential sweep rates (in order of increasing current in the chronovoltammogram) 1, 5, 10, 20, 50, and 100 mV s^{-1}. (I) Current and (E) potential.

For the case of reversible dissolution, the data of [7, 8] were used to obtain the dependence of i on τ and stage rates at polarization $\Delta E \gg RT/F$ in the first region:

Table 1. Kinetic characteristics of active dissolution of zinc

Additive no.	i_e, A m^{-2}	$Q \times 10^2$, A m^{-2} s$^{-1/2}$	γ_1, A m^{-2} s$^{1/2}$	i_{sd}, A m^{-2}	γ_2, A m^{-2} s$^{1/2}$
No additive	0.43	3.9	3.02	0.10	1.54
1	0.28	2.1	2.38	0.07	1.32
5	0.12	0.4	2.29	0.06	1.24

$$i = i_e - Q\tau^{1/2} = i_e[1 - 2i_e(\pi i_{nd})^{-1}], \quad (1)$$

$$Q = 2i_e^2(\pi\gamma_1)^{-1}, \quad (2)$$

$$i_{nd} = nF(c_S - c_0)(D/\pi\tau)^{1/2} = \gamma_1\tau^{-1/2}, \quad (3)$$

where c_S and c_0 are, respectively, the surface and volume concentrations of Zn(II), and D is the diffusion coefficient.

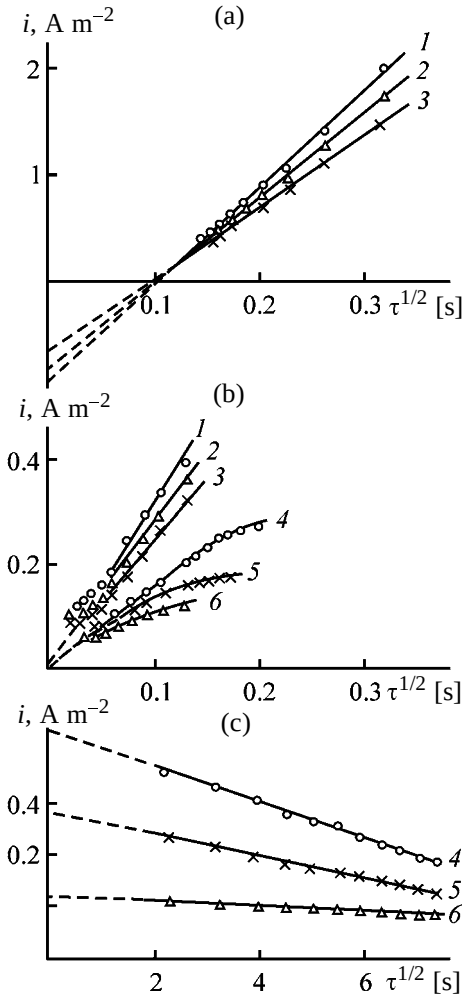

Fig. 3. Anodic chronoammograms measured in (*1*, *4*) straight solution and solutions with additive nos. (*2*, *6*) 5 and (*3*, *5*) 1. Concentration of additives 10^{-4} M; the same for Fig. 4. (*i*) Current density and (τ) time. Potential, V: (*1*–*3*) –0.5 and (*4*–*6*) –1.05. (a–c) For explanation, see text.

It follows from Eq. (2) that

$$\gamma_1 = 0.64i_e^2Q^{-1}. \quad (4)$$

The data of Fig. 3c were used to determine, using Eqs. (1)–(4), the main kinetic characteristics (Table 1).

In the second region, in which $i \approx i_{nd}$, the dependence of i on τ is described by Eq. (3), which makes it possible to find γ_2 from the straight line i–$\tau^{1/2}$ (Fig. 3b). Comparison of the values of γ_1 and γ_2 (Table 1) shows that γ decreases with time. To a first approximation, this can be attributed, in accordance with Eq. (3), to an increase in c_0 with time. Since the dissolution occurs at E = –1.05 V, which is close to E_p = –1.02 V, it can be assumed, with account of the model of concurrent processes of metal dissolution and oxygen chemisorption [9], that a passive film is formed in the course of time, which may be a second reason for a decline in γ because of the decreasing effective value of D. This conclusion is supported by the close values of steady-state i at E equal to –1.05 and –0.5 V (Fig. 3b).

When an anodic chronoammogram is measured at E = –0.5 V, weak areas of air-formed oxide are strengthened by the anodic oxide, and the decaying process of rearrangement of the oxide–hydroxide film leads to a decrease in i. It has been noted [9] that time dependences of i for other metals and of the rates of formation of surface layers on coatings are described, in the general case, by the equation

$$i = i_0 + \gamma\tau^{-\beta}, \quad (5)$$

where i_0, γ, and β are constants, with β equal to 0.5 [10, 11] or 1 [11, 12].

The process on zinc in a borate buffer solution occurs in two stages, which is indicated by two straight lines i–$\tau^{-1/2}$ (Figs. 3a, 3b); the constants of Eq. (5) are listed in Table 2. After the second stage, a steady-state current i_s is attained.

Taking into account the diffusion-kinetic control over dissolution of zinc in the active state at small τ, the role of inhibitors can be played by surfactants,

Table 2. Constants of Eq. (5) describing the anodic chronoammogram of passive dissolution of zinc

Additive no.	$-i_e$, A m^{-2}	γ, A m^{-2} s$^{1/2}$	β	i_s, A m^{-2}
		$\tau < 60$ s		
No additive	0.19	8.4	0.5	–
1	0.13	7.0	0.5	–
5	0.16	7.8	0.5	–
		$\tau > 60$ s		
No additive	0	3.0	0.5	0.11
1	0	2.4	0.5	0.08
5	0	2.7	0.5	0.09

which make lower i_s, and also by film-forming and complexing agents, which diminish, respectively, the effective and true value of D. According to Table 1, substituted pyridinium perchlorates are rather versatile. They hinder both stages of the process, this being more pronounced for the charge-transfer stage, for which the values of K for additive nos. 1 and 5 are equal to, respectively, 1.5 and 3.6. The hindrance to the stationary-diffusion stage remains virtually unchanged on passing from mixed ($K \approx 1.3$) to diffusion ($K \approx 1.2$) control. The additives make longer the time during which the type of control changes (Fig. 3b). Therefore, K increases somewhat, to 1.4–1.6, in the stationary mode.

In the passive state, a certain protective effect would be expected for compounds whose particles can be incorporated into a film, changing its structure and healing its defects. Substituted pyridinium perchlorates mainly affect the value of γ, but do so to a lesser extent than in the active region, and the values of K, equal to 1.1–1.2 in the nonstationary mode, remain virtually unchanged in passing to the stationary mode (K = 1.2–1.3).

The effect of E on K for pyridinium salts was evaluated, with account of the nature of the zinc dissolution process, on the basis of polarization measurements (Table 3).

Table 3 reveals a characteristic feature of the influence exerted by the additives. The more pronounced the protective effect in the active region, the weaker the same effect in the passive region and the stronger the stimulation of local passivation. Presumably, this is due to competition of adsorption of surfactants and passivation in accordance with the model described in [9]. On areas occupied by chemisorbed inhibitor particles, chemisorption of oxygen and subsequent formation of a passivating oxide–hydroxide film are hindered. As a result, the overall influence exerted by the inhibitor and the film decreases with increasing E. This effect is the stronger, the easier the chemisorption of particles in the active region. Naturally, the weakening of the protective properties of the passive film favors local depassivation under the action of activator anions. The role of these anions can be played by ClO_4^- ions of pyridinium salts.

The regular trend in the variation of K within the series of the additive studied (Table 3) created a prerequisite for use of a correlation based on the linear free energy relationship. Here, several approaches are possible. Attempts to use reference values of σ constants of substituents for polysubstituted compounds within the additive scheme failed to give positive results. Using values of K for the stationary reaction series when performing the correlation, as it was done

Table 3. Values of K for substituted pyridinium perchlorates in relation to their structure and potential E. Concentration of additives 10^{-4} M

E* range	$-E$, V	K for indicated additive						
		no. 2	no. 3	no. 1	no. 7	no. 6	no. 4	no. 5
$E < E_p$	1.06	1.7	1.6	1.8	2.0	2.2	3.4	4.9
$E = E_p$	1.02	1.5	1.4	1.6	1.9	2.1	3.3	3.9
$E_p < E < E_{tp}$	0.96	1.5	1.6	1.7	2.0	2.1	2.7	3.1
$E = E_{tp}$	0.90	1.5	1.5	1.7	1.5	1.2	1.1	1.1
$E_{tp} < E < E_{pt}$	0.60	1.6	1.4	1.5	1.3	1.3	1.2	1.1
$E \geq E_{pt}$	0.20	1.1	0.9	0.9	0.7	0.6	0.5	0.4
$E > E_{pt}$	0.00	0.9	0.9	0.6	0.5	0.4	0.3	0.2

* E_{tp}, potential of total passivation; E_{pt}, pitting potential at which a rise in i with time is observed; E_{pt} decreases steadily from –0.1 to –0.4 V in going successively from additive no. 2 to additive no. 5.

Table 4. Characteristics of electronic absorption spectra of substituted pyridinium perchlorates in borate buffer solution

Additive no.	λ, nm	$f \times 10^4$, $mol^{-1}\ cm^{-2}$	$GD_p \times 10^{20}$, $mol^{-1}\ cm^{-1}$
2	275	1.4	3.4
3	275	1.8	4.5
1	275	2.2	5.5
7	318	3.3	9.6
6	278	4.1	10.4
4	315	8.0	23.2
5	315	9.7	27.9

for similar compounds for the case of inhibition of acid corrosion of metals, is too formalized. Therefore, the relationship between K and some parameters of the electronic absorption spectra of dissolved additives was considered by analogy with [14, 15]. This correlation is based on the concept of surfactant chemisorption in the electronically excited state [16]. The excitation energy of π electrons is characterized by the wavelength λ of the longest-wave absorption band in the UV part of the electronic spectrum [17]. The probability of transition of the system from the ground state to excited state, determined by the oscillator strength f, is one more factor, in addition to that energy-related, which strongly affects the chemisorption. The state of polarization of the electronic transition is indicated by such a complex characteristic as

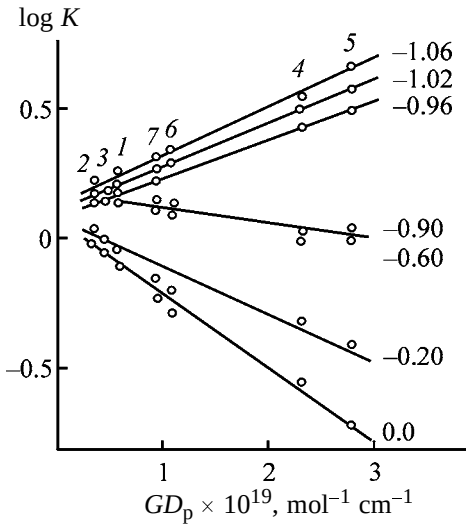

Fig. 4. log K vs. GD_p. (K) Ratio of the anode current densities in a straight solution and that with an additive; (GD_p) product of the possible degeneracy of the upper and lower states by the dipole strength of the electronic transition. Digits at lines correspond to potentials (V); the same for Fig. 5. Digits at points correspond to numbers of additives.

the product of the dipole strength of the transition, D_p, by the possible degeneracy G of the upper and lower states [18]:

$$GD_p = 0.124 \times 10^{-12} f\lambda. \quad (6)$$

The characteristics mentioned are listed in Table 4.

The correlation expressions relating K to λ and f to GD_p have the general form [13, 14]

$$\log K = \log K_{0,x} + æ_x(X - X_0), \quad (7)$$

where X stands for λ, f, or GD_p; $K_{0,x}$ and $æ_x$ are the constants of the reaction series; $\lambda_0 = 275$ nm, $f_0 = 1.4 \times 10^{-4}\ mol^{-1}\ cm^{-2}$, and $GD_p = 3.4 \times 10^{-20}\ mol^{-1}\ cm^{-1}$ are the values of the characteristics taken as standard to rule out far extrapolation of K.

The applicability of relations of the type (7) is illustrated by plots in Fig. 4, and Table 5 lists the constants of the reaction series and correlation coefficients r. The values of K for determining K_0, æ, and r are taken from Table 3.

Table 5 shows that the worst correlation is obtained between log$K$ and λ. This becomes understandable when account is taken of the fact that λ is less sensitive to the nature of substituents (Table 4) than K (Table 3). In accordance with the above-mentioned change in K on passing from active to passive zinc dissolution (Table 3), the sign of the constants æ changes to the opposite. In this same transition, a decrease in r is observed, which may be due to influence of unaccounted-for factors. In particular, the methyl-substituted additives from the beginning of the series (nos. 1–3) can more readily find their way into the forming oxide film, compared with the other, phenyl-substituted additives. To the transition mentioned corresponds a reversal of the sign of the surface charge ($E^{Zn}_{q=0} = -0.82$ V [19]) from negative to positive, which favors a π-electron interaction and can change the surface orientation of particles.

The effect of the additives strongly depends on their concentration, which was demonstrated for compound no. 2, $KClO_4$, and mixture of these (Figs. 1 and 5). At more negative E, additive no. 2 acts as an adsorption inhibitor, for which characteristic straight lines log$K$–log$c$ with slopes changing in the same direction as K were obtained (Fig. 5a). Potassium perchlorate behaves similarly up to $c = 5 \times 10^{-4}$, after which K starts to decrease. Possibly, this is due to the fact that the anions are characterized by U-shaped dependences of the rate of metal dissolution on c [20].

Table 5. Constants of the reaction series of substituted pyridinium perchlorates and correlation coefficients *r*

$-E$, V	$K_{0,\lambda}$	$K_{0,f}$	$K_{0,GD}$	$æ_\lambda \times 10^{-2}$	$æ_f \times 10^{-2}$	$æ_{GD} \times 10^{-20}$	r_λ	r_f	r_{GD}
1.06	1.8	1.6	1.6	0.6	5.4	1.8	0.726	0.985	0.989
1.02	1.6	1.5	1.5	0.6	5.1	1.8	0.768	0.983	0.993
0.96	1.7	1.6	1.6	0.4	3.4	1.2	0.789	0.967	0.984
0.90	1.5	1.5	1.5	–0.2	–2.1	–0.7	0.554	0.899	0.876
0.60	1.4	0.7	1.5	–0.2	–1.5	–0.5	0.797	0.884	0.917
0.20	0.9	0.9	0.9	–0.5	–4.5	–1.6	0.744	0.940	0.926
0.00	0.7	0.8	0.8	–0.8	–6.9	–2.4	0.726	0.934	0.945

When $E \approx -0.7$ V is reached, anodic-anionic activation is observed, which is especially clearly manifested at $c > 3 \times 10^{-4}$ M (Figs. 1 and 5b). After a significant rise in i in the range W from -0.35 to -0.50 V, a virtually limiting anodic current is reached.

In order to eliminate anionic effects at potentials corresponding to the active–passive transition, binary mixtures of additive no. 2 and $KClO_4$ with constant total concentration of 1 mM were studied. In the absence of K^+ ions, this would make it possible to evaluate the influence exerted by the concentration of the pyridinium cation. However, the value of K for $KClO_4$ exceeds unity (Fig. 5c). Experiments with $LiClO_4$ demonstrated that the values of K for this additive are unity in the active region and virtually coincide with those in the presence of $KClO_4$ in passivation. This suggests that ClO_4^- ions play an important part in passivation, and K^+ ions, in hindrance to active dissolution. Therefore, the effect of the mixture can be, to a first approximation, considered in terms of joint adsorption of potassium and pyridinium cations. Their mutual influence was evaluated using the known method [21]

$$\delta = K_{\text{no. 2} + KClO_4}(K_{\text{no. 2}} K_{KClO_4})^{-1}, \qquad (8)$$

where the subscripts denote the additives used.

If the coefficient of mutual influence $\delta > 1$ at $K > 1$, the effects exerted by the inhibitors are mutually enhanced. Under the conditions studied, even though the additives belong to different types of compounds, they compete and mutually weaken the influence of each other, since $\delta < 1$ (Fig. 5e). The minimum values of δ correspond to a mixture with $c_{\text{no. 2}} = c_{KClO_4} = 5 \times 10^{-4}$ M. The extreme values of K for potassium perchlorate and for the mixture are observed at this same value of c_{KClO_4}. In agreement with the above-mentioned competition between surfactant adsorption and passivation, the dependences of K of a mixture on its composition exhibit the opposite behavior in the active region and in passivation (Fig. 5d). This transition is accompanied by weakening of the competitive

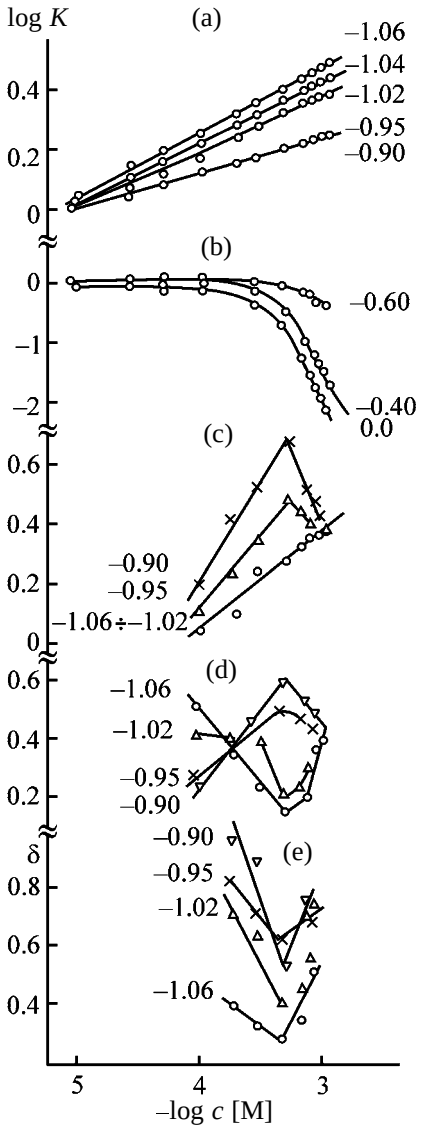

Fig. 5. log$K$ for (a, b) additive no. 2, (c) $KClO_4$, and (d) mixture of these, and also (e) δ vs. log$c$ for (a, b) additive no. 2 and (c–e) $KClO_4$. Total concentration of additives in the mixture 10^{-3} M. (K) Ratio of anode current densities in a straight solution and that with an additive, (δ) coefficient of mutual influence of additives in the mixture, and (c) concentration.

Table 6. Value of K in relation to E and nature of salt anion. Salt concentration 1 mM

$-E$, V	Value of K for indicated salts		
	$KClO_4$	KCl	KBr
1.06–1.02	2.4	2.0	1.5
0.95	2.3	4.1	4.3
0.90	2.2	1.8	3.0
0.80	2.4	2.3	3.1
0.50	0.020	0.016	0.015
0.00	0.006	0.006	0.006

action of the additives (Fig. 5e).

In the presence of KCl and KBr, the polarization curves are similar to those shown in Fig. 1 for pyridinium and potassium perchlorates; the corresponding values of K are listed in Table 6.

Compared with $KClO_4$, KCl and, especially, KBr additives hinder active dissolution to a lesser extent and are more effective in passivation; they lower the potential of local depassivation by 100 mV and accelerate somewhat this process. The limiting anodic current is virtually independent of the nature of salt.

CONCLUSIONS

(1) In the active state, zinc dissolves in the initial period of time with comparable rates of ionization and nonstationary diffusion; then the second of these becomes rate-limiting and, finally, gives way to stationary diffusion. Substituted pyridinium perchlorates hinder ionization to a greater extent.

(2) In the passive region, the time dependence of the dissolution rate is characterized by two portions. The sequence of pyridinium salts arranged in order of their increasing inhibiting action changes to the opposite one when zinc passes from the active to passive state, which is due to competition of two processes: chemisorption of additives and passivation by oxygen.

(3) It is advisable to correlate the performance of substituted pyridinium perchlorates in dissolution of zinc with parameters of the long-wave absorption band in the UV part of the electronic absorption spectrum of the dissolved additives.

(4) Mixtures of potassium and substituted pyridinium perchlorates give lower values of K in active dissolution of zinc, and higher values in passivation and in the passive state. Irrespective of the type of the process, the mixtures are characterized by mutual weakening of the influence exerted by the constituent compounds. This weakening is the most pronounced for the 1 : 1 composition.

REFERENCES

1. Kuznetsov, Yu.I. and Kuznetsova, I.G., *Zashch. Met*., 1986, vol. 22, no. 3, pp. 474–478.
2. Abd El Aal, E.E., *Corros. Sci*., 2000, vol. 42, no. 1, pp. 1–16.
3. Galus, Zb., *Teoretyczne podstawy elektroanalisy chemicznej*, Warsaw: Naukowe, 1971.
4. Grushevskaya, S.N. and Vvedenskii, A.V., *Zashch. Met*., 1999, vol. 35, no. 4, pp. 346–354.
5. Grigor'ev, N.B., Gedvillo, I.A., and Bardina, N.G., *Elektrokhimiya*, 1972, vol. 8, no. 3, pp. 409–412.
6. Popova, S.S., Solov'eva, N.D., and Savel'eva, E.A., *Elektrokhimiya*, 1982, vol. 18, no. 6, pp. 716–720.
7. Marshakov, I.K., Vvedenskii, A.V., Kondrashin, V.Yu., and Bokov, G.A., *Anodnoe rastvorenie i selektivnaya korroziya splavov* (Anodic Dissolution and Selective Corrosion of Alloys), Voronezh: Voronezh. Gos. Univ., 1988.
8. Ekilik, V.V., Komakhidze, M.G., Berezhnaya, A.G., and Sudorgin, N.G., *Zashch. Met.*, 1997, vol. 33, no. 4, pp. 384–388.
9. Lazorenko-Manevich, R.M., Sokolova, L.A., and Kolotyrkin, Ya.M., *Elektrokhimiya*, 1995, vol. 31, no. 3, pp. 235–243.
10. Lilin, S.A., Balmasov, A.V., Shmukler, M.V., and Rumyantsev, E.M., *Zashch. Met*., 1996, vol. 32, no. 4, pp. 432–436.
11. Novakovskii, V.M. and Ovcharenko, V.I., *Zashch. Met*., 1968, vol. 4, no. 6, pp. 656–664.
12. Bondareva, T.P. and Novakovskii, V.M., *Zashch. Met*., 1970, vol. 6, no. 2, pp. 207–209.
13. Ekilik, V.V. and Grigor'ev, V.P., *Priroda rastvoritelya i zashchitnoe deistvie ingibitorov korrozii* (Nature of Solvent and Protective Action of Corrosion Inhibitors), Rostov-on-Don: Rostov. Gos. Univ., 1984.
14. Grigor'ev, V.P., Kuznetsov, V.V., Ekilik, V.V., and Shelepin, O.E., *Zh. Prikl. Khim*., 1969, vol. 42, no. 7, pp. 804–809.
15. Grigor'ev, V.P. and Ekilik, V.V., *Khimicheskaya struktura i zashchitnoe deistvie ingibitorov korrozii* (Chemical Structure and Protective Action of Corrosion Inhibitors), Rostov-on-Don: Rostov. Gos. Univ., 1978.
16. Trapnell, B.M.W., *Chemisorption*, London: Butterworth, 1955.
17. Rao, C.N.R., *Ultra-Violet and Visible Spectroscopy; Chemical Applications*, London: Butterworth, 1961.
18. *Chemical Applications of Spectroscopy*, West, W., Ed., New York: Interscience, 1956.
19. Rotinyan, A.L., Tikhonov, A.I., and Shoshina, I.A., *Teoreticheskaya elektrokhimiya* (Theoretical Electrochemistry), Leningrad: Khimiya, 1981.
20. Kolotyrkin, Ya.M., *Zashch. Met*., 1967, vol. 3, no. 2, pp. 131–144.
21. Pogrebova, I.S., *Ukr. Khim. Zh*., 1982, vol. 48, no. 12, pp. 1275–1280.

Russian Journal of Applied Chemistry, Vol. 76, No. 11, 2003, pp. 1759–1763. Translated from Zhurnal Prikladnoi Khimii, Vol. 76, No. 11, 2003, pp. 1809–1813.

APPLIED ELECTROCHEMISTRY AND CORROSION PROTECTION OF METALS

Corrosion Behavior in Alkaline Media of Steel with Various Conversion Coatings in Concrete

G. Bikulčius, O. Girčiene, and V. Burokas

Institute of Chemistry, Vilnius, Lithuania

Received November 27, 2002; in final form, May 2003

Abstract—The corrosion behavior in alkaline media of St.3 steel with various conversion coatings in concrete was studied.

Reinforced concrete structures are widely used in construction of buildings and bridges. It is traditionally believed that steel in concrete is protected by passivation compounds formed in the strongly alkaline medium in pores (pH 12.6 at 25°C). However, carbon dioxide CO_2 present in the Earth's atmosphere enhances the corrosiveness of the medium toward reinforced concrete structures working under normal and humid conditions [1–5]. Penetration of carbon dioxide into concrete leads to its carbonation. Acid gases, e.g., SO_2, Cl_2, NO_2, etc., are frequently present in working spaces. Their interaction with concrete occurs similarly to the carbonation process. It has been established that the pH of the pore liquid decreases to 10.5 and less at high humidity in the presence of acid gases or chloride ions. It was shown in [6] that the threshold concentration of chloride ions at which iron corrosion begins depends on pH. With decreasing pH, the continuity of the protective layer on steel, which is composed of iron oxide γ-Fe_2O_3, is disturbed [1]. According to the results obtained by most of researchers, the corrosion rate of steel in carbonated concrete is the highest at periodic moistening of structures or in the case of condensate formation [2, 4, 5]. This problem has been studied extensively [6–10]. Analysis of published data makes it possible to state that steel is in the passive state only in uncarbonated concrete at low concentrations of chlorides.

Steel is commonly protected from corrosion with paint-and-varnish materials, electroplated and immersion coatings composed of Zn and its alloys, and conversion coatings deposited prior to painting. In [11], it was suggested to subject zinc coatings, in order to improve their corrosion resistance, to anodizing in solutions containing silicates, tetraborates, and alkali. The resulting anodic coating enhances by 20% the hardness of the zinc coating, exhibits good adhesion to the base, and possesses excellent corrosion-protective properties.

Conversion phosphate coatings [12–14] are films composed of difficultly soluble salts $Zn_3(PO_4)_2 \cdot 4H_2O$, $Fe_3(PO_4)_2 \cdot 2H_2O$, and $Zn_2Fe(PO_4)_2 \cdot 2H_2O$, formed in reaction of the metal with free phosphoric acid and with acidic Zn and Fe phosphates.

The phosphate layer formed improves the adhesive and protective properties of paint-and-varnish coatings and hinders corrosion when the paint film is damaged. Phosphate coatings are classified into two groups: crystalline coatings based on zinc phosphate, with mass of 1.4–7.5 g m^{-2}, and amorphous, based on the $FePO_4$, with mass of 0.2–1.4 g m^{-2}. Corrosion tests in a salt-spray chamber (5% NaCl) demonstrated that the corrosion resistance of steel with crystalline and amorphous phosphate coatings increases by a factor of several tens [15]. With properly chosen composition of the phosphating solution and conditions of its application, phosphate coatings with prescribed properties can be obtained in any particular case. Apparently, a certain structure and composition of a phosphate layer must correspond to each method of phosphating.

The aim of this study was to analyze the corrosion behavior in alkaline media of steel protected with various conversion coatings in concrete.

EXPERIMENTAL

The solutions used were prepared using analytically pure chemicals. The working electrodes were made of St.3 steel. Polarization curves were measured in the potentiodynamic mode at potential sweep rate of 0.1 mV s^{-1} in an aerated 0.1 M NaOH + 0.1 M NaCl solution at 25°C. A platinum electrode served as auxiliary electrode, and saturated silver chloride

1070-4272/03/7611-1759$25.00

Table 1. Composition of solutions and phosphating conditions

Phosphating	Composition,* M	pH	T, °C	τ, min	m, g m^{-2}
F11 crystalline	Zn^{2+} 10.084, Ca^{2+} 0.03, PO_4^{3-} 0.17, NO_3^- 0.2	2.4–2.6	45–55	10	3–5
FA5O amorphous	PO_4^{3-} 0.16, MoO_4^{2-} 0.0005	4.7–5.2	45–50	5	0.4–0.8
F36 black	Zn^{2+} 0.17, PO_4^{3-} 0.34, NO_3^- 0.28	2.2–2.4	45–55	10	8–10
F16 amorphous black	PO_4^{3-} 0.13, NO_3^- 0.28	1.8–2.0	18–20	0.5–2.0	0.4–0.8

* Concentration of Se^{4+}, Cu^{2+}, and Ni^{2+} salts (color modifiers), M: F36 0.048, F16 0.35.

Ag/AgCl electrode, as reference. Prior to each measurement, samples were kept for 15 min in the solution under study. The corrosion current density was found by extrapolation of the Tafel portions of the anodic and cathodic polarization curves. Numerous studies have shown that the passivity of steel is commonly accompanied by a positive shift of the electrode potential of the metal. Therefore, the corrosion potential E_{cor} of steel in concrete can serve as indicator of its state. In measurements in concrete, the variation of E_{cor} of steel with time τ was studied. A saturated

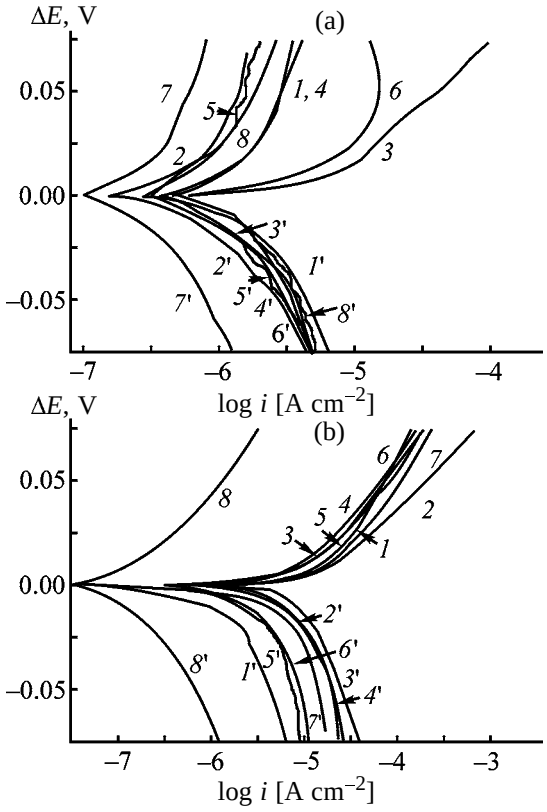

Fig. 1. (*1*–*8*) Anodic and (*1*′–*8*′) cathodic polarization curves obtained on St.3 steel in aerated 0.1 M NaOH solution containing 0.1 M NaCl at pH (a) 13 and (b) 9. Potential sweep rate V_s = 0.1 V s^{-1}. (*i*) Current density and (Δ*E*) polarization. (*1*) No coating; conversion coating: (*2*) FA–As–Al, (*3*) F16, (*4*) FA–As, (*5*) FA50(*n*), (*6*) F36, (*7*) FA50, and (*8*) F11.

$Cu/CuSO_4$ electrode served as reference. All the potentials are given in the hydrogen scale.

The composition of the electrolyte used to deposit conversion coatings onto steel plates, component concentrations, deposition modes, and coating masses are listed in Table 1.

Part of samples with amorphous phosphate coatings were dried at 100°C for 1 h (FA50), and another part remained untreated ([FA50(*n*)]. Silicate anodizing [11] of steel samples coated with FA50 was performed in a solution of composition (g l^{-1}): NaOH 30, $Na_2B_4O_7$ 90, and Na_2SiO_3, at solution temperature not exceeding 25°C in the course of 10 min with ac current of 20 A dm^{-2} for FA–As, and with ac and, additionally, pulsed current for FA–As–Al.

Reinforced concrete samples in the form of cylinders were made from portland cement of composition (%): SiO_2 21.4, Al_2O_3 3.9, Fe_2O_3 2.2, CaO 62.5, MgO 0.5, SO_3^{2-} 4.7, Na_2O 0.8, K_2O 0.6, and Cl^- 0.3, and steel reinforcement ($10 \times 10 \times 0.5$ mm St.3 steel plate). Cement cylinders 50 mm in diameter and 50 mm high were formed from a mixture with cement : sand ratio of 1 : 3 and water : cement ratio of 1 : 2. A steel plate with various conversion coatings was embedded in concrete cylinder at a height of 30 mm. Such a reinforced concrete sample was kept in a mold for 24 h. Then it was extracted, stored under laboratory conditions for 84 h, and placed in water or a 3.5% solution of NaCl in such a way that its lower part (10 mm) was submerged. With the cylinder in this position and good aeration of the external medium, diffusion of the solution into concrete is ensured, to the level of the steel plate. The potential of the steel reinforcement with various conversion coatings was measured daily over the course of 33 days. The degree of concrete carbonation was determined using the phenolphthalein indicator [12].

The values of i_{cor} of the samples under study in an aerated NaOH solution containing 0.1 M NaCl at pH 13 (Fig. 1a) and 9 (Fig. 1b), found by extrapolation of the Tafel portions of the anodic and cathodic

Table 2. Electrochemical parameters* of St.3 steel with conversion coatings in NaOH solutions containing 0.1 M NaCl

Coating	b_A, mV	b_C, mV	i_{cor}, A cm^{-2}	b_A, mV	b_C, mV	i_{cor}, A cm^{-2}
	pH 13			pH 9		
No coating	170	120	1.4×10^{-6}	72	104	1.3×10^{-5}
F16	57	158	3.2×10^{-6}	39	144	1.2×10^{-5}
FA50(*n*)	160	130	9.1×10^{-7}	56	233	8.0×10^{-6}
FA–As	125	80	8.9×10^{-7}	55	140	9.1×10^{-6}
FA–As–A1	221	76	6.8×10^{-7}	50	107	1.3×10^{-5}
F36	160	118	5.0×10^{-7}	87	105	5.4×10^{-6}
F11	106	104	4.4×10^{-7}	59	84	1.4×10^{-7}
FA50	174	76	3.0×10^{-7}	49	150	4.6×10^{-6}

* b_A and b_C are the anodic and cathodic Tafel constants.

polarization curves in the $\log i$–ΔE coordinates, are listed in Table 2. It can be seen that at pH 13 the lowest corrosion currents are observed for steel samples with F11 and FA50 coatings, and the highest, for samples without conversion coating and with F16 coating. With the solution pH decreasing to 9, i_{cor} grows by an order of magnitude for all of the samples studied (from 10^{-7}–10^{-6} A cm^{-2} at pH 13 to 10^{-6}–10^{-5} A cm^{-2} at pH 9). The only exception are samples with F11 coating, for which i_{cor} at pH 9 is 1.4×10^{-7} A dm^{-2} (Table 2). Thus, the lowest corrosion currents at pH 13 or 9 are observed for samples with conversion coatings F11 and FA50. Changes in the solution pH also affect the anodic (b_A) and cathodic (b_C) Tafel constants. At pH 13, b_A varies from 57 to 221 mV, and b_C, from 76 to 158 mV. At pH 9, b_A = 39–87 mV and b_C = 84–233 mV (Table 2).

Before carrying out measurements with steel in concrete, the rate of concrete carbonation was measured with phenolphthalein indicator. It was established experimentally that only in 7 days the pH value of the pore liquid in concrete decreased to 10 and/or less (pH ~9). The electrode potentials of samples without conversion coating and with F11, FA50, and F36 coatings, embedded in concrete, were measured in an NaOH solution (pH 13) (Fig. 2a) or 3.5% NaCl solution (pH ~9) (Fig. 2b) during 33 days.

Measurements of the dependence E_{cor}–τ for reinforced concrete samples submerged in an NaOH solution (pH 13) demonstrated that the potential of steel without conversion coating (Fig. 2a, curve *1*) decreases from 0 to –30 mV in the first 5 days, and then, during the following 28 days, gradually increases to 30 mV. A similar behavior was observed for steel with various conversion coatings. In the case of an FA50 coating (Fig. 2a, curve *4*), E_{cor} increases to 140 mV in 33 days. In the case of an F36 coating (Fig. 2a, curve *2*), E_{cor} decreases from 70 to –150 mV

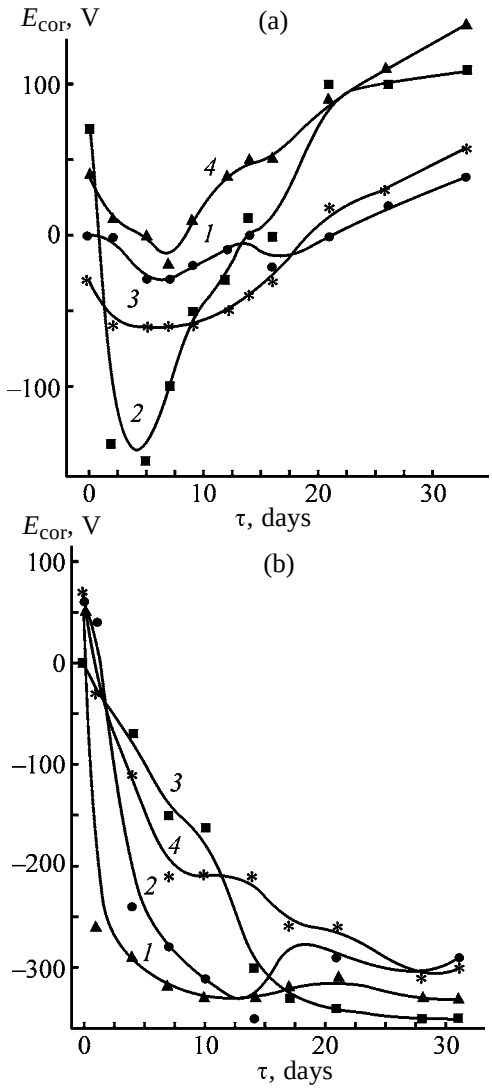

Fig. 2. Corrosion potential E_{cor} of St.3 steel with various conversion coatings in concrete vs. time τ of keeping in (a) NaOH and (b) 3.5% NaCl solutions. pH: (a) 13 and (b) 9. (*1*) Without coating; conversion coating: (*2*) F36, (*3*) F11, and (*4*) FA50.

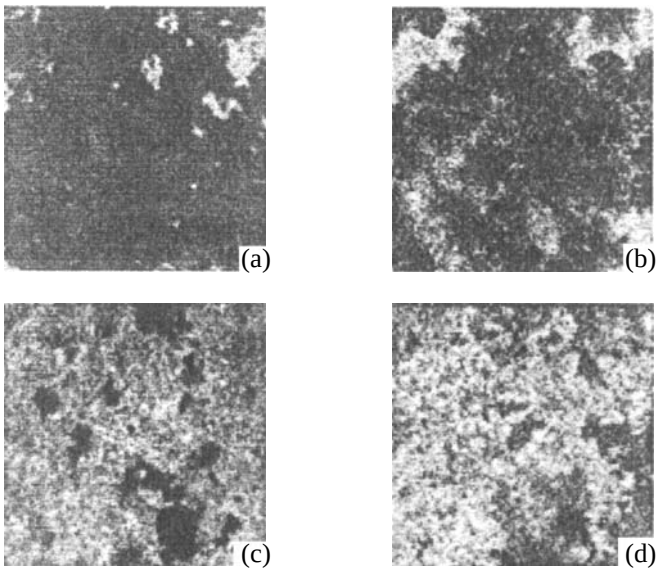

Fig. 3. Surface micrograph of St.3 with various conversion coatings after keeping in a 3.5% NaCl solution for 59 days. (a) Without coating; conversion coating: (b) F36, (c) F11, and (d) FA50.

during the first 5 days, then starts to grow to become 110 mV after 20 days of tests, and remains virtually unchanged during the subsequent 13 days. It should be noted that a steeper run of the E_{cor}–τ curve is observed in the given case. According to the results obtained, FA50 coatings show the highest corrosion resistance.

A study of the dependence E_{cor}–τ in a 3.5% NaCl solution (pH ~9) demonstrated that, in all cases, a rather steep decrease in E_{cor}, from 0–60 mV to the value ranging from –200 to –340 mV, is observed in the first 10–15 days (Fig. 2b). During the remaining 15–20 days, E_{cor} fluctuates within the range from –300 to –350 mV. However, the corrosion potential of samples with FA50 coating is more positive during 33 days than the E_{cor} of the other samples under study (Fig. 2b, curve *4*). This suggests that the FA50 coating has the best protective properties.

St.3 carbon steel can be represented, in the media under study over the whole range of potentials, as a system of the type metal–oxide or metal–metal phosphate, although the composition and structure of corrosion products may be more complex [14, 17]. It was established that the best protective properties in an NaOH solution containing no chloride ions (pH 13) are exhibited by the FA50 conversion coating (Fig. 2a, curve *4*). In a 3.5% NaCl solution (pH ~9), all the conversion coatings studied disintegrate during 33 days (Fig. 2b). However, the disintegration of the FA50 conversion coating (Fig. 2b, curve *4*) occurs at a lower rate.

Figures 3a–3d show surface micrographs of steel samples extracted from concrete after 59 days of tests in a 3.5% NaCl solution. The samples without conversion coating and with F36 coating are completely corroded (Figs. 3a, 3b). The F11 and FA50 coatings (Figs. 3c, 3d) exhibit better protective properties, and, therefore, St.3 steel is less subject to corrosion. Using the above results of the electrochemical measurements, it was established the lowest corrosion currents are observed in an NaOH solution containing 0.1 N NaCl at pH 13 and 9 for samples with F11 and FA50 conversion coatings (Table 2). A study of steel in concrete placed in water (pH 13) or 3.5% NaCl solution demonstrated that preference is to be given to FA50 coatings, since they exhibit the best protective properties.

CONCLUSIONS

(1) The lowest corrosion currents in an NaOH solution containing 0.1 M NaCl at pH 13 and 9 are observed for St.3 steel samples with conversion phosphate coatings F11 and FA50.

(2) Among the coatings studied, amorphous phosphate conversion coating FA50 ensures the best corrosion protection of a steel reinforcement in concrete placed in NaOH solution (pH 13) or 3.5% NaCl solution (pH ~9).

REFERENCES

1. Page, C.L. and Treadaway, K.W.J., *Nature*, 1982, vol. 297, no. 5, pp. 109–114.
2. Komokhov, P.G., Latypov, V.M., Vagapov, R.F., and Latypova, T.V., *Izv. Vyssh. Uchebn. Zaved., Stroit.*, 1998, no. 3, pp. 113–119.
3. Saques, A.A. and Kranc, S.C., *Corrosion*, 1992, vol. 48, no. 8, pp. 624–633.
4. Moskvin, V.M., Ivanov, F.M., Alekseev, S.N., and Guzeev, E.A., *Korroziya betona i zhelezobetona, metody ikh zashchity* (Corrosion of Concrete and Reinforced Concrete and Methods for Their Protection), Moscow: Stroiizdat, 1980.
5. Alekseev, S.N., Ivanov, F.M., Modry, S., and Schissl, P., *Dolgovechnost' zhelezobetona v agressivnykh sredakh: Sovmestnoe izdanie SSSR–ChSSR–FRG* (Longevity of Reinforced Concrete in Corrosive Media: Joint Publication by USSR, CSSR, and FRG), Moscow: Stroiizdat, 1990.
6. Li, L. and Sagues, A.A., *Corrosion*, 2001, vol. 57, no. 1, pp. 19–28.

7. Caballero, C.E., Sanchez, E., Cano, U., *et al*., *Corrosion Rev*., 2000, vol. 18, nos. 2–3, pp. 105–112.
8. Foulkes, F.R. and McGrath, P., *Cem. Concr. Res*., 1999, vol. 29, pp. 873–883.
9. Videm, K. and Myrdal, R., *Corrosion*, 1997, vol. 53, no. 9, pp. 734–742.
10. Wheat, H.G. and Eliezer, Z., *Corrosion*, 1985, vol. 41, no. 11, pp. 640–645.
11. Shih, H.C., Shyr, F.Y., Hsu, J.W., *et al*., *Plat. Surf. Finish*., 1999, no. 1, pp. 104–107.
12. Kozlova, L.A. and Okulov, V.V., *Gal'vanotekh. Obrab. Poverkhn*., 1999, vol. 7, no. 2, pp. 27–34.
13. Kozlova, L.A. and Okulov, V.V., *Gal'vanotekh. Obrab. Poverkhn*., 2000, vol. 8, no. 1, pp. 37–41.
14. Freeman, D.B., *Phosphating and Metal Pretreatment*, Cambridge (England): Woodhead-Faulkner, 1986.
15. Gladkovas, M., Burokas, V., Martusiene, A., and Bucinskiene, D., *Chemija*, 2001, vol. 12, no. 12, pp. 114–118.
16. Loto, C.A., *Corrosion*, 1992, vol. 48, no. 9, pp. 759–763.
17. Kaesche, H., *Die Korrosion der Metalle. Physikalisch-chemische Prinzipien und aktuelle Probleme*, Berlin: Springer, 1979.

Russian Journal of Applied Chemistry, Vol. 76, No. 11, 2003, pp. 1764–1768. Translated from Zhurnal Prikladnoi Khimii, Vol. 76, No. 11, 2003, pp. 1814–1818.

APPLIED ELECTROCHEMISTRY AND CORROSION PROTECTION OF METALS

Corrosion-Protective Properties of *N*-Phenacylmethylpyridinium Bromides

R. I. Yurchenko, I. S. Pogrebova, T. N. Pilipenko, and E. M. Kras'ko

Kiev Polytechnic Institute, National Technical University of Ukraine, Kiev, Ukraine

Received July 1, 2003

Abstract—The inhibiting action of *N*-phenacylmethylpyridinium bromides on corrosion of carbon steel in a 3 M sulfuric acid solution was studied. A relationship between the structure of the compounds under study and their corrosion-protective properties was revealed. Compounds ensuring high degree of corrosion protection of steel in acid media were found.

Despite that the relationship between the structure of organic compounds and their corrosion-protective properties have been studied for a relatively long time [1–3], this problem still remains topical. Particularly promising is a search for effective corrosion inhibitors among substances exhibiting the so-called intramolecular synergism [4–6]. This effect consists in that the presence of functional groups of varied nature in the inhibitor molecule enables multidimensional action on the corrosion process and ensures effective protection by the inhibitor.

As objects of study were chosen phenacylmethylpyridinium bromides **I**–**XI**, which are of interest in that they are simultaneously quaternary pyridinium salts and aromatic carbonyl compounds, i.e., belong to such types of organic compounds whose inhibiting action is well known [1, 2, 7].

Compounds **I**–**XI** were synthesized by alkylation of 2-substituted pyridines with the corresponding ω-bromoacetophenones:

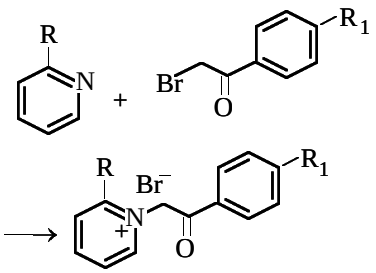

I–**XI**

where R = H, CH_3, NH_2, $COCH_3$; R_1 = H, CH_3, OCH_3, Br, Cl, NO_2.

The presence in these compounds of a methylene bridge separating the pyridinium and benzoyl moieties makes it possible to act upon each of them separately by varying the substituents R and R_1 and to reveal factors positively affecting the inhibiting action of the molecule as a whole.

EXPERIMENTAL

Compounds **I**–**IV** were synthesized by published procedures; compounds **V**–**XI** were uknown previously, and their structure was confirmed by IR and ^1H NMR spectroscopy.

2-Amino-1-phenacylmethylpyridinium bromide V, 2-amino-1-(4-methylphenacyl)methylpyridinium bromide VII, 2-amino-1-(4-methoxyphenacyl)methylpyridinium bromide VIII, 2-amino-1-(4-bromophenacyl)methylpyridinium bromide IX, 2-amino-1-(4-chlorophenacyl)methylpyridinium bromide X, and 2-amino-1-(4-nitrophenacyl)methylpyridinium bromide XI. Solutions of equimolar amounts (0.02 M) of 2-aminopyridine and appropriate ω-bromoacetophenone in ethyl acetate were mixed. The reaction mixture was refluxed for 3 h for **V** and **VII** and for 5 h for **IX**–**XI**. The next day, the reaction mixture was treated with ether, and the precipitate formed was separated and recrystallized from ethanol–ether. For pyridium bromides **V** and **VII**–**XI**, the yields (%) and melting points (°C) are as follows: **V**, 82, 218–220; **VII**, 75, 191–193; **VIII**, 80, 232–234; **IX**, 77, 215–217; **X**, 82, 220–222; and **XI**, 60, 252–254.

2-Acetyl-1-phenacylmethylpyridinium bromide VI. A mixture of equimolar amounts (0.02 M) of 2-acetylpyridine and ω-bromoacetophenone was heated to 125–130°C for 20 min and treated with a minor

1070-4272/03/7611-1764$25.00

Table 1. Hindrance factors γ and degree *Z* of corrosion protection of 08KP steel in 3 M H_2SO_4 solution in the presence of phenacylmethylpyridinium bromides **I**–**XI**

Compound	R	R_1	20°C		40°C		60°C		80°C	
			γ	*Z*, %	γ	*Z*, %	γ	*Z*, %	γ	*Z*, %
I	H	H	11.3	91.1	12.7	92.1	221.2	99.5	88.3	98.7
II	H	NO_2	1.7	41.2	2.2	54.5	–	–	15.7	93.6
III	CH_3	H	15.5	93.5	18.7	94.7	209.1	99.5	150.4	99.3
IV	CH_3	NO_2	2.3	56.5	2.9	65.5	–	–	21.7	95.4
V	NH_2	H	23.7	95.8	29.0	96.5	200.3	99.5	144.6	99.3
VI	$COCH_3$	H	7.6	86.8	10.4	90.4	262.8	99.6	198.3	99.5
VII	NH_2	CH_3	26.5	96.2	34.1	97.1	413.6	99.8	207.1	99.5
VIII	NH_2	OCH_3	32.0	96.4	35.4	97.1	643.2	99.8	626.7	99.8
IX	NH_2	Br	3.4	70.6	3.6	72.2	25.4	96.1	63.0	98.4
X	NH_2	Cl	1.8	44.4	2.2	54.5	23.8	95.8	60.0	98.3
XI	NH_2	NO_2	9.7	89.7	12.3	91.9	44.9	97.8	31.3	96.8

amount of ethanol; the precipitate formed was separated. Yield 35%, mp 198–200°C (from ethanol–ether).

To evaluate the corrosion-protective properties of the compounds under study, the hindrance factors γ and the degree *Z* of corrosion protection of steel were determined in the presence of 1×10^{-2} M of inhibitors in 3 M H_2SO_4 solutions at 20, 40, 60, and 80°C. The corrosion was monitored gravimetrically using 08KP steel samples with the working area of 14×10^{-4} m^2. The test duration was 24 h at 20°C, 2 h at 40 and 60°C, and 1 h at 80°C. Polarization curves were measured in the potentiodynamic mode at the potential sweep rate of 2 mV s^{-1} on a steel electrode in the initial and inhibited sulfuric acid solutions.

The test performed demonstrated that most of the compounds under study show noticeable inhibiting properties which are largely determined by the nature of substituents in their molecules (Table 1).

As is known [7], adsorption of quaternary pyridinium salts may occur both through electrostatic attraction of the pyridinium cation to the negatively charged metal surface and via specific π interaction of the pyridine with the metal. Attempts were made, by introducing substituents of varied electronic nature into the position 2 of the pyridine ring of **I** and thereby changing the charge on the nitrogen atom and the π-electron density of the pyridine ring, to reveal the role played by the pyridinium moiety of the molecule and evaluate the effect of the substituents introduced on the inhibiting effect of the forming compounds. It was found that, in going from **I** and **II** to the corresponding compounds with a CH_3 group heading the series of electron-donor substituents, the hindrance factor of steel corrosion grows somewhat. It increases at 20°C from 11.3 to 15.5 for compounds **I** and **III** and from 1.7 to 2.3 for **II** and **IV**. In the case of such a relatively strong electron-donor substituent as NH_2 group, the protective effect is enhanced substantially, with the corrosion hindrance factor for **V** and **XI** being 23.7 and 9.7, respectively.

This can be accounted for by the electronic influence of the amino group on the π system of the pyridine ring, which favors its π-electronic interaction with the steel surface. Also possible is the direct involvement of the amino group in free or protonated state in adsorption processes. On introducing a CH_3CO group into position 2 of the pyridine ring (compound **VI**), the corrosion hindrance factor decreases to 7.6.

It was established that the observed changes in the inhibiting action of **I, III, V**, and **VI** are strictly determined by the electronic nature of substituents R. There exists a linear relationship (r = 0.994) between the corrosion hindrance factors for these compounds and the constants σ_c^0 characterizing the combination of the mesomeric and π-induction effects of the substituents R [8]. The fact that this dependence is observed suggests that adsorption of the compounds studied onto steel at room temperature is due to π-electronic interaction of the pyridinium ring with the metal surface, favored by the presence of electron-donor substituents in the pyridinium ring. This also indicates that the amino group in **V** is not involved directly in the adsorption, and the decisive role is played by its influence on the π system of the pyridine ring.

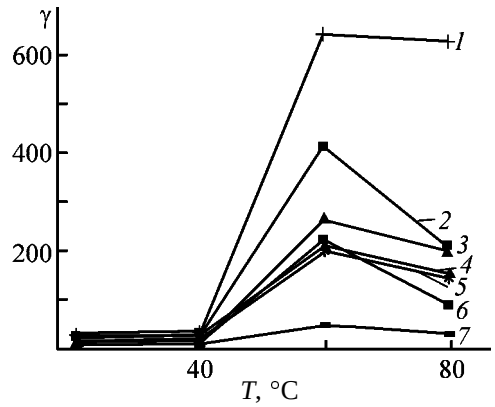

Fig. 1. Hindrance factor γ vs. temperature *T* in corrosion of 08KP steel in a 3 M solution of H_2SO_4 in the presence of 1×10^{-2} M phenacylmethylpyridinium bromides. Compound: (*1*) **VIII**, (*2*) **VII**, (*3*) **VI**, (*4*) **III**, (*5*) **V,** (*6*) **I**, and (*7*) **XI**.

It should be noted that the linear dependence γ–σ_c^0, observed for compounds **I**, **III**, **V**, and **VI**, is also preserved at 40°C, but the correlation coefficient falls in this case to 0.985. At 60°C, the inhibiting action of the compounds studied increases dramatically (Table 1), but the γ–σ_c^0 relationship is strongly disturbed, being completely eliminated at 80°C. Possibly, raising the temperature leads to manifestation in the corrosion process of a number of other factors. This may be, e.g., reorientation of molecules bound to the metal surface via the π system of the pyridinium moiety, enhancement of the role played by electrostatic interaction of pyridinium cations with the metal surface, and increasing share of the specific adsorption of compounds via the carbonyl group.

As is known [1, 2], the corrosion hindrance under the action of carbonyl compounds is mainly due to involvement of the oxygen from the carbonyl group in adsorption processes because of the presence of a substantial electron density on this atom. Electron-donor substituents make higher the nucleophilicity of the oxygen atom of the carbonyl group, thereby enhancing the donor–acceptor interaction of carbonyl compounds with the metal surface, whereas electron-acceptor substituents passivating the carbonyl group make this interaction weaker. Introduction into the *para* position of the benzene ring of **V** of CH_3 or CH_3O groups, which exhibit electron-donor effect, enhances the protective action of the inhibitor, with the result that the corrosion hindrance factor increases to 26.5 and 32.0 for **VII** and **VIII**, respectively, at 20°C. If these substituents are replaced with a bromine or chlorine atom, the corrosion-protective effect decreases dramatically, with the corrosion hindrance factor for **IX** and **X** being as low as 3.4 and 1.8, respectively.

A comparison of the protective effects of compounds **I**, **III**, and **V** and the corresponding nitro derivatives **II**, **IV**, and **XI** demonstrated that introduction of an NO_2 group into the *para* position of the benzene ring makes their inhibiting action weaker. Since the nitro group is a much stronger electron acceptor than a bromine or chlorine atom, it would be expected that the protective properties should be completely eliminated on replacing these atoms with a nitro group. However, it was found that such a replacement not only fails to make the hindrance factor lower, but even raises it substantially. For example, the corrosion hindrance factor for **XI** is 9.7.

Variation of the substituents R_1 revealed for compounds **V**, **VII**, **IX**, and **X** at 20 and 40°C a correlation between their σ_1 constants and γ values, with the correlation coefficients equal to, respectively, 0.998 and 0.990. The exception are compounds **VIII** and **XI**. Possibly, the substituents R_1 in these compounds are involved, in addition to exerting influence on the carbonyl group and the π system of the benzene ring, in some other processes. For **VIII**, this may be, e.g., independent involvement of the MeO group in the free or protonated form in adsorption, whereas in **XI**, as also in **II** and **IV**, the observed corrosion hindrance, probably, results from the combined influence exerted on corrosion both by these compounds themselves and by the corresponding amino compounds, which could be formed under the experimental conditions.

The results of the corrosion tests demonstrated that, with the temperature increasing to 60°C, the inhibiting action of most of the compounds studied increases substantially (Table 1) and remains rather high at 80°C. The observed temperature dependence of the inhibiting effect of the compounds studied (Fig. 1) is probably associated with a change in the mechanism of their adsorption onto the metal and a transition from physical (or first-order specific) adsorption to chemisorption as a result of the enhanced donor–acceptor interaction between the carbonyl oxygen and *d* levels of iron. A certain decrease in the inhibiting action of some compounds at 80°C is possibly due to desorption of inhibitors from the metal surface, resulting from the high rate of metal dissolution at this temperature.

Voltammetric measurements on steel in the presence of compounds **V**, **VIII**, and **XI** demonstrated that these compounds are inhibitors of mixed type, which inhibit both the cathodic and anodic reactions of the corrosion (Fig. 2). Under stationary conditions, they

affect the process to a greater extent by shifting the free corrosion potential E_f of steel in the positive direction. The hindrance factors calculated from the intersection of the Tafel portions of polarization curves for **V**, **VIII**, and **XI** are, respectively, 22.5, 29.2, and 4.0, and those for **V** and **VIII** are close to those obtained from gravimetric measurements (Table 1).

The nature of substituents in these compounds strongly affects the run of the cathodic polarization curves, and to a lesser extent, that of the anodic curves. The influence of compound **XI** containing a nitro group on the cathodic reaction is low, which may be due to its partial reduction on the steel surface. The extent to which compound **XI** affects the cathodic reaction of steel corrosion decreases markedly when the electrode potential is shifted in the negative direction, which may also be due to the reduction of **XI**. Inhibitors **V** and **VIII** enhance substantially the electrode polarization of the cathodic reaction of the corrosion process, thereby markedly changing the run of the cathodic curves at high polarizations. When the electrode potential is shifted in the negative direction, inhibition of the cathodic reaction of the corrosion process is enhanced in their presence. This can be accounted for by an increase in adsorption of **V** and **VIII** onto steel and their reorientation on the metal surface, which ensures formation of a more closely packed protective layer of an inhibitor [7].

The strongest influence on the rate of acid corrosion of metals is commonly exerted by the energetic ($\gamma_{\Delta\Psi_1}$) and blocking (γ_θ) inhibition effects, whose contribution to the overall corrosion hindrance factor can be calculated using a system of equations reported in [7]. The corrosion hindrance associated with the appearance of an additional step of potential, $\Delta\Psi_1$, can be calculated using simple kinetic relations taking into account the Tafel slopes of the polarization curves, b_c and b_a, and the shift of the free corrosion potential, ΔE_f, caused by the inhibitor (Table 2).

A comparison of the experimental (γ_e) and calculated (γ_c) hindrance factors demonstrated that the compounds studied hinder acid corrosion of steel mainly by the energetic mechanism, and the effect of blocking of the metal surface is only of secondary importance in their presence. As also for other cation-like compounds, this is probably due to the presence in the phenacylmethylpyridinium bromides of pyridinium cations ensuring the appearance at the metal–solution interface of a positive adsorption step of potential. The excess of γ_c over γ_e, observed for some compounds, is possibly due to the influence exerted on ΔE_f by a number of additional factors: conjugated reduction of oxygen, occurring in an acid medium in the presence of effective inhibitors; selective adsorption of surfactants on active centers of the metal; etc.

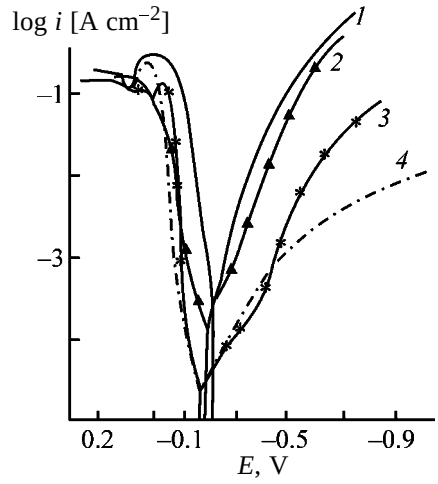

Fig. 2. Polarization curves measured on 08KP steel in a 3 M solution of H_2SO_4 at 20°C in the presence of 1×10^{-2} M phenacylmethylpyridinium bromides. (*i*) Current density and (*E*) potential (vs. standard hydrogen electrode). (*1*) Supporting electrolyte solution; compound: (*2*) **XI**, (*3*) **VIII**, and (*4*) **V**.

CONCLUSIONS

(1) Phenacylmethylpyridinium bromides are effective inhibitors of acid corrosion of steel, whose protective action depends on the nature of substituents present in these compounds.

(2) The inhibiting properties of the compounds under study are enhanced by electron-donor sub-

Table 2. Experimental (γ_e) and calculated (γ_c) corrosion hindrance factors for 08KP steel in a 3 M solution of H_2SO_4 in the presence of **V**, **VIII**, **IX**, and **XI**

Compound	*c*, M	E_f, mV	γ_e	γ_c^*
V	1×10^{-2}	60	23.7	26.8
	4×10^{-3}	56	23.2	21.4
	1.6×10^{-4}	45	17.0	11.8
	6.4×10^{-4}	17	2.6	2.5
VIII	1×10^{-2}	71	32.0	48.9
IX	1×10^{-2}	21	3.4	3.2
XI	1×10^{-2}	50	9.7	10.2
	4×10^{-3}	31	7.8	5.4

* It was taken in calculations that $\gamma_c = 10^{K\Delta\Psi}1$, $K = b_c/b_0(b_a + b_c)$, $\Delta\Psi_1 = \Delta E_c/[1 - b_c b_a/b_0(b_a + b_c)]$, where b_c and b_a are the Tafel slopes of the cathodic and anodic polarization curves in a 3 M solution of H_2SO_4, $b_0 = 2.3RT/F$ [7].

stituents introduced both in the pyridinium and in benzoyl moieties of their molecules and weakened by electron-acceptor substituents. The key role in the corrosion-protective action of the compounds under study at room temperature is the pyridinium moiety, with the corrosion hindrance by the energetic inhibition mechanism, and the benzoyl moiety of the molecule ensures their chemisorption and high performance at elevated temperatures. Such a polyfunctionality of phenacylmethylpyridinium bromides allows them to preserve their strong inhibiting action in a 3 M solution of sulfuric acid in a wide range of solution temperatures (20–80°C).

(3) The most effective of the compounds studied are 2-amino-1-phenacylmethylpyridinium bromide **V**, 2-amino-1-(4-methylphenacyl)methylpyridinium bromide **VII**, and 2-amino-1-(4-methoxyphenacyl) methylpyridinium bromide **VIII**.

REFERENCES

1. Grigor'ev, V.P. and Ekilik, V.V., *Khimicheskaya struktura i zashchitnoe deistvie ingibitorov korrozii* (Chemical Structure and Protective Action of Corrosion Inhibitors), Rostov-on-Don: Rostov. Univ., 1978.
2. Reshetnikov, S.M., *Ingibitory kislotnoi korrozii metallov* (Inhibitors of Acid Corrosion of Metals), Leningrad: Khimiya, 1986.
3. Ivanov, E.S., *Ingibitory korrozii metallov v kislykh sredakh: Spravochnik* (Inhibitors of Metal Corrosion in Acid Media: Reference Book), Moscow: Metallurgiya, 1986.
4. Antropov, L.I., *Zashch. Met.*, 1977, vol. 13, no. 4, pp. 387–399.
5. Pogrebova, I.S., *Effekty sinergizma pri ingibirovanii korrozii metallov* (Synergism in Inhibition of Metal Corrosion), Kiev: Znanie, 1980.
6. Antropov, L.I., Makushin, E.M., and Panasenko, V.F., *Ingibitory korrozii metallov* (Inhibitors of Metal Corrosion), Kiev: Tekhnika, 1981.
7. Antropov, L.I. and Pogrebova, I.S., *Itogi Nauki, Ser.: Korroz. Zashch. Korroz.*, 1973, vol. 2, pp. 27–112.
8. Zhdanov, Yu.A. and Minkin, V.I., *Korrelyatsionnyi analiz v organicheskoi khimii* (Correlation Analysis in Organic Chemistry), Rostov-on-Don: Rostov. Univ., 1966.

Russian Journal of Applied Chemistry, Vol. 76, No. 11, 2003, pp. 1769–1771. Translated from Zhurnal Prikladnoi Khimii, Vol. 76, No. 11, 2003, pp. 1819–1822.

CATALYSIS

Synthesis of a Mixed Catalyst for Sulfuric Acid Production Using Various Wastes

L. A. Nefedova, S. A. Lavrishcheva, E. I. Dobkina, and S. M. Kuznetsova

St. Petersburg State Technological Institute, St. Petersburg, Russia

Received February 13, 2003

Abstract—The structure of mixed catalysts for sulfuric acid production, with various types of raw materials as supports, was studied by electron microscopy.

Sulfuric acid is widely used in production of mineral fertilizers, dyes, explosives, and other chemical products. One of the main directions in the progress of sulfuric acid technology is development of new more effective catalysts and optimization of the existing catalysts [1].

Mixed catalysts for sulfuric acid production of the SVD type are the most widely used in our country. They contain vanadium in the highest oxidation state, alkaline promoters, and natural diatomite as support [2]. However, an urgent problem is extension of the scope of raw materials, in particular, replacement of natural diatomite by other materials. Furthermore, the problem of utilization of spent catalysts becomes more and more pressing. Finally, to increase the final conversion of sulfur dioxide and the productivity of contact apparatus, it is necessary to develop improved catalysts active at both high and low temperatures. This study is aimed at solving the above problems.

To study what types of raw materials could be appropriate as supports, we prepared three samples (Table 1): sample nos. 1 and 2 were prepared from diatomite of the Inza deposit, and sample no. 3, from the waste from electrothermal smelting of crystalline silicon Si_w (98–99% SiO_2, trace amounts of alkali metal oxides, and Al_2O_3). Into sample nos. 2 and 3, we additionally introduced the spent contact mass of SVD catalysts. The catalysts were prepared similarly to SVD, by dry mixing of components [diatomite support and vanadium(V) oxide] and promoters [alkali metal oxides]. Apart from traditional promoter, K_2O, we used a rubidium promoter (rubidium production waste). After molding, the catalysts were dried and then calcined for 4 h at 550°C.

The results (Table 1) show that sample no. 2 has the optimal content of components in the charge, ensuring the maximal activity over the entire temperature range. The high activity of this catalyst at 485 and 420°C arises from additional introduction of a rubidium promoter, which makes lower the viscosity of the molten active component and decreases the degree of the vanadium(V) reduction [1, 2].

Apparently, the low activity of the catalyst based on Inza diatomite (sample no. 1) without additional promoter may be due to the high Al_2O_3 content (up to 12 wt %) in this raw material. As a result, potassium ions of the molten active component are removed from the melt in the form of potash alum, and crystalline V_2O_5 is separated [1, 2].

Owing to a unique combination of alkali metal oxides in the silicate waste, the catalyst based on spent SVD and Si_w (sample no. 3) is active in a wide temperature range even without additional promotion.

Table 1. Characterization of support samples

Sample no.	Charge composition, wt %					Activity X, % at indicated T, °C	
	Inza diatomite	SVD_{sp}	V_2O_5	Rb_w	Si_w	420	485
1	89.3	–	10.7	–	–	18.0	78.0
2	51.4	34.3	10.3	4.0	–	53.0	87.5
3	–	44.6	10.7	–	44.7	50	87.5

1070-4272/03/7611-1769$25.00

Table 2. Structural characteristics of catalysts*

Sample no.	ρ_{true}, g cm^{-3}	ρ_{app}, g cm^{-3}	V_{por}, cm^3 g^{-1}	Pore radius, nm		
				r_{min}	r_{max}	r_{av}
1	2.16	1.41	0.27	45	1050	547
2	2.39	1.04	0.55	6.5	3500	1753
3	2.39	1.03	0.44	7.5	1000	503

* (ρ_{true}) True density, (ρ_{app}) apparent density, and (V_{por}) pore volume.

As known, the chemical composition is not the only factor determining the catalyst activity. The activity also depends on the inner surface area determined by the pore structure [2]. Therefore, we studied the pore structure of the samples synthesized by different procedures.

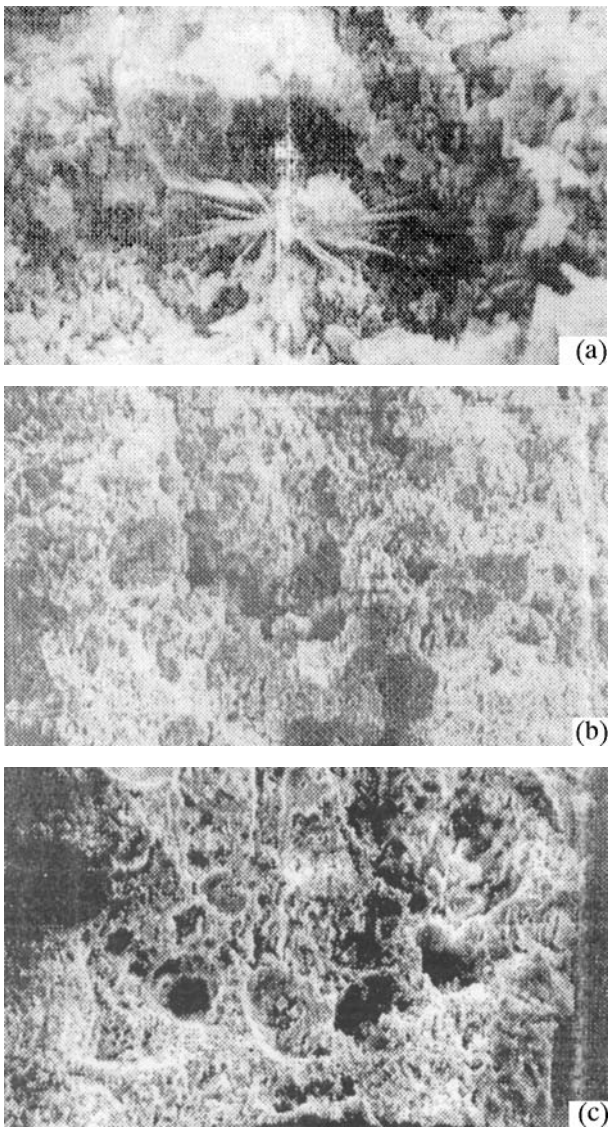

Fig. 1. Electron micrographs of sample nos. (a) 1, (b) 2, and (c) 3. Magnification 500×.

The data obtained by mercury porosimetry are presented in Table 2.

As seen, the catalysts have a multidisperse structure [1–3]. Coarse pores ensuring access of reagents and back diffusion of reaction products are present along with small pores making the corresponding contribution to the surface area.

The pore structure was also studied by electron microscopy on a Napolab 7 scanning electron microscope (Opton, Germany). The electron micrographs of the catalyst based on Inza diatomite (sample no. 1) and the catalyst into which SVD spent contact mass and a rubidium promoter were additionally introduced (sample no. 2) are shown in Fig. 1.

The electron-microscopic study shows that, for the sample synthesized from Inza diatomite without additional introduction of SVD spent catalyst and a rubidium promoter, the distribution of the active component throughout the catalyst grain is nonuniform (Fig. 1a). Owing to higher content of M_2O_3 oxides in the Inza diatomite, potassium ions of the melt are removed from the melt in the form of potash alum, and crystalline V_2O_5 is separated.

The surface tension forces accompanying crystallization of the active component cause the melt to move toward crystallization centers. After heat treatment, agglomerations of the active component crystals reside in the place of drops (Fig. 1a, the center of micrograph).

As compared to the sample prepared without spent contact mass and a rubidium promoter, the modified catalyst (sample no. 2) has a coarser-pore structure (Fig. 1b).

The electron-microscopic examination of the catalyst containing silicate waste (sample no. 3, Fig. 1c) shows that its pores are coarser than those in sample no. 1 but smaller than those in catalyst no. 2.

The distribution of elements of the catalyst active components, V and K ions in particular, over the support surface was studied on an electron-beam scanning microscope with a Kevex microanalyzer.

In the case of the catalyst synthesized without spent SVD and a rubidium promoter (sample no. 1), the distribution of K and V ions over the polished section is nonuniform (Fig. 2, I).

The catalyst modified with a rubidium promoter (sample no. 2) is more uniform (Fig. 2, II). This is

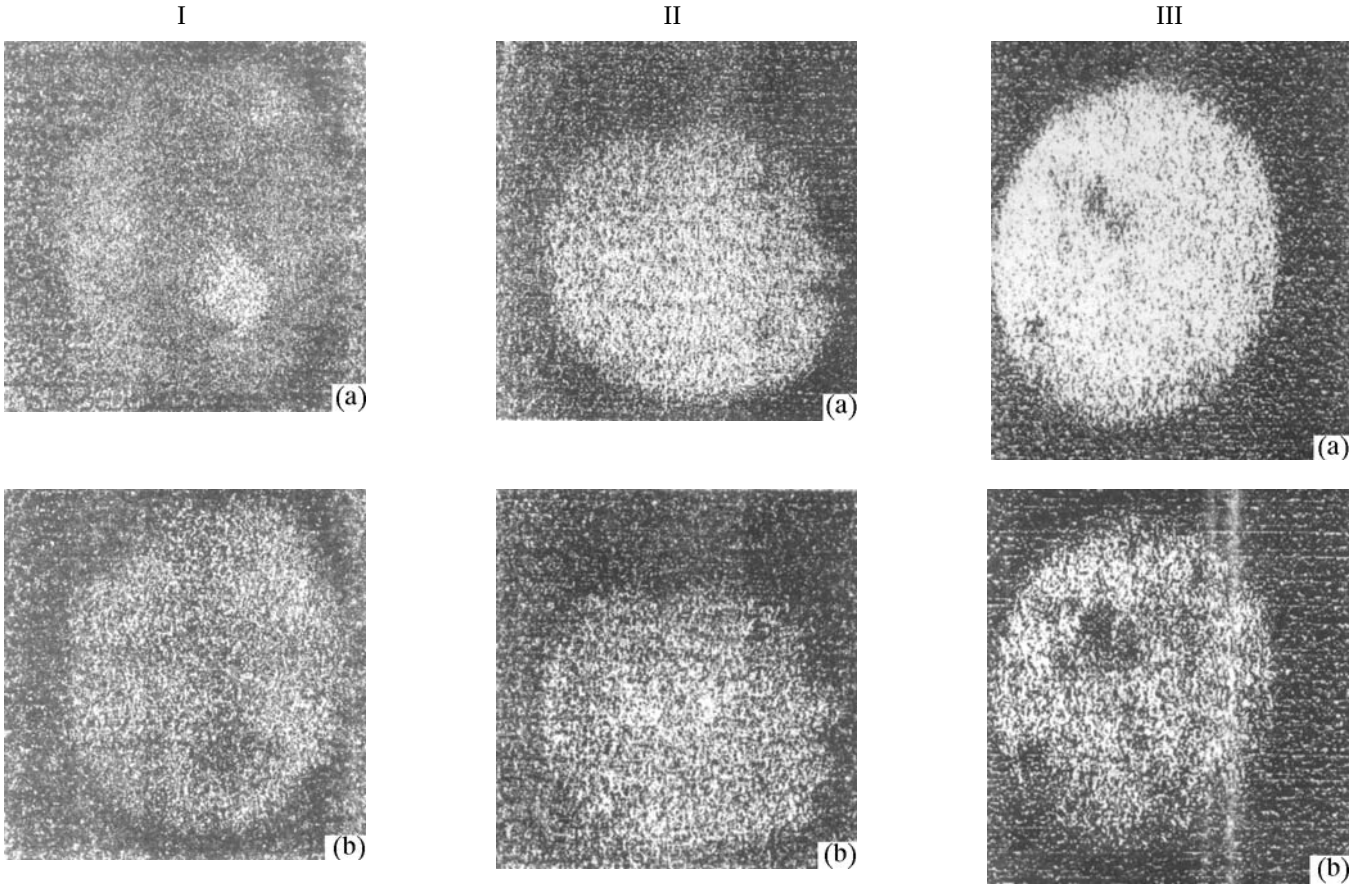

Fig. 2. The distribution of (a) vanadium and (b) potassium elements throughout the catalyst grain. Sample no.: (I) 1, (II) 2, and (III) 3.

apparently due to the lower content of Inza diatomite and, correspondingly, of M_2O_3 oxides.

The same pattern is observed with the catalyst containing a silicate component (sample no. 3; Fig. 2, III). Probably, the presence of alkali metal oxides in Si_w completely compensates the negative effect produced by the minor amount of Al_2O_3 present in it. Moreover, alkali metal oxides present in a large amount lower the melting point and viscosity of the active component, which results in its uniform distribution over the inner surface.

Thus, we have prepared catalysts (sample nos. 2 and 3) active in a wide temperature range ($X_{420°C}$ = 50–53, $X_{485°C}$ = 87–88%) owing to unique chemical composition, multidisperse pore structure, and uniform distribution of the active component over the inner surface of grains.

Hence, partial or complete replacement of diatomite by other raw materials seems feasible; it would also favor the waste utilization.

CONCLUSIONS

(1) A possibility of using silicate promoter (waste) as a new support for SVD catalyst was examined. It is appropriate to introduce rubidium production waste as promoter. (2) The catalysts synthesized are active in a wide temperature range ($X_{420°C}$ = 50–53, $X_{485°C}$ = 87–88%) owing to unique chemical composition, multidisperse pore structure, and uniform distribution of the active component over the inner surface of grains.

REFERENCES

1. Boreskov, G.K., *Geterogennyi kataliz* (Heterogeneous Catalysis), Moscow: Nauka, 1986.
2. Mukhlenov, I.P., Dobkina, E.I., Deryuzhkina, V.I., and Soroko, V.E., *Tekhnologiya katalizatorov* (Catalyst Technology), Leningrad: Khimiya, 1989.
3. Vasil'ev, B.T., and Otvagina, M.I., *Tekhnologiya sernoi kisloty* (Sulfuric Acid Technology), Moscow: Khimiya, 1985.

Russian Journal of Applied Chemistry, Vol. 76, No. 11, 2003, pp. 1772–1775. Translated from Zhurnal Prikladnoi Khimii, Vol. 76, No. 11, 2003, pp. 1823–1826.

CATALYSIS

Influence of Preparation Conditions on Properties of a Copper-Containing Catalyst for Electrocatalytic Oxidation of Acetone

Yu. V. Tsarev, A. E. Dmitriev, and V. V. Kostrov

Ivanovo State University of Chemical Engineering, Ivanovo, Russia

Received April 3, 2003

Abstract—Stages of synthesis of a copper-containing catalyst for electrocatalytic oxidation of acetone in waste gases were studied. The course of the extrusion and calcination and their influence on electrocatalytic oxidation of acetone on the catalyst synthesized were analyzed.

Traditionally, waste gases and air are purified to remove volatile organic compounds (VOCs) by thermal afterburning, catalytic oxidation, sorption, and a sorption-catalytic method [1]. Together with the conventional methods, such techniques as, e.g., VOC oxidation in barrier discharge plasma are also used [2]. Thermal afterburning and sorption purification to remove VOC involve high maintenance expenditure, secondary pollution of the environment with nitrogen oxides, and difficult utilization of the caught components. Advantageous in this regard are sorption-catalytic and catalytic methods, including catalytic oxidation of VOCs under nonstationary conditions [3]. Platinum or oxide (less expensive) catalysts are used in oxidation. As oxide catalysts commonly serve catalysts containing copper(II) and manganese(IV) oxides [4]. Supported catalysts are fabricated using oxides of aluminum, titanium, etc. Activated carbon is occasionally used as support [5]. In this study, primary attention is given to analysis of synthesis stages of a copper-containing catalyst for electrocatalytic decontamination of hydrocarbon-containing gases, which is prepared using technical carbon (TC) as support.

The catalyst was prepared using TC of PM-750 brand. Molded TC grains were impregnated with $Cu(NO_3)_2$ solutions of concentration 100–200 g l^{-1} and mixed with basic copper carbonate $(CuOH)_2CO_3$, with the subsequent addition of a plasticizer (1.25–5.00% solution of polyvinyl alcohol). Further, the catalyst was molded at the optimal molding humidity in the form of grains 0.5–1 mm in size, and the grains were calcined in a CO_2 flow at 350°C.

The rheological characteristics of the molding paste were determined with a plasticity meter with an in-parallel-shifted plate of the Tolstoy design. The structural-mechanical characteristics were calculated from kinetic curves of deformation development and served as a basis for making a complete structural-mechanical analysis of disperse systems and obtaining information about the viscoelastoplastic properties and stability of dispersed structures in the molding paste. The strains were calculated using the Maxwell–Shvedov–Kelvin equation. The strains are related to $P = 1 \times 10^5$ Pa and $\tau = 1000$ s. The sum of relative elastic, viscoelastic, and plastic deformations served to determine to which of the six structural-mechanical types by S.P. Nechiporenko belongs a given molding paste [6].

A thermogravimetric analysis of catalyst samples was carried out on a Q-1500D derivatograph at a heating rate of 5 deg min^{-1}. As a model gas mixture served air containing 1–2 g m^{-3} acetone vapor. The concentration of acetone in the gas–air mixture was determined by nephelometry on a KFK-2MP photoelectrocolorimeter at a wavelength of 320 nm [7]. The conversion of acetone on the catalyst samples synthesized was determined in an isothermal plug-flow reactor. The tests were performed with ac electric voltage applied to the catalyst. The total specific surface area of the catalysts was determined on a Tsvet-211 sorption meter [8]. The surface area of the catalysts was measured by low-temperature selective sorption of helium. The sorption measurements were performed in pulsed mode at –136°C. An X-ray phase analysis of the catalyst samples was carried out on a DRON-UM1 diffractometer with a CuK_α tube (λ = 0.154 nm). The interplanar spacings d were calculated using RFA software written in BASIC. The compounds obtained were identified on the basis of their

1070-4272/03/7611-1772$25.00

Table 1. Structural-mechanical properties of catalysts prepared by mixing basic copper carbonate with TC, with addition of a plasticizer (PVC)

Parameter	Sample		
	A	*B*	*C*
Elastic modulus E_1, MPa	0.48	3.00	3.43
Viscoelastic modulus E_2, MPa	0.56	3.00	8.01
Highest plastic viscosity η_1, MPa s	0.65	1.57	1.58
Plasticity $\prod_c$, s^{-1}	2.9	1.19	1.19
Elasticity λ, fraction units	0.46	0.50	0.30
Relaxation period θ, s^{-1}	2500	1050	658
Fraction of elastic strain ε_{el}, %	38.7	25.6	14.6
Fraction of viscoelastic strain ε_{ve}, %	32.9	25.6	6.26
Fraction of plastic strain ε_{pl}, %	28.4	48.8	79.1

interplanar spacings and comparison of these with the published data [8]. Changes in the phase composition of the samples, depending on their preparation conditions, were judged from the intensity of the most characteristic reflections. The products formed in electrocatalytic oxidation were determined by their absorption with hexane and analysis of the resulting mixture on a SATURN-2000R gas chromatograph–mass spectrometer.

Since molding of TC-based grains is rather a complicated task, the rheological characteristics of the catalyst samples (40% CuO and 60% TC) were studied in relation to the content of the plasticizer, polyvinyl alcohol (PVC). The results obtained by experimental data processing are listed in Table 1 and shown in Fig. 1. It is demonstrated that, with the content of PVC from 5.0 wt % for sample *A* and to 2.5 and 1.25 wt % for samples *B* and *C*, respectively, the structural-mechanical type of the catalyst paste prepared for extrusion changes correspondingly. Sample *A*, which can be related to zero structural-mechanical type, is characterized by medium values of the elastic and viscoelastic moduli (0.48 MPa, 0.56 MPa) and relaxation period of 2500 s^{-1}. Samples *B* and *C* can be related to fourth and fifth structural-mechanical types, in which plastic deformations predominate. Sample *B* is characterized by medium value of the elastic and viscoelastic moduli (3.0 MPa) and relaxation period of 1050 s^{-1}, and sample *C*, by high values of the elastic and viscoelastic moduli (3.43, 8.01 MPa) and short relaxation period (658 s^{-1}). The best sample for extrusion molding is sample *A* of the catalyst of zero structural-mechanical type. For the given sample, the relative elastic, viscoelastic, and plastic strains lie within the range of optimal values (shown by the circle in Fig. 1).

To determine conditions of thermal treatment of the catalyst samples synthesized, they were studied by thermogravimetry. The results obtained in thermogravimetric measurements are shown in Figs. 2 and 3. The experimental data suggest that, for the catalyst samples impregnated with copper nitrate solutions, the decomposition temperature of copper nitrate decreases from 180–220 to 60–90°C (Figs. 2a, 2b). This is, in all probability, due to the presence of highly dispersed TC, which can accelerate the process in question. By contrast, for the catalyst samples prepared by mixing TC with basic copper carbonate $(CuO)_2CO_3$ (Fig. 3), the decomposition temperature of the basic Cu(II) carbonate increases somewhat from 260 to 330°C. All the catalysts prepared are characterized (Figs. 2, 3) by weight loss in the temperature range 350–900°C, which is due to burning-out of TC contained in a sample. The catalyst samples prepared by impregnation with a copper nitrate solution start to lose weight

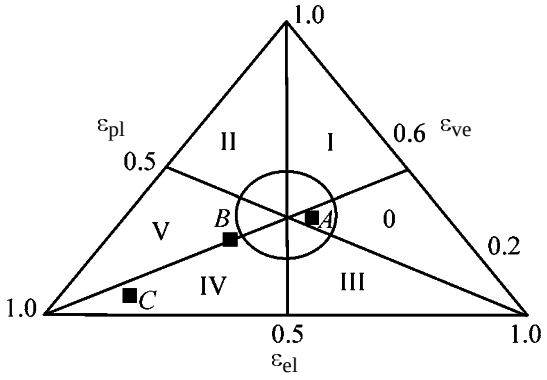

Fig. 1. Diagram of development of viscoelastoplastic strains in the catalyst samples prepared. (ε_{el}, ε_{pl}, ε_{ve}) Fractions of elastic, plastic, and viscoelastic strains, respectively. PVC content (wt %): (*A*) 5.0, (*B*) 2.5, and (*C*) 1.25.

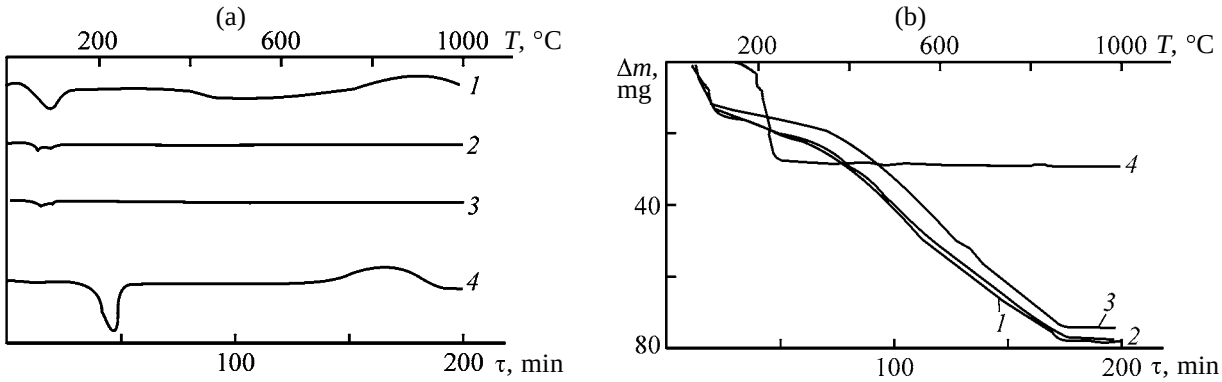

Fig. 2. (a) DTG curves and (b) TG curves of catalyst samples prepared by impregnation with copper nitrate solutions. (*T*) Temperature, (τ) time, and (Δ*m*) weight loss; the same for Fig. 3. Samples impregnated at 80°C for 1 h with $Cu(NO_3)_2$ solution (g l^{-1}): (*1*) 200, (*2*) 150, and (*3*) 100; (*4*) $Cu(NO_3)_2$ sample.

at temperatures 100–150°C lower than those for samples obtained by mixing with the basic Cu(II) carbonate $(CuOH)_2CO_3$.

In the experiments, the specific surface area of the catalyst samples was determined. The experimental data (Table 2, Figs. 4 and 5) indicate that the decrease in the degree of acetone conversion on catalyst samples calcined at high temperature is not caused by catalyst caking, since the specific surface areas of the samples calcined at 350 and 700°C are the same. The high specific surface area of the catalyst sample containing 60 wt % CuO is, in all probability, due to decomposition of basic Cu(II) carbonate, whose content in the catalyst is high. The specific surface area (35 $m^2 g^{-1}$) of the catalyst sample containing no copper oxide is virtually equal to the specific surface area of the starting TC (35 $m^2 g^{-1}$), which indicates the absence of any pronounced influence of the mixing and molding procedures on the specific surface area of the catalyst.

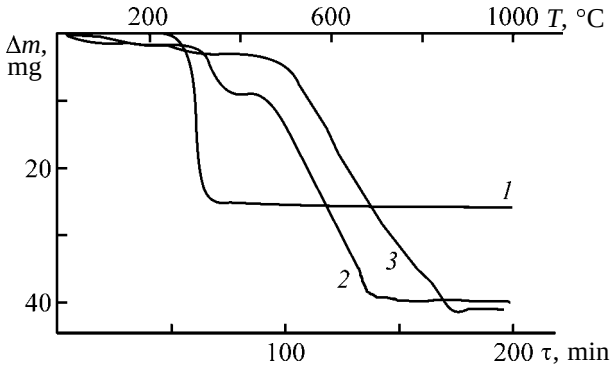

Fig. 3. TG curves of catalyst samples obtained by mixing TC with basic copper(II) carbonate. $(CuOH)_2CO_3$ content (wt %): (*1*) 100, (*2*) 40, and (*3*) 10.

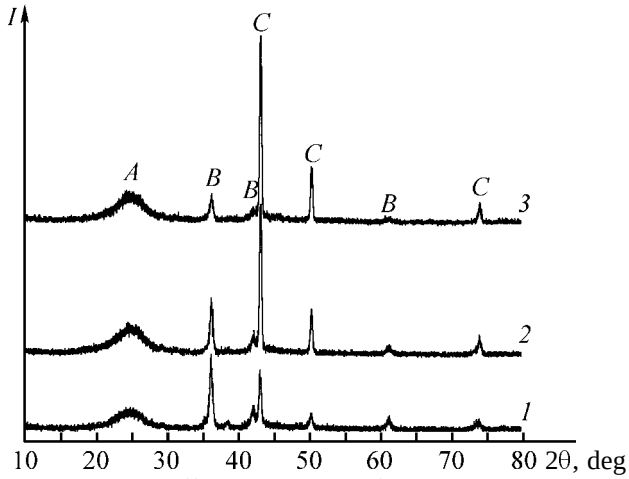

Fig. 4. X-ray diffraction patterns of a catalyst sample containing 20 wt % CuO, calcined at (*1*) 350, (*2*) 500, and (*3*) 700°C. (*I*) Intensity and (θ) Bragg angle. (*A*) TC, (*B*) CuO (Cu_2O), and (*C*) metallic copper.

To determine the phase composition of the catalyst samples synthesized, they were subjected to X-ray phase analysis. Samples with 20% content of the active component, calcined at 350, 500, and 700°C, were studied. Comparison of the experimental diffraction patterns (Fig. 4) with reference data for various compounds showed that the samples contained crystalline CuO (*B*; 2θ = 62°) or Cu_2O (*B*, 2θ = 36°). With increasing calcination temperature, the amount

Table 2. Specific surface area of catalyst samples

Sample no.	Calcination temperature, °C	CuO, %	S_{sp}, $m^2 g^{-1}$
1	700	20	28
2	500	20	37
3	350	20	28
4 (TC)	–	0	38
5	350	60	47
6 (TC)	350	0	35

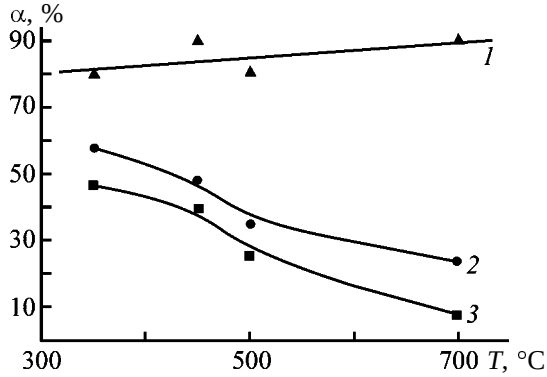

Fig. 5. Degree of acetone conversion α vs. calcination temperature *T* of the catalyst. Input electric power (W cm^{-3}): (*1*) 4, (*2*) 2, and (*3*) 0.6.

of the crystalline phase of these compounds decreases, since the intensities of peaks characteristic of these compounds become lower. The decrease in the amount of copper oxides is due to their reduction in a catalyst at high temperature to metallic copper (*C*; 2θ 43°, 51°). Correspondingly, in the X-ray diffraction patterns the intensity of peaks associated with metallic copper grows with temperature. The catalyst support, TC (*A*), in the catalyst is in amorphous or weakly crystalline state, which can be judged from the halo corresponding to a diffraction angle 2θ = 25°.

A study of the extent to which acetone is converted on the catalyst samples obtained demonstrated (Fig. 5) that, for specific input electric power of less than 2 W cm^{-3}, the degree of acetone conversion decreases with increasing catalyst calcination temperature. Consequently, a conclusion can be made that, in electrocatalytic oxidation of acetone, the CuO and Cu_2O phases enhance the influence exerted by the electric power. The phase of metallic copper has no effect on electrocatalytic oxidation of acetone. For input electric power exceeding 2 W cm^{-3}, the calcination temperature does not affect the degree of acetone conversion on the catalyst. This can accounted for by the prevalent influence of the electric component at high specific input power. These modes are characterized by predominance of plasma-enhanced catalytic processes, since effects characteristic of plasma formation are observed under these conditions.

CONCLUSIONS

(1) Rheological characteristics of catalyst samples were obtained, which indicate that making lower the percentage content of plasticizer (polyvinyl alcohol) impairs viscoelastoplastic properties of the catalysts.

(2) Thermogravimetric studies of the samples yielded information about the temperatures of decomposition of copper nitrate and basic Cu(II) carbonate and of burning-out of technical-grade carbon, which makes it possible to select calcination conditions for copper-containing catalysts synthesized on the basis of technical-grade carbon.

(3) The calcination temperature has no effect on the specific surface area of the samples, since this parameter is the same, and equal to 28 m^2 cm^{-3}, for samples calcined at 350 and 700°C.

(4) An X-ray phase analysis revealed that the decrease in the catalytic activity of the catalyst samples with increasing calcination temperature is due to reduction processes occurring in the catalyst at high temperatures and leading to formation of metallic copper, which is inactive in acetone oxidation.

REFERENCES

1. Popova, N.M., *Katalizatory ochistki gazovykh vybrosov promyshlennykh proizvodstv* (Catalysts for Purification of Industrial Waste Gases), Moscow: Khimiya, 1991.
2. *Ekologiya i kataliz: Sbornik nauchnykh trudov* (Ecology and Catalysis: Coll. of Sci. Works), Novosibirsk: Nauka, 1990.
3. Bugaev, S.P., Kuvshinov, V.A., Sochugov, N.S., and Khryapov, P.A., *Zh. Prikl. Khim.*, 1996, vol. 69, no. 6, pp. 965–969.
4. Oxide Catalysts Withstand Very High Temperatures, *Chem. Eng.* (USA), 1999, vol. 106, no. 12, p. 761.
5. Park, B.-J. and Parks, E.-J., *J. Mater. Sci. Lett.*, 1999, vol. 18, no. 19, pp. 1607–1609.
6. Ziabicki, A., *Fundamentals of Fibre Formation. The Science of Fibre Spinning and Drawing*, London: Wiley, 1976.
7. Peregud, E.A. and Gernet, E.V., *Khimicheskii analiz vozdukha promyshlennykh predpriyatii* (Chemical Analysis of Air in Industries), Leningrad: Khimiya, 1970.
8. *Powder Diffraction File, Data Cards, Inorganic Section Sets 1–34, JCPDS*, Swarthmore, Pennsylvania (USA), 1948–1984.

Russian Journal of Applied Chemistry, Vol. 76, No. 11, 2003, pp. 1776–1783. Translated from Zhurnal Prikladnoi Khimii, Vol. 76, No. 11, 2003, pp. 1827–1833.

ENVIRONMENTAL PROBLEMS OF CHEMISTRY AND TECHNOLOGY

Mathematical Simulation of Ozonosphere Perturbations in Spacecraft Launches

O. V. Yatsenko

Don State Technical University, Rostov-on-Don, Russia

Received March 13, 2003

Abstract—Factorial analysis of the results obtained in numerical simulation of ozone layer depletion by spacecraft was carried out. The mechanism, chemical agents, and kinetic characteristics responsible for the dynamics of ozone level in the perturbed region were studied. A mathematical model of the processes, intended for engineering-ecological estimates, was suggested.

The topicality of structural-informational development of mathematical models (MM) of ozone layer depletion by spacecraft is due to a significant rise in the anthropogenic impact of this kind. The principal factors in this case are the following: steadily increasing number of launches and their increasingly diverse geography; use of phased-out solid-propellant carrier rockets for injection of objects into upper layers of the atmosphere and into space; possibility of successful use in the near future of an aerospace plane intended to simplify the procedure dramatically and raise the intensity of space flights. In the situation at hand, the simulating capacities of the existing models and, in particular, those described in [1–3] are insufficient. However, the capacity of modern personal computers and the possibilities of information technologies enable improvement of these models both in their mathematical structure and in the database for simulation.

A detailed analysis of studies concerned with destruction of the ozone layer by launches of carrier rockets was made in [1]. It is admitted that the most important factor of the influence exerted by carrier rockets on the photochemistry of the ozone layer is the trail cloud formed via mixing of the propulsive jet with background gases. Another important result [1] is associated with analysis of modern MMs of photochemical processes in a stratosphere perturbed by spacecraft. According to [1], most of MMs of this kind are characterized by common structural-informational imperfections and/or limitations: (1) simplified mathematical formulation of the kinetics–diffusion problem or the so-called box model of photochemical transformations and turbulent transfer of reagents in the rocket trail; (2) inclusion into the kinetic scheme of a comparatively small number of reactions dominating in the photochemistry of unperturbed stratosphere and supposedly retaining their relative significance in the case when the stratosphere is perturbed by spacecraft. Therefore, it is impossible to obtain, in terms of the known MMs, answers to a number of questions concerning, in particular, the adequacy of the modeling process itself and of the identification of physicochemical mechanisms involved in breakdown and regeneration of the stratospheric O_3. For example, a detailed MM of photochemical processes in the ozonosphere was suggested in [2]. Based on the model of [2], a set of computer simulations [3] was performed in order to determine the scale-dynamic characteristics of perturbations in launches of Proton carrier rockets, which use 1,1-dimethylhydrazine and N_2O_4 as propellant components. However, beyond the scope of these studies remained the problems associated with mechanisms by which the rocket trail acts upon the ozonosphere and with the adequacy of MM to real processes, whose understanding becomes increasingly important because of the rise in the number of launches and the growing diversity of carrier rockets and propellants used.

The present study is devoted to (1) essential structural improvement of the models [2, 3]; (2) assessment of the adequacy of the modified MM and prototype models [1–3] to real processes of ozone breakdown in the rocket trail; (3) identification of mechanisms of ozone loss in the trail cloud of liquid-propellant rockets; (4) construction of a minimum MM [4] for practical estimates of parametric perturbations of the ozonosphere and radiation field, caused by launches of various types of liquid-propellant rockets.

1070-4272/03/7611-1776$25.00

A structural modification of the diffusion model [3] consists in using a transfer–dissipation equation of more general form: first, the box model is replaced by a discrete diffusion one, and, second, the initial gas-dynamic stage of interaction between the propulsive jet and the ambient gas is taken into account. This shifts the start of simulation from the instant of termination of the gas-dynamic expansion–deceleration–mixing of the propulsive jet with stratospheric gases in the model [3] to the beginning of exhaust of combustion products from nozzles.

The discrete diffusion model assumes that, by the instant of exhaust, the component concentrations in the rocket trail are characterized by step-like distribution along the jet radius. The model considers N concentric ranges uniform in chemical composition and temperature, bounded by circles with radii R_1, $R_1 \times 2^{1/2}$, ..., $R_1 N^{1/2}$ and evolving following the same law $R_n = R_1(t) N^{1/2}$, $n = 1 \ldots N$. In the case, the masses of gas within the zones thus defined can be considered always the same with accuracy sufficient for the purposes mentioned, and the initial concentrations of ith combustion product in nth zone, c'_{in}, can be specified by the distribution

$$c'_{in} = c'_{i1} \frac{e^{-2(n-1)N}}{e^{2/N} - e^{4/N-2}}. \quad (1)$$

Apparently, the box model of diffusion [3] is a particular case of the step-like or discrete diffusion model at $N = 1$.

The preserved simulation limitations of the model, which are determined by the nature of atmospheric turbulence [3, 5], constitute several hours for forecast longevity. Thus, the suggested MM can describe parametric perturbations with fast photochemistry, to which belong perturbations of the ozone layer by liquid-propellant rockets.

The discrete diffusion MM of interaction between the propulsive jet trail and substances of the stratosphere is expressed by the equations

$$\frac{dc_{in}}{dt} = f(c_{kn}, T_n) + [(c_{in-1} - 2c_{in} + c_{in+1})/2 + (0.44\pi R_n)^{-1} (m/u_0\rho)^{1/2} c'_{in}] \frac{d\ln V}{dt}, \quad (2)$$

$$\frac{dT_n}{dt} = \frac{1}{C_V} \Sigma f_i(c_{kn}, T_n) \Delta H_i + [(T_{n-1} - 2T_n + T_{n+1})/2 + (0.44\pi R_n)^{-1} (m/u_0\rho)^{1/2} T'_n] \frac{d\ln V}{dt}, \quad (3)$$

$$\frac{dc_{iN+1}}{dt} = f_i(c_{kN+1}, T), \quad (4)$$

$$c_{i0} = c_{i2}, \quad \frac{d\ln V}{dt} = \frac{d\ln V_n}{dt} = 2\frac{d\ln R_n}{dt},$$

$$R_1 = \{[R_0 + (0.22/w)(mu_0/\rho)^{1/2} \ln(1 + wt/R_0)^{2/3}] + (\xi t/3)\}^{3/2},$$

where $n = 1 \ldots N$ is the number of a chemically and thermodynamically uniform region, with $n = N + 1$ corresponding to unperturbed stratosphere; c_{in}, f_i, and ΔH_i, concentration, rate of formation (decomposition) in chemical reactions, and standard heat of formation of ith substance, respectively; T_n, temperature; C_V, specific heat of the stratospheric gas; $R_n(t) = R_1(t) n^{1/2}$, radius, and $V_n = V_n(t)$, running volume of nth zone contaminated by the rocket trail; m, u_0, and ρ, flow rate of the propellant, outflow velocity of the propulsive jet, and density of ambient air, respectively; w and ξ, rocket motion velocity and coefficient of turbulent dissipation of the solar energy [3]; R_0, radius of the channel displaced by the rocket; the primed concentration and temperature variables correspond to the parameters of the propulsive jet proper, which are imparted to the stratosphere through deceleration–mixing.

In contrast to the models of [1, 3], Eqs. (1)–(4) contain terms related to the initial gas-dynamic stage of formation of the contaminated region. After the initial stage of evolution of the discharge is over, MMs (1)–(4) reduce to the model of [3]. It is important that the chemical unit of the model is nonisothermal: changes in the temperature in the reaction zone are affected not only by mixing processes, but also by energy parameters of the occurring chemical transformations, which determine the kinetics of the initial gas-dynamic stage of interaction.

The constants of photoreactions forming the material flows f_i in Eqs. (2)–(4) were calculated preliminarily and used in simulating the evolution of the rocket trail in the form taking into account the diurnal variations in solar illumination [3]:

$$\left.\begin{aligned} k_k^{ph}(H,t) &= k_k^{ph0}(H) \sin^2(\pi l/\tau), \quad 2n\tau < t < 2n\tau + \tau, \\ k_k^{ph}(H,t) &= 0, \quad 2n\tau + \tau < t < 2n\tau + 2\tau, \end{aligned}\right\} \quad (5)$$

where $k_k^{ph0}(H)$ is the effective constant of kth photochemical reaction at the instant of time corresponding

Relative content of a component in the propulsive jet of liquid-propellant rockets

Ozone-depleting product	Fuel pair			
	$N_2(CH_3)_2H_2 + N_2O_4$	$N_2H_4 + N_2O_4$	$C_{14}H_{30} + O_2$	$H_2 + O_2$
OH, I stage	8.1×10^{-8}	9.3×10^{-8}	8.3×10^{-8}	1.8×10^{-7}
NO, I stage	3.0×10^{-7}	5.1×10^{-7}	–	–
OH, II stage	7.7×10^{-9}	9.0×10^{-9}	7.9×10^{-9}	2.3×10^{-8}
NO, II stage	–	–	–	–

Note: All other components of the propulsive jet affect the kinetics of O_3 breakdown insignificantly, as demonstrated below.

to the highest solar altitude, i.e., at noon; H is the altitude; $\tau = 24$ h.

The possibility of such a solution of the problem is due to the fact that the perturbation of the ozone layer in launches of liquid-propellant rockets is insignificant, which allows use of unperturbed constants of photoreactions and radiation field of the Sun. The resulting limitations mainly refer to the level of O_3 perturbation, which must not exceed 20%. Stronger perturbations lead to a shift of the O_3 concentration maximum, enhanced heating of lower lying layers, and disturbance of stratification; possibly, they cause vertical mixing. The fact that the perturbation level of the ozonosphere in launches of liquid-propellant rockets is insufficient for initiating the above processes has been confirmed by many numerical calculations, e.g., in [1, 3].

The informational improvement of the previous models consists in that both the range of photochemical reactions taken into account and the variety of propellants allowed by the numerical simulation become wider. In particular, each of the reactions described in [3] is now accompanied by a reverse reaction and the constants of oppositely directed transformations are thermodynamically matched. The final kinetic scheme of photoinduced transformations comprises 932 reactions between 74 components and photons in the wavelength range 180–700 nm.

Among the possible fuel–oxidant pairs, MM considers, together with the traditional pair 1,1-dimethylhydrazine + N_2O_4, also $N_2H_4 + N_2O_4$, $H_2 + O_2$, and $C_{14}H_{30} + O_2$. The chemical composition of the propulsive jet, calculated on the assumption of complete combustion of the components, partial dissociation of products, and "frozen" reactions in gas exhaust from the nozzle, is presented in the table (for components essential for the kinetics of ozone transformations).

The improvements of the model extended the range of its validity, as regards the temporal factor, to the instant of propulsive gas exhaust from the nozzle, and, as regards the variety of vehicles and nature of their impact on the ozonosphere, to possibility of adequate description of all the potential hazards among the modern and the most promising spacecraft. This makes it possible to use this model for revealing and classifying the threats to the state of the ozone layer, resulting from the economic use of the space and upper atmosphere, and to develop recommendations for reducing the environmental risk and damage inflicted by impacts of this kind.

The MM was tested for mathematical adequacy and correctness of its computer implementation in accordance with a complex procedure [3]. The correctness of mathematical formulation, reliability of the information database, and adequacy of software were verified. Model calculations of the known parameters of the ozonosphere and, in particular, the altitude profiles of minor gas components of the stratosphere (MGCS), and comparison of the results obtained with data of other authors confirm that the model suggested is well substantiated and reliable.

Practically important results obtained in testing the predecessors of the given MM [2, 3, 6] are the following: (1) altitude profiles of some poorly studied MGCS (Figs. 1a, 1b) [2, 3], calculated for the first time; (2) solution of the disputable issue concerning the diurnal kinetics of NO_2 in the ozone layer and the elementary reactions governing this kinetics [6]; (3) establishment of the important role played by excited O_2^* species in the kinetics of stratospheric ozone [2]; (4) substantiation of the validity of dividing the model into two independent submodels, of radiation-induced transfer and chemical kinetics, and also calculation of the effective constants of photoreactions [2]; and (5) evaluation of the impact of a single launch of a Proton-type rocket [6] (Figs. 2a, 2b).

Fundamentally new results obtained in terms of models (1)–(5) are the following: (1) the initial gasdynamic stage of formation of the trail cloud is in-

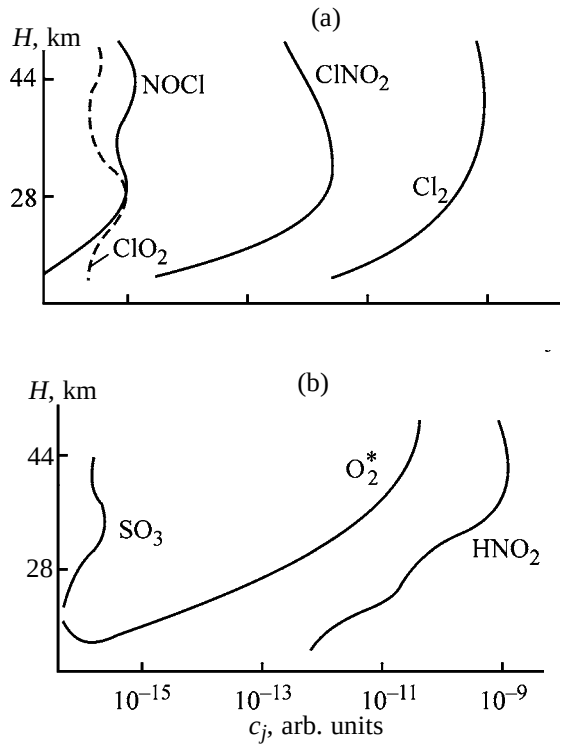

Fig. 1. Altitude (daytime) profiles of poorly studied components of the stratosphere. The O_2^* concentration is reduced by a factor of 10. (*H*) Altitude and (c_j) relative concentration of a component.

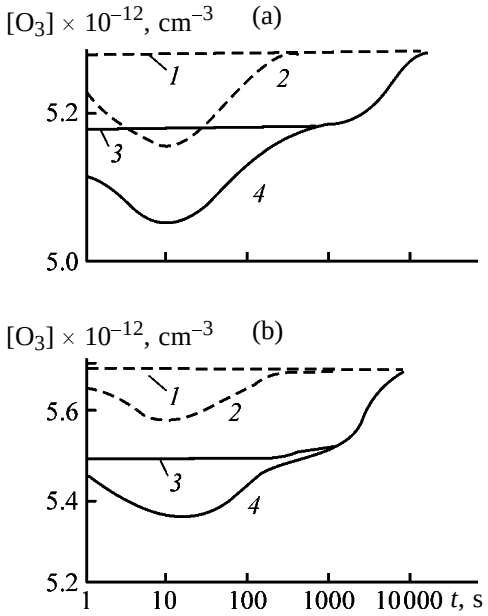

Fig. 2. Dynamics of the ozone concentration [O_3] in the stratosphere upon a single rocket launch at altitudes of (a) 25 and (b) 30 km. (*t*) Time. Curves *2* and *4* describe the evolution of the ozone concentration in a region of stratosphere contaminated when a rocket passed it at noon and midnight, respectively; curves *1* and *3* determine the dynamics of diurnal variations of [O_3] in unperturbed stratosphere (curve *1*, beginning at midnight; curve *2*, at noon).

significant for the overall process of O_3 breakdown; (2) box models are applicable to solution of the problem of evolution of the rocket trail in the stratosphere; (3) temperature perturbations in the rocket trail are insignificant; (4) the models developed can be used as tools for computer simulation of multiple launches of diverse types of liquid-propellant rockets; (5) the physicochemical mechanism of O_3 breakdown by combustion products of liquid propellants can be identified; (6) the influence of a number of components in the propulsive jet on the kinetics of atmospheric ozone is insignificant; (7) simplified MM for rough calculations and estimates can be constructed.

Result 1 was obtained in a set of calculations in terms of models (1)–(5) with $N = 1$ and that described in [3]. By the instants of time corresponding to 1–3 s after exhaust of the propulsive jet, the gas-dynamic parameters and the chemical composition of the contaminated region, yielded by models (1)–(5), approached to within ~30% the values obtained by analytical estimates and chosen as initial conditions in calculating identical perturbation in terms of the model of [3]. In later stages, the kinetic curves obtained in terms of models (1)–(5) and [3] for all the components important for the photochemistry of ozone coincided within the calculation error. This indicates that the chemistry of O_3 loss is not affected by fast processes in the initial gas-dynamic stage of formation of a rocket trail and, simultaneously, confirms the validity of the simplified MMs of the kinetics–diffusion type [1, 3].

Fact 2 was established by comparing the results of calculations with identical initial conditions (of perturbation) and $N = 1$, 3, and 5. This comparison suggests that raising the number of individually considered zones does not reveal any new effects. Conversely, it becomes possible, for liquid-propellant rockets, to detail the results of simulations in terms of the box model *a posteriori*, by analytical methods of mathematical physics. It is noteworthy that this fact is due to the relative small perturbations of the stratosphere kinetics in single launches of typical liquid-propellant rockets. In practice, using the box model saves computational resources, e.g., by shortening 100-fold the time in which a solution is found numerically by passing from $N = 5$ to $N = 1$ and obviating numerous concomitant difficulties.

The smallness of the temperature component of the

stratospheric perturbations on completion of the jet deceleration–mixing stage, mentioned above as result 3 and expressed as a short-time cooling of the trail cloud by fractions of a degree, is also a consequence of the low level and short duration of the initiating impact.

Practical result 4, obtained in terms of specialized CASE-technologies of physicochemical kinetics [3], consists of a software for widely used personal computers, which implements the concepts of the present study, and the most important results [1–3]. In computer implementation of the MM, the function of a source is developed both for simulations of several repeated launches from the same site and for varied physical nature of a contaminant and method of its introduction. In this stage, the following forms of the source function are allowed: hypersonic propulsive jet, liquid drop dispersed in flight, explosion cloud, and combinations of these. The first type of source corresponds to the goals of the present study; second, to contamination of the ozonosphere with unburned components of liquid propellants; and third, to products of their forced explosive elimination.

Result 5 and the ensuing results 6 and 7 are aimed at avoiding, wherever possible, complicated simulations and at replacing them with approximate analytical calculations or simple calculations on personal computers using the standard engineering mathematics software.

The principal hypothesis underlying the model of O_3 breakdown is as follows. The propulsive exhaust of rockets contains one or several components of those exerting predominant influence on the loss of O_3 under natural conditions, with the concentrations of these components in the rocket trail much exceeding the background values. As a result of strongly accelerated loss of O_3, its concentration in the perturbed zone is "adjusted" to the concentration of the ozone-depleting components, with the relative deviation of the ozone concentration from the unperturbed level being comparatively low (≤20%). Since the level of ozonosphere perturbation by components depleting O_3 is assumed to be rather high, its decrease cannot occur exclusively via stratospheric chemistry, being also determined by turbulent dissipation of the trail cloud.

To the above hypothesis, qualitatively accounting for the kinetic of perturbed O_3 in Fig. 2, corresponds, in the simplest variant, the equation

$$\frac{d[\tilde{O}_3]}{dt} = -\frac{k[O_3]_0 c_0}{(1+bt)^3} - \frac{3b[\tilde{O}_3]}{1+bt}, \qquad (6)$$

where c_0 is the effective initial concentration of ozone, which is assumed to be comparatively stable chemically or long-lived; k, the rate constant of O_3 loss; $b = \xi/3R_{gd}^{2/3}$, the constant of turbulent smearing of the trail [3]; R_{gd}, the rocket trail radius upon completion of the gas-dynamic deceleration of the jet; $[\tilde{O}_3] = [O_3] - [O_3]_0$, the deviation of the ozone concentration from the background value $[O_3]_0$.

A solution to (5) is given by

$$[\tilde{O}_3] = \frac{[\tilde{O}_3]_0 - k[O_3]_0 c_0 t}{(1+bt)^3}, \qquad (7)$$

where $[\tilde{O}_3]$ is the primary nonchemical, through dilution of the stratosphere by combustion products, deviation of the ozone concentration from the background value, and c_0 is the initial concentration of the depleting agent.

According to Eq. (7), the degree and dynamics of O_3 perturbation are affected by three parameters: level of perturbation by ozone-depleting agent (agents) and time factors responsible for removal of the depleting agent via chemical reactions and turbulent dissipation. The competition of the reactions of O_3 loss and diffusion forms the temporal dynamics of perturbed ozone, qualitatively coinciding with that in Figs. 2a and 2b.

Finer formulations also take into account the chemical loss and/or generation of the ozone-depleting substance by means of an analytical equation similar to (6). In particular, detailed analysis of the numerical solution for Proton rocket requires that the mechanism (6) should be discarded for the following reasons. In MM (6), the minimum concentration of O_3 occurs at the instant of time $t^*_{gd} = 1/2b$, corresponding to the characteristic duration of turbulent dissipation of the rocket trail. For rockets of the type under consideration, the gas-dynamic scale t^*_{gd} varies from 65 s at altitude of 20 km to 190 s at the upper boundary of the stratosphere. Direct integration of Eqs. (1)–(5) leads to much shorter times of extremal concentration of ozone, from 10 to 75 s, respectively. Thus, the O_3-depleting agent is a highly active substance, which enters into various reactions at a severalfold higher rate, compared with its dissipation in a purely mechanical way.

The apparent mathematical formulation of the case described is as follows:

$$\frac{d[\tilde{O}_3]}{dt} = -k[O_3]_0 c_0 - \frac{3b[\tilde{O}_3]}{1+bt}, \qquad (8)$$

$$\frac{dc}{dt} = -k_1 c_\Sigma c - k_2 c^2 - \frac{3bc}{1+bt}, \quad c(0) = c_0 \qquad (9)$$

(k_1 and k_2 are the rate constants of chemical loss of the depleting substance, and $k_1 c_\Sigma$ is the effective relative rate of depleting agent loss in first-order reactions). These equations reflect both the adjustment of the O_3 kinetics to that of the depleting agent and the kinetics of depleting agent proper, which is consumed in bimolecular first- and second-order reactions with rate constant $t^*_{ch.k} = (k_1 c_\Sigma + k_2 c_0)^{-1}$. Solutions to Eqs. (8) and (9) can be obtained in finite form in the case of predominance of one of the mechanisms of depleting agent loss, i.e., at $k_1 c_\Sigma \gg k_2 c_0$, or, vice versa, $k_1 c_\Sigma \ll k_2 c_0$. In particular, for chemical loss of depleting agent via a first-order reaction, the dynamics of ozone is given by

$$[\tilde{O}_3] = \frac{k[\tilde{O}_3]_0 c_0 (e^{-k_1 c_\Sigma t} - 1)(k_1 c_\Sigma)^{-1} + [\tilde{O}_3]_0}{(1+bt)^3}. \qquad (10)$$

It can be readily seen that the results of (7) and (10) coincide at short times; however, it follows from Eq. (10) that, at $t \approx t^*_{ch.k}$, the decrease in the concentration of the depleting agent switches off the loss channel. In other words, the characteristic lifetime of ozone-destroying substances is included in the key parameters of the problem. A similar situation takes place for loss of depleting agent in binary recombination.

Model (9), (10), combined with kinetic curves and input data of [3], makes it possible to reliably identify as main O_3-depleting agents the following two species: OH and NO radicals. Both these species (i) contain valence-unsaturated atom, (ii) have radical structure and, correspondingly, high chemical activity, and (iii) are present in propellant combustion products and in the propulsive jet in amounts much exceeding the background.

For the first stage of a Proton carrier rocket, the perturbation in NO is about 200%, and that in OH exceeds four orders of magnitude. With account of the relative importance of both the channels and the corresponding reaction constants, this makes it possible to completely disregard the chemical loss of NO and regard as the main channel of OH removal from the stratosphere the bimolecular reactions of the type OH + OH $\rightarrow$ Products, with the characteristic constant $k_2 \approx 10^{-11}$ cm^3 s^{-1}. It is also possible to obtain the extremal time for the state of depleted ozonosphere, $t^*_{ch.k} \approx 10$–30 s, in good agreement with the results of a numerical simulation [3, 6]. It should be noted that this result contradicts the conclusion of [1] about the dominating role of NO in the breakdown of stratospheric ozone. However, the authors of [1] used simplified kinetic schemes of the chemical cycles in the stratosphere and also the integration procedure based on splitting of the problem by the small-parameter method, which is unacceptable in the case of large strongly nonlinear systems.

When the second stage of the rocket is working, the amount of discharged OH decreases, and there is no discharge of NO at all. However, the relative perturbation of the concentration profile at altitudes of 40–45 km and its duration in daytime launches are greater, which is due to outstripping decrease in the efficiency of OH elimination by chemical reactions in view of the high rarefaction of the atmosphere upon opening at high altitude of a channel for photochemical reproduction of OH from water, hydrogen peroxide, and other products of binary reactions between OH radicals. This tendency is confirmed by comparison of the constants of photochemical and purely chemical reactions with OH [2] at different altitudes.

The significance of the influence exerted by OH and NO radicals discharged by a rocket on the breakdown kinetics of stratospheric ozone was verified both via perturbation of the initial data (regular for the candidates for depleting agents and random for all other components of propulsive exhausts) and by numerical characterization of the leading (in the sense of material circulation) reactions involving O_3.

It is noteworthy that, for a chemically stable depleting agent, e.g., a chlorine-containing substance, Eqs. (6) and (7) should be used as the working MM, with the instant of the minimum content of ozone in the rocket trail determined exclusively by transfer process; models (6), (7) and (8)–(10) well account for the results of detailed computer simulations [3, 6] and give estimates of the O_3 perturbation by liquid-propellant rocket, which are one to one and a half orders of magnitude lower than those predicted by [7]. The possible reason for these discrepancies is the imperfect algorithmic implementation of the MM and strongly limited kinetic schemes of atmospheric transformations [7] as compared to the models used in [2, 3, 6], which manifest themselves in a distortion of the physical meaning and dynamic characteristics of the perturbation process.

Figures 3a and 3b show the dynamics of an integral perturbation of O_3 at altitudes in the range 20–50 km, caused by a single launch of a Proton rocket, which is calculated in terms of MM (1)–(5). It can be seen that the impact has local nature, is short, and its level is

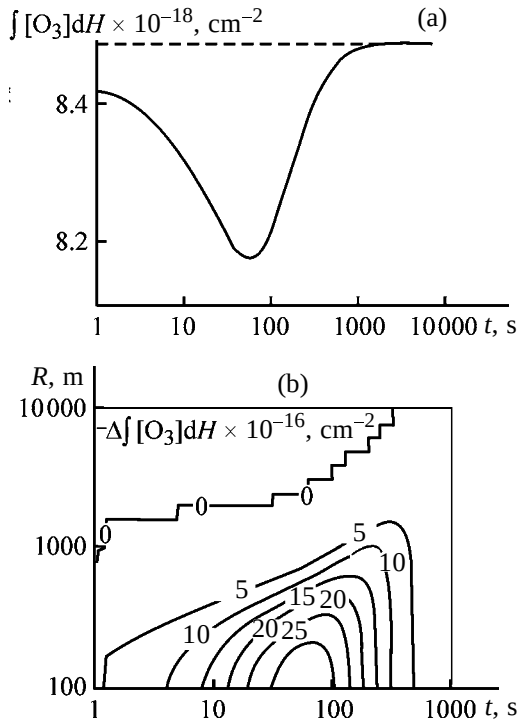

Fig. 3. Variation in space and time of the total content of ozone in the stratosphere in a single rocket launch. ($\int[O_3]dH$) Integral perturbation of ozone content along height, (R) radius of the contaminated zone, and (t) time. (a) Dynamics obtained in the box approximation [calculation by (1)–(5) at $N = 1$] and (b) that according to discrete-diffusion model (1)–(5) at $N = 5$.

low, which fully justifies the phenomenological assumptions made in constructing the MM. Nonlocal impact and dissipation processes depress the level and make longer the duration of an integral (over the range 20–50 km) perturbation to ~4% and 70 s, respectively (see, for comparison, the local perturbation parameters in Figs. 2a and 2b).

It is also important that the result of action of different fuel–oxidant pairs is qualitatively the same, and the perturbation level is proportional to the amount of OH radicals discharged.

The validity of the simplified approach (8)–(10) was confirmed by results of a test numerical simulation for a Proton rocket with kerosene–oxygen fuel: the error in the reproduction by the model of the data of detailed computations in terms of MM (1)–(5) does not exceed 20%. This allows use of elementary models of the type (8)–(10) for evaluation of the integrated impact of multiple launches of liquid-propellant rockets by various scenarios.

The inapplicability of the models presented here to direct simulation of the kinetics of the ozonosphere perturbed by solid-propellant rockets is due to the fact that, in this case, the main combustion products are chlorine-containing substances which catalyze ozone breakdown and, therefore, are not subject to chemical loss within the ozone layer. Here, the mechanisms by which the perturbation is localized and subsequently dissipated are processes of global atmospheric circulation, and, therefore, parametric estimates of the impact are to be based on a knowledge of the corresponding space and time scales. In this case, the decrease in the content of ozone in the atmosphere is found in terms of a simpler model [2], which disregards local turbulent transfer, but, simultaneously, assumes a higher (corresponding to the perturbation level) concentration of chlorine as an MGCS component, compared to the background.

Detailed calculations of the O_3 concentration fields, induced both by single and by multiple launches of liquid-propellant rockets of the same and different types, can be performed not only using MM (1)–(5) at $N = 5$ and more, but also in terms of a box approximation and elementary models of the (8)–(10) type, with subsequent smearing of the steplike profile into a Gaussian curve. The calculation errors associated with such an approach do not exceed 20%.

CONCLUSIONS

(1) The mathematical model of perturbations in the stratosphere, caused by rocket launches, was modified and used to identify the mechanism of ozone breakdown by combustion products of liquid propellants and suggest methods for approximate engineering-ecological estimates of the scale and level of impacts of this kind for various operation scenarios.

(2) A computer simulation confirmed, on the whole, the validity of the previously employed simulation models, made wider the range of situations that can be simulated, and, simultaneously, enabled more detailed simulation.

(3) The insignificant impact of liquid-propellant rockets on the stratospheric chemistry and, in particular, the ozone cycle was confirmed.

REFERENCES

1. *Ekologicheskie problemy i riski vozdeistviya raketno-kosmicheskoi tekhniki na okruzhayushchuyu prirodnuyu sredu: Spravochnoe posobie* (Ecological Problems and Risks Associated with the Impact of Rockets and Spacecraft on the Environment: Reference Book), Adushkin, A.V., Ed., Moscow: Ankil, 2000.

2. Gubanov, E.V., Davletshin, R.F., and Yatsenko, O.V., Photochemical Model of Stratosphere Contaminated by Exhausts of Liquid-Propellant Carrier Rockets, *Preprint of Moscow Inst. of Engineering Physics*, Moscow, 1993. no. 1.
3. Yatsenko, O.V. and Zagorodnyuk, V.T., *Komp'yuternoe modelirovanie zadach prikladnoi fiziko-khimicheskoi dinamiki* (Computer Simulation of Problems of Applied Physicochemical Dynamics), Rostov-on-Don: Severo-Kavkazskii Nauchnyi Tsentr Vysshei Shkoly, 2001.
4. Moiseev, N.N., *Ekologiya chelovechestva glazami matematika* (Ecology of the Mankind in Mathematician's View), Moscow: Molodaya Gvardiya, 1988.
5. Kolesnichenko, A.V. and Marov, M.Ya., *Turbulentnost' mnogokomponentnykh sred* (Turbulence in Multicomponent Media), Moscow: Nauka, 1999.
6. Davletshin, R.F. and Yatsenko, O.V., *Izv. Vyssh. Uchebn. Zaved., Sev.-Kavk. Region, Estestv. Nauki*, 1995, no. 2, pp. 54–62.
7. Tishin, A.P., Aleksandrov, E.L., Rodionov, A.V., *et al.*, *Khim. Fiz.*, 1993, vol. 12, no. 9, pp. 1184–1225.

Russian Journal of Applied Chemistry, Vol. 76, No. 11, 2003, pp. 1784–1786. Translated from Zhurnal Prikladnoi Khimii, Vol. 76, No. 11, 2003, pp. 1834–1836.

ENVIRONMENTAL PROBLEMS OF CHEMISTRY AND TECHNOLOGY

Flocculation Power of Chitosan and Its Derivatives in Mixtures with Anionic Flocculants

V. A. Izvozchikova, N. V. Pastukhova, S. A. Ryabov, Yu. D. Semchikov, L. A. Smirnova, and A. E. Mochalova

Lobachevsky Nizhni Novgorod State University, Nizhni Novgorod, Russia

Received October 28, 2002

Abstract—The flocculation properties of chitosan (cationic component) and its copolymers with (meth)acrylic acid were studied. The flocculation power of grafted chitosan copolymers with dimethylaminoethyl methacrylate in mixtures with an anionic polyacrylic flocculant was evaluated.

In most cases, treatment of industrial and domestic wastewaters is based on flocculation of negatively charged dispersions [1]. The range of cationic flocculants commercially produced in Russia is limited to synthetic (co)polymers based on amino derivatives of acrylic and methacrylic acids, vinylpyridines, and polyethylene amines. Expansion of the assortment and performance of cationic flocculants is still urgent. In this respect, much promise is shown by chitosan [CTS, β-(1 → 4)-2-amino-2-deoxy-*D*-glucose], the product of deacetylation of the natural polymer chitin. Chitosan is widespread in nature; it comes second after cellulose among polysacharides, and it can form chelates [2].

In this work, we studied the flocculation power of CTS, grafted copolymer of chitosan with dimethylaminoethyl methacrylate (DMAEM) dimethyl sulfate and their mixtures with anionic polyacrylic flocculant (PAF, copolymer of acrylamide with sodium methacrylate). The latter product is probably a terpolymer due to partial uncontrolled hydrolysis of acrylamide units.

EXPERIMENTAL

In our work we used CTS* (molecular weight 1.4×10^5, degree of deacetylation 0.82), grafted copolymer of CTS with DMAEM dimethyl sulfate prepared by radical polymerization [3], and PAF.

The flocculant solutions were prepared by dissolution of CTS and its copolymer in 1–2% aqueous acetic acid, and PAF was dissolved in water.

The flocculation power of compounds was studied using model and real systems. The model systems were dispersions of clay, kaolin, and Redoxide dye in water with the concentration of the dispersed phase of 0.5 wt %; industrial and domestic wastewaters were used as real systems.

The flocculation power was evaluated spectrophotometrically by changes in the optical transmission (%) of the suspension with time. The aqueous suspensions were prepared by dispersion of the appropriate system in distilled water for 30 min with stirring at 180–200 rpm. Then, the suspensions were placed into a cell of an FEK-M photocolorimeter, the required amount of a flocculant was added, the mixture was stirred, and the optical transmission of the system was recorded.

First we determined the optimal concentrations of polymeric flocculants and found that it was $\sim 10^{-3}$, $\sim 10^{-4}$, and 10^{-6}% for CTS, its grafted copolymer, and PAF, respectively. At higher concentrations, the dispersions are stabilized. This is confirmed by the data given in Fig. 1, which suggest that the grafted copolymer is the most effective single-component flocculant.

The flocculating power of macromolecular compounds can be enhanced by "double addition" of the flocculant [1]. It is considered that agglomerates formed on adding the first portion of the polymer solution become coarser upon addition of the second portion; as a result, the clarification rate of the dispersion is higher than at the single-stage procedure. It seemed advisable to use different compounds, e.g., cationic and anionic flocculants in the first and second stages, respectively. We suggested that the formation of interpolymeric complexes between a cationic poly-

* Purchased from the Sonat Company, Moscow, Russia.

1070-4272/03/7611-1784$25.00

mer sorbed on dispersed particles and linear macromolecules of an anionic flocculant would increase the efficiency of the dispersion sedimentation [3]. Such a structure can be described as a "bunch on the branch". Thus, the dispersions were treated by three different modes: (1) copolymers were added simultaneously, (2) CTS was added before PAF, or (3) PAF was added before CTS.

The performance of various flocculants in clarification of the clay suspensions is illustrated in Fig. 2. As seen, the flocculant mixtures showed higher flocculation performance as compared to individual components, and the best result was observed for mode 1 (CTS : DMAEM = 5 : 1). We proposed that, in this case, labile networks of macromolecules of the grafted (cationic) and random (anionic) copolymers are formed, and the dispersed particles are trapped by this network and aggregate in it. It should be taken into account that these networks do not spread through the whole solution, and their size is comparable with the size of the particle aggregates. We found that the above mixture acts as efficient flocculant at pH 2–9.

Based on the data obtained for model systems, we tested the flocculant mixtures in clarification of the industrial and domestic wastewaters.

The electrokinetic potential of the disperse phase in wastewaters was determined by electrophoresis using a Ken device. It was found that the colloidal particles were negatively charged and the electrokinetic potential was about 70 mV. This fact explains high stability of industrial wastewaters; they are stable without flocculation and clarification for several months (D = 2–3). Since the dispersed particles are negatively charged, first the cationic and then the anionic flocculants were added. It should be noted that, in contrast to the model tests, no clarification was observed on adding the flocculant mixture. Upon addition of CTS or its grafted copolymer, coarse "curdled" bunches were formed, which did not precipitate in 1 h. After addition of the anionic flocculant, we observed the densification of the initial loose aggregates and their sedimentation in 3–4 min (Fig. 3). Apparently, in this case, the coagulation–flocculation mechanism is realized providing formation of the structures of "bunch on the branch" type. Since the light transmission of the industrial wastewaters was very low ($D \gg 1$ depending on the tank), the flocculation efficiency of the double-stage addition of the polymers in question was estimated at 14–26 depending on the molecular weight of the flocculants:

$$\tau = V/V_0 - 1,$$

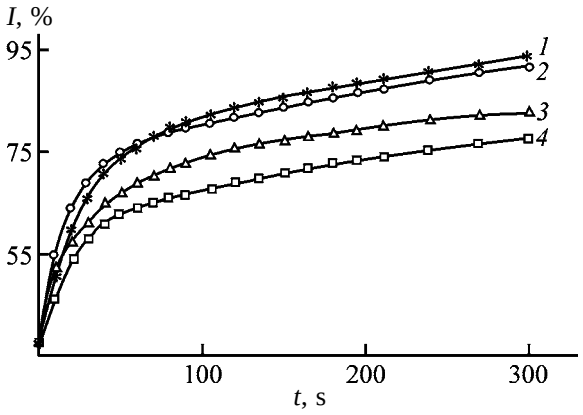

Fig. 1. Optical transmission I of 0.5% clay dispersion in water as a function of time t in the presence of (*1*) grafted copolymer CTS–DMAEM (10^{-4}%), (*2*) CTS (10^{-3}%), (*3*) PAF (10^{-6}%), and (*4*) without flocculant.

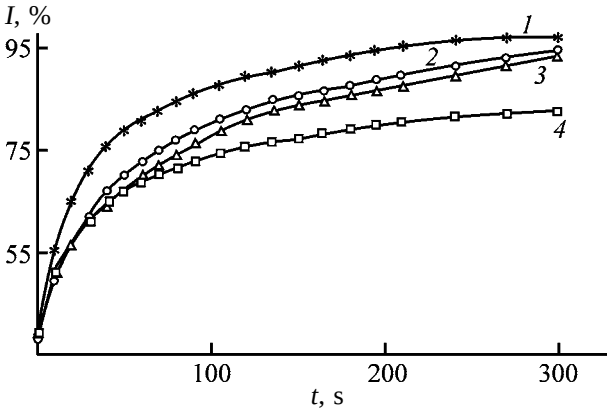

Fig. 2. Optical transmission I of 0.5% clay dispersion in water as a function of time t in the presence of PAF (10^{-6}%) and CTS–DMAEM (10^{-4}%) mixture at the CTS: DMAEM ratio of (*1*) 5 : 1 and (*2*) 1 : 1; (*3,4*) dependences obtained, respectively, with CTS (10^{-3}%) and PAF (10^{-6}%) taken separately.

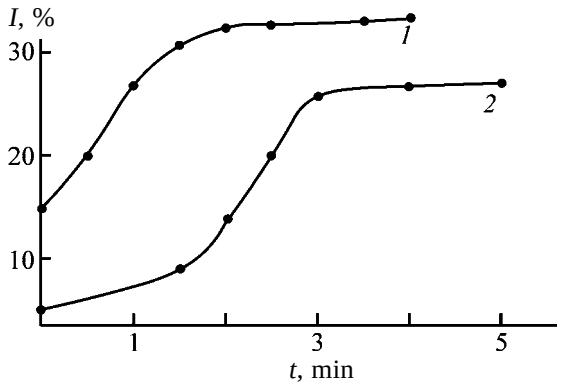

Fig. 3. Kinetics of the wastewater clarification by flocculant mixtures based on (*1*) CTS (molecular weight 2×10^5, 10^{-3}%)–PAF (5×10^{-3}%) and (*2*) CTS (2×10^4, 2×10^{-2}%)–PAF (5×10^{-2}%). (*I*) Light transmission and (*t*) time.

where V and V_0 are the clarification rates of the dispersion in the presence of flocculant and without it, respectively.

CONCLUSIONS

(1) The flocculation powers of chitosan and its grafted copolymer with dimethylaminoethyl methacrylate dimethyl sulfate in their mixtures with anionic acrylic polymer were compared, and a synergistic effect was revealed. To attain the highest flocculation power, the flocculants should be added successively, first the cationic and then the anionic polymers.

(2) The clarification efficiency of the industrial wastewaters is 14–26.

REFERENCES

1. Izvozchikova, V.A., Knyazeva, T.E., Myasnikova, I.B., *et al*., Abstracts of Papers, *Vserossiiskaya nauchno-prakticheskaya konferentsiya "Ekonomicheskie i tekhnologicheskie aspekty sinteza i primeneniya polimernykh flokulyantov dlya ochiski khozyaistvennykh, bytovykh i stochnykh vod i obezvozhivaniya osadkov" (Flok-2000)*, (Russian Scientific and Practical Conf. "Economical and Practical Aspects of Synthesis and Use of Polymeric Flocculants for Treatment of Municipal and Industrial Wastewaters and for Dehydration of Precipitates" (Flok 2000)), Dzerzhinsk, May 23–26, 2000, pp. 9–10.
2. Baran, A.A. and Teslenko, A.Ya., *Flokulyanty v biotekhnologii* (Flocculants in Biotechnology), Leningrad: Khimiya, 1990.
3. Odian, G., *Principles of Polymerization*, New York: McGraw-Hill, 1970.

Russian Journal of Applied Chemistry, Vol. 76, No. 11, 2003, pp. 1787–1791. Translated from Zhurnal Prikladnoi Khimii, Vol. 76, No. 11, 2003, pp. 1837–1841.

ORGANIC SYNTHESIS AND INDUSTRIAL ORGANIC CHEMISTRY

Reduction of 4-Nitrosodiphenylamine with Sodium Hydroxy- and Aminoalkanesulfinates

Yu. V. Polenov, E. V. Egorova, and S. G. Ryazantseva

Ivanovo State Chemical Engineering University, Ivanovo, Russia

Received March 13, 2003

Abstract—The kinetics of reduction of 4-nitrosodiphenylamine with sodium alkanesulfinates were studied, and the reaction mechanism was suggested.

Reduction of 4-nitrosodiphenylamine (NDPA) to 4-aminodiphenylamine (ADPA) is of great practical importance, since ADPA is an intermediate product in preparation of antioxidants. In particular, condensation of ADPA with acetone yields 4-isopropylaminodiphenylamine (commercial name Diafen FP) [1], which is thermal stabilizer for polyethylene, polystyrene, and synthetic rubber, inhibitor of tarring of motor fuel, and stabilizer of leaded gasolines. In recent years, derivatives of alkanesulfinic acids containing various substituents at the first carbon atom were found to be highly promising in reduction of organic nitro and nitroso compounds. The feature of these compounds is the presence of abnormally long C–S bond, which under certain conditions ruptures to form active intermediates having high reducing power: SO_2^{2-} and $S_2O_4^{2-}$ ions and $\dot{S}O_2^-$ radical anions [2]. The use of sodium hydroxymethylsulfinate as a reducing agent allows preparation of ADPA from NDPA in almost quantitative yield [3]. The mechanism of this reaction was thoroughly studied. It was shown that the initial substance can be reduced both with sulfoxylate anions and directly with hydroxymethanesulfinate molecules [4]. The absence of side reactions allows reliable determination of the rate constants of the stages involving decomposition of the reducing agent and the reaction of sulfoxylate anions with the oxidant. These parameters can be used for optimizing processes involving such reducing agents.

In this connection, it is appropriate to study the possibility of NDPA reduction with derivatives of alkanesulfinic acids with the aim to compare their reactivity and performance and also to elucidate the process mechanism.

EXPERIMENTAL

NDPA was prepared by threefold recrystallization of the commercial product from ethanol.

Sodium hydroxymethanesulfinate (SHMS), sodium hydroxyethanesulfinate (SHES), and sodium aminomethanesulfinate (SAMS) used as reducing agents were prepared by the procedures described in [5, 6]. The concentrations of their solutions were determined by iodometric titration [7].

NDPA was reduced directly in the colorimeter cell, which was placed into a temperature-controlled jacket connected to a UT-2 thermostat (the temperature was maintained with the accuracy of ±0.5°C). The reaction rate was determined by measuring the optical density of the NDPA solution at λ = 400 nm, which corresponds to the absorption maximum in its electronic spectrum. It was found preliminarily that the reaction products and the reducing agent do not absorb light at this wavelength. The optical density was measured on a KFK-2 spectrophotometer equipped with an Shch-1516 digital dc voltmeter.

All kinetic measurements were carried out at more than thousand-fold excess of the reducing agent, which provides practically constant concentration of the reducing agent in the course of the experiment.

Preliminary experiments showed that the reaction of NDPA with SHMS in aqueous alkaline solution yields a compound that can be isolated by distillation in a vacuum at approximately 200°C. The melting point of this compound is 66–67°C, the half-wave reduction potential on a dropping mercury electrode $E_{1/2}$ = –0.23 V (anodic wave), and the appearance of the product corresponds to published data for ADPA [8, 9].

To determine the stoichiometry of the reaction between SHMS and NDPA, we mixed the solutions of these compounds in 1 M aqueous NaOH. The resulting mixture was kept under argon at 73°C until decolorization, after which the SHMS content was determined iodometrically.

1070-4272/03/7611-1787$25.00

Table 1. Determination of the stoichiometric ratio of the reactants in reduction of NDPA with SHMS. Initial amount of NDPA 0.0147 mol

ν^{*}_{SHMS}	ADPA obtained	ν^{**}_{SHMS}	NDPA : SHMS*	Yield of ADPA, %
mole				
0.7178	0.0138	0.0799	1 : 1.9	94
0.1078	0.0145	0.0769	1 : 2.1	99
0.1051	0.0145	0.0742	1 : 2.1	99

* Before reaction.
** After reaction.

Table 1 shows that, under these conditions, ADPA is formed in quantitative yield, with the ratio of the reacted NDPA and SHMS being 1 : 2. Qualitative analysis showed that, in the course of reduction, sulfite sulfur is formed.

These results suggest the stoichiometric reaction equation

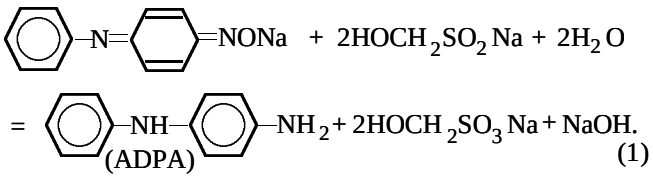

(1)

SHMS and SAMS are analogs of sodium hydroxymethanesulfinate [1]. Hence, there is good reason to believe that the reduction of NDPA with SHES and SAMS proceeds by a stoichiometric equation similar to Eq. (1).

The kinetic curves of NDPA reduction with various reducing agents are shown in Fig. 1. Contrary to reduction of 2-nitro-2'-hydroxy-5'-methylazobenzene (NAB) [10], the reaction between alkanesulfinates and NDPA proceeds without an induction period, with the reaction order with respect to the oxidant being fractional.

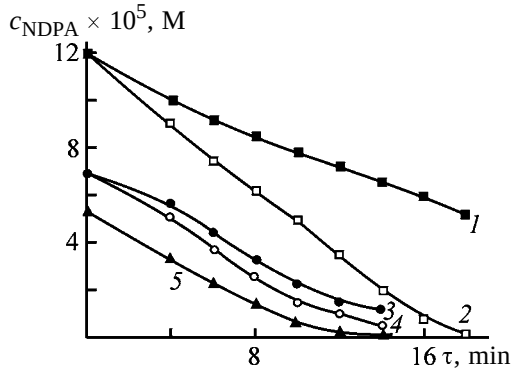

Fig. 1. Kinetic curves of NDPA reduction. (c_{NDPA}) NDPA concentration; (τ) time. (*1*, *2*) SHMS, 309 K, c_{red} = 0.5519, c_{OH^-} = 0.37 M; (*3*, *4*) SHES, 303 K, c_{red} = 0.071, c_{OH^-} = 0.6 M; (*5*) SAMS, 313 K, c_{red} = 0.414, c_{OH^-} = 1.02 M. (*2*, *4*, *5*) In the absence of additives; addition of the corresponding aldehyde, M: (*1*) 0.21 and (*3*) 0.02.

It is well known that reactions involving SHMS are inhibited by formaldehyde. This is due to the fact that the reducing species in some cases are not the molecules of the reducing agent but the products of their decomposition, sulfoxylate ions, formed by the reversible reaction [1]

$$HOCH_2SO_2^- \rightleftarrows HSO_2^- + CH_2O. \quad (2)$$

Addition of formaldehyde and acetaldehyde inhibits the reaction in question (Fig. 1, curves *1* and *3*), and at sufficiently high concentrations of the additives the reaction order with respect to NDPA becomes equal to 1 (Fig. 2a).

However, attempts to completely inhibit the reaction by adding aldehydes, as in the case of NAB and indigocarmine, failed [10, 11]. For example, in reduction of SHMS, the reaction rate on adding formaldehyde decreases by 60% at maximum, and with further addition of formaldehyde it remains constant. For SAMS, according to the equation of its decomposition with rupture of the C–S bond, aminomethanol should be an additive shifting the equilibrium to formation of nondissociated reducing agent molecules:

$$NH_2CH_2SO_2^- + OH^- \rightleftarrows SO_2^- + NH_2CH_2OH. \quad (3)$$

Aminomethanol does not exist in the free state [12]; therefore, it is impossible to carry out experiments with its addition to SAMS.

For all the reducing agents studied, the reaction rate varies in direct proportion to the concentration of the reducing agent (Fig. 2b) both in the presence of aldehydes and without them.

The above experimental data suggest that reduction of NDPA with derivatives of alkanesulfinic acids proceeds by two parallel pathways: direct reaction of NDPA with molecules of reducing agent (associative pathway) and reaction with the products of decomposition of reducing agent molecules, sulfoxylate anions (dissociative pathway). Based on the above and also published data [13], which note that the nitroso group is reduced in steps, we can propose the following reaction pattern (for SHMS as an example):

Associative pathway

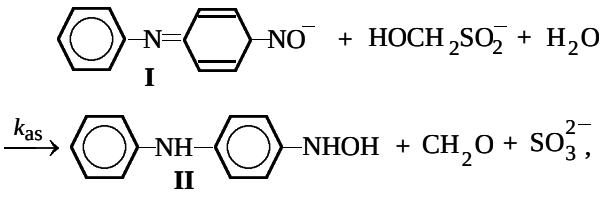

(4)

$$\mathbf{II} + HOCH_2SO_2^- \rightarrow ADPA + HOCH_2SO_3^{2-}. \quad (5)$$

Dissociative pathway

$$HOCH_2SO_2^- + OH^- \underset{-k_1}{\overset{k_1}{\rightleftarrows}} SO_2^{2-} + CH_2(OH)_2,^1 \quad (6)$$

$$\mathbf{I} + HSO_2^- + 2H_2O \xrightarrow{k_2} \mathbf{II} + SO_3^{2-}, \quad (7)$$

$$\mathbf{II} + HSO_2^- + 2H_2O \rightarrow ADPA + HSO_3^{2-}. \quad (8)$$

Since in the presence of aldehyde the reaction order with respect to the reducing agent and NDPA is equal to 1, we can assume that, in the associative pathway, reaction (4) will be the limiting stage and the subsequent fast stage (5) will not affect the overall rate of the process. The first reaction order with respect to the reducing agent in the absence of aldehyde additions and the inhibiting effect of the aldehydes suggest, by analogy with reduction of NAB, that in reduction by the dissociative pathway the limiting stage is cleavage of the reducing agent molecules (6). Applying the steady-state concentration method to stages (6) and (7), and considering the associative pathway, we obtain the kinetic equation

$$v_{ov} = -\frac{dc_{NDPA}}{dt} = v_{dis} + v_{as} = \frac{k_1 k_2 c_{NDPA} c_r c_{OH^-}}{k_{-1} c_a + k_2 c_{NDPA}} + k_{as} c_{NDPA} c_r, \quad (9)$$

where v_{ov}, v_{dis}, and v_{as} are the overall reaction rate and the reaction rates by dissociative and associative pathways, respectively (mol l^{-1} s^{-1}); c_{NDPA}, c_{OH^-}, c_r, and c_a are concentrations of NDPA, hydroxide ions, reducing agent, and aldehyde (or aminomethanol), respectively (M); k_1 and k_{-1} are the rate constants of stage (6) (l mol^{-1} s^{-1}); k_2 and k_{as} are the rate constants of stages (7) and (4), respectively (l mol^{-1} s^{-1}).

Equation (6) can be experimentally verified for the reducing agents studied by analogy with reduction of NAB with SHMS [10].

[1] Methylene glycol is hydrated form of formaldehyde in alkali solution.

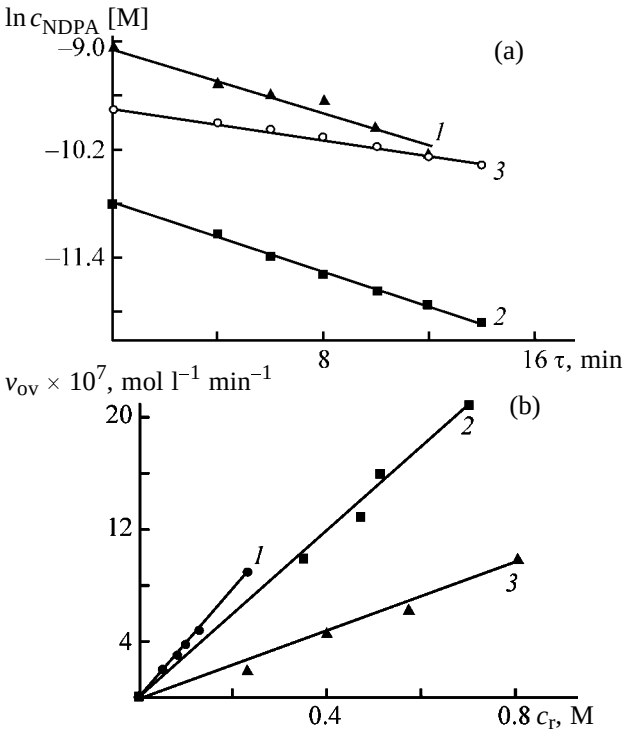

Fig. 2. Dependences of (a) $\ln c_{NDPA}$ on duration of NDPA reduction τ and (b) the reaction rate v_{ov} on concentrations of the reducing agents c_r: (a) (*1*) SHMS, 309 K, c_r = 0.5519, c_{OH^-} = 0.37, c_a = 0.21 M; (*2*) SHES, 303 K, c_r = 0.0634, c_{OH^-} = 0.17, c_a = 0.013 M; (*3*) SAMS, 303 K, c_r = 0.4088, c_{OH^-} = 0.86 M. (b) (*1*) SHES, 283 K, c_{OH^-} = 0.5, $c_{NDPA} = 2.5 \times 10^{-5}$, $c_a = 5 \times 10^{-5}$ M; (*2*) SAMS, 303 K, c_{OH^-} = 0.75, $c_{NDPA} = 2 \times 10^{-5}$; (*3*) SHMS, 308 K, c_{OH^-} = 0.37, $c_{NDPA} = 2.5 \times 10^{-5}$, c_a = 0.21 M.

For this purpose, based on the results of experiments performed at aldehyde concentrations sufficient to suppress pathways (6)–(8), we found k_{as} values (Table 2). Then, from the difference between the overall rate v_{ov} and the rate by the associative pathway v_{as}, we evaluated the reaction rates by the dissociative pathway v_{dis}, entering into the linear form of the kinetic equation

$$\frac{1}{v_{dis}} = A + \frac{Bc_a}{c_{NDPA}}, \quad (10)$$

Table 2. Kinetic parameters of NDPA reduction with sodium alkanesulfinates

Reducing agent	T = 283 K		T = 293 K	
	k_{as}	k_1	k_{as}	k_1
	l mol^{-1} s^{-1}			
SHMS	9.5×10^{-4}	1.13×10^{-9}	1.3×10^{-3}	2.5×10^{-9}
SHES	1.13×10^{-3}	2.2×10^{-7}	5.5×10^{-3}	3.5×10^{-6}
SAMS	6.7×10^{-5}	6.7×10^{-9}	3.17×10^{-4}	1.43×10^{-8}

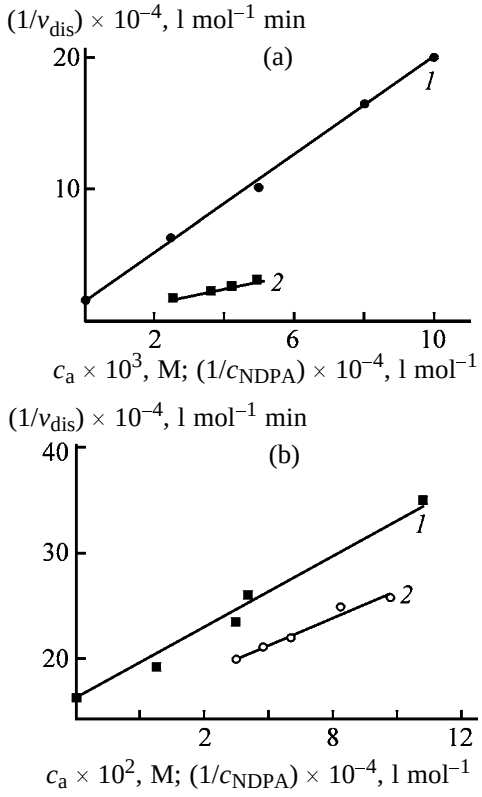

Fig. 3. Reciprocal reaction rate by dissociative pathway $1/v_{dis}$ as a function of (*1*) concentration of aldehydes c_a and (*2*) reciprocal concentration of NDPA $1/c_{NDPA}$: (a) SHES, 283 K; c_r = 0.1064, c_{OH^-} = 1.8; (*1*) $c_{NDPA} = 2.5 \times 10^{-5}$, (*2*) c_a 3.6×10^{-3} M; (b) SHMS, 308 K; c_r = 0.5519, c_{OH^-} = 0.37; (*1*) $c_{NDPA} = 6 \times 10^{-5}$, (*2*) $c_a = 3.6 \times 10^{-2}$ M.

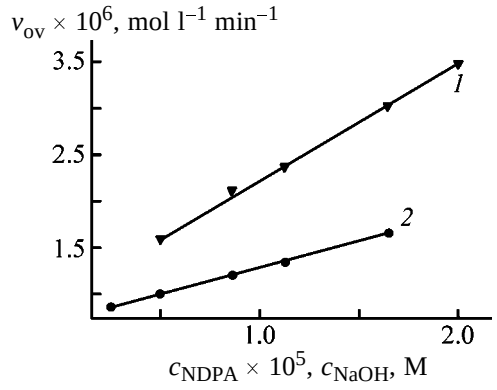

Fig. 4. Rate of NDPA reduction with HAMS v_{ov} as a function of (*1*) NDPA concentration c_{NDPA} and (*2*) concentration of hydroxide ions c_{OH^-} at 303 K. c_r (*1*) 0.468 and (*2*) 0.409; (*1*) c_{OH^-} = 0.75; (*2*) $c_{NDPA} = 2 \times 10^{-5}$ M.

where $A = 1/(k_1 c_r c_{OH^-})$, $B = k_1/(k_1 k_2 c_r c_{OH^-})$.

The linearity of the plots in the coordinates $1/v_{dis}$–c_a at c_{NDPA} and c_{OH^-} = const and $1/v_{dis}$–$1/c_{NDPA}$ at c_a and c_{OH^-} = const (Fig. 3) confirms the validity of Eq. (10).

Table 3. Kinetic parameters of NDPA reduction with SAMS

T, K	$v_{ov} = f(c_{OH^-})$		$v_{ov} = f(c_{NDPA})$	
	$k_{as} \times 10^3$	$k_1 \times 10^8$	$k_{as} \times 10^3$	$k_1 \times 10^8$
	l mol^{-1} s^{-1}			
303	1.5 ± 0.3	2.3 ± 0.6	1.1 ± 0.2	4.0 ± 1.0
308	2.6 ± 0.3	4.0 ± 1.0	2.5 ± 0.5	4.0 ± 1.0
313	6.0 ± 1.0	6.0 ± 1.0	4.0 ± 0.8	6.0 ± 2.0

Table 4. Angular coefficients of dependences $v_{ov} = f(c_r)$ for NDPA reduction with SAMS

T, K	Angular coefficient	
	evaluation by Eq. (1)	experimental
303	3.02×10^{-6}	2.88×10^{-6}
308	6.14×10^{-6}	5.2×10^{-6}
313	7.01×10^{-6}	7.86×10^{-6}

From the initial ordinates of the above linear dependences, equal to the parameter *A* in Eq. (10), we evaluated the rate constants k_1 (Table 2).

As mentioned above, it is impossible to study how aminomethanol inhibits NDPA reduction with SAMS by shifting the equilibrium of decomposition of SAMS molecules by reaction (3). However, the experimental data obtained suggest that two-pathway scheme of reduction is realized in the case of this reducing agent also and it is possible to determine the same kinetic parameters that as in the case of SHMS and SHES.

The dependences of the rate of NDPA reduction with SAMS on the concentrations of NaOH and NDPA are shown in Fig. 4. The observed linear dependences with positive initial coordinates are in good agreement with the kinetic model proposed. Assuming that $k_{-1} c_a \ll k_2 c_{NDPA}$, Eq. (9) is simplified:

$$v_{ov} = k_1 c_r c_{OH^-} + k_{as} c_{NDPA} c_r. \qquad (11)$$

The equation adequately describes the experimental data presented in Figs. 2 and 4.

The rate constants and activation energies were evaluated by least-squares treatment of these dependences for various concentrations of the reducing agent and sodium hydroxide and various temperatures (Table 3). Using the rate constants listed in Table 3,

we evaluated the angular coefficient of the dependence $v_{ov} = f(c_r)$ by Eq. (11) and compared with the experimental data (Fig. 2b) (Table 4). Satisfactory agreement of these results additionally confirms the adequacy of the proposed kinetic model. From the temperature dependences of the rate constants listed in Table 3, we evaluated the activation energies for the associative and dissociative pathways to be 106 ± 10 and 53 ± 2 kJ mol^{-1}, respectively.

It should be noted in conclusion that the found rate constants k_1 (Table 2) characterize the ease of the rupture of the C–S bond in alkanesulfinate molecule. From the above data, the reducing agents can be ranked in the following order with respect to stability: SHES < SAMS < SHMS.

CONCLUSION

Based on the kinetic data for reduction of 4-nitrosodiphenylamine with sodium hydroxymethanesulfinate, sodium hydroxyethanesulfinate, and sodium aminomethanesulfinate, the kinetic equations were obtained. These equations suggest that the reaction proceeds by two parallel pathways: direct reaction of the substrate with reducing agent molecule (associative pathway) and reaction with the product of reducing agent decomposition, sulfoxylate anion (dissociative pathway).

REFERENCES

1. Budanov, V.V. and Makarov, S.V., *Khimiya serosoderzhashchikh vosstanovitelei* (Chemistry of Sulfur-Containing Reducing Agents), Moscow: Khimiya, 1994.
2. Makarov, S.V., Reactivity of Sulfur- and Oxygen-Containing Reducing Agents with C–S Bond, *Doctoral Dissertation*, Ivanovo, 2000.
3. USSR Inventor's Certificate no. 1158561.
4. Polenov, Yu.V. and Budanov, V.V., *Izv. Vyssh. Uchebn. Zaved., Khim. Khim. Tekhnol.*, 1988, vol. 31, no. 4, pp. 40–43.
5. Makarov, S.V., Budanov, V.V., and Shalimova, G.V., *Zh. Prikl. Khim.*, 1985, vol. 58, no. 5, pp. 1098–1102.
6. Makarov, S.V., Sokolova, I.N., and Budanov, V.V., *Zh. Obshch. Khim.*, 1985, vol. 55, no. 4, pp. 724–730.
7. Budanov, V.V., *Khimiya i tekhnologiya vosstanovitelei na osnove sul'foksilovoi kisloty (rongalit i ego analogi)* [Chemistry and Technology of Reducing Agents Based on Sulfoxylic Acid (Rongalite and Its Analogs)], Moscow: Khimiya, 1984.
8. *Sputnik khimika* (A Guide for Chemist), Blokh, M.A., Ed., Leningrad: ONTIKhimteor, 1935.
9. Sarsenbaeva, G.L., Avrutskaya, I.A., and Fioshin, M.D., *Elektrokhimiya*, 1977, vol. 13, no. 2, pp. 290–293.
10. Sokolova, I.N., Budanov, V.V., Polenov, Yu.V., and Polyakova, I.R., *Izv. Vyssh. Uchebn. Zaved., Khim. Khim. Tekhnol.*, 1983, vol. 26, no. 7, p. 822.
11. Budanov, V.V., Sokolova, I.N., Solov'eva, L.B., and Mel'nikova, B.N., *Izv. Vyssh. Uchebn. Zaved., Khim. Khim. Tekhnol.*, 1974, vol. 17, no. 7, pp. 993–997.
12. Nesmeyanov, A.N. and Nesmeyanov, N.A., *Nachala organicheskoi khimii* (Principles of Organic Chemistry), Moscow: Khimiya, 1974, vol. 1.
13. *The Chemistry of the Nitro and Nitroso Groups*, Feuer, H., Ed., New York: Wiley, 1969, part 1.

Russian Journal of Applied Chemistry, Vol. 76, No. 11, 2003, pp. 1792–1794. Translated from Zhurnal Prikladnoi Khimii, Vol. 76, No. 11, 2003, pp. 1842–1844.

ORGANIC SYNTHESIS AND INDUSTRIAL ORGANIC CHEMISTRY

Preparative Synthesis of 4,4'-Bis[5-alkyl(aryl)benzoxazol-2-yl]biphenyls

V. K. Ol'khovik, Yu. V. Matveenko, G. V. Kalechits, A. A. Pap, A. A. Zenyuk, and E. D. Skakovskii

Institute of Chemistry of New Materials, National Academy of Sciences of Belarus, Minsk, Belarus

Received April 4, 2003

Abstract—An attempt was made to prepare 4,4'-bis[5-alkyl(aryl)benzoxazol-2-yl]biphenyls by reaction of dimethyl 4,4'-biphenyldicarboxylate with substituted *o*-aminophenols in a high-boiling solvent in the presence of boric acid.

Compounds containing an oxazole fragment exhibit a set of valuable properties [1]. In particular, benzoxazoles are used in production of heat-resistant polymers [2], scintillators [3, 4], and fluorescent whiteners [5–7]. Of considerable interest as optical whiteners are bis(benzoxazoles) in which benzoxazole cores are linked via an ethylene, aromatic, or heterocyclic bridge. These compounds exhibit high heat resistance and lightfastness; they are used for whitening of virtually all polymeric materials. Synthesis of new compounds of this series and their study in the context of specific applications remain urgent problems.

Studies on synthesis of substituted benzoxazol-2-yl compounds in which benzoxazole cores are linked to biphenyl are relatively few [8, 9], although introduction of an additional aromatic core into the conjugation chain should enhance the whitening effect. One of promising routes to bis(benzoxazoles) containing a biphenyl bridge is that starting from dimethyl 4,4'-biphenyldicarboxylate **I**, which became a cheap and readily available substance after development of an efficient procedure for its recovery from dimethyl terephthalate production waste [10]. The known procedures for preparing 4,4'-bis(benzoxazol-2-yl)biphenyl derivatives are based on condensation of 4,4'-biphenyldicarboxylic acid or its chloride with substituted *o*-aminophenols. The reaction is performed in two steps (formation of acid arylamides followed by cyclodehydration) or in one step, with polyphosphoric acid used as solvent and cyclizing agent. The yields of the target products, depending on the solvent and cyclizing agent used, did not exceed 68% [9]. Isolation of the pure target product involves prolonged (many hours) extraction, which is a significant drawback.

The goal of this study was development of a procedure for preparing 4,4'-bis[5-alkyl(aryl)benzoxazol-2-yl]biphenyls ensuring high yield and purity of the target product, involving no aggressive cyclization agents and sophisticated purification procedures, and starting from readily avaliable ester **I**. We studied the reactions of **I** with various *o*-aminophenols **IIa**–**IId** in high-boiling solvents in the presence of boric acid [11] (Table 1).

4,4'-Bis(benzoxazol-2-yl)biphenyl derivatives were prepared by the scheme

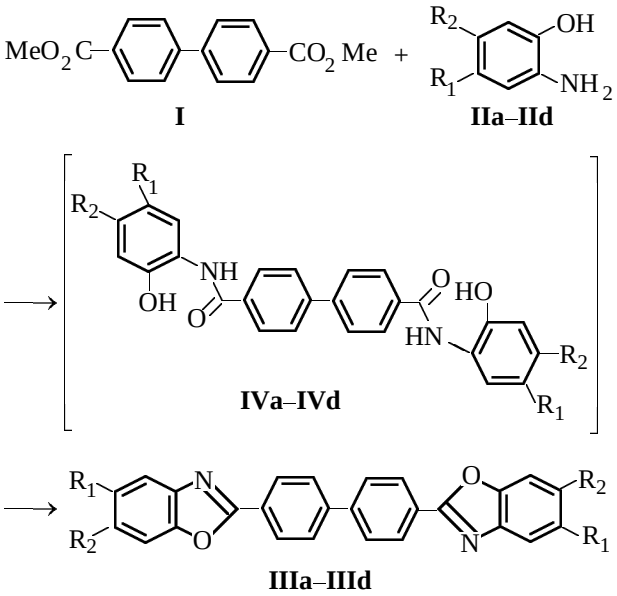

The characteristics of **IIIa**–**IIId** are listed in Table 2.

As solvents we used dimethylformamide, dimethylacetamide (DMA), diheptyl ether, diphenyl ether, and

1070-4272/03/7611-1792$25.00

Table 1. Yield of bis(benzoxazoles) **IIIa**–**IIId** in cyclization of ester **I** with aminophenols **IIa**–**IId** as influenced by reaction conditions

Reaction	Bihenyl : diphenyl ether : pyridine	Diphenyl ether : pyridine	Boric acid, mol %	*T*, °C	τ, h	Yield, %
I + **IIa** = **IIa**	1 : 5 : 1	–	100	250	12	80.7
I + **IIb** = **IIIb**	2.3 : 10 : 1 (Dinil)	–	80	260	12	89.7
I + **IIc** = **IIIc**	1 : 20 : 2	–	100	250	12	88.8
I + **IIa** = **IIIa**	–	10 : 1	100	250	10	92.4
I + **IIa** = **IIIa**	–	10 : 1	20	260	20	63.0
I + **IId** = **IIId**	1 : 100 : 10	–	100	250	12	78.3
I + **IIa** = **IIIa**	1 : 4 : 1	–	50	250	17	73.0
I + **IIa** = **IIIa**	–	10 : 1	50	250	15	87.5
I + **IIa** = **IIa**	2.3 : 10 : 1 (Dinil)	–	100	250	10	91.0
I + **IIb** = **IIIb**	–	30 : 1	75	250	24	86.4
I + **IIc** = **IIIc**	1 : 50 : 2	–	100	250	12	79.1
I + **IIa** = **IIIa**	Diheptyl ether : pyridine = 8 : 1		100	250	17	54.0

Table 2. Yields, constants, and elemental analyses of **IIIa**–**IIId**

Compound	R	Yield, %	T_m, °C	λ_{max}, nm	Found, %/Calculated, %			Formula	Molecular weight
					C	H	N		
IIIa	R^1 = Me, R^2 = H	92.4	336–338	437	81.54/80.75	4.67/4.84	6.27/6.23	$C_{28}H_{20}N_2O_2$	416.48
IIIb	R^1 = Ph, R^2 = H	89.7	305–306	440	83.97/84.43	4.21/4.47	4.87/5.18	$C_{38}H_{24}N_2O_2$	540.62
IIIc	R^1 = *t*-Bu, R^2 = H	88.8	293–295	447	82.18/81.57	7.06/6.44	5.10/5.60	$C_{34}H_{32}N_2O_2$	500.4
IIId	R^1 = H, R^2 = Me	78.3	336–338	435	80.23/80.75	4.16/4.84	6.67/6.73	$C_{28}H_{20}N_2O_2$	416.48

Dinil (a mixture of 26.5% biphenyl and 73.5 δiphenyl ether). In amide solvents and diheptyl ether, the reaction is very slow, because their boiling point is too low for the efficient reaction. Table 1 shows that the ratio between ester **I** and boric acid strongly affects the yield of bis(benzoxazoles) **IIIa**–**IIId**. Complete conversion is attained with an equimolar amount of the catalyst. At lower concentrations of boric acid and optimal reaction temperatures, the yield is as low as 63%. The reaction can be accelerated by adding an equimolar amount of pyridine; in this case, the maximal yield at 250–260°C is attained in 10–12 h. The highest yield of **IIIa**–**IIId** is attained in diphenyl ether (91%) or Dinil (92%) at the component ratio **I** : (**IIa**–**IId**) : pyridine : Dinil = 1 : 2 : 1 : 5 and 100 mol % amount of boric acid.

Compounds **IIIa**–**IIId** can be readily isolated from the reaction mixture as follows. The mixture is cooled to 150–180°C, diluted with DMA, refluxed for 2 h, and then cooled to 80–90°C. Under these conditions, the reaction product crystallizes. It is filtered off and washed on the filter with hot DMA. Compounds **IIIa**–**IIId** are colorless or light yellowish powders insoluble in water and aqueous acids and alkalis and sparingly soluble in organic solvents.

The reaction mechanism involves initial formation of amides **IVa**–**IVd** followed by their cyclization with formation of the benzoxazole fragment, as demonstrated by the example of reaction of **I** with **IIa**. The IR spectrum of the intermediate amide **IVa** contains NH stretching bands at 3320 and 3270 cm^{-1}, NH bending band at 1560 cm^{-1}, and amide $\nu_{C=O}$ band at 1680 cm^{-1}.

The composition of benzoxazoles **IIIa**–**IIId** was confirmed by elemental analysis, and their structure was determined by IR and ^1H NMR spectroscopy.

The IR spectra are consistent with the suggested structures. Transformation of **I** into **IIIa**–**IIId** results in disappearance of a strong band at 1730 cm^{-1} and appearance of a strong band at 1565–1580 cm^{-1}, with the bands of aromatic structures being preserved. The band at 1565–1580 cm^{-1} belongs to vibrations of the –N=C–O– fragment in the ring [12]. A strong band at 1470–1480 cm^{-1} is apparently due to conjugation of the biphenyl fragment with the benzoxazole core of the molecule. The stretching vibration bands of the C–H bonds of the aromatic rings are observed at 3060–3020 cm^{-1}.

In the ^1H NMR spectra of **IIIa**–**IIId**, the protons of the biphenyl fragment give doublets at 7.73–7.78 (4H) and 8.15–8.21 ppm (4H), with the coupling constant of 8.0 Hz. The benzoxazolyl protons give multiplets at 7.15–7.60 ppm (4,6,7-H, 6H). The C^5–CH_3 protons in **IVa** give a singlet at 2.24 ppm; C^6–CH_3 protons in **IVd**, a singlet at 2.26 ppm; C^5–$C(CH_3)_3$ protons in **IIIc**, a singlet at 1.08 ppm (18H); and C^5–Ph protons in **IIIb**, a multiplet at 6.92–7.38 ppm (10H). Bis(benzoxazoles) **IIIa**–**IIId** are luminophores emitting in the blue range, with the fluorescence maximum at 435–440 nm (Table 1).

EXPERIMENTAL

The ^1H NMR spectra were recorded on a Tesla BS-587A spectrometer (100 MHz, internal reference HMDSO, δ scale, solvent CF_3COOD). The IR spectra were taken on a Specord M-80 spectrophotometer in the range 400–4000 cm^{-1} using KBr pellets. The fluorescence spectra were measured on a Fluorat 02-Panorama spectrometer, λ_{exc} = 350 nm. The melting points were measured with a Boetius stage.

The reaction progress was monitored, and the product purity checked, by TLC on Silufol DC-Plastikfolien Rieselgel 60 F_{254} plates, eluent toluene–ether, 3 : 1.

4,4'-Bis[5-alkyl(aryl)benzoxazol-2-yl]biphenyls IIIa–IIId. The reaction vessel was charged with 30.0 g (0.11 mol) of ester **I**, 0.22 mol of substituted aminophenol **IIa**–**IId**, 100 ml of Dinil, 10 ml of pyridine, and 6.2 g (0.1 mol) of boric acid; a nitrogen flow was passed. The mixture was heated with continuous stirring to 160–170°C and kept at this temperature for 3 h until the volatiles (methanol, water, pyridine, etc.) were completely distilled off. Then the temperature was raised to 250–260°C and kept at this level for 10–12 h. After the reaction completion, the mixture was cooled to 150–180°C, diluted with 100 ml of DMA, and refluxed for 2 h. After cooling to 80–90°C, the precipitate was filtered off, washed on the filter with hot DMA, and dried in a vacuum.

CONCLUSIONS

(1) 4,4'-Bis[5-alkyl(aryl)benzoxazol-2-yl]biphenyls are formed in quantitative yield by the reactions of dimethyl 4,4'-biphenyldicarboxylate with substituted *o*-aminophenols in a high-boiling solvent (diphenyl ether or Dinil) in the presence of boric acid and pyridine at 250–260°C for 10–12 h.

(2) High-purity substituted bis(benzoxazoles) can be prepared by this procedure in one step in high yield.

REFERENCES

1. *Condensation Monomers*, Stille, J.K. and Campbell, T.W., Eds., New York: Wiley–Interscience, 1972.
2. Turchi, I.J. and Dewar, M.J.S., *Chem. Rev.*, 1975, vol. 75, no. 2, p. 389.
3. Dorlas, A. von, Schellhammer, G.-W., and Schroeder, J., *Angew. Chem.*, 1975, vol. 87, no. 19, pp. 693–707.
4. Nyilas, E. and Pinter, J.L., *J. Am. Chem. Soc.*, 1960, vol. 82, no. 3, pp. 609–611.
5. *Heterocyclic Compounds*, Elderfield, R.C., Ed., New York: Wiley, 1957, vol. 5.
6. *The Chemistry of Synthetic Dyes*, Venkataraman, K., Ed., New York: Academic, 1971, vol. 6.
7. Leaver, J.H. and Milligan, B., *Dyes Pigments*, 1984, vol. 5, no. 1, pp. 109–144.
8. UK Patent 1319763.
9. US Patent 3314894.
10. Belarussian Patent Application a19990093.
11. Belarussian Patent 5137.
12. Bassignana, P., Cogrossi, C., Gandino, M., and Merli, P., *Spectrochim. Acta*, 1965, vol. 21, no. 3, pp. 605–613.

Russian Journal of Applied Chemistry, Vol. 76, No. 11, 2003, pp. 1795–1797. Translated from Zhurnal Prikladnoi Khimii, Vol. 76, No. 11, 2003, pp. 1845–1847.

ORGANIC SYNTHESIS AND INDUSTRIAL ORGANIC CHEMISTRY

Synthesis of Dehydroabietic Chloride

S. R. Kushnir, N. V. Borisova, A. B. Radbil', E. N. Shmidt, I. N. Iosilevich, and B. A. Radbil'

Lesma Research and Promotion Limited Liability Company, Nizhni Novgorod, Russia
Central Research and Design Institute of Wood-Chemical Industry, Federal State Unitary Enterprise, Nizhni Novgorod, Russia
Institute of Organic Chemistry, Siberian Division, Russian Academy of Sciences, Novosibirsk, Russia

Received May 27, 2003

Abstract—The possibility of converting dehydroabietic acid into the chloride by treatment with $SOCl_2$, PCl_3, and PCl_5 was examined.

Diterpenic (resin) acids are monocarboxylic acids of the hydrophenanthrene series; their only available source is rosin. Their reactions involve the hydrophenanthrene core (especially owing to the presence of conjugated double bonds) and carboxy group. Therefore, it is possible to prepare from rosin diverse valuable derivatives.

The chemical structure and properties of the main representatives of resin acids and their most important derivatives have been comprehensively studied [1–3]. A distinctive feature of resin acids is the presence of the carboxy group at the tertiary carbon atom. Therefore, with resin acids, many reactions characteristic of aliphatic carboxylic acids (formation of esters, salts, amides, nitriles, etc.) are sterically hindered and require severe conditions: high temperatures close to the decomposition point (280–300°C), elevated pressure, etc.

The reactivity of carboxylic acids can be enhanced by converting the carboxy group into a more reactive group. In this connection, it seems promising to prepare resin acid anhydrides and chlorides, which can be converted into the required derivatives more readily than the initial acids.

However, preparation of resin acid anhydrides also involves certain problems, since the reaction requires contact of two carboxy groups at tertiary carbon atoms [4]. Furthermore, anhydrides are less reactive than acid chlorides.

Data on synthesis and properties of resin acid chlorides are scarce and contradictory. In particular, crystalline tetrahydroabietic chloride (mp 69.5°C) was prepared by the reaction of the acid with thionyl chloride [5]. Treatment of levopimaric acid with PCl_3 in the presence of pyridine gave the corresponding acid chloride; it, however, was not isolated pure [6]. Preparation of abietic and dehydroabietic chlorides was attempted in [4, 7, 8]. It was noted that treatment of abietic acid with $SOCl_2$ gave virtually no acid chloride; therefore, subsequent experiments were performed with PCl_5 as halogenating agent. The purity of the resulting abietic and dehydroabietic chlorides isolated as viscous oily liquids was low (50–75 wt % main substance). Goryaev *et al.* [9] reported that $SOCl_2$ did chlorinate dehydroabietic acid; the product was obtained as yellow oil decomposing during distillation and was identified by IR spectroscopy.

Here we report on the synthesis of dehydroabietic chloride **I** in 90–98% yield by treatment of dehydroabietic acid **II** with $SOCl_2$, PCl_3, or PCl_5:

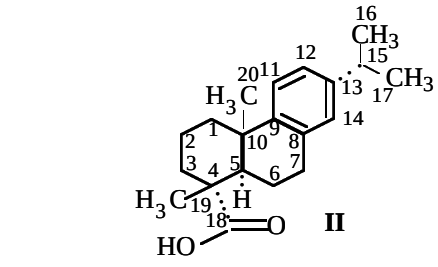

II

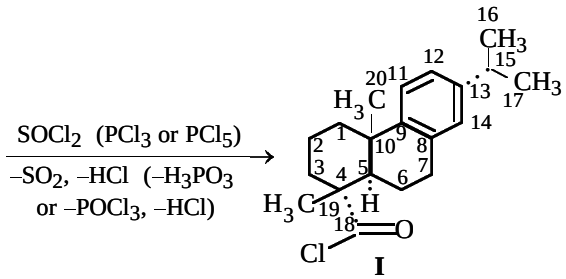

I

1070-4272/03/7611-1795$25.00

The rates of formation of chloride **I** with different chlorinating agents differ considerably. On mixing of **II** with PCl_5 at room temperature, the reaction is so fast that variation of the reactant concentrations cannot be monitored. With $SOCl_2$ and PCl_3, the reaction rates are comparable and depend on temperature. The reaction progress was monitored by IR spectroscopy: The concentration of **I** in reaction mixture samples taken at definite intervals was evaluated from the growing intensity of the C=O band of the chloride at 1790 cm^{-1}, with simultaneous monitoring of a decrease in the intensity of the carboxyl C=O band at 1690 cm^{-1}.

The experimental data are satisfactorily fitted by the kinetic equation of an irreversible second-order reaction. The apparent reaction constants calculated from this equation ($k_{app} \times 10^5$, l mol^{-1} s^{-1}) are as follows (with the temperature, °C, given in parentheses): $SOCl_2$, 6.2 ± 0.3 (40), 32.9 ± 1.8 (50), 50.0 ± 2.9 (60), and 78.9 ± 3.4 (70); PCl_3, 4.1 ± 0.2 (30), 6.0 ± 0.3 (40), 31.1 ± 1.4 (50), and 72.9 ± 3.5 (60). The apparent activation energies of the reactions of **II** with $SOCl_2$ and PCl_3 are 73 ± 1 and 86 ± 1 kJ mol^{-1}, respectively.

The main substance content in the resulting chloride **I** is 99.2–99.5% (GLC data). It is a light-colored highly viscous slowly crystallizing liquid. The product is stable in storage in a sealed vessel; it crystallizes within 30–40 days. The crystals of **I** isolated by double recrystallization from acetone and single recrystallization from hexane melt at 44.5–45°C. The molecular weight of the product, according to mass spectrometry, is 318.17522, which corresponds to the formula $C_{20}H_{27}ClO$ (318.17503). The weight fraction of chlorine, determined according to [10], is 10.4% (calculated for $C_{20}H_{27}ClO$ 11.2%).

The UV spectrum of **I** contains well-defined bands at about 268 and 275 nm, characteristic of acid **II** and corresponding to absorption of the aromatic core. The IR spectrum of **I** contains a pronounced band at 1790 cm^{-1}, corresponding to absorption of the C=O bond in acyl chlorides [11] and absent in the spectrum of **II**.

The ^1H NMR spectra of **I** and **II** are virtually identical; some differences are observed in the ^{13}C NMR spectra.

Chloride **I** is not noticeably hydrolyzed in the cold, which allows removal of excess halogenating agents and the mineral acids forming in the synthesis by washing with water. Compound **I** is readily soluble in toluene, trichloroethylene, carbon tetrachloride, diethyl ether, and dioxane. The product is thermally stable and starts to decompose at a measurable rate only at 140°C; it enters into reactions typical of all acid chlorides.

The results of this study were used for developing a commercial process for production of resin acid chlorides and their mixtures.

EXPERIMENTAL

Dehydroabietic acid **II** was isolated by recrystallization [12] from disproportionated oleoresin rosin commercially produced according to TU (Technical Specifications) 13-00281074-265–95, revision 1. We used acid **II** with mp 172°C (mp 172.5–173°C [13]) containing 98 wt % main substance (GLC data). The halogenating agents and other chemicals were of chemically pure or analytically pure grade and were used without additional purification.

The IR spectrum was recorded in CCl_4 on a Perkin–Elmer 1310 spectrophotometer (NaCl cells, layer thickness 1.05 mm), and the UV spectrum, on a Specord M-40 spectrophotometer in hexane. The ^1H and ^{13}C NMR spectra were recorded on a Bruker AC-200 spectrometer in $CDCl_3$, and the mass spectra, on a Finnigan MAT-8200 spectrometer.

The melting point was determined in a capillary according to GOST (State Standard) 14618.12–78 with a PTP device.

Resin acid methyl esters were analyzed by GLC (Chrom 5 device) following the procedure described in [14, 15], using methyl margarate as internal reference. The relative error of single analysis at a confidence level of 0.95 was within ±2%. The results of five replicate runs were averaged. The mixture components were identified by addition of authentic reference samples and by comparison of the relative retention time with published data.

Reaction of dehydroabietic acid II with $SOCl_2$. Acid **II** (10 g, 0.033 mol) was gradually added to a solution of 6.6 g (0.056 mol) of $SOCl_2$ in 50 ml of toluene. The solution was stirred for 20 h at 20°C, after which the solvent and excess $SOCl_2$ were distilled off at a pressure of 0.08 MPa. The remaining yellow-brown viscous oil (10.3 g, yield 97.3%) was stored at 20–25°C for 30 days. After double recrystallization from acetone and single recrystallization from hexane, crystalline product **I** was obtained; mp 44.5–45°C. IR spectrum, ν, cm^{-1}: 1790 (C=O).

Found: *M* 318.17522 (by mass spectrometry).
$C_{20}H_{27}ClO$.
Calculated: *M* 318.17503.

^{1}H NMR spectrum, δ, ppm (*J*, Hz): 1.20 s (C^{10}–CH_3), 1.29 d (C^{15}–$2CH_3$, *J* 7), 1.31 s (C^4–CH_3), 2.31 m (H^5), 2.93 m (H^7), 6.87 s (H^{14}), 7.0 d (H^{11}, *J* 5), 7.15 d (H^{12}, *J* 5). ^{13}C NMR spectrum, δ, ppm: 37.7 t (C^1), 18.4 t (C^2), 35.9 t (C^3), 58.0 s (C^4), 44.9 d (C^5), 21.8 t (C^6), 29.9 t (C^7), 134.5 s (C^8), 146.3 s (C^9), 37.1 s (C^{10}), 124.3 d (C^{11}, C^{12}), 146.2 s (C^{13}), 127.1 d (C^{14}), 33.6 d (C^{15}), 24.1 q (C^{16}, C^{17}), 181.7 s (C^{18}), 17.9 q (C^{19}), 25.2 q (C^{20}).

^{13}C NMR spectrum of acid **II**, δ, ppm: 37.8 t (C^1), 18.4 t (C^2), 36.6 t (C^3), 47.3 s (C^4), 44.4 d (C^5), 21.6 t (C^6), 29.8 t (C^7), 134.5 s (C^8), 146.6 s (C^9), 36.7 s (C^{10}), 123.9 d (C^{11}), 123.7 d (C^{12}), 145.6 s (C^{13}), 126.7 d (C^{14}), 33.3 d (C^{15}), 23.8 q (C^{16}, C^{17}), 185.3 s (C^{18}), 16.1 q (C^{19}), 25.0 q (C^{20}).

Reaction of dehydroabietic acid II with PCl_3. Acid **II** (10 g, 0.033 mmol) was gradually added to a solution of 3.1 g (0.023 mol) of PCl_3 in 40 ml of toluene. The reaction was performed for 20 h at room temperature. Then the mixture was washed with water, $NaHCO_3$ solution (two times), and again water to neutral reaction of the wash waters. The toluene solution was dried over Na_2SO_4, after which the solvent was removed at a pressure of 0.08 MPa. Compound **I** was obtained as a viscous oily product (yield 9.8 g, 92.5%) which did not crystallize even on adding a seed. The IR spectrum of the product contained a band at 1790 cm^{-1} characteristic of acyl chlorides [11]. Other functional groups were not revealed spectrophotometrically.

Reaction of dehydroabietic acid II with PCl_5. A solution of 5 g (0.017 mol) of **II** in 25 ml of diethyl ether was added to 5 g (0.024 mol) of PCl_5 over a period of 2 h. The mixture was allowed to stand for 20 h at room temperature. Then it was washed with water, $NaHCO_3$ solution (two times), and again water to neutral reaction of the wash waters. The ether layer was dried over Na_2SO_4, and the solvent was distilled off at a pressure of 0.08 MPa. The remaining acid chloride **I** was a light yellow viscous mass which did not crystallize even on adding a seed. The IR spectrum of the product contained a band at 1790 cm^{-1} characteristic of acyl chlorides [11]. Other functional groups were not revealed.

CONCLUSION

Dehydroabietic chloride (yield 90–98%; main substance content 99.2–99.5 wt %, GLC data; mp 45°C) was prepared by treatment of dehydroabietic acid with PCl_3, PCl_5, or $SOCl_2$.

REFERENCES

1. Sandermann, W., *Naturharze Terpentinöl-Tallöl: Chemie und Technologie*, Berlin: Springer, 1960.
2. Mayo, P. de, *Mono- and Sesquiterpenoids*, New York: Interscience, 1959.
3. Pentegova, V.A., Dubovenko, Zh.V., Raldugin, V.A., and Shmidt, E.N., *Terpenoidy khvoinykh rastenii* (Terpenoids of Coniferous Plants), Novosibirsk: Nauka, 1987.
4. Bardyshev, I.I., *Zh. Org. Khim.*, 1999, vol. 35, no. 1, pp. 48–63.
5. Belov, V.N. and Kustova, S.D., *Zh. Org. Khim.*, 1954, vol. 28, no. 24, pp. 1087–1094.
6. Lloyd, W.D. and Hedrick, U.W., *J. Org. Chem.*, 1963, vol. 28, no. 4, pp. 1156–1157.
7. Strizhakov, O.V., Anhydrides of Resin Acids and Rosin, *Cand. Sci. Dissertation*, Minsk, 1983.
8. Paderin, V.Ya., Nitriles and Amino Derivatives of Resin Acids and Rosin, *Cand. Sci. Dissertation*, Minsk, 1972.
9. Goryaev, M.I., Sharipova, F.S., Tikhonova, L.K., *et al.*, *Izv. Akad. Nauk Kaz. SSR, Ser. Khim.*, 1977, no. 2, pp. 68–71.
10. Schöniger, W.S., *Microchim. Acta*, 1959, no. 3, p. 670.
11. Nakanishi, K., *Infrared Absorption Spectroscopy*, Tokyo: Nankido, 1962.
12. Halbrook, N.J. and Lowrence, R.V., *J. Org. Chem.*, 1966, vol. 31, no. 9, pp. 4246–4247.
13. Chudinov, S.V., Trofimov, A.N., Uzlov, G.A., *et al.*, *Spravochnik lesokhimika* (Wood Chemist's Handbook), Moscow: Lesnaya Prom–st., 1987.
14. Kosyukova, L.V. and Dunaev, V.S., *Khim. Drev.*, 1983, no. 4, pp. 101–105.
15. Kosyukova, L.V. and Dunaev, V.S., *Zh. Anal. Khim.*, 1989, no. 9, pp. 1622–1624.

Russian Journal of Applied Chemistry, Vol. 76, No. 11, 2003, pp. 1798–1802. Translated from Zhurnal Prikladnoi Khimii, Vol. 76, No. 11, 2003, pp. 1848–1852.

MACROMOLECULAR CHEMISTRY AND POLYMERIC MATERIALS

Thermodynamics of Oligomerization of Glutaric Aldehyde with Amino Acids

N. P. Kuznetsova, O. A. Pisarev, R. N. Mishaeva, and L. R. Gudkin

Institute of Macromolecular Compounds, Russian Academy of Sciences, St. Petersburg, Russia

Received July 3, 2003

Abstract—Condensation of glutaric aldehyde with amino acids to form oligomers of glutaric aldehyde was studied by differential microcalorimetry and analysis for the functional groups.

Carbonyl–amine reactions are important biochemical reactions used, in particular, for chemical modification of proteins with glutaric aldehyde (GA). The mechanism of this process is poorly understood owing to a complex structure of peptides and a great number of possible reaction pathways. In this work we studied this process with an example of simpler systems.

Condensation of bifunctional GA with amino acids involves several parallel fast steps. In neutral aqueous solutions, the aldehyde group of GA reacts with the nonionized amino group of an amino acid to form Schiff base (rate constant $\sim 4 \times 10^{-3}$ s^{-1}). Parallel aldol condensation of the second aldehyde group of GA, activated by the first reaction, stabilizes the Schiff base. This reaction yields α,β-unsaturated GA oligomers with conjugated ethylene and aldehyde double bonds. Trimers of GA are mainly formed (rate constant $\sim 0.2 \times 10^{-3}$ s^{-1}) [1, 2].

When the molar ratio of functional groups [CHO/NH_2] ranges from 0.5 to ~4–6, single amino group is spent per three aldehyde group to form GA oligomer with three aldehyde and one carboxy groups:

$$\underset{\text{Amino acid}}{HOOC–R–NH_2} + 3\underset{\text{GA}}{[O=CH–(CH_2)_3–HC=O]}$$

$$HOOC–R–N=CH–(CH_2)_3–[\underset{\displaystyle HC=O}{\underset{|}{HC}}=C–(CH_2)_2]_2–HC=O$$

At a large GA excess ($[CHO/NH_2]_0 \gg 4$ mol/mol), 5–6 aldehyde groups and more are spent per a reacted amino group [5].

Our pervious study shows that, in aqueous neutral solutions of GA, a zwitterion of amino acid is rapidly deprotonated (recharged) to form the nucleophilic nonionized aminogroup, which is atypical for neutral solutions of free amino acids. The rate constant of deprotonation of the zwitterion (0.1–0.2 s^{-1}) is higher by three orders of magnitude than that of its condensation. The resulting amino acid anions containing carboxy group can catalyze oligomerization of GA bound to the amino acid. With excess GA, pure GA oligomers can be formed in the solution.

To determine the conditions under which GA is condensed with amino acids by only two main pathways, namely, Schiff base formation and GA oligomerization, we used microcalorimetry and chemical analysis of the functional groups of the products.

EXPERIMENTAL

Reaction of GA with differently charged amino acids [glycine (monoaminoacetic acid), lysine (α,ε-diaminocaproic acid), and glutamic acid (α-aminoglutaric acid) was studied at 21°C in neutral aqueous solutions at the molar ratio of aldehyde and amino groups $[CHO/NH_2]_0$ ranging from 0.5 to 7.0 mol/mol. The amino acid concentration and the volume of the reaction mixture were constant. The reactants were mixed and samples of the reaction mixture were taken at definite time intervals. The content of free amino groups was determined by reaction with 2,4,6-trinitrobenzenesulfonic acid [6], and the content of aldehyde groups, by differential pH-metry with hydroxylamine hydrochloride [7]. The number of functional groups converted into stable Schiff bases was estimated by the difference between the initial and current ($[\Delta CHO]_t$, $[\Delta NH_2]_t$) content of these groups. Commercial 25% aqueous solution of GA was purified on activated carbon. The purity was estimated from the ratio of optical densities at two wavelengths D_{235}/D_{280} =

1070-4272/03/7611-1798$25.00

Table 1. Consumption of functional groups in the course of condensation of GA with lysine, glycine, and glutamic acid

t, min	$[\Delta NH_2]_t/[\Delta NH_2]_0$, %	$[CHO]_t/[CHO]_0$, %	$[\Delta CHO/\Delta NH_2]_t$, mol/mol	Fraction of $[CHO]_t$, %
Lysine, $[CHO/NH_2]_0$ = 4.3 mol/mol				
10	70.3	46	2.8	35/65*
20	78.6	53	2.9	34/66
30	81.4	59	3.2	32/68
40	83.0	59	3.1	32/68
60	84.0	67	3.5	30/70
Glycine, $[CHO/NH_2]_0$ = 5.3 mol/mol				
10	45.8	38	3.5	28/72
20	72.6	45	3.2	31/69
30	77.1	–	–	–
40	82.0	47	3.0	33/67
60	86.0	55	3.4	29/71
Glutamic acid, $[CHO/NH_2]_0$ = 5.0 mol/mol				
10	10	21	10.4	10/90
20	12	28	12	10/90
30	14	30	11	9/91
40	20	31	7.7	13/87
60	30	38	6.3	16/84
1 day	86	83	4.8	20/80

* Fraction of $[CHO]_t$ spent for Schiff base formation in aldol condensation.

0.4–0.5, measured on an SF-26 spectrophotometer. Glutaric aldehyde was stored in an acidified (pH 3) aqueous solution at 4°C. Under these conditions, GA was in the monomeric and hydrated forms.

The heat effects of the reaction of GA with glycine were determined by microcalorimetry on a DAK 1-1 calorimeter at 21°C and 101.3 kPa. The reagent mixer was described in [8]. The differential heat effects in time t, ΔH_t, were estimated from the areas under the microcalorimetric curves measured from zero time to time t:

$$\Delta H_t = \int_0^t \Delta H \mathrm{d}t.$$

The integral heat effects ΔH_0 were determined after the stationary thermal conditions were attained, by integration in the range from 0 to t_{eq}. The calculations were performed by the equation

$$\Delta H_0 = \int_0^{t_{eq}} \Delta H \mathrm{d}t.$$

The determination error of the heat effects at the 95% confidence level was ±2%.

The number of amino groups of amino acids, reacted in time t, $[\Delta NH_2]_t$, should be equal to that of stable aldimine bonds of the Schiff base. Superstoichiometric consumption of aldehyde groups $[\Delta CHO]_t - [\Delta NH_2]_t$ can be due to GA oligomerization. As seen from Table 1, at the initial ratio of the aldehyde groups and amino groups of lysine (α,ε-diaminocaproic acid) and glycine (monoaminoacetic acid) $[CHO/NH_2]_0$ = 4–5 mol/mol, the ratio of reacted groups $[\Delta CHO/\Delta NH_2]_t$ remains constant (~3 mol/mol) up to the reaction completion. About 70% of amino groups are spent within the first 10–20 min and 84–86%, within 1 h.

About 30% of reacted aldehyde groups are spent for formation of stable Schiff bases with the amino acid; the other 70% are involved in aldol condensation of GA. Data for the GA–glutamic acid system are given for comparison. The presence of two carboxy groups at the α- and γ-positions can substantially decelerate conversion of this acid into nucleopilic agent with nonionized amino group. At the same time, the Schiff base derived from a dibasic acid catalyses more strongly the GA oligomerization in solution. In this case, the Schiff base formation is inhibited and 90% of GA is spent for aldol condensation within

Table 2. Consumption of aldehyde and amino groups and enthalpy of reaction of GA with glycine at different reaction times

$[CHO/NH_2]_0$, mol/mol	*t*, min	$[\Delta NH_2]_t$, mmol	$[\Delta CHO]_t$, mmol	$[\Delta CHO/\Delta NH_2]_t$, mol/mol	$[\Delta CHO]_t - [\Delta NH_2]_t$, mmol	Q_t,* J
0.5	1	0.03	0.08	2.4	0.05	–0.2
	10	0.06	0.14	2.3	0.08	–1.5
1.0	1	0.06	0.14	2.4	0.08	–0.4
	10	0.09	0.27	2.9	0.18	–2.9
	30	0.11	0.31	2.7	0.19	–4.0
2.0	1	0.05	0.20	4.1	0.15	–0.3
	10	0.14	0.42	3.0	0.28	–2.1
	30	0.16	0.53	3.3	0.37	–3.1
	60	0.18	0.58	3.3	0.40	–3.6
4.0	1	0.10	0.28	2.8	0.18	–0.6
	10	0.20	0.58	3.0	0.38	–5.0
	30	0.23	0.77	3.3	0.54	–9.5
	60	0.26	0.85	3.3	0.59	–12.4
7.0	1	0.08	0.24	3.1	0.16	–0.2
	10	0.19	0.72	3.9	0.53	–1.6
	30	0.24	1.32	5.5	1.08	–3.8
	60	0.26	1.96	7.4	1.70	–11.0

* Differential thermal effect.

10 min. This can be due to the third reaction: oligomerization of GA (at its excess in the reaction mixture) in the solution, catalyzed by the carboxyl-containing products. It should be noted that the GA pentamer bonded with glutamic acid was isolated by gel chromatography from the products of reaction of GA with glutamic acid [5]. The other aldehyde groups may be involved in GA oligomerization in the solution. When the products of condensation of the amino acid with GA oligomers are accumulated in a large amount in the solution, the remaining aldehyde groups can be spent for formation of condensation products free of aldehyde groups.

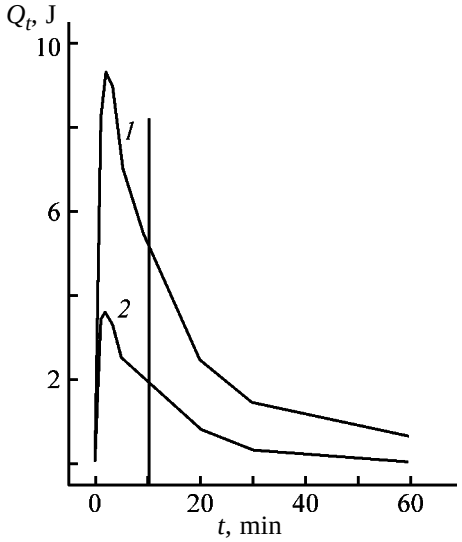

Fig. 1. Heat of reaction Q_t of GA with glycine at 21°C as a function of time *t*. Initial ratio of the functional groups of the reactants $[CHO/NH_2]_0$ (mol/mol): (*1*) 0.5 and (*2*) 4.0.

The results of the study of condensation of GA with glycine at the ratio of the functional groups of the reactants $[CHO/NH_2]_0$ from 0.5 to 7 mol/mol are presented in Table 2. When the ratio is small (0.5 and 1.0), GA is completely consumed in 10 and 30 min, respectively. The ratio between reacted aldehyde groups of GA and reacted amino groups of glycine $[\Delta CHO/\Delta NH_2]_t$ 10 min after the reaction start is 5–7 at $[CHO/NH_2]_0$ = 7.0 and 3 at lower initial ratio.

We studied condensation of GA with glycine by differential microcalorimetry. In these experiments, the time dependence of the reaction enthalpy was measured at different concentrations of the initial components. In all cases, the reaction is exothermic. The differential heat effect of the reaction at the initial ratio of the functional groups of the components of 5 and smaller (Tables 1, 2) can be normalized to the number of moles of the resulting GA–glycine oligomer (gly–GA_3, molecular weight 293). The time dependence of the reaction enthalpy is shown in Fig. 1. The heat release is maximal in 1–2 min after the reaction start. The reaction is complete in 1 h. The time

Table 3. Thermodynamic parameters of reaction of GA with glycine at 21°C

$[CHO/NH_2]_0$, mol/mol	t, min	ΔH_t, kJ mol^{-1}	$\Delta H_t/\Delta H_0$, %	K_{bond}, mol^{-1}	$\ln K_{bond}$	ΔG	$T\Delta S$	ΔS, J mol^{-1} deg^{-1}
						kJ mol^{-1}		
0.5	1	–6.9	10.3	8.9	2.2	–5.3	–1.5	–5.1
	6	–20.9	31.1	37.3	3.6	–8.8	–12.0	–40.0
	10	–32.6	48.8	94.4	4.5	–11.1	–21.4	–72.0
	30	–55.2	82.5	–	–	–	–	–
1.0	1	–8.0	16.0	6.8	1.9	–4.6	–3.4	–11.0
	6	–22.6	73.3	39.9	3.7	–9.0	–13.6	–46.0
	10	–32.6	75.9	68.7	4.2	–10.3	–22.2	–75.5
	30	–39.8	97.0	–	–	–	–	–
2.0	1	–4.6	31.0	3.8	1.3	–3.2	–1.4	–4.7
	6	–12.2	69.0	13.3	2.6	–6.3	–5.9	–20.0
	10	–14.2	70.5	26.4	3.3	–8.0	–6.2	–21.0
	30	–17.5	96.0	84.1	4.4	–10.8	–6.7	–22.8
4.0	1	–6.7	12.1	3.0	1.1	–2.7	–4.0	–13.6
	6	–21.9	39.0	7.6	2.0	–5.0	–16.9	–57.0
	10	–26.3	48.0	16.9	2.8	–6.9	–19.4	–66.0
	30	–36.8	81.6	48.0	3.9	–9.5	–27.4	–93.0
	60	–42.6	95.0	110.6	4.7	–11.5	–31.1	–106.0

dependence of the differential enthalpy ΔH_t of the reaction of GA with glycine is shown in Fig. 2. At the initial ratio of the functional groups from 0.5 to 4, the shape of the curves within the first 10 min is similar (excluding the ratio of 2 and 7 mol/mol), which indicates the similar reaction mechanism is all these cases. At longer reaction time, the curves diverge owing to occurrence of various side reactions. It should be noted that the differential enthalpy ΔH_t measured in the first 10 min ranges from 50 to 75% of the total heat effect ΔH_0 (Table 3).

The integral ΔH corresponding to the equilibrium reaction mixture (in ca. 1 h) can be normalized to the amounts (moles) of both the GA–glycine oligomer (gly–GA_3) and glycine amino groups converted into the Schiff bases. The resulting dependences of ΔH_0 on the initial number of the aldehyde and amino groups are shown in Fig. 3. Curve *1* shows how the enthalpy changes assuming that only the Schiff bases are formed. Curve *2* is the dependence assuming that the reaction yields only the product of condensation of glycine with GA trimer. The minimal enthalpy, equal in the both cases, is registered at the initial ratio of the functional groups $[CHO/NH_2]_0 = 2$ (or in the range from 1 to 4 mol/mol/). Outside this range, the curves go apart owing to parallel occurrence of side reactions. At the glycine excess (the left branch of the curve), glycine can be added to the double bonds of the condensation product (Michael reaction). At high GA content in the initial mixture (right branch of the curve), the reaction products containing carboxy groups catalyze oligomerization of GA in the solution, which is not the case in solutions of pure GA.

The difference between ΔH_0 of the two curves can be assigned to the enthalpy of aldol condensation to form GA oligomers.

In the course of the reaction, a dynamic equilibrium between initial reactants and reaction products is attained. The rate constant of formation of the glycine–GA trimer derivative can be calculated at all reaction times by the equation:

$$K_{bind} = [gly–GA_3]/[gly]_{free}[GA]_{free}.$$

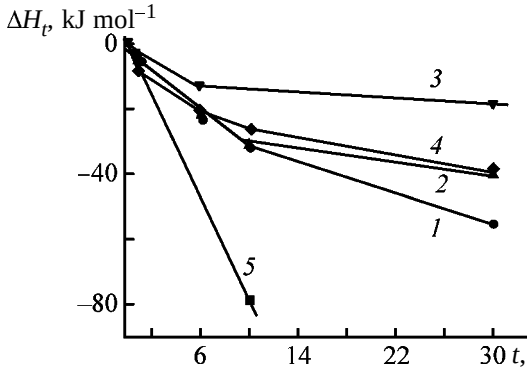

Fig. 2. Differential enthalpy ΔH_t of the reaction of GA with glycine as a function of reaction time t. Initial molar ratio of the functional groups of the reactants $[CHO/NH_2]_0$: (*1*) 0.5, (*2*) 1.0, (*3*) 2.0, (*4*) 4.0, and (*5*) 7.0.

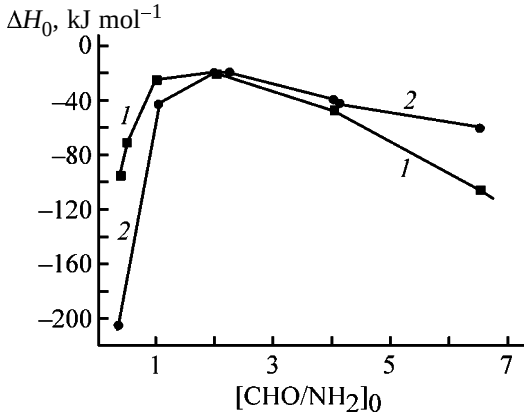

Fig. 3. Integral enthalpy ΔH_0 of the reaction of GA with glycione as a function of the initial molar ratio of the functional groups of the reactants $[CHO/NH_2]_0$. T = 21°C, t = 1 h. ΔH_0 normalized to the (*1*) number of moles of spent amino groups of glycine and (*2*) number of moles of the condensation product of glycine with GA trimer (gly–GA_3).

The Gibbs energy of the reaction was calculated from this constant by the equation $\Delta G = -RT\ln K_{bind}$, and the reaction entropy, by the equation $\Delta G = \Delta H - T\Delta S$. The results are summarized in Table 3. In the course of the reaction, K_{bind} increases and hence $-\Delta G$ also increases. The dependences of ΔH_t and $-T\Delta S$ on the ratio of the functional groups are similar. The negative values of these functions are minimal at $[CHO/NH_2]_0$ = 2 mol/mol. Probably, htis ratio is the most favorable for formation of pure gly–GA_3.

CONCLUSIONS

(1) Oligomerization of glutraic aldehyde with amino acids was studied by differential microcalorimetry and analysis for aldehyde and amino groups. Pure condensation product of amino acid (glycine) with the trimer of glutaric aldehyde is formed at the initial ratio of the functional groups of the reactants of 2 or the ratio of [glutaric aldehyde]/[glycine] = 1.0 mol/mol.

(2) At the ratio of the functional groups from 0.5 to 5 mol/mol, two parallel reactions, formation of stable Schiff bases from glutaric aldehyde and the amino acid and oligomerization of glutaric aldehyde catalyzed by the reaction products containing carboxy groups, mainly occur within the first 10–20 min of the process.

REFERENCES

1. Kuznetsova, N.P., Mishaeva, R.N., and Gudkin, L.R., *Zh. Prikl. Khim.*, 1999, vol. 72, no. 7, pp. 1171–1177.
2. Kuznetsova, N.P., Mishaeva, R.N., Pisarev, O.A., and Gudkin, L.R., *Zh. Prikl. Khim.*, 2000, vol. 73, no. 5, pp. 796–801.
3. Richard, F.V. and Knowles, J.R., *J. Mol. Biol.*, 1968, vol. 37, no. 1, pp. 231–233.
4. Margel, S. and Rembaum, A., *Macromolecules*, 1980, vol. 3, no. 1, pp. 19–24.
5. Kuznetsova, N.P., Gudkin, L.R., and Mishaeva, R.N., *Zh. Prikl. Khim.*, 2002, vol. 75, no. 6, pp. 991–997.
6. Fields, R., *Biochem. J.*, 1971, vol. 124, no. 3, pp. 581–590.
7. Roe, H.R. and Mitchel, G., *Anal. Chem.*, 1951, vol. 23, no. 12, pp. 1758–1760.
8. Pisarev, O.A. and Samsonov, G.V., in *Termodinamika khimicheskikh soedinenii* (Thermodynamics of Chemical Compounds), Gor'kii: Gor'k. Gos. Univ., 1988, pp. 104–109.

Russian Journal of Applied Chemistry, Vol. 76, No. 11, 2003, pp. 1803–1806. Translated from Zhurnal Prikladnoi Khimii, Vol. 76, No. 11, 2003, pp. 1853–1856.

MACROMOLECULAR CHEMISTRY AND POLYMERIC MATERIALS

Platinum-Containing Polymeric Nanocomposites Derived from Porous Polyacrylates

T. I. Izaak, O. V. Babkina, T. N. Drebushchak, and G. M. Mokrousov

Tomsk State University, Tomsk, Russia
Novosibirsk State University, Novosibirsk, Russia
Molecular Design and Environmentally Safe Processes Research Center, Novosibirsk, Russia
Institute of Chemistry of Solids and Mechanochemistry, Novosibirsk, Russia

Received July 8, 2003

Abstract—The dependence of the electrical conductivity of a platinum-containing polymeric nanocomposite on the number of sorption–reduction cycles was studied, as well as its thermal properties.

Nanoparticles, whose properties differ from those of macroparticles, are widely used in electrocatalysis, photocatalysis, electrophotography, as components of magnetic memory, etc. [1–3]. For example, the use of electrodes coated with polymeric films with immobilized platinum group metal nanoparticles [4, 5] increases the currents of hydrogen and oxygen liberation from aqueous solutions at relatively low content of the platinum metal catalyst. The structure of matrices usually used for preparing metal-containing polymeric nanocomposites consists of a system of interpenetrating pores providing higher specific surface area and easy penetration of reagents in the bulk of the matrix and determining the growth conditions of the metal particles. Among these materials are porous polyethylene prepared by localized crazing [6], perfluoroalkanelsulfonic acid (Nafion trade name) with communicating ionic regions (nonuniformities) formed by sulfonate groups [7], cross-linked polyacrylates with carboxy functional groups, etc. Catalytically active metal nanoparticles are introduced by sorption and reduction of the metal ions in a porous polymeric matrix (PPm) which can be considered as nanoreactor [8]. Immobilization of growing particles on the polymer prevents their aggregation. Association of the metal cation with functional groups of the polymer plays an important role in the formation of nanoparticles [9].

In this work, we used a polymeric matrix prepared by copolymerization of methyl methacrylate (MMA) with potassium methacrylate (KMA) in the presence of polyethylene glycol (PEG) as an inert solvent and blowing agent. The polymerization product is a gel whose porous structure is formed by phase separation via macro- and microsyneresis [10]. The parameters of the porous structure are controlled by variation of the component ratio in the initial mixture. At a high degree of dilution of the ionic monomer (KMA) with a mixture of MMA and PEG, the growing gel is collapsed into a microgel at the critical point of phase separation, i.e., macrosyneresis occurs. In this case, polyethylene glycol acts as a dispersion medium.

In the course of polymerization, the polymeric particles agglomerate to form a heterogeneous gel consisting of the blowing agent and copolymer. In the course of polymerization at a high concentration of the ionic monomer forming salt cross-links, the liquid phase of PEG, at a definite density of cross-links, forms dispersed drops inside the growing gel, i.e., microsyneresis occurs. In this case, PEG is partially retained in the gel phase owing to formation of hydrogen bonds between OH groups of PEG and the oxygen atoms of the carboxy groups of the copolymer. The growing structure also contains two continuous phases: blowing agent and the copolymer.

Porous materials prepared by macro- and microsyneresis of polymeric gels have different pore size distribution. Pores formed in the course of macrosyneresis are larger [10]. Since the blowing agent forms a continuous phase, it can be extracted from the matrix to form a porous polymer which exhibits cation-exchange properties owing to the presence of carboxy groups.

In this work we studied sorption and reduction of platinum(IV) ions in porous polyacrylate matrices of different structures. The properties of the polymeric matrix before and after platinum reduction and proper-

1070-4272/03/7611-1803$25.00

Table 1. Composition and properties of porous polyacrylate composites*

Sample no.	[MMA]/[PEG]	c_{KMA}, g ml^{-1}	Π, %	$c_{CO_2^-}$	SC
				mmol g^{-1}	
1	0.66	0.076	61.0	0.45	0.72
2	0.51	0.141	65.4	0.47	0.76
3	0.66	0.148	70.8	0.79	1.04

* (Π) Porosity and (SC) sorption capacity for platinum.

ties of the platinum-containing polymeric nanocomposites were also studied.

EXPERIMENTAL

The porous polymeric matrix was prepared by block copolymerization of MMA with KMA at 70°C in the presence of PEG-200 polyethylene glycol and using benzoyl peroxide as an initiator. Polyethylene glycol was extracted with water in a Soxhlet apparatus for 10 h. The thickness of the resulting copolymers was 15 mm. Platinum cations were sorbed on PPM from aqueous solutions of platinum(IV) chloride at room temperature and then were reduced to metal with hydrazine hydrate by the Paal procedure. The electrical conductivity of the composites σ (S cm^{-1}) was measured with an E-711 apparatus operating at 1000 Hz ac current. The IR spectra of thin wet films were recorded on a Specord-M80 spectrometer. To determine the platinum content, the nanocomposites were pyrolyzed at 800°C, and metallic platinum was dissolved. The platinum content was determined photometrically on a KFK-3 photometer by the relatively sensitive procedure with tin chloride [11]. Thermal analysis curves of the initial and the platinum-containing polymeric matrices were recorded on a Q-1500 MOM derivatoraph (Hungary) in air. The samples (40–45 mg) were heated from 25 to 700°C at a rate of 10 deg min^{1}. X-ray diffraction patterns were obtained on a D8 GADDS diffractometer (Bruker) in the range 2θ = 5°–75° using CuK_α radiation. The particle size was calculated by the Debye–Scherrer equation [12]. The content of CO_2^- groups in the polymer was determined by potentiometric titration.

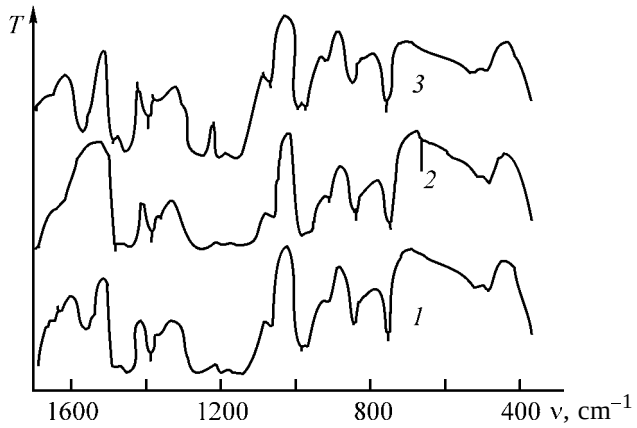

Fig. 1. IR spectra: (*T*) transmission and (ν) wave number. Matrix: (*1*) polymeric, (*2*) with sorbed platinum, and (*3*) with reduced platinum.

The polymeric samples were prepared at different [MMA] : [PEG] ratios and different content of carboxy groups, determined by the KMA concentration in the initial mixture. At high KMA concentrations (Table 1, sample nos. 2 and 3), the phases are separated in the system by the microsyneresis mechanism to form mainly micropores invisible with an electron microscope. At a low salt concentration, the macroporous structure is formed by macrosyneresis.

Platinum nanoparticles were prepared in the polymer bulk in two steps: (1) sorption of $PtCl_4$ from aqueous solution at room temperature, followed by sorption of the reducing agent (hydrazine hydrate) from toluene solution at 5°C, and (2) reduction of platinum ions by flash heating of the polymer in hexane to 60°C.

This procedure was used to exclude migration of platinum(IV) ions to the reduction front, causing nonuniform distribution of platinum nanoparticles in the bulk of the polymer. Polymeric composites were washed with distilled water to remove the reduction products. We experimentally found that the time required to attain the equilibrium in the PPM–$PtCl_4$ solution system depended on the syneresis type: 2 h for sample nos. 2 and 3 and 30 min for sample no. 1.

In solutions, $PtCl_4$ forms an acid, $H_2[PtCl_4(OH)_2]$. It is unclear how this complex anion is sorbed on the polymer exhibiting cation-exchange properties. We suggest that one or two OH groups of the anion are substituted with the carboxy groups of the polymer. In the IR spectrum of PPM (Fig. 1), the band of free CO_2^- groups is present at 1560 cm^{-1}. After coordina-

tion of the platinum complex anions, this band completely disappears and the band of coordinated CO_2^- group appears at 1640 cm^{-1}. After reduction to metallic platinum, the band at 1560 cm^{-1} appears again, i.e., noncoordinated carboxy groups are regenerated and can be involved in repeated chemisorption. As seen from Table 1, the concentration of the CO_2^- ion-exchange groups is lower than the sorption capacity of the matrix for platinum ions. Probably, platinum chloride is also absorbed in the polymeric matrix by a mechanism other than ion exchange. This assumption is confirmed by the fact that the IR spectrum of PPM kept in an aqueous solution of $PtCl_4$ contains the band at 670 cm^{-1} assigned to the stretching vibrations of the Pt–Cl bond of the complex anion. The pore structure of the polymer affects the mobility of these weakly bonded anions and hence affects the size of platinum nanoparticles.

Hexachloroplatinic acid is reduced with hydrazine hydrate by the following reaction:

$$H_2[PtCl_4(OH)_2] + N_2H_4 \cdot H_2O$$

$$\rightarrow N_2H_5H[PtCl_4(OH)_2]$$

$$\rightarrow H[PtN_2H_4Cl_3(OH)_2] \rightarrow Pt(0) + N_2\uparrow.$$

Nitrogen is liberated from the pores of the polymeric matrix and nanoparticles of metallic platinum are formed. Dispersions of metal-containing polymeric composites in 2-methoxyethanol are stable for several months.

The typical X-ray diffraction pattern of the polymeric matrix containing 10 wt % Pt is shown in Fig. 2. The fact that only platinum reflections and board reflections of the polymer at 13.8° and 30° are present in the pattern suggests the absence of side products. The average size of crystallites calculated from the (111) reflection is 4 nm. The particle size is almost independent of both the polymer structure and its sorption capacity. Since the equilibrium in the PPM–PCl_4 solution is attained slowly, the mobility of platinum ions sorbed by the non-ion-exchange mechanism is strongly restricted. Hence, surface complexes between platinum ions and carboxyate anions of the polymer can be considered as dissociated to a negligible extent, compared to bulk aqueous solution.

Since the CO_2^- groups are regenerated after platinum reduction, repeated sorption–reduction cycles of platinum(IV) ions are possible. The electrical conductivity of the nanocomposite increases with increasing

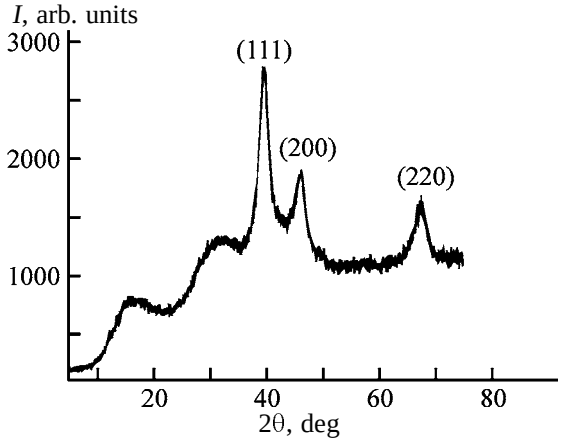

Fig. 2. Typical X-ray diffraction pattern of platinum-containing nanocomposite. (*I*) Intensity and (θ) Bragg angle.

content of platinum nanoparticles, which is important for preparing electrodes from these materials. The results of the first four sorption–reduction cycles are presented in Table 2. As seen from Table 2, the electrical conductivity of the composite increases with increasing content of platinum nanoparticles. However, the value of the conductivity indicates that the percolation threshold was not reached.

We studied the thermal properties of the polymeric matrix and platinum–polymer composites. The most intense thermal degradation of PPM by depolymerization [13] was observed at 340–370°C. At the same time, thermal analysis curves of the platinum nanocomposites contain a strong exothermic peak in this range, which is absent in the thermal analysis curves of pure polyacrylates. This is probably due to platinum-catalyzed oxidation with atmospheric oxygen of the monomer formed by depolymerization. The maximum of thermal degradation of the PPM is shifted to 390–420°C. Thermolysis of PPM is completed at 670°C. The weight loss of the platinum nanocomposite stops at 460°C. Its decomposition products contain carbon compounds.

Table 2. Sorption–reduction cycles of platinum in sample no. 1

Cycle no.	σ, S cm^{-1}	Pt concentration, mmol g^{-1} of polymer
1	3.8×10^{-4}	0.72
2	1.9×10^{-3}	0.79
3	1.9×10^{-3}	1.17
4	2.3×10^{-3}	2.1

CONCLUSIONS

(1) Platinum-containing polymeric nanocomposites were prepared by sorption and reduction of platinum ions in the bulk of porous polyacrylates with different structures.

(2) The average size of platinum particles, determined by X-ray diffraction, is 4 nm.

ACKNOWLEDGMENTS

This work was financially supported by the Integration Federal Target Program (grant no. Ch0069).

REFERENCES

1. Sergeev, G.B., *Usp. Khim.*, 2001, vol. 70, pp. 915–933.
2. Bukhtiyarov, V.I. and Slin'ko, M.G., *Usp. Khim.*, 2001, vol. 70, pp. 165–181.
3. Moon, J.-S., Park, K., and Kim, J.-H., *Appl. Catal. A: General*, 1999, vol. 184, pp. 41–48.
4. Podlovchenko, B.I. and Andreev, V.N., *Usp. Khim.*, 2002, vol. 71, pp. 950–966.
5. Toshiyuki, A., Kazuhiro, H., and Yukihide, S., *Eur. Polym. J.*, 2001, vol. 37, pp. 753–761.
6. Trofimchuk, E.S., Yablokova, M.Yu., Nikonorova, N.I., *et al.*, *Vysokomol. Soedin., Ser. B*, 2001, vol. 43, pp. 1251–1256.
7. Hsu, W.Y. and Gierke, T.D., *Macromolecules*, 1982, vol. 15, pp. 101–109.
8. Pomogailo, A.D., Rozenberg, A.S., and Uflyand, I.E., *Nanochastitsy matallov v polimerakh* (Metal Nanoparticles in Polymers), Moscow: Khimiya, 2000.
9. Sergeev, G.B., Kiryukhin, M.V., Bakhov, F.N., and Sergeev, V.G., *Vestn. Mosk. Univ., Khim.*, 2001, vol. 42, no. 5, pp. 308–314.
10. Okay, O., *Prog. Polym. Sci.*, 2000, vol. 25, no. 6, pp. 711–719.
11. Marczenko, Z., *Kolorymetryczne oznaczanie pierwiastkow*, Warsaw: Naukowa-Techniczne, 1968.
12. Kovba, L.M. and Trunov, V.K., *Rentgenofazovyi analiz* (X-ray Phase Analysis), Moscow: Mosk. Gos. Univ., 1969.
13. Shibaev, L.A., Antonova, T.A., Vinogradova, L.V., *et al.*, *Zh. Prikl. Khim.*, 1998, vol. 71, no. 5, pp. 835–842.

Russian Journal of Applied Chemistry, Vol. 76, No. 11, 2003, pp. 1807–1812. Translated from Zhurnal Prikladnoi Khimii, Vol. 76, No. 11, 2003, pp. 1857–1862.

MACROMOLECULAR CHEMISTRY AND POLYMERIC MATERIALS

Dehydration of Organic Solvents by Evaporation through Membranes Based on Polyelectrolytic Complexes

Yu. P. Kuznetsov, E. V. Kruchinina, L. A. Nud'ga, V. A. Petrova, A. M. Bochek, G. V. Shishkina, and N. A. Matveeva

Institute of Macromolecular Compounds, Russian Academy of Sciences, St. Petersburg, Russia

Received June 18, 2003

Abstract—Evaporation of binary aqueous–organic mixtures through composite membranes with coatings based on polyelectrolytic complexes including different combinations of polyelectrolytic polycations and polyanions was studied. The possibility of efficient dehydration of organic solvents by their pervaporation was demonstrated.

Production of organic solvents (aliphatic alcohols, ketones, esters, etc.) includes their dehydration in the final stage. This procedure is complicated by the fact that these organic solvents form, as a rule, aqueous azeotropic mixtures. In the common processes, dehydration of these organic solvents is carried out by power-consuming distillation combined with additional chemical treatment. At the same time, it is known that organic solvents, including azeotropic mixtures, can be dehydrated by pervaporation (evaporation through membranes of diffusion type). The dehydration by this technique is less power-consuming and is carried out without chemical treatment at lower temperature.

When preparing pervaporation membranes, the following hydrophilic polymers are used: some cellulose derivatives, polyacrylic acid (PAA), polyvinyl alcohol, aromatic polyimides, and polyamides and their derivatives [1–5]. These polymers contain specific ionic or nonionic functional groups (hydroxy, sulfo, carboxy, amino) which are responsible for selective transfer of water molecules through pervaporation membranes. Published data show that the most efficient in dehydration of organic compounds by pervaporation are membranes with coating films based on polyelectrolytic complexes (PECs) consisting of polycations and polyanions.

The principles of the choice of polyanions and polycations suitable for preparing polyelectrolytic pervaporation membranes, procedures for their preparation, and structural features and permeability of the membranes were discussed in [6–12]. These works showed also that the pervaporation membranes prepared from PECs of similar chemical composition can considerably differ in their permeability. This difference can be caused by differences in the content of polycation and polyanion in the polyelectrolytic complex, in their molecular weights, in the time of membrane preparation (in advance or immediately before pervaporation), in the temperature of thermal treatment, and in other factors. The permeability and selectivity of pervaporation membranes is influenced by procedures used for their preparation. In this work we used the composite membranes (CMs) with coating films based on known and new PECs obtained by different combinations of polycations and polyanions.

EXPERIMENTAL

Polyanion-containing agents used in our experiments were as follows: PAA with molecular weight (MW) 1×10^7, sulfoethyl cellulose (SEC) with MM 240×10^3 and the degree of sulfonation γ 41 or 100 (per 100 glucose units), carboxymethyl cellulose (CMC) with MW 91.5×10^3 and γ = 46, and poly(2-acrylamido-2-methylpropane)sulfonic acid (PSA) with MW 4×10^6. Chitosan (Ch) with MW 185×10^3 (degree of deacetylation 80%) and quaternized poly(2-dimethylaminoethyl) methacrylate (PDM) with MW of 14×10^6 were used as sources of polycations.

When preparing the composite membranes, commercial ultrafilter based on UMP-20 aromatic polyamide was used as support.

The PAA/Ch stoichiometric polyelectrolytic complex and the complexes with the PAA/Ch ratios of 2/1 and 1/2 were prepared using 0.1–0.2 and 0.5–1.0%

1070-4272/03/7611-1807$25.00

solutions of PAA and Ch, respectively, in 30% aqueous acetic acid.

To prepare the composite membranes based on PECs in advance, a thin layer of aqueous PEC of appropriate composition was applied to a support, which was followed by drying, keeping in excess of distilled water for 1 day, and repeated drying [8]. Hereinafter, the membranes prepared in advance will be referred to as the homogeneous composite membranes.

The PAA/Ch composite membranes can be prepared also immediately before pervaporation. In this case, a thin layer of 0.1–0.2% aqueous PAA was applied to the support surface and dried at 20°C, after which this layer was coated with a thin layer of 0.5–1.0% Ch in 2% aqueous acetic acid. The resulting coating film was kept for appropriate time and then dried. Hereinafter, the membranes of this type will be referred to as the laminated membranes.

In our experiments we also used the laminated selective composite membranes based on other composite polyelectrolytic complexes: PDM/SEC (prepared from 0.1–0.2% aqueous PDM and 0.5–10% aqueous SEC), PDM/CMC (prepared from 0.2% aqueous PDM and 1.5% aqueous CMC), and a ternary PSA/PDM/PAA membrane (prepared from 0.2% aqueous PSA, PDM, and PAA). When preparing these complexes, the separate components were applied to the support in the order corresponding to their position in the complex designation. The composite membranes with coatings based on single polymers were used as references.

All the experiments on pervaporation of aqueous–organic solutions were carried out on a temperature-controlled laboratory device with stirring at the residual pressure above the membrane of 0.2 mbar. The effective surface area of the membranes was 6.2 cm^2. The vaporous permeate that passed through a membrane was condensed in a trap cooled with liquid nitrogen. The condensate was weighed, and the transmembrane vapor flow rate ($\prod$, kg m^{-2} h^{-1}) was calculated.

In our experiments we studied dehydration of binary aqueous–organic (ethanol, 2-propanol, acetone, methyl ethyl ketone, ethyl acetate, and methyl acetate) mixtures with water content of up to 55 wt %. The permeate composition was determined by refractometric or chromatographic (0.5-m column packed with Porapak Q) methods. The selectivity factor of the pervaporation separation was calculated by the equation

$$\alpha = (X_A/X_B)/(Y_A/Y_B),$$

where X_A and X_B are the weight content of water and organic substance in the permeate, and Y_A and Y_B are the weight content of water and organic substance in the initial aqueous–organic mixture.

It is known that Ch/PAA poyelectrolytic complexes can be used for preparing efficient homogeneous pervaporation membranes [8, 11]. For example, the stoichiometric and nonstoichiometric complexes of this type were used as 50-μm coatings in pervaporation of aqueous 2-propanol or dioxane to remove water [11]. These experiments showed that, with membranes containing PAA with MW 2×10^5, only nonstoichiometric membranes [Ch/PAA ratios 2/1, 1/2 and 1/3] exhibit high dehydration power. In contrast, according to the data reported in [8], the membranes of both types, homogeneous and laminated, based on stoichiometric Ch/PAA complexes, exhibit high selectivity in pervaporation of aqueous ethanol of approximately azeotropic composition to remove water. It was shown also that, with increasing PAA molecular weight from 9×10^4 to 45×10^4, the separation factor significantly increases, whereas the vapor flow rate decreases. In evaporation of water–ethanol mixtures through the membranes based on polyelectrolytic complexes of PAA and several polymeric quaternary ammonium salts [10], the permeability and selectivity increase with increasing PAA molecular weight (to 4×10^6).

In this work we prepared polyelectrolytic complexes of different types from ultra-high-molecular-weight PAA, PSA, and PDM. The pervaporation characteristics of homogeneous PAA/Ch membranes with the PAA/Ch ratios of 2/1, 1/1, and 1/2 are listed in Table 1. This table also gives the pervaporation characteristics of known PAA/Ch homogeneous membranes with PAA of different molecular weights and characteristics of membranes prepared from PAA and Ch as single component, which are of interest because there are published data on similar membranes [1, 2, 13].

The comparison of the data on separation of water–ethanol mixtures by evaporation through our composite membrane no. 1 and its known analog no. 2 (Table 1) shows that these membranes have comparable selectivity factors α, but the evaporation rate through our membrane is noticeably higher. We believe that the advantage of membrane no. 1 is caused, all factors being the same, by smaller thickness of its coating due to ultrahigh molecular weight of PAA in its composition. The decisive role of this factor is confirmed by the pervaporation data reported in [10, 13] where the membranes based on PAA of identical molecular weight as single component (Table 1, CM no. 8) and in combination with various polymeric

Table 1. Pervaporation characteristics of composite membranes with coatings prepared from PAA and Ch as single components and from homogeneous PAA/Ch complexes at 40°C

CM no.	PAA/Ch ratio	Initial mixture		Permeate, H_2O, wt %	Π, kg m^{-2} h^{-1}	α_{H_2O}
		H_2O, wt %	organic component			
1	1/1	10	Ethanol	99	0.55	891
2	1/1*	10	″	99.2	0.2 (30°C)	1117
3	1/1	12	2-Propanol	93	2.4	98
4	1/1	8	Acetone	99	1.0	1140
5	2/1	8	″	83	0.99	56
6	1/2	8	″	89	0.98	93
7	PAA	10	Ethanol	95	0.44	171
8	PAA**	10	″	99	1.6	891
9	PAA	8	Acetone	99	0.6	1140
10	PAA**	10	″	97	2.4	291
11	Ch	8	″	8	14.0	1
12	Ch***	10	Ethanol	99.8	0.1 (60°C)	6500

* PAA with MW 45×10^4 [8]. ** Aromatic polyamido imide support [13]. *** Cross-linked Ch [1].

bases were studied. These data show (Table 1, CM no. 3) that the membrane based on stoichiometric PEC exhibits low selectivity for water–2-propanol mixture. The similar negative effect found in [7] was attributed to breakdown of stoichiometric CMs in aqueous solutions enriched in 2-propanol. Table 1 (CM nos. 7, 9 and 11) shows that the selectivity of membranes with coatings prepared from PAA as single component considerably exceeds that of the membranes prepared from non-cross-linked chitosan. It should be noted that the selectivity of membranes based on chitosan or polyacrylic acid of relatively low molecular weight can be improved by their chemical cross-linking (Table 1, CM no. 12). The membranes based on PAA with molecular weight exceeding 1×10^6 exhibit fairly high selectivity without cross-linking [1, 8]. Thus, when preparing pervaporation membranes based on individual PAA or on its polyelectrolytic complexes, the use of PAA of ultrahigh molecular weight is preferable.

We found that, in pervaporation of a water–acetone mixture through homogeneous membranes with coating film prepared from stoichiometric PEC or individual PAA, the dehydration of acetone is highly efficient (Table 1, CM nos. 4 and 9). These results are consistent with the basic relations concerning contribution of the thermodynamic factors to the pervaporation selectivity. The main factor responsible for efficient separation of water from ethanol and acetone in pervaporation of water–ethanol (acetone) mixtures is the difference between the water permittivity (80.1) and that of ethanol and acetone (24.3 and 20.7, respectively). In pervaporation of aqueous–organic mixtures with identical water content, the dehydration is the more efficient, the larger the difference between water and the organic component in polarity. With lowering polarity of the organic component, its interaction with the polar coating weakens and, therefore, the selectivity of dehydration is improved. It should be noted that the efficiency of the pervaporative separation is also a function of the difference in the diffusion coefficients of the compounds being separated. In pervaporative dehydration, this factor is controlled by the difference between kinetic diameters of organic and water molecules, among which the kinetic diameter of water molecule, as a rule, is smaller.

It was of interest to study the difference between the pervaporation characteristics of membranes with homogeneous and laminated coating films. These effects were studied in evaporation of water–acetone mixtures with widely varied water content through stoichiometric PAA/Ch membranes (Figs. 1, 2).

The PAA/Ch composite membranes (homogeneous and laminated) used in our experiments exhibit high permeability and selectivity. As seen from Fig. 1, the acetone content in the permeate does not exceed 1 wt % at widely varied initial water content. This figure shows that the efficiency of separation of water–acetone mixtures by pervaporation (curve *1*) considerably exceeds the separation efficiency in a common open evaporation (curve *2*).

The pervaporation is also less power-consuming process than open evaporation, especially in separation of aqueous–organic mixtures with low water content. This is due to the fact that, in distillation, all

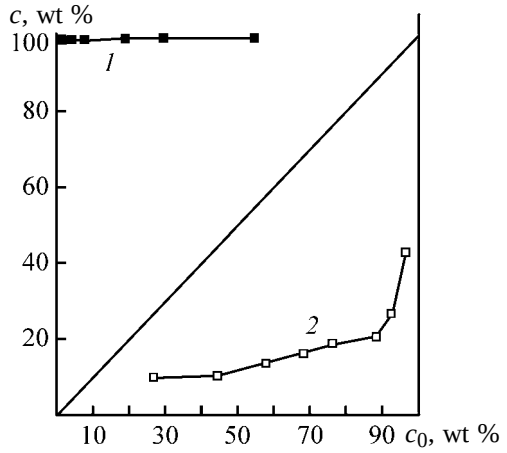

Fig. 1. Water content c in (*1*) permeate (evaporation through PAA/Ch membrane irrespective of the membrane type) and (*2*) in the vapor phase (common open evaporation) as a function of the initial water content c_0 in the water–acetone mixture at 20°C.

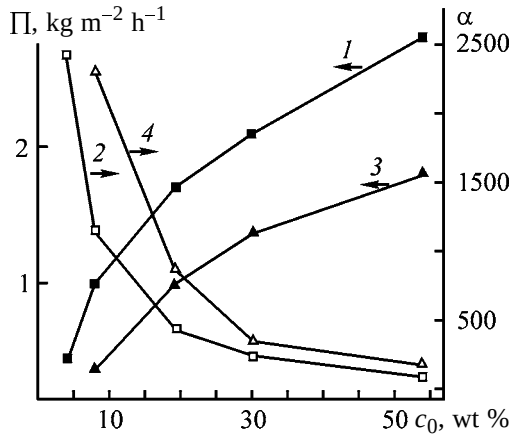

Fig. 2. (*1, 3*) Vapor flow rate ∏ and (*2, 4*) selectivity factor α at 40°C as functions of the water content c_0 in the initial water–acetone mixture. Membranes: (*1, 2*) PAA/Ch stoichiometric homogeneous and (*3, 4*) PAA/Ch stoichiometric laminated.

volatile components are transferred to the vapor phase, whereas in pervaporation water molecules are selectively transferred through the membrane.

Figure 2 shows that, with increasing water content in the water–acetone mixture, the transmembrane vapor flow increases and the pervaporation selectivity decreases. Under these conditions, the PAA/Ch laminated membrane exhibits higher selectivity and lower permeability than homogeneous membranes (Fig. 2, curves *4* and *3*, respectively). These data show that the procedures used for preparing pervaporation membranes affect their permeability and selectivity.

It should be noted that, when preparing the laminated membranes, it is difficult to control their chemical composition and the layer thickness. In this case, we can only suggest the polyelectrolytic complexes are formed, because these membranes, like stoichiometric homogeneous membranes, ensure efficient water removal from water–acetone mixture with a water content of 50% and more. At the same time the membranes prepared from individual PAA are suitable for dehydration only at low water content in acetone (Table 1). When the water content exceeds 20 wt %, these membranes completely lose their selectivity.

When preparing the PAA/Ch laminated coating film, a thin layer of PAA/Ch polyelectrolyte complex is formed over the layer of unchanged PAA. Although this membrane has reduced permeability, when water–acetone mixture passes through its multilayer structure, the selective transfer of water molecules is reached at widely varied water content in the initial mixture. The similar selectivity is attained by the membranes prepared from individual PAA (Table 1). In this case, the selectivity for water can be attributed to formation of hydrogen bonds between PAA and the surface polar molecules of the polyamide support. It will be shown below that, with less polar polyacrylonitrile used as support instead of polyamide, the permeability increases to a level close to that of the homogeneous membranes.

Comparison of procedures used for preparing homogeneous and laminated pervaporation membranes shows that, as a whole, the membranes with laminated coatings are preferable. The main drawbacks of preparing the homogeneous membranes are the necessity of using concentrated acidic PAA and Ch solutions and prolonged washing of the resulting coatings with water. Therefore, in further experiments we used the PAA/Ch laminated membranes.

The lamination technique provides especial advantage in preparing PDM/SEC, PDM/CMC, and PSA/PDM/PAA membranes containing components unstable even in weakly acidic solutions. The presence of polyelectrolytic complexes in the multilayer coating films is confirmed by the fact that, in application of individual anionic (except for PAA) and cationic polymeric agents to a support, the selective pervaporation membranes are not formed. Of particular interest are the laminated membranes with ternary PSA/PDM/PAA coatings consisting of ultra-high-molecular-weight polymeric components. This coating can be applied to a support as a very thin 0.1-μm uniform film exhibiting high permeability. In this coating, the polycationic layer (PDM) is located between two polyanionic layers of different types. We believe that the PSA/PDM and PDM/PAA polyelectrolytic complexes are formed at interfaces.

Table 2. Separation of dilute aqueous acetone solutions by evaporation through laminated composite membranes of different compositions

CM no.	PEC type	H_2O, wt %		Π, kg m^{-2} h^{-1}	α_{H_2O}	$\alpha\Pi$
		initial mixture	permeate			
1	PAA/Ch	8	99	0.37	1140	422
		4	99	0.16	2380	381
1–1	PAA/Ch*	8	99.3	0.94	1630	1534
2	PDM/SEC	8	95	1.9	218	414
	(γ = 41)	4	96	0.9	577	519
3	PDM/SEC	8	93	2.4	153	367
	(γ = 100)	4	94	1.4	377	527
4	PDM/CMC	8	98.5	1.05	755	793
		4	98.5	0.6	1578	947
5	PSA/PDM/PAA	8	99.5	2.3	2290	5267
		4	99.5	1.5	4780	7170
6	Simplex**	9	99.6	2.4 (50°C)	2518	6043

* Applied to polyacrylonitrile support. ** Prepared from SEC and poly(dimethyldiallylammonium chloride) [9].

Our experimantal data on pervaporative separation of acetone-rich water–acetone mixtures with laminated composite membranes of different compositions are listed in Table 2. To evaluate the generalized characteristic of the membrane performance reflecting both the selectivity and permeability, we used the productivity factor $\alpha\Pi$. Table 2 shows that this factor, being approximately identical for CM nos. 1–3, noticeably increases in going to PDM/CMC membranes, and for ternary membrane PSA/PDM/PAA it becomes commensurable with that of the best of known analogs (Table 2, CM no. 6).

We found that the productivity factor of PAA/Ch laminated membrane with the coating applied to a polyacrylonitrile support with porous chracteristics close to those of the polyamide ultrafilter (Table 2, CM nos. 1–1) exceeds the productivity factor of PAA/Ch membrane with the coating applied to a polyamide support (Table 2, CM no. 1). The productivity factor of this membrane also exceeds that of the PAA/Ch homogeneous membrane (1140 kg m^{-2} h^{-1}) (CM no. 4, Table 1). We believe that these effects are caused by the fact that PAA interacts with the polyacrylonitrile support more weakly than with the polyamide support. Thus, the chemical features of a support material substantially influence the membrane productivity factor. We do not rule out also that high permeability of ternary composite membrane no. 5 (Table 2) is caused not only by its small thickness and ultrahigh molecular weight of its polymeric constituents, but also by the order of application of the laminated coating film to the polyamide support.

The service life of a pervaporation membrane was determined in long-term (530 h) evaporation of a water (1.5 wt%)–acetone mixture through laminated membrane no. 2 (Table 2). In these experiments, the removal of methanol traces present in acetone (130 ppm) was monitored by IR spectroscopy. This problem is important from practical viewpoint. Our tests showed that the membrane exhibits the stable permeability in the course of long-term pervaporation. Upon successive evaporation of the water–acetone mixture through three identical membranes, the water and methanol contents were decreased to 0.3 wt % and 80 ppm, respectively.

The published data on pervaporative dehydration of organic solvents mainly concern water–aliphatic alcohol mixtures. At the same time, it was of interest to elucidate whether the pervaporation can be used for dehydration of a wider set of organic solvents, including aqueous azeotropic mixtures. With this aim, we studied water removal from aqueous 2-propanol, methyl ethyl ketone (MEK), methyl acetate, and ethyl acetate (EtAc) by their evaporation through several laminated composite membranes (Table 3).

Table 3 shows that the most versatile are the membranes with the coating based on the PAA/Ch complex. These membranes efficiently dehydrate all the aqueous–organic mixtures studied by us. The permeability of these membranes for water, all other factors being the same, depends on the nature of the organic solvent. For organic solvents under consideration, the membrane permeability decreases in the order EtAc > acetone > ethanol. We believe that the decrease in

Table 3. Separation of aqueous–organic mixtures by evaporation through laminated membranes of different compositions at 40°C

CM no.	PEC type	Initial mixture		Permeate, wt % H_2O	Π, kg m^{-2} h^{-1}	α_{H_2O}
		H_2O, wt %	organic solvent			
1	PAA/Ch	7.5	MEK	99	1.4	1222
		10		99	2.6	892
		3.3	EtAc	99.5	1.0	5850
		6.2	MeAc	99.5	1.3	3015
		12	2-Propanol	99	0.3	728
2	PDM/SEC (γ = 41)	3.7	MEK	97	1.5	842
		7.5	MEK	Azeotrope	7.1	–
		7	EtAc	〃	7.4	–
3	PDM/CMC	7.5	MEK	99	1.7	1220
		9.4	EtAc	94	2.5	150
4	PSA/PDM/PAA	5	MEK	99.5	1.5	3783
		10	EtAc	Azeotrope	5.2	–

permeability is caused by formation of water associates with ethanol and acetone and their lack in the case of ethyl acetate. The similar effects were found in [4] for membranes with the coating prepared from a sulfonated aromatic polyamide. Table 3 shows also that, in evaporation of the aqueous–organic mixtures through a PSA/PDM/PAA ternary laminated membrane, especially efficient dehydration is reached for acetone and MEK.

CONCLUSIONS

(1) New types of composite pervaporation membranes ensuring the efficient dehydration of aliphatic alcohols, ketones, and esters were prepared by different combinations of polyanions and polycations.

(2) The permeability and selectivity of the pervaporation membranes is a function of the polyelectrolyte complex type, molecular weight of polyanions and polycations, and chemical features of polymeric support material.

(3) The permeation characteristics of the pervaporation membranes with coating films prepared from ultra-high-molecular-weight polyacrylic acid and Chitosan is a function of procedure of preparing the polyelectrolytic complex.

ACKNOWLEDGMENTS

The authors are grateful to A.V. Zinenkov for assistance in measuring the service life of pervaporation membranes.

This work was financially supported by the Russian Foundation for Basic Research (project no. 03-03-32 379).

REFERENCES

1. Mochizuki, A., Amiya, S., Sato, Y., *et al.*, *J. Appl. Polym. Sci.*, 1990, vol. 40, pp. 633–643.
2. Choi, H.S., Hino, T., Shikata, M., *et al.*, *J. Membr. Sci.*, 1992, vol. 72, pp. 259–266.
3. Huang, R.Y.M. and Rhim, J.W., *Polym. Int.*, 1993, vol. 30, pp. 123–128.
4. Kirsh, Yu.E., Vdovin, R.A., Fedotov, Yu.A., *et al.*, *Vysokomol. Soedin., Ser. A*, 1996, vol. 38, no. 2, pp. 330–336.
5. Yanagishita, H., Maejima, C., Kitamoto, D., and Nakane, T., *J. Membr. Sci.*, 1994, vol. 86, pp. 231–240.
6. Semenova, S.I., Ohya, H., and Soontarapa, K., *Desalination*, 1997, vol. 110, pp. 251–286.
7. Smirnova, N.N. and Fedotov, Yu.A., *Membrany*, 2002, no. 14, pp. 60–68.
8. Shieh, J.-J. and Huang, R.Y.M., *J. Membr. Sci.*, 1997, vol. 127, pp. 185–202.
9. Richau, K., Schwarz, H.H., Apostel, R., and Paul, D., *J. Membr. Sci.*, 1996, vol. 113, pp. 31–41.
10. Karakane, H., Tsuyomoto, M., Maeda, Y., and Honda, Z., *J. Appl. Polym. Sci.*, 1991, vol. 42, pp. 3229–3239.
11. Ageev, E.P., Kotova, S.L., Skorikova, E.E., and Zezin, A.B., *Vysokomol. Soedin.*, 1996, vol. 38, no. 2, pp. 323–329.
12. Lenk, W. and Meier-Haask, J., *Desalination*, 2002, vol. 148, pp. 11–16.
13. RF Patent 2 088 320.

Russian Journal of Applied Chemistry, Vol. 76, No. 11, 2003, pp. 1813–1816. Translated from Zhurnal Prikladnoi Khimii, Vol. 76, No. 11, 2003, pp. 1863–1867.

MACROMOLECULAR CHEMISTRY AND POLYMERIC MATERIALS

Rheological and Electrophysical Properties of Dispersions Based on Thermally Treated Magnetite and Aqueous Emulsions of Water-Soluble Polymers in Transformer Oil

T. G. Lazareva and E. V. Shinkareva

Institute of General and Inorganic Chemistry, National Academy of Sciences of Belarus, Minsk, Belarus

Received April 23, 2003

Abstract—Rheological, electrophysical, and sorption properties of magnetite dispersions modified with water-soluble polymers were studied as influenced by the temperature of heat treatment in the 300–600°C range.

Composites sensitive to mechanical and magnetic fields can be prepared from fluid systems with dispersed fillers modified with water-soluble polymers. Such materials can be used as antivibrators, acoustic sensors, measurement devices, and shock absorbers [1]. Filler particles are modified by sorption of water-soluble polymer on their surface; in this case, additional treatment, such as heating or water sorption, can affect the filler properties. It is known that thermal treatment can affect the crystal structure of the polymer or cause more profound degradation with formation of new bonds. The oxidation and degradation processes begin on heating in air to 170–220°C, whereas the carbon structure is formed at temperatures higher than 500°C.

Previously, we studied the rheological properties of magnetite dispersions in transformer oil as influenced by conditions of the filler surface modification with water vapor and solutions of water-soluble polymers such as polyvinyl alcohol (PVA) and carboxymethyl cellulose [2]. We proposed that modification of the magnetite surface with water-soluble polymers plasticized with water molecules can yield systems exhibiting both plasticity and dilatancy, which is due to the formation of a network of hydrogen bonds in the mechanical field and subsequent structuring of the system with increasing shear stress, with anisotropic orientation of filler particles.

In this work we studied the rheological, electrophysical, and sorption properties of magnetite dispersions modified with a water-soluble polymer as influenced by the temperature of heat treatment (300–600°C).

EXPERIMENTAL

In our work we used dry transformer oil as dispersion medium and finely ground pure-grade magnetite (5–10 μm particle size) dried at 100±5°C for 5 h. Modification was performed as follows: magnetite was mixed with 5 and 20% solutions of PVA (16/1 brand) and a 0.5% solution of carboxymethyl cellulose (Na-CMC, 70/300 brand); the PVA–magnetite ratio was 5 and 10, and the Na-CMC–magnetite ratio, 2.5 (bath ratio). The mixtures were dried at 100±5°C for 5 h and treated for 2 h at 300–600°C. Then, the sorption of water vapor by the resulting magnetite composites was studied. These samples were stored at ambient temperature for 20 days in desiccators at the relative humidity of 30, 60, 80, and 100%, maintained by saturated solutions of appropriate salts.

The viscosity was measured on a Rheotest-2 rotary viscometer in the shear rate range 3–1312 s^{-1} (5 wt % solution concentration).

The conductivity of dispersions based on the pretreated composite of magnetite and water-soluble polymer was measured on an HI 9032 (Hanna Instruments) stationary conductometer at 20±5°C.

The dependences of the viscosity η of 5% magnetite dispersions modified with 5% PVA solution and treated at 300–600°C on the shear rate τ_v are shown in Fig. 1. As seen, thermal treatment of modified magnetite does not affect the modes of the fluid flow as compared to the untreated filler. The viscosity of such fluid systems increases up to a certain limit; such systems exhibit the dilatancy. Sorption of water vapor by the treated magnetite–PVA composite changes the fluid flow mode: η decreases with increasing τ_v. As a result, the viscosity at small shear rates increases; the higher the water content, the greater the system viscosity. After heating to 300°C at sorption degree of 2.2%, the maximal viscosity η_{max} is 32 mPa s, and at 600°C and sorption degree of 10.4%, 55 mPa s. At a shear stress >1 Pa, the viscosity is independent of

1070-4272/03/7611-1813$25.00

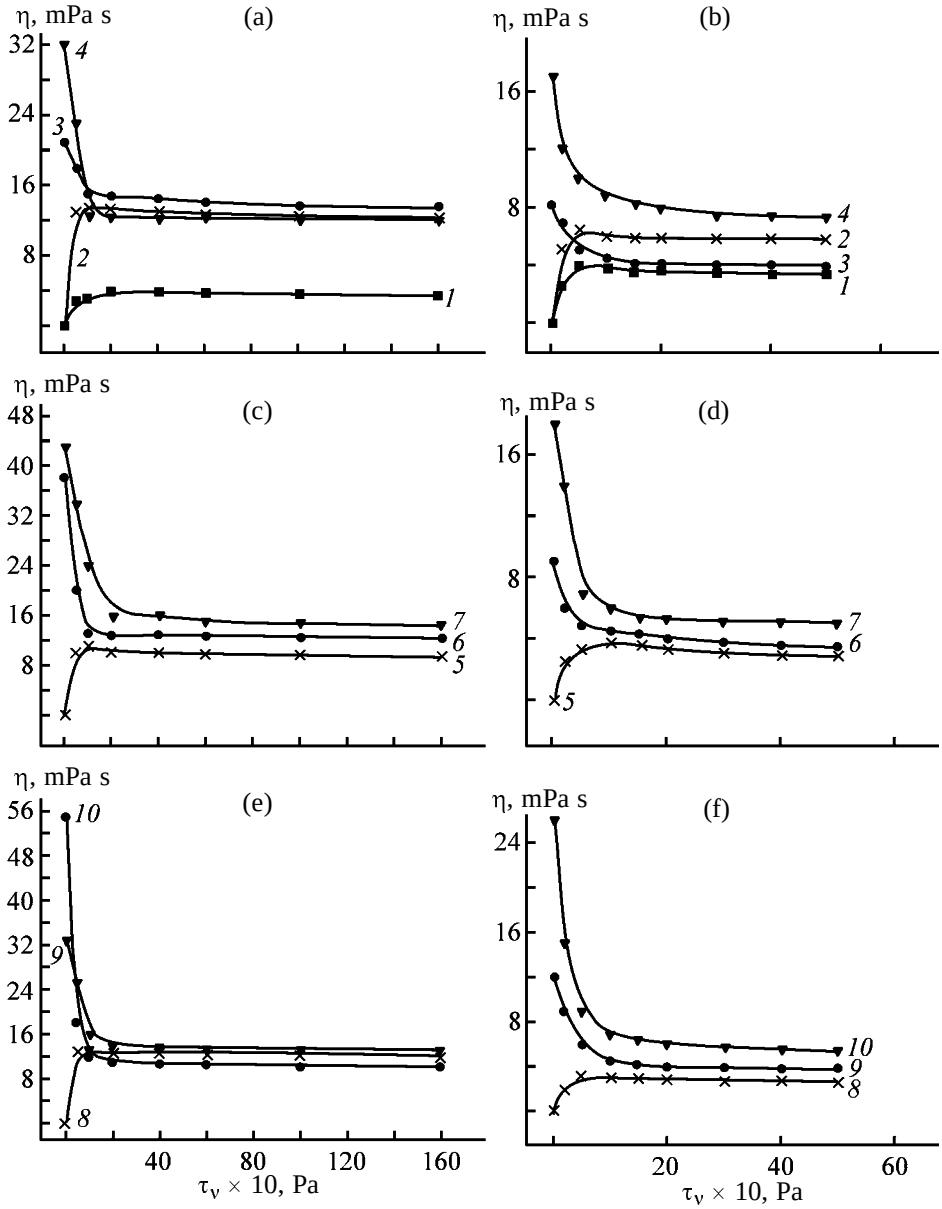

Fig. 1. Dynamic viscosity η as a function of the shear stress τ_v at (a, c, e) 30 and (b, d, f) 70°C for 5 wt % magnetite dispersion in transformer oil. Magnetite modified with 5% PVA solution. Filler: (*1*) untreated, (*2*, *5*, *8*) thermally treated, and (*3*, *4*, *6*, *7*, *9*, *10*) thermally treated and modified with water vapor; the same for Fig. 2. Temperature of thermal treatment, °C: (*2*–*4*) 300, (*5*–*7*) 400, and (*8*–*10*) 600; the same for Fig. 2. Water content, %: (*3*) 1.0, (*4*) 2.25, (*6*) 1.58, (*7*) 9.84, (*9*) 2.20, and (*10*) 10.43.

the water vapor sorption by filler particles. The thermal treatment of the magnetite–PVA composite with steam provides formation of the structure more sensitive to water vapor and causes a significant increase in the system viscosity. It should be noted that the flow curves recorded for 5%-magnetite dispersions modified with 20% PVA, heated to 300–600°C, and plasticized with water molecules are similar to those given above.

The dependences of the viscosity η of 5% magnetite dispersions modified with 0.5% Na-CMC solution and treated at 300–600°C on the shear rate τ_v are shown in Fig. 2. As seen, thermal treatment at 300°C of the magnetite–Na-CMC composites does not affect the shape of the flow curves; the viscosity η increases up to certain limit. With increasing temperature to 400–600°C, the shape of the flow curves of magnetite dispersion changes, and a maximum appears at τ_v = 0.2–0.5 Pa; there are sections in which the fluid viscosity decreases (plasticity) or increases (dilatancy). With penetration of additional water molecules in the magnetite–Na-CMC composite treated at 300–600°C,

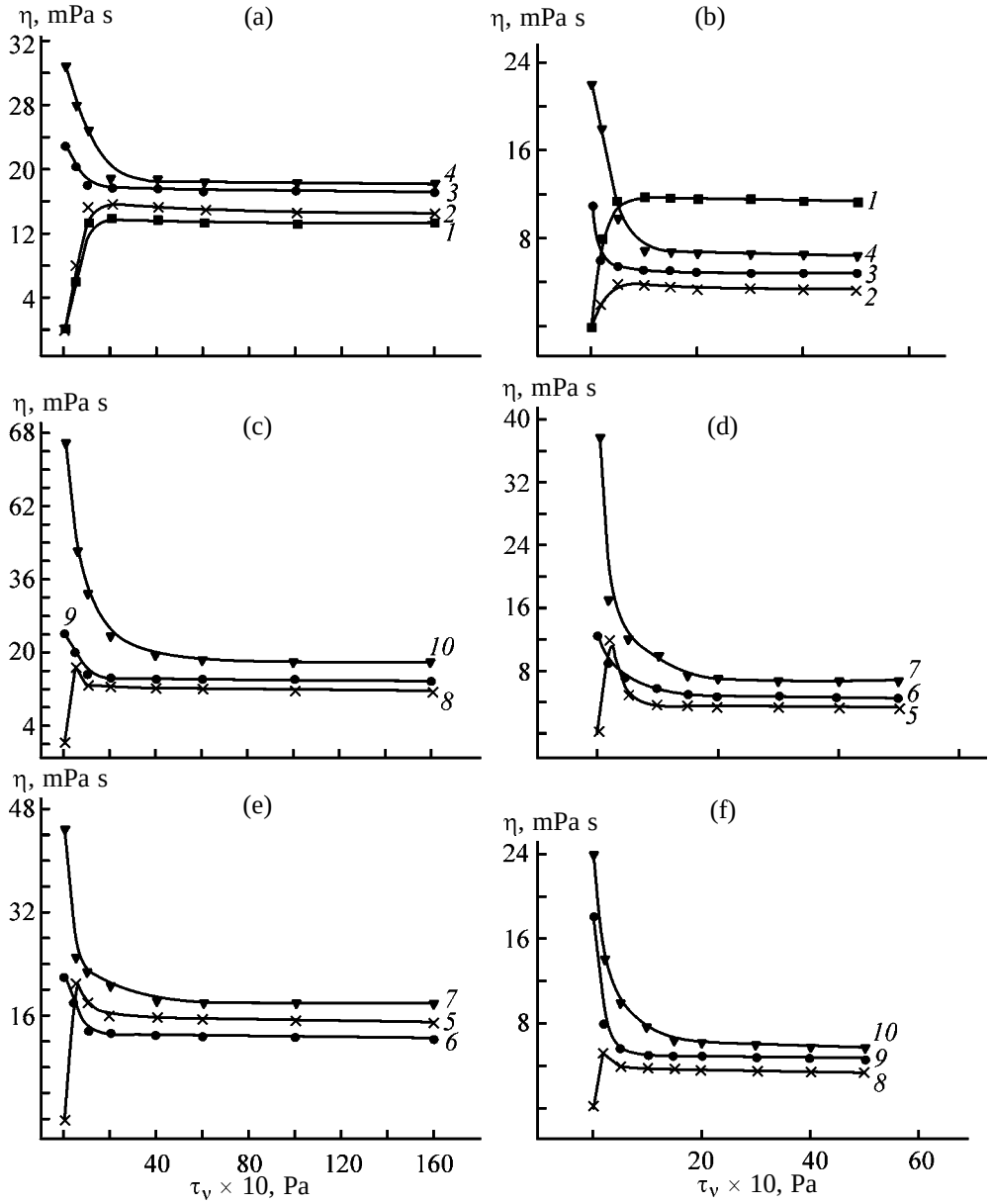

Fig. 2. Dynamic viscosity η as a function of the shear stress τ_v at (a, c, e) 30 and (b, d, f) 70°C for 5 wt % magnetite dispersion in transformer oil. Magnetite modified with 0.5% Na-CMC solution. Water content, %: (*3*) 0.7, (*4*) 1.8, (*6*) 1.4, (*7*) 1.9, (*9*) 1.34, and (*10*) 4.0.

the flow mode strongly changes. With increasing shear stress, the dispersion viscosity decreases. However, at small shear stresses (up to 2×10^{-2} Pa) the system viscosity first increases and then decreases, in contrast to untreated filler and magnetite–Na-CMC composite plasticized with water molecules, for which the peak in the flow curves is observed at greater τ_v (up to 2–4 Pa). Upon heating of magnetite modified with 0.5% Na-CMC solution at 300°C and subsequent treatment with water vapor (1.8% water content), the viscosity increases to 33 mPa s at maximum (system temperature 30°C); upon heating to 400°C, at 1.9% water content, to 45 mPa s, and upon heating to 600°C, at 4.0% water content, to 66 mPa s.

The thermal treatment of the magnetite–water-soluble polymer system affects it hydrophilicity. The sorption capacity of the thermally treated samples is greater than that of the untreated sample, and this effect is observed in the entire water vapor pressure range studied. The greatest increase in the sorption capacity is observed after heating to 600°C. In this case, the sorption of water vapor in the magnetite–PVA system comprises 2.2% (30% relative humidity)

Table 1. Sorption capacity of the thermally treated magnetite–water-soluble polymer composite

Thermal treatment		Relative air humidity, %	Sorption time, days	Water content, %
T, °C	τ, h			
Modified with 0.5% solution of Na-CMC, 70/300 brand				
100	2	30	20	0.3
		60	20	0.6
		80	20	0.8
		100	20	8.8
300	2	30	20	0.7
		60	20	1.5
		80	20	1.8
		100	20	12.3
400	2	30	20	1.4
		60	20	1.6
		80	20	1.9
		100	20	16.0
600	2	30	20	1.4
		60	20	2.0
		80	20	3.4
		100	20	4.0
Modified with 5% solution of PVA, 16/1 brand				
100	2	30	20	0.1
		60	20	0.3
		80	20	1.0
		100	20	8.2
300	2	30	20	1.0
		60	20	1.2
		80	20	2.2
		100	20	20.0
400	2	30	20	1.8
		60	20	2.6
		80	20	9.8
		100	20	21.3
600	2	30	20	2.2
		60	20	3.3
		80	20	10.3
		100	20	25.8

and 10.4% (80%), whereas for magnetite–Na-CMC composites it is 1.3 (30%) and 4.0% (80%). With decreasing treatment temperature to 300°C, the sorption capacity decreases, but it remains higher than that of the untreated filler. The sorption capacity with respect to water vapor of the magnetite–PVA composites is 1.0 (30) and 2.25 (80%) and of the magnetite–Na-CMC, 0.7 (30%) and 1.8 (80%) (Table 1). The effects observed are probably due to changes in the nature of intra- and intermolecular interactions and to related changes in the molecular mobility in the thermally treated magnetite–water-soluble polymer composites, and also to the formation of a carbon structure.

Table 2. Conductivity of dispersions based on thermally treated magnetite–water-soluble polymer composite

Modifying agent	Treatment temperature, °C	Specific conductivity, μS cm^{-1}
5% solution of PVA, 16/1 brand	100	133.5
	300	158.7
	400	215.8
	600	366.9
20% solution of PVA, 16/1 brand	100	132.6
	300	154.6
	400	224.3
	600	425.8
0.5% solution of Na-CMC, 70/300 brand	100	132.9
	300	129.5
	400	147.6
	600	230.4

We also studied the suitability of the dispersions based on thermally treated magnetite–water-soluble polymer composites as conducting materials. For example, thermal treatment of the filler in air at 300–600°C increases its conductivity (Table 2).

Thus, our experimental data suggest that the structural and rheological properties of the magnetite–water-soluble polymer system can be controlled by additional thermal treatment and sorption of water vapor.

CONCLUSION

Thermal treatment at 300–600°C and sorption of water vapor increase the conductivity of magnetite particles modified with water-soluble polymers and change the flow mode of fluids based on them under the mechanical stress. As a result, the systems exhibiting both plasticity and dilatancy are formed depending on modification conditions, which allows preparation of systems with controlled flow mode in the mechanical field.

REFERENCES

1. Jiang, F.O., Wang, Z.W., Wu, J.Y., and Zhow, L.W., Abstracts of Papers, *Int. Conf. on Electro-Rheological Fluids, Magneto-Rheological Suspensions, and Their Applications*, Yonezawa (Japan), July 22–25, 1997, p. 163.
2. Lazareva, T.G., Shinkareva, E.V., and Prodan, S.A., *Zh. Prikl. Khim.*, 2001, vol. 74, no. 6, pp. 1002–1005.

Russian Journal of Applied Chemistry, Vol. 76, No. 11, 2003, pp. 1817–1821. Translated from Zhurnal Prikladnoi Khimii, Vol. 76, No. 11, 2003, pp. 1868–1872.

MACROMOLECULAR CHEMISTRY AND POLYMERIC MATERIALS

Role of the Chemical and Physical Networks in Formation of a Complex of Elastic and Dissipative Properties of Epoxy-Phenolic Binders

Yu. N. Smirnov, T. E. Shatskaya, and V. I. Natrusov

Institute for Problems of Chemical Physics, Russian Academy of Sciences, Chernogolovka, Moscow oblast, Russia
Stekloplastik Scientific Production Association, Russian Joint-Stock Company, Kryukovo, Moscow oblast, Russia

Received July 16, 2002; in final form, July 2003

Abstract—A study was made of the elastic and dissipative properties of epoxy-phenolic network polymers in which the ratio of the chemical and physical cross-links was controlled by varying the ratio of epoxy and phenol groups in the initial compositions.

Machine building development demands nonmetallic polymer composite materials (PCMs) characterized by high elasticity and strength. Specific conditions of exploitation of articles manufactured from PCMs pose additional requirements on them. They must exhibit high dynamic and static fatigue resistance, high fracture resistance, and other characteristics associated with the ability of the polymer matrix (PM) in PCMs to dissipate the mechanical loading energy [1]. This necessitates directed control of the elastic and relaxation (dissipative) properties of not only articles manufactured from composites as integral structures [2, 3] but also of the PM in separate.

The aim of this work was to elucidate how the chemical and physical networks affect formation of the elastic and relaxation properties of epoxy-phenolic polymers (EPPs) when the ratio of different cross-linking bonds is varied by varying the ratio of the epoxy and phenol groups in the initial composition being cured.

EXPERIMENTAL

We studied an epoxy-phenolic compound based on resorcinol diglycidyl ether (RDGE) purified by vacuum distillation and an SF-0113 novolac phenol–formaldehyde resin (PFR) [TU (Technical Specifications) 6-05-031-509–74] with a drop point T_d = 75–90°C and a free phenol content under 0.5 wt % [4]. As tertiary amine we used *N*,*N*-diethylaniline efficiently accelerating reactions of epoxides with phenol and secondary alcohol groups [5].

The elastic and relaxation dynamic characteristics of EPPs were studied by the bending resonance vibration method on a setup similar to that described in [6]. The static mechanical characteristics, i.e., tensile strength σ_t, Young modulus E_t, and breaking strain ε_t, were determined on a 1231-U tensile-testing machine at the clamp movement rate of 1 mm min^{-1}. The samples for testing were molded in vacuum molds supplied with dumbbell-like fluoroplastic inserts (to damp the shrinkage strains) with a 30-mm-long working unit. Prior to tests, the samples were annealed for 3 h in VM-1 vacuum oil at 160°C, which was followed by cooling at a 0.2 deg min^{-1} rate. The annealing was controlled with a polarization setup. The surface fracture energy γ (identified with the fracture viscosity [7]) was estimated by cleaving trapezoidal samples having a longitudinal groove according to the procedure described in [8, 9].

Three-dimensional cross-linking of network epoxy polymers occurring in the glassy state at room temperature is effected by various bonds: chemical covalent (stable) and physical (labile at the given temperature). The labile physical bonds linking the chemical structure elements are so important that one can speak of a network of physical bonds having its own specific features and governing, for a significant part, the set of physicomechanical properties of epoxy polymers. Among physical labile bonds, the most important are hydrogen bonds characterized by a cohesion energy of 29–40 kJ mol^{-1} [10]. Cured epoxy resins contain abundant secondary alcohol groups yielded by opening of epoxy rings in polycondensa-

1070-4272/03/7611-1817$25.00

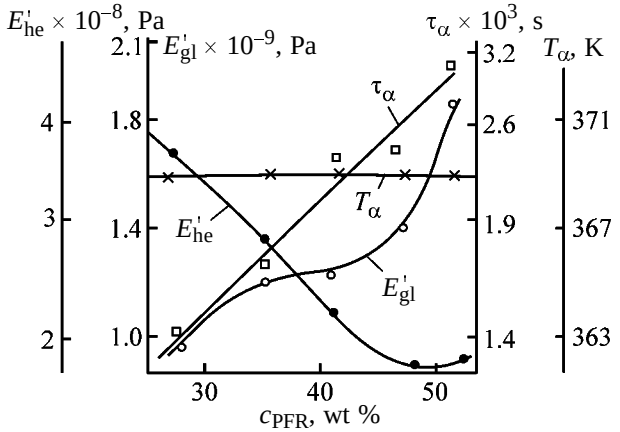

Fig. 1. Variation of the shear modulus in hyperelastic (E'_{he}) and glassy (E'_{gl}) states, α-transition temperature T_α, and α-transition relaxation time τ_α with the content of PFR c_{PFR} in epoxy-phenolic compound.

tion. Thus, the hydrogen bonds formed by these groups can be treated as the major effective cross-linking sites of the labile physical network, supplementing the chemical linking of the structural elements of the polymer.

A specific feature of curing of epoxy resins with polyphenols, in particular, PFRs [11], is that it allows control of the content of the secondary alcohol groups and, thereby, the number of effective linking sites of the physical network. For example, at equimolar ratio of the epoxy and phenol groups in the initial compound, the epoxy groups at moderate temperatures react, for the most part, with phenol groups, if the latter are sterically accessible [12]:

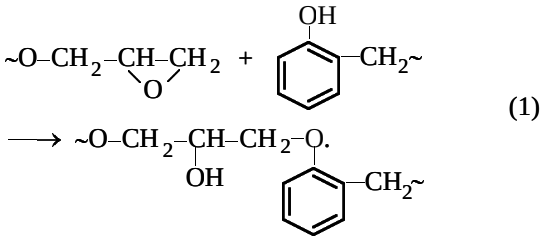

(1)

When taken in excess over the phenol groups, the epoxy groups can also react with the secondary alcohol groups, especially at elevated temperatures and in the presence of tertiary amines catalyzing this reaction [5]:

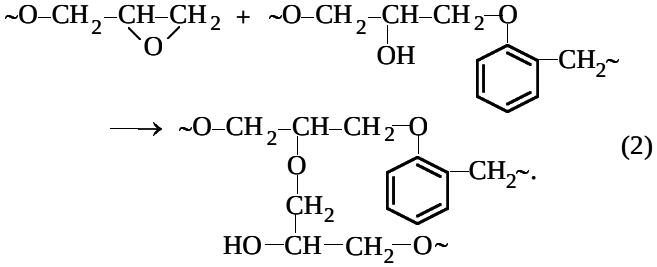

(2)

In this case, a chemical cross-link appears instead of a secondary alcohol group, which is a linking site of a labile physical network. Evidently, with increasing mass fraction of PFR, the density of the chemical cross-links should decrease, and the number of the physical linking sites, increase. It should be noted that, in this work, in the presence of *N*,*N*-diethylaniline and at stepwise increase in the curing temperature, virtually all the epoxy and phenol groups reacted. This enabled more correct elucidation of how the contents of different types of bonds providing three-dimensional cross-linking (physical and chemical; their contents vary in opposite directions) affect the behavior of EPPs under mechanical loading in different modes. With a view to development of polymeric materials exhibiting high strength when subjected to dynamic and static loads, it is important, above all, to elucidate how the changes in the nature of the cross-linking bonds affect the energy of the cohesion interaction of the structural units and their energy dissipation ability. It is believed [13] that these factors make the greatest contribution to the resistance of polymeric materials to high mechanical loads.

The EPP samples with varied content of PFR were subjected to mechanical tests of two kinds, dynamic and static. In the first case, we studied the temperature dependences of the dynamic elasticity modulus E' and the mechanical loss tangent $\tan\delta$. Figure 1 shows that, with increasing PFR content in the initial composition, the dynamic elasticity modulus tends to increase in the glassy state (E'_{gl}, 300 K) and to decrease in the hyperelastic state of EPP (E'_{he}, 420 K). These findings are in line with the views on the deciding influence of the physical bonds on the glassy state and of the chemical bonds on the hyperelastic state of network polymers [6].

It should be noted that other researchers also reported that the dynamic elasticity moduli in the glassy and hyperelastic states vary in the opposite directions [14, 15] in the case of epoxy–amine polymers in which the cross-linking density of the chemical network was controlled by varying the structure of the initial epoxy oligomer. It was supposed [14, 15] that increasing the distance separating the chemical cross-linking sites in epoxy polymers characterized by a high cross-linking density tends to increase the number of physical contacts. In our case, increase in the content of the secondary alcohol groups in parallel with increase in the distance separating the cross-links tends to additionally enhance the effect exerted by physical links.

Thus, increase in the dynamic elasticity modulus in

the glassy state with increasing PFR content and, consequently, the number of labile physical links indicate that the cohesion energy of interaction between the structural units of EPPs grows [16].

The dissipative properties of EPPs can be assessed from their relaxation spectra using different parameters. The first parameter is the internal friction background (IFB) for which one conventionally takes the mechanical loss tangent measured at room temperature, $\tan\delta_{25}$, i.e., at the temperature at which the strength of these polymers is tested. The IFB can serve as an indicator of the structural organization and intermolecular interaction in polymers [17]. The second parameter is the energy dissipated during the α-relaxation process [18] involving large-scale segmental molecular motion. This parameter is conventionally estimated as the intensity (or height) of the α peak in the maximum, i.e., as $\tan\delta_{max}$, or, more precisely, as the α-peak area, which is approximated by the product of $\tan\delta_{max}$ by the FWHM of the α peak $\Delta_{1/2}$ [18]. The energy dissipated during the α process can also be estimated indirectly, using the parameters of segmental mobility of the PM such as, e.g., the effective activation energy U_α [19] or the α-relaxation time τ_α [20]. Notably, the energy dissipated during the α process can affect the room-temperature strength of the PM [20].

Since it is difficult to correctly estimate $\Delta_{1/2}$ and U_α, we took $\tan\delta_{25}$, $\tan\delta_{max}$, and τ_α as relaxation (dissipation) dynamic indicators.

Figure 2 shows that, with decreasing PFR content, i.e., with increasing number of the chemical cross-links, $\tan\delta_{25}$ and, hence, the IFB tend to linearly grow. This is in line with the observed decline in the dynamic elasticity modulus in the glassy state and, evidently, means that the local molecular mobility tends to grow with increasing number of the chemical bonds owing to weakening of the intermolecular interaction [6]. At the same time, $\tan\delta_{max}$ tends to linearly decline with increasing number of the chemical cross-links, and this is accompanied by a decrease in the α-process peak area. This could also be due to a decrease in the large-scale segmental molecular mobility owing to an increase in the density of the chemical cross-links. However, this contradicts the following data. First, the temperature corresponding to the α-peak maximum remains virtually unchanged (Fig. 1), while it is known [21, 22] that the glass transition point of epoxy polymers typically increases with increasing chemical cross-linking density. Evidently, this is due to mutual compensation of the opposite changes in the number of different types of

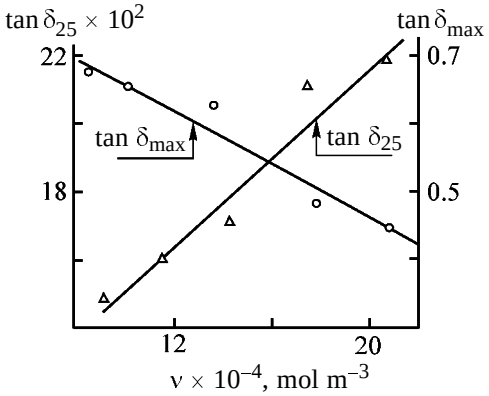

Fig. 2. Variation of the mechanical loss tangent at room temperature ($\tan\delta_{25}$) and in the α-transition maximum ($\tan\delta_{max}$) with the number of the chemical cross-links ν.

cross-links (and, possibly, to increase in the content of the aromatic rings in the PFR structure).

Second, the τ_α parameters calculated from the resonance condition in the α-peak maximum tend to decrease with increasing number of the chemical cross-links (Fig. 1). This means that the segmental molecular mobility, on the contrary, tends to grow with increasing density of the chemical cross-links. Therefore, a decrease in the mechanical losses (weakening of the dissipative properties) during the α process with increasing chemical cross-linking density is due to increase, rather than decrease, in the molecular mobility because of weakening of the intermolecular interaction. In turn, enhancement of the dissipative properties of EPPs with increasing number of labile physical cross-links is, evidently, due to increase in the effective size of the kinetic units of the α-relaxation process owing to increase in the interchain cooperativity of the segmental motion.

Thus, the dynamic mechanical tests showed that, with increasing PFR content in the initial composition, i.e., with increasing number of physical and decreasing number of chemical cross-links, not only the dynamic elasticity moduli in the glassy and hyperelastic states, but also the mechanical loss tangent in the glassy state (IFB) and in the region of the α transition from the glassy to hyperelastic state vary in the opposite directions. In transition from the glassy to hyperelastic state, the cohesion and dissipative properties of EPPs vary in the opposite directions.

Static tensile tests yielded the following characteristics: E_t, σ_t, ε_t, and γ. Figure 3 shows that, with increasing PFE content, σ_t, ε_t, and γ tend to increase, and E_t remains unchanged.

Let us attempt to analyze in a simplified way these results using the known Griffits formula of the critical

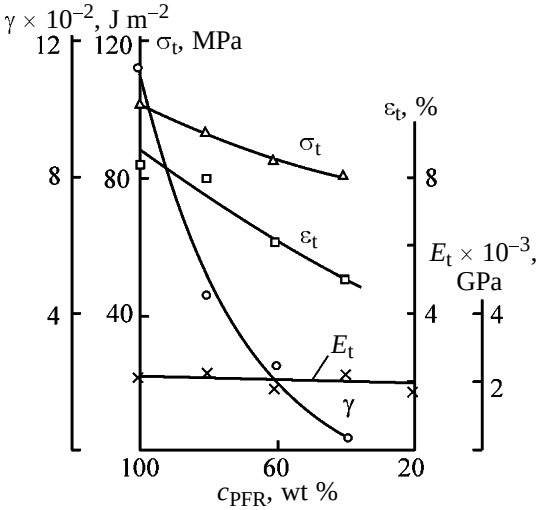

Fig. 3. Variation of the physicomechanical properties of epoxy-phenolic polymers: surface fracture energy γ, tensile strength σ_t, breaking strain ε_t, and Young modulus E_t, with the PFR content c_{PFR} in the epoxy-phenolic composition.

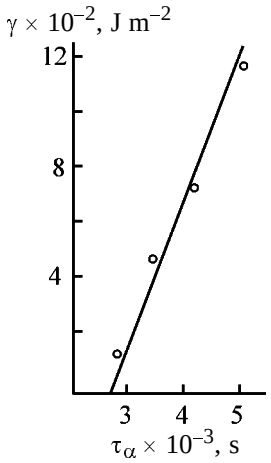

Fig. 4. Variation of the surface fracture energy γ with the α-transition relaxation time τ_α.

strength [13]

$$\sigma_c r = 2E\gamma/\pi l_{cr},$$

where E is the Young modulus; γ, specific surface energy; and l_{cr}, critical defect size.

This formula interrelates the major parameters governing the strength of solid materials: elasticity parameter E, relaxation (dissipative) parameter represented by γ [13] (identified, according to the published data, with the fracture viscosity [7, 9]), and the parameter l_{cr} characterizing the structure defects. The latter parameter was calculated by substituting into formula (1) the experimental E_t, σ_t, and γ values. It should be noted that l_{cr} is directly proportional to γ.

The fact that the relaxation and structural parameters vary in the same direction (as early reported in [5, 8]), in combination with larger l_{cr} parameters incomparable with the sizes of the supramolecular formations in EPPs [12], can suggest that l_{cr} characterizes the size of the critical structural defect in the preruptured, rather than in the initial, state. Hence, the above-mentioned correlation can have the following physical sense at the micromechanical level: The stronger the relaxation (dissipative) properties of PMs, the greater external mechanical load applied to the material is required for preliminary initiation of the catastrophic rupture event via rapid growth of the propagating main crack forming a new surface and the greater deformation work is spent for the preliminary growth of the greatest structural defect to the critical size or for preliminary opening of the crack to the critical state. This deformation energy should be added to the surface fracture energy proper.

Thus, the specific surface fracture energy of polymers reflects, to a significant extent, the relaxation ability of the material, i.e., its ability for viscous dissipation of mechanical energy at the top of the propagating crack owing to plastic deformation of the adjacent regions.

Notably, there is no correlation between the strength parameters and IFB, and there is a linear correlation between γ and τ_α (Fig. 4). The physical sense of this correlation at the molecular level, evidently, consists in the following. Despite low (room) temperature of static cleavage tests, large-scale molecular motion substantially contributes to fracture via forced plastic flows at the mouth of the propagating crack. The greater the effective sizes of the kinetic units participating in the relaxation process, the greater volume they occupy (the greater proportion of the fluctuation free volume they need [23]), the greater should be the volume of the plastic zone at the top of the propagating crack, and the greater the dissipated energy.

Thus, increase in the number of labile physical cross-links and the parallel decrease in the number of the chemical cross-links are responsible for the EPP fracture delocalization at the microlevel. This means that larger microvolumes of the material are involved into fracture (increase in γ and l_{cr}). At the macrolevel, this is manifested in growth of ε_t and also of the total deformation energy A_d including the fracture energy, which is estimated from the integral area enclosed by the fracture curve [5]. Therefore, in the case of static tests, the suggested approach involving variation of different types of cross-links in EPP also affords more efficient dissipation of the mechanical energy. Evi-

dently, increase in the EPP strength with increasing PFR content is due to enhancement of the dissipative properties of these polymers.

CONCLUSIONS

(1) Dynamic tests showed that increase in the content of phenol–formaldehyde resins in epoxy-phenolic polymers tends to increase eventually the content of labile physical and decrease the content of stable chemical cross-links in the resulting three-dimensional network polymer.

(2) Dynamic and static tests suggest enhancement of the elastic and dissipative properties of these polymers in the glassy state and their weakening in the hyperelastic state.

(3) Analysis of the role of the dissipative properties of epoxy-phenolic polymers at the local and large-scale (segmental) levels of the molecular mobility of the polymer matrix during fracture upon extension of these materials shows the following. Articles subjected to large dynamic loads need the maximal amount of labile physical bonds and, thus, the maximal content of phenol–formaldehyde resins. Articles operating at elevated temperatures, when the deciding role is played by chemical covalent bonds, need a reduced content of phenol–formaldehyde resins and, thus, an increased density of the chemical cross-links.

ACKNOWLEDGMENTS

This work was financially supported by the Russian Foundation for Basic Research and the Regional Foundation (project no. 01-03-97009, r 2001 for near-Moscow region).

REFERENCES

1. Bartenev, G.M., *Prochnost' i mekhanizm razrusheniya polimerov* (Strength and Failure Mechanisms of Polymers), Moscow: Khimiya, 1984.
2. Smirnov, Yu.N., Magomedov, G.M., and Dzhamaeva, N.M., *Plast. Massy*, 1999, no. 7, pp. 28–34.
3. Smirnov, Yu.N., Magomedov, G.M., and Dzhamaeva, N.M., *Zh. Prikl. Khim.*, 2002, vol. 75, no. 1, pp. 113–119.
4. *Spravochnik po plasticheskim massam* (Reference Book on Plastics), Kataev, V.N., Popov, V.A., and Sazhin, B.I., Eds., Moscow: Khimiya, 1975, vol. 2.
5. Smirnov, Yu.N. and D'yankova, S.L., *Zh. Prikl. Khim.*, 2000, vol. 73, no. 5, pp. 819–825.
6. Perepechko, I.I., *Akusticheskie metody issledovaniya polimerov* (Acoustic Methods of Investigation of Polymers), Moscow: Khimiya, 1973.
7. Kulik, S.G., Elastification of Epoxy Polymers Aimed To Increase the Fracture Viscosity of Composite Materials Thereof, *Cand. Sci. Dissertation*, Moscow, 1979.
8. Volkov, V.P., Evdokimenko, N.M., Kartsovnik, V.I., *et al.*, *Mekhan. Polim.*, 1978, no. 2, pp. 248–251.
9. Trostyanskaya, E.B., Babaevskii, P.G., and Kulik, S.G., *Vysokomol. Soedin., Ser. A*, 1979, vol. 21, no. 6, pp. 1328–1333.
10. Andreevskaya, G.D. *Vysokoprochnye orientirovannye stekloplastiki* (High-Strength Oriented Fiber Glass Plastics), Moscow: Nauka, 1966.
11. Lee, H. and Nevill, K., *Handbook of Epoxy Resins*, New York: McGraw-Hill, 1967.
12. Smirnov, Yu.N. and Volkov, V.P., *Zh. Prikl. Khim.*, 2002, vol. 75, no. 4, pp. 625–632.
13. *Fracture of Nonmetals and Composites*, Liebowitz, H., Ed., New York: Academic, 1972, vol. 7, part 2.
14. Perepechko, I.I. and Kvacheva, L.A., *Vysokomol. Soedin., Ser. A*, 1971, vol. 13, no. 1, pp. 124–127.
15. Hata, H. and Kumanotani, J., *J. Appl. Polym. Sci.*, 1971, vol. 15, no. 11, pp. 2371–2375.
16. Shteinberg, V.G., Efremova, A.I., and Rozenberg, B.A., *Vysokomol. Soedin., Ser. A*, 1979, vol. 21, no. 6, pp. 1259–1263.
17. Bartenev, G.M. and Zelenev, Yu.V., *Vysokomol. Soedin., Ser. A*, 1975, vol. 14, no. 5, pp. 998–1009.
18. Smirnov, Yu.N., Magomedov, G.M., and Dzhamaeva, N.M., *Zh. Prikl. Khim.*, 2002, vol. 75, no. 1, pp. 113–119.
19. Aharoni, S.M., *J. Appl. Polym. Sci.*, 1972, vol. 16, no. 12, pp. 3275–3284.
20. Smirnov, Yu.N., Irzhak, V.I., and Rozenberg, B.A., *Vysokomol. Soedin., Ser. B*, 1983, vol. 25, no. 12, pp. 914–916.
21. Ponomareva, T.I., Irzhak, V.I., and Rozenberg, B.A., *Vysokomol. Soedin., Ser. A.*, 1978, vol. 20, no. 2, pp. 597–602.
22. Salamatina, O.B., Akopyan, E.L., Rudnev, S.N., *et al.*, *Vysokomol. Soedin., Ser. A.*, 1983, vol. 25, no. 1, pp. 179–195.
23. Smirnov, Yu.N., Natrusov, V.I., Ponomareva, T.I., and Shatskaya, T.E., *Plast. Massy*, 1985, no. 10, pp. 19–21.

Russian Journal of Applied Chemistry, Vol. 76, No. 11, 2003, pp. 1822–1828. Translated from Zhurnal Prikladnoi Khimii, Vol. 76, No. 11, 2003, pp. 1873–1879.

MACROMOLECULAR CHEMISTRY AND POLYMERIC MATERIALS

Formation of Strength Properties of Model Glue Joints Based on Epoxy–Amine Binders Cured by Polycondensation Mechanism

Yu. N. Smirnov and V. N. Korotkov

Institute for Problems of Chemical Physics, Russian Academy of Sciences, Chernogolovka, Moscow oblast, Russia

Received May 22, 2002; in final form, September 2003

Abstract—The kinetics of formation of strength properties were studied for a model glue joint based on epoxy–amine binder cured by the polycondensation mechanism at various temperatures. The binder curing kinetics were monitored. In the course of curing, shrinkage defects were studied and the glue joint fracture surface was examined.

In [1–3], we attempted chemical designing of high-strength epoxy-amine binders (EABs) for fiber glass plastics by combining the structural contributions from polycondensation and polymerization curing mechanisms. It was shown in [1, 3] that, with attaining the optimal structural microheterogeneity of the materials combined, this markedly enhances the cohesion strength of EABs, particularly their breaking strain, and also the fracture work. This makes these materials especially attractive as binders for composites [4]. However, high cohesion strength of the polymer matrix in a composite should be combined with high adhesion strength with respect to the reinforcing filler surface [5]. Studying the adhesion strength formation during composite molding is essential for chemical designing of high-strength fiber glass plastics. It is important to elucidate how different structural contributions from the combined different three-dimensional cross-linking processes affect the origination, number, and size of shrinkage and thermal defects, the corresponding strains, and their relaxation processes.

As known [6–8], in models simulating the three-dimensionally strained state of the matrix in composite materials, shrinkage strains arising in the course of curing of epoxy systems are responsible for shrinkage defects of the cohesion, adhesion, and mixed types. The type and pattern of evolution of shrinkage defects in the course of curing depend on the sequence of the two processes cross-linking the polymer matrix, namely, gelation (formation of a network of chemical bonds) and glass transition (formation of a network of labile physical bonds). As known [9, 10], the sequence of these processes is governed by the curing temperature, as well as by the chemical composition of the binder [11].

The aim of this work was to elucidate how the shrinkage defects and relaxation (dissipative) properties of the base epoxy–amine compound cured by the polycondensation mechanism affect formation of the strength properties of the model composites and their fracture in the course of curing. This is particularly important in view of the fact that shrinkage defects arising immediately during formation of articles from composite materials (CMs) are able of transformation in the course of cooling under thermal strains into extremely dangerous defects such as critical Griffits defects [12]. The latter stimulate further cohesion and adhesion fracture processes in CM articles operating under loads.

EXPERIMENTAL

Strength properties of the composites were studied with a glue joint model (GJM) obtained by gluing two $60 \times 25 \times 6$-mm glass plates. The plates were arranged crosswise and separated with an insert made of a fluoroplastic film to control the glue seam thickness (~120 μm). A hole cut in the insert allowed control of the glue joint area (d = 5 mm). The binder was poured into the hole in the insert, and the plates were pressed with a 250-g load and placed into a special stand and then into an oven. After keeping in the oven for a certain time, a batch of six samples was cooled to room

1070-4272/03/7611-1822$25.00

temperature. The remaining samples were cooled for some more time. Some samples were glued with pure epoxy resins without curing agent. The resins were heated to 120°C, poured into the hole in the insert, whereupon the plates were laid, pressed with a load, and cooled at a rate of 0.5 deg min^{-1}. The tensile strength of the glue joint σ_{glue} was determined at 20°C by extending the GJM with cross-shaped clamps at a rate of 3 mm min^{-1}. The average σ_{glue} was estimated from the data obtained in tests with six samples.

As the basic binder we used a compound based on ED-20 epoxy–4,4'-isopropylidenediphenol resin and *m*-phenylenediamine (*m*-PDA). The curing kinetics of the individual binder were studied calorimetrically on an EK-2 low-inertia calorimeter [13], using a torsion pendulum (torsion mass 9 g; a 60-mm-long VM-1 glass thread containing 25 wt % binder as the working unit); on a Rheotest-II viscometer [plate–cone design; gelation time at various temperatures was determined by extrapolating the linear section, corresponding to a sharp viscosity growth, to the abscissa (time axis) and, additionally, as the time of achievement of a conventional viscosity of 4000 P]; and tensometrically, on a setup described in [14].

Shrinkage defects were observed immediately during the isothermal synthesis in long glass tubes [8], when chemical shrinkage in the middle of the tubes creates an all-sided extended state [15] similar to the strained state of a matrix in a fibrous composite [7]. A fairly high adhesion between the system being cured and the glass surface afforded the initial shrinkage cohesion defects which further, under certain conditions, evolved into adhesion exfoliates.

Figure 1 presents typical kinetic plots of σ_{glue} for the ED-20 + *m*-PDA binder at curing temperatures lower than the limiting glass transition point for this system (155°C).

Unexpectedly, the run of these curves proved to significantly differ from that of the curing kinetic curves. For example, a characteristic feature of the time dependence of σ_{glue} was a maximum in the initial stage of the binder curing, preceding the gelation stage (the corresponding gelation onset time is indicated in the abscissa with arrows). Notably, the subsequent sections are characterized by steadily low σ_{glue}. At the same time, further growth and attainment of saturation by the σ_{glue} vs. time plot seems to naturally stem from development and further inhibition of the binder curing due to its vitrification (hardening). Figure 1 shows that the time of attainment of the maximum, σ_{glue}^{max}, tends to decrease and the corresponding σ_{glue}^{max}, σ_{glue}^{min}, and $\sigma_{glue}^{\leftarrow\infty}$, to increase with increasing experimental temperature T_{cur}. At T_{cur} = 100°C (Fig. 1, curve *3*), the previously observed σ_{glue} maximum is virtually degenerated. Notably, similar nontrivial variation of the glue joint strength was revealed for binders with other compositions such as, e.g., *N*,*N*,*N*',*N*'-tetraglycidyl-3,3'-dichloro-4,4'-diaminodiphenylmethane (EKhD grade)–aniline, ED-20–4,4'-diaminodicyclohexylmethane, and ED-20–benzyldimethylamine.

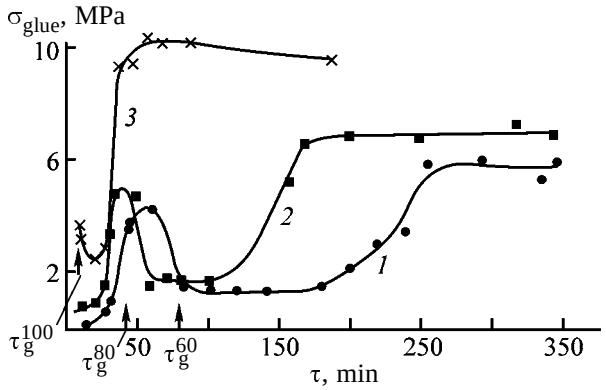

Fig. 1. Glue joint strength σ_{glue} as a function of the curing time τ. (τ_g) Gelation time; the same for Fig. 2. *T*, °C: (*1*) 60, (*2*) 80, and (*3*) 100.

Curing was studied at temperatures of 40–120°C differing from both the test temperature (20°C) and the limiting glass transition point (155°C). Therefore, when analyzing the pattern of variation of the glue joint strength in the course of curing, it is necessary to take into account the fact that the binder in the GJM before the tests can generally change its physical state by five different pathways: liquid state (LS) at $T_{cur} \rightarrow$ LS at T_{test}, LS at $T_{cur} \rightarrow$ glassy state (GS) at T_{test}, LS at $T_{cur} \rightarrow$ hyperelastic state (HES) at $T_{cur} \rightarrow$ HES at T_{test}, LS at $T_{cur} \rightarrow$ HES at $T_{cur} \rightarrow$ GS at T_{test}, LS at $T_{cur} \rightarrow$ GS at $T_{cur} \rightarrow$ GS at T_{test}.

Realization of particular pathway depends on the sequence of the two cross-linking processes, gelation and glass formation, for a given composition of the binder and specific curing and test temperatures.

The glue joint strength should be determined, above all, by the physical state of the binder in GJM at T_{test} (LS, HES, or GS) governing the elasticity modulus on GJM extension. However, essential is also the final physical state of the binder at T_{cur}, which determines the nature of the transition on cooling to T_{test} and, hence, the free excess volume and its distribution over holes (voids) [16, 17], as well as the residual (shrinkage and particularly thermal) internal stresses. Thus, σ_{glue} can vary in the course of curing

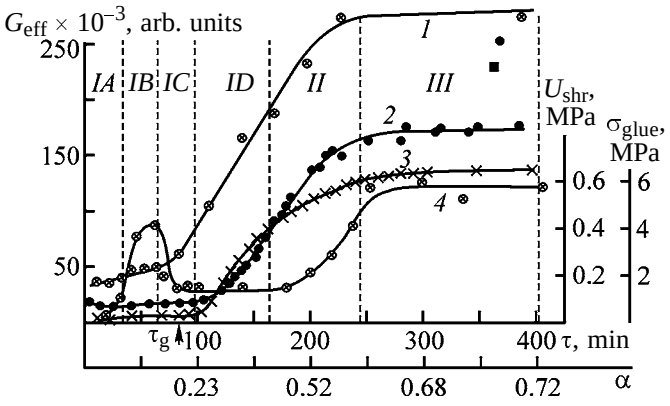

Fig. 2. Variation of the effective elasticity modulus G_{eff} at (*1*) 20°C (G_{eff}^{20}) and (*2*) 60°C (G_{eff}^{60}), and (*3*) shrinkage stresses U_{shr} and (*4*) glue strength σ_{glue} with time τ and conversion α. Fracture time intervals: (*IA–ID*) cohesion, (*II*) cohesion–adhesion, and (*III*) adhesion.

not only with the conversion of the functional groups and cross-linking density but also with the physical history of the binder in GJM.

Figure 2 combines the results of the kinetic studies at T_{cur} = 60°C. It should be noted that, to distinguish more clearly between the two cross-linking processes, we studied gelation in separate, on a highly sensitive rotation viscometer. The kinetic viscosity curves exhibited a typical run [18, 19] and consisted of two sections corresponding to slow and fast viscosity growth, respectively. The gelation onset time τ_g^T (T is the temperature, °C) in these curves was estimated by extrapolating to abscissa (time axis) the linear section corresponding to fast growth. In Figs. 1 and 2, the respective τ_g^T values are shown with arrows at the abscissa, and the corresponding temperatures are indicated. Glass transition (hardening) of the binder at room and other temperatures was studied with a less sensitive torsion pendulum adjusted to recording changes in the torsion rigidity of the thread due to the liquid–glass transition only. The growth of the binder viscosity in the initial curing stages is due to enhancement of its dissipative properties (the ability of dissipating energy during the relaxation process) in the liquid state. In this work, we did not estimate the dissipative (relaxation) properties of the binder in the hyperelastic and glassy states and gave them only general consideration. Curve *1* in Fig. 2 shows how the effective elasticity modulus at room temperature, G_{eff}^{20}, varies with swinging of the thread of the torsion pendulum at room temperature. Notably, in these experiments the set of impregnated threads was kept at 60°C for a certain time. Next, one of the threads was cooled for a certain time to room temperature, at which G_{eff}^{20} was measured.

Curve *2* in Fig. 2 shows how the elasticity modulus at T_{cur} = 60°C, G_{eff}^{60}, varies with thread swinging. The G_{eff}^{60} growth onset at τ = ~115 min corresponds to the glass transition onset. Notably, this time coincides with the hardening time determined for the system by the method of penetration of a glass rod into the binder being cured. The attainment of saturation by curve *2* at τ = ~240 min suggests that glass transition virtually terminates at this curing temperature.

To elucidate how the physical state (LS, HES, or GS) of the binder in the GJM affects the glue joint strength in various stages of the chemical and physical cross-linking, we will analyze the whole set of the kinetic data and also the pattern of fracture of the glue interlayer in the GJM. This pattern can be derived from optical studies of the fracture surface image at ×10 magnification. Notably, in the course of curing the loaded GJM undergoes fracture of three major types: (*I*) cohesion, (*II*) cohesion–adhesion, and (*III*) adhesion. These fracture types generally correspond to the defects arising from spontaneous fracture of the binder due to shrinkage strains directly at T_{cur} [6–8]. Thermal strains in the course of cooling and the external load do not principally affect the GJM fracture pattern at T_{test}.

In early curing stages (until ~30 min), the binder at T_{cur} and T_{test} occurs in the viscous-flow LS, and upon cooling its viscosity increases only. The cohesion fracture of GJM has a liquid nature. During separation of the plates, bubbles are formed and degrade (Fig. 3a). The time interval corresponding to this type of cohesion fracture is designated in Fig. 2 as section *IA*. A minor σ_{glue} growth is due to the viscosity growth in the course of curing.

Within 35–60 min, the binder at T_{cur} and T_{test} also occurs in the LS. Upon cooling to T_{test}, the viscosity markedly increases, but the G_{eff}^{20} growth rate remains unchanged (Fig. 2, curve *1*). The cohesion fracture in this stage has a plastic nature and is characterized by weakly manifested surface relief features. This fracture type is illustrated in Fig. 3b, and its corresponding time interval is indicated as section *IB* in Fig. 2. This section is characterized by a major primary growth of the glue joint strength.

In the 65–90 min interval, the binder, occurring in the LS at T_{cur}, exhibits the onset of transition to the solid state upon cooling. A fairly sharp inflection appears in curve *1*. At T_{cur}, the viscosity begins to rapidly grow to a conventional value of 4000 P (at 60°C

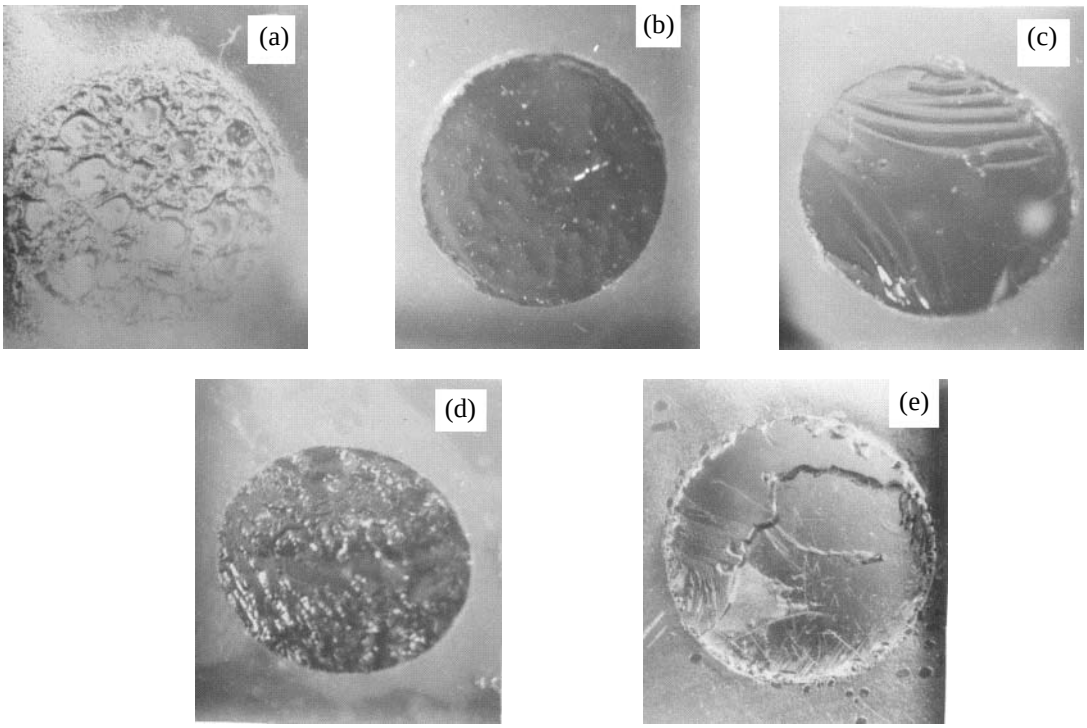

Fig. 3. GJM fracture surface image. τ, min: (a) 0–25, (b) 25–65, (c) 65–90, and (d) 90–160, and (e) 160–240.

within 83 min); no growth of shrinkage stresses is observed (Fig. 2, curve *3*). Shrinkage defects in the tubular model samples do not form yet, but the glue joint strength drastically decreases. From the time at which σ_{glue} begins to decrease till that at which it attains saturation, fracture is brittle by nature and exhibits clear shear bands typical for GJMs glued with low-molecular-weight glassy substances (e.g., ED-8 glassy epoxy resin). This fracture type is illustrated by Fig. 3c, and its corresponding time interval is indicated as section *IC* in Fig. 2. The inflection in curve *1*, transformation of the binder into brittle state, and a sharp decrease in the glue strength directly indicate the onset of glass transition of the binder at T_{test}. Notably, this is the first physical transition in the binder manifested at room temperature. The conversion of the binder attained by that time can be treated as critical for attaining the GS of the binder (α_{ph1}) [19]. This parameter is of practical importance for predicting the life of intermediate prepregs in storage.

To tentatively analyze variation of the glue joint strength within the *IA*–*IC* intervals, we will take advantage of the Griffits formula for the critical strength σ_{cr} [12]:

$$\sigma_{cr} = (2E\gamma/\pi l_{cr})^{1/2}$$

were E is Young modulus; γ, specific surface energy; and l_{cr}, critical defect size.

This formula interrelates the major factors governing the strength of solid materials: elasticity factor E, the l_{cr} factor characterizing the structural defectiveness, and the γ-relaxation (dissipative) factor (according to Berry [12]). This equation was already used for analyzing the glue joint strength of elastomers [21]. It suggests that a sharp increase in the glue joint strength in going from section *IA* to *IB* cannot be due only to enhancement of the flexible properties of the binder, as the G_{eff}^{20} growth rate in curve *1* (Fig. 2) remains unchanged. Thus, with invariant structural defectiveness factor, the growth of the glue joint strength should, evidently, be due to growth of the dissipative factor γ (owing to the binder viscosity growth). At the same time, a sharp decrease in the glue joint strength in going from section *IB* to *IC* (when the fracture mechanism changed from plastic to brittle) should, evidently, be attributed to a decrease in the dissipative factor owing to the change in the physical state of the glue interlayer. It should be noted that transition from plastic to brittle fracture means transition from fracture involving relaxation processes characterized by viscous energy dissipation and, correspondingly, large γ values, to fracture characterized by small γ values, which are virtually equal to the energy of new surface formation proper.

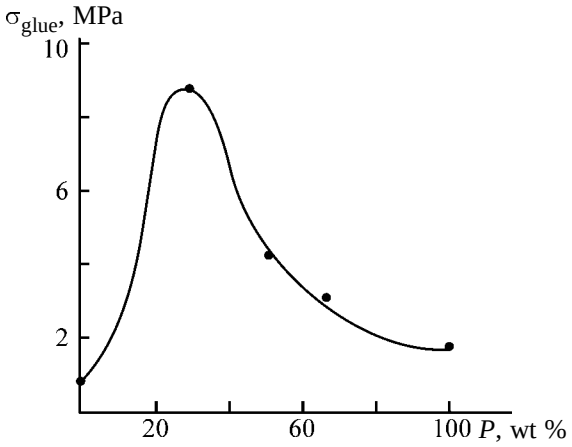

Fig. 4. Variation of the glue joint strength σ_{glue} with the content P of ED-16 and ED-8 epoxy resins.

The changes in the physical state of the binder in early curing stages were reproduced by plates glued with straight epoxy resins ED-16 (simulating a highly viscous liquid medium) and ED-8 (simulating fully glassy medium at room temperature).

Figure 4 shows that, on varying the ED-16-to-ED-8 resin ratio, σ_{glue} passes through a prominent maximum at 25 wt % of ED-8, with σ_{glue} being fairly high at a maximum.

Thus, the changes in the glue joint strength and in the GJM fracture pattern in the *IA*–*IC* intervals can be treated as due to the changes in the physical state of the binder at T_{test} owing to partial chemical transformations of the initial compound, namely, formation of linear chains or local microgels, rather than to the onset of the chemical cross-linking with formation of a macrogel. The microgels can be formed in the case of microheterogeneous chemical cross-linking.

It is believed [22] that formation of microgel structures is much less probable (and, correspondingly, the degree of microheterogeneity of the network structure is smaller) in the case of polycondensation than in the case of radical polymerization [23]. However, under the actual conditions [low curing temperature and high viscosity, sharply increasing during vitrification (hardening) of the binder], the probability of microheterogeneous cross-linking of the binder should be fairly high [24–26]. The microheterogeneous nature of the network structure of the binder in the HES can be responsible for microheterogeneous structure of the binder in the GS upon cooling, when locally vitrified microvolumes of the binder can be distributed in a highly viscous liquid medium and act as viscous energy dissipation sites. Their growth in number before complete transition of the binder to the glassy state (which can be treated as percolation) should initially favor substantial enhancement of the dissipative properties of the binder followed by their weakening upon transition of the binder to completely solid (brittle) state. This process resembles fracture of amorphous-crystalline polymers depending on the size and number of crystallites [27].

Within 90–180 min (*ID*, *II*), the observed pattern of variation of the glue joint strength was unexpected. Despite doubling of the conversion of the functional groups within this interval, σ_{glue} remains unchanged. The GJM fracture in this interval is plastic by nature, when the microrelief features of the fracture surface are more pronounced (Fig. 3d; Fig. 2, section *II*). At the same time, in the case of the tubular model samples, shrinkage stresses begin to grow at T_{cur}, and shrinkage defects appear. Also, glass transition of the binder begins and intensively develops at T_{cur} (G_{eff}^{60} grows; Fig. 2, curve *2*). Within this time interval, a secondary physical transition is manifested in the binder due to formation of a macronetwork of physical bonds (glass formation) at T_{cur}. The critical degree of the transition was estimated at 0.63. At T_{test}, the elasticity of the binder in the GS continues to substantially grow (curve *1*).

The reasons for the lack of growth of the glue joint strength in the time interval of interest still remain to be fully understood. The above-presented formula suggests two major factors responsible for the σ_{glue} invariance. The growth of the elasticity factor and the constancy of the relaxation factor can involve the compensation growth of the defectiveness factor (including growth of the sizes of the defects and internal strains localized in their vicinity). This is in line with the growth of the number and size of the shrinkage defects and shrinkage stresses observed within the interval of interest in the case of tubular model samples. The growth of the elasticity factor can also be compensated by a decrease in the relaxation factor. However, this seems less probable in the considered stage of the physical and chemical cross-linking of the binder when the gel fraction has already started to form. In terms of the model of microheterogeneous cross-linking of the binder, γ can be treated as constant, under assumption that a uniform macronetwork structure has not yet formed in this stage. The binder consists of unlinked microgels and at T_{cur} occurs essentially in a highly viscous LS, rather than in the HES. Upon cooling, the binder entirely transforms to the GS with presumably globular structure. Evidently, this specifically predetermines the cohesion fracture mechanism for GJM, with prominent surface microrelief features. The glass formation in the binder,

which began at T_{cur}, is accompanied by "freezing-out" of the mobility of the largest microstructure units. This, evidently, is responsible for even greater localization of the chemical cross-linking and yields microstructure units with a small dimensionality, with the concentration of elastically active chains remaining virtually unchanged.

Within the time interval from the glass transition onset (115 min) to virtual completion (260–270 min), the conversion of the functional groups of the binder increases from 0.3 to 0.65. Nevertheless, the final macrostructurization (monolithization) of the binder can proceed as a physical process of vitrification of a microheterogeneous medium by formation of physical intermolecular contacts between glassy microvolumes based on the most strongly cross-linked microgels that already lost their mobility, rather than as a chemical process of formation of an infinite network of covalent bonds. Evidently, at low curing temperatures, the onset of monolithization of the binder, i.e., formation of a macronetwork of physical bonds or macrovitrification at T_{cur}, is specifically responsible for the secondary growth of the glue joint strength.

At higher curing temperatures, the secondary growth of σ_{glue}, taking into account the growth of the elasticity factor E and defectiveness factor l_{cr}, can be due to the outrunning enhancement of the dissipative properties of the binder owing to accelerated growth of the gel fraction content.

Notably, the section corresponding to rapid secondary growth of σ_{glue} begins approximately in the middle of the section corresponding to the G_{eff}^{60} growth at T_{cur}. The enhancement of the elastic properties of the binder during glass formation owing to chemical cross-linking is similar, in principle, to that of elastic dynamic properties of network polymers during glass transition upon cooling. In the latter case, the average change in the elastic properties during glass transition typically corresponds to the maximum mechanical losses in the polymer [28]. The enhancement of the dissipative properties and, correspondingly, of the binder strength is specifically responsible for transition from cohesion to adhesion fracture for GJM, as suggested by the appearance of adhesion defects in the transition region *II* in Fig. 3e, observed in tubular model samples.

After the GJM fracture changes eventually to adhesion mechanism (~240 min, α = 0.62) until attaining the limiting conversion at 60°C (α_∞ = 0.72, ~420 min), the growth of the elasticity moduli in swinging at 20 and 60°C virtually terminates, as well as the growth of shrinkage stresses and glue joint strength, but in tubular samples the adhesion defects continue to slowly grow. Transformation of the functional groups of the binder and growth of the content of the gel fraction seem to be responsible for further enhancement of the strength of the binder and, thus, of the GJM. But the limiting stage of the GJM fracture is fracture along the glass–binder interface. The above-presented formula suggests that, with a constant elasticity factor, the growth of the relaxation factor is compensated by that of the defectiveness factor (with the adhesion defects dominating). Also, further growth of the degree of the binder curing in the glassy state can deteriorate the relaxation characteristics of the glue interlayer, enhance localization of stresses near the glass–binder interface, and increase the importance of the adhesion factors.

Evidently, the adhesion contribution to the GJM strength and the adhesion defects are specifically responsible for a fairly low limiting glue joint strength. For the actual curing temperature range and glue composition range, it was estimated at 6–20 MPa, and the strength of the binders proper, at 60–90 MPa. This requires paying particular attention to strengthening of the glass–gluing seam interface in further studies.

CONCLUSIONS

(1) With ED-20–*m*-phenylenediamine compound cured by the polycondensation mechanism as a binder, the glue joint exhibits substantially nonmonotonic variation of the strength during isothermal curing. This is due to the action of two relaxation processes in the glue interlayer (vitrification of the binder at room and curing temperatures) and gelation, as well as to changes in the fracture mechanism of the model glue joint.

(2) The first strength maximum for the model glue joint corresponds to transition of the binder from the viscous-flow to glassy state. It is due to the action of two competitive factors: enhancement of the dissipative properties due to viscosity growth because of proceeding of the curing reaction and hardening and, correspondingly, transformation of the binder to brittle state at the test temperature. These findings are interpreted in terms of the model of microheterogeneous cross-linking of the binder.

(3) A fairly long section characterized by a low and virtually constant σ_{glue}^{min} value is, evidently, due to growth of the contribution from shrinkage defects and stresses.

(4) The revealed initial growth and further decline of the strength of the model glue joints is of practical importance: Forced cooling of glued and, correspondingly, glass fiber plastic articles in the appropriate time interval can produce dangerous defects irremovable by further heating.

(5) Worsened relaxation characteristics of the binder and concentration of thermal stresses at the glass–polymer interface predetermines inevitable transition to adhesion fracture of the model glue joints, thus decreasing the overall strength of the glue joint.

ACKNOWLEDGMENTS

This work was financially supported by the Russian Foundation for Basic Research jointly with the Regional Foundation (project no. 01-03-97009, r2001 for near-Moscow region).

REFERENCES

1. Smirnov, Yu.N., Komarov, B.A., and Kushch, P.P., *Plast. Massy*, 2001, no. 9, pp. 26–29.
2. Smirnov, Yu.N., Komarov, B.A., Kushch, P.P., *et al*., *Plast. Massy*, 2001, no. 11, pp. 6–12.
3. Smirnov, Yu.N., Komarov, B.A., Kushch, P.P., *et al*., *Zh. Prikl. Khim*., 2002, vol. 75, no. 2, pp. 274–285.
4. Enikolopyan, N.S., *Zh. Vses. Khim. O–va. im. D.I. Mendeleeva*, 1978, vol. 23, no. 3, pp. 243–245.
5. Gorbatkina, Yu.A., *Adgezionnaya prochnost' v sistemakn polimer–volokno* (Adhesion Strength in Polymer–Fiber Systems), Moscow: Khimiya, 1987.
6. Chekanov, Yu.A. Korotkov, V.N., Rozenberg, B.A., *et al*., *J. Mater. Sci*., 1993, vol. 28, no. 12, pp. 3860–3867.
7. Korotkov, V.N., Chekanov, Yu.A., and Rozenberg, B.A., *Vysokomol. Soedin., Ser. A*, 1994, vol. 36, no. 4, pp. 684–689.
8. Chekanov, Yu.A., Korotkov, V.N., Djavadjan, Dj.A., and Bogdanova, L.M., *Polymer*, 1995, vol. 36, no. 10, pp. 2013–2019.
9. Enns, J.B. and Gillham, J.K., *J. Appl. Polym. Sci*., 1983, vol. 28, no. 11, pp. 2567–2574.
10. Wisanrakkit, G. and Gillham, J.K., *J. Appl. Polym. Sci*., 1990, vol. 41, no. 12, pp. 2885–2892.
11. Chekanov, Yu.A., Defect Formation in Curing of Epoxy Resins, *Cand. Sci. Dissertation*, Chernogolovka, 1995.
12. *Fracture. An Advanced Treatise*, Liebowitz, H., Ed., New York: Academic, 1972. Translated under the title *Razrushenie*, Moscow: Mir, 1976, vol. 7, part 2, p. 24.
13. Dzhavadyan, E.A., Galyuk, O.S., and Rozenberg, B.A., *Zavod. Lab*., 1979, no. 3, pp. 228–230.
14. Korotkov, V.N., Chekanov, Yu.A., Smirnov, Yu.N., and Zenkov, I.D., *Vysokomol. Soedin., Ser. A*, 1996, vol. 38, no. 6, pp. 1025–1029.
15. Korotkov, V.N., *Vysokomol. Soedin., Ser. A*, 1997, vol. 39, no. 4, pp. 630–639.
16. Salamatina, O.B., Vinnik, R.N., Artemenko, S.A., *et al*., *Vysokomol. Soedin., Ser. A*., 1981, vol. 23, no. 1, pp. 23–31.
17. Smirnov, Yu.N., Ponomareva, T.I., Irzhak, V.I., and Rozenberg, B.A., *Vysokomol. Soedin., Ser. B*, 1982, vol. 24, no. 2, pp. 128–131.
18. Smirnov, Yu.N., Kruzhkova, S.V., Shatskaya, T.E., and Natrusov, V.I., *Plast. Massy*, 2002, no. 6, pp. 18–23.
19. Dzhavadyan, E.A., Irzhak, V.I., and Rozenberg, B.A., *Vysokomol. Soedin., Ser. A*, 1999, vol. 41, no. 4, pp. 623–627.
20. Smirnov, Yu.N., Shatskaya, T.E., Natrusov, V.I., and Lapitskii, V.A., *Plast. Massy*, 1986, no. 7, pp. 24–27.
21. Gent, A.N., *J. Polym. Sci*., 1971, vol. 9, no. 2, pp. 283–288.
22. *Polymer Networks'91*, Dusek, K. and Kuchanov, S.I., Eds., Utrecht: VSP, 1992, p. 7.
23. Korolev, G.V., Mogilevich, M.M., and Golikov, I.V., *Setchatye poliakrilaty* (Network Polyacrylates), Moscow: Khimiya, 1995.
24. Bogdanova, L.M., Dzhavadyan, E.A., Irzhak, V.I., and Rozenberg, B.A., *Vysokomol. Soedin., Ser. B*, 1979, vol. 21, no. 9, pp. 683–686.
25. Irzhak, V.I., Peregudov, N.I., and Rozenberg, B.A., *Dokl. Akad. Nauk SSSR*, 1982, vol. 263, no. 3, pp. 362–365.
26. Zuttgert, K.E. and Bourt, K., *Prog. Colloid Sci*., 1978, vol. 64, no. 1, pp. 38–43.
27. Gul', V.E., *Struktura i prochnost' polimerov* (Structure and Strength of Polymers), Moscow: Khimiya, 1971.
28. Perepechko, I.I., *Akusticheskie metody issledovaniya polimerov* (Acoustic Methods of Investigation of Polymers), Moscow: Khimiya, 1973.

Russian Journal of Applied Chemistry, Vol. 76, No. 11, 2003, pp. 1829–1831. Translated from Zhurnal Prikladnoi Khimii, Vol. 76, No. 11, 2003, pp. 1880–1882.

MACROMOLECULAR CHEMISTRY AND POLYMERIC MATERIALS

Uranyl Sulfoxide Complexes as Photoinitiators of Polymerization of Methyl Methacrylate and Epoxy Acrylate Oligomers

E. M. Battalov, G. V. Leplyanin, and Yu. I. Murinov

Institute of Organic Chemistry, Ufa Scientific Center, Russian Academy of Sciences, Ufa, Bashkortostan, Russia

Received April 16, 2003

Abstract—Photoinitiation activity of uranyl sulfoxide complexes in polymerization of methyl methacrylate and epoxy acrylate derived from ED-16 and acrylic acid, and also the postirradiation effects in photopolymerization of these monomers were studied.

The behavior of uranyl salts in radical polymerization is of interest. These compounds are inactive in the thermal initiation of polymerization, but they are fairly active photoinitiators [1]. In this work, we studied photopolymerization of methyl methacrylate (MMA) initiated with uranyl sulfoxide complexes, which are infinitely soluble in MMA monomer.

EXPERIMENTAL

Methyl methacrylate was purified to remove the stabilizer by the method described in [3]. Uranyl sulfoxide complexes were synthesized by the method of [3]. Polymerization was performed in the bulk at a temperature controlled with ±0.05°C accuracy. The photopolymerization kinetics was studied dilatomertically with molybdenum glass dilatometers. Epoxy acrylate polymer was synthesized as in [4]. A PRK-4 mercury lamp was used as a UV source; the distance between the light source and reactor was 14 cm in all experiments. The dynamic viscosity was measured with a Rheotest 2.1 device. The spectra of the samples were recorded on a Specord UV VIS spectrophotometer.

Whyte and Melville were the first who studied uranyl salts as photopolymerization initiators [5]. They found that, at low concentrations of uranyl sulfate, the rate of photopolymerization of vinyl acetate and methacrylic acid is proportional to the square root of the salt concentration. Okamura and Motoyama [6] confirmed this dependence when studying vinyl acetate photopolymerization activated with uranyl nitrate and oxalate in the systems with water and acetic acid. They observed reduction of U(VI) to U(IV) and assumed the following reaction scheme taking into account the presence of water:

$$UO_2^{2+} + 2H_2O \rightarrow U^{4+} + 2OH^- + 2OH^{\cdot}.$$

Simionescu *et al.* [7] studied photopolymerization of acrylonitrile in the presence of uranyl salts and found that the initiation activity decreases in the series $UO_2SO_4 > UO_2(OAc)_2 > UO_2(NO_3)_2$.

Polymerization occurs by radical mechanism, and the polymer obtained has amorphous structure. The subsequent studies [8–10] on using uranyl salts as polymerization photoinitiators were aimed at comprehensive elucidation of the initiation mechanism.

The kinetic curves of MMA polymerization in the presence of uranyl nitrate sulfoxide complex under UV irradiation are shown in Fig. 1. As seen, the polymerization rate increases by a factor of approximately

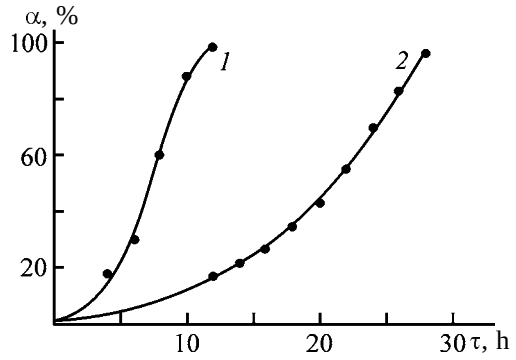

Fig. 1. Kinetic curves of MMA polymerization at 50°C (*1*) in the presence of 0.05 wt % $UO_2(NO_3)_2 \cdot 2$DASO (DASO is diamyl sulfoxide) and (*2*) without additions. (α) Conversion and (τ) time; the same for Fig. 4.

1070-4272/03/7611-1829$25.00

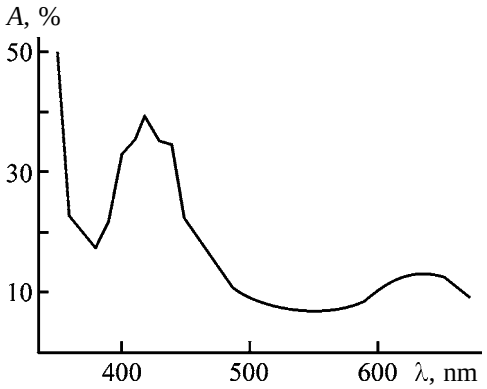

Fig. 2. Transmittance spectrum of MMA (d = 5 mm) in the presence of 0.08 wt % $UO_2(NO_3)_2 \cdot 2DHSO$ (DHSO is dihexyl sulfoxide). (A) Transmittance and (λ) wavelength.

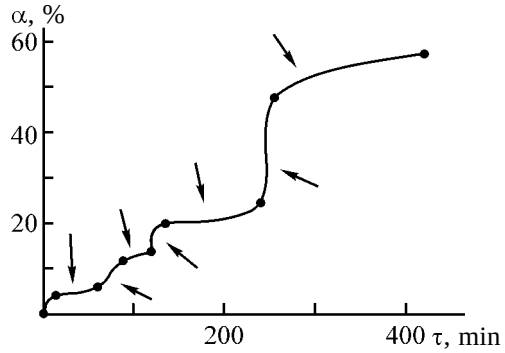

Fig. 3. Kinetics of MMA photopolymerization in the presence of 0.05 wt % $UO_2(NO_3)_2 \cdot 2DASO$ under the irradiation at λ = 430 nm (arrows bottom-up) and λ = 600 nm (arrows top-down) at 50°C. (α) Conversion and (τ) time.

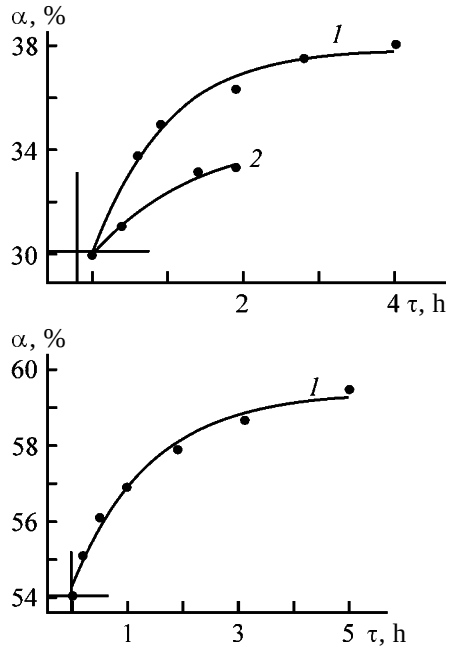

Fig. 4. Kinetic curves of postirradiation effects in MMA polymerization at 50°C in the presence of 0.5 wt % (*1*) $UO_2 \cdot (NO_3)_2 \cdot 2DASO$ and (*2*) diacetyl at various conversions.

2, i.e., this complex exhibits photoinitiation activity. The photoinitiation mechanism probably involves sensitization of polymerization of vinyl monomers with uranyl (sulfate, nitrate, oxalate, etc.) and was discussed previously in numerous papers [5–10]. The following photoinitiation mechanism presented in [6] is apparently the most realistic:

$$UO_2^{++} \xrightarrow{+h\nu} [UO_2^{++}]^*, \quad (1)$$

$$[UO_2^{++}]^* \rightarrow UO_2^{++} + \Delta, \quad (2)$$

$$[UO_2^{++}]^* \rightarrow UO_2^{++} + h\nu^1, \quad (3)$$

$$[UO_2^{++}]^* + M \rightarrow [UO_2^{++} + M]^*, \quad (4)$$

$$[UO_2^{++} + M]^* \rightarrow UO_2^{++} + M^*, \quad (5)$$

$$[UO_2^{++} + M]^* \rightarrow UO_2^{++} + R^*, \quad (6)$$

$$M^* + M \rightarrow 2R_1^{\cdot}, \quad (7)$$

$$M^* \rightarrow \Delta^1, \quad (8)$$

$$R_1^{\cdot} + M \rightarrow R_2^{\cdot}, \quad (9)$$

$$R_m^* + R_n^* \rightarrow P_m + P_n. \quad (10)$$

Photoinitiation occurs only under the action of light with λ = 430 nm, which is absorbed by the central atom of the complex (Fig. 2). The kinetic curves of MMA polymerization in the presence of a uranyl nitrate sulfoxide complex under irradiation with light at 430 and 600 nm are shown in Fig. 3. As seen, the rate of MMA polymerization in the presence of the amy sulfoxide complex under irradiation by light with the wavelength in the region of uranyl absorption (Fig. 2) is higher compared to irradiation at the wavelength of the ligand absorption. This suggests the major role of uranyl in the polymerization initiation. Probably, sensitization with uranyl complexes proceeds just by the above scheme. The stepwise character of polymerization under irradiation by light with different wavelengths suggests different polymerization rates and the possibility of performing the reaction in the controllable mode.

It should be noted that the MMA polymerization in the presence of uranyl complexes is accompanied by strong postirradiation effects. For comparison, the postirradiation effect of such well-known photoinitiator as diacetyl is shown in Fig. 4. The reason of this effect is poorly understood.

Afterpolymerization is also characteristic for epoxy acrylate oligomers, e.g., ED-16-AA (products of reaction of diepoxide ED-16 with acrylic acid) after short UV irradiation, especially in the presence of uranyl

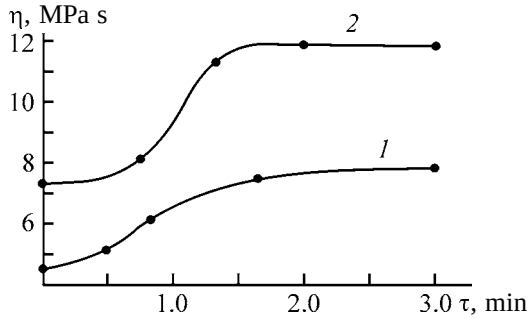

Fig. 5. Kinetic curves of dynamic viscosity η of epoxy acrylate oligomer ED-16-AA after UV irradiation for 15 s in the presence of (*1*) 1.0 wt % benzophenone and (*2*) 0.08 wt % $UO_2(NO_3)_2 \cdot 2DASO$ at 60°C. (τ) Time; the same for Fig. 6.

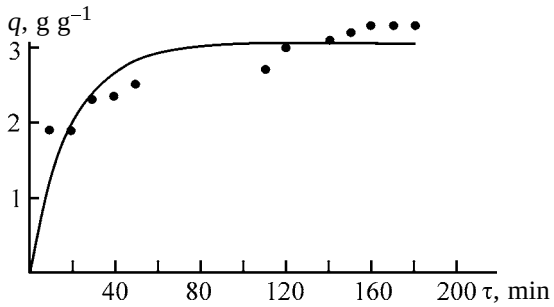

Fig. 6. Kinetics of swelling *q* in trichloroethylene of epoxy acrylate polymer ED-16–AA prepared in the presence of uranyl nitrate sulfoxide complex. UV irradiation of the initial oligomer 15 min.

nitrate sulfoxide complex (Fig. 5). Benzophenone as a photoinitiator gives a weaker postirradiation effect. Variation of the dynamic viscosity of this oligomer in time after 15 s of preliminary UV irradiation is an indirect evidence of postpolymerization in the presence of photoinitiators. In the system studied, there are no mechanisms other than postpolymerization under the action of long-lived radicals that could be responsible for variation of the dynamic viscosity.

The kinetics of swelling of the epoxy acrylate polymer prepared by photopolymerization in the presence of uranyl nitrate complex with petroleum sulfoxides is shown in Fig. 6. As seen, this polymer weakly swells in trichloroethylene and is classed with cross-linked products.

Thus, uranyl sulfoxide complexes are photoinitiators of MMA polymerization and of photoinduced cross-linking of epoxy acrylate oligomers. Cross-linked polymeric products are formed under irradiarion of epoxy acrylate oligomers in the presence of uranyl sulfoxide complexes. Polymerization of both MMA and epoxy acrylate oligomers is accompanied by increased postirradiation effects as compared to standard photoinitiators (dibenzoyl, diacetyl, benzophenone).

CONCLUSIONS

(1) Uranyl sulfoxyde complexes are fairly efficient photoinitiators of polymerization of methyl methacrylate and epoxy acrylate oligomer.

(2) The monomers studied show increased afterpolymerization effect.

(3) The polymerization rate can be controlled by varying the irradiation wavelength.

REFERENCES

1. Leplyalin, G.V., Battalov, E.M., and Murinov, Yu.I., *Vysokomol. Soedin*., 1988, vol. 30, no. 3, pp. 223–226.
2. *Monomery* (Monomers), Korshak, V.V., Ed., Vol. 1, Moscow, 1951.
3. Nikitin, Yu.E., Kolosnitsyn, V.S., Murinov, Yu.I., and Baranovskaya, E.M., *Neftekhimiya*, 1976, vol. 16, no. 3, pp. 299–303.
4. Zadontsev, B.P., Baranovskii, L.A., and Baranovskaya, N.F., *Epoksiakrilovye smoly: Obzor informatsii. Khimicheskaya promyshlennost'. Epoksidnye smoly i materially na ikh osnove* (Epoxy Acrylic Resins: Information Review. Chemical Industry. Epoxy Resins and Derived Materials), Moscow: NIITEKhIM, 1981.
5. Whyte, R.B. and Melville, H.W., *J. Soc. Dyers Colour*., 1949, vol. 65, pp. 705–708.
6. Okamura, S. and Motoyama, T., *Mem. Fac. Eng. Kyoto Univ*., 1959, vol. 21, pp. 312–321.
7. Simionescu, C., Feldman, D., and Hrihorov, M., *Rev. Chim. Acad. Rep. Popul. Roum*., 1962, vol. 7(2), pp. 1293–1310.
8. Mahadevan, V. and Santappa, M., *J. Polym. Sci*., 1961, vol. 2, pp. 361–378.
9. Venkatarao, K. and Santappa, M., *J. Polym. Sci*., 1967, vol. 5, pp. 637–649.
10. Venkatarao, K. and Santappa, M., *J. Polym. Sci*., 1970, vol. 8, pp. 3429–3433.

Russian Journal of Applied Chemistry, Vol. 76, No. 11, 2003, pp. 1832–1834. Translated from Zhurnal Prikladnoi Khimii, Vol. 76, No. 11, 2003, pp. 1883–1885.

MACROMOLECULAR CHEMISTRY AND POLYMERIC MATERIALS

Diffusion Modification of Polymethyl Methacrylate with Oligoglycol Acrylates

L. A. Abdrakhmanova, V. Kh. Fakhrutdinova, and V. G. Khozin

Kazan State Architectural and Building Academy, Kazan, Tatarstan, Russia

Received June 18, 2003

Abstract—The structural transformations of oligoglycol acrylates in the surface layers of polymethyl methacrylate were studied.

Surface bursting resulting in development of cracks with the depth of 1–2 mm and more ("silver" formation) is characteristic of polymethyl methacrylate (PMMA) plexiglass. Under conditions of artificial and natural aging, evaporation of low-molecular-weight substances, and action of various factors, significant defects are formed, altering the physicomechanical, optical, and other characteristics of plexiglasses. Factors deteriorating the strength of the surface layer of glass play an extremely important part in appearance of "silver." The appearance of "silver" is especially affected by almost all organic solvents.

The real method of strengthening the surface layers is creation of gradient interpenetrating networks (IPNs) [1–3], blends of three-dimensional polymers in which concentrations of components vary through the cross section of the sample. Introduction of oligoglycol acrylates of various structures, polymers based on which are characterized by increased softening point and hardness [4], into the surface layers of PMMA allows production of materials of the gradient semi-IPN type with enhanced performance.

Diffusion swelling of PMMA in oligoglycol acrylates, ethylene glycol dimethacrylate (EGDMA), triethylene glycol dimethacrylate (TEGDMA), and polyethylene glycol dimethacrylate (PEGDMA), was carried out at 37, 42, and 50°C. The degree of swelling of PMMA in the oligomers is presented in Table 1. The kinetic curves of PMMA swelling in acrylates at 50°C are shown in Fig. 1.

Table 1 shows that, with increasing molecular weight (correspondingly, with decreasing fraction of acrylate groups in oligomer molecules), the degree of swelling increases. Apparently, the rate of polymerization of oligoglycol acrylates increases with decreasing their molecular weight, which results in an increase in the viscosity of oligoglycol acrylates in the course of diffusion and, correspondingly, in a decrease in swelling.

To identify the spectra of the gradient PMMA, we recorded the IR spectra of polyglycol acrylates prepared by polymerization of the corresponding oligomers. The spectra of the diffusion-modified PMMA at various depths of the samples were obtained by laser spectroscopy.

The characteristic bands for polyglycol acrylates based on EGDMA are 1639 and 1283 cm^{-1}, up to 1283.5 for PEGMA, and 1283.6 cm^{-1} for TEGMA. The band at 988.2 cm^{-1} in the spectrum of PMMA was selected as the reference for calculations.

Processing of the spectra and determination of the intensity ratio of the characteristic bands to the reference band at 988.2 cm^{-1} at various depths from the sample surface allowed determination of the relative content of oligomers in the surface layers of the samples. The results are presented in Table 2.

As follows from Table 2, the dependence of the oligomer concentration on the depth of its penetration into the PMMA matrix has a maximum (Fig. 2). For

Table 1. Degree of swelling of PMMA α in oligomers

T_{sw},* °C	Oligomer	α, wt %, at indicated treatment duration, min		
		30	60	90
37	EGDMA	0.8	2.3	4.3
	TEGDMA	–	–	–
	PEGDMA	7.2	11.4	16.2
50	EGDMA	1.9	6.6	10.4
	TEGDMA	7.8	11.8	13.5
	PEGDMA	15.4	18.0	20.8

* T_{sw} is the swelling temperature.

1070-4272/03/7611-1832$25.00

Table 2. Relative content of oligomers in the surface layers of PMMA (swelling at 50°C)

Distance from the sample surface, μm	Intensity ratio of the characteristic bands to the band at 988.2 cm^{-1}		
	EGDMA	TEGDMA	PEGDMA
2	1.50	–	–
5	1.50	–	–
10	1.60	–	–
30	1.80	–	2.60
50	1.85	2.45	1.15
60	1.85	2.30	0.07
100	1.60	1.98	Absent
200	0.90	0.95	″
240	0.70	0.75	″
500	0.22	0.30	″
540	0.18	Absent	″

TEGDMA and PEGDMA, the range of variation is narrow, since in the surface layers we failed to reveal the band characteristic for PMMA (988.2 cm^{-1}).

The data obtained show that, the higher the molecular weight of oligoglycol acrylate, the smaller the depth of its penetration into the PMMA matrix. A comparison of these data with the results listed in Table 2 suggests higher local concentration of the oligomers with the higher molecular weight (PEGDMA and TEGDMA) in the surface layers, since the greater degree of swelling corresponds to the smaller penetration depth.

To explain why the dependence of the oligomer concentration on the penetration depth has a maximum, we studied structural transformations of oligoglycol acrylates in the surface layers of PMMA. To identify the resulting structures, we recorded the ^1H NMR spectra.

The treatment of the ^1H NMR spectra and determination of the intensity ratio of the characteristic signals to the reference signal confirmed polymerization of the oligomer in the surface layers, which is observed only when a "threshold" concentration of the oligomer in the surface layer is reached. The local concentration of the oligomer in the surface layers at which polymerization begins is approximately 15–20 wt %; this corresponds to the degree of swelling of the polymer in oligoglycol acrylate of 6–9 wt %. With a further increase in the degree of swelling, the fraction of nonpolymerized oligomer in the surface layers decreases owing to its conversion into the network polymer (Fig. 3).

Polymerization of the oligomer is also confirmed by the results of studying the molecular mobility in the surface layers of PMMA. At the degree of swelling more than 10%, the mobility of the oligomeric component decreases (Fig. 4) owing to curing. With increasing degree of swelling, the fraction of the component corresponding to the mobility of oligomer in

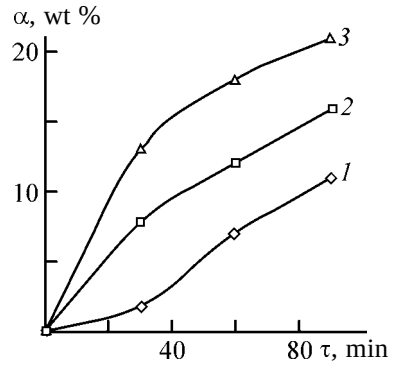

Fig. 1. Kinetic curves of PMMA swelling in oligoglycol acrylates at 50°C: (α) degree of swelling and (τ) time. (*1*) EGDMA, (*2*) TEGDMA, and (*3*) PEGDMA; the same for Fig. 2.

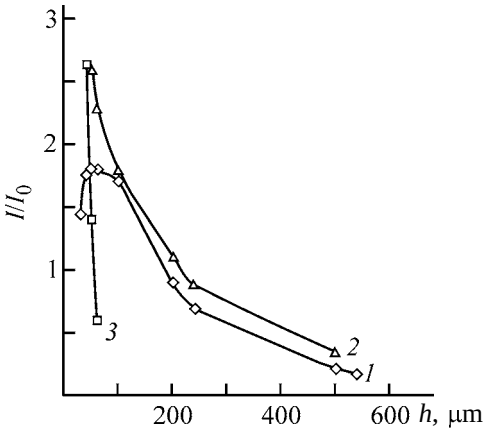

Fig. 2. Relative content of oligomers in the surface layers of PMMA from the evidence of laser Raman spectroscopy (the 1283.2 cm^{-1}/988.2 cm^{-1} intensity ratio). (I/I_0) Relative intensity and (*h*) penetration depth.

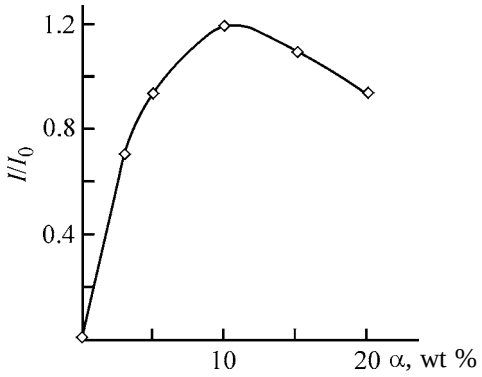

Fig. 3. Relative content of EGDMA (from the evidence of ^{1}H NMR) as a function of the degree of swelling of PMMA α. (I/I_0) Relative intensity.

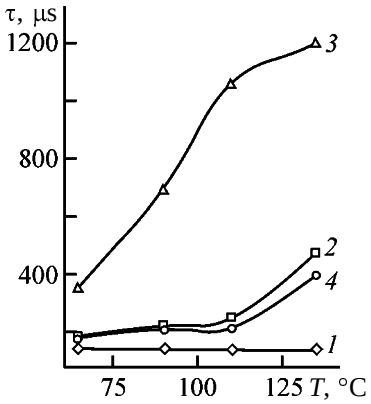

Fig. 4. Transverse spin–spin relaxation time τ of the surface layers of PMMA modified with EGMA at 50°C as a function of temperature *T*. Degree of swelling (wt %): (*1*) 1.9, (*2*) 3.6, (*3*) 8.1, and (*4*) 20; the same for Fig. 5.

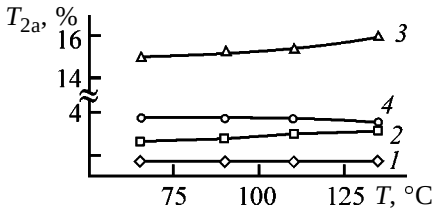

Fig. 5. Population of the mobile component T_{2a} of surface layers of PMMA modified with EGMA at 50°C as a function of temperature *T*.

PMMA increases to the threshold concentration and then starts to decrease (Fig. 5).

Thus, the forming structure of gradient polymers is largely governed by the depth of penetration of the oligomeric modifying agent into the surface layer and the degree of its curing in this layer.

EXPERIMENTAL

In the experiments we used PMMA of the Altuglas brand with the following physicochemical characteristics: d = 1188 kg m^{-3}, n_D^{20} = 1.4900, T_g = 100°C; EGDMA with d = 1080 kg m^{-3} and n_D^{20} = 1.4540; TEGDMA with d = 1092 kg m^{-3} and n_D^{20} = 1.4600; PEGDMA with d = 1099 kg m^{-3} and n_D^{20} = 1.4900; benzoyl peroxide in the amount of 0.3% (with respect to oligoglycol acrylate) was used as polymerization initiator.

The structure of gradient PMMA was analyzed by IR and laser spectroscopy. The IR spectra were recorded on a Perkin–Elmer 2000 FI-IR spectrometer.

The spectra of diffusion-modified PMMA at various depths of the samples were obtained by the laser spectroscopy on a Raman DILOR XY spectrometer with multichannel detection, equipped with a microscope and a video image (excitation of platinum at 458 μm, XYZ with manual or automatic monitoring of excitation zone). The composition of gradient layers was studied at various depths from the surface up to 550 μm (with a step of 1 μm in the automatic mode).

To study the molecular mobility in the surface layers of PMMA (samples of surface layers of modified PMMA in powdered form), we used pulse NMR at 64 MHz.

The ^{1}H NMR spectra were recorded on a Bruker spectrometer operating at 100 MHz using acetone-d_6 as a solvent.

CONCLUSIONS

(1) With increasing molecular weight (correspondingly, with decreasing fraction of acrylate groups in oligomer molecules), the degree of swelling of polymethyl methacrylate in oligomers increases. For ethylene glycol dimethylacrylate, the oligomer concentration as a function of the depth of its penetration into the polymethyl methacrylate matrix passes through a maximum.

(2) Polymerization of oligomers in the polymethyl methacrylate matrix is observed only when their threshold concentration in the surface layers, approximately 15–20 wt %, is reached.

REFERENCES

1. Lipatov, Yu.S., *Vysokomol. Soedin., Ser. A*, 1975, vol. 17, no. 4, pp. 937–940.
2. Dror, M., Elsable, M., and Berry, G., *J. Appl. Polym. Sci.*, 1981, vol. 26, no. 6, pp. 1741–1757.
3. Karabanova, L.V., Sergeeva, L.M., Lutsyk, E.D., and Kuznetsova, V.P., *Vysokomol. Soedin., Ser. A*, 1996, vol. 38, no. 10, pp. 1700–1705.
4. Berlin, A.A., Kefeli, T.Ya., and Korolev, G.V., *Polietherakrilaty* (Polyether Acrylates), Moscow: Nauka, 1967.

Russian Journal of Applied Chemistry, Vol. 76, No. 11, 2003, pp. 1835–1838. Translated from Zhurnal Prikladnoi Khimii, Vol. 76, No. 11, 2003, pp. 1886–1889.

MACROMOLECULAR CHEMISTRY AND POLYMERIC MATERIALS

Epoxy Polymers Containing Coordinated Rare-Earth Metal Ions

L. M. Amirova, V. P. Fomin, and R. R. Amirov

Tupolev Kazan State Technical University, Kazan, Tatarstan, Russia
Kazan State University, Kazan, Tatarstan, Russia

Received May 6, 2003

Abstract—Solid, optically transparent polymers with a high (up to 25 wt %) content of coordination-bound rare-earth elements were prepared by curing glycidyl esters of phosphorus acids with rare-earth metal salts.

There are two main lines in the use of metal compounds in preparation of epoxy polymers [1–3]. Salts and other metal compounds catalyze curing of epoxy oligomers [1, 2] and can be latent hardeners, e.g., for preparation of single-component epoxy compounds. Large amounts of metal ions can improve such properties of epoxy polymers as adhesion, bending strength, crack resistance, water absorption, and softening point [2, 3]. Nevertheless, introduction of metal ions into epoxy resins is complicated because of low solubility of their inorganic compounds (oxides, salts). This problem is usually solved using salts with organic anions or metal complexes. However, introduction of noticeable amounts of large organic ions and molecules together with metals can worsen the polymer parameters and requires special study.

Among metal ions introduced into epoxy polymers, we can emphasize rare-earth elements (REE). REE-containing polymers arouse growing interest, which is caused by the possibility of producing various optical devices (waveguides, optical amplifiers, lasers) on their base [4]. The use of epoxides as polymeric matrices is caused by a set of their favorable physicomechanical properties providing good performance. However, polymers prepared by curing of commercial epoxy–4,4'-isopropylidenediphenol oligomers show insufficient optical characteristics, softening point, and refractoriness.

It was shown previously that polymers based on glycidyl esters of phosphorus acids (GEP) combine high physicomechanical and thermal properties and refractoriness with good optical characteristics [5–8]. In addition, phosphoryl groups in GEP molecules can form additional coordination bonds with multicharged metal ions (including REE ions), similarly to trialkyl phosphates, which are well-known extractants [9]. This suggests the possibility of introducing large amounts of REE ions into such epoxy polymers.

In this work we studied formation of GEP-based solid, optically transparent polymers with required refractive index and high (up to 25 wt %) concentrations of coordination-bound REE ions.

EXPERIMENTAL

GEPs of the general formula

$$RP(OCH_2CH{-}CH_2)_2,$$
$$\quad\|\quad\quad\quad\backslash\ /$$
$$\quad O\quad\quad\quad\ O$$

where R is $(OCH_2CH{-}CH_2)_2$ (**I**), OCH_3 (**II**), CH_3 (**III**), synthesized as in [10] and analytically pure or chemically pure grade REE chlorides, nitrates, and sulfates (Y, Sc, La, Pr, Nd, Gd, Tb, Dy, Ho, Er, Tm, Yb, Lu) were used.

Glycidyl esters of phosphorus acids were dried by water distillation in a vacuum for 1 h at 60–70°C. The REE salts were used in the form of crystal hydrates or dehydrated samples. Polymers were prepared by stirring at 25°C phosphorus-containing glycidyl ester with REE salt in 100 : (0.5–50) weight ratio (as calculated for cation content) until the salt completely dissolved; curing was performed at 40–80°C.

The viscosity of mixtures of REE salt and GEP was determined according to GOST 10587–84 as the time of outflow of a definite volume of the mixture through a VPZh-1 viscometer capillary with a diameter from 0.54 to 5.1 mm.

1070-4272/03/7611-1835$25.00

Gel times τ_{gel} of compounds of GEPs **I**–**III** with MX_3, glass transition points T_g, and hardnesses H of polymers

LnX_3,* wt %	T_{cur}, °C	τ_{gel}, h			T_g, °C			H, MPa		
		I	**II**	**III**	**I**	**II**	**III**	**I**	**II**	**III**
					$Gd(NO_3)_3$					
0.5	40	7.1	8.0	9.1	62	60	57	136	134	133
10	40	4.2	5.1	6.4	95	91	84	142	138	137
25	40	2.3	3.4	4.6	110	105	98	148	143	140
0.5	60	6.5	7.4	8.1	68	65	60	137	135	132
10	60	3.4	4.3	5.4	99	96	90	145	141	139
25	60	1.5	2.5	3.2	115	110	102	151	149	148
0.5	80	5.1	6.2	7.4	72	69	64	139	136	134
10	80	2.5	3.5	4.1	105	100	96	148	145	141
25	80	1.1	2.3	2.8	120	111	106	155	153	150
					$GdCl_3$					
0.5	40	8.0	8.9	10.2	60	58	55	135	132	131
10	40	4.2	5.5	8.1	89	84	81	140	135	134
20	40	2.5	3.8	4.2	106	100	94	145	140	139
0.5	60	7.2	8.3	9.1	66	64	62	136	133	132
10	60	3.6	4.6	6.2	99	96	92	144	140	138
20	60	2.1	3.1	5.8	112	110	105	148	146	145
0.5	80	6.2	7.2	8.2	71	70	67	137	135	134
10	80	2.7	3.8	5.5	103	100	95	145	143	140
20	80	1.4	2.4	3.4	117	114	110	150	145	144
					$Gd_2(SO_4)_3$					
0.5	40	9.2	10.6	11.8	60	58	55	134	131	129
8	40	4.9	6.4	7.6	87	80	79	137	135	134
15	40	3.2	4.1	5.3	100	118	90	140	138	136
0.5	60	8.4	9.6	10.7	65	63	60	136	132	130
8	60	4.3	5.3	6.8	92	90	88	139	137	135
15	60	2.5	3.4	4.7	110	102	98	142	140	138
0.5	80	7.0	8.3	9.7	70	68	65	137	135	133
8	80	3.2	4.1	5.9	100	98	92	140	139	136
15	80	2.1	3.0	4.6	115	110	105	142	141	140

* Content as calculated for cation.

The glass transition point T_g was determined by a thermomechanical method with a PTB-1 device. The heating rate was 50 deg h^{-1} at static loading (P = 9.8–39.2 N) of cylindrical samples 8 mm in diameter and 11 mm high.

The hardness of samples was measured with a PMT-3 microdurometer.

The IR spectra of samples were recorded on a Specord IR-75 spectrometer, and UV-VIS spectra, on a Lambda EZ210 (Perkin–Elmer) spectrophotometer.

After mixing metal salt with phosphorus-containing glycidyl esters **I**–**III**, the viscosity of the system gradually increases. The process rate depends on the salt content, cation, anion, GEP structure, temperature, and moisture content. The time dependences of the viscosity of REE salt–**I** mixtures for two concentrations of holmium and ytterbium nitrates are shown in Fig. 1. With gadolinium salts as examples, the gel time is presented in the table as a function of curing temperature, anion, and GEP structure. As seen, the gel time decreases in the orders **III** > **II** > **I** and sulfate > chloride > nitrate. The temperature rise and increase in salt concentration also accelerate gelation. In the series of REE cations, no regular trends in the curing rates were revealed.

The curing was monitored by IR spectroscopy. The IR spectra of gadolinium sulfate solution in triglycidyl

phosphate and of the cured polymer are shown in Fig. 2. Metal ions open the epoxy ring, which follows from disappearance of the band at 920 cm^{-1}. Simultaneously, new bands at 1640 and 1290 cm^{-1} appear. The first of them can be assigned to vibrations of C–O–M bonds [11] formed by opening of the epoxy ring with REE ion. The band at 1290 cm^{-1} belongs to ether bonds C–O–C.

In the presence of REE ions, two mechanisms of epoxy ring opening are possible. At a low cation content, catalytic homopolymerization (with formation of C–O–C ether bonds) proceeds. At high REE salt concentrations, along with homopolymerization, epoxy ring opening can occur by binding of the metal ion (with formation of C–O–M bonds) and growth of the polymer chain. It was established by DSC that small (0.5–5 wt parts) amounts of REE triflates catalyze DGEBA polymerization with complete cross-linking at 120– 200°C [12]. From the temperature dependences of the dielectric loss tangent, we determined the glass transition points of polymers: 108.8, 95.1, 124.8, 110.5, and 93.1°C for the samples prepared with Yb^{3+}, La^{3+}, Ce^{4+}, Dy^{3+}, and Sm^{3+}, respectively.

It was found that the intensity ratio of the bands at 1290 and 1640 cm^{-1} decreases as the REE content increases. This shows that homopolymerization, prevailing at a low content of metal ions [12], gives way to the metal-coordination mechanism at high REE concentrations.

Reactions of **I**–**III** with REE salts yield hard polymers with the hardness of 130–150 MPa (see table).

The polymers prepared were studied thermomechanically. Figure 3 shows the thermomechanical curves of triglycidyl phosphate cured at 40°C with various amounts of yttrium nitrate. As seen, the glass transition point increases and deformation decreases with increasing salt concentration. The T_g values found from thermomechanical curves are also listed in the table.

The table shows that, for metal-coordinated polymers based on bi- and trifunctional GEPs, T_g differs only slightly. At low metal concentrations, this can be caused by the fact that in homopolymerization, characteristic for this concentration range, the three functional groups of triglycidyl phosphate are not fully converted. This is indicated by relatively low glass transition points. At high concentrations of metal ions, small differences in the glass transition and hardness for bi- and trifunctional GEPs can be explained by the fact that the thickness of the polymer network is determined by cross-links produced by coordination

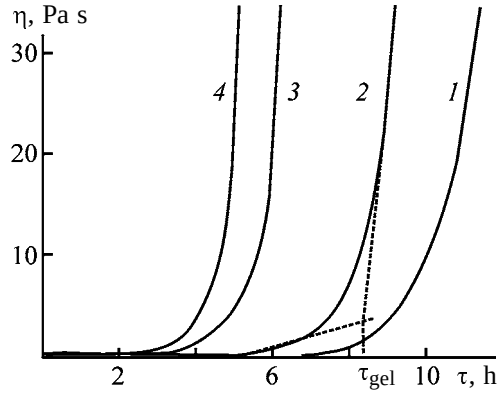

Fig. 1. Increase in viscosity η of $M(NO_3)_3$–**I** mixtures in time τ at 40°C. M: (*1*, *3*) Ho and (*2*, *4*) Yb. Salt content as calculated for cation (wt %): (*1*, *2*) 1 and (*3*, *4*) 10.

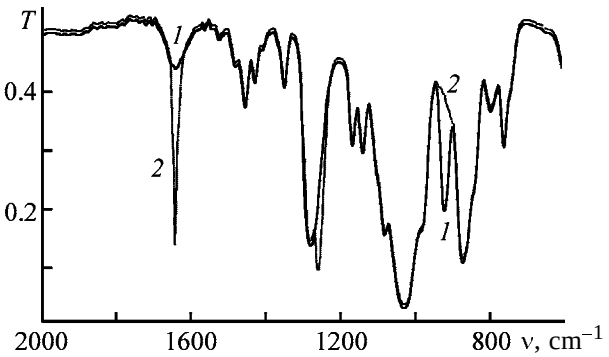

Fig. 2. IR spectrum of $Gd_2(SO_4)_3$–**I** system (*1*) after mixing and (*2*) after curing at 40°C for 6 h. (*T*) Transmittance and (ν) wave number. Salt content as calculated for cation 5 wt %.

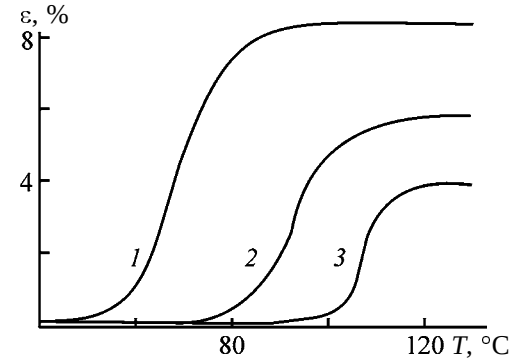

Fig. 3. Thermomechanical curves of the polymer based on $Y(NO_3)_3$ and GEP **I**, prepared at 80°C. (ε) Deformation and (*T*) temperature. Salt content as calculated for cation (wt %): (*1*) 1, (*2*) 5, and (*3*) 10.

of REE cations, whose coordination numbers are close [11].

As noted above, polymers doped with REE are of great interest as materials for optics and quantum electronics. Polymers obtained in reactions of GEPs **I**–**III**

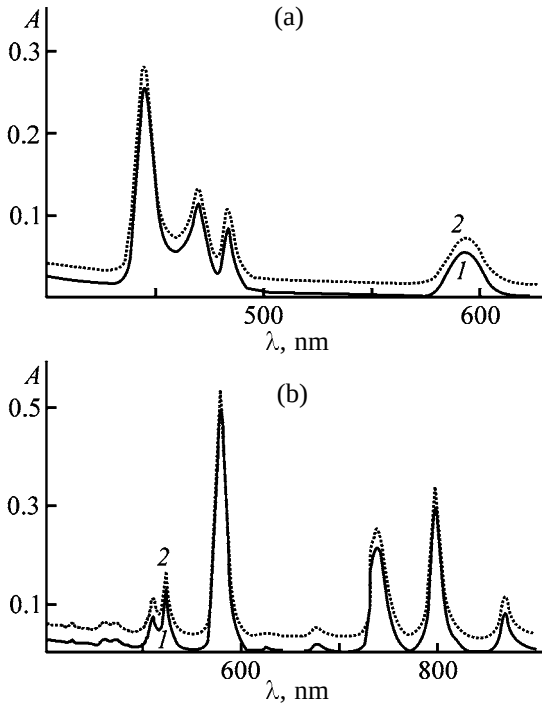

Fig. 4. Electronic absorption spectra of $M(NO_3)_3$–**I** liquid systems and (*2*) polymers on their base, cured at 40°C. (*A*) Optical density and (λ) wavelength. M: (a) Pr and (b) Nd. Salt content as calculated for cation 10 wt %.

with REE salts exhibit high transparency with 98–99% transmittance in the visible range for the materials based on La^{3+}, Y^{3+}, Sc^{4+}, Yb^{3+}, Tb^{3+}, Gd^{3+}, and Lu^{3+}. For the materials with REE ions absorbing in the visible range, we recorded the corresponding spectra. Some of them for liquid and cured REE-containing samples are shown in Fig. 4. As seen, curing does not affect the location and width of bands and weakly affects the background absorption. The spectra obtained have a better resolution as compared to the spectra given in [13] for glasses doped with the same REE, which are used as fiber amplifiers and lasers [14]. Thus, epoxy polymers doped with REE show promise as optical materials.

CONCLUSIONS

(1) The possibility of formation of metal-coordinated polymers in reaction of glycidyl esters of phosphorus acids with REE salts was demonstrated.

(2) Polymers obtained were characterized by electronic and IR spectroscopy and thermomechanically.

ACKNOWLEDGMENTS

The work was financially supported in part by the joint program of CRDF and Ministry of Education of the Russian Federation "Basic Education and Higher School" (BRHE, REC-007).

REFERENCES

1. Shode, L.G., Mirenskii, R.B., and Sorokin, M.F., *Lakokras. Mater. Ikh Primen*., 1986, no. 5, pp. 36–39.
2. Hamerton, I., Howlin, B.J., and Jepson, P., *Coord. Chem. Rev*., 2002, vol. 224, no. 1, pp. 67–85.
3. Amirova, L.M., *Elementoorganicheskie i metallkoordinirovannye epoksidnye polimery: sintez, svoistva, primenenie* (Organometallic and Metal-Coordinated Epoxy Polymers: Synthesis, Properties, and Use), Kazan: Novoe Znanie, 2003.
4. US Patent 5 657 156.
5. Amirova, L.M., Shageeva, I.K., and Stroganov, V.F., *Zh. Prikl. Khim*., 2001, vol. 74, no. 8, pp. 1328–1331.
6. Amirova, L.M. and Sakhabieva, E.V., *Zh. Prikl. Khim*., 2001, vol. 74, no. 10, pp. 1692–1695.
7. Amirova, L.M., Saifutdinov, R.Kh, Magsumova, A.F., and Amirov, R.R., *Zh. Prikl. Khim*., 2001, vol. 74, no. 11, pp. 1881–1884.
8. Amirova, L.M., Andrianova, K.A., Bukharaev, A.A., and Fomin, V.P., *Zh. Prikl. Khim*., 2002, vol. 75, no. 9, pp. 1505–1508.
9. *Gidrometallurgiya* (Hydrometallurgy), Laskorin, B.N., Ed., Moscow: Metallurgiya, 1976.
10. Rizpolozhenskii, N.I., Boiko, L.V., and Zvereva, M.A., *Dokl. Akad. Nauk SSSR*, 1964, vol. 155, no. 5, pp. 1137–1139.
11. *Koordinatsionnaya khimiya redkozemel'nykh elementov* (Coordination Chemistry of Rare-Earth Elements), Spitsyn, V.I. and Martynenko, L.I., Eds., Moscow: Mosk. Gos. Univ., 1974.
12. Castell, P., Galia, M., Serra, A., *et al*., *Polymer*, 2000, vol. 41, no. 24, pp. 8465–8474.
13. Kolobkov, V.P. and Petrovskii, G.T., *Opt.-Mekh. Prom*., 1971, no. 3, pp. 53–60.
14. Miyajima, Y., Komukai, T., Sugawa, T., and Yamamoto, T., *Opt. Fiber Technol*., 1994, no. 1, pp. 35–47.

Russian Journal of Applied Chemistry, Vol. 76, No. 11, 2003, pp. 1839–1843. Translated from Zhurnal Prikladnoi Khimii, Vol. 76, No. 11, 2003, pp. 1890–1894.

MACROMOLECULAR CHEMISTRY AND POLYMERIC MATERIALS

Flocculation of a Synthetic Rubber Latex with Homopolymers and Copolymers of *N*-Vinylcaprolactam and *N*-Vinylimidazoles

G. V. Shatalov, V. N. Verezhnikov, E. V. Churilina, V. A. Kuznetsov, and T. N. Poyarkova

Voronezh State University, Voronezh, Russia

Received March 19, 2003

Abstract—Flocculation of a latex of SKS-30 ARK commercial rubber with homopolymers and copolymers of *N*-vinylcaprolactam, 1-vinyl-2-methylimidazole, and its quaternization product was studied. The flocculating power of the nonionic polymers in acid solution was evaluated. The performance of the copolymers grows with increasing content of cationic units in the macromolecules and on adding an acid.

An urgent problem in rubber production is development of methods of salt-free coagulation of latexes with synthetic and natural polymers, including proteins [1, 2]. An important advantage of coagulants based on natural products is that they are nontoxic and environmentally friendly. Protein hydrolyzates used as coagulating additives in industry [3, 4] are unstable in storage and nonuniform in composition; they also have other drawbacks. The undesirable properties of protein products are partially eliminated by performing coagulation with addition of salts. Promising coagulants for latexes are synthetic polymers with an amide (peptide) bond, containing ionic groups in the macrochain. These groups enhance the coagulation power of macromolecular compounds.

It is known [5] that polymers based on *N*-vinylcaprolactam (VC), containing an amide bond in the ring, are low-toxic and capable of complexation; their aqueous solutions have the lower critical solution point in the temperature interval of functioning of living bodies. Lozinskii *et al.* prepared a "protein-like copolymer" from VC and 1-vinylimidazole [6] with the structure resembling that of a globular protein. It was shown previously that 2-methylimidazole (MI) used in production of drugs, polymeric materials, and other products is suitable for latex coagulation [7].

In this work, we studied coagulation of a latex of SKS-30 ARK commercial rubber with a VC homopolymer and its copolymers with *N*-vinylimidazoles. As comonomers we used 1-vinyl-2-methylimidazole (VMI) and 1-vinyl-2-methyl-3-propylimidazolium iodide (VII). This choice was governed by the ease of preparing these monomers from readily available 2-methylimidazole (MI).

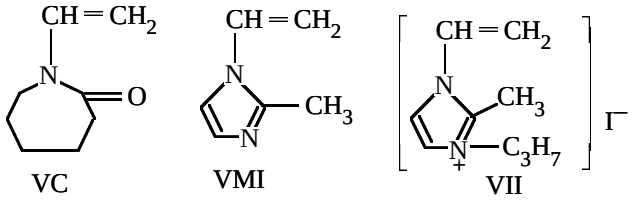

VC VMI VII

EXPERIMENTAL

VC (mp 33–34°C, bp 92–93°C/1 mm Hg) was prepared from caprolactam, acetaldehyde, and alcohol by the procedure described in [8]. VMI was prepared by thermal dehydration of 1-(2'-hydroxyethyl)-2-methylimidazole with a mixture of KOH and NaOH (1 : 1 by weight) at 150–160°C in the presence of hydroquinone. Fractionation yielded VMI with bp 64–66°C at 4 mm Hg and n_D 1.5250, which agrees with reference data [9].

Synthesis of 1-(2'-hydroxyethyl)-2-methylimidazole involved the reaction of MI with oxirane in DMF. Vacuum fractionation of the reaction mixture gives a product with mp 64–65°C (from ethyl acetate).

VII was prepared by quaternization of VMI with propyl iodide. A solution of VMI in absolute ethyl acetate was mixed with C_3H_7I at 5°C, stirred for 1 h, and allowed to stand for 12 h at the same temperature. The product was recrystallized from isobutyl alcohol and dried in a vacuum; mp 129–130°C, in agreement with published data [10].

1070-4272/03/7611-1839$25.00

Poly-*N*-vinylcaprolactam (PVC) and poly-1-vinyl-2-methylimidazole (PVMI) were prepared by radical polymerization in isopropanol at 70°C. The monomer concentration was 3.0 M, and the initiator [azobis(isobutyronitrile), AIBN] concentration, 3.0×10^{-2} M. Under such conditions, we prepared PVC with $M_\eta = 2.65 \times 10^4$, and at [VC] = 4.5 M, with $M_\eta = 8.2 \times 10^4$. PVC with $M_\eta = 3.5 \times 10^4$ was prepared by polymerization in benzene solution at 50°C for 5 h at [AIBN] = 1.5×10^{-2} M. The polymers were precipitated with hexane and vacuum-dried at 55–60°C. The molecular weights M_η were calculated from the intrinsic viscosities [η] by the formula $[\eta] = 1.5 \times 10^{-4} M_\eta^{0.68}$ [5]. PVMI had [η] = 0.17 dl g^{-1} in C_2H_5OH at 25°C.

The radical copolymerization of VC with VII was performed in ethanol, and that with VMI, in isopropanol (total concentration of comonomers 1 M) under conditions of thermal initiation (70°C, [AIBN] = 1×10^{-2} M). The mole fractions of the comonomers in the mixture were varied from 0.1 to 0.9. The products were precipitated with hexane and dried similarly to the homopolymers. Over the entire composition range, [η] of the homopolymers was 0.10–0.12 dl g^{-1} (for VC–VII in CH_3OH and VC–VMI in H_2O) at 25°C.

The copolymer compositions were determined by IR spectroscopy, from the intensity ratio of the absorption bands in the regions of 1635 (C=O vibrations of the VC units) and 1440 cm^{-1} (vibrations of the imidazole ring [11]).

Coagulation experiments were performed with a latex of commercial SKS-30 ARK rubber prepared with an emulsifying system based on disproportionated tall oil [12].

The coagulation power of the polymeric products was evaluated gravimetrically (by the weight of the coagulum formed) and visually (by the serum transparency). Coagulation was performed in a stirred flask containing 20 ml of a latex solution containing 1% dispersed phase (dry residue 18.65%). After thermostating at room temperature, the prescribed amount of an aqueous solution of a polymer was added with stirring. The consumption of the acidifying agent (2.0% sulfuric acid) was 15 kg t^{-1} rubber. The resulting coagulum was separated from the serum, washed with water, and dried to constant weight at 75–80°C.

Experiments on latex coagulation were performed with PVC (M_η 26.5×10^3 and 3.5×10^6) and with VC–VMI (VC mole fraction 0.57) and VC–VII (VC mole fraction 0.57 and 0.66) copolymers.

Since data on VC (M_1)–VII copolymers are lacking, we studied their radical copolymerization in ethanol under conditions of thermal initiation. From the data on composition of the copolymers obtained at low (up to 5–7%) conversions, we calculated analytically [13] the apparent copolymerization constants: $r_1 = 0.54 \pm 0.07$ and $r_2 = 0.03 \pm 0.02$. Thus, r_1 and r_2 differ considerably, with VII showing relatively low ($r_2 \approx 0$) activity. This is due to the fact that VII is charged, which prevents its addition to the propagating macroradical bearing like-charged units and favors addition of VC units.

We found that VC–VII copolymers with the VC mole fraction exceeding 0.55 are water-soluble like PVC of widely varied M_η. As the content of VC units decreases, the products become water-insoluble because of increased content of hydrophobic VII units.

The coagulation performance of the polymers was evaluated from the rubber flocculation curves, i.e., from the dependences of the weight fraction φ of the recovered polymer on the flocculant concentration *c*.

VC homopolymers differing in M_η and the VC–VMI copolymer without acidification showed no flocculating power. Nonionic PVMI tested for comparison behaved similarly. The curves of rubber recovery with PVC, PVMI (Fig. 1a), and VC–VMI copolymer (Fig. 1b, curve *8*) pass through a maximum (flocculation optimum), i.e., their shape is typical of flocculation of negatively charged sols (including latexes) with nonionic polymers and cationic polyelectrolytes [14, 15]. A decrease in the efficiency of rubber recovery at flocculant concentrations above the optimum is accounted for, according to the existing concepts [16], by restabilization of the system due to recharging of particles (addition of polyelectrolytes) and/or formation on their surface of a dense layer of adsorbed hydrophilic macromolecules, exerting a stabilizing effect (addition of nonionic polymeric flocculants).

The appearance of the flocculating power in an acidic solution may be due to two factors. First, the aggregative stability of the latex decreases owing to hydrolysis of carboxyl-containing surfactants (salts of fatty and other acids) to form insoluble and virtually nondissociating carboxylic acids showing no protective effect. In the process, the charge and potential of the particles and the thickness of the electrical double layer should decrease. As a result, the particles become able to approach each other to a distance at which the thickness of the adsorption layer of the macromolecules is sufficient for formation of interparticle bridges [16].

Second, the flocculating effect of PVC and VC–VMI copolymer, and also of PVMI in an acid solution may be associated with appearance of positively charged sites in the macromolecules due to protonation. In polymers containing VMI units, the protonation can occur at nucleophilic pyridine-like nitrogen atoms of the imidazole ring [17]. The protonation of azoles at the nitrogen atoms containing lone electron pairs in interaction with mineral acids is indicated in [18]. This is also suggested by the previously revealed [7] dramatic enhancement of the coagulating power of 2-methylimidazole in acid solution upon addition of increasing amounts of sulfuric acid.

In PVC and its copolymers, the possible protonation site in acid solutions is the C=O group of lactam units. This process was detected experimentally with a related polymer, polyvinylpyrrolidone [19], by NMR spectroscopy. According to [19], in acid solutions, at pH < 4, the ^{13}C NMR signal of the carbonyl carbon atom is regularly shifted downfield with increasing acidity. This suggests an increase in its positive charge and may be due to protonation of the carbonyl oxygen atom. Protonation of PVC is confirmed by certain experimental data. For example, with hydrogen ions in the latex replaced by Na^+ ions in an equimolar amount, the flocculation efficiency is extremely low, φ = 1–3% (Fig. 1, curve *4*). Hence, specifically appearance of cationic groups in PVC macromolecules, rather than an increase in the ionic strength of the medium, is the decisive factor responsible for coagulation. The efficiency of rubber recovery is also very low when an acid is added without a flocculant, whereas an increase in the acid concentration in the presence of PVC causes a sharp growth of φ (Fig. 1, curves *9* and *10*), presumably due to increasing protonation of the polymer macromolecules.

Thus, PVC (like PVMI) in acid solutions acquires the properties of a cationic polyelectrolyte. Its addition to a latex under these conditions should result in chemical binding of surfactant (stabilizer) anions with the cationic centers of flocculant macromolecules to form insoluble ionic complexes exhibiting no stabilizing effect. Such an interaction was detected nephelometrically in the presence of an acid in aqueous solutions of a mixture of PVC with Leukanol[1] [a nonhydrolyzable (in contrast to soaps) stabilizer present in latexes] (Fig. 2). Figure 2 shows that, as the acid concentration is increased, the turbidity first grows slightly and then sharply, suggesting formation of particles

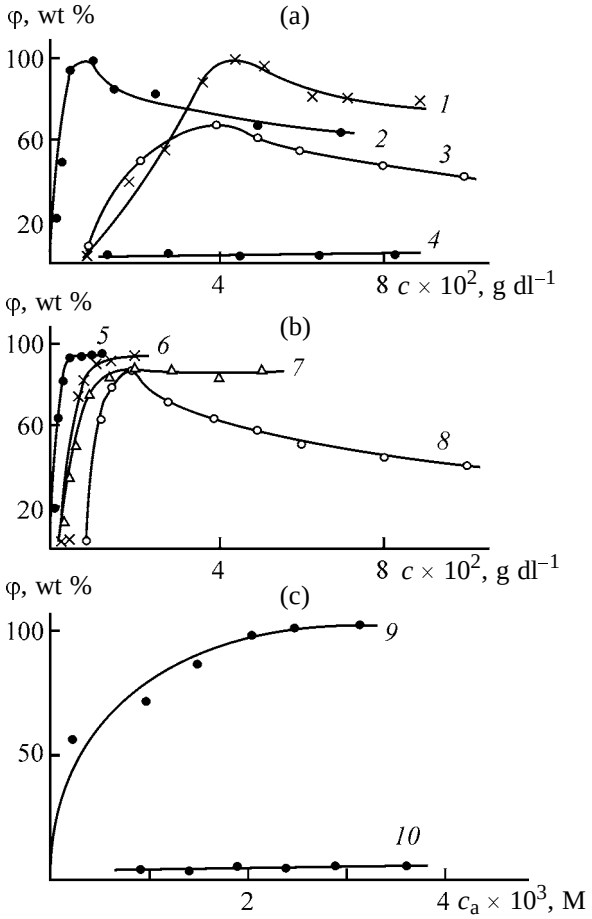

Fig. 1. Weight percentage of the recovered rubber φ as a function of the concentration of (a) homopolymers (*c*), (b) copolymers (*c*), and (c) acid (c_a). (*1*, *4*) PVC (M_η = 3.5×10^6), (*2*) PVMI, (*3*) PVC ($M_\eta = 2.65 \times 10^4$), (*5*, *7*) VC (mole fraction 0.66)–VII copolymer, (*6*) VC (mole fraction 0.57)–VII copolymer, (*8*) VC (mole fraction 0.57)–VMI copolymer, and (*9*) PVC ($M_\eta = 8.2 \times 10^4$). (*4*) NaCl concentration 3×10^{-3} M. H_2SO_4 concentration, M: (*1–3*, *5*, *8*) 1.5×10^{-3} and (*4*, *6*, *7*) 0. PVC concentration ($M_\eta = 8.2 \times 10^4$): (*9*) 2.2×10^{-3} and (*10*) 0.

of the insoluble oligomer–polymer complex [20]. In the absence of an acid, no interaction is observed in a wide range of Leukanol concentrations (Fig. 2, curve *2*).

It should be noted that, at the acid concentrations used in flocculation experiments (Fig. 2, point in curve *2* denoted with a circle), there is no noticeable increase in the turbidity. This fact apparently suggests that, under these conditions, the degree of protonation is low and the concentration of the forming complex is below the solubility limit at which the new phase starts to precipitate.

Thus, appearance of positive charges in polymer

[1] A mixture of sodium salts of an oligomeric product formed by condensation of β-naphthalenesulfonic acid with formaldehyde.

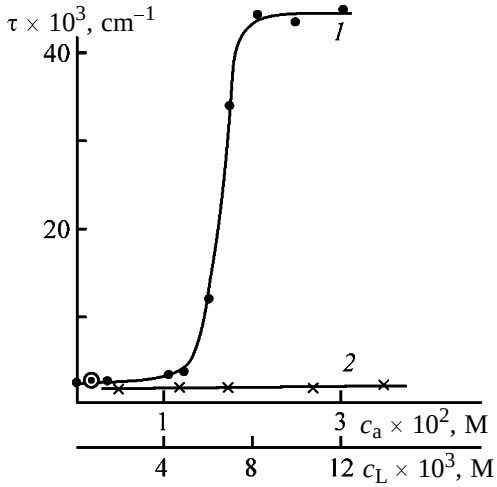

Fig. 2. Turbidity τ (*1*) of solution of PVC (M_η = 8.2 × 10^4)–Leukanol mixture (3.6 × 10^{-3} M each) as a function of H_2SO_4 concentration c_a and (*2*) of PVC solution (3.6 × 10^{-3} M) as a function of the Leukanol concentration c_L in the absence of the acid.

macrochains in acid solutions results in manifestation of the neutralization mechanism of flocculation, along with the bridging mechanism. The neutralization mechanism involves binding of surfactant (stabilizer) anions with cationic groups of the flocculant macromolecules.

Comparison of the curves for PVC and PVMI (Fig. 1a) shows that the polymer with an imidazole ring exhibits a stronger flocculating effect. This is indicated by the fact that the optimal flocculating concentration of PVMI (9.4 × 10^{-3} g dl^{-1}) is considerably lower than that of PVC (3.9 × 10^{-2} and 5.3 × 10^{-2} g dl^{-1} for samples with M_η = 2.65 × 10^4 and 3.5 × 10^6, respectively). The higher flocculating activity of PVMI and VC–VMI copolymers is due to the presence in the macromolecules of more basic imidazole rings which are protonated in acid solutions more efficiently than caprolactam units.

The influence of the molecular weight of the polymers on their flocculating effect was considered with PVC samples differing in M_η by a factor of more than 1000. We found that the floculation efficiency noticeably grew with increasing average molecular weight of PVC (with the sample having M_η = 3.5 × 10^6, the coagulum yield in the flocculation optimum is 100%, whereas with the relatively low-molecular-weight sample it is about 70%). Such a trend is characteristic of nonionic and weakly charged polymers (with which PVC in a weakly acidic solution can be classed) and is not observed with highly charged polyelectrolytes [15, 16].

Copolymers of VC with VII exhibit a higher flocculating power compared to PVC. Figure 1 (curves *5*–*7*) show that, on adding VC–VII copolymers to the latex, the yield of the recovered rubber sharply grows, reaching a virtually constant limiting value, φ_∞, starting from a certain critical concentration c_∞ of each copolymer. The flocculating power grows (c_∞ decreases, φ_∞ increases) on acidification (Fig. 1, curves *5* and *7*) and with increasing content of VII units in the macromolecules (curves *6*, *7*). This is due to an increase in the number of cationic groups in macrochains, which enhances the contribution of the neutralization factor to the latex destabilization. Furthermore, there is no restabilization branch in the flocculation curves obtained with the copolymers. This suggests a decrease in the adsorbability of copolymer macromolecules with hydrophilic charged groups. In the ascending portions of the flocculation curves, the adsorption of macromolecules is provided by electrostatic forces. After neutralization of the surface charge, such phenomena as further adsorption, densification of the adsorption layer of macromolecules, and enhancement of its protective function cease to be manifested, and the system remains strongly destabilized with excess copolymer also.

Thus, coagulation of a latex of a synthetic rubber can be effected with nonionic PVC and VC–VMI copolymer in acid solutions; copolymers of VC with a cationic monomer, VII, exhibit a flocculating effect in the absence of acid also, and this effect is enhanced upon acidification.

CONCLUSIONS

(1) Products of homopolymerization of *N*-vinylcaprolactam with a wide range of molecular weights and water-soluble copolymers with 1-vinyl-2-methylimidazole and 1-vinyl-2-methylpropylimidazolium iodide exhibit flocculating power and can be used for recovery of a synthetic rubber from a latex.

(2) Copolymers of *N*-vinylcaprolactam with *N*-vinylimidazole derivatives exhibit stronger flocculating effect than poly-*N*-vinylcaprolactam.

REFERENCES

1. Papkov, V.N., Sigov, O.V., Rogozina, T.E., *et al.*, *Prozv. Ispol'z. Elastom.*, 2000, no. 6, pp. 3–6.
2. Moiseev, V.V., Popova, O.K., Kosovtsev, V.V., and Evdokimova, O.A., *Primenenie belkov pri poluchenii elastomerov: Tematicheskii obzor* (Use of Proteins in

Production of Elastomers: Topical Review), Moscow: TsNIITEneftekhim, 1985.

3. USSR Inventor's Certificate no. 1 065 424.
4. Popova, O.K., Gulyaeva, N.A., Evdokimova, O.A., *et al.*, *Prom–st. Sint. Kauchuka*, 1985, no. 8, pp. 9–10.
5. Kirsh, Yu.E., *Poli-N-vinilpirrolidon i drugie poli-N-vinilamidy* (Poly-*N*-vinylpyrrolidone and Other Poly-*N*-vinylamides), Moscow: Nauka, 1998.
6. Lozinskii, V.I., Simenel, I.A., Kurskaya, E.A., *et al.*, *Dokl. Ross. Akad. Nauk*, 2000, vol. 375, no. 5, pp. 637–640.
7. Verezhnikov, V.N., Nikulin, S.S., and Garshin, A.P., *Zh. Prikl. Khim.*, 1997, vol. 70, no. 12, pp. 2052–2055.
8. Kuznetsov, V.A., Shatalov, G.V., and Sorokatyi, S.Yu., Abstracts of Papers, *I Vserossiislaya konferentsiya po khimii geterotsiklov pamyati A.N. Kosta* (I Russian Conf. on Chemistry of Heterocycles, Dedicated to the Memory of A.N. Kost), Suzdal, 2000, p. 46.
9. Shatalov, G.V., *Monomery i polimery s azol'nymi i azinovymi tsiklami* (Monomers and Polymers with Azole and Azine Rings), Voronezh: Voronezh. Gos. Univ., 1984.
10. Salamone, J.C., Israel, S.C., Taylor, P., and Snider, B., *Polymer*, 1973, vol. 14, no. 12, pp. 639–644.
11. Konsulov, V.B. and Mladenov, I., *Vysokomol. Soedin., Ser. B*, 1979, vol. 21, no. 9, pp. 679–682.
12. Kirpichnikov, P.A., Averko-Antonovich, L.A., and Averko-Antonovich, Yu.O., *Khimiya i tekhnologiya sinteticheskogo kauchuka* (Chemistry and Technology of Synthetic Rubber), Leningrad: Khimiya, 1987.
13. Ezrielev, A.I., Brokhina, E.L., and Roskin, E.S., *Vysokomol. Soedin., Ser. A*, 1969, vol. 11, no. 8, pp. 1670–1680.
14. Verezhnikov, V.N., Nikulin, S.S., Poyarkova, T.N., *et al.*, *Zh. Prikl. Khim.*, 2000, vol. 73, no. 10, pp. 1720–1724.
15. Verezhnikov, V.N., Nikulin, S.S., Poyarkova, T.N., *et al.*, *Zh. Prikl. Khim.*, 2002, vol. 75, no. 3, pp. 472–476.
16. Baran, A.A., *Polimersoderzhashchie dispersnye sistemy* (Polymer-Containing Disperse Systems), Kiev: Naukova Dumka, 1986.
17. Ivanskii, V.I., *Khimiya geterotsiklicheskikh soedinenii* (Chemistry of Heterocyclic Compounds), Moscow: Vysshaya Shkola, 1978.
18. Gorkovenko-Spirina, O.P., Formation and Properties of Solutions of Tetrazole-Containing Polymers, *Cand. Sci. Dissertation*, Irkutsk, 2002.
19. Kirsh, Yu.E., Semina, N.V., Yanul', N.A., *et al.*, *Zh. Fiz. Khim.*, 1994, vol. 68, no. 9, pp. 1584–1586.
20. Kashlinskaya, P.E., Verezhnikov, V.N., and Poyarkova, T.N., *Zh. Prikl. Khim.*, 1991, vol. 64, no. 1, pp. 218–220.

Russian Journal of Applied Chemistry, Vol. 76, No. 11, 2003, pp. 1844–1849. Translated from Zhurnal Prikladnoi Khimii, Vol. 76, No. 11, 2003, pp. 1895–1900.

MACROMOLECULAR CHEMISTRY AND POLYMERIC MATERIALS

Preparation and Properties of Polymers Derived from Epoxy Resins and Oligochelatotitanophenylenesiloxanes

A. L. Suvorov, L. D. Dul'tseva, G. I. Ovchinnikova, E. A. Khrustaleva, N. Yu. Ostanina, and V. I. Abramova

Institute of Organic Synthesis, Ural Division, Russian Academy of Sciences, Yekaterinburg, Russia

Received April 14, 2003

Abstract—Oligochelatotitanophenylenesiloxanes of various structures were suggested as curing agents for epoxy resins. The compound formulas and curing conditions were chosen so as to ensure the maximal degree of cross-linking and hence the best physicomechanical properties of the polymers.

Preparation of polymers derived from epoxy resins and oligochelatotitanoarylenesiloxanes of the general formula

$$-[Ti(Ch)_2-O-Si(CH_3)_2-Ar-Si(CH_3)_2-O]_n-, \quad (1)$$

where Ch is a chelating ligand and Ar is phenylene, *p,p'*-diphenylene, or *p,p'*-oxydiphenylene, was reported in [1].

In this work we studied the reactions of oligochelatotitanoarylenesiloxanes with epoxy resins and the properties of the resulting polymers as influenced by the chemical structure of the curing agent and its content in the compound.

Experiments were performed with ED-20 epoxy–4,4'-isopropylidenediphenol resin (epoxide number 21.3), which was purified by filtration followed by vacuum drying, and oligochelatotitanoarylenesiloxanes prepared by heterofunctional condensation of bis(dimethoxysilyl)benzene with appropriate bis(chelato)dialkoxytitanium [2]. The characteristics of the oligochelatotitanoarylenesiloxanes prepared are listed in Table 1.

We found that the compounds containing various amounts of oligochelatotitanoarylenesiloxanes do not lose solubility after prolonged (for up to a year) storage at room temperature. However, in the course of storage, as in the case of epoxy–titanopolyether compounds [3, 4], their viscosity grows, though to a considerably lesser extent (Fig. 1). This may be due both to chemical reactions of the epoxy groups with the functional groups of the curing agent and to intermolecular interaction of the components [4, 5].

Curing of epoxy–chelatotitanophenylenesiloxane compounds starts at a noticeable rate at 160–200°C depending on the structure of the curing agent and its content in the compound. The process is manifested as a sharp ascent in the DTA curves [6]. Since curing of epoxy resins is an exothermic process, the compounds were heated stepwise from 150 to 200 or 220°C depending on the curing agent content. The curing time at each temperature was varied from 1 to 6 h, so as to ensure the maximal degree of cross-linking (content of soluble fraction ≤2%) and obtain high-quality cavity-free samples (Table 2).

The reaction of oligochelatotitanoarylenesiloxanes with the epoxy resin was studied by IR spectroscopy. Compounds were heated in a chosen stepwise curing mode, and at each temperature samples were taken to record the spectrum. Changes in the spectra became noticeable at 170°C. The bands at 920 and 865 cm^{-1}, characteristic of the epoxy group [7], decreased in intensity and fully disappeared at 200°C. In the range 900–920 cm^{-1}, there are also bands originating from

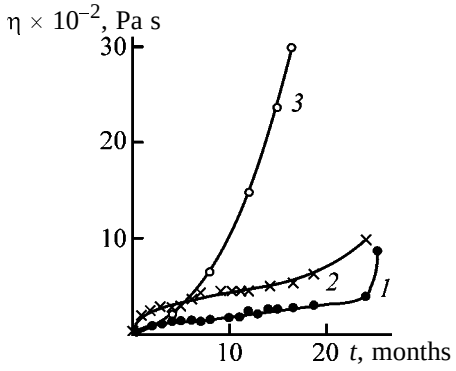

Fig. 1. Variation of the viscosity η in the course of storage at room temperature of epoxy compounds based on (*1*, *2*) oligomer **I** and (*3*) titanium polyether. (τ) Time. Curing agent content, %: (*1*, *3*) 10.0 and (*2*) 20.0.

1070-4272/03/7611-1844$25.00

Table 1. Characteristics of oligo[bis(chelato)titanophenylenetetramethyldisiloxanes] $-[-Ti(Ch)_2-O-Si(CH_3)_2-C_6H_4-Si(CH_3)_2-O]_n-$

Oligomer	Chelating ligand (Ch)	Found, %/Calculated, %		Molecular weight			*n* in formula, found	*T*,* °C
		Ti	Si	determination method	found	calculated (per unit)		
I	Acetylacetone	11.94/11.94	10.18/10.18	ITEC, DMF	955	470.5	2.03	60–80
II	Dibenzoylmethane	6.80/6.66	7.64/7.81	ITEC, benzene	1480	718.8	2.06	150–170
III	8-Quinolinol	8.54/8.54	10.21/10.21	Ebullioscopy, THF	1116	560.6	1.99	150–160

* Temperature of mixing with the epoxy resin.

Table 2. Compositions and properties of polymers derived from ED-20 and oligo[bis(chelato)titano-*p*-phenylenetetramethyldisiloxanes]*

c, mol mol^{-1}	c_c, wt %	Curing mode	M_s, g mol^{-1}	ΔG, kcal mol^{-1}	log τ	T_V, °C	*a*, kJ m^{-2}	Strength, MPa		
								σ_c	σ_t	σ_b
Oligomer **I**										
22.0	5	1	–	–	–	–	13.7	101.0	38.0	117.5
10.5	10	III	945	–	–	325	25.0	115.5	74.0	123.0
8.5	12	II	–	–	–	–	15.5	142.0	80.0	178.5
6.6	15	II	470	20.7	–0.87	320	14.0	105.0	67.0	140.0
4.7	20	II	–	–	–	–	10.0	–	60.0	134.5
3.5	25	II	–	17.9	–2.52	290	12.0	111.0	64.0	132.0
2.7	30	III	–	15.5	–3.95	286	12.5	100.0	23.5	100.0
Oligomer **II**										
33.7	5	I	–	13.4	–5.13	–	7.0	117.0	57.0	106.5
16.0	10	II	1130	10.8	–6.65	355	12.0	117.5	53.0	145.5
10.0	15	II	490	18.4	–2.26	330	13.4	120.0	77.5	152.5
7.0	20	II	700	–	–	330	2.2	115.0	42.0	91.5
5.3	25	II	–	–	–	–	1.2	132.0	32.5	100.0
Oligomer **III**										
12	10	I	880	–	–	296	17.8	110.0	83.0	134.0
10.0	12	II	–	20.8	–0.81	–	–	–	63.5	160.0
7.8	15	II	600	–	–	295	15.0	113.0	67.0	127.8
5.5	20	III	750	–	–	286	14.0–17.0	110.0	53.0	127.5
4.0	25	II	–	–	–	–	10.0	–	70.0	160.0

* (*c*) Content of ED-20 in the compound, mol mol^{-1} curing agent; (c_c) content of curing agent in the compound; (T_V) Vicat softening point; (*a*) specific impact resilience; (σ_c, σ_t, σ_b) compression, tensile, and bending strength at the yield point, respectively.

** (I) 150°C, 1 h; 160°C, 1 h; 170°C, 1 h; 180°C, 3 h; 190°C, 3 h; 210°C, 1 h; 220°C, 3 h; (II) 150°C, 4 h; 160°C, 3 h; 170°C, 3 h; 180°C, 3 h; 190°C, 3 h; 200°C, 3 h; (III) 150°C, 1 h; 160°C, 1 h; 170°C, 1 h; 180°C, 3 h; 190°C, 3 h; 200°C, 6 h.

the stretching vibrations of the ≡Si–O– bond in the ≡Ti–O–Si≡ fragment [8]. The absence of bands at 920 and 865 cm^{-1} in the spectra of the cured samples shows that not only the epoxy groups but also the ≡Ti–O–Si≡ groups are fully consumed. Also, in the compounds with the oligomers containing acetylacetonate (**I**) and dibenzoylmethanate (**II**) ligands at titanium, the bands at 1720 and 1745 cm^{-1}, usually characteristic of carbonyl groups in esters and ketones [7], appear at 170°C and grow in intensity on further heating. Similar changes in the spectra were observed on heating of a model mixture of dibutoxytitanium bis(acetylacetonate) or bis(dibenzoylmethanate) with phenyl glycidyl ether under similar conditions (temperature, time). The bands at 1720–1745 cm^{-1} continued to grow even after full consumption of the epoxy

groups. The bands characteristic of the oxirane ring virtually fully disappear in the presence of even catalytic amounts of the chelate component. With the oligomer containing 8-quinolinolato substituent (**III**), no absorption appears at 1720–1745 cm^{-1}.

The changes observed in the IR spectra suggest that curing of the epoxy resin with oligochelatotitanoarylenesiloxanes involves the reaction of epoxy groups with the ≡Ti–O–Si≡ bonds by the following scheme:

$$-[Ti(Ch)_2-O-Si(CH_3)_2-Ar-Si(CH_3)_2-O]_n- + n\underset{\backslash\ O\ /}{CH_2-CHR'} \quad (2)$$
$$\rightarrow -[Ti(Ch)_2OCH(R')-CH_2O-Si(CH_3)_2ArSi(CH_3)_2-O]_n-,$$

and also polymerization of epoxy groups.

The suggested scheme of the reaction of the epoxy resin with oligochelatotitanoarylenesiloxanes is confirmed by an increase in absorption in the range 1040–1140 cm^{-1}, characteristic of compounds containing ≡Si–O–C≡ and ≡C–O–C≡ fragments [7].

Yatluk *et al.* showed [9] that heating of titanium complexes with β-dicarbonyl compounds to 150–200°C causes transformations of the chelating ligand to give ketones and esters. They are formed by Claisen retrocondensation of free ligands which, in turn, are released in reaction with alcohols formed by decomposition of the alkoxy groups in the titanium complex. Similar transformations probably occur when the OH groups of the epoxy resin react with the chelating ligand of the curing agent. Initially the epoxy resin adds to the curing agent molecule, displacing the chelating ligand:

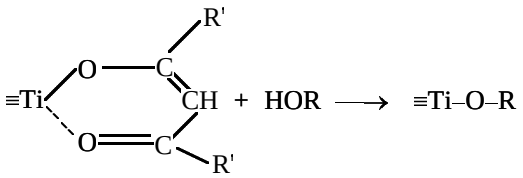

$$+ R'CC(=O)CHR'OH, \quad (3)$$

where R is the epoxy resin residue; R' = CH_3, C_6H_5.

Then the resin reacts with the free ligand along the pathway of Claisen retrocondensation:

$$R'-COCH_2COR' + HR \rightarrow R'COOR + CH_3COR' \quad (4)$$

This process accounts for appearance of the ester absorption bands in the spectra of the cured product. The forming ketones, acetone or acetophenone, are apparently removed from the sample in the course of curing. It was shown for the acetylacetonate curing agent that curing is accompanied by up to 1.3% weight loss, in agreement with data of [9].

The density of the polymeric network was calculated from the thermomechanical curves by the method described in [10]. The results of calculating the molecular weight M_s of the chain segment between the cross-linking points are listed in Table 2. Depending on the composition and structure of the curing agent, M_s varies from 470 to 1130; the minimal values of M_s and hence the thickest networks are provided by the compounds containing 6–10 mol of the resin per mole of the curing agent.

This conclusion agrees with the dielectric properties of the cured polymer samples. The maximum in the temperature and frequency dependences of tanδ corresponds to the region of dipole-segmental loss, as it is manifested above the glass transition point of the polymers. From these data, we calculated the relaxation time logτ and the activation energy ΔG^* of the dipole-segmental process [3, 11]. The results are listed in Table 2. It is seen that, in the examined range of the polymer compositions, the least mobile networks (largest logτ and ΔG^*) are formed in curing of the compounds containing 6.6–10 mol of the resin per mole of the curing agent.

The thickest polymer networks, as a rule, determine the highest glass transition points T_g. The concentration dependence of T_g^d calculated from the temperature and frequency dependence of tanδ for the polymers derived from oligomer **II** is shown in Fig. 2. The same figure shows the T_g^t values (superscripts d and t refer to data obtained by the dielectric and thermomechanical data, respectively). The heights of the high elasticity plateaus, D_{he}, found from the thermomechanical curves, are plotted in Fig. 3. In all the cases, $T_g^t > T_g^d$, which is due to relaxation phenomena in the polymers. Despite similar mechanisms of the dielectric and mechanical phenomena, the nature of glass transition in these cases is different. Large loads permanently acting on a sample hamper relaxation in polymer and cause accumulation of strains, shifting the glass transition point (determined from the thermomechanical curves) to higher temperatures [12]. At the same time, T_g^d is determined by extrapolation of the temperatures at which tanδ (at a given frequency) is maximal to a frequency of 1 Hz. Hence, T_g^d corresponds to the temperature of structural glass transition corresponding to the equilibrium conditions. However, both methods show that high values of T_g and low

values of D_{he} are exhibited by polymers obtained by curing of a compound whose composition provides formation of the thickest network (10 mol of the resin per mole of the curing agent).

The physicomechanical properties of the polymers are listed in Table 2. The bending (σ_b) and tensile (σ_t) strength is plotted vs. composition in Fig. 4. It is seen that the dependences pass through maxima at the molar ratio of 8–10 mol of the resin per mole of the curing agent, i.e., at the compound formulas ensuring formation of the thickest network. Figure 4 also shows that, for the polymers derived from **II**, the strength maximum is slightly shifted toward higher resin content. The polymers derived from **I** have the highest σ_b and σ_t values. In the composition range differing from the optimum, the polymers also exhibit high strength. At a higher content of the curing agent, the stronger polymers are obtained with **I**, and at a lower content, with **I**.

For the polymers derived from **III**, there is no clear correlation between the properties and compound formula, which may be due to an additional effect of the nitrogen-containing ligand on the curing [13].

Thus, our studies showed that the polymers derived from the epoxy resin and oligochelatotitanophenylenesiloxanes have the highest density of cross-linking and the best physicomechanical characteristics at the molar ratio of the resin to the curing agent of 6.6–10. In this composition range, the physicomechanical properties of the polymers are similar to those of epoxy–titanopolyether polymers [3, 14]. At the same time, the polymers derived from the epoxy resin and oligochelatotitanophenylenesiloxanes have higher (by 90° on the average) softening point.

To accelerate curing of epoxy–chelatotitanophenylenesiloxane compounds, we used accelerators differing in the chemical nature: 2,4,6-tris(dimethylaminomethyl)phenol (UP-606/2), NaI, and a complex of dibenzo-18-crown-6 with KI (DBC). These catalysts were added in amount of 1 wt % to the compounds, which allowed the maximal temperature to be decreased by 40–50°C, and the curing time, by a factor of 2–3. The properties of the polymers obtained from one of the compounds with **II** in the presence of catalysts are listed in Table 3. It is seen that the physicomechanical properties of the products are similar to those of the polymers of the same compositions obtained without a catalyst. The softening point of the polymers and the working life of the compounds decrease (the latter, from 6 to 1 month).

The epoxy–chelatotitanophenylenesiloxane compounds were used as bases of adhesives for gluing ferrite–Sitall (devitrified glass) rods. The strength of the glued rods at static cantilever bending, σ_{cb}, is given in Table 3. It is seen that the strength of rod gluing with the compounds under consideration is as high as with epoxy–titanopolyether compounds [15].

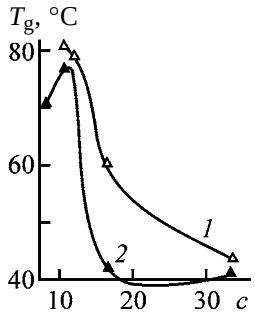

Fig. 2. Glass transition point T_g of polymers derived from ED-20 resin and oligomer **II** as a function of the compound formula. Determination method: (*1*) thermomechanical and (*2*) dielectric. (*c*) Molar ratio of ED-20 to **II**; the same for Fig. 3.

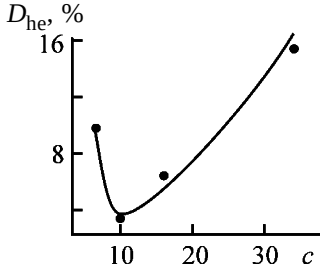

Fig. 3. Height of the high elasticity plateau D_{he} of polymers derived from ED-20 resin and oligomer **II** as a function of the compound formula.

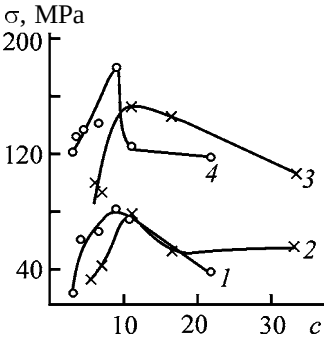

Fig. 4. (*1*, *2*) Tensile and (*3*, *4*) bending strength σ of polymers as a function of the compound composition. (*c*) Molar ratio of ED-20 to the oligomer. Curing agent: (*1*, *4*) **I** and (*2*, *3*) **II**.

EXPERIMENTAL

The components were combined by vigorous stirring at 60–170°C depending on the chemical structure of the curing agent (Table 1), followed by evacuation

Table 3. Properties of polymers prepared from ED-20 and oligomer **II** (10 wt %) in the presence of 1 wt % catalyst

Polymer no.	Catalyst	Curing mode*	Strength, MPa				a, kJ m^{-2}	T_V, °C
			σ_c	σ_t	σ_b	σ_{cb}		
1	UP-606/2	IV	117.0	70.0	129.0	71.5	10.0	340
2	Na1	V	129.0	–	–	113.3	–	–
3	DBC	V	110.0	–	–	97.0	–	275
4	No catalyst	II	117.5	53.0	145.5	82.5	10.0	355

* (IV) Heating from 20 to 150°C over a period of 2 h; 150°C, 3 h; (V) 120°C, 1 h; 130°C, 1 h; 140°C, 1 h; 150°C, 1 h; 160°C, 2 h; (II) see Table 2.

at 80°C for 30–40 min. The compounds contained 5–30 wt % curing agent, which corresponds to 33.7–2.7 mol of the resin per mole of the curing agent.

The viscosity η of the compounds was measured by the falling ball method at 25°C.

The IR spectra of the initial components, compounds kept at definite temperatures for definite periods, and cured polymers were measured on a UR-20 spectrophotometer with KBr, NaCl, and LiF prisms; the samples were prepared as mulls in mineral oil or 2% solutions in CH_2Cl_2.

The DTA curves were recorded on an OD-102 derivatograph at a heating rate of 5 deg min^{-1} in air.

The soluble fraction in the cured samples was determined by prolonged extraction with acetone in a Soxhlet apparatus.

The compression (σ_c), tensile (σ_t), and bending (σ_b) strength was determined with FM-250 and ZDM-5/91 tensile-testing machines, and the specific impact resilience a, on an MK-05 pendulum impact machine.

Thermomechanical measurements were performed on a device with a constant load of 8 kg cm^{-2}. The thermomechanical curves are plots of the strain D (%) vs. temperature. From these plots, we determined the glass transition point of the polymers T_g^t and estimated the height of the high elasticity plateau D_{he} [16]. The Vicat softening point T_V was determined on the same device as the temperature at which a rod with a tip area of 1 mm^2 sank into a sample to a depth of 1 mm under a load of 5 kg.

The dielectric properties (dielectric loss tangent $\tan\delta$ and dielectric permittivity ε') were determined with a TR-9701 bridge in the frequency range 0.5–200 kHz at 20–200°C.

CONCLUSIONS

(1) Oligochelatotitanophenylenesiloxanes prepared by heterofunctional condensation of bis(dimethyloxysilyl)benzene with appropriate bis(chelato)dialkoxytitanium were used as curing agents for ED-20 epoxy–4,4'-isopropylidenediphenol resin.

(2) Reactions of epoxy groups with functional groups of the curing agents were studied by IR spectroscopy. Conditions ensuring formation of the maximally cross-linked polymers were found.

(3) The best properties are exhibited by the polymers prepared from compounds with the molar ratio of the resin to the curing agent of 6.6–10.

(4) Adhesives based on epoxy–chelatotitanophenylenesiloxanes ensure high strength of glued ferrite–Sitall rods.

REFERENCES

1. USSR Inventor's Certificate no. 1086783.
2. USSR Inventor's Certificate no. 303334.
3. Suvorov, A.L., Suvorova, A.I., Dul'tseva, L.D., *et al.*, *Vysokomol. Soedin., Ser. A*, 1978, vol. 20, no. 1, pp. 2592–2600.
4. Dul'tseva, L.D., Suvorov, A.L., Mitrofanov, B.V., *et al.*, in *Abrazivnye instrumenty s polimernymi i keramicheskimi svyazuyushchimi: protsessy polucheniya i primenenie* (Abrasive Tools with Polymeric and Ceramic Binders: Fabrication and Use), Sverdlovsk: Ural. Nauchn. Tsentr Akad. Nauk SSSR, 1982, pp. 73–79.
5. Romanovskii, G.K., Tsitokhtsev, R.A., Rapoport, L.Ya., and Petrov, G.N., *Vysokomol. Soedin., Ser. A*, 1975, vol. 17, no. 11, pp. 2512–2516.
6. Abramova, V.I., Dul'tseva, L.D., Suvorov, A.L., *et al.*, *Plast. Massy*, 1986, no. 1, p. 58.
7. Bellamy, L.J., *The Infra-Red Spectra of Complex Molecules*, New York: Wiley, 1957.
8. Zeitler, V.A. and Brown, J.A., *J. Phys. Chem.*, 1957, vol. 61, p. 1174.
9. Yatluk, Yu.G., Chernyak, S.V., Suvorov, A.L., *et al.*,

Zh. Obshch. Khim., 2001, vol. 71, no. 6, pp. 1027–1029.

10. Paramonov, Yu.M., Artemov, V.N., and Klebanov, M.S., *Sb. Tr. Nauchno-Proizv. Ob"ed. "Plastik,"* 1977, issue 3, pp. 81–86.
11. Kauzman, W., *Rev. Mod. Phys.*, 1942, vol. 43, p. 219.
12. Sogolova, T.I. and Slonimskii, G.L., *Zh. Vses. Khim. O–va. im. D.I. Mendeleeva*, 1961, vol. 6, no. 4, pp. 389–393.
13. Dul'tseva, L.D., Yatluk, Yu.G., Suvorov, A.L., *et al.*, Abstracts of Papers, *III Vsesoyuznaya konferentsiya po khimii i fizikokhimii oligomerov (Odessa, 23–25 sentyabrya 1986 g.)* (III All-Union Conf. on Chemistry and Physical Chemistry of Oligomers (Odessa, September 23–25, 1986)), Chernogolovka: Otd. Inst. Khim. Fiz. Akad. Nauk SSSR, 1986, p. 2178.
14. USSR Inventor's Certificate no. 523913.
15. USSR Inventor's Certificate no. 812817.
16. Tsetlin, B.L., Gavrilov, V.I., Velikovskaya, N.A., and Kochkin, V.V., *Zavod. Lab.*, 1956, no. 22, pp. 352–355.

Russian Journal of Applied Chemistry, Vol. 76, No. 11, 2003, pp. 1850–1854. Translated from Zhurnal Prikladnoi Khimii, Vol. 76, No. 11, 2003, pp. 1901–1905.

MACROMOLECULAR CHEMISTRY AND POLYMERIC MATERIALS

Influence of Concentration and Molecular Characteristics of Copolymers of Acrylamide with Sodium Acrylate on the Thoms Effect in Oil-in-Water Emulsions

V. A. Myagchenkov and S. V. Chichkanov

Kazan State Technological University, Kazan, Tatarstan, Russia

Received April 12, 2003

Abstract—The effect of the concentration and molecular parameters of random copolymers of acrylamide and sodium acrylate on their performance as additives reducing the hydraulic resistance of turbulent flows in oil-in-water emulsions is quantitatively studied.

Water-soluble acrylamide (co)polymers are widely used in various stages of petroleum recovery, transportation, and refinery, particularly, as functional additives to control wellbore shale or to extend bentonite clay, as friction reducers to improve the performance of drilling facilities and transportation pipelines, and also for smoothing the profile of water injection well, oil dewatering and desalination, clean-up of equipment and pipelines to remove paraffin deposits, oily water clarification, etc. [1–3].

High-molecular-weight ionic and nonionic acrylamide (co)polymers prove to be among the most effective polymeric additives for reducing the hydraulic resistance of turbulent flows in oil-in-water and water-in-oil emulsions (Thoms effect) [1, 4]. The performance of polymeric additives as antiturbulence agents depends on a number of parameters, primarily on the polymer concentration and molecular characteristics [5, 6].

In this work, for such compositionally complex dispersion systems as oil-in-water (O/W) dispersions, we analyzed how the molecular weight (M) and M polydispersity of the polymeric additive, anionic acrylamide copolymer, influences the Thoms effect. It should be pointed out that the available information on the influence of the M polydispersity on the performance of copolymers as antiturbulence additives is limited, being not always correct [5, 6]. Only the behavior of cationic acrylamide copolymer in aqueous dispersions was studied systematically [7].

In this connection, one should take into account the fact that many chemical and physicochemical properties (including the Thoms effect) of copolymers depend not only on M and M polydispersity, but also on the mean composition of macromolecules $\bar{\alpha}$ and α polydispersity [8]. This problem, typical of common methods used for synthesis of random copolymers, such as ion and radical copolymerization and polymer-analogous reactions [9], was not given due attention in interpreting experimental data on the Thoms effect in dispersions containing random copolymers as additives.

An additional argue for the necessity of consideration of the influence of $\bar{\alpha}$ and α polydispersity on the resultant macroscopic Thoms effect in oil emulsions with ionic random copolymers of acrylamide and sodium acrylate as additives is that these parameters strongly affect the conformation state of the macroanions. In this work, in order to *a priori* exclude the effect of such characteristics of a polymeric additive as the $\bar{\alpha}$ and α polydispersity on the turbulent flow of oil emulsions, we used an unconventional method, mild ultrasonic disintegration (USD), for synthesis of the copolymer samples [10, 11].

EXPERIMENTAL

Anionic acrylamide copolymers differing in M, but similar in $\bar{\alpha}$ and α polydispersity were synthesized using USD from Alcoflood 1175A random copolymer of acrylamide and sodium acrylate [M_0 10.8×10^6; α 21.5% (weight percentage of ionic groups)]. As in [11, 12], USD synthesis of the copolymers was carried out with an UZDN-1 ultrasonic disintegrator at a frequency of 22×10^3 Hz in 0.1 M aqueous solution under specially selected mild conditions. In experiments we varied the ultrasonic field power and exposure time. Without taking into account the type of

1070-4272/03/7611-1850$25.00

terminal groups and chemical nature (acrylate or amide) of the polymer units where the macromolecular chain is broken, a simplified mechanism of ultrasonic disintegration in synthesis of the copolymer samples with various M can be presented as

$$\text{–(–A–)}_n\text{–(–B–)}_m\text{–} \rightarrow \text{–(–A–)}_{n_1}\text{–(–B–)}_{m_1}\text{–}$$
$$+ \text{–(–A–)}_{n_2}\text{–(–B–)}_{m_2}\text{–} + \cdots + \text{–(–A–)}_{n_1}\text{–(–B–)}_{m_1}\text{–}$$
$$+ \cdots + \text{–(–A–)}_{n_k}\text{–(–B–)}_{m_k}\text{–} + \dot{Z},$$

where A = CH_2–$\underset{\displaystyle CONH_2}{\underset{|}{CH}}$; B = –$CH_2$–$\underset{\displaystyle COO^-Na^+}{\underset{|}{CH}}$; $\dot{Z}$ are radicals inactive with respect to the rupture of the skeleton carbon–carbon bonds, whose nature appears to be inessential in analysis of general relationships of USD; $\sum_{i=1}^{k} n_i = n$, and $\sum_{i=1}^{k} m_i = m$.

As expected, with increasing exposure time, the number of breaks per macromolecule increased, and the degree of polymerization ($n_i + m_i$) of the polymer fragments formed in the course of USD decreased.

Mild conditions that were selected for USD allowed exclusion from consideration of such difficultly controllable reactions involving functional groups of the macromolecules as depolymerization and interchain interaction. It was demonstrated in particular experiments that USD of random copolymers of acrylamide and sodium acrylates could be interpreted in terms of the theory of random polymer degradation without depolymerization [13, 14]. Particularly, according to [13], the M polydispersity of USD products [estimated using the degradation scheme as the difference in ($n_i + m_i$) for the whole set of k fractions of the investigated copolymer] should follow the Flory statistics, and, therefore, the Schultz parameter $F = 1$ [14]. The USD procedure used permitted separation of eight samples with the maximal ($M_{max} = M_0$) and minimal (M_{min}) molecular weights differing by more than two orders of magnitude. The M_x of copolymer samples obtained in the course of USD was estimated by Eq. (1) using the initial sample with $M = M_0$ and $[\eta] = [\eta]_0$ as a reference ([η] is the intrinsic viscosity in 0.5 M NaCl).

$$M_x = M_0([\eta]_x/[\eta]_0)^{1/a}, \quad (1)$$

where a is the exponent in the Staudinger–Mark–Houwink equation (2).

$$[\eta] = kM^a. \quad (2)$$

We assumed $a = 0.814$ for all the samples of copolymers of acrylamide and sodium acrylate with $\alpha = 21.5\%$ [15].

For all the copolymers separated in the course of USD, $M_x \geq M_{min} = 0.08 \times 10^6$, suggesting that, for any fraction of any sample, $n_i + m_i > 500$. In accordance with concepts of the binary copolymerization theory [8, 16], the above inequality is equivalent, to a first approximation, to the fulfillment of relationships (3) for copolymer samples obtained upon USD.

$$\frac{n_1}{n_1 + m_1} = \frac{n_2}{n_2 + m_2} = \cdots = \frac{n_i}{n_i + m_i} = \cdots = \frac{n_k}{n_k + m_k}$$
$$= \frac{n}{n + m}. \quad (3)$$

It follows from these equalities that all the random copolymers of acrylamide and sodium acrylate obtained upon USD are identical not only in $\bar{\alpha}$, but also in the compositional nonuniformity, i.e., α polydispersity [8].

Also we used the ultrasonic disintegrator to obtain stable 10% O/W emulsions from dewatered and degassed crude oil (Aptugai oilfield, Perm oblast). Into a 300-ml conical flask containing fixed volumes of oil and water, a stabilizer was added in amount of 2% relative to the oil volume. The mixture was stirred for a short time on a magnetic stirrer and ultrasonicated for 15 min. As demonstrated by the microscopic data, the resulting emulsions were quite uniform with the particle size ranging from 0.7 to 1 μm, and no remarkable separation of the emulsion was observed in 10 days.

The performance of a polymeric antiturbulence additive in complex dispersion systems like oil emulsions can be correctly evaluated from the difference between the linear flow velocities across a capillary with (v) and without the additive (v_0) using a relative dimensionless parameter T [17]:

$$T = (v - v_0)/v_0. \quad (4)$$

The optimal capillary size for measuring the Thoms effect T in oil emulsions was determined in special experiments to be 0.5×38 mm (Reynolds number of water $Re = 5.2 \times 10^3$). Therefore, we measured the weights of emulsions with (m) and without (m_0) the additive, passed through the capillary in 30 s. The weights were measured on an A&D single-arm electronic balance (Japan). Under these conditions, Eq. (4)

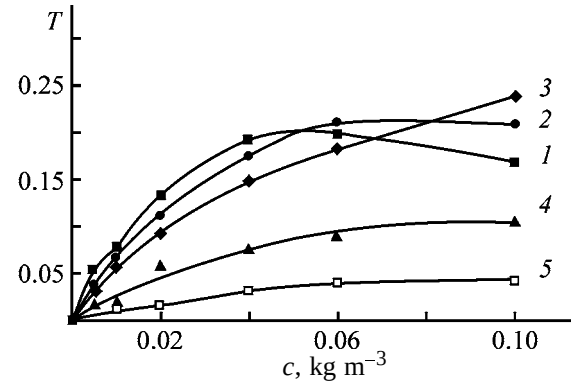

Fig. 1. Thoms effect T as a function of the concentration c of anionic acrylamide copolymers with various M. $M \times 10^{-6}$: (*1*) 10.80, (*2*) 5.08, (*3*) 3.30, (*4*) 1.07, and (*5*) 0.83.

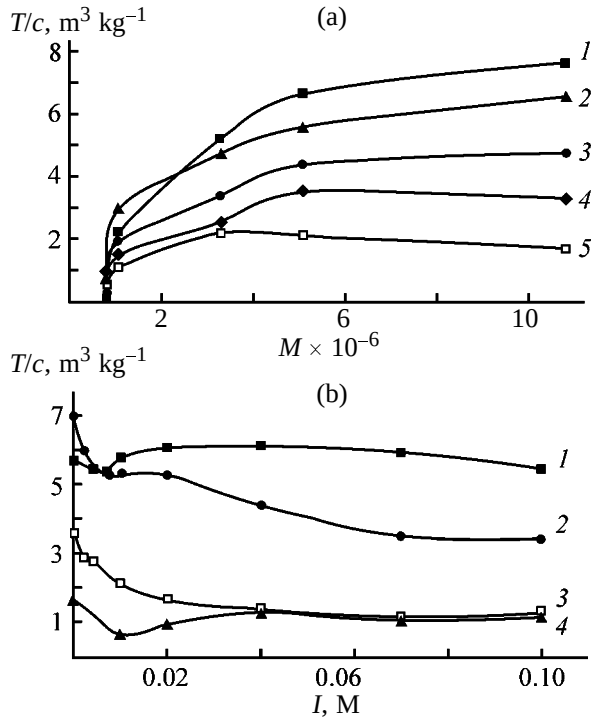

Fig. 2. Reduced Thoms effect T/c as a function of (a) molecular weight M of copolymers at various concentrations and (b) solution ionic strength I at c = 0.1 kg m^{-3}. (a) c (kg m^{-3}): (*1*) 0.01, (*2*) 0.02, (*3*) 0.04, (*4*) 0.06, and (*5*) 0.1. (b) $M \times 10^{-6}$: (*1*) 10.8, (*2*) 5.08, (*3*) 1.07, and (*4*) 0.83.

can be rewritten as

$$T = (m - m_0)/m_0. \quad (5)$$

To elucidate the performance of a specific (co)polymer as an antiturbulence additive for oil emulsions, it is necessary to analyze the effects of at least the (co)polymer concentration c and M on T. The concentration dependences of T are shown in Fig. 1 for several samples of anionic acrylamide copolymers with various M. As seen, the general concepts of the Thoms effect theory [5, 7] are valid in oil emulsions also, i.e., T increases with increasing c and M. To gain a better insight into the rheology of oil emulsions with polymeric additives, it was advisable to study the effect of each next portion of the additive on the macroscopic effect. In so doing, we pass from the parameter T to the reduced Thoms effect $\gamma = T/c$ [7, 14]. It is obvious that the higher γ, the higher the efficiency of a fixed portion of a polymeric antiturbulence additive, all other conditions being equal. As an illustration, Fig. 2 shows the reduced Thoms effect as a function of M for various concentrations of the polymeric additive. With increasing c, γ regularly decreases, especially in the case of the highest-molecular-weight sample with $M = M_0$, i.e., as c increases, the antiturbulence effect of the next portions of the additive decreases. It is clear from these results that the concentration dependence of the reduced Thoms effect should be necessarily taken into account in optimization of high-speed pipeline transportation of oil emulsions containing polymeric additives.

In recovery and transportation of crude oil as an O/W emulsion, the dispersion medium contains various electrolytes, primarily, salts, whose concentration amounts to several percents [18]. Therefore, the effect of the ionic strength on T is of not only scientific, but also practical interest. In this work we used NaCl as a supporting electrolyte. As seen from Fig. 2, T in O/W emulsions depends on the ionic strength of the dispersion medium, the dependence being less pronounced as compared to aqueous solutions [19]. In the emulsions, the electrolytic effect is reflected, most likely, in modification of the electrical double layer around the stabilized particles of the dispersed phase.

Figure 3 clearly shows the trend in the specific viscosity of O/W emulsions containing anionic acrylamide copolymers with various M and also the electrolyte. The adsorption coefficient β of anionic acrylamide copolymers in O/W emulsions was estimated from the viscometric data using Eq. (6)

$$\beta = \frac{\eta_{sp}^0 - \eta_{sp}}{\eta_{sp}^0} \frac{c}{S_{sp}(1 - q)}, \quad (6)$$

where S_{sp} is the specific surface area of 1 m^3 of the dispersed particles (for spherical particles $S_{sp} = 3/R$, where R is the particle radius); η_{sp}^0 and η_{sp}, specific viscosities of aqueous solutions of the copolymers (c = 0.1 kg m^{-3}) before and after contact with the

dispersed particles, respectively; and q, volume fraction of the aqueous phase in the emulsion.

The coefficient β thus obtained appeared to be comparatively small (2×10^{-2} mg m^{-2}). It is natural to attribute such a low β in O/W emulsions to strong electrostatic repulsion between similarly charged macroanions of the copolymer and anions of the stabilizer forming an adsorption layer of the potential-determining ions on the surface of the dispersed particles. Furthermore, the quite high T and $\gamma = T/c$ in O/W emulsions in the presence of the anionic acrylamide copolymers give an additional, indirect evidence in favor of this concept.

Except for [7], the extensive literature on various aspects of the Thoms effect contains practically no systematic quantitative information of the influence of the M polydispersity and compositional polydispersity on T. In this work, the samples of random copolymers of acrylamide with sodium acrylate were identical in $\bar{\alpha}$ and α polydispersity. Therefore, no fundamental problems could arise in preparing systems with fixed $\overline{M} = 3.3 \times 10^6$ and various M polydispersity. The composition of the systems with $\overline{M} = 3.3 \times 10^6$ was estimated as in [7]. As a quantitative criterion for evaluation of the M polydispersity of the copolymers we used the Schultz parameter F [7, 19] defined as

$$F = (\overline{M}_w/\overline{M}_n) - 1 = \sum_{i=1}^{k} \omega_1 M_1 \sum_{i=1}^{k} (\omega_i/M_i) - 1, \quad (7)$$

where $\overline{M}_w$ and $\overline{M}_n$ are the weight-average and number-average molecular weights of the systems, and ω_i, weight fraction of the ith component of the mixture, i.e., of a copolymer with $M = M_i$ (k is the number of copolymer kinds in the mixture).

Higher F in a given mixture compared to the reference is indicative of its greater M polydispersity.

The concentration dependences of T are given in Fig. 4 for a series of the most typical copolymer mixtures with fixed $\overline{M} = 3.3 \times 10^6$. It is clearly seen that the resultant macroscopic Thoms effect correlates with the M polydispersity of oil-in-water emulsions.

In Fig. 5, the Thoms effect is plotted as a function of the Schultz parameter F in O/W emulsions at various ionic strengths. The presence of a maximum and a minimum in this plot suggests complexity of the turbulent flow mode in this system, which is reflected primarily in nonadditive contributions of copolymers with various M to the resultant macroscopic Thoms effect. Knowingly not touching upon a very complicated and in a number of points debatable mechanism

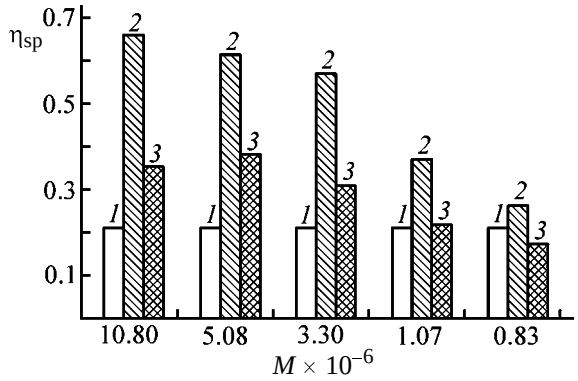

Fig. 3. Specific viscosity histogram for the system oil emulsion–polymer–electrolyte: (*1*) emulsion, (*2*) emulsion–polymer (0.1 kg m^{-3}), and (*3*) emulsion–polymer (0.1 kg m^{-3})–electrolyte (0.1 M NaCl).

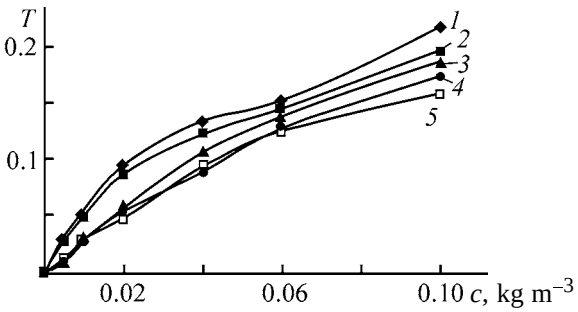

Fig. 4. Thoms effect T as a function of the additive concentration c. F: (*1*) 1, (*2*) 5.16, (*3*) 1.45, (*4*) 2.07, and (*5*) 3.71.

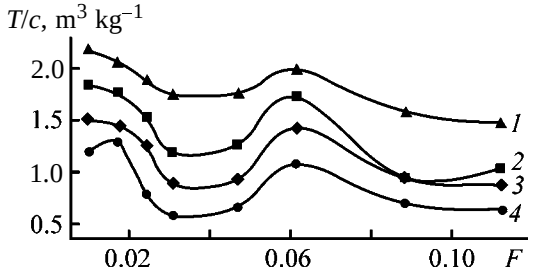

Fig. 5. Reduced Thoms effect T/c as a function of the M polydispersity F (c = 0.1 kg m^{-3}). I (M): (*1*) 0, (*2*) 0.002, (*3*) 0.01, and (*4*) 0.1.

of turbulent flow of O/W emulsions in multicomponent systems with water-soluble anionic acrylamide copolymer additives, it may be established that, apart from traditional control tools of the process, there is an unconventional approach based on control of the M and α polydispersities of a copolymer additive [7]. Without question, carrying out intensive experimental and theoretical studies in this direction will promote development and application of optimal regimes of high-speed pipeline transportation of oil emulsions with additives based on water-soluble acrylamide (co)polymers.

CONCLUSION

Samples of copolymers identical in the composition and polydispersity, but having different molecular weights were obtained by ultrasonic disintegration of macromolecules at the skeleton carbon–carbon bonds.

REFERENCES

1. Poraiko, I.N., *Primenenie poliakrilamida v tekhnologicheskikh protsessakh, svyazannykh s dobychei nefti: Tematicheskii nauchno-tekhnicheskii obzor* (Applications of Polyacrylamide in Petroleum Recovery: A Topical Review), Moscow: VNIIOENG, 1974.
2. Ibragimov, G.Z., Sorokin, V.A., and Khisamutdinov, N.M., *Khimicheskie reagenty dlya dobychi nefti* (Oilfield Chemicals), Moscow: Nedra, 1986.
3. Barabanov, V.P. and Krupin, S.V., *Vodorastvorimye polimery i ikh primenenie: Uchebnoe posobie* (Water-Soluble Polymers and Their Applications: A Textbook), Kazan: Kazan. Khim.-Tekhnol. Inst., 1984.
4. Small, S.R., *Neft' Gas Neftekhim. Rubezh.*, 1986, no. 7, pp. 60–63.
5. Nikolaev, A.F. and Okhrimenko, G.I., *Vodorastvorimye polimery* (Water-Soluble Polymers), Leningrad: Khimiya, 1979.
6. Abramova, L.I., Baiburdov, T.A., Grigoryan, E.P., *et al.*, *Poliakrilamid* (Polyacrylamide), Moscow: Khimiya, 1992.
7. Myagchenkov, V.A., Chichkanov, S.V., Proskurina, V.E., and Myagchenkov, A.V., *Zh. Prikl. Khim.*, 2002, vol. 75, no. 9, pp. 1517–1520.
8. Myagchenkov, V.A. and Frenkel', S.Ya., *Kompozitsionnaya neodnorodnost' sopolimerov* (Composition Nonuniformity in Copolymers), Leningrad: Khimiya, 1988.
9. Shur, A.M., *Vysokomolekulyarnye soedineniya* (Macromolecular Compounds), Moscow: Vysshaya Shkola, 1981.
10. Myagchenkov, V.A., Krikunenko, O.V., and Churikov, F.I., *Ul'trazvukovaya destruktsiya vodorastvorimykh (so)polymerov* (Ultrasonic Degradation of Water-Soluble (Co)polymers), Kazan: Kazan. Khim.-Tekhnol. Inst., 1998.
11. Myagchenkov, V.A. and Krikunenko, O.V., *Vysokomol. Soedin., Ser. A*, 1995, vol. 37, no. 1, pp. 44–49.
12. Myagchenkov, V.A., Panarin, E.F., Yunusov, O.A., *et al.*, *Dokl. Ross. Akad. Nauk*, 1992, vol. 324, no. 4, pp. 826–829.
13. Berlin, A.A., Khakimdzhanova, M.A., Karmilova, L.V., and Enikolopyan, N.S., *Vysokomol. Soedin.*, 1968, vol. 10, no. 7, pp. 1496–1501.
14. Berlin, A.A., Vol'fson, S.A., and Enikolopyan, N.S., *Kinetika polimerizatsionnykh protsessov* (Polymerization Kinetics), Moscow: Khimiya, 1978.
15. Klein, J. and Conrad, K.D., *Makromol. Chem.*, 1978, vol. 179, pp. 1635–1638.
16. *Copolymerization*, Ham, G.E., Ed., New York: Interscience, 1964.
17. Myagchenkov, V.A., Chichkanov, S.V., Proskurina, V.E., and Krupin, S.V., *Georesources*, 2002, no. 6, pp. 19–23.
18. Tronov, V.P., *Promyslovaya podgotovka nefti* (Oil Treating), Kazan: Fen, 2000.
19. Myagchenkov, V.A. and Chichkanov, S.V., *Zh. Prikl. Khim.*, 2003, vol. 76, no. 5, pp. 842–846.

Russian Journal of Applied Chemistry, Vol. 76, No. 11, 2003, pp. 1855–1857. Translated from Zhurnal Prikladnoi Khimii, Vol. 76, No. 11, 2003, pp. 1906–1908.

BRIEF COMMUNICATIONS

Precipitation of Titanium(IV) and Iron(III) Phosphates from Sulfuric Acid Solutions

L. G. Gerasimova and M. V. Maslova

Tananaev Institute of Chemistry and Technology of Rare Elements and Mineral Raw Materials, Kola Scientific Center, Russian Academy of Sciences, Apatity, Murmansk oblast, Russia

Received March 13, 2003

Abstract—Conditions for the precipitation of phosphates from solutions of titanium(IV) sulfate containing iron(III) were studied. The precipitation of components and the mechanism of the phase formation in the system under study were considered in relation to the $TiO_2 : Fe_2O_3$ ratio in the starting solution.

Titanium(IV) phosphates are well-known synthetic products used for obtaining high-quality white paper and light-resistant plastics, for filling construction and paintwork materials, and also as sorbents. Each of these fields imposes specific demands on the composition and properties of the product, which depend on the composition of the raw materials and conditions of the synthesis.

Titanium(IV) phosphates are usually obtained from sulfuric-hydrochloric acid titanium-containing solutions by adding phosphoric acid [1–3]. If process solutions containing impurities of other ions apart from titanium(IV) are used for this purpose, the target product can be contaminated with these impurities because of the equal solubility of their phosphates or of their sorption on the surface of the titanium phosphate precipitate.

In this work we studied the conditions for the precipitation of titanium(IV) and iron(III) phosphates from sulfuric acid solutions containing various quantities of these components. Such solutions are obtained by the sulfuric acid processing of titanium-containing raw materials: sphene, perovskite, and ilmenite. In particular, sphene solutions intended for obtaining pigment titanium dioxide by thermal hydrolysis contain 150–250 g l^{-1} TiO_2 and up to 5 g l^{-1} Fe_2O_3; perovskite solutions, up to 20 g l^{-1} Fe_2O_3; and ilmenite solutions, up to 100 g l^{-1} Fe_2O_3 [4–6]. Wastewater to be treated contains up to 10 g l^{-1} TiO_2 and from 5 to 80 g l^{-1} iron (in terms of Fe_2O_3).

The following data were the prerequisites for our study. Titanium(IV) forms a hydrated solid phase on adding H_3PO_4 to its solutions over a wide range of their concentration and acidity. The number of aqua groups in the precipitate depends on the conditions of its preparation [7, 8]. At the same time, hydrated iron(III) phosphates under the action of phosphoric acid are precipitated from sulfuric acid solutions to a small extent [9–11]. The mechanism of the formation of the phosphate solid phase in mixed iron–titanium solutions is poorly understood.

In our study we used a titanium(IV) sulfate solution (concentrations of TiO_2 and H_2SO_4 1.75 and 4.25 M, respectively) prepared by dissolving titanium(IV) hydroxide in sulfuric acid, and also a solution of iron(III) sulfate (Fe_2O_3 concentration 0.625 M). We stirred the solutions (the starting volume of the solutions corresponded to a specified $TiO_2 : Fe_2O_3$ ratio) for 30 min and added concentrated H_2SO_4 up to 4.5 M. We used 81% solution of H_3PO_4 as a precipitant. Its consumption corresponded to the molar ratio $(TiO_2 + Fe_2O_3) : P_2O_5 = 1 : 1$. We added phosphoric acid to the solution under study gradually over a period of 0.5–1 h with stirring and heating (T = 80°C). Then the suspension was allowed to stand for 2 h, after which the precipitate was separated from the liquid phase and washed with water to pH 7. We determined the composition of the liquid phase (the contents of TiO_2, Fe_2O_3, and P_2O_5) by chemical analysis, and the composition of the solid phase, by the X-ray spectral analysis. For this purpose, we calcined the precipitates at 800°C. We studied the structure of the precipitates by optical microscopy, IR spectroscopy, and X-ray phase analysis.

Figure 1 shows the effect of the starting composition of the solution on the degree of passing of the components into the precipitate on adding H_3PO_4. The TiO_2/Fe_2O_3 concentration ratio was chosen as the characteristic of the solution.

1070-4272/03/7611-1855$25.00

Characteristics of phosphate precipitates separated from sulfuric acid titanium solutions in the presence of iron(III)

TiO_2/Fe_2O_3 molar ratio*	Composition of precipitates, wt %			Moisture content, %	Calcination loss, %	$TiO_2 : Fe_2O_3 : P_2O_5 : H_2O$ molar ratio
	TiO_2	Fe_2O_3	P_2O_5			
0.25	33.6	0.55	31.1	65.1	77.6	1 : 0.01 : 0.6 : 10
0.33	27.5	0.53	35.9	62.4	71.2	1 : 0.01 : 0.7 : 12
0.50	25.9	0.45	38.3	71.3	82.3	1 : 0.01 : 0.8 : 15
4	30.4	0.45	28.1	54.9	66.0	1 : 0.006 : 0.5 : 10
12	34.4	0.53	33.4	55.8	67.3	1 : 0.007 : 0.6 : 9
20	34.4	0.66	34.6	58.1	70.0	1 : 0.009 : 0.6 : 9
26	37.0	0.66	38.0	59.0	71.3	1 : 0.008 : 0.6 : 9

* In the starting solution.

In the range of titanium(IV) concentrations in the solution corresponding to the ratio TiO_2/Fe_2O_3 = 4–20 (the Fe_2O_3 concentration is 0.0625 M and does not change), at the above-noted H_3PO_4 consumption, titanium(IV) is precipitated almost completely. For TiO_2/Fe_2O_3 = 4, the degree of iron(III) precipitation increases from 30 to 55% (in terms of Fe_2O_3) as the titanium(IV) concentration in the solution increases. Under similar conditions, no precipitate is formed from the solution of pure iron(III) sulfate. We emphasize that about 50% of H_3PO_4 (in terms of P_2O_5) is not involved in the reaction and remains in the liquid phase. For a low titanium(IV) concentration in the solution under study (0.125 M in terms of TiO_2) and the ratio TiO_2/Fe_2O_3 = 0.25–0.5, the phosphate precipitate contains from 3 to 7% Fe_2O_3. The degree of titanium(IV) precipitation decreases as the concentration of iron(III) increases.

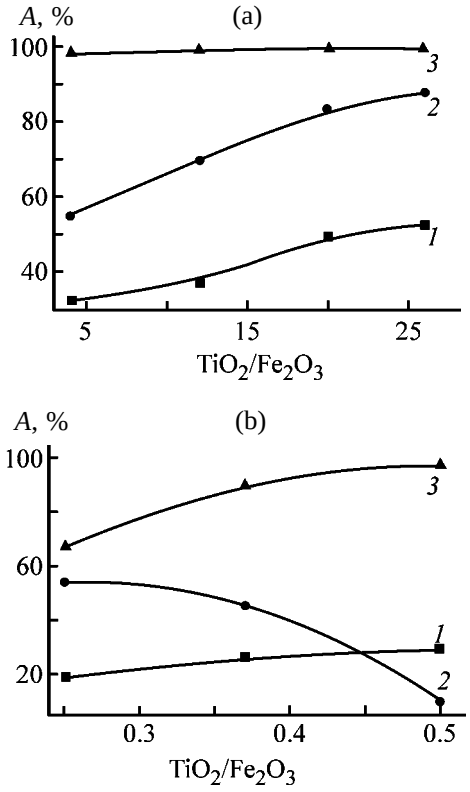

Fig. 1. Degree of precipitation of the main components *A* as a function of the TiO_2/Fe_2O_3 molar ratio in solution. Content in the starting solution, M: (a) Fe_2O_3 0.065 and (b) TiO_2 0.125. (*1*) Fe_2O_3, (*2*) P_2O_5, and (*3*) TiO_2.

On the basis of the data from [12, 13], we may state that titanium(IV) and iron(III) are combined into a pseudocomplex in sulfate solutions. Its presence affects the titanium(IV) precipitation and the composition of the resulting precipitate. The data of crystallooptical analysis suggest that the precipitates consist of two phases. The impurity phase seems to be based on the iron–titanium complex (its study was beyond the scope of this work). Since the degree of iron(III) precipitation is lower than the maximal degree, we can suggest that the composition and stability of such complexes depend on the composition of the starting mixed solutions. As the titanium(IV) concentration in the starting mixture increases, the amount of iron(III) bound to titanium(IV) and, as a consequence, the degree of iron(III) precipitation grow also. In the case of a considerable excess of iron(III) relative to titanium(IV), the stability of iron–titanium complexes increases, which hampers the formation and further precipitation of hydrated titanium phosphate. In this case, the degree of iron(III) precipitation is about 25% (in terms of Fe_2O_3).

The compositions of the precipitates isolated from the iron–titanium sulfate system under study on adding phosphoric acid are given in the table. Since the precipitates are very poorly crystallized, the X-ray and IR data do not offer a sufficiently precise information on their phase composition and character of bonds. Therefore, we determined the composition of the

precipitates by chemical analysis. The samples were first dried at 105°C and then calcined at 850°C. In so doing, we determined the moisture content and calcination loss (see table).

Comparison of the compositions of the filtrates obtained after separating the phosphate precipitate and of the final products allows the following conclusions. At a high starting concentration of TiO_2, iron(III) precipitated from the solution has a low solubility in water; its content in the final product corresponds to the degree of its precipitation in the presence of H_3PO_4. The content of iron(III) precipitated from the solutions with its high concentration does not correlate with the degree of its precipitation. Iron(III) seems to be sorbed on the active surface of the phosphate precipitate, and its washing with water results in its desorption and passing into washing water.

CONCLUSION

On adding orthophosphoric acid into iron–titanium sulfuric acid solutions, precipitates are formed over a wide range of titanium(IV) and iron(III) concentrations. These precipitates consist mainly of hydrated titanium(IV) phosphate with an impurity of iron(III) phosphate, which does not exceed 0.66% in terms of Fe_2O_3. At a high iron(III) concentration in the solution, it is sorbed on the surface of hydrated titanium(IV) phosphate particles. However, the sorption involves no chemical reaction. The data obtained can be used for separating titanium(IV) and iron(III) in acid sulfate solutions.

REFERENCES

1. Tananaev, I.V., Rozanov, I.A., Avduevskaya, K.A., *et al*., *Fosfaty chetyrekhvalentnykh elementov* (Phosphates of Tetravalent Elements), Moscow: Nauka, 1972.
2. Spitsyn, V.I. and Ippolitova, E.A., *Zh. Anal. Khim*., 1951, vol. 4, no. 1, pp. 5–14.
3. Dolmatov, Yu.D. and Bulavina, Z.N., *Zh. Prikl. Khim*., 1974, vol. 47, no. 7, pp. 1498–1503.
4. Motov, D.L. and Maksimova, G.K., *Sfen i ego khimicheskaya pererabotka na titanovye pigmenty i napolniteli* (Sphene and Its Chemical Processing into Titanium Pigments and Fillers), Leningrad: Nauka, 1983.
5. Goroshchenko, Ya.G., *Fiziko-khimicheskie issledovaniya pererabotki redkozemel'nykh titanoniobatov sernokislotnym metodom* (Physicochemical Studies of Processing Rare-Earth Titanoniobates by Sulfuric Acid Method), Moscow: Akad. Nauk SSSR, 1960.
6. Belen'kii, E.F. and Riskin, I.V., *Khimiya i tekhnologiya pigmentov* (Chemistry and Technology of Pigments), Leningrad: Khimiya, 1974.
7. Bortun, A., Jaimez, E., Llavona, R., *et al*., *Mater. Res. Bull*., 1995, vol. 30, no. 4, pp. 413–420.
8. Bereznitski, Y., Jaroniec, M., Bortun, A., *et al*., *J. Colloid Interface Sci*., 1997, vol. 191, pp. 442–448.
9. Zabrodskii, V.N., Prokshin, N.E., and Zemskova, L.M., *Radiokhimiya*, 1998, vol. 40, no. 2, pp. 142–145.
10. Eshchenko, L.S., Pechkovskii, V.V., and Novikov, O.V., *Izv. Akad. Nauk BSSR, Ser. Khim*., 1978, no. 2, pp. 68–72.
11. Filatova, L.N., Shelyakina, M.A., Plachinda, A.S., and Makarov, E.F., *Zh. Neorg. Khim*., 1976, vol. 21, no. 10, pp. 2715–2720.
12. Goroshchenko, Ya.G., *Khimiya titana* (Chemistry of Titanium), Kiev: Naukova Dumka, 1970.
13. Konotopchik, K.U., Mechanism and Kinetics of the Synthesis of Titanium Dioxide for Radioceramics, *Cand. Sci. (Chem) Dissertation*, Sverdlovsk, 1979.

Russian Journal of Applied Chemistry, Vol. 76, No. 11, 2003, pp. 1858–1859. Translated from Zhurnal Prikladnoi Khimii, Vol. 76, No. 11, 2003, pp. 1909–1910.

BRIEF COMMUNICATIONS

Choice of a Stabilizer for the Reaction of KOH with Hydrogen Peroxide To Produce Potassium Superoxide

N. F. Gladyshev, S. I. Dvoretskii, D. V. Zhdanov, M. A. Ul'yanova, and Yu. A. Ferapontov

Tambov Research Chemical Institute, Federal State Unitary Enterprise, Tambov, Russia

Received April 1, 2003

Abstract—A stabilizer for the reaction of KOH and H_2O_2 yielding potassium superoxide was proposed. The stabilizer does not affect the main consumer properties of the regenerative product based on KO_2.

Potassium superoxide KO_2 is the most widely used substance for self-contained human respiratory apparatus. The use of KO_2 is based on its capability to chemisorb moist carbon dioxide, generating oxygen required for breathing [1].

Development of a new process for KO_2 production involved certain problems related to the process conditions and qualitative composition of the final product. One of these problems is considered in this paper.

EXPERIMENTAL

According to the suggested process [1–4], potassium superoxide is produced from potassium hydroxide and hydrogen peroxide by their mixing in the molar ratio $H_2O_2 : KOH = 1.75 : 1$ with subsequent disproportionation of the intermediate adduct $K_2O_2 \cdot 2H_2O_2$ in a spray-type reactor. The process can be described by the following reaction equations:

$$2KOH + 3H_2O_2 = K_2O_2 \cdot 2H_2O_2 + 2H_2O, \quad (1)$$

$$K_2O_2 \cdot 2H_2O_2 = 2KO_2 + 2H_2O. \quad (2)$$

The reaction of hydrogen peroxide with potassium hydroxide is strongly exothermic under normal conditions and is accompanied by decomposition of the peroxide products and evolution of atomic oxygen. Therefore, to carry out the process, it is necessary either to cool the reaction area, which requires additional power consumption, or to add a stabilizer. By the stability of various solutions of peroxide compounds is meant the capability to preserve their available oxygen (decrease in the absolute content of available oxygen should not exceed 0.5 wt %) for a long time.

The best stabilizers of concentrated alkaline solutions of H_2O_2 are $Na_4P_2O_7$, magnesium salts of mineral acids, and certain organic compounds [5–10].

Up to now, there are no strict scientific principles for the choice of stabilizers for H_2O_2 solutions preventing their decomposition [6]. Therefore, the stabilizers are mainly chosen empirically depending on the composition of a particular solution containing H_2O_2 or other peroxides. Since H_2O_2 alkaline solution is used further for obtaining potassium superoxide and the regenerative product thereof, the suitable stabilizers should meet certain requirements concerning their toxicity, thermal stability, chemical resistance to atomic oxygen, etc. Organic compounds are unsuitable as stabilizers for H_2O_2 alkaline solutions because of the possibility of their oxidation with potassium superoxide, accompanied by burning and explosion. Among inorganic salts, magnesium sulfate and $Na_4P_2O_7$ are the best stabilizers of H_2O_2 alkaline solutions. These compounds were used in this work to obtain potassium superoxide and the regenerative product thereof.

A specified amount of a stabilizer was dissolved in a 50% H_2O_2 solution. The solution was placed in a reactor cooled with tap water stream, and a 50% KOH solution was added slowly with stirring. We found that KOH reacts with H_2O_2 under these conditions without decomposition of peroxide products (simple acid–base interaction) at the molar ratios $H_2O_2 : MgSO_4 \geq 700 : 1$ and $H_2O_2 : Na_4P_2O_7 \geq 590 : 1$. According to the chemical analysis [11], the available oxygen content in the resulting solution is close to that calculated theoretically. It is known from the literature that each stabilizer has its own critical concentration up to which it is effective. A greater amount of the stabilizer could even promote peroxide solution decomposition [7]. Furthermore, the process being developed for producing KO_2 requires that the H_2O_2 alkaline solutions be stable for no less than one day. Therefore, to choose the optimal concentration of a stabilizer for

1070-4272/03/7611-1858$25.00

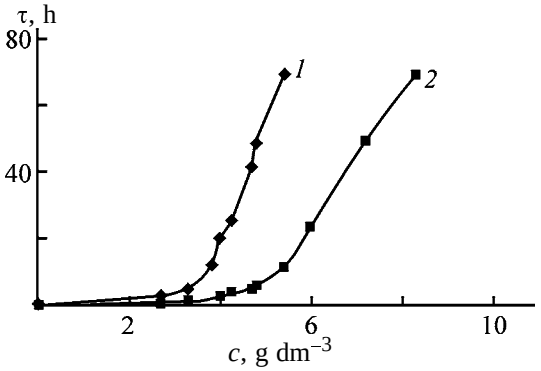

Time τ of stability of H_2O_2 alkaline solution as a function of the stabilizer concentration *c*: (*1*) $MgSO_4$ and (*2*) $Na_4P_2O_7$.

the H_2O_2 alkaline solution, we studied how the time of stability of the resulting solution depends on the stabilizer content in the starting H_2O_2 solution. The results are shown in the figure.

These data show that the amount of $MgSO_4$ per unit volume of the starting H_2O_2 solution, required for the stabilization of the reaction between H_2O_2 and KOH and for the further storage of the resulting solution, is less than that of sodium diphosphate, all other things being equal. Therefore, $MgSO_4$ is preferable as the stabilizer. In addition, $MgSO_4$ is more readily available and cheaper than $Na_4P_2O_7$.

According to the experimental data [2], $MgSO_4$ does not affect the qualitative composition of the final product, i.e., when hydrogen peroxide stabilized with $MgSO_4$ is used, the product obtained by the above-described technique is the same as the product obtained from H_2O_2 without adding magnesium sulfate (all other factors being the same). This conclusion is confirmed by chemical analysis.

It was found that, with magnesium sulfate used as a stabilizer for the reaction of H_2O_2 with KOH, granulated KOH could be used instead of the 50% KOH solution. In this case, peroxide products did not decompose either.

Our experiments showed that, with time, the resulting H_2O_2 alkaline solution acquired a distinct yellow color suggesting the presence of superoxide ion. That is, colorless diamagnetic peroxide ions O_2^{2-} disproportionate directly in the solution to give colored paramagnetic superoxide ions O_2^-. We found no indications on this phenomenon in the available literature. Kazarnovskii [12] studied this process only for solid compounds. To confirm the occurrence of this process in solution, we started the magnetic susceptibility measurements. The preliminary results confirm the presence of diamagnetic ions in the resulting H_2O_2 alkaline solutions. It should be noted that superoxide ions remain stable in aqueous solution under study for a rrelatively long time. This is important, because all superoxides are known to readily decompose on contact with water to the corresponding alkali with oxygen evolution.

CONCLUSIONS

(1) A study of the stability of potassium peroxide peroxosolvate solutions by chemical analysis showed that the solution stabilized with $MgSO_4$ (in the molar ratio $MgSO_4 : H_2O_2 = 1 : 750$) remains stable for one day at temperatures of up to 25°C.

(2) Diamagnetic peroxide ions O_2^{2-} disproportionate to give paramagnetic superoxide ions O_2^- directly in solution.

REFERENCES

1. Morachevskii, A.G., Beloglazov, I.N., and Kasymbaev, B.A. *Kalii: svoistva, proizvodstvo, primenenie* (Potassium: Properties, Production, Applications), Moscow: Ruda i Metally, 2002.
2. Ferapontov, Yu.A., Simanenkov, S.I., Gur'ev, A.A., *et al.*, *Vestn. Tambov. Gos. Tekh. Univ.*, 2001, vol. 7, no. 3, pp. 422–426.
3. Zhdanov, D.V., Ferapontov, Yu.A., and Gur'ev, A.A., *Tr. Tambov. Gos. Tekh. Univ.*, 2001, issue 8, pp. 210–219.
4. Ferapontov, Yu.A., Zhdanov, D.V., and Gladyshev, N.F., *Sbornik trudov XV mezhdunarodnoi nauchnoi konferentsii "Matematicheskie metody v tekhnike i tekhnologiyakh"* (Proc. XV Int. Scientific Conf. "Mathematical Methods in Industry and Technology"), Tambov, 2002, vol. 3, pp. 161–166.
5. Schumb, W.C., Satterfield, Ch.N., and Wentworth, R.L., *Hydrogen Peroxide*, New York: Reinhold, 1955.
6. *Khimiya i tekhnologiya perekisi vodoroda* (The Chemistry and Technology of Hydrogen Peroxide), Seryshev, G.A., Ed., Leningrad: Khimiya, 1984.
7. Pozin, M.E. *Perekis' vodoroda i perekisnye soedineniya* (Hydrogen Peroxide and Peroxide Compounds), Moscow: Goskhimizdat, 1951.
8. FRG Patent 594806.
9. UK Patent 433470.
10. US Patent 405532.
11. Seyb, E., and Kleinberg, J., *J. Am. Chem. Soc*, 1951, vol. 73, p. 2308.
12. Kazarnovskii, I.A., *Dokl. Akad. Nauk SSSR*, 1975, vol. 221, no. 2, pp. 353–356.

Russian Journal of Applied Chemistry, Vol. 76, No. 11, 2003, pp. 1860–1861. Translated from Zhurnal Prikladnoi Khimii, Vol. 76, No. 11, 2003, pp. 1911–1912.

BRIEF COMMUNICATIONS

Optimization of *tert*-Butyl Perbenzoate Purification

I. A. Solodova, I. P. Gorokhova, V. V. Zakhvatov, G. M. Salikhova, E. V. Maryanina, and Ch. B. Medvedeva

Kazan'orgsintez Open Joint-Stock Company, Kazan, Tatarstan, Russia

Received March 26, 2003

Abstract—Purification of *tert*-butyl perbenzoate with an $Na_2S_2O_5$ solution was studied.

tert-Butyl perbenzoate (TBPB) is widely used as high-temperature polymerization initiator in production of polyethylene, polystyrene, and vinyl acetate plastics. The quality of commercial TBPB is determined by its purity, i.e., by the degree of removal of numerous impurities: *tert*-butyl hydroperoxide (TBHP), di-*tert*-butyl peroxide (DTBP), benzoic acid (BA), *tert*-butyl alcohol (TBA), benzotrichloride (BTC), etc.

The major impurities in TBPB prepared by the two-step procedure [1] are DTBP, TBHP, and BA. In the first step (preparation of TBHP sodium salt), DTBP is removed by washing with benzine in which DTBP dissolves better than TBHP sodium salt. In the second step, TBPB is prepared from TBHP sodium salt and benzoyl chloride; the product is purified to remove TBHP with an NaOH solution [1]. The TBHP sodium salt formed in the process is removed from TBPB by subsequent washings with water. In practice, to obtain TBPB meeting TU (Technical Specifications) 6-05-1997–85 (main substance content no less than 98.5%, TBHP content no more than 0.1%), the reaction product is usually washed with five or six portions of NaOH solution and four portions of water to pH 6–8.

This procedure is time-consuming (it takes a half of the total time for the whole cycle of TBPB production). Therefore, development of a more efficient procedure for TBPB purification is an urgent problem.

The use of a sulfite buffer solution for washing of hydroxy-*tert*-alkyl peroxyesters is mentioned in patents [2, 3], mainly devoted to synthesis of peroxides.

In this work we studied purification of TBPB with an $Na_2S_2O_5$ solution.

tert-Butyl perbenzoate was washed with 33 wt % NaOH solution. The alkali content in the product being purified was 2.6 wt %. The number of alkaline washing runs n_{OH^-} was varied from 0 to 5. After that, TBPB was washed with one portion of 8% $Na_2S_2O_5$ and up to four portions of water.

In the course of purification, we determined the TBHP content before and after purification and monitored the pH of the aqueous extract. The purified TBPB was analyzed for the content of the main sub-

Influence of the number of washing runs n on the impurity content c in TBPB (initial pH 11)

n_{OH^-}	c_{TBHP}, wt %		$n_{Na_2S_2O_5}$	After washing with $Na_2S_2O_3$		n_{H_2O}	After washing with H_2O			
	after main reaction	after OH^- washing		pH of TBPB	c_{TBHP}, wt %		pH of TBPB	c_{TBPB}	c_{TBHP}	c_{BA}
								wt %		
0	1.4	–	1	3.0	0.24	4	4.0	97.8	0.22	0.44
1	1.4	0.37	1	5.0	0.06	4	6.0	98.8	0.06	0.36
2	1.5	0.22	1	5.4	0.02	1	6.6	99.5	0.02	0.23
3	1.4	0.18	1	5.6	0.02	1	6.5	99.6	0.02	0.24
4	1.5	0.16	1	6.0	0.02	1	6.8	99.3	0.02	0.26
5	1.7	0.10	1	6.2	0.02	1	6.7	99.6	0.02	0.26
5	1.6	0.10	0	–	–	4	8.0	98.5	0.1	0.47

1070-4272/03/7611-1860$25.00

stance, TBHP, and BA. TBPB was determined by iodometric titration in the presence of $CuCl_2$ in isopropyl alcohol–acetic acid; TBHP, by iodometric titration in methanol–toluene in the presence of pyridine; and BA, by high-frequency titration with an alkali solution. The analytical data are listed in the table.

Purification with an $Na_2S_2O_5$ solution without preliminary washings with NaOH is inefficient, as it leads to a decrease in the main substance content. Apparently, in an acid solution, TBPB decomposes to form benzoyl chloride, which is subsequently hydrolyzed to BA.

The table shows that, as the number of OH^- washing runs is increased, the TBHP content in TBPB decreases. The required level of purity is attained only after $n_{OH^-} = 5$. If OH^- washing is followed by treatment with an $Na_2S_2O_5$ solution, one alkaline washing is sufficient to attain the required purity. This is probably due to the fact that, on the one hand, in alkaline washings NaOH binds free TBHP, and, on the other hand, alkaline medium promotes hydrolysis of TBPB to TBHP and BA. This assumption is also confirmed by the fact that treatment with an $Na_2S_2O_5$ solution decreases the BA content in TBPB. Washing of TBPB with an $Na_2S_2O_5$ solution decreases the pH of the TBPB being purified from 11.0 to 5.4–6.2, which makes washing of TBPB with water more efficient and allows the number of washing runs to be decreased.

Thus, purification of TBPB with an $Na_2S_2O_5$ solution in combination with alkaline washings is more efficient, as it improves the purity of the commercial product and reduces the purification time and the volume of wash waters.

The purification procedure developed can be recommended for commercial use.

CONCLUSION

Treatment of *tert*-butyl perbenzoate with an $Na_2S_2O_5$ solution improves the quality of the commercial product and reduces the purification time.

REFERENCES

1. Rakhimov, A.I., *Khimiya i tekhnologiya organicheskikh perekisnykh soedinenii* (Chemistry and Technology of Organic Peroxides), Moscow: Khimiya, 1979.
2. US Patent 4 486 580.
3. US Patent 4 634 753.

Russian Journal of Applied Chemistry, Vol. 76, No. 11, 2003, pp. 1862–1863. Translated from Zhurnal Prikladnoi Khimii, Vol. 76, No. 11, 2003, pp. 1913–1914.

BRIEF COMMUNICATIONS

Effect of Transition Metal Diketonates on Oxidation of Sunflower-Seed Oil

Zh. V. Shmyreva, L. V. Moiseeva, L. F. Ponomareva, Yu. E. Zelenskaya, and T. Yu. Dolgova

Voronezh State University, Voronezh, Russia

Received June 2, 2003

Abstract—Effect of transition metal (Mn, Fe, Co, Ni, Cu, Zn) diketonates on oxidation of sunflower-seed oil with atmospheric oxygen was studied.

Among a number of transition metal complexes, diketonates are of interest due to capability to catalyze oxidation of hydrocarbons. It is known that the catalysis direction can change, with oxidation catalysts becoming inhibitors.

In this work, the data on the effect of 20 transition metal (Mn, Fe, Co, Ni, Cu, Zn) β-diketonates of series **I**–**VI** on the catalysis direction in oxidation of sunflower-seed oil with atmospheric oxygen were summarized and correlated to reveal how the activity depends on the ligand structure and metal type:

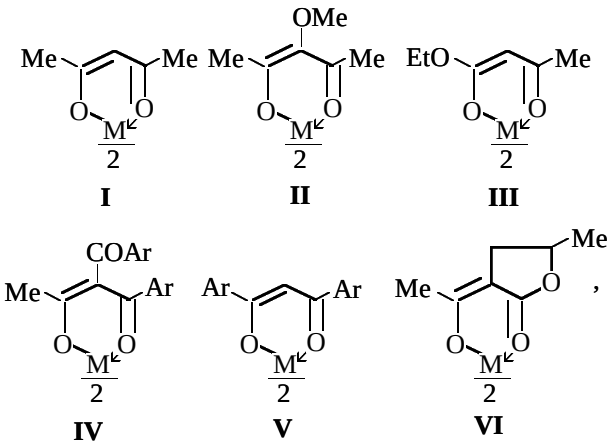

where **I** are complexes with acetylacetone; **II**, with metoxyacetylacetone; **III**, with acetoacetic ester; **IV**, with acetylbenzoylmethane; **V**, with dibenzoylmethane; and **VI**, with α-aceto-γ-methyl-γ-butyrolactone chelates.

The choice of the oxidation substrate was determined by its practical significance in study of oxidative degradation of edible oils and pharmaceuticals [1]. For series **I**–**VI**, by an example of copper and nickel complexes, we considered the effect of ligand, and for series **I** and **VI**, the effect of metal type. The relative activity constant K_{rel} determined as

$$K = \omega_{O_2(chel)}/\omega_{O_2(oil)},$$

where $\omega_{O_2(chel)}$ is the rate of atmospheric oxygen uptake at substrate oxidation in the presence of metal complex and $\omega_{O_2(oil)}$ the rate of oxygen uptake without additives (ml min^{-1}), is the quantitative characteristic of the metal complex catalytic activity.

In other words, K_{rel} is a factor by which the rate of oxygen uptake with a definite volume of the substrate changes in the presence of a metal diketonate. Correspondingly, the inequality $K_{rel} > 1$ indicates a positive catalytic effect of the metal complex, and $K_{rel} < 1$, inhibiting effect (negative catalysis). The data obtained are listed in Tables 1 and 2.

Comparison of K_{rel} for copper and nickel chelates **I**–**VI** reveals higher sensitivity of the nickel complexes to the ligand structure as compared to copper complexes. For example, for Ni-**III** and Ni-**IV**, the activity gets inverted ($K_{rel} < 1$), while copper chelates with all ligands show only positive catalytic activity. It is interesting that, whereas the Cu-**IV** complex

Table 1. Influence of the ligand structure on the catalytic activity of Cu and Ni diketonates **I**–**VI**

M	K_{rel}					
	I	**II**	**III**	**IV**	**V**	**VI**
Cu	2.5	3.2	3.2	1.3	3.1	2.7
Ni	1.4	1.3	0.7	2.8	1.3	0.2

1070-4272/03/7611-1862$25.00

Table 2. Influence of the metal type on the chelate activity in oxidation of sunflower-seed oil

Diketonate	K_{rel}					
	Mn	Fe	Co	Ni	Cu	Zn
I	2.8	1.8	4.4	1.4	2.5	0.7
VI	0.4	0.2	0.3	0.2	2.7	0.6

show decreased activity, the Ni-**IV** complex exhibits increased activity. For the Ni-**III** and Ni-**VI** chelates, $K_{rel} < 1$, indicating activity inversion.

A previous study of the activity of transition metal chelates with **VI** [2] in oxidation of dehydroabietic acid reveal a substantial dependence of the oxidation rate on the metal type.

The relative activities of series **I**–**VI** are compared in Table 2. As seen, K_{rel} sharply decreases for complexes with **VI**, excluding the copper chelate, i.e., the activity inversion takes place virtually irrespective of the metal. In the case of complexes **I**, the activity of chelates decreases in the order Co > Mn > Cu > Fe > Ni, Zn, which mainly agrees with data of [3]. It is known [4] that the electrode potential of the metal ion and the complex stability are factors determining the catalytic activity of the chelate. For acetylacetonates **I**, the activity variation does not correlate with any of the above parameters.

Thus, for diketonates studied, the variation of the ligand structure can be accompanied by changes in the direction of catalytic activity in sunflower-seed oil oxidation, which substantially broadens possible applications of these complexes.

EXPERIMENTAL

The synthesis of transition metal chelates and their structures are described in [5]. Acetylacetonates **I** were prepared similarly. Metal chelates with **II**–**V** were prepared as in [6].

The metal chelate activity was estimated in oxidation of the unrefined sunflower-seed oil with atmospheric oxygen without initiator at $60 \pm 0.1°C$; A metal chelate concentration did not exceed 10^{-3} M. The measurement results were treated by the method described in [7]. For all measurements, $r \geq 0.97$, which shows that the volume of oxygen taken up v_{O_2} linearly depends on time:

$$v_{O_2} = f(\tau) \equiv y = kx + b,$$

where x is the time of uptake; y, amount of oxygen taken up; and k, proportionality coefficient, $k = \tan\alpha = dv_{O_2}/d\tau = \omega_{O_2}$, where ω_{O_2} is the rate of oxygen uptake.

CONCLUSIONS

The catalytic activity of transition metal β-diketonates in oxidation of sunflower-seed oil with atmospheric oxygen was studied, and high activity of copper chelates, independent of the ligand structure, was revealed. The possibility of inversion of the catalytic activity depending of the metal chelate structure was found.

REFERENCES

1. Kastornykh, M.S., Selezneva, G.D., Rogovskii, T.A., and Sinitsina, V.F., *Pishch. Prom.*, 1990, no. 11, pp. 67–69.
2. Malikov, B.F., Luk'yanova, L.F., Ponomarev, F.G., *et al.*, *Dokl. Akad. Nauk SSSR*, 1978, vol. 241, no. 4, pp. 856–857.
3. Sychev, A.Ya., Reibel', I.M., and Stoyanova, N.I., *Zh. Fiz. Khim.*, 1970, vol. 44, pp. 2419–2420.
4. Nizel'skii, Yu.M., *Kataliticheskie svoistva β-diketonatov metallov* (Catalytic Properties of Metal β-Diketonates), Kiev: Naukova Dumka, 1983, pp. 7–28.
5. Ponomarev, F.G. and Trishin, Yu.G., in *Sintez i issledovanie svoistv kompleksnykh soedinenii* (Synthesis and Study of Properties of Complex Compounds), Voronezh, 1973, issue 1, p. 121.
6. Shlifer, G.A., *Kompleksoobrazovanie v rastvorakh* (Complex Formation in Solutions) Moscow: Khimiya, 1964.
7. Zaitsev, I.A., *Vysshaya matematika* (Higher Mathematics), Moscow: Vysshaya Shkola, 1991, pp. 368–374.

Russian Journal of Applied Chemistry, Vol. 76, No. 11, 2003, pp. 1864–1866. Translated from Zhurnal Prikladnoi Khimii, Vol. 76, No. 11, 2003, pp. 1915–1917.

BRIEF COMMUNICATIONS

Chromatographic Properties of Silica Gel Packing Materials as Influenced by Polymeric Coating

S. S. Airapetyan and A. G. Khachatryan

Yerevan State University, Yerevan, Armenia

Received December 3, 2002; in final form, May 2003

Abstract—Some chromatographic properties of microspheric silica gels coated with copolymer of polystyrene, *p*-divinylbenzene, and allyl alcohol were studied. The measurements were performed by reverse-phase high-performance liquid chromatography using modified C_8 and C_{18} phases with secondary silanization with trimethylchlorosilane.

Development of new procedures improving structural and chromatographic parameters of packing materials for chromatographic columns, including silica gel, remains urgent. At present, it seems impossible to propose a principally novel process for preparing packing materials based on silica gel for high-performance liquid chromatography (HPLC) to meet all the chromatographic requirements. Therefore, another approach is preferred: modification of known systems, e.g., coating of the silica gel surface with a polymeric material. As a result, systems exhibiting the properties of both silica gel and coating polymer are obtained. This can decrease or even completely eliminate the solubility of silica gel, making it applicable in aqueous and, especially, in alkaline aqueous solutions.

Several procedures are used to deposit polymeric layers on silica gel supports [1–11], macroporous glasses [12, 13], and diatomite [14]. Coating of non-silica gel supports (e.g., aluminum oxide, zirconium dioxide, and carbon glass) with polymeric layers is described in [15]. For this purpose, both natural [3, 4, 10, 11] and synthetic [1, 2, 5–9, 12–15] polymers are used.

In some works on polymeric coatings, primary attention is given to covalent binding of the polymeric coating with a support surface [8–11]. At the same time, it is believed [1] that there is no pronounced difference between systems with polymeric coatings bound to the support surface and encapsulating this surface.

In this work we studied the possibility of improving some chromatographic properties of packing materials based on silica gel microspheres by their coating with an appropriate polymer.

EXPERIMENTAL

As starting materials for column packing we used microspheric silica gels (MSs) prepared by hydrothermal modification of the initial MS, which, in turn, was obtained by the procedure given in [16].

The modes of hydrothermal treatment (HT) of the initial MS for preparing macroporous samples and the pore properties of the resulting silica gels are listed in Table 1. The size distribution of these MSs are shown in the figure.

The polymeric layer was applied to MS by polymerization of an adsorption layer of the monomer mixture in the presence of benzoyl peroxide (BP), whose content was about 3–5 wt % of the total weight of monomers. The porous support was impregnated with a solution of the monomer mixture in acetone with subsequent removal of the solvent at room temperature. The polymerization initiator PB was added simultaneously with the monomers, providing poly-

Table 1. Preparation conditions and porosity characteristics of microspheric silica gels*

Mode of hydrothermal treatment				Porosity characteristics	
τ, h	pH	*T*, °C	$SiO_2 : H_2O$**	*S*, $m^2\ g^{-1}$	*V*, $cm^3\ g^{-1}$
–	–	–	–	250	0.58
2	7.5	100	1 : 12	230	0.58
2	8.0	120	1 : 12	120	0.58
2	8.0	150	1 : 12	75	0.58
4	8.0	200	1 : 12	45	0.58

* (*S*) Specific surface area and (*V*) pore volume.
** Weight ratio.

1070-4272/03/7611-1864$25.00

Table 2. Main chromatographic properties of microspheric silica gels

Type of packing material*	Polymer content, wt %	k		Performance, TP m^{-1}		Acetonitrile : water**	p, MPa
		benzene	toluene	benzene	toluene		
Si-100 + C_8 + TMCS	–	2.045	3.352	44426	52480	1 : 1	10.4
	12.2	1.806	2.763	71200	73747	1 : 1	9.6
Si-200 + C_8 + TMCS	–	1.560	2.333	26640	38693	1 : 1	8.7
	10.7	1.337	1.879	51984	65147	1 : 1	9.1
Si-200 + C_{18} + TMCS	–	1.789	2.976	50708	60046	1 : 1	9.0
	8.7	1.439	2.323	57492	76867	1 : 1	8.6
Si-300 + C_8 + TMCS	–	1.382	2.265	34998	38780	2 : 3	8.3
	7.3	1.235	1.762	54677	60327	2 : 3	9.4
Si-500 + C_8 + TMCS	–	1.471	2.440	34553	35192	7 : 13	6.8
	4.4	1.352	1.823	53380	57385	7 : 13	7.9

* Number at Si indicates the average pore size, Å.
** Weight ratio.

merization in the sample bulk. After solvent removal, the resulting dry powder was transferred into a sealed flask and placed in an oven.

Polymerization was carried out in an oven in two stages: first the sample was heated at 80–85°C for 8–10 h and then at 130°C for 3–4 h. The resulting sorbent was washed with hot dimethylformamide (DMF) to remove the homopolymers and initial monomers and dried with acetone on the filter. Then, the sorbent was modified with silanes to prepare C_8 and C_{18} phases on the surface according to [1], with additional silanization with trimethylchlorosilane (TMCS).

We used chemically pure grade styrene, allyl alcohol, and *p*-divinylbenzene (12 : 5 : 3 monomer weight ratio), chemically pure grade acetone, and chromatographic grade acetonitrile, water, and test mixture (uracil, benzene, and toluene).

The pore characteristics were determined by mercury porosimetry (Pore Sizer 9300 porosimeter) and by sorption of benzene vapor.

The HPLC analysis was performed on a Biotronic BI 8100 device equipped with a Spectro Monitor 5000 detector based on a photodiode matrix and a UV detector (λ = 254 nm); the flow rate of the mobile phase in all the tests was 1 ml min^{-1}. In the tests, we used the 4.6 × 150-mm columns; the other chromatographic parameters are listed in Table 2. As a test mixture we used the mixture of uracil, benzene, and toluene with $x : y : z$ weight ratio.

As seen from the figure, in preparation of the wide-pore MS samples by hydrothermal treatment of the initial silica gel, the pore size distribution becomes broader, which affects the chromatographic properties.

The performance of the columns packed with MS containing C_8 phase with respect to toluene sharply decreases on passing from Si-100 + C_8 (52480 TP m^{-1}) to Si-200 + C_8 (38693 TP m^{-1}), with the difference of 13788 TP m^{-1}, whereas on passing from Si-200 + C_8 to Si-500 + C_8 the difference is only 3501 TP m^{-1} (Table 2). This fact indicates that the main structural changes occur on substitution of Si-100 by Si-200. After attainment of the Si-200 structure, further structural changes on passing to Si-500 do not significantly affect the performance of the columns packed with these MSs. Similar trends are observed with benzene.

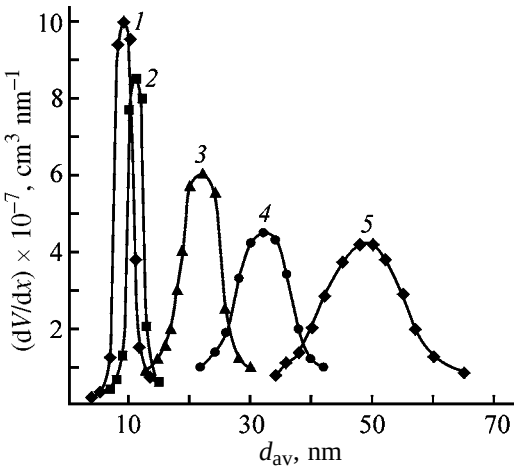

Pore distribution dV/dx in MS with respect to the pore size d_{av} determined by mercury porosimetry. (*1*) Initial MS; HT conditions: (*2*) pH 7.5, 100°C, 2 h; (*3*) pH 8.0, 120°C, 2 h; (*4*) pH 8.0, 150°C, 2 h; and (*5*) pH 8.0, 200°C, 4h.

The average increase in the column performance with respect to toluene after coating of the silica gel packing with a polymeric layer is about 20 000 TP m^{-1}, i.e., the column performance is improved by a factor of 1.5.

As seen from Table 2, on passing from Si-100 + polymer + C_8 to Si-200 + polymer + C_8, the column performance decreases by 6800 TP m^{-1}, which comprises 11.7 and 13.2% of the performance of the columns based on Si-100 + polymer + C_8 and Si-200 + polymer + C_8, respectively. At the same time, on passing from Si-100 + C_8 to Si-200 + C_8, the difference is 13 787 TP m^{-1} or 26.3%. In going from Si-200 + polymer + C_8 to Si-300 + polymer + C_8 and finally to Si-500 + polymer + C_8, the difference in performance is 4820 and 2942 TP m^{-1}, respectively. This suggests that the polymeric coating levels the differences in the sorbent structure after its hydrothermal modification, and no sharp drop in the column performance on passing from Si-100 + polymer + C_8 to Si-200 + polymer + C_8 packing material is observed. Moreover, on passing from Si-200 + polymer + C_8 to Si-500 + polymer + C_8, the column performance smoothly decreases, whereas in the case of Si-200 + C_8–Si-500 + C_8, such a trend is not observed.

On passing from Si-200 + C_{18} to Si-200 + polymer + C_{18}, the column performance with respect to toluene increases by a factor of 1.28 (16 821 TP m^{-1}). This fact suggests that the C_{18} phase improves the silica gel structure owing to the increase in hydrophobicity (the C_{18} phase is more hydrophobic than the C_8 phase) and in the content of organic phase on the silica gel surface.

The increase in the column performance after coating with the polymer is due to more uniform size distribution, because in this case polymer closes the finer pores.

The sorption capacity k of the columns packed with polymer-coated silica gel should obviously decrease because the pore volume and specific surface area of silica gel decrease with increasing amount of the polymer deposited. The decrease in the specific surface area depends on the silica gel structure and, to a lesser extent, on the content of the polymeric coating.

We found that, for deposition of the polymeric coating, it is advisable to use silica gel with a more open structure (with a greater pore volume, ≥ 0.75 cm^3 g^{-1}).

CONCLUSIONS

(1) The quality of the packing materials for high-performance liquid chromatography based on microspheric silica gels is improved by deposition of a polymeric layer on their surface; on average, the column performance increases by a factor of 1.5.

(2) Certain decrease in the capacity of the columns based on these sorbents is due to the decrease in the pore volume and specific surface area with increasing content of the polymer deposited.

REFERENCES

1. *Modifitsirovannye kremnezemy v sorbtsii, katalize i khromatografii* (Modified Silica Gels in Sorption, Catalysis, and Chromatography), Lisichkin, G.V., Ed., Moscow: Khimiya, 1986.
2. Zubakova, L.B., Borisova, V.N., Koroleva, S.K., *et al.*, *Zh. Prikl. Khim.*, 1987, vol. 60, no. 7, pp. 1491–1494.
3. Zubakova, L.B., Borisova, V.N., Koroleva, S.K., *et al.*, *Zh. Prikl. Khim.*, 1986, vol. 59, no. 5, pp. 1182–1184.
4. USSR Inventor's Certificate no. 10 618 282.
5. Hanson, M., Unger, K.K., Mant, C.T., and Hodges, R.S., *J. Chromatogr.*, 1992, vol. 599, pp. 65–75.
6. Lemque, R., Vidal-Madyar, C., Racine, M., *et al.*, *J. Chromatogr.*, 1991, vol. 553, pp. 165–177.
7. Hanson, M., Unger, K.K., and Schomburg, G., *J. Chromatogr.*, 1990, vol. 517, pp. 269–284.
8. Ivanchev, S.S., Dmitrienko, A.V., Demidova, V.A., and Dabagova, A.G., *Vysokomol. Soedin., Ser. A*, 1985, vol. 27, no. 5, pp. 1086–1093.
9. Ivanchev, S.S., Dmitrienko, A.V., Polozov, B.V., *et al.*, *Plast. Massy*, 1982, no. 10, pp. 20–21.
10. Ivanchev, S.S., Dmitrienko, A.V., Demidova, V.A., and Shadrina, N.E., *Vysokomol. Soedin., Ser. A*, 1986, vol. 28, no. 10, pp. 2095–2100.
11. Ivanchev, S.S., Dmitrienko, A.V., Polozov, B.V., *et al.*, *Zh. Prikl. Khim.*, 1983, vol. 56, no. 11, pp. 2553–2559.
12. Ivanov, A.E., Grin, M.E., Zhil'tsov, V.V., *et al.*, *Prikl. Biokhim. Mikrobiol.*, 1990, vol. 26, no. 6, pp. 810–847.
13. USSR Inventor's Certificate no. 1 477 439.
14. UK Patent 1 602 432.
15. Hanson, M. and Unger, K.K., *Trends Anal. Chem.*, 1992, vol. 1, no. 10, pp. 368–372.
16. USSR Inventor's Certificate no. 1 443 248.

Russian Journal of Applied Chemistry, Vol. 76, No. 11, 2003, pp. 1867–1869. Translated from Zhurnal Prikladnoi Khimii, Vol. 76, No. 11, 2003, pp. 1918–1920.

BRIEF COMMUNICATIONS

Calix[4]resorcinols as Stabilizers for Rubber Stocks Based on Butadiene–Acrylonitrile Rubbers

S. V. Bukharov, E. A. Teregulova, G. N. Nugumanova, N. A. Mukmeneva, F. K. Miryasova, A. R. Burilov, M. A. Pudovik, I. L. Nikolaeva, E. M. Kasymova, and A. I. Konovalov

Kazan State Technological University, Kazan, Tatarstan, Russia
Arbuzov Institute of Organic and Physical Chemistry, Kazan Scientific Center, Russian Academy of Sciences, Kazan, Tatarstan, Russia

Received February 21, 2003

Abstract—Modification of tetramethylcalix[4]resorcinol with dimethylaminomethyl and 3,5-di-*tert*-butyl-4-hydroxybenzyl fragments was studied. The antioxidative activity of these macrocyclic stabilizers in rubber stocks based on butadiene–acrylonitrile rubber was examined.

Phenolic stabilizers are relatively little used in rubber stocks, as they are apparently inferior in the protective effect to *p*-phenylenediamine derivatives. At the same time, a major advantage of phenolic stabilizers is that, in contrast to amines, they do not alter or alter only slightly the color of rubber items; also, they are nontoxic and low-volatile and are difficultly washed out.

Macrocyclic phenolic stabilizers, in particular, calix[4]resorcinols, are a new group of phenolic stabilizers. Tetramethylcalix[4]resorcinol **I** appeared to be suitable as antioxidant for vulcanized rubbers based on butadiene–acrylonitrile rubbers [1, 2].

In this work we studied the antioxidative activity exhibited in rubber stocks based on butadiene–acrylonitrile rubbers by modified tetramethylcalix[4]resorcinols **II** and **III** containing in *o*-positions of the aromatic rings dimethylaminomethyl or 3,5-di-*tert*-butyl-4-hydroxybenzyl fragments:

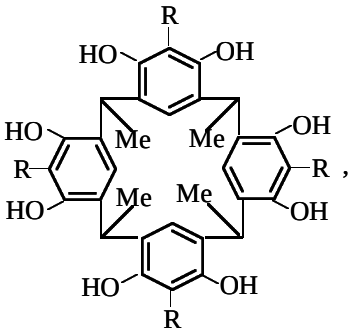

where R = H (**I**), CH_2NMe_2 (**II**), or $CH_2C_6H_2(Bu\text{-}t)_2$-3,5-OH-4 (**III**).

It is known that introduction of dimethylaminomethyl groups into the molecule of **I** appreciably facilitates its oxidation [3]. Therefore, compound **II** should be a much more effective trap of peroxy radicals, compared to unsubstituted calixarene **I**.

Compound **III** contains phenolic groups differing in the reactivity. This should enhance the inhibiting performance in radical oxidation processes. Stabilizer **III** was prepared by the reaction of **I** with 3,5-di-*tert*-butyl-4-hydroxybenzyl acetate **IV** in the presence of formic acid. The mixture formed in the course of the reaction contains 70% calixarene **III** and 30% 2,4,6-tris(3,5-di-*tert*-butyl-4-hydroxybenzyl)resorcinol **V**:

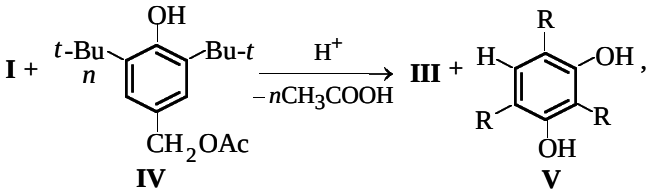

where R = $CH_2C_6H_2(Bu\text{-}t)_2$-3,5-OH-4.

It was shown previously [4] that, in the presence of strong mineral acids ($HClO_4$, H_2SO_4), the content of **III** in the reaction mixture does not exceed 30%.

The compositions of commercial rubber stocks containing as stabilizers *N*-isopropyl-*N*'-phenyl-*p*-phenylenediamine (Diafen FP) or its mixture with 2,2,4-trimethyl-1,2-dihydroquinoline (Acetonanil),

1070-4272/03/7611-1867$25.00

Table 1. Composition of rubber stocks based on SKN-18 and SKN-26 rubbers

Component*	Content, wt parts per 100 wt parts of rubber	
	SKN-18	SKN-26
Zinc oxide	4	3
Sulfenamide Ts	1	0.7
N,*N*-Dithiodimorpholine	2	–
Thiuram D	1	–
Stearic acid	1	1
Carbon black	120	40
EDOS plasticizer	45	–
Sulfur	–	1.5
Stabilizer	4	2

* Sulfenamide Ts is *N*-cyclohexyl-2-benzothiazolylsulfenamide; Thiuram D, tetramethylthiuram disulfide; EDOS plasticizer, a mixture based on dioxane alcohols; stabilizer, compounds **I**–**III**, **V**, **III** + **V**, Diafen FP, or Acetonanil.

calixarenes **I**–**III**, benzylated resorcinol **V**, and a mixture of **III** and **V** obtained in the course of the reaction of **I** with **IV** are listed in Table 1. The results of physicomechanical tests of these stocks are listed in Table 2. The performance of the stabilizers was evaluated by relative changes in the nominal tensile strength σ, relative elongation at break ε, and elongation set θ, occurring upon thermal oxidative aging.

Table 2 shows that, in the rubber stock of thiuram vulcanization with a high filler content, modified calixarenes **II** and **III** somewhat surpass **II** and Diafen FP (amine stabilizers) as regards preservation of σ, but are inferior to the latter additives with respect to preservation of ε. In the rubber stock of sulfur vulcanization with a low filler content, exhibiting better physicomechanical properties, calixarenes **II** and **III** inhibit thermal oxidative degradation more effectively than **I** and are comparable in this respect with Diafen FP (Table 2).

EXPERIMENTAL

In our study, we used commercial samples of butadiene–acrylonitrile rubbers SKN-18 and SKN-26. Rubber stocks were prepared in two steps with a Brabender plasticorder with the mixing chamber volume of 50 cm^3. In the first step, the rubber, carbon black, and other components, except the vulcanizing group, were mixed at 130°C. In the second step, the vulcanizing group was added. The total mixing time was 7 min, and the rotor rotation rate, 35 rpm. The rubber stocks based on SKN-18 and SKN-26 were vulcanized at 143°C for 30 and 40 min, respectively.

Physicomechanical tests were performed with a Tensometer T-10 tensile-testing machine (Monsanto).

The ^{1}H NMR spectra were recorded on a Varian Gemini-200 spectrometer (200 MHz) relative to residual protons of deuterated solvents.

4,6,10,12,16,18,22,24-Octahydroxy-5,11,17,19-tetra(3,5-di-*tert*-butyl-4-hydroxybenzyl)-2,8,14,20-tetramethylpentacyclo[19.3.1.1^{3,7}.1^{9,13}.1^{15,19}]octacosa-1(25),3,5,7(28),9,11,13(27),15,17,19(26),21,23-dodecaene III. Formic acid (65 ml) was added to a solution of 3 g (5.5 mmol) of **I** and 6.9 g (24.8 mmol) of **IV** in 55 ml of acetone. The mixture was allowed to stand at 20°C for 1 day. Then it was poured into 100 ml of water, and an $NaHCO_3$ solution was added to pH 5–6. A mixture of products (7.75 g) was obtained, containing, according to the ^{1}H NMR spectrum, compounds **V** and **III** in a molar ratio of 3 : 7. It was dissolved in 25 ml of benzene, and 170 ml of hexane was added. Compound **III** was obtained; yield

Table 2. Effect of stabilizers on properties of vulcanized rubbers based on SKN-18 and SKN-26

Parameter	Stabilizer					
	control*	**I**	**II**	**III**	**V**	**III** + **V**
σ, MPa	14.0 (21.2)**	13.7 (23.5)	13.3 (18.0)	12.7 (20.1)	13.2 (20.5)	14.7 (21.6)
ε, %	129 (314)	148 (320)	117 (244)	133 (308)	156 (310)	129 (280)
θ, %	4 (8)	3 (9)	4 (8)	4 (8)	4 (10)	3 (8)
ε'/ε***	0.89 (0.87)	0.89 (0.78)	0.94 (1.06)	0.91 (0.95)	0.81 (0.95)	0.89 (0.88)
θ'/θ***	0.95 (0.69)	0.98 (0.60)	0.75 (0.82)	0.80 (0.62)	0.81 (0.77)	0.62 (0.69)

* For vulcanized rubber based on SKN-18, Diafen FP : Acetonanil (1 : 3); for that based on SKN-26, Diafen FP.
** The values for SKN-26 are given in parentheses.
*** (ε', θ') Values obtained after thermal oxidative aging at 100°C for 72 h.

2.6 g (33%), mp 230°C (dec.). ^{1}H NMR spectrum $CDCl_3$), δ, ppm: 1.39 s (72H, CMe_3), 1.77 d (12H, Me, $^3J_{HH}$ 7.0 Hz), 3.89 s (8H, CH_2), 4.60 q (4H, CH, $^3J_{HH}$ 7.0 Hz), 5.08 s (4H, OH), 6.34 s (8H, OH), 7.00 s (8H, Ar–H), 7.33 s (4H, Ar–H).

Found, %: C 77.65; H 8.65.
$C_{92}H_{120}O_{12}$.
Calculated, %: C 77.97; H 8.47.

4,6,10,12,16,18,22,24-Octahydroxy-5,11,17,19-tetrakis(dimethylaminomethyl)-2,8,14,20-tetramethylpentacyclo[19.3.1.1^{3,7}.1^{9,13}.1^{15,19}]octacosa-1(25),3,5,7(28),9,11,13(27),15,17,19(26),21,23-dodecaene II and 2,4,6-tris(3,5-di-*tert*-butyl-4-hydroxybenzyl)resorcinol V were prepared as described in [5] and [6], respectively.

CONCLUSION

Modification of tetramethylcalix[4]resorcinol with dimethylaminomethyl and 3,5-di-*tert*-butyl-4-hydroxybenzyl fragments afforded macrocyclic stabilizers with enhanced antioxidative activity, exceeding that of the starting tetramethylcalix[4]resorcinol, toward rubber stocks based on butadiene–acrylonitrile rubbers.

ACKNOWLEDGMENTS

The study was financially supported by the Russian Foundation for Basic Research (project no. 02-03-33037).

REFERENCES

1. Ehrhardt, D., *Gummi, Fasern Kunststoffe*, 1992, vol. 45, no. 5, pp. 231–239.
2. Ehrhardt, D., *Gummi, Fasern Kunststoffe*, 1992, vol. 45, no. 7, pp. 358–361.
3. Yanilkin, V.V., Ryzhkina, I.S., Morozov, V.I., *et al.*, *Zh. Obshch. Khim.*, 2001, vol. 71, no. 3, pp. 409–414.
4. Bukharov, S.V., Nugumanova, G.N., Mukmeneva, N.A., *et al.*, *Zh. Obshch. Khim.*, 2002, vol. 72, no. 8, pp. 1405–1406.
5. Yoh-ichi, M. and Tahanao, M., *Tetrahedron Lett.*, 1993, no. 46, pp. 7433–7436.
6. US Patent 4173541.

Russian Journal of Applied Chemistry, Vol. 76, No. 11, 2003, pp. 1870–1872. Translated from Zhurnal Prikladnoi Khimii, Vol. 76, No. 11, 2003, pp. 1921–1923.

BRIEF COMMUNICATIONS

Sulfonated Petroleum Polymeric Resins as Plasticizers for Cement Mortars

V. P. Lesnyak, L. V. Gaponik, V. P. Mardykin, and F. N. Kaputskii

Research Institute of Physicochemical Problems, Belarussian State University, Minsk, Belarus

Received July 1, 2003

Abstract—Sulfonation of petroleum polymeric resins based on the C_9 fraction with various suilfonatic agents was studied, and procedure was developed for preparing sulfonated resins. The possibility of using sulfo resins as effective plasticizers for concrete was examined.

Sulfonation of hydrocarbon polymers is one of effective modification procedures extending the application field of these materials. Introduction of sulfo groups makes polymers hydrophilic, which allows their use as water-soluble components of various formulations.

Efficient sulfonation procedures were developed for polymers and copolymers of ethylene and styrene [1–3]. In the case of petroleum polymeric resins (PPSs), which are multicomponent systems involving about ten kinds of monomeric units, sulfonation procedures virtually have not been studied. Petroleum polymeric resins are today one of the most promising and cheapest synthetic substitutes of vegetable oils and rosins. These products are prepared from by-products of oil pyrolysis and are widely used in production of synthetic drying oils, oil–resin lacquers, and components of various paint-and-varnish, adhesive, rubber, and other formulations. However, PPR-based products are, as a rule, soluble only in aromatic hydrocarbons and alkyl halides and insoluble in water, which restricts their applications. Modification of PPRs by sulfonation will give environmentally friendlier water-soluble film-forming agents and plasticizers.

Our studies resulted in development of a waste-free process for production of PPRs and petroleum polymerizate (PP), an analog of petroleum polymeric drying oil, by cationic polymerization of the C_9 fraction. There products are intended for use as film-forming agents in paint-and-varnish production [4–6].

The goal of this work was to study sulfonation of PPRs and prepare from them a plasticizing additive to cement mortars.

Published data and preliminary experiments on sulfonation of styrene oligomer (molecular weight 1000–3000) revealed the regular trends and optimal conditions of the process and allows us to find the best sulfonating agents (SAs) for PPRs of molecular weights 500 and 800 [7].

Sulfonation was performed under mild conditions (at 0–35°C) in a halogenated hydrocarbon solvent. As sulfonating agents we used 10–34% oleum, liquid SO_3, acetyl sulfate, chlorosulfonic and sulfuric acids, and 2 : 1 and 1 : 1 SO_3–dioxane complexes. The latter agents appeared to be the most effective. The complex $2SO_3 \cdot$dioxane was prepared at 0–5°C in a reactor equipped with a power-driven stirrer, a dropping funnel, and a thermometer, by slowly adding 1,4-dioxane to a solution of SO_3 in chloroform. To the resulting complex of SO_3 with dioxane or to another SA, a solution of PPR or PP in chloroform was added over a period of 2–3 h with vigorous stirring. After adding the whole amount of PPR (or PP), the mixture was stirred for an additional 1 h and then diluted with water and neutralized with sodium carbonate. The aqueous and organic layers were separated in a separatory funnel. The aqueous layer was filtered and dialyzed for 24 h. The purified solution was evaporated on a rotary evaporator to obtain sulfo-PPR (SPPR).

The influence of the reactant ratio on the SPPR yield and content of HSO_3 groups is illustrated by the table. Sulfonation of PPR with sulfuric acid yields a product that is virtually insoluble in water, probably owing to formation of sulfone derivatives. With acetyl sulfate, oleum, or liquid SO_3 used as sulfonating agents, partially water-soluble products were obtained, but their yield and content of sulfo groups were lower as compared to the resins sulfonated with SO_3–dioxane complexes and chlorosulfonic acid.

The reactant ratio noticeably affects the content of

1070-4272/03/7611-1870$25.00

Sulfonation of PPR and PP with the complex $2SO_3 \cdot$dioxane, chlorosulfonic acid, and oleum

Run no.	Sulfonating agent	M_n^* of PPR	SA : PPR weight ratio	SPPR yield, % %	Content of HSO_3 groups, mmol g^{-1}
1	$2SO_3 \cdot$dioxane	500	1.6 : 1	55	4
2	″	500	2 : 1	90	4
3	″	500	3 : 1	75	5
4**	″	500	3 : 1	98	4
5**	″	500	3 : 1	86	5
6	″	800	3 : 1	76	6
7	″	800	5 : 1	85	6
8	″	800	7 : 1	70	6
9	HSO_3Cl	800	1.4 : 1	42	6
10	″	800	2.1 : 1	43	6
11	Oleum	500	3 : 1	30	7

* (M_n) Number-avegare molecular weight.
** In run nos. 4 and 5, PP containing 70 and 80 wt % PPR, respectively, was sulfonated.

the sulfo groups introduced and the yield of the water-soluble resin (run nos. 1–3). The product containing the sulfo group in each monomeric unit can be prepared only with excess sulfonating agent (run nos. 3–10). Sulfonation of PPR with a SO_3–dioxane complex at less than 2 : 1 SA : PPR ratio gives a water-soluble product in a lower yield (run no. 1); therefore, it is appropriate to use the complex $2SO_3 \cdot$dioxane at the SA : PPR weight ratio from 2 : 1 to 5 : 1. With chlorosulfonic acid used for sulfonation (run nos. 9 and 10), the SPPR yield is lower than in run nos. 6–8, at comparable degree of sulfonation. In sulfonation of the resin of molecular weight 500 with oleum, the SPPR yield is considerably lower compared to sulfonation with a complex of SO_3 with dioxane, but the content of HSO_3 groups is higher by a factor of almost 2 (run nos. 3, 11). In sulfonation of petroleum polymerizate, the SPPR yield strongly depends on the resin concentration, whereas the content of sulfo groups is virtually the same (run nos. 3–5).

SPPR sample nos. 6–10 were tested as plasticizers for cement mortars.[1] The results showed that these SPPRs ensure the same or even higher mobility of mortars, compared to S-3 superplasticizer. Sulfo resins enhance the early strength of concrete to a greater extent (at equal mortar mobility), whereas plasticizers behaving as surfactants (including S-3) cause an opposite effect (the strength of concrete after 3-day setting is shown in the figure). Furthermore, SPPR additives accelerate setting and alter the hardening kinetics.

[1] Experiments were performed under the guidance of V.V. Tur (Brest State Technical University).

We also found that the plasticizing effect of SPPRs strongly depends on their degree of sulfonation, decreasing as the content of sulfo groups grows. The best results were obtained with SPPR no. 6. Electron microscopic examination suggests that sulfo resin molecules favor an increase in the content of crystallization centers and make the size of ettringite crystals and their distribution in the cement stone structure more uniform.

As compared to nonplasticized samples and those plasticized with S-3, the concretes obtained with SPPR additives are more uniform; they have higher density and considerably lower autogenic shrinkage strain [8].

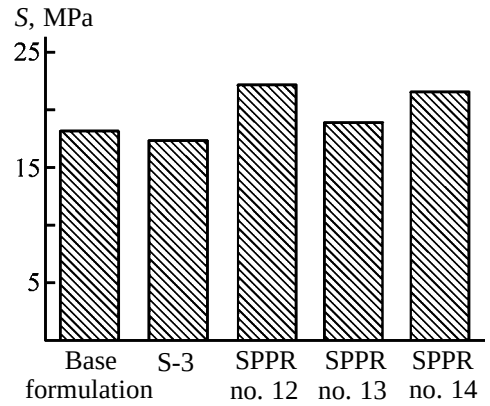

Effect of plasticizer on the compression strength S of concrete. SPPR sample nos. 12–14 were prepared by sulfonation of PPR (M_n = 600) with the complex $2SO_3 \cdot$dioxane, HSO_3Cl, and SO_3, respectively; content of HSO_3 groups 2, 2, and 3 mmol g^{-1}, respectively.

CONCLUSIONS

(1) A procedure was developed for sulfonation of petroleum polymeric resins and petroleum polymerizate with various sulfonating agents (a complex of SO_3 with 1,4-dioxane, chlorosulfonic acid, oleum), allowing control of the content of sulfo groups in the product. Samples of water-soluble sulfo resins with the molecular weight of 1000–1500 and different degrees of sulfonation were prepared.

(2) The sulfonated petroleum polymeric resins can be used as effective concrete plasticizers.

REFERENCES

1. Gilbert, E.E., *Sulfonation and Related Reactions*, New York: Interscience, 1965.
2. *Entsiklopediya polimerov* (Polymer Encyclopedia), Kabanov, V.A., Ed., Moscow: Sov. Entsiklopediya, 1974, vol. 2, pp. 874–881.
3. Fedtke, M., *Reaktionen an Polymeren*, Leipzig: Grundstoffindustrie, 1985.
4. Kaputskii, F.N., Mardykin, V.P., Gaponik, L.V., *et al.*, *Zh. Prikl. Khim.*, 2002, vol. 75, no. 6, pp. 1024–1026.
5. Kaputskii, F.N., Mardykin, V.P., Gaponik, L.V., *et al.*, in *Materialy Mezhdunarodnoi nauchno-tekhnicheskoi konferentsii "Razrabotka importozameshchayushchikh tekhnologii i materialov v khimicheskoi promyshlennosti"* (Proc. Int. Scientific and Technical Conf. "Development of Import-Replacing Processes and Materials in Chemical Industry"), Minsk, December 20–22, 1999, pp. 142–146.
6. Kostyuk, S.V., Lesnyak, V.P., Gaponik, L.V., *et al.*, in *Materialy Mezhdunarodnoi nauchno-tekhnicheskoi konferentsii "Novye tekhnologii retsiklinga vtorichnykh resursov"* (Proc. Int. Scientific and Technical Conf. "New Processes for Recycling of Secondary Resources"), Minsk, October 24–26, 2001, pp. 44–47.
7. Lesnyak, V.P., Kaputskii, F.N., Mardykin, V.P., *et al.*, in *Materialy Mezhdunarodnoi nauchno-tekhnicheskoi konferentsii "Novye tekhnologii v khimicheskoi promyshlennosti"* (Proc. Int. Scientific and Technical Conf. "New Processes in Chemical Industry"), Minsk, November 20–22, 2002, pp. 64–67.
8. Tur, V.V., Kaputskii, F.N., and Ignasheva, O.E., in *Materialy Vtoroi Mezhdunarodnoi nauchno-prakticheskoi konferentsii "Beton i zhelezobeton v tret'em tysyacheletii"* (Proc. Second Int. Scientific and Practical Conf. "Concrete and Reinforced Concrete in the Third Millenium"), Rostov-on-Don, 2002, pp. 342–348.

Russian Journal of Applied Chemistry, Vol. 76, No. 11, 2003, pp. 1873–1880. Translated from Zhurnal Prikladnoi Khimii, Vol. 76, No. 11, 2003, pp. 1924–1931.

HISTORY OF CHEMISTRY AND CHEMICAL TECHNOLOGY

175 Years of Manufacture of Platinum Metals in Russia

The history of platinum manufacture in Russia and the development of research in this field have been the subject of several papers [1–6]; however, all of these cover the period of time before the 1940s. For various reasons, the manufacture of these metals in later period has not been discussed. Here we consider, after a brief review of the main stages of development of the manufacture of platinum-group metals on the basis of the Ural deposits, materials related to manufacture of platinum and concomitant elements from sulfide copper–nickel ores of the Norilsk deposit.

As far back as the early XVIII century, the Europe was well aware of the existence of platinum, which was imported from South America only. The annual production and consumption of platinum were within 320–560 kg. In Russia, platinum-containing samples of osmious iridium were found in gold fields of Upper Iset and Neiva districts in the Urals only in 1819. This stimulated further prospecting for platinum deposits. Purely platinum placers were discovered in the Gornaya Blagodat district in 1824, and in Nizhni Tagil district in the Urals in 1825. By order of the minister of finance, count E.F. Kankrin (1774–1845), who stimulated in every possible way prospecting for, and mining of platinum, all the metal ("raw" platinum) was delivered to St. Petersburg. Samples were analyzed at the laboratory of the Mining Military College (now Mining Institute) by V.V. Lyubarskii (1795–1852). Previously, in 1823, he also analyzed samples of osmious iridium. Having graduated from the Mining Military College in 1816, Lyubarskii worked for several years at laboratories of Ural plants, and then, in 1820–1827, at the laboratory of the Mining Military College, which was rebuilt and expanded in 1826 and later merged with the laboratory of the Department of Mining and Salt Affairs to become United Laboratory of the Department of Mining and Salt Affairs, Mining Military College, and Mining Apothecary [7]. The new laboratory was headed by P.G. Sobolevskii (1781–1841), who played an outstanding part in the development of processes for industrial refining of platinum and production of ductile platinum [7–9]. Sobolevskii graduated from a military educational institution (1798) and then was first in military and then in state service; in 1817–1824, he was an engineer at the Kama–Votkinsk iron-making plant, and in 1819, became manager of the plant. In 1824, Sobolevskii returned to St. Petersburg and took part in the organization of the United Laboratory and remained its head till the end of his life. For his scientific merits, he was elected corresponding member of the St. Petersburg Academy of Sciences in 1830.

Sobolevskii and Lyubarskii developed a relatively simple, but, at the same time, rather efficient method for refining of raw platinum and its conversion into ductile metal and laid foundations of powder metallurgy [10]. From May till November 1826, about 1600 kg of raw platinum was processed. In 1828, export and trading of raw platinum were prohibited. In the same year, Russia started mintage of platinum coins, which continued till 1845. During this period of time, the production of raw platinum markedly increased, to become 3490 kg in 1843. Before that time, platinum and its compounds had been studied in Russia by A.A. Musin-Pushkin (1760–1805), a chemist, mineralogist, honorary member of the St. Petersburg Academy of Sciences (since 1796), and vice-president of Berg Kollegiya (Mining Board) [11]. In 1797–1805, he published 23 papers devoted to platinum and suggested an original method for production of ductile platinum. Musin-Pushkin's studies favored the development of methods for analysis and refining of platinum metals in Russia.

To the most important events associated with studies of platinum metals belongs the discovery of ruthenium in 1844 by K.K. Klaus (1796–1864), a professor of Kazan University. Klaus started research in chemistry of platinum metals, which led to this discovery, in 1841. Having headed the chair of pharmacy at Dorpat University on returning in 1852 to his native Dorpat (now Tartu, Estonia), he continued studies in chemistry of ruthenium, osmium, and other platinum-group metals [12, 13]. Klaus wrote fundamental monographs *Issledovaniya ostatkov Ural'skoi platinovoi rudy i metalla ruteniya* (Studies of Residues of Ural Platinum Ore and Ruthenium Metal, 1845) and *Materialy k khimii platinovykh metallov* (Materials for Chemistry of Platinum Metals, 1854). The first of these was awarded the Demidov prize by the St. Petersburg Academy of Sciences. A hundred years after,

1070-4272/03/7611-1873$25.00

K.K. Klaus.

Klaus's works were republished in the series *Klassiki nauki* (Classics of Science).

Klaus suggested new techniques for refining of platinum metals, described methods for their tests for purity, considered properties of a large number of compounds of these metals, and suggested procedures for analysis of "platinum residues." In contrast to his predecessors, who studied separate problems of chemistry and metallurgy of platinum, Klaus created the chemistry of platinum metals of that time [4].

From 1841 till 1867, platinum was refined at St. Petersburg Mint. After mintage of platinum coins was terminated (June 1845), export of platinum obligatorily refined at the Mint was allowed. Thus, the refining works continued to exist in Russia, but it terminated in 1867 when export of raw platinum was allowed.

In 1879, platinum refining was commenced in limited amounts (130–150 kg in a year) at the Tentelevskii chemical plant (St. Petersburg). However, this plant, and also another small plant refining platinum in St. Petersburg, belonged to foreigners. About 10–13% of platinum produced at the Urals was refined. As noted in [4], 92% of investment into the Ural platinum industry belonged to foreigners. At the same time, the Ural platinum fields gave more than 90% of world's platinum.

Quite a number of known Russian geologists were engaged in studies of platinum deposits in the Urals. A.A. Inostrantsev (1843–1919), a professor of St. Petersburg University, published in 1893–1894 studies of bedrock deposits in the Nizhni Tagil district. By that time, only placer deposits were used in the Urals. Bedrock deposits, whose disintegration produced placers, had not been studied. The geology of bedrock deposits was also the subject of a study by Academician A.P. Karpinskii (1846–1936), published in 1893. During many years, the platinum deposits of the Urals were studied by N.K. Vysotskii (1864–1932), a geologist from St. Petersburg. The platinum deposits of the Nizhni Tagil district were described in a paper by N.A. Zavaritskii (1884–1952), published in 1909. A number of Ural platinum deposits were described by F.Yu. Levinson-Lessing (1861–1939), a professor of St. Petersburg Polytechnic Institute, in his publications of 1909–1910.

In the field of chemical analysis of minerals containing platinum metals, much was done by B.G. Karpov (1870–1940). Having graduated from the St. Petersburg University (1896) with first-degree diploma, he started to work as chemist-analyst at the Geological Committee (St. Petersburg). Already in 1900, Karpov established for the first time, together with A.A. Antipov (1858–1911), the presence of uranium in the geological material from Fergana province. In the same year, he was sent to a business trip abroad for further improvement of his skills and worked at H. Le Chatelier's laboratory (1850–1936) in Paris. Beginning in 1907, Karpov specialized in analysis of platinum metals. He wrote a manual *O metodakh analiza samorodnoi platiny* (On Methods for Analysis of Native Platinum) and made several hundred analyses of both native platinum and platinum ores from Ural deposits [4, 14].

In the late XIX century, Professor N.S. Kurnakov (1860–1941, academician since 1913) carried out at the chemical laboratory of the Mining Institute studies in chemistry of complex compounds of platinum-group metals [6, 15, 16]. Already the first scientist's communication devoted to this subject, on "products of thiourea combination with platinum salts" (1889), aroused much interest among chemists. The results of the study were included by D.I. Mendeleev (1834–1907) in the fifth edition of *Osnovy khimii* (Fundamentals of Chemistry). Later (1889–1893), these studies were continued. It was emphasized in the monograph [15] that Kurnakov was the first among Russian scientists to appreciate the coordination theory of A. Werner (1866–1919), an outstanding Swiss chemist, later a Nobel Prize laureate (1913). The results of Kurnakov's studies in the field of chemistry of complex compounds were summarized in a separate collection of works [17].

At the turn of the XX century, it became clear that chemistry of platinum metals is intimately associated with chemistry of coordination compounds. Platinum metals form various complex compounds characterized by high stability. Already in the beginning of the XX century, investigations carried out by L.A. Chugaev shifted the center of research in the field of complex compounds and also in chemistry of platinum metals to Russia [6]. Chugaev graduated from the natural department of the physicomathematical faculty at Moscow University in 1895. The initial period of his scientific activities was devoted to studies of organic compounds. In 1903, Chugaev defended his master dissertation "Studies in the Field of Terpenes and Camphor." However, his doctoral dissertation "Studies in the Field of Complex Compounds" (1906) was devoted to synthesis and studies of properties of compounds formed by a number of metals, including platinum and palladium, with imides and α-dioximes. In the following years, Chugaev's interests were focused exclusively on the chemistry of coordination compounds. Chugaev was a professor of the Moscow Higher Technical School (1904–1908) and extraordinary (since 1908) and ordinary (since 1911) professor of the St. Petersburg University [18].

As already noted, Russia was the main supplier of platinum to the world market at the beginning of the XX century, but platinum refining was not performed on due scale. The question of necessity for organization of industrial refining of Ural raw platinum was raised by Russian scientists more than once; however, this was hindered by the existing Russia's treaty commitments. The export of raw platinum was completely prohibited only after the beginning of World War I.

In July 1914, the government made a contract with the management of the Joint-Stock Society of Nikolae-Pavda mining district to build and equip in accordance with the requirements of modern technology a refining plant in Yekaterinburg with annual output capacity of no less than 450 poods (~7400 kg) and manufacture simple articles from refined platinum [5, 6, 19]. The government surrendered its rights to build a state-owned plant for platinum refining to the joint-stock society.

In February 1915, the Permanent commission for analysis of natural productive forces of Russia (KEPS) was organized by decision of the Academy of Sciences, and Academician V.I. Vernadsky (1863–1945) was appointed its chairman, and Academician Kurnakov, its vice-chairman. In his keynote address devoted to the goals of the Commission, Vernadsky mentioned that, for Russia's natural resources to be used properly, "it is necessary to go Russia's own way without using as prescriptions the achievements of the West or America... We must search not only for sources of new natural productive forces in our country, but also for methods and procedures for their use, and devise these methods" [20].

L.A. Chugaev.

N.N. Baraboshkin.

In August 1915, the Nikolae-Pavda joint-stock society invited mining engineer N.N. Baraboshkin (1880–1935) to head work on building of a refining plant in Yekaterinburg. N.N. Baraboshkin entered the Mining Institute in St. Petersburg in 1899 and graduated therefrom in 1914, having worked during his education period in gold and platinum fields of the Urals and Siberia and at other metallurgical plants. Beginning in 1911, he made a great number of analy-

O.E. Zvyagintsev.

ses of platinum metals at a laboratory of the Mining Institute. Karpov's paper [21] mentions that "It is necessary to mention as one of the most outstanding representatives of Kurnakov's analytical school N.N. Baraboshkin, who applied to the greatest extent his analytical talents to studies of analysis of platinum ore and products of its processing. These studies... brought to him honorable fame and key position at... the refining plant." In 1914–1915 at the Mining Institute, N.N. Baraboshkin was engaged, together with N.I. Podkopaev (1872–1930), in improvement of methods for platinum refining, with the result that the Klaus–Baraboshkin method was devised and later used for a long time at the refining plant [6, 22]. At the beginning of 1916, a temporary laboratory for refining and production of technical-grade spongy platinum, headed by N.N. Baraboshkin, was put into operation. In October of the same year, the construction of the first Russia's refining plant was, for the most part, finished. The commonly accepted official data of its starting-up is October 10 (23), 1916, when the Ministry of Trade and Industries approved a special "Instruction" regulating all aspects of the functioning of the new plant. From November 1916 till November 1917, 900 kg of platinum was refined; by the beginning of 1918, the output capacity of the refining plant reached 400 kg of platinum per month and increased gradually. However, on February 6 (19), 1918, the plant was nationalized and soon was closed. The civil war suspended work on platinum refining, but the plant was not evacuated and all the equipment remained intact. Mainly owing to N.N. Baraboshkin's efforts, the refining plant resumed its work in the spring of 1920. Soon, other metals started to be produced together with platinum: palladium in 1922, iridium in 1923, rhodium in 1925, osmium in 1927, and ruthenium in 1930. Manufacture of extra-brand platinum was started in 1928, melting of platinum to obtain platinum bullion, in 1923, and manufacture of platinum alloys and fabrication of articles from platinum and platinum alloys, in 1928.

Professor N.N. Baraboshkin was one of organizers of higher metallurgical education in the Urals, headed metallurgical chairs at the Ural Polytechnic Institute, and dealt with a wide variety of issues related to manufacture of copper and nickel at plants of the Ural region [19, 23–25].

The achievements in refining of platinum and associated metals were closely related to wide-scale studies carried out, in the first place, in Petrograd. On Chugaev's initiative supported by academicians Kurnakov and A.E. Fersman (1883–1945), the Institute of Platinum and Other Noble Metals (Platinum Institute) was organized in Petrograd in April 1918 [26, 27]. This made it possible to unite specialists working in the field of chemistry of platinum metals at laboratories of the University, Mining and Polytechnic Institutes, and some other institutions. The explanatory memorandum devoted to the organization of the institute read: "Platinum-group metals, i.e., platinum, iridium, rhodium, palladium, osmium, and ruthenium, constitute the exclusive national treasure of the Russian state, since more than 95% of the whole world's production of placer platinum falls on Russia..." [4]. Chugaev was appointed the first director of the Platinum Institute. The aims of the Institute, formulated by its director, were diverse and extensive, with the development of methods for separation of platinum and associated metals and their manufacture in pure state occupying the first place [28]. After the untimely death of Chugaev in September 1922, Kurnakov was elected director of the Institute. During the entire period of his scientific activities, Kurnakov was incessantly interested in platinum and other platinum-group metals: in their complex compounds, manufacture technology, alloys on their base, and use of the metals and alloys in various fields of technology.

In 1922, the State Association of plants producing and processing platinum, Uralplatina of VSNKh (Supreme Council for National Economy), was created. In agreement with this association, the Platinum Institute engaged itself in a number of investigations in the field of refining and analysis of platinum metals. To accomplish these tasks, two commissions were organized at the Institute: that of refining, headed by

Kurnakov, and analytical, headed by Karpov. A number of known specialists working at the Platinum Institute were, simultaneously, members of both the commissions: S.F. Zhemchuzhnyi (1873–1929), O.E. Zvyagintsev (1894–1967), and V.V. Lebedinskii (1888–1956). A detailed report about the activities of the Platinum Analytical Commission can be found in [21]. A major contribution to the organization of joint work of Uralplatina and the Platinum Institute was made by Zvyagintsev, an engineer at Uralplatina in 1922 to 1926 and later one of the leading Russian specialists in chemistry, geochemistry, and technology of platinum metals, the author of a number of monographs and books on history of chemistry [29].

In 1923–1925, KEPS, Russian Academy of Sciences, initiated publication of capital work of N.K. Vysotskii [30], devoted to deposits, production, and refining of platinum in Russia. Results obtained in studies carried out by staff members of the Institute of Platinum and in other investigations in the field of chemistry of platinum metals appeared on regular basis in *Izvestiya Instituta* (Transactions of the Institute), which started to be published in 1920.

In 1919, in lower reaches of the Yenisei River, beyond the Polar circle, prospecting for deposits of coal and other minerals was commenced, with only rather scarce relevant information available. The expedition was led by N.N. Urvantsev (1893–1985), a young mining engineer and graduate of the Tomsk Technological Institute [31]. The systematic studies carried out in the following years on the southern periphery of the Taimyr tundra led to discovery of a coal field and deposits of copper–nickel ores containing platinoids, which constituted the mineral and energy base for Norilsk mining-and-smelting combine. The decision to construct the combine was made by the Council of People's Comissars of the USSR on June 23, 1935. The implementation of the plan was entrusted to Chief Administration of Prison Camps (GULAG). The exceedingly severe climate of the Polar region made construction under the ever-frost conditions a very complicated task. Nevertheless, first hundreds of tons of raw nickel were obtained in 1939, production of electrolytic nickel commenced in the spring of 1942, that of electrolytic copper, in 1943, and that of cobalt, in 1944. As nickel and copper were produced, platinoid-containing sludges were accumulated.

On April 7, 1939, the country's leadership made a decision to construct a refining plant in Krasnoyarsk. The construction and functioning of the plant were also entrusted (till 1953) to NKVD (People's Comissariat for Internal Affairs). The construction site was chosen with participation of Zvyagintsev. The design was made by specialists of the Soyuznikel'olovoproekt Institute (now Gipronikel' Institute, St. Petersburg), with participation of specialists from the Institute of General and Inorganic Chemistry, Russian Academy of Sciences, and Mining Institute. Professors N.P. Aseev (1871–1952), K.F. Beloglazov (1887–1951), N.S. Greiver (1900–1971), and Yu.V. Morachevskii (1894–1961) took part in extensive studies of the behavior of platinum metals in processing of sulfide copper–nickel ores, carried out at the Leningrad Mining Institute.

The refining plant in Krasnoyarsk was constructed in severe war years; however, already in November 1942, the first batch of sludges formed in nickel electrolysis was delivered to the plant for processing. On March 23, 1943, first platinum (1291 g) and palladium (3235 g) were produced on the pilot installation from Norilsk sludges. This date is considered the birthday of the Krasnoyarsk Refining Plant (Krasnoyarsk Plant of Nonferrous Metals since 1967). On June 1, 1943, the plant commenced manufacture of finished products in conformity with the established State plan. In May 1944, manufacture of rhodium was started. In January 1945, the main shop for refining of platinum and palladium was put into operation and large-scale manufacture of these metals was commenced. In 1946–1947, melting of platinum and palladium was made possible and manufacture of these metals in the form of bullion was organized. In November 1946, recovery of ruthenium by distillation with ammonium persulfate was started. In 1948, processing of Ural placer platinum and secondary raw materials containing precious metals was organized. In May 1950, a technology for electrochemical recovery of gold from solutions to give commercial technical-grade metal was developed. In 1952, a method for electrochemical recovery of rhodium from solutions of its pure salt was introduced into practice [32].

In September 1994, Russia's largest goldsmith's work was created, and in 1996, and effective technology for gold and silver refining was developed.

Together with the traditional research centers at which sulfide copper–nickel ores and chemistry of platinum-group metals were studied, scientists and specialists exiled to Krasnoyarsk (professors I.Ya. Bashilov and S.M. Anisimov) or detained there (professors R.L. Myuller and V.V. Nedler, engineers K.K. Beloglazov, A.P. Sergeev, A.N. Fedorova, and others) much helped to staff members of the plant during its early years, in 1943–1953, in developing

the technology for processing of novel types of raw materials and refining of platinum metals.

I.Ya. Bashilov (1892–1953) studied at the Petrograd Polytechnic Institute. Already in 1921, he, together with V.G. Khlopin (1890–1950, member of the Academy of Sciences of the USSR since 1939), developed and implemented a technology for production of radium and other valuable components (uranium, vanadium) from the ore delivered from Central Asia (Fergana). In 1932, he created and headed the chair of rare metals at the Moscow Institute of Fine Chemical Technology. In the same tear, Bashilov was appointed scientific supervisor of the Institute of Rare Metals (Giredmet). In August 1938, professor Bashilov, one of those who organized the industry of radioactive and rare metals in Russia, was groundlessly repressed and, on finishing his detention term in June 1943, sent to Krasnoyarsk, to the refining plant [32–35]. First, he worked as researcher and then as head of the research department of the Central factory laboratory. Despite the previous conviction, which was not expunged, Bashilov was awarded a State Prize in 1948. Already after the scientist's death, the decision of the Special Board of NKVD of February 14, 1939, was repealed by the Supreme Court of the USSR on January 30, 1957 "because of the absence of a crime."

S.M. Anisimov (1901–1970), a disciple of a prominent metallurgist V.Ya. Mostovich (1880–1935) and a professor of the North-Caucasian Mining-and-Smelting Institute (Vladikavkaz), was repressed in 1941, served his sentence at Norilsk labor camps, and then worked at the Krasnoyarsk Refining Plant. He did much in organizing at the plant an assay laboratory for analyzing raw, and other industrial, materials with low content of noble metals. Anisimov paid much attention to training plant's staff members for assay techniques and carried out a number of technological studies [32]. In 1954, Anisimov was fully rehabilitated, returned to Vladikavkaz, and headed the chair of metallurgy of noble and rare metals at the same institute as before.

Head of the chair of electrochemistry at Leningrad University, professor R.L. Myuller (1899–1964) was sentenced to 10 years of imprisonment for "anti-Soviet propaganda" [36, 37]. In 1946–1949, Myuller demonstrated, together with specialists from the plant, the possibility of using electrochemical methods in various stages of the refining process. A shop for fractional electrolysis operated at the plant for a long time. Such methods as cathodic deposition of metallic rhodium from solutions of hexachlororhodic acid and electrochemical purification of iridium solutions proved to be successful [32].

In 1956, after full rehabilitation, Myuller resumed his rather successful scientific activities at the Leningrad University.

V.V. Nedler (1908–1997), a known physicist-spectroscopist from Moscow, served his four years term of imprisonment in Krasnoyarsk. His contribution to implementation of spectral analysis at the plant and personnel training is invaluable. In the early 1950s, spectral analysis became the most important method for monitoring processes, testing the quality of finished products, and analyzing other materials at a plant. On returning to Moscow, Nedler, a doctor of chemical science, professor, and State Prize laureate, worked successfully at Giredmet Institute for many years [38]. The organization at the plant of a research department, which actually functioned as an applied-research institute, was much assisted by scientists from the Institute of General and Inorganic Chemistry, Academy of Sciences of the USSR: Academician I.I. Chernyaev, corresponding members of the Academy of Sciences of the USSR Lebedinskii and N.K. Pshenitsyn, Professor A.M. Rubinshtein, and, especially, Professor Zvyagintsev. I.I. Chernyaev (1893–1966), a disciple and follower of Chugaev, graduated from the Petrograd University in 1915, worked at the Institute of Platinum in 1918–1934 and at the Institute of General and Inorganic Chemistry, Academy of Sciences of the USSR beginning in 1934; in 1941–1966 he was director of the Institute. Chernyaev was a prominent specialist in chemistry of complex compounds and discoverer of the *trans* effect. The methods for osmium recovery from ore and production of high-purity platinum, developed by Chernyaev, are used in the industry. Beginning in 1918, Lebedinskii and N.K. Pshenitsyn (1891–1961), graduates from St. Petersburg (Petrograd) University and Chugaev's disciples, worked at the Institute of Platinum and at the Institute of General and Inorganic Chemistry, Academy of Sciences of the USSR. The main Lebedinskii's investigations were devoted to methods for production and refining of rhodium. Pshenitsyn made a major contribution to analytical chemistry of platinum metals and developed an industrial method for iridium recovery [16, 26].

Of promise and interest are investigations in the field of electrocrystallization and refining of platinum metals with molten electrolytes, carried out the most extensively at the Institute of High-Temperature Electrochemistry, Russian Academy of Sciences, Yekaterinburg and also at the Yekaterinburg Plant for Proc-

essing of Nonferrous Metals (former Refining Plant). These studies were initiated and supervised by Academician A.N. Baraboshkin (1925–1995), N.N. Baraboshkin's son [39].

Platinum-group metals play an important part both in monetary reserves of states an in quite a number of diverse, and newest branches of technology [40]. Platinum metals, and also their alloys and compounds, are irreplaceable in electronics, radio engineering, instrument building, chemical and petrochemical industries, space and nuclear engineering, medicine, and goldsmith's works. Platinum and platinum–rhenium catalysts are used in manufacture of high-octane gasoline and numerous monomers for manufacture of synthetic rubber and other synthetic materials. Platinum metals and their alloys are used in fuel cells, microelectronics, growth of single crystals of precious gems, and special glass making. Alloys of platinum with rhodium and palladium neutralize noxious components of exhaust gases of internal combustion engines.

By the end of the XX century, the share of Russia and Republic of South Africa (RSA) exceeds 92% of world's production of platinum metals and 96% of their resources [41]. However, the structures of resources and production in these countries differ significantly. Platinum predominates in RSA ores and its output is approximately twice that of palladium. By contrast, the palladium resources in raw materials in Russia much exceed those of platinum, and, therefore, producing a comparable amount of palladium, our country lags far behind RSA (by a factor of more than 4.5) in production of platinum. An analysis of the world market of platinum metals in the 1990s was made in [41]. During the period from 1993 to 1998, the world consumption of platinum-group metals increased by 74% (from 263 to 458 tons), and that of platinum, by 41.7% (from 126 to 179 tons).

In Russia, more than 98% of the proven resources of platinum-group metals is concentrated in the Arctic zone, with more than 95% of these metals manufactured from sulfide copper–nickel ores of the Norilsk industrial region [40, 42, 43]. The factors determining the unique properties of Norilsk platinoid–copper–nickel ores have been analyzed by D.A. Dodin *et al*. [43, 44]. However, the fraction and quality of ores rich in platinum metals delivered to the Norilsk mining-and-smelting combine decreases gradually. In this context, much attention is given by the program "Platinum of Russia" (1992) to studies of new, untypical of Russia, kinds of platinum-containing raw materials [40, 44–46].

Russia possesses sufficient natural resources for extending the existing, and creating new, sources of raw materials for production of platinum metals and raising their manufacture in order to ensure the leading position in the world market in the XXI century.

REFERENCES

1. Zvyagintsev, O.E., *Izv. Inst. Izuch. Platiny*, 1927, no. 5, pp. 5–22.
2. Fritsman, E.Kh., *Izv. Inst. Izuch. Platiny*, 1927, no. 5, pp. 23–74.
3. Zvyagintsev, O.E., in *Materialy po istorii otechestvennoi khimii* (Materials on History of Domestic Chemistry), Moscow: Akad. Nauk SSSR, 1950, pp. 122–134.
4. Zvyagintsev, O.E., *Tr. Inst. Ist. Estestvozn. Tekh*., 1955, vol. 6, pp. 160–204.
5. Shabarin, S.K., *Izv. Akad. Nauk SSSR, Otd. Tekh. Nauk*, 1952, no. 10, pp. 1512–1519.
6. Fedorenko, N.V., *Razvitie issledovanii platinovykh metallov v Rossii* (Development of Studies of Platinum Metals in Russia), Moscow: Nauka, 1985.
7. Stepanov, N.I., *Izv. Inst. Izuch. Platiny*, 1927, no. 5, pp. 75–84.
8. Plotkin, S.Ya., *Petr Grigor'evich Sobolevskii*, Moscow: Nauka, 1966.
9. Sobolevskii, P.G., *Izv. Inst. Platiny Drug. Blagorodn. Met*., 1927, no. 5, pp. 206–219.
10. Plaksin, I.N., in *Russkie uchenye v tsvetnoi metallurgii* (Russian Scientists in Nonferrous Metallurgy), Moscow: Metallurgiya, 1948, pp. 92–108.
11. Raskin, N.M., *Apollos Apollosovich Musin-Pushkin*, Leningrad: Nauka, 1981.
12. Menshutkin, B.N., *Izv. Inst. Izuch. Platiny*, 1928, no. 6, pp. 1–10.
13. Ushakova, N.N., *Karl Karlovich Klaus*, Moscow: Nauka, 1972.
14. Lebedinskii, V.V., *Izv. Sekt. Izuch. Platiny, Akad. Nauk SSSR*, 1945, no. 18, pp. 5–7.
15. Solov'ev, Yu.I., *Nikolai Semenovich Kurnakov: 1860–1941*, Moscow: Nauka, 1986.
16. Solov'ev, Yu.I., *Istoriya khimii v Rossii* (History of Chemistry in Russia), Moscow: Nauka, 1985.
17. Kurnakov, N.S., *Trudy po khimii kompleksnykh soedinenii* (Works on Chemistry of Complex Compounds), Moscow: Akad. Nauk SSSR, 1963.
18. Zvyagintsev, O.E., Solov'ev, Yu.I., and Starosel'skii, P.I., *Lev Aleksandrovich Chugaev*, Moscow: Nauka, 1965.
19. Naboichenko, S.S., *Metallurg Nikolai Baraboshkin* (Metallurgist Nikolai Baraboshkin), Yekaterinburg: Ural'sk. Univ., 2001.

20. Vernadsky, V.I., *O blizhaishikh zadachakh Komissii po izucheniyu proizvoditel'nykh sil Rossii* (On Nearest Goals of the Commission for Analysis of Productive Forces in Russia), Petrograd, 1915.
21. Karpov, B.G., *Usp. Khim.*, 1936, vol. 5, nos. 7–8, pp. 1153–1159.
22. Zvyagintsev, O.E., *Izv. Sekt. Izuch. Platiny Akad. Nauk SSSR*, 1936, no. 13, pp. 5–7.
23. Deryagin, P.I., *Tsvetn. Met.*, 1967, no. 10, pp. 102–104.
24. Derevyankin, V.A. and Deryagin, P.I., *Izv. Vyssh. Uchebn. Zaved., Tsvetn. Metall.*, 1980, no. 6, pp. 89–90.
25. Morachevskii, A.G., *Zh. Prikl. Khim.*, 2002, vol. 75, no. 4, pp. 699.
26. Solov'ev, Yu.I., *Institut obshchei i neorganicheskoi khimii im. N.S. Kurnakova Rossiiskoi Akademii nauk: Istoricheskii ocherk* (Kurnakov Inst. of General and Inorganic Chemistry, Russian Acad. Sci.: Historical Sketch), Moscow: Nauka, 1993.
27. *Organizatsiya nauki v pervye gody Sovetskoi vlasti 1917–1925: Sbornik dokumentov* (Science Organization in the First Years of the Soviet Power, 1917–1925, Coll. of Documents), Leningrad: Nauka, 1968, pp. 136–139.
28. Chugaev, L.A., *Izv. Inst. Platiny Drug. Blagorodn. Met.*, 1920, no. 1, pp. 1–11.
29. Pichkov, V.N. and Solov'ev, Yu.I., *Zh. Neorg. Khim.*, 1974, vol. 19, no. 7, pp. 1723–1728.
30. Vysotskii, N.K., *Platina i raiony ee dobychi* (Platinum and Regions of Its Mining), Petrograd: Komiss. Estestv. Proizv. Sil, Ross. Akad. Nauk, 1923, part 1, pp. 1–108; part 2, pp. 109–344; part 3, pp. 345–392; 1925, part 4, pp. 393–629.
31. Urvantsev, N.N., *Noril'sk: Istoriya otkrytiya i osvoeniya medno-nikelevykh rud Sibirskogo severa* (Norilsk: History of the Discovery and Development to Commercial Level of Copper–Nickel Ores of Northern Siberia), Moscow: Nedra, 1969.
32. *I vstal zavod nad Eniseem* (A Plant Appeared over Yenisei), Graiver, B.M., Compiler, Krasnoyarsk: Platina, 1998.
33. Polishchuk, V.R., *Repressirovannaya nauka* (Repressed Science), Yaroshevskii, M.G., Ed., Leningrad: Nauka, 1991, vol. 1, pp. 352–366.
34. Morachevskii, A.G., *Ocherki ob uchenykh-khimikakh Sankt-Peterburgskogo politekhnicheskogo instituta* (Essays about Chemists from St. Petersburg Polytechnic Institute), St. Petersburg: Sankt-Peterb. Gos. Politekh. Univ., 2002.
35. Morachevskii, A.G., *Zh. Prikl. Khim.*, 2003, vol. 76, no. 8, pp. 1400–1402.
36. Nemilov, S.V., *Fiz. Khim. Stekla*, 1999, vol. 25, no. 2, pp. 121–129.
37. Morachevskii, A.G., *Zh. Prikl. Khim.*, 1999, vol. 72, no. 7, pp. 1226–1228.
38. *Zavod. Lab.*, 1997, no. 8, p. 60.
39. Morachevskii, A.G., Polyakov, E.G., and Strangrit, P.T., *Zh. Prikl. Khim.*, 2000, vol. 73, no. 10, pp. 1737–1738.
40. Chernyshov, N.M., *Soros. Obraz. Zh.*, 1998, no. 5, pp. 72–76.
41. Nekrasov, E. and Stavskii, A., *Met. Evrazii*, 1999, no. 6, pp. 84–86.
42. Genkin, A.D., Distler, V.V., Gladyshev, G.D., *et al.*, *Sul'fidnye medno-nikelevye rudy Noril'skikh mestorozhdenii* (Sulfide Copper–Nickel Ores of Norilsk Deposits), Moscow: Nauka, 1981.
43. Dodin, D.A., Dyuzhikov, O.A., Kravtsov, V.F., *et al.*, in *Platina Rossii: Problemy razvitiya mineral'no-syr'evoi bazy platinovykh metallov: Sbornik nauchnykh trudov* (Platinum of Russia: Problems of Development of Mineral Resources of Platinum Metals: Coll. of Sci. Works), Moscow: Geoinformmark, 1994, pp. 18–41.
44. Dodin, D.A., Chernyshov, N.M., Dyuzhikov, O.A., *et al.*, in *Platina Rossii: Problemy razvitiya mineral'no-syr'evoi bazy platinovykh metallov: Sbornik nauchnykh trudov* (Platinum of Russia: Problems of Development of Mineral Resources of Platinum Metals: Coll. of Sci. Works), Moscow: Geoinformmark, 1994, pp. 5–17.
45. Greiver, T.N. and Petrov, G.V., *Tsvetn. Metall.*, 1999, nos. 8–9, pp. 7–10.
46. Petrov, G.V., Greiver, T.N., and Lazarenkov, V.G., *Sovremennoe sostoyanie i tekhnologicheskie perspektivy proizvodstva platinovykh metallov iz khromitovykh rud* (Present-Day State and Technological Prospects for Manufacture of Platinum Metals from Chromite Ores), St. Petersburg: Nedra, 2001.

A. G. Morachevskii

Russian Journal of Applied Chemistry, Vol. 76, No. 11, 2003, pp. 1881–1882. Translated from Zhurnal Prikladnoi Khimii, Vol. 76, No. 11, 2003, pp. 1932–1933.

BOOK REVIEWS

Tarasov, A.V., Besser, A.D., Mal'tsev, V.I., and Sorokina, V.S., *Metallurgicheskaya pererabotka vtorichnogo svintsovogo syr'ya* (Metallurgical Processing of Secondary Lead)

Tarasov, A.V., Ed., Moscow: Gintsvetmet, 2003, 224 pp.

In the recent decade, exceedingly close attention has been given in all the economically developed countries to utilization of lead battery scrap. This problem, which is very important economically and environmentally, is made particularly pressing by the global rise in the number of automobiles and other vehicles using lead batteries, high toxicity of lead, and depletion of lead ore deposits. By the end of the XX century, the annual world's output of lead exceeded 6 million tons, with no less than 55% of the whole manufactured amount of lead constituted by secondary metal, which is mainly obtained in processing of spent lead batteries. No less than 70% of lead produced in the world is consumed in manufacture of lead batteries. On the completeness of collection and utilization of battery scrap depends the possibility of satisfying the demand of the world's leading countries for lead. The aforesaid refers to Russia in full measure.

The monograph by A.V. Tarasov and co-authors comprises a foreword, introduction, eight chapters, and bibliographic list containing 243 references to various publications.

A brief foreword (p. 6) notes that the short supply of lead and its alloys in Russia was among the reasons for decrease in manufacture of lead batteries and their increased import. The introduction (pp. 7 and 8) justly emphasizes that the overall expenditure for manufacture of lead and its alloys and compounds from secondary lead raw materials and the impact of the methods for its processing on the environment are much lower than that in their production from ore raw materials. Provided that an efficient system for battery collection and processing is organized, the dependence of Russia on imported lead and its alloys and concentrates can be eliminated.

Chapter 1 of the monograph (pp. 9–14) analyzes data on the present state of manufacture and consumption of lead. Unfortunately, data on the dynamics of manufacture and consumption of lead in Russia in the last decade, the more so for the earlier period, are virtually lacking. Chapter 2 (pp. 15–21) characterizes secondary lead-containing raw materials. The main attention is given to lead battery scrap and wastes of battery plants. These kinds of secondary lead can be processed together. Chapter 3 (pp. 22–48) is devoted to preparation of secondary lead-containing raw materials for the basic metallurgical procedures. The chapter considers transportation of lead batteries, discharge and processing of electrolyte, cropping of batteries into fractions, desulfurization (desulfation) of the oxide–sulfate fraction with caustic soda or soda ash, manufacture of commercial sodium sulfate as by-product, and utilization of organic components of battery scrap.

Chapter 4 (pp. 48–81) discusses the main processes occurring in pyrometallurgical processing of secondary lead and the appropriate apparatus. Unfortunately, the authors fail to present with due clarity the physicochemical essence of reduction processes and do not use the known results of numerous studies of these processes. The same chapter considers slags and mattes, typically produced in manufacture of lead by pyrometallurgical methods, and smelting processes in furnaces of various types. Chapter 5 (pp. 81–161), occupying the central place in the monograph, describes the basic flowsheets for processing of secondary lead-containing raw materials: melting of uncropped lead batteries in shaft furnaces after discharge of electrolyte, melting of separate fractions of lead battery scrap in reverberatory or rotating furnaces, electrosmelting, and other known procedures. The authors give numerous examples from domestic and foreign practice.

Chapter 6 (pp. 161–185) describes processes for refining of lead obtained from secondary raw materials. The authors restrict the consideration to analysis of widely known procedures for pyrometallurgical purification to remove antimony, arsenic, tin, and

1070-4272/03/7611-1881$25.00

copper impurities and of electrolytic refining with a hydrofluorosilicic electrolyte. New promising procedures specially developed for refining of secondary lead are not discussed in the monograph. Chapter 7 (pp. 185–204) presents information about hydrometallurgical methods for processing of battery scrap. Chapter 8 (pp. 204–211) considers environmental and economical aspects of lead manufacture from secondary raw materials.

Numerous deviations from the commonly accepted rules of bibliographic description may hinder use of the, on the whole, rather informative list of references.

The monograph by Tarasov and co-authors will be indubitably of interest for specialists working at research and development organizations dealing with processing of secondary lead-containing raw materials.

A. G. Morachevskii

Russian Journal of Applied Chemistry, Vol. 76, No. 11, 2003, p. 1883. Translated from Zhurnal Prikladnoi Khimii, Vol. 76, No. 11, 2003, p. 1934.

INFORMATION

Jubilee Scientific Conference "Gerasimov Readings"

In tribute of the centennial anniversary of the birthday of Yakov Ivanovich Gerasimov (23.09.1903–17.03.1983), a known physical chemist, corresponding member of the Academy of Sciences of the USSR, and laureate of a State Prize, the jubilee scientific conference "Gerasimov Readings" was held at the Lomonosov State University in Moscow on September 29–30, 2003. The conference was organized by the Chemical Faculty of Moscow State University (MGU), Scientific Council of the Russian Academy of Sciences for Chemical Thermodynamics and Thermochemistry, and Scientific Council of the Russian Academy of Sciences for Physicochemical Foundations of Semiconductor Materials Science, with financial support by the Russian Foundation for Basic Research and a number of other institutions. The organizing committee of the conference was headed by the Dean of the Chemical Faculty, Academician V.V. Lunin and his deputies, Academician Yu.D. Tret'yakov and Professor G.F. Voronin.

The scientific program included seven plenary reports, poster sessions in six sections, and round table on use of computers in chemical research and teaching of chemistry. Lunin and Tret'yakov took part in the opening session of the conference. The report by N.A. Smirnova (St. Petersburg State University) "Thermodynamics of Complex Fluid Systems at St. Petersburg University: Research and Teaching" was devoted to a wide variety of thermodynamic problems dealt with at the Chemical Faculty of St. Petersburg State University. Particular attention was given to thermodynamics of solutions of various kinds and to thermodynamics of surface phenomena. O.M. Poltorak (MGU) considered in his report the problems associated with teaching of chemical thermodynamics within the modern course in physical chemistry. The report by Voronin (MGU) "Unused Possibilities of Chemical Thermodynamics" analyzed the main directions of development of chemical thermodynamics in the XX century. J. Hertz (Université Henry Poincarè, Nancy I, France), a known scientist in the field of thermochemistry of metal alloys, considered in his report the basic research in the field of thermodynamics, mainly carried out in the XIX century by Carnot, Clapeyron, Thomson, Clausius, Gibbs, Ostwald, Le Chatelier, Duhem, de Dondet, Boltzmann, and Planck. In particular detail were considered the activities of Sadi Carnot (1796–1832), a French engineer and physicist, one of the founders of thermodynamics.

The report by F.A. Kuznetsov (Institute of Inorganic Chemistry, Siberian Division, Russian Academy of Sciences, Novosibirsk) was devoted to the role of chemical thermodynamics in semiconductor materials science. The report by Yu.V. Tsvetkov (Baikov Institute of Metallurgy and Materials Science, Russian Academy of Sciences, Moscow) considered Ya.I. Gerasimov's studies in the field of theoretical metallurgy and their influence on the subsequent research. The author developed (together with E.K. Kazenas) a procedure and apparatus used to obtain experimental data on thermodynamics of evaporation and dissociation of oxides of a great number of metals. Studying the thermodynamics of transfer of components of the metallurgical raw materials into the gas phase is of particular importance for the development of plasma metallurgy. E.P. Ageev (MGU) illustrated his report devoted to the career and research activities of Gerasimov by a large number of interesting photographs.

Numerous poster reports were grouped into six sections: (I) general and academic problems of chemistry and chemical thermodynamics; (II) thermodynamic properties of substances; (III) phase equilibria and transformations; (IV) physical chemistry of solutions and melts; (V) theoretical and semiempirical methods for calculation and evaluation of physicochemical parameters of substances; and (VI) adsorption, kinetics, and catalysis. Abstracts of papers of the jubilee scientific conference "Gerasimov Readings" were published as a separate edition.

A. G. Morachevskii and L. B. Tsymbulov

1070-4272/03/7611-1883$25.00

Russian Journal of Applied Chemistry, Vol. 76, No. 12, 2003, pp. 1885–1890. Translated from Zhurnal Prikladnoi Khimii, Vol. 76, No. 12, 2003, pp. 1937–1942.

INORGANIC SYNTHESIS AND INDUSTRIAL INORGANIC CHEMISTRY

Liquid Fertilizers Based on Dolomite, Nitric Acid, and Ammonia

A. Sviklas and R. Shlinkshene

Kaunas Technological University, Lithuania

Received May 6, 2003

Abstract—Solubility in the system $Ca(NO_3)_2$–$Mg(NO_3)_2$–NH_4NO_3–H_2O was studied by the visual-polythermic method. The crystallization curves and the chemical composition of the solid phase were determined. The chemical composition of solutions with crystallization temperature of 0°C was calculated. A technological scheme for production of liquid fertilizers containing nitrogen, calcium, and magnesium was proposed.

The world's production of concentrated combined fertilizers, e.g., nitroammophosphates, increases, whereas the fraction of fertilizers with secondary macronutrient elements decreases. Cultivation of a number of agricultural cultures involves deficiency of bound calcium, magnesium, and sulfur [1–3], which is partially compensated for by use of nitrophoska and superphosphates. However, in many cases it is more expedient to use liquid fertilizers. Of particular interest is use of dolomite[1] $CaCO_3 \cdot MgCO_3$, which contains up to 30% CaO and 20% MgO, as a raw material for manufacture of liquid fertilizers containing calcium and magnesium.

The agrochemical efficiency of chemically unprocessed dolomite is low, as it is almost insoluble in water. Milled dolomite is used in agriculture only for neutralization of acid soils.

Products formed in dolomite processing with orthophosphoric acid can be used as fertilizers in neutral or alkaline soils [5]. Production of suspended fertilizers by reacting dolomite with various inorganic compounds has been reported [6, 7]. However, calcium and magnesium phosphates are virtually not used in production of liquid fertilizers at all because of their low solubility [8].

Readily water-soluble calcium and magnesium nitrates obtained by decomposition of dolomite with nitric acid can be the best components of calcium- and magnesium-containing liquid fertilizers. There are published data on application of the product formed in the reaction between dolomite and nitric acid as an additive in the production of ammonium nitrate [9]. However, data on phase equilibria in the ternary systems $M(NO_3)_2$–NH_4NO_3–H_2O (M = Ca, Mg) and $Ca(NO_3)_2$–$Mg(NO_3)_2$–H_2O systems [10–14] are insufficient for creating liquid calcium-, magnesium-, and nitrogen-containing fertilizers.

The aim of this study was to analyze the possibility of manufacturing liquid fertilizers containing simultaneously nitrogen, calcium, and magnesium by decomposition of dolomite with nitric acid, with the subsequent neutralization of the resulting product with ammonia water.

To achieve this objective, it was necessary to study the solubility in the system $Ca(NO_3)_2$–$Mg(NO_3)_2$–NH_4NO_3–H_2O, to determine the chemical composition of liquid calcium, magnesium, and nitrogen-containing fertilizers, and to suggest a technological scheme for manufacture of liquid fertilizers.

To study the solubility, we used analytically pure $Ca(NO_3)_2 \cdot 4H_2O$, $Mg(NO_3)_2 \cdot 6H_2O$, and NH_4NO_3 and distilled water.

The content of calcium, magnesium, iron, and aluminum in terms of their oxides was determined by chelatometry; that of ammonia nitrogen, by the formaldehyde method; and that of nitric nitrogen, by the permanganate method. The concentration of silicon oxide and the amount of crystallization water were determined gravimetrically [15, 16].

[1] There are deposits of dolomite (about 180 million cubic meters) in northern Lithuania [4], but this mineral is virtually not used in agriculture as a fertilizer.

1070-4272/03/7612-1885 $25.00 © 2003 MAIK "Nauka/Interperiodica"

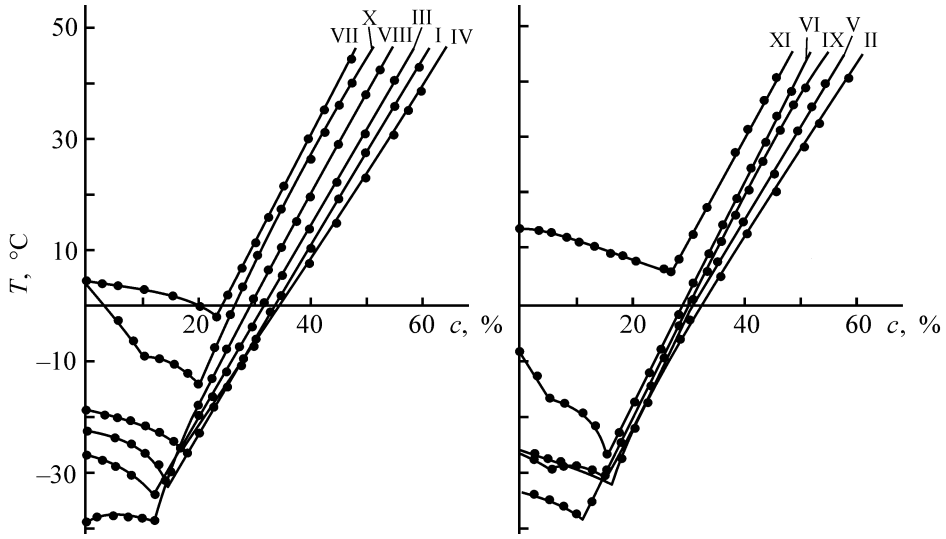

Fig. 1. Polythermal sections I–XI of solutions of the system $Ca(NO_3)_2$–$Mg(NO_3)_2$–NH_4NO_3–H_2O. (T) Temperature and (c) content of NH_4NO_3.

The following physicochemical methods of analysis were used in the study: atomic-absorption electrothermopyrographic spectrometry (Perkin–Elmer Zeeman 3030 spectrometer [17, 18]), IR spectrometry (Specord M-80 spectrometer, KBr pellets, compaction duration 5 min [19]), thermogravimetry (Du Pont Instruments 990 Thermal Analyzer, heating rate 10 deg min [20]), and X-ray phase analysis (DRON-3 instrument with a cobalt anode, range of diffraction angles 0–166.5°, measurement error not exceeding 0.5% [21]).

To obtain liquid fertilizers under laboratory conditions, we used technical-grade nitric acid (58%), ammonia water (25%), and dolomite[2] containing 53.21% $CaCO_3$ and 42.88% $MgCO_3$. The content of admixtures in dolomite was as follows (wt %): Fe_2O_3 1.71, Al_2O_3 0.10, SiO_2 2.10, Mn 1.76×10^{-2}, Zn 2.71×10^{-2}, Cr 1.54×10^{-3}, Cu 3.34×10^{-4}, Ni 2.81×10^{-4}, Co 8.51×10^{-4}, Mo 2.50×10^{-4}, Cd 9.79×10^{-5}, Pb 4.69×10^{-6}, Se $< 1 \times 10^{-6}$, and Hg $< 1 \times 10^{-6}$. The crystallization temperatures of solutions were determined by visual-polythermic method [22].

Table 1. Chemical composition of sections of the system $Ca(NO_3)_2 + Mg(NO_3)_2 + H_2O \rightarrow NH_4NO_3$

Section	Composition, wt %		
	$Ca(NO_3)_2$	$Mg(NO_3)_2$	H_2O
I	21	14	65
II	21	15	64
III	23	16	61
IV	25	10	65
V	25	14	61
VI	25	22	53
VII	27	23	50
VIII	30	14	56
IX	30	15	55
X	30	20	50
XI	35	20	45

Taking into account the composition of dolomite (ratio of calcium and magnesium oxides), we studied the dependence of the crystallization temperature of solutions with varied ratio of calcium and magnesium nitrates on the concentration of ammonium nitrate (0 to 60%) in the temperature range from full freezing up to 40°C. The solubility in 11 sections $x Ca(NO_3)_2 + y Mg(NO_3)_2 + z H_2O \rightarrow NH_4NO_3$ (Table 1) was determined by the visual-polythermic method.

Polythermal sections I–XI are shown graphically in Fig. 1. The crystallization curves in the selected range of concentrations and temperatures had one or two inflection points associated with phase transitions.

Using a centrifuge-refrigerator (at low crystallization temperatures T_{cr}) or a Nutsche filters (at crystallization temperatures higher than 0°C), we isolated the crystals obtained at the temperatures corresponding to the inflection points and in characteristic ranges of polytherms and then subjected them to chemical and instrumental analysis. An examination of the obtained experimental and published [10–14] data

[2] Pyatrashunai (northern Lithuania).

Table 2. Chemical composition of solutions and solid phases in the system $Ca(NO_3)_2$–$Mg(NO_3)_2$–NH_4NO_3–H_2O

Composition of solution, %				$Mg(NO_3)_2 \cdot 6H_2O + NH_4NO_3 + Ca(NO_3)_2 \cdot 2H_2O \cdot NH_4NO_3$ solid phase				
$Ca(NO_3)_2$	$Mg(NO_3)_2$	NH_4NO_3	H_2O	Ca^{2+}	Mg^{2+}	NH_4^+	NO_3^-	H_2O
15.52	10.80	32.50	41.18	6.00*/6.49	3.04/3.89	5.40/5.84	59.00/60.39	24.13/23.38

* Numerator, found; denominator, calculated.

on the solubility in the ternary systems $M(NO_3)_2$–NH_4NO_3–H_2O (M = Ca, Mg) and $Ca(NO_3)_2$–$Mg(NO_3)_2$–H_2O demonstrated that binary crystal hydrates are formed as a result of the crystallization. Table 2 shows, as an example, results of chemical analysis of the solid phase in section III at crystallization temperature of 0°C.

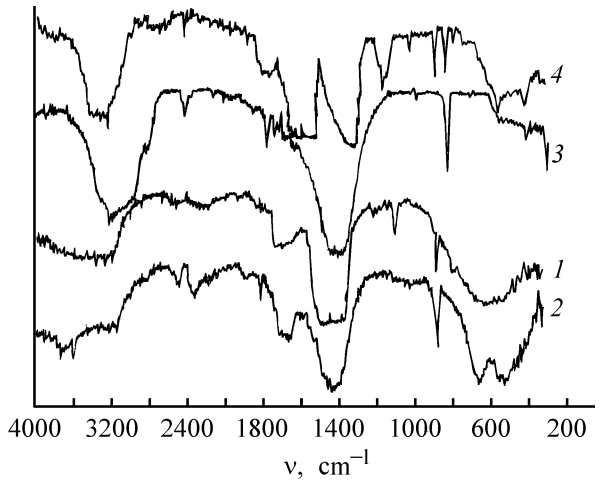

Fig. 2. IR spectra of (*1*) $Ca(NO_3)_2 \cdot 4H_2O$, (*2*) $Mg(NO_3)_2 \cdot 6H_2O$, (*3*) NH_4NO_3, and (*4*) solid phase in section III of the system $Ca(NO_3)_2$–$Mg(NO_3)_2$–NH_4NO_3–H_2O at crystallization temperature of 0°C. (ν) Wave number.

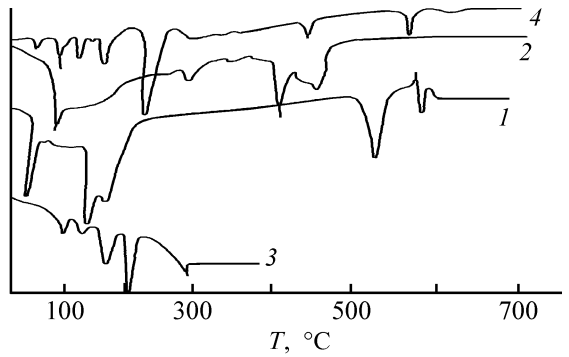

Fig. 3. DTG curves of (*1*) $Ca(NO_3)_2 \cdot 4H_2O$, (*2*) $Mg(NO_3)_2 \cdot 6H_2O$, (*3*) NH_4NO_3, and (*4*) solid phase in section III of the system $Ca(NO_3)_2$–$Mg(NO_3)_2$–NH_4NO_3–H_2O at crystallization temperature of 0°C. (*T*) Temperature.

Apparently, these data closely coincide with those calculated from the stoichiometry. To confirm these results, we used various instrumental methods: IR spectrometry, X-ray diffraction analysis, and thermography (Figs. 2–4).

The IR spectra of calcium nitrate tetrahydrate and magnesium nitrate hexahydrate (Fig. 2, curves *1* and *2*)

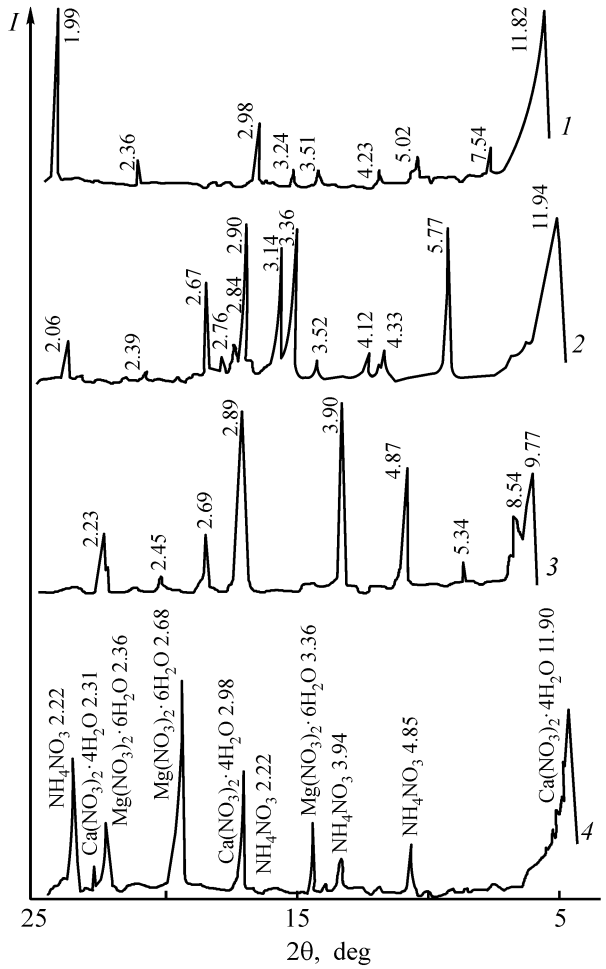

Fig. 4. X-ray diffraction patterns of (*1*) $Ca(NO_3)_2 \cdot 4H_2O$, (*2*) $Mg(NO_3)_2 \cdot 6H_2O$, (*3*) NH_4NO_3, and (*4*) solid phase in section III of the system $Ca(NO_3)_2$–$Mg(NO_3)_2$–NH_4NO_3–H_2O at crystallization temperature of 0°C. (*I*) Intensity and (2θ) Bragg angle.

Table 3. Characteristics of ?bending (?inflection?) points in the system $Ca(NO_3)_2$–$Mg(NO_3)_2$–NH_4NO_3–H_2O

Section	Solution composition, wt %				T_{cr}, °C	Solid phase*
	$Ca(NO_3)_2$	$Mg(NO_3)_2$	NH_4NO_3	H_2O		
I	17.75	11.83	15.50	54.92	–32.5	I + Mg · 6H + A + A · Ca · 2H
II	17.698	12.64	15.75	53.92	–31.5	〃
III	20.36	14.16	11.50	53.98	–33.8	I + Mg · 9H + Mg · 6H + A + A · Ca · 2H
IV	20.62	8.25	17.50	53.63	–26.1	I + Mg · 6H + Ca · 4H + A + A · Ca · 2H
V	23.75	13.30	5.00	57.95	–27.8	I + Mg · 9H + Mg · 6H + Ca · 4H
	21.25	11.90	15.00	51.85	–29.0	Mg · 6H + Ca · 4H + A + A · Ca · 3H
VI	23.75	20.90	5.00	50.35	–16.5	Mg · 6H + Ca · 4H
	21.25	18.70	15.00	45.05	–26.5	Mg · 6H + Ca · 4H + A + Ca · 3H
VII	20.92	17.83	22.50	38.75	–2.5	Mg · 6H + Ca · 4H + Ca · 3H
VIII	26.25	12.25	12.50	49.00	–38.5	I + Mg · 9H + Mg · 6H + Ca · 4H + A + Ca · 3H
IX	26.70	13.35	11.00	48.95	–37.3	I + Mg · 9H + Mg · 6H + A + A · Ca · 2H
X	27.00	18.00	10.00	45.00	–9.3	Mg · 6H + Ca · 3H
	24.00	16.00	20.00	40.00	–14.0	Mg · 6H + Ca · 3H + A · Ca · 2H
XI	25.87	14.78	26.10	33.25	+6.3	Mg · 6H + Ca · 3H + A · Ca · 4H

* I is ice; A, NH_4NO_3; Mg · 6H, $Mg(NO_3)_2 \cdot 6H_2O$; Mg · 9H, $Mg(NO_3)_2 \cdot 9H_2O$; Ca · 3H, $Ca(NO_3)_2 \cdot 3H_2O$; Ca · 4H, $Ca(NO_3)_2 \cdot 4H_2O$; A · Ca · 2H, $NH_4NO_3 \cdot Ca(NO_3)_2 \cdot 2H_2O$; A · Ca · 3H, $NH_4NO_3 \cdot Ca(NO_3)_2 \cdot 3H_2O$; A · Ca · 4H, $NH_4NO_3 \cdot Ca(NO_3)_2 \cdot 4H_2O$.

contain absorption peaks of the NO_3^- group at 750–1050 and 1330–1420 cm^{-1}, and the spectrum of ammonium nitrate (Fig. 2, curve *3*), that of the NH_4^+ group at 3100 cm^{-1}. These vibrations are characteristic of pure components of the system, but, with certain deviations, they can also be seen in the spectrum of the solid phase being analyzed (Fig. 2, curve *4*).

The DTG curves of pure compounds (Fig. 3, curves *1–3*) show dips corresponding to endothermic effects: 95, 300, and 410–460°C for $Mg(NO_3)_2 \cdot 6H_2O$; 40, 140–160, and 500°C for $Ca(NO_3)_2 \cdot 4H_2O$; 100, 130, 170, and 205°C for NH_4NO_3. The same dips at temperatures slightly changed owing to the formation of crystal hydrates of binary salts were found in the DTG curves of the compound under analysis (Fig. 3, curve *4*).

A comparison of the interplanar spacings in the X-ray diffraction patterns of the substance under analysis (Fig. 4, curve *4*) and pure substances (Fig. 4, curves *1–3*) revealed certain disagreements. It is necessary to note that the X-ray diffraction pattern of the solid phase contains all the main peaks with *d/n* values (Å): 1.190, 0.305, and 0.231 for calcium nitrate; 0.359, 0.268, and 0.236 for magnesium nitrate; 0.483, 0.398, and 0.222 for ammonium nitrate. Thus, we can conclude that binary salts containing calcium and magnesium crystal hydrates and also ammonium nitrate are present in the solid phase.

A comparison of the results of chemical and instrumental analyses with published data on the solubility of salt systems identified the following compounds in the solid phase: NH_4NO_3, $Mg(NO_3)_2 \cdot 6H_2O$, $Mg(NO_3)_2 \cdot 9H_2O$, $Ca(NO_3)_2 \cdot 3H_2O$, $Ca(NO_3)_2 \cdot 4H_2O$, $NH_4NO_3 \cdot Ca(NO_3)_2 \cdot 2H_2O$, $NH_4NO_3 \cdot Ca(NO_3)_2 \cdot 3H_2O$, and $NH_4NO_3 \cdot Ca(NO_3)_2 \cdot 4H_2O$. The characteristics of inflection points in the range studied in the system $Ca(NO_3)_2$–$Mg(NO_3)_2$–NH_4NO_3–H_2O are shown in Table 3.

It is seen that the crystallization temperature at the transition points varies widely, within the range –38.5…+6.3°C. The crystallization temperature at inflections in various sections grows with increasing concentration of ammonium.

Using the data obtained (isotherm 0°C), we found that the maximum concentration of nutrients in solutions with various N : CaO : MgO ratios is as follows (%): N (total) 16.13, CaO 7.59, MgO and 5.06 (Table 4). For the CaO : MgO ratio corresponding to dolomite, higher concentrations of nutrients are observed in the solution containing (wt %): NH_4NO_3 28.20, 17.95 $Ca(NO_3)_2$, 15.80 $Mg(NO_3)_2$, and 38.05 H_2O (pH 4.4). The chemical composition, concentra-

Table 4. Characteristics of solutions crystallized at 0°C in the system $Ca(NO_3)_2$–$Mg(NO_3)_2$–NH_4NO_3–H_2O

Section	Solution composition, wt %				Concentration of nutrients, wt %			pH
	NH_4NO_3	$Ca(NO_3)_2$	$Mg(NO_3)_2$	H_2O	N	CaO	MgO	
I	33.70	13.92	9.28	43.10	15.92	4.73	2.51	4.1
II	32.45	14.19	10.13	43.23	15.69	4.82	2.74	4.2
III	32.40	15.55	10.82	41.23	16.04	5.29	2.92	4.0
IV	34.60	16.35	6.54	42.51	16.13	5.56	1.77	4.4
V	30.30	17.42	9.76	42.52	15.42	5.92	2.64	4.2
VI	28.20	17.95	15.80	38.05	15.92	6.10	4.27	4.4
VII	18.50	22.00	18.75	40.75	13.78	7.48	5.06	3.8
	24.10	20.49	17.46	37.95	15.24	6.97	4.71	3.7
VIII	29.55	21.14	9.86	39.45	15.81	7.19	2.66	4.1
IX	29.50	21.15	10.58	38.77	15.93	7.19	2.86	4.2
X	2.75	29.18	19.45	48.62	9.62	9.92	5.25	4.8
	25.55	22.33	14.89	37.23	15.57	7.59	4.02	4.2

tions of nutrients, and pH of solutions having crystallization temperature of 0°C are listed in Table 4.

According to the data obtained, the mixture containing 16% bound nitrogen, 6% calcium (in terms of CaO), and 4% magnesium (in terms of MgO) is the optimal liquid fertilizer among those prepared by decomposition of dolomite with nitric acid, followed by treatment of the resulting acid product with ammonia water. As the temperature of saturated solutions increases, the concentration of nutrients grows only slightly. At 20 and 30°C the effect of salting-out of calcium and magnesium nitrates manifests itself. Thus, summer solutions are distinguished by increased concentration of nitrogen, but lowered concentrations of CaO and MgO.

Samples of liquid fertilizers that contain calcium, magnesium, and bound nitrogen were prepared under laboratory conditions, and their physicochemical properties were studied. Dolomite was decomposed under the optimal conditions reported in [23]: the highest degree of decomposition is reached with 45–55% HNO_3, 0.5–1.0-mm dolomite fraction, reaction dura-

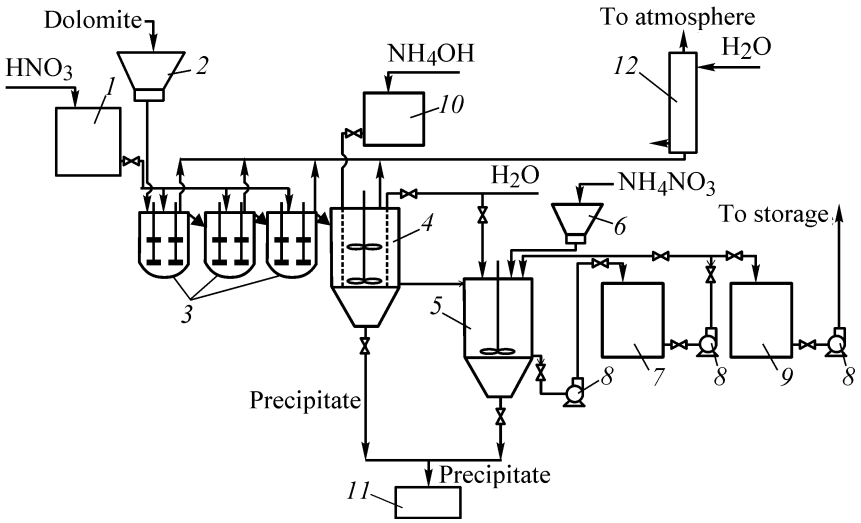

Fig. 5. Technological scheme of production of liquid fertilizers from dolomite, nitric acid, and ammonia: (*1*) tank for nitric acid, (*2*) bunker with dolomite, (*3*) reactors with elliptical bottom, (*4*) neutralization vessel, (*5*) coagulation vessel, (*6*) bunker with ammonium nitrate, (*7*) intermediate tank, (*8*) rotary pumps, (*9*) vessel for fertilizers, (*10*) tank with ammonia water, (*11*) slime bunker, and (*12*) packed absorber.

tion of 40–60 min, temperature of 50–60°C, and HNO_3 consumption of 120% relative to the stoichiometry. The product of dolomite decomposition with nitric acid contained, after its neutralization with ammonia, an aqueous solution of ammonium, calcium, and magnesium nitrates.

The main physicochemical parameters of this liquid fertilizer were as follows: crystallization temperature –3.3°C, pH 5.4, density 1281 kg cm^{-3}, dynamic viscosity 5.47 P, refractive index 1.440, and electrical conductivity 0.109 S cm^{-1}. Apparently, these parameters conform to the commonly accepted requirements to liquid fertilizers. Such a liquid fertilizer can be used as a special fertilizer for hothouse cultures, flowers, and fruit cultures.

We distinguished the following main technological stages of production of liquid fertilizers: decomposition of dolomite with nitric acid, neutralization of acidic solution, its standardizing with respect to nitrogen content, removal of precipitate, and conservation. A technological scheme for production of liquid fertilizers (Fig. 5) was supported on the basis of the results obtained.

CONCLUSIONS

(1) A study of solubility in the system $Ca(NO_3)_2$–$Mg(NO_3)_2$–NH_4NO_3–H_2O revealed the chemical composition of liquid fertilizers (%): NH_4NO_3 28.20, $Ca(NO_3)_2$ 17.95, $Mg(NO_3)_2$ 15.80, and H_2O 38.05. This chemical composition corresponds to the liquid-fertilizer brand 16-0-0-6CaO-4 MgO.

(2) A technological scheme for production of liquid nitrogen-, calcium-, and magnesium-containing fertilizers was supported.

REFERENCES

1. Rinkis, G.Ya. and Nollendorf, V.F., *Sbalansirovannoe pitanie rastenii makro- i mikroelementami* (Balanced Feed of Plants with Macro- and Microelements), Riga: Zinatne, 1982.
2. Koren'kov, D.A., *Produktivnoe ispol'zovanie mineral'nykh udobrenii* (Productive Usage of Mineral Fertilizers), Moscow: Rossel'khozizdat, 1985.
3. *Agrochemija* (Agricultural Chemistry), Vaišvila, Z., Ed., Kaunas: Lututè, 1999.
4. *Lietuvos dolomitas: Lietuvos pramones ir prekybos ministerijos ir Lietuvos chemiku draugijos leidinys*, 1994, p. 5–19.
5. *Osnovy tekhnologii kompleksnykh udobrenii* (Fundamentals of the Technology of Combined Fertilizers), Kononov, A.V., Ed., Moscow: Khimiya, 1988.
6. Polish Patent 267 235.
7. Czechoslovak Inventor's Certificate, no. 207 849.
8. *Tekhnologiya fosfornykh udobrenii* (Technology of Phosphate Fertilizers), Evennchik, S.D. and Brodskii, A.A., Eds., Moscow: Khimiya, 1987.
9. *Spravochnik azotchika* (Handbook of Nitrogen-industry Worker), Mel'nikov, E.Ya., Ed., Moscow: Khimiya, 1987.
10. Zenin, S.E., Obozhin, V.N., and Perfil'eva, O.G., *Uchenye zapiski Buryat-Mongol'skogo pedagogicheskogo instituta* (Transactions of Buryat-Mongol Pedagogical Institute), 1960, issue 19.
11. Flatt, R., Brunisholz, G., and Muhlethaler, R., *Helv. Chim. Acta.*, 1961, no. 6, pp. 1582–1584.
12. Lamberger, I. and Paris, R., *Bull. Soc. Chim.*, 1950, no. 5, pp. 546–549.
13. Protsenko, P.I., Brykova, N.A., and Moshchenskaya, L.A., *Zh. Prikl. Khim.*, 1969, vol. 42, no. 6, pp. 1250–1255.
14. Goloshchapov, M.V., *Izv. Voronezh. Ped. Inst.*, 1955, no. 16.
15. *Tekhnicheskii analiz i kontrol' v proizvodstve neorganicheskikh veshchestv* (Technological Analysis and Monitoring in Production of Inorganic Substances), Moscow: Vysshaya Shkola, 1976.
16. *Osnovy analiticheskoi khimii: Prakticheskoe rukovodstvo* (Fundamentals of Analytical Chemistry: Manual), Zolotov, Yu.A., Ed., Moscow: Vysshaya Shkola, 2001.
17. Khavezov, I. and Tselev, D., *Atomno-absorptsionnyi analiz* (Atomic-absorption Analysis), Moscow: Khimiya, 1983.
18. Ewing, G.W., *Instrumental Methods of Chemical Analysis*, New York: McGraw–Hill, 1987.
19. Nakamoto, K., *Infrared and Raman Spectra of Inorganic and coordination compounds*, New York: Wiley & Sons, 1986.
20. Berg, L.G., *Vvedenie v termografiyu* (Introduction to Thermography), Moscow: Nauka, 1969.
21. *Rukovodstvo po rentgenovskomu issledovaniyu mineralov* (Manual of X-ray Analysis of Minerals), Frank-Kamenetskii, V.A., Ed., Leningrad: Nedra, 1975.
22. Eraizer, L.N. and Kaganskii, I.M., *Zavod. Lab.*, 1967, no. 1, p. 119.
23. Šlinkšienè R. and Sviklas A., *Cheminè Technologija*, 1995, no. 2, pp. 31–33.

Russian Journal of Applied Chemistry, Vol. 76, No. 12, 2003, pp. 1891–1895. Translated from Zhurnal Prikladnoi Khimii, Vol. 76, No. 12, 2003, pp. 1943–1947.

INORGANIC SYNTHESIS AND INDUSTRIAL INORGANIC CHEMISTRY

Technology for Joint Production of Bromine and Lithium Bromide from Brines from Siberian Platform

A. D. Ryabtsev, N. P. Kotsupalo, L. A. Serikova, L. T. Menzheres, and E. V. Mamylova

Ekostar-Nautekh Close Corporation, Novosibirsk, Russia

Received April 8, 2003

Abstract—Two methods for obtaining bromine and lithium bromide from highly mineralized brines enriched with lithium- and bromine-containing compounds, with Li : Br atomic ratio of 0.4–0.8, were studied. These methods are based on a combination of the technique for production of bromine and sorption recovery of lithium from brines to give eluates, LiCl solutions.

Lithium bromide is an expensive reagent in short supply, which is in high demand in the market of lithium products. The prospects for high demand for this compound is mainly associated with its use in refrigeration engineering and in manufacture of heat pumps.

Most of the existing industrial techniques for manufacture of LiBr are based on the reaction of lithium hydroxide or carbonate with hydrobromic acid [1, 2] or elementary bromine in an aqueous medium in the presence of a reducing agent, e.g., hydrogen peroxide [3] or ammonia [4]. The common shortcoming of these methods is the high cost of LiBr obtained, which is due to the fact that expensive commercial lithium compounds, hydrobromic acid, and liquid bromine are used in the process. At present, HBr and Br_2 are manufactured in Russia in limited amounts and mainly from imported raw materials. In this context, development of more economic methods for production of LiBr from new kinds of raw materials is rather a topical task.

As comparatively low-cost and available raw material for production of both liquid Br_2 and LiBr can serve highly mineralized brines from the Siberian platform, which contain considerable amounts of compounds of lithium and bromine simultaneously. The lithium to bromine atomic ratio in brines of this type is 0.4–0.8, and, therefore, only part of bromine contained in a brine, rather than its whole amount, is required for obtaining LiBr. The remaining part can be used to manufacture liquid Br_2 as commercial product.

The most promising technique for processing of brines of this kind is that combining two main technological procedures: production of bromine and selective recovery of lithium ions to give lithium products. Of the known industrially used techniques for manufacture of bromine, the best applicable to the case in question is that based on steam induced desorption of elementary bromine after oxidation of bromide ions with chlorine. However, an important shortcoming of this technique is the necessity for use of liquefied chlorine, which is ecologically unsafe and involves difficulties in its transportation, storage, and use. To improve the ecological and economic characteristics of this technique, the authors suggest to oxidize bromide ions with chlorine obtained by anodic oxidation of chlorine ions contained in the brine, rather than with liquefied chlorine. Such a technology, based on electrochemical oxidation of Br^- ions with anodic chlorine, combined with steam-induced desorption of the Br_2 formed, is, presumably, the most promising for large-scale manufacture of Br_2[1] [5].

A sorption technique based on use of an inorganic lithium-selective sorbent $LiCl \cdot 2Al(OH)_3 \cdot mH_2O$ (DGAL-Cl) has been developed for recovery of lithi-

[1] For manufacture of Br_2 from brines from the Siberian platform.

1070-4272/03/7612-1891 $25.00 © 2003 MAIK "Nauka/Interperiodica"

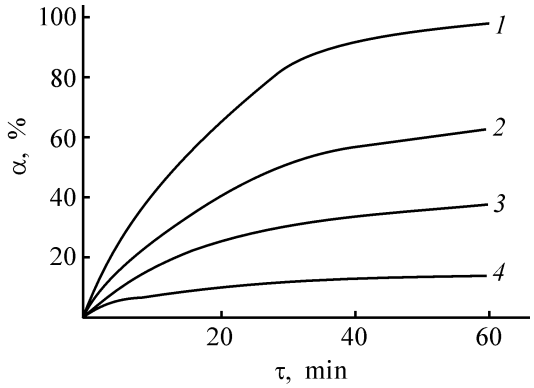

Fig. 1. Kinetic curves for the degree α of bromine absorption by LiOH solution in the presence of a reducing agent from bromine–air mixture with varied content of Br_2. (τ) Time. Br_2 content $c \times 10^2$ in air (g l^{-1}): (*1*) 25.7, (*2*) 16.2, (*3*) 9.7, and (*4*) 3.7.

um ions from highly mineralized brines [6]. In this method, lithium ions are recovered from the brine in the form of a selective-sorption eluate, a dilute LiCl solution with concentration of 7–10 kg m^{-3}, which contains a certain admixture of calcium and magnesium compounds removable by an appropriate purification procedure.

In elaboration of the techniques developed for recovery of lithium and bromine ions from brines of the Znamenskoe deposit (Irkutsk oblast), two new technological procedures were suggested for joint production of LiBr and elementary bromine. The first of these combines a procedure for manufacture of bromine and that for production of LiOH or Li_2CO_3 from selective-sorption eluates. A LiOH solution can be obtained by electrochemical conversion of a lithium chloride solution or its mixture with lithium carbonate [7, 8], and Li_2CO_3 slurry, by carbonization of a LiOH solution with carbon dioxide. Lithium bromide is obtained by bromination of lithium hydroxide or carbonate. As a brominating agent in the given method serves bromine vapor evolving from bromine water formed in isolation of bromine in the stage of steam desorption [1].

The second variant also includes a technique for production of liquid bromine; however, it is suggested to obtain LiBr directly from selective-sorption eluates (LiCl solutions) by ion exchange in desorption of lithium ions from the cation-exchange resin with a hydrobromic acid solution obtained by reduction of liquid bromine in an aqueous medium. Thus, the aim of this study was to make comparative analysis of the two suggested technological procedures for joint production of Br_2 and LiBr from natural brines.

EXPERIMENTAL

Laboratory studies were carried out with model solutions imitating the composition of a brine[2] with average composition (g l^{-1}): LiCl 2.5, NaCl 6.1, KCl 8.2, $MgCl_2$ 115, $CaCl_2$ 335, and Br^- 9.3; Li : Br atomic ratio 0.5. In studying multicomponent systems containing Br^0, Br^-, and Cl^-, analysis of solutions and the gas phase was performed using methods commonly accepted in manufacture of bromine [9]. The content of chloride ions in solutions was determined by mercurimetric titration, and that of calcium and magnesium ions, by trilonometry [10]; lithium ions were analyzed by flame photometry on an SP-9 spectrophotometer [11].

The first technological variant employs bromine water as a brominating agent. To obtain bromine vapor, bromine water was placed in a flask thermostated at 50°C. The flask was connected to absorbing vessels filled, depending on the aim of an experiment, with LiOH solution or Li_2CO_3 slurry. Bromine vapor was driven-off from bromine water with air from a compressor, with the content of bromine in the bromine–air mixture varied from 0.04 to 0.26 kg m^{-3}. The concentration of the LiOH solution was 50 g l^{-1}, the liquid to solid phase ratio (l : s) in the Li_2CO_3 slurry was varied from 3 to 11. As a reducing agent was used carbamide, with its amount varied in the range 0.75–1.5 relative to that required by the stoichiometry for reduction of elementary bromine to the bromide ion in accordance with the equations describing the chemical reactions

$$3Li_2CO_3 + 3Br_2 + CO(NH_2)_2 = 6LiBr + N_2\uparrow + 4CO_2\uparrow + 2H_2O, \quad (1)$$

$$6LiOH + 3Br_2 + CO(NH_2)_2 = 6LiBr + N_2\uparrow + CO_2\uparrow + 5H_2O. \quad (2)$$

As is known, the rate of bromine absorption by solutions of alkali or alkali metal carbonates is determined by the resistance of the boundary gas layer [1], being proportional to the bromine concentration in the gas phase. Figure 1 shows kinetic curves for the degree of bromine absorption by a LiOH solution from a bromine–air mixture with varied content of Br_2. As would be expected, the process is the faster and the degree of bromine absorption the greater, the higher the bromine concentration in the bromine–air mixture. The isotherm of bromine absorption is linear in the concentration range under study.

[2] Znamenskoe deposit (Irkutsk oblast).

With Li_2CO_3 slurry used to obtain lithium bromide, it was established that the concentration of the resulting LiBr solution increases with decreasing l : s ratio in the slurry, which is indicated by the data presented below:

The l : s ratio in slurry	11	7	4	3
LiBr concentration, g l^{-1}	125	246	381	440

Consequently, the l : s ratio is to be lowered for obtaining more concentrated LiBr solutions.

In the experiments, highly concentrated LiBr solutions with concentration of 400 g l^{-1} and more were obtained from saturated LiOH solutions and Li_2CO_3 slurry. In both cases, a certain excess of a reducing agent, about 20% relative to the stoichiometry of reactions (1) and (2), is necessary for more complete absorption of the bromine vapor. On the basis of the studies performed, technological Scheme 1 for obtaining LiBr with bromine vapor used as brominating agent has been developed [12].

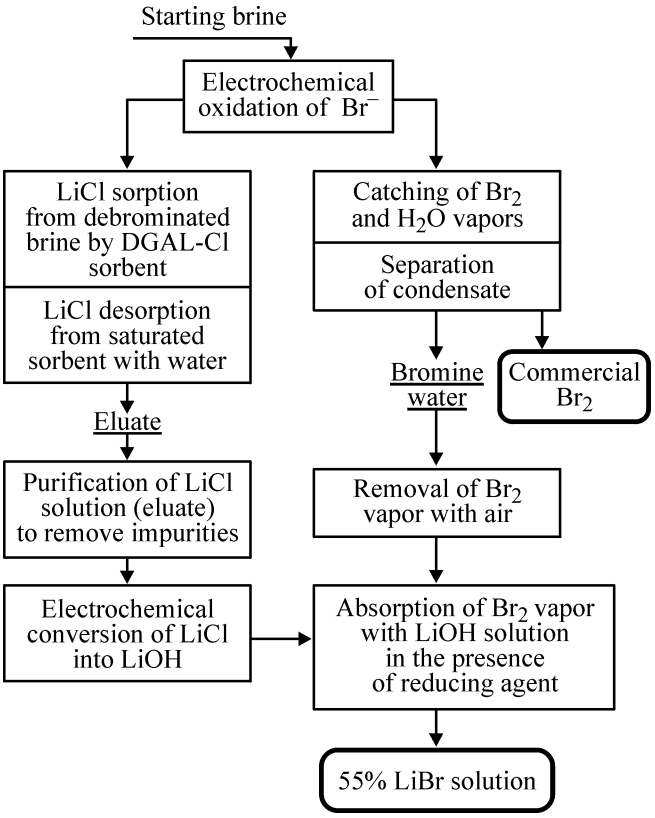

Scheme 1.

The second method for producing LiBr directly from eluates obtained from brine as LiCl solutions is based on sorption of lithium ions by a KU-2×8 cation-exchange resin in the H^+ form, with its subsequent desorption with hydrobromic acid to give a LiBr solution. Laboratory studies were carried out with model LiCl solutions in distilled water, with the concentration of lithium ions in the solutions varied from 3 to 1500 mg l^{-1}. Sorption was performed at room temperature in a glass column 60 mm high and 1.09 cm in diameter, packed with 50 cm^3 of KU-2 × 8 cation-exchange resin at bed height of 54 cm. The kinetics of sorption of lithium ions by the cation-exchange resin was studied by the dynamic method. A solution to be passed through the sorption stage was fed from below upwards by a dosage pump, with the linear flow velocity W of the solution varied from 7.4 to 26 m h^{-1}. The cation-exchange resin saturated with lithium ions was washed to remove chloride ions with demineralized water, after which lithium ions were desorbed with a HBr solution. The process in which LiBr is obtained can be described by the following ion-exchange reactions

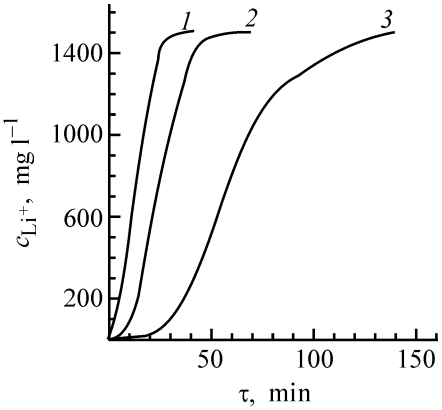

Fig. 2. Output curves of lithium ion sorption by KU-2×8 cation-exchange resin at different linear flow velocities of the solution. (c_{Li^+}) Concentration of Li^+ ions and (τ) time. W (m h^{-1}): (*1*) 26, (*2*) 15, and (*3*) 7.4.

$$R\text{–}H^+ + Li^+_{sol} \rightarrow R\text{–}Li^+ + H^+_{sol}, \quad (3)$$

$$R\text{–}Li^+ + H^+_{sol} \rightarrow R\text{–}H^+ + Li^+_{sol}. \quad (4)$$

In the initial stage of dynamic studies, output curves of lithium ion sorption by the cation-exchange resin were obtained at different flow velocities of a LiBr solution with concentration of 9.2 g l^{-1}, which corresponded to lithium ion concentration of 1500 mg l^{-1}. The dependences obtained (Fig. 2) made it possible to determine the time necessary for complete saturation of the cation-exchange resin and its dynamic exchange capacity (DEC), and to calculate the working zone height $H_{w.z}$ for each case. The sorption was performed in the plug-flow mode, which made it pos-

Table 1. Basic parameters of the process of lithium ion sorption by KU-2×8 cationite

Flow velocity of LiCl solution through cationite, W, m h^{-1}	Time elapsed till complete saturation of cationite with Li^+, τ, min	DEC, mg-equiv ml^{-1}	$H_{w.z}$, m
7.4	135	1.78	0.64
15.0	60	1.61	0.77
26.0	35	1.58	0.89

Table 2. Basic technological characteristics of the process of lithium ion desorption from saturated cationite with HBr solutions

c_{HBr}, M	Degree of Li ion desorption, %	Concentration of the resulting LiBr solution, g l^{-1}	Degree of utilization of the desorbing solution, %
0.7	41.0	62.5	99.2
1.5	72.0	129.3	99.2
2.0	98.5	174.0	100
2.2	98.8	184.6	96.5
2.5	98.9	187.2	86.1

sible to use in the calculations the Michaels–Treible formula [13]:

$$H_{w.z} = H_b \frac{\tau_{eq} - \tau_{br}}{\tau_{eq} - (1 - \phi)(\tau_{eq} - \tau_{br})},$$

where H_b is the height of the fixed bed of the cation-exchange resin (m); τ_{eq}, the time in which a concentration equal to $0.95\,c_{in}$ appears after the cationite bed (h); τ_{br}, the time in which a breakthrough concentration equal to $0.05\,c_{in}$ appears after the cationite bed (h); ϕ, the symmetry parameter of the curve.

It was established in the experiments that raising W leads to an increase in $H_{w.z}$, with the dependence being linear. As expected, the capacity characteristics of the cation-exchange resin decrease somewhat, as also does the degree of lithium ion sorption from solutions, with increasing flow rate of the solution. It should be added that the dynamic exchange capacity of the cation-exchange resin in the concentration range of lithium ions in LiCl solutions (3–1500 mg l^{-1}), used in this study, remains virtually constant, being equal to 1.6 mg-equiv ml^{-1} (Table 1).

Lithium ions were desorbed from the cationite in three stages with HBr solutions at l : s = 1 : 1 for each stage by Scheme 2 modeling the process of continuous counterflow desorption (horizontal arrows denote the flow of the cation-exchange resin, and vertical arrows, that of the desorbing HBr solution). It was established experimentally that the optimal HBr concentration in the desorbing solutions is 2.0–2.2 M. As can be seen from the data in Table 2, only this concentration ensures the most complete (~99%) recovery of lithium ions from the cation-exchange resin and the maximum concentration of LiBr in the final desorbate. Use of more concentrated hydrobromic acid solutions for desorption of lithium ions is inexpedient because of the low extent of their utilization.

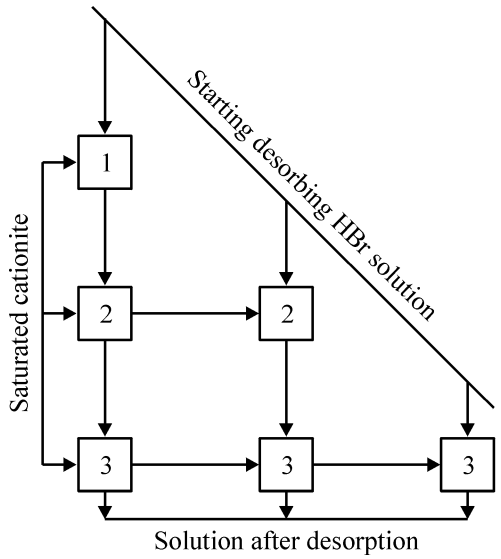

Scheme 2.

HBr solutions of required concentration were obtained by reacting elementary bromine with a reducing agent in an aqueous medium. The most appropriate reducing agents for this purpose are hydrazine, carbamide, and their derivatives, which form as a result of a redox reaction inert gaseous substances, N_2 and CO_2:

$$2Br_2 + N_2H_4 = 4HBr + N_2\uparrow. \quad (5)$$

The synthesis was carried out at room temperature under conditions of continuous metering-out of liquid bromine and agitation of the reaction mass until its total decoloration, which indicated the completion of the reaction. It was established experimentally that reaction (5) proceeds in strict conformity with the stoichiometry, with no excess of reagents required. This method for obtaining lithium bromide has been patented [14], its technological flowsheet is represented by Scheme 3. A solution of hydrobromic acid was used as brominating agent [14].

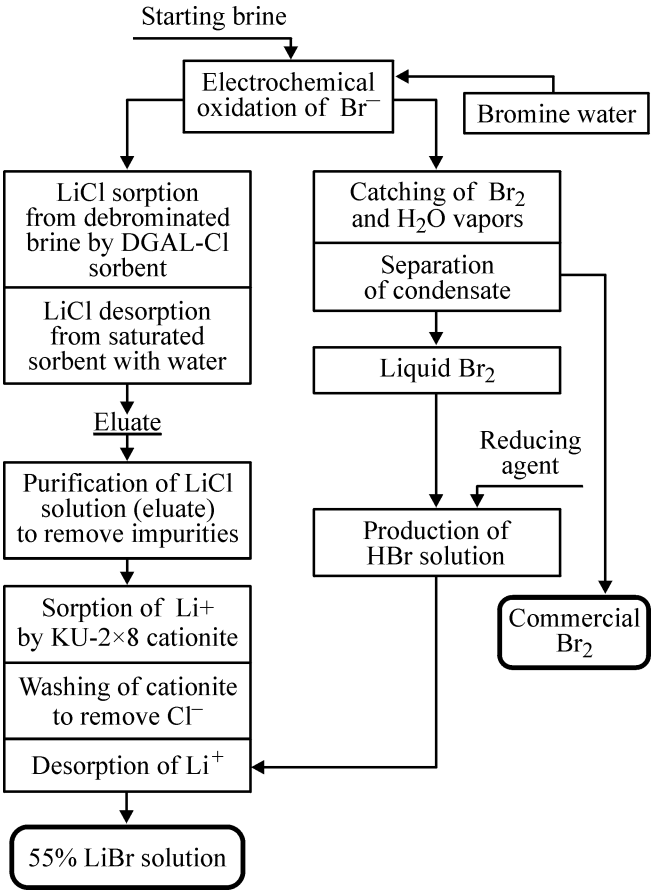

Scheme 3.

As already mentioned, both the methods yield two commercial products, Br_2 and LiBr, within a single technological scheme. It should be noted that, on the whole, the second method for LiBr manufacture directly from selective-sorption eluates obtained in the initial stages of brine processing is simpler and less expensive than the first technique, which involves power-intensive stages of LiOH or Li_2CO_3 production, which require intricate equipment. As for the choice of the optimal method for obtaining LiBr, it is determined by specific features and conditions of a particular production shop being designed or by availability of low-cost Li_2CO_3.

Combined schemes for joint production of Br_2 and LiBr from brines make it possible to lower substantially the manufacturing cost of the products obtained.

CONCLUSIONS

(1) Two variants of a technology for joint production of Br_2 and LiBr with bromine vapor or hydrobromic acid as brominating agents were developed.

(2) The second technique, which does not require additional expenditure for conversion of LiCl into LiOH or Li_2CO_3 for catching of bromine vapor, is simpler and less expensive.

REFERENCES

1. Ksenzenko, V.I. and Stasinevich, D.S., *Khimiya i tekhnologiya broma, ioda i ikh soedinenii* (Chemistry and Technology of Bromine, Iodine, and Their Compounds), Moscow: Khimiya, 1995.
2. USSR Inventor's Certificate, no. 597639.
3. USSR Inventor's Certificate, no. 929557.
4. USSR Inventor's Certificate, no. 1038282.
5. RF Patent 2171862.
6. RF Patent 2050330.
7. RF Patent 2157338.
8. RF Patent 2193008.
9. Polyanskii, N.G., *Analiticheskaya khimiya broma* (Analytical Chemistry of Bromine), Moscow: Nauka, 1980.
10. Morachevskii, Yu.V. and Petrova, E.M., *Metody analiza rassolov i solei* (Methods for Analysis of Brines and Salts), Moscow: Khimiya, 1964.
11. Poluektov, N.S., Meshkova, S.B., and Poluektova, E.N., *Analiticheskaya khimiya elementov: Litii* (Analytical Chemistry of Elements: Lithium), Moscow: Nauka, 1975.
12. RF Patent 2205796.
13. Kel'tsev, N.V., *Osnovy adsorbtsionnoi tekhniki* (Fundamentals of Adsorption Technology), Moscow: Khimiya, 1984.
14. RF Patent 2157339.

Russian Journal of Applied Chemistry, Vol. 76, No. 12, 2003, pp. 1896–1899. Translated from Zhurnal Prikladnoi Khimii, Vol. 76, No. 12, 2003, pp. 1948–1951.

INORGANIC SYNTHESIS AND INDUSTRIAL INORGANIC CHEMISTRY

Optimization of Gas-Extraction Recovery of Osmium Tetroxide from Aqueous Solutions

L. A. Ushinskaya, M. Yu. Stashok, O. V. Rodinkov, and L. N. Moskvin

Mekhanobr Engineering Analyte Closed Corp. Regional Analytic Center, St. Petersburg, Russia
St. Petersburg State University, St. Petersburg, Russia

Received July 16, 2003

Abstract—Dynamic gas extraction of osmium tetroxide from aqueous solutions was studied. The possibility of shortening substantially the duration of the stage of gas-extraction recovery of OsO_4 by reasonable choice of temperature, flow rate of extracting gas, and sample volume was also considered. The coefficients of OsO_4 distribution between the aqueous and gas phases were determined in the temperature range 20–90°C.

The absence of highly selective reagents for photometric determination of osmium and its low concentrations in objects to be analyzed create a need for preliminary concentration and separation of osmium from accompanying admixtures [1–3]. The unique property of osmium to form a volatile tetroxide is most commonly used to separate it from other metals. Osmium is frequently isolated as tetroxide by evaporation or gas extraction. Gas-extraction separation of osmium from other metals is in considerable use not only in analytic practice but also in industrial production of this metal [2, 4].

The search for more perfect schemes for distilling off osmium tetroxide has resulted in that a procedure for gas-diffusion recovery of osmium has been developed [5]. However, this scheme failed to solve the major problem of sample preparation for the determination of osmium, since it could not make shorter the time required for osmium isolation, which commonly takes more than an hour [2, 4, 5]. The possibility of optimizing the stage of osmium recovery in the form of its tetroxide is limited by the lack of published data on the coefficients of OsO_4 distribution in the liquid–gas system over a wide temperature range or any quantitative information about the effect of various factors on the efficiency of gas-extraction recovery.

The aim of this study was to search for the conditions under which the time of gas-extraction recovery of osmium is the shortest by revealing factors that affect the coefficients of osmium tetroxide distribution between the aqueous and gas phases.

EXPERIMENTAL

The osmium concentration in solution was determined by a spectrophotometric method based on the formation of a colored complex of osmium with thiourea [1]. We measured the optical density of colored solutions at a wavelength of 480 nm on a Karl Zeiss Specord M 40 spectrophotometer (Jena, Germany).

We prepared working aqueous solutions of OsO_4 immediately before experiments by saturating aqueous phases with OsO_4 vapor. For this purpose, we bubbled air through an alkaline solution of OsO_4, prepared from a standard solution in Richter's apparatus, and directed the resulting air flow into Zaitsev's absorbing apparatus filled with distilled water or sulfuric acid solution, depending on the required composition of the aqueous phase. The concentration of osmium in the thus prepared working solutions was determined spectrophotometrically by the above-mentioned procedure with the use of thiourea.

We determined the coefficients of OsO_4 distribution in the gas–liquid system by the known procedure, which determines the decrease in the component concentration in the working solution after passing a specified volume of an extracting gas through this solution [6]. Zaitsev's absorbing apparatus (bubbler) with the working solution was placed in a liquid thermostat, with temperature maintained constant to within ±0.1°C. To maintain a constant flow rate of the extracting gas (air or nitrogen) through the bubbler, we used a gas flow controller from the gas preparation unit of a gas chromatograph. The flow rate of the extracting gas

1070-4272/03/7612-1896 $25.00 © 2003 MAIK "Nauka/Interperiodica"

was measured with a soap-film flowmeter and maintained constant using a rotameter at the bubbler inlet. We measured the time with a stop-watch. The coefficient of OsO_4 distribution was calculated by the formula: [6]

$$K = W_G t/[V_L \ln(c_L^0/c_L)]. \quad (1)$$

Here K is the distribution coefficient, equal to the ratio of the OsO_4 concentration in the liquid phase to its concentration in the gas phase at equilibrium; W_G, the volumetric flow rate of the extracting gas ($cm^3\ min^{-1}$); t, the duration of bubbling (min); V_L, the solution volume (cm^3); c_L^0 and c_L, the starting and final concentrations of OsO_4 in the working solution ($mg\ l^{-1}$).

The relative error in determining K by the above-mentioned procedure is, with account of the error in measuring the flow rate of the extracting gas and other quantities appearing in formula (1), 5% at number of measurements $n = 4$ and confidence coefficient $P = 0.95$.

In the general case, the distribution coefficient of any component in a liquid–gas system depends on its concentration. The nonlinearity of the interphase distribution isotherm becomes significant at a certain concentration of the component, when the nonideal nature of the solution begins to show itself. For extremely diluted solutions, which corresponds to an overwhelming majority of cases of gas-extraction recovery of osmium from solutions, the concentration dependence of the distribution coefficient can, as a rule, be disregarded [6]. Our experiments showed that the coefficient of OsO_4 distribution between the aqueous and gas phases is independent of the OsO_4 concentration in aqueous solutions over the whole concentration range (30–500 $mg\ l^{-1}$), and its numerical value at 20°C is 950 ± 50. In this case, K is independent of which extracting gas (air or nitrogen) is used for OsO_4 extraction.

It has been shown previously that, for liquid–gas systems, the distribution coefficient of a volatile substance with limited solubility in a liquid can be rather easily estimated *a priory* if the saturated vapor pressure and the solubility of the substance at a given temperature are known [7]:

$$K = RTdP_0. \quad (2)$$

Here R is the universal gas constant ($dm^3\ Pa\ mol^{-1}\ K^{-1}$); T, temperature (K); P_0, the saturated vapor pressure at the temperature specified (Pa); d, the solubility of the substance in the liquid at this temperature ($mol\ dm^{-3}$).

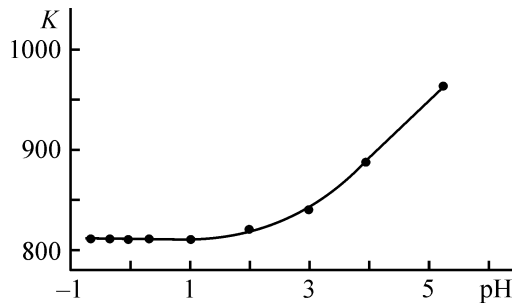

Fig. 1. Effect of pH on the coefficient of OsO_4 distribution K between aqueous and gas phases at 20°C.

Below, the coefficients of OsO_4 distribution in a water–air system, found experimentally and calculated by formula (2) on the basis of published data on OsO_4 properties [8], are compared:

T, °C	K_{exp}	K_{calc}
18	990 ± 50	910
25	720 ± 40	680

Taking into account that formula (2) is based on the assumption that the phases are ideal, we can conclude that the correspondence between the experimental and calculated K values is reasonable.

The most important factors affecting K are the nature of the liquid phase and the temperature, whereas the nature of the gas phase, in which intermolecular interaction forces are negligibly small, hardly affects this parameter. Figure 1 shows how the coefficient of OsO_4 distribution depends on the pH value of aqueous solutions. As would be expected with account of the weakly acid properties of osmium tetroxide ($K_1 = 6.3 \times 10^{-3}$, $K_2 = 6.8 \times 10^{-13}$), K is virtually independent of the hydrogen ion concentration within the pH range in which OsO_4 is almost completely in the molecular form.

It is a common knowledge that raising the temperature leads to a substantial decrease in K and to a corresponding increase in the efficiency of gas-extraction recovery. The table illustrates the effect of temperature on the coefficients of OsO_4 distribution. In addition to data for purely aqueous solutions, the table lists those for a sulfuric acid solution, since various forms of osmium in aqueous solutions are rather frequently oxidized to OsO_4 in a sulfuric acid medium. It can be seen from the table that heating from room temperature to 90°C results in a decrease in the distribution coefficient by almost a factor of 30 for both neutral and sulfuric acid solutions. The temperature

Coefficients of OsO_4 distribution, K, in the liquid–gas system at various temperatures

T, °C	K	
	1*	2*
20	950 ± 50	810 ± 40
30	620 ± 30	450 ± 20
40	360 ± 20	290 ± 15
50	210 ± 11	170 ± 9
60	115 ± 6	93 ± 5
70	70 ± 4	65 ± 3
80	50 ± 3	40 ± 2
90	34 ± 2	27.0 ± 1.4

* 1, distilled water; 2, 1 M solution of H_2SO_4.

dependences of the distribution coefficient (Fig. 2) are close to the theoretical dependences. They are straight lines in the $\ln K$–$1/T$ coordinates.

The flow rate of the extracting gas is one more factor, in addition to an increase in temperature, that can intensify the gas-extraction recovery. All other conditions being the same, the higher the flow rate of the extracting gas, the greater the amount of a volatile component extracted from a solution in unit time. However, raising the flow rate of the extracting gas through a solution being analyzed is reasonable only to those values at which the interphase equilibrium in the liquid–gas system has enough time to be attained. Figure 3 shows how the flow rate of the extracting gas affects the distribution coefficient calculated by formula (1) in terms of the equilibrium model of dynamic gas extraction.

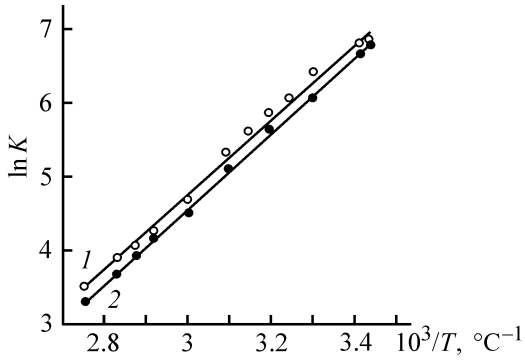

Fig. 2. Logarithm of the coefficient of OsO_4 distribution in the liquid–gas system, $\ln K$, vs. temperature T. (*1*) Distilled water and (*2*) 1 M solution of H_2SO_4.

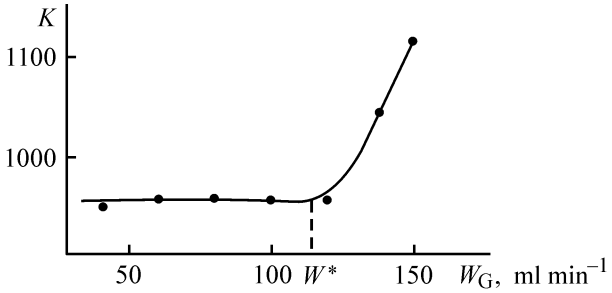

Fig. 3. Effect of the flow rate W_G of the extracting gas on the coefficient K of OsO_4 distribution between aqueous and gas phases. V_L = 2.0 ml, temperature 20°C.

As follows from Fig. 3, K is independent of the flow rate of the extracting gas, W_G, at $W_G \le 120$ ml min^{-1}. At greater flow rates, K starts to increase with W_G. This circumstance indicates that the interphase equilibrium has no enough time to be attained in this region. Similar dependences were obtained for other solution volumes V_L in the bubbler in the range 1–10 ml. The only difference is that the value of W_G^*, at which deviation from the equilibrium conditions of gas-extraction recovery begins, varies in direct proportion to the solution volume.

The ratio V_L/W_G is the time during which the extracting gas is in contact with the bulk of the solution. On this basis, we can conclude that the minimum time required for an equilibrium interphase distribution of OsO_4 to be established between the liquid and gas phases is $V_L/W_G^* = 2.0$ ml : 120 ml min^{-1} = 1 s.

Using the equilibrium model of dynamic gas extraction and the resulting formula (1), we can calculate the time R necessary for a prescribed degree of gas-extraction recovery of OsO_4 from the solution to be attained:

$$R = (1 - c_L/c_L^0). \quad (3)$$

Substituting c_L/c_L^0 from Eq. (3) into formula (1) and making simple rearrangements, we obtain

$$t = (KV_L/W_G)\ln[1/(1 - R)]. \quad (4)$$

If we set the flow rate of the extracting gas as $W_G = W_G^*$ and take into account that $V_L/W_G^* = 1$ s, we obtain the following approximate relationships for calculating the necessary duration t (s) of the stage of gas-extraction recovery of OsO_4 from aqueous solutions:

$$t \approx 3K \quad (\text{for } R = 0.95), \quad (5)$$

$$t \approx 4.6K \quad (\text{for } R = 0.999). \quad (6)$$

To verify the validity of expressions (5) and (6), we found experimentally the time necessary for 95%

recovery of OsO_4 from 5 and 10 ml of 1 M sulfuric acid solution at 90°C (K = 27) and air flow rates of 300 and 600 ml min^{-1}, respectively. In both cases, this time was 90 ± 5 s, in satisfactory agreement with the calculated value (81 s).

CONCLUSION

The duration of the stage of gas-extraction recovery of osmium from aqueous solutions in the form of its volatile tetroxide does not exceed several minutes at reasonable choice of temperature, flow rate of extracting gas, and sample volume. This creates favorable conditions for development of fast procedures for photometric determination of osmium in aqueous media and, in particular, that for flow-through injection analysis.

REFERENCES

1. Ginzburg, S.I., Ezerskaya, N.A., Prokof'eva, I.V., *et al.*, *Analiticheskaya khimiya platinovykh metallov* (Analytical Chemistry of Platinum Metals), Moscow: Nauka, 1972.
2. Beamish, F.E., *The Analytical Chemistry of the Noble Metals*, Oxford: Pergamon, 1966.
3. Sandell, E.B., *Colorimetric Determination of Traces of Metals*, New York: Interscience, 1959.
4. Khvostova, V.P. and Shlenskaya, V.I., *Analiz i tekhnologiya blagorodnykh metallov* (Analysis and Technology of Noble Metals), Moscow: Metallurgiya, 1971.
5. Varshal, G.M., Koshcheeva, I.Ya., Tyutyunnik, O.A., *et al.*, *Zh. Anal. Khim.*, 1998, vol. 53, no. 2, pp. 131–135.
6. Vitenberg, A.G. and Ioffe, B.V., *Gazovaya ekstraktsiya v khromatograficheskom analize: Parofaznyi analiz i rodstvennye metody* (Gas Extraction in Chromatographic Analysis: Vapor-Phase Analysis and Related Methods), Leningrad: Khimiya, 1982, pp. 8–43.
7. Rodinkov, O.V. and Moskvin, L.N., *Zh. Anal. Khim.*, 1995, vol. 50, no. 2, pp. 164–166.
8. Sinitsin, N.M., Kunaev, A.M., Ponamareva, E.I., *et al.*, *Metallurgiya Osmiya* (Metallurgy of Osmium), Alma-Ata: Nauka KazSSR, 1981.

Russian Journal of Applied Chemistry, Vol. 76, No. 12, 2003, pp. 1904–1908. Translated from Zhurnal Prikladnoi Khimii, Vol. 76, No. 12, 2003, pp. 1956–1960.

INORGANIC SYNTHESIS AND INDUSTRIAL INORGANIC CHEMISTRY

Synthesis of Monolithic Silica Gel in Alkaline Medium

N. N. Khimich, L. A. Koptelova, L. A. Doronina, and I. A. Drozdova

Grebenshchikov Institute of Silicate Chemistry, Russian Academy of Sciences, St. Petersburg, Russia

Received May 22, 2003

Abstract—The influence exerted by the basicity and nucleophilicity of a number of organic amines on the formation of a monolithic silica gel by the organic sol-gel method was studied.

During several years, the fundamental aspects of tetramethoxysilane (TMOS) hydrolysis and polycondensation of the forming compounds have been studied in order to obtain a monolithic silica gel SiO_2. The composition of the sol–gel system ensuring the formation of a three-dimensional network with minimum content of organic impurities has been optimized by varying the chemical nature of DCCA (drying control chemical additives) reagents introduced into the system [1], catalysts [2], and solvents of the sol–gel process [3]. However, acid-catalyzed sol–gel synthesis was considered in all cases.

Catalysis of an organic sol–gel process in an alkaline medium was described in [4], mainly with the aim to synthesize nanodispersed SiO_2 particles [5, 6]. However, only few publications have been concerned with the fundamental aspects of formation of a monolithic SiO_2 gel in the presence of bases [7, 8], with catalysis performed in both cases by adding an ammonia solution to the sol–gel system. In [9], the influence exerted by a number of organic amines on TMOS hydrolysis and polycondensation of the forming compounds was studied in order to obtain monodisperse SiO_2 nanoparticles. In this case, the catalytic process occurs under conditions of strong dilution of TMOS with water and ethanol (TMOS : water : ethanol ≈ 1 : 25 : 100), which is favorable for formation of an ensemble of dispersed particles [4].

In the present study, the influence exerted by basicity and nucleophilicity of a number of organic amines on TMOS hydrolysis and polycondensation of the forming compounds under conditions of a limited amount of water and ethanol relative to that of the forming SiO_2 gel was analyzed, possibility of synthesizing a monolithic gel under the given conditions was determined, and preparative methods for this synthesis were developed.

EXPERIMENTAL

For a study of TMOS hydrolysis and polycondensation of the forming compounds under alkaline conditions the following chemically and thermally stable aromatic amines were chosen: 3-fluoropyridine (**1a**), pyridine (**1b**), and 2-picoline (**1c**), and tertiary cyclic amines: 4-methyl morpholine (**1d**), 1-methylpiperidine (**1e**), and 1-ethyl-2,2,6,6-tetramethylpiperidine (**1f**):

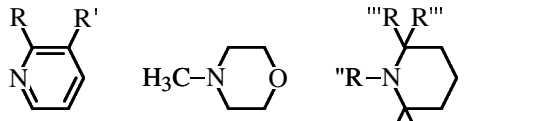

1a–**1c** **1d** **1e**, **1f**

where R = H, R' = F (**1a**); R = R' = H (**1b**); R = CH_3, R' = H (**1c**); R" = CH_3, R"' = H (**1e**); R" = C_2H_5, R"' = CH_3 (**1f**).

The choice of the amines used is not accidental. This becomes apparent when comparing the ionization constants of their conjugated acids, pK_a:

$$:NR_3 + H_2 \rightleftarrows HN^+R_3 + OH^-.$$

The boiling points and pK_a constants of these amines are listed below [for comparison, the corresponding constants for ammonia (**1g**) are also presented]:

Amine	pK_a	bp, °C
1a	3.0 [10]	30–31/4 mm
1b	5.247 [10]	115
1c	5.997 [10]	128
1d	7.41 [11]	115.4
1e	9.97 [12]	106
1f	11.13 [13]*	82–83/10 mm
1g	9.25 [14]	

* The pK_a value is given for 1,2,2,6,6-pentamethylpiperidine; for 1-ethyl-2,2,6,6-tetramethylpiperidine the pK_a value must be about the same or somewhat higher.

1070-4272/03/7612-1904 $25.00 © 2003 MAIK "Nauka/Interperiodica"

All the compounds used, TMOS and the amines, were purified by distillation on a rectification column with efficiency of 10 theoretical plates in a vacuum with residual pressure of 760–10 mm Hg. Compounds **1b**–**1e** are commercial preparations; trifluoropyridine **1a** and 1-ethyl-2,2,6,6-tetramethylpiperidine **1f** were synthesized using the procedures described in [15] and [16], respectively.

To prepare sol–gel systems **1a**–**1g**, TMOS (1 equiv), ethanol (1 equiv), and a catalyst were mixed in the order specified above and water was added under vigorous agitation with a magnetic stirrer. In the case of pyridine **1b**, 2-picoline **1c**, or 2-fluoropyridine **1a**, water was added at room temperature; for more basic amines, 4-methyl morpholine **1d**, 1-methylpiperidine **1e**, 1-ethyl-2,2,6,6-tetramethylpiperidine **1f**, or ammonia **1g**, this was done under cooling to –10°C. The ratios of amines **1a**–**1g** used as catalysts in preparing the corresponding gels **2a**–**2g** are listed below:

Gel	**2a**	**2b**	**2c**	**2d**	**2e**	**2f**	**2g**
Amine	**1a**	**1b**	**1c**	**1d**	**1e**	**1f**	**1g**
Ratio	0.1	0.1	0.1	0.02	0.01	0.01	0.01

The resulting solutions were placed in hermetically sealed polypropylene test tubes 15 mm in diameter (5 test tubes for each gel) and heated at 70°C for 6 days. Then the hermetic stoppers of the test tubes were replaced with stoppers with apertures (1 mm in diameter) and humid gels were dried in the following temperature mode: heating from 70 to 80°C in 2 h, keeping at 80°C for 22 h, heating from 80 to 100°C in 2 h, keeping at 100°C for 22 h, heating from 100 to 120°C in 2 h, and keeping at 120°C for 20 h. Gels **2b** and **2f** were additionally heated in glass test tubes from 120 to 150°C in 5 h and kept at this temperature for 20 h. This yielded samples **3b** and **3f**.

For the resulting gels **1a**–**1g**, the open porosity W_{op} and apparent density d_{app} (Archimedes method, with toluene as saturating fluid) were determined. The gelation point t (h) was found at 70°C as the time after which the sol lost its fluidity. The hardness of the samples was measured on a PMT-3 microhardness meter. Derivatograms were measured on a Q-1500D derivatograph (Hungary) in the temperature range extending to 1000°C at heating rate of 20 deg min^{-1}. The percentage content of SiO_2 in the gels obtained was determined gravimetrically, and the content of carbon was found by measuring the electrical conductivity of a $Ba(OH)_2$ solution serving as absorber of CO_2 formed upon burning the samples in oxygen. An electron-microscopic study of the gels was performed on an EM-125 instrument at accelerating voltage of 75 kV with cellulose–carbon replicas prepared on freshly cleaved surfaces of the gels obtained. The porous structure of the samples was studied by analyzing adsorption–desorption isotherms of ethanol on a McBain spring vacuum balance [17].

Physicochemical characteristics of the gels obtained

Sol–gel system	t, h	SiO_2, %	C, %	d_{app}, g cm^{-3}	W_{op}, %	Hardness, kg mm^{-2}
2a	0.77	88	2.05	1.07	46.8	32.6
2b	0.18	89.5	3.35	0.73	63.2	11.1
3b	–	92.4	4.10	0.61	69.4	9.8
2c	0.13	90	4.55	0.66	66.7	15.7
2d	0.02	92	1.75	–	–	9.4
2e	<0.01	91	1.45	0.58	71.3	9.2
2f	<0.01	91	2.70	0.65	67.9	15.4
3f	–	93	2.50	–	–	–
2g	<0.01	94	1.0	–	–	10.0

Samples **2a** and **2b** were monolithic transparent cylinders; systems **2c**, **2d**, and **3b**, somewhat opalescent partly cracked cylinders; systems **2e**–**2g** and **3f**, completely cracked samples.

The table lists the physicochemical characteristics of the resulting gels.

It can be seen from the table that the density and hardness of the samples synthesized decreases and their porosity increases as the basicity of the amines used as catalysts becomes higher. In this case, the content of SiO_2 in the gel matrix shows, according to the derivatographic data in Fig. 1, the opposite trend, i.e., grows, with the gelation time t of the sol-gel system simultaneously decreasing. Such a change in t in going from sample **2a** to samples **2e**–**2g**, which even occurs upon a pronounced decrease in the amine concentration, can be readily accounted for by an increase in the rates of reactions of hydrolysis of the $Si–OCH_3$ bond [4].

$$\equiv Si–OCH_3 + H_2O \xrightarrow{OH^-} \equiv Si–OH + CH_3OH \quad (1)$$

and condensation of the forming silanols into siloxanes [4]

$$\equiv Si–OH + HO–Si\equiv \underset{(III)}{\overset{(II)}{\rightleftarrows}} \equiv Si–O–Si\equiv + H_2O.$$

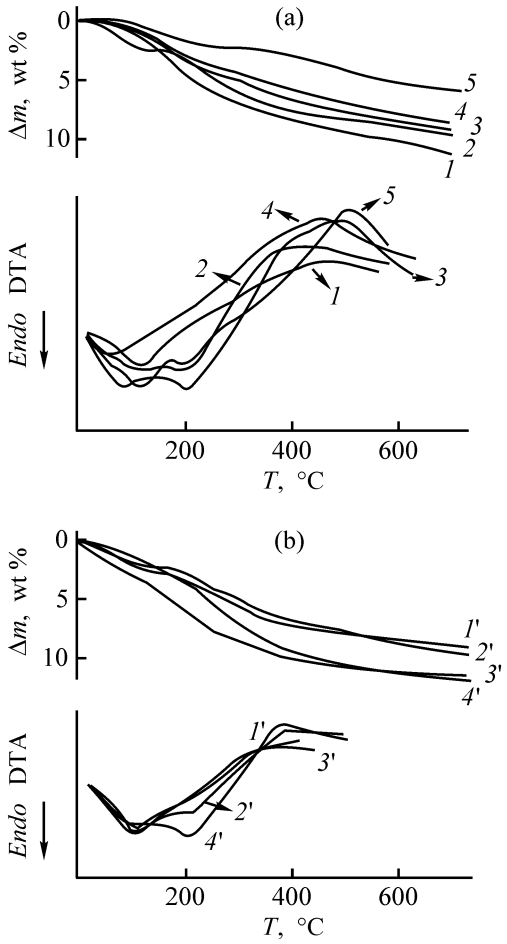

Fig. 1. DTA and TG data for (*1*–*5*, respectively) gels **2a**–**2c**, **2e**, **2g** and (*1'*–*4'*, respectively) gels **2b**, **2f** and **3b**, **3f**. (Δm) Mass loss and (T) temperature.

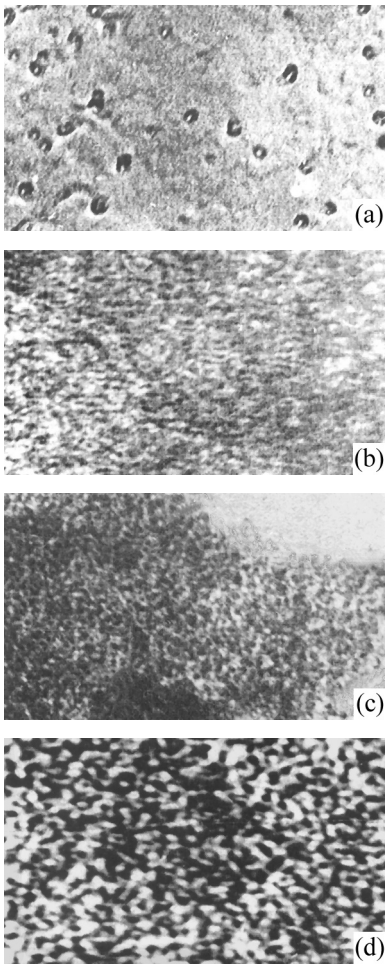

Fig. 2. Electron micrographs of gels (a) **2a**, (b) **2b**, (c) **2e**, and (d) **2f**. Magnification 120000.

Of much more interest is analysis of DTA curves (Fig. 1a) in order to determine the content of SiO_2 and carbon in the gel matrix (see table). As can be seen from an analysis of the intensities of these curves in the temperature range 400–600°C, which correspond to exothermic effects of burning-out of unhydrolyzed methoxy groups in the gel matrix, the number of these groups is the greatest when strongly basic amines are used as catalysts of the sol–gel process, i.e., in samples **2e** and **2g**. The rise in the intensity of this band in the case of gel **2f**, with a simultaneous increase in the content of carbon, should be attributed to lower volatility of amine **1f** as compared with the other bases used. In contrast to the other bases, amine **1f** simply remains in the gel matrix upon its being dried. In this case, the total amount of carbon in these samples (see table) is much lower than that in samples **2b** and **2c**. It seems reasonable to assume that the main part of carbon in the last two gels is contained in the form of volatile organic compounds remaining in the gel matrix after drying. Indeed, the DTA curves of these gels show two extrema [in contrast to the DTA curves of gels **2e** and **2g**] related to intense endothermic evaporation effects.

Comprehensive quantitative analysis of gels **2a**–**2g** is rather complicated; however, analysis of DTA curves and general considerations lead to the following conclusions. Apparently, residual amounts of methanol, water, and catalyst, retained in pores of the matrix by strong hydrogen bonds, remain in the gels after drying at 120°C. To their removal from the structure corresponds the first endothermic effect in the DTA curves of gels **2a**–**2g**. The second endothermic effect, probably, corresponds to removal of volatile organic compounds of silicon, which are formed when amines **1b** or **1c** are used as catalysts of the sol–gel process. These compounds are, apparently, characterized by low molecular weight, which allows them to easily leave a matrix being heated.

Such a disproportionation of alkoxysilanes to give the starting TMOS or low-molecular-weight siloxane has been described when studying the mechanisms of the sol–gel process [18]. When strong bases are used, no low-molecular-weight siloxanes are formed. In this case, it can be seen from the DTA curves that the evaporation of the solvents of the sol–gel process is immediately followed by burning-out of methoxylyl groups ≡Si–OM.

Finally, the attribution of the existence of the second dip in the DTA curves just to the process of evaporation of volatile siloxanes (rather than to evaporation of the excess amount of an amine used) can be confirmed by analysis of data for gels **2a**–**2c**. The content of carbon in the matrix of sample **2a** is much lower than that in gels **2b** and **2c**, although the volatilities of 3-fluoropyridine, pyridine, and 2-picoline are about the same. The second dip in the DTA curve, which is characteristic of gel **2b**, is virtually not observed at all in gel **3b** (Fig. 1b), with the content of carbon in the gel matrix remaining virtually unchanged. It is apparent that, in this case, volatile siloxanes are simply transformed into siloxanes with higher molecular mass. In passing from gel **2f** to gel **3f**, the run of the corresponding DTA curves is not changed (Fig. 1b).

Gels **2b** and **2c** still remain monolithic, whereas with stronger bases used as catalysts of the sol–gel process [gels **2d**–**2g**], the samples obtained completely crack in drying despite the increased amount of SiO_2 in the gel matrix and lowered content of carbon. The reason for such a behavior of the samples synthesized can be understood when studying their microstructure (Figs. 2 and 3).

It follows from the electron micrographs of gels **2a**, **2b**, **2e**, and **2f** in Fig. 2 that the monolithic structure of gel **2a**, which is, on the whole, characteristic of the sol–gel process in an acid medium, contrasts with the cellular structure of gel **2b** and even looser structure of gels **2e** and **2f**. These distinctions become even more apparent when studying the porosity of the samples synthesized (Fig. 3). Analysis of the data in Fig. 3 shows a clearly pronounced dependence of the pore size distribution on the basicity of a catalyst for different sol–gel systems. For comparison, data for a sol–gel process performed in the presence of acetic acid are show (Fig. 3, curve *1*).

The mechanisms of sol–gel processes of TMOS hydrolysis and polycondensation of the resulting compounds and those by which particles of colloid silica are formed have been described in detail [4, 19]. Apparently, gel **2a** is formed by the polymeric mechanism, which is characteristic of processes occurring in the acid medium, and gels **2d**–**2g**, by the corpuscular mechanism, in which the possibility of coarsening of SiO_2 particles is due to the occurrence of reaction (III). The mechanism by which gels **2b** and **2c** are formed has intermediate nature, with the Si–O–Si bonds between separate particles partly preserved, which is responsible for the monolithic character of gels **2b** and **2c**. The number of Si–O–Si bonds is small, and it is this fact that accounts for the low density and hardness of these monoliths. The use in the process of a sterically hindered base with lowered nucleophilicity, amine **1f**, does not lead to any significant changes in the parameters of the resulting gel **2f**, in contrast to the sol–gel process of TMOS hydrolysis and polycondensation of the forming compounds under conditions of strong TMOS dilution with water and ethanol [9].

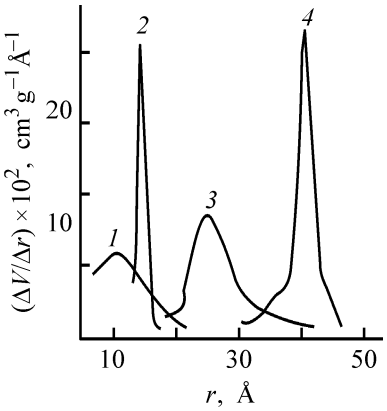

Fig. 3. Curves describing pore volume V distribution with respect to pore radii r for (*2*–*4*, respectively) gels **2a**, **2b**, and **2d**. (*1*) Sol–gel process in acid medium (acetic acid).

CONCLUSIONS

(1) A novel method for synthesis of porous SiO_2 xerogels is suggested. This method employs amines as catalysts, with the pore size controlled by the basicity of a catalyst used.

(2) Irrespective of the concentration of tetramethoxysilane, the mechanism of the sol–gel process is determined solely by the nature of a catalyst. In the case of weakly basic amines, a mixed polymeric–corpuscular mechanism is operative, which enables synthesis of monolithic SiO_2 xerogels.

(3) In alkaline catalysis under the action of strong bases, the dispersed phase has the form of an ensemble of weakly bound SiO_2 particles, which gives no way of obtaining monolithic samples.

REFERENCES

1. Khimich, N.N. and Stolyar, S.V., *Zh. Prikl. Khim.*, 1998, vol. 71, no. 10, pp. 1590–1595.
2. Khimich, N.N., Venzel', B.I., Drozdova, I.A., and Suslova, L.Ya., *Dokl. Akad. Nauk*, 1999, vol. 366, no. 3, pp. 361–363.
3. Khimich, N.N., Venzel', B.I., Drozdova, I.A., and Koptelova, L.A., *Zh. Prikl. Khim.*, 2002, vol. 75, no. 7, pp. 1125–1130.
4. Brinker, C.I. and Scherer, G.W., *Sol–Gel Science*, New York: Acad., 1990.
5. So Jae-Hyun, Yang Seung-Man, Kim, C., and Hyun, J.C., *Colloids Surfaces A: Physicochem. Eng. Aspects*, 2001, vol. 190, pp. 89–98.
6. Sung Kyoo Park, Ki Do Kim, and Hee Taik Kim, *Colloids Surfaces A: Physicochem. Eng. Aspects*, 2002, vol. 197, pp. 7–17.
7. Hæreid, S., Nilsen, E., and Einarsrud, M.-A., *J. Non.-Cryst. Solids*, 1996, vol. 204, no. 3, pp. 228–234.
8. Pajonk, G.M., Venkateswara, Rao A., Sawant, B.M., and Parvathy, N.N., *J. Non.-Cryst. Solids*, 1997, vol. 209, no. 1, pp. 40–50.
9. Khimich, N.N., Zvyagil'skaya, Yu.V., Zhukov, A.N., and Us'yarov, O.G., *Zh. Prikl. Khim.*, 2003, vol. 76, no. 6, pp. 904–908.
10. *Beilstein Handbook of Organic Chemistry: Fifth Supplementary Series*, Berlin: Springer, 1989, vol. 20, part 5.
11. *Beilstein Handbook der Organischen Chemie: Drittes und Viertes Ergänzungswerk*, Berlin: Springer, 1983, vol. 27, part 1.
12. *Beilstein Handbook of Organic Chemistry: Fifth Supplementary Series*, Berlin: Springer, 1988, vol. 20, part 2.
13. *Beilstein Handbook of Organic Chemistry: Fifth Supplementary Series*, Berlin: Springer, 1988, vol. 20, part 4.
14. Gordon, A.J. and Ford, R.A., *The Chemist's Companion, A Handbook of Practical Data, Techniques and References*, New York: Wiley–Interscience, 1972.
15. Roe, A. and Hawkins, G.F., *JACS*, 1947, vol. 69, no. 10, pp. 2443–2444.
16. Berg, S.S. and Cowling, D.T., *J. Chem. Soc. (C)*, 1971, pp. 1653–1658.
17. Venzel', B.I. and Svatovskaya, L.G., *Fiz. Khim. Stekla*, 1994, vol. 20, no. 4, pp. 523–528.
18. Klemperer, W.G. and Ramamurthi, S.D., *Better Ceramics Through Chemistry III*, Brinker, C.J., Clark, D.E., and Ulrich, D.R., Eds., Pittsburgh: Mat. Res. Soc., 1988.
19. Iler, R.K., *The Chemistry of Silica*, New York: Wiley–Interscience, 1979.

Russian Journal of Applied Chemistry, Vol. 76, No. 12, 2003, pp. 1909–1913. Translated from Zhurnal Prikladnoi Khimii, Vol. 76, No. 12, 2003, pp. 1961–1965.

PHYSICOCHEMICAL STUDIES OF SYSTEMS AND PROCESSES

A Simple Criterion of Thermodynamic Similarity for Molecular Inorganic Compounds

I. B. Sladkov

St. Petersburg State Technical University, St. Petersburg, Russia

Received November 12, 2002; in final form, October 2003

Abstract—The new determining criterion of thermodynamic similarity was suggested and used to obtain correlations that ensure reliable prediction of the physicochemical properties of molecular inorganic compounds on the basis of a single experimental characteristic of a substance, its boiling temperature.

The accumulation of reference information lags far behind the needs of science and technology for data on the physicochemical properties of substances. Because the experimental determination of properties is frequently a complicated task, it becomes even more important to determine the lacking data by calculation. Presently, such methods use the thermodynamic similarity theory as a theoretical basis [1].

The similarity theory originates from the reduced Van der Waals equation, from which the law of corresponding states follows. The concept of the corresponding states, which appeared as a consequence of the reduced Van der Waals equation, further became separated from the particular form of the equation of state and transformed into a method for prediction of the physicochemical properties of substances in terms of the similarity theory [2].

The similarity theory is based on the generalized form of the reduced equation of state

$$Y_{red} = f(T_{red}, V_{red}), \quad (1)$$

where Y_{red} is an invariant that represents the dimensionless form of the property to be determined using the law of the corresponding states. Such an invariant may be a dimensionless combination of any physicochemical properties.

Equation (1) means that, in terms of the dimensionless parameters, the physicochemical behavior of similar substances must be identical. This gives reason to believe that Eq. (1) is the criterion equation of thermodynamic similarity. The criterion equation in the form (1) is referred to as the two-parameter form of the law of corresponding states.

As is known from the similarity theory, criterion equations can be applied solely to identical objects. Correspondingly, Eq. (1) is only applicable to thermodynamically similar substances.

To judge whether or not the thermodynamic similarity is the case, one commonly uses the dimensionless parameters named the determining criteria of thermodynamic similarity. In the absence of such criteria, Eq. (1) has a very narrow applicability range, being solely suitable for small groups of substances exhibiting rather rigorous thermodynamic similarity. To extend the applicability range of Eq. (1), a determining criterion A is introduced as its additional argument to give a three-parameter form of the law of corresponding states

$$Y_{red} = f(T_{red}, V_{red}, A). \quad (2)$$

Establishing the determining criteria of thermodynamic similarity is a rather complicated task. It is this circumstance that explains why more than half a century passed between the formulation of the law of corresponding states and its practical application (in the form of methods for approximate calculation of physicochemical properties). In the mid-1950s, several criteria of the same kind were suggested, among which the Pitzer acentric factor gained the widest acceptance [3]. The correlations developed on the basis of the acentric factor have found wide application for predicting properties of organic substances.

The use of the acentric factor in the case of inorganic molecular compounds meets certain difficulties, which are caused both by the specific features of the prediction method [4] and by the fact that the correlations based on the acentric factor cannot be applied to strongly polar substances and associated liquids [3].

1070-4272/03/7612-1909 $25.00 © 2003 MAIK "Nauka/Interperiodica"

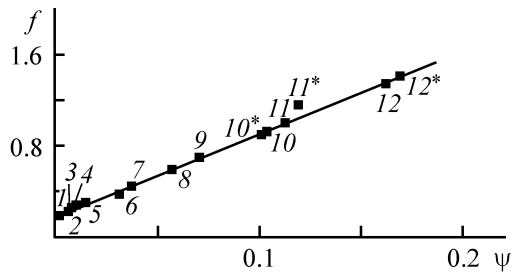

Fig. 1. Relation between the criteria f and ψ. *Digits at points* denote the sample nos. in Table 1, and *digits with asterisk*, those in Table 2; the same for Figs. 2 and 3.

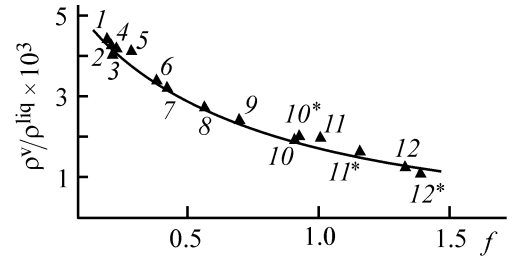

Fig. 2. Relation between the criterion f and the vapor to liquid density ratio ρ^{v}/ρ^{liq} at the boiling point.

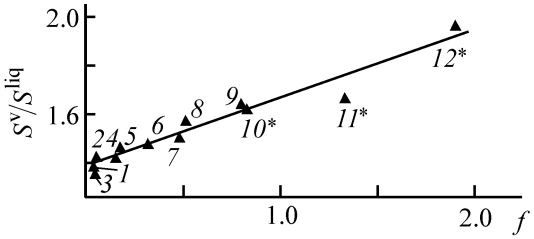

Fig. 3. Relation between the criterion f and the ratio of the standard entropies of gas and liquid, S^{v}/S^{liq}.

It has been suggested to use in characterizing the thermodynamic similarity of inorganic molecular compounds the determining criterion named the factor of complexity of the intermolecular interaction (ψ-factor) [5]. This factor is calculated from the boiling temperature T_b and the molar volume of a liquid at the boiling point, V_b ($cm^3\ mol^{-1}$):

$$\psi = 0.01 \ln T_b - 0.122 \ln V_b + 0.006.$$

A number of correlations have been developed on the basis of the ψ-factor for predicting the physicochemical properties of molecular inorganic liquids [6]. Many of these allow calculation of physicochemical properties with nearly experimental error.

Although data on the molar volume of a liquid at its boiling point are available for many substances (e.g., in a reference book [6]), the boiling points of a molecular liquid is its most readily available characteristic. Accordingly, it would be of particular importance to have, for little-studied substances, a determining criterion that could be calculated solely from the boiling point of a substance under consideration.

The method used to establish the ψ-factor [5] was applied to obtain a new determining criterion of thermodynamic similarity, defined by the equation

$$f = \ln T_b - 1.1 \ln \Pi - 4. \quad (3)$$

It should be emphasized that the parachor Π is calculated from data on the parachor increments for different elements. The calculation procedure and all the necessary tabulated data were reported in [6].

Prior to considering the calculation of physicochemical properties with the use of the criterion f, let us note that the determining criteria f and ψ are correlated (Fig. 1), with high correlation factor ($R = 0.9967$):

$$f = 7.3\psi + 0.2.$$

The existence of the above correlation is of major practical importance, because it allows estimation of the polarity of a little-studied substance on the basis of the only experimental parameter, its boiling temperature. The values of the ψ-factor, which characterize the boundaries between substances with different polarities, can be used to obtain the following values of the criterion f for characterizing the polarity: $0 < f < 0.5$ for nonpolar and weakly polar substances (e.g., $SiCl_4$ and BBr_3), $0.5 < f < 0.9$ for moderately polar substances (e.g., $CrCl_2O_2$ and IF_5), and $f > 0.9$ for strongly polar substances (e.g., HCl and NH_3).

Being the determining criterion of thermodynamic similarity, the parameter f must correlate with the invariants of the physicochemical properties. This is well confirmed both graphically (Figs. 2 and 3) and by the analytical relations (4)–(9) presented below.

Let us list the expressions derived for calculating various physicochemical properties with the use of the parameter f as the determining criterion.

Molar volume of a liquid at its boiling point

$$V_b = (-6.2f + 31.2)\Pi^{0.94}. \quad (4)$$

Critical temperature

$$T_{cr} = T_b/(0.667 - 0.055f^{0.5}). \quad (5)$$

Table 1. Physicochemical properties of substances

Substance no.	Substance	f	ψ	Π, $J^{1/4}\,cm^{5/2}\,mol^{-1}$	T_b, K	V_b, $cm^3\,mol^{-1}$	T_{cr}, K	V_{cr}, $cm^3\,mol^{-1}$	P_{cr}, MPa
1	$SiCl_4$	0.20	0.001	4.30	330.5	121.2	507.0	326.3	3.73
2	$GeCl_4$	0.22	0.005	4.49	356.2	124.1	552.0	330.0	3.83
3	$SiBr_4$	0.22	0.005	5.30	425.9	143.6	663.2	382.1	4.00
4	SnI_4	0.23	0.006	7.40	622.5	195.8	968.0	530.0	4.30
5	$SiHCl_3$	0.29	0.013	3.67	305.2	102.8	479.0	268.2	4.17
6	BBr_3	0.39	0.030	3.93	364.2	103.3	581.0	280.0	4.84
7	VCl_3O	0.43	0.036	4.14	399.9	105.9	636.1	290.1	5.17
8	$CrCl_2O_2$	0.57	0.056	3.56	389.0	88.3	610.0	240.0	5.60
9	IF_5	0.70	0.070	3.07	377.6	76.5	603.1	209.1	6.80
10	SO_2	0.93	0.102	1.80	263.1	43.9	430.6	122.0	7.88
11	HCl	1.01	0.112	1.23	188.1	30.8	324.7	87.6	8.26
12	NH_3	1.33	0.162	1.15	239.7	25.0	405.5	72.0	11.35

Table 2. Error Δ in calculating physicochemical properties

Substance no.	Substance	ΔV_b	ΔH_b	ΔT_{cr}	ΔV_{cr}	ΔP_{cr}	Substance no.	Substance	ΔV_b	ΔH_b	ΔT_{cr}	ΔV_{cr}	ΔP_{cr}
		%							%				
1	$SiCl_4$	–2.5	–2.0	1.4	–2.2	4.6	7	VCl_3O	2.5	1.3	–0.4	–1.4	–2.7
2	$GeCl_4$	–1.4	–3.0	0.7	0.1	5.8	8	$CrCl_2O_2$	3.4	–2.8	1.9	3.4	2.4
3	$SiBr_4$	–0.4	3.3	0.2	1.1	3.6	9	IF_5	0.8	–5.2	0.8	0.5	–4.4
4	SnI_4	–0.30	–4.5	0.4	–0.4	3.1	10	SO_2	0.8	–1.6	–0.5	–0.8	–2.2
5	$SiHCl_3$	–2.9	–2.2	–0.1	0.7	1.5	11	HCl	–1.6	8.8	–5.3	–5.2	–3.4
6	BBr_3	0.8	4.0	–0.9	0.8	–1.0	12	NH_3	4.8	1.6	–2.1	0.3	–0.1

It can be readily seen that, at $f \to 0$, Eq. (5) transforms into the known Guldberg rule, which is observed for nonpolar substances.

Critical volume

$$V_{cr} = V_b(2.69 + 0.05f). \quad (6)$$

At $f \to 0$, Eq. (6) yields the known Hertz rule, which is valid for nonpolar substances.

Van der Waals constant

$$b = V_b(0.2f + 1.12). \quad (7)$$

Critical pressure

$$P_{cr} = 1.039\,T_{cr}/b. \quad (8)$$

Enthalpy of vaporization at the boiling point

$$\Delta H_b = RT_b \ln(10.255T_{cr}/b)/(1 - T_b/T_{cr}). \quad (9)$$

The potentialities of the new criterion are illustrated for 12 substances belonging to different classes and having different polarities. The physicochemical properties of these substances were taken from a reference book [6] (see Table 1). The mean errors in calculating the above properties by Eqs. (4)–(9) are listed in Table 2.

The data presented show that the calculated and the experimental values are in good agreement. It is important to note that the prediction error is virtually polarity-independent.

The data array was expanded to 50 substances.[1] All the data necessary for calculation were taken from

[1] The 50 substances whose properties were included into the expanded data array are the following: CH_4, B_2H_6, GeH_4, SnH_4, CF_4, MoF_6, WF_6, UF_6, BCl_3, CCl_4, $TiCl_4$, PCl_3, PCl_5, $BiCl_3$, S_2Cl_2, $MoCl_5$, PBr_3, $SmBr_4$, BI_3, SiI_4, CCl_3F, CBr_2F_2, $CBrF_3$, $SiBrCl_3$, $SiBr_2Cl_2$, $PClF_2$, PCl_2F, $NClF_2$, $SiHBr_3$, PCl_3O, PBr_3O, SCl_2O, ClO_3F, WCl_4O, and CO; the remaining 15 substances are listed in Tables 1 and 4.

Table 3. Verification of the accuracy of the methods used for calculating physicochemical properties

Property	Mean error, %		Maximum error, %	
	Δ^*	Δ^{**}	Δ^*	Δ^{**}
V_b	1.9	1.9	5	6
ΔH_b	3.0	2.7	9	10
T_{cr}	1.3	1.5	5	6
V_{cr}	1.5	2.1	4	6
P_{cr}	2.9	3.1	7	11

* Data array for 12 substances.

** Data array for 50 substances.

Table 4. Error in calculating the entropy by Eq. (10) [7]

Substance no.	Substance	f	S^{liq}	S^g	Δ, %
			J mol^{-1} K^{-1}		
1	$SiCl_4$	0.20	239.8	331.0	1.1
2	$GeCl_4$	0.22	245.6	347.8	–1.2
3	$SiBr_4$	0.22	277.9	377.5	3.0
4	$SnCl_4$	0.24	258.6	364.9	–0.7
5	$SiHCl_3$	0.29	227.7	313.4	2.3
6	BBr_3	0.39	228.9	324.3	0.8
7	VCl_3O	0.43	236.4	344.0	–1.3
8	$CrCl_2O_2$	0.57	222.0	328.0	–0.2
9	IF_5	0.70	224.7	338.5	1.0
10	AsF_3	0.91	178.2	295.5	6.1
11	BrF_3	1.16	181.2	293.0	0.1
12	N_2H_4	1.38	121.6	238.7	–2.2

Table 5. Influence of acentric factor ω on error Δ in calculating the critical parameters

Substance no.	Substance	ω	ΔT_r	ΔV_{cr}	ΔP_{cr}
1	BCl_3	0.150	–0.5	–2.9	2.2
2	BF_3	0.420	6.7	7.2	4.5
3	H_2O	0.344	–0.8	–12.6	17.1
4	Re_2O_7	0.601	8.8	0.4	0.9
5	NO_2	0.860	14.6	3.9	20.4

a reference book [6]. As can be seen from Table 3, that a 4-fold extension of the data array leaves virtually unchanged the error in prediction of the physicochemical properties considered. This points to high reliability of the data on the error of the correlations presented.

The criterion suggested can also be used for predicting the thermodynamic properties of substances. For example, there is a clearly pronounced correlation between the ratio S^{liq}/S^g of the standard entropies (at 298 K) of a substance in the liquid and gaseous states and the parameter f (Fig. 2). This correlation, expressed by

$$S^{liq}/S^g = (0.18f^2 + 1.385), \quad (10)$$

can be used to predict the entropy of a phase state of a substance (liquid or gas) from the entropy of the other state. The errors of such a prediction are listed in Table 4. Here, the set of substances is somewhat different from that of Table 1, because some substances (SO_2, HCl, NH_3) do not exist in the liquid state at T = 298 K and P = 1 atm (101 325 Pa).

Molecular inorganic compounds with widely different intermolecular interactions are represented in the set of the substances studied, including nonpolar, moderately polar, and highly polar substances. For all these substances, the criterion suggested ensures rather high accuracy of prediction of their physicochemical properties.

To gain clearer insight into the potentialities of the criterion suggested, it is appropriate to consider the limiting case of prediction, when substances with the most complex intermolecular interaction are under study. To such substances belong associated liquids, which are characterized by the presence of hydrogen bonds and high values of the acentric factor. The errors in calculating the critical parameters for such substances are listed in Table 5. It can be seen that there is no unambiguous pattern in this case: the calculation error may be either low or rather large (this mainly refers to the critical pressure).

The increase in error is presumably due to poorer accuracy in calculating the parachor (for substances with hydrogen bonds the additivity of the parachor is violated) and, consequently, the parameter f. At the same time, with account of the fact that prediction of physicochemical properties with the use of the parameter suggested is based on the only input property (boiling point), application of the parameter f to the above substances, too, may be of practical importance.

CONCLUSIONS

(1) A determining criterion that considerably extends the potentialities of the thermodynamic similar-

ity theory for prediction of physicochemical properties of little-studied substances was suggested.

(2) The similarity criterion was used to obtain the correlations that ensure reliable prediction of physicochemical properties on the basis of the only characteristic of a substance, its boiling temperature.

REFERENCES

1. Filippov, L.P., *Podobie svoistv veshchestv* (Similarity of Substance Properties) Moscow: Mos. Gos. Univ., 1978.
2. Filippov, L.P., *Zakon sootvetstvennykh sostoyanii* (The Law of Corresponding States), Moscow: Mos. Gos. Univ., 1983.
3. Reid, R.C. and Sherwood, T.K., *The Properties of Gases and Liquids. Their Estimation and Correlation,* New York: McGraw–Hill, 1966, 2nd ed.
4. Sladkov, I.B. and Prokopenko, O.A., *Zh. Prikl. Khim.*, 1997, vol. 70, no. 10, pp. 1606–1611.
5. Sladkov, I.B., *Teplofizicheskie svoistva veshchestv i materialov* (Thermophysical Properties of Substances and Materials), Moscow: Izd. Standartov, 1986, vol. 23, pp. 69–84.
6. Morachevskii, A.G. and Sladkov, I.B., *Fiziko-khimicheskie svoistva molekulyarnykh i neorganicheskikh soedinenii* (Physicochemical Properties of Molecular and Inorganic Compounds) St. Petersburg: Khimiya, 1996.
7. Ruzinov, L.P. and Gulyanitskii, B.S., *Ravnovesnye prevrashcheniya metallurgicheskikh reaktsii* (Equilibrium Transformations of Metallurgical Reactions), Moscow: Metallurgiya, 1975.

Russian Journal of Applied Chemistry, Vol. 76, No. 12, 2003, pp. 1914–1919. Translated from Zhurnal Prikladnoi Khimii, Vol. 76, No. 12, 2003, pp. 1966–1970.

PHYSICOCHEMICAL STUDIES OF SYSTEMS AND PROCESSES

Calculation of the Enthalpy of Sublimation by the QSPR Method with the Use of a Fragment Approach

N. I. Zhokhova, I. I. Baskin, V. A. Palyulin, A. N. Zefirov, and N. S. Zefirov

Moscow State University, Moscow, Russia

Received December 23, 2002; in final form, June 2003

Abstract—The enthalpies of sublimation of organic compounds belonging to various classes were studied for the first time in terms of the fragment approach based on the QSPR (Quantitative Structure–Property Relationships) method. The applicability of this technique to calculation of this parameter was demonstrated and a model that makes it possible to predict the enthalpy of sublimation of compounds on the basis of descriptors taking into account the fragment composition of a molecule was suggested.

The enthalpy of sublimation, $\Delta_{sub}H$, is the enthalpy of a transition of a substance from the solid state directly (without melting) to the gaseous state [1]. This property is of certain practical interest for the chemistry of the crystalline state and, in particular, for resolving the problems associated with dispersion of dyes and discoloration of materials, and such ecological problems as transport of organic contaminants in the atmosphere, etc. [1–5]. Determining the enthalpy of sublimation, $\Delta_{sub}H$, or other thermodynamic parameters experimentally requires application of expensive and time-consuming procedures. Therefore, considerable attention has been given in the literature both to theoretical calculational techniques and to empirical QSPR (Quantitative Structure–Property Relationships) methods for estimating these characteristics. For example, the enthalpies of sublimation have been obtained by calculating crystal packings [1–3]. For QSPR, methods of regression analysis [1], neural networks [1], and 3D-QSAR (CoMFA) [4, 5] methods have been used. In the case of a regression analysis with learning sample containing 62 compounds (control sample of 10 compounds), a three-parameter equation has been obtained, in which the number of carbon atoms, and also the number of donors and acceptors of the hydrogen bond, were used as descriptors [1].

In 1990, the FRAGMENT software was developed. This program can generate sets of fragments: chains (1–9 atoms), cycles (3–6-membered), and several types of branched fragments [6–11]. Each atom in a fragment is designated in dependence on the type of atom, the number of H atoms bonded to it, and the bonding environment, which makes it possible to take into account in adaptable manner the multiple bonds, functions, heteroatoms, etc. The FRAGMENT program has been successfully used in the QSAR/QSPR software package EMMA [11–19] and neural-network software package NASAWIN [20–23].

In previous studies concerned with QSAR/QSPR [(Quantitative Structure–Activity Relationships)/(Quantitative Structure–Property Relationships)], fragment descriptors have been widely used both for QSPR (chromatographic retention indices [18], boiling point [18], polarizability [24], density, viscosity, and saturated vapor pressure [25] for widely diverse classes of compounds) and for QSAR [11, 19]. A point of principle should be noted: if a set of compounds is sufficiently large for constructing a statistically significant model, then any topological index can be replaced with a set of fragment descriptors [26]. The advantage of fragment descriptors consists in the clearness and easy structural interpretation of the results of QSAR/QSPR. In this study, fragment descriptors are used to carry out a QSPR analysis of the enthalpy of sublimation.

As model experimental database of the enthalpies of sublimation (Database 1) were chosen the data reported in [1]: learning sample of 62 compounds and control sample of 10 structures (compound nos. 63–72). The complete sample comprised molecules with known crystal structure, which contain C, H, O, and N atoms, including aliphatic and aromatic hydrocarbons, their oxo and aza derivatives, carboxylic acids, amide and amino acids, cyanides, quinones, and heterocycles. The input and verification of Database 1

1070-4272/03/7612-1914 $25.00 © 2003 MAIK "Nauka/Interperiodica"

were performed using MEOW and BASTET software [24]. The advantage of the given sample of compounds is that the enthalpies of sublimation can be calculated for this set in three ways: (1) by theoretical calculation of crystal packings (with the statistical parameters $n = 62$, $r^2 = 0.971$, $s = 0.939$ kcal mol^{-1}, maximum error 3.5 kcal mol^{-1}), (2) by regression analysis (with the following statistical parameters: three descriptors, $n = 62$, $r^2 = 0.92$, $s = 1.6$ kcal mol^{-1}, maximum error 8.9 kcal mol^{-1}, average error of prognosis 2.8 kcal mol^{-1}), and (3) with a neural network (with the following parameters for the best model: seven hidden neurons, $n = 62$, $r^2 = 0.865$, $s = 2.2$ kcal mol^{-1}, maximum error 10.1 kcal mol^{-1}, average error of prognosis 36 kcal mol^{-1}). This constitutes a sound basis for comparison, even though the sample is not too large.

The MEOW and BASTET software was used to create Database 2 (88 compounds), by adding to Database 1 experimental data of [2] and excluding duplicates, and Database 3 (104 compounds), by adding to Database 2 experimental data of [4] for chlorinated diphenyls (15 structures) and excluding duplicates. The inclusion of chlorinated phenyls is due both to the importance of this type of compounds, which find wide application as insulating materials and fire retardants, and to the desire to extend the structural diversity of the sample by covering chlorine-containing compounds.

The QSPR modeling was performed using QSAR software EMMA [18, 19] and NASAWIN [20–22]. The fragment descriptors were calculated by FRAGMENT software (modified version distinguished by a greater number of types of fragments and more versatile classification of atoms [11, 23]), with the following restrictions imposed: chain length was 1–6; fragment descriptors were selected both automatically and manually; in selecting mutually correlated descriptors, those correlated to the greatest extent with the property were chosen.

Let us consider the comparative results of QSPR. The table lists characteristics of the models devel-

Statistical parameters of QSPR models for the enthalpy of sublimation, based on fragment descriptors for Databases 1–3

Parameter	Descriptor									
	1	2	3	4	5	6	7	8	9	10
Model no. 1*										
Learning sample, compound nos. 1–62										
R^2	0.5584	0.7331	0.9235	0.9403	0.9468	0.9520	0.9577	0.9610	–	–
s	5.62	4.41	2.38	2.12	2.02	1.94	1.83	1.78	–	–
F	76	81	233	224	199	182	174	163	–	–
Maximum error,(1) kcal mol^{-1}	13.15 (46)	14.47 (50)	8.08 (4)	6.41 (36)	6.26 (36)	6.33 (36)	6.61 (36)	6.17 (36)	– –	– –
Control sample, compound nos. 63–72										
R^2 progn.	0.6310	0.7762	0.7688	0.6708	0.6684	0.6593	0.6954	0.6140	–	–
Prognosis error, kcal mol^{-1}:										
average	3.7	2.7	2.7	3.3	3.2	3.3	3.1	3.3	–	–
maximum	7.6 (64)	5.9 (64)	7.3 (70)	7.4 (64)	7.7 (64)	7.8 (64)	7.4 (64)	8.5 (64)	–	–
Model no. 2**										
Learning sample, compound nos. 1–62, 73–92, 94–96, 98–101, 103, 104										
R^2	0.4886	0.6803	0.8523	0.8734	0.8878	0.8980	0.9072	0.9151	0.9214	0.9296
s	5.36	4.26	2.92	2.71	2.57	2.46	2.37	2.28	2.20	2.10
F	85	94	167	148	135	123	116	110	106	106
Maximum error,(1) kcal mol^{-1}	15.2 (46)	15.2 (50)	10.1 (4)	8.1 (75)	6.5 (28)	6.2 (28)	6.7 (75)	6.8 (75)	6.1 (36)	6.5 (36)

Table. (Contd.)

Parameter	Descriptor									
	1	2	3	4	5	6	7	8	9	10
Model no. 2**										
Control sample, compound nos. 63–72, 93, 97, 102										
R^2 progn.	0.6563	0.7607	0.7518	0.7105	0.7319	0.7365	0.7233	0.7303	0.7319	0.7294
Prognosis error, kcal mol^{-1}:										
average	2.73	2.42	2.41	2.70	2.57	2.69	2.75	2.72	2.72	2.74
maximum	7.3	6.1	7.7	7.6	7.4	7.4	7.7	7.6	7.5	7.8
	(68)	(70)	(70)	(70)	(70)	(70)	(70)	(70)	(70)	(70)
Model no. 3***										
Learning sample, compound nos. 1–35, 37–62, 64, 70, 73–92, 94–96, 98–101, 103, 104										
R^2	0.4786	0.6714	0.8450	0.8656	0.8802	0.8908	0.9004	0.9094	0.9161	0.9235
s	5.39	4.30	2.97	2.78	2.64	2.54	2.44	2.34	2.27	2.18
F	83	91	160	140	126	116	109	104	100	98
Maximum error,(1) kcal mol^{-1}	15.2	15.2	10.0	8.1	7.5	7.5	7.8	7.5	7.5	7.7
	(46)	(50)	(4)	(75)	(70)	(70)	(70)	(70)	(70)	(70)
Control sample, compound nos. 36, 63, 65–69, 71–72, 93, 97, 102										
R^2 progn.	0.7554	0.8488	0.8161	0.7796	0.7989	0.7982	0.7783	0.8027	0.7994	0.7905
Prognosis error, kcal mol^{-1}:										
average	2.18	1.98	2.16	2.43	2.31	2.46	2.56	2.37	2.37	2.42
maximum	7.3	5.4	5.9	5.6	5.6	5.9	6.3	5.9	6.1	6.5
	(68)	(71)	(36)	(36)	(36)	(36)	(36)	(36)	(36)	(36)

(1) Given in parentheses are the numbers of compounds for which the maximum error is presented; the enumeration corresponds to that in Databases 1–3, which can be provided by the authors if requested.

* Model no. 1: descriptor 1: fr_1 is the number of arbitrary atoms; descriptors 2, 3: fr_2, fr_3 are the numbers of fragments of the types =CR−OH and N_{sp^3}−C=O, respectively; descriptor 4; fr_4 is te number of simple bonds in a molecule, •−•; descriptors 5–8: fr_5, fr_6, fr_7, fr_8 are the numbers of fragments of the types RC_{Ar}÷$C_{Ar}H$÷$C_{Ar}H$÷$C_{Ar}R$, NH_2, •=•−•−•−•=•, and CH_3, respectively.

** Model no. 2: descriptor 1: fr_1 is the number of arbitrary atoms; descriptors 2–10: fr_2, fr3, fr_4, fr_5, fr_6, fr_7, fr_8, fr_9, fr_{10} are the numbers of fragments of the types =CR−OH, N_{sp^3}−C=O, CH_2−CH_2−CH_2−CH_2, =CR−C_{Ar}(÷$C_{Ar}H$)$_2$, =CR−CH_2, C_{Ar}−C_{Ar}(÷$C_{Ar}R$)$_2$, C−C−C−C=, •−•−•−•−•÷•, C−C−C−C=O, respectively.

*** Model no. 3: descriptor 1: fr_1 is the number of arbitrary atoms; descriptors 2–10: fr_2, fr_3, fr_4, fr_5, fr_6, fr_7, fr_8, fr_9, fr_{10} are the numbers of fragments of the types =CR−OH, N_{sp^3}−C=O, CH_2−CH_2−CH_2−CH_2, =CR−C_{Ar}(÷$C_{Ar}H$)$_2$, C_{Ar}−C_{Ar}(÷$C_{Ar}R$)$_2$, =CR−CH_2, C−C−C−C−C, •−•−•−•÷•, C−C−O−C=O, respectively.

oped on the basis of the fragment descriptors. First, a QSPR model was constructed (see table, Model no. 1) using the same sample as that in [1], i.e., 62 compounds were taken as learning sample and 10 compounds (63–72) for prognosis purposes (Database 1). It can be seen from the table that a satisfactory statistics, which is comparable with that in [1] and provides a reasonable prognosis (Model no. 1), is obtained with fragment descriptors 3–5. Interestingly, descriptor 1 (number of nonhydrogen atoms) models the first descriptor of [1], and the following two fragment descriptors indirectly model the number of centers forming hydrogen bonds (as in [1]).

It is also of interest that formic acid (15.2 kcal mol^{-1} for learning sample) and adamantane (14.30 kcal mol^{-1} for control sample) fall out of the correlation, irrespective of the number of descriptors. In other words, fragment descriptors fail to reflect structural features of these compounds, which are important for prognostication of the enthalpy of sublimation.

Formic acid is the first member of the homologous series of acids, with Database 1 containing data (kcal mol^{-1}) for acetic (16.3), propionic (17.7), oleic (19.2), and valeric acids (20.2). In going from formic to valeric acid, the enthalpy of sublimation shows monotonic linear variation, which, presumably, obviates the question of experimental error in determining the value of $\Delta_{sub}H$ and may be due to the fact that the models include no descriptors that would reflect the tendency toward variation of the enthalpy of sublimation in the series of carboxylic acids.

It is noteworthy that adamantane has nearly spherical molecule and is highly volatile, and the absence of its derivatives and analogues from the learning sample leads to unsatisfactory prognosis. It should be emphasized in this context that, despite separate discussions, no rigorous scientific approach to the division of a sample into learning and control samples has been reported in the literature.

Naturally, with Database 3 available, it was of interest to obtain a QSPR model, using an extended learning sample. For this purpose, compound nos. 1–62 (Database 1), 73–88 (Database 2), and 13 compounds of the series of chlorinated diphenyls were used as a learning sample. The control sample included, in accordance with [1], the same 10 compounds (63–72), but was supplemented with three compounds belonging to the series of chlorinated diphenyls: two compounds used for prognostication in [4], namely, 2,2',5-trichlorodiphenyl (23.8 kcal mol^{-1}) and 2,2',5,5'-tetrachlorodiphenyl (24.1 kcal mol^{-1}), and also 2,2',3,3',4,4',6-heptachlorodiphenyl (29.3 kcal mol^{-1}). Thus, the learning sample comprised 91 compounds, and the control sample, 13 compounds. The QSPR model constructed (see table, Model no. 2) is distinguished by good prognosticating capacity, which exceeds that of Model no. 2 and makes it possible to predict the property under study for compounds belonging to the series of chlorinated diphenyls. The average error of prognostication varies from 2.4 kcal mol^{-1} (model based on three descriptors) to 2.7 kcal mol^{-1} (model based on eight descriptors).

It is also of interest that compound no. 70 (dimethylglyoxime, 23.2 kcal mol^{-1}), which falls out of the correlation for the control sample, remains in this position upon inclusion of a varied number of descriptors into the model. This fact may indicate that either the experimental data are to be refined or this compound (dihydroxylated diazadiene) is to a certain extent unique among the structures in Database 3.

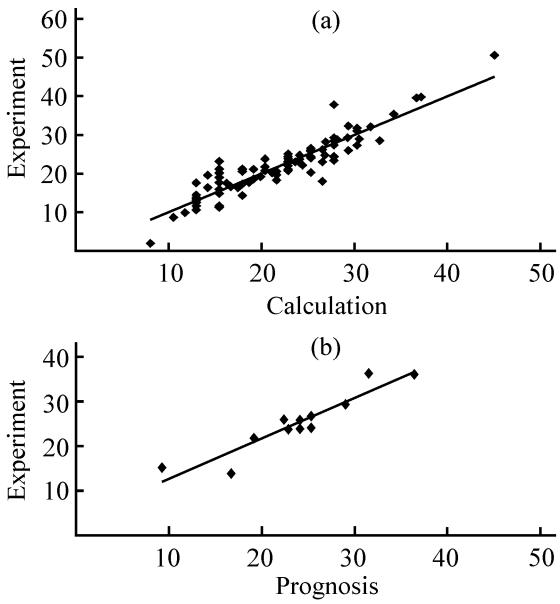

Scatter diagram of calculated and experimental enthalpies of sublimation (kcal mol^{-1}) for (a) learning and (b) control samples of Database 3 in accordance with the linear-regression model [Eq. (1)].

Finally, the above consideration of the structures that fall out of the correlation gave rise to an idea to change the learning and control samples in the following way: two structures, adamantane and dimethylglyoxime were transferred from the control to the learning sample, and formic acid, contrariwise, from the learning to the control sample. Thus, the learning sample comprised 92 compounds, and the control sample, 12 compounds. The QSPR model constructed (see table, Model no. 3) has the best prognosticating capacity, compared with the set of the linear-regression models described.

The equation corresponding to the model based on three fragment descriptors (Model no. 3), which is characterized by the maximum value of the Fisher criterion and high prognosticating capacity, is presented below

$$\Delta_{sub}H_{calc} = +5.57 + 1.23fr_1 + 6.92fr_2 + 6.95fr_3, \quad (1)$$

$n = 104$, $r^2 = 0.8540$, $s = 2.97$, F = 160, average error (absolute value) of prognostication 2.16 kcal mol^{-1}, where fr_1 is the number of any nonhydrogen atoms, •; fr_2, the number of fragments of the type =CR–OH; fr_3, the number of fragments of the type N_{sp^3}–C=O.

The figure shows the scatter of the experimental and calculated enthalpies of sublimation, which agrees with the given model.

The maximum errors in prognostication of the enthalpy of sublimation (kcal mol^{-1}) are observed for formic acid (5.9) and pentaerythritol tetranitrate (4.8); for the learning sample, octadecane (10), dibenzoylmethane (8.6), dimethylglyoxime (7.7), and nitrogen (6) fall out of the correlation. The deviations from the correlation for formic acid and dimethylglyoxime remain the same, which supports the above explanations for both these cases.

In the next stage, the applicability of the fragment approach to prognostication of the enthalpies of sublimation of organic compounds with QSPR models constructed using artificial neural networks was analyzed [27]. A three-layer feed-forward back-propagation neural network produced using the software package NASAWIN [28] was chosen for this purpose. The input layer of the network comprised eight neurons in accordance with the number of descriptors preliminarily selected using a procedure for step-by-step linear regression analysis of descriptors. Two neurons were placed in the internal layer, since their greater number leads, when working with the given database, to strong "overlearning," and smaller number, to construction of a model that does not differ fundamentally from the linear-regression model. The output layer comprised a single neuron that corresponded to the property being prognosticated. As the learning algorithm was taken the "generalized delta rule" [27], with the learning rate parameter equal to 0.25 and learning "instant" parameter of 0.9. The learning process was terminated when the minimum prognostication error was achieved for the control sample.

The differences between the statistical parameters of linear-regression and neural-network models obtained on the basis of the same fragment descriptors are insignificant. At the same time, inclusion of descriptors selected as a result of the neural-network procedure makes it possible to improve the quality of the models. For example, it was possible to construct, for the learning and control samples of the linear-regression Model no. 3 (see table), a model with the best prognosticating capacity among all the models obtained (average prognostication error 1.66 kcal mol^{-1}, $R^2 = 0.8308$, $RMS_{learn} = 3.9364$, $RMS_{progn} = 2.1964$). The model is based on eight descriptors: descriptor 1: fr_1, –• (number of nonhydrogen atoms); descriptors 2–8: fr_2, fr_3, fr_4, fr_5, fr_6, fr_7, fr_8, the number of fragments of the type =CR–OH, N_{sp^3}–C=O, •–•=• (chain of three arbitrary atoms), $C_{Ar}÷C_{Ar}R÷C_{Ar}$ (÷ is an aromatic bond), CH_3–C–C, CH_2–(C=)–OR, CH_2–CH_2–CH_2, respectively.

As in the preceding cases, the strongest deviations from correlation in the control sample are characteristic of pentaerythritol tetranitrite (5.34 kcal mol^{-1}) and formic acid (1.95 kcal mol^{-1}).

Thus, the enthalpies of sublimation of organic compounds belonging to various classes were studied for the first time using the fragment approach based on the QSPR method. It was shown that the models for calculation of the enthalpy of sublimation, obtained using this technique, have parameters comparable with, and, in some cases, exceeding those of the regression equations reported in the literature. In other words, the model suggested makes it possible to prognosticate the enthalpy of sublimation of compounds with the use of descriptors taking into account the fragment composition of a molecule.

REFERENCES

1. Charlton, M.H., Docherty, R., and Hutchings, M.G., *J. Chem. Soc. Perkin Trans. 2*, 1995, pp. 2023–2030.
2. Gaezzotti, A., *J. Phys. Chem.*, 1991, vol. 95, pp. 8948–8955.
3. Gaezzotti, A., *J. Am. Chem. Soc.*, 1989, vol. 111, pp. 1835–1843.
4. Puri, S., Chickos, J.S., and Welsh, W.J., *J. Chem. Inf. Comput. Sci.*, 2002, vol. 42, pp. 109–116.
5. Puri, S., Chickos, J.S., and Welsh, W.J., *J. Chem. Inf. Comput. Sci.*, 2002, vol. 42, pp. 299–304.
6. Baskin, I.I., Palyulin, V.A., and Zefirov, N.S., Abstracts of Papers, *Mezhvuzovskaya konferentsiya "Molekulyarnye grafy v khimicheskikh issledovaniyakh"* (Intercoll. Conf. "Molecular Graphs in Chemical Research"), Kalinin, 1990, p. 5.
7. Baskin, I.I., Palyulin, V.A., and Zefirov, N.S., Abstracts of Papers, *I Vsesoyuznaya konferentsiya po teoreticheskoi organicheskoi khimii* (I All-Union Conf. On Theoretical Organic Chemistry), Volgograd, 1991, p. 557.
8. Palyulin, V.A., Baskin, I.I., Petelin, D.E., and Zefirov, N.S., Abstracts of Papers, *10th Eur. Symp. on Structure-Activity Relationships: QSAR and Molecular Modelling*, Barcelona, 1994, B257.
9. Palyulin, V.A., Baskin, I.I., Petelin, D.E., and Zefirov, N.S., *QSAR and Molecular Modelling: Concepts, Computational Tools and Biological Applications*, Sanz, F., Giraldo, J., and Manaut, F., Eds., Prous Science Publishers, Barcelona, 1995, p. 51.
10. Palyulin, V.A., Radchenko, E.V., Baskin, I.I., *et al.*, Abstracts of Papers, *11th Eur. Symp. on QSAR: Computer Assisted Lead Finding and Optimization*, Lausanne, 1996, 31A.

11. Zefirov, N.S. and Palyulin, V.A., *J. Chem. Inf. Comput. Sci.*, 2002, vol. 42, pp. 1112–1122.
12. Petelin, D.E., Palyulin, V.A., and Zefirov, N.S., *Dokl. Akad. Nauk SSSR*, 1992, vol. 324, pp. 1019–1022.
13. Pivina, T.S., Sukhachev, D.V., and Maslova, L.K., *Dokl. Akad. Nauk SSSR*, 1993, vol. 330, pp. 468–472.
14. Sukhachev, D.V., Pivina, T.S., Shlyapochnikov, V.A., *et al., Dokl. Akad. Nauk SSSR*, 1993, vol. 328, pp. 188–189.
15. Sukhachev, D.V., Pivina, T.S., Zhokhova, N.I., *et al., Izv. Akad. Nauk, Ser. Khim.*, 1995, pp. 1653–1656.
16. Sukhachev, D.V., Pivina, T.S., Zhokhova, N.I., and Zefirov, N.S., *Izv. Akad. Nauk, Ser. Khim.*, 1995, pp. 1657–1660.
17. Sukhachev, D.V., Pivina, T.S., Zhokhova, N.I., *et al., Izv. Akad. Nauk, Ser. Khim.*, 1995, pp. 1661–1665.
18. Zefirov, N.S. and Palyulin, V.A., *J. Chem. Inf. Comput. Sci.*, 2001, vol. 41, pp. 1022–1027.
19. Zefirov, N.S., Petelin, V.A., Palyulin, V.A., and McFarland, J., *Dokl. Akad. Nauk SSSR*, 1992, vol. 327, pp. 504–508.
20. Baskin, I.I., Palyulin, V.A., and Zefirov, N.S., *QSAR and Molecular Modelling: Concepts, Computational Tools and Biological Applications*, Sanz, F., Giraldo, J., and Manaut, F., Eds., Prous Science Publishers, Barcelona, 1995, p. 30.
21. Halberstam, N.M., Baskin, I.I., Palyulin, V.A., and Zefirov, N.S., Abstracts of Papers, *Int. Symp. CACR-96*, Moscow, 1996, p. 37.
22. Baskin, I.I., Palyulin, V.A., and Zefirov, N.S., *J. Chem. Inf. Comput. Sci.*, 1997, vol. 37, pp. 715–721.
23. Artemenko, N.V., Baskin, I.I., Palyulin, V.A., and Zefirov, N.S., *Dokl. Akad. Nauk SSSR*, 2001, vol. 381, pp. 203–206.
24. Zhokhova, N.I., Baskin, I.I., Palyulin, V.A., *et al., Izv. Akad. Nauk, Ser. Khim.*, 2002, no. 5, p. 1005.
25. Artemenko, N.V., Baskin, I.I., Palyulin, V.A., and Zefirov, N.S., *Izv. Akad. Nauk, Ser. Khim.*, 2002, no. 1, pp. 19–27.
26. Baskin, I.I., Skvortsova, M.I., Stankevich, I.V., and Zefirov, N.S., *J. Chem. Inf. Comput. Sci.*, 1995, vol. 35, pp. 527–531.
27. Zupan, J. and Gasteiger, J., *Neural Networks in Chemistry*, Weinheim: Wiley–VCH, 1999.
28. Baskin, I.I., Halberstam, N.M., Artemenko, N.V., *et al.*, Abstracts of Papers, *14th Eur. Symp. on Quantitative Structure–Activity Relationships (Euro QSAR 2002)*, Bournemouth, 2002, p. 173.

Russian Journal of Applied Chemistry, Vol. 76, No. 12, 2003, pp. 1920–1924. Translated from Zhurnal Prikladnoi Khimii, Vol. 76, No. 12, 2003, pp. 1971–1975.

PHYSICOCHEMICAL STUDIES OF SYSTEMS AND PROCESSES

Thermochemistry of Lappaconitine Hydrobromide and Its Analogues

B. K. Kasenov, Zh. K. Tukhmetova, A. Zh. Turmukhambetov, Sh. B. Kasenova, E. S. Mustafin, S. M. Adekenov, and L. A. Krichevskii

Institute of Phytochemistry, Ministry of Education and Science of the Republic of Kazakhstan, Karaganda, Kazakhstan

Received July 15, 2003

Abstract—Isothermal calorimetry was applied to study the heats of dissolution of lappaconitine hydrobromide at varied dilution. The data obtained were used to calculate the standard enthalpy of dissolution of $C_{32}H_{44}N_2O_8 \cdot HBr$ in an infinitely diluted (standard) aqueous solution. The heats of combustion and melting of $C_{32}H_{44}N_2O_8 \cdot HBr$ were calculated using approximate methods. A combination of experimental and calculation techniques was used to find the standard heats of formation of lappaconitine hydrobromide and its 33 analogues.

Studying the thermochemical and thermodynamic properties of alkaloids is of certain theoretical and practical interest for directed synthesis of these compounds with prescribed properties.

The alkaloid lappaconitine is an ester of triatomic amino alcohol lappaconine and *N*-acetylanthranilic acid; the structural formula of lappaconitine hydrobromide (allapinine) is given below [1]:

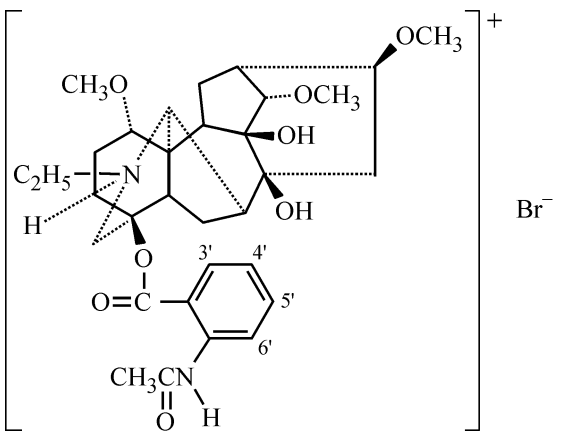

It should be emphasized that, until now, neither experimental nor estimated values of the thermochemical and thermodynamic constants of this theoretically and practically important alkaloid and its derivatives are available in the literature.

In view of the aforesaid, the aim of this study was to analyze experimentally the thermochemical properties of lappaconitine hydrobromide and to use the data obtained to find, by combining calculation procedures, the standard enthalpies of formation of $C_{32}H_{44}N_2O_8 \cdot HBr$ and its analogues.

The enthalpy of dissolution of lappaconitine hydrobromide $C_{32}H_{44}N_2O_8 \cdot HBr$ in water was studied calorimetrically under isothermal conditions on a DAK-1-1A calorimeter. The theory of, and procedure for a calorimetric study were described in detail in [2–5]. The DAK-1-1A commercial differential automated calorimeter has the following main technical characteristics: working temperatures 25–200°C, cartridge volume 8 cm^3, error in measuring heat release energy ≤20 μW. The calorimeter measures the integral heat flux outgoing from the calorimetric cartridge, in which a substance is being dissolved, through the differentially connected thermocouples and the massive central unit of the microcalorimeter. The rated error in determining the heat effects is ±2.0%.

The experimental errors and the uniformity of variance in determining the heat effects were calculated using the Student and Bartlett criteria.

The heat of combustion of lappaconitine hydrobromide was calculated using the Karas and Frost methods [7], and the heat of fusion was found from an empirical equation recommended in [8].

The values of $\Delta_f H^0_{298.15}$ for analogues of $C_{32}H_{44}N_2O_8 \cdot HBr$ were calculated using the system of enthalpy increments for anions [9, 10].

1070-4272/03/7612-1920 $25.00 © 2003 MAIK "Nauka/Interperiodica"

EXPERIMENTAL

The commercial lappaconitine hydrobromide chosen for the calorimetric study (M = 665.6 g mol^{-1} [11]) was of analytically pure grade (>99.0% main substance) and had melting point of 225°C (with decomposition), in conformity with the data of [11].

The homology-based technique was used to index the powder X-ray diffraction pattern of $C_{32}H_{44}N_2O_8 \cdot HBr$. It was found that $C_{32}H_{44}N_2O_8 \cdot HBr$ crystallyzes in the tetragonal system with the following lattice constants: a = 12.26, c = 10.72 Å; V^0 = 1611.3 Å^3; Z = 2; $\rho_{X\text{-ray}}$ = 1.41, and ρ_{pycn} = 1.38 ± 0.04 g cm^{-3}.

The enthalpy of dissolution of lappaconitine hydrobromide in water was determined experimentally at dilutions of 1 : 36000, 1 : 44000, and 1 : 50000 (moles of a salt : moles of water) with automated heat compensation. The heat effects were recorded with a KSP-4 potentiometer and, simultaneously, with an IP-4 high-precision integrator. A substance under study (weighed on an analytical balance to the fourth decimal place) was introduced in a metallic ampule, which was then inserted into a metallic cartridge with the solvent. The time of preliminary thermostating of the solvent and the substance was 2 h. The zero drift of the integrator did not exceed 3 units in the last digit position in 100 s. The substance under study dissolved when the ampule was submerged in the solvent.

The instrument was tested by measuring the heat of dissolution of thrice-recrystallized KCl at dilutions of 1 : 1600, 1 : 2400, and 1 : 3200 (moles of a salt : moles of water). The resulting averaged heat of KCl dissolution in water at 25°C (17860 ± 283 J mol^{-1}) was in satisfactory agreement with the recommended values (17577 ± 34 [13] and 17489 ± 371 [14] J mol^{-1}), obtained at the same temperature with accuracy of 1.6 and 2.0%, respectively.

Table 1 lists the calorimetrically determined heats of lappaconitine hydrobromide dissolution at various dilutions.

The experimentally found enthalpies of dissolution of $C_{32}H_{44}N_2O_8 \cdot HBr$ at varied dilution were further used for calculating the ΔH^0 of its dissolution at standard (infinite) dilution. A mathematical processing of the experimental data established that the dependence of the enthalpy of dissolution (kJ mol^{-1}) on the molal concentration $\sqrt{m}$ is described, similarly to [15], by the equation

$$\Delta H^m_{diss} C_{32}H_{44}N_2O_8 \cdot HBr = 6.02 - 93.13\sqrt{m}. \quad (1)$$

Table 1. Heat effect and molar enthalpy of $C_{32}H_{44}N_2O_8 \cdot HBr$ dissolution in water at varied dilution*

$C_{32}H_{44}N_2O_8 \cdot HBr$, g	Q, J	ΔH^m, kJ mol^{-1}
Dilution 1 : 36000		
0.0051	0.018	2.35
0.0049	0.018	2.44
0.0053	0.019	2.39
0.0050	0.018	2.40
0.0051	0.018	2.35
	Average	2.39 ± 0.05
Dilution 1 : 44000		
0.0041	0.016	2.60
0.0042	0.017	2.69
0.0040	0.016	2.66
0.0040	0.016	2.66
0.0042	0.017	2.69
	Average	2.66 ± 0.04
Dilution 1 : 50000		
0.0039	0.017	2.90
0.0038	0.017	2.98
0.0039	0.018	3.07
0.0037	0.017	3.06
0.0038	0.016	2.80
	Average	2.96 ± 0.14

* Dilution, mole of a salt : mole of H_2O; the same for Table 2.

By solving this equation, the standard enthalpy of lappaconitine hydrobromide dissolution in an infinitely diluted aqueous solution was found to be 6.02 ± 0.17 kJ mol^{-1}. This value is of great theoretical and practical importance for calculating the standard heats of formation of various lappaconitine derivatives.

Further, the enthalpies of interaction between an aqueous solution of $C_{32}H_{44}N_2O_8 \cdot HBr$ and crystalline silver nitrate were determined in the reaction

$$C_{32}H_{44}N_2O_8 \cdot HBr\ (\text{solution},\ nH_2O) + AgNO_3(\text{s.}) = C_{32}H_{44}N_2O_8H^+\ (\text{solution},\ nH_2O) + NO_3^-\ (\text{solution},\ nH_2O) + AgBr(\text{s.}) - \Delta H^0_{int}. \quad (2)$$

Table 2. Enthalpies of interaction of an aqueous solution of $C_{32}H_{44}N_2O_8 \cdot HBr$ with $AgNO_3$ at varied dilution

$AgNO_3$, g	Q, J	$-\Delta H^0$, kJ mol^{-1}
Dilution 1 : 36 000		
0.0013	0.307	40.11
0.0012	0.285	40.34
0.0013	0.309	40.37
0.0013	0.312	40.77
0.0013	0.317	41.42
	Average	40.60 ± 0.64
Dilution 1 : 44 000		
0.0011	0.275	42.47
0.0011	0.266	41.08
0.0010	0.249	42.30
0.0010	0.247	41.96
0.0011	0.271	41.85
	Average	41.93 ± 0.67
Dilution 1 : 50 000		
0.0010	0.253	42.98
0.0010	0.244	43.21
0.0010	0.258	42.83
0.0009	0.232	43.79
0.0009	0.233	43.98
	Average	43.56 ± 0.54

Table 3. X-ray diffraction characteristics of AgBr

d, Å	I/I_0
2.975 (3.333)*	8 (7)*
2.874 (2.886)	100 (100)
2.040 (2.041)	73 (36)
1.737 (1.742)	3 (2)
1.664 (1.667)	20 (15)
1.442 (1.444)	8 (7)

* Published data [16] are given in parentheses.

The $AgNO_3$ crystals subjected to a calorimetric study were of analytically pure grade. Table 2 lists the results obtained in determining the ΔH^0 of the interaction.

The mass of the resulting crystalline precipitate of AgBr had, after its being dried, a mass totally corresponding to the theoretical yield. This indicates that lappaconitine hydrobromide completely dissociated upon dissolution in water. The same conclusion follows from X-ray diffraction data for AgBr (Table 3) formed in reaction (2), which were in full agreement with reference data [16].

To calculate $\Delta_f H^0_{298.15}$ for $C_{32}H_{44}N_2O_8 \cdot HBr$, its standard heat of combustion was evaluated using the Karas and Frost methods [7], which are the most appropriate techniques for taking into account the contributions of different groups to the heat of combustion. The resulting averaged heat of $C_{32}H_{44}N_2O_8 \cdot HBr$ combustion was –18 318 ± 619 kJ mol^{-1}, with relative calculation error of 3.4%. The standard enthalpy of formation of (molten) $C_{32}H_{44}N_2O_8 \cdot HBr$ was calculated from the ΔH^0 of combustion by the Hess cycle by the reaction

$$2C_{32}H_{44}N_2O_8 \cdot HBr_{(l)} + 78.5O_{2(g)} = 64CO_{2(g)} + 45H_2O_{(l)} + 2N_{2(g)} + Br_{2(g)} \quad (3)$$

to be –718 kJ mol^{-1}. It should be emphasized that the Karas and Frost methods are only applicable to calculation of ΔH^0 of combustion of liquid hydrocarbons. The data required for calculating $\Delta_f H^0_{298.15}$ of $C_{32}H_{44}N_2O_8 \cdot HBr_{(l)}$ by scheme (3), with the exception of ΔH^0 of combustion, were taken from [17].

In view of the fact that lappaconitine hydrobromide is in the crystalline state at 298.15 K, its $\Delta_f H^0_{298.15}$ is to be calculated for the solid state. For this purpose, ΔH^0_{melt} of $C_{32}H_{44}N_2O_8 \cdot HBr$ was estimated using the empirical equation [8]:

$$\Delta H^0_{melt} = 44.4T_{melt} - 4400, \quad (4)$$

which is commonly used for strongly polar halide compounds. The value of ΔH^0_{melt} of $C_{32}H_{44}N_2O_8 \cdot HBr$, found using Eq. (4), is 17.7 kJ mol^{-1}. The equation

$$\Delta_f H^0_{298.15}C_{32}H_{44}N_2O_8 \cdot HBr_{(s)} = \Delta_f H^0_{298.15}C_{32}H_{44}N_2O_8 \cdot HBr_{(l)} - \Delta H^0_{melt} \quad (5)$$

was used to calculate the standard enthalpy of $C_{32}H_{44}N_2O_8 \cdot HBr_{(cr)}$ formation to be –736.0 kJ mol^{-1}.

Further, the ΔH^0 of $C_{32}H_{44}N_2O_8 \cdot HBr$ dissolution at infinite dilution (6.02 kJ mol^{-1}) was used to calculate the standard enthalpy of $C_{32}H_{44}N_2O_8 \cdot HBr$ formation in the standard aqueous solution by the equation

$$\Delta_f H^0_{298.15}C_{32}H_{44}N_2O_8 \cdot HBr \text{ (solution, } H_2O\text{, standard state)} = \Delta_f H^0_{298.15}C_{32}H_{44}N_2O_8 \cdot HBr_{(s)} + \Delta H^0_{solv} \quad (6)$$

to be –730 kJ mol^{-1}. The relation

$$\Delta_f H^0_{298.15}C_{32}H_{44}N_2O_8H^+ \text{ (solution, } H_2O\text{, standard state)} = \Delta_f H^0_{298.15}C_{32}H_{44}N_2O_8 \cdot HBr \text{ (solution, } H_2O\text{, standard state)} - \Delta_f H^0_{298.15}Br^- \text{ (solution, } H_2O\text{, standard state)}, \quad (7)$$

was used to calculate, on the basis of the data obtained and the reference value of $\Delta_f H^0_{298.15}$ (solution, H_2O, standard state), the standard enthalpy of formation of the $[C_{32}H_{44}N_2O_8H]^+$ ion in a standard aqueous solution to be –599.0 kJ mol^{-1}. The value obtained by the calculation was used to calculate $\Delta_f H^0_{298.15}$ for other lappaconitine derivatives. In [9, 10], a system of thermochemical enthalpy increments was developed. This system makes it possible to calculate standard heats of formation of compounds in the crystalline state by the equation

$$\Delta_f H^0_{298.15}M_m(X_\alpha O_\beta)_n = [m\Delta_f H^0_{298.15}(M^{n+}, \text{ solution, } H_2O, \text{ standard state})]K + n\Delta_f H^i_{298.15})X_\alpha O_\beta^{m-}, \quad (8)$$

where $\Delta_f H^i_{298.15}$ is the enthalpy increment for the anion, and K is the proportionality factor.

To calculate $\Delta_f H^0_{298.15}$ of the compounds by Eq. (8), it suffices to know the $\Delta_f H^0_{298.15}$ (solution, H_2O, standard state) of the cation, whereas the coefficients K and $\Delta_f H^i_{298.15}$ for the anions are tabulated; the accuracy of the calculation is ±5.0%. For the lappaconitine derivatives, Eq. (8) can be represented as (for the example of $C_{32}H_{44}N_2O_8 \cdot HNO_3$):

$$\Delta_f H^0_{298.15}C_{32}H_{44}N_2O_8 \cdot HNO_{3(s)} = [\Delta_f H^0_{298.15}C_{32}H_{44}N_2O_8H^+ \text{ (solution, } H_2O\text{, standard state)}]K + \Delta_f H^i_{298.15}NO_3^-. \quad (9)$$

Table 4 lists the values of $-\Delta_f H^0_{298.15}$ for 33 lappaconitine derivatives, calculated using Eq. (9).

CONCLUSIONS

(1) The enthalpies of lappaconitine hydrobromide dissolution in water at varied dilution were determined experimentally for the first time. The values obtained were used to calculate by indirect methods the standard enthalpy of $C_{32}H_{44}N_2O_8 \cdot HBr$ dissolution, $\Delta_f H^0_{298.15}$ of $[C_{32}H_{44}N_2O_8H]^+$ (solution, H_2O, standard state), standard enthalpy of formation of molten and crystalline $C_{32}H_{44}N_2O_8 \cdot HBr$, its heat of combustion, and heat of fusion.

(2) The standard heats of formation of 33 lappaconitine derivatives were calculated.

Table 4. Standard heats of formation of lappaconitine derivatives

Compound	$-\Delta_f H^0_{298.15}$, kJ mol^{-1}
$C_{32}H_{44}N_2O_8 \cdot HF$	913
$C_{32}H_{44}N_2O_8 \cdot HCl$	747
$C_{32}H_{44}N_2O_8 \cdot HI$	638
$C_{32}H_{44}N_2O_8 \cdot HClO_4$	747
$C_{32}H_{44}N_2O_8 \cdot HClO_3$	740
$C_{32}H_{44}N_2O_8 \cdot HBrO_3$	727
$C_{32}H_{44}N_2O_8 \cdot HJO_3$	877
$[C_{32}H_{44}N_2O_8H]_2S$	1026
$[C_{32}H_{44}N_2O_8H]_2SO_4$	2092
$[C_{32}H_{44}N_2O_8H]_2S_2O_3$	1872
$[C_{32}H_{44}N_2O_8H]_2Se$	1080
$[C_{32}H_{44}N_2O_8H]_2SeO_4$	1764
$[C_{32}H_{44}N_2O_8H]_2TeO_4$	2001
$[C_{32}H_{44}N_2O_8H]_2SO_3$	1800
$[C_{32}H_{44}N_2O_8H]_2SeO_3$	1649
$[C_{32}H_{44}N_2O_8H]_2TeO_3$	1685
$C_{32}H_{44}N_2O_8 \cdot HNO_3$	819
$C_{32}H_{44}N_2O_8 \cdot HNO_2$	711
$[C_{32}H_{44}N_2O_8H]_3PO_4$	3006
$[C_{32}H_{44}N_2O_8H]_4P_2O_7$	4602
$[C_{32}H_{44}N_2O_8H]_3AsO_4$	2638
$[C_{32}H_{44}N_2O_8H]_2CO_3$	1842
$[C_{32}H_{44}N_2O_8H]_2C_2O_4$	2018
$C_{32}H_{44}N_2O_8 \cdot HAlO_2$	1489
$C_{32}H_{44}N_2O_8 \cdot HBO_2$	1315
$C_{32}H_{44}N_2O_8 \cdot HReO_4$	1456
$C_{32}H_{44}N_2O_8 \cdot HMnO_4$	1199
$[C_{32}H_{44}N_2O_8H]_2Cr_2O_7$	2761
$[C_{32}H_{44}N_2O_8H]_2CrO_4$	2091
$[C_{32}H_{44}N_2O_8H]_2WO_4$	2287
$[C_{32}H_{44}N_2O_8H]_2MoO_4$	2100
$C_{32}H_{44}N_2O_8 \cdot HVO_3$	1514
$C_{32}H_{44}N_2O_8 \cdot HNbO_3$	1691

ACKNOWLEDGMENTS

The study was supported by the Foundation for Science, National Academy of the Republic of Kazakhstan [grant for Research Project "Instruments for Physicochemical Studies," no. 2-2-2.4-2 (31)-II, 11.03.2003].

REFERENCES

1. Dzhakhangirov, F.N., Sokolov, S.F., and Verkhratskii, A.N., *Allapinin – novyi protivoaritmicheskii preparat rastitel'nogo proiskhozhdeniya* (Allapinine, a New Antiarrhythmic Preparation of Plant Origin), Tashkent: FAN, 1993.
2. Skuratov, S.M., Kolesov, V.P., and Vorob'ev, A.F., *Termokhimiya* (Thermochemistry), Moscow: Mos. Gos. Univ., 1964, vol. 1.

3. Calvet, E. et Prat, H., *Microcalorimetrie. Applications Physico-Chemiques et Biologiques*, Paris: Masson, 1956.
4. Topor, N.D. and Suponitskii, Yu.L., *Usp. Khim.*, 1984, vol. 53, no. 9, pp. 1425–1462.
5. Calvet, E., *Zh. Fiz. Khim.*, 1959, no. 6, pp. 1161–1175.
6. Spiridonov, V.P. and Lopatkin, A.A., *Matematicheskaya obrabotka fiziko-khimicheskikh dannykh* (Mathematical Processing of Physicochemical Data), Moscow: Mos. Gos. Univ., 1970.
7. Kazanskaya, A.S. and Skoblo, V.A., *Raschety khimicheskikh ravnovesii* (Calculation of Chemical Equilibria), Moscow: Vysshaya Shkola, 1974.
8. Morachevskii, A.G. and Sladkov, I.B., *Termodinamicheskie raschety v metallurgii* (Thermodynamic Calculations in Metallurgy), Moscow: Metallurgiya, 1985.
9. Kasenov, B.K., Abishev, D.N., and Bukharitsyn, V.O., *Termokhimiya arsenatov shchelochnykh metallov* (Thermochemistry of Alkali Metal Arsenates), Almaty: Nauka, 1988.
10. Kasenov, B.K., Aldabergenov, M.K., and Pashinkin, A.S., *Termodinamicheskie metody v khimii i metallurgii* (Thermodynamic Methods in Chemistry and Metallurgy), Almaty: Rauan, 1994.
11. Shakirov, R., Telezhenetskaya, M.V., Bessonova, I.A., *et al.*, *Khim. Prirod. Soedin.*, 1996, no. 4, pp. 615–681.
12. Kovba, L.M. and Trunov, V.K., *Rentgenofazovyi analiz* (X-Ray Phase Analysis), Moscow: Mos. Gos. Univ., 1969.
13. Mishchenko, K.P. and Poltoratskii, G.M., *Termodinamika i stroenie vodnykh i nevodnykh rastvorov elektrolitov* (Thermodynamics and Structure of Aqueous and Nonaqueous Electrolyte Solutions), Leningrad: Khimiya, 1976.
14. *Termicheskie konstanty veshchestv: Spravochnik* (Thermal Constants of Substances: Reference Book), Glushko, V.P., Ed., Moscow: Nauka, part 1, 1981; part 3, 1982.
15. Krestov, G.A., *Termodinamika ionnykh protsessov v rastvorakh* (Thermodynamics of Ionic Processes in Solutions), Leningrad: Khimiya, 1984.
16. X-Ray Powder Data File, *American Society for Testing and Materials (ASTM)*, 1972.
17. Ryabin, V.A., Ostroumov, M.A., and Svit, T.F., *Termodinamicheskie svoistva veshchestv* (Thermodynamic Properties of Substances), Leningrad: Khimiya, 1977.

Russian Journal of Applied Chemistry, Vol. 76, No. 12, 2003, pp. 1925–1929. Translated from Zhurnal Prikladnoi Khimii, Vol. 76, No. 12, 2003, pp. 1976–1980.

SORPTION AND ION-EXCHANGE PROCESSES

Sorption of Heavy Metals from Model Solutions with Amine-Containing Chemisorption Polyamide Fiber

T. V. Druzhinina, L. M. Smolenskaya, and M. A. Struganova

Kosygin Moscow State Textile University, Moscow, Russia
Belgorod State Technological Academy, Belgorod, Russsia

Received July 19, 2002; in final form, September 2003

Abstract—Sorption of Cu(II), Ni(II), Zn(II), and Cr(VI) ions with POLAN-OG sorbent was studied. The capacity and kinetic characteristics of the sorbent in hydrochloric acid and chloride solutions were determined.

Complexing ion exchangers occupy a leading position among sorption-active polymeric materials. Their use is diverse, from waste-free high technologies to solution of environmental problems. Recently, there has been a steady trend toward use of fibrous complexing sorbents for concentration and recovery of microelements from aqueous media and process solutions in analytical monitoring. The fibrous materials based on cellulose, polyacrylonitrile, polyvinyl alcohol, polycaproamide (PCA) and their copolymers show high performance in recovery of heavy metals, including platinum group metals, and radionuclides [1, 2]. In addition, they exhibit higher kinetic characteristics as compared to granulated or porous sorbents [3]; metals sorbed can be relatively readily desorbed with acids, and these sorbents can be used repeatedly in sorption–desorption cycles.

It is known [4] that the complexing properties of polymeric ion exchangers depend not only on the kind offunctional groups, but also on the polarizability of atoms bound to these groups, distribution of ligand groups along the polymer chain, and other factors. This allows preparation of fibrous complexing ion exchangers with a wide spectrum of the sorption properties, in particular, by polymer-analogous transformations. A variety of fibrous chemisorption materials (fibers, nonwoven materials, cloths) allow variation of the chemisorption equipment design.

Commercially available fibrous sorbents do not meet the demand for such materials in solving environmental problems, both in assortment and in production volume. Therefore, synthesis of new sorption fibers, study of their properties, and assessment of specific application fields are topical. In this study, we examined the sorption properties and kinetics of sorption of heavy metal ions with chemisorption polyamide fiber POLAN-OG. This material differs from the known chemisorption fibers in the chemical composition, structure, nature of functionally active groups, and advanced production technology.

A fibrous sorbent with the static exchange capacity (SEC) with respect to HCl of 1.73 mmol mol^{-1} was prepared by polymer-analogous transformation of polycaproamide (PCA) fiber with grafted polyglycidyl methacrylate (PGMA) under the action of aqueous hydrazine hydrate [5]. The chemisorption fiber has the following chemical structure.

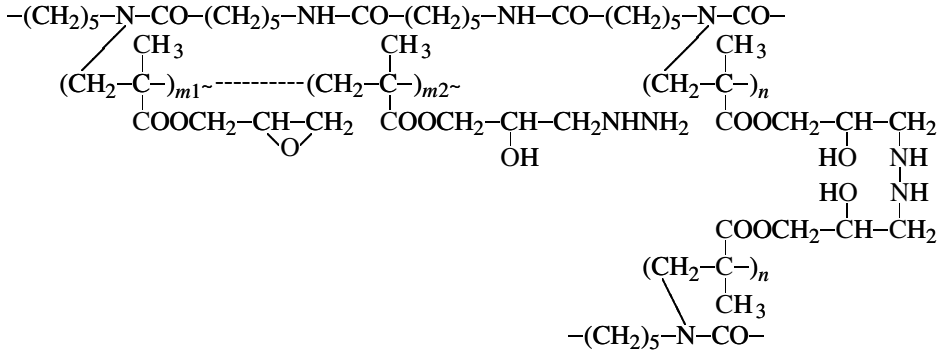

1070-4272/03/7612-1925 $25.00 © 2003 MAIK "Nauka/Interperiodica"

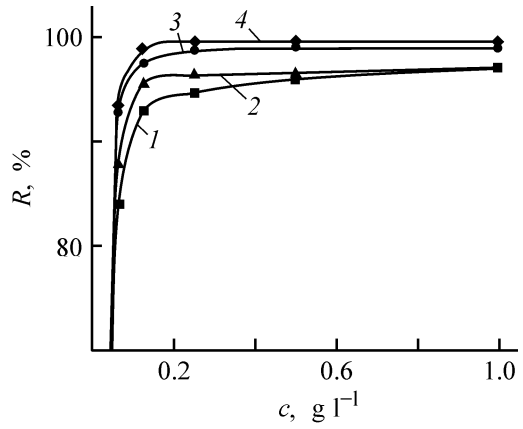

Fig. 1. Degree of recovery of metal ions, *R*, from solutions with amine-containing polyamide fiber vs. heavy metal ion concentration *c*. Sorption conditions: sorption time 60 min, *L*/*S* ratio 100, pH 5. Ion recovered: (*1*) Cu(II), (*2*) Cr(VI), (*3*) Ni(II), and (*4*) Zn(II).

Ionogenic functional groups NH and NH_2 in the coordination-active (deprotonated) state form the outer coordination sphere and play the role of ligands toward ions being sorbed.

Electron-microscopic studies have shown [1] that grafted PMGA is distributed over the surface of the polycaproamide fiber. Therefore, the chemically active hydrazide groups introduced are accessible in chemisorption, and the mass exchange is fast. In addition, hydrophobic grafted chains of carbon-chain PMGA protect the fibrous PCA matrix and thus increase the sorbent resistance toward aggressive media. The use of physically active grafted copolymers, e.g., PCA–PMGA as the starting material in obtaining fibrous chemisorbents, has a number of technological advantages as compared to widely described chemisorption fibers based on random copolymers (fibers of VION type [6]): problems with preparing the fiber from copolymers with insufficient fiberforming ability and necessity for cross-linking of such fibers to make them insoluble are eliminated [1, 7].

Although certain processes for treatment of wastewater from electroplating shops have been developed, and there are a lot of publications on this issue [8–11], the problem of efficient removal of heavy metal ions to the level of maximum permissible concentration remains urgent. In this study, we studied the sorption of transition metal ions [Cu(II), Ni(II), Zn(II), and Cr(VI)] contained in the process solutions of electroplating shops with PCA–PMGA copolymers.

The sorption was performed under static conditions from model solutions with metal ion concentrations of 1 g l^{-1} and lower at a solution volume (ml) to fibrous sorbent weight (g) ratio (*L*/*S*) equal to 100. The content of metal ions in the solution was determined spectrophotometrically with a Specord M-40 spectrophotometer. The optical density ε of the solution with introduced reagent picramine before and after addition of fibrous sorbent was measured at λ = 550 nm and solution layer thickness *l* = 5 cm. The content of sorbed metal ions was determined using a calibration plot.

The static capacity of the fibrous sorbent (g g^{-1}) was found by the formula

$$\mathrm{SC} = \frac{(c_0 - c_1)V}{p \times 1000},$$

where c_0 is the initial metal ion concentration, (g l^{-1}); c_1, the metal ion concentration after sorption (g l^{-1}); *V*, the solution volume (ml); and *p*, the sorbent weight (g).

The specific surface area (S_{sp}) of the chemisorption fiber was determined gravimetrically (in a desiccator) with water vapor as adsorbate [12]. To compare the values of S_{sp} obtained by the sorption method in the dessicator and on a device equipped with a Mackbain balance [13], we used polycaproamide fiber as reference. The S_{sp} value was found to be 66 $m^2 g^{-1}$, in good agreement with the reference value of 70 $m^2 g^{-1}$.

We found that the fibrous sorbent exhibits high absorptive power with respect to Ni(II) and Zn(II) even in dilute solutions (0.125 g l^{-1}) (Fig. 1). The degree of metal ion recovery *R* reaches 99%, which makes expedient use of the POLAN-OG fiber in sorption of trace amounts of these metals. A somewhat lower *R*, 93 and 95.5%, was obtained for solutions containing Cu(II) and Cr(VI) ions, respectively, at their concentration of 0.125 g l^{-1}.

At solution volume to fibrous sorbent weight ratios of 50–500 and metal ion concentration of 0.1 g l^{-1}, the *R* value decreases only slightly with increasing solution volume. Upon a tenfold increase in the *L*/*S* ratio, *R* decreases by 3%, at most, from 99.6 to 96.6%. This trend is preserved for all the solutions studied.

The sorption efficiency substantially depends on the sorption kinetics. The kinetic curves of sorption of Cu(II), Ni(II), and Cr(VI) ions are shown in

Figs. 2a–2c. The equilibrium distribution of metal ions between the fiber and solution is reached in a short time (20–30 min) within a wide range of concentrations at room temperature. Such a short time is due to the high specific surface area of the chemisorbent, 40 $m^2 g^{-1}$, and to the fact that chemically active groups are mostly situated in the surface layers of the fiber [1]. The degree of metal ion recovery reaches high values, 98% for Cu(II) and Cr(VI) and 100% for the other ions studied, in sorption from 1 $g l^{-1}$ solutions.

The high degree of Cu(II) recovery (99% in 30 min) is also achieved in sorption from solutions with concentrationstypical of natural water, 0.001–0.0005 $mg l^{-1}$ [maximum permissible concentration of Cu(II) in water of fish ponds is 0.001 $mg l^{-1}$], which demonstrates high sorption characteristics of this fibrous chemisorbent. Since wastewater from electroplating shops may differ not only in composition, but also in acidity, the effect of pH on the metal ion sorption should be studied. In addition, it is known that the main part of basic ligand groups have strong affinity for hydrogen ions, since the energy of the $L^- \rightarrow H^+$ coordination bond is higher than that of the $L^- \rightarrow M^{n+}$ bond. This leads to substantial influence of the H^+ concentration on complexation of ionogenic groups. The $R = f(\text{pH})$ curves (Fig. 3) show that, under the conditions studied, the sorption of 3*d*-element ions is the most efficient within the pH 5–7 range. The degree of metal ion recovery sharply decreases to 20–40% with increasing solution acidity. This is caused by a decrease in the concentration of coordination-active (nonprotonated) ionogenic groups in the fiber phase and by a change in their electron-donor properties. Since the chemisorption fiber was used in the sorption process in the OH form, the solution pH increased owing to partial transfer of OH^- ions to the solution in complexation.

The change in color of the complexing ion exchanger allows quantitative estimation of the sorption of Cu(II) and Ni(II) ions. At pH > 5, the degree of metal ion recovery is higher, and accordingly, the intensity of color of the fibrous chemisorbent increases as compared to the color of the sorbent at pH < 5. In accordance with the known coordination properties of transition metal ions [Cu(II), Ni(II), Zn(II)] [14] in the systems studied, ML_4 complexes are formed in the course of sorption on the fiber containing NH and NH_2 groups. Because of the polymeric structure of the fiber ligand groups, their irregular distribution along the chain, and the heterogeneity of the system in which the metal ions are recovered, interchain complex formation (rather than intramolecular coordination) is the most probable:

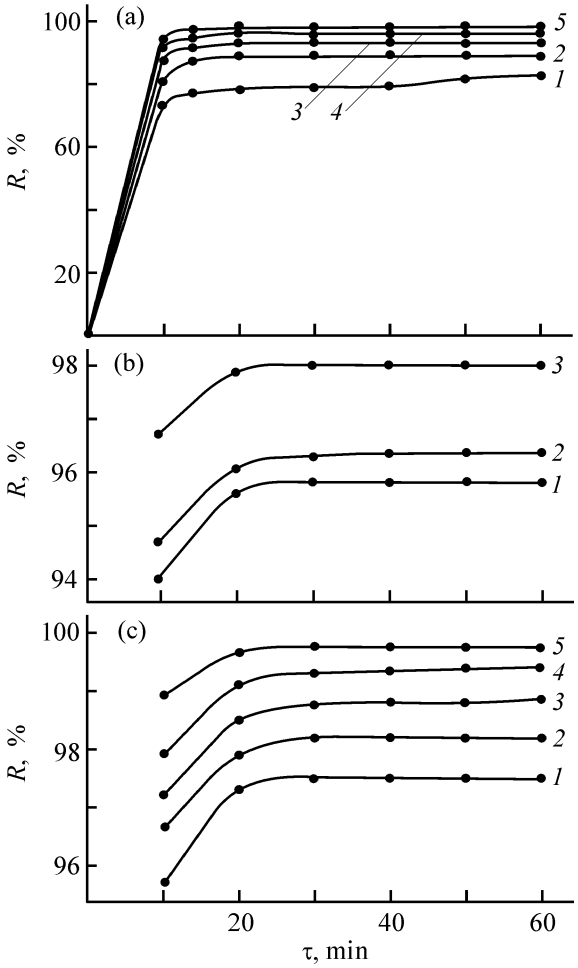

Fig. 2. Kinetics of sorption of (a) Cu(II), (b) Cr(VI), and (c) Ni(II) with chemisorption polyamide fiber. Sorption conditions: *L*/*S* ratio 100, pH 5. (*R*) Degree of metal ion recovery and (τ) sorption time. Concentration ($g l^{-1}$): Cu(II) and Ni(II), (*1*) 0.0625, (*2*) 0.125, (*3*) 0.25, (*4*) 0.5, and (*5*) 1.0; Cr(VI), (*1*) 0.125, (*2*) 0.5, and (*3*) 1.0.

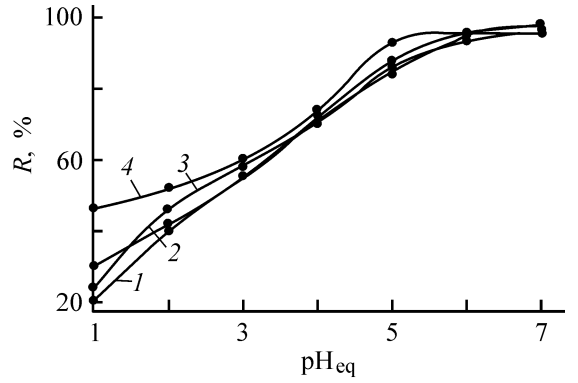

Fig. 3. Degree of transition metal ion recovery *R* with amine-containing fibrous chemisorbent as a function of pH. Sorption conditions: sorption time 24 h, *L*/*S* ratio 100, metal ion concentration 1.0 $g l^{-1}$. Ion being recovered: (*1*) Cu(II), (*2*) Ni(II), (*3*) Zn(II), and (*4*) Cr(VI).

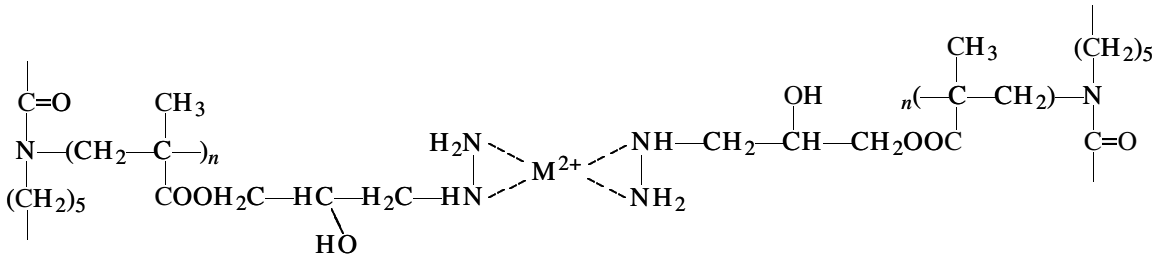

The complexation in sorption of Cr(VI) involves chromium reduction to Cr(III), which is probably due to the presence of hydrazide groups, which exhibit reductive properties ($E^0_{Cr_2O_7^{2-}/2Cr^{3+}}$ = 1.33 V and $E^0_{N_2H_4/N_2}$ = –1.16 V). Initially, the fiber becomes brown and then it acquires a dingy green color, which is characteristic of Cr(III) complexes. The brown color is probably due to mixing of the orange-red color of the $Cr_2O_7^{2-}$ ion and green color of Cr(III) formed by partial reduction of Cr(VI) on the sorbent. The reduction of $Cr_2O_7^{2-}$ ion on the surface of POLAN-OG fibrous sorbent has not been studied previously.

One of parameters of sorption with complexing ion exchangers is the distribution coefficient of the metal ion in the sorbent–sorbate system, which gives important information about the applicability of a chemisorbent.

The distribution coefficients of metal ions, *D*, calculated for sorption at various equilibrium pH values are listed in the table. The table shows that, for all the metal ions studied, *D* values grow with increasing pH. The highest *D* values were obtained for Zn(II) and Cr(VI) at pH 7.

To estimate the selectivity of sorption with the fibrous sorbent studied, we recovered metal ions from aqueous solution containing a mixture of Cu(II), Ni(II), Zn(II), and Cr(VI) in the concentration of 0.25 g l^{-1}. The *D* values obtained are listed below.

Ion	Cu^{2+}	Ni^{2+}	Zn^{2+}	Cr(VI)
$D \times 10^{-3}$, ml g^{-1}	9.9	9.8	9.9	9.4

As seen, the POLAN-OG fiber virtually equally sorbs all the metal ions studied (the *D* values do not differ substantially) and hence does not exhibit selectivity in this system. The distribution coefficients increase, as the metal ion concentration decreases, which is caused by the shift of the reaction equilibrium toward complexation.

The sorption capacity (SC) of POLAN-OG fiber measured for 1 g l^{-1} solutions is given below.

Ion	Cu^{2+}	Ni^{2+}	Zn^{2+}	Cr(VI)
SC, mg g^{-1}	98.36	99.24	99.44	98.40
SC, mmol g^{-1}	1.54	1.69	1.52	1.89

As seen, the POLAN-OG fibrous sorbent is characterized by fairly high SC with respect to 3*d*-element ions. It is inferior to POLIORGS-35 fiber in sorption of copper(II), but its SC with respect to zinc and nickel is considerably higher, by a factor of 1.5 and 2, respectively [2]. The degree of water decontamination to remove zinc ions is comparable with that obtained with VION chemisorption fiber [16]. The SC of POLAN-OG fiber increases in the order Zn(II) < Cu(II) < Ni(II) < Cr(VI).

CONCLUSIONS

(1) Fibrous complexing ion exchangers based on a graft copolymer of polycaproamide and polyglycidyl methacrylate, which contains hydrazide groups (POLAN-OG), has sorption capacity with respect to Cu(II), Ni(II), Zn(II), and Cr(VI) ions of about 1.52–1.89 mmol g^{-1} and virtually quantitatively (97–

Distribution coefficients of heavy metal ions at various pH (sorption conditions: sorption time 24 h, *L*/*S* ratio 100, metal ion concentration 1 g l^{-1})

Ion	$D \times 10^{-2}$, ml g^{-1}, at indicated pH						
	1	2	3	4	5	6	7
Cu^{2+}	0.25	0.67	1.22	2.45	6.69	16.7	32.3
Ni^{2+}	0.43	0.72	1.22	2.45	6.14	19.0	19.0
Zn^{2+}	0.32	0.85	1.38	2.57	7.33	19.0	49.9
Cr(VI)	0.85	1.08	1.50	2.89	13.3	24.0	32.3

100%) recovers them from 0.5–1.0 g l^{-1} aqueous solutions.

(2) A scheme of coordination binding of metal ions with nitrogen-containing ligand groups of the polymeric chemisorption fiber is suggested.

(3) The POLAN-OG fiber exhibits no selectivity with respect to copper(II), nickel(II), chromium(VI), and zinc(II) ions and can be recommended for their group recovery or for metal ion sorption from individual solutions.

REFERENCES

1. Druzhinina, T.V. and Nazar'ina, L.A., *Khim. Volokna*, 1999, no. 4, pp. 8–16.
2. Myasoedova, G.V., Nikoshina, V.A., Molochnikova, N.P., and Lileeva, L.V., *Zh. Anal. Khim.*, 2000, vol. 55, no. 6, pp. 611–615.
3. Zverev, M.P., *Ekol. Prom. Ross.*, 1997, no. 4, pp. 35–38.
4. Saldadze, K.I. and Kopylova-Valova, V.D., *Kompleksoobrazuyushchie ionity (kompleksity)* [Complex Ion Exchangers (Complexites)], Moscow: Khimiya, 1980.
5. Druzhinina, T.V. and Struganova. M.A., *Khim. Volokna*, 2001, no. 1, pp. 6–9.
6. Barash, A.N., Zverev, M.P., Kalyanova, N.F., *et al., Khim. Volokna*, 1984, no. 3, pp. 17–19.
7. Gulina, L.V., Grigoryan, E.A., Gabrielyan, G.A., and Gal'braikh, L.S., *Khim. Volokna*, 2002, no. 6, pp. 55–61.
8. Skvortsov, N.G. and Kolosova, G.M., *Zh. Prikl. Khim.,* 1995, vol. 68, no. 2, pp. 328–330.
9. Zhukov, A.A., Zholobova, L.V., and Kuznetsov, N.P., *Ekol. Prom. Ross.*, 1998, no. 2, pp. 17–19.
10. Borisenko, Z.V., Mubarakshin, G.M., and Nachinkin, O.I., *Khim. Volokna*, 1997, no. 2, pp. 52–54.
11. Plokhov, S.V. and Barinova, N.A., *Ekol. Prom. Ross.*, 2001, no. 9, pp. 9–11.
12. Andrichenko, Yu.D., Druzhinina, T.V., Afanas'eva, I.S., and Litvinova, T.A., *Khim. Volokna*, 1982, no. 4, pp. 40–41.
13. Litvinova, T.A., Bogacheva, T.I., Andrichenko, Yu.D., and Druzhinina, T.V., *Khim. Volokna*, 1984, no. 1, pp. 20–21.
14. Pavlov, N.N., *Teoreticheskie osnovy obshchei khimii* (Theoretical Principles of General Chemistry), Moscow: Vysshaya Shkola, 1978.
15. Pauling, L.C., *General Chemistry*, San Francisco: Freeman, 1954.
16. Zverev, M.P., *Khim. Volokna*, 2002, no. 6, pp. 67–75.

Russian Journal of Applied Chemistry, Vol. 76, No. 12, 2003, pp. 1930–1935. Translated from Zhurnal Prikladnoi Khimii, Vol. 76, No. 12, 2003, pp. 1981–1986.

APPLIED ELECTROCHEMISTRY AND CORROSION PROTECTION OF METALS

Influence of Cobalt Intercalation on Processes in a Nickel–Zinc Battery with Nickel Oxide Electrode Fabricated from Spherical Nickel Hydroxide

Z. P. Arkhangel'skaya, T. B. Kas'yan, M. M. Loginova, and L. B. Raikhel'son

Akkumulyatornaya Kompaniya Rigel' Open Joint-Stock Company, St. Petersburg, Russia

Received March 6, 2003

Abstract—The influence of cobalt on processes that occur in a nickel oxide electrode of a nickel–zinc battery, fabricated from spherical nickel hydroxide on foamed nickel support, was studied.

A considerable progress has been made recently in improving the nickel oxide electrode (NOE) of the conventional power cells with alkaline electrolyte (nickel–cadmium and nickel–metal hydride). This resulted from simultaneous optimization of the morphological and electrochemical parameters of nickel hydroxide by imparting spherical shape to its particles and by modifying its structure with cobalt additives [1].

The electrodes made of spherical nickel hydroxide show better working capacity when charged and discharged in intensive modes and have stable electrochemical parameters in cycling. The anodic oxidation of the active paste of NOE, which contains incorporated cobalt compounds, occurs at low current expenditure for oxygen evolution, especially with lithium added simultaneously [2]. It was noticed that the strongest increase in the NOE activity is achieved in the presence of cobalt compounds.

It has been established, when analyzing the mechanism by which cobalt affects the NOE properties, that its incorporation into the structure of nickel hydroxides changes the nature of protonic bonds in it, which is accompanied by delocalization of protons [3].

In more recent studies [4, 5], the specific properties of nickel hydroxide modified with cobalt are accounted for by the formation, in the course of NOE forming, of intercalation compounds $Ni_{1-x}Co_xOOH$ (at x = 0.03–0.28), whose conductivity is higher by three orders of magnitude than that of $Ni(OH)_2$. This intercalation compound is revealed by Raman spectroscopy (its presence in $Ni(OH)_2$ can be judged from the intensity of the line at 515 cm^{-1} [4]). The dependence of the electron (proton) exchange on cobalt content per nickel atom in conversion from $Ni(OH)_2$ to NiOOH is described by a curve peaked at 1.1–1.2, the values attained at Co/(Ni + Co) = 0.07. This result was obtained in studying electrodes made of highly dispersed spherical $Ni(OH)_2$ (particle size 250 Å [4]. Virtually the whole amount of spherical $Ni(OH)_2$ used in power cells consists of particles with radii ranging from several to 20–30 μm. In this case, the exchange is characterized by values of 0.85–0.95 [1].

EXPERIMENTAL

In this study, we analyzed specific features of processes occurring on NOE made of spherical nickel hydroxide in NTs-25 nickel–zinc (NZ) batteries. Nickel hydroxide used in the study contained 5–6% cobalt and 3% zinc. Zinc, which is the conventional additive to spherical nickel hydroxide, is introduced to prevent formation in the course of charging of the gamma phase of NiOOH, which has irregular and easily destructible structure.

The active paste was deposited onto a foamed nickel support, and then the electrodes were compacted and dried.

A degree of compaction of the assembly that is necessary for stable reversible operation of the negative electrode was ensured when assembling batteries with the NOE under study, in contrast to the case of metal-ceramic (MC) electrodes. This was done by varying the relative thicknesses and capacities of the positive and negative electrodes at the their constant total thickness in the assembly and by using an appropriate set of separators.

1070-4272/03/7612-1930 $25.00 © 2003 MAIK "Nauka/Interperiodica"

Table 1. Parameters of the NTs-25 batteries under study, with a positive electrode made of spherical nickel hydroxide and containing cobalt as additive

Variant of assembly	Electrode thickness, mm		Number of electrodes in an assmebly		Theoretical capacity, A h		Ratio of Zn/NOE capacities
	Zn	NOE	Zn	NOE	Zn	NOE	
I	1.25	0.95 × 2	8	7	95	50	1.9
II	1.25	0.80 × 2	9	9	107	46	2.3
III	1.25 × 2	0.95 × 2	4 × 2 + 2	5	118	36	3.3

For most of the batteries under study, the NOE on a foamed nickel support had the same thickness as the MC electrodes; in some experiments, we used thinner electrodes, with their number in the battery assembly changed simultaneously. The positive electrodes were used in pairs.

The negative electrodes in differently assembled batteries were of the same design, but contained different amounts of the active paste.

For this purpose, the middle electrodes in the assembly of type III were paired. The electrolyte volume was 105 ml for all types of batteries. The basic parameters of the batteries are listed in Table 1.

Since the zinc electrode is insensitive to the forming modes, the primary goal of the study was to optimize the forming modes for the positive electrodes.

A study of the properties of $Ni_{1-x}Co_xOOH$ compounds revealed that they are formed under conditions of anodic polarization of an NOE containing $Co(OH)_2$ as additive at rather high oxidation rates (currents of 0.1–0.5 A) [5]. In this case, the oxidation occurs to give an intercalation compound with mosaic structure. The intercalated compound also remains stable under steady-state conditions and in the case of cathodic polarization of the NOE, but is reduced to give $Co(OH)_2$ when the potential is lowered to 0.1–0.0 V (relative to the Hg/HgO electrode in the same solution) [5]. Further lowering of the NOE potential is accompanied by even deeper reduction of cobalt hydroxide. As a result, metallic cobalt, which is inactive under the conditions of operation of the positive electrode, can be formed in the NOE at negative potentials.

Based on the results of electrochemical, X-ray diffraction, and electron-microscopic studies, it was recommended in [5] to charge NOE made of spherical nickel hydroxide in rather intensive modes, with excess charge imparted in the forming cycles, and to discharge it without allowing the final potential of the positive electrode to decrease below a certain value. As noted in studies devoted to this problem, a high degree of its charging is achieved in 2–3 cycles, with the capacity equal to 150% of the theoretical value in terms of the Ni^{2+} to Ni^{3+} conversion imparted in each cycle [1].

The data of [6] clearly show that the NOE of the type considered should be formed with excess charge imparted. In this study, the effect of cobalt on the processes occurring in the electrode was studied using potentiodynamic cycling, with the potential varied stepwise. This allowed evaluation of the contribution from each individual process in charging of the electrode, depending on the amount of cobalt added, conditions of its introduction, and forming mode.

In charging of the electrode under study, which was made of spherical nickel by its codeposition with cobalt hydroxide, Co(II) is converted to Co(III) in the first cycle, with the structural transformation and oxidation of a part of nickel occurring simultaneously. In the process, the capacity spent for formation of the intercalation compound is approximately twice that necessary for charging of cobalt.

In the course of the subsequent discharge, the capacity spent for the formation of this complex is not returned, since the complex is not reduced under the standard operation conditions. In addition, the final period of charging is accompanied by oxygen evolution. All these circumstances lead to discrepancy between the capacity imparted in the first charging and the discharge capacity.

In the second cycle, charging occurs more effectively at lower potential, which is due to the influence exerted by cobalt intercalation. However, in this case too, the whole amount of the active paste is only involved in the process after an excess charge is imparted, compared with the value calculated for the Ni(II) to Ni(III) conversion [6].

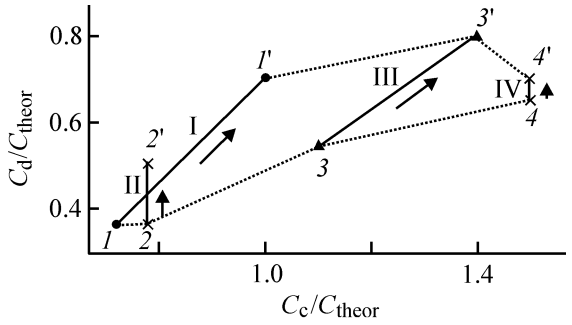

Fig. 1. Effect of charging capacity on the coefficient of utilization of the active paste in an NOE made of spherical nickel hydroxide in forming of NTs-25 batteries in modes I–IV. (C_d/C_{theor}) Ratio of discharge to theoretical capacity and (C_c/C_{theor}) ratio of charging to theoretical capacity; the same for Fig. 2. Cycle: (*1*–*4*) first and (*1*'–*4*') second.

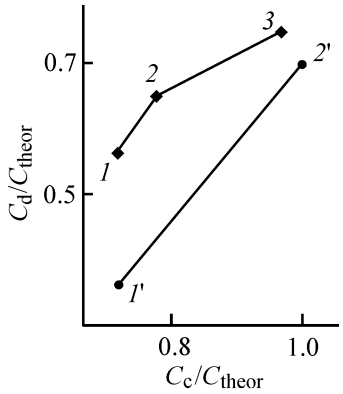

Fig. 2. Coefficient of utilization of the active paste of NOE made of spherical nickel hydroxide with varied density vs. charging capacity in forming of NTs-25 batteries. Cycle no.: (*1*, *1*') first, (*2*, *2*') second, and (*3*) third. NOE density (g cm^{-3}): (*1*–*3*) 2.7 and (*1*'–*2*') 2.5.

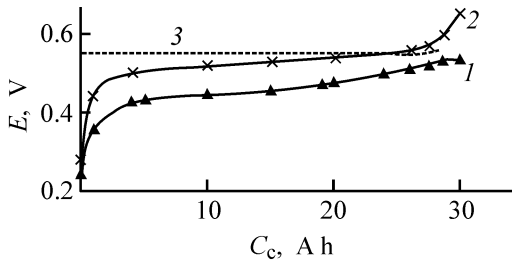

Fig. 3. Variation with cycling of the potential E of NOE (*1*) with and (*2*) without cobalt and (*3*) potential of oxygen evolution. Charging current 5 A. (C_c) Charging capacity.

The concepts concerning the conversion conditions and further effective influence of cobalt on the electrochemical processes on NOE, formulated for the case of nickel-metal hydride batteries, were taken into account when studying the NZ battery only in the part regarding the inadmissibility of overcharging of the zinc electrode. The forming modes with different ratios of charging to theoretical capacity C_c/C_{theor} were chosen based on the negative to positive electrode capacity ratios in Table 1. The results obtained, summarized in Fig. 1, refer to a 0.95–1-mm-thick NOE with active paste density of 2.5 g cm^{-3}.

The first charging of the batteries was done with currents corresponding to $0.06-0.1\,C$, i.e., in more prolonged modes as compared with those recommended in [5]. This is due to the considerable thickness of the electrodes used in NZ batteries. Four forming modes were tested, which differed in the charging capacities C_c/C_{theor}. The largest coefficient of utilization of the active paste in the first cycle (0.65) was achieved after imparting a charge capacity of $1.5\,C_{theor}$ (forming variant IV). After the second charging, the maximum value of C_c/C_{theor}, equal to 0.8, was obtained after a charging capacity of $1.4\,C_{theor}$ was imparted in the course of 8–10 h (Fig. 1, variant III).

The coefficient of utilization of the active paste in the first forming cycle grows with its density increasing to 2.7 g cm^{-3} (Fig. 2). This is presumably due to improvement of the conductivity in the solid phase. However, the degree of charging increased in the second cycle only slightly and, therefore, a third forming cycle was required. But even in this case, the current utilization coefficient was lower than the maximum value obtained at active paste density of 2.5 g cm^{-3} (Fig. 1, variant III).

The forming mode at which the capacities equal to 1.1 and $1.4\,C_{teor}$ are imparted in, respectively, the first and second cycles was chosen on the basis of the results obtained. The degree of charging of the active paste, obtained in this case, is 0.8, which is much lower than that in nickel–cadmium and nickel–metal hydride batteries ($0.95\,C_{rat}$). The possible reason is that zincate ions are incorporated into the structure of nickel hydroxide from the electrolyte, thereby being involved in the conversion of the active paste [7]. In the first cycle, when the electrolyte if free of zincate ions, the degree of NOE charging grows steadily with increasing charging capacity, but the effect achieved tends to disappear in the second cycle.

In the subsequent cycling of NZ batteries, the utilization coefficient of the active paste remains at the level reached, and the effect of zincate ions is not manifested during a certain period. This makes it possible to reveal specific features of the processes associated with cobalt intercalation. The stationary potential of an NOE containing cobalt additive is shifted toward negative values relative to that for NOE made of pure nickel hydroxide. Correspondingly, their charging potentials (Fig. 3) and the battery voltages are different, too [7, 8].

Another specific feature of an NOE modified with cobalt is its ability, acquired in the course of forming, to be charged in more intensive modes. The current utilization is the highest at a final charging potential of 0.52–0.54 V (battery voltage 1.92–1.93 V), which is lower than the 0.55–0.6 V potential (battery voltage 1.98–2.05 V) commonly used for charging of batteries with NOE containing no cobalt additive. Despite that the NOE capacity continues to grow with increasing final charging potential, the current utilization coefficient decreases and, simultaneously, the consumption of current for oxygen evolution increases.

The tolerance to fast charging is the important advantage of NZ batteries with NOE made of spherical nickel hydroxide, which is topical for power cells intended for vehicles. With a 0.6–0.8-mm-thick NOE, batteries of this kind can be charged in 2–5 h.

The results obtained in studying deep discharge of NOE, at which the NOE potential shifts toward negative values as far as the potential of hydrogen evolution (–1.1 V), which corresponds to a battery voltage of 0–0.1 V (Fig. 4), are characteristic of the transformations occurring with cobalt compounds. A charging that follows a deep discharge occurs at a lower potential equal to 0.35–0.37 V (battery voltage 1.75 V) in its initial stage, which confirms that NOE oxidation proceeds by another mechanism. In the cycle following the deep discharge, the NOE capacity decreases by 15–20 %.

Repeated deep discharges of the batteries are accompanied by further decrease in the NOE capacity, which points to gradual degradation of its active paste [8]. If the final discharge potential is not allowed to be lower than the minimum value of 0–0.1 V (battery voltage 1.2 V), the electrochemical characteristics of NOE remain constant during a long time, i.e., the forming intercalation compound $Ni_{1-x}Co_xOOH$ is not decomposed under these conditions.

Apart from the phenomena considered, which are associated with intercalation processes, the electrode made of spherical nickel hydroxide reveals other essential features imparting new properties to this electrode. A very important result illustrating the specificity of the processes occurring on NOE made of spherical nickel hydroxide was obtained in [7, 8]. In cycling of NZ batteries, the uniformity of the active paste distribution over the zinc electrode surface was considerably improved, compared with that in a battery with MC-supported NOE. No tendency toward "loss of shape" was observed on the negative electrode after 200 cycles [8]. At the same time, in batteries with an NOE on an MC support, tested under the analogous conditions, the loss of active paste in the upper part of the electrode surface is commonly as great as 50% [9].

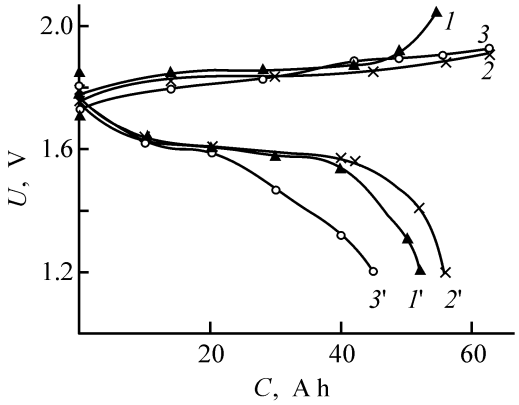

Fig. 4. Variation of the potential U in the course of (*1*–*3*) charging and (*1*'–*3*') discharge of an NTs-25 battery, following the discharge to a voltage of (*2*, *2*') 1.2 V and (*3*–*3*') 0.0–0.1 V. (*C*) capacity. (*1*, *1*') Control cycle.

The reasons for zinc redistribution on the negative electrode of an NZ battery being cycled have been studied extensively. The observed loss of shape is commonly attributed to processes occurring on the zinc electrode itself or in the electrolyte, without taking into account the effect of NOE. Only in [9], data were obtained, indicating that this phenomenon is certainly associated with the nonuniformity of current distribution over the NOE surface. This nonuniformity is responsible for a similar current distribution over the surface of the negative electrode, too, and, eventually, leads to dissolution of zinc in the upper part of the electrode and to its local passivation.

A clearly pronounced improvement of the state of the zinc electrode in its joint operation with NOE made of spherical nickel hydroxide, all other factors being the same, can be accounted for by specific features of the processes occurring on the positive electrode of this type. The high conductivity of the active paste in the presence of cobalt, established in [4, 5], plays a certain role in the changes observed, by making less significant the difference in conductivity between $Ni(OH)_2$ and NiOOH. At the same time, the observed effect cannot be accounted for solely by this factor, since introduction of other electrically conducting additives into NOE (e.g., graphite) does not lead to any results of this kind.

Probably, the observed ability of cobalt additives to level the current distribution over the surface of NOE can be attributed to the effect produced by cobalt on the intercalation hysteresis of protons

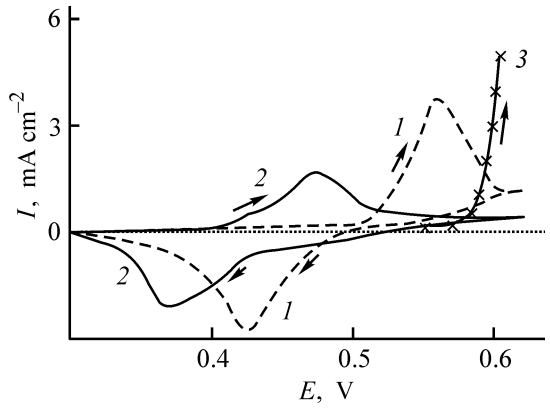

Fig. 5. Cyclic voltammetric curves for NOE (*1*) not containing and (*2*) containing cobalt as additive [10] and (*3*) curve for oxygen evolution. (*I*) Current and (*E*) potential.

under conditions of its anodic and cathodic polarization [10].

We established in this study that the voltammetric charging–discharge hysteresis loops are shifted, upon incorporation of cobalt into the NOE structure, to lower potentials by approximately 120 mV, with the distance between their peaks decreasing from 90 mV (for "pure" NOE) to 50 mV (for an electrode containing cobalt hydroxide). This shift makes the difference between the potentials of NOE oxidation and oxygen evolution greater, which creates more favorable conditions for separation of these processes in battery charging.

The voltammetric curves (*1, 2*) obtained in studying the hysteresis of protons on NOE with and without cobalt [10] are shown schematically in Fig. 5. The values of current refer solely to the *I–E* curve for oxygen evolution, since, according to the authors' data, the position of the peak, a critical parameter for the problem under consideration, is independent of the potential sweep rate and current. The anodic and cathodic portions of the voltammetric curves are shifted by 0.085 V toward positive values, with account taken of the change in the potential of the mercury oxide reference electrode on passing from a 1 M KOH electrolyte used in [10] to a 7 M KOH electrolyte in the present study. The voltammetric curves show that, in principle, the intercalation hysteresis of protons can affect the current distribution in the case of anodic polarization of NOE.

It can be seen that, for pure NOE containing no cobalt (Fig. 5, curve *1*), the peak potential of the anodic current is approximately the same as the potential of the onset of oxygen evolution (Fig. 5, curve *3*). In this case, the oppositely varying currents consumed for the main and side processes cancel out each other to a certain extent in the most overcharged region. In this region, the total current remains constant or increases only slightly, whereas the fraction of current consumed for oxygen evolution grows.

For NOE containing cobalt as an additive, the peak potential of the anodic polarization current on the voltammetric curve is shifted to more negative values (Fig. 5, curve *2*). Therefore, the decrease in current is not compensated for by oxygen evolution. In this case, a decrease in current in a certain area of the electrode must be accompanied by an increase in current in its less charged areas, whose potential is still lower than the value corresponding to the peak in the voltammetric curve, i.e., the currents will be equalized automatically.

The difference in the positions of the peak potentials of the anodic and cathodic currents in the voltammetric curves (Fig. 5) is in agreement with the data according to which the discharge potential (Fig. 3) of batteries with NOE modified with cobalt is lower than that of batteries with NOE containing no cobalt [7, 8].

CONCLUSIONS

(1) Nickel–zinc batteries with a nickel oxide electrode made of spherical nickel hydroxide acquired new properties associated with the intercalation effect of the cobalt additive contained in nickel hydroxide. The conversion of nickel hydroxide to an electrically conducting intercalation compound made it possible to charge the nickel oxide electrode in shorter modes, with high coefficient of current utilization for the main process and its insignificant consumption for oxygen evolution.

(2) The best separation of the main and side processes is provided by the shift of the stationary potential of the nickel hydroxide electrode made of spherical nickel hydroxide toward negative values, compared with the potential of pure nickel hydroxide electrode. This makes the difference between the potentials of the main oxidation process and oxygen evolution larger.

(3) The change in the voltammetric characteristic of the nickel oxide electrode, caused by the effect of cobalt intercalation on the hysteresis of protons, makes the anodic current distribution over the electrode surface more uniform. This leads to a more uniform distribution of the current density over the surface of the zinc electrode, too, and decelerates the processes leading to loss of its shape.

REFERENCES

1. Yu, C.Z, Lai, W.H., Yan, G.J., and Wu, J.Y., *J. Alloys Compounds*, 1999, vols. 293–295, pp. 784–787.
2. Malandin, O.G., Rakhovskaya, S.M., Vasev, A.V., *et al., Elektrokhimiya*, 1980, vol. 16, no. 7, pp. 1041–1044.
3. Ezhov, B.B., Malandin, O.G., and Rakhovskaya, S.M., *Elektrokhimiya*, 1984, vol. 20, no. 1, p. 140.
4. Audemer, A., Delahaye, A., Farhi, R.J., *et al., J. Electrochem. Soc.*, 1997, vol. 144, no. 8, pp. 2614–2620.
5. Pralong, V., Delahay-Vidal, A., Beaudoin, B., *et al., J. Electrochem. Soc.*, 2000, vol. 147, no. 4, pp. 1306–1313.
6. Pralong, V., Chabre, Y., Delahay-Vidal, A., and Tarascon, J.-M., *Solid State Ionics*, 2002, vol. 147, pp. 73–84.
7. Arkhangel'skaya, Z.P., Kas'yan, T.B., Loginova, M.M., and Raikhel'son, L.B., *Zh. Prikl. Khim.*, 2003, vol. 76, no. 6, pp. 953–958.
8. Loginova, M.M., Kas'yan, T.B., Arkhangel'skaya, Z.P., and Raikhel'son, L.B., *Zh. Prikl. Khim.*, 2002, vol. 75, no. 6. pp. 779–782.
9. Alekseeva, M.E., Arkhangel'skaya, Z.P., Ivanova, R.P., *et al., Zh. Prikl. Khim.*, 1998, vol. 71, no. 6. pp. 940–945.
10. Podolske, Ta K. and Newman, J., *J. Electrochem. Soc.*, 1999, vol. 146, no. 8, pp. 2769–2779.

Russian Journal of Applied Chemistry, Vol. 76, No. 12, 2003, pp. 1936–1941. Translated from Zhurnal Prikladnoi Khimii, Vol. 76, No. 12, 2003, pp. 1987–1991.

APPLIED ELECTROCHEMISTRY AND CORROSION PROTECTION OF METALS

Potential and Current Distributions in Chlorine Diaphragm Electrolyzers with Gas Removal from the Back Side of External Electrodes and Possibility of Electrolysis Intensification

G. G. Tul'skii, A. K. Gorbachev, and A. Yu. Brovin

Khar'kovskii Politekhnicheskii Institut National Technical University, Kharkov, Ukraine

Received August 21, 2002; in final form, September 2003

Abstract—The cell voltage balance components of monopolar and bipolar electrolyzers were analyzed on the basis of calculations in terms of a mathematical model of the potential and current distributions along the cell height and tests of a laboratory electrolyzer of industrial height. Ways to diminish energy expenditure and to intensify diaphragm electrolysis of aqueous sodium chloride solutions were substantiated theoretically and experimentally.

Further improvement of the electrochemical production of chlorine and sodium hydroxide by diaphragm electrolysis of aqueous sodium chloride solutions remains a topical task, since about 50% of the world output of these products is manufactured in this way. Therefore, despite the fact that membrane electrolysis of aqueous sodium chloride solutions [1] is a promising technique, improving the diaphragm electrolysis is of practical and theoretical interest.

In [2, 3], a procedure was suggested for calculating the potential and current distributions along the height of vertical diaphragm chlorine electrolyzers with account of the gas-filling of the anolyte. The influence exerted by the electrical resistance of the current-carrying support of the anode on the potential and current distributions along the height of a vertical chlorine electrolyzer, in which an asbestos diaphragm is deposited on the cathode grid, hydrogen is removed from the back side of the grid cathode, and chlorine is released into the interelectrode space (BGK-50 and DM-50 electrolyzers).

However, a no less important factor that affects the potential and current distributions and, moreover, hinders intensification of electrolysis is the gas-filling of the anolyte [3]. A possible way to diminish the effect of gas-filling on the current distribution along the electrolyzer height is to remove chlorine from the back side of a gas-permeable external electrode, as this is done in membrane electrolyzers [1]. For this purpose, it was suggested in [4] to use an additional diaphragm tightly pressed against the external perforated or gridlike anode.

The aim of our study was to analyze the potential and current distributions along the height of a vertical diaphragm chlorine electrolyzer with gas removal from the back side of external electrodes and to assess the possibility of intensifying further the electrolysis of aqueous sodium chloride solutions and diminishing the specific power consumption in this process.

The equivalent electrical circuit of such a cell is shown in Fig. 1. To develop a mathematical model of the electrolyzer, we divide a cell with parallel electrodes into n parts, as this was done in [2], and regard each part as a closed electric circuit with current supply at $x = 0$ for all the circuits. Therefore, the voltage applied to this circuit is the same for all the circuits and equal to the voltage across the cell. The dependence of the polarization on current density in a narrow range of variation of this parameter (1000–2000 A m^{-2}) can be approximated with a straight line. In this case, the voltage balance at any point x along the height of a monopolar cell with gas removal from the back side of the external electrodes is constituted by the following components

$$E = E^{eq}_{Cl_2/Cl^-} - E^{eq}_{H_2O/H_2} + \eta_{Cl_2} + \eta_{H_2} + U_d + U_{ad} + U_{el} + E_{diff} + U_a + U_c + U_{cont}, \quad (1)$$

where $E^{eq}_{Cl_2/Cl^-}$ and $E^{eq}_{H_2O/H_2}$ are the equilibrium electrode potentials; η_{Cl_2} and η_{H_2}, the overvoltages of

1070-4272/03/7612-1936 $25.00 © 2003 MAIK "Nauka/Interperiodica"

chlorine and hydrogen evolution; U_d, U_{ad}, and U_{el}, the voltage drops across the main (cathode) diaphragm, additional (anode) diaphragm, and electrolyte, respectively; E_{diff}, the diffusion potential; U_a, U_c, and U_{cont}, the voltage drops across the anode, cathode, and contacts, respectively.

According to published data [5–7], the dependence of the overvoltage of gas evolution on the current density is described by the equations

$$\eta_{Cl_2} = 0.100 + 0.028\log i_a, \quad (2)$$

$$\eta_{H_2} = 0.240 + 0.100\log i_c, \quad (3)$$

where i_a and i_c are the cathode and anode current densities.

As in [2], these equations can be approximated with a linear dependence in a narrow range of current densities (250–3000 A m^{-2}) of practical interest. Using the least-squares procedure, we obtained the following equations

$$\eta_{Cl_2} = \Delta E_a + p_a i_a = 0.051 + 0.130 i_a, \quad (4)$$

$$\eta_{H_2} = \Delta E_c + p_c i_c = 0.286 + 0.340 i_c, \quad (5)$$

where ΔE_a and ΔE_c are the constant components of the anode and cathode polarization, and p_a and p_c are the coefficients of their variable components (Ω cm^2).

According to the equivalent circuit (Fig. 1), a current I_0 is applied to the anode at point $x = 0$. Taking into account the fact that the conditions and parameters of electrolysis are the same across the cell width, we can relate the current load to unit anode width. Let us denote the current flowing across the cross-section of the anode at a height x from the point of current supply by I; then, we have the following expression for the current flowing through the electrolyte, I_{el}

$$I_{el} = I_0 - I. \quad (6)$$

The density of the current flowing through the electrolyte at any point x along the electrode height is given by

$$i = \frac{dI_{el}}{dx} = -\frac{dI}{dx}. \quad (7)$$

Taking into account (7), we can rewrite Eqs. (4) and (5) as

$$\eta_{Cl_2} = \Delta E_a - p_a\frac{dI}{dx} = 0.051 - 0.130\frac{dI}{dx}, \quad (8)$$

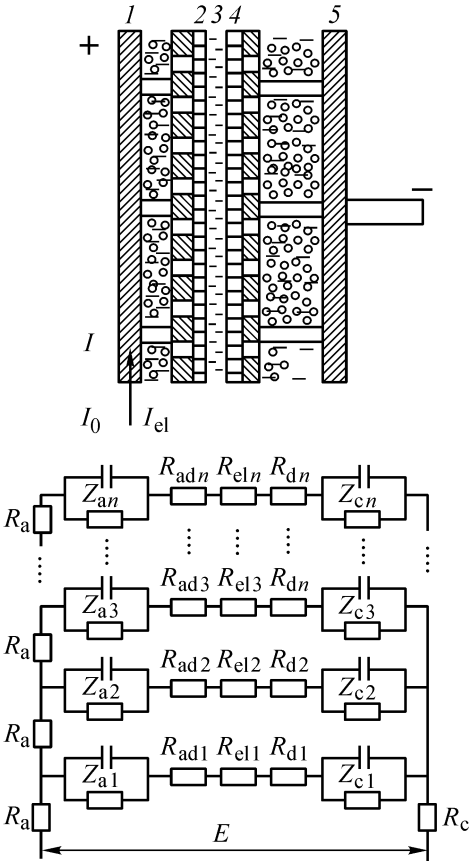

Fig. 1. Equivalent electrical circuit of a monopolar cell with gas removal from the back side of gas-permeable electrodes. (*1*) External grid anode, (*2*) additional anode diaphragm, (*3*) anolyte, (*4*) diaphragm, and (*5*) external grid cathode; the same for Fig. 4.

$$\eta_{H_2} = \Delta E_c - p_c\frac{dI}{dx} = 0.086 - 0.340\frac{dI}{dx}. \quad (9)$$

The equation for the voltage drop across the anolyte at its zero gas-filling takes the form

$$U_{el} = -\frac{dI}{dx}R_0, \quad (10)$$

where R_0 is the reduced resistance of the anolyte at zero gas-filling (Ω cm^2).

The voltage drop across the diaphragm is given by

$$U_d = -\frac{dI}{dx}R_d, \quad (11)$$

where R_d is the reduced resistance of the diaphragm (Ω cm^2).

The voltage drop across the additional (anode) diaphragm is given by

$$U_{ad} = -\frac{dI}{dx}R_{ad}, \quad (12)$$

where R_{ad} is the reduced resistance of the additional diaphragm ($\Omega\,cm^2$).

Using Ohm's law for an anode fragment of unit height, we obtain

$$\frac{dU_a}{dx} = IR_a, \quad (13)$$

where R_a is the electrical resistance of this fragment.

Integrating expression (13), we obtain an equation that describes the ohmic loss of voltage along the anode height:

$$U_a = R_a\int_0^x I\,dx. \quad (14)$$

Substitution of the values of the voltage balance components (8)–(12) and (14) into Eq. (1) gives

$$E - E_{const} = R_a\int_0^x I\,dx - \frac{dI}{dx}(p_a + p_c + R_{diff} + R_{ad} + R_0), \quad (15)$$

where $E_{const} = E^{eq}_{Cl_2/Cl^-} - E^{eq}_{H_2O/H_2} + E_{diff} + \Delta E_a + \Delta E_c + \Delta U_c + U_{cont}$ is the overall voltage balance constant.

Differentiating Eq. (15) and making certain rearrangements, we have

$$\frac{d^2I}{dx^2} = I\sqrt{\frac{R_a}{p_a + p_c + R_{diff} + R_{ad} + R_0}} = \beta^2 I. \quad (16)$$

The solution to a differential equation of this kind is the function

$$I = A\,ch\,\beta x + B\,sh\,\beta x, \quad (17)$$

where A and B are coefficients found from boundary conditions;

$$\beta = \sqrt{\frac{R_a}{p_a + p_c + R_{diff} + R_{ad} + R_0}}. \quad (18)$$

At $x = 0$ I $= I_0$, $A = I_0$; at $x = h$ $I = 0$, $B = -I_0\dfrac{\cosh\beta h}{\sinh\beta h}$.

Substituting the values of A and B into Eq. (17), we obtain an equation that can be used for calculating the current density

$$I = I_0\frac{\sinh[\beta(h - x)]}{\sinh\beta}. \quad (19)$$

Differentiating (19), we have the following equation for the current density

$$-\frac{dI}{dx} = i = \beta I_0\frac{\sinh[\beta(h - x)]}{\sinh\beta}. \quad (20)$$

Substituting I from Eq. (19) into Eq. (14), we obtain the dependence of voltage drop on x along the anode height for the boundary conditions $x = 0$, $U_a = 0$

$$U_a = \frac{I_0R_a}{\beta\sinh\beta h}\{\cosh\beta x - \cosh[\beta(h - x)]\}. \quad (21)$$

The relations (19)–(21) make it possible to calculate how the current, current density, and voltage drop across the anode vary along the height of a monopolar cell with gas removal from the back side of gas-permeable electrodes.

Using the mathematical model obtained, we studied the potential and current distributions along the height of an electrolyzer cell with gas removal from the back side of gas-permeable electrodes on laboratory electrolyzers of industrial height ($H \approx 900$ mm) with units of BGK-50/25 and DM-50 industrial electrolyzers. The design of a laboratory electrolyzer was described in [3].

A new feature in the design of the laboratory electrolyzer is that an additional polypropylene diaphragm, tightly pressed against the frontal side of the external anode, was used to ensure removal of evolving chlorine to behind the back side of the external perforated anode. The removal of the evolving chlorine from the back side of the gas-permeable anodes made it possible to work with a virtually gas-free anolyte and, therefore, to diminish the interelectrode distance to 6 mm, of which 2.5–3 mm was occupied by an asbestos diaphragm. In this cell, brine is fed into the interdiaphragm space, which ensures a uniform flow across the cathode diaphragm.

The reduced resistance of the additional anode diaphragm was 0.98 $\Omega\,cm^2$ at a current density of 1450 A cm^{-2}. The reduced resistance of the anolyte decreased by 1.67 $\Omega\,cm^2$, compared with BGK-50/25, and by 1.17 $\Omega\,cm^2$, compared with DM-50, at average current densities of 1450 and 1675 A m^{-2}, respectively.

The experimental current density distribution along the height of the laboratory electrolyzer (points) and that calculated using the mathematical model are presented in Fig. 2. For comparison, the current distribution in a BGK-50/25 industrial electrolyzer is shown by a dashed line. These data demonstrate a satisfactory agreement between the experimental and calculated dependences, which gives reason to conclude that the mathematical model we developed is adequate to the processes occurring in real electrolyzers with gas removal from the back side of gas-permeable electrodes. The bends in the current distribution curves can be attributed to nonuniformity of the cross-section of the ORTA current lead along its height for the electrolyzer types mentioned.

The absence of gas-filling in the interelectrode space leads to a more uniform current density distribution along the electrolyzer height. The ratio of the initial to final current density was 1.35 for laboratory electrolyzers assembled with the use of units of BGK-50/25 industrial electrolyzers and 1.28 for DM-50 at average current densities of 1450 and 1675 A m^{-2}, respectively. The remaining nonuniformity of the current density distribution is only associated with the nonuniformity of voltage drop across the anode. The variation of the variable voltage balance components along the height of the laboratory electrolyzers described here is shown in Fig. 3.

The voltage drop across the anolyte, $U_{el} + U_{ad}$, decreased in the experimental electrolyzers, compared with their industrial analogues, from 0.47 to 0.22 V for BGK-50/25 and from 0.29 to 0.23 V for DM-50; the voltage across the electrolyzers at working current densities was 3.28 and 3.33 V, respectively. The more pronounced effect obtained with the additional anode diaphragm for a BGK-50/25-based electrolyzer is due to considerable ohmic voltage loss in the anolyte because of the larger interelectrode distance and greater working height of the anode, compared with those in the electrolyzer based on DM-50.

The ohmic voltage loss in diaphragm electrolysis of aqueous sodium chloride solutions can be decreased to a minimum with a bipolar cell design with gas removal from the back side of gas-permeable electrodes. This cell differs from the previously described monopolar cells in that its anode and cathode have lateral current leads to the external electrodes. An asbestos diaphragm at the cathode and an additional polypropylene diaphragm at the anode ensure removal of the evolving gases from the back side of gas-permeable electrodes. The feed brine is delivered into the interdiaphragm space. The equivalent electrical circuit of the cell described is shown in Fig. 4.

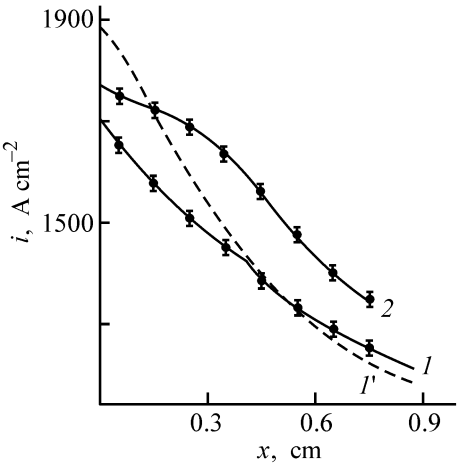

Fig. 2. Distribution of the current density i along the height x of cells of different types with gas removal from the back side of electrodes, obtained on (*1*, *2*) laboratory and (*1'*) industrial electrolyzers. Cell type: (*1*, *1'*) BGK-50/25 and (*2*) DM-50. *Lines*, calculation; *points*, experiment.

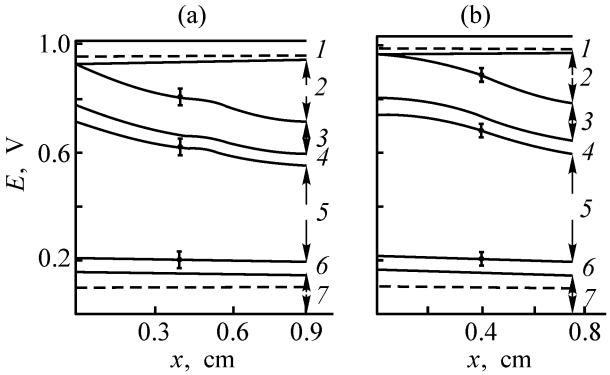

Fig. 3. Variation of the variable voltage balance components along the height of a laboratory electrolyzer with gas removal from the back side of electrodes, fabricated with the use of units of various industrial electrolyzers. (*E*) Sum of variable voltage balance components and (*x*) anode height. (a) BGK-50/25 and (b) DM-50. (*1*) Anode overvoltage; voltage drops across (*2*) anode, (*3*) anode diaphragm, (*4*) anolyte, (*5*) cathode diaphragm, and (*6*) cathode; (*7*) cathode overvoltage.

In accordance with the equivalent electrical circuit, the voltage balance equation for the given bipolar cell has the form

$$E - E_{const} = U_{el} + U_d + U_{ad} + i(p_a + p_c). \quad (22)$$

Substituting Eqs. (8)–(12) into expression (22), we obtain

$$E - E_{const} = -\frac{dI}{dx}(p_a + p_c + R_d + R_{ad} + R_0). \quad (23)$$

Comparative characterization of different types of cells in diaphragm chlorine electrolyzers fabricated with the use of the same units*

Cell type	I, A	H, cm	Current density, A m^{-2}			U_{cell}, V	d, mm
			i_0	i_{av}	i_{fin}		
Monopolar:							
BGK-50/25	1276	88	1883	1450	1185	3.50	12
DM-50	1256	76	1883	1675	1323	3.35	8
with gas removal from the back side	1276	88	1692	1450	1252	3.28	2
of gas-permeable electrodes	1256	76	1772	1675	1355	3.32	2
Bipolar with gas removal from the back	1276	88	1450	1450	1450	3.18	2
side of gas-permeable electrodes	1256	76	1675	1675	1675	3.27	2

* i_0, i_{av}, i_{fin}, the initial, average, and final current density, respectively; U_{cell}, cell voltage; d, interelectrode distance.

From Eq. (23) follows the relation for the current density

$$-\frac{dI}{dx} = \frac{E - E_{const}}{p_a + p_c + R_d + R_{ad} + R_0}. \quad (24)$$

In accordance with Eq. (24), the current density in a bipolar cell of a vertical diaphragm chlorine electrolyzer is independent of the electrode height and remains constant for any point along the electrolyzer height. For example, under the electrolysis conditions used in the preceding calculations (E = 3.5, E_{const} = 2.47 V; p_a = 0.13, p_c = 0.34; R_d = 3, R_{ad} = 0.33, and R_0 = 0.98 Ω cm^2) the current density will be 2150 A cm^{-2}, which exceeds by nearly a factor of 1.5 the average current density in BGK-50/25. In electrolysis with average current density of 1450 A cm^{-2}, the voltage across the bipolar cell we suggested will be 3.18 V. Hence follows that use of a bipolar cell design in a vertical chlorine electrolyzer instead of the monopolar one will make it possible to intensify the process 1.5-fold at the same energy expenditure or to diminish the energy consumption by 235–245 kW h per 1 ton of NaOH (100%) at the same current load on the electrolyzer.

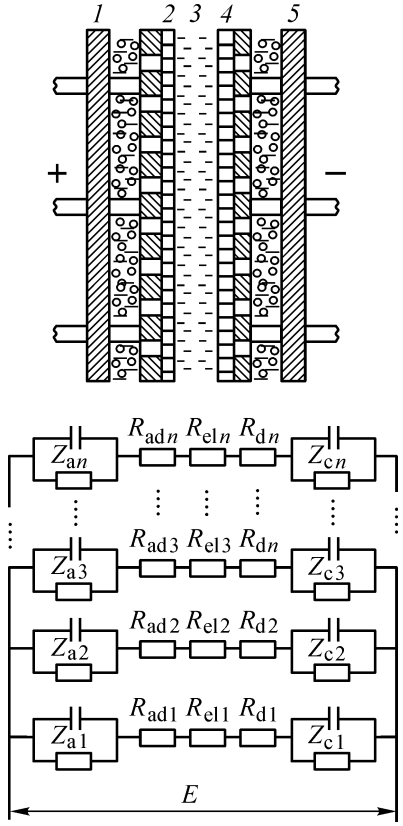

Fig. 4. Equivalent electrical circuit of a bipolar cell.

Comparative characteristics of different types of cells of vertical chlorine electrolyzers fabricated using units of BGK-50/25 and DM-50 industrial electrolyzers are listed in the table.

Use of the monopolar cell design in a chlorine electrolyzer with gas removal from the back side of gas-permeable electrodes makes it possible to decrease considerably the specific power consumption and to improve the current density distribution along the height of a cell of this kind. A more uniform current density distribution offers an opportunity to intensify the process of electrolysis by raising the working current densities. It is possible to further intensify the chlorine diaphragm electrolysis and to diminish the specific electric power consumption if a bipolar cell design with gas removal from the back side of gas-permeable electrodes is used. The requirement of a uniform current density distribution does not restrict the height of such a bipolar cell, which enable a considerable intensification of the diaphragm electrolysis of aqueous sodium chloride solutions.

With the problem of a diaphragm with lower specific electrical resistance under electrolysis conditions resolved, the bipolar design of a chlorine diaphragm electrolyzer becomes the most promising in the development of new chlorine electrolyzers.

CONCLUSIONS

(1) The main reason for nonuniformity in the potential and current distributions along the height of monopolar cells in industrial diaphragm chlorine electrolyzers is the gas-filling of the electrolyte and low electrical conductivity of the titanium ORTA current leads.

(2) Up to 90% of the ohmic voltage loss in electrolysis of an aqueous sodium chloride solution is that in the anode, electrolyte, and diaphragm.

(3) The minimum ohmic voltage loss and the best potential and current distributions are observed in a bipolar cell with gas removal from the back side of the external gas-permeable electrodes.

REFERENCES

1. Mazanko, A.F., Kamar'yan, G.M., and Romashin, O.P., *Promyshlennyi membrannyi elektroliz* (Industrial Membrane Electrolysis), Moscow: Khimiya, 1989.
2. Gorbachev, A.K. and Tul'skii, G.G., *Zh. Prikl. Khim.*, 1999, vol. 72, no. 5, pp. 779–785.
3. Gorbachev, A.K. and Tul'skii, G.G., *Zh. Prikl. Khim.*, 1997, vol. 70, no. 9, pp. 1459–1465.
4. USSR Inventor's Certificate, no. 1528815.
5. Kolotyrkin, Ya.M. and Shub, D.M., *Itogi nauki i tekhniki: Elektrokhimiya* (Advances in Science and Technology: Electrochemistry), Moscow: VINITI, 1982, vol. 20, pp. 3–43.
6. Krishtalik, L.I., Kokoulina, D.V., and Erenburg, R.G., *Itogi nauki i tekhniki: Elektrokhimiya* (Advances in Science and Technology: Electrochemistry), Moscow: VINITI, 1982, vol. 20, pp. 77–111.
7. El'tsev, V.A., Vorob'eva, G.A., Yurkov, L.I., *et al.*, *Zh. Prikl. Khim.*, 1980, vol. 53, no. 1, pp. 128–132.

Russian Journal of Applied Chemistry, Vol. 76, No. 12, 2003, pp. 1942–1945. Translated from Zhurnal Prikladnoi Khimii, Vol. 76, No. 12, 2003, pp. 1992–1994.

APPLIED ELECTROCHEMISTRY AND CORROSION PROTECTION OF METALS

Contact Deposition of Copper Powders onto Zinc in H_2SO_4–$CuSO_4$ and H_2SO_4–$CuSO_4$–$ZnSO_4$ Solutions and Their Morphology

O. I. Kuntyi, Z. O. Znak, and I. V. Dyug

Lvivska Politekhnika National University, Lviv, Ukraine

Received July 29, 2003

Abstract—The contact extraction of copper in the form of dispersed powders onto compact zinc from H_2SO_4–$CuSO_4$ and H_2SO_4–$CuSO_4$–$ZnSO_4$ solutions was studied. The influence exerted by acidity and temperature of the solution on the rate and time of cementation, specific consumption of metallic zinc, and morphology of copper deposits was investigated.

The increasing demand for dispersed metal powders [1] stimulates the development of new technologies, especially those using secondary raw materials. This is in the first place topical for copper powders occupying the leading position in volume of production among nonferrous metals [2]. Reprocessing of secondary copper, e.g., of copper–zinc-containing catalysts of KSO and KSO-F brands yields $ZnSO_4$–H_2SO_4–$CuSO_4$ solutions, from which copper and zinc are successively extracted electrochemically. At the same time, complete electrochemical extraction of copper is uneconomical, and, to prevent contamination of zinc with copper, the metal should be only extracted after thorough purification of the solution to remove copper ions by cementation [3]. Taking into account the considerable volumes of this kind of processing, it is reasonable to precipitate copper to obtain cement powders that can be successfully used in powder metallurgy [4].

This study is concerned with contact deposition of dispersed copper powder onto compact zinc in model technological solutions formed in integrated reprocessing of secondary copper raw.

EXPERIMENTAL

The contact precipitation of copper was performed and the kinetic relationships of the process were studied, along with the morphology of dispersed powder, using H_2SO_4–$CuSO_4$ and H_2SO_4–$CuSO_4$–$ZnSO_4$ solutions, which model technological solutions used reprocessing of copper-containing raw materials and spent copper–zinc catalysts. The initial solutions contained (mol dm^{-3}): $CuSO_4$ 0.2, H_2SO_4 0.1–2.0, and $ZnSO_4$ 0–0.8. The cementation was performed on a disc-shaped zinc electrode 30 mm in diameter in a thermostated vessel containing 0.2 dm^3 of the solution, in the temperature range 20–60°C under constant agitation. The disc was situated at the vessel bottom, with its working face upwards. The electrodes were trimmed with a fine emery paper and degreased with alcohol prior to each test. In the course of cementation, the solutions were sampled at regular intervals of time for analysis by the standard iodometric method for the content of copper. After the contact deposition of copper was complete, the dispersed powder was washed with a 0.1 N H_2SO_4 solution, water, and ethanol, and then dried in a vacuum. The morphology of the copper powders obtained was studied with a JEOL T-20 scanning electron microscope.

The results of the study show that, at the initial concentration of 0.2 mol dm^{-3} $CuSO_4$, the morphology of the copper deposits obtained by the contact method depends on the H_2SO_4 concentration. It was established that the dispersity of the copper powder grows with increasing acidity. At the same time, no influence of indifferent ions and, in particular, Zn^{2+} on the dispersity of copper deposits was revealed up to a $ZnSO_4$ concentration of 0.8 mol dm^{-3}.

Under the given cementation conditions, the primary structural units of the cement deposit are globular particles, which form conglomerates with varied spa-

1070-4272/03/7612-1942 $25.00 © 2003 MAIK "Nauka/Interperiodica"

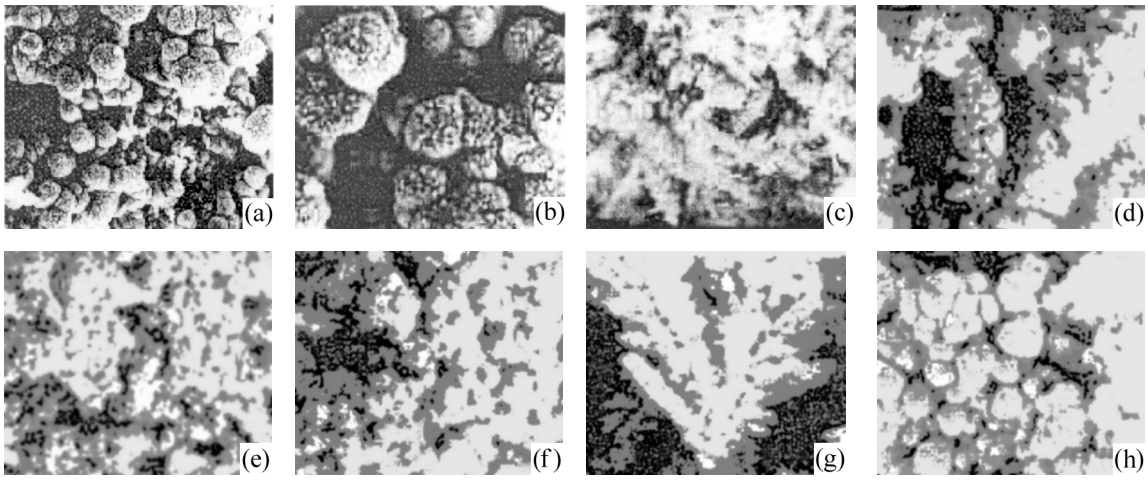

Fig. 1. Electron micrographs of copper powders deposited by the contact method onto zinc in a 0.2 M $CuSO_4$ solution of various compositions. H_2SO_4 concentration (mol dm^{-3}): (a, b) 0.25, (c, d, g, h) 0.5, and (e, f) 2.0. Temperature (°C): (a–f) 2 and (g, h) 50. Magnification: (a, c, e) 1000, (b) 2000, and (d, f–h) 3000.

tial structure (Fig. 1). The size of the primary particles depends on the ratio of rates of nucleation and growth of crystalline copper nuclei, which to a certain extent correlates with the content of H_2SO_4 in solution. With increasing sulfuric acid concentration, the contribution of the conjugate reaction of hydrogen evolution becomes more pronounced. As a result, the degree of surface blocking by hydrogen increases, thus making slower the growth rate of nuclei of the metal being deposited. In addition, the intensified hydrogen evolution facilitates renewal of the surface of zinc owing to a decreased adhesion of the cement deposit to the metal. Hence, with increasing acidity, the rate of nucleation becomes higher, whereas the rate of nucleus growth decreases. For example, at a H_2SO_4 concentration of 2 mol dm^{-3} the particle size does not exceed 10 μm, whereas at the 0.25 mol dm^{-3} concentration, particles up to 40 μm in diameter are formed.

In the second stage, the globular particles, which are structural elements of the copper deposit formed in the first stage, are layered to form conglomerates as the second spatial step of formation of the cement deposit. Starting with the H_2SO_4 concentration of 0.5 mol dm^{-3}, growth of dendrite-like deposits is observed (Figs. 1c, 1d, and 1g), which can be related to the third stage of deposit formation. This can be accounted for by a considerable adsorption of H_3O^+ on the forming copper particles, with the subsequent electroreduction of hydrogen. As a result, the copper deposit, probably, grows as in the case of electrolysis in the mode of deposition of a dispersed copper powder [2]. In deformation, the forming dendrites are easily disintegrated into conglomerates of the second stage.

It is clearly seen that the primary structural elements decrease in size as the cement deposit grows (Figs. 1c, 1d, 1g, and 1h). This is due to a decrease in the concentration of copper ions in the course of cementation.

It was established that the size of the primary structural elements decreases somewhat with increasing temperature, which can be accounted for by the acceleration of hydrogen electroreduction on the copper being deposited. At the same time, no strong effect of temperature on the spatial form of the cement deposits was observed.

The acid concentration also strongly affects the kinetic properties and the process parameters in obtaining a copper powder in purification of zinc sulfate solutions. With the H_2SO_4 concentration increasing to 2 mol dm^{-3}, the cementation rate becomes faster (Fig. 2a), and the process duration, shorter (see table). This is due to the increasing share of the conjugate reaction of hydrogen reduction. This, firstly, facilitates the diffusion of the electrolyte toward the surface of zinc; secondly, makes larger the area of the cementing metal, owing to the appreciable etching of its surface; and, thirdly, prevents formation of an insoluble film of the $xZnSO_4 \cdot Zn(OH)_2$ salt of variable composition on this surface.

The dispersed powder deposited by the contact method in the form of small conglomerates is easily detached from the zinc surface, which also ensures

Rate V, cementation time τ, and specific yield of copper powder by zinc, SY^{*}_{Cu}, at various concentrations of H_2SO_4 and $ZnSO_4$ and temperatures (initial concentration of $CuSO_4$ 0.2 mol dm^{-3})

Test no.**	T, °C	$[H_2SO_4]$, mol dm^{-3}	$V \times 10^3$, mol dm^{-3} min^{-1}	τ, min	SY_{Cu}, mol %
1	20	0.25	3.2	90	88
2	20	0.5	4.7	78	69
3	20	0.5	3.9	83	74
4	20	1.0	6.7	70	43
5	20	2.0	7.4	45	33
6	20	3.0	7.1	42	27
7	30	0.5	4.8	75	59
8	40	0.5	5.1	70	53
9	50	0.5	7.0	72	52
10	50	0.5	6.9	60	58
11	60	0.5	6.9	60	55

* $SY_{Cu} = (\nu_{Cu}/\nu_{Zn}) \times 100$, where ν_{Cu} and ν_{Zn} are the number of moles of copper deposited by the contact method and of dissolved zinc, respectively.

** Solution used in test nos. 3 and 10 contained (mol dm^{-3}): H_2SO_4 0.5 and $CuSO_4$ 0.8.

a large working area of the cementing metal. At the same time, the specific yield of the copper powder considerably decreases with increasing sulfuric acid concentration (table).

With increasing temperature, the cementation rate grows to reach its maximum value at 50°C, with the subsequent deceleration of the process. The time of complete cementation (see table, Fig. 2) decreases to the minimum value at 50°C. This is associated with the increasing rate of the chemical reaction of zinc with H_2SO_4.

The presence of $ZnSO_4$ somewhat hinders cementation at 20°C (Fig. 2a, curve *3*). However, this effect manifests itself to a lesser extent at higher temperatures, and is not virtually observed at 50°C (Fig. 2b, curve *6*). The inhibiting effect of indifferent ions at their high concentrations is due to electrostatic repulsion forces [5]. Analysis of the results obtained shows that the effect of indifferent zinc ions is mainly compensated for by etching of the surface of the cementing metal, i.e., by a sharp increase in the active surface area.

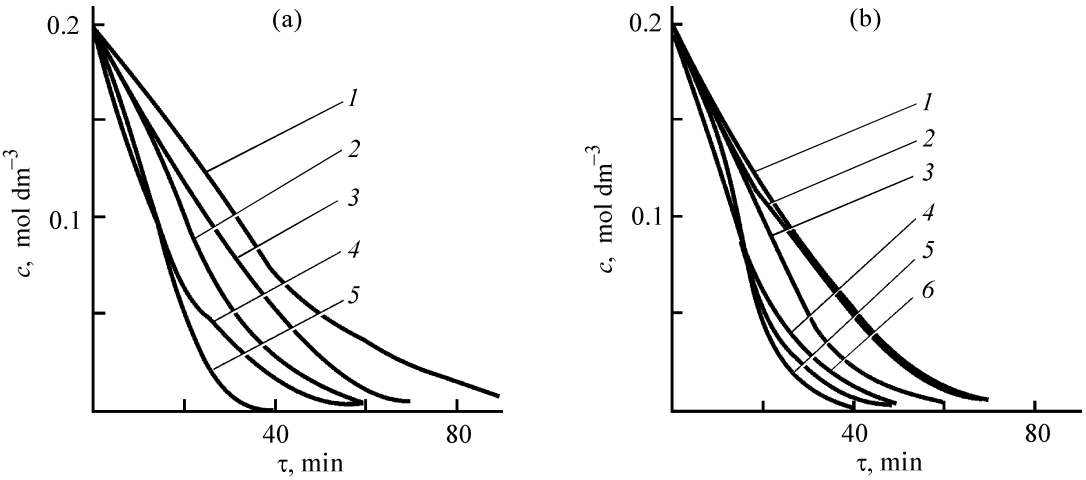

Fig. 2. Influence of (a) H_2SO_4 concentration and (b) temperature on the kinetics of contact deposition of copper onto zinc in a 0.2 M $CuSO_4$ solution of various compositions. (c) Concentration of Cu^{2+} ions in solution and (τ) time. (a) Temperature 20°C. H_2SO_4 concentration (mol dm^{-3}): (*1*) 0.25, (*2, 3*) 0.5, (*4*) 1.0, and (*5*) 2.0. $ZnSO_4$ concentration (mol dm^{-3}): (*1, 2, 4, 5*) 0, and (*3*) 0.8. (b) H_2SO_4 concentration 0.5 mol dm^{-3}. Temperature (°C): (*1*) 20, (*2*) 30, (*3*) 40, (*4, 6*) 50, and (*5*) 60. $ZnSO_4$ concentration (mol dm^{-3}): (*1–5*) 0 and (*6*) 0.8.

CONCLUSIONS

(1) The cementation of copper on zinc from H_2SO_4–$CuSO_4$ and H_2SO_4–$CuSO_4$–$ZnSO_4$ technological solutions formed in processing of secondary copper- and copper–zinc-containing raw materials is suitable for obtaining finely dispersed copper powders.

(2) The optimal concentration of sulfuric acid is 0.5 mol dm^{-3}, with the $ZnSO_4$ content not limited. The temperature does not affect strongly the morphology of the dispersed copper powder within the range 20–50°C.

REFERENCES

1. Levina, D.A. and Chernyshev, L.I., *Poroshk. Metall.*, 2001, nos. 3/4, pp. 124–126.
2. Nichiporenko, O.S., Pomosov, A.V., and Naboichenko, S.S., *Poroshki medi i ee splavov* (Copper and Copper–Alloy Powders), Moscow: Metallurgiya, 1988.
3. Yavors'kii, V.T., Kalimon, Ya. A., Znak, Z.O., *et al., Sbornik nauchnykh statei k IV Mezhdunarodnoi nauchno-prakticheskoi konferentsii "Problemy sbora, pererabotki i utilizatsii otkhodov,"* (Proc. of the IV Int. Sci.-Pract. Conf. "Collection, Processing, and Utilization of Wastes"), Odessa: Odessk. Tsentr. Nauchn. Tekhn. Ekspl. Inst., 2002, pp. 234–235.
4. Pekhovech, V.A., Panteleev, V.N., and Godes, A.I., *Poroshk. Metall.*, 1967, no. 4, pp. 38–41.
5. Alkatsev, M.I., *Protsessy tsementatsii v tsvetnoi metallurgii* (Cementation in Nonferrous Metallurgy), Moscow: Metallurgiya, 1981.

Russian Journal of Applied Chemistry, Vol. 76, No. 12, 2003, pp. 1946–1950. Translated from Zhurnal Prikladnoi Khimii, Vol. 76, No. 12, 2003, pp. 1995–1999.

CATALYSIS

Use of Cobalt(II) Phthalocyanine Sulfonates in Gas Purification To Remove Hydrogen Sulfide

G. A. Faddeenkova and N. N. Kundo

Boreskov Institute of Catalysis, Siberian Division, Russian Academy of Sciences, Novosibirsk, Russia

Received August 12, 2002

Abstract—Experiments on liquid-phase oxidation of H_2S with oxygen in the presence of catalysts, cobalt phthalocyanine sulfonates [$CoPc(SO_3Na)_n$], were performed on a laboratory static installation in order to find conditions under which a stationary oxidation mode can be established at pH ≥ 8. The influence exerted by additional introduction of a soluble salt of Mn^{2+} ($MnSO_4$, $MnCl_2$) into the reaction mixture at various pH values was studied.

Cobalt(II) phthalocyanine sulfonates [$CoPc(SO_3Na)_n$] are active catalysts for liquid-phase oxidation of H_2S with oxygen [1–3], which can be successfully used in liquid oxidative processes for purification of various gases to remove hydrogen sulfide. Liquid oxidative methods for gas purification include H_2S absorption with an aqueous solution that contains an alkaline agent and a catalyst and catalytic oxidation of the thus caught H_2S with atmospheric oxygen.

In a weakly alkaline medium (pH 7.3–8.0), the absorbed H_2S, which is in the form of HS^- ions, is oxidized in the presence of $CoPc(SO_3H)_n$ at a high rate by the polysulfide mechanism [1]. The main oxidation products are elementary sulfur and thiosulfates [1]. HS^- ions are oxidized via redox transitions $Co(II)Pc(SO_3H)_n + HS^- \rightleftarrows Co(I)Pc(SO_3H)_n$ The oxidation mechanism is described by the scheme

$$Co(II)Pc(SO_3Na)_n + HS_n^- \rightarrow Co(I)Pc(SO_3Na)_n + HS_n^{\bullet} + H^+, \quad (1)$$

$$2HS_n^{\bullet} \rightarrow S_{2n}^{2-} + 2H^+, \quad (2)$$

$$2Co(I)Pc(SO_3Na)_n + 0.5O_2 + 2H^+ \rightarrow 2Co(II)Pc(SO_3Na)_n + H_2O, \quad (3)$$

$$HS^- + S_{2n}^{2-} \rightarrow HS_n^- + S_{(n+1)}^{2-}. \quad (4)$$

In alkaline solutions (pH > 11), HS^- ions are oxidized through oxygen activation via formation of [$Co(III)Pc(SO_3Na)_n \cdot O^{2-}$] complexes [4], i.e., via the redox transitions [1, 4, 5]

$$Co(II)Pc(SO_3Na)_n \rightleftarrows Co(III)Pc(SO_3Na)_n.$$

In this case, the catalyst activity is more than an order of magnitude lower [1], with sulfites and sulfates formed as a result of oxidation. It should be noted that, in gas purification to remove H_2S, it is important to obtain elementary sulfur, since it is easily separated from the absorbing solution.

At pH 8–11, lower rates of liquid-phase oxidation of H_2S are commonly observed in the presence of $CoPc(SO_3Na)_n$, compared with those at pH 7.3–8.0 and pH > 11. The rate of oxidation and the composition of the oxidation products formed at pH 8–11 are even affected by minor changes in the process parameters {pH value, presence of oxidation (semi)products, such as S^0 and SO_3^{2-} ions [6]}.

In gas purification to remove H_2S, it is necessary to maintain a stationary oxidation mode of oxidation of H_2S being caught. The purification process should be stable in an as wide fluctuation range of the purification process parameters as possible, and, primarily, it should be stable against accumulation of oxidation products and semiproducts.

The aim of this study was to find conditions that make it possible to establish a stationary mode of liquid-phase oxidation of H_2S with oxygen in the presence of catalysts $CoPc(SO_3Na)_n$ at pH 8–11, to select optimal oxidation conditions, and to perform test purification of petroleum gas to remove H_2S on a pilot installation.

EXPERIMENTAL

Experiments on liquid-phase oxidation of H_2S were performed on a static laboratory installation [6].

1070-4272/03/7612-1946 $25.00 © 2003 MAIK "Nauka/Interperiodica"

For the experiments, Na_2S and Na_2SO_3 solutions and solutions of the catalysts $Co(II)Pc(SO_3Na)_2$ and $Co(II)Pc(SO_3Na)_4$ were prepared. The content of Na_2SO_3 and $Na_2S_2O_3$ in the working solutions was determined by iodometry [7], and the concentration of the catalysts, cobalt(II) phthalocyanine sulfonates, by spectrophotometry [6]. The pH value of a solution being oxidized was maintained constant by introducing a phosphate buffer solution.

The rate of NaHS oxidation in the static installation was determined volumetrically from the oxygen absorption, and also from changes in the iodometrically found concentration of NaHS in the reaction mixture [7]. The completion of NaHS oxidation was indicated both by termination of oxygen absorption and by the absence of HS^- ions in the reaction mixture, which was determined using lead indicator paper [8]. The content of oxidation products, Na_2SO_3 and $Na_2S_2O_3$, in the reaction mixture was found iodometrically [7]. The presence of elementary sulfur in the oxidation products in the static installation was determined visually, and the amount of sulfur formed, spectrophotometrically [9]. The overall balance of oxidation products in the static installation correlated with the amounts of oxidized NaHS and oxygen consumed for oxidation.

The concentration of H_2S in an unpurified petroleum gas was found by means of chromatography. The absence of H_2S in a purified gas was established visually, using a lead indicator paper moistened with water and placed in the gas flow [8]. The content of the products formed in oxidation of the H_2S caught, Na_2SO_3 and $Na_2S_2O_3$, was determined iodometrically [7], and the absence of Na_2SO_4 in the absorbing solution was established using $BaCl_2$ [10]. The content of elementary sulfur in the absorbing solution was found spectrophotometrically [9], and the concentration of soda ($NaHCO_3$ + Na_2CO_3), by titration with sulfuric acid [11]. The overall balance of the amount of products formed in oxidation of the H_2S caught in the absorbing solution correlated with the total amount of H_2S caught by the installation for purification of petroleum gas to remove H_2S.

Figures 1a and 1b show the results of experiments on liquid-phase oxidation of H_2S in the presence of catalysts, $CoPc(SO_3Na)_2$ and $CoPc(SO_3Na)_4$, at pH 8.0 and 10.2, performed on the static installation.

As can be seen from Fig. 1a, introduction of already a second portion of the substrate results in that the process becomes steady-state, being characterized by rather high oxidation rate [especially in the presence of $CoPc(SO_3Na)_4$]. In the experiments with

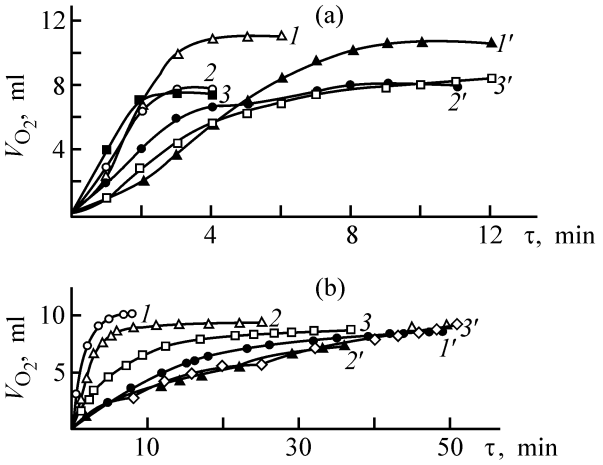

Fig. 1. Kinetics of liquid-phase oxidation of H_2S with oxygen in the presence of a catalyst, (*1–3*) $CoPc(SO_3Na)_4$ or (*1'–3'*) $CoPc(SO_3Na)_2$ at pH value of (a) 8.0 and (b) 10.2. T = 25°C, P_{O_2} = 101 kPa, V_Σ = 20 ml, $[CoPc(SO_3Na)_n]$ = 5 mg l^{-1}. (V_{O_2}) Oxygen volume and (τ) process duration; the same for Figs. 2–4. Concentration $[H_2S]_0$ (M): (*1*, *1'*) 2.4×10^{-2}, (*2*, *2'*) 4.8, and (*3*, *3'*) 7.2.

the initial concentration of H_2S (curves *1* and *1'*), the main oxidation product was $Na_2S_2O_3$ and, in part, elementary sulfur. The increase in the oxidation rate and sulfur yield upon repeated introduction of the substrate being oxidized into the oxidized reaction mixture (curves *2* and *2'*) is due to the fact that the elementary sulfur formed in the initial experiments maintains a high concentration of polysulfide ions in the reaction mixture through the reaction

$$HS^- + (n - 1)S^0 = HS_n^-. \quad (5)$$

The high running concentration of polysulfide ions in the reaction mixture favors the liquid-phase oxidation of H_2S by the polysulfide mechanism. The yield of S^0 in NaHS oxidation is about 60%, and that of $Na_2S_2O_3$, approximately 40% (curves *2* and *2'*). The kinetic curves *2*, *3* and *2'*, *3'*, which describe liquid-phase oxidation of H_2S, are very close. This is accounted for by the fact that the oxidation products S^0 and $Na_2S_2O_3$, which are accumulated in the solution, have no inhibiting effect on the liquid-phase oxidation of H_2S [6]. Thus, a stationary mode of liquid-phase oxidation of H_2S in the presence of catalysts, cobalt(II) phthalocyanine sulfonates $CoPc(SO_3Na)_n$, is ensured at pH 8.0.

The process of liquid-phase oxidation of H_2S at pH 10.2 (Fig. 1b) does not become steady-state upon repeated charging of the substrate: the time of oxida-

Table 1. Calculated equilibrium compositions of an absorbing solution of soda in purification of an H_2S-containing gas ($[H_2S] = 0.3$, $[CO_2] = 2.5$ vol %; $P_{gas} = 101$ kPa)

pH value	Concentration, M			
	$NaHCO_3$	Na_2CO_3	NaHS	Na_2S
8.0	3.17×10^{-2}	1.47×10^{-4}	2.22×10^{-3}	1.6×10^{-7}
8.5	0.100	1.47×10^{-3}	7×10^{-3}	1.6×10^{-6}
9.0	0.317	1.47×10^{-2}	2.22×10^{-2}	1.6×10^{-5}
9.5	1.00	0.147	0.07	1.6×10^{-4}
10.0	3.17	1.47	2.22×10^{-1}	1.6×10^{-3}

tion increases upon introduction of each subsequent portion of the substrate into the reaction mixture. The elementary sulfur formed in the initial experiment (curve *1*) dissolves afterwards (curves *2* and *3*): in runs with the $CoPc(SO_3Na)_2$ catalyst, no sulfur was formed at all. At pH 10.2, an intermediate oxidation mechanism is operative [4], in which a major part of polysulfide ions formed in reactions (1)–(4) is noncatalytically oxidized to SO_3^{2-} ions. Sulfite ions accumulated in the absorbing solution increasingly disrupt the polysulfide oxidation mechanism by decomposing the sulfide ions:

$$(n - 1)SO_3^{2-} + HS_n^- = (n - 1)S_2O_3^{2-} + HS^-. \quad (6)$$

In the experiments performed at pH 10.2, the liquid-phase oxidation of H_2S did not become steady-state. Therefore, absorbing solutions of this composition cannot be recommended for use in gas purification to remove hydrogen sulfide.

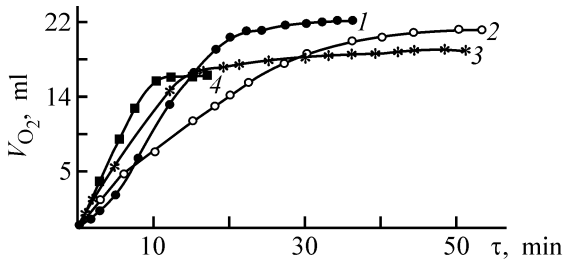

Fig. 2. Kinetics of oxidation with oxygen of alkaline aqueous solutions of NaHS in the presence of catalysts, $CoPc(SO_3Na)_2$, $CoPc(SO_3Na)_4$, and $MnSO_4$. $T = 25°C$, $P_{O_2} = 101$ kPa, pH 11.3, $V_\Sigma = 20$ ml, $[H_2S]_0 = 2.4 \times 10^{-2}$ M. Concentration (M): (*1*) $[MnSO_4] = 0.5 \times 10^{-3}$, (*2*) $[CoPc(SO_3Na)_2] = 10$, (*3*) $[CoPc(SO_3Na)_4] = 10$; (*4*) $[CoPc(SO_3Na)_4] = 10$ mg l^{-1}, $[MnSO_4] = 0.5 \times 10^{-3}$ M.

The disodium salt of disulfonic acid of cobalt phthalocyanine, $CoPc(SO_3Na)_2$, is used in air purification to remove H_2S [12, 13]. In this case, a sufficient capacity of a weakly alkaline absorbing solution for H_2S is ensured both by the alkalinity of the absorbing solution and by the high activity of the catalyst $CoPc(SO_3Na)_2$. In purification of oxygen-free gases, the capacity of the absorbing solution for sulfur depends solely on the alkalinity of the absorbing solution. Table 1 lists calculated equilibrium compositions of a soda solution at various pH values of the solution in purification of a gas containing H_2S.

As follows from the data in Table 1, raising the pH of the absorbing solution from 8.0 to 10.0 leads to an increase in the equilibrium content of H_2S being caught in the absorbing solution by two orders of magnitude (H_2S is present in solutions at pH 8–10 mainly as HS^- and S^{2-} ions). Therefore, it is necessary to use absorbing solutions with the highest possible pH value in purification of oxygen-free gases to remove H_2S with $CoPc(SO_3Na)_n$. Consequently, it is important to select the conditions at which H_2S is oxidized in solutions with the highest possible pH value in the stationary mode by the polysulfide mechanism, to give elementary sulfur as a result of oxidation.

The process of liquid-phase oxidation of H_2S at pH 10.2 (Fig. 1b) does not become steady-state because of the accumulation of the oxidation semiproduct Na_2SO_3 in the absorbing solution. To pass to a stationary oxidation mode, it is necessary to restrict the accumulation of SO_3^{2-} ions in the reaction mixture.

It is known that manganese compounds are active catalysts for liquid-phase oxidation of H_2S and oxidation of sulfite ions to sulfate ions. In this study, it is suggested to introduce soluble Mn^{2+} salts into the reaction mixture in addition to the $CoPc(SO_3Na)_n$ catalyst.

Figure 2 shows data on oxidation of alkaline aqueous solutions of NaHS with oxygen in the presence of the $CoPc(SO_3Na)_2$, $CoPc(SO_3Na)_4$, and $MnSO_4$ catalysts.

Addition of Mn_2^+ salts to the $CoPc(SO_3Na)_4$ catalyst (Fig. 2, curve *4*) makes shorter the time of complete NaHS oxidation, from 48 to 14 min. Also, the composition of the oxidation products is changed: the volume of oxygen consumed for complete oxidation of the reaction mixture decreases from 19.6 to 16.4 ml. In the simultaneous presence of $CoPc(SO_3Na)_4$ and $MnSO_4$, elementary sulfur is formed in NaHS oxidation. In the presence of only one of these catalysts, $MnSO_4$ (Fig. 3, curve *1*) or $CoPc(SO_3Na)_4$ (Fig. 3, curve *3*), no elementary sulfur is formed in NaHS oxidation.

Table 2. Results obtained in purification of petroleum gas on the pilot installation (amount of petroleum gas being purified 0.76 $m^3\ h^{-1}$, air flow rate 2.4 $m^3\ h^{-1}$, solution circulation rate 47 $l\ h^{-1}$, time of oxidative regeneration of solution 12.8 min, $MnCl_2$ concentration 80 $mg\ l^{-1}$, purified gas contains no H_2S, regenerated solution contains HS^- ions)

τ, min	H_2S content in unpurified gas, vol %	Amount of H_2S caught by 1 l of solution, g	Solution pH		Content of indicated substance in absorbing solution			
			after absorber	after regenerator	$NaHCO_3$, $g\ l^{-1}$	Na_2CO_3, $g\ l^{-1}$	$Na_2S_2O_3$, $g\ l^{-1}$	$CoPc(SO_3Na)_4$, $mg\ l^{-1}$
135	2.34	0.57	8.4	8.8	14.9	4.77	111	22
495	1.36	0.38	8.8	9.0	10.8	5.3	102	22
180	1.63	0.4	8.6	9.0	–	–	–	–
505	2.55	0.64	8.5	8.8	6.89	4.62	108	8.0
960	1.99	0.49	8.7	8.9	6.84	3.68	112	8.4

Figures 3 a 4 show the kinetic curves obtained in experiments on NaHS oxidation in the presence of $MnSO_4$ and $CoPc(SO_3Na)_4$ catalysts at pH 11.0 and 11.85, respectively. In these experiments, the stage of oxidative regeneration of the absorbing solution was simulated by multiple introduction of the substrate into an oxidized solution.

At pH 11.0 and 11.85, the process of liquid-phase oxidation of H_2S becomes steady-state already after a second introduction of the substrate. The main oxidation products are elementary sulfur and thiosulfates. Thus, simultaneous use of two catalysts, $CoPc(SO_3Na)_4$ and Mn^{2+}, must ensure a stationary mode of liquid oxidative purification of oxygen-free gases to remove H_2S.

Petroleum gas was purified to remove H_2S by the liquid oxidative method on the pilot installation. The initial absorbing solution contained $CoPc(SO_3Na)_4$ and $MnCl_2$ catalysts, and also sodium thiosulfate, carbonate, and bicarbonate.[1]

The gas to be purified was fed into the bottom part of an absorber packed with iron chips and was washed there in the counterflow mode with the absorbing solution.

The gas purified to remove H_2S was directed from the upper part of the absorber through a spray catcher to the flare, and the absorbing solution saturated with hydrogen sulfide was delivered to the bottom part of the regenerator, an apparatus with a continuous bubbling bed. In the regenerator, air was bubbled through the solution and the H_2S caught was oxidized. The regenerated solution was delivered from the upper part of the regenerator to the upper part of the absorber. The elementary sulfur formed as a a result of oxidation was floated to the solution surface in the regenerator and was removed therefrom as sulfur foam.

Table 2 presents the results obtained in purification of petroleum gas to remove H_2S with $CoPc(SO_3Na)_4$ and $MnCl_2$ catalysts.

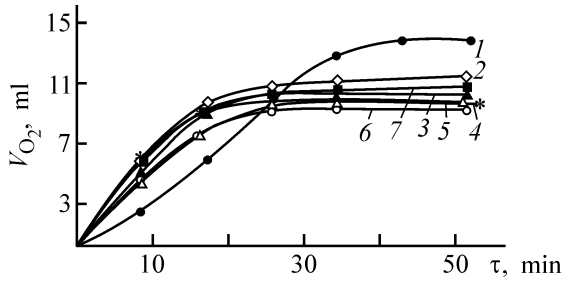

Fig. 3. Kinetics of NaHS oxidation with oxygen in the presence of $CoPc(SO_3Na)_4$ and $MnSO_4$ catalysts. T = 25°C, P_{O_2} = 101 kPa, pH 11.0, V_Σ = 20 ml, $[CoPc(SO_3Na)_4]$ = $10^{-2}\ mg\ l^{-1}$, $[MnSO_4]$ = 0.5×10^{-3} M. (*1*) $[NaHS]_0$ = 2.4×10^{-2} M, (*2–7*) reaction mixture after the preceding experiment, into which NaHS was introduced in amount equal to its initial content in the reaction mixture.

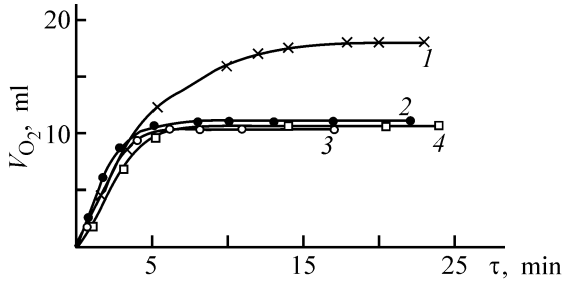

Fig. 4. Kinetics of oxidation of aqueous alkaline solutions of NaHS with oxygen in the presence of $CoPc(SO_3Na)_4$ and $MnSO_4$ catalysts. T = 25°C, P_{O_2} = 101 kPa, pH 11.85, V_Σ = 20 ml, $[CoPc(SO_3Na)_4]$ = $10\ mg\ l^{-1}$, $[MnSO_4]$ = 0.5×10^{-3} M. (*1*) $[NaHS]_0$ = 2.4×10^{-2} M, (*2–4*) reaction mixture after the preceding experiment, into which NaHS was introduced in amount equal to its initial content in the reaction mixture.

[1] The tests were performed by staff members of the VNIPIgazpererabotka Institute (Krasnodar) with participation of one of the authors of this paper.

It follows from the data in Table 2 that complete gas purification was observed at sufficiently high loads in terms of H_2S to be purified (up to 0.6 g H_2S l^{-1}). At solution pH 8.4–9.0, the purification mode was stable. The yield of sulfur was about 90%.

CONCLUSIONS

(1) It was shown that the process of liquid oxidative purification of oxygen-free gases to remove H_2S with cobalt phthalocyanine sulfonates as catalysts is stable if accumulation of SO_3^{2-} ions in the absorbing solution is prevented.

(2) If manganese chloride $MnCl_2$ was used, together with the $CoPc(SO_3Na)_4$ catalyst, on a pilot installation, petroleum gas containing 1.4 to 2.6 vol % H_2S was completely purified to remove H_2S. In this case, the capacity of the absorbing solution for H_2S was up to 0.6 g l^{-1}, with the yield of elementary sulfur obtained in the process of purification equal to about 90%.

REFERENCES

1. Kundo, N.N. and Keier, N.P., *Kinet. Kataliz*, 1970, vol. 11, no. 1, pp. 91–99.
2. Simonov, A.D., Keier, N.P., Kundo, N.N., *et al.*, *Kinet. Kataliz*, 1973, vol. 14, no. 4, pp. 988–992.
3. Stuchinskaya, T.L., Maizlish, V.E, Kundo, N.N., and Smirnov, R.P., *Zh. Prikl. Khim.*, 1993, vol. 66, no. 5, pp. 1039–1043.
4. Abel, E.W., *Chem. Commun.*, 1971, no. 9, pp. 449–450.
5. Wagnerova, D.M., Schwertnerova, E., and Veprek-Šišska, J., *Coll. Czech. Chem. Commun.*, 1974, vol. 39, no. 8, pp. 1980–1988.
6. Faddeenkova, G.A. and Kundo, N.N., *Zh. Prikl. Khim.*, 1979, vol. 52, no. 10, pp. 2161–2165.
7. Karyakin, Yu.V. and Angelov, I.I., *Chistye khimicheskie veshchestva* (Pure Chemical Substances), Moscow: Khimiya, 1974.
8. *TU* (Technical Specification) *2061–49, Lead Indicator Paper*.
9. Lazarev, V.I. and Kostrikov, V.I., *Zh. Anal. Khim.*, 1970, vol. 25, no. 3, pp. 553–555.
10. Kreshkov, A.P., *Osnovy analiticheskoi khimii* (Fundamentals of Analytical Chemistry), Moscow: Khimiya, 1976, vol. 1, 4th ed.
11. Kreshkov, A.P., *Osnovy analiticheskoi khimii* (Fundamentals of Analytical Chemistry), Moscow: Khimiya, 1970, vol. 2, 3rd ed.
12. Vasilevskaya, L.S. and Golyand, S.M., *Zh. Prikl. Khim.*, 1978, vol. 51, no. 8, pp. 1887–1889.
13. Rybakov, L.A., Afanas'ev, Yu.M., Shimko, I.G., and Chinennaya, S.K., *Khim. Volokna*, 1984, no. 6, pp. 12–14.

Russian Journal of Applied Chemistry, Vol. 76, No. 12, 2003, pp. 1951–1954. Translated from Zhurnal Prikladnoi Khimii, Vol. 76, No. 12, 2003, pp. 2000–2003.

ENVIRONMENTAL PROBLEMS OF CHEMISTRY AND TECHNOLOGY

Cationic Polymers as Organic Coagulants in Water Treatment at Heat and Electric Power Plants

V. F. Kurenkov, E. L. Gogolashvili, I. V. Molgacheva, and A. I. Gaisina

Kazan State Technological University, Kazan, Tatarstan, Russia

Tatarenergo Joint-Stock Company, Kazan, Tatarstan, Russia

Energoprogress Engineering Center, Kazan, Tatarstan, Russia

Received June 2, 2003

Abstract—The efficiency of water treatment with organic coagulants (cationic polymers) and calcium hydroxide (alkalizing agent) in combination with iron(II) sulfate (mineral coagulant) was studied as influenced by the nature and concentration of an organic coagulant and concentration of a mineral coagulant.

Coagulation treatment of natural water to remove coarse and colloidal admixtures is an important stage of water pretreatment at heat and electric power plants (HEPPs). Pretreatment is usually performed with various salts of Al(III), Fe(II), and Fe(III) (mineral coagulants); for simultaneous water softening, this process is often combined with liming [$Ca(OH)_2$ is added to the treated water].

To intensify the treatment after liming and coagulation, natural water was treated with Praestol high-molecular-weight polyacrylamide flocculants [1]. The use of flocculants at the water-treatment installation the Kazan HEPP-2 improved the quality of water passed through ion-exchanging filters in further stages of water treatment and was economically efficient.

In the recent decades, organic polymeric coagulants have found increasing application; these water-soluble cationic polymers are mainly used for treatment of wastewater and more complete dehydration of precipitates. Positively charged macromolecules of organic coagulants interact with negatively charged pollutant particles in water, causing their destabilization and rapid flocculation to form coarser aggregates. Mineral coagulants are less expensive, but organic coagulants provide more efficient removal of colloidal and dispersed particles. It should be noted that, in the absence of mineral coagulants, the salt content in purified water would be lower, which, in turn, should decrease the load on the ion-exchange filters and the mineralization of wastewater. Moreover, the concentrations of organic coagulants required for water treatment are significantly smaller than those of mineral compounds; they can be used in a wide pH range and do not affect the acidity of the medium.

Organic coagulants for water treatment are widely used in the Republic of South Africa [2]. The long-time use of organic coagulants (Zetafloc LP526 polyamines) significantly improved the quality of drinking water and decreased its cost. Its has been found [2] that the best results are obtained in a narrow concentration range of organic coagulants, whereas the overcharge of a mineral coagulant does not affect the quality of purified water.

Good results have been obtained with Kemazur 4535 organic coagulant in the stage of water pretreatment at a water-desalinating electrodialysis installation of a cement plant in Tunisia [3]. The water fed into this installation was characterized by wide fluctuations of the content of colloidal and dispersed particles, and the optimal charge of the organic coagulant and flocculant substantially improved the quality of desalinated water and prolonged the service life of the filters. It should be noted that the organic coagulants are most widely used in North America, in contrast to Europe, where various inorganic coagulants are preferred [4].

Previously [5], we studied the water treatment with organic coagulants formed by degradation of high-molecular-weight cationic Praestols [copolymer of

1070-4272/03/7612-1951 $25.00 © 2003 MAIK "Nauka/Interperiodica"

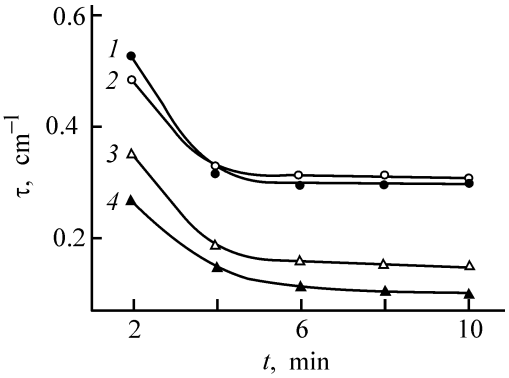

Fig. 1. Turbidity τ vs. the sedimentation time *t* of natural water in the presence of various coagulants. Concentrations: $Ca(OH)_2$ 3.0 mg-equiv l^{-1}, $FeSO_4$ 10 mg l^{-1}, and organic coagulant 1 mg l^{-1}. Coagulants: (*1*) $Ca(OH)_2$ + $FeSO_4$, (*2*) *1* + FL 15, (*3*) *1* + FL 28 P3, and (*4*) *1* + FL 45C.

acrylamide (AA) with *N*-acrylamidopropyl-*N*,*N*,*N*-trimethylammonium chloride (APTMAC)]. The resulting low-molecular-weight cationic Praestols improve the efficiency of water treatment, but comparison of their effect with that of water-soluble polymers of other classes, e.g., poly-2-hydroxypropylenedimethylammonium chlorides and polydiallyldimethylammonium chloride, is advisable.

In this study, we analyzed the performance of poly-2-hydroxypropylenedimethylammonium chlorides and polydiallyldimethylammonium chloride (organic coagulants) used in combination with calcium hydroxide in the presence and absence of iron(II) sulfate (mineral coagulant).

EXPERIMENTAL

In the tests, we used cationic poly-2-hydroxypropylenedimethylammonium chlorides FL 15 (M_η = 7×10^4) and FL 28 P3 (M_η = 4×10^5) and polydiallyldimethylammonium chloride FL 45C [M_η = $(1–3) \times 10^5$] purchased from SNF FLOERGER company (France):

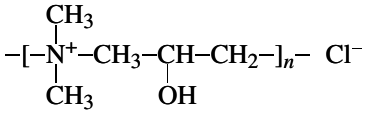

(FL 15; FL 28 P3)

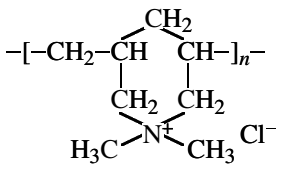

(FL 45C)

Iron(II) sulfate $FeSO_4 \cdot 7H_2O$ [technical-grade green vitriol, GOST (State Standard) 6981–75] and a saturated solution of construction lime $Ca(OH)_2$ (GOST 9179–77) were used as coagulants. The initial and purified water was analyzed using chemically pure and analytically pure grade reagents; all solutions were prepared in distilled water. The experiments were performed using river water samples taken at the water scoop of the Kazan HEPP-2 (total hardness 3.8 mg-equiv l^{-1}, alkalinity 2.4 mg-equiv l^{-1}, permanganate oxidizability (PO) 11.0–17.3 mg O l^{-1}, and total content of iron 159–240 mg l^{-1}).

The coagulation tests were carried out by the standard procedure [6] and by sedimentation analysis, using an LAM-1 laboratory turbidity analyzer [7]. The optimal charges of $Ca(OH)_2$ and $FeSO_4$ solutions were calculated in conformity with regulations [6]. The tests were performed as follows. First, natural water samples (150 cm^3) were placed in cylinders with ground-glass stoppers, and then the reagents were added in the following order: $Ca(OH)_2$ solution, mineral coagulant, and, finally, organic coagulant. All the reagents were added successively at 1-min intervals. Then the mixture was agitated by carefully mixed turning-over the cylinder five times (to preserve the sludge structure), poured into a cylindrical optical cell, and the variation of the optical density of the resulting suspension with time was recorded. The measurements were carried out in the same cylinder at a depth of 90 mm from the surface (λ 670 nm, *l* 35.2 mm).

First, we analyzed the effect of organic coagulants on the sedimentation of the disperse phase in natural water after its treatment with calcium hydroxide and mineral coagulant. Figure 1 shows how the water turbidity varies in the absence (curve *1*) and in the presence of various organic coagulants (curves 2–4). The tests were carried out at constant concentrations of $Ca(OH)_2$, $FeSO_4$, and polymers. As seen, the turbidity of water considerably decreases upon addition of organic coagulants owing to intensive sedimentation of the dispersed particles. Comparison of the data of Fig. 1 at τ = const shows that the effect on the suspension clarification increases in the order FL 15 < FL 28 P3 < FL 45C (passing from curve *2* to curve *4*, Fig. 1).

A chemical analysis of the initial and purified water showed that organic polymers do not affect the pH and hardness of water being treated, and only PO values and iron content decrease. Therefore, we evaluated the effect of organic coagulants on the removal of iron compounds and natural organic compounds from natural water. The total content of organic compounds and iron in water was determined from the PO

values (mg O l^{-1}) and by photometry, respectively. The analyses of the initial and clarified water were performed using the known procedures [8]. The effect of the concentration of the organic coagulants on the PO values and content of iron in water is illustrated in Tables 1 and 2, respectively. As seen from these data, the efficiency of water treatment increases with increasing concentration of the organic coagulant. It should be noted that the content of organic and iron compounds decreases even with small additions of organic coagulants.

We also compared the results of water treatment upon substitution of the mineral compound with organic coagulant at optimal and decreased concentrations of iron(II) sulfate. The optimal charge of iron(II) sulfate of 40 mg l^{-1} was determined by analysis of the initial water and confirmed by special coagulation tests. The results obtained are listed in Table 3. It can be seen that lowering the charge of iron(II) sulfate from 40 to 10 mg l^{-1} leads to a decrease in the efficiency of water treatment, i.e., the content of residual iron in the treated water grows. Upon substitution of the mineral coagulant with FL 54C, the efficiency of water treatment improves, this organic coagulant provides more complete removal of organic compounds and iron from water as compared with the effect of the mineral coagulant at its optimal charge of 40 mg l^{-1}.

Figure 2 shows the effect of FL 45C organic flocculant on PO (curve *1*) and content of iron compounds (curve *2*). These parameters of the water treatment efficiency upon addition of the optimal charge (40 mg l^{-1}) of the mineral coagulant are 58 and 69% of the initial values, respectively. As seen from Fig. 2, addition of even insignificant amounts of organic coagulant provides better purification of water as compared with the mineral coagulant.

Our experimental data show that the mineral coagulant $FeSO_4$ can be replaced with with an organic coagulant in pretreatment of water at heat and electric power plants. In this case, use of water-soluble cationic polymers FL 15, FL 28 P3, and FL 45C not only provides more complete removal of impurities but also decreases the salt content in the wastewater. For example, at $FeSO_4$ concentration of 40–50 mg l^{-1}, the content of sulfate ions in water increases by 5–20 g m^{-3}. Moreover, we should remember that, in the flood period, the coagulant is usually taken in a double amount, which increases the pollution of water with sulfate ions. In the subsequent stages of water pretreatment, the ion-exchange filters sorb the sulfate anions, but in the course of filter regeneration they pass into wastewater. Thus, use of organic coagulants significantly decreases the salt content in wastewater and improves the environmental situation at wastewater discharge sites.

Table 1. Oxidizability PO of the clarified water as influenced by the concentration of organic coagulants, c_{oc} ($FeSO_4$ 10 mg l^{-1}, PO of initial water 8.48 mg O l^{-1})

Polymer brand	PO (% of the initial value) at indicated c_{oc}, mg l^{-1}				
	0	0.1	1.0	5.0	10.0
FL 15	81	81	65	62	53
FL 28 P3	81	52	50	47	41
FL 45C	81	61	61	36	41

Table 2. Content of iron in the clarified water as influenced by the concentration of organic coagulants c_{oc} ($FeSO_4$ 10 mg l^{-1}, total content of iron compounds in initial water 198 mg l^{-1})

Polymer brand	Iron concentration (% of the initial value) at indicated c_{oc}, mg l^{-1}				
	0	0.1	1.0	5.0	10.0
FL 15	78	55	55	44	53
FL 28 P3	78	64	56	35	27
FL 45C	78	66	52	34	42

Table 3. Efficiency of water treatment with mineral ($FeSO_4$) and organic (FL 45C) coagulants (initial water: PO 14.8 mg O l^{-1} and iron content 204 mg l^{-1})

Charge, mg l^{-1}		Purified water	
$FeSO_4$	FL 45C	PO, % of the initial	Fe_{tot}, % of the initial
40	–	58	69
10	–	52	99
–	5	32	27

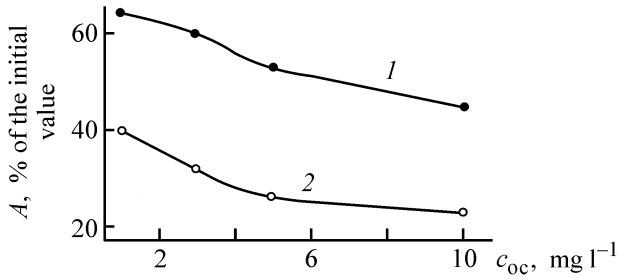

Fig. 2. Quality parameters of clarified water, A: (*1*) permanganate oxidizability and (*2*) total iron content, vs. the concentration of FL 45C organic coagulant, c_{oc}. $Ca(OH)_2$ content 3.0 mg-equiv l^{-1}.

CONCLUSIONS

(1) Poly-2-hydroxypropylenedimethylammonium chlorides FL 15 and FL 28 P3 and polydiallyldimethylammonium chloride FL 45C can be used as effective organic coagulants in the stage of water pretreatment at heat and electric power plants.

(2) The turbidity of water and the content of organic impurities and iron compounds in water decrease upon its treatment with organic coagulants in combination with calcium hydroxide both with and without iron(II) sulfate mineral coagulant.

REFERENCES

1. Kurenkov, V.F., Gogolashvili, E.L., Saifutdinov, R.R., *et al., Zh. Prikl. Khim.*, 2001, vol. 74, no. 9, pp. 1551–1554.
2. Nozaic, D.J., Freese, S.D., and Thompson, P., *Water Sci. Technol. Water Supply*, 2001, vol. 1, pp. 43–50.
3. Bouguecha, S. and Dhahbi, M., *Desalination*, 2002, vol. 151, pp. 75–86.
4. Shelley, S.A., *Chem. Eng. (USA)*, 1997, vol. 104(6), pp. 63–64, 66.
5. Kurenkov, V.F., Gogolashvili, E.L., Molgacheva, I.V., *et al., Zh. Prikl. Khim.*, 2003, vol. 76, no. 5, pp. 800–803.
6. *Rukovodyashchie ukazaniya po izvestkovaniyu vody na elektrostantsiyakh* (Master Guideline on Liming of Water at Heat and Electric Power Plants), Moscow: STsNTI, 1973.
7. Kurenkov, V.F., Gogolashvili, E.L., and Isakov, A.A., in *Struktura i dinamika molekulyarnykh sistem: Sbornik statey* (Structure and Dynamics of Molecular Systems: Collection of Papers), Ioshkar-Ola: 2001, issue 8, part 2, pp. 116–120.
8. *Unifitsirovannye metody analiza vod* (Standard Methods of Water Analysis), Lur'e, Yu.Yu., Ed., Moscow: Khimiya, 1973.

Russian Journal of Applied Chemistry, Vol. 76, No. 12, 2003, pp. 1955–1957. Translated from Zhurnal Prikladnoi Khimii, Vol. 76, No. 12, 2003, pp. 2004–2007.

ORGANIC SYNTHESIS AND INDUSTRIAL ORGANIC CHEMISTRY

Base-Catalyzed Autocondensation of Cyclohexanone

P. K. Trakhanov, V. S. Kruk, and Yu. V. Maksimuk

Research Institute of Physicochemical Problems, Belarussian State University, Minsk, Belarus

Received May 6, 2003

Abstract—Autocondensation of cyclohexanone in air at 119–137°C, catalyzed with a solid alkali, was studied.

Cyclohexanone is an intermediate in industrial organic synthesis. Its characteristic feature is tendency to undergo autotransformations yielding a series of products [1]. In synthesis of caprolactam [2] and adipic acid [3], autocondensation is a side reaction, whereas in the first step of industrial synthesis of 2-phenylphenol (a bactericide) [4–6] or 2-cyclohexylcyclohexanol (a fragrance) [7], this is the principal process. To improve the existing processes involving cyclohexanone and develop new ones, it is appropriate to study the kinetic features of its autocondensation, primarily with the aim to obtain input data for simulation of flowsheets and process equipment.

The condensation is nonselective and yields a mixture of isomers; the resulting compounds with double bonds are not quite stable. Therefore, not all of the products of deep autocondensation of cyclohexanone have been identified. Compounds **I**–**III** have been studied in most detail [1, 8–10].

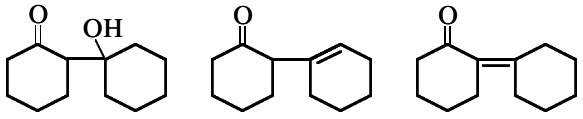

I **II** **III**

Formation of condensation products containing three and more rings was considered in [11–13]. The autocondensation is reversible, and, at elevated temperatures, compounds **II** and **III** are hydrolyzed back to cyclohexanone in the presence of water. The kinetic (in the range 180–290°C) and thermodynamic characteristics of this reaction, which is very important for processing by-products from caprolactam production [14], have been considered previously [15–17].

Data on liquid-phase autooxidation of cyclohexanone under various conditions are summarized in Table 1. It is seen that the major influence on the reaction rate is exerted by the temperature and catalyst. Virtually no data are available for the interval from 80 to 210°C in which the majority of industrial processes are performed. In this study, we examined the kinetics of cyclohexanone autocondensation in air at 119–137°C, catalyzed with a solid alkali.

EXPERIMENTAL

The kinetics of liquid-phase aldol condensation of cyclohexanone was studied in a laboratory installation consisting of a round-bottomed three-necked glass flask fully immersed in a thermostat with silicone oil.

Table 1. Kinetics of liquid-phase autocondensation of cyclohexanone

T, °C	Catalyst/solvent	Other conditions	Analytical method	References
25	Aqueous NaOH	Analysis of aqueous and organic layers	IR	[8]
30–70	Alcoholic or aqueous-alcoholic KOH	Preliminary purging with argon	^{1}H NMR	[9]
80	–/–	Under N_2,	GLC	[18]
	–/CCl_4	in the dark,		
	–/CCl_4 + DPPH*	with removal of water		
119–137	KOH(cr.)/–	In air, with removal of water	GLC	This work
210±0.5 (0.6 MPa)	Al, Fe oxides/decalin	Under N_2, without removal of water	GLC	[19]

* DPPH is 1,1-diphenyl-2-picrylhydrazyl (inhibitor of radical reactions).

1070-4272/03/7612-1955 $25.00 © 2003 MAIK "Nauka/Interperiodica"

Table 2. Kinetic study of base-catalyzed autocondensation of cyclohexanone

T, °C	τ, min	Cyclohexanone, wt %	Condensation products, wt %		
			II + III	**IV**	**V**
119	5	98.7	1.2	0.1	0.1
	10	96.9	2.9	0.1	0.1
	20	93.6	6.0	0.1	0.3
	40	90.9	8.6	0.2	0.3
	80	87.6	11.6	0.2	0.5
	160	84.2	14.7	0.5	0.6
125	5	98.1	1.8	0.1	0.1
	10	96.0	3.8	0.1	0.1
	20	92.1	7.5	0.2	0.2
	42	88.4	11.0	0.3	0.3
	84	85.0	14.5	0.5	0.5
	160	81.4	17.3	0.6	0.7
129	5	95.9	3.7	0.2	0.1
	10	92.7	6.9	0.2	0.3
	20	89.4	10.0	0.3	0.4
	40	85.8	13.0	0.5	0.5
	80	81.7	17.0	0.6	0.7
	160	76.7	21.4	0.9	0.9
133	5	95.0	4.0	0.2	0.1
	10	92.0	6.9	0.2	0.2
	20	88.5	11.3	0.3	0.3
	40	84.4	14.4	0.4	0.2
	80	79.0	18.2	0.6	0.5
	160	72.3	25.3	1.4	1.0
137	5	92.4	7.1	0.3	0.2
	10	90.2	9.3	0.2	0.3
	20	86.0	13.2	0.4	0.5
	40	79.6	18.7	0.8	0.8
	80	68.0	28.7	1.7	1.5
	160	56.0	38.2	3.5	2.4

The flask was equipped with a reflux condenser with a Dean–Stark trap, a high-speed glass stirrer with a glass hydroseal, and a control thermometer. The temperature in the flask was maintained with an accuracy of ±0.2°C.

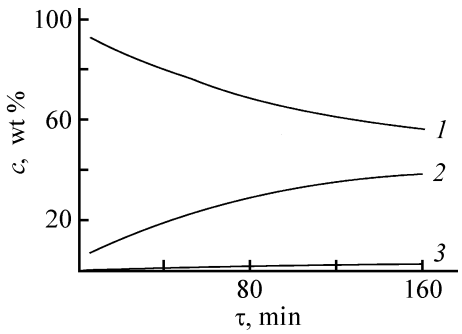

Fig. 1. Variation of the concentrations *c* of (*1*) cyclohexanone and of its condensation products (*2*) **II + III** and (*3*) **IV** with time τ at 137°C.

Five experiments were performed at 119, 125, 129, 133, and 137°C. The flask was charged with 240 ml of purified cyclohexanone (main substance content >99.5%), which was preliminarily kept at the experimental temperature for 40 min. Granulated KOH (chemically pure grade), 2.4 g, was added with vigorous stirring. The time of mixing of the alkali with cyclohexanone was considered to be the start of the process. Samples of the reaction mixture (2–3 ml) were taken with a glass syringe 5, 10, 20, 40, 80, and 160 min after the start of the reaction. The samples were transferred into glass test tubes containing 1-tetradecene (pure grade, distilled). The reaction in a withdrawn sample was stopped by rapid cooling. Preliminary experiments showed that change in the reactant concentrations after rapid cooling to –20°C was negligible.

The amount of water collected in the Dean–Stark trap was insignificant. The maximum amount was about 5 ml at the highest experimental temperature (137°C). Therefore, despite the fact that the distillate was an azeotropic mixture of water and cyclohexanone, changes in the amount of cyclohexanone in the flask were negligible.

Samples were analyzed by gas–liquid chromatography (GLC) on a Tsvet-800 device (flame ionization detector; 2000 × 3-mm steel column packed with Chromaton N-Super + 3% OV-1; column temperature schedule: 140°C, 25 min; heating to 190°C at a rate of 25 deg min^{-1}; 190°C, 35 min; vaporizer and detector temperatures 200°C; carrier gas nitrogen).

According to our results and those of Kim et al. [11], GLC makes it possible to determine the ratios of condensation products differing in the number of cyclohexane rings, but not the ratios of particular isomers, because the products undergo isomerization in the chromatographic column in the course of the analysis. Thus, we determined the total amount of products with two (**II + III**, retention time 10 min), three (**IV**, 35 min), and more (**V**, 52 min) cyclohexane rings. This assignment was based on the retention times of authentic samples of **II** [16], **III** [20], *cis*-2,6-di(1-cyclohexen-1-yl)cyclohexanone (a representative of compounds **IV**) [13], 2,6-dicyclohexylidencyclohexanone [21], and dodecatriphenylene (a representative of compounds **V**) [22]. Compound **I** is thermally unstable [10] and decomposes in the course of the kinetic experiment.

The concentrations of cyclohexanone and its condensation products (Table 2) were calculated from the chromatograms using 1-tetradecene (retention time 5 min) as internal reference [23].

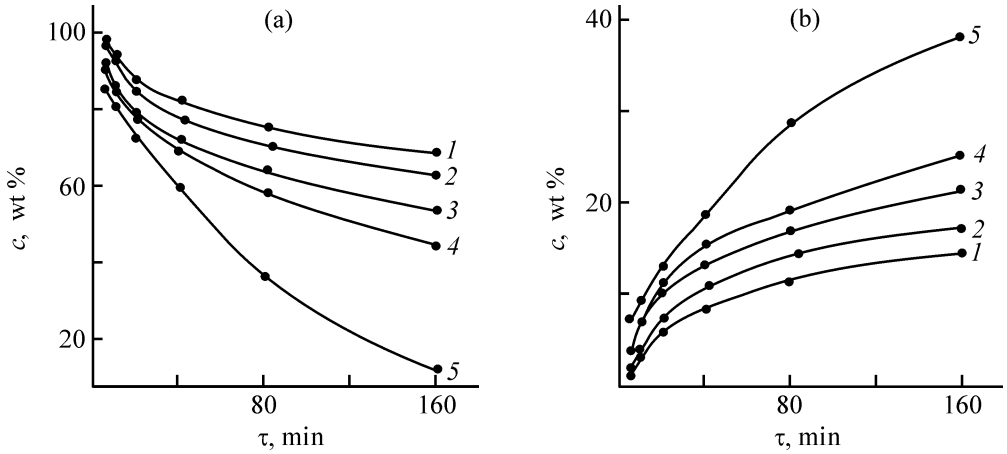

Fig. 2. Variation of the concentrations c of (a) cyclohexanone and (b) **II** + **III** with time τ of autocondensation at (*1*) 119, (*2*) 125, (*3*) 129, (*4*) 133, and (*5*) 137°C.

The kinetic curves of consumption of cyclohexanone and accumulation of condensation products are shown in Figs. 1 and 2. The reaction order evaluated from these curves is abnormally high for all the temperatures except 137°C. We failed to interpret the kinetic curves in terms of formal kinetics and to suggest the condensation mechanism; apparently, several reactions occur simultaneously.

CONCLUSIONS

(1) A procedure was developed for GLC analysis of products of cyclohexanone autocondensation, which differ in the number of cyclohexanone rings.

(2) The temperature dependences of the concentrations of the starting cyclohexanone and reaction products in autocondensation in air were obtained. The reaction is accompanied by formation of "heavy" condensation products in the entire temperature range studied (119–137°C); at 137°C, their amount reaches 4.5% in 2 h.

REFERENCES

1. Svetozarskii, S.V. and Zil'berman, E.N., *Usp. Khim.*, 1970, vol. 39, no. 7, pp. 1173–1189.
2. *Proizvodstvo kaprolaktama* (Production of Caprolactam), Ovchinnikov, V.I. and Ruchinskii, V.R., Eds., Moscow: Khimiya, 1977.
3. Freidlin, G.N., *Alifaticheskie dikarbonovye kisloty* (Aliphatic Dicarboxylic Acids), Moscow: Khimiya, 1978.
4. Gorchakova, E.N., Sibarov, D.A., Fedorov, V.S., and Proskuryakov, V.A., *Zh. Prikl. Khim.*, 1994, vol. 67, no. 9, pp. 1471–1475.
5. US Patent 4088702.
6. GB Patent 1480326.
7. USSR Inventor's Certificate, no. 1735262.
8. Baeva, V.P., Iogansen, A.V., Kurkchi, G.A., and Furman, V.M., *Zh. Org. Khim.*, 1974, vol. 10, no. 7, pp. 1446–1448.
9. Ufimova, G.A., Shutova, I.V., Shapiro, Yu.E., *et al., Zh. Org. Khim.*, 1989, vol. 25, no. 6, pp. 1201–1204.
10. Iogansen, A.V., Kurkchi, G.A., Baeva, V.P., *et al., Zh. Org. Khim.*, 1971, vol. 7, no. 10, pp. 2509–2511.
11. Kim, A.M., Markov, A.F., Mamatyuk, V.I., and Emiryan, A.A., *Izv. Vyssh. Uchebn. Zaved., Khim. Khim. Tekhnol.*, 1986, vol. 29, no. 10, pp. 37–40.
12. Pettit, G.R., Thomas, E.G., and Herald, C.L., *J. Org. Chem.*, 1981, vol. 46, no. 21, pp. 4167–4171.
13. Bell, T.W., Vargas, J.R., and Crispino, G.A., *J. Org. Chem.*, 1989, vol. 54, no. 8, pp. 1978–1987.
14. Krasnykh, E.L., Glazko, I.L., Sokolov, A.B., *et al., Khim. Prom–st.*, 2002, no. 6, pp. 53–54.
15. Richer, P. and Bešta, J., *Chem. Prum.*, 1958, vol. 8, no. 2, pp. 62–64.
16. Marachuk, L.I., Kozyro, A.A., Simirskii, V.V., *et al., Zh. Prikl. Khim.*, 1992, vol. 65, no. 4, pp. 875–880.
17. Sharov, K.T., Rozhnov, A.M., Zakrevskii, V.M., *et al., Zh. Prikl. Khim.*, 1982, vol. 55, no. 8, pp. 1896–1897.
18. Kaim, A., Kaminski, J., and Kolodziejski, W., *Acta Chim. Hung.*, 1988, vol. 125, no. 1, pp. 141–145.
19. Vit, Z., Nordek, L., and Malek, J., *Coll. Czech. Chem. Commun.*, 1982, vol. 47, pp. 2235–2245.
20. Reese, J., *Ber.*, 1942, vol. 42, no. 4, pp. 384–394.
21. Munk, P. and Plesek, J., *Coll. Czech. Chem. Commun.*, 1957, vol. 22, no. 5, pp. 1691–1694.
22. Svetozarskii, S.V., Zil'berman, E.N., and Razuvaev, G.A., *Zh. Obshch. Khim.*, 1959, vol. 29, no. 5, pp. 1454–1457.
23. Gol'berg, K.A. and Vigdergauz, M.S., *Vvedenie v gazovuyu khromatografiyu* (Introduction to Gas Chromatography), Moscow: Khimiya, 1990.

Russian Journal of Applied Chemistry, Vol. 76, No. 12, 2003, pp. 1958–1961. Translated from Zhurnal Prikladnoi Khimii, Vol. 76, No. 12, 2003, pp. 2008–2011.

ORGANIC SYNTHESIS AND INDUSTRIAL ORGANIC CHEMISTRY

Chlorophyll and Its Derivatives, Chlorins and Porphyrins, as a Promising Class of Environmentally Friendly Dyes

B. D. Berezin, M. B. Berezin, A. P. Moryganov, S. V. Rumyantseva, and N. S. Dymnikova

Institute of Chemistry of Solutions, Russian Academy of Sciences, Ivanovo, Russia

Received October 15, 2002; in final form, September 2003

Abstract—The possibilities of using pheophorbid (*a*), chlorin e_6, its copper complex, 6-*N*-(2-aminoethylamido)chlorin e_6 dimethyl ester, and its complexes with Cu(II), Ni(II), Co(II), and Zn(II) as dyes for cellulose, acetate, and wool fibers were studied.

Chlorophyll is not only one of the most important "life complexes" in photosynthesis, but also the most abundant environmentally clean natural dye. Chlorophyll has been actively studied for several decades, mainly as a compound initiating the photochemical step of photosynthesis [1–7]. Its potential as a source of environmentally clean tetrapyrrole dyes has not received due attention. There are only reports on the use of chlorophyll as a food dye and also as a household dye for imparting color and other useful properties to cleansing agents (toilet soap) and tooth-pastes [8].

Our goal was to search for suitable chlorophyll derivatives and appropriate conditions for dyeing fibrous materials of various origins.

It is known that industrially used synthetic organic dyes are environmentally hazardous not only in production, but also in the use of the dyed textiles. Apparently, tetrapyrrole macrocyclic dyes based on synthetic porphyrins and phthalocyanines are environmentally much more friendly:

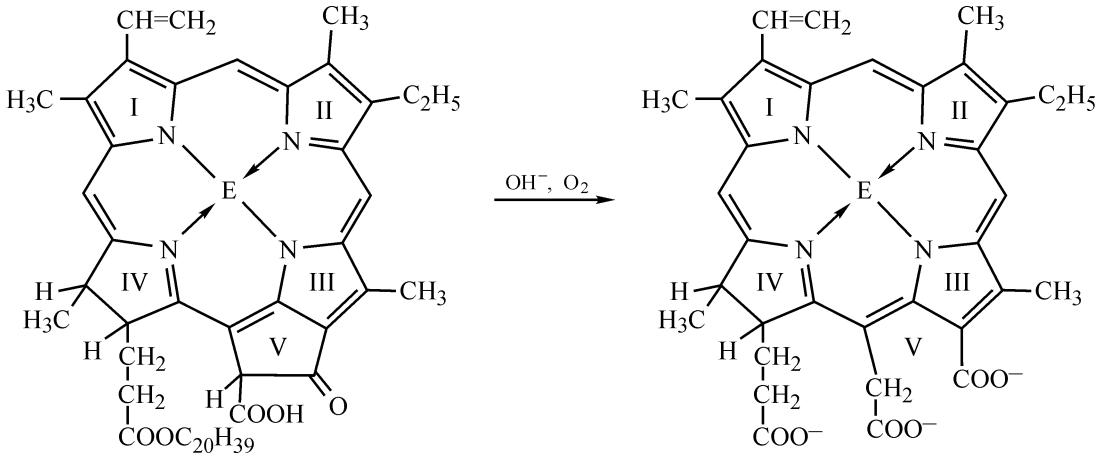

E = 2H, chlorophyll ligand;
E = M, metallochlorophyll

E = 2H, chlorin e_6;
E = M, metallochlorin e_6

Porphyrin dyes based on tetra(*p*-chloromethylphenyl)porphine [9], its ammonium, sulfonium [10], and thiosulfo derivatives [11], and also on tetra(*p*-methylpyridinio)octaphenyltetraazaporphine [12] were tested and showed good results as active dyes for polyamide fibers and as cationic dyes for wool, polyamide, polyacrylic, and cellulose fibers. Unfortunately, the study failed to go beyond the stage of lab tests. A particular place among tetrapyrrole compounds was occupied by pigments and water-soluble dyes based on

1070-4272/03/7612-1958 $25.00 © 2003 MAIK "Nauka/Interperiodica"

phthalocyanines. Their applications and physicochemical properties are discussed [13–15]. The production of phthalocyanine pigments and dyes is not environmentally friendly. However, ready pigments based on metall-free phthalocyanine and its Cu(II), Co(II), Ni(II), and Al(III) complexes are absolutely resistant to alkalis, moderately concentrated acids, and atmospheric oxygen. Therefore, phthalocyanines are the most harmless in service among synthetic dyes [13].

We performed experiments on dyeing of cotton fabric and of wool and acetate fibers with metal derivatives [Cu(II), Zn(II), Co(II), Ni(II) complexes] of pheophorbid, chlorin e_6, and its aminoethylamide dimethyl ester (at carboxy groups in 6- and γ-positions). The pretreatment of the textiles and dyes and the finishing were performed as recommended in [16–23].

EXPERIMENTAL

Pheophorbid, chlorin e_6, and 6-*N*-(2-aminoethylamido)chlorin e_6 dimethyl ester were prepared from pheophytin recovered from the acetone extract of nettle leaves. Pheophorbid (H_2Pb) was prepared by hydrolyis of the phytol residue of pheophytin with concentrated HCl [6]. The electronic absorption spectrum of the compound are in agreement with published data [4]. Chlorin e_6 (H_2Chln e_6) was prepared from pheophorbid by opening of ring E with a 30% solution of KOH in methanol [6]:

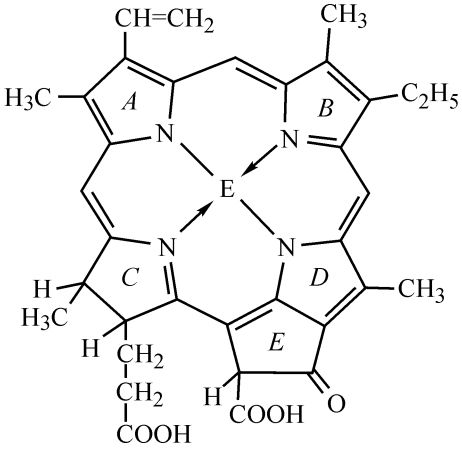

Metallopheophorbids: E = Cu(II), Zn(II), Co(II), Ni(II)

6-*N*-(2-aminoethylamido)chlorin e_6 dimethyl ester was prepared from pheophorbid dimethyl ester in ethylenediamine solution. The electronic absorption spectrum of the product is in agreement with published data [4]. The compounds were tested in dyeing wool and cotton and acetate fibers.

Before dyeing, wool was pretreated with $Na_2Cr_2O_7$ as follows. A wool sample was placed in a solution containing sodium bichromate (4 wt % relative to the fiber) and 5% acetic acid (bath ratio 25). The solution was gradually heated to boiling and boiled for 1 h. Then the bath was cooled, and the wool was washed, dried, and dyed. Since hydrophobic H_2Pb and H_2Chln e_6 are poorly soluble in neutral aqueous solutions, dyeing was performed in 5% aqueous ammonia. With 6-*N*-(2-aminoethylamido)chlorin e_6 dimethyl ester, dyeing was performed in a weakly acidic solution (pH 4). The dyeing solution contained 2.5 g l^{-1} H_2Chln e_6 or its derivatives [CuChln e_6, 6-*N*-(2-aminoethylamido)chlorin e_6 dimethyl ester, or its Cu complex]. In dyeing of wool with 6-*N*-(2-aminoethylamido)chlorin e_6 dimethyl ester, 10 g l^{-1} of $MgSO_4$ was added to improve fixation of the dye. The wool sample was kept in the boiling dyeing bath for 30 min. The dyed samples were washed with hot water (70°C), detergent solution (5 g l^{-1}), and cold water and then dried. Samples dyed with chlorin ligand had intense green-brown color; those dyed with CuChln e_6 were blue-green; with H_2Pb, light green-brown; and with 6-*N*-(2-aminoethylamido)chlorin e_6 dimethyl ester, khaki.

In dyeing of wool with H_2Chln e_6 and 6-*N*-(2-aminoethylamido)chlorin e_6 dimethyl ester, followed by keeping for 1 min in aqueous $Cu(CH_3COO)_2$, the resulting color was intense blue-green in the first case and yellow-green in the second.

6-*N*-(2-Aminoethylamido)chlorin e_6 dimethyl ester was tested as a dye for acetate fiber at a bath ratio of 25. For this purpose, the fiber sample was treated for 30 min in a boiling bath containing 2.5 g l^{-1} of the dye and 10 g l^{-1} of $MgSO_4$. As a result, the fiber acquired the khaki color. Subsequent treatment with aqueous solutions of $Cu(CH_3COO)_2$ and $Ni(CH_3COO)_2$ imparted to the sample intense apple-green color, and upon treatment with $Co(CH_3COO)_2$ and $Zn(CH_3COO)_2$ solutions this color was very weak.

Chlorin H_2Chln e_6 was also tested for dyeing of cotton fabric and printing on it. Dyeing was performed by impregnation with the dye solution, followed by thermal fixation of the dye (bath ratio 25). For dyeing of cotton, 2 g l^{-1} of H_2Chln e_6 was dissolved in water containing 5 g l^{-1} of NaOH and 40 g l^{-1} of NaCl. The sample was padded at room temperature for 1 min. The dye was fixed by two methods. After squeezing, the fabric was either placed for 10 min in an oven heated to 150°C or treated for 10 min with steam in a steaming unit at 103–105°C. The samples became green-yellow. The degree of fixation of the dye on the fabric was determined with a photocolorimeter.

Longer (30 min) steam treatment impaired fixation of the dye. Addition of urea (150 g l^{-1}) to the dyeing bath, followed by steam treatment of the fabric for 30 min, also resulted in worse fixation of the dye. The effect of urea on the uptake and fixation of dyes is ambiguous [24]. It is only obvious that the effect of urea is specific and strongly depends on a particular dye and its concentration in the dyeing bath.

Then, we performed a series of experiments on dyeing a cotton fabric with CuChln e_6 (2 g l^{-1}) by padding with addition of urea (150 g l^{-1}). We found that CuChln e_6 is fixed on fabric worse than H_2Chln e_6 does. To obtain more intense color, padding was performed with H_2Chln e_6. After squeezing, the sample was treated with aqueous $Cu(CH_3COO)_2$, washed with hot water, a detergent solution, and cold water, and dried. The sample had an intense green color. Steaming is not appropriate.

We also tested printing with chlorin e_6. The printing paste consisted of H_2Chln e_6 solution (2.5 g l^{-1}) in 1% aqueous NaOH, mixed with 12% starch thickener. With carboxymethyl cellulose thickener used instead of starch thickener, the fixation of the dye on the fabric was better.

The use of chlorophyll proper (MgChl) as technical dye involves several serious problems. First, chlorophyll and its metal analogs are readily soluble in organic solvents, so that these dyes are easily removed from fibers. Chlorophyll and its metal analogs are unstable to alkaline treatments (laundering): The cyclopentenone ring is opened, and water-soluble metallochlorins are formed. Furthermore, chlorophyll is insufficiently stable in acidic solutions, dissociating with the release of Mg^{2+} [26, 27]:

$$MgChl + 2H_3O^+(2H^+_{solv}) \rightarrow Mg^{2+} + H_2Chl.$$

All these factors prevent straight use of chlorophyll as a dye. However, these difficulties can be overcome [5, 25–31] by modifying chlorophyll molecules. Chlorophyll ligand (H_2Chl) can be readily converted into metal porphyrins difficultly soluble in organic solvents, or into their ionic species. The cyclopentenone ring in H_2Chl and in its phytol-free analog, pheophorbid H_2Pb, transforms in strongly alkaline solutions into other, hydrophobic functional groups [6]. Chlorins and porphyrins obtained from chlorophyll readily form stable complexes with *d* metals. The coordinated metals are not released under conditions of dyeing and use of textiles; furthermore, they can form extra coordination bonds [32] with functional groups of natural and synthetic polymers, thus ensuring their stronger binding with the fiber. Also, *d* metals incorporated in metallochlorins e_6, their functional derivatives, and metalloporphyrins deactivate singlet oxygen $^1O_2$, an agent destroying dyes and fibers, and exert a photostabilizing effect on macrocyclic dyes [32, 33].

Thus, our experiments on dyeing of cellulose, acetate, and wool fibers with chlorophyll dyes gave encouraging results. Bright stable colors were obtained. The tint depends on cation in metal-containing chlorins. Furthermore, metals exert auxochromic and photostabilizing effects on the chlorin chromophore; they enhance the affinity of chlorin for the fiber [33]. The dyes exhibit a weak chemical affinity for cellulose fibers. This is due to low chemical affinity of the π system and functional groups (CO_2R, COOH, C=O, $CH=CH_2$, Alk, CH_2NH_2) of the dyes to functional groups of cellulose (–O–, –OH) and, possibly, also to the low ability of bulky macrocyclic π systems (chlorins, porphyrins, phthalocyanines) to penetrate deep into cotton fiber. However, chemical modification of chlorins, porphyrins, and their metal derivatives [6] may allow preparation of active dyes suitable for high-quality dyeing to obtain green, red, and pink colors.

CONCLUSIONS

(1) Chlorophyll derivatives pheophorbid (*a*), chlorin e_6, 6-*N*-(2-aminoethylamido)chlorin e_6 dimethyl ester, and their Cu(II) and Ni(II) complexes can be considered representatives of a new class of chlorophyll dyes for dyeing of cellulose, wool, and acetate fibers.

(2) In dyeing of wool, chlorin e_6 has advantages over pheophorbid (*a*); to obtain more intense color of cotton fabric and articles from wool fiber, it is appropriate to use chlorin e_6 or 6-*N*-(2-aminoethylamido)chlorin e_6 dimethyl ester, with subsequent treatment with aqueous solutions of Cu(II) or Ni(II) salts.

REFERENCES

1. Chirkov, Yu.G., *Fotosintez: dva veka spustya* (Photosynthesis: Two Centuries Later), Moscow: Znanie, 1981.
2. *The Photochemical Apparatus; Its Structure and Function, Report of Symp. Held June 16–18, 1958, Upton*, New York: Brookhaven National Laboratory, 1959.
3. Fischer, H. and Orth, H., *Die Chemie des Pyrrols*, Leipzig: Akademie, 1937, vol. 2, part 1.

4. Gurinovich, G.P., Sevchenko, A.N., and Solov'ev, K.N., *Spektroskopiya khlorofilla i rodstvennykh soedinenii* (Spectroscopy of Chlorophyll and Related Compounds), Minsk: Nauka i Tekhnika, 1968.
5. Berezin, B.D., *Koordinatsionnye soedineniya porfirinov i ftalotsianina* (Coordination Compounds of Porphyrins and Phthalocyanine), Moscow: Nauka, 1978.
6. Koifman, O.I., Askarov, K.A., and Berezin, B.D., *Porfiriny: struktura, svoistva, sintez* (Porphyrins: Structure, Properties, and Synthesis), Enikolopyan, N.S., Ed., Moscow: Nauka, 1985.
7. Godnev, T.N., *Khlorofill: ego stroenie i obrazovanie v rastenii* (Chlorophyll: Its Structure and Formation in Plants), Minsk: Akad. Nauk Bel. SSR, 1963.
8. Humphrey, A., *Food Chem.*, 1980, vol. 5, no. 1, pp. 57–67.
9. USSR Inventor's Certificate, no. 990777.
10. USSR Inventor's Certificate, no. 1028672.
11. USSR Inventor's Certificate, no. 1260377.
12. USSR Inventor's Certificate, no. 1578161.
13. Thomas, A. and Moser, F., *Phthalocyanine Compounds*, New York: Reinhold, 1963.
14. Berezin, B.D., Physicochemical Properties of Coordination Compounds of Phthalocyanine, *Doctoral Dissertation*, Kiev, 1965.
15. Berezin, B.D. and Enikolopyan, N.S., *Metalloporfiriny* (Metalloporphyrins), Moscow: Nauka, 1988.
16. Mel'nikov, B.N., Moryganov, A.P., and Kalinnikov, Yu.A., *Teoriya i praktika vysokoskorostnoi fiksatsii krasitelei na tekstil'nykh materialakh* (Theory and Practice of Rapid Fixation of Dyes on Textiles), Moscow: Legprombytizdat, 1987.
17. Stepanov, B.I., *Vvedenie v khimiyu i tekhnologiyu organicheskikh krasitelei* (Introduction to Chemistry and Technology of Organic Dyes), Moscow: Khimiya, 1984.
18. Leonova, N.A., Mel'nikov, B.N., and Berezin, B.D., *Izv. Vyssh. Uchebn. Zaved., Khim. Khim. Tekhnol.*, 1970, vol. 13, no. 9, pp. 1346–1349.
19. Leonova, N.A., Mel'nikov, B.N., and Berezin, B.D., *Izv. Vyssh. Uchebn. Zaved., Khim. Khim. Tekhnol.*, 1970, vol. 13, no. 11, pp. 1653–1655.
20. Leonova, N.A., Mel'nikov, B.N., and Berezin, B.D., *Izv. Vyssh. Uchebn. Zaved., Khim. Khim. Tekhnol.*, 1971, vol. 14, no. 3, pp. 93–95.
21. Shkrobysheva, V.I., Berezin, B.D., Mel'nikov, B.N., *et al.*, *Vopr. Nov. Tekhnol. Sherst. Prom–sti.*, 1974, no. 28, pp. 111–114.
22. Kalinnikov, Yu.A., Mel'nikov, B.N., and Berezin, B.D., *Izv. Vyssh. Uchebn. Zaved., Khim. Khim. Tekhnol.*, 1980, vol. 23, no. 3, pp. 336–339.
23. Mel'nikov, B.N., Berezin, B.D., and Kalinnikov, Yu.A., *Izv. Vyssh. Uchebn. Zaved., Khim. Khim. Tekhnol.*, 1981, vol. 24, no. 5, pp. 623–626.
24. Mel'nikov, B.N. and Moryganov, P.V., *Primenenie krasitelei* (Applications of Dyes), Moscow: Legkaya Industriya, 1971, p. 262.
25. Rashidova, S.T., Processing of Chlorophyll Recovered from Silkworm Excretions To Obtain Metalloporphyrins and Physicochemical Properties of These Products, *Cand. Sci. Dissertation*, Ivanovo, 1983.
26. Lapshina, O.V., Spectroscopy and Transformation Kinetics of the Enol Form of Chlorophyllic Acid and Its Complexes, *Cand. Sci. Dissertation*, Ivanovo, 1976.
27. Berezin, B.D. and Lapshina, O.B., *Zh. Fiz. Khim.*, 1974, vol. 48, no. 2, pp. 303–307.
28. Karmanova, L.P., Kinetics and Mechanism of Dissociation of Metalloporphyrins in Organic Proton-Donor Media, *Cand. Sci. Dissertation*, Ivanovo, 1974.
29. Berezin, B.D., Drobysheva, A.N., and ?Karmanova, L.P., *Zh. Fiz. Khim.*, 1976, vol. 50, no. 5, pp. 1194–1198.
30. Koifman, O.I. and Berezin, B.D., *Izv. Vyssh. Uchebn. Zaved., Khim. Khim. Tekhnol.*, 1972, vol. 15, no. 1, p. 147.
31. Berezin, B.D., Volkova, N.I., and Karavaeva, E.B., *Zh. Neorg. Khim.*, 1974, vol. 19, no. 11, p. 3053.
32. Venediktov, E.A., Influence of the Molecular Structure on Physicochemical Interaction of Porphyrins and Metalloporphyrins with Molecular Oxygen, *Cand. Sci. Dissertation*, Ivanovo, 1980.
33. Berezin, B.D. and Drobysheva, A.N., *Zh. Fiz. Khim.*, 1968, vol. 42, no. 8, pp. 2092–2096.

Russian Journal of Applied Chemistry, Vol. 76, No. 12, 2003, pp. 1962–1964. Translated from Zhurnal Prikladnoi Khimii, Vol. 76, No. 12, 2003, pp. 2012–2014.

ORGANIC SYNTHESIS AND INDUSTRIAL ORGANIC CHEMISTRY

Binding of Copper(II), Cobalt(II), and Nickel(II) Cations with Humic Acids and Their Sodium Salts in Aqueous Media

V. N. Kislenko and L. P Oliinyk

L'vovskaya Politekhnica National University, Lviv, Ukraine

Received December 19, 2002; in final form, January 2003

Abstract—Binding of Cu(II), Co(II) and Ni(II) cations to humic acids and their sodium salts was studied in aqueous media at pH 3–6 by spectrophotometry and potentiometric titration technique.

Humic acids are the main organic component of soils. They are polyfunctional substances containing carboxy, hydroxy and amino groups. Among these functional groups, the carboxy groups prevail. These functional groups are responsible for binding of metal cations and, in particular, heavy metal cations. The influence of the medium on the complexing of humic acids with heavy metals is an environmentally important problem. It has been found that binding of double-charged metals to humic acids depends on particular metal [1]. For example, the amount of lead and cadmium bound to humic acids varies in direct proportion to the metal concentration in solution, whereas the binding of zinc passes through a maximum. According to [2–4], the carboxy and amino groups of humic acids form chelates with heavy metal cations. The amount of copper(II) bound to humic acids grows with increasing initial copper(II) concentration and pH [5].

In this study, we examined the binding of copper(II), cobalt(II), and nickel(II) to humic acids and their sodium salts.

EXPERIMENTAL

In our experiments, we used $CuSO_4$, $CoCl_2$, and $NiSO_4$ of chemically pure grade and humic acids produced by the Olaine Plant of Chemicals [TU (Technical Specification) 10P 316–69]. The solubility of humic acids grows with pH increasing from 3 to 8. At pH lower than 3, the solubility of humic acids slightly increases owing to protonation of the amino groups. The titration curve of humic acids with aqueous alkali shows that humic acids contain free carboxy groups (titrated approximately at pH 7) and carboxy groups bound to amino groups (titrated at pH 11). In the curve of back titration of aqueous humic acid ammonium salt, there is a bending point at pH 7. The calculated concentration of free and bound carboxy groups in humic acids is 1.9 and 1.7 mmol g^{-1}, respectively.

Our experiments on interaction of humic acids with transition metal cations were carried out as follows. An aqueous suspension of humic acids or an aqueous solution of their sodium salt was mixed with aqueous metal salt being studied and kept for a day with stirring. The resulting suspension was centrifuged for 20 min at 8000 rpm and then the solution of a metal salt with humic acids was separated from the insoluble precipitate. At pH < 5, the concentration of humic acids in the solution after centrifugation was within the limits of the experimental error. After separation of the solid precipitate of the transition metal humates, the concentration of copper(II) and cobalt (II) in the aqueous phase was determined from the absorption of their ammonia complexes at 540 and 490 nm, respectively. The concentration of metal bound to humic acids was determined as the difference between its initial and final concentrations in the liquid phase.

In aqueous suspension, humic acids behave as ion exchangers. Therefore, on adding NaCl or $CaCl_2$ to an aqueous dispersion of humic acids, the pH of the dispersion decreases, and the pH remains unchanged after separation of the suspension by centrifuging. This fact shows that the metal cations are strongly bound to humic acid species by replacing hydrogen ions. Titration of a humic acid suspension with NaCl and $CaCl_2$ solutions shows (Fig. 1) that, at the bending point, the maximum extent of binding of metals to humic acids is attained at the ratio of the metal chloride to humic acids of 7.9 and 25 mmol g^{-1} for NaCl

1070-4272/03/7612-1962 $25.00 © 2003 MAIK "Nauka/Interperiodica"

and $CaCl_2$, respectively. The amount of metal bound to humic acids was calculated from the difference of the pH values of the initial humic acid (HA) suspension and that at the bending point. These values are 1.0 and 1.2 mmol g^{-1} HA for sodium and calcium cations, respectively. We believe that, at suspension pH of approximately 3, mixed calcium humate-chloride salts are formed. Since the total content of carboxy groups in the humic acids, determined by titration with NaOH, is 3.6 mol g^{-1}, our results show that only some portion of the carboxy groups of humic acids interact with sodium and calcium cations.

The titration curve of aqueous $CuSO_4$ with a humic acid suspension (pH 2.8) shows (Fig. 2, curve *2*) that the minimum pH is approximately equal to pH of the initial humic acid suspension. A bend occurs in the titration curve at $\nu[(CuSO_4)/m_{HA}]$ = 1.6 mmol g^{-1}, which exceeds that in titration of aqueous NaCl and $CaCl_2$. Comparison of the titration curves of $CuSO_4$ with humic acid and sodium humate (Fig. 2, curves *2* and *3*) shows that the position of the bending point is independent of the initial pH of these titrating solu tions, although the minimum pH in the titration curves grows with increasing initial pH of titrants. When titrating aqueous sodium humate (pH 7.9) with aqueous $CuSO_4$, the minimum pH in the titration curve is close to the pH value corresponding to $CuSO_4$ hydrolysis (3.8–4.6). Although the titration curves (Fig. 2, curves *2* and *3*) differ in the minimal pH values, the corresponding $\nu[(CuSO_4)/m_{HA}]$ ratios are equal. Under the conditions corresponding to the bending point, insoluble copper humates precipitate.

We found that the amount of copper bound to humic acids in the precipitate grows virtually in direct proportion to the $CuSO_4$ concentration in the solution (Fig. 3). This fact shows that the distribution of Cu(II) cations between the aqueous phase and the solid phase of humic acid suspension [formation of copper(II) humate] is an equilibrium process. With pH increasing from 4.0 to 4.6, the slopes of these straight lines become steeper (Fig. 3, curves *1* and *2*), i.e., this equilibrium is shifted toward copper(II) humate formation. At pH of about 7 and low copper(II) concentration, water-soluble copper(II) humates are formed. With the copper(II) concentration increasing at pH of about 7, a mixture of copper(II) humate and Cu(II) hydroxide precipitates. This precipitate contains up to 40 mmol Cu(II) g^{-1} HA, which considerably exceeds the concentration of carboxy groups in the humic acid suspension (3.6 mmol g^{-1} HA). This fact shows that, under these conditions, poorly soluble basic copper(II) humates are formed.

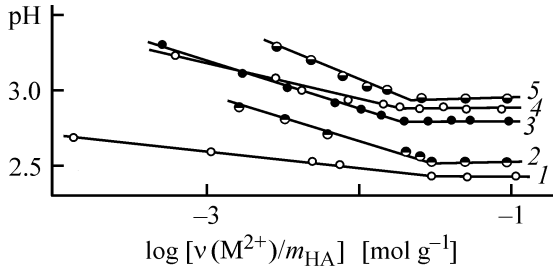

Fig. 1. Curves of potentiometric titration of humic acids with (*1*, *2*, and *5*) $CaCl_2$ and (*3*, *4*) NaCl aqueous solutions $\nu(M^{2+})/m_{HA}$. Metal chloride concentration 10 wt %. Humic acid concentration in suspension (wt %): (*1*) 10, (*2*, *3*) 5, and (*4*, *5*) 2.

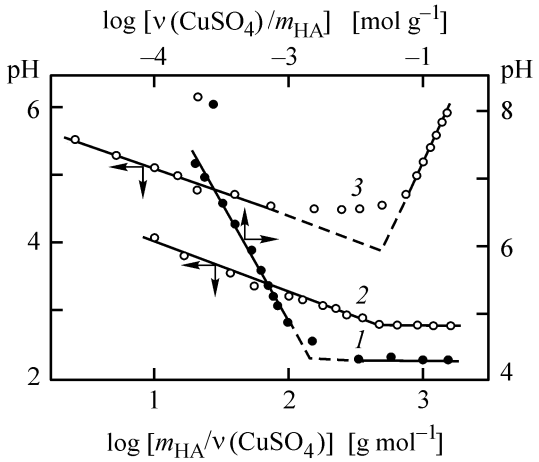

Fig. 2. Curves of potentiometric titration of (*1*) aqueous sodium humates (pH 7.8) with aqueous $CuSO_4$, (*2*) aqueous $CuSO_4$ with humic acid suspension (10 wt %, pH 2.8), and (*3*) aqueous $CuSO_4$ with sodium humate solution (pH 7.6). $\nu(CuSO_4)/m_{HA}$ is the ratio of $CuSO_4$ to humic acids. $CuSO_4$ concentration (wt %): (*1*) 7.9, (*2*) 1.9, and (*3*) 3.95. Sodium humate concentration (wt %): (*1*) 1.2 and (*3*) 5.

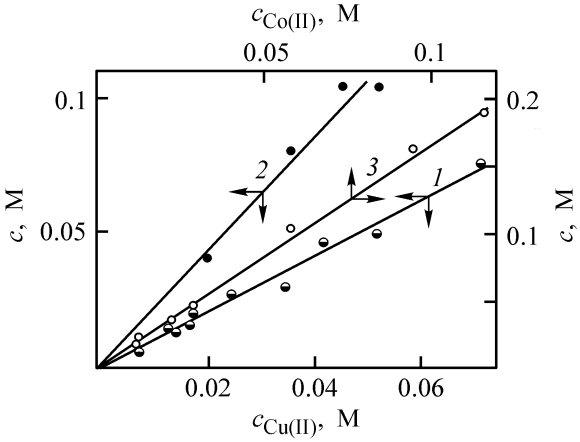

Fig. 3. Plot of the concentration c of (1, 2) copper(II) and (3) cobalt(II) bound to humic acids in suspension vs. the concentration of these metals, $c_{Cu(II)}$, $c_{Co(II)}$, in the solution. Initial concentration of humic acids, g l^{-1}: (*1*, *3*) 2.5 and (*2*) 1.25. pH: (*1*) 4.0 and (*2*, *3*) 4.6.

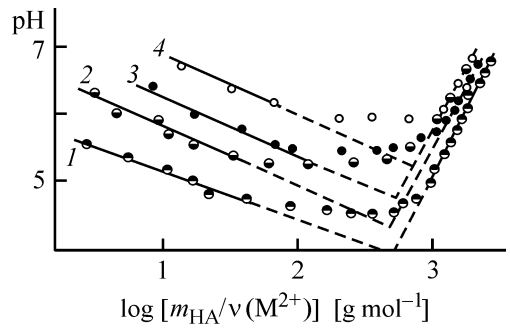

Fig. 4. Curves of potentiometric titration of solution of (*1*) $CuSO_4$, (*2*, *3*) $CoCl_2$, and (*4*) $NiSO_4$ with aqueous sodium humate with the initial pH 7.6. Concentration of titrated salt (wt %): (*1*) $CuSO_4$ 0.395, (*2*) $CoCl_2$ 2.0, and (*3*) $NiSO_4$ 0.25. Sodium humate concentration (wt %): (*1*) 5 and (*2*–*4*) 10.

The curves of potentiometric titration of cobalt(II), nickel(II), and copper(II) with aqueous sodium humate (initial pH 7.6) have a similar shape (Fig. 4). These curves show that, on adding first small portions of sodium humate, pH decreases. We believe that this acidification is caused by displacement of protons of both the free carboxy groups and protonated amino groups of humic acids by the metal cations. On further addition of sodium humate, pH first remains approximately constant and then sharply increases. The minimum pH in these curves increases in the order copper(II) < cobalt(II) < and nickel(II), i.e., in the same order in which grows the pH of conversion of these cations into their hydroxides. At the same time, the bending points in these titration curves occur at approximately equal $\nu(M^{2+})/m_{HA}$ ratios: copper(II) 1.6, cobalt(II) 2.0, and Ni(II) 1.4. We believe that the flat lower portion of the potentiometric titration curves is due to formation of basic metal humates. We found that, like copper(II), the amount of cobalt(II) bound to humic acids at pH 4.6 increases in direct proportion to the equilibrium cobalt(II) concentration in the liquid phase (Fig. 3, curve *3*). The slope of this plot (1.67) is smaller than that for copper(II) (2.42). We believe that this difference is due to the fact that basic Co(II) humates are less stable than basic copper(II) humate at pH 4.6. This difference is also in line with our assumption of formation of basic metal humates and is consistent with the known fact that copper(II) hydroxide, as compared to cobalt(II) hydroxide, is formed at lower pH.

CONCLUSIONS

(1) Humic acids and sodium humates are bound with double-charged transition metal cations in aqueous solutions within the pH range 3–5. The amount of transition metal bound to humic acids grows with the pH increasing from 4.0 to 4.6.

(2) The bending point in the curve of potentiometric titration of double-charged transition metal cations with humic acids and sodium humates occurs at $\nu[(M^{2+})/m_{HA}]$ ratios equal to 1.6, 2.0, and 1.4 mmol g^{-1} for copper(II), cobalt(II), and nickel(II), respectively; its position only slightly depends on the initial pH of the titrants.

REFERENCES

1. Ricca, G., Pastorelli, C., and Severini, F., *The Role of Humic Substances in the Ecosystems and in the Environmental Protection*, Drozd, J., Gonet, S.S., Senesi, N., and Weber, J., Eds., Wroclaw: PTSH, 1997, pp. 175–181.
2. Tipping, E., *Geochim. Cosmochim. Acta*, 1981, vol. 45, no. 1, pp. 191–199.
3. Xu, H., Ephraim, J., Ledin, A., and Allard, B., *Sci. Tot. Environ.*, 1989, vol. 81/82, no. 3, pp. 653–660.
4. Cao, Y., Gankin, M., and Betterton, E., *Environ. Health Perspect.*, 1995, vol. 103, no. 1, pp. 29–32.
5. Benedetti, M.F., *Environ. Sci. Technol.*, 1995, vol. 29, no. 2, pp. 446–457.

Russian Journal of Applied Chemistry, Vol. 76, No. 12, 2003, pp. 1965–1970. Translated from Zhurnal Prikladnoi Khimii, Vol. 76, No. 12, 2003, pp. 2015–2021.

MACROMOLECULAR CHEMISTRY AND POLYMERIC MATERIALS

Thermal Desorption of Covalently Bound Fullerene C_{60} from Poly-*N*-vinylpyrrolidone Films

A. O. Pozdnyakov, E. Yu. Melenevskaya, O. V. Ratnikova, and B. M. Ginzburg

Institute of Machine Science Problems, Russian Academy of Sciences, St. Petersburg, Russia

Institute of Macromolecular Compounds, Russian Academy of Sciences, St. Petersburg, Russia

Received July 15, 2003

Abstract—Kinetics of formation of thermolysis products in heating of thin films of poly-*N*-vinylpyrrolidone and of poly-*N*-vinylpyrrolidone with covalently bound fullerene C_{60} was studied by thermal desorption mass spectrometry.

Since fullerene C_{60} (C_{60}) exhibits biological activity, synthesis of its water-soluble forms and, in particular, polymer–C_{60} systems, is a topical task [1–4]. These are two types of fullerene-containing polymers in which C_{60} is bound to water-soluble macromolecules by covalent or noncovalent bonds. Poly-*N*-vinylpyrrolidone (PVP) is a nonionic water-soluble amphiphilic polymer that can form complexes with molecules of diverse structures and polarities [5]. Poly-*N*-vinylpyrrolidone is produced commercially and is widely used in medicine [6]. Fullerene C_{60} supported by this polymer can be used in biological studies [7]. Some features of the interaction between C_{60} and PVP are known. A radical ion donor–acceptor complex in the PVP–C_{60} system has been detected by ESR spectroscopy [8]. The formation of donor–acceptor bonds between C_{60} and the carbonyl groups of PVP has been confirmed by ^{13}C NMR studies [9].

The structure and properties of solutions of PVP–C_{60} systems are determined by the type of the PVP–C_{60} interaction and the nature of a solvent. As determined by the method of Rayleigh scattering, solutions of PVP–C_{60} complexes contain domains whose size is determined by the balance of the attractive forces between C_{60} molecules and repulsive force between the macromolecules [10]. It should be noted that the degree of heterogeneity of composite and nanocomposite polymer systems is an important parameter affecting their properties. However, there are only a few methods for measuring this parameter. At the same time, this parameter is required to correlate the structure and the properties of these systems and to develop techniques for their synthesis.

The high sensitivity of mass spectrometry and thermal desorption mass spectrometry (TDMS) to a molecule flow in the gas phase allows determination of the weight loss by the polymer–C_{60} system in the course of C_{60} desorption. The sensitivity of other common methods of thermal analysis (e.g., thermogravimetry) is substantially lower, and these methods are unsuitable for this purpose. The type of polymer–fullerene bonding and the structural state of C_{60} (X-ray-amorphous or crystalline) were determined by TDMS from the curves of thermal desorption of C_{60} and the thermolysis products of the polymeric matrix [11–15]. In this study we examined thermal desorption of fullerene C_{60} from PVP–C_{60} systems prepared by different procedures and analyzed the thermolysis products of PVP.

EXPERIMENTAL

Samples of PVP and PVP containing C_{60} bound by covalent bonds (PVP–cov-C_{60}) were prepared by radical polymerization in toluene, using asobis(isobutyronitrile) (AIBN) of pure grade [TU (Technical Specification) 6-09-3840–74]. Trace amount of water were removed from AIBN in a vacuum [16]. *N*-Vinylpyrrolidone (N-VP) was dried over KOH and distilled under reduced pressure. The middle fraction was degassed. A fullerene powder with 98% C_{60} was kept in a vacuum at 100°C. The toluene solutions of C_{60} were prepared by the procedure described in our previous study [17]. Copolymerization of N-VP and C_{60} was performed in toluene at 60°C in the presence of AIBN as an initiator.

1070-4272/03/7612-1965 $25.00 © 2003 MAIK "Nauka/Interperiodica"

Properties of PVP and its complex with C_{60}*

Properties	Sample	
	PVP	PVP–cov-C_{60}
C_{60} content, wt %	–	1.6
MW_{peak} (MEC)	$>90 \times 10^3$	6×10^3
MW_{LS} in water	–	10×10^3
MWD	4.9	2.2
MW_{SD}	–	10^3

* MW_{peak} is the number-average molecular weight corresponding to the maximum content of macromolecules in the molecular-weight distribution (MWD) determined by exclusion chromatography; MW_{LS} is the weight-average molecular weight determined from light scattering; and MW_{SD} is the number-average molecular weight determined by the sedimentation procedure.

Fullerene C_{60} traps free radicals and inhibits copolymerization. This leads to termination of in the early stages in the case of simultaneous component mixing. The monomer conversion is about 20%. To increase the copolymer yield, AIBN was introduced in two steps. Half of the whole amount of AIBN was added at room temperature and the reaction mixture was stirred for 1 h. Then a toluene solution of C_{60} was added, and the reaction mixture was heated at 60°C for 100 h. After that, the remaining portion of AIBN was added, and the copolymerization was continued for the same time. Then PVP–cov-C_{60} was isolated.

The copolymer, formed in 70–90% yield was reprecipitated from diethyl ether, dissolved in distilled water, and lyophilically dried. Polyvinylpyrrolidone prepared by copolymerization in toluene in the presence of AIBN and commercial fractionated PVP with molecular weight (MW) of about $(10–12) \times 10^3$ were used as references. The PVP fraction with MW = 12×10^3 was additionally dried in a vacuum (residual pressure 10^{-6} mm Hg) at 140°C for 10–15 h. The molecular weights of PVP and PVP–cov-C_{60} copolymer were determined by microcolumn exclusion chromatography (MEC) and by the method of Rayleigh scattering (see table).

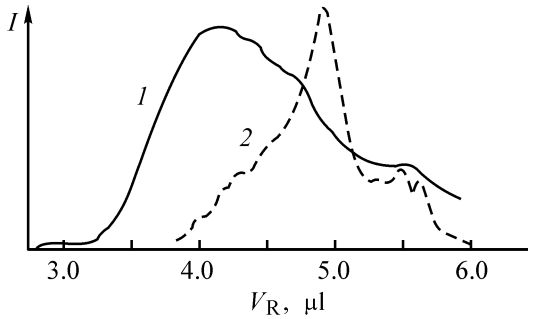

Fig. 1. HPLC pattern of PVP–cov-C_{60} solution in chloroform measured with (*1*) refractometric detection and (*2*) photometric detection (λ = 260 nm, 0.5 × 400-mm Ultrastyrogel 1000 column, chloroform as an eluent, elution rate 3 μl min^{-1}). (*I*) Intensity and (V_R) retention volume.

The glass transition point of PVP $T \sim 180$°C [18].

Complexes of PVP with C_{60}, in which PVP is bound to C_{60} by noncovalent bonds (PVP–C_{60}) were prepared from a benzene solution of these components [19]. The fullerene content in the complex thus obtained may be higher than 1%. In this study, we used the complex containing about 1.7% C_{60}.

Samples of PVP, PVP–cov-C_{60}, and PVP–C_{60} were studied by TDMS. Thin films with a definite thickness were prepared as follows. An aliquot of a dilute solution of PVP–cov-C_{60} or PVP–C_{60} in distilled water or toluene was applied to an oxidized tantalum support-heater equipped with a thermocouple. To minimize the contact of the polymer with water, dried PVP was applied by hatching a support with a sample. The coated support was dried for 5 min at room temperature under a reduced pressure (~700 mm Hg) in a VT6060T vacuum oven (Kendro Laboratory Products) and then placed in a vacuum chamber of MKh-1320 magnetic mass spectrometer (energy of ionizing electrons 75 eV). Thermal desorption experiments were performed in a vacuum with residual pressure of $\sim 10^{-7}$ mm Hg.

The composition of PVP complexes with C_{60} was examined in our previous study by thin-layer chromatography (THC) using toluene as an eluent [16]. The presence of free fullerene was detected only in pure C_{60} and PVP–C_{60}. The absence of free C_{60} in PVP–cov-C_{60} was confirmed by UV spectra of solutions of C_{60} and PVP–cov-C_{60} in chloroform [16]. Naturally, PVP–cov-C_{60} contains large amounts of C_{60} bound to the initiator radicals formed after the second addition of AIBN.

It should be noted that, in these systems, C_{60} is bound to radicals of the initiator and polymer by covalent bonds; their number may range from 1 to 3–4 [16]. We suggest that products are formed with both polymer and initiator radicals, initiator radicals only, and polymer radicals only. A study of PVP–cov-C_{60} solution by two-detector exclusion chromatography confirmed its nonuniformity (Fig. 1). As seen from the chromatogram, the C_{60} content in the low-molecular-weight fractions is high. Apparently, PVP with higher molecular weight is formed after the second addition of the initiator, since the contribution of chain termination reaction decreases owing to the lowering

of the activity of C_{60} that reacted in the first polymerization step. Thus, our chromatographic study demonstrated that the polymerization product is not uniform and contains PVP homopolymer, a series of fullerene-containing PVPs with different numbers of macromolecules with different molecular weights, and structures containing radicals of both the polymer and initiator or only initiator radicals.

The mass spectrum of volatile thermolysis products (VTP) contains signals of vinylpyrrolidone VP (m/z = $56_{100\%}$, $111_{50\%}$, $28_{47\%}$, $27_{25\%}$, $41_{18\%}$), pyrrolidone Pr (m/z = $85_{100\%}$, $42_{42\%}$, $41_{36\%}$, $28_{32\%}$, $30_{29\%}$, $56_{16\%}$) and trace amounts of water (m/z = $18_{100\%}$). The main lines of these compounds and their relative intensities (lower index) are in parentheses. The ratios of VP and Pr formed in thermolysis of PVP and PVP–cov-C_{60} differ in a wide temperature range. A typical mass spectrum of VTP of these samples is shown in Figs. 2a and 2b, respectively. The intensity of the Pr lines in the spectrum of VTP of PVP is the highest, which indicates that elimination of side pyrrolidone groups prevails. On the contrary, PVP–cov-C_{60} is mainly thermolyzed by depolymerization to form VP monomer.

To gain deeper insight into thermolysis of these samples, we recorded the temperature dependences of the rate of formation of the VP monomer $dN_{VP}/d\tau$, pyrrolidone ring $dN_{Pr}/d\tau$, and C_{60} molecules $dN_{C_{60}}/d\tau$ (N_i is the current amount of product liberated from the sample; τ is the time). The kinetics of formation of the thermolysis products was monitored by the line of their molecular ions M^+ 111, 85, and 720, respectively. The samples were heated at a rate of about 7 deg s^{-1}.

The temperature dependences of the rate of liberation of VP $dN_{VP}/d\tau$ from predried PVP and PVP–cov-C_{60} are shown in Fig. 3. It should be noted that, since different radicals are grafted to PVP–cov-C_{60}, only a shift of T_{max} of thermal desorption steps, but not their contribution, can be interpreted. In the case of PVP–cov-C_{60}, the low-temperature peak at T_{max} ~ 290°C is observed along with a high-temperature peak at T_{max} ~ 480°C.

The low-temperature peak is due to rupture of the PVP–C_{60} covalent bond in PVP–cov-C_{60}. This bond is located at the β-position with respect to the double bond of C_{60} and is weak. A similar low-temperature peak has been observed in thermolysis of polystyrene with grafted C_{60} groups [13]. The activation energy of rupture of this bond, calculated from the temperature dependence of the rate of monomer desorption in the low-temperature step (T_{max} ~ 290°C), is about 80 kJ mol^{-1}. The total activation energy of VP formation in thermolysis of dry PVP is ~170 kJ mol^{-1}. It is difficult to calculate the activation energy of PV formation in the high-temperature step of PVP–cov-C_{60} thermolysis, since this step overlaps with the low-temperature step.

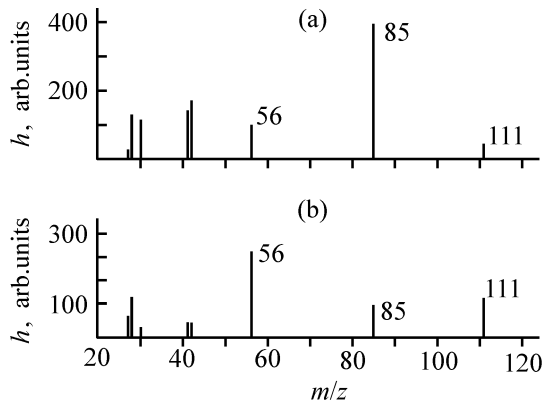

Fig. 2. Fragment of mass-spectrum obtained after thermal treatment of (a) PVP and (b) PVP–cov-C_{60} at ~320°C. (h) Relative peak intensity and (m/z) molecular weight to charge ratio.

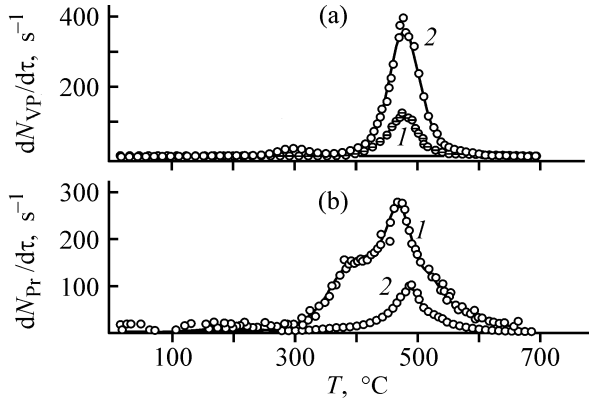

Fig. 3. Rate of formation of (a) VP $dN_{VP}/d\tau$ and (b) Pr $dN_{Pr}/d\tau$ vs. the temperature T of thermal treatment of predried films of (*1*) PVP and (*2*) PVP–cov-C_{60}.

The temperature dependence of the rate of Pr formation, $dN_{Pr}/d\tau$, in the course of thermolysis of PVP–cov-C_{60} films and predried PVP are shown in Fig. 3. As can be seen from Fig. 3, Pr is formed in a wider temperature range (100–700°C) than VP. It should be noted that, at low temperatures, liberation of Pr from PVP predried in a vacuum and applied by the dry procedure is less intense. Poly-*N*-vinylpyrrolidone contains trace amounts of N-VP and 2-pyrrolidone, which are mainly removed by prolonged heating in a vacuum [20]. It is natural to assume that pyrrolidone is released from dry PVP owing to the presence of strongly bound water in the polymer [18]. We suggest that liberated VP undergoes acidic hydrolysis, since the pH of the aqueous PVP solution is ~5.5. The hy-

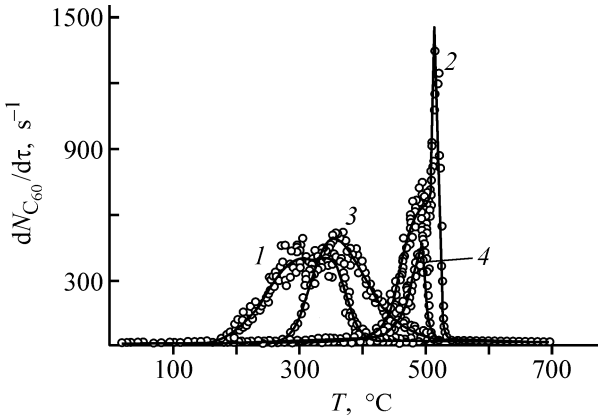

Fig. 4. Rate of C_{60} desorption, $dN_{C_{60}}/d\tau$, vs. the temperature T of thermal treatment of (*1*) 20-nm films of pure C_{60}, applied from a toluene solution to the metal surface, PVP–cov-C_{60} films applied from (*2*) aqueous and (*3*) toluene solutions, and (*4*) PVP–C_{60} film.

drolysis continues until water is present in the system. Water molecules form strong hydrogen bonds with the oxygen atoms of the carbonyl groups and are, apparently, retained in the polymer up to its complete degradation.

The temperature dependences of the rate of C_{60} desorption, $dN_{C_{60}}/d\tau$, from films applied from an aqueous solution of PVP–C_{60}, PVP–cov-C_{60} films applied from aqueous and toluene solutions, and 200-Å films of C_{60} applied from saturated toluene solution of C_{60} to the metal support are shown in Fig. 4. The film of pure C_{60} was studied for comparison, since thermal desorption of C_{60} is not complicated in this case by C_{60} diffusion in the polymeric matrix. The thermogram of thermal desorption of C_{60} from PVP–cov-C_{60} contains a dome-shaped peak at 380–500°C and a sharp peak at 500–530°C. Low-temperature desorption of C_{60} is accompanied by degradation of the macromolecules to form VP and Pr (Figs. 3 and 4). In addition, a comparative kinetic study of C_{60} desorption from a film of pure C_{60} on a metallic support and from PVP–cov-C_{60} film demonstrated that C_{60} molecules are formly retained by the PVP matrix until they diffuse to the polymer–vacuum interface. The total activation energy of low-temperature (380–500°C) desorption of C_{60} (~110 kJ mol^{-1}) is close to that for other polymer–C_{60} complexes bound by covalent bonds [21]. If the low-temperature desorption of C_{60} is caused by rupture of the covalent bonds, the lower activation energy of C_{60} desorption as compared to that of PVP degradation should be due to the fact that the PVP–C_{60} covalent bond is weaker than the C–C bonds in a PVP macromolecule. The high-temperature peak (500–530°C) of C_{60} desorption is absent in the thermogram of PVP–cov-C_{60} films applied from a toluene solution. In this case, C_{60} desorption starts at temperatures lower than those of the onset of PVP depolymerization (Fig. 3a). These data confirm that the mechanisms of high- and low-temperature desorption of C_{60} differ.

The difference in the mechanisms of high- and low-temperature desorption may be due to formation of donor–acceptor bonds of the fullerene both with the macromolecule grafted to it and with free PVP present in the sample. In addition, as we shown previously [19], donor–acceptor bonds and radical ions [8] are formed after exhaustive removal of the solvent (toluene) from the PVP–C_{60} system. Occurrence of these processes in the course of PVP–cov-C_{60} thermolysis cannot be ruled out *a priori*.

In concentrated aqueous solutions of PVP–C_{60} complexes, aggregation to form fractal structures was revealed by small-angle neutron scattering [22, 23]. At relatively high fullerene content in the complex (more than 1%), phase separation occurs and micellar structures composed of fullerene agglomerates with a polymer shell are formed. At the same time, in toluene, which is bad solvent for PVP, its macromolecules are contracted, which prevents contact between the components. Hence, the probability of formation of PVP–C_{60} donor–acceptor bonds in toluene is very low, and the thermal desorption of C_{60} from a PVP–C_{60} film applied from toluene solutions should be similar to that from other polymers, e.g., poly(methylmethacrylate).

In this stage of the study, we suggest that the difference between the thermal desorption of C_{60} from PVP–cov-C_{60} films prepared from toluene and aqueous solutions is due both to different strengths of interaction of these components and different degrees of fullerene aggregation. The high-temperature peak at 500–530°C can be assigned to desorption of C_{60} molecules bound by donor-acceptor bonds or forming radical ions with appreciable charge transfer from the carbonyl oxygen of PVP to C_{60} (negative charge on C_{60} prevents its desorption from the polymer). The content of these C_{60} molecules, roughly estimated by integration of the desorption rate in the high-temperature step, is about 10% of the total fullerene amount in the sample.

The fact that the temperature dependence of C_{60} formation in the course of thermolysis of PVP–C_{60} film (Fig. 4, curve *4*) shows only the high-temperature peak (T_{max} is slightly lower than that for PVP–cov-C_{60}) and does not contain the dome-shaped peak at 380–500°C, which is present in the thermogram of PVP–cov-C_{60}, confirms our assumption that the high-

temperature step is caused by rupture of donor–acceptor bonds between C_{60} and the polymer. The fullerene content in the complex is about 1.7%, i.e., is higher than the critical concentration (1%) at which, in accordance with the data of small-angle neutron scattering [22, 23], dense micellar structures can be formed. It should be noted that, at the temperatures of desorption of the fullerene from PVP–C_{60} film applied from an aqueous solution [22, 23], the PVP–C_{60} covalent bonds are ruptured and the degree of heterogeneity of the film is determined by the C_{60} content in the system.

Although chemical transformations in solutions that contain PVP and C_{60} and in films applied from these solutions are complex, we suggest the following simplified scheme describing the heterogeneous structure of PVP–cov-C_{60} and PVP–C_{60} films, as well as the temperature transformations of this structure.

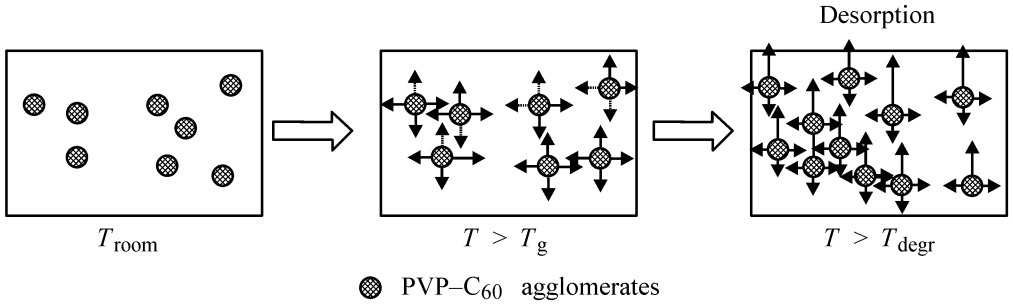

Fullerene desorption from PVP–C_{60} agglomerates is difficult, since they are encapsulated in the PVP matrix, which is preserved up to complete thermolysis of the polymer. As a result, the high-temperature peak of C_{60} desorption appears at 500–530°C (Fig. 4). The low-temperature peak (380–500°C) in the thermogram of PVP–cov-C_{60} is caused both by rupture of C_{60}–PVP covalent bonds and desorption of separate nonbonded C_{60} molecules or C_{60} molecules present in loose agglomerates. If the initial system becomes heterogeneous after formation from solution on the support, complex competitive processes determined by the reactivity and interdiffusion of the components will occur on further heating. The diffusion can be accelerated at temperatures higher than the glass transition point $T_{g.}$ The TDMS data discussed above suggest heterogeneous structure of the examined films is caused by agglomeration in the initial solutions is retained up to the temperature of PVP thermal degradation, $T_{degr.}$ The heterogeneous structure of these systems will be studied in more detail in our further works.

CONCLUSIONS

(1) Curves of thermal desorption of fullerene C_{60} from poly-*N*-vinylpyrrolidone bound to C_{60} by covalent bonds were recorded, as well as the curves of formation of thermolysis products of poly-*N*-vinylpyrrolidone films applied from different solvents.

(2) In the sample applied from an aqueous solution, fullerene is firmly retained in the poly-*N*-vinylpyrrolidone matrix up to the decomposition temperature of poly-*N*-vinylpyrrolidone. This interaction is independent of the bonding type in the initial poly-*N*-vinylpyrrolidone–C_{60} system.

(3) The unusual high-temperature peak of C_{60} desorption is due to rupture of the donor-acceptor bonds between the fullerene and the carbonyl oxygen of the pyrrolidone ring in the poly-*N*-vinylpyrrolidone matrix.

(4) The mechanism of thermolysis of the systems examined and the mechanism of thermal desorption of C_{60} from them is determined both by the type of poly-*N*-vinylpyrrolidone-C_{60} bonds and the solvent used for film preparation. The degree of aggregation of C_{60} and its derivatives increases when water is used as the solvent.

ACKNOWLEDGMENTS

We are grateful to the Humboldt Foundation for placing vacuum oven at our disposal. This study was financially supported by "Urgent Directions in Physics of Condensed Matter" State research program ("Fullerenes and Atomic Cluster" direction), Russian Foundation for Basic Research (project no. 03-03-32633), and OEMMPU program no. IG-03 of the Russian Academy of Sciences.

REFERENCES

1. *Fullerenes: Chemistry, Physics and Technology*, Kadish, K.M. and Ruoff, R.S., Eds., New York: Wiley–Interscience, 2000.

2. Da Ros, T., and Prato, M., *Chem. Commun.*, 1999, pp. 663–669.
3. Burley, G.A., Keller, P.A., and Pyne, S.G., *Fullerene Sci. Technol.*, 1999, vol. 7, no. 6, pp. 973–1001.
4. Guldi, D. and Prato, M., *Acc. Chem. Res.*, 2000, vol. 33, pp. 695–703.
5. Kirsh, Yu.E., *Poli-N-vinilpirrolidon i drugie poli-N-vinilamidy* (Poly-*N*-vinylpyrrolidone and Other Poly-*N*-vinylamides), Moscow: Nauka, 1998.
6. Kirsh, Yu.E., *Khim.-Farm. Zh.*, 1983, vol. 17, no. 6, pp. 711–721.
7. Kiselev, O.I., Kozeletskaya, K.N., Melenevskaya, E.Yu., *et al.*, *Mol. Mater*, 1998, vol. 11, pp. 121–124.
8. Khairullin, I.I., Chen, Y.-H., and Hwang, L.-P., *Chem. Phys. Lett.*, 1997, vol. 275, pp. 1–7.
9. Vinogradova, L.V., Melenevskaya, E.Yu., Hachaturov, A.S., *et al.*, *Polymer Sci.*, 1998, vol. 40, no. 11, pp. 1152–1159.
10. Sushko, M.L., Tenhu, H., and Klenin, S.I., *Polymer*, 2002, vol. 43, no. 9, pp. 2769–2775.
11. Pozdnyakov, A.O., Ginzburg, B.M., Pozdnyakov, O.F., and Redkov, B.P., *Zh. Prikl. Khim.*, 2000, vol. 73, no. 1, pp. 134–136.
12. Shibaev, L.A., Antonova, T.A., Vinogradova, L.V., *et al.*, *Pis'ma Zh. Tech. Fiz.*, 1997, vol. 23, no. 18, pp. 87–92.
13. Pozdnyakov, A.O., Pozdnyakov, O.F., Redkov, B.P., *et al.*, *Pis'ma Zh. Tekh. Fiz.*, 1996, vol. 22, no. 18, pp. 57–60.
14. Pozdnyakov, A.O., Ginzburg, B.M., Pozdnyakov, O.F., *et al.*, *Pis'ma Zh. Tekh. Fiz.*, 2000, vol. 26, no. 17, pp. 46–52.
15. Ginzburg, B.M., Pozdnyakov, A.O., Zgonnik, V.N., *et al.*, *Pis'ma Zh. Tekh. Fiz.*, 1996, vol. 22, no. 4, pp. 73–77.
16. Zgonnik, V.N., Vinogradova, L.V., Melenevskaya, E.Yu, *et al.*, *Zh. Prikl. Khim.*, 1997, vol. 70, no. 9, pp. 1538–1542.
17. Zgonnik, V.N., Vinogradova, L.V., Melenevskaya, E.Yu, *et al.*, *Zh. Prikl. Khim.*, 1995, vol. 68, no. 1, pp. 99–105.
18. Lebedeva, T.L., Fel'dshtein, M.M., Kuptsov, S.A., and Plate, N.A., *Vysokomol. Soedin., Ser. A*, 2000, vol. 42, no. 9, pp. 1504–1523.
19. Ratnikova, O.V., Melenevskaya, E.Yu., Zgonnik, V.N., and Mokeev, M.V., *Zh. Prikl. Khim.*, 2003, vol. 76, no. 10, pp. 1663–1668.
20. Kopeikin, V.V., Santuryan, Yu.G., and Danilova, M.Ya., *Khim.-Farm. Zh.*, 1988, no. 10, pp. 1253–1256.
21. Pozdnyakov, O.F., Redkov, B.P., and Pozdnyakov, A.O., *Pis'ma Zh. Tekh. Fiz.*, 2002, vol. 28, no. 24, pp. 53–57.
22. Lebedev, V.T., Torok, Gy., Len, A., *et al.*, Abstracts of Papers, *6th Biennial Int.–l Workshop "Fullerenes and Atomic Clusters,"* St. Petersburg, June 30–July 4, 2003, p. 208.
23. Lebedev, V., Torok, Gy., Cser, L., *et al.*, *J. Appl. Crystallogr.*, 2003, vol. 36, pp. 646–648.

Russian Journal of Applied Chemistry, Vol. 76, No. 12, 2003, pp. 1971–1973. Translated from Zhurnal Prikladnoi Khimii, Vol. 76, No. 12, 2003, pp. 2022–2024.

MACROMOLECULAR CHEMISTRY AND POLYMERIC MATERIALS

Copolymerization of 1-Vinyl-1,2,4-triazole with 2-Hydroxyethyl Methacrylate

T. G. Ermakova, N. P. Kuznetsova, and K. A. Maksimov

Favorskii Institute of Chemistry, Siberian Division, Russian Academy of Sciences, Irkutsk, Russia
Irkutsk State Technical University, Irkutsk, Russia

Received July 10, 2003

Abstract—Radical copolymerization of 1-vinyl-1,2,4-triazole with 2-hydroxyethyl methacrylate in dimethylformamide and ethanol, initiated with azobis(isobutyronitrile), was studied. The copolymerization constants of this pair of monomers at low conversions and the microstructure parameters were determined. New highly hydrophilic thinly cross-linked copolymers were prepared from these monomers in the presence of cross-linking agents.

The interest in polymerization and copolymerization of vinylazoles [1–3] and, in particular, 1-vinyl-1,2,4-triazole (VT) steadily grows. The VT homopolymer, thanks to its unique properties (nontoxicity, high hydrophilicity, chemical stability, complexing power, heat resistance) shows promise for food industry, engineering, and medicine [4, 5]. In turn, polymerization of 2-hydroxyethyl methacrylatye (HEOMA) and its copolymerization with other vinyl comonomers have been fairly well studied. These (co)polymers are widely used for biological purposes and for fabrication of various medical items [6–8].

No data are available on copolymerization of VT with HOEMA, although the possibility of combining the valuable properties of both monomers is very attractive. Synthesis of new copolymers derived from VT and HOEMA would extend the assortment of nontoxic hydrophilic polymeric materials and open up new prospects for using them in medicine.

In this study, we examined the relative reactivities of VT and HOEMA in their binary radical copolymerization in DMF and ethanol, and also some properties of the resulting copolymers.

EXPERIMENTAL

1-Vinyl-1,2,4-triazole was prepared as described previously [9], by the reaction of 1,2,4-triazole with acetylene under pressure in the system KOH–dioxane. The product was distilled in a vacuum; bp 48°C at 3 mm Hg, n_D^{20} 1.5100. HOEMA was purified as described in [10] and distilled in a vacuum; bp 80°C at 3 mm Hg, n_D^{20} 1.4538.

Copolymerization was performed in ethanol and DMF in the presence of azobis(isobutyronitrile) (AIBN) as initiator at 60°C for 5 h. The monomer concentrations were 1 M, and the initiator concentration, 1×10^{-2} M. The molar ratio of the comonomers was varied from 2 : 8 to 9 : 1. The copolymers were isolated, reprecipitated into acetone from DMF solution, filtered off, and vacuum-dried to constant weight. The composition of copolymers was determined by elemental analysis from the nitrogen content. The IR spectra were recorded on a Specord UR-75 spectrometer in the range 400–4000 cm^{-1}; copolymer samples were prepared as KBr pellets. The intrinsic viscosity of copolymers in DMF was measured with an Ubbelohde viscometer at 20°C by the dilution method. A turbidimetric titration was performed on a KFK-2 device. The copolymerization constants were calculated by the Fineman–Ross and Kelen–Tudos methods [11] using the program from [12]. The microstructure parameters of the copolymers were calculated from the copolymerization constants [13]. A thermogravimetric analysis of samples was performed with an MOM derivatograph (Hungary) in air at a heating rate of 5 deg min^{-1}; the maximum temperature was 700°C.

Copolymerization of VT with HOEMA in DMF and alcohol yielded white powdered products soluble in dipolar organic solvents. The formation of true

1070-4272/03/7612-1971 $25.00 © 2003 MAIK "Nauka/Interperiodica"

Table 1. Copolymerization of VT with HOEMA in DMF and ethanol (60°C; 5 h; [VT] + [HOEMA] = 1, [AIBN] = 10^{-2} M)

Composition, mole fraction				Yield, %	[η], dl g^{-1}	T_{dec}, °C
starting mixture		copolymer				
VT	HOEMA	VT	HOEMA			
Dimethylformamide						
0.2	0.8	0.09	0.91	84	0.15	140–145
0.5	0.5	0.24	0.76	76	0.69	250–263
0.8	0.2	0.46	0.54	43	1.17	>300
0.9	0.1	0.59	0.41	37	1.35	>300
Ethanol						
0.2	0.8	0.05	0.95	79	0.08	190–195
0.5	0.5	0.17	0.79	61	0.19	218–220
0.8	0.2	0.37	0.60	52	0.53	>300
0.9	0.1	0.57	0.43	50	1.09	>300

copolymers follows from the monotonic run of the turbidimetric titration curve, which has no plateaus characteristics of mechanical blends of homopolymers.

The analytical and IR data prove that the polymeric chain is formed by opening of the double bonds in vinyl groups of both comonomers. New copolymers containing triazole and hydroxyethyl methacrylate units were obtained:

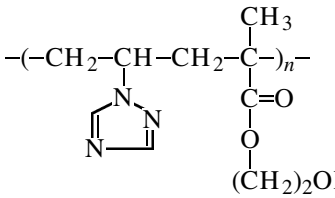

The IR spectra of the synthesized copolymers, contain no absorption bands at 960 and 1650 cm^{-1}, which are characteristic of vinyl groups, are absent. The bands characteristic of the N–H stretching vibrations in triazole at 3300–3400 cm^{-1} are absent, too. At the same time, all the absorption bands of the triazole ring (bending at 670, 1010, 1130, and 1280 cm^{-1}; stretching at 1120, 1430, and 1510 cm^{-1}), as well as the C=O stretching bands in HOEMA (1720 cm^{-1}) are preserved.

Table 1 shows that, as the VT content in the starting monomer mixture is increased, the yield decreases, but the intrinsic viscosity and decomposition point grow, with the latter becoming higher than 300°C.

Analysis of the copolymers shows that, irrespective of the molar ratio of the comonomers, the copolymers are enriched in the HOEMA units, which is consistent with the copolymerization constants (Table 2).

The calculated copolymerization constants of the comonomers show that VT is less active than HOEMA. The decreased reactivity of VT in copolymerization with some unsaturated compounds has been noted previously [1, 14] and was accounted for by polarization of the vinyl group under the influence of the triazolyl substituent.

The higher reactivity of HOEMA [like methyl methacrylate (MMA) and fluorinated methacrylates], compared to VT, may be due to relative stability of the hydroxyethyl methacrylate radical in which the radical center is conjugated with both carboxy and methyl groups. The activity factors are known to grow in going from MMA to higher alkyl acrylates and methacrylates [15]. The quantities $1/r_1$ (Table 2), which characterize the activity of HOEMA to the macroradical with the VT terminal unit confirm that the neutral HOEMA molecules react at a higher rate with the VT radical than with the HOEMA radical. The product of activity constants r_1r_2, equal to 0.22 in DMF and 0.16 in ethanol, shows a tendency toward alternation of VT and HOEMA units in the copolymers. Calculation of the intramolecular distribution of units in the macrochain (see figure) shows that the chains mainly consist of blocks of the more active comonomer, HOEMA, separated by single VT units. As the VT content in the starting monomeric mixture

Table 2. Copolymerization constants of VT (M_1) with HOEMA (M_2)

M_2	Solvent	r_1	r_2	r_1r_2	$1/r_1$	$1/r_2$
HOEMA	DMF	0.09	2.40	0.22	11.11	0.42
	Ethanol	0.06	2.66	0.16	16.67	0.38
MMA*	DMF	0.62	1.48	0.92	1.61	0.68
4-FAMA**	DMF	0.23	1.77	0.41	4.35	0.56
8-FAMA**	DMF	0.25	2.42	0.61	4.00	0.41

* MMA is methyl methacrylate; Q_1 = 0.35, e_1 = 0.08; data of [14].

** 4-FAMA is 2,2,3,3-tetrafluoropropyl methacrylate, and 8-FAMA, 2,2,3,3,4,4,5,5-octafluoropropyl methacrylate [1].

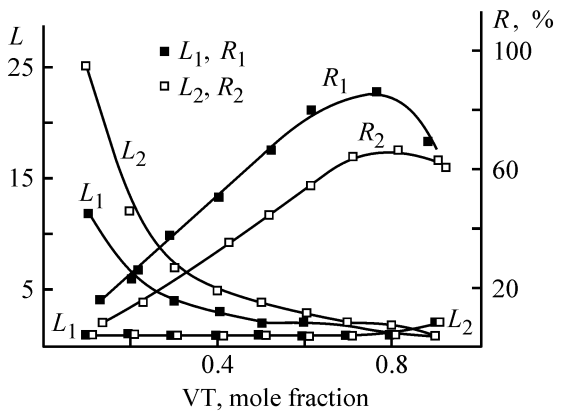

Mean lengths of blocks of similar units L and block structure parameter R vs. the VT mole fraction in the starting monomer mixture. Copolymerization in (*1*) DMF and (*2*) ethanol.

is increased, the length of its blocks grows, and, at the VT mole fraction of 0.75–0.85, the copolymer microstructure becomes close to the alternating structure, which corresponds to the maximum value of the block structure parameter R.

New thinly cross-linked copolymers were prepared by copolymerization of VT with HOEMA in the presence of AIBN and cross-linking agents (0.25 mol %), divinylbenzene and *N*,*N*'-methylenebisacrylamide, at 120°C. The polymerizate is a transparent solid block. The network copolymers are stable up to 240°C according to thermogravimetric analysis. When heated to 260°C, they undergo slow thermal degradation with 10% weight loss. Fast degradation starts at 325°C and is accompanied by 60% weight loss. Above 420°C, the degradation becomes slower, and the residue burns out at 700°C. The thinly cross-linked copolymers prepared have a high refractive index (≥1.5200) and softening point of 110°C; they withstand contact with 0.1 N NaOH and HCl for a week. Hydrated transparent gels with water absorption of 40–75% were obtained.

CONCLUSIONS

(1) Radical copolymerization of 1-vinyl-1,2,4-triazole with 2-hydroxyethyl methacrylate yielded new copolymers containing triazole and hydroxyethyl methacrylate units, soluble in dipolar organic solvents.

(2) 1-Vinyl-1,2,4-triazole is less active in copolymerization.

(3) New thinly cross-linked heat-resistant highly hydrophilic copolymers of 1-vinyl-1,2,4-triazole with 2-hydroxyethyl methacrylate and a cross-linking agent were prepared. These copolymers exhibit high refractive index and are resistant to acid and base hydrolysis; they show promise as raw materials for medicine.

REFERENCES

1. Kuznetsova, N.P., Kanitskaya, L.V., Fedorov, S.V., and Ermakova, T.G., *Vysokomol. Soedin., Ser. B*, 2001, vol. 43, no. 9, pp. 1565–1569.
2. Shagun, V.A., Toryashinova, D.S., Kuznetsova, N.P., and Ermakova, T.G., *Vysokomol. Soedin., Ser. A*, 2002, vol. 44, no. 2, pp. 1–9.
3. Kizhnyaev, V.N. and Vereshchagin, L.I., *Usp. Khim.*, 2003, vol. 72, no. 2, pp. 159–181.
4. Zinchenko, V.I., Makarov, A.S., Lopyrev, V.A., *et al.*, *Pivo Napit.*, 1999, no. 4, pp. 58–59.
5. Voronkov, M.G., Lopyrev, V.A., Kukharskaya, E.V., *et al.*, *Zh. Prikl. Khim.*, 1985, vol. 58, no. 1, pp. 178–180.
6. Lavrov, N.A., *Zh. Prikl. Khim.*, 1992, vol. 65, no. 8, pp. 1896–1901.
7. Jayakrishman, A., *Polymer*, 1990, vol. 31, no. 7, pp. 1339–1342.
8. Asadov, Z.G. and Aliev, V.S., *Usp. Khim.*, 1992, vol. 61, no. 5, pp. 1002–1019.
9. Ermakova, T.G., Tatarova, L.A., and Kuznetsova, N.P., *Zh. Obshch. Khim.*, 1997, vol. 67, no. 5, pp. 859–861.
10. Lavrov, N.A., Sautin, S.N., Bondarenko, V.M., and Nikolaev, A.F., *Vysokomol. Soedin., Ser. B*, 1979, vol. 21, no. 1, pp. 21–23.
11. Kelen, T. and Tudos, F., *React. Kinet. Catal. Lett.*, 1974, no. 1, p. 487.
12. Deryabina, G.I., *Laboratornyi praktikum po khimii VMS: Radikal'naya polimerizatsiya i sopolimerizatsiya: Uchebnoe posobie* (Practical Laboratory Course of Macromolecular Chemistry: Radical Polymerization and Copolymerization: Textbook), Kuibyshev: Kuibyshev. Gos. Univ., 1988.
13. Zil'berman, E.N., *Vysokomol. Soedin., Ser. B*, 1979, vol. 21, no. 1, pp. 33–36.
14. Tatarova, L.A., Morozova, I.S., Ermakova, T.G., *et al.*, *Vysokomol. Soedin., Ser. A*, 1983, vol. 25, no. 1, pp. 14–17.
15. *Copolymerization*, Ham, G.E., Ed., New York: Interscience, 1964.

Russian Journal of Applied Chemistry, Vol. 76, No. 12, 2003, pp. 1974–1977. Translated from Zhurnal Prikladnoi Khimii, Vol. 76, No. 12, 2003, pp. 2025–2027.

MACROMOLECULAR CHEMISTRY AND POLYMERIC MATERIALS

Quantitative Aspects of Competition of Substitution and Addition Pathways in Chlorination of Synthetic Rubbers

V. A. Alferov, V. A. Aver'yanov, and A. A. Goryacheva

Tula State University, Tula, Russia

Received July 1, 2003

Abstract—The competition of substitution and addition pathways in chlorination of SKDN-N, LKN-S, SKDS-N, and NMPB synthetic rubbers in chloroform was studied.

Chlorinated rubbers are of particular importance owing to the unique properties of materials prepared on their basis, such as adhesive composites, paint-and-varnish coatings, heat-insulating materials, and covulcanizates with common rubbers [1–6]. For example, adhesives based on chlorinated rubbers are widely used in various branches of national economy thanks to their high adhesion to various surfaces, elasticity of joints, chemical stability, and low inflammability. Covulcanizates of chlorinated and nonchlorinated rubbers exhibit higher fire, heat, and ozone resistance and enhanced physicomechanical properties [1]. Rubbers and oligobutadienes are widely used as binders that exhibit high strength and heat resistance as compared with the known analogue [2].

The optimal combination of the properties of the resulting materials is ensured by reasonable balance between the amount of chlorine in the rubber and the number of the residual multiple bonds. Fire resistance, chemical stability, and elasticity of the resulting materials grow with increasing chlorine content. However, at a more complete chlorination the amount of the residual double bonds becomes smaller, which adversely affects the strength of a material. At small amount of the residual double bonds, covulcanization between chlorinated and unchlorinated rubbers becomes impossible. Therefore, we examined in this study the competition of the substitution and addition pathways in chlorination as a factor controlling the ratio of the content of chlorine incorporated into the rubber macromolecule to that of the residual double bonds.

EXPERIMENTAL

We used SKDN-N, LKN-S, SKDS-N, and NMPB synthetic rubbers; their chlorination was carried out in chloroform without initiation. In all the cases, the content of rubbers in the chloroform solution was 5 wt %.

The reaction was performed in a glass reactor equipped with a water jacket, a bubbler for chlorine supply, a reflux condenser, and a thermometer. Gaseous chlorine from a cylinder was passed through a Tishchenko bottle with concentrated sulfuric acid and mixed with argon (1 : 1 molar ratio), and the resulting gaseous mixture was passed through the bubbler and fed into the reactor. The constant supply of chlorine was maintained with a manostat, and the rate of chlorine supply was monitored with a rheometer. The temperature of the reaction mixture was maintained by circulating water heated to a required temperature through the water jacket of the reactor. Unreacted chlorine and hydrogen chloride contained in the output gas were trapped with an aqueous solution of potassium iodide at the reactor outlet. At the end of the experiment, the reactor was purged for 40 min to remove chlorine and hydrogen chloride. Then, the solvent was removed from the reaction mixture on a rotary evaporator, and the residue was dried in a vacuum to constant weight. The iodine formed in the reaction between potassium iodide and chlorine in aqueous solution was titrated with a 0.1 N $Na_2S_2O_3$ solution, and the concentration of absorbed HCl was determined by titration with a 0.2 M NaOH solution in

1070-4272/03/7612-1974 $25.00 © 2003 MAIK "Nauka/Interperiodica"

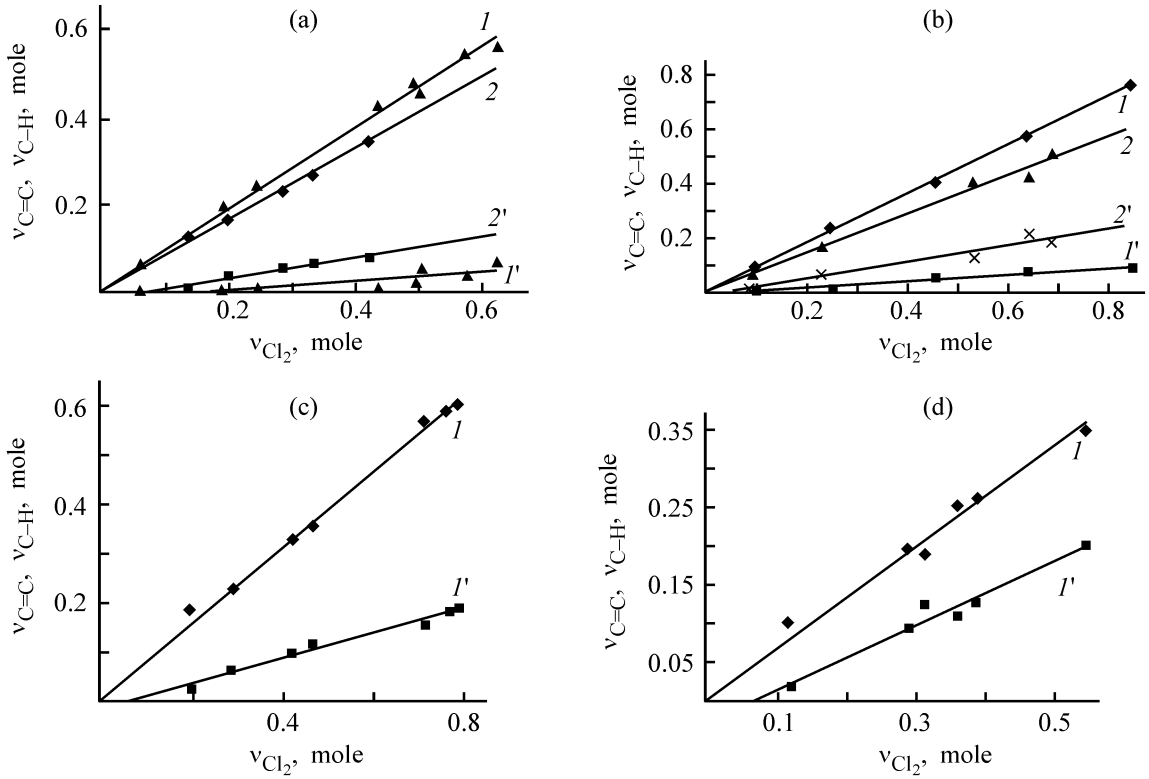

Fig. 1. Dependences of chlorination degree of the C=C and C–H bonds in (a) SKDN-N, (b) SKDS-N, (c) LKN-S, and (d) NMPB rubbers on the overall degree of chlorination. ($\nu_{C=C}$, ν_{C-H}) Content of chlorinated bonds per rubber monomer unit and (ν_{Cl_2}) amount of chlorine taken up per rubber monomer unit; the same for Fig. 2. Chlorination pathway: (*1, 2*) addition and (*1*', *2*') substitution. Temperature, °C: (a) (*1*, *1*') 20 and (*2*, *2*') 58; (b) (*1*, *1*') 15 and (*2*, *2*') 58, and (c, d) 58.

the presence of phenolphthalein. Then, the number of the C–Cl bonds formed in the rubber by substitution chlorination was evaluated. Using these data and the weight of chlorinated rubber, we determined the content of chlorine and the number of chlorinated double bonds in the samples.

The results of chlorination of SKDN-N and SKDS-N rubbers in chloroform are shown in Figs. 1a and 1b as the dependences of the number of moles of the chlorinated C=C and C–H bonds per mole of the monomeric unit ($\nu_{C=C}$, ν_{C-H}) on the number of moles of chlorine taken up per rubber monomer unit (ν_{Cl_2}). As seen, the number of the chlorinated C=C and C–H bonds linearly increases with increasing degree of chlorination. In all the systems studied, the addition pathway in chlorination prevails.

The relative contribution of the addition pathway in chlorination of SKDN-N rubber at 20°C is about 85%. With increasing temperature the contribution of the addition pathway in chlorination decreases, and at 58°C it becomes 71%, which allows preservation of a fairly large amount of the residual double bonds at high degrees of chlorination. At the degree of chlorination, $\nu_{Cl_2} > 0.75$, required to obtain rubber materials with the necessary consumer properties, the content of the residual double bonds is more than 40% of their initial content.

Similar results were obtained for SKDS-N rubber. High-temperature chlorination shows more promise as it ensures the most favorable ratio between the amount of chlorine incorporated in the rubber macromolecule and the content of the residual double bonds. Thus, the chlorination of LKN-S and NMPB rubbers was performed at the maximum temperature of 58°C corresponding to the boiling point of chloroform (Figs. 1c, 1d). The results are similar to those obtained for SKDN-N and SKDS-N rubbers, but in the case of NMPB rubber, the contribution of the substitution pathway in chlorination is greater and, thus, a greater fraction residual double bonds is retained in the rubber (e.g., about 50% at $\nu_{Cl_2} > 0.75$).

Hence, NMPB rubber is of particular importance for modification.

Our analysis of the ν_{C-H}–ν_{Cl_2} dependences showed that their rise begins not from the origin of coordinates, but at some threshold degree of chlorination,

Parameters of Eqs. (1) and (2) for rubber chlorination

Rubber	*T*, °C	α	β	γ	γ/α
SKDN-N	20	0.9 ± 0.03	–0.29 ± 0.02	0.133 ± 0.02	6.767
	58	0.78 ± 0.01	–0.01 ± 0.01	0.23 ± 0.02	3.391
LKN-S	58	0.77 ± 0.02	–0.015 ± 0.02	0.253 ± 0.05	3.043
SKDS-N	15	0.87 ± 0.04	–0.02 ± 0.04	0.159 ± 0.05	5.472
	58	0.71 ± 0.05	–0.01 ± 0.09	0.30 ± 0.14	2.367
NMPB	58	0.66 ± 0.05	–0.03 ± 0.03	0.41 ± 0.09	1.610

which is probably due to the free-radical mechanism of the substitution chlorination of the C–H bonds. It is known that the efficiency of induction of substitution chlorination by chloroalkenes increases with increasing degree of chloroalkene chlorination [7].

This approach can be probably extended to rubber macromolecules. At the beginning of the process, their initiation activity is very low; moreover, the initial stage of the free-radical chlorination (as also that of any free-radical reaction), which involves accumulation of free radicals, is not steady-state. With increasing degree of chlorination, the initiating power of macromolecules increases, but the content of the double bonds decreases owing to the addition of chlorine. The opposite effects of these factors can account for the linearity of the ν_{C-H}–ν_{Cl_2} dependences.

The resulting dependences of $\nu_{C=C}$ and ν_{C-H} on ν_{Cl_2} can be approximated by linear equations

$$\nu_{C=C} = \alpha\nu_{Cl_2}, \quad (1)$$

$$\nu_{C-H} = \beta + \gamma\nu_{Cl_2}. \quad (2)$$

The parameters of the above equations, obtained by the least-squares method [8], are listed in the table.

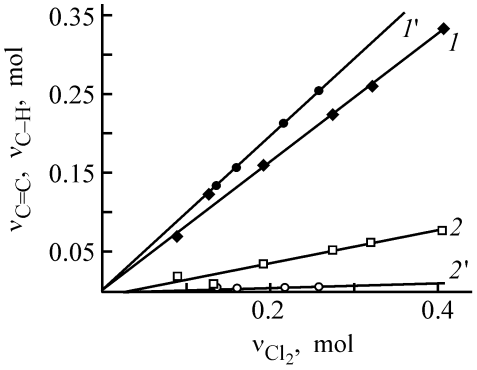

Fig. 2. Degree of chlorination of the (*1*, *1*') C=C and (*2*, *2*') C–H bonds in SKDN-N rubber vs. the overall degree of chlorination in the (*1*', *2*') presence and (*1*, *2*) absence of the inhibitor (5 wt % of the total rubber weight).

The γ/α ratio should obviously correspond to the ratio of the rate constants of the addition and substitution pathways in chlorination.

The difference in the activation energies of these pathways, evaluated from the γ/α ratios at different temperatures, is 14.66 and 15.43 kJ mol^{-1} for SKDN-N and SKDS-N rubbers, respectively. These results are in good agreement with the data on the competitive chlorination of the C=C and C–H bonds under the conditions of free-radical chlorination of tetrachloroethene and 1,2-dichloroethane [9].

The radical-chain mechanism of the reactions studied was confirmed by the data on inhibition of SKDN-N rubber chlorination in the presence of 2,6-di-*tert*-butyl-4-methylphenol. The results are shown in Fig. 2 as dependences of $\nu_{C=C}$ and ν_{C-H} on ν_{Cl_2} in the presence of the inhibitor and without it. It can be seen that, in the presence of the inhibitor, the substitution chlorination, which proceeds exclusively by the free-radical mechanism, is strongly suppressed. At the same time, the increase in the contribution of the addition pathway is due to the fact that this chlorination pathway is not suppressed by the inhibitor.

CONCLUSION

The dependences obtained can be used to determine the content of bound chlorine and the number of residual double bonds in the rubber. The value of these parameters of chlorination, attained in the experiments with the rubbers, make them promising for production of valuable materials and composites.

REFERENCES

1. Ronkin, G.M., Mazanko, A.F., and Romashin, O.P., in *Nauchnye trudy NII Sintez* (Scientific Papers of the Sintez Research Institute), Moscow, 1996, pp. 445–503.

2. Mogilevich, M.M., Turov, B.S., Morozov, Yu.M., *et al., Zhidkie uglevodorodnye kauchuki* (Liquid Hydrocarbon Rubbers), Moscow; Khimiya, 1983.
3. Cataldo, F., *J. Appl. Polym. Sci.*, 1995, vol. 58, no. 11, pp. 2063–2065.
4. Dontsov, A.A., Lozovik, G.Ya., and Novitskaya, S.P., *Khlorirovannye polimery* (Chlorinated Polymers), Moscow: Khimiya, 1979.
5. JPN Patent 06 116 303.
6. US Patent 5 143 180.
7. Serguchev, Yu.A., Barabash, V.V., and Stetsyuk, T.A., Abstracts of Papers, *4 Vsesoyuzonaya nauchnaya konferentsiya "Sovremennoe sostoyanie i perspektivy razvitiya teoreticheskikh osnov proizvodstva khlororganicheskikh produktov"* (4th All-Union Conf. "Modern State and Prospects of Development of Theoretical Basis for Production of Chlorinated Organic Products"), Baku, 1985, pp. 31–32.
8. Doerfel, K., *Statistik in der analytischen Chemie*, Leipzig: Leuna-Merseburg, 1966.
9. Aver'yanov, V.A., Ryl'tsova, S.V., and Alferov, V.A., *Kinet. Katal.*, 1997, vol. 38, no. 1, pp. 20–25.

Russian Journal of Applied Chemistry, Vol. 76, No. 12, 2003, pp. 1978–1982. Translated from Zhurnal Prikladnoi Khimii, Vol. 76, No. 12, 2003, pp. 2028–2032.

MACROMOLECULAR CHEMISTRY AND POLYMERIC MATERIALS

Effect of Allyl Substitution in Chitosan on the Structure of Graft Copolymers

L. A. Nud'ga, V. A. Petrova, and M. F. Lebedeva

Institute of Macromolecular Compounds, Russian Academy of Sciences, St. Petersburg, Russia

Received July 4, 2003

Abstract—The kinetics of graft polymerization of vinyl acetate on allyl chitosan samples with varied content of allyl groups, initiated with ammonium peroxodisulfate, was studied.

Graft polymerization of vinyl monomers on polysaccharides allows preparation of hybrid copolymers combining the properties of natural and synthetic polymers, e.g., biocompatibility and thermoplasticity. Such copolymers show promise as biomaterials.

Graft polymerization of vinyl acetate (VA) on chitosan in acetic acid solution, initiated with ammonium peroxodisulfate, yielded self-stabilized emulsions. The process kinetics was studied; it was found that the reaction rate only weakly depends on the concentrations of chitosan and initiator and is proportional to the VA concentration. An examination of the thermomechanical properties of the copolymers with different degrees of grafting showed that, at longer grafting time, partially cross-linked structures are obtained. Alkaline treatment of the grafted polyvinyl acetate resulted in transfer of the copolymer into solution or its transformation into a gel (in the case of the cross-linked copolymer) through hydrolysis of acetate groups. The hydrolysis kinetics was studied. The final product was a copolymer of chitosan with polyvinyl alcohol [1]. Despite the 100% conversion of the monomer and high degree of grafting, the grafting efficiency did not exceed 50%, i.e., grafting and homopolymerization of VA occurred at different rates. It has been shown previously that the use of cellulose ethers with a small content of allyl groups sharply enhances the efficiency of grafting of vinyl monomers and the content of grafted chains [2].

In this study we examined the effect of allyl substituents in chitosan on the parameters of graft polymerization of VA and structure of the resulting copolymer.

EXPERIMENTAL

Allyl chitosan (ACAN) with the degrees of allyl substitution, γ_A, of 4, 9, 25, and 38 was prepared as described in [3].

Vinyl acetate was distilled twice; the fraction with bp 72.5–72.8°C was used. Ammonium peroxodisulfate (APS) was recrystallized from water.

Graft polymerization of VA was performed as follows. A calculated amount of water was added to a definite portion of a 4% solution of ACAN in 2% acetic acid to obtain the required ACAN concentration. The mixture had pH 3.6. Then a definite amount of VA was added; the mixture was vigorously stirred to obtain an emulsion and heated to 60°C. The calculated amount of APS was added, with the stirring being continued. This instant of time was considered to be the start of the reaction. Samples of the reaction mixture were taken at regular intervals; the reaction in these samples was stopped by adding acetone. The precipitate was filtered off on a Schott filter placed in a Soxhlet apparatus. The homopolymer was separated from the precipitate by exhaustive extraction with acetone, followed by solvent evaporation in a rotary evaporator. The copolymer yield was determined by weighing the filter with the precipitate after drying in a vacuum at 60°C.

The degree of grafting, C (%), was calculated by the formula

$$C = [(g_1 - g_0)/g_0] \times 100,$$

where g_0 is the ACAN weight in the sample, and g_1, the copolymer weight in the sample.

1070-4272/03/7612-1978 $25.00 © 2003 MAIK "Nauka/Interperiodica"

The grafting efficiency E (%) was calculated as the ratio of the weight of the grafted PVA to the total weight of the polymerized monomer:

$$E = (g_1 - g_0)/(g_1 - g_0 + g_2) \times 100,$$

where g_2 is the weight of VA homopolymer in the sample.

The yields Q_1 and Q_2 of the grafted polymer and homopolymer were calculated as the ratios of the weight of the corresponding polymer to the weight of the monomer taken in the reaction; the conversion K was calculated as $Q_1 + Q_2$.

To isolate the grafted polymer, the purified copolymer was treated for 24 h with a mixture of concentrated acetic acid and 60% sodium nitrite solution at a solid-to-liquid ratio of 1 : 10. Such treatment resulted in deamination and depolymerization of chitosan. The homopolymer was filtered off and heated with 1 N HCl at 100°C for 1 h; the resulting solution was dialyzed against water to negative reaction for chloride ions. The dialyzate was lyophilically dried. The isolated grafted polymer was polyvinyl alcohol (PVAl). Its molecular weight was calculated from the intrinsic viscosity [η] (dl g^{-1}) in water at 25°C by the formula [4]

$$[\eta] = 1.40 \times 10^{-2} M^{0.60}.$$

The number of grafted chains N per 100 monomeric units was calculated by the formula

$$N = g_1(166 + 40x) \times 100/M_i g_0,$$

where $(166 + 40x)$ is the molecular weight of the ACAN monomeric unit with the degree of deacetylation of 0.88 and degree of allyl substitution $x = \gamma_A/100$; M_i is the molecular weight of grafted PVA, which is calculated from the molecular weight of PVAl, determined as described above.

The thermomechanical properties of graft copolymers were studied by the penetration method at a heating rate of 1 deg min^{-1} and a load of 0.1 kg mm^{-2}.

The kinetics of graft polymerization of VA on ACAN was studied in relation to the content of unsaturated groups and concentrations of the monomer, initiator, and ACAN (Fig. 1). The kinetic curves of graft polymerization on ACAN with varied content of allyl groups are similar. Their shape shows that the grafting starts without induction period, occurs fast, and is complete in 15 min. Within this time, all the grafting parameters (degree and efficiency of grafting, monomer conversion) reach their maximum values,

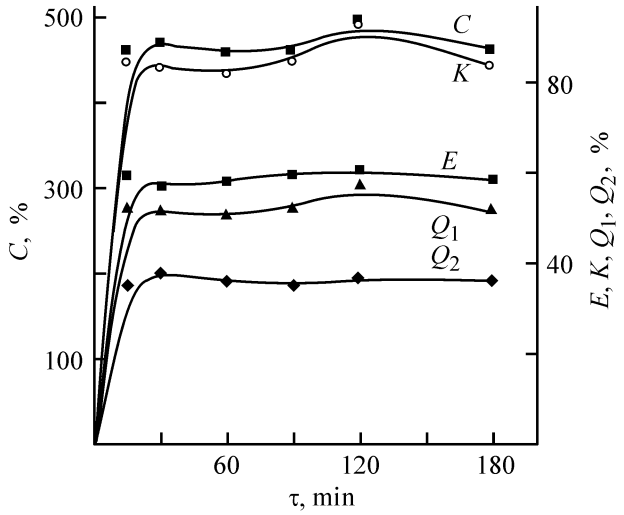

Fig. 1. Kinetic curves of graft polymerization of VA on $ACAN_{\gamma=13}$. [ACAN] = 6 mM; [VA] = 1 M; [APS] = 3 mM; 60°C. (C) Degree of grafting, (E) grafting efficiency, (K) monomer conversion, (Q_1) yield of the grafted polymer, (Q_2) yield of the homopolymer, and (τ) time.

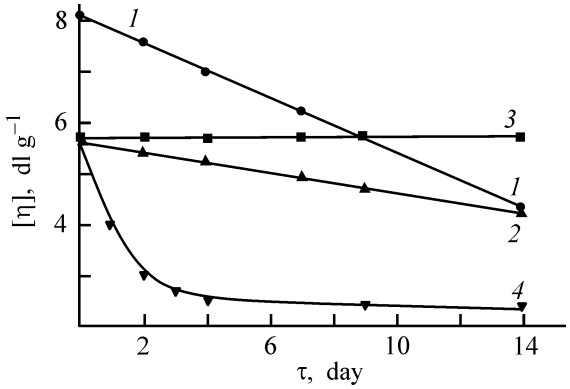

Fig. 2. Variation with time of the intrinsic viscosity [η] of (*1*) chitosan, (*2*) $ACAN_{\gamma=13}$, (*3*) $ACAN_{\gamma=30}$, and (*4*) $ACAN_{\gamma=30}$ in the presence of 3 mM APS. 20°C.

and the secondary processes starting subsequently only weakly affect these parameters.

With ACAN, the absolute degree of grafting increases by a factor of 2, compared to graft polymerization of VA on chitosan, and the grafting efficiency, by a factor of 1.5 even at $\gamma_A = 13$ (480 against 240% and 60 against 40%, respectively), which suggests that the allyl groups are involved in initiation of the graft polymerization. This has been shown previously in studies of graft polymerization of vinyl monomers on allyl hydroxyethyl cellulose (AHOEC) [2]. Initiation can occur via formation of peroxy groups at the allyl α-C atom, with their subsequent decomposition, and(or) via proton abstraction from the allyl α-CH_2 group by the radical ion generated by decomposition of APS.

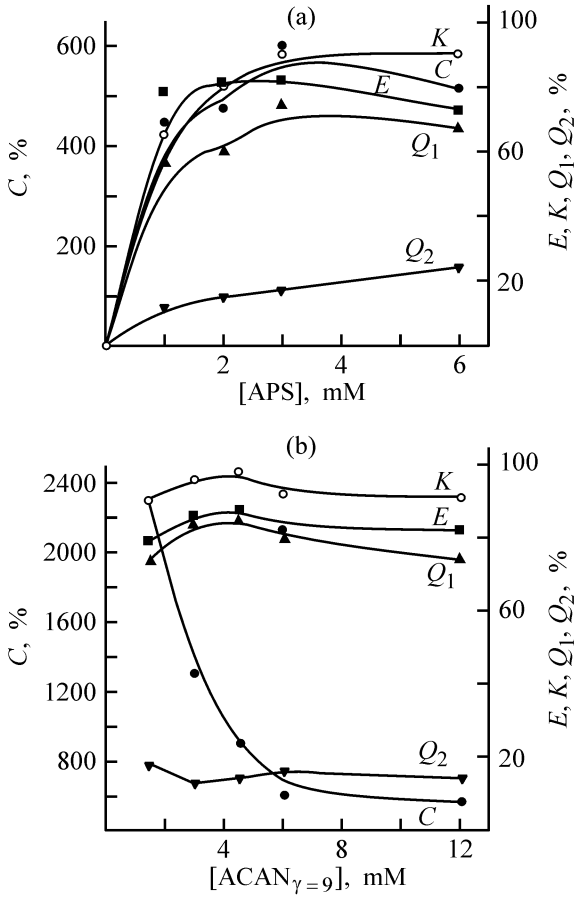

Fig. 3. Degree C and efficiency E of grafting, monomer conversion K, and yields of the grafted polymer Q_1 and homopolymer Q_2 vs. the concentrations of (a) APS and (b) $ACAN_{\gamma=9}$. 60°C; 15 min; [VA] = 1.0 M; (a) $[ACAN_{\gamma=9}]$ = 6 mM; (b) [APS] = 1.0 mM.

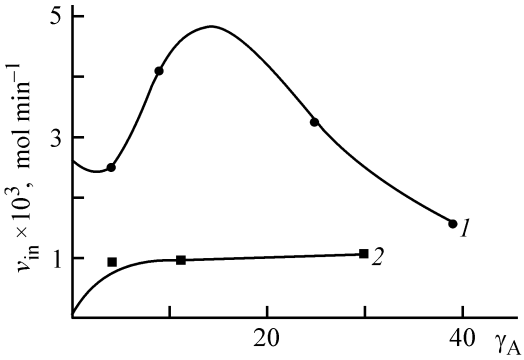

Fig. 4. Initial rate of graft polymerization v_{in} of VA on (*1*) ACAN and (*2*) AHOEC vs. the allyl group content γ_A.

The occurrence of radical oxidation processes in ACAN solutions is indicated by measurements of the intrinsic viscosity of ACAN with various degrees of ally substitution in the course of storage of 3% ACAN solutions in 0.33 M acetic acid at 20°C. The curves of [η] against time (Fig. 2) show that chitosan undergoes hydrolytic and oxidative degradation in the solution, with a decrease in [η] (curve *1*). In the $ACAN_{\gamma=13}$ solution, the degradation is slower (curve *2*), and in the $ACAN_{\gamma=30}$ solution, [η] does not change noticeably with time (curve *3*). Since all the three polymers contain in the backbone glucoside bonds unstable in acid solutions, the constancy of [η] in the $ACAN_{\gamma=30}$ solution suggests a dynamic equilibrium between the degradation and cross-linking of $ACAN_{\gamma=30}$ macromolecules, which occurs as a result of recombination of radicals that arise at the allyl α-CH_2 group. Addition of 3 mM APS to the solution drastically accelerates the degradation (curve *4*) owing to additional generation of peroxy radicals by the reaction of the initiator with the allyl group. In the presence of VA, the additional peroxy radicals act as propagation points of the grafted chain. The combination of the two initiation mechanisms results in that the initial grafting rate grows with increasing γ_A.

The degree and efficiency of grafting considerably grow with the initiator concentration increasing up to [APS] = 3 mM (Fig. 3a). At the same time, an increase in the ACAN concentration results in a sharp decrease in the degree of grafting, without affecting the other parameters (Fig. 3b).

Comparison of the initial rate v_{in} of VA grafting on AHOEC and ACAN (Fig. 4) as a function of γ_A shows that, firstly, v_{in} of grafting on ACAN is higher than that on AHOEC at any γ_A, owing to the activating effect of the chitosan amino groups on the VA double bond. Secondly, the curves differ in shape: With AHOEC, v_{in} tends to weakly grow, whereas with ACAN it passes through a maximum. Inhibition of the reaction on ACAN at $\gamma_A > 15$ may be due to the occurrence of cross-linking within microemulsion particles. Apparently, the presence of a large amount of propagation points results in the occurrence of cross-linking from the very beginning of the reaction, which prevents diffusion of the monomer inside the microemulsion drops. This assumption is confirmed by the fact that the states of the reaction system differ, depending on γ_A, even 15 min after the reaction onset. The copolymerizate is an emulsion at low γ_A (4 or 9), a gel at γ_A = 23 and a two-phase system at γ_A = 38. A similar effect is exerted by an increase in the concentration of allyl groups because of the growing ACAN content, even at small γ_A.

Allylchitosan is a diphilic polymer containing both hydrophilic (hydroxy and amino) and hydrophobic (allyl) groups. At the beginning of the reaction, when VA is dispersed in ACAN solution, a microemulsion is formed. This microemulsion is stabilized by hy-

Table 1. Content of grafted PVA chains, *N*, and degree of their polymerization, DP, (reaction conditions: 60°C, 15 min)

γ_A	[APS], mM	[VA], M	DP	N^*	γ_A	[APS], mM	[VA], M	DP	N^*	γ_A	[APS], mM	[VA], M	DP	N^*
0	3.0	1.0	230	2.6	9	1.0	1.0	200	4.6	9	3.0	0.5	80	2.1
4			254	3.4		3.0		200	5.5			1.0	254	5.5
9			200	5.5		6.0		200	5.2			2.0	350	5.0

* Per 100 monomeric units of ACAN.

Table 2. Determination of the reaction orders of graft polymerization of VA on $ACAN_{\gamma=9}$ (reaction conditions: 60°C, 15 min)

[VA], M	[APS], mM	$[ACAN_{\gamma=9}]$, mM	log [*C*]	*v* of reaction, mmol min^{-1}	log *v*	tan α
0.25	3.0	6.02	–0.6021	9.5924×10^{-5}	–4.0181	1.70
0.50			–0.3010	6.2255×10^{-4}	–3.2058	
2.00			0.3010	6.4177×10^{-3}	–2.1926	
1.0	1.0	6.02	–3	3.3090×10^{-3}	–2.4803	0.05
	2.0		–2.6990	3.3253×10^{-3}	–2.4782	
	6.0		–2.2218	3.6220×10^{-3}	–2.4410	
1.0	3.0	1.5	–2.8239	4.1523	–2.3817	–0.10
		3.0	–2.5229	4.2293	–2.3737	
		12.0	–1.9208	4.8045	–2.3184	

drophobic interaction of VA molecules with ACAN allyl groups; the ACAN hydrophilic groups are oriented toward the aqueous medium. On adding an initiator, grafting and homopolymerization of VA start within such a microparticle When the amount of propagation points is relatively small (γ_A 4 or 9), the grafted PVA chains do not interact with one another, at least in the first 15 min of the reaction, and the reaction system remains an emulsion. As the content of grafted chains increases (γ_A 13 and 25), the probability of interaction of the propagating chains grows, and a gel is formed in 15 min; at $\gamma_A = 38$, a thick network of cross-linked grafted PVA is formed. At high degrees of grafting, the microemulsion particles get inverted, and the system undergoes segregation. The longer the grafting process, the higher the degree of cross-linking. Therefore, the monomer conversion varies only weakly at reaction times longer than 30 min, and the degree and efficiency of grafting slightly grow because of the incorporation of the homopolymer into the grafted chains by the recombination mechanism.

We were able to determine the number of grafted PVA chains, *N*, only in the range of γ_A from 0 to 9; we revealed a correlation of *N* with γ_A (Table 1). The molecular weight of grafted PVA is independent of the initiator and ACAN concentrations but is determined by the monomer concentration. At high γ_A, the molecular weight could not be determined because of the strong cross-linking.

To calculate the reaction orders with respect to each reactant from the kinetic curves, we determined the initial rates at three concentrations of each reactant (at constant concentrations of the two other reactants) and plotted the concentration dependences of the rates in the logarithmic coordinates. The reaction orders were determined as the slopes of the straight lines obtained. The results are listed in Table 2. We obtained the following equation for the rate of VA grafting to ACAN:

$$v_{in} \sim [VA]^{1.70}[APS]^{0.05}[ACAN]^{-0.10}.$$

Comparison with the corresponding equation for VA grafting to chitosan (CAN) [1],

$$v_{in} \sim [VA]^{1.08}[APS]^{0.04}[CAN]^{-0.02}$$

shows that, with ACAN, the order with respect to the monomer is appreciably higher, which is quite consistent with the presumed participation of ACAN allyl groups in grafting initiation.

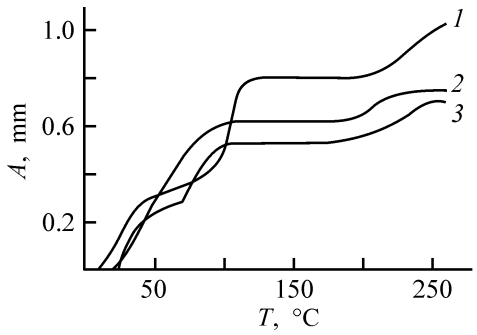

Fig. 5. Thermomechanical curves of graft copolymers: (*A*) strain and (*T*) temperature. (*1*) PVA–$ACAN_{\gamma=9}$ and (*2*, *3*) PVA–$ACAN_{\gamma=30}$. Degree of grafting, %: (*1*) 570 and (*2*, *3*) 450. Grafting time, min: (*1*, *3*) 180 and (*2*) 15.

The presence of cross-linked structures in the copolymers prepared on highly substituted ACAN samples is confirmed by the thermomechanical curves (Fig. 5). Two clearly pronounced thermal transitions are seen: The first one, at about 20°C, corresponds to melting of the grafted PVA chains, and the second, at about 210°C, to softening of the copolymer. The height and length of the plateau in the thermomechanical curves furnish information about the degree of copolymer cross-linking. The copolymer prepared on $ACAN_{\gamma=9}$ shows higher strain than those prepared on $ACAN_{\gamma=30}$; the strain is the lower, the longer the grafting. Hence, the density of cross-linking increases with γ_A and with the grafting time.

Thus, ACAN controls the structure of the graft copolymer: We obtained comb-shaped copolymers at low values of γ_A (4, 9), thinly cross-linked structures at medium γ_A (23), and three-dimensional thickly cross-linked networks at higher γ_A.

CONCLUSIONS

(1) A kinetic study of the graft polymerization of vinyl acetate on allyl chitosan showed that the content of allyl groups in the chitosan samples affects the initial reaction rate, number of grafted polyvinyl acetate chains, and structure of the graft copolymer.

(2) The kinetic orders of graft polymerization with respect to the monomer, initiator, and allyl chitosan were determined. The reaction orders with respect to the initiator and allyl chitosan are zero, and that with respect to the monomer is close to 2.

REFERENCES

1. Nud'ga, L.A., Petrova, V.A., Lebedeva, M.F., and Petropavlovskii, G.A., *Zh. Prikl. Khim.*, 1996, vol. 69, no. 7, pp. 1194–1199.
2. Nud'ga, L.A., Plisko, E.A., and Petropavlovskii, G.A., *Zh. Prikl. Khim.*, 1989, vol. 62, no. 11, pp. 2569–2672.
3. Nud'ga, L.A., Petrova, V.A., Denisov, V.M., and Petropavlovskii, G.A., *Zh. Prikl. Khim.*, 1991, vol. 64, no. 1, pp. 229–232.
4. Dien, H.A., *J. Polym. Sci.*, 1954, vol. 12, pp. 414–438.

Russian Journal of Applied Chemistry, Vol. 76, No. 12, 2003, pp. 1983–1987. Translated from Zhurnal Prikladnoi Khimii, Vol. 76, No. 12, 2003, pp. 2033–2037.

MACROMOLECULAR CHEMISTRY AND POLYMERIC MATERIALS

Simulation of the Kinetics of Plasticizer Extraction with Ethanol

A. V. Dedov

Mosiskozh Open Joint-Stock Company, Moscow, Russia

Received August 12, 2003

Abstract—The main approaches to simulation of the migration kinetics of ingredients from polymers were considered. The mathematical models used for predicting the kinetics of diffusion-controlled migration processes were analyzed.

Extraction of plasticizer from polyvinyl chloride (PVC) deteriorates the polymer characteristics and also has an adverse environmental impact. A decrease in the plasticizer content in PVC makes higher its glass transition point and impairs the consumer properties of articles thereof. A number of plasticizers are toxic, which limits their permissible content in liquids. Reliable prediction of the kinetics of extraction of plasticizers from PVC often allows estimation of the service life of a polymeric article and control over the content of ingredients in the environment.

An analysis of the models used for predicting the kinetics of migration of ingredients from polymers revealed two major approaches to development of such models. One approach consists in processing of the experimental results and derivation of empirical equations [1–5]. The other approach utilizes the mathematical techniques developed to describe processes similar to migration of ingredients from polymers, such as heat loss from solids [6] and diffusion of low-molecular-weight substances in polymers [7].

The validity of empirical models is determined by the large body of experimental data. However, their use is usually limited to specific experimental conditions. This approach requires that the dependences of the coefficients in empirical equations on characteristics of plasticizers should be established [3, 4]. A knowledge of the temperature dependences of the coefficients makes empirical equations suitable for conditions differing from those in accelerated tests of PVC [3].

Equations constituting mathematical models use a parameter characterizing the transfer of plasticizers from the bulk to the surface or escape of an ingredient from the surface of the material to the environment. The kinetics of transfer of a plasticizer in a polymer is governed by the diffusion rate, and the parameter characterizing the escape of the plasticizer from the polymer surface depends on the state of aggregation of the environment. For PVC brought in contact with air, the volatility of the plasticizer serves as such parameter [6]. For PVC brought in contact with liquids or solids capable of absorbing the escaped plasticizer, the coefficient of diffusion of the ingredient in the medium is suitable as such parameter. This approach to simulation of the migration kinetics requires determining the limiting stage of the process, for which purpose there are still no fully adequate calculational procedures [8]. A multitude of models is used now for predicting the migration kinetics of ingredients introduced for various purposes, so that a model suitable for the given specific service conditions of a polymeric article and specific nature of an ingredient.

The aim of this study was to simulate the kinetics of extraction of dioctyl phthalate (DOP) and dibutyl phthalate (DBP) from PVC with ethanol.

The validity of mathematical models was assessed by comparing their predictions with the experimental results reported in [9–12]. These studies were concerned with extraction of DOP and DBP with ethanol at different temperatures and different initial contents of the plasticizer in PVC. The extraction kinetics were shown to depend on the rate of diffusion of an ingredient in PVC, which eliminates the need to determine the limiting stage of the process. Given below are the equations constituting the mathematical models used for predicting the migration kinetics of ingredients introduced for various purposes in the case of a diffusion-controlled process:

$$\frac{M_\tau}{M_0} = 2.26\sqrt{\frac{D\tau}{\delta^2}}, \quad (1)$$

1070-4272/03/7612-1983 $25.00 © 2003 MAIK "Nauka/Interperiodica"

$$\frac{M_\tau}{M_0} = 1 - \frac{8}{\pi}\exp\left(-\frac{4\pi^2 D\tau}{\delta^2}\right), \quad (2)$$

$$\tau_i = \alpha_i \frac{l^2}{D}, \quad (3)$$

$$\frac{M_\tau}{M_0} = 4\left(\frac{D\tau}{\pi}\right)^{0.5}\frac{1}{\delta}. \quad (4)$$

Here, M_τ is the amount of an ingredient, which migrates out of the polymer within a time τ; M_0, the initial content of the ingredient in the polymer; D, the coefficient of diffusion of the ingredient in the polymer; τ_i, the time of migration of ith portion of the ingredient initially contained in the polymer; a_i, a constant coefficient independent of the nature of the ingredient; δ, the thickness of a polymeric article; and l, the parameter relating the conditions of contact between the polymer and the environment to the thickness of the material ($2l = \delta$ and $l = \delta$ in the cases of one- and two-sided contact, respectively).

We give unified designations to the variables in Eqs. (1)–(4), which may differ from those used in the original papers.

Equations (1) and (2) were used for predicting the migration kinetics of the plasticizer for plasticized PVC brought in contact with unplasticized PVC [13] and air [14]. Equation (3) served for predicting the migration kinetics of plasticizers [15, 16] and stabilizers [17–19], and Eq. (4), for describing the kinetics of extraction of stabilizers from polyolefins [7].

It can be seen that it is difficult to analyze Eqs. (1)–(4) in such a form. It is more convenient to have all the equations in the form (3) and use for this purpose the coefficient a_i, which is directly proportional to the time of migration of a certain portion of the plasticizer. The parameter $1/a_i$ can be used for evaluating the migration rate of a certain portion of the plasticizer for a polymer contacting with various media.

Equations (1), (2), and (4), which include the film thickness as a variable, are intended for predicting the kinetics of migration of ingredients in the case of a two-sided contact of the polymer with the environment. In Eq. (3), the type of contact of the polymer with the environment is expressed via parameter l, and after replacing it with δ in accordance with $2l = \delta$, Eq. (3) takes the form

$$\tau_i = \frac{a_i \delta^2}{4D}. \quad (5)$$

The parameters a_i in Eqs. (3) and (5) are governed by the preset M_τ/M_0 ratio, which does not enter into them in the explicit form. In this study, we do not consider the method for calculation of the coefficient a_i; it was described in detail in [6]. For Eqs. (1), (2), and (4), the coefficients a_i are equal to constants appearing in the corresponding equations at preset M_τ/M_0 ratios. The coefficients a_i calculated for Eqs. (1), (2), (4), and (5) are listed in Table 1. Notably, in the case of extraction of a plasticizer with ethanol at one-sided

Table 1. Comparison of the adequacy of the models in predicting the kinetics of plasticizer extraction with ethanol

Plasticizer	Q,* wt. part	T, °C	References	$D \times 10^9$, $cm^2\ s^{-1}$	a_i for indicated M_τ/M_0				
					0.1	0.2	0.3	0.4	0.5
DBP	50	10	[9]	0.23	0.16	0.72	1.45	2.62	4.90
	50	25	[9]	1.3	0.12	0.52	1.43	2.00	4.90
	50	30	[9]	3.6	0.16	0.75	1.80	3.00	4.90
	50	60	[9]	8.9	0.17	0.75	1.45	3.00	4.90
DOP	33	45	[10]	4.9	0.17	0.76	1.77	3.13	4.90
	43	50	[11]	11.0	0.23	1.03	1.40	2.65	4.90
	50	25	[9]	2.9	0.23	0.80	1.75	3.12	4.90
	60	30	[10]	7.5	0.43	1.03	1.81	2.84	4.90
	60	45	[10]	15.0	0.52	1.55	2.32	3.40	4.90
	60	55	[10]	44.0	0.63	1.26	2.22	3.28	4.90
	100	45	[10]	95.0	0.54	1.63	2.45	3.27	4.90
Calculation by indicated equation:									
(1)					0.20	0.78	1.76	3.13	4.90
(2)					2.60	2.90	3.28	3.69	4.12
(5)					0.10	0.38	0.95	1.60	4.00
(4)					0.20	0.78	1.77	3.14	4.90

* Q is the initial content of the plasticizer in PVC, wt parts per 100 wt parts of the polymer.

contact between the liquid and the polymer, the coefficient a_i increases fourfold, compared to the two-sided contact.

In this study, we do not analyze models predicting the kinetics of extraction of plasticizers from PVC with fuels [11, 12] and alcohols [20]. A drawback of these models is that their equations include an additional variable, the equilibrium content of ingredient in the liquid, which depends on the chemical nature and temperature of the liquid [9–12, 20].

The models analyzed in this study were developed under certain assumptions, the most common of which are the constancy of the diffusion coefficient throughout the migration process and immediate and permanent escape of the evolved ingredient from the polymer surface into the environment. However, in extraction of the plasticizer from PVC, the diffusion coefficient D may vary in a certain stage of the process. This is due to glass transition in the polymer [11, 12] or in its surface layer [21] after migration of a certain portion of the plasticizer. When the polymer is in contact with air, these amounts of the plasticizer can be easily calculated [1]; extraction of ingredient may involve a counterflow of the liquid into the polymer, and this may exert varied influence on the glass transition of the material.

As to immediate escape of an ingredient from the polymer surface, this is of less importance for the plasticizer extraction kinetics. This follows from [10, 11], where it was shown that the rates of extraction of the plasticizer with alcohols at vigorous stirring and in a stagnant liquid rapidly approach each other. Along with the aforesaid, the accuracy of prediction of the plasticizer extraction kinetics depends on the PVC brand, composition of the material, and the conditions of manufacturing articles thereof [9].

The diversity of models hinders analysis of their validity by the previously applied method of comparison of the experimental and calculated τ_i values [15–19]. In this study, we solved the inverse problem, namely, calculated the coefficients a_i (Table 1) from the experimental data on the extraction kinetics and compared them with those calculated by Eqs. (1), (2), (4), and (5). In our calculations, we used the experimental data; the τ_i parameters were obtained from the kinetic dependences characteristic of extraction of plasticizers. We calculated the diffusion coefficient of the plasticizer in PVC for the two-sided contact of the polymer with alcohol by the equation [22]

$$D = 0.049\frac{\delta^2}{\tau_{0.5}}, \quad (6)$$

Here, $\tau_{0.5}$ is the time corresponding to extraction of 50% of the initial amount of the plastisizer contained in the polymer, or to $M_\tau/M_0 = 0.5$.

Comparison of the parameters a_i calculated by Eqs. (1), (2), and (4) shows how the plasticizer migration kinetics varies with the state of aggregation of the environment (Table 1). Under identical conditions, the plasticizer migration rate is the lowest when PVC is in contact with air [the coefficient a_i from Eq. (2) is greater than those from Eqs. (1), (2) and (4)]. The revealed dependence of the plasticizer migration kinetics on the state of aggregation of the environment, namely, the greater rate of the process in the case of contact of PVC with liquids and solids, compared to its contact with air, is supported by the experimental data [1].

At the same time, the use of Eq. (5) for predicting the plasticizer migration kinetics implies its independence from the state of aggregation of the environment. It should be noted that Eq. (5) was intended specifically for predicting the kinetics of the stabilizer migration from polyolefins. Testing the adequacy of Eq. (5) in predicting the kinetics of the plasticizer migration from PVC suggests that the value of the coefficient a_i is to be corrected (raised) [15].

The dependence of the calculated coefficient a_i on the state of aggregation of the environment is the most pronounced in the initial stage of migration, at $M_\tau/M_0 \le 0.3$. With increasing time of migration, the calculated a_i values get closer, except that calculated using Eq. (5). However, at $M_\tau/M_0 = 0.5$, the coefficients a_i calculated by different equations differ much less significantly.

For $M_\tau/M_0 = 0.5$, the parameters a_i calculated using different equations (Table 1) are equal or close to 0.049 in Eq. (4). At the same time, Table 1 shows that, at $M_\tau/M_0 \ne 0.5$, D varies with the equation chosen for its calculation.

The values of a_i, derived from experimental data, also differ significantly in the initial stage of extraction of the plasticizer and get close at $M_\tau/M_0 \ge 0.3$ (Table 1). The divergence of the coefficients a_i in the initial stage of extraction can be attributed to the experimental inaccuracies in monitoring the migration of relatively small amounts of a plasticizer and in processing the plots constructed on a small scale.

Processing the experimental values of a_i by the Table-Curve program yielded a mathematical expression, which can be substituted into Eq. (5), making it suitable for predicting the kinetics of DOP and DBP extraction with ethanol at various stages of the process.

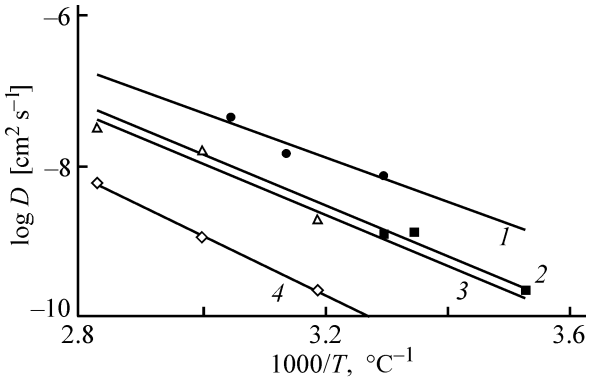

Temperature dependence of the diffusion coefficient D of (*1, 3*) DOP and (*2, 4*) DBP for (*1, 2*) extraction and (*3, 4*) evaporation.

$$\tau_i = 0.19\left(\frac{M_\tau}{M_0}\right)^2 \frac{\delta^2}{D}, \quad (7)$$

Here, M_τ/M_0 varies from 0 to 1.

The correlation coefficient for Eq. (7) was estimated at 0.92, which is sufficient for tentative calculation of the kinetics of DOP and DBP extraction with ethanol.

The established temperature dependences of the coefficient of the plasticizer diffusion in PVC (see figure) increase the potential of Eq.(7). The figure also presents the temperature dependences of the plasticizer diffusion coefficient in the case of contact of the polymer with air (the corresponding D values are marked with open rhombs and squares). These data were obtained for samples that initially contained 65 wt. parts of ingredient per 100 wt parts of PVC and were subjected to a high vacuum [23]. Table 2 lists the characteristics of the DOP and DBP diffusion under various conditions of use of a polymeric article, which were obtained using the Arrhenius equation. The figure and Table 2 suggest a higher rate of the plasticizer diffusion in extraction from PVC, compared to the case of the polymer contacting air.

Table 2. Characterization of diffusion of plasticizers in PVC for various conditions of use of the polymeric article

Plasticizer	Content in PVC, wt. parts	Extraction		Evaporation*	
		E_a, kJ mol^{-1}	$\log D_0$	E_a, kJ mol^{-1}	$\log D_0$
DOP	60	55.9	1.41	77.3	3.0
DBP	50	55.9	0.74	73.5	3.2

* Initial content of plasticizer 65 wt. parts per 100 wt. parts of PVC.

To conclude, the kinetics of DOP and DBP extraction from PVC with ethanol is most adequately simulated by Eqs. (1) and (4). The precision of simulating the kinetics of migration of an ingredient in the case of a polymer brought in contact with various media is strongly dependent on the conditions under which the coefficient of diffusion of the ingredient in the polymer is determined.

CONCLUSION

Models that most adequately predict the kinetics of extraction of a plasticizer from polyvinyl chloride were identified. The specific features of the plasticizer diffusion in the case of polymer brought in contact with air or ethanol were elucidated.

REFERENCES

1. Thinius, K., *Chemie, Physik und Technologie der Weichmacher*, Leipzig: Grundstoffeindustrie, 1963.
2. Kovacic, T. and Mrklic, Z., *Thermochim. Acta*, 1998, vol. 322, no. 2, pp. 129–135.
3. Dedov, A.V., Bablyuk, E.B., and Nazarov, V.G., *Vysokomol. Soedin., Ser. B*, 2000, vol. 42, no. 5, pp. 884–886.
4. Dedov, A.V. and Nazarov, V.G., *Vysokomol. Soedin., Ser. B*, 2001, vol. 43, no. 9, pp. 1574–1577.
5. Kovacic, T. and Mrklic, Z., *Thermochim. Acta*, 2002, vol. 381, no. 1, pp. 49–60.
6. Calvert, P. and Billingham, N., *J. Appl. Polym. Sci.*, 1979, vol. 24, no. 3, pp. 357–370.
7. Sancher, I.C., Chang, S.S., and Smith, L.E., *Polym. News*, 1980, vol. 6, no. 6, pp. 249–259.
8. Dedov, A.V. and Nazarov, V.G., *Vysokomol. Soedin., Ser. B*, 2002, vol. 44, no. 4, pp. 729–732.
9. Kompouris, E.M., Regas, F., and Rokotas, S., *Polymer*, 1975, vol. 16, no. 11, pp. 840–844.
10. Messadi, D. and Vernaud, J.M., *J. Appl. Polym. Sci.*, 1982, vol. 27, no. 9, pp. 3945–3955.
11. Papaspyrides, C.D., *Polymer*, 1986, vol. 27, no. 12, pp. 1967–1970.
12. Papaspyrides, C.D., *J. Appl. Polym. Sci.*, 1986, vol. 32, no. 12, pp. 6025–6032.
13. Chamberlin, R. and Harrison, A., *Polym. Age*, 1972, no. 9, pp. 331–333, p. 341.
14. Gumargalieva, K.Z., Zaikov, G.E., and Semenov, S.A., *Vysokomol. Soedin., Ser. A*, 1998, vol. 40, no. 10, pp. 1551–1553.
15. Nazarov, V.G., Dedov, A.V., Semenov, A.A., and

Zhdanova, O.A., *Vysokomol. Soedin., Ser. B*, 1991, vol. 32, no. 12, pp. 927–933.

16. Nazarov, V.G., Dedov, A.V., and Semenov, A.A., *Vysokomol. Soedin., Ser. A*, 1994, vol. 36, no. 1, pp. 80–84.
17. Nazarov, V.G. and Dedov, A.V., *Zh. Prikl. Khim.*, 1998, vol. 71, no. 2, pp. 316–319.
18. Dedov, A.V. and Nazarov, V.G., *Zh. Prikl. Khim.*, 2001, vol. 74, no. 5, pp. 865–866.
19. Dedov, A.V. and Nazarov, V.G., *Plast. Massy*, 2001, no. 12, pp. 41–42.
20. Duvis, T., Karles, G., and Papaspyrides, G.D., *J. Appl. Polym. Sci.*, 1991, vol. 42, no. 1, pp. 191–198.
21. Taverded, J.L. and Vernaud, J.M., *Eur. Polym. J.*, 1986, vol. 22, no. 12, pp. 959–962.
22. Malkin, A.Ya. and Chalykh, A.E., *Diffuziya i vyazkost' polimerov: Metody issledovanii* (Diffusion and Viscosity of Polymers: Methods of Investigation), Moscow: Khimiya, 1979.
23. Shtarkman, B.N., *Plastifikatsiya polivinilkhlorida* (Plasticization of Polyvinyl Chloride), Moscow: Khimiya, 1975.

Russian Journal of Applied Chemistry, Vol. 76, No. 12, 2003, pp. 1988–1992. Translated from Zhurnal Prikladnoi Khimii, Vol. 76, No. 12, 2003, pp. 2038–2042.

MACROMOLECULAR CHEMISTRY AND POLYMERIC MATERIALS

Viscosity of Blends of Pectins of Various Origins with Ethylene–Vinyl Acetate Copolymers

A. I. Suvorova, I. S. Tyukova, E. A. Smirnova, and A. L. Peshekhonova

Ural State University, Yekaterinburg, Russia

Moscow State University of Applied Biotechnology, Moscow, Russia

Received July 8, 2003

Abstract—The rheological properties of ethylene–vinyl acetate copolymers of various compositions in blends with pectins of various origins (pectins recovered from apple pulp, watermelon peel, and citrus fruits) were studied. The degrees of swelling of blend films in water were measured.

The interest in studying properties of blends of natural polymers with chemical derivatives of cellulose and with synthetic polymers is dictated by the demand for new compounds suitable for development of biodegradable materials. Such materials become more and more needed in production of polymeric items with short service periods (packaging films and items, package for cosmetics and household chemical products, films for agriculture) [1–3]. The most frequently used natural polymer is starch, a renewable natural polysaccharide consisting of 1,4-α-*D*-glucopyranose units.

Pectins, like starch, are renewable natural raw materials; they are recovered from fruits and vegetables [4, 5]. Pectins are polymers of 1,4-α-*D*-galacturonic acid the contain partially esterified carboxy groups. Blends of pectins with other polymers have been only examined in few studies. In particular, pectin–starch blends have been shown to be similar to synthetic polymers in mechanical properties [6]. The rheological properties of 5% aqueous solutions of citrus pectin isolated from lemon seeds and peel, and also of blends of this pectin with polyvinyl alcohol and polyvinylpyrrolidone were studied in [7]. It was noted that these systems showed non-Newtonian flow behavior; addition of a vinyl polymer to a pectin solution caused its viscosity to increase.

In development of materials for biodegradable packaging films and other consumable items, blends containing hydrophobic polymers are of particular interest, since one of the main functions of packaging is protection from external moisture. In particular, ethylene–vinyl acetate copolymers (EVACs) whose macromolecules contain both hydrophobic methylene groups and hydrophilic vinyl acetate units are rather widely used in production of protective films for foodstuffs. However, EVACs virtually do not degrade in the environment. Addition of natural polysaccharides, pectins, to these copolymers imparts to them biodegradability. The presence of vinyl acetate units (15 to 28–30%) in EVACs should favor formation of stable blends with polar hydrophilic pectin molecules.

In this study, we examined the rheological properties of two EVAC samples containing pectins of various origins as biodegradable additives; we also analyzed how these blends interact with water. Data on the rheological properties of polymer blends allow assessment of the possibility and conditions of preparing from these blends consumable polymeric articles (primarily packaging films) that would rapidly degrade in the nature. In development of biodegradable materials, it is important to study not only the rheological properties of materials, but also their interaction with water, since biodegradation is more intensive in the presence of moisture. Therefore, for a series of EVAC–pectin blends, we studied swelling of films in water, since the equilibrium swelling and swelling rate furnish information on the interaction of blends with water, necessary for the development of materials degrading under the action of environmental factors.

EXPERIMENTAL

Experiments were performed with two EVAC samples containing 15 (EVAC1) and 25% (EVAC2) vinyl acetate units. The content of these units was deter-

1070-4272/03/7612-1988 $25.00 © 2003 MAIK "Nauka/Interperiodica"

Characteristics of polymers studied

Polymer	Content of vinyl acetate groups in EVAC and ester groups in pectins, %	T_m of EVAC and T_{dec} of pectins, °C	[η], dl g^{-1}, at 25°C	MW	Degree of crystallinity, %
EVAC1	15	92.6	0.72 in chloroform	–	27
EVAC2	24	77.0	0.68 in chloroform	–	16
Watermelon pectin	85	175.0	2.36 in water	12.6×10^5	Fully amorphous
Citrus pectin	75	160.0	1.14 in water	5.0×10^5	15
Apple pectin	75	170.0	1.56 in water	7.3×10^5	20

mined by analysis of the products of base hydrolysis of the copolymers in a mixed solvent (hexanol–xylene) [8]. As measure of molecular weights (MWs) of EVACs we used the intrinsic viscosities [η] of the copolymer solutions in chloroform, since calculation by the Mark–Kuhn–Houwink equation is in this case impossible. We used three pectin samples recovered from apple pulp, watermelon peel, and citrus fruits. The intrinsic viscosities of pectins were determined from the viscosities of their aqueous solutions. The resulting values of [η] and molecular weights of the polymers are listed in the table. The composition of pectins was studied by IR spectroscopy. The spectra were recorded on a Perkin–Elmer spectrometer in the 1000–3900 cm^{-1} range using a KBr prism. The spectra contained bands assignable to carbonyl (1750 cm^{-1}) and methoxy (1450 cm^{-1}) groups characteristic of pectins, and also broad bands of hydroxy groups at 3400–3450 cm^{-1}, typical of all polysaccharides [9–11]. All the pectins studied had about the same content of ester groups (see table).

The structure of the polymers was characterized by X-ray diffraction. Measurements were made with a DRON-2.0 diffractometer in the 2θ range 15°–50° with Cu_{K_α} radiation (λ 0.1542 nm). The diffraction patterns of pectins were measured with powdered samples. EVACs were studied as thin (~50 μm) films prepared by heating under a pressure of 15 MPa. The sample structure was characterized by the degree of crystallinity (see table), which was determined as the ratio of the area under the diffraction peak to the total area under the X-ray scattering curve in the angle range under consideration.

To find the conditions for measuring the viscosity of pectin–EVAC blends, we determined by DTA the melting points of the copolymer samples. The thermal behavior of pectins was characterized by thermogravimetric analysis with a Q-1500D derivatograph (MOM, Hungary) in the range 20–240°C. Pectins, like other polysaccharides, do not pass reversibly to the viscous-flow state, since their melting points exceed the decomposition points [12]. The temperatures of the onset of intense degradation of natural pectins are listed in the table.

Samples for rheological studies were prepared by blending a weighed portion of pectin with pulverized EVAC. Blends containing 5–20 wt % pectin were heated for 2 h at 50°C and then compacted at 140°C and a pressure of 15 MPa. Samples had a cylindrical shape; the diameter of their base corresponded to the diameter of the working channel of the viscometer (0.8 cm). Samples of blends were semitransparent, with embedded pectin particles visible with a microscope, i.e., the blends were heterogeneous. The viscosity of EVAC–pectin blends was measured with an MV-2 capillary microviscometer with the capillary length to radius ratio of 25 : 1. Under these conditions, the entrance effect could be disregarded in calculations [13]. The viscosity was measured at stresses of 500–3000 Pa, shear rates of 10^{-1}–10^1 s^{-1}, and temperature of 110°C, which exceeded the melting points of the EVAC samples used and was 50°C lower than the temperature at which the pectins started to degrade.

The interaction of polymer blends with water was evaluated by the extent of equilibrium swelling, which was determined gravimetrically with films prepared by compaction under the same conditions as for rheological tests. To accelerate the swelling, the measurements were performed at 50°C.

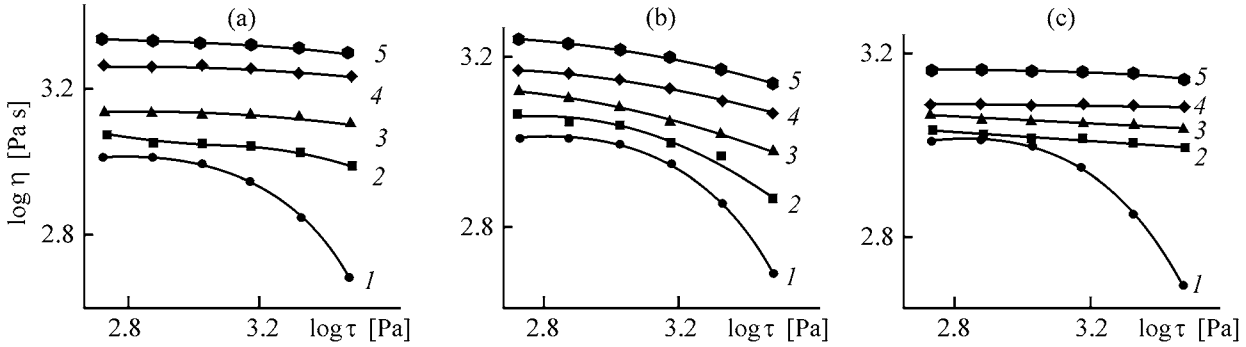

Fig. 1. Flow curves of EVAC2 blends with (a) watermelon, (b) citrus, and (c) apple pectins. (η) Effective viscosity and (τ) shear stress. Pectin content in blends, wt %: (*1*) 0, (*2*) 5, (*3*) 10, (*4*) 15, and (*5*) 20.

Figure 1 shows the flow curves of the blends of EVAC-2 with (a) watermelon, (b) apple, and (c) citrus pectins. The EVAC1 sample was studied only in a blend with watermelon pectin. The dependences obtained for this system are similar to those shown in Fig. 1. It is seen that all the blends behave as non-Newtonian fluids. The dependence of the viscosity on the shear stress was the most pronounced for pure EVAC. As the pectin content is increased, the blends become less flowable, their viscosity grows, and the slope of the curves relative to the abscissa decreases, i.e., the viscosity becomes less dependent on the shear stress. Such trends are known for polymeric systems filled with disperse fillers, in which introduction of a filler results in that, in the flow, the structure of the system is not disturbed by the stress [14].

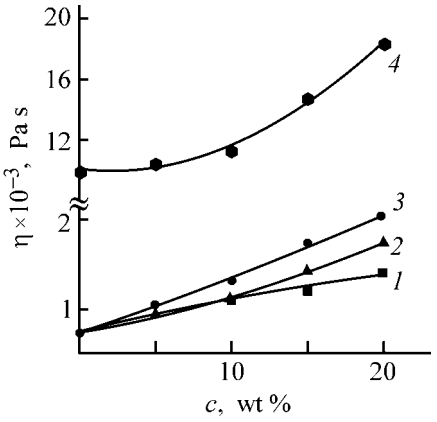

Fig. 2. Effective viscosity η of EVAC2 blends with (*1*) citrus, (*2*) apple, and (*3*) watermelon pectins and (*4*) EVAC-1 blend with watermelon pectin vs. the pectin concentration *c*. Shear stress 2100 Pa.

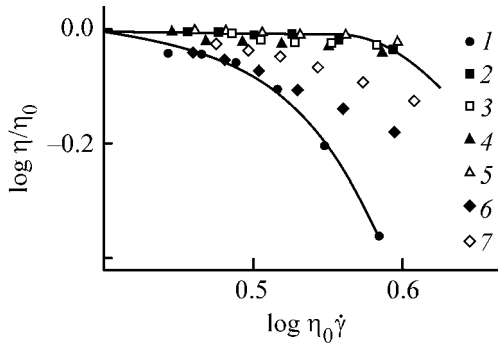

Fig. 3. Flow curves of EVAC2–pectin systems in reduced coordinates: (η/η_0) normalized effective viscosity and ($\eta_0\dot{\gamma}$) shear rate. (*1*) EVAC, (*2*, *3*) EVAC–watermelon pectin, (*4*, *5*) EVAC–citrus pectin, and (*6*, *7*) EVAC–apple pectin. EVAC : pectin ratio: (*2*, *4*, *6*) 90 : 10 and (*3*, *5*, *7*) 80 : 20.

Figure 2 shows the dependence of the effective viscosity of polymer blends on the pectin content. It is seen that, as the pectin concentration is increased, the viscosity of the blends with both EVAC1 and EVAC2 grows. Blends of EVAC2 with different pectins differ in the viscosity only slightly (Figs. 1, 2). The influence of the pectin origin can be revealed by comparing curves *1*–*3* in Fig. 2 and the data in the table. The viscosity of EVAC-2–pectin blends is the higher, the higher the molecular weight of the pectin. The degree of esterification of the natural polymer, similar for apple and citrus pectins (see table), apparently, does not have a decisive effect on the viscosity of blends with EVACs. Comparison of the effective viscosities of blends containing different copolymers (Fig. 2, curves *3*, *4*) with similar molecular weights shows that the viscosity is more sensitive to the content of vinyl acetate units in EVAC than to the pectin origin.

By extrapolating the viscosity coefficients obtained to zero shear stress, using the procedure described in [15], we calculated for the EVAC2–pectin systems the highest Newtonian viscosities η_0 and then, using the concept of invariance of rheological data [13, 15], plotted them in the normalized coordinates. The log–log plots of the normalized effective viscosity η/η_0 vs. shear rate $\dot{\gamma}\eta_0$ for blends of EVAC2 with three pectins are shown in Fig. 3. It is seen that the experimental data on the reduced effective viscosity for all

the three systems containing pectins of different origins form a relatively narrow zone of values at different shear stresses. The existence of such a dependence for normalized effective viscosity of the systems at hand suggests that the relaxation properties of the EVAC2 melt containing pectins of different origins should be described by a common functional dependence characterizing the similarity of the relaxation spectra of these systems [13, 15].

The rheological data show that addition of pectins recovered from various plants results mainly in increased viscosity and hindered flow. The absolute values of viscosity of the blends remain within the limits characteristic of the flow of melts of industrial thermosoftening plastics in the course of molding [16].

Addition of natural polymers to synthetic polymers is aimed to enhance the degradability of utilized polymeric items upon their disposal in soil. An important prerequisite for efficient degradation under the action of a complex of natural agents is the ability of a material to interact with soil moisture. Therefore, we evaluated the swellability of EVAC2–watermelon pectin blends in water. Figure 4 shows the kinetic curves of swelling in water at 50°C of films formed from EVAC2 and its blends. The kinetic curves are typical of systems with limited swelling; the amount of absorbed water grows in proportion to the pectin content. However, as seen from the slopes of the initial portions of the curves, the swelling rates and equilibration time are similar for all the compositions. This is due to the fact that, in the systems studied, the low-polar component, EVAC, prevails, and polar hydrophilic pectin plays the role of a filler enhancing the water-absorption power of the blend films. The dependence of the limiting degree of swelling on the pectin content in the films is shown in Fig. 5.

Thus, addition of pectins as fillers to EVAC results in formation of systems more capable of swelling in water than pure EVAC. This is important from the viewpoint of biodegradation of such systems under natural conditions (disposal of used items in soil).

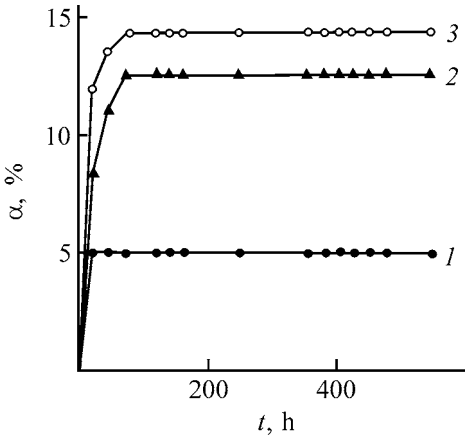

Fig. 4. Kinetic curves of swelling of EVAC2–watermelon pectin blends in water at 50°C. (α) Degree of swelling and (*t*) time. EVAC2 : pectin: (*1*) 100 : 0, (*2*) 90 : 10, and (*3*) 80 : 20.

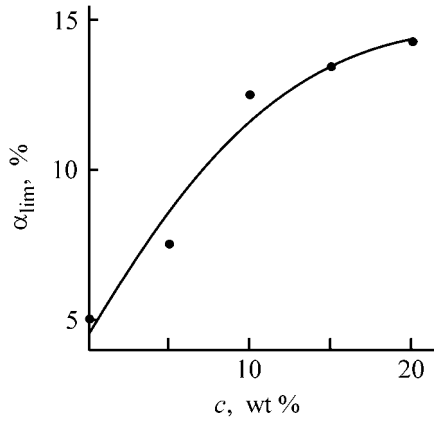

Fig. 5. Limiting degree of swelling α_{lim} of EVAC2–watermelon pectin blends in water at 50°C vs. the pectin concentration *c*.

CONCLUSIONS

(1) Natural polysaccharides, pectins, irrespective of their specific plant origin, when added to ethylene–vinyl acetate copolymers, increase their viscosity to an extent growing with the pectin concentration. The viscosity remains within the limits characteristic of processing of synthetic polymers. The pectin origin (apple pulp, watermelon peel, citrus fruits) affects the rheological properties of pectin blends with ethylene–vinyl acetate copolymers to a lesser extent than does variation of the content of acetate groups in the synthetic component. Pectins enhance the swellability of blends in water, which should positively affect their biodegradability under natural conditions.

(2) Among the systems studied, the optimal rheological characteristics in combination with sufficient water-absorption power are exhibited by blends of the copolymer containing 25% vinyl acetate groups with watermelon pectin. These blends can be used to prepare biodegradable polymeric films and other consumable materials.

REFERENCES

1. Vasnev, V.A., *Vysokomol. Soedin.*, 1997, vol. 39, no. 12, pp. 2073–2089.

2. Suvorova, A.I., Tyukova, I.S., and Trufanova, E.I., *Usp. Khim.*, 2000, vol. 69, no. 5, pp. 454–503.
3. Fomin, V.A. and Guzeev, V.V., *Plast. Massy*, 2001, no. 2, pp. 42–46.
4. Coffin, D.R. and Fishman, M.L., *J. Agricult. Food Chem.*, 1993, pp. 1192–1197.
5. Bastioli, C., *The Wiley Enciclopedia of Packaging Technology*, Brody, A.L. and Marsh, K.S., Eds., Wiley, 1977, 2nd ed., pp. 77–83.
6. Coffin, D.R. and Fishman, M.L., *J. Appl. Polym. Sci.*, 1994, vol. 54, pp. 1311–1320.
7. Rashidova, S.Sh., Voropaeva, I.L., Mukhamedzhanova, M.Yu., *et al.*, *Zh. Prikl. Khim.*, 2002, vol. 75, no. 7, pp. 1159–1163.
8. Popova, G.S., Budtov, V.N., and Ryabikova, V.I., *Analiz polimerizatsionnykh plastmass* (Analysis of Polymerization Plastics), Leningrad: Khimiya, 1988.
9. Filippov, M.P. and Shaleshurina, S.A., *Izv. Vyssh. Uchebn. Zaved., Pishch. Tekhnol.*, 1972, vol. 86, no. 1, pp. 186–189.
10. Turakhozhaev, M.T., Khodzhaeva, M.A., Ivanova, I.A., *et al.*, *Khim. Prirodn. Soedin.*, 1999, no. 5, pp. 570–572.
11. Kacurakova, M., Capek, P., Sasinkova, V., *et al.*, *Carbohydr. Polym.*, 2000, vol. 43, pp. 195–203.
12. Henseke, G., *Zucker Chemie*, Berlin: Akademie, 1966.
13. Malkin, A.L. and Chalykh, A.E., *Diffuziya i vyazkost' polimerov: Metody izmereniya* (Diffusion and Viscosity of Polymers: Measurement Methods), Moscow: Khimiya, 1979.
14. Lipatov, Yu.S., *Fizicheskaya khimiya napolnennykh polimerov* (Physical Chemistry of Filled Polymers), Moscow: Khimiya, 1977.
15. Torner, R.V., *Teoreticheskie osnovy pererabotki polimerov* (Theoretical Principles of Polymer Processing), Moscow: Khimiya, 1977.
16. *Osnovy tekhnologii pererabotki plastmass* (Principles of Plastic Processing), Kuleznev, V.N. and Gusev, V.K., Eds., Moscow: Khimiya, 1995.

Russian Journal of Applied Chemistry, Vol. 76, No. 12, 2003, pp. 1993–1997. Translated from Zhurnal Prikladnoi Khimii, Vol. 76, No. 12, 2003, pp. 2043–2047.

MACROMOLECULAR CHEMISTRY AND POLYMERIC MATERIALS

Structural Changes Induced in Flax Cellulose by Alkaline Treatment

M. I. Voronova, S. N. Petrova, T. N. Lebedeva, O. N. Ivanova, A. N. Prusov, and A. G. Zakharov

Institute of Chemistry of Solutions, Russian Academy of Sciences, Ivanovo, Russia

Received April 3, 2003

Abstract—Treatment of flax cellulose with NaOH was studied.

Because of the limited resources of cotton cellulose, a growing attention has been paid in recent years to production of cellulose from unconventional annually renewable plant raw materials such as flax, jute, hemp, etc. Practical implementation of the corresponding processes requires knowledge of structural changes occurring in cellulose in the course of treatments and in conversion into cellulose ethers and esters.

The interaction of alkali metal hydroxides with regenerated cellulose has been studied quite thoroughly; much less understood are the structural changes in cellulose in cellulose-containing plant raw materials. Therefore, the aim of this study was to analyze structural transformations induced in flax cellulose by alkaline treatment.

EXPERIMENTAL

In the study, we examined intermediate flax fibers after mechanical separation from boon.

Natural flax fibers were beaten in a dry crushing mill with shock-pulse loading (loading velocity 40 m s^{-1}). By virtue of the ventilation effect, the flax is carried away with the air flow, accelerated by spreaders to 40–120 m s^{-1}, and knocked against beaters. In this stage, flax is broken into linen fiber and boon, which are then separated in a cyclone separator.

Fiber samples were treated with NaOH at various temperatures for 1 h at a liquor ratio of 1 : 10. The swelling of the fibers and sorption of water and alkali were determined as in [1]. A weighed portion of air-dry cellulose with a fixed moisture content, taken to with accuracy of 0.0002 g, was placed in a specially designed vessel for swelling runs, poured over with NaOH, and allowed to stand at a fixed temperature for 15 min. Then NaOH-treated cellulose was centrifuged for 10 min at 8000 rpm. It was demonstrated in preliminary experiments that the indicated temperature, swelling, and centrifugal drying conditions are sufficient for equilibration in the cellulose–NaOH–water system. Samples after centrifugation were weighed and analyzed for absorbed NaOH by titration with 0.1 N H_2SO_4 (samples were allowed to stand in distilled water for up to 3 h before titration). For each NaOH concentration, the result was obtained as an average of three replicate runs to within 10%.

Also, we studied structural changes induced in cellulose by alkaline treatment. Samples of NaOH-treated cellulose were washed to neutral reaction and dried to constant weight. Then the thus obtained samples were analyzed for α-cellulose [2], concomitant compounds (lignin [3] and hemicelluloses [2]), degree of polymerization DP [2], water retention [4] and water-absorbing capacity [5]. Structural transformations in cellulose were also monitored by recording IR spectra on an Avatar 360 FT-IR ESP spectrophotometer over the range 400–4000 cm^{-1} in KBr pellets (1 mg per 100 mg KBr).

Interaction of a cellulose-containing material with NaOH involves absorption of NaOH and water (swelling), formation of alkaline cellulose, and dissolution of low-molecular-weight fractions (hemicelluloses) and noncellulose components. Figure 1 shows characteristics of flax cellulose swollen in NaOH solutions with various concentration, including the swelling (swollen cellulose to absolutely dry cellulose weight ratio) and uptakes of NaOH and water (number of absorbed NaOH and H_2O molecules in centrifuged alkaline cellulose per cellulose unit).

1070-4272/03/7612-1993 $25.00 © 2003 MAIK "Nauka/Interperiodica"

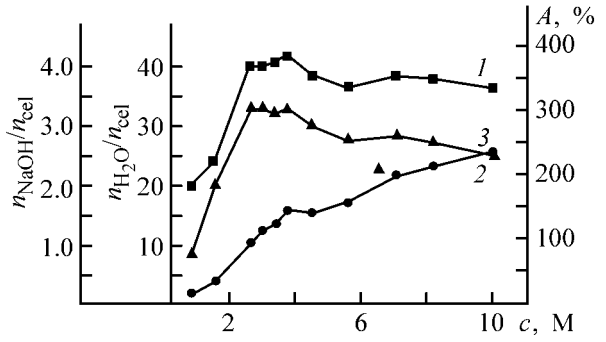

Fig. 1. Swelling *A* of flax cellulose vs. the NaOH concentration *c*. (n_{NaOH}/n_{cel}, n_{H_2O}/n_{cel}) Numbers of the NaOH and H_2O molecules in centrifuged alkaline cellulose per cellulose unit. (*1*) Swelling, (*2*) absorption of NaOH, and (*3*) absorption of water.

The swelling of cellulose and cellulose-containing materials has been long studied. However, the swelling mechanism remains to be conclusively established. One thing is clear: alkaline cellulose is not formed by the reaction with an alkali without swelling, e.g., in an anhydrous alcohol.

The swellability of a cellulose-based material can be characterized by the weight or volume swelling [6], linear expansion of a fiber, etc. Uptake of an alkali and water by cellulose can be determined directly, as in this study, or indirectly [7]. The swellabilities determined by different methods sometimes differ considerably. However, the shapes of the dependences of the swelling and alkali and water uptake on the alkali concentration are independent of the determination procedure. The swelling by weight increases with increasing NaOH concentration, and the corresponding dependence curve shows a peak through a maximum at NaOH concentration of 2–3 M. Figure 1 shows that this behavior correlates with the water uptake. With increase in the NaOH concentration above 3 M, the content of water in the sample decreases (curve *3*), while that of NaOH continues to increase (curve *2*).

The position of the peak depends on the origin of cellulose (flax or wood) and treatment [6, 8]. It is difficult to conclude unambiguously what factors, the degree of purification of the initial material or crystallinity index (CI), are decisive. In our case, the swelling curve of untreated flax fibers (lignin content 16%; cellulose, 72%; hemicelluloses, 6%; DP 4700; and CI 0.6) virtually coincides with that of refined sulfate wood cellulose (lignin content <1%; cellulose, 95%; hemicelluloses, 3–4%; DP 1800; and CI 0.55) [1]. It may be suggested that the swelling curve and the position of the peak are largely determined by parameters of the alkaline solution rather than by structural characteristics of a cellulosic material.

The effect of the alkali concentration in solutions on the swelling of cellulose is usually accounted for by hydration of ions as the main factor [9]. According to the hydrated-ion model, an ion is bound in solution to a fixed number of solvent molecules to form discrete first, second, etc. coordination spheres [10]. The number of bound solvent molecules is determined by the sum of the coordination number (the most probable number of solvent molecules in the first coordination sphere of an ion) and the number of solvent molecules forming the second and more remote coordination spheres. The experimental hydration numbers obtained by different methods differ considerably. The coordination number of ions is a more definite quantitative parameter. The coordination numbers of Li^+, Na^+, and K^+ are 4, 6, and 8, respectively. However, the swellability of cellulose in the corresponding alkalis increases in the reverse order. According to [8], the swellability of cellulose in various alkalis is as follows (%): cotton cellulose: 800 in KOH, 1100 in NaOH, and 1200 in LiOH; and wood cellulose: 1300 in LiOH, 1220 in NaOH, and 850 in KOH. Therefore, the swelling is associated with total hydration of the ions rather than with that of their first hydration sphere.

Based on the X-ray diffraction and spectroscopic data, the authors of [11–13] found that the second hydration sphere around the Li^+ and Na^+ ions consists of 12 water molecules. By the effect on the structure of water, Li^+ and Na^+ are classified with positively hydrated ions (mean residence time of water molecules near an ion is longer than that in the bulk of water). The K^+ ion, demonstrating a weaker capability to form the second hydration sphere in solutions, [14] was classified with the negatively hydrated ions. On the basis of the available data, one may suggest that the hydration shells around the Li^+, Na^+ and K^+ ions include 16 (4 + 12), 18 (6 + 12) and 8 (8 + 0) water molecules, respectively. Accordingly, the alkali metal concentrations at which water in solutions is totally bound to form hydration shells of the ions are as follows (M): LiOH 3.2 (8.28%), NaOH 3.08 (10.99%), and KOH 6.5 (28.7%).

As seen, the hydration number and nature of hydration of the Li^+, Na^+, and K^+ ions are markedly different, which should be reflected in the curves of cellulose swelling and alkali and water uptake. According to [8], the alkali concentration of the maximum cellulose swelling in various alkalis is as follows (M): cotton cellulose: LiOH 4, NaOH 4.5, and KOH 5.8; and wood cellulose: LiOH 2.5, NaOH 2.5, and KOH 6.0. Therefore, the positions of the swelling maxima

are close to the alkali metal concentrations at which water is totally bound to form hydration shells of the ions.

Progressive binding of water with increasing alkali concentration should be accompanied by structural and energy changes in the hydrates. The experimental data suggest that this is a stepwise process. For example, according to the NMR relaxation data [15, 16], the initially octahedral first hydration sphere of Na^+ becomes tetrahedral with increasing NaOH concentration. A similar effect has been observed in X-ray diffraction study of 2–3 M aqueous NaOH and NaCl [13].

Thus, the peaks in the swelling and NaOH and water uptake curves, as well as the appearance of peaks of alkaline cellulose in the X-ray diffraction patterns, i.e., penetration of NaOH into the crystalline regions of the cellulose structure, correspond to an NaOH concentration at which the hydration shell around the Na^+ ion undergoes a structural rearrangement. The initially octahedral first coordination sphere transforms into that of the tetrahedral type, which, presumably, initiates transformation of the second hydration sphere, too.

The structural transformations occurring in the cellulose-containing plant raw material after removal of NaOH and drying was monitored by the optical density ratios in the IR spectra. Levdik *et al*. [17] have demonstrated, using the X-ray diffraction data, that the change in the D_{1375}/D_{1325} ratio in cellulose, observed after alkaline treatment, is associated with the transformation of the cellulose structure from cellulose I to cellulose II. Our results show (Fig. 2a) that the transformation starts at an NaOH concentration of 2.0 M and comes to the end at that of 3.0 M, which corresponds to the maximum swelling range of cellulose (Fig. 1).

Over the range 2–3 M, the degree of structural transformation is virtually a linear function of the NaOH concentration. The transformation into cellulose II occurs only when the initial system of hydrogen bonds in highly ordered regions of the cellulose structure breaks down. Otherwise, the native modification (cellulose I) is restored after removal of NaOH by washing with water. The absorption at 3000–3700 cm^{-1} in the IR spectra of cellulose characterizes the stretching vibrations of the H-bonded hydroxy groups, and the D_{3360}/D_{2920} ratio, the hydrogen bonding strength in cellulose [18]. It follows from the dependence of the D_{3360}/D_{2920} ratio on the NaOH concentration (Fig. 2b) that the strength is at a minimum at 2.0–2.5 M and starts to increase again above 3 M, reflecting the formation of a new system of hydrogen bonds (cellulose II).

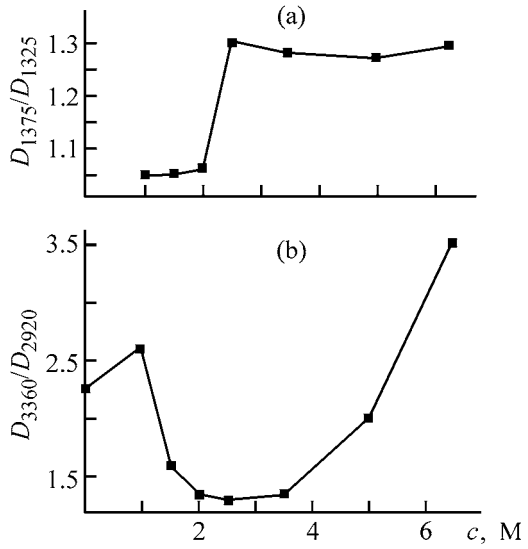

Fig. 2. (a) D_{1375}/D_{1325} as a measure of the cellulose I/cellulose II conversion and (b) D_{3360}/D_{2920} as a measure of the hydrogen bonding strength in flax cellulose vs. the NaOH concentration c.

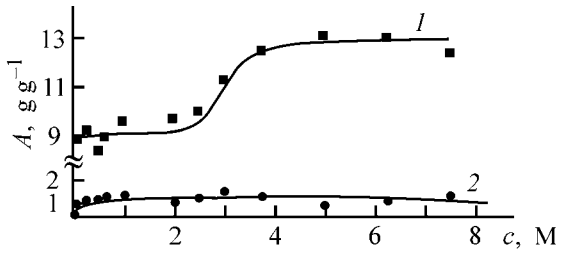

Fig. 3. (*1*) Water absorption and (*2*) retention of flax cellulose after alkaline treatment vs. the NaOH concentration c. (A) Water content.

X-ray diffraction studies of cellulose II [19] revealed that its structure with mixed conformation of the hydroxymethyl groups is characterized by a more developed system of hydrogen bonds as compared to cellulose I in which only one conformation exists. This feature leads to high stability of the system of hydrogen bonds, which, in turn, provides high resistance of cellulose II to dissolution in alkalis and Cadoxene [21]. However, the equilibrium water uptake is higher in cellulose II as compared to cellulose I. As seen from Fig. 3 (curve *1*), the water uptake abruptly changes at NaOH concentration corresponding to the structural transition. The water uptake determined by the procedure described in [4] is independent of the crystal modification (Fig. 3, curve *2*).

It is known that alkaline treatment of cellulose decreases its DP [9]. The dependence of DP of flax

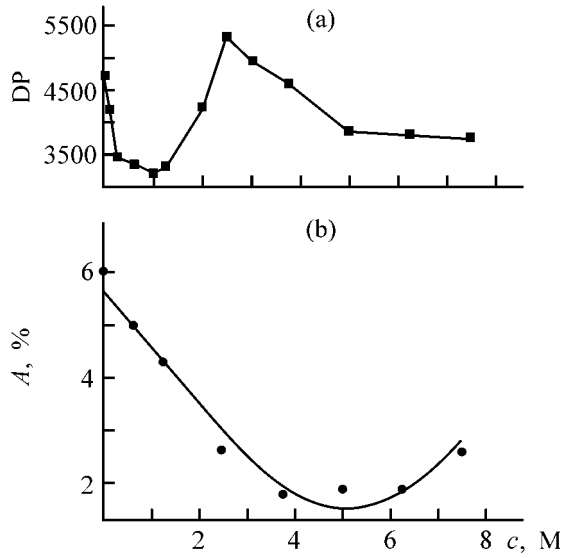

Fig. 4. (a) Degree of polymerization DP and (b) hemicellulose content *A* in flax cellulose samples after alkaline treatment vs. of the NaOH concentration *c*.

cellulose on the NaOH concentration has a maximum within the range 2–3 M (Fig. 4a).

In our opinion, such a dependence is a result of cellulose degradation (breakdown of the glucoside bonds) and transfer of low-molecular-weight fractions to the solution. The DP is at a maximum at NaOH concentrations corresponding to the strongest swelling of cellulose (Fig. 1). In this concentration range, i.e., under conditions favoring the strongest swelling, there is no steric hindrance to dissolution, and the removal of low-molecular-weight fractions and even hemicellulose with higher DP dominates. At NaOH concentrations below 1.5 M, the degree of swelling is still low, and above 4 M, it is no longer sufficiently high, which makes the transfer of hemicelluloses from cellulose fibers into the solution difficult because of the steric hindrance. This decreases the mean DP and increases the hemicellulose content in linen cellulose treated at high NaOH concentration (Fig. 4b).

Thus, the NaOH concentration range 2–3 M provides the minimum energy of hydrogen bonding in cellulose (Fig. 2b) and, as a result, the cellulose I/cellulose II transformation occurs (Fig. 2a) [22]. In this case, the maximum removal of lower-molecular-weight fractions of cellulose makes higher the mean DP in the insoluble fraction.

CONCLUSIONS

(1) The presence of concomitant compounds (lignin, hemicelluloses, etc.) in untreated linen cellulose has no significant effect on the structural transformation occurring in cellulose under the action of NaOH, contrary to, e.g., regenerated wood cellulose (sulfate pulping).

(2) The extrema in the dependences of the parameters characterizing structural changes in cellulose under the action of NaOH (swelling, transformation of cellulose I into cellulose II, hydrogen bonding strength, and degree of polymerization) are found within the NaOH concentration range 2–3 M. It is suggested that, over this range, structural rearrangement in the Na^+ hydration shell facilitates penetration of the alkali into the crystalline regions of the cellulose structure.

REFERENCES

1. Arkhangel'skii, D.N. and Yushkova, T.V., in *Protsessy studneobrazovaniya v polimernykh sistemakh: Mezhvuzovskii nauchnyi sbornik* (Gelation in Polymer Systems: Intercollegiate Scientific Coll.), Saratov: Saratov. Gos. Univ., 1985, part 2, pp. 41–49.
2. *Analiticheskii kontrol' proizvodstva iskusstvennykh volokon: Spravochnoe posobie* (Analytical Control in Artificial Fiber Production: A Handbook), Dibrova, A.K. and Matveev, V.S., Eds., Moscow: Khimiya, 1986.
3. *Spravochnik khimicheskoi tekhnologii obrabotki l'nyanykh tkanei* (Handbook of Chemical Finishing of Linen Fabric), Fridlyand, G.I., Ed., Moscow: Legkaya Industriya, 1973.
4. Jayme, G. and Roffael, E., *Papier*, 1970, vol. 24, no. 4, pp. 181–186.
5. *GOST* (State Standard) *5556–81: Medicinal Absorbent Cotton: Method for Determination of the Absorbing Capacity*.
6. Reizin'sh, R.E., Chernyavskaya, S.A., Laka, M.G., and Klyavin'sh, Z.V., *Khim. Drev.*, 1984, no. 6, pp. 45–48.
7. Serkov, A.T., *Khim. Volokna*, 2000, no. 2, pp. 11–15.
8. Rogovin, Z.A., *Khimiya tsellyulozy* (Cellulose Chemistry), Moscow: Khimiya, 1972.
9. Klenkova, N.I., *Struktura i reaktsionnaya sposobnost' tsellyulozy* (Cellulose Structure and Reactivity), Leningrad: Nauka, 1976.
10. *Ionnaya sol'vatatsiya* (Ion Solvation), Krestov, G.A., Ed., Moscow: Nauka, 1987.
11. Mishchenko, K.P. and Poltoratskii, G.M., *Termodinamika i stroenie vodnykh i nevodnykh rastvorov elektrolitov* (Thermodynamics and Structure of Aqueous and Nonaqueous Electrolyte Solutions), Leningrad: Khimiya, 1976.
12. Heinje, G., Luck, W.A.P., and Heinzinger, K., *J. Phys. Chem.*, 1987, vol. 91, no. 2, pp. 331–338.

13. Dorosh, A.K., *Struktura kondensirovannykh system* (Structure of Condensed Systems), Lviv: Vishcha Skola, 1981.
14. Skryshevskii, A.F., *Strukturnyi analiz zhidkostei i amorphnykh tel* (Structural Analysis of Liquids and Amorphous Bodies), Moscow: Vysshaya Shkola, 1980.
15. Dorosh, A.K., in *Termodinamika i stroenie rastvorov: Mezhvuzovskii sbornik* (Solution Thermodynamics and Structure: Intercollegiate Coll.), Ivanovo: Ivan. Gos. Univ, 1977, p. 25.
16. Lyashchenko, A.K., *Izv. Akad. Nauk SSSR, Ser. Khim.*, 1973, no. 2, pp. 287–292.
17. Levdik, I.Yu., Dobrovol'skaya, I.P., Dobrynin, N.A., *et al.*, *Khim. Drev.*, 1989, no. 1, pp. 32–35.
18. Levdik, I.Yu., Inshakov, M.D., Misyurova, E.P., and Nikitin, V.N., *Khim. Drev.*, 1988, no. 3, pp. 109–116.
19. Zhbankov, R.G. and Kozlov, P.V., *Fizika tsellyulozy i ee proizvodnykh* (Physics of Cellulose and Its Derivatives), Minsk: Nauka i Tekhnika, 1983.
20. Ioelovich, M.Ya. and Karlivan, V.P., *Khim. Drev.*, 1986, no. 1, pp. 18–25.
21. Gaivoronskii, A.V., Nagrodskii, R.A., Talmud, S.L., *et al.*, *Zh. Prikl. Khim.*, 1975, vol. 48, no. 3, pp. 602–605.
22. Nikitin, V.M., Obolenskaya, A.V., and Shcheglov, V.P., *Khimiya drevesiny i tsellyulozy* (Wood and Cellulose Chemistry), Moscow: Lesnaya Prom–st., 1978.

Russian Journal of Applied Chemistry, Vol. 76, No. 12, 2003, pp. 1998–2002. Translated from Zhurnal Prikladnoi Khimii, Vol. 76, No. 12, 2003, pp. 2048–2052.

MACROMOLECULAR CHEMISTRY AND POLYMERIC MATERIALS

Carboxymethyl Cellulose Amides and Their Properties

N. M. Zabivalova, A. M. Bochek, L. M. Kalyuzhnaya, E. N. Vlasova, and B. Z. Volchek

Institute of Macromolecular Compounds, Russian Academy of Sciences, St. Petersburg, Russia

Received June 11, 2003

Abstract—Single-stage synthesis of carboxymethyl cellulose amides was studied. The influence exerted by introduction of amide groups with bulky alkyl radicals on the thermodynamic affinity of mixed cellulose ethers for a solvent and their solubility in water was evaluated.

There is growing interest in associated polymer systems based on environmentally friendly biodegradable natural polymers. Among derivatives of cellulose, its water-soluble ethers and esters are widely used in manufacture of detergents, oil production (drilling muds), and textile, paint-and-varnish, food, cosmetic, and fragrance industries. These are methyl cellulose (MC), hydroxypropyl cellulose (HPC), hydroxypropyl methyl cellulose (HPMC), methyl ethyl cellulose (MEC), and some others cellulose ethers and esters.

Among ionic derivatives of cellulose, carboxymethyl cellulose sodium salt (NaCMC) is most widely used. Carboxymethyl cellulose is a typical polyelectrolyte [1, 2]. Its application field can be extended by chemical modification.

Two major methods are known to be used for chemical modification of partially substituted cellulose ethers. The first is introduction of new functional groups at the free hydroxy groups in the anhydroglucose units, and the second, selective modification of the already present substituents.

It is of significant scientific and practical interest to synthesize CMC amides (CMCAs) and study the effect of newly introduced substituents on the thermodynamic affinity of the resulting products for water. CMCAs can be synthesized by the reaction of amines with CMC acid chloride [3–5] or CMC in the H form (HCMC) [6]. By varying the molecular weight and degree of substitution in CMC and also the nature of an amine and degree of amidation, new cellulose derivatives soluble in water and organic solvents can be synthesized. New mixed ethers of cellulose can behave as polyacids, weak polybases, nonionic materials, or polyampholytes.

In this study, we examined the synthesis of CMCA by the reaction of amines with the carboxy groups of HCMC.

EXPERIMENTAL

As starting materials we used two NaCMC samples: CMC synthesized in laboratory (degree of polymerization DP_η 360; degree of substitution DS 0.32) and commercial NaCMC (degree of polymerization DP_η 630; degree of substitution DS 0.80). CMC with low DS was chosen with the aim to refine conditions for CMCA synthesis and to study the effect of introduction of small amounts of new functional groups on the thermodynamic affinity of the resulting derivatives for water. With the commercial NaCMC sample, we studied the effect of large amounts of new functional groups on the solubility of CMCA in water. In amidation, we used decylamine.

Samples of NaCMC may contain, as impurities, low-molecular-weight chlorides of the starting reactants used in carboxymethylation of cellulose. To remove foreign compounds, the sample was pretreated in a Soxhlet apparatus with hot 70% aqueous isopropanol for 4 h to negative reaction for chloride ($AgNO_3$) and then vacuum-dried at 50°C for 12 h. The DS_{Na} and DP_η were determined with thus pretreated samples.

CMCA was synthesized by reaction (1).

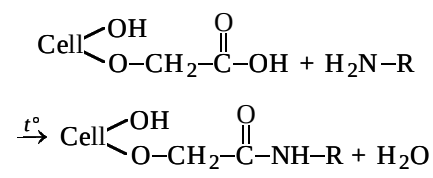

(1)

1070-4272/03/7612-1998 $25.00 © 2003 MAIK "Nauka/Interperiodica"

The reaction conditions were selected so as to obtain a set of water-soluble mixed cellulose ethers. NaCMC samples were initially converted into the H form by treatment with 20% HCl in 70% ethanol, washed to negative reaction for chloride ($AgNO_3$), and dried to constant weight in a vacuum oven at 60°C for 12 h. The degree of amidation (DA) in the resulting CMCA was estimated by Eq. (2).

$$DA = \frac{179y}{14 \times 100 - 139y}, \quad (2)$$

where y is the nitrogen content (wt %); 179, the molecular weight of the HCMC (DS 0.32) unit; and 139, the increase in the molecular weight of HCMC after introduction of one decylamine group.

Nitrogen was determined by the Kjeldahl method [7].

The solubility of CMCA was determined as follows. A weighed portion of CMCA required for preparation of 1% solution (corrected for the moisture content in CMCA) was stirred in distilled water at room temperature for 6 h. The solution was filtered through a Schott filter no. 2 (pore size 40–90 μm). The precipitate was washed on the filter with water and dried at 105°C to constant weight. The solubility was estimated by Eq. (3).

$$S = \left(1 - \frac{g_2 - g_3}{g_1}\right) \times 100, \quad (3)$$

where g_1, g_2, and g_3 are the weights (g) of the polymer taken for dissolution, filter with the precipitate, and filter, respectively.

The sorption of solvent vapor on CMCA at 293 K was measured at a solvent saturation pressure on a McBain quartz spring balance (sensitivity 1 mg mm^{-1}) with accuracy of about 0.01%.

Infrared spectra of mixed cellulose ethers were recorded on a Bruker FS-88 FTIR spectrometer in KBr pellets.

Table 1 shows the conditions of synthesis of CMCA from HCMC with DS 0.32. The reaction was carried out at 140°C. To decrease the polymer degradation rate, the synthesis was performed in xylene at a liquor ratio of 4 and 13. In carrying out the reaction, we varied the reaction time and amount of decylamine (recalculated to 1 mol of carboxy groups of the polymer). A fixed amount of decylamine was added to HCMC in xylene, and synthesis of CMCA was carried out at elevated temperature with stirring. After the reaction was complete, the samples were washed with 70% aqueous ethanol to remove the amine salt sorbed on the polymer. The washing was repeated five times with fresh portions of the ethanol solution. The completeness of removal of the unchanged amine was controlled by the IR absorption band of the amine salt according to the procedure described in [6].

Table 1. Synthesis of CMCA from CMC (DS 0.32)

Run no.	τ, h	Amount of amine, mol mol^{-1}	Liquor ratio	N, %	DA	Sorption of water vapor, g g^{-1}
1*	–	–	–	–	–	2.203
2	3	1 : 1	4	0.76	0.105	1.517
3	1	1 : 0.5	13	0.15	0.019	1.856
4	2	1 : 0.5	13	0.20	0.026	1.687
5	3	1 : 0.5	13	0.41	0.055	1.680
6	1	1 : 1	13	0.34	0.045	1.785
7	2	1 : 1	13	0.48	0.064	1.776
8	3	1 : 1	13	0.50	0.066	1.764

* Run with NaCMC (DS 0.32).

It should be pointed out that the NaCMC sample with DS 0.32 is highly soluble in water, which is caused by the uniform distribution of substituents [8]. Commercial NaCMC is readily soluble in water at DS 0.40 and higher. The synthesis of the amides is influenced by the liquor ratio and amount of decylamine taken for reaction (recalculated to 1 mol of carboxy groups of the polymer). As seen, DA grows with increasing amount of the amine in the reaction mixture, at the same reaction time (experiment nos. 2, 5, 8). With increasing liquor ratio, DA decreases as a result of a decrease in the amine concentration in the reaction mixture.

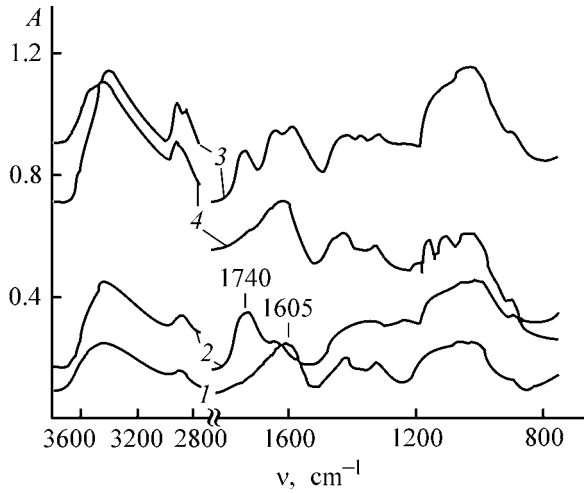

Fig. 1. FTIR spectra: (*1*) NaCMC, (*2*) HCMC, (*3*) amidated HCMC (DA 0.066), and (*4*) amidated NaCMC (DA 0.066). Initial CMC with DS 0.32. (*A*) Absorption and (ν) wave number; the same for Figs. 2 and 4.

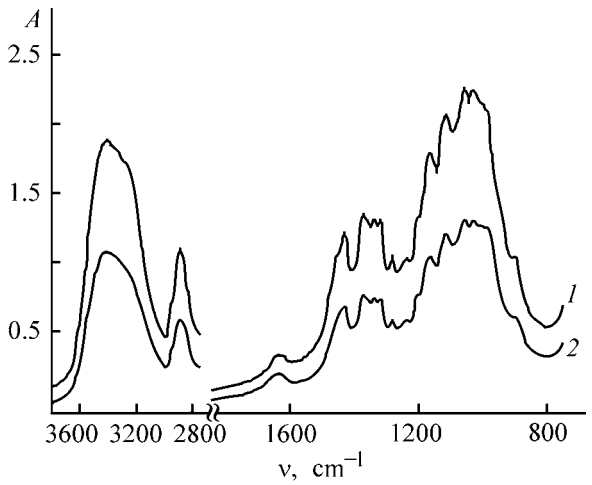

Fig. 2. FTIR spectra of cotton cellulose: (*1*) after amidation and (*2*) that after subsequent saponification. Reaction time 3 h.

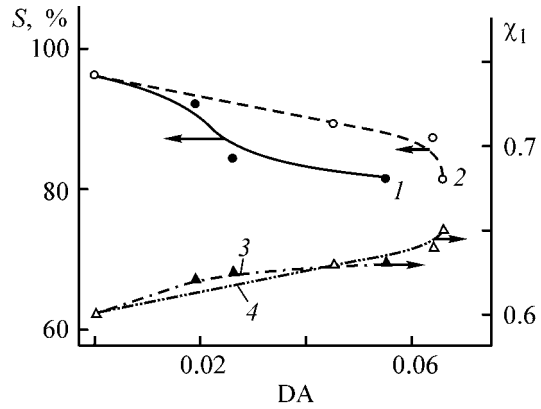

Fig. 3. (*1*, *2*) Solubility *S* of CMCA in water and (*3*, *4*) polymer–solvent interaction parameter χ_1 in the system CMCA–water vs. DA. CMCA samples were prepared from CMC with DS 0.32. Amount of decylamine added (mol mol^{-1} COOH groups of CMC): (*1*, *3*) 0.5 and (*2*, *4*) 1.0.

The chemical analysis data (determination of DA from the nitrogen content) were confirmed by the FTIR spectra of the initial NaCMC, HCMC, and the resulting amides, which contain ionized and free carboxy groups (Fig. 1).

The IR spectrum of regenerated cotton cellulose is characterized by broad adsorption band at 3000–3700 cm^{-1} (free and H-bonded OH groups of the polymer) and a symmetrical band at 2900 cm^{-1} (CH_2 and CH groups of cellulose) [9]. The IR spectrum of NaCMC (Fig. 1) shows a band at 1597–1605 cm^{-1}, assigned to antisymmetrical vibrations of the ionized carboxy groups COO– [6]. On passing to HCMC, an absorption band of COOH at 1740 cm^{-1} and a shoulder at 1647 cm^{-1} are observed [10]. The amide group has absorption bands at 1650 cm^{-1} (amide I) and 1515–1570 cm^{-1} (bending vibrations of the NH group) [11].

As the CO bands of the amide and COOH groups (1647 cm^{-1}) are close, we recorded IR spectra of CMCA, in which unchanged carboxy groups occur in the H form (spectrum no. *3*) and Na form (spectrum no. *4*). As seen, in the case of HCMC amide, characteristic bands of COOH are observed at 1740 cm^{-1}, and amide bands, at 1640–1650 and 1570 cm^{-1}. After conversion of free carboxy groups into the Na form, the CO band of the amide group appears as a shoulder. The band at 1570 cm^{-1} is not observed because of the small amount of the amide groups in CMCA, as demonstrated below. Furthermore, after substitution of even a small amount of the carboxy groups with amide groups, we observed splitting of the band at 2900 cm^{-1}, which should be assigned to additional CH_2 groups of the primary amine used in amidation. The absorption bands at 2875 and 2925 cm^{-1} are assigned to symmetrical and antisymmetrical vibrations of the CH_2 groups of the substituent, respectively [11].

It should be pointed out that, a shoulder at 3180 cm^{-1} is observed in the range of absorption of the OH groups (3000–3700 cm^{-1}), which suggests hydrogen bonding with the NH groups of the amide [11]. Thus, the IR spectra of the CMCA samples confirm the results of chemical analysis.

Under conditions similar to those used in synthesis of CMCA, amines may react with the hydroxy groups of the polymer (such a reaction is used in synthesis of cellulose carbamates [12]). To check the possibility of formation of an amide by the reaction of the amine with the hydroxy groups, cotton linter was treated with the reaction mixture under the same conditions as CMC was. The FTIR spectra of cotton cellulose after amidation and subsequent saponification are shown in Fig. 2. No absorption bands typical of the amide groups are observed in the spectra, which suggests that the amine reacts with the carboxy groups of the polymer essentially by reaction (1).

Since we used decylamine as an amidating agent, it may be expected that introduction of such a bulky radical into the CMC molecule will alter the thermodynamic affinity of the polymer for water. Therefore, we studied the solubility of the resulting products in water and estimated the Flory–Huggins polymer–solvent interaction parameter χ_1, using the water vapor sorption method (Fig. 3). The interaction parameter χ_1 was calculated by Eq. (4).

$$\ln a_1 = \ln(p_1/p_1^0) = \ln(1 - \varphi_2) + \varphi_2 + \chi_1\varphi_2^2, \quad (4)$$

where a_1 is the solvent activity and p_1/p_1^0, relative pressure of the solvent vapor.

The experiments were carried out at a saturated vapor pressure of water, i.e., $a_1 = p_1/p_1^0 = 1$ and $\ln a_1 = 0$.

The volume fraction of the polymer was estimated by Eq. (5).

$$\varphi_2 = \frac{1}{1 + \frac{d_2}{d_1}(\Delta W)}, \quad (5)$$

where ΔW is the sorption of water (g g^{-1}), and d_1 and d_2, the densities of water and the polymer, respectively.

The densities of CMCA samples were calculated theoretically [13].

Figure 3 shows that introduction of a small amount of amide groups containing a long alkyl radical in the CMC macromolecules (DA ≤ 0.06) does not decrease significantly the solubility of CMCA in water. At DA > 0.06, the solubility of mixed cellulose ethers remarkably decreases. The observed steady increase in χ_1 suggests a decrease in the thermodynamic affinity of CMCA for water.

Table 2 summarizes the results of synthesis of CMCA from commercial CMC. At a liquor ratio of 4, the major part of the reaction mixture is absorbed by the sample. As a result, the polymer macrochains suffer a remarkable oxidative degradation at 140°C. To optimize the synthesis conditions, we varied the liquor ratio. The minimum degradation was observed at a liquor ratio of 13, but in this case, the consumption of chemicals is the highest. A liquor ratio of 10 was accepted as the optimum.

As determination of nitrogen in CMCA samples by the Kjeldahl method takes a long time, we studied the possibility of determining DA by the conductometric titration. Determination of the carboxy groups in CMC takes about 1.0–1.5 h. The DS in the initial CMC was determined from the amount of the carboxy groups, using back titration [2]. Then we determined unchanged carboxy groups in the resulting CMCA. The DA was found as the difference

$$DA = DS_{CMC} - DS_{CMCA}.$$

Table 2. Synthesis of CMCA samples from CMC with DS 0.80 (reaction time 3 h; amount of decylamine added 1 mol mol^{-1} COOH groups)

Run no.	Liquor ratio	N, %	DA		Water vapor sorption, g g^{-1}
			Kjeldahl method	conductometric titration	
1*					2.240
2	4	0.58	0.58	0.50	0.687
3	6	0.61	0.61	0.58	0.759
4	10	0.67	0.67	0.63	0.776
5	13	0.65	0.65	0.60	0.825

* Run with NaCMC (DS 0.80).

As seen (Table 2), both methods used for determining DA provide similar results. It should be pointed out that conductometric titration is applicable only to CMCA samples with DA >0.2. For samples with lower DA (Table 1), we obtained considerable discrepancies in the DA values estimated from the nitrogen content and from conductometric titration data.

At high DA, the FTIR spectra shows the characteristic amide band at 1650 cm^{-1} (Fig. 4). The band at 1550 cm^{-1} appears as a shoulder, which becomes more pronounced with increasing DA. Substitution of more than half of the carboxy groups in CMC strongly decreases the CMCA solubility in water and the thermodynamic affinity of the polymer for the solvent (Fig. 5). The resulting CMCA samples demonstrate a limited solubility in aqueous-organic solvents.

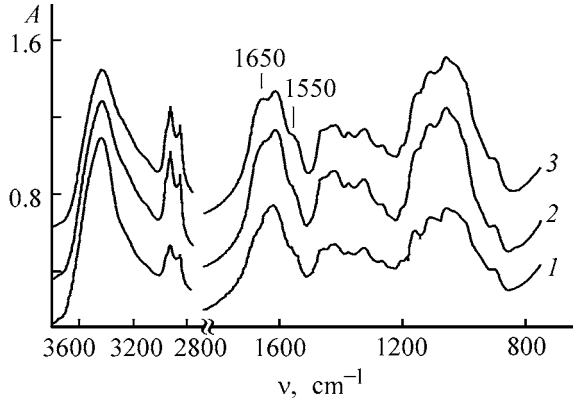

Fig. 4. FTIR spectra of CMCA samples. DA: (*1*) 0.50, (*2*) 0.58, and (*3*) 0.63.

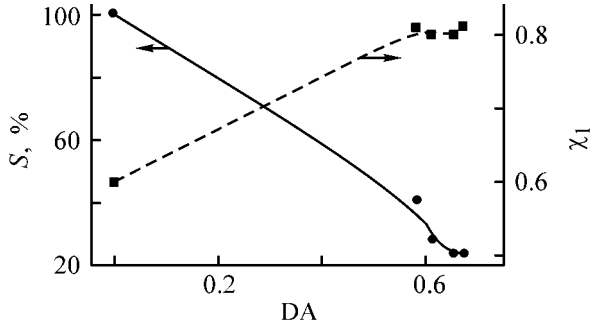

Fig. 5. Solubility S of CMCA in water and polymer–solvent interaction parameter χ_1 in the systems CMCA–water vs. DA. CMCA samples were prepared from CMC with DS 0.80. Amount of decylamine added 1 mol mol^{-1} COOH groups of CMC.

Comparison of Tables 1 and 2 shows that, under similar conditions of CMC amidation (temperature, liquor ratio, amount of the amine added), DA can be controlled by varying DS in the initial CMC.

Finally, the degree of amidation and physicochemical characteristics (solubility in water and aqueous-organic solvents) of CMCA can be controlled by varying the DS in the initial CMC and the structure of an amine.

CONCLUSIONS

(1) Optimal conditions are determined for single-stage synthesis of carboxymethyl cellulose *N*-decylamide (*N*-decylaminocarboxymethyloxycellulose).

(2) Amidation of carboxymethyl cellulose is affected by characteristics of the initial CMC, the amount of the amine added, and liquor ratio.

(3) Small degree of amidation has no considerable effect on the solubility of carboxymethyl cellulose in water. At high DA, the solubility in water is very low, but the products become soluble in aqueous-organic solvents.

REFERENCES

1. Yusupova, L.D., Bochek, A.M., and Petropavlovskii, G.A., *Zh. Prikl. Khim.*, 1994, vol. 67, no. 7, pp. 1187–1191.
2. Bochek, A.M., Yusupova, L.D., Zabivalova, N.M., *et al., Zh. Prikl. Khim.*, 2002, vol. 75, no. 4, pp. 659–663.
3. Sun'-Tun, Derevitskaya, V.A., and Rogovin, Z.A., *Vysokomol. Soedin.*, 1959, vol. 1, no. 8, pp. 1178–1183.
4. Kinstler, O.B. and Porsham, M.L., *Izv. Akad. Nauk Latv. SSR, Ser. Khim.*, 1977, no. 6, pp. 737–742.
5. Klem, D., Scnaberrauch, M., and Geschwend, G., *Wiss. Z., Friedrich Schiller Univ., Jena Naturwiss. R.*, 1985, nos. 5–6, pp. 34–39.
6. Petropavlovskii, G.A., Larina, E.I., and Borisova, T.I., *Cellulose Chem. Technol.*, 1984, vol. 187, no. 3, pp. 283–292.
7. Klimova, V.A., *Osnovnye mikrometody analiza organicheskikh soedinenii* (Basic Methods for Microanalysis of Organic Compounds), Moscow: Khimiya, 1967.
8. Petropavlovskii, G. A., *Gidrofil'nye chastichno zameshchennye efiry tsellyulozy i ikh modifikatsiya putem khimicheskogo sshivaniya* (Hydrophilic Partially Substituted Cellulose Ethers and Their Modification by Chemical Cross-Linking), Leningrad: Nauka, 1989.
9. Zhbankov, R.G., *Infrakrasnye spektry tsellyulozy i ee proizvodnykh* (Infrared Spectra of Cellulose and Its Derivatives), Minsk: Nauka i Tekhnika, 1964.
10. *Cellulose and Cellulose Derivatives*, Bikales, N.M. and Segal, L., Eds, New York: Wiley, 1971.
11. Bellamy, L.J., *The Infrared Spectra of Complex Molecules*, London: Wiley, 1954.
12. Petropavlovskii, G. A. and Zimina, T.R., *Zh. Prikl. Khim.*, 1994, vol. 67, no. 5, pp. 705–721.
13. Sewell, R.A., *J. Appl. Chem.*, 1953, vol. 3, pp. 71–80.

Russian Journal of Applied Chemistry, Vol. 76, No. 12, 2003, pp. 2003–2008. Translated from Zhurnal Prikladnoi Khimii, Vol. 76, No. 12, 2003, pp. 2053–2058.

MACROMOLECULAR CHEMISTRY AND POLYMERIC MATERIALS

Variation of Composition and Submicroscopic Structure of Pine Wood in Potash-Sulfite Cooking

G. A. Pazukhina and O. P. Kovaleva

State Forestry Engineering Academy, St. Petersburg, Russia

Received January 27, 2003

Abstract—Variation of submicroscopic structure and also the behavior of phenolic compounds and polysaccharides of pine wood under conditions of potash-sulfite cooking were studied.

Delignification of pine wood by the traditional sulfite procedure is hampered by the presence of phenolic compounds and their derivatives, such as pinosylvin (3,5-dihydroxystilbene), its monomethyl ether, and flavone compounds of the phenolic type (pinocembrin, pinobanksin, etc.) in the heartwood. Phenolic compounds, entering into the condensation with lignin, inhibit its dissolution to the point of complete termination. Combined alkaline-sulfite procedures of cellulose production allow recovery of various plant raw materials. In so doing, wood is separated into fibers with yield higher by 10% than that in the traditional sulfite cooking, and the yield of cellulose increases by 7–8% due to the stabilization of carbohydrates to acid hydrolysis [1]. This is cased by the differences in the topochemistry of wood delignification processes.

It has been shown previously [2, 3] that, in soda-sulfite cooking of spruce wood, the *P* and S_1 layers of the cell wall of wood are subjected to a directed chemical action. As a result of swelling and subsequent contraction of wood with variation of pH of the cooking liquor at the interface of intercellular substances, microfissures and subcapillaries are formed, which provides early separation of wood residue into fibers and production of cellulose with high morphologic homogeneity. Sodium and potassium compounds can be used as a soluble base for combined alkaline-sulfite delignification [1, 4–6].

The aim of this study was to examine the variation of chemical composition and submicroscopic structure of ordinary pine (*Pinus silvestris*) wood in potassium-sulfite cooking.

EXPERIMENTAL

For chemical analysis of pine wood and wood residue, we used a 0.25–0.50-mm sawdust fraction. The lignin content in wood, wood residue, and cellulose was determined by treatment with sulfuric acid [7]; the cellulose content, by the nitric acid-alcohol method [7]; the content of pentosans, by the bromide-bromate method [7]; and the content of substances extracted with hot water, ethyl ether, and acetone, by the procedure described in [7].

For cooking we used pine wood chips 20–25 mm long, 20–25 mm wide, and 2–5 mm thick. The cooking was carried out in an electrically heated 2.5 dm^3 autoclave. Before cooking, the chips were treated with saturated steam at 100°C for 15 min, after which the chips were impregnated with a 45 g dm^{-3} (in the K_2O units) K_2CO_3 solution at 50°C for 80 min and gage pressure of 0.9 MPa. After completion of impregnation and withdrawal of the draining K_2CO_3 solution, sulfurous acid containing 0.3% (in the K_2O units) potassium base and 8% total SO_2 was introduced into the autoclave. The temperature schedule was as follows: heating to 145°C for 45 min and cooking at this temperature until an intermediate product with a given content of lignin was obtained [8].

The total volume of submicroscopic capillaries (TVSC) was measured by determining the water volume in capillaries inaccessible to polymer macromolecules in moist samples of wood and cellulose. For this purpose, lateral sections of the initial wood and wood residue, 0.2 mm thick, were prepared on a microtome. Polyethylene glycol with the number-

1070-4272/03/7612-2003 $25.00 © 2003 MAIK "Nauka/Interperiodica"

average molecular weight of 40 000 was used as a polymer. The concentration of aqueous solutions of polyethylene glycol was measured with an ITR-1 interferometer. By evaluating the amount of water "inaccessible" to the soluble polymer Q, we determined the point of fiber saturation, which characterizes the total volume of submicroscopic capillaries of cellulose fibers swollen in water ($cm^3\ g^{-1}$) [9].

The amount of water inaccessible to the polymer was evaluated by the formula [9]

$$Q = \frac{W+q}{P}\left[1 - \frac{W}{W+q}\,\frac{c_{in}}{c_{fin}}\right],$$

where W is the weight of the polyethylene glycol solution (g); P, weight of absolutely dry sample (g); q, the weight of water contained in the sample (g); and c_{in} and c_{fin}, the initial and final concentrations of polyethylene glycol solution (%).

The volume of the cell walls (VCW) was evaluated by the formula

$$VCW = (TVSC + 1/1.45)K_y,$$

where K_y is the yield coefficient for wood residue or cellulose determined as the ratio of the weight of the wood residue or cellulose to the weight of the initial absolutely dry wood, and 1.45 is the specific volume of the wood substance ($g\ cm^{-3}$).

The water-retaining power (WRP) of cellulose and wood residue was determined by centrifugation and evaluated from the amount of water retained in fiber shells (% of the weight of absolutely dry wood residue) [10]. The carbohydrate composition of the samples and wood residues was determined by gas–liquid chromatography [7].

The pine wood sample selected for the study had the volume ratio of the heartwood and sapwood parts of wood of 58 and 42%, respectively.

As seen from Table 1, the heartwood and sapwood parts of pine wood differ appreciably in density and chemical composition. The heartwood contains more lignin and extractable substances but less cellulose and pentosans. The presence of significant amounts of extractable substances of the phenolic type (1.8 wt %), extracted with acetone after treatment with ethyl ether, in the heartwood did not allow complete delignification of this sample of pine by the traditional sulfite procedure: as a result of cooking, dark-colored cellulose was obtained in a total yield of 46.4 wt %, with the content of wood residue of 15.4 wt %.

The series of potash-sulfite cookings with sampling of wood residue at certain intervals yielded intermediate products with lignin content from 29.0 to 5.7 wt % in the total yield of 96.7 to 48.1 wt %. As seen from Fig. 1, the TVSC and WRP increase in treatment of pine wood with saturated steam for 15 min. In parallel, the content of extractable substances and acetyl groups decreases by 32 and 12 wt %, respectively (Table 2).

During impregnation, penetration of K_2CO_3 solution into the wood substance is accompanied by its swelling. The layer S_3, which is the layer of secondary cell wall, situated most closely to the lumen, contacts the solution first. To the middle plate, the solution penetrates mainly through the apertures of edged pores. As a result of swelling of cell walls, a developed system of submicroscopic capillaries is formed. The degree of swelling of wood substance can be indirectly judged from the variation of TVSC, VCW, and WRP. At insignificant decrease in the yield of wood residue (by 1.7 wt %) in treatment with solution of potassium carbonate, the TVSC increases by 13 vol %, VCW, by 3.5 vol %, and WRP, by 24 wt %. The rather weak swelling of pine wood substance under the action of K_2CO_3 solution is accounted for by the features of this type of wood, such as the high content of resinous substances, which decrease the permeability

Table 1. Characteristics and chemical composition of pine wood

Characteristic	Heartwood part	Sapwood part	Wood as a whole
Density, $kg\ m^{-3}$	520	470	490
Composition, wt %:			
cellulose	41.9	50.5	45.5
lignin	32.2	26.5	29.8
pentosans	6.9	7.6	7.2
substances extracted with:			
hot water	5.5	4.4	5.0
ethyl ether	7.0	4.8	6.0
acetone after extraction with ethyl ether	1.8	–	1.0

Table 2. Variation of composition of pine wood in treatment with K_2CO_3 solution

Treatment no.	τ, min	Yield, % of the weight of absolutely dry wood	Lignin, wt %		Extractable substances, % of the weight of absolutely dry wood		Acetyl groups, wt %	
			of the weight of absolutely dry wood	of the initial content in wood	ethyl ether	acetone after extraction with ethyl ether	of the weight of absolutely dry wood residue	of the initial content in wood
Initial wood		100.0	29.8	100.0	6.0	1.00	2.27	100.0
Treatment with steam								
1	15	96.7	29.0	94.1	4.1	0.83	2.10	89.5
Treatment with K_2CO_3 solution								
2	15	96.0	28.4	91.5	3.6	0.62	2.06	88.9
3	30	95.8	28.0	90.0	2.2	0.30	1.99	85.4
4	60	95.4	27.9	89.3	–	–	1.65	70.1
5	80	95.0	27.9	88.9	1.8	0.22	1.54	64.4

Table 3. Variation of composition of pine wood in sulfite stage of cooking

Treatment no.	τ, min (T, °C)	Yield, % of the weight of absolutely dry wood		Lignin, wt %		Extractive substances, % of the weight of absolutely dry wood	
		total	sorted cellulose	of the weight of absolutely dry wood residue	of the initial content in wood	ethyl ether	acetone after extraction with ethyl ether
Heating to final temperature							
6	15 (70)	95.3	–	28.0	89.6	2.3	0.26
7	30 (110)	94.8	–	27.1	86.2	2.7	0.22
8	45 (145)	84.0	–	27.0	76.1	2.8	0.18
Keeping at 145°C							
9	30	71.6	21.2	23.3	56.0	2.5	0.18
10	60	61.1	29.0	16.5	33.8	2.5	0.17
11	90	55.2	36.3	12.5	23.2	2.5	0.16
12	120	51.7	43.3	8.6	14.9	2.6	0.16
13	150	48.1	45.7	5.7	9.2	2.6	0.17

of wood and the state of edged pores of heartwood. It is well known that heartwood differs from sapwood in the predominance of pores closed by toruses, which hampers impregnation.

As the K_2CO_3 solution penetrates into the capillary-porous system, the wood is subjected not only to physical but also to chemical action of this solution. Deacetylation of wood, which started in the stage of steam treatment, is enhanced in treatment with potassium carbonate solution: the content of acetyl groups decreases by additional 25 wt % (Table 2, treatment no. 5). The deacetylation is somewhat accelerated with increasing treatment duration, which is due to improvement of the conditions of wood impregnation through removal of extractable substances.

Treatment of pine wood with K_2CO_3 solution provides dissolution of more than 70 wt % of the substances extracted with ethyl ether and decreases the content of phenolic compounds, which is indirectly suggested by the decrease from 0.83 to 0.22 wt % in the content of substances extracted with acetone after extraction with ethyl ether. After completion of the stage of alkaline treatment of wood, the free-draining solution of K_2CO_3 is fully removed, and only a part of the solution, filling the capillary-porous system of wood, is involved in the sulfite stage. During the first 15 min of the sulfite stage of cooking, i.e., during heating to 70°C, K_2CO_3 reacts with H_2SO_3, which is accompanied by a decrease in the pH of the medium. As can be seen from Table 3 and Fig. 1, during this

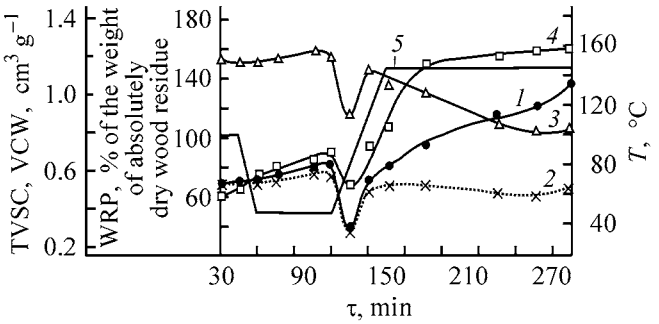

Fig. 1. Variation of TVSC of (*1*) wood residue and (*2*) initial wood, (*3*) WRP, and (*4*) VCW in potash-sulfite cooking. (*T*) Temperature and (τ) time; the same for Figs. 2 and 3; (*5*) temperature regime of cooking.

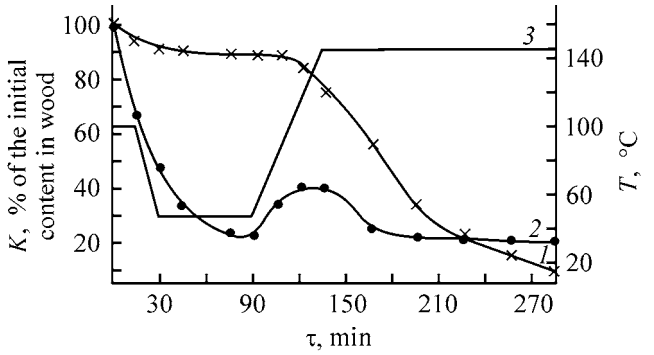

Fig. 2. Variation of content *K* (*1*) lignin and (*2*) resin in potassium-sulfite cooking. (*3*) Cooking temperature.

period the TVSC significantly decreases (by 53%), and the VCW decreases from 87 to 66%. The decrease in TVSC is caused by significant contraction of cell walls of wood (WRP decreases from 1.19 to 0.88 $cm^3 g^{-1}$ of wood residue). The abrupt decrease in the degree of swelling of cell walls is apparently favored by deresinification of tracheids of pine wood in the stage of treatment with K_2CO_3 solution. With further heating, the TVSC, WRP, and VCW of wood residue increase again owing to hydrolysis of polysaccharides and dissolution of their hydrolysis products, and also to formation of solid lignosulfonic acid having hydrophilic properties.

During keeping at the final temperature, sulfonation of lignin is enhanced, its dissolution is accelerated, and carbohydrate components are swollen and partially dissolved. When the final temperature of potash-sulfite cooking is reached, with the development of the system of submicroscopic capillaries continuing, the WRP decreases, which is caused by dissolution of significant amounts of lignin, hemicelluloses, and in part, cellulose.

As can be seen from Table 3, the yield of wood residue somewhat increases within 15 min after supply of sulfurous acid to cooking, presumably owing to uptake of sulfur (sulfonation of lignin) and also to an increase in the content of extractable substances (by 31 wt %) through their precipitation from solution in substitution of the alkaline medium for acidic medium. During heating to 145°C, the yield of wood residue significantly decreases (to 84 wt %) owing dissolution of lignin and readily hydrolyzable carbohydrates. During cooking at the final temperature, the yield of wood residue rapidly decreases, which is caused by dissolution of sulfonated lignin.

After keeping for 30 min at the final temperature, the wood residue is divided into two portions: sorted cellulose (21.2 wt %) and wood residue (50.4%). As can be suggested, the sorted cellulose is formed from sapwood, which contained less lignin and no phenolic compounds among its extractable substances. After longer cooking at the final temperature, the content of sorted cellulose increases and that of wood residue decreases. After the completion of cooking, the total yield of cellulose was 48.1 wt %, with the content of wood residue equal to 2.4 wt %.

It should be noted that, for pine wood delignification by the potash-sulfite procedure, there is no so-called point of desintegration into fibers. The disintegration of wood residue into fibers was extended in time owing to the presence of readily cooked sapwood and difficulty cooked heartwood. The dynamics of lignin dissolution during cooking are complicated. Treatment of wood with saturated steam weakens the bonds between carbohydrate and lignin macromolecules, which favors removal of approximately 6 wt % of lignin from wood with a condensate being formed. During treatment with K_2CO_3 solution, approximately 5 wt % of lignin is dissolved additionally. In the initial stage of sulfite cooking, lignin is not dissolved, since a certain degree of sulfonation is required for lignin to pass into sulfurous acid solution. With increasing temperature, the lignin dissolution accelerates. As a result, when the final temperature is reached, an additional 13 wt % of lignin passes into the solution. The rate of lignin dissolution is the highest during the first hour of keeping at the final temperature, after which the process decelerates. The deceleration of delignification is due to the fact that, by this instant of time, sapwood has got free of the main part of lignin, while delignification of heartwood still continues.

The variation of the content of substances extractable with acetone in the wood residue and cellulose is shown in Fig. 2. After steaming, 34 wt % of resinous substances is removed from wood, and after treatment

with K_2CO_3 solution, 42 wt % of resinous substances passes into the solution. However, after complete withdrawal of draining solution of potassium carbonate and supply of a sulfurous acid, the resin content in the wood residue increases. This is due to the fact that extractable substances dissolved in the alkaline solution, whose certain volume is retained in wood, partially reprecipitate in wood capillaries when pH and temperature change. In the course of subsequent sulfite cooking, the extractable substances slowly pass into the solution. In separation of sorted cellulose and wood residue, it was found that the wood residue contains a large amount of resinous substances. After the cooking is complete, approximately 20% of the initial amount of extractable substances is contained in wood.

Tables 2 and 3 show that the content of phenolic compounds (acetone extract after pretreatment of wood residue and cellulose with ethyl ether) gradually decreases in the course of potash-sulfite cooking. In the first stage of cooking (treatment with saturated steam or and K_2CO_3 solution), up to 80 wt % of the initial amount of phenolic compounds in wood is recovered from pine chips, including 60 wt % in alkaline treatment. In the stage of sulfite cooking, the wood substance continues be feed of phenolic compounds with increasing temperature, but a part of these compounds (0.18% of the weight of absolutely dry cellulose) remains in the fiber. The high content of resinous substances of the phenolic type in the resulting cellulose does not allow its exhaustive delignification. From this sample of highly resinous freshly felled pine wood, cellulose with the lignin weight fraction of 5.7% was produced.

The deacetylation of wood in its treatment with potassium carbonate solution and the swelling and contraction of cell walls of wood, proceeding under conditions of potassium-sulfite cooking, provide favorable conditions for stabilization of carbohydrate components to the action of sulfurous acid. As can be seen from Fig. 3, the first 15-min step of treatment of pine wood with K_2CO_3 solution causes an insignificant loss of readily hydrolyzable polysaccharides as a result of hydrolysis of galactopyranose (25 wt %) and arabinofuranose (22 wt %) side monomeric units of glucomannan and xylan, respectively. After the completion of alkaline treatment, 55 wt % of galactopyranose and 50 wt % of arabinofuranose units are eliminated, and these units are virtually absent in the early stages of sulfite cooking. The increased hydrolytic stability of glucomannan in comparison with other hemicellulose components of wood is retained during most part of the sulfite cooking. After the cooking was complete,

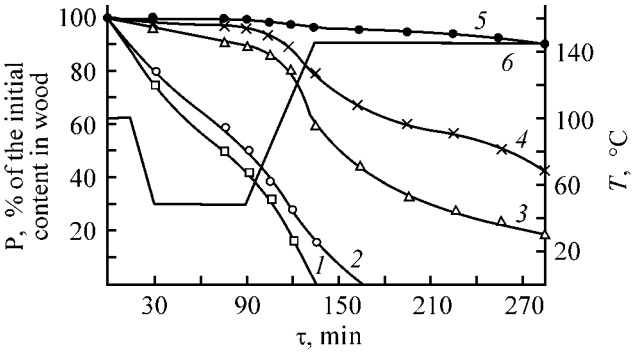

Fig. 3. Variation of the content of polysaccharides P in wood residue in potassh-sulfite cooking: (*1*) galactan, (*2*) arabinane, (*3*) xylan, (*4*) mannan, and (*5*) glucan; and (*6*) cooking temperature.

cellulose contained 41.7 wt % of glucomannan and 19.3 wt % of xylan relative to their initial amount in wood. In the course of sulfite cooking, the content of glucan decreases insignificantly owing to dissolution of glucomannan and, in part, cellulose.

The behavior of hemicelluloses in potassium-sulfite cooking is largely determined by distinctions in delignification of heartwood and sapwood. Decelerated delignification of heartwood results in degradation of a part of polysaccharides of sapwood, more readily liberating the main amount of lignin. Therefore, contrary to spruce wood, the increase in the yield of commercial cellulose in delignification of pine wood by potassium-sulfite cooking is significantly weaker owing to stabilization of carbohydrate components with respect to acidic hydrolysis in the sulfite stage of cooking.

CONCLUSIONS

(1) Under conditions of potash-sulfite cooking, pretreatment of pine wood with saturated steam and K_2CO_3 solution gives rise to a system of submicroscopic capillaries owing to swelling and removal of individual components of wood. This treatment allows recovery of up to 80 wt % of phenolic compounds contained in wood, which significantly facilitates the subsequent sulfite delignification.

(2) On adding sulfurous acid to pine chips impregnated with K_2CO_3, the cell walls of wood undergo contraction. With increasing temperature of cooking, lignin and carbohydrates begin to dissolve.

(3) In delignification of pine wood by the traditional potash-sulfite procedure, degradation of wood residue to fibers is extended in time owing to the difference in rate of delignification between heartwood and sapwood.

(4) Under conditions of potassium-sulfite cooking of pine wood, the stability of glucomannan to acid hydrolysis is increased.

ACKNOWLEDGMENTS

The authors are greateful to A.P. Treiman for the help determining the submicroscopic structure of wood.

REFERENCES

1. Pazukhina, G.A., *Stupenchatye metody proizvodstva tsellyulozy* (Step Procedures of Cellulose Production), Moscow: Lesnaya Prom–st., 1990.
2. Pazukhina, G.A., Purina, L.T., Brentse, A.A., and Treimanis, A.P., *Khim. Drev.*, 1981, no. 4, pp. 19–23.
3. Pazukhina, G.A., Treimanis, A.P., and Akimova, I.V., *Khim. Drev.*, 1979, no. 3, pp. 13–17.
4. USSR Inventors' Certificate, no. 520 430.
5. USSR Inventors' Certificate, no. 1 304 456.
6. USSR Inventors' Certificate, no. 1 716 837.
7. Obolenskaya, A.V., El'nitskaya, Z.P., and Leonovich, A.A., *Laboratornye raboty po khimii drevesiny i tsellyulozy* (Laboratory Manual on Chemistry of Wood and Cellulose), Moscow: Ekologiya, 1991.
8. Kovaleva, O.P., Potash-Sulfite Cooking of Pine Wood, *Cand. Sci. Dissertation*, St. Petersburg, 1991.
9. Treimanis, A.P., Gromov, V.S., and Kampuse, A.A., *Khim. Drev.*, 1975, no. 4, pp. 22–29.
10. Hopner, Th., Jayme, G., and Ulrich, J., *Papier*, 1965, vol. 9, nos. 19–20, pp. 476–482.

Russian Journal of Applied Chemistry, Vol. 76, No. 12, 2003, pp. 2009–2013. Translated from Zhurnal Prikladnoi Khimii, Vol. 76, No. 12, 2003, pp. 2059–2063.

MACROMOLECULAR CHEMISTRY AND POLYMERIC MATERIALS

Formation of Strength Properties of Model Glue Joints Based on Epoxy-Amine Binders Operating by the Polymerization Mechanism

Yu. N. Smirnov, B. A. Komarov, T. E. Shatskaya, and V. I. Natrusov

Institute of Problems of Chemical Physics, Russian Academy of Sciences, Chernogolovka, Moscow oblast, Russia

Stekloplastik Scientific and Production Association, Open Joint-Stock Company, Kryukovo, Moscow oblast, Russia

Received June 16, 2002; in final form, May 2003

Abstract—The kinetics of curing of an epoxy-amine compound by the polymerization mechanism were studied at various temperatures by isothermal calorimetry and rheokinetic procedures. The resulting kinetic data were correlated with the patterns of variation of the adhesion strength of glass–epoxy-amine compound–glass glue joints, of shrinkage stresses, and shrinkage defects, as well as with the nature of the glue joint failure.

In [1–3], we attempted chemical design of high-strength epoxy-amine binders for fiber glass plastics by optimal combination of the structural contributions from polycondensation and polymerization processes to the cohesion strength of the binders proper. Studying the adhesion strength formation in curing of compounds is also essential for designing the chemical structure of the binder for high-strength fiber plastics.

It is important to elucidate how the structural contributions from a combination of different processes of three-dimensional cross-linking of binders (glues) affect the origination, number, and extent of shrinkage and thermal defects, as well as the corresponding stresses and their relaxation processes. This will allow optimization of the molding mode for high-strength composites.

Earlier [4], we have elucidated how the strength properties of model glue joints (MGJs) vary in the course of curing of epoxy-amine compounds by the polycondensation mechanism. Unexpectedly, the time dependence of the glue joint strength σ_{glue} of MGJs proved to be complex. In early curing stages (preceding gelation), σ_{glue} of the GLMs initially grew, then passed through then maximum, and a decreased. Further, σ_{glue} remained unchanged, then grew, and finally approached a constant limiting value.

This complex pattern of variation of the glue joint strength of MGJs in the course of isothermal curing was attributed to two relaxation transitions in the glue interlayer, which are due to physical (glass transition of the binder at the curing and test temperatures) and chemical (gelation) processes, as well as to shrinkage and thermal stresses and the corresponding defects affecting the failure mechanism of adhesion joint.

The aim of this study was to examine the glue joint strength as influenced by the kinetic features of the polymerization curing of the epoxy-amine compound. This process was studied by isothermal calorimetry and rheokinetic procedures, namely, rotation viscometry, tensimetry, and a procedure utilizing a torsion pendulum.

EXPERIMENTAL

As the binder we used a compound based on ED-20 epoxy-4,4'-isopropylidenediphenol resin and benzyldimethylamine (BDMA). The curing kinetics of the individual binder were studied calorimetrically on an EK-2 low-inertia calorimeter with a torsion pendulum (torsion mass 9 g; a 60-mm long VM-1 glass thread containing 25 wt % binder as the working unit) and on a Rheotest-II viscometer [plate-cone design; gelation time at various temperatures was determined by extrapolating the linear portion corresponding to a sharp viscosity growth to the abscissa (time) axis and, additionally, as the time in which a conventional viscosity of 4000 Pa is reached]. The shrinkage stresses were determined tensimetrical-

1070-4272/03/7612-2009 $25.00 © 2003 MAIK "Nauka/Interperiodica"

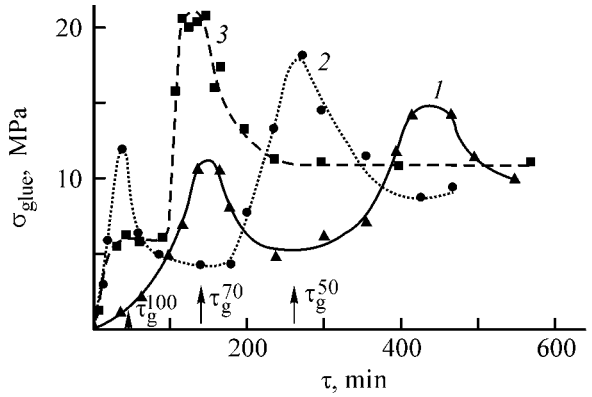

Fig. 1. Glue joint strength σ_{glue} vs. the curing time τ for ED-20 + BDMA compound. (τ_g^T) Gelation time, min, for the corresponding T_{cur}; the same for Fig. 2. *T*, °C: (*1*) 50, (*2*) 70, and (*3*) 100.

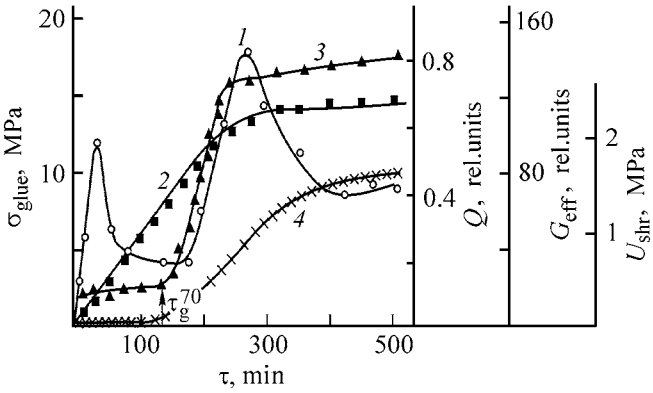

Fig. 2. Variation of (*1*) glue joint strength σ_{glue}, (*2*) conversion *Q* of the functional groups, (*3*) effective elasticity modulus G_{eff}, and (*4*) shrinkage stress U_{shr} with the curing time τ at 70°C.

ly [5]. The glue joint strength of MGJs was determined by the procedure described in detail in [6].

Shrinkage defects were observed directly during isothermal synthesis in long glass tubes [7]. A fairly high adhesion between the system being cured and the glass surface gave rise to initial shrinkage cohesion defects which further, under certain conditions, evolved into adhesion exfoliates.

Figure 1 presents typical kinetic plots for the glue joint strength σ_{glue} at curing temperatures T_{cur} of 50, 70, and 100°C, which are lower than the limiting glass transition point T_{gl}^{∞} of the epoxy-amine compound cured by the polymerization mechanism (T_{gl}^{∞} = 106°C [8]). Figure 1 shows that the time dependences of σ_{glue} for a polymer binder (glue) operating by the polymerization mechanism have two maxima. They tend to shift to smaller times with rising curing temperature; at high T_{cur} the initial maximum finally decays, like in the case of compounds cured by the polycondensation mechanism [4]. Comparison of the results from studies of the glue joint strength in the course of curing of different types of epoxy-amine compounds poses a number of questions as to the reasons for (1) appearance of the initial peak in the glue strength vs. time plots for different types of glue compounds; (2) decrease in σ_{glue} rather than leveling-off (like in the case of polycondensation mechanism) after the secondary growth of the glue joint strength in the case of glue compounds cured by polymerization mechanism; and (3) a much greater strength of a glue joint for compounds cured by polymerization mechanism, despite its lower cohesion strength.

To elucidate the reasons for the appearance of two glue strength peak, let us consider the time dependence of σ_{glue} at 70°C (Fig. 2) together with the analogous dependences for such curing parameters as the current conversion of the functional groups of the glue compound *Q*, the effective torsion elasticity modulus G_{eff}, and the shrinkage stress U_{shr}. Figures 1 and 2 (where the gelation times τ_{gel} for the corresponding T_{cur} are shown with arrows) clearly demonstrate that, in all cases of polymerization curing, the primary glue joint strength maximum precedes the onset of gelation. Notably, this occurs at a time when there is no noticeable growth of shrinkage stress, shrinkage defects are not formed at the curing temperature, and glass transition at T_{cur} is not recorded by the torsion pendulum.

Evidently, like in the case of polycondensation curing, the initial peak in the plot of the glue joint strength against the curing time appear for physical reasons. We have found earlier [4] that the initial growth of the glue joint strength is due to enhancement of the viscous (dissipative) properties of the binder owing to the onset of its transition from the liquid to glassy state at the test (room) temperature. This is indicated by a sharp growth of the viscosity of the compound at room temperature, which is due to the physical process of transition of the binder to the glassy state. Notably, the effective activation energy of this process is much lower than that of the chemical transformations [9]. Therefore, at low curing temperatures, the physical (glass transition) process in the binder may run a head of the chemical (gelation) process, and at higher curing temperatures, on the contrary, it may lag behind. Consequently, the viscosity growth may be due to both physical and chemical processes [8, 9]. In this context, the subsequent decrease in σ_{glue} is, evidently, due to curing and, accordingly, to embrittlement of the binder, which is completely vitrified at room temperature. We emphasize that both the primary glass transition of the glue

compound cured at room temperature and its secondary glass transition at the curing temperature are treated as prolonged processes [4].

The secondary growth of the glue joint strength is, evidently, due to an increase in the gel fraction content or in the degree of cross-linking, which favors simultaneous enhancement of the elastic and relaxation (dissipative) properties of the glue compound. This is indicated by a sharp rise in the viscosity of the compound owing to the chemical gelation process and also by a noticeable increase in the effective elasticity modulus G_{eff} at T_{cur} (Fig. 2, curve *3*). Notably, the onset of a steep rise in G_{eff} at τ = 150 min is due to the onset of glass transition in the binder. This time corresponds to the beginning of hardening of the binder, as indicated by the penetration method.

Figure 2 shows that the glue joint strength rapidly grows till at 270th–280th min. Diring this same time interval, G_{eff} reaches its limiting values and the conversion curve *2* levels off. This suggests that the stage of intensive chemical and physical (relaxation processes) transformations of the glue composition at the given curing temperature terminates. It could be expected that the glue joint strength should also attain a limiting value, like in the case of the compound cured by the polycondensation mechanism (the more so that the chemical and physical transformations of the binder are not complete even in 600 min). This is indicated by increments, though small, in G_{eff} and Q, seen in Fig. 2. However, despite the increase in these parameters of the curing processes, the glue joint strength clearly tends to decrease after 300 min. Notably, this is typical of all the temperatures studied (Fig. 1).

This is understandable if we take into account that, starting from 150th min, shrinkage defects in long glass tubes tend to noticeably grow and at τ = 280 min they begin to transform into adhesion defects through exfoliation of the binder from the walls of the glass tubes. Also, the shrinkage stress U_{shr} tends to grow steadily throughout the 600-min period (Fig. 2, curve *4*). Evidently, it is the enhancement of internal stresses and increase in the degree of defectiveness of the binder after sharp deceleration of the chemical cross-linking that are responsible for the secondary decrease in the glue joint strength. Along with the above-mentioned factors, the relaxation characteristics of the binder can additionally decrease within 300–600 min due to physical aging [1], i.e., afterpacking of the network structure and the corresponding decrease in the free volume fraction.

Let us discuss why these factors do not exert similar influence in the case of a system cured by the polycondensation mechanism. Above all, the highest attainable strengths of the glue joints in the case of binders operating by the polymerization mechanism substantially (by a factor of 2–2.5) exceed the maximum strength of the glue joint in the case of the system cured by the polycondensation mechanism [4]. This may be due to two major factors. First, it is known [8, 11] that initiation of the polymerization curing typically requires a hydroxyl-containing accelerator acting as a proton donor:

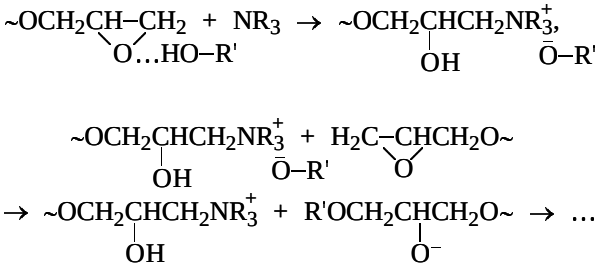

It is seen that, in the first (initiation) stage, a proton is transferred from the hydroxyl-containing HO–R' fragment to the oxygen atom in the epoxy group to form a new hydroxy group and alkoxy anion. In the second stage (polymerization proper), the alkoxy anion (free or as part of an ion pair) attacks the epoxy ring and gets incorporated into the network structure. This scheme suggests that the hydroxy groups contained in the borosilicate glass [12], particularly in its surface layers, can also be involved in the polymerization process to form a chemical bond between the binder and the glass surface. At the same time, it is well known [13–16] that the formation of a chemical bond between the polymer matrix and the substrate surface substantially increases the adhesion strength.

It is known [8, 17] that tertiary amines of the BDMA type are not incorporated into the chemical structure of the network and can act as typical plasticizers, which increase the molecular mobility in the polymer matrix and improve its relaxation ability with respect to internal stresses and excess free volume [3, 17, 18]. To elucidate the possible influence exerted by such a plasticizer as a tertiary amine on the glue joint strength, we carried out the following experiments. Into the glue compound cured by the polycondensation mechanism, which contained ED-20 and *m*-phenylenediamine (*m*-PDA), we introduced 2.5, 5.0, 10, or 15 wt % of a typical plasticizer, dibutyl phthalate (DBP). The glue joint strength was studied for the resulting compounds on keeping the MGJ at

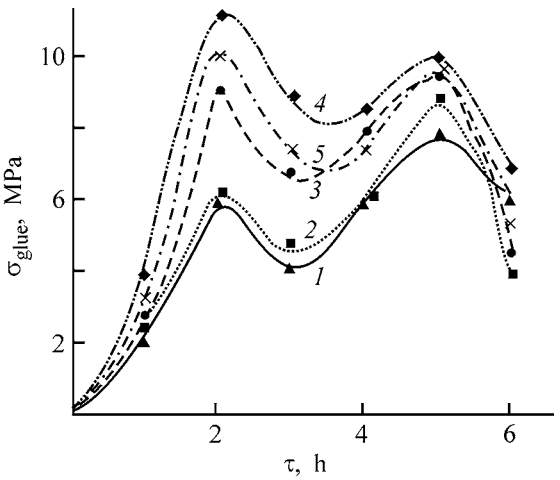

Fig. 3. Variation of the glue joint strength σ_{glue} of the ED-20 + *m*-PDA compound with the curing time τ at 70°C. DBP concentration, wt %: (*1*) 0, (*2*) 2.5, (*3*) 5.0, (*4*) 10, and (*5*) 15.

80°C for 1, 2, 3, 4, 5, and 6 h. Figure 3 shows that the time dependences of σ_{glue} pass through two maxima. With increasing DBP concentration, the glue joint strengths at the maxima tend to increase, with the most significant rise in σ_{glue} observed for the initial maximum. This confirms the assumption that such a plasticizer as tertiary amine exerts physical influence on the glue joint strength for the compound cured by the polymerization mechanism.

A more pronounced influence of the plasticizer on the initial maximum of the glue joint strength is, evidently, due to the specific features of the MGJ failure in the initial stages of curing (cross-linking) of the glue compound transforming to the glassy state at T_{test}. Optical microscopic studies within the time interval corresponding to the appearance of the initial maximum of the glue joint strength showed that, for glue compounds cured by both the polymerization and polycondensation [4] mechanisms, failure at the beginning of curing has a cohesion nature, and the glue interlayer disintegrates like a viscous liquid. Further, a cohesion-plastic failure is observed in the region corresponding to the primary rise in σ_{glue}, and in the region corresponding to the primary decline in σ_{glue}, a cohesion-brittle failure with typical shear bands is observed. Upon introduction of a plasticizer, the range of brittle failure shifts to longer curing times. This is probably due to the fact that the plasticizer increases the molecular mobility of the compound, thus shifting the instant of vitrification to longer times and, thereby, to higher conversion of the functional groups. Evidently, the plasticizer decreases the degree of brittleness of low-molecular-weight glassy binder that has not yet formed a chemically cross-linked three-dimensional structure.

Notably, in the portion of curve *1* between the two glue joint strength peaks, i.e., at minimum values of σ_{glue}, there is another portion corresponding to a cohesion-plastic failure with more pronounced microprofile of the fracture surface. Next, from the beginning of the secondary rise portion to the second σ_{glue} peak, the failure has mixed cohesion–adhesion nature. In all the above-described cases, the nature of failure of the glue compounds cured by the polymerization and polycondensaion mechanisms is about the same. However, upon attainment of the secondary σ_{glue} maximum, the types of failure of these two compounds begin to differ sharply: For the binder operating by the polymerization mechanism, the cohesion failure is observed once again, but this concerns the glass plate rather than the polymer matrix with glass pieces contacting the polymer matrix torn off. This is particularly typical of high curing temperatures, since it follows from Fig. 1 that, with increasing T_{cur}, the σ_{glue}^{max} values tend to increase. These findings clearly illustrate the known enhancement of the strength of adhesion to glass fiber in the case of binders operating by the polymerization mechanism [3, 16, 19, 20]. This validates the idea that the contributions of polymerization and polycondensation to the overall curing process should be optimally combined in order to make high the cohesion and adhesion components of the glass fiber strength [1–3].

CONCLUSIONS

(1) With a binder operating by the polymerization mechanism (ED-20 + benzyldimethylamine), the adhesion strength of a glue joint of glass plates increases by a factor of 2–2.5.

(2) A substantial growth of the glue joint strength is due to combination of two factors: chemical, i.e., formation of a chemical bond between the binder operating by the polymerization mechanism and the glass surface, and physical, i.e., placticizing (relaxation) effect of the tertiary amine acting as initiator.

(3) The major difference in the failure mechanisms for glue joints in the case of systems cured by the polymerization and polycondensation mechanisms is the cohesion failure of the glued plates in the former case.

(4) These findings allow chemical design of high-strength fiber plastics by varying the ratio of the contributions of polycondensation and polymerization to the overall curing process.

ACKNOWLEDGMENTS

This study was financially supported by the Russian Foundation for Basic Research jointly with the Regional Foundation (project no. 01-03-97009, r2001 for near-Moscow region).

REFERENCES

1. Smirnov, Yu.N., Komarov, B.A., and Kushch, P.P., *Plast. Massy*, 2001, no. 9, pp. 26–29.
2. Smirnov, Yu.N., Komarov, B.A., Kushch, P.P., *et al.*, *Plast. Massy*, 2001, no. 11, pp. 6–12.
3. Smirnov, Yu.N., Komarov, B.A., Kushch, P.P., *et al.*, *Zh. Prikl. Khim.*, 2002, vol. 75, no. 2, pp. 274–285.
4. Smirnov, Yu.N. and Korotkov, V.N., *Zh. Prikl. Khim.*, 2003, vol. 76, no. 11, pp. 1873–1879.
5. Korotkov, V.N., Chekanov, Yu.A., Smirnov, Yu.N., and Zenkov, I.D., *Vysokomol. Soedin., Ser. A.*, 1996, vol. 38, no. 6, pp. 1025–1029.
6. Smirnov, Yu.N., Golodkova, F.M., and Korotkov, V.N., *Plast. Massy*, 1999, no. 12, pp. 19–23.
7. Chekanov, Yu.A., Korotkov, V.N., Djavadjan, Dj.A., and Bogdanova, L.M., *Polymer*, 1995, vol. 36, no. 10, pp. 2013–2017.
8. Dzhavadyan, E.A., Bogdanova, L.M., Irzhak, V.I., and Rozenberg, B.A., *Vysokomol. Soedin., Ser. A*, 1997, vol. 39, no. 4, pp. 591–599.
9. Smirnov, Yu.N., Kruzhkova, S.V., Shatskaya, T.E., and Natrusov, V.I., *Plast. Massy*, 2002, no. 6, pp. 18–23.
10. Plazek, D.J. and Frund, Z.N., *J. Polym. Sci., Part B: Polym. Phys.*, 1990, vol. 28, no. 3, pp. 431–448.
11. Kushch, P.P, Komarov, B.A., and Rozenberg, B.A., *Vysokomol. Soedin., Ser. A*, 1979, vol. 21, no. 8, pp. 1697–1703.
12. Andreevskaya, G.D. *Vysokoprochnye orientirovannye stekloplastiki* (High-Strength Oriented Fiber Glass Plastics), Moscow: Nauka, 1966.
13. Berlin, A.A. and Basin, V.E., *Osnovy adgezii polimerov* (Basics of Polymer Adhesion), Moscow: Khimiya, 1969.
14. Bikerman, Ya.O., *Usp. Khim.*, 1972, vol. 41, no. 8, pp. 1431–1464.
15. *Composite Materials*, Broutman, L.J. and Krock, R.H., Eds., vol. 6: *Interfaces in Polymer Matrix Composites*, Plueddemann, E.P., Ed., New York: Academic, 1974.
16. Gorbatkina, Yu.A., *Adgezionnaya prochnost' v sistemakn polimer–volokno* (Adhesion Strength in Polymer–Fiber Systems), Moscow: Khimiya, 1987.
17. Lee, H. and Nevill, K., *Handbook of Epoxy Resins*, New York: McGraw-Hill, 1967.
18. Smirnov, Yu.N., Golodkova, F.M., and Ponomareva, T.I., *Zh. Prikl. Khim.*, 2000, vol. 73, no. 4, pp. 634–638.
19. Smirnov, Yu.N. and D''yankova, S.L., *Zh. Prikl. Khim.*, 2000, vol. 73, no. 5, pp. 819–825.
20. Partansky, A.M., *Epoxy Resins*, Washington: Dow Chemical, 1970.

Russian Journal of Applied Chemistry, Vol. 76, No. 12, 2003, pp. 2014–2016. Translated from Zhurnal Prikladnoi Khimii, Vol. 76, No. 12, 2003, pp. 2064–2066.

Professor Vladimir Avgustovich Kind (To 120th Anniversary of His Birthday)

V.A. Kind, and engineer and pedagogue, made an outstanding contribution to the science of construction materials, the training of specialists in technology of binders, and the development of the cement industry. All his pedagogical and scientific activities were closely associated with higher school institutions of St. Petersburg, Polytechnical and Technological Institutes.

Vladimir Avgustovich Kind was born on October 3 (September 20), 1883, into the family of the manager of Avzyano-Petrovskie ironworks and steel-making plant in the former Verkhe-Ural'skii uyezd (district) of Orenburg Province. The parents of the scientist-to-be, Avgust Kind and his wife Amaliya, were born in Alsace-Lotharingia, a part of Germany in 1871–1918. V.A. Kind was educated at Kazan Nonclassical Secondary School, which he finished with success in 1902. In the same year, he entered, having passed the competition of school-leaving certificates, the electrochemical subdepartment of the metallurgical department at the newly opened St. Petersburg Polytechnical Institute. In those years, N.A. Menshutkin, N.S. Kurnakov, and F.Yu. Levinson-Lessing were among professors; A.A. Baikov, V.A. Kistyakovskii, P.P. Fedot'ev, and a number of other scientists, later widely known, were beginning their pedagogical activities.

In 1908, V.A. Kind graduated from the institute as an engineer metallurgist. Already when being a student, V.A. Kind published his first scientific study "Reactions between Carbamides and Chlorous Salts." Having graduated from the institute, V.A. Kind started teaching at the chair of analytical and organic chemistry at the Polytechnical Institute, headed at that time by B.N. Menshutkin (1874–1938). Till 1916, V.A. Kind's scientific interest were focused on studies and description of oil fields in Southern Russia, oil refining, and technical analysis of oil. Beginning in 1916 and till the end of V.A. Kind's life, his scientific activities were devoted to study of construction materials and binders. The "Society for Promotion of the Development of Portland Cement Industry" was organized in St. Petersburg. Not abandoning his pedagogical activities, V.A. Kind became society manager and editor of the *Portland-Tsement* (Portland Cement) journal (published till 1918).

In 1919, the chemical faculty was organized at Petrograd Polytechnical Institute on the basis of the electrochemical subdepartment of its metallurgical department (faculty). The faculty included chairs (laboratories) of general chemistry, physical chemistry, theoretical electrochemistry, technical electrochemistry, mineral technology, geology, mineralogy, and some others. Professor P.P. Fedot'ev (1864–1934) was appointed the dean of the chemical faculty. On V.A. Kind's initiative, and with his direct participation, a silicate department was organized at the new faculty to train engineers for cement, ceramic, and glass-making industries. A large laboratory of artificial silicates, the first of this kind in St. Petersburg, was created at the silicate department. The laboratory was concerned with the technology of binders and ceramics. Beginning in 1922, V.A. Kind also delivered a course of lectures on construction materials at the construction engineering faculty of the Polytechnical Institute. In 1927, he became professor.

In 1930, the higher school institutions of Leningrad were subjected to a shake-up. The chemical faculty of Leningrad Polytechnical Institute was included in Leningrad Technological Institute. V.A. Kind and his co-workers and colleagues constituted the main part of the staff members of chairs of the silicate profile at the Technological Institute, those of binders, ceramics, glass, and physical chemistry of silicates. V.A. Kind

1070-4272/03/7612-2014 $25.00 © 2003 MAIK "Nauka/Interperiodica"

headed the chair of binders at Leningrad Technological Institute till 1938. Simultaneously, he continued to head the chair of construction materials at the Polytechnical Institute. Under the severe conditions of that time, V.A. Kind managed to create a prominent scientific school and to organize training of specialists in technology of binders , ceramics and glass. Among V.A. Kind's pupils and closest associates were such well-known, in the future, specialists as V.F. Zhuravlev, Ya.V. Klyucharov, S.D. Okorokov, V.V. Yurganov, and V.A. Kind's son, V.V. Kind. V.A. Kind maintained permanent close friendship with academicians A.A. Baikov (1870–1946), D.S. Belyankin (1876–1953) and corresponding members of the Academy of Sciences of the USSR, N.N. Kachalov (1883–1961) and P.P. Budnikov (1885–1968).

V.A. Kind started his active research activities in 1919–1920 at the laboratory of silicates at the chemical faculty of Petrograd Polytechnical Institute and, later, at laboratories of quite a number of institutions, which appeared and disappeared. Nevertheless, V.A. Kind's studies were systematic and interrelated and resolved important problems of manufacture and use of binders. One the first areas of V.A. Kind's research was devoted to use of shale in calcination of portland cement and application of shale ash in manufacture of construction materials. A large series of scientist's studies, which were continued for more than 15 years, were devoted to comprehensive analysis of natural and artificial hydraulic acid additives to various cements. First of all, methods for evaluating the "activity" of additives were developed on the basis of chemical processes that occur in hydration of the most important classes of cements. Particularly important was the fact that V.A. Kind substantiated the possibility of using acid blast-furnace slags as hydraulic additives. This area of V.A. Kind's scien tific activities was analyzed in ample detail by P.P. Budnikov [1].

Of high theoretical and practical importance are V.A. Kind's studies in the field of alumina cements, whose hardening is based on hydration of calcium aluminates. As far back as 1925, V.A. Kind presented at the All-Union Congress on construction materials a report on main prerequisites for manufacture of alumina cements from Tikhvin bauxites. In 1928, V.A. Kind became a member of a special commission for alumina cement. On the basis of the experimental studies carried out by the scientist and his co-workers, a decision was made to manufacture the alumina cement by blast-furnace smelting.

Beginning in 1931, V.A. Kind supervised research at the laboratory of construction materials of the All-Union Research Institute of Hydraulic Engineering and at the laboratory of binders of the Technological Institute. The attention of the first of these two laboratories was focused on problems associated with production of a hydraulic concrete with high water resistance, low shrinkage, weak exothermic effect, high water-impermeability, which would satisfy all the requirements to hydraulic concrete. At the laboratory of the Technological Institute, the chemistry of cements and the influence exerted by their chemical and mineralogical composition on the processes of hardening and the working characteristics of the cements were studied with active participation of students. One of the last V.A. Kind's studies, carried out together with his pupil, V.F. Zhuravlev (1907–1952), was devoted to use of D.I. Mendeleev's Periodic law in classification of chemical compounds with respect to their binding properties (*Zh. Prikl. Khim.*, 1938, no. 5). The authors established that binding properties are observed in chemical compounds that are similar in structure to calcium silicates and aluminates. Later, research in this area was continued by Zhuravlev.

V.A. Kind wrote quite a number of textbooks and monographs, which became widely known and exerted strong influence on the training of specialists and the development of the cement industry in the country. They include: *Instruksii po opredeleniyu aktivnosti gidravlicheskikh dobavok* (Recommendations for determining the Activity of Hydraulic Additives) (together with S.I. Druzhinin and S.D. Okorokov, Moscow, 1931), *Khimicheskaya kharakteristika portlandtsementa* (Chemical Characterization of Portland Cement) (Moscow, 1932), *Spetsial'nye svoistva stroitel'nykh rastvorov* (Special Properties of Mortars) (together with Okorokov *et al*., Moscow, 1933), *Spetsial'nye tsementy* (Special-Purpose Cements) (Moscow, 1932, 1st ed.; 1936, 2nd ed.), *Stroitel'nye materialy (ikh poluchenie, svoistva i primenenie)* (Construction Materials: Manufacture, Properties, and Use) (together with Okorokov, Moscow, 1934), and *Putstsolanovye tsementy* (Puzzolan Cements) (together with Baikov *et al*., Moscow 1936). Among these books, *Stroitel'nye materialy* (Construction Materials) is a textbook of unique information value, largely based on original research of that time, including studies by V.A. Kind and his pupils.

Vladimir Avgustovich Kind suddenly died on February 12, 1938, in Leningrad. Prematurely passed away an excellent person, talented engineer and researcher, pedagogue beloved by his pupils, and organizer and supervisor of research collectives. To his career and pedagogical and scientific activities were

devoted a spacious obituary, written by P.P. Budnikov [1], Okorokov's paper [2], small book by I.L. Znachko-Yavorskii and I.G. Savelov [3], and other publications [4–8]. In [2, 3], a list of the most important V.A. Kind's works was presented.

REFERENCES

1. Budnikov, P.P., *Zh. Prikl. Khim.*, 1938, vol. 11, no. 5, pp. 807–810.
2. Okorokov, S.D., *Tr. Len. Politekhn. In–ta*, 1949, no. 1, pp. 111–119.
3. Znachko-Yavorskii, I.L. and Savelov, I.G., *K istorii razvitiya otechestvennoi nauki i tekhniki proizvodstva tsementa* (The History of the Development of Domestic Science and Technology of Cement Manufacture), Frunze: Maktep, 1974.
4. Tsement, 1938, no. 5, pp. 2–4.
5. Zhuravlev, V.F., Okorokov, S.D., and Val'berg, G.S., *Tsement*, 1948, no. 3, pp. 6–8.
6. Okorokov, S.L., *Tsement*, 1967, no. 4, p. 13.
7. Okorokov, S.D. and Sychev, M.M., *Tsement*, 1970, no. 8, pp. 20–21.
8. *Uchenye LTI imeni Lensoveta* (Scientists of Lensovet Technological Institute in Leningrad), Leningrad: Len. Tekhnol. Inst. im. Lensoveta, 1987.

A. G. Morachevskii

Russian Journal of Applied Chemistry, Vol. 76, No. 12, 2003, p. 2017. Translated from Zhurnal Prikladnoi Khimii, Vol. 76, No. 12, 2003, p. 2072.

ANNIVERSARIES

Mikhail Mikhailovich Koton (To His 95th Birthday)

On December 29, 2003, Mikhail Mikhailovich Koton, doctor of chemical science and corresponding member of the Russia Academy of Sciences, is 95.

Mikhail Mikhailovich can be rightfully named "archpastor" of the domestic chemical science, who guided representatives of several generations of scientists working in the filed of chemistry and physics and technologists specializing in polymers.

Mikhail Mikhailovich is still full of creative aspirations, he is honorary director of the Institute of Macromolecular Compounds, Russian Academy of Sciences, whose acting head he had been for nearly thirty years, and leader of a scientific school recognized with a grant from the President of the Russian Federation.

Mikhail Mikhailovich made an invaluable contribution to the research concerned with the problem of thermally stable polymers. The concepts of the ways to synthesize polyimides and the relationship between their structure and properties, developed under his supervision, made it possible to manufacture in our country virtually all types of materials (electrically insulating films, strengthening fibers, membranes for separation of gases and fluids, protective coatings and interlayer insulation for electronic devices, etc.) exhibiting stable operation at temperatures of 300°C and more.

In recent years, members of Mikhail Mikhailovich's scientific school have been developing a new generation of binders for construction composites and new polymeric materials for laser technologies, to be used in optoelectronics and photonics.

Mikhail Mikhailovich was born, and spent his young years at the town of Peterhof, a place that is closely associated with Russia's history and culture.

He spent all days of the Leningrad siege in the besieged city and worked at the laboratory of local air defense. He was elected a deputy of the Leningrad City Council. For many years he had been a member of the Editorial board and Deputy Editor-in-Chief of Zhurnal Prikladnoi Khimii (Russian Journal of Applied Chemistry). Mikhail Mikhailovich is a person of perfect humanity and high moral, which constitute the notion of St. Petersburg culture and way of life.

The Editorial board and the editorial staff of Zhurnal Prikladnoi Khimii heartily congratulate Mikhail Mikhailovich on his jubilee and wish him sound health and success in implementation of his scientific ideas.

Staff members of the Institute of Macromolecular Compounds, Editorial board and editorial staff of Zhurnal Prikladnoi Khimii

1070-4272/03/7612-2017 $25.00 © 2003 MAIK "Nauka/Interperiodica"

Russian Journal of Applied Chemistry, Vol. 76, No. 12, 2003, pp. 2018–2019. Translated from Zhurnal Prikladnoi Khimii, Vol. 76, No. 12, 2003, pp. 2068–2069.

BOOK REVIEWS

Pastukhov, E.A., Vatolin, N.A., Lisin, V.L., Denisov, V.M., and Kachin, S.V., *Difraktsionye issledovaniya stroeniya vysokotemperaturnykh splavov* (Diffraction Analysis of the Structure of High-Temperature Melts), Yekaterinburg: Ur. Otd. Ross. Akad. Nauk, 2003, 353 pp.

The monograph by E.A. Pastukhov and co-authors analyzes and summarizes results obtained in diffraction studies of high-temperature metallic, oxide, sulfide, and halide melts. As is known, most of the substances studied in these classes retain, in the liquid state at the melting point and even when overheated to considerably higher temperatures, a certain short-range order that is close to the structure of these same substances in the solid state. However, no rigorous theory that would describe the atomic coordination and properties of various substances in a wide temperature range has been developed for liquid phases as yet. The primary role in studying the structure of liquid high-temperature systems is played by analysis of the short-range order by diffraction techniques and computer simulation.

Previously, N.A. Vatolin, an academician of the Russian Academy of Sciences, and Pastukhov, a corresponding member of the Russian Academy of Sciences, already published a monograph with similar content.[1] During the 20 years that have elapsed since that time, a vast body of new experimental data has been accumulated and new concepts have appeared. The book comprises an introduction, seven chapters, conclusion and bibliographic list with 469 references to domestic and foreign publications.

The introduction (pp. 5–7) emphasizes that the vast body of data on thermodynamic, kinetic, and physical properties of binary metallic and ionic melts, accumulated by now, confirms the theoretical concept of similarity between the nearest coordination of particles in the melt and in the solid state. The advances in the development of the theory of liquid state and the improve accuracy and information value of the diffraction experiment made it possible to calculate the interatomic interaction potential and thermodynamic and transport properties of melts from the structural factor and the radial distribution function. The first chapter (pp. 8–51) gives notion of the basic characteristics of the liquid state, to which belong short-range order, thermal motion of atoms, radial distribution function and structural factor, and potential of pairwise interaction. The second chapter (pp. 52–69) is devoted to X-ray structural analysis as applied to melts. Although X-ray, electron, and neutron diffraction techniques yield close diffraction patterns, the authors restrict the consideration to X-ray diffraction analysis as the more widely used method.

The third chapter (pp. 70–185), which occupies the central place in the monograph, contains information about diffraction studies of metallic melts. Compared with the already mentioned edition of 1980, the number of metals and alloys considered has increased. Unfortunately, the authors did not specify the criteria used in selecting the systems to be discussed; quite a number of liquid alloys with strong interaction between the components, for which the diffraction patterns are known, are not mentioned in the monograph. The fourth chapter (pp. 186–258) is devoted to oxide and some other oxygen-containing melts. In contrast to metallic systems, oxide melts, as a rule, have a considerable fraction of covalent bonding, which leads to certain specific features in radial distribution curves. A small fifth chapter (pp. 259–270) presents the results of studies of sulfide melts. Copper, iron, and thallium sulfides are considered. The sixth chapter (pp. 271–304) discusses the specific features of the structure of molten halides. The seventh chapter (pp. 305–329) is of generalizing nature. It analyzes the fundamental aspects of how the above-mentioned structural parameters change upon melting. In the conclusion (pp. 330–333), the authors emphasize once more, on the basis of the whole body of the material presented, that, as regards the effect of temperature on the structure, the liquid state is a natural extension of the crystalline state. The results obtained

[1] Vatolin, N.A. and Pastukhov, E.A., *Difraktsionnye issledovaniya stroeniya vysokotemperaturnykh splavov* (Diffraction Analysis of the Structure of High-Temperature Melts), Moscow: Nauka, 1980, 188 pp.

1070-4272/03/7612-2018 $25.00 © 2003 MAIK "Nauka/Interperiodica"

in studying liquid alloys with strong interaction between the components (silicides, germanides, and aluminides of transition metals) point to the existence of regions retaining a short-range order that corresponds to the structures of the most stable high-temperature phases present in the phase diagram. Some semiquantitative estimates are made. For example, it is noted that raising the temperature to 400–700°C above the liquidus line affects the short-range order parameters only slightly. The degree of dissociation in melting is estimated to be 10–20% for the most stable compounds, which show a singular peak in the melting curve, and 40–70% for compounds with broad peaks and relatively moderate melting points.

The structural transformations in the liquid state, associated with a change in the coordination number, are similar to polymorphic transformations, which occur in solids when the number of nearest neighbors decreases or increases and accordingly, the interatomic distance changes.

The monograph by Pastukhov and co-authors is of indubitable interest for a wide audience of specialists in physical chemistry of the disordered state; it can also be of use for postgraduate students, masters, and undergraduate students specialized in this field.

A. G. Morachevskii